Global COE Program
International Urban Earthquake Engineering Center
for Mitigating Seismic Mega Risk

8CUEE CONFERENCE PROCEEDINGS

8th International Conference on Urban Earthquake Engineering

Center for Urban Earthquake Engineering
Tokyo Institute of Technology

Tokyo Tech
CUEE

Executive and Program Committee

Toru Takeuchi (Chair)
Shizuo Hayashi
Kikuo Ikarashi
Hideki Kaji
Kazuhiko Kasai
Saburoh Midorikawa
Chitoshi Miki
Junichiro Niwa
Tatsuo Ohmachi
Ryuzo Ohno
Toshihiro Osaragi
Hiroyasu Sakata
Jiro Takemura
Kohji Tokimatsu
Yutaka Yokoyama
Satoshi Yamada
Akira Wada

Global COE program entitled **"International Urban Earthquake Engineering Center for Mitigating Seismic Mega Risk"**

Center for Urban Earthquake Engineering (CUEE), Tokyo Institute of Technology

CUEE O-okayama Office TEL/FAX: +81-(0) 3-5734-3200
CUEE Suzukakedai Office TEL/FAX: +81-(0) 45-924-5576/5199
URL: http://www.cuee.titech.ac.jp

PREFACE

I am delighted to convene our 8th International Conference on Urban Earthquake Engineering here in Tokyo on March 7th and 8th, 2011, once again welcoming numerous distinguished experts and guests from around the world. The conference has been held annually in Tokyo since fiscal year 2003 under the auspices of two major consecutive Center of Excellence (COE) programs, both headquartered at the Center for Urban Earthquake Engineering (CUEE) here at Tokyo Tech. These are the 21st Century COE program entitled "Evolution of Urban Earthquake Engineering" (FY 2003-2007) and the subsequent Global COE program entitled "International Urban Earthquake Engineering Center for Mitigating Seismic Mega Risk" launched in fiscal year 2008.

The current program aims not only to promote research to mitigate the seismic "mega" risk confronting vast and numerous modern cities in earthquake regions throughout the world, but also to produce next-generation practitioners and researchers whose task it will be to develop new strategies and practices for seismic risk reduction. Therefore, this 8CUEE once again seeks to promote our twin goals of intensive information dissemination and technology transfer, all in furthering the very active international network that is directed toward our young researchers in this field, through a sustained international collaborative effort.

The Eighth Conference offers a platform not only to share common interests and new information and technologies in the field of Urban Earthquake Engineering but also to share our collective research and educational outcomes, while expediting and strengthening the worldwide network for Earthquake Engineering. The Conference is to feature state-of-the-art technical presentations as well as an agenda of some 250 oral presentations on various themes relevant to Urban Earthquake Engineering, with participation comprising

scientists, engineers, researchers, and active planners of divers generations, including both younger researchers as well as graduate students. This conference also includes Special Sessions and Best Presentation Awards for Young Researchers. To facilitate conference participation of young researchers, postdoctoral fellows and PhD students, travel grants have been awarded this year again to some forty individuals studying or working at collaborating institutions.

This conference will be capped by two Special Lectures in honor of the retirement from Tokyo Tech of Professors Akira Wada and Tatsuo Ohmachi, both of whom have dedicated themselves and their professional activities to the progress of our discipline, not to mention the promotion of a robust faculty in the field of Earthquake Engineering at TiTech. We would like to express both our profound respect and heartfelt appreciation for their accomplishments and efforts. In closing, we hope that the Eighth Conference will prove a rich and stimulating opportunity for all participants, who inclusive of divers generations are dedicated to Urban Earthquake Engineering.

Kohji Tokimatsu
Global COE Program Leader and
Director of CUEE, Tokyo Tech

Table of contents

Paper ID Page

Keynote Lectures

08-076 Achieving Resiliency with Seismic Isolation 1
Stephen Mahin, Kenneth Ogorzalek, and Tracy Becker

02-142 Challenges in Estimating the In-situ Strength of Liquefied Soil 9
Ross W. Boulanger and I. M. Idriss

15-023 Seismic Behaviour of Large Dams During Recent Earthquakes and Current State of Seismic Design Criteria for Large Dams 15
Martin Wieland

15-098 Reflections on Evolution of Near-field Earthquake Engineering 21
Tatsuo Ohmachi

10-311 Wise Dynamic Testing for Enhanced Understanding of Structures 31
Akira Wada, Mineo Takayama, and Satoshi Yamada

Engineering Seismology

12-291 Earthquake Risk Assessment and Corresponding Contingency Plans of the Major Cities of Bangladesh 37
A. S. M. Maksud Kamal

01-229 Major Ground Motion Research Programs at the Pacific Earthquake Engineering Research Center (PEER) 47
Yousef Bozorgnia

01-069 Statistical Features of Short-period and Long-period Near-source Ground Motions 51
Masumi Yamada, Anna H. Olsen, and Thomas H. Heaton

01-112 Strong Motion Record Observed at Concepcion during the 2010 Chile Earthquake 61
Saburoh Midorikawa and Hiroyuki Miura

01-009 Correlation of Strong Ground Motion and Estimations of Seismic Hazard and Loss for Large Areas and Critical Elements of Network 65
Vladimir Sokolov and Friedemann Wenzel

01-206 Preliminary Study of New Attenuation Relationship for Response Spectra on Seismic Bedrock Including near Source Data 75
Hongjun Si, Saburoh Midorikawa, Hideaki Tsutsumi, Akemi Noda and Toshiyuki Masatsuki

01-223 On the Effective Earthquake Early Warning Systems for Both Distant and Near Events 79
Yutaka Nakamura

12-179 Evaluation of SRSND Simulator Againts Fragility Curves for Pisco Quake 89
Carlos Zavala, Zenón Aguilar, and Miguel Estrada

Paper ID		Page
14-181	Land Use Evaluation Using Satellite Imagery for Urban Inventories *Miguel Estrada, Hiroyuki Miura, Fumio Yamazaki, and Saburoh Midorikawa*	93
01-102	Evaluation of Building Damage Areas of the 2006 Central Java, Indonesia Earthquake Detected from Satellite Optical Images *Hiroyuki Miura, Saburoh Midorikawa, and Norman Kerle*	97
15-071	Building Damage and Tsunami Inundation GIS Datasets after the 2010 Chile Earthquake *Yoshihisa Maruyama, Fumio Yamazaki, Shizuko Matsuzaki, Hiroyuki Miura, and Miguel Estrada*	103
01-116	A New Data Logger with Large Dynamic-range to Observe from Microtremors to Strong Motions *Masayuki Araki, Hitoshi Morikawa, Takamori Ito, Masachika Tanigawa, and Keitaro Matsumoto*	109
18-280	Ground Motion and Tsunami Simulation for the Great 1707 Hoei, Japan, Earthquake *Takashi Furumura, Kentaro Imai, and Takuto Maeda*	115
01-083	Nonlinear Site Response of the 2008 Wenchuan, China Earthquake From Time-frequency Analysis *Kuo-Liang Wen, Jyun-Yan Huang , Xiaojun Li, Zhenghua Zhou, and Ruizhi Wen*	121
01-182	Estimation of Shallow 2D S-wave Velocity Profile from Waveform Inversion of Seismic Refraction Data *Hiroaki Yamanaka and Yasutomo Yamauchi*	127
01-028	Earthquake Input Motion to High-rise Building in the Western Part of Kobe City During the 1995 Hyogo- ken Nanbu Earthquake *Masayuki Nagano and Jianjing Zhao*	133
11-012	Sensitivity of Ground Response Analysis to Shear Wave Velocity Profile *Pulpong Pongvithayapanu*	143
01-208	Site Characterization in the Greater Bangkok by Microtremor Observations *Nakhorn Poovarodom and Nonthakorn Plalinyot*	151
14-156	Introduction of the Geological Database for TSMIP *Chun-Hsiang Kuo, Kuo-Liang Wen, Hung-Hao Hsieh, and Kai-Wen Kuo*	157
01-064	Effects of Water Layer on Seismogram Synthesis in Kanto Basin Area based on a Hybrid Boundary Element Method: Numerical Implementation *Zheng-HuaQian, Hiroaki Yamanaka, and Sohichi Hirose*	165
01-100	A Preliminary Study on Variability of Earthquake Ground Motions due to Random Inhomogeneity in Propagation Path *Yoshiyuki Sato and Saburoh Midorikawa*	171
01-021	Reevaluation of Deep Underground Structures in the Tokyo Metropolitan Area, Using Dominant Periods of H/V of Coda Waves Observed by MeSO-NET *Seiji Tsuno, Hiroaki Yamanaka, Shin'ichi Sakai, Naoshi Hirata, Keiji Kasahara, Hisanori Kimura, and Tamotsu Aketagawa*	179

Paper ID Page

07-106 Seismic Response Estimation of Nuclear Power Plant Model Based on Fault-structure System 183
Pher Errol B. Quinay, Tsuyoshi Ichimura, Muneo Hori, M.L.L. Wijerathne, and Akemi Nishida

01-139 Evaluation of Coseismic Displacements in the Near-field from Strong-motion Seismometers. Analysis of Four Recent Large Earthquakes 189
E. H. Javelaud, S. Inoue, A. Furukawa, and T. Ohmachi

01-202 Broadband Source Model for the 2009 L'Aquila, Italy, Earthquake 193
Natalia Poiata, Kazuki Koketsu, Alessandro Vuan, and Hiroe Miyake

01-052 The Possibility of Trap Wave and Site Effect in the Longitudinal Valley of Eastern Taiwan..... 199
Kuei-Mei Lin, Kuo-Liang Wen, Chun-Te Chen, and Jyun-Yan Huang

01-053 Analysis of the Site Effect in Chianan Plain from the 2010 Jiasian, Taiwan, Earthquake 205
Fei-Wen Cheng, Kuo-Liang Wen, Chun-Te Chen, and Jyun-Yan Huang

01-121 Estimation of Shallow S-wave Velocity Structure in Damascus City, Syria, Using Microtremor Exploration..... 211
Hussam Eldein Zaineh and Hiroaki Yamanaka

01-123 Surface Waves on an Exponentially Varying Transversely Isotropic Elastic Medium due to a Subsurface Point Load..... 219
Priza Kayestha, Takatsugu Konno, and Anil C. Wijeyewickrema

01-113 Determination of Shallow Shear-wave Velocity Profiles and Site Amplification in Metro Manila, Philippines Using Microtremor Array Observations..... 227
Rhommel Grutas and Hiroaki Yamanaka

01-148 Estimation of Surface-wave Group Velocity in the Kanto Basin using Seismic Interferometory of Long-term Microtremors..... 233
Kosuke Chimoto and Hiroaki Yamanaka

01-051 Coseismic Deformation of the 2008 Wenchuan, China Earthquake Calculated from Strong Motion Data..... 237
Jyun Yan Huang, Kuo Liang Wen , Chun Te Chen, and Sheng Chung Su

01-075 2D Finite Difference Modeling of Wave Propagation of the 2010 JiaSian, Taiwan, Earthquake..... 243
Chun-Te Chen and Kuo-Liang Wen

Geotechnical Earthquake Engineering

02-045 Seismic Performance of Earth Slopes 247
Ellen M. Rathje, George Antonakos, and Gokhan Saygili

02-097 Application of Discrete Element Method in Geogrid and Aggregate Interaction in a Reinforced Unpaved Roadway..... 255
Wen-Chao Huang

Paper ID Page

02-195 Finite Deformation Analysis of Earthquake Induced Damage to Breakwater during 1995 Hyogoken-nanbu Earthquake 261
Kyohei Ueda, Susumu Iai, and Tetsuo Tobita

02-082 Performance Based Seismic Design Method of Gravity Quay Walls..... 271
Heba Kamal, Mona Aid, and Amira Abdel Rahman

02-107 Centrifuge Model Tests on Dynamic Behavior of Quay Wall Backfilled with Granular Treated Soil..... 279
Yoshiyuki Morikawa, Hidenori Takahashi, Kimitoshi Hayano, and Youtao Okusa

02-313 Centrifuge Model Test of Fault Rupture Propagation in Alluvial Deposit 285
Jiro Takemura, Yukie Ishii, Yusuke Hara and Osamu Kusakabe

02-218 Basic Study for Simulation of Behavior of Soil due to Cyclic Loading using Particle Method..... 293
Tomohide Takeyama

02-115 Seismic Hazard for Maximum Shear Stresses in Soil Layers at Oakland International AirportI 299
Tadahiro Kishida

02-001 Ground Settlements and Earth Pressures around Embedded Foundations Subjected to Strong Ground Shaking 305
Kohji Tokimatsu, Shuji Tamura, Kazushi Tohyama, Hiroko Suzuki, and Hiroyuki Yoshida

02-192 Dynamic Soil-structure-interaction of Shallow Foundations on Dry Sand - A Centrifuge Based Study 311
S.K. Haigh, C.M. Heron, U. Cillingir, and S.P.G Madabhushi

02-128 Impulsive Vertical Acceleration Caused by Foundation Uplift during Earthquake..... 319
Shuji Tamura, Keisuke Adachi, and Kohji Tokimatsu

02-150 Effects of Sway-Rocking Motion on Pile Stresses during Large Shaking Table Tests..... 327
Hiroko Suzuki and Kohji Tokimats

02-006 Effects of Pile Rigidity on Response of Base-isolated Structure during Soil Liquefaction Based on Centrifuge Tests 333
Takenori Hida and Shuji Tamura

02-036 Comparative Study on Effect of Liquefiable Soil-structure Interaction by Shaking Table Test 341
Peizhen Li, Xiuqiang Li, and Xilin Lu

02-026 Dynamic Centrifuge Model Test of Pile-supported Building with Semi-rigid Pile Head Connections in Liquafiable Soil 349
Sadayuki Ishizaki, Kohji Tokimatsu, and Toshiaki Nagao

02-204 Seismic Response of Pile Foundation in Sloping Ground..... 355
Akihiro Takahashi and Takaho Yamazaki

Paper ID Page

02-353 Aging Effect on Liquefaction Strength and Cone Resistance of Fines-containing Sand Investigated in Triaxial Apparatus 359
Takaji Kokusho, Yohta Nagao, and Fumiki Ito

02-091 Estimating Shear Modulus vs Strain From Field Measurements 365
Daniel E. Torres, Giovanna Biscontin, and Jose M. Roesset

02-015 E-Defense Shaking Table Tests for Geotechnical Engineering Research Projects
- Summary of the First Phase and Introduction of Test Series in the Second Phase - 371
Yohsuke Kawamata, Kentaro Tabata, Manabu Nakayama, and Koichi Kajiwara

02-230 The Generalized Scaling Law for Liquefiable Sand Deposit
- Causes of Discrepancy at Low Centrifugal Accelerations - 379
Tetsuo Tobita and Susumu Iai

02-266 Blast-induced Liquefaction for Earthquake Studies 389
Michael Eller and Scott A. Ashford

02-094 Centrifuge Modeling on the Seismic Responses of Sandy Deposit with a Thin Silt Seam 395
Chung-Jung Lee, Yue-Chen Wei, Hon-Chen Lien, and Hui-Tsyr Chen

02-275 Performance-based Post-liquefaction Settlement Hazard Evaluation 401
Steven L. Kramer and Yi-Min Huang

02-037 Geotechnical Aspects of the 2010 Darfield (New Zealand) Earthquake 407
Rolando P Orense, Michael J Pender, Liam M Wotherspoon, and Misko Cubrinovski

15-188 Liquefaction-induced Damage in Christchurch City Caused by the 2010 Darfield Earthquake, New Zealand..... 417
Takashi Kiyota, Mitsu Okamura, Hirofumi Toyota, Misko Cubrinovski, and Rolando P. Orense

15-176 Strong Ground Motions and Site Effects of the 2010 Chile Earthquake 425
Toru Sekiguchi, Nelson Pulido, Gaku Shoji, Jorge Alba, and Fernando Lázares

03-065 Seismic Risk Performance of Urban Transportation Systems Considering Site Effects and Interaction With the Built Environment 433
Sotirios Argyroudis and Kyriazis Pitilakis

03-145 Pipeline Failure in Earthquakes: Should Active Fault Traces BE Considered a Serious Hazard to Buried Pipelines? 441
Francesca Draper, William Mahoney, Suresh Dash, and Subhamoy Bhattacharya

01-243 Estimation of Site Effects based on Recorded Data and the Ground Motion Attenuation Relationship 449
H. S. Kuyuk, K. Koketsu, H. Miyake, H. Si, Y. Fukushima, H. Ghasemi, and R. Ibrahim

02-025 Numerical Simulations of a Centrifuge Test to Study Void-redistribution and Shear-localization Effects 455
Ronnie Kamai and Ross W. Boulanger

Paper ID Page

02-120 Centrifuge Modeling on Uplift Behavior of Immersed Tunnel Embedded in Liquefied Soils 461
Yu-Chen Wei, Wen-Ya Chuang, Wen-Yi Hung, Huei-Tsyr Chen, and Chung-Jung Lee

02-265 Centrifuge Testing of Rocking Foundations on Saturated and Submerged Sand 467
Jacquelyn Allmond, Lijun Deng, and Bruce Kutter

02-132 Failure Mechanisms of Shallow Foundation under Combined Loadings 473
Michael Cocjin, Sakae Seki, and Osamu Kusakabe

02-141 Inclusion of Axial Load on Bending Response of Pile in Liquefiable Soils 483
Domenico Lombardi, Suresh R. Dash, and Subhamoy Bhattacharya

02-170 Simulation of Three-Dimensional Nonlinear Behavior of Soil-Pile-Structure in Large Shaking Table Tests 489
Youhao Zhou, Hiroyuki Yoshida, Hiroko Suzuki, Yasushi Nukui, and Kohji Tokimatsu

02-250 Seismic Analysis of Coupled Soil-pile-structure Interaction using Finite Elements 495
Mahmoud N. Hussien, Tetsuo Tobita, and Susumu Iai

02-197 The Effect of Loading Rate on Bearing Capacity of Pile Foundations 501
Koji Watanabe and Osamu Kusakabe

02-228 Effect of Arch Action on Pseudo-Static Response of Urban Mountain Tunnel at Relatively Shallow Depth in Soft Ground 509
Shuhei Shibayama, Akihiro Takahashi, and Osamu Kusakabe

02-302 Displacement of Tunnels in Liquefied Sand Deposits 517
Siau Chen Chian and Santana Phani Gopal Madabhushi

02-017 Stiffness and Poisson's Ratio Evaluation on Granular Materials by Elastic Wave Measurements on Laboratory Specimen 523
Laxmi Prasad Suwal, Reiko Kuwano, Junichi Koseki and Takeshi Sato

02-340 Effects of Initial Static Shear on Shear Strain Localization Characteristics of Sand in Undrained Cyclic Torsional Shear Tests 531
Gabriele Chiaro, Takashi Kiyota, and Junichi Koseki

02-205 Dynamic Characteristics of the Surface Soils in Lima, Peru 537
Diana Calderon, Toru Sekiguchi, Zenon Aguilar, Fernando Lazares, and Shoichi Nakai

02-169 Simulations of Strong Ground Motions Recorded at Three Stations in Kashiwazaki City during the 2007 Niigata-ken Chuetsu-oki Earthquake 543
Kota Katsumata, Kohji Tokimatsu, and Hiroshi Arai

03-022 Reliability Assessment of Tehran Province Gas Distribution Pipeline System during Liquefaction 551
Danesh Nourzadeh, Khosrow Bargi, and Shiro Takada

03-255 Seismic Performance of a System of Interdependent Lifeline and Infrastructure Components 557
Jacopo Selva, Kalliopi Kakderi, Maria Alexoudi, and Kyriazis Pitilakis

Paper ID Page

02-072 Study of Ground Response of Three Cities of Kathmandu Valley of Nepal Using Microtremor Observations 567
Youb Raj Paudyal, Ryuichi Yatabe, and Netra Prakash Bhandary

18-087 Numerical Study on Scour Problem Induced by Tsunami Flood 577
Tso-Ren Wu, Chung-Yue Wang, Meng-Zhi Chen, Ray Shyan Wu, and Yuan-Fan Tsai

03-038 The Seismic Mitigation Assessment of LNG Tank by 3D Numerical Simulation 583
Ruifu Zhang, Dagen Weng, and Weibo Ni

Structural Concrete

04-281 Behavior of FRP-Confined Capsule-shaped RC Columns under Lateral Loading 591
Kiang Hwee Tan, Tamali Bhowmik, and T. Balendra

07-158 Seismic Performance of a Coupled Wall with High Performance Fiber Reinforced Concrete 597
Chung-Chan Hung

04-099 Rapid Recovery Technique by Using Fiber Reinforced Composite for Damaged RC Column under Seismic Loading 601
Minoru Kunieda, Yasushi Umeda, Naoshi Ueda, and Hikaru Nakamura

04-251 Structural Behavior of Deep Beam with Deteriorated Anchorage of Main Reinforcement 607
Akira Hosoda, Hiroshi Kaneko, and Misato Yuzurio

04-270 Evaluation of Shear Resisting Mechanism of Partially Corroded RC Beams 615
Tomohiro Miki and Yasuhito Takeuchi

04-079 Evaluation Method for Load-carrying Capacity of Incompletely-grouted PC Girders with Broken Tendons 621
Ken Watanabe, Toshiya Tadokoro, and Yukihiro Tanimura

04-110 Deformability Models for Shear Critical Reinforced Concrete Members 629
Sung-Gul Hong

04-305 Effect of Crack Configuration, Axial Load, and Shear Reinforcement upon Hysteresis Characteristics of High-strength RC Columns 639
Yasuji Shinohara and Shizuo Hayashi

04-194 A Simplified Numerical Approach to Cumulated Damage Effects on Seismic Performance of Existing RC Frame Structures 649
Jiang Qian, Wei Huang, and Binbin Zhuang

04-007 Non-linear FE Analysis of Post-tensioned Precast Concrete Wall 653
Ohmura Tetsuya and Gregory G. Deierlein

04-226 Seismic Behavior of L-Shaped Core-Walls 657
Susumu Kono, Kohei Sakamoto, Kazuma Inada, and Masanobu Sakashita

04-119 Development of an Energy Dissipation Device for Prestressed Concrete Members 665
Yasushi Sanada, Yuta Sashima, and Hiroki Sugiura

Paper ID Page

08-217 Response of High Performance Fiber Reinforced Concrete Infill Panels Retrofitting Steel Moment-resisting Frames 671
Sarah L. Billington, Dimitrios G. Lignos, Joan V. Hanson, and Daniel Moreno-Luna

04-077 Damage Investigation of Reinforced Concrete Buildings at the 2010 Chile Earthquake..... 679
Taiki Saito, Susumu Kono, Koichi Kusunoki, Yousok Kim, Tomoya Matsui, Masanori Tani, Yo Hibino, Carlos Zavala, and Patricia Gibu

04-070 Seismic Fragility Analysis of RC Frame Structures 687
Huanjun Jiang, Junjie Mao, Xilin Lu, and Linzhi Chen

04-114 Study on Influences of Construction Joints and Multi-layered Longitudinal Bars on Restoring Force Characteristics in R/C Cantilever Beams 695
Koshiro Nishimura

04-093 Experimental Study on Bonding Action with Neutron Diffraction Technique..... 701
Koichi Kusunoki, Kenji Kabayama, Tomohisa Mukai, Yuichi Hatanaka, Hiroshi Suzuki, and Akira Tasai

07-040 Vibration Characteristics of Traditional Adobe-quincha Buildings Located at Lima Historic Centre 707
C. Cuadra, C. Zavala, A. Abe, T. Saito, and S. Sugano

07-089 Experimental Shear Strength of Squat Masonry Shear Walls..... 713
Mohamed A. ElGawady,and Jamal Elmapruk

04-143 Shear Strengthening for Reinforced Concrete Beams using ECC Panels 723
Koji Matsumoto, Asami Yamamoto, and Junichiro Niwa

04-061 Applicability of Tension Softening Curves for the Contribution of Steel Fibers to Shear Resistance of RSF Beams..... 729
Pitcha Jongvivatsakul, Ken Watanabe, Koji Matsumoto, and Junichiro Niwa

04-059 Experimental Study on Diagonal Compressive Capacity of Reinforced Concrete Beams using High Strength Materials 735
Patarapol Tantipidok, Koji Matsumoto, Ken Watanabe, and Junichiro Niwa

04-066 Experimental Response of Steel Fiber Reinforced Concrete Knee Joints of Rigid-framed Railway Bridges Under Cyclic Loading..... 743
Kabir Shakya, Koji Matsumoto, and Junichiro Niwa

04-166 Seismic Vulnerability and Structural Retrofitting of Municipal Theatre of Lima, Peru..... 749
R. Proaño, L. Quiro, and C. Zavala

07-177 Dynamic Identification of Rehabilitated Masonry Building by Ambient and Forced Vibration Tests 757
Rafik Taleb, Farid Bouriche, Mehdi Boukri, and Fouad Kehila

04-189 A Study on Failure Mechanism of RC Structures with Specially Shaped Columns with Consideration of Diaphragm Using PushOver Analysis 765
Pu Yang, Xiaoliang Wang, Hongliu Xia, Yi Liu, Wei Wei, and Akira Wada

Paper ID Page
04-233 Attempts at Simulating Membrane Effects in Slabs Using Finite Element Analysis 771
Saurabh Prasad and Tara C. Hutchinson
04-239 Reinforced Concrete Beam-column Joint Strengthened by Ferrocement..... 779
B. Li and Eddie S.S. Lam
04-248 Evaluation of the Damage Observed in a Reinforced Concrete Wall Building during the February 27, 2010 Chile Earthquake 789
Fabian Rojas and James Anderson
04-260 Preliminary Collapse Assessment of the Torre Alto Rio Building in The Mw = 8.8 February 27, 2010 Chile Earthquake 799
Zeynep Tuna and John W. Wallace
04-095 Development of Partially Tube-confined Reinforced Concrete Ductile Moment Frame 805
Yuntian Wu, Yan Xiao, Yingmin Li, Shuyan Ji, and Akira Wada
04-084 Estimation of Peak Impact Force due to Impact of Tsunami Water-borne Shipping Containers on RC Columns 811
M. A. K. M. Madurapperuma and Anil C. Wijeyewickrema
04-276 Flexural Behavior of Belled Pile with High-strength Longitudinal Reinforcement..... 819
Yo Hibino, Yasuji Shinohara, and Shizuo Hayashi
04-190 Seismic Damage Mechanism Control of RC Ductile Frames from a Stiffness Point of View 825
Zhe Qu, Lieping Ye, and Akira Wada
11-086 Seismic Analysis of RC Structure under Multiple Earthquakes 831
Bin Wang, Huanjun Jiang, and Xilin Lu
07-193 Analytical Investigation on Seismic Behavior of Connections Between Precast RC Columns and Steel Beams 837
Qiyun Zhu and Xilin Lu
04-288 A Fundamental Study on Structural Performance of CES Shear Wall with Different Anchorage Condition of Wall Reinforcement 843
Tomoya Matsui, Suguru Suzuki, and Hiroshi Kuramoto

Steel Structure

05-155 Braced Frames for Seismic Design in Urban Areas 851
Charles W. Roeder, Dawn E. Lehman, Po-Chien Hsiao, and Keith Palmer
05-041 Seismic Design of Recent Project in Tokyo Tech O-okayama Campus 857
Toru Takeuchi
05-216 Experimental and Analytical Validation of a Seismic Retrofit System for Existing Steel Moment-resisting Frames 865
Dimitrios G. Lignos, Daniel M. Moreno-Luna, and Sarah L. Billington
01-164 Factors Influencing the Progressive Collapse of Frame Structures and Sensitivity of the Collapse to These Factors 875
Liping Liu, Pei Cao, Yingmin Li, Akira Wada, Mingkui Xiao, and Yangbing Liu

Paper ID Page

05-042 Collapse Behavior and Ultimate Earthquake Resistance of Weak Column Type Multi Story Steel Frame under Bi-axial Ground Motion 881
Satoshi Yamada and Yuko Shimada

05-167 Effect of Yielding of Roof Members on Seismic Response Behavior of Double Layer Lattice Domes 885
Tomohiko Kumagai, Toru Takeuchi, and Toshiyuki Ogawa

10-285 The AISC 2010 Seismic Provisions for Composite Structures: Towards an Application of PBD Principles for Innovative Connections 891
Roberto T. Leon and Jong Wan Hu

05-033 Experimental Evaluation of Composite Effects on Structural Behavior of Panel Zone 899
Shoichi Kishiki and Satoshi Yamada

07-096 Cyclic Behaviour of Steel Tube-reinforced Concrete Composite Walls with High Axial Force Ratio 905
Xiaodong Ji, Jiaru Qian, and Zao Jiang

05-125 Experimental Study on the Development of a Tubular Damper For Use in Bolt Joints 915
Seiji Mukaide, Daiki Imoto, Nobuhiro Nagayama, and Motohide Tada

05-081 A Sensitivity Study of Bolt Tension Effect on Seismic Response of Special Bolted Moment Frames 921
Atsushi Sato and Chia-Ming Uang

05-175 Which Spectral Shape Really Matter to Predict Nonlinear Structural Response: Application to Steel Frames 927
Edén Bojórquez, Iunio Iervolino, and Alfredo Reyes-Salazar

05-122 Plastic Deformation Capacity of Structural Steel under Various Axial Strain Histories 935
Yu Jiao, Satoshi Yamada, and Shoichi Kishiki

05-104 Elasto-plastic Behavior of RHS Columns under Bi-axial Bending Moments 941
Yuko Shimada and Satoshi Yamada

05-016 Investigation of Cyclic Deterioration Behavior of RHS-Columns 947
Takanori Ishida, Yuko Shimada, and Satoshi Yamada

05-034 Proposal of Elastic Buckling Strength Formula for Columns in Steel Moment Frames Considering Anti-Symmetric Axial Forces Generated by Horizontal Loads 953
AkinobuTakada, Motohide Tada, Seiji Mukaide, and Yoshikazu Araki

05-014 Shear Resistance of Exposed Column Bases in Steel Braced Frames 963
Hayato Asada, Shoichi Kishiki, and Satoshi Yamada

05-157 Strength Evaluation of Interface Weld of Gusset Plate Connections 969
Yao Cui, Hayato Asada, Shoichi Kishiki, and Satoshi Yamada

08-054 Seismic Damping Controlled Shear Wall System and Its Design Methodology 977
Chao Pan and Dagen Weng

05-212 Development of a Self-centering Steel Plate Shear Wall 985
Patricia M. Clayton, Jeffrey W. Berman, Tyler Winkley, and Laura N. Lowes

Paper ID Page

10-031 Nonlinear Seismic Response of Steel Concentrically Braced Frames using Endurance Time Method 993
M. A. Hariri Ardebili, Y. Zarringhalam, M. Yahyai, and M. Mirtaheri

05-225 A Method to Detect Structural Damage Using High-frequency Seismograms 1003
Vanessa M. Heckman, Monica D. Kohler, and Thomas H. Heaton

05-273 Dynamic Analysis of a Full-scale Four-story Steel Building Experimented to Collapse by Strong Ground Motions 1009
Tran Tuan Nam and Kazuhiko Kasai

05-133 Performance of Steel Self-centering Braced Frame System During Intense Earthquake and Aftershock Ground Motions 1015
Nathan Brent Chancellor, David A. Roke, Richard Sause, James M. Ricles, and Nathaniel P. Gonner

05-357 Computer Modeling of Special Concentrically Braced Frame Structural Systems 1023
Po-Chien Hsiao, Dawn E. Lehman, and Charles W. Roeder

05-344 Three-Dimensional Tests of Two-story, One-bay by One-bay, Steel Concentric Braced Frames 1033
Keith Palmer, Charles Roeder, Taichiro Okazaki, Carol Sheiled, and Dawn Lehman

05-336 A Method for the Damage Assessment of Single-layer Latticed Shells by Performing Static Stability Analysis Twice 1041
Dabin Yang, Yigang Zhang, and Jinzhi Wu

05-047 Effect of Brace Fracture on Seismic Performance of Braced Frame 1049
Ryota Matsui and Toru Takeuchi

01-018 Comparison Study on Damage Potential of Synthetic and Recorded Ground Motions 1059
Shiling Pei, John W. van de Lindt, Stephen Hartzell, and Nicolas Luco

Bridge

06-245 Seismic Design of Highway Bridges in California 1067
Lian Duan

06-310 Seismic Behavior of Curved Steel-girder Highway Bridges 1075
Ian G. Buckle, Eric V. Monzon, and Ahmad M. Itani

06-184 Seismic Performance of Twin-cell Hollow Composite Members 1085
H.-L. Hsu and R.-Z. Lee

06-271 Scale Effects of Reinforced Concrete Columns under Shake Table Testing: Phase I - Full Scale Test Results 1089
José I. Restrepo, Matthew J. Schoettler, Gabrielle Guerrini, David E. Duck, and Francesco Carrea

05-307 Response of Bridge under Seismic Load Including Collisions 1097
Eiki Yamaguchi and Keita Yamada

Paper ID Page
06-290 Performance-based Seismic Assessment of Skewed Bridges 1103
Farzin Zareian, Ertugrul Taciroglu, Peyman Kaviani, Curt B. Haselton, and Pere Pla-Junca
06-063 Shear Behavior of Segmental Concrete Beams with Draped External Tendons 1111
Dinh Hung Nguyen, Koji Matsumoto, Tsuyoshi Hasegawa, and Junichiro Niwa
06-105 Seismic Performance of a Full-seize Polypropylene Fiber Reinforced Cement Composite Bridge Column Based on E-Defense Shake Table Excitations 1117
Kazuhiko Kawashima, Richelle Zafra, Tomohiro Sasaki, Koichi Kajiwara, and Manabu Nakayama
08-144 Advanced Precast Concrete Dual-shell Steel Columns 1125
Gabriele Guerrini and José I. Restrepo
06-220 Combined Actions on Reinforced Concrete Bridge Piers 1131
Thomas M. Frankie and Daniel A. Kuchma
06-264 Bonding Behavior of CFRP Sheet-steel Connections Using for Seismic Retrofit of Highway Bridge Columns 1137
Guangfeng Zhang, Jun-ichi Hoshikuma, and Junichi Sakai
13-247 Modeling of Pitting Corrosion in Reinforced Concrete Bridge Columns for Time-varying Seismic Risk Assessment 1143
Anirudh S. Rao, Michael D. Lepech, and Anne S. Kiremidjian

Timber

07-101 Seismic Properties of Japanese Traditional Wooden Pagodas - Static Loading Test and Free Vibration Test of a Small Scale Model - 1149
Eisuke Nishikawa and Hidekazu Nishizawa
07-135 Structural Collapse Analysis of Light-frame Wood Shear Walls under Earthquake Motions 1157
Weichiang Pang, Seyed Masood Hassanzadeh Shirazi, John van de Lindt, and Shiling Pei
07-283 Earthquake Response Analysis of Timber Structure with Passive Control Scheme by Detailed Frame Model 1167
Kazuhiro Matsuda, Kazuhiko Kasai , and Hiroyasu Sakata
07-171 A Basic Study on Dynamic Property and Seismic Response of Timber Structure with Flexible Floor and Uni-axial Stiffness Eccentricity 1175
Yoshihiro Yamazaki, Kazuhiko Kasai, and Hiroyasu Sakata

Response Control

08-298 Probabilistic Evaluation of Collapse Potential of Structures with Magneto-Rheological (MR) Dampers 1185
Yunbyeong Chae, James M. Ricles, and Richard Sause

Paper ID Page

10-272 Use of Response Modification and Modular Construction Technologies for Next-generation Nuclear Power Plants 1193
Bozidar Stojadinovic, Eric Keldrauk, and Michael Mieler

07-312 The Seismic Responses of 14-Story RC Structures Installed with Three-pin Steel Damper... 1201
Huei-Tsyr Chen, Yung-Feng Su, and Hsun-Hua Tang

08-062 Retrofit of Soft Story Structure Using Seismic Isolation Technology 1205
Lieping Ye, Peng Pan, Yujun Qi, Zhenhua Pan, Haiyun Cao, and Shichun Zhao

07-185 Fundamental Study on Probabilistic Evaluation of the Ultimate State of Base Isolated Structures 1211
Toshiyuki Nakazawa, Zhe Qu, Arata Miyoshi, Shoichi Kishiki, and Akira Wada

10-136 Seismic Design for a Resilient and Sustainable Society 1217
Victor Zayas

50-339 China-Japan (NSFC-JST) Research on Use of Dampers for Repair of RC Building Damaged During 2008 Wenchuan Earthquake Part 1: Analytical Simulation Based on Full-Scale Damper Tests 1227
Xilin Lu, Kazuhiko Kasai, Dagen Weng, Wuchuan Pu, Ying Zhou, and Akira Wada

08-282 China-Japan (NSFC-JST) Research on Use of Dampers for Repair of RC Building Damaged During 2008 Wenchuan Earthquake Part 2: Design Method for RC Building Repair Using Dampers 1237
Kazuhiko Kasai, Xilin Lu, Wuchuan Pu, Dagen Weng, Akira Wada, and Ying Zhou

08-131 Torsional Vibration Control of High-rising Structure with Large Local Space by Using Bidirectional TMD 1247
Bin Zhao, Hui Gao, and Xilin Lu

08-222 Achieving Enhanced Seismic Performance of Tall Buildings Through Base Isolation..... 1253
Troy A. Morgan and Kazuhiko Kasai

05-304 Concepts for the Design of Mass Isolated Steel Buildings..... 1261
Luis E. Peternell-Altamira, and Gary T. Fry

07-073 Response Behaviour of Isolated Buildings to Earthquake Excitations Considering Soil Flexibility 1271
Sayed Mahmoud and Per-Erik Austrell

04-103 Nonlinear Seismic Response of Base-isolated Buildings Considering Pounding 1277
Deepak Raj Pant and Anil C. Wijeyewickrema

11-296 Pounding of Base Isolated Structures Considering Inelastic Behavior of Superstructure..... 1285
Parisara Thiravechyan, Troy A. Morgan, and Kazuhiko Kasai

07-138 Modelling Hybrid Base Isolation Systems for Free Vibration Simulations 1293
Anastasia Athanasiou and Giuseppe Oliveto

04-268 Seismic Isolation of Tall Cantilever Wall Buildings using One or More Isolation Planes..... 1303
Vladimir Calugaru and Marios Panagiotou

Paper ID Page

01-246 Shaking Table Test Study of Sympathetic Vibration in Base Isolation Structure 1311
Yuxiang Xu, Yuhua Zhu and Wensheng Lu

08-221 A Design Approach for Seismic Vibration Control of RC Building Structures Using Visco-elastic Damper 1321
Wuchuan Pu and Kazuhiko Kasai

08-172 Seismic Response Analysis of Steel Moment Frames with Viscoelastic Dampers Based on Quasi-linear Motion Mechanism 1327
Jaedo Kang and Hiroshi Tagawa

10-032 A Simplified Design Method for Energy-dissipated Structure with Viscous Dampers 1335
Chao Zhang, Da G. Weng, and Xi L. Lu

11-209 Seismic Performance of a Steel Self-centering Moment Resisting Frame: MCE-Level Hybrid Simulations and Quasi-static Pushover Experiments 1345
Ying-Cheng Lin, James M. Ricles, and Richard Sause

08-027 Bio-inspired Passive Actuator for Structural Control 1355
Chun-Hung Lin, Paul K. Hansma, and Henry T.Y. Yang

08-293 Development of Simplified Design Procedure for Structures with Magneto-rheological (MR) Dampers 1363
Yunbyeong Chae, Baiping Dong, James M. Ricles, and Richard Sause

Monitoring

01-252 Seismic Instrumentation of Buildings by the California Strong Motion Instrumentation Program 1373
Moh-jiann Huang and Anthony F. Shakal

11-207 Strong Motion Observation for Buildings by Building Research Institute 1379
Toshihide Kashima and Shin Koyama

11-240 Building Health Monitoring and Diagnosis from Earthquake Response Records 1385
Chi-Chang Lin, Jer-Fu Wang, and Ging-Long Lin

19-295 Observation of Strong Earthquake Motion at Public Works by NILIM 1393
Shojiro Kataoka

19-163 A New Approach for Strong-motion Observation using Low-cost Sensors in Collaboration with Nonprofessional Partners 1397
Jun Tobita and Nobuo Fukuwa

Non-structural Components

09-174 Development of Shake Table Motions for Simulation of the Seismic Response of Nonstructural Systems 1403
Manos Maragakis , Arash E. Zaghi , Siavash Soroushian , Ahmad Itan, and Gokhan Pekcan

Paper ID Page

09-354 Shaking Table Test for the Examination of the Pounding Phenomenon between Sprinkler Heads and Ceilings 1411
Kunio Mizutani and Shojiro Motoyui

09-297 Mechanical Characteristics of Metal Joint Parts in Japanese Style of Ceiling 1415
Shojiro Motoyui, Yasuaki Sato, Yuichiro Shimizu, and Tomonari Koshikawa

09-355 Ceiling Damage in the 2010 Canterbury Earthquake 1421
Gregory MacRae, James Hair and Rajesh P Dhakal

Design & Standards

16-284 Role of Standards and Regulations for Buildings 1427
Jun Kanda

10-224 Guidelines for Performance-Based Seismic Design of Tall Buildings 1433
J. P. Moehle, Y. Bozorgnia and R. O. Hamburger

01-068 Near Fault Earthquakes of Medium Magnitude: The Case of the Athens 1999 Event 1439
C. Spyrakos, E. Skiada, and I. Taflampas

10-162 Recent Revision of China Code for Seismic Design of Building Structures 1447
Yingmin Li, Qian Tan, Akira Wada, Pu Yang, Hongliu Xia, Liping Liu, Yuntian Wu, Shuyan Ji, Zhe Qu, Nina Zheng, and Jun Han

15-211 Historical Review of the Italian Seismic Code from the perspective of the 2009 L'Aquila Earthquake 1455
Giuseppe Oliveto and Luis D Decanini

11-080 Development and Implementation of Mega Urban Earthquake Damage Assessment and Reconstruction Program: 2010 Haiti Earthquake 1465
H. Kit Miyamoto and Amir S. Gilani

11-258 Seismic Separation of Adjacent Building 1473
James Anderson and Fabian Rojas

10-078 Evaluation of the Policies for Seismic Retrofit of Buildings 1481
Shoichi Ando

12-010 Seismic Vulnerability Index Method: Algerian Case Studies 1489
Mahmoud Bensaibi, Fouzia Djaalali, Fatma I. Belheouane, Omar Amellal, and Nacim Yousfi

10-361 Revitalization of Circular Concrete Columns by High Performance Ferrocement 1495
Ivy F.Y. Ho and Eddie S.S. Lam

11-048 Improvement of Parallel Computing Performance of Integrated Earthquake Simulation 1505
M. L. L. Wijerathne, M. Hori, T. Ichimura, and T. Kabeyazawa

11-004 An Improvement in Estimating the Seismic Responses of One-way Unsymmetric Plan Tall Buildings 1511
Mehdi Poursha, Faramarz Khoshnoudian, and A.S. Moghadam

Paper ID Page

11-117 Development of IT Triage System (Tracy) to Share Regional Disaster Medical Information ... 1519
Muneyoshi Numada, Yasunori Hada, Miho Ohara, and Kimiro Meguro

10-237 A Performance-based Framework for Design and Evaluation of Communities Subject to Hazards ... 1529
Michael Mieler and Bozidar Stojadinovic

09-044 Ceiling Fragility of Japanese Ceiling Systems ... 1535
YasuakiSato, Gregory A. MacRae, Rajesh P. Dhakal, and Shojiro Motoyui

Tsunami

18-035 Residual Horizontal Displacement of Water Particles in the Vicinity of Tsunami Source ... 1541
Mikhail A. Nosov

18-108 Field Survey of the 2010 Tsunami in Chile ... 1547
Shunichi Koshimura, Masashi Matsuoka, Masafumi Matsuyama, Takumi Yoshii, Erick Mas, Cesar Jimenez, and Fumio Yamazaki

18-299 Field Survey for 2010 Chilean Earthquake and Tsunami Disaster in Ports and Coasts ... 1559
Shigeo Takahashi, Takahiro Sugano, Takashi Tomita, Taro Arikawa, Daisuke Tatsumi, Hiroaki Kashima, Susumu Murata, Yoshihiro Matsuoka, and Tomoaki Nakamura

18-140 The Tsunami of Camana 2001 ... 1567
Cesar Jimenez, Bruno Adriano, Shunichi Koshimura, and Yushiro Fujii

18-200 On Submarine Landslide Caused by the Suruga Bay Earthquake ... 1573
Hiroyuki Matsumoto, Toshitaka Baba, and Yoshiyuki Kaneda

18-137 Numerical Model of Dynamics of Compressible Ocean in Tsunami Source: Sensitivity to Input Parameters ... 1579
Sergey V. Kolesov

18-160 Validation of Tsunami Inundation Modelling for the June 23, 2001 Peru Earthquake ... 1585
Bruno Adriano, Shunichi Koshimura, and Yushiro Fujii

18-152 The Tsunami Vulnerability Assessment in Peru using the Index of Potential Tsunami Exposure ... 1591
Hideaki Yanagisawa, Koshimura Shunichi, Yuji Yagi, Yushiro Fujii, Gaku Shoji, and Cesar Jimenez

Human Behavior

17-309 Walking Experiment Considering Scattered Goods and Blackout in Walkways of High Rise Buildings after an Earthquake ... 1597
Akihiko Hokugo, Ai Sekizawa, Hiroaki Notake, U Hiroi, and Daisuke Ooiwa

17-178 Constructive Loop Model of Management for Pre-Quake Mitigation and Post-Quake Rehabilitation ... 1603
Haruyuki Fujii

Paper ID Page
17-151 Human Behavior of Building Reconstruction and Fireproofing of Cities 1609
Toshihiro Osaragi and Yumi Nakata
17-126 Static and Dynamic Emergency Evacuation Guidance for Complex Building Geometries 1615
Chih-Yuan Chu
17-159 Residents Adaptation of Post Disaster Housing: The Role of Physical Environment for Social Interaction 1621
Syam Rachma Marcillia
17-147 Development of a Method for Detecting Vulnerable Area by Urban Texture 1627
Xue Ma and Ryuzo Ohno

Risk Management
16-219 Socio Economic Disaster Risk Assessment of ASEAN Countries 1633
Sushil Gupta and Jerry Velasquez
12-124 Seismic Risk Evaluation Based on Digital Mapping of a Romanian Urban Area 1639
Ana-Maria Toma and Gabriela M. Atanasiu
16-165 Strategic Firefighting Operation to Mitigate Fire Damage Risk in a Near-field Earthquake in the Metropolis of Tokyo - Analysis of the Relationship between the Timing of the Switch to Firefighting Operation and Damage Reduction - 1647
Eiichi Itoigawa
14-146 Rescheduling Timetables of Taiwan High-speed Rail System using Optimization and Decision Tree 1655
Ting-Wu Ho, Te-Che Chen, Nailah Firdausiyah, Chia-Ying Lin, Ssu-Min Tseng, and Chien-Cheng Chou
16-263 Study of Self-risk Management of Local Residents for Earthquake Disaster 1661
Masami Kobayashi
16-008 Long-run Effects of a Disaster: Measuring the Economic Impacts of the Kobe Earthquake 1667
Yasuhide Okuyama
19-127 Earthquake Preparedness and BCM in Japan 1675
Shinichi Okabe
16-050 Quantitative Risk Analysis Approach for BCP (Business Continuity Planning) Decision Making against Earthquakes 1679
Satoru Nishikawa
16-238 “Disaster Prevention” and Business Continuity: Linguistic and Cultural Pitfalls for Implementing Effective BCM in Japan 1687
Nathan Lee Rhoden and Shinji Hosotsubo
16-154 Tokyo Inland Earthquakes and Business Continuity of Companies/Organization 1693
Hiroaki Maruya

Paper ID Page

16-262 Business Continuity Planning at Universities
-A Case Study on Tokyo-Tech Suzukakedai Campus- 1699
Hideki Kaji, Tatsuo Ohmachi, Saburoh Midorikawa, Hiroaki Maruya, and Masaki Fujioka

12-259 Seismic Risk and Damage Cost Analysis of Mid-rise Base Isolated Buildings in Peru..... 1707
Luis A. Bedrinana and Taiki Saito

12-134 An Integrated Earthquake Impact Assessment System 1713
Sheng-Lin Lin, Amr S. Elnashai, and Billie F. Spencer, Jr.

01-109 Local Site Effects on Damage of Historical Monuments in Istanbul during the 1894 Marmara Sea, Turkey, Earthquake..... 1721
Masashi Morita, Saburoh Midorikawa, Atilla Ansal, and Barbaros Çetiner

01-180 A study on Expected Distribution of Lead Time by Earthquake Early Warning in Japan..... 1729
Hidetoshi Yoshinari, Miho Ohara, and Kimiro Meguro

11-278 An Automated Decision-making System Framework for Earthquake Early Warning System Applications 1737
Stephen Wu and James L. Beck

8CUEE CONFERENCE PROCEEDINGS
8th International Conference on Urban Earthquake Engineering
March 7-8, 2011, Tokyo Institute of Technology, Tokyo, Japan

ACHIEVING RESILIENCY WITH SEISMIC ISOLATION

Stephen Mahin[1], Kenneth Ogorzalek[2], and Tracy Becker[2]

1) Professor and Director, Pacific Earthquake Engineering Research Center, University of California, Berkeley, USA
2) Graduate Student, Dept. of Civil & Environ. Engineering, University of California, Berkeley, USA
mahin@berkeley.edu, tcbecker@berkeley.edu, kogorzalek@berkeley.edu

Abstract: Safety of occupants is of paramount importance in the design of any structure, but increasing attention is being placed on achieving structures that are also resilient. Such structures are intended to return to service quickly following a major earthquake, in some cases immediately. Such concerns may focus on structures and lifelines critical to a community's needs in the aftermath of an earthquake, but may also focus on continuity of important business and organizational activities, preservation of social and technological services (schools, communications, power, etc.), and allowing citizens to "shelter-in-place" while repairs are made to residential structures. In this paper, research to improve the resilience of buildings and bridges are highlighted. For buildings, effective approaches to minimize damage to structural and nonstructural components are stressed. In the case of bridge structures, approaches are examined whereby highway and rail bridges can be used immediately following a major earthquake to facilitate emergency response and promote rapid recovery. Results of shaking table tests, nonlinear dynamic analyses and economic evaluations are presented.

1. INTRODUCTION

Many researchers and practitioners worldwide are working to develop economical systems that can dependably permit engineered facilities to continue functioning even following a large seismic event. Such solutions are critical in the case of facilities such as hospitals, emergency command centers, and lifeline systems needed for emergency response and recovery. Moreover, the types of facilities where post-earthquake functionality should be maintained can be quite extensive, if consideration is given to facilities needed to ensure rapid recovery of a community or organization. For example, the San Francisco Planning and Urban Research Association (SPUR, 2009) has indicated that many schools, residential buildings, and even retail and commercial buildings are necessary to provide the housing and services that would enable a community to function following an earthquake. Similarly, the vitality and perhaps viability of a business depends on its ability to provide continuous service to its customers. Increasingly, there is increasing recognition that the traditional approach of designing "ductile" structures for collapse prevention is not sufficient in a modern society. Solutions that can with confidence preserve operations, or provide the promise of minimizing the disruption and cost of repairs following major earthquakes, are needed.

To minimize post-earthquake disruption, a structure or system must be able to limit the damage occurring in structural and nonstructural components, and should not exhibit permanent displacements. Structures could simply be made stronger so that they remain essentially elastic for the level of earthquake for which resilience is desired. However, this strength-based approach (1) requires more materials that add to the cost and carbon footprint of the structure, and (2) results in higher accelerations that necessitate special attention in the design of nonstructural components, equipment and contents. While many types of structures that behave nonlinearly are being explored to enhance resilience, many share the following characteristics: (1) they are designed with an explicit nonlinear deformation mechanism that has only a modest strength in order to reduce cost as well as in-structure accelerations, (2) they incorporate highly durable and/or easily replaceable energy dissipation devices to reduce forces and displacements in structural and nonstructural elements not associated with the nonlinear deformation mechanism, and (3) they exhibit self-centering characteristics that minimize permanent lateral and vertical displacements of the structure.

Systems being considered include ones with beams, columns, walls, braces and systems that exhibit origin-oriented hysteretic loops (Fig. 1a); this behavior is often achieved by use of a combination of yielding or friction to provide hysteresis and use of gravity or post-tensioning to provide self-centering capabilities. In some cases special materials, such as shape memory alloys, can be used alone to provide these hysteretic characteristics.

Another approach is to install viscous damping devices. When installed in flexible systems that remain essentially elastic during the response, viscous dampers can be quite effective in reducing forces, accelerations and drifts in the structure. However, traditional design approaches do not focus on limiting drifts and accelerations to levels necessary

to achieve resilience.

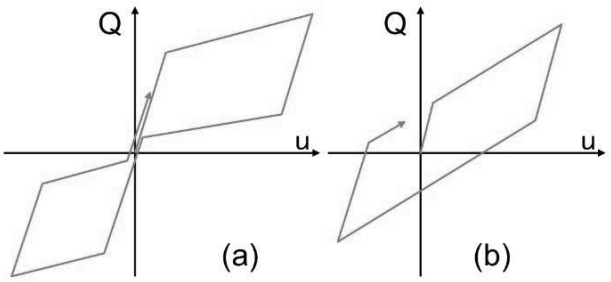


Figure 1 Hysteretic Loop Shapes for (a) Self-Centering Elements and (b) Traditional Isolation Devices

Viscous dampers, and elements having self-centering characteristics are typically installed pervasively throughout a structure. Where large nonlinear deformations are expected during the dynamic response, such systems may limit forces and accelerations experienced by structural and nonstructural elements, but they may not be able to limit displacement-related damages.

An alternative approach is seismic isolation. While seismic isolation has been in use for several decades, design codes and guidelines are often formulated to provide seismic performance comparable to fixed base buildings. While it is presumed that isolated buildings perform better than traditional structures, generally building codes permit substantial damage in the event of major earthquakes.

In this paper, several new approaches to seismic isolation of buildings and bridges are presented where resilience is considered as a prime design criterion. In such cases, isolators are provided with special hysteretic loops to limit accelerations and forces that can be developed by the supported structure, and where the structure and isolators have little or no residual displacement.

2. ISOLATED BUILDINGS

For resilience, it is convenient to consider a limit on story drifts. The drift limit should prevent significant yielding of the structural elements that might result in damage requiring inspection and repair, and permanent residual displacements. Drift should also be limited to prevent damage to nonstructural elements that are sensitive to relative displacements between stories. It can be shown on the basis of first principles that steel braced frames will begin to buckle or yield bracing elements at a story drift ratio of about 0.25% to 0.4% drift, where as moment frames in steel or concrete will yield at a drift ratio around 0.9% to 1.25%. Many types of cladding and partitions begin to display damage at a drift ration of about 0.3% with significant damage occurring by a drift ratio of 1%. Thus, in setting design criteria it is necessary to consider drift limits considering likely damage to both structural and nonstructural elements. From the above example, it is technically feasible, and perhaps economical, to isolate a moment resisting frame, but it is likely that substantial damage will occur in partitions, cladding, elevators and so on, before the structural system yields. Thus, depending on the type of nonstructural elements utilized, braced frames (or shear walls or other stiff systems) may be more consistent with the requirement of limiting damage to nonstructural components. However, it may not be necessary to preclude all damage to nonstructural elements during the resilience targeted event, so long as continued functionality is preserved and the occupants are able to "shelter-in-place" during repairs.

Many types of nonstructural elements, equipment and contents are sensitive to in-structure accelerations. To prevent acceleration related damages, it is necessary to consider a limit of floor level accelerations, or on the characteristics of pseudo-acceleration spectrum at each floor. For simplicity, we might consider a design were in the floor level accelerations are limited to 0.4g, though other values may be appropriate for certain types of elements and equipment.

While near or completely elastic behavior in the portions of the facility away from the isolation plane will eliminate the possibility of residual displacement in those locations. Some isolation systems may tend to have residual displacements. The acceptability of residual displacement in the isolation system following an intense earthquake should be carefully considered. If accounted for in the initial design with regards to accessibility and functionality of utilities, residual displacements in the isolators may not impair post-earthquake functionality, and thus be acceptable. Re-centering an isolated building following an earthquake may be economical in certain cases if needed. In other cases, isolators can be designed to minimize residual isolator displacements.

For resilient designs, it is necessary to identify a level of shaking at which resilience is desired. This may be expressed as a fraction of the maximum considered earthquake, or in terms of the confidence with which resilience can be achieved over the life of the structure (i.e., 50% confidence that the facility will remain operational following an earthquake having a 10% probability of exceedence in 50 years, or a 90% confidence that the structure will be inoperable due to earthquakes for less than 3 days during the life of the structure). It is expected that different facilities will likely have different criteria, depending on their use and importance to the community or owner. For example, some structures would be expected to be operable immediately, while others might be acceptable in terms of resiliency if their function is restored within 90 days. In all cases, a high confidence of collapse resistance is assumed. For the purposes of this paper, resiliency for the maximum considered event is targeted, consistent with important or critical facilities.

2.1 Isolation Systems

It has been noted that the design of isolated structures can be problematic due to the apparent over-conservativeness of some design provisions, and also because of challenges encountered when designing isolated systems to resist intense near-field ground motions. To resist

large near-fault ground shaking, relatively large and strong isolators are often necessitated to control displacements and maintain isolator stability. In these cases, isolators may not act effectively, especially for small events, and require relatively large design forces and trigger excessive accelerations in the superstructure [Morgan and Mahin, 2007]. Similarly, traditional designs have relied on isolation systems that have essentially bilinear hysteretic loop shapes with effective periods in the 2-3 sec. range (Fig. 1b). This type of isolator may develop large forces (and thereby drifts and accelerations) in the supported structure due to the large lateral isolator displacements that may develop in large earthquakes. Thus, efforts are underway to improve isolation for small events, limit drifts for larger events, and reduce floor accelerations.

Several approaches are being pursued at Berkeley and elsewhere to overcome these impediments to resilience, including novel combinations of elastomeric isolators and nonlinear viscous dampers. Another promising approach is the newly developed Triple Pendulum Slider [Earthquake Protection Systems, 2007]. This device has three independent pendulum mechanisms (Fig. 2).

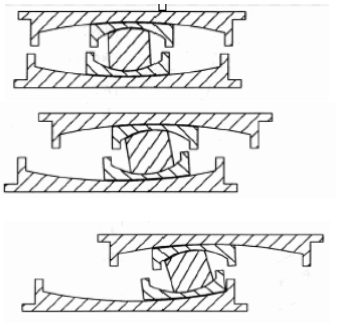


Figure 2 Triple Pendulum Bearing

By strategically selecting friction coefficients and the effective radius for each pendulum mechanism, hysteretic characteristics can be optimized for occasional, rare and very rare events (Fig. 3). Figure 4 shows hysteretic loops for different combinations of friction coefficients and radii.

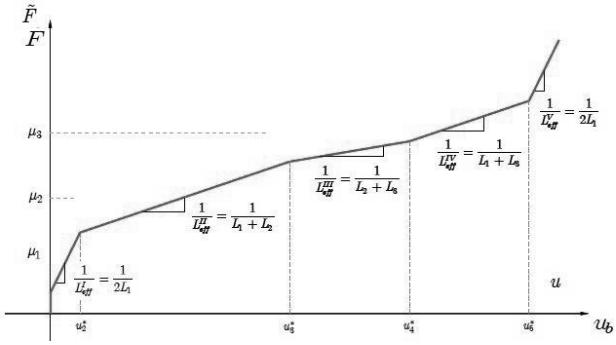


Figure 3 Envelop Force-Displacement Relation for TP isolators

One advantage of isolators of all kinds is that their behavior is highly repeatable. This is in part due to the high quality manufacturing processes and quality control tests of production bearings, but also in large part due to the simplicity of the underlying physical processes. For example, recent tests were done using TP isolation bearings, under linear, circular, square and figure eight displacement histories. A mixed kinematic/plasticity model was able to reproduce the test results with a high degree of accuracy as seen in Figure 5 (Becker and Mahin, 2011).

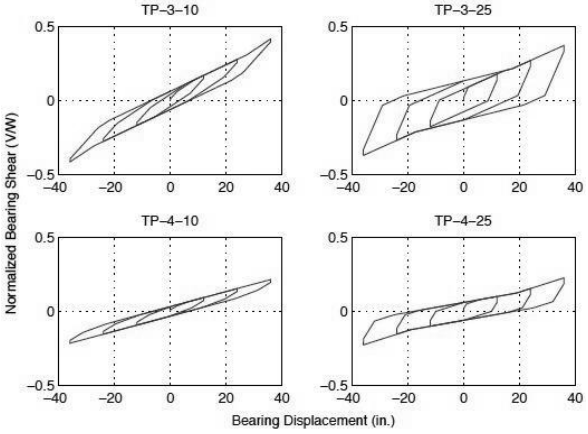


Figure 4 Representative Hysteretic Loops

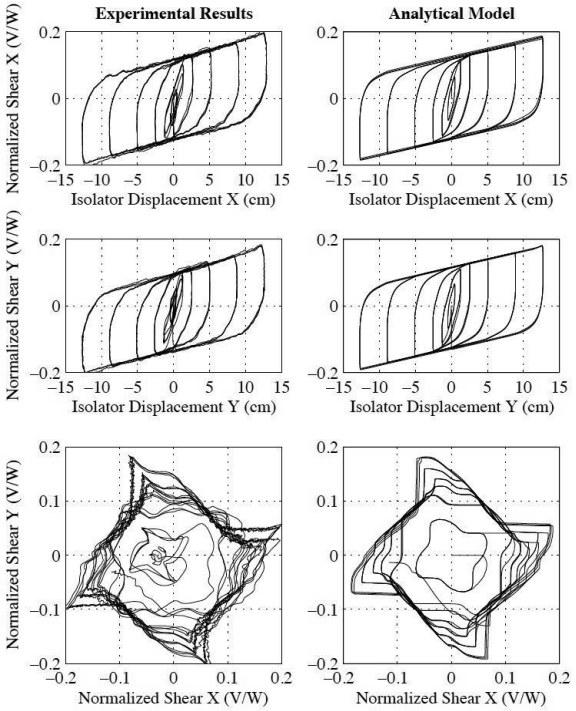


Figure 5 Comparison of Test and Numerical Response of TP isolators under square displacement excursions in the XY plane.

2.2 Isolated Building Tests and Analyses

Tests (Fig. 6) and analyses (Morgan and Mahin, 2011) demonstrate that the devices can be designed to achieve about the same isolator displacements for a large event, but with smaller drifts and accelerations in the superstructure and with a far greater degree of isolation during smaller events (Fig. 3) [Morgan and Mahin, 2011].

Numerical simulations were conducted of a three-story structure similar to that shown in Fig. 5 subjected to the suite of SAC ground motions corresponding to a 2% probability

of exceedence at a site in metropolitan Los Angeles (Somerville, 1997). For TP bearings with an effective period of 4 seconds and damping of 10% (see TP-4-10 plot in Fig. 4) the computed median isolator displacement is 770 mm, but the peak median story drift is less than 0.4% and the peak median floor level acceleration is less than about 20% g. Thus, for this type of isolation, high confidence of resilience can be obtained for even MCE level excitations.



Figure 6 Test of 3-Story Isolated Building

3. ISOLATED BRIDGES

Seismic isolation is especially easily to implement for bridges where decks are attached to the supporting columns and abutments via elastomeric or other bearings. To develop improved understanding of the behavior of seismically isolated bridges and gain confidence in design methods, a series of tests and analyses of isolated bridges has been recently completed at Berkeley (e.g., Anderson, 2003). These studies included a variety of different isolator types, bridge dynamic properties, and earthquake characteristics. Three generic types of isolator bearings were considered, including lead rubber bearings, high damping bearings, and friction pendulum bearings. Extensive studies were made to characterize bearings subjected to 3D loading, and to assess the effects of aging. Bridge systems tested include one and two span bridges having substructure periods ranging from nearly zero to more than 2 seconds. More than a dozen bridge configurations were tested to assess the effects of mass eccentricity, stiffness eccentricity, bridge substructure period, bearing type, in-situ variations in bearing properties, yielding of supporting columns, and earthquake excitations. One of the bridge models tested appears in Fig. 7.

Such experimental results were used to develop improved numerical models of the isolation bearings, and to assess the sensitivity of system response to different design parameters, and to uncertainties in these parameters. Various provisions of the AASHTO Guideline Specification [1999] such as those related to treatment of bidirectional excitations were assessed in Anderson and Mahin [2003, 2004]. Overall, good performance was noted for all of the isolated systems studied.



Figure 7 Shaking Test specimen of simple supported bridge with different substructure stiffness

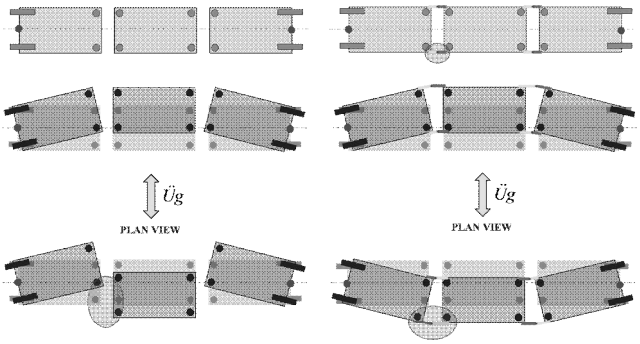
The technology of seismic isolation has been proven beneficial for suppressing vibrations to the superstructure due to period elongation. By allowing a majority of the energy to be dissipated within the isolation layer, structural forces and accelerations are attenuated, thereby providing an attractive system for protecting the structural and non-structural components. This is vitally important because recent implications of seismic isolation have involved long-span bridge structures. However, an isolated bridge system will inherently develop relative displacements between adjacent bridge decks, thereby damaging non-structural components such as expansion joints. Therefore, seismically isolating a bridge must also incorporate a method to control the relative displacements between bridge decks while still preserving the desired seismic response of the bridge system. Segmental Displacement Control (SDC) design was recently introduced by Earthquake Protection Systems of Vallejo, California, to achieve this goal and provide a more resilient bridge system. This concept is the subject of intense investigation.

3.1 Segmental Displacement Control Concept

As an innovative concept to isolated bridge systems, SDC design, developed by Earthquake Protection Systems (EPS), originated to evade seismic damage of long highway and railway bridges, thereby preserving the functionality after a major earthquake. Using seismic isolation concepts previously stated, the decoupled superstructure decks are connected at the expansion joints by lock-up guide devices. This device contains user defined properties in accordance with the performance of the isolated bridge system and its fundamental demands. However, the primary purpose of the lock-up guide is to resist the relative transverse displacement between bridge decks, thereby allowing for protection of the

non-structural components and a more resilient structural system.

In perspective of relative transverse displacement, the concept of SDC is shown in Figure 1, where the fundamental behavior of an isolated bridge with three decks is displayed in plan view. The dotted horizontal line references the centerline of the bridge and is parallel to longitudinal motion. The middle bridge deck is fully supported by bearings that allow longitudinal and transverse displacement, shown as circles. However, the end bridge decks are restrained in the transverse direction characterizing a typical configuration for a highway or railway bridge, shown as rectangles. Only three bridge decks are displayed in the conceptual figure because of experimental reference presented later on and the emphasis of relative transverse displacement. A real-life bridge would typically have more decks in series that are fully supported by bearings with longitudinal and transverse freedom, which resembles the middle deck in Figure 8.



(a) (b)

Figure 8 Segmental Displacement Control Design Concept Plan View: (a) Unrestrained Decks, and (b) Restrained Decks

As seen in Figure 8 (a), the bridge decks are not restrained to one another. Therefore, any seismic excitation in the transverse direction will impose relative transverse displacement between the bridge decks, inducing further damage to the non-structural components. However, Figure 8 (b) displays a pair of lock-up guides between two adjacent decks, thereby mitigating the relative transverse displacement between bridge decks and defining the mode shapes for the superstructure. These mode shapes are characteristic of longer periods and therefore produce lower forces at the hinged connections. It is noteworthy to mention that the number and position of the lock-up guides used between adjacent decks is user defined, as a single lock-up guide located at the centerline of the bridge is another option. The latter would resemble a similar connection for train cars and is in intended for future study. For the experiment presented within this paper, the lock-up guide configuration in Figure 8 (a) and (b) is investigated.

Another function of the lock-up guide is to allow a prescribed amount of longitudinal translation between adjacent decks. This translation will allow thermal movement of the bridge but during a major event or when the prescribed longitudinal displacement capacity is exceeded, the connection "locks up", providing a restraining stiffness that is characteristic of the lock-up guide dimensions and material properties. Locking up the bridge system is not only beneficial for non-structural components, but also for reducing the probability of bridge deck unseating.

3.2 Lock-Up Guide

With the concepts of SDC, the underlying behavior depends on the characteristics and design of the lock-up guide. Figure 9 shows the specific experimental lock-up guide AutoCAD sketch-up used for this research, where each end of the lock-up guide is fixed to two separate and adjacent bridge decks.

The lock-up guide contains three steel plates, or fingers, that overlap each other and are joined through a slotted-pin connection. The slot has a displacement capacity that is user defined to the performance of the bridge system in the longitudinal direction, for instance the different requirements for highway, freight railway, and high-speed railway bridges. Thermal expansion is allowed, yet for a major earthquake, the pin will "lock up" in the slot. Transverse displacement is restricted by the stiffness of the pin and the surrounding fingers strength. As seen in Figure 9, the vertical displacement and the rotations about the X and Y axes are restrained based on material stiffness. However, the lock-up guide does have the capacity to rotate about the Z axis more than 90 degree, which greatly exceeds the rotation capacity of a real bridge. The specific theoretical coordinate axes used in the Figure 9 are used based on correlation with experimental axes, where the Y axis is orientated longitudinal to the experimental bridge.

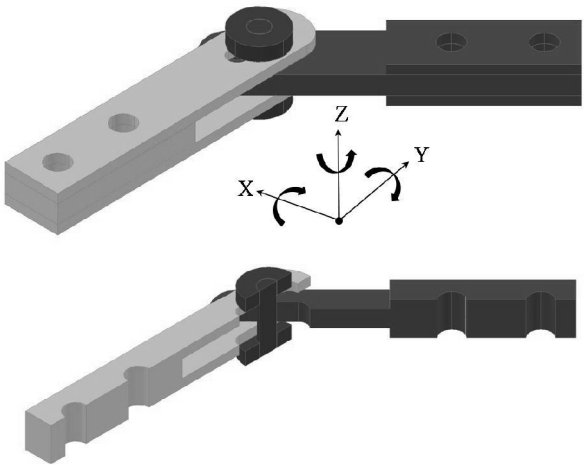


Figure 9 AutoCAD Sketch-Up of Lock-Up Guide

In transition from the end deck to the middle deck, it is important for the lock-up guide not to interfere with the performance of the isolation bearings, meaning that the displacement capacity of the slot is not less than the longitudinal distance vector for maximum rotation of the end deck. Though, based on free body dynamics of a bridge system containing lock-up guides, isolated bearing displacement is expected to be less when compared to a

system without lock-up guides.

In the longitudinal direction, force-displacement of the lock-up guide is preliminary modeled as a gap followed by elastically perfectly plastic (EPP) behavior. The stiffness and yield point are based on the dimensions of the lock-up guide. It is noteworthy to mention that once the slot is maximized, behavior of lock-up guide fingers can produce a hardening effect.

3.3 Segmental Displacement Control Experimental Results

To validate the effectiveness of SDC design for isolated bridges, an experimental program was designed to implement a series of ground motions on a shake table to a quarter scaled isolated bridge, where a direct comparison between an isolated bridge and an isolated bridge with installed lock-up guides was studied. Particular attention was also directed to the behavior of the triple and single friction pendulum isolation bearings. After research tests were completed, a public demonstration of the effectiveness and efficiency of SDC design was held at the Richmond Field Station, Berkeley, CA, where the final specimen displayed an innovative railroad expansion track on top of the isolated bridge. The following figures display a completed experimental specimen and an AutoCAD sketch up of the isolated bridge.

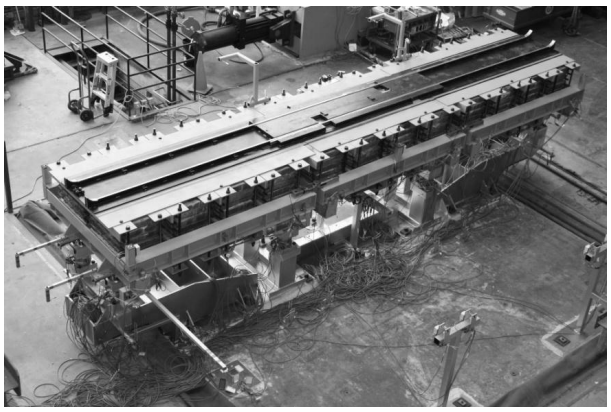


Figure 10 Scaled Experimental Isolated Bridge with Lock-Up Guides Installed

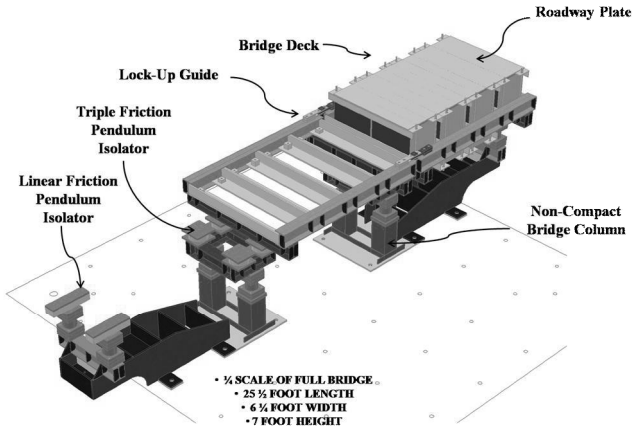


Figure 11 AutoCAD Sketch Up of Dissected Isolated Bridge with Lock-Up Guides Installed

Conclusions of the experiment resulted in large relative displacements seen for the isolated bridge with no lock-up guide. This is expected because of the difference in deck fundamental periods. After implementing 1994 Northridge, CA, Sylmar XYZ ground motion, the maximum transverse relative displacement between bridge decks was approximately 1.6", as seen in Figure 5, correlating to 6.4" for a full scale bridge. This amount of full scale displacement will most likely damage the expansion joints. However, the experiment with the lock-up guide installed shows smaller relative transverse displacements, which is critical to prevent damage to non-structural components. It is noteworthy to mention that Figure 5 does not account for relative rotation correction, which would lead to even smaller relative transverse displacements.

Overall observations suggest SDC has great potential for preserving non-structural components and a more resilient bridge system because of reduced transverse relative displacement between bridge decks. However, experimental tests also poise attention to decreased triple friction pendulum bearing displacement. Knowledge of this observation must be accounted for in an isolated bridge design.

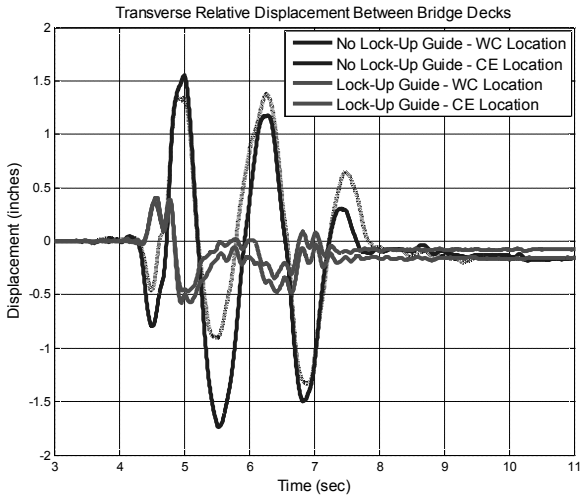


Figure 12 Transverse Relative Displacement Between Bridge Decks

4. CONCLUSIONS

The technology and design approaches described in this paper provide several alternative ways to achieve durable building and transportation structures that increase post-earthquake serviceability and reduce the need for repair. By permitting structures to undergo significant inelastic deformations during seismic events, yet suffer little damage that would require post-earthquake repairs and impair operability, structural engineers can achieve designs that are durable, dependable, and economical in terms of initial construction cost and the potential losses that might occur in the event of a damaging earthquake. As such, these approaches address the basic principles articulated by sustainable design and seismic resiliency.

Additional research is needed to refine these concepts,

especially with regards to (1) reducing cost and increasing speed of construction, (2) reducing the societal and ecological impacts of construction, (3) and refining concepts such as those presented herein and developing more generally applicable design guidelines.

Acknowledgements:

The authors acknowledge support from the Transportation Systems Research Program of the Pacific Earthquake Engineering Research Center. In addition, this paper includes work supported by the National Science Foundation under Grant No. CMMI-0724208. Any opinions, findings, and conclusions expressed here are those of the authors and do not necessarily reflect the views of the sponsors.

References

Anderson, E. (2003). "Performance-Based Design of Seismically Isolated Bridges," Doctoral Thesis, University of California, Berkeley, CA, 881 pp.

Anderson, E. and Mahin, S. (2004). "An Evaluation Of Bi-Directional Earthquake Shaking On The Provisions of the AASHTO Guide Specifications For Seismic Isolation Design," *Proceedings,* 13WCEE, Vancouver.

Earthquake Protection Systems (2007). *Product Description,* Mare Island, CA.

Becker, T.C. and Mahin, S. (2011), "Experimental and Analytical Study of the Bi-directional Behavior of the Triple Pendulum Isolator, EESD (in press).

SPUR (2009), "The Resilient City: A new framework for thinking about disaster planning in San Francisco," Urbanist, San Francisco Planning and Urban Research Association, February 2009.

Morgan, T. and Mahin, S. (2007). "Enhancing the performance capabilities of seismically isolated buildings using multi-stage friction pendulum sliding bearings," *Proceedings*, World Forum on Smart Materials and Smart Structures Technology (SMSST '07), Chongqing & Nanjing, China.

Morgan, T.A. and S.A. Mahin, (2010), "Achieving reliable seismic performance enhancement using multi-stage friction pendulum isolators," *Earthquake Engineering and Structural Dynamics* 39 (13).

Morgan, T. and Mahin, S. (2011), The Use of Innovative Base Isolation Systems to Achieve Complex Seismic Performance Objectives, PEER Report, Pacific Earthquake Engineering Research Center, University of Calif., Berkeley (in press).

8CUEE CONFERENCE PROCEEDINGS
8th International Conference on Urban Earthquake Engineering
March 7-8, 2011, Tokyo Institute of Technology, Tokyo, Japan

CHALLENGES IN ESTIMATING THE IN-SITU STRENGTH OF LIQUEFIED SOIL

Ross W. Boulanger[1], and I. M. Idriss [2]

1) Professor, Dept. of Civil and Environmental Engineering, Univ. of California, Davis, CA
2) Professor Emeritus, Dept. of Civil and Environmental Engineering, Univ. of California, Davis, CA
rwboulanger@ucdavis.edu, imidriss@aol.com

Abstract: The in-situ residual strength of liquefied soil is an important factor in the evaluation of earthquake-induced deformations and post-earthquake stability for many geotechnical structures and it is a topic with considerable technical uncertainty. Limitations in the case history database and limitations in our understanding of, and ability to numerically simulate, the mechanisms of strength loss associated with pore water pressure diffusion and void redistribution constitute the major challenges in estimating the in-situ residual strength of liquefied soils. These aspects are described and discussed.

1. INTRODUCTION

The in-situ residual strength (S_r) of cohesionless or nonplastic soils liquefied by earthquake shaking is an important factor in evaluations of earthquake-induced deformations and post-earthquake stability for many geotechnical structures. For example, the slide in the upstream shell of the Lower San Fernando Dam in 1971 (Fig. 1) was attributed to liquefaction induced strength loss.

Procedures for estimating the residual shear strength continue to represent an area of significant technical uncertainty. Procedures have included laboratory testing of field samples obtained by frozen sampling techniques (e.g., Robertson et al. 2000) or by high-quality tube sampling techniques coupled with approaches for correcting the shear strength for the estimated volume changes that occur during sampling and testing (e.g., Poulos et al. 1985, Castrol et al. 1992). Empirical correlations based on back-analyses of liquefaction flow slide case histories (e.g., Seed 1987) have been preferred for practice, in part because they implicitly account for void redistribution and other in-situ mechanisms of strength loss that laboratory element testing cannot recreate.



Fig. 1. Slide in the upstream shell of the Lower San Fernando Dam in 1971 (CA DSOD files)

Challenges in advancing procedures for estimating residual shear strengths include limitations in the case history database and in our understanding of, and ability to numerically simulate, the mechanisms of strength loss associated with pore water pressure diffusion and void redistribution. These challenges are described and discussed in this paper.

2. CASE HISTORY DATABASE

It is often necessary in practice to estimate S_r for liquefiable soils spanning a greater range of in-situ relative densities than are represented in the flow slide case history database. For example, the schematic cross-section of an earth embankment dam in Fig. 2 shows a potential slope failure passing through the dam shell with a representative $(N_1)_{60}$ = 20 and the underlying alluvium with a

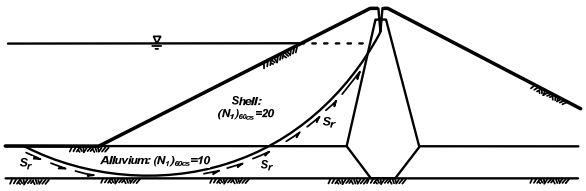


Fig. 2. Schematic of an earth dam with two zones in which liquefaction may be triggered by strong earthquake shaking (Boulanger and Idriss 2011).

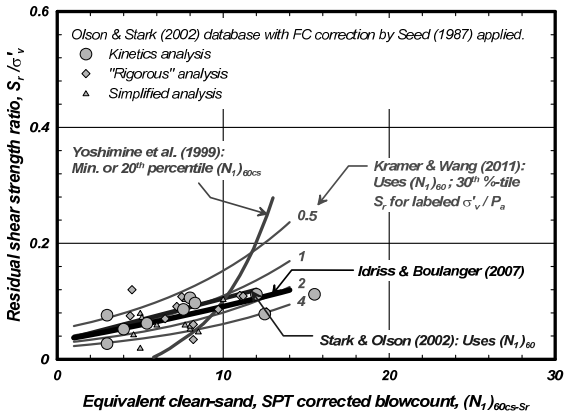


Fig. 3. Comparison of some SPT-based residual shear strength ratio correlations over the range of available case history data (Boulanger and Idriss 2011).

representative $(N_1)_{60}$ = 10. The case history database of flow slides only contains cases with $(N_1)_{60}$ values less than about 14; thus, the shell material in this example is outside the range of the case history data. However, if a liquefaction triggering analysis shows that both zones are expected to liquefy during strong earthquake shaking, then the analysis of post-earthquake stability requires that estimates be made for the shear resistance in both zones.

The range of the case history data, as interpreted by Olson and Stark (2002) and incorporating the fines adjustment recommended by Seed (1987), and some recent correlations for S_r/σ'_v- are presented in Fig. 3. This figure is illustrative of the range of conditions covered by the available databases. The information in Fig. 3 indicates: (1) the $(N_1)_{60cs}$ values are limited to less than about 14, and (2) the residual shear strength ratios are mostly limited to less than about 0.12, which is also generally less than about 20% of the pre-earthquake drained strength for these types of soils.

The four correlations shown in Fig. 3 illustrate the range of approaches used by different investigators. The Olson and Stark (2002) correlation for S_r/σ'_v is based on representative $(N_1)_{60}$ values without a fines content correction and is expressly limited to $(N_1)_{60}$ less than or equal to 12 (i.e., close to the limit of the available data). The Idriss and Boulanger (2007) correlation is based on representative, equivalent clean sand $(N_1)_{60cs}$ values computed using the fines content correction by Seed (1987), and closely follows the Olson and Stark (2002) correlation in this range of $(N_1)_{60cs}$ values. The Kramer and Wang (2011) correlation uses representative $(N_1)_{60}$ values without a fines correction, includes a dependency on confining stress, and spans across the other two correlations. The Yoshimine et al. (1999) correlation (as presented in Wride et al. 1999) is based on the minimum or 20th percentile $(N_1)_{60cs}$ value, uses the Seed (1987) fines correction, and tends to bound the data with a sharply upward-curving relationship. Despite their differences, the four correlations are consistent in indicating that the post-liquefaction shear resistance of a cohesionless soil with a representative $(N_1)_{60}$ value less than about 14 can be expected to be between 5% and 20% of its pre-earthquake drained strength, assuming a drained friction angle ranging from about 28 to 34 degrees.

3. MECHANISMS

An important challenge faced in practice is deciding how to extrapolate these correlations to $(N_1)_{60}$ or $(N_1)_{60cs}$ values greater than 14. Some of the technical issues involved in guiding this extrapolation are discussed below.

It is first useful to revisit the various definitions that have been used in the literature for the shear strength of liquefied soils. The ultimate shear resistance, or critical state strength, that is measured in undrained laboratory element tests may be denoted as S_{CS}, whereas the quasi-steady state shear resistance, which corresponds to a local minimum in the stress-strain curve from an undrained laboratory element test, may be denoted as S_{QSS}. The S_{QSS} generally coincides with the soil's transition from an incrementally contractive to an incrementally dilative response in undrained shearing, which has been termed phase transformation (Ishihara 1993). Residual shear strength, S_r, refers to the shear resistance that a liquefied soil mobilizes in the field, which can be complicated by void redistribution, particle mixing, and other field mechanisms that are not replicated in laboratory element tests. These three "strengths" are fundamentally different from a mechanics standpoint, and thus maintaining a distinction is essential.

The undrained response of saturated sand for a range of initial relative densities (D_R) and consolidation stresses in direct simple shear loading is illustrated by the results in Fig. 4 for Fraser river sand by Vaid and Sivathayalan (1996) and

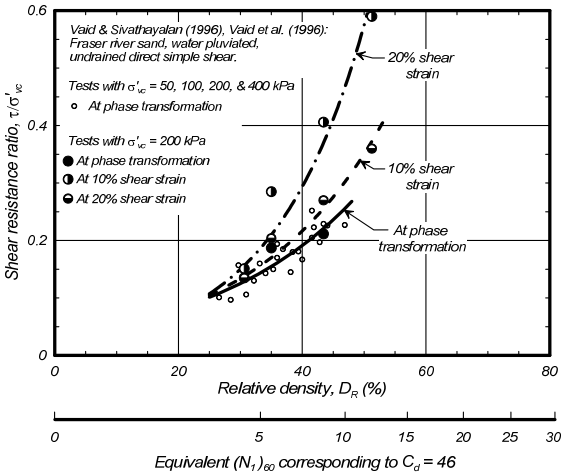


Fig. 4. Undrained shear resistance ratios mobilized in direct simple shear tests on Fraser river sand (Boulanger and Idriss 2011).

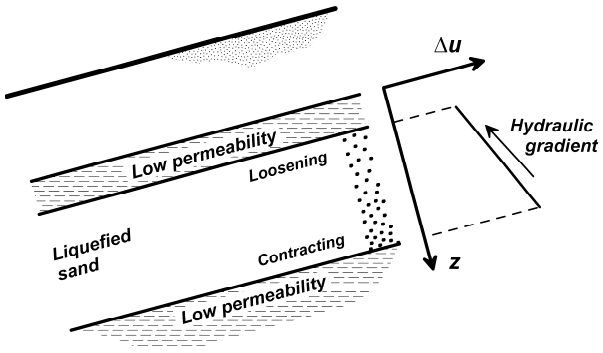


Fig. 5. Schematic of void redistribution in a confined sand layer due to upward seepage driven by earthquake-induced excess pore water pressure gradients (after Whitman 1985)

Vaid et al. (1996). The normalized shear resistance, τ/σ'_{vc}, for this sand at σ'_{vc} of 50 to 400 kPa are plotted versus D_R showing that: (1) τ/σ'_{vc} at phase transformation is relatively independent of σ'_{vc} for σ'_{vc} ranging from 50 to 400 kPa, and (2) τ/σ'_{vc} increases with both increasing D_R and increasing shear strain beyond phase transformation. These data are consistent with the trends in other laboratory testing programs (e.g., Ishihara 1993, 1996; Yoshimine et al. 1999) in showing that as the sand nears D_R of 50-60%, its dilative tendencies at σ'_{vc} less than 400 kPa result in the undrained shear resistance at large strains in simple shear exceeding the drained strength.

Relationships developed from laboratory element tests have been converted to correlations with SPT $(N_1)_{60}$ or CPT q_{c1N} values by a number of investigators. The equivalent $(N_1)_{60}$ can be related to relative density, as suggested by Meyerhof (1957), using:

$$\left(N_1\right)_{60} = C_d \left(D_R\right)^2 \qquad (1)$$

where the parameter C_d depends on the soil characteristics (e.g., Cubrinovski and Ishihara 1999). A typical value for clean sands is $C_d = 46$ (Idriss and Boulanger 2004), and this value was used to compute the equivalent $(N_1)_{60}$ values presented along the axis beneath the laboratory test data shown in Fig. 4. Thus, the undrained shear resistance of saturated sands, at σ'_v less than about 400 kPa, is shown to increase sharply as $(N_1)_{60}$ exceeds values of about 12-16. Procedures developed in this manner are based on the assumption that the in-situ void ratio will not increase (or relative density decrease) in a critical zone or layer in response to the transient pore water seepage that occurs as excess pore water pressures dissipate during and after earthquake shaking.

Void redistribution, as described by Whitman (1985), can develop where pore water seepage driven by earthquake-induced excess pore water pressure gradients causes localized loosening of the liquefied soil. This localized loosening can cause S_r to be much lower in the field than would be obtained from laboratory tests of samples at the pre-earthquake void ratio. These situations require the presence of a soil layer of significantly lower permeability overlying the liquefied soil layer, thereby impeding the outward seepage, as illustrated schematically for an infinite slope in Fig. 5.

The factors affecting void redistribution have been demonstrated through a range of physical modeling studies (e.g., Kokusho 1999, 2000, 2003, Kulasingam et al. 2004, Malvick et al. 2008) and analytical modeling studies (e.g., Yang and Elgamal 2002, Naesgaard et al. 2005, Seid-Karbasi and Byrne 2007). Shaking table tests by Kokusho (1998), for example, have illustrated how transient pore water seepage can cause dramatic strength loss and slope deformations after shaking has ceased. The four images in Fig. 6 are from a video of a fully submerged sand model with two horizontal silt seams (the white layers) showing: (a) the geometry before the start of shaking, (b) the geometry after shaking has stopped and pore water seepage from the sand below the silt seams is just starting to break up through the silt seams along the glass side walls of the container, (c) the geometry as the lower silt seam and overlying sand are weakened by the upward pore water flow and begin to flow both laterally and down the adjacent slope, and (d) the geometry as deformations are nearing their final values. These images suggest that the upward pore water seepage from the liquefied sand layer below the silt seams, after shaking had ceased, was a major factor causing the silt seams and overlying sand to flow laterally. The third image also shows the lower white silt seam initially translating out over the adjacent muddy water, illustrating how hydroplaning and intermixing with the adjacent water can accentuate the flow deformations experienced by unstable, submerged slopes. These observed mechanisms of strength loss in liquefied soils (i.e., pore water pressure and void redistribution; hydroplaning; and water entrainment) are some of the factors that complicate the back-calculation of meaningful strengths in case histories that involve submerged slide masses.

An important consequence of void redistribution is that the in-situ S_r of a liquefied soil depends not only on soil properties (e.g., densities and permeabilities), but also on the dynamic loading conditions (e.g., intensity and duration) and all the factors that affect the pore pressure dissipation process (e.g., layer thicknesses, geometry, slope angles). This means that the pre-earthquake SPT penetration resistance or pre-earthquake void ratio cannot be expected to provide a sufficient basis for accurately predicting S_r.

The potential influence of localized loosening of sand on the relationship between the shear resistance ratio (τ/σ'_{vc}) and the pre-earthquake $(N_1)_{60}$ is illustrated by a simple example shown in Fig. 7. The baseline curve in this figure corresponds to the undrained monotonic shear resistance of Fraser river sand in direct simple shear loading to 20% shear strain, as shown previously in Fig. 4. The equivalent $(N_1)_{60}$ values were computed from the D_R values using $C_d = 46$ for both Figs. 4 and 7. The other curves in Fig. 7 correspond to cases where void redistribution has caused the in-situ D_R to change by ΔD_R relative to the pre-earthquake

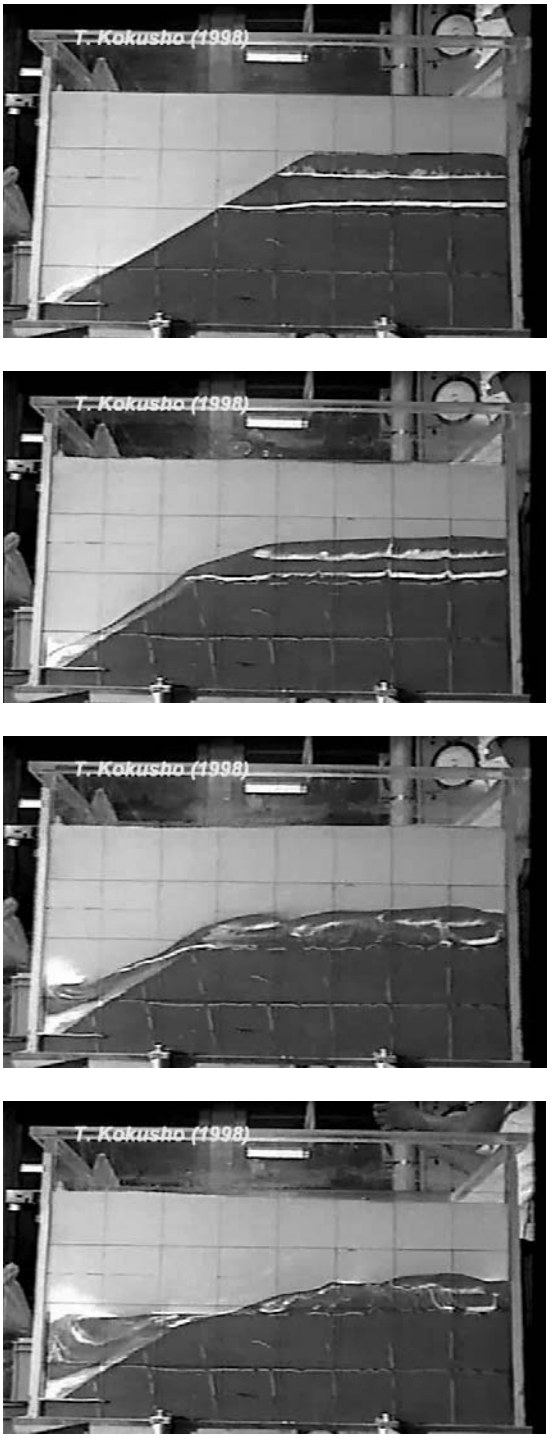


Fig. 6. Images of shaking table test by Kokusho (1998)

value. For example, the baseline curve gives τ/σ'_{vc} = 0.41 at a pre-earthquake D_R = 45% and $(N_1)_{60}$ = 9.3. If void redistribution produced ΔD_R = -0.2, the new D_R = 25% would correspond to a $(N_1)_{60}$ = 2.9 and τ/σ'_{vc} = 0.11. This reduced τ/σ'_{vc} value would, however, be plotted against the pre-earthquake $(N_1)_{60}$ = 9.3, which is why loosening causes the curves to shift downward and to the right in Fig. 7. For Fraser river sand at a pre-earthquake D_R = 45%, a ΔD_R = -0.2 would correspond to a volumetric strain of only -3.4%. This simple example illustrates how changes in D_R caused by void redistribution can strongly affect the expected relationship between S_r and the pre-earthquake $(N_1)_{60}$ values.

The potential for significant void redistribution can be expected to decrease as the soils become denser. Physical and analytical studies show that as the D_R of a sand deposit increases, the potential for void redistribution-induced strength loss decreases sharply because: (1) the consolidating portions of the deposit release less water because the post-liquefaction reconsolidation strains are smaller, and (2) the dilating portions of the deposit can accommodate the influx of more water without localizing because the sand has a greater dilatancy.

Numerical simulations of the void redistribution process are complicated by a number of factors, including limitations in commonly-available site characterization data and computational challenges in modeling coupled diffusion and localization processes (e.g., Seid-Karbasi and Byrne 2007; Kamai and Boulanger 2011). Further research on numerical simulations of this process and detailed validation studies continue to be an important need in this area.

4. DISCUSSION

Two possible scenarios were considered by Idriss and Boulanger (2007, 2008) in guiding the extrapolation of S_r/σ'_v correlations to $(N_1)_{60}$ values greater than 14, as illustrated in Fig. 8. The first scenario corresponds to conditions where the effects of void redistribution are expected to be negligible; e.g., the field conditions and stratigraphy are such that the post-earthquake pore water seepage will not be impeded by lower-permeability layers and thus the dissipation of excess pore pressures is expected to lead to densification of soils at all depths (in-situ void ratios decrease). In this case, the in-situ post-liquefaction shear resistance can be expected to be reasonably represented by relationships developed with consideration of laboratory element test results. This scenario was the basis for the upper curve which bends strongly upward at $(N_1)_{60cs}$ values of 15-17 in Fig. 8, which Idriss and Boulanger (2007) recommended only for those cases where void redistribution effects are expected to be negligible.

The second scenario in Fig. 8 corresponds to conditions where the effects of void redistribution can be significant; e.g., the field conditions and stratigraphy are such that the post-earthquake pore water seepage will, or could be, impeded by an overlying lower-permeability layer. In this scenario, the potential for void redistribution-induced loosening and strength loss may be judged to represent a serious possibility. In such a situation, the potential increases in void ratio near an impeded drainage boundary would mean that relationships guided primarily by the results of laboratory element tests could significantly over-estimate the in-situ shearing resistance (e.g., Fig. 7). For this scenario, Idriss and Boulanger (2007) recommended a lower relationship which curves more gently upward, eventually approaching drained strengths at an $(N_1)_{60cs}$ of about 32; this latter point on the residual strength curve was selected to agree with the limits of liquefaction triggering curves.

The two scenarios presented by Idriss and Boulanger (2007) present an opportunity for discussing a few technical issues regarding the development of procedures for estimating Sr.

- Can the absence of observations of flow slides in cohesionless soils with $(N_1)_{60}$ or $(N_1)_{60cs}$ values greater than about 14 be taken as evidence that in-situ shear strengths can always be expected to steeply increase as $(N_1)_{60}$ or $(N_1)_{60cs}$ values increase above 14?
- Are the mechanisms of in-situ void redistribution and particle intermixing sufficiently well understood that we know when it will, or will not, be significant? Can we omit these mechanisms in the development of procedures that will be used in practice?
- Are the case history data sufficiently well constrained or the mechanisms of strength loss sufficiently well understood to determine whether a strength (S_r) model, strength ratio (S_r/σ'_v) model, or a hybrid model is the most appropriate?

These and other questions regarding the estimation of residual shear strength warrant further discussions, and likely will continue to be topics for debate for years to come. In the meantime, further research on understanding and bounding the significance of void redistribution and other mechanisms of strength loss are needed to resolve concerns and advance this aspect of our practice.

5. CONCLUDING REMARKS

Challenges in advancing the procedures for estimating the in-situ residual shear strength of liquefied soils were described and discussed. These include limitations in the empirical case history data and in our understanding of, and ability to numerically simulate, the mechanisms of strength loss associated with pore water pressure diffusion and void redistribution. Additional research and evaluations are needed for advancing our understanding and treatment of this important area of practice.

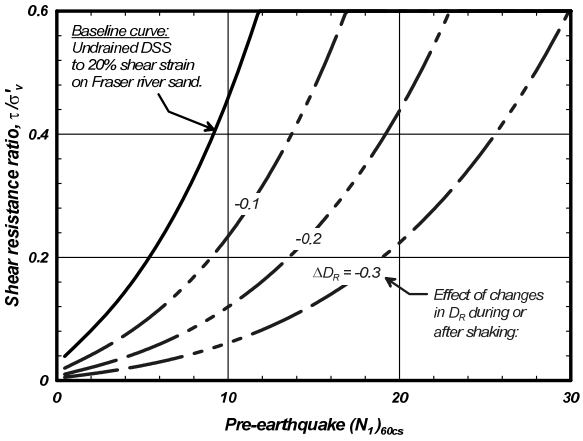


Fig. 7. Example of how changes in D_R caused by void redistribution could affect the relationship between the shear resistance ratio and pre-earthquake penetration resistances

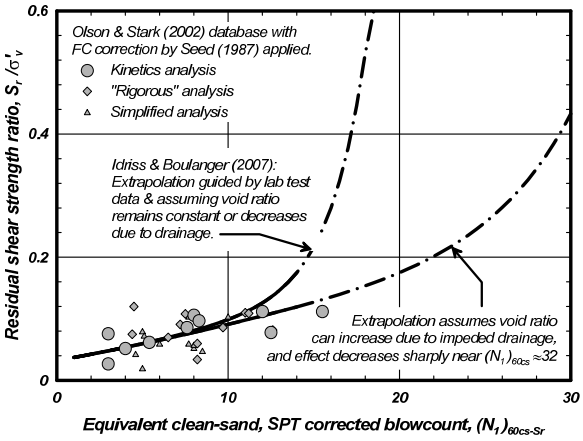


Fig. 8. SPT-based correlation for cohesionless soils at σ'_{vc} < 400 kPa by Idriss and Boulanger (2007) (from Boulanger and Idriss 2011)

References:

Boulanger, R. W., and Idriss, I. M. (2011). "Cyclic failure and liquefaction: Current issues." Proc., 5th International Conference on Earthquake Geotechnical Engineering, Santiago, Chile.

Castro, G., Seed, R. B., Keller, T. O., and Seed, H. B. (1992). "Steady-state strength analysis of Lower San Fernando dam slide." Journal of Geotechnical Engineering, ASCE, 118(3), 406-427.

Cubrinovski, M., and Ishihara, K., (1999). "Empirical correlation between SPT N-value and relative density for sandy soils." Soils and Foundations, Japanese Geotechnical Society 39(5), 61–71.

Idriss, I. M., and Boulanger, R. W. (2007). "SPT- and CPT-based relationships for the residual shear strength of liquefied soils." Earthquake Geotechnical Engineering, 4th International Conference on Earthquake Geotechnical Engineering–Invited Lectures, K. D. Pitilakis, ed., Springer, Netherlands, pp.1–22.

Idriss, I. M., and Boulanger, R. W. (2008). *Soil liquefaction during earthquakes*. Monograph MNO-12, Earthquake

Engineering Research Institute, Oakland, CA, 261 pp.
Ishihara, K. (1993). "Liquefaction and flow failure during earthquakes." Geotechnique 43(3), 351–415.
Ishihara, K. (1996). *Soil behaviour in Earthquake Geotechnics*. Oxford University Press Inc., New York.
Kamai, R., and Boulanger, R. W. (2011). "Numerical simulations of a centrifuge test to study void redistribution and shear localization effects." Proc., 8th International Conference on Urban Earthquake Engineering, Tokyo Institute of Technology, Tokyo, Japan.
Kokusho, T. (1998). Video of shaking table tests, Geotechnical Engineering Laboratory, Chuo University, http://www.civil.chuo-u.ac.jp/lab/doshitu/top/top_en.html.
Kokusho, T. (1999). "Water film in liquefied sand and its effect on lateral spread." J. Geotechnical Eng., ASCE 125(10), 817–26.
Kokusho, T. (2000). "Mechanism for water film generation and lateral flow in liquefied sand layer." Soils and Foundations 40(5), 99–111.
Kokusho, T. (2003). "Current state of research on flow failure considering void redistribution in liquefied deposits." Soil Dynamics and Earthquake Engineering 23(7): 585-603.
Kramer, S. L., and Wang, C. H. (2011). "A hybrid model for estimation of the residual strength of liquefied soil." Submitted for review.
Kulasingam, R., E. J. Malvick, Boulanger, R. W., and Kutter, B. L. (2004). "Strength loss and localization of silt interlayers in slopes of liquefied sand." Journal of Geotechnical and Geoenvironmental Engineering 130(11): 1192-1202.
Malvick, E. J., Kutter, B. L., and Boulanger, R. W. (2008). "Postshaking shear strain localization in a centrifuge model of a saturated sand slope." Journal of Geotechnical and Geoenvironmental Engineering, ASCE, 134(2), 164-174.
Meyerhof, G. G. (1957). "Discussion on research on determining the density of sands by spoon penetration testing." Proceedings, 4th International Conference on Soil Mechanics and Foundation Engineering, London, Vol. 3, pp. 110.
Naesgaard, E., Byrne, P. M., Seid-Karbasi, M., and Park, S. S. (2005). "Modeling flow liquefaction, its mitigation, and comparison with centrifuge tests." Proceedings, Performance Based Design in Earthquake Geotechnical Engineering: Concepts and Research, Geotechnical Earthquake Engineering Satellite Conference, Osaka, Japan, September 10, pp. 95–102.
Olson, S. M., and Stark, T. D. (2002). "Liquefied strength ratio from liquefaction flow case histories." Canadian Geotechnical J. 39, 629–47.
Poulos, S. J., Castro, G., and France, J. W. (1985). "Liquefaction evaluation procedure." J. Geo-technical Eng., ASCE 111(6), 772–91.
Robertson, P. K., Wride, C. E., List, B. R., Atukorala, U., Biggar, K. W., Byrne, P. M., Campanella, R. G., Cathro, C. D., Chan, D. H., Czajewski, K., Finn, W. D. L., Gu, W. H., Hammamji, Y., Hofmann, B. A., Howie, J. A., Hughes, J., Imrie, A. S., Konrad, J.-M., Kupper, A., Law, T., Lord, E. R. F., Monahan, P. A., Morgenstern, N. R., Phillips, R., Piche, R., Plewes, H. D., Scott, D., Sego, D. C., Sobkowicz, J., Stewart, R. A., Watts, B. D., Woeller, D. J., Youd, T. L., and Zavodni, Z. (2000). "The Canadian liquefaction experiment: an overview." Canadian Geotechnical J. 37, 499–504.
Seed, H. B. (1987). "Design problems in soil liquefaction." J. Geotechnical Eng., ASCE 113(8), 827–45.
Seid-Karbasi, M., and P. M. Byrne (2007). "Seismic liquefaction, lateral spreading, and flow slides: a numerical investigation into void redistribution." Canadian Geotechnical Journal, Vol. 44, No. 7, pp 873-890.
Vaid, Y. P., and Sivathayalan, S. (1996). "Static and cyclic liquefaction potential of Fraser Delta sand in simple shear and triaxial tests." Canadian Geotechnical J. 33, 281–89.
Vaid Y. P., Sivathayalan, S., Eliadorani, A., and Uthayakumar, M. (1996). Laboratory testing at UBC CANLEX Report, Department of Civil Engineering, University of British Columbia.
Whitman, R. V. (1985). "On liquefaction." Proceedings, 11th International Conference on Soil Mechanics and Foundation Engineering, San Francisco, CA, A.A. Balkema, pp. 1923–926.
Wride, C. E., McRoberts, E. C., and Robertson, P. K. (1999). "Reconsideration of case histories for estimating undrained shear strength in sandy soils." Canadian Geotechnical J. 36, 907–33.
Yang, Z., and A. W. Elgamal (2002). "Influence of Permeability on Liquefaction-Induced Shear Deformation." Journal of Engineering Mechanics, Vol. 128, No. 7, pp 720-729.
Yoshimine, M., Robertson, P. K., and Wride, C. E. (1999). "Undrained shear strength of clean sands to trigger flow liquefaction." Canadian Geotechnical J. 36, 891–906

8CUEE CONFERENCE PROCEEDINGS
8th International Conference on Urban Earthquake Engineering
March 7-8, 2011, Tokyo Institute of Technology, Tokyo, Japan

SEISMIC BEHAVIOUR OF LARGE DAMS DURING RECENT EARTHQUAKES AND CURRENT STATE OF SEISMIC DESIGN CRITERIA FOR LARGE DAMS

Martin Wieland

Chairman, Committee on Seismic Aspects of Dam Design, International Commission on Large Dams (ICOLD)
Poyry Energy Ltd., Zurich, Switzerland
martin.wieland@poyry.com

Abstract: The following, relatively recent earthquakes had a major impact on large dams: (i) the 2001 Bhuj (M=7.5) earthquake in Gujarat province, India has affected or damaged some 245 earthen dams, most of them used for irrigation and water supply; (ii) the 2008 Wenchuan (M=8.0) earthquake in Sichuan province, China has damaged 1803 dams and reservoirs and 403 hydropower plants with an installed capacity of 3.3 GW; and (iii) the 2010 Maule (M=8.8) earthquake in Chile has strongly shaken some 13 large dams. Among these events the lessons learnt from the Wenchuan earthquake are the most significant ones as this earthquake has also affected RCC and concrete face rockfill dams. The main conclusions from these recent earthquakes are discussed. Moreover, the current state of seismic design criteria for large dams of the International Commission on Large Dams is presented.

1. INTRODUCTION

In recent years, three important earthquakes have occurred, which have damaged different types of dams, i.e.

(i) the 2001 Bhuj (M=7.5) earthquake in Gujarat province, India has affected or damaged some 245 earthen dams, most of them used for irrigation and water supply;

(ii) the 2008 Wenchuan (M=8.0) earthquake in Sichuan province, China has damaged 1803 dams and reservoirs and 403 hydropower plants with an installed capacity of 3.3 GW, most of the dams were small dams but also a few dams with heights exceeding 100 m and run-of-river power plants were affected; and

(iii) the 2010 Maule (M=8.8) earthquake in Chile has strongly shaken and affected some 13 large dams. Moreover, during recent earthquakes in Japan a large number of dams had to be inspected according to current regulations.

The lessens learnt from the Wenchuan earthquake are the most significant ones for the dam industry as this earthquake has affected both roller compacted concrete and concrete face rockfill dams, i.e. dams which are being built in increasing numbers and whose earthquake resistance had not yet been tested by previous earthquakes. Moreover, a large concrete gravity dam under construction was also severely shaken. The main conclusions and lessons learnt from the Wenchuan earthquake are discussed in the subsequent sections.

2. WENCHUAN EARTHQUAKE

2.1 Effects on Large Dams

Sichuan province is the province with the largest hydropower potential in China with some 6678 dams and reservoirs.

The Wenchuan earthquake is the earthquake, which has affected more dams than any other earthquake before, i.e. 1803 dams and reservoirs and 403 hydropower plants. It is also the most important seismic event, which occurred since the creation of the earthquake committee of the International Commission on Large Dams (ICOLD) some 40 years ago.

2.1.1 Shapai arch dam

During the Wenchuan earthquake the 132 m high Shapai arch dam, the world's highest roller compacted concrete (RCC) arch dam, was subjected to strong ground shaking.

The dam is a three-centered arch structure with vertical upstream face. The crest length and thickness are 250.25 m and 9.5 m respectively. The maximum thickness at the base is 28 m. The dam is located 30 km away from the epicenter and during the earthquake the reservoir was at normal water level. There are two vertical contraction joints and two induced joints with a spacing of about 50 m. The dam is founded on granite and granodiorite and was completed in 2003. The seismic design of the dam was based on a horizontal peak ground acceleration of 0.138 g.

During the author's visit in early April 2009 no signs of damage could be observed, however, the reinforced concrete elevator building on the crest and the superstructures of the intake towers suffered some damage, which was repairable. The powerhouse located several kilometers downstream was severely damaged by the impact of rocks originating from high elevations in the steep mountains. The movement joint of the penstock across the river failed, causing flooding of

the powerhouse.

2.1.2 Zipingpu concrete face rockfill dam

The 156 m high Zipingpu concrete face rockfill dam (CFRD) is one of the largest CFRDs in China and one of the key projects for water supply and irrigation for the Chengdu basin. The dam was completed in 2006 and represented the latest CFRD technology in China. The dam was designed for an intensity of VIII (Chinese scale), with a design peak ground acceleration of 0.26 g. The epicentral distance of the dam was 17 km. During the earthquake the reservoir level was low and its volume was 200 Mm^3. Under normal operation conditions the reservoir volume is 1100 Mm^3. The crest of the dam and the concrete face were damaged. Of greatest interest was the damage to the concrete face and waterproofing system which consisted of damage of the waterstop and the offset of the horizontal joint between the second and third stage slab construction.

After the earthquake the maximum settlement at the dam crest was 735 mm and the horizontal deflection in downstream direction was 180 mm. The cross-canyon deformation of both abutments was 102 mm.

Because of the low water level in the reservoir at the time of the earthquake, it is difficult to estimate what the earthquake behaviour of the dam, the concrete face, and the waterproofing system would have been if the reservoir was full.

2.2 Earthquake Hazard

The Wenchuan earthquake has clearly demonstrated that earthquakes are multiple hazards, which can affect large dam projects in many different ways. The seismic hazard includes the following:

- ground shaking causing vibrations in dams, appurtenant structures and equipment, and their foundations;
- fault movements in the dam foundation or discontinuities in dam foundation near major faults which can be activated causing structural distortions;
- fault displacement in the reservoir bottom causing water waves in the reservoir or loss of freeboard;
- rockfalls causing damage to gates, spillway piers (cracks), retaining walls (overturning), surface powerhouses (cracking and puncturing), electro-mechanical equipment, penstocks, masts of transmission lines, etc.
- mass movements (landslides and rockfalls) into the reservoir causing impulse waves and overtopping of dams;
- mass movements blocking rivers and forming landslide lakes whose failure may lead to overtopping of downstream run-of-river power plants or the inundation of powerhouses with equipment;
- mass movements blocking access roads to dam sites and appurtenant structures and
- ground movements and settlements due to liquefaction or densification of soil, causing distortions in dams and appurtenant structures.

Surface water waves in the reservoir and long-period reservoir oscillations (seiches) caused by ground movements are of lesser importance for the earthquake safety of a dam. Although overtopping of the dam crest is possible such as in the case of the 1959 Hebgen Lake earthquake in Montana, USA.

Usually the dam engineers are focusing on the ground shaking and neglect the other aspects. Therefore, it is recommended to prepare a hazard matrix in which along one axis the different hazards are listed and along the other one the different structures, elements and components of the dam project.

It is well known that ground shaking affects all structures (above and below ground), elements and components at the same time, whereas the other hazards listed above may only affect some of them. However, the Wenchuan earthquake has shown that in the epicentral region where thousands of rockfalls and slides occurred, the damage due to rockfalls was very serious. Some of the dam sites were not accessible for several months. For example the Shapai arch dam site was inaccessible by road and heavy construction equipment for about 10 months.

2.3 Main Lessons Learnt from Wenchuan Earthquake

Strong earthquakes can affect a large area and many dams may be subjected to strong ground shaking. This has been the case for the Wenchuan earthquake. Different types of dams have been damaged; therefore the lessons learnt from this earthquake will be relevant for the whole dam industry.

During the Wenchuan earthquake the problem of mass movements (mainly rockfalls in very steep mountains) and landslide lakes have shown to be very important new features of strong earthquakes.

In addition, an unprecedented large number of dams and run-of-river power plants have been affected by this earthquake. The Wenchuan earthquake has confirmed and demonstrated that dams, spillways and appurtenant structures must be able to withstand the multiple effects of strong earthquakes.

3. SEISMIC DESIGN CRITERIA

3.1 Background on Seismic Design of Dams

Large concrete dams have been among the first structures that have been designed against earthquakes since the 1930s, however, the knowledge about their seismic safety is actually poor, because most of them were designed using seismic design criteria and methods of dynamic analysis that are considered obsolete today. Earthquake loading was represented by a pseudo-static force expressed as the product of a seismic coefficient and the weight of the structure, acting in upstream-downstream direction plus a hydrodynamic force acting on the upstream face of the dam. This type of analysis did not consider the dynamic characteristics of the dam, although both, inertia forces and the hydrodynamic pressure were taken into account.

A significant step forward was achieved when in 1989 ICOLD published Bulletin 72 entitled Selecting Seismic Parameters for Large Dams, where new seismic design criteria were specified for dams. Accordingly, new dams

should comply with this guideline, which sets minimum seismic design criteria for dams and safety-relevant elements. This guideline has been revised in 2010. The basic concept is that the dam has to be designed for the Operating Basis Earthquake (OBE) and the Safety Evaluation Earthquake (SEE). The terms Maximum Credible Earthquake (MCE) and Maximum Design Earthquake (MDE) defined in the 1989 version of the guideline have been replaced by Safety Evaluation Earthquake (SEE).

The seismic design of dams is based on two different elements, i.e.

(i) dynamic analysis of dam subjected to OBE and SEE ground motions; and

(ii) proven design concepts and guidelines to ensure that the dam will perform well under strong earthquake action.

It is a misconception to believe that a dam with conceptual deficiencies can be made safe by using sophisticated seismic analysis tools. Powerful analysis software is available today to perform such analyses. However, the reliability of analyses is limited by the uncertainties in the seismic input, dynamic material properties, limitations in numerical modeling etc. Moreover, most computer programs for the inelastic dynamic analysis of dams are still in the research and development phase and have not been tested in practice. Although in dam engineering the behaviour of dams shall be analysed as realistically as possible, this is a difficult task for the strongest earthquake ground motion, because of the lack of observational data of modern dams, which have experienced such earthquakes. Because of these reasons and due to the fact that each dam is a prototype it is very difficult to generalize observations obtained from a few dams.

Finally, we should not underestimate the importance of the quality of the construction works on the earthquake performance of large dam projects..

3.2 Seismic Design Criteria for Dam Projects

In practice the seismic design criteria for the main structures, components and equipment of a typical hydro power plant must be defined. The following design earthquake motions are used:

(i) Construction level earthquake for temporary structures (CE): A typical return period of the CE for appurtenant structures is 50 years. For cofferdams and critical construction stages of concrete dams with blocks of variable height the CE is larger than that for appurtenant structures and can be selected based on risk considerations.

(ii) Design basis earthquake for appurtenant structures (DBE): The DBE can be selected based on earthquake codes for buildings and other structures. The seismic design shall then be performed following the corresponding building code taking into account the local soil conditions, the importance factors assigned to different types of appurtenant structures and using ductility/behaviour factors for different structural elements and systems specified in the code. If the code allows, then site-specific design response spectra can be used. In Europe, the return period of the DBE ground motion is 475 years. In North America the DBE is based on a reference return period of 2475 years.

(iii) Operating Basis Earthquake (OBE): The OBE has a return period of145 years. No structural damage is accepted, i.e. stresses in concrete dams must remain within allowable stresses. The OBE represents a serviceability limit state and is basically an economical criterion, which is of primary interest for the dam owner.

(iv) Safety Evaluation Earthquake (SEE): The SEE has no specific return period but 10,000 years are often used for large dams. The return period of the SEE is also determined based on the seismic risk of a dam. For example in Switzerland the return periods of the SEE ground motions are as follows: 10,000 years for dam category I (large dams with reservoir depth exceeding 40 m or a reservoir volume exceeding one million m3), 5,000 years for dam category II (medium size dams with reservoir depths in the range of 5 to 40 m), and 1000 years for dam category III (all other dams also including those with a height of less than 5 m). Category I and II dams are under control of the federal authorities.

Structural damage (cracks, deformations) is accepted for the SEE as long as there is no uncontrolled release of large quantities of water from the reservoir. The SEE is relevant for dam safety.

For the safety-relevant elements such as the bottom outlet and the spillway gates, which must be operable after the SEE, no damage and inelastic deformations are accepted, which would obstruct operation of these elements. Power supply and control units for the operation of these elements must also be intact after the SEE.

Thus the seismic performance criteria for the bottom outlet and spillway gates are stricter than thos of the dam body as they must be operable so that the reservoir can be lowered, and a moderate flood can still be released safely after a major earthquake.

Accordingly, the following safety classes of the different structures, elements and components can be defined:

(i) Safety class 1 includes elements and components, which must remain in an operable state after the ground motion of the SEE, i.e. bottom outlet and spillway gates.

(ii) Safety class 2 includes the dam body and other water retaining elements, which must be able to retain the water in the reservoir after the SEE until the water in the reservoir can be lowered if the dam experiences structural damage.

(iii) Safety class 3 includes mainly appurtenant structures such as the powerhouse, switchyard, transmission towers etc., which have to be able to withstand a design ground motion that is less severe than that of the SEE.

(iv) Safety class 4 includes non-critical structures like office buildings, storage facilities etc., which may be designed according to building code regulations.

(v) Furthermore, special seismic design criteria have to be established for temporary structures (cofferdams, river diversion structures etc.) and for critical construction phases.

For the seismic analysis and design of the hydro-mechanical and electro-mechanical equipment the design ground motions at the supports of these components have to be used. These support motions at the dam crest may be completely different from the earthquake ground motion at the rock surface obtained from the seismic hazard analysis.

4. SEISMIC ANALYSIS OF DAMS

4.1 Concrete Dams

For the analysis of a dam subjected to the OBE ground motion, linear-elastic dynamic analysis methods developed in the 1970s are still suitable. The great advantage of such analyses is that two engineers solving the same problem should get the same answers, if the geometry, material properties and boundary conditions are the same. Today such analyses seem to be straightforward, however, there are still problems with the realistic modeling of the dynamic interaction effects of the dam with the reservoir and the foundation rock, the material damping and the effect of non-uniform ground motions especially in the case where three-dimensional analyses are needed.

In the case of the SEE ground motions, some structural damage is accepted, which is usually characterized by inelastic phenomena, e.g. joint opening, formation of cracks, hysteretic behaviour of materials, sliding and rocking motions, etc. The inelastic dynamic analyses are much more demanding and complex than any linear-elastic analyses, and besides experience and engineering judgment a thorough understanding of the main inelastic features governing the dynamic response are needed. In addition, these analyses require an in depth knowledge of the numerical limitations of the nonlinear algorithms involved.

Many engineers still try to avoid nonlinear seismic analyses, for example, by assuming high damping values or considering too low SEE ground motions in order to reduce the dynamic response, so that a linear-elastic analysis could be justified. It is, however, expected that there will be an increasing demand for nonlinear dynamic analyses of dams in the future.

4.2 Embankment Dams

The first dynamic response analysis of an earth dam was made by Mononobe et al. already in 1936. Earth dam design prior to the 1960s was mainly empirical using judgment guided by past experience. However, there was a severe lack of precedence of dams which had been subjected to strong shaking by an earthquake.

Basically, the seismic safety and performance of embankment dams is assessed by investigating the following aspects:

- permanent (inelastic) deformations experienced during and after an earthquake (e.g., loss of freeboard);
- stability of slopes during and after the earthquake, and dynamic slope movements;
- build-up of excess pore water pressures in embankment and foundation materials (soil liquefaction);
- damage to filter, drainage and transition layers (i.e., whether they will function properly after the earthquake);
- damage to waterproofing elements in dam and foundation (core, upstream concrete face or asphalt membrane, geotextiles, grout curtain, diaphragm walls in foundation, etc.,);
- vulnerability of dam to internal erosion after formation of cracks or formation of loose material zones due to high shear (shear bands);
- vulnerability of hydromechanical equipment to ground displacements and vibrations; and,
- damage to intake and outlet works (safe release of the water from the reservoir may be jeopardized after the earthquake).

Different material models can be used for the inelastic dynamic analysis of dams. Today the most widely used method for the seismic analysis of embankment dams is the equivalent linear method developed in the early 1970s. In this method the shear strain-dependent shear modulus and damping ratio are taken into account in an iterative process using linear-elastic dynamic analyses.

5. THE ROLE OF ICOLD IN THE EARTHQUAKE SAFETY OF LARGE DAMS

The Committee on Seismic Aspects of Dam Design is one of ICOLD's oldest technical committees, which at present comprises dam and earthquake experts from 32 different countries from all continents. It has prepared a number of guidelines on various aspects of seismic analysis, design and seismic monitoring of dams. These guidelines are considered as seismic guidelines in most countries which do not have any specific codes or regulations for dams. Since 1984 the following guidelines have been prepared (Wieland, 2003):

- Bulletin 52 (1986): Earthquake analysis procedures for dams (Report prepared on behalf of the Committee on analysis and design of dams of ICOLD, O. C. Zienkiewicz, R. W. Clough, H. B. Seed),
- Bulletin 62 (1988): Inspection of dams following earthquakes – guidelines (revised in 2008),
- Bulletin 72 (1989): Selecting seismic parameters for large dams (revised in 2010),
- Bulletin 112 (1998): Neotectonics and dams,
- Bulletin 113 (1999): Seismic observation of dams,
- Bulletin 120 (2001): Design features of dams to effectively resist seismic ground motion,
- Bulletin 123 (2002): Earthquake design and evaluation of structures appurtenant to dams, and
- Bulletin 137 (2011): Reservoirs and seismicity: state of knowledge.

Bulletin 137 is concerned with reservoir-triggered seismicity which has attracted much attention in connection with large dam projects and it has also been argued that the Wenchuan earthquake was triggered by the reservoir stored by the Zipingpu dam although there is no evidence, which supports this allegation. An expert team of ICOLD and the Chinese National Committee on Large Dams, which visited

some of the large dams affected by the Wenchuan earthquake in spring 2009 has not found any link between this earthquake and the Zipingpu reservoir.

The publication with the greatest impact on the seismic design of dams is Bulletin 72, which was revised in 2010. In this guideline the concept of two earthquake level for the seismic design of dams was introduced internationally, i.e. the Operating Basis Earthquake (OBE) and the Safety Evaluation Earthquake (SEE) ground motions. Today, most dams are designed against earthquakes using this concept, which can be considered as the minimum seismic design requirement for dams.

Bulletin 120 complements Bulletin 72 as it includes conceptual features for the seismic design of dams, which are extremely important as it is well-known that it will be difficult to have a dam to perform well during an earthquake when the basic seismic design concepts are not observed.

6. CONCLUSIONS

The importance of the seismic load case in the design of dams has changed considerably. Rational concepts of the ground motion a dam has to be able to withstand have been developed, i.e. a dam must be able to withstand the SEE ground motion. Furthermore, we have to realise that all structures, elements and components of a hydropower plant will be subjected to ground shaking if an earthquake occurs. Therefore, all of them have to be checked and designed for earthquake action.

Moreover, the Wenchuan earthquake has clearly shown that the seismic hazard is a multiple hazard, and all of them have to be considered.

Simple nonlinear analyses methods are still widely used for the seismic analysis of dams, such as the Newmark sliding block method and the equivalent linear method for the analysis of the embankment dams. These methods are, however, nearly 40 years old.

The methods for nonlinear dynamic analysis of dams are, however, still under development. Nonlinear seismic analyses need substantial engineering judgment. The proper formulation of the goals of the seismic analysis is probably the most difficult task required to ensure that such an analysis can actually ‘succeed’. Relatively simple models should be preferred to complex models employing nonlinear constitutive laws using parameters that are either not available or very hard to determine.

References:

ICOLD, (1986). Earthquake analysis procedures for dams by O. C. Zienkiewicz, R. W. Clough, H. B. Seed, Bulletin 52, Committee on Seismic Aspects of Dam Design, ICOLD, Paris.

ICOLD, (1988/2008). Inspection of dams following earthquakes – guidelines, Bulletin 62, Committee on Seismic Aspects of Dam Design, ICOLD, Paris (rev. 2008).

ICOLD, (1989/2010). Selecting seismic parameters for large dams, Bulletin 72, Committee on Seismic Aspects of Dam Design, ICOLD, Paris.

ICOLD, (1998). Neotectonics and Dams, Bulletin 112, Committee on Seismic Aspects of Dam Design, ICOLD, Paris.

ICOLD, (1999). Seismic observation of dams, Bulletin 113, Committee on Seismic Aspects of Dam Design, ICOLD, Paris.

ICOLD, (2001). Design features of dams to effectively resist seismic ground motion, Bulletin 120, Committee on Seismic Aspects of Dam Design, ICOLD, Paris.

ICOLD, (2002). Earthquake design and evaluation of structures appurtenant to dams, Bulletin 123, Committee on Seismic Aspects of Dam Design, ICOLD, Paris.

ICOLD, (2011). Reservoirs and seismicity: state of knowledge (in print), Bulletin 1137, Committee on Seismic Aspects of Dam Design, ICOLD, Paris.

Mononobe, N., Takata, A. & Matumura, M., (1936). Seismic stability of the earth dam. Trans. 2nd Congress on Large Dams, Washington, D.C. Q. VII, pp.435-444.

Wieland M., (2003). Seismic Aspects of Dams, General Report Q.83, Trans. 21st Int. Congress on Large Dams, Vol. 3, Montreal, Canada.

8CUEE CONFERENCE PROCEEDINGS
8th International Conference on Urban Earthquake Engineering
March 7-8, 2011, Tokyo Institute of Technology, Tokyo, Japan

REFLECTIONS ON EVOLUTION OF NEAR-FIELD EARTHQUAKE ENGINEERING

Tatsuo Ohmachi

Professor, Department of Built Environment, Tokyo Institute of Technology, Japan
Ohmachi@enveng.titech.ac.jp

Abstract: Reflecting on his 32 years of teaching and research at Tokyo Tech, the author addresses an urgent necessity to establish a new field of study; namely, near-field earthquake engineering. Several landmark events that motivated the author to devote himself to the field, as well as more recent events that the author was actively associated with are summarized.

1. INTRODUCTION

It was July 1, 1979 when I moved to Tokyo Institute of Technology (Tokyo Tech) from the Electric Power Development Co. Ltd. (EPDC), and joined the earthquake engineering laboratory as Associate Professor. My boss was Professor Hiroyoshi Kobayashi who had been engaged in hazard assessment and mapping of ground motion intensity in the event of the expected Tokai earthquake, with a the help of his doctoral student, S. Midorikawa.

In the previous year, 1978, the Large Scale Earthquake Countermeasures Act came into effect in Japan. A main target of this act is the Tokai earthquake which is supposedly imminent and expected to occur beneath Suruga Bay where an earthquake of magnitude (M) 8 or larger has not occurred since 1854. Following this Act, instrumentation arrays were set up to monitor precursors of an earthquake and data from the arrays are telemetered to Tokyo where the Japan Meteorological Agency would review the data and decide whether a meeting of the Earthquake Assessment Committee should be convened.

Discussions with Professor Kobayashi and his colleagues deeply impressed me with their hazard assessment work, applying the state-of-the art technology to a seismic fault model with site-dependent geological conditions. Since then, I have been motivated to study near-field earthquake engineering. In the following sections, I discuss several landmark earthquake events listed in Table 1 that motivated me to devote myself to the near-field earthquake engineering in chronological order.

2. LANDMARK EARTHQUAKE EVENTS

2.1 The 1984 Nagano-ken Seibu earthquake (M6.8), Japan

In early January, 1985, I had an opportunity to investigate damage to a tunnel running zigzag across the source area of the Nagano-ken Seibu earthquake which occurred on September 14, 1984. The tunnel is a headrace tunnel for hydroelectric power generation, having a horseshoe-shaped cross section about 3 m in diameter. Tunnel damage was mainly horizontal shear cracking of the concrete lining and concentrated at three different locations along the tunnel. To my surprise, the three damage locations were on a straight line having an orientation consistent with a mechanism solution of the earthquake, as shown in Fig. 1. On this basis, it was estimated that the tunnel damage had been caused by subsurface faulting, and that the straight line was evidence of the faulting, although no trace of the faulting was found on the ground surface.

Table 1 Landmark events in near-field earthquake engineering

Year	Landmark Earthquake Events	Special Features
1984	Nagano-ken Seibu (M6.8), Japan	Tunnel damage and upthrow of boulders
1985	Michoacan (M8.1), Mexico	Uplift of seabed at Caleta de Campos
1990	Luzon Island (M7.8), Philippines	Fault trace on ground surface
1994	Northridge (M6.7), USA	High acceleration exceeding 1 g
1995	Hyogo-ken Nanbu (M7.2), Japan	Jumping of bell house and Level 2 motion
1999	Chi-chi (M7.5), Taiwan	Collapse of a concrete gravity dam
2000	Tottori-ken Seibu (M7.3), Japan	Sudden Change in reservoir water level
2003	Tokachi-Oki (M8.0), Japan	Tsunami generation observed by JAMSTEC
2008	Iwate-Miyagi Nairiku (M7.2), Japan	Strong motion records of about 4 g and nonlinear response of a rockfill dam

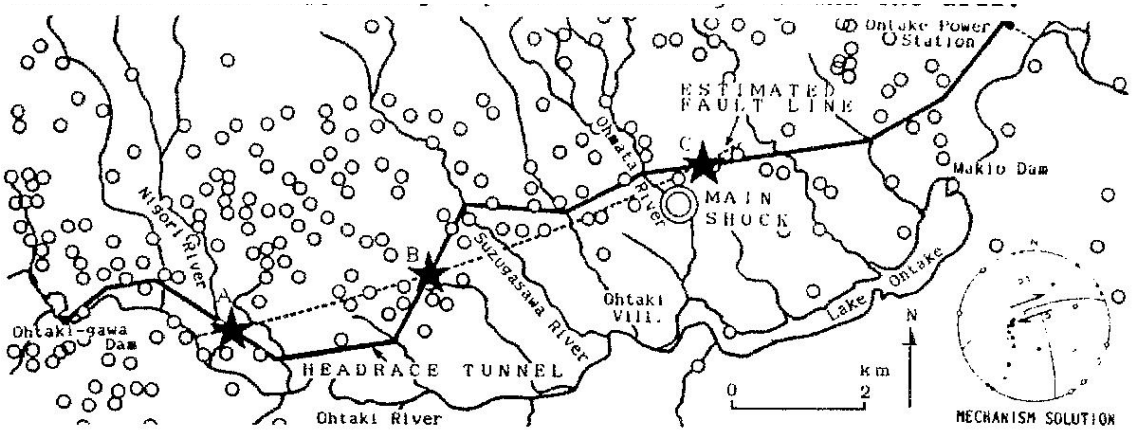


Fig. 1 Location map of earthquake damage to the headrace tunnel, Japan

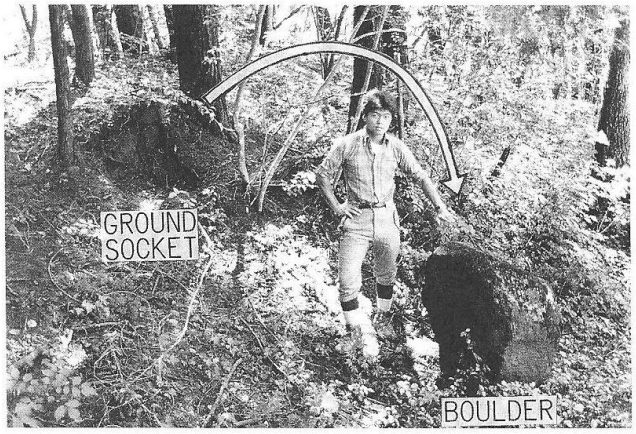


Fig. 2 Upthrow of a boulder in the near-field of the 1984 earthquake, Japan

In August, 1985, we made a presentation of the tunnel investigation (Kobayashi et al., 1985) at a poster session of the 23rd general assembly of International Association of Seismology and Physics of the Earth's Interior (IASPEI) which was held in Tokyo. In the next booth, there was another poster presentation dealing with upthrow of boulders observed in the near-field of the same earthquake (Umeda et al., 1985). I was very much interested in their presentation in which extremely high peak ground acceleration (PGA) as much as 1 to 10 g where g is acceleration due to gravity, was estimated from the jumping. Though PGA of 1.25 g had already been observed at the Pacoima dam during the 1971 San Fernando earthquake (M6.6), I felt the estimated PGA of 10G was unbelievable. What is worse, the estimated PGA was increased to 8 to 16 g later (Umeda et al., 1987). A site investigation which included the areas where upthrow of boulders were reported was conducted by my colleagues, later, as shown in Fig. 2.

2.2 The 1985 Michoacan earthquake (M8.1), Mexico

The Michoacan earthquake occurred on September 19, 1985, along the Pacific coast of Mexico. While my colleagues went out to Mexico city for the earthquake investigation, I stayed back in my laboratory and found a paper by Newmark on upthow of objects during earthquakes (Newmark, 1973) which states "although it is necessary that the actual acceleration of a near-surface object be greater than the acceleration of gravity for it to move upward relative to the ground, this is not necessarily an indication that the general vertical ground acceleration is indeed greater than that of gravity". This is because the upward movement or upthrow takes place when the earthquake response of the objects exceeds the acceleration of gravity. Inspired by this paper, I collected things available in my room such as steel balls and a sponge rubber mat, and repeated shake-table experiments by trial and error.

Finally, I succeeded to demonstrate the jumping of steel balls which were originally embedded in hollows of the sponge rubber mat, only by horizontal table motion. The experiments were followed by numerical simulations shown in Figs. 3 and 4. In Fig. 4, it is interesting to note that maximum response accelerations in both horizontal and vertical directions were in excess of 10 g, while the ground motion acceleration was less than 1.5 g.

In January, 1986, I visited the source area of the Michoacan earthquake as a member of the Japan Society of Civil Engineers (JSCE) investigation team. At Caleta de Campos, one of the inhabitants told us that the sea surface had settled down significantly after the earthquake. In fact it could be observed as a shell line about 1m 1 m above the sea surface, as shown in Fig. 5, which was, in our estimation, caused by the uplift of the seabed as a result of the seismic faulting. Later we were pleased to find that earthquake ground displacement calculated from strong motion records showed an uplift similar to that observed by us.

2.3 The 1990 Luzon Island earthquake (M7.8), Philippines

On July 16, 1990, a major earthquake occurred in the central part of Luzon Island, Philippines. In Dagupan city,

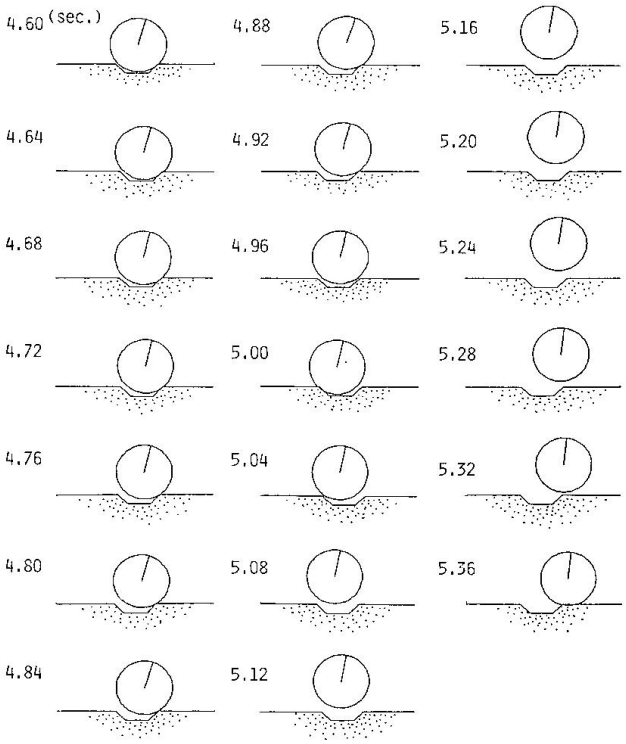


Fig. 3 Snapshots of numerical simulation of upthrow of objects

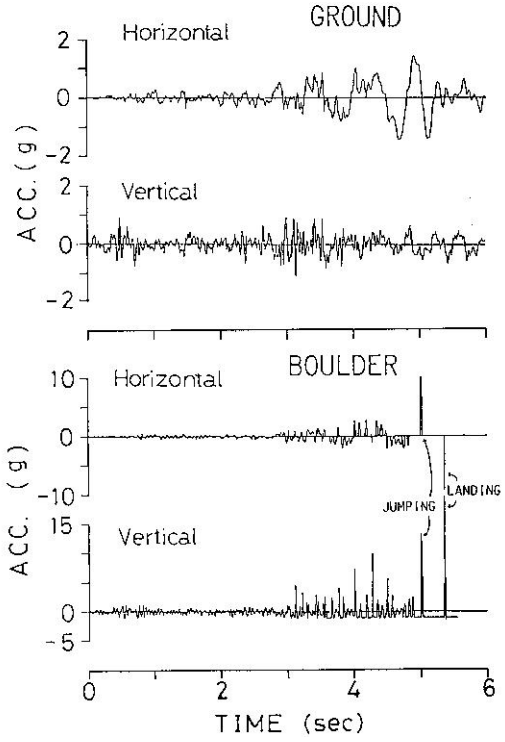


Fig. 4 Time histories of the numerical simulation



Fig. 5 Uplift of seabed witnessed at Caleta de Campos, Mexico

many building were damaged by soil liquefaction, while a refurbished hotel building in Baguio city had collapsed due to the intense earthquake shaking. For the first time in my life, I observed a seismic fault that had appeared on the ground surface, in the suburbs of Digdig town (Fig. 6).

2.4 The 1994 Northridge earthquake (M6.7), USA

Before the dawn of January 17, 1994, this earthquake occurred in the middle of the San Fernando Valley, California. At Tarzana strong motion station 5 km distant from the epicenter, the PGA was 1.82 g and 1.18 g in the



Fig. 6 Surface rupture witnessed in the suburbs of Digdig town, Philippines

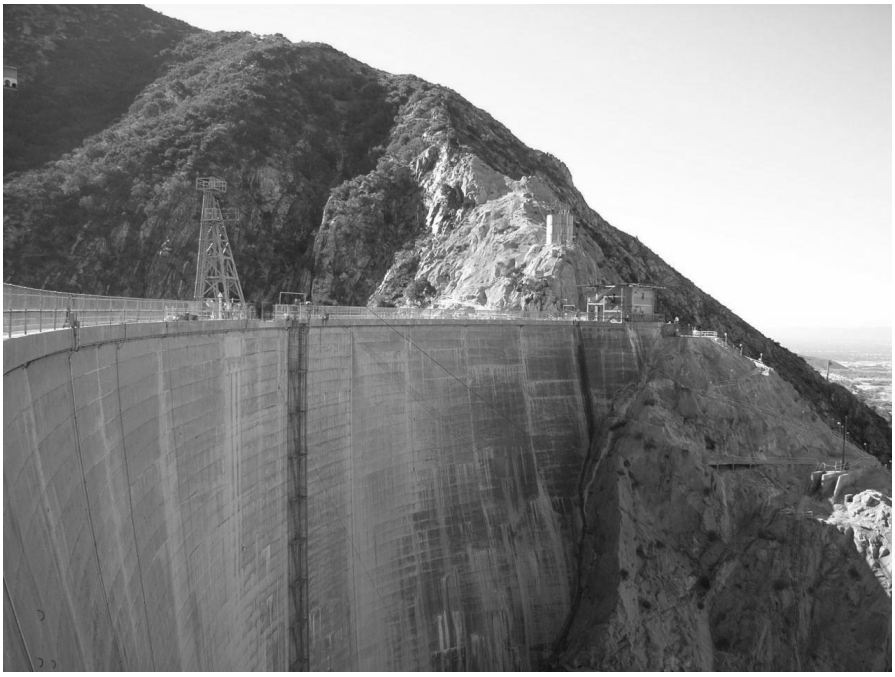


Fig 7 Left bank of the Pacoima arch dam, USA

horizontal (H) and vertical (V) directions, respectively. Despite such high accelerations, surprisingly, little damage was observed around the station.

On the left bank of the Pacoima dam which is a 111 m high arch dam, the PGA was 1.53 g and 1.39 g in the horizontal (H) and vertical (V) directions, respectively. It is noted that in the 1971 San Fernando earthquake (M6.6), an earthquake acceleration of 1.25 g (H) was recorded, which was the first time in history that accelerations exceeding 1 g were observed. Since then, the 1971 earthquake records have been widely discussed and it has been concluded that the high acceleration was attributable to the effect of the narrow ridge shown in Fig. 7, where the accelerometers were installed. This conclusion was further confirmed by the 1994 earthquake because PGA observed at another rock station at the dam site was 0.54 g (H) and 0.43 g (V), respectively.



Fig. 8 A Japanese bell house that was uplifted during the 1995 earthquake, Japan

2.5 The 1995 Hyogo-ken Nanbu earthquake (M7.2), Japan

Similar to the Northridge earthquake, the Hyogo-ken Nanbu earthquake occurred before dawn on a winter day on January 17, 1995. I was amazed to see the serious damage to different types of civil engineering structures. The damage suggested ground motion intensities much higher than those used in traditional seismic designs of structures, which was demonstrated by several strong motion recordings of the main shock in and around Kobe city.

Meanwhile on Awaji Island, no strong motion recording was recovered, even though some areas were assigned the highest seismic intensity 7 on the Japan Meteorological Agency (JMA) scale. On being informed that the uplifting of a Bell House shown in Fig. 8 had been observed at Saimyo-ji temple located in an intensity 7 area, I could not help visiting that location for more detailed information. This was because, as shown in Fig. 9, I had studied the uplifting of a Bell House several years before the 1995 earthquake, and learned that it could provide much information associated with earthquake ground motion (Ohmachi et al, 1997).

Following the 1995 earthquake, the Japan Society of Civil Engineers (JSCE) issued the "Proposal on Earthquake Resistance for Civil Engineering Structures" three times in May 1995, January 1996 and June 2000. One of the requirements of the proposals is to consider two levels of earthquake input motion for seismic design of structures; namely, Level 1 and Level 2 motions. I took part in drafting the proposals on the Level 2 motion (Fig. 10) and studied earthquake input motion in detail during that time.

Based on these experiences, I was involved in the formulation of the Guideline for Seismic Safety Evaluation of Dams (Draft) issued in 2005, and the Revised Guideline

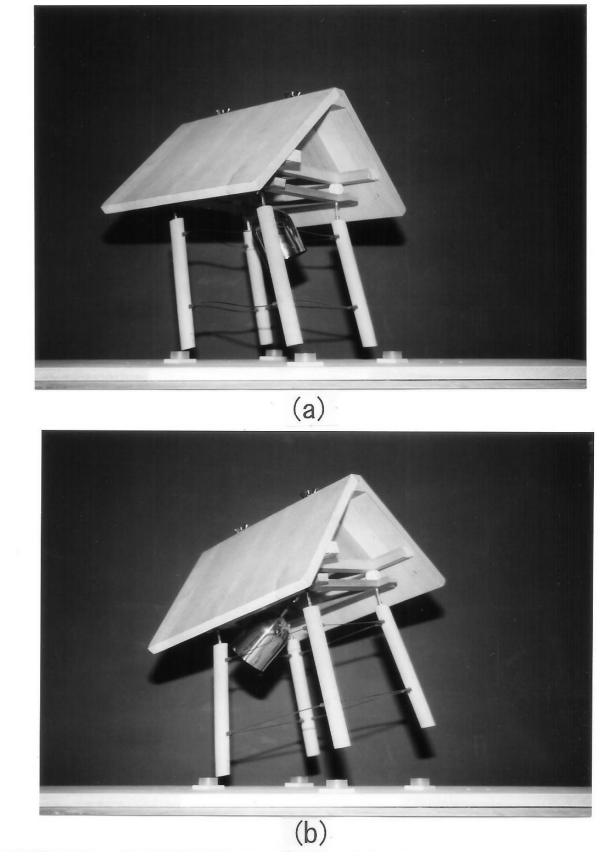


Fig. 9 A shake-table experiment for the upthrow of a bell house

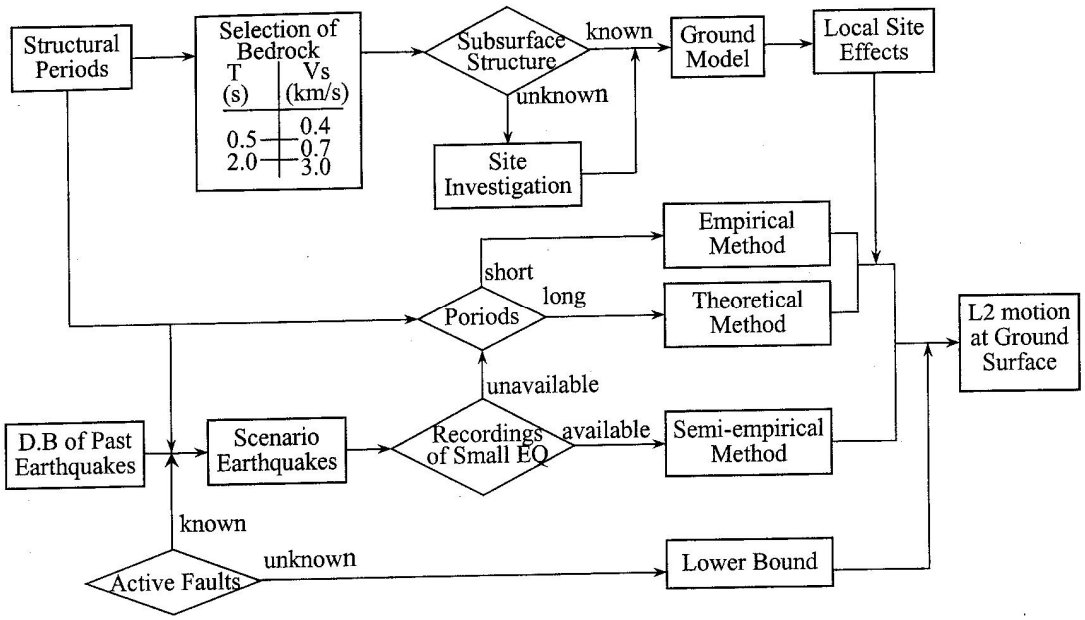


Fig. 10 Flowchart to formulate Level 2 earthquake motions (Ohmachi,1999)



Fig. 11 The Shih-kang dam collapsed by the 1999 earthquake, Taiwan

for Seismic Safety Evaluation of Water Works issued in 2010.

2.6 The 1999 Chi-chi earthquake (M7.5), Taiwan

Among several cases of dams damaged by the Chi-chi earthquake, the most severe case was the collapse of the Shih-Kang dam. It was a 357 m long concrete gravity dam, equipped with 18 spillway gates and 2 sediment flushing gates. Due to dislocation along the ramified seismic fault planes, the right half side of the dam and intake tunnel on the left bank side were crushed completely with 7.5 m and 3.5 m differences in level, respectively. Figure 11 shows the Shih-Kang dam severely damaged by the earthquake.

2.7 The 2000 Tottori-ken Seibu earthquake (M7.3), Japan

This earthquake occurred on October 6, 2000, in the western part of Tottori prefecture. The Kasho dam located in the near field of this earthquake, is a 46.6 m high concrete gravity dam constructed in 1989. Strong motion accelerometers at the dam registered a peak acceleration of

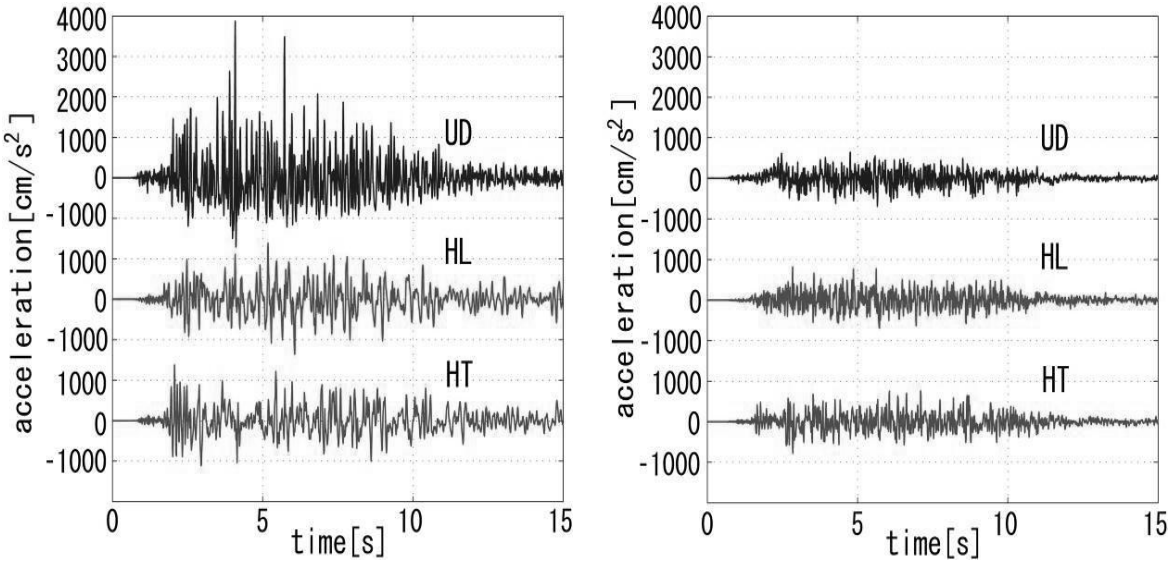


Fig. 12 Three-component acceleration records at IWTH25 station:
(a) surface record (left) and (b) borehole record at a depth of 260m (right)

2051 gal at the top of the dam and 531 gal in the lower inspection gallery (Japan Commission of Large Dams, 2002). Despite such high accelerations, the dam did not suffer serious damage, the only damage was cracking of the concrete floor in the sub-gate control room. Although no increase in water leakage was recorded, the water level of the reservoir suddenly dropped 6 cm immediately after the main shock. The reasons for the drop in water level were not clear and raised concern among dam engineers.

On hearing about this drop in water level, I recalled the radiation pattern of a strike-slip of a point source faulting, and tried to attribute the drop in the water level to the change in the slope of the reservoir bed. In fact according to a ground survey conducted around the reservoir, there was a slight decrease in the slope of the ground surface. Moreover, integration of the acceleration records in the gallery gave a permanent uplift of about 5 cm, and a 34.9 m long plumb line installed in a vertical shaft within the dam showed a change in the slope of the dam. To my satisfaction, these observed changes in the slope were in fairly good agreement with those from a numerical simulation using a seismic fault model.

2.8 The 2003 Tokachi-oki earthquake (M8.0), Japan, and tsunami

The Tokachi-oki earthquake (M8.0) occurred off the southeastern coast of the Tokachi district at 04:50 on September 26, 2003. In the source area, an offshore monitoring system deployed by Japan Agency for Marine-Earth Science and Technology (JAMSTEC) succeeded in recording detailed data associated with the tsunami generation process for the first time in history. Analysis of the JAMSTEC monitoring data showed that three kinds of water waves were involved in the dynamic tsunami generation process; that is, water pressure waves of short period, a tsunami of long period, and preceding waves of intermediate period.

Since 1995, we have developed the "dynamic tsunami simulation technique", which takes into account both the dynamic seabed displacement and acoustic effects of the seawater. Through the dynamic simulation, the three kinds of water waves were predicted, but had to be validated by actually observed data. In this context, the JAMSTEC data was very important not only for general scientific purposes but also for our study on near-field tsunamis which aims to develop state-of-the-art technology for an effective tsunami warning system.

2.9 The 2008 Iwate-Miyagi Nairiku earthquake (M7.2), Japan

This earthquake occurred on June 14, 2008 near the boundaries of Iwate and Miyagi prefectures. During the earthquake, extremely high accelerations were recorded at the KiK-net IWTH25 station, as shown in Fig. 12. The peak acceleration in the vertical component of the surface record in Fig. 12(a) was about 4 g and the upward vertical acceleration was much larger than the downward counterpart, while in the borehole record at a depth of 260 m in Fig. 12(b), the upward and downward accelerations have symmetric vertical amplitudes. Some researchers have suggested that the asymmetric large amplification in the vertical acceleration is because the ground surface was tossed into the air during the main shock like a body on a trampoline (Aoi et al., 2008, and Yamada et al., 2009).

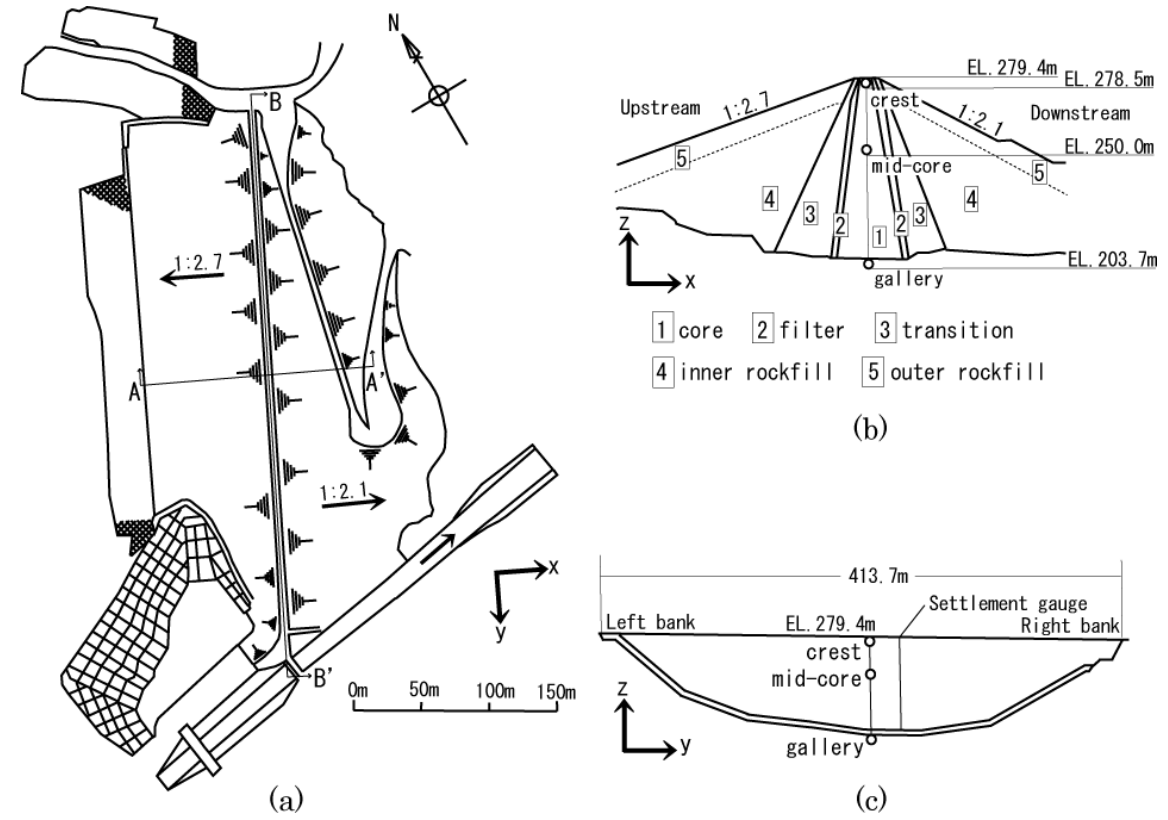


Fig. 13 (a) Plan, (b) cross section A-A' and (c) cross section B-B' of the Aratozawa dam with seismometers located at crest, mid-core and gallery. Arrows with x, y and z indicate positive directions of observed accelerations

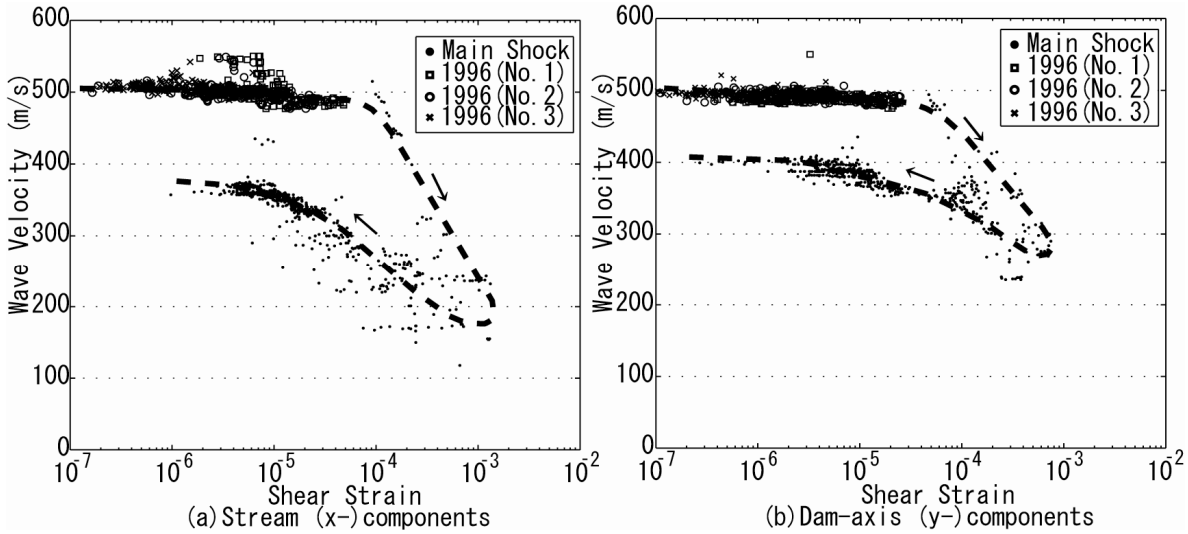


Fig. 14 Strain dependent shear wave velocities evaluated from strong motion records

Field investigations, shake-table experiments, and numerical simulations were conducted to reproduce the acceleration time histories of the surface record. The vertical component of the surface record looks similar to the one from the simulation shown in Fig. 4, but dissimilar in detail. Thus, we concluded that probably the influence of the interaction of the station house with the underlying ground had been included in the surface record.

During the earthquake, the Aratozawa dam which is a 74.4 m high rockfill dam with a central clay core (Fig. 13),

was severely shaken but suffered only minor damage. The earthquake acceleration exceeded 10 m/s^2 at the gallery, inducing large shear strains in excess of 10^{-3}. Due to the large strains, the shear wave velocity and shear modulus showed a significant decrease from their initial values, as shown in Fig. 14. The full recovery of the decreased wave velocity took almost one year.

3. CONCLUDING REMARKS

In most earthquakes, the strongest ground motions are observed in the near-field, where not only the number of casualties is largest, but also devastation of human society is most serious. Hence, in earthquake prone countries like Japan, it is well known that the near-field of a major earthquake which by definition is located in the vicinity of causative seismic fault is the most dangerous and vulnerable area. Due to scarcity of detailed observation data, the causes and effects of the near-field earthquakes (NOT CLEAR) have not been fully understood to date even by experts in earthquake engineering. However, since the 1995 Hyogo-ken Nanbu earthquake which is often referred to as the Kobe earthquake, this situation has changed significantly, at least in Japan. At the present time, systematic observation arrays for earthquakes have been set up throughout Japan, including arrays for tsunamis which are in the process of being formed, along the Pacific coast of Japan. We are often surprised to see observed data from these arrays, which are sometimes beyond our expectations and filled with inspiration for new ideas.

For these reasons, I would like to draw attention to the urgent necessity to establish a new field of study, namely, near-field earthquake engineering (直下地震工学 in Japanese). It is my firm conviction that research in near-field earthquake engineering will never fail to enrich traditional earthquake engineering, and make effective significant contributions to reduce earthquake risk in our society as well.

Acknowledgements:

The author has benefited from many useful discussions with professors and his colleagues of Tokyo Tech including: late Hiroyoshi Kobayashi, Saburoh Midorikawa, Takumi Toshinawa, Shusaku Inoue and Anil C. Wijeyewickrema.

References:

Aoi, S., Kunugi, T. and Fujiwara H. (2008), "Trampoline Effect in Extreme Ground Motion," *Science*, Vol. 322, 727-730.

Kobayashi, H., Ohmachi, T. and Midorikawa, S. (1985), "Traces of Subsurface Faulting of the Western Nagano Earthquake of 1984, P-12-10, IASPEI.

Newmark, N.M. (1973), "Interpretation of apparent upthrow of objects in earthquakes," *Proceedings of 5th World Conference on Earthquake Engineering*, Paper No.294.

Ohmachi, T., Kawamura, M., Yasuda, S., Mimura, C., and Nakamura, Y. (1988), "Damage due to the 1985 Mexico earthquake and the ground conditions," *Soils and Foundations*, Vol. 28, No.3, 149-159.

Ohmachi, T. and Midorikawa, S. (1992), "Ground-motion intensity inferred from upthrow of boulders during the 1984 Western Nagano Prefecture, Japan, earthquake," *Bulletin of the Seismological Society of America*, Vol. 82, No.1, 44-60.

Ohmachi, T. (1994), "Lessons learned from the 1994 Northridge earthquake, California earthquake," *Proc. JSCE* No. 492/VI-23, 1-12, 1994. (in Japanese)

Ohmachi, T. Midorikawa, S. and Honda, M. (1997), "Jumping of bell houses caused by near-field.ground motion. Case histories and shaking table experiment," short communication, *Earthquake Engineering and Structural Dynamics*, Vol. 26, 657-665.

Ohmachi, T. (1999), "Formulation of Level 2 earthquake motions for civil engineering structures, *Proc. 7th US-Japan Workshop on Earthquake Resistant Design of Lifeline Facilities and Countermeasures against Liquefaction*, Technical Report MCEER-99-0019, 497-506.

Ohmachi, T. (2000), "On damage to dams due to the 1999 Chichi earthquake," *Dam Engineering,* Vol. 10, No. 2, 138-150.

Ohmachi, T., Kojima, N., Murakami, A. and Komaba, N. (2003), "Near field effects of hidden seismic faulting on a concrete dam," *Jour. Natural Disaster Science*, Vol. 25, No. 1, 7-15.

Ohmachi, T. and Inoue, S. (2008), "Dynamic tsunami generation process observed in the 2003 Tokachi-oki, Japan, earthquake," *Advances in Geoscience*, Vol. 18, 159-168.

Ohmachi, T., Inoue, S., Mizuno, K. and Yamada, M. (2010), "A realistic model to reproduce the extreme acceleration observed at the Kik-Net IWTH25 station during the 2008 Iwate-Miyagi Nairiku earthquake," *Proc. 13th Japan Earthquake Engineering Symposium*.

Ohmachi, T. and Tahara, T. (2011), "Effects of the Iwate-Miyagi Nairiku earthquake in 2008, Japan on a central clay core rockfill dam, *Proc. General Assembly of ICOLD* (in press).

Umeda, Y. Kuroiso, A, Ito, K., Iio, Y. and Muramatsu, I. (1985), "High acceleration region and rupture zone of the Western Nagano Prefecture earthquake, 1984," P12-9, IASPE.

Umeda, Y. Kuroiso, A, Ito, K., Iio, Y. and Muramatsu, (1987), "High accelerations produced by the Western Nagano Prefecture, Japan, earthquake of 1984," *Tectonophysics* 141, 335-343.

8CUEE CONFERENCE PROCEEDINGS
8th International Conference on Urban Earthquake Engineering
March 7-8, 2011, Tokyo Institute of Technology, Tokyo, Japan

WISE DYNAMIC TESTING FOR ENHANCED UNDERSTANDING OF STRUCTURES

Akira Wada[1], Mineo Takayama[2], and Satoshi Yamada[3]

1) Professor, Structural Engineering Research Center, Tokyo Institute of Technology, Japan
2) Professor, Department of Architecture and Building Engineering, Fukuoka University, Japan
3) Associate Professor, Structural Engineering Research Center, Tokyo Institute of Technology, Japan
wada@serc.titech.ac.jp, mineot@fukuoka-u.ac.jp, naniwa@cv.titech.ac.jp

Abstract: In this decade, large shaking tables were installed at the UC San Diego in USA and the E-Defense in Japan. The bed of the E-defense can support 1200 metric tons and 20m tall structures. This is very large comparing to the past facility and is very strong machine, but actual buildings are bigger and taller than the one that could be on the table. Total weight of a tall building will be heavier over 100,000 metric tons and height of a tall building is higher than 300m in Japan and800m in the world.
Researchers can test only 5 story buildings at the E-defense and test 10-story buildings but very small floor area at the UCSD. We cannot test actual buildings. Then, we need new wise ideas for understanding and knowing the behaviors of actual large structures due to large earthquakes. We will discuss the history of Japanese researches and introduce 4 wise and innovative dynamic tests.

1. EARTHQUAKE ENGINEERING GROWING BY PAST SEVERE DISASTERS

Before Galileo Galilee had written "Two New Sciences", the first textbook of structural mechanics about 370 years ago, we have not any equation for knowing strength of a beam or a column, but humankind is wise and has some intuition. Old carpenters or old contractors could built very beautiful buildings and architectures such as Pyramids in Egypt, Parthenon in Greece, Pantheon in Rome or 5 story pagodas in Japan and so on more than 1000 or 2000 years ago. These buildings have very good performance for a long time, but many buildings were also collapsed by many reasons. In some cases, engineers in the ancient time learned better construction technology by observing collapses and failures. In the 20th century, we have had many severe earthquake disasters and we have learned much from these events and understood the structure behavior better under earthquakes.

a. Building structures have to have adequate lateral strength.
b. Structural members and total structures have to have some deformability.
c. A structure has to have enough integrity.
d. Supporting own gravity weight after an earthquake is fundamental importance.
e. Location of construction, soil condition, and foundation are also fundamental importance.
f. Soil-structure interaction has significance influence to a response of a structure. In some cases, beneficial effect would be, but other case, adverse effect would be to the responses of the structure.
g. A pattern of maximum response of story shear forces could be defined for an earthquake event, but it also changes due to characteristics of earthquakes such as frequency content. The enemy cannot be defined in our science.
h. Strong columns and weak beams structure is preferable.
i. Strong shear-walls or steel braces are very effective to increase seismic capacity.
j. Negative slope of stiffness makes a structure instable.
k. Not only horizontal movements but also rotation along Z-axis has strong effect to collapse behavior of a structure.
l. Joints of beam to column or joints of brace to beam-column are very important. Details are very important.
m. Supplemental damping devices increase a seismic capacity. Passive controlled structure is one of good seismic structure examples.

This paper was presented as a keynote address in the 3rd international conference on advances in experimental structural engineering being held concurrently with the PEER annual meeting and the Loma Prieta earthquake 20th commemorative symposium in October 2009.

n. Seismic isolation is also one of good seismic structure examples
o. Three important roles of seismic design are 1) Preventing collapse of building to save human life, 2) Reparable structure after an earthquake to keep a building property, 3) Keeping a function of building to reduce business interruption due to an earthquake. If possible, we, structural engineers, want to make a building that can cover these three roles.
p. Expectation of public for a good earthquake performance is growing up year by year.
q. Resilience of life, city and country is next important words for structural engineers.

2. ENGINEERS MUST KNOW WHAT WILL HAPPEN BEFORE IT HAPPENS

Structural engineers want to know how a building behaves when an earthquake hits it in future. They have to know what will happen in the building that they are designing and building. We can test beams, columns and joints of these members taking a part from actual building structures. When we have enough research money, we can test two-story to several story of whole building structure. Regretfully, we cannot test more than ten story-building structures, since we have not large enough testing laboratory in the world.

We have an analytical approach using high-speed computers to be able to know the structural behavior under earthquake loadings. When we can grasp the mechanical properties of structural members and structural frames through the results of individual component tests, we can make a mathematical nonlinear model in the computer. Calculation itself has not any problem now, because that we can use high-speed and large-capacity computers. Then we can get a lot of information from the calculated results.

The structural test is the induction process, but the numerical analysis is the deduction process. The structural design is also deduction process and synthetic approach. This is very important. We are using many engineering products such as mobile phones, automobile cars, airplanes and so on, these products are made by mass-production and these functions are checked right after when consumers start to use. On the contrary to these products, building structures are made individually. Since a severe earthquake may be occurred rarely, actual performance can be revealed only when the earthquake happens.

Humankind has built many buildings and many big cities. But not all we have done are based on our experiences. Then we have to know what will happen in the actual building structures in future earthquake event by any possible ways before any troubles happen. The static tests and the dynamic tests should give us a lot of important information and important knowledge.

3. AIMS OF STRUCTURAL TESTS AND NEEDS OF REALISTIC TESTS

As discussed above, the structural tests give us important knowledge and many ideas. We do not need to explain more why we do structural tests. Structural materials such as concrete, steel and other materials can be changed to increase strength. Structural engineering is a field of design works and, the innovative engineers will make new structures or new structural systems beyond those we had past. Then we have to test the structures or new structural systems.

a. Understanding and knowing the structures better.
b. Making safer structures, more economical structures and higher performance structures.
c. Finding weak point of our structures before an actual earthquake hits them.
d. Avoiding failures and increasing the reliability of the structures.
e. Getting the government permission of new ideas.
f. Making a design guideline, a design standard and a design code.
g. Increasing sympathetic friends of engineers and researchers understanding about new ideas and new deign.
h. Persuading the building owners about our design and persuading general public about new ideas.
i. Increasing understanding of the structural behavior for young students and young engineers. The experimental test is good experience for young people.

For these aims, realistic dynamic tests are most effective method and they have strong visual persuasive power. In this paper, we would like to introduce some examples of our researches in last 30 years.

4. TINY SEISMIC ISOLATED STRUCTURES WITH HORIZONTAL HEAVY INERTIA MASSES

Professors Hideyuki Tada and Mineo Takayama have tested tiny seismic isolated structures using also small

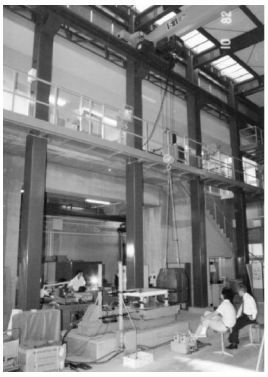




Photo 1 & 2 Tiny seismic isolated structure with heavy iron weight

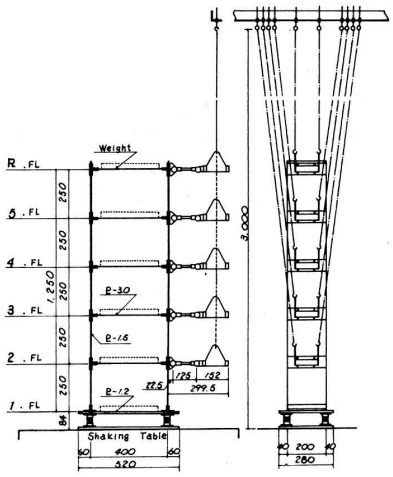


Figure 1 5-story seismic isolated structure and 5-horizontal inertia masses

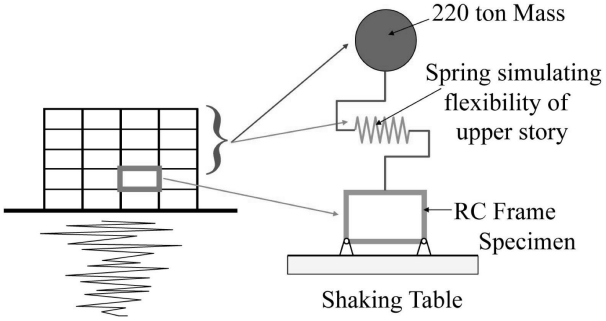


Figure 2 Additional mass and flexibility

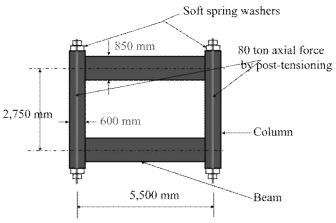


Figure 3 Introduction of column axial forces

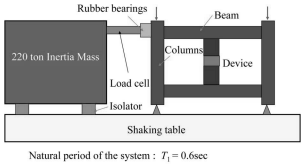


Figure 4 Elevation view during test

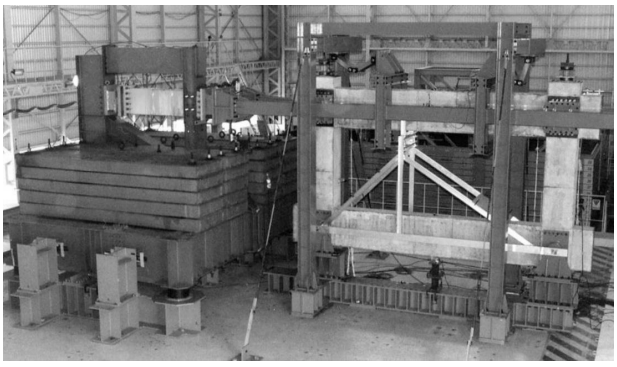


Photo 3 Very heavy steel inertia weight and reinforced concrete frame

supporting one floor and the diameter of the rubber is only shaking table in October 1982. 4 rubber bearings were 30mm. Fundamental natural period is too short because that the floor is light and stiffness of rubber is little high. In many cases, small specimens have short natural period. At that time, they could not capture the typical behavior of seismic isolated structures. They needed heavy horizontal inertia weight. Then, 5 metric-tons iron weight hanged from crane was connected to the side of the specimen. Fundamental natural period of the total system become long enough to show the dynamic behavior of seismic isolated structure as shown in Photo-1 and Photo-2. Next step, the same research group has done 5-story seismic isolated structure using same idea as shown in Fig-1. This system has 5-separated horizontal inertia masses hanged from the high tower in the laboratory.

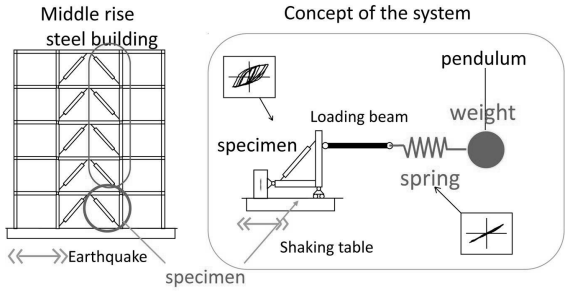


Figure 5 Model steel frame and a specimen with inertia weight and spring

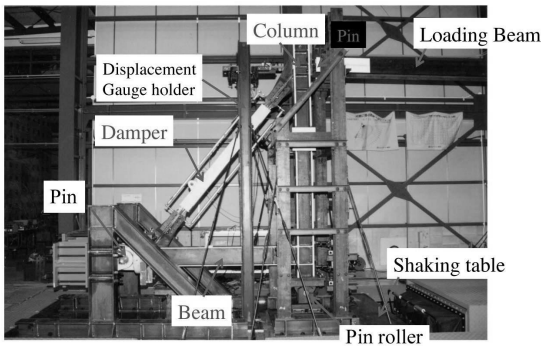


Photo 4 Beam, column and buckling restrained brace on the shaking table

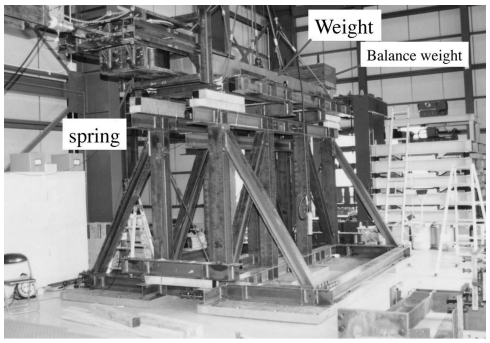


Photo 5 Inertia iron weight and spring of 2 rubber bearings

5. SEISMIC RETROFITTED REINFORCED CONCRETE FRAMES ADDED SUPPLEMENTAL DAMPERS

The research team of Dr. Masanori Iiba and Professors Satsuya Soda, Eiichi Inai, Hiroshi Kuramoto and Akira Wada has done reinforced concrete frames having supplemental dampers with horizontal inertia mass set on 4 flexible rubber bearings at the large-scale earthquake simulator of the National Research Institute for Earth Science and Disaster Prevention in 1998. The reinforced concrete frames we tested were designed by old Japanese building code and seismic capacities were not adequate. But we could get many useful data and BBC took a film of our tests and broadcasted to the world through the program called "Tomorrow's World".

6. PASSIVE CONTROLLED STEEL FRAMES WITH HORIZONTAL INERTIA MASS

The research team of Professors Satoshi Yamada, Masayoshi Nakashima, Toru Takeuchi and Akira Wada has done steel frames having supplemental dampers with horizontal inertia mass hanged from the crane beam at the shaking table of the Disaster Prevention Research Institute, Kyoto University in 1999. We tested only one story frame taken from a several story steel frame. Horizontal weight simulates other part of story of the original building. Soft spring made of rubber bearings simulates flexibility of other part of the original frame. Total system composed of the specimen frame, soft spring and horizontal mass has 0.6 natural period. We could test many frames using this system with not much research money.

7. COLLAPSE TESTS OF VERY SMALL STEEL FRAMES IN HIGH GRAVITY CIRCUMSTANCE OF CENTRIFUGE MACHINE

The centrifuge machines have been used for the static or dynamic stability tests in the research field of soil mechanics and foundation engineering. When the specimen size is 1/10 of the actual scale of a structure, total weight of the structure become 1/1000, but sectional area of the member is only 1/100. Then, stress level become 1/10 of actual stress in the structure. Nonlinear effect of the structural member cannot be treated correctly in the 1/10 specimen. P-delta effect becomes also very small when the specimen's weight is too light. The research group of Dr. Hideo Katsumata, Professors Satoshi Yamada and Akira Wada have done the collapse tests of very small steel frames in the very high gravity circumstance of centrifuge machine at the Technical Research Institute of Obayashi Corporation. 3, 12 and 30 story steel frames have tested here. The centrifuge could produce 100G gravity and the testing container could have a 2m high specimen. We could test 200m tall buildings using this strong machine theoretically. Since the scale of a specimen is 1/100, it was very difficult to make the specimen precisely.

7.1 3-Story Weak Columns and Strong Beams Steel Frame

The first try was a test of a 3-story steel frame shown in Fig.6 and Photo 7. The frame had 4 columns in every floor, sectional shape of all columns was 1mm thickness and20mm diameter tube. Beams were very strong. Then, the shear capacity of each floor was equal. We took the test under 30G and shake the container horizontally. Finally, the columns at ground floor were broken, just after that, second and third floor collapsed. Most dangerous collapse mode was happened. We took several valuable video movies.

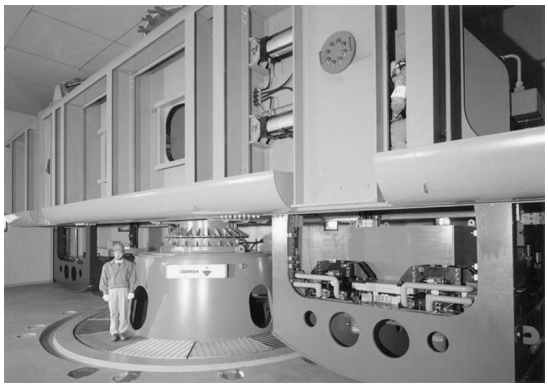


Photo 6 Big centrifuge and container at the Obayashi Technical Research Institute

7.2 12-Story Strong Columns and Weak Beams Steel Frame

The second try was 12-story frame. The frame was made as weak beams and strong columns structure. We took the test under 60G and shake the container horizontally. It had perfect vibrations under medium horizontal acceleration. Next, we applied large horizontal acceleration to the container, then the frame become unstable as shown in Photo 9. Finally, the whole frame was perfectly collapsed as shown in Photo 10.

7.3 30-Story steel frame having center wall and strong outrigger beam

The third try was 30story frame having a center wall and a strong outrigger at middle height. We took the test under 60G and shake the container. The relationships of story shear and story deformation getting from the test were very beautiful, almost all stories yielded and ductility factors were around 2 to 3. The center wall and the outrigger were very effective to control the vibration mode. These members should increase the seismic capacity of the building structures.

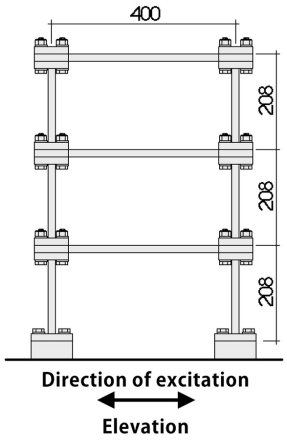


Figure 6 3-story steel frame composed of 4 tube columns and 4 rigid beams

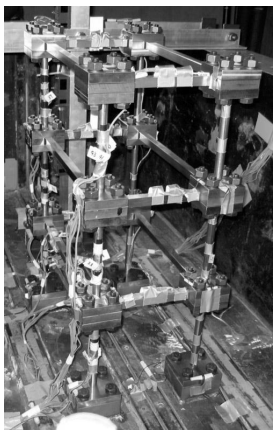


Photo 7 3-story steel frame in the container of the centrifuge machine

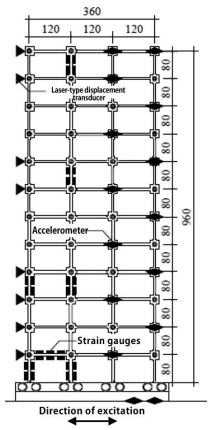


Figure 7 12-story steel frame

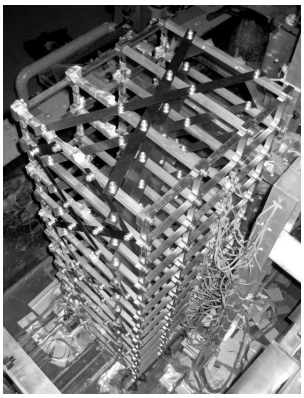


Photo 8 12-story frame in the container

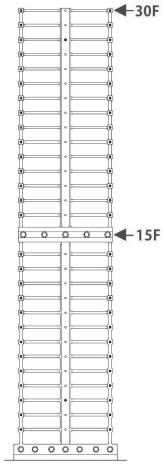




Figure 8 30-story steel frame



Photo 9 Loss the stability of frame just before collapse

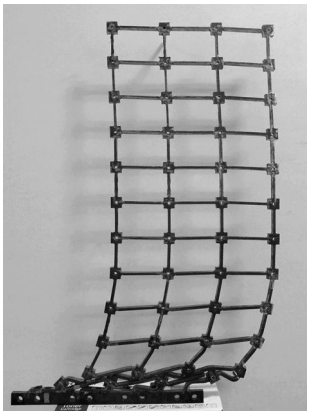


Photo 10 Final collapse of 12 story frame

Photo 11 30-story frame

8. CONCLUSIONS

Actual buildings become bigger and larger every year, and many cities in the world are growing larger every year. Structural engineers must engineer safer buildings and safer cities for people. We have to know how the structures behave under strong earthquakes. We need to do not only the static structural test but also dynamic test. But often, the test facilities have some limitation. Researchers and engineers have to use these facilities under the combination with deep thinking and innovative ideas.

After the Loma Prieta Earthquake in 1989, many professors and engineers discussed about the performance based earthquake engineering. Japan experiences 20% of strong earthquakes in the world, but only 1% to 2% buildings are constructed by using seismic isolation or passive controlled devices. We need to promote these new technologies and increase the number of practical applications in not only Japan but also in all countries exposed to the earthquake risk.

References:

Iiba, M., Inai, E., and Kuramoto, H. 2002. Full-scale shaking table tests on dynamic failure of reinforced concrete building using old seismic regulation. *Journal of Structure Construction Engineering*. Architectural Institute of Japan. Tokyo, Japan. (in Japanese)

Iiba, M., Inai, E., Kuramoto, H., and Wada, A. 2005. Shaking table tests on partial full-scale reinforced concrete frames with shear failure in colimns using inertial loading equipment. *Proceedings, The First International Conference on Advances in Experimental Structural Engineering*. Nagoya, Japan.

Kuramoto, H., Iiba, M., and Wada, A. 2002. A seismic evaluation method for existing reinforced concrete buildings retrofitted by response controlling techniques. *Journal of Structure Construction Engineering*. Architectural Institute of Japan. Tokyo, Japan.

Tada, H., and Takayama, M., et al. 1983. Small model tests of seismic isolated structures. S*ummaries of Technical Papers of Kyushu Chapter Architectural Research Meeting*, Architectural Institute of Japan, Fukuoka, Japan. (in Japanese)

Yamaguchi, M., Yamada, S., Ogihara, M., Ogihara, M., Narikawa, M., Takeuchi, T., Maeda, Y., and Wada, A. 2000. Earthquake resistant performance of moment resistant steel frames with damper. *Proceedings*, *Behavior of steel structures in seismic*

areas. STESSA2000. Montreal, Canada.

Yamaguchi, M., Yamada, S., Maeda, Y., Ogihara, M., Takeuchi, T., Narikawa, M., Nakashima, M., and Wada, A. 2001. A shaking table test procedure simulating earthquake responses of actual structures -Seismic performance of moment resisting steel frame with damper part 1-. *Journal of Structure Construction Engineering*. Architectural Institute of Japan. Tokyo, Japan. (in Japanese)

Yamaguchi, M., Yamada, S., Maeda, Y., Ogihara, M., Takeuchi, T., Narikawa, M., Nakashima, M., and Wada, A. 2001. Evaluation of seismic performance of partial frames using the shaking table test -Seismic performance of moment resisting steel frame with damper part 2-. *Journal of Structure Construction Engineering*. Architectural Institute of Japan. Tokyo, Japan. (in Japanese)

Wada, A., Yamada, S., Takazawa, M., Seki, M., Katsumata, H., Higuchi, S., and Okuda, H. 2006. Earthquake collapse tests of miniature steel frame model using large centrifuge machine. *Proceedings*, *8th U.S. National Conference on Earthquake Engineering, 100 Anniversary Earthquake Conference*. San Francisco, California.

8CUEE CONFERENCE PROCEEDINGS
8th International Conference on Urban Earthquake Engineering
March 7-8, 2011, Tokyo Institute of Technology, Tokyo, Japan

Earthquake Risk Assessment and Corresponding Contingency Plans of the Major Cities of Bangladesh

A. S. M. Maksud Kamal

Professor, Department of Geology, Dhaka University and Urban Risk Reduction Specialist
Comprehensive Disaster Management Programme (CDMP)
maksud.kamal@cdmp.org.bd

Abstract: Comprehensive Disaster Management Programme (CDMP) of the Ministry of Food and Disaster Management (MoFDM), Government of Bangladesh took a component to assess earthquake risks and to develop spatial contingency plan for risk management of the three major cities, viz., Dhaka, Chittagong and Sylhet city corporations of the country. Following five steps were undertaken to accomplish seismic risk assessment: fault mapping and modeling, determination of ground shaking in PGA, development of fragility curves for the building typology, assessment of their vulnerability and generation of risk scenarios through deterministic and probabilistic seismic hazards. Later on, contingency plans have been developed based on damage scenarios for national level, all major responding organizations and respective city corporations. Contingency plan at national level developed following UN cluster system that reflects emergency coordination mechanism between the lead and support agencies belonging to each cluster. Contingency plan of the major responding organizations detailed-out the rules and responsibilities of all relevant organizations to response during emergency, while the GIS-based city level contingency plans illustrate spatial lay-out regarding rescue and evacuation operations. The plans are placed to the organizations through government mechanism to make their use optimal and effective during emergency through repeated simulation drills.

1. INTRODUCTION

Bangladesh is regarded as a supermarket for natural disasters. Flood, cyclone, storm-surges, river erosion, landslides, drought, earthquake and climate induced hazards can be named. Though the country has not been jolted by devastating earthquake in the last one hundred years,, historical evidences reveal that eight big earthquake occurred with magnitude >7.0 in and around Bangladesh in the last 250 years. Great Indian earthquake of 12 June, 1897 (magnitude≈ 8.3-8.7) though had its epicenter about 230 kilometers away from Dhaka, but caused extensive damages mostly in the north-eastern part of the country. Moreover, during 2007-2009, the country got very minor to moderately low seismic disturbances more than 130 times. Being located in the seismotectonic regime of youngest Himalayan mountainous terrain, the countries stretching across this mountainous belt are hotbed for seismic activity due to the existences of geological plate boundaries and the corresponding development of active fault zones in the region. Considering the potential threat of the earthquake hazards, Comprehensive Disaster Management Programme (CDMP) of the Disaster Management and Relief Division (DMRD), Ministry of Food and Disaster Management (MoFDM) has been taken initiatives to assess earthquake risks of the major cities viz., Dhaka, Chittagong, Sylhet and subsequently develop the scenario-based contingency plan and introduce other interventions to reduce the seismic vulnerability of the country. This study also supports government to take decision on enhancing or developing the policy instruments towards ensuring a resilient urban built environment.

2. STUDY AREA

UN-HABITAT (2008/2009) analyses show that 17 per cent of the cities of the developing world experienced very high growth rates of 4 percent or more. The major cities of Bangladesh have been experiencing the same rate or more population influx with rapid horizontal extension of the urbanized areas. With an urban growth rate more than 4 percent annually, Dhaka, which already hosts more than 13 million people, is one of the fastest but unplanned growing cities in Southern Asia, and is projected to accommodate more than 20 million by 2025. Likely, Chittagong and Sylhet are also accommodating around 4 percent growth of population with lateral extension of the township areas. Due to phenomenal growth of the building stocks after the independence in 1971, good number buildings constructed before development and approval of building code in 1993, poor construction practices without following building code, urban sprawling on unsuitable land, high population density and narrow road networks in the

cities, poor capacities of the major responding organizations during the period of emergency and minor awareness among city dwellers multiply the earthquake vulnerability of the cities mentioned. Considering the rapid unplanned urbanization and potential threat of seismic hazard, three major cities, viz, Dhaka, Chittagong and Sylhet city corporations (Figure 1) are considered for seismic risk assessment in the view point of disaster risk management.

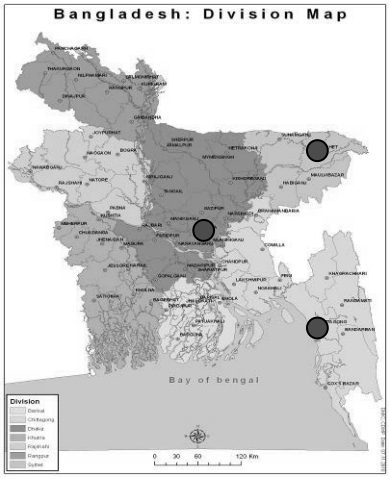


Figure 1: The red dots indicate the study area

3. SEISMIC HAZARD ASSESSMENT

3.1 Time-predictable fault modeling for characteristic earthquake

Characteristic earthquake is defined as the one that has constant recurrence period and displacement on the specific fault. It is well-known that active fault generates characteristic earthquakes. If the time of the latest and penultimate events on the active fault is revealed, the recurrence period and the elapsed time since the latest event are known and the probability of future earthquake occurrence can be estimated. This is a kind of prospect of future earthquake occurrence based on the time- predictable model. The time-predictable model on an active fault can be estimated if at least the occurrence periods of two historical earthquakes are known. In Bangladesh, the historical earthquakes are not well-documented. Successful trench investigations have not been conducted before accomplishing this study. Based-on historical evidences of seismicity (Figure 2), literature-reviews, high resolution 3-D satellite image (CORONA and SPOT) interpretations, field survey and trench investigations in potential target sites, C^{14} dating of 24 samples led to develop a time predictable fault model (Wells and Coppersmith, 1994) for the active fault of the country. Three active faults have been identified in the, viz., Plate Boundary Fault (PBF is divided into 3 segments), Dauki Fault and Madhupur Blind Fault. Figure 3 and 4 represent the active faults and trench investigations while table-1 shows that result of time predictable fault model. Fault model is suggested on the basis of the present information which need revision in future based on more detailed investigations.

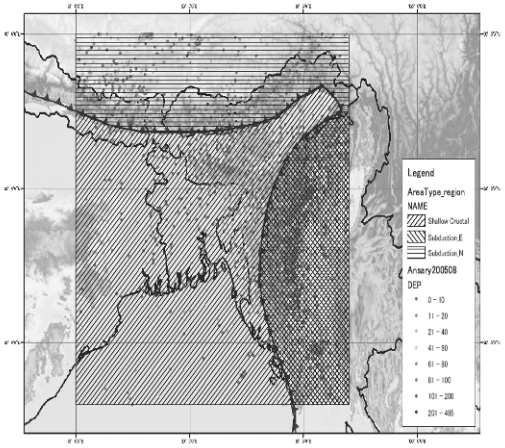


Figure 2: Historical seismicity in and around Bangladesh

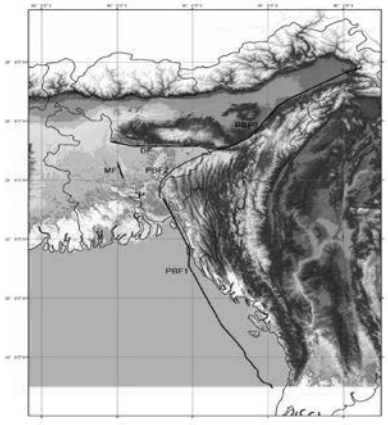


Figure 3: Major active fault locations in the country

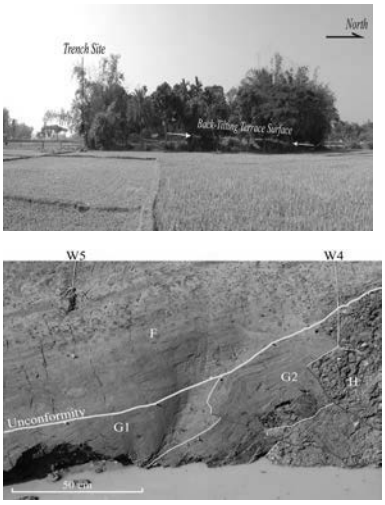


Figure 4: a: Elected back-lilted terrace at Gobrakhali b: West wall of the trench showing fault displacement

Table 1: Time predictable fault model of Bangladesh

Segment		Events	Observed Recurrence Period	Elapsed Time since Last Event (years)	50 year Prob. Time-Dependent (%)	Estimated Magnitude (Mw)	Length (km)
Plate Boundary Fault (PBF)	PBF-1	**AD 1762** AD 680 to 980 [1)] BC 150 to AD 60BC 1395 to 740	900	246	1.1	8.5	795
	PBF-2	before 16th century	> 900	> 508	> 6.7	8.0	270
	PBF-3	before 16th century	> 900	> 508	> 6.7	8.3	504
Dauki Fault (DF)		AD 1897 AD 1500 to 1630 (AD 1548 ?)	349	111	7.0	8.0	233
Madhupur Blind Fault (MF)		AD 1885	350	123	8.7	7.5	60
Non-characteristic but relating to fault (PBF-2, PBF-3, DF)		AD 1918 (PBF-2) AD1869, 1943, 1954, 1988 (PBF-3) AD 1664, 1923, 1930 (DF)	20	-	-	7.0 - 7.4	-

The time of events, recurrence period, elapsed time since the latest event and the 50 years probability of future earthquake occurrence for each active fault are shown in in the Table. The Brownian Passage Time (BPT) model is adopted as the probability density function. The aperiodicity α is presumed to be 0.5 followed after Parsons (2004) etc.

3.2. Baserock and Seismic Motion Analysis

The deterministic approach was adopted for the earthquake motion estimation in this study. The earthquake motion for engineering seismic baserock and sub-surface layer amplification were determined separately. Four formulas from Next Generation Ground Motion Attenuation Model (NGA, 2008) are applied and average value was used. The stochastic Green's function study (Kamae et.al., 1991) was also conducted for verification. The amplification by sub-surface soil layers was evaluated by the amplification factor which was decided by average shear wave velocity from ground surface to 30 meters depth. The ground of each grid was classified based on the modified National Earthquake Hazard Reduction Program (NEHRP) provisions. The amplification factors of NEHRP provisions were verified by the response analysis at 19 points through PS loggings.

The PGA, PGV and Sa (h=5%, T=0.3 and 1.0 sec) at engineering seismic baserock (Vs30=760m/sec) reflected that in Dhaka the PGA in Dhaka is 130 to 230 gals for MF (Figure). The most important earthquake in Chittagong is PBF-1 where PGA is estimated 650 to 770 gal. The most important earthquakes in Sylhet are DF and PBF-2. PGA by DF is 180 to 240 gal and 160 to 240 gal by PBF-2.

The PGA, PGV and Sa (h=5%, T=0.3 and 1.0 sec) at ground surface were calculated. The PGA in Dhaka by MF is 220 to 410 gal. The PGA in Chittagong by PBF-1 is 600 to 770 gal where amplification of surface layer is very little or deamplified because of non-linearity of soils. The PGA in Sylhet by DF is 270 to 420 gal and 230 to 420 gal by PBF-2. Figure 5, 6 and 7 represents the base rock motion, ground amplifications and ground motions at Dhaka for different faults.

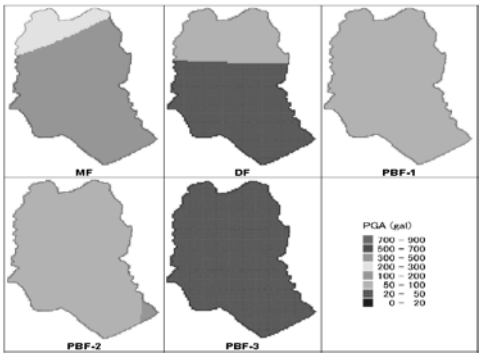


Figure 5: Base rock motion in Dhaka

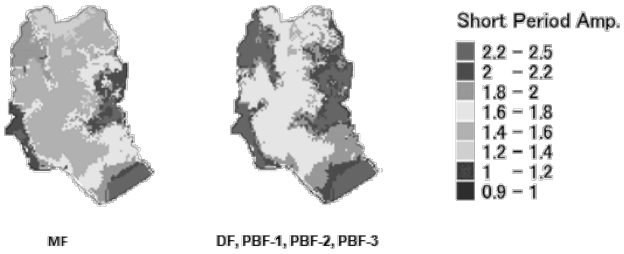


Figure 6: Ground amplification for PGA and Sa (0.3) in Dhaka

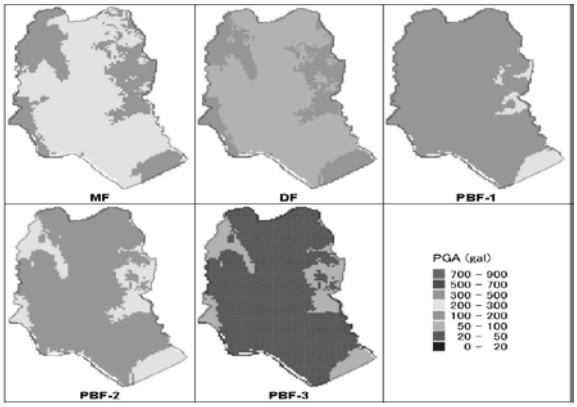


Figure 7: Ground surface motion at Dhaka

4. SEISMIC VULNERABILITY ASSESSMENT

To assess the vulnerability of the exposures building stocks, lifelines and essential facilities database in GIS were developed using high resolution satellite images as well as field survey. It is estimated that there are 326,000, 182,000, and 52,000 buildings in Dhaka, Chittagong, and Sylhet City Corporation areas respectively (Figure 8 and 9). Afterwards, building stocks were differentiated into structural types. Such as, in Dhaka city corporation area, reinforced concrete and masonry buildings are 85000 and 180,000 respectively.



Dhaka Chittagong Sylhet

Figure 8: Building footprints

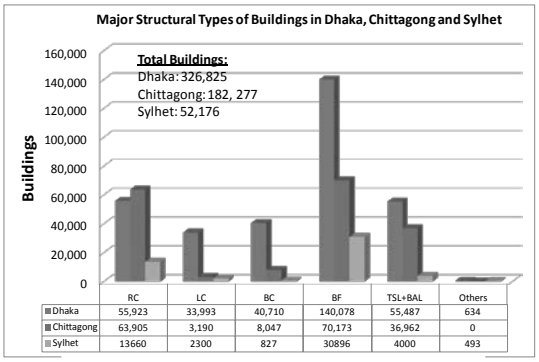


Figure 9: Building typology

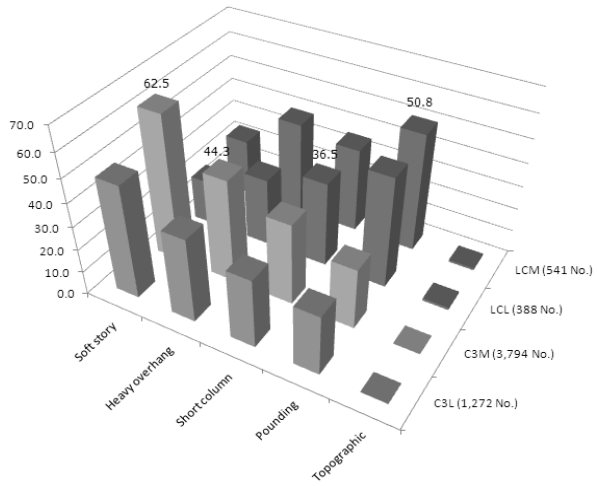


Figure 10: Relationship between the vulnerability factor and structural types in Dhaka

To asses the vulnerability of the building, three level survey were conducted in this study. The vulnerability factors considered in level one survey were number of stories, occupancy class, structural type, number of occupants during the day and the night, age of the building, presence of soft story, presence of heavy overhangs, shape of the building in plan view (rectangular, narrow rectangular, irregular), shape of the building in elevation view (regular, setback, and narrow tall), pounding possibility, building in slope land, visible ground settlement, presence of short columns, visible physical condition (poor/average/good). Figure 10 represent the relationship between the vulnerability factors and structural types. In the Level-2 survey, a sketch of the building plan at the ground story, the dimensions of columns, concrete and masonry walls were measured. Level-3 survey was conducted for dynamic measurement on few selected buildings in three cities. Main objective of this survey is to understand the behavior of different types of buildings during earthquake. For dynamic measurement of buildings, micro tremor, schmidt Hammer, ferro Scanner,

vibration shaker, hydraulic Jack with Deflection Meter were used.

For the lifeline inventory mainly for transportation and utility system were conducted. In the 3 cities, transportation system consists of (1) highway transportation system, (2) railway transportation system, (3) bus transportation system, and (4) ferry transportation system. While utility system consists of (1) potable water system, (2) natural gas system, (3) electricity power system, and (4) communication system, and for Dhaka (5) waste water or sewage network. The lifeline inventory in Dhaka City Corporation area includes over 1270 kilometers of highway road, 10 highway bridges, and pipe line lengths for portable water, waste water and natural gas are 1100, 630 and 830 kilometers respectively. While in Chittagong, the lifelines include 639 kilometers of highway road, 4 highway bridges, and 792 kilometers of potable water and gas pipes. In Sylhet, the lifelines include 148 kilometers of highway road, 2 highway bridges, and 268 kilometers of potable water and gas pipes.

Utilizing the same methodology for lifeline inventory, essential facility inventory was developed. The essential facility inventories in this study consist of 3 categories: (1) Medical care facilities, i.e. hospital and medical clinic, (2) emergency response facilities, i.e. police station, fire station and emergency operation center and (3) schools. There are 600 hospitals, 2700 schools, 10 fire stations, 62 police stations and 18 emergency response agency offices in Dhaka City Corporation area. While in Chittagong, there are 162 hospitals, 1033 schools, 12 fire stations, 11 police stations and 11 emergency response agency offices. And in Sylhet, there are 87 hospitals, 211 schools, 2 fire stations, 6 police stations, and 9 emergency response agency offices.

Based on the vulnerability factors of the building stocks and lifelines, vulnerability maps were developed which show the characteristics of the buildings, essential facilities, and lifelines that make them susceptible to the damaging effects of earthquake. From the collected database and vulnerability maps, the major findings regarding to the seismic vulnerability of building, lifeline and essential facilities can be summarized as the followings: The vulnerability factor which is the most common in Dhaka city is soft story (52%). The common vulnerability factor in both Chittagong and Sylhet city is heavy overhang (38% and 46%, consequently). Among occupancy classes in all city corporation areas, residential class is the major proportion. Their proportions are 80.0%, 82.0% and 85.0% in Dhaka, Chittagong and Sylhet, respectively. Among structural type of non-engineered buildings from the survey results, brick in cement mortar masonry with flexible roof is the most common type in all cities. For engineered buildings, concrete frame with masonry infill walls is the most common class. From the survey results, age of buildings has been related to structural types. For example, it was found that most buildings with concrete slab-column frames are constructed less than 10 years. On the other hand, most masonry buildings with concrete floors ages more than 10 years. Also, light reinforced concrete buildings (LC) are found to be older than reinforced concrete buildings. As expected, all residential types have an average number of occupants per floor area in the daytime less than the nighttime; nevertheless, the other occupancy classes as commercial, industrial, government and education have the number of occupants in the daytime more than the nighttime.

5. RISK ASSESSMENT

Risk is the conditional probability and magnitude of damage occurs on the exposures to a hazard event. For assessing the seismic risk the fragility functions (capacity of the buildings to withstand during different level of strong ground motions) has been developed for the structural types of the buildings and life line systems. For instances for the development of fragility functions of the building stocks following vulnerability factors are considered: number of story, presence of soft-story and torsional irregularities as determined by infill wall arrangement, presence of heavy-overhangs, Presence of soft-story as determined by 1st story height, variation in concrete strength. Combing the fragility functions of the buildings and infrastructures with the hazard maps (ground shaking of the scenario earthquakes) building damages and functionality of the lifelines and critical infrastructures were estimated using a software known as Hazard United States (HAZUS). Before calculating the damage scenarios, HAZUS has been customized considering the Bangladesh perspectives. To run the assessment, city corporation wards are divided into smaller area called cluster to generate detail level of statistical data for corresponding analysis. In Dhaka city corporation area, 552 clusters are generated in 91 wards. While, 41 wards of Chittagong city corporation are divided into 285 clusters, and 27 wards of Sylhet City Corporation into 82 clusters.

Risk assessment reveals that if an earthquake occurred at Madhupur fault with magnitude 7.5, about 72,000 buildings (Table-2) will be totally damaged during this time. It is estimated that about 140000 buildings will be completely damaged at 8.5 magnitude earthquake originated from plate boundary fault-1. During an earthquake at 8.0 magnitude originated from Dauki fault about 25000 buildings will be damaged beyond repair. There will be severe damage to essential

facilities like Hospital, schools, police stations after different level of earthquakes in Dhaka, Chittagong and Sylhet. For instances, here, damage scenarios are shown for Dhaka calculated for Madhupur fault earthquake. This earthquake will cause moderately to complete damage at about 250 hospital or clinics, 1300 schools as well as 30 police and 4 fire service stations (Table- 3). In Dhaka there are about 60000 hospital beds available for use. On the day after the earthquake, it is estimated that only 24,200 hospital beds (41%) will be available for use by patients already in the hospital and those injured by the earthquake. After one week, 54% of the beds will be back in service. By 30 days, 72% will be operational. During this period there will be around 80 leaks and 270 breaks in water supply system, 100 leaks & 360 breaks in waste water system and 60 leaks & 190 breaks in gas supply network.

Table 2: Expected Building Damage by Building Type in Dhaka City Corporation Area: Scenario Case 1 (Madhupur fault)

Dhaka : Case 1										
	None		*Slight*		*Moderate*		*Extensive*		*Complete*	
	Count	*(%)*	*Count*	*(%)*	*Count*	*(%)*	*Count*	*(%)*	*Count*	*(%)*
Steel	*8*	*0.01*	*14*	*0.03*	*125*	*0.24*	*324*	*0.98*	*948*	*1.31*
Concrete	*101,832*	*81.51*	*17,066*	*39.47*	*15,152*	*28.50*	*12,866*	*38.81*	*38,648*	*53.44*
Masonry	*6,353*	*5.09*	*10,784*	*24.94*	*26,558*	*49.95*	*17,328*	*52.26*	*21,611*	*29.89*
Thin Shed and Bamboo	*16,745*	*13.40*	*15368*	*35.55*	*11,331*	*21.31*	*2,635*	*7.95*	*11,108*	*15.36*
Total	*124,939*		*43,232*		*53,166*		*33,153*		*72,316*	

Table 3: Expected Damage to Essential Facilities in Dhaka City Corporation Area: Scenario case1

Dhaka : Case 1				
Classification	Total	Facilities		
		At Least Moderate Damage >50%	Complete Damage >50%	With Functionality >50% on day 1
Hospitals	600	241	10	224
Schools	2,737	1,173	90	895
EOCs	18	8	2	7
Police Stations	62	30	0	15
Fire Stations	10	4	0	3

Madhpur Fault earthquake will generate a total of 30 million tons of debris. If the debris tonnage is converted to an estimated number of truckloads, it will require 1,200,000 truckloads (@25 tons/truck) to remove the debris generated by the earthquake. Only the building related economic losses for this earthquake are estimated more than 6000 million USD.

Risk assessment has been calculated for Dhaka, Chittagong and Sylhet for all possible earthquakes to be originated in the three fault lines, viz, Madhupr fault, Dauki fault and Plate Boundary faults. This is first effort in Bangladesh to conduct hazard, vulnerability and risk assessment through seismic microzonation mapping of the cities. Characterizations (recurrence period and magnitude determinations) and further identifications of the fault zones, accurate buildings and lifelines system vulnerability assessment and fragility functions development of the buildings are highly crucial in this context. Consecutive studies will further improve the results definitely. Once the hazard scenarios are changed, vulnerability and risk will also bring updated results.

The objective of assessing the risk scenarios were to develop the scenario-based spatial contingency plans for addressing the systematic and realistic approach of preparedness and responses during the period of emergency.

6. DEVELOPMENT OF EARTHQUAKE CONTINGENCY PLAN

6.1 Concept of Contingency Plan

Usually many agencies are involved in accomplishing the activities for preparedness, response and early recovery to reduce the risk of any big

disasterous event. Experiences have shown that all agencies need to work together *under a well-designed and fully-coordinated plan for optimum and efficient preparedness, response and early recovery, usualy known as Contingency Plan*, in a systematic manner so that their capacities and resources are best utilized to fulfil the need complimenting and supplementing other agencies. Realizing the need of coordinated and comprehensive emergency response, United Nations has been promoting its humanitarian response activities in a cluster approach. This approach is proved to be effective and efficient in responding to recent disasters, for instances, the response during October 8, 2005 Kashmire earthquake in Pakistan. Hence, it has been assumed that this concept of response operations in functional clusters be applied in Bangladesh also in case of possible earthquake disaster.

6.2 Contingency Plan Developed for Major Responding Agencies Of Bangladesh

From CDMP-I initiatives, scenario-based contingency plans have been developed for national level, three city corporations (Dhaka, Chittagong and Sylhet) and *key major responder agencies*- viz., Armed Forces Division (AFD), Fire Service & Civil Defense (FSCD), Directorate General of Health Services (DGHS), Disaster Management Bureau (DMB), and Directorate of Relief and Rehabilitation (DRR) to respond first during any emergency. Figure 11 illustrate the development procedures of contingency plan. Moreover, lifelines & utilities (Dhaka Power Distribution Company Limited, Dhaka Water Supply and Sewerage Authority, Titas Gas Transmission and Distribution Company Limited, Bangladesh Telecommunication Company Limited), and humanitarian assistance providers have also been addressed in the contingency planning process. These plans adopt scenario-based contingency planning approach that involves the development of specific scenarios through the hazard, vulnerability mapping and damage estimations. In the formulation process of the plan, the main focus is given to the worst case scenario by assuming that- if plan is developed for the worst case making it flexible, then there shall have the preparation for anything, anytime.

6.3 Funtionability of National Earthqauke Contingency Plan

Under National Earthquake Contingency Plan, all response activities are grouped into nine relevant operational functional clusters based on the similarity of works, normal time and disaster time mandates of different relevant organizations and possible complimentarity in the resources and capacities. Beside emergency opeartions, preparedness and early recovery actvities are also assigned for each functional clusters to reduce the earthqauke vulnerability to a certain manageable level. The proposed operational

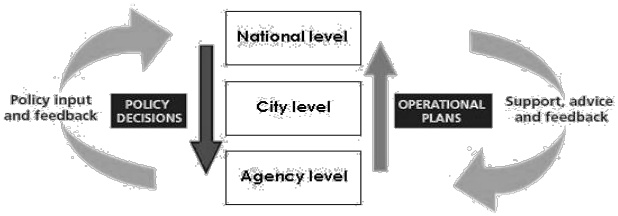


Figure 11: Development procedures of contingency plan

functional clusters with lead and support agencies under National Earthqauke Contingency Plans are: Emergency Operations Cluster 1– Overall Command and Coordination (lead–Disaster Management Bureau), Emergency Operations Cluster 2 – Search, Rescue and Evacuation (lead-fire service and Civil Defence), Health Cluster- (Director General of Health services), Relief Services (Food, Nutrition and other Relief) cluster (lead-Directorate of Relief and rehabilitation), Shelter (including Camp Management) cluster (lead-DMB), Water Supply, Sanitation and Hygiene Cluster (lead-Local Government Bodies: City Corporations/pourashava), Restoration of Urban Services Cluster (lead-Local Government Bodies: City Corporations/pourashava, Transport (Road, Rail, Air, Sea) Cluster (lead-BRTA, BIWTA, Bridge Authority, Security and Welfare Cluster (lead-Bangladesh Police). The role of Armed Force Division is actively associated with all the clusters as support agencies.

6.4 Agency Level Contingency Plan (A Case Study)

With regard to each functional cluster, spatial planning requirements in terms of locating facilities at appropriate locations, need assessment based on spatial coverage, identifying alternative locations and routes for emergency supplies, identifying emergency evacuation routes and places for

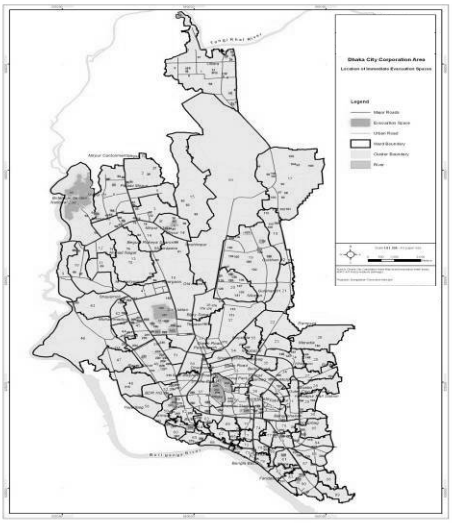


Figure 12: Possible open spaces in Dhaka

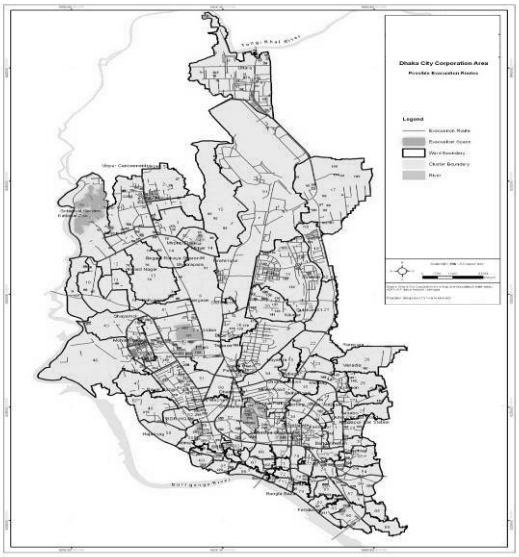


Figure 13: Possible open evacuation roads in Dhaka

temporary shelters and medical facilities, pre-positioning of facilities etc. have been identified and mapped under GIS environment that would enable the key emergency responders to act in a coordinated as well as cohesive way. For instances, the total number of displaced population needing temporary shelter has been estimated at around 870,000 within the Dhaka city during Madhupur earthquake. This is estimated as 50% of the displaced people need immediate shelter after the earthquake and the remaining 50% will manage their shelter in their relatives and other places. Open spaces within the city corporation area that are more than 2500 square meters (area with capacity for sheltering 500 families or more) are mapped and their shelter capacities are calculated. The total open spaces within Dhaka City area have only about one fourth capacity of the total population needing shelters. Figure 12 and 13 show open spaces and evacuation routes to be used during emergency.

The population evacuated in immediate shelter requires about 3800 cubic meters of emergency water with the rate of 15 liters per capita per day. The populations who are taken outside require about 9,200 cubic meters of water per day. So the total emergency water needed in the emergency shelters is about 13,000 cubic meters per day. Pre-positioning of this amount of the water at the above planned spaces is before earthquake is the most appropriate way to provide immediate emergency water. To manage toilets in the immediate shelters spaces is the main challenge related to sanitation. Sphere standard demand one toilet for each 20 people in the emergency shelter. The calculation shows that about 12,700 toilets are needed in the open spaces within Dhaka City and additional 30,700 toilets need to plan for the people of Dhaka who need immediate shelter outside Dhaka city. The total number of skilled/trained workers required for repairing the potable water and waste water system within Dhaka city corporation area after an earthquake is about 1800 people per day to repair the system within 7 days. If it is planned to repair in 14 days, it require about 900 skilled workers per day and require about 420 people working per day to repair the system in 30 days time. Skilled workers required to repair overhead water tank and waste water treatment plant is not calculated here, as it require thousands of skilled workers if planned to repair within a month, which is practically not possible even if planned. It requires 3-6 months to repair the overhead tanks and treatment plant, even if the required manpower is available. The total estimated cost require for repairs is about 27 Million US Dollars. It is assumed that the repair cost for the waste water treatment plant, probability of which to be functional after the earthquake is 40-50% has been assumed that 25% of the replacement cost. Priorities for recovery of different components within the system are also made in this plan.

6.5 Contingency Plan is the Living Document

The contingency plans have been developed with around 30 interactive meetings with the agencies. Moreover, two workshops have been conducted in national level to validate the plans. The plan is a measure of the quality of the process. A good planning process will produce a good plan. Even though the earthquake that occurs may be very different from the one planned for, the plan will still be useful. A good contingency plan ensures better preparedness for any emergency that may occur, even one that is very different from the scenario in the plan. Legal provisions and organizational set up, functional response roles and responsibilities assigned for the agency, operating procedures guideline and readiness checklists are also outlined in this plan. Contingency plans are the living documents. With the increase of knowledge and resources, the plan can be updated. Disaster Management and Relief Division (DMRD) of the Ministry of Food and Disaster Management have forwarded the plan to the respective organizations. In order to understand and operate the plan, trainings on incident command system and restoration of lifelines within shortest possible time have been provided to the professionals of the major responding organizations. To cope with emergency situations, organizations are planning to exercises the plan through simulation drills.

7. CONCLUSION

The Government of Bangladesh (GoB) has made a gradual shift in disaster management towards a comprehensive risk reduction approach that recalls and learns from past experience in order to anticipate and reduce the impact of future risks. The traditional

disaster management model focusing on disaster relief and recovery has done little to redress these rising levels of risk. The Ministry of Food and Disaster Management, has (through Comprehensive Disaster Management Programme-CDMP) adopted a more holistic approach that embraces processes of hazard identification and mitigation, community preparedness, integrated response efforts and where relief and recovery activities are planned within an all-risk management framework that seeks to raise the capacities of at-risk communities while lowering their vulnerability to specific hazards. Following the mission and vision of the Government of Bangladesh (GoB), this study is one of the outputs under Earthquake and Tsunami preparedness component of CDMP-I. The study addresses the earthquake hazard, vulnerability, risk and damage assessment following the standard methodology. Then using the scenario-based risk assessment, sub-sequent mitigation/contingency plans have been developed for the major responding organizations, city corporations and national level. The contingency plans which address the gaps and needs are being utilized for re-strengthening the preparedness and response mechanisms of the relevant organizations. Moreover, following the guidelines of contingency plans, various awareness raising activities has been launched and policy instruments are being updated and developed aiming to escalate better understanding to implement the documents in practices at all level.

Acknowledgement:
Thanks are extended to Asian Disaster Preparedness Center (ADPC) and its partner organizations OYO International Corporation (OIC), Japan and National Society for Earthquake Technology (NSET), Nepal who develop the documents of this article under the direct technical support and supervision of the author. The author would also like to acknowledge Geological Survey of Bangladesh (GSB), Geology Department, University of Dhaka; Civil Engineering Department, Bangladesh University of Engineering and Technology and other GoB organizations that came forward to develop the documents of this paper. Final acknowledgment must render to the Ministry of Food and Disaster Management, Government of Bangladesh and donor agencies (UNDP, EC, DFID) who provide both administrative and financial supports to produce the documents given in the article. Thanks are also offered to the individuals who contributed in this study.

References:

Abrahamson N. and W. Silva. (2008), "Summery of NGA ground motion relation", Earthquake Spectra, Vol. 24, issue 1, page 67-97.

Kamae, K., K. Irikura and Y. Fukuchi. (1991), "Strong Motion Prediction during Large Earthquake based on the Scaling Law of the Earthquake", J. Struct. Constr. Eng., AIJ, No. 430, 1-9.

Persons, T. (2004), "Recalculated probability of M $\geqq$ 7 earthquakes beneath the Sea of Marmara", Turkey. J. Geophys. Res., 109, B05304, doi:10.1029/2003JB002667.

UN Habitat (2008/2009), States of the World Cities (2008/2009); Harmonies cities, UN Habitat.

Wells, D. L. and K. J. Coppersmith. (1994), "New Empirical Relationships among Magnitude, Rupture Length, Rupture Width, Rupture Area, and Surface Displacement", Bull. Seismol. Soc. Am., 84, 974-1002.

8CUEE CONFERENCE PROCEEDINGS
8th International Conference on Urban Earthquake Engineering
March 7-8, 2011, Tokyo Institute of Technology, Tokyo, Japan

MAJOR GROUND MOTION RESEARCH PROGRAMS AT THE PACIFIC EARTHQUAKE ENGINEERING RESEARCH CENTER (PEER)

Yousef Bozorgnia

Executive Director, PEER, University of California, Berkeley, California, USA
yousef@berkeley.edu

Abstract: At the Pacific Earthquake Engineering Research Center (PEER) there are three major ground motion research programs: (a) Update of ground motion prediction equations (GMPEs) for shallow crustal earthquakes in active tectonic regions (NGA-West2); (b) development of next generation attenuation relationships for stable continental regions (NGA-East); and (c) global GMPEs for the Global Earthquake Model (GEM). This paper presents an overview of these "mega" research programs.

1. INTRODUCTION

The Pacific Earthquake Engineering Research Center (PEER), with headquarters at the University of California, Berkeley, has traditionally had major research projects on the engineering characterization of ground motions. PEER's ground motion projects are part of a larger research theme for Performance-Based Earthquake Engineering (PBEE). Currently there are three major ground motion research programs at PEER: (a) Update of ground motion prediction equations (GMPEs) for shallow crustal earthquakes in active tectonic regions (NGA-West2); (b) development of next generation attenuation relationships for stable continental regions (NGA-East); and (c) global GMPEs for the Global Earthquake Model (GEM). This paper presents an overview of these mega programs at PEER.

2. NGA-WEST 2

In 2003, PEER initiated a large research project to develop next generation attenuation relationships for shallow crustal earthquakes in active tectonic regions (NGA-West1). The project concluded in 2008, and provided two important practical deliverables: (1) a strong motion database of recorded ground motions, and (2) a set of peer-reviewed ground motion prediction equations (GMPEs), or what engineers call attenuation models. Many researchers, practitioners, and organizations throughout the world are now using the NGA-West1 models. For example, NGA programs are either being initiated or planned for areas such as Japan, Taiwan, and Europe.

The NGA-West1 database is one of the largest strong motion databases in the world. It includes over 10,000 components of ground motion recordings from all over the world along with their associated metadata, such as moment magnitude, six different source-to-site distance measures, fault mechanism, shallow site characteristics, depth to bedrock, among others.

The NGA-West1 GMPEs represent a major advancement in ground motion prediction made possible by the extensive update of the PEER strong-motion database and the supporting studies on 1-D ground motion simulation, 1-D site response, and 3-D basin response sponsored by PEER (Power et al., 2008). The NGA-West1 generated five GMPEs: Abrahamson & Silva (2008), Boore & Atkinson (2008), Campbell & Bozorgnia (2008), Chiou & Youngs (2008), and Idriss (2008). These models superseded the previous GMPEs developed by the five developers, and are capable of predicting ground motions for magnitudes up to 8.5 and distances out to 200 km. Style of faulting, hanging wall and footwall effects, linear and nonlinear site effects and depth to basement rock (basin depth) are among features incorporated in most of the NGA-West1 models. The NGA-West1 models went through an extensive peer-review process by the US Geological Survey (USGS), and three of the models were adopted by the USGS for the 2008 edition of the US National Seismic Hazard Maps (Petersen et al., 2008).

As successful as the original NGA-West1 program was, there are some additional and complementary ground motion issues and supporting topics that could not be addressed in the program due to time constraints. The goal of a follow-up study, NGA-West2, is to fill these gaps. Specifically, the NGA-West2 is addressing the following technical issues.

2.1 Directivity Models for NGA Relationships

The original plan for the development of the NGA-West1 ground motion relationships was to develop the models in two steps: (a) to develop the NGA models without

explicitly including near-fault directivity effects; and (b) to subsequently examine the near-fault directivity effects and add additional terms to the NGA-West1 relationships to incorporate such near-fault effects. Step (a) of the NGA-West1 development was completed, and PEER is now examining the near-fault directivity effects to be added to the NGA models.

2.2 Directionality of Ground Motions

Direction (azimuth) and relative amplitudes of the maximum and minimum horizontal ground motions at a site located close to an active fault are important in determining the damage and loss to a structure. For example, at sites very close to active faults, the fault-normal direction can experience significantly larger intermediate- and long-period ground motions than the fault-parallel direction. The ground motions estimated from the current NGA-West1 models are for the average ("geometric mean") of the two horizontal components. PEER is examining these directionality effects and will incorporate these effects into the NGA-West2 models.

2.3 Models for Vertical Ground Motions

The ground motions estimated from the current NGA-West1 models are for the average ("geometric mean") of the two horizontal components. Some structural and non-structural components are sensitive to the vertical input motion, especially in near-source areas. PEER is developing new ground motion prediction equations for the vertical component.

2.4 Updating NGA Models for Small Magnitude Data

In the last few years, there have been a large number of ground motion recordings for low-magnitude events. Preliminary analysis of a limited subset of these recordings have indicated that the NGA-West1 models may over-predict low magnitude ground motions. PEER is collecting thousands of low-magnitude California recordings to update NGA models.

2.5 Updating NGA Models for Moderate & Large Magnitude Data

In the last few years, there have been important moderate and major shallow crustal (i.e., non-subduction type) earthquakes in California and other active tectonic regions throughout the world that can be used to verify and/or enhance the current NGA-West1 models. Examples of such events are the 2004 Pakfield (California) earthquake as well as recent events in Japan, Italy and China with magnitudes as large as 7.9. These new recordings can serve to validate the large-magnitude scaling characteristics of the NGA models.

2.6 Scaling of NGA Models for Damping

The current NGA-West1 models for linear-elastic spectra are for 5% viscous damping. In reality, structural and non-structural systems can have different damping ratios than 5%, depending on the system type and level of input ground motions. Current guidelines to translate the 5% damped elastic spectra to other damping values pre-date the NGA project and are possibly outdated. PEER is developing a new damping model that can be used to adjust the 5% damped spectral predicted by the NGA models to other damping values.

2.7 Development of Epistemic Uncertainty Model for NGA

There is a need to add an epistemic ("model to model") uncertainty that is not necessarily captured by the use of multiple NGA models. There is currently no consensus epistemic uncertainty model to use with the NGA models. In this task, PEER will develop a consensus epistemic uncertainty model for the NGA models that can be used by all users of these models.

2.8 Further Development of Site Response in NGA

The current state of the practice in some seismic hazard analyses is to: (a) perform a probabilistic hazard analysis using the NGA models for NEHRP B/C boundary site conditions corresponding to V_{S30} =760 m/sec, and (b) apply the NEHRP site coefficients to adjust the estimated NGA ground motions to the desired NEHRP site class. The issue with this process is that: (a) the NEHRP site coefficients were developed over a decade ago, long before the NGA models; and (b) the NEHRP site coefficients are inconsistent with those predicted by the site terms included in the NGA models. In this task, PEER is examining the discrepancy between the NEHRP site coefficients and the site factors predicted by the NGA models and attempt to resolve any discrepancy.

3. NGA-EAST PROGRAM

The goal of NGA-East program is to develop next generation GMPEs for stable continental regions (such as Central & Eastern North-America). The NGA-East includes seven working groups (WGs) each of which is focused on a specific technical area. The WGs support the NGA-East program by providing guidance on research needs and/or research products. Below is a short overview of the main tasks associated with each Working Group.

Database WG: To develop an exhaustive database of recorded motions in Central & Eastern North-America (CENA) and other Stable Continental Regions (SCRs), with the associated metadata.

Path/Source WG: To develop regionalized models for correlated sets of source (stress-drop) and path parameters (attenuation and Q).

Simulations WG: To coordinate the validation and forward modeling of ground motion simulation, considering different methods. The Simulations WG relies on input from the Database, Path/Source, and Geotechnical WGs.

Geotechnical WG: To develop a simplified model to remove site effects from recorded dataset; define the reference rock shear wave velocity and kappa values, and

the range of conditions to which they apply. The Geotechnical WG is also tasked to develop a site effects model for NGA-East.

Sigma WG: To develop standard deviation models for the NGA-East project. This WG uses information from all the WGs.

Vertical Motions WG: To develop models for V/H ratios to be applied to the horizontal ground motion models. This WG relies on information from the Database WG.

GMPE Developers WG: To develop a suite of GMPEs for CENA.

The NGA-East and NGA-West2 program are interacting with each other, especially for the Vertical and Sigma WGs.

4. GLOBAL GMPEs FOR GEM

Building on the most recent advances in the field, the global GMPEs program has gathered a distinguished international team of experts to use a unified, transparent and collaborative approach to select a harmonized suite of GMPEs that can be used at the global and regional levels.

The program is coordinated by PEER and sponsored by the Global Earthquake Model (GEM), an international organization with the mission to engage the global community in the design, development and deployment of state-of-the-art models and tools for earthquake risk assessment worldwide.

Based on a systematic and consistent set of evaluation criteria, existing GMPEs for each major tectonic environment will be screened and selected by the research teams. The selected GMPEs will provide a consistent platform for the ground motion component of the GEM hazard model(s). The GEM program at PEER is organized into the following tasks:

Task 1A: *Define of a consistent strategy for modeling ground motions.* The issues that are addressed in this subtask are as follows: (i) consistency in the model parameters (magnitude, distance, style-of-faulting, site classification, etc.) and in the ground motion parameters (PGA, PGV, spectral acceleration, etc.); (ii) balancing the approaches to modeling ground motions (e.g. empirical versus numerical simulations). The working group will develop a consistent strategy for developing global ground motion models for active crustal regions, subduction zones and stable continental regions.

Task 1B: *Examine methods for estimation of site effects in parametric ground motion models.* The parametric ground motion models all use some simplified site classification method to account for the site effects. To apply the ground motion models requires having estimates of the site classification for the entire region of interest. Therefore, an efficient method for estimating the site classification, consistent with the classification used in the ground motion models, will be completed by correlating available site classifications with other parameters that are available for the entire region.

Task 2: *Compile and critically review GMPEs.* In this task, recent sets of candidate GMPEs will be compiled and reviewed. The GMPEs will be representative of the global (worldwide) data sets for four tectonic categories of earthquakes:

(a) shallow crustal earthquakes in active tectonic regions,
(b) shallow crustal earthquakes in stable continental regions,
(c) subduction zone interface and intraslab (Wadati-Benioff) earthquakes.
(d) volcanic earthquakes.

Task 3: *Select or derive a global set of GMPEs*. In this task, the GMPEs compiled and screened in Task 2 will be reviewed, adjusted (if needed) and selected as the Global GMPEs. For each tectonic region, the selection and adjustment will be based on review of the applicability to a wide range of magnitude, distance and so forth, and the compatibility of the GMPEs with the recorded regional ground motion data.

Task 4: *Include near-fault effects.* A working group will provide recommendations regarding correction of GMPEs for near-fault effects, including directivity and directionality. The working group for this task will examine various existing adjustments of GMPEs to include near-fault effects.

Task 5: *Build a database of waveforms.* There will be three databases of recorded waveforms for different tectonic environments:

(a) A very comprehensive database for shallow crustal earthquakes in active tectonic regions has already been developed by PEER. As mentioned previously, under the NGA-West2 program, the database is significantly being improved and expanded. The new database will be available through PEER web site.

(b) A database of waveforms for stable continental regions (SCRs) developed within the scope of the NGA-East program, and will be made available through PEER web site.

(c) A waveforms database for subduction regions will be provided through the PEER website.

Task 6: *Design the specifications to compile a global database of soil classification.* In this task, a working group will propose a set of *specifications* to compile consistent global database of geological soil classifications based on V_{s30} and designed to be consistent with the soil categories in the NEHRP and EuroCode 8 building codes.

5. CONCLUDING REMARKS

PEER is coordinating three “mega” research programs on different aspects of ground motion hazards. These programs are multi-disciplinary involving geologists, seismologists, geotechnical and structural engineers. The ground motion hazard programs at PEER also include academicians, practicing engineers and end-users. Such strong collaborative efforts among various disciplines and sectors have proven to yield high quality final products, and a greater impact on the earthquake engineering and scientific communities.

Acknowledgements:

The ground motion research programs at PEER are funded by California Earthquake Authority (CEA), California Department of Transportation (Caltrans), Pacific Gas & Electric Company (PG&E), Nuclear Regulatory Commission (NRC), Department of Energy (DOE), Electric Power Research Institute (EPRI), and Global Earthquake Model (GEM). Supports of the sponsors are gratefully appreciated. The Center for Urban Earthquake Engineering (CUEE) in Tokyo Institute of Technology is gratefully acknowledged for inviting the author to present this paper.

References:

Abrahamson, N. A., and Silva, W. J. (2008), "Summary of the Abrahamson & Silva NGA Ground Motion Relations," *Earthquake Spectra* **24**, 67–97.

Boore, D. M., and Atkinson, G. M. (2008), "Ground-Motion Prediction Equations for the Average Horizontal Component of PGA, PGV, and 5%-Damped PSA at Spectral Periods between 0.01 s and 10.0 s," *Earthquake Spectra* **24**, 99–138.

Campbell, K. W., and Bozorgnia, Y. (2008). NGA Ground Motion Model for the Geometric Mean Horizontal Component of PGA, PGV, PGD and 5% Damped Linear Elastic Response Spectra for Periods Ranging from 0.01 to 10 s," *Earthquake Spectra*, **24**, 139–171.

Chiou, B. S. J., and Youngs, R. R. (2008), "Chiou-Youngs NGA Ground Motion Relations for the Geometric Mean Horizontal Component of Peak and Spectral Ground Motion Parameters," *Earthquake Spectra* **24**, 173–215.

Idriss, I. M. (2008), "An NGA Empirical Model for Estimating the Horizontal Spectral Values Generated by Shallow Crustal Earthquakes," *Earthquake Spectra* **24**, 217–242.

Petersen, M. D., Frankel, A. D., Harmsen, S. C., Mueller, C. S., Haller, K. M., Wheeler, R. L., Wesson, R. L., Zeng, Y., Boyd, O. S., Perkins, D. M., Luco, N., Field, E. H., Wills, C. J., and Rukstales, K. S. (2008). *Documentation for the 2008 Update of the United States National Seismic Hazard Maps*, *U.S. Geological Survey Open-File Report 2008-1128*.

Power, M., Chiou, B., Abrahamson, N., Bozorgnia, Y., Shantz, T., and Roblee, C. (2008), "An Overview of the NGA Project," *Earthquake Spectra*, **24**, 3–21.

8CUEE CONFERENCE PROCEEDINGS
8th International Conference on Urban Earthquake Engineering
March 7-8, 2011, Tokyo Institute of Technology, Tokyo, Japan

STATISTICAL FEATURES OF SHORT-PERIOD AND LONG-PERIOD NEAR-SOURCE GROUND MOTIONS

Masumi Yamada[1], Anna H. Olsen[2], and Thomas H. Heaton[3]

1) Assistant Professor, Kyoto University, Uji, Japan
2) Researcher, University of Colorado at Boulder, Boulder, US
3) Professor, California Institute of Technology, Pasadena, US
masumi@eqh.dpri.kyoto-u.ac.jp, anna.olsen@colorado.edu, heaton_t@caltech.edu

Abstract: This study collects recorded ground motions from the near-source region of large earthquakes and considers to what extent this historic record can inform expectations of future ground motions at similar sites. The distribution of observed peak ground acceleration (PGA) is well approximated by the lognormal distribution, and we expect the observed distribution to remain unchanged with the addition of data from future earthquakes. However, the distribution of peak ground displacements (PGD) will likely change after a well recorded large earthquake. Specifically we expect future observations of PGD greater than those previously recorded. We use seismic scaling relations to motivate the expected distribution of PGD as uniform on the logarithmic scale, or at least fat-tailed. Since PGA does not scale with fault rupture area or slip on the fault, there are no such scaling relations to predict the observed distribution of PGA. The observed records show that there is essentially no correlation between PGD and PGA for near-source ground motions from large events. The large uncertainty in a future value of PGD in the near-source region of a large earthquake exists despite the ability of earth scientists to accurately model long-period ground motions. In contrast, the relative certainty in a future value of PGA exists despite the inability to model short-period ground motions reliably. The stability of the observed distribution of PGA with respect to new ground motion records enables us to predict the distribution of future PGA and to calculate the probability of exceeding the largest recorded PGA.

1. INTRODUCTION

The current practice of seismic structural design assumes an expectation of future ground motions. An engineer first defines the likely and most severe ground motions that may excite a structure at a particular site in its anticipated lifetime. Then the engineer specifies a lateral force resisting system with a capacity sufficient to withstand these expected demands. This approach to design problems works well if the definition of future ground motions is reliable. Unfortunately, predicting the future is a notoriously difficult endeavor.

Past experience primarily informs the seismic design of structures. ASCE 7-05, the standard adopted by the 2006 International Building Code for seismic design, requires the use of at least three recorded ground motion time histories for structural designs based on seismic response histories (American Society of Civil Engineers, 2006). If there are fewer than three appropriate recorded ground motions, simulated motions may be used to meet the requirement. Also, structural engineers develop their judgments through their own experiences and the experiences of their predecessors. Experience and the historic record may be necessary, but not sufficient, evidence for anticipating the future ground motions at a given site. This study considers the extent to which recorded ground motions can inform the prediction of future ground motions.

Throughout this study we distinguish ground motions dominated by short-period versus long-period energy content. All seismic ground motions can be decomposed according to the relative amounts of energy in harmonic waves of every period. Generally speaking, the energy in ground motions from smaller, more frequent earthquakes is mostly from the short-period content, whereas the energy in ground motions from larger, less frequent earthquakes is primarily in the long-period content. This distinction between short- and long-period energy also categorizes a structure as short- or long-period according to the structure's fundamental period. The lateral force-resisting system of a structure with a short fundamental period tends to be susceptible to short-period ground motions. Similarly, a structural system with a long fundamental period is particularly sensitive to long-period ground motions.

This study collects recorded ground motions from the near-source region of large earthquakes and considers to what extent this historic record can inform expectations of future ground motions at similar sites. We find that future peak ground accelerations (a good intensity measure for short-period ground motions) can be readily predicted from existing records, but the experience of past large earthquakes does not adequately predict future peak ground displacements (a good intensity measure for long-period

ground motions). These observations directly affect the design of structures, since building codes rely explicitly or implicitly on recorded ground motions: existing measures of peak ground acceleration from records are a reliable predictor of future peak ground accelerations, but future peak ground displacements may differ significantly from measures of peak ground displacement from existing records.

2. DATA

We collect ground motions from ten historic earthquakes to generate distributions of observed peak ground acceleration and displacement. Specifically, we use ground motions only from earthquakes with magnitudes greater than 6.0 and from sites in the near-source. We define the near-source region to be within 10 km of the surface projection of the fault rupture. We choose this number because it is small enough to demonstrate the source scaling, but large enough to include a sufficient number of records to characterize the statistics. We disregard the soil class at the instrumented sites.

Table 1 lists important features of the data set. The earthquakes include the major events in the years 1979 through 2004. The data set covers a range in moment magnitude from 6.0 to 7.8, with wide gaps between 6.0 and 6.5 and between 6.9 and 7.3. Nonetheless, the data well represent the ground motions of interest. The Chi-Chi and Parkfield earthquakes are well recorded, each with over forty near-source records. (In fact, the Chi-Chi strong ground motion data set is the largest for a major earthquake [Shin and Teng, 2001].) However, the Landers, Hyogoken-nanbu, Izmit, and Denali ruptures are poorly recorded, since each has fewer than five near-source records. Table 1 also lists the focal depth of each hypocenter, ranging from 12.0 km to 21.2 km, as well as the fault rupture model used to define the near-source area.

We obtained ground acceleration time histories from several databases around the world. The COSMOS Virtual Data Center, which includes the California Strong Motion Instrumentation Program and the United States Geological Survey seismic networks, was the source for ground motions from the Imperial Valley, Loma Prieta, Landers, Northridge, Denali, and Parkfield earthquakes. The ground motions for the Hyogoken-nanbu earthquake were from: the Japan Meteorological Agency; the Committee of Earthquake Observation and Research in the Kansai Area in Japan (Toki *et al.*, 1995); and the Japan Railway Institute, whose records were scanned and digitized by Wald (1996). (Seismometers in the CEORKA network record velocity, but CEORKA processes the records to provide acceleration time histories.) The national strong-motion network in Turkey recorded ground motions in the Izmit earthquake (Akkar and Gülkan, 2002), and we collected them from two sources: the Earthquake Research Department of the General Directorate of Disaster Affairs in Turkey (Earthquake Research Department, 2004); and the COSMOS Virtual Data Center, which archived records from the National Earthquake Monitoring Center, Kandilli Observatory and from the Earthquake Research Institute, Boğaziçi University. The Central Weather Bureau Seismic Network in Taiwan recorded the ground motions for the Chi-Chi earthquake, and Lee *et al.* (2001) disseminated them. The K-NET (Kyoshin Net, 1996) and KiK-net (KiK-net, 2000) seismic networks, operated by the National Research Institute for Earth Science and Disaster Prevention in Japan, were our sources for the strong ground motions of the Niigataken-chuetsu earthquake.

The geographic distributions of instrumented sites in the near-source regions are not uniform. The density of sites per near-source area is not constant for all events, and the sites do not evenly represent all near-source regions. For nine of the ten earthquakes used in this study, Yamada *et al.* (2007) showed the sites in comparison to the fault rupture surface projection and the near-source region. As examples of particularly poor distributions of instrumented sites (for our purposes), many of the ground motions from the 1979

Table 1 Earthquake Data Set Used for the Near-Source Ground Motion Analysis

Earthquake	M_w	N	Focal Depth (km)	Fault Model
1979 Imperial Valley	6.5	14	12.0	Hartzell and Heaton (1983)
1989 Loma Prieta	6.9	8	19.0	Wald *et al.* (1991)
1992 Landers	7.3	1	15.0	Wald and Heaton (1994)
1994 Northridge	6.6	17	16.8	Wald *et al.* (1996)
1995 Hyogoken-Nanbu	6.9	4	20.3	Wald (1996)
1999 Izmit	7.6	4	17.0	Sekiguchi and Iwata (2002)
1999 Chi-Chi	7.6	42	21.2	Ji *et al.* (2003)
2002 Denali	7.8	1	15.0	Tsuboi *et al.* (2003)
2004 Parkfield	6.0	47	12.0	Ji *et al.* (2004)
2004 Niigataken-Chuetsu	6.6	9	13.0	Honda *et al.* (2005)

Moment magnitude (M_w) and focal depth are cited from the Harvard Centroid Moment Tensor solution. The preliminary determination of the epicenter is used for the focal depth. The number of near-source records for each earthquake (N) is also tabulated. The fault models are used to define near-source stations.

Imperial Valley earthquake are from sites forming a line perpendicular to the fault, and most ground motions from the 1999 Chi-Chi earthquake are from sites on the foot wall. Despite the non-uniform geographic distribution of the recorded ground motions, we treat each record as a sample of the ground movement in the near-source region.

To determine the peak ground acceleration and displacement of a recorded ground motion, we process each time history. We first remove the bias from the acceleration record by subtracting the mean of the pre-event interval. Then we integrate twice to generate the displacement time history. We remove the longest period content of the displacement time history with a fourth-order Butterworth filter (13.3 s corner period) to avoid problems caused by a shift in the baseline. Filtering in this way can produce a peak ground displacement smaller than what would have been calculated from the unfiltered record. Nonetheless, these filtered records still contain rich long-period content. We then find the square root of the sum of the squares of the north-south and east-west components at each time step of the record. The peak ground measure is the largest such value over all time steps. This measure of peak ground motion is also known as the vector amplitude (Kanno *et al.*, 2006). Yamada (2007) compared PGAs and PGDs calculated from the horizontal components or from the vertical component and found that they have a similar trend with respect to moment magnitude. We use only the horizontal components to calculate the peak values since most engineered structures are more vulnerable to lateral than vertical excitation.

In addition to the recorded ground motions, we also consider a recurrence of the 1906 San Francisco earthquake. We use the simulated ground motions generated by Aagaard *et al.* (2008) closest to sites in the California Integrated Seismic Network as of December 2007. To be consistent with the choice of recorded ground motions, we only include sites within 10 km of the historic rupture on the San Andreas fault. These selection criteria result in 87 "records" of a recurrence of the 1906 San Francisco earthquake. These ground motions are long period (periods greater than 2 s), so we use a fourth-order Butterworth filter (25.0 s corner period) and calculate only the peak ground displacement of each record.

3. OBSERVED DISTRIBUTIONS OF PGA AND PGD

For our collected set of recorded ground motions, Figure 1 plots the peak ground accelerations and displacements as functions of the moment magnitude of the generating earthquake. Each data point is denoted with a symbol, and the least squares regression lines for the peak ground measures as functions of magnitude are shown. At each magnitude, the peak ground acceleration (PGA) and peak ground displacement (PGD) data are approximately lognormally distributed about their respective regression lines. Note that PGA saturates at magnitudes greater than 6.0, as evidenced by the approximately zero slope of the regression line. The saturation of short-period ground

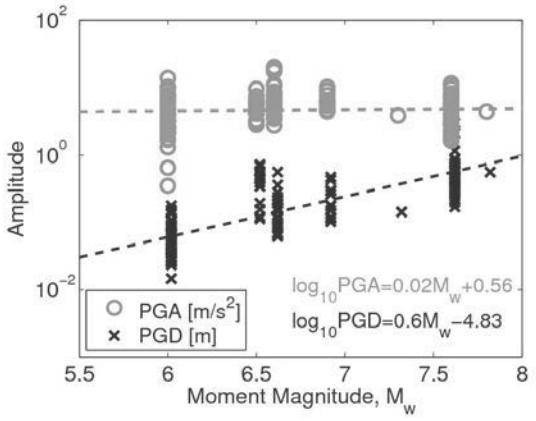


Figure 1 Near-source PGA and PGD as a function of moment magnitude. The dashed lines are least-squares regression lines for the two intensity measures, and the equations for these lines are also given.

motions in the near-source has been observed previously by Rogers and Perkins (1996) and Somerville (2003). In contrast, the logarithm of PGD increases linearly with respect to magnitude, with a slope of 0.6. Previous studies have discussed this linear trend (e.g., Wells and Coppersmith, 1994; Campbell and Bozorgnia, 2008). We expect this slope to be in the range of 0.5 to 0.75 based on the following argument.

Given the definition of seismic moment, M_0, ($\log M_0 = \log \mu + \log S\bar{D}$) and the relationship between seismic moment and moment magnitude, M_w, ($\log M_0 = 2/3(M_w + 10.73)$), we find:

$$\log S\bar{D} = 2/3(M_w + 10.73) - \log \mu , \qquad (1)$$

where S is the rupture area, $\bar{D}$ is the average slip, and μ is the crustal rigidity. If we assume the rupture area is approximately the square of the rupture length (reasonable for small to moderate earthquakes [Aki, 1972; Kanamori and Anderson, 1975]) and PGD is proportional to the average slip, (1) implies that:

$$\log PGD = 1/2 M_w + \text{a constant.}$$

If we assume the rupture area is proportional to the rupture length (reasonable for large earthquakes, [Scholz, 1982]) and PGD is proportional to the average slip again, Equation (1) then implies that:

$$\log PGD = 3/4 M_w + \text{another constant.}$$

Thus we expect the slope of the relationship between the logarithm of PGD and moment magnitude to be between 0.5 and 0.75 for the combination of moderate and large earthquakes.

As mentioned previously, PGA is known to saturate at magnitudes greater than 6, and the logarithm of PGD is known to increase linearly with respect to magnitude. Thus, there is essentially no correlation between these two

intensity measures for near-source ground motions from large events. Figure 2 plots PGA versus PGD for the near-source records used in this study and for additional far-source records. The far-source PGDs and PGAs are from ground motions recorded in magnitude greater than 6 earthquakes at distances greater than 10 km from the fault. Unlike the far-source records, the near-source PGD and PGA are very weakly correlated.

Figure 3 compares the marginal distributions of PGA and PGD to a base-10 lognormal distribution. The histogram of the PGA data is consistent with a lognormal distribution: on a logarithmic scale, the PGA data are clearly peaked, symmetric about the mean, and have thin tails. This observation is consistent with Figure 1 since the mean PGA is approximately constant for magnitudes greater than 6.0, and the PGA data appear to be lognormally distributed about the mean with constant variance. The near-source PGA of earthquakes with magnitude greater than 6.0 can be approximated by the lognormal distribution:

$$p(PGA) = \frac{1}{0.56 PGA\sqrt{2\pi}} e^{-[\ln PGA - \ln 4.64)^2 / 0.64]}, \qquad (2)$$

where ln represents the natural logarithm. The histogram of the PGD data, however, is inconsistent with a lognormal distribution: on a logarithmic scale, the PGD data are roughly uniform over the range of observed PGD. The PGD data are not peaked because the mean PGD is correlated with magnitude. At a given magnitude, the PGD data appear lognormally distributed, but since the mean increases with magnitude, the projection of the data as a marginal distribution becomes more uniform than peaked.

Figures 4 and 5 are histograms of the PGA and PGD data, respectively. For the PGA data, we show a subset of the observed data with the Chi-Chi data removed as well as the full data set. The distribution of the subset without the Chi-Chi data appears lognormal. The addition of the Chi-Chi data does not change the shape of the distribution; including the Chi-Chi PGA data simply increases the height of the histogram. This exercise suggests that a lognormal

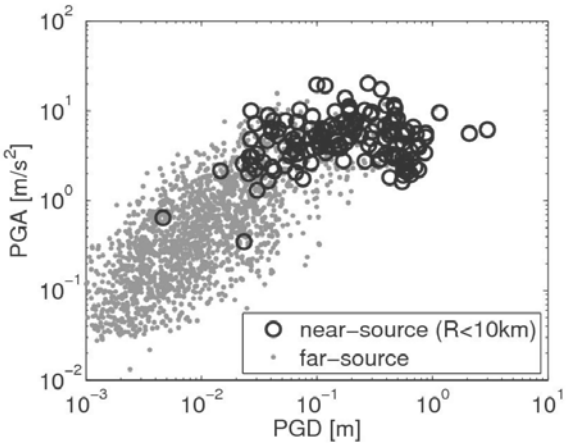


Figure 2 Relationship between PGD and PGA. The near-source records are the same data used in this study. The far-source records are the records from earthquakes with magnitude greater than 6.0.

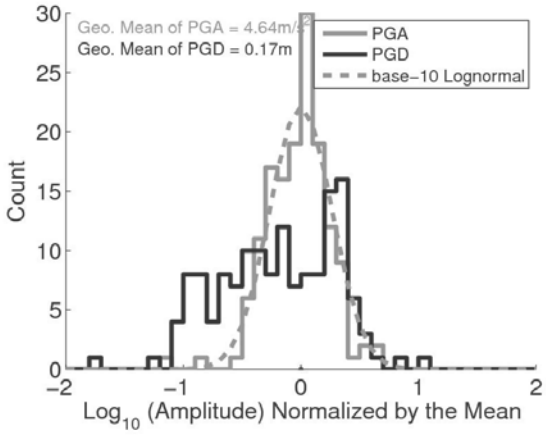


Figure 3 Comparison of observed near-source PGA and PGD histograms to a base-10 lognormal distribution. The lognormal distribution shown has a geometric mean (4.64 m/sec^2) and geometric standard deviation (1.77 m/sec^2) calculated from the PGA data.

distribution is a good approximation for existing, recorded PGA at near-source sites in earthquakes with magnitudes greater than 6.0, and this distribution will remain approximately lognormal with the addition of future data. The saturation of PGA at large magnitudes supports our claim: since the mean and standard deviation of PGA are approximately constant for each large earthquake, data from future earthquakes will also have the same mean and standard deviation and thus cannot change the shape of the PGA distribution.

Now consider the observed distribution of PGD in Figure 5. Similar to the analysis of the PGA data, we show the distribution of PGD for a subset of our recorded data set that does not include ground motions from the Chi-Chi earthquake. This distribution is roughly uniform on a logarithmic scale over the range of this subset. Adding the PGDs from the Chi-Chi earthquake extends the range of PGD at large values; there are several PGDs from the

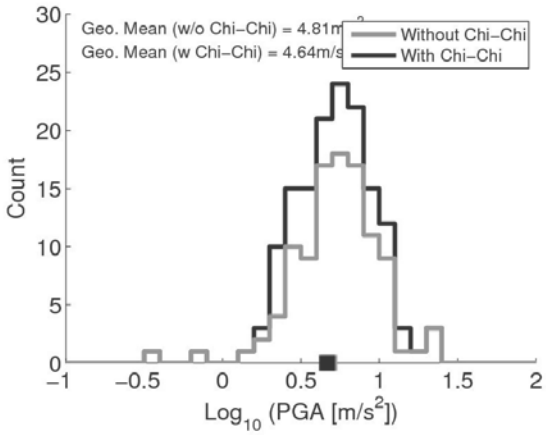


Figure 4 Histogram of the near-source PGA for earthquakes with magnitude greater than or equal to 6.0. The black and gray lines are histograms of the full data set with and without the Chi-Chi earthquake records, respectively. The squares on the horizontal axis indicate the geometric mean of each component, and their values are shown on the plot.

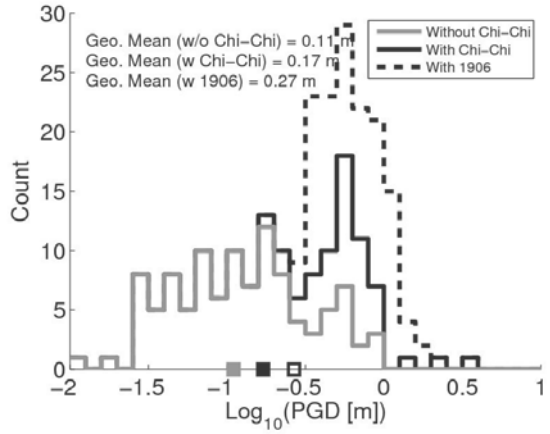


Figure 5 Histogram of the near-source PGD for earthquakes with magnitude greater than or equal to 6.0. The black and gray lines show the distribution of recorded PGD in our data set with and without the Chi-Chi observations, respectively. The dashed lines augment the recorded data set with an imagined repeat of the 1906 San Francisco earthquake. The squares on the horizontal axis indicate the geometric mean of each set of data, and the values are listed in the plot.

Chi-Chi ground motions that are larger than observations from other large earthquakes. The spread in the distribution of observed near-source PGD widens notably with the inclusion of this single earthquake.

We use a simulation of ground motions in the 1906 San Francisco earthquake to imagine the effect of the next large, well-recorded earthquake on this distribution of PGD. If the 1906 earthquake recurred and was recorded with existing instrumentation, Figure 5 shows the effect on the "observed" distribution. The simulated data add to the histogram at the largest observed PGDs. In other words, many of the simulated PGDs are in the range of the largest recorded PGDs. Certainly the next large, well-recorded earthquake will not be a repeat of the 1906 San Francisco earthquake, but a future rupture has the potential to produce numerous recorded ground motions with PGDs at the high end of, or greater than, those recorded at present.

Earthquakes with magnitudes greater than 6.0 change the observed distribution of PGD, either by extending the distribution or by adding data at previously recorded values. The increase of PGD with magnitude (Figure 1) helps to explain this point. Although PGD is lognormally distributed at a given magnitude, the mean of the logarithm of PGD increases linearly with magnitude. Thus, the magnitude of each event determines where its observed PGDs add to the distribution of PGD from all events, either beyond the observed range or within it. This finding is in contrast to our statements about the distribution of PGA: records from future, well-recorded earthquakes will not change the observed distribution of PGA, whereas they may change—and many change substantially—the observed distribution of PGD.

4. THEORETICAL DISTRIBUTIONS OF PGA AND PGD

In this section we first use empirical scaling relationships to derive the expected marginal distribution of PGD in the near-source region of large earthquakes. First, we assume that the number of earthquakes N with magnitudes greater than M is given by the Gutenberg-Richter relationship:

$$N = 10^{a-bM} = \int_M^\infty N_M \, dM \,, \qquad (3)$$

where N_M is the number of earthquakes with magnitude between M and $M + \Delta M$. In a different form,

$$N_M = \frac{dN}{dM} = b\ln(10)10^{a-bM} = 10^{A-bM} \,, \qquad (4)$$

where $10^A = b\ln(10)10^a$, a constant. The moment magnitude can be rewritten in terms of the seismic moment, M_0, which is equal to the product of the crustal rigidity, μ, average slip on the fault, $\bar{D}$, and the area of fault rupture, S:

$$M_w = 2/3\log_{10} M_0 - 10.73 = 2/3\log_{10}(\mu \bar{D} S) - 10.73 \,.$$

Thus,

$$N_M = 10^{A+10.73b} 10^{-2/3b\log_{10}(\mu \bar{D} S)} = c(\bar{D}S)^{-2/3b} \,,$$

where $c = 10^{A+10.73b}\mu^{-2/3b}$, a constant.

One of two assumptions can be made at this point, depending on the size of the earthquake. For moderate earthquakes, the fault rupture length, L, is approximately equal to the fault rupture width, which implies that the fault rupture area is approximately L^2. For large earthquakes, the rupture length is much larger than the approximately constant rupture width, which implies that the rupture area is proportional to the rupture length. We also assume in both cases that the average slip on the fault is proportional to the length of the fault rupture. Thus,

$$N_M \propto (\bar{D}L^2)^{-2/3b} \approx \bar{D}^{-2b} \quad \text{if } S \approx L^2 \quad \text{(moderate events)}$$
$$N_M \propto (\bar{D}L)^{-2/3b} \approx \bar{D}^{-4/3b} \quad \text{if } S \approx L \quad \text{(large events)}$$

The total rupture area for all earthquakes of magnitude M is:

$$N_M S \approx N_M \propto \bar{D}^{-2b}\bar{D}^2 = \text{constant for } b = 1,$$
$$N_M S \propto \bar{D}^{-4/3b}\bar{D} = \bar{D}^{-1/3b} \quad \text{for } b = 1.$$

Assuming a uniform geographic distribution of seismic instrumentation, Equation (5) implies that the total number of near-source records at a particular magnitude is either constant or weakly dependent on magnitude, depending on the assumed geometry of the fault rupture. Furthermore, the peak ground displacement in the near-source is proportional to the average slip on the fault (Aagaard *et al.*, 2001). These results can be combined with the observations from Figure 1 to generate a rough approximation of the marginal probability density function for the logarithm of PGD.

If we assume the rupture area is approximately square

(that is, consider moderate earthquakes), then the total number of near-source records is constant for all magnitudes. Given enough time, all magnitude 6 earthquakes will produce the same number of near-source records as all magnitude 7 earthquakes or all magnitude 8 earthquakes. Figure 6 (top) combines this result with the observations that the mean PGD increases with magnitude and PGD is lognormally distributed at a given magnitude. The resulting marginal distribution of PGD is approximately uniform because the total number of recorded ground motions is constant for all magnitudes.

Alternatively, if we assume the rupture length is much larger than the rupture width (that is, consider large earthquakes), then the total number of near-source records decreases with magnitude, since magnitude depends on average slip. Figure 6 (bottom) shows the relative number of near-source ground motions at each magnitude given that the total number is proportional to the mean PGD raised to the negative one-third power. The resulting marginal distribution of PGD is not uniform, but it is also not lognormal; it is something in-between the two.

We cannot develop a similar argument for the marginal distribution of PGA because the relationship between PGA and faulting is not clear. At this time, seismologists are developing finite element models to simulate broadband ground motions and thus predict PGA in the near-source region. However, these models require sophisticated fault and velocity models to propagate short-period seismic waves or require a stochastic description of PGA. Unlike PGD, which can be related to slip on the fault, it is difficult to use a fundamental, physical understanding of faulting and wave propagation to predict PGA. Yamada *et al.* (2007) shows that the distribution for near-source PGA seems to be compatible with the hypothesis that the total radiation of high-frequency energy scales with the rupture area. This hypothesis is consistent with the observation that the PGA weakly depends on the slip on the fault.

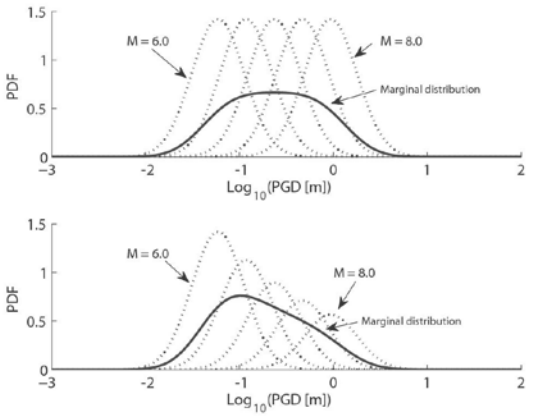


Figure 6 Theoretical marginal distribution of PGD. Seismic scaling relations predict that the number of recorded PGDs at a given magnitude in the near-source region is constant (top, moderate earthquakes) or weakly dependent on magnitude (bottom, large earthquakes). Given enough observations, the resulting, expected marginal distribution of PGD more closely resembles a uniform—not normal—distribution on the logarithmic scale.

5. A PARADOX

This discussion of predicting PGA and PGD from the fundamentals of faulting and wave propagation leads directly to a paradox: the PGA in a future earthquake can be easily predicted from past earthquakes even though short-period ground motions cannot be easily simulated, whereas the PGD in a future earthquake cannot be predicted even though long-period ground motions are routinely simulated. Given only the information that a site is in the near-source of an earthquake with magnitude greater than 6.0, the recorded ground motions used in this study show that PGA is well approximated by a lognormal distribution, but the distribution of the logarithm of PGD is roughly uniform with an unknown point of truncation. Thus, using past observations of ground motions can produce a relatively certain prediction of PGA and a quite uncertain prediction of PGD. This is in contrast to the present capabilities of simulating ground motions. Long-period ground motions can be readily generated from models of faults and seismic velocity structures. Currently, however, generating short-period ground motions is not routinely done as it requires much more detailed models or stochastic descriptions.

The resolution of this paradox considers the assumed information. Simulating ground motions assumes a magnitude and either generates a slip distribution (dynamic source modeling) or assumes a slip distribution (kinematic source modeling). Our study of recorded ground motions assumes only that the earthquake has a magnitude greater than 6.0. Knowing the magnitude does not help predict the PGA since PGA saturates with magnitude, but knowing the magnitude helps to predict PGD since the logarithm of PGD is proportional to the magnitude.

However, we need to predict more than the magnitude of future events; the near-source PGD is best predicted by slip on a near-by segment of a fault.

Thus, the ability of seismologists to generate reliable long-period ground motions (and thus reliable predictions of PGD) in an earthquake of known magnitude does not imply that they can predict the PGD in the next large-magnitude earthquake, unless they can also reliably predict slip.

6. IMPLICATIONS FOR SEISMIC RISK

Engineers often use ground motion intensity measures in place of full time histories to predict seismic structural responses. Although the interaction of the complete ground motion time history with the structure defines the response, a characteristic of the ground motion—as measured by the intensity measure—is often sufficient to predict the structural response for many types of structures. The most common intensity measure is spectral acceleration at the fundamental period of the structure (abbreviated $S_a(T_1)$). Other scalar and vector intensity measures based on spectral

quantities have been proposed as well (e.g., Baker and Cornell, 2005; Luco and Cornell, 2007). For six- or twenty-story, steel, moment-resisting frames, Olsen (2008) showed that, among the considered intensity measures, the peak inter-story drift ratio was best predicted by $S_a(T_1)$, assuming that the lateral force-resisting system was not compromised. However, large permanent drifts and collapse due to P-Δ are predicted better by a combination of large peak ground velocity (PGV) and PGD. Near-source ground motions with large PGDs are almost always accompanied by large PGVs. Thus, in the near-source region, PGDs are often associated with simulated collapse. Thus, although $S_a(T_1)$ is widely used as an intensity measure, there is evidence that an alternate intensity measure may predict structural response better, depending on the structure type and response of interest.

The maximum value of the appropriate intensity measure likely to be experienced at a site is often of interest for seismic risk assessment. This maximum value depends on an expectation of future ground motions, which is informed by existing recorded ground motions as well as the current understanding of the physical mechanisms. This study shows that the maximum likely PGA within 10 km of a fault that produces a magnitude greater than 6.0 earthquake can be reliably derived from a lognormal distribution, since the empirical marginal distribution of such PGAs is stable with respect to new records and consistent with a lognormal distribution. Determining the maximum likely PGD in the same geographic region is more problematic given the available recorded ground motions with large PGDs. This study shows that the current empirical marginal distribution of PGD is fat-tailed, if not uniform on a logarithmic scale to a physical limit. This physical limit has not yet been determined, and simulation of ground motions from plausible large earthquakes (for example, the repeat of the 1906 San Francisco earthquake) suggests that the next large, well-recorded earthquake will contribute several measured PGDs between the current largest recorded PGDs and the suspected physical limit. Given this evidence, we find the calculation of the maximum likely PGD difficult—if not impossible—given the current knowledge.

These results have a direct bearing on seismic risk assessment. If the appropriate intensity measure for a structural response of interest is PGA, then recorded ground motions with the largest observed PGAs can be used as representative of future ground motions with the largest PGAs. The predicted structural responses based on existing large PGAs would be reliable even after the next large earthquake. However, if the appropriate intensity measure is PGD, the largest observed PGDs may not be representative of the future largest PGDs. Consequently, structural responses based on the largest recorded PGDs may not be representative of structural responses in the future largest PGDs. Consider tall buildings as an example. Their response to ground motions with PGDs of 0.2 m or 2 m or 10 m range from elastic to catastrophic failure. If this type of building is located within 10 km of an earthquake with magnitude greater than 6, each response is roughly equally likely if each level of ground motion is approximately equally likely. This study provides evidence to caution against assuming that recorded ground motions with the largest PGDs are representative of unrecorded or future ground motions with the largest PGDs.

This study supports the argument made in Heaton (2007). Among other questions, Heaton (2007) asks whether the current structural design philosophy of performance-based earthquake engineering is appropriate for the design of long-period structures. PBEE assumes that the reliability of a structure's performance—be it, seismic response or lifetime cost—can be predicted during the design phase. Heaton (2007) points out that such a reliability analysis is credible only if the hazard is well-described by a knowable and finite uncertainty. The present study suggests that a future PGA (and thus the peak amplitude of short-period ground motions) is readily predictable from past records with a known, finite uncertainty. In contrast, a future PGD (or peak amplitude of long-period ground motions) cannot be anticipated with certainty because first, each large earthquake changes the observed marginal distribution of PGD, and second, the uncertainty of this distribution at present is quite large.

7. CONCLUSIONS

For ground motions recorded within 10 km of a fault producing an earthquake with magnitude greater than 6.0, the observed distribution of peak ground acceleration is lognormal, but the observed distribution of peak ground displacement is approximately uniform on a logarithmic scale, or at least fat-tailed. We expect the distribution of PGA to remain approximately lognormal with the addition of data from future earthquakes. However, the distribution of PGD will likely change after a well-recorded large earthquake, and specifically we expect the range of recorded PGD to expand at the largest values. The observed records show that there is essentially no correlation between PGD and PGA for near-source ground motions from large events.

Seismic scaling relations motivate the expected distribution of PGD as uniform on the logarithmic scale, or at least fat-tailed. This result implies that every peak ground displacement is approximately equally likely at a given site—to a physical limit—even though an earthquake large enough to produce large displacements is infrequent. There are no such scaling relations to predict the lognormal distribution of PGA because PGA does not scale with fault rupture area or slip on the fault. The large uncertainty in a future value of observed PGD exists despite the ability of earth scientists to accurately model long-period ground motions. In contrast, the certainty in a future value of PGA exists despite the inability to model short-period ground motions reliably.

The design of short-period structures with modern building codes is reliable in part because earthquakes with magnitude greater than 6 produce a stable marginal distribution of PGA with respect to future earthquakes. The mean and standard deviation of PGA in the next large

earthquake can be predicted reliably from the historic distribution of PGA. The design of long-period structures, however, should not rely on the same argument: the observed marginal distribution of PGD may change after the next well-recorded large earthquake. The emphasis on recorded ground motions for structural design using seismic response histories assumes that future ground motions will be sufficiently similar to recorded ground motions. This study demonstrates that this assumption is not valid. Thus, there must be a different approach to the design of long-period structures that does not rely heavily on past observations of PGD to predict future amplitudes of long-period ground motions. This approach should acknowledge that, for any site in the near-source region of a major fault, every PGD is similarly likely in the logarithmic sense. That is, 1 m of future peak ground displacement is approximately as likely as 10 m of future peak ground displacement. The optimal design of long-period structures should be the most economical design that is robust in large ground motions.

Acknowledgements:

We are deeply appreciative of comments provided by the Associate Editor and reviewers. We acknowledge all institutions providing strong motion records, especially the COSMOS data center, Southern California Earthquake Center (SCEC) data center, National Research Institute for Earth Science and Disaster Prevention (NIED), and Japan Meteorological Agency (JMA). David Wald of the United States Geological Survey and Hiroo Kanamori of the California Institute of Technology helped obtain data for the Hyogoken-nanbu earthquake. Egill Hauksson provided the California Integrated Seismic Network (CISN) station list. This research was supported by the United States Geological Survey and Promoting Science and Technology (SCF) commissioned by the Ministry of Education, Culture, Sports, Science and Technology of Japan.

References:

Aagaard, B. T., T. M. Brocher, D. Dolenc, D. Dreger, R. W. Graves, S. Harmsen, S. Hartzell, S. Larsen, K. McCandless, S. Nilsson, N. A. Petersson, A. Rodgers, B. Sjögreen, and M. L. Zoback (2008). Ground-motion modeling of the 1906 San Francisco earthquake, part II: Ground-motion estimates for the 1906 earthquake and scenario events, *Bull. Seismol. Soc. Am.* 98, no. 2, 1012–1046.

Aagaard, B., J. Hall, and T. Heaton (2001). Characterization of near-source ground motions with earthquake simulations, *Earthq. Spectra* 17, no. 2, 177–207.

Aki, K. (1972). Earthquake mechanism, *Tectonophysics* 13, no. 1–4, 423–446.

Akkar, S., and P. Gülkan (2002). A critical examination of near-field accelerograms from the Sea of Marmara region earthquakes, *Bull. Seismol. Soc. Am.* 92, no. 1, 428–447.

American Society of Civil Engineers (2006). Minimum Design Loads for Buildings and Other Structures, ASCE/SEI 7-05, Reston, Virginia.

Baker, J. W., and C. A. Cornell (2005). A vector-valued ground motion intensity measure consisting of spectral acceleration and epsilon, *Earthq. Eng. Struct. Dyn.* 34, 1193–1217.

Campbell, K., and Y. Bozorgnia (2008). NGA ground motion model for the geometric mean horizontal component of PGA, PGV, PGD and 5 ranging from 0.01 to 10 s, *Earthq. Spectra* 24, 139–171.

Earthquake Research Department (2004). ftp://angora.deprem.gov.tr/, General Directorate of Disaster Affairs, Republic of Turkey Ministry of Public Works and Settlement.

Hartzell, S. H., and T. H. Heaton (1983). Inversion of strong ground motion and teleseismic waveform data for the fault rupture history of the 1979 Imperial Valley, California, earthquake, *Bull. Seismol. Soc. Am.* 73, no. 6A, 1553–1583.

Heaton, T. H. (2007). Will performance-based earthquake engineering break the power law?, *Seism. Res. Lett.* 78, no. 2, 183–185.

Honda, R., S. Aoi, N. Morikawa, H. Sekiguchi, T. Kunugi, and H. Fujiwara (2005). Ground motion and rupture process of the 2004 Mid Niigata Prefecture earthquake obtained from strong motion data of K-NETand KiK-net, *Earth Planets Space* 57, 527–532.

Ji, C., K. K. Choi, N. King, K. M. Larson, and K. W. Hudnut (2004). Co-seismic slip history and early afterslip of the 2004 Parkfield earthquake (Abstract S53D-04), *Eos Trans. Am. Geophys. Union* 85, no. 47 (Fall Meet. Suppl.), S53D-04.

Ji, C., D. V. Helmberger, D. J. Wald, and K.-F. Ma (2003). Slip history and dynamic implications of the 1999 Chi-Chi, Taiwan, earthquake, *J. Geophys. Res.* 108, no. B9, 2412, doi 10.1029/2002JB001764.

Kanamori, H., and D. Anderson (1975). Theoretical basis of some empirical relations in seismology, *Bull. Seismol. Soc. Am.* 65, no. 5, 1073–1095.

Kanno, T., A. Narita, N. Morikawa, H. Fujiwara, and Y. Fukushima (2006). A new attenuation relation for strong ground motion in Japan based on recorded data, *Bull. Seismol. Soc. Am.* 96, no. 3, 879–897.

KiK-net (2000). http://www.kik.bosai.go.jp/, National Research Institute for Earth Science and Disaster Prevention, Japan.

Kyoshin Net (1996). http://www.k‐net.bosai.go.jp/, National Research Institute for Earth Science and Disaster Prevention, Japan.

Lee, W. H. K., T. C. Shin, K. W. Kuo, K. C. Chen, and C. F. Wu (2001). CWB free-field strong-motion data from the 21 September Chi-Chi, Taiwan, earthquake, *Bull. Seismol. Soc. Am.* 91, no. 5, 1370–1376.

Luco, N., and C. A. Cornell (2007). Structure-specific scalar intensity measures for near-source and ordinary earthquake ground motions, *Earthq. Spectra* 23, no. 2, 357–392.

Olsen, A. H. (2008). Steel moment-resisting frame responses in simulated strong ground motions: Or how I learned to stop worrying and love the big one, Ph.D. Thesis, California Institute of Technology.

Rogers, A., and D. Perkins (1996). Monte Carlo simulation of peak acceleration attenuation using a finite-fault uniform-patch model including isochrone and extremal characteristics, *Bull. Seismol. Soc. Am.* 86, no. 1A, 79–92.

Scholz, C. (1982). Scaling laws for large earthquakes: Consequences for physical models, *Bull. Seismol. Soc. Am.* 72, no. 1, 1–14.

Sekiguchi, H., and T. Iwata (2002). Rupture process of the 1999 Kocaeli, Turkey, earthquake estimated from strong-motion waveforms, *Bull. Seismol. Soc. Am.* 92, no. 1, 300–311.

Shin, T.-C., and T.-l. Teng (2001). An overview of the 1999 Chi-Chi, Taiwan, earthquake, *Bull. Seismol. Soc. Am.* 91, no. 5, 895–913.

Somerville, P. (2003). Magnitude scaling of the near fault rupture directivity pulse, *Phys. Earth Planet. Inter.* 137, no. 1, 201–212.

Toki, K., K. Irikura, and T. Kagawa (1995). Strong motion records in the source area of the Hyogoken-Nanbu earthquake, January 17, 1995, Japan, *J. Nat. Disaster Sci.* 16, no. 2, 23–30.

Tsuboi, S., D. Komatitschb, C. Ji, and J. Tromp (2003). Broadband modeling of the 2002 Denali fault earthquake on the Earth simulator, *Phys. Earth Planet. Inter.* 139, no. 3–4, 305–313.

Wald, D. J. (1996). Slip history of the 1995 Kobe, Japan, earthquake determined from strong motion, teleseismic, and geodetic data, *J. Phys. Earth* 44, 489–503.

Wald, D. J., and T. H. Heaton (1994). Spatial and temporal

distribution of slip for the 1992 Landers, California, earthquake, *Bull. Seismol. Soc. Am.* 84, no. 3, 668–691.

Wald, D. J., T. H. Heaton, and K. W. Hudnut (1996). The slip history of the 1994 Northridge, California, earthquake determined from strongmotion, teleseismic, GPS, and leveling data, *Bull. Seismol. Soc. Am.* 86, no. 1B, S49–S70.

Wald, D. J., D. V. Helmberger, and T. H. Heaton (1991). Rupture model of the 1989 Loma Prieta earthquake from the inversion of strong-motion and broadband teleseismic data, *Bull. Seismol. Soc. Am.* 81, no. 5, 1540–1572.

Wells, D., and K. Coppersmith (1994). New empirical relationships among magnitude, rupture length, rupture width, rupture area, and surface displacement, *Bull. Seismol. Soc. Am.* 84, no. 4, 974–1002.

Yamada, M. (2007). Early warning for earthquakes with large rupture dimension, Ph.D. Thesis, California Institute of Technology.

Yamada, M., T. Heaton, and J. Beck (2007). Real-time estimation of fault rupture extent using near-source versus far-source classification, *Bull. Seismol. Soc. Am.* 97, no. 6, 1890–1910.

8CUEE CONFERENCE PROCEEDINGS
8th International Conference on Urban Earthquake Engineering
March 7-8, 2011, Tokyo Institute of Technology, Tokyo, Japan

STRONG MOTION RECORD OBSERVED AT CONCEPCION DURING THE 2010 CHILE EARTHQUAKE

Saburoh Midorikawa[1] and Hiroyuki Miura[2]

1) Professor, Department of Built Environment, Tokyo Institute of Technology, Japan
2) Assistant Professor, Department of Built Environment, Tokyo Institute of Technology, Japan
smidorik@enveng.titech.ac.jp, hmiura@enveng.titech.ac.jp

Abstract: The 2010 Maule, Chile earthquake (Mw8.8) produced many strong motion records. At Concepcion where many high-rise buildings suffered severe damage, a strong motion accelerogram with long period contents was observed. In this paper, local site effects on the record are examined based on the microtremor and aftershock record. The relation between the building damage and ground motion characteristics is also discussed.

1. INTRODUCTION

A gigantic earthquake with Mw8.8 occurred in Chile on February 27, 2010. The effects of the earthquake were observed over a wide area with a length of more than 500 km. The numbers of affected people and damage houses are about 2 millions and 370,000, respectively (Elnashai et al. 2011). The monetary loss is roughly estimated at 30 billion US$. The earthquake also produced many strong motion records. Among the records, a record with large amplitude and longer period was observed at Concepcion where many high-rise buildings had severe damage. In this paper, we examine the characteristics of the record in relation to local site effect and building damage.

2. OUTLINE OF EARTHQUAKE AND STRONG MOTION RECORDS

Large earthquakes have frequently occurred along the coast of Chile due to subduction of the Nasca plate to the continental plate. The 2010 Maule, Chile earthquake occurred in the seismic gap along the coast of Chile where the last large earthquake (M8.5) occurred in 1835 (Beck et al. 1998). The magnitude of the earthquake is 8.8 in Mw and the length of the aftershock area is approximately 500km. The fault models of the earthquake have been proposed by several researchers. For example, Poiata and Koketsu (2010) estimated a reverse fault model with a strike and dip of 11° and 18°, respectively. The fault length is estimated to be 450-500 km long. Figure 1 shows the surface projection of the slip distribution. The maximum fault slip is 9 m.

Strong motion records from the Maule earthquake are obtained by two strong motion networks such as RENADIC [Red Nacional de Acelerógrafos del Departamento de Ingeniería Civil de la Universidad de Chile] (Boroschek et al. 2010) and RSN [Red Sismologica Nacional by Dept. Geophysics of the University of Chile] (Barrientos 2010). Figure 2 shows the distribution of the peak horizontal accelerations in the epicentral region. The peak accelerations higher than 0.3 g are observed at many sites.

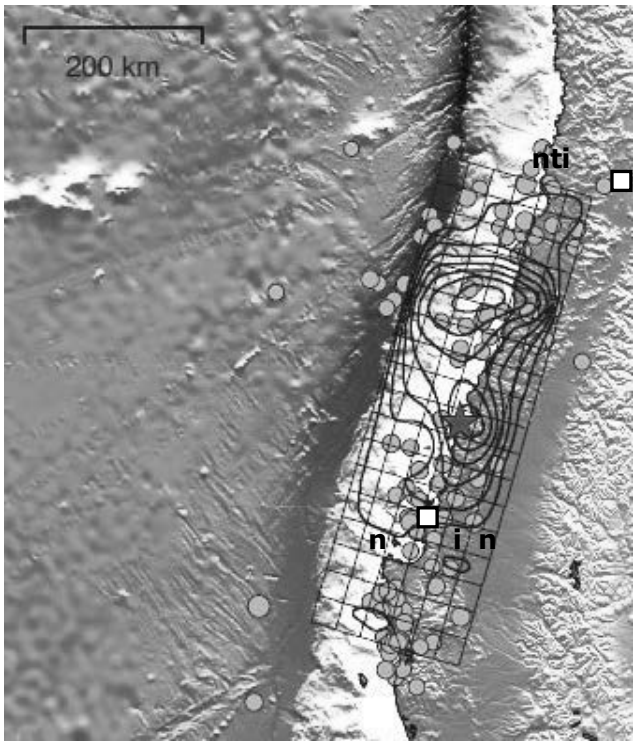


Figure 1 Fault Model (Poiata and Koketsu 2010)

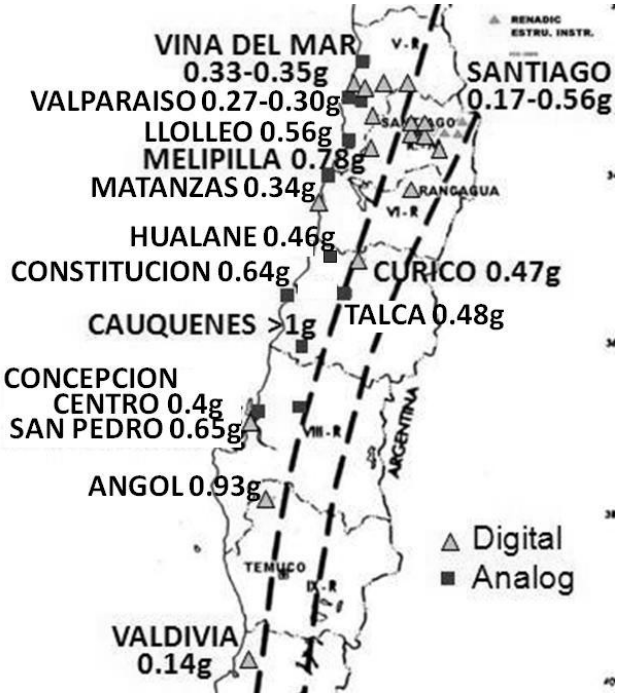


Figure 2 Distribution of Peak Horizontal Accelerations

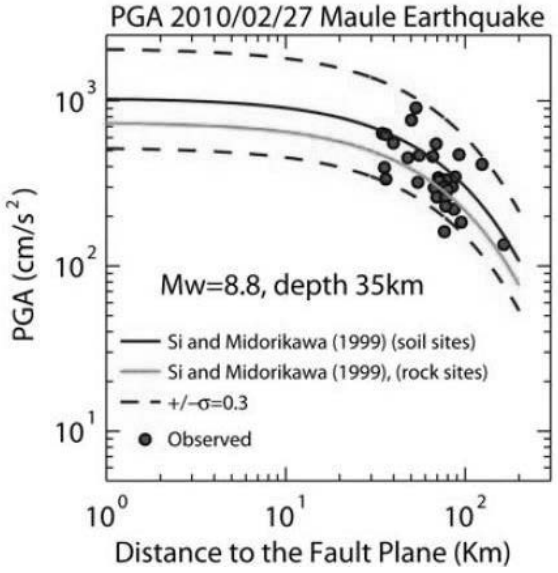
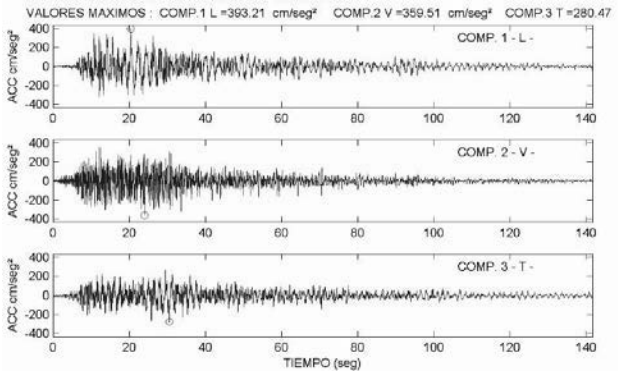


Figure 3 Attenuation of Peak Horizontal Accelerations (Pulido et al. 2011)

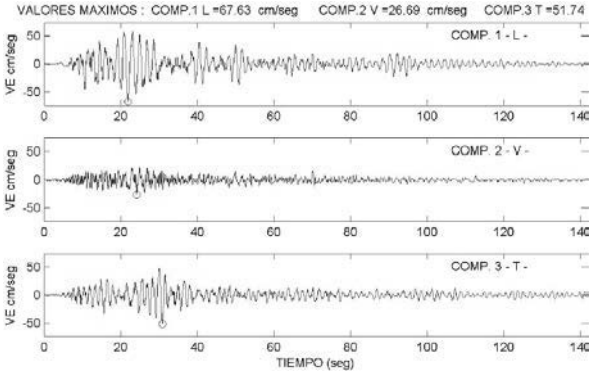
Figure 3 shows the attenuation of the peak horizontal acceleration (Pulido et al. 2011). In the figure, the curve from the empirical relationship by Si and Midorikawa (2000) is also plotted. The data from the earthquake is consistent with the existing relationship.

3. STRONG MOTION RECORD AT CONCEPCION

Among the strong motion records, an accelerogram observed at the downtown of Concepcion where many high-rise buildings suffered severe damage, has large amplitude and longer period contents. Figure 4 shows the acceleration and velocity time histories of the record. The peak horizontal acceleration and velocity are about 0.4g and 70 cm/s, respectively. The record was obtained at the basement floor of a three-story school building. The building suffered moderate damage.



(a) acceleration



(b) velocity

Figure 4 Acceleration and velocity Time Histories of Record at Concepcion (Boroschek et al. 2010)

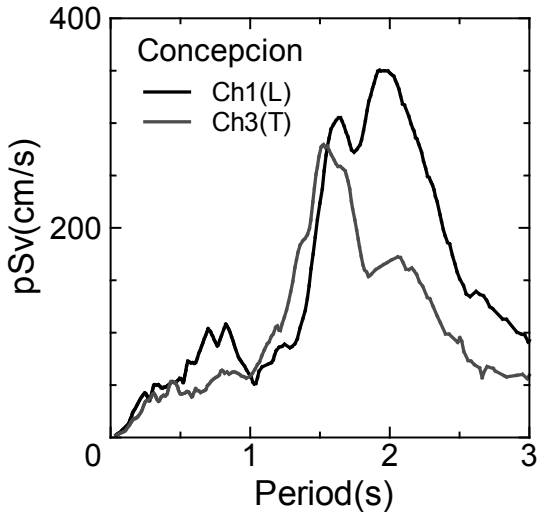


Figure 5 Pseudo Velocity Response Spectra (h=0.05)

Figure 5 shows the pseudo velocity response spectra of

the record (h=0.05). In the spectra, there are two strong peaks at periods of 1.5 and 2 seconds. At the peaks, the response amplitudes are very high such as about 350 cm/s at period of 2 seconds. The high response value is comparable with those of the records at Kobe in the 1995 earthquake and at Mexico City in the 1985 earthquake, where catastrophic damage was observed.

4. LOCAL SITE CONDITIONS AT CONCEPCION

To examine the local site effect, the microtremor measurement was conducted at the site. Figure 6 shows the overall response of the measurement system which is almost constant with ground velocity up to 2 seconds. As shown in Fig. 7, the H/V spectral ratio of microtremor has peaks at periods of 1 and 1.5 seconds. During the measurement, a small aftershock record was observed by chance. Figure 8 shows the aftershock record, indicating the predominant period of 1 to 1.5 seconds.

The surface soil of Concepcion consists of sand, and the estimated depth to the bedrock is 100 m or more. Table 1 shows the estimated velocity profile (Nicolau del Roure et al. 1980). The shear-wave velocity of surface soils is about 200 m/s. Figure 9 shows the computed amplification factor from the soil model, showing the predominant period of 1.5 sec.

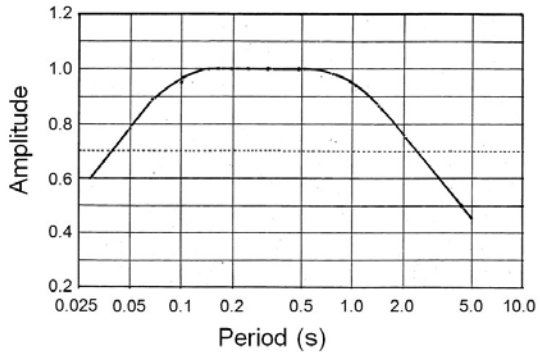


Figure 6 Overall Response of Measurement System

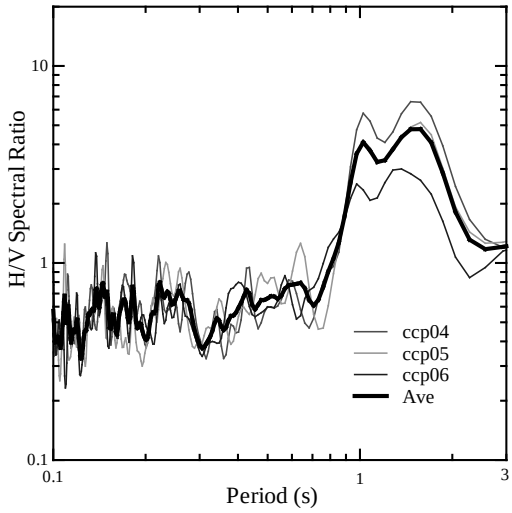
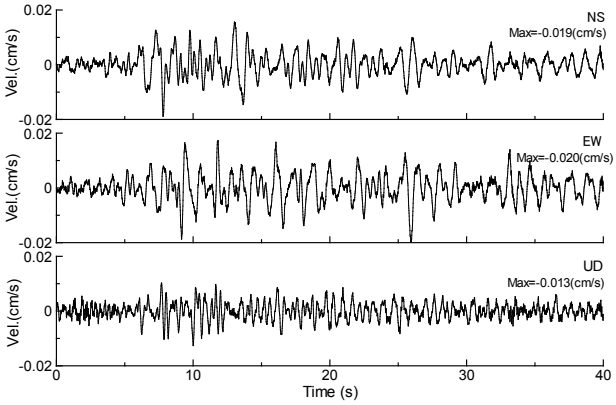
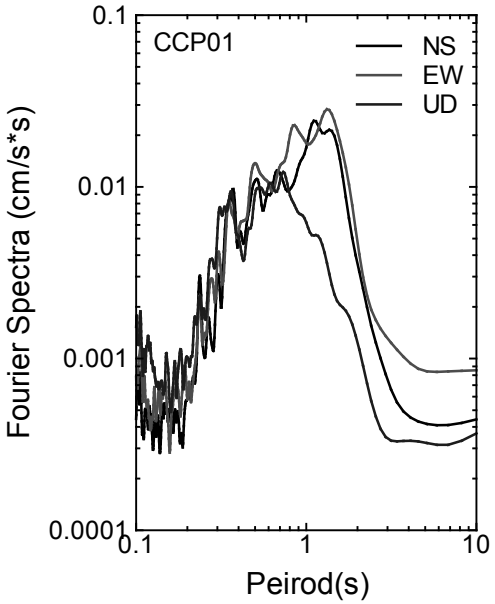


Figure 7 H/V Spectral Ratio of Microtremor



(a) velocity time history



(b) Fourier spectra

Figure 8 Aftershock Record on March 31, 2010

Table 1 Soil Profile Model (Nicolau del Roure et al. 1980)

		ρ	

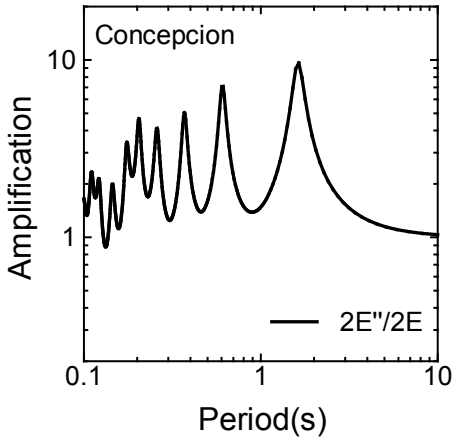


Figure 9 Computed Amplification Factor

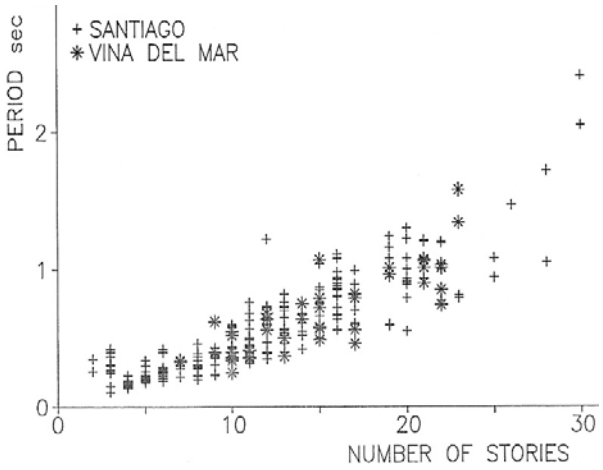


Figure 10 Number of Story vs. Period of Buildings from Ambient Vibration Test (Midorikawa 1990)

The results of the microtremor, the aftershock record and the computed amplification factor show strong local site effects at the site. In the results, the strong peaks are commonly found at periods of 1 and 1.5 seconds. The periods are 40 to 50 percents shorter than those in the strong motion records. As the period during strong shaking will be longer due to nonlinear soil response, the predominant periods of the strong motion record can be explained by local site effects.

In the city, more than seventy buildings suffered severe damage (Municipality of Concepcion 2010). High-rise buildings with 15 to 20 stories seem to be prominent in the damaged buildings. Figure 10 shows the relationship between the story number and vibration period of RC buildings from the ambient vibration test in Chile (Midorikawa 1990).

The period of the 15 to 20 story building which is prominent in the damage building seems 0.5 to 1 sec. at the ambient motion level. At the strong motion level, the period becomes longer due to nonlinear building response, suggesting that resonance of the building response with ground motion may have occurred during the earthquake. Importance of seismic microzoning studies is reconfirmed to evaluate local site effects for damage assessment in urban areas.

5. CONCLUSIONS

The 2010 Maule, Chile earthquake (Mw8.8) produced many strong motion records. Among them, an accelerogram observed at the downtown of Concepcion where many high-rise buildings suffered severe damage, has large amplitude and longer period contents. The pseudo velocity response spectrum has peaks at periods of 1.5 and 2 seconds, and the amplitudes are very high such as about 350 cm/s at period of 2 seconds. The predominant periods of the strong motion record correspond to those of the microtermor, the aftershock record and the computed amplification factor, suggesting strong local site effects. The periods also coincide with the vibration periods of high-rise buildings which suffered severe damage. This suggests that resonance of the building response with ground motion may have occurred during the earthquake. Importance of seismic microzoning studies in urban areas is reconfirmed.

Acknowledgements:

The authors express their gratitude to Profs. R. Riddell and E. Cruz, and Mr. N. Maureira, Catholic University of Chile, and Profs. Y. Kitagawa, K. Kobayashi and K. Katori, the JAEE-AIJ reconnaissance team for their cooperation in the field survey.

References:

Barrientos, S. (2010), "Terremoto Cauquenes 27 Febrero 2010," Servicio Sismologico, Universidad de Chile, 20pp. (in Spanish).

Beck, S. et al. (1998), "Source characteristics of historic earthquakes along the central Chile subduction zone," *Journal of South American Earth Sciences*, **11**, 115-129.

Boroschek, R. et al. (2010), "Maure Region Earthquake February 27, 2010 Mw=8.8," *RENADIC REPORT 10/08 Rev.1*, Civil Engineering Department, Faculty of Mathemathics and Physical Sciences, University of Chile.

Elnashai, A. S. et al. (2011), "The Maule (Chile) Earthquake of February 27, 2010. Consequence Assessment and Case Studies," *MAE Center Report No.10-04*. 190pp

Midorikawa, S. (1990), "Ambient Vibration Tests of Buildings in Santiago and Vina del Mar," *DIE No.90-1*, Departamento de Ingenieria Estructural, Pontificia Universidad Catolica de Chile, 169pp.

Municipality of Concepcion (2010), "Informe Parcial Edificios de 3 o Mas Pisos Segun Condiciones Estructurales," http://www.concepcion.cl/ (in Spanish).

Nicolau del Roure, R. G. et al. (1980), "Caracteristicas de la Amplificacion Sismica en la Ciudad de Concepcion," *3as. Jornadas Chilenas de Sismologia e Ingenieria Antisismica*, C.4.1-C.4.18 (in Spanish).

Poiata, N. and K. Koketsu (2010). "Source process inversion of teleseismic body waves," http://outreach.eri.u-tokyo.ac.jp/2010/03/201003_centralchile/.

Pulido, N. et al. (2011), "Earthquake Source Process and Site Effects of Strong Motion Stations of the 2010 Chile Mega-Earthquake," *2010 Chile Earthquake and Tsunami Technical Report*, JST-JICA SATREPS TEAM, 1-9.

Si, H. and Midorikawa, S. (2000), "Attenuation Relationships of Peak Acceleration and Velocity Considering Effects of Fault Type and Site Condition," *Proceedings of the 12th World Conference on Earthquake Engineering*, 532-1-532-6.

8CUEE CONFERENCE PROCEEDINGS
8th International Conference on Urban Earthquake Engineering
March 7-8, 2011, Tokyo Institute of Technology, Tokyo, Japan

CORRELATION OF STRONG GROUND MOTION AND ESTIMATIONS OF SEISMIC HAZARD AND LOSS FOR LARGE AREAS AND CRITICAL ELEMENTS OF NETWORK

Vladimir Sokolov[1] and Friedemann Wenzel[2]

1) Senior Researcher, Geophysical Institute, Karlsruhe Institute of Technology, Karlsruhe, Germany
2) Professor, Geophysical Institute, Karlsruhe Institute of Technology, Karlsruhe, Germany
Vladimir.Sokolovi@kit.edu, Friedemann.Wenzel@kit.edu

Abstract: Recent studies have shown that the proper treatment of ground-motion variability and, particularly, the correlation of ground motion are essential for the estimation of the seismic hazard, damage and loss for distributed portfolios. We analyzed the effects of variations in parameters of the correlation components on such estimations using Taiwan area as the example. A scenario earthquake modeling, probabilistic seismic hazard assessment (PSHA), and a portfolio containing a set of hypothetical building and bridges were used for the purpose. We showed that the impact of ground-motion correlation on seismic loss and damage estimation depends on level of hazard and probability level of interest (return period). On the other hand, the relative influence of each type of correlation (between-earthquake and spatial correlations) is not equal. Thus, for practical estimations we should emphasize the following. If information on correlation models is not available, it is necessary to obtain upper and lower bound estimates by assuming the extreme characteristics of correlations (the perfect correlation and the uncorrelated ground motion). If the difference between the bound estimates cannot be neglected, one should make correspondent assumptions about the correlation based on reported models and results of their application.

1. INTRODUCTION

During last decade an increasing attention has been focusing on studies of ground-motion correlation. The term is related to similarity of ground-motion aleatory variability, or residuals between observations and results of modelling, during different earthquakes and different locations. The proper treatment of ground-motion correlation, which contains the between-earthquake and the site-to-site (spatial) components, is essential for the estimation of seismic hazard, damage and loss for widely located building assets (portfolios) and spatially distributed structures (lifelines).

Several studies analyzed the influence of ground-motion uncertainty and correlation on characteristics of loss distribution considering particular scenario earthquakes (e.g. Lee et al. 2004; Lee and Kiremidjian 2007; Molas et al. 2006; Goda and Atkinson 2009; Crowley et al. 2008; Sokolov and Wenzel 2010) and multiple events in probabilistic hazard and loss analysis (e.g. McVerry et al. 2004; Wesson and Perkins 2001; Park et al. 2007; Goda and Hong 2008, 2009).

The parameters of ground-motion correlation may vary over wide ranges, and it is still necessary to analyze the relative influence of the variation on estimations of aggregated loss for a portfolio (widely located constructions of several types) and on characteristics of joint hazard and damage. Sokolov and Wenzel (2010), using a single (scenario) earthquake, compared the effects of variations in parameters of the between-earthquake correlation and in the spatial (site-to-site) correlation on the seismic loss and damage estimations for hypothetical portfolio and critical elements of a network. In this work we perform similar sensitivity analysis for a case of multiple earthquakes, i.e. for the case of probabilistic seismic hazard assessment (PSHA) and loss estimations. Taiwan Island has been chosen as the test case for this study because of relatively high seismicity and previous experience in earthquake hazard modelling, which can be used as the source of necessary data and for comparison of results. Seismic hazard model has been constructed and probabilistic seismic hazard and loss analysis has been performed using Monte Carlo technique.

2. GROUND MOTION CORRELATION

It has become common practice to separate the total ground-motion aleatory variability into two independent components, namely, the earthquake-to-earthquake (between-earthquake) variability and the site-to-site (within-earthquake) variability. The between-earthquake variability results from event-specific factors that have not been included in the predictive model. The within-earthquake variability is determined mostly by peculiarities in the propagation path and local site conditions,

The ground-motion parameter Y at n locations during m earthquakes is represented by

$$\log Y_{i,j} = f(e_i, p_{i,j}, s_{i,j}) + \eta_i + \varepsilon_{i,j} \quad (1)$$

where e_i denotes variables that are properties of the earthquake source; $p_{i,j}$ are the properties of propagation path; $s_{i,j}$ are the properties of site location j during earthquake i; and f is a suitable function that describes the dependence of the mean value of ground-motion parameter $\overline{Y}_{i,j}$ on the magnitude, distance, local site conditions, etc. The random variables η_i and $\varepsilon_{i,j}$ represent the between-earthquake and within-earthquake components of variability (independent and normally distributed with variances σ_η^2 and σ_ε^2), respectively. The value of η_i is common to all sites during a particular earthquake i, and the value of $\varepsilon_{i,j}$ depends on the site. Assuming the independence of the two random terms, the total aleatory variance σ_T^2 is given by $\sigma_T^2 = \sigma_\eta^2 + \sigma_\varepsilon^2$.

The between-earthquake correlation of earthquake ground motion, or the similarity of ground-motion variability during different earthquakes, is determined by the relation between the components of variability (Wesson and Perkins 2001):

$$\rho_\eta = \sigma_\eta^2 / \sigma_T^2 = \sigma_\eta^2 / (\sigma_\eta^2 + \sigma_\varepsilon^2) \quad (2)$$

At the same time, two close sites may exhibit correlation of ground-motion residuals during an earthquake due to the commonality of wave paths (within-earthquake site-to-site correlation), which depends on the site separation distance Δ. The site-to-site (or spatial) correlation function $\rho_\varepsilon(\Delta)$ is usually represented as

$$\rho_\varepsilon(\Delta) = \exp(a\Delta^b), \quad (3)$$

where a and b are the region-dependent coefficients. The so-called "correlation distance" R_C may be considered a characteristic of the correlation (Wang and Takada 2005). The correlation distance shows the site-to-site distance for which the correlation coefficient $\rho_\varepsilon(\Delta)$ decreases up to 1/e = 0.368. For earthquake i and site j, the total correlation in $\varepsilon_{i,j}$ values is the following (e.g. Park et al. 2007):

$$\rho_T(\Delta) = \rho_\eta + \rho_\varepsilon(\Delta)(\sigma_\varepsilon^2 / \sigma_T^2) \quad (4)$$

.

The modern ground-motion attenuation equations (e.g. New Generation Attenuation models, NGA) allow the recognition of the between-earthquake correlation, because the equations include specification of the between-earthquake and within-earthquake components of variability (e.g. Douglas 2003, 2006; Abrahamson et al. 2008). The site-to-site correlation should be empirically evaluated for a given area. A dense observation of records from numerous earthquakes is necessary for analysis of the site-to-site correlation structure; therefore, such correlations investigated only for areas of dense strong-motion network: California, Japan and Taiwan (see review of recent studies in Sokolov et al. 2010). Analysis of the site-to-site correlation in Taiwan, which has been performed by Sokolov et al. (2010), revealed that the correlation structure is highly dependent on the local geology (see Figure 1), as well as on peculiarities of the propagation path (azimuth-dependent attenuation).

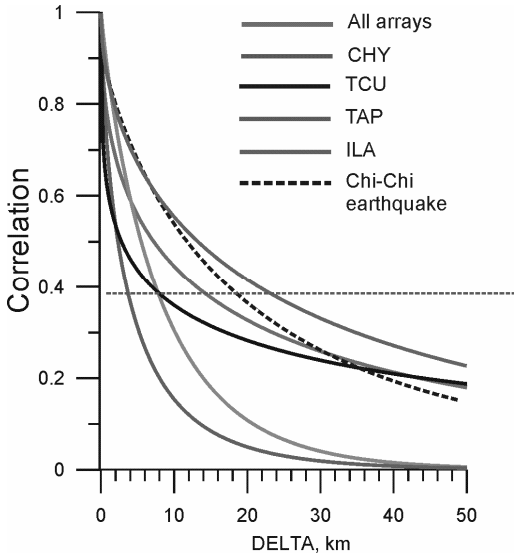


Figure 1. Site-to-site intra-event (spatial) correlation functions $\rho_\varepsilon(\Delta)$ estimated for particular strong-motion arrays in Taiwan using the data from moderate-to-large earthquakes ($M_W > 6.0$) in Taiwan (Sokolov et al. 2010). CHY array – thick sediments; TCU array - stiff soils in extended hilly areas; TAP array - triangular asymmetric alluvium-filled Taipei basin; ILA array - Quaternary alluvial Ilan basin. The data from all arrays were used for the case of the Chi-Chi earthquake. Red dashed line show the level of 1/e = 0.368.

3. ESTIMATION OF SEISMIC HAZARD

3.1 The Approach

In this work we applied the Monte-Carlo approach (e.g. Ebel and Kafka 1999) for seismic hazard and loss assessments. This approach, as it has been stated by Bommer and Crowley (2006), is consistent with the real nature of ground-motion variability. The large numbers of earthquake scenarios that are compatible with the seismicity model are triggering to sample the magnitude and spatial distribution of seismicity, as well as the distribution of ground motion for each event as defined by the aleatory variability. Each scenario generates a random combination of input parameters from their respective distributions, giving one possible model solution. This process is repeated many times, generating alternative model solutions. As the number of iterations increases it is possible to estimate the probability distribution function of the model solution. The approach

is suitable as a method for studying correlated hazard or so-called 'joint hazard' at various points of spatially distributed systems, (e.g. Rhoades and McVerry 2001).

The seismic source model describes as completely as possible, both spatially and temporarily, the process of earthquake occurrence in a region. The Monte Carlo process is used for generation of synthetic catalogues. Each synthetic catalogue represents a version of what could occur in the way of earthquakes in that region in the next years that would be consistent with past behaviour. Each epicenter within the source zone is determined randomly accepting that any location within the source zone has an equal probability of being the epicenter of the next earthquake. The depth of the given earthquake source is also generated randomly. The magnitude value is determined randomly against the magnitude-frequency distribution for that source zone.

For each generated event in the synthetic earthquake catalogue, ground-motion parameter at selected sites is calculated using (a) the appropriate ground-motion prediction equation and (b) two random draws from the standard normal probability distribution: the between-earthquake variability for the earthquake and the within-earthquake variability at each site (Bommer and Crowley 2006; Crowley and Bommer 2006). For a given earthquake, the influence of the between-earthquake variability will be the same through the region of interest, whilst the influence of the within-earthquake variability will be different at each site. The spatial correlation is also considered. From observation of the seismic effect of a very large number of simulations, probabilities can be calculated by merely counting the number of results exceeding a critical value.

3.2 The Input Data

Tectonic setting and seismicity of Taiwan are described in detail elsewhere (see, for example, review in Tsai et al. 1987; Campbell et al. 2002; Cheng et al. 2010). In this study we considered only crustal seismicity (earthquake depth less than 35 km) and we accepted the source zonation scheme given by Loh and Jean (1997) (Figure 2). Seismicity in each zone was analyzed separately to determine the magnitude frequency parameters in the form of linear Gutenberg-Richter law. Obviously, it is not possible to assume that parameters of seismicity sharply change at borders of the zones and a smoothing procedure is applied. A uniform distribution for earthquake depth has been accepted in calculations.

The ground motion-prediction equation for the calculation was used in the following form, which was recently proposed for Taiwan (Sokolov et al. 2010):

$$\ln PGA = -3.07 + 0.83M_W - 1.33\ln[R + 0.15\exp(0.54M_W)] + 0.0023R \pm \sigma_T \quad (5)$$

where PGA is measured in units of g, and R is the hypocentral distance in km. In our analysis we jointly consider both the components of aleatory variability (between-earthquake and within-earthquake) and the site-to-site (spatial) correlation. The total standard deviation σ_T is considered as a magnitude-dependent quantity assuming. gradually decreasing σ_T from 0.66 (M_W 5.0) to 0.50 (M_W 8.0).

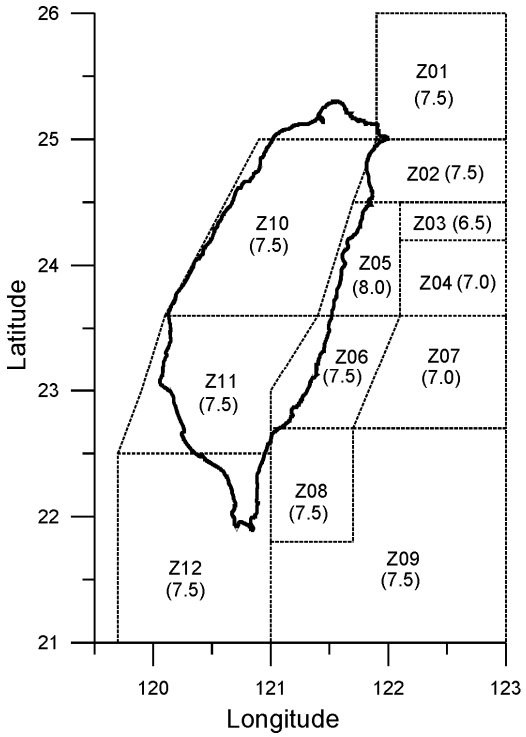


Figure 2. Source zonation scheme (Loh and Jean 1997). Values of maximum magnitude are shown in parentheses.

3.3 Modelling of Correlated Ground Motion

The following models of spatial correlation are applied (see also Sokolov and Wenzel 2010). First, we used the following values of between-earthquake correlation $\rho_\eta = \sigma^2{}_\eta / \sigma^2{}_T$: 0.09, 0.31, and 0.50. The correlation distances R_C, which characterize the spatial correlation (equation 3), vary from 5 km to 30 km. The accepted ranges of between-earthquake correlation and spatial correlation may be treated as reliable because they correspond to the observed values (see review in Sokolov and Wenzel 2010). We also consider the extreme cases, where all the variability is between earthquakes (all-between, $\sigma_\varepsilon = 0, \rho_\eta = 1.0$); where all the variability is within earthquakes (all-within, $\sigma_\eta = 0, \rho_\eta = 0.0$); and a case of spatially uncorrelated ground motion (no-spatial), for which coefficient of spatial correlation $\rho_\varepsilon(\Delta)$ equals to zero for all separation distances Δ > 0 km, and $\rho_\varepsilon(\Delta) = 1$ for Δ = 0 km. The all-between case corresponds to application of conventional PSHA (Cornell 1968), in which the ground-motion variability is implicitly assumed to be entirely between-earthquake component (e.g. Bommer and Crowley 2006).

When modeling the correlated ground-motion field, in addition to the median value $\overline{Y}_{ij}$, we need to generate the standard normal variates (errors) of η_i and $\varepsilon_{i,j}$.

The dependence structure among the variates is described by the total correlation coefficients (equation 4) and the correlation matrix Σ. The correlation matrix Σ is defined as follows:

$$\Sigma = \begin{pmatrix} 1 & \rho_{12} & \cdots & \rho_{1k} \\ \rho_{21} & 1 & \vdots & \rho_{2k} \\ \vdots & \vdots & \vdots & \vdots \\ \rho_{k1} & \rho_{k2} & \cdots & 1 \end{pmatrix} \quad (6)$$

where ρ_{ij} is the correlation coefficient calculated for the sites separated by a distance Δ. Descriptions of the procedure for generation of *k*-site random field of ground-motion error values that are spatially correlated may be found in many sources (e.g. Johnson 1987; Park et al. 2007). The generation consists of the following steps. First, a vector of independent standard normal variates **U**= [U_1, U_2, …., U_k] with standard deviation σ_T, or **U** ~ $N_k(0, \sigma_T^2)$, is generated. Then, a correlation matrix Σ is constructed and a Cholesky decomposition is applied to represent the correlation matrix Σ as the matrix product of matrix **B** and its transposition $\mathbf{B}^T$, i.e., $\Sigma = \mathbf{B}\,\mathbf{B}^T$. The required vector **X** is obtained as **X=BU**. These X_j values are added to the median ground-motion term $\overline{Y}_{ij}$ to obtain a realization of spatially correlated ground motions. Figure 3 shows examples of modeled ground-motion residuals for two models of spatial correlation.

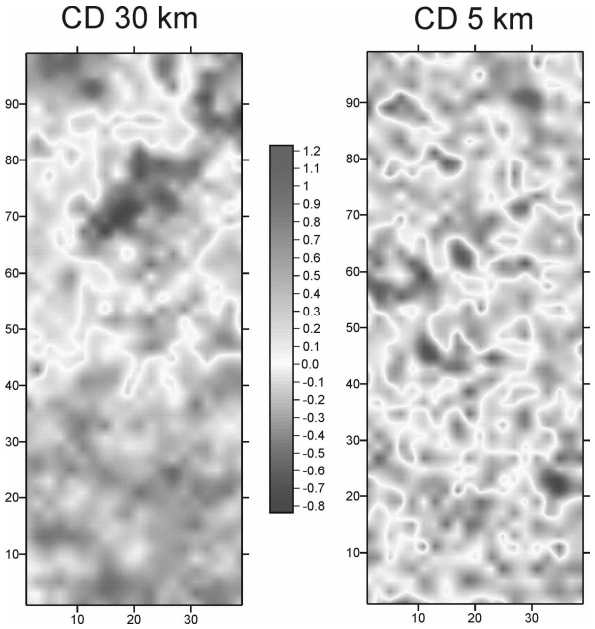


Figure 3. Examples of distribution of spatially-correlated ground motion residuals (natural logarithm of g – acceleration of gravity) modeled for two values of correlation distance (CD)

3.4 Results of Probabilistic Seismic Hazard Assessment

Monte Carlo technique was used to generate 1000 stochastic 2000-year catalogues of earthquakes with magnitudes $M_W \geq 4.75$; each catalogue contains more than 17500 events. One ground motion random field (PGA) was generated for each earthquake using the selected correlation model. The hazard rates, i.e., the annual probability of exceedence of PGA values at the individual sites were computed from the statistics of the simulated earthquakes. Figure 4 shows PGA map for 475-year return period (i.e. 10 % probability of exceedence in 50 years) and hazard curves for particular sites – large cities: Taipei, Taichung, Hualien, Chiai, and Taitung.

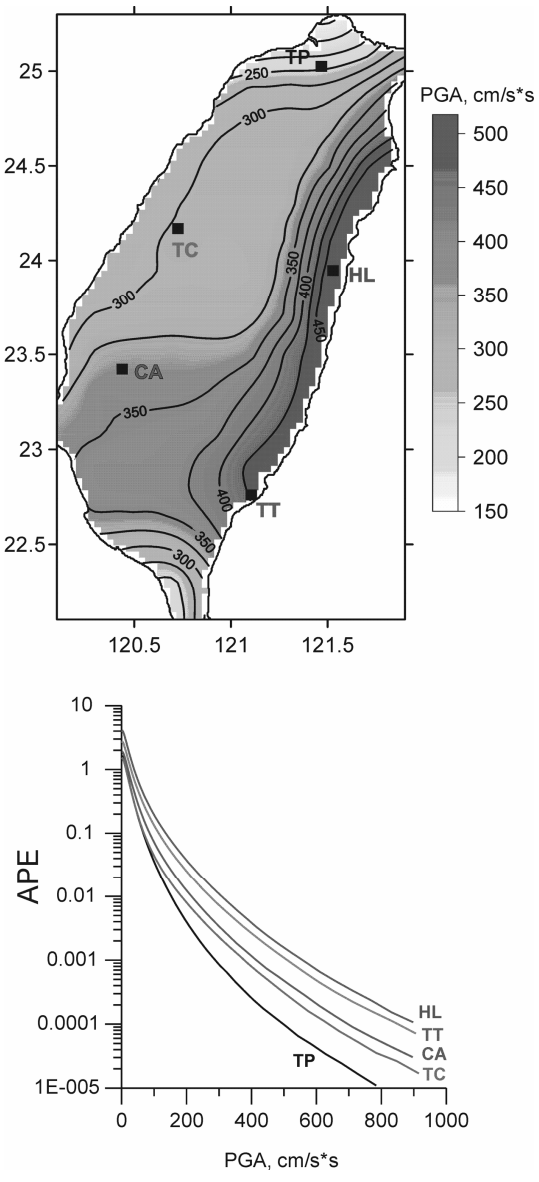


Figure 4. PGA scheme for return period of 475 years. The hazard curves (annual probability of exceedence of PGA values) are shown for sites Taipei (TP); Taiching (TC), Hualien (HL), Chiai (CA), and Taitung (TT).

The PSHA map, which is based only on the regional sources, reveals that the hazard level increases from the northwest to the southeast and southwest; the hazard is highest along the eastern coast of Taiwan. Our results show a good agreement with the previous assessments, which were performed using the Cornell's (Cornell 1968) approach (e.g. Sokolov et al. 2001; Campbell et al. 2002; Cheng et al. 2007, 2010).

Some applications require assessing the probability that a specific event will occur during certain condition at least once or that several such events will occur simultaneously. For example, there may be an interest in knowing whether the vulnerable elements of a lifeline network (e.g. bridges, local substations of power supply network, etc.) are likely to be simultaneously affected by shaking of sufficient strength to disable them or at least one element will be damaged causing the failure of the system (e.g. Rhoades and McVerry 2001; McVerry et al. 2004). To analyze such cases, we considered a few models of sites distribution with different distances between the sites. An example is shown in Figure 5a.

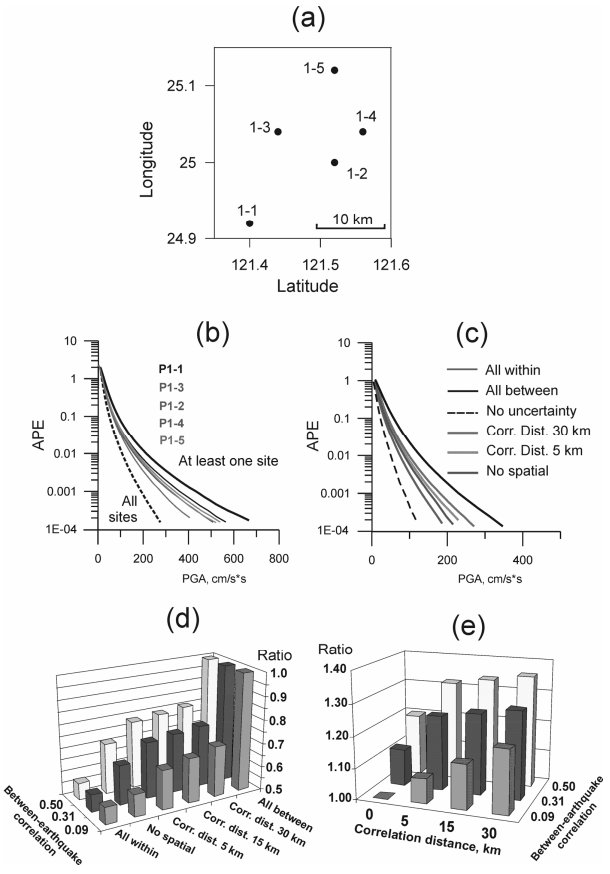


Figure 5. Analysis of joint hazard, Taipei area (low hazard). (a) The model of sites distribution. (b) Comparison of hazard curves, between-earthquake correlation $\rho_\eta = 0.31$. (c) Joint exceedence, influence of spatial correlation, $\rho_\eta = 0.31$. (d, e) Relative influence of the correlation components on joint exceedence. The base value (*see text*) corresponds to Ratio = 1.0.

The examples of hazard curves, i.e. the annual probability of exceedence of a given PGA threshold for the considered sites separately, for at least one site, and for all sites simultaneously (joint hazard), are shown in Figure 5bc (Taipei area). As can be seen from Figure 5b, the return period for joint exceedence (all sites) is larger than the return periods for the individual sites. At the same time, the return periods for the individual sites are larger than the return period for the at least one exceedence. The assumptions of all-between-earthquake (ABE) variability and all-within-earthquake (AWE) variability, depending on the case of interest, provide upper and lower bound estimates (see also Rhoades and McVerry 2001; McVerry et al. 2004). For at least one exceedence, the relative changes between the bound estimates, i.e. ratios AWE / ABE, do not exceed 20 %, while for joint exceedence the difference between the bound estimates vary between 80 % and 100 % (Figure 5d).

Influence of the spatial correlation, parameters of which vary within considered realistic ranges, is shown in Figure 5c. The influence may be characterized by relative changes of ground-motion parameter (PGA) for particular annual probability of exceedence (APE), or by changes of APE for particular PGA threshold, when varying the correlation components. Here we used the first variant (same APE, changes of PGA) and analyzed the changes comparing with a base value, which corresponds to the case of smallest considered between-earthquake correlation ($\rho_\eta = 0.09$) and spatially uncorrelated ground motion ($R_C = 0$ km, no-spatial).

For the at least one exceedence, the changes in characteristics of between-earthquake correlation ρ_η and the site-to-site correlation $\rho_\varepsilon(\Delta)$ reveals only a slight influence on the PGA estimations for particular annual probability of exceedence. When considering joint exceedence, variations in the correlation distances R_C , as well as variations in the between-earthquake correlation ρ_η , would considerably change the PGA estimations (Figure 5e).

On one hand, the combined effect of variations in the correlation components depends on return period (annual probability of exceedence), i.e. the relative changes increase with the increase of return period. On the other hand, the relative impact of the particular correlation component taken alone (i.e. only between-earthquake correlation or only site-to-site correlation) is the largest in the case of the smallest correlation coefficient of the other component.

As expected (see also McVerry et al. 2004), a set of closely located sites is characterized by the higher frequency of joint exceedence of a given PGA threshold than a set with relatively large distance between sites. In general, the probability of at least one exceedence is approaching the probability of joint exceedence, while the distance between considered sites is decreasing. However it should be noted that this effect has been observed in our study for the case of areal source zones.

3. ANALYSIS OF LOSS AND DAMAGE

For loss analysis we selected the areas of 10 km x 10 km at the location of Taipei (low hazard) and Hualien (high hazard) cities (see Figure 4). The areas were divided into cells of 1 km x 1 km and the random values of ground motion parameter were calculated for the centers of the cells. On one hand, the increase of resolution (or the decrease of the cell dimensions) would increase the calculation time. On the other hand, the dimensions of a cell should be much lower than the smallest considered correlation distance (R_C 5 km) in our analysis. Bal et al. (2010) analyzed the influence of the geographical resolution of the exposure data on the variability of loss estimations. They showed that the results of loss estimation are relatively insensitive to the spatial resolution of the building stock for exposure at grid sizes less than 2 km x 2 km. It has been supposed that all cells contain the same number of hypothetical buildings, which are typical for Taiwan (Liao et al. 2006), namely: steel-braced frames of four to seven stories.

In this study, we use the methodology, which is based on fragility functions (e.g. HAZUS, FEMA 2003), for loss estimation. A fragility function defines the exceedence of a damage state for a given level of ground shaking. Five damage states are considered: None, Slight, Moderate, Extensive and Complete. The probability of being or exceeding a damage state DS_i is modelled with a cumulative lognormal distribution- Details of the procedure, definitions and assumptions are described in Sokolov and Wenzel (2010).

The development of damage-loss functions for various types of structures is a demanding task. Such conversions have been performed using the regional damage ratio models based either on (a) Modified Mercalli intensities that were calculated directly (McVerry et al. 2004) or estimated from the PGA values (Molas et al. 2006), or on (b) pseudo-spectral acceleration (Park et al. 2007; Goda and Hong 2008). To minimize the effects of errors in the estimation of the replacement cost, we did not consider the conversion of damage to monetary loss. The mean cost ratio (MCR) was calculated in our study by integrating the results of calculation for every particular building.

Examples of loss exceedence curves, i.e. the annual probability of exceedence (APE) of a given mean cost ratio (MCR) threshold, are shown in Figure 6a. The assumptions of all-between-earthquake (ABE) and all-within-earthquake (AWE) variability provide upper and lower bound estimates of MCR values. The difference between the estimates depends on level of hazard and on annual probability of exceedence (return period). For example, the results obtained for low hazard area (Taipei) and for return periods less that 300 years showed a negligible difference between the extreme variants of correlation. For return period 475 years, the difference (ratio ABE / AWE) is about 1.60 for the Taipei area (low hazard) and 1.90 for the Hualien area (high hazard). Obviously, the ratio should depend also on the type of considered constructions (e.g. seismic design level).

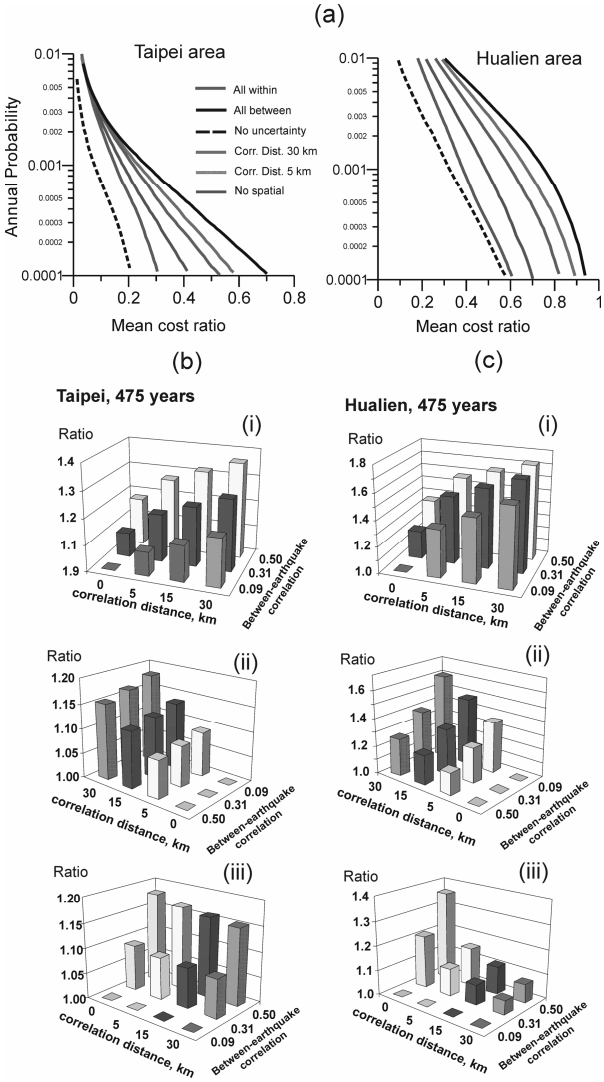


Figure 6. Mean damage ratio, influence of correlation components. (a) Loss exceedence curves, between-earthquake correlation $\rho_\eta = 0.31$. (b, c) relative influence of the correlation components. (i) combined influence; (ii) influence of spatial correlation; (iii) influence of between-earthquake correlation.

The MCR values estimated for particular return periods may vary over wide ranges when considering different characteristics of the between-earthquake correlation and the spatial correlation. Figures 6b and 6c show quantitative description of the MCR variations relative to the base values. First (Figure 6bc-i), the base value has been assigned to the smallest considered between-earthquake correlation ($\rho_\eta = 0.09$) and spatially uncorrelated ground motion (R_C = 0 km). The variations in the loss estimations due to a combined influence of the between-earthquake correlation and the spatial

correlation may be as high as 35% for area of low hazard (Taipei) and 75% for area of high hazard (Hualien).

Second, we separately compared the variations of loss estimations caused by to spatial correlation $\rho_\varepsilon(\Delta)$ alone (Figure 6bc-ii) and by to between-earthquake correlation ρ_η alone (Figure 6bc-iii). On one hand, the relative impact of the particular correlation component taken alone (i.e. between-earthquake correlation or site-to-site correlation) also depends on the level of hazard, i.e. the impact is larger for the high-hazard area (Hualien) than that for the low-hazard area (Taipei). On the other hand, the relative impact of the particular correlation component is the largest in the case of the smallest correlation coefficient of the other component.

As the example, let us consider Hualien area, return period 475 years (Figure 6c). The full-scale variations in the between earthquake correlation (i.e. ρ_η from 0.09 to 0.5) would increase the MCR values by 35 % in the case of no spatial correlation (R_C = 0 km) and by less than 10 % in the case of considerable spatial correlation (R_C = 30 km). Correspondingly, the full scale variations in the spatial correlation (i.e. R_C from 0 km to 30 km) would increase the MCR values by almost 60 % in the case of smallest between-earthquake correlation ($\rho_\eta = 0.09$) and by 22 % in the case of largest between-earthquake correlation ($\rho_\eta = 0.5$).

We also analyzed the case when it is necessary to estimate probability (return period) that several critical elements of a network (e.g. bridges) would be damaged simultaneously (joint damage) or at least one element would be damaged causing the failure of the system. For this purpose, we considered a system of three bridges located within the high-hazard territory (Hualien area). Two models of location of the bridges were constructed, which are characterized by different distances between the bridges (Figure 7a), namely: the model B1, distances vary from 10 km to 14 km; the model B2, distances vary from 2.1 km to 2.3 km.

The classification of typical bridges in Taiwan is given by Liao and Loh (2004), and we used the Type 4C bridge (Table 1 in Liao and Loh 2004). The damage level was accepted as equal to or greater than 20% of the replacement cost (damage ratio 0.2). The expected time of bridge outage for this damage level (extensive damage) is between 3 weeks and 3 months (Mander 1999). Details of the procedure, definitions and assumptions are described in Sokolov and Wenzel (2010). Note that here we did not consider uncertainties arising from the damage factor (Stergiou and Kiremidjian 2006) and correlated damage states conditioned in ground motion (Lee and Kiremidjian 2006).

Figures 7b and 7c show estimations of return periods for the cases when at least one bridge will be damaged (Figure 7b) and all bridges will be damaged simultaneously (Figure 7c). For at least one damaged bridge, the possible variations (within realistic range) in the correlation components may be neglected. When considering joint damage (Figure 7c), variations in the correlation distances R_C, as well as variations in the between-earthquake correlation ρ_η, would considerably change the estimations of return period. The assumptions of all-between-earthquake (ABE) variability and all-within-earthquake (AWE) variability provide the lower and the upper bound estimates. The relative changes between the bound estimates, i.e. ratios ABE / AWE are about 14 times and 18 times for the models B1 and B2 correspondingly. As expected, the system of closely located bridges (model B2) is characterized by the smaller return period of joint damage than the system (model B1) with relatively large distance between sites.

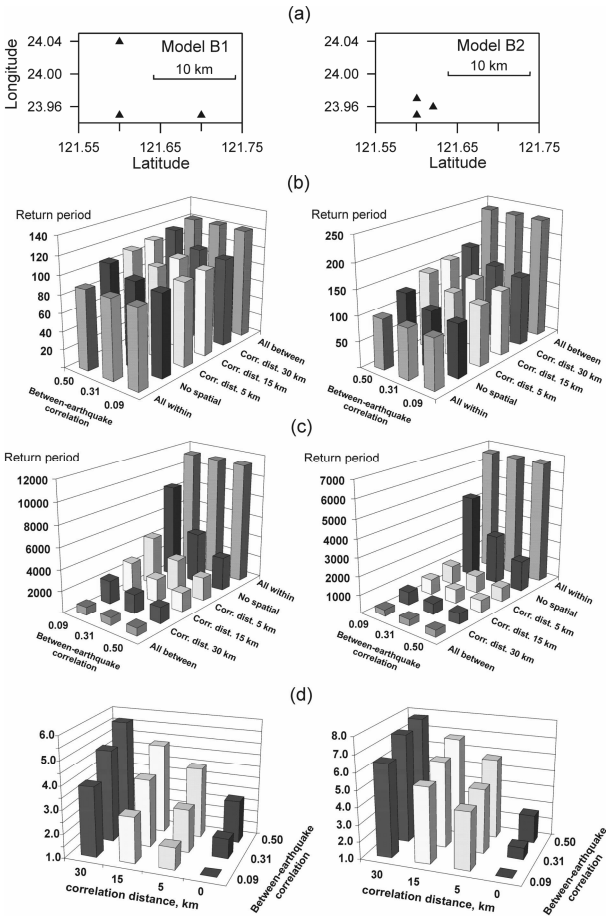


Figure 7. Analysis of joint damage for a set of bridges (Hualien area) considering influence of the correlation components. (a) The models of bridges distribution. (b) Damage of at least one bridge. (c) Damage of all bridges (joint damage). (d) Influence of the correlation components on return period of joint damage.

The relative influence of the correlation components on the return period of joint damage (Figure 7d) has been analyzed by comparison of the estimations with the base value, which corresponds to the case of the smallest considered between-earthquake correlation ($\rho_\eta = 0.09$) and spatially uncorrelated ground motion (R_C = 0 km). On one hand, the realistic full-scale variations in the

correlation components may lead to considerable alterations (up to 6-8 times) in estimations of return period. On the other hand, the site-to-site correlation plays more important role in the estimations than the between-earthquake correlation, especially for the case of closely located bridges (model B2). Thus, when analyzing joint damage for a set of closely located critical elements of a network, the possible variations in the between-earthquake correlation may be neglected if the spatially correlated ground motions are used.

3. CONCLUSIONS

A model for probabilistic seismic hazard and loss estimation using Monte Carlo approach has been developed for Taiwan region. The model is based on previous experience in earthquake hazard modeling in the region. The framework has been used for sensitivity analysis of the impact of variation of characteristics of ground-motion correlation components on probabilistic estimates of seismic loss and damage for extended objects (hypothetical portfolio) and critical elements (e.g. bridges) of a network. It has been recently found that, on one hand, consideration of a realistic correlation model of seismic excitation is especially important in seismic loss estimation and that, on the other hand, the parameters of ground-motion correlation may vary over wide ranges.

The results of the modeling show that the proper consideration of (a) the between-earthquake correlation and (b) the parameters of spatial correlation is essential for the estimation of seismic losses for distributed portfolios. Both types of ground-motion correlation affect the probability of joint damage of critical components and the characteristics of loss distribution for a portfolio. The peculiarities of the influence were analyzed and are described in literature. In our work, we showed that, on one hand, the impact depends on level of hazard and probability level of interest (return period), and that, on the other hand, the relative influence of each type of correlation is not equal. Obviously, characteristics of the analyzed portfolio or parameters of critical elements of a network (e.g. seismic design level of construction and mutual location of elements) may be of considerable importance.

Thus, supporting and extending the conclusions and recommendations made, for example, by Rhoades and McVerry (2001) and Goda and Hong (2008), we should emphasize the following. If information on correlation models is not available, first, it is necessary to obtain upper and lower bound estimates by assuming the extreme characteristics of correlations (the perfect correlation and the uncorrelated ground motion). Second, if the difference between the bound estimates cannot be neglected, one should make correspondent assumptions about the correlation based on reported models and results. However it is necessary to bear in mind that the spatial correlation of ground motion, in principle, depends on the chosen ground motion model. On the other hand, the correlation structure depends on the local geology as well on peculiarities of the propagation path (azimuth-dependent attenuation) (e.g. Sokolov et al. 2010). Thus, a single generalized model of spatial correlation may not be adequate for large areas.

We realize, of course, that there are several limitations of our study. Our findings have been obtained using the areal model of seismic zones without consideration of influence of linear (fault) sources. Proximity to the active faults may considerably affect the results of hazard and loss estimation. We did not consider epistemic uncertainty in all inputs to the assessment, which usually is incorporated using the logic tree approach. The damage analysis in our study was based only on peak ground acceleration, and it included some arbitrary assumptions about the parameters of fragility curves. Obviously, for practical calculations requiring the estimation of the absolute values of loss, these simplified assumptions have to be reconsidered.

Acknowledgements:

The authors would like to thank Julian J. Bommer for his thoughtful comments and suggestions. Chin-Hsun Yeh provided necessary data used in this study. This work was sponsored by Deutsche Forschungsgemeinschaft (DFG), Germany, project WE 1394/14-1

References:

Abrahamson, N., Atkinson, G., Boore, D., Bozorgnia, Y., Campbell, K., Chiou, B., Idriss, I.M., Silva, W., and Youngs, R. (2008), "Comparison of the NGA ground-motion relations", *Earthquake Spectra,* **24**(1), 45-66, doi: 10.1193/ 1.2924363.

Bal, I. E., Bommer, J. J., Stafford, P. J., Crowley H., and Pinho, R. (2010), "The influence of geographical resolution of urban exposure data in an earthquake loss model for Istanbul", *Earthquake Spectra*, **26**(3), 619-634, doi: 10.1193/1.3459127.

Bommer, J. J. and Crowley, H. (2006), "The influence of ground-motion variability in earthquake loss modeling", *Bulletin of Earthquake Engineering,* **4**(3), 231-248, doi: 10.1007/ s10518-006-9008-z

Campbell, K. W., Thenhaus, P. C., Barnard, T. P., and Hampson, D. B. (2002), "Seismic hazard model for loss estimation and risk management in Taiwan", *Soil Dynamics and Earthquake Engineering*, **22**: 743-754.

Cheng, C. T., Chiou, S. J., Lee, C. T., and Tsai, Y. B. (2007), "Study of probabilistic seismic hazard maps of Taiwan after Chi-Chi earthquake", *Journal of GeoEngineering*, **2**(1), 19-28.

Cheng, C. T., Lee, C. T., Lin, P. S., Lin, B. S., Tsai, Y. B., and Chiou, S. J. (2010), "Probabilistics earthquake hazard in metropolitan Taipei and its surrounding regions", *Terrestial, Atmospheric and Oceanic Sciences (TAO)*, **21**(3), 429-446, doi: 10.3319/TAO.2009.11.11.01(TH)

Cornell, C. A. (1968), "Engineering seismic risk analysis", Bulletin of Seismological Society of Americs, **58**, 1583-1606.

Crowley, H. and Bommer, J. J. (2006), "Modelling seismic hazard in earthquake loss models with spatially distributed

exposure", *Bulletin of Earthquake Engineering*, **4**, 249-273, doi: 10.1007/s10518-006-9011-4.

Crowley, H., Bommer, J. J., and Stafford, P. J. (2008), "Recent developments in the treatment of ground- motion variability in earthquake loss model", *Journal of Earthquake Engineering* 12(S): 71-80, doi: 10.1080/136324608 02013529.

Douglas, J. (2003), "Earthquake ground motion estimation using strong-motion records: a review of equations for estimation of peak ground acceleration and spectral ordinates", *Earth Science Reviews*, **61**, 43-104.

Douglas, J. (2006), *"Errata and additions to "Ground motion estimation equations 1966-2003",* BRGM/RP-54603-FR.

Ebel, J. E. and Kafka, A. L. (1999); "A Monte Carlo approach to seismic hazard analysis", *Bulletin of Seismological Society of America*, **89**, 854-866.

FEMA (2003) *HAZUS-MH MRS, Technical manual*, Federal Emergency Management Agency, Washington DC.

Goda, K. and Atkinson, G. M. (2009), "Probabilistic characterization of spatially correlated response spectra for earthquakes in Japan", *Bulletin of Seismological Society of America*, **99**, 3003-3020, doi: 10.1785/0120090007.

Goda, K. and Hong, H. P. (2008), "Estimation of seismic loss for spatially distributed buildings", *Earthquake Spectra*, **24**, 889-910, doi: 10.1193/1.2983654.

Goda, K and Hong, H. P. (2009), "Deaggregation of seismic loss of spatially distributed buildings", *Bulletin of Earthquake Engineering*, **7**, 255–272, doi: 10.1007/s10518-008-9093-2

Johnson, M. E. (1987), "*Multivariate statistical simulation*". Wiley Series in Probability and Mathematical Statistics, Los Alamos National Laboratory, Los Alamos, NM.

Lee, R., Kiremidjian, A. S., and Stergiou, E. (2004), "Uncertainty and correlation of network components losses for a spatially distributed system". *Proceedings of the 13th World Conference on Earthquake Engineering,* Vancouver, Canada, August 1-6, 2004; Paper 989.

Lee, R. and Kiremidjian, A. S. (2007), "Uncertainty and correlation for loss assessment of spatially distributed systems", *Earthquake Spectra*, **23**, 753-770, doi: 10.1193/ 1.2791001.

Liao, W. I. and Loh, C. H. (2004), "Preliminary study of the fragility curves for highway bridges in Taiwan", *Journal of Chinese Institute of Engineers*, **27**(3), 367-375

Liao, W. I., Loh, C. H., and Tsai, K. C. (2006), "Study of the fragility of building structures in Taiwan", *Natural Hazards,* **37**(1-2), 55-69, doi: 10.1007/s11069-005-4656-x.

Loh, C. H. and Jean, W. Y. (1997), "Seismic zoning on ground motion in Taiwan area", *Proceedings of 14th International Conerence. on Soil Mechanics and Foundation Engineering*, Germany, 6-12 September, 1997, 71–79.

Mander, J. B. (1999), "*Fragility curve development for assessing the seismic vulnerability of highway bridges*". University at Buffalo, State University of New York, MCEER Research Progress and Accomplishments, Research Summary 1997-1999. Available in http://mceer.buffalo.edu/ publications/resaccom/99sp01/chl0mand.pdf

McVerry, G. H., Rhoades, D. A., and Smith, W. D. (2004), "Joint hazard of earthquake shaking at multiple locations", *Proceedings of the 13th World Conference on Earthquake Engineering*, Vancouver, Canada, August 1-6, 2004. Paper 646.

Molas, G. L., Anderson, R., Seneviratna, P., and Winkler, T. (2006), "Uncertainty of portfolio loss estimates for large earthquakes", *Proceedings of First European Conference on Earthquake Engineering and Seismology*, Geneva, Switzerland, 3-8 September 2006: Paper 1117

Rhoades, D. A., and McVerry, G. H. (2001), "Joint hazard of earthquake shaking at two or more locations", *Earthquake Spectra,* **17**(4), 697-710, doi: 10.1193/1.1423903

Park, J., Bazzurro, P., and Baker, J. W. (2007), "Modeling spatial correlation of ground motion intensity measures for regional seismic hazard and portfolio loss estimations". *Applications of Statistics and Probability in Civil Engineering* (Kanda, Takada & Furuta, eds.), Taylor & Francis Group, London, 1-8.

Sokolov, V., Loh, C. H., and Wen, K. L. (2001), "Site-dependent input ground motion estimations for the Taipei area: a probabilistic approach", *Probabilistic Engineering Mechanics*, **16**(2), 177-191

Sokolov, V., Wenzel, F., Jean, W. Y., and Wen, K. L. (2010), "Uncertainty and spatial correlation of earthquake ground motion in Taiwan". *Terrestial, Atmosperic and Oceanic sciences (TAO)*, **21**(6), 905-921, doi: 10.3319/ TAO.2010.05.03.01(T)

Sokolov, V., and Wenzel, F. (2010), "Influence of spatial correlation of strong ground-motion on uncertainty in earthquake loss estimation", *Earthquake Engineering and Structural Dynamics*, Online first, DOI: 10.1002/eqe.1074

Stergiou, E. and Kiremidjian, A. S. (2006), "*Treatment of uncertainties in seismic risk analysis of transportation systems*", The John A. Blume Earthquake Engineering Center, Report 154.

Tsai, C. C. P., Loh, C. H., and Yeh, Y. T. (1987), "Analysis of earthquake risk in Taiwan based on seismitectonic zones", *Memoir of the Geological Society of China*, 9, 413-446.

Wang, M. and Takada, T. (2005), "Macrospatial correlation model of seismic ground motions", *Earthquake Spectra*, **21**(4), 1137-1156, doi: 10.1193/1.2083887.

Wesson, R. L. and Perkins, D. M. (2001), "Spatial correlation of probabilistic earthquake ground motion and loss", *Bulletin of Seismological Society of America*, 91, 1498-1515, doi: 10.1785/0120000284

8CUEE CONFERENCE PROCEEDINGS
8th International Conference on Urban Earthquake Engineering
March 7-8, 2011, Tokyo Institute of Technology, Tokyo, Japan

PRELIMINARY STUDY OF NEW ATTENUATION RELATIONSHIP FOR RESPONSE SPECTRA ON SEISMIC BEDROCK INCLUDING NEAR SOURCE DATA

Hongjun Si[1], Saburoh Midorikawa[2], Hideaki Tsutsumi[3], Akemi Noda[4], and Toshiyuki Masatsuki[4]

1) Head, Seismic Engineering Division, Kozo Keikaku Engineering Inc., Japan
2) Professor, Center for Urban Earthquake Engineering, Tokyo Institute of Technology, Japan
3) Director, Japan Nuclear Energy Safety Organization, Tokyo, Japan
4) Engineer, Seismic Engineering Division, Kozo Keikaku Engineering Inc., Japan
shj@kke.co.jp, smidorik@enveng.titech.ac.jp, tsutsumi-hideaki@jnes.go.jp, akemi-noda@kke.co.jp, toshi-masatsuki@kke.co.jp

Abstract: Prediction of the response spectra for the strong motion on seismic bedrock based on an attenuation relationship is very important for the earthquake mitigation and the nuclear power plant safety. So far, since the data are rarely derived on seismic bedrock, it remains many difficulties to develop an attenuation relationship on seismic bedrock directly. In this study, we have developed a response spectra database on seismic bedrock include the following data: (1) Data directly estimated from the recordings derived at the vertical array at KiK-net stations at which the bottom seismograph is located on seismic bedrock with Vs over 2km/sec; (2) Recordings derived at hard rock sites in RK-NET and dam sites; (3) Near source data estimated using the substructure model and an equivalent linear method for records at K-NET and KiK-net sites. Based on this database, we developed a new attenuation relationship for response spectra on seismic bedrock, including the near source records. This paper presents the preliminary results of the development of the attenuation relationship.

1. INTRODUCTION

Prediction of the response spectra for the strong motion on seismic bedrock based on an attenuation relationship is very important for the earthquake mitigation and the nuclear power plant safety. So far, since the data are rarely derived on seismic bedrock, it remains many difficulties to develop an attenuation relationship on seismic bedrock directly.

In this study, we develop a response spectra database on seismic bedrock include the following data: (1) Data directly estimated from the recordings derived at the vertical array at KiK-net stations at which the bottom seismograph is located on seismic bedrock with Vs over 2km/sec; (2) Recordings derived at hard rock sites in RK-NET and dam sites; (3) Near source data estimated using the substructure model and an equivalent linear method for records at K-NET and KiK-net sites. Based on this database, we develop a new attenuation relationship for response spectra on seismic bedrock, including the near source records. This paper presents the preliminary results of the development of the attenuation relationship.

2. DATA

We choose 28 earthquakes, with Mw over 5.5 and 3 or more records per event on hard rock are obtained, to establish the new attenuation relationship for response spectra on bedrock, among the 47 events we collected. There are 13 crustal earthquakes, 6 inter-plate earthquakes, and 9 intra-plate earthquakes in the database. Table 1 show the earthquakes used in this study. The moment magnitude ranged from 5.5 to 8.3. Figure 1 shows the histogram of the earthquake type and plot of moment magnitude vs. the focal depth.

The strong motion data used in this study are derived at stations in KiK-net, K-NET, and F-NET by National Research Institute for Earth Science and Disaster Prevention (NIED), RK-NET by Central Research Institute of Electric Power Industry (CRIEPI), and the dam observation stations by Japan Commission on Large Dams (JCOLD), National Institute for Land and Infrastructure Management (NILIM) and the Miyagi prefecture. Only the data recorded or estimated on hard rock are used.

For the strong motion derived by KiK-net, the stations at which the bottom seismograph located on the bedrock where Vs >2km/s are selected for estimating the strong motion on bedrock. Generally, the strong motion observation system at stations in KiK-net is a vertical array observation system, at each station, seismograph installed both on the ground surface and on the bottom of the borehole. In this study, the stations at where the bottom of the borehole reaches the bedrock with shear wave velocity over 2 km/sec are selected as the candidate stations for the

estimation of strong motion. For the purpose, we firstly identified the properties of the soil materials in the borehole by fitting the transfer function defined as the ratio of the Fourier spectra of the seismic wave recorded at ground surface and the bottom of the borehole. Then the strong motions on bedrock are estimated from the records on ground surface of the borehole. Almost all the records from KiK-net are derived by using this method. Figure 2 shows the example of the result of the identification of material of the borehole and the estimated strong motion on seismic bedrock.

Finally, for the 28 target earthquakes, 521 records on bedrock are derived. For the near source area, however, since the data derived are not sufficient, 27 records with a fault distance under about 20km are used by evaluating the site effects between the seismic bedrock and ground surface based on an equivalent linear method, while the velocity structure are derived from the database by NIED.

In the database, the distance definitions used in this study are fault distance and the equivalent hypocentral distance (EHD). In this paper we only show the results for horizontal component and fault distance

Figure 3 shows the distribution of M_w and fault distance of the records in our database. From this figure, many near field strong motion can be confirmed in our database

3. REGRESSION MODEL

3.1 Attenuation model for deep earthquake

Midorikawa and Ohtake (2002) proposed a model with a different attenuation rate for shallow and deep earthquake. For understanding the physical base of the above model, we performed a numerical simulation to check the attenuation rate for shallow and deep earthquake. The simulation is summarized as follows.

(1) *Method*: a 2D FDM is used for the simulation. Simulation model is designed as a 300km in horizontal direction (X axes) and 90km in vertical direction (Z axes), divided by meshes with size of 0.1km by 0.1km. The velocity structure used in the simulation is JMA2001 model, which is a standard model used to determine source location of the earthquakes occurred in Japan. Figure 4 shows the distribution of Vp and Vs of JMA2001 model.

(2) *Target earthquake*: An Mw6 reverse earthquake is assigned as the target earthquake. Depths of the earthquakes are set to 10km, 20km, 50km and 70km. a simple triangle source function with a duration of 1 sec is used in the simulation. Seismic waves are calculated at receivers with distances ranged from about 10km - 280km.

(3) *Results*: Figure 5 shows the attenuation rate of PGV for the four scenario earthquakes. From the figure, the different attenuation rates at far stations are confirmed between the shallow earthquakes (focal depth of 10km and 20km) and the deep earthquakes (50km and 70km). This result suggests the different attenuation rate should be included in the regression model.

3.2 Model used in this study

As discussed above, the following model is adopted as the regression model in this study. For coefficient of C and k, since no sufficient data for the estimation, we adopt the values used by Si and Midorikawa (1999).

$$
\begin{aligned}
&\log SA(T) = b(T) + g(X) - kX + \varepsilon(T) \\
&b(T) = a(T)M_w + \sum d_i(T)S_i + h(T)D \\
&g(X) = \left\{ \begin{array}{l} -\log(X + C);\ D \le 30km \\ 0.6\log(1.7D + C) - 1.6\log(X + C);\ D > 30km\ \&\ X \ge 1.7D \end{array} \right\} \\
&C = 0.0055 \cdot 10^{0.5M_w},\ T < 0.5s \\
&= 0.0028 \cdot 10^{0.5M_w},\ T \ge 0.5s \\
&k = 0.003,\ T < 0.5s \\
&= 0.002,\ T \ge 0.5s
\end{aligned}
\qquad (1)
$$

Where, SA(T) shows GMTRotI50, an average response spectra proposed by Boore et al. (2006) for horizontal components, and response spectra for vertical components. X shows fault distance or EHD. D shows the focal depth, S_i is a category variable, shows the earthquake type defined as crustal, inter- and intra-plate earthquake, the same as that used in Si and Midorikawa (1999). In this paper, we only show the results for GMTRotI50 and the fault distance.

4. RESULTS

We performed a two-step regression analysis. Firstly b (T) is decided; then regression on a (T), d_i (T), and h (T) simultaneously. For the periods longer than 5s, only the earthquakes with Mw over 6 are used. The weighting schemes are as follows: 8 for distance ≤ 25km; 4 for ≤50km; 2 for ≤ 100km. For events: 8 for No. of records ≥ 30;4 for ≥ 20; 2 for ≥ 10.

Figure 6 shows the coefficient derived in this study. From the figure, a (T), the coefficients of Mw increase with period T, and the coefficients d_i (T) for intra-plate generally decrease with T, these represents the common knowledge about the effects of seismic source on ground motion, implicating the results are reasonable. The coefficient of focal depth, h (T), varies in the range of 0.003 to 0.009, also show reasonable results by comparing with the previous studies, e.g., for PGA or PGV.

Figure 7 shows the comparison of the most important coefficient a (T), with recent previous studies. From the figure, the results in this study show almost the same values as the others, e.g., Uchiyama and Midorikawa (2006), Kanno et al. (2006). This implicated that, the results in this study are reasonable.

Figure 8 shows examples of the predicted response spectra by using our new model. The response spectra are calculated under the following condition: a crustal event, at a fault distance of 20km; Mw of the target earthquakes are 6, 7 and 8. From the results, it can be confirm that, (1) the amplitudes increase with Mw; (2) corner frequency increases with Mw too. Generally the predicted response spectra are considered as reasonable.

5. CONCLUSIONS

In this study, we construct a database of response spectra on seismic bedrock. Based on the database, we derived a new attenuation relationship of response spectra on bedrock. The standard deviation is considerable small. Comparison with other studies show our results are consistent with the recent previous studies, implicating our model is reasonable.

Acknowledgements:

The authors acknowledge supported by the Research Found from an incorporated administrative agency, Japan Nuclear Energy Safety Organization. The strong motion data is provided by the KiK-net, K-NET and F-NET by NIED, RK-NET by CRIEPI, Dam records by JCOLD, NILIM, and the Miyagi prefecture. Figures are plotted by Plots. Part of the regression analysis is performed using the R language. The authors thank Professor Tatsuo Ohmachi, Dr. Yoshiaki Shiba, Dr. Shojiro Kataoka, Dr. Changjiang Wu, Dr. Hiroyuki Yamada for their fruitful suggestion. The thanks also go to Akihiro Sawaii, Toshio Kuriyama, Dr. Reiko Tajima and the other colleagues in KKE for their great help.

References:

Boore, D.M., Watson-Lamprey, J., and Abrahamson, N. A. (2006) "GMRotD and GMRotI: Orientation-independent measures of ground motion," *Bulletin of the Seismological Society of America*, **96**, 1502-1511.

Kanno, T., Narita, A., Morikawa, N., Fujiwara, H., and Fukushima, Y. (2006) "A New Attenuation Relation for Strong Ground Motion in Japan Based on recorded data," *Bulletin of the Seismological Society of America*, **96**(3), 879-897.

Midorikawa, S., and Ohtake, Y. (2002), "Attenuation relationships of peak ground acceleration and velocity considering attenuation characteristics for shallow and deeper earthquakes," *Proceedings of 11th Japan Earthquake Engineering Symposium*, **1**, 609-614.

Sato, T. Okawa, I., Nishikawa, T., Sato, T., and Seki, M. (2010), "Prediction of waveforms of long-period ground motions for hypothetical earthquakes using empirical regression relations of response spectra and phase spectra," *J. Struct. Constr. Eng. AIJ*, **649**, 521-530 (in Japanese).

Table 1 Earthquakes used in this study

EQ. No.	EQ. NAME	Initial Date	Time	Mw	Depth	Fault Type	Number of Data
1	Nihon-kai Chubu	1983.05.26	11:59	7.8	6.0	Inter	3
2	Eastern Off Chiba	1987.12.17	11:08	6.7	30.0	Intra	10
3	Off Kushiro	1993.01.15	20:06	7.6	105.0	Intra	8
4	Off Noto-hanto	1993.02.07	22:27	6.3	15.0	Crustal	3
5	Hokkaido-Nansei-Oki	1993.07.12	22:17	7.7	10.0	Inter	4
6	Hokkaido-Toho-Oki	1994.10.04	22:22	8.3	35.0	Intra	5
7	Sanriku-Haruka-Oki	1994.12.28	21:19	7.7	35.0	Inter	11
8	Hyogo-ken Nanbu	1995.01.17	5:46	6.9	10.0	Crustal	34
9	North-Western Kagoshima	1997.03.26	17:31	6.1	6.0	Crustal	3
10	North-Western Kagoshima	1997.05.13	14:38	6.0	7.0	Crustal	3
11	Izu Hanto Toho-Oki	1998.05.03	11:09	5.5	3.0	Crustal	8
12	Western Tottori	2000.10.06	13:30	6.8	11.0	Crustal	55
13	Geiyo	2001.03.24	15:27	6.7	51.0	Intra	40
14	Miyagi-ken Oki	2002.11.03	12:37	6.4	46.0	Inter	21
15	Hyuganada	2002.11.04	13:36	5.7	35.0	Intra	9
16	Miyagi-ken Oki	2003.05.26	18:24	7.0	71.0	Intra	33
17	Northern Miyagi	2003.07.26	0:13	5.5	12.0	Crustal	14
18	Northern Miyagi	2003.07.26	7:13	6.1	12.0	Crustal	13
19	Tokachi Oki	2003.09.26	4:50	8.0	35.0	Inter	16
20	Chuetsu	2004.10.23	17:56	6.6	10.0	Crustal	30
21	Kushiro-oki	2004.11.29	3:32	7.0	48.0	Inter	5
22	Western Fukuoka	2005:03:20	10:53	6.6	9.0	Crustal	27
23	Miyagi-ken Oki	2005.08.16	11:46	7.1	42.0	Inter	42
24	Chuetsu-oki	2007.07.16	10:13	6.6	10.0	Crustal	23
25	Ibaraki-oki	2008.05.08	1:45	6.8	51.0	Inter	11
26	Iwate-Miyagi Nairiku	2008.06.14	8:43	6.9	10.0	Crustal	36
27	Northern Iwate	2008.07.24	0:26	6.8	108.0	Intra	24
28	Surugawa	2009.08.11	5:07	6.2	23.0	intra	30

Si, H. and Midorikawa, S. (1999), "New attenuation relationship for peak ground acceleration and velocity considering effects of fault type and site condition," *J. Struct. Constr. Eng. AIJ*, **523**, 63-70 (in Japanese).

Yoshida, N. (1995), "DYNEQ, A computer program for dynamic response analysis of level ground by equivalent linear method," *http://boh0709.ld.infoseek.co.jp/*.

Uchiyama, Y. and Midorikawa, S. (2006), "Attenuation relationship for response spectra on engineering bedrock considering effects on focal depth," *J. Struct. Constr. Eng. AIJ*, **606**, 81-88 (in Japanese).

Ueno, H., Hatakeyama, S., Akegata, T., Funasaki, J., and Hamada, N. (2002), "Improvement of hypocenter determination procedures in the Japan Meteorological Agency," *Q. J. Seismol.*, **65**, 123-134.

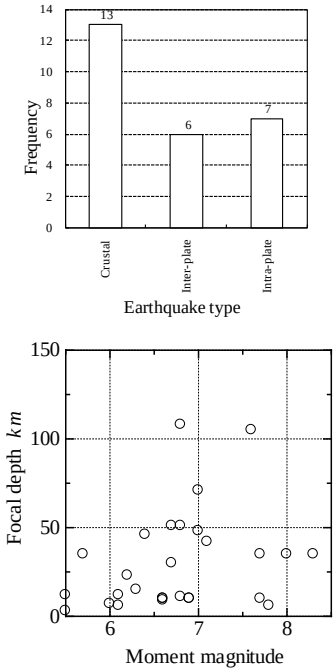


Figure 1 histogram of the earthquake type (upper) and the plot of moment magnitude vs. the focal depth (lower)

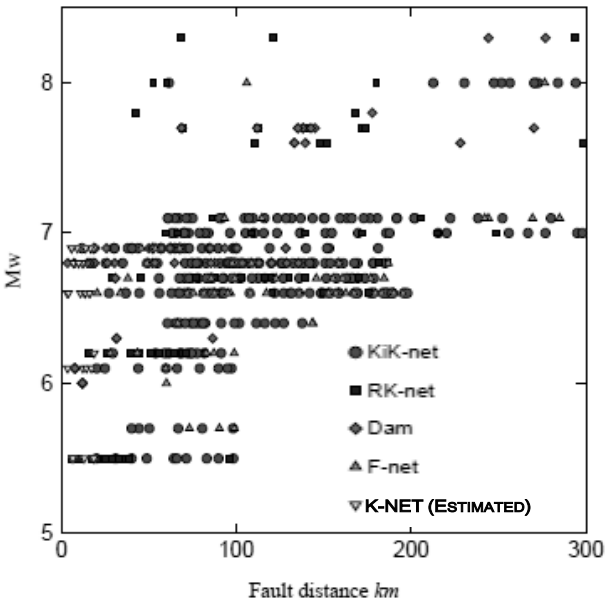


Figure 2 Distribution of Mw vs. fault distance

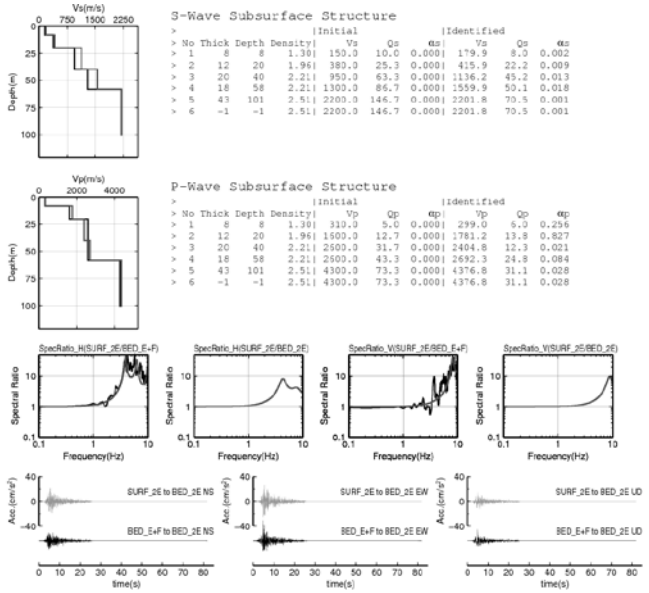


Figure 3 Example of results for identification of borehole materials and the estimated strong motion on bedrock. Top and second row panels: initial model (black) and identified model (red) for horizontal and vertical motion; third row panels show fitting of the identified and observed transfer function (left: horizontal, right: vertical component. Fourth row: estimated seismic wave on bedrock using surface and underground seismogram.

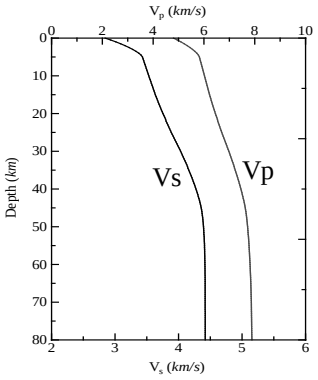


Figure 4 the JMA2001 model (Ueno et al, 2002)

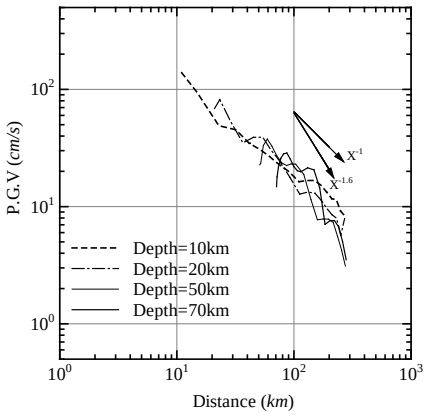


Figure 5 Attenuation rate of PGV of the synthetic seismic wave

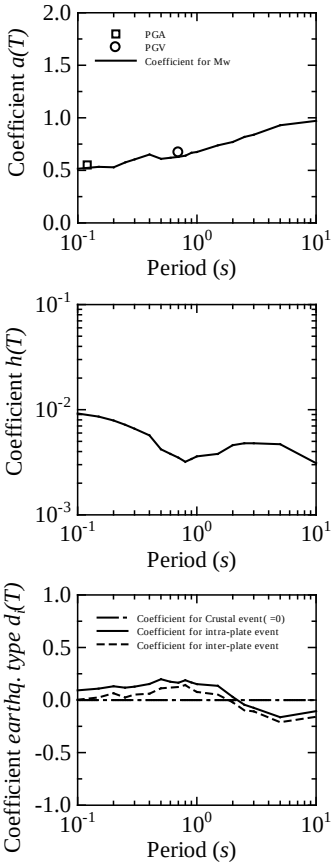


Figure 6 Coefficients a (T), h (T) and d (T)

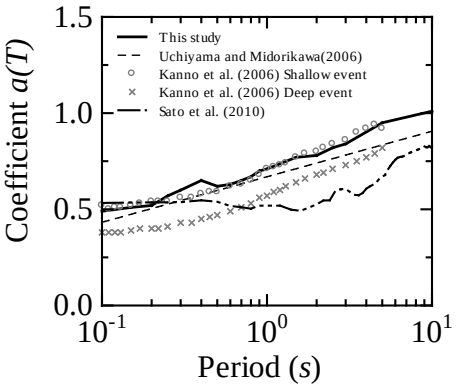


Figure 7 Comparison of the coefficient a (T) with the recent previous studies.

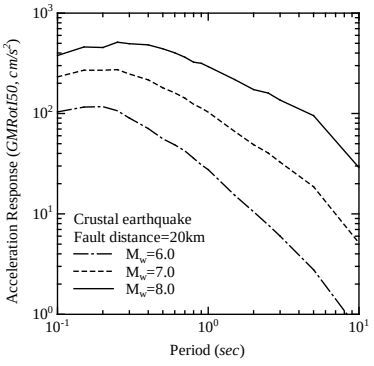


Figure 8 Predicted response spectra based on the results

8CUEE CONFERENCE PROCEEDINGS
8th International Conference on Urban Earthquake Engineering
March 7-8, 2011, Tokyo Institute of Technology, Tokyo, Japan

ON THE EFFECTIVE EARTHQUAKE EARLY WARNING SYSTEMS FOR BOTH DISTANT AND NEAR EVENTS

Yutaka Nakamura

President, System and Data Research, Tokyo, JAPAN
Visiting Professor, Dept. of Built Environment, Tokyo Institute of Technology, Yokohama, JAPAN
yutaka@sdr.co.jp

Abstract: This paper describes the truly effective early warning systems with simulated results for disaster prevention against distant and near events. And the role of national or public organizations in earthquake disaster prevention will be discussed.

1. INTRODUCTION

It is clear that the basic countermeasure against earthquake strong motion is to reinforce buildings and other structures. However, even enough counter-measured facilities against expected strong motion un-expecting accidents may be occurred. Against the un-expecting accidents, the earthquake early warning system, *UrEDAS*, Urgent Earthquake and Detection and Alarm System, was developed 25 years ago. At first the system was adopted for the Seikan under-sea-tunnel as an earthquake information system in 1988, and then fully operated for safety of the Tokaido Shinkansen from 1992. After that we are developing and improving our systems on the experiences of the Kobe earthquake and etc., as the technical innovation group for the EEW, Earthquake Early Warning. As the results of our activities, *FREQL*, Fast Response Equipment against Quake Load, was developed. At the start of the *UrEDAS* operation, the processing time of warning was three seconds after the P-wave detection. Now the processing time of *FREQL* is shortened to 0.1 second in minimum. This shortened processing time makes possible to issue a quick alarm over one second leading for large motion against even an under earthquake. Although this time margin is very short, it is expected that significant effects will be generated for facilities operated under the ultimate situation as the bullet train or the elevator system of high-rise buildings. The ultimate EEW system as *FREQL* is useful for rescue activities just after the earthquake damage to prevent the second disaster by large aftershocks.

In 1992 Nakamura's Group of *RTRI*, Railway Technical Research Institute, proposed a project of *UrEDAS* network with 2000 stations not only for earthquake disaster prevention, but also for working as a node of communication network when natural disaster occurred. In 1992, TV news of NHK, Nihon Hoso Kyoukai (Japan Broadcasting Corporation) announced that a trial operation of EEW information service for Tokyo metropolitan area with UrEDAS information will start in 1993. But this project was not realized mainly because of objection of *JMA*, Japan Metrological Agency. *JMA* started the similar project in 2005 using a system developed by themselves. In this paper, not only the EEW of Japan, but also the present state of the information for earthquake disaster prevention will be described.

2. CONCEPT OF EEW

There are two kinds of earthquake alarms as illustrated in **Figure 1**. One is the "On-Site Alarm" which is an alarm based on observations close to the objects to be warned. The other one is the "Front Alarm" which is an alarm based on observations near the epicentral area, which is then used for the warning in possible damage areas away from the epicenter. Because the latter alarm concept requires the use of communication networks, it is also sometimes called

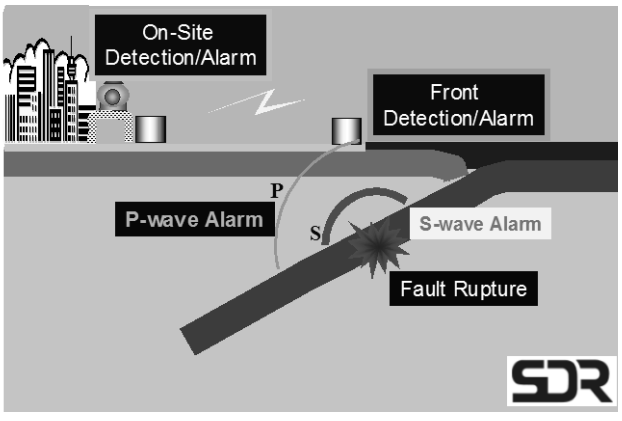


Figure 1 Concept of an EEW system

"Network Alarm". Both alarm types described can make use of two different triggers, also called "alarms". One is the trigger/alarm exceeding a preset level, the so-called "S-wave Alarm" or "Triggered Alarm"; the other one is the trigger/alarm during the preliminary motion, the so-called "P-wave Alarm".

3. *UrEDAS*

The idea of disaster mitigation by the EEW depends on the progress of science and technology during 19 and 20 centuries. Earthquake is a vibration caused by the results of the crust destruction. Although the earthquake prediction obviously brings numerous benefits to the disaster prevention, this kind of destructive phenomena is a stochastic phenomenon and is impossible to predict its occurrence with enough accuracy and reliability applicable to disaster prevention. Instead of the prediction the EEW is close up for disaster prevention.

The idea to minimize the direct effects of earthquakes by developing an early warning system was first published by Dr. J. D. Cooper (1868) with the aim of earthquake disaster prevention in San Francisco. It is interesting for me that he describes the idea of EEW based on the failure of the Japanese earthquake prediction method using a magnet at an earthquake in 1868. After Cooper various similar ideas has been proposed, but Cooper's and the other ideas were never realized and then basically forgotten.

About 100 years after Dr. Cooper's publishing, independently a similar idea was born from an idle talk at a tea time of an university laboratory. This is the detection system before 10 seconds for Tokyo metropolitan area proposed by Dr. Hakuno et al (1972). At the same time, many institutions and agencies including *JMA* started to research a possible EEW based on the existing automatic earthquake observation system consisting of a network of many monitoring stations.

JNR, Japanese National Railways, had also started to research possible EEW based on the same concept as *JMA*, while Nakamura at the *RTRI* of *JNR*, started to develop a different concept in 1979, using only a single station. He completed the prototype *UrEDAS*, pronounced "Yuredasu" meaning "shaking begins" in Japanese. This was the first actual P-wave detection and alarm system worldwide and was published in Nakamura (1984).

The main *UrEDAS* functions are the estimation of magnitude and location, vulnerability assessment and issuing warnings within a few seconds using initial P-wave motion at a single station. Unlike other automatic seismic observation systems, *UrEDAS* does not have to transmit the observed waveform in realtime to a remote processing or centralized system and is therefore comparatively simple. *UrEDAS* calculates parameters such as back azimuth, predominant frequency for magnitude evaluation and vertical to horizontal ratio for discrimination between P and S waves, using the amplitude for each sample in realtime. These calculations are processed in realtime without storing waveform data. The amount of processing of *UrEDAS* is almost constant regardless of whether or not an earthquake is occurring, so the number of computational processes does not increase in the event of an earthquake. Then UrEDAS does not cause any system down after big earthquake.

UrEDAS can issue its alarm based on the *M-Δ* diagram in **Figure 2** immediately after the earthquake detection. The *M-Δ* diagram is derived from past damage experience to JNR facilities and equipment and aids in decreasing the number of false or needless alarms. This kind of alarm is referred to as the *M-Δ* Alarm. *UrEDAS* can also assist in decisions to safely restart train operations based on the detailed earthquake parameters.

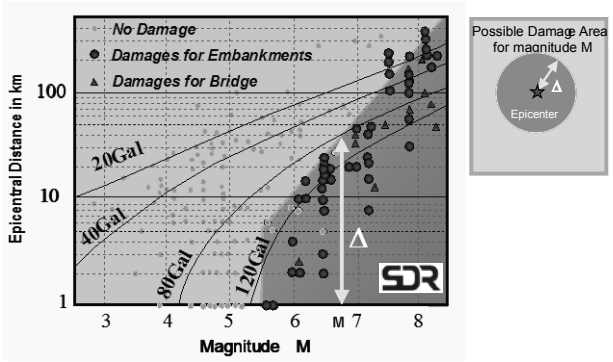


Figure 2 M-Δ diagram

After an initial testing period, the development of *UrEDAS* for routine use was completed and trial operations for the protection of the Shinkansen line, the bullet train, in central Japan were carried out commencing in 1990. These trials led to the implementation of some additional capabilities and functionality of *UrEDAS*. In 1992, *UrEDAS* started routine operations with full functionality for the Tokaido Shinkansen line (Nakamura, 1996). These *UrEDAS* issue a P-wave warning with a processing time of just three seconds after detecting the P-wave.

Other organizations, such as *JMA*, continued their research and development but without implementing operational systems. This made *JNR* the only agency to implement an operational and functioning actual warning system in the 20th Century.

4. THE 1995 KOBE EARTHQUAKE AND *Compact UrEDAS*

After the 1995 Kobe earthquake, it was recognized that an even shorter warning time would lead to even more effective realtime disaster mitigation. To achieve this, *UrEDAS* was developed further with the aim of being able to issue warnings within about one second after the detection of a damaging earthquake. The resulting system was the *Compact UrEDAS* which became available in 1997 (Nakamura, 1998) and commenced routine operations for the Tohoku, Joetsu and Nagano Shinkansen lines in 1998.

In contrast to *UrEDAS* which estimates the destructiveness of the earthquake from the earthquake's parameters, *Compact UrEDAS* derives this from the earthquake motion directly 'in realtime' and then issues the

alarm, if required. To estimate earthquake dangerousness, the power density *PD* (W/kg) of the earthquake vibration is calculated from the inner product of the acceleration vector $\boldsymbol{a}$ (cm/s^2) and the velocity vector $\boldsymbol{v}$ (cm/s). As this value is a large number, it is normally expressed in terms of the Destructive Intensity (*DI*) defined as the logarithm of absolute value of this inner product (*LPD*, logarithm of the power density) as Eq. (1). The concept of *DI* is illustrated in **Figure 3**.

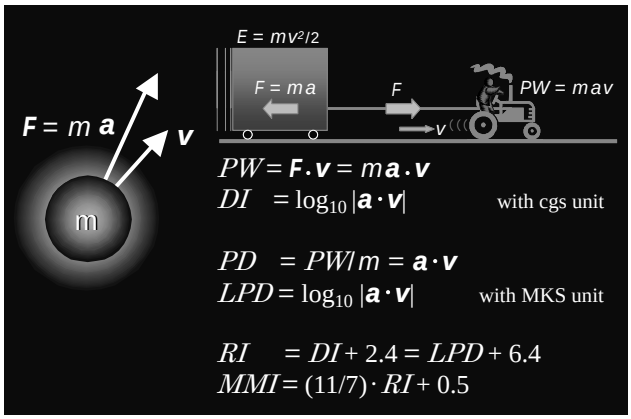


Figure 3 Relationship between various earthquake

$$DI = \log |\boldsymbol{a}\cdot\boldsymbol{v}| = LPD + 4.0 \qquad (1)$$

The maximum value of *DI* during an event, DI_{max} relates to the earthquake damage and is similar to the instrumental intensity scale of *JMA*, I_{JMA}, with the constant difference of 2.4, and corresponds to *MMI*, the Modified Mercalli Intensity. These indices are referred as *RI*, Realtime Intensity, and *MMI*, respectively.

$$RI = DI + 2.4 \qquad (2)$$
$$MMI = (11/7)RI + 0.5 = (11/7)DI + 4.27 \qquad (3)$$

I_{JMA} can only be calculated after earthquake termination according to its artificial definition without physical background. Contrary to this, *DI* is defined as the logarithm of Power Density multiplied by a constant. Power Density is a physical variable related closely to earthquake damage. *DI* can be calculated in realtime and its value increases immediately after the P-wave arrival. Because *DI* is sensitive to the P-wave arrival, it can be used to define a P-wave alarm. **Figure 4** shows the change of *RI* as a function of time with the acceleration waveform and the change of *SI*, Spectral Intensity. *RI* is more sensitive than both, the acceleration and *SI*, because the value of *RI* increases drastically at the P-wave detection, about one second prior to the other indices.

When the P-wave arrives, *RI* increases dramatically, followed by a further but slower increase until the arrival of the S-wave, by which time it reaches its maximum, called RI_{max}. The *PI*-value is defined as the maximum *RI* within *t* seconds after P-wave detection. This *PI*-value seems to be applicable as a trigger for the P-wave alarm. Furthermore, it is possible to estimate RI_{max} from the *PI*-value approximately.

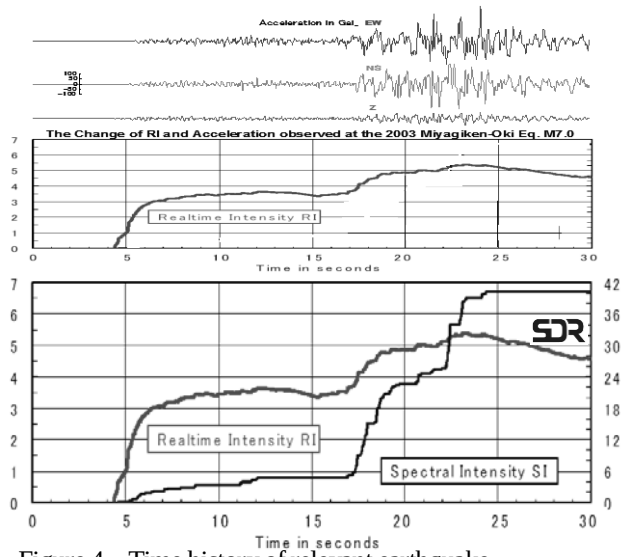


Figure 4 Time history of relevant earthquake

Because each facility has its own withstanding intensity level, each customer can determine the *PI*-value as the trigger of the P-wave alarm. In other words, with the continuous observations of *RI*, an earthquake alarm can be issued efficiently and the damage can be estimated reliably. In fact, the *PI*-value with its physical meaning of power related to destructiveness and dangerousness of the earthquake can thus be used for a P-wave alarm as realized in the *Compact UrEDAS* and *FREQL* (explained later in detail).

The function of the *Compact UrEDAS* is to issue an early warning for the area close to the instrument based on the risk of the detected earthquake motion, which is different from the alarm from the *UrEDAS* to the area of possible damage based on the estimated location and magnitude of the detected earthquake. The target area of the *UrEDAS* alarm is about 200 km around the location of the instrument, while that of the *Compact UrEDAS* alarm is only about 20km around the instrument. Thus, to maximize the effectiveness of the warning system, an ideal strategy is to use the *UrEDAS* (front alarm or network alarm) to respond to more distant large earthquakes and use the *Compact UrEDAS* (on-site alarm) to respond to nearby earthquakes.

5. EXAMPLE OF A SUCCESSFUL EEW BY *Compact UrEDAS*

The derailment of one Shinkansen train during the 2004 Niigata-ken Chuetsu Earthquake (M6.8) impressively demonstrated the effectiveness and benefits of the early warning system for Shinkansen train operations. The fact that there were no fatalities or injuries to the passengers and crew of the train is clearly a result of the availability of the early warning system. The circumstances and course of events of the derailment are described in the following. **Figure 5** shows a summary and timeline of the events.

The train line is built on many viaducts, and two of them with different characteristics are joined at 300m from

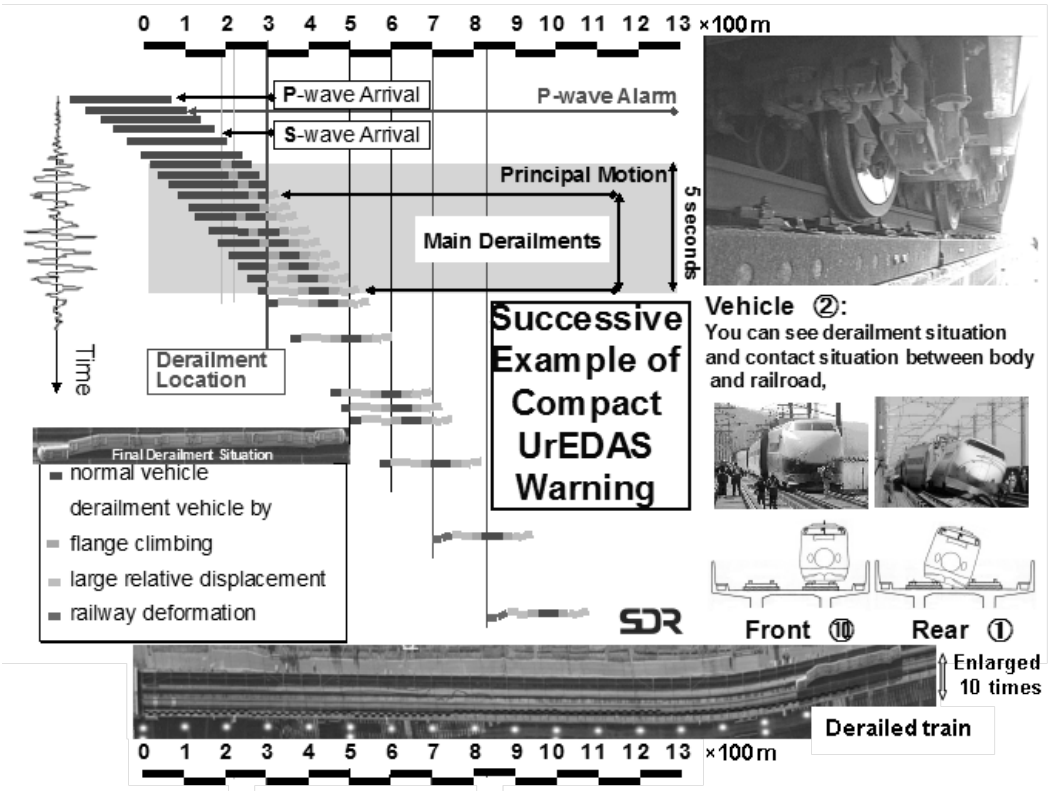


Figure 5 The Shinkansen Derailment during the 2004 Niigata-Ken Chuetsu Earthquake

the tunnel exit including the snow-shade (the 300m point hereafter). The earthquake effects on these viaducts were different from each other. When the train passed the 300m point, it is likely that the train derailed, because the joints in the rail tracks underwent different displacements.

The power supply to the train was interrupted by the P-wave alarm of the *Compact UrEDAS* installed at the substation (SS), 11km from the epicenter of the earthquake. The alarm was triggered about 2.5 seconds before the arrival of the S-wave at the location of the train. The large motion started one more second after that. So the P-wave alarm preceded the onset of the large motion by about 3.5 seconds. Without the automatically initiated emergency breaking triggered by the alarm the train would have arrived at the 300m point earlier and more vehicles would have passed that point during the large motion. With the very real possibility of the rails buckling while the train passed over them at great speed, this most probably would have caused a much more serious derailment destroying the rails completely which then might well have led to the train overturning.

If this happened to the lead vehicles, it could have been as catastrophic as the accident of the German ICE (InterCity Express) high-speed train in 1998 (Wikipedia). Consequently, although the derailment could not be prevented, this certainly illustrates the usefulness of the warning system impressively.

A subsequent simulation of the alarm behavior of a *FREQL* system using the recorded waveform showed that the train would have received the P-wave alarm another 0.8 seconds earlier, if a *FREQL* had been installed in Shin-Kawaguchi SS, because the *FREQL* would have issued the P-wave alarm already 0.2 seconds after the P-wave detection.

There are several more examples of successful warnings by *UrEDAS* or *Compact UrEDAS* in 1995, 2003, 2005 and as detailed in Nakamura and Saita (2007).

6. *JMA*'S EEW

In about the Year 2000, *JMA* started research on a single site detection system with the Railway Technical Research Institute. Their system concept was basically similar to the ideas behind the *UrEDAS*. However, in contrast to the *UrEDAS* which is a direct realtime system, the *JMA* development adopted an intermittent processing system by determining the necessary parameters using stored waveform data of several seconds duration to fit the estimated function. As such, *JMA*'s centralized system gathered information of each site and re-processed it using the stored information from many sites, and then issued an alarm, if necessary.

Therefore, *JMA*'s EEW can be regarded as a network-type alarm system that requires a normally functioning telecommunications network. Except for the cases of extremely deep earthquake events, the combination of processing time and telecommunication time (the time it takes for the observations to reach the central system) is too long to issue a meaningful alarm for the possible epicentral damaged area before the large earthquake motion from a nearby earthquake or an epicentral earthquake starts.

Therefore, this system is unable to issue a warning before the onset of the large earthquake motion at the damaged area. In some cases, the warning was even issued after termination of the earthquake motion. In the case of the 2008 Iwate-Miyagi-Nairiku Earthquake, for instance, it was impossible for the system to issue the warning for the damaged area.

7. ULTIMATE EEW SYSTEM: *FREQL*

The functions of *UrEDAS* and *Compact UrEDAS* were combined which not only reduced the size and weight of the system, but also improved its functionality. This development was completed in 2005 and given the name *FREQL*. In Japanese, *FREQL*, pronounced "furekkuru", means "wave coming". *FREQL* shortened the processing time required to issue an *UrEDAS* /P-wave alarm - based on the estimated earthquake parameters from three seconds (for *UrEDAS*) to one second. The previously minimum time for issuing a P-wave alarm based on the dangerousness of the detected earthquake motion by the *Compact UrEDAS* of one second was improved by the *FREQL* to just 0.2 seconds and further to 0.1 seconds in 2009. This enables *FREQL* to issue an alarm before a large earthquake motion even in the case of the epicentral area.

FREQL is not only very valuable in the detection of the initial quake, but is also used during rescue operations after the main shock by detecting, and warning for possible aftershocks. For instance, the Tokyo Fire Department Hyper Rescue Team pulled out a small child from underneath debris from a land slide during the 2004 Niigataken-Chuetsu Earthquake. After that they had contacted us for using *FREQL* to keep the safety of the rescue staff during the high risk of aftershocks. Based on their request, a portable version of the *FREQL* was developed in 2005, improving the system's capabilities further and making it more compact.

The Hyper Rescue Team examined *FREQL* not to cause false alarm because of the working heavy equipments. And also functional examination with the high quality three dimensional shaking table made skeptic person understand that *FREQL* should be useful for earthquake disaster prevention.

The portable *FREQL* is now in use by many fire departments nationwide, even accompanying international disaster rescue teams, such as to the 2006 Pakistan Earthquake and the 2008 Sichuan Earthquake, see **Figure 6**.



Figure 6 FREQL used by Japanese International Rescue Team at the Sichuan Earthquake

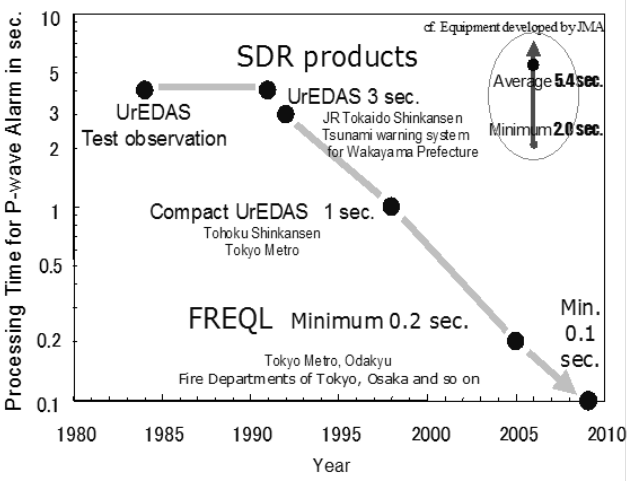


Figure 7 Processing Time of the EEW systems

Table 1 Comparison between SDR and JMA methods

Method	Products	P, S-wave Recognition	Processing Time Interval	Magnitude M from	Epicentral Distance Δ from	Warning based on	Alert Issueing after Trigger	Development / Practical Use
SDR	*UrEDAS*	Yes	1/100 s.	Initial Period*	Initial Amplitude and M (S-P Time after S)*	M-Δ	Set to 3 s.	1984/1989～
	Compact UrEDAS					Initial *RI*	Set to 1 s.	1997/1998～
	FREQL					Initial *RI* / M-Δ	Min. 0.1 s./ 1s.**	2003/2004～
	AcCo-PS					Initial *RI* / M-Δ	Min. 0.2 s./ 1s.**	2007/2008～
JMA		No?	1 s.	Amplitude and Δ	Initial Gradient of Amplitude	Estimated Sesmic Intensity	Average 5.4 s. (Minimum 2 s.)	2004/2007～

* except *Compact UrEDAS*.

** corresponds to warning based on Initial *RI* / M-Δ, respectively.

RI: Realtime Seismic Intensity.

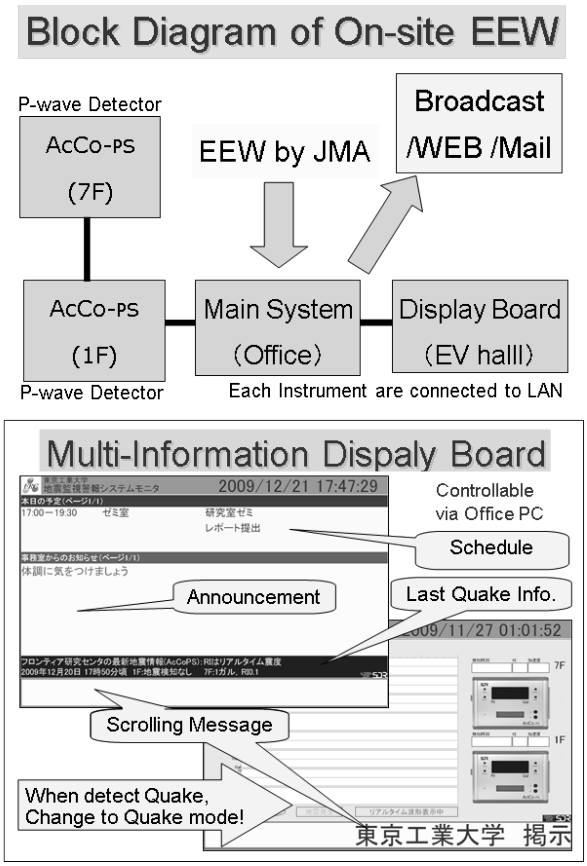


Figure 8 Block diagram of On-site EEW in Suzukakedai Campus of Tokyo Tech.

Rescue teams involved in the aftermath of the 2008 Iwate-Miyagi-Nairiku Earthquake also benefited greatly from the portable *FREQL*.

FREQL were used also in some private railway companies in Tokyo metropolitan area for EEW, and are testing now in a nuclear power plant, semiconductor facilities and so on. We expect in near future *FREQL* will be actively involved in plants and worksites to mitigate earthquake damage.

The alarm processing time of EEW Systems explained above is shown in **Table 1** and **Figure 7**, is the comparison of each EEW's functions.

Tokyo Institute of Technology has started operation of unique earthquake information system integrated with a display board. Normally this system shows general campus information with recent earthquake observed information. And if *AcCo-PS*, P-wave warning device with *FREQL* function, detects an earthquake, this system shows waveform and *RI* and *PGA* with frequency range between 0.1 Hz and 5 Hz (*5HzPGA*), see **Figure 8**.

8. SIMULATIONS OF *FREQL* ALARM

In this section simulated examples will be presented for damaged earthquakes; big near event, near event and huge distant event.

8.1. A Big Near Event

The 2008 Iwate-Miyagi-Nairiku Earthquake, M7.2 and 8 km depth, was occurred in north-east of Japan at 14th June 2008, around 8:43 of local time. This earthquake caused severe damage in the epicentral area, yet *JMA*'s EEW system was unable to issue an alarm before the start of shaking in the damaged area within approximately *25* km of the epicenter. **Figure 9** shows the time of the actual alarms issued by *JMA*'s EEW and compares them with alarms which an on-site *FREQL* system would have been able to issue, based on a simulation using the recorded waveforms. The depth of this earthquake was approximately 8km below the surface. The alarm from *JMA*'s EEW was issued *3.5* seconds after the event detection to the primary customer and one second later to the public, which is equivalent to about *10* seconds after the earthquake occurrence. Although the timing of the alarm in this case was faster than the averaged processing time of *5.4* seconds (see Figure 7), the

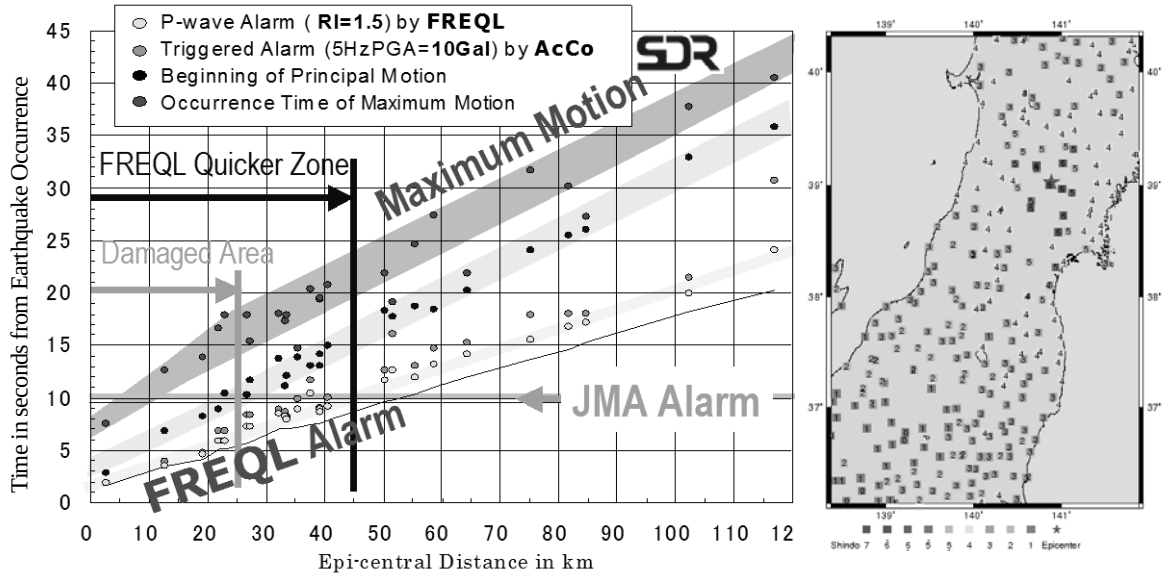


Figure 9 Comparison of EEW timing between JMA and FREQL/AcCo for the 2008 Iwate-Miyagi-Nairiku Earthquake

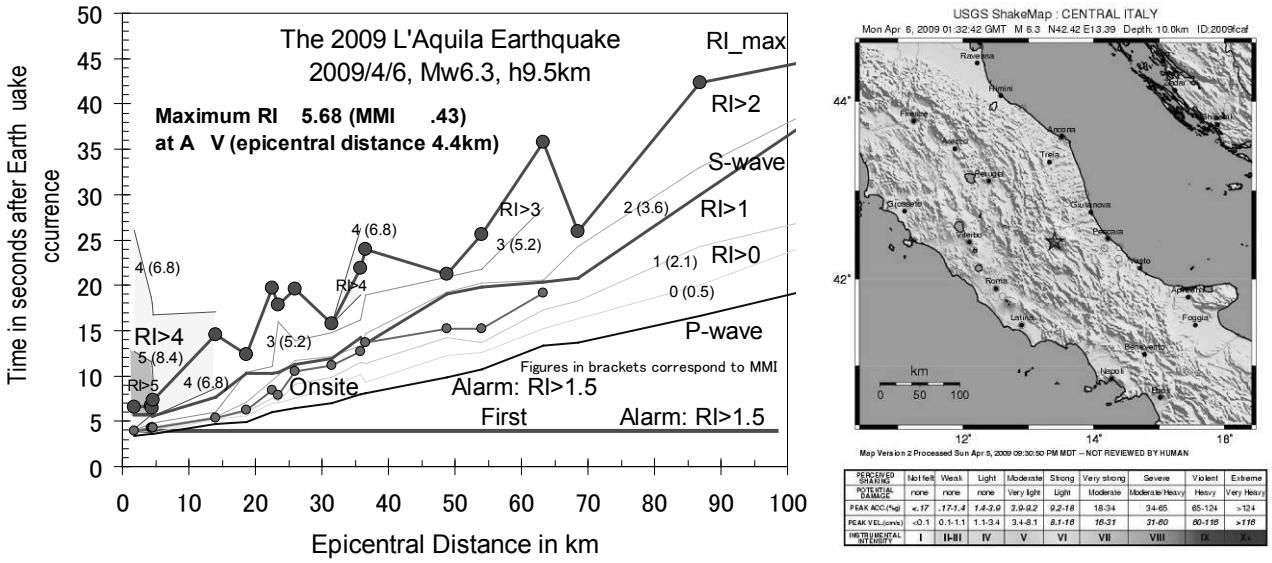


Figure 10. Timings of P wave arrival, FREQL warning, S-wave arrival and Maximum motion arrival: RI means Realtime Seismic Intensity; figures in brackets are corresponding to MMI.

warning was still only delivered after the beginning of the strong motion. In contrast to this, *FREQL* is expected to issue an alarm *0.2* seconds after the P-wave detection in the damaged area, i.e. the time margin before the beginning of the strong motion is several seconds, even at the epicenter itself.

In general, one can safely state that the on-site alarm issued by the *FREQL* is faster than that issued by *JMA*'s EEW within an area of about *50* km from the epicenter. For epicentral distances over *50* km, the on-site EEW of the *FREQL* is issued more than *10* seconds before the onset of strong motion. The average processing time of *JMA*'s EEW is *5.4* seconds, but to transmit the information from the detecting site to the processing center and the warning to the user will take some additional seconds. Typically, the transmitting time from the detecting site to the processing center, and from there to the users is estimated to be a total of around two seconds, increasing the time difference between receiving the warning from *JMA* and from *FREQL* even more. The experience of the 2008 Iwate-Miyagi-Nairiku Earthquake confirms this finding for locations with over 100km of epicentral distance. Until today, there has been no example where *JMA*'s EEW was able to effectively be used for disaster prevention by means of early warning

8.2. A Near Event-1

The 2009 L'Aquila Earthquake, M6.3 and 9.5 km depth, was occurred in central Italy at 6th April 2009. This earthquake caused severe damage in the epicentral area.

Figure 10 shows a result of simulation for the 2009 L'Aquila earthquake using strong motion records. According to this figure, FREQL was expected to get a few seconds as a leading time at even epicentral area. It is very short time, but during the leading time people could be evacuate into some sturdy desk before falling down the floor or the ceiling. It is needless to say that the most important measure is to build the structures enough earthquake-proof. Even after the reinforcement against the earthquake, because there is still risk on the falling objects, the repeated emergency drills are essential to acquire the image of the damage situation after the earthquake for the reasonable countermeasures. Anyway there is no system to issue the earthquake alarm quicker than on-site FREQL, so it is advisable to take proper countermeasures without exaggerating the effect of EEW.

8.3. A Near Event-2

The 2010 Jiansian Earthquake, M6.4 and 23 km depth, was occurred in mountain area of southern Taiwan at 4th March 2010, 8:18:52.14 of local time, according to the *CWB*, Central Weather Bureau. **Figure 11** shows distribution map of seismic intensity *RI* and *5HzPGA*. The strong motion was observed at the plane area apart from epicenter and damage was occurred in this area. This interested phenomenon was strongly reflected by the amplification of the sedimentary

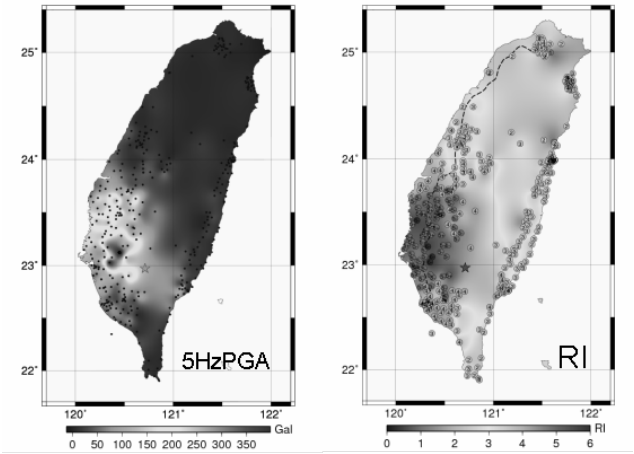


Figure 11 Distribution of Realtime Seismic Intensity and 5HzPGA of the 2010 Jiansian Earthquake, Taiwan

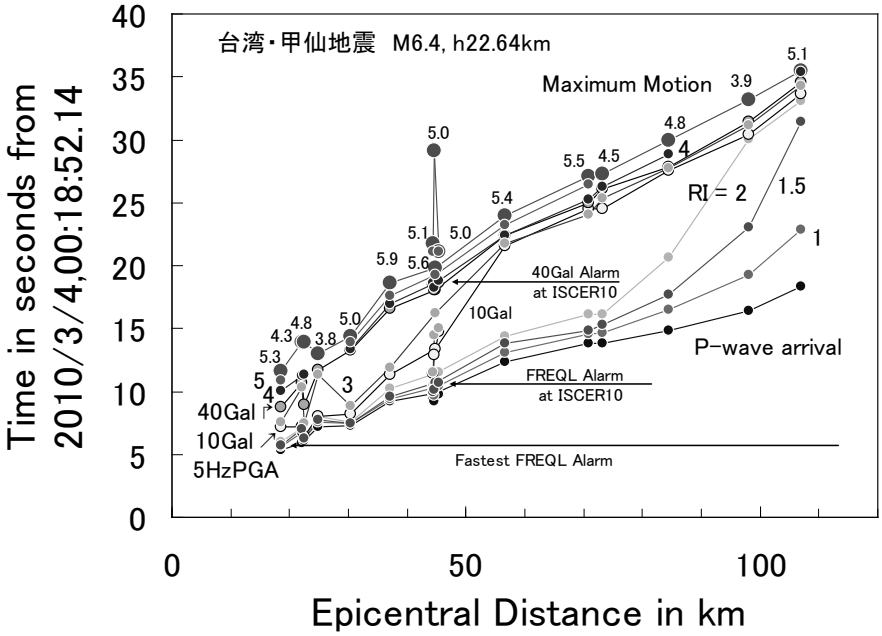


Figure 12 Simulation Result of FREQL Alarm for the Jiansian Earthquake

surface ground on the plane. In the area a running Taiwan Shinkansen train with 300km/h was derailed, but no injured passenger and no damage to the structures.

Figure 12 shows a simulation result of *FREQL* alarm using strong records of the *CWB* with changing of the *RI*. The 40 Gal alarm, which is a triggered alarm over 40 Gal of 5HzPGA, was issued at 8:19:10 to the derailed train. *FREQL* alarm should be issued at 8:19:02, 8 seconds earlier than the 40 Gal alarm. *FREQL* alarm issued *0.8* seconds after P wave detection proceeding to the strong motion with over *7* seconds. It is clear that the *FREQL* alarm proceeding to the strong motion with over three seconds at even the focal area.

8.4. A Huge Distant Event

A huge earthquake, Mw 8.8 and 47 km depth, with tsunami was occurred along the coastline of Chili in 27th February 2010, 3:34 of local time. **Figure 13** shows a simulated result using the waveform data set of Chili University. According to this the strong motion over *5* of *RI*, correspond to *8* of *MMI*, were maintained several tens seconds even at several *100* km apart from epicenter. This is the property of a huge earthquake of almost M_w *9*. The on-site alarm by *FREQL* in focal area will be issued just after P wave detection. In the area far from the epicenter, the on-site alarm by *FREQL* will be delayed from P wave detection. But the leading time proceeding to the strong motion over *4* of *RI*, correspond to *7* of *MMI*, were estimated as follows; over *7* seconds for the focal area and several tens seconds for distant area. Of course the leading time of a network alarm by *FREQL* will be longer, but the on-site alarm by *FREQL* will be present enough leading time needless communication facilities which often broken at big disaster occurrence.

9. WHAT INFORMATION IS REQUIRED FOR EARTHQUAKE DISASTER MITIGATION?

From the operational side, there are three pieces of information relevant to realtime earthquake assessment:

(1) an early warning before the onset of the strong shaking for the area of certain damage,
(2) information before the shaking starts about the area that will not be damaged, and
(3) a precise and detailed estimate of the location and extent of the area where serious damage can be expected.

The most important issue for public agencies is to have a reliable assessment as listed in Item (3) above, so that rescue activities in the damaged areas can be initiated immediately. For the public agencies it is impossible to deliver information as under Item (1) due to the long processing and communication times. Only on-site early warnings can deliver that information. In general, the early warning can only be used to trigger individual or locally based social group help or action. Governmental assistance will mainly focus on the rescue work in the seriously damaged areas evaluated by information as under Item (3). Information as under Item (2) has no relevance to damage, and is unnecessary information for disaster prevention. For most events, unfortunately, *JMA*'s EEW seems usually only capable to deliver information as under Item (2).

The warning must be delivered rapidly and be accompanied by information for a rational response to the event. The information as under Item (3) above is essential to decide on such actions. It is important to receive rapid and

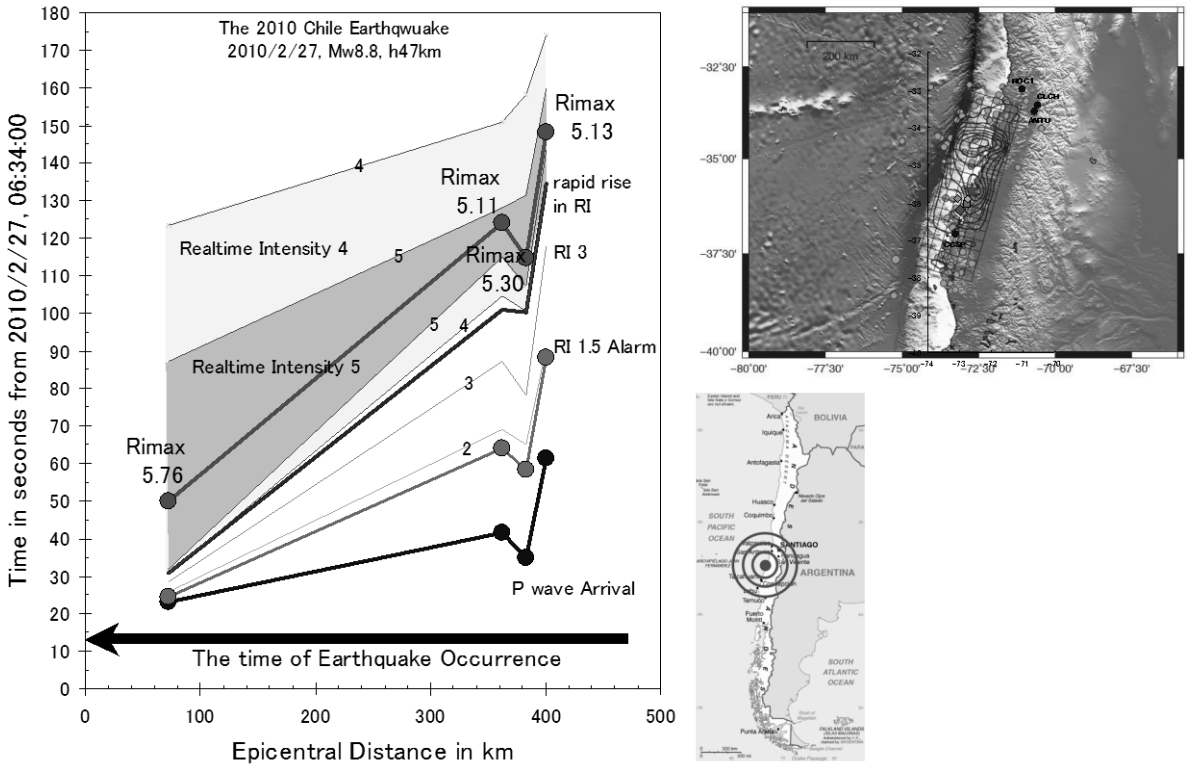


Figure 13 Simulation Result for the 2010 Chile Earthquake of Mw 8.8

accurate earthquake information from organizations such as JMA in Japan, but it is also important not to restrict the delivery of the information as under Item (3) from other organizations, such as local universities or Institutions.

As mentioned above, the best possible earthquake assessment (made in realtime) is essential information to specify the extent and location of the seriously damaged area, to enable the implementation of immediate and appropriate emergency response directly after the event. While earthquake observation systems designed for scientific research must be able to determine the exact location of the events, *UrEDAS* has deliberately been designed to estimate the earthquake parameter only in an approximate way to be able to issue the warning and the required response action in the shortest possible time.

Public organizations should deliver information on the earthquake parameters not only for the main shock but also for aftershocks as soon as possible. However, from the viewpoint of earthquake disaster prevention, it is more important to deliver accurate earthquake information as quickly as possible rather than to deliver a "late" early warning. For the most appropriate and quick response after the earthquake, the "actual observed" seismic motion as intensity, not an estimated value, is the most important information because the degree of damage can be estimated from it.

10. PROBLEMS IN THE DELIVERY OF EARTHQUAKE WARNINGS BY THE NATIONAL AUTHORITIES

If only one authority can issue warnings, all organizations and the general public must rely on it. This leads to the general public, as well as organizational managers develop the habit of waiting for the information from the authority instead of using some reasonable self-management for protection and mitigation. On the other hand, if other organizations are also permitted to issue warnings, all involved must be aware of that they do this on their own risk and must take full responsibility for their warnings and possible consequences.

If issuing warnings is based on a law or regulation, organizations and individuals responsible for issuing warnings develop a strong tendency to wait with the warning until the last moment (which may be too late). On the organizational level, promulgation of such warnings might be slowed down for fear of reprisals or bad reputation.

In Japan, this trend is quite obvious in the ways in which tsunami warnings or cautions are given. By law, only *JMA* is permitted to issue tsunami information in the form of an official tsunami warning. However, as it is commonly seen on TV news in Japan, the source of such tsunami information is not clear and in most cases, the accuracy of the information on which the warning is based is doubtful. This situation can lead to a considerable lack of reliability with many false warnings and cautions, commonly know as the "crying wolf syndrome".

It became very obvious that an *M7* class earthquake causes catastrophic damage especially in the area close to the epicenter. Although *M7* class earthquakes are quite common in Japan, it is a potentially fatal flaw in the warning system that the *JMA*'s EEW cannot issue a timely and accurate estimate of the large motion in the catastrophically

damaged area. If the early warning for the large motion is delayed too long (for whatever reason) it becomes meaningless.

For *M8* class events (which occur statistically once every several tens of years in Japan), the *JMA*'s EEW seems to be capable to issue a warning with a useful time margin for the strong motion. Yet such a warning is only useful, if it is readily available for the damaged area more than *50* km from the epicenter. This, however, might not be the case, because in such a serious situation it is quite possible that the information is lost or delayed by problems in the communication system. In contrast, an on-site alarm system is, by definition, not exposed to these problems and can issue a warning or alarm before the onset of the large earthquake motion.

On-site alarm equipment such as the *FREQL*, is capable to issue the alarm in as short a time as *0.1* seconds after the P-wave and can thus issue the warning before the onset of the large earthquake motion, even for locations close to the epicenter. If then a local FM radio station would broadcast the *FREQL* information, there would be a time margin for preventative action within the damaged area. Unfortunately, after December 2007, there is a hesitation for implementing of such a system because it might violate a law restricting the authority to issue warnings to *JMA*.

11. CONCLUDING REMARKS

Realtime earthquake warning was initially aimed at disaster prevention for the train system in Japan, but is by now used in many other environments as well. To be of wide-ranging benefit, the time margin of the warning must be very short on a time scale of seconds to enable quick action by the general public, such as to seek shelter (like under a sturdy desk) or to evacuate immediately to a pre-determined safety zone. The disaster prevention activity must be based on the actual seismic motion in the surrounding area, not an estimated one or one for some other location.

It is an open question whether or not an appropriate earthquake early warning system is in place in Japan today. Clearly, there has not been much discussion about this issue until today. It seems that the (so far futile) attempt to develop a reliable earthquake prediction system is getting much more attention than the fact that an effective and reliable earthquake early warning system is a reality and readily available.

It is clear that the primary preventative action by the people at the time of the earthquake is to keep away from places where they could be hit by falling or loose objects. To be able to do this obviously requires a timely and immediate warning to be issued.

The earthquake information including warning is not effective for disaster prevention to be provided exclusively as a national project. A warning cannot prevent the possible collapse of structures, but it can most definitely assist people evacuating from collapsing facilities. A prompt and reliable earthquake warning should become part of the daily life of the people in Japan. National organizations should be able to specify the area of expected catastrophic damage accurately and initiate rescue operations without delay based on information from responsible and capable organizations in realtime.

Acknowledgment:

The author wishes to thank Tokyo Fire Department for their cooperation in the implementation the systems: *FREQL*-based early warning system. The simulation described in this article used the waveform data from K-NET and KiK-net of NIED, National Institute of Earth Science for Disaster Prevention, Dr. Kai-Wen Kuo of the Central Weather Bureau of Taiwan and Mr. Jerry Li of Taiwan High Speed Rail Corporation. I wish to express my sincere thanks to all individuals that contributed to this paper.

References:

Cooper, J. D. (1868), "Earthquake indicator", San Francisco Daily Evening Bulletin, 3rd November 1868.

Hakuno, M. (1972), H. Takahashi, "Earthquake warning system 10 seconds before the strong motion (in Japanese)", Shizen, September 1972.

Nakamura, Y. (1988), "On the urgent earthquake detection and alarm system (UrEDAS)", Proceedings of 9th World Conference on Earthquake Engineering, Vol.VIII, 673-678.

Mori, J., Wald, D. J. and Wesson, R. L. (1995), "Overlapping fault planes of the 1971 San Fernando and 1994 Northridge, California earthquakes", Geophys. Res. Lett, 22(9), 1033-1036

Nakamura, Y. (1996), "Real-time information systems for hazards mitigation", Proceedings of 11th World Conference on Earthquake Engineering.

Nakamura, Y. (1998), "A new concept for the earthquake vulnerability estimation and its application to the early warning system", Early Warning Conference 98 in Potsdam, Germany.

Saita, J. and Nakamura, Y. (2003), "UrEDAS: The Early Warning System for Mitigation of Disasters Caused by Earthquakes and Tsunamis", in: J. Zschau, A, Kuppers (Eds.), Early warning Systems for Natural Disaster Reduction, Springer, 453-460.

Nakamura, Y. (2007) and Saita, J., "FREQL and AcCo for a Quick Response to Earthquake", in: P. Gasparini,G. Manfredi, J. Zschau (Eds.), Earthquake Early Warning Systems, Springer, 308-324.

Wikipedia: "Eschede train disaster", http://en.wikipedia.org/wiki/Eschede_train_disaster

Nakamura, Y. and Saita, J. (2007), "UrEDAS, the Earthquake Warning System: Today and Tomorrow", in: P. Gasparini,G. Manfredi, J. Zschau (Eds.), Earthquake Early Warning Systems, Springer, 249-281.

Nakamura, Y., Saita, J. and Satoh, T. (2010): "On an earthquake early warning system (EEW) and its applications", Soil and Dynamics and Earthquake Engineering, doi:10.1016/j.soildyn.2010.04.012

Data source of strong ground motion records of the 2009 L'Aquila earthquake: http://itaca.mi.ingv.it/ItacaNet/ http://earthquake.usgs.gov/earthquakes/shakemap/global/shake

8CUEE CONFERENCE PROCEEDINGS
8th International Conference on Urban Earthquake Engineering
March 7-8, 2011, Tokyo Institute of Technology, Tokyo, Japan

EVALUATION OF SRSND SIMULATOR AGAINTS FRAGILITY CURVES FOR PISCO QUAKE

Carlos Zavala[1)], Zenón Aguilar[2)], and Miguel Estrada[3)]

1) Professor, CISMID, Structural Lab, Faculty of Civil Engineering Universidad Nacional de Ingeniería, Lima, Peru
2) Professor, CISMID, Geotechnical Lab Faculty of Civil Engineering Universidad Nacional de Ingeniería, Lima, Peru
3) Professor, CISMID, Geomantic Lab Faculty of Civil Engineering Universidad Nacional de Ingeniería, Lima, Peru
czavala@amauta.rcp.net.pe, zaguilar@zergeosystemperu.com, estrada@uni.edu.pe

Abstract: An evaluation of the seismic response of structures using SRSND simulator developed for compute damage ratio in terms of repair cost on housing at Pisco is presented. The simulator consider the implementation of a simple algorithm for compute the seismic response of a building base on material, story height, state of conservation of the building and irregularities. The damage is compute by comparison with a damage matrix based on test results and also post quake survey developed after Pisco quake on Pisco city. Also fragility curves results for the same city has been developed by the authors and is used as comparison parameter for evaluation of the SRSND simulator results. Good agreement between both results has been found. Therefore confidence in the use of the simulator as a tool to predict losses on cities after a quake is shown.

1. INTRODUCTION

On the estimation of seismic risk analysis of cities, there are different parameters used as output of the process. The more likely used is the damage cost or the cost of reposition of the damage structures. Other parameters are the probability of damage for deterministic type of structure, the amount of collapse housing by material type and others. The evaluation of each of the output parameters need the evaluation of probability approach or empirical regression analysis based on damage survey after the event. Each of these results is linked with earthquake acceleration on a characteristic soil. Therefore, the evaluation of the seismic response of a building and the determination of the damage level need the knowledge of the soil condition, probable acceleration on the site, material influence, number of stories of the building, basic geometry and other input parameters.

In this paper a seismic response simulator with damage level estimation (Simulador Respuesta Sísmica y Nivel de Daño SRSND in Spanish) is presented. This simulator is used as a tool to predict the cost of reposition for a damage level as a consequence of an input acceleration of the ground. The development of the simulator, the input data on for the model and the parameters used on the quake response are presented. Then the validation if the model is performed by comparison with field survey results and also fragility curves developed from the survey of Pisco city after August 15th 2007 earthquake.

2. ESTIMATION OF SEISMIC RESPONSE

For the estimation of the seismic response on an approximate method is developed based on the peak ground acceleration of the soil where the structure has been build. For that purpose seismic hazard of the location is used as a first input. Next a catalog of building types that represent the study zone is needed. Therefore a field survey for typify the buildings must be developed. On the survey several variables are consider: seismic demand acceleration, material of the building, number of stories, structural predominant system, state of conservation, irregularities of plant, height and shape. Then we use the methodology propose by Miranda, that use a series of βi index to produce the seismic response based on a product of βi by the spectral displacement (Sd) for the predominant period of the building, divided by the height of the building(H), to reproduce the maximum inter story drift during an earthquake:

$$\left(\frac{\Delta\delta_j}{h_j}\right)=\frac{\beta_1\beta_2.\beta_3\beta_4}{H}S_d$$

The index β1, is an modal participation factor approximation given as a function of the story number:

$$\beta_1=\frac{3N}{2N+1}$$

The index β2, is a ratio between the approximate maximum drift (calculate as SDOF system) against the drift on real system:

$$\beta_2=\frac{\max\left(\frac{\Delta\delta_j}{h_j}\right)}{\left(\frac{U_r}{H}\right)}$$

The index β3 is the reatio between the force response (F^x) with the over resistance of the structure (F) formulated as a function of the assign ductility (μ) for the type of structural system:

$$\beta_3 = \frac{U^x + \Delta U^x}{U} = \frac{F^x.\mu}{F}$$

The index β4 produce an approximation of the ratio between the inelastic drift and the elastic drift that provide an approximate measure of the ductility:

$$\beta_4 = \frac{\varphi_{inelastic}}{\varphi_{elastic}}$$

The estimation of the period of the structure is the base for this diagnosis, which is extremely dependant of the type of building and number of stories. Therefore the drift in each story can be approximate and by comparison of drift limits based on experimental approach, the estimation of damage level using a damage matrix will produce the reposition cost of the building.

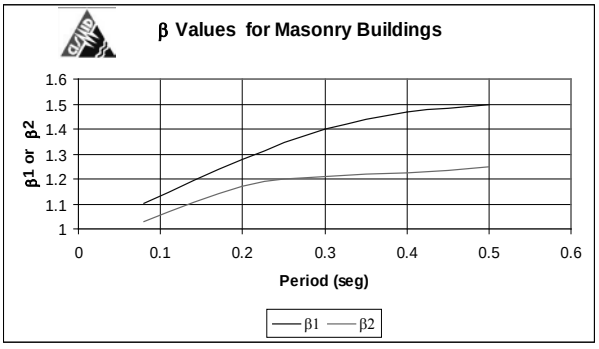


Figure 1: Values of β1 and β2 parameters

This procedure has been automated in our SRSND simulator to provide under a seismic scenario the estimation of the damage level of a city. For the βi values, multiple analysis of typical houses and ductility consideration has been calibrated with test results. Figure 1 shows the values of β1 and β2 for masonry buildings. Figure 2 presents the values of β3 factor as function of the period of the structural system considering assigned ductility (μ) of 6. Figure 3 presents the values of for β4 as function of the assigned ductility.

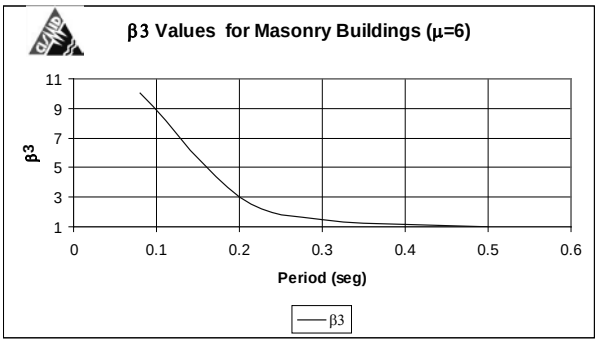


Figure 2: The β3 factor

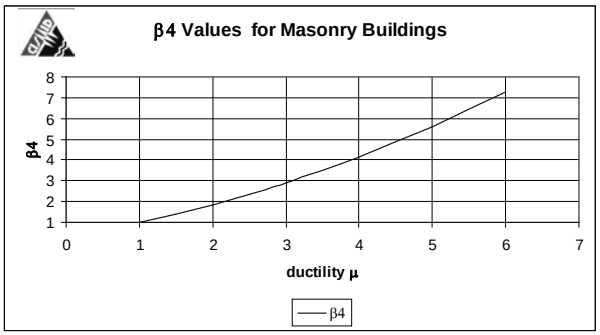


Figure 3: The β4 values as function of ductility

After the evaluation of the seismic response, the damage level can be computed using the following matrix:

Drift (Δδj/hj)	Damage Level	Occurrence
1/2000-1/1000	Non damage	none
1/800	Light damage	Initial crack
1/350	Severe damage	Diagonal open
> 1/200	Collapse	Non

3. VALIDATION OF SRSND WITH PISCO QUAKE FIELD SURVEY

On August 15th 2007 an earthquake of magnitude 8.0 Mw, stroke the south coast of Peru with epicenter at Latitude -13.49° and Longitude: -76.85° with depth of 26 Km. located 74 Km. west of Pisco city. The quake kill 593 persons, with 1,291 injured, and 48,208 collapse houses, and near 90,000 affected houses.

The authors with the support of professors and students of the Faculty of Civil Engineering of the National University of Engineering carried out a field survey on the Pisco city involved in the present report with the financial aid of Inter-American Development Bank (IDB) and World Bank (WB). Pisco city is located on the coast. However the damage characterization depends of the demand and also the site conditions where different kinds of soil profiles were found.

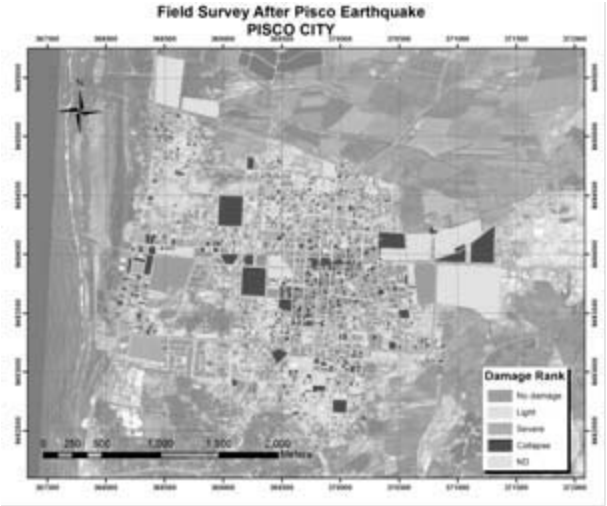


Figure 4: Results of Damage Survey in Pisco

Pisco has areas of soft soil represented by a mix of sand with gravel with high level of humidity and also a middle soil with gravel and compact sand. A campaign was developed to study Pisco city, to implement the damage characterization, and record the data on a GIS system.

Figure 4 presents the damage survey in Pisco city performed by CISMID. Here the red color represents the collapsed structures, in orange the severe damage buildings, in yellow slight damage and light green non damage structures.

Using the field survey data, the simulator SRSND performed the risk analysis results in terms of reconstruction cost using the damage matrix. Figure 3 and Figure 4 have a good agreement, showing that the simulator can emulate the response of the buildings and provide the cost of reconstruction.

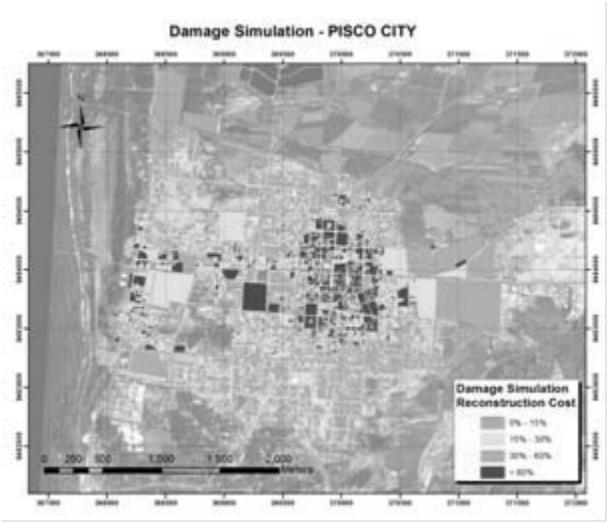


Figure 5: Damage simulation in terms of reconstruction cost

4. FRAGILITY CURVES FROM SURVEY DATA AND VALIDATION OF SRSND

In order to know the fragility of the structural systems damage under Pisco earthquake an analysis of the survey data has been performed in order to compute the probability of damage under an assigned peak ground acceleration. We must mentioned that one of our limits was the difficulty to have a representative soil profile during the quake, because the few records of after shocks and also the few stations that record these events.

Figure 6 shows the results of field survey on Pisco City, by damage for each type of material used in the city. From the total of adobe buildings, 82% collapsed, following by quincha buildings with 65% of collapse. Masonry buildings suffer less from the strike of the quake (slight damage and non damage) with 70% of them without high demand.

If we consider the total of buildings of Pisco city, Figure 7 presents the percentage considering the total number of the buildings. The adobe buildings that collapsed in the city represents 15% of the total and the masonry buildings that collapsed represents 10.7% of the total of housing.

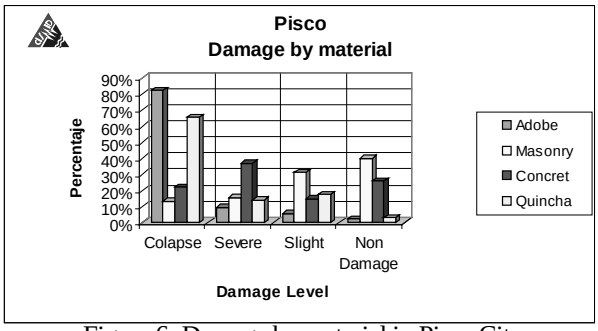


Figure 6: Damage by material in Pisco City

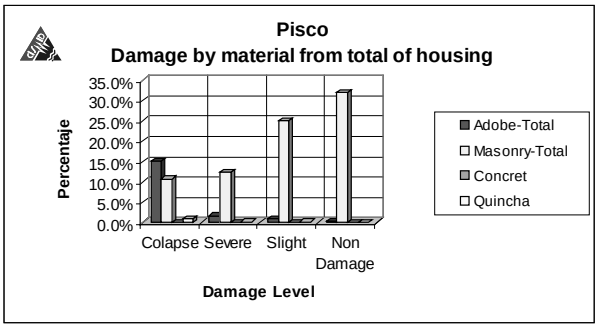


Figure 7: Damage related with total

In Pisco city the adobe structures suffer more than other materials. Also masonry buildings had less damage than the adobe but collapse in this case are more related with the soil profile and demand acceleration during the earthquake.

Mainly in Pisco city soil profile presents three big groups of peak ground acceleration: 0.42g, 0.462g and 0.588g. Under these demands buildings will experiment a probability of damage. Correlating these accelerations with the data of survey, soil profile and also material type we developed fragility curves for adobe structures and masonry structures, presented in Figure 8.

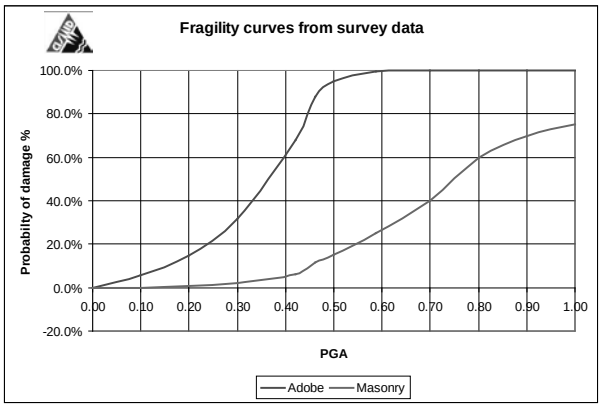


Figure 8: Fragility curves for adobe and masonry

Using these curves the probability of damage of each building can be computed. Then the results show that three groups were generated: 3118 buildings had less than 10% of probability of damage. Among 5193 buildings have a damage probability between 10 to 30 %, and 1866 buildings

have a damage probability over 60%. This last situation means collapse and cost of reposition is 100%.

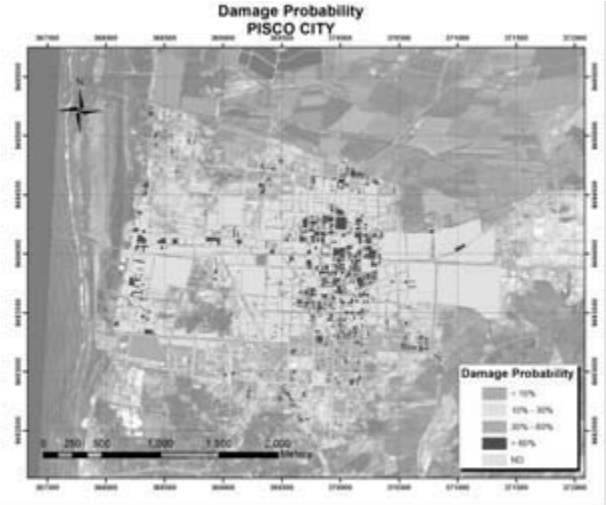


Figure 9: Damage Probability from Fragility Curves

Figure 9 presents the results of the damage probability in each building of Pisco city, considering the fragility curves presented in Figure 8. Here is possible to see the agreement with the SRSND and also the field survey results. These verified the simulation performed by SRSND and also validate the use of the developed fragility curves from survey and soil profile data.

5. CONCLUSIONS

- A simulator for the seismic response of buildings using survey data and approximation parameters βi has been presented. The simulator perform an approximate methodology based on a SDOF system that used the predominant period of the building to compute the seismic response and damage level.
- To compute the earthquake response the spectral displacement must be computed using the predominant period. Then with the use of the same parameter, the constant βi are computed for an assigned ductility. Curves for each parameter are introduced for the case of masonry buildings.
- For validation of the SRSND simulator a comparison with the damage survey after Pisco earthquake was performed. Here a good agreement among colors on Figure 4 and Figure 5, give a trustable results from the simulation
- Also survey results after Pisco earthquake is presented. Mainly the damage due to the earthquake in Pisco City has been caused by the soil conditions that may amplify the seismic waves, on building materials, like adobe, that have a bad behavior against seismic forces and construction quality that do not comply with the standards.
- As a consequence of 15/8/2007 Pisco quake, damage on housing occurs at Pisco, were the most damage construction system was the adobe walls house with 82% of collapse in Pisco.
- Masonry housing experiment less damage than adobe due to the confinement of the walls, with only 10% of collapse in Pisco.
- It is evident the correspondence between the damage levels and the soil conditions; therefore, soil profile of urban areas constitutes a very important tool for city planning and reconstruction plans.
- Damage levels were presented in a matrix related with drift values. These values can be correlated with the type of damage and also with the cost of retrofit its damage. It means the cost of restoration.
- It is demonstrated that even in a case of a strong ground motion if the masonry buildings are built following the national standards they do not collapse, given as result the safety of their occupants.

Acknowledgements:

The authors acknowledge support from Inter American Development Bank (IDB) and World Bank (WB) for the support this research. Also our gratitude to the Secretary of First Ministry Board to trust on our Institution in the development of this microzoning studies. Our gratitude to all our staff members, specially our young researchers who collaborated in the field survey and implementation of GIS data.

References:

CISMID-FIC-UNI. (2007). Microzoning of Pisco, San Luis de Cañete and Huaytara. Report for Inter American Development Bank (IDB) and Secretary of the Presidency of First Minister (PCM), Lima, PERU.

CISMID-FIC-UNI. (2008). Microzoning of Tambo de Mora and Chincha Baja. Report for World Bank (WB) and FORSUR Ministry of Housing, Lima, PERU.

Journal of Structural Engineering ASCE (July 2002) .Approximate Lateral Drift Demands in Multistory Buildings with Non uniform Stiffness - Eduardo Miranda and Carlos J. Reyes.

Journal of Structural Engineering ASCE. (1999.) Approximate lateral deformation demands in multistory buildings – Miranda Eduardo.

Carlos Zavala y Ricardo Proaño – XIV Congreso de Ingeniería Civil Iquitos Perú (Octubre 2003.)Estimación rápida de la Respuesta Sísmica en base a sistemas de un grado de libertad para el calculo de vulnerabilidad sísmica (in Spanish).

CISMID/FIC/UNI/ (Noviembre 2007) - Carlos Zavala SRSND Simulador Respuesta Sísmica y Nivel de Daño (in Spanish).

8CUEE CONFERENCE PROCEEDINGS
8th International Conference on Urban Earthquake Engineering
March 7-8, 2011, Tokyo Institute of Technology, Tokyo, Japan

LAND USE EVALUATION USING SATELLITE IMAGERY FOR URBAN INVENTORIES

Miguel Estrada[1], Hiroyuki Miura[2], Fumio Yamazaki[3], and Saburoh Midorikawa[4]

1) Associate Professor, Faculty of Civil Engineering, National University of Engineering, Peru
2) Assistant Professor, Department of Built Environment, Tokyo Institute of Technology, Japan
3) Professor, Department of Urban Environment Systems, Graduate School of Engineering, Chiba University, Japan
4) Professor, Department of Built Environment, Tokyo Institute of Technology, Japan
estrada@uni.edu.pe, hmiura@enveng.titech.ac.jp, yamazaki@tu.chiba-u.ac.jp, smidorik@enveng.titech.ac.jp

Abstract: To evaluate the seismic vulnerability of an urban area it is necessary to know the type of buildings or the actual land use over it. The development of building inventory is costly and time consuming, therefore, in Peru only few municipalities may have the capacity to develop such a kind of work. In this paper it is discussed the use of high resolution images to infer the type of social class and consequently the type of house or building typified by its major characteristics, based on two characteristics: the number of pools and the concentration of vegetation that exist in each block of the area under study.

1. INTRODUCTION

Peru is located in a seismic prone area and the development of the cities are so fast and do not pay attention to the regulation on building constructions, so it is of interest to study the type of building on urban area to know their vulnerability in case of an extreme earthquake. One of the main data source to assess the type and condition of the building are the census or inventory data that is developed for the local governments. In most of the municipalities in Peru there is not a policy to develop this kind of data, not only because of lack of economic resources but also because the absence of technical people that can understand the problem and conduct this work. Therefore it is necessary to develop a methodology to carry out a fast inventory of buildings and to recognize their vulnerability against earthquakes. Recently high resolution imagery is becoming more accessible, not only because price, but also because multiple satellites are observing the earth surface constantly given a rich source on information about the land use. Lima city is characterized by people of different social classes; these social classes may indicate the type of building where they live, in terms of quality and if they followed the regulations during the construction of the building. Low class people generally they construct their houses by themselves, as they can and without following the regulations of the National Building Code.

In this study it is proposed to used high resolution satellite imagery to recognize the social class of the people by identify some characteristics of their houses like pools and greenness and thus to classify the vulnerability of the urban area. Finally the land information is integrated with PRISM sensor data to identify areas that are built over important slope to evaluate also hazard of these area.

2. UMBRELLA PROJECT

This research is under the project "Enhancement of Earthquake and Tsunami Disaster Mitigation Technology in Peru" the purpose of this project is to developed technologies and measures for prediction and mitigation of earthquake/tsunami disasters caused by large-magnitude inter-plate earthquakes occurring off the coast of Peru.

This project is divided into five active groups. Group 1 will research on seismology and geotechnical issues, and give the final response of the soils. Group 2, will study the source, effects and countermeasures of tsunamis produced by an earthquake. Group 3, will identify the most typical building problems and will propose retrofitting methods or will give some advises to improve the actual building code. Group 4, will develop methodologies to identify the land use, by using the satellite imagery and integrating all the information in a GIS platform to assess the risk of the building as well as to develop a methodology for fast assessment of the damaged area by an earthquake or tsunami. Finally, Group 5 will take the entire group's output and will disseminate this knowledge and propose policies for a sustainable development of the population. This project is under the support of Japan International Cooperation Agency, Japan Science and Technology Agency, Peruvian International Cooperation Agency. And the institutions directly involved in this study are the Chiba University and Tokyo Institute of Technology, from the Japanese side and the Japan Peru Center for Earthquake Engineering Research and Disaster Mitigation, National University of Engineering, from the Peru side.

3. STUDY AREA

The area of study is the district of La Molina in Lima Peru. This district has a population of approximately 130000 habitants. This district is very special in Lima Metropolitan area, because here it can be found people of different social classes and therefore different construction type and building quality. Another issue in this district is that it is growing very fast and the new developed urban area is taking place on terrain with important slope. Because soil conditions, buildings in this district have suffered of important damage in past earthquakes, therefore it is important to know the type of building that are built on this area. In Figure 1 it can be seen the location and extension of La Molina district, that is located in the middle east of Lima. Although this is a district with relatively good economical resources, the situation of the cadastral information is still in the beginning stage that is why it is necessary to use another source of information to evaluate and assess the type of buildings.

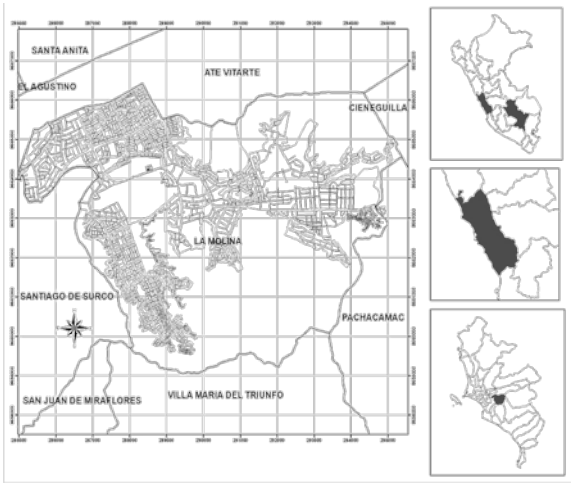


Figure 1. District of La Molina in Lima, Peru.

4. DATA CHARACTERISTICS

The date used in this work is the multispectral Worldview 2 which major characteristics are shown in Table 1.

Table 1. Worldview 2 scene characteristics.

Characteristic	Value
Acquisition date	March 11, 2010
Number of bands (M – P)	8 – 1
Rows/Columns (M – P)	4031/5463 – 16124/21852
Bits per pixel	16
Spatial resolution	2.0 m MS/0.5 m PAN
Wavelength (nm):	
- Coastal (Band 1)	- 427 nm
- Blue (Band 2)	- 478 nm
- Green (Band 3)	- 546 nm
- Yellow (Band 4)	- 608 nm
- Red (Band 5)	- 659 nm
- Red edge (Band 6)	- 724 nm
- NIR 1 (Band 7)	- 831 nm
- NIR 2 (Band 8)	- 908 nm

As we can see in Table 1 the number of multispectral bands that are included in one image is good enough to detect many materials over the earth surface. This advantage is taken as the base for the analysis. In this research Worldview 2 images were selected instead of Ikonos (Cook et. al., 2000) images because two reasons: first: there is a better resolution 0.50 m vs. 0.60 m, and second spectral resolution in case of Worldview 2 has more sensibility as it can be seen in Figure 2.

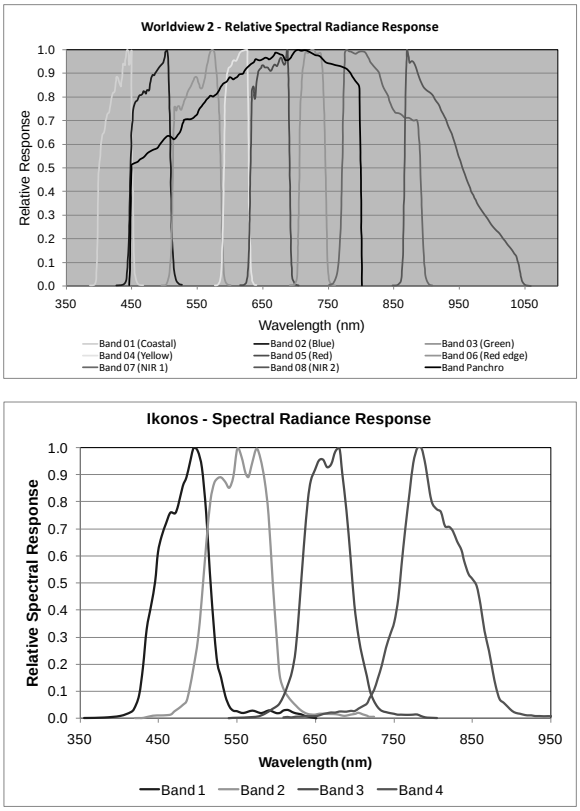


Figure 2. Spectral response comparison between Worldview 2 and Ikonos images.

5. METHODS AND PROCEDURES

To assess the seismic vulnerability of an urban area can be done by evaluating of housing census data, but it has the drawback that that method cannot be generalized, one approach based on contextual analysis of image and GIS data is presented by Ebert et al (2008) where an approach based on proxy variables that were derived from high resolution optical and laser scanning data was applied, in combination with elevation information and existing hazard data social class we investigate the location of swimming pool within an urban area. Another approach for building inventory is presented by Dutta et. al (2005) where very high resolution satellite optical data from Quickbird satellite with object-oriented classification scheme was used for an overall

accuracy of 85% in detailed classification of urban land cover.

In La Molina district it can be found different types of land use depending on the social classes. As it is shown in Figure 3, high social class area (a) has an important green area and important features are the pools inside of the lot, middle class area (b) has also important green area but no pools, and low class area has few vegetation and no pools. Therefore if pools and vegetation can be detected in an automatic manner we could infer the type of social class in the area and as consequence the social vulnerability of it.



(a) (b) (c)

Figure 3. Difference between land use in La Molina.

For mage classification exits a bunch of methods, mainly classified into two big groups: unsupervised and supervised methods. One of the methods of supervised classification is described by Mohd et. al. (2007) the Spectral Angle Mapper (SAM) this is a physically-based spectral classification that uses an n-dimensional angle to match pixels to training pixel area. The algorithm determines the spectral similarity between two spectra by calculating the angle between them, treating them as vectors in a space with axes equal to the number of bands. Smaller angles represent closer matches to the training pixels.

Luc et. al. (2005) depicts how to obtain the angle between two spectra that are being compared. In Figure 4 it can be seen, in a three bands dimension space, if spectral angle (θ) is small then the tested (t) and reference (r) spectral vectors are similar. In Eq. 1, we can see the numerical calculation, where the angle θ is a kind of correlation value between two samples in an n-dimensional spectral space.

$$\theta = \cos^{-1}\left(\frac{\sum_{i=1}^{n} t_i r_i}{\sqrt{\sum_{i=1}^{n} t_i^2 \sum_{i=1}^{n} r_i^2}}\right) \qquad \text{Eq. 1}$$

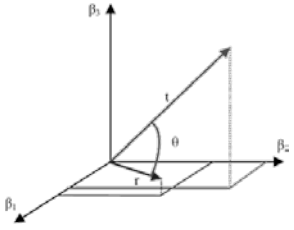


Figure 4. r reference spectra vector, t spectra vector to be compared, θ spectral angle .

Pixels that are in pools are selected as trained pixels. Pixels were selected over the image, and their spectral response was analyzed. Figure 5, shows how the pixels were selected and the average of the digital number of these pixels.

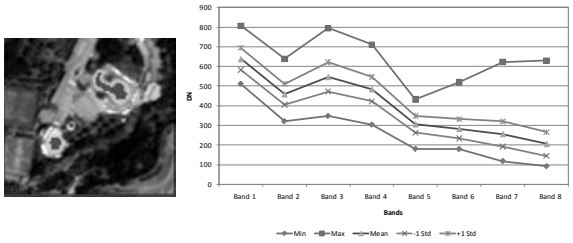


Figure 5. Trained pixels and their spectral response.

Another parameter that was used is the NDVI to detect the concentration of vegetation in the area.

6. RESULTS

The SAM method for classification gave good results and the pools could be detected, the number of pools in one block where automatically counted and the image was transferred to GIS map and then classified by this number.

Additionally, the NDVI also was calculated and the number of pixels that represent vegetation where counted in each block.

Figure 6 shows the thematic map considering the number of pools by block, it can be seen that there are some areas where the number of pools is considerable given areas of high class. In Figure 7, is presented the thematic map representing the concentration of vegetation in each block, high concentration of vegetation indicates high class, while very low concentration may indicate low class.

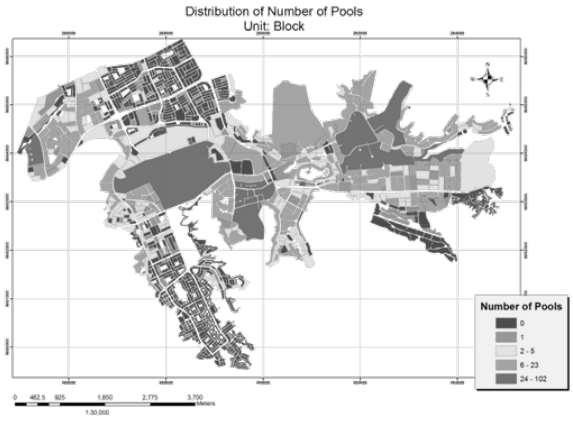


Figure 6. Classified map indicating the number of pools by block.

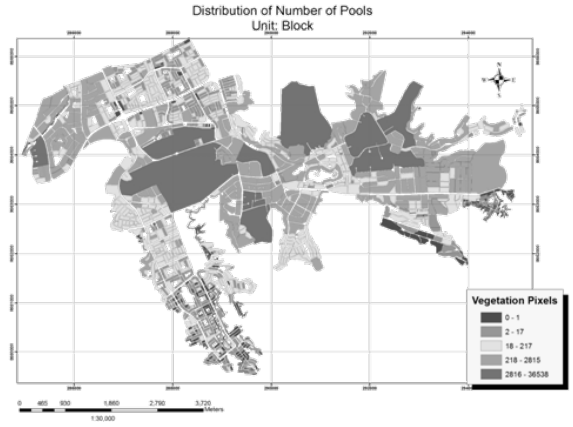


Figure 7. Classified map indicating the number of vegetation pixels by block.

Also it was conducted a field survey for verification of the results given good agreement with the two indexes. In Figure 8, it can be seen that for different type of land use it is possible to correlate the number of pools and the NVDI.

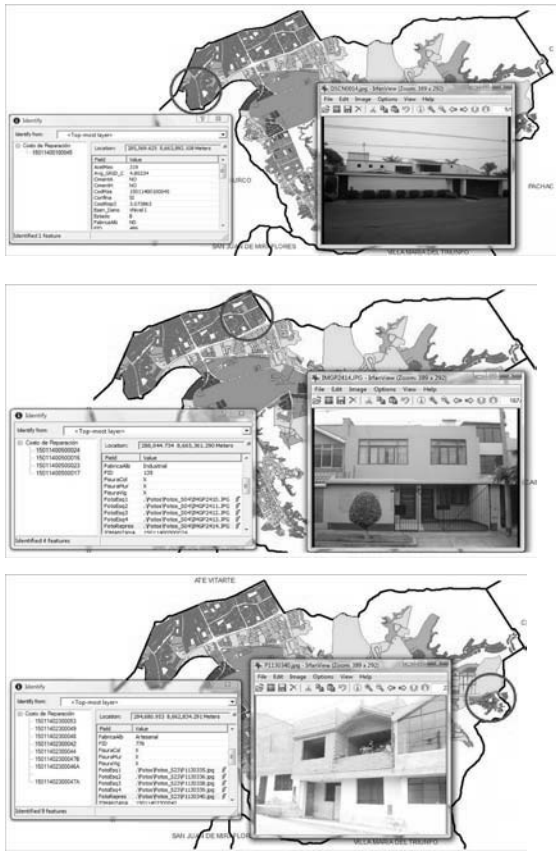


Figure 8. Field survey of different sectors.

3. CONCLUSIONS

It can be shown that from satellite information it can be inferred the type of social class based on two characteristics of the urban area: the number of pools and the concentration of vegetation. While the number of pools and the concentration of vegetation is high it is and indicative that the social class of the people who live there is high and therefore their houses may be well constructed, while on the other side where pools do not exist and the vegetated area is minor may indicate a social class where the construction of the houses may have not follow the standards and therefore their seismic vulnerability could be considerable.

Acknowledgements:

The authors would like to thank to the Japan Science and Technology Agency and Japan International Cooperation Agency for the support in acquiring the satellite data and the field survey..

References:

Cook , M., Peterson , B., Dial , G., Gerlach , F., Hutchins , K., Kudola, R. and Bowen, H., (2000), "IKONOS Technical Performance Assessment", Space Imaging, LLC.

Dutta, D., Serker, K. and Warnitchai, P., (2005), "Use of VHR Remote Sensing Imagery for Urban Building and Infrastructure Inventory Database for Disaster Risk Analysis", Map India 2005, Geomatics 2005.

Ebert, A., Kerle, N. and Stein, A. (2008), "Urban social vulnerability assessment with physical proxies and spatial metrics derived from air- and spaceborne imagery and GIS data", Nat Hazards 48:275–294.

Luc, B., Deronde, B., Kempeneers, P., Debruyn, W. and Provoost, S. (2005), "Optimized Spectral Angle Mapper classification of spatially heterogeneous dynamic dune vegetation, a case study along the Belgian coastline", The 9th International Symposium on Physical Measurements and Signatures in Remote Sensing, Beijing.

Mohd, H., Suhaili, A. and Mansor, S. (2007), "The Performance of Maximum Likelihood, Spectral Angle Mapper, Neural Network and Decision Tree Classifiers in Hyperspectral Image Analysis", Journal of Computer Science 3 (6): 419-423.

8CUEE CONFERENCE PROCEEDINGS
8th International Conference on Urban Earthquake Engineering
March 7-8, 2011, Tokyo Institute of Technology, Tokyo, Japan

EVALUATION OF BUILDING DAMAGE AREAS OF THE 2006 CENTRAL JAVA, INDONESIA EARTHQUAKE DETECTED FROM SATELLITE OPTICAL IMAGES

Hiroyuki Miura[1)], Saburoh Midorikawa[2)], and Norman Kerle[3)]

1) Assistant Professor, Dept. of Built Environment, Tokyo Institute of Technology, Japan
2) Professor, Center for Urban Earthquake Engineering, Tokyo Institute of Technology, Japan
3) Assistant Professor, International Institute for Geo-Information Science and Earth Observation (ITC), Netherlands
hmiura@enveng.titech.ac.jp, smidorik@enveng.titech.ac.jp, kerle@itc.nl

Abstract: In order to estimate the building damage distribution of the 2006 Central Java, Indonesia earthquake, a procedure of pixel-based damage detection is applied to the optical satellite images observed before and after the earthquake. The satellite FORMOSAT-2 images with the resolution of 2m are used. The comparison of the images shows that the digital numbers in severely damaged area in the post-event image is higher those in pre-event image. In the analysis, the pixels of the image are classified into vegetation, bare ground and built-up areas. The damaged areas are detected by differential of the digital numbers in the built-up areas. The estimated damage distribution is validated by comparing with the GIS building damage data obtained by the field survey. The result shows that the severely damaged areas are well detected by the analysis. In the densely vegetated area, however, the damage is underestimated because the buildings are obscured by trees.

1. INTRODUCTION

In a destructive earthquake, man-made structures such as buildings and infrastructures would be severely damaged over a wide area. As basic information for early-stage recovery activities, it is necessary to identify the damage distribution as soon as possible after an earthquake. Since remote sensing can easily capture the real world from the air at a time, the remote sensing technology is a promising tool for early damage assessment and has been applied in various post-earthquake activities (Rathje and Adams, 2008). For rapid damage identification, it is important to develop a computer-based image analysis to automatically or semi-automatically detect damaged areas from satellite images.

Pixel-based image analysis is one of the major change detection techniques from remote sensing data (Lunetta and Elvidge, 1998). In pixel-based change detection, each pixel is assigned to "change" pixel or "non-change" pixel based on the characteristics of the pixel between two-date images. The technique had been also applied to detect earthquake damage (e.g., Kohiyama and Yamazaki, 2005). In these damage detection studies, difference and/or correlation of digital number (DN) or edge intensity between the pre- and post-event images is used. The areas where these indices are significantly changed after the event are extracted as damaged areas.

There would be two factors of false detections in the pixel-based change detection. The one is that difference of projection direction of buildings and their shadows between two images may produce lots of false detections when using the images whose observation angles such as off-nadir angles are different each other. The other is that change detection for whole pixels in the images may produce not only the change related to earthquake damage but also non-earthquake change (e.g., seasonal vegetation change). For the former factor, the use of images whose off-nadir angles are same may reduce such false detections. For the latter factor, false detections would be reduced by extracting built-up areas in advance and detecting changes only from the built-up areas.

For more accurate automatic damage identification, a procedure of pixel-based damage detection is proposed in consideration of the two problems shown above and applied to optical satellite images observed before and after the 2006 Central Java, Indonesia earthquake. The satellite FORMOSAT-2 images with the spatial resolution of 2m are used because the satellite observes with constant off-nadir angle. To accurately detect the damage of buildings, pixels of the images are firstly classified into three categories; vegetation, bare ground and built-up areas. The damage areas are estimated by the differential of DN in the extracted built-up areas between the pre- and post-event images. The detected damage distribution is validated by comparing with the building damage data obtained by field survey.

2. CHARACTERISTICS OF SATELLITE IMAGES

The destructive earthquake in Java Island, Indonesia occurred at 05:54AM on May 27, 2006 (M_W6.3) caused severe damage in the central Java province. The epicenter

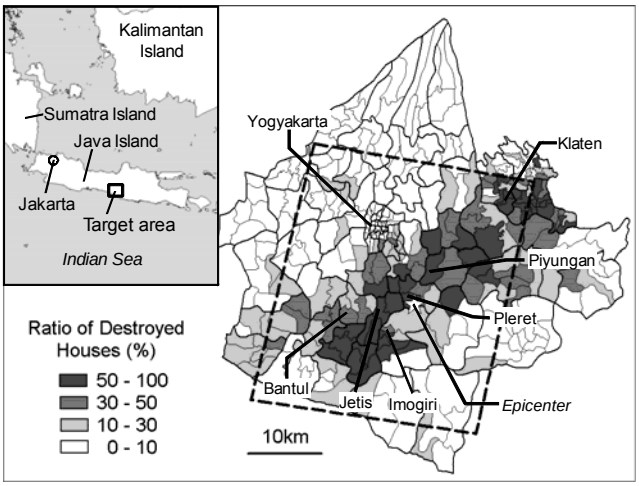


Fig. 1 Target Area with Village-level Damage Ratios

of the earthquake is located in 15km southeast from Yogyakarta, a major city of the central Java. The number of deaths and injured people was approximately 5,700 and 37,000, respectively. The number of destroyed buildings was more than 300,000. The monetary loss was about 3 billion US$ (Karnawat et al., 2008).

Figure 1 shows the location of the epicenter and distribution of ratio of destroyed houses by village-level damage statistics compiled by the regional governments approximately one month after the earthquake (IFRC, 2006). The damage ratio is higher than 50% not only in the epicentral areas such as Prelet and Jetis but also in the northeastern areas about 30km far from the epicenter such as Klaten. The dotted square in Fig. 1 shows the target area of this study.

Figures 2 show the pre- and post-event satellite images used in this study. The FORMOSAT-2 images observed before and after the earthquake are used. The pre- and post-event images were observed in May 18 and June 11, 2006, respectively. The panchromatic image is used as the pre-event image because multi-spectral image was not acquired in the target area before the earthquake. The panchromatic and pan-sharpened images from the multi-spectral image are used as the post-event image. The spatial resolution of the images is 2m.

Figures 3 (a) and (b) show the close-ups of the pre- and post-event panchromatic images in severely damaged area. According to the field survey by Architectural Institute of Japan (2007), about 90% of the residential houses are severely damaged in the settlement located at the central part of the image. Figure 3(c) indicates a cross-section of the DN of the images along the dotted line in the figures. In the severely damaged area, the DN in the post-event is remarkably higher than that in the pre-event. The collapsed buildings produce lots of rubble piles such as wall bricks on the surface ground. Since the reflectance of brick is higher than that of roof tile (Miura et al., 2007), the difference of the reflectance of the materials results the differential of the DN. Therefore, the differential of the DN between the images is used to detect the building

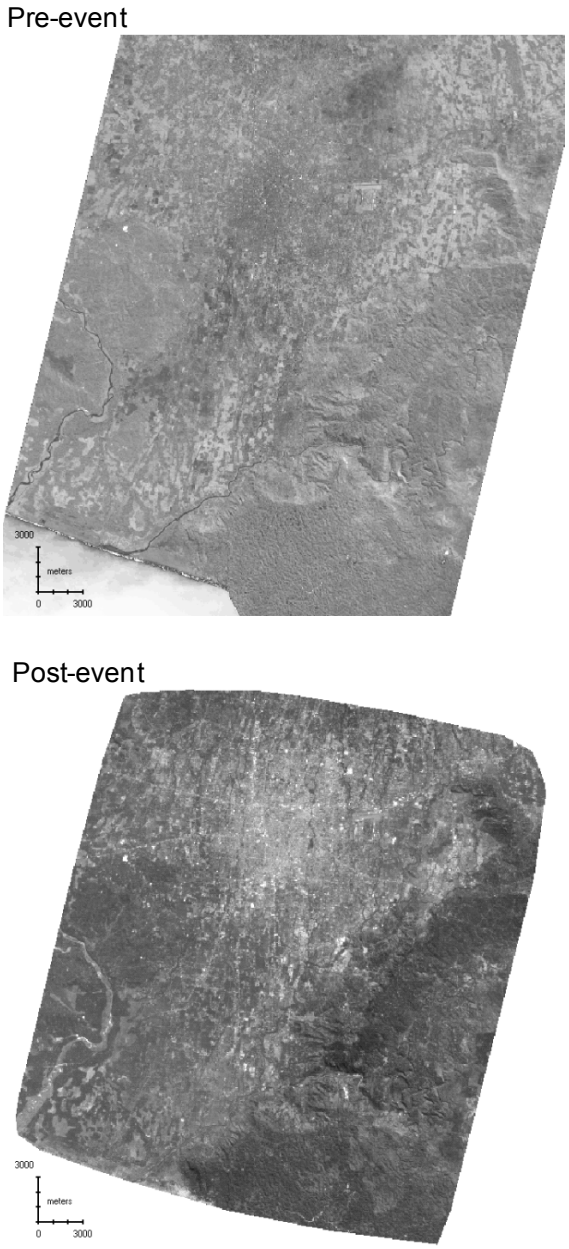
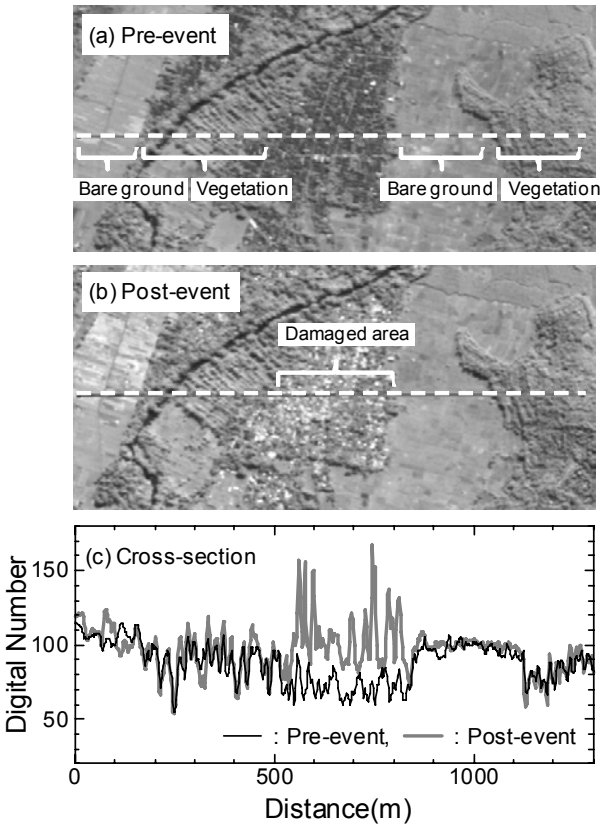


Fig. 2 Comparison of Pre- and Post-event Images

damage areas in this study.

3. DAMAGE DETECTION

Figure 4 shows the flowchart of the damage detection procedure employed in this study. In order to detect building damage in built-up areas, the pixels of the images are classified into vegetation, bare ground and built-up areas. First, vegetated areas are extracted by thresholding of NDVI (Normalized difference vegetation index) calculated from post-event pan-sharpened image. NDVI is defined as the difference in pixels between near infrared band image and red band image divided by their sum. A higher NDVI indicates a higher density of green leaves in a pixel. Figures 5 (a) and (c) indicate the distribution and the



Figs. 3 Comparison of Pre- and Post-event Images

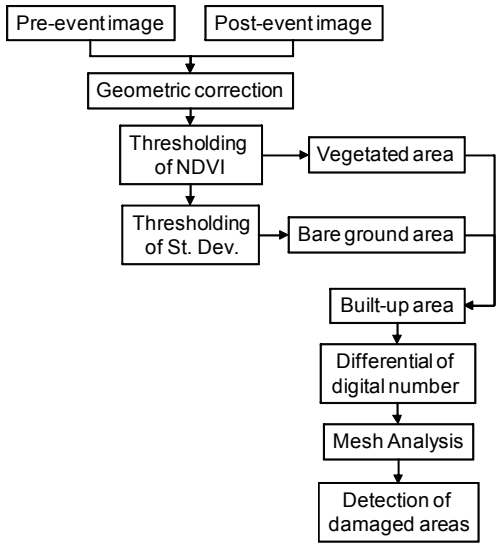
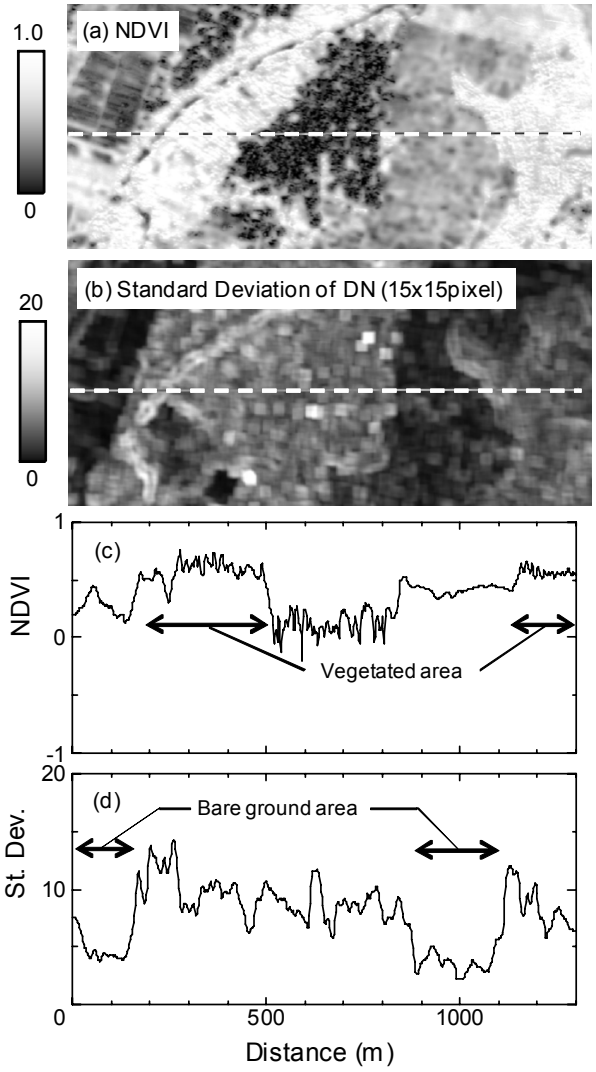


Fig. 4 Flow of Damage Detection

cross-section of NDVI in the area shown in Figs. 3. The threshold value of NDVI is selected by comparing the distribution of NDVI and the vegetated area. In this study, the pixels whose NDVI is higher than 0.4 are classified into vegetated areas.

Second, bare ground areas are extracted by thresholding of standard deviation (SD) of the DN in a windowed area calculated from pre-event panchromatic image. Because



Figs. 5 NDVI and SD Images

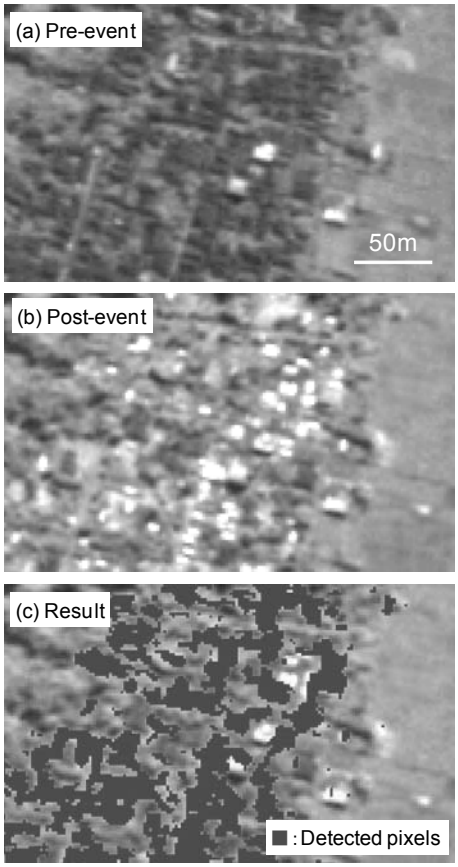
homogeneous materials such as soil are uniformly distributed in bare ground, the variation of the DN in bare ground areas is lower than that in built-up areas. The SD that is one of the texture indices is used to extract the bare ground areas. By considering that the size of buildings in the target area is from 5 to 30m and the size of bare ground is from several tens to hundreds meters, the window size for the calculation of the SD is determined at 30x30m (15x15pixels). Figures 5 (b) and (d) indicate the distribution and the cross-section of the SD. The threshold value of SD is selected by comparing the distribution of the SD and the bare ground areas. The pixels whose SD is lower than 6.0 are classified into bare ground areas.

Finally, built-up areas are extracted by subtracting the vegetated areas and bare ground areas from the whole area. The differential of the DN in the built-up areas is calculated and the thresholding is applied to the differential. From the comparison of the difference image and the distribution of damaged areas, the pixels whose differential of the DN is larger than 20 is extracted as the damaged areas. Figures 6 shows the distribution of the detected pixels. Red pixels

indicate the detected pixels, showing the damaged area is well detected in the analysis.

The detected pixels would correspond to rubble piles produced from collapsed buildings. This indicates that the severely damaged or collapsed buildings can be detected but moderately and slightly damaged buildings cannot be detected by the image analysis.

In order to identify the extent of the detected pixels, the number of the detected pixels is evaluated by 200m-mesh map. Figure 7 shows the distribution of the detected areas. Figure 8 shows the distribution of damage ratios of destroyed houses calculated from the village-level damage statistics (IFRC, 2006). In the epicentral area such as Pleret and Jetis whose damage ratio is more than 70%, many pixels are well detected by the image analysis. Also in the northeastern area such as Klaten that are severely damaged, many pixels are detected as damage. On the contrary, in the southern area such as Pundong and Bambang Lipuro, the number of the detected pixels is rather smaller while the area is also severely damaged according to the damage statistics.



Figs. 6 Result of Damage Detection

4. VALIDATION

In order to quantitatively evaluate the result of the damage detection, the estimated damage distribution is compared to building-by-building damage data obtained in field surveys by Gadjar Mada University in Yogyakarta. The data includes the location of building, building use, structure, material of roof, number of floors and damage level (Kerle, 2010). The damage is classified into three categories; Collapse/Heavy damage (Collapse), Moderate damage and Slight damage. About 50,000 buildings in the epicentral area were investigated. Approximately 95% buildings of the surveyed buildings are one-story residential buildings. Almost 65% of the buildings are classified into collapse, 15% and 20% are classified into moderate and slight damage, respectively.

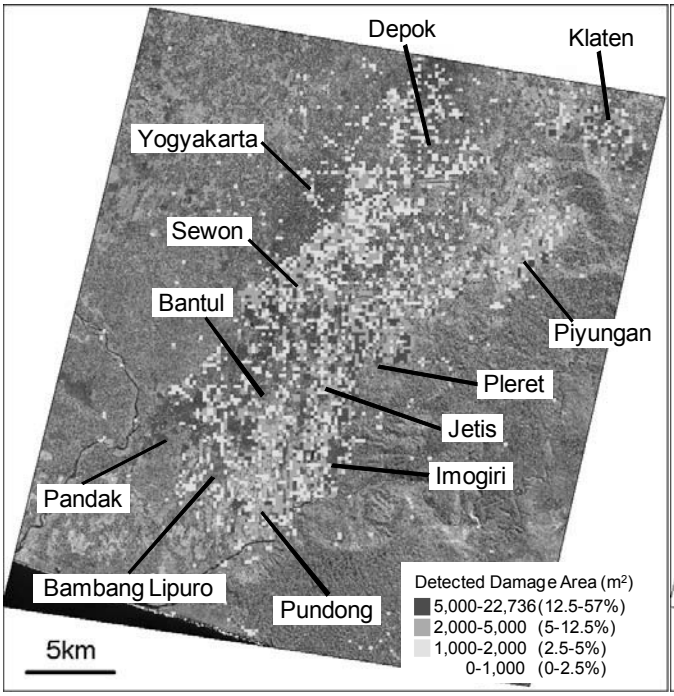


Fig. 7 Distribution of Detected Pixels

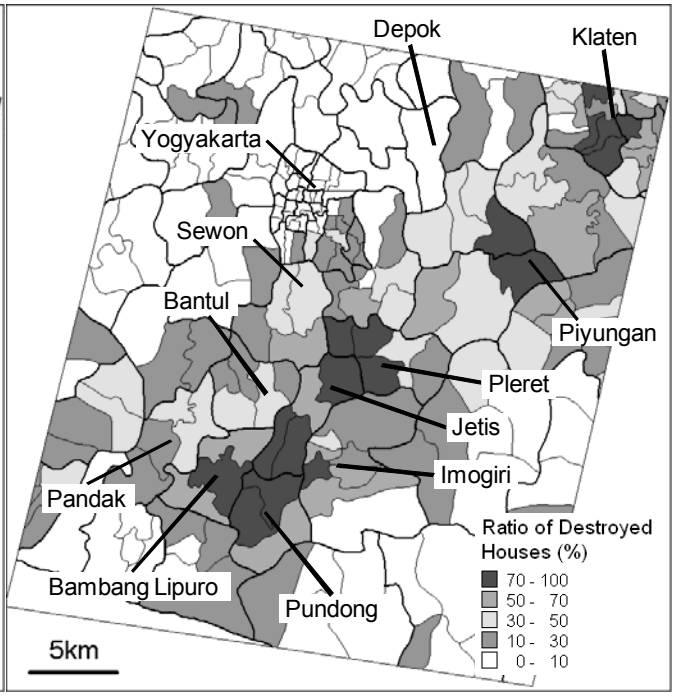


Fig. 8 Village-level Damage Distribution

From the comparison of the damage data and the actual building distribution in satellite images, the survey was conducted for settlement-by-settlement and unsurveyed settlements are situated in next to the surveyed settlements. In the surveyed settlements, almost all the buildings seem to be investigated. Since the size of the settlements is usually more than 200m, the damage rate can be properly evaluated by 200m-mesh map. Figure 9 shows the distribution of the number of collapsed buildings obtained in the field surveys. The data covers Prelet, Jetis, Imogiri, Bantul and does not cover Yogyakarta and Klaten.

Figures 10 (a), (b) and (c) show the close-ups of the pre-, post-event image and the damage detection in a built-up area. The damage data is illustrated by points in Fig. 10(b). Red, yellow and green points represent collapsed, moderately damaged and slightly damaged buildings, respectively. In Fig. 10(c), red, blue, orange and green pixels represent damaged, undamaged, bare ground and vegetated areas, respectively. In this mesh, about 170 buildings are collapsed and the damaged areas are almost successfully detected by the image analysis. Figures 10 (c)-(e) show the close-ups in a vegetated area. While many buildings are collapsed in the dotted circle in the figure, the damaged areas are mis-detected and classified into vegetated areas by the image analysis. As

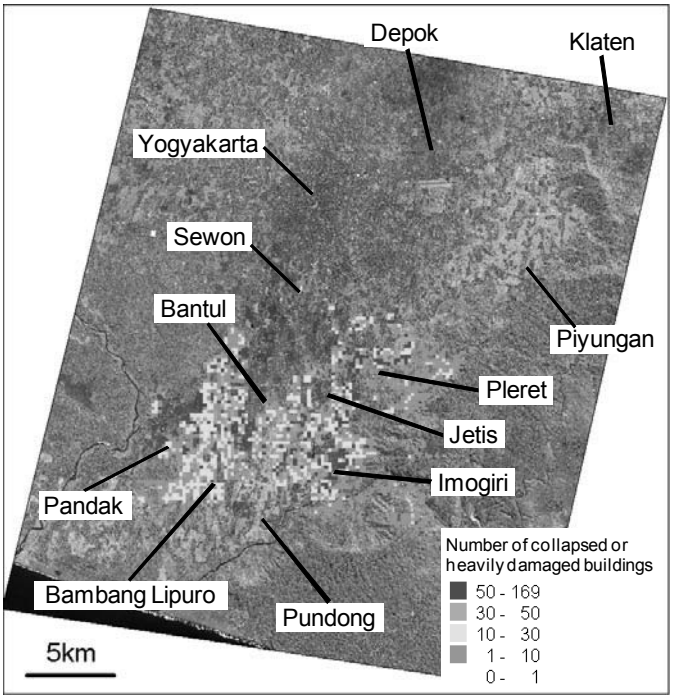
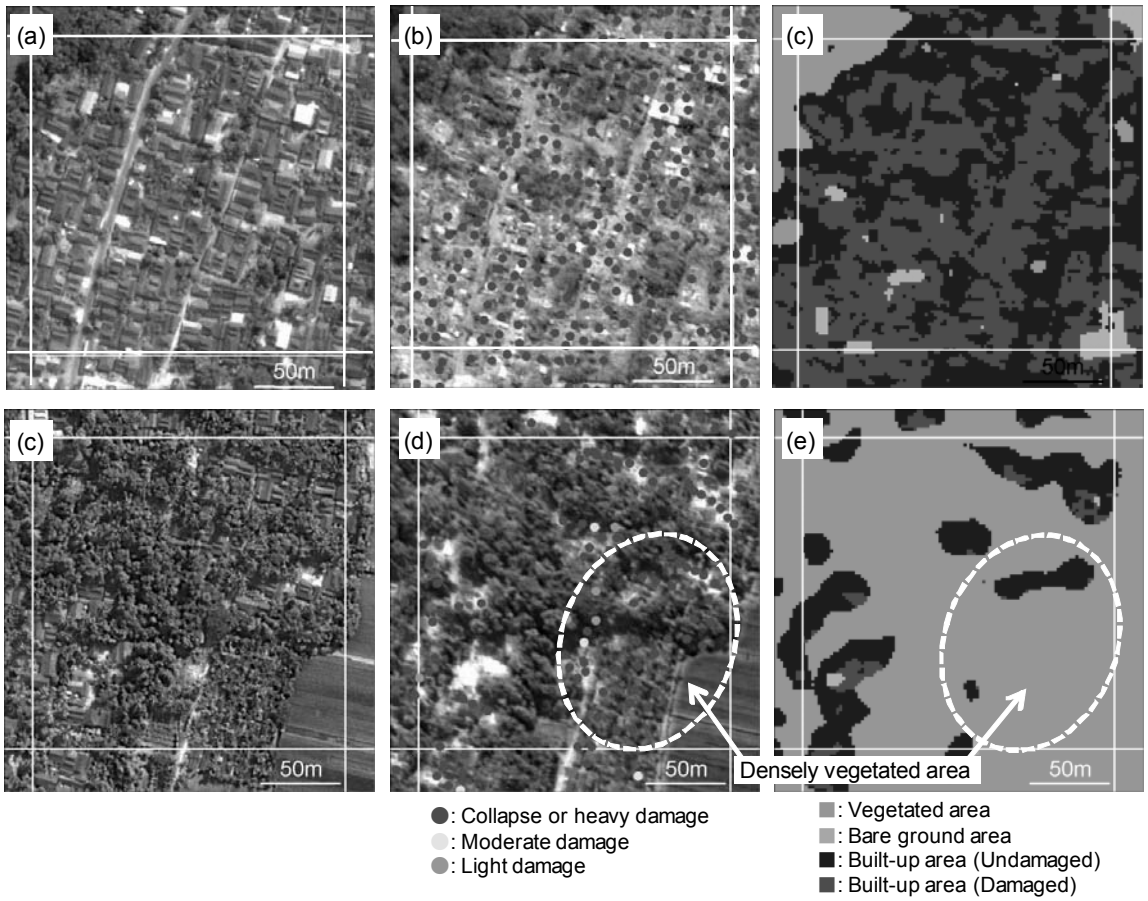
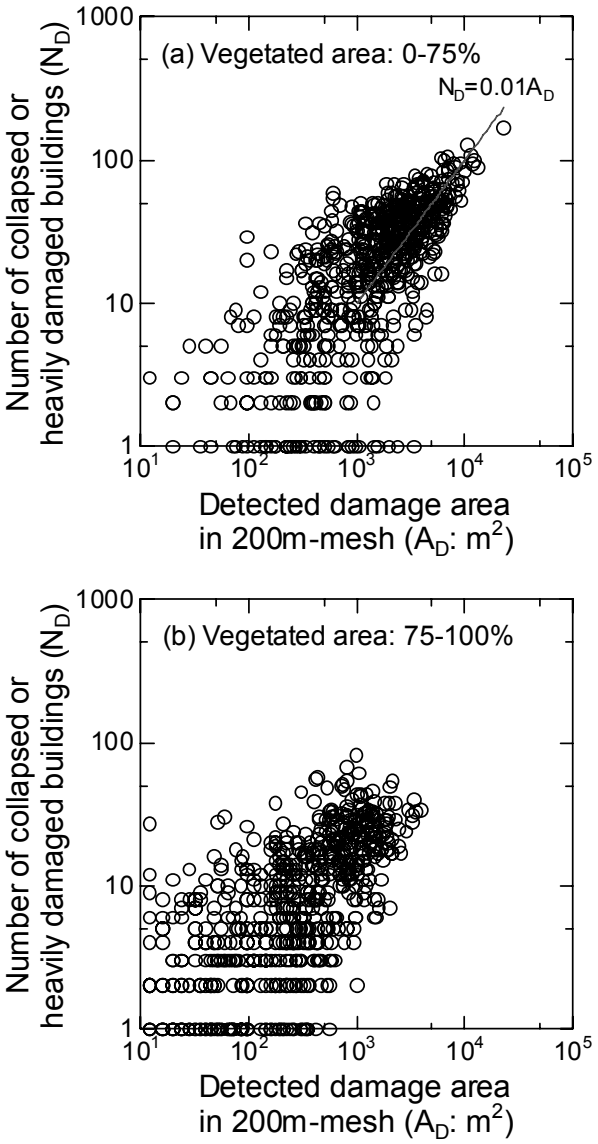


Fig. 9 Distribution of Collapsed Buildings by Field Survey



Figs. 10 (a) Pre-event, (b) Post-event, (c) Result of Damage Detection in Built-up Area
(c) Pre-event, (b) Post-event, (c) Result of Damage Detection in Vegetated Area



Figs. 11 Relationship between Detected Area by Image Analysis and Number of Collapsed Buildings

shown in the images, most of the area is covered with vegetation such as trees. Since the building roofs are obscured by trees in the densely vegetated areas, it is difficult to identify the damaged buildings from the satellite image. The dense vegetation might be a cause of the underestimation of the damage.

If the detected pixels represent collapsed buildings, the detected areas should be proportional to the product of number and size of the collapsed buildings. Since the data for building size is not available, the relationship between the damage area detected in the image analysis and the number of the collapsed buildings in each 200m mesh is examined. As shown in Figs. 10, since the damage in vegetated areas might be underestimated, the relationships are examined by considering the percentage of vegetated areas in each mesh.

Figures 11(a) and (b) show the relationships for the meshes whose percentage of vegetation is (a) less than 75% and (b) more than 75%, respectively. The correlation of the relationship is clearer observed in the less vegetated areas such as Fig. 11(a) than in the densely vegetated areas such as Fig. 11(b). Approximate line of the relationship is plotted in Fig. 11(a). From the approximate line, average detected area per a collapsed building is estimated to 100 square meters. The average size of residential buildings in the target area is about 5 to 10 meters. The detected area per a collapsed building is a little bit larger than the average size of a building because the detected areas may include rubble piles scattered around the buildings.

5. CONCLUDING REMARKS

Image analysis for building damage detection is applied to the pre- and post-event FORMOSAT-2 images to estimate the damage distribution of the 2006 Central Java, Indonesia earthquake. In the damage detection, built-up areas are firstly extracted from the images. The damaged areas are estimated from the differential of the DN in the built-up areas. The comparison of the estimated damage distribution and the building damage data by the field survey indicates that severely damaged areas are well detected although the damage is underestimated in the densely vegetated areas.

Acknowledgements:

This study is supported by the Global COE Program "International Urban Earthquake Engineering Center for Mitigating Seismic Mega Risk" sponsored by Ministry of Education, Culture, Sports, Science and Technology (MEXT), Japan.

References:

Architectural Institute of Japan, (2007), "*Report on the Damage Investigation of the 2006 Central Java Earthquake"*, 296pp.

International Federation of Red Cross (IFRC), (2006), "*Damage Distribution and Preliminary Needs Assessment"*, http://www.reliefweb.int/library/documents/2006/IFRC/ifrc-idn-20jun.xls.

Karnawati, D. *et al.*, (2008), "*The Yogyakarta Earthquake of May 27*, 2006", Star Publishing Company Inc.

Kerle, N., (2010), "Satellite-Based Damage Mapping Following the 2006 Indonesia Earthquake –How Accurate Was It?", *International Journal of Applied Earth Observation and Geoinformation*, 12(6), 466-476.

Kohiyama, M. and Yamazaki, F., (2005), "Image Fluctuation Model for Damage Detection Using Middle-Resolution Satellite Imagery", *International Journal of Remote Sensing*, 26(24), 5603-5627.

Lunetta, R. S. and Elvidge, C. D., (1998), "*Remote Sensing Change Detection –Environmental Monitoring Methods and Applications"*, Ann Arbor Press, 318pp.

Miura, H. *et al*., (2007), "Identification of Damaged Areas due to the 2006 Central Java, Indonesia, Earthquake Using Satellite Optical Images", *Proceedings of 2007 Urban Remote Sensing Joint Event*, Paper No. DIS4.

Rathje, E. M. and Adams, B. J., (2008), "The Role of Remote Sensing in Earthquake Science and Engineering: Opportunities and Challenges", *Earthquake Spectra*, 24(2), 471-492.

8CUEE CONFERENCE PROCEEDINGS
8th International Conference on Urban Earthquake Engineering
March 7-8, 2011, Tokyo Institute of Technology, Tokyo, Japan

BUILDING DAMAGE AND TSUNAMI INUNDATION GIS DATASETS AFTER THE 2010 CHILE EARTHQUAKE

Yoshihisa Maruyama[1)], Fumio Yamazaki[2)], Shizuko Matsuzaki[3)], Hiroyuki Miura[4)], and Miguel Estrada[5)]

1) Associate Professor, Department of Urban Environment Systems, Chiba University, Japan
2) Professor, Department of Urban Environment Systems, Chiba University, Japan
3) Graduate Student, Department of Urban Environment Systems, Chiba University, Japan
4) Assistant Professor, Department of Built Environment, Tokyo Institute of Technology, Japan
5) Associate Professor, Japan Peru Center for Earthquake Engineering and Disaster Mitigation, National University of Engineering, Peru
ymaruyam@tu.chiba-u.ac.jp, yamazaki@tu.chiba-u.ac.jp, 10td0309@graduate.chiba-u.jp, hmiura@enveng.titech.ac.jp, estrada@uni.edu.pe

Abstract: This paper presents the results of a field survey conducted by the authors after the 2010 Chile earthquake. The authors visited the affected area about a month after the earthquake. The GIS datasets for the damage levels of buildings in Talca and the tsunami-inundated areas in Talcahuano, Dichato, and Constitución are constructed in this study, and a series of fundamental analyses are performed using a digital elevation model (DEM). Further, the usefulness of satellite images captured after the earthquake to detect damaged buildings in Talca is discussed using the GIS datasets constructed in this study.

1. INTRODUCTION

The 2010 Chile earthquake occurred off the coast of the Maule Region of Chile on February 27, 2010, at 03:34 local time (06:34 UTC) with a magnitude of 8.8 on the moment magnitude scale. The epicenter was offshore from the Maule Region, approximately 335 km southwest of Santiago, the capital of Chile, and 105 km north-northeast of Chile's second largest city, Concepción. It is reported that a severe ground motion with the Modified Mercalli Intensity (MMI) scale of VII was felt widely in Chile and that the extensive damage was caused by the ground shaking and tsunami (USGS, 2010). The total economic loss estimates range from USD 15 to 30 billion, which correspond to 10% to 15% of Chile's real GDP (Bray and Frost 2010). According to the report on the scene, the actual death toll was 486 as of March 8, 2010, and approximately 370,000 homes were damaged.

The authors visited the affected area about a month after the event as part of an international research project "Enhancement of earthquake and tsunami disaster mitigation technology in Peru" (Yamazaki *et al.* 2010), which is under the research program "Science and Technology Research Partnership for Sustainable Development (SATREPS)" (JST 2008) supported by the Japan Science and Technology Agency (JST) and the Japan International Cooperation Agency (JICA). The lessons learned from the 2010 Chile earthquake are expected to apply to the earthquake disaster mitigation technologies in Peru because the two countries have common regional tectonics and social surroundings.

Three teams of Japanese and Peruvian researchers were dispatched by the SATREPS project to carry out field surveys. In this paper, the results of the field survey performed by Damage Assessment Group and Disaster Mitigation Plan Group are presented. The spatial damage data, topographical maps, and satellite images provided by different institutions are compiled by the geographical information system (GIS), and the primitive analyses are conducted to reveal the characteristics of the tsunami-inundated areas in view of elevations and damage incidents to adobe and unreinforced masonry buildings, which are also widely seen in Peru.

2. OUTLINE OF FIELD SURVEY

The authors arrived in Santiago on April 2, 2010. We drove to Concepcíon the next day and visited the tsunami-affected areas of Talcahuano, Dichato, and Constitución. We moved to Talca on April 7 and left Santiago on April 8. Before leaving, we visited Valparaíso and Viña del Mar. Figure 1 shows the locations of the cities that we visited during the survey.

Figure 2 shows the route of our field survey in Santiago

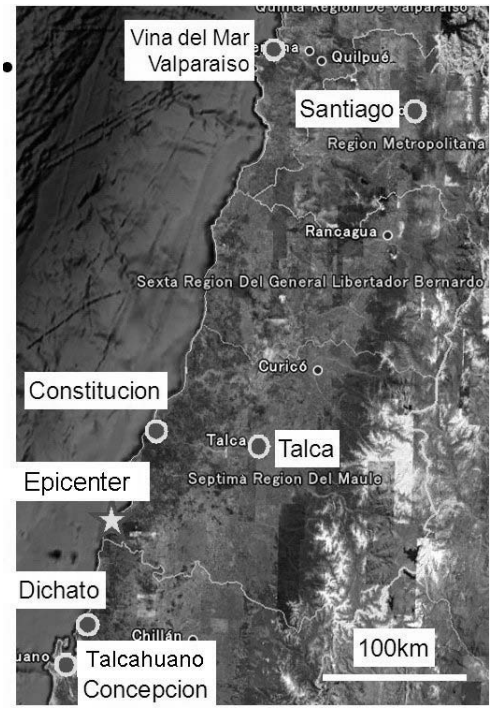


Figure 1 Locations of cities visited by the authors





Figure 2 Survey route and field photos in Santiago—April 2, 2010

and some field photographs. The route was recorded by a portable GPS device during the survey and the location of the photo shooting could be identified as the location data were embedded in the Exchangeable Image File Format (EXIF). An RC building with 20 stories constructed in 2003 suffered from shear failures in columns and walls at the first and the second stories. A collapsed highway bridge and an





Figure 3 Survey route and field photos in Concepcíon—April 4, 2010





Figure 4 Survey route and field photos in Dichato—April 5, 2010

RC building with the collapsed first floor were found. The locations of these sites are also shown in the survey route in Fig. 2.

Figure 3 shows the survey route in Concepcíon. An RC

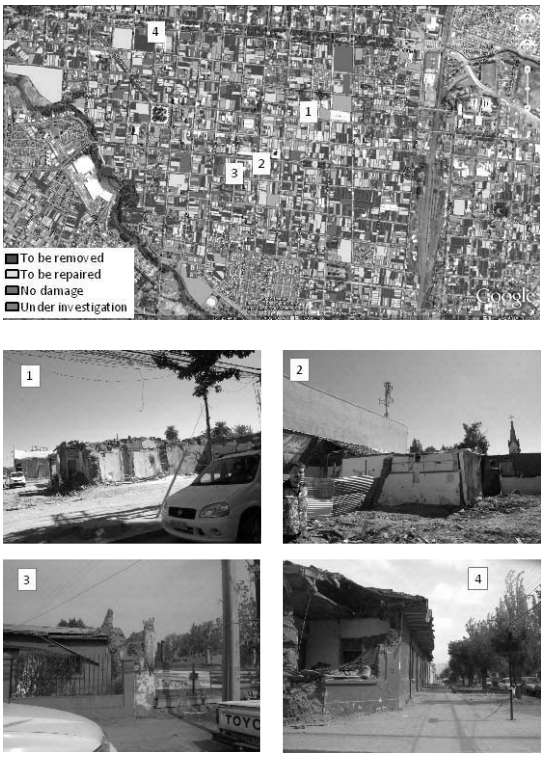


Figure 5 GIS file to show the damage levels of buildings in Talca and locations of field photos

building with the damaged middle floor was found at the site numbered 1. An RC building with 15 stories had collapsed completely at the site numbered 2. The road bridges collapsed at sites 3 and 4. The temporary bridge girder was constructed two days after the earthquake at site 3. Although the photos are not shown in this paper, the adobe and unreinforced masonry constructions were severely damaged in the urban area.

Figure 4 shows the survey route in Dichato. It is reported that more than 80% of the built-up area in Dichato suffered from tsunami (Humboldt State University Preliminary Tsunami Survey Team, 2010). As shown in the field photos, the buildings collapsed because of the tsunami waves. A ship was conveyed against the river flow because of the tsunami and eventually found at site 3.

3. CONSTRUCTION OF GIS FOR BUILDING DAMAGE AND TSUNAMI-INUNDATED AREA

3.1 Building Damage GIS in Talca

Talca is the capital of both Talca Province and Maule Region. Its population is approximately 200,000, and it is approximately 250 km south of Santiago and 60 km northwest of the epicenter of the 2010 Chile Earthquake. According to USGS (2010), Talca was affected with a severe ground motion with the MMI scale of VII.

During our survey, we interviewed officials from Maule Regional Office to investigate the damage of buildings. As a result of our interview, an image file that shows the damage levels of buildings was provided. The polygons, which

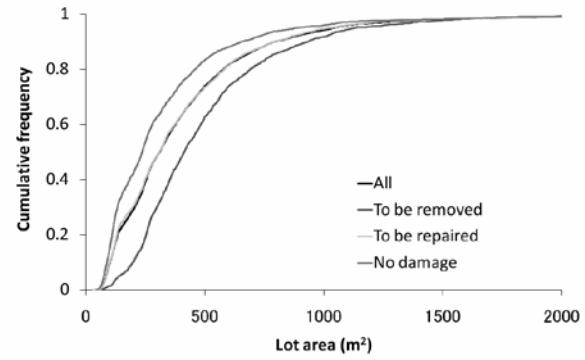


Figure 6 Cumulative frequencies of the areas of building lots with respect to the damage level

indicate the building lots, are classified into four levels, namely, to be removed, to be repaired, no damage, and under investigation. It should be noted that the image file was compiled with the damage dataset as of March 31, 2010.

In this study, the location of the image file was established in terms of map projections. The satellite image and road data presented in Google Earth were employed as a base map to georeference the image file. Then, the image file was converted to a GIS file with polygons to identify the damage levels of buildings. Figure 5 shows the developed GIS file presented by Google Earth and some field photos to show the examples of damaged buildings.

In all, 5617 polygons were projected to the map coordinate system. 1559 (27.8%), 1872 (33.3%), and 1864 (33.2%) buildings were classified as to be removed, to be repaired, and no damage, respectively. The typical construction types in Talca are adobe and unreinforced masonry buildings, which are primarily used for older constructions with 2–4 stories (dating back to before the 1960s–70s). Modern buildings that were designed according to the current codes suffered minor, repairable damage, while a large number of adobe and unreinforced masonry constructions suffered significant damage (MCEER, 2010).

Figure 6 shows the cumulative frequencies of the areas of building lots with respect to the damage level. The mean of all the georeferenced areas was approximately 430 m^2 and was almost equal to that of the areas associated with the buildings to be repaired. The mean of the lot areas of the buildings to be non-damaged was approximately 340 m^2, which was considerably smaller than that of the buildings to be removed. On the basis of the results, it has been speculated that the newer buildings are constructed in relatively small lots; however, the construction periods are not available at this moment.

Recent advancements in remote sensing technologies and their applications have made it possible to use remotely sensed imagery for estimating the damage distribution due to natural disasters. Among them, high-resolution optical satellite imagery, which has become available in the last decade, has made satellite remote sensing more useful in disaster management since even the damage status of individual buildings can be identified (Saito *et al.* 2004, Yamazaki *et al.* 2005). Figure 7 compares the pre- and



(a) Pre-event (Jan. 1, 2008)



(b) Post-event (March 10, 2010)



(c) GIS data

Figure 7 Comparison between pre- and post-event satellite images to detect affected buildings

post-event high-resolution optical satellite images with the GIS dataset shown in Fig. 5. As for the pre- and post-event images, the image captured by QuickBird on January 1, 2008, which is presented in Google Earth, and that captured by WorldView-2 on March 10, 2010, are employed in this study. A comparison of the pre- and post-event images revealed that some of the affected buildings could be visually detected, but not all the damaged ones could be identified appropriately. Since the post-event image was captured with the large off-Nadia angle (40.3°), the quality of image is not sufficient for visual damage inspection. Moreover, the number of affected buildings whose roofs had completely collapsed is small in Talca. Hence, it can be concluded that the damaged buildings in Talca are difficult to be detected through visual damage inspection using satellite images.

3.2 Development of GIS for Tsunami-Inundated Area

Various institutions released the maps to show the damage distribution at their Web sites after the 2010 Chile earthquake. The tsunami-inundated areas interpreted from satellite and aerial images were published by National Office of Emergency of the Interior Ministry (ONEMI) of Chile

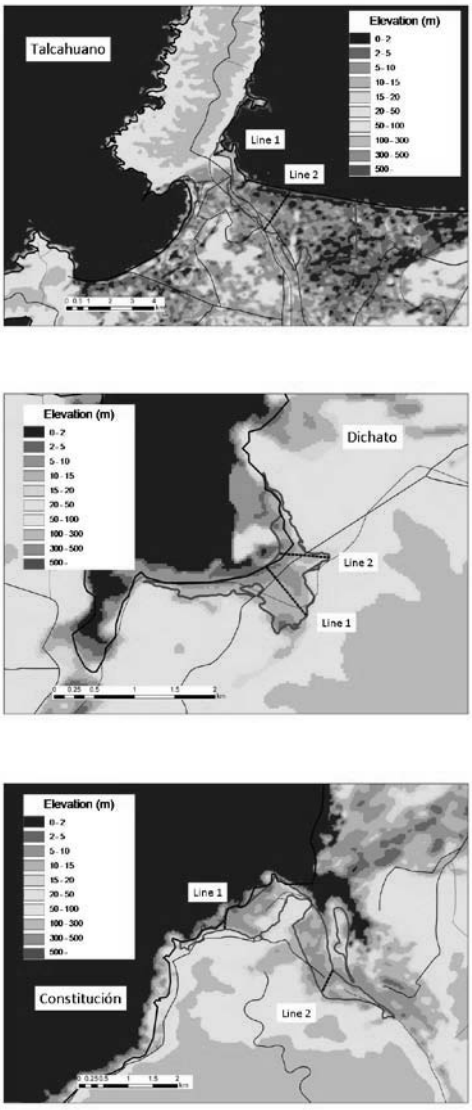


Figure 8 Tsunami-inundated areas in Talcahuano, Dichato, and Constitución

(SNIT 2010). On the basis of the maps, the number of affected buildings and that of causalities were estimated.

In this study, the tsunami-inundated areas were projected onto a map coordinate system, and the topographical conditions were evaluated in terms of the elevation. The inundated areas in Talcahuano, Dichato, and Constitución were converted to the GIS data and compared with the digital elevation model (DEM). The DEM employed in this study is the ASTER Global Digital Elevation Model (GDEM) developed by the Ministry of Economy, Trade, and Industry (METI) of Japan and the United States National Aeronautics and Space Administration (NASA) (ERSDAC 2009). The ASTER GDEM is a highly accurate DEM covering all the land on earth with the spatial resolution of 30 m.

Figure 8 shows the tsunami-inundated areas in Talcahuano, Dichato, and Constitución and the distributions of the elevation derived from the ASTER GDEM. The elevations in the inundated areas are lower than 20 m on the

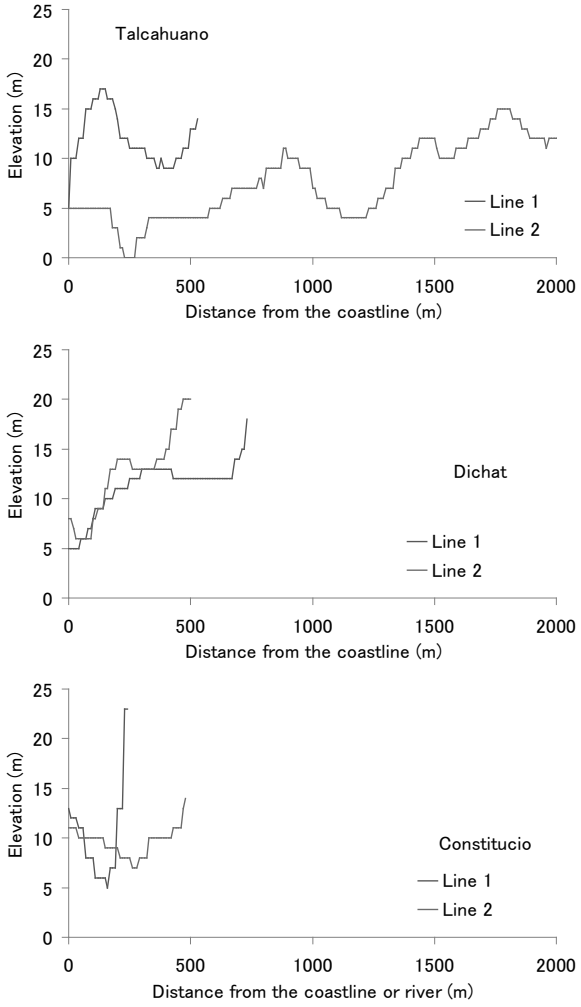


Figure 9 Elevations along the transverse lines set in Fig. 8

whole except for a certain area in Constitución. As shown in the figure, we set the two traverse lines in each inundated area. The elevations were extracted along the two lines. The extracted elevations are illustrated in terms of the distance from the coastline in Fig. 9. As for Line 2 in Constitución, the elevations are presented with respect to the distance from the Maule River. The relatively low elevations and slow grades result in long travel distances of the tsunami wave. According to Line 2 in Talcahuano, the tsunami wave could travel approximately 2000 m from the coastline. Line 1 in Constitución was assigned to identify the surveyed site by Imamura *et al.* (2010). According to their report, the tsunami runup height was 28.3 m at the site. Since the DEM used in this study is a global dataset that consists of 30-m grid cells, the elevation at the site is estimated to be approximately 23 m. The slope is estimated to be approximately 67% and is almost equivalent to that reported by Imamura *et al.* (2010), which is 63.5%.

As shown in Fig. 10, the inundation depth was measured at several sites in the three cities. The inundation depth along the beachfront street in Talcahuano was larger than 150 cm, but a depth of 55 cm was observed in its bystreet (site 4). Figure 11 summarizes the measurements in the three cities. The inundation depth is presented with

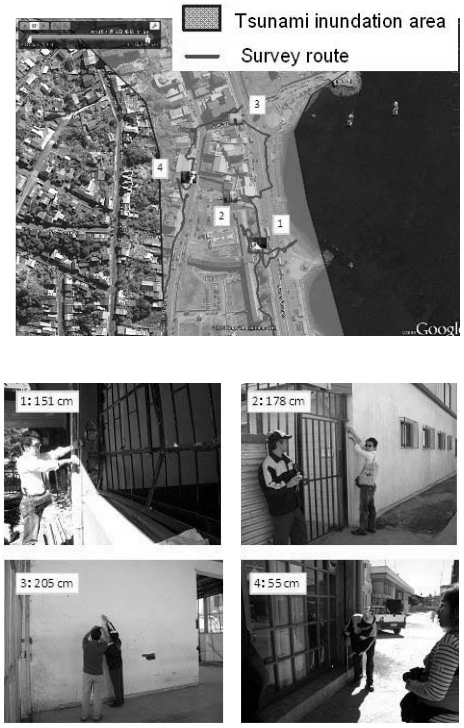


Figure 10 Measurement of tsunami inundation depth in Talcahuano

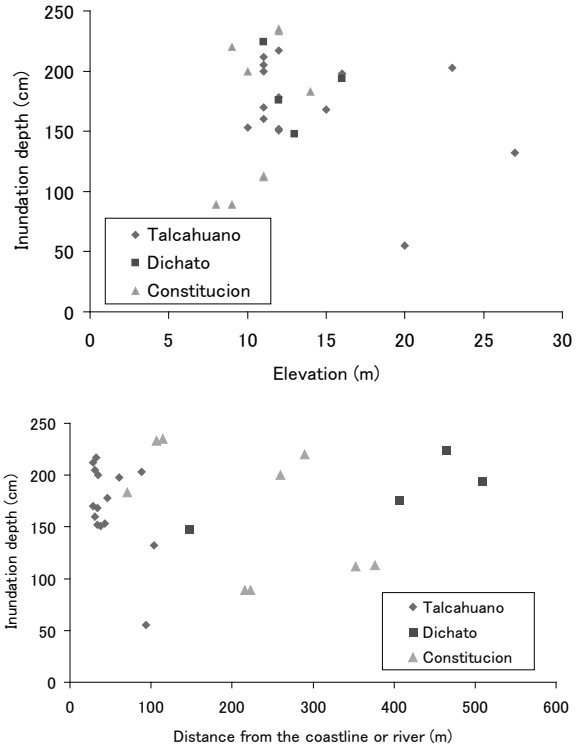


Figure 11 Summary of the measurement of tsunami inundation depth

respect to the elevation and the distance from the coastline. As for the results in Constitución, the records are shown with respect to the distance from the Maule River. A clear tendency is not seen in the relationship between the tsunami inundation depth and the elevation. The recorded depth in

Talcahuano and Constitución decreased with an increase in the distance from the coastline or the river; however, this tendency is not seen from the records in Dichato because of the insufficient number of measurements.

4. CONCLUSIONS

In this paper, the results of a field survey conducted after the 2010 Chile earthquake by the authors during April 2–8, 2010, are presented. The GIS dataset for the building damage in Talca was developed by establishing the location of the image file in terms of map projections. The usefulness of high-resolution satellite images to detect the building damage in Talca was investigated with the aid of the constructed GIS dataset. Moreover, the tsunami inundation maps published by ONEMI were georeferenced, and the characteristics of the inundated areas were evaluated in view of the elevation.

According to the relationship between the building damage levels and the lot areas, the mean of the areas associated with the non-damaged buildings was the smallest, while the mean of the areas associated with the buildings to be removed was the largest. In Talca, modern buildings that were designed according to the current codes suffered minor, repairable damage, while a large number of adobe and unreinforced masonry constructions, which were built in the 1960s–70s, suffered significant damage. On the basis of these circumstances, it has been speculated that the newer buildings may be constructed in relatively small lots; however, the construction periods are not available at this moment. According to the results of a visual damage inspection using pre- and post-event satellite images, it was concluded that the damaged buildings in Talca could not be appropriately detected because of their damage patterns and the quality of the post-event satellite image.

A comparison of the georeferenced tsunami-inundated areas with the elevations obtained from the ASTER GDEM revealed that the elevations in the inundated areas were lower than 20 m on the whole except for a certain area. A clear tendency was not seen in the relationship between the tsunami inundation depth and the elevation. The recorded inundation depth in Talcahuano and Constitución decreased with an increase in the distance from the coastline or the river.

These findings of our field survey after the 2010 Chile earthquake will be expanded in the earthquake and tsunami disaster mitigation technology in Peru through the SATREPS project.

Acknowledgements:

The authors would like to express their sincere gratitude to the Japan Science and Technology Agency (JST) for the financial support in conducting the field survey under the SATREPS project "Enhancement of earthquake and tsunami disaster mitigation technology in Peru" (Principal Investigator: Prof. Fumio Yamazaki, Chiba University).

References:

Bray, J. and Frost, D. (2010), "Geo-engineering Reconnaissance of the 2010 Maule, Chile Earthquake."

Earth Remote Sensing Data Analysis Center (ERSDAC). (2009), ASTER GDEM, http://www.gdem.aster.ersdac.or.jp/

Humboldt State University Preliminary Tsunami Survey Team (2010), http://www.eqclearinghouse.org/20100227-chile/.

Imamura, F., Fujima, K. and Arikawa, T. (2010), "Field Survey of the 2010 Chilean Tsunami," http://www.jsce.or.jp/committee /eec2/eq_report/201003Chile/Imamura.pdf.

Japan Science and Technology Agency (JST) (2008), http://www.jst.go.jp/global/english/index.html.

MCEER (2010), "Preliminary Damage Reports from the Chile Earthquake February 27, 2010," http://mceer.buffalo.edu /research/Reconnaissance/Chile2-27-10/damage-reports.asp.

The National System of Coordination of Territorial Information (SNIT). (2010), http://hosting.snit.cl/terremoto2010/

Saito, K., Spence, R., Going, C. and Markus, M. (2004), "Using High-Resolution Satellite Images for Post-Earthquake Building Damage Assessment: A Study Following the 26 January 2001 Gujarat Earthquake," *Earthquake Spectra*, Vol. 20, No. 1, 145-169.

U.S. Geological Survey. (2010), http://earthquake.usgs.gov/ earthquakes/shakemap/global/shake/2010tfan/.

Yamazaki, F., Zavala, C., Nakai, S., Koshimura, S., Saito, T. and Midorikawa S. (2010), "Enhancement of Earthquake and Tsunami Disaster Mitigation Technology in Peru: A SATREPS Project," *Proceedings of the 7th International Conference on Urban Earthquake Engineering*, 1501-1506.

Yamazaki, F., Yano, Y. and Matsuoka, M. (2005), "Visual Damage Interpretation of Buildings in Bam City Using QuickBird Images Following the 2003 Bam, Iran, Earthquake," *Earthquake Spectra*, Vol. 21, No. S1, 329-336.

8CUEE CONFERENCE PROCEEDINGS
8th International Conference on Urban Earthquake Engineering
March 7-8, 2011, Tokyo Institute of Technology, Tokyo, Japan

A NEW DATA LOGGER WITH LARGE DYNAMIC-RANGE TO OBSERVE FROM MICROTREMORS TO STRONG MOTIONS

Masayuki Araki[1)], **Hitoshi Morikawa**[2)], **Takamori Ito**[3)], **Masachika Tanigawa**[4)], **and Keitaro Matsumoto**[5)]

1) President, aLab Co.Ltd, Japan
2) Associate Professor, Department of Built Environment, Tokyo Institute of Technology, Japan
3) Postdoctral Research Fellow, Earthquake Research Institute, The University of Tokyo, Japan
4) Graduate Student, Department of Built Environment, Tokyo Institute of Technology, Japan
5) Under Graduate Student, Department of Civil and Environmental Engneering, Tokyo Institute of Technology, Japan
morika@enveng.titech.ac.jp

Abstract: A new data logger is developed to use for microtremor and strong motion measurement. Especially, to know the deep structure, we need to handle microtremors in low frequency range: that is, lower than 1 Hz. In this frequency range, not only power of microtremors is very small, but the sensitivity of sensor is generally critical. A data logger with very low noise and high resolution is required for this purpose. Of course, we can find very expensive systems with high performance in noise and resolution, though, they are not so suitable for the microtremor survey, usually. We, thus, introduce some traditional but new features and complete a new system. Basic performances of the new systems are examined and discuss the aplicability to the observations in fields.

1. INTRODUCTION

To know deep ground structure, microtremor surveys are carried out. For this purpose, we need precise information with respect to phase for surface waves (for example, Okada (2003), Matsushima and Okada (1990), Morikawa *et al.* (2004)). Generally speaking, the power of microtremors in low frequency range is definitely smaller than ones in high frequency range. The sensor sensitivity, however, is very low in low frequency range and the S/N (signal-to-noise ratio) of analogue circuit is very bad because of 1/f noise, which is called sometime pink noise. This means that we have many difficulties to observe precisely microtremors in low frequency rawnge to apply them to the estimation of deep ground structure.

Recently, many kinds of small sensors are provided and many of them works based on sophisticated feedback system. They usually announce that they have flat response to very low frequency range, sometimes to DC (direct current, that is, 0 Hz). They have some analogue circuit for feedback system, thus, they cannot escape from the 1/f noise, especially, as signal level is very low.

To avoid the problems relating to 1/f noise, we may use a moving-coile-type (MC-type) sensor, which has classical and simple system. Because MC-type sensor does not have any noise caused by power supply and analogue circuits: this means 1/f noise free. If we use MC-type sensors, we can concentrate to develop a data logger with very low noise. Of course, we have to consider the high output impedance of MC-type sensors, but we may keep still advantages over feedback-type sensors, which is contaminated by the noise from analogue circuits in sensors.

Considering the above situations, we have tried to develop a new data logger with very low noise and high dynamic range, using three analogue-to-digital converter (ADC) for one singnal. Recently, the cost of ADC is decreased drastically for consumer use, thus, we can possibly complete this products with low costs. We discuss the performance of our new data logger: especially, the noise level in low frequency range.

2. BASIC CONCEPTS FOR DESIGN

Generally, a MC-type velocity sensor has enough sensitivity to vibration whose period is ten times to the natural period of its pendulum. Thus, the target performance of our data logger is set that it can keep enough S/N against microtremors with ten times longer period range than the natural period of a sensor.

For a MC-type velocity sensor, the response in longer period range than natural period of sensor decrease in 6 dB/oct. in a case where its damping ratio is set 0.7. This means that the sensitivity of sensor is half at twice period of natural period and about 1/10 of sensitivity at ten times of period. For example, in a case where we have a sensor with sensitivity of 1V/kine (kine = cm/s) and with natural period of 0.5 seconds, its sensitivity is only 0.1

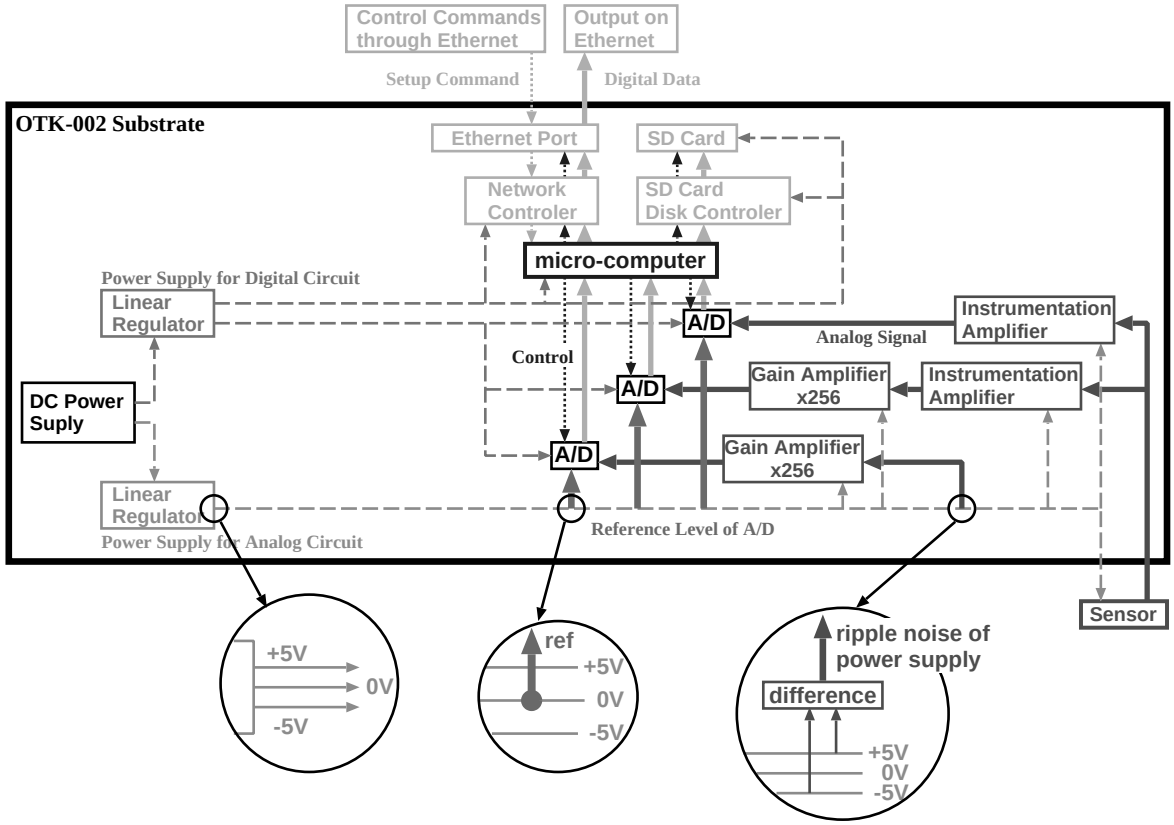


Figure 1 Block diagram of a new data logger. Colors denote different properties of lines such as signals, power supplys, and so on.

V/kine at 5 seconds. Power of microtremors depends on ground structure, though, sometimes we may have to observe the microtremors whose maximum value is only 0.5 mkine ($= 0.5 \times 10^{-3}$ cm/s) on slightly hard soil ground, for example. In this case, we have to log the signal of only 0.5 mV. This value must be obtained in the most sensitive range for sensors: in the above example, it should be around 0.5-second microtremors. Thus, we have to record precisely a signal with at most 100 μV at 5-second microtremors. This means that enough S/N is required to 10-μV signal for 5-second microtremors.

On the other hand, in a case where the input gate voltage to ADC is $\pm$10 V and word length is 24 bit, the minimum value to represent the signal is about 1 μV. Thus, if we use 24bit ADC to manage $\pm$10V, the signal of microtremors in long period range, such as 5 seconds, may be contaminated by quantized noise. Furthermore, since the effective resolution of 24-bit ADC is less than 22 bit, we cannot record precisely 10-μV signal.

To consider the above many problems, we decided our concepts for the design of a new data logger as follows:

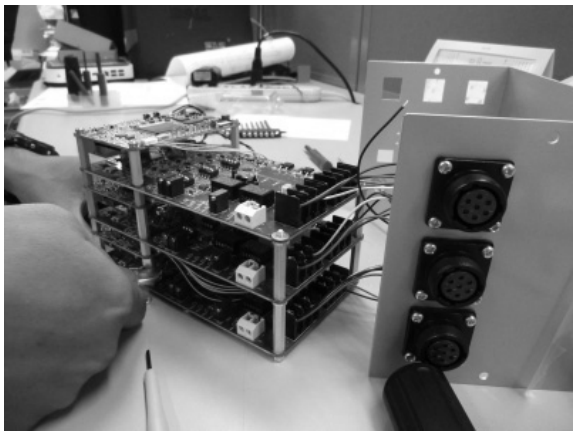
- hybrid system by means of three 24-bit ADCs,
  - direct signal (hereafter, 'x1 signal') to first ADC of three,
  - 256 times gained signal ('x256 signal') to second ADC, and
  - ripple noise of power supply ('x256 power') with 256 times gain to thrid ADC,
- using distinct series-type regulators for analogue and digital circuits to reduce noise from power supply.
- considering the operability and general versatility, power supply circuits for feedback-type sensors and a special circuits to calibrate a MC-type sensor are mounted.

The block diagram of trial production is shown in Figure 1. This figure shows a substrate for one signal component.

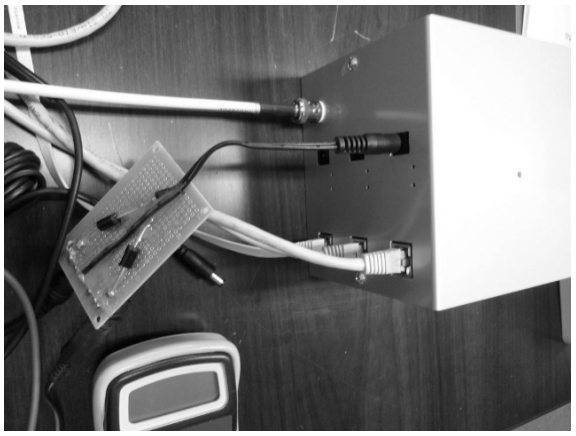
The originality of this logger is located at the three ADCs as shown in the figure. Especially, recording the ripple noise of power supply is the new idea to improve the S/N of system. The record of ripple noise of power supply will play an important role as the reference of signals.

ADC requires a reference level of 0V and the ground line (GND) for analogue power supply is used as reference. This reference level fluctuates randomely and degradation of S/N is caused by this fluctuations mainly. This fluctuations are inputted to third ADC as differences of positive and negative power supply lines.

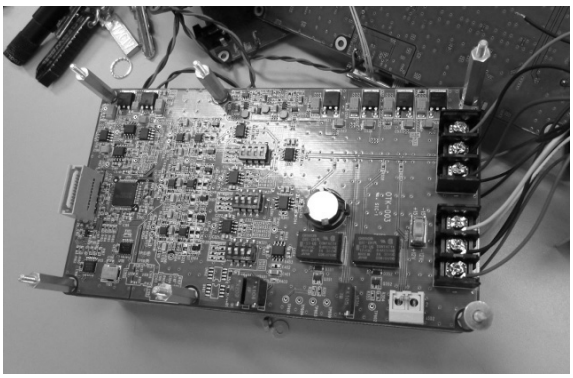
The thrid ADC to record ripple noise of power supply can contribute to simplify the system. Since the data logger records ripple noise always, we can monitor the condition of system. We do not need to mount any temperature compensation circuits and some other specially designed power supply circuits: as a result, quality of the recorded signal is independent of power supply unit and we do not care types of power supply. To obtain the good



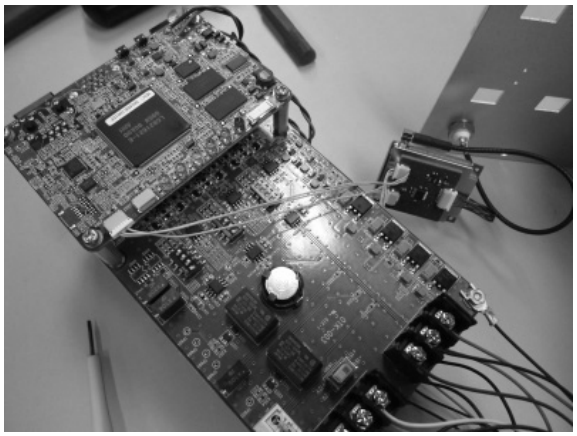
(a) Construction of substrate



(b) Exterior of opposite side of (a)



(c) Substrate for input and analogue circuit



(d) Substrate for control and digital circuit

Figure 2 Details of the new data logger

S/N records, we just remove the recorded ripples from the records of signal.

The parallel recoding of signal with different gain is conventional idea to keep large dynamic range. This type of data logger could be found in many of classical analogue data recorders, though, recently, we can find very few for digital loggers. However, this type of logging system is reasonable recently, because the cost of ADC is drastically reduced and ADC can be synchronized readily using clock signal from GPS (global positioning system). Considering these situations, we decided use three ADCs for one signal.

In a case where the level of x256 signal is enough large and saturate the upper level of ADC, we can use the data of x1 signal. From this, this system has apparently 32 bit resolution, that is, 24 + 8. Of course, we have to consider the loss of efficient resolution of ADC such as about 22 bit resolution when 10ms of sampling interval. However, this is enough large dynamic range to record the microtremors and strong ground motions.

We would like to emphasize again that the points of this logger is recoding of ripple noise of power supply. This idea comes true the amazing S/N, dynamic range, and low cost.

3. TRIAL PRODUCTION OF DATA LOGGER

Following the concepts descrived in the previous section, a trial production is made. To reduce the cost, we used some products developed for IT-Kyoshin Kei (IT-Kyoshin Kei Research Group, 2010): a substrate for microprocessor to control the system, circuit design for anti-aliasing filter, and so on. On the other hand, instrumentation and gain amplifier circuits at input stage and power supply circuits are newly developed.

To record three components of microtremors and/or strong ground motion, nine-channel ADCs are required, though the microprocessor to control system has not enough power to manage all the nine channels. Thus, we apply three substrates for three components of signals, which are developed for IT-Kyoshin Kei and include four-channel ADC and its controller.

Details of a traial production are shown in Figure 2. System for one component of signal consists of two substrates: the one is large and the other is small. For three components of data, totally six substrates are used as shown in Figure 2(a).

Large substrate mounts input stage and ADC (see Figure 2(c)). First, the signal passes an instrumentation amplifier to compensate the input impedance and is inputted into gain amplifier with 256 times. After that, the signal

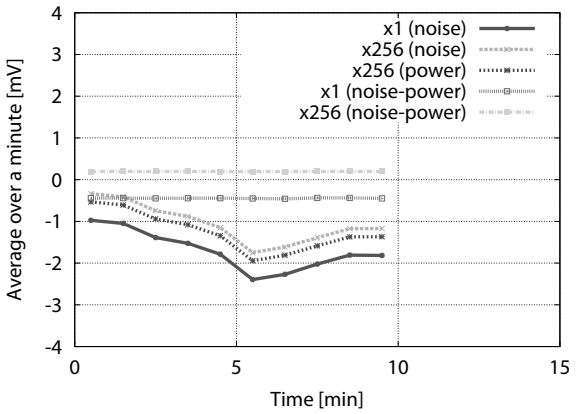


Figure 3 One-minute averages of self-noise. To obtain this data, we short the input connectors and average the data for each one minute. 'x1' and 'x256' stand for different gains, '(noise)' and '(power)' for self-noise and ripple noise of power supply, respectively. Furthermore, '(noise-power)' denotes the data without the ripple noise, which can be caluculated from the self-noise ('noise') minus ripple noise ('power'). '-' in 'noise-power' means minus. Large drift of mean values are observed for 'noise' and 'power', but 'noise-power' is completely corrected and stable.

goes through the Bessel filter with second order and 40-Hz cut off frequency for anti-aliasing and moves to ADC. Since the input stage is designed as fully balanced circuit (differential circuit), the signal is received as three lines, that is, positive, negative, and ground lines. This substrate has also own power supply system, whose location on the substrate is decided considering influences to the analogue signals.

Small substrate includes microprocessor to control system: writing data to SD card, receiving command through the ethernet controller, communicating ADC and GPS clock signal generator, and so on (see Figure 2 (d)). The GPS receiver unit is also shown at right-upper side in the photo. Three microprocessors follow this GPS clock signal and are synchronized mutually.

This system works by 12V DC power supply and spends 2100-mA (700 mA x 3) current at most (see Figure 2(b)). In a case of standalone mode, that is, no communications through network and connected to MC-type sensors, it can save much power and spends about 1200 mA (400 mA x 3).

4. PERFORMANCE TEST

To observe the self-noise of system and discuss S/N, the input connectors are shorted and records signals. For observation, we have to adjust the zero-level using trimmers, however, the zero-level is not stable, because of temperature and some other reasons. One-minute averages of self-noise are shown in Figure 3. In this figure, the vertical axis is shown in mV and the upper three lines in legend show x1 signal, x256 signal, and x256 power, respectively. The lower two lines show the data "x1 signal minus (x256 power)/256" and "x256 signal minus x256 power." In this figure, we use a word 'noise' instead of 'signal,' because we deal with the self-noise.

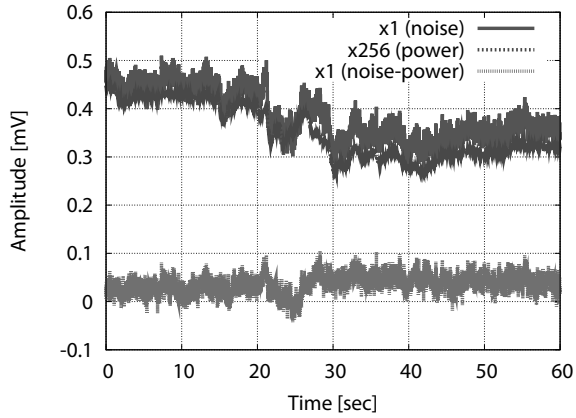
The large drifts are observed for '(noise)' and '(power)': the level of drifts is a few mV in peak-to-peak. This means that we cannot observe any signal of microtremors, whose level must be less than a mV. In this case, self-noise should be same as the ripple noise of power supply and, then, '(noise-power)' should be zero always. As shown in Figure 3, the fluctuation of '(noise-power)' is very small without small offset. We do not care this kind of offset, which depends on the adjustments of the trimmers, because we can remove it easily using numerical analysis.

Figure 4 shows time histories of self-noise. In this case, 'x256 noise' should coinside with 'x256 power', however, small diferences are observed as shown in Figure 4(b). 'x256 noise - x256 power' is very stable and the noise with long period is almost removed. 'x1 noise - (x256 power)/256' is also stable but we can find much noise in short period, which may be caused by a kind of quantitave noise.

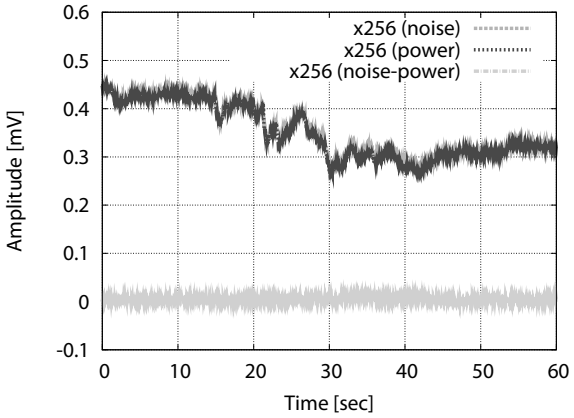
Next, we calculate the Fourier spectrum of self-noise as shown in Figure 5. To calculate the Fourier amplitudes, we use 80-second durations and averaging the 'raw' spectra. The vertical axis is not normalized by the duration and, then, the dimension is same as time histories. In Figure 5(a), red marks show the 'raw' spectra for each duration, and green line is their average. 1/f noise can be observed clearly for 'x1 noise' in lower frequency range than 1 Hz. However, the noise level is flat and horizontal, which is like a white noise, in higher frequency range than a few Hz. This may be caused by quantitative noise of ADC, because the self-noise level is very small and its amplitude cannot reach 8 bit.

The averaged Fourier amplitudes for another data are shown in Figure 5(b). It is observed that 'x256 power' shows the properties of 1/f in lower frequency range than 10 Hz and 'x256 noise - x256 power' shows 1/30 to 1/50 lower level than 'x256 noise': that is, the noise floor of 'x256 noise' is reduced to about 30 to 36 dB (5 to 6 bits in digital). This means that 'x256 power' works very well to reduce the noise in lower frequency range.

Since the amplitude of 'x256 noise - x256 power' is about a few μV, the system covers the dynamic range of 126 dB (21 bits) using only 'x256 signal'. Thus, we use the low gain data, which is 'x1 signal', we can keep huge dynammic range 174 dB (29 bits = 21 + 8 bits), overall. Unfortunately, we cannot converge the high (x256) and low (x1) gain signals because of the small differences of offset and drifts between high and low gain signals. As a result, we have realized 29-bit dynamic range and 24-bit resolution. It should be noted that the above property includes perfomance of analogue circuits, namely, this is not a theoretical specification of ADC.

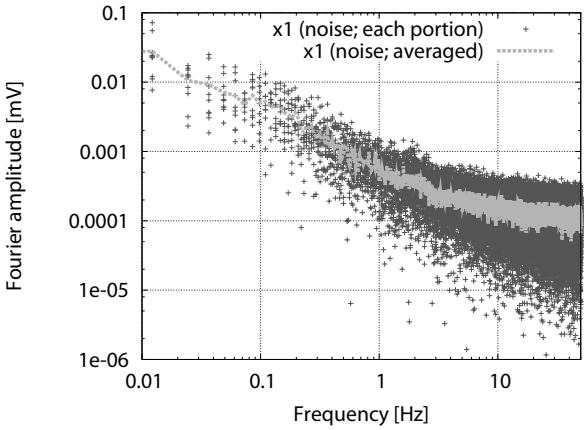


(a) low gain (x1)

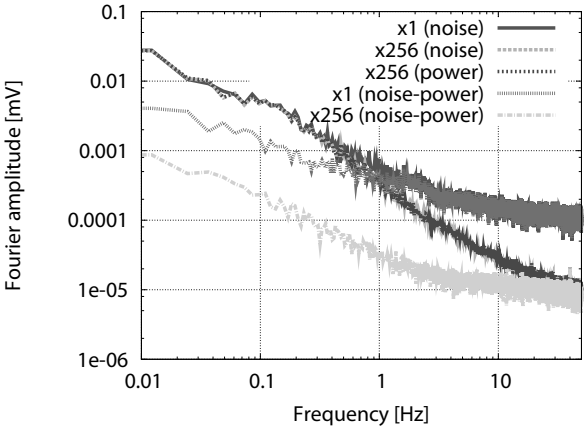


(b) high gain (x256)

Figure 4 Time histories of self-noise of the data logger. The colors in legend corresponds to Figure 3. After removing the ripple noise of power supply, which is '(power)', the fluctuations with long period are disappeared and the data is stable.



(a) Fourier amplitude of direct (x1) input of self-noise.



(b) Fourier amplitudes of self-noise under different conditons.

Figure 5 Fourier amplitude of self-noise of the data logger. The vertical axis is not normalized by the duration of data. Thus, the dimention of vertical axis is same as the time histories. In panel (a), red marks are 'raw' spectra for 80-second duration and green line is averaged spectrum. In panel (b), the meanings of colors and legend are same as Figure 3.

5. CONCLUSIONS

We have developed a new data logger with huge dynamic range and very low noise. In this system, we apply three-channel ADC for one component of signal to record low and high gain signals and ripple noise of power supply. It is observed that the thrid ADC to record the ripple noise of power supply contributes to reduce the 1/f noise, through the performance test of the logger.

Consequently, the noise is reduced to about 30 to 36 dB (5 to 6 bits) and the overall dynamic range is more than 170 dB (29 bits). Furthermore, we apply the consumer-use ADC and reduce the cost.

For further developements, we try to use this new data logger under the various situations and examine its performance.

Acknowledgements:

We are deeply grateful to Professor H.-T. Chen of National Central University, Taiwan for his kind support to our experiments in NCU.

References:

Okada, H. (2003), *The Microtremor Survey Method*, Geophysical Monograph Series, No. 12, Society of Exploration Geophysicists, Tulsa, Oklahoma.

Matsushima, T. and Okada, H. (1990), "Determination of Deep Geological Structures under Urban Areas using Long-Period Microtremors," *Butsuri-Tansa*, **43**, 21–33.

Morikawa, H., S. Sawada, and J. Akamatsu (2004), "A method to estimate phase velocities of Rayleigh waves using microseisms simultaneously observed at two sites," *Bull. Seismol. Soc. Am.*, **94**(3), 961–976.

IT-Kyoshin Kei Research Group (2010), http://wwweic.eri.u-tokyo.ac.jp/ITKyoshin/Kenkyukai/index.html

8CUEE CONFERENCE PROCEEDINGS
8th International Conference on Urban Earthquake Engineering
March 7-8, 2011, Tokyo Institute of Technology, Tokyo, Japan

GROUND MOTION AND TSUNAMI SIMULATION FOR THE GREAT 1707 HOEI, JAPAN, EARTHQUAKE

Takashi Furumura[1], Kentaro Imai[2], and Takuto Maeda[3]

1) Professor, CIDIR, Interfaculty Initiative in Information Studies / Earthquake Research Institute, The University of Tokyo, Japan
2) Research Associate, Tsunami Engineering Laboratory, Disaster Control Research Center, Tohoku University, Japan
3) Project Researcher, CIDIR, Interfaculty Initiative in Information Studies / Earthquake Research Institute, The University of Tokyo, Japan
furumura@eri.u-tokyo.ac.jp, imai@tsunami2.civil.tohoku.ac.jp, maeda@eri.u-tokyo.ac.jp

Abstract: The source rupture area of the 1707 Hoei earthquake which occurred along the Nankai Trough, off southwestern Japan, should be extend further, to the Hyuga-nada, more than 70 km beyond the currently accepted location at the westernmost end of Shikoku in order to explain many recent findings such as those for geodetic data and geological investigations in coastal area and large tsunami in Kyushu, Japan. Numerical simulation of the tsunami using a new source-rupture model for the Hoei earthquake explains the distribution of the very high tsunami observed along the Pacific coast from western Shikoku to Kyushu more consistently with tsunami run-up into Ryujin Lake at Kyushu. It is known that the tsunamis from the 684 Tenmu, 1361 Shokei, and 1707 Hoei earthquakes deposited sand in Ryujin Lake, but lesser tsunamis from other earthquakes were unable to reach the lake. This irregular behavior suggests that, in addition to the regular Nankai Trough earthquake cycle of 100-150 years, there may be a hyper-earthquake cycle of 300-500 years. These greater earthquakes produce the larger tsunamis from western Shikoku to Kyushu than we expect for future Nankai Trough earthquake.

1. INTRODUCTION

Great inter-plate earthquakes have occurred at the Nankai Trough at a recurrence interval of approximately 100 to 150 years due to the subduction of the Philippine Sea plate beneath southwestern Japan (Fig.1).

In the recorded history of the Nankai Trough earthquakes the 1707 Hoei earthquake (hereafter called the Hoei earthquake) was the largest shock in modern Japanese history. It killed more than 20,000 people due to its strong ground motion and the tsunami associated with the earthquake. The fault rupture area of the Hoei earthquake has been thought to spread from Suruga Bay to the westernmost end of Shikoku, which is often referred as a worst-case scenario for the Nankai Trough earthquake.

The source rupture histories of the recent 1944 Tonankai and 1946 Nankai earthquakes were examined extensively based on the analysis of modern instrumental data, such as tide gauge records of tsunami waveforms, seismograms, and geodetic data. However, the source model of the historical Hoei earthquake in 1707, on the other hand, have mostly been deduced from descriptions of earthquake phenomenon in ancient documents such as shaking felt by humans, damage to houses, and visual measurements of tsunami inundation or tsunami run-up height, and pattern of ground elevation an subsidences.

Recently, geological surveys of earthquake-related lacustrine sediment in seashore lakes along the Pacific coast from Shikoku to Kyushu endeavor to clarify the tsunami history of the historical and pre-historical Nankai Trough earthquakes. Ryujin Lake is one such onshore lake that has tsunami-induced oceanic deposits (hereafter called tsunami

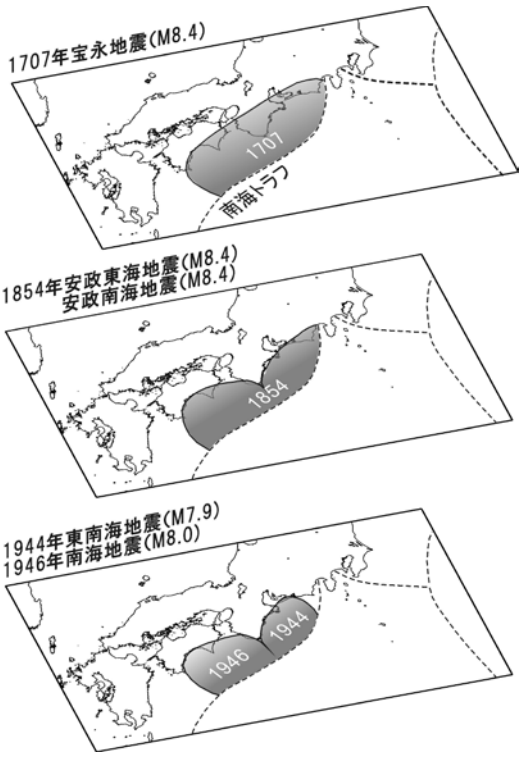


Figure 1 History of the Nankai Trough earthquake and source rupture area of recent three earthquake sequences of 1944/1946 Showa Tonankai/Nankai, 1854 Ansei, and 1707 Hoei earthquakes.

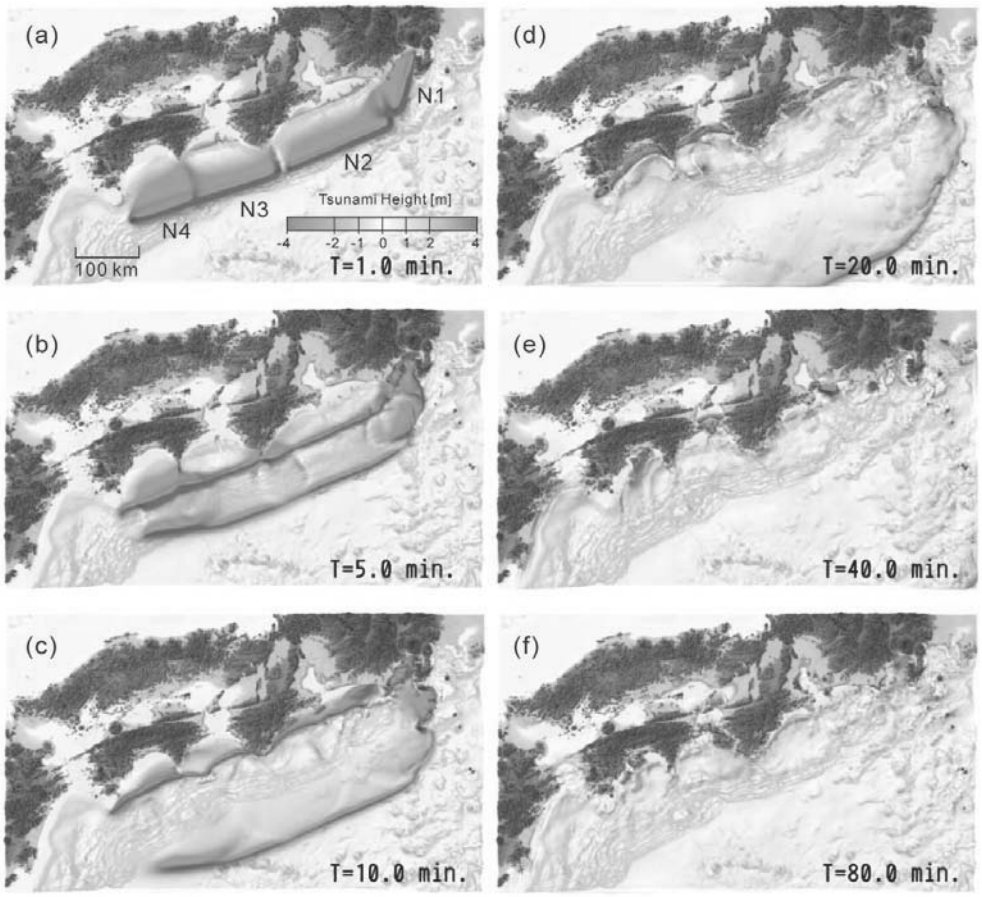


Figure 2 Snapshots of the tsunami propagation for the 1707 Hoei earthquake at T = 1.0, 5.0, 10.0, 20.0, 40.0, and 80.0 min. Red and blue colors indicate uplift and subsidence of the sea surface, respectively

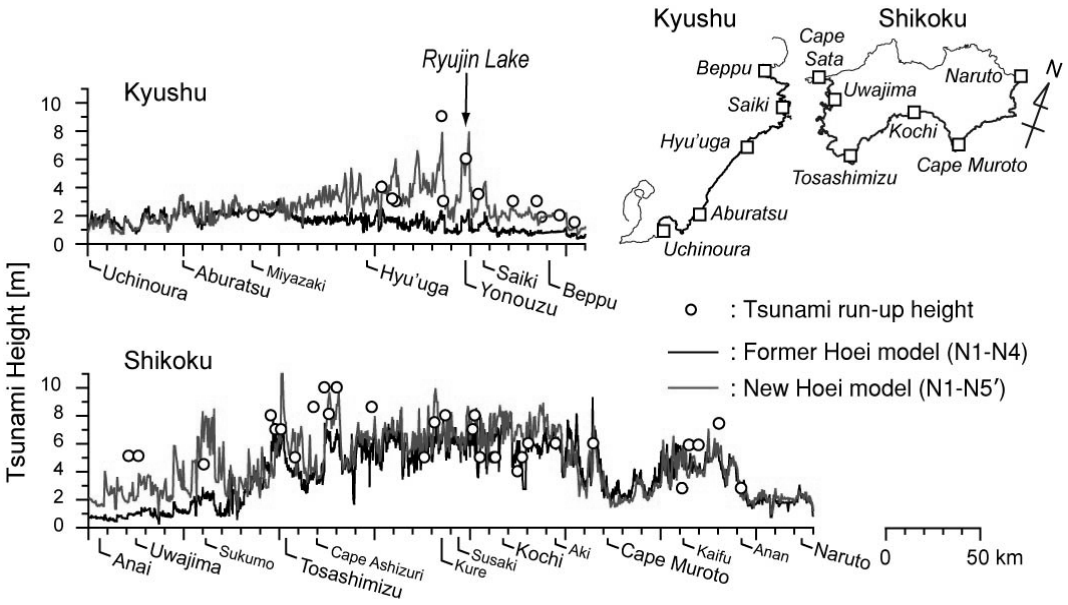


Figure 3 Maximum height of tsunami derive by the tsunami simulation for the former Hoei earthquake source model (black) and new source model (red) comparing with observation (circles).

lakes), located along the coast of the Hyuga-nada in

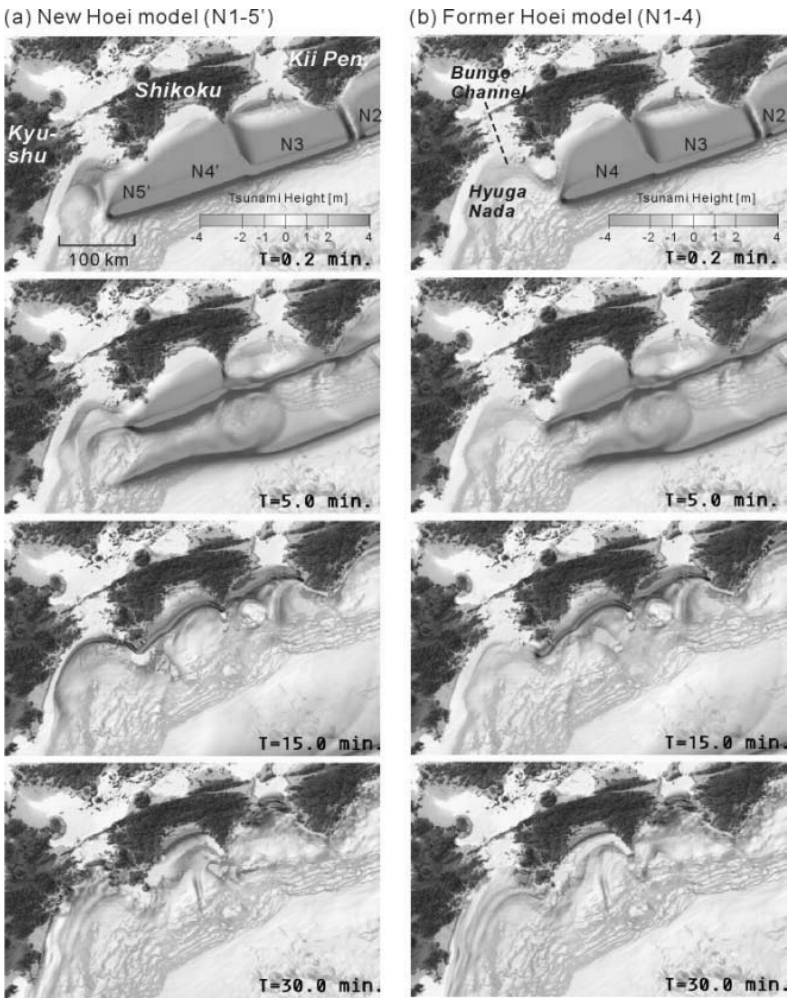


Figure 4 Snapshots of tsunami propagation from the Kii Peninsula to Kyushu (a) New Hoei earthquake model with fault segments N1 to N5 (b) former Hoei model (after An'naka et al., 2003) with fault segments N1 to N4.

Kyushu. Ryujin Lake has a thick cover of marine deposits, including coarse-grained sea sands and marine sediments containing oceanic plankton carried by Nankai Trough earthquake, not every 100 to 150 years, but were only deposited in the 1707 Hoei earthquake, the 1361 Shohei earthquake, and the 684 Tenmu earthquakes, probably associated with larger tsunamis than usual. Also, recent findings in the historical documents claim that the height of the tsunami during the Hoei earthquake at the village of Yonouzu, near Ryujin Lake, was more than 10 m, which is very much larger than regular tsunamis associated with the earthquake.

The data from the Japanese GEONET nation-wide GPS network illustrating the current ground deformation pattern of undergoing recovery process of post- Nankai Trough earthquake and studies on inter-plate coupling along the Nankai Trough using this data reveal strong interplate coupling along the Nankai Trough extends to Hyuga-nada

Following these new findings and supporting instrumental data, we will reexamine the source model for the Hoei earthquake and extended the source-rupture area 70 km eastward to the Hyuga-nada from the westernmost end of Shikoku.

We will demonstrated by tsunami simulation that our new source Hoei earthquake source model can explains large tsunami observed in Kyushu and tsunami inundation into Ryujin Lake more consistently than previous models.

2. TSUNAMI SIMULATION FOR THE 1707 HOEI EARTHQUAKE

We first conducted tsunami simulation for the Hoei earthquake using a source model of An'naka et al. [2003] which consists of four fault segments (N1 to N4) extending from Suruga Bay to the westernmost end of Shikoku, a total length of 605 km.

Vertical ground deformation due to fault rupture of the N1 through N4 fault segments are calculated using the program following Mansinha and Smylie [1975]. The result show large ground upheavals of up to 2 m above the shallowest end of the source fault segment on the trench side

and some of upheaval can be found on land, including at Cape Muroto, Cape Shiono, and along the coast of Suruga Bay. On the other hand, large surface subsidence of as much as 2 m is found widely on land in a narrow belt zone extending from Shizuoka to the westernmost end of Shikoku. These are consistent with the observed ground deformation pattern of the Hoei earthquake.

Using the results of the coseismic ground deformation pattern, we conducted a tsunami simulation. The area of the simulation is 540 km by 860 km which has been discritized by a nested mesh model that connects gradually 30 m, 90 m, and 270 m mesh model to allow efficient simulation of the tsunami in heterogeneous bathymetry. The bathymetric model was provided by the Central Disaster Mitigation Council, Cabinet Office, Government of Japan. Then propagation of the tsunami and tsunami run-up are calculated based on a finite-difference method (FDM) of a nonlinear, long-wave tsunami model [Goto and Ogawa, 1997].

Snapshots of tsunami propagation obtained from the simulation are illustrated in fig. 2 at time T = 1, 5, 10, 20, 40, and 80 min from the time the earthquake started. The snapshots shows that the radiation of tsunamis from rectangular fault sources is very strong in the direction perpendicular to the trough axis, while it is very weak in the direction parallel to the trough. As the tsunami approaches the shore, its speed decreases suddenly and its height increases very drastically. The onshore height of the tsunami, more than 8 m, is several times larger than the height of the initial tsunami above the source area along the Pacific coast from the westernmost end of Shikoku to Hyuga-nada. The tsunami lasts for several tens of minutes after the earthquake and a number of tsunami trains are captured within Tosa Bay.

Distribution of maximum simulated tsunami height is illustrated in fig. 3. From historical records, tsunami heights of 9 m at Tosa Shimizu and Ashizuri Cape and more than 4 m along the coast from Ashizuri Cape to Hyuga-nada are known to have occurred. The simulated maximum tsunami height along the Pacific coast from Tosa Bay to Suruga Bay generally agrees well with observed tsunami run-up during the Hoei earthquake [e.g., Hatori, 1974, 1985; Murakami et al., 1996]. However, the height of the simulated tsunami from western Shikoku to Hyuga-nada in Kyushu is less than half of the actual height observed. For example, historical archives document that at Yonouzu village, at the northern end of Hyuga-nada, the tsunami was more than 10 m and killed 18 people [Chida et al, 2003. Yet the simulated tsunami height at Yonouzu is less than 4 m, much shorter than the tsunami experienced with the Hoei earthquake.

3. REVISION OF THE SOURCE MODEL FOR THE 1707 HOEI EARTHQUAKE

In order to better explain the height of the Hoei earthquake tsunami from Cape Ashizuri to Hyuga-nada, we revised the present source model of the Hoei earthquake developed by An'naka et al. [2003] based on the findings of a number of recent geodetic and geological investigations of the Nankai Trough.

Ten years of data from the nationwide GEONET GPS network illustrates pattern of vertical ground deformation of 2 mm/year has occurred on land from Enshu-nada to Hyuga-nada. This pattern of vertical ground movement is considered to illustrate the process of recovery of ground surface deformation due to the Nankai Trough earthquakes. We also consulted recent studies on the spatial distribution of inter-plate coupling rates along the Nankai Trough [e.g., Hashimoto, 2009] based on the inversion of the GEONET data. It shows that an area of strong inter-plate coupling with high coupling ratios is found from Suruga Bay to Hyuga-nada, more than 100 km beyond the westernmost end of Shikoku which we have considered the evidence that seismic energy is now accumulating to cause a large earthquake in the future.

Following these new findings, we revised the source-rupture model for the Hoei earthquake and extended the border of the Hoei earthquake source segments from the westernmost end of Shikoku to Hyuga-nada, where strong inter-plate coupling has been found.

We set a 70 km by 120 km subfault segment, N5, on the west of the N4 subfault segment and extended the source rupture area of the Hoei earthquake to Hyuga-nada. The ground surface deformation pattern derived using subfaults N1 to N5 agrees well with our expectation of gentle (40 cm) ground subsidence in the area around Yonozu and Ryujin Lake, where large tsunami attacked, and some subsidence of the ground surface at Cape Ashizuri as noted by Kawasumi (1950). It also corresponds well to the present ground elevation field derived from the GEONET.

We then conducted a tsunami simulation using the revised source model of the Hoei earthquake to see the contribution of the N5 subfault segment in increasing simulated tsunami height along the coast from Shikoku to Kyushu. Snapshots of tsunami propagation are compared in fig. 4 with that for the former source model. Maximum simulated tsunami heights for the new model are compared with those of the former model in fig.3. The comparison clearly demonstrates the development of a larger tsunami with heights of 5 m to over 10 m over a wide area along the Pacific coast from the westernmost end of Shikoku to Hyuga-nada due to the N5 subfault. The height of the tsunami due to the N5 fault is very strong to spread large tsunami wavefront from Cape Ashizuri to Hyuga-nada.

The maximum tsunami height along the coast near Ryujin Lake as calculated by the present simulation is 6 m, while it is a maximum of 2 m for the former Hoei earthquake source model. Thus, larger tsunami at Yonozu and tsunami run-up into Ryujin Lake might occur when the Nankai Trough fault rupture extends to Hyuga-nada, but not during events like the 1854 Ansei Nankai and 1946 Showa Nankai earthquakes, in which the fault rupture did not extend past the westernmost end of Shikoku. Our newly simulated tsunami height of approximately 6 m but not as high as 10 m at Ryujin Lake also confirms the interpretation

of Okamura et al. [2004] that larger tsunami inundation occurred in the Ryujin lake though narrow channel connecting lake and sea but tsunami did not overtopping of beach hills that are 10 m high.

4. CONCLUSION

Of the series of repeating megathrust earthquakes in the Nankai Trough, the Hoei earthquake is considered to be the most damaging, with its linkage of Tokai, Tonankai and the Nankai earthquakes, and fault ruptures extending from Suruga Bay to the westernmost end of Shikoku, about 600 km in length [An'naka et al., 2003].

However, the recent discovery of the thick cover of tsunami-induced deposits caused by the Hoei earthquake has overturned our understanding. The existence of the tsunami deposits in the onshore lakes in Kyushu was not well explained by the expected ground deformation pattern produced by the former Hoei earthquake source model where the fault rupture stopped at the westernmost end of Shikoku. The source model also failed to explain the larger tsunami experienced during the Hoei earthquake from Cape Ashizuri to Hyuga-nada.

An inferred property of the present crustal deformation pattern illustrated by the GEONET GPS measurements and a number of studies on inter-plate coupling along the Nankai Trough subduction zone based on the GPS data indicate that Hyuga-nada may also be in the area of the Nankai Trough earthquake nucleation zone. Following these new geological and geodetic findings, we revised the source model of the Hoei earthquake by introducing a new subfault segment at Hyuga-nada on the western side of Nankai earthquake segment.

We succeeded in explaining development of the large tsunami from Cape Ashizuri to Hyuga-nada with maximum tsunami heights of 5 to 10 m that attack along the Pacific coast from the westernmost end of Shikoku to Hyuga-nada. This agrees with the heights of tsunamis observed along the Pacific coast from Cape Ashizuri to Hyuga-nada during the Hoei earthquake [Hatori, 1974, 1985; Murakami, 1996] very consistently.

The extension of the source rupture area to Hyuga-nada would produce increased shaking in Kyushu. Exactly what the intensity was in Kyushu in 1707 is unclear; we are unaware of any historical documents that permit a meaningful comparison of intensities of the 1707 and 1856 earthquakes.

The linkage process between different subfaults in Nankai Trough earthquakes of more than 700 km and described by at least five fault segments may contribute significantly to the severity of the disaster, especially the tsunamis. Researchers have claimed that delayed rupture between subfaults amplifies tsunami height over a wide area due to overlap of individual tsunamis from different fault segments [Kawata et al., 2003; Imai et al., 2010]. We should be prepared for a diversity of rupture processes during future earthquakes along the Nankai Trough.

Finally, this study suggests that earthquake rupture extent along the Nankai Trough may not be as limited as previously described: as combinations of subfaults to produce Nankai, Tonankai, or Tokai earthquakes. The Hoei earthquake was a much larger event in which rupture spread as far as Hyuga-nada. Such larger events do not occur during the regular Nankai Trouh earthquake cycle of 100-150 years, but may occur in a hyper-earthquake cycle of 300 to 500 years. The larger tsunami and tsunami deposits at Ryujin Lake in Kyushu left by large tsunamis from the 684 Tenmu, 1361 Shohei, and 1707 Hoei earthquakes, attest to such a hyper-earthquake cycle.

Acknowledgements:

This study was conducted under support of the Research Project "Improvements in strong ground motion and tsunami simulation accuracy for application to realistic disaster prevention of Nankai Trough megathrust earthquakes" of the Ministry of Education, Culture, Sports and Technology of Japan. We thank to the Central Disaster Mitigation Council, Cabinet Office, Government of Japan and Yonouzu Promotion office, Oita Prefecture, Japan to provide bathymetry map data.

References:

An'naka, T., K. Inagaki, H. Tanaka, and K. Yanagisawa (2003), “Characteristics of great earthquakes along the Nankai trough based on numerical tsunami simulation”, Journal of Earthquake Engineering, JSCE, CD-ROM.

Chida, N., S. Takamiya, H, Hamada, T. Tomimatsu, and S. Mitarai (2003), “Historical materials of the tsunamis in Yonouzu village, southerm part of Oita prefecture, southwest Japan, which were caused by earthquakes of October 28, 1707 and Nobember 24, 1854”, Res. Bull. Fac. Educ. & Welf. Sc., Oita Univ, 129-143.

Goto, C., and Y. Ogawa, “(IUGG/IOC TIME PROJECT), Numerical method of tsunami simulation with the leap-frog scheme, Part 1 Shallow water theory and its difference scheme, Intergovernmental Oceanographic Commission, Manuals and Guides”, No.35, 43p., 1997.

Hashimoto, C., T. Sagiya, and M. Matsuura (2009), “Interplate coupling in southwest Japan inferred from GPS data inversion”, Abst. SSJ Meet., A32-08.

Hatori, T. (1974). "Sources of large tsunamis in southwest Japan." J. Seismol. Soc. Japan 27, 10-24.

Hatori, T. (1985), “Field investigation of Historical tsunamis along the east coast of Kyushu, West Japan”, Bull. Earthq. Res. Inst. Univ. Tokyo, 60, 439-459.

Imai, K., K. Satake, and T. Furumura (2010), "Amplification of tsunami heights by delayed rupture of great earthquakes along the Nankai trough", Earth Planets Space, 62, 427-432, 2010.

Kawasumi, H. (1950), “Crustal deformations as deduced from mareographic data”, Publ. Shikoku-Tiho Sogo-Kaihatsu Shingikai (Committee for the Synoptic Development of the Shikoku District).

Kawata, Y., S. Suzuki, and T. Takahashi (2003), “An effect of giant earthquake scenarios at the Nankai trough on a tsunami hazard”, Proceedings of Coastal Engineering, JSCE, 50, 326-330.

Mansinha, L., and D. E. Smyli (1971), “The displacement fields of inclined faults”, Bull. Seism. Soc. Am., 61, 1433-1440.

Murakami, H., T. Shimada, S. Itoh, N. Yamamoto, and J. Ishizuka (1996), “Reexamination of the heights of the 1606, 1707 and 1854 Nankai Trsunamis along the coast of Shikoku Island”, J. SNDS, 15-1, 39-52.

Okamura, M., Matsuoka, H, Chida, N., and K. Shimazaki (2004), "Recurrence intervals of super Nankai earthquakes", Abst. Fall Meet. Seism. Soc. Japan, A027.

Omori, F. (1913), “An account of the destructive earthquakes in Japan. Publ. Earthquake Invest. Comm.”, 68B, 1-179.

8CUEE CONFERENCE PROCEEDINGS
8th International Conference on Urban Earthquake Engineering
March 7-8, 2011, Tokyo Institute of Technology, Tokyo, Japan

NONLINEAR SITE RESPONSE OF THE 2008 WENCHUAN, CHINA EARTHQUAKE FROM TIME-FREQUENCY ANALYSIS

Kuo-Liang Wen[1)], Jyun-Yan Huang [2)], Xiaojun Li[3)], Zhenghua Zhou[4)], and Ruizhi Wen[5)]

1) Professor, Institute of Geophysics, National Central University, Taiwan, R.O.C.
Division Head, National Center for Research on Earthquake Engineering, Taiwan, R.O.C.
2) PhD Student, Institute of Geophysics, National Central University, Taiwan, R.O.C.
3) Research Fellow, Institute of Geophysics, China Earthquake Administration, China
4, 5) Research Fellow, Institute of Engineering Mechanics, China Earthquake Administration, China
wenkl@earth.ncu.edu.tw, 986402005@cc.ncu.edu.tw, beerli@vip.sina.com, bjsmoc@163.com, ruizhi@iem.net.cn

Abstract: A magnitude M_s=8.0 earthquake occurred on May 12, 2008 in Sichuan, China. Surface rupture and severe damage were observed during the great event. Liquefaction also reported in the Chengdu plain. The nonlinear soil response should be occurred during the strong shaking of this event. During the Wenchuan earthquake, National Strong Motion Observation Network System of China obtained a large number of acceleration records from the main shock (~ 460 free-field strong motion stations). In this study, the strong motion records are used to identify the nonlinear site effects during the 2008 Wenchuan, China earthquake. The horizontal-to-vertical spectral ratio has become popular in study of the site effect and the determination of the predominant period of a site. Wen et al. (2006a) extended this method to identify the nonlinear soil response during strong motion events. Due to only the main shock records are available now, we can identify the soil response is linear or nonlinear based on variation of the predominant frequency with time using the moving window spectral ratio method.

1. INTRODUCTION

Nonlinear site effects, such as an increase in damping and reduction in shear wave velocity as input strength increases, are commonly recognized in the dynamic loading of soils from geotechnical models. During the findings of recent years indicate that nonlinear site effects are more common than previously recognized in strong-motion seismology (Beresnev and Wen, 1996). Direct seismological evidences of nonlinear site effects were reported by using the spectral ratio techniques of soil-to-rock or surface-to-borehole station pair (Wen *et al.* 1994, 1995; Beresnev *et al.* 1995a, 1995b).

A magnitude M_s=8.0 Wenchuan, China earthquake occurred at 14:28 of May 12, 2008 (Local time). It caused 69,197 people killed and 215,000 buildings totally damaged. The surface rupture along the Yingshow-Beichuan fault and Kuanshian-Chiangyio fault (Longmenshan fault system) are about 240 and 70 km length, respectively. During the Wenchuan earthquake, National Strong Motion Observation Network System of China obtained a large number of acceleration records from the main shock (~ 400 free-field strong motion stations). Therefore, a lot of high quality data had been recorded that triggered by this disaster event (Figure 1). The Wenchuan earthquake not only directly caused heavy damages on the structure and huge human life loss near the epicenter area, but also induced the secondary damages to the buildings in that region (Zhang et al. 2008). From the field surveys, many places, such as Chendo, Deryang, and Menyang area (Figure 2, Yuan et al. 2009; Du and Xing 2010), show the soil liquefaction were related to local geology and intensity. It implies that the nonlinear soil response should occur pervasively in those areas. The normal spectral ratio method of a two-station pair can not apply to this large alluvium area. In this study, the horizontal-to-vertical (H/V) method was used to study the nonlinear site response during the 2008 Wenchuan, China earthquake.

2. METHOD USED TO IDENTIFY NONLINEAR SITE RESPONSE

Nonlinear site effects, such as an increase in damping and reduction in shear wave velocity as input strength increases, are commonly recognized in the dynamic loading of soils from geotechnical models. During the findings of recent years indicate that nonlinear site effects are more common than previously recognized in strong-motion seismology. Direct seismological evidences of nonlinear site effects were reported by using spectral ratio techniques (Wen 1994). Nakamura (1989) proposed a hypothesis that microtremor site effects can be determined by simply evaluating spectral ratio of horizontal versus vertical components of motion observed at the same site. Lermo and Chávez-García (1993) shows that this method can use to

earthquake record for studying the site effect. Wen *et al.* (2006a) using the horizontal-to-vertical spectral ratio method to identify nonlinear site response. The results show the applicability of H/V technique for nonlinear site response identification. In this study, we calculated the H/V ratios of the Wenchuan mainshock record at each station and compared the variation of the predominant frequency with time using the moving window spectral ratio method to identify the site response at each station during the 2008 Wenchuan, China earthquake.

3. RESULTS OF THE NONLINEAR SITE RESPONSE ANALYSIS

3.1 H/V Ratios in the Liquefaction Area

Many places had observed soil liquefaction after the 2008 Wenchuan earthquake (Yuan et al. 2009; Du and Xing 2010). Figure 3a shows the time-frequency H/V spectra of the near-fault station 51SFB. The ratio shows clearly de-amplification and dominant frequency shift effect in the strong motion portion. The ratio of Window C (Figure 3b), with PGA = 23.31 gals, seems move back to linear response.

Station 51WCW (汶川臥龍) recorded very high peak ground acceleration (953.79 gals on Window B). Figure 4a shows the time-frequency H/V spectra of 51WCW. The dominant frequency shift to lower frequency is clearly shown in the results of the 2048 points window for the two strong motion portions (Windows B and D). For the latter portion of weak motion part, the dominant frequency shift back to higher frequency (Figure 4b).

After analyzed the data of the stations in Figure 1b during the Wenchuan, China earthquake, the results were shown in Figure 5. Red symbols show the station has strong nonlinearity, purple symbols show the station has weak nonlinearity, blue symbols show the station did not have nonlinear effect. The results show that the nonlinear site effects existed in most near fault area. The liquefaction areas are within the nonlinear soil response area (Figure 6).

3.2 Quantitative analysis of nonlinearity

In previous study, the strong and weak motion's H/V spectral ratios are compared to show the nonlinearity qualitatively. Some stations are not easy to clarify it had nonlinear response or not. So, Wen et al. (2006b) identify the nonlinearity, quantitatively, by the deviation between the H/V spectral ratios of strong and weak motions. Which was calculated as follow:

$$d(f) = \frac{s(f) - w(f)}{\sigma(f)} * 100\% \qquad (1)$$

where *s(f)* is the H/V ratio of the strong motion event, *w(f)* and $\sigma(f)$ are H/V ratio of the weak motion event and its standard deviation. Noguchi and Sasatani (2008) proposed to use the quantitative index of nonlinear site response DNL (degree of nonlinear site response) defined as follow:

$$\mathrm{DNL} = \sum \left| \log\left(\frac{R_{strong}(f)}{R_{weak}(f)} \right) \right| \bullet \Delta f \qquad (2)$$

where R_{strong} and R_{weak} are H/V spectral ratio of the strong and weak motions, and sum it from 0.5 to 20 Hz frequency band.

Due to only the main shock data are available now, so as that shown in Figures 3b and 4b, the different windows from the main shock records are used to quantitatively analyze the H/V ratios of strong and weak motion. The DNL values are calculated from the strong motion window (e.g. window B in Figures 3 and 4) and the weak motion window (final later portion as window C in Figure 3). Figure 7 compare the DNL values and the PGAs on window B for that station. It clearly show that when PGA greater than about 100 gal, the strong motion records will show nonlinear effect.

4. CONCLUSIONS AND DISCUSSIONS

Liquefaction hazard occurred in the epicenter area during the May 12, 2008 Wenchuan, China earthquake. In this study, the horizontal-to-vertical spectral ratio method is used to identify the nonlinear site effects during the earthquake. The results show that the nonlinear site effects existed in most near fault area. The liquefaction areas are within the nonlinear soil response area. The DNL between the H/V ratios of strong motion and weak motion are calculated in the frequency band of 0.5~20 Hz. The DNL value has positive relationship with PGA value. The stations, with nonlinear site response, seems on the range of DNL > 3.0 and PGA > 100 gal. The DNL analysis use the strong and weak motion portion on the same record, after receiving the weak motion record from the small magnitude after shocks, we can check the results again.

Due to the site condition of each strong motion station is not clear at the moment, only simply separated as soil and rock site. If it can have more detail information, for example the Vs30, then we can compare the DNL value with Vs30. This information will be useful for engineering application.

Acknowledgements:

The authors would like to thank China Strong Motion Networks Center, Institute of Engineering Mechanics, China Earthquake Administration for providing the strong motion data of the 2008 Wenchuan, China earthquake. This study has been supported by the National Science Council, Taiwan, R.O.C. under the grant no. NSC 99-2116-M-008-023.

References:

Beresnev, I.A., Wen, K.L., and Yeh, Y.T. (1995a), "Nonlinear Soil Amplification: Its Corroboration in Taiwan," *Bull, Seism. Soc. Am.*, **85**, 496-515.

Beresnev, I.A., Wen, K.L., and Yeh, Y.T. (1995b), "Seismological Evidence for Nonlinear Plastic Ground Behavior During Large Earthquakes," *Soil. Dyn. Earthquake Eng.*, **14**, 103-114.

Beresnev, I.A. and Wen, K.L. (1996), "Nonlinear Ground Response - a Reality? (A Review)," *Bull. Seis. Soc. Am.*, **86**(6), 1964-1978.

Du, G.Y. and Xing, X.C. (2010), "Research on the Soil Liquefaction

in the Piedmont Region of the Longmen Mountain," *Hydrogeology and Engineering Geology*, **37**(1), 108-112.
Lermo, J. and Chávez-García F.J. (1993), "Site Effect Evaluation Using Spectral Ratios With Only One Station," *Bull, Seism. Soc. Am.*, **83**, 1574-1594.
Nakamura, Y. (1989), "A Method for Dynamic Characteristics Estimation of Subsurface Using Microtremor on the Ground Surface," *QR of RTR1*, **30**(1), February.
Noguchi, S. and Sasatani, T. (2008), "Quantification of Degree of Nonlinear Site Response," *Proc. 14WCEE*, P028, No.03-03-0049.
Wen, K.L. (1994), "Non-linear Soil Response in Ground Motions," *Earthq. Eng. Struct. Dyn.*, **23**(6), 599-608.
Wen, K.L, Beresnev, I.A., and Yeh, Y.T. (1994), "Nonlinear Soil Amplification Inferred From Downhole Strong Seismic Motion Data," *Geophys. Res. Lett.*, **21**, 2625-2628.
Wen, K.L., Beresnev, I.A., and Yeh, Y.T. (1995), "Investigation of Non-linear Site Amplification at Two Downhole Strong Ground Motion Arrays in Taiwan," *Earth. Eng. Struct. Dyn.*, **24**, 313-324.
Wen, K.L., Chang, T.M., Lin, C.M., and Chiang, H.J. (2006a), "Identification of Nonlinear Site Response Using the H/V Spectral Ratio Method," *Ter. Atm. Oce.*, **17**(3), 533-546.
Wen, K.L., Chang, T.M., Lin, C.M., and Chiang, H.J. (2006b), "Identification of Nonlinear Site Response During the 1999, Chi-Chi, Taiwan Earthquake From the H/V Spectral Ratio," *Proc. of Third Int. Symp. on the Effects of Surface Geology on Seismic Motion, Grenoble, France, 30 Aug. - 1 Sep. 2006*, Paper No.: 012, ESG2006, V.1, 225~232.
Yuan, X.M.，Cao, Z.Z., Sun，R.，Chen, L.W., Meng，S.J., Dong, L., Wang，W.M., Meng，F.C., Chen，H.J., Zhang，J.Y., and Cai, X.G. (2009), "Preliminary Research on Liquefaction Characteristics of Wenchuan 8.0 Earthquake," *Chinese Journal of Rock Mechanics and Engineering*, **28**(6), 1288-1296.
Zhang, Y.S., Lei, W.Z., Shi, J.S., Wu, S.R., and Wang, X.L. (2008), "General Characteristics of 5.12 Earthquake-induced Geohazards in Sichuan," *Journal of Geomechanics*, **14**(2), 109-116.

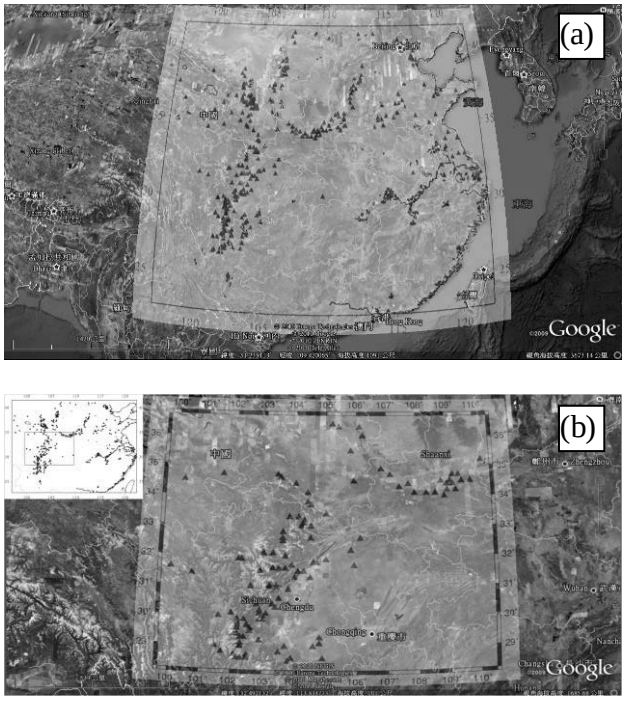


Figure 1 (a) Strong motion station distribution in China; (b) Stations used in this study.

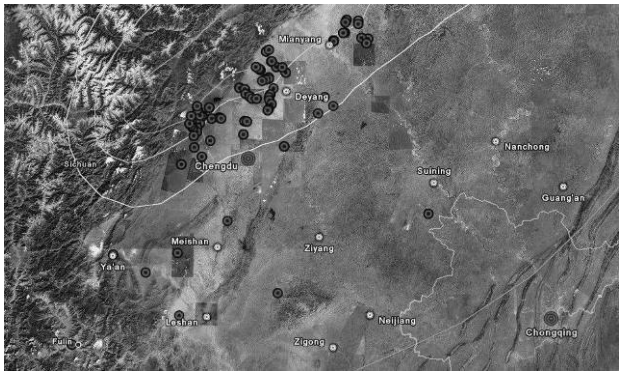


Figure 2 Liquefaction distribution near fault rupture area. Solid red dots show the village has liquefaction (Yuan *et al.* 2009).

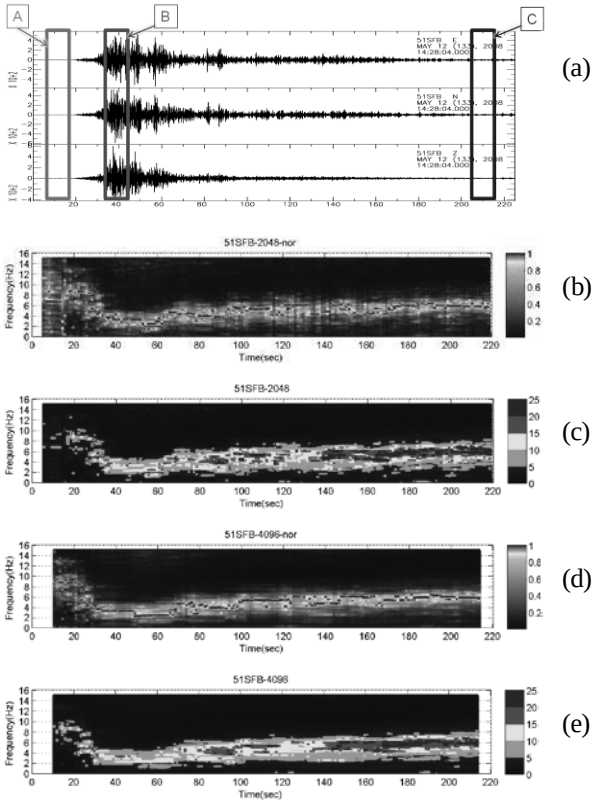


Figure 3a Time variation spectral ratio of the station 51SFB (什邡八角), (a)A-Window, B-Window, and C-Window position; Others are time-frequency spectra for (b) 2048 points window and normalized, (c) 2048 points window and no normalize, (d) 4096 points window and normalized, (e) 4096 points and no normalize.

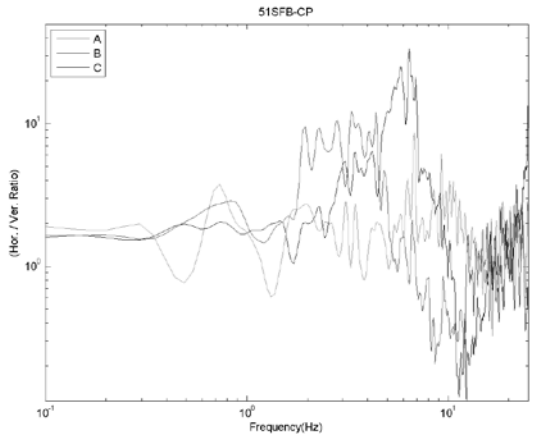


Figure 3b H/V ratio for different time windows of the station 51SFB.

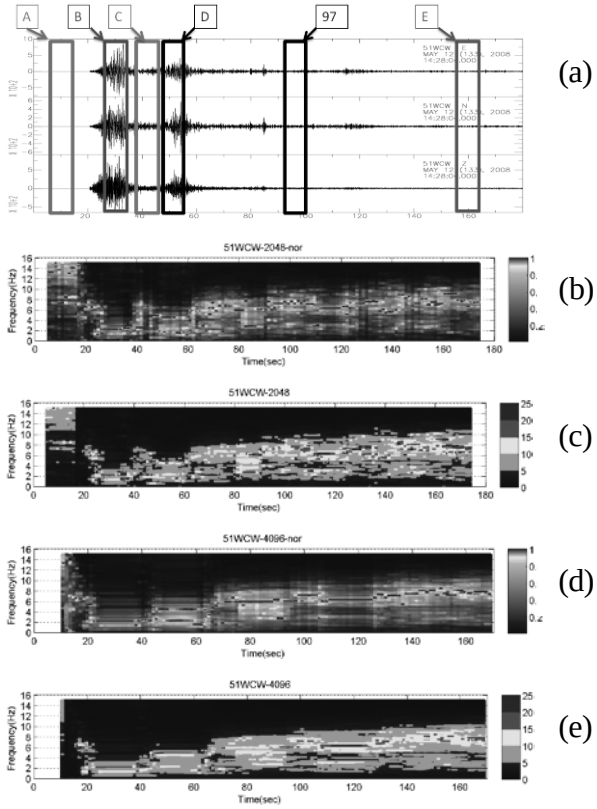


Figure 4a Time variation spectral ratio of the station 51WCW (汶川臥龍), (a)A-Window, B-Window, and C-Window position; Others are time-frequency spectra for (b) 2048 points window and normalized, (c) 2048 points window and no normalize, (d) 4096 points window and normalized, (e) 4096 points and no normalize.

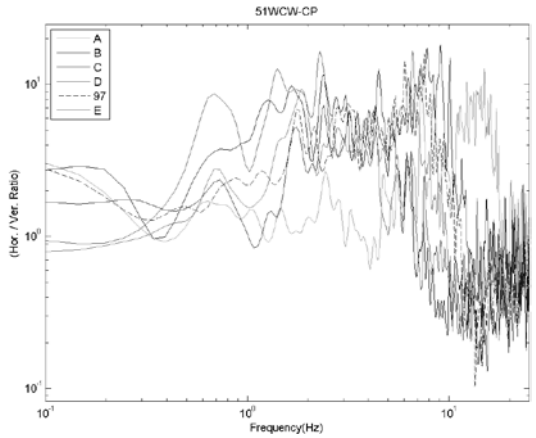


Figure 4b H/V ratio for different time windows of the station 51WCW.

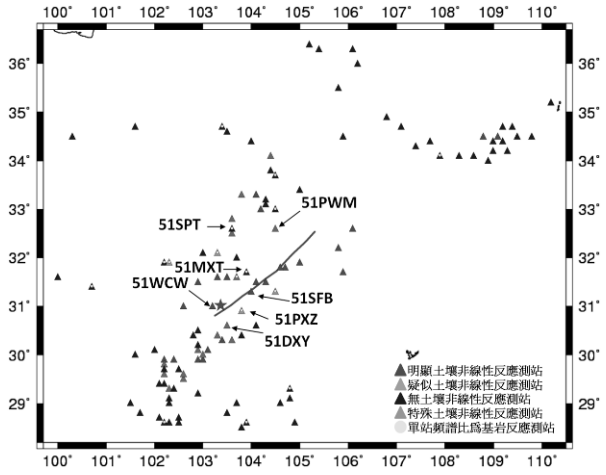


Figure 5 Station distribution of the strong (red), weak (purple), no (blue), and special (green) nonlinear response. Yellow symbol shows the H/V ratio is the type of rock site.

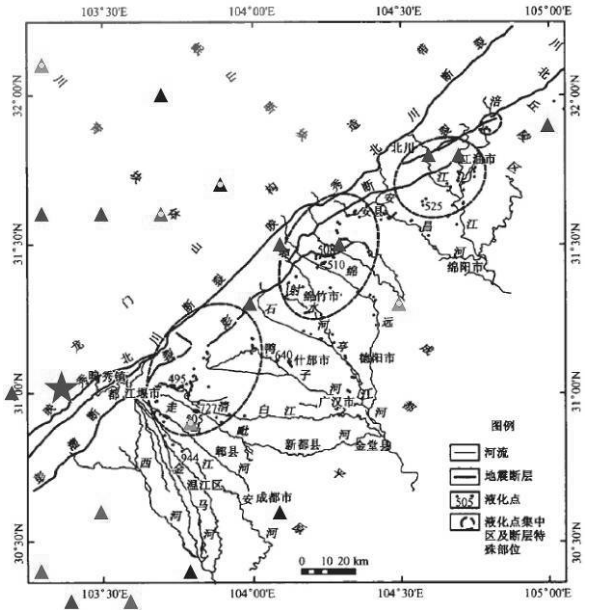


Figure 6 Liquefaction distribution near fault rupture area. Three circles show the dense liquefied areas from Du and Xing 2010.

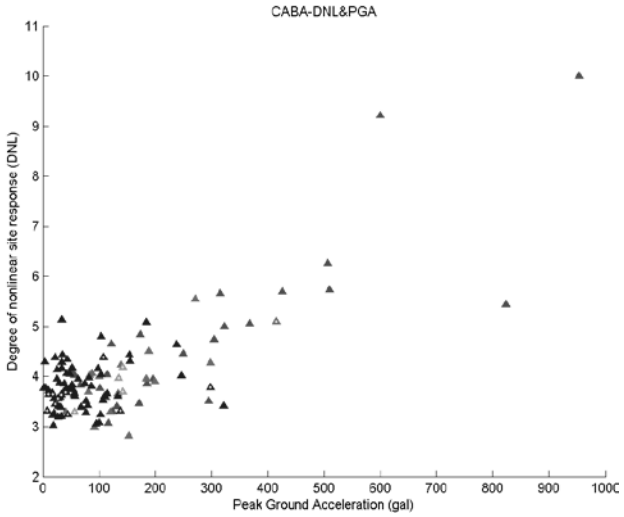


Figure 7 Relationship between the DNL and peak ground acceleration for Windows B and C.

8CUEE CONFERENCE PROCEEDINGS
8th International Conference on Urban Earthquake Engineering
March 7-8, 2011, Tokyo Institute of Technology, Tokyo, Japan

ESTIMATION OF SHALLOW 2D S-WAVE VELOCITY PROFILE FROM WAVEFORM INVERSION OF SEISMIC REFRACTION DATA

Hiroaki Yamanaka[1] and Yasutomo Yamauchi[2]

1) Associate Professor, Dept. of Environmental Science and Tech., Tokyo Institute of Technology, Japan
2) Graduate Student, Dept. of Environmental Science and Tech., Tokyo Institute of Technology, Japan
yamanaka@depe.titech.ac.jp

Abstract: We proposed a waveform inversion to deduce a 2D S-wave velocity profile for shallow soil layers from SH-wave data obtained in a refraction survey. The waveform inversion method is based on the approach by Takekoshi and Yamanaka (2009). Preprocessing of SH wave data is included in our methods to eliminate the effects of source time function for a wave generator in the refraction seismics. The wave data at each site are deconvolved using the observed data at a reference station. The misfit function is defined as differences between the calculated and observed waveforms after the deconvolution process and it is minimized with a hybrid heuristic search method. Theoretical SH-wave is generated from a finite difference computation of SH-wave propagating in a 2D inhomogeneous media. We conducted numerical experiments using synthetic SH-wave data in two shallow soil models. The inversions of the synthetic data could reconstruct the true models very well indicating a validity of the method. We, then, applied the waveform inversion to actual SH-wave data obtained at 8 stations in a shallow refraction exploration. The obtained 2D profile is similar to that from a conventional travel time analysis.

1. INTRODUCTION

S-wave velocity distribution in ground is one of the important factors to estimate local site amplification at a site covered with soft soils, such as basin and reclaimed area. Several kinds of S-wave velocity measurements are available for the purpose of estimation of site amplification. One of the major methods is PS-logging using bore measurements. Although we can determine an accurate S-wave velocity distribution from the logging, surveying cost would be more expensive than surface explorations techniques. The microtremor exploration is one of the important techniques to deduce S-wave velocity profile of soils with low cost, and has been applied in various kinds of S-wave exploration in earthquake engineering (e.g., Arai and Tokimatsu et al., 2005,). The microtremor technique is used to determine a 1D profile of S-wave velocity. This can not be used for a site with irregular interfaces or strong lateral heterogeneity of S-wave velocity.

Tomographic inversions of travel times of S-wave generated with artificial sources can be used to map inhomogeneous S-wave velocity. Surface wave However, it is required to prepare many travel time data from many sensors along a surveying line. This is one of the disadvantages in the methods based on tomographic inversions. Recently, surface waves in the refraction data are used in shallow S-wave profiling from dispersion analysis (e.g., Hayashi and Suzuki, 2004). Since travel times of initial S-wave are not used in the surface wave method, it is easily applied in noisy urban area. Although a two-dimensional image of S-wave velocity can be derived from the surface wave method, it is required to prepare many observed stations for detailed imaging. Furthermore separation of surface wave modes must be done before the dispersion analysis, when higher mode surface waves have larger or similar amplitudes to the fundamental modes. Takekoshi and Yamanaka (2009) have proposed a waveform inversion technique using shallow seismic refraction data to a 2D inhomogeneous S-wave profile. The effectiveness of the method was examined using numerical experiments.

In this study we applied the waveform inversion technique by Takekoshi and Yamanaka (2009) to actual data obtained in shallow seismic refraction exploration for mapping a 2D S-wave velocity model. First, we show a flow for data pre-processing of observed data before the inversion. We then conduct numerical test of the data processing and inversion using numerical data. Finally we applied the technique to the actual data.

2. METHOD

2.1 Pre-processing of Data

Characteristics of SH-waves observed in refraction survey are controlled with physical parameters of ground and source effects of wave-generator. We usually use plank-hammering to generate SH-waves. It is not easy to

estimate source time function and radiation patterns of such sources from observed data. Therefore, these source effects must be moved from observed data to retrieve effects of subsurface structure. A deconvolution technique is applied to the SH-waves. The spectrum, of SH-wave observed at site *j*, $O_j(\omega)$ is divided with that at a reference site,*r*, $O_r(\omega)$ as

$$\frac{O_j(\omega)}{O_r(\omega)} = \frac{S(\omega)G_j(\omega)}{S(\omega)G_r(\omega)} = \frac{G_j(\omega)}{G_r(\omega)}. \quad (1)$$

This processing provides a ratio of Green's function between the two sites in the time domain, $D_j^o(t)$. In actual processing the following equation is used to avoid numerical instability.

$$D_j^o(t) = \mathrm{F}^{-1}\left[\frac{O_j(\omega)O_r^*(\omega)}{O_r(\omega)^2 + \varepsilon}\right], \quad (2)$$

where F^{-1} and * mean the inverse Fourier transform and complex conjugate. ε is a small value and to be 0.1% of averaged amplitude of observed data. We also apply band-pass filtering during this processing in the frequency domain.

2.2 Parameterization of Soil Model

S-wave velocity structure of shallow soils is modeled using the parameterization by Takekoshi and Yamanaka (2009) as shown in Figure 1.

A soil model consists of surface layers over a basement having a constant S-wave velocity that is one of the unknown parameters in the waveform inversion. The surface layers are divided into layers separated by the interfaces. For example, the model in Figure 1c has three surface layers. The depth shape of each interface is described with basis functions by Aoi et al. (1995). Using linear combination of a basis function ck(x) and a coefficient pk, the interface depth d(x) at location x is written as

$$d(x) = \sum_k^L p_k c_k(x) \quad (3)$$

where *L* is number of basis function. The basis function is defined as

$$c_k(x) = \begin{cases} 1/2 + 1/2\cos(\pi/\Delta(x - x_k)) & x_{k-1} \le x \le x_{k+1} \\ 0 & otherwise \end{cases} \quad (4)$$

where Δ and x_k are constant given in advance. The interface depth parameters are defined for each interface of a multi-layered model. The unknown parameters to be determined on the waveform inversion are the coefficients p_k in the equation (3) with respect to the interface shape. In order to model lateral variation of S-wave velocity in surface layers, it is divided into blocks as can be seen in Figure 1c. S-wave velocity for each block is also one of the parameters in the inversion. In order to stabilize the inversion we used smoothing of the S-wave velocity of the blocks in each layer with a weighted 3-points smoothing operation.

The unknown parameters to be determined in the inversion are P_k, S-wave velocities of all the blocks in surface layers and S-wave velocity of the basement. For example, if we use 15 basis functions for each interface, total number of the unknown parameters for the model in Figure 1 are 76 (15*3P_k, 10*3+1 S-wave velocities).

The above-mentions parameterization of the subsurface structure can allow to model soils layers separated by geologically discontinuous interfaces with S-wave variations. We therefore assume small variations of S-wave velocities in the blocks that belong to the same layer in the inversion. This can be implemented with making narrow search limits of the S-waves for the blocks.

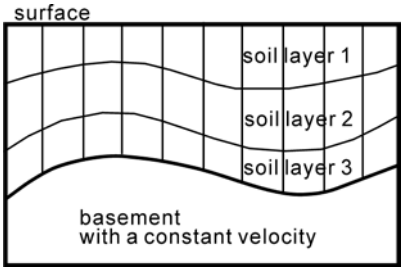


Figure 1. Schematic illustration for parameterization of subsurface structural model in the waveform inversion.

2.3 Definition of Misfit

The misfit function to be minimized in the inversion is defined using observed and theoretical traces to determine the model parameters. The misfit, *E*, is calculated from

$$E = \frac{1}{M}\sum_{j=2}^{M}\frac{\sum_{i=1}^{N}\left[\overline{D_j^o(t_i)} - \overline{D_j^c(t_i)}\right]^2}{\sum_{i=1}^{N}\left[\overline{D_j^o(t_i)}\right]^2} \quad (5)$$

where $Dj^o(t)$ and $Dj^c(t)$ are the observed and calculated SH-waves after the devonvolution processing. *N* is the number of stations along the surveying line.

In the calculation of the misfit, synthetic SH-waves are generated using finite difference approximation of a 2.5D equation of motion of SH-waves. The 2.5D equation of motion due to SH-waves is numerical solved with 4th-order and 2nd-order central finite difference approximation in space and time. The staggered finite difference grid is used in the approximation. The absorbing and sponge buffer conditions are subjected in the non-physical boundaries in the bottom, left and right sides of a finite difference grid model. The free surface condition is applied in the upper boundary of the model.

2.4 Inversion Algorithm

It is expected that the misfit function has a complex multi-model shape. An appropriate initial model is required

in the least-squared inversions, because of the local search characteristics. However, we often have no a priori knowledge on subsurface structure, especially for shallow near-surface soils. We therefore applied global search algorithms to minimize the misfit function in this study.

Heuristic approaches are one of the global search algorithms used in various kinds of geophysical inversions, such as GA and SA (e.g., Yamanaka, 2005). Since the heuristic inversion methods require many numbers of forward calculations, the heuristic approaches are not so often applied in inversions with relatively heavy forward computations. We however used the hybrid heuristic method proposed by Yamanaka (2007), because the method is capable to find the optimal model with less computational efforts than those for the conventional heuristic algorithms. Details can be shown in Takekoshi and Yamanaka (2009).

3. NUMERICAL TEST OF INVERSION

3.1 Two-Layer Model with Inclined Interface

Figure 2a shows a two-dimensional S-wave velocity model used in numerical experiment of the waveform inversion including data pre-processing. The model consists of a surface layer and basement with S-wave velocities of 200 and 500m/s, respectively. The model is digitized with grid points having a cell size of 0.2m. We calculated synthetic SH-waves at 8 sites on the surface at interval of 5meters in this model using the FD code. A point source having time function of Ricker wavelet with frequency of 30 Hz is set on the surface at distance of 10 meters from the left end of the model. Figure 3 shows the calculated SH-waves after the deconvolution processing. We used the data at 0 meters as the reference motion in the preprocessing. These waves were used as synthetic data in the numerical experiments. Reflected phases and surface waves can be identified in the waveforms.

In the waveform inversion, two-layer model is assumed with 20 blocks in the surface layer. The interface is model using 20 coefficients of Pk in the above equation. Total number of the unknown parameters is 41 in this numerical test. 10 inversions using different initial values of random number generator were conducted, and acceptable models were estimated from the all models examined in the 10 inversions. Average of the minimum misfits in the 10 inversions is shown in Figure 4 with its standard deviations at each generation. The minimum misfit decreases gradually with in the 130 generations, then it does significantly over the 150 generations. It suggests that the models around the global minimum model are sampled by the inversion. Figure 2b shows a model averaged of the minimum models from the 10 inversions. Their standard deviation is also shown in Figure 2c, by which we can understand stability of the inversions. The inverted model is almost the same as the true model with differences of basement depth in the left side from the source. This part is not constrained in the inversion because of no existence of observed data. The small standard deviation in Figure 2c indicates that model with the global minimum misfit is found in the inversion. Figure 3 also compares observed SH-waves with those for the inverted model. The two SH-waves are in agreement with each other.

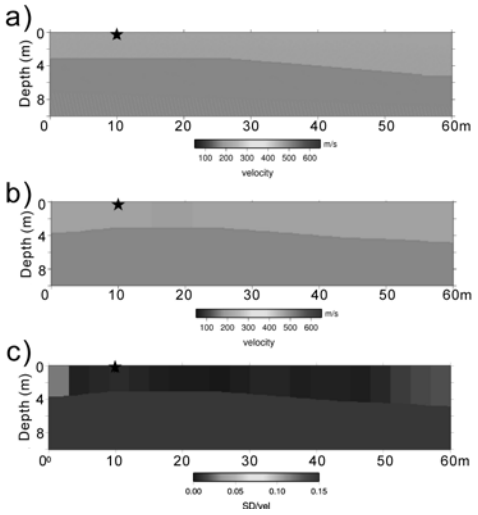


Fig.2. 2D S-wave velocity models in numerical experiments. The top model is assumed to generate synthetic observed data in Fig.3, and middle model is derived from inversion of the synthetic waveforms. The bottom shows the standard deviation of the S-wave velocity at each block in the inverted models from 10 inversions using different initial values of a random number generator. A star in each figure shows the source location.

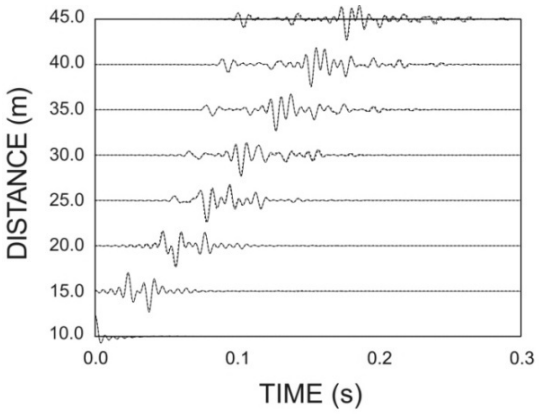


Fig.3. Comparison of synthetic observed waveforms (solid line) with theoretical waveforms for inverted model (broken line) in numerical experiment using a model in Fig.2. Each trace indicates SH-wave after deconvolution processing and is normalized with its maximum value.

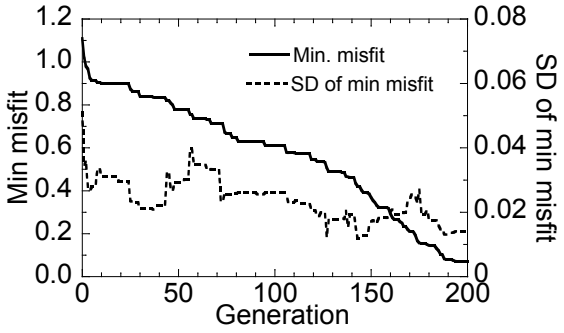


Fig.4. Variation of average of the minimum misfits at each generation from 10 inversions with different initial values of a random number generator (solid line) with its standard deviation (broken line) in numerical experiment using a model in Fig.2.

3.2 Three-Layer Model with blind layer

The second numerical experiment was conducted using a three-layer model with a blind layer. It is noted that a blind layer can not be identified in conventional travel time analysis of seismic refraction data. Figure 5 shows the model assumed in the second numerical experiment consisting of two layers over the basement. The top layer has a higher velocity then that of the second layer. Therefore the thickness of the top layer can not be known in the conventional travel time analysis. In the inversion, each interface is modeled by 20 Pks, and the surface layers are model with 20 blocks.

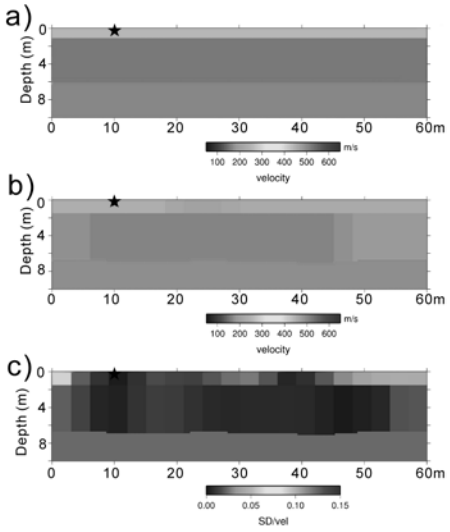


Fig.5. 2D S-wave velocity models in numerical experiments. The top model is assumed to generate synthetic observed data in Fig.6, and the middle model is derived from inversion of the synthetic waveforms. The bottom shows the standard deviation of the S-wave velocity at each block in the inverted models from 10 inversions using different initial values of a random number generator. A star in each figure shows the source location.

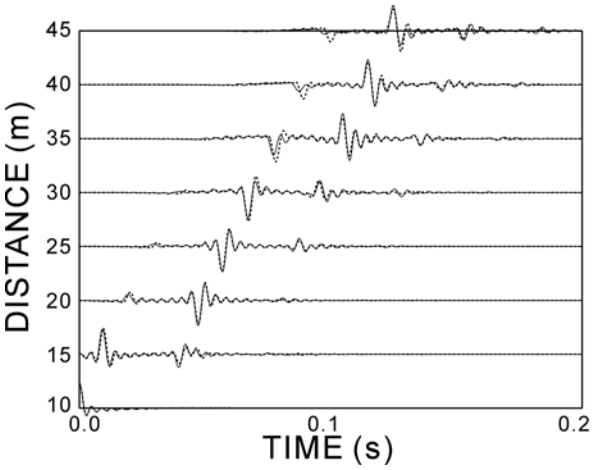


Fig.6 Comparison of synthetic observed waveforms (solid line) with theoretical waveforms for inverted model (broken line) in numerical experiment using a model in Fig.5. Each trace indicates SH-wave after deconvolution processing and is normalized with its maximum value.

The inverted model and standard deviations are shown in Figures 5b and 5c. Although the basement depth in the inverted model is slightly deeper than that of the true model, the blind top layer is well reconstructed with the inverted model. The comparisons of SH-waves for the true and inverted models are displayed in Figure 6. The agreement between the two SH-waves is well except for the amplitudes for the reflected phase at 0.1 second at sites of 35 to 45 meters. This might be caused by the slight different of the basement depth.

4. APPLICATION TO ACTUAL DATA

4.1 Measurements

The measurement was conducted at a sports ground of our university in Yokohama as shown in Figure 7. The surveying line is 35 meters long. 8 horizontal sensors with natural frequency of 10 Hz were installed at interval of 5 meters along the line. Four sources were served long the line; two were placed at the two ends of the surveying line, and the others are located at offset distance of 20 meters from the two ends. SH-waves were generated with plank hammering of the wooden plate at the sources, and recorded at every 0.5 msec with a digital recorder. Each data were stacked 20 times to increase S/N ratio.

The observed SH-waves from the sources at 0 and 35 meters are displays in Figure 8. Two traces shown at each site are the SH-waves from hitting of the wooden plate in the right and left directions to identify SH-waves with different polarity. From the arrival times of the initial onsets of the SH-waves we conducted conventional travel time analysis as shown in Figures 9a and 9b. The basement with an

S-wave velocity of 460 m/s is overlain by the surface layer with an S-wave velocity of 260m/s and thickness of about 10 meters. The 2D model is relatively simple without any strong lateral variation and steep interfaces.

4.2 Waveform Inversion

We conducted waveform inversion for the SH-waves generated from the source at 0 meters. We used the SH-waves observed at the site of 0 meters as the reference data in the deconvolution processing. In the forward calculation, we again used the Ricker wavelet with a frequency of 20 Hz. A three-layer model is modeled with 10 interface coefficients and 10 blocks in the surface layers. Totally 41 unknown parameters were to be determined in the inversion.

Figure 10a and 10b shows the inverted model and its standard deviations. The inverted model is very simple as expected in the model by conventional analysis. The surface layers have small lateral velocity variations. The average S-wave velocities of the surface layers are 230 and 360 m/s, respectively. The depth to the basement with an S-wave velocity of 477 m/s is about 12 meters in entire of the surveying line. The small standard deviation in Figure 10b clearly indicated the inversion found models near the global minimum misfit. The S-wave velocities for the top layer and the basement are similar to those from the conventional travel time analysis as shown in Figure 9. The existence of the second layer can not be found in the travel time analysis. The depth to the basement is 2 meter deeper than the inverted model.

Figure 11 compares observed and calculated SH-waves. Synthetic SH-waves for the model from the conventional travel time analysis is also shown in the figure. The large phases in the observed SH-waves are well reconstructed with the synthetic SH-waves for the inverted model. However, the SH-waves calculated for the travel time analysis can not well explain the large later phases.

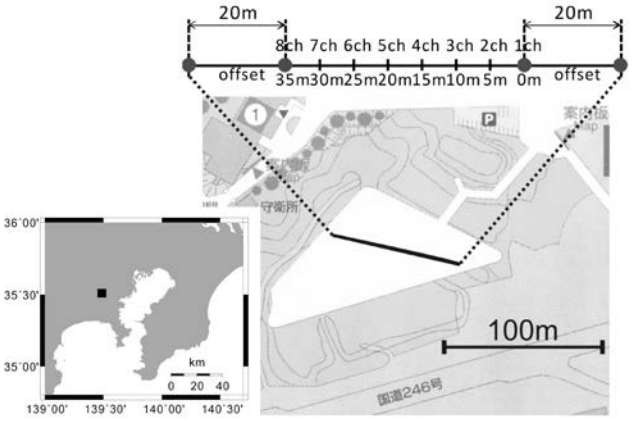


Figure 7. Location of observation sites of shallow refraction exploration. Four circles along the surveying line show shot points to generate SH-waves.

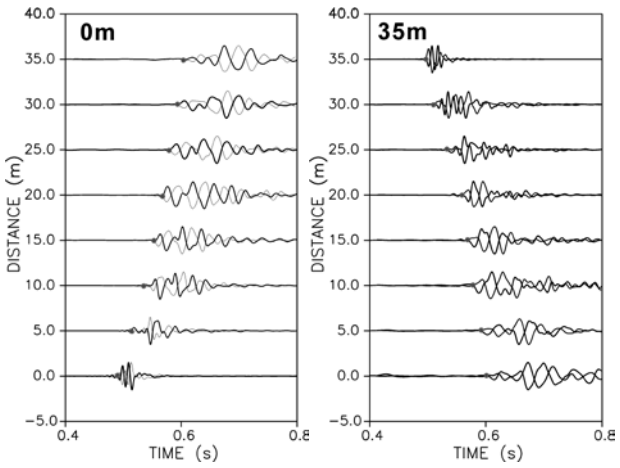


Figure 8 Observed SH-waves and their spectra. The top figures show SH-waves observed along the surveying line due to shots at distances of 0m and 35m. The attached circles in the traces indicate arrivals of initial motions. The lower figure shows spectra of SH-waves due to a shot at 0 m.

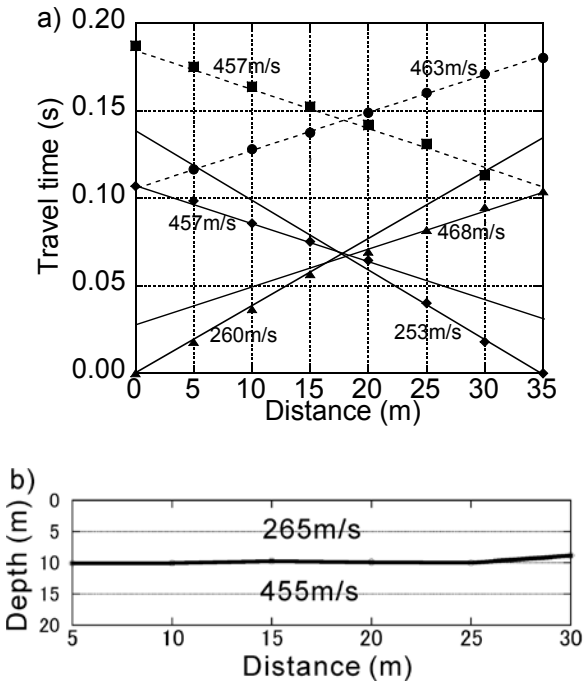


Figure 9 Results of conventional analysis of travel time of initial motions. Top is the travel time diagram and bottom is S-wave velocity model along surveying line.

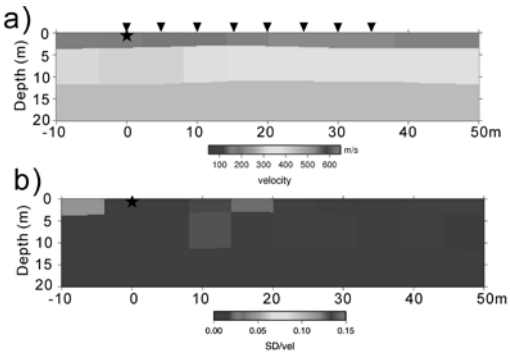


Fig.10. 2D S-wave velocity models from inversion of observed SH-waves in Fig.13. The top model (a) is an inverted 2D model from SH-waves at 8 stations, and middle model (b) the standard deviation of the S-wave velocity at each block in the inverted models from 10 inversions for the inverted model. A star in each figure shows the source location.

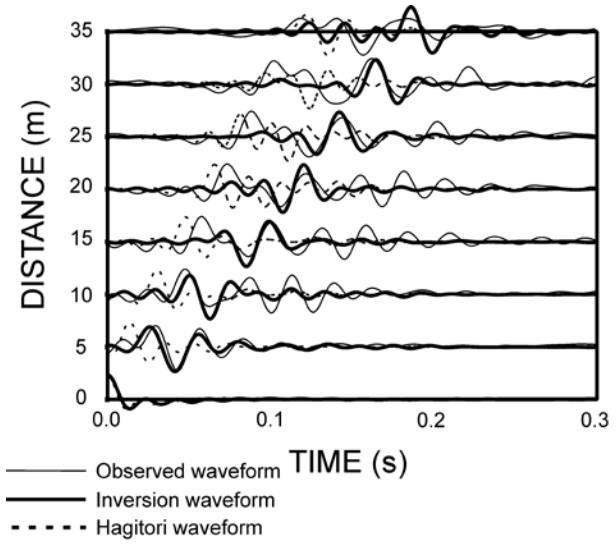


Fig.11. Comparison of observed waveforms (thin-solid line) with theoretical waveforms for inverted model in Fig.12a (thick-solid line) and model from conventional travel time analysis in Fig.10 (broken line). Each trace indicates SH-wave after deconvolution processing and is normalized with each maximum value.

5. CONCLUSIONS

We proposed an inversion technique of SH-waves observed in shallow seismic refraction explorations to deduce 2D inhomogeneous models of shallow soils. In the method we added pre-processing of the observed data by introducing deconvolution using reference station to eliminate the effects of sources. The other part of the inversion is almost the same as Takekoshi and Yamanaka (2009). We conducted numerical experiments of the waveform inversion using synthetic data. The effectiveness of the method is clearly shown from the numerical experiment for the model having a blind layer. We also applied the technique to actual refraction data, and could determine a model that fits more the observed SH-waves than the model from the conventional travel time analysis. These results clearly indicate effectiveness of the waveform inversion technique. We will try to apply our technique various kinds of shallow soils explorations to examine its applicability.

Acknowledgements:

The authors acknowledge support from the GCOE project of the Japan Ministry of Education, Culture, Sport, Science, and Technology (MEXT). We also thank graduate students who helped in field work of seismic explorations.

References:

Aoi, S., T. Iwata, K. Irikura, and F. J. Sanchez-Sesma（1995）: Waveform inversion for determining the boundary shape of a basin structure, Bull. Seism. Soc. Am., 85, 1445-1455.

Arai, H. and Tokimatsu, K.: S-Wave Velocity Profiling by Joint Inversion of Microtremor Dispersion Curve and Horizontal-to-Vertical (H/V) Spectrum, Bull. Seism. Soc. Am., 95, 1766-1778, 2005.

Hayashi, K., and H. Suzuki（2004）: CMP cross-correlation analysis of multi-channel surface-wave data: Exploration Geophysics, 35, 7 - 13 ; Butsuri-Tansa, 58, 7 -13 ; Mulli-Tamsa, 7, 7-13.

Takekoshi, M., and H. Yamanaka (2009) : Waveform inversion of shallow seismic refraction data using hybrid heuristic search method, Exploration Geophysics, 40, 99-104 ; Butsuri-Tansa, 62, 99-104 ; Mulli-Tamsa, 12, 99-104.

Yamanaka, H (2005), "Comparison of performance of heuristic search methods for phase velocity inversion in shallow surface wave methods," Journal of Environmental and Engineering Geophysics, 10, 163-173.

Yamanaka H. (2007), "Inversion of surface-wave phase velocity using hybrid heuristic search method," Geophysical Exploration (Butsuri Tansa), 60, 265-275 (in Japanese).

8CUEE CONFERENCE PROCEEDINGS
8th International Conference on Urban Earthquake Engineering
March 7-8, 2011, Tokyo Institute of Technology, Tokyo, Japan

EARTHQUAKE INPUT MOTION TO HIGH-RISE BUILDING IN THE WESTERN PART OF KOBE CITY DURING THE 1995 HYOGO-KEN NANBU EARTHQUAKE

Masayuki Nagano[1] and Jianjing Zhao[2]

1) Professor, Department of Architecture, Tokyo University of Science, Japan
2) Graduate Student, Department of Architecture, Tokyo University of Science, Japan
nagano-m@rs.noda.tus.ac.jp, j7109638@ed.noda.tus.ac.jp

Abstract: The deep basin-edge structure beneath Kobe City is a plausible cause of ground motion amplification in the damage belt during the 1995 Kobe earthquake. Strong motions were recorded at two neighboring sites, Takatori and Shin-Nagata, located in the western part of the damage belt. The latter site, which was the basement of a high-rise building, recorded motion less than half the amplitude observed at the former site. This difference has gone unresolved in terms of the relationship between the level of ground motions and actual damage. This paper investigated input earthquake motion to the high-rise building at Shin-Nagata during the 1995 Kobe earthquake. Spatial variation of ground motions in the western part of Kobe City was examined using a 3-D finite difference method that considered both the seismic fault and the 3-D subsurface structure, which played an important role in the difference in ground motion level at the two sites. A 2-D underground model estimated the loss of input motion due to the constraint of an embedded rigid base, which contributed to the reduction of the observed motion associated with the site-specific nonlinearity of the surrounding surface soil.

1. INTRODUCTION

The 1995 Hyogo-ken Nanbu, Japan earthquake (hereafter, referred to as the 1995 Kobe earthquake) killed more than 6,000 people. Strong ground shaking during the earthquake devastated numerous structures, including old wooden houses. Most of the structural damage was spatially concentrated in the "heavily damaged belt zone," which corresponds to a Japanese seismic intensity scale of 7 (Japan Meteorological Agency (JMA) scale). Figure 1 illustrates this zone, which is a 1-2-km-wide area between Rokko Mountain and Osaka Bay. Ground velocity waveforms obtained from records of the event contain large-amplitude pulses with a predominant period of about 1, which is caused in the rupture process by a seismic fault beneath Kobe City.

One plausible explanations for the peculiar damage pattern observed is the existence of a basin-edge structure in the deep subsurface soil beneath Kobe City (e.g., Motosaka & Nagano 1997). Kobe City is located just within the border of the Osaka Plain, and the level of the seismic bedrock abruptly drops off at the foot of Rokko Mountain.

Although more than 16 years have passed, damage caused by the 1995 Kobe earthquake has been the icon for natural disaster prevention with regard to seismology, earthquake engineering, and civil/structural engineering. Nevertheless, some issues remain unresolved from the standpoint of the relationship between observed ground motion and actual damage.

Strong ground motion were recorded in and around the heavily damaged belt zone in Kobe City during the main shock. In the western part of the worst-hit area, two strong ground motion records were obtained for Takatori (TKT) and Shin-Nagata (SNT). The former is a record of ground surface motion (Nakamura et al., 1996). The latter is from the first basement level of the 25-story steel reinforced concrete (SRC) building shown in Figure 2 (Yasui et al. 1998). The SNT record includes the effects of the soil-structure interaction (SSI). The amplitudes of the ground motions at two sites are quite different, even though both sites, which are separated by about 1 km, are within the damage belt.

Figure 3 shows the velocity waveforms and pseudo-velocity spectra at the two sites rotated to the fault-normal (FN) direction as a principal axis N150E and N140E, for TKT and SNT, respectively.

The ground motion record from the TKT site is one of the most important records of the Kobe earthquake because the peak ground velocity (PGV) exceeded 1.5 m/s, the largest ground velocity reported in Japan at that time. Its waveform is pulse-like with a predominant period of about 1 s. In contrast, the PGV at SNT is approximately 0.6 m/s, which is less than half of that at TKT. This difference applies to both the PGV and the response spectra. Accelerometer data at SNT were slightly saturated during the main shock, however, this introduced only a minor error in the velocity

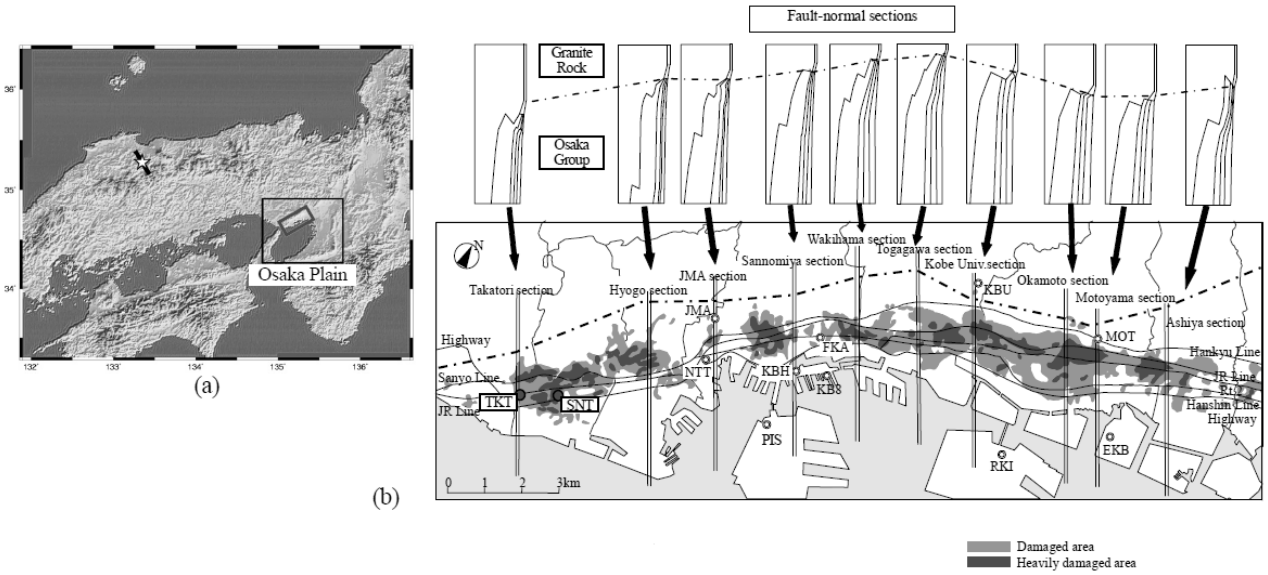


Figure 1. Location of Kobe City, Japan, and the damage belt during the 1995 Kobe earthquake. (a) Kobe City is located in the western part of Honshu Island, Japan. The thick inclined rectangle in (a) corresponds to area (b) the heavily damaged belt zone. A dash-dotted line indicates the structural boundary between rock and sediments along Rokko Mountain. Fault-normal sections of a deep underground structure for 2-D analyses are illustrated. Takatori (TKT) and Shin-Nagata (SNT) are about 1 km apart and are both located in the western part of the damage belt. (Nagano & Yamada, 2002)

waveforms because the duration of the saturation was limited. The peak ground acceleration (PGA) loss is estimated to be about 10% of the restored accelerometer data (Yasui et al. 1998).

These observations suggest the need to address several different questions. Why is there such a large discrepancy between the two records in very short distance? Is there any variance in the characteristics of the ground motion amplification due to deep or shallow geological conditions? Is there any significant loss of foundation input motion due to the embedded basement of the building?

This paper focuses on earthquake input motion to the high-rise building at SNT during the 1995 Kobe earthquake using three approaches: (1) a 3-D finite difference method (FDM) to elucidate the spatial variations considering both the seismic fault and the 3-D basin-edge structure; (2) amplification characteristics using recorded motions after the 1995 Kobe earthquake at SNT, and (3) the foundation input motion analysis, considering the strong nonlinearity of the surrounding surface soil.

2. SPATIAL VARIATION OF GROUND MOTIONS IN THE WESTERN PART OF KOBE CITY

2.1 Methodology and Modeling

Strong ground motions in the western part of Kobe City are evaluated using a 3-D FDM that considers both the seismic fault and the 3-D basin-edge structure in the western part of the Osaka Plain.

Figure 4(a) shows the finite difference (FD) modeling region. The lengths of planar regions are 32 and 42 km in the NS and EW directions, respectively. The velocity structure is referred from geological data from the Osaka Prefecture

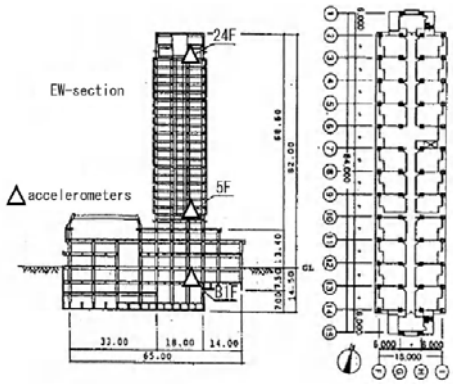


Figure 2. High-rise SRC building constructed at SNT, and the location of accelerometers. The seismograms in Figure 3 were obtained at the first basement floor level. The section plan is illustrated in the EW direction. (after Yasui et al. 1998)

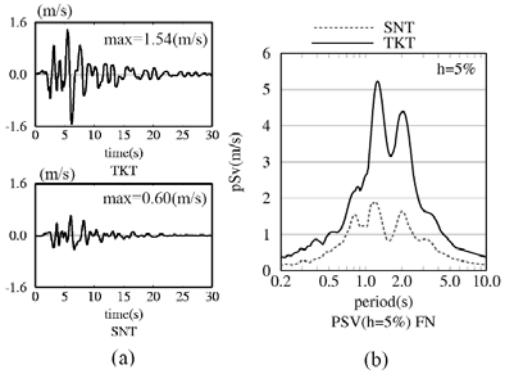
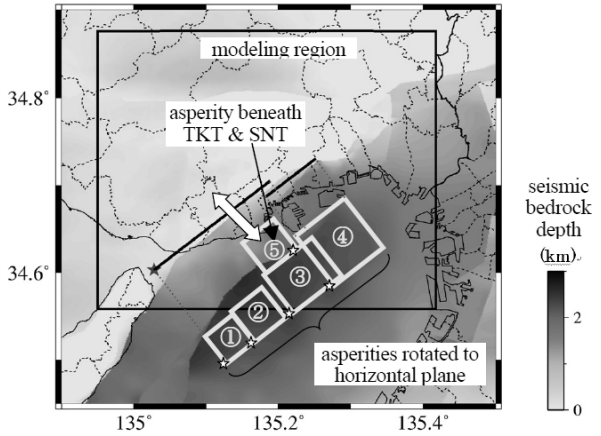
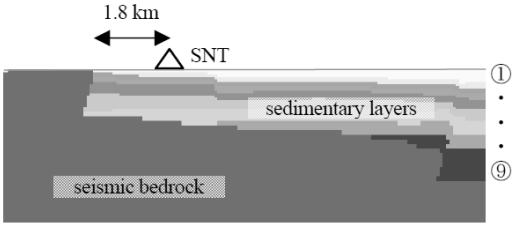


Figure 3. Seismograms at TKT and SNT during the 1995 Kobe earthquake. (a) Velocity waveforms and (b) pseudo-velocity response spectra.

(2006), where the thrust-type basin-edge structure is properly modeled along the Rokko Mountain. Sediments on seismic bedrock are modeled in nine layers from 0.4 to 1.2 km/s for V_S, as shown in Table 1. Figure 4 (b) shows a cross section of the underground structure through SNT in N135E direction. Seismic bedrock abruptly drops off at the boundary between rock and sediments.



(a) Depth contour of seismic bedrock and seismic faults beneath Kobe City



(b) Cross section of the underground structure through SNT corresponding to the arrow in (a)

Figure 4. Underground structure in the Kobe area including the modeling region for 3-D FDM and seismic fault

Table 1 Physical parameters of sediment layers

	V_S(m/s)	V_P(m/s)	ρ(t/m^3)
Sediment-1	400	1620	1.77
Sediment-2	500	1790	1.94
Sediment-3	600	1910	2.00
Sediment-4	700	2010	2.00
Sediment-5	800	2120	2.04
Sediment-6	900	2280	2.06
Sediment-7	1000	2430	2.15
Sediment-8	1100	2590	2.19
Sediment-9	1200	2750	2.20
Basement rock	3200	5400	2.66
Crust	3500	6000	2.8
	3800	6600	3.0
	4500	6800	3.2

Table 2 Source parameters

No.	Strike (deg.)	Dip (deg.)	Onset time (s)	Seismic moment (Nm)	Peak slip rate(m/s)	Depth of rupture onset (km)
1	53	90	0.00	0.61×10^{18}	8	16
2	53	90	1.61	1.43×10^{18}	8	16
3	53	90	3.75	2.61×10^{18}	2	16
4	233	85	6.10	3.43×10^{18}	3	14
5	53	90	4.94	1.46×10^{18}	4	10

rake angle: 180° , rupture velocity: 2.8 km/s

A numerically efficient FD technique that combines non-uniform and discontinuous grids is applied for 3-D wave propagation analysis (Nagano, 2004). The entire soil region is divided into two regions at a specific depth modeled by different non-uniform grids. Grids in the bottom region, for bedrock, are coarser than those in the top region, which included sediment. This significantly reduces the number of grids. The boundary between the two regions is set at a depth of 4.1 km. The minimum grid spacing is 50 m; therefore, synthetic motions with a frequency component up to 1.6 Hz can be properly evaluated.

The source model is characterized by the five asperities (Matsushima & Kawase, 2009), as shown in Figure 4(a) and Table 2. Asperity No. 5 exists in a shallow region, just beneath the western part of Kobe City, including TKT and SNT, significantly contributes to amplification of the strong ground motions at two sites. All calculated velocity waveforms and recorded ground motions are low-pass filtered at 1.6Hz.

2.2 Simulation of Ground Motions at TKT and SNT and Their Spatial Variations

Synthesized ground motions at TKT and SNT were compared with records in Figures 5 and 6 and rotated in fault-normal direction, N140E. The 3-D FDM reproduces the ground motion at TKT in terms of both peak velocity

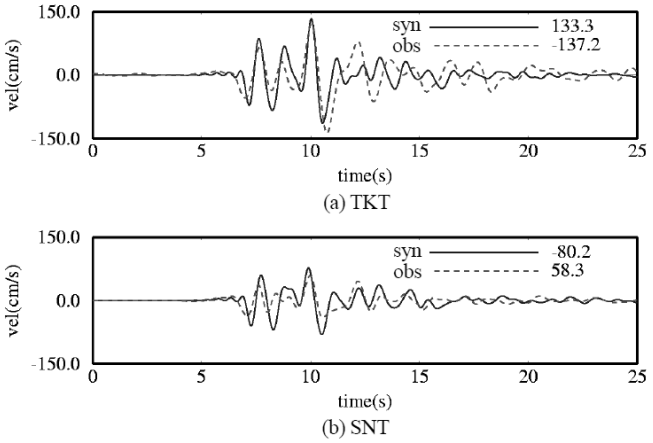


Figure 5. Comparison of synthesized and observed velocity waveforms in the FN direction at TKT and SNT.

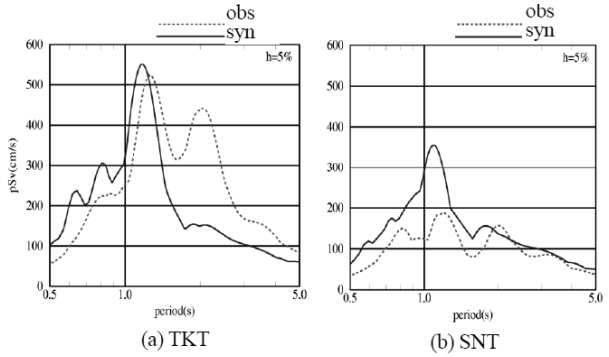


Figure 6. Comparison of pseudo-velocity spectra(h = 5 %) in the FN direction at TKT and SNT.

and the spectral peak with a 1.2 s period. The amplitude of the synthetic motion at SNT is 0.6 times that of TKT, which is still overestimated, but consistent with the observed relationship.

Figure 7 shows the peak velocity contour in the FN direction for the western part of Kobe City. A high-amplitude region spreads in Nagata and Suma Ward. In the western part of Hyogo Ward, the peak ground velocity (PGV) is small. This is consistent with the distribution shown in Figure 1. Figure 8(a) plots the peak velocity distributions in the FN section through TKT and SNT. The horizontal axis x is the distance from the boundary between rock and sediments to the coast. PGV amplitude peaks can be seen in where x = 1-2 km, corresponding to the damaged belt zone. TKT is located at edge of the peak region, while SNT is outside the peak region. This amplification appears to be due to constructive interference of multi-passing waves in the basin-edge structure, as shown in Figure 4 (b).

The PGV distribution is slightly different from the incidence of a plane shear wave (S wave), in that the location of the peak moves to the edge and the peak area is narrow. These are consequences of the rupture directivity effects of the asperity beneath TKT and SNT. Figure 8(b) compares the calculated PGV distribution with the actual damage ratio of the wooden structure in the same region,

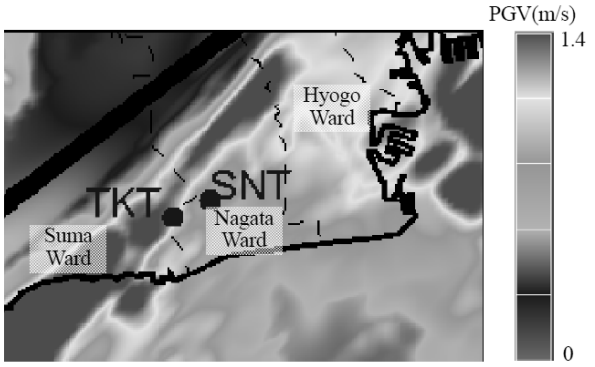
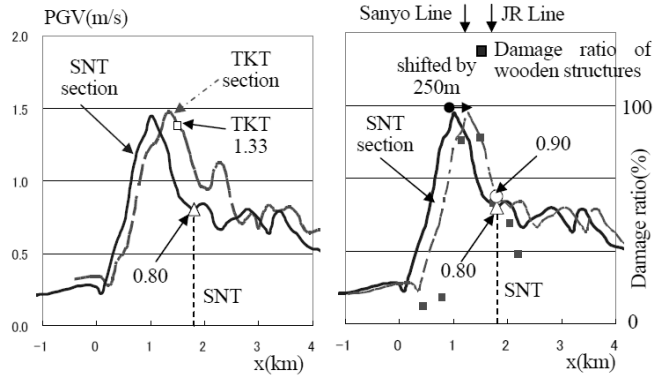


Figure 7. Contour distribution of PGV in the FN direction in western Kobe City.



(a) PGV Distribution (b) Comparison with damage ratio of wooden structures in SNT section

Figure 8. PGV distributions in the FN sections through TKT and SNT and comparison with the damage ratio of wooden structures along the SNT section.

according to a detailed survey (Inoue et al, 1996). Heavily damaged area can be seen between the Sanyo and JR Lines. The damage ratio around SNT is smaller than that in the most devastated area. 3-D FDM results indicate a peak location nearer to the mountain side than to the actual damage peak. Shifting the calculated PGV distribution by 250 m to the bay side provides better consistency with the actual damage ratio, as shown in Figure 8(b).

One reason for this inconsistency is the modeling of the deep subsurface structure. In the geological model of the Osaka Prefecture (2006), only one bedrock step exists at the structural boundary. According to the detailed survey based on reflection exploration (Huzita & Sano, 1996, Sano, 1998), another latent fault exists in the sediment side, adjacent to the rock-sediment border, resulting in two bedrock steps. This difference in basin-edge modeling could be one reason for the peak location shift of the PGV distribution. Even when PGV distribution in the 3-D FDM is shifted to the coast, the PGV at SNT is estimated at 90 cm/s, which is smaller than that at TKT.

Results by 3-D FDM suggest that large-amplitude discrepancies in the records for TKT and SNT are partly due to the spatial variations of the ground motion in very short distance in the FN direction, due to the coupling effects of a rupture of the asperity beneath, and a step-like bedrock boundary. Other reasons for the significant reduction of ground motion at SNT need to be explored because the calculated amplitude at SNT is still overestimated compared with the observed motion, as shown in Figures 5 and 6.

3. AMPLIFICATION CHARACTERISTICS BASED ON OBSERVED GROUND MOTION

3.1 Observation Sites at and around SNT

After the 1995 Kobe earthquake, strong motion seismometers were installed at several sites around SNT, as shown in Figure 9. Ground motions were recorded during numerous events, even though amplitude levels were much smaller than those during the 1995 Kobe earthquake. Seismograms at SNT were recorded in the SRC building and their structural response characteristics were also

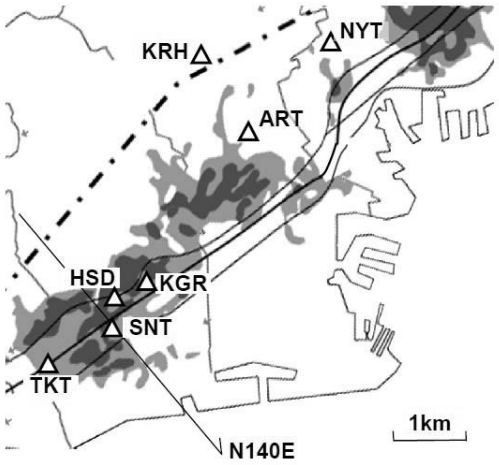


Figure 9. Observation sites for strong ground motions in the western part of the Kobe urban area.

investigated in detail (Nakamura, 2003).

Using these records, site characteristics at SNT can be roughly estimated by calculating the transfer functions between the other sites. Here, we selected 12 events in Table 3, for which seismic records at SNT and surrounding sites were obtained simultaneously.

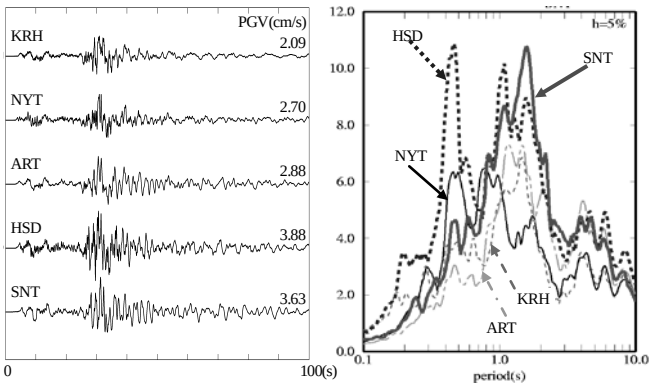
All motions are rotated to the building axis, i.e., longitudinal direction, N335E, corresponding to the FN direction, and the transverse direction, N65E, corresponding to the fault-parallel (FP) direction.

3.2 Ground Motions during the 2000 Tottori-Ken Seibu Earthquake

During the 2000 Tottori-ken Seibu earthquake (No.4 in Table 3), the JMA seismic intensity scale in Nagata was 4—the largest recorded since the 1995 Kobe earthquake. Figure 10 shows velocity seismograms and pseudo-velocity spectra (h = 5%) in the FN direction for five sites, including SNT. The PGV distribution along the FN section, including SNT, is plotted in Figure 11. The plots also include PGVs of the ground motions recorded in the Higashi-Nada area, the eastern part of the Kobe urban area, for comparison. The horizontal axis is taken as the distance from the structural edge between rock and sediment.

Table 3 Event list used in this study

No.	Date and Epicenter	M_J	JMA Int level at Nagata	neighboring site
1	1999.07.15 Osaka Bay	3.9	Ⅲ	HSD
2	1999.08.02 South Osaka	3.9	Ⅱ	HSD
3	1999.08.21 North Wakayama	5.6	Ⅲ	HSD
4	2000.10.06 Tottori-ken Seibu	7.3	Ⅳ	HSD
5	2001.03.24 Geiyo	6.7	Ⅲ	HSD
6	2001.08.25 South Kyoto	5.4	Ⅲ	HSD
7	2004.09.05 Off Kii Pen.	7.1	Ⅲ	KGR
8	2004.09.05 Off Tokaido	7.4	Ⅲ	KGR
9	2005.02.14 East-South Osaka	4.1	Ⅱ	KGR
10	2007.04.15 Mid Mie	5.4	Ⅱ	KGR
11	2008.04.17 Osaka Bay	4.1	Ⅲ	KGR
12	2008.04.18 Osaka Bay	3.7	Ⅱ	KGR



(a) Velocity waveforms (b) Pseuso Velocity Spectra(h=5%)

Figure 10. Velocity waveforms and response spectra in the FN direction of seismograms at five sites in the western part of Kobe city during the 2000 Tottori-Ken Seibu earthquake.

The PGV gradually increases from KRH and NYT near the structural border, to the sites in the sediment and coastal area. A long-period component, around 5 s, was predominant in ground motions in Kobe during the 2000 Tottori-ken Seibu earthquake (Nagano, 2004), leading to a gradual increase of the PGV distribution to the coastal area from mountain side, as indicated by the trend in Higashi-Nada area (Nagano et al., 2003). On the other hand, the recorded motion at SNT was smaller than at HSD, 300 m toward the mountain, in terms of the PGV and a short-period component of less than 1 s. These could be the results of the constraint on the ground motion by the embedded basement.

3.3 Site Characteristics at SNT and Neighboring Sites

The nearest observation sites to SNT are Hosoda-Cho (HSD) and Kagura-Cho (KGR) under the JMA. The seismometer at HSD was in operation until 2001, and then moved to KGR, 500 m to the east from HSD, after 2002. Both sites were located in the damage belt during the 1995

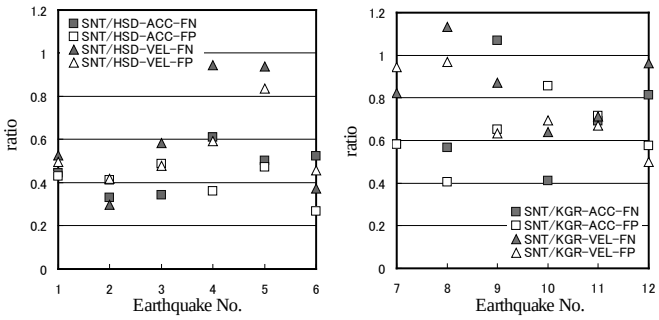


Figure 12. PGV and PGA ratios of SNT to neighboring sites after the 1995 Kobe earthquake

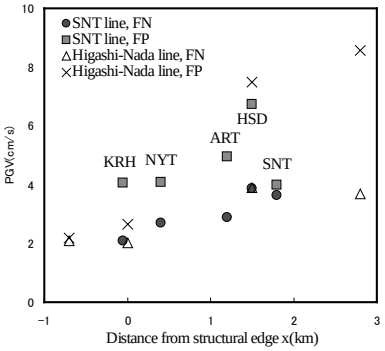
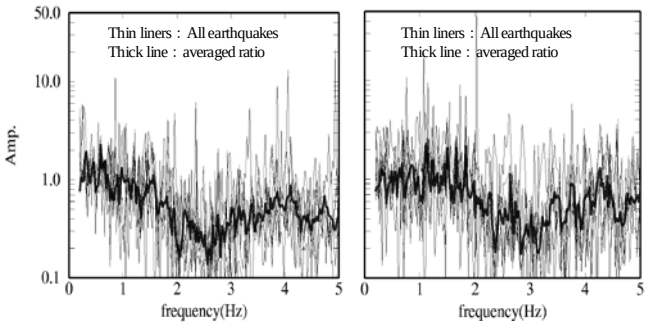


Figure 11. Peak velocity distribution in the FN section during the 2000 Tottori-Ken Seibu earthquake.



(a) SNT/HSD (b) SNT/KGR

Figure 13. Fourier amplitude ratios at SNT to neighboring sites in the FN direction after the 1995 Kobe earthquake

Kobe earthquake. Using seismograms simultaneously recorded at SNT, HSD, and KGR, shown in Table 3, PGA and PGV ratios are plotted in Figure 12. Ground motions at SNT are in general smaller than either of the other two sites. The ratios of PGA are smaller than the PGV ratios, corresponding to a large reduction of the high-frequency component, as shown in Figure 10.

Figure 13 traces the Fourier amplitude ratios, SNT/HSD and SNT/KGR for each of six earthquakes, as well as averaged data. The amplitude ratio is less than one in the frequency range above 2 Hz, due to the input loss effect of the embedded foundation. On the other hand, the reduction of ground motion is not as noticeable at frequencies below 2 Hz, which was predominant during the 1995 Kobe earthquake, as shown in Figure 3. Therefore, it is rather difficult to account for the reduction in ground motion at SNT during the 1995 Kobe earthquake only using the recorded motion observed during small amplitude events that occurred after the Kobe earthquake. The constraint effect of the embedded basement around 1 s is small when the ground motion level is small, and the surrounding soft soil is linear.

4. FOUNDATION INPUT MOTION CONSIDERING SITE NONLINEARITY OF SURROUNDING SOIL DURING MAIN-SHOCK

4.1 Underground Structure Model Including Embedded Basement

Reduction of the seismic motion at SNT was analyzed in terms of the loss of input motion due to a rigid foundation embedded in soft surface soil. The 2-D model in Figure 14 serves used as the subsurface structure passing through SNT in the FN direction. This underground model has two soft surface layers on the engineering bedrock (V_S=500 m/s) and another latent fault, the Kariyaoki Fault, adjacent to the basin edge. This geometry and layers are slightly different from the 3-D model previously used, but were calibrated in aftershock simulations by Nagano et al. (1998).

The basement of the building was 84 m long in the FN direction and 14.5 m deep. Rigid, massless solid elements are embedded in the upper layer of soft surface soil in the 2-D underground model.

The transfer function of SNT/HSD is calculated for a vertically incident SV-wave and compared in Figure 15 with the recorded motions from Figure 13(a). The 2-D finite element method (FEM) results explain to some extent, the recorded motions up to 1.2 Hz. In the higher frequency range, the fluctuation of the curve is large in the 2-D FEM, compared with the observed fluctuation.

Foundation input motion is also evaluated by 2-D FEM as a transfer function of the basement divided by the free field motion at SNT obtained from a 2-D model without a basement. The input motion decreases in the frequency range above 1.2 Hz. This amplitude reduction is not seen in the lower frequency range; thus, it is difficult to explain the reduction in ground motion at SNT during the 1995 Kobe earthquake using linear soil properties.

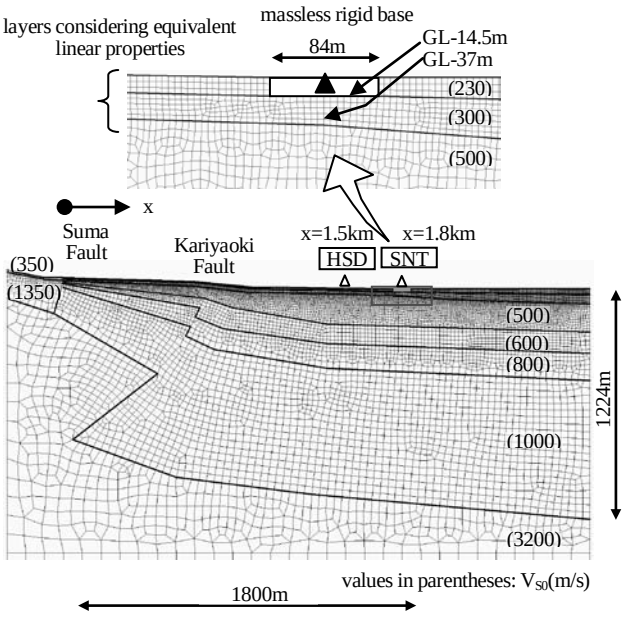


Figure 14. Underground structure used in the 2-D FE model to evaluate foundation input motion at SNT.

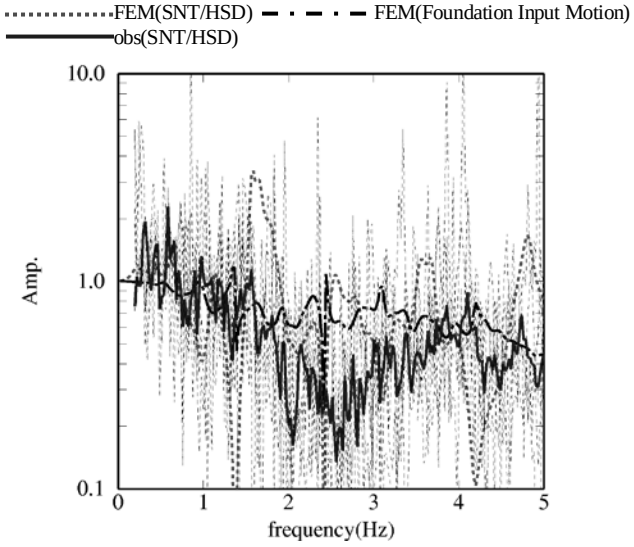


Figure 15. Transfer functions of the foundation at SNT and comparison with observation.

Table 4 Detailed S-wave structure beneath SNT

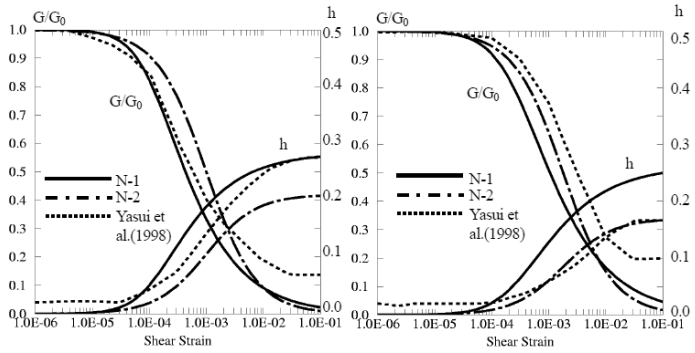
No.	V_{S0}(m/s)	ρ(t/m^3)	Thickness(m)	Upper depth(m)	Nonlinear characteristics
1	125.0	1.8	2.8	0	sand
2	210.2	1.8	2.2	2.8	sand
3	209.7	1.8	1.8	5.0	clay
4	324.3	1.9	4.1	6.8	sand
5	229.2	1.8	3.1	10.9	clay
6	337.0	1.9	3.4	14.0	sand
7	271.9	1.8	4.4	17.4	clay
8	313.9	1.8	4.5	21.8	sand
9	278.3	1.8	3.5	26.3	clay
10	296.0	1.8	7.2	29.8	clay
11	450.0	1.9	—	37.0	—

4.2 Equivalent Soil Properties During the 1995 Kobe Earthquake

Yasui et al. (1998) carried out a detailed analysis of the dynamic soil-structure interaction (SSI) problem at the SNT site. They simulated nonlinear structural response using records for three floors (B1F, 5F, 24F) in the building, along with ground motions on the free-field surface, based on an iterative scheme that included nonlinearity of the surrounding soil. The peak structural response at the first floor was estimated to be 23% less than the free-field motion for peak acceleration, and 10% less for peak velocity. The estimated PGV for the free field at SNT is 0.65 m/s, which is still less than half the PGV at TKT.

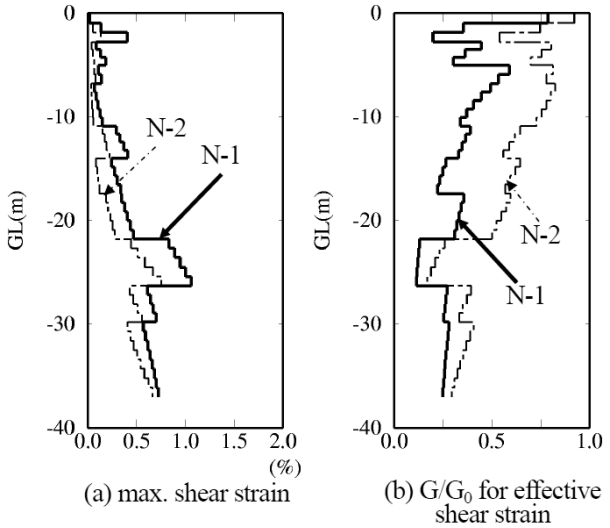
In Yasui et al. (1998), equivalent soil properties were determined using an iterative scheme based on data records at SNT. This approach helps ensure that the site nonlinearity associated with the surrounding soil is taken into account in the SSI analysis. The average ratio of the equivalent S-wave velocity, V_{Se}, to the initial S-wave velocity, V_{S0}, is 0.84 in the soft surface layers on engineering bedrock.

Table 3 provides the detailed S-wave structure beneath SNT, and the equivalent soil properties of surface layers were evaluated by time-domain nonlinear analysis. Outcropped motion on the Osaka Group layers at TKT (peak acceleration is 6.17m/s^2, and peak velocity is 1.37m/s) serves as input motion to the one-dimensional soil column at GL-37m. Considering the relationship between SNT and TKT from the 3-D FDM, its amplitude is reduced to 60% of the original motion.



(a) sand (b) clay

Figure 16 Nonlinear characteristics of surface soil



(a) max. shear strain (b) G/G_0 for effective shear strain

Figure 17. Distribution of maximum shearing strain and reduction of shearing stiffness in depth

Two cases of standard soil nonlinearities, e.g., the N-1 (Osaki et al., 1978) and N-2 (Koyamada et al., 2005) models, are referred in the time-domain nonlinear analysis and evaluation of equivalent soil properties. In both models, averaged parameters for sand and clay were given for the Ramberg-Osgood model and the Hardin-Drnevich model, respectively. Curves of G/G_0-γ, h-γ are illustrated in Figure 16 for two models, compared with Yasui et al.(1998).

Figure 17 shows the distribution of maximum shearing strain and reduction of shearing stiffness in the depth direction, as results of the nonlinear analyses of the 1-D soil column. Averaging G/G_0 in the soft soil part estimated the coefficients for the reduction of V_S as 0.56 and 0.72 for N-1 and N-2, respectively. These values are smaller than the 0.83 used in Yasui et al.(1998). In the N-1 model, stiffness degrades more rapidly with an increase of shearing strain, resulting in a larger shearing strain in the nonlinear analysis than for the N-2 model.

4.3 Foundation Input Motion Embedded in Soft Surface Soil

Next, input motion analysis studied three cases of equivalent soil properties. CASE-1 used the original linear properties and CASE-2 employed the average coefficient for the reduction of V_S from Yasui et al. (1998), i.e., 0.83. A smaller V_S, 0.56, evaluated using the N-1 model was used in CASE-3. The same coefficients and damping ratio were applied for each layer in both CASE-1 and CASE-2.

Transfer functions of the foundation input motion for a vertically incident SV-wave are plotted in Figure 18. In CASE-1 and CASE-2, the decrease in amplitude is small for frequencies below 1 Hz. It is hard to account for a reduction of ground motion amplitude at SNT based on these first two cases. In CASE-3, a small trough appeared at around 0.8 Hz in the foundation input motions. The foundation response seems reduced as a result of the constraint of a rigid base on the waves in the soft surface layers, especially due to the constraint effect at the sides of the rigid base.

To assess the effect of foundation input loss on the

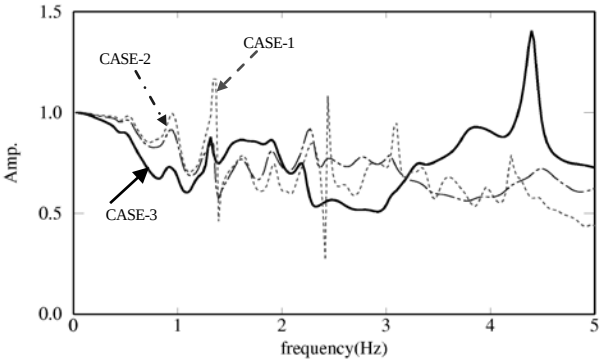
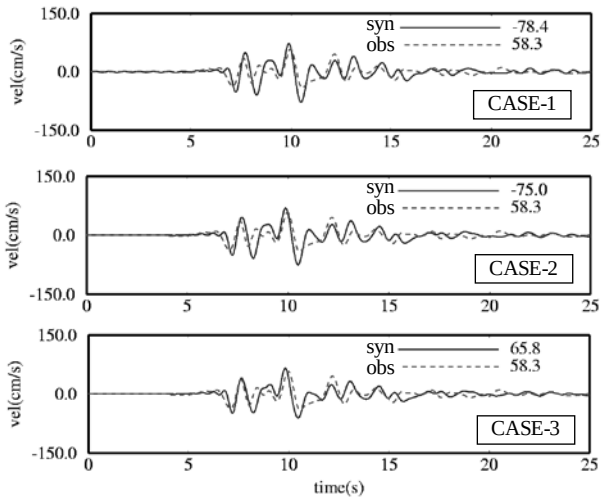
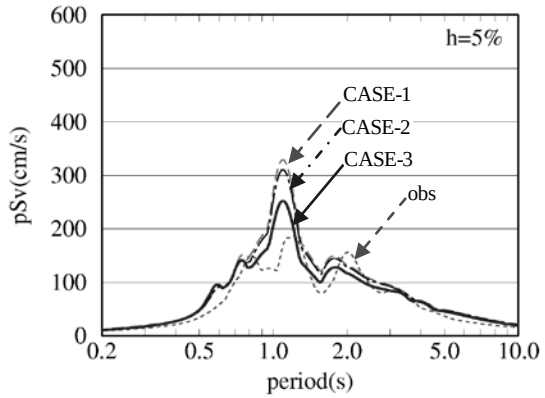


Figure 18. Transfer functions of foundation input motions to free surface motions for three cases



(a) Velocity Seismograms



(b) Pseudo velocity spectra (h=5%)

Figure 19. Comparison of calculated foundation input motion and observed motion at SNT. (a) velocity seismogram, and (b) the pseudo velocity spectra (h=5%).

seismograms, the responses of a rigid foundation at SNT were evaluated. Although SNT, calculated by 3-D FDM, is ground motion on an outcrop of engineering bedrock, we refer it as free field motion for convenience, then multiply it by the transfer function given in Figure 18. Figure 19 shows the calculated velocity seismograms and the response spectra.

For CASE-1, the peak velocities remained almost the same as for the original ground motion, implying that the kinematic effect of a rigid foundation alone cannot account for the large reduction at SNT. In CASE-2, which uses the site nonlinearity in Yasui et al. (1998), both the velocity waveform and response spectrum were almost the same level as in CASE-1. The peak velocity in CASE-3 was reduced to 0.66 m/s, almost the same as the observed ground motion.

CASE-3 still overestimates the actual motion at SNT, however, the loss of foundation input motion due to the strong site nonlinearity of the surrounding soil partially accounts for a significant reduction of the recorded motion at SNT in comparison with TKT.

5. CONCLUSIONS

This paper investigated input earthquake motion to the high-rise building at Shin Nagata (SNT) during the 1995 Kobe earthquake to determine the cause of the large discrepancy in motion between SNT and Takatori (TKT). Three approaches were used: a 3-D finite difference method evaluated the spatial variations, considering both the seismic fault and the 3-D basin-edge structure; studying the amplification characteristics using recorded motions after the 1995 Kobe earthquake at SNT; and foundation input motion analysis took into account the strong nonlinearity of surrounding surface soil.

Conclusions are summarized below.

(1) 3-D FDM showed that the large discrepancy in amplitudes from the records of TKT and SNT is partly due to the spatial variation of the ground motions in a very short distance in the FN direction, resulting from the coupling effects of a rupture in the asperity and step-like bedrock structure. The peak ground velocity at SNT is 0.6 times of that at TKT.

(2) It is difficult to account for the reduction in ground motion at SNT during the 1995 Kobe earthquake using only the recorded motions observed in the small amplitude events after the Kobe earthquake. The constraint effect of the embedded basement around 1s is small when the ground motion level is small and the surrounding soft soil is linear.

(3) The loss of foundation input motion due to the strong site nonlinearity of the surrounding soil partially accounts for a significant reduction in the recorded motion at SNT in comparison with TKT.

Acknowledgements:

The authors would like to thank the West Japan Branch Office of the Urban Renaissance Agency for providing strong motion data at SNT. Comments from Dr. Mitsuru Nakamura, Ohbayashi Corporation, on the observation system at SNT were useful. We also used the data of K-NET, JMA, and the Railway Technical Research Institute.

References:

Motosaka, M. & Nagano, M. (1997), "Analysis of amplification characteristics of ground motions in the heavily damaged belt zone during the 1995 Hyogo-ken Nanbu earthquake", *Earthquake Engineering and Structural Dynamics*, 26: 377-393.

Nakamura, Y., Uehan, F., and Inoue, H. (1996), "Waveform and its Analysis of the 1995 Hyogo-Ken-Nanbu Earthquake (II)" (in Japanese), *JR Earthquake Information*, 23d, Railway Technical Research Institute.

Yasui, Y., Iguchi, M., Akagi, H., Hayashi, Y. & Nakamura, M. (1998), "Examination of effective input motion to structures in heavily damaged zone in the 1995 Hyogo-Ken Nanbu earth-quake" (in Japanese), *J. Struct. Constr. Eng.*, AIJ, 512, 111-118.

Nagano, M. & Yamada, A. (2002), "Amplification characteristics of ground motions adjacent to boundary of 3D basin-edge structure" (in Japanese), *J. Struct. Constr. Eng.*, AIJ, 560, 51-58.

Osaka Prefecture (2006) "Geological survey on Osaka Plane" (in Japanese), CD-ROM offered by R&D in the Field of Earthquake and Disasters Reduction, MEXT.

Nagano, M. (2004), "Evaluation of Strong Ground Motions in Kobe Area During the 2000 Tottori-ken Seibu Earthquake Using 3D

Finite Difference Method with Variable Grid Spacing and Time Increment" (in Japanese), *J. Struct. Constr. Eng.*, AIJ, 580: 43-50.

Matsushima, S. & Kawase, H. (2009) "Re-evaluation of strong motion and damage of wooden houses in Kobe City during the 1995 Kobe earthquake" (in Japanese). *Journal of Structural Engineering*, AIJ. 537-543.

Huzita, K. & Sano, M. (1996), "Hanshin-Awaji earthquake disaster and the Rokko Movements" (in Japanese). *Kagaku*, 66:793-805.

Sano, M. (1998), "Underground structures and active hidden faults in Osaka Basin" (in Japanese). 11th Seminar of Fault Research & Information Center. 6-23.

Inoue, R., Suzuki, S. Kudo, K., Takahashi, M., and Sakaue, M. (1996), "A Detailed Survey on the Damage of Buildings During the Hyogoken Nanbu (Kobe) Earthquake with References to Aftershock Data and Geology", *Proc. of 11th WCEE*, No.1253.

Nagano, M., Ohno, S., Kikuchi, R. and Kobayashi, H. (2003), "Simulation Analysis of Seismograms Recorded at Deep Vertical Array and Effects of Irregularity of Bedrock Shape" (in Japanese), *J. Struct. Constr. Eng.*, AIJ, 570: 45-52.

Nakamura, M. (2003), "Amplitude Dependence Evaluation of Modal Parameters through Earthquake Observation on a SRC High-rise Building" (in Japanese), *Technical Papers of Annual Meeting*, AIJ, B2, 949-950.

Nagano, M., Kudo, K. & Takemura, M. (1999) "Simulation analyses of the array strong motion records from the after-shocks of the 1995 Hyogo-ken Nanbu earthquake (M_J= 7.2) regarding the irregularity of the underground structure in Nagata Ward, Kobe" (in Japanese), *Zisin* 2, 52: 25-41.

Ohsaki, Y., Hara, A. and Kiyota, Y. (1978), "Stress-Strain Model of Soils for Seismic Analysis" (in Japanese), *Proc. of 5th JEES*, 679-704.

Koyamada, K. (2005), "Effects of soil nonlinearity on evaluation of site response" (in Japanese). *Proceedings of the 32nd Symposium of Earthquake Ground Motion*, AIJ, 97-104.

8CUEE CONFERENCE PROCEEDINGS
8th International Conference on Urban Earthquake Engineering
March 7-8, 2011, Tokyo Institute of Technology, Tokyo, Japan

SENSITIVITY OF GROUND RESPONSE ANALYSIS TO SHEAR WAVE VELOCITY PROFILE

Pulpong Pongvithayapanu

Lecturer, International Maritime College, Kasetsart University, Si Racha campus, Thailand
pulpong@src.ku.ac.th

Abstract: The sensitivity of ground response analysis to shear wave velocity profiles was calibrated for Bangkok subsoil. The shear wave velocity was obtained from down-hole seismic tests conducted at several locations in Bangkok. Conventional shear wave profiles were obtained that expressed variation of the shear wave as step functions against depth. A new interpretation method was proposed, which exhibited the influence of effective in-situ overburden stress on the profile. Furthermore, a simple linear correlation between shear wave velocity and depth was obtained. Both profiles produced no significant difference in ground response analysis. The proposed correlation was simple, portable and therefore suitable for many practitioners.

1. INTRODUCTION

One of the most important input parameters used in ground response analysis using either the equivalent linear method or the nonlinear method is the shear wave velocity (V_s) at low strain. Determination of V_s is becoming a normal part of dynamic site evaluation studies. V_s, measured either by in-situ or laboratory techniques, is a soil property used to determine the maximum shear modulus, G_{max}, or the stiffness of deposit soils. The field measurement of V_s at low strain can be carried out by several methods, such as seismic reflection and refraction, seismic cross-hole, seismic down-hole (up-hole) and seismic cone tests. V_s can be determined by laboratory measurement, for instance, using the bender element test, which can be performed in a conventional triaxial apparatus or with an odometer device. To attain a reliable V_s profile from such direct V_s measurements requires experience and engineering judgment, as well as complicated experimental instrumentation. In addition, the determination of the in-situ V_s is uncertain, due to the unpredictability of local variations in soil deposits and anisotropic stress conditions. Furthermore, the use of in-situ determination of V_s in several areas is scarce. Thus, in addition to direct measurement of V_s, many researchers have put much effort both in the field and the laboratory to approximate V_s using empirical relationships between V_s and various soil properties.

As mentioned previously, V_s can be estimated by other means. Hardin (1963) correlated V_s with the effective confining pressure and void ratio. Fumal (1978) related V_s with depth and Dickenson (1994) proposed a nonlinear relationship between V_s and undrained shear strength for soils in the San Francisco Bay area. The correlation based on the SPT *N-value* and V_s has been well formulated by many scholars, such as Ohsaki (1973) and Imai (1982). Though the precision of the V_s value attained by these correlations may vary greatly, it would still be useful in areas where the measurement of V_s has not been broadly explored.

In Thailand, the Bangkok Metropolitan Area (BMA), which includes the capital city with a population of approximately 10 million people, is known as an area of low seismic activity. The closest potentially active faults are in the west of Thailand, about 200 to 300 km away. More active seismic sources in Burma are between 600 km and 1,000 km from the BMA. However, the BMA is situated on a soft clay layer. This uppermost layer of soft marine clay (usually referred to as "soft Bangkok clay") is about 15 to 18 m thick. Underneath this soft clay layer are layers of stiff clay and sand, respectively. It is widely recognized that "soft clay", if encountered by medium to high seismic forces, can amplify the earthquake ground motion 3-6 times, in terms of peak ground acceleration (*PGA*).

To perform a complete seismic site response analysis, the V_s profile is one of the crucial input parameters that has to be determined. Though the low strain amplitude shear modulus of soft Bangkok clay has been determined already in the laboratory by Shibuya (1999), Teachavorasinskun and Amornwithayalax (2002) and Teachavorasinskun et al. (2002), the in-situ value has not been broadly determined. Therefore, an available in-situ V_s profile is suitable and should be adopted in the ground response analysis of the BMA. Since 1995, many scholars have measured the V_s profile around the BMA by various conventional methods. Shibuya (1997) obtained V_s profiles using the seismic cone test. Ashford (1997 and 2000) conducted a series of down-hole seismic tests along the north–centre–southeast of the BMA (Figure 1) and also estimated V_s from specific field and laboratory soil data using a number of published

empirical correlations, which were then developed into a generalized V_s profile. Moreover, the V_s profile obtained from the conventional methods appeared to have some variations, resulting in over- or under- estimation, because of a lack of suitably accurate values for some parameters in the V_s calculation. Teachavorasinskun (2004) interpreted the down-hole seismic tests of Ashford (1997 and 2000) by adding a correction to the V_s calculation, which acknowledged the surface distance of the point of wave generation in the down-hole tests. The linear increase of V_s with depth can be observed from this study. This proposed simple linear correlation between V_s and depth around the BMA is an essential, practical and portable component for further research. This useful correlation may at least contribute to the relative uniformity of subsoil conditions around the BMA.

The current study aimed to compute the site response in terms of Peak Ground Acceleration (*PGA*) and the soil amplification factor of the generalized subsoil around the BMA, by employing a linear V_s profile depicted by practical simple correlation (Teachavorasinskun, 2004) and comparing it with the step function V_s profile developed by estimation and in-situ measurements from earlier studies, such as Ashford (1997) and Warnitchai (2001). The one-dimensional site response analysis program, DEEPSOIL V3.7, developed at the University of Illinois at Urbana-Champaign by Professor Youssef M.A. Hashash and his students was adopted for the current study.

2. GROUND RESPONSE ANALYSIS

It is generally recognized that ground response analysis can determine, to some extent, the performance of the local soil conditions of a specific area that been shaken by a medium to strong earthquake. Some soils, especially those containing soft clay, might amplify (though some might de-amplify) the earthquake ground motions to about 3-6 times the *PGA*. Therefore, in an area located on layers of thick soft clay, such as Mexico City, the San Francisco Bay area and the BMA, particular attention should be paid to prevent damage, as well as loss of human life. A complete idealized ground response analysis can be categorized into three major steps: 1) the analysis of the rupture mechanisms, that is the fault characteristics and the direction of rupture propagation relative to the site at the source of an earthquake; 2) the analysis of the propagation of shear waves triggered by the fault through the bedrock below the site of interest; and 3) the analysis of the surface ground motion influenced by the local soil conditions above the bedrock. While the source mechanisms, as well as source-to-site behavior are somewhat crucial in ground response analysis, the local soil conditions always play an important role in the determination of surface ground motion as influenced by any seismic force. Another reason to simplify the ground response analysis is that in some countries, such as Thailand, information on the fault characteristics within or near the country is very limited. Therefore, the problem of ground response analysis can be simplified to the determination of the soil response to the motions of the bedrock directly beneath it.

In order to undertake ground response analysis, many soil parameters need to be entered into the program. Those parameters include the unit weight of soil, geometry (soil thickness), soil damping characteristics and shear modulus or V_s profiles. The appropriate input bedrock motion is vital in the analysis. The frequency content parameter and the duration of earthquake motion appear to have a substantial effect on the response of local soil conditions.

2.1 Generalized Soil Profile and Basic Soil Properties of the BMA

The generalized soil profiles and the basic soil properties of the BMA used in this research were based on data obtained from the literature (Ashford, 1997 and 2000; Shibuya, 2003; Teachavorasinskun, 2004) with some adjustments (Figure 2). It is recently known that the BMA is composed of layers of soft-to-stiff clay and medium-to-dense sand in the topmost 80 m. It is also recognized that BMA subsoil is relatively uniform throughout the entire area. The generalized soil profile of the BMA consists of five layers of different thicknesses and properties of subsoil underlain by elastic bedrock. The first layer of soft clay is 15 m thick. The second layer contains the first stiff clay and is 10 m thick and is over the first dense sand which is 15 m thick. The fourth layer is a second layer of stiff clay with a thickness of 5 m. The last layer of the generalized soil profile is the second dense sand layer with a thickness of 35 m. It should be noted that the properties of the bedrock profile under the BMA area vary in the range of 550 to 2,000 m in depth and are not exactly identified. The aquifer system above this bedrock is known to be very complex (Brand, 1976) and no rock outcrop is located in the area. A variety of bedrock types, such as gneiss and quartzite have been identified (Shibuya, 2003). Therefore, in this analysis, the bedrock was simplified to be just under the generalized soil profile of the BMA with a unit weight of 23.60 kN/m^3, with V_s being about 1,000 m/s.

2.2 Shear Wave Velocity Profile of the BMA

In this study, the sensitivity of the V_s profile on the estimation of ground response analysis of BMA was evaluated by exploiting the generalized (best-estimated) V_s profile developed by Ashford (1997 and 2000), called a step V_s profile, and the linear V_s profiles developed by Teachavorasinskun (2004) as comparative V_s profiles in the analysis (Figure 2). The step V_s profile was derived from the specific field and laboratory soil data from nine sites around the BMA, using several published empirical correlations, and then the estimates were confirmed by referring to actual in-situ V_s measurements at another six sites, namely, AIT and SIIT (north of the BMA), Chula 1 and 2 (in the centre of the BMA) and Nong Gu Hao and Lad Krabang (south of the BMA) using a down-hole method. The step V_s profile is a conventional step-function profile extensively employed in the representation of in-situ measurement of V_s from various measurement methods, including down-hole seismic and

seismic cone tests. However, it has been recently recognized that an erroneous profile can occur if some of the parameters are ignored in the surface distance of wave generation in the V_s calculation. In addition, the measurement method itself gives a variation in V_s. The V_s value obtained from the seismic cone test was greater than that measured by the cross-hole seismic method. Therefore, in uniform layers of subsoil, as occur in the BMA, the new simple correlation between V_s and depth interpreted and corrected from the existing data of down-hole seismic tests can be used to represent the V_s profile more simply and practically. Figure 2 represents the step V_s and the simple V_s profiles. It can be discerned from Figure 2 that the simple V_s profiles seem to be at the boundary values of the step V_s profile. It is also noticeable that the boreholes of Chula 1 and 2 and of AIT and SIIT are in the north and centre of the BMA, while the Nong Gu Hao and Lad Krabang boreholes are in the southeast of the BMA. The linear V_s profiles of Chula 1 and 2, as well as for the AIT and SIIT sites, are almost similar. In addition, an almost-parallel line between Nong Gu Hao and Lad Krabang sites could be observed. As a result, only two of these profiles, (Chula 1 and 2 and Nong Gu Hao sites), were selected as the linear V_s profiles in the analysis.

2.3 Soil Models for Ground Response Analysis

The cyclic properties of clay, the shear modulus reduction curve and the damping ratio, employed in this equivalent linear analysis were taken from Teachavorasinskun et al. (2002). They proposed a hyperbolic equation of the equivalent shear modulus degradation curve as well as a damping ratio versus the single amplitude shear strain curve for soft-to-medium Bangkok clay (Figure 3). The shear modulus curves show that the proposed curve of soft Bangkok clay by Teachavorasinskun et al. (2002) agrees well with the curves by Vucetic (1991) with a plastic index (*PI*) range of 15-50. It should be noted that the typical range of *PI* for soft Bangkok clay is between 30 and 60. The curve of Hardin (1972) over-estimates somewhat the shear modulus reduction curve of soft Bangkok clay. For soft Bangkok clay, the damping ratio curve, PI = 30, from Vucetic (1991) was adopted, because in a previous investigation by Teachavorasinskun et al. (2002), no unique relationship resulted from the damping ratio test results, due to the dependency of the damping ratio on some cyclic load characteristics, specifically the rate of loading and the initial confining pressure. The soil modulus and damping factor curves produced by Seed (1970) were used in the response analyses for sand.

2.4 Input Motions

The strong ground motion time histories were selected based on the frequency content as well as the epicentral distance from the available strong motion databases, namely the COSMOS virtual data center and the USGS National Strong-Motion Project (NSMP). The BMA study area is quite far from any current, known, potentially active faults in the western part of Thailand (approximately 200-300 km). Though those active faults can produce an earthquake of about M_w = 7.8 (Teachavorasinskun and Pongvithayapanu, 2006), owing to the path and distance effects, the high frequency content of the earthquake wave will be filtered and attenuated as it travels through the soil layers and bedrock underneath the BMA. For this reason, the relatively low frequency but long shaking duration of the 1999 Hector Mine earthquake (on October 16, 1999 at 2:46:44 am near California, USA) was picked as an input source for this analysis. However, an earthquake motion of relatively high frequency content, such as the 1988 Burma-India border earthquake, was also employed to observe the effect of the frequency content parameter in this ground response analysis. The characteristics, the motion time histories and the Fourier amplitude spectrum of these two earthquake scenarios are shown in Table 1 and Figure 4. The high frequency content of the 1988 Burma-India border earthquake can be observed from the relationship of the Fourier amplitude spectrum against frequency. In contrast, the 1999 Hector Mine earthquake had a relatively low frequency content.

2.5 Peak Acceleration Profiles and Amplification Ratio

It can be seen from the results of site response analysis that there were no significant trends in the peak acceleration, amplification ratio and pseudospectral acceleration (*PSA*) between the step V_s profile and linear V_s profiles employed in this study. For the peak acceleration throughout the entire depth of the generalized BMA subsoil profile, the difference was very small at depths below 40 m, especially with the input motion of low frequency content. However the high frequency content of earthquake input motion gave slightly more divergent results between those of the three V_s profiles, particularly near the ground surface. The complete results of peak acceleration profiles are plotted in Figure 5. The results for the amplification ratio show that the BMA subsoil of various V_s profiles could be amplified by high frequency input motion about 4-6 times in terms of *PGA* and by low frequency input motion about 4-7 times in terms of *PGA*. The step V_s profile and linear V_s profiles of the AIT & SIIT sites resulted in almost the same amplification ratio (Figure 6). The peak amplification ratio occurred in the frequency range between 0.5 and 1 Hz. Figure 7 shows the elastic response spectra in terms of *PSA* with 5% damping, which indicates clearly that for all the V_s profiles there was not much difference in the shape of the *PSA* response spectra.

3. CONCLUSIONS

From the one-dimensional ground response analysis of the BMA using the equivalent linear method and various V_s profiles, it can be inferred from the computed results that the simple linear V_s profile against depth could be used with a certain degree of satisfaction to predict some of the ground response parameters, such as peak ground acceleration, amplification ratio and the response spectrum. It should be acknowledged that the ground response analysis can be strongly influenced by the V_s profile. However in some areas, such as where there is low seismic activity from earthquakes,

experimental and in-situ test data of basic dynamic properties of the subsoil are somewhat scarce, a simple linear correlation of the V_s profile against depth could be employed to estimate the ground response analysis around such areas. Because of the fairly uniform layers of subsoil conditions underneath the BMA, the linear and practical correlations can capably represent the V_s profile through a finite depth of subsoil layers. In addition, it could be observed that the frequency content and the peak acceleration of input earthquake motion significantly affected the ground response analysis results, especially with regard to values of the amplification ratio and response spectra.

Acknowledgements:

The authors would like to express their sincere gratitude to Professor Masayuki Hyodo, Geotechnical Engineering Division, Department of Civil and Environmental Engineering, Yamaguchi University, Ube, for having accepted the first author as a foreign researcher and inspiring him to complete this work.

References:

Ashford, S.A., Jakrapiyanun, W., and Lukkunaprasit, P. (1997), "Amplification of earthquake ground motions in Bangkok," Report CU/CE/EVR 1997.002, Chulalongkorn University, Bangkok, Thailand.

Ashford, S.A. (2000), "Shear wave velocity testing at Chulalongkorn University and SIIT, Bangkok, Thailand," Test Report No. TR-2000/15. University of California, San Diego.

Bardet, J.P., Iichi, K., and Lin, C.H. (2000), "EERA – A computer program for equivalent-linear earthquake site response analyses of layered soil deposits," EERA Manual, University of Southern California.

Brand, E.W. and Balasubramaniam, A.S. (1976), "Soil compressibility and land subsidence in Bangkok," *Proceedings of the Second International Symposium on Land Subsidence*, Anaheim, California, 13-17, December, 1976, IAHS-AISH Publication No. 121.

Dickenson, S.E. (1994), "The dynamic response of soft and deep cohesive soils during the Loma Prieta earthquake of October 17, 1989," Ph.D. Dissertation, University of California, Berkeley.

Fumal, T.E. (1978), "Correlations between seismic wave velocities and physical properties of near-surface geologic materials in the Southern San Francisco Bay region, California," USGS Open-File Report 78-1067, Reston, VA: US Geological Survey.

Hardin, B.O. and Richart, F.E. (1963), "Elastic wave velocities in granular soils," *Journal of Soil Mechanics and Foundations Division*, Proceedings of the American Society of Civil Engineers 89 (SM1, February), 33-65.

Hardin, B.O. and Drnevich, V.P. (1972), "Shear modulus and damping in soils: Design equations and curves," *Journal of Soil Mechanics and Foundations Division*, Proceedings of the American Society of Civil Engineers **98**(7), 667-692.

Imai, T. and Tonouchi, K. (1982), "Correlation of N-value with S-wave velocity and shear modulus," *Proceedings of the 2nd European Symposium on Penetration Testing*, Amsterdam, 67-72.

Ohsaki, Y. and Iwasaki, R. (1973), "On dynamic shear moduli and Poisson's ratios of soil deposits," *Soils and Foundations*, **13**(4), 61-73.

Seed, H.B. and Idriss, I.M. (1970), "Soil moduli and damping factors for dynamic response analyses," Report No. EERC 70-10, Earthquake Engineering Research Center, University of California, Berkeley.

Shibuya, F., Tanaka, H., Tanaka, M. and Hamonche, K. (1997), Bi-country cooperative research programme on geotechnical engineering properties of Bangkok clay. Chishitsu-to-Chosa 72, 44-51.

Shibuya, S. and Tamrakar, S.B. (1999), "In-situ and laboratory investigations into engineering properties of Bangkok clay," *Proceedings of International Symposium Characterization of Soft Marine Clays*, Bothkennar, Drammen, Quebec and Ariake Clays, Balkema, Yokosuka, Japan, 107-132.

Shibuya, S. and Tamrakar, S.B. (2003), "Engineering propoerties of Bangkok clay," *Proceedings of Characterisation and Engineering Properties of Natural Soils*, Tan, T. S. (Editors), Vol. 1, Swets & Zeitlinger, Lisse.

Teachavorasinskun, S. and Amornwithayalax, T. (2002), "Elastic shear modulus of Bangkok clay during undrained triaxial compression," *Geotechnique,* **52**(7), 537-540.

Teachavorasinskun, S., Thongchim, P., and Lukkunaprasit, P. (2002), "Shear modulus and damping of soft Bangkok clays," *Canadian Geotechnical Journal*, **39**(5), 1201-1208.

Teachavorasinskun, S. and Lukkunaprasit, P. (2004), "A simple correlation for shear wave velocity of soft Bangkok clays," *Geotechnique*, **54**(5), 323-326.

Teachavorasinskun S. and Pongvithayapanu P. (2006), "Study for determination of ground motion parameters for Hutgyi Hydropower Project," Final Report (Part II), The Electrical Authority of Thailand.

Warnitchai, P., Sangarayakul C., and Ashford, S.A. (2001), "Seismic hazard in Bangkok due to distant earthquakes," *Proceedings of the Joint Workshop on Urban Safety Engineering 2001*, September 21-22, 2001, AIT, Thailand, The University of Tokyo, Japan.

Youssef, M.A. Hashash. (2009), "User Manual and Tutorial of DEEPSOIL V3.7," Department of civil and environmental engineering, University of Illinois at Urbana-Champaign, July 27, 2009.

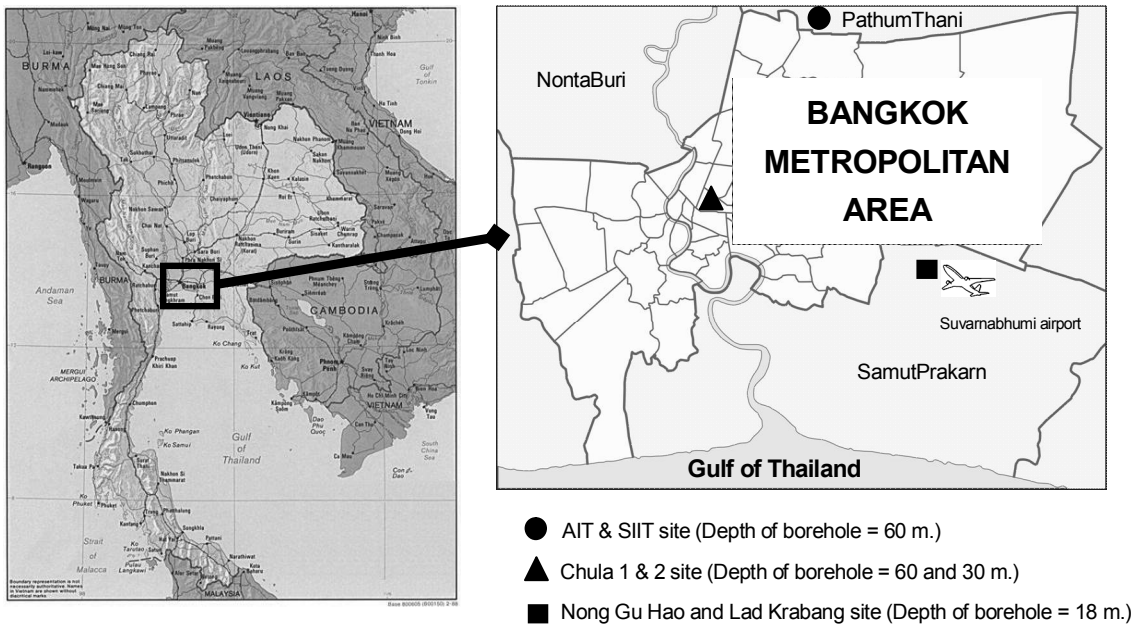


Figure 1 The location of down-hole seismic tests along the north-center-southeast of the Bangkok Metropolitan Area (BMA), Thailand (Ashford, 1997 and 2000)

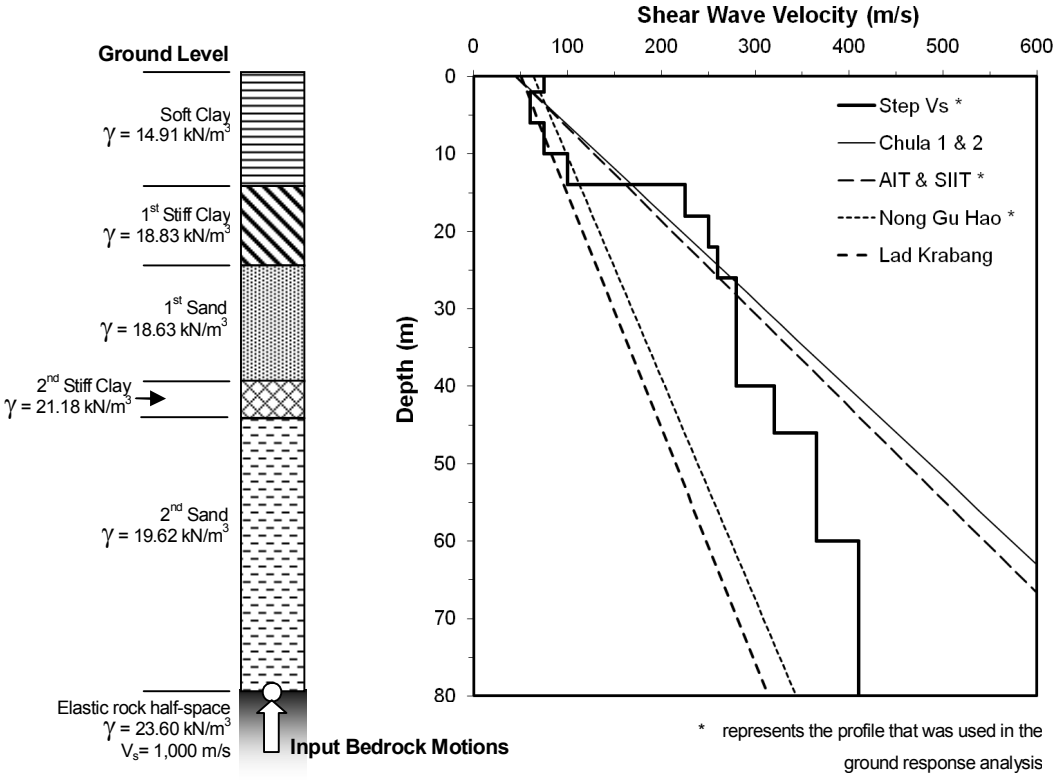


Figure 2 Generalized subsoil and shear wave velocity profile of the BMA.

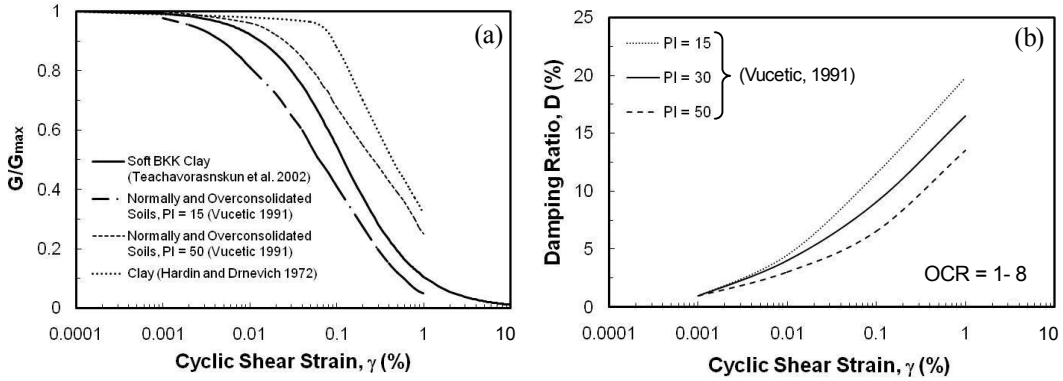


Figure 3 (a) The shear modulus reduction curve of soft Bangkok clay and (b) the damping ratio of normally consolidated and overconsolidated (OCR = 1-8) soils reproduced from Teachavorasinskun et al. (2002), Vucetic (1991) and Hardin (1972).

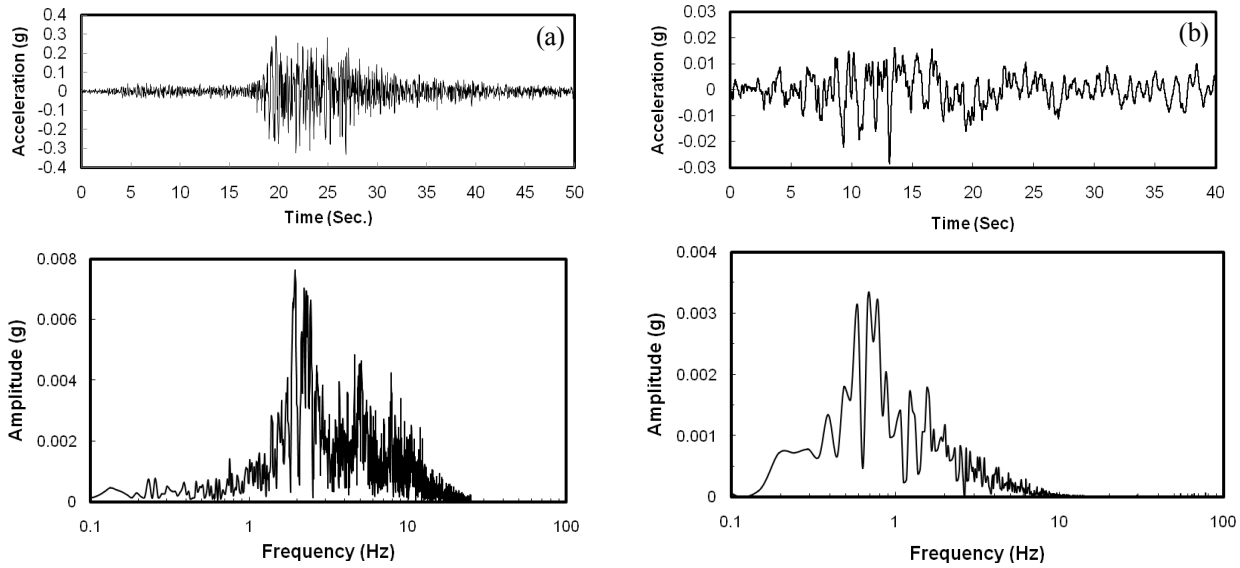


Figure 4 Time history and Fourier amplitude spectrum for:
a) 1988 Burma-India border earthquake; and b) 1999 Hector Mine earthquake.

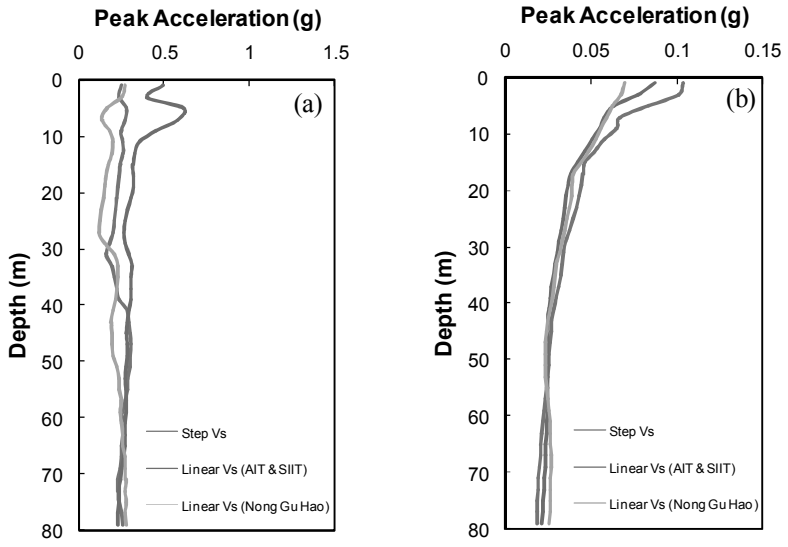


Figure 5 Peak acceleration profiles of the BMA from various soil profiles with:
a) 1988 Burma-India border earthquake; and b) 1999 Hector Mine earthquake.

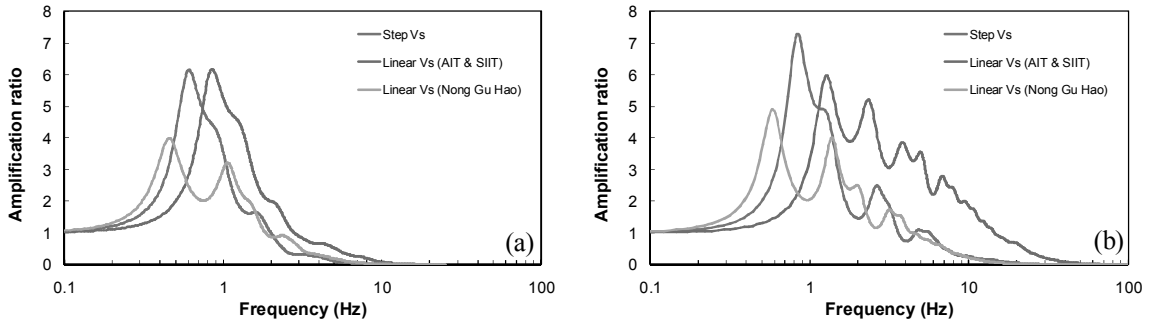


Figure 6 Amplification ratio of BMA from various soil profiles for
a) 1988 Burma-India border earthquake and b) 1999 Hector Mine earthquake

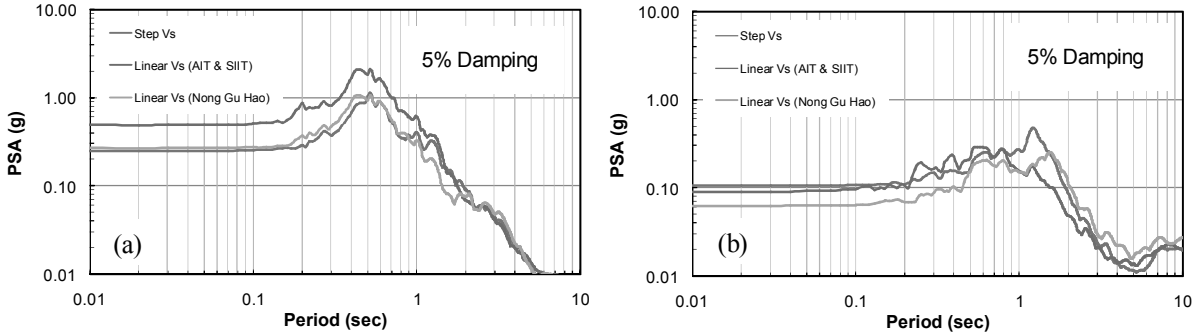


Figure 7 Elastic response spectra (5 % damping) of the BMA from various soil profiles for:
a) 1988 Burma-India border earthquake; and b) 1999 Hector Mine earthquake.

Table 1 Characteristics of earthquake motion from the 1988 Burma-India border and the 1999 Hector Mine earthquakes

Events	**Properties of Recorded Earthquake Motion**		
	M_w	Epicenter distance (km)	Peak Acceleration (g)
1988 Burma-India border	7.3	210	0.331
1999 Hector Mine	7.1	208	0.028

8CUEE CONFERENCE PROCEEDINGS
8th International Conference on Urban Earthquake Engineering
March 7-8, 2011, Tokyo Institute of Technology, Tokyo, Japan

SITE CHARACTERIZATION IN THE GREATER BANGKOK BY MICROTREMOR OBSERVATIONS

Nakhorn Poovarodom[1] and Nonthakorn Plalinyot[2]

1) Associate Professor, Faculty of Engineering, Thammasat University, Pathumthani, Thailand
2) Graduate Student, Faculty of Engineering, Thammasat University, Pathumthani, Thailand
pnakhorn@engr.tu.ac.th, nonthakorn_plalinyot@hotmail.com

Abstract: Bangkok and its vicinity have substantial risks from distant earthquakes arises due to the ability of the underlying thick soft clay to amplify ground motions. The seismic regulation and design standards for buildings have been issued and updated occasionally according to the recent assessment of seismic hazards whilst site characterization for evaluation of seismic wave amplification has been primitively investigated. This research aims to quantitatively investigate site characteristics of subsoils by economical and practical technique of microtremor observations. The technique of single point observation with Horizontal-to-Vertical spectral ratio (H/V) method to estimate the predominant period and the technique of array observation with Spatial Autocorrelation (SPAC) technique for exploration of shear wave velocity profile are conducted for 36 sites in approximately 80 km by 80 km area. The results of shear wave velocity profiles are firstly compared with the available results from previous researches and they are found to be in good agreement. Site classifications based on the predominant period and the average shear wave velocity are presented and discussed with distribution of thickness of soft clay and geotechnical properties. Relations among average shear wave velocity from surface to different depth and predominant periods are investigated for their consistencies.

1. INTRODUCTION

Local site conditions can substantially influence the characteristics of ground shaking, such as amplitude, frequency content, duration, and earthquake damages. Several examples from catastrophic earthquakes have revealed that ground motion intensity can be amplified, frequency contents become narrow band, and duration of shaking can be lengthened due to a seismic interaction of soft shallow soil layers with deep basin structure below at the site. The local site effects are taken into account for seismic design by classifying site into categories based upon the geotechnical properties of the site and different levels of design ground motion are provided. The famous site characterization scheme has been established by the National Earthquake Hazard Reduction program (NEHRP 2004) and widely accepted in many countries. The average of shear wave velocity from the surface to 30-m depth (V_{S30}) is adopted as the key index for site classification. Recent studies have discussed on limitation on using V_{S30} to predict site amplification (Gallipoli and Mucciarelli 2009) and attempted to include site predominant period obtained by Horizontal-to-Vertical spectral ratio (H/V) study (Lang and Schwartz 2006)

Bangkok and the vicinity area, with more than ten million populations, is located about 120 to 300 km from low to moderate seismicity faults and 400 to 1000 km from highly active Sumatra subduction zone. The area is situated on a large plain underlain by the thick alluvial and deltaic sediments of the Chaophraya Basin. This plain consists of thick soft clay, about 15 to 20 m in the metropolitan area. The problem of soil amplification of ground motions of Bangkok is, therefore, appears to be susceptible to the teleseismic earthquakes. In fact, occasional events of tremors generated from remote earthquake were felt and caused chaos to Bangkok residents. The seismic regulation and design standards for building was firstly issued in 1997 and recently updated according to improvement of researches (DPT 2009). Among these pertinent tasks, site characterization for evaluation of seismic wave amplification has been primitively investigated. Owing to the limited information, this research aims to quantitatively investigate site characteristics of subsoils by economical and practical technique of microtremor observations. The technique of single point observation with Horizontal-to-Vertical spectral ratio (H/V) method to estimate the predominant period and the technique of array observation with Spatial Autocorrelation (SPAC) technique for exploration of shear wave velocity profile down to about 100 m are conducted for 36 sites in approximately 80 km by 80 km area.

2. MICROTREMOR OBSERVATION TECHNIQUES

The conventional approach for shear wave survey such as PS logging tests with boreholes has crucial disadvantages

as it is costly and time consuming. On the other way, microtremor observations have been raised up as a tool for evaluating site effects. This technique has several advantages; economical, environment friendly for urban area and effective for low or moderate seismicity area. In this study, the microtremor measurements, which can be readily conducted on the ground surface without drilling any borehole, are conducted for extensive surveys in the Greater Bangkok area to provide site characteristics useful for ground motion evaluation. The technique of single point microtremor observation with Horizontal-to-Vertical spectral ratio (H/V) method is applied to estimate the predominant period and the technique of array microtremor observation with Spatial Autocorrelation (SPAC) technique is applied for exploration of shear wave velocity profile.

2.1 Horizontal to Vertical Spectral Ratio Method (H/V spectral ratio)

This technique was proposed by Nakamura (1989) to interpret records of microtremors for the dominant period of subsoil sediments and also the estimated amplification level. In this method, the ratios of horizontal to vertical Fourier Spectra of microtremors are used to eliminate the source effect. This technique requires the horizontal and vertical component of microtremors measured at a single station only. The H/V spectrum plots are obtained by taking the ratio of the Fourier Spectra of the horizontal to the Fourier Spectra of the vertical component, as shown in equation 1.

$$\text{H/V spectrum} = \frac{\sqrt{F_{NS} \times F_{EW}}}{F_{UD}} \tag{1}$$

where F_{NS}, F_{EW} and F_{UD} are the Fourier amplitude spectra in the north-south, east-west and up-down directions, respectively. The peak of the H/V spectrum plot is interpreted as predominant period and amplification ratio. In spite of the wide popularity of the H/V spectral ratio method, there exists inconsistency of the assumption used in this method with theory. Nakamura's method assumes that microtremors are composed of body waves and thus is theoretically inconsistent with the results that show that microtremors are composed of surface waves. However, a number of researches have experienced that the H/V spectral ratio can be utilized to estimate the predominant period of a site, and it has broadly been applied to evaluate site effect and seismic microzonation.

2.2 Spatial Autocorrelation Method (SPAC method)

This technique was proposed by Aki (1957) based on the relationship between the temporal and spatial spectra of waves to obtain phase velocity dispersion curve. The basis of SPAC method is to simultaneously record the vertical component of microtremors for several positions to obtain Rayleigh wave samples propagating from a wide range of azimuthal angles. The coherency spectrum can then be computed for any pair of sensor in the array to evaluate the correlation among them to determine phase velocity characteristic which is dispersive. The coherencies for all measurement pairs having the same spatial distance are then azimuthally averaged to provide the spatial autocorrelation coefficients of inter-station distance r, $\rho(\omega, r)$. By assuming that, the wave energy propagates with only one velocity at each frequency, ω, it can be shown that the spatial autocorrelation coefficient for a circular array is given by (Aki, 1957, Okada, 2003):

$$\rho(\omega, r) = J_0\left(\frac{\omega r}{c(\omega)}\right) \tag{2}$$

where J_0 is the Bessel function of the first kind with the zero-th order and $c(\omega)$ is the (dispersive) phase velocity at frequency ω for the Rayleigh waves with the fundamental mode. From the dispersion relation of phase velocity and frequency, the results from field observations are then compared with those derived theoretically from a horizontally layered earth model by iteration procedure. The results of best-fit shear wave velocity–depth profile can be determined from the inversion analysis, in which this study applies the technique developed by Yokoi (2005) which employs the combination of Down Hill Simplex Method with Very Fast Simulated Annealing.

3. FIELD OBSERVATIONS AND ANALYSIS OF DATA

3.1 Area of Study

The investigated area is located within latitudes 13° 30' N to 14° 5' N and longitudes 100° 5' E to 100° 50' E, covering Bangkok and the vicinity provinces named Nakhon Pathom in the west, Nonthaburi and Pathumthani in the north, Samut Sakhon and Samut Prakan in the south. The area lies on a large alluvial plain of delta area where two main rivers, Chaopraya and Tha Chin, empty into the Gulf of Thailand in the south. Figure 1 shows the investigated area where 36 observation sites are distributed almost evenly inside.



Figure 1 Area of Study

3.2 Microtremor Observation

The measurement system consists of a portable data acquisition with 24 bit A/D converter and four units of the three components, moving coil type, velocity sensor with 2-second natural period. The sensors are connected to the data acquisition unit through cables. Before conducting measurement in each site, huddle test was performed for coherency and phase differences among the sensors. The applicable range of frequency was identified as from 0.8 to 17 Hz. At each record, data was recorded for 20 minutes with sampling frequency of 200 Hz. The data was divided into segment of 4096 data points and used for the analysis.

The arrangement of sensors for SPAC observation was selected as equilateral triangular array where one unit is placed at the center of circular and the other three are on the perimeter as shown in Figure 2. Four array arrangements were set for each site, with radius (r) of 9, 25, 35 and 50 m. In addition, pairs of peripheral stations with inter-station distance $\left(\sqrt{3}r\right)$ of 15.9, 43.3, 60.6 and 86.6 m are also included for calculating of SPAC coefficients. The maximum depth for inversion analysis was set to 90 m. The data of single station measurement were used to determine H/V spectrum ratio.

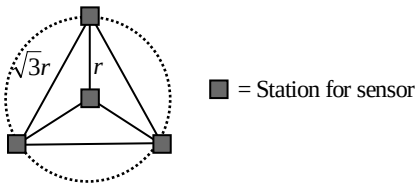


Figure 2 Arrangement of sensors for array observation

4. Results and Discussions

4.1 Comparison of V_{S30} with different techniques

First, the average of shear wave velocities from the surface to 30-m depth (V_{S30}) obtained by this study were compared with results from several techniques done by previous researchers. The number of pervious tests is limited which include seismic downhole tests by Palasri and Ruangrassamee (2009) named as D1 and Ashford (2000) named as D2, microtremor with frequency-wave number (F-k) spectral analyses by Arai and Yamazaki (2002) named as FK and multichannel analysis of surface waves method named as MASW. This research conducted the measurement at approximately the same location of total 7 sites. The results of V_{S30} are compared and shown in Figure 3. Despite the fact that results are not exactly identical for all tests, they are found to be in good agreement among different techniques employed.

The study remarks on a simple way to estimate V_{S30} from dispersion curve, without inversion analysis. Konno et. al. (2007) proposed that the phase velocity of Rayleigh wave with wave length of 40 m (C_{40}) can be used to approximate V_{S30}. The results from this study are presented in Figure 4 in which the applicability of the approximation technique can be clearly observed in spite of some degree of under estimation existed.

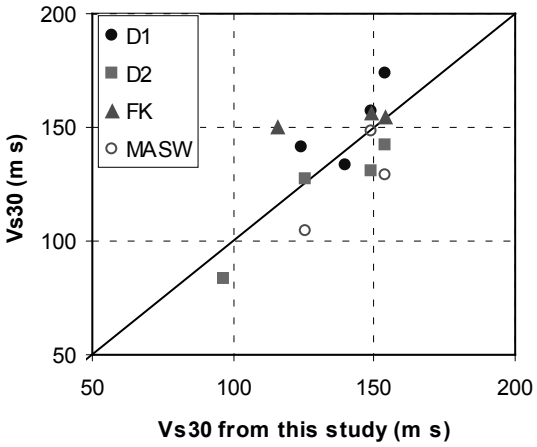


Figure 3 Comparison of V_{S30} obtained from this study and other techniques

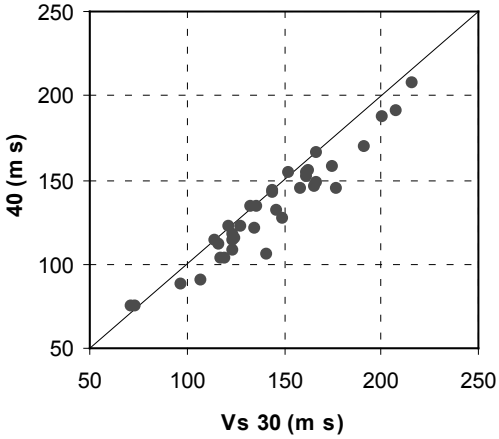


Figure 4 Comparison of V_{S30} obtained from this study and its estimation by phase velocity with wave length of 40 m

4.2 Results from Microtremors and Soil Data

The shear wave velocity and predominant period obtained from microtremor of 36 sites are discussed with soil profile classification in this area. Tuladhar (2003) used the boring log data to classify soil profile into several classes, which is re-drawn in Figure 5 and 6 for the profile and location of area, respectively.

Soil class A (A1, A2 and A3) has larger depths of soft soil layers (16 to 20 m). For class B (B1, B2 and B3), the thickness of soft clay is about 10 to 14 m. Soft clay is followed by first stiff clay and first sand for these soil classes. In soil class C (C1 and C2), which represents area nearby the boundary of the plain, the first layer is medium stiff clay about 8 to 10 m, and follow by first stiff clay or first sand layer.

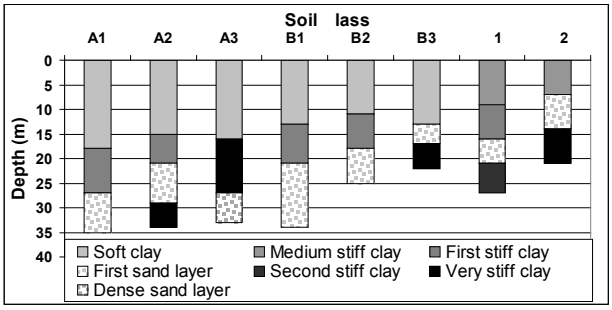


Figure 5 Generalized Soil Profiles in the Study Area

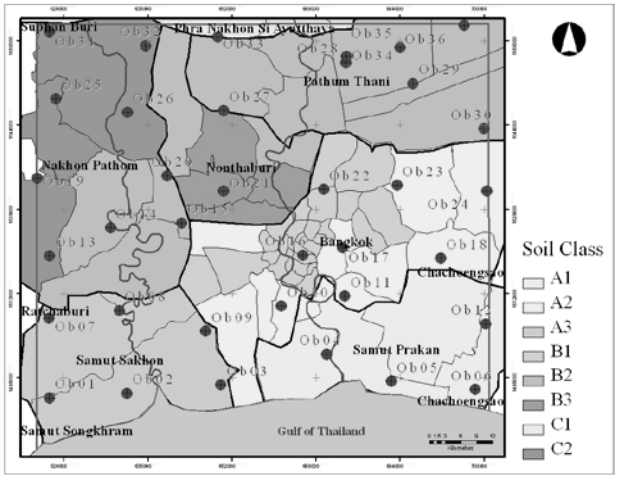


Figure 6 Location of Soil Classification Area

The results of average of shear wave velocity from the surface to 30-m depth (V_{S30}) and predominant period (T_P) are depicted in Figure 7 and 8, respectively.

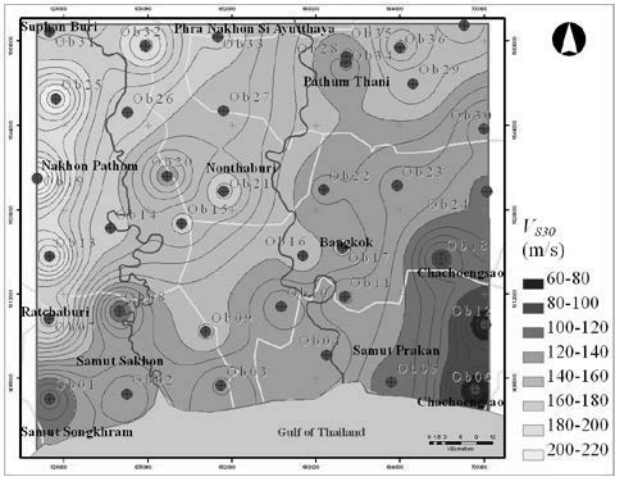


Figure 7 Map of V_{S30} for the Greater Bangkok

The variation of the values can be clearly distinguished where V_{S30} varies from 70 to 220 m/s and T_P varies from 0.4 to 1.1 second. The area with lowest V_{S30} and longest T_P is located in the south-east part where soil class is A1, which contains the deepest layer of soft soil. Area along the Gulf of Thailand exhibits low V_{S30} and long T_P, which is also consistent with properties of soil class A1, A2 and A3. For soil class B1, B2 and B3, V_{S30} is increased and T_P is shortened as soil becomes stiffer. The hardest soil type in this study located in the north-west part, class C2, yields highest V_{S30} and shortest T_P.

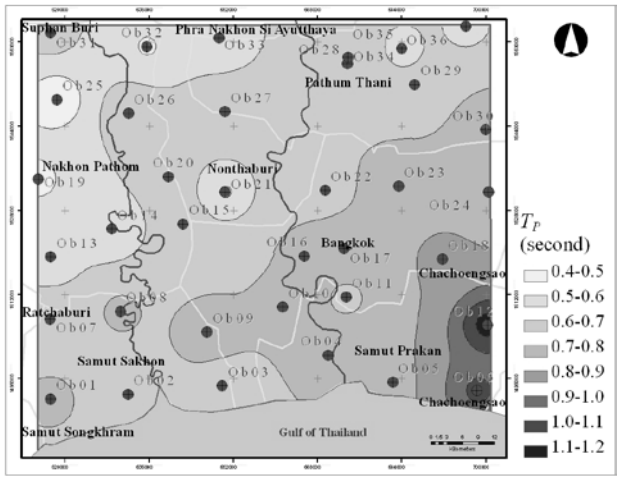


Figure 8 Map of Predominant Period for the Greater Bangkok

4.3 Discussion on Average Shear Wave Velocity and H/V Spectral Ratio

The microtremor technique provides both information on velocity structure of and predominant period of subsoil. There have been discussions on the latter result obtained by ambient H/V spectral technique since this technique is theoretical inconsistent by the assumption on type of wave mainly composed in the signal. In addition, shallow shear wave profiles, V_{S10}, was proposed for an economical site classification scheme (Gallipoli and Mucciarelli 2009). The following discussion provides relations among the average shear wave velocity at different depth, 10 m to 90 m, and the predominant periods obtained in this study. Figure 9 shows V_{S30} plotted in the abscissa and V_{S10}, V_{S50}, V_{S70}, and V_{S90} in the ordinate. From these relations, results from regression analysis in a form of $y=ax^b$ and the coefficient of determination (R^2) are provided in Table 1. It can be clearly noticed that, except V_{S10}, deeper shear wave velocities correlated well with V_{S30} by nearly linear relationship. The map of V_{S10} is shown in Figure 10 which could be misleading because V_{S10} is highly influenced by the uppermost layer of soft clay. This finding is contradicted to the investigation in Gallipoli and Mucciarelli 2009 which is resulted from different geological conditions.

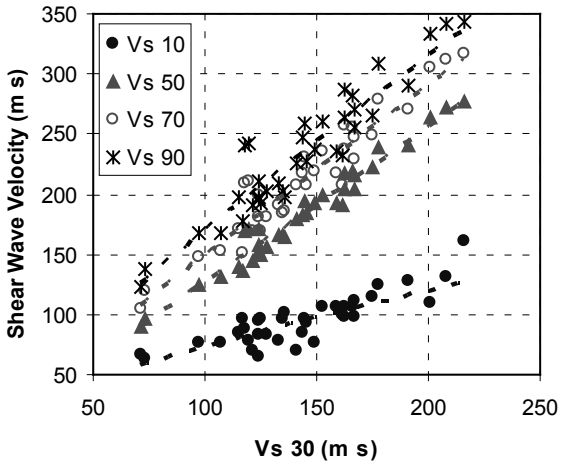


Figure 9 Relations among V_{S30} and V_{S10}, V_{S50}, V_{S70}, V_{S90}

Table 1 Results of Regression Analysis for V_{S30} and V_{S10}, V_{S50}, V_{S70}, V_{S90}

Type	a	b	R^2
V_{S10}	2.86	0.705	0.682
V_{S50}	1.19	1.01	0.963
V_{S70}	1.76	0.964	0.916
V_{S90}	2.78	0.892	0.893

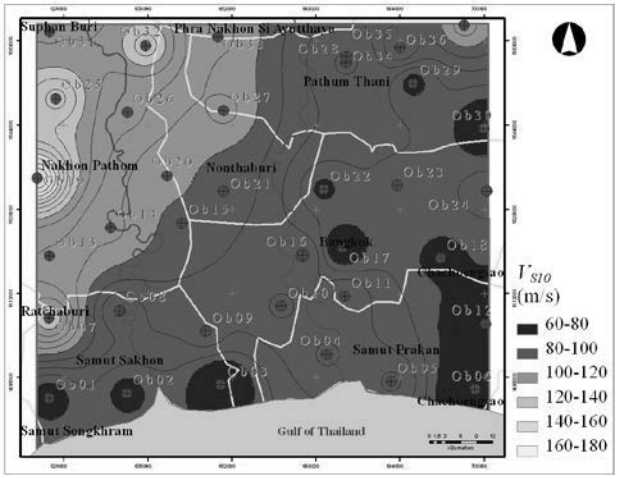


Figure 10 Map of V_{S10} for the Greater Bangkok

Figure 11 shows predominant frequencies $(1/T_P)$ plotted in the abscissa and V_{S10}, V_{S30}, V_{S50}, V_{S70}, and V_{S90} in the ordinate. Table 2 provides results from regression analysis in a form of $y=ax^b$ and the coefficient of determination (R^2). It can be noticed again that, except V_{S10}, deeper shear wave velocities correlated well with the predominant frequencies by nearly linear function. This could support the applicability of H/V spectral ratio technique that the information of deep ground structure can be achieved where the uppermost layers do not absolutely dominate the results.

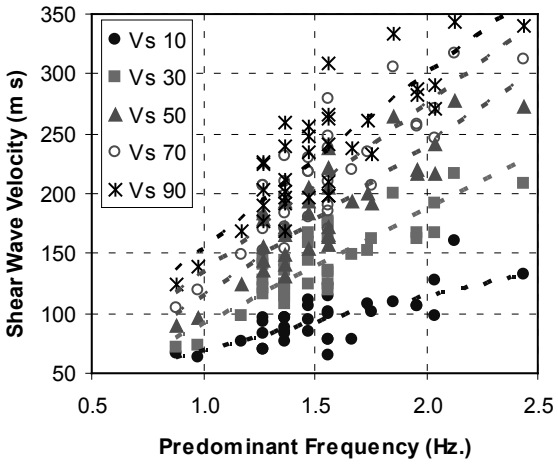


Figure 11 Relations among Predominant Period and V_{S10}, V_{S30}, V_{S50}, V_{S70}, V_{S90}

Table 2 Results of Regression Analysis for Predominant Period and V_{S10}, V_{S30}, V_{S50}, V_{S70}, V_{S90}

Type	a	b	R^2
V_{S10}	69.0	0.730	0.521
V_{S30}	91.7	1.03	0.747
V_{S50}	115	1.07	0.759
V_{S70}	135	1.03	0.742
V_{S90}	154	0.958	0.734

4. CONCLUDING REMARKS

Site characterizations in the Greater Bangkok by microtremor observation are presented in this paper. From 36 observation sites in 80 by 80 km^2 area, shear wave velocity profiles, by SPAC method, and predominant periods, by H/V spectral ratio method, are presented and discussed with soil classification based on boring log data. The area along the Gulf of Thailand and the south-east part of the study area exhibit very low V_{S30} of 70 m/s and long predominant period of 1.1 second while high V_{S30} of 220 m/s and short predominant period of 0.4 second are found the north-west part. This characterization is in accordance with generalized information from boring log data of soil layers.

The relations among the average shear wave velocity at different depth, 10 m to 90 m, and the predominant periods are discussed. It was shown that shallow shear wave velocities to 10 m depth, influenced by thick soft clay in this study, were not reasonably correlated with deep shear wave velocities. The predominant periods were shown to be able to represent shear wave velocity profiles down to 90 m.

Acknowledgements:

This study is a part of research project supported by the Thailand Research Fund, research number RDG5330026, the 2011 research fund from the National Research Council of Thailand and the 2009 Thailand Toray Science Foundation Research Grant. The sources of support are gratefully acknowledged. The authors express their sincere thanks to Mr. Amornthep Jirasakjamroonsri, Mr. Narakorn Boontem and Mr. Trin Boonngam for their assistances. The authors are grateful to Dr. Toshiaki Yokoi (Building Research Institute, Japan) for his valuable consultations on microtremor techniques.

References:

Aki K. (1957), "Space and Time Spectra of Stationary Stochastic Waves, with Special Reference to Microtremors", *Bulletin of the Earthquake Research Institute*, No. 22 , 415–456.

Arai H., and Yamazaki F. (2002), Exploration of S-Wave Velocity Structure Using Microtremor Arrays in the Greater Bangkok, Thailand, EDM Technical Report No.15, Earthquake Disaster Mitigation Research Center.

Ashford S.A. (2000), Shear Wave Velocity Testing at Chulalongkorn University and SIIT Bangkok, Thailand. Test Report No. TR-2000/15, University of California, San Diego, Department of Structural Engineering, Structural Systems Research Project.

Building Seismic Safety Council (2004), NEHRP Recommended Provisions for Seismic Regulations for New Buildings and Other Structures, Part 1: Provisions (2003 Edition), FEMA 450, Federal Emergency Management Agency, Washington, D.C.

Department of Public Works and Town & Country Planning (DPT) (2009), "Standard for Earthquake Resistant Design of Buildings, DPT standard 1302" (in Thai).

Gallipoli M.R. and Mucciarelli M. (2009), "Comparison of Site Classification from VS30, VS10, and HVSR in Italy" ", *Bulletin of the Seismological Society of America*, 99(1), 340-351.

Konno K., Suzuki T., Kamata Y., and Nagao T. (2007), "Estimation of Average S-wave Velocity of Ground Using Microtremors at Strong-Motion Sites in Yokohama", *Journal of Japan Society of Civil Engineering*, 63, 639-654 (in Japanese with English abstract).

Lang D.H., and Schwarz J. (2006), "Instrumental Subsoil Classification of Californian Strong Motion Sites based on Single-Station Measurements", *Proc. of the 8th U.S. National Conf. of Earthquake Engineering*, San Francisco, Paper No. 120.

Morikawa H., Sawada S., and Akamatsu J. (2004), "A Method to Estimate Phase Velocity of Rayleigh Waves Using Microseisms Simultaneously Observed at Two Sites", *Bulletin of the Seismological Society of America*, 94(3), 961-976.

Nakamura Y. (1989), "A Method for Dynamic Characteristics Estimation of Subsurface using Microtremor on the Ground Surface", *Q. Rep. Railw. Tech. Res. Inst.* 30, No. 1, 25–33.

Okada H. (2003), "The Microtremor Survey Method (translated by Koya Suto)", Geophysical Monograph Series, No.12, Society of Exploration Geophysicists.

Palasri C. and Ruangrassamee A. (2009) , "Relations among Shear Wave Velocity, SPT-N Value and Undrained Shear Strength of Soil in Bangkok and the North of Thailand", *Proc. of the 14th National Convention on Civil Engineering, Thailand*. (in Thai)

Tuladhar R. (2003), "Classification of Soil Profile and Seismic Response Analysis (Elastic) in the Greater Bangkok Area", Internal Report, Structural Engineering Field of Study, Asian Institute of Technology, Thailand.

Yokoi T. (2005), "Combination of Down Hill Simplex Algorithm with Very Fast Simulated Annealing Method-an Effective Cooling Schedule for Inversion of Surface Wave's Dispersion Curve", *Proc. of the Fall Meeting of Seismological Society of Japan*. B049.

8CUEE CONFERENCE PROCEEDINGS
8th International Conference on Urban Earthquake Engineering
March 7-8, 2011, Tokyo Institute of Technology, Tokyo, Japan

INTRODUCTION OF THE GEOLOGICAL DATABASE FOR TSMIP

Chun-Hsiang Kuo[1)], Kuo-Liang Wen[2, 3)], Hung-Hao Hsieh[4)], and Kai-Wen Kuo[5)]

1) Associate Research Fellow, National Center for Research on Earthquake Engineering, Taiwan, ROC
2) Professor, Institute of Geophysics, National Central University, Taiwan, ROC
3) Division Manager, National Center for Research on Earthquake Engineering, Taiwan, ROC
4) Assistant Research Fellow, National Center for Research on Earthquake Engineering, Taiwan, ROC
5) Director, Seismology Center, Central Weather Bureau, Taiwan, ROC
chkuo@ncree.narl.org.tw, wenkl@earth.ncu.edu.tw, hhhsieh@ncree.narl.org.tw, kuo@ss2.cwb.gov.tw

Abstract: The **E**ngineering **G**eological **D**atabase for **T**SMIP (EGDT) was constructed by the National Center for Research on Earthquake Engineering (NCREE) and the Central Weather Bureau (CWB) in Taiwan from 2000 to 2010. SPT-N (Standard Penetration Test) values were obtained by in-situ experiment; otherwise, the critical physical characteristics of soils, such as void ratio, specific gravity, effective size, liquid limit, etc., were being measured from the samples, as well as the soils were classified according to the USCS. P and S wave velocity profiles were also measured by a suspension PS-logging system. The drilled depths in this project must exceed 35 m to ensure that Vs30 is able to be measured; moreover, several boreholes were drilled over 50 m or 100 m according to the annual contract stipulations. Nevertheless, some boreholes drilled in the first or second year do not reach the required 30 m. The database contains 469 surveyed stations, which are about 69% (469/682) of the free-field TSMIP network. We therefore used the database to evaluate the empirical Vs equations for different areas, as well as the station sites were classified according to the Vs30 criterion of NEHRP. Everyone can search or apply for the data from the website: http://geo.ncree.org.tw/.

1. INTRODUCTION

Site effect is a very important issue in both seismology and earthquake engineering. Different characteristics of near surface layers cause various effects at sites. The so-called Vs30, the average shear wave velocity of the top 30 meters, is a well-known parameter used on defining the hardness of sites. Anderson et al. (1996) indicated that layers of the depth in top 30 meters have a considerable influence on the characteristic of the ground motion generated. Vs30 was further recommended as a significant parameter for recent building code (BSSC 2001; Dobry et al. 2000); moreover, it was used by the Next Generation Attenuation of ground motions project (NGA) in strong ground motion prediction studies (Power et al. 2008; Chiou et al. 2008). It should be noted that the strong motion recordings in Taiwan were also included in the NGA database by the executive - Pacific Earthquake Engineering Research Center (PEER).

For collecting high-quality instrumental recordings of strong ground motion caused by earthquakes, the Taiwan Strong Motion Instrumentation Program (TSMIP) was carried out by the CWB from 1991. Most of the stations were installed in the metropolitan districts of Taiwan for earthquake hazard reduction. These data were really useful for understanding earthquake source mechanism and improving seismic design of buildings, as well as studying seismic wave propagation, including local site effect.

In order to use the collected strong motion recordings more effectively and precisely on earthquake engineering, the NCREE and the CWB had established a free-field strong motion drilling project to construct the EGDT since 2000. 469 free-field strong motion stations had been surveyed in the past decade.

439 of the 469 surveyed stations included wave velocity profiles and most of the profiles reached a depth of 30 m, so that the site classification was done according to the Vs30 criterion of NEHRP Provision. In the process, Vs30 values were estimated by a reliable extrapolation for the profiles did not reach 30 m. Otherwise, we also analyzed the relations between shear-wave velocity (Vs), N value, and depth to evaluated empirical Vs equations in different regions of Taiwan.

2. ENGINEERING GEOLOGICAL DATABASE FOR TSMIP

2.1 Summary of the EGDT

Taiwan Island results from the collision of the Philippine Sea Plate and the Eurasian Plate. The rate of the subduction system is still about 80 mm/yr today, which made a four-kilometer-high mountain belt and high uplift rate of 5-7 mm/yr in marine terrace (Liew et al. 1993), as well as high seismicity in and around the island. Otherwise, Taiwan was considered suffering the highest erosion rate in the world (Koppes and Montgomery 2009). That is why the geology, topography, and seismicity are various and

complex in Taiwan.

After the destructive Chi-Chi earthquake, the variable geological conditions at strong motion stations were considered must to be known, and then the site effect might be assessed. The work will be an important reference material to reduce the hazard from another possible earthquake in the future.

In the first year, 2000, the surveyed focused on the co-stations of TSMIP and Taiwan Rapid Earthquake Information Release System (RTD). Then the stations located on the Western Plain were surveyed in 2001. Surveyed stations achieved a number of 469 until 2010, about 69% (469/682) of the free-field TSMIP network (Figure 1).

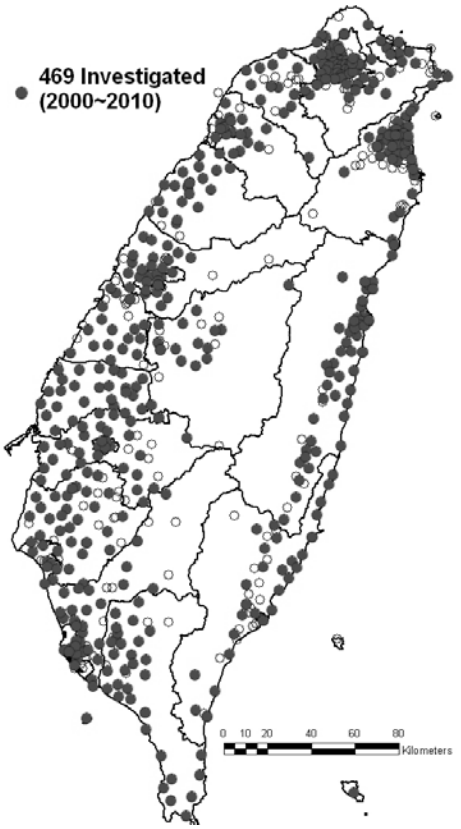


Figure 1 Distribution of the free-field TSMIP stations. The red circles are surveyed station whereas the open ones are still not.

The investigations of TSMIP included drawing surface chart nearby, in-situ standard penetration test, experiments of critical physical characteristics for soils in laboratory, such as void ratio, specific gravity, effective size, liquid limit, grain size distribution size, Atterberg index, etc., as well as the soils were classified according to the Unified Soil Classification System (USCS). Otherwise, P and S wave velocities were also measured using a suspension PS-logging system. Sampling rate of the suspension PS-logging system can up to 2.5 μs and frequency of the velocity measurement is 0.5 or 1 m per point. Some boreholes drilled in the first and second year did not reach the required 30 m, thus the drilled depth in the project was stipulated 35 m at least to ensure that Vs30 is able to be measured after 2001. Furthermore several boreholes were drilled over 50 m or 100 m according to the annual contract stipulations. However, there were still a few velocity profiles did not reach 30 m due to borehole collapse after 2001. 22 boreholes were drilled larger than 50 m in the database and the deepest one is 150 m at TCU138.

All of the in-situ procedures and sampling are under the criteria of American Society for Testing and Materials (ASTM) in this project. The core sampling was made for colluvium, gravel formation, and rock formation, but not for soil layers. During drilling process, SPT was carried out every 1.5 meters (every 3 to 5 meters in gravel layer) or when encountered the interface of different materials; moreover, disturbed samples were also sampled at the same time. The following physical characteristics and soil classification were executed under the ASTM criteria in a laboratory certificated by the Taiwan Accreditation Foundation (TAF).

After drilling, the borehole was casing a PVC pipe and then the gap between PVC pipe and borehole was grouted. Suspension PS-logging system has two receivers at a fixed distance of 1 m, as well as a source was integrated in a tube. That is why the continuous measurement and velocities at depth were capable by this system. P and S wave velocities were calculated by the differences of arrival times (Figure 2).

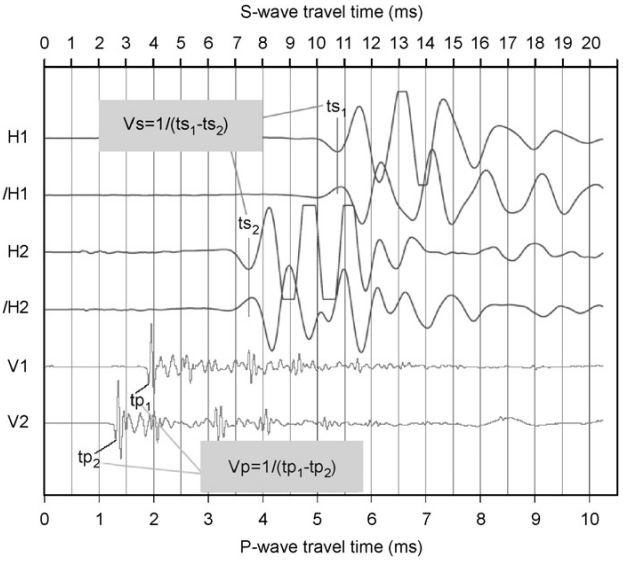


Figure 2 Illustration of the suspension PS-logging method. Vs and Vp were calculated from the formulas on the sketch. (After Kuo et al. 2009, Fig. 9)

2.2 Requested Data Format

The data we provided now included six parts, they are strata description, result of soil physical property tests, P and S wave velocities, SPT-N values, strata profiles and coordinates, and plan view and photos, respectively. They are free for request and provided in Excel format. Figure 3 showed an example at TCU083. Some supplements, such as raw data (ORG format) of PS-logging system, photo of core

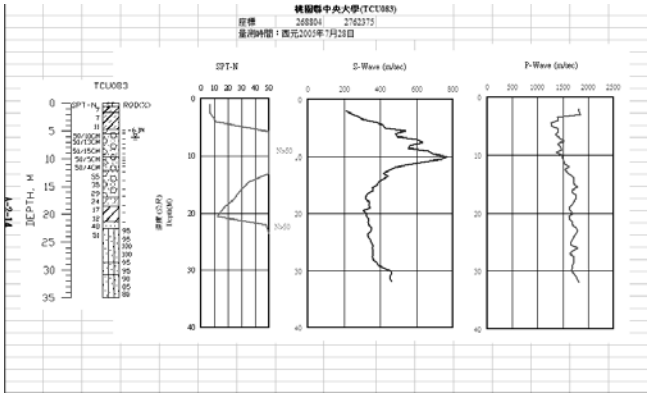
samples, and aerial photographs (Figure 4) were also free, but a further application procedure is needed.

鑽孔編號	深度(m)	SPT-N	USCS	土壤描述	取樣編號	Gravel%(ASTM)
TCU083	0		SF	棕色粉土質黏土,夾混凝土塊、少量細砂及垃圾-回填層	S-0	
TCU083	0.6		CL	紅棕色粉土質黏土,偶夾小礫石及樹根,中度稠密	S-0	
TCU083	1.05	7	CH		S-1	0
TCU083	1.7		CL	紅棕色粉土質黏土,中度稠密至稠密	S-0	
TCU083	2.55	7	CH		S-2	0
TCU083	4.05	11	CH		S-3	0
TCU083	4.75		GW	灰色或棕灰色,后英質礫石,夾紅棕色粉土質黏土,極密實,礫石和漂度高	S-0	
TCU083	5.45		GW	灰色或棕灰色,后英質礫石,夾紅棕色粉土質黏土,極密實,礫石和漂度高	S-0	
TCU083	5.8	50/10	GP-GM		S-4	66
TCU083	6.9	50/13	GM		S-5	52
TCU083	8.55	50/15	GM		S-6	43
TCU083	9.6		GW	灰色或棕灰色,后英質礫石,夾紅棕色粉土質黏土,極密實,礫石和漂度高	S-0	
TCU083	10.05	50/5	GM		S-7	41
TCU083	11.55	50/4	GP-GM		S-8	69
TCU083	12.05		SM	黃棕色,礫石,夾細砂及粉土,密實	S-0	
TCU083	13.05	55	SM		S-9	0
TCU083	14.55	35	SM		S-10	0
TCU083	16.05	29	SM		S-11	8
TCU083	16.9		SM	黃棕色,粉土質砂,夾灰色粉土及黏土	S-0	
TCU083	17.55	24	SM		S-12	2
TCU083	18.6		CH	黃棕色,粉土質黏土,夾少量細砂	S-0	
TCU083	19.05	17	CH		S-13	0
TCU083	20.55	12	CH		S-14	0
TCU083	21.2		SM	黃棕色,粉土質砂,夾粉土質黏土	S-0	
TCU083	22.05	48	SM		S-15	0
TCU083	22.5		SS	黃棕色至暗灰砂岩夾頁岩,中至高度風化,膠結差,泥質極弱	S-0	
TCU083	23.55	51	SM		S-16	0
TCU083	28.6		SS	黃棕色,細砂岩間夾灰色至黃棕色泥岩,中至高度風化,膠結性差至尚可,泥質極弱至弱	S-0	
TCU083	30.85		SS	黃棕色,粗至極粗粒砂岩夾礫石,中度至高度風化,膠結差至尚可,泥質極弱至弱	S-0	

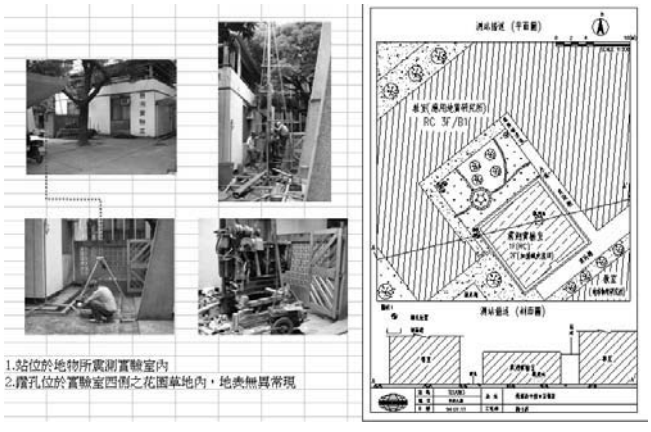
(a) Strata description at TCU083.

Sand%(ASTM)	Silt%(ASTM)	Clay%(ASTM)	D_{10}(mm)	D_{20}(mm)	D_{30}(mm)	D_{60}(mm)	乾密度(t/m³)	含水量(%)	比重	過程(%)	塑性指數(%)
5	47	48	0.000	0.000	0.006	0.010	1.91	22	2.72	59	33
6	44	50	0.000	0.001	0.005	0.012	1.87	33	2.72	69	40
12	35	53	0.000	0.000	0.003	0.012	1.87	27	2.72	69	40
23	9	2	0.069	2.634	12.248	16.325	1.88	18	2.66	-	NP
32	10	6	0.052	0.470	5.296	9.728	2.02	14	2.67	-	NP
38	13	6	0.025	0.269	1.626	6.592	2.06	15	2.67	-	NP
38	17	4	0.029	0.212	0.547	5.329	1.94	22	2.67	-	NP
21	8	2	0.101	4.161	12.429	16.686	2.21	13	2.67	-	NP
58	31	11	0.004	0.053	0.157	0.181	2.16	15	2.67	-	NP
62	27	11	0.004	0.062	0.172	0.210	2.04	17	2.67	-	NP
53	29	10	0.005	0.053	0.169	0.213	2.11	18	2.68	-	NP
71	20	7	0.008	0.107	0.227	0.285	2.02	19	2.66	-	NP
11	57	32	0.000	0.004	0.011	0.020	1.77	25	2.72	52	32
27	56	17	0.003	0.009	0.030	0.054	1.93	29	2.70	63	39
83	13	4	0.026	0.168	0.230	0.272	1.97	20	2.66	-	NP
81	16	3	0.040	0.155	0.179	0.192	1.53	41	2.66	-	NP

(b) Soil physical properties at TCU083.

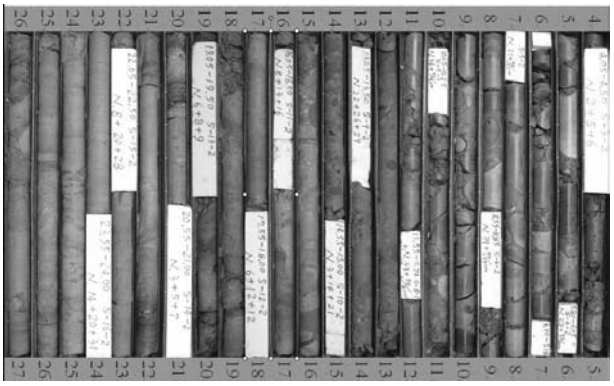


(c) Soil column, N value, S wave, and P wave profiles at TCU083 (from left to right).

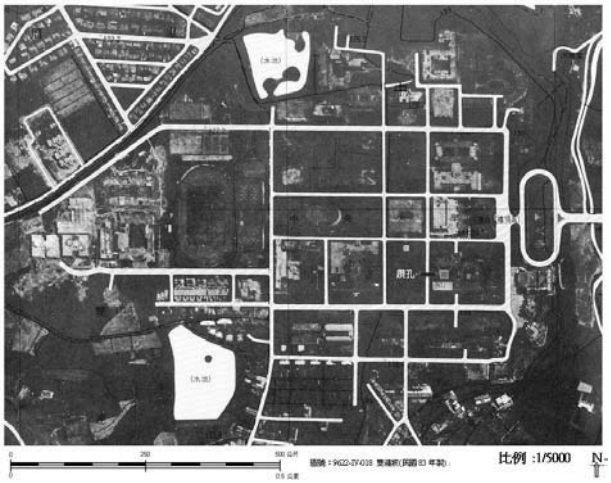


(d) Photos and plan view at TCU083.

Figure 3 An example of requested data at TCU083.



(a) Photo of the cores at TCU083.



(b) The aerial photograph of TCU083.

Figure 4 An example of supplements at TCU083.

3. CHARACTERISTICS OF NEAR-SURFACE STRATA

This section exhibited the studies about the characteristics of the near-surface strata. They might be significant reference materials for site effect and strong motion prediction researches. However, the data used by the following empirical Vs equations and Vs30 extrapolations were until 2009. The last drilled results of 2010 were only adopted on the site classification now.

3.1 Empirical Vs Equations

Many researchers had evaluated empirical equations of shear wave velocity because of the efficiency and economy. Fourteen representative results (Ohsaki and Iwasaki 1973; Hamilton 1976; Imai 1977; Ohta and Goto 1978; Seed and Idriss 1981; Sykora and Stoke 1983; Lee 1992; Pitilakis et al. 1999; Japan Road Association 2002; Chen et al. 2003; Holzer et al. 2005, Chapman et al. 2006; Hasabcebi and Ulusay 2007; Lee and Tsai 2008) were shown in Table 1. Those researches established relations among soil indexes. We are following the method proposed in the previous article (Kuo et al. 2011) to evaluate empirical Vs equations

in other regions of Taiwan. The codes of TSMIP stations were given according to the abbreviations of seven regions of Taiwan, which are TAP, TCU, CHY, KAU, TTN, HWA, and ILA. Kuo et al. (2011) evaluated the equations for TAP (Taipei Basin) and ILA. The present study evaluated the equations in other five regions using the data of EGDT, and the results were shown in Table 2 as well as the published results in TAP and ILA (Kuo et al. 2011). It should be noted that the empirical equations in Table 2 using the data until 2009, however, they might be some different after the data of 2010 is joined. However, the equations can only be applied to the strata shallower than or equal to 50 m as well as N smaller than 50 because of our data collection.

Because empirical equations in HWA and TCU passed the rule of thumb test, but failed in stepwise selection, we could not implement multivariable analysis for the data of the two regions due to multicollinearity. There are only a few data sets in HWA and TTN (fewer than 200 data sets), so that we did not consider the soil types or it might be unreasonable in statistics. The empirical equations were plotted together in Figure 5. The empirical Vs equations in Figure 5 were displayed as a function of N that we let the parameter of depth as 20 meters. The S wave velocity in TTN and HWA are obviously larger than in other regions. This phenomenon reflects the real geological background of Taiwan.

Table 1 Fourteen representative empirical equations of shear wave velocity quoted by this study.

Author	Regression equation	Soil type	Samples
Ohsaki and Iwasaki (1973)	$Vs=82N^{0.39}$	All	220
Hamilton (1976)	$Vs=128D^{0.28}$	Mud	29 sites
Imai (1977)	$Vs=91N^{0.337}$	All	943
	$Vs=80.6N^{0.331}$	Sand	151
	$Vs=102N^{0.292}$	Clay	183
Ohta and Goto (1978)	$Vs=62.14N^{0.219}D^{0.23}\times$ 1.000	Clay	300
	1.091	Fine sand	
	1.029	Medium sand	
	1.073	Coarse sand	
	1.151	Sand & gravel	
Seed and Idriss (1981)	$Vs=61N^{0.5}$	All	-
Sykora and Stokoe (1983)	$Vs=100.5N^{0.29}$	Sand	-
Lee (1992)	$Vs=71.9(D+1)^{0.39}$	SM	126
	$Vs=86.1N^{0.116}(D+1)^{0.244}$	CL	265
	$Vs=82.8N^{0.134}(D+1)^{0.233}$	ML	100
	$Vs=84.5N^{0.118}(D+1)^{0.246}$	CL/ML	365
Pitilakis et al. (1999)	$Vs=145(N_{60})^{0.178}$	Sand	15 sites
	$Vs=132(N_{60})^{0.271}$	Clay	
JRA (2002)	$Vs=100N^{1/3}$ $(1\leqq N\leqq 25)$	Clay	-
	$Vs=80N^{1/3}$ $(1\leqq N\leqq 50)$	Sand	
Chen et al. (2003)	$Vs=163.59+4.09D+2.2(N_1-N_{1,avg})$	All	45 sites
Holzer et al. (2005)	$Vs=75.2+3.99D$	Mud	135
Chapman et al.(2006)	$Vs=85.13N^{0.153}\sigma_v{}'^{0.147}$	Sand	223
	$Vs=92.25N^{0.266}\sigma_v{}'^{0.072}$	Clay	154
Hasancebi and Ulusay (2007)	$Vs=90N^{0.309}$	All	97
	$Vs=90.8N^{0.319}$	Sand	
	$Vs=97.9N^{0.269}$	Clay	
Lee and Tsai (2008)	$Vs=137.153N^{0.229}$	All	28 sites
	$Vs=98.07N^{0.305}$	Sand	15 sites
	$Vs=163.15N^{0.192}$	Silt and Clay	15 sites

Table 2 Empirical Vs equations in seven regions of Taiwan.

Region	Empirical Vs equation	Soil type	Samples
TAP	$Vs=93.11N^{0.242}D^{0.136}$	sand	221
	$Vs=114.55N^{0.168}D^{0.143}$	clay and silt	498
TCU	$Vs=138.46N^{0.2201}$	sand	250
	$Vs=185.59N^{0.1872}$	clay and silt	204
ILA	$Vs=169.04+4.46N+0.59D$	all	641
HWA	$Vs=219.96N^{0.1593}$	all	166
CHY	$Vs=158.981+1.641N+2.836D$	sand	738
	$Vs=148.34+2.523N+2.993D$	clay and silt	723
KAU	$Vs=163.049+3.84N+2.558D$	sand	382
	$Vs=165.967+2.614N+2.849D$	clay and silt	341
TTN	$Vs=233.35N^{0.171}D^{0.088}$	all	48

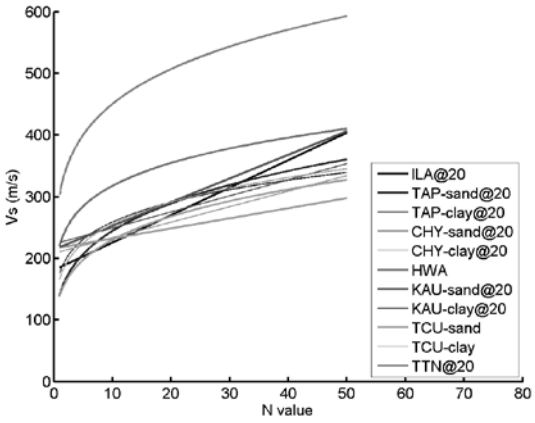


Figure 5 Empirical Vs equations in different regions of Taiwan. The marker "@20" indicates the curve is at the depth of 20 meters.

3.2 Extrapolations of Vs30

53 of the 439 drilled boreholes did not reach 30 m in the EGDT. It will be a problem when calculating Vs30 for not only the stations in Taiwan, but also those in other countries. The earlier article (Kuo et al. 2011) discussed this problem and then compared three frequently used techniques, which are least square of single station (LSS), statistical extrapolation (STS), and bottom constant velocity (BCV). They indicated BCV is the most accurate method for stations in TAP and ILA regions.

Based on the procedure of Kuo et al. (2011), we further compared the accuracy of the techniques using the boreholes (until 2009) attain to 30 m. 367 boreholes were used in the examination by using an error percentage (Err%):

$$Err\%=\frac{\sum|V_{rel}-V_{est}|/V_{rel}}{n}\times 100\% \qquad (1)$$

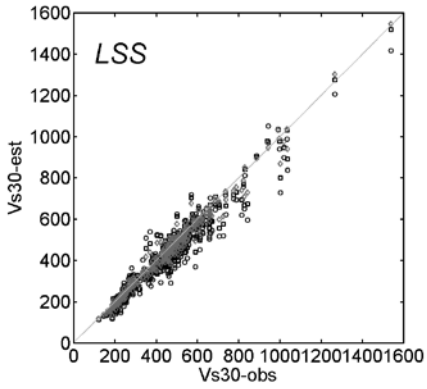
Where V_{rel} is the measured S wave velocity, V_{est} is estimated S wave velocity by extrapolations, and n is the number of data. The error percentages were showed in Table 3 and indicated the same result as Kuo et al. (2011), that is, obviously BCV is the most accurate and stable extrapolation in the regions.

In addition, Figure 6 illustrated the estimated Vs30 (y-axis) by the three extrapolations (Figure 6(a) ~ (c)) as well as the estimated results by Lee and Tsai (2008) (Figure

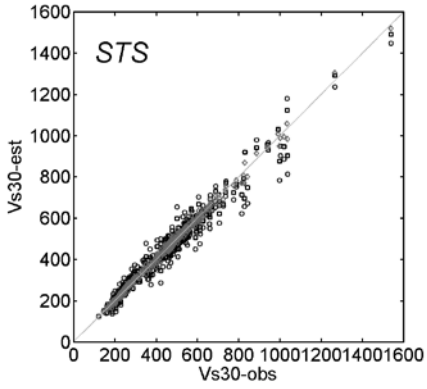
6(d)) versus the real Vs30 (x-axis) obtained by PS-logging for the 367 boreholes. The assumed depths of 15, 20, and 25 m were represented as open blue circles, open black squares, and open magenta diamonds, respectively. The discrepancies between the estimated and real Vs30 decrease as assumed depths increase in Figure 6(a) ~ (c). Otherwise, the divergences of BCV are the least. The phenomena indicated again the error is becoming smaller as depth increasing, and BCV can get the best Vs30. Figure 6(d) denoted the results of Lee and Tsai (2008) still have large disagreements even if the largest estimated Vs30 had been restricted by a value of about 800 m/s. It should be noted that Lee and Tsai (2008) also used the data of EGDT but only until 2005 as well as other 4885 engineering boreholes in their geo-statistical method.

Table 3 The Err% obtained from extrapolations at three assumed depths. The percentages after "±" are the standard deviations.

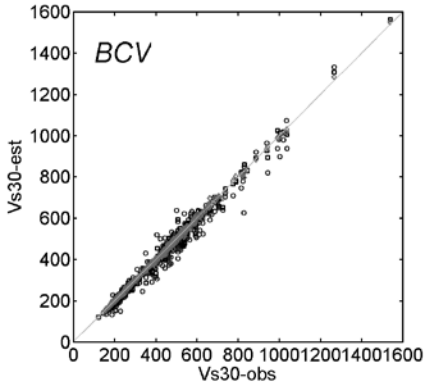
Assumed depth	Mean Err% of 367 boreholes		
	LSS	STS	BCV
15 m	11.26% ±8.03%	7.37% ±6.61%	6.66% ±5.69%
20 m	8.06% ±6.15%	4.68% ±4.05%	3.12% ±2.85%
25 m	5.69% ±4.41%	2.17% ±1.95%	1.17% ±1.27%



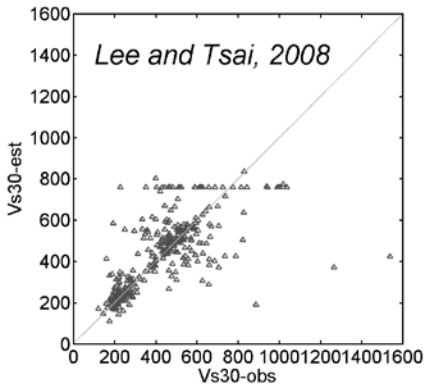
(a) Estimated Vs30 by LSS versus real Vs30.



(b) Estimated Vs30 by STS versus real Vs30.



(c) Estimated Vs30 by BCV versus real Vs30.



(d) Estimated Vs30 by Lee and Tsai (2008) versus real Vs30.

Figure 6 Estimated Vs30 by different methods (y-axis) versus real Vs30 obtained by PS-logging measurements (x-axis).

3.3 Site Classification of Drilled TSMIP Stations

Site classifications were achieved for the 439 drilled TSMIP stations according to the Vs30 criteria of NEHRP (Table4). Vs30 were estimated by BCV for these stations did not be drilled to 30 m. The results were illustrated in Figure 7. There are one of class A, 29 of class B, 200 of class C, 193 of class D, and 16 of class E. In Taiwan, most stations belong to class C and D (89.5%); the others are only 10.5%. Stations of class D and E mainly distributed on plains and basins with unconsolidated sediments; stations of class C are located on northwestern Taiwan and around the Central Mountain and the Coast Range; stations of class B are mostly located on the north of Taiwan and several on mountain areas; the unique class A in the database only appears in the Coast Range.

Table 4 Site class Definition of NEHRP in terms of Vs30 and brief geological descriptions.

NEHRP site class	Description	Range of *Vs*30 (m/s)
A	Hard rock	$Vs30 > 1500$
B	Firm to hard rock	$1500 \geq Vs30 > 760$
C	Dense soil and soft rock	$760 \geq Vs30 > 360$
D	Stiff soil	$360 \geq Vs30 \geq 180$
E	Soft soil	$180 > Vs30$

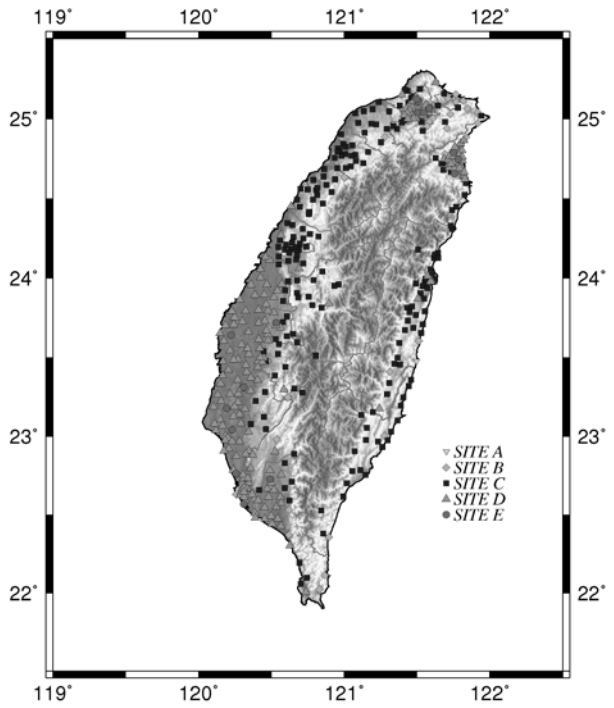


Figure 7 Distributions and site classifications of 439 drilled free-field TSMIP stations in Taiwan.

4. CONCLUSIONS

The goal of this article is to introduce the Engineering Geological Database for TSMIP in Taiwan, as well as the main results investigated recently by ourselves. The empirical Vs equations could offer important information about near-surface velocity profiles for calculation of seismic wave propagation, like SHAKE; otherwise, the Vs30 provided the significant parameter of site effect in earthquake engineering, and also for strong ground motion prediction.

Many organizations applied for the data of EGDT, such as the United States Geological Survey, the University of Southern, PEER, the State University of New York, the Tokyo Institute of Technology, the Karlsruhe University, the Carleton University, the University of Sheffield, the China Earthquake Administration, and local institutes in Taiwan. Dozens of researches which used the data has been published; include SCI articles, EI articles, proceedings of conferences, master and Ph.D. thesis, and technical reports. For example, the amount of published SCI journal articles is 11 (Huang et al. 2005, 2007, 2009; Wang et al. 2006; Sokolov et al 2007; Wen et al, 2008; Lee and Tsai 2008; Pavlenko and Wen 2008; Kuo et al. 2009, 2011; Lin et al. 2009). Those articles might make you more understand about the database and give you some ideas of using the data.

Acknowledgements:

It is gratefully acknowledged that the EGDT was constructed by many participants in the past decade. Additionally, the authors thank Dr. Cheng-Chao Lee for providing many helpful reference materials.

References:

Anderson, J.G., Lee, Y., Zeng, Y., and Day, S. (1996), "Control of Strong Motion by the Upper 30 Meters," *Bulletin of the Seismological Society of America*, **86**(6), 1749-1759.

Building Seismic Safety Council, BSSC (2001), "NEHRP Recommended Provisions for Seismic Regulations for New Buildings and Other Structures," Washington, DC.

Chapman, M.C., Martin, J.R., Olgun, C.G., and Beale, J.N. (2006), "Site Response Models for Charleston, South Carolina, and Vicinity Developed from Shallow Geotechnical Investigations," *Bulletin of the Seismological Society of America*, **96**(2), 467-489.

Chen, M.H., Wen, K.L., and Loh, C.H. (2003), "A Study of Shear Wave Velocities for Alluvium Deposits in Southwestern Taiwan," *Journal of Chinese Institute of Civil and Hydraulic Engineering*, **15**(4), 667-677.

Chiou, B., Darragh, R., Gregor, N., Silva, W. (2008), "NGA Project Strong Motion Database," *Earthquake Spectra*, **24**(1), 23-44.

Dobry, R., Borcherdt, R.D., Crouse, C.B., Idriss, I.M., Joyner, W.B., Martin, G.R., Power, M.S., Rinne, E.E., and Seed, R.B. (2000), "New Site Coefficients and Site Classification System Used in Recent Building Seismic Code Provisions," *Earthquake Spectra*, **16**, 41–67.

Hamilton, E. (1976), "Shear Wave Velocity versus Depth in Marine Sediments: A Review," *Geophysics*, **41**(5), 985-996.

Hasancebi, N. and Ulusay, R. (2007), "Empirical Correlations between Shear Wave Velocity and Penetration Resistance for Ground Shaking Assessments," *Bulletin of Engineering Geology and Environment*, **66**, 203-213.

Holzer, T.L., Bennett, M.J., Noce, T.E., Padovani, A.C., Tinsley, III J.C. (2005), "Shear-Wave Velocity of Surficial Geologic Sediments: Statistical Distributions and Depth Dependence," *Earthquake Spectra*, **21**(1), 161-177.

Huang, M.W., Wang, J.H., Hsieh, H.H., Wen, K.L., and Ma, K.F. (2005), "Frequency-Dependent Sites Amplifications Evaluated from Well-Logging Data in Central Taiwan," *Geophysical Research Letter*, **32**, L21320.

Huang, M.W., Wang, J.H., Hsieh, H.H., and Wen, K.L. (2009), "High Frequency Site Amplification Evaluated from Borehole Data in the Taipei Basin," *Journal of Seismology*, **13**(4), 601-611.

Huang, M.W., Wang, J.H., Ma, K.F., Wang, C.Y., Hung J.H., and Wen, K.L. (2007), "Frequency-Dependent Sites Amplifications with $f \geqq 0.01$ Hz Evaluated from Velocity and Density Models in Central Taiwan," *Bulletin of the Seismological Society of America*, **97**(2), 624-637.

Imai, T. (1977), "P- and S-wave Velocities of the Ground in Japan," *Proceedings of the 9th International Conference on Soil Mechanics and Foundation Engineering*, Tokyo, Japan, July 10-15, Vol. 2, pp. 257-260.

Japan Road Association (2002), "Specification for Highway Bridges, Part V: Seismic Design," Tokyo, Japan, 406 pp.

Koppes, M. N. and Montgomery, D.R. (2009), "The Relative Efficacy of Fluvial and Glacial Erosion over Modern to Orogenic Timescales" *Nature Geoscience*, **2**, 644-647.

Kuo, C.H., Cheng, D.S., Hsieh, H.H., Chang, T.M., Chiang, H.J., Lin, C.M., and Wen, K.L. (2009), "Comparison of Three Different Methods in Investigating Shallow Shear-Wave Velocity Structures in Ilan, Taiwan," *Soil Dynamics and Earthquake Engineering*, **29**(1), 133-143.

Kuo, C.H., Wen, K.L., Hsieh, H.H., Chang, T.M., Lin, C.M., and Chen, C.T. (2011), "Evaluating Empirical Regression Equations for Vs and Estimating Vs30 in Northeastern Taiwan," *Soil Dynamics and Earthquake Engineering*, **31**(3), 431-439.

Lee, C.T. and Tsai, B.R. (2008), "Mapping Vs30 in Taiwan," *Terrestrial, Atmospheric and Oceanic Sciences*, *19*(6), 671-682.

Lee, S.H.H. (1992), "Analysis of the multicollinearity of regression

equations of shear wave velocities," *Soils and Foundations*, **32**(1), 205-14.

Liew, P.M., Pirazzoli, P.A., Hsieh, M.L., Arnold, M.., Barusseau, J.P., Fontugne, M., and Giresse, P. (1993), "Holocene Tectonic Uplift Deduced from Elevated Shorelines, Eastern Coastal Range of Taiwan," *Tectonophysics*, **222**, 55-68.

Lin, C.M., Chang, T.M., Huang, Y.C., Chiang, H.J., Kuo, C.H., and Wen, K.L. (2009), "Shallow S-Wave Velocity Structures in the Western Coastal Plain of Taiwan," *Terrestrial, Atmospheric and Oceanic Sciences*, **20**(2), 299-308.

Ohsaki, Y. and Iwasaki, R. (1973), "On Dynamic Shear Moduli and Poisson's Ratio of Soil Deposits," *Soils and Foundations*, **13**(4), 61-73.

Ohta, Y. and Goto, N. (1978), "Empirical Shear Wave Velocity Equations in Terms of Characteristic Soil Indexes." *Earthquake Engineering and Structural Dynamics*, **6**, 167-87.

Pavlenko, O.V. and Wen, K.L. (2008), "Estimation of Nonlinear Soil Behavior During the 1999 Chi-Chi, Taiwan, Earthquake," *Pure and Applied Geophysics*, **165**(2), 373-407.

Pitilakis, K., Raptakis, D., Lontzetidis, K., Tika-vassilikou, T., and Jongmans, D. (1999), "Geotechnical and Geophysical Description of Euro-Seistests, Using Field and Laboratory Tests, and Moderate Strong Ground Motions," *Journal of Earthquake Engineering*, **3**(3), 381-409.

Power, M., Chiou, B., Abrahamson, N., Bozorgnia, Y., Shantz, T., and Roblee, C. (2008), "An Overview of the NGA Project," *Earthquake Spectra*, **24**(1), 3-21.

Seed, H.B. and Idriss, I.M. (1981), "Evaluation of Liquefaction Potential of Sand Deposits Based on Observations of Performance in Previous Earthquakes," *Proceedings of the Conference on In Situ Testing to Evaluate Liquefaction Susceptibility*, ASCE, pp. 81-544.

Sokolov, V.Y., Loh, C.H., and Jean, W.Y. (2007), "Application of Horizontal-to-Vertical (H/V) Fourier Spectral Ratio for Analysis of Site Effect on Rock (NEHRP-class B) Sites in Taiwan," *Soil Dynamics and Earthquake Engineering*, **27**(4), 314-323.

Sykora, D.E. and Stokoe, K.H.II. (1983), "Correlations of In Situ Measurements in Sands of Shear Wave Velocity, Soil Characteristics and Site Conditions," Report GR 83-33, Civil Engineering Department, University of Texas at Austin, 484 pp.

Wang, G.Q., Tang, G.Q., Boore, D.M. Burbach, V.N., Jackson, C.R., Zhou, X.Y., and Lin, Q.L. (2006), "Surface Waves in the Western Taiwan Coastal Plain from an Aftershock of the 1999 Chi-Chi, Taiwan, Earthquake," *Bulletin of the Seismological Society of America*, **96**(3), 821-845.

Wen, K.L., Lin C.M., Chiang, H.J., Kuo, C.H., Huang, Y.C., and Pu, H.C. (2008), "Effect of Surface Geology on Ground Motions: the Case of TAP056," *Terrestrial, Atmospheric and Oceanic Sciences*, **19**(5), 451-462.

8CUEE CONFERENCE PROCEEDINGS
8th International Conference on Urban Earthquake Engineering
March 7-8, 2011, Tokyo Institute of Technology, Tokyo, Japan

EFFECTS OF WATER LAYER ON SEISMOGRAM SYNTHESIS IN KANTO BASIN AREA BASED ON A HYBRID BOUNDARY ELEMENT METHOD: NUMERICAL IMPLEMENTATION

Zheng-Hua Qian[1)], Hiroaki Yamanaka[2)], and Sohichi Hirose[3)]

1) G-COE PD, Dept. of Environmental Science and Technology, Tokyo Institute of Technology, Japan
2) Professor, Dept. of Environmental Science and Technology, Tokyo Institute of Technology, Japan
3) Professor, Dept. of Mechanical and Environmental Informatics, Tokyo Institute of Technology, Japan
qian.z.aa@m.titech.ac.jp, yamanaka@depe.titech.ac.jp, shirose@cv.titech.ac.jp

Abstract: In our previous work (Qian et al, 2010), we presented the theory of a hybrid boundary element method which can be applied to study the effects of liquid layer on seismogram synthesis in multi-layered solid/liquid media. In this paper, we show the numerical implementation of the method and state a step-by-step procedure of applying the algorithm to a general multilayered fluid-solid media. First, two models containing irregular fluid-solid interfaces are used to test the validity of the method. Then, a preliminary application is conducted in the Kanto basin area by a realistic model for the Kanto basin including sea water. The difference appearing in the synthetic seismograms due to the presence of the water layer can be clearly observed. This kind of synthesis could help us understand the influence of water layer on the seismic ground motion at land, in which seismologists may be mostly interested.

1. INTRODUCTION

This work is the second part of a series study about water effects on seismogram synthesis in multilayered media with irregular interfaces. In the first part of the series study (Qian et al, 2010; hereafter referred to as article I), we have developed and presented the theoretical formulation of an extended synthesis method for simulating seismoacoustic scattering by an irregular fluid-solid interface within a multilayered medium. As the second part of the series study, the present article will be devoted to assessing the validity of the formulation obtained earlier and showing its applicability. For the sake of continuity of the presentation, we shall first briefly summarize the theory and fundamental formulas needed in the present article. We shall then test its validity by comparing the results calculated using our formulation with the existing results by the reflection/transmission matrix method (Okamoto and Takenaka, 1999), two fluid-solid models are used for this testing: one is an elastic half space containing a basin-like water layer, and the other one is an elastic half space containing a flat water layer with a basin. Finally, as a preliminary application of our formulation, we shall simulate the wave propagation in a realistic Kanto basin model including sea water layer to see how much is changed in the synthetic seismograms due to the appearance of the water layer.

2. SUMMARY OF THE ALGORITHM

2.1 Solution procedure

In this subsection, we shall briefly summarize the theory developed in article I and describe the procedures of its implementation. The problem to be considered is illustrated in Fig. 1. In this model, there are L homogeneous layers $\Omega^{(i)}$ (i=1, 2, …, L) over a half-space, among which the ith layer is bounded by two irregular interfaces $\Gamma_{(i-1)}$ and $\Gamma_{(i)}$ (Throughout the paper, the superscript with round brackets is used for layer index and the subscript with round brackets for interface index). The uppermost layer is water which is assumed to be linear, incompressible liquid without viscosity. An arbitrary seismic source is embedded in the sth layer. The properties of an arbitrary solid layer $\Omega^{(i)}$ are described by the elastic constants $\lambda^{(i)}$, $\mu^{(i)}$ and mass density $\rho^{(i)}$. As shown in article I, this problem has been theoretically solved by using a hybrid boundary element method. This method can be regarded as an extension of the approach (Ge and Chen, 2007 and 2008), combining the traditional boundary element method with the global reflection/transmission matrix propagators (Chen, 1990 and 1995), which was originally developed for efficient seismogram synthesis in multilayered solid media with irregular interfaces. The procedure of applying the introduced algorithm to calculate a seismic ground motion in a general irregular multilayered water-solid medium can be summarized as follows.

Step 1 By using the free surface condition calculate the global matrix propagators in the uppermost layer, i.e. the water layer, by the following equation

$$\begin{pmatrix}\mathbf{D}_{qq}^{(1)}\\ \mathbf{D}_{pq}^{(1)}\end{pmatrix}=\left(-\mathbf{G}_{(1)}^{(1)}\quad \mathbf{H}_{(2)}^{(1)}\right)^{-1}\mathbf{G}_{(2)}^{(1)}, \tag{1}$$

where **H** and **G** are the coefficient matrices obtained by integrating the fundamental solutions of the potential problem (Balas et al, 1989) over elements at both interfaces $\Gamma_{(i)}$ and $\Gamma_{(i+1)}$. The detailed definitions of the global matrix propagators **D** can refer to our previous work (Qian et al, 2010). Suppose each interface is discretized into *N* elements, the global matrix propagators obtained in Eq. (1) obviously have the dimension *N*×*N*. (Here, one important point is that the form of Eq. (1) is different from those used to obtain global matrix propagators in solid layers since the wave propagation problem in the water layer is taken as a potential problem and no shear waves exist.)

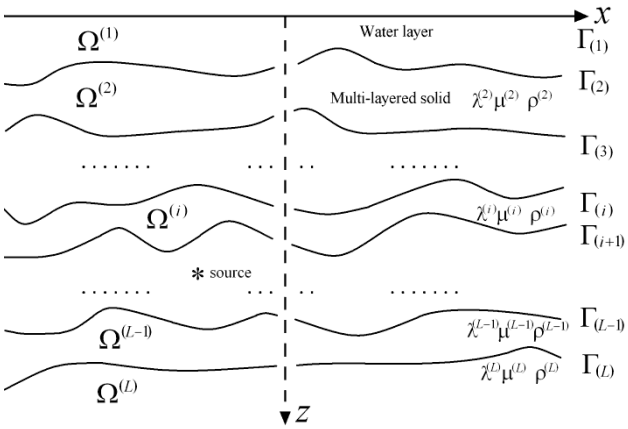


Fig. 1 A multi-layered water/solid model with irregular interfaces

Step 2 By using the continuity conditions at the liquid-solid interface (Medina and Dominguez, 1989), extend the global matrix propagators obtained in Step 1 into the same dimension as those defined in solid layers, i.e. 2*N*×2*N*,

$$\mathbf{D}_{tu}^{(1)}=\rho_{\mathrm{f}}\omega^2\begin{bmatrix}\mathbf{D}_{pq}^{(1)}\cdot\mathbf{N}_1^{\mathrm{e}}\cdot(\mathbf{N}_1^{\mathrm{e}})^{\mathrm{T}} & \mathbf{D}_{pq}^{(1)}\cdot\mathbf{N}_2^{\mathrm{e}}\cdot(\mathbf{N}_1^{\mathrm{e}})^{\mathrm{T}}\\ \mathbf{D}_{pq}^{(1)}\cdot\mathbf{N}_1^{\mathrm{e}}\cdot(\mathbf{N}_2^{\mathrm{e}})^{\mathrm{T}} & \mathbf{D}_{pq}^{(1)}\cdot\mathbf{N}_2^{\mathrm{e}}\cdot(\mathbf{N}_2^{\mathrm{e}})^{\mathrm{T}}\end{bmatrix}, \tag{2}$$

where ρ_{f} is the mass density in the water layer and ω is the angular frequency. The matrices $\mathbf{N}_1^{\mathrm{e}}$ and $\mathbf{N}_2^{\mathrm{e}}$ are defined as follows:

$$\mathbf{N}_1^{\mathrm{e}}=\begin{bmatrix}n_1^{\mathrm{e}1} & n_1^{\mathrm{e}2} & \cdots & n_1^{\mathrm{e}N}\\ n_1^{\mathrm{e}1} & n_1^{\mathrm{e}2} & \cdots & n_1^{\mathrm{e}N}\\ \vdots & \vdots & \ddots & \vdots\\ n_1^{\mathrm{e}1} & n_1^{\mathrm{e}2} & \cdots & n_1^{\mathrm{e}N}\end{bmatrix}, \tag{3a}$$

$$\mathbf{N}_2^{\mathrm{e}}=\begin{bmatrix}n_2^{\mathrm{e}1} & n_2^{\mathrm{e}2} & \cdots & n_2^{\mathrm{e}N}\\ n_2^{\mathrm{e}1} & n_2^{\mathrm{e}2} & \cdots & n_2^{\mathrm{e}N}\\ \vdots & \vdots & \ddots & \vdots\\ n_2^{\mathrm{e}1} & n_2^{\mathrm{e}2} & \cdots & n_2^{\mathrm{e}N}\end{bmatrix}, \tag{3b}$$

in which n_1^{e} and n_2^{e} are the components of the unit normal vector of the neighboring solid layer at element 'e'.

Step 3 Use the extended global matrix propagator obtained in Step 2 to calculate the global matrix propagators in the neighboring solid layer, i.e. $\Omega^{(2)}$, by

$$\begin{pmatrix}\mathbf{D}_{uu}^{(2)}\\ \mathbf{D}_{tu}^{(2)}\end{pmatrix}=-\left(\mathbf{H}_{(2)}^{(2)}-\mathbf{G}_{(2)}^{(2)}\mathbf{D}_{tu}^{(1)}\quad \mathbf{G}_{(3)}^{(2)}\right)^{-1}\mathbf{H}_{(3)}^{(2)}. \tag{4}$$

Then use the global matrix propagators obtained in Eq. (4) to calculate the global matrix propagators in the other solid layers below $\Omega^{(2)}$ until the layer neighboring the seismic source layer by

$$\begin{pmatrix}\mathbf{D}_{uu}^{(i)}\\ \mathbf{D}_{tu}^{(i)}\end{pmatrix}=-\left(\mathbf{H}_{(i)}^{(i)}-\mathbf{G}_{(i)}^{(i)}\mathbf{D}_{tu}^{(i-1)}\quad \mathbf{G}_{(i+1)}^{(i)}\right)^{-1}\mathbf{H}_{(i+1)}^{(i)}, \tag{5}$$

where i = 3, 4, …, s−1 with s denoting the seismic source layer.

Step 4 In case of a plane wave incidence problem or a seismic source located at the bottom layer, skip this step and jump to Step 5. Otherwise, calculate the global matrix propagators in the bottom layer by using the radiation conditions at infinity, we thus have

$$\begin{cases}\mathbf{D}_{uu}^{(L)}=0\\ \mathbf{D}_{tu}^{(L)}=\left(\mathbf{G}_{(L)}^{(L)}\right)^{-1}\mathbf{H}_{(L)}^{(L)}.\end{cases} \tag{6}$$

Use the global matrix propagators obtained in Eq. (6) to calculate the global matrix propagators in the solid layers which are above the bottom layer but below the seismic source layer by

$$\begin{pmatrix}\mathbf{D}_{uu}^{(i)}\\ \mathbf{D}_{tu}^{(i)}\end{pmatrix}=-\left(\mathbf{H}_{(i+1)}^{(i)}+\mathbf{G}_{(i+1)}^{(i)}\mathbf{D}_{tu}^{(i+1)}\quad -\mathbf{G}_{(i)}^{(i)}\right)^{-1}\mathbf{H}_{(i)}^{(i)}, \tag{7}$$

where $i = L-1, L-2, \ldots, s+1$.

Step 5 Substitute all the global matrix propagators obtained in the above steps into the simultaneous matrix equation in the seismic source layer and solve the problem by

$$\left(\mathbf{H}_{(s)}^{(s)}-\mathbf{G}_{(s)}^{(s)}\mathbf{D}_{tu}^{(s-1)}\right)\mathbf{u}_{(s)}+\left(\mathbf{H}_{(s+1)}^{(s)}+\mathbf{G}_{(s+1)}^{(s)}\mathbf{D}_{tu}^{(s+1)}\right)\mathbf{u}_{(s+1)}=\mathbf{F}, \tag{8}$$

where $\mathbf{u}_{(s)}$ and $\mathbf{u}_{(s+1)}$ are the displacement solutions at the upper and lower interfaces of the source layer, respectively.

Step 6 Obtain the displacement solutions at the fluid-solid interface by the global matrix propagators defined in Step 3 by the recursive relation

$$\mathbf{u}_{(2)}=\mathbf{D}_{uu}^{(2)}\mathbf{D}_{uu}^{(3)}\cdots\mathbf{D}_{uu}^{(s-1)}\mathbf{u}_{(s)}. \tag{9}$$

Step 7 Execute the Fast Fourier Transform (FFT) on the displacement solutions obtained in Eq. (9) to get the seismic

ground motion in time domain finally.

2.2 Technical note on fluid-solid continuity conditions

In this subsection, we shall present one technical note on the application of the continuity conditions at the fluid-solid interface. In general, the unit normal vector at the fluid-solid interface can be defined in two ways: one is defined as the outward unit normal vector of the solid layer and the other is defined as the outward unit normal vector of the fluid layer, as shown in Fig. 2.

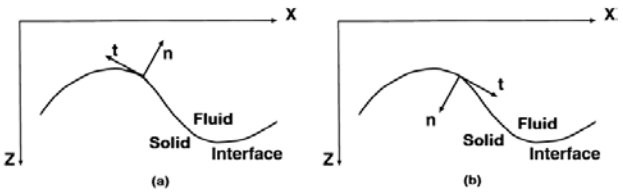


Fig. 2 Geometry of a fluid-solid interface. **n** and **t** are the unit normal and tangential vectors of the interface.

The extension equation of the global matrix propagators in Step 2 will be changed depending on which way is used to define the unit normal and tangential vectors at the fluid-solid interface. Equation (2) stated in Step 2 corresponds to the case shown in Fig. 2(a). In case of the selection of Fig. 2(b), the extension equation will be changed into

$$\mathbf{D}_{tu}^{(1)} = -\rho_{\mathrm{f}}\omega^2 \begin{bmatrix} \mathbf{D}_{pq}^{(1)} \cdot \mathbf{N}_1^{\mathrm{e}} \cdot (\mathbf{N}_1^{\mathrm{e}})^{\mathrm{T}} & \mathbf{D}_{pq}^{(1)} \cdot \mathbf{N}_2^{\mathrm{e}} \cdot (\mathbf{N}_1^{\mathrm{e}})^{\mathrm{T}} \\ \mathbf{D}_{pq}^{(1)} \cdot \mathbf{N}_1^{\mathrm{e}} \cdot (\mathbf{N}_2^{\mathrm{e}})^{\mathrm{T}} & \mathbf{D}_{pq}^{(1)} \cdot \mathbf{N}_2^{\mathrm{e}} \cdot (\mathbf{N}_2^{\mathrm{e}})^{\mathrm{T}} \end{bmatrix}, \quad (10)$$

where all the elements of the matrices $\mathbf{N}_1^{\mathrm{e}}$ and $\mathbf{N}_2^{\mathrm{e}}$ need to be changed consequently. This technical note looks no big deal, but it plays an important role in the numerical implementation.

3. NUMERICAL IMPLEMENTATION

3.1 Validity Tests

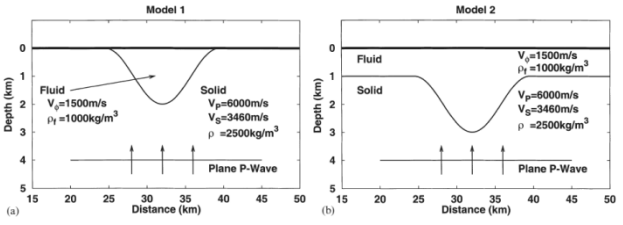


Fig. 3 The two models used to test the introduced algorithm

Before applying the introduced algorithm to practical problems, we should test its validity by comparing our numerical results with the existing solutions. However, we do not have exact (analytic) solutions for problems of irregularly layered structures, so it is important to compare the results of completely different numerical methods to ensure validity. For such purpose, we calculate the case of a plane *P* wave vertically incident onto irregularly layered fluid-solid structures in the two models, as shown in Fig. 3. The detailed values of the structural parameters can refer to the work (Okamoto and Takenaka, 1999). In their work, the existing results for the two models calculated by the reflection/transmission matrix method are available to make the necessary comparison.

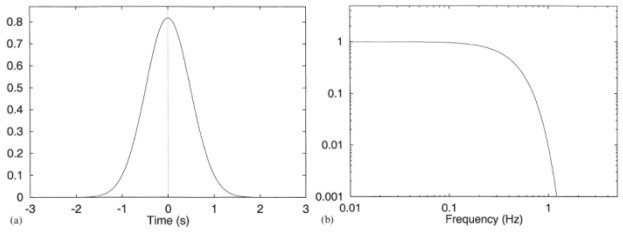


Fig. 4 The time function and its spectral amplitude used in our test calculations (Okamoto and Takenaka, 1999)

The time function of the input plane wave is

$$f(t) = \begin{cases} \sqrt{\alpha/\pi}\exp(-\alpha t^2), -T_s/2 \le t \le T_s/2 \\ 0, \qquad\qquad t \ge T_s/2\,,\ t \le -T_s/2 \end{cases}, \quad (11)$$

where the pulse duration T_S is set to 4.2 s and α is set to 2.1. Its shape and spectrum are shown in Fig. 4.

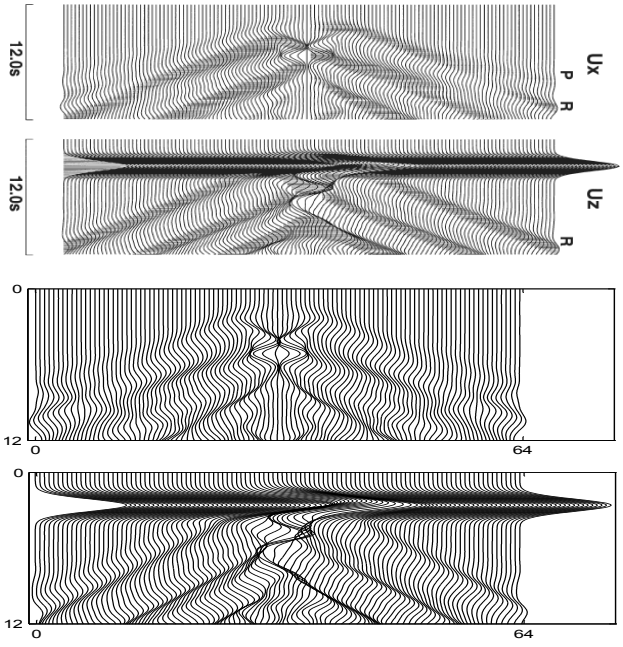


Fig. 5 Time responses along the fluid-solid interface of Model 1: the one on top calculated by the reflection/ transmission matrix method, and the one at bottom calculated by the present method.

Model 1. Figure 5 shows the displacements of both horizontal and vertical components along the fluid-solid interface of Model 1. The one on top is calculated by the reflection/transmission matrix method in the work (Okamoto and Takanaka, 1999). And the one at bottom is calculated by the present hybrid boundary element method. Inside the

irregular part of the model, i.e., the basin structure, the large-amplitude multiple reflections in the water basin are well observed in the waveforms calculated by both the present method and the reflection/transmission matrix method. Both the scattered *P* waves (P) and a *Rayleigh* wave (R), which are indicated in the top plot, can also be well and clearly observed in our calculated seismograms.

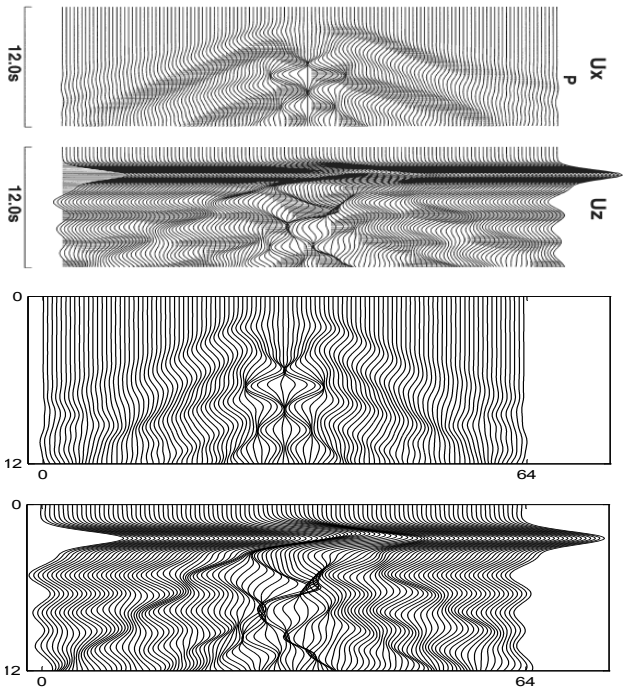


Fig. 6 The same as Fig. 5, but for Model 2.

Model 2. Figure 6 shows the displacements of both horizontal and vertical components at the fluid-solid interface of Model 2. In this case, the 'observation points' are all located at the water layer bottom. The one on top is calculated by the reflection/transmission matrix method in the work (Okamoto and Takenaka, 1999). And the one at bottom is calculated by the present hybrid boundary element method. Again, the synthetic seismograms calculated by both methods agree with each other very well. The periodic multiple reflections at the flat portion of the water layer are clearly observed and interfered by the scattered waves from the inside of the irregular part of the model, which are modeled very well by both methods.

The above two testing calculations show the validity of the present method and the correctness of our computational program, respectively. Next, we shall start a preliminary application to a realistic model in Kanto basin area.

3.2 Preliminary Application to a Realistic Model

In this subsection, we consider a relatively complex model, as shown in Figure 7. The model consists of a water layer on the top and three solid layers bonded by irregular interfaces. Table 1 shows the detailed parameters of each layer in the model. A vertically incident *SV* wave is taken into account for this synthesis. The time function of the incident plane wave is a Ricker wavelet defined as (Ricker, 1977)

$$u(t) = (2\pi^2 f_c^2 t^2 - 1)\exp(-\pi^2 f_c^2 t^2), \qquad (12)$$

where f_c is the characteristic frequency of the wavelet and t is the time. Observation points are placed along the fluid-solid interface.

Table 1 Parameters of each layer in the model

Parameter / Layer	Vp (km/s)	Vs (km/s)	Mass density (g/cm^3)
Water layer	1.5	0	1.0
Solid layer 1	1.84	0.50	1.8
Solid layer 2	2.40	1.00	2.0
Solid layer 3	3.00	1.50	2.3

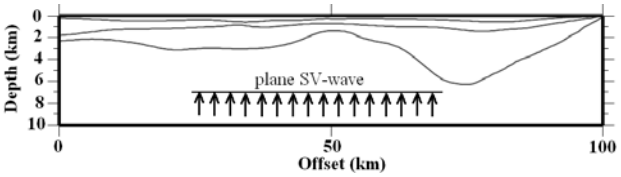


Fig. 7 The 2-D underground profile from Tokyo (139.765827/35.681421) to Simoda (138.89719/34.64911)

Figure 8 presents the horizontal displacements along the fluid-solid interface due to a vertically incident *SV* wave in the multilayered structure shown in Fig. 7. The one on the top of Fig. 8 is for the case when the first layer in Fig. 7 is empty, while the one at the bottom of Fig. 8 is for the case when the first layer in Fig. 7 is filled with water. From the comparison between the two seismograms, we can see that there are only minor differences for the cases with and without the water layer. This is understandable since our incident wave is a vertically shear wave which does not propagate in the water layer. A further comparison between the two cases is conducted for the seismogram at one point close to the leftmost side, which is shown in Fig. 9. It can be readily seen that the major waveform remains very similar and only its amplitude is reduced a little bit in the case of the appearance of the water layer.

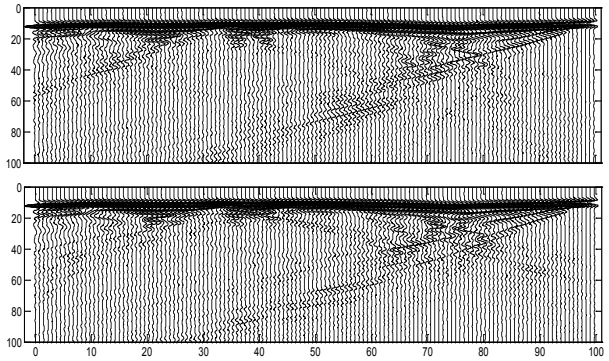


Fig. 8 Horizontal displacement along the fluid-solid interface due to a vertically incident *SV* wave: the case without water layer and the one with water layer.

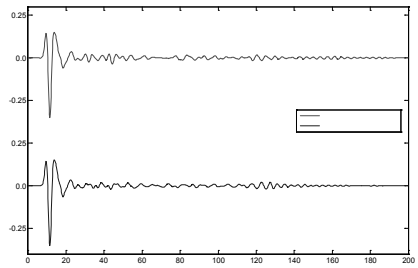


Fig. 9 Horizontal displacement at the point 10 km away from the leftmost side

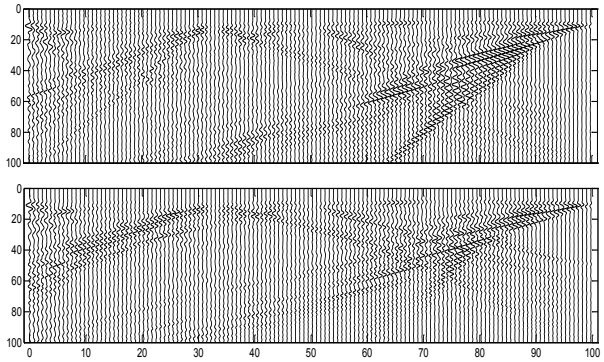


Fig. 10 As Fig. 8, but for vertical displacement

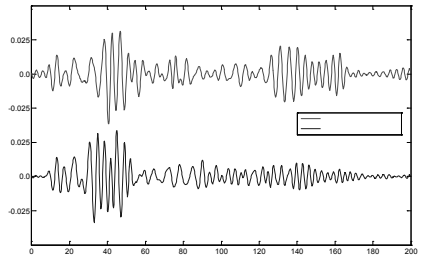


Fig. 11 As Fig. 9, but for vertical displacement

Figure 10 presents the vertical displacements along the fluid-solid interface in the multilayered structure. Different from the case of the horizontal displacement, the comparison between the two seismograms in Fig. 10 shows that large change occurs in the vertical displacement component due to the appearance of the water layer and the main change appears in the later arrival waves. A detailed illustration on the seismograms at the same point as that shown in Fig. 9 is presented in Fig. 11, which confirms the observation in Fig. 10. This is due to the fact that water waves are more easily excited by the vertical component in the case of a vertically incident *SV* wave, which may be contrary to the case of a *P* wave incidence.

Since the structure shown in Fig. 7 is very complex, it is still very difficult to interpret the synthetic seismograms completely. Here, we just show a preliminary attempt to look into the change appearing in the synthetic seismograms due to the presence of the water layer.

4. CONCLUSIONS

In this paper, we show the numerical implementation of the hybrid boundary element method which is an extension of the approach originally developed for seismogram synthesis in multilayered solid media. The extended method can be applied to study the effects of water layer on seismic ground motion in multilayered media. A step-by-step procedure of applying the algorithm to a general multilayered fluid-solid media is stated in detail. Then two models containing an irregular fluid-solid interface are used to test the validity of the formulation and the computation program, resulting in a good agreement with the results calculated by the reflection/transmission matrix method. Finally, a preliminary application is conducted by a realistic model in Kanto basin area including the sea water at Tokyo bay. The difference appearing in the synthetic seismograms due to the presence of the water layer can be clearly observed. This kind of synthesis could help us understand the influence of water layer on the seismic ground motion at land, in which seismologists may be mostly interested.

Acknowledgements:

The authors are very grateful to the support of the Global COE Program entitled "International Urban Earthquake Engineering Center for Mitigating Seismic Mega Risk", Tokyo Institute of Technology.

References:

Qian, Z.-H., Yamanaka, H. and Hirose, S. (2010), "Effects of water depth variation on seismogram synthesis in Oceanic structures based on a hybrid boundary element method," Proceedings of the Joint Conference of 7th CUEE & 5th ICEE, 309-316.

Okamoto, T. and Takenaka, H. (1999), "A reflection/transmission matrix formulation for seismoacoustic scattering by an irregular fluid-solid interface," *Geophysical Journal International*, 139, 531-546.

Ge Z.X. and Chen X.F. (2007), "Wave propagation in irregularly layered elastic models: a boundary element approach with a global reflection/transmission matrix propagators," *Bulletin of the Seismological Society of America*, 97, 1025-1031.

Ge Z.X. and Chen X.F. (2008), "An efficient approach for simulating wave propagation with the boundary element method in multilayered media with irregular interfaces," *Bulletin of the Seismological Society of America*, 98, 3007-3016.

Chen, X.F. (1990), "Seismogram synthesis for multi-layered media with irregular interfaces by global generalized reflection/ transmission matrices method-I. Theory of 2D SH case," *Bulletin of the Seismological Society of America*, 80, 1696-1724.

Chen, X.F. (1995), "Seismogram synthesis for multi-layered media with irregular interfaces by global generalized reflection/ transmission matrices method-II. Applications for 2D SH case," *Bulletin of the Seismological Society of America*, 85, 1094-1106.

Balas, J., Sladek, J. and Sladek, V. (1989), "Stress Analysis by Boundary Element Methods," Elsevier., New York.

Medina, F. and Dominguez, J. (1989), "Boundary elements for the analysis of the seismic response of dams including dam-water-foundation interaction effects. I," *Engineering Analysis with Boundary Elements*, 6, 153-163.

Ricker, N.H. (1977), "Transient waves in visco-elastic media," Elsevier, Amsterdam.

8CUEE CONFERENCE PROCEEDINGS
8th International Conference on Urban Earthquake Engineering
March 7-8, 2011, Tokyo Institute of Technology, Tokyo, Japan

A PRELIMINARY STUDY ON VARIABILITY OF EARTHQUAKE GROUND MOTIONS DUE TO RANDOM INHOMOGENEITY IN PROPAGATION PATH

Yoshiyuki Sato [1] and Saburoh Midorikawa [2]

1) Chief Researcher, Research and Development Institute, Takenaka Corporation, Japan
2) Professor, Department of Built Environment, Tokyo Institute of Technology, Japan
satou.yoshiyukia@takenaka.co.jp, smidorik@enveng.titech.ac.jp

Abstract: In this study inhomogeneity in seismic propagation paths is focused on as a cause of variability of observed seismic ground motion and preliminary evaluation by numerical simulations has been done. First strength and correlation length of inhomogeneity of seismic velocity in propagation path were inferred based on KiK-net observation records in order to set up realistic models for numerical simulations for inland earthquakes. It was revealed that the estimated inhomogeneity was greater than values in previous studies. It may reflect the strong inhomogeneity in the shallow part of the upper crust. Then numerical simulations were performed in order to study the influence of the strong inhomogeneity on seismic wave. 3D random inhomogeneous models were set up and the finite difference method was applied to obtain velocity time histories in the random media. As a result relatively large fluctuation in peak ground velocity has been observed. The result implies the importance of inhomogeneity in propagation path as a cause of seismic ground motion.

1. INTRODUCTION

Empirical attenuation relations are often utilized for practical prediction of ground motion, but large fluctuation has been observed between the observed values and the attenuation relation. The fluctuation measured as common logarithmic standard deviation of attenuation relation is about 0.2～0.3(Midorikawa and Ohtake 2003). As the value of fluctuation of ground motions has great influence on probabilistic seismic hazard analysis which provides basic data for disaster prevention or seismic risk evaluation, more refined evaluation of the fluctuation is an important problem. Observed seismic ground motion consists of three factors; the source, path and site effect. The contribution of each factor to the total fluctuation has to be evaluated for modeling of the fluctuation more physically. In this study the path effect on variability of seismic motion is focused on.

Though the seismic path is modeled as homogeneous medium in general, PS-logging data in deep boreholes have suggested that random fluctuation of seismic velocity exists in one geological layer (Shiomi et al. 1997). Also coda wave arriving after direct P or S wave can be interpreted as scattered wave generated by inhomogeneity in the propagation path and the calculated envelope of coda wave based on scattering theory can satisfactory explain observed records (Sato and Yamashita 2001).

Inhomogeneity in the path can also affect the variability of seismic ground motion. The effect has been evaluated based on numerical simulations because analytical solution like envelopes has not been obtained yet. For example Shapiro and Kneib(1993) performed the finite difference simulations assuming that the path medium velocity has random fluctuation. As a result they have shown that the amplitude of calculated waves fluctuates and the fluctuation becomes greater with increasing distance. Hoshiba(2000) also simulated plane waves in medium having random velocity distribution and has shown that the fluctuation has peak value at certain distance after which the fluctuation decrease in turn unlike the result of Shapiro and Kneib(1993). Although it is recognized that numerical simulations can evaluate the characteristics of waves in random medium as the above examples, value of fluctuation and dependency on distance are needed to be studied more quantitatively by accumulating simulation cases.

In order to perform realistic simulations one of the most important problems is setting up of parameters of inhomogeneity. Generally random inhomogeneity is expressed by two parameters, the strength (ε) and correlation length (a) of velocity fluctuation. In the past simulation analyses these parameters are thought to be assumed referring to values inferred from observation records. The inferred parameters in past studies seem to range in relatively wide value. For example Wu and Aki (1988) arranged the ε and a values estimated by past studies in various regions in the world. If limited to values in the lithosphere, ε and a respectively changes in the range from one to two orders. Sato et al.(2008) has shown that the fluctuation of calculated waves varies with the change of assumed ε and a by means of 3D finite difference simulations.

As the change of ε or a may result from the difference of regions or scale of regions, it is important to use

inhomogeneous parameters inferred in accordance with the objective of simulations. In this study aiming at simulating seismic waves in relatively short distance by inland shallow earthquakes, ε and a in propagation path are inferred based on seismic observation records. Then numerical simulations are performed assuming the inferred parameters in order to study preliminary the influence of inhomoogeneity on seismic ground motions.

2. ANALYSIS METHOD TO INFRER INHOMGENEOUS PARAMETERS

2.1 Earthquake Observation Data

KiK-net records were used in this study. KiK-net is a seismograph network consisting of about 700 observation sites located nationwide in Japan. At each observation site two seismograph are installed; one at the surface and the other at the bottom of borehole. In order to extract information of inhomogenity in the propagation path observation sites were selected under the condition that the underground seismometers reaches the depth of base rock. The base rock here means so-called "earthquake bedrock" which has S wave velocity more than about 3 km/s. 24 sites were found to meet the above condition and 3 sites of them have been selected for analysis considering the quantity and quality of the observed records. The selected sites are SMNH01(Hakuta, Shimane Prefecture), GIFH09(Hashima, Gifu Prefecture) and MYGH01(Sendai, Miyagi Prefecture). The S wave velocity at the depth of a borehole seismometer of each site is 2.80km/s, 3.04km/s and 3.26km/s respectively.

The analyzed records were selected from records satisfying the conditions; the hypocenteral distance is equal to or less than 80km and the depth is equal to or less than 50km. Also condition that the magnitudes of earthquakes, Mj, are less than or equal to 5 is added so that the shape of wave can be simply pulse-like, which is one of the assumptions of analysis method mentioned later. The specifications of analyzed earthquakes and the distribution of epicenters are shown in Table 1 and Figure 1. The number of used earthquakes at each site is 12, 6 and 4 respectively. The events used at SMNH01 are aftershocks of the Western Tottori Prefecture earthquake in 2000 (M_j7.3), so more short-distance records have been obtained than other two sites.

The records of underground seismometers include down going waves reflected from upper sedimentary layers. The effects have to been removed before analysis. To perform this operation the structure of sedimentary layers is

Table 1 The Analyzed Earthquakes in This Study

SMNH01

No.	date	time	Latitude (°)	Longitude (°)	Depth (km)	Mj	No.	date	time	Latitude (°)	Longitude (°)	Depth (km)	Mj
1	2000/10/06	18:54	35.270	133.352	12	3.7	7	2000/11/10	19:09	35.307	133.323	10	3.3
2	2000/10/06	19:57	35.270	133.345	13	4.0	8	2001/04/19	8:51	35.302	133.298	9	3.2
3	2000/10/06	23:13	35.292	133.290	7	4.1	9	2001/08/11	17:29	35.278	133.328	8	3.6
4	2000/10/07	18:32	35.310	133.323	8	3.9	10	2002/03/06	7:12	35.280	133.333	8	4.5
5	2000/10/17	22:10	35.290	133.300	7	3.7	11	2003/04/18	20:01	35.290	133.332	11	3.5
6	2000/10/18	0:00	35.312	133.322	9	3.4	12	2003/12/13	22:07	35.223	133.307	11	3.8

GIFH09

No.	date	time	Latitude (°)	Longitude (°)	Depth (km)	Mj
1	1999.11.29	21:34	35.093	136.997	51	4.7
2	2000.03.03	9:23	35.171	136.717	16	3.6
3	2001.09.22	18:11	35.035	136.927	41	4.2
4	2003.09.11	0:30	35.441	136.295	38	3.8
5	2005.01.09	18:59	35.315	136.847	13	4.7
6	2005.12.28	14:52	35.182	136.710	13	3.8

MYGH01

No.	date	time	Latitude (°)	Longitude (°)	Depth (km)	Mj
1	2001/01/27	16:54	38.331	140.605	13	3.4
2	2001/02/04	20:51	38.325	140.612	11	3.2
3	2007/04/05	20:39	38.202	141.148	12	4.5
4	2007/04/12	22:50	38.198	141.147	12	4.5

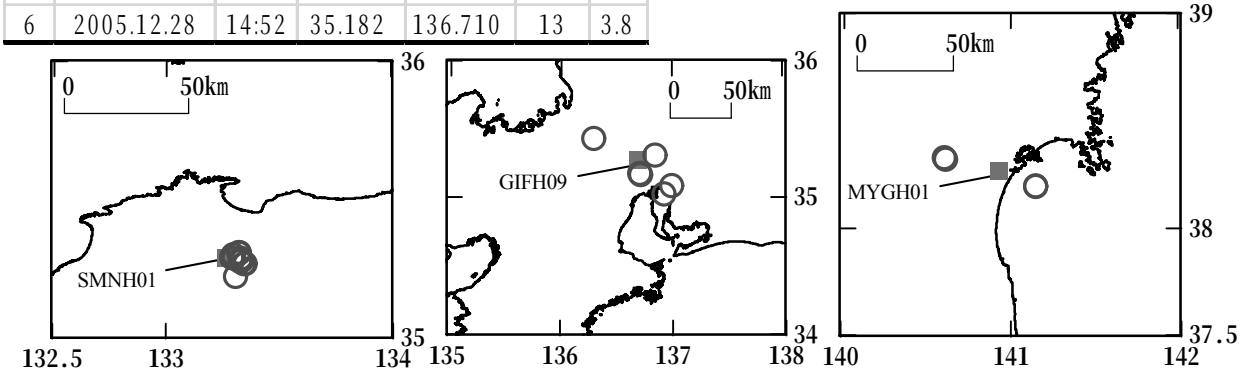


Figure 1 Distribution of Earthquakes Analyzed in This Study

needed. Although the P and S wave velocity (*Vp, Vs*) and thickness of layers beneath KiK-net sites have been made public as PS-logging data, dumping characteristics of the layers (*Q* values) are not included in these models. Also PS-logging data might have some errors from real *Vp, Vs* values. In order to infer *Q* values and improve *Vp, Vs* values we perform inversion analyses of transmission functions calculated from the vertical array records.

As mentioned above the vertical array of KiK-net consists of only two seismometers, so usual method in which one component, for example the transverse component of S wave portion, is inverted may be insufficient to resolve material properties of multiple layers. We used method of Sato et al. (2003) to infer reliable velocity and *Q* values. This method inverts three kind of records simultaneously; transmission function of transverse component of S wave, transmission function of vertical component of P wave and H/V spectral ratio. H/V spectral ratio is defined here as Fourier spectral ratio of radial component to vertical component of P wave of surface records.

The inferred parameters are *Vp, Vs, Qp, Qs* and incident angle at the base rock. The thickness of each layer is same as that of PS-logging data. *Q* value is assumed to depend on both frequency and Vs and is modeled based on Kobayashi et al.(1999) as following.

$$1/Qs = 1/(\alpha \cdot Vs \cdot f^{\beta}) + 1/(\beta \cdot Vs) \qquad (1)$$

In eq. (1) f is frequency (Hz) and α and β are unknown parameters to be inferred by inversion. *Qp* is assigned as *Qs*/2 based on Yoshida et al.(2002).

Based on the inferred underground model the effect of sedimentary layers is removed from the borehole record. One dimensional SH wave theory is used to evaluate transmission function of sedimentary layers and the Fourier spectrum of transverse component is divided by the transmission function to get the time history records at base rock when upper sedimentary layers are removed.

2.2 Estimation of Inhomogenious Parameters

The pulse width of seismic wave radiated from the source is broadened with increasing distance due to scattering in the propagation path. Saito et al.(2002) theoretically obtained mean squared(MS) envelopes of ground motion, *I(r,t)*, in three dimensional inhomogeneous media having the Gaussian type autocorrelation function(ACF) as

$$I(r,t) = 1/(4\pi R^2 t_M) \cdot \pi^2/2 \cdot \sum_{n=1}^{\infty} (-1)^{n+1} n^2 \exp[(-\pi^2/4) n^2 (t-R/V_0)/t_M] \qquad (2)$$

$$t_M = \pi^{1/2} \varepsilon^2 R^2 /(2aV_0) \qquad (3)$$

where R is hypocenral distance, t is lapse time and V_0 is average *S wave* velocity in the random medium.

The inhomogeneous parameters, a and ε can be inferred as ε^2/a by comparing the MS envelopes calculated by using eqs. (2) and (3) with those of observed records. Envelopes of observed records are calculated based on the method of Dziwonski et al.(1969). Basically fitting of calculated and observed MS envelopes is performed in 1 sec width time window started from the onset of S wave. Appropriate ε^2/a value is searched by nonlinear least square method in which the sum of squared residuals between calculated and observed envelopes is minimized.

3. RESULTS OF INFERERENCE OF INHOMOGENEITY

3.1 Inferred Ground Motion at Bed Rock

The observation records used for inferring underground structures are selected so that the variation of geometrical incident angles, which are calculated from epicentral distance and depth of the hypocenter, is within 20 degree. As a result, from four to eight records has been selected at each observation site. The logarithm averages of transmission functions and H/V spectral ratios from each earthquake record are set as targets of inversions. As an example Figure 2 shows the fitting of calculated and observation records. The estimated underground model produces better fitting than the PS logging model. At other two sites good fitting has also been obtained. The estimated underground models are shown in Table 2.

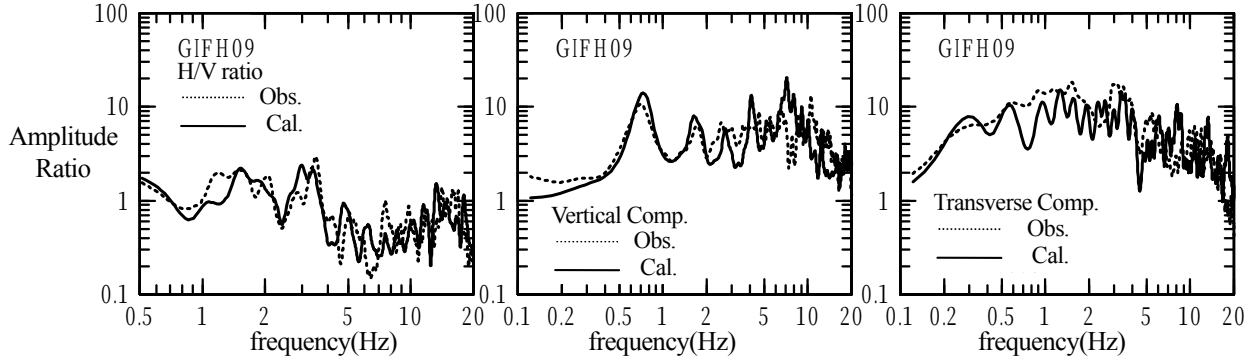


Figure 2 Fitting of observed spectral ratios and calculated ones based on the inferred underground model inferred by inversion analysis (GIFH09)

Table 2 Inferred Underground Structures by Inversion Analysis

SMNH01

No.	Tick-ness (m)	density (g/cm^3)	Vs(m/s) PS	Vs(m/s) Inver-sion	Vs/Qs
1	4	1.72	290	231	1/0.011f+1/0.091
2	7	1.72	290	231	
3	11	1.88	550	514	1/0.0036f+1/0.51
4	20	2.2	1200	1416	
5	12	2.36	1900	2054	
6	-	2.52	2800	2800	1/0.032f+1/0.34

GIFH09

No.	Tick-ness (m)	density (g/cm^3)	Vs(m/s) PS	Vs(m/s) Inver-sion	Vs/Qs
1	12	1.65	140	136	1/0.073f+1/0.14
2	138	1.76	340	292	
3	100	1.85	470	448	
4	90	1.94	670	656	
5	380	2.12	1030	1175	1/0.027f+1/0.52
6	-	2.57	3040	3040	1/0.053f+1/0.37

MYGH01

No.	Tick-ness (m)	density (g/cm^3)	Vs(m/s) PS	Vs(m/s) Inver-sion	Vs/Qs
1	50	1.73	210	239	1/0.058f+1/0.33
2	60	1.89	560	527	
3	140	2.2	1750	1410	1/0.054f+1/0.23
4	450	2.52	2450	2798	1/0.015f+1/0.43
5	-	2.61	3260	3260	1/0.011f+1/0.084

Some examples of the estimated bed rock records based on the inferred underground model are shown in Figure 3. The waves are S wave transverse components of velocity records and band pass filter between 1 to 5 Hz was applied. The bed rock records show relatively short duration time and are simple in shape.

3.2 Inferred Inhomogeneous Parameters

Some examples of fitting results between calculated and observed MS envelopes are shown in Figure 4. Envelopes in this figure are normalized to each maximum amplitude. Inferred ε^2/a for each record is shown in each figure. The ε^2/a values have fluctuation as large as about one order. Relation between ε^2/a and hypocentral distance is shown in Figure 5 where ε^2/a decreases with increasing distance. As all three observation sites seem to obey the same distance dependency, this trend may originate from common characteristics of inhomgeneous structure in the crust.

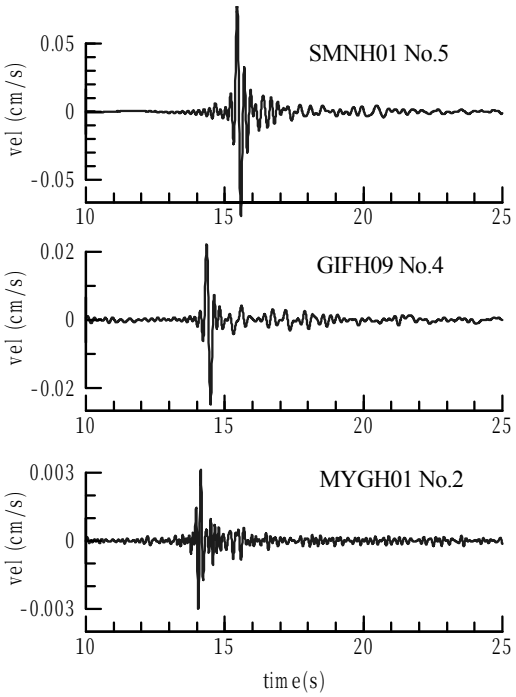


Figure 3 Examples of Inferred Ground Motion at Bedrock

In order to investigate the cause of the dependency of ε^2/a on distance comparison with results in past studies are done. Kosuga(2001) reviewed values of a and ε inferred in worldwide regions. In Figure 6 values of a and ε in the crust reviewed by Kosuga(2001) is plotted as symbols noted "past studies". Inferred ε^2/a in this study are also shown as straight lines. They are classified according to hypocentral distance (R). The ε^2/a values inferred from records with $R \geqq 10$km seem to have almost same distribution range as that of a and ε of previous studies. On the other hand the ε^2/a values inferred from records with R <10km are larger than previous studies. Larger value of ε^2/a can be seen in other studies. For example Yoshimoto et al.(1997) estimated ε^2/a as 8×10^{-3} km^{-1} in Nikko area, Japan by using records of small earthquakes with R less than about 15km. This value is larger than the usual values which are inferred by using records with R of tens or hundreds of kilometers. The ε^2/a by Yoshimoto et al.(1997) is near the value obtained from records with R<10km in this study. From these results it is indicated that earthquake records with smaller R may have stronger effects of scattering .

3.3 Inferred Model of Inhomogeneity

Kosuga(2001) founded that correlation distance (a) in the upper mantle becomes larger than in the crust based on reviewed results of past studies, although the strength of velocity fluctuation (ε) do not so differ in the upper mantle and in the crust. Flatte and Wu (1988) also indicated that the lower mantle has lager correlation distance than that of the upper crust based on the observation records at NORSAR which is a large horizontal array with aperture as large as about 100km. Yoshimoto et al.(1997) inferred a =300～800m, ε=0.05～0.08 based on the above mentioned ε^2/a value estimated in Nikko area. Yoshimoto et al.(1997)

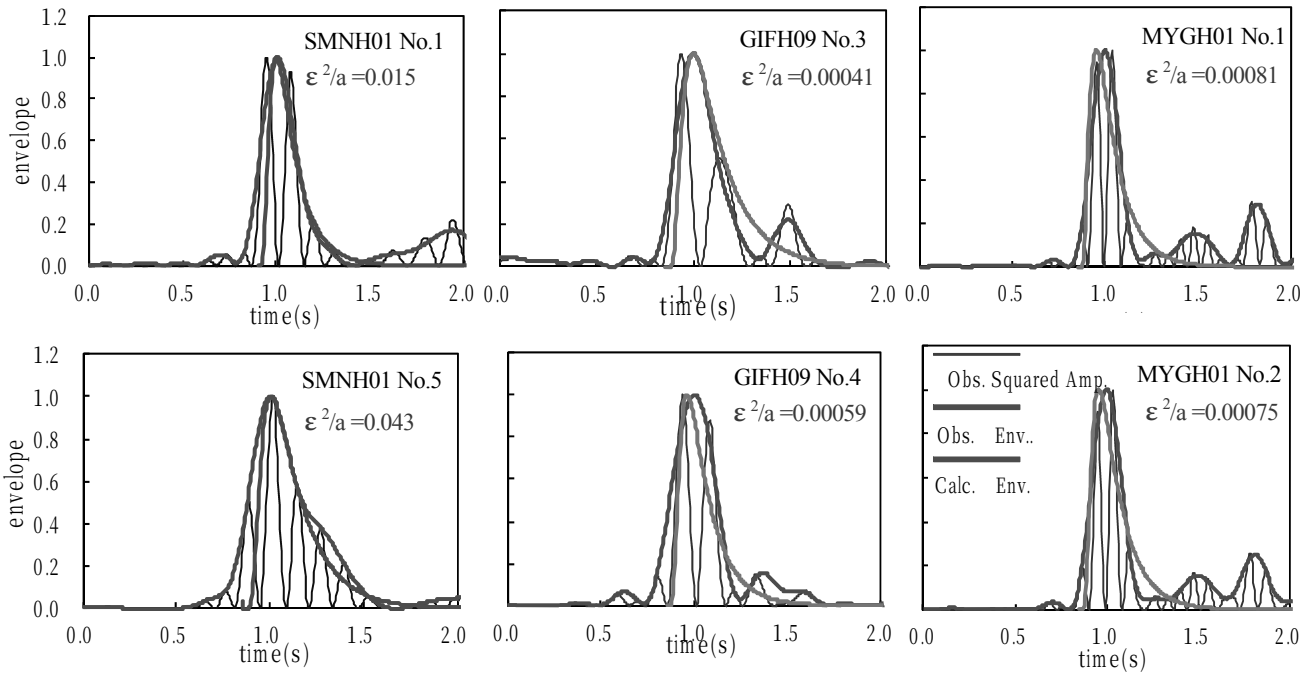


Figure 4 Examples of Fitting of Observed and Calculated Envelopes

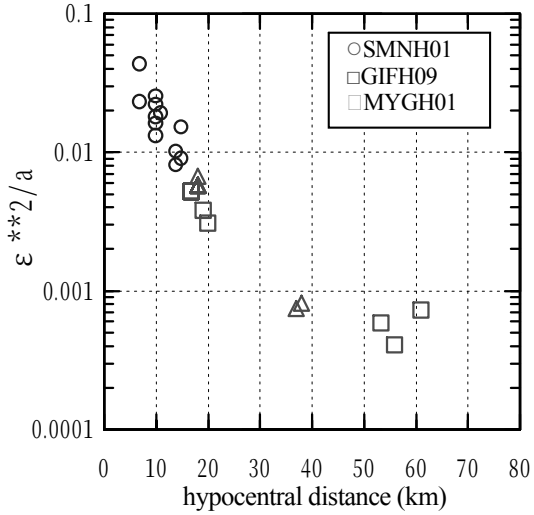


Figure 5 Relation between ε²/a and Hypocentral Distance

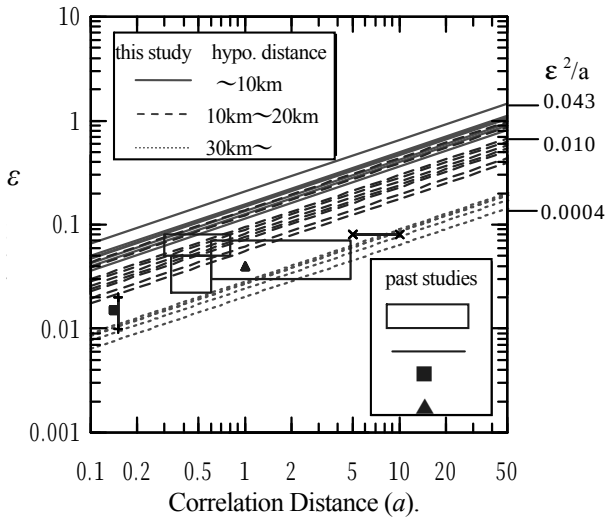


Figure 6 Comparison of Inferred a and ε in This Study with Values in Past Studies

pointed out that the cause of large ε^2/a may be strong inhomogeneity in the shallow part of the upper crust. Those results means that characteristics of inhomogeneity changed with depth and the inferred ε^2/a in this study with relatively smaller value may reflect deeper portion in the crust.

As to earthquake records in short distance the effect of path in the shallow crust with strong inhomogeneity may become larger because the ratio of path length passing in the region to the total distance becomes larger than that of records of far events. This can result in the dependence of ε^2/a on distance shown in Figure 5. To verify this assumption a simple examination was done as follows. The crust was modeled as Figure 7 in which the upper and the lower portion have different ε^2/a. The travel path from a hypocenter to an observation site is expressed as a straight line under the assumption that seismic velocity do not differ in the two regions. The ratio of length of path in the upper layer (r_1) to the total path length (R) was evaluated. The relation between r_1/R and ε^2/a is shown in Figure 8 supposing the thickness of the upper layer h_1 is 10km. Value of ε^2/a seems to increase with increasing r_1/R except for two values obtained at MYGH01. This means that the longer the seismic wave travel path in shallower part of the crust becomes, the stronger the effect of inhomogeneity. As the thickness of the upper layer h_1 is uncertain, several h_1 values were assumed. But the lenear relation between r_1/R and ε^2/a is better in the case of h_1=10km. Although h_1 cannot be inferred definitely the assumption that inhomogeneity of the shallow part of crust is greater than that of deeper part will be supported by the above result.

Figure 8 suggests value of ε^2/a used for numerical simulations. When seismic ground motion in relatively small distance are simulated the value of ε^2/a about 0.01 may be appropriate.

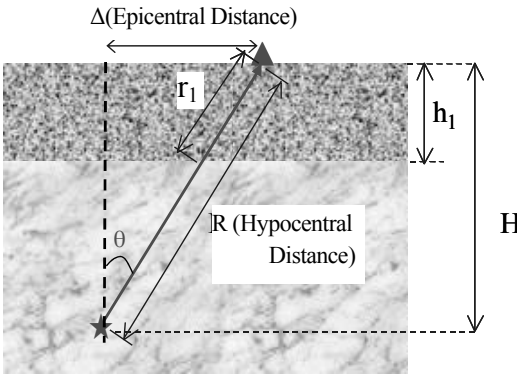


Figure 7 Supposed Structure of Inhomogeneity in Shallow Part of the Crust

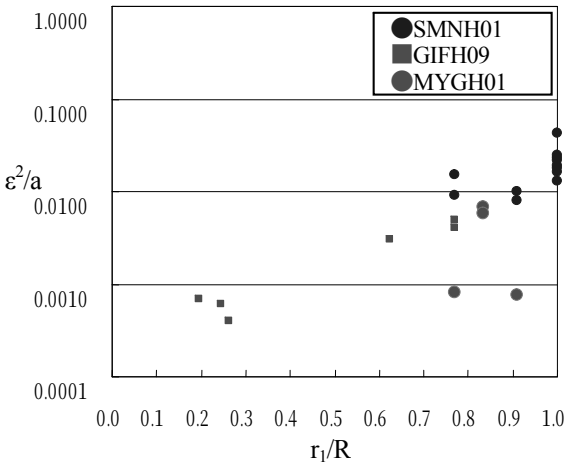


Figure 8 Relation between r_1/R of Figure 7 and ε^2/a

4. NUMERICAL SIMULATIONS

4.1 Method of Simulations

Preliminary numerical simulations were performed in order to study the influence of the strong heterogeneity on seismic ground motion variability. The finite difference method are applied assuming 3D inhomogeneous medium shown in Figure 9. The size of model is 45km×45km×10km corresponding to the shallow part of crust in which strong inhomogeneity has been inferred. The inhomogeneity in the medium is generated as following. The seismic velocity in the medium is expressed as

$$V(\boldsymbol{x}) = V_0(1 + n(\boldsymbol{x})) \qquad (4)$$

where $V(\boldsymbol{x})$ means velocity of Vp or Vs at position $\boldsymbol{x}$ in the 3D medium. V_0 is average velocity of V_P or Vs and $n(\boldsymbol{x})$ means fluctuation of velocity. In this study V_P, Vs were set as 6.7km/s, 3.7km/s respectively. $n(\boldsymbol{x})$ was generated from auto-correlation function (ACF) R(r) based on Hoshiba(2000). ACF of the Gaussian function type was assumed here as follows.

$$R(\boldsymbol{r}) = \langle n(\boldsymbol{x})n(\boldsymbol{x}+\boldsymbol{r}) \rangle = \varepsilon^2 exp(-|\boldsymbol{r}|^2/a^2) \qquad (5)$$

where $\boldsymbol{r}$ means distance vector between arbitrary two points in the medium and $\langle\ \rangle$ means averaging operation. After $R(\boldsymbol{r})$ are evaluated assuming ε and a, $n(\boldsymbol{x})$ can be produced by Fourier transforming of $R(f)$ assuming the phase is random. According to eq. (4) Vp, Vs value of each grid is assigned. Density was assumed not to have fluctuation and has constant value of 2.8g/cm^3. ε^2/a is set to 0.01 based on the result in this study shown in Figure 7 and Figure 8.

A point source was assumed at 5km depth with focal mechanism of vertical fault with pure strike slip. The source time function is assumed to be a smoothed ramp function with rise time τ. Hereafter $1/\tau$ is expressed as f_0 to be referred as central or predominant frequency of waves. The grid interval is 0.05km to make possible to calculate up to 8Hz waves.

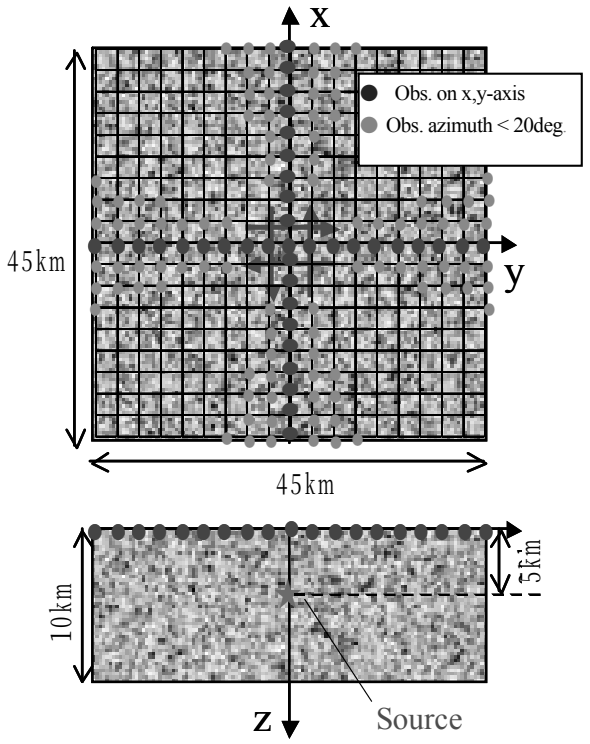


Figure 9 Numerical Simulation Model

4.2 Results of Simulations

Examples of calculated waves in the case of f_0=2Hz and 5Hz are shown in Figure 10 and 11. Simulated waves in homogeneous media are also shown for comparison. In these figures simulated waves at grids on y-axis are selected considering the radiation pattern of the source. In the case of assumed source mechanism, the x- and y-axis are in the direction of node of P wave radiation pattern. The amplitude of S wave is maximized on the contrary and only transverse component is generated in these directions. The calculated waves in homogeneous medium show such theoretical characteristics. Also the shape of waves in homogeneous medium does not change with increasing distance. On the other hand in the case of inhomogenous medium, not only x-component but also y- and z-component are generated. Also shown are later phases after main pulses of direct S waves. These are coda waves by scattering. The coda waves become more prominent in the case of f_0=5Hz than in the case of f_0=2Hz. In the case of f_0=5Hz the amplitude and duration of coda waves increase with distance clearly. These

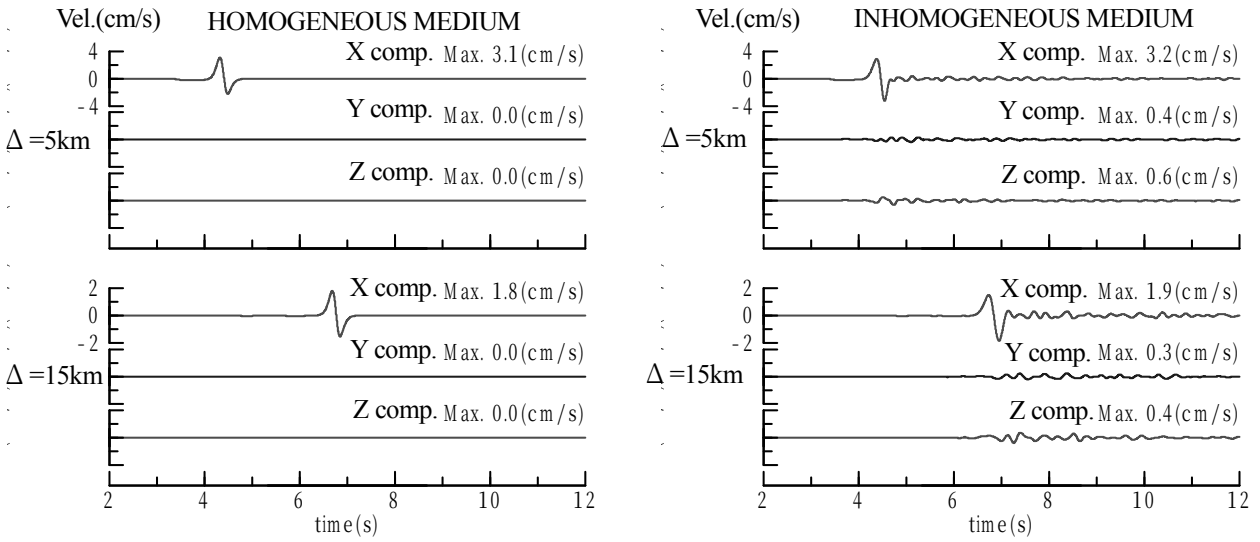


Figure 10 Examples of Calculated Velocity Waves (f_0 = 2Hz) Δ: Epicentral Distance

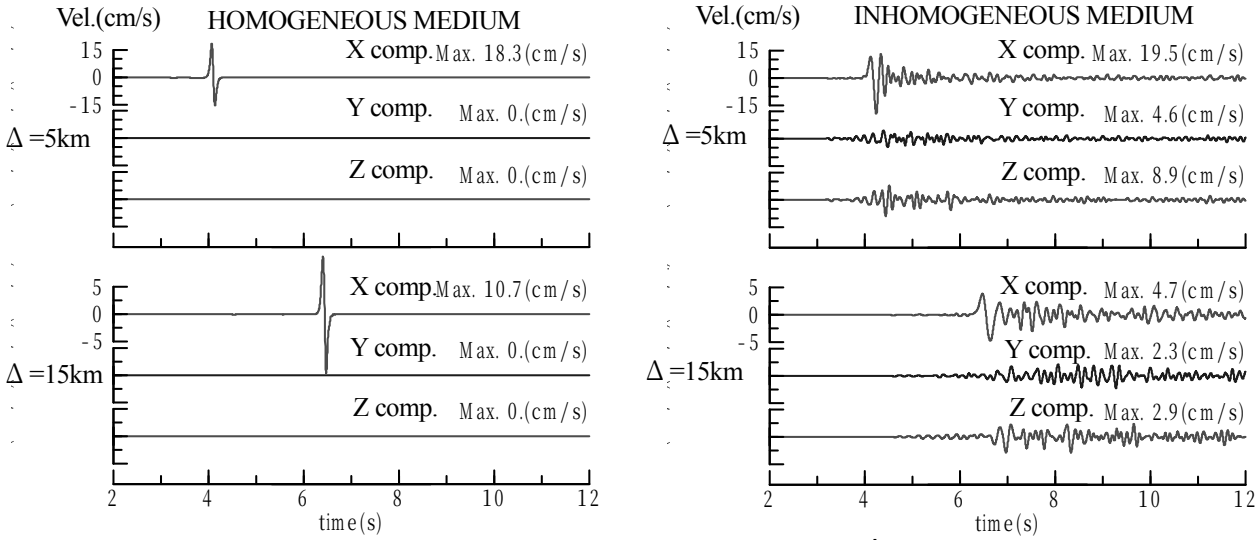


Figure 11 Examples of Calculated Velocity Waves (f_0 = 5Hz) Δ: Epicentral Distance

phenomena are also observed in real seismic records.

The amplitude of simulated wave in inhomogeneous medium differs from that of wave in homogeneous medium as shown in Figure 10 and 11. This means that inhomgeneity affects variability of seismic ground motion. In order to investigate the effect quantitatively the peak ground velocity (PGV) of simulated waves was evaluated and arranged. As mentioned above the effects of radiation pattern of the source is included in the waves. So in this study the ratio of PGV of simulated waves in inhomogeneous media to that of waves in homogeneous media was evaluated. As the difference of amplitude originated from source is canceled by this operation, the fluctuation of ratio means the effects in propagation path. In order to avoid sampling from grids located in the direction of near the node of S wave radiation, only the grids contained in the range where the azimuth angle from the origin is below 20 degree were selected as shown in Figure 9. Transverse component synthesized from two horizontal components was used to calculate the ratio.

The ratios were arranged as relation to hypocentral distance and are shown in Figure 12. In both cases of f_0=2 Hz and f_0=5Hz the ratios in an average decrease with increasing distance. The dependency is clearer in the 5Hz case and is thought to be scattering attenuation by inhomogeneity. As the fluctuation of ratios around the average attenuating trend corresponds to variability caused by path effect, we first regressed the linear decreasing trend by the least squared method. Then the residuals between the ratios in Figure 12 and the values by the regressed equation were calculated to evaluate the standard deviation of them. The common logarithm standard deviations (σ) in the case of f_0=2Hz and 5Hz are 0.09 and 0.17 respectively. Considering that the standard deviation of attenuation relations is σ=0.2 ~0.3 on an average, the σ of our simulations implies the possibility that the inhomogeity in propagation path has relatively large contribution to the total cause of variability of observed seismic ground motion.

As ε and a corresponding to the large ε^2/a value (0.01), which is inferred to reflect the characteristic of shallow part of the crust, were assumed in the whole propagation media, the σ's evaluated here might be somewhat overestimated. So we are planning simulations assuming the two layered model as Figure 7. By using such a model simulation may become more realistic and we can obtain basic data to study

dependence of σ on distance and frequency quantitatively.

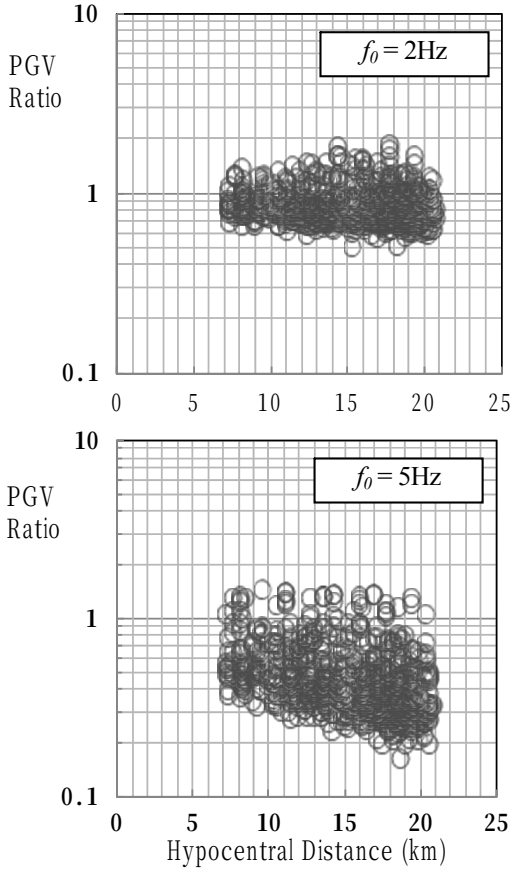


Figure 12 Relation between Ratios of PGV (Inhomogeneous/ homogeneous) and Hypocentral Distance.

5. CONCLUSIONS

Preliminary evaluation of variability of seismic ground motion caused by inhomogeneity in propagation path has been done by numerical simulations. First, strength (ε) and correlation length (a) of inhomogeneity of seismic velocity in propagation path were inferred based on KiK-net records to set up realistic models for numerical simulations for inland earthquakes. The estimated ε^2/a depends on distance and the values for short distance records are clearly greater than common values in previous studies. It may reflect the strong inhomogeneity in the shallow part of the upper crust. Then numerical simulations were performed assuming 3D random inhomogeneous media assuming inhomogneity with property based on the ε^2/a value estimated for short distance. The simulated waves explained characteristics of coda waves well. Based on the calculated waves, common logarithm standard deviation (σ) of fluctuation of peak ground velocity was evaluated. As for 2Hz and 5Hz waves σ estimated as about 0.1 ～ 0.2. The result implies the possibility that the inhomogneity in propagation path has relatively large contribution to the total cause of variability of observed seismic ground motion. In further study we are planning to accumulate simulation cases in order to evaluate dependence of the variability on distance and frequency..

Acknowledgements:

The authors acknowledge National Research Institute for Earth Science and Disaster Prevention (NIED) for providing KiK-net records.

References:

Dziewonski, A., Bloch, S. and Landisman, M. (1969), "A Technique for the Analysis of Transient Seismic Signals", Bulletin of the Seismological Society of America, **59**(1), 1969, 427-444.

Flatte, S. M. and Wu. R. S. (1988), "Small-Scale Structure in the Lithosphere and Athenosphere Deduced from Arrival Time and Amplitude Fluctuations at NORSAR", Journal of Geophysical Research, **93**, 6601-6614.

Hoshiba, M. (2000), "Large Fluctuation of Wave Amplitude Produced by Small Fluctuation of Velocity Structure", *Physics of the Earth and Planetary Interiors*, **120**, 201-217.

Kobayashi, K., Kyuke, H., Uetake,T., Mashimo, M. and Kobayashi, H. (1999), "Estimation of Q Value for Soil Layers by Simultaneous Inversion of Transfer Functions at Many Sites: Part 3 Investigation on Basic Equation of Q Value", *Summaries of Technical Papers of Annual Meeting 1999*, Architectural Institute of Japan, **B-2**(Structures Ⅱ), 253-254. (in Japanese)

Kobayashi, K., Uetake, T., Mashimo, M. and H. Kobayashi (2000), "Estimation of Deep Underground Velocity Structures by Inversion of Spectral Ratio of Horizontal to Vertical Component in P-wave Part of Earthquake Ground Motion", *Proceedings of the 12th World Conference on Earthquake Engineering*, Paper No. 2658.

Kosuga, M. (2001), "Random Inhomogeneities in the Lithosphere Inferred from Coda Analysis", *Zishin Second Series*, the Seismological Society of Japan, **54**(1), 127-145. (in Japanese)

Midorikawa, S. and Ohtake, Y. (2003), "Empirical Analysis of Variance of Ground Motion Intensity in Attenuation Relationships," *Journal of Japan Association for Earthquake Engineering*, Japan Association for Earthquake Engineering, **3**(1), 59-70. (in Japanese)

Sato, H. and Yamashita, T. (2001), "Prospect of the Study on Seismic-wave Scattering", *Zishin Second Series*, the Seismological Society of Japan, **54**(1), 65-76. (in Japanese)

Sato, Y., Kobayashi, K. and Uetake, T. (2008), "Influence of velocity fluctuation in seismic wave path on fluctuation of earthquake ground motion", *Summaries of Technical Papers of Annual Meeting 2008*, Architectural Institute of Japan, **B-2**(Structures Ⅱ), 763-764**.** (in Japanese)

Sato, Y., Yoshida, H., Kobayashi, K., Uetake, T. and Yashiro, K. (2003), "Inversion of Q_P and Q_S Values of Sedimentary Layers by Using Borehole Array Data", *Summaries of Technical Papers of Annual Meeting 2003*, Architectural Institute of Japan, **B-2**(Structures Ⅱ), 187-188**.** (in Japanese)

Saito, T., Sato, H. and Ohtake, H. (2002), "Envelope Broadening of Spherically Outgoing Waves in Three-Dimensional Random Media Having Power Law Spectra", *Journal of Geophysical Research*, **107**(No.B5), ESE 3-1 - ESE 3-16.

Shapiro, S. A. and Kneib, G. (1993), "Seismic Attenuation by Scattering: Theory and Numerical Results", *Geophysical Journal International*, **114**, 373-391.

Shiomi, K. , Sato, H. and Ohtake, M. (1997), "Broad-band power-law spectra of well-log data in Japan, *Geophysical Journal International*, **130**, 57-64.

Yoshida, H. and Kobayashi, K. (2002), "Relationship between Qp and Qs Values in Sedimentary Layers", *Summaries of Technical Papers of Annual Meeting 2002*, Architectural Institute of Japan, **B-2**(Structures Ⅱ), 183-184. (in Japanese)

Yoshimoto, K. , Sato, H. and Ohtake, M.(1997), "Short-Wavelength Crustal Heterogeneities in the Nikko Aera, Central Japan, Revealed from the Three-Component Seismogram Envelope Analysis", Physics of the Earth and Planetary Interiors, **104**, 63-73.

Wu, R. S. and Aki, K. (1988), "Seismic Wave Scattering in Three-Dimensionally Heterogeneous Earth", *Pure and Applied Geophyics*, **128**, 1-6.

8CUEE CONFERENCE PROCEEDINGS
8th International Conference on Urban Earthquake Engineering
March 7-8, 2011, Tokyo Institute of Technology, Tokyo, Japan

REEVALUATION OF DEEP UNDERGROUND STRUCTURES IN THE TOKYO METROPOLITAN AREA, USING DOMINANT PERIODS OF H/V OF CODA WAVES OBSERVED BY MESO-NET

Seiji Tsuno[1)], Hiroaki Yamanaka[1)], Shin'ichi Sakai[2)], Naoshi Hirata[2)], Keiji Kasahara[2)], Hisanori Kimura[3)], and Tamotsu Aketagawa[4)]

1) Int.-Dis. Grad. Sch. of Sci. and Eng., Tokyo Institute of Technology, Japan
2) Earthquake Research Institute, University of Tokyo, Japan
3) National Research Institute for Earth Science and Disaster Prevention, Japan
4) Hot Springs Res. Inst. of Kanagawa Prefecture
tsuno.s.aa@m.titech.ac.jp, yamanaka@depe.titech.ac.jp

Abstract: We reevaluated deep underground structures in the Tokyo Metropolitan Area, using dominant periods of H/V spectral ratios of coda waves observed by MeSO-net. At first, we verified the stability of H/V of earthquake ground motions by applying the time-frequency analysis and understanding the differences of H/V calculated by several earthquake recording data. The results of those processes showed that coda waves were mainly composed of surface waves. The variability of H/V of coda waves calculated by 9 earthquakes larger than Mj 6.5 was quite small. Consequently, we concluded that dominant periods of H/V of coda waves would be useful for creating a 3-D subsurface velocity structural model. Finally, we compared the dominant periods of H/V of coda waves obtained by MeSO-net with the velocity structures in the Tokyo Metropolitan Area proposed by Yamanaka and Yamada (2006).

1. INTRODUCTION

The high-density seismic observation network at more than 200 stations, called MeSO-net (Sakai and Hirata, 2009), has been being installed at an interval distance of about 5 km in the Tokyo Metropolitan Area. By comparing numerical predictions with earthquake ground motions observed by MeSO-net, we found that the previous 3-D underground velocity structural model in the Tokyo Metropolitan Area (Yamanaka and Yamada, 2006) was still not constrained enough to accurately predict the observed earthquake ground motions for long periods larger than 1 second. Therefore, to improve the 3-D underground velocity structural model especially for bedrock and/or a deep boundary between layers, we evaluated the relationship between dominant periods of H/V spectral ratios of earthquake ground motions and underground velocity structures in the Tokyo Metropolitan Area.

2. H/V SPECTRAL RATIO OF EARTHQUAKE GROUND MOTIONS

2.1 Data set

To evaluate the relationship between dominant periods of H/V spectral ratios of coda waves and deep underground structures, we used earthquake recording data at about 170 sites by MeSO-net in the Tokyo Metropolitan Area. For analyzing long periods of earthquake ground motions larger than 10 seconds, we selected 9 earthquakes larger than Mj 6.5 occurred in and around Japan. List of earthquakes used in this study is shown in Table 1. Locations of hypocenters of the earthquakes and MeSO-net are shown in Figure 1.

Table 1 Details of earthquakes used in this study

No.	Origin time	Location of Hypocenter	Latitude	Longitude	Hypo. dist.	Depth	Magnitude
1	2009/8/9, 19:56	Off the south coast of Tokaido	33.1 N	138.5 E	250 km	340km	Mj 6.9
2	2009/8/11, 5:07	Suruga Bay	34.8 N	138.5 E	150 km	20 km	Mj 6.6
3	2009/8/13, 7:49	Off the east coast of Hachijojima	33.0 N	140.8 E	250 km	40 km	Mj 6.5
4	2009/8/17, 9:05	Ryukyu Islands	23.4 N	123.6 E	2000 km	50 km	Mj 6.7
5	2009/8/17, 19:10	Ryukyu Islands	23.3 N	123.7 E	2000 km	40 km	Mj 6.6
6	2009/10/30, 16:03	In the sea off Amami Oshima	29.2 N	129.9 E	1200 km	60 km	Mj 6.8
7	2010/2/27, 5:31	In the sea off Okinawa Island	25.9 N	128.7 E	1450 km	40 km	Mj 7.4
8	2010/3/14, 17:08	Offshore Fukushima prefecture	37.7 N	141.9 E	250 km	40 km	Mj 6.6
9	2010/4/26, 11:59	Ryukyu Islands	22.2 N	123.8 E	2000 km	50 km	Mj 6.6

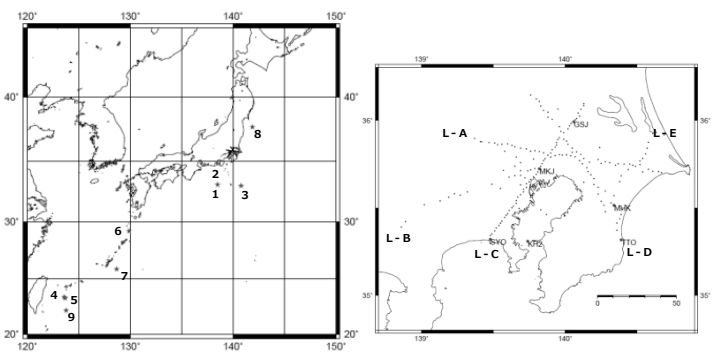


Figure 1 (Left) Hypocenters of earthquakes (Right) Locations of MeSO-net used in this study

2.2 Time-frequency analysis

To understand the discrepancy of H/V spectral ratios obtained by different wave types (e.g. body waves and surface waves), we verified time-variations of H/V spectral ratios, by performing the time-frequency analysis (Gabor transform with Gaussian time window of 20 seconds.). In this paper, we defined the division of geometric mean between horizontal components by a vertical component as H/V spectral ratio. Velocities and H/V spectral ratio at MKJ during off the east coast of Hachijojima earthquake (2009/8/13, Mj 6.5) are shown in Figure 2 and Figure 3, respectively.

In the early arrival from 100 to 200 seconds, a period less than 4 second is dominated for H/V spectral ratio in Figure 3. On the other hand, a period of 5 to 10 second is dominated in the later phase from 200 to 600 seconds. The discrepancy of those dominant periods is caused by the complexity of wave fields during earthquake ground motions. In generally, early arrivals consist of body waves and later phases consist of surface waves.

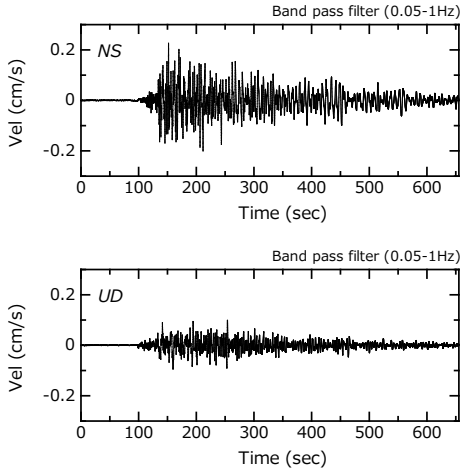


Figure 2 Velocities of NS and UD components by BWF between 1 and 20 seconds at MKJ during off the east coast of Hachijojima earthquake (2009/8/13, Mj 6.5)

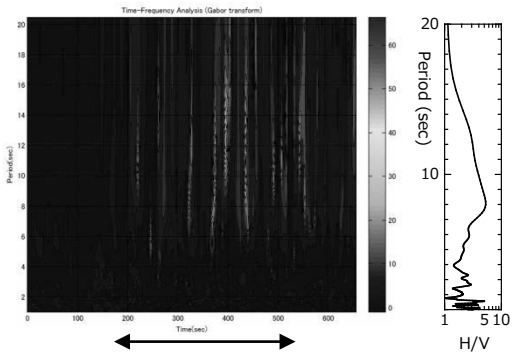


Figure 3 (Left) Gabor transform of H/V spectral ratio at MKJ using Gaussian time window of 20 seconds (Off the east coast of Hachijojima earthquake, 2009/8/13, Mj 6.5) (Right) H/V spectral ratio of coda waves in a duration shown with a closed arrow in the left figure

2.3 Similarity to H/V spectral ratio of microtremors

We compared H/V spectral ratios of coda waves with H/V spectral ratios of microtremors. As examples, H/V spectral ratios of coda waves and microtremos are shown in Figure 4. The similarity of both H/V spectral ratios means that coda waves used in this study are composed of surface waves as well as microtremors. However, the difference of the two H/V spectral ratios for periods larger than 5 seconds is due to the noise of vertical sensors.

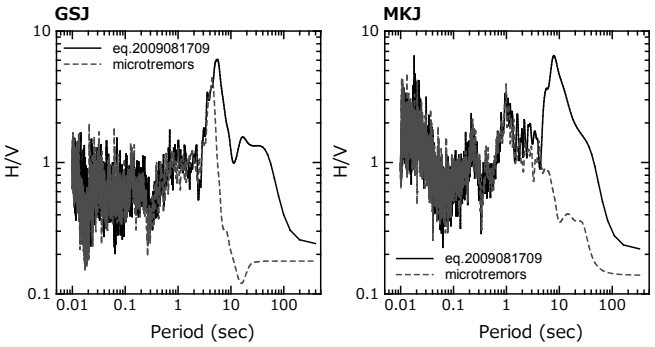


Figure 4 Comparison of H/V spectral ratios of coda waves (2009/8/17, Mj 6.7) with those of microtremors at GSJ and MKJ

2.4 Comparison with R/V spectral ratio

We compared the H/V spectral ratios of coda waves with R/V spectral ratios, as shown in Figure 5 using the earthquake recording data of off the east coast of Hachijojima earthquake (2009/8/13, Mj 6.5). Although the dominant periods of the H/V and R/V spectral rations are quite similar, the amplitudes have a slight difference for the peak because H/V spectral ratios have an influence from Rayleigh waves as well as Love waves. In the case of using H/V spectral ratios, we need to consider the contribution of Love waves despite less influence than Rayleigh waves.

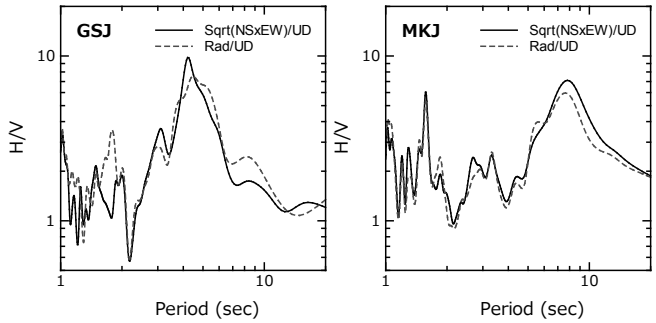


Figure 5 Comparison of H/V spectral ratios with R/V spectral ratios at GSJ and MKJ, during off the east coast of Hachijoima earthquake (2009/8/13, Mj 6.5)

2.5 Stability of H/V spectral ratios derived from different earthquakes

H/V spectral ratios averaged by 9 different earthquakes (See Table 1) are shown in Figure 6. Average of H/V spectral ratios has a quite small variability; therefore, it reflects the underground structure beneath the site. We could

accurately determine dominant periods of H/V spectral ratios at all the stations, using the average of H/V spectral ratios as shown in Figure 6. Theoretical ellipticities of fundamental mode Rayleigh waves calculated by the S-wave velocity models (Yamanaka and Yamada, 2006) are also shown in Figure 6. The agreement between the average of the H/V spectral ratios and the theoretical one at MKJ indicates that the structural model is well constraint at this site. On the other hand, the slight difference between the averaged and the theoretical H/V spectral ratios (e.g. GSJ and MHK) requires that the structural model beneath these sites will be improved.

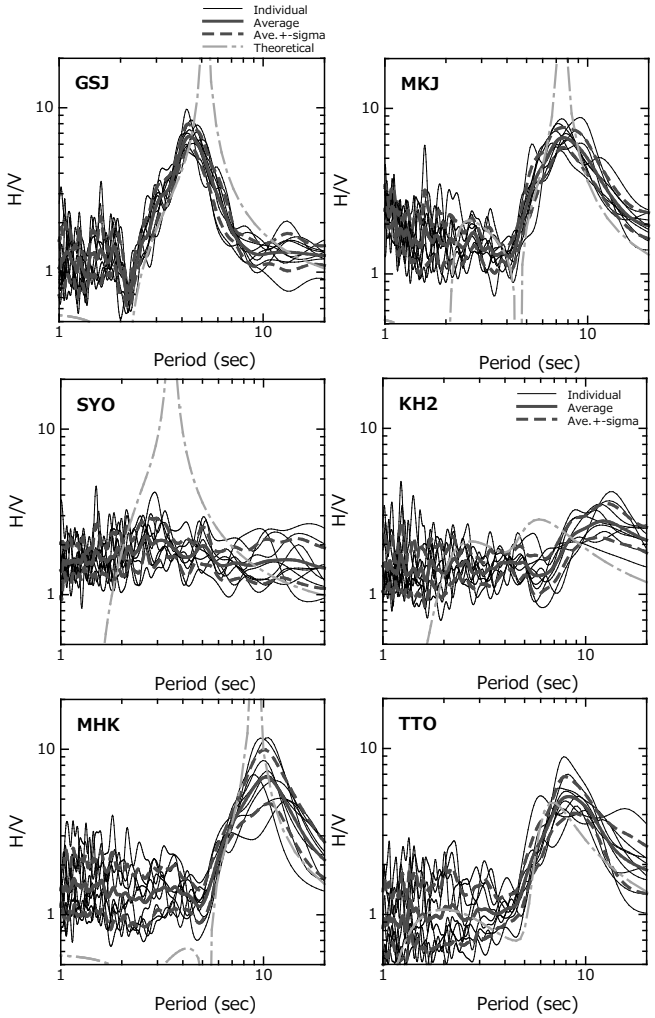


Figure 6 H/V spectral ratios at GSJ, MKJ,SYO, KH2, MHK and TTO (See Figure 1) (Black line: individual H/V, red line: averaged, red dot line: +- σ , green broken line: theoretical)

3. RELATIONSHIP BETWEEN H/V SPECTRAL RATIOS OF CODA WAVES AND DEEP UNDERGROUND STRUCTURES

Distribution of dominant periods of H/V spectral ratios using MeSO-net data is shown in Figure 7. Most of H/V spectral ratios in the Tokyo Metropolitan Area have periods larger than 5 seconds, due to deep underground structures (Yamanaka and Yamada, 2006). In particular, periods larger than 8 seconds are dominated in the west side of the Tokyo Bay and the north of the Boso Peninsula. This tendency is a good agreement with depths of seismic bedrock estimated by array microtremors observations (Yamanaka and Yamada, 2006).

In Figure 8, we compared dominant periods of H/V spectral ratios with theoretical dominant periods of fundamental mode Rayleigh waves calculated by using Yamanaka and Yamada's model, for 5 cross sections shown in Figure 1. Although both dominant periods in Figure 8 have the same tendency, they don't agree with each other in detail. In Line C, for example, the theoretical dominant periods by Yamanaka and Yamada's model underestimate those observed. The dominant periods of H/V spectral ratios matched well for sites where shallow basin structures are located; however, dominant periods of H/V spectral ratios didn't match well for sites where deep basin structures are located. Yamanaka and Yamada's model is based on phase velocities of Rayleigh waves estimated by array microtremors observations; therefore, the uncertainty of underground structural model is increased when a phase velocity is not obtained for long periods.

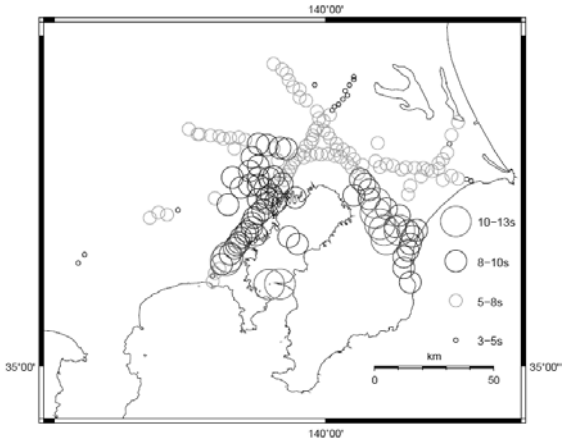


Figure 7 Distribution of dominant periods of H/V spectral ratios in MeSO-net

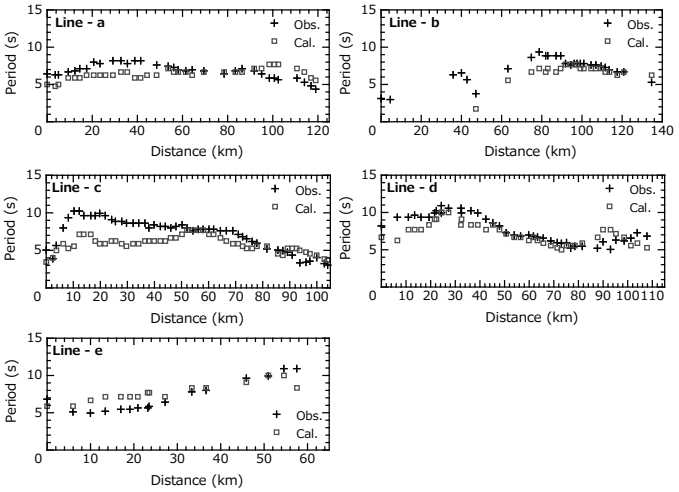


Figure 8 Comparison of dominant periods of H/V spectral ratios observed by MeSO-net with those calculated by Yamanaka and Yamada's model

4. DISCUSSIONS

We examined wave types of coda waves used for the calculations of H/V spectral ratio. Here, we focus on a duration of 312 to 335 seconds in which H/V spectral ratio is dominated during off the east coast of Hachijojima earthquake (2009/8/13, Mj 6.5; See Figure 3). H/V spectral ratios and those Fourier spectra from 312 to 335 seconds at MKJ are shown in Figure 9. The Fourier amplitudes of vertical motions from 322 to 328 seconds are decreasing at a period of around 8 seconds; therefore, H/V spectral ratio has a certain peak. Particle motions of NS - UD components from 317 to 327 seconds processed by a bandpass filter at periods between 8 and 20 seconds are retrograde (See Figure 10). On the other hand, particle motions processed by a bandpass filter at periods between 5 and 8 seconds are prograde. These wave motions strongly support that the vertical and radial motions are composed of Rayleigh waves propagating from the south to north as shown in Figure 11.

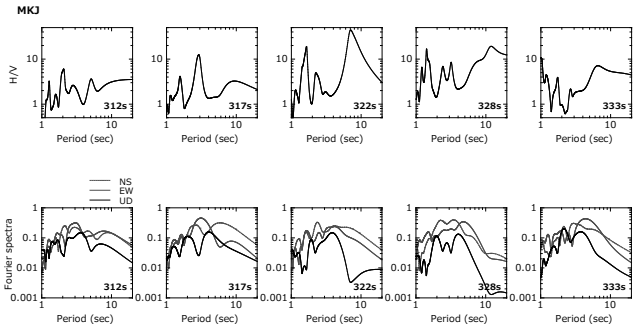


Figure 9 H/V spectral ratios and those Fourier spectra (312-333 second) at MKJ, during off the east coast of Hachijojima earthquake (2009/8/13, Mj 6.5)

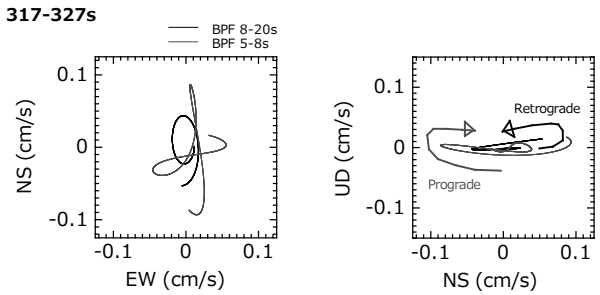


Figure 10 Particle motions among horizontal and vertical components at MKJ from 317 to 327 seconds during off the east coast of Hachijojima earthquake (2009/8/13, Mj 6.5)

5. CONCLUSIONS

Coda waves used in this study were mainly composed of surface waves consisting of both Rayleigh waves and Love waves. The variability of H/V spectral ratio of coda waves observed by 9 earthquakes larger than Mj 6.5 was quite small. Consequently, we concluded that dominant periods of H/V of coda waves would be useful for creating a 3-D underground velocity structural model to predict long period ground motions. In the case of using amplitudes of H/V of coda waves, we would need to include the amplitude of Love waves. In Yamanaka and Yamada's model, which is based on phase velocities of Rayleigh waves obtained by array microtremors observations, there are still uncertainties in the data obtained from deep basin structures when phase velocities for long periods are not obtained by array microtremors recording data.

As a next step, we aim to improve the velocity structural models in the Tokyo Metropolitan Area, by applying the inversion of ellipticities of Rayleigh waves for H/V of coda waves observed by MeSO-net. Also, we will simulate long periods of strong ground motions in the area, using the improved velocity structural models.

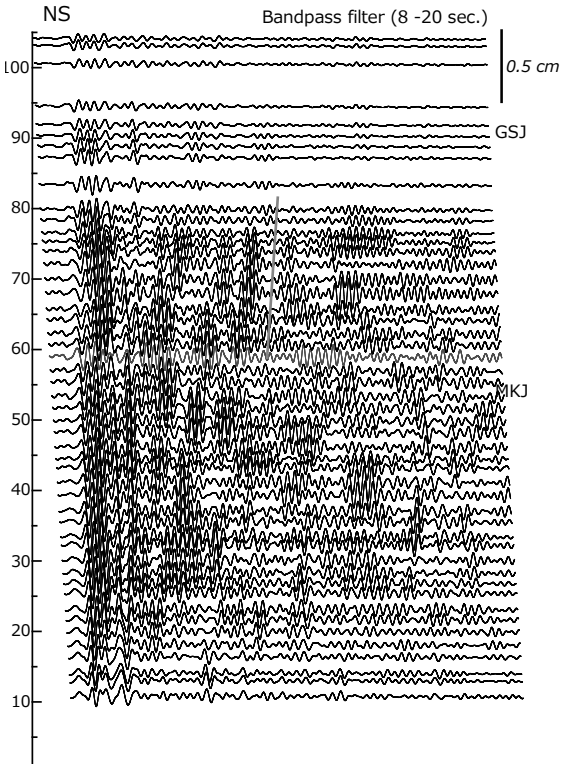


Figure 11 Time series of displacement (BWF 8-20 seconds) for NS component at a cross section of Line C from the south-west to the north-east

Acknowledgements:

We used earthquake recording data obtained by MeSO-net. This work is one part of 'Special project for earthquake disaster mitigation in the Tokyo Metropolitan Area' supported by Ministry of Education Culture, Sports, Science and Technology, Japan.

References:

Sakai, S. and Hirata, N. (2009), "Distribution of the metropolitan seismic observation network", Bull. Earthq. Res. Inst. Univ. Tokyo, Vol. 84, pp.57-69.

Yamanaka, H. and Yamada, N. (2006), "Modeling 3D S-wave velocity structure of Kanto basin for estimation of earthquake ground motion", BUTSURI-TANSA, Vol. 59, No. 6, pp.549-560.

8CUEE CONFERENCE PROCEEDINGS
8th International Conference on Urban Earthquake Engineering
March 7-8, 2011, Tokyo Institute of Technology, Tokyo, Japan

SEISMIC RESPONSE ESTIMATION OF NUCLEAR POWER PLANT MODEL BASED ON FAULT-STRUCTURE SYSTEM

Pher Errol B. Quinay[1)2)], Tsuyoshi Ichimura[3)], Muneo Hori[4)], M.L.L. Wijerathne[5)], and Akemi Nishida[6)]

1) Postgraduate student, Department of Civil Engineering, The University of Tokyo, Japan
2) Fellow of Advanced Science, Computational Science and e-Systems, Japan Atomic Energy Agency, Japan
3) Associate Professor, Earthquake Research Institute, The University of Tokyo, Japan
4) Professor, Earthquake Research Institute, The University of Tokyo, Japan
5) Assistant Professor, Earthquake Research Institute, The University of Tokyo, Japan
6) Principal Research Engineer, Computational Science and e-Systems, Japan Atomic Energy Agency, Japan
equinay2@eri.u-tokyo.ac.jp, ichimura@eri.u-tokyo.ac.jp, hori@eri.u-tokyo.ac.jp, lalith@eri.u-tokyo.ac.jp, nishida.a@jaea.go.jp

Abstract: In this study, we extend the application of the fault-structure system (FSS) analysis to seismic response estimation of a model of nuclear power plant (NPP). FSS is a system that can account for the variability of earthquake input and the corresponding seismic response. In FSS, an integrated analysis of the seismic wave propagation and NPP response is conducted, which include three-dimensional (3D) modeling of the fault rupture process, interaction of seismic wave with the complicated crust structure, effect of geologic setting within immediate vicinity of the NPP, and response of NPP structure. In solving the FSS, the Macro-Micro Analysis procedure (Ichimura and Hori, 2009a) is adopted to efficiently handle the resolution required for geologic- and engineering-length scale simulations. A 3D FEM code based on hybrid grid is developed to gain flexibility in handling mesh modeling and the resulting computational cost. A validation of the method is performed by a reproduction of an earthquake event on actual 3D crust structure. A scenario earthquake simulation is conducted for a fault-plane rupture close to the NPP model. Results show that by employing the FSS, a realistic response of the NPP can be obtained with respect to the scenario setting. Future targets for improvement are also discussed.

1. INTRODUCTION

Seismic response of large-scale structures such as nuclear power plants (NPP) is complicated due geometrical irregularities that conform to the function of different components of such facility. The use of numerical methods for analysis is widely-accepted, and improvements in computational resources are leading to development of more sophisticated analysis tools. Following this development, emphasis should also be placed on the earthquake input to the structure because this input is affected by the radiation characteristics of rupture of the source, the effect of geologic layers, subsurface velocity layers in the soft basin, and site effects such as surface topography. Thus, each earthquake scenario is unique in terms of phase and amplitude characteristics which are significant factors to account for in seismic response of structures such as NPPs.

The FSS is a system that can account for the variability of earthquake input and the corresponding seismic response. Though the FSS is a promising tool for analysis, it demands a heavy computational environment especially if considering 3D problems. It should be mentioned that different methods exist in the literature to address this difficulty (as examples, Domain Reduction Method (Bielak, et. al, 2003); Macro-Micro Analysis (MMA) (Ichimura and Hori, 2009a)). Among these methods, the MMA (Ichimura and Hori, 2009a) is one of the most promising analysis tool because of its rigorous mathematical foundation while maintaining robustness in implementation to actual problems. MMA efficiently solves the FSS by decomposing the problem into two scales, and satisfying the accuracy required in both scales in solving the problem. In this study, the extension of applicability of the MMA for NPP seismic analysis is examined.

2. METHODOLOGY

2.1 Equations for Macro-Micro Analysis

As earlier mentioned, the FSS includes 3D modeling of the earthquake source rupture, the wave propagation through the irregular crust, effect of geologic structure near the structure, and finally, the seismic response of the structure. It should be observed that two length scales are being considered when solving the FSS – the geologic and engineering, and the spatial dimensions would vary from about 10^5 meters for the domain size for seismic wave propagation to about 10^{-1} meters for the mesh to conform to structure component size. Thus, if to be solved directly (all

components are solved at once), the computational cost can increase considerably which may not be practical to run in any present computational environment.

The MMA addresses this difficulty by applying perturbation technique to the elastodynamic problem,

$$d_i\left(c_{ijkl}d_l\left(u_k\right)\right)-\rho\ddot{u}_j=0 \quad , \quad (1)$$

where c_{ijkl} is the component of elasticity tensor, ρ is mass density, u_k is displacement component, d_i is partial differentiation, and $\dot{(\ )}$ is time differentiation. The singular perturbation expansion method (Smith, 1985) expands the solution u_k of the wave equation as,

$$u_k \approx u_k^{(0)}+\varepsilon u_k^{(1)}+\ldots \quad , \quad (2)$$

where $u^{(0)}$ is solution at low resolution, $u^{(1)}$ is solution at high resolution, and $\varepsilon=X_i/x_i$ is a very small parameter (<<1) that relates the slow spatial variable, X to fast-changing variable, x.

The use of Equation (2) on Equation (1) results to two equations that first, computes the solution in the domain of the slow spatial variable, and then refines this solution using the properties near the structure:

$$D_i\left(C_{ijkl}D_l u_k^{(0)}\right)-R\ddot{u}_j^{(0)}=0 \quad , \quad (3)$$

$$d_i\left(c_{ijkl}\left(d_l u_k^{(1)}+d_l u_k^{(0)}\right)\right)-\rho\left(\ddot{u}_j^{(1)}+\ddot{u}_j^{(0)}\right)=0 \quad , \quad (4)$$

where D_i is differentiation with respect to X_i , R is the effective density, and C_{ijkl} is the equivalent elasticity tensor in the domain of the slow spatial variable. In MMA, Equation (3) is called the Macro analysis and Equation (4) is called the Micro analysis. The reader is referred to (Ichimura and Hori, 2006) for details of the derivation of Equations (3) and (4). Figure 1 shows the schematic of the MMA.

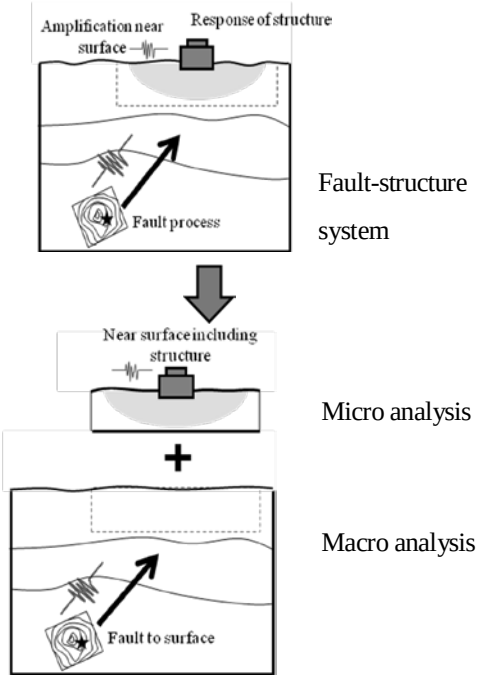


Figure 1. Schematic of MMA: decomposition of FSS to two-step procedure, Macro and Micro analysis.

2.2 Computing the Macro analysis

The "Macro" analysis is carried out to obtain the low resolution solution at geologic-length scale. This includes modeling the earthquake generation and propagation through the crust structure. Earthquake generation is modeled as double couple point source(s) with a specific source time function, rise time, magnitude and moment tensors. Modeling the propagation includes accounting for the irregular crust structure, basin velocity structures, and their respective layer properties (pressure and shear wave velocities, density, and quality factor). Following Equation (3), the spatial component is discretized using the Galerkin method and temporal component is discretized using Newmark-β (β=1/4) method to arrive at the following equation for implementation to computer code:

$$\left(\mathbf{K}+\frac{2}{\Delta t}\mathbf{C}+\frac{4}{\Delta t^2}\mathbf{M}\right)\mathbf{u}^{n+1}= \left(\frac{2}{\Delta t}\mathbf{C}+\frac{4}{\Delta t^2}\mathbf{M}\right)\mathbf{u}^{n}+\left(\mathbf{C}+\frac{4}{\Delta t}\mathbf{M}\right)\mathbf{v}^{n}+\mathbf{M}\mathbf{a}^{n}+\mathbf{f}^{n} \quad , \quad (5)$$

where **K**, **C**, **M**, **u**, **v**, **a**, **f**, n, Δt are stiffness, Rayleigh damping, mass matrices, displacement, velocity, acceleration, external force vectors, temporal counter, and time step size, respectively.

2.3 Computing the Micro analysis including NPP model

To include the site-specific response, the "Micro" analysis is carried out as described in Equation 4. Here, a small region near the structure is considered and the low resolution obtained in Macro analysis is refined to account for the settings near the structure to be analyzed. Such refinement of solution is a main point of perturbation methods. Discretization in space using the Galerkin method and in time using Newmark-β (β=1/4) method, we arrive at the equation similar to Equation (5) without the external force term.

2.3 FEM coding of the Macro and Micro Analysis

As mentioned, solving the FSS using the direct analysis can result to large computational cost. However, even though a significant reduction has been achieved in decomposition to two scales, the computation cost is still high. In the developed MMA code, several computing techniques were used in mesh modeling and time integration. Mesh modeling employs a background cell to efficiently place finite elements and reduce inefficient tetrahedral elements (elements with low aspect ratio). The background cell also determines the voxel (Koketsu, 2004) locations, and based on location in the layers, may invoke the octree technique (Bielak, 2005) to determine its efficient dimension. In the analysis,, the element-by-element (EBE) technique (Wenget and Hughes, 1985) is implemented to avoid global assembly of stiffness matrix. The EBE is implemented to the preconditioned gradient method (PCG) with a specified criterion for convergence.

For the details of the Macro and Micro analysis and implementation of the computating techniques mentioned, the reader is referred to the following related papers (Ichimura and Hori, 2006, Ichimura and Hori, 2007, Ichimura and Hori, 2009a, Ichimura and Hori, 2009b).

3. Application Examples

3.1 Validation of earthquake simulator: Reproduction of observed earthquake

To check the validity of the code to simulate earthquake as input to NPP, a reproduction of observed earthquake is conducted. A region that includes a large part of Tokyo, as shown in Figure 2 (with details in Table 1), is chosen as the simulation region, and layer properties are as derived by Tanaka et al. (2006). A recent earthquake is selected (F-NET) which was observed in several seismic stations (K-Net). This earthquake is modeled as a double-couple point source with settings as given in Table 2. Equation (5) is used to compute the response at seismic stations. The target accuracy is 0.5 Hz. Time step size is 0.01 seconds and 10 elements is used for one wavelength. The iterative solver is PCG method with convergence criteria of $1x10^{-6}$.

Table 1. Layer material properties used in reproduction of observed earthquake (Tanaka et al. 2006)

Layer	P-wave velocity (m/s)	S-wave velocity (m/s)	Density (kg/m3)	Quality factor
1	1850	500	1950	60
2	2560	1000	2150	150
3	3200	1700	2300	200
4	5800	3360	2700	500
5	6600	3700	2800	600
6	8040	4480	4400	800

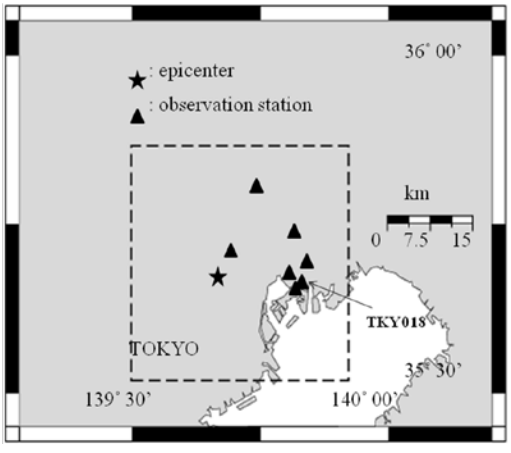


Figure 2. Target region, earthquake epicenter (shown as star), and observation points (shown as black triangels) for the reproduction of observed earthquake. Arrow points to Station TKY018.

Table 2. Observed earthquake properties (K-net)

Date	2010/05/09
Latitude	35.6757 N
Longitude	139.6613 E
Depth	26.73 km
Source time function	$M_o(2t^2/T_o^2)$ $0 \le t \le T_o/2$
	$M_o(1-2(t-T_o)^2/T_o^2)$ $T_o/2 \le t \le T_o$
	M_o $t \ge T_o$
Magnitude	Mw = 3.8
Strike, Dip, Rake	253°, 17°, 39°
Rise time, To	0.18 sec

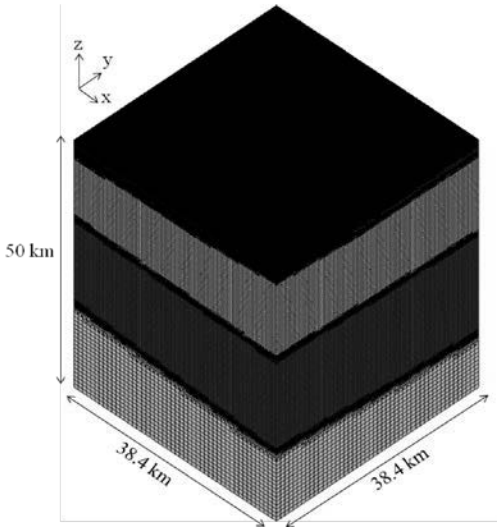


Figure 3. Resulting 3D model of the actual crust structure (Tanaka, 2006) using the modeling code of Macro analysis. The minimum element size is 100 m.

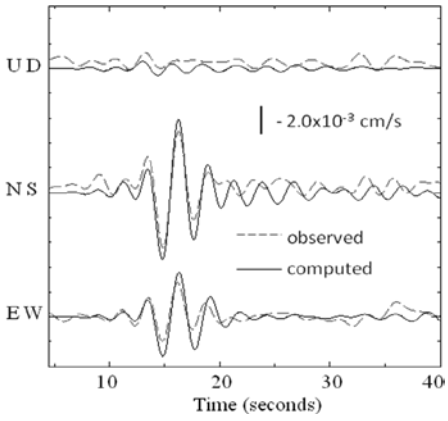


Figure 4. Comparison of observed and computed results at Station TKY 018. The results are band-pass filtered (0.1 – 0.5 Hz).

As observed in Figure 3, a good agreement between the observed and computed seismograms has been obtained. Similar agreement has also been obtained in the comparison for other seismic stations. This validates the applicability of the Macro analysis code for earthquake simulation from fault to surface in geologic-length scale.

3.2 Earthquake scenario example: Nuclear power plant seismic response estimation

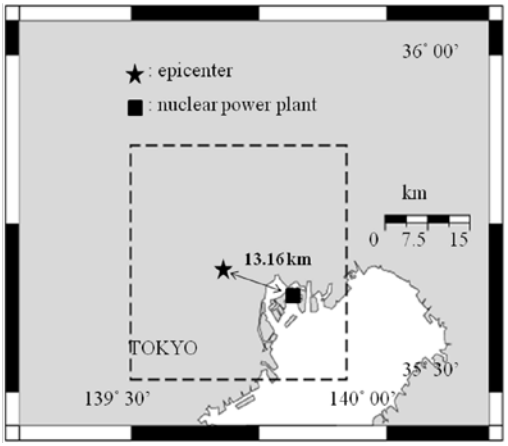


Figure 5. Target region, earthquake epicenter, and NPP (shown as star and square marks).

Table 3. Material properties

Material	P-wave velocity (m/s)	S-wave velocity (m/s)	Density (kg/m3)	Quality factor
Engineered fill	1500	400	1600	50
NPP	3373	2127	2500	200

Table 4. Scenario earthquake properties

Hypocenter depth	30.0 km
Rupture speed	2.0 km/s
Source time function	$M_o(2t^2/T_o^2)$ $0 \le t \le T_o/2$
	$M_o(1-2(t-T_o)^2/T_o^2)$ $T_o/2 \le t \le T_o$
	M_o $t \ge T_o$
Magnitude	$M_w = 5.3$
Strike, Dip, Rake	30^o, 45^o, 60^o
Rise time, To	1.0 sec

In this section, the MMA is applied to seismic response estimation of NPP model. The target accuracy is 0.5 Hz. The same simulation domain and crust layer properties as 3.1 are used. The time increment is 0.01 seconds and total simulation time is 40.96 seconds. The criterion used for numerical accuracy is ten (10) elements per wavelength for the target accuracy. Figure 5 shows the problem setting where the epicenter is about 13.16 km from the NPP. The rupture plane is about 1.2 km x 1.2 km in dimensions and dips at 45^0 from the horizontal plane (see Figure 8). The hypocenter depth is about 30 km and rupture propagation speed from the hypocenter is 2.0 km/s. In this scenario, the moment magnitude is about 75% of scenario for Kanto region as presented in CDPC report (2004).

Figures 6 and 7 show the Micro model (with location of soft soil and NPP) and the NPP meshed model, respectively. Tables 3 and 4 give the details of the material properties of the soft soil layer and NPP, and the properties of the scenario earthquake modeled as fault-plane rupture.

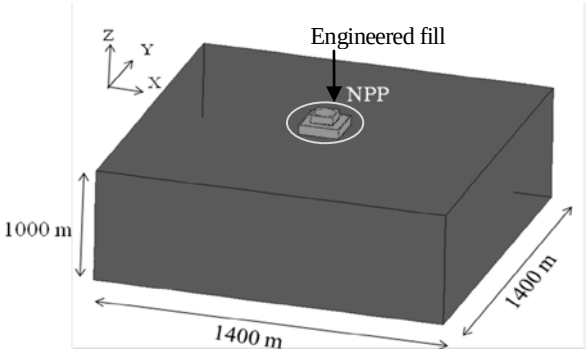


Figure 6. Micro model. NPP structure is at the center of the model. An engineered fill encloses the NPP at about 40 meters on each side.

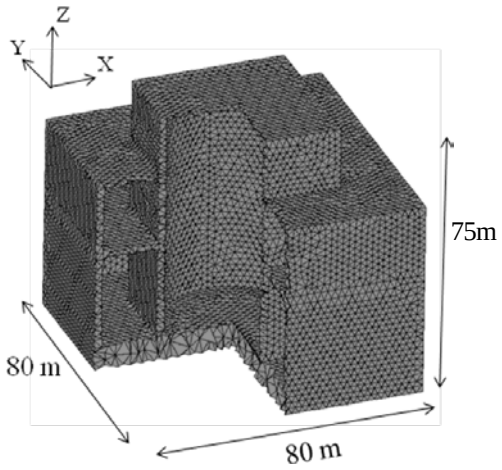


Figure 7. Model of NPP used in the simulation. Mesh size is 2.0 m. Embedment to soil is 36.0 meters from the base.

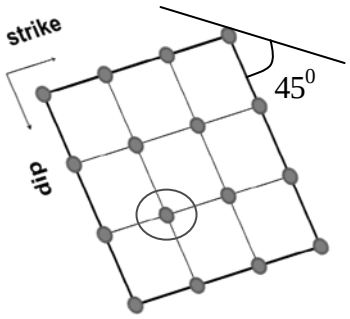


Figure 8. Fault-plane rupture modeled as 16 point sources with different rupture starting time. Distance between adjacent point sources is 400 m. Details are as given in Table 4. Red circle shows the hypocenter.

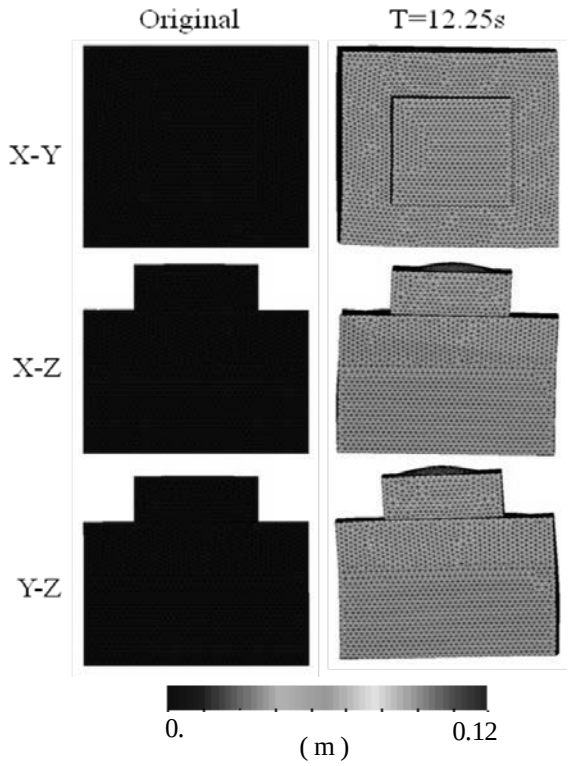


Figure 9. NPP structure deformation at time, T = 12.25 seconds (deformation x2000). Color bar shows displacement.

It is emphasized that the application of FSS for seismic analysis of NPP is advantageous because it can simulate the realistic behavior of this structure with respect to the given earthquake scenario and actual geologic and near vicinity settings. Because the analysis is based on 3D models, the 3D effect of the wavefield on the NPP structure is inherently accounted for. As shown in Figure 9, deformation of the NPP can be examined simultaneously from which critical locations in the structure can be determined. The capability to observe these deformations using analysis tools such as MMA is significant when designing new structures and analyzing existing ones.

To extend the applicability further for in-depth analysis of NPP structures, this study hopes to integrate fracture analysis based on particle discretization scheme (Hori et al. 2005). Moreover, to further reduce the computation time in modeling and analysis, hybrid-parallelization (shared and distributed memory) is presently being implemented to the MMA codes.

4. CONCLUSIONS

We have presented a FSS approach for seismic response estimation of NPP structures. FSS includes 3D modeling of the fault rupture process, interaction of seismic wave with the complicated crust structure, effect of geologic setting within immediate vicinity of the NPP, and response of NPP structure. To solve the FSS, a multiscale approach – Macro-Micro Analysis is used, allowing for feasibility of implementation to present available computational resource. To validate the earthquake input to the NPP model, a recent earthquake in Kanto region is reproduced. This is then extended to seismic response estimation of NPP under a scenario earthquake.

Acknowledgements:

The authors acknowledge support from the Japan Atomic Energy Agency and CREST project.

References:

Ichimura, T., Hori, M. (2009a), "Structural Seismic Response Analysis based on Multiscale Approach of Computing Fault-Structure System," *Earthquake Engineering and Structural Dynamics*, 38, 439-455.

Bielak, J., Loukakis, K., Hisada, Y., Yoshimura, C. (2003), "Domain Reduction Method for three-dimensional earthquake ground motion modeling in localized regions, Part I: Theory," Bulletin of Seismological Society of America, Vol. 93, No.2, pp. 817-824.

Smith, D.R.(1985), "Singular Perturbation Theory, An Introduction with Applications," Cambridge University Press: Cambridge.

Ichimura, T., Hori, M. (2006), "Macro-micro analysis method for wave propagation in stochastic media," Earthquake Engineering and Structural Dynamics, 35, 419-432.

Koketsu, K. Fujiwara, H., Ikegami, Y. (2004), "Finite Element Simulation of Seismic Ground Motion with a Voxel Mesh," Pure and Applied Geophysics, Vol. 161, pp.2183-2198.

Bielak, J., Ghattas, O., Kim, E.J.(2005), "Parallel Octree-based Finite Element Method for Large-Scale Earthquake Ground Motion Simulation," Computer Modeling in Engineering and Sciences, Vol. 10, 99-112.

Wenget, J.M., and Hughes, T.J.R., (1985) "Solution Algorithms for Nonlinear Transient Heat Conduction Analysis Employing Element-by-Element Iterative Strategies," Comput. Methods Appl. Mech. Eng., 52, 711-815.

Ichimura, T., Hori, M., Kuwamoto, H. (2007), "Earthquake Motion Simulation with Multiscale Finite-Element Analysis on Hybrid Grid," Bulletin of Seismological Society of America, Vol. 97, No. 4, 1133-1143.

Ichimura, T., Hori, M., Bielak, J. (2009b), "A Hybrid Multiresolution Meshing Technique for Finite Element Three-dimensional Earthquake Ground Motion Modeling in Basins Including Topography," Geophysical Journal International. 177, 1221-1232.

Tanaka, Y., Miyake, H., Koketsu, K., Furumura, T., Hayakawa, T., Baba, T., Suzuki, H.,Masuda, T., (2006) "The DaiDaiToku Integrated Model of the Velocity Structure beneath the Tokyo Metropolitan Area (2)," Abstracts of the Japan Geoscience Union Meeting, S116-P014.

F-net Broadband Seismograph Network, Japan National Research Institute for Earth Science and Disaster Prevention, http://www.fnet.bosai.go.jp/freesia/

K-net Kyoshin Network, Broadband Seismograph Network, Japan National Research Institute for Earth Science and Disaster Prevention, http://www.k-net.bosai.go.jp

Central Disaster Prevention Council (CDPC) (2004), Working Report on Near-field Earthquake beneath Central Tokyo, http://www.bousai.go.jp/jishin/chubou/shutochokka/12/shiryo2-2.pdf (in Japanese).

Hori, M., Oguni, K., Sakaguchi, H. (2005), "Proposal of FEM implemented with particle discretization for analysis of failure phenomena," Journal of the Mechanics and Physics of Solids. Vol.53, pp.681-703.

Abe, H.(2007), "Outline of Japanese Seismic Design Review Guide of Nuclear Power Reactor Facilities," Japan Nuclear Energy Safety Organization.

8CUEE CONFERENCE PROCEEDINGS
8th International Conference on Urban Earthquake Engineering
March 7-8, 2011, Tokyo Institute of Technology, Tokyo, Japan

EVALUATION OF COSEISMIC DISPLACEMENTS IN THE NEAR-FIELD FROM STRONG-MOTION SEISMOMETERS. ANALYSIS OF FOUR RECENT LARGE EARTHQUAKES

E. H. Javelaud[1)], S. Inoue[2)], A. Furukawa[3)], and T. Ohmachi[4)]

1) Former Research Student, Department of Built Environment, Tokyo Institute of Technology, Japan
2) Research Associate, Department of Built Environment, Tokyo Institute of Technology, Japan
3) Graduate Student, Department of Built Environment, Tokyo Institute of Technology, Japan
4) Professor, Department of Built Environment, Tokyo Institute of Technology, Japan
Emmanuel.Javelaud@ens-lyon.org, shusaku@enveng.titech.ac.jp, ohmachi@enveng.titech.ac.jp, furukawa.a.aa@m.titech.ac.jp

Abstract: Detailed analysis of the low frequency content of accelerations recorded in the near-field of four large Japanese earthquakes showed that it is possible to obtain realistic estimates of coseismic displacement time histories. Nearby GPS records are used as a check of the method. The displacements obtained for each earthquake by the two independent methods are given here in terms of maps of residual displacements, with an aim at stressing the usefulness of the proposed methodology.

1. INTRODUCTION

The determination of coseismic displacements from strong-motion seismometers is needed for various purposes including tsunami prediction, estimation of ground strain, design of structures and deep foundations. Deriving displacements from strong-motion seismometers records, rather than obtaining them from direct measurements such as from GPS stations, is interesting because of the large number of accelerometers already deployed, including in a wide range of places, such as the bottom of boreholes, within structures or on the seabed.

The methodology we use to estimate the displacement time-histories from strong-motion records was first described in Javelaud et al. (2005). A detailed description of the method including its limitations can be found in Javelaud et al. (2011).

It has so far been used in studies related to the evaluation of ground strain (Ohtake 2006 and 2007), estimation of the coseismic residual tilt of structures (Javelaud et al., 2006) and coseismic displacement time-histories (Javelaud et al., 2005, 2010 and 2011; Inoue et al., 2007; Furukawa et al., 2010a and 2010b).

In this paper, the displacements time-histories derived from accelerations recorded during four recent and large Japanese earthquakes are compared with those obtained by nearby GPS stations, as a check of the method. Map of residual displacement estimated for four large earthquakes are gathered here with an aim at showing the efficiency of the proposed methodology in different earthquake situations.

2. EARTHQUAKES STUDIED

The four Japanese earthquakes studied are the 2004 Niigata-ken Chuetsu earthquake, the 2007 Noto Hanto Earthquake, the 2007 Niigata-ken Chuetsu-oki Earthquake and the 2008 Iwate-Miyagi Nairiku Earthquake.

TABLE 1 MAIN CHARACTERISTICS OF THE EARTHQUAKES STUDIED

Earthquake	Fault type	Maximum acceleration recorded (cm/sec^2)	M_{JMA}
2004 Niigata-ken Chuetsu earthquake	Reverse	> 1000	6.8
2007 Noto Hanto Earthquake	Reverse	> 1300	6.9
2007 Niigata-ken Chuetsu-oki Earthquake	Reverse	> 700	6.9
2008 Iwate-Miyagi Nairiku Earthquake	Reverse	3866	7.2

TABLE 2 STUDIED EARTHQUAKES AND RELATED REFERENCES

Earthquake	General information	GPS
2004 Niigata-ken Chuetsu earthquake	Asano and Iwata (2009), Honda et al. (2005).	GSI (2004)
2007 Noto Hanto Earthquake	Hiramutsu et al. (2008)	GSI (2007,a)
2007 Niigata-ken Chuetsu-oki Earthquake	Tabuchi et al. (2008), Miyake et al. (2010)	GSI (2007,b)
2008 Iwate-Miyagi Nairiku Earthquake	Suzuki et al. (2010)	GSI (2008)

Brief summary of the studied earthquakes' characteristics are given in Table 1, while references about their mechanisms and source of the GPS residual displacement data are given in Table 2. The strong-motion records come from two networks, the Japanese nationwide K-Net and KiK-Net networks. A few records from the Japanese Meteorological Agency have also been used.

3. MAP OF RESIDUAL DISPLACEMENTS

Maps of residual displacement (Figure 1 to 4) were drawn for each earthquake (Murakami, 2008; Inoue et al., 2009; Javelaud et al., 2010; Furukawa et al., 2010) and the displacement derived from acceleration records compared with those obtained from GPS data.

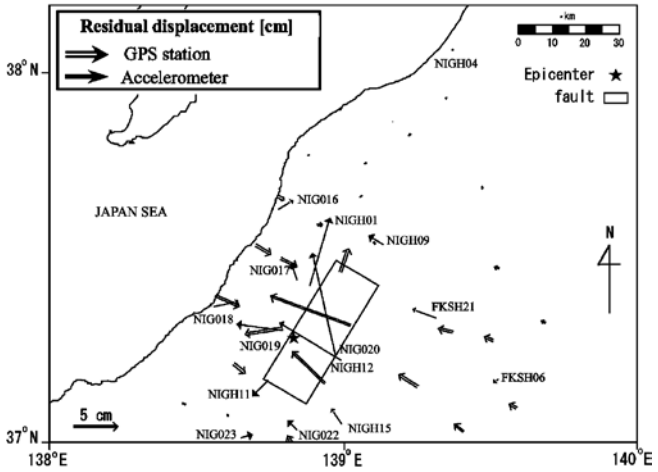


Figure 1 Comparison of coseismic residual displacement obtained from strong-motion seismometers and surrounding GPS stations during the 2004 Niigata-ken Chuetsu earthquake, Japan

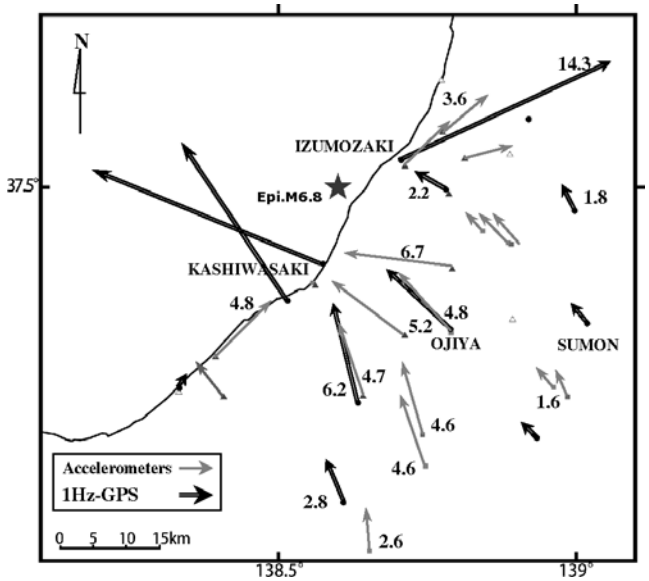


Figure 2 Comparison of coseismic residual displacement obtained from strong-motion seismometers and surrounding GPS stations during the 2007 Niigata-ken Chuetsu-Oki earthquake, Japan

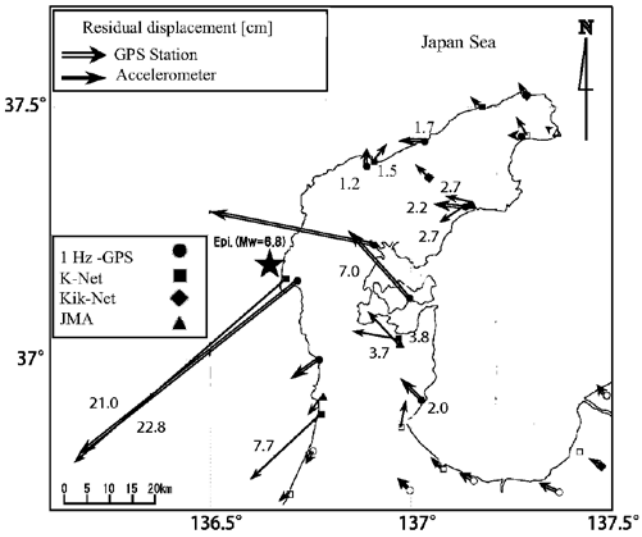


Figure 3 Comparison of coseismic residual displacement obtained from strong-motion seismometers and surrounding GPS stations during the 2007 Noto Hanto earthquake, Japan

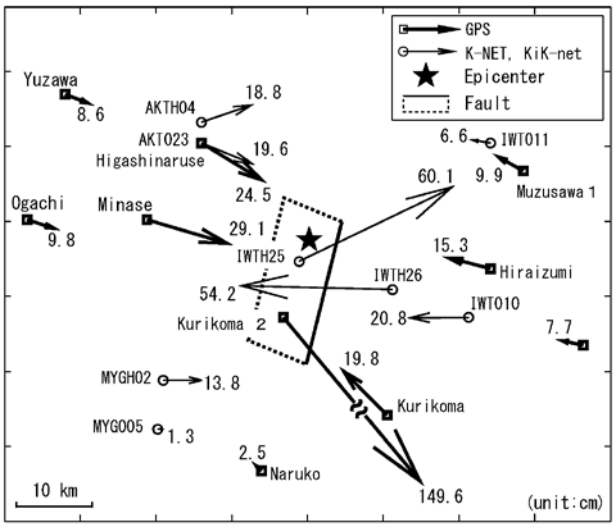


Figure 4 Comparison of coseismic residual displacement obtained from strong-motion seismometers and surrounding GPS stations during the 2008 Iwate-Miyagi Nairiku earthquake, Japan

The four maps above show the coseismic residual displacement obtained at both GPS stations and from acceleration records. In these four areas hit by large earthquakes, there are some collocated GPS and strong-motion stations: at those places, the residual displacements obtained by the two methods are very close in amplitudes and directions, which is an important result considering that the instruments are not sealed on a same concrete footing but at best distant by a few hundred meters. At other places, the residual displacements obtained by the two methods are consistent considering the distance between the instruments and the varying field of displacement.

4. DISCUSSION AND CONCLUSIONS

Estimating displacement time-histories from accelerations records is difficult because strong-motion records of translational accelerations are contaminated during the recording process by instrumental noise, mainly by 1/f semiconductor noise, and by the simultaneous record of the instrument's tilt.
This addition of noise to the translational accelerations includes the addition of long period noise, which makes the estimation of the displacement time histories by double integration difficult to perform and the results of double integration of accelerations series often uncertain.

The proposed methodology is described in detail elsewhere, such as in Javelaud et al.(2011), but could be summarized as follow:
In a first step, the records' low frequency content is visualized. To obtain the Fourier transform of the signal, computers perform their Discrete Fourier Transform (D.F.T.). This provides a discrete representation of the signals' Fourier content but not the continuous visualization necessary to obtain a detailed representation of their low frequency content. Long zero pads are therefore first added to the acceleration records so that the Discrete Fourier Transform performed by computer provides the Discrete Time Fourier Transform of the records (Oppenheim and Schafer, 2010), i.e. allows the user to visualize all the low frequency information that the acceleration records contains.
Then, the 1/f semiconductor noise is estimated from ambient vibration noise records or from records of small aftershocks that occurred short before or after the main event.
Also, any residual tilt shall be recorded after the main part of the shaking as a constant acceleration lasting until the end of the record. It shall therefore have a typical shape in the Fourier domain that should be distinguishable from the low frequency content of the acceleration record and from the 1/f semiconductor noise.

The importance of these three terms (translational acceleration, 1/f semiconductor noise and residual tilt) is evaluated before processing the acceleration time-histories:
- far from the epicenter, the 1/f semiconductor noise may dominate the acceleration record and so an estimate of the displacement can be obtained if the corner frequency at which the 1/f noise dominates the acceleration is small enough.
- in the near-field, removing the residual tilt is often all what is needed to obtain stable and reliable displacement time-histories. The effect of the oscillatory part of the tilt is indeed assumed to have little effect on the displacement time-histories. This assumption may not be valid in the very near-field of the largest earthquakes (Furukawa, 2010; Javelaud et al., 2011). Further studies (Furukawa, 2011) are currently performed to investigate these records with very large amplitude, reaching for example nearly 4000 cm/sec^2 during the 2008 Iwate-Miyagi Nairiku Earthquake.

We believe that the records obtained from the thousand of strong-motion seismometers already deployed in Japan can be also used immediately following earthquakes to obtain additional information such as quick estimations of the residual displacements but also to provide background data for the design of structures close to capable fault and more realistic tsunami prediction.

Acknowledgements:

The authors are grateful to the Center for Urban Earthquake Engineering (CUEE) in Tokyo Institute of Technology for organizing this conference. The accelerograms used were provided by the National Research Institute for Earth Science and Disaster Prevention (Tsukuba, Japan) through the K-Net (www.k-net.bosai.go.jp) and KiK-Net (www.kik.bosai.go.jp) networks, and by the Japanese Meteorological Agency, while GPS measurements were provided by GSI (Geographical Survey Institute, Ministry of Land, Infrastructure and Transport, Ibaraki, Japan).

References:

Asano, K., and T. Iwata (2009). "Source Rupture Process of the 2004 Chuetsu, Mid-Niigata Prefecture, Japan, Earthquake Inferred from Waveform Inversion with Dense Strong-Motion Data", Bull. Seismol. Soc. Am. **99**, 123-140.

Furukawa A., Inoue S. and Ohmachi T. (2010a). "Verification of a quantitative method to estimate coseismic displacements in near-field from strong-motion accelerographs (in Japanese)", *Japan Society of Civil Engineers 2010 Annual Meeting*, I-326.

Furukawa A., Ohmachi T. and Inoue S. (2010b), "Need to improve the Seismic Deformation Method in application to near-field earthquakes", Proc. the Second Symposium on Disaster Mitigation of Lifelines considering System Interactions, 64-69.

Furukawa A. (2011). "Relation between observed ground displacement in the near-field and ground displacement based on Seismic Deformation Method" *Master thesis, Tokyo Institute of Technology.*

Geographical Survey Institute (2004). 2004 Niigata-ken Chuetsu earthquake.) www.gsi.go.jp/WNEW/PRESS-RELEASE/2004/1024-3-1.gif

Geographical Survey Institute (2007a). 2007 Noto Hanto Earthquake) http://www.gsi.go.jp/BOUSAI/isikawa-index.html

Geographical Survey Institute (2008). 2008 Iwate-Miyagi Nairiku Earthquake) http://www.gsi.go.jp/johosystem/johosystem60036.html

Hiramatsu, Y., Moriya K., Kamiya T., Kato M. and Nishimura T. (2008), "Fault model of the 2007 Noto Hanto earthquake estimated from coseismic deformation obtained by the distribution of littoral organisms and GPS: Implication for neotectonics in the northwestern Noto Peninsula", Earth. Planets Space, **60** (9), 903-913.

Honda R, Aoi S, Sekiguchi H, Morikawa N, Kunugi T and Fujiwara H. Ground Motion and Rupture Process of the 2004 Mid Niigata Prefecture Earthquake Obtained from Strong Motion Data of K-NET and KIK-NET. www.k-net.bosai.go.jp/k-net/topics/niigata041023, date of access: 2011/01/16.

Inoue S., Murakami Y., and Ohmachi T. (2007). "Evaluation of the near-field ground displacements based on numerical simulation, strong motion records and GPS records (in Japanese)", *Proc. 6th Annual Meeting of Japan Association for Earthquake Engineering*, 218-219.

Javelaud, E.H., Kubo, G., Ohmachi, T. and Inoue. S. (2005). "Coseismic ground displacement due to the 2004 Niigata-ken Chuetsu earthquake, Japan." *Proc. 4th Annual Meeting of Japan Association for Earthquake Engineering*, 312-313.

Javelaud, E.H., Ohmachi T., and Inoue S. (2006). "A quantitative method to estimate the coseismic residual tilt from strong-motion records", *Proc. 30th Annual Meeting of San-daigakuin*, 5-6.

Javelaud, E. H., Ohmachi T., Murakami Y. and Inoue S. (2010). A quantitative approach to estimate coseismic displacements in the near-field from strong-motion accelerographs: example of the 2007 Niigata-ken Chuetsu-Oki earthquake, Japan. *Joint Conference Proceedings of the 7th International Conference on Urban Earthquake Engineering (7CUEE) & 5th International Conference on Earthquake Engineering (5I*CEE).

Javelaud, E.H., Ohmachi T., and Inoue S. (2011). A Quantitative Approach For Estimating Coseismic Displacements In The Near Field From Strong-Motion Accelerographs. *Bulletin of the Seismological Society of America*, 101(3) (accepted).

Murakami Y. (2008). "Evaluation of near field displacements." *Master thesis, Tokyo Institute of Technology.*

Miyake, H., K. Koketsu, K. Hikima, M. Shinohara, and T. Kanazawa (2010), "Source fault of the 2007 Chuetsu-oki, Japan, Earthquake", Bull. Seismol. Soc. Am., **100**, 384-391.

Oppenheim A. and R. Schafer (2010). Discrete-Time Signal Processing, *Pearson, Third edition, 1132pp.*

Ohtake, K. (2006). Near-field earthquake displacements of the non-liquefiable ground relevant to damage to buried pipelines. *Doctor thesis. Tokyo Institute of Technology.*

Ohtake K., Ohmachi T. (2007) Near-field earthquake displacements of the non-liquefiable ground relevant to damage to buried pipelines. *5th AWWARF/JWWA Water System Seismic Conference.*

Suzuki W., Aoi S., and H. Sekiguchi (2010). Rupture Process of the 2008 Iwate–Miyagi Nairiku, Japan, Earthquake Derived from Near-Source Strong-Motion Records. Bull. Seismol. Soc. Am. 100, (1), 256–266,

Tabuchi, H., T. Harada, and K. Ishibashi (2008). "A southeasterly-dipping static fault model of the 2007 Niigata-ken Chuetsu-oki, Japan, earthquake based on crustal movements, tsunamis, aftershock distribution and neotectonics", Report of Research Center for Urban Safety and Security, Kobe University **3**, 1-10.

8CUEE CONFERENCE PROCEEDINGS
8th International Conference on Urban Earthquake Engineering
March 7-8, 2011, Tokyo Institute of Technology, Tokyo, Japan

BROADBAND SOURCE MODEL FOR THE 2009 L'AQUILA, ITALY, EARTHQUAKE

Natalia Poiata[1], Kazuki Koketsu[2], Alessandro Vuan[3], and Hiroe Miyake[4]

1) Graduate Student, Earthquake Research Institute, University of Tokyo, Japan
2) Professor, Earthquake Research Institute, University of Tokyo, Japan
3) Researcher, Istituto Nazionale di Oceanografia e Geofisica Sperimentale, Trieste, Italy
4) Assistant Professor, Earthquake Research Institute, University of Tokyo, Japan
natalia@eri.u-tokyo.ac.jp, koketsu@eri.u-tokyo.ac.jp, avuan@inogs.it, hiroe@eri.u-tokyo.ac.jp

Abstract: The 2009 L'Aquila, Italy, earthquake (M_w 6.3) caused severe damage to the city of L'Aquila and tens of villages of the Abruzzo region, killing over 300 people. The mainshock was followed by a significant aftershock activity that extended more than 30 km in northwest-southeast direction. This earthquake provided an unprecedented for a normal faulting event amount of seismological records. During the mainshock, several of the near-fault stations located on the hanging wall of the causative fault experienced ground shakings that exceeded the level prescribed by the design spectra (e.g., Eurocode8) in the period up to 1 s. We studied the source process of the 2009 L'Aquila earthquake in both low- and broadband frequency ranges. The low-frequency (0.05-0.5 Hz) source model was determined by the waveform inversion of the near-field strong motion data, resulting in a slip distribution characterized by an asperity located about 8 km southeast from the hypocenter. The broadband (0.2-10.0 Hz) source characteristics were further determined by employing the empirical Green's function method. Here we discuss the comparison of the derived source characteristics and their influence on the spatial variability of the observed ground motions.

1. INTRODUCTION

The L'Aquila earthquake (Fig. 1) occurred on 6 April 2009 at 01:32:40 UTC in the Abruzzo region of Central Apennines, Italy. According to the Istituto Nazionale di Geofisica e Vulcanologia of Italy (INGV) the earthquake was generated by normal faulting on a fault system running parallel to the axis of the Apennine mountains and had a moment magnitude (M_w) of 6.3. The updated location of hypocenter was estimated to be 2 km westward from the city of L'Aquila at 42.3476°N, 13.3800°E, and depth of 9.46 km (INGV, 2009). This M_w 6.3 event caused severe damage to the city of L'Aquila and tens of villages of the Abruzzo region located in the middle Aterno Valley. Although this magnitude was not among the largest to have occurred in the Apennines, the 2009 L'Aquila earthquake can be considered one of the most disastrous events there (Tertulliani, 2009). As was estimated by the May of 2009, 305 person lost their lives and over 1500 were injured, and thousands of buildings and houses were destroyed and damaged. This represents the highest death toll due to an earthquake in European Union since the 1980 Irpinia event, and the highest economic loss due to the seismic activity since the 1999 Athens earthquake (Papanikolaou *et al.*, 2010). According to the damage estimates, 47% of houses in the epicentral area were damaged and 20% of those were heavily damaged. Most of the damage occurred within the city of L'Aquila, located close to the hypocenter, and the villages of Paganica and Onna, located further southeast.

The 6 April 2009 L'Aquila mainshock was a largest event in a seismic sequence that started a few months earlier. The mainshock was followed by a significant aftershock activity that extended over the length exceeding 30 km in northwest-southeast direction (Fig. 1).

The 2009 L'Aquila earthquake provided an unprecedented amount of seismological records form a normal faulting event, making the study of its source process an important issue for understanding and quantifying the seismic hazard due to normal faulting events. The mainshock and aftershocks have been recorded by several local and regional seismic networks. The records from the Italian strong-motion network (RAN), operated by the Department of Civil Protection were integrated into the ITalian Accelerometric Archive (ITACA) and made available over the internet. Fifty-eight strong motion stations in the distance range from 1.7 km to 277 km provided the high quality digital acceleration records of the mainshock. The near-fault stations at epicentral distances of 1.7 to 5.0 km) on the hanging wall side recorded largest horizontal PGA values ranging from 0.35 to 0.65 g. These stations are also characterized by vertical PGAs as large as the horizontal ones. The largest PGA of 662 cm/s^2 was recorded at the AQV station in the Aterno valley. Stations located on the foot wall side recorded only PGAs less than 0.15 g. According to some of the Italian seismologists this event represents the third largest earthquake recorded by strong-motion instruments in Italy, after the 1980 M_w 6.9 Irpinia and the 1976 M_w 6.4 Friuli earthquakes (Akinci *et al.*, 2010).

The comparison of the 5% damped velocity response

spectra estimated from the records of the 2009 L'Aquila mainshock recorded at the near-fault stations located on the hanging wall of the causative fault with the design spectra prescribed by the Eurocode 8 (EC8) showed that both the horizontal and vertical components generally exceeded the spectral ordinates of the design spectra (Fig. 2). This can explain the widespread damage of the buildings observed in the near-fault area.

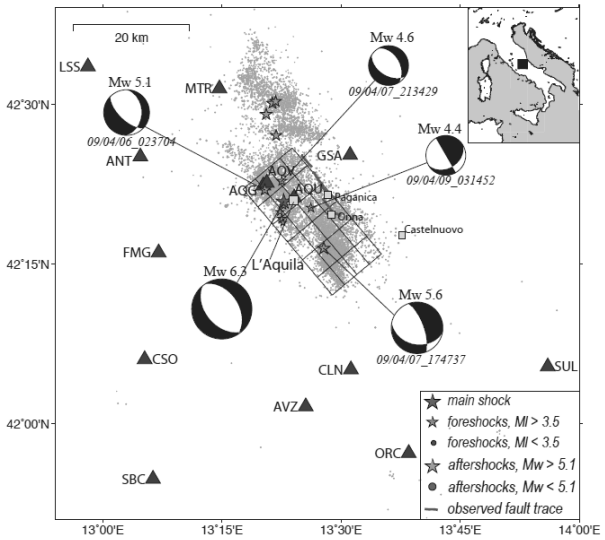


Figure 1. Map view of the L'Aquila area showing the distribution of the strong motion stations of RAN network that recoded the mainshock and are located within the epicentral distance of 50 km from the epicenter (blue triangles). The black rectangles represent the surface projection of the fault plane determined from the waveform inversion analysis.

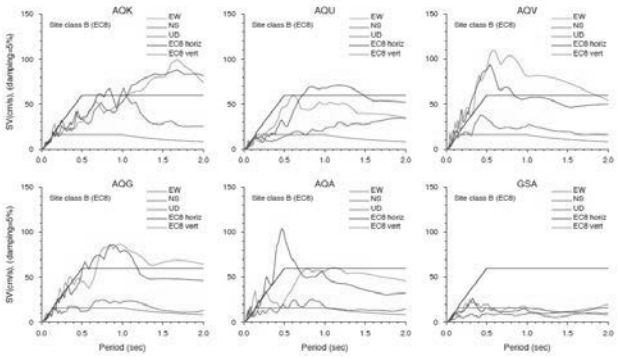


Figure 2. Comparison of three component recorded velocity response spectra (5% damping) with the pseudo-velocity response spectra prescribed by the EC8 for the horizontal and vertical components for 10% exceedance probability in 50 years.

2. SOURCE PROCESS INFERRED BY STRONG MOTION INVERSION

We developed a rupture model for the L'Aquila event in a frequency range of 0.05-0.5 Hz through the waveform inversion of near-field strong motion data applying the multiple-time-window linear waveform inversion method of Yoshida *et al.* (1996). We used three component velocity records from the stations located within the distance of 55 km from the epicenter (Fig. 1). To account for the geological complexity of the area, a set of 1-D stratified velocity models were determined for each station by the forward modeling of the available aftershock records (Fig. 1) assuming the finite duration point source approximation and calculating the theoretical Green's functions by the extended reflectivity method of Kohketsu (1985).

A number of studies including coseismic surface rupture observations (Falcucci *et al.*, 2009; Boncio *et al.*, 2010; EMERGEO Working Group, 2010), geodetic data (e.g., Atzori *et al.*, 2009; Anzidei *et al.*, 2009) and distribution of the relocated aftershocks (Chirabba *et al.*, 2009) confirmed that 2009 L'Aquila earthquake was a result of a normal faulting along the northwest-southeast oriented, southwest dipping Paganica fault. Taking into account these analyses we assumed that rupture occurred on a single fault plane dipping towards southwest, and adopted the location of the rupture starting point corresponding to the revised hypocenter of INGV. The orientation of the fault plane is based on the best fit solution Poiata *et al.* (2009). We set the fault plane dimensions of 24 km in length by 16 km in width by referring the aftershock distribution of INGV. The fault was then discretized into 6 × 4 subfaults, each with an area of 4 km in length by 4 km in width. Figure 1 illustrates the described fault settings by showing the surface projection of the assumed fault plane. The best values of the hypocenter depth and fault orientation (strike and dip angles) were determined during the strong motion inversion analysis through the grid search procedure. We estimated as well the rupture propagation velocity V_r minimizing the residuals between observed and synthetic velocity ground motions (Fig. 3).

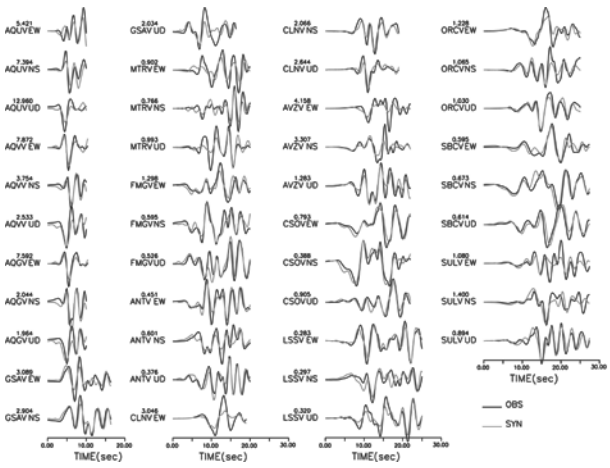


Figure 3. Comparison of the observed (black traces) and synthetic (red traces) ground velocities for the low-frequency strong motion source model. The numbers above the station codes indicate the maximum amplitudes of observation in cm/s.

The slip distribution of our best model from the strong motion inversion shows a major asperity located about 8 km southeast from the hypocenter beneath the town of Onna (Fig. 4e). The total seismic moment corresponding to the model is 0.373 x 10^{19} Nm (M_w 6.3) and the optimal depth of the rupture starting point is found to be 8.2 km. The overall source duration is around 14 s, and the rupture velocity is estimated at 2.0 km/s. The pure normal faulting mechanism of the strong motion model (Fig. 4d) and the precise fault orientation correspond to the values of strike and dip of 140° and 46°, respectively.

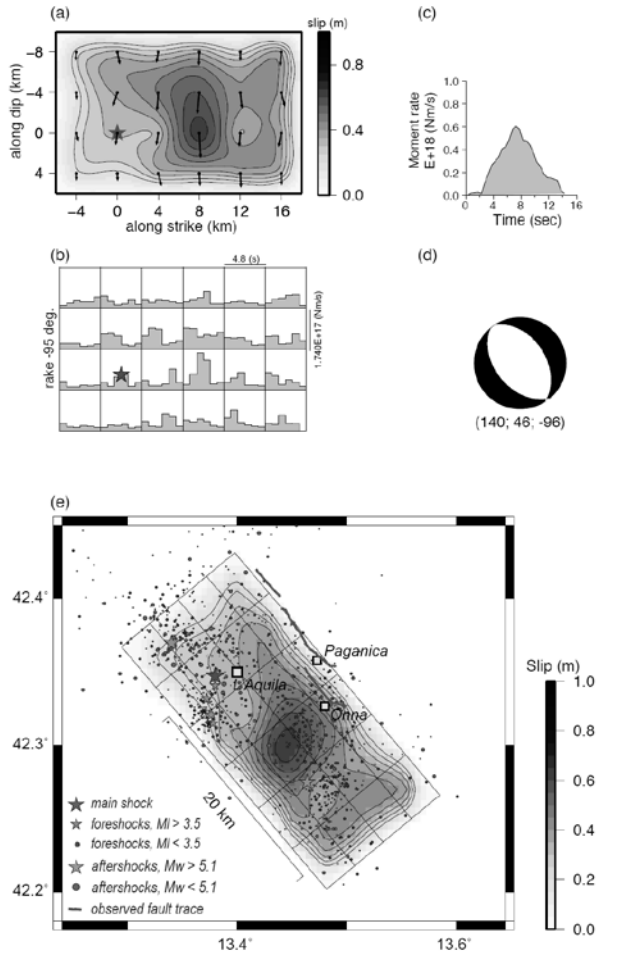


Figure 4. Results of the strong motion waveform inversion. (a) Slip distribution plotted at contour intervals of 0.05 m. The red star indicates the hypocenter. The arrows denote slip vectors of the hanging wall relative to the footwall. (b) Moment-rate functions of each subfault for the resultant direction of the rake angle. The red star indicates the hypocenter. (c) Total moment-rate function. (d) Focal mechanism solution corresponding to the slip distribution of (a). (e) Surface projection of the slip distribution (a) on the map. The contour interval is 0.05 m. The red star indicates the rupture starting point, orange and blue stars show the locations of the strongest foreshocks and aftershocks respectively; orange and blue dots the other foreshocks and aftershocks for a one week period following the mainshock. Red thick line show the location of the observed coseismic breakages modified after Boncio *et al.* (2010).

The source model and the location of the main asperity are in agreement with the results presented by other authors (Atzori *et al.*, 2009; Cirella *et al.*, 2009) as well as the aftershock distributions.

3. BROADBAND SOURCE MODELING USING THE EMPIRICAL GREEN'S FUNCTION METHOD

One of the principal goals of the source processes estimations is to provide the source model capable of reproducing broadband ground motions in the near source region with accuracy enough for engineering purposes. For frequencies higher than 1 Hz, the deterministic simulations of ground motions are limited by the deficit of the precise information about the velocity structure, and the complexity of the source description. A useful approach to overcome these difficulties is to estimate ground motions of an earthquake using the records of smaller events as the empirical Green's function.

We applied this empirical Green's function (EGF) method of Irikura (1986) to estimate the broadband source model for the 2009 L'Aquila mainshock in the frequency range of 0.2-10 Hz. For the source parameter estimation the aftershock form 7 April 2009 (21:34:29; one day from the mainshock) with the magnitude M_w 4.6 was selected as the empirical Green's function. The initial location of the SMGA was assumed based on the location of the asperity determined from the low-frequency inversion analysis. We further determined the parameters of the high-frequency SMGA such as: number and size of subfaults, rupture velocity, rise time of source time function and stress drop, by applying spectral fitting method (Miyake *et al.*, 1999) and forward modeling of the observed broadband ground motions for the selected mainshock-aftershock pair.

The size of the SMGA of the mainshock was found to be 8.0 km in length by 5.2 km in width with the rupture starting point located in its northwestern part. The rupture was estimated to have propagated predominantly towards the southeast and up-dip, in agreement with the result from the source inversion of strong motion data. The rupture velocity was determined to be 2.9 km/s. The validation of the estimated source parameters was made by comparison of the synthetic waveforms of acceleration, velocity, and displacement with the observed ones for four closest stations (Fig. 5) as well as five other stations located at larger epicentral distances. The estimated source model reproduced well the ground motion pulses in the velocity and displacement components of the stations located on the hanging wall side of the causative fault. The results of the analysis for 2009 L'Aquila earthquake indicate that a SMGA coincides with the asperity that was estimated from the low-frequency waveform inversion (Fig. 6).

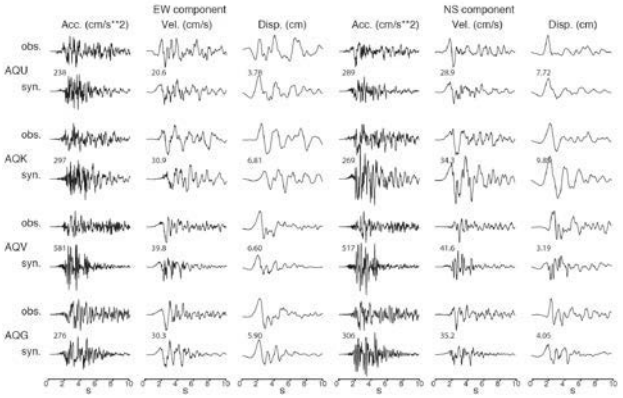


Figure 5. Comparison of the observed and synthetic broadband ground motions for four closest stations used for the estimation of the parameters of SMGA. The numbers aligned the station codes indicate the maximum amplitudes of observation.

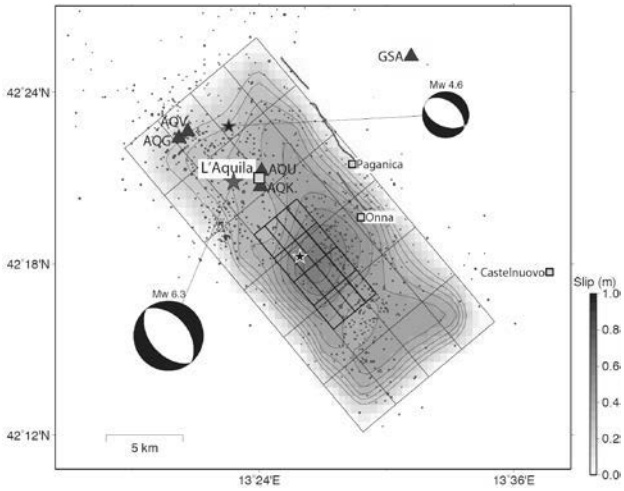


Figure 6. Map view of the near-source region of the 2009 L'Aquila earthquake showing the relative location for the surface projection of SGMA determined from the EGF analysis (black rectangles), and the slip distribution determined from the strong motion inversion. The red star represents the location of the mainshock and the black star with red contour represents the location of the EGF event. The focal mechanisms and seismic moments determined by INGV are also shown. The rest of the components are the same as shown in Fig. 1.

4. CONCLUSIONS

We presented a source model of the L'Aquila earthquake, determined from the waveform inversion of strong motion data in the frequency range of 0.05-0.5 Hz, and the broadband modeling using the EGF method in the frequency range of 0.2-10 Hz. The resulted source model; location of the main asperity and the SMGA (Figs. 4 and 6) are in agreement with the results presented by other authors (Cirella *et al.*, 2009; Atzori *et al*., 2009) as well as the aftershock distributions. We confirmed that the location of the main slip area southeast from the hypocenter is the robust feature of the inversion. This SMGA is in agreement with the existing empirical source scaling relationships for inland crustal earthquakes implying a stress drop of around 10 MPa (e.g., Miyake *et al.*, 2003). This feature is also in agreement with the study of Bindi *et al*. (2009), confirming that the 2009 L'Aquila earthquake provided a stress drop that corresponds to the events recorded in the Central and Southern Apennines.

The results of our analysis show as well correlation with the observed macroseismic intensities reported by INGV. The maximum MCS intensities of IX-X are reported southeast of the hypocentral location, with the value of X corresponding to the city of Onna.

References:

Akinci, A., Malagnini, L., Sabetta, F. (2010), "Characteristics of the Strong Ground Motions from the 6 April 2009 L'Aquila Earthquake, Italy," *Soil Dyn. Earth. Eng.*, **30**, 320-335.

Anzidei, M., Boschi, E., Cannelli, V., Devoti, R., Esposito, A., Galvani, A., Melini, D., Pietrantonio, G., Riguzzi, F., Sepe, V., and Serpelloni, E. (2009), "Coseismic Deformation of the Destructive April 6, 2009 L'Aquila Earthquake (Central Italy) from GPS Data," *Geophys. Res. Lett.*, **36**, L17307, doi:10.1029/2009GL039145.

Atzori, S., Hunstad, I., Chini, M., Salvi, S., Tolomei, C., Bignami, C., Stramondo, S., Trasetti, E., Antonioli, A., and Boschi, E. (2009), "Finite Fault Inversion of DInSAR Coseismic Displacement of the 2009 L'Aquila Earthquake (Central Italy)," *Geophys. Res. Lett.*, **36**, L15305, doi:10.1029/2009GL039293.

Bindi, D., Pacor, F., Luzi, L., Massa, M., and Ameri, G. (2009), "The M_w 6.3, 2009 L'Aquila Earthquake: Source, Path and Site Effects from Spectral Analysis of Strong Motion Data," *Geophys. J. Int.*, **179**, 1573-1579.

Boncio, P., Pizzi, A., Brozzetti, F., Pomposo, G., Lavecchia, G., Di Naccio, D., and Ferrarini, F. (2010), "Coseismic Ground Deformation of the 6 April 2009 L'Aquila Earthquake (Central Italy, Mw6.3)," *Geophys. Res. Lett.* **37**, L06308, doi:10.1029/2010GL042807.

Chiarabba, C., Amato, A., Anselmi, M., Baccheschi, P., Bianchi, I., Cattaneo, M., Cecere, G., Chiaraluce, L., Ciaccio, M. G., De Gori, P., De Luca, G., Di Bona, M., Di Stefano, R., Faenza, L., Govoni, A., Importa, L., Lucente, F. P., Marchetti, A., Margheriti, L., Mele, F., Michelini, A., Monachesi, G., Moretti, M., Pastori, M., Piana Agostinetti, N., Piccinini, D., Roselli, P., Seccia, D., and Valoroso, L. (2009), "The 2009 L'Aquila (Central Italy) M_w 6.3 Earthquake: Main Shock and Aftershocks," *Geophys. Res. Lett.* **36**, doi:10.1029/2009GL039627.

Cirella, A., Piatanesi, A., Cocco, M., Tinti, E., Scognamiglio, L., Michelini, A., Lomax, A., and Boschi, E. (2009), "Rupture History of the 2009 L'Aquila (Italy) Earthquake from Non-Linear Joint Inversion of Strong Motion and GPS Data," *Geophys. Res. Lett.*, **36**, L19304, doi:10.1029/2009GL039795.

EMERGEO Working Group (2010), "Evidence for Surface Rupture Associated with the M_w 6.3 L'Aquila Earthquake Sequence of

April 2009 (central Italy)," *Terra Nova*, **22**, 43-51.

Falcucci, E., Gori, S., Peronace, E., Fubelli, G., Moro, M., Saroli, M., Giaccio, B., Messina, P., Naso, G., Scardia, G., Sposato, A., Voltaggio, M., Galli, P., and Galadini, F. (2009), "The Paganica Fault and Surface Coseismic Ruptures due to the April 6, 2009 Earthquake (L'Aquila, Central Italy)," *Seismol. Res. Lett.*, **80**, 940-950.

Irikura, K. (1986), "Prediction of Strong Acceleration Motions using Empirical Green's Function," *Proc. 7th Japan Earthq. Eng. Symp.*, 151-156.

Istituto Nazionale di Geofisica e Vulcanologia (INGV) (2009), "Location of April 6, 2009 Earthquake Updated with all the Available Data;" http://www.ingv.it.

Kohketsu, K. (1985), "The Extended Reflectivity Method for Synthetic Near-Field Seismograms," *J. Phys. Earth*, **33**, 121-131.

Miyake, H., Iwata, T., and Irikura, K. (1999), "Strong Ground Motion Simulation and Source Modeling of the Kagoshima-ken Hokuseibu Earthquakes of March 26 (M_{JMA} 6.5) and May 13 (M_{JMA} 6.3), 1997, using Empirical Green's Function Method," *Zisin2*, **51**, 431-442 (in Japanese with English abstract).

Miyake, H., Iwata, T., and Irikura, K. (2003), "Source Characterization for Broadband Ground-Motion Simulation: Kinematic Heterogeneous Source Model and Strong Motion Generation Area," *Bull. Seismol. Soc. Am.*, **93**, 2531-2545.

Papanikolaou, I. D., Lekkas, E. L., and Fountoulis, O. G. (2009), "Preliminary Report on the L'Aquila M_w=6.2 (M_L=5.8) Earthquake (6th April 2009) Abruzzo, Central Apennines, Italy," http://dtag.geol.uoa.gr/~dtag/assets/File/Preliminary%20report.pdf.

Poiata, N., Koketsu, K., Vuan, A., and Miyake, H. (2009), "Rupture Process of the 2009 L'Aquila, Italy, Earthquake Inferred from the Inversion of Multiple Seismological Datasets," *Eos Trans. AGU*, **90**(52), Fall Meet. Suppl., Abstract U13C-04.

Tertulliani, A., Rossi, A., Cucci, L., and Vecchi, M. (2009), "L'Aquila (Central Italy) Earthquakes: The Predecessors of the April 6, 2009 Event," *Seismol. Res. Lett.*, **80**, 1008-1013.

Yoshida, S., Koketsu, K., Shibazaki, B., Sagiya, T., Kato, T., and Yoshida, Y. (1996), "Joint Inversion of Near- and Far-Field Waveforms and Geodetic Data for the Rupture Process of the 1995 Kobe Earthquake," *J. Phys. Earth.*, **44**, 437-454.

8CUEE CONFERENCE PROCEEDINGS
8th International Conference on Urban Earthquake Engineering
March 7-8, 2011, Tokyo Institute of Technology, Tokyo, Japan

THE POSSIBILITY OF TRAP WAVE AND SITE EFFECT IN THE LONGITUDINAL VALLEY OF EASTERN TAIWAN

Kuei-Mei Lin[1], Kuo-Liang Wen[2], Chun-Te Chen[3], and Jyun-Yan Huang[3]

1) Master student, Institute of Geophysics, National Central University, Taiwan, R.O.C.
2) Professor, Institute of Geophysics, National Central University, Taiwan, R.O.C.
3) PhD Candidate, Institute of Geophysics, National Central University, Taiwan, R.O.C.
986202006@cc.ncu.edu.tw, wenkl@earth.ncu.edu.tw, 956402004@cc.ncu.edu.tw, 986402005@cc.ncu.edu.tw

Abstract: The Longitudinal valley is the convergent boundary of Eurasian Plate and Philippine Sea Plate. Located between the Central Range and Coastal Range, the valley was linear, narrow, and near the north-south direction. There are numerous earthquakes and many active faults here, and the underground active tectonics are very complicated. The previous studies provided us a better understanding of structures and seismotectonics in the Longitudinal valley. The fracture zone could be regarded as a low-velocity zone, and seismic energy will trapped in this low-velocity zone. In this study, the trapped waves were identified from the observed seismograms based on the characteristics list (Li *et al.* 1998, Ben-Zion 1998) and the amplitude, particle motion, and dominant frequency were also analyzed. Finally, the site effects in the Longitudinal valley were discussed in this study.

1. INTRODUCTION

Taiwan is located along the plate boundary between the Eurasian Plate and the Philippine Sea Plate. Collision between the two plates takes place along the Longitudinal valley (LV) with a highly convergence rate of 82 mm/yr. The Longitudinal valley is considered as the collision suture between the two plates. Its tectonic implications and seismicity have long been a primary research focus in the central eastern Taiwan. The crust beneath the Longitudinal valley was unusually thinner than that beneath other parts in Taiwan (Kim et al. 2005, Kim et al. 2006, Liang et al. 2007).

The LV is sandwiched between the Central Range and the Costal Range. It is shown in Figure 1. It is about 160 km long and less than 10 km wide in most places. And it's filled with Quaternary sediment. The geological condition in LV is relatively soft in contrast to the stiff eastern and western range. Li (2004) reported that a fracture zone may form a low-velocity zone and trap some waves inside the fault. From the regional geology setting, we want to know if the Longitudinal valley can trap waves just like a low-velocity zone.

The seismicity in central collision zone is relatively low in contrast to the very active northern and southern collision zone. The Longitudinal valley was reported with complex tectonics along different segment of the LV. We also collect the earthquakes data and stations' information to analyze the site effect in the area.

2. DATA AND METHOD

2.1 Data Source

Strong ground-motion data obtained by the Taiwan Strong-Motion Instrumentation Program (TSMIP) are used to investigate site effect. The TSMIP accelerograph network currently consists of more than 650 free-field stations. Seismic signals digitized at 24 bits and 200 samples per second for three-component stations. And the maximum range of records is ±2g. All the arrival time and earthquake-location files from 1999 to 2009 reported by the Central Weather Bureau (CWB) have been collected and analyzed in this study.

The Chengkung earthquake (M_L = 6.42) occurred on December 10, 2003 at a focal depth of 17.73 km, as reported by the CWB. The main shock occurred at 23.0667°N and 121.3982°E along the eastern coast of Taiwan near the town of Chengkung. This earthquake resulted in slight damage of buildings and constructions of nearby harbor facilities, leading to limited property loss. We collected 98 P-wave arrival times recorded by stations of Hualien and Taidong for this event. And we take this earthquake as a target to discuss the trapped wave. The selected earthquake and stations are plotted in Figure 2.

2.2 Trap Wave Analysis

The Chengkung earthquake and its aftershock sequence occurred along an east-dipping seismic zone beneath the Coastal Range in southern LV (Kim et al. 2006, Hao et al. 2007). Recent studies of strong ground motion and coseismic GPS observation suggested that the 2003 Chengkung earthquake sequence along this east-dipping

fault was most probably related to the Chihshang fault. And maybe seismic waves could be trapped in this east-dipping seismic zone.

Joints and cracks are distributed around the fault plane with a high density (Scholz et al. 1993). When the wavelengths of the seismic wave are longer than the scale of each crack, the total elastic property of the material can be considered as a homogeneous zone (O'conell and Budiansky 1974, Hudson 1980). Hence, the trapped waves that travel within the fault-zone can be expected. The fault-zone trapped waves have some characteristics (Li et al. 1998, Ben-Zion 1998):

(1) Large amplitude within a fault zone;
(2) Particle motion polarized into the fault-parallel direction;
(3) Propagating along the fault zone;
(4) Normal dispersion;
(5) Dominant frequency that almost corresponds to the frequency showing the minimum phase velocity.

We identify trapped waves from observed seismograms based on the characteristics listed above. An example of observation of fault-zone trapped wave is shown in Figure 3. We can find that the fault-zone trapped wave with large amplitude arrival after the S wave. From the cross seismic array, each seismogram is synchronized with the onset of the direct S-wave arrival. The amplitude of the trace in fracture zone is relatively large than others.

2.3 H/V ratio

The waveform data recorded by seismic station is mainly influenced by source effect, path effect and site effect. Traditionally, reference-site method was used to discuss the local site effect. Nakamura (1989) found that it can only use the Horizontal-to-Vertical (H/V) spectral ratio of surface station to get the site effect in the station location easily.

At the same time, Huang and Teng (1999) also confirmed that the amplification is similar to one when the reference station is the rock station. And Hsieh (2001) proved the H/V ratio of good rock station will approach a constant by analyzed several downhole accelerometer arrays in Taiwan. In general, H/V ratio of rock station is often affected by regional structure. The value is not stable but will slightly similar to a constant.

3. RESULTS

3.1 Trap Wave

The acceleration data of station HWA005 for Chengkung earthquake exhibits phase with large amplitudes after S waves in the Figure 4. And we further to analyze the particle motions for direct P wave and the waves after S arrival (Figure 5). We find that the particle motion of P wave shows basically a vertical movement. And the particle motion of the wave after S wave displays an east-west movement. That seems like the wave after S wave is a reflected wave due to tectonic. Accordingly, compared with the stations in the north of station HWA005 and found stations HWA017, HWA029 and HWA059 had same phenomenon that movement seems to shift from directly approach in the northeast-southwest (before 60 sec in Figure 6) to approximate in the east-west (after 60 sec in Figure 6). Stations HWA016, HWA020, and HWA052 also showed similar tendency. And stations HWA018, HWA031, HWA035, and HWA051 were not so clear. All stations' data were shown in Figure 6.

3.2 Dominant Frequency

After basic data processing, include baseline correction and filter, the H/V ratios of every station are calculated, and then picked out the dominant frequency for each station. The dominant frequency is the frequency has the greatest impact of site amplification.

In this study, we selected the dominant frequency based on:

(1) The frequency with high magnification;
(2) Some stations have several bands with magnification. In such cases, we may (a) choose the lower frequency band if the low- frequency with higher magnification; (b) choose the lower frequency band if several bands with similar magnification; (c) choose the high frequency band if the high-frequency with higher magnification.
(3) After pick out the dominant frequency of each station, we will compare with the dominant frequency of nearby station and revise.

In general, there is not much difference between adjacent stations. It is because the subsurface structure may not exist significant change. The sample of pick out dominant frequency is shown in Figure 7.

4. DISCUSSIONS AND CONCLUSIONS

From the results of analyzing the particle motions, we found some stations in the LV displayed that the direction of wave propagation changed by structure in 2003 Chenkung earthquake. The direction of wave shift from near northeast-southwest or north-south to approach east-west. Most of them were located in the north of station HWA005. But from the time domain, the amplitude of those stations didn't reveal as in Figure 3. The maximum amplitude is 25.073 gals in station HWA005. It is mainly because the complex structure beneath the LV. We suspect that the seismic wave propagated along the LV fault zone.

Stations in the south of HWA005 have large amplitude of P and S wave, but they didn't receive obvious fault zone trapped wave or resonant wave by alluvium. That may be mixed by strong S wave or the time was too short to produce trapped wave. On the other hand, the changes of direction in the station HWA005 and others to the north could be due to the thick alluvium beneath the stations. The seismic wave propagated along the fault zone to the alluvial plain of northern LV and trapped and resonated in there. The stations HWA031, HWA033, and HWA051 on the eastern of northern LV are near to the surface exposure of Luehmei

fault. Their particle motions almost similar. And stations on the western of northern LV show obvious change of direction of wave propagation. The wave resonance in alluvium may come from fault zone of LV, which located in the eastern boundary of northern LV. The seismic wave resonated by the alluvium, so the stations HWA005, HWA020, HWA052, HWA059, HWA017, HWA029, and HWA016 all had significant change of direction of wave propagation.

It is noticeable that HWA032 and HWA035 didn't show clear change of wave direction. From the drilling data of station HWA035, the structure nearby the station can be considered as a more rigid stratum. And from the drilling data of station HWA006 which near by HWA005, the structure in the vicinity of HWA006 is a softer stratum and has thicker alluvium. That may be the reason for the different results between the station HWA035 and HWA005. Another noticeable is the station HWA018. In addition to HWA018, stations had obvious change of wave propagation in that area. From the drilling data, the structure beneath the station has divided into upper and lower levels by a thin soft layer. It may be the cause of difference behavior in contrast to nearby station.

We further analysis particle motions of six stations. The results are shown in Figure 8. The direction of wave propagation was significantly different at before 60 seconds and after. Those are particularly clear at stations HWA005 and HWA038. The movement displays a northeast-southwest direction at the window before 60 seconds. After 60 seconds, the movement shift to about an east-west or north-south direction. The station closer to the epicenter shows unobvious tendency. Next we want to choose smaller earthquakes to analyze in the future. Hope the trapped wave can identify more clearly, and to link the geological structure.

Figure 9 compare the dominant frequency result and that from microtremor measurement by Huang (2009). Near the Hualien and Taidong cities, both have low dominant frequency. The Hualien and Taidong cities are alluvial plains, the resonance frequency is relatively lower than other places in the study area. The value of dominant frequency is less than 4 Hz. The dominant frequency value is about 3.5-5.5 Hz in most places of LV. The value of dominant frequency shows greater than 6.5 Hz in the southern part of LV. Because the lack of drilling data, we have to do further investigation to check the reason of high dominant frequency value. From the drilling data, we can find that the high value in the eastern of Coastal Range is mainly due to the thin alluvium. Huang's study use intensive microtremor measurements distributed in LV. So his result can provide better control inside of LV than our results. However, our station network has a bigger distribution range from LV to Coastal Range. Our results reveal that the dominant frequency value is greater than 4 Hz for the most part of eastern Coastal Range. The largest value is reach to 10~20Hz.

Acknowledgement:

The authors are grateful to the Central Weather Bureau of Taiwan for providing arrival time and drilling data from their seismic network. This study was supported by National Science Council of Taiwan under the grants no. NSC98-2116-M-008-008 and NSC 99-2116-M-008-023.

References:

Ben-Zion, Y. (1998), "Properties of Seismic Fault Zone Waves and Their Utility for Imaging Low-velocity Structures," *J. Geophys. Res.*, **103**, 12567-12585

Hudson, J.A. (1980), "Wave Speeds and Attenuation of Elastic Waves in Material Containing Cracks," *Geophys. J. R. Astr. Soc.*, **64**, 133-150

Huang, H.C. and Teng, T.L. (1999), "An Evaluation on H/V Ratio vs. Spectral Ratio for Site Response Estimation Using the 1994 Northridge Earthquake Sequence," *Pure & Applied Geophysics*, **156**, 631-649

Hao, K.C., Wu, Y.M., Chen, Y.G., and Chen, R.Y. (2007), "2003 Mw6.8 Chengkung Earthquake and Its Related Seismogenic Structures," *Journal of Asian Earth Sciences*, **31**, 332-339

Hsieh, H.H. (2001), "A Study of Horizontal-to-Vertical Spectral Ratio by Using the Downhole Accelerometer Array in Taiwan," Master degree thesis, National Central University, Taiwan

Huang, J.Y. (2009), "Using Microtremor Measurement to Study the Site Effect in Taiwan Area," Master degree thesis, National Central University, Taiwan

Kim, K.H., Chiu, J.M., Pujol, J., Chen, K.C., Huang, B.S., Yeh, Y.H., and Shen, P. (2005), "Three-dimensional Vp and Vs Structural Models Associated with the Active Subduction and Collision Tectonics in the Taiwan Region From 3-D Seismic Tomography," *Geophys. J. Int.*, **162**, 204-220

Kim, K.H., Chiu, J.M., Pujol, J., and Chen, K.C. (2006), "Polarity Reversal of Active Plate Boundary and Elevated Oceanic Upper Mantle Beneath the Collision Suture in Central Eastern Taiwan," *Bull. Seism. Soc. Am.*, **96**, 796-806

Li, Y.G., Aki, K., Vidale, J.E., and Alvarez, M.G. (1998), "A Delineation of the Nojima Fault Ruptured in the M7.2 Kobe, Japan, Earthquake of 1995 Using Fault Zone Trapped Wave," *J. geophys. Res.*, **103**, 7247-7263

Li, Y.G. (2004), "Low-velocity Damaged Structure of the San Andreas Fault at Parkfield From Fault Zone Trapped Waves," *Geophysical Research Letters*, **31**.

Liang, W.T., Chiu, J.M., and Kim, K.H. (2007), "Anomalous Pn Wave Observed in Eastern Taiwan: Implications of A Thin Crust and Elevated Oceanic Upper Mantle Beneath the Active Collision-zone Suture," *Bull. Seism. Soc. Am.*, **97**, 1370-1377

Nakamura, Y. (1989), "A Method for Dynamic Characteristics Estimation of Subsurface Using Microtremor on the Ground Surface," *QR of RTRI*, **30**, 25-33

O'Connell, R.J. and Budiansky, B. (1974), "Seismic Velocities in Dry and Saturated Cracked Solid," *J. Geophys. Res.*, **79**, 5412-5426

Scholz, C.H., Dawers, N.H., Yu, J.Z., and Anders, M.H. (1993), "Fault Growth and Fault Scaling Laws: Preliminary Results," *J. Geophys. Res.*, **98** 21591-21961

Mizuno, T. (2003), "The Subsurface Observation of Fault-zone Trapped Waves: Applications to Investigations of the Deep Structure of Active Faults," *Bull. Earthq. Res. Inst.*, **78**, 91-106.

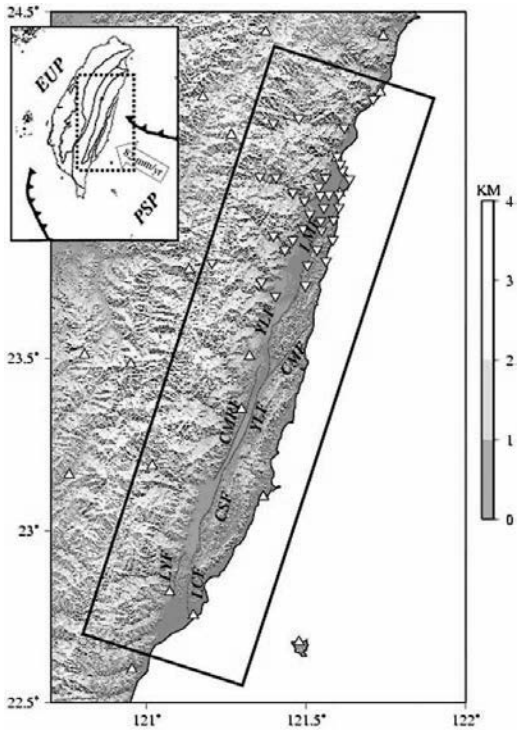


Figure 1 Topography map of the collision zone in central eastern Taiwan showing the collision zone suture (the Longitudinal Valley, LV), oceanic frontal arc (the Coastal Range, COR), and the uplifted continental crust (the Central Range, CR) (Kim et al. 2006).

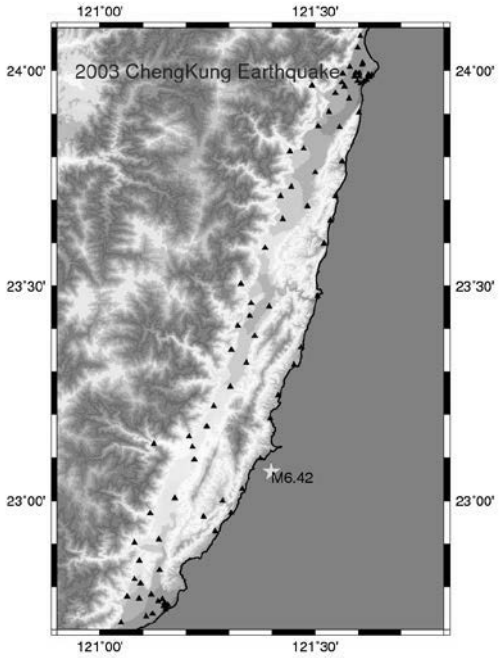


Figure 2 The 2003 Chengkung earthquake and stations used in this study. Yellow star is the epicenter location and black triangles are seismic stations.

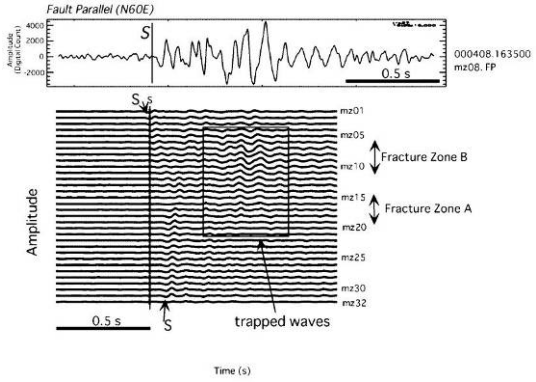


Figure 3 An example of observations of fault-zone trapped waves (Mizuno 2003).

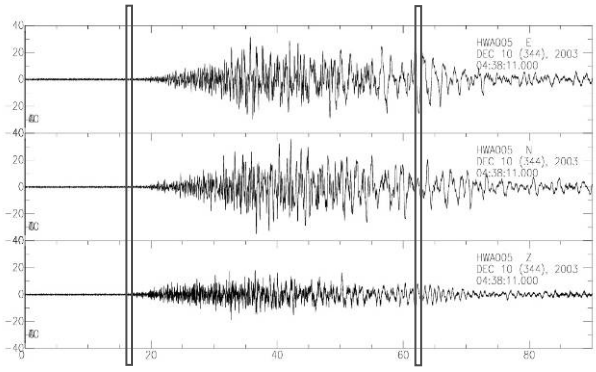


Figure 4 The waveform of station HWA005 for 2003 Chengkung earthquake. We cut two time windows to analyze the particle motion. First time window is at 15.9-16.9s for direct P wave. Second time window is at 62-63s for the wave having large amplitude after S wave.

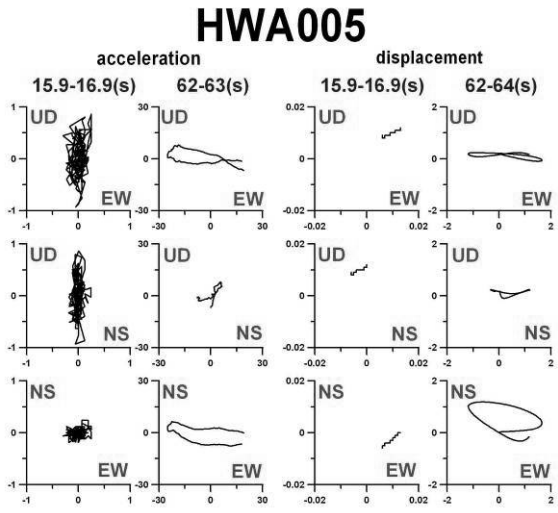


Figure 5 The particle motion of station HWA005 in different time windows. The left side of the figure is 1sec time window for direct P wave. The right side is 1sec time window for the wave after the S wave.

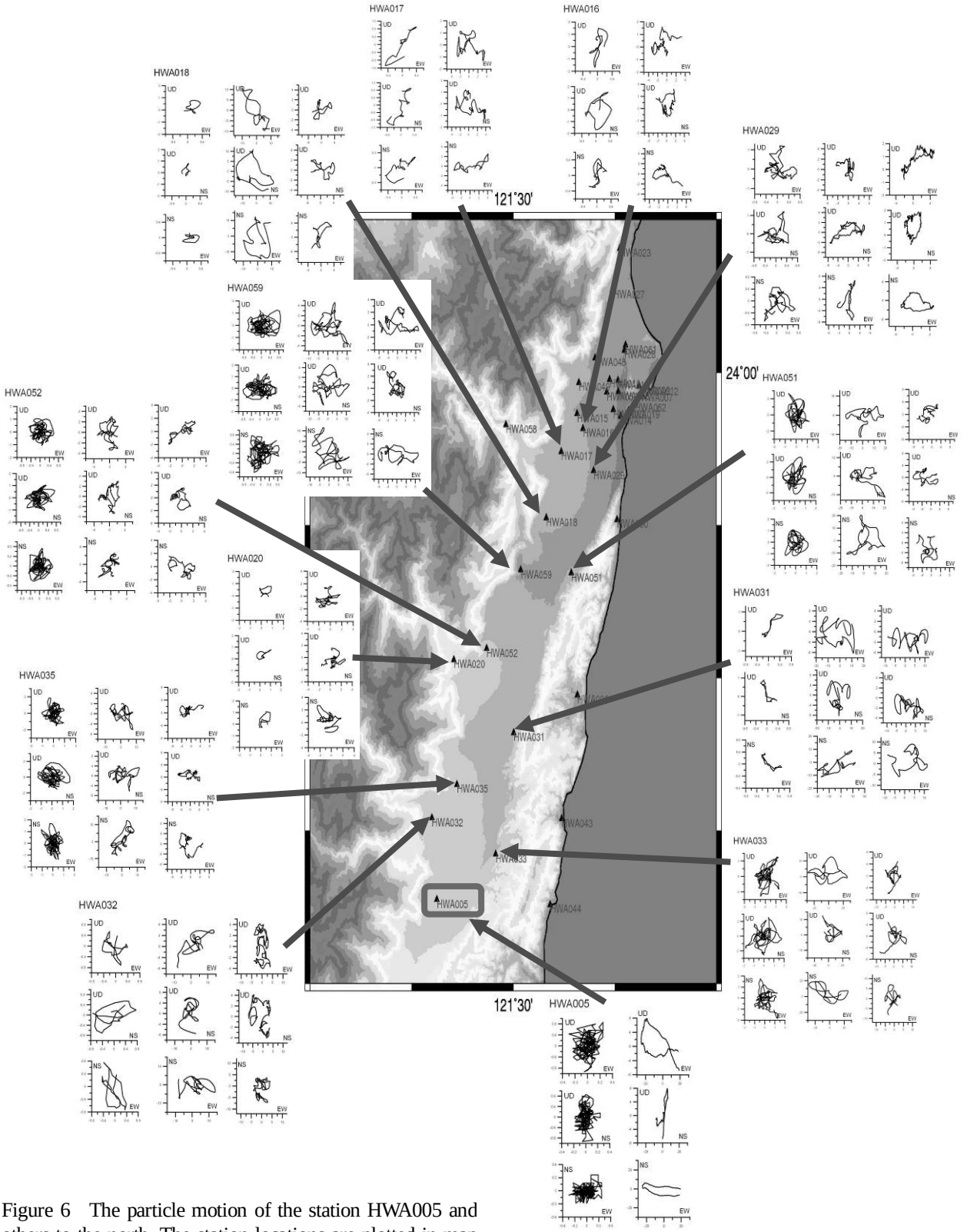


Figure 6 The particle motion of the station HWA005 and others to the north. The station locations are plotted in map view.

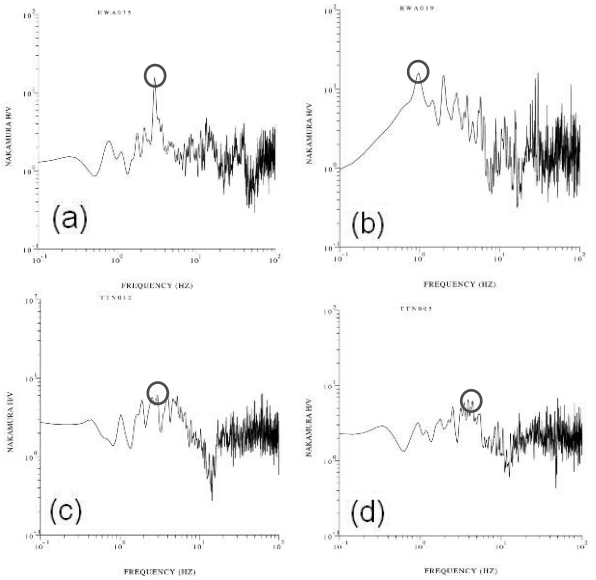


Figure 7 Examples of picking results of dominant frequency.

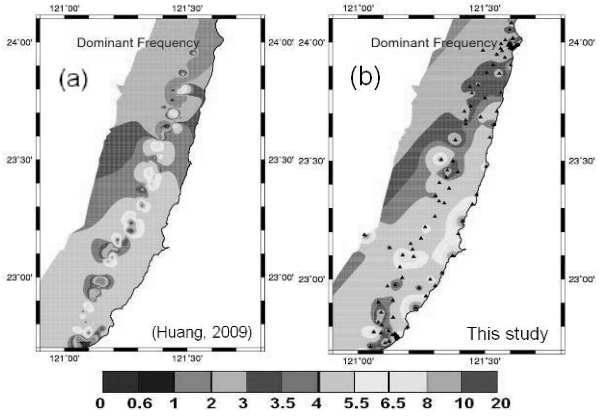


Figure 9 The dominant frequency distributions in the LV area. (a) Result from Huang (2009), (b) Average of the five selected earthquakes from this study.

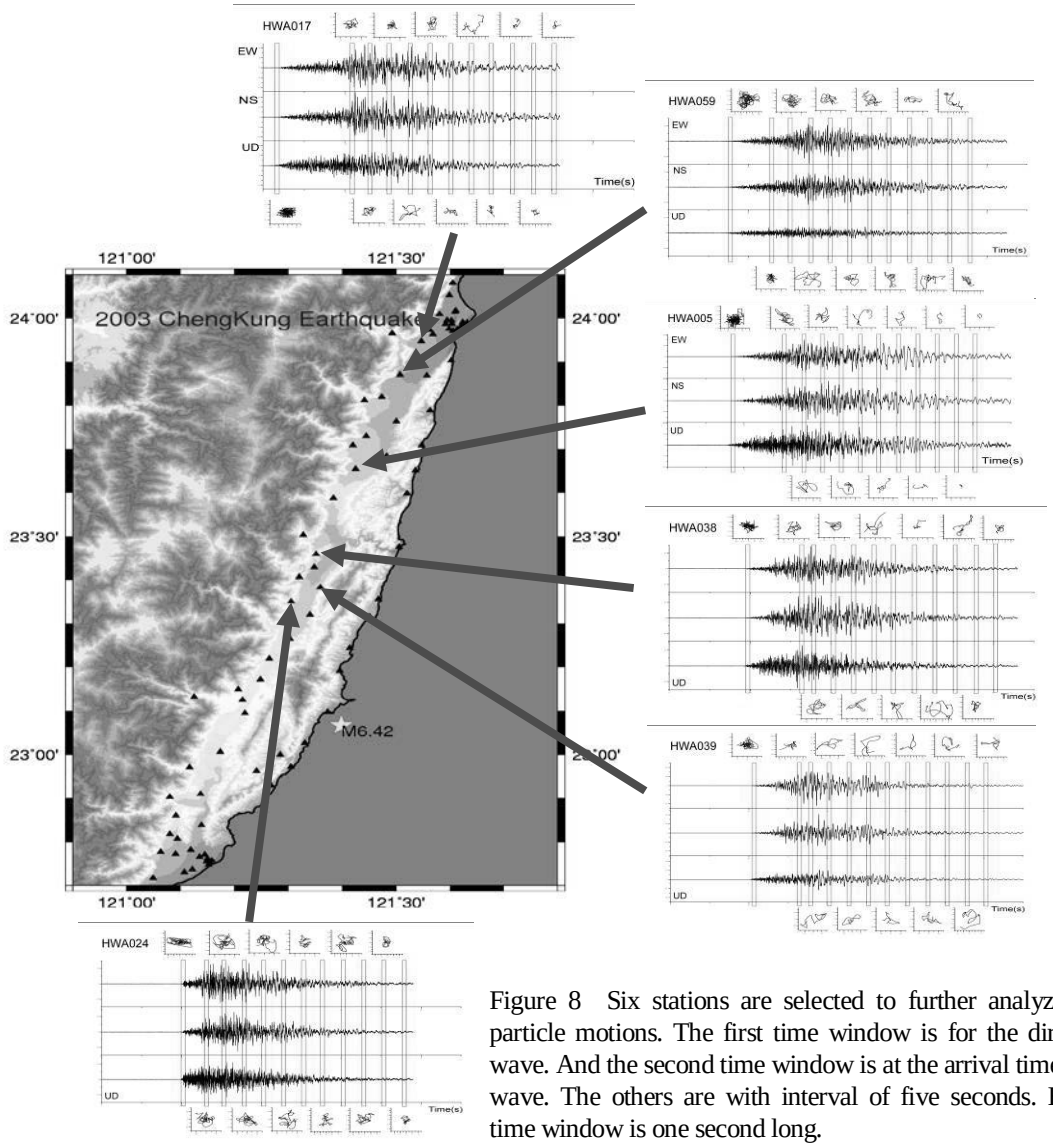


Figure 8 Six stations are selected to further analyze the particle motions. The first time window is for the direct P wave. And the second time window is at the arrival time of S wave. The others are with interval of five seconds. Every time window is one second long.

8CUEE CONFERENCE PROCEEDINGS
8th International Conference on Urban Earthquake Engineering
March 7-8, 2011, Tokyo Institute of Technology, Tokyo, Japan

ANALYSIS OF THE SITE EFFECT IN CHIANAN PLAIN FROM THE 2010 JIASIAN, TAIWAN, EARTHQUAKE

Fei-Wen Cheng[1)], Kuo-Liang Wen[2)], Chun-Te Chen[3)], and Jyun-Yan Huang[3)]

1) Master student, Institute of Geophysics, National Central University, Taiwan, R.O.C.
2) Professor, Institute of Geophysics, National Central University, Taiwan, R.O.C.
3) PhD Candidate, Institute of Geophysics, National Central University, Taiwan, R.O.C.
986202007@cc.ncu.edu.tw, wenkl@earth.ncu.edu.tw, 956402004@cc.ncu.edu.tw, 986402005@cc.ncu.edu.tw

Abstract: The Jiasian earthquake occurred on March 4th, 2010 and it was a large earthquake (M_L 6.4) occurred on land in Taiwan. There were 96 people injured but no one died. It also caused a high speed rail car derail, soil liquefaction, and some structures damage. The event of the high speed train was noticed by public and it is the first case of high speed rail derailed due to earthquake in Taiwan.

We utilize the strong motion data from Jiasian earthquake and using the Horizontal-to-Vertical (H/V) spectral ratio method to analyze the site effect in the Chianan Plain. The dominant frequency contour from strong-motion data was compared with the results from dense microtremor measurement (Huang 2009), and they showed good agreement with each other. Finally, due to there's a train of Taiwan High Speed Rails went off the track in our study region. The strong-motion records near the accident location was analyzed and method was proposed to improve the alarm system.

1. INTRODUCTION

The March 4th, 2010 Jiasian, Taiwan earthquake is an inland shallow earthquake with magnitude M_L=6.4 and focal depth 22.6 km. It caused many structures damage, soil liquefaction, high speed rail car went off the rail and about 90 people injured.

Taiwan is located on the plate boundary between the Eurasian plate and the Philippine Sea plate, in a region of high seismicity (Figure 1). The subduction zone is active in the east and south of Taiwan, in the Ryukyu and Manila-Luzon arc-trench system. There are many earthquakes occurred every year in Taiwan. In the past, nearly a dozen destructive earthquakes have occurred in Taiwan, including the Meishan earthquake (M_L=7.1, 1906), the Hisnchu-Taichung earthquake (M_L=7.1, 1935), and the Chi-Chi earthquake (M_L=7.3, 1999). Most of people living in the western Taiwan, and is the important place of economy develop, so if a large earthquake happen in this region, it will have big influence in Taiwan.

The Jiasian earthquake data used in this study are from the free-field strong-motion stations operated by Central Weather Bureau (CWB). The Horizontal-to-Vertical (H/V) spectral ratio method was used to conduct the site effect analysis in this study for the Chianan Plain (Figure 2).

2. Data

From 1990, the dense earthquake monitoring network called Taiwan Strong Motion Instrumentation Program (TSMIP) was operated by CWB, Taiwan, and there are 688 free field strong-motion stations involved now. Furthermore, the Real-Time Digital stream output system (RTD) involved 109 stations were constructed by CWB since1995 for real time location and shake map (Figure 3). The average accelerograph station spacing is about 5 km except Central Mountain Range. Most of these accelerographs are run at 200 samples/sec with 16-bit resolution at least and the dynamic range at ± 2g.

In this study, we use the data in the Chianan Plain from the Jiasian earthquake. Totally, about 130 stations triggered by this event in this area are shown in Figure 2.

3. Method

The factors affect the ground motions are quit complex. The main factors are source, path, and local site effects. Spectral ratio analysis is a simple method for studying site effects. The spectral ratio from soil and rock station pair was used to analyze the resonance frequency of the soil layer and the amplification factor in traditionally.

Choosing a perfect rock station in a wide alluvium plain is difficult. If choose a wrong rock station, such as at mountain of the top or valley, it will be affected by the topography. Nakamura (1989) proposed a single station spectral ratio method, using microtremor data to study the resonance frequency of a shallow soil layer. Field and Jacob (1993) and Lachet and Bard (1994) evaluated this single

station spectral ratio method by using theoretical calculation. Lermo and Chávez-García (1993) applied this method to S waves. Because find the perfect reference stations is difficult in this region, we used a single station spectral ratio method in this study. Assuming S_H and S_V are the horizontal and the vertical spectra on the surface. The H/V ratio S_M :

$$S_M = \frac{S_H}{S_V} \quad (1)$$

To take advantage of equation (1), we may realize the site effect in Chianan Plain.

4. Result

4.1 Dominant frequency

Cutting a 5~10 sec time window of S wave to obtain H/V spectral ratio. After that, the dominant frequency and related amplitude value of the H/V spectrum are picked. The rules of dominant frequency selection were varied from person to person. In this study, the rules are as follows:

1. Choosing the highest of the H/V ratio to be the dominant frequency.
2. If the H/V ratio had the same peak value in the frequency of over two, we may choose the lower frequency.

To avoid the interference of noise the dominant frequency we choosed were between 0.4~20 Hz. Figure 4 is the example of H/V spectra. The left spectrum is the result of station CHY115. The dominant frequency is 2.38 Hz and the related H/V ratio is 41.07. The right spectrum is the result of station KAU087. The dominant frequency is 6.86 Hz and the related H/V ratio is 11.09.

Figure 5 shows the dominant frequency distribution in the Chianan Plain. The 0.3 to 3 Hz low frequency regions are located near the coastal plain. Most intermediate frequency band of 3 ~ 6.5 Hz are surrounding the basin and the regions near the tableland, hill, and mountain. Others are high dominant frequency areas, greater than 6.5 Hz. The regions are mainly at the mountain area where mainly are the rock stations.

4.2 Amplification Effects

Except the dominant frequency can picking from the H/V ratio, it also can be used to understand the spacial variation of the site amplification on different frequency bands. In order to avoid the unusual peak of the H/V ratio, the average H/V ratio in the 1 Hz frequency band were calculated. Figures 6a ~ 6d show the examples of the results for frequency 0.4~1 Hz, 2~3 Hz, 5~6 Hz, and 10~11Hz, respectively.

The higher amplification contours areas occurred on deeper alluvium at lower frequency band. At higher frequency band, the higher amplification contours areas occurred shift to near the piedmont (Figure 6). As the frequencies increase, the distributions of higher H/V ratio areas shifted toward the areas of shallow soil.

5. Discussions and Conclusions

5.1 Compare with The Result of Microtremor

Huang (2009) used the microtremor measurement to study the site effect in Taiwan area. We compared the results of strong-motion and microtremor by the distribution of dominant frequency (Figure 7). The lower frequencies are mainly along the regions of coast or the alluvial plain. Toward the mountain area, the dominant frequencies are higher. And the results of the two measurements are similar but the result of strong-motion is about 0.5~1 Hz higher (Figure 5 and Figure 7). In the Figures 5 and 7, the red triangles and the block crosses are the free-field strong-motion stations and microtremor stations, respectively. We may see that there are some strong-motion stations located near the mountain region, but microtremor stations were not. Therefore, the dominant frequencies of the strong-motion are higher in the nearby mountain region. The microtremor stations are denser than strong-motion stations in the plain area. Consequently, the map in Figure 5 seems higher in some areas. It may caused by local geological variations.

5.2 Damages versus Site Amplification

There were many structures destroyed in Jiasian earthquake. The majority are elementary and junior high schools. Therefore, the distribution of destructive schools are plotted to discuss the relationship between damages and site amplification.

It usually use 10 derived by storeys to estimate the resonance frequency of the structure. Figure 6a and Figure 8 are the site amplification at the frequencies of 1~2 Hz and 4~5 Hz, respectively. Damage structures are separated to two kinds by the stories of schools, the white symbols are 1~3 stories, yellow symbols are equal or greater than 4 stories, and the light blue symbols are the stories not known. The stars show the buildings are serious damage and the diamonds are only a little damage. The school buildings are serious damage near the epicenter area. Further more, the damaged schools are within the areas of high magnification. And the higher stories schools are damaged at the high amplification area of low frequencies, in contrast, to the lower stories schools are damaged at the high amplification area of higher frequencies. For example, Kaohsiung is an urban area, the most schools are higher (greater than or equal to 4), and the serious damaged schools are located in the high amplification areas of 1-2 Hz (Figure 9).

5.3 The Event of High Speed Rail Train Derailed

The event of the high speed train, TN#T110, was noticed by public and it is the first case of high speed train derailed due to earthquake in Taiwan. After the sensor received the seismic data, when the ground acceleration is equal or greater than 40 gal, then the alarm system of the Taiwan High Speed Rails will be triggered and started to

stop the train.

Because we did not have the strong-motion data of high speed rail, we selected the station CHY099 which near the alarm station to be as the alarm sensor's station of high speed rail. Based on the time of the high speed rail derailed, it shows the surface wave arrived (Figure 10). Seems the surface wave has some relationship with the train derailed, but it need more study.

Due to the earthquake alarm system are along the rail route, the time is short to brake when the train received the message that PGA ≥ 40 gal. Station CHY061 is the closest station to the epicenter (Figure 11), therefore assuming the earthquake warning system also setting at CHY061. Using the velocity structure (Lin 2009), we could obtain the P wave arrival time difference is 6.14 sec. The average response time of the alarm system from 6 trains of this event is 3.14 sec. If the brake time was stable, it will have 14.61 sec more to brake before station CHY099 received the PGA ≥ 40 gal message and the train velocity can be reduce from 298 km/hr to 245.90 km/hr. If the high speed rail can install the earthquake alarm system at the strong-motion stations in the future, it will increase much more time to brake the trains and decrease the probability of derail.

Acknowledgement:

The authors are grateful to the Central Weather Bureau of Taiwan for providing the arrival time and drilling data of their seismic network. This study was supported by National Science Council of Taiwan under the grants no. NSC98-2625-M-008 and NSC 99-2116-M-008-023.

References:

Chang, C.P., Angelier, J., and Huang, C.Y. (2000), "Origin and Evolution of a Me´lange: The Active Plate Boundary and Suture Zone of the Longitudinal Valley, Taiwan," *Tectonophysics*, **325**, 43–62.

Field, E.H. and Jacob, K.H. (1993), "The Theoretical Response of Sedimentary Layers to Ambient Seismic Noise," *Geophysical Research Letters*, **20**, 2925-2928.

Hung, J.Y. (2009), "Using Microtremor to Study The Site Effect in Taiwan Area," *NCU*.

Lachet, C. and Bard, P.Y. (1994), "Numerical and Theoretical Investigations on the Possibilities and Limitations of Nakamura`s Technique," *J. Phys. Earth*, **42**, 377-397.

Lermo, J. and Chávez-García, F.J. (1993), "Site Effect Evaluation Using Spectral Ratios With Only One Station," *Bull, Seism. Soc. Am.*, **83**, 1574-1594.

Lin, C.M. (2009), "Shallow Velocity Structure, Site Effect and 3D Seismic Wave Simulation of the Western Plain of Taiwan," *NCU*.

Nakamura, Y. (1989), "A Method for Dynamic Characteristics Estimation of Subsurface Using Microtremor on The Ground Surface," *QR of RTR1*, **30** (1).

Wen, K.L., Shin, T.C., and Wu, Y.M. (2009), "Earthquake Early Warning Technology Progress in Taiwan," *Journal of Disaster Research*, **4** (4)

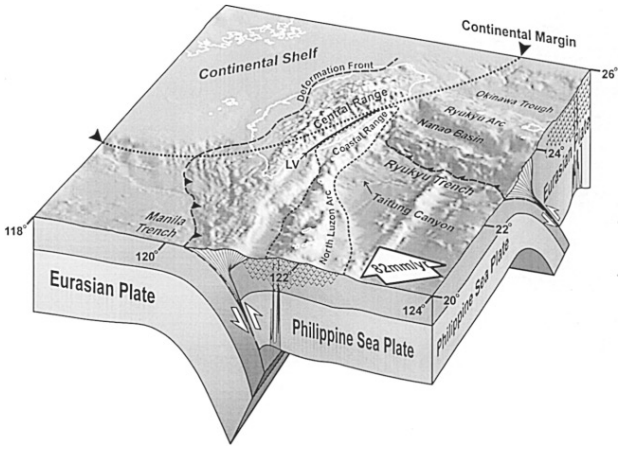


Figure 1 Tectonic setting in the Taiwan plate boundary zone. The Philippine Sea plate moves 82 mm/yr toward northwest direction. (Chang et al. 2000).

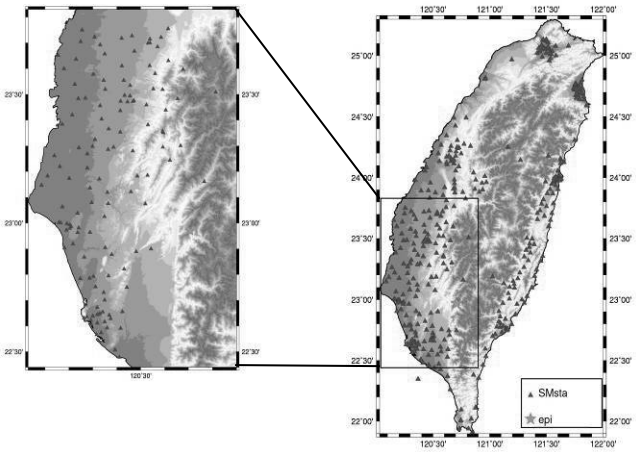


Figure 2 Left is the region in this study, Chianan Plain. In this figure, the red triangles are the free-field stations which were received the records from Jiasian earthquake, and the green star is the epicenter.

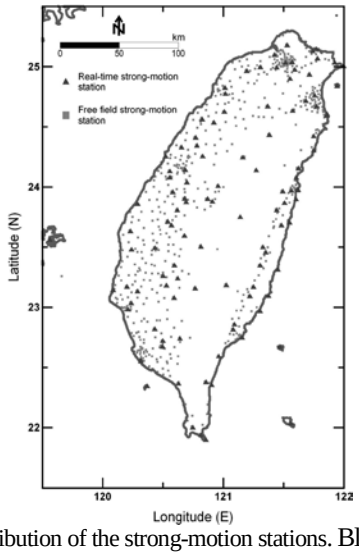


Figure 3 Distribution of the strong-motion stations. Blue triangles are RTD strong-motion station and grey rectangles are free-field strong-motion stations. (Wen et al. 2009).

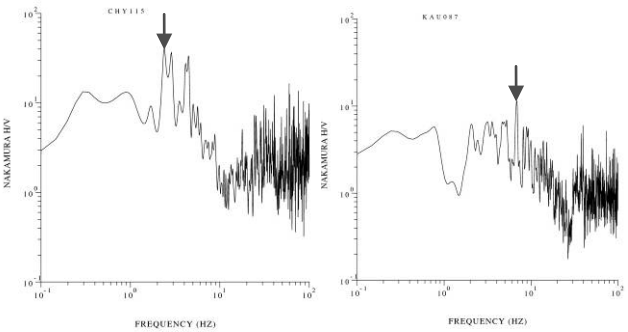


Figure 4 Examples of the H/V spectra. The left is the station of CHY115 and the right is the KAU087.

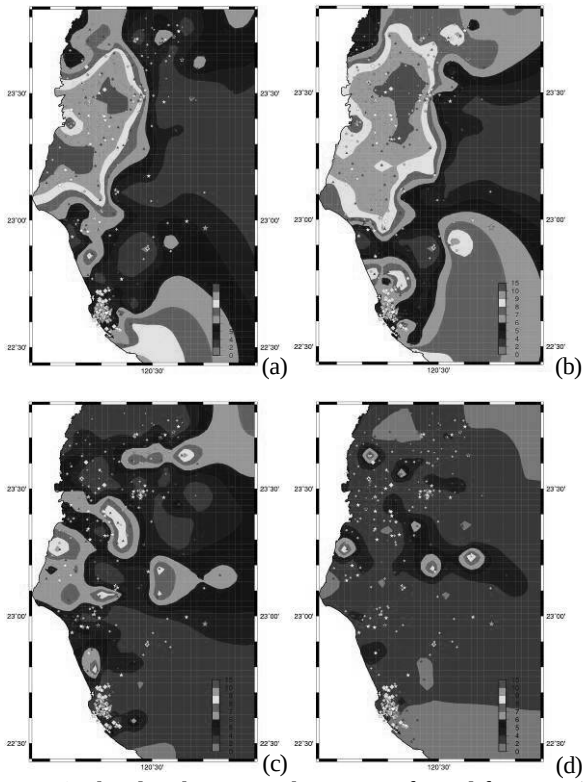


Figure 6 The distribution in the space of amplification. (a) 0.4~1 Hz (b) 1~2 Hz (c) 5~6Hz (d) 10~11 Hz. The green star is the location of epicenter.

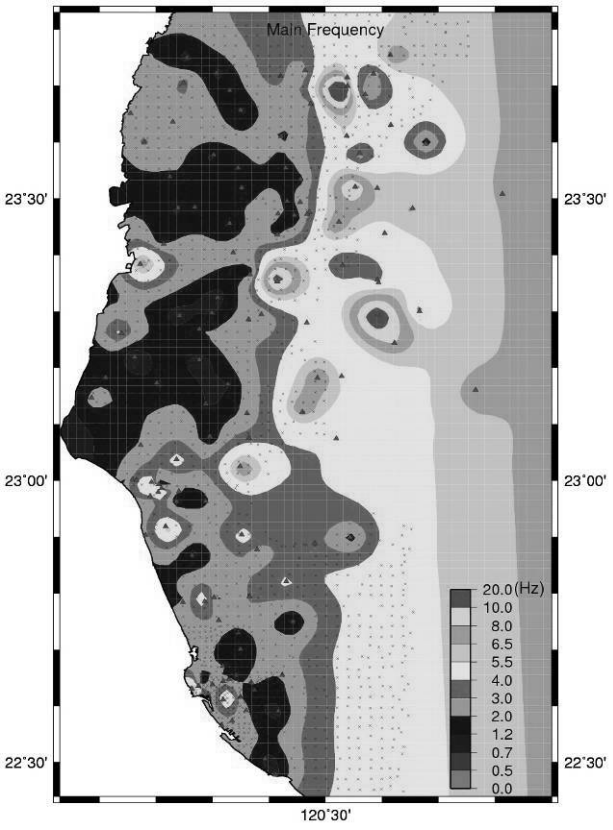


Figure 5 The dominant frequency distribution in Chianan Plain. The red triangles represent the free-field strong-motion stations. The block crosses are microtremor stations.

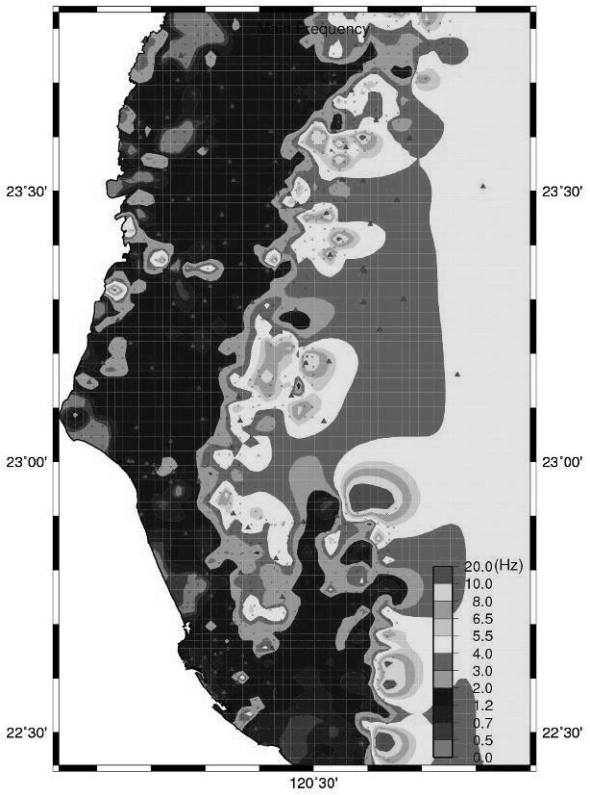


Figure 7 The dominant frequency distribution in Chianan Plain from the microtremor data. (Huang 2009) The red triangles represent the free-field strong-motion stations. The block crosses are microtremor stations.

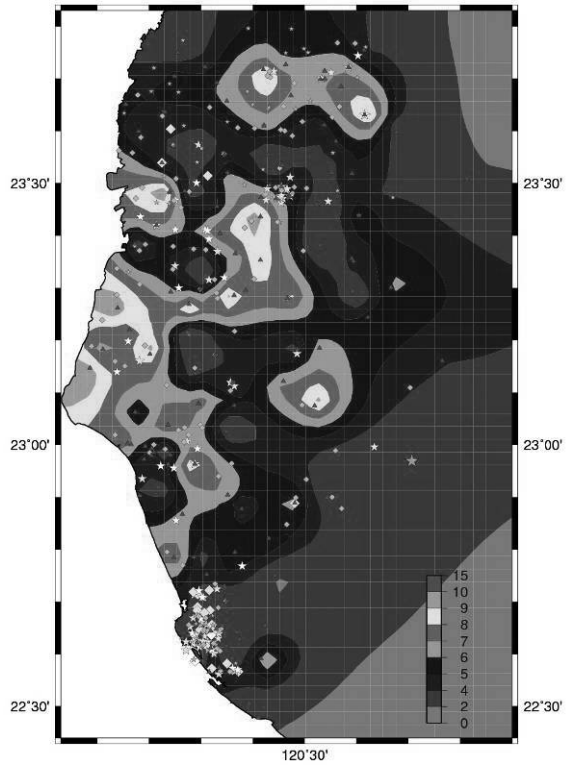


Figure 8 The maps of amplification, and the frequencies are 4~5 Hz. The green star is the location of epicenter.

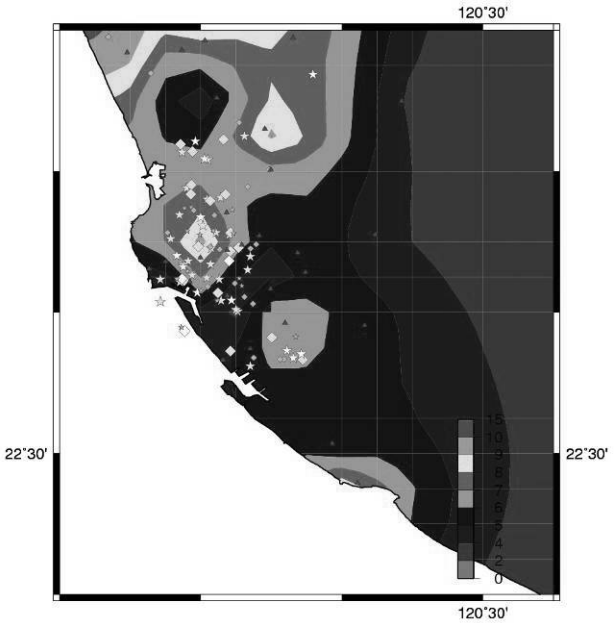


Figure 9 The maps of amplification, and the frequencies are 1~2 Hz in Kaohsiung City.

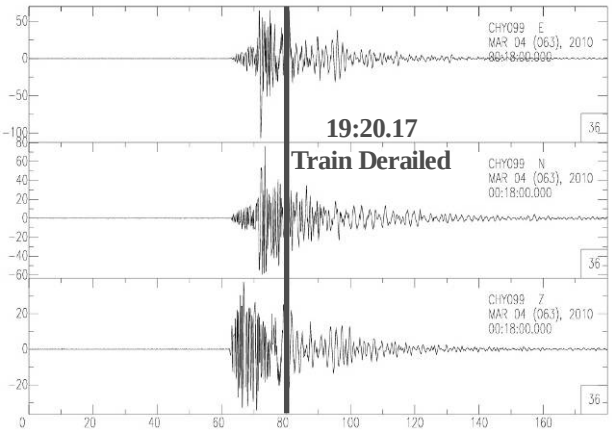


Figure 10 The waveform recorded at strong-motion station CHY099.

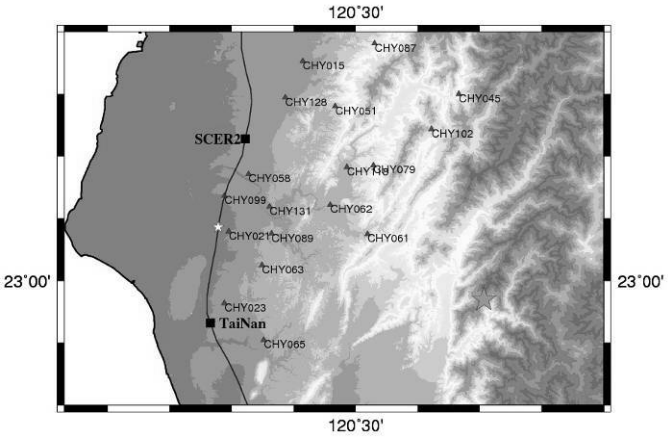


Figure 11 The distribution of strong-motion station (red triangles). The green star is the epicenter, the write is the point of train derailed, and the blue line is the rail.

8CUEE CONFERENCE PROCEEDINGS
8th International Conference on Urban Earthquake Engineering
March 7-8, 2011, Tokyo Institute of Technology, Tokyo, Japan

ESTIMATION OF SHALLOW S-WAVE VELOCITY STRUCTURE IN DAMASCUS CITY, SYRIA, USING MICROTREMOR EXPLORATION

Hussam Eldein Zaineh[1] and Hiroaki Yamanaka[2]

1) Doctoral Candidate, Dept. of Environmental Science and Technology, Tokyo Institute of Technology, Japan
2) Professor, Dept. of Environmental Science and Technology, Tokyo Institute of Technology, Japan
Zaineh.h.ab@m.titech.ac.jp, yamanaka@depe.titech.ac.jp

Abstract: Array measurements of microtremors were carried out at thirty sites in Damascus city, Syria to estimate S-wave velocity structures of shallow soil formations for site effect analysis. The microtremor data were recorded by 6 vertical-component seismometers distributed along the circumferences of two circles as well as one 3-component seismometer deployed in the center. The phase velocities were estimated at each site from the vertical components of recorded microtremor data by using Spatial Autocorrelation method (SPAC). Then, Genetic Simulated Annealing Algorithm technique was applied for inversion of the phase velocities to estimate the 1-D S-wave velocity structures beneath the considered sites. Inverted Vs profiles are not uniform in Damascus city and the results show a shallow soft layer (~200 m/s) appeared in the Eastern part of the city as well as the Central part along Barada River. This layer is controlling the amplification factors in the city and high amplification was mainly observed at the locations having this layer. The inversion results also show that the depth to the engineering bedrock (~750 m/s) is very shallow along foothills of Mt. Qasyoun in the north-west and along the foothills of Mt. El-Mane and Mt. El-Madani in the far south. Then the depth increases towards the center of the city and towards the east. The maximum depth to the engineering bedrock was observed in the southern part of Damascus. To validate the results of inversion, the spectral ratios between the horizontal and vertical components (H/V) of the recorded microtremor data at the central seismometer has been compared with the computed H/V ratios of the fundamental-mode Rayleigh-waves based on the respective Vs structure. The results showed a good agreement in the period range of (0.05s - 0.5s). In this period range, the clear H/V peaks in the central and eastern part of the city are due to the overall effect of the velocity contrast between layers in this area. Moreover, the average S-wave velocity for the top 10 m of soils (V_{S10}) shows a better correlation with the averaged site amplification in the period range (0.1s - 1.0s) than V_{S30} which indicates that V_{S10} can be a better proxy for site amplification in the case of Damascus city.

1. INTRODUCTION

Damascus city, located in the south-western part of Syria (Fig. 1a), is a capital city with a large trade, industry, culture and transport activities and more than five million people live in Damascus and its suburb. Serghaya Fault, as a branch of Dead Sea Fault System (DSFS), has a length of 200 km and located approximately along the Syrian-Lebanese border, about ~30 km north-west of Damascus (M. Meghraoui et al. 2003, F. Gomez et al. 2003). Serghaya Fault is considered as the main source of seismic potential for the city and through the last 2000 years, many destructive earthquakes occurred in the region and caused much causality in Damascus city and its vicinity; one of the most documented events occurred in 1759 with a magnitude of ~7.4 (Ambraseys and Barazangi, 1989). Historical records suggest that DSFS, which is quiescent at present, is capable of producing relatively large earthquakes (Ambraseys, 2009). Syrian Seismic Design Regulations, are officially established in 1995 and revised in 2004, require an information on S-wave velocity structure for estimating the site coefficient (S) as in the 1995 code or estimating the seismic coefficients (C_a and C_v) as in the 2004 code. Since Syrian cities have lack of information on subsurface structure (S-wave velocity structure), it is so complicated task to define the site classification according to the Syrian codes.

Globally, S-wave velocity has been recognized as one of the important soil properties in earthquake and civil engineering. Therefore, knowledge of geometry and shear wave velocities of soil deposits and basement is one of the key parameters controlling the amplification of seismic motion. Also, this knowledge is required for the solution of many significant problems in earthquake engineering such as design earthquake motions and soil-structure interaction and therefore most of the building codes required the knowledge of S-wave structure. Array technique using microtremors is an important exploration method which becomes very attractive and useful for microzonation and site effects studies in urbanized areas. This exploration method was established after the pioneering work done by Aki 1957. The wide spreading of the microtremor technique is due to its low cost compared with other

conventional geophysical prospecting, as well as its applicability even in big and crowded cities. Array records of long-and short-period microtremors have been applied successfully to delineate both the deep and shallow S-wave velocity structures of various sedimentary basins (e.g. Asten and Henstridge, 1984; Matsushima and Okada, 1990; Yamanaka et al., 1994; Kawase et al., 1998; Satoh et al., 2001; Scherbaum et al. 2003) located in highly populated urban areas, like Damascus city. In this exploration method, Rayleigh-wave phase velocities are estimated from vertical components of array records of microtremors, and then the subsurface structure is estimated by the Rayleigh-wave inversion.

The main objective of this study is to estimate the shallow S-wave velocity Structure in Damascus city. We also discuss site effects in the city using S-wave velocity profiles obtained from microtremor data.

2. TOPOGRAPHY AND GEOLOGY OF THE STUDIED AREA

Damascus city occupies the mostly part of Dimashq basin (Damascus basin). Dimashq basin is located to the south-western part of Syria and extends between 33°00´ to 33°50´ N and 36°00´ to 36°50´ E. The north-western part of the area was formed after many tectonic evolutions that affected the region and started in Mesozoic period. As a result, many folding structures are appeared (Palmyra subzone and Anti Liban subzone) as Mt. Qasyoun and Mt. El-Qalamoun which bounded Dimashq basin at the north-west (Ponikarov, 1963). Elevation points vary within the limits of 1.500 -1900 m and the relative elevations amount to 500-700 m. The south-eastern part of the area is quite different from the folded mountain system. It is the Drouz depression zone characterized by typically platform dislocations and intensive basaltic volcanism, with shallow-seated pre-Cambrian basement as Mt. El-Mane which bounded the basin at the far south (Ponikarov et al., 1963). The highest point is about 1000 m and relative elevation here amount to 300-400 m. Actually, the basin is filled by deposits of the surrounded heights and deposits carried by Barada River (Nahr Barada) which flows through the basin and forms the lowland of the basin (The geological map of Syria, explanatory notes, Dimashq sheet, 1963).

The geological map of Damascus (Fig. 1b) shows different type of geological formations. Cretaceous (Turonian, C_r) and Paleogene (Middle Eocene, P_g) formations appeared in the north-west of the city along Mt. Qasyoun and Mt. El-Qalamoun. The outcropping basalt rock (Middle Miocene, B_N) appeared in the far south along Mt. El-Mane and Mt. El-Madani. While the main part of the city lies on the sedimentary basin (Dimashq basin) represented mainly by the upper quaternary deposits (Q_3) (Geological map of Syria, Dimashq sheet, 1963) as well as the recent alluvial deposits (Q_4) which have very limited areal exposure along Barada River (Geological Map of Syria, North of Damascus sheet, 1998). In general, the upper quaternary deposits (Q_3) represented by Proluvial and Lacustrine formations which are the most dominant exposures. Lacustrine deposits appear in the further east of Damascus and form the basin of El-Oteibeh Lake. While Proluvial deposits forms the fan of Damascus in the intermountain area, (Geological Map of Syria, Dimashq sheet, 1963).

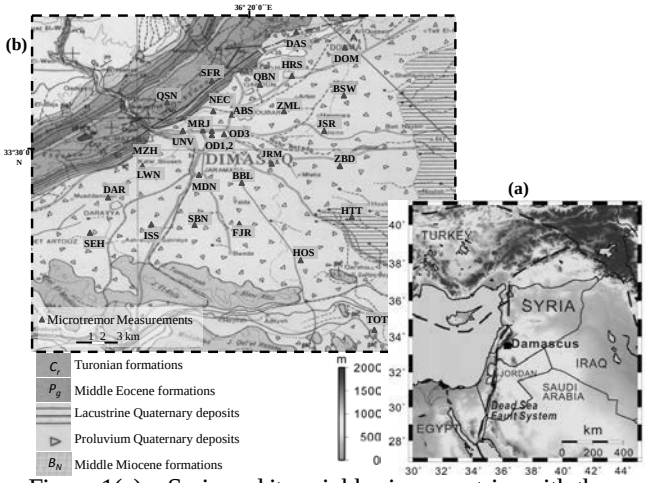


Figure 1(a) Syria and its neighboring countries with the location of Damascus city. (b). Locations of the microtremor survey sites (red triangles) presented on the geological map of Damascus city. (The geological map of Syria, 1963)

3. ARRAY MEASUREMENT OF MICROTREMORS

The site locations for the array measurement of microtremors are shown in Figure 1b. We conducted array measurements at 30 sites in the city of Damascus. The selection of these sites is based on the geological conditions of the city as well as the results of microtremor H/V spectral ratios (*Zaineh et al. 2009*). Measurements at 26 sites were conducted at Dimashq Basin (Q_3 zone). Namely, UNV, MRJ, OD1, OD2, OD3, NEC and ABS sites are located at the central part of Damascus. DAS, HRS and QBN sites are located in the north. BBL and MDN sites are located at the south-central of Damascus while LWN, DAR and SEH sites are located at the western part. All these sites have short to medium peak period of H/V spectral ratios. JRM, ZML, DOM, BSW, JSR, ZBD and HTT sites are situated at the eastern part while HOS, FJR, SBN and ISS sites are located in the south. These sites, also conducted at Damascus basin (Q_3 zone), have medium to long peak period of H/V. The remaining measurements (MZH, QSN and SFR) were conducted along Mt. Qasyoun where paleogene and cretaceous formations appeared (these sites have almost a flat H/V spectral ratio curves), as well as one measurement (TOT) at the south east of the city (location of TOTH seismic station) where young basalt rocks are outcropping (Fig. 1b).

All measurements were taken using circular array configuration which consists of 7 recording stations. For each array measurement, a 3-components accelerometer (#1 in Fig. 2) was deployed in the center and 6 vertical accelerometers were distributed along the circumference of two circles. Stations #2, #3 and #4 distributed along the circumference of the inner circle while #5, #6 and #7

distributed along the outer one. Both of these circles have the same center and the radius of inner circle is half of the outer one as it shown in Figure 2. Two array measurements of 7 stations were carried out in each site (large and small arrays) for better resolution with a duration of 20 minutes for each. The size of large array varies from 12 meters to 40 meters depending on the available open space at the selected site. The small array (1.5 m the smallest one) was deployed for better resolution at the up most soil layers, while the large one is for deeper soil layers. A simultaneous recording at 7 stations was carried out for about 20 minutes for each array. The microtremor data were recorded by 24 bit A/D wireless portable recorders with 100 samples per second attached to 7 accelerometers manufactured by Mitsutoyo (Japan) having flat characteristic period range of 0.01 sec to 14 sec.

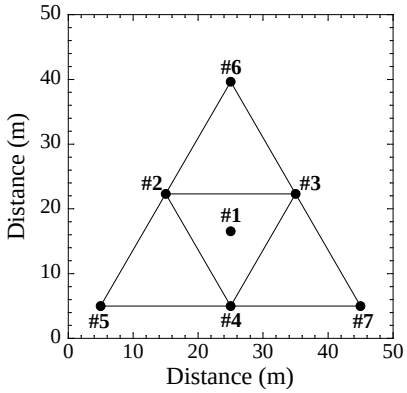


Figure 2. Large Array Configuration at HTT site.

4. DATA PROCESSING

4.1 Estimation of Phase Velocity

For the estimation of phase velocity, each observed vertical-component records were divided into time segments of 81.92 sec in length after removing the locally generated noise. We estimate the phase velocities of Rayleigh waves by Spatial Autocorrelation (SPAC) method (*e.g. Okada, 2003*). The SPAC method requires ambient-noise records obtained in a circular array of stations with one station at the center. This geometry allows the computation of the cross-correlation between many station pairs at the same inter-station distance, *r*, and sampling many different azimuths at the recording site. The correlation coefficients, $\rho(r, \omega)$ as a function of frequency (ω), are computed as the normalized cross-correlation between all station pairs separated a distance *r* and averaged over all azimuths, θ. Assuming stationary of microtremors, Aki (1957) showed that

$$\rho(r,\omega) = \frac{1}{2\pi \emptyset(r=0,\omega)} \int_0^{2\pi} \emptyset(r,\theta,\omega)\, d\theta$$

$$= J_0\left(\frac{r\omega}{c(\omega)}\right) \qquad (1)$$

where $\emptyset(r=0, \omega)$ is the average autocorrelation function at the center of the array, $\emptyset(r, \theta, \omega)$ is the cross-correlation function between the records obtained at coordinates (r, θ) and the record obtained at the center of the circle, $c(\omega)$ is the phase velocity at frequency ω at the site, and $J_0(\cdot)$ is the Bessel function of first kind and order zero. In this equation, the only unknown parameter is the phase velocity, $c(\omega)$, which can be obtained from the inversion of the correlation coefficients. Further details about SPAC method can be found in the literature *(e.g. Okada, 1987, 2003; Morikawa et al. 2004; Chavez-Garcia et al. 2005).*

The observed phase velocity dispersion curves show big differences from site to site and they can be categorized to three different groups ***a, b,*** and ***c*** (Fig. 3). *Group* ***a*** represents the sites located in the central and eastern part of Damascus. The value of observed phase velocities for these sites ranged from 200 m/s to 700 m/s and the phase velocity curves have narrow period range from 0.03 s to 0.2 s except for HTT site which has a wider period range up to 0.5 s (Fig. 3a). *Group* ***b*** represents the sites located in the south and south-central of the city. The phase velocity curves of these sites have a wider period range (0.03 s to 0.5 s) than group ***a*** (Fig. 3b). The sites in these two groups are located at the same geological formation (Q_3 zone). While *group* ***c*** represents the sites located along Mt. Qasyoun with different geological formations (Q_3, C_r *and* P_g) as well as TOT site located at the south-eastern part of Damascus in the region of outcropping basalt (B_N). *Group* ***c*** sites (Fig. 3c) have high phase velocities (up to 1000 m/s) with more narrow period range from 0.03s to 0.15s. Figures 3a and b show the variations of the observed phase velocities for the sites located at the same geological formations while figure 3c shows the variation of the observed phase velocities for the sites located at different geological formations. The results show that the value of phase velocity decreases from the foothills of Mt. Qasyoun toward the east and the south. The period range of the observed phase velocity curves decreases in the same direction too. These clear differences are an indication of a significant variation in the shallow soil formations in Damascus city.

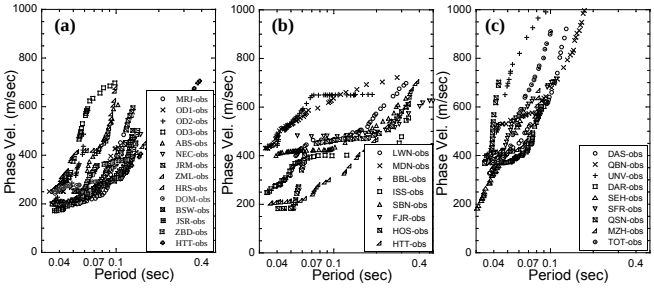


Figure 3. Comparison of the observed Rayleigh wave phase velocities for ***a*** sites located at the central and east, ***b*** sites located at the south and south-central; and ***c*** sites located in the north-west of Damascus along Mt. Qasyoun as well as TOT site in the south-east.

4.2 Inversion of Phase-Velocity Data

The phase-velocity data were inverted by Genetic Simulated Annealing Algorithm technique, which is a hybrid inversion technique introduced by H. Yamanaka, (2007) as global optimizing method. In this technique, a 1-D soil profile is searched by minimizing the misfit between

observed and inverted phase velocities. 10 inversions with 100 generations were conducted using different seeds of random numbers where good model with smaller misfit survive more in the next generation while bad models are replaced by newly generated ones and so on, (*Yamanaka and Ishida, 1996; H. Yamanaka, 2007).*

Open circles and solid lines in Figure 4 show the observed and inverted phase velocities for the models in Figure 3. The sites are shown in Figures 4 a-1 to a-3, belong to the group ***a*** in Figure 3 and located at central and eastern part of the city. The sites in b-1 to b-3 belong to the group ***b*** and located at south and central-south while the sites in c-1 to c-3 belong to the group ***c*** and located in the north-west along Mt. Qasyoun. It is confirmed that the misfit between the observed and inverted phase velocities is fairly good for all the sites. Thus we succeeded to estimate the shallow structure down to the engineering basement with an S-wave velocity of ~750 m/sec for all the sites. While deeper structure (~1250m/sec) was estimated only in few sites that belong to the groups ***b*** and ***c*** (UNV, QBN, DAS etc.).

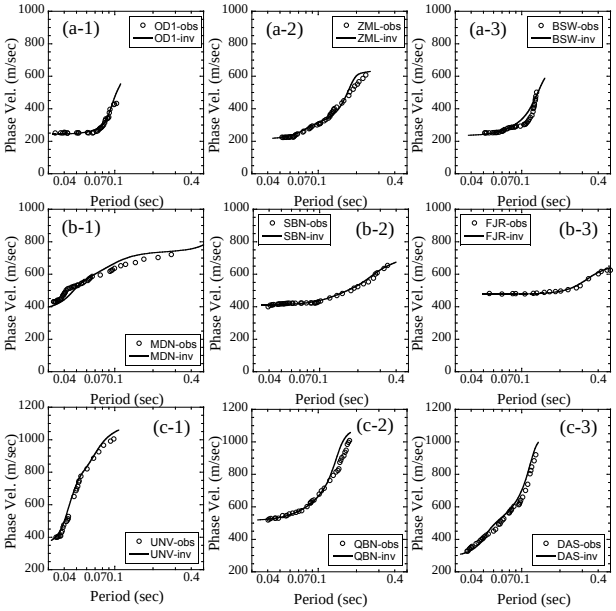


Figure 4. Comparison between the inverted phase velocity (circles) and observed one for some sites belong to different groups.

5. RESULTS

5.1 S-Wave Velocity Structure

As it is mentioned previously, subsurface structural model corresponding to the minimum misfit between the observed and inverted phase velocities was selected as inverted 1-D soil profile for each site. The results show that the shallow soils are not uniform in Damascus city and there is a wide variation in both S-wave velocity and thickness of shallow soil layers. According to our results, the city can be divided into three regions as following (Fig. 5):

*Center and east region (**a** region)* (Fig. 5a), the features of the S-wave velocity structure in this region is as following:

- The first layer is a shallow soft layer with a very low S-wave velocity (~ 200 m/s) with the thickness ranged from ~ 5 m in the center (MRJ, OD2 and OD3) and becomes about ~10 m in the eastern part of the city.
- The second layer has a low velocity (~350 m/s) with thickness ranged from ~7 m in the central part and becomes ~20 m in the eastern part (BSW, ZBD and HTT). The second layer (~ 350 m/s) is disappeared in OD1, OD2 and OD3 sites while it is replaced by higher velocity layer (~500 m/s) in HRS and HTT sites.
- The third layer is the engineering bedrock with S-wave velocity of ~750 m/s.

Generally, the depth to the engineering bedrock is increasing from 10 m in the central part along Barada River and becomes about 30 m in the eastern part as it is shown in Figure 6.

*South and central-south region (**b** region)* (Fig. 5b), the features of the S-wave velocity structure in this region is as following:

- FJR and SBN sites has a thick layer with a high S-wave velocity (~500m/s) overlain the engineering bedrock.
- HOS and ISS sites has a very thin soft layer (~200m/s) and a thick high velocity layer (~500m/s) overlain the engineering bedrock.
- MDN and LWN sites have a thin low velocity layer (~350m/s) overlain the high velocity layer (~500m/s) and the engineering bedrock.
- BBL site has a thin low velocity layer (~350m/s) overlain the engineering bedrock.

The depth to the engineering bedrock is increasing from 20 m in the central-southern part (MDN and BBL) towards the southern part and becomes at relatively deeper depth (~80 m) underneath ISS, FJR and HOS sites as it is shown in Figure 6.

*Foothills region (**c** region)* (Fig. 5c), this region located along Mt. Qasyoun (north-west) and along Mt. El-Madani and Mt. El-Mane (far south), the engineering bedrock in the north-west area is covered by one low velocity layer (~ 350 m/s) as in DAR, MZH, UNV and QSN sites, or by two layers (~350 m/s and ~500 m/s) as in DAS and SFR sites while in QBN site, the engineering bedrock is covered by a high velocity layer (~500 m/s). SEH site has a very thin soft layer (~200m/s) overlain the engineering bedrock. While TOT site in the south-east of Damascus, has a thin low velocity layer (~350 m/s) overlain the engineering bedrock. Generally, the subsurface distribution of the S-wave velocity revealed the engineering bedrock at a relatively shallow depth (less than 10 m) in this region as it is shown in Figure 6.

Figure 6 shows the contour maps for the depth to the engineering bedrock presented on the elevation map of Damascus city. Circles, squares, and triangles denote the sites of ***a, b,*** and ***c*** regions respectively. Generally, the depth is less than 10 m in the foothills region (***c** region*) along Mt. Qasyoun in the north-west and along Mt. El-Madani and Mt. El-Mane in the far south. The depth increases towards the basin from 10 m in the central part of the city to 30 m in the east and becomes at a relatively deeper depth (~80 m) underneath ISS, FJR and HOS sites in the south.

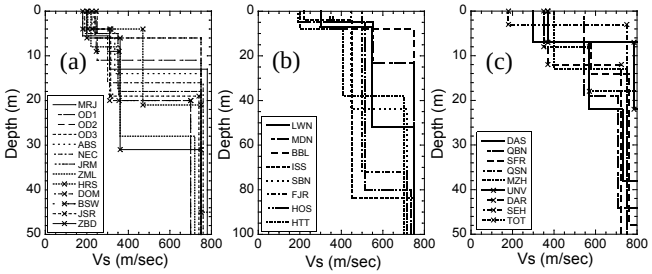


Figure 5. Comparison of the inverted 1-D soil profiles for **a** sites located at central and east, **b** sites located at the south and south-central, and **c** sites located in the north-west as well as TOT site located in the south-east of Damascus.

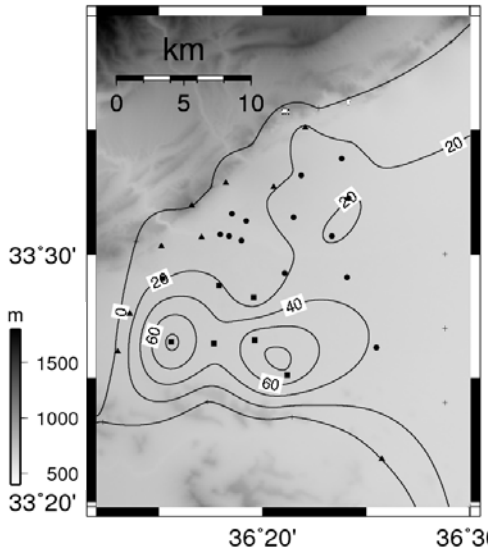


Figure 6. Contour Map for the depth to the engineering bedrock (m) presented on the elevation map. Circles, squares, and triangles denote sites of ***a, b*** , and ***c*** regions respectively

5.2 Site Amplification Factor

Using the inverted 1-D soil profiles (Fig. 5), site amplification factor was calculated by following one-dimensional shear wave propagation theory (*Schnabel et al., 1972*) for vertically incident S-wave. Here we consider the engineering bedrock as a half space since this layer has appeared in all soil profiles. Figure 7 compares the theoretical amplification factors for ***a*** sites located at the central and eastern region, ***b*** sites located in the south and south-central region, and ***c*** sites located in the foothills region. Figure 8(a) shows the contour map of the averaged site amplification for period range from 0.1 s to 1.0 s presented on the elevation map of Damascus city and Figure 8(b) shows the contour map for the fundamental predominant periods of the site amplification factors.

Regarding our results, ***a*** region (Fig. 7a) has the highest site amplification among the regions due to the presence of the soft layer (~200 m/s) near the surface which controlling the site amplification in this region. While the fundamental predominant periods of the amplification factors in this region, increases from 0.15 sec in the central part of the city to 0.3 sec in the east (circles in the Fig.8). For ***b*** region (Fig. 7b), the overall site amplification in this region is higher than it in ***c*** region. The fundamental period of the amplification factors in ***b*** region, increases from 0.15 sec in the central-south to 0.6 sec in the southern part of the city underneath ISS, FJR and HOS sites (squares in the Fig. 8). While ***c*** region (Fig. 7c), has the lowest site amplification and the shortest predominant periods (less than 0.15 sec) of the amplification factors among the regions (triangles in Fig. 8).

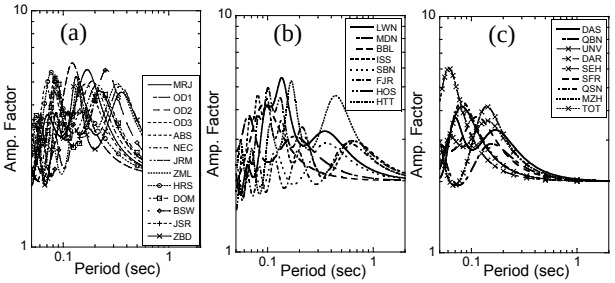


Figure 7. Comparison of the theoretical amplification factors for ***a*** sites located in the central and eastern region, ***b*** sites located in the south and south-central region, and ***c*** sites located in the foothills region.

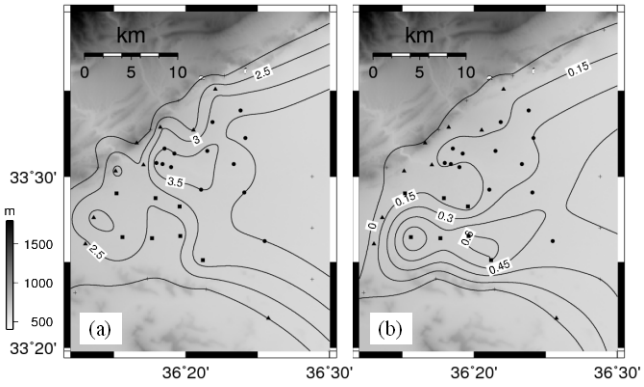


Figure 8(a). Contour map of the averaged site amplification for period range (0.1 s – 1.0 s) presented on the elevation map. (b). Contour Map for the fundamental period of the amplification factors (sec). Circles, squares, and triangles denote sites of ***a, b,*** and ***c*** regions respectively

5.3 Horizontal-to-Vertical Spectral Ratio

The horizontal-to-vertical $(H/V)_o$ spectral ratios at all measurement sites were determined from the observed microtremor data recorded at the 3-components accelerometer (#1 in Fig. 2) deployed in the center of each array measurement. These values are next compared with the computed $(H/V)_c$ spectral ratios of the fundamental-mode Rayleigh waves based on the obtained S-wave velocity structure. Solid and dotted lines in Figure 9 show the observed and computed H/V spectral ratios for the 1-D soil profiles in Figure 5. Figures 9 (1) to (3) show the results of some ***a*** sites located in the central and eastern part of Damascus (region ***a***). Figures 9 (4) to (6) show the results of some ***b*** sites situated in the south and central-south (region ***b***) while Figures 9 (7) to (9) show the results of some ***c*** sites located in the north-west along Mt. Qasyoun (region ***c***). The results of these Figures show that the overall peak period characteristics of the observed $(H/V)_o$ are in close agreement with the computed $(H/V)_c$ in the period range

from 0.05 sec to about 0.5 sec. Generally, the sites of ***a*** region exhibit a clear peak due to the high velocity contrast in these sites while the sites of ***b*** and ***c*** regions have almost a flat H/V spectral ratio of the observed and computed one in the period range of 0.05 sec to about 0.5 sec. As an exception, SEH, ISS, and HOS sites (located in ***b*** and ***c*** regions) exhibit a short period peak (less than 0.1 s) because of the high velocity contrast due to the presence of a thin soft layer (~200 m/s) near the surface. The mismatch between $(H/V)_o$ and $(H/V)_c$ for longer period range (period > 0.5 sec) can be attributed due to the lack of deep soil layers in our soil models, thereby indicating the limitation of the method used in this study.

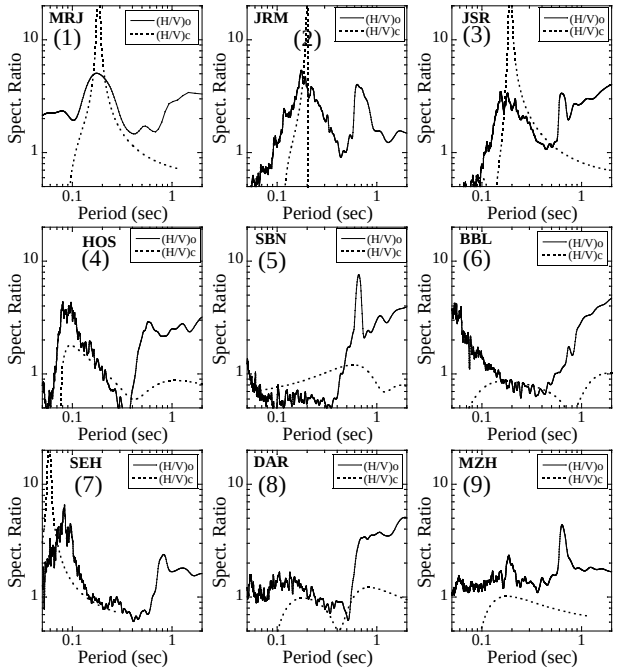


Figure 9. The comparison of the observed $(H/V)_o$ spectral ratios of microtremor data (solid line) with the computed $(H/V)_c$ spectral ratios of the fundamental-mode Rayleigh waves (dotted line)

6. DISCUSSION

6.1 V_{S30} and V_{S10} *vs.* Site Amplification

The average of shear-wave velocity from the surface to 30 m depth (V_{S30}) is adopted as international standard for soil classification. It was proposed in the United States under the National Earthquake Hazard Reduction Program (NEHRP). In fact, many U.S. building codes now require V_{S30} for site classification and Syrian building code 2004 which based on UBC97 has the same requirement of V_{S30} for site classification. Since the NEHRP classification was based on data from the western United States (*Borcherdt 1992, 1994*), we should confirm the validity of the NEHRP site classification in the case of Damascus city. Therefore, V_{S30} was compared with the averaged site amplification for a period range from 0.1s to 1.0s. Figure 10(a) shows the correlation between the V_{S30} and the averaged site amplification. A slight correlation with a scattered relationship was observed between the V_{S30} and the averaged site amplification and almost all our sites are belonging to the same class (class C) according to the NEHRP classification (Table 1). Then, we compared between the V_{S10} (the average of shear wave velocity for the top 10 meters of soils) with the averaged site amplification for the same period range. Figure 10(b) shows the correlation between the V_{S10} and the averaged site amplification. In the case of V_{S10}, a much better correlation was observed with the averaged site amplification which illustrate that V_{S10} can be a better proxy for the site amplification than V_{S30} with less economic and logistic efforts. The fact that V_{S10} could be a better proxy for the site amplification than V_{S30} in Damascus city can be interpreted due to the shallow low velocity layer (~200 m/s) which controlling the site amplification as it is mentioned previously. Table 1 reports Latitude, Longitude, Elevation, V_{S30}, V_{S10}, NEHRB Class, Geological index, Site predominant period of the site amplification, and the averaged site amplification for period range from 0.1s to 1.0s.

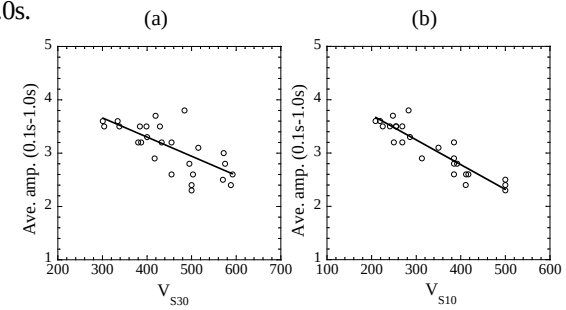


Figure 10(a). Correlation between the V_{S30} and the averaged site amplification. (b). Correlation between the V_{S10} and the averaged site amplification for all sites located in the upper quaternary deposits zone (Q_3)

Table 1. Latitude, Longitude, Elevation, V_{S30}, V_{S10}, NEHRB Class, Geological index, Site predominant period, and the averaged site amplification

Site ID	Latitude	Longitude	Elevation (m)	V_{S30}	V_{S10}	NEHRB Class	Geology Index	Period (sec)	Ave. A_{mpl} (0.1s - 1.0s)
HTT	33.437176°	36.424798°	634	338	225	D	Q_3	0.4	3.5
ZBD	33.484384°	36.401168°	647	304	241	D	Q_3	0.4	3.5
BSW	33.537408°	36.402325°	649	334	209	D	Q_3	0.3	3.6
JSR	33.512041°	36.388949°	652	387	269	C	Q_3	0.2	3.2
HOS	33.418736°	36.353208°	654	400	286	C	Q_3	0.6	3.3
DOM	33.564253°	36.396803°	657	380	269	C	Q_3	0.2	3.2
JRM	33.487230°	36.351019°	665	384	255	C	Q_3	0.2	3.5
ZML	33.524978°	36.358211°	682	301	219	D	Q_3	0.3	3.6
OD3	33.509123°	36.316405°	687	484	283	C	Q_3	0.1	3.8
ABS	33.522236°	36.320094°	689	429	269	C	Q_3	0.2	3.5
MRJ	33.513242°	36.299376°	691	419	248	C	Q_3	0.2	3.7
OD1	33.512181°	36.306552°	694	433	250	C	Q_3	0.2	3.2
NEC	33.527222°	36.308765°	697	399	255	C	Q3	0.2	3.5
OD2	33.510265°	36.307039°	697	484	283	C	Q_3	0.1	3.8
BBL	33.470845°	36.326301°	668	575	392	C	Q_3	0.1	2.8
TOT	*33.361887°*	*36.429033°*	*683*	*572*	*372*	*C*	B_N	*0.1*	*3.0*
ISS	33.440919°	36.259903°	687	417	313	C	Q_3	0.7	2.9
HRS	33.552960°	36.364250°	701	455	385	C	Q_3	0.1	3.2
LWN	33.483526°	36.253027°	703	455	385	C	Q_3	0.1	2.6
DAR	33.459943°	36.226702°	706	515	350	C	Q3	0.1	3.1
DAS	33.584778°	36.367628°	714	495	385	C	Q_3	0.2	2.8
MZH	*33.505369°*	*36.252047°*	*740*	*515*	*350*	*C*	P_g	*0.1*	*3.1*
SFR	*33.547835°*	*36.303989°*	*809*	*542*	*385*	*C*	C_r	*0.1*	*2.9*
FJR	33.442093°	36.326885°	659	500	500	C	Q_3	0.6	2.3
SBN	33.440035°	36.294330°	672	500	500	C	Q_3	0.4	2.4
MDN	33.478828°	36.298217°	689	503	412	C	Q_3	0.1	2.6
SEH	36.298217°	36.217047°	708	588	411	C	Q_3	0.1	2.4
UNV	33.511307°	36.284259°	710	592	417	C	Q_3	0.1	2.6
QBN	33.545180°	36.342131°	723	570	500	C	Q_3	0.1	2.5
QSN	*33.532547°*	*36.276567°*	*1108*	*592*	*417*	*C*	C_r	*0.1*	*2.6*

6.2 Comparison with Geological Data

As it is mentioned previously, the basin of Damascus is filled mainly by the deposits of the surrounded heights represented by the proluvial deposits which form Dimashq fan as well as the lacustrine deposits which form the basin of El-Oteibeh Lake in the far east of the basin. Dimashq fan is characterized by a monotonous lithological composition, i.e., yellow-grey loams with intercalations of angular predominantly lime-stone pebbles near the mountain ridges. But, further from the mountain ridges and closer to the central part, proluvium is represented by loess-like loams which are laterally replaced by lacustrine deposits. In the outer portion of Dimashq fan, on the boundary with the lacustrine plain (Fig. 1b), alternation of the lacustrine deposits with proluvial pebble-beds and loams were observed in many wells (*Geological map of Syria, 1963*). In addition, the recent alluvial deposits (Q_4) have very limited areal exposure along Barada River which flows through the basin (*Geological map of Syria, 1998*). This, illustrate that the quaternary deposits in the eastern part of the basin as well as the central part along Barada River are different from other locations near to the mountain ridges. Also our results show that the low S-wave velocity layers were mainly observed in the eastern part of Damascus city as well as the central part along Barada River. Figure 11 shows the comparisons in general sense between the 1-D soil profiles obtained from inversion (right) with the nearest geological borehole profile (left) for different 4 locations in the city. The distance between both profiles in MRJ site (Fig. 11(a)) is about 200 m; the last layer in the geotechnical borehole profile (Dense Conglomerates with SPT number of 59) represents the engineering bedrock in our results (with S-wave velocity of ~750 m/s). In NEC site (Fig. 11(b)), the distance between the two profiles is about 1000 m; the engineering bedrock is represented by the lower quaternary layer (Clay & Sand) in the geological profile. For MZH site (Fig. 11(c)), the distance is about 1500 m between the two profiles and the engineering bedrock is represented by the cretaceous layer (limestone). While for SEH site (Fig. 11(d)), the engineering bedrock is represented by the fractured basalt layer and the distance between the inverted 1-D soil profile and the geological one is about 800m. Generally, there is a very good agreement between the inverted profiles and geological profiles which confirm the validity of our results.

7. CONCLUSIONS

Array measurements of Microtremors were performed at thirty sites to estimate the S-wave velocity structure of shallow soil formations in the city of Damascus, Syria. As a result we succeeded to estimate the shallow structures down to the engineering bedrock with an S-wave velocity of ~750 m/sec.

The inversion results show that the engineering basement is located at a shallow depth (less than 10 m) for sites located in the foothills region along Mt. Qasyoun in the north-west and along Mt. El-Madani and Mt. El-Mane in the far south. The depth increases gradually toward the center of the basin (~15 m) and toward the east (~30 m) and becomes at a relatively deeper depth (~80 m) underneath ISS, FJR and HOS sites in the south.

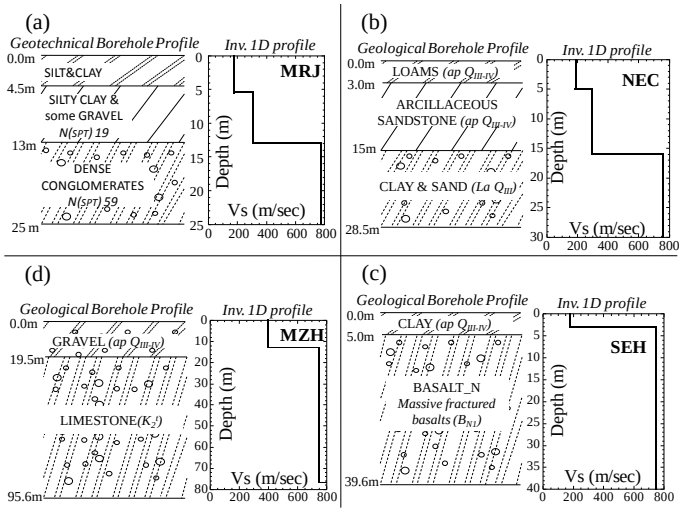


Figure 11. Comparisons between the inverted 1-D soil profile and nearest geological borehole profile at different 4 sites in Damascus city; (a) and (b) represent MRJ and NEC sites respectively, located in the center and east region; (c) represents MZH site located in the foothills region along Mt. Qasyoun; and (d) represents SEH site located in the foothills region along Mt. El-Madani.

The shallow structure is not uniform in Damascus city and there is a wide variation in both S-wave velocity and thickness of shallow soil layers. The results show a shallow soft layer (~200 m/s) appeared in the central and eastern region (***a*** region). This layer is controlling the amplification factors in the city and high amplification was mainly observed at the sites having this layer.

To validate the S-wave structures obtained from the inversion, the spectral ratios between the horizontal and vertical components (H/V) of the recorded microtremor data has been compared with the computed H/V ratios of the fundamental-mode Rayleigh-waves based on the respective Vs structure. The results show a good agreement in the period range from 0.05s to 0.5s. The mismatch outside this period range (period>0.5s) can be attributed due to the lack of deep soil layers in our soil models.

To validate the NEHRP site classification in the case of Damascus city, the average of shear wave velocity for the top 30 m of soils (V_{S30}) has been compared with the averaged site amplification. The results show a slight correlation with a scattered relationship between the V_{S30} and the averaged site amplification. In the other hand, the V_{S10} show a much better correlation with the averaged site amplification that suggest V_{S10} as a better proxy for site amplification than V_{S30} in the case of Damascus city with less economic and logistic efforts due to the fact that site amplification is controlled by a very shallow low velocity layer near the surface.

Acknowledgement:

This research is a part of cooperative project between Tokyo Institute of Technology (Japan) and National Earthquake Center in Syria with a financial support from Grants-in-Aid for Scientific Research by Ministry of Education, Culture, Sports, Science and Technology in Japan. Also we acknowledge the financial support of Center for Urban Earthquake Engineering (CUEE) under the G-COE program of Tokyo Institute of Technology. We are really indebted to Prof. SASANO and Prof. SEO as well as Drs. FOUJITA and MORITA from Tokyo Institute of Technology for their highly intensive support in the preparation and execution of the field survey. We would like to send our appreciation to Prof. Dr. Mohamad Daoud, Director General of National Earthquake Center in Syria for supporting us during our survey in Syria. Also, we like to express our thanks to Syrian team who participated in field survey especially, Mr. Ibrahim R., Miss. Dakkak R., Miss. Khalil A.and Miss. Nkshbndy D.and all team members for their efforts.

References:

Ambraseys N.N., (2009) Earthquakes in the Mediterranean and Middle East –A Multidisciplinary Study of Seismicity up to 1900.

Ambraseys N.N., and M. Barazangi, (1989) The 1759 earthquake in the Bekaa Valley: implications for earthquake hazard assessment in the Eastern Mediterranean region, J. geophys. Res., 94, 4007–4013

Asten M. W., and J. W. Henstridge, (1984) Array estimator and the use of microseism for the reconnaissance of sedimentary basins, Geophysics 49, 1828–1837

Aki K., (1957) Space and time spectra of stationary stochastic waves, with special reference to microtremors, Bull. Earthq. Res. Inst. Tokyo Univ. 35, 415–456

Borcherdt R. D., (1992) Simplified site classes and empirical amplification factors for site-dependent code provisions, in Proc. NCEER, SEAAOC, BSSC Workshop on Site Response during Earthquakes and Seismic Code Provisions, November 18-20, Univ. of Southern California, Los Angeles, California

Borcherdt R. D., (1994) Estimates of site-dependent response spectra for design (methodology and justification), Earthq. Spectra 10, 617–653.

Chavez-Garcia F.J., M. Rodriguez, and W. R. Stephenson, (2005) An alternative approach to the SPAC analysis of microtremors: exploiting the stationarity of noise, Bull. Seism. Soc. Am., 95, 1, 277-293.

Gomez, F., M. Meghraoui, A. N. Darkal, F. Hijazi, M. Mouty, Y. Suleman, R. Sbeinati, R. Darawcheh, R. Al-Ghazzi, and M. Barazangi, (2003) Holocene faulting and earthquake recurrence along the Serghaya branch of the Dead Sea fault system in Syria and Lebanon, Geophys. J. Int., 153, 658–674.

Kawase H., T. Satoh, T. Iwata, and K. Irikura, (1998) S-wave velocity structures in the San Fernando and Santa Monica areas, in Proc. of the 2nd International Symposium on Effects of Surface Geology on Seismic Motions, Yokohama, Japan, Vol. 2, 733–740.

Matsushima T., and H. Okada, (1990) Determination of deep geological structures under urban areas, BUTSURI-TANSA (J. Soc. Explor. Geophys. Jpn.) 43, 21–33.

Ministry of Industry, Department of Geological and Mineral Researches, Geological Map of Syria, (1963) geological map of Syria, I-36-XII I-37-VII, Dimashq Sheet scale 1:200,000, 1963.

Ministry of Petroleum and Mineral Resources, General Est. of Geology and Mineral Resources, Geological map of Syria, (1998) geological map of Syria, North of Damascus sheet scale 1:50,000, 1998.

Meghraoui M., F. Gomez, R. Sbeinati, J. V. Woerd, M. Mouty, A. N. Darkal, Y. Radwan, I. Layyous, H. Al-Najjar, R. Darawcheh, F. Hijazi, R. Al-Ghazzi, and M. Barazangi, (2003) Evidence for 830 years of seismic quiescence from palaeoseismology, archaeosesimology, and historical seismicity along the Dead Sea fault in Syria, Earth planet. Sci. Lett., 210, 35–52.

Morikawa H, S. Sawada, and J. Akamatsu, (2004) A method to estimate phase velocities of Rayleigh waves using microseisms simultaneously observed at two sites, Bull. Seism. Soc. Am., 94, 3, 961–976.

Okada H., T. Matsushima, and E. Hidaka, (1987) Comparison of spatial auto correlation method and frequency-wave number spectral method of estimating the phase velocity of Rayleigh waves in long-period microtremors, Geophys. Bull. Hokkaido Univ. 49, 53–62 (in Japanese with English abstract).

Okada H., (2003) The microtremor survey method, Society of Exploration Geophysicists.

Ponikarov V.P., (1963) Explanatory Notes on the Geological Map of Syria, Scale 1:500,000, Part 1 Stratigraphy, Igneous Rocks and Tectonics. Ministry of Geology, Russia.

Schnabel P.B., J. Lysmer, H.B. Seed, (1972) SHAKE: a computer program for earthquake response analysis of horizontally layered sites, Report No. EERC72-12, University of California, Berkeley.

Satoh T., H. Kawase, and S. Matsushima, (2001) Estimation of S-wave velocity structures in and around the Sendai basin, Japan using array records of microtremors, Bull. Seism. Soc. Am. 91, 206–218.

Scherbaum F., K. G. Hinzen, and M. Ohrnberger, (2003) Determination of shallow shear wave velocity profiles in the Cologne, Germany using ambient vibrations, Geophys. J. Int. 152, 597–612.

Takekoshi M. and Yamanaka H., (2009) Waveform inversion of shallow seismic refraction data using hybrid heuristic search method, Exploration Geophysics, 40, 99-104. (vol. 62, Butsuri-Tansa, 2009. P. 99-104; Vol. 12, Mulli-Tamsa, 2009. P. 99-104).

Yamanaka H., M. Takemura, H. Ishida, and M. Niwa, (1994) Characteristics of long-period microtremors and their applicability in exploration of deep sedimentary layers, Bull. Seism. Soc. Am. 84, 1831–1841.

Yamanaka H. and Hiroshi I., (1996) Application of Genetic Algorithms to an inversion of surface-wave dispersion data, vol. 86, Bulletin of Seismological Society of America, 1996. No. 2. p. 436-444.

Yamanaka H., (2007) Inversion of surface-wave phase velocity using hybrid heuristic search method, vol. 60, Butsuri-Tansa (Geophysical exploration), 2007. P. 265-275. (In Japanese)

Zaineh H. E., Khalil A., Nkshbndy D., Daoud M., Semman N., Dakkak M., Yasmeneh R., Deep R., Elsafady R. and Mahmood F., (2010) Preliminary Seismic Micro-Zoning Study for Damascus City by Using Microtremors, Proceedings of 14th European Conference on Earthquake Engineering, Ohrid, Macedonia.

8CUEE CONFERENCE PROCEEDINGS
8th International Conference on Urban Earthquake Engineering
March 7-8, 2011, Tokyo Institute of Technology, Tokyo, Japan

SURFACE WAVES ON AN EXPONENTIALLY VARYING TRANSVERSELY ISOTROPIC ELASTIC MEDIUM DUE TO A SUBSURFACE POINT LOAD

Priza Kayestha[1)], Takatsugu Konno[2)], and Anil C. Wijeyewickrema[3)]

1) Graduate Student, Department of Civil and Environmental Engineering, Tokyo Institute of Technology, Japan
2) Former Student, Department of Civil and Environmental Engineering, Tokyo Institute of Technology, Japan
3) Associate Professor, Department of Civil and Environmental Engineering, Tokyo Institute of Technology, Japan
kayestha.p.aa@m.titech.ac.jp, konno.t.ad@m.titech.ac.jp, wijeyewickrema.a.aa@m.titech.ac.jp

Abstract: Surface waves generated by a subsurface point load in a transversely isotropic elastic medium with elastic constants and mass density varying exponentially with depth are studied in this paper. The axis normal to the free surface is the axis of symmetry. The surface wave in this case is dispersive which is in contrast to the homogeneous case in which the Rayleigh surface wave is non-dispersive. The elastodynamic reciprocity theorem, which provides an integral relation between two elastodynamic states of same body, has been used to determine the unknown coefficients in the expressions for the displacement and stress components. Numerical results for beryl rock have been presented.

1. INTRODUCTION

Studies have shown that Rayleigh surface waves recorded during earthquakes or underground explosions are dispersive in nature, a characteristic which is different from the context of a homogeneous half-space given by Lord Rayleigh. Numerous studies were carried out with many number of layers to refine the model, until the inhomogeneous nature of the half-space as a continuous variation of the material properties was considered practical (Ewing et al. 1957). The aim of this paper is to obtain the analytical solution for seismic wave propagation in an inhomogeneous transversely isotropic elastic half-space. Rayleigh surface wave being the most devastating wave during an earthquake, the focus of this study is to analyze the surface waves generated due to a time-harmonic subsurface horizontal point load at a depth $x_3 = z_0$ from the free surface (see Figure 1).

The elastodynamic reciprocity theorem was used to determine the surface waves generated by a subsurface point load of arbitrary direction in an isotropic, homogeneous, elastic half-space in Achenbach (2000b). The same theory has been used by Achenbach (2000a) for axisymmetric wave motion generated by point load excitation in an isotropic elastic layer, by Achenbach and Xu (1999) to determine displacements excited by a point load of arbitrary direction in an isotropic elastic layer and by Kulkarni and Achenbach (2008) to determine surface waves generated by a line load in an inhomogeneous transversely isotropic half-space. Recently, this theorem was used by Kayestha et al. (2010) to study axisymmetric surface waves generated due to a time-harmonic vertically applied point load in a transversely isotropic, inhomogeneous elastic half-space.

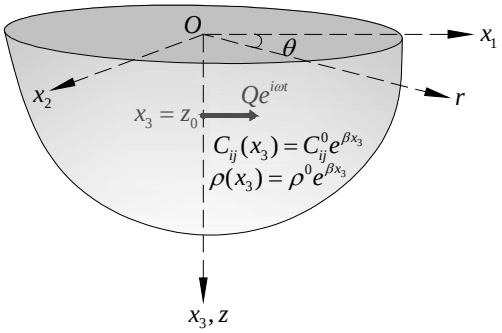


Figure 1 Inhomogeneous transversely isotropic elastic half-space subjected to a subsurface time-harmonic horizontal point load.

In the present paper too, the elastodynamic reciprocity theorem has been used to study surface waves generated by a subsurface harmonic horizontal point load in an inhomogeneous transversely isotropic elastic half-space. This method makes it possible to solve the point load generated surface wave field with an analytical approach, which provides explicit expressions for components of displacements and stresses. Numerical results for beryl rock have been presented.

2. GOVERNING EQUATIONS

For a transversely isotropic elastic solid the stress

components are given in terms of the displacement gradients as (see Ting 1996),

$$\begin{aligned}
\sigma_{11} &= C_{11}(x_3)\frac{\partial u_1}{\partial x_1} + C_{12}(x_3)\frac{\partial u_2}{\partial x_2} + C_{13}(x_3)\frac{\partial u_3}{\partial x_3},\\
\sigma_{22} &= C_{12}(x_3)\frac{\partial u_1}{\partial x_1} + C_{11}(x_3)\frac{\partial u_2}{\partial x_2} + C_{13}(x_3)\frac{\partial u_3}{\partial x_3},\\
\sigma_{33} &= C_{13}(x_3)\frac{\partial u_1}{\partial x_1} + C_{13}(x_3)\frac{\partial u_2}{\partial x_2} + C_{33}(x_3)\frac{\partial u_3}{\partial x_3},\\
\sigma_{23} &= C_{44}(x_3)\left(\frac{\partial u_2}{\partial x_3} + \frac{\partial u_3}{\partial x_2}\right),\\
\sigma_{13} &= C_{44}(x_3)\left(\frac{\partial u_1}{\partial x_3} + \frac{\partial u_3}{\partial x_1}\right),\\
\sigma_{12} &= C_{66}(x_3)\left(\frac{\partial u_1}{\partial x_2} + \frac{\partial u_2}{\partial x_1}\right),
\end{aligned} \tag{1}$$

where $C_{66}(x_3) = \left[C_{11}(x_3) - C_{12}(x_3)\right]/2$ and σ_{ij}, u_i are components of stress tensor and displacement vector, respectively. Since the elastic half-space is inhomogeneous, elastic constants C_{ij} depend on depth x_3. The equations of motion in the absence of body forces can be written as

$$\sigma_{ij,j} = \rho(x_3)\ddot{u}_i, \tag{2}$$

where ρ is the mass density which also varies with the depth x_3.

3. SURFACE WAVES

For time-harmonic motion displacement components can be expressed in general forms as (Achenbach 1998)

$$\begin{aligned}
u_\alpha(x_1,x_2,x_3,t) &= \frac{1}{k}V(x_3)\frac{\partial \phi}{\partial x_\alpha}(x_1,x_2)e^{i\omega t}, \quad (\alpha = 1,2),\\
u_3(x_1,x_2,x_3,t) &= W(x_3)\phi(x_1,x_2)e^{i\omega t},
\end{aligned} \tag{3}$$

where x_1 and x_2 are Cartesian coordinates, $k = \omega/c$ is wavenumber and $\phi(x_1,x_2)$ is a dimensionless function which is the solution of Helmholtz's equation,

$$\frac{\partial^2 \phi}{\partial x_1^2} + \frac{\partial^2 \phi}{\partial x_2^2} + k^2\phi = 0. \tag{4}$$

In what follows the time-harmonic factor $e^{i\omega t}$ is omitted. Substituting the stress components from Eq. (1) and the displacement components from Eq. (3) in the equations of motion given in Eq. (2), results in two coupled ordinary differential equations given by

$$\begin{aligned}
&-kC_{11}V(x_3) + \left(C_{13} + C_{44}\right)\frac{dW}{dx_3} + \frac{1}{k}C_{44}\frac{d^2V}{dx_3^2}\\
&+\frac{\rho\omega^2}{k}V(x_3) + \frac{dC_{44}}{dx_3}\left[\frac{1}{k}\frac{dV}{dx_3} + W(x_3)\right] = 0,
\end{aligned} \tag{5}$$

$$\begin{aligned}
&-k^2\left[\frac{1}{k}\left(C_{44} + C_{13}\right)\frac{dV}{dx_3} + C_{44}W(x_3)\right] + C_{33}\frac{d^2W}{dx_3^2}\\
&+\rho\omega^2 W(x_3) - k\frac{dC_{13}}{dx_3}V(x_3) + \frac{dC_{33}}{dx_3}\frac{dW}{dx_3} = 0.
\end{aligned} \tag{6}$$

Elastic constants and mass density are assumed to vary exponentially with depth and are expressed as $C_{ij}(x_3) = C_{ij}^0 e^{\beta x_3}$ and $\rho(x_3) = \rho^0 e^{\beta x_3}$, where β is the parameter representing the inhomogeneous behavior of the half-space. For surface waves propagating in the half-space defined by $x_3 \geq 0$ seeking solutions of Eqs. (5) and (6) in a general form given by $V(x_3) = \bar{V}e^{-px_3}$ and $W(x_3) = \bar{W}e^{-px_3}$ and substituting the expressions of elastic constants and mass density results in two homogeneous equations yields

$$\begin{aligned}
&\left[-kC_{11}^0 + \frac{\rho^0\omega^2}{k} - \beta\frac{p}{k}C_{44}^0 + \frac{p^2}{k}C_{44}^0\right]\bar{V}\\
&+\left[\beta C_{44}^0 - p\left(C_{13}^0 + C_{44}^0\right)\right]\bar{W} = 0,
\end{aligned} \tag{7}$$

$$\begin{aligned}
&-\left[\beta k C_{13}^0 - kp\left(C_{13}^0 + C_{44}^0\right)\right]\bar{V}\\
&-\left[k^2C_{44}^0 - \rho^0\omega^2 + \beta p C_{33}^0 - p^2C_{33}^0\right]\bar{W} = 0.
\end{aligned} \tag{8}$$

In order for non-trivial solution to exist, determinant of the coefficients must vanish, which yields the characteristic equation

$$M_1\gamma^4 + M_2\gamma^2 + M_3 = 0, \tag{9}$$

where

$$\begin{aligned}
&M_1 = C_{33}^0C_{44}^0,\ M_2 = \Gamma - \frac{\beta^2}{2k^2}C_{33}^0C_{44}^0,\\
&M_3 = RS - \frac{\beta^2}{4k^2}\left[C_{44}^0\left(\rho^0c^2 - C_{44}^0\right) + \right.\\
&\left. C_{33}^0\left(\rho^0c^2 - C_{11}^0\right) + \left(C_{44}^0 - C_{13}^0\right)^2\right] + \frac{\beta^4}{16k^4}C_{44}^0C_{33}^0,
\end{aligned} \tag{10}$$

in which

$\Gamma = \left(C_{13}^0 + C_{44}^0\right)^2 + \left(\rho^0c^2 + C_{11}^0\right)C_{33}^0 + \left(\rho^0c^2 + C_{44}^0\right)C_{44}^0$,
$R = \rho^0c^2 - C_{11}^0$, $S = \rho^0c^2 - C_{44}^0$ and $\gamma = p/k - \beta/(2k)$.

For the characteristic equation, there exist two positive real roots of γ for certain restricted range of β/k and are given by

$$\gamma_1 = s_1 - \frac{1}{2}\frac{\beta}{k}, \quad \gamma_2 = s_2 - \frac{1}{2}\frac{\beta}{k}, \tag{11}$$

where s_1 and s_2 correspond to two solutions for p/k. The corresponding forms of $V(x_3)$ and $W(x_3)$ then can be written as

$$V(x_3) = V_1 e^{-s_1 k x_3} + V_2 e^{-s_2 k x_3}, \tag{12}$$

$$W(x_3) = m_1 V_1 e^{-s_1 k x_3} + m_2 V_2 e^{-s_2 k x_3}, \tag{13}$$

where

$$m_i = \frac{\gamma_i^2 C_{44}^0 + \rho^0 c^2 - C_{11}^0 - \frac{1}{4}\frac{\beta^2}{k^2} C_{44}^0}{(C_{13}^0 + C_{44}^0)\gamma_i - \frac{1}{2}\frac{\beta}{k}(C_{44}^0 - C_{13}^0)}, \quad i = 1, 2. \tag{14}$$

The relevant components of stress $\sigma_{ij}(x_1, x_2, x_3)$ can be expressed as

$$\begin{aligned}
\sigma_{33} &= e^{\beta x_3}\left(-C_{13}^0 k V(x_3) + C_{33}^0 \frac{dW(x_3)}{dx_3}\right)\phi, \\
\sigma_{13} &= e^{\beta x_3} C_{44}^0 \left(\frac{1}{k}\frac{dV(x_3)}{dx_3} + W(x_3)\right)\frac{\partial \phi}{\partial x_1}, \\
\sigma_{23} &= e^{\beta x_3} C_{44}^0 \left(\frac{1}{k}\frac{dV(x_3)}{dx_3} + W(x_3)\right)\frac{\partial \phi}{\partial x_2}.
\end{aligned} \tag{15}$$

The traction free boundary conditions on the surface $x_3 = 0$ are

$$\sigma_{33}(x_1, x_2, 0) = \sigma_{13}(x_1, x_2, 0) = \sigma_{23}(x_1, x_2, 0) = 0. \tag{16}$$

Substituting Eq. (15) in Eq. (16) yields

$$\begin{aligned}
&(m_1 - m_2)\left(s_1 s_2 C_{33}^0 + C_{13}^0\right) \\
&\quad + (s_2 - s_1)\left(C_{13}^0 + m_1 m_2 C_{33}^0\right) = 0.
\end{aligned} \tag{17}$$

This equation is dispersive due to the appearance of the dispersion parameter β/k in m_i and s_i $(i = 1, 2)$. In order to ensure that surface waves decay exponentially with depth, ratios of β/k has to be restricted. The ratios for which Eq. (9) has exactly two positive real roots satisfies the decay conditions, so if γ_1 and γ_2 denote these two roots, then they both satisfy the condition

$$\gamma_i > \frac{1}{2}\left|\frac{\beta}{k}\right|, \tag{18}$$

which ascertain that both the displacements and stresses decay to zero as $x_3 \to \infty$. Thus, the displacement components of surface waves traveling in the inhomogeneous transversely isotropic half-space are

$$\begin{aligned}
u_\alpha &= \frac{D}{k}\left(e^{-s_1 k x_3} - \frac{s_1 - m_1}{s_2 - m_2} e^{-s_2 k x_3}\right)\frac{\partial \phi(x_1, x_2)}{\partial x_\alpha} e^{i\omega t}, \\
u_z &= D\left(m_1 e^{-s_1 k x_3} - m_2 \frac{s_1 - m_1}{s_2 - m_2} e^{-s_2 k x_3}\right)\phi(x_1, x_2) e^{i\omega t},
\end{aligned} \tag{19}$$

where $\alpha = 1, 2$ and D is an unknown multiplying constant of length dimension.

4. SURFACE WAVES GENERATED BY A HORIZONTAL POINT-LOAD EXCITATION

The time-harmonic horizontal point-load Q parallel to the free surface is applied at $x_1 = x_2 = 0$, $x_3 = z_0$ as shown in Figure 1. In this case, unlike Kayestha et al. (2010), the problem is no longer axially symmetric and the θ dependence also needs to be considered during the analysis. Solutions for displacement components in general form are based on Eq. (19). For analysis, cylindrical coordinate system $(x_1 = r\cos\theta,\ x_2 = r\sin\theta,\ x_3 = z)$ has been introduced as x_3-axis is perpendicular to the plane of symmetry. In cylindrical coordinate system, Eq. (19) can be re-written as

$$\begin{aligned}
u_r(r, z) &= \frac{D}{k} u(z)\frac{\partial \phi(r)}{\partial r}, \\
u_z(r, z) &= D w(z)\phi(r),
\end{aligned} \tag{20}$$

where

$$u(z) = \left(e^{-s_1 k z} - \frac{s_1 - m_1}{s_2 - m_2} e^{-s_2 k z}\right),$$

$$w(z) = \left(m_1 e^{-s_1 k z} - m_2 \frac{s_1 - m_1}{s_2 - m_2} e^{-s_2 k z}\right), r = \left(x_1^2 + x_2^2\right)^{1/2}$$ and

Eq. (4) becomes

$$\frac{\partial^2 \phi(r)}{\partial r^2} + \frac{1}{r}\frac{\partial \phi(r)}{\partial r} + k^2 \phi(r) = 0. \tag{21}$$

The solution for $\phi(r, \theta)$ of Eq. (21) can be written as (see Achenbach, 2003)

$$\phi(r, \theta) = \Psi(kr)\cos\theta. \tag{22}$$

Equation (21) then takes the form

$$\frac{d^2\Psi}{dr^2}+\frac{1}{r}\frac{d\Psi}{dr}+\left(k^2-\frac{1}{r^2}\right)\Psi=0. \tag{23}$$

From the asymptotic expansion of Hankel functions, the relevant solution of $\Psi(r)$ for outgoing and incoming waves can be given as

$$\Psi(kr)=H_1^{(2)}(kr), \tag{24}$$

and

$$\Psi(kr)=H_1^{(1)}(kr), \tag{25}$$

respectively. Using Eqs. (22) and (24) the corresponding components of displacement and stress can thus be written as

$$u_r=\frac{1}{k}Du(z)H_1^{(2)\prime}(kr)\cos\theta, \tag{26}$$

$$u_z=Dw(z)H_1^{(2)}(kr)\cos\theta, \tag{27}$$

$$u_\theta=-\frac{1}{kr}Du(z)H_1^{(2)}(kr)\sin\theta, \tag{28}$$

$$\sigma_{rr}=De^{\beta z}\left[\Delta_1\left(\frac{1}{kr^2}H_1^{(2)}(kr)-\frac{1}{kr}H_1^{(2)\prime}(kr)\right)+\Delta_2H_1^{(2)}(kr)\right]\cos\theta, \tag{29}$$

$$\sigma_{zz}=De^{\beta z}\Delta_3H_1^{(2)}(kr)\cos\theta, \tag{30}$$

$$\sigma_{rz}=\frac{D}{k}e^{\beta z}\Delta_4H_1^{(2)\prime}(kr)\cos\theta, \tag{31}$$

$$\sigma_{\theta\theta}=-De^{\beta z}\left[\Delta_1\left(\frac{1}{kr^2}H_1^{(2)}(kr)-\frac{1}{kr}H_1^{(2)\prime}(kr)\right)-\Delta_5H_1^{(2)}(kr)\right]\cos\theta, \tag{32}$$

$$\sigma_{\theta z}=-\frac{D}{kr}e^{\beta z}\Delta_4H_1^{(2)}(kr)\sin\theta, \tag{33}$$

$$\sigma_{r\theta}=De^{\beta z}\Delta_1\left(\frac{1}{kr^2}H_1^{(2)}(kr)-\frac{1}{kr}H_1^{(2)\prime}(kr)\right)\sin\theta, \tag{34}$$

where the prime denotes differentiation with respect to the argument and

$$\Delta_1=2C_{66}^0u(z),$$

$$\Delta_2=\left(C_{13}^0\frac{dw(z)}{dz}-kC_{11}^0u(z)\right),$$

$$\Delta_3=\left(C_{33}^0\frac{dw(z)}{dz}-kC_{13}^0u(z)\right),$$

$$\Delta_4=C_{44}^0\left(\frac{du(z)}{dz}+kw(z)\right),$$

$$\Delta_5=\left(C_{13}^0\frac{dw(z)}{dz}-kC_{12}^0u(z)\right). \tag{35}$$

5. USE OF ELASTODYNAMIC RECIPROCITY

Elastodynamic reciprocity has been used to obtain the unknown constant D introduced in Eq. (19). Considering two distinct time-harmonic states A and B of same frequency, reciprocity relation can be written as

$$\int_V\left(f_i^Au_i^B-f_i^Bu_i^A\right)dV=\int_S\left(u_i^A\sigma_{ij}^B-u_i^B\sigma_{ij}^A\right)n_j\,dS, \tag{36}$$

where f_i^A, f_i^B are body forces, u_i^A, u_i^B are displacement components and $\sigma_{ij}^A, \sigma_{ij}^B$ are stress components in states A and B, respectively, while n_j are the components of the outward normal to boundary S. For state A, displacement and stress components due to the point-load can be given as in Eqs. (26)-(34) but with $k_R=\omega/c_R$, where c_R is the Rayleigh surface wave speed. For state B, a virtual wave system consisting of the sum of outgoing and incoming waves is considered. Thus, the final displacement components after obtaining the constant D is given by,

$$u_r=-\frac{1}{4i}\frac{Qu^R(z_0)}{I}u^R(z)H_1^{(2)\prime}(k_Rr)\cos\theta, \tag{37}$$

$$u_\theta=\frac{1}{4i}\frac{Qu^R(z_0)}{Ir}u^R(z)H_1^{(2)}(k_Rr)\sin\theta, \tag{38}$$

$$u_z=-\frac{k_R}{4i}\frac{Qu^R(z_0)}{I}w^R(z)H_1^{(2)}(k_Rr)\cos\theta, \tag{39}$$

$$\sigma_{rr}=-\frac{k_R}{4i}\frac{Qu^R(z_0)e^{\beta z}}{I}\left[\Delta_1\left(\frac{1}{k_Rr^2}H_1^{(2)}(k_Rr)-\frac{1}{k_Rr}H_1^{(2)\prime}(k_Rr)\right)+\Delta_2H_1^{(2)}(k_Rr)\right]\cos\theta, \tag{40}$$

$$\sigma_{rz}=-\frac{1}{4i}\frac{Qu^R(z_0)}{I}e^{\beta z}\Delta_4H_1^{(2)\prime}(k_Rr)\cos\theta, \tag{41}$$

$$\sigma_{zz} = -\frac{k_R}{4i}\frac{Qu^R(z_0)}{I}e^{\beta z}\Delta_3 H_1^{(2)}(k_R r)\cos\theta, \tag{42}$$

$$\sigma_{\theta z} = \frac{1}{4i}\frac{Qu^R(z_0)}{I\,r}e^{\beta z}\Delta_4 H_1^{(2)}(k_R r)\sin\theta, \tag{43}$$

$$\sigma_{r\theta} = -\frac{k_R}{4i}\frac{Qu^R(z_0)}{I}e^{\beta z}\Delta_1 \left(\frac{1}{k_R r^2}H_1^{(2)}(k_R r) - \frac{1}{k_R r}H_1^{(2)\prime}(k_R r)\right)\sin\theta, \tag{44}$$

where $D = -\frac{k_R}{4i}\frac{Qu^R(z_0)}{I}$,

$I = \int_0^\infty e^{\beta z}\left[u^R(z)\Delta_2 - w^R(z)\Delta_4\right]dz$, $u^R(z)$ and $w^R(z)$ are defined just after Eq. (20).

6. NUMERICAL RESULTS

In this section numerical results are given for beryl rock (see Table 1). The dispersion curve for beryl rock obtained from Eq. (17) is shown in Figure 2(a). In addition, the positive real roots γ_1 and γ_2 of Eq. (9) are also plotted as a function of β/k. From a detailed calculation, it has been found that in the range $-2.210 \le \beta/k \le 0.164$, Eq. (9) have exactly two positive roots and thus Figure 2(a) shows the plot of non-dimensional surface wave speed c/c_T where $c_T^2 = C_{44}^0/\rho^0$, in this range of β/k. In addition, Figure 2(b) shows a variation of γ_1 and γ_2 with β/k which satisfies the condition given in Eq. (18) ensuring exponential decay of both the stresses and displacements, as the roots γ_1 and γ_2 are above the limit $\beta/2k$.

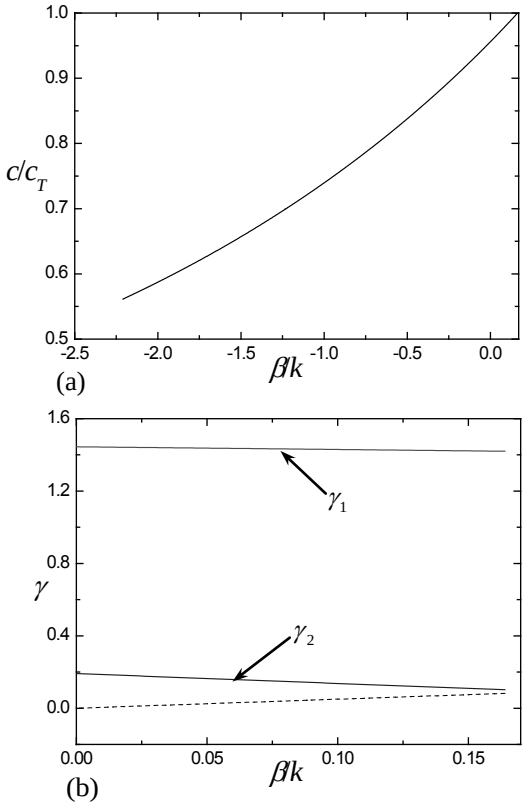


Figure 2 Beryl rock: Variations with the dispersion parameter β/k of (a) the surface wave speed and (b) the parameters γ_1 and γ_2 appearing in Eq. (9) (the dashed line is plot of $\gamma = \beta/2k$).

Table 1 Material constants

Material	$\bar{C}_{11}$	$\bar{C}_{13}$	$\bar{C}_{33}$	$C_{44}\times10^4$ (N/mm^2)	ρ (g/cm^3)
Beryl rock[a]	4.13	1.01	3.62	1.00	2.63

[a] Rajpakse and Wang (1993), $\bar{C}_{ij} = C_{ij}/C_{44}$.

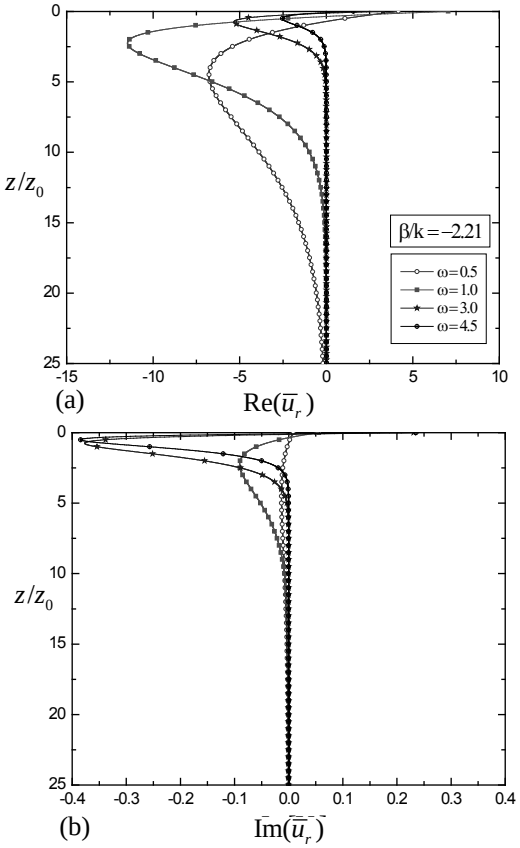


Figure 3 Normalized radial displacement $\bar{u}_r(0.1, z)$ along z-axis for $\beta/k = -2.21$, (a) real part and (b) imaginary part.

Figures (3) and (4) show the variation of radial displacement $\bar{u}_r = z_0 u_r C_{44}^0/Q$ along the depth direction at different non-dimensional frequencies ω for the inhomogeneous parameter $\beta = -2.21k$ and $\beta = 0.1k$,

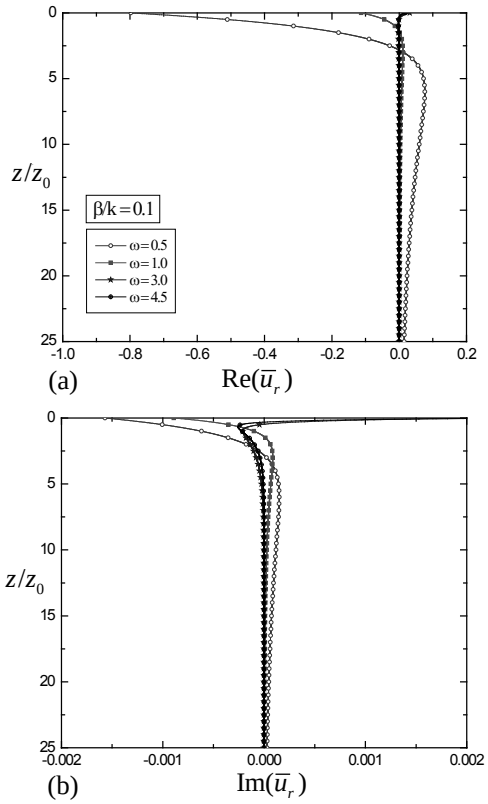


Figure 4 Normalized radial displacement $\bar{u}_r(0.1, z)$ along z-axis for $\beta/k = 0.1$, (a) real part and (b) imaginary part.

respectively. When the value of β is negative as seen in Figure (3), density and stiffness of the material decreases with depth thus resulting in less resisting capacity of the material. Besides, for positive value of β shown in Figure (4) density and stiffness increases with depth resulting in higher resisting capacity of the material. Thus, comparing Figures (3) and (4) it can be seen that the absolute values of displacements are much larger in Figure (3) than in Figure (4). In Figures (3) and (4), the displacement profile show changes in sign with the increasing depth; however, this feature is not clearly visible in Figure (4).

Since the half-space is subjected to time-harmonic radial loading at a depth of $z/z_0 = 1$, a distinct feature of displacement profile can be seen in Figure (3). Displacement profile in Figure (3) shows large absolute displacement values around the periphery of loaded point. For frequency $\omega = 3.0$, the peak displacement is noted exactly at $z/z_0 = 1$, however, for other frequencies it is noted at other depths. It can be seen that the displacement decays rapidly with increasing depth in both Figures (3) and (4). Thus from Figures (3) and (4), it can be noted that the degree of anisotropy of the material has significant influence on both real and imaginary parts.

Figures (5) and (6) show the variation of normalized vertical displacement $\bar{u}_z = z_0 u_z C_{44}^0 / Q$ along the depth direction at different non-dimensional frequencies ω for the inhomogeneous parameter $\beta = -2.21k$ and

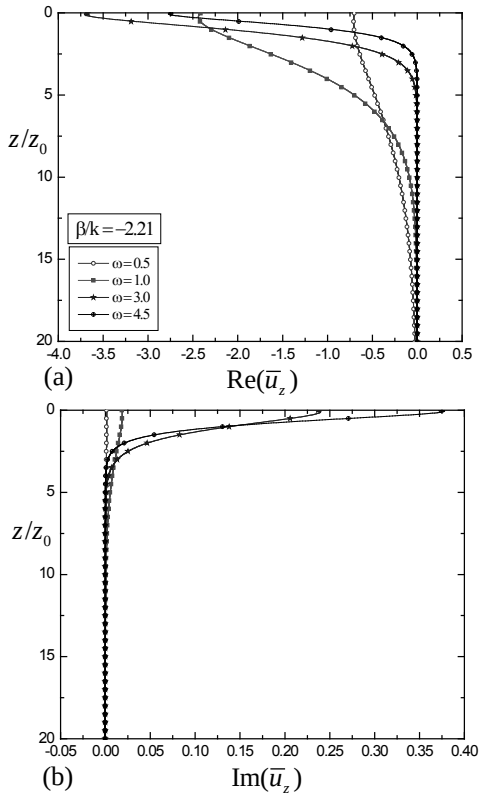


Figure 5 Normalized vertical displacement $\bar{u}_z(0.1, z)$ along z-axis for $\beta/k = -2.21$, (a) real part and (b) imaginary part.

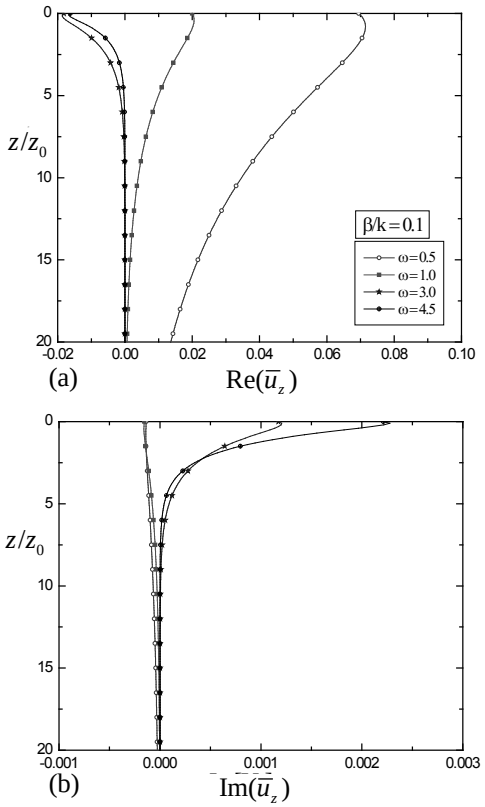


Figure 6 Normalized vertical displacement $\bar{u}_z(0.1, z)$ along z-axis for $\beta/k = 0.1$, (a) real part and (b) imaginary part.

$\beta = 0.1k$, respectively. As mentioned earlier, in this case too absolute values of displacements in Figure (5) are much larger than Figure (6) for both real and imaginary parts. The nature of displacement profile is similar to Rayleigh surface waves which is an expected feature for vertical displacement profile. The influence of frequency also has significant effect on the displacement profile. $\mathrm{Im}(\overline{u}_z)$ increases with an increase of frequency in both Figures (5) and (6), however, the variation of $\mathrm{Re}(\overline{u}_z)$ with ω is quite complicated. It can be seen in vertical displacement profile that the degree of anisotropy of the material has significant influence on both real and imaginary parts as was observed in radial displacement profile.

7. SUMMARY AND CONCLUSIONS

Explicit analytical solutions and numerical results are presented for displacement components of an inhomogeneous transversely isotropic elastic half-space subjected to a time-harmonic horizontal subsurface point-load. Elastodynamic reciprocity theorem is used in conjunction with an appropriately selected auxiliary elastodynamic solution to determine surface wave motions. It has been noted that the degree of inhomogeneity influence the results of displacement components significantly. The decay of the displacements with increasing depth is in general smooth.

Acknowledgements:

The first author is pleased to acknowledge a Monbukagakusho (Ministry of Education, Culture, Sports, Science and Technology, Japan) scholarship for graduate students. Financial support from the Center for Urban Earthquake Engineering (CUEE) through the GCOE Program "International Urban Earthquake Engineering Center for Mitigating Seismic Mega Risk," is gratefully acknowledged.

References:

Achenbach, J. D. (1998), "Lamb waves as thickness vibrations superimposed on a membrane carrier wave", *Journal of the Acoustical Society of America*, Vol. **103**(5), 2283-2286.

Achenbach, J. D. (2000a), "Calculation of wave fields using elastodynamic reciprocity", *International Journal of Solids and Structures*, **37**, 7043-7053.

Achenbach, J. D. (2000b), "Calculation of surface wave motions due to a subsurface point force: An application of elastodynamic reciprocity", *Journal of the Acoustical Society of America*, **107**(4), 1892-1897.

Achenbach, J. D. (2003), *Reciprocity in Elastodnamics*, Cambridge Monographs on Mechanics, Cambridge University Press.

Achenbach, J. D. and Xu, Y. (1999), "Wave motion in an isotropic elastic layer generated by a time- harmonic point load of arbitrary direction", *Journal of the Acoustical Society of America*, Vol. **106**(1), 83-90.

Ewing, W. M., Jardetzky, W. S. and Press, F. (1957), *Elastic Waves in Layered Media*, New York, NY: McGraw-Hill.

Kulkarni, S. S. and Achenbach, J. D. (2008), "Application of the reciprocity theorem to determine line-load-generated surface waves on an inhomogeneous transversely isotropic half-space", *Wave Motion*, Vol. **45**, 350-360.

Kayestha, P., Konno, T. and Wijeyewickrema, A. C. (2010), "Surface waves due to subsurface point load excitation in an inhomogeneous transversely isotropic elastic medium," *The 3rd Asia Conference on Earthquake Engineering (3ACEE)*, CD-ROM Paper No. ACEE-P-108.

Rajapakse, R. K. N. D. and Wang, Y. (1993), "Green's functions for transversely isotropic elastic half space", *ASCE Journal of Engineering Mechanics*, Vol. **119**(9), 1725-1744.

Ting, T. C. T. (1996), *Anisotropic Elasticity: Theory and Applications*, New York, Oxford University Press.

8CUEE CONFERENCE PROCEEDINGS
8th International Conference on Urban Earthquake Engineering
March 7-8, 2011, Tokyo Institute of Technology, Tokyo, Japan

DETERMINATION OF SHALLOW SHEAR-WAVE VELOCITY PROFILES AND SITE AMPLIFICATION IN METRO MANILA, PHILIPPINES USING MICROTREMOR ARRAY OBSERVATIONS

Rhommel Grutas[1)] and Hiroaki Yamanaka[2)]

1) Graduate Student, Dept. of Environmental Sci. and Tech, Tokyo Institute of Technology, Japan
2) Associate Professor, Dept. of Environmental Sci. and Tech, Tokyo Institute of Technology, Japan
grutas.r.aa@m.titech.ac.jp, yamanaka@depe.titech.ac.jp

Abstract: This paper presents the shear-wave (S-wave) velocity structures and site amplification of 32 sites covering all geologic settings in Metro Manila. We applied the passive microtremor array measurement using spatial autocorrelation (SPAC) to cover large area within a short period of time. An expanding double circular array composed of seven vertical portable seismometers is set up to measure Rayleigh type ground surface motions of microtremors and to come up with surface wave phase velocities in the form of dispersion curve. We used hybrid genetic algorithms for the inversion of surface waves to provide Vs structures. Thus, a 3D depth configuration of engineering bedrock is shown to evaluate the deepest alluvium deposits in the metropolis. The engineering bedrock is defined for this study to have S-wave of about 600 m/s. A one-dimensional analysis was applied to evaluate amplification using the revealed S-wave velocity profiles. The obtained variation in the site amplification factors and formulated regression equation provided information on the site response in the Metro Manila.

1. INTRODUCTION

Identification of velocity structures has been the interest of earthquake engineers to be able to evaluate theoretically the strong ground motions and site responses. Being able to model the dynamic characteristics of the underground structures are beneficial inputs to ground shaking hazard analysis. In the study of local site response in a metropolis, knowledge of sedimentary layers is important and a detailed approach requires sufficient distribution of boreholes with information regarding S-wave velocities.

Metro Manila, the capital of the Philippines is composed of 16 cities and one municipality. It has been considered as high risk to large earthquakes due to its surrounding active faults and trenches. Metro Manila is transected by 135 km long right lateral strike slip fault that is capable of producing a single earthquake event with a magnitude range of 7.3-7.7 (Rimando and Knuepfer, 2006). This fault (West Valley Fault) traverses the boundary of the Central Plateau and Marikina Valley with a sharp offset of several ten meters in elevation. Based on geomorphologic features (Gervasio, 1968), Metro Manila is divided into three categories; the Coastal Lowland, Central Plateau and Marikina Valley. The Coastal Lowland and Marikina Valley have deep quaternary alluvium sediments from the deposition of rivers, deltaic deposits and coastal deposits, whereas the Central Plateau covers tuffaceous sediments and pyroclastic flow deposits.

In this study, we conducted short period microtremor array measurements in 32 sites to make a detailed investigation of the shallow sedimentary layers by covering the major geologic settings in Metro Manila. Essential procedures require the extraction of Rayleigh waves from microtremors in the form of phase velocity dispersion curves by using Spatial Autocorrelation (SPAC) method and applied a hybrid genetic algorithms method for the inversion to infer the shallow S-wave velocity structures.

2. MICROTREMOR MEASUREMENT

Array observations of microtremors were carried out at 32 sites within Metro Manila on September 2009 and March 2010 (Fig. 1), totaling to nine surveyed days at an average of 3 to 4 sites per day. The surveyed sites were government establishments, private lands and school grounds that have open fields for easy deployment of circular arrays. The instruments used in the survey are portable accelerometers. Seven vertical sensors were used featuring Mitsutoyo 6A1 products with a period range of 0.01 to 14 s, with attached 24-bit analog-to-digital recorder that takes 100 samples per seconds. Each sensor was paired by a data recorder that transmits data to a laptop using wireless network. A software package installed in the laptop controls the setting and the duration of the recording. This set up enable easy viewing of real-time waveforms and quick assessment of sensors' sensitivities. The arrangements of six sensors were placed in the vertices of two equilateral triangles inscribed in a circle with the 7th sensor at the center. The sizes of the array were

selected according to the availability of the space at the site and limitation of signals from the wireless network. Due to this reason, the circular arrays were set up with a maximum length of sides of the triangle at 32 m. Two recording set-ups were deployed at each site by changing from the largest to smallest circular array. The shortest length of the side of the triangle for the smallest array that allows us to achieve a better definition of shallow layers is 1.5 m. The time for one recording took 30 to 40 minutes long.

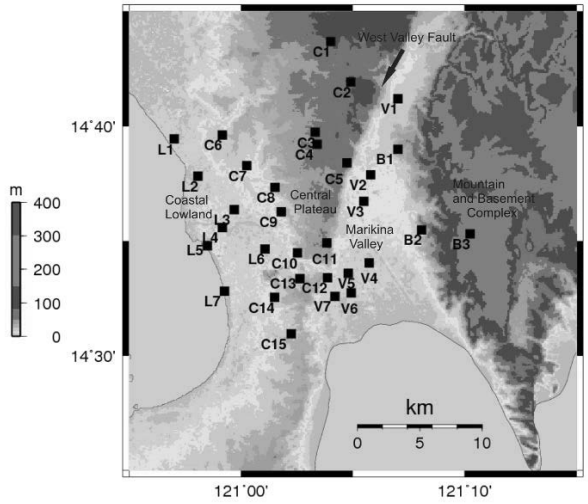


Figure 1 Map showing locations of microtremor sites. Sites have coded letters representing (L) Coastal Lowland, (C) Central Plateau, (V) Marikina Valley, and (B) Basement area

3. SPATIAL AUTOCORRELATION (SPAC)

The SPAC method by Aki (1957) and Okada (1987) was employed in the processing of microtremor array data in order to identify phase velocity dispersion curve. The SPAC method analyzes ambient vibration records from an array of stations. The SPAC method in practice requires a circular array consisting of 3 or more circumferential stations and one at the center (Okada, 2006). Hence, for practical use, it is sufficient enough in SPAC applications to provide phase velocities by arranging 3 sensors in the tip of equilateral triangle inscribe in a circle and one sensor at the center (Kudo *et al.*, 2002). By setting up the array of vertical components of microtremor instrument, the phase velocities of Rayleigh waves could be estimated by computing the SPAC coefficients calculated from various combinations of station distances as a function of frequency, and averaged azimuthally for the selected time segments. Thus, cross correlation functions is computed between pairs of stations, and averaged for different station pairs at the same inter-station distance.

The SPAC coefficients can be directly calculated in a frequency domain using the Fourier Transform of the observed microseism, denoted by equation

$$\rho(r,\omega) = \frac{1}{2\pi}\int_0^{2\pi} \frac{R_e[S_{CX}(\omega,r,\theta)]}{\sqrt{S_C(\omega)\cdot S_X(\omega,r,\theta)}}\,d\theta \qquad (1)$$

where $R_e[\ ]$ stands for the real part of a complex value, and $S_C(\omega)$ and $S_X(\omega,r,\theta)$ are the power spectral densities of microtremors at sites C(0,0) and X (r,θ) respectively, and $S_{CX}(\omega,r,\theta)$ is the cross spectrum between ground motions at these two sites.

Further details of the SPAC method can be found in literatures (e.g. Okada, 1987, 2006; Kudo *et al.*, 2002; Chavez-Garcia *et al.*, 2005).

4. ANALYSIS AND INTERPRETATION

Phase velocities of Rayleigh waves are estimated from vertical components of microtremors. The SPAC coefficients were calculated for various combinations of station distances, as a function of frequency, and averaged azimuthally for the selected time segments. The SPAC coefficients provide a good average in the phase velocity of propagating waves in the array for a fixed distance between two stations at various frequencies.

Ideally, the larger the circular microtremor array the deeper sediments and most likely higher phase velocity will be deduced, but because of limitations in the area and accessibility, some sites could be surveyed only for a relatively small array with low expectation of reaching bedrock at sites having deep alluvium cover. For example the site L4 in Fig. 2 has a phase velocity that reaches only to a maximum of 350 m/s. In order to deal with dispersion curves that did not reach the engineering bedrock (Vs~600 m/s) we considered the input parameters of nearby sites that have phase velocity of engineering bedrock and with same geologic composition.

As shown in Fig. 2 dispersion curves of phase velocity in Coastal Lowland are distinct to have been covered by soft layer of alluvium. The Central Plateau shows abrupt steep slope on dispersion curves and in most cases the phase velocity start with a value higher than 200 m/s which clearly exhibits the top hard soil layer. Other steep dispersion curves of phase velocity in Central Plateau that have less than 200 m/s justify that a thin layer of soft sediment exist underlain by hard soil.

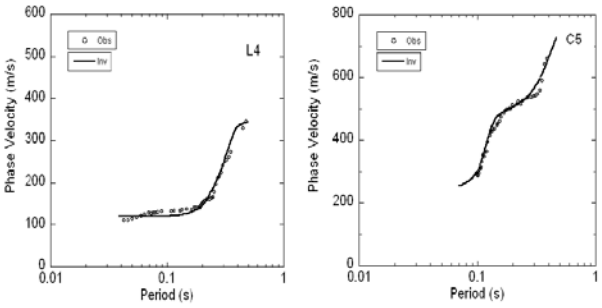


Figure 2 Comparison between observed phase velocity of microtremors (circular dotted line) and inverted surface wave phase velocity using hybrid genetic algorithms (solid line). Site L4 and C5 are located in Coastal Lowland and Central Plateau, respectively.

4.1 Inversion of surface waves using hybrid genetic algorithms

In order to extract the subsurface structural model from surface wave dispersion curve we applied Hybrid Genetic Algorithms (HGAs) as an inversion technique. SPAC utilizes the Rayleigh wave's surface propagation and considering that it propagates in a horizontally layered half-space. Dispersion curve of Rayleigh wave phase velocity is inverted into a 1-D shear wave velocity profile using HGAs based on the method of Takekoshi and Yamanaka (2009). In the HGAs inversion, subsurface structural models are searched by minimizing the misfits that is defined by L1-norm of differences between observed and inverted phase velocities. We conducted 10 inversions with 100 generations using different seeds of random numbers where good model with smaller misfit survive more in the next generation while bad models are replaced by newly generated models. The searched horizontally-layered models were considered to be an isotropic, homogenous unit characterized by four parameters: thickness (h), density (ρ), P-wave velocity (Vp) and shear-wave velocity (Vs). The unknown parameters in the HGAs inversion are S-wave velocity and thickness. The density is fixed while the P-wave is derived using an empirical relation with S-wave. In the inversion we searched for an optimal combination of S-wave velocity and thickness for each layer and they are digitized as 8-bit binary strings.

4.2 Shear wave velocity structures

The inferred S-wave velocity profiles at 32 sites in Metro Manila using the HGA's inversion of the phase velocity from SPAC of microtremors are presented here. The four major classifications based on geomorphic characteristics are enumerated as follows: Coastal Lowland, Central Plateau, Marikina Valley and Basement area. This study defines the engineering bedrock as having S-wave velocity of about 600 m/s. This assumption considered all the S-wave velocities that fall within the range of 500 m/s to 900 m/s as engineering bedrock.

Coastal Lowland (L) has a geological classification of Quaternary alluvium. As shown in Fig. 3, sites L1 and L2 have thin (~5 m) low velocity (Vs~90 m/s) layers existing near the surface, but high-velocity (Vs~600 m/s) layers are prevalent along shallow depth. The existence of the low velocity layers in these areas are considered to be from coastal deposits and some reclaimed land at close proximity to the coast. Because of high velocity contrast between the layers, it is possible to have high site amplification in these areas. The sites L4 and L5 located in Manila City, have the deepest sedimentary layers of 52 and 60 m, respectively. These results further contribute details to the study of Daligdig and Besana (1993) who discussed and mapped out the distribution of alluvial cover in the Manila area where the thickest accumulation of fine sediments exceeds 20 m. Documented damages of buildings during the 1968 Casiguran Earthquake could be seen in this area, as well as in areas nearby Pasig River where a distinct clustering of damaged buildings was noted (Omote *et al.*, 1969). Sites L3, L6, and L7 have thin (~3 to 11 m) low velocity (Vs~78 to 135 m/s) layer underlain by another layer (2 to 18 m) above the bedrock (Vs~600 m/s).

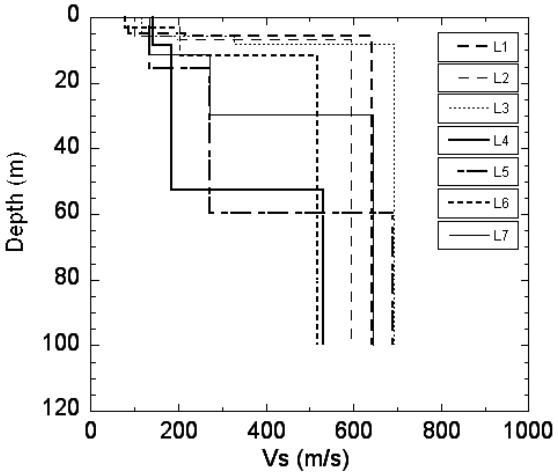


Figure 3 Inferred shear-wave velocity structures at Coastal Lowland by applying HGAs in the inversion of observed phase velocity dispersion curves.

The Marikina Valley (V) has the same geological classification as Coastal Lowland. From north where V1 is located in the upper stream of Marikina River to site V7 in the south shows clear variations of thicknesses in the near-surface layer from 19 to 64 m, respectively. Site V1 has a Quaternary alluvium thickness of 19 m with low velocity (Vs~200 m/s) layer underlain by engineering bedrock (Vs~600 to 800 m/s). The existence of layers with high velocities can be compared to the one identified by Matsuda *et al.* (2000) who used N-value of more than 50 that were obtained from Standard Penetration Test (SPT) of 80 borehole records in Marikina Valley. Also, the depth of around 30 m of N>50 in Manggahan, Pasig City is congruent with the microtremor array observations derived in this study.

The area of Central Plateau that covers the majority of Metro Manila is composed of tuffaceous sediments and pyroclastic flow deposits. It has high elevation compared to Coastal Lowland and Marikina Valley. Due to its composition, Central Plateau has layers with high velocity (Vs~500 to 1100 m/s) at shallow depth. The lower S-wave velocity sediment in Central Plateau reaches to a maximum depth of 20 m before engineering bedrock (Vs~600 m/s) is located. Sites C6, C7 and C9, which are located near the boundary of geologic contact between Quaternary alluvium deposits and tuffaceous sediments, have engineering bedrock at depths 10, 13, and 12 m, respectively. In these sites Quaternary alluvium deposits are thin and then become thicker towards the coast of Manila Bay. The site C15 is located in the southern part of the Central Plateau. It has soft sediments at 12 m underlain by a thicker layer with high velocity of about 500 m/s.

Basement area (B) or Basement complex is mainly mountainous area to the east of Metro Manila. Three sites were measured in this area namely B1, B2 and B3 at elevations of 25 m, 44 m and 198 m, respectively. B1 is a rock site located near the boundary of Marikina Valley consisting of a thin (~10 m) low velocity (Vs~200 m/s) uppermost layer underlain by a 15 m thick, second layer that has S-wave velocity of 470 m/s and, a third layer of high velocity (Vs~730 m/s). In site B2, it shows to have a thin (~17 m) low velocity (Vs~140 m/s) layer near the surface and a high velocity (Vs~1900 m/s) underlying at shallow depth. Site B2 is near to the borehole site with a basement (Vs~2000 m/s) at the depth of 20 m (Yamanaka *et al.*, 2002). Site B3 has thin (~5 m) low velocity (Vs~160 to 330 m/s) layer followed by a high velocity (Vs~2700 m/s). Site B3 is significant for the study of deep sediments in Metro Manila because it inferred the seismic basement rock that has S-wave velocities of 2700 to 3000 m/s.

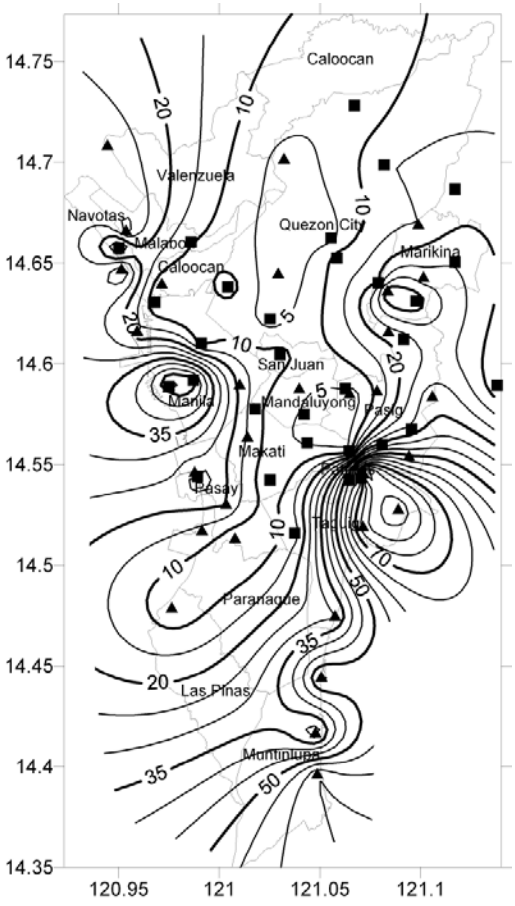


Figure 4 Three-dimensional (3-D) map of engineering bedrock (Vs~600 m/s) in and around Metro Manila from the combined data of microtremor observations (square) and boreholes (triangle).

The engineering bedrock in Metro Manila is summarized by a three-dimensional (3-D) contour map of engineering bedrock depths, with S-wave velocity of about 600 m/s. Further addition of borehole data from Metro Manila Earthquake Impact Reduction Studies (MMEIRS, 2004) lead to the refinement of 3-D contour map of engineering bedrock in Metro Manila. The deepest engineering bedrocks are found in Manila and Taguig-Pateros areas as shown in Fig. 4. Those areas have alluvium sediments with a depth of 50 – 90 m. The deep Quaternary alluvium on these two basins was deposited by the Pasig River that crosses the Central Plateau and connects the two basins. While in Marikina Valley the majority of deposition in the southern part came from Marikina River.

4.3 Site amplifications

This study calculated the 1-D amplification factors of S-waves propagating vertically in the shear-wave velocity profiles. As shown in Fig. 5 the amplification factors of Coastal Lowland and Marikina Valley have a dominant peak in the range of 0.20 to 1.15 s. The thinner upper layer of low velocity in sites L1 and L2 corresponds to the predominant peak at 0.24 s. Hence, the thicker low velocity layer of site L4 leads to the dominant peak at 1.15 s. Therefore, the thicker the sediment the longer period is expected. The same case also appeared in the amplification factors of Marikina Valley that it has a very clear variations of thicknesses on the upper layer from site V1 (north) to site V7 (south). Site V1 has a dominant peak at 0.3 s while V7 has a dominant peak at 1.2 s. Coastal Lowland and Marikina Valley are susceptible to high amplifications for earthquake events having period ranges from 0.24 to 1.0 s. The maximum amplification amplitude for Coastal Lowland reaches 8.1 at period of 0.24 s and in Marikina Valley to have amplification of 7.9 at the period of 1.2 s.

In Central Plateau, it is expected that the amplification levels are generally low than those from Coastal Lowland and Marikina Valley because of its tuffaceous characteristics. Central Plateau has a low period of less than 0.20 s, making it a distinct characteristic of a stable site to have engineering bedrock. The average amplification deduced for Central Plateau in this study is 6.0 at the period of 0.1 s. It is clearly pointed out that the amplifications of Coastal Lowland and Marikina Valley have a difference factor of 2 compared to the amplification of Central Plateau. Thus, considering the Central Plateau as a reference site, the intensity level of ground shaking in Coastal Lowland and Marikina Valley could be increased by factor of two when there is a significant earthquake event that will strike Metro Manila.

The Basement area (B) has similar characteristics of Central Plateau, but relatively smaller in amplification. In Basement area, the maximum amplification that was identified is 4.5 at period 0.17 s from site B1 which is located near the boundary of Marikina Valley. Site B3 has an amplitude of 4 at period of 0.1 s. Site B3 is significant compared to all microtremor sites in this study because it has a shear wave velocity layer reaching almost 3000 m/s which is categorized as basement complex or seismological bedrock. This site B3 can be used as a stable reference site for understanding site response and future understanding of much deeper sediments in Metro Manila.

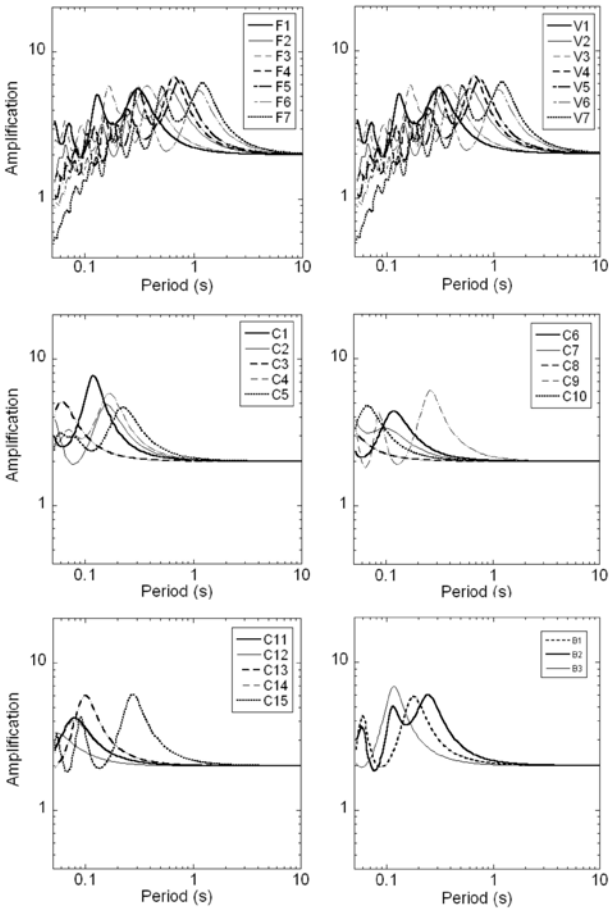


Figure 5 Amplifications of different geomorphic classifications in Metro Manila with the reference of engineering bedrock (Vs~600 m/s) as a half space model at the bottom layer.

4.4 Relationship of amplifications to Vs30

The most common parameter adopted worldwide for the seismic code, also in the National Structural Code of the Philippines (NSCP) (ASEP, 2001), is the average shear-wave velocity in the top 30 m of subsoil (Vs30). For this study, we derived regression equation of the calculated site amplification based on the Vs30

$$Ave.Amp = (687/Vs_{30})^{0.476} \quad (2)$$

where $Ave.Amp$ is the average amplification of a site and Vs_{30} is the average shear-wave velocity of the upper 30 m from the ground.

Focusing on the S-wave velocity of surface deposits that play a significant role in site amplification, comparison was made to other regression equation as shown in Fig. 6. Borcherdt (1994) developed a method to estimate site amplification from the average shear-wave velocity in the upper 30 m that is characterized by short (0.1-0.5 s) and mid-period (0.4-2.0 s) amplification. Also, Borcherdt work has been incorporated into the 1997 Uniform Building Code. As show in Fig. 6, our result coincides with the short period amplification of Borcherdt (1994). As compared to earthquake records, it is expected that the result of amplification for shallow S-wave velocity profiles is relatively low compared to the results derived by Fujimoto and Midorikawa (2006) because their amplification includes the effect of deeper profiles. However, the reference engineering bedrock in this study has S-wave velocity of around 600 m/s. Recently, Yamanaka *et al.* (2010) derived different correlation equation with respect to different periods using strong motion records in Metro Manila. As shown in Fig. 6, it would imply that the amplification in short period (0.14 s) of Yamanaka *et al*. (2010) shows higher amplification values compared to the result of this study. But interestingly, comparing the regression equation, the difference in amplification is almost twice and parallel to each other. More likely, this is the effect of basement rock that lies underneath Metro Manila having S-wave velocity of 3000 m/s. For a much deeper sedimentary layers amplification computation, the identified seismic basement rock (Vs~3000 m/s) of site B3 will be a suitable reference site. The effect of identified higher S-wave velocity value for basement rock will have an increase in amplitude value in amplification and will also give amplification in the longer periods because it is underlain by deeper sedimentary layers.

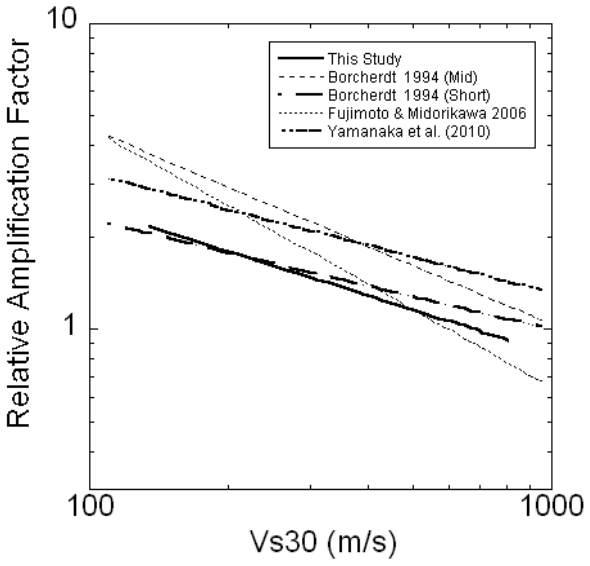


Figure 6 Comparison of result from this study using microtremor observation to various authors who used strong motion records to derived correlations between Vs30 and relative amplification factors.

5. CONCLUSIONS

Presented in this article are the wide area of coverage for microtremor surveys and the shallow S-wave velocity profiles of 32 sites covering all geologic conditions in Metro Manila. The results for the inferred S-wave velocity profiles are consistent with the investigations of the available borehole data, which significantly contributes to the

refinement of map of the depth of engineering bedrock. It is possible that some observed differences in interface depth and S-wave velocity estimation are affected by a significant distances between the borehole and microtremor sites. The deepest Quaternary alluvium in Coastal Lowland and Marikina Valley was located in Manila and Pateros-Taguig area making it distinct and critical areas for site response. We propose to classify these two catch basins as a separate group from Coastal Lowland and Marikina Valley and to be characterized as important areas considering site effects. Therefore, the four classifications namely: Coastal Lowland; Central Plateau; Marikina Valley; and Basement area, will be classified to six characteristics including these two deep alluvium basins. The area of boundary for these two separated classes will be at contour depth of 30 and 50 m in Coastal Lowland and Marikina Valley, respectively. In Marikina Valley, the identified area with deep alluvium corresponds to landfill classification as the Delta.

Site amplifications are provided to better understand the effect of geologic condition and thickness of Quaternary alluvium to the predominant period of amplifications. The Coastal Lowland and Marikina Valley show a predominant periods in the range of 0.2 to 1.2 s, while the Central Plateau and Basement area exhibit predominant periods about 0.2 s and below. Thus, site amplification is computed using the engineering bedrock of Central Plateau with S-wave velocity of about 600 m/s as a reference. The analysis with respect to the Vs30 was also evaluated and the different site classes in reference to NEHRP were obtained. A correlation between average amplification and Vs30 shows good agreement with the Borcherdt's (1994) short period regression, but as compared to the regression for earthquake records it shows a low level of amplification. Hence, this difference will be further assessed in the future by identifying the deeper sedimentary layers underlain by basement bedrock (Vs~3000 m/s). This paper presented briefly the result of local site effect focusing on the shallow velocity structures, especially Vs30 which has greater effect in engineering structures.

Acknowledgement:

The authors acknowledge support from the Japan Ministry of Education, Culture, Sport, Science, and Technology (MEXT) for establishing the Center for Urban Earthquake Engineering (CUEE) in Tokyo Institute of Technology. We thank also Philippine Institute of Volcanology and Seismology (PHIVOLCS) for providing the logistics and accommodations during our survey in the Philippines on Sept 2009 and March 2010. The authors also acknowledge Ansai, T., Capistrano, R.K., Deocampo, J.B., Fallarme, J.P, Niiro, R., Tiglao, R., and Yamauchi, Y. for their help in the survey set ups during fieldworks.

References:

Aki, K. (1957), "Space and time spectra of stationary stochastic waves, with special reference to microtremors". *Bulletin of the Earthquake Research Institute*.35, 415-456.

Association of Structural Engineers of the Philippines- ASEP (2001), "National Structural Code of the Philippines 2001. *5th edition ASEP"*. Manila, Philippines.

Borcherdt, R.D. (1994), "Estimates of site-dependent response spectra for design (Methodology and Justification)", *Earthquake Spectra*, 10 (4), 617-653.

Chavez-Garcia, F.J., Rodriguez, M., and Stephenson W. R. (2005), "An alternative approach to the SPAC analysis of microtremors: Exploiting stationary of noise". *Bull. Seism. Soc. Am.***95**,1, 277-293.

Daligdig, J., and Besana, G. (1993), "Seismological Hazards in Metro Manila. *Natural Disaster Prevention and Mitigation in Metropolitan Manila". Department of Science and Technology, Philippine Institute of Volcanology and Seismology (DOST-PHIVOLCS)*, 9-41.

Fujimoto, K., and Midorikawa, S. (2006), "Relationship between Average Shear-Wave Velocity and Site Amplification Inferred from Strong Motion Records at Nearby Station Pairs". *Proceedings of the sixth volume of Japan Association for Earthquake Engineering,* (In Japanese, with English abstract) No. 1, 11 -22.

Gervasio, F.C. (1968), "The Geology, Structures and Landscape Development of Manila and Suburbs". *The Philippine Geologist*. 22, 178-192.

Kudo, K., Kanno, T., Okada, H., Ozel, O., Erdik, M., Sasatani, T., Higashi, S., Takahashi, M., and Yoshida, K. (2002), "Site specific issues for strong ground motions during the Kocaeli, Turkey Earthquake of August 17, 1999, as inferred from array observations of microtremors and aftershocks". *Bull. Seism. Soc. Am*,92, 448-465.

Matsuda,I., Enomoto, T., Banganan, E. L., and Narag, I. C. (2000), "Regional Division of Marikina Valley and Coastal Lowland, Metro Manila on the Basis of Soil Condition". *Proceedings International Workshop on the Integration of Data for Seismic Disaster Mitigation in Metro Manila.* 43-62.

Metro Manila Earthquake Impact Reduction Study (MMEIRS) (2004), "MMEIRS Final Report Volume 1 Execute Summary, March 2004", http://www.pdc.org/mmeirs/html/mmeirs-home.jsp (last accessed December 2010).

Okada, H. (2006), "Theory of efficient array observations of microtremors with special reference to the SPAC method". *Exploration Geophysics*, 37, 73-85.

Okada, H., Matsushima, T., and Hidaka, E. (1987), "Comparison of Spatial Autocorrelation Method and Frequency-Wavenumber Spectral Method of Estimating the Phase Velocity of Rayleigh Waves in Long-Period Microtremors". *Geophysical Bulletin of Hokkaido University, Sapporo, Japan* (In Japanese). No.49, 53-62.

Omote, S., Osawa, Y., Skimmer, I., and Yoshimi, Y. (1969), "Philippines: Luzon Earthquake of 02 August 1968". *Paris: UNESCO*. 541 pp.

Rimando, R., and Knuepfer, P. (2006), "Neotectonics of the Marikina Valley Fault System (MVFS) and tectonic framework of structures in Northern and Central Luzon, Philippines". *Tectonophysics*. 415,17-38.

Takekoshi, M., and Yamanaka, H. (2009), "Waveform inversion of shallow seismic refraction data using hybrid heuristic search method". *Exploration Geophysics*, **40, 99**-104.

Yamanaka, H., Midorikawa, S., Kinugasa, Y., Bautista, B., and Rimando, R. (2002), "Estimationof Seismic Risk in Metro Manila, *Metro Manila": In search of a Sustainable Future, Editors; Tatsuo Omachi and Emerlinda Roman, Published by the Japan Society for the Promotion of Science (JSPS) Manila Project in collaboration with the University of the Philippines Press,388 pages*, 301-326.

Yamanaka, H., Ohtawara, K., Grutas, R., Tiglao, R., Lasala, M., Narag, I., and Bautista, B. (2010), "Estimation of Site Amplification in Metropolitan Manila, Philippines, for Earthquake Ground Motion Records".*SEG* (in press).

8CUEE CONFERENCE PROCEEDINGS
8th International Conference on Urban Earthquake Engineering
March 7-8, 2011, Tokyo Institute of Technology, Tokyo, Japan

ESTIMATION OF SURFACE-WAVE GROUP VELOCITY IN THE KANTO BASIN USING SEISMIC INTERFEROMETORY OF LONG-TERM MICROTREMORS

Kosuke Chimoto[1)] and Hiroaki Yamanaka[2)]

1) Graduate Student, Interdisciplinary Graduate School of Science and Engineering, Tokyo Institute of Technology, Japan
2) Assistant Professor, Interdisciplinary Graduate School of Science and Engineering, Tokyo Institute of Technology, Japan
chimoto.k.aa@m.titech.ac.jp, yamanaka@depe.titech.ac.jp

Abstract: It has already been demonstrated that an estimate of the Green's function can be obtained from the cross correlation of long-term ambient noises between two stations, and it can be possible to extract interstation surface wave group velocity. We had observation of microtremors in the southern Kanto basin including IZU peninsula, to validate the existing three dimensional S-wave velocity model of deep sediments. Obtained data were processed for estimating the Green's functions by cross correlation between two stations. The result shows that the estimated Green's functions propagate by the different velocities because of the complexity of geology of this area. Furthermore, they have specific azimuthal dependence. Finally, we estimated the Rayleigh and Love wave velocity from the estimated Green's function assuming a straight path. The result was compared with the theoretical ones calculated from 2D models of an existing basin model of the deep sedimentary layers. The result compares favorably with theoretical ones in the basin area. However, there are significant differences in the IZU peninsula.

1. INTRODUCTION

It is known that long-period strong ground motion is amplified in a large sedimentary basin. Tokyo metropolitan area locates over Kanto basin with a scale of about 200× 200km large and a depth is more than 4km. Therefore it is important to estimate amplification effects in the large and deep basin. Accordingly, some subsurface structure models were proposed to predict strong ground motion including Kanto basin (e.g. Yamanaka & Yamada, 2006). Although They carried out validation of their models by simulating observed ground motion during small events, they still have difficulty to validate such models due to uncertainty of source and subsurface structure out of the basin.

Seismic interferometory is used for estimating Green's function between two sites. This method is one of passive imaging method because it doesn't need special sources (e.g. earthquake or artificial source). Main data processing is cross correlating long-term ambient noises at two sites (Snieder, 2004).

Recent studies showed possiblily to retrieve surface wave of Green's function from long-term ambient noises (e.g. Shapillo and Campillo, 2004). As shown in Shapiro et al. (2005), it is also possible to use estimated traveltimes from cross correlations for a Rayleigh wave tomographic inversion.

In this study, we applied seismic interferometory to estimate and validate its subsurface model for the Kanto basin. First we conducted observation of long-term ambient noises around Kanto basin and Izu peninsula. Observed microtremor data are processed with a procedure based on seismic interferometory and we estimated traveltime of each Green's functions at the periods of 2-6s. Traveltimes were used for estimating averaged group velocities between two observation sites. We compared group velocities and theoretical ones calculated from Yamanaka and Yamada (2006). The observed group velocities are well explained by the theoretical ones in the Kanto basin, but we found discrepancy in the Izu peninsula. To understand subsurface structure regionally, we conducted surface wave tomography.

2. ESTIMATING GROUP VELOCITIES

2.1 Extracting Green's Function

In order to apply seismic interferometory, we started long-term continuous observation of ambient noises from March 2008 in the southern Kanto region as shown in Figure 1. We have already got cross correlation functions from the data of these observation. Data procedure is described in Yamanaka et al. (2010) precisely. Here we roughly show about data processing. First, in order to extract surface waves, band-pass filter is applied to the data with the period of 2 – 6s. Then, one-bit data clipping is used to reduce the influence of nonstationaly event like earthquake (e.g. Gerstoft et al., 2006). Finally we cross correlate the data at two sites. Since Love and Rayleigh waves appear in the horizontal component, we rotated the horizontal components into the radial(R) and transverse(T) components. Figure 2

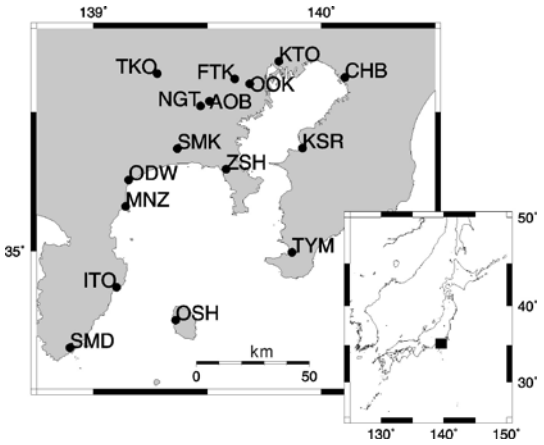


Fig.1. Observation Sites.

shows an example of cross correlation functions. As there are three components data at each site, we can get nine cross correlations after all. When source distribution is spatially uniform, positive waveform and negative waveform will be same (Snieder, 2004), but estimated Green's functions are not always symmetry. Fig. 3 shows all cross correlations against the inter-station distances and azimuths. This also show asymmetry of cross correlations. Gerstoft et al. (2006) showed most of the noise originates from microseisms from the direction of the ocean in California, U.S.A.. Our results also suggest this azimuthal dependence caused microseisms from ocean.

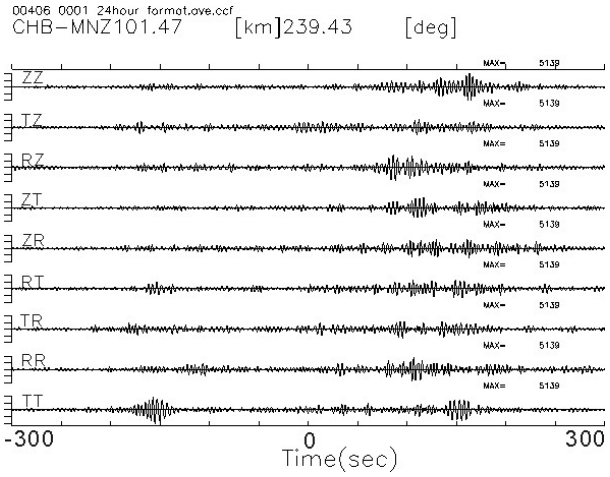


Fig.2. An example of cross correlations at 9 components. Z, R and T means Vertical, Radial and Transeverse, respectively.

2.2 Estimation of Group Velocity

We estimate group velocities using a multiple-filter technique (Dziewonski et al., 1969). The positive and negative cross correlations are firstly averaged to enhance Signal to Noise Ratio and then narrow bandpass filtered. We can see dispersive wave-trains in the cross correlation on vertical, radial, and transverse components (Fig.4). This result shows that we can get the Rayleigh and Love wave Green's function from ambient noises. Then we estimated

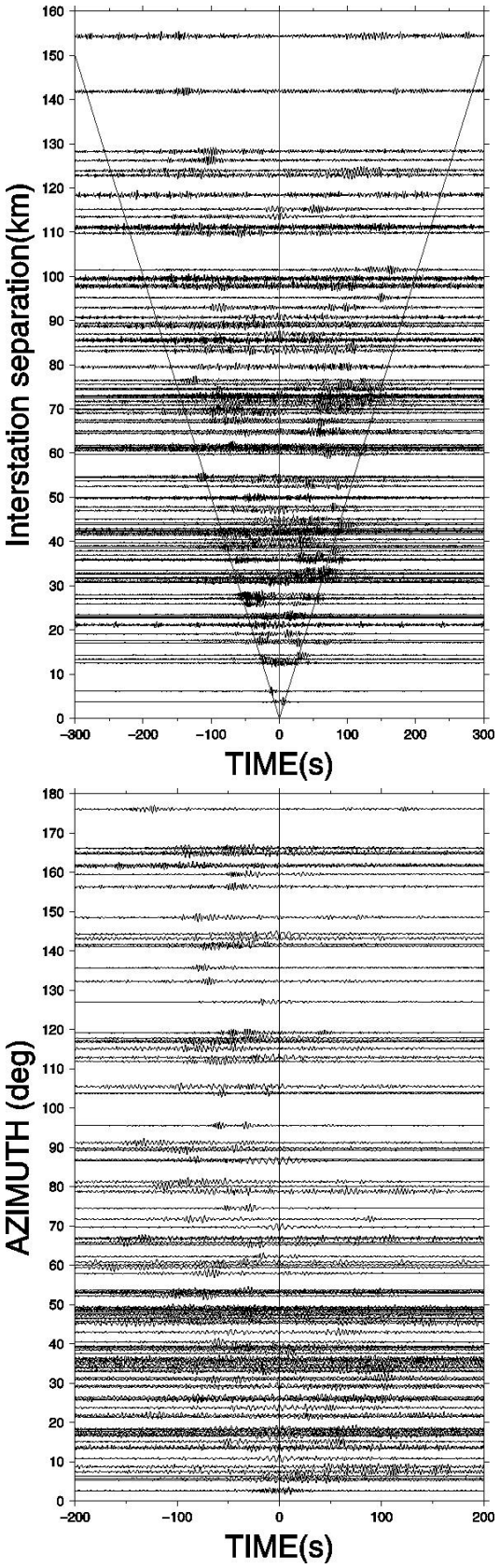


Fig.3. All cross correlations against distance (top) and azimuth (bottom). Vecolity of 1.5 km/s is shown in the top figure.

traveltime of fundamental mode of Rayleigh and Love wave, respectively. Rayleigh and Love wave's group velocity are estimated by assuming straight ray path.

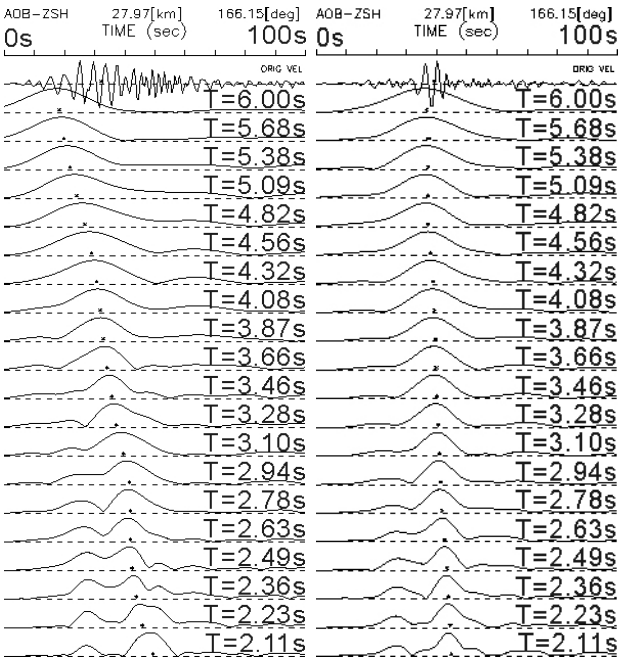


Fig. 4. The result of multiple filter analysis. Wave-form at top shows original cross correlation. ZZ (left) and TT (right) component are shown.

2.3 Comparing observed and calculated group velocity

We compared the observed group velocity and theoretical one calculated from Yamanaka and Yamada (2006). Two-dimensional model along two sites is divided into 500m segments. Each segment were assumed lateral model. Theoretical fundamental group velocities of Rayleigh and Love waves are calculated at each segment. Finally, theoretical averaged group velocity is obtained from those group velocities.

Figure 5 showes good agreement between observed and theoretical group velocities of the Rayleigh and Love waves in the Kanto basin. However the comparisons in the other area shows discrepancy between them. For example, Figure 6 shows group velocity between SMD and MNZ crossing Izu peninsula. This result clarifies inappropriateness of subsurface structure model in this region. In this way, we can validate two dimensional model not using earthquake nor artificial source.

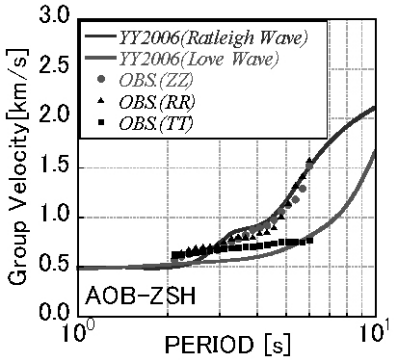


Fig. 5 Comparison of observed and theoretical group velocity (AOB-ZSH)

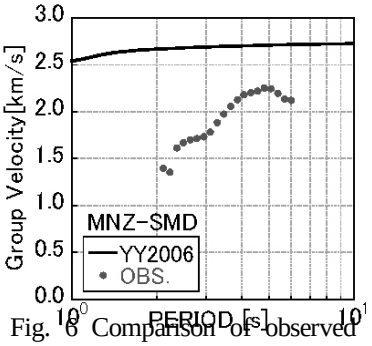


Fig. 6 Comparison of observed and theoretical group velocity (MNZ-SMD)

3. TOMOGRAPHIC INVERSION

3.1 Surface wave tomography

In this section, we consider about three-dimensional model. As shown by Bensen et al. (2008), if we have a lot of observation sites, we can conduct tomographic inversion based on seismic interferometory. Southern Kanto area is divided into 0.125° ×0.125° cells having constant group velocity in tomographic inversion, as indicated in Figure 7. the propergation paths are assumed to be completely straight paths. In order to construct tomography map, we applied a back projection technique using slowness at each period as an unknown parameter. Traveltimes are estimated in section 2 and an initial model is made based on those traveltimes. The nonlinear tomographic inversion is solved by iteratively conducting linear inversion, Simultaneous Iterative Reconstruction Technique (SIRT). Iteration is continued until residual becomes the minimum.

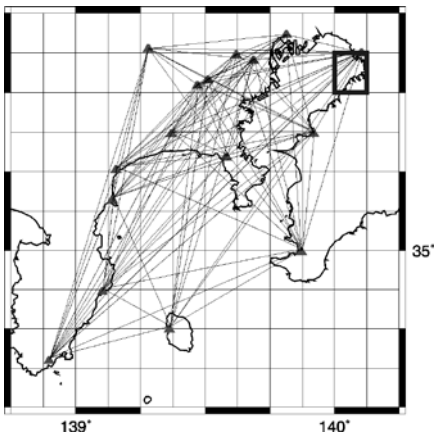


Fig. 7 Cell dividing and ray path coverage for tomographic inversion. Rectangular area shows tomographic inverted area in Fig.10,

3.2 Results

Figure 8 shows Rayleigh wave tomography map at period of 6s. This map clearly shows regional difference of group velocity. We can identify high velocity area such as Kanto mountain, Izu and Miura peninsula. We can also find low velocity area such as Tokyo, Sagami bay and Central Kanto basin. This result compares favorably with Section 2.

We conducted this surface wave tomography among the period of 2- 6s including Love waves (Fig.9). Estimated group velocities at each cell are used for tomographic inversion.

Rayleigh wave group velocity and Love wave group velocity are simultaneously inverted using Genetic Algorithm (Yamanaka and Ishida, 1996) to estimate a one-dimensional S-wave velocity at each cell subsurface model. The determined model including Chiba-city is shown in Figure 10. The comparison between the observed and theoretical phase velocities is shown in Figure 11. The theoretical phase velocity well explains the observed one.

4. CONCLUSIONS

Seismic interferometory using continuous microtremor data were applied in the Kanto basin and Izu peninsula. More than 150days observed data were used for extracting Green's functions. We used the multiple filter analysis for estimating group velocities at period of 2-6s. observed and theoretical group velocity comperes favarly, but we found discrepancy in Izu peninsula. We conducted tomographic inversion using SIRT. The result showed regional differences of group velocities.

Acknowledgements:

Some observation sites were set at other research observatories. We thank those who provide to us.

References:

Bensen, G.D., Ritzwoller M.H. and Shapiro, N.M. (2008). Broadband ambient noise surface wave tomography across the united states. *J. Geophys. Res*, **113**, B05306,, doi:10.1029/ 2007JB005248

Dziewonski, A. Bloch, S. and Landisman, M. (1969). A thechnique for the analysis of transient seismic signals. *Bull. Seis. Soc. Am.*, **59**(1), 427-444.

Gerstoft, P., Sabra, K.G., Roux, P., Kuperman, W.A. and Fehler, M.C. (2006). Green's functions extracting and surface-wave tomography from microseisms in southern California, *Geophysics*, **71**(4), SI23-SI31.

Shapiro, N.M. and Campillo, M. (2004). Emergence of broadband Rayleigh waves from correlations of the ambient noise, *Geophys. Res. Lett.* **31**, L07614, doi: 10.1029/2004GL019491.

Shapiro, N.M, Campillo, M., Stehly, L. and Ritzwoller, M. H. (2005). High-Resolution Surface-Wave Tomography from Ambient Seismic Noise. *Science*, **307**(11), 1615-1618.

Snieder, R. (2004). Extracting the Green's function from the correlation of coda waves: A derivation based on stationary phase, *Physical Review E*, **69**, 046610.

Yamanaka,H. and Ishida, H. (1996). Application of genetic algorithms to an inversion of surface-wave dispersion data, *Bull. Seis. Soc. Am.*, **86** 436-444.

Yamanaka, H. and Yamada, N. (2006). Modeling 3D S-wave velocity structure of Kanto basin for estimation of earthquake ground motion, *Butsuri-Tansa (Geophysical exploration)*, **59**(6), 549-560 (in Japanese).

Yamanaka, H. (2010). Estimation of surface-wave group velocity in the southern Kanto area using seismic interferometoryic processing of continuous microtremor data. *Butsuri-Tansa (Geophysical exploration)*, submitted.

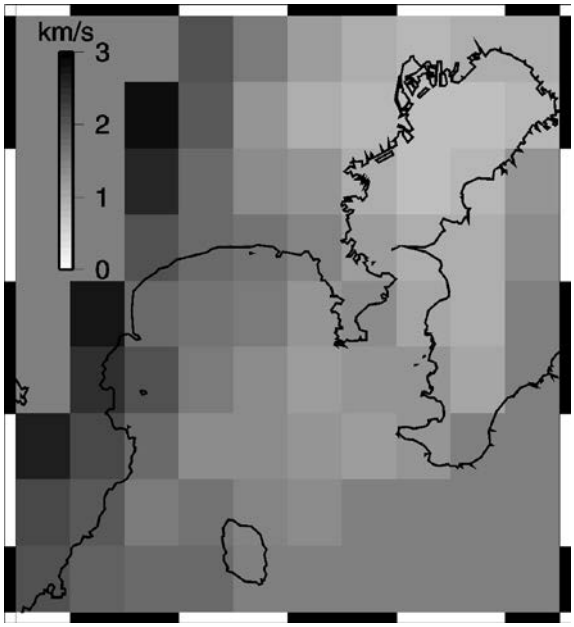


Fig.8. 6s Rayleigh wave tomography map

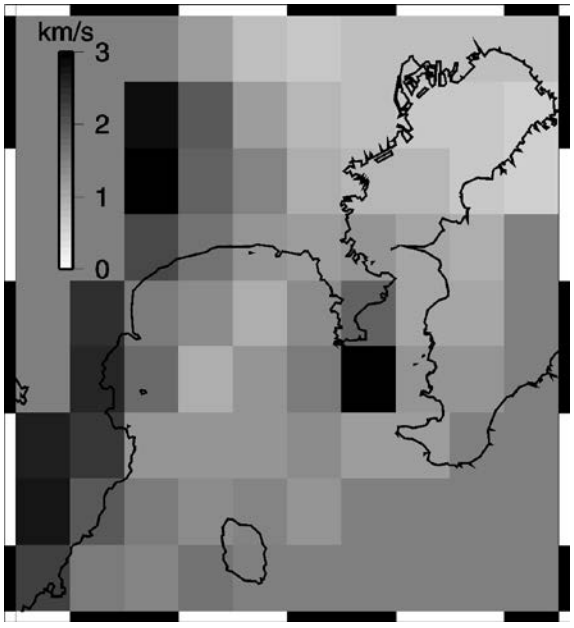


Fig. 9. 6s Love wave tomography map

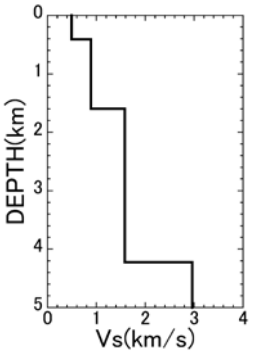


Fig. 10. 1D structure model at rectangular area showed in Fig.7.

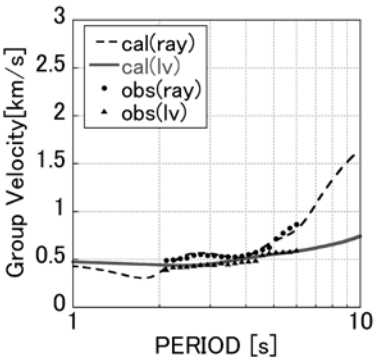


Fig. 11. Result of joint inversion using GA at rectangular area showed in Fig.7.

8CUEE CONFERENCE PROCEEDINGS
8th International Conference on Urban Earthquake Engineering
March 7-8, 2011, Tokyo Institute of Technology, Tokyo, Japan

COSEISMIC DEFORMATION OF THE 2008 WENCHUAN, CHINA EARTHQUAKE CALCULATED FROM STRONG MOTION DATA

Jyun Yan Huang[1], Kuo Liang Wen[2) 3)], Chun Te Chen[4], and Sheng Chung Su[4]

1) PHD student, Institute of Geophysics, National Central University, Taiwan
2) Professor, Institute of Geophysics, National Central University, Taiwan
3) Research fellow, National Center for Research on Earthquake Engineering, Taiwan
4) PHD candidate, Institute of Geophysics, National Central University, Taiwan
986402005@cc.ncu.edu.tw, wenkl@earth.ncu.edu.tw, 956402004@cc.ncu.edu.tw, scsu@scman.cwb.gov.tw

Abstract: On May 12, 2008, there was an Ms 8.0 earthquake occurred in Wenchuan, China region. The earthquake inflicted severe damage in China, especially in the near-fault region. The mainshock was recorded by over four hundreds strong motion stations in whole China, and there were over sixty stations near Longmenshan fault. In this study, the method which was modified from Wu and Wu (2007) was used to correct the baseline of each strong motion record for near fault stations. After three-parts-correction and double integral, the co-seismic displacements were found from strong motion data only. The results were compared with that from GPS measurements. Finally, there were some near fault records showed the baselines can divided into more than three parts. So in this study, the appropriateness of applying Hilbert-Huang Transform (HHT) method to find each divided time points was also discussed.

1. INTRODUCTION

There were some problems in strong motion records which were using digital instrument during huge earthquake, especially in near-fault region. The baseline of each record was drifted during large shaking from ground tilting (Graizer 2005), instrument impact or seriously permanent displacement occurred. Iwan et al. (1985) mentioned that the processes of baseline drifting could divide into three parts, and the corrected method could base on the slope of these three lines in velocity records.

Boore (2001) then tested and verified the difference corrected results from changing the length of the corrected lines. The results showed the unsuitable divided time choosing would lead great divergence. Wu and Wu (2007) built up a try and error method to choose divided times. In this study, the baseline correction method was modified from Wu and Wu (2007) and reduced some men-made decisions for semi-automatically choosing the most suitable divided times.

After three parts baseline correction, the ground motions of each station in Sichuan from 2008 great Wenchuan earthquake were corrected. And the co-seismic deformation results were corresponding to the GPS measurements including directions and quantity in near fault region.

Anyway, the three part baseline correction model would not appropriate for all the data when the baseline drift was greater than three parts. Huang et al. (1998) mentioned a Hilbert-Huang Transform (HHT) method which can expertly decompose different frequency signal. And commonly the baseline offsets were treated as the very low frequency signal. So in this study, a given waveform with obviously offset were built. The given waveforms were decomposed into several modes by HHT method and try to find out the divided time and offset.

2. METHODS AND DATA PROCESSING

2.1 Semi-Auto Three Parts Baseline Correction Method

Iwan et al. (1985) mentioned the baseline drifting models were associated with starting time of the strong shaking T1 and the end of shaking time T2. Wu and Wu (2007) then added another possible model, which was associated with another important time T3. T3 time means the end of great shaking and the ground started to become stable. (Figure 1, Wu and Wu 2007) In order to verify the suitability of each T1 and T2 time, they determined a parameter f (Eq. 1) :

$$f = \frac{|r|}{|b| \bullet \sigma} \tag{1}$$

This f value was calculated for corrected displacement data of the time history after T3 to the end. Where r: linear correlation coefficient, verified the data was scattered or not. b: the slope of regression line, verified the baseline was flat

or not. σ: variation coefficient, verified the baseline was stable or not .

In this study, the baseline correction method was modified from Wu and Wu (2007, Figures 2 and 3). The variable range for T1 and T2 were applied and semi-auto calculation collocated with try-and-error process was used. After calculated the f-value for different T1, T2 pairs, the time pair with greatest f-value were the final target. The simple linear correction was done from least square fitting with the best time pair in the end.

2.2 Hilbert-Huang Transform

Huang et al. (1998) mentioned a signal analysis method called Hilbert-Huang Transform (HHT) and which was clever at processing non-stationary or non-sinusoidal signal. And the men-made non-sinusoidal signal and real seismic records could finely decompose into several intrinsic mode function (IMF) components with different frequency composition. And the characteristic of each IMF was that the greater the IMF component, the lower the frequency content. (Ray et al. 2003) The HHT method was consisted of two parts: the Empirical Mode Decomposition (EMD) method and the instantaneous frequency in the Hilbert spectral analysis. In this study, the EMD method was used to decompose the given waveform. The procedures can be described as the original signal minus the average envelope lines for several times to get an IMF mode and repeated the process for the residual parts to get the higher IMF mode. Finally, the procedures were ended when the residual parts became a monotone function.

2.3 The Given Waveform

In this study, the given waveform was composed of a 5 Hz sinusoidal wave and a wave package which will attenuate with time. One or two obvious offset were added in this waveform for different situation. (Figure 4) The equation was as followed:

$$y = \frac{600}{0.141} * \sin(\pi t) * \exp(-8t) * \sin(10\pi t) \qquad (2)$$

Where the unit of y was acceleration ground motion (gal.), the obvious offsets were set on 5 seconds in Figure 4 (a) for a two parts baseline drifting model and were set on 5 and 20 seconds in Figure 4 (b) for a three parts baseline drifting model.

3. DISCUSSIONS AND CONCLUSIONS

3.1 Results for the Near-Fault Region During the 2008 Wenchuan Earthquake

The co-seismic deformation values were calculated from the corrected displacement records (Figure 3 (b), the range of double arrow showed) in different components. (NS, EW, Z) And the results were combined into vectors of permanent displacement in near-fault region. The results then compared with the GPS co-seismic deformation from The Project of Crustal Movement Observation Network of China (2008) (Figure 5). They showed a good agreement in vector directions and scales. Figure 6 were the example of corrected waveforms and which were compared the permanent displacement value with nearest GPS station.

The calculated displacement values were greater than 150 cm near the fault (Figure 5). Chang et al. (2008) used the teleseismic records and applied a quick-inversion method to calculate the slip rate on fault plane for Wenchuan earthquake (Figure 7 (a)). In this study, the two regions which had the greatest slip value were showed a good agreement with Chang et al. (2008) on the permanent displacement contour (Blue stars in Figure 7 (b)).

3.2 Results From EMD Process for Given Waveforms

Several IMF components which were decomposed from the given waveform model by EMD process was shown in Figure 8 and Figure 9.

For the two parts baseline drifting models (Figure 4 (a)), IMF components of the greater offset one (Figure 8 (a)), the obviously offset (30 gal.) were appeared at 5 seconds from the given waveform. And it could be found in component IMF2 and IMF3 after EMD decomposition, there were a significant discontinuity occurred at around 5 seconds. It is worthy to mention that the final value of the highest mode (IMF13) will converge toward the original given offset (30 gal). It was considered that whether these characteristics will occur when the offset is small or not. A smaller offset (6 gal) in the same drifting time was decomposed in Figure 8 (b). The discontinuity at 5 seconds in IMF2 and IMF3 and the converged offset in IMF13 still can be found.

For the three parts baseline drifting models (Figure 4 (b)), the IMF components of co-aspect offsets one (Figure 9 (a)), the offsets were occurred at 5 seconds (30 gal) and 20 seconds (10 gal). These drifting times could be found at lower IMF component (IMF2 and IMF3) as the results of two parts baseline drifting models. The final offset in the highest mode (IMF13) was only indicated the second offset (10 gal). Finally, for the IMF components of opposite offsets one (Figure 9 (b)), the offsets were at 5 seconds (30 gal) and 20 seconds (-10 gal). The amplitude of the second drifting time in IMF2 was become much higher than the co-aspect one, and the final offset for IMF13 converged on -10 gal.

3.3 Conclusions

The corrected permanent displacement which was using the semi-auto three part baseline correction method had a good agreement with GPS results for the data of 2008 great Wenchuan earthquake. The permanent displacement contour showed the distribution of correct displacement, which were corresponded with the inversion results of slip model (Chang et al. 2008).

Due to the purpose that there's a problem about the real strong motion might be a multiple drifting model, the suitability of that applying HHT method to identify the drifting time and offset value were tested in this study. For the results of two parts and three parts drifting models, the EMD components showed the drifting time in lower mode

and the final offset will be at the end of the highest mode. If the offsets were opposite with each other for three parts model, the amplitude of the indicated dividing time in second IMF component was much higher than the co-aspect one.

Acknowledgement:

We express our deeply appreciative to Dr. C. F. Wu of the Central Weather Bureau, Taiwan for providing the Three-Parts Baseline correction code. We also wish to thank China Strong Motion Networks Center, Institute of Engineering Mechanics, China Earthquake Administration for providing the near fault seismic data during 2008 Wenchuan, China earthquake. This study was supported by the National Science Council under grant numbers NSC98-2625-M-008-010 and NSC 99-2116-M-008 -023.

References:

Boore, D. M. (2001), "Effect of Baseline Corrections on Displacements and Response Spectra for Several Recordings of the 1999 Chi-Chi, Taiwan, Earthquake", *Bulletin of the Seismological Society of America*, **91**(5), 1199–1211.

Chang, Y., Phon, Y. P., Xu, L. S., Chou, C. H., and Chan, Y. T. (2008), "The Rupture Process and It's Time History about Wenchuan Great Earthquake, 2008", *Science in China*, **38**(10), 1186-1194. (in Chinese)

Graizer, V. M. (2005), "Effect of Tilt on Strong Motion Data Processing", *Soil Dynamics and Earthquake Engineering*, **25**, 197–204.

Huang, N. E., Zheng, S., Long, S. R., Wu, M. C., Shih, H. H., Zheng, Q., Yen, N. C., Tung, C. C., and Liu, H. H. (1998), The Empirical Mode Decomposition and Hilbert Spectrum for Nonlinear and Nonstationary Time Series Analysis, *Proc. R. Soc. London*, Ser. A, **454**, 903–995.

Iwan, W. D., Moser, M. A., and Peng, C. Y. (1985), "Some Observations on Strong-Motion Earthquake Measurement Using a Digital Accelerograph", *Bulletin of the Seismological Society of America*, **75**(5), 1225-1246.

Ray, R. Z., Shuo, M., Erdal, S., and Stephen, H. (2003), "Hilbert-Huang Transform Analysis of Dynamic and Earthquake Motion Recordings", *Journal of engineering mechanics*, **129**(8), 861-875.

The Project of Crustal Movement Observation Network of China (2008), "The Coseismic Displacement Fields of Wenchuan Ms 8.0 Earthquake Occurrence in 2008 Using GPS Data" , *Science in China* , **38**(10), 1195-1206.(in Chinese)

Wu, Y. M. and Wu, C. F. (2007), "Approximate Recovery of Coseismic Deformation from Taiwan Strong-Motion Records", *J. Seismol.*, **11**, 159–170.

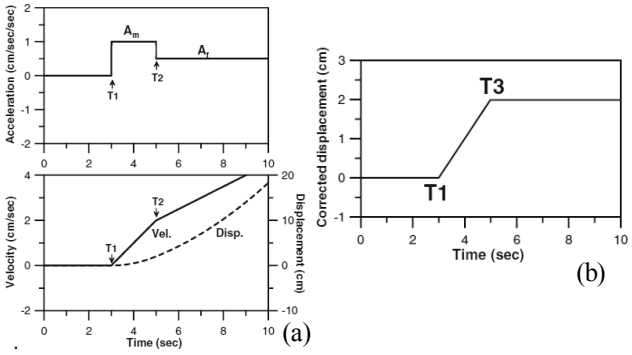


Figure 1 (a)Three parts baseline drifting model. Top: acc. Bottom: vel. and disp.(b)T3 time in displacement. (Wu and Wu 2007)

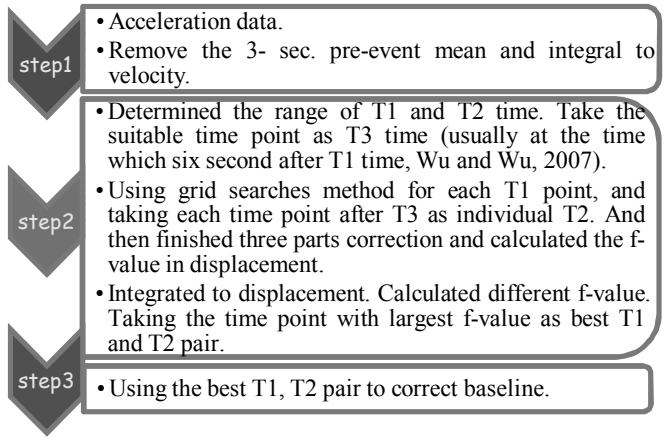


Figure 2 The flow chart of the data processing in this study.

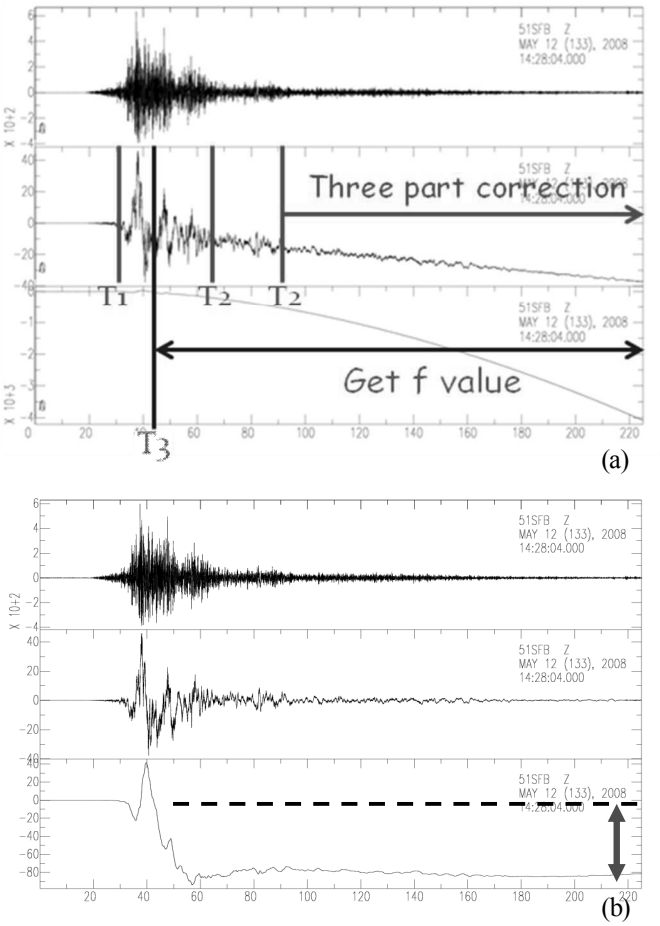


Figure 3 (a) Uncorrected vertical component record of station 51SFB. (b) Corrected record of station 51SFB, red arrow means the calculated permanent displacement. Top: acc. data. Middle: vel. data. Bottom: disp. data.

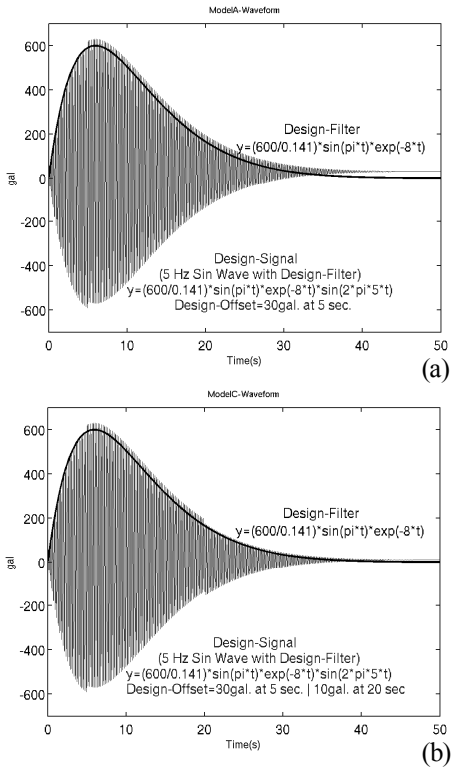


Figure 4 The given waveform with obviously offset. (a) two parts baseline drifting, the offset was at 5 sec. (b) three parts baseline drifting, the offsets were at 5 and 20 sec.

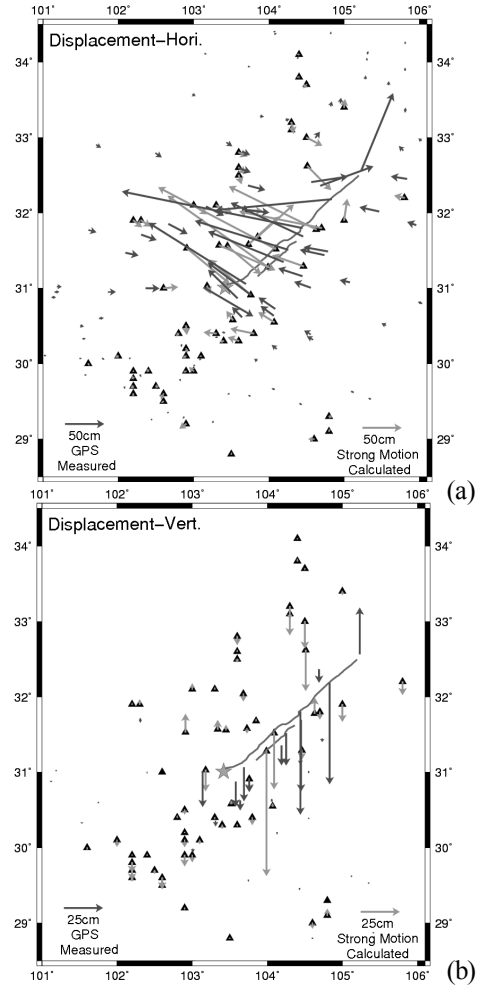


Figure 5 The distribution of co-seismic permanent displacements from this study and GPS measurement. Red arrows: GPS measurement. ; Green arrows: permanent displacement form corrected strong motion data. ; Black triangle: strong motion stations (a) Horizontal component . (b) Vertical component.

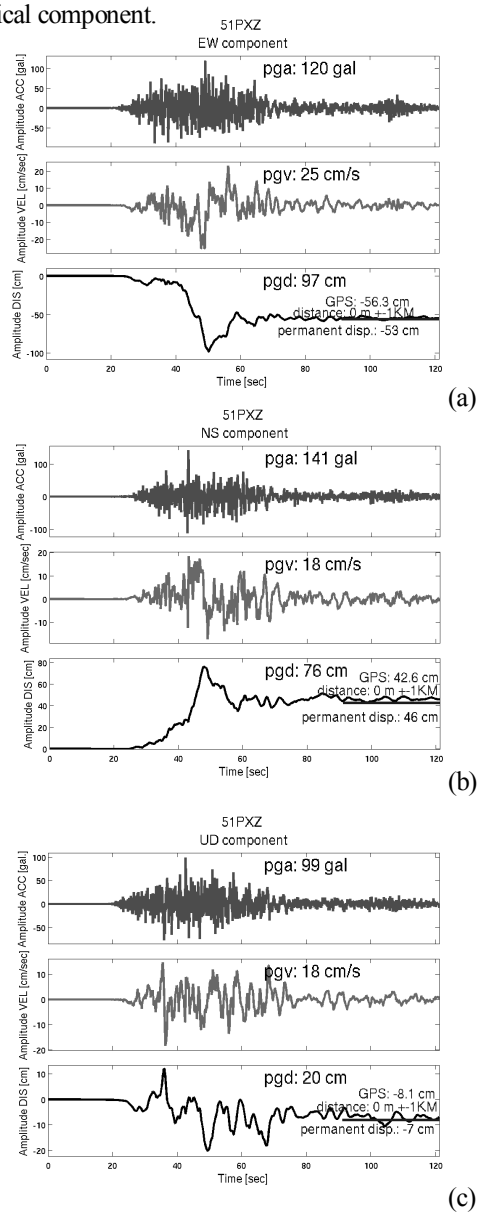


Figure 6 The corrected strong motion data, Top: acc. Middle: vel. Bottom: disp. Blue line: permanent displacement value in nearest GPS station. (a)E-W (b) N-S (c) U-D component.

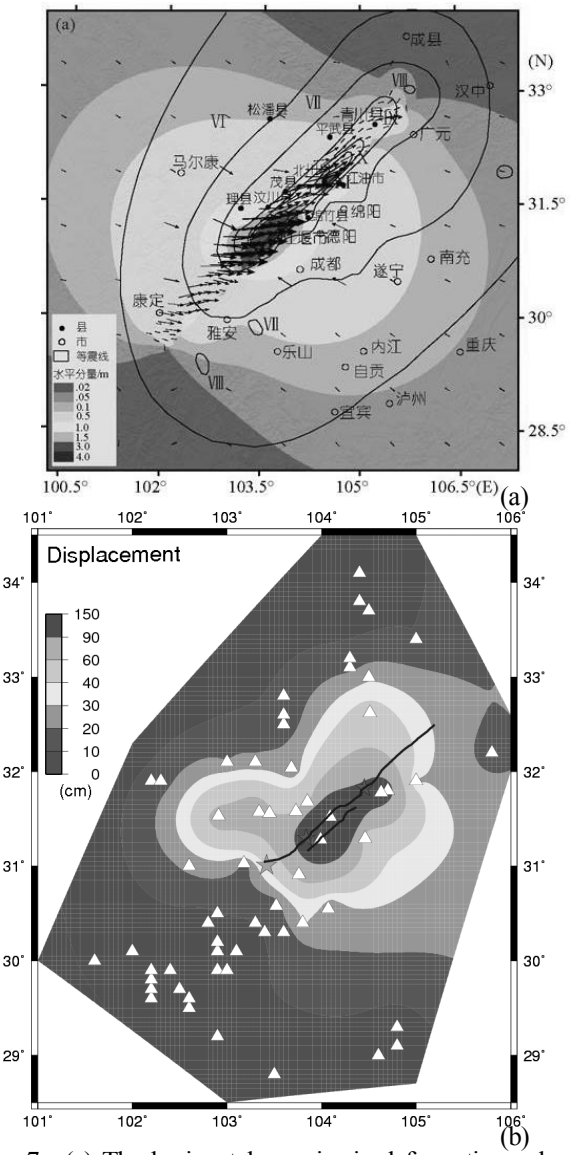
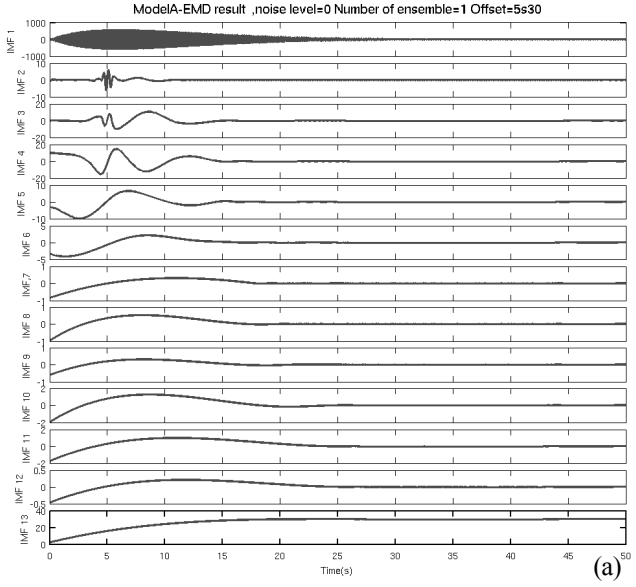


Figure 7 (a) The horizontal co-seismic deformation value in near-fault region during 2008 Wenchuan main shock. (Chang et al. 2008) (b) The distribution of corrected co-seismic permanent displacement values.



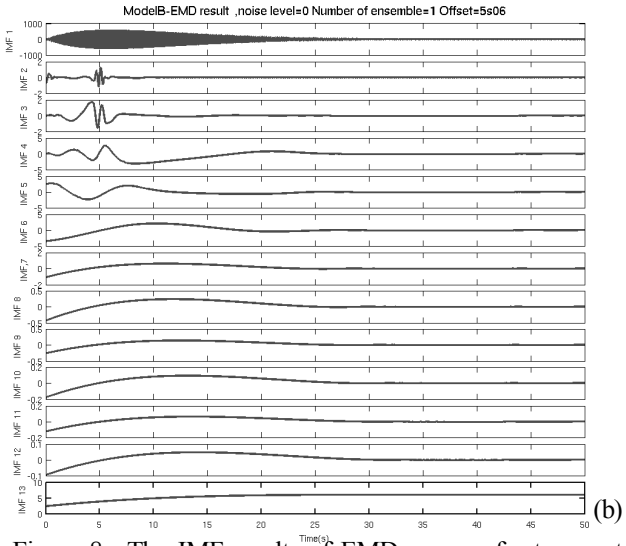


Figure 8 The IMF results of EMD process for two parts baseline drifting models, from top to bottom were different IMF components which represented different frequency content.(a) The obviously offset was at 5 seconds and it's 30 gal. (b) The obviously offset was at 5 seconds and it's 6 gal.

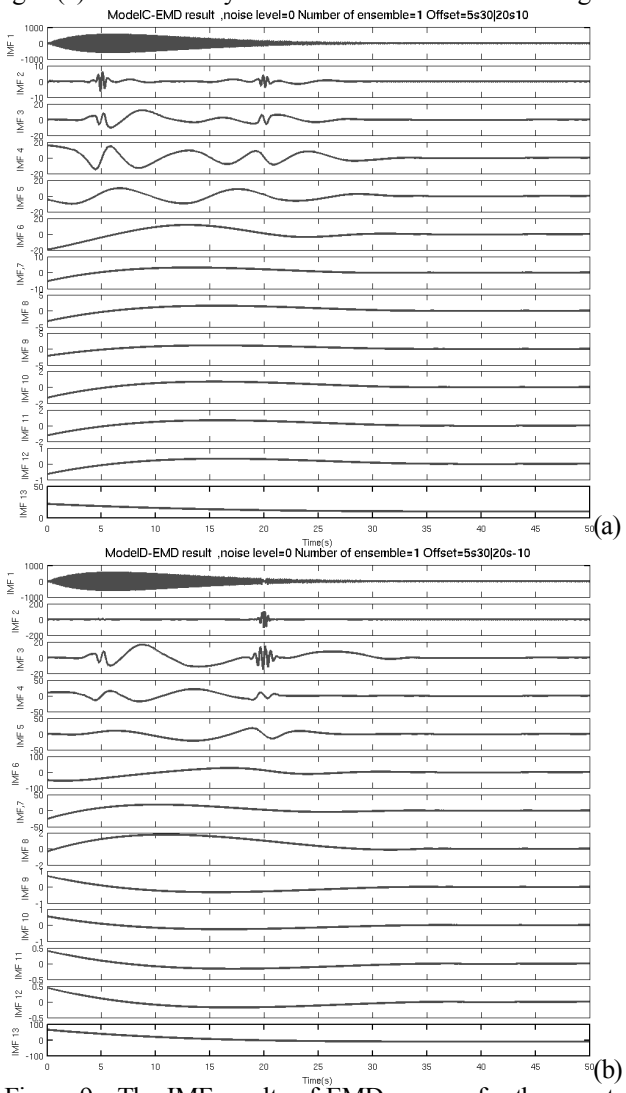


Figure 9 The IMF results of EMD process for three parts baseline drifting models.(a) The obviously offset was at 5 seconds (30 gal.) and 20 seconds (10 gal.). (b) The obviously offset was at 5 seconds (30 gal.) and 20 seconds (-10 gal.).

8CUEE CONFERENCE PROCEEDINGS
8th International Conference on Urban Earthquake Engineering
March 7-8, 2011, Tokyo Institute of Technology, Tokyo, Japan

2D FINITE DIFFERENCE MODELING OF WAVE PROPAGATION OF THE 2010 JIASIAN, TAIWAN, EARTHQUAKE

Chun-Te Chen[1] and Kuo-Liang Wen[2]

1) PhD Candidate, Institute of Geophysics, National Central University, Taiwan
2) Professor, Institute of Geophysics, National Central University, Taiwan
956402004@cc.ncu.edu.tw, wenkl@earth.ncu.edu.tw

Abstract: The 2010 JiaSian M_L 6.4 earthquake occurred on March 4, 2010 at 00:18:52 UTC. The epicenter was located in southern Taiwan (22.969°N 120.707°E) at the depth 22.6 km. This was the most powerful earthquake in the Kaohsiung area since recent hundred years. The quake did not cause death, but injured 96 people. Several building was collapsed during main shock and aftershock. Six trains of THSR (Taiwan High Speed Rail) were disrupted, and one was de-railed while in an emergency braking. This is the first de-railed accident of THSR caused by earthquake. The strong ground shaking also induced the soil liquefaction near the Xinhua town and close to the THSR bridge pier. Fortunately the soil liquefaction did not cause any building damage. In this study we use 2D finite-difference method to simulating the wave propagation of the JiaSian earthquake. The results of the simulation demonstrate that the long duration surface wave of the west ChiaNan plain resulting from the multi-pathing waves trapped in the top Pleistocene formation. Synthetic PGVs were good fit with the observations. We believe the simulation can be applied to understanding the strong ground motions expected for future earthquake.

1. INTRODUCTION

Taiwan is located on the boundary between the Philippine Sea Plate and the Eurasian Plate. The seismicity in the Taiwan is very high. During the 20th century occurred many large and destructive earthquakes close to the ChiaNan plain. For example M_L=7.1 on 1941 December 17, M_L=7.1 on 1946 December 5 and M_L=6.3 on 1964 January 18. So, southwestern Taiwan has always been considered as probably to occur next big earthquake area. Taiwan is covered with a dense strong motion network array that is operated within the frame of the Taiwan Strong Motion Instrumentation Program (TSMIP) conducted by the Central Weather Bureau (CWB). These recorded events make this study possible to compare with the simulation and the observation. From the results of the microtremor array research (Lin et al. 2009) and seismic tomography (Wu et al. 2007), we can construct a geometry model to estimate the seismic wave propagations for the area of ChiaNan plain. In this study we perform 2D Finite-Difference simulations of the ChiaNan plain for the M_L = 6.4 2010 March 4 JiaSian earthquake. We analyze the synthetic waveform, peak ground velocity (PGVs), 2 dimension wave propagation snapshots for three 2D profiles. This enables us to understand how the surface wave generated and predicting the ground motions. We except the results can provide to the future seismic hazard mitigation for the southwestern Taiwan.

2. METHOD

2.1 2010 March 4 JiaSian Earthquake

On 2010 March 4, a M_L = 6.4 (M_w = 5.97) earthquake occurred near the JiaSian seismic station17 km to the southeast. This was the most powerful earthquake in the Kaohsiung area since recent hundred years. The intensity reach to 6 and the maximum peak ground acceleration recorded over 460 gal at the CHY062. Shaking map and the stations distribution shown in the Figure 1. The quake caused several building collapsed and one high speed rail train was de-railed. We found near the west part of the ChiaNan plain excite significant long period and long duration ground motions at periods of about 2-4 sec. The quake was strong enough to trigger about 390 stations of TSMIP network. Therefore, this event provides us enough observations to study the ground motion characteristic and suitable for comparison of observation and simulation. In this study we simulate 2D wave propagation for three profiles to see how the surface waves generate.

2.2 ChiaNan Plain Velocity Model

The ChiaNan plain located in the southern part of the western coastal plain of Taiwan. It's a low, flat and the largest plain in Taiwan. The plain was filled by alluvium deposits, which resulted in flat-lying Quaternary layers. The detail structure of the plain was study by seismic reflection survey (Pan 1967, 1968) and the shallow velocity structure was estimated from surface to a depth of 3 km by the

microtremor array measurement (Lin et al. 2009). In this study, we combined the shallow layers velocity and the three main interface's depth (Plio-Pleistocene, Pliocene, and Miocene formations) to create the shallow layer 2D velocity model. We give the S velocity 0.3 km/s and P velocity 1.8 km/s between surface to Plio-Pleistocene interface, Plio-Pleistocene to Pliocene is 0.53 and 2 km/s, Pliocene to Miocene is 1.7 and 3.2 km/s, respectively. Then we embedded the shallow 2D model into the Taiwan area subsurface model by Wu et al. (2007) derived from seismic tomography. Figure 2 display the 2D velocity model used in this study.

Density model is also need for the Finite Difference simulation that is calculated from P wave velocities after Glaznev et al. (1996). The convert equation is given as Eq.(1) and Eq.(2) below :

when V_p less than 5500 m/s:

$$density = 2933 - 518 \times \ln(|vp - 7.595|) \quad (1)$$

when V_p large or equal 5500 m/s:

$$density = 1656 + 1068 \times \ln(|vp - 3.18|) \quad (2)$$

Totally we created three 2D profiles velocity model crossed the epicenter and TSMIP station CHY131, CHY021, and CHY023, respectively (Figure 3). Each model has a width 80km and depth 40km.

2.3 Numerical Modeling

We use a 2D Finite-Difference method (Bohlen 2002) for wave propagation simulation. Our simulations are calculated by 4th order standard staggered grid. Damping and one way absorbing boundary (Cerjan et al. 1985) is applied at the left/right, front/back and the bottom to avoid the interference of reflection waves. The calculations are performed on the IBM x3550 supercomputer "Vger" of the center for Computational Geophysics, National Central University. Vger has 108 computing nodes 432 CPUs, calculating performance approach to 3.5TFlops. Our model dimension is 80 × 40 km, grid size is 20 × 20 meters. Therefore, there are 4000 × 2000 = 8,000,000 girds in one model. Estimate *Q* values model are calculated from the S wave velocity model. $Q_p = 0.15 \times V_s$ and $Q_s = 0.1 \times V_s$, where V_s is in meter/sec. We run the code in the supercomputer use two nodes eight processors for each simulation. Total real time of calculating is about 11 hours. Detail modeling parameters are list in Table 1. We set the source as a double coupling point source. The moment tensor calculated respectively depends on the different azimuth of these profiles. The depth of the source was set to 18 km (BATS) and 22.6 km (CWB). After comparing the waveforms simulated by the different depth. We decide to use the result from the source on depth of 18 km because the result has a better fitting between the observation and the simulation than the result from the depth of 22.6 km

3. RESULT

3.1 Observed and Simulated PGVs

We compare observed and simulated waveforms and peak ground velocity. The observed and the simulated data were all filtered (0.05 Hz-1.0Hz) and rotated to radial and transverse component respectively. We also use 2D to 3D conversion (Miksat et al. 2008) to make the amplitude and waveform correction from 2D simulation. The results of the three stations those nearest to the epicenter CHY061, CHY131and CHY089 are good fit with the waveform pattern and the peak ground velocity in horizontal component (Figure 4). In general, the vertical component fit is not so good. However, it's difficult to obtain a very good fit in vertical component from simulating. Figure 5 displays observed and simulated velocity waveforms for the stations that far away the epicenter and located on the soft alluvium layer. The PGVs and durations still had a good fit in the horizontal components. The modeling results also show the velocity waveform has a surface wave generated for the station CHY016 and CHY115. Although the pattern of the waveform is not good fit, the 2D simulating still provide us a good way to study the wave propagation and ground motion prediction.

3.2 Wave Fields

Figure 6 display the snapshots of the 2D wave field for the profile CHY131. The snapshots show the waves into a sub Miocene structure (40-50km) during 12-20 sec did not generated the surface wave and caused short duration. When the waves come into the Pliocene formation the surface wave generated clearly and caused the long duration by the distance increase. Not only the profile CHY131 the other profiles also showed the similar phenomenon. The velocity of the Plio-Pleistocene layer is more slow and soft, but it seems has less influence in our simulation. That is because the Plio-Pleistocene layer is very thin (about 100m) the response of the frequency may be large than 1 Hz. Another reason is our grid size of the model 20 meters is not enough small to analyze such a thin structure. For all this we also found how the surface wave generated very depends on the structure. The surface wave generated almost immediately at the edge of the Pliocene formation for CHY131 and CHY021 model. But this phenomenon did not occur on CHY023 model. The surface wave generated at about 10 kilometers away from the Pliocene formation edge. Figure 7 show the pseudo array radial seismograms of three profiles respectively. The comparing result indicated the shape of the Pliocene interface plays an important role to control the wave propagation and the PGVs value.

4. CONCLUSION

Our simulations for the JiaSian earthquake on ChiaNan plain show a good fit with observed and simulated PGVs on radial component. Indicating our numerical modeling is suitable to predicting the ground motions for the area. Even though the vertical simulated PGVs were always overestimate. These may caused by the *Q* values model are estimated roughly from the V_s. We believe to modulate the attenuate model can solve this and obtain a good fit for

vertical PGVs. The snapshots of the wave propagation show the surface wave generated by the shape change of the top layer's interface. The phenomenon also appears in the observation. Unfortunately the observation is not enough along our profile.

We only discuss the velocity waveforms up to 1 Hz in this study. Because we apply a simple velocity model to the top layers. In the further we expect to combine the borehole drilling data and other detail velocity information to create a high resolution velocity model. This may provide us to obtain a higher frequency (up to 3 Hz) of the synthetic waveforms. The result should be a good solution for investigate the wave propagation behavior and predict the ground motion.

Acknowledgements:

We thank Thomas Bohlen for providing 2D Finite-Difference code. We also thank Central Weather Bureau for providing the TSMIP data. The simulations were computed on the "Vger" supercomputer of the center for Computational Geophysics, National Central University. This study is supported by National Science Council, ROC, under the grant no. NSC 98-2116-M-008-008、NSC-99-2116-M-008-023.

References:

Bohlen, T., (2002), "Parallel 3-D viscoelastic finite-difference seismic modeling," *Computers @ Geopsciences*, Vol. **28**, No. 8, 887-889.

Cerjan, C., Kosloff, D., Kosloff, R., & Reshef, M. (1985), "A nonreflecting boundary condition for discrete acoustic and elastic wave equations," *Geophysics*, **50**, 705–708.

Glaznev, V.N., Raevsky, A.B.&Skopenko, G.B., (1996), "A three-dimensional integrated density and thermal model of the Fennoscandian lithosphere," *Tectonophysics*, **258**, 15–33

Lin, C. M., T. M. Chang, Y. C. Huang, H. J. Chiang, C. H. Kuo, and K. L. Wen* (2009), "Shallow S-wave velocity structures in the western coastal plain of Taiwan," *Terr. Atmos. Ocean Sci.*, **22**, 2, 299-308. doi: 10.3319/TAO.2007.12.10.01(T).

Pan, Y. S., (1967), "Interpretation and seismic coordination of the Bouguer gravity anomalies over west-central Taiwan," *Petrol. Geol. Tai wan*, **5**, 99-115.

Pan, Y. S., (1968), "Interpretation and seismic coordination of the Bouguer gravity anomalies obtained in south western Taiwan," *Petrol. Geol. Tai wan*, **6**, 197-208.

Miksat J., M¨uller T. M. and Wenzel F., (2008), "Simulating three-dimensional seismograms in 2.5-dimensional structures by combining two-dimensional finite difference modelling and ray tracing," *Geophys. J. Int.*,**174**,309-315,doi: 10.1111/j.1365-246X. 2008.03800.x

Wu, Y. M., C. H. Chang, L. Zhao, J. B. H. Shyu, Y. G. Chen, K. Sieh, and J. P. Avouac (2007), "Seismic tomography of Taiwan: Improved constraints from a dense network of strong-motion stations," *Journal of Geophysical Research*, **112**, B08312, doi:10.1029/2007JB004983.

Table 1 Modeling parameters

Parameter	value
Horizontal grid size (m)	20
Vertical grid size (m)	20
Horizontal Dimension (km)	80
Vertical Dimension (km)	80
Number of grid points (H)	4000
Number of grid points (V)	2000
Number of time steps	140000
Simulation time (sec)	140

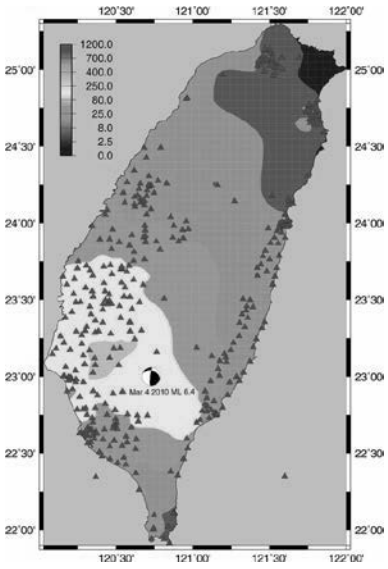


Figure 1 Shaking map of the JiaSian earthquake. Red triangles are the TSMIP stations.

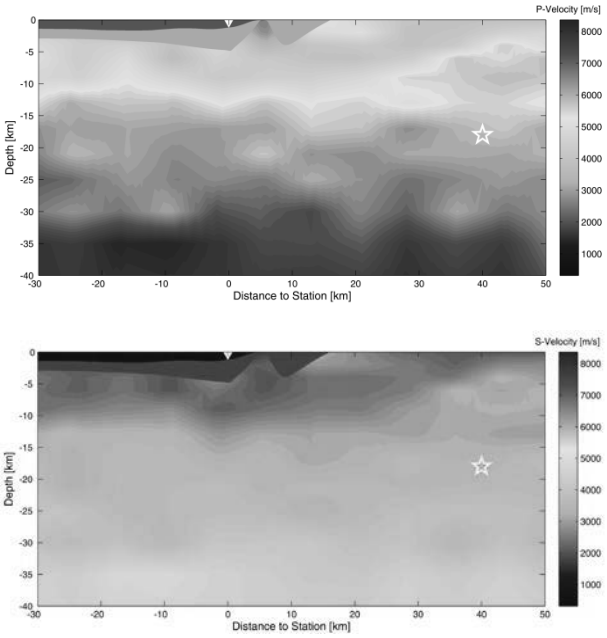


Figure 2 P wave velocity and S wave velocity model. Dimension is 80 km in width 40 km in depth. White triangle is the CHY131 location, star is the source location.

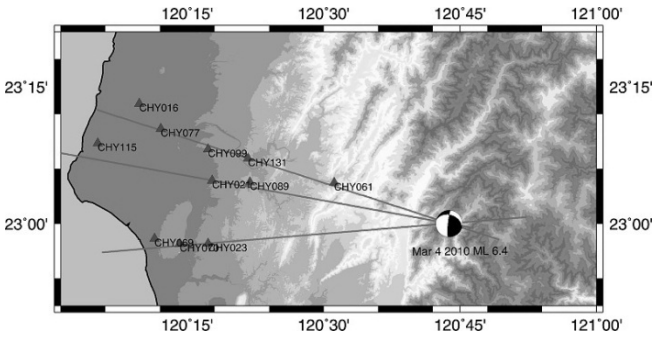


Figure 3 Location of the three profiles.

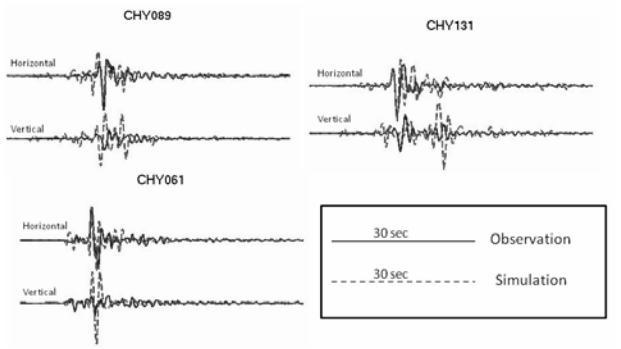


Figure 4 Comparison between observed and simulated velocity waveforms for three stations nearest to the epicenter.

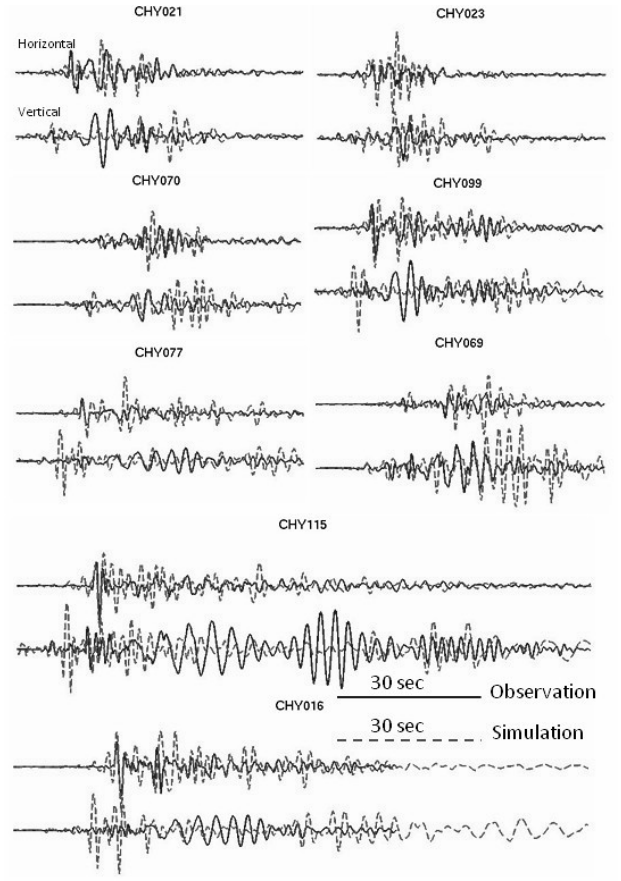


Figure 5 Comparison between observed and simulated velocity waveforms for other stations.

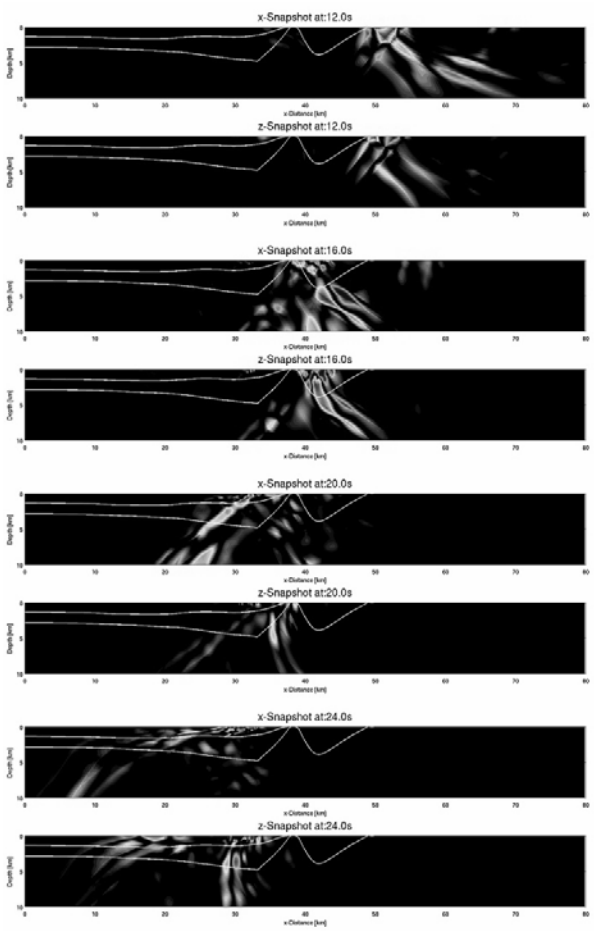


Figure 6 Profile CHY131 snapshots of the radial and vertical component of the simulated velocity wavefield for 12-24 sec. The color map scaled to the maximum velocity.

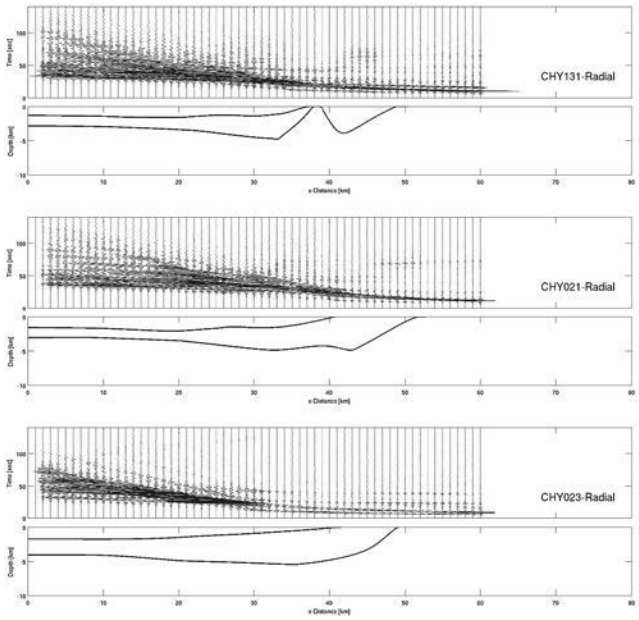


Figure 7 Synthetic pseudo array radial seismograms along three profiles. Top first black line is the interface of the Pliocene formation; second black line is the Miocene interface.

8CUEE CONFERENCE PROCEEDINGS
8th International Conference on Urban Earthquake Engineering
March 7-8, 2011, Tokyo Institute of Technology, Tokyo, Japan

SEISMIC PERFORMANCE OF EARTH SLOPES

Ellen M. Rathje[1)], George Antonakos[2)], and Gokhan Saygili[3)]

1) Professor, Department of Civil, Architectural, and Environmental Engineering, University of Texas at Austin, TX, USA
2) Graduate Student, Department of Civil, Architectural, and Environmental Engineering, University of Texas at Austin, TX, USA
3) Geotechnical Engineering, Norwegian Geotechnical Institute, Inc., Houston, TX USA
e.rathje@mail.utexas.edu, antonakosg@gmail.com, gokhan.saygili@ngi-inc.com

Abstract: Permanent sliding displacement represents a common damage parameter for evaluating the seismic performance of earth slopes. Empirical models for the sliding displacement of shallow (rigid) sliding masses have demonstrated that including both peak ground acceleration and peak ground velocity improves the displacement prediction and reduces its uncertainty. These empirical displacement models have been recently modified for application to flexible sliding masses, where the dynamic response of the sliding mass is important. This unified framework includes predicting the seismic loading for the sliding mass in terms of the maximum seismic coefficient (k_{max}) and the maximum velocity of the seismic coefficient-time history (k-vel_{max}). The predictive models are a function of the peak ground acceleration (PGA), peak ground velocity (PGV), the natural period of the sliding mass (T_s), and the mean period of the earthquake motion (T_m). The empirical predictive models for sliding displacement utilize k_{max} and k-vel_{max} in lieu PGA and PGV, and include a term related to the natural period of the sliding mass. This unified framework provides a consistent approach for predicting the sliding displacement of rigid (T_s=0) and flexible (T_s>0) slopes. This paper summarizes these new developments for predicting permanent sliding displacements of slopes and provides comparisons between the new model and existing models.

1. INTRODUCTION

Permanent sliding displacement represents a common damage parameter for evaluating the seismic stability of slopes. This displacement represents the cumulative, downslope movement of a sliding mass due to earthquake shaking. The magnitude of sliding displacement relates well with observations of seismic performance of slopes (e.g., Jibson et al. 2000), and thus has been a useful parameter in seismic design and hazard assessment.

Figure 1 outlines the process commonly used to compute the earthquake-induced sliding displacement (D) of a slope with yield acceleration, k_y (k_y = seismic coefficient that when multiplied by the weight of the sliding mass and applied to the slope yields a factor of safety of 1.0). If the sliding mass is relatively shallow and stiff, a rigid sliding block analysis is appropriate. In this case, the natural period of the sliding mass (T_s) is essentially zero and the dynamic response of the sliding mass can be ignored. The seismic loading is simply the acceleration-time ($a - t$) history at the base of the sliding mass, with the destabilizing force-time history (F(t))on the slope equal to the $a - t$ history (in units of gravity, g) times the weight of the sliding mass. Seismic loading parameters for the slope can be derived that represent various ground motion characteristics (GM) of an acceleration-time history, such as the peak ground acceleration (PGA), peak ground velocity (PGV), Arias Intensity (I_a), etc. The seismic loading parameters are used, along with the k_y of the slope, to predict D from empirical models (e.g., Jibson 2007, Saygili and Rathje 2008).

Deeper and/or softer sliding masses are flexible and have natural periods greater than zero, such that the rigid sliding block model is not appropriate. In these cases, the dynamic response of the flexible sliding mass must be taken into account (Figure 1). Two-dimensional finite element analysis can be used to model this dynamic response, or alternatively the sliding mass at its maximum thickness can be modeled as a one-dimensional soil column. Previous research (e.g., Rathje and Bray 2001, Vrymoed and Calzascia 1978) has shown that the one-dimensional simplification provides an adequate estimate of the seismic loading for deeper sliding masses. A decoupled sliding block analysis (e.g., Makdisi and Seed 1978, Bray and Rathje 1998) computes the dynamic response of the sliding mass and uses the results of the dynamic response analysis to compute the sliding displacement. The seismic loading time history for the sliding mass is related to the seismic coefficient (k)-time history, in which k represents the average acceleration within the sliding mass. The destabilizing force-time history (F(t)) is then simply equal to the k-time history times the weight of the sliding mass.

It has become common practice to use rigid sliding block analyses for sliding masses with T_s below some threshold, while using a flexible sliding block analysis for T_s greater than some threshold (Jibson 2010). In actuality, the response of slopes does not abruptly change from rigid to

flexible at some value of T_s, but rather there is a transition from rigid to flexible behavior as T_s increases. This paper summarizes a recently developed unified framework that models the full range of dynamic response conditions from rigid through flexible sliding mass behavior (Rathje and Antonakos 2010). This unified approach predicts the seismic loading parameters and permanent displacements of sliding masses as a function of T_s (as defined by the one-dimensional period computed for the maximum thickness of the sliding mass), such that the approach tracks the response from rigid conditions ($T_s = 0$) to very flexible conditions ($T_s >> 0$). The unified model is also built upon recently the developed empirical model for rigid sliding displacement (i.e., Saygili and Rathje 2008) that uses PGA and PGV to predict sliding displacement. The unified approach is described in this paper, and the predicted sliding displacements are compared with those from previously published models.

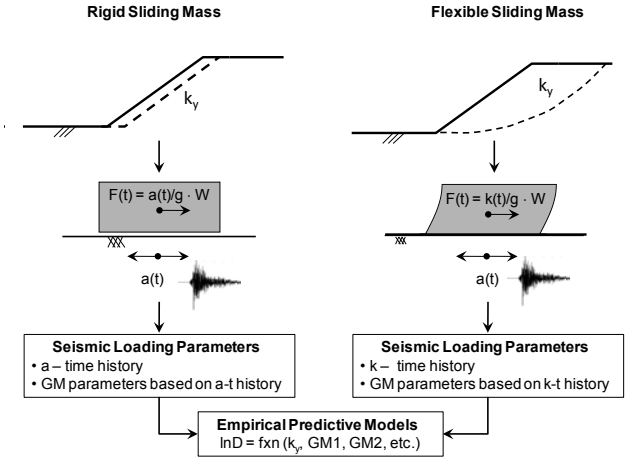


Figure 1 Procedures for computing earthquake-induced sliding displacements for rigid and flexible sliding masses.

2. RIGID SLIDING BLOCK DISPLACEMENTS

Saygili and Rathje (2008) presented a suite of empirical predictive models for the sliding displacement of rigid slopes, and recommended two models: (1) a PGA model that only includes PGA and k_y in the displacement prediction and a (2) PGA, PGV model that includes PGA, PGV, and k_y. Rathje and Saygili (2009) slightly modified the PGA model from Saygili and Rathje (2008) by adding a term related to earthquake magnitude (M). The recommended single (scalar) parameter model is the (PGA, M) model from Rathje and Saygili (2009), and the recommended two (vector) parameter model is the (PGA, PGV) model from Saygili and Rathje (2008). For simplicity, these models are called the SR08/RS09 models.

Figure 2 plots predicted values of D from the SR08/RS09 models as a function of k_y for different earthquake scenarios of M = 6, 7, and 8, each with a site-to source distance (R) equal to 5 km and rock site conditions (i.e., V_{s30} = average shear wave over the top 30 m = 760 m/s) Ground motion parameters for these scenarios were generated using the ground motion prediction equations from the Next Generation Attenuation project for PGA and PGV (the average from 4 different models was used) and using the Rathje et al. (2004) relationship for the Mean Period (T_m). These values are listed in Table 1. Predicted values of D are shown in Figure 2 for both the (PGA, M) and (PGA, PGV) models. Generally, the (PGA, PGV) model predicts smaller displacements than the (PGA, M) model, with the difference as large as 65% for the M=8 scenario. These differences are caused by the fact that the empirical displacement models were developed based on displacements computed from acceleration-time histories recorded on both rock and soil. Because soil motions tend to have larger PGV values than rock motions for the same PGA and the (PGA, M) model does not include the effects of PGV, the (PGA, M) model predicts larger displacements than the (PGA, PGV) model for rock sites. The (PGA, PGV) model does not have the same issue because it uses a PGV as a separate independent variable and thus directly accounts for the differences in PGV for rock and soil motions.

Table 1 Ground motion parameters for each earthquake scenario

M	R (km)	PGA (g)	PGV (cm/s)	T_m (s)
6.0	5.0	0.26	15.1	0.37
7.0	5.0	0.35	30.0	0.45
8.0	5.0	0.42	50.3	0.47

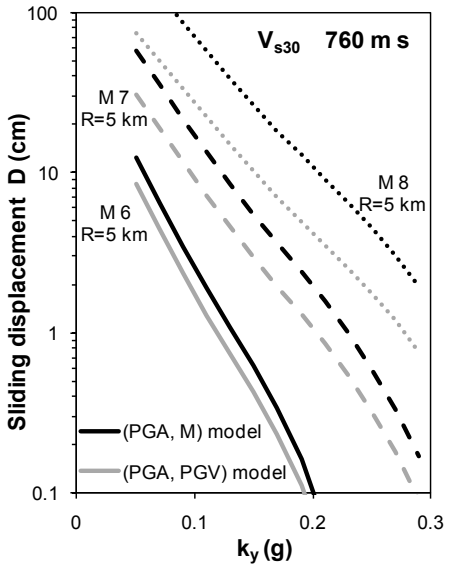


Figure 2 Rigid sliding block displacements calculated from the SR08/RS09 (PGA, M) and (PGA, PGV) models for different earthquake scenarios and site conditions.

In addition to the differences in median displacements from the (PGA, M) and (PGA, PGV) models, there are

significant differences in the standard deviations of the predictions. The standard deviation (σ_{lnD}) for each model increases with increasing k_y/PGA, with values ranging between 0.75 and 1.0 (in natural log units) for the (PGA, M) model (Rathje and Saygili 2009), and values ranging between 0.4 and 0.9 for the (PGA, PGV) model (Saygili and Rathje 2008). Thus, there is significantly less uncertainty in the displacement prediction when PGV is used in the displacement calculation.

One limitation of the SR08/RS09 empirical models is that they only represent rigid sliding block conditions. Rathje and Antonakos (2010) developed a framework similar to SR08/RS09 for flexible sliding conditions and this model is summarized in the next section. Because of the superiority in the (PGA, PGV) model over the (PGA, M) model, only the (PGA, PGV) model will be discussed.

3. MODEL FOR FLEXIBLE SLIDING BLOCK DISPLACEMENTS

3.1 Seismic Loading Parameters for Flexible Sliding Masses

For a rigid sliding mass, the acceleration-time history represents the seismic loading for the sliding mass and this acceleration-time history can be characterized by its PGA and PGV. The recorded acceleration- time history from the GIL067 station during the 1989 Loma Prieta (M=6.9) earthquake is shown in Figure 3(a) (PGA = 0.36 g), and the velocity-time history derived from numerical integration of the acceleration-time history is shown in Figure 3(b) (PGV = 29 cm/s). For a rigid sliding mass subjected to the GIL067 motion, the characteristics of the both the acceleration and velocity time history will influence the level of induced displacement.

The seismic loading for a flexible sliding mass subjected to the GIL067 motion is not the acceleration-time history, because of the dynamic response of the sliding mass. Rather, the seismic loading is the k-time history (e.g., Seed and Martin 1966, Bray and Rathje 1998), which represents the average acceleration within the sliding mass as well as the shear force at the base of the sliding mass. Consider the dynamic response of a 30-m thick sliding mass (H = 30 m) with a shear wave velocity of 250 m/s (V_s = 250 m/s) and associated site period of 0.5 s (T_s= 4H/V_s = 0.5 s). The k-time history for this site, computed using one-dimensional, equivalent-linear site response analysis, is shown in Figure 3(c). Note that the k-time history displays much less high frequency motion than the acceleration-time history due to the averaging of accelerations within the sliding mass. Additionally, its peak value (k_{max}) is smaller than the input PGA (k_{max} = 0.12 g vs. PGA = 0.36 g). k_{max} represents the appropriate seismic loading parameter for this flexible sliding mass.

In the same way that an acceleration-time history is numerically integrated to generate a velocity-time history, the k-time history can be numerically integrated to generate a velocity-time history of the k-time history. This velocity is called k-vel and it provides information regarding the frequency content of the k-time history. The maximum value of the k-vel-time history is called k-vel_{max}. As expected, the k-vel-time history contains less high frequency motion than the velocity-time history. Surprisingly, however, the value of k-vel_{max} (31 cm/s) is similar to the value of PGV (29 cm/s). Because the integrated k-vel-time history is influenced by both the amplitude and frequency content of the k-time history, the increase in long period motion in the k-time history is balanced by the reduction in its peak such that k-vel_{max} is similar in amplitude to PGV.

To use the SR08/RS09 predictive models for flexible sliding blocks, the appropriate seismic loading parameters must be specified. Based on the above descriptions, k_{max} should be used to replace PGA in the SR08/RS09 models and k-vel_{max} should be used to replace PGV. Predictive models for k_{max} and k-vel_{max} are required such that engineers do not need to perform dynamic response analysis to estimate these seismic loading parameters.

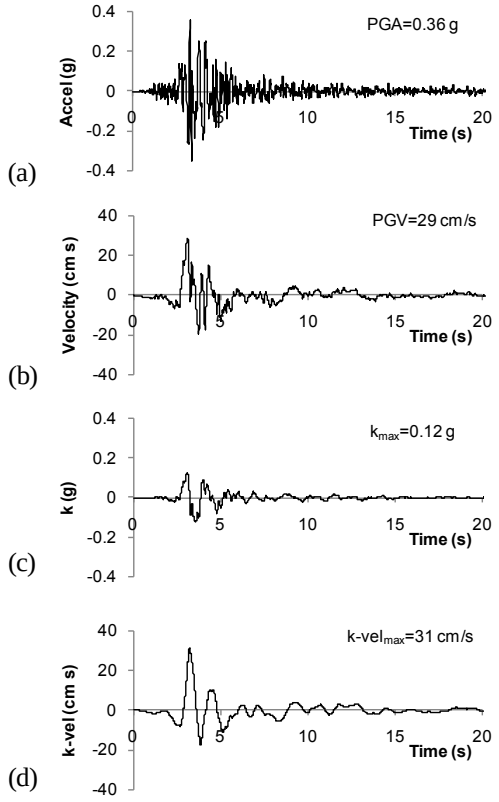


Figure 3 (a) Acceleration and (b) velocity-time histories for a rigid sliding mass, and (c) k-time history and (d) k-vel-time history for a flexible sliding mass with T_s=0.5 s.

3.2 Predictive Models for k_{max} and k-vel_{max}

Predictive models for k_{max} and k-vel_{max} were developed based on one-dimensional site response calculations of five sliding masses subjected to 80 input motions. These calculations were performed using the equivalent-linear site response code Strata (Kottke and Rathje 2008). The sites consisted of one 15-m profile (V_s = 400 m/s), two 30-m profiles (V_s = 400 m/s and 250 m/s) and two 100-m profiles

(V_s = 400 m/s and 265 m/s). The resulting values of site period (T_s) are 0.15 s, 0.30 s, 0.48 s, 1.0 s, and 1.5 s, respectively. The 80 input motions represented motions from earthquakes M = 6 to 7.9 and recorded a distances between 0.1 and 60 km. The input PGA values ranged from 0.02 to 1.0 g, and the input PGV values ranged from 1.2 cm/s to 70 cm/s. k-time histories were computed at the base of each one-dimensional site profile, from which k_{max} and k-vel_{max} values were derived. Further details about the analyses performed can be found in Rathje and Antonakos (2010) and Antonakos (2009).

The computed k_{max} values were normalized by the input PGA and k_{max} / PGA is plotted versus T_s/T_m in Figure 4(a), and several important observations can be made. First, k_{max} / PGA approaches 1.0 as T_s/T_m approaches 0.1. This trend is consistent with k_{max} = PGA for rigid sliding masses, and indicates that T_s/T_m = 0.1 essentially represents rigid sliding conditions. Next, k_{max} is greater than the PGA at moderate period ratios (T_s/T_m = 0.1 to 0.7), while k_{max} is smaller than the PGA at larger period ratios. The data in Figure 4(a) are shown for different ranges of input PGA. These data indicate that the ratio of k_{max} / PGA decreases with increasing input PGA.

A predictive equation for k_{max} / PGA was developed by Rathje and Antonakos (2010) to model these trends. This model predicts $\ln(k_{max}/PGA)$ as a function of $\ln[T_s/T_m]$ and PGA.

For $T_s/T_m \geq 0.1$:

$$\ln(k_{max}/PGA) = (0.459 - 0.702 \cdot PGA) \cdot \{ \ln([T_s/T_m]/0.1) \} + (-0.228 + 0.076 \cdot PGA) \cdot \{ \ln([T_s/T_m]/0.1) \}^2 \quad (1)$$

For $T_s/T_m < 0.1$:

$$\ln(k_{max}/PGA) = 0$$

The standard deviation for this model in natural log units is 0.25. The model predications from equation (1) are shown in Figure 4(a) for PGA = 0.1, 0.3, and 0.7 g. These predictions fit the computed data well. Given the predicted value of k_{max} / PGA and the input motion PGA, k_{max} is estimated.

The additional information required predictive models is for k-vel_{max}. Figure 4(b) shows the computed values of k-vel_{max} normalized by the input PGV and plotted versus T_s/T_m. The k-vel_{max} / PGV data display similar trends to the k_{max} / PGA data. The data indicate k-vel_{max} equal to PGV at very small period ratios ($T_s/T_m \leq$ 0.2 in this case), k-vel_{max} greater than PGV at smaller period ratios (T_s/T_m = 0.2 to 1.5), and k-vel_{max} less than PGV at larger period ratios. The range of period ratios where k-vel_{max} / PGV > 1.0 is larger than the range of period ratios where k_{max} / PGA > 1.0. Again, there is an input amplitude effect, with smaller values of k-vel_{max} / PGV observed at larger values of input PGA. However, this input amplitude effect is not pronounced at smaller period ratios.

A predictive model for k-vel_{max} / PGV was developed by Rathje and Antonakos (2010) with a similar functional form to equation (1). The predictive model for k-vel_{max} / PGV is given by:

For $T_s/T_m \geq 0.2$:

$$\ln(\text{k-vel}_{max}/PGV) = (0.240) \cdot \{ \ln([T_s/T_m]/0.2) \} + (-0.091 - 0.171 \cdot PGA) \cdot \{ \ln([T_s/T_m]/0.2) \}^2 \quad (2)$$

For $T_s/T_m < 0.2$:

$$\ln(\text{k-vel}_{max}/PGV) = 0$$

The standard deviation for this model in natural log units is 0.25. The model predications from equation (2) are shown in Figure 4(b) for input PGA = 0.1, 0.3, and 0.7 g. Again, the predictions fit the computed data well.

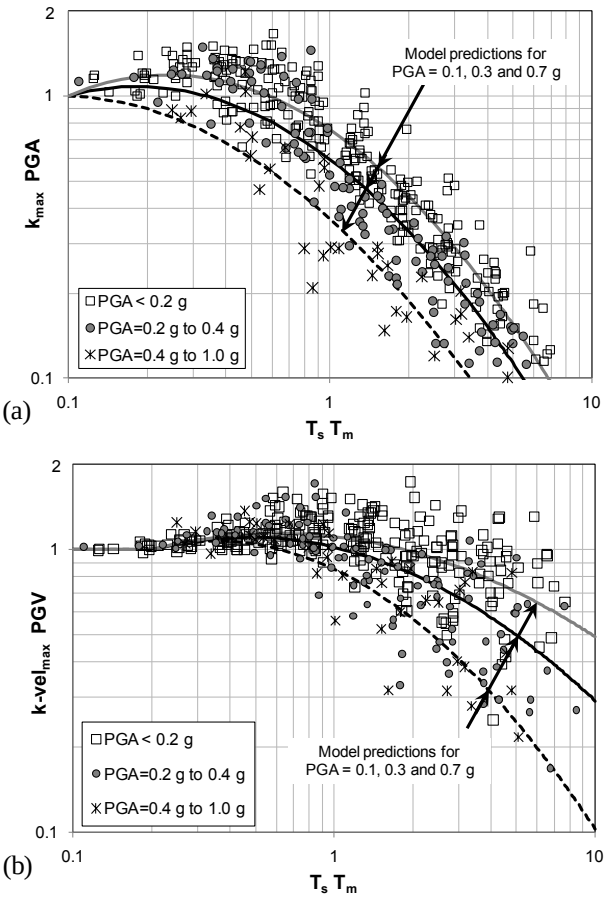


Figure 4 (a) Computed values of k_{max}/PGA vs. T_s/T_m along with model predictions and (b) computed values of k-vel_{max}/PGV vs. T_s/T_m along with model predictions.

Bray and Rathje (1998) developed a predictive model for k_{max} that uses a power law relationship to predict a normalized k_{max} (k_{max} / [NRF·PGA]) as a function of T_s/T_m. The power law relationship results in a log-linear relationship between k_{max} and T_s/T_m for a constant value of PGA. The PGA normalization effectively scales k_{max} linearly with PGA, although the nonlinear response factor (NRF) recommended by Bray and Rathje (1998) takes into account some nonlinear scaling. Bray and Rathje (1998) state that their model is appropriate for T_s/T_m greater than 0.5. Predicted values of k_{max} from equation (1) (Rathje and

Antonakos 2010) are compared to the predictions from Bray and Rathje (1998) in Figure 5 for input PGA values of 0.2 and 0.8 g. For PGA=0.2 g, the Bray and Rathje (1998) predictions agree favorably with Rathje and Antonakos (2010) in the period range of 0.5 to 2.0 where the log-linear shape is most valid. At larger period ratios the Bray and Rathje (1998) model predicts larger values of k_{max}. The second-order polynomial used in Rathje and Antonakos (2010) more accurately models the variation of k_{max} / PGA over a wide range of period ratios. For PGA=0.8 g, the Bray and Rathje (1998) model is consistently larger than Rathje and Antonakos (2010), although the difference is most pronounced at large period ratios. This difference indicates that the NRF factor incorporated in Bray and Rathje (1998) does not model as much soil nonlinearity as Rathje and Antonakos (2010).

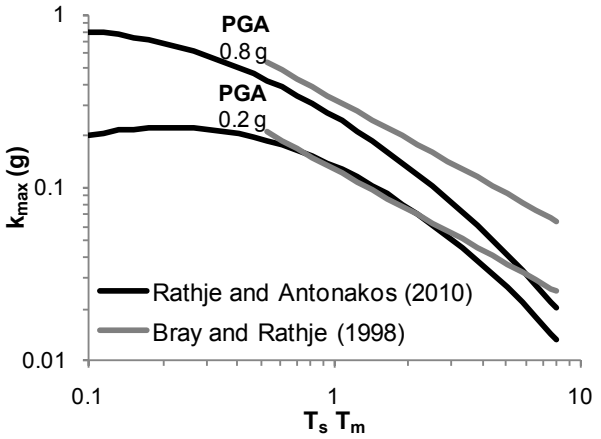


Figure 5 Comparison of k_{max} predictions from Rathje and Antonakos (2010) and Bray and Rathje (1998)

3.3 Predictive Model for Flexible Displacements

Rathje and Antonakos (2010) computed decoupled sliding displacements using the calculated k-time histories for the five sites and 80 input motions (400 time histories). Displacements were calculated for k_y = 0.04, 0.08, 0.12, and 0.16. The resulting dataset included 569 non-zero values of displacement (i.e., instances where $k_y < k_{max}$). Additionally, rigid sliding block displacements were computed for the 80 input time histories and the four values of k_y for comparison with the median values predicted by the SR08/RS09 empirical models.

The Rathje and Antonakos (2010) approach for computing the displacement of a flexible sliding mass is based on first computing the sliding displacement using the SR08/RS09 empirical models with k_{max} used in lieu of PGA and k-vel_{max} used in lieu of PGV. This value of displacement is then further modified based on the period of the sliding mass (T_s). The modifications developed by Rathje and Antonakos (2010) are based on comparisons of the computed displacements from the calculated k-time histories and the predicted displacements from the SR08/RS09 empirical models using the values of k_{max} and k-vel_{max} of the calculated k-time histories. These comparisons showed that the SR08/RS09 empirical models underestimated the sliding displacement of flexible sliding masses such that the displacement must be increased. Rathje and Antonakos (2010) developed modifications for both the (PGA, M) and (PGA, PGV) models, but only the (PGA, PGV) modification is given here. The resulting modification to the SR08/RS09 (PGA, PGV) model to account for flexible sliding is:

For $T_s \leq 0.5$:

$$\ln(D_{flexible}) = \ln(D_{PGA,PGV}) + 1.42 \cdot T_s \quad (3)$$

For $T_s > 0.5$:

$$\ln(D_{flexible}) = \ln(D_{PGA,PGV}) + 0.71$$

where $D_{PGA,PGV}$ represents the median displacement predicted by the (PGA, PGV) SR08/RS09 rigid sliding block model and T_s is the natural period of the sliding mass. For the calculation of $D_{PGA,PGV}$, k_{max} is used in lieu of PGA and k-vel_{max} is used in lieu of PGV. These values can be estimated from equations (1) and (2).

After modification of the displacement predictions, the standard deviation of lnD (σ_{lnD}) was estimated. A linear relationship is used to predict σ_{lnD} for flexible sliding masses for the (PGA, PGV) model:

$$\sigma_{lnD} = 0.40 + 0.284 \cdot k_y/k_{max} \quad (4)$$

4. PREDICTIONS OF SLIDING BLOCK DISPLACEMENT

4.1 Example Application

To illustrate the application of the Rathje and Antonakos (2010) model for predicting the dynamic response and sliding displacement of slopes, consider the following example. The critical sliding mass for a slope is 20-m thick with an average V_s = 400 m/s and resulting T_s = 0.2 s. The k_y is equal to 0.1. The design event is M = 8 and R = 5 km, with the input rock motions described in Table 1. Based on the site and ground motion characterizations, T_s/T_m = 0.43.

Equations 1 and 2 are used to predict k_{max} and k-vel_{max} based on the PGA (=0.42 g), PGV (=50 cm/s), and T_s/T_m (=0.43). Using these values, equation (1) predicts k_{max}/PGA = 0.84, while equation (2) predicts k-vel_{max}/PGV = 1.09. Thus, the seismic loading parameters for this sliding mass are predicted as:

$$k_{max} = 0.84 \cdot 0.42 \text{ g} = 0.35 \text{ g} \quad (5)$$

$$\text{k-vel}_{max} = 1.09 \cdot 50 \text{ cm/s} = 55 \text{ cm/s} \quad (6)$$

Using the seismic loading parameters of k_{max} = 0.35 g and k-vel_{max} = 55 cm/s along with k_y = 0.1, the SR08/RS09 (PGA, PGV) model predicts 23.7 cm. This value then is adjusted using the modification for flexible sliding given in

equation (3). For T_s = 0.2 s, the modification from equation (3) is:

$$\ln(D_{flexible}) = \ln(23.7\text{ cm}) + 1.42 \cdot 0.2 \quad (7)$$

This expression predicts a median displacement value of 31.5 cm for flexible sliding conditions. In all cases, the modification in equation (3) increases the displacement.

To estimate the + 1 standard deviation displacement, the standard deviation (σ_{lnD}) is estimated from equation (4). For this example k_y = 0.1 and k_{max} = 0.35 g, which results in k_y/k_{max} = 0.28. Using equation (4), σ_{lnD} =0.48 and the resulting +1 σ_{lnD} displacement is:

$$\ln(D_{flexible,\,+1\sigma lnD}) = \ln(D_{flexible,median}) + \sigma_{lnD} \quad (8)$$

$$\ln(D_{flexible,\,+1\sigma lnD}) = \ln(31.5) + 0.48 \quad (9)$$

$$D_{flexible,\,+1\sigma lnD} = 50.9\text{ cm} \quad (10)$$

4.2 Comparison with Previous Models

Bray and Travasarou (2007) also developed a model to predict the sliding displacement of rigid and flexible slopes. This model uses only a single ground motion parameter to characterize the seismic loading, $S_a(1.5T_s)$, which is defined as the input rock response spectral acceleration at a period equal to 1.5 times the natural period of the sliding mass. The seismic loading parameter for the sliding mass (i.e., k_{max}) is not computed directly in this approach, such that the condition of $k_y \geq k_{max}$ (i.e., no sliding and D = 0 cm) is not explicitly checked. To circumvent this issue, Bray and Travasarou (2007) include a statistical model for the probability that the displacement is equal to zero (i.e., $k_y \geq k_{max}$) that is a function of k_y and $S_a(1.5T_s)$.

Median sliding displacements were computed using both the Rathje and Antokankos (2010) and Bray and Travasarou (2007) models for comparison. These displacements were computed for two ground motion scenarios (M=7, R=5km and M=8, R=5 km) and two values of k_y (0.05 and 0.1) over a range of T_s equal to 0.0 to 1.0 s. For the Rathje and Antonakos (2010) calculations, the required input ground motion parameters are PGA and PGV, and they are given in Table 1 for the earthquake scenarios. The Bray and Travasarou (2007) model requires $S_a(1.5T_s)$, such that the full input acceleration response spectrum was computed using the Next Generation Attenuation project ground motion prediction equations. $S_a(1.5T_s)$ was computed for each value of T_s by linear interpolation of the acceleration response spectrum around the period of $1.5T_s$.

Figure 6 shows plots of the displacements predicted by the two models as a function of T_s. These displacement spectra show how the flexible sliding block displacements vary with T_s for a given ground motion scenario and k_y. For both models the displacement spectra show that the maximum displacement occurs at T_s around 0.1 s to 0.2 s. In this period range the dynamic response of the sliding mass increases the seismic loading, which results in more displacement. As T_s increases beyond 0.2 s, the seismic loading starts to decrease and the resulting displacements also decrease.

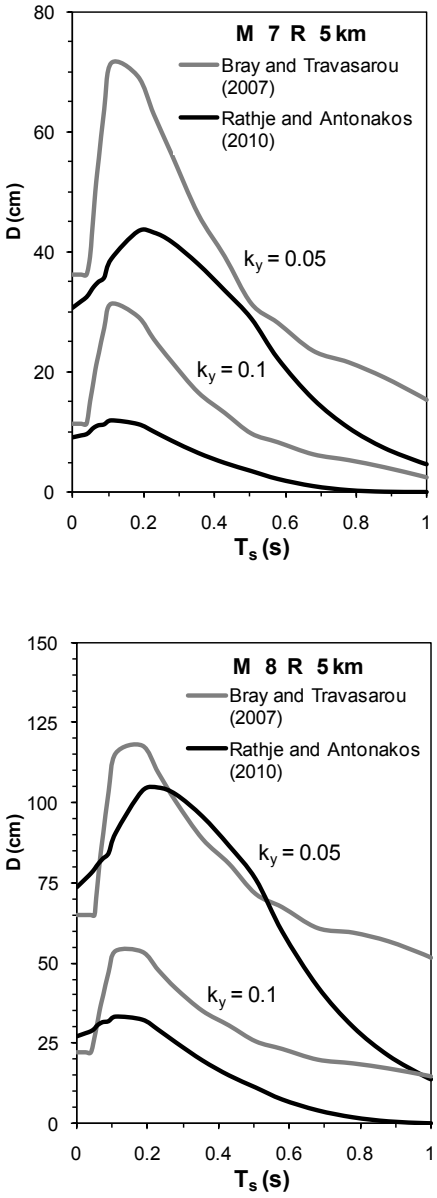


Figure 6 Comparison of displacements from Rathje and Antonakos (2010) and Bray and Travasarou (2007) models

Figure 6 generally shows that Bray and Travazarou (2007) model predicts larger displacements than Rathje and Antonakos (2010) model. At the period of peak displacement, the Bray and Travasarou (2007) model predicts between 1.3 times larger displacement (M=8, R=5 km, and k_y = 0.05) and 2.6 times larger displacement (M=7, R=5 km, and k_y = 0.1) than the Rathje and Antonakos (2010) model. This large difference at the peak is controlled by the very steep increase in displacement that occurs between Ts = 0.0 and 0.2 s for the Bray and Travasarou (2007) model. The maximum difference between the two models occurs at longer periods, where the Rathje and Antonakos (2010) model tends towards zero displacement and the Bray and

Travasarou (2007) maintains relatively large values (Figure 6). The predictions of k_{max} from Rathje and Antonakos (2010) indicate that the displacements should tend towards zero here because k_{max} becomes close to, or less than, k_y. While Bray and Travasarou (2007) attempt to account for this issue by predicting the probability that the displacement is equal to 0.0, this probability never exceeded 0.3 for the cases considered here. For the median displacement to be equal to zero, this probability would need to be equal to or greater than 0.5.

The differences in the displacements predicted by the Rathje and Antonakos (2010) and Bray and Travasarou (2007) models are a function of various features of the two models. The more distinct peak produced by the Bray and Travasarou (2007) model is caused by the use of the spectral acceleration as the input ground motion parameter. The maximum spectral acceleration is typically about 2.0 to 2.5 times larger than the PGA, such that the seismic loading at $T_s \sim 0.1$ to 0.2 s is significantly larger than it is at $T_s = 0.0$ s and leads to a rapid increase in displacement with increasing T_s. The increase in seismic loading with T_s for the Rathje and Antonakos (2010) model is more gradual, as shown by the k_{max}/PGA data in Figure 4, and thus the model predicts a more gradual increase in displacement with increasing T_s. The larger displacements predicted by the Bray and Travasarou (2007) model may be a result of using only one ground motion parameter (i.e., $S_a(1.5T_s)$) in the predictive equations and using rock and soil motions to compute the sliding displacements upon which the model is based. Rathje and Antonakos (2010) observed that the Saygili and Rathje (2009) model that uses (PGA, M) predicted larger displacements than the (PGA, PGV) model, and ascribed this difference to the fact that the (PGA, M) model did not adequately account for frequency content differences between rock and soil motions. While $S_a(1.5T_s)$ certainly provides more frequency content information than PGA, it appears that it does not provide as much information as PGV.

5. CONCLUSIONS

This paper summarizes recent work by Rathje and Antonakos (2010) to develop a unified empirical model to predict the sliding displacements of rigid and flexible sliding masses. The unified model is an extension of the empirical models for rigid sliding masses developed by Saygili and Rathje (2008) and Rathje and Saygili (2009). The main advancements contributed by the SR08/RS09 models include: (1) the addition of a frequency content parameter (PGV) to better predict displacements and (2) a better description of the standard deviation associated with the prediction of sliding displacements. This paper focused on summarizing and comparing the Rathje and Antonakos (2010) based that is based on (PGA, PGV).

The unified approach involves first predicting the seismic loading parameters for a potential sliding mass, and then using these seismic loading parameters to predict sliding displacement. The seismic loading parameters are given by k_{max} and k-vel_{max}, defined as the maximum value of the k-time history and the maximum velocity of the k-time history, respectively. The predictive model for k_{max} is a function of PGA and T_s/T_m and the predictive model for k-vel_{max} is a function of PGV, PGA, and T_s/T_m. To predict sliding displacement, k_{max} is used in lieu of PGA and k-vel_{max} is used in lieu of PGV in the SR08/RS09 (PGA, PGV) model.

In addition to the change in seismic loading parameters, the SR08/RS09 (PGA, PGV) model must be further modified to account for the differences in frequency characteristics between acceleration-time histories and k-time histories. This modification is a function of T_s and increases the predicted displacement.

Comparisons between the Rathje and Antonakos (2010) model and a previously published model of Bray and Travasarou (2007) show that the Rathje and Antonakos (2010) model predicts smaller displacements, in general. These smaller displacements result from the important frequency content information provided by PGV.

Acknowledgements:

The authors acknowledge support from the Japan Ministry of Education, Culture, Sport, Science, and Technology (MEXT) for establishing the Center for Urban Earthquake Engineering (CUEE) in Tokyo Institute of Technology. This support makes possible the forthcoming international conference, as well as international joint research projects and exchange programs with overseas universities.

References:

Antonakos, G. (2009), *"Models of Dynamic Response and Decoupled Displacements of Earth Slopes during Earthquakes"*, M.S. Thesis, University of Texas at Austin, Austin, TX.

Bray, J.D. and E.M. Rathje 1998. "Earthquake-Induced Displacements of Solid-Waste Landfills," *Journal of Geotechnical and Geoenvironmental Engineering*, American Society of Civil Engineers, **124**(3), 242-253.

Bray, J.D. and Travasarou, T. (2007), "Simplified Procedure for Estimating Earthquake-Induced Deviatoric Slope Displacements", *Journal of Geotechnical and Geoenvironmental Engineering*, American Society of Civil Engineers, **133**(4), 381-392.

Jibson, R.W. (2007), "Regression models for estimating coseismic landslide displacement", *Engineering Geology*, **91**, pp. 209-218.

Jibson, R.W. (2010), "Methods for assessing the stability of slopes during earthquakes—A retrospective", *Engineering Geology*, doi:10.1016/j.enggeo.2010.09.017.

Jibson, R.W., E.L. Harp and J.A. Michael (2000), *"A Method for Producing Digital Probabilistic Seismic Landslide Hazard Maps*", Engineering Geology, **58**, 271–289.

Kottke, E.M. and E.M. Rathje (2008), "Technical Manual for Strata," *PEER Report 2008/10*, Pacific Earthquake Engineering Research Center, University of California at Berkeley, 84 pp.

Makdisi, F.I. and H.B. Seed (1978), "Simplified Procedure for Estimating Dam and Embankment Earthquake Induced Deformations", *Journal of the Geotechnical Engineering Division*, American Society of Civil Engineers, **104**(GT7), 849-867.

Rathje, E.M. and Bray, J.D. (2001), "One and Two Dimensional Seismic Analysis of Solid-Waste Landfills," *Canadian Geotechnical Journal*, **38**, 850-862.

Rathje, E.M. and G. Saygili (2009), "Probabilistic assessment of earthquake-induced sliding displacements of natural slopes",

Bulletin of the New Zealand Society for Earthquake Engineering, **42**(1), 18-27.

Rathje, E.M., and Antonakos, G., (2010), "A unified model for predicting earthquake-induced sliding displacements of rigid and flexible slopes," *Engineering Geology*, doi:10.1016/ j.enggeo.2010.12.004.

Saygili, G. and E.M. Rathje (2008), "*Empirical Predictive Models for earthquake-Induced Sliding Displacements of Slopes*", Journal of Geotechnical and Geoenvironmental Engineering, American Society of Civil Engineers, **134**(6), 790-803.

Rathje, E.M., F. Faraj, S. Russell and J.D. Bray (2004), "*Empirical Relationships for Frequency Content Parameters of Earthquake Ground Motions*", Earthquake Spectra, Earthquake Engineering Research Institute, **20**(1), 119-144.

Vrymoed, J.L. and Calzascia, E.R. (1978), "Simplified Determination of Dynamic Stresses in Earth Dams," *In* Proceedings, *Earthquake Engineering and Soil Dynamics Conference*, American Society of Civil Engineers, 991-1006.

8CUEE CONFERENCE PROCEEDINGS
8th International Conference on Urban Earthquake Engineering
March 7-8, 2011, Tokyo Institute of Technology, Tokyo, Japan

APPLICATION OF DISCRETE ELEMENT METHOD IN GEOGRID AND AGGREGATE INTERACTION IN A REINFORCED UNPAVED ROADWAY

Wen-Chao Huang

Assistant Professor, Department of Civil Engineering, National Central University, Jhongli City, Taiwan
wenchaoh@ncu.edu.tw

Abstract: For wet or soft subgrades in an unpaved roadway system, it is usually difficult for the roadway to meet design expectation due to high potential of excessive rut depth. One way to treat the wet or soft subgrade condition is to employ geogrid reinforcement in the unpaved roadway system. In this study the interaction between geogrid and aggregate material was investigated through discrete element method. The aggregate material in the discrete element model is assumed to be consisted of cylinders, while due to the reinforcing characteristic of geogrid reinforcement, it is assumed to be consisted of unmovable grids.
Results showed that the inclusion of geogrid reinforcement at the interface of aggregate layer and the subgrade layer limits the lateral movement of the aggregate material, while when no geogrid reinforcement was included in the roadway system, the deformation of the aggregate layer shows pattern of lateral and upward movement. Due to the patterns and amounts of movement observed in the models, the deformation expressed at the surface of the aggregate layer has shown improvement comparing to unreinforced model.

1. INTRODUCTION

The presence of wet or soft subgrade soils in roadway construction has been a major issue of concern in the geotechnical area for a long time. What is generally meant by wet or soft subgrade in this study is a soft soil deposit that constitutes a poor foundation for roadways, because of its fine grain size and high water content associated with low density. Such characteristics result in high deformability, low permeability, and low shear strength. In consequence, the bearing capacity of these subgrades is very low. For pavements built on such poor foundation conditions, this lead prematurely to excessive permanent deformation, rutting, and cracking. Currently, the methods to address wet and soft subgrade conditions include excavation-substitution, soil improvement with chemical additives, and mechanical reinforcement with geosynthetics. In particular, the use of geosynthetics, such as geotextiles and geogrids, is a practice that has been used since the 1970s. The study presented in this paper is devoted to the use of geogrids in unpaved roads.

Geogrids are large aperture meshes made of plastic polymers. They are placed horizontally on the subgrade and backfilled with compacted aggregate. As a tensile-resistant reinforcement, geogrids can provide mechanical support and added stiffness to the aggregate layer. Geogrid reinforcement spreads the load more broadly to the subgrade, thus improved performance in terms of bearing capacity and deformation is achieved.

In this study, application of discrete element method (DEM) to examine the mechanisms of geogrid reinforcement is proposed. From the microscopic view of the aggregate particles in the sense of discrete element method, the reinforcing mechanisms such as lateral restraint, and the enhanced stiffness of the aggregate layer is easily to be observed with the installation of geogrid reinforcement. The main reinforcing mechanisms of the geosynthetic reinforcement are discussed in the following section.

2. REINFORCING MECHANISMS

2.1 Tensile Membrane

The tensile membrane effect (Figure 1) is a major mechanism in weak subgrade reinforcement. Application of concentrated vertical load to the aggregate layer surface produces compression of the subgrade. As a result, the geosynthetic deflects and tensile forces are developed. This provides additional vertical support to the aggregate and lightens pressure on the subgrade. Tensile membrane effect can also contribute to spreading vertical load over a wider area of subgrade and, consequently, increasing the bearing capacity.

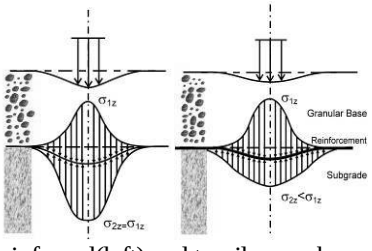


Figure 1 Unreinforced(left) and tensile membrane effect in reinforced case(right)

A number of analytical or numerical models have been proposed to quantify this mechanism in two dimensional plane strain conditions. Analyses suggest the tensile membrane effect would be maximized when high modulus geosynthetics are used and the subgrade is very soft (Bourdeau, 1989). Miura et al. (1990) performed laboratory tests to investigate the influence of geogrid tensile modulus. According to their experimental results, improved performance was related to the magnitude of strain measured in the geogrid during loading. Field test results also showed that the improvement was obtained in terms of rut depth reduction when using higher modulus geogrids, although not to the same level as would be obtained from the laboratory tests.

2.2 Lateral Restraint

Lateral restraint (Figure 2) is a reinforcement mechanism that does not require geosynthetic deflection. Under the vertical compressive pressure, particles in the aggregate layer and the soft subgrade tend to spread away from the loaded area. If the geosynthetic has sufficient interface shear resistance and tensile stiffness, friction or tangential interaction between soil and geosynthetic counteract this movement of the particles. This induces tension in the geosynthetic and enhances lateral confining stresses in the aggregate layer and the subgrade. Because confining stresses are increased, compressive stiffness and resistance of both the aggregate layer and the subgrade are improved by the lateral restraint mechanism. It was shown using X-ray radiography of reinforced soil experiments that the tensile membrane and lateral restraint actions are not independent from each other but they can develop simultaneously in two-layer systems reinforced at the interface. (Bourdeau et al. 1990) Lateral restraint was also recognized as a major function of reinforcement in multilayered reinforced soil. (Bourdeau and Ashmawy, 2002) In a recent case study of reconstructed road where geosynthetic composites were installed, it was observed that the enhanced confinement of aggregate contributed to reduction of the rut depth (Al-Qadi et al., 2000).

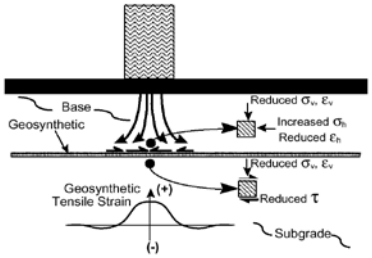


Figure 2 Principle of lateral restraint action (modified from Perkins, 1997)

2.3 Passive Anchorage

Passive anchorage is a necessary condition for tensile membrane effect as well as lateral restraint to develop effectively. Tensile forces in the geosynthetics need to be balanced by mobilized anchorage resistance. Interface shear resistance is a combination of surface friction and grain/geosynthetic interlock. Pullout tests are used for simulating and quantifying in the laboratory soil-geosynthetic interaction in the passive anchorage zone. Laboratory test suggests that the tensile strain in a geogrid decreases, due to anchorage effect, with increasing radial distance from the loading plate to approximately twice the radius of the plate, i.e. 10 to 15 in (Haas et al. 1988). Thus, relatively short anchorage length is sufficient to allow tensile forces be mobilized in a geogrid. However, this is not the case with geotextile reinforcement where longer anchorage length may be needed because interface shear strength between geotextile and soil is typically lesser than that of a geogrid with interlocking aggregates.

2.4 Interlocking of Aggregate and Geogrids

Interlocking of aggregate and geogrid as shown in Figure 3 can be effective under cyclic loading due to traffic. With repetitive loadings from the surface, the aggregate particles are rearranged and moved to a denser state. The relative size of aggregate material and geogrid openings are needed to be properly chosen such that the interlocking can be developed effectively.

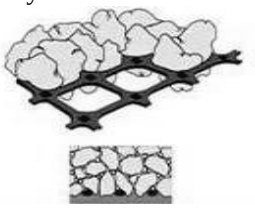


Figure 3 Interlocking of aggregate and geogrid

Additional compaction effort can also be achieved when the interlocking between aggregate and geogrid is formed. As aggregate particles are stuck inside the apertures of geogrid, the tensile membrane effect provides lateral restraint as mentioned previously; hence the resultant stress acted on the subgrade clay layer is reduced. The consequence of this condition is that the excessive pore water pressure induced by the stress increment after each cycle of loading on subgrade clay layer can be dissipated in a more effective way; therefore the subgrade clay layer can become stronger with effective compaction behavior.

3. MODEL FORMULATION

Because of the enhancement effect from geogrid reinforcements to the aggregate layer which consisted of mostly individual particles, it is of interest to investigate the effects through the application of discrete element method (DEM). The advantage of employing DEM in the unpaved roadway system is that the aggregate material behaves like a number of individual cylinders. The reinforcing mechanisms as mentioned in section 2 are therefore to be investigated through the observation of aggregate cylinder movements both qualitatively and quantitatively under either unreinforced or reinforced cases. The commercial software - Particle Flow Code 2D (PFC 2D) developed by Itasca, Inc. is employed for analysis in this study. Due to the nature of two dimensional analysis of PFC 2D, we have assumed that the particles and walls are cylinders and plates, which may

not be a perfect modeling of the real case. However, the 2D analysis result can provide an insight toward the behavior of the aggregate material with geogrid reinforcement installed.

To simplify the unreinforced/reinforced condition in the discrete element model, the following models are established for analyses:

(a) aggregate particles rest on a frictional surface.
(b) aggregate particles rest on a series of continuous small particles.
(c) aggregate particles rest on pairs of smaller particles which is not subject to move in both the horizontal and vertical directions. This case is used to simulate the geogrid reinforced case.

The particles as mentioned above are simulated as cylinders in the models and generated randomly in a predetermined space (formed by boundaries – or walls), and then gravity force is applied to the system in order to simulate the effect of geostatic stress, another wall with limiting width simulating the foundation footing is moving downward at a certain velocity within a period of time until a given distance is achieved.

The geometry of the discrete element model is illustrated in Figure 4. The aggregate layer consisted of 300 cylinders with radius ranging from 0.14 m to 0.28 m. The grids are assumed to be consisted of a series of two smaller cylinders with radius 0.1 m. The spacing of the grid is 1.2 m (center to center).

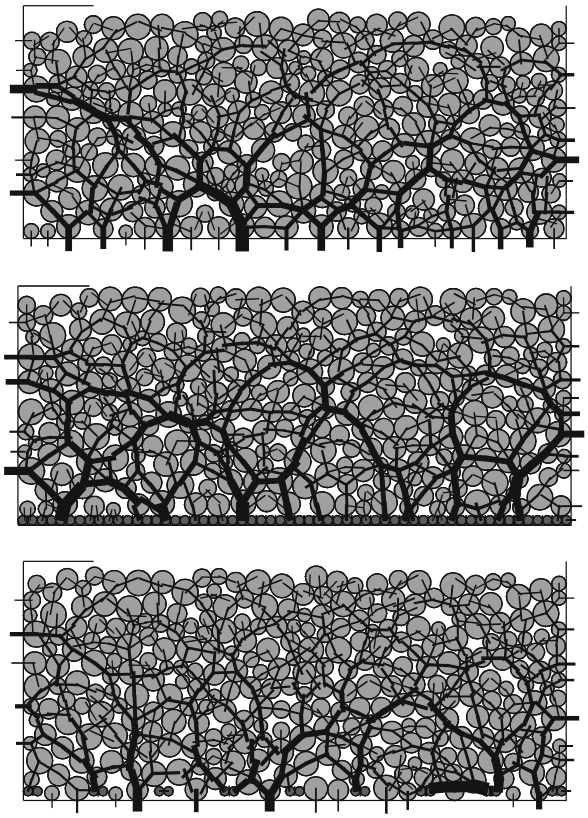


Figure 4 Discrete element model with gravity force applied (top: control model, unreinforced; middle: unreinforced case; bottom: reinforced case)

The velocity of the loading plate is 0.5 mm/sec downward. Due to the requirement of stabilization of the discrete element modes, a total number of 1500 time steps for the unreinforced case and 8000 time steps for the reinforced case are applied to whole system. The contact forces generated during the "loading" period are then recorded and discussed, as well as the moving direction of each particle especially those below the foundation footing.

4. RESULTS AND DISCUSSION

4.1 Contact forces

After the gravity force is applied to the system, it is found that the contact forces (shown in the figure as black lines) are increasing with depth, as shown in Figure 4 under different cases. Out of the three cases shown in Figure 4, the reinforced case showed stress concentration above some geogrid locations. Due to this condition, the induced gravity force was also reduced in the locations adjacent to stress concentration areas, and thus the stress transferred to the subgrade layer is also reduced.

After force equilibrium is achieved in the gravity-applied system, the loading plate is then lowered at a constant speed and the development of contact forces between cylinders is recorded as shown in Figure 5. In the unreinforced case, the stress is distributed within a wider range and concentrated at the corner of the loading plate. In the reinforced case, the contact forces are more concentrated, especially under the loading plate. Most of the contact forces are balanced by the geogrid reinforcement in the reinforced cases, while in the unreinforced case, the forces are balanced by the cylinder-wall friction which is not as effective as in the reinforced case.

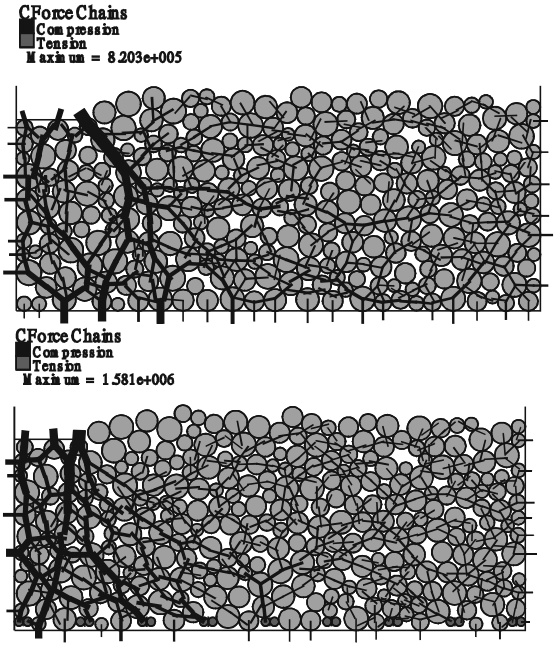


Figure 5 Contact forces in unreinforced (top) and reinforced cases (bottom)

The forces are recorded when similar plate displacements are achieved. In the unreinforced case, the

maximum contact force is about 820 kN at the edge of the loading plate. In the reinforced case, the maximum contact force is 1483 kN, which is evenly distributed below the loading plate. From the examination of contact forces developed in the above cases, it is therefore understood that the induced stiffness (equivalent of force divided by displacement) in the reinforced case is much larger than that in the unreinforced case. In the reinforced case, due to the limitation of lateral movement of the geogrid cylinders, the forces are balanced by the reaction provided by the geogrid reinforcement.

From the above results, we have expected that the reinforcing mechanisms from geogrid reinforcements are therefore developed gradually. First of all, with gravity force before the external loading is applied to the system, some of the contact forces are already balanced by the geogrid reinforcement (Figure 4 bottom one, the arching effect on the right). The location might be random; however, this condition can reduce the potential stress increment onto the subgrade clay layer. Secondly, as the loading plate is moving downward onto the aggregate layer, the contact forces are balanced by the geogrid with the particles directly above it. Since the local stiffness of the aggregate material is enhanced due to geogrid reinforcement, the propagation of enhanced stiffness of the aggregate material is moving upward to the area below the loading plate as the loading plate is pushed down further. This procedure creates a limited force-concentrated area compared to the unreinforced case. In this area, the local stiffness is enhanced significantly due to the geogrid reinforcement.

As mentioned above, the requirement for interlocking of aggregate particle and the geogrid reinforcement is needed to ensure the effectiveness of geogrid reinforcement. Without effective interlocking of aggregate particles and geogrid aperture, lateral restraint and tensile membrane effect cannot be activated sufficiently. In order for the geogrid reinforcement to have the most beneficial effect, proper aperture opening size and aggregate size needs to be chosen accordingly, a common suggestion is to make sure that the aggregate size is about 1/2 to 1/3 of aperture opening size. (AASHTO)

4.2 Particle movements

In the previous section, the contact forces for unreinforced and reinforced cases are discussed. When taking a look at the displacement vector in the cases shown in Figure 6, it is found that for all the cases, the cylinders that are right outside the loading plate have a tendency to move counterclockwise, the only different phenomenon that has been observed is the range of the heaving of the particles close to the surface. In the unreinforced control case, the overall heaving of the particles extends to a greater depth and extends more horizontally to the right (this can be observed from the vector at the bottom of the unreinforced case). In the unreinforced case with fine particles below, the aggregate particles that are moving outward extend to almost the boundary of the model while in the reinforced case, the moving particles extend to only half of the space and the remaining particles almost remain immobilized.

The most important effect of the geogrid reinforcement can be observed in this analysis as well. From the vectors of the unreinforced case, it is found that at the bottom of the model, a noticeable horizontal displacement can be observed, in the controlled unreinforced case, it even extends more to the right. In the reinforced case, it is found that the "lateral restraint effect" of the reinforcement has most significant effect below and right outside of the loading plate. Although the assumption of the "geogrid reinforcement" which is consisted of several "unmovable cylinders" may not be realistic in the actual practice, it provides us an insight from this extreme case.

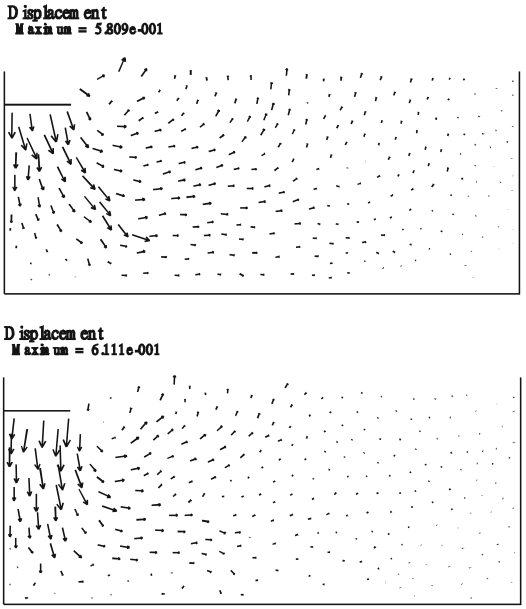


Figure 6 Displacement vector of aggregate cylinders (top: unreinforced; bottom: reinforced case)

When observing from the particle moving directions, it is shown that in the reinforced case, especially the rectangular area under the loading plate, most of the particles are confined horizontally, i.e. only vertical movements are permitted during loading. This condition explains the effect of lateral restraint and its consequences of enhanced confinement. As mentioned previously, the particles that are stuck in the geogrid apertures are confined laterally and vertically. As loading plate is moving downward, the lateral and vertical movement of the particles is less-limited such that particles below the loading plate started to express some degree of vertical and horizontal displacement. This condition can be observed apparently when comparing unreinforced and reinforced cases.

4.3 Contamination of particles

One condition that can deteriorate the performance of the unpaved roadway system is the contamination of subgrade clay layer and aggregate base layers. When finer particles penetrate into the voids of coarse particles, the original friction angle of the aggregate layer can be reduced significantly. Moreover, the drainage function of the aggregate layer can be hindered when clogging condition initiates. However, with the geogrid reinforcement installed at the interface of aggregate and subgrade clay layer, the

interlocking of the aggregate particle and the geogrid aperture may prevent the fine particles from moving upward, and thus the friction angle of the aggregate particles could be retained.

A DEM model is assumed to consist of a finer subgrade layer with 600 cylinders and an aggregate base layer with 100 cylinders. In order to simulate the pumping of fine particles, we have assumed that the fine particles are moving upward, that is, by moving the bottom of the boundary upward, as shown in Figure 7. The openings of the geogrid reinforcement are assumed to consist of a series of two small cylinders with radius 0.1 m. The spacing of the openings is 1.2 m (center to center). Unreinforced and reinforced cases are analyzed in order to compare the results qualitatively. The unreinforced case is achieved by just eliminating the cylinders that represent the geogrids, as shown in the top one of Figure 7. The amount of movement of the wall is kept constant so that the illustrations are comparable.

It is found both in the unreinforced and reinforced cases that the finer cylinders cannot move any further upward since they are blocked by coarser cylinders which represent the aggregate material, only a small amount of the finer cylinders squeezed into the voids that are at the interface, no other finer cylinders moved upward beyond this boundary. In terms of the "contaminated" zones in these two cases, in the reinforced case it is found that the contaminated zone is wide-spread all over the interface while in the reinforced case, the "contaminated" zones are somehow confined by the grids as can be seen in the bottom one of Figure 7 that some of the aggregate particles get stuck between the grids and this provides a barrier to prevent any other aggregate particles around that zone from moving down.

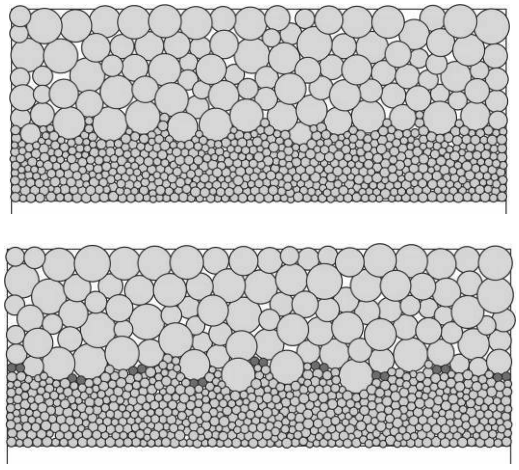


Figure 7 Fine particle movements in unreinforced (top) and reinforced (bottom) cases

This simulation of pumping of fine particles may not be too realistic since the ratio of void size in the coarser layer to the size of the finer layer is chosen due to the analysis limitation of the software in this study. Meanwhile, the loading is a load-unload mono cycle procedure that the contamination behavior of the soils may be more significant when more cycles of loading are applied. However, this simulation gives an idea about how the grids play a role to maintain the aggregate particles (by forming an arched zone) and prevent the particles above it from moving down into the subgrade layer, and vice versa. Although in Figure 7 not all the aggregate particles are retained by the geogrids in the reinforced case, the contaminated zone is somehow confined due to the presence of the geogrids.

5. CONCLUSIONS

A common approach to improve the performance of the unpaved roadway system with soft subgrade is to install geogrid reinforcement. Typically the incompetent soft subgrade clay material can be excavated partially, and a certain amount of aggregate material is backfilled with geogrid reinforcement positioned on top of the aggregate material. After this step is completed, another layer of aggregate material is placed and compacted.

As mentioned previously, the reinforcement effect provided by geogrid in the unpaved roadway system comes from several mechanisms: (1) tensile membrane effect; (2) lateral restraint; (3) passive anchorage and (4) interlocking of aggregate material and geogrid openings. In this study, the discrete element method (DEM) is used to analyze the mechanisms of geogrid reinforcement in an unpaved roadway from the viewpoints of individual particles of both the aggregate and geogrid material.

First of all, from the resultant contact forces recorded below the loading plate when comparing the unreinforced and reinforced cases, an approximate 50% increase of contact force to reach similar plate settlement is required for the reinforced case. Therefore, the local stiffness of the reinforced case was increased significantly when geogrid reinforcement is added. What was meant by local stiffness is that for reinforced case, most of the increased contact forces between cylinders were located right below the loading plate, only in the area below the loading plate and close to the geogrid reinforcement can we find the enhanced area extended slightly outward.

When checking from the movements of the cylinders, it is found that in the reinforced case, the aggregate cylinders tend to move within a limited range in the area under the loading plate both horizontally and vertically. Due to the assumption that the geogrid (which is consisted of unmovable cylinders) has very high stiffness, the aggregate cylinders are stuck (interlocked) in the apertures of the geogrid with very minor lateral deformation. When interlocking of aggregate material and geogrid aperture is formed at the interface, progressive interlocking between aggregate cylinders is initiated such that an enhanced confinement effect of the aggregate layer is appeared. The above condition explains that a higher resultant contact force may be required to reach similar plate settlement in the reinforced case.

Another effect of geogrid reinforcement in the system is to prevent the contamination of the coarse and fine particles. With the interlocking effect of the geogrid reinforcement, the aggregate material forms a barrier such that the finer clay particles have fewer tendencies to penetrate into the aggregate layer above. Meanwhile, the aggregate material was also retained on the geogrid apertures to prevent the clay

layer from being contaminated.

To ensure the best effect of the geogrid reinforcement, relative sizes of aggregate material and geogrid apertures need to be properly chosen such that interlocking can be initiated at the interface. With the propagation of enhanced areas that contain confined aggregate material, the local stiffness of the aggregate material is increased below the loading plate, and therefore the resulting settlement can be reduced.

Acknowledgements:

The author acknowledges the support from Purdue Research Foundation. During the study of the presented work, the author also would like to express thankfulness to Professor Bourdeau, an associate professor in Department of Civil Engineering at Purdue University.

References:

Haas, R., J. Wall, and R.G. Carroll (1988), "Geogrid Reinforcement of Granular Bases in Flexible Pavements," *Transportation Research Record*, Washington D.C., 19-27.

Miura, N. , A. Sakai, Y. Taesiri, T. Yamanouchi, and K. Yasuhara (1990), "Polymer Grid Reinforced Pavement on Soft Clay Grounds," *Geotextile and Geomembranes*, **9**, 99-123.

Bourdeau, P.L., and A. Ashmawy (1996), "Response of a Woven and a Nonwoven Geotextile to Monotonic and Cyclic Simple Tension," *Geosynthetics International*, **2**(4), 493-515.

Perkins, S. W. , and M. Ismeik (1997), "A Synthesis and Evaluation of Geosynthetic-Reinforced Base Layers in Flexible Pavements: Part 1," *Geosynthetics International*, **4**(6), 549-604.

Al-Qadi, I.L., and J.J. Hughes (2000), "Field Evaluation of Geocell Use in Flexible Pavement," *Transportation Research Record*, **1313**, 26-35.

Bourdeau, P.L., and A.K. Ashmawy (2002), "Fatigue limit load in triaxial tests of geotextile-reinforced soil," *Geosynthetics : state of the art, recent developments : proceedings of the seventh International Conference on Geosynthetics*. Nice, France, 1233-1236.

Bourdeau, P.L., and J.I. Amundaray (2005), "Non-parametric simulation of geotechnial variability," *Geotechnique*, **55**(2), 95-108.

8CUEE CONFERENCE PROCEEDINGS
8th International Conference on Urban Earthquake Engineering
March 7-8, 2011, Tokyo Institute of Technology, Tokyo, Japan

FINITE DEFORMATION ANALYSIS OF EARTHQUAKE INDUCED DAMAGE TO BREAKWATER DURING 1995 HYOGOKEN-NANBU EARTHQUAKE

Kyohei Ueda[1], Susumu Iai[2], and Tetsuo Tobita[3]

1) Researcher, Earthquake and Structural Dynamics Group, Port and Airport Research Institute, Japan
2) Professor, Disaster Prevention Research Institute, Kyoto University, Japan
3) Assistant Professor, Disaster Prevention Research Institute, Kyoto University, Japan
ueda-k@pari.go.jp, iai@geotech.dpri.kyoto-u.ac.jp, tobita@geotech.dpri.kyoto-u.ac.jp

Abstract: In order to verify the applicability of strain space multiple mechanism model based on finite strain (both total Lagrangian (TL) and updated Lagrangian (UL)) formulations, seismic response analyses are performed on Breakwater No.7 in Kobe Port during 1995 Hyogoken-Nanbu earthquake. Both infinitesimal and finite deformation analyses are performed to examine the effect of geometrical nonlinearity. As an input dilatancy parameter in the model, two types of undrained shear strength (20 kPa and 40 kPa) are adopted according to the results of undrained triaxial compression tests. The settlements at the top of the caisson in the infinitesimal deformation analyses are 3.62 m and 2.89 m for the undrained shear strength of 20 kPa and 40 kPa, both of which exceed the upper limit of measurements (2.6 m). In contrast, the computed settlements in the TL/UL formulations with the undrained shear strength of 20 kPa and 40 kPa are 2.46/2.46 m and 1.93/1.88 m, respectively, both of which fall inside the measured range (between 1.4 and 2.6 m). The results confirm that the TL and UL formulations are numerically equivalent and the effect of geometrical nonlinearity has to be accurately considered in predicting the seismic response of port structures such as breakwaters.

1. INTRODUCTION

During the Hyogoken-Nanbu earthquake of 1995, Kobe Port was shaken by a strong ground motion having peak ground accelerations of 0.54 and 0.45 g in the horizontal and vertical directions, respectively (Inagaki et al., 1996). Many port structures in Kobe Port, most of which were classified into a rigid block type made of concrete caissons, were damaged. Caisson type quay walls moved up to 5 m toward the sea. Composite breakwaters settled down about 2 m without significant horizontal movement.

Japan has been repeatedly hit by major earthquakes such as Tokachi-Oki (2003) and Niigata Chuetsu (2004) earthquakes after the Hyogoken-Nanbu earthquake. In the next 30 years, it is predicted that Japan will be hit by some major earthquakes (e.g., Tokai and Tonankai earthquakes), which are likely to cause serious damage to port structures. In order to propose effective measures against such major earthquakes, it is very important to predict the damage of port structures due to major earthquakes accurately and verify their seismic performance appropriately.

In order to estimate the seismic damage, various simplified methods have been proposed. However, most of such simplified methods, in which the action of soil is idealized through earth pressure, subgrade reaction force and bearing capacity, can't directly take into account the characteristics of earthquake motion and the variation in soil behavior due to liquefaction. Actual seismic response of port structures, in particular, is a result of dynamic soil-structure interaction, which is much more complicated than considered in such simplified methods. The soil behavior should be interpreted through the dynamic soil-structure interaction process due to earthquake shaking.

Effective stress analysis by finite element method is one of effective means for taking into account the complex behavior of soil. In particular, a strain space multiple mechanism model can take into account the effect of rotation of principal stress axis directions, the effect of which is known to play an important role in the cyclic behavior of sand (Iai et al., 1992). However, the formulation of this model has been carried out based on the infinitesimal strain theory, and thereby the model has difficulty in analyzing large deformation and rotation. This is why the strain space multiple mechanism model has been extended based on two types of finite strain formulations (total and updated Lagrangian) to take into account the effect of geometrical nonlinearity for large deformation analyses (Ueda, 2009; Iai et al., 2010c).

The objective of this study is to examine how well the model, which has capability to take into account the effect of geometrical nonlinearity, can simulate the induced damage to Breakwater No. 7 in Kobe Port during 1995 Hyogoken -Nanbu earthquake and to verify the applicability of the model to seismic response of port structures.

2. SUMMARY OF DAMAGED BREAKWATER

Breakwater No. 7, which is the target of numerical simulation in this study, is located south of Rokko Island in Kobe Port as shown in Fig. 1. A typical cross section and deformed configuration of the breakwater are shown in Fig. 2. The breakwater is a composite type, which consists of a concrete caisson installed on foundation rubble without backfill and embedment, and was constructed on decomposed granite soils, which were backfilled into the area excavated from the original alluvial clay layer. The clay layer reaches a thickness of up to 25 m at the southern front, in which Breakwater No.7 is located, in Kobe Port. During 1995 Hyogoken-Nanbu earthquake, the breakwater induced the settlement of about 1.4 m to 2.6 m. However, the horizontal displacements of the breakwater were less than tens of centimeters. The deformation configuration suggests that the caisson was settled down into the foundation rubble due to the liquefaction or degradation of the loose deposit and the gravity force of the caisson itself, and the settlement also dragged down the rubble and pushed it into the loose deposit below it.

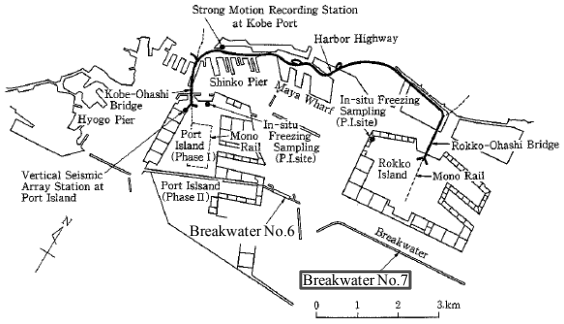


Figure 1 Location of Breakwater No. 7 in Kobe Port (modified after The Great Hanshin-Awaji Earthquake Survey Editorial Board (1998))

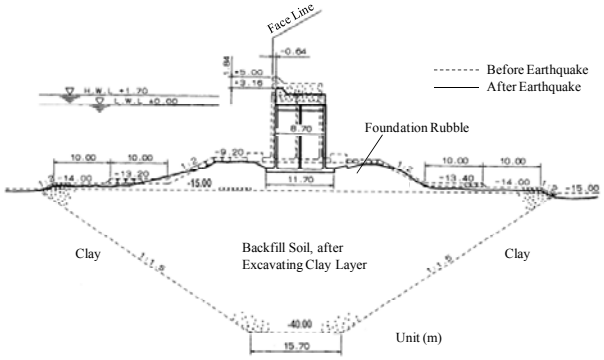


Figure 2 Location of Breakwater No. 7 in Kobe Port (modified after Iai et al. (1998))

3. CONSTITUTIVE MODEL OF SOILS

3.1 Generalized Multiple Mechanism Model Based on Infinitesimal Deformation Theory

An effective stress model proposed by Iai et al. (1992), which is called "Multiple mechanism model", has been extended as a generalized form, which is called "Cocktail glass model", by introducing a new stress-dilatancy relationship (Iai et al., 2010a and b).

With the effective stress and strain vectors in plane strain condition expressed as

$$\boldsymbol{\sigma}' = \left\{ \sigma'_x \quad \sigma'_y \quad \tau_{xy} \right\}^{\mathrm{T}} \tag{1}$$

$$\boldsymbol{\varepsilon} = \left\{ \varepsilon_x \quad \varepsilon_y \quad \gamma_{xy} \right\}^{\mathrm{T}} \tag{2}$$

the integrated form of the constitutive relation is given by

$$\boldsymbol{\sigma}' = -p\mathbf{I} + \sum_{i=1}^{I} q^{(i)} \left\langle \mathbf{t}^{(i)} \otimes \mathbf{n}^{(i)} \right\rangle \Delta\omega \tag{3}$$

$$\left\langle \mathbf{t}^{(i)} \otimes \mathbf{n}^{(i)} \right\rangle = \mathbf{t}^{(i)} \otimes \mathbf{n}^{(i)} + \mathbf{n}^{(i)} \otimes \mathbf{t}^{(i)} \tag{4}$$

where p denotes effective confining pressure (isotropic stress), $\mathbf{I}$ denotes second order identity tensor, q denotes virtual simple shear stress, $\mathbf{n}$ denotes a unit vector along the direction of the branch between the particles in contact with each other, $\mathbf{t}$ denotes a unit vector normal to $\mathbf{n}$.

The volumetric strain ε and the virtual simple shear strain γ are defined as follows:

$$\varepsilon = \mathbf{I} : \boldsymbol{\varepsilon} \tag{5}$$

$$\gamma^{(i)} = \left\langle \mathbf{t}^{(i)} \otimes \mathbf{n}^{(i)} \right\rangle : \boldsymbol{\varepsilon} \tag{6}$$

where the double dot symbol defines double contraction. In order to take into account the effect of volumetric strain due to dilatancy ε_{d}, effective volumetric strain ε' is introduced by

$$\varepsilon' = \varepsilon - \varepsilon_{\mathrm{d}} \tag{7}$$

Dilatancy in Equation (7) is decomposed into contractive component $\varepsilon_{\mathrm{d}}^{\mathrm{c}}$ and dilative component $\varepsilon_{\mathrm{d}}^{\mathrm{d}}$ as

$$\varepsilon_{\mathrm{d}} = \varepsilon_{\mathrm{d}}^{\mathrm{c}} + \varepsilon_{\mathrm{d}}^{\mathrm{d}} \tag{8}$$

The time derivative of both sides of Equation (3) yields the incremental constitutive equation as follows:

$$\dot{\boldsymbol{\sigma}}' = \mathbb{C} : \dot{\boldsymbol{\varepsilon}} \tag{9}$$

where

$$\begin{aligned} \mathbb{C} = {} & K_{\mathrm{L/U}} \mathbf{I} \otimes \mathbf{I} + \sum_{i=1}^{I} G_{\mathrm{L/U}}^{(i)} \left\langle \mathbf{t}^{(i)} \otimes \mathbf{n}^{(i)} \right\rangle \otimes \left\langle \mathbf{t}^{(i)} \otimes \mathbf{n}^{(i)} \right\rangle \Delta\omega \\ & - K_{\mathrm{L/U}} \mathbf{I} \otimes \mathbf{I}_{\mathrm{d}} + \sum_{i=1}^{I} \left(H_{\mathrm{L/U}}^{(i)} + L_{\mathrm{L/U}}^{(i)} \right) \left\langle \mathbf{t}^{(i)} \otimes \mathbf{n}^{(i)} \right\rangle \otimes \mathbf{I} \Delta\omega \\ & - \sum_{i=1}^{I} \left\langle \mathbf{t}^{(i)} \otimes \mathbf{n}^{(i)} \right\rangle \otimes \left(H_{\mathrm{L/U}}^{(i)} \mathbf{I}_{\mathrm{d}} + L_{\mathrm{L/U}}^{(i)} \mathbf{I}_{\mathrm{d}}^{\mathrm{c}} \right) \Delta\omega \end{aligned} \tag{10}$$

The increments of the dilative and contractive components of dilatancy are given as follows:

$$\dot{\varepsilon}_{\mathrm{d}}^{\mathrm{d}} = \mathbf{I}_{\mathrm{d}}^{\mathrm{d}} : \dot{\boldsymbol{\varepsilon}} \tag{11}$$

$$\dot{\varepsilon}_{\mathrm{d}}^{\mathrm{c}} = \mathbf{I}_{\mathrm{d}}^{\mathrm{c}} : \dot{\boldsymbol{\varepsilon}} \tag{12}$$

where

$$\mathbf{I}_{\mathrm{d}}^{\mathrm{d}} = \sum_{i=1}^{I} \frac{\gamma^{(i)} / \gamma_{\mathrm{v}}}{1 + \left| \gamma^{(i)} / \gamma_{\mathrm{v}} \right|} \mathrm{M}_{\mathrm{fv}} \left\langle \mathbf{t}^{(i)} \otimes \mathbf{n}^{(i)} \right\rangle \Delta\omega \tag{13}$$

$$\mathbf{I}_{\mathrm{d}}^{\mathrm{c}} = -\sum_{i=1}^{I} \mathrm{M}_{\mathrm{v}} \left(1 - \left(\frac{G_{\mathrm{L/U}}^{(i)}}{G_{\mathrm{L0}}} \right) \right) \left| \left\langle \mathbf{t}^{(i)} \otimes \mathbf{n}^{(i)} \right\rangle \right|^{*} \Delta\omega \tag{14}$$

For more details, refer to Iai et al. (2010b).

3.2 Finite Strain Formulation of Generalized Multiple Mechanism Model in Reference Configuration

The generalized multiple mechanism model described in the previous section has been extended based on finite strain formulation (Ueda, 2009; Iai et al., 2010c). In the finite strain formulation of the model, the unit vector $\mathbf{N}$ along the direction of the branch and the unit vector $\mathbf{T}$ normal to $\mathbf{N}$ are defined in the reference configuration of the material. These vectors are assumed to change their direction and magnitude into $\mathbf{n}$ and $\mathbf{t}$ in the current configuration through the deformation gradient $\mathbf{F}$ as follows:

$$\mathbf{n} = \mathbf{F}\mathbf{N} \tag{15}$$

$$\mathbf{t} = \mathbf{F}\mathbf{T} \tag{16}$$

$$\mathbf{F} = \frac{\partial \mathbf{x}}{\partial \mathbf{X}} \tag{17}$$

where the motion of the material transforms the initial position vector $\mathbf{X}$ defined in the reference configuration to the current position vector $\mathbf{x}$ defined in the current configuration.

The material description of integrated form of the strain space multiple mechanism model in the reference configuration is given by using the second Piola-Kirchhoff effective stress $\mathbf{S}'$ as follows:

$$\mathbf{S}' = \mathbf{S}'_{p} + \mathbf{S}'_{q} = -Jp\mathbf{C}^{-1} + J^{-1}\mathbb{Q} : \overline{\mathbf{S}} \tag{18}$$

where $\mathbf{C}$ and J denote the right Cauchy-Green tensor and Jacobian determinant ($= \det \mathbf{F}$). The fourth-order tensor $\mathbb{Q}$ and the second-order tensor $\overline{\mathbf{S}}$ in Equation (18) are respectively defined by

$$\mathbb{Q} = \mathbb{N} - \frac{1}{2}\mathbf{C}^{-1} \otimes \mathbf{C} \tag{19}$$

$$\overline{\mathbf{S}} = \sum_{i=1}^{I} Jq^{(i)} \left\langle \mathbf{T}^{(i)} \otimes \mathbf{N}^{(i)} \right\rangle \Delta\omega \tag{20}$$

Incremental form of the constitutive equation in the reference configuration is derived by taking the material time derivative of both sides of Equation (18) as

$$\dot{\mathbf{S}}' = \mathbb{C} : \dot{\mathbf{E}} = \left(\mathbb{C}_{p} + \mathbb{C}_{q} \right) : \dot{\mathbf{E}} \tag{21}$$

where

$$\begin{aligned} \mathbb{C}_{p} = {} & J\left(K_{\mathrm{L/U}} - p\right)\mathbf{C}^{-1} \otimes \mathbf{C}^{-1} \\ & + 2Jp\mathbf{C}^{-1} \odot \mathbf{C}^{-1} - JK_{\mathrm{L/U}}\mathbf{C}^{-1} \otimes \mathbf{C}_{\mathbf{d}}^{-1} \end{aligned} \tag{22}$$

$$\begin{aligned} \mathbb{C}_{q} = {} & J^{-1}\left[\mathbb{Q} : \overline{\mathbb{C}}_{q} + \left(\mathbf{C} : \overline{\mathbf{S}} \right) \tilde{\mathbb{Q}} \right] \\ & - \left(\mathbf{C}^{-1} \otimes \mathbf{S}'_{q} + \mathbf{S}'_{q} \otimes \mathbf{C}^{-1} \right) \end{aligned} \tag{23}$$

$$\overline{\mathbb{C}}_{q} = \sum_{i=1}^{I} J \left\langle \mathbf{T}^{(i)} \otimes \mathbf{N}^{(i)} \right\rangle \otimes \mathbf{C}_{q}^{(i)-1} \Delta\omega \tag{24}$$

$$\begin{aligned} \mathbf{C}_{q}^{(i)-1} = {} & q^{(i)}\mathbf{C}^{-1} + G_{\mathrm{L/U}}^{(i)} \left\langle \mathbf{T}^{(i)} \otimes \mathbf{N}^{(i)} \right\rangle \\ & + H_{\mathrm{L/U}}^{(i)} \left(\mathbf{C}^{-1} - \mathbf{C}_{\mathbf{d}}^{-1} \right) + L_{\mathrm{L/U}}^{(i)} \left(\mathbf{C}^{-1} - \mathbf{C}_{\mathbf{dc}}^{-1} \right) \end{aligned} \tag{25}$$

$$\tilde{\mathbb{Q}} = \mathbf{C}^{-1} \odot \mathbf{C}^{-1} - \frac{1}{2}\mathbf{C}^{-1} \otimes \mathbf{C}^{-1} \tag{26}$$

The dilative and contractive components of dilatancy in the reference configuration are given through a derivation analogous to that in the infinitesimal strain formulation as follows:

$$\dot{\varepsilon}_{\mathrm{d}}^{\mathrm{d}} = \mathbf{C}_{\mathrm{dd}}^{-1} : \dot{\mathbf{E}} \tag{27}$$

$$\dot{\varepsilon}_{\mathrm{d}}^{\mathrm{c}} = \mathbf{C}_{\mathrm{dc}}^{-1} : \dot{\mathbf{E}} \tag{28}$$

where

$$\begin{aligned} \mathbf{C}_{\mathrm{dd}}^{-1} = {} & J^{-1} \sum_{i=1}^{I} \left(\frac{\gamma^{(i)} / \gamma_{\mathrm{v}}}{1 + \left| \gamma^{(i)} / \gamma_{\mathrm{v}} \right|} \right) \mathrm{M}_{\mathrm{fv}} \\ & \times \left(\left\langle \mathbf{T}^{(i)} \otimes \mathbf{N}^{(i)} \right\rangle - \frac{1}{2}\gamma^{(i)}\mathbf{C}^{-1} \right) \Delta\omega \end{aligned} \tag{29}$$

$$\mathbf{C}_{\mathrm{dc}}^{-1} = -\sum_{i=1}^{I} \mathrm{M}_{\mathrm{v}} \left(1 - c_{1} \left(\frac{G_{\mathrm{L/U}}^{(i)}}{G_{\mathrm{L0}}} \right) \right) \left| \left\langle \mathbf{T}^{(i)} \otimes \mathbf{N}^{(i)} \right\rangle \right|^{*} \Delta\omega \tag{30}$$

3.3 Finite Strain Formulation of Generalized Multiple Mechanism Model in Current Configuration

The spatial description of integrated form in the current configuration is obtained through the push-forward operation (Holzapfel, 2001) of the material description in Equation (18) as follows:

$$\boldsymbol{\sigma}' = \boldsymbol{\sigma}'_p + \boldsymbol{\sigma}'_q = -p\mathbf{I} + J^{-1}\mathbb{Z} : \overline{\boldsymbol{\sigma}} \tag{31}$$

where $\boldsymbol{\sigma}'$ denotes the Cauchy effective stress and

$$\mathbb{Z} = \mathbb{N} - \frac{1}{2}\mathbf{I} \otimes \mathbf{I} \tag{32}$$

$$\overline{\boldsymbol{\sigma}} = \sum_{i=1}^{I} q^{(i)} \left\langle \mathbf{t}^{(i)} \otimes \mathbf{n}^{(i)} \right\rangle \Delta\omega \tag{33}$$

With the Oldroyd stress rate of the Kirchhoff effective stress (Holzapfel, 2001), incremental form of the strain space multiple mechanism model in the current configuration is given as follows:

$$\mathrm{Oldr}\left(J\boldsymbol{\sigma}'\right) = J\mathbb{C} : \mathbf{d} = J\left(\mathbb{C}_p + \mathbb{C}_q\right) : \mathbf{d} \tag{34}$$

where $\mathbf{d}$ denotes the rate of deformation tensor and

$$\mathbb{C}_p = \left(K_{\mathrm{L/U}} - p\right)\mathbf{I} \otimes \mathbf{I} + 2p\mathbb{N} - K_{\mathrm{L/U}}\mathbf{I} \otimes \mathbf{I}_{\mathrm{d}} \tag{35}$$

$$\mathbb{C}_q = J^{-1}\left[\mathbb{Z} : \overline{\mathbb{C}}_q + \mathrm{tr}\overline{\boldsymbol{\sigma}}\mathbb{Z}\right] - \left(\mathbf{I} \otimes \boldsymbol{\sigma}'_q + \boldsymbol{\sigma}'_q \otimes \mathbf{I}\right) \tag{36}$$

$$\overline{\mathbb{C}}_q = \sum_{i=1}^{I} \left\langle \mathbf{t}^{(i)} \otimes \mathbf{n}^{(i)} \right\rangle \otimes \mathbf{I}_q^{(i)} \Delta\omega \tag{37}$$

$$\begin{aligned} \mathbf{I}_q^{(i)} &= q^{(i)}\mathbf{I} + G_{\mathrm{L/U}}^{(i)} \left\langle \mathbf{t}^{(i)} \otimes \mathbf{n}^{(i)} \right\rangle \\ &\quad + H_{\mathrm{L/U}}^{(i)} \left(\mathbf{I} - \mathbf{I}_{\mathrm{d}}\right) + L_{\mathrm{L/U}}^{(i)} \left(\mathbf{I} - \mathbf{I}_{\mathrm{d}}^{\mathrm{c}}\right) \end{aligned} \tag{38}$$

The dilative and contractive components of dilatancy in the current configuration are defined as follows:

$$\dot{\varepsilon}_{\mathrm{d}}^{\mathrm{d}} = \mathbf{I}_{\mathrm{d}}^{\mathrm{d}} : \mathbf{d} \tag{39}$$

$$\dot{\varepsilon}_{\mathrm{d}}^{\mathrm{c}} = \mathbf{I}_{\mathrm{d}}^{\mathrm{c}} : \mathbf{d} \tag{40}$$

where

$$\begin{aligned} \mathbf{I}_{\mathrm{d}}^{\mathrm{d}} &= J^{-1} \sum_{i=1}^{I} \left(\frac{\gamma^{(i)} / \gamma_{\mathrm{v}}}{1 + \left|\gamma^{(i)} / \gamma_{\mathrm{v}}\right|} \right) \mathrm{M}_{\mathrm{fv}} \\ &\quad \times \left(\left\langle \mathbf{t}^{(i)} \otimes \mathbf{n}^{(i)} \right\rangle - \frac{1}{2}\gamma^{(i)}\mathbf{I} \right) \Delta\omega \end{aligned} \tag{41}$$

$$\mathbf{I}_{\mathrm{d}}^{\mathrm{c}} = -\sum_{i=1}^{I} \mathrm{M}_{\mathrm{v}} \left(1 - c_1 \left(\frac{G_{\mathrm{L/U}}^{(i)}}{G_{\mathrm{L0}}} \right) \right) \left| \left\langle \mathbf{t}^{(i)} \otimes \mathbf{n}^{(i)} \right\rangle \right|^{*} \Delta\omega \tag{42}$$

For more details, refer to Ueda (2009) or Iai et al. (2010c).

4. OUTLINE OF FINITE ELEMENT ANALYSIS

4.1 Determination of Model Parameters

The strain space multiple mechanism model described in the previous chapter has 15 parameters for the analysis of liquefaction; three specify volumetric mechanism, three specify shear mechanism, and the rest control liquefaction and dilatancy.

The parameters for defining the characteristics of volumetric and shear deformation are shown in Table 1. They were determined as following the past analytical study (Fujii et al., 2008). The parameters r_K and l_K in Table 1, which are defined only for the backfill soil (viz. decomposed granite soil), control the bulk modulus for liquefaction analysis and were determined according to the volumetric strain of the undisturbed soil samples after undrained cyclic triaxial tests (The Third District Port Construction Bureau, 1997).

Table 1 Model parameters for deformation characteristics

Soil Type				Parameters for deformation characteristics						
				volumetric mechanism			shear mechanism			
	ρ (t/m^3)	n	σ_{ma}' (kPa)	K_{ma} (kPa)	r_K	l_K	G_{ma} (kPa)	φ_f (°)	c (kPa)	h_{max}
Alluvial Clay	1.70	0.45	143.0	195500	-	-	74970	30.00	0.0	0.30
Foundation Rubble	2.00	0.45	98.0	469000	-	-	180000	40.00	0.0	0.30
Backfill Soil	1.80	0.45	98.0	220872	0.11	2.0	84695	39.67	0.0	0.24

The rest of 15 parameters, which specify the characteristics of liquefaction and dilatancy, are defined only for the backfill soil as shown in Table 2. They were determined by referring to the liquefaction resistance curves, which were obtained from undrained cyclic triaxial tests of decomposed granite soil taken from the reclaimed ground in Rokko Island (see Fig.1), as shown in Fig. 3. The relative density of the decomposed granite soil was 67 % to 77 %. An example on the simulated cyclic behavior of the backfill soil is given in Fig. 4. The parameter q_{us} in Table 2, which is undrained shear strength for describing the steady state of sand (e.g., Yoshimine and Ishihara (1998)), was determined from undrained monotonic triaxial compression tests. According to Hyodo et al. (1997), the undrained shear strength of decomposed granite soil with relative density of 80 % in Rokko Island is about 20 kPa and 40 kPa ($=q/2$) depending on initial confining pressure as shown in Fig. 5. In the following analysis, without considering the effect of initial confining pressure on undrained shear strength, both 20 kPa and 40 kPa were simply adopted as the undrained shear strength of the backfill soil.

Table 2 Model Parameters for Dilatancy

Soil Type	Parameters for dilatancy								
	φ_p (°)	ε_d^{cm}	r_{ε_d}	r_{ε_d}	q_1	q_2	S_1	c_1	q_{us} (kPa)
Backfill Soil	28.0	0.45	1.20	0.90	1.00	1.00	0.005	1.65	20.0 40.0

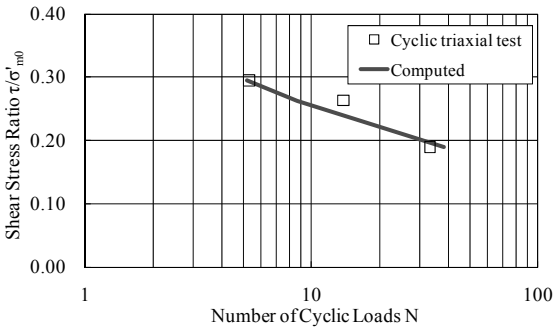


Figure 3 Liquefaction resistance curve

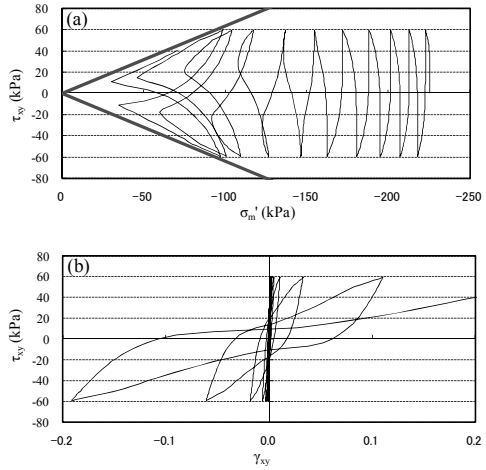


Figure 4 Computed results of cyclic shear; (a) Effective stress path, (b) Stress strain relation

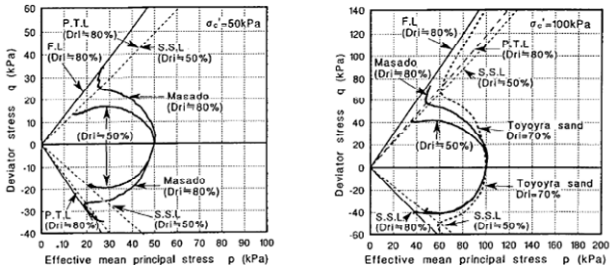


Figure 5 Effective stress path in undrained monotonic triaxial compression test (Hyodo, 1997)

4.2 Modeling of Structures and Sea Water

The concrete caisson was idealized by linear plane elements, which have been extended for large deformation analysis based on the concept of multiple shear mechanism (Ueda et al, 2009). The parameters of the plane elements are shown in Table 3. The relative sliding and separation between the foundation rubble and the concrete caisson was taken into account by introducing joint elements.

The sea water was modeled as incompressible fluid and formulated as an added mass matrix considering the equilibrium and continuity of the fluid at the solid-fluid interface (Zienkiewicz, 2000).

Table 3 Model Parameters for structures

Structure Type	Density	Young's modulus	Poisson ratio
	ρ (t/m^3)	E (kPa)	ν
Caisson	2.1	2.23×10^7	0.17
Upper Concrete	2.3	2.94×10^7	0.17
Footing	2.1	2.94×10^7	0.17

4.3 Initial and boundary conditions and input motion

The finite element mesh for numerical analysis is shown in Fig. 6. Before the seismic response analysis, a static (self-weight) analysis was performed with gravity force under drained condition to simulate the initial stress acting in-situ before the earthquake.

During the seismic response analysis, the seismic wave should be appropriately simulated to transmit from the analysis domain with the finite elements to the outside field. In order to take into account this effect, the side boundaries were idealized by viscous dampers.

With these boundary conditions, seismic response analyses were performed on Breakwater No.7. As an input motion, both of the horizontal (NS) and vertical (UD) components of the earthquake motion recorded at Port Island during 1995 Hyogoken-Nanbu earthquake, shown in Fig. 7, were adopted through the deconvolution by the equivalent linear method for obtaining the incident waves. In this research, EW component of the horizontal waves, the direction of which is parallel to the longitudinal direction of Breakwater No.7, was not considered.

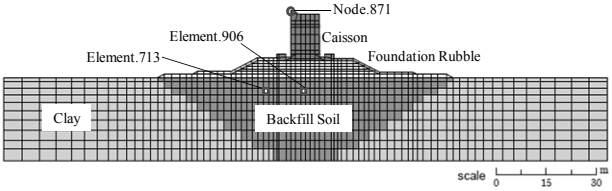


Figure 6 Finite element mesh for numerical analysis

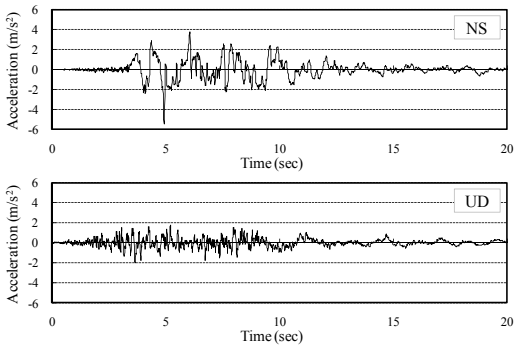


Figure 7 Input acceleration

The seismic response analyses were performed under undrained conditions. The numerical time integration was done by the Wilson-θ method (θ=1.4) using a time step of 0.01 seconds. Rayleigh damping (α =0.0 and β =0.002), which is proportionally decreasing with the degree

of cyclic mobility, was used to ensure stability of the numerical solution process. Selective reduced integration was adopted for Gauss integration using four nodes isoparametric elements.

In computation, both an infinitesimal deformation analysis and finite deformation analyses were performed to compare the effect of geometrical nonlinearity. In the finite deformation analyses, we employed both total Lagrangian (TL) formulation with material description based on reference configuration (see Section 3.2) and updated Lagrangian (UL) formulation with spatial description based on current configuration (see Section 3.3).

5. RESULTS OF THE ANALYSIS

5.1 Seismic response and deformation

The computed settlements at the top (Node.871, see Fig. 6) of the breakwater in the infinitesimal and finite deformation analyses are compared in Fig. 8. For both the infinitesimal and finite deformation analyses, the settlements are negatively correlated with the undrained shear strength. In other words, the settlement decreases as the undrained shear strength becomes larger. The figure shows that the results in the infinitesimal deformation analyses for the case of q_{us} =20 kPa and 40 kPa are 3.62 m and 2.89 m, respectively, both of which exceed the upper limit of measurements (2.6 m). In contrast, the settlements in the finite deformation analysis based on TL formulation are 2.46 m and 1.93 m for the case of q_{us} =20 kPa and 40 kPa, respectively, both of which fall within the measured range from 1.4 m to 2.6 m. The results in the UL formulation show the same tendency and no significant difference from those in the TL formulation for each undrained shear strength, which suggests that both formulations are not only theoretically but also numerically equivalent to each other. The figure also indicates that the difference between the settlements in the infinitesimal and finite deformation analyses, which is due to the effect of geometrical nonlinearity, increases as the undrained shear strength becomes smaller. The difference in the case of q_{us} =20 kPa is about 1.2 times as large as that in the case of q_{us} =100 kPa, which suggests that it is preferable to carry out the finite deformation analysis by taking into account geometrical nonlinearity, in particular, when the undrained shear strength used as an input parameter is small.

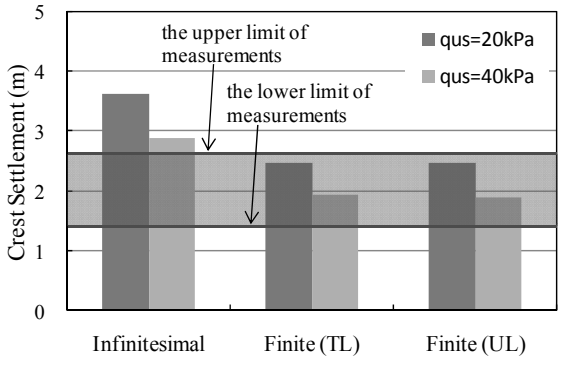


Figure 8 Comparison between computed settlements at the top of Breakwater No. 7

The computed horizontal displacements at the top of the breakwater are shown in Fig. 9. All of the results exceed the average of measurements. However, the differences are less than 0.6 m and of little consequence compared to the dimension of the breakwater. Unlike the settlements shown in Fig. 8, the horizontal displacements increase as the undrained shear strength becomes larger. This is because the deformation mode, in particular, about the inclination of the caisson during shaking in the case of q_{us} =40 kPa is slightly different from that in the case of q_{us} =20 kPa as described hereinafter.

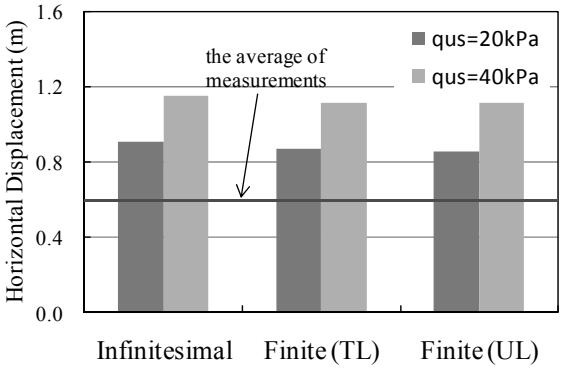


Figure 9 Comparison between computed horizontal displacements at the top of Breakwater No. 7

The computed deformations of the breakwater after shaking in the case of q_{us} =20 kPa are shown in Fig. 10, in which solid lines illustrate the deformed meshes with reference to the original configuration in broken lines. In both the infinitesimal and finite deformation analyses, the deformation mechanism is similar to that mentioned earlier in Chapter 2. However, it seems that the extent of deformed region in the infinitesimal deformation analysis becomes more widespread than the observation, in particular, in the vicinity of the foundation rubble around the caisson, while the deformation mode in the finite deformation analyses is consistent with the observation. By comparison, the results in the case of q_{us} =40 kPa are shown in Fig. 11. The deformation mechanism is considered to be the same as that in the case of q_{us} =20 kPa although the extent of deformation is slightly different from that in Fig. 10. Compared to the results in the case of q_{us} =20 kPa, the caisson sinks down with a slightly larger inclination in the case of q_{us} =40 kPa, which may be affected by the difference of stress states in the backfill soil just below the caisson. As mentioned earlier about the settlements, the TL and UL formulations are also equivalent to each other about the deformed configuration in both Fig. 10 and Fig. 11.

The computed accelerations and displacements at the top of the breakwater in the case of q_{us} =20 kPa are shown in Fig. 12. The first and second rows in the figure show that both the horizontal and vertical accelerations are hardly affected by the difference of analytical methods (e.g., infini-

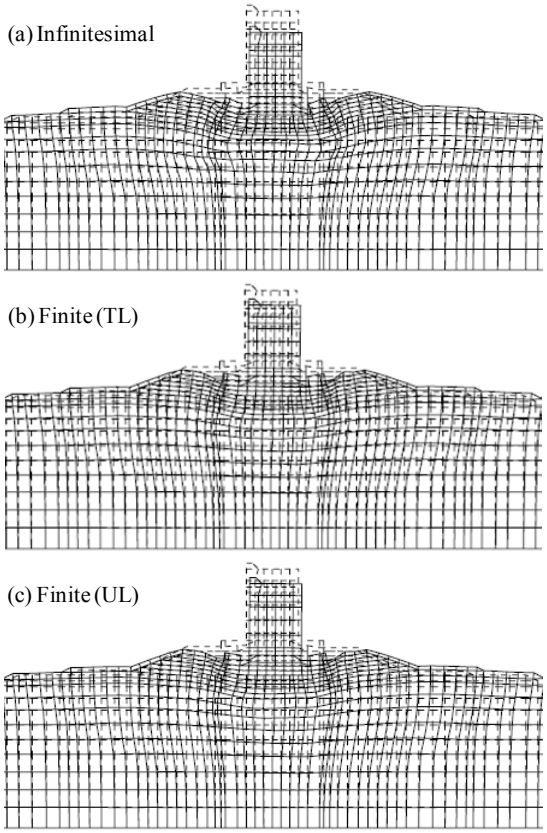


Figure 10 Computed deformation after shaking (q_{us} =20 kPa)

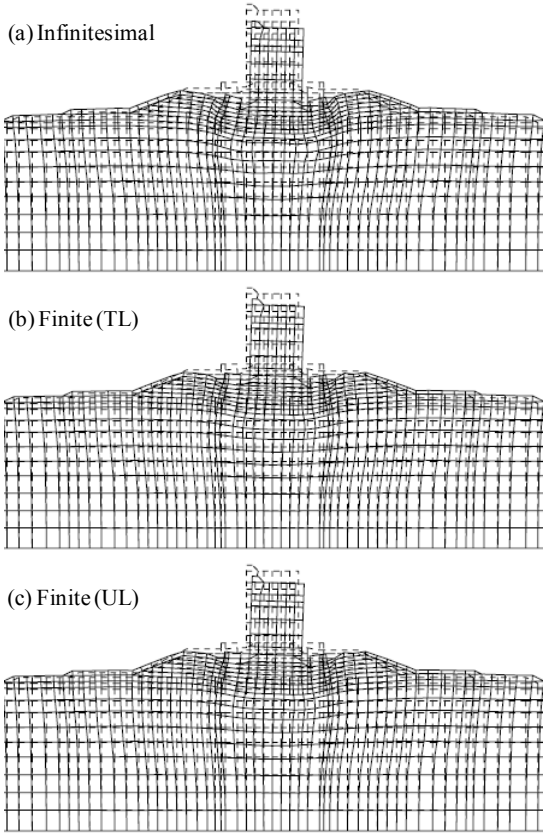


Figure 11 Computed deformation after shaking (q_{us} =40 kPa)

tesimal or finite deformation analysis). The vertical displacements shown in the fourth row gradually accumulate and reach the residual values shown in Fig .8 while the horizontal displacements shown in the third row are oscillating due to shaking. As shown in Fig. 13, the same tendencies about accelerations and displacements are recognized in the case of q_{us} =40 kPa. Comparison between the first rows in Fig. 12 and Fig. 13 indicates that the horizontal acceleration at the top of the caisson is more attenuated after about 6 seconds as the undrained shear strength in the backfill soil becomes smaller, which causes the difference of the horizontal displacements shown in the third rows and Fig. 9. The attenuation is attributed to the decrease of effective stress, which is equivalent to the build-up of excess pore water pressure under the condition that total stress is constant, in the backfill soil just below the caisson.

5.2 Excess pore water pressure

The computed excess pore water pressure ratios (= $1-\sigma'_{m}/\sigma'_{m0}$) at the end of shaking in the case of q_{us} =20 kPa and 40 kPa are shown in Fig. 14 and Fig. 15, respectively. In the both figures, the excess pore water pressure ratios in the infinitesimal deformation analysis are a little lower than those in the finite deformation analyses, in particular, in the area just below the foundation rubble far away from the caisson. The settlements of the caisson in the

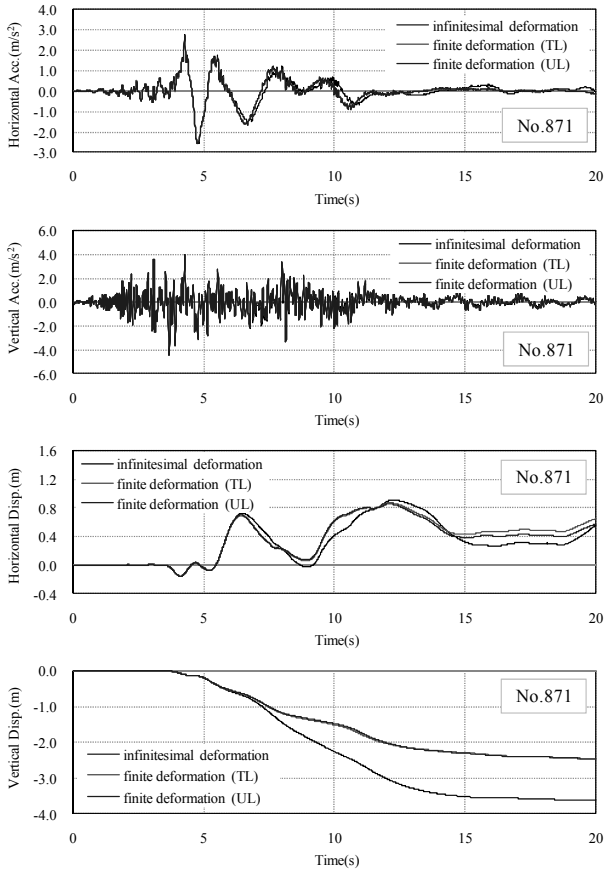


Figure 12 Time history of computed accelerations and displacements (q_{us} =20 kPa)

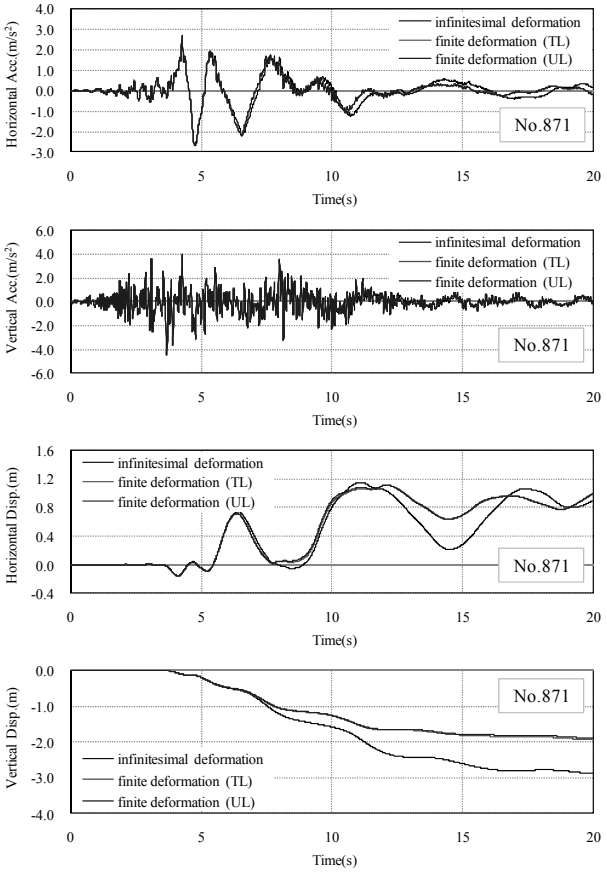


Figure 13 Time history of computed accelerations and displacements (q_{us} =40 kPa)

infinitesimal deformation analysis, however, are larger than those in the finite deformation analyses for each undrained shear strength as mentioned earlier in Fig. 8, which suggests that the difference of the settlements is more directly affected by the effect of geometrical nonlinearity (e.g., difference of the relationship between displacements and strains in simple terms) rather than by the difference of the excess pore water pressure ratios. In major parts of the backfill soil below and in the vicinity of the caisson, which affects the behavior of the caisson most susceptibly, the excess pore water pressure ratios in Fig. 14 are slightly higher than those in Fig. 15. This is why the settlement of the caisson in the case of q_{us} =20 kPa is larger than that in the case of q_{us} =100 kPa as shown in Fig. 8. As mentioned earlier about the settlements, Fig. 14 and Fig. 15 confirm that the TL and UL formulations are equivalent to each other about the excess pore water pressure ratios.

5.3 Effective stress path and stress-strain relationship

The computed effective stress paths and stress-strain relations are shown in Fig. 16 and Fig. 17 for the elements in the backfill soil below the caisson (see Fig. 6). The filled circles and triangles represent the initial stress state before shaking and the finial stress state after shaking, respectively. The maximum shear stress τ and mean effective stress σ'_{m} in the effective stress paths for the finite deformation

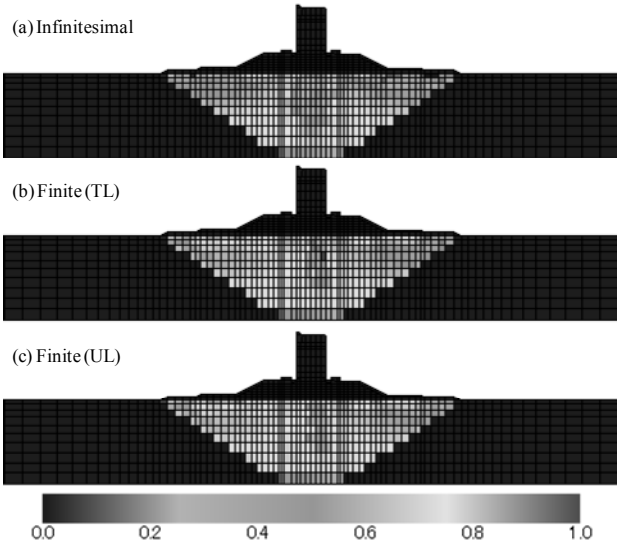


Figure 14 Computed distribution of excess pore water pressure ratio (q_{us} =20 kPa)

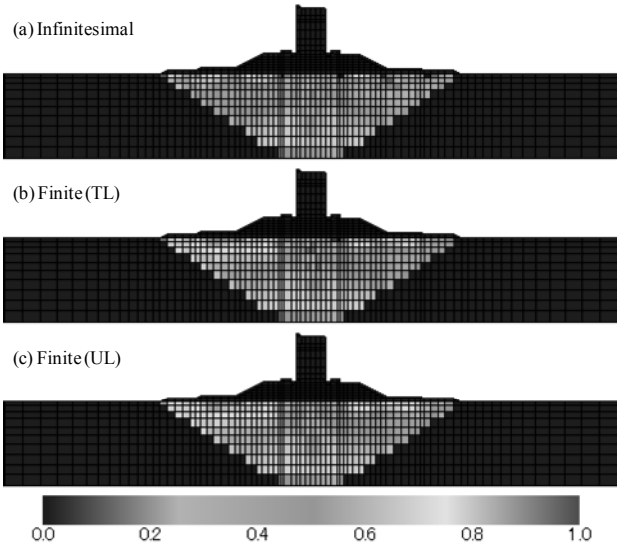


Figure 15 Computed distribution of excess pore water pressure ratio (q_{us} =40 kPa)

analyses (both the TL and UL formulations) are given as follows:

$$\tau = \sqrt{\left(\left(\sigma'_{11} - \sigma'_{22}\right)/2\right)^2 + \left(\sigma'_{12}\right)^2} \tag{43}$$

$$\sigma'_{\mathrm{m}} = \left(\sigma'_{11} + \sigma'_{22}\right)/2 \tag{44}$$

where $\sigma'_{11}, \sigma'_{12}, \sigma'_{22}$ are the components of Cauchy effective stress. The computed second Piola-Kirchhoff effective stress and Green-Lagrange strain in the TL formulation are converted into Cauchy effective stress and Euler-Almansi strain. Both of Fig. 16 and Fig. 17 confirm that the stress paths and stress-strain relations obtained in the

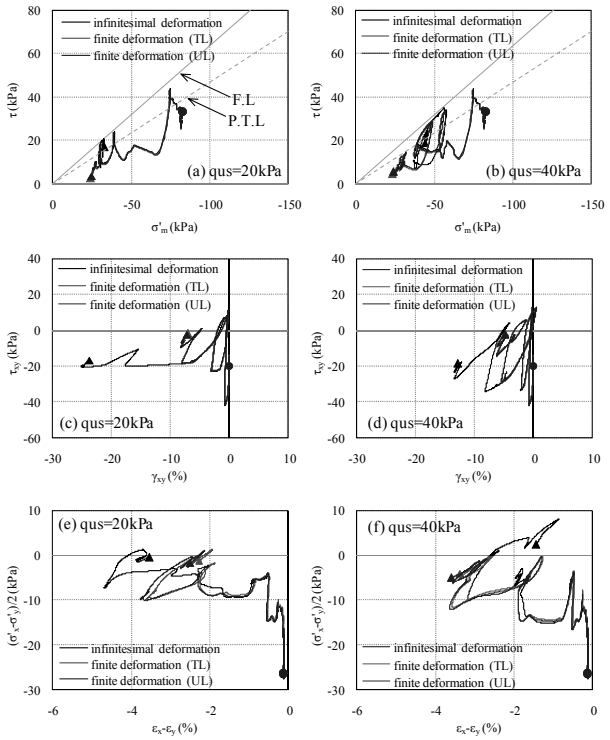


Figure 16 Computed effective stress path and stress-strain relations (for element No. 713)

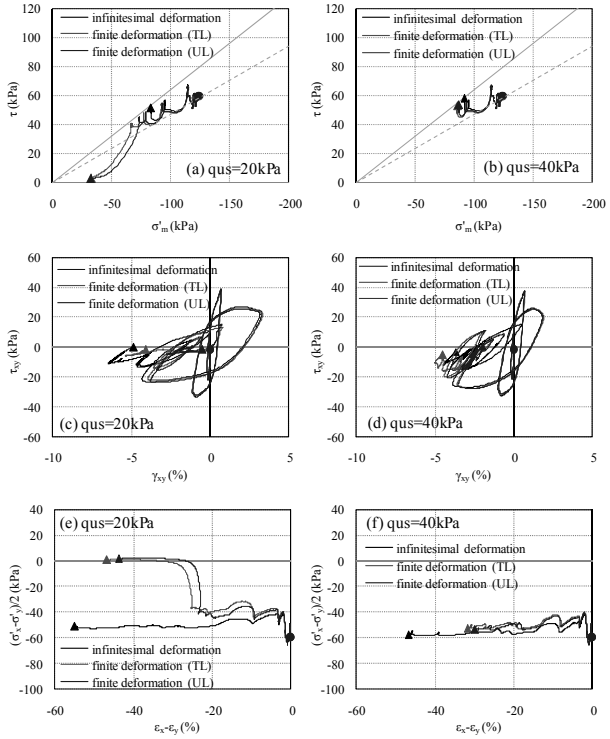


Figure 17 Computed effective stress path and stress-strain relations (for element No. 906)

TL formulation are nearly identical to those in the UL formulation. Thus, we can say for sure that the TL and UL formulations are not only theoretically but also numerically equivalent to each other. In what follows, we discuss in detail.

The initial stress states in Fig. 16(a) are the same as those in Fig. 16(b) because the undrained shear strength doesn't affect the results of the self-weight analysis performed under drained condition. In addition, the initial stress states are equivalent regardless of the analytical method, which suggests that the effect of geometrical nonlinearity is hardly induced in the self-weight analysis, and are relatively close to the failure line (F.L) even before shaking due to the overburden pressure of the caisson by gravity. We obtain the same consequence in Fig. 17(a) and (b). As shown in Fig. 16(a) and (b), the difference of undrained shear strength significantly affects the effective stress paths except for the initial point in both the infinitesimal and finite deformation analyses. In the area beyond the phase transformation line (P.T.L) and below the maximum shear stress of 40 kPa, the results for the case of q_{us} =40 kPa exhibit dilative behavior under cyclic shear loading while those for the case of q_{us} =20 kPa show contractive behavior. In both Fig. 16 and Fig. 17, the effective stress paths of the infinitesimal deformation analysis are consistent with those of the finite deformation analyses except for the last portion, in which the effective stress paths in the finite deformation analyses generally show a tendency to get closer to the origin (viz., fully liquefied condition) than those in the infinitesimal deformation analysis do.

Comparison between the stress-strain relations for the case of q_{us} =20 kPa in Fig. 16 and Fig. 17 suggests that the deformation mechanism of the backfill soil directly below the caisson (e.g., element No. 906) differs from that at the same depth away from the caisson (e.g., element No. 713) regardless of the analytical method. The former is dominated by deviatoric strain as shown in Fig. 16(c) and (e), and the latter depends mainly on shear strain as shown in Fig. 17(c) and (e). We can recognize the same tendency in the case of q_{us} =40 kPa. However, the absolute maximum values of shear and deviatoric strain in the case of q_{us} =40 kPa are generally less than their counterparts in the case of q_{us} =20 kPa for both the infinitesimal and finite deformation analyses.

The stress-strain relations in Fig. 16 and Fig. 17 confirm that the infinitesimal deformation analysis is virtually the same as the finite deformation analyses for small strain range. However, as shown in Fig. 16(c) and (d), the results of the infinitesimal deformation analysis become different from those of the finite deformation analyses beyond the absolute value of the shear strain of about 10 % due to the effect of geometrical nonlinearity. The threshold value is similar to the results obtained in simulation for soil behavior during monotonic and cyclic simple shear (Ueda, 2009; Iai et al., 2010c). However, we can recognize some discrepancy between the infinitesimal and finite deformation analyses even in the area below the threshold value in Fig. 17(c) and (d). This may be because the relations are affected by stress and strain conditions of the surrounding soils. Figures 17(e) and (f) confirm that the effect of geometrical

nonlinearity becomes obvious beyond the deviatoric strain level of about 20 % and 30 %. The discrepancy in Fig. 16(e) and (f), which is visible beyond the deviatoric strain level of about 3 %, is considered to depend on stress and strain conditions of the surrounding soils as well as in the shear stress-strain relations.

6. CONCLUSIONS

In this study, infinitesimal and finite deformation analyses were performed on the seismic response of Breakwater No.7 in Kobe Port during 1995 Hyogoken-Nanbu earthquake in order to verify the applicability of an effective stress model. The model used in the analyses was a strain space multiple mechanism model, which has been extended based on finite strain (both total and updated Lagrangian) formulations to take into account the effect of geometrical nonlinearity. As an input dilatancy parameter in the model, two types of undrained shear strength (q_{us} =20 kPa and 40 kPa) were adopted according to the results of undrained triaxial compression tests. Primary conclusions of this study are summarized as follows:

For the both cases of q_{us} =20 kPa and 40 kPa, the settlements at the top of the breakwater exceeded the upper limit of measurements in the infinitesimal deformation analyses while those in the finite deformation analysis (both the total and updated Lagrangian formulations) fell inside the measured range. In both the infinitesimal and finite deformation analyses, the computed settlements increased as the undrained shear strength became smaller. In addition, the difference of the settlements between the infinitesimal and finite deformation analyses also increased with the decrease in the undrained shear strength. Thus, it is preferable to perform the finite deformation analysis by considering geometrical nonlinearity, in particular, when the undrained shear strength is small.

All of the computed results (e.g., deformation, stress path, and stress-strain relationship) indicated that the total and updated Lagrangian formulations are not only theoretically but also numerically equivalent to each other, which demonstrated the validity of the computer programming for finite deformation analysis. We conclude that in order to predict accurately the seismic response of port structures such as breakwaters by finite element method, it is necessary to carry out the analysis by considering the effects of not only material nonlinearity but also geometrical nonlinearity with total or updated Lagrangian formulations.

Acknowledgements:

The authors would like to thank the members of the FLIP consortium (Secretariat: Coastal Development Institute of Technology) for providing some analytical input data (e.g., the finite element mesh and input wave) to carry out this study.

References:

Fujii, N., Iai, S., Noumi, A,. Ozutsumi, O., and Sawada, S. (2008), "Effective Stress Analysis Considering Steady State of Sandy Soil on Caisson Breakwater Damaged by Hyogoken-Nanbu Earthquake," The 43rd Japan National Conference on Geotechnical Engineering, Hiroshima, 1809-1810 (in Japanese).

Holzapfel, G.A. (2001), "Nonlinear Solid Mechanics," John Wiley&Sons.

Hyodo, M., Aramaki, N., Tokuhara, Y., Kikuchi, S., Nakata, Y., and Murata, H. (1997), "Undrained Cyclic Shear Characteristics of Decomposed Granite Soil in Rokko Island," Proceeding of JSCE, **582**(III-41), 87-98 (in Japanese).

Iai, S., Ichii, K., Liu, H., and Morita, T. (1998), "Effective Stress Analyses of Port Structures," Soils and Foundations, Special Issue, 97-114.

Iai, S., Matsunaga, Y., and Kameoka, T. (1992), "Strain Space Plasticity Model for Cyclic Mobility," Soils and Foundations, **32**(2), 1-15.

Iai, S., Ozutsumi, O., and Tobita, T. (2010a), "Evolution of Induced Fabric in a Strain Space Multiple Mechanism Model for Granular Materials," The 45th Japan National Conference on Geotechnical Engineering, Matsuyama, 343 -344 (in Japanese).

Iai, S., Tobita, T., Ozutsumi, O., and Ueda, K. (2010b), "Dilatancy of Granular Materials in a Strain Space Multiple Mechanism Model," International Journal for Numerical and Analytical Methods in Geomechanics (in print).

Iai, S., Ueda, K., Tobita, T., and Ozutsumi, O. (2010c), "Finite Strain Formulation of a Strain Space Multiple Mechanism Model for Granular Materials," International Journal for Numerical and Analytical Methods in Geomechanics (submitted).

Inagaki, H., Iai, S., Sugano, T., Yamazaki, H. and Inatomi, T. (1996), "Performance of caisson type quay walls at Kobe Port," Soils and Foundations, Special Issue, 119-136.

Taylor, D.W. (1948), "Fundamentals of Soil Mechanics," John Wiley&Sons.

The Great Hanshin-Awaji Earthquake Survey Editorial Board (1998), "The Great Hanshin-Awaji Earthquake Survey, Analysis of the Cause of Damage in Civil Engineering Structures, Ground and Earth Structures, Port and Coastal Structures," Maruzen Co., Ltd.

The Third District Port Construction Bureau of Transport Ministry and Kiso-Jiban Consultants Co., LTD. (1997), "Soil Test Report of Kobe Port."

Toyota, H., Nakamura, K., and Kazama, M. (2004), "Shear and Liquefaction Characteristics of Sandy Soils in Triaxial Tests," Soils and Foundations, **44**(2), 117-126.

Ueda, K. (2009), "Finite Strain Formulation of a Strain Space Multiple Mechanism Model for Granular Materials and its application," Doctoral Thesis, Kyoto University, Japan (in Japanese).

Ueda, K., Iai, S., Tobita, T., and Ozutsumi, O. (2009), "Finite Strain Formulation of Elastic Body Based on Multiple Shear Mechanism," Annuals of Disaster Prevention Research Institute, Kyoto University, **52**(B), 383-394 (in Japanese).

Yoshimine, M., and Ishihara, K. (1998), "Flow Potential of Sand during Liquefaction," Soils and Foundations, **38**(3), 189-198.

Zienkiewicz, O. C., Taylor, R. L., and Zhu, J. Z. (2000), "The Finite Element Method : Its Basis and Fundamentals," Sixth Edition, Elsevier.

8CUEE CONFERENCE PROCEEDINGS
8th International Conference on Urban Earthquake Engineering
March 7-8, 2011, Tokyo Institute of Technology, Tokyo, Japan

PERFORMANCE BASED SEISMIC DESIGN METHOD OF GRAVITY QUAY WALLS

Heba kamal[1], Mona Aid[2], and Amira Abdel Rahman[3]

1) Assistant Professor, Soil Mechanics &Geotechnical Engineering Institute, Housing & Building National Research Center, Egypt
2) Professor, Soil Mechanics &Geotechnical Engineering Department Housing & Ain Shams University, Egypt
3) Professor, Soil Mechanics &Geotechnical Engineering Institute, Housing & Building National Research Center, Egypt

Abstract: Recently strong earthquakes around the world caused serious disasters for port structures. It shows the shortcoming of current design and construction procedures and the needs to develop the performance based guidelines for seismic design. The performance-based seismic design method has taken in the seismic design standards of buildings and bridges. However, port structures still use working stress design method. There are lots of improvements needed to be done to upgrade the current design codes. This research discusses the performance-based seismic design process of port structures, including the performance objective, design method, and seismic estimation. The seismic capability of gravity quay walls at different cases histories are studied by using performance-based seismic design method. Afterwards, seismic performance of gravity quay walls is studied through effective stress analysis by varying structural and geotechnical parameters of quay walls under various levels of shaking. This research will be useful for future seismic design of gravity quay walls.

1. INTRODUCTION

Experience at ports has demonstrated that waterfront retaining structures are highly susceptible to earthquake-induced damage. A significant percentage of the damage is due to the liquefaction of adjacent soils. In the case of caisson-type quay walls subjected to earthquake excitation, typical damage modes are found out to be seaward displacement, settlement and tilting as shown in Figure 1. In several cases, ground deformations associated with liquefaction-induced failure of caissons have extended as much as 150 m into backland areas damaging waterfront components and suspending port operations (Inagaki et al., 1996; PHRI, 1997; Werner; 1998; PIANC, 2001; Iai, 2005).

In order to develop a simplified technique for estimating seismically-induced deformations of gravity quay walls "caisson-type" this research focused on field performance data, as well as numerical analyses. The authors have utilized a numerical model, validated with well-documented case histories, for parametric studies of seismic performance of gravity quay walls. The results of this study have been synthesized into practice oriented design charts for estimating the lateral deformations of gravity quay walls.

2. NUMERICAL MODEL

The computer program FLAC (Itasca, 2005) was used in this study. The FLAC program employs an explicit finite difference method for modeling nonlinear static and dynamic problems in two dimensions.

The numerical modeling has been analyzed under plane strain and fluid–mechanical interaction conditions. The soil modeling was performed using an effective stress based Mohr-Coulomb constitutive model. The elastic behavior of the soil was defined by the bulk and shear modulus, and the shear strength is defined by the friction angle and the cohesion. For the quay wall, the concrete caisson has been modeled by linear elastic elements, with soil–structure interfaces modeled by joint interfaces. The lateral boundaries of the model were modeled as free field boundaries and set a distance of seven times the caisson height to eliminate boundary effects on the computed pattern of soil deformations.

In this analysis, the Finn and Byrne model of FLAC 2D has been used to carry out coupled dynamic groundwater flow calculations (Itasca, 2005). This analysis which takes into account the effects of seismically induced pore water pressures was used to investigate the degree and extent of liquefaction

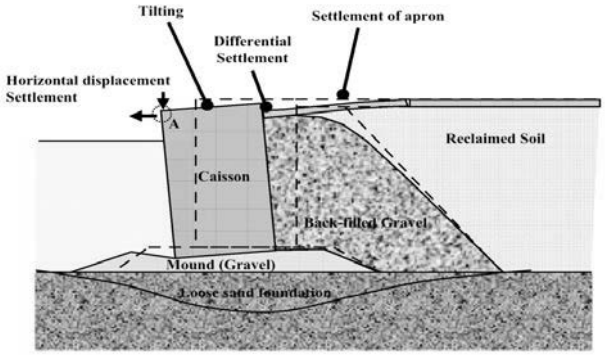


Figure 1 Parameters of damage criteria for gravity quay walls

3. VALIDATION OF THE NUMERICAL MODEL

An early stage of the research involved the validation of the numerical analysis procedure for modeling the seismic performance of concrete caissons. Requisite data for the case studies included: the geometry of the caisson, foundation

pad and backfill, acceleration time histories recorded near the site, site specific geotechnical data, and pre- and post-earthquake wall geometry. After an extensive review of the literature six case studies were selected, including: a wharf at Akita Port during the MJMA 7.7 1983 Nihonkai Chubu Earthquake Japan (Hamada, 1992), two wharves at Kushiro Port during the MJMA 7.8 1993 Kushiro Oki Earthquake Japan (Iai et al., 1994), two wharves at Kobe Port during the Mw 6.9 1995 Hyogoken-Nanbu Earthquake Japan (Inagaki et al., 1996), and one wharf at Taichung port during the Mw 7.6 1999 Chi-Chi Earthquake Taiwan (Chen and Hwang, 2000).

As an example of the seismic performance of a concrete caisson, typical damage at Rokko Island, Kobe Port is shown in Figure 2. This lateral and vertical deformation was common at the port in the aftermath of the 1995 Hyogoken Nanbu earthquake. The portion of the berth illustrated in Figure 2 was modeled using FLAC and the results of this study are shown in Figure 3.

The results of the numerical analyses were consistent with the measured displacements as shown in Table 1. The case studies have been particularly useful for calibrating the numerical model, evaluating the uncertainty associated with the model, and assessing the applicability of the model for computing the dynamic behavior of gravity quay walls.

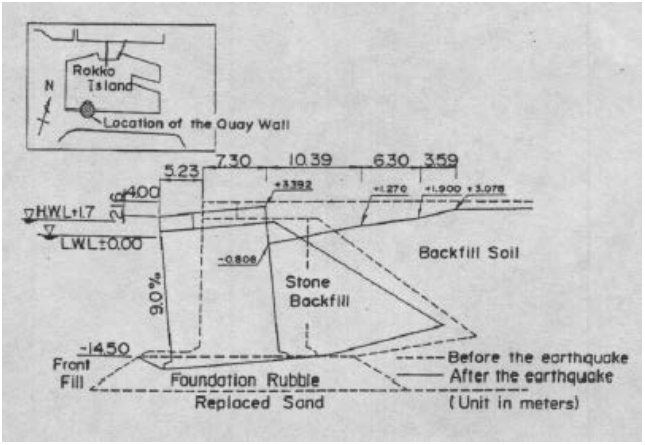


Figure 2 Deformation of caisson at Rokko Island (Inagaki et al., 1996)

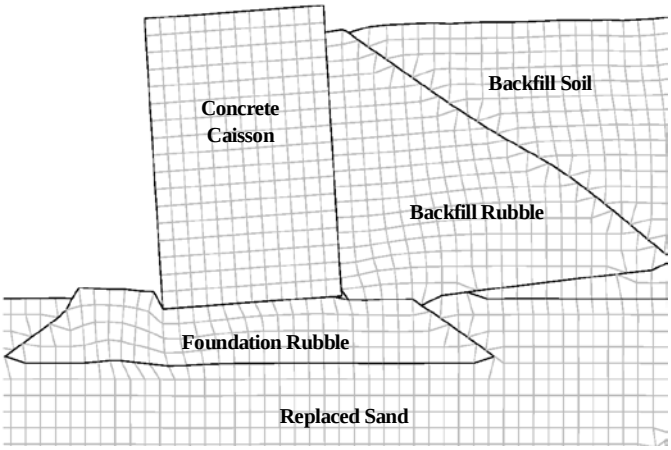


Figure 3 Deformed mesh of Rokko Island Model

4. SEISMIC PERFORMANCE EVALUATION CHARTS

4.1 Limitation of the Advanced and Empirical Methods

Although the applicability of the effective stress analysis method for seismic performance evaluation of caisson type quay walls was verified with case histories, it is difficult to conduct effective stress analyses for all varieties of quay walls considered during the design procedure due to the limitation of costs and time. Furthermore, the effective stress method needs many input parameters and the calibration of which is not easy. It is necessary to become accustomed with the program in Advance if one wants to use, and practicing the parameter calibration and executing the numerical simulation is time consuming. Therefore, it is desirable to establish a simple but robust estimation technique for deformation of gravity quay walls and to confirm the numerical results in some cases.

For gravity quay walls, a conservative relation between seismic coefficients and the level of input motion needed to cause damage to quay walls was proposed based on the case histories (Noda et al., 1975). Furthermore, a simplified damage evaluation technique using seismic coefficients was developed (Uwabe et al., 1983). However, these studies are only applicable in the cases without liquefaction and it is difficult to take into account the effect of subsoil conditions below and behind quay walls. The applicability of the sliding block concept for this purpose was examined (Mohajeri et al., 2004); however, experimental results revealed the complexity of the behavior of caisson walls, and the sliding block concept does not work well for such a complex behavior.

To overcome this problem, simplified seismic performance evaluation charts based on parametric studies using effective stress analyses are proposed.

4.2 Parametric Study Using a Structurally Simplified Model

4.2.1 Parameters characterizing gravity quay walls

The factors governing the seismic performance of a caisson-type quay wall include wall dimensions, the thickness of the soil deposit below the wall and liquefaction resistances of subsoil below and behind wall, as well as the levels of seismic shaking at the base layer. In this study, the soil deposit below the wall was represented by a sand backfill used to replace the original soft clay deposit in order to attain the required bearing capacity. The effects of this soil deposit on the deformation of a caisson-type quay wall may be approximately the same as those of a natural sand deposit below the wall; thus, the results of the parametric study may be applicable not only for the quay wall with sand replacement studied here but also for a quay wall constructed on a natural sandy deposit.

Table 1 Summary of case history data

Case Studies	Xd* (m)			Yd** (m)		
	Predicted	Measured	Average	Predicted	Measured	Average
Nihonkai-Chubu Earthquake Akita Port	1.3	0.8~1.5	1.2	0.35	N/A	N/A
Kushiro-Oki Earthquake	0.26	0.17~0.30	0.24	0.40	0.27~0.47	0.37
Pier 2 (without soil improvement) Pier 3 (with soil improvement)	0.14	0.06~0.24	0.15	0.08	0.05~0.13	0.09
Hyogoken-Nanbu Earthquake	2.8	2.3~3.2	2.75	1.2	0.8~1.1	0.95
Port Island Rokko Island	4.3	3.9~5.2	4.55	2.2	1.4~2.2	1.8
Chi-Chi Earthquake Taichung Harbor Berth No. 3	1.0	0.162~1.6	0.95	0.5	0.1~1.0	0.55

Note: * seaward lateral displacements at the top of the caisson
** settlements at the top of the caisson

The standard cross section of the caisson used for the parametric study is shown in Figure 4. Major cross-sectional dimensions were specified by the width (W) and the height (H) of the caisson wall and by the thickness of subsoil (D1) and thickness of the backfill (D2). A width-to-height ratio of the caisson wall (aspect ratio; W/H) is one of the most important

parameters in conventional seismic design and correlates with the seismic coefficients used in the pseudo-static method as shown in Figure 5, which is based on Japanese case histories. The width-to-height ratio (W/H) was thus considered a major parameter in this study. The

parameters used in this study were W/H = 0.50, 0.65, 0.90, 1.05, 1.20, which correspond to the seismic coefficients of Kh range from 0.05 to 0.30, which is the range of interest for port engineers (PIANC, 2001).

In this study, the peak acceleration of the input seismic excitation assigned at the base layer is the north-south direction of Kobe vertical seismic array. This motion is scaled to six different acceleration values ranging from 0.1g to 0.6g. Figure 6 shows the time history of north south direction of Kobe Earthquake applied at the base of the model at -32m.

The thickness of the liquefied soil deposit below the wall (D1) was specified by a ratio with respect to the wall height (H), ranging from D1/H = 0.0 (i.e. a rigid base layer located immediately below the wall) to D1/H = 1.0 (i.e. thick soil deposit below the wall). The thickness of the liquefied soil deposit behind the wall (D2) was specified by a ratio with respect to the wall height (H), ranging from D2/H = 0.0 (i.e. a non liquefied soil layer) to D2/H = 1.0 (i.e. a liquefied soil layer with depth equal to the height of the wall).

Other geometrical conditions assumed for the effective stress analyses include: wall height H= 13m water level = 2 m lower than the top of the wall, thickness of the rubble mound = 4m.

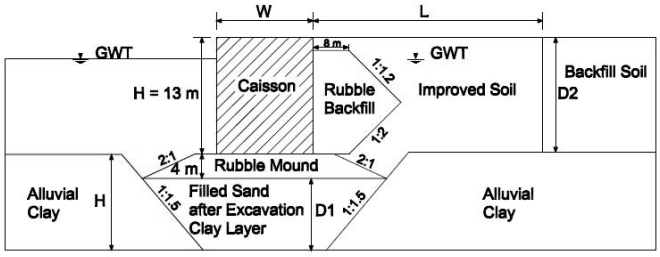


Figure 4 Typical cross section of gravity quay wall for parametric study

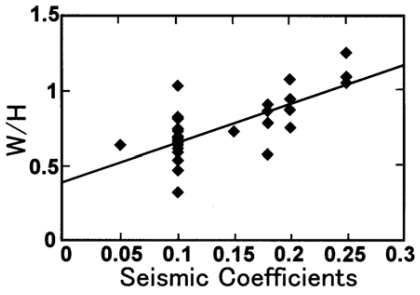


Figure 5 Correlation between the width-to-height ratio (W/H) and seismic coefficients (Ebeling. and Morrison,1992)

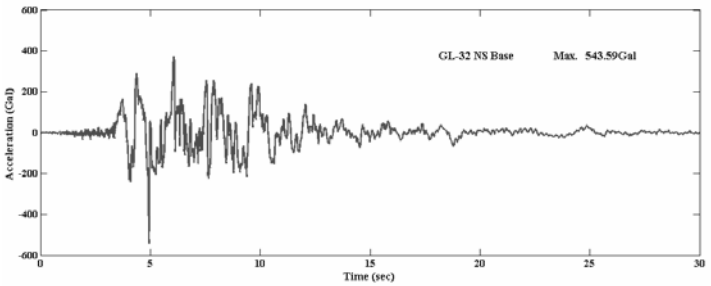


Figure 6 Time history of input ground acceleration (Inagaki et al.,1996)

4.2.2 Geotechnical conditions and parameters

The geotechnical conditions of the soil deposits below and behind the wall were assumed to be the same, represented by the equivalent SPT-N value (the corrected SPT-N value for the effective vertical stress of 65 kPa of an equivalent relative density). The equivalent SPT-N value has been widely used for the assessment of liquefaction potential (PHRI, 1997). The geotechnical model parameters determined by the equivalent SPT-N value are summarized in Table 2. The assumed relative density (Dr) for each equivalent SPT-N value, which was given in the process of the simplified procedure, is also shown in Table 2 as a reference. The range of densities used can be correlated with the corrected standard penetration resistances of 5 to 25 in soil.

4.3 Parameter Sensitivity and Charts

The results of the parametric study were summarized in terms of the residual horizontal displacement (d) at the top of the wall. The residual horizontal displacement was normalized with respect to the wall height (H). The effects of the major parameters on the normalized residual horizontal displacement (d/H) are discussed as follows.

4.3.1 Width-to-height ratio (W/H)

As seen from Figure 7 at SPT N = 5 increasing the width to height ratio (W/H) leads to significant decrease in the normalized lateral displacement (d/H), especially for W/ H = 1.05 and 1.02 and at higher input excitation level 0.4g, 0.5g and 0.6g. Similar trends are shown in Figure 8 and Figure 9 for SPT N = 10 and 15 respectively. However, in Figure 10 at SPT N =20 and Figure 11 at SPT N= 25 increasing the width to height ratio (W/H) leads to negligible effect n the o normalized lateral displacement (d/H) at any excitation level for different soil conditions (i.e W/H = 1.05 is considered as the optimum).

4.3.2 Input excitation Level (g)

Increasing the input excitation level lead to significant increase of the lateral normalized displacements (d/H) and normalized vertical displacements especially for the SPT N values of 5 and 10.In case of width to height ratio (W/H) (from 0.50, 0.65, 0.90) the normalized horizontal displacement (d/H) for moderate earthquakes (i.e g = 0.2 to 0.3) and high earthquakes (i.e g = 0.4 to 0.6) is within the range 0.05 to 0.13 and 0.13 to 0.30 respectively. These ranges of normalized horizontal displacements (d/H) are consistent with the normalized horizontal displacement, which proposed by PIANC 2001 whatever the value of SPT.

In case of width to height ratio (W/H) >1.00 the normalized horizontal displacement (d/H) for moderate earthquakes (i.e g = 0.2 to 0.3) and high earthquakes (i.e g = 0.4 to 0.6) is within the range 0.02 to 0.04 and 0.04 to 0.13 respectively.

4.3.3 SPT-N value

The effects of the equivalent SPT N value are shown in Figure 7 to Figure 11 for width-to-height ratio (W/H) 0.50, 0.65, 0.90, 1.05 and 1.20. For W/H=0.50 and W/H=0.65 increasing the SPT N value leads to decrease the normalized lateral displacement and it can be shown clearly for higher input excitation level 0.4g , 0.5g and 0.6g. This trend is the same for W/H = 1.05 and 1.20.

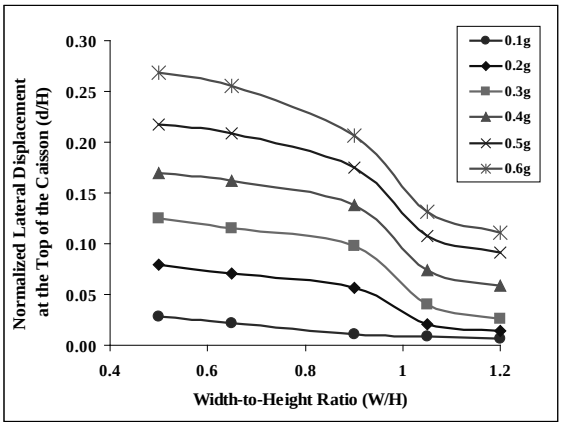


Figure 7 Effects of the width-to-height ratio W/H on normalized lateral displacement (d/H) (for SPT N value of 5) at D1/H=1.0

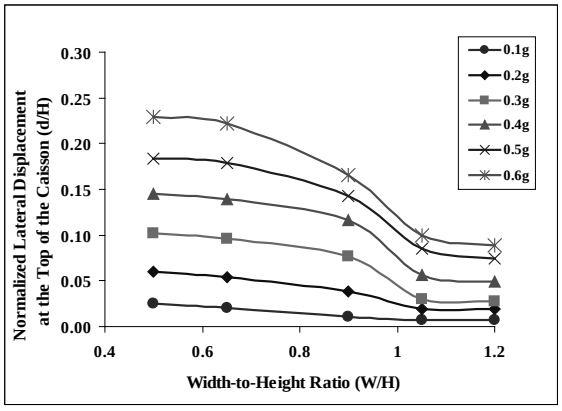


Figure 8 Effects of the width-to-height ratio W/H on normalized lateral displacement (d/H) (for SPT N value of 10) at D1/H=1.0

Table 2 Geotechnical Model Parameters of Sand for Parametric Study

SPT N values	ρ_d (kg/m^3)	ϕ (deg)	G (Pa)	K (Pa)	Dr (%)	C1	C2
5	1500	35	3.50E7	7.59E7	41	1.164	0.344
10	1500	38	5.82E7	1.26E8	55	0.49	0.82
15	1600	40	8.18E7	1.77E8	66	0.29	1.38
20	1700	41	1.06E8	3.17E8	77	0.21	1.90
25	1800	42	1.30E8	3.91E8	85	0.16	2.50

Note: ρd=dry density; φ =friction angle; G= shear modulus; K=bulk modulus; C1 and C2 = Finn model constant

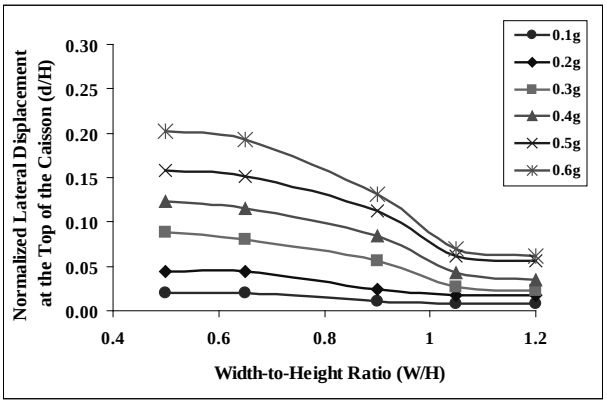


Figure 9 Effects of the width-to-height ratio W/H on normalized lateral displacement (d/H) (for SPT N value of 15) at D1/H=1.0

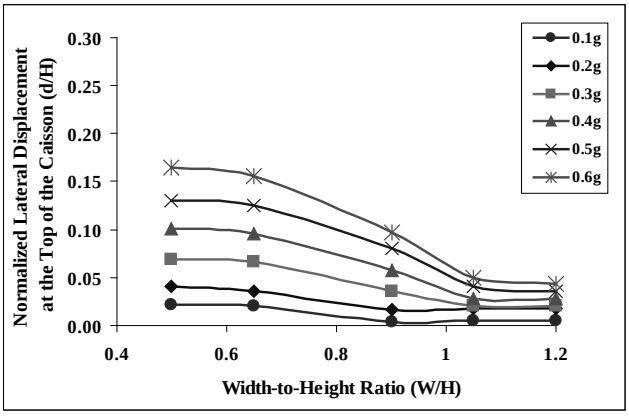


Figure 10 Effects of the width-to-height ratio W/H on normalized lateral displacement (d/H) (for SPT N value of 20) at D1/H=1.0

4.3.4 Thickness of soil deposit below wall (D1/H)

The effects of the thickness of the soil deposit below the wall is shown in Figure 12 for W/H=0.90. There is a linear relation between D1/H and d/H as D1/H reaches 0.5 the rate of change greatly increases particularly for g above 0.4. This comment is the same for different N values up to 25 which clarify that the thickness of a soil deposit below the wall and its SPT N values are two important factors that affect the displacement.

The thickness of the soil deposit below the wall significantly affects the displacement. For a wall built on a thick soil deposit (D1/H> 0.50), the effects of the equivalent SPT N values of the soil below and behind the wall are significant.

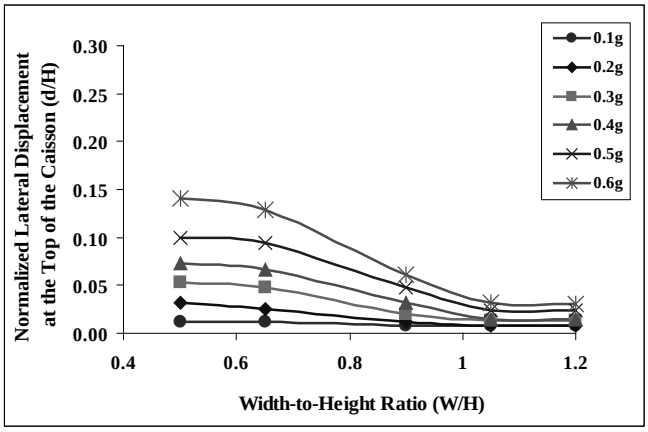


Figure 11 Effects of the width-to-height ratio W/H on normalized lateral displacement (d/H) (for SPT N value of 25) at D1/H=1.0

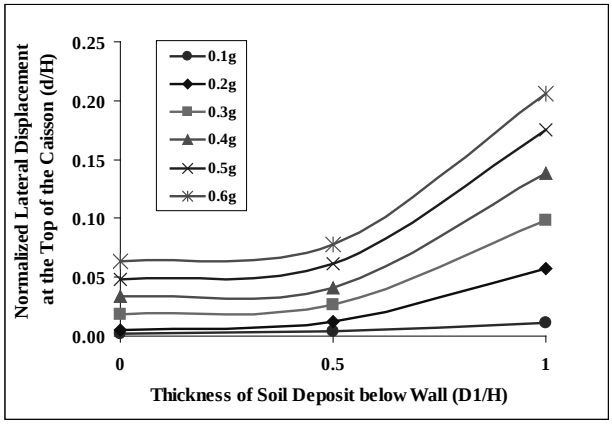


Figure 12 Effects of thickness of soil deposit below the wall (D1) on normalized lateral displacement (d/H) (for SPT N value of 5) at W/H=0.90

4.3.5 Thickness of backfill soil (D2/H)

The effects of the thickness of backfill soil behind the wall is shown in Figure 13 W/H=0.90 and at D1/H=1.0. When the level of excitation is high, significant increase in the displacement is recognized for D2/H> 0.50 and for smaller SPT N values, this clarify that the existence of a soil deposit behind the wall and its SPT N values are two important factors that affect the displacement.

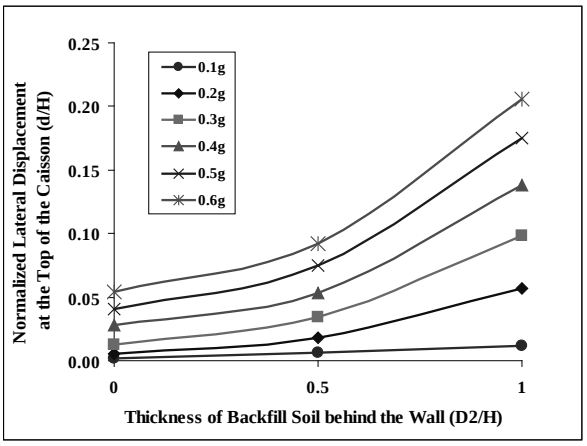


Figure 13 Effects of thickness of backfill (D2) on normalized lateral displacement (d/H) (for SPT N value of 5) at W/H=0.90 and D1/H=1.0

4.4 Procedures for Evaluating Wall Displacement

Based on the results of the parametric study shown in the previous section, a simple procedure is easily developed for evaluating the displacement of gravity quay walls. The flow chart for the simplified procedure is shown in Figure 14. In this procedure, the displacement is evaluated with respect to the parameters in the order of their sensitivity to the displacement.

5. CONCLUSIONS

This investigation had highlighted the following pertinent aspects of the seismic design and performance of gravity quay walls.

1. The proposed nonlinear, effective stress analysis has been proved that it is a more appropriate method to simulate the seismic performance of the caisson as compared to conventional design approaches. It is more efficient especially when excess pore pressure generation and liquefaction have occurred in the backfill.
2. Among the parameters considered in this study, the most sensitive parameter affecting the quay wall displacement under a prescribed level of shaking was the range of SPT-N values of subsoil below and behind the wall. Second was the thickness of backfill soil (D2/H). Thirdly was the thickness of the soil deposit below the wall (D1/H). Fourthly was the width to height ratio (W/H).
3. The factors of safety computed with standard pseudo-static design methods are not adequately correlated with the wall deformations to facilitate estimates of seismically-induced lateral deformations. Therefore, deformation based analyses which account for the generation of excess pore pressures in the backfill are recommended.
4. Simplified design charts have been developed to aid in the performance based seismic design of gravity quay walls.

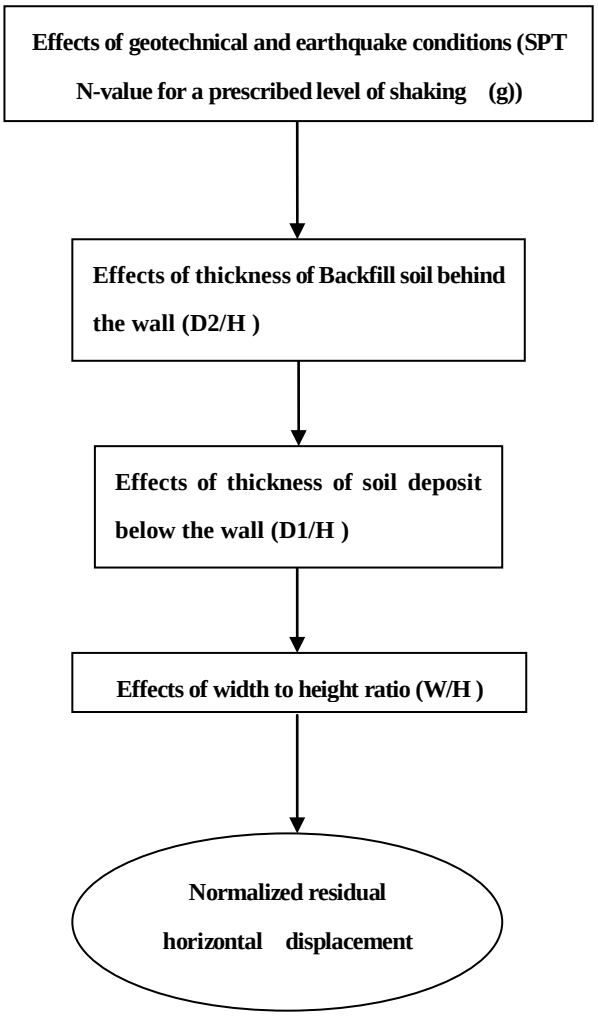


Figure 14 Procedure for evaluate the quay wall displacement

References:

Chen, H. and Hwang, S (2000), "Preliminary Analysis for Quay wall Movement in Taichung Harbour during the September 21, 1999, Chi-Chi Earthquake." Earthquake Engineering and Engineering Seismology, pp. 43-55.

Ebeling, R.M. and Morrison, E.E. (1992), "The Seismic Design of Waterfront Retaining Structures." U.S. Naval Civil Engineering Laboratory, Port Hueneme, CA. Technical Report ITL-92-11. NCEL TR- 939, 329 p.

Hamada, H. (1992), "Large Ground Deformations and Their Effects onLifelines: 1983 Nihonkai-Chubu Earthquake", Technical Report NCEER-92-0001, Case Studies of Liquefaction and

Lifeline Performance during Past Earthquakes, Volume 1.
Iai, S., Matsunaga, Y., Morita, T. , Sakurai , H., Oishi , H., Ogura , H., Ando , Y., Tanaka, Y., and Kato, M.(1994), "Effects of Remedial Measures against Liquefaction at 1993 Kushiro-Oki Earthquake." Proceedings of the Fifth US-Japan Workshop on Earthquake Resistant Design of Lifeline Facilities and Countermeasures Against Site Liquefaction. T.D. O'Rourke and M. Hamada (eds.). National Center for Earthquake Engineering Research. NCEER-94-0026. Statue University of New York, Buffalo, NY. pp 135-152.
Iai, S. (2005),"Remediation of Liquefiable Soils for Port Structures in Japan- Analysis, Design and Performance" Journal of Earthquake Engineering, Volume 9, No. 1, pp. 77–103.
Inagaki, H., Iai, S., Sugano, T., Yamazaki, H. and Inatomi, T. (1996), "Performance of caisson type quay walls at Kobe port." Soils and Foundations, Special Issue on Geotechnical Aspects of the January 17 1995 Hyogoken-Nambu Earthquake, pp119-136.
Itasca Consulting Group. (2005), "User's Manual for FLAC, Version 5.0." Itasca. Minneapolis, Minnesota.
Mohajeri, M., Ichii, K. and Tamura, T., (2004), "Experimental study on sliding block concept for caisson walls" Journal of waterway, port, coastal and ocean engineering, ASCE, Vol. 130, issue 3, pp. 134-142.
Noda, S., Uwabe, T. and Chiba, T. (1975), "Relation between seismic coefficient and ground acceleration for gravity quay wall", Report of the port and harbor research institute, Vol. 14, No. 4 (in Japanese)
PIANC, International Navigation Association (2001), "Seismic Design Guidelines for Port Structures." Balkema, 474 p.
PHRI, Port and Harbour Research Institute (1997), "Handbook on Liquefaction Remediation of Reclaimed Land, Balkema." 312 p.
Uwabe, T.(1983), "Estimation of earthquake damage deformation and cost of quay walls based on earthquake damage records" Technical note of the port and harbor research institute, No. 473 (in Japanese)
Werner, S.D. (1998), "Seismic Guidelines for Ports." Technical Council on Lifeline Earthquake Engineering, Monograph No. 12, ASCE.

8CUEE CONFERENCE PROCEEDINGS
8th International Conference on Urban Earthquake Engineering
March 7-8, 2011, Tokyo Institute of Technology, Tokyo, Japan

CENTRIFUGE MODEL TESTS ON DYNAMIC BEHAVIOUR OF QUAY WALL BACKFILLED WITH GRANULAR TREATED SOIL

Yoshiyuki Morikawa[1], Hidenori Takahashi[2], Kimitoshi Hayano[3], and Youtao Okusa[4]

1) Head of Soil Stabilization Group, Port and Airport Research Institute, Japan
2) Chief of Design Division, Yokohama Port and Airport Technology Investigation Office (MLIT), Japan
3) Associate Professor, Faculty of Engineering, Yokohama National University, Japan
4) Student of Graduate School of Engineering, Yokohama National University, Japan
morikawa@pari.go.jp, takahashi-h83ab@pa.ktr.mlit.go.jp, hayano@ynu.ac.jp, b0543040@ynu.ac.jp

Abstract: In order to maintain the depth of waterways and sea basins, huge amounts of soft clayey soil are dredged at many ports every year in Japan. In recent years, it has become more difficult to secure disposal areas for dredged soil due to environmental and economical restrictions. The effective use of the dredged soils is therefore required. Granular treated soil, which is dredged clay mixed with cement and polymer, has been developed as a countermeasure against this background and expected to be practical uses for reclamation, backfill or subsoil materials. In this study, a series of dynamic centrifuge tests on applicability of granular treated soil to quay-wall backfill was conducted. The test results indicated that backfill of granular treated soil can reduce lateral displacement of caisson and that such backfill is resistant to liquefaction because of its high permeability.

1. INTRODUCTION

In order to maintain waterways and sea basins, huge amounts of soft clayey soil are dredged at many ports every year in Japan. The dredged soil is dumped at disposal sites in coastal areas as reclamation material. In recent years, however, it has become more difficult to secure disposal areas for dredged soil and subsoil due to environmental restrictions and economic factors. The effective use of these dredged soils is therefore required.

Dredged clay usually has relatively low strength and requires long period for consolidation. Therefore, dredged soil cannot be used without improvement such as solidification. The granulation technique was proposed as a method of improving dredged soil (Kiyota et al. 2000; Kawai et al. 2002). In this technique, dredged soil is mixed with cement and polymer and converted into high-strength particles. Dredged soil improved by granulation technique (hereinafter referred to as "granular treated soil") is a light weight material comparing with sand or gravel because of trapped air inside its particles. The granular treated soil is therefore expected to be used for load embankment, backfill of quay wall and retaining wall, and subsoil material of artificial tidal flat (Amano et al. 2002; Takahashi et al. 2008). Furthermore, granular treated soil is resistant to liquefaction, because it has high permeability because of its relatively large particle size of 1 to 10 mm. Against this background, the authors initiated a project to promote effective use of granular treated soil.

This paper reports the applicability of the granular treated soil for backfill with caisson-type quay walls. A series of centrifuge model tests was performed to investigate the dynamic vibration characteristics of backfill reclaimed with granular treated soil. In these tests, sand was also used for backfill in order to compare with granular treated soil. The results of these tests indicated that backfill consisting of granular treated soil can reduce earth pressure behind caisson and lateral displacement of caisson due to its low unit weight, and that such backfill is resistant to liquefaction because of its high permeability. Furthermore, the effects of phase lag and wave reduction were observed in backfill of granular treated soil. These results show that an isolation effect in ground reclaimed with granular treated soil can be expected.

2. MODEL GROUND PREPARATION

2.1 Granular Treated Soil

The material of the granular treated soil used was marine clay (called Kawasaki clay) dredged at Kawasaki Port. The materials for treatment of the clay were water-soluble chelating polymer (partially neutralized polyacrylate), which was used to reduce the water content of the clay, and ordinary Portland cement used as a solidification agent. The mix ratios of the polymer and the cement were 0.1% and 5%, respectively, of the dry weight of the clay. The Kawasaki clay was stirred into a homogeneous slurry while its water content was adjusted to be 60%, which

was slightly higher than its liquid limit (w_L = 48.6%). The slurry was then mixed with the polymer for two minutes followed by five minutes of mixing with the cement using a small blade mixing machine. This length of mixing time was needed to ensure a homogeneous condition for the mixture, which was further re-mixed for a minute one hour after the first mixing to prevent re-bonding between its particles. After being mixed thoroughly, the materials were then cured in trays covered with plastic sheeting to maintain a constant water content in a steady-temperature room at 20°C.

Table 1 and Figure 1 show the physical properties and photos of backfill materials, respectively. Soma sand was excavated in the Fukushima Prefecture area of Japan and used for comparison with granular treated soil. Figure 2 shows grain size distribution curves for Kawasaki clay and backfill materials. It can be seen that the D_{50} and D_{10} values of granular treated soil are larger than those of Kawasaki clay and Soma sand. Accordingly, granular treated soil can be expected to have high permeability.

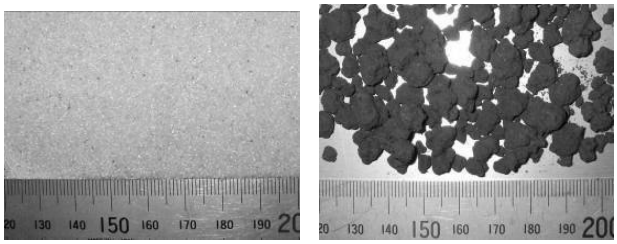
Table 1 Physical Properties of Backfill Materials

(a) Soma Sand (Cat. 5)

ρ_s (g/cm^2)	D_{50} (mm)	U_c	e_{max}	e_{min}
2.66	0.24	1.5	0.979	0.623

(b) Granular Treated Soil

ρ_s (g/cm^2)	Maximum particle size (mm)	D_{50} (mm)	D_{10} (mm)	U_c
2.80	0.24	5.1	2.2	3.0



(a) Soma Sand (b) Granular Treated Soil

Figure 1 Backfill Materials

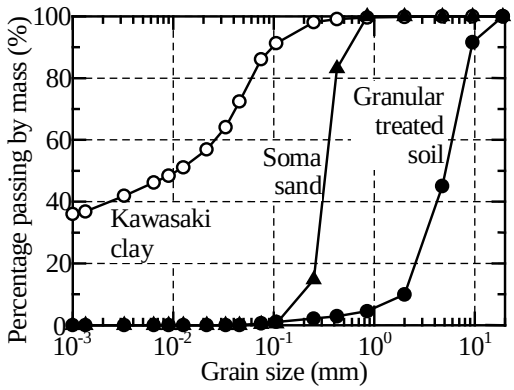


Figure 2 Grain Size Distribution Curves of Kawasaki Clay and Backfill Materials

2.2 Model Test Apparatus and Model Ground Preparation

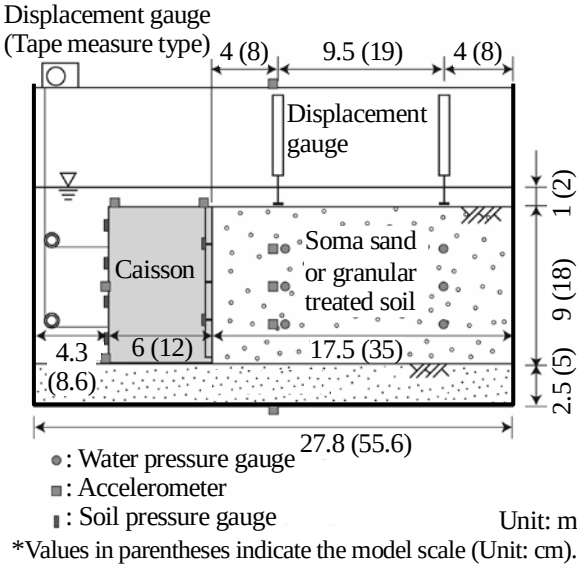
The geotechnical centrifuge used was the PARI centrifuge, which has a radius of 3.8 m, a maximum payload of 2.7 metric tons and a maximum acceleration of 113 G. The details of the centrifuge were described by Kitazume & Miyajima (1995). In this study, shaking table tests were carried out in a centrifugal acceleration field of 50 G.

A schematic representation of the model ground is illustrated in Figure 3, which shows the prototype scale corresponding to the centrifugal acceleration. The specimen container used had rigid sidewalls and a width of 20 cm, a height of 40 cm and a length of 55.6 cm. Membranes coated with grease were placed on inside surfaces of the specimen container to reduce friction between the container and the model ground.

Before preparing the model ground in the specimen container, accelerometers and water pressure gauges were placed precisely at designated depths from the ground surface with the help of fine fishing lines, rubber bands and acrylic plates. After the container had been filled with sand, the fishing lines were cut.

The foundation layer was made of Soma sand poured using a sand hopper, which was placed high enough that the ground density was not influenced by the reduction in the falling height of sand as the specimen container filled up. The relative density of the foundation layer was 90 - 93%.

A caisson model was placed on the foundation layer. This caisson model had a width of 19.5 cm, a height of 18 cm, a length of 12 cm and a unit weight of 18.8 kN/m^3. The centre of mass of the caisson model coincided with its centroid. The caisson model also had four pressure plates on backfill side as shown in Figure 4. The vertical and horizontal force behind the caisson model can be measured by load cells attached inside the pressure plates (Vertical force was not measured because the membrane was also put on the backfill side of the caisson model.)



*Values in parentheses indicate the model scale (Unit: cm).

Figure 3 Schematic View of Model Ground

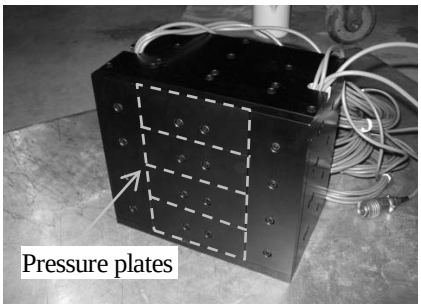


Figure 4 Pressure Plates of the Caisson Model

Table 2 Test Cases

	Backfill material	Initial relative density (%)	Void ratio *e*
Case 1	Granular treated soil	-	3.08
Case 2	Soma sand (Cat. 5)	95	0.73
Case 3		53	0.90

The conditions of the backfill are shown in Table 2. In Case 1, backfill was reclaimed with loose granular treated soil, which was poured from a height of 0 cm. The height of the backfill of granular treated soil was made so that its surface corresponded to the height of the caisson after self-weight consolidation and compaction as outlined below. In Cases 2 and 3, Soma sand was used as a backfill material. It was poured in the same manner as the foundation layer, and the relative density was controlled.

Then, the ground was saturated by difference of water head levels in a centrifugal acceleration field of 20 G. It was confirmed that saturated ground can be obtained by this method (Takahashi et al. 2006). A viscous fluid, which is an aqueous solution of cellulose ethers (Brand name: METOLOSE), was used for saturation. The kinematic viscosity of the solution was controlled to 50 cSt in consideration of similitude of the phenomena of the dynamic deformation of ground and the dissipation of excess pore water pressure in a centrifugal acceleration field of 50 G.

The model ground prepared was set up in the centrifuge facility and subjected to a centrifugal acceleration field of 50 G. After the target acceleration was reached, self-weight consolidation was conducted before the shaking table test to stabilize the backfill against stress induced by such acceleration.

After self-consolidation, several vibrations of 20 sinusoidal waves with a frequency of 100 Hz (corresponding to 2 Hz on the prototype scale) were applied. The amplitude of the input waves was increased in a stepwise manner. During each step, the displacement of the caisson and settlement of the backfill were measured using displacement gauges, and the response acceleration and pore water pressure were measured using embedded accelerometers and water pressure gauges, respectively. Furthermore, the horizontal force behind the caisson was also measured by load cells attached inside the pressure plates.

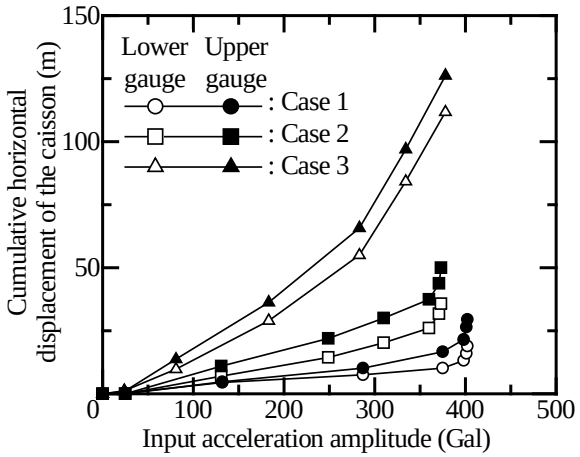


Figure 5 Relationship between Cumulative Horizontal Displacement of the Caisson Top and Input Acceleration Amplitude

3. RESULTS OF MODEL TESTS

3.1 Cumulative Displacement

Figure 5 compares the amounts of displacement on the prototype scale to highlight the relationships between the cumulative horizontal displacement of the caisson and the input acceleration amplitude. The cumulative displacement was evaluated from the position of the caisson before the first step of the shaking table test, although small displacement was observed until the target acceleration was reached.

In all cases, cumulative displacement increased with higher inputs of acceleration amplitude. Displacement in Case 3 was considerably larger than that in the other cases. It can be thought that the large displacement seen in this case was caused by liquefaction in the backfill of loose Soma sand and high earth pressure, as discussed later. The displacement in Case 1 was reduced to half that seen in Case 2 when the input acceleration was large. It can be considered that the earth pressure from the backfill of granular treated soil during vibration was lower than that from dense sand because of its low unit weight and small response acceleration, as outlined in the next section.

The relationships between cumulative settlement of the backfill behind the caisson and input acceleration amplitude are shown in Figure 6 on the prototype scale. Settlement was obtained at 4 m and 13.5 m (8 cm and 27 cm on the model scale) behind the caisson. The settlement of the backfill shown in Figure 6 contains deformation component caused by displacement of the caisson as well as densification component. In all cases, settlement of the backfill increased with higher values of input acceleration amplitude. In particular, the settlement in Case 3 was larger than that seen in the other cases; this was considered to be a result of liquefaction of backfill. The settlement seen in Case 1 was greater than that in Case 2. Furthermore, in Case 1, the difference between settlement at 4m and 13.5 m behind the caisson was smaller than that in Case 2. These facts indicate

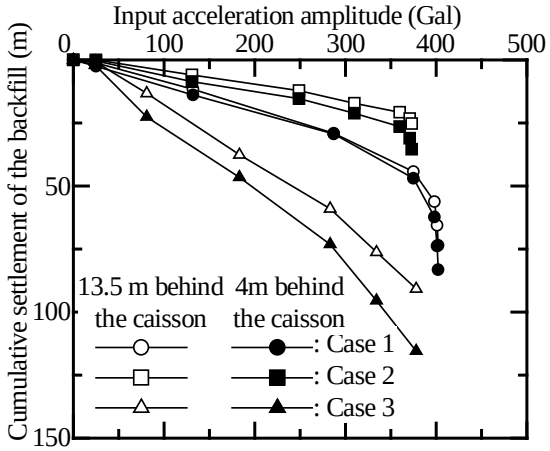


Figure 6 Relationship between Cumulative Settlement of the Backfill and Input Acceleration Amplitude

the high compressibility of granular treated soil, because the displacement of the caisson in Case 1 was smaller than that in Case 2. The high compressibility of granular treated soil is a pending issue to be resolved.

3.2 Response Acceleration

Time histories of response acceleration during the shaking table tests are shown in Figures 7 and 8 on the prototype scale, except for Case 3, in which the response acceleration was unreliable due to liquefaction of the backfill. A limited span (2 sec. on the prototype scale) of the time histories is plotted to facilitate understanding of phase lag and the amplitude of response acceleration.

In Figure 7 (a), a phase lag and amplification were observed in the response acceleration of the backfill and the caisson. It can be thought that the phase lag was caused by low stiffness of the backfill, because the submerged unit weight of the granular treated soil was low (γ' = 4.4 kN/m^3) in comparison with that of dense Soma sand (γ' = 9.2 kN/m^3). When the input acceleration amplitude was large, the response acceleration of the upper part of the backfill and the caisson fell out of step with the input acceleration (Figure 7 (b)). The phase lag increased and acceleration amplitude was reduced, which indicates that stiffness of the backfill of granular treated soil was significantly degraded during vibration because of large strain.

In Figure 8 (a), the response acceleration of the backfill was amplified, but no phase lag was observed. When the input acceleration amplitude was large, the response acceleration of the upper part of the backfill and the caisson included a phase lag. However, the acceleration was amplified in contrast to Case 1 (Figure 7 (b)).

The reduction of acceleration amplitude in the backfill of granular treated soil can be regarded as a kind of isolation effect. The backfill of granular treated soil can be expected to reduce acceleration at the surface.

3.3 Excess Pore Water Pressure

Figure 9 shows time histories of the excess pore water pressure ratio during the shaking table tests. The excess pore

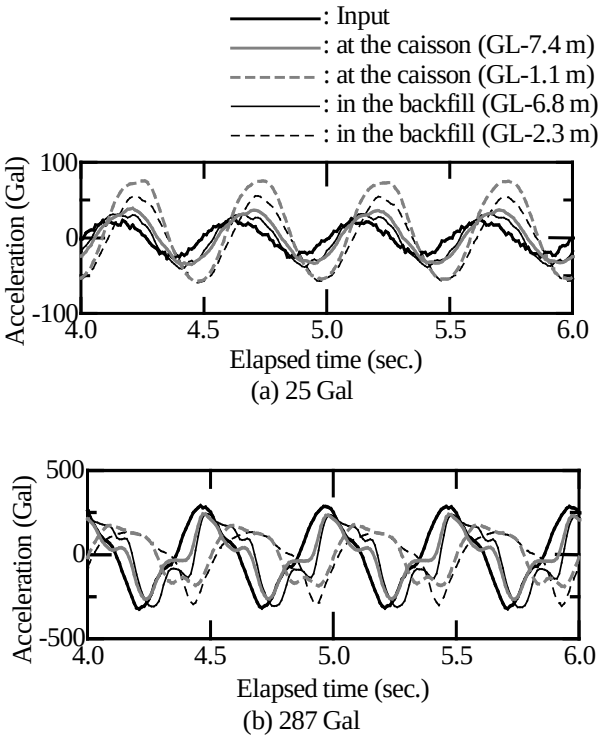


Figure 7 Time Histories of Response Acceleration (Case1)

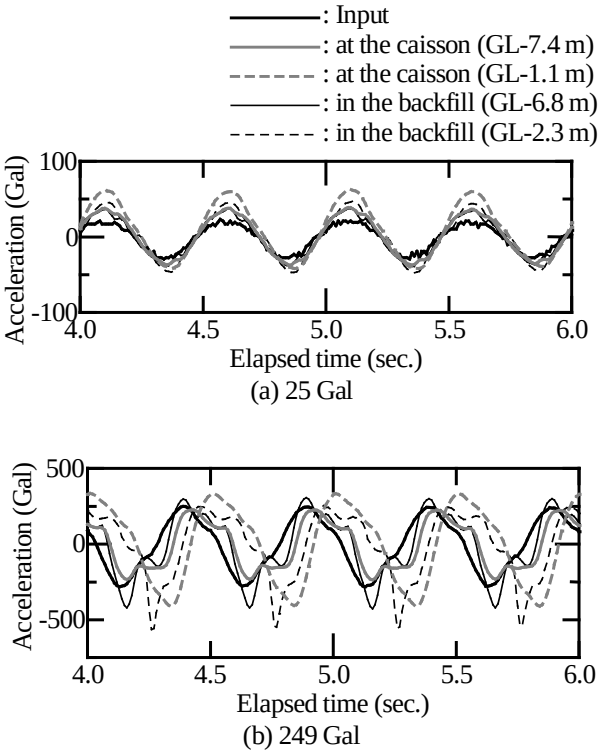


Figure 8 Time Histories of Response Acceleration (Case2)

water pressure shown in the figure was measured at GL-2.3 m and 4 m behind the caisson. The ratio is the excess pore water pressure normalized by the effective overburden pressure. These time histories show simple moving averages of data within the wave length because the ratio shows sharp

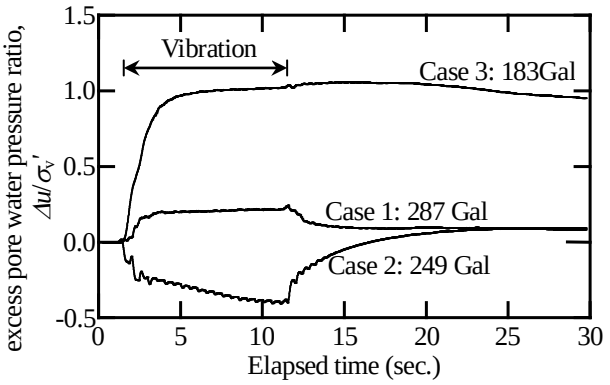


Figure 9 Time Histories of Pore Water Pressure Ratio

fluctuations.

In Case 2, the excess pore water pressure ratio shows a negative value. This can be considered as suction induced by outward displacement of the caisson and dilatancy of dense sand. On the other hand, in Case 3, the backfill of loose Soma sand was found to be liquefied, as the excess pore water pressure ratios reached about 1.0. In Case 1, liquefaction was not observed and the excess pore water pressure ratio increased slightly to 0.24. Furthermore, no suction was observed. This behaviour of the excess pore water pressure in Cases 1 resulted from the high permeability of the granular treated soil, which can be considered highly applicable for quay-wall backfill as a countermeasure against liquefaction.

3.4 Earth pressure behind the caisson

Figure 10 shows distributions of the earth pressure behind the caisson before the first and third vibration. Fluctuation range of the earth pressure during the third vibration is also shown in the figure. The dynamic water pressure is contained in the fluctuation range, but the hydrostatic pressure is not included. The earth pressure before vibration and its maximum value during vibration in Case 1 are smaller than that in Case 2. It can be noted that the backfill reclaimed by granular treated soil instead of dense sand can reduce the earth pressure behind the caisson, because it depends on the response acceleration of the backfill as well as unit weight. The maximum value of the earth pressure during vibration in Case 3 was larger than that in other cases, which was caused by liquefaction.

Figure 11 shows relationships among the total earth pressure, inertia force and dynamic water pressure, which induces the outward displacement of the caisson. (Inertia force, of which positive direction is outward, was evaluated from the acceleration measured at the middle height of the caisson.) The resultant force of these three components to slide the caisson is also shown in the figure as broken line. Resultant forces to slide the caisson of Cases 1, 2, and 3 were 380, 460, and 560 kN/m^2, respectively. It can be thought that the horizontal displacement of the caisson shown in Figure 5 depends on the resultant force. The total earth pressure and inertia force shows positive correlation in Case 3. This correlation is in accord with the results of

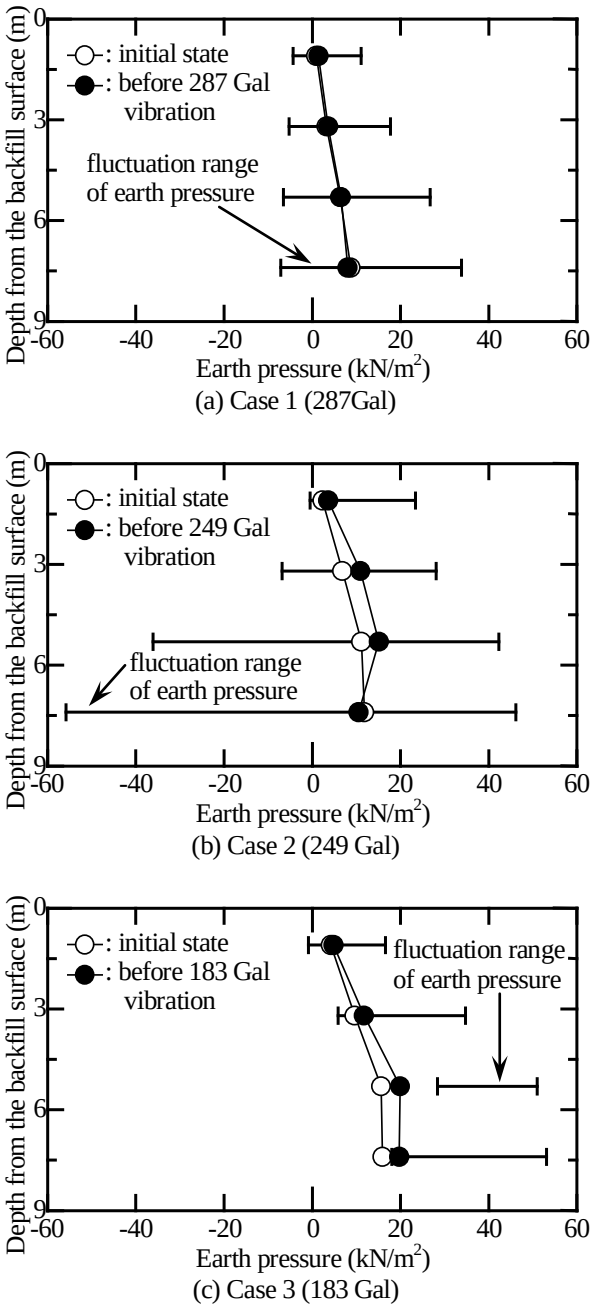


Figure 10 Distribution of Earth Pressure

Kohama et al. (1998), which is the earth pressure and inertia force cooperate together to slide the caisson when liquefaction occurs. In Case 1, the positive correlation between the total earth pressure and inertia force is also observed. It can be thought that this behaviour was caused by stiffness degradation of the backfill. The resultant force in Case 1 was smaller than that in other cases. Therefore, the horizontal displacement of the caisson in Case 1 was reduced in spite of synchronization of the total earth pressure and inertia force. On the other hand, in Case 2, it is because the maximum values of total earth pressure and inertia force were not simultaneous that the horizontal displacement of the caisson was small despite relatively large resultant force to slide the caisson.

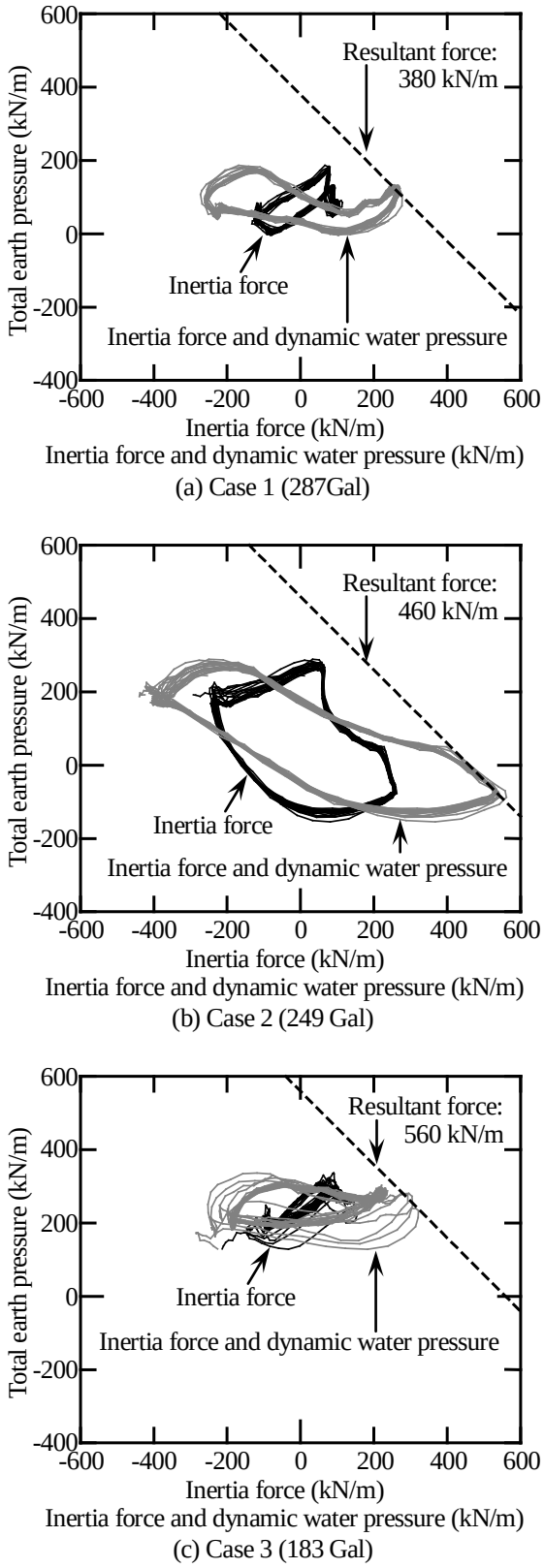


Figure 11 Relationship between Inertia Force and Earth Pressure during Vibration

4. CONCLUSIONS

In this study, dynamic centrifuge tests on the applicability of granular treated soil for quay-wall backfill were conducted. As results of the tests, the response acceleration amplitude and the earth pressure behind the caisson was reduced. This leads to reduction of the horizontal displacement of the caisson. Furthermore, Liquefaction was not observed in the backfill of the granular treated soil, which resulted from its high permeability. The granular treated soil can be considered to have high applicability to the quay-wall backfill in terms of a countermeasure against liquefaction.

Acknowledgements:

The authors wish to express their sincere gratitude to Dr. S. Nishimura (Hokkaido University) who developed the model of the caisson used here. They also thank Mr. K. Takehana (Geo-design Co. Ltd) for providing technical support in conducting a major part of the model test.

References:

Amano, K., Nishikawa J., Sato, A. and Koyanagawa, T. (2002). "Applicability of granulated coal ash for materials," *Proceedings of the 37th Japan national conference on geotechnical engineering*, 701-702 (in Japanese).

Kawai, S. Shiota, K. and Eguchi, S. (2002). "Development of grain solidification technology of the dredged soil using coal ashes," *Proceedings of the 57th Japan society of civil engineers annual meeting* (CD-ROM) (in Japanese).

Kitazume, M. and Miyajima, S. (1995). "Development of PHRI Mark II geotechnical centrifuge," *Technical Note of Port and Harbour Research Institute*, (817), 1-33.

Kiyota, M., Tutumi, T., Kurosaka, H., Murakami, Y., Morisaki, S. and Nakamura, N. (2000). "Study on technique to recycle excavated soil," *Proceedings of the 35th Japan national conference on geotechnical engineering*, 1083-1084 (in Japanese).

Kohama, E., Miura, K., Yoshida, N., Ohtsuka, N., and Kurita, S. (1998). "Instability of Gravity Type Quay Wall Induced by Liquefaction of Backfill During Earthquake," *Soils and Foundations*, **38** (4), 71-83.

Takahashi, H., Kitazume, M., Ishibashi, S. and Yamawaki, S. (2006). "Evaluating the saturation of model ground by P-wave velocity and modeling of models for a liquefaction study," *International Journal of Physical Modelling in Geotechnics*, **6**(1), 13-25.

Takahashi, H., Ichikawa, E., Kitazume, M., Nishimura, D. and Hasegawa M. (2008). "Centrifuge shaking table tests on sheet pile quay wall back-fill with granulated soil," *Proceedings of the 8th national symposium on ground improvement*, 255-260 (in Japanese).

Takahashi, H., Ichikawa, E., Ohkusa, Y., Hayano, K. and Morikawa, Y. (2009). "Compressive characteristics of lean-mixed granular cement treated soil," *Proceedings of the 8th symposium on Environmental geotechnical engineering*, 147-150 (in Japanese).

8CUEE CONFERENCE PROCEEDINGS
8th International Conference on Urban Earthquake Engineering
March 7-8, 2011, Tokyo Institute of Technology, Tokyo, Japan

CENTRIFUGE MODEL TEST OF FAULT RUPTURE PROPAGATION IN ALLUVIAL DEPOSIT

Jiro Takemura[1], Yukie Ishii[2], Yusuke Hara[2] and Osamu Kusakabe[3]

1) Associate Professor, Department of Civil Engineering, Tokyo Institute of Technology, Japan
2) Graduate Student, Department of Civil Engineering, Tokyo Institute of Technology, Japan
3) Professor, Department of Civil Engineering, Tokyo Institute of Technology, Japan
jtakemur@cv.titech.ac.jp, ishii.y.aa@m.titech.ac.jp, hara.y.af@m.titech.ac.jp, kusakabe@cv.titech.ac.jp

Abstract: A fault simulator was newly designed and manufactured for centrifuge study on the structure in or on the soils over dip-slip fault. The design specifications are (1) the simulator can function under 50 G with the surcharge pressure of 500kPa, (2) maximum offset of 30 mm with the dip angle of 60^o can be achieved at the bottom of model soil, (3) both normal and reverse faulting can be generated and adequate force is available for generating reverse faulting, (4) the front face is transparent to observe the model ground during centrifuge tests. This paper describes the newly developed fault simulator and its functions and performance. Some results obtained from an initial test series are also presented. In the initial tests, the effects of overburden stress, type of faults, namely, reverse and normal faulting, and contact conditions between the base rock and the soil, on the rupture propagation and associated ground deformation were studied.

1. INTRODUCTION

The behaviour of alluvial deposits subjected to fault displacement of the base rock is one of the major concerns for almost all structures within fault zone. An understanding the fault rupture propagation through soils would assist engineers in siting and designing the critical structures, such as, building, bridges, tunnels and buried pipes, in the regions where soils overlie active or potentially active fault.

Well and Coppersmith (1994) complied 421 historical earthquakes and selected 244 earthquakes with reliable source parameters. They produced empirical relationships among magnitude, rupture length, rupture width, rupture area, and surface displacement. From indicative fault rupture field studies, Bray et al. (1994) suggested that the characteristics of subsoil overlying the bedrock fault strongly influence the observed fault rupture propagation in the soil.

To compensate the shortcoming of the field study, that is, the lack of well documented field data on the behaviour of subsoil due to the bedrock fault, and to study the mechanisms involved in the fault rupture propagation, both 1G and centrifuge model tests have been performed for several decades. Roth et al. (1981) conducted centrifuge model tests to observe the pattern of shear ruptures in a 6-m alluvial deposit caused by a bedrock fault movement. Cole and Lade (1984), and Lade et al. (1984) performed an extensive 1G experimental study on the shapes and locations of failure surfaces propagating through dense and loose sand caused by a fault movement. They observed that larger vertical displacements are required to form a complete failure surface throughout the sand layer under reverse fault conditions, compared to those under normal fault conditions. El Nahas et al. (2006) developed a centrifuge model setup which can simulate normal and reverse faults, using a triangle shape base block supported by two hydraulic cylinders. Using the centrifuge test results obtained from this simulator and finite element analyses, Anastasopoulos et al. (2007) discussed fault rupture propagation through sand. Ha et al. (2006) developed a two-section split-container for centrifuge modeling of ground deformation by faulting. They reported the results of centrifuge model tests using this container on the effect of permanent ground deformation caused by strike-slip faults on buried pipes.

Numbers of physical model tests have contributed for understanding the mechanisms of fault rupture propagation, behavior of geotechnical structures subjected to the ground deformation by the fault, and the effects of various factors on them. However, there are still remaining factors which have not been well investigated by physical model, for example, the effect of depth of the alluvium overlying the bedrock fault, especially on behavior of the soils at the large depth under a large overburden pressure and the conditions of interface between the base rock and overlying alluvium.

This paper describes a newly developed dip-fault simulator in a centrifuge, by which a large overburden pressure can be applied to the model soil. Some results obtained from an initial test series are also presented. In the initial tests, studied were the effects of overburden stress and type of faults, namely, reverse and normal faulting, and contact conditions between the base rock and the soil, on the rupture propagation and associated ground deformation.

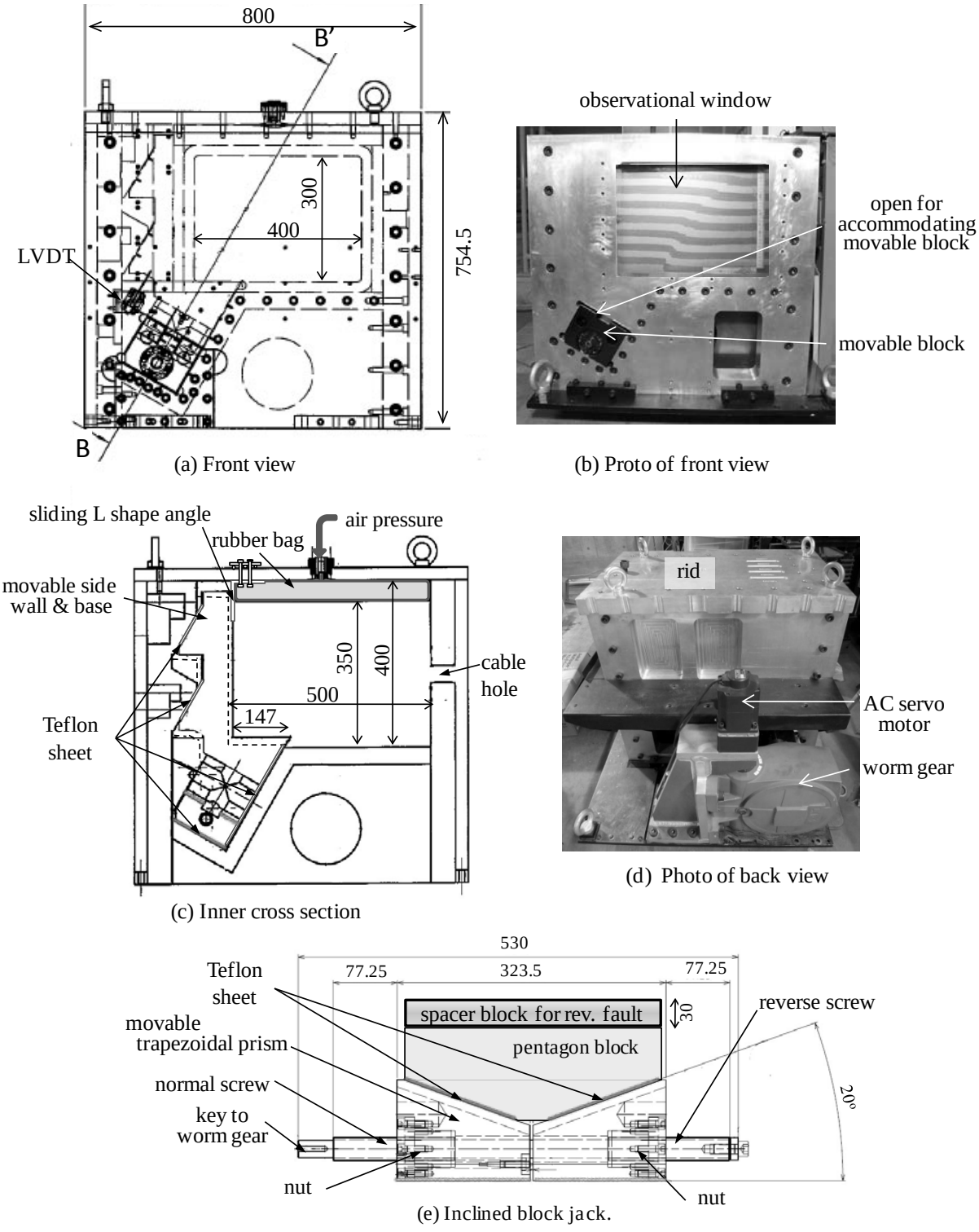


Figure 1 Details of fault simulator

2. FAULT SIMULATOR AND CENTRIFUGE MODEL TEST

2.1 Fault Simulator

A fault simulator was newly designed and manufactured for Mark III Centrifuge at the Tokyo Institute of Technology (Takemura et al., 1999) for centrifuge study of underground structures in soils over dip-slip faults. Specific conditions considered in the design of simulator and soil container are (1) the simulator can function under 50 G with the surcharge pressure of 500kPa, (2) maximum offset of 30 mm with the dip angle of 60^o can be imposed, (3) both normal and reverse faulting can be generated and adequate force is available for generating reverse faulting under the maximum surcharge pressure, (4) the front face is

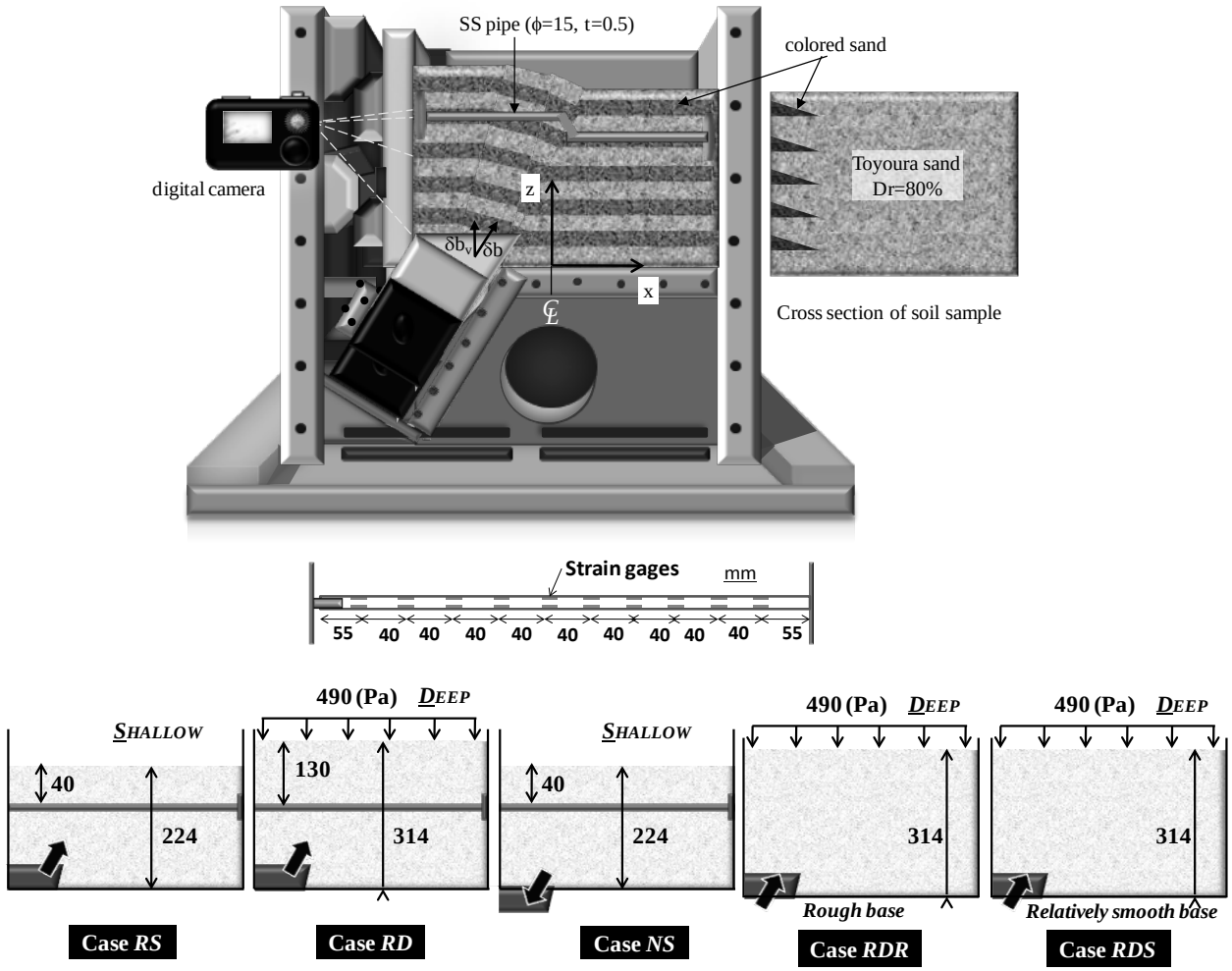


Figure 2 Test setup , and test cases with buried pipe

Table 1 Specification of fault simulator

overall dimensions	L800 x W 600 x H755 mm
Inside container dimensions	L500 x W300 x H350 mm
Weight of simulator	627 kg without soil sample
Max. Offset	30mm for normal and reverse
Actuating system	AC Motor (AC100 4.7A) => 1/50 reduction gear Torque 28N.m =>1/50 worm gear => inclined block (20^o) driven by screw (20^o, P5mm) jack
Max thrust force of jack	230kN
Thrust rate of jack	0 - 2.18mm/min
Dip angle	60 degree
Max surcharge pressure	500kPa

transparent to observe the model ground during centrifuge tests, (5) inner dimensions of the container should be large as much as possible, but the whole test system can be housed in a space available in the swing platform.

Specification of the fault simulator is given in Table 1. Details of fault simulator are shown in Figure 1. The simulator accommodates a container for model ground, which has internal dimensions of 500mm long, 400mm wide

Table 2 Specification of Toyoura sand used in the test

Specific gravity :Gs	2.65
Average grain size: D_{50}	0.16 mm
Max. void ratio	0.997
Min. void ratio	0.609
Relative density	80%

and 300mm deep, made of aluminum alloy. Left side wall and base is movable, which is made from an ingot of the alloy to have an accuracy of the shape. Displacement of the movable wall and base is restricted in the direction of the horizontal angle of 60^o by the inclined guide and the brackets (Figure 1(c)). Fault actuating system consisting of an AC servo-motor with 1/50 reduction gear, a 1/50 reduction worm gear, and a screw jack can create the maximum thrust force of 230kN in a relatively small space beneath the container. The screw jack consists of a rod with normal and reverse screws at the rear and front parts respectively, two trapezoidal prisms, and a pentagon steel block as shown in Figure 1 (e). The trapezoidal blocks are

connected to the rear and front screws of the rod through nuts. With this combination the two trapezoidal prisms move back and forth in the opposite direction, which actuates the pentagon block and the movable side wall & base upward and downward with a dip angle of 60°, simulating reverse and normal faulting, respectively.

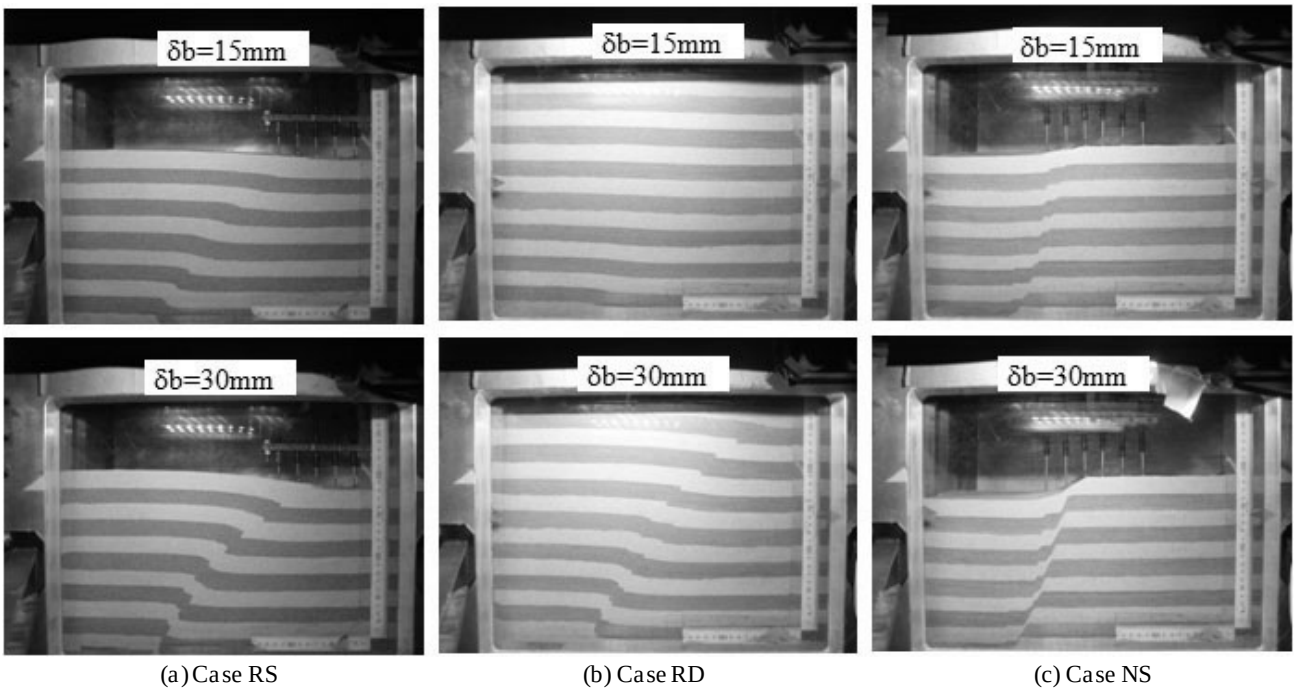
A cubic shape rubber bag can be placed on the top of the model ground to apply the maximum surcharge pressure of 500 kPa. To support the pressure of the rubber bag, a rid made of aluminum is fixed to the top of simulator (Figure 1(c)). The front plate of the model container has a rectangular glass window of 400mm wide, 300mm high and 40mm thick, through which the propagation of fault rupture and ground deformation can be viewed (Figure 1(b)).

2.2 Model Preparation and Test Procedures

Using the fault simulator, an initial test series was performed on sand with a buried steel pipe. Figure 2 shows a setup for the test without surcharge and the test cases. Three test cases with pipe are presented in this paper as shown in Figure 2, namely Case RS (reverse faulting and shallow pipe), Case RD (reverse faulting and deep pipe) and Case NS (normal faulting and shallow pipe). In 50G centrifugal acceleration adopted in the tests, the thickness of model ground and pipe cover depth for RS and NS are 11.2m and 2m respectively. Although the model thickness of RD is 15.7m, the overburden stress is equivalent to those of about 40m for the dry sand used in the test. In addition to the three tests, two reverse faulting tests, Cases RDS and RDR were conducted for the sand model with the same dimensions and surcharge as Case RD, but without pipe. Different roughness was made at the container base, namely, frictional condition for Case RDR, which was created by an abrasive paper and less frictional condition with aluminum surface for Case RDS.

Typical test procedures are as follows: (i) fix a model buried pipe to the right side wall; (ii) pour dry Toyoura sand (Table 2) into the container by air pluviation method with a target relative density of 80% to the predetermined height. Every 20mm thickness, colored Toyoura sand is poured adjacent to the front window to create alternate layers with 20 mm thick each for clear identification of the failure surface in the front view (Figure 2); (iii) for Cases RD, RDS and RDR, place the rubber bag on the surface of the model sand layer; (iv) After bolted the top rid onto the container, feed the air pressure to the rubber bag; (v) mount the completed model on the swing platform ready for centrifugal acceleration; (vi) having reached 50G acceleration, activate the fault simulator by the speed of 2.18mm/min to the maximum offset of δb =30mm; (vii) during the faulting period, capture the front view by a digital camera located in front of the front face.

The digital image taken by the camera is used for Particle Image Velocimetry (PIV) processing (White et al., 2003). The model pipe (Figure 2) used in the test is made of stainless steel with outer diameter of 15mm and thickness of 0.5mm, which is equivalent to 750mm diameter and 25mm thick pipe in a prototype. Ten pairs of strain gages are attached to the inner top and bottom surfaces of the pipe with 40mm interval to measure the bending strain of the pipe. The model pipe has a circular flange at the right end, with which the pipe is rigidly fixed to the side wall. On the other a solid circular bar with a flange is inserted to the left end of the pipe. This left flange was attached to the left wall to create a slider. With this slider no extra axial force is induced to the pipe due to the faulting.



(a) Case RS (b) Case RD (c) Case NS

Figure 3 In flight photos of deformation and rupture propagation in sand due to dip slip faulting

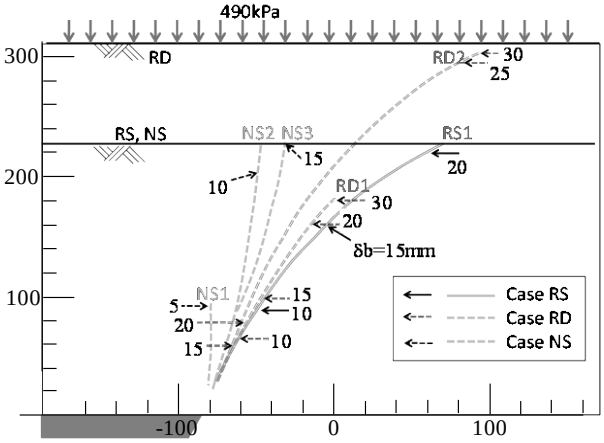


Figure4 Observed rupture surface at δb=30mm and location of rupture end at various δb. The arrow points the location of rupture end at δb shown.

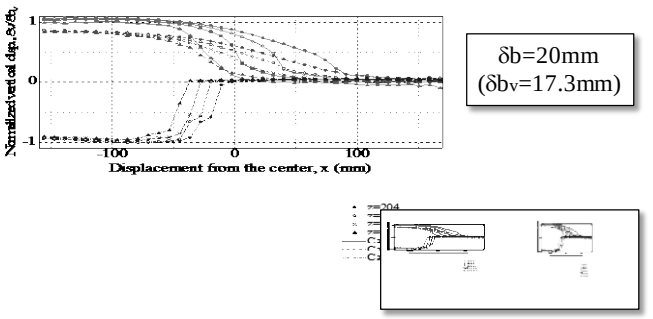


Figure 5 Profiles of vertical displacement normalized by vertical component of dip slip fault.

3. TEST RESULTS AND DISCUSSIONS

3.1 Fault Rupture Propagation in Sand

During the faulting period, digital image of the front view of the model ground was captured every 1mm displacement of the movable wall and base (δb), which corresponds to the base rock movement along the dip. The in-flight photos of Cases RS, RD and NS at δb=15mm and 30mm are shown in Figure 3. Shape of the rupture surface could be approximated by log-spiral as suggested by Cole and Lade (1984). However, the number and propagation rate of the rupture surface depend on the type of fault and vertical stress of the ground.

From the captured image, propagations of rupture surfaces were traced as shown in Figure 4. In the figure the rupture surfaces observed at the end of the faulting (δb=30mm) are compared for three test cases. The locations of the rupture end at every 5mm of δb are also indicated for each rupture surface. From the figure the followings are confirmed.

1) Rupture propagation rate to the base movement (δb) was greater in the order of Cases NS, RS and RD. 2) The rupture surfaces caused by reverse faulting at the same distance from the container base sloped lower for the shallow case (NS) than the deeper case (RD). 3) Only one rupture surface reached to the ground surface for the reverse faulting, while for the normal faulting two surfaces reached to the ground surface. 4) For the normal faulting, a vertical rupture (NS1) initiated at small base movement but its propagation terminated at δb=5mm. Second one (NS2) appeared and reached to the surface in a small increment of δb from 5 to 10mm at the foot wall side, which was followed by the third one (NS3) at the further foot wall side.

The possible reasons for 1) and 2) is the difference of stress-strain relation which is affected by the stress condition and the confining stress. For the normal faulting, the soil is horizontally expanded, while for the reverse faulting the soil is compressed. Although the stress increment on the failure surface depended on the degree of dilation and the dip angle, the stress of the soil for the normal fault is relatively small and close to active condition compared to those for the reverse fault which have a large stress increase in passive condition. As a result, soils for the normal fault have smaller failure stain than those for the reverse fault, requiring small relative movement for creating shear band for the former than the latter. Difference of dilation of soil between high and low confining stress could explain the difference between Case RS and Case RD. In the previous studies (El Nahas, et al.,2006; Lee and Hamada, 2005), similar results to 3)and 4) were reported. Some previous 1 g model experiments (Cole and Lade,1984; Lee and Hamada, 2005) showed the secondary rupture surface for the normal fault in the hanging wall side for the relatively low dip angles. In Case NS with relatively steep dip angel of 60°, the secondary rupture and the resultant graben were not observed.

3.2 Vertical Deformation of the Ground due to Faulting

The propagation of fault rupture causes deformation in the alluvium over the bedrock. For the case of dip-slip fault with a relatively steep dip angle, like the condition of the test (60°), the vertical differential movement is one of the most critical concerns for the structures constructed in or on the ground. The displacement of the ground induced by the model fault offset was measured from the photos taken by the digital camera using PIV technique with Geo PIV (White and Take, 2003). It should be noted that patch size adopted in the PIV analysis was 64 pixels, equivalent to about 9mm, to have a reliable measurement. However, due to this relatively large patch size, discontinuous deformation might be underestimated. Vertical displacement, δv, profiles at various vertical distances from the base measured at δb=20mm are compared in Figure 5. The displacement is normalized by the vertical component of fault movement, δb_v. The horizontal variation of vertical displacement was more continuous for the reverse faults than the normal fault, and also for Case RD than Case RS. The maximum vertical displacements are almost the same as δb_v for Case RS and Case NS, while for Case RD the vertical displacements were smaller than δb_v. Clear discontinuities can be seen in the profile at the hanging wall side for all depths for the normal fault. In the reverse fault cases, discontinuities were also observed at the hanging wall side

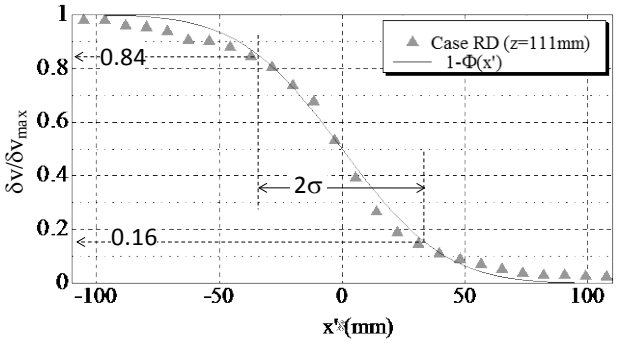


Figure 6 Approximation of vertical displacement profile by cumulative distribution function Φ.

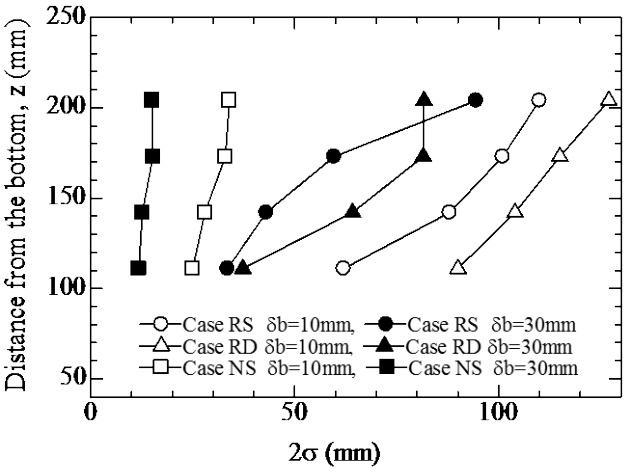
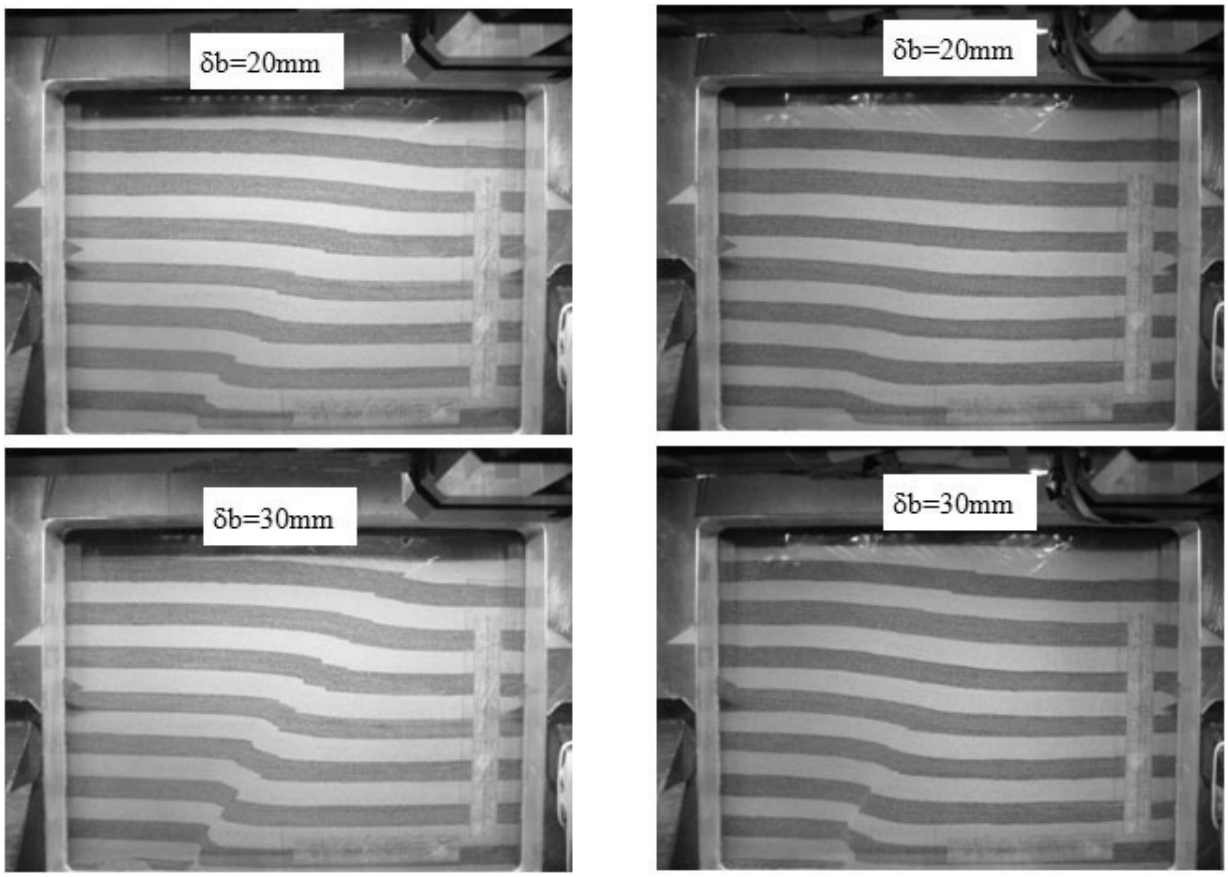


Figure 7 Variation of differential settlement width in terms of 2σ



(a) Case RDR (b) Case RDS

Figure 8 In flight photos of deformation and rupture propagation in sand by to reverse faulting with different base rock-sand interface.

especially for the shallower depth.

Figure 6 shows a typical vertical displacement profile for the case of continuous variation. In the ordinate the δv, is normalized by the maximum value, δv_{max}, and in the abscissa the horizontal coordinate, x', at $\delta v / \delta v_{max}=0.5$ is taken as zero. As can be seen in the figure, the normalized profile can be approximated by cumulative distribution function *Φ*. 2σ (where σ is standard deviation), which is obtained by the method shown in the figure, can be considered as one of the indices representing the width of steep differential vertical displacement. The variations of 2σs obtained from the normalized profile with the distance from the bottom of the container are compared for the three tests at δb=10 and 30mm in Figure 7. The width of differential settlement was larger in the order of Cases RD, RS and NS. The width became larger as the distance from

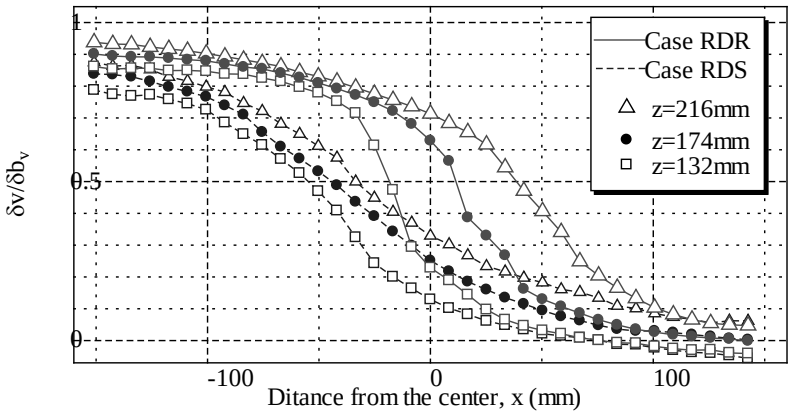


Figure 9 Profiles of normalized vertical displacement in sand by reverse faulting with different base rock-sand interface.

the bottom increased especially for the reverse fault, and it became narrower as the fault offset increased, which is attributed to the concentration of deformation due to the rupture propagation.

3.3 Effect of Interface between Base Rock and Sand.

The movement of bed rock by a dip fault has a horizontal component, which causes shear stresses on the rock surface against horizontal compression and extension for the reverse and normal faulting respectively. In order to the effect of the shear forces mobilized at the interface between the base and sand for the relatively deep depth, the reverse faulting tests were conducted with two different interface conditions, namely high frictional (Case RDR) and less frictional (Case RDS) as explained in 2.2.

The in-flight photos taken at δb=20mm and 30mm are shown in Figure 8. For the case with rough base, clear rupture or discontinuous deformation was propagated from the edge of the fault offset to the upper portion of the sand at δb=20mm. At δb=30mm, new rupture surfaces emerged in hanging wall side above the old one and finally reached to the sand surface. On the other hand for the case with relatively smooth base surface, although vertical movement was extended to the upper portion, no clear rupture surface was observed at δb=20mm. Even at δb=30mm, ground rupture took place at limited depth. It is noted that the rupture surface was not emerged from the edge of the fault offset but at hanging wall side slightly from the edge.

Figure 9 depicts the profiles of the normalized vertical displacement, $\delta v/\delta b_v$, measured for δb=30mm at various vertical distances from the base for the cases with rough base and relatively smooth base conditions. From the figure, the effect of interface condition between the base and sand on the deformation of sand due to the reverse fault can be clearly seen. In the case with the frictional base the differential vertical displacement was more significant than that of the less frictional case and the vertical displacement largely extended to the foot wall side compared to the less frictional case. It could be attributed to larger horizontal compression for the latter case than the former. This horizontal compression at the base of hanging wall can be also a reason for the rupture emerging at the hanging wall side for Case RDS as shown in Figure 8.

4. CONCLUSIONS

A fault simulator was newly developed, which can simulate dip-slip fault in a centrifuge. The simulator has a soil container of inner dimensions of 500mm long, 300mm wide and 350 deep, which functions with full of soil with the surcharge pressure of 500kPa under 50G centrifugal acceleration. Maximum relative displacement of 30 mm with the dip angle of 60^o can be imposed both for normal and reverse faulting. From the initial tests using the fault simulator on the rupture propagation and deformation in dry sand, the following conclusions were drawn.

(1) Shape of the rupture surface could be approximated by log-spiral. Rupture propagation rate to bedrock dip-slip movement is larger for normal faulting than reverse faulting. The rupture surfaces propagation by the reverse fault are affected by the overburden pressure; the deeper the depth is, the smaller the propagation rate and the lower the rupture surface. Only one rupture surface reached to the surface for the reverse fault cases, while for the normal fault case two surfaces reached to the ground surface.

(2) Width of differential settlement was wider for the reverse fault than the normal fault, and for the shallow depth than the deep depth. The width became larger as the distance from the bottom increased especially for the reverse fault, and it became narrower as the fault offset increased, which is attributed to the concentration of deformation due to the rupture propagation.

(3) The frictional condition at the interface between base rock and sand affects rupture propagation and the deformation in sand due to the reverse fault. High frictional condition with large mobilized shear force at the base creates clear rupture surfaces with larger differential vertical displacement in sand compared to less frictional condition with small shear force. This difference could be attributed to larger horizontal compression for the latter case than the former.

Acknowledgements:

The authors gratefully acknowledge the funding for this research from Japan Society for the Promotion of Science (JSPS) as Grant-in-Aid program.

References:

Anastasopoulos, I., Gazetas, G., Bransby, M.F. Davies, M.C.R. and El Nahas, A. (2007). "Fault rupture propagation through sand: Finite-Element analysis and validation through centrifuge experiments", *J. Geotech & Geo-env. Engrg, ASCE*, **133**(8), 943-958.

Bray, J. D., Seed, R. B., Cluff, L. S., and Seed, H. B. (1994). "Earthquake fault rupture propagation through soil" *J. Geotech. Engrg, ASCE.*, **120**(GT3), 543–561.

Cole, D.A. and Lade, P.V. (1984). "Influence zones in alluvium over dip-slip faults", *J. Geotech. Engrg, ASCE*, **110**(5), 599-615.

El Nahas, A., Bransby, M.F. and Davies, M.C.R. (2006). "Interaction between normal fault rupture and rigid strong raft", *Proc. Physical modeling in Geotechnics, Hong Kong*, 337-342.

Ha, D., Abdoun, T., O'rourke, M., Van Laak, P., O'rourke, T., and Stewart, H. (2006). "Split-container for centrifuge modeling of permanent ground deformation effects on buried pile system", *Proc. Physical modeling in Geotechnics, Hong Kong*, 729-734.

Lade, P.V., Cole, D.A. and Cummings, D. (1984). "Multiple failure surfaces over dip-slip faults", *J. Geotech. Engrg, ASCE*, **110**(5), 616-627.

Lee, J.W. and Hamada, M. (2005). "An experimental study on earthquake fault rupture propagating through a sandy soil deposit", *Journal of Structural Engineering/Earthquake Engineering, JSCE*, 22(1), 1s-13s.

Roth, W.H., Scott, R.F. and Austin, I.(1981). "Centrifuge modeling of fault propagation through alluvial soils", *Geophysical Research Letters*, 561-564.

Takemura, J., Kondoh, M., Esaki, T., Kouda, M. and Kusakabe, O. (1999). "Centrifuge model tests on double propped wall excavation in soft clay", Soils and Foundation, **39**(3), 75-87.

Well, D. L, and Coopersmith, K. J. (1994). "New Empirical Relationships among Magnitude, Rupture Length, Rupture Width, Rupture Area, and Surface Displacement", *Bulletin of the Seismological Society of America*, **84**(4), 974-1002.

White, D. J., Take, W. A., and Bolton, M. D. (2003). "Soil deformation measurement using particle image velocimetry (PIV) and photogrammetry", *Geotechnique*, **53**(7), p.619-631.

White, D. J. and Take, W. A. (2003). "GeoPIV, 7.6 ed", *Cambridge University Engineering Department*, 2003.

8CUEE CONFERENCE PROCEEDINGS
8th International Conference on Urban Earthquake Engineering
March 7-8, 2011, Tokyo Institute of Technology, Tokyo, Japan

BASIC STUDY FOR SIMULATION OF BEHAVIOR OF SOIL DUE TO CYCLIC LOADING USING PARTICLE METHOD

Tomohide Takeyama[1)]

1) Assistant Professor, Department of Civil Engineering, Tokyo Institute of Technology, Japan
takeyama.t.aa@m.titech.ac.jp

Abstract: Smoothed particle hydrodynamics (SPH), as a particle method, was originally proposed for modeling astrophysical phenomena, and later widely extended for applications to problems of continuum solid and fluid mechanics. In the SPH method, the problem domain is represented by a set of arbitrarily distributed particles which possess material properties and move according to the governing conservation equations. The field variables are approximation, the formulation of SPH is not affected by the arbitrariness of the particle distribution. Therefore it can naturally handle problems with extremely large deformation. In this research, applying this method, the behavior of soil due to cyclic loading is simulated.

1. INTRODUCTION

The Smoothed Particle Hydrodynamics (SPH) was originally proposed for modeling astrophysical phenomena by Lucy (1977). In the present it is widely used for applications to problems of fluid mechanics. In the SPH method, the problem domain is represented by particles. The field variables are calculated at the position of particles. These particles move according to the governing equations. The SPH method is one of meshless Lagrangian method. Therefore it can naturally handle problems with extremely large deformation such as liquefaction or land slide which is hardly simulated by FEM. Additionally,

In order to apply the SPH method to the geotechnical problems, the simple simulations employed the Modified Cam-Clay model with subloading surface as the constitutive model were carried out in this research.

2. SPH Method

2.1 Formulation of SPH

Smoothed Particle Hydrodynamics (SPH) was developed by Lucy (1977) and Gingold and Monaghan (1983) for the simulation of astrophysical problems. SPH is the method to evaluate the field variables such as density, velocity and so on at the arbitrary time by regarding the continuum as particle aggregate as shown in Figure 1.

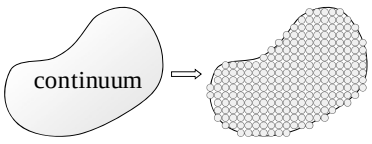


Figure 1 Basic concept of Smoothed Particle Hydrodynamics (SPH)

According to SPH formulation, a function at an arbitrary point $f(\mathbf{x})$ is interpolated in an integral form as

$$f(\mathbf{x}) = \int_{\Omega} f(\mathbf{x}')W(\mathbf{x}-\mathbf{x}',h)dV\,. \tag{1}$$

In the equation (1), Ω is the domain of integral that contains $\mathbf{x}$. The function $W(\mathbf{x}-\mathbf{x}',h)$ is so-called the smoothing kernel function. In the smoothing kernel function, h is the smoothing length defining the influence area of the smoothing kernel function. It should satisfy following conditions. The first one is the normalization condition. The integral of smoothed kernel function become 1.

$$\int_{\Omega} W(\mathbf{x}-\mathbf{x}',h)dV = 1\,. \tag{2}$$

The second one is the Delta function condition. In the limit for $h \to 0$, the smoothing kernel function become the Dirac delta function.

$$\lim_{h\to 0} W(\mathbf{x}-\mathbf{x}',h) = \delta(\mathbf{x}-\mathbf{x}')\,. \tag{2}$$

The third one is the compact condition. The smoothing kernel function becomes 0 outside a certain area.

$$W(\mathbf{x}-\mathbf{x}',h) = 0\,, \text{ when } |\mathbf{x}-\mathbf{x}'| > \kappa h \tag{3}$$

where κ is a constant. According to this condition, the value of function inside the circle (2D) or sphere (3D) with radius of κh is influence in calculating $f(\mathbf{x})$ by the equation (1). In the other words, it is not necessary to

consider the variables outside the domain which is called a support domain. Therefore the cost of computation can makes small.

The integral representation for $f(\mathbf{x})$ can be spatially descretized by particle approximation as

$$f(\mathbf{x}) \approx \sum_{j=1}^{N} \frac{m_j}{\rho_j} f(\mathbf{x}_j) W(\mathbf{x}-\mathbf{x}_j, h). \quad (4)$$

The subscript j iterates over all particles neighboring the particle i. N is the number of particles neighboring the particle i. m_j, ρ_j and $\mathbf{x}_j$ are the mass, the density and the position of particle j respectively. Therefore a field quantity at the position of particle i, $\phi_i = \phi(\mathbf{x}_i)$ can be written as

$$\phi_i = \sum_{j=1}^{N} \frac{m_j}{\rho_j} \phi_j W_{ij} \quad (5)$$

where

$$W_{ij} = W(\mathbf{x}_i - \mathbf{x}_j, h). \quad (6)$$

In order to simulate the motion of particles, the spatial derivative of field quantity is required. The spatial derivative of a function is obtain by substituting $\nabla f(\mathbf{x})$ with $f(\mathbf{x})$ in equation (1), which gives

$$\nabla f(\mathbf{x}) = \int_\Omega \{\nabla f(\mathbf{x}')\} W(\mathbf{x}-\mathbf{x}', h)\, dV. \quad (7)$$

Applying the Gaussian divergence theorem to the equation (7), the following equation is obtained.

$$\nabla f(\mathbf{x}) = \int_S f(\mathbf{x}') W(\mathbf{x}-\mathbf{x}', h)\, \mathbf{n}\, dS - \int_\Omega f(\mathbf{x}') \nabla W(\mathbf{x}-\mathbf{x}', h)\, dV. \quad (8)$$

S is the surface of support domain and $\mathbf{n}$ is the normal vector. The first term of right hand side of equation (8) becomes 0 due to the compact condition. As well as the procedure to descretize $f(\mathbf{x})$, the spatial derivative of a function is approximated as

$$\nabla f(\mathbf{x}) \approx -\sum_{j=1}^{N} \frac{m_j}{\rho_j} f(\mathbf{x}_j) \nabla W(\mathbf{x}-\mathbf{x}_j, h). \quad (9)$$

The spatial derivative of field quantity at the particle i, $\nabla\phi_i = \nabla\phi(\mathbf{x}_i)$ is written as

$$\nabla\phi_i = \sum_{j=1}^{N} \frac{m_j}{\rho_j} \phi_j \nabla_i W_{ij}. \quad (10)$$

2.2 Smoothing kernel function

In SPH method, a cubic spline function is widely adopted as the smoothing kernel function.

$$W(R,h) = \alpha_d \begin{cases} 2/3 - R^2 + R^3/2 & 0 \le R < 1 \\ (2-R)^3/6 & 1 \le R < 2 \\ 0 & R \ge 2 \end{cases} \quad (12)$$

where $R = |\mathbf{x}-\mathbf{x}'|/h$, $\alpha_d = 1/h$, $15/7\pi h^2$ and $3/2\pi h^3$ in one, two and three dimensional space. α_d is defined so that the unity condition is satisfy. The spatial derivative of smoothing kernel function is described as

$$\nabla W(R,h) = \frac{\alpha_d}{h^2} \begin{cases} -2 + 3R/2 \\ -2/R + 2 - R/2 \\ 0 \end{cases} \begin{matrix} 0 \le R < 1 \\ 1 \le R < 2 \\ R \ge 2 \end{matrix} (\mathbf{x}-\mathbf{x}'). \quad (13)$$

The smoothing kernel function $W(R,h)$ and the spatial smoothing kernel function $\nabla W(R,h)$ adopted the cubic spline function are shown in Figure 2.

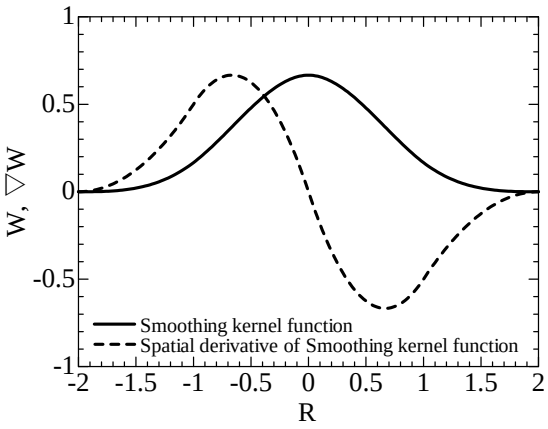


Figure 2 The smoothing kernel function and its spatial derivative

2.3 Governing equations

The governing equations in calculating the behavior of continuum are as follows.

$$\rho\dot{\mathbf{v}} = \nabla\cdot\boldsymbol{\sigma} + \rho\mathbf{g} \quad (14)$$

$$\dot{\rho} = -\rho\nabla\cdot\mathbf{v} \quad (15)$$

$$\dot{\boldsymbol{\sigma}} = \mathbf{C}^{ep} : \dot{\boldsymbol{\varepsilon}} \quad (16)$$

The equations (14), (15) and (16) are the equation of motion, the conservative low of mass and the constitutive equation respectively. ρ, $\mathbf{v}$, $\mathbf{g}$, $\boldsymbol{\sigma}$, $\boldsymbol{\varepsilon}$ and $\mathbf{C}^{ep}$ are density, velocity, acceleration of gravity, stress tensor, strain tensor and elasto-plastic constitutive tensor.

The divergence of $\boldsymbol{\sigma}/\rho$ is described as

$$\nabla \cdot \left(\frac{\boldsymbol{\sigma}}{\rho} \right) = \frac{1}{\rho} \nabla \cdot \boldsymbol{\sigma} - \frac{\boldsymbol{\sigma}}{\rho^2} \cdot \nabla \rho \,. \tag{17}$$

Applying the equation (10) to the left hand side and the second term of right hand side of equation (17), following equations are obtained.

$$\left\langle \nabla \cdot \left(\frac{\boldsymbol{\sigma}}{\rho} \right) \right\rangle_i = \sum_{j=1}^{N} \frac{m_j}{\rho_j} \frac{\boldsymbol{\sigma}_j}{\rho_j} \cdot \nabla_i W_{ij} \tag{18}$$

$$\left\langle \frac{\boldsymbol{\sigma}}{\rho^2} \nabla \cdot \rho \right\rangle_i = \frac{\boldsymbol{\sigma}_i}{\rho_i^2} \cdot \sum_{j=1}^{N} \frac{m_j}{\rho_j} \rho_j \nabla_i W_{ij} \tag{19}$$

By substituting the equations (18) and (19), the divergence of stress dividing by density at the position of particle i can be written as

$$\left\langle \frac{1}{\rho} \nabla \cdot \boldsymbol{\sigma} \right\rangle_i = \sum_{j=1}^{N} m_j \left(\frac{\boldsymbol{\sigma}_i}{\rho_i^2} + \frac{\boldsymbol{\sigma}_j}{\rho_j^2} \right) \cdot \nabla_i W_{ij} \,. \tag{20}$$

The equation of motion (14) can be descretized.

$$\frac{D\mathbf{v}_i}{Dt} = \sum_{j=1}^{N} m_j \left(\frac{\boldsymbol{\sigma}_i}{\rho_i^2} + \frac{\boldsymbol{\sigma}_j}{\rho_j^2} \right) \cdot \nabla_i W_{ij} + \mathbf{g} \tag{21}$$

Therefore, we can calculate the acceleration of particle i from the mass, the density, the coordinates and the stress tensor at each particle which is contained in the support domain of particle i based on the equation (21). As well as the equation of motion, the conservative low of mass (15) can be descretized as

$$\frac{D\rho_i}{Dt} = \sum_{j=1}^{N} m_j \left(\mathbf{v}_i - \mathbf{v}_j \right) \cdot \nabla_i W_{ij} \,. \tag{22}$$

The strain rate is described as follows based on the small strain theorem.

$$\dot{\boldsymbol{\varepsilon}} = -\frac{1}{2} \left(\nabla \otimes \mathbf{v} + \mathbf{v} \otimes \nabla \right) \tag{23}$$

$\nabla \otimes \mathbf{v}$ can be descretized by particle approximation as

$$\left\langle \nabla \otimes \mathbf{v} \right\rangle_i = \sum_{j=1}^{N} \frac{m_j}{\rho_j} \nabla_i W_{ij} \otimes \mathbf{v}_j \,. \tag{24}$$

In order to symmetrize, by subtracting

$$\sum_{j=1}^{N} \frac{m_j}{\rho_j} \nabla_i W_{ij} \otimes \mathbf{v}_i \,, \tag{25}$$

we can obtain

$$\left\langle \nabla \otimes \mathbf{v} \right\rangle_i = \sum_{j=1}^{N} \frac{m_j}{\rho_j} \nabla_i W_{ij} \otimes \left(\mathbf{v}_j - \mathbf{v}_i \right). \tag{26}$$

The benefit of this symmetrization is the reduction of errors arising due to the inconsistency of particles. The strain rate is descretized as

$$\dot{\boldsymbol{\varepsilon}}_i = -\frac{1}{2} \sum_{j=1}^{N} \frac{m_j}{\rho_j} \left\{ \nabla_i W_{ij} \otimes \left(\mathbf{v}_j - \mathbf{v}_i \right) + \left(\mathbf{v}_j - \mathbf{v}_i \right) \otimes \nabla_i W_{ij} \right\} \tag{27}$$

In coding the SPH method, some special treatments is employed for enhancing the stability properties of numerical algorithms. The first one is the artificial viscosity. The formulation of SPH induces the unphysical oscillations in the numerical result. Monaghan and Gingold (1983) applied it to SPH to remove this unphysical oscillations. This Monaghan type artificial viscosity is the most widely used so far in the SPH literatures. The detailed formulation is as follows.

$$\Pi_{ij} = \begin{cases} \dfrac{-\alpha \bar{c} \phi + \beta \phi^2}{\bar{\rho}} & \left(\mathbf{v}_i - \mathbf{v}_j \right) \cdot \left(\mathbf{x}_i - \mathbf{x}_j \right) < 0 \\ 0 & \left(\mathbf{v}_i - \mathbf{v}_j \right) \cdot \left(\mathbf{x}_i - \mathbf{x}_j \right) \geq 0 \end{cases} \tag{28}$$

where

$$\phi = \frac{\bar{h} \left(\mathbf{v}_i - \mathbf{v}_j \right) \cdot \left(\mathbf{x}_i - \mathbf{x}_j \right)}{\left| \mathbf{x}_i - \mathbf{x}_j \right|^2 + \left(0.1 \bar{h} \right)^2} \tag{29}$$

$$\bar{h} = \left(h_i + h_j \right) / 2 \,, \quad \bar{\rho} = \left(\rho_i + \rho_j \right) / 2 \,, \quad \bar{c} = \left(c_i + c_j \right) / 2$$

In the above equation, α, β are constants. c is the speed of sound. The second one is XSPH technique proposed by Monaghan (1994). In XSPH method, the position of particles is updated according to the following equation.

$$\frac{d\mathbf{x}_i}{dt} = \mathbf{v}_i - \varepsilon \sum_{j=1}^{N} \frac{m_j}{\rho_j} \left(\mathbf{v}_i - \mathbf{v}_j \right) W_{ij} \tag{30}$$

where ε is a constant. It is clear that the velocity of neighboring particle contributes in updating the position of the particle i. Therefore the XSPH technique can keep the particles more orderly and avoid the penetration between approaching particle.

2.3 Constitutive equation

The constitutive equation employed in this research is the Modified Cam-Clay model (MCC) proposed by Roscoe et al. (1968). The yield function of MCC model is described as

$$f = \mathrm{M}D\ln\frac{p'}{p'_0} + \mathrm{M}D\ln\left\{1+\left(\frac{q}{\mathrm{M}p'}\right)^2\right\} - \varepsilon_v^p = 0 \qquad (31)$$

in which the plastic volumetric strain ε_v^p plays a role of hardening parameter. M is the critical state parameter defined by Roscoe, Schofield and Thurairajah (1963). D is the coefficient of dilatancy proposed by Shibata (1963). p', p'_0 and q are the effective mean stress, the effective mean stress in the pre-consolidated state and the deviatoric stress. The yield surface of MCC model in ax-symmetric stress plane is shown in Figure 3.

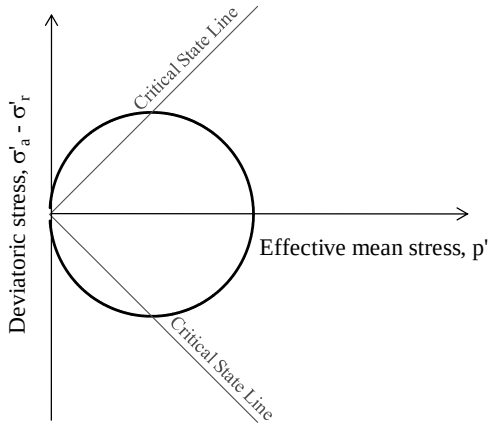


Figure 3 Yield surface of Modified Cam-Clay model in axi-symmetric stress plane

If the stress state is inside the yield surface, a non-linear elastic stress-strain relationship is applied.

$$\dot{\boldsymbol{\sigma}}' = \mathbf{C}^e : \dot{\boldsymbol{\varepsilon}}^e \qquad (32)$$

where

$$\mathbf{C}^e = K\mathbf{1}\otimes\mathbf{1} + 2G\mathbf{A} \qquad (33)$$

In the equation (33), K and G are elastic bulk modulus and elastic shear modulus. $\mathbf{1}$ is Croneker's delta. $\mathbf{A} = \mathbf{I} - (\mathbf{1}\otimes\mathbf{1})/3$ is 4th order deviatoric tensor where I is 4th order identity tensor. Applying the associate flow rule to the consistency condition $df = 0$, the stress-strain relationship in elasto-plastic state is obtained as

$$\dot{\boldsymbol{\sigma}} = \mathbf{C}^{ep} : \dot{\boldsymbol{\varepsilon}} \qquad (16)$$

where

$$\mathbf{C}^{ep} = \mathbf{C}^e - \frac{\mathbf{C}^e : \partial f/\partial\boldsymbol{\sigma}' \otimes \partial f/\partial\boldsymbol{\sigma}' : \mathbf{C}^e}{\mathbf{1} : \partial f/\partial\boldsymbol{\sigma}' + \partial f/\partial\boldsymbol{\sigma}' : \mathbf{C}^e : \partial f/\partial\boldsymbol{\sigma}'}. \qquad (34)$$

During the earthquake, the shear deformation occurs in the ground and the pore water pressure arises due to the dilatancy. Thus the effective mean stress decreases. And then the liquefaction occurs when the effective mean stress becomes 0. Therefore it is need that the constitutive model can represent at least the decrease of the effective mean stress in undrainage shear deformation by cyclic load. However, the constitutive model which I mentioned above cannot represent this feature. In order to represent that feature, the subloading surface proposed by Hashiguchi et al. (1998) is employed in this research. The subloading surface is always inside the normal yield surface and the current stress is on the subloading surface. The plastic strain is developed although the stress is inside the normal yield surface by applying subloading surface. Therefore the reduction of effective pressure due to cyclic load can be calculated. The function of subloading surface is as follows.

$$f = \mathrm{M}D\ln\frac{p'}{p'_0} + \mathrm{M}D\ln\left\{1+\left(\frac{q}{\mathrm{M}p'}\right)^2\right\} - \varepsilon_v^p - MD\ln R = 0 \qquad (35)$$

where $R = p'_y / p'_c$ is called the similarity ratio of subloading surface which indicates the ratio of size between the subloading surface and normal yield surface. The subloading surface of $R = 0.8$ and the normal yield surface on axi-symmetric stress plane are shown in Figure 4.

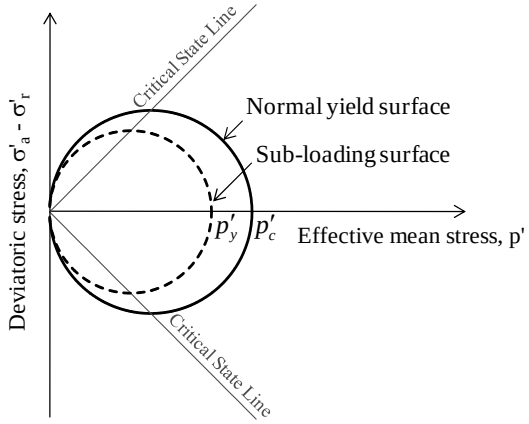


Figure 4 Subloading surface and normal yield surface in axi-symmetric stress plane

The similarity ratio R change according to the developing low which is also proposed by Hashiguchi et al. (1998)

$$\dot{R} = -\frac{m}{D}\ln R\left\|\dot{\boldsymbol{\varepsilon}}^p\right\| \qquad (36)$$

where m is the parameter which controls the speed of the subloading surface to achieve the normal yield surface.

3. Result of simulation

In this chapter, the simulation result of constant volume shear test applied cyclic load by using SPH method. The material parameters used in the simulation are listed in Table 1.

Table 1 Material parameters used in the simulation

Critical state parameter	M	1.00
Irreversible ratio	Λ	0.80
Coefficient of dilatancy	D	0.08
Poisson's ratio	ν'	0.33
Compression index	λ	0.20
Void ratio at pre-consolidated state	e_0	1.00
Earth pressure at rest at pre-consolidated state	K_0	1.00
Earth pressure at rest at initial	K_i	1.00
Vertical stress at pre-consolidated state (kPa)	σ'_{v0}	98.0
Vertical stress at initial (kPa)	σ'_{vi}	98.0
Parameter for sub-loading surface	m	2.0

In the simulation, the increment of time is set to be 1.0×10^{-7} sec. The number of step is 1000000, the number of particles is 6160. The computation time is not so long because calculation process is parallelized by GPUs (Graphic Processing Units).

3.1 Constant volume shear test

The simulation of constant volume shear test are performed. The initial configuration of particles is shown in Figure 5. The height and width of specimen is 0.1m and 0.06m.

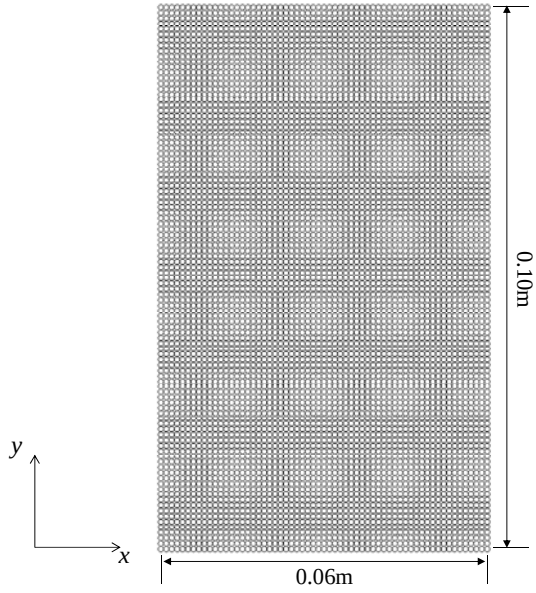


Figure 5 Initial configuration of particles (6060 particles)

The displacements are given at particles which placed on the boundary of specimen. In order to simulate the cyclic loading, given displacements are turned to opposite direction when the deviatoric strain is over 1.5%. Figure 6 shows the velocity vectors in compression shearing and extension shearing process. Figure 7(a) and (b) are shown the stress path and stress-strain relationship of the particle which is located the center of specimen.

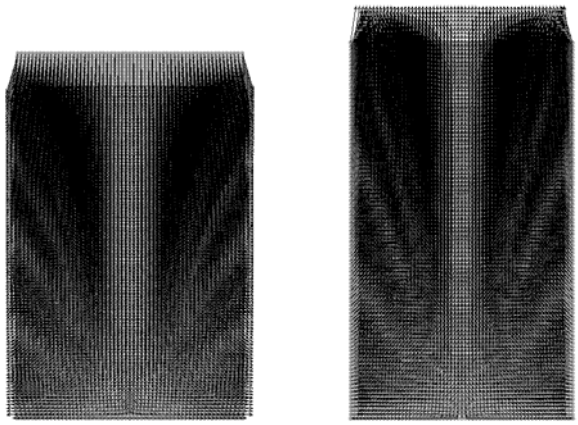


Figure 6 Velocity vectors of particles in compression shearing process: right hand side, extension shearing process: left hand side

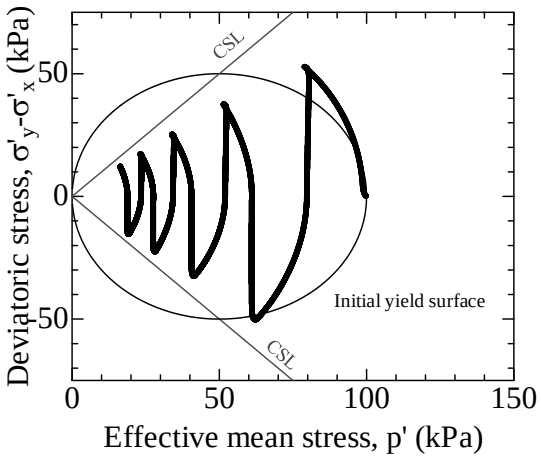


Figure 7(a) Effective stress path

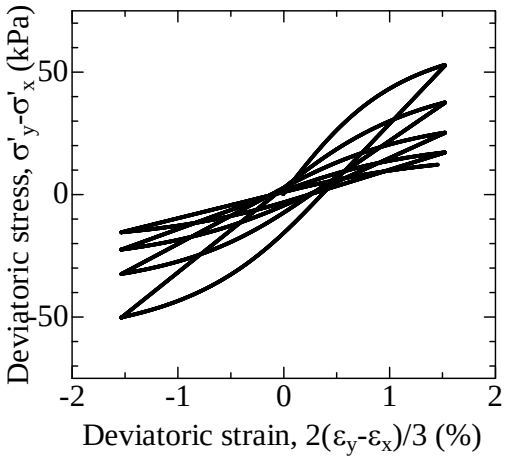


Figure 7(b) Stress-strain relationship

The reduction of effective mean stress due to cyclic load can be simulated as shown in Figure 7(a). The reduction

of the shear modulus during cyclic deformation also can be seen in Figure7(b).

4. CONCLUSIONS

In this research, the simulations of constant volume shear test employed the Modified Cam-Clay model with subloading surface as the constitutive model was performed by using the SPH method.

It is confirmed that the decrease of effective mean stress and the shear modulus during cyclic deformation can be reproduced by this method.

In order to applying this method to more practical geotechnical problems, it is necessary to develop the method which can solve the soil/water coupled problem. That is the future work.

Acknowledgements:

The authors acknowledge support from the Japan Ministry of Education, Culture, Sport, Science, and Technology (MEXT) for establishing the Center for Urban Earthquake Engineering (CUEE) in Tokyo Institute of Technology.

References:

Shibata, T., (1963), "On the volume changes of normally consolidated clays," *Annuals of Disaster Prevention Research Institute*, Kyoto University, **6**, 128-134. in Japanese.

Roscoe, K.H., Schofield, A.N. and Thurairajah, A., (1963), "Yeilding of clays in states wetter than critical," *Geotechnique*, **13**(3), 250-255.

Roscoe, K.H. and Burland, J.B., (1968), "On the generalized stress-strain behavior of 'wet' clay," *Engineering Plasticity*, Cambridge University, 535-609.

Lucy, L.B., (1977), "Numerical approach to testing the fission hypothesis," *Astronomical Journal*, **82**, 1013-1024.

Monaghan, J.J. and Gingold, R.A., (1983), "Shock simulation by the particle method SPH," *Journal of Computational Physics*, **52**, 374-389.

Monaghan, J.J., (1994), "Simulating Free Surface Flows with SPH," *Journal of Computational Physics*, **110**, 399-406.

Hashiguchi, K. and Chen, Z.P., (1998), "Elastoplastic constitutive equation of soils with the subloading surface and rotational hardening," *International Journal for Numerical and Analytical Methods in Geomechanics*, **22**, 197-277.

8CUEE CONFERENCE PROCEEDINGS
8th International Conference on Urban Earthquake Engineering
March 7-8, 2011, Tokyo Institute of Technology, Tokyo, Japan

SEISMIC HAZARD FOR MAXIMUM SHEAR STRESSES IN SOIL LAYERS AT OAKLAND INTERNATIONAL AIRPORT

Tadahiro Kishida

JST-JICA Assistant Professor, Graduate School of Engineering, Chiba University, Japan
tkishida@faculty.chiba-u.jp

Abstract: Seismic shear stresses in soil layers are studied at Oakland International Airport where thick Young Bay Mud deposit exists under the landfill. Site response analyses are performed with the wide range of input ground motions to compute maximum shear stresses in soil layers. Stress reduction coefficients are calculated from the site response analyses and compared with the predictive equations. Regression analyses are performed for maximum shear stresses and those intensities are incorporated into the probabilistic seismic hazard analysis to describe the variations of ground motion intensities with the depth. Conditional mean spectra are calculated with 10 % probability of exceedance in 50 years, and the methodology to calculate the design spectra with the conditional probability distribution is described.

1. INTRODUCTION

Oakland International Airport is located at 7 km south of the central city of Oakland providing the service for more than 10 million people and 700 thousand tons of cargo for a year. The construction of airport was started at 1927 and expanded until middle of 1960's. At the early stage of construction, the airport was built with the dredged sand and clay over the Young Bay Mud in San Francisco East Bay. Since the airport is located at 8 km west of Hayward Fault and 20 km east of San Andreas Fault, the relatively high seismic intensity is expected with the amplification of seismic wave by thick Young Bay Mud deposit.

As a typical design procedure, maximum shear stresses in soils layers are calculated for the design ground motions to estimate the liquefaction potential and seismic deformations. Simplified procedure, which is suggested by Seed and Idriss (1971), uses the peak ground acceleration (PGA) and stress reduction coefficient (r_d) to estimate the maximum shear stresses in soil layers. PGA is generally obtained by the probabilistic seismic hazard analysis (PSHA) and r_d is calculated given PGA and earthquake magnitude from disaggregation results. However, ground motion intensity changes for maximum shear stresses in soil layers since those depends on the depth of soil layer and earthquake magnitude or ground motion frequency (Idriss (1999), Cetin et al. (2004), Kishida et al. (2009)). Therefore, it is important to understand the variation of ground motion intensities in providing the design spectra.

This paper describes the characteristics of maximum shear stress distributions at Oakland International Airport by performing the site response analysis with the equivalent linear method of SHAKE (Schunable, 1972), and those results are compared with the simplified procedure for estimating the maximum shear stress distribution. The vector intensities of maximum shear stresses are introduced as a linear combination of spectral accelerations, and those intensities are incorporated into the probabilistic seismic hazard analysis. Effects of variation of ground motion intensities are described by the conditional mean spectra and the rational procedure for calculating the design spectra from the probabilistic seismic hazard analysis are presented.

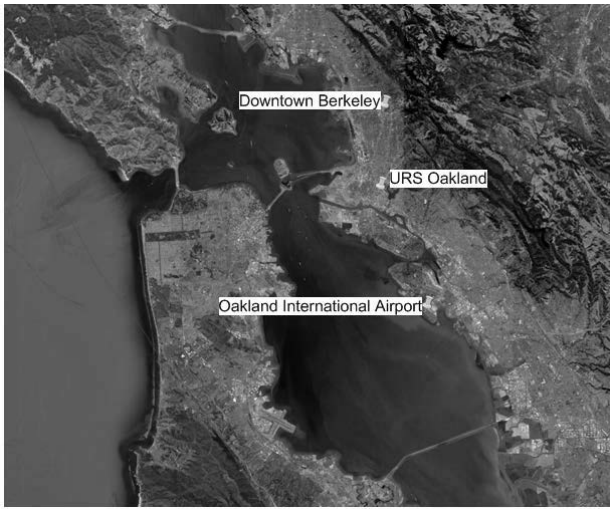


Figure 1. Location of Oakland International Airport

2. MAXIMUM SHEAR STRESSES IN SOIL LAEYRS

2.1 Site Conditions

Oakland International Airport is located at the San Francisco East Bay as shown in Figure 1. Airport is surrounded by the perimeter dike to protect from the

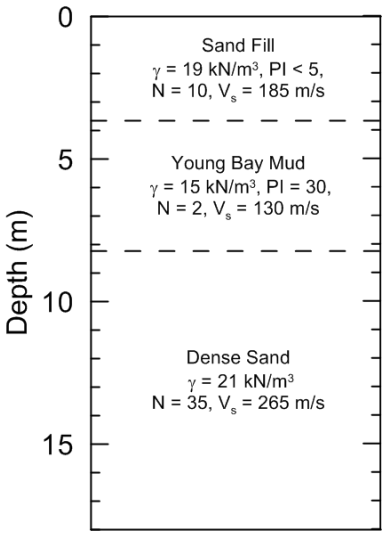


Figure 2. Representative Soil Profile

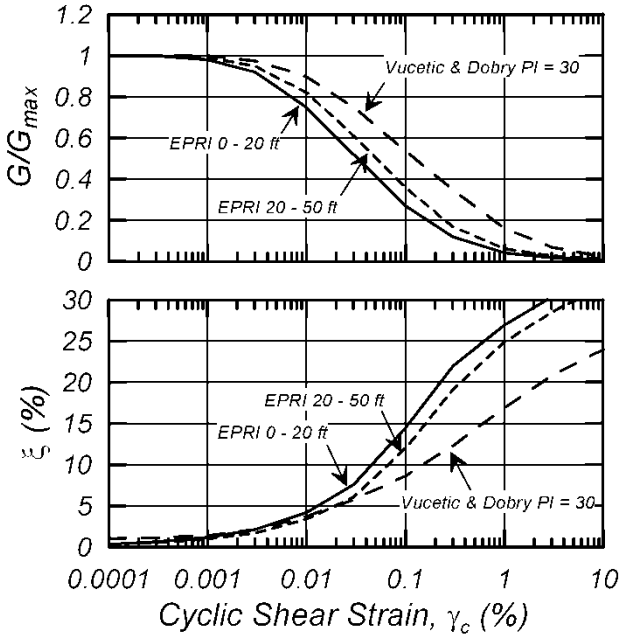


Figure 3. Modulus Reduction and Damping Ratio

flooding and wind surge, and runway is located about 180 m away from the perimeter dike. Figure 2 shows the representative soil profile and properties near the runway. At the ground surface, landfills were 3 to 5 m thick and comprised primarily of sands and silts which had SPT blow counts (N) of 6 to 20. Young Bay Mud layers were 3 to 8 m thick showing the very soft clay characteristics with Plasticity Index (PI) of 17 to 50. Young Bay Mud layers were sometimes underlain by a layer of stiff silty clays, which is called as Old Bay Mud, to dense sand layers those had N values of 20 to 50. Unit weight (γ) for the landfill, Young Bay Mud, and underlying dense sand deposits ranged from 17 to 22 kN/m^3, 14.5 to 16 kN/m^3, and 20 to 22 kN/m^3, respectively.

2.2 Site Response Analyses

Site response analyses were performed by SHAKE91 (Idriss and Sun, 1992) with the soil profile in Figure 2.

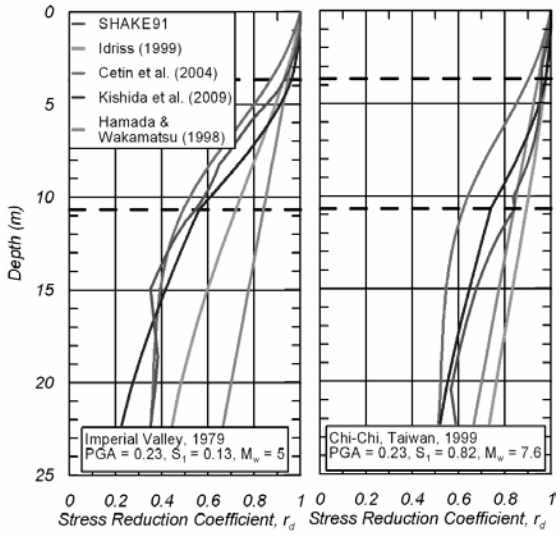


Figure 4. Variation of Stress Reduction Coefficient

Figure 3 shows the modulus reduction curves and damping ratio curves for sand layers from EPRI (1993), and Young Bay Mud from Vucetic and Dobry (1989). More than 2,500 input ground motions were selected from PEER strong motion database (PEER, 2005) from Site conditions of D (NEHRP, 2003). Figure 4 shows the representative analysis results showing the variation of r_d by SHAKE with the comparison of predicted values by Kishida et al. (2009), Idriss (1999), Cetin et al. (2004), and Hamada and Wakamatsu (1998), where r_d is defined as follows.

$$r_d = \frac{\tau_{\max} g}{\sigma_{vo} PGA} \tag{1}$$

SHAKE results clearly show two physical trends for the variation of r_d. One is that the reduction of r_d is relatively small in sand layers compare to that in Young Bay Mud layer. This is because that the sand layer tends to behave rigidly with a shorter period of a soil column by high shear wave velocity than Young Bay Mud layer. The other trend is that r_d becomes higher with the increase of earthquake magnitude due to the increase of predominant period of ground motions, by which a soil columns also tends to behave rigidly.

These physical trends can be evaluated for the presented predictive equations. Kishida et al. (2009), Idriss (1999), and Cetin et al. (2004) include the ground motion period or magnitude effects, but Hamada & Wakamatsu (1998) does not consider those effects. Kishida et al. (2009) and Cetin et al. (2004) includes the soil profile effects those tend to reduce the r_d values with the decrease of shear wave velocities, but Idriss (1999) and Hamada and Wakamatsu (1998) do not consider those effects.

Figure 5 shows the variation of residuals against depth where residuals are defined as differences between maximum shear stresses by SHAKE and estimated values by predictive equations in natural logarithm. Figure 5 also shows the expected values of residuals obtained by fitting residuals with smooth spline function. It is noted that Idriss

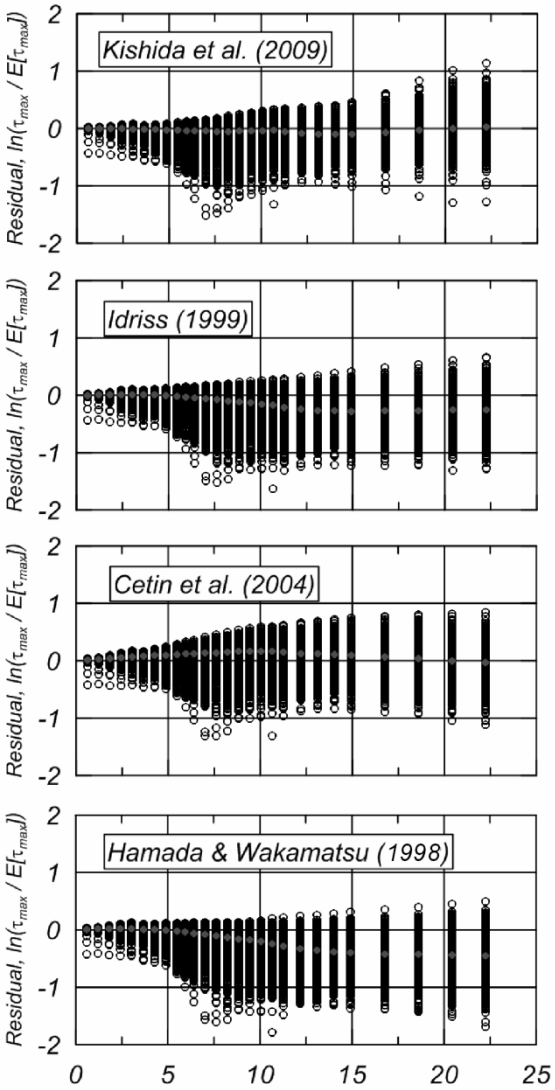


Figure 5. Variations of Residuals of r_d

(1999) and Hamada & Wakamatsu (1998) tend to overestimate the maximum shear stresses beneath the Young Bay Mud layer by 24% and 33%, respectively since these equations do not consider the effects of soft soil layers. It is also observed that the equation by Cetin et al. (2004) underestimates the maximum shear stress by 6% at the depth of 3 m and that bias increases up to 19% at the depth of 10 m. One of the reasons for this bias is because that Cetin et al. (2004) consider the soft layer effects by averaging shear wave velocities for upper 12 m instead of considering the period changes in soil columns. Kishida et al. (2009) shows the smallest bias that overestimates 10% at the depth of 14 m. It is mentioned that equations by Kishida et al. (2009), Idriss (1999) and Hamada and Wakamatsu (1998) do not have any bias in a sand layer less than 3.5 m depth, but Cetin et al. has a bias. Although these observations are obtained based on the single soil profile, those are explained by physical understandings of soil responses.

3. SEISMIC HAZARD ANALYSIS AND DESIGN SPECTRA

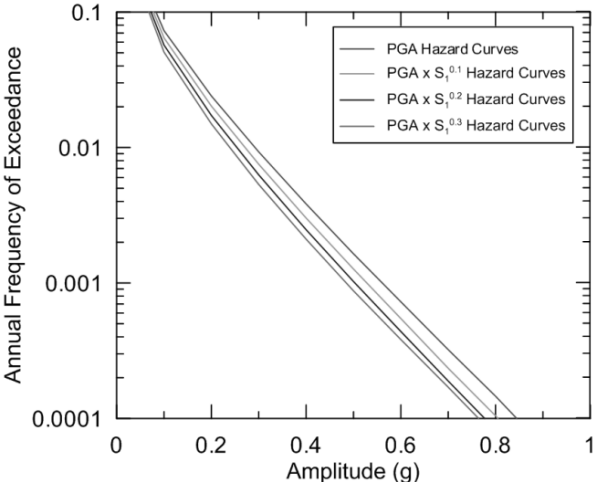


Figure 6. Seismic Hazard Curves for Vector Intensities

3.1 SEISMIC HAZARD OF VECTOR INTENSITIES

Regression analyses were performed for maximum shear stresses at depth of 3, 6, and 18 m after the site response analyses. Following equations are obtained with predictor variables of PGA and S_1 where S_1 is defined as $S_a(1.0)$ divided by $S_a(0.2)$ (Kishida et al., 2009).

$$\ln \tau_{\max} = \begin{bmatrix} 4.00 \\ 4.57 \\ 5.15 \end{bmatrix} + \begin{bmatrix} 1.00 \\ 0.992 \\ 0.964 \end{bmatrix} \ln PGA + \begin{bmatrix} 0.0184 \\ 0.0926 \\ 0.238 \end{bmatrix} \ln S_1 \qquad (2)$$

where τ_{max} is in the unit of kPa. It is noted that the fractional contribution of S_1 to PGA for the maximum shear stresses increases with the increase of depth from 0 to 0.25, which indicates that the longer period of ground motions becomes more important for the deeper soil layer.

Probabilistic seismic hazard analyses were performed for these intensities with the fault parameters obtained from URS Corporation, Oakland (Wong, 2010) after the study by Working-Groups on California Earthquake Probabilities (WGCEP, 2002). Attenuation relationships for ground motion intensities of maximum shear stresses are obtained as follows, those are expressed as a linear combination of spectral accelerations.

$$E[\ln I] = \mathbf{c}'\boldsymbol{\mu} \qquad (3)$$

$$\sigma_I^2 = \mathbf{c}'\mathbf{V}^{1/2}\boldsymbol{\rho}\mathbf{V}^{1/2}\mathbf{c} \qquad (4)$$

where $\mathbf{c}$ and $\mathbf{u}$ are vectors of coefficients for the linear combination and expected values of spectral acceleration. Matrix of $\mathbf{V}$ and $\boldsymbol{\rho}$ are diagonal matrix of standard deviations and correlation matrix of spectral accelerations, respectively. In the analysis, the attenuation relationships by Abrahamson and Silva (2008) with the correlation relationships by Baker and Jayaram (2008) are used.

Figure 6 shows the variation of hazard curves for ground motion intensities with different combinations of S_1 and PGA. It is noted that hazard values slightly decrease with the increase of S_1 to PGA since S_1 is generally smaller than 1.0.

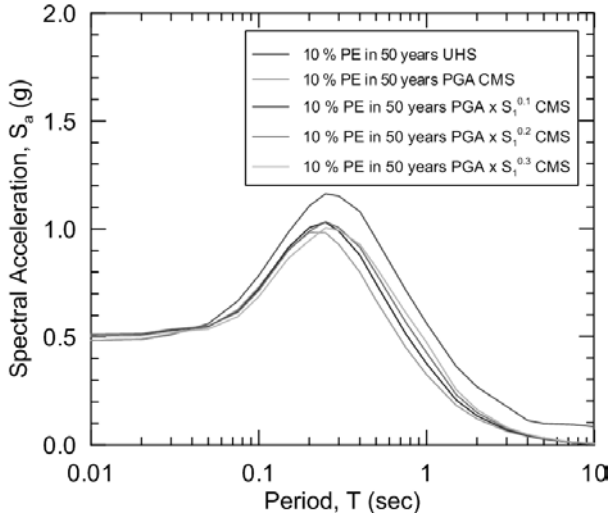


Figure 7. Variation of Conditional Mean Spectra

Based on these results, maximum shear stresses can be directly estimated by substituting the hazard values from Figure 6 into Equation (2). For example, the maximum shear stress at 6 m depth with the 10 % probability of exceedance in 50 years is obtained as follows.

$$\tau_{\max} = \exp\left[4.57 + 0.992\left(\ln PGA \cdot S_1^{0.0933}\right)\right] = \exp\left[4.57 + 0.992\left(\ln 0.45\right)\right] = 44 \quad (5)$$

The calculated shear stress by Equation (2) with the hazard value in Figure 6 will provide the same value to that by the simplified procedure if the soil layer exists at the ground surface, but deviate with the increase of the depth of soil layers.

3.2 CONDITIONAL MEAN SPECTRA

Effects of variation of seismic intensity with depth are further illustrated with the conditional mean spectra, those are calculated as follows.

$$\ln \mathbf{S_a} = E\left[\ln \mathbf{S_a}\right] + \boldsymbol{\Sigma}\left(\sigma_I^2\right)^{-1}\left(\ln I - E\left[\ln I\right]\right) \quad (6)$$

where, σ_I is a standard deviation of ground motion intensity and $\boldsymbol{\Sigma}$ is a vector of the covariance between spectral accelerations and ground motion intensity. Figure 7 shows Uniform Hazard Spectra (UHS) and the variation of conditional mean spectra (CMS) obtained by Equation (6) given the hazard values at 10 % probability of exceedance in 50 years. It is noted that the relatively longer period component around 0.7 second increases and the shorter period component around 0.1 second decreases with the increase of the contribution of S_1. This is corresponding to the fact that the longer period of components in ground motions tends to be more important with the increase of the depth for soil layers. Therefore, it is understood that the general design procedures do not envelop the range of ground motion intensities in a soil column since that uses the PGA from seismic hazard analysis with the earthquake magnitude from disaggregation results. It is also mentioned

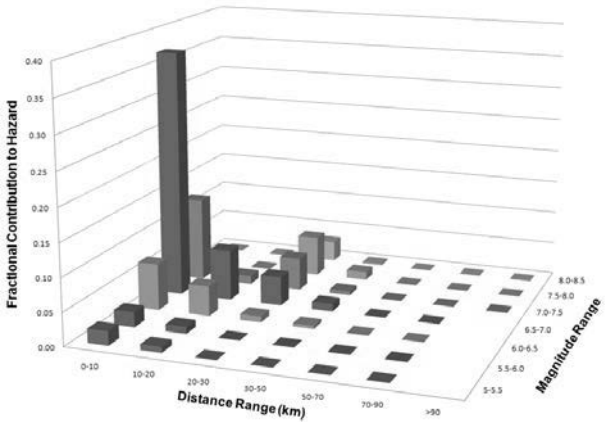


Figure 8. Disaggregation of Hazard for PGA

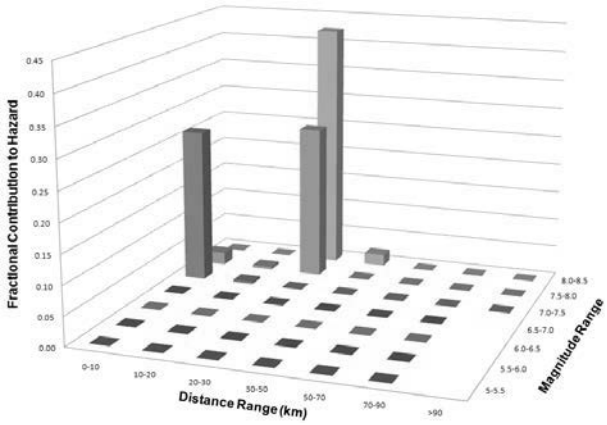


Figure 9. Disaggregation of Hazard for S_a(3.0)

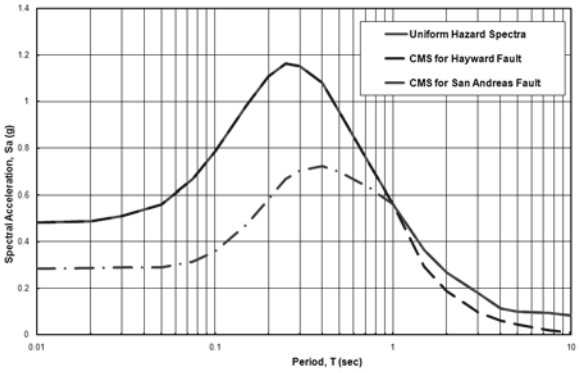


Figure 10. Conditional Mean Spectra for Hayward Fault and San Andreas Fault

that this discussion never been applied if the earthquake magnitude is used as a ground motion characteristic since there is no conditional probability distributions for spectral accelerations given PGA and earthquake magnitude.

3.3 DESIGN SPECTRA

Figure 8 and 9 shows the disaggregation results of hazard curves at 10 % probability of exceedance in 50 years for PGA and S_a(3.0). There are two distinguished sources around magnitude of 6.5 with distance of 10 km, and 7.5 with distance of 20 km, those are corresponding to Hayward fault and San Andreas Fault. It is observed that Hayward

fault is a dominant source of the hazard value of PGA, and San Andreas Fault is a dominant source of $S_a(3.0)$. Therefore, it is conservative if the uniform hazard spectra are used in a design procedure, but will be unconservative if the conditional mean spectra given the spectral acceleration at the specific period are used as discussed in the previous section, which method is similar to that discussed by Baker (2010). Therefore, it is reasonable to cover the range of spectral accelerations in Uniform Hazard Spectra for Hayward Fault and San Andreas Fault separately in producing the conditional mean spectra since the ground motion intensity changes with a depth of the soil layer and there is a wide range of possible consequences of seismic deformations as discussed by Idriss and Boulanger (2008).

Figure 10 shows the conditional mean spectra given the range of Uniform Hazard Spectra for each fault with the expected earthquake magnitude and distance. It is noted that the conditional mean spectra are lower than Uniform Hazard Spectra if the earthquake scenario is not the major contribution to the seismic hazard value. As a result, two spectral accelerations are generated for Hayward Fault and San Andreas Fault for the design purpose to cover the variation of seismic intensities in a soil column.

4. CONCLUSIONS

This paper describes the variation of seismic intensities for maximum shear stresses in soil layers at Oakland International Airport where thick Young Bay Mud deposit exists under the landfill. Variation of stress reduction coefficients (r_d) are studied by performing the site response analysis with the comparison of predictive equations. Regression analyses were performed for maximum shear stresses in soil layers and the variation of ground motion intensities with depth is described. Seismic hazard analyses were performed for vector intensities of maximum shear stresses, and those variations are illustrated with conditional mean spectra showing the different ground motion characteristics with depth. The methodology to obtain the design spectra from uniform hazard spectra was presented when the hazard was contributed by multi earthquake scenarios for different periods.

Acknowledgements:

This study is supported by Japan Science Technology and Japan International Corporation Agency. Author acknowledges the comments by Ivan Wang at URS Corporation, Oakland for the fault systems in California.

References:

Abrahamson, N. A. and Silva, W. J. (2008), "Summary of the Abrahamson and Silva NGA Ground-motion Relations," Earthquake Spectra, 24: 67-97.

Baker, J. W. (2010). "The Conditional Mean Spectrum: A Tool for Ground Motion Selection," Journal of Structural Engineering, American Society of Civil Engineers, Posted ahead of print 26 February 2010 (in press).

Baker, J. W. and Jayaram, N. (2008), "Correlation of Spectral Acceleration Values from NGA Ground Motion Models," Earthquake Spectra, 24: 299-317.

Cetin, K. O., Seed, R. B., Der Kiureghian, A., Tokimatsu, K., Harder, L. F., Kayen, R. E., and Moss, R. E. S. (2004), "Standard Penetration Test-based Probabilistic and Deterministic Assessment of Seismic Soil Liquefaction Potential", J. Geotechnical and Geoenvironmental Eng., ASCE 130(12), 1314–340.

Cornell, C.A. (1968), "Engineering seismic risk analysis," Bulletin of Seismic Society of America, 58, 1583-1606.

Electric Power Research Institute (EPRI) (1993), "Guidelines for Site Specific Ground Motions," Rept. TR-102293, 1-5, Pala Alto, California.

Hamada, M. and Wakamatsu, K. (1998), "Mechanism of Lateral Spread for Liquefied Soil Layer," 10th Japan Earthquake Engineering Symposium Panel Discussion, 147-152. (in Japanese)

Idriss, I. M. and Boulanger, R. W. (2009), "Soil Liquefaction during Earthquakes," Earthquake Engineering Research Institute MNO-12.

Idriss, I. M. and Sun, J. I. (1991), "SHAKE91 A Computer Program for Conducting Equivalent Linear Seismic Response Analyses of Horizontally Layered Soil Deposits," Center for Geotechnical Modeling, Department of Civil and Environmental Engineering, University of California, Davis .

Idriss, I. M., (1999), "An Update to the Seed-Idriss Simplified Procedure for Evaluating Liquefaction Potential", in Proceedings, TRB Workshop on New Approaches to Liquefaction, Publication No. FHWA-RD-99-165, Federal Highway Administration.

Kishida, T., Boulanger, R. W., Abrahamson, N. A., Driller, M. W., and Wehling, T. M. (2009a). "Seismic Responses of Levees at the Sacramento-San Joaquin Delta", Earthquake Spectra, EERI, Vol. 25(3), 557-582.

Kishida, T., Boulanger, R. W., Abrahamson, N. A., Driller, M. W., and Wehling, T. M. (2009b). "Site Effects at the Sacramento-San Joaquin Delta". Earthquake Spectra, EERI, Vol. 25(2), pp.301-322.

National Earthquake Hazards Reduction Program (NEHRP) (2003), "Recommended provisions for seismic regulations for new buildings and other structures with accompanying commentary," Building Seismic Safety Council for Federal Emergency Management Agency, Washington, D.C.

Pacific Earthquake Engineering Research Center (2005), "Next Generation Attenuation (NGA) Strong Ground Motion Database," University of California, Berkeley, http://peer.berkeley.edu/nga/index.html

Schnabel, P. B., Lysmer, J., and Seed, H. B. (1972). "SHAKE: A Computer Program for Earthquake Response Analysis of Horizontally Layered Sites." Rep. No. EERC/72-12, Earthquake Engineering Research Center, Univ. of California, Berkeley, California.

Vucetic, M., and Dobry, R. (1991), "Effect of Soil Plasticity on Cyclic Response," Journal of Geotechnical Engineering, American Society of Civil Engineers, **117**(1), 117, 89–107.

Wong, I. (2010), personal communication, URS Corporation, Oakland.

Working Group on California Earthquake Probabilities (2003). Earthquake Probabilities in the San Francisco Bay Region: 2002–2031, USGS Open-File Report 03-214.

8CUEE CONFERENCE PROCEEDINGS
8th International Conference on Urban Earthquake Engineering
March 7-8, 2011, Tokyo Institute of Technology, Tokyo, Japan

GROUND SETTLEMENTS AND EARTH PRESSURES AROUND EMBEDDED FOUNDATIONS SUBJECTED TO STRONG GROUND SHAKING

Kohji Tokimatsu[1], Shuji Tamura[2], Kazushi Tohyama[3], Hiroko Suzuki[4], and Hiroyuki Yoshida[5]

1) Professor, Tokyo Institute of Technology, Japan
2) Associate Professor, Disaster Prevention Research Institute, Kyoto University, Japan
3) Student, Tokyo Institute of Technology, Japan
4) Assistant Professor, Tokyo Institute of Technology, Japan
5) Chief, Arch. & Struct. Eng. Operation Center, Tokyo Electric Power Services Co., Ltd., Japan
kohji@o.cc.titech.ac.jp

Abstract: Dynamic centrifuge shaking table tests were performed using soil-foundation-superstructure models to examine ground settlement distribution around a building subjected to strong ground shaking as well as earth pressure acting on embedded foundations during and after shaking. Based on the test results and discussions, the following conclusions are made: (1) The dynamic passive earth pressure acting on a rigid wall during strong shaking increases with increasing ground acceleration and becomes almost equal to the value estimated by the Mononobe-Okabe method only when the ground acceleration exceeds about 6 m/s^2 accompanied by a shear strain of about 2.5 % (2) The static earth pressure acting on a rigid wall after strong shaking may vary from less than to more than twice the original "at rest" value, depending on the stress state developed on each side of the foundation and (3) The ground settlement along the excitation direction increases towards the building, due to strong soil-structure interaction that prevails within a horizontal distance of 0.3-0.6 times the foundation embedment, creating a steeper dipping slope in dense sand than in loose sand.

1. INTRODUCTION

The Niigata-ken Chuetsu-oki earthquake (Mj=6.8) that occurred on July 16, 2007, with an epicenter off the Niigata Prefecture affected the coastal areas of the southwestern Niigata prefecture, including Kashiwazaki city and Kariwa village as well as the Kashiwazaki-Kariwa nuclear power plant of Tokyo Electric Power Company (TEPCO). A matter of utmost concern was the performance of the Kashiwazaki-Kariwa nuclear power plant during and after the earthquake. The peak ground acceleration recorded at the site was as large as 12.2 m/s^2. Three reactors in full operation as well as one in a start-up state were automatically shutdown and all the critical structures seemed to be in good condition; however, a fire broke out around a house electric transformer and many non-critical structures as well as incidental components such as pipes and ducts were damaged, retarding the re-operation of the plant. The major cause of the damage seems to be not only the near field strong ground motions but also the settlements of backfill around the critical buildings.

Based on the field reconnaissance made after the quake, Tokimatsu (2007) showed that: (1) ground settlements appeared to occur wherever backfilled with sand particularly near the critical buildings, causing unacceptable settlements of numerous non-critical structures and incidental components such as pipes and ducts, all of which were directly founded on the backfill and (2) the ground settlement was particularly larger near the building and tended to decrease rapidly with distance from the building, suggesting that soil-structure interaction significantly affected the resulting ground settlement variation.

Ishihara (2009) pointed out that when a soil deposit in contact with a vertical rigid wall is shaken horizontally, the soil near the wall will fall down into the aperture created at the interface and will be compressed and packed by the relative movement of the outer soil mass, thereby exerting a greater earth pressure on the wall. There is some concern, therefore, that dynamic soil-foundation interaction would produce an earth pressure which is by far greater than the pressure at rest, or even more than the pressure normally considered in the design of walls against seismic shaking (Ishihara, 2009). A little is known, however, about ground settlement variation around a building with embedded spread foundation subjected to extremely strong shaking and the resulting effects on earth pressures during and after shaking.

The objective of this paper is to examine the ground settlement distribution around a building subjected to strong ground shaking as well as earth pressure acting on the embedded foundation during and after shaking. For this purpose, two series of centrifuge shaking table tests were

performed in which a building with spread foundation is embedded into either a loose or dense sand layer and founded on the underlying dense sand layer.

2. CENTRIFUGE SHAKING TABLE TEST SETUP AND PROCEDURE

In order to investigate ground settlements and earth pressure changes around an embedded foundation during and after strong ground shaking, two series of centrifuge shaking table tests (series L and D) were performed at a centrifugal acceleration of 50*g* using the geotechnical centrifuge at the Disaster Prevention Research Institute, Kyoto University. Figure 1 shows the test setup and instrumentation for series L prepared in a laminar shear box with inner dimension of 450 mm (length) × 150 mm (width) × 200 mm (height). Dry Toyoura sand (D_{50}=0.21 mm) was pluviated to form a 142 mm thick dense sand layer with D_r=90%. A foundation-superstructure model was then placed directly on the surface of the dense sand. Dry Toyoura sand was further pluviated to form an additional 52 mm thick loose sand layer around the building so as to embed the foundation into the ground to a depth of 52 mm. The relative density of the surface layer surrounding the embedded foundation was 40 %.

Series D was done with identically the same test setup and instrumentation as series L but with only one exception: the relative density of the surface layer surrounding the embedded foundation was 90 % instead of 40%. The internal friction angle of Toyoura sand is ϕ=36° for D_r =40% and ϕ=42° for D_r=90%.

The foundation was made of aluminum alloy having a dimension of 124 mm (length) x 64 mm (width) x 60 mm (height). The surface of the foundation was rough with a static friction coefficient of 0.69 against Toyoura sand. The superstructure was of rigid brass with a dimension of 82 mm long x 58 mm wide x 50 mm high which was connected to the foundation with two plates 35 mm high. The masses of the foundation and superstructure were 1.0 kg and 2.0 kg, respectively. The natural frequency and the damping ratio of the superstructure under the fixed base condition were about 105 Hz and 0.5%.

The foundation was modeled so that normal and shear forces acting on the base and both lateral sides of the foundation can be measured separately. This is achieved by securing small two-axis load cells (Tokyo Sokki Kenkyujo Co., Ltd.) behind the base and lateral side plates of the foundation as shown in Fig. 1 (Tamura et al, 2011). The base of the foundation consists of two separate plates of equal size, each connected to one two-axis load cell, while each of the left and right lateral surfaces of the foundation consists of one plate connected to another two-axis load cell.

The input motion used for the tests was Rinkai92, which is a synthesized ground motion for the Tokyo Bay area. According to the similitude law, the time axis of the motion was scaled down to a factor of 1/50. Shaking table tests were conducted in four consecutive stages with increasing acceleration amplitude of the input motion from about 0.7, 1.5, 3.7, to 6.5 m/s^2. During the shaking table tests, the horizontal accelerations of the superstructure and the foundation as well as those in the soil and the vertical accelerations of the foundation and the ground surface and the base of the laminar shear box were measured along with the forces acting on the base and both sides of the foundation. All data presented hereafter are of prototype scale, unless otherwise noted.

3. CENTRIFUGE SHAKING TABLE TEST RESULTS AND DISCUSSIONS

3.1 Time Histories of Selected Values

Figures 2 and 3 show the time histories of selected parameters including: the horizontal acceleration of the input motion, the ground surface and at depth of 1.5 m, foundation and superstructure; the earth pressures on both side of the foundation, horizontal relative displacement between the foundation and the ground; and the shear stress and shear strain at a depth of 1.5 m for series L and D subjected to the largest input motion with a peak acceleration of 6.5 m/s^2. The horizontal ground acceleration time histories were double integrated to determine their horizontal displacement time histories. The horizontal relative displacement between the foundation and the ground was determined by subtracting one from the other in the time domain. The corresponding shear strain time history was determined by dividing the differential horizontal displacement by the distance between the ground surface and a depth of the base of the foundation. The corresponding shear stress time history was calculated by integrating the product of horizontal acceleration and mass density of the soil with depth. It is to be noted that the displacement time histories shown in this paper correspond to the dynamic component and do not reflect the permanent one.

The maximum horizontal accelerations of the foundation for series L and D were about 5 m/s^2, which are apparently smaller than those of the ground surface (about 7 m/s^2), suggesting soil-structure interaction effects. Not only the peak horizontal accelerations of the superstructure and foundation, but also the earth pressure acting on the

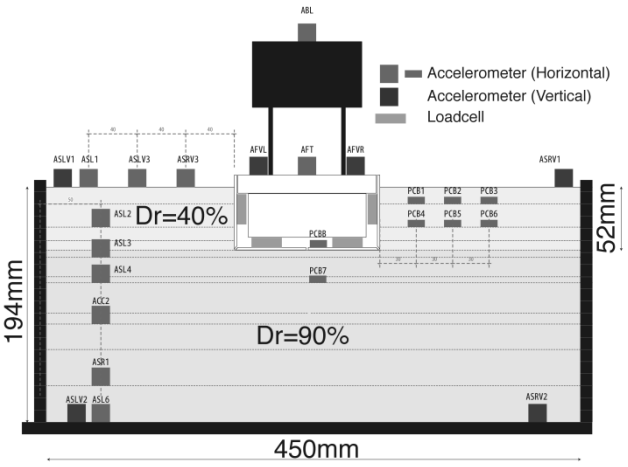


Figure 1 Test setup in laminar shear box (Series L)

foundation are almost the same in the two tests, in spite of the difference in soil density around the foundation between the two tests.

3.2 Dynamic Earth Pressures

Figures 4 and 5 show the relation of the dynamic earth pressures acting on both sides of the foundation with the relative displacement between the foundation and soil for series L and D subjected to the largest input motion with a peak acceleration of 6.5 m/s^2. When the foundation pushes the soil on the right thereby increasing positive relative displacement, the earth pressure on the right increases with decreasing earth pressure on the left. This creates a passive side stress condition on the right with an active side stress condition on the left. When the foundation pushes the soil on the left, all stress conditions are reversed.

The peak earth pressure occurring at each peak relative displacement is slightly larger on the left than on the right. The earth pressure coefficients corresponding to the largest earth pressure are 8 to 9 on the left side and 6 to 7 on the right side, irrespective of the relative density of the surface layer. The reason why the earth pressure becomes independent of relative density is unknown but may be due to densification of loose sand and dilatation of dense sand due to cyclic loading. The reason why the passive earth pressure coefficient is larger on the left side is also unknown but it may be associated with a possible permanent displacement that might have prevailed on the left side of the foundation.

Figure 6 shows the relation of the maximum passive side earth pressure coefficient with the maximum ground acceleration at a depth of 1.2 m during each excitation.

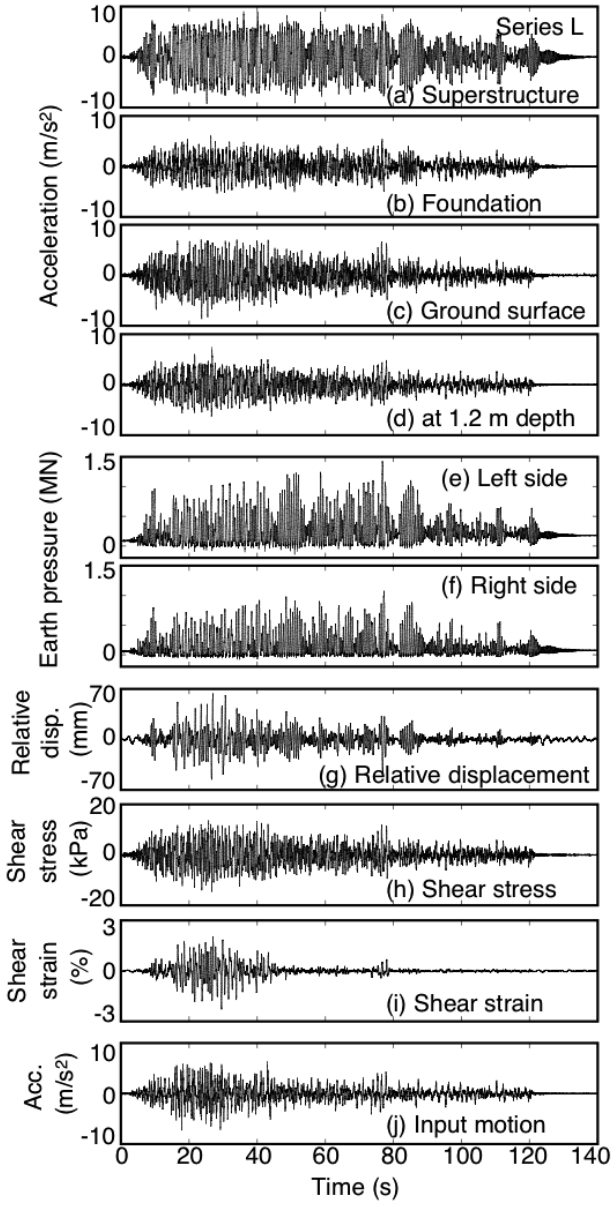


Figure 2 Time histories of selected parameters for series L with input acceleration of 6.5 m/s^2

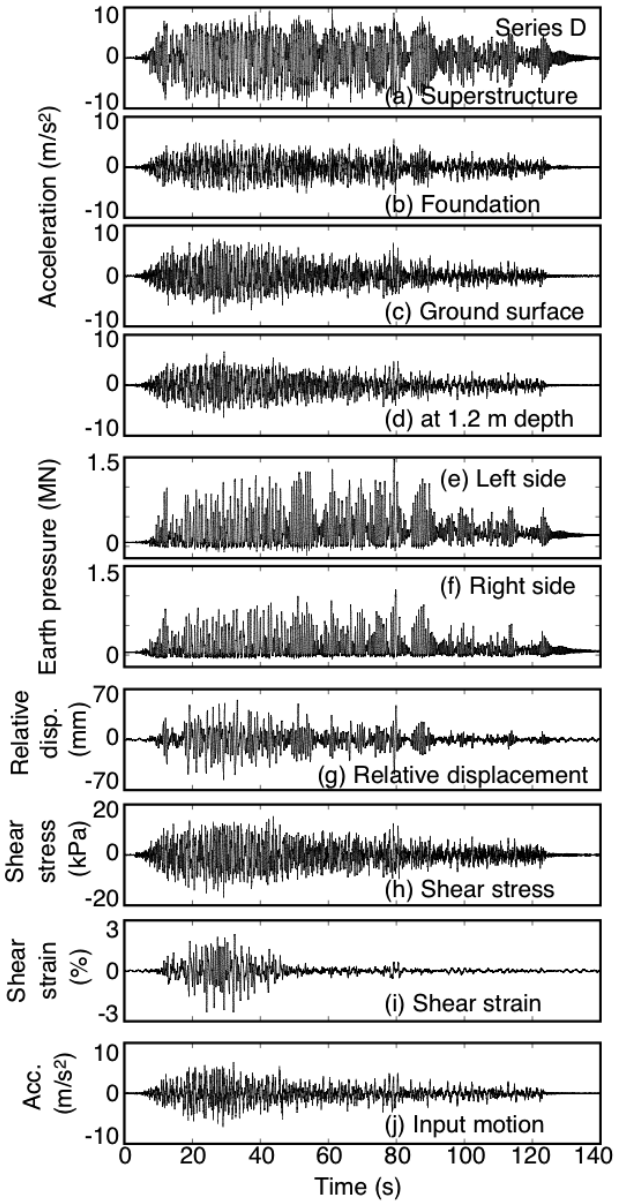


Figure 3 Time histories of selected parameters for series D with input acceleration of 6.5 m/s^2

Also shown in the figure with lines are the relation determined by the Mononobe-Okabe (1924) method with $\delta=2\phi/3$. The observed passive side earth pressure coefficients at the final excitation with a ground acceleration of about 6 m/s^2 accompanied by a shear strain of 2.5% are consistent with those determined by the Mononobe-Okabe (1924) method. The observed passive side earth pressure coefficients at other excitation with smaller input motions are, however, far less than those determined by the Mononobe-Okabe (1924) method. This is probably because the relative displacement between the soil and foundation was significantly less than that required to mobilize the full passive earth pressure.

3.3 Ground Settlement Distribution

Figures 7 and 8 illustrate the settlement distribution around the building for the two series after the final shaking. Despite almost the same response between the two tests, the settlement distributions from the two tests are significantly different from each other in the following aspects:

(1) The ground settlements away from the building along the excitation direction as well as those along the orthogonal direction for series L with Dr= 40% are about 5 mm (10 % of the thickness of the surface layer), while those for series D with Dr= 90% are almost zero. These settlements mainly reflect one-dimensional volume change of the surface layer due to cyclic loading.

(2) The ground settlement along the direction parallel to the excitation tends to increase towards the building, whereas those along the orthogonal direction do not show such a trend. The former trend is probably caused by strong soil-structure interaction that occurs along the direction of excitation. They increase from about 5 mm to 10 mm (20 % of the thickness of the surface layer) over a distance of 0.4-0.6 times the embedment depth in series L, creating a gentler slope (about 1/5) for loose sand. In contrast, it increases from about zero to 10 mm over a distance of 0.3-0.4 times the embedment depth in series D,

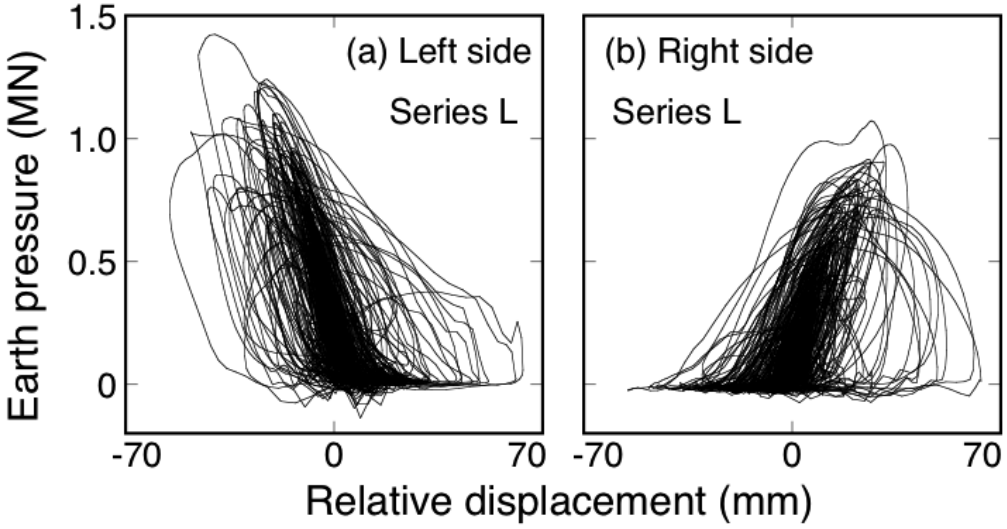


Figure 4 Relation between dynamic earth pressures acting on both sides of foundation and relative displacement between foundation and soil for series L

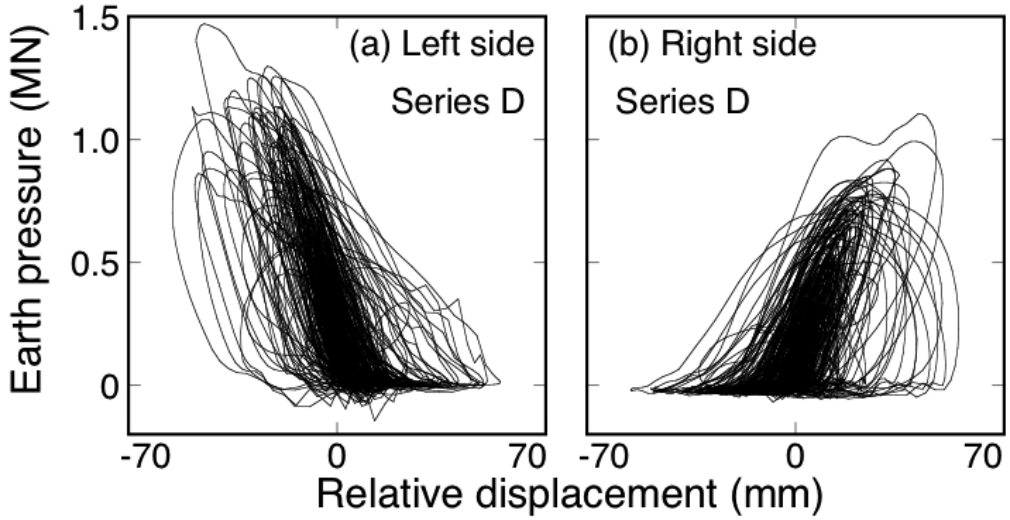


Figure 5 Relation between dynamic earth pressures acting on both sides of foundation and relative displacement between foundation and soil for series D

creating a steeper slope (about 1/2) for dense sand.

(3) A close examination of the ground settlement along the direction of shaking further indicates that the ground heaves at the left edge of the building, causing the largest ground settlement slightly away from the building rather than at the edge of the building. Such ground heave does not occur on the right side of the building. The difference in ground settlement distribution between both sides of the building may be associated with the difference in stress condition between the two sides of the foundation after shaking, i.e., the passive side stress state may develop on the left with the active side stress state on the right.

Assuming an active thrust created behind the embedded wall using the internal friction angle of Toyoura sand (ϕ =36° for Dr =40% and ϕ =42° for Dr =90%), the affected distance would be 0.51 and 0.45 times the embedment depth for series L and D, respectively. These values are consistent with those observed in the tests, suggesting that the ground settlements affected by dynamic soil-structure interaction would be mainly limit to the active thrust created behind the embedded wall.

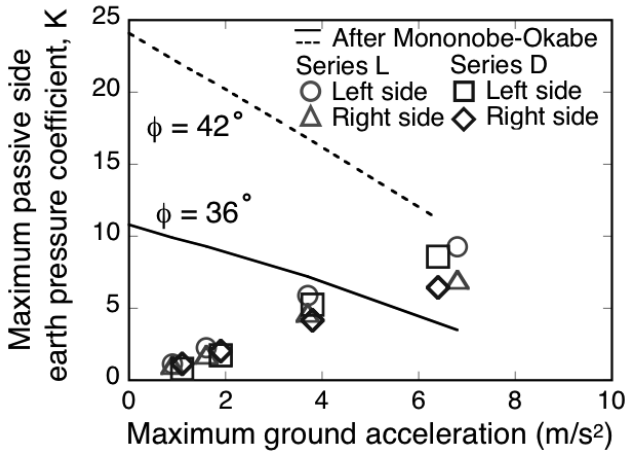


Figure 6 Relation of maximum passive side earth pressure coefficient with maximum ground acceleration at a depth of 1.2 m during each excitation

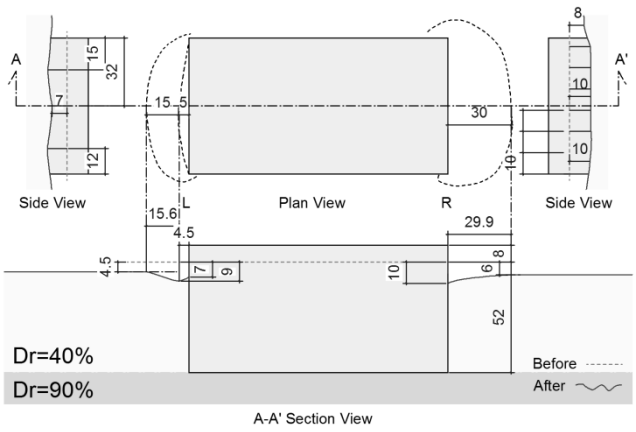


Figure 7 Ground settlements around building after final excitation for series L (Dr =40%, Model scale in mm)

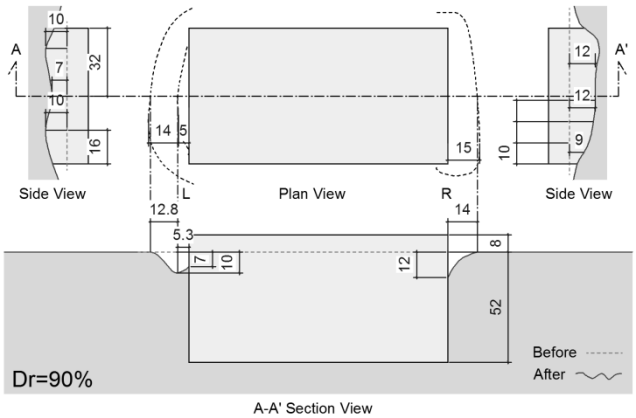


Figure 8 Ground settlements around building after final excitation for series D (Dr =90%, Model scale in mm)

3.4 Earth Pressures after Strong Shaking

Figure 9 shows the relation of earth pressure coefficients on both sides of the foundation after each excitation against the maximum shear strain developed in the surface layer during the excitation. The observed earth pressure coefficients after the final excitation that induced a shear strain on the order of 2.5 % in the surface layer are about 1.2 on the left and 0.4 on the right side, with an average value of about 0.8, which is significantly greater than the initial value of about 0.5. This seems in general

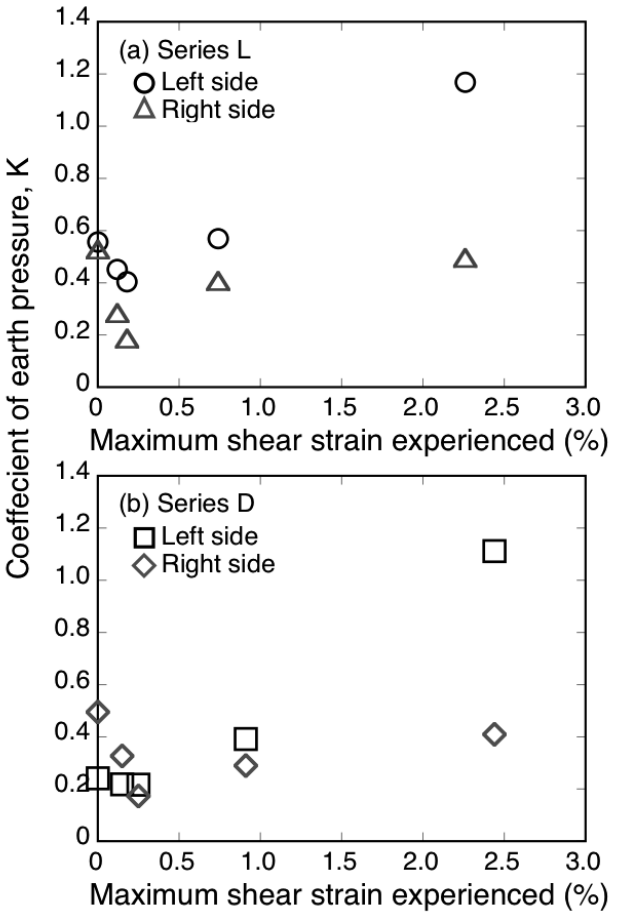


Figure 9 Relation of earth pressure coefficients on both sides of foundation after each excitation against maximum shear strain experienced

consistent with the finding by Youd and Craven (1975) that the earth pressure coefficient at rest of a sand increased from 0.3 to 0.8 when subjected to one hundred cycles of shear strain of about 1 %. The earth pressure coefficients after other excitation with a smaller peak acceleration, however, seem to decrease from the original "at-rest" value, which is inconsistent with the finding by Youd and Craven (1975).

The reason why the earth pressure coefficient at the end of last shaking varies from less than to more than twice the original "at rest" value is probably due to a possible permanent displacement that might have prevailed on the left side of the foundation. It is conceivable from the ground displacement pattern shown in Figures 7 and 8 that, after the end of the final excitation, the passive side stress state might have developed on the left of the foundation with the active side stress state on the right.

4. CONCLUSIONS

Dynamic centrifuge shaking table tests were performed using the soil-foundation-superstructure model to examine ground settlement distribution around a building subjected to strong ground shaking and earth pressures acting on its embedded foundation during and after shaking. Based on the test results and discussions, the following conclusions are made:

(1) The dynamic passive earth pressure acting on a rigid wall during strong shaking increases with increasing ground acceleration but becomes almost equal to the value estimated by the Mononobe-Okabe method only when the ground acceleration exceeds 6 m/s^2 accompanied by a shear strain of about 2.5 %.

(2) The static earth pressure acting on a rigid wall after strong shaking may vary from less than to more than twice the original "at rest" value, depending on the stress state developed on each side of the foundation at the end of shaking.

(3) The ground settlements away from the building along the excitation direction as well as those along the orthogonal direction would mainly reflect one-dimensional volume change characteristics of the surface layer due to cyclic loading.

(4) The ground settlement along the excitation direction increases towards the building, mainly due to strong soil-structure interaction that prevails near the building. This creates a slope dipping to the building with a slope angle much larger in dense sand than in loose sand. The horizontal distance within which the ground dips to the building due to dynamic soil-structure interaction is about 0.3-0.6 times the foundation embedment depth. The affected distance is well explained by assuming the active thrust behind the wall of the embedded foundation.

References:

Ishihara, K. (2009): New challenges in geotechnique for ground hazards due to intensity strong earthquake shaking, Earthquake and Tsunami, Geotechnical, Geological, and Earthquake Engineering, 2009, Volume 11, 91-114, DOI: 10.1007/978-90-481-2399-5_7.

Mononobe, N. (1924): Notes on the Vertical Motion of an Earthquake and on the Vibration of Structures, Journal of the civil engineering society, 10 (5), pp.1063-1094. (In Japanese)

Okabe, S. (1924): General Theory on Earth Pressure and Seismic Stability of Retaining Wall and Dam, Journal of the civil engineering society, 10 (6), pp. 1277-1323.

Tamura, S., Adachi, K., and Tokimatsu, K. (2011): Impulsive Vertical Acceleration Caused by Foundation Uplift during Earthquake, Proceedings of 8th International Conference on Urban Earthquake Engineering, March 2011, Tokyo Institute of Technology, 8pp.

Tokimatsu, K. (2007): Geotechnical problems in the 2007 Niigata-ken Chuetsu-oki earthquake, Geotechnical Earthquake Engineering and Soil Dynamics IV (GSP 181, ASCE), pp. 1-30, (doi 10.1061/40975(318)212).

Youd, L. Y. and Terry N. Craven, T. N. (1975): Lateral Stress in Sands During Cyclic Loading, Journal of the Geotechnical Engineering Division, Vol. 101, No. 2, pp. 217-221.

8CUEE CONFERENCE PROCEEDINGS
8th International Conference on Urban Earthquake Engineering
March 7-8, 2011, Tokyo Institute of Technology, Tokyo, Japan

DYNAMIC SOIL-STRUCTURE-INTERACTION OF SHALLOW FOUNDATIONS ON DRY SAND – A CENTRIFUGE BASED STUDY

S.K. Haigh[1)], C.M. Heron[2)], U. Cillingir[3)], and S.P.G Madabhushi[4)]

1) University Lecturer, Department of Engineering, University of Cambridge, Cambridge, United Kingdom
2) PhD Student, Department of Engineering, University of Cambridge, Cambridge, United Kingdom
3) Research Associate, Department of Engineering, University of Cambridge, Cambridge, United Kingdom
4) Reader in Geotechnical Engineering, Department of Engineering, University of Cambridge, Cambridge, United Kingdom
skh20@cam.ac.uk, cmh78@cam.ac.uk, uc206@cam.ac.uk, mspg1@cam.ac.uk

Abstract: This paper presents the results of a series of dynamic centrifuge model tests investigating the behaviour of single degree of freedom structures founded on dry sand. The paper highlights the benefits that can be accrued from allowing deformation between the building foundation and the soil. Specifically, rocking of the foundation can both dissipate energy through damping and can isolate the superstructure from large peak accelerations by lifting off from the soil below. This behaviour is examined by means of moment-rotation loops derived from centrifuge model test data which illustrate the variation in behaviour for different bearing pressures and earthquake characteristics.

1. INTRODUCTION

The seismic design of shallow foundations is well established, however there are improvements to the current design practice which can yet be made. The disconnection between structural and geotechnical engineering in seismically active regions has resulted in a design practice which can be inefficient and is potentially inadequate. This research project aims to tackle this problem by investigating the behaviour of the soil-foundation interface and how this affects the response of the building superstructure. Soil-structure interaction provides a potential means to dissipate energy and to isolate the structure from the full magnitude of the earthquake shaking. However the misconceptions associated with allowing movement in the soil-structure interface have thus far prevented this from being fully exploited. Current design codes generally advise that the foundation be designed in such a way as to act rigidly with the soil that it is founded on. Rubber bearings and other structural isolation techniques are often implemented at great cost to isolate the superstructure from the foundation. With a complete soil-foundation-structure analysis, the soil itself can be used to achieve results comparable to structural isolation techniques with a greatly reduced cost.

The majority of geotechnical failures involving shallow foundations are associated with soil liquefaction. The research presented here involves dry sand beds. Geotechnical failures are much rarer with dry sand, the main issue being excessive settlements. Far more common is the structural failure of a superstructure on shallow foundations sited on dry sand. One such example from the 2005 Pakistan Earthquake was presented by Ali et al. 2010, the failure being shown in Figure 1.



Figure 1 Damage from the 2005 Pakistan Earthquake
Ali et al. (2010)

Much research has already been conducted into shallow foundations subject to dynamic shaking. However, much of that research focused on saturated problems where liquefaction is important. The majority of that research also studied simple strip foundations with no superstructure mass. The benefits of studying the entire superstructure-foundation-soil system have recently been recognised and an increasing amount of research is being conducted to investigate the overall system behaviour.

A significant volume of research has focused on deriving an analytical mechanism to model the soil-structure interface. Many questions have arisen with the approaches

taken including whether a trapped wedge is present under the shallow foundation. None of the proposed mechanisms in the literature has so far been heavily scrutinised by comparison with centrifuge model test data, nor has the actual mechanism ever been observed during centrifuge modelling by, for example, conducting particle image velocimetry (PIV) (White et al. 2003) on images collected with a high speed camera. However, one mechanism which has been verified by 1g testing is that proposed by Paolucci and Pecker (1997) entitled 'Mec 2'. Testing conducted at 1g by Knappett et al. (2006) utilising PIV to measure foundation soil movements found that Mec 2 modelled the deformation mechanism accurately. There have also been significant numbers of centrifuge studies conducted to investigate the same problem. Earlier research such as that conducted by Zeng and Steedman (1998) was focused on estimating settlements resulting from dynamic shaking. More recent research has focused on the soil-structure interaction, involving allowing displacement to occur between the soil and foundation. The resulting rocking and sliding of the foundation as well as the structures' self-centering characteristics have been investigated by Gajan and Kutter 2008. Further work is required, however, to ensure an analytical mechanism can be proposed which could be used by industry and to ensure that any proposed mechanism has been tested robustly against a wide range of loading scenarios through physical modelling studies. Furthermore, methods to quantify energy dissipation in the soil-structure interface need developed.

2. METHODOLGY

A series of four centrifuge tests were conducted using the 10m Turner Beam Centrifuge at the University of Cambridge. To induce dynamic shaking in the models, a Stored Angular Momentum (SAM) Actuator (Madabhushi et al. 1998) was used. The tests were run at a nominal centrifugal acceleration of 50 g. During dynamic tests, boundary effects can influence the response of the specimen being tested, hence, to minimise these effects an Equivalent Shear Beam (ESB) box was used. An ESB box consists of Aluminium rings connected, and separated with layers of rubber. The stiffness of the ESB box used in this series of tests was tuned to match the natural frequency of a sand column with a voids ratio of 0.77 (I_D=58% for Hostun sand) at 50g.

Models were prepared with dry Hostun HN31 sand at a target relative density of either 50% or 80%. Sand pouring was completed using an automatic sand pourer (Madabhushi et al. 2006) to ensure uniformity throughout the depth of the sand column .

During pouring of the sand, an array of piezoelectric accelerometers and micro-electromechanical system (MEMS) accelerometers were located at specified locations to allow the response of the sand column to be monitored during shaking. Further accelerometers were attached to the model structures to track their dynamic response. Linear variable differential transformer (LVDT) displacement transducers were used to monitor the settlement of the structures and free-field surface. The model layout is shown in Figure 2.

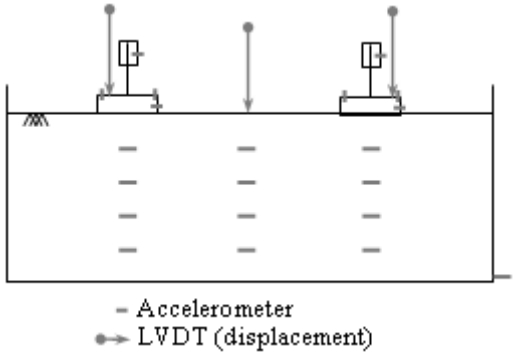


Figure 2 Instrumentation layout

The prototype structure modelled in these tests is an isolated raft footing with an approximately three storey superstructure subjected to lateral shaking along one axis. Lumped mass single degree of freedom structures were placed on the sand surface during the first two tests as shown in Figure 2. For the second set of tests, sway frame single degree of freedom structures were used as they were considered more representative of the prototype being modelled in terms of the rocking-sliding response during shaking. The reasoning for this will not be discussed here. All the model structures had a model foundation size of 80mm x 80mm (4m x 4m at prototype scale). Two model structures with bearing pressures of 50kPa and 100kPa were placed on the sand surface with no embedment for each test. The model structures were tuned to have a fixed base natural frequency of 50 Hz.

Each model was subjected to three earthquakes. The first was a small amplitude 50 Hz shake with a peak ground acceleration (PGA) of 8g (0.16g prototype). This was followed by a larger fixed amplitude shake at 50 Hz with a PGA of 16g (0.32g prototype). These were followed by a sine-sweep earthquake in which the frequency was dropped from 60 Hz to 0 Hz with fixed displacement amplitude and hence a decreasing acceleration magnitude. Data was acquired during each test at a sampling frequency of 4 kHz.

3. OVERVIEW OF RESPONSE

3.1 Settlements

The settlement of a structure will be affected by the bearing pressure that it exerts on the ground and the relative density of the soil. By reference to Figure 3 it can be seen that the settlement traces did respond as expected. Figure 3 shows data for the small structure (50kPa) during the larger 50Hz earthquake. The structure settled by 3.95mm (200mm prototype scale (PS)) on loose sand and only 0.67mm (35mm PS) when sited on dense sand. The free-field settlement follows the structural settlements in pattern however, again, as would be predicted, the differential settlement between the structure and free-field are greater for loose sand, as shown in the lower plot on Figure 3.

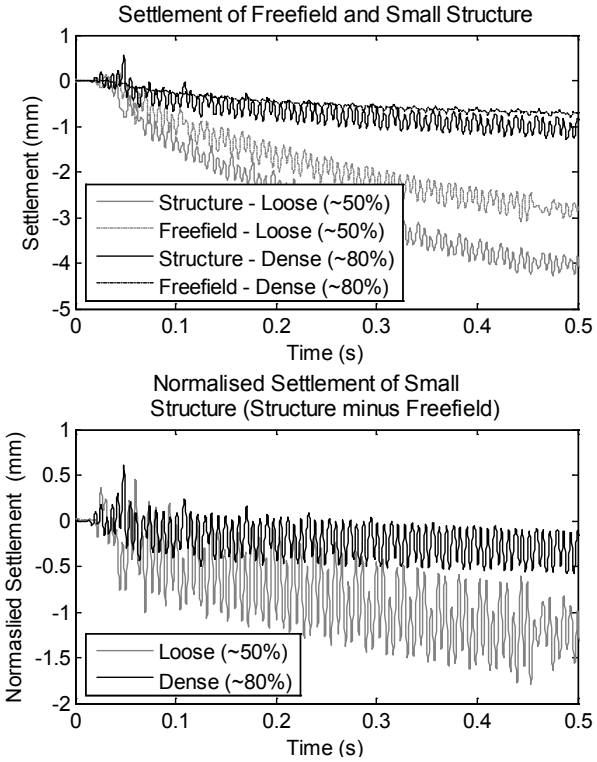


Figure 3 Variation in settlement of 50kPa model structure located on sands beds of varying relative density

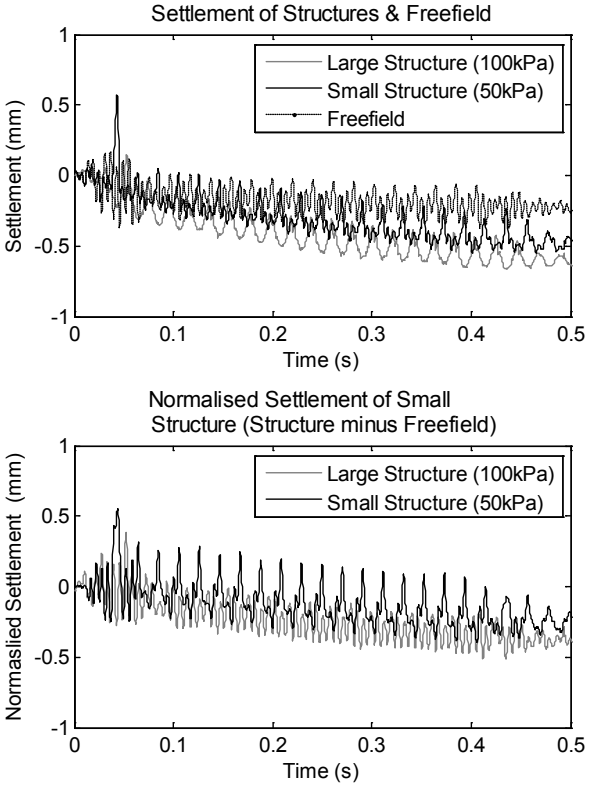


Figure 4 Variation of settlement of model structures with varying bearing pressure

Assuming uniform conditions under a foundation and hence no differential settlements occurring across the footprint of the structure, the most common damage associated with seismic induced settlements is to the services supplying the structure. It is therefore perhaps more relevant to quote differential settlements relative to the free-field. In this case, those settlements were 1mm (50mm PS) and 0.2mm (10mm PS) for the loose and dense sand models respectively. This level of settlement is more relevant and much more modest that the total settlement values quotes above.

Another property affecting settlements is the bearing pressure of the structure. The effect of bearing pressure on a dense sand model is shown in Figure 4. The total settlement values were 0.5mm (25mm PS) and 0.6mm (30mm PS) for the 50kPa and 100kPa structures respectively. Differential ultimate settlements relative to the free-field were 0.3mm (15mm PS) and 0.4mm (20mm PS) respectively. These settlement values are well within the serviceability limit state of current design practice.

3.2 Frequency Response

By analyzing the data collected during the sine-sweep shaking, the natural frequency of the superstructure-foundation-soil (SFS) system can be determined. Figure 5 shows the response of the superstructures of the lumped mass SDOF structures sited on dense sand during a sine-sweep earthquake. It can be clearly seen that the peak amplitude response of both superstructures occurs when the input acceleration magnitude has dropped significantly. As the frequency reduces during the sine-sweep earthquakes, the spike in response of the superstructures is being driven by the input frequency passing through the natural frequency of the SFS system. At this spike in response, it would be expected that the input frequency and superstructure vibration frequency would be the same. The lower plots on Figure 5 display the frequencies present in the input and superstructure accelerations during the period of peak superstructure response. It can be observed that indeed the input and superstructure frequencies do match during the period of peak response.

In the methodology section of this paper, it was specified that the model structures had a fixed base natural frequency of 50Hz. The natural frequencies of the SFS systems as determined from Figure 5 are much lower than this at 39Hz and 43Hz for the large and small structures respectively. Basic mechanical vibration theory tells us that the higher the mass the lower the natural frequency for the same stiffness of system. Therefore the observed response is as would be predicted. What this highlights is the importance of carrying out a coupled structure-foundation-soil analysis when designing buildings in seismically prone areas. If the foundation had been assumed to act rigidly with the soil beneath and hence a fixed base analysis conducted of the structure, the frequency at which the building is most vulnerable would have been significantly overestimated. Soil-structure interaction must be taken into consideration when conducting any seismic design or analysis.

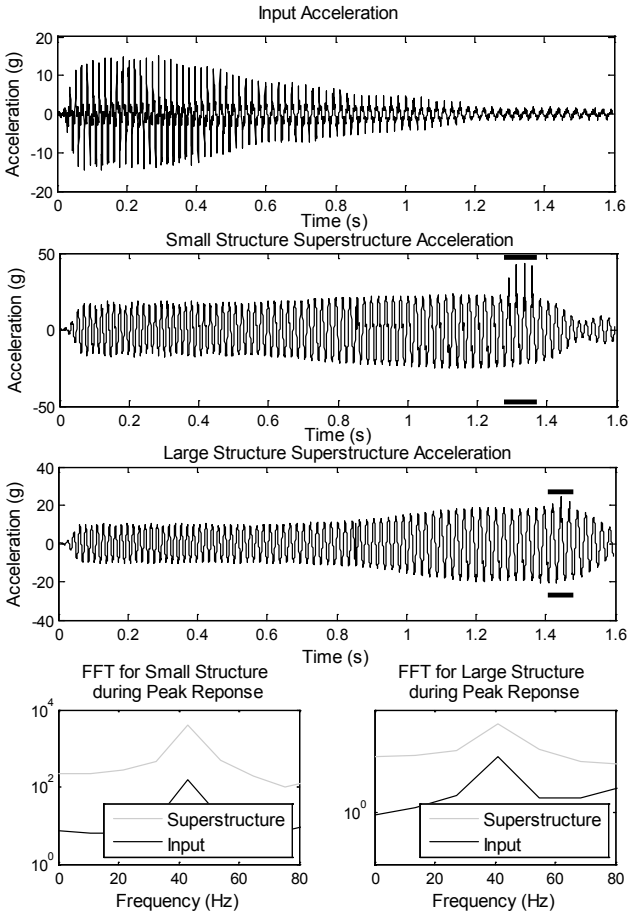


Figure 5 Natural frequency of soil-structure system for larger and smaller model structures

4. MOMENT-ROTATION DERIVATION

The impact of the foundation performance on the behaviour of the structure can be quantified by investigating the relationship between the foundation rotation and the moment being applied to the soil.

The acceleration of the superstructure and resulting d'Alembert force result in a moment being applied by the foundation onto the sand beneath. Further, the rotational moments of inertia of the superstructure and the foundation add to this moment. These moments result in a rotation of the foundation with one edge lifting off and the other embedding into the sand. Lift-off of footings is not commonly allowed for in seismic design codes, instead, foundations are designed to be large enough to act rigidly with the ground beneath, allowing neither rotation nor sliding. The benefits of allowing such relative motion between the foundation and the soil will be discussed later.

In generating the moment-rotation loops presented in the following section, the rotations were calculated using the double-integral of two vertical accelerometers which were located on either edge of the foundation. A problem with calculating the rotation with this method is that heavy filtering of the acceleration signals is required in order for the integral not to drift. This filtered results in reduction in the peak displacements and hence the peak rotations being evaluated. This problem will be solved in future tests, however, for this analysis, qualitative comparisons can still be made between the moment-rotation plots, although when examining the plots presented later in this paper, it must be remembered that more accurate loops would be stretched outwards in the horizontal direction. The same vertical accelerometers also allowed the rotational mass moment of inertia to be calculated. The acceleration of the superstructure measured during shaking was multiplied by the mass of the superstructure to provide a force and further multiplied by the distance between the centre of the superstructure and the soil to provide a moment value.

The usefulness of the moment-rotation loops is that the area within the loops provides a representation of the energy dissipation. The slope of the loops also provides an indication of the rotational stiffness of the foundation system.

5. BEHAVIOUR OF MOMENT-ROTATION LOOPS

Comparison of moment rotation loops from different tests allows the effects of three different parameters on the soil-foundation interaction to be investigated.

5.1 Bearing Pressure

Increasing the bearing pressure of the model structure has a two fold effect. The larger bearing pressure results in an increase in small strain stiffness of the sand beneath the footing due to the higher confining stress. In addition, the increased bearing pressure means an increased superstructure mass and hence an increased moment being applied to the foundation when subjected to the same magnitude of acceleration.

Figure 6 shows the moment-rotation loops for the two SDOF model structures during a test on loose sand. For clarity, the moment-rotation loops shown are only for the middle third of the shaking duration. It is observed that the moment applied by the smaller (50kPa) structure is indeed smaller than that for the larger structure (100kPa).

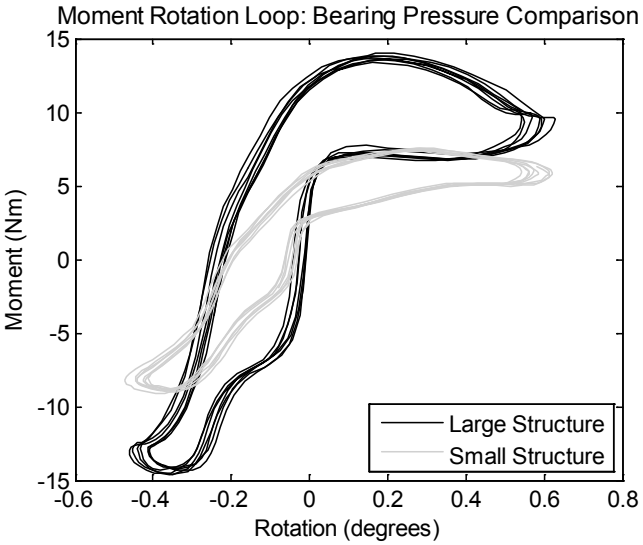


Figure 6 Variation of moment-rotation plot with bearing pressure

The superstructure to foundation mass (SSFM) ratios are the same and the centres of gravity are similar for both model structures. The lighter structure's superstructure is therefore half the mass of the larger structure's superstructure. It could be assumed that both superstructures would experience similar acceleration magnitudes. However, the large structure applies a moment which is only approximately 50% higher than that of the smaller structure. When the acceleration traces are examined, it is observed that the larger superstructure experiences an acceleration which is about 25% smaller in magnitude than the smaller superstructure. As shown earlier the natural frequency for the two structure-soil systems are different. Given that this model was shaken at 50 Hz and the smaller system's natural frequency is 45 Hz, (compared to 39 Hz for the larger system), this proximity of the excitation frequency to the natural frequency will result in greater superstructure acceleration.

There is one further moment component which should be added into the calculation. This is created when the foundation lifts off at one edge and hence the centre of the contact area moves. The self-weight of the structure thus applies a moment about the new foundation centre. This effect is not included in this analysis as the instrumentation was inadequate to determine the centre of rotation. It is interesting to observe that the peak rotation is the same for both structures, a result which is consistently seen across all the tests conducted thus far. This limit on rotation, independent of bearing pressure could be a function of the self-centering nature of the structures. With similar centres of mass and SSFM ratios, it would be expected that the self-centering and d'Alembert forces would balance each other at a similar level of rotation, however this assumes an equal acceleration magnitude in each of the superstructures which we have already seen not to be true. Therefore, in reality the peak rotations may turn out to be marginally different between the two structures and the apparent identical peak rotations shown in Figure 6 may be a function of the data processing and filtering. This will be examined in future tests when the rotations are measured more accurately.

The area within moment-rotation loops gives an indication of the energy dissipated. When the area within the loops for the entire duration of shaking is calculated, it is found that the larger structure dissipated more than twice the energy of the smaller structure. Once again, this would be expected due to its mass being doubled. The larger structure's increased mass will also result in it coupling more rigidly with the sand beneath through frictional forces and hence more energy will be transmitted into the structure.

5.2 Frequency Effects

As discussed in the previous section, the excitation frequency has a major impact on the response of the structures. During one test with the sway frame structures, an additional earthquake was fired with a frequency of 40Hz but with a peak ground acceleration the same as that of the smaller 50Hz earthquake. This allowed the consequence of moving the excitation frequency closer to the natural frequency of the structure to be examined. Figure 7 shows the moment-rotation loops for these two earthquakes for the small structure only. The results show that the loops for the lower frequency earthquake extend much further along the x-axis showing peak rotations increasing three-fold over the rotations experienced during the 50Hz earthquake. This result is not hugely surprising but is rather alarming given, as discussed previously, that fixed base analysis would have shown the structural vulnerability at 50Hz. The energy dissipated during the 40Hz earthquake was almost twice that dissipated during the 50Hz earthquake.

Another variation between the two moment-rotation loops is the apparent change in small strain stiffness between the two earthquakes. It would seem that the higher frequency earthquake resulted in a higher stiffness between the footing and the soil. The loops plotted are again for the middle third of the earthquakes only. The loops have a similar stiffness during the initial couple of cycles of shaking. Therefore, a potential explanation for the variation in small rotation stiffness is that the large soil strains result in increased softening in the soil-structure interface when the structure suffers large rotation amplitudes due to resonance.

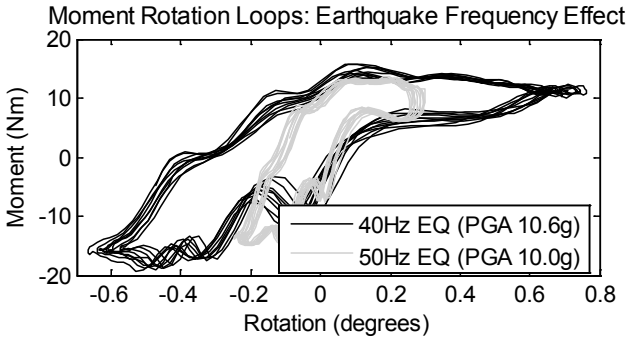


Figure 7 Variation of moment-rotation plot with frequency

5.3 Acceleration Magnitude

Increasing the input acceleration magnitude would be expected to increase the accelerations measured on the structure and hence to increase the moment applied by the structure through the foundation to the soil beneath. Consequently the rotations would also be expected to increase. Figure 8 shows the moment-rotation loops for the small sway frame structure during a test on dense sand. As can be observed, there is only a marginal increase in the applied moment when the larger (16.5g PGA, 0.3g PS) earthquake is fired. However, the rotations increase significantly being approximately twice those experienced during the smaller earthquake (10.0g PGA, 0.2g PS). It is clear therefore that the extra energy being input during the larger earthquake is not being transmitted upwards through the foundation and into the structure. This may be due to the existence of a threshold moment above which lift-off of the foundation occurs giving a very low rotational foundation stiffness. This appears to agree with the shapes of the

moement-rotation loops derived for these experiments. This marginal increase in applied moment demonstrates the foundation system's ability to isolate the building from high accelerations due to high-magnitude earthquakes. The larger rotations resulted in increased energy dissipation during the larger earthquake of 250% compared to the energy dissipation during the smaller earthquake. If the building could be constructed in such a way as to cope with significant rotations during the earthquake, this could offer significant benefits as an earthquake mitigation technique.

It might be expected that a reduction in small strain stiffness would be observed during the larger earthquake compared to the smaller earthquake due to increased shear modulus degradation. However, the slopes of the loops at small strains are very similar for both earthquakes. During the same test two sine-sweep earthquakes of varying magnitude were fired. During the larger magnitude sine-sweep earthquake the natural frequency of the system was found to be 38 Hz compared to 42 Hz during the smaller sine-sweep earthquake. Given that the masses involved remained the same, this reduction in natural frequency during the larger earthquake can only be attributed to a reduction in the stiffness of the soil-structure interface. This change of natural frequency of 10% would correspond to a change in stiffness of approximately 20%. Given the shapes of the moment-rotation loops as currently derived, this small change in stiffness would be difficult to observe.

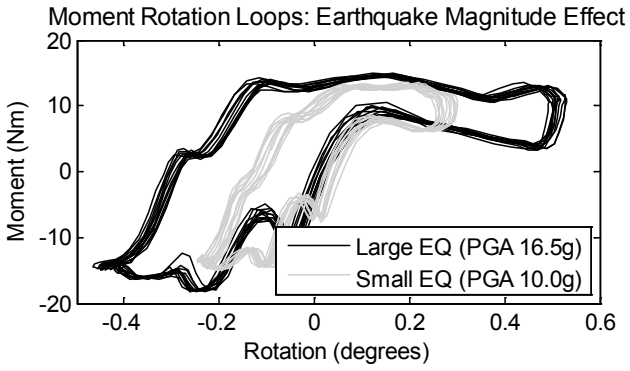


Figure 8 Variation of moment-rotation plot with acceleration

6. CONCLUSIONS

The results of an initial analysis of experiments involving single degree of freedom structures on shallow foundations have been presented. The importance of soil-structure interaction analysis when conducting seismic design due to the major impact the interaction has on the natural frequency of the system has been demonstrated. It was observed that the natural frequency of the system could vary by up to 20% when sited on the sand surface compared to the fixed base natural frequency.

In addition, the coupling of the foundation with the ground beneath is very important. Increasing the displacement and hence acceleration does not directly result in proportionally increased accelerations in the structure owing to the ability of the structure to lift off and rock. This lack of connection is therefore advantageous as it reduces the energy transmission in the structure and hence reduces the ductility requirements of the structure. There are two ways this disconnection between the foundation and the soil can manifest itself. Firstly though relative sliding between the foundation and the soil. This sliding process isolates the structure from the full magnitude of shaking of the soil beneath but also dissipated energy in the process. The degree of relative sliding has not yet been measured but will be in forthcoming centrifuge tests. Secondly the foundation can rock on the sand beneath, as has been observed in the tests conducted thus far. This again dissipated large amounts of energy. Neither of these methods have been included into seismic design due to the fear of excessive settlements, permanently rotated structures and toppling of the structure during rocking. Even when an earthquake was fired at the natural frequency of the system, these model structures never developed large permanent rotations, nor did they reach any degree of rotation which could result in toppling of the structure. In fact, allowing the structure to rock and dissipate the energy through plastic deformation of the soil is particularly safe due to the self centering characteristic which both prevents complete collapse and also minimizes permanent rotations. Establishing a plastic hinge in the soil will not result in permanent deformations whereas a plastic hinge developing within the structure will result in complete collapse.

Future work on this project will allow more accurate moment-rotation loops to be plotted. This will then allow for the confirmation and/or modification of the theories derived thus far based on the current results. The ultimate aim of this research is to derive a general analytical mechanism which is capable of modeling the soil-structure interface in detail and to encourage the development of foundation designs in which deformation is permitted in order to minimize inertial loads on the superstructure.

Acknowledgements:

The authors would like to acknowledge the support of the European Union Framework 7 Project SERIES.

References:

Ali, S., Ali, L. and Ammar, M. (2010), "Geotechnical aspects of recent Pakistan earthquakes," *Proceedings of the 5th International Conference on Recent Advances in Geotechnical Earthquake Engineering and Soil Dynamics and Symposium in Honor of Prof. I.M. Idriss*, Paper No. EQ 3.

White, D.J., Take, W.A. and Bolton M.D. (2003), "Soil deformation measurement using particle image velocimetry (PIV) and photogrammetry," *Géotechnique*, **53**(7), 619–631.

Paolucci, R. and Pecker, A. (1997), "Seismic bearing capacity of shallow strip foundations on dry soils," *Soils and Foundations*, **37**(3), 95–105.

Knappett, J.A., Haigh, S.K. and Madabhushi, S.P.G. (2006), "Mechanisms of failure for shallow foundations under earthquake loading," *Soil Dynamics and Earthquake Engineering*, **26**(2-4 SPEC. ISS.), 91–102.

Zeng, X. and Steedman, R.S. (1998), "Bearing capacity failure of shallow foundations in earthquakes," *Géotechnique*, **48**(2),

235-256.

Gajan, S.A. and Kutter, B.L. (2008), "Capacity, settlement, and energy dissipation of shallow footings subjected to rocking," *Journal of Geotechnical and Geoenvironmental Engineering*, **134**(8), 1129–1141.

Madabhushi, S.P.G., Schofield, A.N. and Lesley, S. (1998), "A new stored angular momentum (SAM) based earthquake actuator," *Proceedings of Centrifuge 98*, pages 111–116.

Madabhushi, S.P.G., Houghton, N.E. and Haigh, S.K. (2006), "A new automatic sand pourer for model preparation at university of Cambridge," *Proceeding of the 6th International Conference on Physical Modeling in Geotechnics*.

8CUEE CONFERENCE PROCEEDINGS
8th International Conference on Urban Earthquake Engineering
March 7-8, 2011, Tokyo Institute of Technology, Tokyo, Japan

IMPULSIVE VERTICAL ACCELERATION CAUSED BY FOUNDATION UPLIFT DURING EARTHQUAKE

Shuji Tamura[1], Keisuke Adachi[2], and Kohji Tokimatsu[3]

1) Associate Professor, DPRI, Kyoto University, Japan
2) Mitsui Fudosan Co., Ltd (Former Graduate Student, Kyoto University), Japan
3) Professor, Tokyo Institute Technology, Japan
tamura@sds.dpri.kyoto-u.ac.jp

Abstract: Dynamic centrifuge tests were performed using soil-footing – superstructure models to investigate the effects of footing uplift on the vertical acceleration of a footing during strong shaking. The horizontal shearing and vertical compressive forces on the base of the footing, as well as the earth pressure and wall friction force on both sides of the footing, were measured carefully using newly developed 2D-load cells. The following conclusions were drawn. (1) The foundation uplift induces vertical acceleration of two types on an embedded footing: "impulsive vertical acceleration" caused by the collision impulse between the foundation and soil and "induced vertical acceleration" caused by the height movement of the gravitational center of structure. (2) The amplitude of the impulsive vertical acceleration, more than 12 m/s^2, is much greater than that of the induced vertical acceleration. (3) When the horizontal superstructure acceleration exceeds about 5 m/s^2, the amplitudes of the impulsive vertical acceleration and the induced vertical acceleration increase dramatically, suggesting that a small earthquake will generate only small vertical acceleration but that an intense earthquake will trigger the foundation uplift and generate extremely high vertical acceleration especially by the collision impulse.

1. INTRODUCTION

A slender building supported by a shallow foundation might be uplifted along with rocking during an intense earthquake. Houser (1963), in his pioneering study of the foundation uplift, suggested that the stability of a tall, slender block subjected to earthquake motion is much greater than would be inferred from its stability against a constant horizontal force. Subsequently, many researchers studied the effects of foundation uplift on the seismic response of structures. Based on numerical analyses, Meek (1975) reported that the uplift engenders a favorable reduction in the structural deformation. Based on model nine-story building frame shaking table tests and two-dimensional numerical analyses, Huckelbridge and Clough (1978) reported that the uplift causes a general reduction in the applied loading. To consider the beneficial effects of foundation uplift, Chopra et al. (1985) proposed a simplified analysis of the structure response associated with foundation uplift.

Meek (1975) also predicted negative effects of foundation uplift, as characterized by collision impulses when the foundation slams into renewed contact with the ground. Based on numerical analyses of reactor buildings subjected to both horizontal and vertical input motions, Muto and Kobayashi (1979) reported that foundation uplift can induce vertical acceleration of two types: a collision impulse caused by the foundation uplift and induced vertical acceleration caused by the height movement of the gravitational center of the structure. They also reported that the former can have greater acceleration amplitude than the latter. Despite numerous numerical analyses, few experimental studies have examined the collision impulse generated by the foundation uplift.

The objective of this study is to examine the vertical acceleration of those two types caused by foundation uplifting that occurs during strong shaking. A dynamic centrifuge test on a superstructure–footing model was performed, with the footing embedded in the sand layer.

2. CENTRIFUGE TEST

2.1 Test Model

A dynamic centrifuge test was conducted using a soil-foundation – superstructure model at 40 × g centrifugal acceleration with the geotechnical centrifuge at the Disaster Prevention Research Institute, Kyoto University. Figure 1 shows the test setup and instrumentation. The soil-footing – superstructure system was prepared in a laminar shear box with inner dimensions of 450 mm

(length) × 150 mm (width) × 200 mm (height). Table 1 presents the weights and dimensions of the footing–superstructure model in the model and prototype scales. The footing was modeled with aluminum alloy of 124 mm (shaking direction) × 64 mm (width) × 52 mm (height). The superstructure modeled with rigid brass of 82 mm (shaking direction) × 58 mm (width) × 50 mm (height) was supported by two 35-mm-high plate springs. The superstructure weight was 2.0 kg. That of the footing was 1.0 kg. The natural frequency and damping constant of the superstructure under the fixed footing condition were, respectively, about 105 Hz and 0.5%. Dry sand was air-pluviated to prepare a uniform soil layer with Dr=90%. Toyoura sand with D_{50}=0.21 mm was used for the test. The soil model heights were 198 mm; the footing was embedded 50 mm into the dry sand layer. The static friction coefficient between Toyoura sand and the footing surface was 0.37.

2.2 Earth Pressure, Base Friction, and Soil-structure Responses Measurements

Figure 2 portrays a detailed cross section of the foundation in the plane parallel to the direction of shaking, with two base plates and two active/passive side plates. Each of these four plates was connected to the main body of the foundation with a newly developed load cell (Tokyo Sokki Kenkyujo Co. Ltd.), as shown in Photo 1, to identify forces acting on the foundation. Each load cell was designed to measure normal and shear forces acting on the attached plate separately. The two load cells on the base plates therefore provided the horizontal shear and vertical forces. The remaining two attached on the side walls provided the earth pressure and wall friction force on the active and passive side plates. The base lines of the forces measured by the load cells were set to zero before the start of centrifuge test.

The shaking test was run using Rinkai92, i.e., a synthesized ground motion for the Tokyo Bay area, as the input horizontal motion with no vertical motion to the base of the container. The peak acceleration was scaled to about 5 m/s^2 in prototype scale. In addition to forces acting on the footing described in the preceding paragraph, the horizontal and vertical accelerations of superstructure, footing, soil and container base were measured, as well as the horizontal and vertical displacement of the footing (Fig. 1). All data presented herein are of prototype scale.

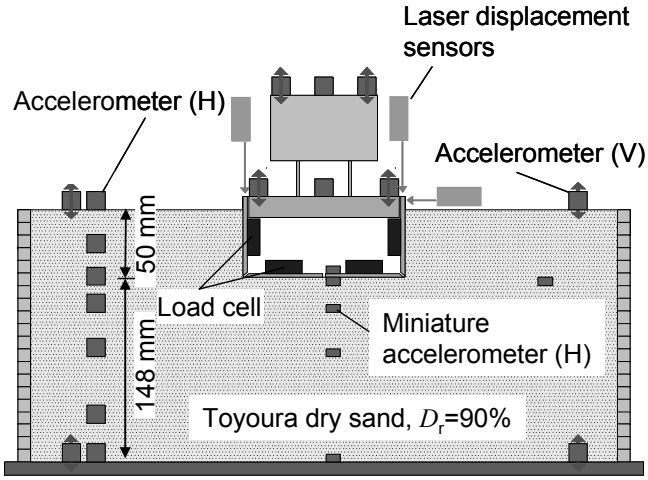


Figure 1 Test model

Table 1 Weights and dimensions of the footing– superstructure model in the model and prototype scale

		Unit	Prototype	Model
Footing	Mass	kg	64,000	1.0
	Length (L×B×H)	m	4.96×2.56×2.08	0.124×0.064×0.052
Structure	Mass	kg	128,000	2.0
	Natural frequency	Hz	3.8	105

3. CENTRIFUGE TEST RESULTS

3.1 Horizontal Acceleration and Footing Rotation

Figure 3 depicts the respective time histories of the horizontal acceleration of the input, the ground surface,

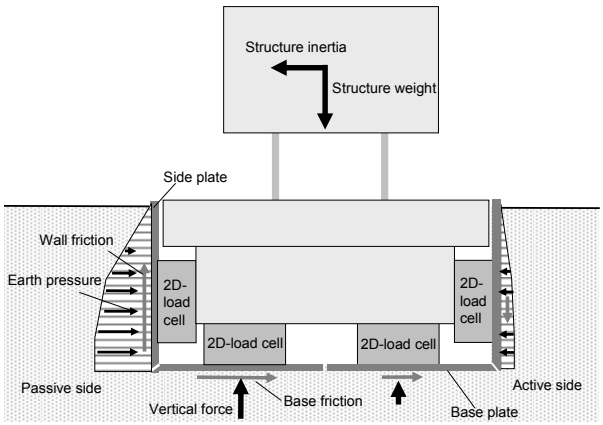
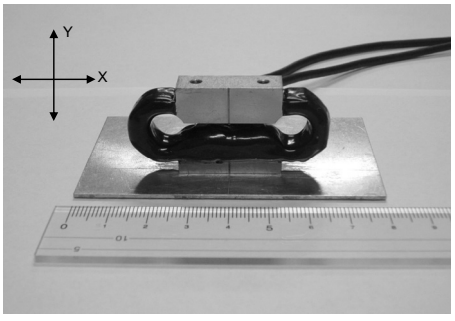


Figure 2 Earth pressure and base friction measurements



Picture 1 Two-directional load cell capable of separate measurements from horizontal and vertical forces

the top of the footing and superstructure, and the footing rotation. The footing rotation was evaluated as the ratio of the relative displacement between the vertical displacements on the left and right sides of the footing, which were calculated by double integration of the accelerations, to the distance between the two sensors (clockwise rotation = positive). The peak horizontal accelerations of the ground surface and the superstructure are, respectively, 7.5 m/s^2 and 8.3 m/s^2. The amplitude of the horizontal superstructure acceleration tends to be nearly constant for T=20–40 s. However, the amplitude of the footing rotation, generated by the superstructure inertia, tends to change with time. The waveform of the footing rotation angle differs greatly from that of the superstructure.

3.2 Vertical Acceleration

Figure 4 shows the time histories of the vertical acceleration of the container base, the ground surface, and the footing, which are the average of the two values measured on the left and right sides and on the left and right sides of footing. The peak average vertical ground surface acceleration is about 2.8 m/s^2 despite extremely small values on the container base (about 0.3 m/s^2). The peak average vertical acceleration of the footing (7.4 m/s^2) is apparently larger than that of the ground surface. The peak vertical accelerations of both sides of the footing were extremely high: greater than 12 m/s^2. It is noteworthy that the positive vertical footing acceleration was spiky and much greater than the negative acceleration.

Figure 5 shows the wavelet frequency spectra of the horizontal acceleration of superstructure and the vertical acceleration of the footing left side. The wavelet frequency spectrum of the vertical acceleration is quite different from that of the horizontal acceleration. The horizontal acceleration always contains low frequency components, from 1 Hz to 3 Hz. On the other hand, the vertical acceleration have wide frequency range from 1 Hz to 20 Hz and occurred intermittently.

To investigate the vertical acceleration of the footing, the relation between the peak vertical acceleration of the footing left side and the predominant frequency at the same instance is shown in Fig. 6. The positive vertical acceleration tends to contain higher frequency component than the negative vertical acceleration. The predominant frequency of the positive high acceleration whose amplitude is greater than 5 m/s^2, is 3-12 Hz. On the other hand, the predominant frequency of the positive high acceleration is 3-7 Hz, which is about two times that of the superstructure horizontal acceleration.

4. VERTICAL ACCELERATION CAUSED BY FOOTING UPLIFT

4.1 Footing Rotation and Vertical Acceleration on Footing

The centrifuge test results show that high vertical acceleration exceeding 12 m/s^2 occurs on the footing in spite of the absence of the vertical input motion. To discuss why such high vertical acceleration was induced on the footing, Fig. 7 depicts selected time histories of important values for a period of 3 s (T=22–25 s) during which the footing rotation has a peak value. These include the horizontal acceleration of the superstructure, vertical accelerations of left and right sides of footing and their average, the vertical shear force acting on active/passive sides (wall friction), the vertical forces acting on the left and right sides of footing base and their sum, and the footing rotation. The vertical solid lines (T=p1, p2) and the dotted lines (T=m1, m2) in the figure correspond respectively to the instants at which the average vertical

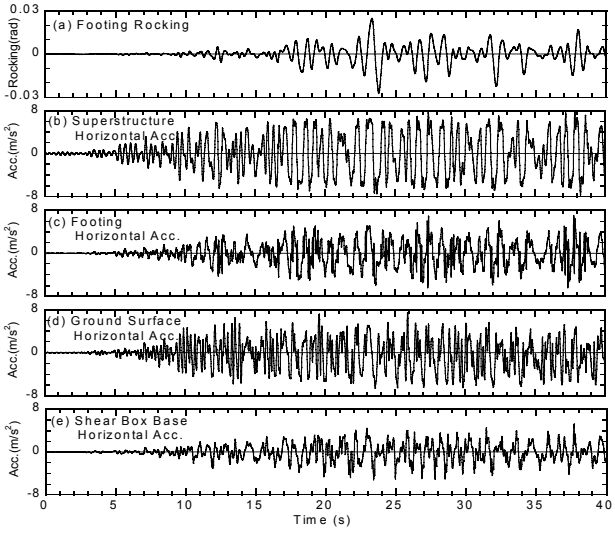


Figure 3 Time histories of horizontal accelerations and footing rotation

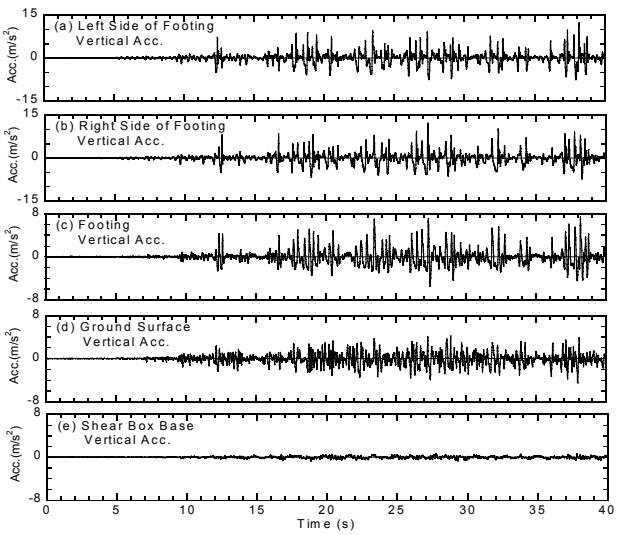


Figure 4 Time histories of vertical accelerations

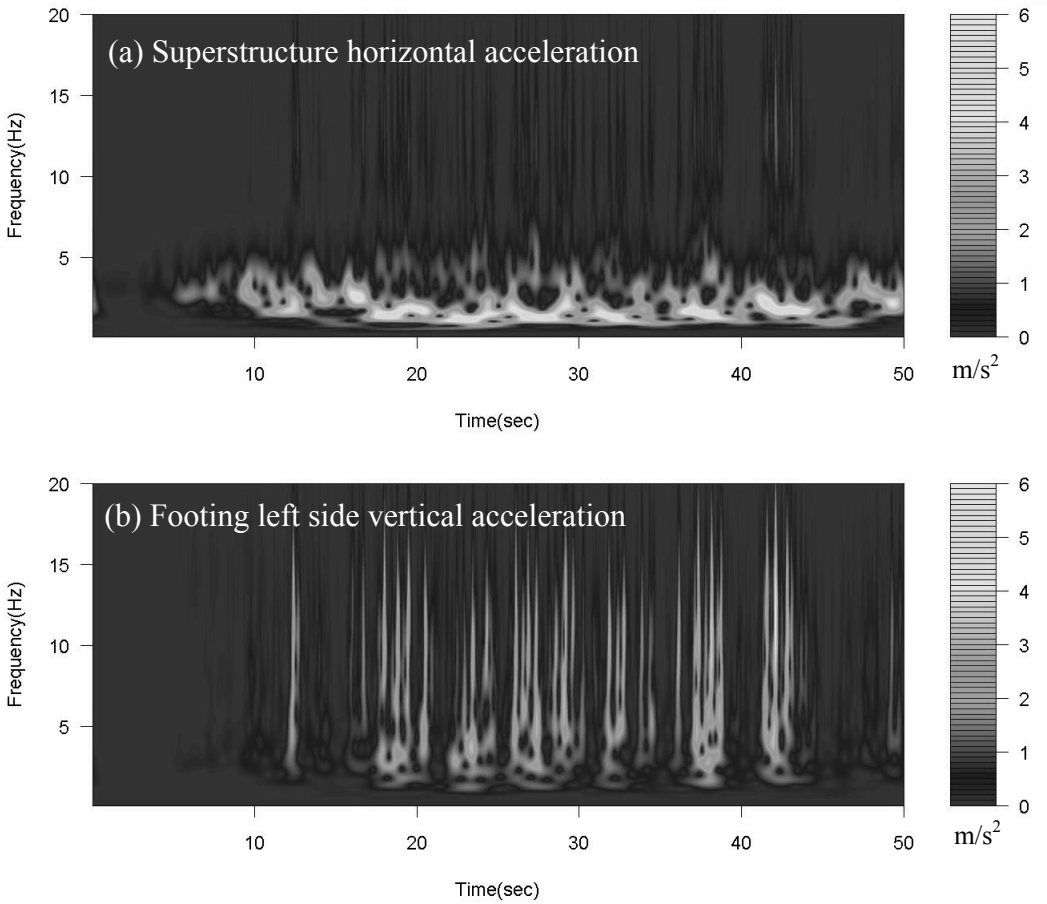


Figure 5 Wavelet frequency spectra of horizontal acceleration of superstructure and vertical acceleration of footing left side

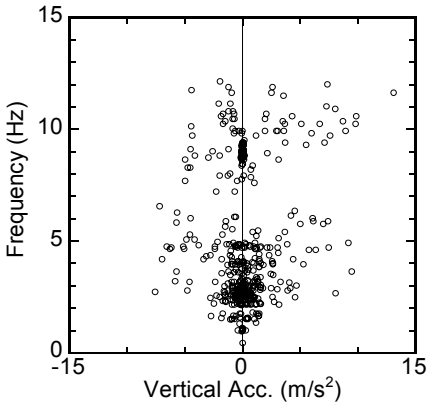


Figure 6 Vertical acceleration peaks of footing left side and frequency at the same instance

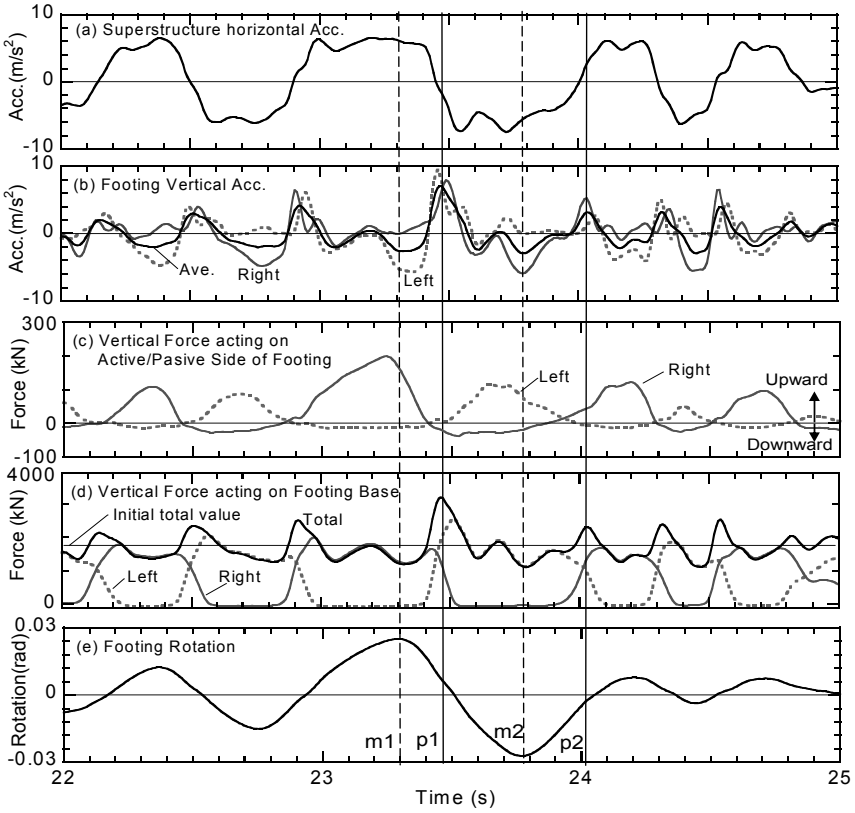


Figure 7 Time histories of footing responses and vertical force acting on the footing base for T=22– 25 s

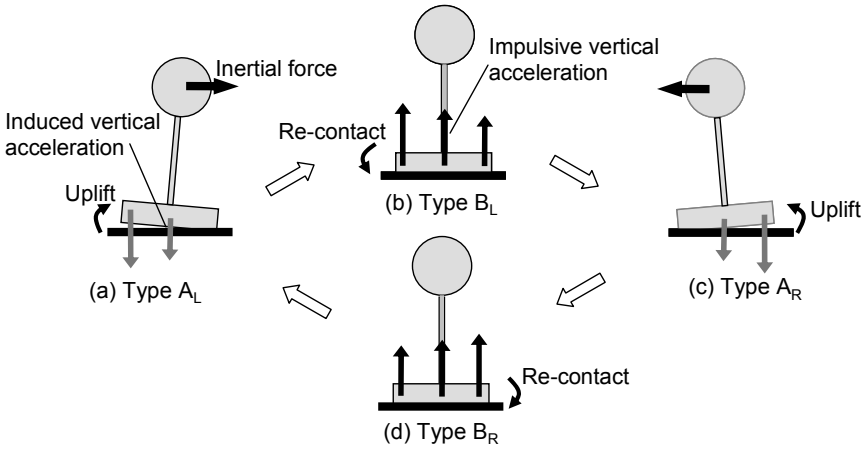


Figure 8 Schematic figure showing footing rotation, superstructure inertia force, and vertical accelerations

acceleration of the footing has a positive peak and negative peak. It is noteworthy that the peak average vertical acceleration is significantly greater on the positive side than on the negative side, as discussed in the following paragraph.

The footing rotation (Fig. 7(e)) has positive peaks at T=m1. The vertical force on the footing base is almost zero on the left side (the blue dotted line in Fig. 7(d)), indicating that the footing was uplifted on this side. The wall friction force on the footing's right side (passive side) has a greater value and acts upward; that on the left side (active side) has a smaller value and acts downward, indicating that the former wall friction reduces the settlement of the footing's right side, but the latter wall friction does not reduce the uplift of the footing's left side. The vertical acceleration on the footing has a large negative peak on the left side (blue dotted line in Fig. 7 (b)), but with a very small value on the opposite (right) side (red solid line in Fig. 7(b)).

The horizontal acceleration of the superstructure and the footing rotation (Figs. 7(a) and 7(e)) has a negative peak at T=m2. The trends observed at this instant, if horizontally reversed, are fundamentally the same as those observed at T=m1. That is, the vertical force on the footing base is almost zero on the right side, indicating that the footing did uplift on this side. The vertical acceleration, in contrast, has a large negative peak on the right side, but was almost zero on the opposite (left) side (Fig. 7(b)), which indicates that the negative vertical acceleration at this instant varies within the foundation. Further examination reveals that the average of the negative peak vertical acceleration (black solid line in Fig. 7(b)) would be approximately half of that occurring at the same instance on either side of the foundation.

In spite of the fact that the horizontal acceleration of the superstructure and the footing rotation are almost zero at T=p1and p2 (Figs. 7(a) and 7(e)), the vertical accelerations on the footing have large positive peaks (Fig. 7 (b)) on both sides. Unlike the instants producing negative peak vertical acceleration, positive peaks do occur on both sides. The average of the positive peak vertical acceleration (black solid line in Fig. 7(b)) would be approximately the same as that occurring anywhere on the foundation. The wall friction forces on the footing's both sides have a small value, probably because an extremely small superstructure inertia causes the earth pressure, which is nearly at rest state.

Based on the findings and discussions presented above, Fig. 8 portrays a schematic diagram showing the relation among the footing rotation, the superstructure inertia force, and the vertical accelerations acting on a shallow foundation. In Types A_L and A_R, a large inertial force acting on the superstructure might trigger an uplifting of the footing on the side opposite to the direction of the inertia force, which could cause varying downward accelerations within the footing. The resultant vertical acceleration is "induced vertical acceleration", the amplitude of which corresponds to the movement of the gravitational center of the structure following the footing uplift (Muto and Kobayashi, 1979). In Types B_L and B_R, with no horizontal inertial force from the superstructure, larger upward accelerations with almost same amplitude develop throughout the footing. The vertical acceleration of this type seems to result from the collision impulse between the footing and soil because it occurs when the footing reattaches to the soil. For that reason, high vertical accelerations occur during strong shaking on the footing without the presence of the vertical input motion, which also explains why the peak average vertical acceleration is significantly greater on the positive side than on

the negative side.

4.2 Impulsive Vertical Acceleration

To discuss the positive vertical acceleration in detail, a free body (mass m) falling from a specific height touches the ground at a velocity v_0, and comes to rest. Based on the law of conservation of momentum, the momentum, mv_0 is equal to an impulse as

$$\int_0^{t_f} F(t)dt = m \cdot v_0 \qquad (1)$$

where F(t) is the impulsive force when the body contacts the soil and t_f is the interval between the contact and the rest. In fact, F(t) can be expressed as follows.

$$F(t) = m \cdot a_v(t) \qquad (2)$$

In that expression, a_v(t) is the impulsive vertical acceleration of the free body. Eqs. (1) and (2) suggest that the impulsive vertical acceleration on the footing caused by the collision impulse depends on the vertical footing velocity immediately before re-attachment.

Figure 9 presents the relation between the peak vertical velocity of the re-contact side of the footing and the corresponding average positive vertical acceleration of the footing. The vertical acceleration increases concomitantly with the vertical velocity, indicating that the positive vertical acceleration was actually generated by the collision impulse between the footing and soil, as predicted numerically by Meek (1975) and Muto et al. (1979). The positive vertical acceleration will be called "impulsive vertical acceleration".

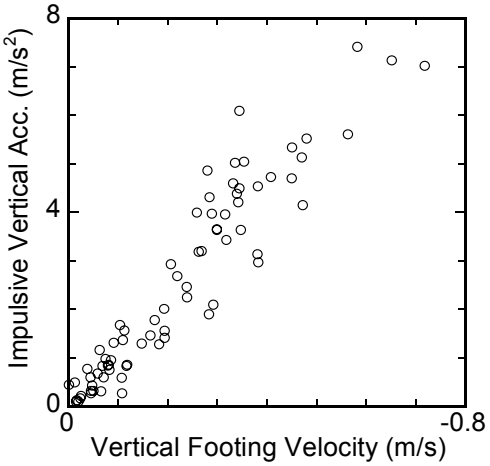


Figure 9 Relation between peak average vertical footing velocity immediately before re-contact and the corresponding average vertical acceleration of footing

5. IMPULSIVE VERTICAL ACCELERATION AND INDUCED VERTICAL ACCELERATION

Figure 10 shows the relation between the preceding peak footing rotation angle and the peak impulsive vertical acceleration on the footing's left and right sides, in addition to the relation between the footing rotation angle and the peak induced vertical acceleration at the same instance. The peak impulsive acceleration tends to increase concomitantly with increased footing rotation angle and exceeds 12 m/s^2. The peak induced vertical motion also tends to increase concomitantly with increased footing rotation angle but reaches an upper limit of about 8 m/s^2. The peak impulsive vertical acceleration

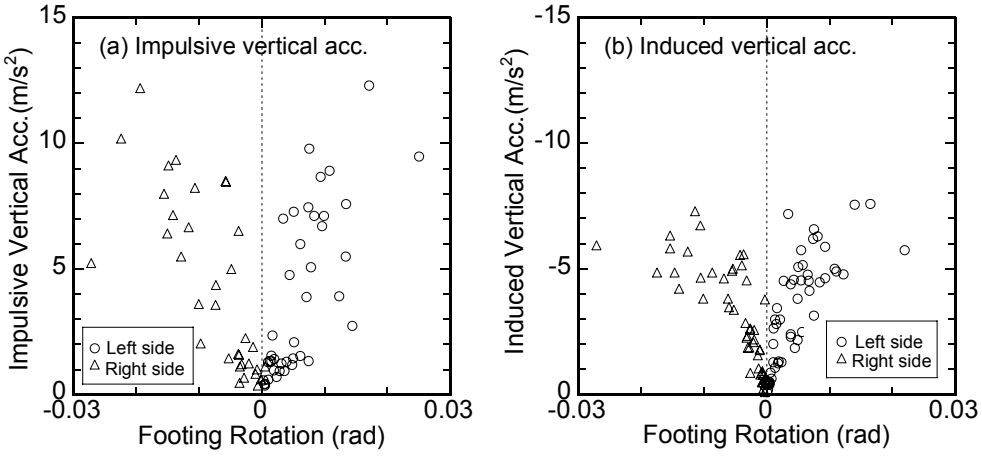


Figure 10 Relation between the preceding peak footing rotation angle and the peak impulsive vertical acceleration, and the relation between the footing rotation angle and the peak-induced vertical acceleration at the same instance

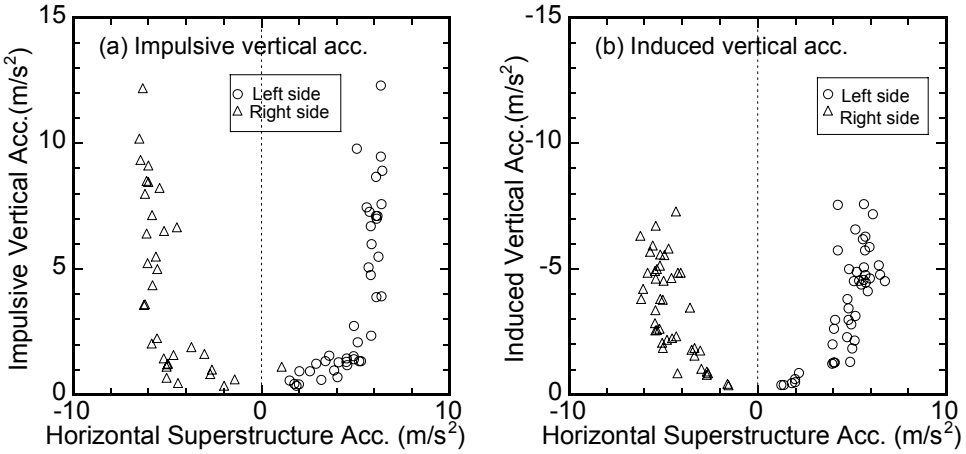


Figure 11 Relation between preceding peak horizontal superstructure acceleration and peak impulsive vertical acceleration, and the relation between peak horizontal superstructure acceleration and peak induced vertical acceleration at the same instance

tends to be larger than that of induced vertical acceleration at the same footing rotation angle, indicating that not only the effects of the induced vertical acceleration but also those of the impulsive vertical acceleration on facilities of important structures such as nuclear plants should be investigated.

Figure 11 portrays the relation between the preceding peak horizontal superstructure acceleration and the corresponding peak impulsive vertical acceleration, in addition to the relation between the horizontal superstructure acceleration and the peak induced vertical acceleration at the same instance. When the horizontal superstructure acceleration exceeds about 5 m/s^2, the amplitudes of the impulsive vertical acceleration and the induced vertical acceleration rise dramatically. The explanation above suggests that a small earthquake will generate only slight vertical acceleration, but that an intense earthquake will trigger the foundation uplift and generate extremely high vertical acceleration, especially because of the collision impulse.

To investigate the effects of horizontal superstructure inertia on the footing rotation, the relation between the peak rotation angle of the footing and the overturning moment of the footing-superstructure at the same instance is presented in Fig. 12. The moment-rotation relationship shows strong non-linear behavior. The footing rotation angle increases significantly when the overturning moment is greater than about 3000 kNm. The overturning moment, 3000 kNm, is mainly caused by the superstructure inertia whose horizontal acceleration amplitude is about 5 m/s^2. This indicates that the footing rotation angle increases rapidly when the superstructure horizontal acceleration amplitude is greater than 5 m/s^2.

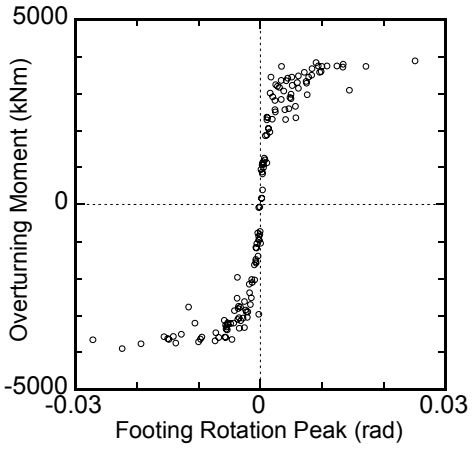


Figure 12 Relation between peak footing rotation and overturning moment of footing-superstructure at the same instance

Therefore, the amplitudes of the impulsive vertical acceleration and the induced vertical acceleration rise dramatically, when the horizontal superstructure acceleration exceeds about 5 m/s^2, as presented in Figs. 10 and 11.

6. CONCLUSION

Dynamic centrifuge tests were performed using soil-footing – superstructure models to investigate the effects of the footing uplift on the vertical acceleration of the footing during strong shaking. The horizontal shearing and vertical compressive forces on the base of the footing, in addition to the earth pressure and wall friction force on both sides of the footing, were measured care-

fully using newly developed 2D-load cells. The following conclusions were drawn.

(1)The foundation uplift induces vertical acceleration of two types on an embedded footing: "impulsive vertical acceleration" caused by the collision impulse between the foundation and soil and "induced vertical acceleration" caused by the height movement of the gravitational center of the structure.

(2)The amplitude of the impulsive vertical acceleration, more than 12 m/s^2, is much greater than that of the induced vertical acceleration.

(3)When the horizontal superstructure acceleration becomes greater than about 5 m/s^2, the amplitudes of the impulsive vertical acceleration and the induced vertical acceleration rise dramatically, suggesting that a small earthquake will generate only small vertical accelerations but that an intense earthquake will trigger the foundation uplift and generate extremely high vertical acceleration, especially by the collision impulse.

(4)The amplitudes of both vertical accelerations increase with the induced rotation angle of the footing.

Acknowledgements:
This study was conducted with the financial support of a Grant-in-Aid for Scientific Research from the Ministry of Education, Culture, Sports, Science and Technology of Japan.

References:

Chopra, A. K. and Yim, S. C. -S. (1985): Simplified Earthquake Analysis of Structures with Foundation Uplift, Journal of Structural Engineering. ASCE, Vol. 111, No. 4, pp. 906–930.

Housner, G. W. (1963): The behavior of inverted pendulum structures during earthquakes, Bulletin of the Seismological Society of America. Vol. 53, No. 2, pp. 403–417.

Huckelbridge, A. A. Jr. and Clough, R. W. (1978): Seismic response of uplifting building frame, Journal of the Structural Division. ASCE, Vol. 104, No. 8, pp. 1211–1229.

Meek, J. W. (1975): Effects of Foundation Tipping on Dynamic Response, Journal of the Structural Division. ASCE, Vol. 101, No. 7, pp. 1297–1311.

Muto, K. and Kobayashi, T. (1979): Nonlinear rocking analysis of nuclear reactor buildings –Simultaneous Horizontal and Vertical Earthquake Inputs, Journal of Architecture and Building Science. AIJ, Vol. 276, pp. 69–77. (in Japanese)

8CUEE CONFERENCE PROCEEDINGS
8th International Conference on Urban Earthquake Engineering
March 7-8, 2011, Tokyo Institute of Technology, Tokyo, Japan

EFFECTS OF SWAY-ROCKING MOTION ON PILE STRESSES DURING LARGE SHAKING TABLE TESTS

Hiroko Suzuki[1] and Kohji Tokimatsu[2]

1) Assistant Professor, Dept. of Architecture and Building Engineering, Tokyo Institute of Technology, Japan
2) Professor, Dept. of Architecture and Building Engineering, Tokyo Institute of Technology, Japan
hsuzuki@arch.titech.ac.jp, kohji@o.cc.titech.ac.jp

Abstract: Effects of sway-rocking motion on pile stresses are estimated through large shaking table tests in which a structure supported by a 3x3 pile group was set in a dry sand deposit prepared in a cylindrical laminar box with a height of 6.5 m and a diameter of 8.0 m. Presence of foundation embedment and input motions were variable in the tests. The test results have shown that foundation embedment restrains sway motion more than rocking motion. As a result, the foundation embedment decreases its displacement but increases ratios of rocking component against sway component. This induces a unique bending strain distribution of piles in which it decreases toward the pile head. This contrasts well with the bending strain distribution without foundation embedment in which it increases toward the pile head. Sway and rocking stiffness increases with decreasing predominant period of input motion, with stiffness increase being more significant in sway than in rocking. This makes effects of rocking motion on pile stresses more significant with shorter period motion than with longer period motion.

1. INTRODUCTION

In order to establish reasonable seismic design of pile foundations, it is important to estimate soil-pile-structure interaction during earthquakes, in which both kinematic forces from the ground and inertial forces from structures act on the piles. Such kinematic and inertial forces depend on various factors, such as foundation embedment and structure response including sway-rocking motions. To estimate effects of sway-rocking motion on soil-structure interaction, many studies have been made based on physical model tests and numerical analyses for spread foundation models (e.g., Toki et al. 1980, Hayashi 1996, Kutter et al. 2010, Tamura et al. 2010). Hayashi (1996) and Kutter et al. (2010) have shown that rocking motion of slender buildings or bridge columns with spread foundation could act as effective energy dissipation components of structure systems. If the structure is founded on piles, its rocking motion might have affected pile stresses. Iiba et al. (2003) has investigated sway-rocking motion of pile-structure systems through shaking table tests. Studies on sway-rocking motion of pile-structure systems based on physical model tests, however, have been rare.

To investigate inertial and kinematic effects on pile groups during three-dimensional shaking, physical tests on soil-pile-structure models were conducted using E-Defense at the Hyogo Earthquake Engineering Research Center of the National Research Institute for Earth Science and Disaster Prevention (NIED) (Tabata and Sato 2006, and Tokimatsu et al. 2007). In the shaking table tests using E-Defense, structure models as well as input motion and its maximum acceleration were variable. The objectives of this study are to investigate factors influencing sway-rocking motion and the effects of sway-rocking motion on pile stresses through the shaking table tests conducted at E-Defense.

2. LARGE SHAKING TABLE TESTS

The E-Defense shaking table platform has a dimension of 15 m length and 20 m width. It is supported on fourteen vertical hydraulic jacks and connected to five hydraulic jacks each in the two orthogonal horizontal directions. A soil-pile-structure model was constructed in a cylindrical laminar box with a height of 6.5 m and a diameter of 8.0 m. The container consists of forty-one stacked ring flames, enabling shear deformation of the inside soil during two-dimensional horizontal shaking. Figures 1 and 2 show the test model prepared in the cylindrical laminar box placed on the shaking table. The superstructure was supported on a 3x3 pile group that penetrated into a dry sand deposit, as shown in Figure 2.

Dry Albany sand, imported from Australia, was used for the sand deposit. The sand had a mean grain size D50 of 0.31 mm. After setting the pile group in the laminar box, the sand was air-pluviated and compacted to a relative soil density of about 70 % so as to form a uniform sand deposit with a thickness of 6.4 m. The natural period of the ground surface was about 0.2 s. Each pile of the pile group was made of stainless steel and had a diameter of

152.4 mm and a wall thickness of 2.0 mm. The piles were set up with a horizontal space of four-pile diameters center to center. Their tips were jointed to the laminar box base with pins and their heads were fixed to a foundation of a weight of 10 tons. The piles were labeled A1 to C3 according to their locations within the pile group, as shown in Figure 2(a).

A total of five test series was conducted, in which the presence of foundation embedment (0.5 m) and of superstructure (28 tons) as well as the natural period of the superstructure were varied. In this study, factors influencing sway-rocking motion and effects of sway-rocking motion on pile stresses are discussed, based on the test series YM and NM. Both had the same superstructure but series YM had foundation embedment but series NM did not.

The tests were conducted under one-, two- or three-dimensional shaking with three different ground motions recorded at (i) Takatori in the 1995 Kobe earthquake (Takatori), (ii) Lincoln School in the 1952 Taft earthquake (Taft) and (iii) Akasaki in the 2000 Tottori earthquake (Tottori). In each test series, either or both of the two horizontal or three-component motions were used as inputs to the shaking table with the largest horizontal acceleration being scaled to 0.3~6 m/s^2. The NS and EW components of the ground motion were applied to the NS and EW directions as shown in Figure 2, with the UD component to the vertical direction. This paper describes the effects of the presence of foundation embedment and input motions on sway-rocking motion and pile stresses based on test series YM and NM with Takatori (TK) or Tottori (TT) motions having maximum horizontal input accelerations of 0.8 m/s^2 under three dimensional loading. These tests are, hereafter, called YM-TT, YM-TK and NM-TK.

Many strain gauges, accelerometers, velocity meters, earth pressure transducers, displacement transducers, settlement meters and load cells, about 900 sensors in total, were placed in the sand deposit as well as on the pile-structure model, as shown in Figure 2. Further details of the test apparatus and procedure have been described elsewhere (Tabata and Sato, 2006).

3. DIFFERENCE IN SOIL-PILE-STRUCTURE RESPONSE BETWEEN MODELS

Figure 3 shows the acceleration response spectra of the superstructure, the foundation, the ground surface and the shaking table for Tests YM-TT, YM-TK and NM-TK. Tottori motion dominates only in the short period range with a sharp spectral peak at less than 0.1 s (YM-TT, Figure 3(a)(b)). In contrast, Takatori motion dominates over the wide period range covering from 0.1 s to 1.0 s (YM-TK, NM-TK, Figure 3(c)-(f)). Figure 4 shows amplitude ratios of the superstructure acceleration with respect to the shaking table acceleration for the three tests. Among the three tests,

Table 1 Test series

	Embedment (0.5 m)	Superstructure (28 tons)	Natural period (s)	Maximum input acceleration (m/s^2)							
				Takatori				Taft and Tottori			
				X	Y	XY	XYZ	X	Y	XY	XYZ
YS	Yes	Yes	0.1 (model S)	0.3, 0.8				-			0.3, 0.8
YL	Yes	Yes	0.6 (model L)								
YN	Yes	No	-								
YM	Yes	Yes	0.2 (model M)					0.3, 0.8			
NM	No	Yes		0.3, 0.8			0.3, 0.8, 6.0, 8.0	-			

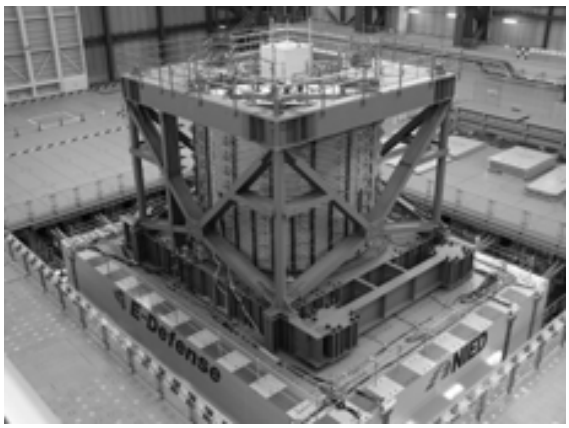


Figure 1 Laminar shear box on shaking table platform

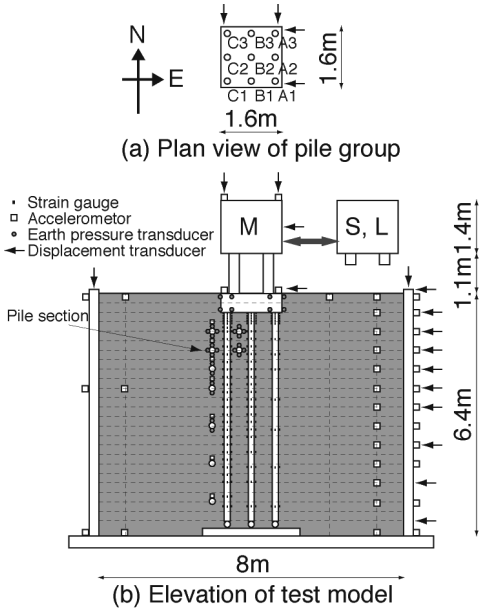


Figure 2 Test model in laminar box

the peak amplitude ratio is the largest in YM-TT and the smallest in NM-TK. It is interesting to note that the period, at which the amplitude ratio takes a peak, is longer in NM-TK than in YM-TT and YM-TK. This suggests that the presence of foundation embedment affects coupled vibration of soil-pile-structure systems.

Figure 5 shows the time histories of bending strains at the head of Pile A1, displacements of foundations and the ground surface and accelerations of superstructures, foundations, the ground surface and the shaking table. Figure 5 indicates that the accelerations and displacements of the ground, the foundation and the superstructure are all larger with Takatori motion (YM-TK, NM-TK) than with Tottori motion (YM-TT) (Figure 5(b)-(f)(i)-(m)(p)-(t)), confirming that the predominant period of input motions affects the soil-structure behavior. A comparison between YM-TK and NM-TK shows that the superstructure acceleration is larger with embedment (YM-TK) than without embedment (NM-TK) but the foundation displacement is smaller when the foundation is embedded (Figure 5(i)(k)(p)(r)). Namely, the foundation embedment decreases the displacement but increases the acceleration as mentioned in the previous study on spread foundations with smooth surface (Tamura et al. 2010).

To investigate the effects of the difference in soil-pile-structure interaction on pile stresses, Figure 6 shows distributions of bending strains with depth for Piles A1, B2 and C3, at instant when the bending strain takes the largest peak in each test. Pile A1 was located on the southeast corner, Pile B2 on the middle and Pile C3 on the northwest corner within a pile group. The bending strain shown in Figure 6 is computed by the sum of NS and EW components. At these instants, the inertial force increases southeastward in all the three tests, making Pile A1 the leading pile and Pile C3 the following pile. As might be expected, Figure 6 indicates that the bending strain is larger in the leading pile than in the trailing pile. These trends confirm that the pile stresses vary within a pile group and that bearing load is the largest in the leading corner pile due to the shadowing effects. A comparison in bending strains

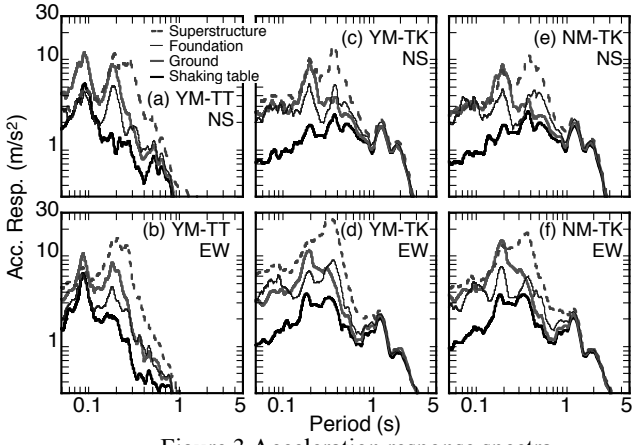


Figure 3 Acceleration response spectra

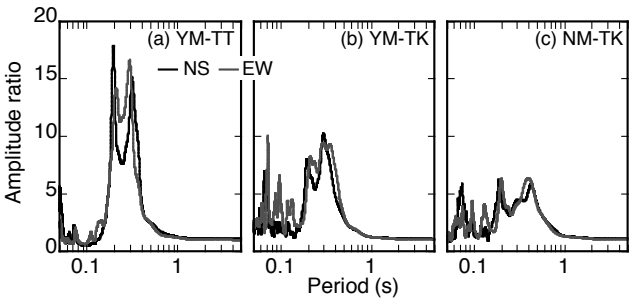


Figure 4 Amplitude ratios of superstructure with respect to input motion

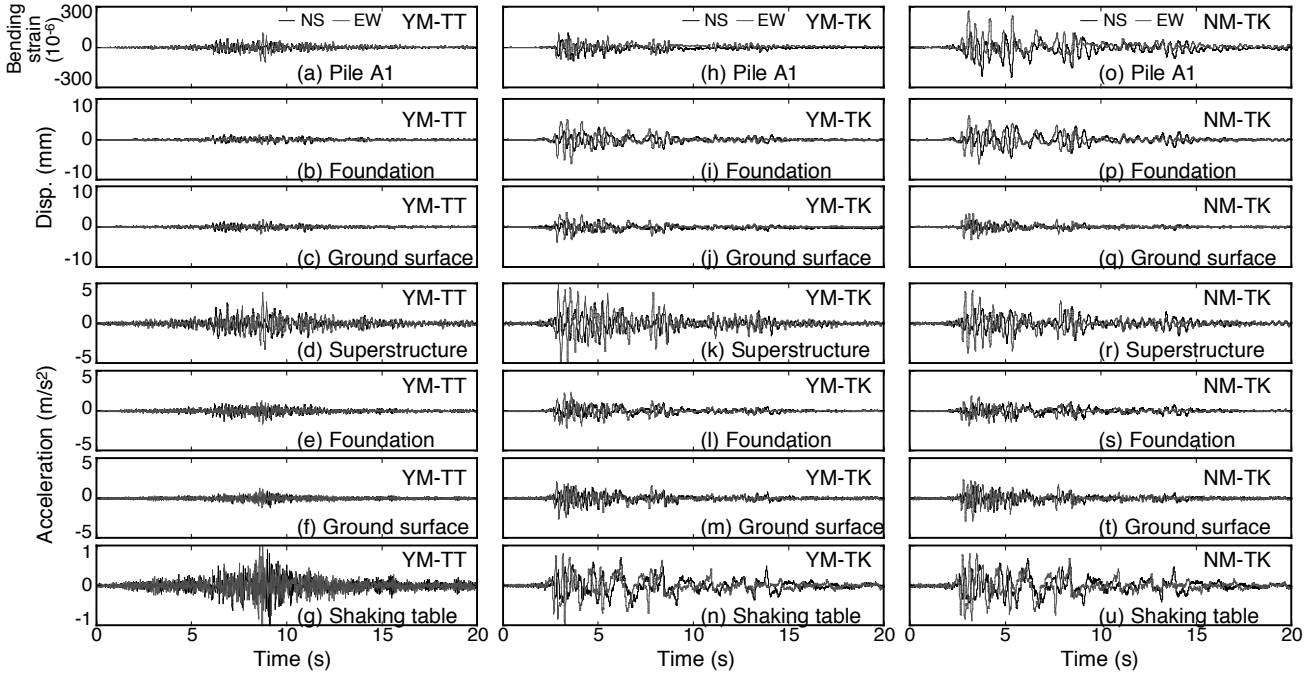


Figure 5 Time histories of major parameters

among the three tests shows that the bending strain in NM-TK is the largest (Figure 6(g)-(i)). This is probably because the foundation embedment affects bending strains in such a way that the earth pressure acting on an embedded foundation reduces the shear force transmitted to pile heads from a superstructure, as mentioned in the previous studies (e.g., Imaoka et al, 1998; Tamura et al, 2002). In contrast, the bending strain in YM-TT is the smallest among the three tests. This is due to its small superstructure acceleration and ground displacement (Figure 3(c)(d)). It is also interesting to note that the bending strain decreases toward pile heads in YM-TT and YM-TK (Figure 6(c)(f)). This contrasts well with the bending strain distribution in NM-TK in which it reaches a peak at the pile head, decreasing with depth (Figure 6(i)). The presence of foundation embedment might have affected the bending strain distributions with depths.

4. SWAY-ROCKING MOTION OF FOUNDATION

Integration of the vertical and horizontal accelerations measured at the four edges on the foundation, yields their vertical and horizontal displacements. The rotational angles of the foundation are then computed from the difference in vertical displacements between the opposite edges of the foundation. Figure 7 shows relation between the inertial force and the rotational angle of a foundation. Figure 7 indicates that the rotational angle of the foundation is related to the inertial force.

Sway and rocking components of the displacements on the top of the foundation are defined by the following equations:

$$Y = Y_S + Y_R \tag{1}$$

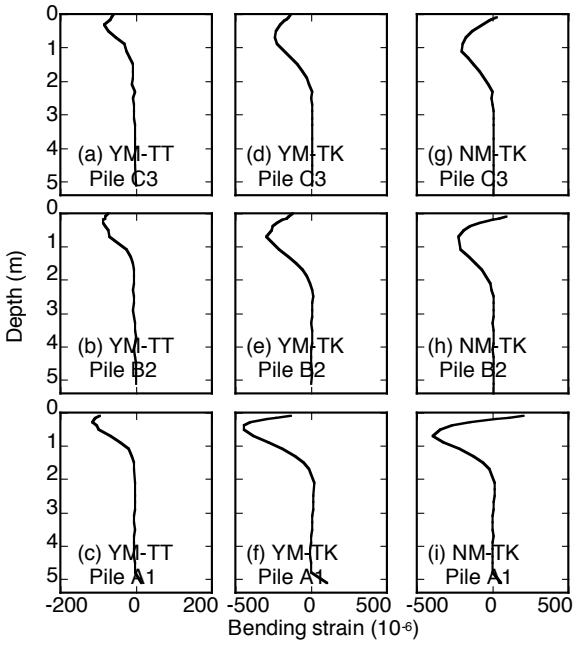


Figure 6 Distributions of bending strains

$$Y_R = \frac{h}{2}\theta \tag{2}$$

in which Y or Y_S is the relative displacement with respect to the ground at the top of the foundation or at the center of the gravity of the foundation, as shown in Figure 8. Y_R is the displacement at the foundation top induced by rotational motion, θ is the rotational angle, and h is the height of the foundation. Since Y can be computed from the observed accelerations of the foundation and the ground surface, and Y_R from Equation (2), Y_S can readily be determined by Equation (1).

Figure 9 shows relations between sway and rocking components in foundation displacements in the three tests. A comparison between YM-TK and NM-TK shows that rocking components are larger but sway components are smaller in YM-TK than in NM-TK (Figure 9(b)(c)). Since the foundation displacement is larger in NM-TK than in YM-TK (Figure 5(i)(p)), the foundation embedment decreases its displacement and thus increases the ratio of rocking components in foundation displacements. The decrease in sway component in foundation displacement in YM-TK is probably caused by the reduction of shear force at pile heads due to earth pressure acting on the embedded foundation. A comparison between YM-TT and YM-TK shows that both rocking and sway components are smaller in YM-TT than in YM-TK (Figure 9(a)(b)), probably due to smaller foundation displacement. In contrast, the ratios of rocking components in foundation displacements are larger in YM-TT than in YM-TK.

A comparison between sway and rocking components in foundation displacement among the three tests (Figure 9) indicates that the difference in bending strain distributions is related to sway-rocking motion of foundations. Namely, in the case with foundation embedment (YM-TT and YM-TK), the increase in rocking component tends to rotate

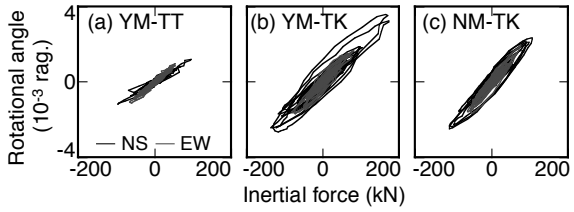


Figure 7 Relationship of inertial force and rotational angle

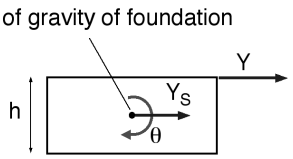


Figure 8 Sway and rocking motions of foundation

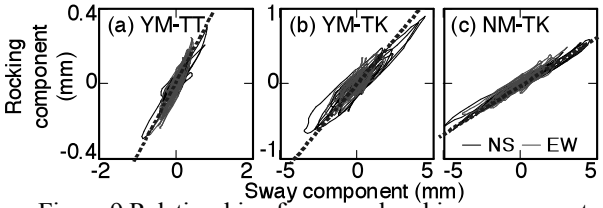


Figure 9 Relationship of sway and rocking components in foundation displacement

the foundation significantly, reducing the bending moment at the pile head. This could induce such a unique trend in which the bending strain does reach a peak at some depth below the pile head rather than at the pile head, thereby decreasing towards the pile head. In contract, the effects of sway motion are significant in the case without foundation embedment (NM-TK), inducing the bending strain distribution in which it reaches a peak at the pile head, decreasing with depth. In addition, a comparison between YM-TT and YM-TK shows that the slope of bending strain below the heads is smaller in YM-TT than in YM-TK.

Figure 10 illustrates the horizontal force, P_Y and the rotational moment, M_X, which are transmitted to the foundation from the superstructure. P_Y and M_X could be estimated by the structure response (Architecture Institute of Japan 1996). Figure 11 shows the relationship between the horizontal force, P_Y and the relative displacements of the gravity center of foundations with the ground and Figure 12 shows the relationship between the rotational moment, M_X and the rotational angles of foundations. The slopes of these relationships correspond to the stiffness of sway and rocking motions. A comparison between YM-TK and NM-TK shows that the rocking stiffness is almost the same but the sway stiffness is larger in YM-TK than in NM-TK (Figures 11 and 12(b)(c)). This suggests that the foundation embedment increases sway stiffness but may not play an important role in controlling rocking stiffness. As a result, sway motion dominates pile stresses in NM-TK but rocking motion dominates pile stresses in YM-TK (Figure 6(d)-(i)).

A comparison between YM-TT and YM-TK shows that sway and rocking stiffness is larger in YM-TT than in YM-TK (Figures 11 and 12(a)(b)). This is related to the previous study on spread foundations (Toki et al. 1980), in which sway and rocking motion decreases, with decreasing predominant period of input motions. In particular, the sway stiffness is significantly large when the predominant period of input motion decreases. As a result, rocking motion dominates pile stresses more significantly in YM-TT than in YM-TT (Figure 6(a)-(f)). This makes the slope of bending strain below the heads smaller in YM-TT than in YM-TK.

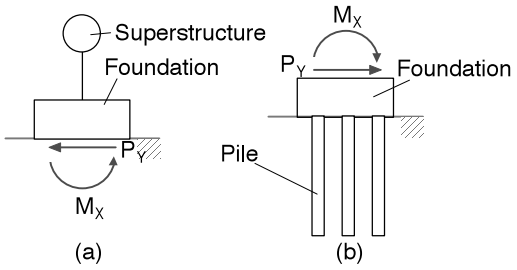


Figure 10 Forces acting on foundation

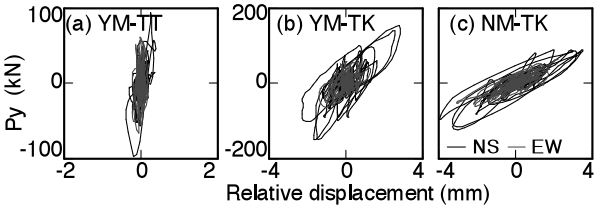


Figure 11 Relationship between relative displacement and horizontal force

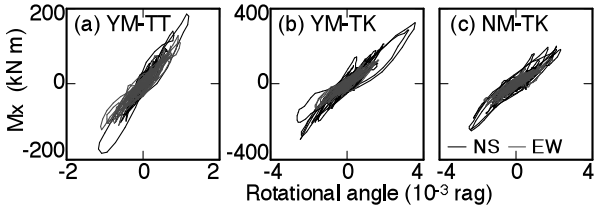


Figure 12 Relationship between rotational angle and rotational moment

5. CONCLUSIONS

To investigate soil-pile-structure interaction during earthquakes, factors influencing sway-rocking motion of pile-structure models and effects of sway-rocking motion on pile stresses are discussed through physical model tests on soil-pile-structure systems using the large shaking table at E-Defense, NIED. The test results and discussions have led to the following conclusions:

Foundation embedment restrains sway motion more than rocking motion. This is because the foundation embedment in these tests increases sway stiffness, but does not play an important role in controlling rocking stiffness. As a result, the foundation embedment decreases its displacement and thereby increasing ratios of rocking components in foundation displacement. In addition, the increased sway stiffness with foundation embedment induces a shorter natural period of the coupled vibration of a soil-pile-structure system and a larger amplitude ratio of the superstructure response than those without foundation embedment.

Rocking motion dominates in a structure with foundation embedment, causing a unique bending strain distribution of piles in which it does reach a peak at some depth below the pile head rather than at the pile head, thereby decreasing towards the pile head. In contract, sway motion dominates in a structure without foundation embedment, making a bending strain distribution, which reaches a peak at the pile head, decreasing with depth.

Sway and rocking stiffness increases with decreasing predominant period of input motion, with the stiffness increase being more significant in sway than in rocking motion. As a result, with decreasing predominant period of input motion, effects of rocking motion on pile stress distributions become significant. This makes the slope angle of bending strain below the heads tend to be smaller with shorter period motion than with longer period motion.

ACKNOWLEDGEMENTS:

The study described herein was made possible through the Special Project for Earthquake Disaster Mitigation in Urban Areas, supported by the Ministry of Education, Culture, Sports, Science and Technology (MEXT). The authors express their sincere thanks to the above organization.

References:

Architecture Institute of Japan (1996), An introduction to dynamic soil-structure interaction, Gihodo Printing, 400 pp.

Hayashi, Y. (1996), "Damage reduction effect due to basemat uplift of building", *Journal of Structural and Construction Engineering*, No. 485, 53-62 (in Japanese).

Iiba, M., Tamori, S. and Kitagawa, Y. (2003), "Fundamental characteristics on seismic effect to pile foundation by shaking table test for model of building-soil interaction system", *Journal of Structural and Construction Engineering*, No. 566, 29-36 (in Japanese).

Imaoka, K., Tokutate, S., Aoyama, K., Fukuwa, N., Iiba, M. and Taga, N. (1998), "Dynamic embedment effects using silicon soil model", *Proc. of 10th Japan Earthquake Engineering Symposium*, 1653-1658 (in Japanese).

Kutter, B. L., Deng, L. and Kunnath, S. (2010), "Estimation of displacement demand for seismic design of bridges with rocking shallow foundations", *Proc. of Fifth International Conference on Recent Advances in Geotechnical Earthquake Engineering and Soil Dynamics*, Paper No. SOAP 11, 11 pp.

Tabata, K. and Sato, M. (2006), Report of special project for earthquake disaster mitigation in urban areas, Ministry of Education, Culture, Sports Science and Technology, 489-554 (in Japanese).

Tamura, S., Tokimatsu, K., Uchida, A., Funahara, H. and Abe, A. (2002), Relation between seismic earth pressure acting on embedded footing and inertial force based on liquefaction test using large scale shear box, *Journal of Structural and Construction Engineering*, No. 559, 129-134 (in Japanese).

Tamura, S., Adachi, K. and Tokimatsu, K. (2010), "Effects of roughness of shallow foundation surface on superstructure response during a strong earthquake", *Proc. of 7th International Conference on Urban Earthquake Engineering and 5th International Conference on Earthquake engineering*, 413-418.

Toki, K., Sato, T. and Miura, F. (1980), "Separation and sliding between soil and structure during strong ground motion", *Journal of the Japan Society of Civil Engineers*, No. 302, 31-41 (in Japanese).

Tokimatsu, K., Suzuki, H., Sato, M. and Tabata, K. (2007), "Three-dimensional shaking table tests on soil-pile-structure models using E-Defense facility", *Proc. of 4th International Conference on Earthquake Geotechnical Engineering*, 11 pp.

8CUEE CONFERENCE PROCEEDINGS
8th International Conference on Urban Earthquake Engineering
March 7-8, 2011, Tokyo Institute of Technology, Tokyo, Japan

EFFECTS OF PILE RIGIDITY ON RESPONSE OF BASE-ISOLATED STRUCTURE DURING SOIL LIQUEFACTION BASED ON CENTRIFUGE TESTS

Takenori Hida[1] and Shuji Tamura[2]

1) Researcher, DPRI, Kyoto University, Dr. Eng.
2) Assoc. Professor, DPRI, Kyoto University, Dr. Eng.
hida-t@sds.dpri.kyoto-u.ac.jp, tamura@sds.dpri.kyoto-u.ac.jp

Abstract: Dynamic centrifuge tests were performed to investigate the effects of pile rigidity on the pile stresses and the seismic response of a base-isolated structure during soil liquefaction. Then pseudo-static analyses and single-degree-of-freedom analyses were conducted. The following conclusions were reached. (1) In cases where the structure inertia is large, the bending moment at pile heads and their tips in the high-rigidity pile case are almost identical to those in the low-rigidity pile case. (2) In cases where the natural period of the base-isolated structure is close to the predominant period of the ground, the shear deformation of the isolator in the high-rigidity pile case is smaller than that in the low-rigidity pile case.

1. INTRODUCTION

In recent years, base-isolated structures have been constructed on soft ground that might undergo liquefaction. In such soils, a base-isolated structure can vibrate sympathetically with long-period seismic ground motion, making the shear deformation of the seismic isolator excessively large. A superstructure might then bump against the retaining wall, damaging an isolator (AIJ, 2001, 2007). Furthermore, leaning of a footing can reduce the lateral stiffness of the laminated rubber bearing (AIJ, 2001). A footing might lean when the pile is damaged. Consequently, the seismic adequacy of a pile of a base-isolated structure during soil liquefaction is important knowledge.

Several reports have described that pile rigidity affects pile stress (e.g., Tokimatsu et al., 2005, Fukutake et al., 2004). However, knowledge of pile rigidity effects on pile stresses and the seismic response of a base-isolated structure during soil liquefaction is limited.

This study investigates pile rigidity effects on the seismic response of a base-isolated structure and the bending moment of the piles. For this purpose, dynamic liquefaction tests on a base-isolated structure-footing model supported by 2 × 2 piles that have high and low bending rigidity were performed using a geotechnical centrifuge. Then pseudo-static analyses and response analyses of single-degree-of-freedom systems were conducted.

2. CENTRIFUGE TEST PERFORMED

Centrifuge tests were performed using 40g centrifugal acceleration with the geotechnical centrifuge at the Disaster Prevention Research Institute, Kyoto University. The test model is presented in Fig. 1. The pile specifications are presented in Table 1. Case 1 is the high-

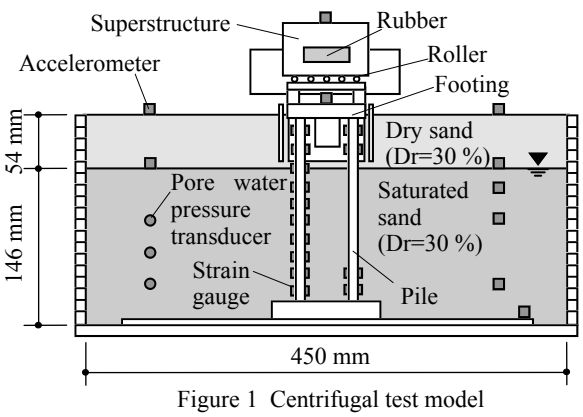


Figure 1 Centrifugal test model

rigidity pile case. Case 2 is the low-rigidity pile case. Piles are of 8 mm diameter and 176 mm length. The footing was supported by 2 × 2 piles. The pile heads were linked rigidly with the footing; their tips were connected rigidly to the base plate. Respective masses of the footing and superstructure were 0.99 kg and 2.0 kg. The superstructure was supported by a roller. To simulate the seismic isolator, the footing and the superstructure were connected by rubber. The natural period and the damping constant of the superstructure under the fixed footing condition were, respectively, 0.125 s and 0.4. The soil used for the tests was Toyoura sand. The relative density of the sand deposit was 30%. The sand deposit was deaerated and Metolose solution with viscosity that was 40 times that of water was infused into the sand deposit. To measure the earth pressure and the sidewall friction acting on the embedded footing, biaxial load cells were set on the footing. Accelerometers were set on the footing, the superstructure, and the ground. The test models were excited using Hachinohe 1968 NS. All data presented in the following sections are adjusted to the prototype scale.

3. TEST RESULTS

Time histories of the excess pore water pressure ra-

Table 1 Pile specification

	Case 1 High rigidity pile	Case 2 Low rigidity pile
Material	Stainless	Aluminum
Shape	Bar	Pipe
Length	176 mm (7.04 m)	176 mm (7.04 m)
Diameter	φ=8 mm (φ=32 cm)	φ=8 mm, t=0.8 mm (φ=32 cm, t=3.2 cm)
E･I	3.85×10^5 Ncm^2 (9.86×10^4 kNm^2)	0.841×10^5 Ncm^2 (2.14×10^4 kNm^2)

( ): prototype scale

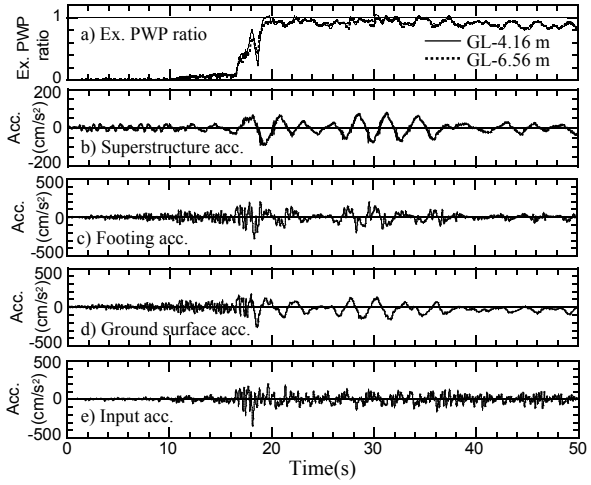


Figure 2 Response of ground, footing and superstructure (Case 1, High rigidity pile)

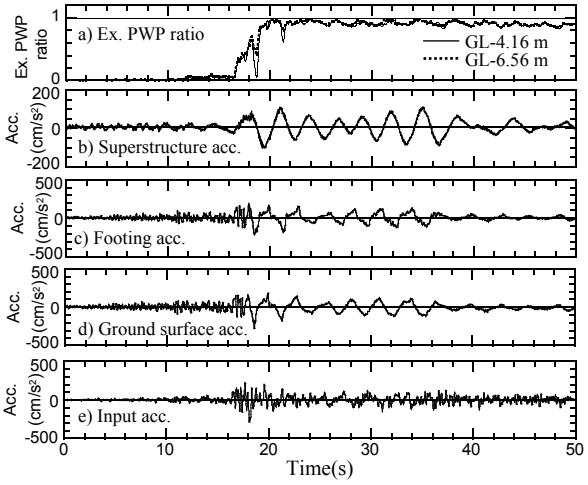


Figure 3 Response of ground, footing and superstructure (Case 2, Low rigidity pile)

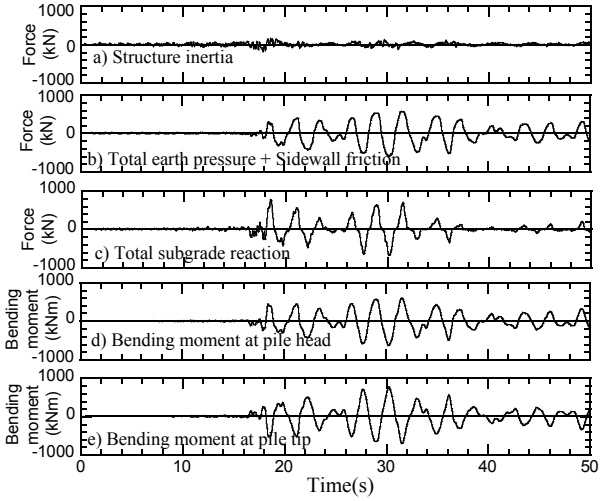


Figure 4 Force and bending moment of pile (Case 1, High rigidity pile)

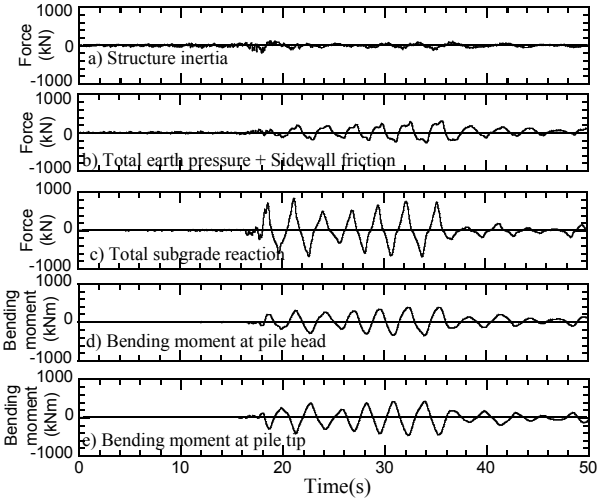


Figure 5 Force and bending moment of pile (Case 2, Low rigidity pile)

tio, superstructure acceleration, footing acceleration, ground surface acceleration, and input acceleration are depicted in Figs. 2 and 3. In both cases, the excess pore water pressure started to increase at 16 s. Ground liquefaction occurred at about 20 s. The amplitude of the superstructure acceleration in Case 2 was greater than that in Case 1. The predominant period of the ground during soil liquefaction was ca. 3 s, which was shorter than the natural period of the superstructure (5 s).

Time histories of the structure inertia (Sum of the superstructure and the footing inertia), the resultant of the total earth pressure and the sidewall friction, the total subgrade reaction (Suzuki et al., 2005) , and the bending moment at pile heads and their tips are shown in Figs. 4 and 5. The total subgrade reaction (Sum of the lateral subgrade reaction acting on the pile) was calculated as the difference between the shear force at pile tips and their heads. The structure inertia was extremely small in both cases. The amplitude of the resultant of the total earth pressure and the sidewall friction, the total subgrade reaction, and the bending moment at pile heads and their tips became extremely large at around 16 s. The amplitude of the resultant of the total earth pressure and the sidewall friction in Case 2 was smaller than that in Case 1. The amplitude of the total subgrade reaction in Case 2 was almost equal to that in Case 1. The bending moment at pile heads and their tips in Case 2 was smaller than those in Case 1.

4. PILE RIGIDITY EFFECTS ON PILE STRESS

To investigate the difference between the bending moment of piles in Case 1 and that in Case 2, the structure inertia, the resultant of the total earth pressure and the sidewall friction, and the total subgrade reaction at the time of maximum bending moment at pile tips are depicted in Fig. 6. The depth distribution of displacement of the ground and the pile is portrayed in Fig. 7. The displacement of the ground was greater than that of the pile and the footing in both cases. Consequently, the total subgrade reaction and the resultant of the total earth pressure and the sidewall friction acted as an external force. The total subgrade reaction in Case 2 was almost identical to that in Case 1. The relative displacement between the ground and the footing in Case 2 was smaller than that in Case 1 because the footing supported by the low-rigidity piles is more likely to follow the ground than that supported by the high-rigidity piles. Consequently, the resultant of the total earth pressure and the sidewall friction in Case 2 was smaller than that in Case 1. As described above, the total subgrade reaction in Case 2 was almost identical to that in Case 1. Moreover, the resultant of the total earth pressure and the sidewall friction in Case 2 was smaller than that in Case 1. Therefore, the bending moments at pile heads and their tips in Case 2 were smaller than those in Case 1.

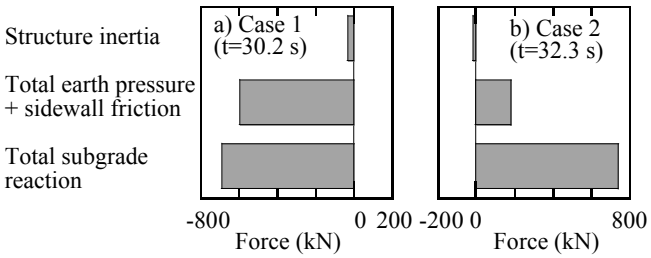


Figure 6 Structure inertia, total earth pressure + sidewall friction and total subgrade reaction

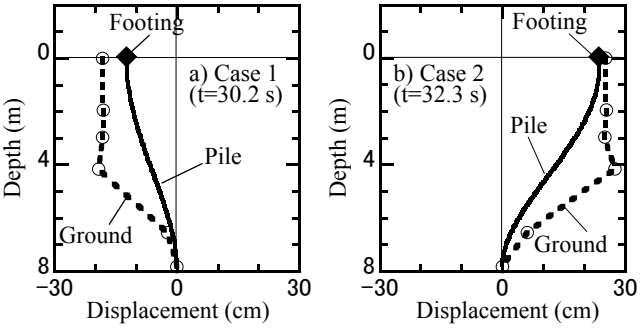


Figure 7 Displacement distributions of ground, footing and pile

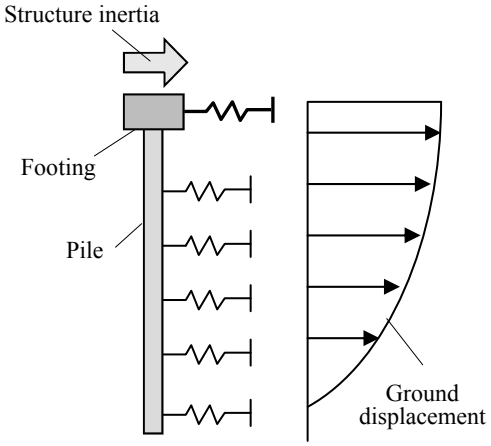


Figure 8 Analysis model of the pseudo-static analysis

5. PSEUDO-STATIC ANALYSIS INCORPORATING FOOTING EMBEDMENT EFFECTS

5.1 Subgrade Reaction, Total Earth Pressure and Sidewall Friction

Pseudo-static analyses were performed to investigate the effects of pile rigidity on the bending moment of the pile. The analysis model is presented in Fig. 8. In this study, the total earth pressure and the sidewall friction acting on the embedded footing were considered as a spring between the ground and the footing placed at the pile head. The subgrade reaction acting on the pile was calculated based on the Recommendations for Design of Building Foundations (AIJ, 2001). The *N*-value was

calculated using the following equation (JRA, 2002)

$$V_S = 80 \cdot N^{1/3} \quad (2)$$

where V_S is the shear wave velocity of the ground, and N is the N-value of the ground. The reduction coefficient of the subgrade reaction by soil liquefaction was set to 0.1.

The ultimate lateral resistance was calculated using the following equation.

$$p_y = 3K_P \gamma z \quad (2)$$

Therein, γ is the unit weight of the soil (kN/m³), z stands for the ground depth (m), and K_P represents the coefficient of passive earth pressure calculated using Rankine's equation. The relation between the relative displacement and the subgrade reaction was approximated as a trilinear function.

The total earth pressure acting on the embedded footing was calculated as shown below (Tokimatsu et al., 2003).

$$P_E = P_{Ep} - P_{Ea} = \frac{1}{2}\gamma H^2 B(K_{Ep} - K_{Ea}) \quad (3)$$

In that equation, γ stands for the unit weight of the soil (kN/m³), H denotes the footing height (m), B represents the footing width (m). Also, K_{Ep} and K_{Ea} respectively signify the coefficient of the earth pressure in passive and active sides. In fact, K_{Ep} and K_{Ea} were calculated using the seismic earth pressure theory by Zhang et al (1998). The relative displacement between the ground and the footing at the active and passive earth pressures are set respectively as 0.5% and 5% of the embedment height of the footing.

The sidewall friction acting on the embedded footing, P_{fs}, is calculated as

$$P_{fs} = \mu P_0 \quad (4)$$

and

$$P_0 = \frac{1}{2}K_0 \gamma H^2 B' \quad (5)$$

In those equations, P_0 signifies the earth pressure at rest (kN), γ stands for the unit weight of the soil (kN/m³), H denotes the footing height (m), B' represents the width of sidewall of the footing (m). Furthermore, K_0 is the coefficient of the earth pressure at rest calculated using Jaky's equation. Finally, μ is the friction coefficient between the ground and the sidewall of the footing, as calculated using the following equation (Tamura et al., 2007).

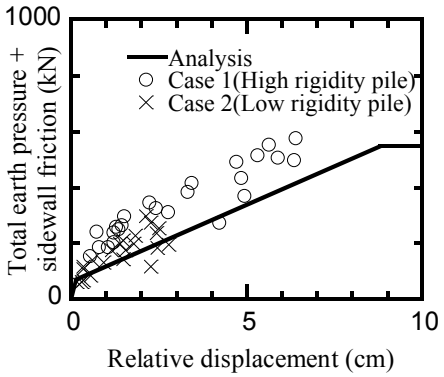


Figure 9 Relation between relative displacement and total earth pressure + sidewall friction

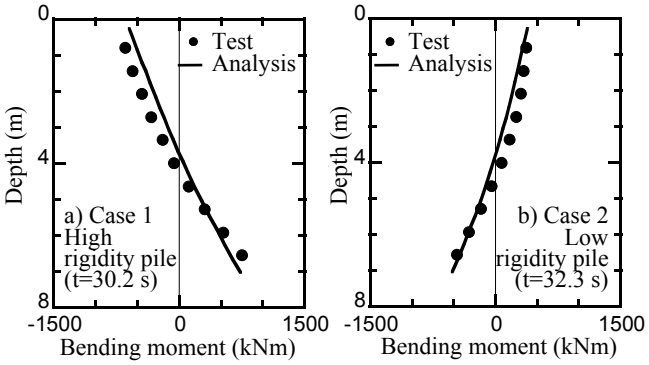


Figure 10 Depth distribution of bending moment

$$\mu = \tan\phi \quad (6)$$

Therein, ϕ is the internal friction angle (34°) of the soil. The relation between the relative displacement and the sidewall friction was set as a bilinear function that reaches constant value (P_{fs}) at 0.15 cm in the relative displacement. In this study, the relation between the relative displacement and the sum of the total earth pressure and the sidewall friction was approximated as a trilinear function. The relation between the relative displacement and the resultant of the total earth pressure and the sidewall friction is shown in Fig. 9. The centrifugal test results are also shown there. The resultant of the total earth pressure and the sidewall friction for analysis approximately agrees with the test results.

Assuming that the structure inertia and the resultant of the total earth pressure and the sidewall friction are evenly allocated to four piles, the analyses were performed for a pile. The ground displacement was set to be constant from the ground surface to 3 m depth. It was approximated by a cosine function from 3 m depth to bottom. The observed structure inertia and the ground surface displacement at the time of maximum bending moment at the pile tip were used for analyses. The structure inertia and the ground displacement were acted on

the pile simultaneously. The analyses were performed using software developed by Kozo Keikaku Engineering Inc.(2009). The depth distribution of the bending moment at the time of maximum bending moment at the pile tip is presented in Fig. 10. The analytical result shows good agreement with the test results in both cases.

5.2 Effects of Structure Inertia on Pile Stresses

To investigate the effects of the structure inertia on pile stress, analyses were performed for cases with various structure inertia. The ground surface displacement was set to 15 cm. In consideration of that the natural period of the superstructure is longer than the predominant period of the liquefied ground, the structure inertia and ground displacement was acted in the opposite phase. The relation between the structure inertia and the bending moment at the pile head is portrayed in Fig. 11. The relation between the structure inertia and the bending moment at the pile tip is presented in Fig. 12. For the case in which the structure inertia is less than 150 kN, the bending moment at pile head and its tip in the high-rigidity pile case are greater than those in the low-rigidity pile case. However, for structure inertia greater than 150 kN, the bending moment at the pile head and its tip in the high-rigidity pile case are almost identical to those in the low-rigidity pile case.

The relation between the structure inertia and relative displacement between the ground and footing is presented in Fig. 13. The minimum relative displacement which required to develop the passive state is also shown in the figure. The relation between the structure inertia and the resultant of the total earth pressure and the sidewall friction is presented in Fig. 14. For the case in which the structure inertia is smaller than 150 kN, the resultant of the total earth pressure and the sidewall friction in the high-rigidity pile case is greater than that in the low-rigidity pile case. For the case in which the structure inertia is greater than 60 kN, the relative displacement in the high-rigidity pile case is greater than the minimum relative displacement which required to develop the passive state. Consequently, the resultant of the total earth pressure and the sidewall friction reached a constant value. For structure inertia larger than 150 kN, the relative displacement in the low-rigidity pile case is larger than the minimum relative displacement which required to develop the passive state. Consequently, the resultant of the total earth pressure and the sidewall friction reached a constant value. Therefore, for structure inertia greater than 150 kN, the resultant of the total earth pressure and the sidewall friction in the high-rigidity pile case accords with that in the low-rigidity pile case.

Secondly, the effects of the structure inertia on the lateral subgrade reaction are investigated. The depth distribution of the subgrade reaction in cases where the structure inertia is 0 kN and 300 kN are presented in Fig. 15. The ultimate lateral resistance calculated using equation (2) is also presented there. The subgrade reaction reaches the ultimate lateral resistance in both cases. The subgrade reaction in the high-rigidity pile case is almost identical to that in the low-rigidity pile case.

As described above, in cases where the structure inertia is small, the lateral subgrade reaction in the high-rigidity pile case is almost identical to that in the low-rigidity pile case. Moreover, the resultant of the total earth pressure and the sidewall friction in the high-rigidity pile case is greater than that in the low-rigidity pile case. Therefore, the bending moment at pile heads and their tips in the high-rigidity pile case are greater than those in the low-rigidity pile case. However, in

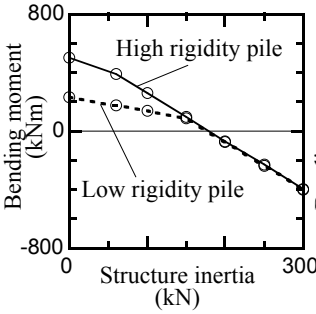


Figure 11 Relation between structure inertia and bending moment at pile head

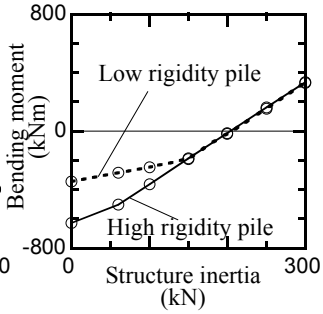


Figure 12 Relation between structure inertia and bending moment at pile tip

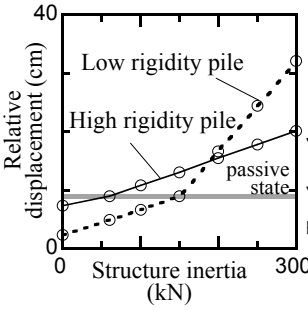


Figure 13 Relation between structure inertia and relative displacement

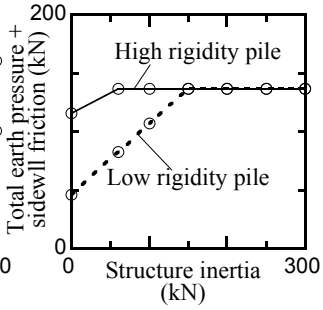


Figure 14 Relation between structure inertia and total earth pressure + sidewall friction

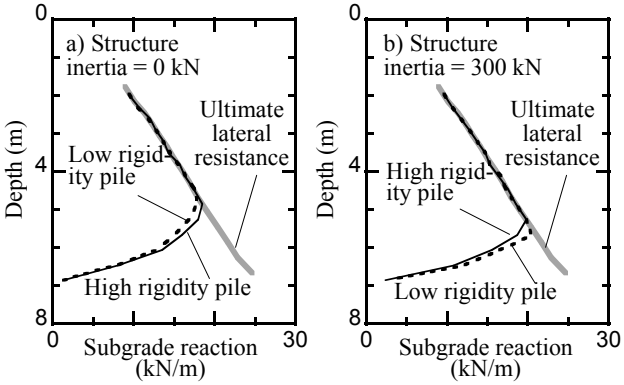


Figure 15 Depth distribution of the subgrade reaction

cases where the structure inertia is large, the subgrade reaction and the resultant of the total earth pressure and the sidewall friction in the high-rigidity pile case are almost identical to those in the low-rigidity pile case. Therefore, the bending moments at pile heads and their tips in the high-rigidity pile case are almost identical to those in the low-rigidity pile case.

6. EFFECT OF PILE RIGIDITY ON SUPERSTRUCTURE SEISMIC RESPONSE

To clarify the cause of which the acceleration in the low-rigidity pile case was greater than that in the high-rigidity pile case (Figs. 2, 3), the acceleration Fourier spectrum of footing, ground surface and shaking table are presented in Fig. 16. The predominant period of the footing was almost identical to that of the ground surface in both cases. Results show that the footing response is strongly affected by the ground response. In the periodic band of 2–5 s, the amplitude of the footing acceleration in the high-rigidity pile case is an intermediary value between that of the ground surface and the shaking table acceleration. On the other hand, in that periodic band, the amplitude of footing acceleration in the low-rigidity pile case was almost equal to that of the ground surface acceleration. This is because the footing behavior when supported by the low-rigidity piles is affected by the ground surface behavior. In the periodic band of 2–5 s, the amplitude of the footing acceleration in the high-rigidity pile case was smaller than that in the low-rigidity pile case. Therefore, the superstructure acceleration in the high-rigidity pile case was smaller than that in the low-rigidity pile case.

To investigate the effect of pile rigidity on the shear deformation of the isolator, seismic response analyses of single-degree-of-freedom systems were conducted. Figure 17 portrays the analytical model. The restoring force characteristic of the isolator was considered to be elastic. That of the damper was considered to be elasto-plastic (AIJ, 2001). The yield shear force coefficient of the damper (α_s) was set to 0.03, 0.04 and 0.05; its yield displacement was set to 1 cm. Viscous damping of the isolator was neglected. As stated previously, the footing response is affected strongly by the ground response. Assuming that the superstructure inertia only slightly affects the footing response, the footing acceleration observed in centrifuge tests was used as the input motion. Figure 18 portrays the relation between the natural period of the structure and the maximum shear deformation of the isolator. The smaller the α_s, the larger the shear deformation. For a natural period of the base-isolated structure of 5 s, The difference between the shear deformation of the isolator in the high-rigidity pile case and that in the low-rigidity pile case is small. In each case, the shear deformation is large for the case in which the natural period of the structure is close to the predominant period of the ground (3 s). That tendency is

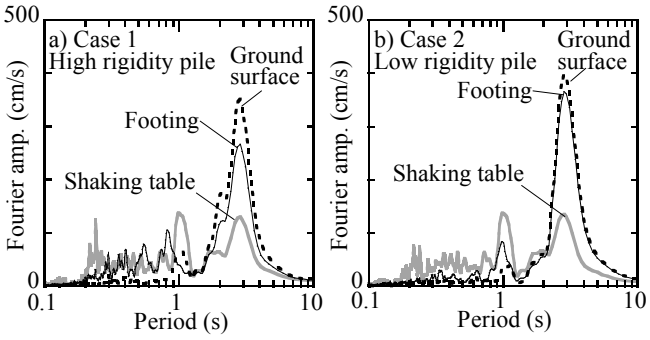


Figure 16 Acceleration Fourier spectrum of footing, ground surface and shaking table

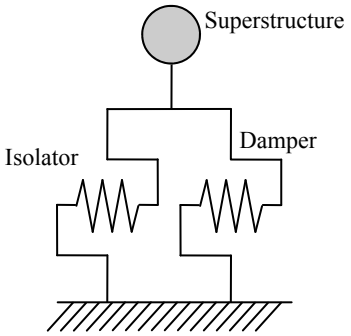


Figure 17 Analytical model

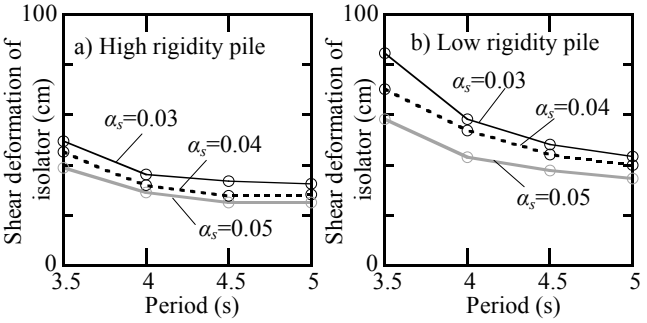


Figure 18 Relation between isolated period and maximum shear deformation of isolator

more apparent in the low-rigidity pile case than in the high-rigidity pile case. For the case in which the natural period of the structure is 3.5 s, the shear deformation in the low-rigidity pile case is much larger than that in the high-rigidity pile case. Particularly, the shear deformation in the low-rigidity pile case reaches about 85 cm when the yield shear force coefficient of the damper is 0.03.

As described above, in cases where the structure inertia is small, the bending moments at pile heads and their tips in the high-rigidity pile case are greater than those in the low-rigidity pile case. In contrast, in cases where the structure inertia is large, the bending moments at pile heads and their tips in the high-rigidity pile case are almost identical to those in the low-rigidity pile case. In cases where the natural period of base-isolated structure is much longer than the predominant

period of the ground, the difference between the shear deformation of the isolator in the high-rigidity pile case and that in the low-rigidity pile case is small. In contrast, in cases where the natural period of the structure is close to the predominant period of the ground, the shear deformation in the high-rigidity pile case is smaller than that in the low-rigidity pile case. Considering those results, the high-rigidity pile is suitable for a base-isolated structure for cases in which the natural period of the base-isolated structure is close to the predominant period of the ground.

7. CONCLUSIONS

Dynamic centrifuge tests were performed to investigate the effects of pile rigidity on the pile stresses and the seismic response of a base-isolated structure during soil liquefaction. Then pseudo-static analyses and single -degree-of-freedom analyses were conducted. They yielded the following conclusions.

For cases where the structure inertia is small, the bending moment at pile heads and their tips in the high-rigidity pile case are greater than those in the low-rigidity pile case. In contrast, in cases where the structure inertia is large, the bending moment at pile heads and their tips in the high-rigidity pile case are almost identical to those in the low-rigidity pile case. For the case in which the natural period of base-isolated structure is much longer than the predominant period of the ground, the difference between the shear deformation of the isolator in the high-rigidity pile case and that in the low-rigidity pile case is small. In contrast, in cases where the natural period of the base-isolated structure is close to the predominant period of the ground, the shear deformation of the isolator in the high-rigidity pile case is smaller than that in the low-rigidity pile case. Considering those results, the high-rigidity pile is suitable for a base-isolated structure for cases in which the natural period of the base-isolated structure is close to the predominant period of the ground.

Acknowledgments:

The authors thank Mr. K. Adachi, a former graduate student of Kyoto University, for assistance with centrifuge tests. This study was conducted with financial support of the Japan Society for the Promotion of Science and The Japan Iron and Steel Federation.

References:

Architectural Institute of Japan (2007), "Structural Response and Performance for Long Period Seismic Ground Motions".

Architectural Institute of Japan (2001), "Recommendation for the Design of Base Isolated Buildings".

Tokimatsu, K., Suzuki, H. and Sato, M. (2005), "Effects of Dynamic Soil-Pile-Structure Interaction on Pile Stress," *Journal of Struct. Constr. Eng.*, AIJ, (587), 125-132 (in Japanese).

Fukutake, K., Ohtsuki, A., Tanaka, H. and Matsuura, A. (2004), "Analytical Evaluation of Ductile Pile for Liquefiable Ground," Symposium on Pile Behavior and Design in Liquefying Soil, JGS (in Japanese).

Suzuki, Y. and Adachi, N.（2005), "Effects of Soil Density on Subgrade Reaction of Pile in Liquefied Soil," *Journal of Struct. Constr. Eng.*, AIJ, (592), 97-104 (in Japanese).

Architectural Institute of Japan (2001), "Recommendations for Design of Building Foundations" (in Japanese).

Japan Road Association (2002), "Specifications for Highway Bridges, Part V, Seismic Design"

Tokimatsu, K., Tamura, S., Miyazaki, M. and Yoshizawa, M.（2003), "Evaluation of Seismic Earth Pressure Acting on Embedded Footing Based on Liquefaction Test Using Large Scale Shear Box," *Journal of Struct. Constr. Eng.*, AIJ,（570）, 101-106 (in Japanese).

Zhang, Jian-Min, Shamoto, Y. and Tokimatsu, K. (1998), "Evaluation of Earth Pressure Under Any Lateral Deformation," *SOILS AND FOUNDATIO*NS, **38**(1), 15-33

Zhang, Jian-Min, Shamoto, Y. and Tokimatsu, K. (1998), "Seismic Earth Pressure Theory for Retaining Walls under any Lateral Displacement," *SOILS AND FOUNDATIONS*, **38**(2), 143-163

Tamura, S., Imayoshi, T. and Sakamoto, T. (2007), "Earth Pressure and Sidewall Friction Acting on an Embedded Footing in Dry Sand Based on Centrifuge Tests," *SOILS AND FOUNDATIONS*, **47**(4), 811-819

Kozo Keikaku Engineering Inc. (2009), "User's Manual for k-PILE"

8CUEE CONFERENCE PROCEEDINGS
8th International Conference on Urban Earthquake Engineering
March 7-8, 2011, Tokyo Institute of Technology, Tokyo, Japan

COMPARATIVE STUDY ON EFFECT OF LIQUEFIABLE SOIL-STRUCTURE INTERACTION BY SHAKING TABLE TEST

Peizhen Li[1], Xiuqiang Li[2], and Xilin Lu[3]

1) Associate Professor, State Key Laboratory of Disaster Reduction in Civil Engineering, Tongji University, P. R. China
2) Master Student, State Key Laboratory of Disaster Reduction in Civil Engineering, Tongji University, P. R. China
3) Professor, State Key Laboratory of Disaster Reduction in Civil Engineering, Tongji University, P. R. China
lipeizh@tongji.edu.cn, lixiuqiang198703@163.com, lxlst@tongji.edu.cn

Abstract: Through comparing the shaking table model test results of liquefiable soil-pile-structure interaction system with that of structure on fixed base, the effects of liquefiable Soil-Structure Interaction (SSI) on dynamic characteristics and seismic responses are studied in this paper. Due to the effect of SSI, the natural frequency of the system in liquefiable soil is lower than that of the structure on fixed base and its damping ratio is larger than that of structure. The mode shapes of system in liquefiable soil are notably different from those of the structure on fixed base, and there exists rocking and swing at the foundation in SSI system. When SSI is considered, the seismic responses such as acceleration, shear force, bending moment and strain are commonly less than those of the structure on fixed base, while displacement of SSI system is larger.

1. INTRODUCTION

Seismic dynamic response of the building is a complicated problem of coupling interaction between the structure and soil through the interface. Soil, foundation and the superstructure vibrate as a whole under earthquakes, bind to each other, and affect each other. Typically, the interaction between the soil and structure contains two-fold meaning, one is the vibration characteristics influence of the superstructure from the soil (including the natural frequency, damping ratio and vibration mode, etc.); the other is the feedback from the superstructure due to the input seismic waves from the soil. Researchers have derived a lot of valuable conclusions from shaking table scale model tests of SSI in liquefiable ground (e.g., Koga et al. 1990, Funahara et al. 2000, Kagawa et al. 2000, Tamura et al .2000, Takahiro et al. 2004, Chen et al. 2003, Feng et al. 2005, Meng et al. 2005, Ling et al. 2006). Studies have shown that seismic soil-structure interaction effect (compared with the structure on fixed base) can be generally summed up as the change of the dynamic characteristics of structure-the extension of natural period, changes in mode shape, damping change (usually increase), changes in seismic response-the internal force and displacement change, changes in movement characteristics of the base. The main conclusions of these studies are obtained through theoretical analysis and calculation, only a small amount of information is from the on-site or laboratory test results. Exploring the soil-structure interaction effect in the elastic stage and elastic-plastic stage through shaking table tests is significant to verify the theories of calculation and analysis.

Sponsored by key projects of National Natural Science Foundation of China, a series of shaking table model tests have been carried out including the dynamic system of soil and high-rise structure using the pile foundation and that of high-rise structure on fixed base not considering SSI (e.g., Chen et al. 1999, Soil Dynamic Laboratory 2001, Lu et al. 2002, Li et al. 2006, Li et al. 2008). The emphasis of this paper will focus on dynamic characteristics and seismic response of structure affected by SSI.

2. BRIEF DESCRIPTION OF SHAKING TABLE MODEL TESTS

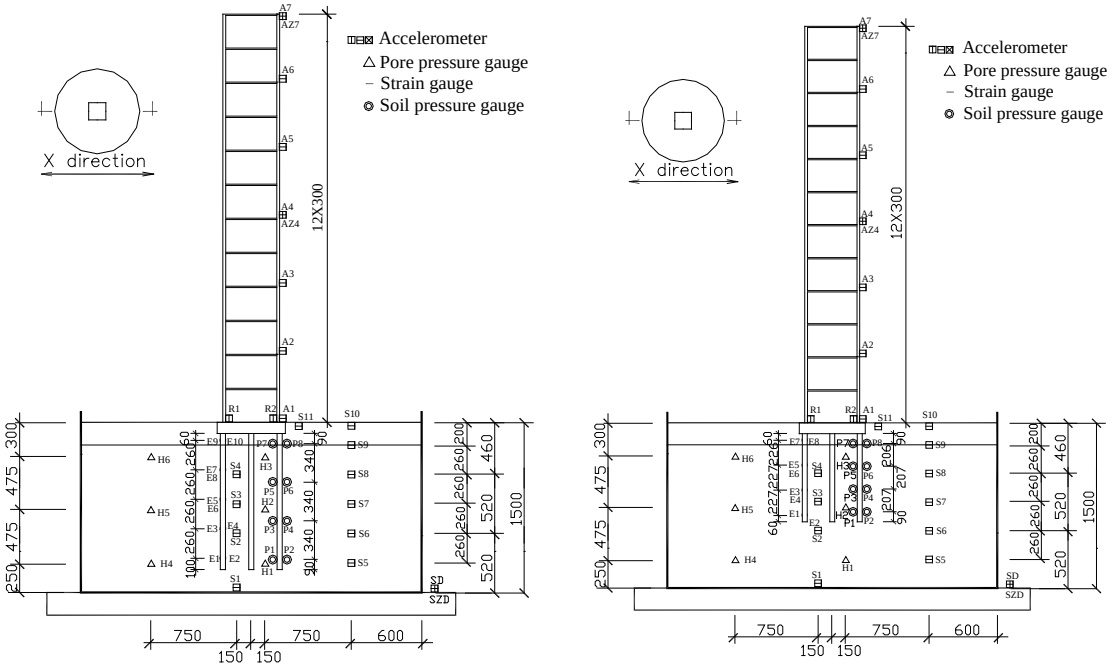
The shaking table model tests of liquefiable soil-pile-structure system have been carried out (called Test PS10L and Test PS10S). The longer piles (1.2m in length) were used as the foundation in Test PS10L and the shorter piles (0.8m in length) were used in Test PS10S. As a comparison, shaking table test of structure on fixed base (called Test S10L) has also been carried out. In these three tests, 12-story reinforced concrete frame structure with single span was employed to simulate the superstructure with the scaling factor of 1/10. The design of 12-story R.C. frame structure used as the superstructure in test S10L was the same as that in test PS10L and PS10S, and the structures were cast synchronously.

Non-gravity model with similitude rules controlled

materials was adopted in present test. Similitude formulas and similitude factors of all physical quantities were induced from Bockingham π theorem. The scales of models were 1/10. The similitude factor of mass density was 1, and the similitude factor of elasticity modulus for structure was 1/2.668. Saturated sand covered by silt clay was used for the soil model. The top layer was silt clay, 0.2m in depth; while the bottom layer was sand, 1.30m in depth. For the foundation of the superstructure, nine piles of a pile group were used.

Because of wave reflection on the boundary, an error called boundary effects will affect the test results. To reduce the boundary effect, a flexible container and proper constructional details were designed for the model test, and the ratio of the ground plane diameter to the structural plane diameter (i.e., D/d) was set at 5 by controlling the size of the structural plane. The cylindrical container was 3000 mm in diameter, and its lateral rubber membrane was 5 mm thick. Reinforcement loops of 4 mm diameter, spaced at 60 mm, were used to strengthen the outside of the container in the tangential direction.

Accelerometers, displacement meter and strain gauges were used to measure the dynamic response of the superstructure, foundation and soil. Pore pressure gauges were embedded in soil to measure the change of pore pressure. Pressure gauges were used to measure the contact pressure between piles and the surrounding soil. Figure 1 shows the arrangement of measuring points. The photo of Test PS10L is shown in Figure 2. The photo of Test S10L is shown in Figure 3.



(a) PS10L (b) PS10S

Figure 1 Sketch of Measuring Point Arrangement

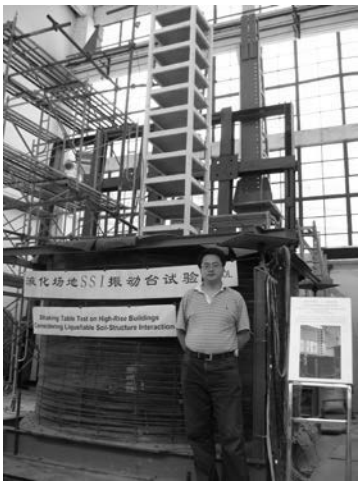


Figure 2 Test PS10L



Figure 3 Test S10L

El Centro wave and Shanghai bedrock wave were used as the input excitation. The peak acceleration value is

inputted according to the corresponding epicentral intensity in the seismic code of China, and the time interval is adjusted according to the similitude relation.

Test loading schedules is shown in Table 1, including 16 excitations. Before and after the altering of inputting acceleration, the White Noise with small amplitude is inputted to observe the change of dynamic characteristics of the system.

Table 1 Test Loading Schedules of Test PS10L, PS10S and S10L

No.	Excitation Code	Acceleration Peak Value (g)		Remarks
		Prototype	Model	
1	1WN	—	0.07	
2、3	EL1、SJ1	0.035	0.131	Basic seismic of 7 degree
4	4WN	—	0.07	
5、6	EL2、SJ2	0.1	0.375	7 degree
7	7WN	—	0.07	
8、9	EL3、SJ3	0.2	0.75	8 degree
10	10WN	—	0.07	
11、12	EL4、SJ4	0.3	1.125	
13	13WN	—	0.07	
14、15	EL5、SJ5	0.4	1.5	
16	16WN	—	0.07	

Note: EL—El Centro wave (unidirectional X); SJ—Shanghai bedrock wave (unidirectional X)

3. TESTS PHENOMENA COMPARISON

By observing and comparing, there exist some similar phenomena between Test PS10L and Test PS10S. The superstructure inclines to some degree after all excitations. The pile is dug out after the test and it can be seen that there are many horizontal cracks along the piles. The crack is dense at the top of the pile and less or none at the tip. The cracks on the two side piles of three rows piles in the vibration direction are much more and larger. However, the cracks on the middle pile are relatively fewer and smaller. The cracks penetrate basically on the plane vertical to the vibration direction and usually not penetrate on the plane horizontal to the vibration direction. The cracks appear to be typical bending cracks. There is almost no crack on the superstructure.

However, on the frame structure on fixed base, the cracks appear much earlier, develop faster. In test S10L, there is not any crack on the structure under the first eight excitations. After the excitation of SJ3, horizontal cracks appear on the east side of the southeast corner column at the 3rd story, and vertical cracks appear on the south part of the east beam, about 0.1mm in width. After the excitation of EL5, original cracks keep on developing. New slight vertical cracks appear on the east part of the south beam at the 1st story, both parts of the north beam at the 1st story, both parts of the beams at the 2nd story, both parts of the south beam at the 3rd story, the east part of the north beam at the 3rd story, both parts of the south beam at the 4th story and the east part of the south beam at the 5th story, and the beams is along the vibration direction. The above vertical cracks develop upwards or downwards, about 0.1~0.2mm in width. Vertical cracks appear on the joint between the southwest column and the south beam at the 6th story, and horizontal cracks appear on the west side of the southwest corner column at the 1st story, the west side of the northwest corner column at the 5th story, the west side of the northwest corner column at the 2nd story, about 0.1~0.2mm in depth. After the excitation of SJ5, vertical cracks appear on the south side of the southwest corner column at the 1st story, the west side of the southwest corner column at the 4th story and the south side of the southwest corner column at the 5th story, about 0.2mm in depth, and original cracks keep on developing.

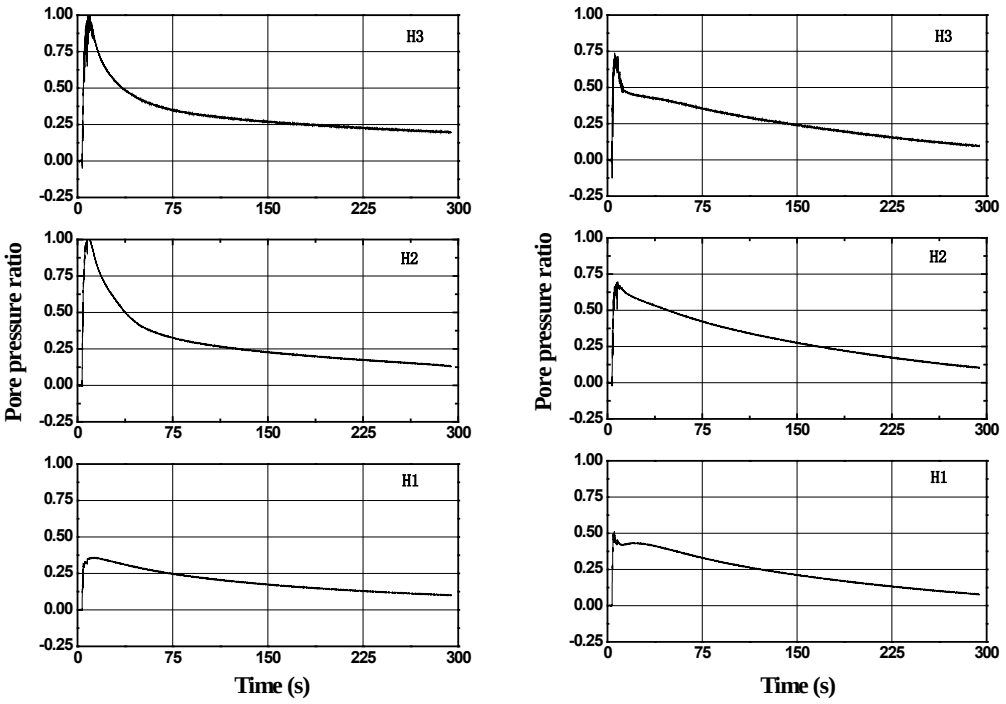
Comparing test PS10L and PS10S on liquefiable soil-pile-structure interaction system with test S10L on fixed base, conclusion can be drawn as follows. There are no cracks appear on the superstructure in SSI system, while some cracks appear on the superstructure with fixed base. This is mainly resulted from the vibration isolation effect of liquefied sand and effect of SSI on foundation motion. The superstructures of test PS10L and test PS10S are supported on the foundation which placed in saturated sand, and the excitations the superstructure received are obviously less than that of the superstructure directly fixed to shaking table.

The change of pore water pressure ratio in the sand soil is obtained by nine high-sensitivity pore water pressure gauge embedded in the sand soil (The arrangement of the measuring points is shown in Figure 1). Figure 4 show the pore water pressure ratio time histories of the measuring points in PS10L and PS10S tests under the excitation of EL3. From the figures, we can see the pore water pressure ratio of some points reach 1.0, which mean sand soil liquefied in the excitation of EL3.

4. STRUCTURAL DYNAMIC CHARACTERISTICS INFLUENCE OF SSI

Table 2 displays the frequency and damping ratio in each phase of these three tests. It can be seen that, with increasing of times and peak acceleration of input excitation, the frequency of model decrease, while the damping ratio

increases. Through comparing the change of model frequency with the change of structural frequency on fixed base, we can see that, the decreasing of structural frequency in test S10L is faster. This is resulted from the different development of crack on structure.



(a) PS10L (b) PS10S

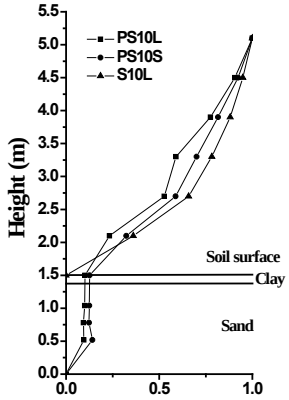
Figure 4 The Pore Pressure Ratio Time History of Different Measuring Points

Table 2 Frequency and Damping Ratio of Three Test Models in Each Phase

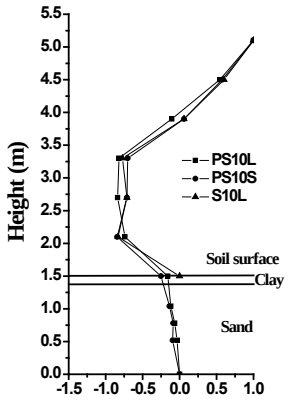
No.	Excitation Code	Test PS10L		Test PS10S		Test S10L	
		Frequency (Hz)	Damping Ratio(%)	Frequency (Hz)	Damping Ratio (%)	Frequency (Hz)	Damping Ratio (%)
1	1WN	2.977	7.01	2.680	10.16	2.977	10.650
4	4WN	2.977	8.08	2.680	11.01	2.977	6.210
7	7WN	2.680	8.33	2.382	10.14	2.680	9.040
10	10WN	2.084	9.10	2.382	9.26	2.084	7.640
13	13WN	1.786	16.53	2.382	8.45	1.489	18.170
16	16WN	1.786	11.19	2.382	8.93	1.191	13.590

With increasing of times and peak acceleration of input excitation, the model frequency of test PS10L, PS10S and test S10L on fixed base all decrease, while damping ratio increase, but the reasons are different. As to SSI system, the change of dynamic characteristics is the common result of soil softening, pile foundation crack development, and the decreasing the structural rigidity, and soil softening is the main factor. As to the structure on fixed base, the change of frequency is only resulted from the appearance and development of crack on beams and columns.

Figure 5 and Figure 6 display the mode shape curves of test PS10L, PS10S and S10L model under the excitation of 1WN and 13WN. From the figures, the main difference of mode shape between test PS10L, PS10S which taking the effect of SSI into account and test S10L which not taking the effect of SSI into account is that there is obvious translational and rotational movement in the foundation of test PS10L, PS10S model. With increasing of excitation times, the soil continues to soften, the translational and rotational movement of the foundation keeps on increasing and the rotational movement is more obvious. The degree of foundation translation and rotation has relation with the soil condition and the foundation type. The first mode shape of the superstructure is mainly shear type, while there are translational and rotational components in test PS10L, PS10S. With increasing of excitation times, the structural cracks at the lower stories develop, the rigidity decreases, and the height of zero point in the mode shape amplitude descends.

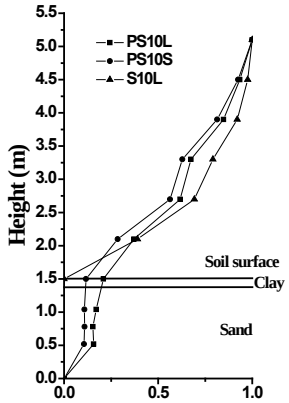


(a) The First Mode Shape
(Under the Excitation of 1WN)

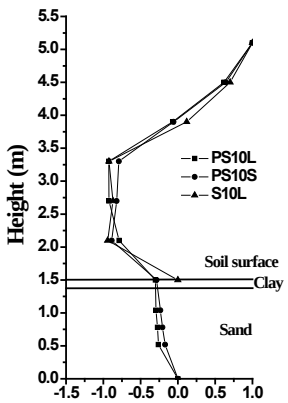


(b) The Second Mode Shape
(Under the Excitation of 1WN)

Figure 5 Contrast of Mode Shape Curves



(a) The first Mode Shape
(Under the Excitation of 13WN)



(b) The Second Mode Shape
(Under the Excitation of 13WN)

Figure 6 Contrast of Mode Shape Curves

5. STRUCTURAL SEISMIC RESPONSE INFLUENCE OF SSI

Due to the effect of SSI on structural dynamic characteristics, there is some change on the seismic response of the superstructure. Through comparison among the structural acceleration response, displacement response, interstory shear, overturning moment and so on, the effect of SSI in liquefied soil is discussed.

In test S10L on fixed base, the frame structure is directly fixed on shaking table. So the input acceleration of the shaking table is the seismic acceleration of free field at the bottom of the structure. In test PS10L and PS10S, the container is fixed on the shaking table. The frame structure is supported on the foundation in soil. So the input vibration travels from the shaking table, through soil and foundation, to the structural bottom. The comparison of seismic response on superstructure between SSI system and fixed base system should be based on the equality of seismic acceleration in free field.

In test, the acceleration record of foundation top for SSI system is not the "free field" motion. It also includes the effect of SSI on foundation motion. Take the record of measuring point S10 which has a certain distance off the foundation as the seismic acceleration of free field in test PS10L and PS10S. Take the input acceleration of the shaking table as the seismic acceleration of free field in test S10L. Adjust the peak acceleration of free field in test S10L to equal to that in test PS10L. Then the seismic response of superstructure of three tests could be compared as follows.

Due to the effect of SSI, there is great difference in crack development on frame structure for three tests (see former test phenomena). But as comparison base, the frame structure of each test should be at the similar state, so the comparison will be held only under the first and the second input excitation when there is not or only very slight crack on the structure.

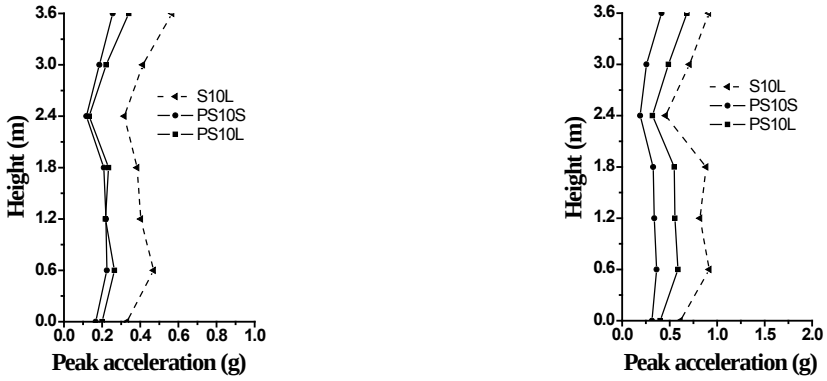
5.1 Acceleration Response

Figure 7 displays the comparison of peak acceleration on structure in three tests. It can be seen that, the acceleration response on superstructure for SSI system is obviously smaller than that on fixed base, and this law doesn't change with increasing of excitation.

5.2 Displacement Response

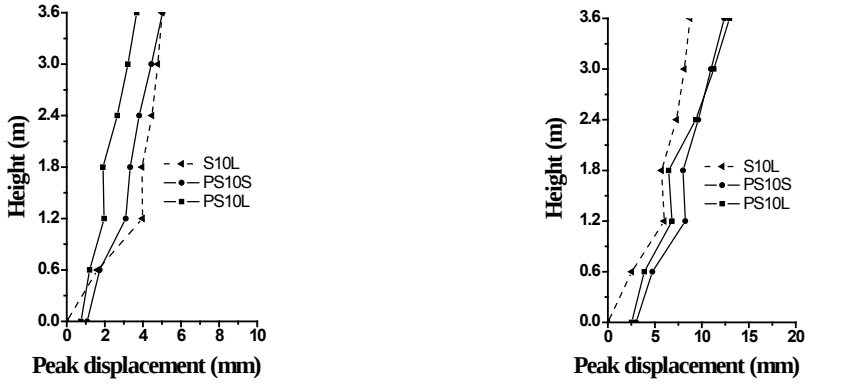
Figure 8 displays the comparison of the displacement peak value on frame structure in three tests. When taking

SSI into account, because the displacement on structure consists of translation and rotation of foundation and structural deformation, the displacement response for SSI system is usually larger than that on fixed base. Under small excitation, the displacement for SSI system differs not much from that on fixed base, and the former is even smaller than the latter. But with increasing of excitation, softening and non-linear development of soil and translational and rotational rigidity descending of pile foundation, the displacement peak value of SSI system is larger than that of fixed base.



(a) Under the Excitation of EL1 (b) Under the Excitation of EL2

Figure 7 Comparison of Peak Acceleration



(a) Under the Excitation of EL1 (b) Under the Excitation of EL2

Figure 8 Comparison of Displacement Peak Value

5.3 Interstory Shear and Overturning Moment

Figure 9 and Figure 10 display the comparison of the interstory shear and overturning moment amplitude on frame structure in three tests. It can be seen that, the interstory and overturning moment on superstructure for SSI system are smaller than that of fixed base, and this law doesn't change with increasing of excitation.

5.4 Strain Response on the Bottom of the Column at the Ground Story

Table 3 displays the comparison of the strain amplitude on the bottom of the column at the ground story in three tests. It can be seen that, the strain on superstructure for SSI system is obviously smaller than that of fixed base.

Table 3 Comparison of Strain on the Bottom of the Column at the Ground Story

Test Code	Under Excitation of El Centro Wave		Under Excitation of Shanghai Bedrock Wave	
	EL1	EL2	SJ1	SJ2
PS10L	109.1	235.5	101.3	216.1
PS10S	75.6	126.8	72.2	66.8
S10L	413.2	625.0	182.9	459.1

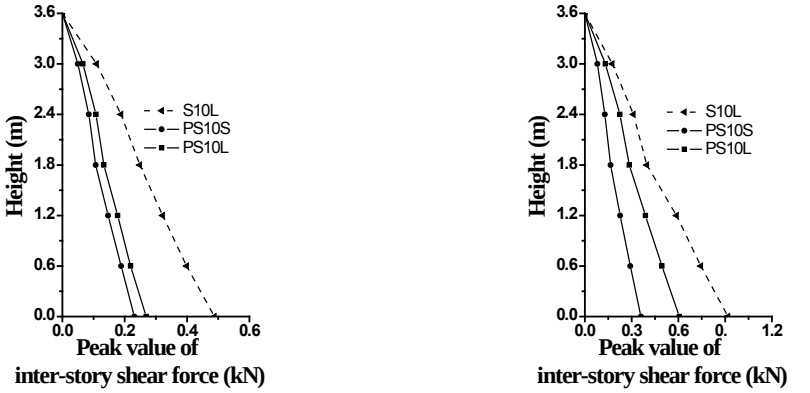
6. CONCLUSIONS

Through comparing the shaking table model test results of liquefiable soil-pile-high-rise structure interaction system with that of high-rise structure on fixed base, the effects of Soil-Structure Interaction (SSI) on dynamic characteristics and seismic response are studied further. Some important findings from the present tests are as follows.

(1) The effect of the dynamic liquefiable soil-structure interaction has relation with many factors. The effect with shorter pile is larger than that with longer pile. The larger the peak acceleration of excitation is, the larger the effect is.

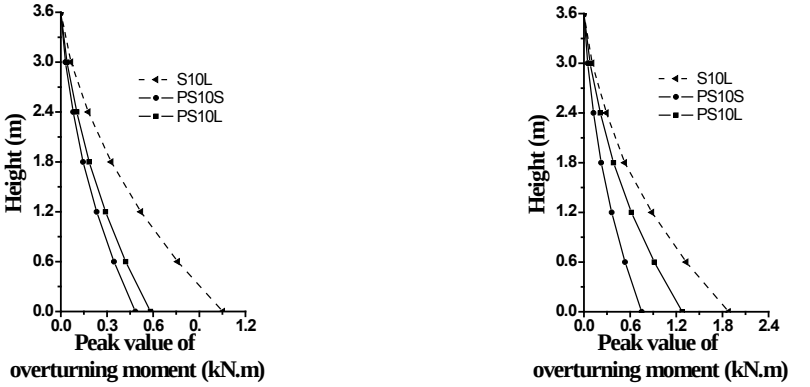
(2) Under the same excitation, compared with the structure on fixed base, the superstructure of SSI system generates cracks much later, smaller and fewer, develops more slowly.

(3) The interaction results in the change of structural dynamic characteristics, the damping ratio increases, and the mode shape changes. Under the same excitation, the acceleration, interstory shear, overturning moment and strain



(a) Under the excitation of EL1 (b) Under the excitation of EL2

Figure 9 Comparison of the Interstory Shear Amplitude



(a) Under the Excitation of EL1 (b) Under the Excitation of EL2

Figure 10 Comparison of the Overturning Moment Amplitude

on the structure when taking SSI into account are always smaller than that on fixed base, while the displacement is larger than that on fixed base.

Acknowledgement:

This project was supported by the key project (Grant No. 51021140006 and 90815029) of the National Natural Science Foundation of China, the project (Grant No. 2007CB714202) of National Basic Research Program of China.

References:

Chen Y Q, Huang W, Lu X L, et al. (1999), "Design of Shaking Table Model Test on Dynamic Soil-structure Interaction System," *Structural Engineers (Supplement)*, 243-248 (in Chinese).

Chen, Y.Q., Lu, X.L., Hou, J.G., et al. (2003), "Shaking table testing on seismic liquefaction of soft soil under building footing," *Engineering Journal of Wuhan University*, **36**(1), 59-64 (in Chinese).

Feng, S.L., Wang, J.H., Guo, J.T., et al. (2005), "A shake table test on the seismic resistance of pile foundation in liquefied soil," *China Civil Engineering Journal*, **38**(7), 92-95 (in Chinese).

Funahara, H., Fujii, S. and Tamura, S. (2000), "Numerical simulation of pile failure in liquefied soil observed in large-scale shaking table test," *12th World Conference on Earthquake Engineering*, Auckland, New Zealand, No.0927.

Li, P. Z., Chen, Y. Q., Lu, X. L., et al. (2006), "Shaking table testing of hard layered soil-pile-structure interaction system," *Journal of Tongji University*, **34**(3), 307-313 (in Chinese).

Li, P. Z., Ren, H. M., Lu, X. L., et al. (2008), "Shaking table tests of dynamic interaction of soil-structure considering soil liquefaction," *14th World Conference on Earthquake Engineering*, Beijing, China, No. 04-01-0024.

Ling, X.Z., Guo, M.Z., Wang, D.S., et al. (2006), "Large-scale shaking table model test of seismic response of bridge of pile foundation in ground of liquefaction," *Rock and Soil Mechanics*, **27**(1), 7-10, 22 (in Chinese).

Lu, X.L., Chen, Y. Q., Chen, B. and Li, P. Z. (2002), "Shaking table model test on dynamic soil-structure interaction system," *Journal of Asian Architecture and Building Engineering*, **1**(1), 55-64.

Meng, S.J., Liu, H.L., Yuan, X.M., et al. (2005), "Experimental study on the mechanism of earthquake-induced differential settlement of building on liquescent subsoil by shaking table," *Chinese Journal of Rock Mechanics and Engineering*, **24**(11), 1978-1985 (in Chinese).

Kagawa, T., Minowa, C., Abe, A. (2000), "EDUS project (earthquake damage to underground structures)," *12th World Conference on Earthquake Engineering*, Auckland, New Zealand, No.0329.

Koga, Y., and Matsuo, O. (1990), "Shaking table tests of embankments resting on liquefiable sandy ground," *Soils Found*, 30, 162-174.

Tamura, S., Suzuki, Y., Tsuchiya, T., et al. (2000), "Dynamic response and failure mechanisms of a pile foundation during soil liquefaction by shaking table test with a large-scale laminar shear box," *12th World Conference on Earthquake Engineering*, Auckland, New Zealand, No.0903.

Takahiro, K., Yoichi, Y., Naoki, T., et al. (2004), "Shaking table testing of liquefiable ground improved by multi-layer solid," *13th World Conference on Earthquake Engineering*, Vancouver, Canada, Paper No. 136.

8CUEE CONFERENCE PROCEEDINGS
8th International Conference on Urban Earthquake Engineering
March 7-8, 2011, Tokyo Institute of Technology, Tokyo, Japan

DYNAMIC CENTRIFUGE MODEL TEST OF PILE-SUPPORTED BUILDING WITH SEMI-RIGID PILE HEAD CONNECTIONS IN LIQUEFIABLE SOIL

Sadayuki Ishizaki[1)], Kohji Tokimatsu[2)], and Toshiaki Nagao[3)]

1) Research Engineer, Technology Center, Taisei Corp., Japan
2) Professor, Center for Urban Earthquake Engineering, Tokyo Institute of Technology, Japan
3) Senior Research Engineer, Technology Center, Taisei Corp., Japan
sada.ishizaki@sakura.taisei.co.jp, kohji@o.cc.titech.ac.jp, toshiaki.nagao@sakura.taisei.co.jp

Abstract: Dynamic centrifuge model tests are conducted using pile-supported building models to investigate the seismic behavior of buildings with semi-rigid pile head connections in liquefiable soil. The dynamic test results show that (1) The semi-rigid pile head connection is effective for reducing the bending moment of piles in liquefied soil; and (2) The maximum acceleration of superstructure with semi-rigid pile head connections is about 40% of that of superstructure with rigid pile head connections in liquefied soil.

1. INTRODUCTION

In these days, various semi-rigid pile head connection methods have been developed that permit the rotation of pile heads as more effective pile design methods. Their effectiveness for reducing damage to piles has been verified by structural tests (Hara et al. 2002, Ohtsuki et al. 2001, Hiraide et al. 2004). The existing researches have, however, made studies focusing only on the static structural properties of pile head connections. Few examples are available of verifying in tests the effectiveness of semi-rigid pile head connection methods for reducing damage using the whole building while considering the dynamic soil-pile-structure interaction. In the previous study by authors (Ishizaki et al. 2006), shaking table tests of pile-supported building model in dry sand were conducted to investigate the seismic behavior of buildings with semi-rigid pile head connection method. In this study, dynamic centrifuge model tests are conducted using pile-supported building model in liquefiable soil to examine the effectiveness of semi-rigid pile head connection method for reducing seismic damage to piles, and the effects on the response of the building.

2. TEST OUTLINE

Dynamic centrifuge model tests are performed using soil-pile-structure systems at 50g centrifugal acceleration. Two soil-pile-structure models are used in the tests; the one is a building model with semi-rigid pile head connections (S-model) and the other is a building model with rigid pile head connections (R-model). The model is prepared in a laminar shear box 560mm in length, 210mm in width and 400mm in depth.

2.1 Models

Figure 1 shows the soil-pile-structure system used in the tests. The soil model is created using Toyora sand, and it consists of two layers with different relative densities. The target relative densities are set at 60% in the upper layer and 90% in the lower layer. The relative densities of the upper layer before excitation are 65% in S-model and 60% in R-model. Therefore the soil model in S-model is more dense than that in R-model. The soil models are saturated with silicon oil with 40 times viscous than water.

The mass of the superstructure is 5.2kg and that of the foundation is 2.7kg. The natural period of the superstructure in small excitation is 0.003s (0.15s in prototype scale). The models of pile and pile head are shown in Figure 2. Pile group consists of 2×2 stainless steel pipes. Each pipe has a diameter of 16mm with a 1mm wall thickness. The elastic coefficient of the pipe is 1.97×10^{8}kN/m^{2}. The pile tips are connected to the base of the laminar box with pin joints. The pile heads are connected to the foundation (pile cap) either semi-rigidly or rigidly according to the model type. In S-model, the foundation is simply placed on the pile heads. In R-model, the pile head is sandwiched between divided sections of foundation and fastened by bolts.

The rotation characteristics at the pile head connections are identified in preliminary static bending tests. A cantilever beam composed of the pile and the foundation is used as a specimen. The pile tip is subjected

to loading and unloading in a direction perpendicular to the axis. The bending moment and the rotation angle at the pile head are measured. Several initial axial forces of 1kN (2.5MN in prototype scale), 0.4kN (1.0MN in the scale) and 1.6kN (4.0MN in the scale) are applied to the semi-rigid pile head connection. Figure 3 shows the relationships between the bending moments and the rotation angles at pile heads in the both pile head connections. In the semi-rigid pile head connection, the initial rigidity is small, and the rotation angle increase drastically as the bending moment increase. The relationship is represented by nearly the same curve either in loading or unloading.The maximum resistance of moment *Mu* is given by the following equation:

$$M_u = \frac{D}{2} \cdot N \qquad (1)$$

in which *D* is the pile diameter, and *N* is the axial force. *Mu* at each axial force is showed in Figure 3. The bending moments at semi-rigid pile head connection are close to the *Mu* for the respective axial forces.

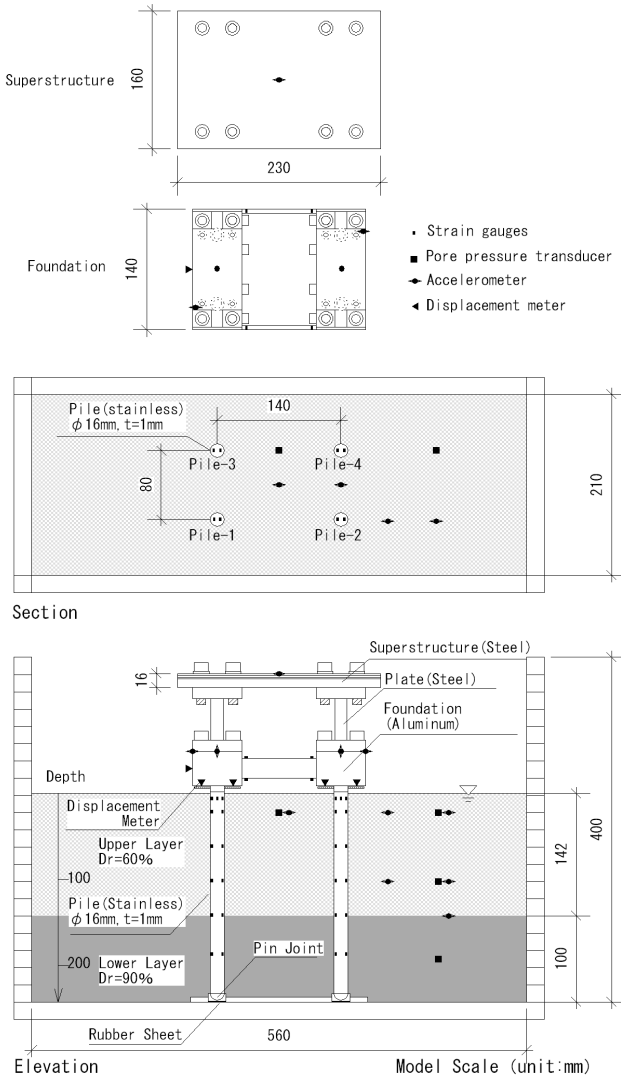


Figure 1 Model Layout

2.2 Measurement Parameters

Measurement parameters are shown in Figure 1, and strain gauges attached to the inner surfaces of piles are shown in Figure 2. The horizontal accelerations of soil and structure, the vertical accelerations of foundation, the strains of piles, the rotation angles of pile heads, and the pore water pressures of soil are measured. The displacements of structure and soil are found by double integration of the accelerations with respect to time.

2.3 Input Motion

Rinkai wave is used as an input motion. The amplitude is adjusted to obtain a maximum horizontal acceleration of 200 cm/s^2 in prototype scale. The initial vibration characteristics of the soil-pile-structure models are identified under tiny vibration.

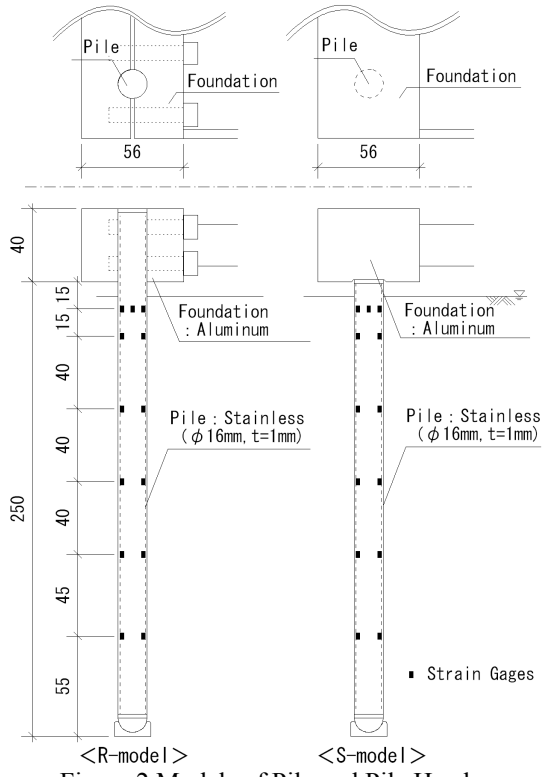


Figure 2 Models of Pile and Pile Head

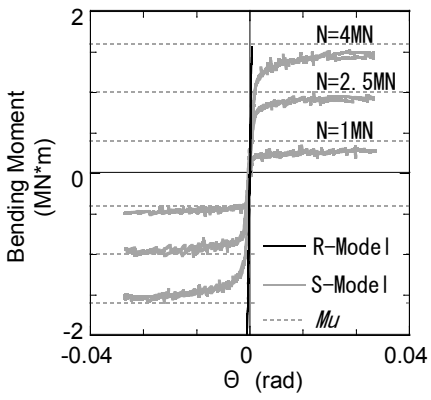


Figure 3 Relationships between Bending Moments and Rotation Angles at Pile Heads in Preliminaly Tests

3. TEST RESULTS AND DISCUSSIONS

All data presented in this section are of prototype scale. The results of excitation using Rinkai with a peak input acceleration of 200 cm/s^2 are compared in S-model and R-model. The initial axial forces on pile heads in S-model are almost the same (Table 1).

3.1 Time Histories of Accelerations, displacements and excess pore water pressures of soil

The time histories of the accelerations of soil and shaking table, the displacements of soil and the excess pore water pressures of soil are shown in Figure 4. The excess pore water pressures of soil at 1.1m and 5.1m depths reach the respective initial effective vertical stresses, then the upper layers are liquefied in the both models. The excess pore water pressure of soil at 5.1m depth in S-model rise later than that in R-model. This is because the relative density of the upper layer in S-model is higher than that in R-model. Therefore the accelerations of soil in S-model decrease after the time of 20s, on the other hand, those in R-model decrease after 12s.

The excess pore water pressures at 9.6m depth in both models reach the initial effective vertical stress at the time of 30s, but decrease gradually during the shaking.

The displacements of soil at 1.1m depth in both models increase drastically during soil liquefaction, especially from 77s to 88s.

3.2 Time Histories of Acceleration of Superstructure, Displacement of Foundation, Bending Moment of Pile Head and Rotation Angel of Pile Head

Figure 5 Shows the time histories of the acceleration of the superstructure, the displacement of the foundation, the bending moment of and the rotation angle of the pile head. The acceleration of the superstructure in S-model agrees with that in R-model before 20s. But after 23s when the soil liquefaction almost occurrs in the upper layer, the acceleration of the superstructure in S-model tends to decrease and delay than that in R-model. After 30s, a maximum acceleration of the superstructure in S-model is 0.47m/s^2 and that in R-model is 1.09m/s^2, i.e., the maximum acceleration of the superstructure in S-model decreases to 40% of that in R-model.

The displacements of the foundations in the two models mostly agree before 20s. However, after 20s, the displacement of the foundation in S-model tends to increase and delay than that in R-model. This tendency is especially clear from 77s to 88s. The displacement of the foundation in S-model corresponds to that of the soil at 1.1m depth in the model after 20s (Fig. 4(b)).

Table 1 Initial Axial Forces on Pile Heads in S-model

Pile	Initial Axial Force	Pile	Initial Axial Force
Pile-3	2100kN	Pile-4	2320kN
Pile-1	2350kN	Pile-2	2200kN

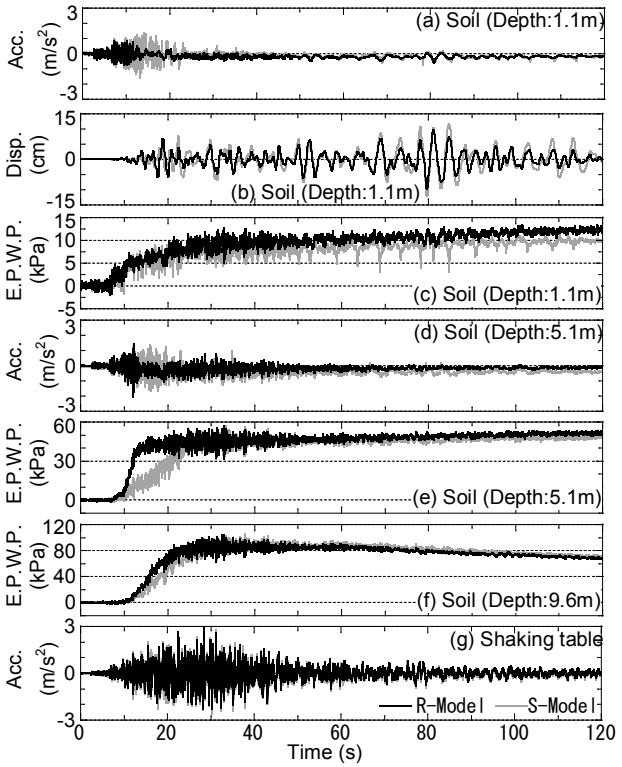


Figure 4 Time Histories of Accelerations, Displacements and Excess Pore Water Pressures of Soil

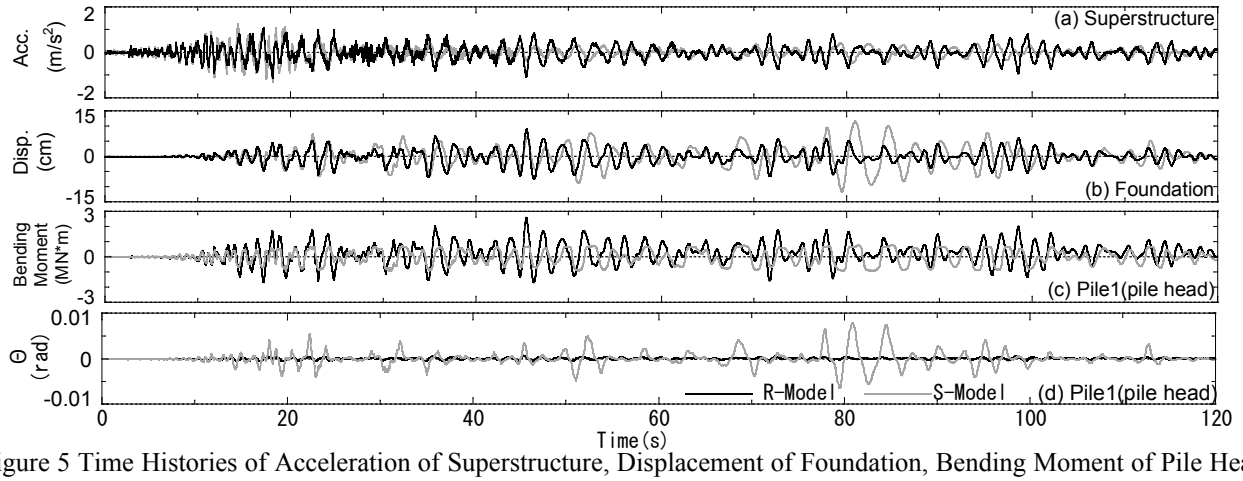


Figure 5 Time Histories of Acceleration of Superstructure, Displacement of Foundation, Bending Moment of Pile Head and Rotation Angel of Pile Head

3.3 Relationships between Bending Moments and Rotation Angles at Pile heads

Figure 6 shows the relationships between the bending moment and the rotation angle at pile head. The semi-rigid pile head connections have lower initial rigidities than the rigid pile head connections as shown in preliminary tests, and exhibit non-linear elastic behavior. And the bending moments in S-model drop steadily than those in R-model. In S-model, *Mu* varies according to the varying axial force due to overturning moment as shown Eq. (1). The moment in the pile subjected to compression is higher than the moment in the pile subjected to pullout force (Fig. (6)). And the rotation angle in the pile subjected to pullout force is larger than that in the other pile subjected to compression.

3.4 Distributions of Bending Moments along Piles

The inertia force is computed from the observed accelerations of the superstructure and the foundation. Figure 7 and 8 show the distributions of bending moments along piles at 18.0s (before liquefaction) and at 77.9s (during liquefaction). And Table 2 shows the inertia force at each second for respective models. At each second, the inertia forces of the two models are almost equal.

At 18.0s (before liquefaction), there are two peaks at pile head and at 9.4m depth in the distributions of bending moments in R-model. And the bending moments at pile heads are considerably higher than those at 9.4m depth. In the S-model that permit the rotations of pile heads, the bending moments at pile heads are lower than those occur in the soil, and those at pile head in R-model. The maximum bending moments that occur in the soil are higher in S-model than those in R-model. Moreover, the depth that the maximum bending moments occur at is shallow in S-model than that in R-model. And in the S-model, the varying axial forces due to overturning moment affect the distributions of bending moments along piles, i.e., the bending moment that occurs in the soil is larger in the pile subjected compression than that in the pile subjected to pullout force.

At 77.9s (during liquefaction), the inertia force is 40% of that at 18.0s. But, in R-model, the pile head bending moments at 77.9s are nearly the same as those at 18.0s. This is mainly because of the soil liquefaction. On the contorary, in S-model, the bending moments that occur in the soil at 77.9s are lower than those occur in the pile heads. This future of the distributions of bending moments at 77.9s is different from that at 18.0s. This is attributed to the reduction of inertia force and the soil liquefaction.

3.5 Distributions of Maximum Bending Moments along Piles

Figure 9 and 10 show the distributions of the maximum bending moments along piles before liquefaction (i.e., 0-25s) and during liquefaction (i.e., 25-120s). And Table 3 shows the maximum inertia forces for the respective periods.

Before liquefaction (i.e., 0-25s), the distributions of bending moments in R-model show two peaks at pile head and at 9.4m depth, but the bending moments at pile head are considerably higher than those at 9.4m depth. In S-model, on the other hand, the bending moments that occur in the soil are slightly higher than those at the pile

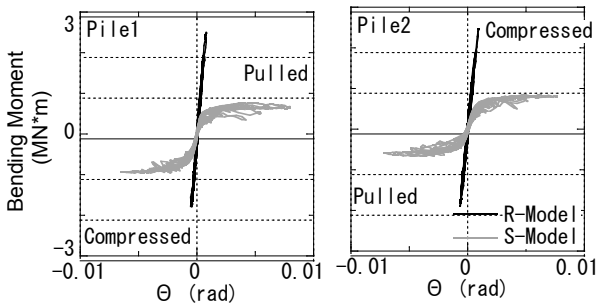


Figure 6 Relationships between Bending Moments and Roration Angles at Pile Heads

Table 2 Inertia Forces

Time	R-model	S-model
18.0s	1035kN	1072kN
77.9s	433kN	420kN

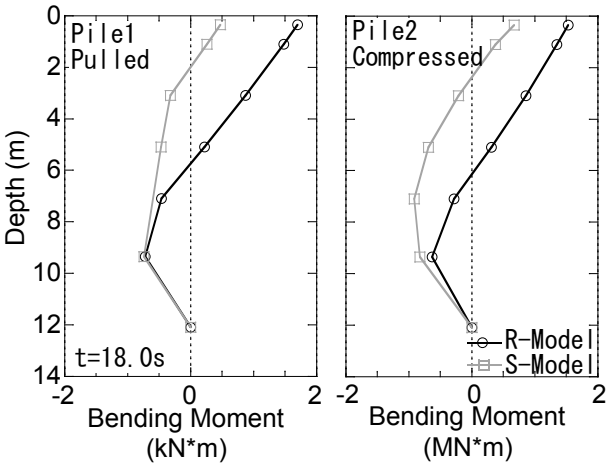


Figure 7 Distributions of Bending Moments along Piles at 18.0s

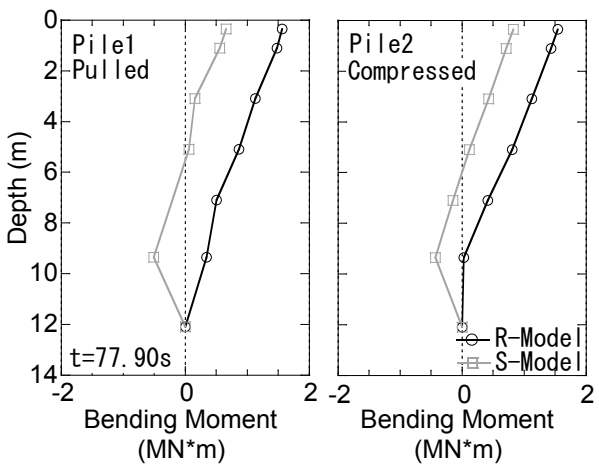


Figure 8 Distributions of Bending Moments along Piles at 77.9s

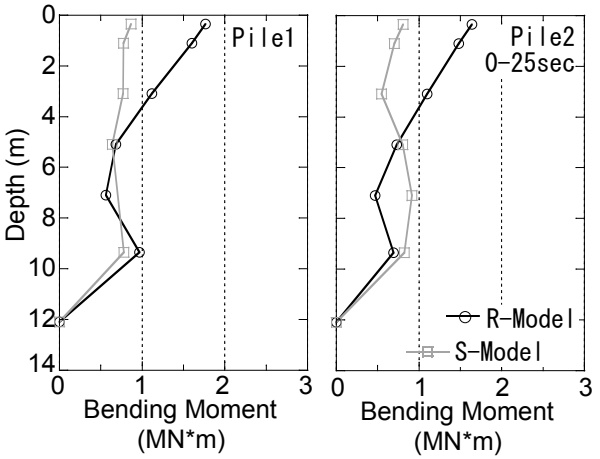


Figure 9 Distributions of Maximum Bending Moments along Piles Before Liquefaction (0-25s)

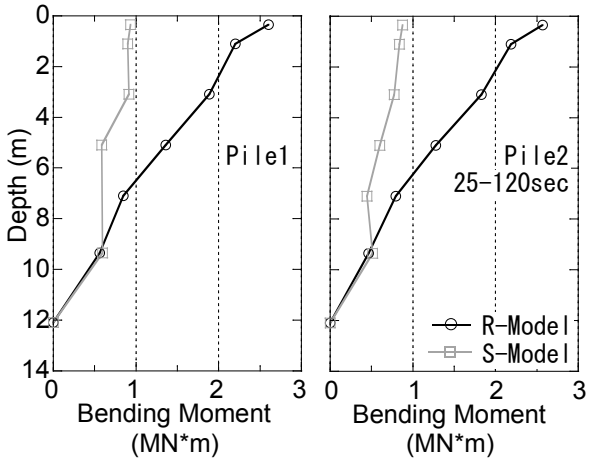


Figure 10 Distributions of Maximum Bending Moments along Piles During Liquefaction (25-120s)

heads. And the bending moments at pile heads in S-model are almost 50% of those at pile heads in R-model.

During liquefaction (i.e., 25-120s), the maximum bending moments those occur in R-model are significantly higher than those before liquefaction. This is attributed to the soil liquefaction because the inertia forces for the respective periods are the same. In S-model, in contrast, the maximum bending moments during liquefaction are lower than those before liquefaction. This is because of the reduction of inertia force and the soil liquefaction. Therefore the maximum bending moment that occurs in S-model decreases to 40% of that occurs in R-model during the whole time of shaking.

4. CONCLUSIONS

Dynamic centrifuge model tests are conducted to investigate the seismic behavior of buildings with semi-rigid pile head connections in liquefiable soil. Two soil-pile-structure models are used in the tests; the one is a building model with semi-rigid pile head connections and the other is a building model with rigid pile head connections. Following conclusions are obtained from comparisons of the two test results.

(1) The maximum acceleration of the superstructure in S-model is almost the same as that in R-model before liquefaction. During liquefaction, on the contrary, the response of the superstructure in S-model tends to decrease and delay than that in R-model.

(2) Before liquefaction, the bending moment at the pile head in S-model is about half of that in R-model. And in S-model, the maximum bending moments occurs in the soil, but is almost the same as that at pile head.

(3) During liquefaction, the maximum bending moment in R-model is higher than that before liquefaction.

Table 3 Maximum Inertia Forces

Period	R-model	S-model
0-25sec (Before Liquefaction)	1056kN	1200kN
25-120sec (During Liquefaction)	1074kN	439kN

This is because of soil liquefaction. In S-model, in contrast, the bending moment that occurs in the soil during liquefaction is lower than that occurs in the soil befofre liquefaction. This is because of the soil liquefaction and the reduction of inertia force. Therefore the maximum bending in S-model is about 40% of that in R-model during the whole time of shaking.

References:

Hara, T. Yasuda, S. Kawabata, I. Komuro, T. Korenaga, T. Tatsuno, S. (2002), "Development of Pile Head-Foundation Joint without Anchorage of Pile Rebar," Summaries of Technical Papers of Annual Meeting, AIJ, C-2, 187-190.

Ohtsuki, A. Tazoh, T. Aoki, T. Mano, H. Isoda, K. Iwamoto, T. Arakawa, N. Ishihara, T. Ohkawa, M. (2001), "A Pile-head Device with Spherical Contact-surface for Decreasing the Bending Moment," Summaries of Technical Papers of Annual Meeting, AIJ, B-2, 451-454.

Hiraide, T. Sugimura, Y. Ohsugi, F. (2004), " Experimental Study on Mechanical Properties of Pile Headjoint for Prestressed High Strength Concrete Piles Using Unbonded Stud Bars," Journal of Structural and Construction Engineering, AIJ, No.581, 71-78.

Ishizaki, S. Majima, M. Nagao, T. Funahara, H. Aoshima, K. (2006), "Shaking Table Tests on Soil-Pile-Structure Models with Semi-Rigid Pile Head Connections," Journal of Structural and Construction Engineering, AIJ, No. 602, 171-177.

8CUEE CONFERENCE PROCEEDINGS
8th International Conference on Urban Earthquake Engineering
March 7-8, 2011, Tokyo Institute of Technology, Tokyo, Japan

SEISMIC RESPONSE OF PILE FOUNDATION IN SLOPING GROUND

Akihiro Takahashi[1)] and Takaho Yamazaki[2)]

1) Associate Professor, Department of Civil Engineering, Tokyo Institute of Technology, Japan
2) Graduate Student, Department of Civil Engineering, Tokyo Institute of Technology, Japan
takihiro@cv.titech.ac.jp, yamazaki.t.ac@m.titech.ac.jp

Abstract: Seismic response of pile foundation in sloping ground was examined through a series of centrifuge model tests. This paper reports test results for the case that involves earthquake-induced large displacement of the sloping ground. Test results reveal that the loss of soil reaction due to the slip in the downslope has more impact on increase of the pile bending moment than the kimenatic load induced by soil mass movement in the upslope within the scope of the study.

1. INTRODUCTION

Diversification of risk is important for business continuity as well as quick disaster recovery after an earthquake. To this end, redundant transportation network is required especially for interurban roads and railways. Construction of the new Tomei Expressway and Chuo Shinkansen (new maglev line) connecting Tokyo and Nagoya in Japan are typical examples. Construction of such bypasses is typically made in mountain area and involves not only the tunnelling but also construction of many bridges. For the latter, construction of foundations in sloping ground is required.

Current design specifications of bridge foundation in sloping ground require stabilization of the sloping ground prior to the bridge construction in Japan (e.g., NERI, 2010). Because of this, movement of the sloping ground is seldom considered in seismic design of the bridge foundation. However, (1) allowable slope displacement deemed to be unharmful to bridge foundations during an earthquake is unclear, (2) displacement-based seismic design is seldom applied for slopes, and (3) seismic foundation-slope interaction is little understood, although many researches have been done for problems related to liquefaction (Martin & Chen, 2005; Takahashi & Takemura, 2005 among others.)

In this study, seismic response of pile foundation in sloping ground was examined through a series of centrifuge model tests. This paper reports test results for the case that involves earthquake-induced large displacement of the sloping ground.

2. TEST PROCEDURES AND CONDITIONS

The setup for centrifuge model tests is illustrated in Fig.1. In centrifuge model tests, slope is made by the Edosaki sand with 90 mm in thickness (2:25 m in prototype scale) with a slope of 1V:1.5H on the assumption that the slope is a colluvium slope or embankment over a sloping soft rock. The base soft rock is made of plates of plasticized polyvinyl chloride, considering the typical stiffness of the soft rock. At first, model piles (instrumented aluminium pipe having 10 mm diameter and 1 mm wall thickness) are installed in the prefabricated hole in the model soft rock and wet sand with a water content of 15% was placed in a model container and was compacted into a layer with 20 mm in thickness to achieve dry density ρ_d=1.4 Mg/m^3 (relative compaction of 80%). This compaction was continued up to the top of slope, while installing accelerometers as shown in Fig.1. After fixing the pile cap, structure (mass of 0.80 kg) and displacement transducers, the completed slope model (see

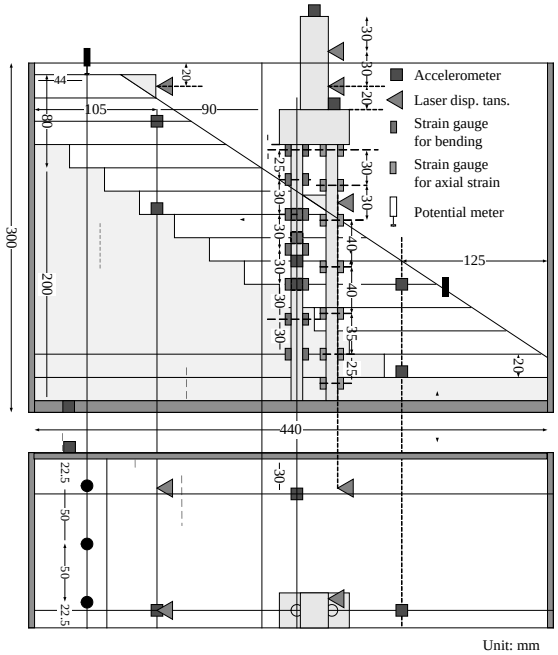
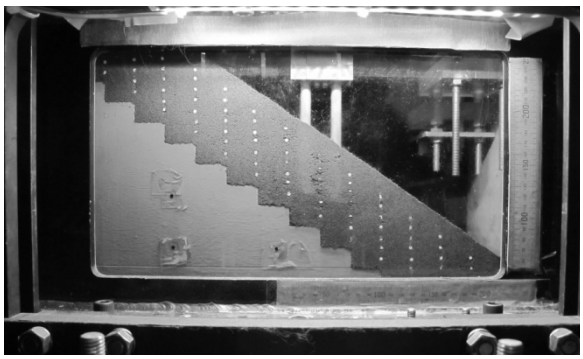
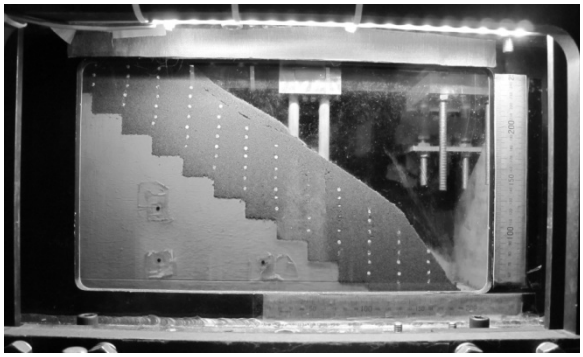


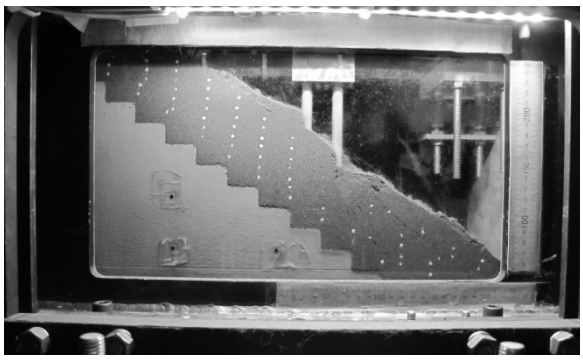
Figure 1 Model setup



(a) Before shaking



(b) Before third shaking (after second shaking with cut slope at the toe)



(c) After all the shakings

Figure 2 Side views of the model

Fig. 2(a)) was mounted on a geotechnical centrifuge, and shake table tests were conducted at 25 g field.

The target structure is a bridge pier supported by steel pipe piles arranged in 1x2 grids (2x2 for full width) with 3*D* spacing, where *D* = diameter of the pile. Weight of the structure supported by piles is determined so that the pile tip load is less than one-third of the ultimate tip resistance for the soft rock. To avoid having complicated slope—pile cap interaction problem, the stuck-out piles were employed. Natural frequency of the structure is around 30 Hz.

Figure 3 shows the typical earthquake motion applied. The earthquake motion is sinusoidal waves of 48 Hz. In total the earthquake motion was applied to the model four times. During the second shot, the surface failure occurred in the upslope of the piled structure as shown in Fig. 2(b). (Since this photo was taken after cutting the toe of the slope

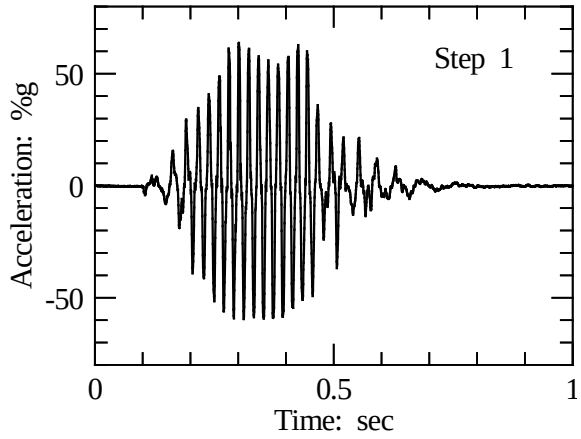


Figure 3 Typical input motion (Step 1)

as mentioned in the following section, the slope near the toe is steeper than the other location, but this portion was not steep when the two earthquake motion was applied for the first stage.) Since catastrophic failure of the slope did not occur in the first two earthquakes, the spinning of the centrifuge was stopped and toe of the slope was steeply cut to have large slope deformation in the following two earthquakes. Visual observation of the model was made from the side transparent window of the container with CCD camera.

3. TEST RESULTS AND DISCUSSIONS

3.1 Displacement of Structure and Slope

Figure 2 shows side views of the model (a) before shaking, (b) after the second shaking and (c) fourth shakings. During the second shaking the surface failure occurred in the upslope of the piled structure (Fig. 2(b)). In the following third and fourth shakings the slope near the toe also failed, resulting in relatively large deformation of the slope as shown in Fig. 2(c).

Time histories of the horizontal displacement of (a) the structure top and (c) the upslope distant from the structure are plotted in Fig. 4 for all the steps. The displacement is normalized by diameter of the model pile. Since the reading of the displacement transducer for the slope went out of range during the second shaking, the reading was reset before restarting spinning of the centrifuge for third and fourth shakings.

Horizontal displacement of the structure accumulates with shaking though its magnitude is small compared to that of the slope. The reasons for the small permanent displacement of the structure are that no plastic deformation occurred in the piles and the piles were firmly embedded in the artificial soft rock.

Unlike the slope stabilizing piles, the piles in this study support the structure, and hence response of the piles is not only affected by kinematic interaction between the slope and piles but also the inertia force of the structure. In the tests, rather smaller vibration of the structure was observed during shaking (see Fig. 4(a).) Possible explanation of the reason for this is as follows: Since the natural frequency of the slope

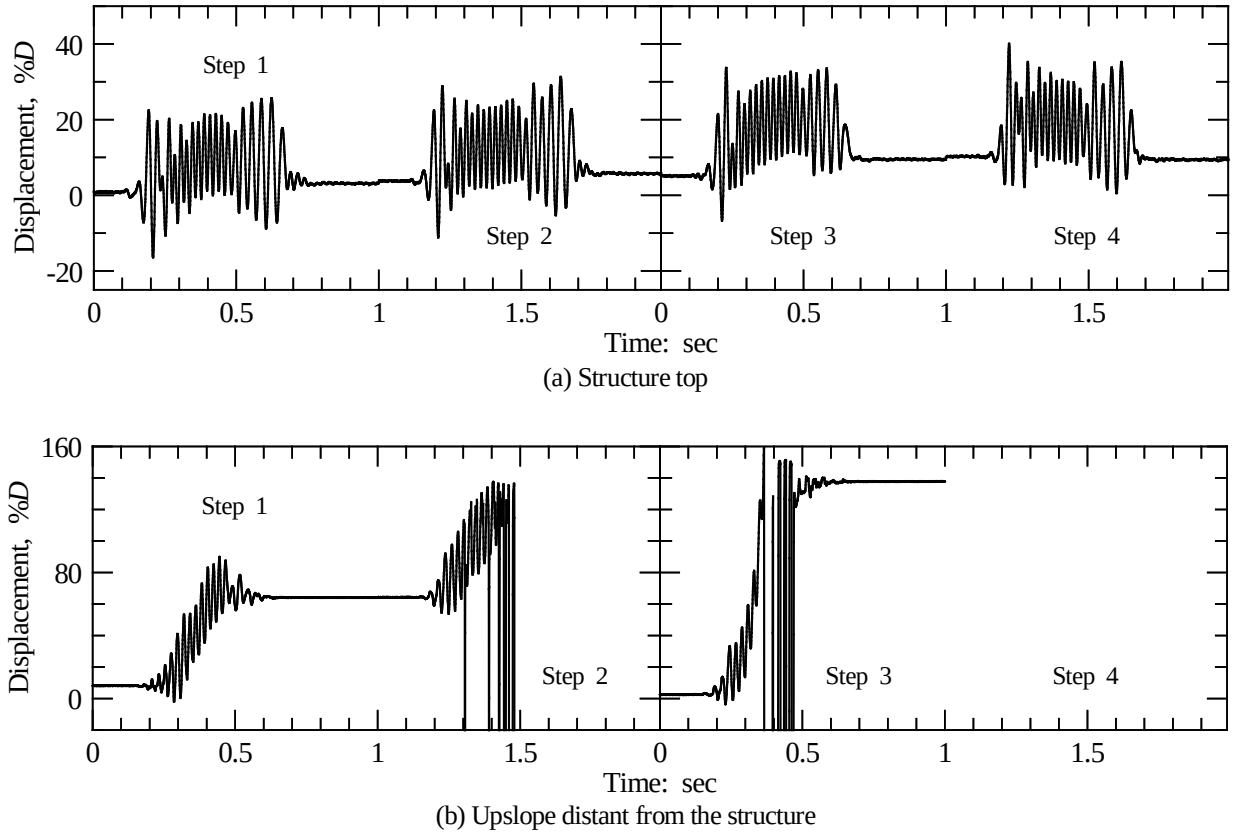


Figure 4 Time histories of the horizontal displacement of the structure and slope

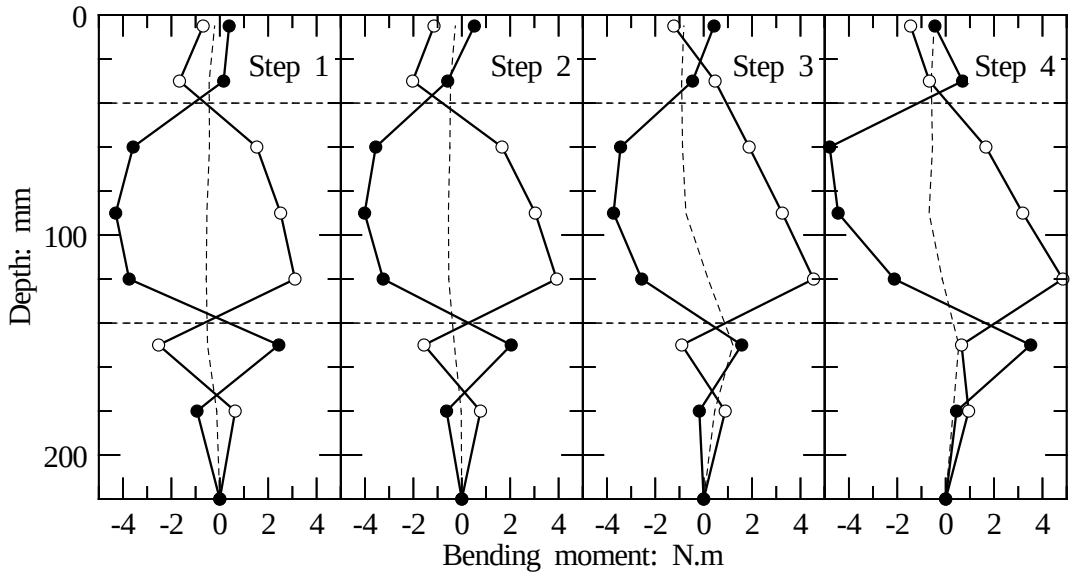


Figure 5 Bending moment profiles at the time when the maximum or minimum value is observed

(> 200 Hz) is larger than the dominant frequency of the input motion (≈ 48 Hz), the slope movement was generally in phase with the input motion, while due to the small natural frequency for the structure (≈ 30 Hz,) the movement of the structure was out of phase with that of the slope. Because of this, dynamic component of the kinematic interaction between the slope and piles acted as constraint rather than promoting vibration of the structure. The larger free vibration of the structure after shaking (see t = 0.5-0.7 or 1.5–1.7 sec in Fig. 4(a)) may support this interpretation.

3.2 Pile Response

Model piles were instrumented and strain gauges on the upslope pile allow us to calculate the bending moment distribution of the pile. The bending moment profiles at the time when the maximum or minimum value is observed are

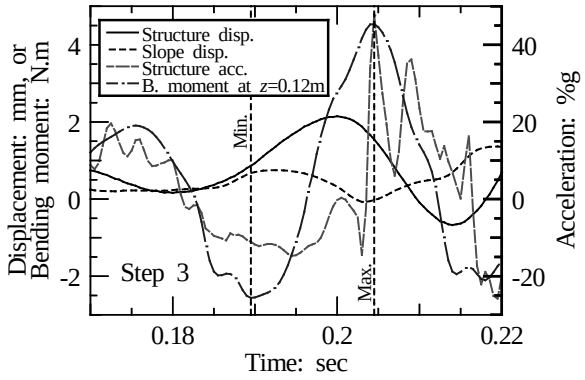


Figure 6 Time histories of displacements of structure and slope, acceleration of structure, and bending moment of pile at z = 120mm (Step 3)

illustrated in Fig. 5 for all the shaking steps. In addition, the bending moment profiles after the shaking are also plotted with the dashed lines in the figure. Irrespective to the shaking step, the maximum (plotted with open circles) or minimum (plotted with filled circles) value was observed at the very beginning of the shaking (around t = 0.2 sec. and 1.2 sec. in Fig. 4.)

In the first shaking step when the permanent displacement of the slope is not so large, the maximum and minimum bending moment profiles are more or less symmetric, while such symmetry is lost in the following shaking steps due to the relatively large permanent displacement of the slope. In the following shaking steps the maximum value increases with shaking and at the fourth shaking step about 50% increase was observed in the mobile layer, i.e., the soil above the soft rock, while such a change was about 10% for the minimum value.

Time histories of displacements of the structure top and slope (upslope distant from the structure), acceleration of the structure bottom, and bending moment of pile at z = 120mm are shown in Fig. 6 for Step 3. The time when the maximum bending moment is observed (t = 0.2045 sec for Step 3) corresponds to the time when the largest inertia force acts on the structure in the donwslope direction and the slope moves to the upslope most. At that moment, the bending moment profile is almost straight in the mobile layer. These indicate that when the maximum bending moment is observed, reaction of the soil mass in the downslope is very small, suggesting that this large bending moment is mainly attributed to the large inertia force of the structure and contribution of the soil mass movement is small.

On the other hand, the time when the minimum bending moment is observed (t = 0.1895 sec for Step 3) corresponds to the time when the structure moves in the downslope direction and the slope moves to the upslope most. This means that the bending moment at this moment is affected by the soil mass movement of the slope. Therefore the depth where the minimum value is observed changes with shaking steps, suggesting that contribution of the slope movement is relatively large.

Due to the small number of measurement points in the soft rock layer, probably the largest value in the layer could not be captured. However the increasing ratio of the peak value in the soft rock layer may be comparable to that in the soil layer above the soft rock.

4. SUMMARY

Seismic response of pile foundation in sloping ground was examined through a series of centrifuge model tests. This paper reports test results for the case that involves earthquake-induced large displacement of the sloping ground. Test results reveal the followings:

(1) Horizontal displacement of the structure accumulates with shaking though its magnitude is small compared to that of the slope.

(2) When the large bending moment is observed in the upslope pile, either (a) the largest inertia force acts on the structure in the donwslope direction and the slope moves to the upslope most, or (b) the structure moves in the downslope direction and the slope moves to the upslope most. The large bending moment is mainly attributed to the large inertia force of the structure in the former, while contribution of the soil mass movement is relatively large in the latter.

(3) The loss of soil reaction due to the slip in the downslope has more impact on increase of the pile bending moment than the kinematic load induced by soil mass movement in the upslope within the scope of the study.

Acknowledgements:
The authors acknowledge financial support from the Japan Iron and Steel Federation for this research.

References:

Nippon Expressway Research Institute (2010), "Design Specification for Expressway," Vol. 2 (in Japanese.)

Martin, G.R. and Chen, C.Y. (2005), "Response of piles due to lateral slope movement," *Computers & Structures*, **83**(8), 588-598.

Takahashi, A. and Takemura, J. (2005), "Liquefaction-induced large displacement of pile-supported wharf," *Soil Dynamics and Earthquake Engineering*, **25**(11), 811-825.

8CUEE CONFERENCE PROCEEDINGS
8th International Conference on Urban Earthquake Engineering
March 7-8, 2011, Tokyo Institute of Technology, Tokyo, Japan

AGING EFFECT ON LIQUEFACTION STRENGTH AND CONE RESISTANCE OF FINES-CONTAINING SAND INVESTIGATED IN TRIAXIAL APPARATUS

Takaji Kokusho[1)], Yohta Nagao[2)], and Fumiki Ito[2)]

1) Professor, Dept. Civil & Environmental Eng., Chuo University, Japan
2) Graduate student, Chuo University, Japan
kokusho@civil.chuo-u.ac.jp

Abstract: Innovative miniature cone penetration and subsequent liquefaction tests are carried out in a modified triaxial apparatus on sand specimens containing fines. A unique curve relating cone resistance q_t and liquefaction strength R_L is obtained for reconstituted specimens, despite the differences in relative density D_r and fines content F_c, quite contradictory to the current liquefaction potential evaluation practice. In order to examine cementation effects on the q_t~R_L, curve, a small amount of cement is added to fines in the sand specimens to simulate a long geological period in a short time, which tends to increase the liquefaction strength R_L more than the penetration resistance q_t, resulting in higher liquefaction strength under the same cone resistance with increasing F_c. Comparative tests on specimens without cement but with overconsolidation or prestraining history carried out in the same way also indicate clear increase in R_L for the same q_t, irrespective of F_c. Thus it is clarified that not the fines content itself but the aging effects such as cementation and prior stress/strain-hisories raise R_L for the same q_t, where F_c plays an important role only for the cementation.

1. INTRODUCTION

Recent case studies have revealed that aging effect plays an important role in seismic liquefaction of sand deposits. Liquefaction have often occurred in backfills and reclaimed ground of young ages in contrast to natural deposits of older than thousands years being stable. The aging effect may include cementation or chemical bonding between soil particles and also mechanical particle rearrangements by prior loading due to overconsolidation, prestraining by previous earthquakes, etc. Also pointed out is that cases are increasing in which sands containing measurable amount of low-plastic fines have liquefied such as in Adapazari, during 1999 Kocaeli earthquake and in Christchurch during 2010 Darfield earthquake in New Zealand in which the aging effect may reflect.

In engineering practice, liquefaction potential is evaluated using penetration resistance in standard penetration tests (SPT) or cone penetration tests (CPT). If sands contain a measurable amount of fines, liquefaction strength is normally raised in accordance to fines content F_c in most liquefaction evaluation methods. This F_c-dependent modification of liquefaction strength may be originated from liquefaction case studies (Tokimatsu and Yoshimi 1983, Seed and De Alba 1984), in which empirical curves correlating back-calculated in situ liquefaction strengths to SPT N_1-values were found strongly dependent on fines content. More directly, Suzuki et al. (1995) carried out CPT tests and soil sampling by in situ freezing technique in the same sand deposits, showing that the higher the fines content the greater the liquefaction strength for the same q_t-value. In contrast to their finding, however, quite a few laboratory tests using reconstituted specimens, having the same relative density D_r (Kokusho 2007) or the same void ratio (Papadopoulou and Tika 2008), have shown that R_L clearly decreases with increasing fines content of low plasticity fines changing F_c=0~30%. Thus, a lack of understanding seems to remain in the current practice for liquefaction potential evaluation in the field in relation with laboratory test results for sands containing fines.

In this paper, systematic experimental studies are addressed, in which a miniature cone penetration and subsequent cyclic loading test were carried out on the same triaxial test specimens (Kokusho et al. 2005). An innovative simple mechanism introduced in a normal cyclic triaxial apparatus by Kokusho et al. (2003) was used enabling a miniature cone to penetrate into the sand specimen at a constant speed. Results from the two sequential tests on the same specimen were compared to develop direct q_t - R_L correlations for sands containing various amounts of fines. The major goal in the present paper is to investigate two types of aging effect; by cementation and by prior loading, and compare them in a series of laboratory tests. For the former aging effect, accelerated tests are carried out by adding a small quantity of cement to reconstituted specimens to simulate cementation or chemical bonding for a geological time span in a short time. For the latter, overconsolidation and prestraining are

given to specimens independently to reproduce prior loading in a long history. In both cases, penetration resistance q_t and liquefaction strength R_L are measured in the same specimens to investigate the aging effect on the q_t - R_L correlations considering fines content as a key parameter.

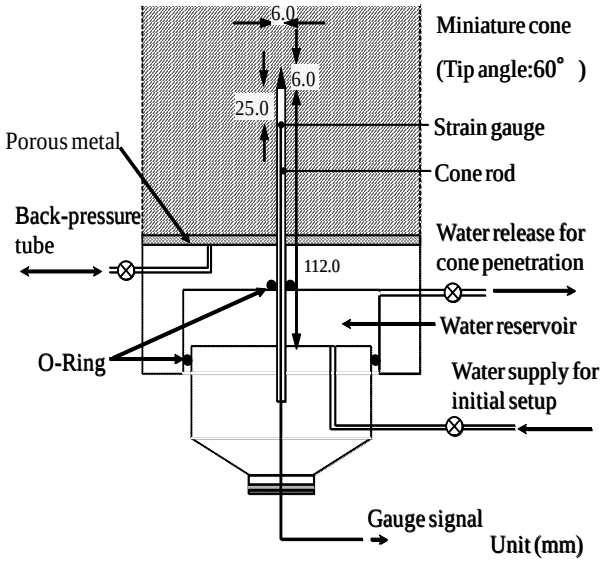
2. TEST APPARUTUS, SOIL MATERIAL & TEST PROCEDURES

In the triaxial apparatus used in this research, the specimen size was 100 mm in diameter and 200 mm in height. In the liquefaction tests, the soil specimen was loaded cyclically by a pneumatic actuator as a stress-controlled test. In order to carry out a cone penetration test in the same specimen prior to the liquefaction tests, a pedestal below the soil specimen was modified as shown in Fig.1, so that a miniature cone can penetrate into the specimen from below. For that goal, the pedestal consists of two parts, a fixed circular base to which the cone rod is fixed and a movable metal cap, through the center of which the cone rod penetrates in the upward direction into the overlying specimen. The annulus between the two parts is sealed by O-rings, enabling the cap to slide up and down by water pressure supplied into a water reservoir in between the two parts (Kokusho et al. 2003). During the test, the pedestal cap is initially set up at the highest level by filling water inside, and the specimen is constructed on it. By opening a valve at the start of the cone penetration, the water in the reservoir is drained by the cell pressure, resulting in the settlement of a total body of the specimen at the top of the pedestal, realizing relative penetration of the cone by 25 mm. The penetration rate is about 2mm per second, much slower than prototype CPT, and is almost constant irrespective of the difference in relative density. The miniature cone is 6 mm diameter and 60 degrees tip angle, about 1/6 smaller in dimension than the prototype cone used in the field. The strain gauges to measure the penetration resistance are glued at the inner wall of the rod tube, 25 mm lower than the foot of the cone.

Beach sand (Futtsu sand) consisting of sub-round particles of hard quality was used in this test. Fines mixed with the sand is silty and clayey soils with low plasticity index of I_p=6 sieved from decomposed granite in reclaimed ground of the Kobe city, Japan. For the test series for cementation, a prescribed quantity of Portland cement was completely mixed with the Masa fine soil to make it with different degree of chemical activity. The cement content C_c, the weight ratio of cement to soil (including fines), varied from 0 to 1.0%, and the fines content F_c including the cement changed from 0 to 30%. This means that the ratio C_c/F_c, a parameter representing chemical activity of fines, varied from 0 to 30%. Then the sand specimen with given F_c was prepared by the wet tamping method to make a given relative density D_r, which was changed in 3 steps, about D_r=30, 50 and 70%. The specimen was then completely saturated with de-aired water, and consolidated under the isotropic effective stress of 98 kPa with the back-pressure of 196 kPa. If cement is added to fines, the consolidation time was controlled exactly 24 hours after wetting, while for tests without cement it was about 2 hours.

For the test series of mechanical loading, the overconsolidation ratio, OCR=4, was applied to the specimen in one group by temporarily increasing the confining pressure up to 392 kPa for 1 hour, while non-destructive axial strain of 2×10^{-2} % in the double amplitude was given 10 thousand cycles to the specimen consolidated under 98 kPa in another group. The volume change due to cyclic straining was minimal.

Then, the specimen was fully saturated by using de-aired water in a double negative pressure method so that



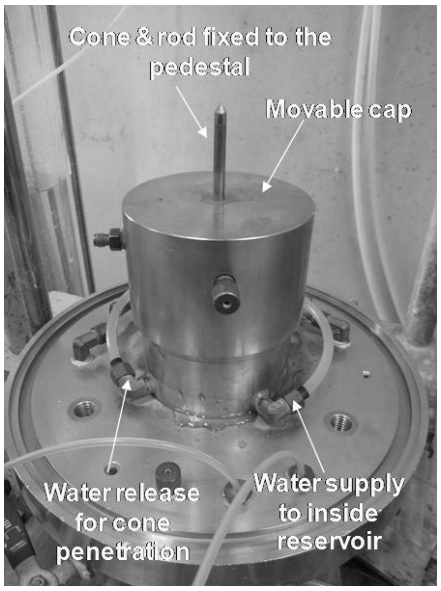


Figure 1. Cross section (right) and Photograph (left) of the modified pedestal in the lower part of triaxial apparatus

the B-value larger than 0.95 was measured, and isotropically consolidated with the effective stress of 98 kPa with the back-pressure of 196 kPa. In the test sequence, the penetration test was first carried out under undrained condition after consolidating the specimen. Then, after releasing pore pressure and reconsolidating it under the same confining pressure again, although the volume change by this procedure was almost negligible, the liquefaction test was carried out on the same specimen. The sinusoidal cyclic axial load applied with the frequency of 0.1 Hz was measured with a load cell in the pressure chamber. The cell pressure and the pore-water pressure were measured with electric piezometers and the axial deformation is measured with LVDT of 50 mm maximum capacity. It may well be suspected that, in such a test sequence, the liquefaction strength is possibly influenced by the preceding cone test and subsequent reconsolidation. However, it was already confirmed in previous research (Kokusho et al. 2005) that the cyclic stress ratio for liquefaction is almost unaffected by the cone test and reconsolidation.

3. TEST RESULTS ON CEMENTATION EFFECT

In the test, relative density D_r, fines content F_c and cement content C_c of the specimen were parametrically changed to investigate their effects on penetration resistance and undrained cyclic strength. Fig.2 shows cone resistance q_t at the top and excess pore-pressure Δu at the bottom, respectively, plotted versus the penetration length obtained in the tests for D_r≈50%, F_c=0, 5, 10, 20% and C_c=0, 0.5, 1.0%. It is clearly observed that q_t for soils without cement (C_c =0) decreases with increasing fines up to F_c =20%. For individual F_c–values, q_t tends to increase more or less with C_c changing from 0 to 1%. The excess pore pressure Δu building up almost linearly with the penetration length tends to increase with increasing F_c, though the change is not so conspicuous.

Fig.3 shows relationships between the stress ratios R_L ($\sigma_d/2\sigma'_c$: σ_d =cyclic stress amplitude, σ'_c =effective isotropic confining stress) versus the number of loading cycles N_c for the double amplitude axial strain ε_{DA}=5% obtained by undrained cyclic loading tests on sand specimens having D_r≈50%, F_c=0, 5, 10, 20%, and C_c=0, 0.5 and 1.0%. Obviously, the increase in fines content tends to reduce liquefaction strength R_L in specimens without cement as already demonstrated by previous researches (e.g. Kokusho 2007). Also indicated in the figure is that the R_L-value increases with increasing cement content for all the fines content F_c and the increment is particular large for F_c =20%.

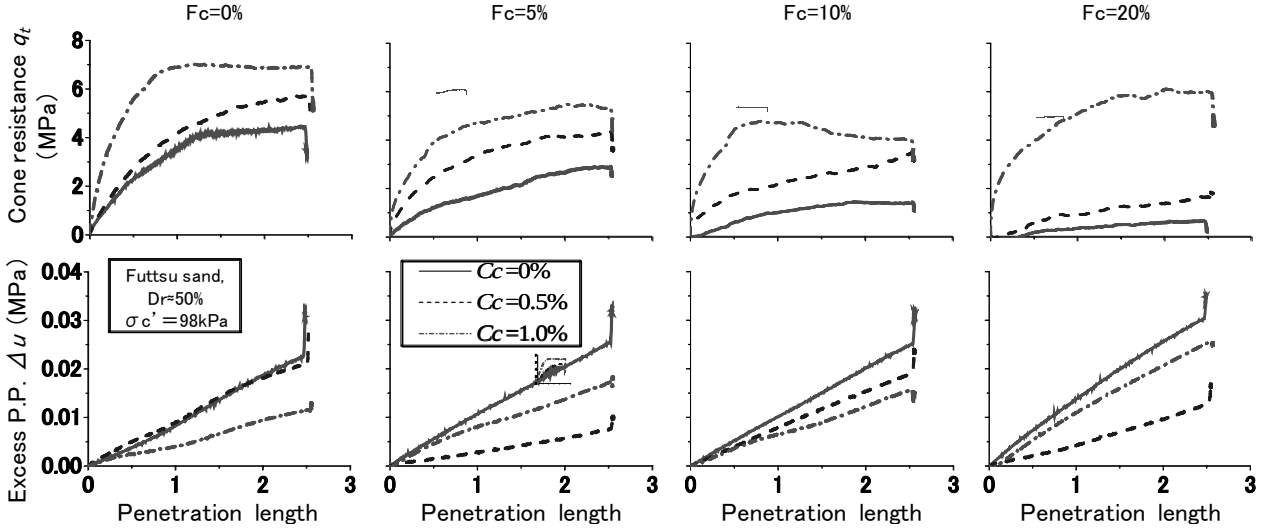


Figure 2 Cone resistance or excess pore-pressure versus penetration length for river sand specimens of D_r≈50% with different consolidation time.

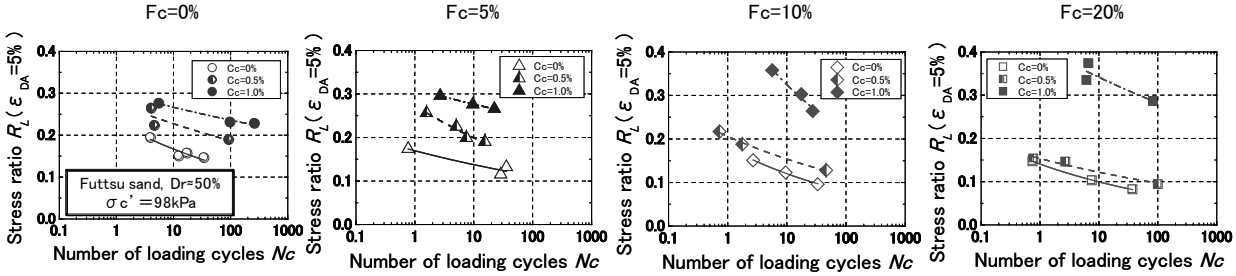


Figure 3 Stress ratios R_L versus number of loading cycles N_c

In Fig. 4, test results for different values of D_r, F_c and C_c are shown on the $R_L \sim q_t$ diagram with different symbols. The liquefaction strength R_L in the vertical axis is defined as the stress ratio $\sigma_d / 2\sigma_c'$ for ε_{DA}=5% and N_c=20 (this research) and N_c=15 (Suzuki et al.). The penetration resistance q_t in the horizontal axis is determined as the maximum value during the penetration. The open symbols (except the star symbols) corresponding to the specimens without cement are located along the thick straight line in the chart despite the wide differences in D_r (30~70%) and F_c (0~30%) as already pointed out in the previous research (Kokusho et al. 2005, 2009). This finding is inconsistent with the current liquefaction potential evaluation practice, because R_L seems to be uniquely determined from q_t irrespective of F_c.

The half-close and close symbols except the stars are all from the accelerated tests on specimens containing cement. Among them, upward triangles, for instance, represent the case F_c=5%, and they move up from the open (C_c =0) to the half-close (C_c =0.5%) further to the full-close symbols (C_c =1.0%) as C_c / F_c changes from 0 to 20% for the same value of F_c =5% as indicated by thin arrows in the diagram. In the similar manner, other symbols move up with increasing C_c or C_c / F_c for the same fines content of F_c =10%, 20% and 30%. Samples with higher value of C_c / F_c may be considered as of longer geological age because higher chemical activity is exerted in the same soil in the accelerated test. This indicates that the cementation effect tends to push up the data points on the $R_L \sim q_t$ diagram from the unique line of no cement and gives higher liquefaction strength under the same cone resistance.

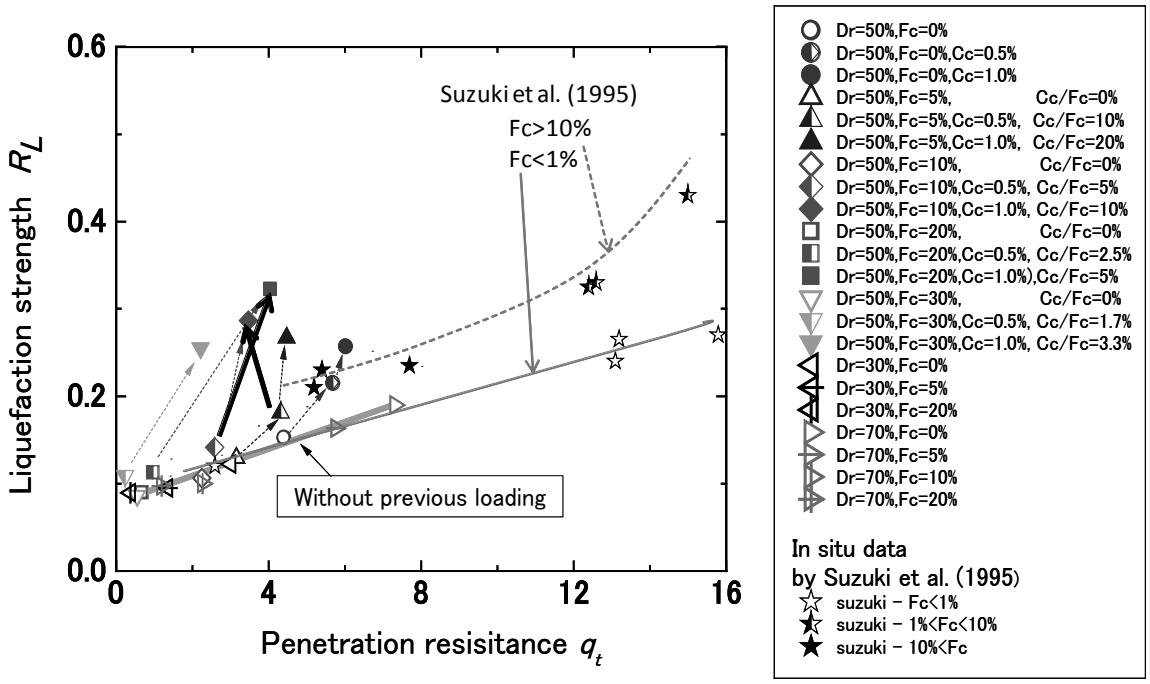


Figure 4 R_L versus q_t relationship for specimens with different cementation effect

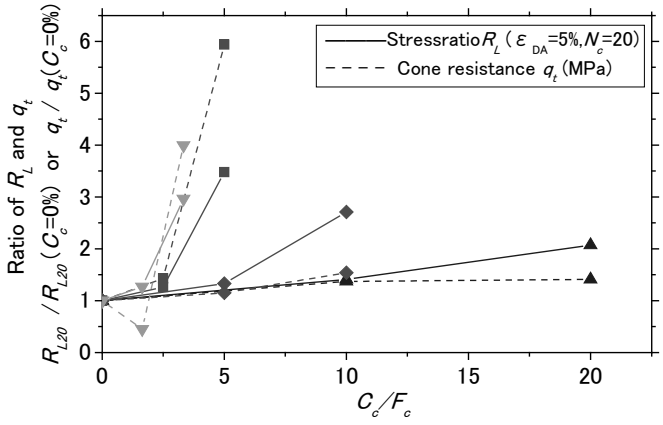


Figure 5 Rate of increase in R_L, q_t versus C_c/F_c

The star symbols in the same figure indicates the R_L~ q_t plots based on field investigations by Suzuki et al. (1995) combining prototype cone tests in situ and undrained cyclic triaxial tests on intact samples recovered from the same soil deposits by in situ freezing technique. It demonstrates a clear difference in the R_L ~ q_t relationships due to different fines contents of $\boldsymbol{F_c}$ <1.0%, $\boldsymbol{F_c}$ =1.0-10% and $\boldsymbol{F_c}$ >10%. Also noted is that the two research results are in a good coincidence not only qualitatively but also quantitatively, particularly in the case without cement, despite a large difference in the cone size and CPT test procedures.

On the other hand, data points with the same $\boldsymbol{C_c/F_c}$ –value, 5% or 10%, can be recognized to shift upward as $\boldsymbol{F_c}$ increases from the unique line of no cement as indicated by the thick arrows in the graph. This indicates that, under the same geological age, higher $\boldsymbol{F_c}$-value results in higher liquefaction strength for the same cone resistance. Thus, the present research results by the accelerated test clearly indicate that not the fines content itself but the cementation effect is responsible for the higher liquefaction strength for larger $\boldsymbol{F_c}$ under the same cone resistance.

Based on the data shown in Fig. 4, the ratio of increase in R_L or q_t is shown versus the $\boldsymbol{C_c/F_c}$ -value with the fines content F_c as a parameter in Fig. 5. With increasing chemical activity, the R_L-value increases more than the q_t-value for $F_c \leq 10\%$, but it is reverse for $F_c \geq 20\%$. Also noted in Fig. 5 is that not only the $\boldsymbol{C_c/F_c}$ -value but also the fines content $\boldsymbol{F_c}$ tends to considerably increase R_L and q_t up to F_c=20% even under the same cement content of $\boldsymbol{C_c}$ =1.0% as demonstrated by the encircled plots but the trend seems to change at F_c=30%. Thus, there seems to be a kind of transition around F_c=20%, in which the increasing trend in R_L or q_t with increasing $\boldsymbol{C_c/F_c}$ -value changes, which may possibly have something to do with soil structure change from sand grain supporting to matrix supporting.

4. TEST RESULTS ON OVERCONSOLIDATION & PRESTRAINING

Test results on reconstituted specimens of D_r≈50% , F_c =0~20%, C_c =0, which experienced either prestraining history of 10 thousand cycles of 2×10^{-2} % double amplitude axial strain or overconsolidation of OCR=4 are plotted with different symbols on the R_L~ q_t diagram in Fig. 6. The open symbols with/without bars are all for the specimens with no prior loading histories as explained before, which are almost aligned in a single unique solid line despite the wide difference in D_r and F_c. If specimens are prestrained, both R_L and q_t increase, and the data points are plotted with half-close symbols. They move upward and rightward as thin dashed arrows from the original points of no prior loading. The all half-close plots may be aligned in a straight dashed line, which tends to converge to the solid line of no prior loading at the left end. In the case of overconsolidation, both R_L and q_t increase again, moving the plots to the full-close symbols from the original open symbols as indicated with thin solid arrows. They are all located above the solid line of no prior loading and may be along a chain-dotted line almost in parallel with the solid line.

Thus, a pair of unique lines seem to exist; one corresponding to prestraining by particular stain amplitude with a given number of cycles and the other corresponding to overconsolidation of particular OCR. They tend to give higher liquefaction strength corresponding to the same penetration resistance q_t than sands without prior loading histories, although the degree of increase is certainly dependent on the specifications of loading. It is obviously seen that these lines are independent of fines content for F_c=0~20%, in a good contrast to the cases for specimens containing a small quantity of cement previously addressed.

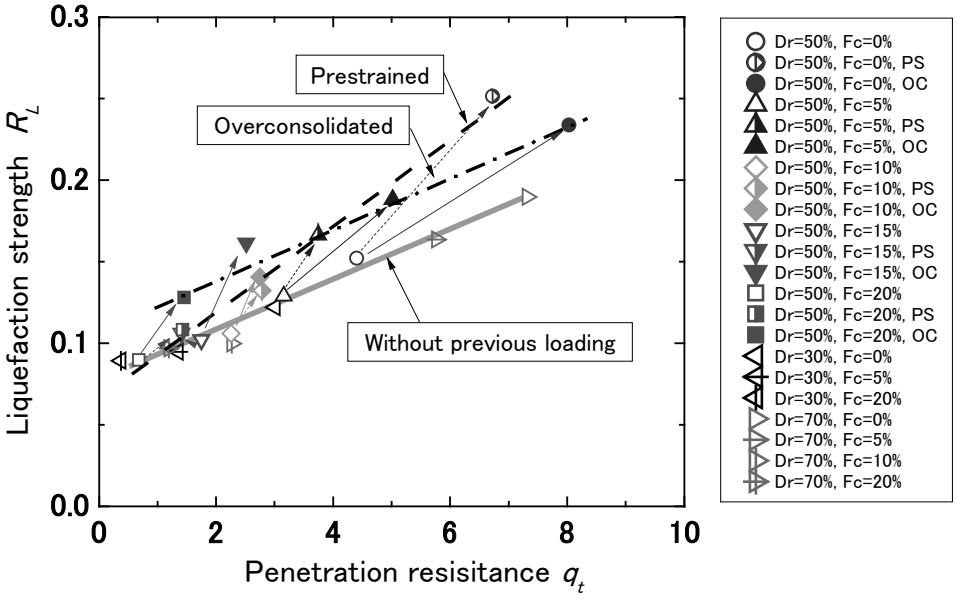


Figure 6 R_L versus q_t relationships for overconsolidated and prestrained specimens (PS: Prestrained, OC: Overconsolidated)

This observation reveals that the two types of the aging effects; by cementation and by prior loading histories such as overconsolidation and prestraining, both tend to increase liquefaction strength under the same penetration resistance on the $R_L \sim q_t$ diagram, though fines content is the major player in determining how much the increase is in the former while it has little effect in the latter. In the current liquefaction potential evaluation, fines content is dealt with as a key parameter to modify liquefaction strength by a certain amount from a standard curve of no fines. This research results indicate that the F_c-dependent modification of R_L should exclusively represent the cementation effect. No logical basis may be justified to consider the effect of prior loading by modifying liquefaction strength as a function of fines content.

5. CONCLUSIONS

A series of experimental study by miniature cone penetration tests and subsequent cyclic loading tests were carried out in the same triaxial test specimen to investigate two types of aging effect on liquefaction strength; by cementation and by prior loading, with fines content F_c as a key parameter. Accelerated tests on the cementation effect using specimens containing a small quantity of cement yielded the following major findings;

- For reconstituted soils without cement, the liquefaction strength R_L is uniquely related to the cone penetration resistance q_t, forming a single $R_L \sim q_t$ line, irrespective of relative soil density D_r and fines content F_c, quite contradictory to the current liquefaction potential evaluation practice.
- This laboratory test result coincides with in situ $R_L \sim q_t$ relation by Suzuki et al.(1995) quantitatively despite clear difference in the test procedures and cone size.
- Specimens with higher value of C_c/F_c (simulating longer geological age) results in higher liquefaction strength under the same cone resistance, indicating that the cementation effect tends to raise the $R_L \sim q_t$ line from that for soils without cement.
- For the same C_c/F_c-value (simulating the same geological age), higher fines content results in higher liquefaction strength under the same cone resistance, which is consistent with the trend found in the field investigations.
- Thus, it is revealed that the reason why higher fines content leads to higher liquefaction strength does not depend on fines content itself but cementation effect, which tends to be pronounced as fines increase.

Another series of tests on the effect of prior loading revealed;

- If specimens are prestrained with medium strain cycles, both R_L and q_t increase, and the plots on the $R_L \sim q_t$ diagram may be approximated by a straight dashed line, which tends to converge to the solid line of no prior loading at the left end. In the case of overconsolidation, both R_L and q_t increase again, and the plots may be aligned along a chain-dotted line almost in parallel with the solid line.
- Thus, the two different unique lines exist, which give higher liquefaction strength under the same penetration resistance q_t than sands of no prior loading. It is obviously seen that these lines are independent of fines content for F_c=0~20%, in a good contrast to the cases in the accelerated tests on specimens containing a small quantity of cement.

Consequently, two types of the aging effects; by cementation (chemical bonding) and by prior loading such as overconsolidation and prestraining, both tend to increase liquefaction strength under the same penetration resistance. However, fines content is the major player in determining how much the increase is in the former while it has little effect in the latter. Thus, the F_c-dependent modification of R_L should represent the cementation effect only, excluding the prior loading effects.

REFERENCES

Kokusho, T., Murahata, K., Hushikida, T. and Ito, N. (2003), Introduction of miniature cone in triaxial apparatus and correlation with liquefaction strength, *Proc. of Annual Convention of JSCE*, III-96, 191-192 (in Japanese).

Kokusho, T., Hara, T., and Murahata, K. (2005), Liquefaction strength of fines-containing sands compared with cone-penetration resistance in triaxial specimens, *Proc. 2nd Japan-US Workshop on Geomechanics*, ASCE Geo-Institute Publication No.156, pp356-373, 2005.

Kokusho, T. (2007), Liquefaction strengths of poorly-graded and well-graded granular soils investigated by lab tests, *4th International Conference on Earthquake Geotechnical Engineering*, Thessaloniki, 159-184, Springer.

Kokusho, T., Ito, F. and Nagao, Y. (2009), Effects of fines and aging on liquefaction strength and cone resistance of sand investigated in triaxial apparatus, *Proc. Earthquake Geotechnical Eng. Satellite Conference*, 17th ICSMGE, Alexandria, Paper No. I.16, CD-publication.

Papadopoulou, A. and Tika, T. (2008), The effect of fines on critical state and liquefaction resistance characteristics of non-plastic silty sands, *Soils & Foundations*, Vol.48, No.5, 713-725, 2008.

Suzuki, Y., Tokimatsu, K., Taya, Y. and Kubota, Y. (1995), Correlation between CPT data and dynamic properties of in situ frozen samples", Proc. 3rd International Conference on Recent Advances in Geotechnical Earthquake Engineering and Soil Dynamics, St. Louis, Vol.1 249-252.

Seed, H. B. and De Alba, P. (1984), Use of SPT and CPT tests for evaluating the liquefaction resistance of sands, Proc. In-situ '86, ASCE Geotechnical Special Publication No.156, 356-373.

Tokimatsu, K. and Yoshimi, Y. (1983), Empirical correlation of soil liquefaction based on SPT N-value and fines content. Soils and Foundations, Vol.23, No.4, 57-74.

8CUEE CONFERENCE PROCEEDINGS
8th International Conference on Urban Earthquake Engineering
March 7-8, 2011, Tokyo Institute of Technology, Tokyo, Japan

ESTIMATING SHEAR MODULUS VS STRAIN FROM FIELD MEASUREMENTS

Daniel E. Torres[1)], Giovanna Biscontin[2)], and Jose M. Roesset[3)]

1) Graduate Research Assistant, Dept. of Civil Engineering, Texas A&M University, College Station, Texas, USA
2) Associate Professor, Dept. of Civil Engineering, Texas A&M University, College Station, Texas, USA
3) Professor, Dept. of Civil Engineering, Texas A&M University, College Station, Texas, USA
gbiscontin@tamu.edu

Abstract: Soil shear modulus non-linearity with strain is routinely measured in the laboratory, usually resulting in normalized curves of G/G_{max}. Since soil moduli at small strains (G_{max}) measured in the laboratory and in situ often differ by considerable amounts, it is customary to rely on field measurements for analysis and design. The nonlinearity is introduced by using the normalized laboratory curves together with the field estimate of G_{max}. Actual evaluation of shear modulus nonlinearity directly in the field has been rare until the recent introduction of large-scale mobile shakers which can apply higher loads and strains to the soil. The proposed method to evaluate shear modulus vs strain in situ involves applying dynamic loads on a surface foundation and measuring the dynamic response of the soil mass beneath the foundation with embedded instrumentation. Linear and nonlinear shear moduli can be estimated by analyzing phase differences of the measured velocity time histories at different locations. However, the choice in defining average strain and shear wave velocity of the wave traveling between any two measurement points will lead to different estimates of shear modulus and level of strain. This paper focuses on illustrating the consequences of these choices through simulated response.

1. INTRODUCTION

Soil shear modulus (G) nonlinearity with strain is routinely measured in the laboratory, usually resulting in normalized curves of shear modulus with its maximum value at very low strain levels. However, soil moduli at small strains (G_{max}) measured in the laboratory and in situ often differ by considerable amounts due to sample disturbance and time effects. Numerous studies have attempted to explain these differences and to provide correction factors that could be applied to the experimental data (i.e., Anderson and Woods 1975). As a result, it is common today, particularly in geotechnical earthquake engineering, to combine values of the shear modulus at low levels of strain determined in the field through geophysical methods with the normalized G/G_{max} curves from laboratory tests, or available in the literature, to obtain the variation of shear modulus with level of strain for nonlinear seismic analyses. The basic assumption is that the relative variation of the shear modulus with strain level is the same in situ and in laboratory tests. Recent studies have raised some questions as to the accuracy of this assumption and have attempted to evaluate shear modulus and its variation with strain using field data such as seismic records from arrays (Zeghal et al. 1995, Chang et al. 1996). Henke and Henke (1993, 2003) developed a torsional cylindrical impulse shear test to determine soil moduli in situ, which consists of intruding a cylinder probe into the soil and generating torsional impulses at selected levels of excitation. Roblee and Riemer (1998) proposed the Downhole Freestanding Shear Device (DFSD), which is designed to create and subsequently test a freestanding soil column at the bottom of a borehole. Safaqah and Riemer (2006) applied the DFSD to estimate nonlinear moduli in situ.

Recently, under the Network for Earthquake Engineering Simulations (NEES) program, the University of Texas at Austin developed mobile shakers (Fig. 1) that are capable of exerting sufficient strain on a larger volume of soil offering the opportunity to measure shear modulus and its variation with strain in a realistic manner (Stokoe et al. 2006, Park 2007, Park 2010). These field tests need to be interpreted carefully to ensure that



Figure 1. Large capacity vibroseis truck, T-Rex, of the University of Texas at Austin.

the desired properties are correct and no bias is introduced in the results. This paper introduces possible issues in data interpretation rising from the estimation of strains and the localized nature of the measurements.

2. FIELD TESTING SETUP

In tests performed at the Fitzpatrick Ranch in Austin Texas by Park (2010) using the dynamic testing equipment developed at The University of Texas at Austin under the auspices of NEES of the National Science Foundation, a 0.90 m circular slab was constructed on the ground and subjected to harmonic loads of different amplitudes (Figure 2). Geophones were installed in and under the footing to investigate the response of the foundation/soil system. The amplitude of the vertical force imposed on the foundation was captured through a load cell placed on the footing. Details of the experimental set up and of the measurements are provided in Park (2010).

The geophones measured particle velocities at various depths under the slab and the displacements at the geophone locations were computed by double integration. The corresponding value of the shear modulus can be determined computing first the shear wave velocity (v_s) from the time lag (Δt) between arrival times at the different depths:

$$v_s = \frac{\Delta z}{\Delta t} \qquad (1)$$

where, Δz is the distance separating two geophones, and then the modulus ($G = \rho v_s^2$) assuming a known value for the soil density ρ.

In the tests under consideration a harmonic force was applied at the top of the footing for sufficient cycles to reach steady-state. Similarly to a cyclic laboratory test, the reference shear strain associated with a shear modulus is the maximum strain in the cycles. Tests were performed at different load amplitudes to evaluate strains and shear modulus at different levels, ideally yielding a G vs γ curve. The reference shear strain can be estimated from the calculated displacements using different approaches. Two simple possible interpretations are to define the reference shear strain as (Figure 3):

$$\bar{\gamma} = \frac{\Delta u_1}{\Delta z} \qquad (2)$$

Or

$$\gamma_a = \frac{\Delta u_2}{\Delta z} \qquad (3)$$

In this paper, two approximations introduced in the estimates of the desired quantities from field data will be evaluated:

1. The determination of the reference strain from the difference between the displacements at two different depths, either at the same time or different times.
2. The determination of the shear wave velocity from the time lag between the maximum displacements.

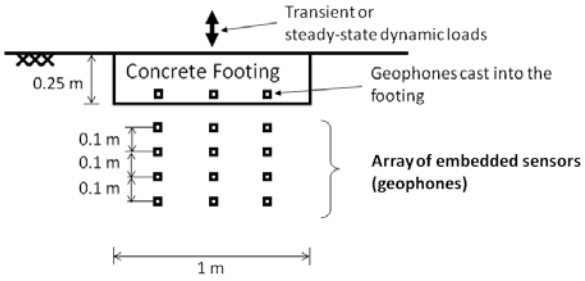


Figure 2 Schematic of the test setup at the Fitzpatrich Ranch in Austin, Texas, USA

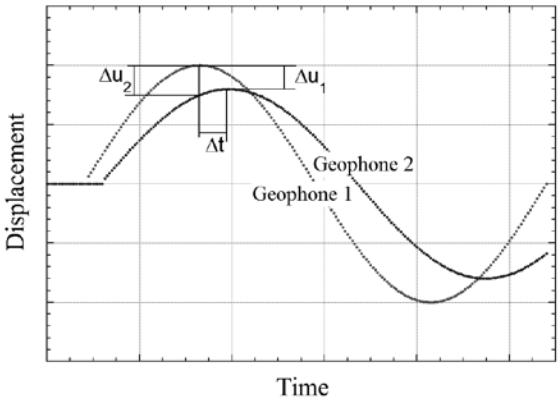


Figure 3 Definition of quantities used in equations (2) and (3).

2. FORMULATION

In this work a cone mode was used to evaluate the significance of the approximations introduced by using displacement time histories calculated from measured velocities. Meek and Veletsos (1974) pointed out that a cone could represent exactly the stiffness of a circular foundation on the surface of an elastic half space. This concept was further developed by Wolf and Deeks (2004), who presented cone solutions for a number of different excitations and layered soil profiles where the properties vary with depth.

Although a shear cone, in which only shear deformations are allowed, will provide the correct values for the horizontal stiffness of a circular mat, it will not reproduce exactly the state of strains and stresses in the soil, since in the real problem a horizontal force will produce both a

horizontal displacement and a small rotation of the foundation, with a fully three dimensional state of stresses. The study presented here, therefore, focuses on one-dimensional propagation of shear waves generated by a harmonic load applied at the surface through a circular footing. While the cone model does not reproduce the true conditions of the tests, including any effects of soil properties varying with depth, the simplifications are justified in view of the interest in evaluating the approximations in interpretation methods, which are usually based on a one-dimensional interpretation. The cone was reproduced with two different discrete models: a series of lumped masses and interconnecting springs and a finite difference using second-order central difference formulation. For the mass-spring model the total mass for each layer is (Torres 2010):

$$M = \frac{\pi}{3}\rho r_o^2 \Delta z \frac{z_i^2 + z_i z_{i-1} + z_{i-1}^2}{z_o^2} \tag{4}$$

with a corresponding spring stiffness

$$k_i = \frac{A_o G}{\Delta z}\frac{z_{i-1} z_i}{z_o^2} \tag{5}$$

with z_i and z_{i-1} the depth of the interface between layer i and i-1 from the cone vertex, z_0 is the distance of the footing from the cone vertex, $\Delta z = z_1 - z_{i-1}$, and A_0 is the area of a footing of radius r_0.

The second-order central difference discretization with mesh size Δz yields:

$$u_{i,n+1} = 2u_{i,n} - u_{i,n-1} + \frac{\Delta t^2}{\rho A_i}\left[(GA)_i \frac{u_{i+1} - 2u_i + u_{i-1}}{\Delta z^2} + \frac{(GA)_{i+1} - (GA)_{i-1}}{2\Delta z}\frac{u_{i+1} - u_{i-1}}{2\Delta z}\right]_n$$

with $u_{i,n}$ as the displacement of the i-th node at time $n\Delta t$.

For both models the bottom was placed at a sufficient distance to guarantee that reflections would not arrive back at the location of interest during the time range under consideration and the time increment Δt was taken small enough to guarantee stability of integration.

2.1 Validation of the implementation

For both approaches, mass-spring model or finite difference implementation, the solution in the linear elastic range should converge to the theoretical solution as the distance between the masses in the first case and the mesh size in the second tend to zero. The computer programs implementing the two models were validated comparing their results to the analytical predictions for the cone. In this validation case the soil deposit was characterized by a shear wave velocity of 100 m/s, a mass density of 2000 kg/m ^{3} and therefore a maximum shear modulus G_{max} of 20 MPa. A footing with a radius of 0.5 m was subjected to harmonic forces with frequencies of 10, 50 and 100 Hz.

For the mass-spring model mesh sizes of 0.05, 0.10 and 0.20 m were considered. The displacements computed at the surface are shown in Figure 4 versus Δz in comparison with the analytical solution.

Mesh sizes of 0.10, 0.05 and 0.01 m were considered for the finite difference model. In order to get accurate results the mesh size for the finite difference model needs to be much smaller than the Δz used with the lumped masses and springs. The results are also shown in Figure 4. Figure 5 shows values of the strains computed with the three models and from the analytical solution. When using a $\Delta z = 0.05$ m for the mass-spring model the strains are obtained at twice the number of points and different depths from those with $\Delta z = 0.1$ m. The results for the mass-spring model with $\Delta z = 0.05$ m and with $\Delta z = 0.01$ m for finite differences are close to the analytical curve, whereas the results with the mass-spring model with $\Delta z = 0.10$ m are slightly lower than the analytical solution.

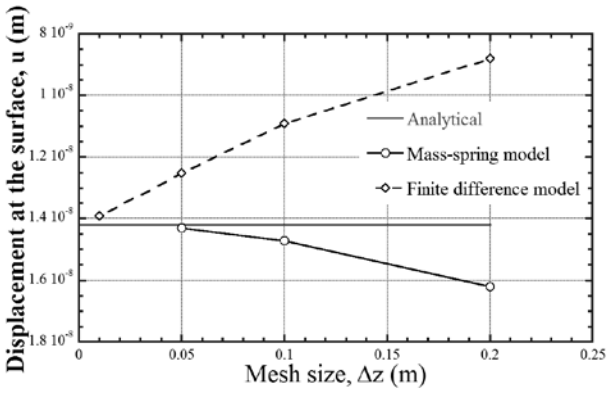


Figure 4 Comparison of displacement at the surface evaluated with the analytical solution and the mass-spring and finite difference models.

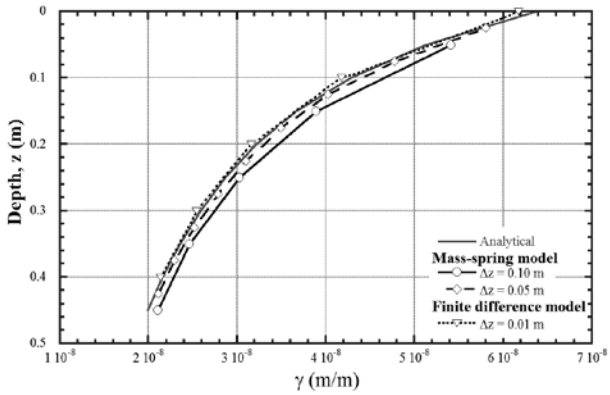


Figure 5 Comparison of strains obtained from the analytical solutions vs calculated with mass-spring and finite difference models.

3. NONLINEAR ANALYSIS

In the nonlinear analysis the soil shear stiffness varies with the level of strain according to the G/G_{max} curve illustrated in Figure 6. The variable shear modulus is implemented in the mass-spring and the finite difference models using a piecemeal linearized approach as proposed by Iwan (1967). The same problem geometry and initial properties were used for the nonlinear analysis as before for the linear analysis. The soil deposit had an initial (at low level of strains) shear wave velocity of 100 m/s, a mass density of 2000 kg/m^3 and therefore a maximum shear modulus G_{max} of 20 MPa. The footing of 0.5 m radius was subjected to harmonic forces with a frequency of 50 Hz and varying amplitudes. The harmonic force amplitudes were 100, 500, 1000, 5000, and 10,000 N for $\Delta z = 0.10$ m. Harmonic force amplitudes for $\Delta z = 0.05$ m were 100, 500, 1000, and 5000 N because for a depth of 0.025 m the strain corresponding to a force of 10,000 N exceeded the maximum strain considered in the G/G_{max} curve.

The propagation velocities were computed from the time interval between the maximum displacements at the different depths as defined in equation (1). Figure 7 shows the agreement between the values of the G/G_{max} versus γ obtained for both approaches when the shear wave velocity between two locations is evaluated for the time interval at which the maximum strain actually occurs between the two points. As expected, the agreement between the assumed material properties and those derived from the computed displacement time histories is excellent. This simply verifies that the codes reproduce correctly the variation of G with γ entered as input.

When the strain between two locations is computed from the difference between the peak displacements at the two locations ($\bar{\gamma}$), we are effectively using an averaged value for the strain that is always going to be smaller than the actual maximum. As shown in Figure 8 the values of the actual normalized shear modulus vs reference strains obtained from the difference between the peak displacements for $\Delta z = 0.1$ m and $\Delta z = 0.05$ m are always to the left of the assumed curve.

The reference strain estimated using Equation (3) is larger than $\bar{\gamma}$ and the normalized shear modulus curve is closer to the assumed values, although still to the left (Figure 9).

Figure 10 compares the assumed normalized shear modulus curve and the values of $v_s^2/\ v_s^2{}_{max}$ computed from the time interval between peak displacements, while γ is the actual maximum shear strain computed by the program. In this case the values of $v_s^2/\ v_s^2{}_{max}$ are always larger than those of the assumed G/G_{max} curve. This indicates that the shear wave velocity computed is an average velocity over time rather than the minimum velocity corresponding to γ.

If then the same values $v_s^2/\ v_s^2{}_{max}$ are plotted vs the strain computed from the difference between peak displacements ($\bar{\gamma}$), as shown in Figure 11, the agreement between estimated and computed curve improves. In this case the errors committed using $v_s^2/\ v_s^2{}_{max}$ and $\bar{\gamma}$ have opposite effect, resulting in a better match, although the estimate is still to the left of the actual values, indicating that the error committed using $\bar{\gamma}$ is larger.

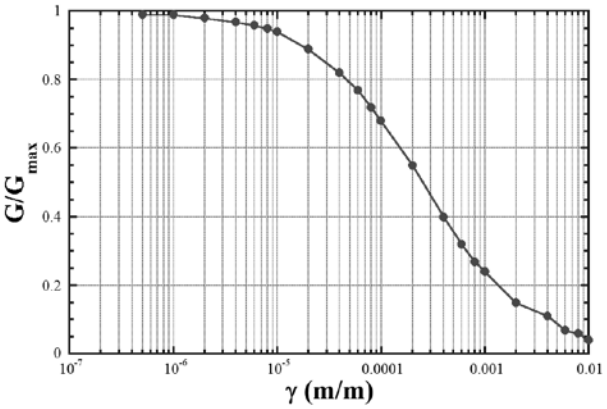


Figure 6 Shear modulus variation with strain for the nonlinear analyses (adapted from Derendeli 2001).

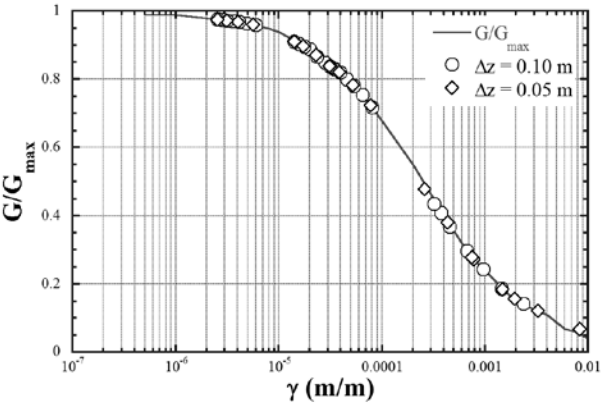


Figure 7 Shear modulus variation assumed and calculated with nonlinear code vs maximum shear strain.

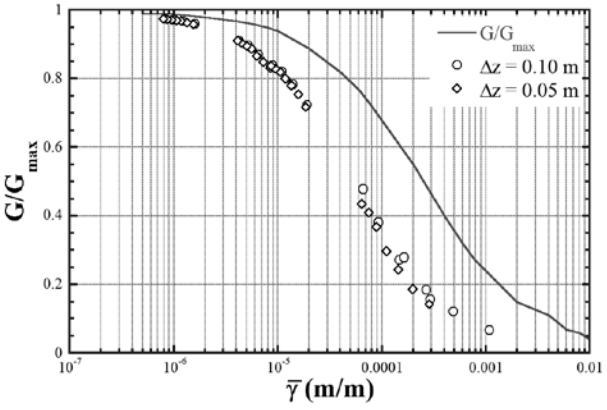


Figure 8 Shear modulus variation with $\bar{\gamma}$.

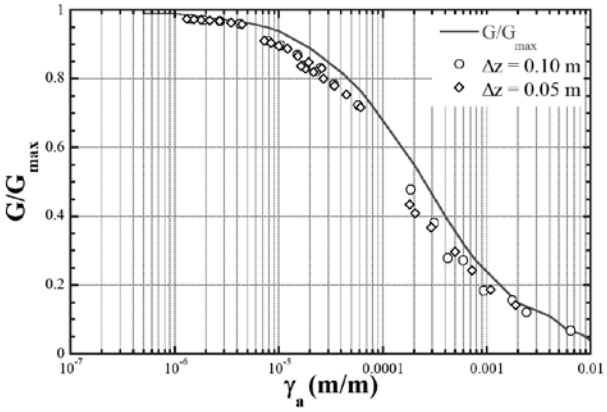


Figure 9 Shear modulus variation with γ_a.

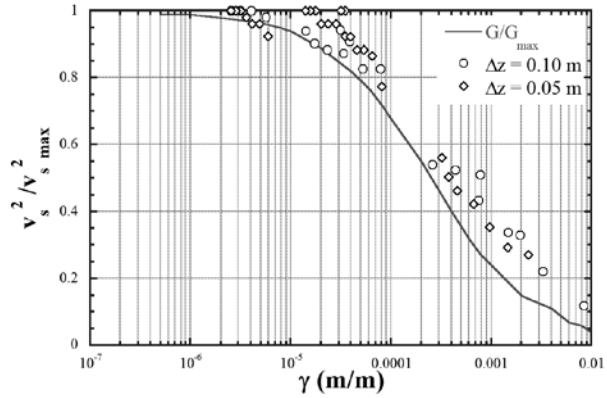


Figure 10 Shear wave velocity ratio variation with γ.

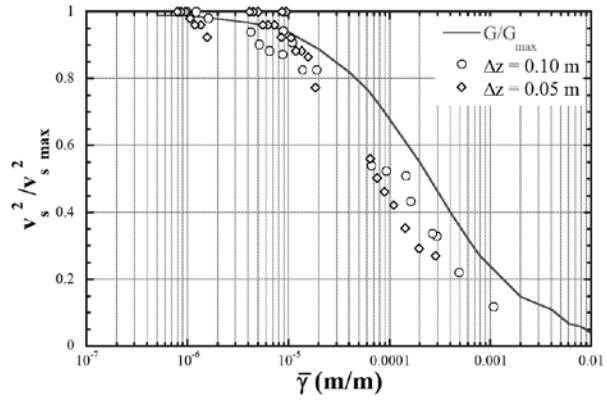


Figure 11 Shear wave velocity ratio variation with $\bar{\gamma}$.

The alternate definition of reference strain using displacements at two geophone locations at the time when the maximum is measured at the one closer to the source, yields higher values and moves the curve to the right (Figure 12), seemingly giving a better estimate of the normalized modulus curve.

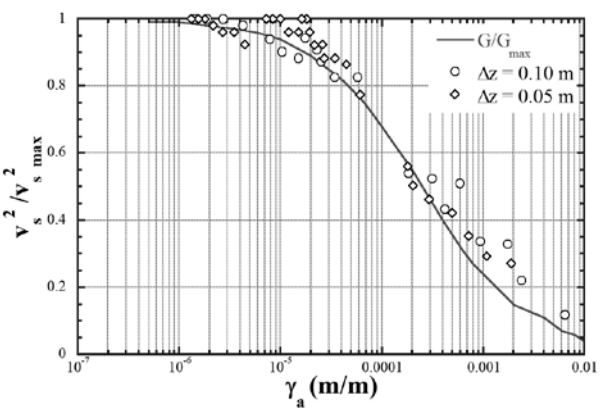


Figure 12 Shear wave ratio variation with γ_a.

3. CONCLUSIONS

The main objective of this study was to evaluate the accuracy of the procedures used in practice to determine soil properties directly from in situ measurements in order to compare them to those reported in the literature from laboratory tests.

For this purpose a shear cone that would reproduce correctly the horizontal stiffness of a circular mat foundation on the surface of an elastic, homogeneous half space, was considered. A number of cases were evaluated increasing the level of the applied harmonic force and using nonlinear springs that would reproduce a specified G/G_{max} vs. γ curve for the soil. Using a similar procedure to that used in field tests, the shear wave velocity between hypothetical receivers and the levels of strain were assessed. The results indicate that the curves obtained from the field tests need to be carefully interpreted since both the shear modulus and the reference strains estimated from field data yield averaged quantities showing a bias toward over- or under- estimation. Even in those cases where the two opposite biases may result in a better estimate, users need to be aware of the potential dangers, since there is no assurance the two errors will always be balanced equally.

Acknowledgements:

This material is based upon work supported by the National Science Foundation under Grant No. CMS-0421275. The support is gratefully acknowledged.

References:

Anderson, D. G. and Woods, R. D. (1975), "Comparison of Field and Laboratory Shear Modulus." *Proc. ASCE conference on In-situ Measurements of Soil Properties*, Vol. I, 69-62

Chang, C.Y., Mok, C.M. and Tang, H.T. (1996), "Interface of dynamic shear modulus from Lotung downhole data," *Journal of Geotechnical Enginnering*, ASCE, 122(8), 657-665.

Darendeli, M. B. (2001). " Development of a New Family of Normalized Modulus Reduction and Material Damping Curves," PhD thesis, The University of Texas at Austin.

Henke, R. and Henke, W. (1993), “Laboratory Evaluation of in situ Geotechnical Torsional Cylindrial Impulse Shear Test for Earthquake Resistant Design”, *Bulletin of the Seismological Society of America*, **83**(1), 245–263.

Henke, R. and Henke, W. (2003), “Selected Issues Regarding the Torsional Cylindrical Impulse Shear Test”, *Bulletin of the Seismological Society of America*, **93**(6), 2516-2530.

Iwan, W. D. (1967). “On a Class of Models for the Yielding Behavior of Continuous and Composite Systems.” *Journal of Applied Mechanics, ASME,* 34(3), 612-617.

Meek, J.W. and Veletsos, A.S. (1974), “Dynamic behaviour of building-foundation systems,” *Earthquake Engineering and Structural Dynamics*, 3(2), 121-138.

Park, K. (2010), “Field Measurements of the Linear and Nonlinear Shear Moduli of Cemented Alluvium Using Dynamically Loaded Surface Footings,” *PhD Thesis*, The University of Texas at Austin.

Roblee, C. and Riemer, M. (1998), “The Downhole Freestanding Shear Device Concept”, *Geotechnical Earthquake Engineering and Soil Dynamics III Conference*, Vol. 1, ASCE, Seattle, Washington, pp 201–212.

Safaqah, O. A. and Riemer, M. F. (2006), “Minimizing Sampling Disturbance Using a New in situ Device”, *Soil Dynamics and Earthquake Engineering*, **26**, 153–161.

Stokoe, K. H., Kurtulus, A., and Park, K. (2006). “Development of Field Methods to Evaluate the Nonlinear Shear and Compression Moduli of Soil.” *Earthquake Geotechnical Engineering Workshop*, Christchurch, New Zealand

Torres, D.E. (2010), “Evaluation of the Procedure Used to Determine Nonlinear Soil Properties In Situ,” *PhD Thesis*, Texas A&M University.

Wolf, J.P. and Deeks, A.J. (2004), “Foundation vibration analysis,” Elsevier, Oxford, UK.

8CUEE CONFERENCE PROCEEDINGS
8th International Conference on Urban Earthquake Engineering
March 7-8, 2011, Tokyo Institute of Technology, Tokyo, Japan

E-DEFENSE SHAKING TABLE TESTS FOR GEOTECHNICAL ENGINEERING RESEARCH PROJECTS - SUMMARY OF THE FIRST PHASE AND INTRODUCTION OF TEST SERIES IN THE SECOND PHASE -

Yohsuke Kawamata[1)], Kentaro Tabata[2)], Manabu Nakayama[3)], and Koichi Kajiwara[4)]

1) Research Fellow, Hyogo Earthquake Engineering Research Center, National Institute for Earth Science and Disaster Prevention
2) Senior Researcher, Ditto
3) Invited Research Fellow, Ditto
4) Deputy Director, Ditto
kawamata@bosai.go.jp, tabata@ bosai.go.jp, m-nakayama@ bosai.go.jp, kaji@bosai.go.jp

Abstract: Since E-Defense opened in 2005, the first phase in the first five years was over at the end of FY 2009, and the second phase got started at the beginning of FY 2010. In the first phase, four geotechnical large-scale shaking table tests out of forty-two test projects at E-Defense were performed; i.e. two soil-pile interaction tests in liquefiable and non-liquefiable soil strata, and two liquefaction-induced lateral spreading tests. Based on these full-scale tests, better understanding on liquefaction effects on soil-pile interaction could be obtained, and potentials of E-Defense testing for geotechnical projects could be validated. In the second phase, another series of geotechnical shaking table tests will be conducted using large-scale models of underground system, such as underground highways and subway. To simulate complicated underground space under mega cities, some structure models will be placed close to others, and connected to different types of structures. This test series can provide fundamental information on seismic performance of underground system. In this paper, descriptions and some results of the tests in the first phase are briefly summarized. In addition, setup plans of the test to be performed in the second phase are available.

1. INTRODUCTION

The Kobe Earthquake, 1995 in Japan damaged a large number of structures, and gave great lessons on seismic design of the structures. The reliability of seismic resistance of the existing structures needed to be verified, and more advanced and reliable design methods needed to be established in order to reduce the risk of earthquakes coming in the near future. To achieve the above goals, one of the most powerful approaches is performance of full- or large-scale experiments.

In light of this, Science and Technology Agency (at present, the Japan Ministry of Education, Culture, Sport, Science, and Technology, MEXT) made a decision to build the research facility with large-scale three-dimensional shaking table belonging to National Research Institute for Earth Science and Disaster Prevention (NIED), Hyogo Earthquake Engineering Research Center, called E-Defense. Three great advantages of the E-Defense testing are; 1) observe "more realistic" situations and phenomena minimizing scale effect, 2) record "more detailed" behavior placing more sensors, 3) perform producing earthquake disaster which provides case histories of "artificial" disasters. Using test results, numerical analyses can be validated and improved. These innovative procedures can contribute to saving human lives and properties from large catastrophic earthquakes all over the world.

Since E-Defense opened in 2005, considerable efforts have been made by coordination and collaboration of many participants, including academic institutions, government researchers, general public, private and industrial organizations. The first five years from the start of its operation FY 2005 through FY 2009, were defined as the first phase, and forty-two shaking tests with various types of structures (Tabata and Kajiwara 2009), including four soil-structure interaction tests were successfully performed in this phase. At the beginning of FY 2010, April 2010, the second phase got started and a new geotechnical engineering research project has been carefully planned now.

In this paper, the introduction of E-Defense research facility and brief summaries of geotechnical engineering research projects performed in the first phase are presented showing some examples. Also, another series of geotechnical experiments to be conducted in the second phase is introduced.

2. SPECIFICATIONS OF TESTING COMPONENTS

First of all, specifications and characteristics of testing components belonging to E-Defense (*i.e.* the shaking table, soil containers) are introduced. These components were used for the first phase tests, and will also be used for the second phase tests.

2.1 E-Defense Shaking Table

The key element of E-Defense is a 20 m by 15 m shaking table (Photo 1). The specifications of the table shown in Table 1 gives the capability of reproducing the seismic motions recorded in the 1995 Kobe earthquake for a 12-MN model structure. Motions in horizontal and vertical directions are controlled using 10 and 14 units of hydraulic actuator, respectively. Because of noise in the hydraulic system, interaction between the shaking table and test specimens, and nonlinear behavior of test specimens, actual table motions are not always identical as target motions. Therefore, some excitations are usually inputted to the table with test specimens prior to tests to observe differences of the table motions and find correction factors at any frequency. Because of high nonlinearity of geo-materials, however, it is not reasonable to input motions to soil-structure specimens before testing, and therefore, motions with no correction are usually applied.

2.2 Soil Containers

Regarding geotechnical testing, E-Defense has two large soil containers, (a) a cylindrical laminar container, and (b) a rectangular rigid container. The former, the cylindrical laminar container has 8 m in diameter and 6.4 m in height, and is composed of 40 laminar rings that can only move horizontally. The latter, the rectangular rigid container is 16 m long, 4 m wide and 5 m high. Those containers have to be chosen with careful considerations on research purpose, target structures, and expected results.

2.3 Sand

Approximately 1000 tons of Albany silica sand is stored in the stock yard at E-Defense. The properties and indices of the sand are presented in Table 2. Details of its deformation characteristics are available in Yasuda *et al.* (2006). The grain size distribution of the sand is shown in Figure 2 with one of Toyoura sand, indicating both the sands show similar distribution. Because the Albany sand was used for tests several times, fine contents may be washed out and particles may be crushed somewhat, and therefore, its characteristics may be slightly changed. To quantify it, another series of laboratory tests (index and deformation characteristics tests) has been conducted. The results will be published in the near future.

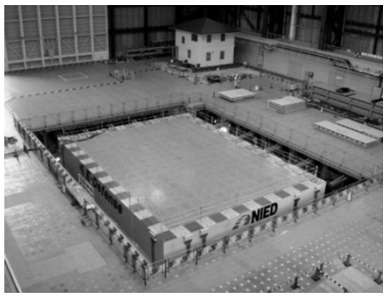


Photo 1. E-Defense shaking table

Table 1. Specifications of the E-Defense shaking table

Table size		20m x 15m	
Loading capacity		12MN	
Maximum performance*		Horizontal (x and y)	Vertical (z)
	acceleration	900gal	1500gal
	velocity	2m/s	0.7m/s
	displacement	±1m	±0.5m
	allowable moment	150MNm	40MNm

* at the maximum load

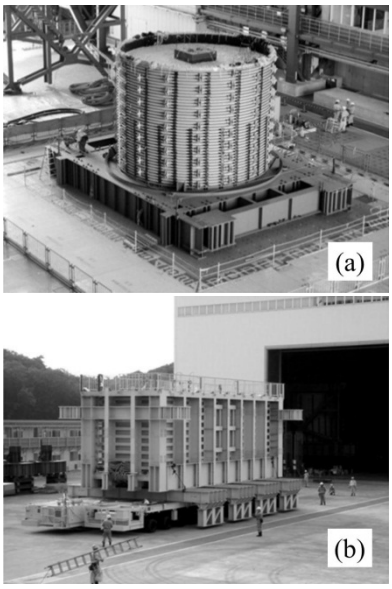


Photo 2. Soil containers for E-Defense testing: (a) cylindrical laminar container, and (b) rectangular rigid container

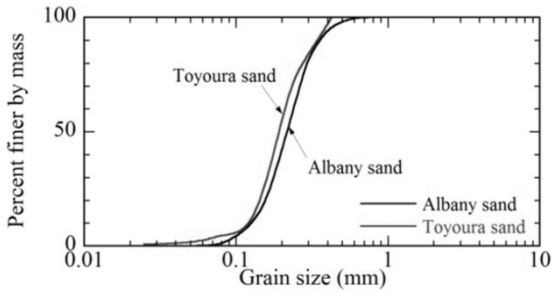


Figure 1. Grain size distributions of Albany silica and Toyoura sand

Table 2. Properties of Albany silica sand

Density of soil particles	$\rho_s = 2.63$ g/cm^3
Maximum void ratio	$e_{max} = 0.783$
Minimum void ratio	$e_{min} = 0.513$
Mean grain size	$D_{50} = 0.20$ mm
Uniformity coefficient	$U_c = 1.64$
Coefficient of curvature	$U'_c = 1.13$

2.4 Sensors and Data Acquisition System

As mentioned above, more than 40 full- or large-scale tests have been performed at E-Defense with various types of structures, and many kinds of measurements have been used to achieve their research goals. Therefore, various types

of sensors and tools fixing positions of these sensors are now available. In geotechnical testing programs, ground displacement, deformation of structures, accelerations in ground and structures, earth pressure acting on the structures, are usually measured, and pore water pressure is also monitored if soil liquefaction is expected. In the first phase tests at E-Defense, strain gauges, displacement transducers, earth pressure gauges, accelerometers, pore water pressure gauges, tilt-meters, and shape-tapes were applied. In addition, a unique three-dimensional displacement measuring system was employed to investigate the motions of the ground surface, the caisson, the footing and the weight of the structure (Tokuyama *et al.* 2007). In this system, displacement is determined by digital video cameras that capture reflective, spherical markers attached to an object. The advantage of the system is to acquire very large displacement that is difficult to measure by a typical displacement transducer.

The data acquisition system has approximately 900 channels. Because various behaviors of test specimens want to be measured, this number of sensors may be short. Therefore, reasonable sensoring plans with the above numbers of sensors are usually developed defining priorities of measurements.

3. PAST RESEARCH PROJECTS

In the first phase of E-Defense, there was a two-year geotechnical testing program as a part of the Special Project for Mitigation of Earthquake Disaster in Urban Areas, called Dai-Dai-Toku in Japanese. In this chapter, some examples of the large-scale tests are briefly described. More details are available elsewhere (*e.g.* Tabata *et al.* 2007).

3.1 Soil-Structure Interaction (SSI) in Level Ground

In order to obtain better understanding on soil-structure interaction and failure mechanism of pile foundations due to earthquake-induced ground motions, a series of large-scale model shaking table tests with a soil-foundation -superstructure system was performed using the E-Defense shaking table in February and August, 2006. In this paper, brief description of the test setup and some examples of the test results are presented.

The specimen for SSI test was built in the cylindrical laminar container (Figure 2). A target structure placed at the center of the container filled with a 6.4 m high non-liquefiable deposit of Albany silica sand with the relative density of 70 %. The target structure consisted of a 28-ton superstructure supported by four 30 cm high columns, a 10-ton footing, and a pile foundation composed of 9 hollow steel piles 5.7 m long, 152 mm in diameter and 2 mm thick. All the piles were fixed at the top to the footing and pinned at the bottom of the container. The four columns supporting the superstructure could be replaced in order to change natural periods of the foundation-superstructure system.

Totally 80 shaking tests were performed with different structures inputting various motions, and the test results from three cases of them are presented herein: Case 1 for the structure with a natural period shorter than the deposit's predominant period (short period structure), Case 2 for the structure with a natural period longer than the deposit's (long period structure), and Case 3 for the structure having a footing and a pile foundation without the superstructure (no superstructure). In Case 1 and 2, columns of rigid steel and vibration isolation rubbers were used in order to adjust the natural period of the structure systems respectively, and all the other specifications, such as shape and weight, were identical. In Case 3, no superstructure and column were placed on the footing. Two-dimensional horizontal motion recorded at JR Takatori Station in the 1995 Kobe earthquake (Nakamura *et al.* 1996) with the maximum acceleration adjusted to approximately 0.8 m/s^2 was applied to the shaking table.

Figure 3 presents the time histories of the table accelerations in x- and y-directions shown in Figure 2, indicating that the table motions in three test cases were almost identical. Nonlinear behaviors of the test specimens and interactions between the hydraulic system, the shaking table, and the test specimens usually affect the table motions, but their influence can be reasonably assumed to be negligible in the above three cases.

Figure 4 shows the time histories of the horizontal inertial force of the superstructure and the footing (*Fy*), and horizontal displacement of the footing in y-direction (*dy*) in Case 1 and 2. In Case 1, since time histories of *Fy* and *dy* have almost the same phase, the inertial force dominates the displacement of the footing. On the other hand, the inertial force in Case 2 has less correlation with the displacement of the footing than Case 1.

The time histories of bending strains in *y*-direction at a depth of 15 cm from the pile head along the center pile defined as B2 (Figure 2) are compared in Figure 5. The values of bending strain of the short period structure (Case 1) appear to be larger than those in the other cases especially at around 6-7 seconds, while the long period structure (Case 2) gives a similar tendency to that of the structure with no superstructure (Case 3). Figure 6 shows profiles of bending strain along Pile B2 in *y*-direction when the maximum strain appeared at 15 cm below the pile head in Case 1-3. From this figure, it is obvious that Case 2 and 3 showed similar strain distributions, while Case 1 gave quite a different profile from the others, and much larger bending strains.

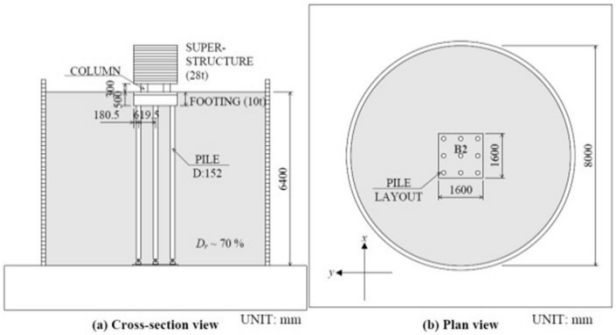


Figure 2. Specimen for SSI test and location of the pile B2

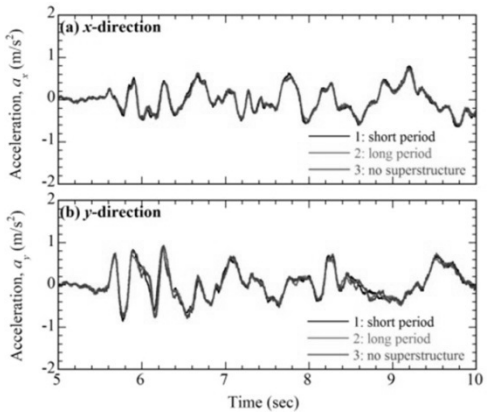


Figure 3. Comparisons of table acceleration time histories in (a) x-direction, and (b) y-direction

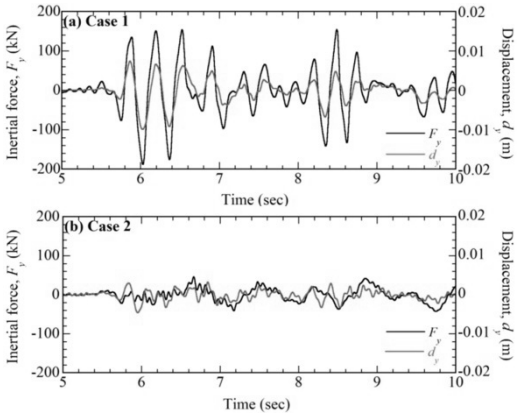


Figure 4. Time histories of horizontal inertial force induced by the superstructure and the footing (*Fy*), and horizontal displacement at the footing (*dy*)

The above comparisons show that the superstructure with long natural period (Case 2) behaved as an isolated structure, and minimized effects of inertial force of the superstructure on the piles. In addition, they indicate the inertial force of the superstructure has a great influence on the bending behavior of the piles. These facts imply that isolated superstructures can improve performance of pile foundations.

3.2 Liquefaction-induced Lateral Spreading

The other series of large-scale model shaking table tests with two different types of quay walls and a pile superstructure system right behind the walls was performed in March and December, 2006. The objectives of this testing series were to produce liquefaction and lateral spreading, and obtain better understanding on process of liquefaction generation, and failure mechanism of a quay wall and pile foundation system behind the walls. This paper briefly describes the test setup and some examples of the results from a test with a caisson type quay wall.

Figure 7 shows the test specimen built in the rectangular container. The specimen consisted of liquefiable deposit, a 2 m high caisson-type quay wall, a 40 cm thick gravel mound beneath the quay wall, and a structure supported by a pile group. The deposit was made of Albany silica sand compacted into 90 % relative density up to 75 cm from the bottom of the container, and 60 % relative density above that. The deposit was divided by the caisson into 2.5 m thick "seaside" and 4.5 m thick "landside". The level of the water table was adjusted to 0.5 m below the landside ground surface saturated with de-aired water before testing. The pile-supported structure was placed behind the caisson, consisting of six hollow steel piles, a footing and a weight representing a superstructure. The six piles were aligned with three parallels to the face line of the caisson in two rows, and fixed to the footing and pinned at the bottom of the container. The 10-ton footing was embedded into the landside deposit to a depth of 0.5 m. The 12-ton weight was placed on the footing, generating inertial force under applied motions.

The horizontal and vertical motions used for this test series were defined based on the 80 % adjusted north-south and up-down motions recorded at JR Takatori Station in the 1995 Kobe earthquake. The horizontal motion was applied in the model's long direction. The peak table accelerations were approximately 6.0 and 1.7 m/s^2 in the horizontal and vertical directions respectively, and the shaking duration was about 41 seconds. Figure 8(a) shows the acceleration time histories of the target and recorded table motions in the first 30 seconds of the shaking. Because the characteristics of the deposit were significantly changed due to liquefaction because of its high nonlinearity, the table control system could scarcely follow such change, and therefore, difference between the target and the actual table motions usually become significant. However, as shown in Figure 8, both shapes of time histories and the Fourier spectrum show reasonable agreement.

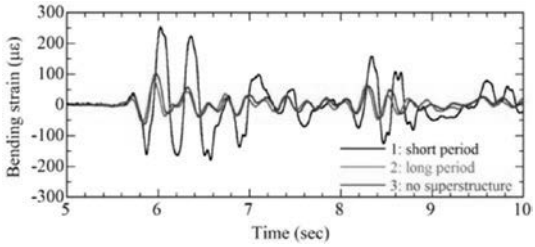


Figure 5. Bending strain time histories of the pile B2

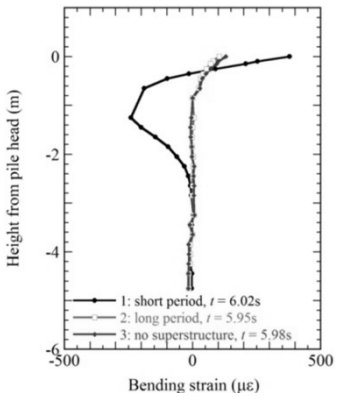


Figure 6. Bending strain distributions along the pile B2

Figure 9 illustrates permanent deformation shape of the test specimen. The caisson tilted toward the seaside at a 25-degree angle with horizontal displacement of approximately 2.0 m and 1.3 m at the top and the bottom, respectively. The mound also moved horizontally with the caisson. Three seaside piles significantly bent at almost the same elevation of the seabed as shown in Photo 3. Figure 9 also shows permanent displacement of the landside ground surface decreased with the distance from the caisson. This trend is similar to some cases observed in the 1995 Kobe earthquake (Ishihara *et al.* 1996). The above observation indicates the test was able to simulate a lateral spreading phenomenon of the liquefied deposit observed in actual damaged sites. The liquefaction and induced lateral spreading also generated approximately 20 cm settlement in the landside deposit, while relatively small settlement was observed at the seaside deposit.

Figure 10 shows the changes of excess pore water pressure, Δu, at four different depths (0.6, 1.7, 2.9 and 3.7 m from the landside ground surface) under the measurement point F indicated in Figure 7. As shown in Figure 10, Δu began to increase at all the depths when the shaking started, and then reached their overburden pressure in about 7 seconds. It shows all the depths of the deposit were fully liquefied. Following this Δu built-up process, Δu dissipation started from the bottom layer to the surface, indicating the liquefied deposit settled from the bottom to the surface. In addition, the Δu dissipation process at any depth provided identical paths from 40 to 100 seconds. This fact indicates the Δu of upper layers began to dissipate when its pressure level reached that of the lower layers.

Figure 11 shows the horizontal displacements of the caisson, the weight and the footing of the pile-supported structure, and their surrounding deposit represented by the measurement point D. Note that the point D was located on the ground surface between the caisson and the footing of the structure (Figure 7). This figure indicates the caisson significantly moved toward the seaside at 10.5 seconds. It is consistent with significant drop of the pore water pressure Δu observed at this time in Figure 10 because the pore water was released from the confinement due to the movement of the caisson. Until the caisson tilted, horizontal displacement toward the seaside at the point D was always smaller than that of the caisson, and those of the weight and the footing were smaller than those of the caisson and the point D. Also, the horizontal displacement changed with nearly the same phase. Just after the caisson significantly tilted at 10.5 seconds, the horizontal displacements of the weight and the footing became the same as one of the point D, and kept increasing together. This observation implies that a major trigger of inclination of the pile-supported structure was tilting of the caisson. Moreover, the horizontal displacement of the weight was identical to that of the footing before 12.5 seconds, and data of the footing was lost at 12.5 seconds because the marker sunk into the water. Considering on the pore water pressure drop at this time in Figure 10, it can be guessed the inclination of the structure toward the waterside started at this point.

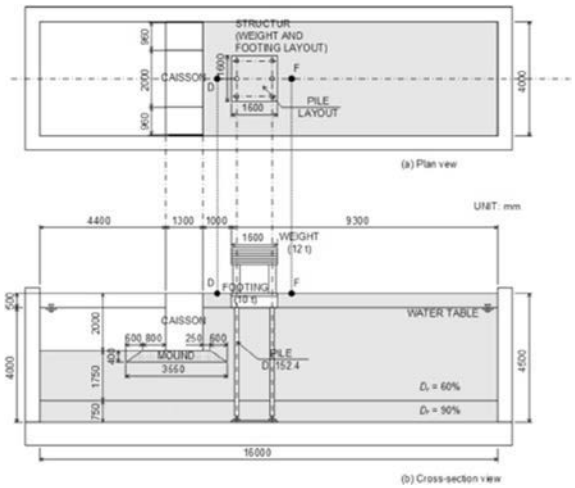
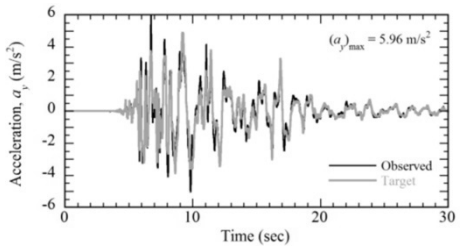
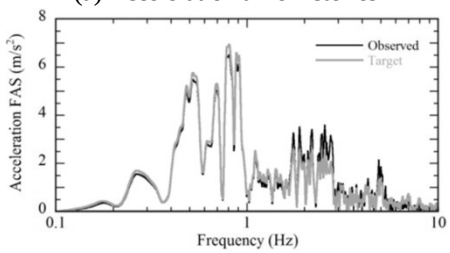


Figure 7. Specimen for lateral spreading test and locations of measurement point D



(a) Acceleration time histories



(b) Acceleration Fourier amplitude spectra

Figure 8. Comparisons between target and observed table motion

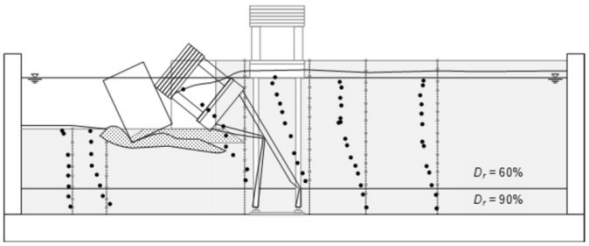


Figure 9. Permanent deformation shape due to liquefaction -induced lateral spreading



Photo 3. Piles yielded at level of the seabed

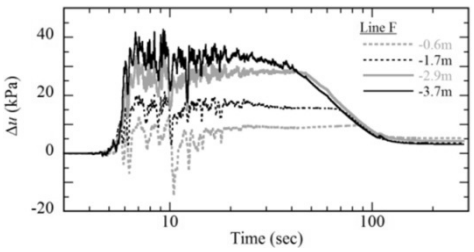


Figure 10. Time histories of excess pore water pressure at various depths at measurement point D

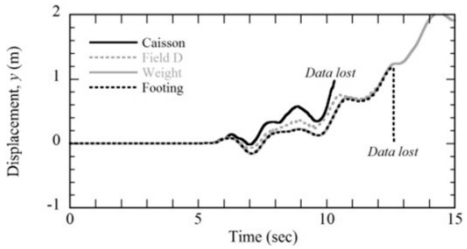


Figure 11. Horizontal displacement of the caisson, measurement point D, the weight, and the footing

3.3 Summaries

Through the Dai-Dai-Toku two-year projects, the following capabilities of the E-Defense testing facility could be validated:

- Reproduction of ground motion records on the table
- Simulation of liquefaction and liquefaction-induced phenomena such as lateral spreading
- Simulation of failure mechanisms on structures (e.g. piles and caissons)
- Preparation and installation of soil, structure models and sensors

Using the above capabilities, another series of large-scale model geotechnical shaking table tests has currently been conducted from FY 2010 through FY 2015. This current research project is briefly introduced in the next chapter.

4. CURRENT RESEARCH PROJECT

In the second phase of E-Defense starting at the beginning of April in 2010, another series of geotechnical engineering large-scale tests will be performed. According to goals of E-Defense, achieving resilient cities, the subject chosen for the second phase tests is “underground transportation system in mega cities”. This chapter presents fundamental descriptions about the project. More details will be published soon.

4.1 Abstract

In mega cities, many types of underground structures, such as underground road networks, subway systems, underground streets and underground parking lots, have been built. Therefore, underground structures beneath mega cities often show very complicated distribution. Subway systems in Tokyo, Osaka, New York and San Francisco Bay Area are great examples. As another example, a part of the road network around Financial District in Boston was buried into the ground to use space on the ground more effectively (Boston Big Dig Project). In addition, there are great projects of building an express railway network in some countries including the United States, and the network may be under ground in existing city areas because of the limit of space above the ground surface. Burying public city functions may be promoted more in the near future for more effective land usage and preservation of the landscape.

Regarding underground structures in mega cities, there are still some uncertainties of their seismic behavior, such as effect of neighboring structures and behavior of connections between different types of structures. In the current design practice, for instance, the effect of neighboring structures needs to be considered only for appropriate choice of construction method (e.g. prevention of unacceptable deformation of existing structures induced by construction of new structures close to the existing ones), not for estimation of their seismic performance. Such uncertainties need to be clarified in order to achieve great resiliency of urban areas against earthquake disasters by controlling risk of losing lives and properties.

In light of this, a large-scale model shaking table test of underground structures will be performed at E-Defense in FY 2011. Because large-scale test specimens can be shaken on the E-Defense large shaking table, scale effect can be relatively eliminated compared with the past experiments with smaller specimens. In addition, more detailed information will be available through the data acquired by large amounts of sensors placed on the large test specimen. As a result, more reasonable understanding on seismic behavior of underground structures, soil-structure and structure-structure interactions can be obtained analyzing the results of this “artificial case history”.

Because E-Defense shaking table tests take lots of time and cost, the best test plan must be built in order to gain more useful results, and therefore, an effective project network needs to be established. Figure 12 shows the current research network for this project, including three important components; i.e. an E-Defense large-scale model test, a small scale model test, and a numerical simulation analysis. Prior to the large-scale test, the numerical analysis, the small-scale 1-g and the centrifuge shaking table tests are conducted in order to gain fundamental information and improve plans of the large-scale tests. After the large-scale test, the small-scale test and the numerical analysis will be

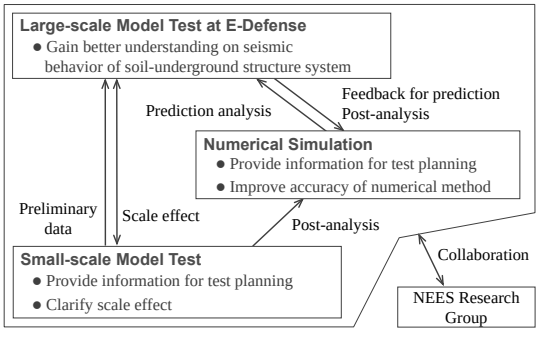


Figure 12. Project network including three important components and research collaboration with NEES

validated comparing results from all the tests and numerical simulation approaches.

In addition to the above important components, representatives of Network for Earthquake Engineering Simulation (NEES) will be involved into this research project. Current collaboration activities and possible future research collaboration are described below.

4.2 Draft of Test Plan

As mentioned above, there are still numbers of uncertainties in seismic behavior of underground structures. However, it is very difficult to perform large-scale tests in many times to reveal all the uncertainties, and therefore, the following three uncertainties are focused in the first large-scale test:

- Damage development at joints between different components such as tunnels, subway stations, vertical shafts and ventilation towers: Because of significant difference of seismic responses among these components, it is expected that damage can be localized at these joints. There are several options on types of joints, such as rigid connection, flexible connection, and connection with no fixity in an axial direction of horizontal components and fixed in the other directions (representing typical shield-shaft connections). Connections to be tested will be determined with careful consideration on types of actual structures, and reliability of data obtained. One of possible options is to use rigid connection in the first test providing results which are easy to analyze, and more complicated connections later.
- Effect of neighboring structures on seismic behavior of underground structures: Since underground space in mega cities has been highly developed, newly constructing structures often have to be designed with very small distance from existing structures. The distance between these structures is one of the significant factors affecting their seismic behaviors. This project will focus on the relationship between the distance of underground structures and magnitude of the effect of these neighboring structures. Distribution of structure specimens will be designed based on results of preliminary tests and simple pre-numerical analyses.
- Seismic behavior of vertical underground structures: Vertical underground structures are generally built through several different types of soil strata. This complexity of soils may significantly affect seismic behavior of the structures. To evaluate effect of ground composing of different types of soil strata on structural response, a vertical structure embedded into a hard soil (*e.g.* cement-mixed soil) stratum underlying a relatively soft cohesionless soil stratum is considered.

Based on these three target uncertainties defined above, one of possible setup plans for the large-scale model test and its dimensions are shown in Figure 13 and 14, respectively. The scale of this test setup is 1/30. It is noticeable that this plan is tentative, and the detailed test plans will be made based on discussion about the results to be obtained in the preliminary small-scale model shaking table test and the following simulation analyses performed prior to the large-scale test.

Materials (*e.g.* stiffness and ductility) and specifications (*e.g.* shape, dimensions, and distribution) of structure models shall be carefully chosen in order to represent typical structures and observe expected phenomenon. Materials which can give fundamental information to be used for quantitative assessment of design code and numerical analyses in small and middle levels of motions, and provide mechanism of failure development in large level of motions are ideal, but the former has higher priority if both are incompatible. Mortal with short fibers, acryl, aluminum, and steel are possible materials.

Sensoring plans shall be designed based on preliminary simulation analyses in order to obtain useful records. Accelerometers, earth pressure gauges, strain gages, shape-tape, tilt-meters and displacement transducers will be used as usual. In addition, applications of fiber optic sensors giving deformation of structures and ground, and tactile sensors showing two-dimensional earth pressure distribution at the surface of the underground structures are under examination.

Two or three levels of motions, such as small-, middle-, and large-levels, will be applied to the test specimen.

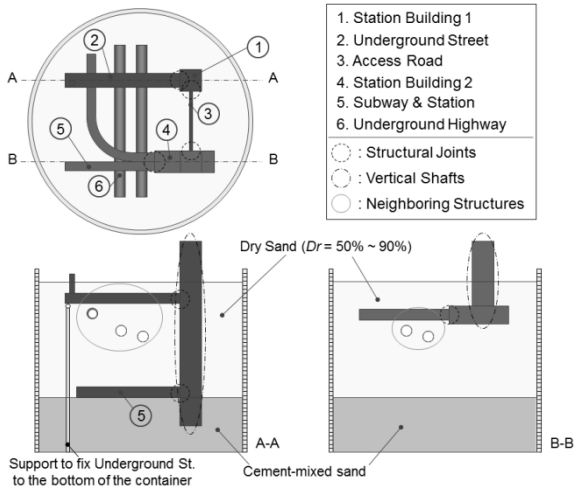


Figure 13. An example of possible test setup

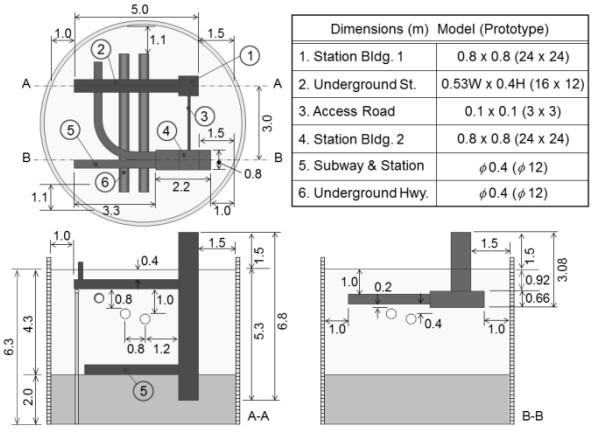


Figure 14. Dimensions of the possible test specimen

Because the height of the specimen is only about 6 m, it is difficult to simulate propagation and amplification processes of motions from the bottom to the top. Therefore, motions recorded at the ground surface in actual earthquake events will be used as large-level motions. To assess dynamic characteristics of the specimen, small-level of white noise or sweep will also be applied. Because three-dimensional behaviors of model structures are expected, especially around connections, various shaking directions will be tested by rotating directions in order to find the most critical direction giving the maximum responses of the structures.

4.3 Collaboration Works with NEES

In July 2005, NIED and NEES concluded Memorandums of Understandings (MOU) covering collaboration activities through 2010. According to the MOU, E-Defense and NEES have held 8 joint meetings as of January 2011, and some collaboration research activities. In 2010, there were three meetings in which the current geotechnical project was discussed; the 9th National and the 10th Canadian Conference on Earthquake Engineering in Toronto, the 8th NEES/E-Defense joint meeting in Miki, and 2010 Quake Summit in San Francisco. In the meetings, Japanese and U.S. geotechnical researchers exchanged opinions about the project, and determined to look for how the both will work together. Currently, a competition of preliminary simulation analysis is considered as one of possible options.

4.4 Test Schedule

This project has been performed for six successive fiscal years, 2010 through 2015. A long term schedule including contents for each fiscal year is shown in Table 3. Details of the second half of this project (FY 2013~ FY 2015) will be made based on the results in the first half (FY 2010 ~ FY 2012).

Also, details of the schedule for the first and second fiscal years are presented in Table 4. The first large-scale model test will be performed in February, 2012. Note that the test setup of the first test shall be finalized by the end of May, 2011 in the current schedule as of January 15, 2011.

Table 3. Project schedule (long term)

Fiscal Year	Contents
2010	Preliminary test for the entire soil-structure system test: - Centrifuge shaking test (scale: 1/50) - Small-scale shaking table test - Laboratory tests of geo-material to be used - Post-simulation analyses of preliminary tests - Planning the large-scale system test to be performed in FY 2011
2011	Entire soil-structure system test: - Pre-simulation analyses - Large-scale model shaking table test at E-Defense (scale: 1/30)
2012	Evaluation of the results from the system test - Post-simulation analyses - Planning the preliminary test for the other large-scale model shaking table test and the prediction analyses
2013 ~ 2015	Small-scale model preliminary shaking table test and large-scale model shaking table test (component test or another system test) Pre- and post-simulation analyses Evaluation of results from the component test Summary of the whole project

Table 4. Project schedule (short term)

Research works	Research meetings in Japan and U.S.
Fiscal Year 2010 (2010/4 ~2011/3) October, 2010 ~ February, 2011: Perform the preliminary tests (Centrifuge, small-scale shaking table tests, and laboratory tests of soil to be used) February, 2011 ~ May, 2011: Make a detailed plan of the system test	July 26-29: 9th National and 10th Canadian Conf. on Eq. Engr. (Toronto) September 17, 18: E-Defense/NEES Planning Meeting (Miki) October 7, 8: NEES Annual Meeting (San Francisco)
Fiscal Year 2011 (2011/4 ~2012/3) June, 2011 ~ January, 2012: Pre-simulation of the large-scale system test November, 2011 ~ February, 2012: Make a test specimen of the entire soil-structure system February, 2012: Perform the large-scale system test at E-Defense	(Undecided) June 9-11: 2011 NEES & MCEER Annual Meeting (Buffalo)

5. CONCLUSIONS

Since E-Defense started its operation, approximately six years have passed. Nowadays, testing knowledge and technique with the E-Defense shaking table have been developed, great connections with international research groups have been established, and various kinds of tools and sensors become available. Using the above advantages, E-Defense will keep distributing more effective and useful data to academic societies.

Acknowledgements:

All the research programs mentioned in this paper are funded by the Japan Ministry of Education, Culture, Sport, Science, and Technology (MEXT). Research committees and researchers concerned give advice, comments on the research projects. All their supports and contributions are greatly acknowledged.

References:

Ishihara, K., Yasuda, S. & Nagase, H., (1996), "Soil characteristics and ground damage", *Soils and Foundations*, Special issue, 109-118.

Nakamura, Y., Uehan, F. and Inoue, H., (1996), "Waveform and its analysis of the 1995 Hyogoken-Nanbu earthquake (II)", *JR Earthquake Information*, 23d., Railway Technical Research Institute, 112, (in Japanese).

Tabata, K. and Kajiwara, K., (2009), "Experimental research on behavior of various structures under earthquake motions at E-Defense", *Proc. 2nd China-Japan Science Forum,* Beijing, China, 205-206.

Tabata, K., Sato, M., Tokimatsu, K., Suzuki, H., and Tokuyama, H., (2007), "Soil-pile-structure interaction during multi-dimensional shaking through physical model tests using E-Defense facility", Proc., 4th Conf. Urban Earthquake Engineering, 841-848.

Tokuyama, H., Tabata, K., Nakazawa, H. & Sato, M., (2007), "Applicability of three-dimensional displacement measure-ment to model ground in large-scale shaking table testing at E-Defense", *The 42nd Annual Symposium of the Japanese Geotechnical Society, Proc. Symp.*, 1643-1644, (in Japanese).

Yasuda, S., Saito, S. and Suzuki, S. (2006), "Effect of confining pressure on liquefaction behavior of sand", *The 61st Annual Symposium of the Japanese Society of Civil Engineers*, *Proc. Symp.*, 547-548, (in Japanese).

8CUEE CONFERENCE PROCEEDINGS
8th International Conference on Urban Earthquake Engineering
March 7-8, 2011, Tokyo Institute of Technology, Tokyo, Japan

THE GENERALIZED SCALING LAW FOR LIQUEFIABLE SAND DEPOSIT - CAUSES OF DISCREPANCY AT LOW CENTRIFUGAL ACCELERATIONS -

Tetsuo Tobita[1] and Susumu Iai[2]

1) Assistant Professor, Disaster Prevention Research Institute, Kyoto University, Kyoto, Japan
2) Professor, Disaster Prevention Research Institute, Kyoto University, Kyoto, Japan
tobita.tetsuo.8e@kyoto-u.ac.jp, iai@geotech.dpri.kyoto-u.ac.jp

Abstract: A series of centrifuge model tests are conducted under the scheme of the modeling of models technique to find issues on the generalized scaling law for dynamic centrifuge tests (Iai et al., 2005). In a series of dynamic tests on a flat, saturated sand layer of 1/100 scale, four different centrifugal accelerations from 5 g to 70 g are employed on the scaled models for which the prototype is uniquely given. The models are exposed to sinusoidal input accelerations with 0.65 Hz and amplitudes of 2.5 m/s^2 and 3.1 m/s^2 in prototype scale. For response during shaking, nearly identical accelerations and excess pore-water pressure buildups are recorded for all the cases in the prototype scale. Discrepancies are found on surface settlements and duration time for dissipation of excess pore-water pressure. The major causes of the discrepancy may be (1) the duration time for the initial consolidation, (2) small value of the shear modulus due to low confining stress in model ground under low centrifugal acceleration, and (3) reduced permeability due to adsorption of viscous fluids on sand particles.

1. INTRODUCTION

Application of the geotechnical centrifuge modeling to design practice was considered in the past (e.g., Craig, 1984); however, with increasing demands on performance-based design of large structures, physical model testing seems to be facing limitations due to modeling techniques and equipment. This is where the breakthrough for physical modeling can be addressed as to directly apply test results of large prototypes to performance-based design practice. This may be one of the challenging topics for the geotechnical centrifuge community to be linked with industry (Terashi et al., 2004; Gaudin et al., 2010).

One of the great advantages of numerical analyses is that response of full-scale structures can be readily simulated, and parametric studies can be conducted just by changing numbers in input files. However, numerical methods are solely validated through results of physical model tests or real-scale behavior of geotechnical structures. Despite the fact that results of numerical analyses are merely an approximation, they have often been used for quantitative evaluation of structural behaviors without comparing results of computation with other numerical or physical models.

Use of a geotechnical centrifuge has an advantage in accurately simulating real-scale behavior in a scaled model by applying the same confining stresses to the model ground as prototypes. In the centrifuge model testing, although structural models have to be small and simplified, the prototype behavior is approximated in accordance with scaling laws (e.g., Garnier et al., 2007), and it qualitatively represents prototype behavior. One of the major obstacles for application of physical modeling results to performance-based design practice is that a specific prototype cannot be tested due to restrictions associated with experimental conditions, such as the size of the model container and scaling effects on materials. For 1-g model testing, to overcome these restrictions, the size of the experimental facility has become larger and larger so that real-scale models can be tested [e.g., E-defense (Tokimatsu et al., 2007), U.C. San Diego (Einde et al., 2004)]. However, for geotechnical structures, development of a larger research facility may still have limitations because, even with such a large facility, physical modeling with foundations and surrounding ground has to be reduced due to factors inherent in a large facility, such as the capacity of the shake table, budget, etc.

Demands for the testing of large prototypes are increasing under the restrictions mentioned above. To resolve such demands and restrictions, Iai et al. (2005) proposed the scaling law by combining the scaling law for centrifuge testing with the one for 1-g dynamic-model testing. They call it the “generalized scaling law” in dynamic centrifuge modeling. The objective of the present study is to investigate and point out issues on the applicability of the scaling law through the technique of “modeling of models” for dynamic behavior of flat, saturated sand deposits.

1.1 Brief review of the generalized scaling law

Scaling factors for physical model tests can be introduced in general forms by choosing a set of basic

physical properties to be independent and deriving the scaling factors for other properties via governing equations of the analyzed system. These primitive forms of scaling factors are listed in row (4) in Table 1. In the concept of the generalized scaling law, a model on a shaking table in a geotechnical centrifuge is considered to be a small-scale representation of a 1-g shaking-table test. Figure 1 visualizes this concept by introducing a virtual 1-g model to which the prototype is scaled down via a similitude for 1-g shaking-table tests (Iai, 1989). The virtual 1-g model is subsequently scaled down by applying a similitude for centrifuge tests to the actual physical model. In this way, the geometric scaling factors applied in 1-g tests (μ) [row (1) of Table 1] can be multiplied with those for centrifuge tests (η) [row (2) of Table 1], resulting in much larger overall scaling factors $\lambda=\mu\eta$ [row (1) of Table 1].

Table 1. Scaling factors (= Prototype/Model) in physical model tests

	(1) scaling factor for 1g test	(2) scaling factor for centrifuge test	(3) partitioned scaling factor	(4) generalized scaling factors
Length	μ	η	$\mu\eta$	λ
Density	1	1	1	1
Time	$\mu^{0.75}$	η	$\mu^{0.75}\eta$	$(\lambda\lambda_\varepsilon/\lambda_g)^{0.5}$
Frequency	$\mu^{-0.75}$	$1/\eta$	$\mu^{-0.75}/\eta$	$(\lambda\lambda_\varepsilon/\lambda_g)^{-0.5}$
Acceleration	1	$1/\eta$	$1/\eta$	λ_g
Velocity	$\mu^{0.75}$	1	$\mu^{0.75}$	$(\lambda\lambda_\varepsilon\lambda_g)^{0.5}$
Displacement	$\mu^{1.5}$	η	$\mu^{1.5}\eta$	$\lambda\lambda_\varepsilon$
Stress	μ	1	μ	$\lambda\lambda_g$
Strain	$\mu^{0.5}$	1	$\mu^{0.5}$	λ_ε
Stiffness	$\mu^{0.5}$	1	$\mu^{0.5}$	$\lambda\lambda_g/\lambda_\varepsilon$
Permeability	$\mu^{0.75}$	η	$\mu^{0.75}\eta$	$(\lambda\lambda_\varepsilon/\lambda_g)^{0.5}$
Pore pressure	μ	1	μ	$\lambda\lambda_g$
Fluid Pressure	μ	1	μ	$\lambda\lambda_g$

Table 2. Generalized scaling factors implemented in the present study

	Scaling factor (Prototype/Model)			
1 G: μ	20	10	2	1.43
Centrifuge: η	5	10	50	70
Length	100	100	100	100
Density	1.00	1.00	1.00	1.00
Time	47.3	56.2	84.1	91.5
Frequency	0.0211	0.0178	0.0119	0.0109
Acceleration	0.200	0.100	0.0200	0.0143
Velocity	9.46	5.62	1.68	1.31
Displacement	447	316	141	120
Stress	20.0	10.0	2.00	1.43
Strain	4.47	3.16	1.41	1.20
Stiffness	4.47	3.16	1.41	1.20
Permeability	47.3	56.2	84.1	91.5
Pore pressure	20.0	10.0	2.00	1.43

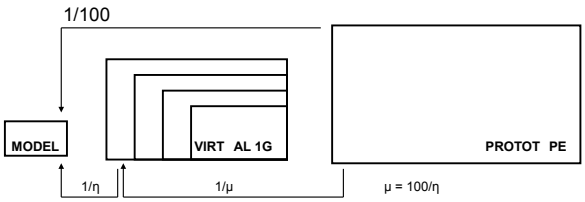


Figure 1. Concept of "modeling of models" applied to the generalized scaling.

2. DYNAMIC CENTRIFUGE TESTS ON FLAT, LOOSE, SATURATED SAND DEPOSIT

To investigate the applicability of the generalized scaling relations described above, a series of dynamic tests was conducted following the principle of "modeling of models." This technique was introduced by Schofield (1980) to assess the behavior of a prototype through repetition of the test at different scales and comparison of the results in prototype scale. In the present study, without changing the actual size of the physical model but varying the virtual 1-g dimension, the overall scaling factor ($\lambda=\mu\eta$) is kept constant (Fig. 1). Here, it is set to a fixed value comprising different combinations of the scaling factors for 1-g model testing, μ, and centrifuge testing, η. Table 2 lists the applied geometric scaling factors as well as frequencies and amplitudes of the input motions employed in the study. In what follows, units are in prototype unless otherwise specified.

2.1 Test cases

Test cases are summarized in Table 3. In the test series referred to Case A, centrifuge tests under 5, 10, 50, and 70 g were employed with the target amplitude of the input acceleration of 2.5 m/s^2. In the tests referred to Case B, centrifugal accelerations of 5, 10, and 50 g are carried out with the target amplitude of the input acceleration of 3.1 m/s^2.

Input waves are sinusoidal, and their frequency is fixed at 0.65 Hz, and duration is 35 s. Note, for example, that a case specified by "50B89" in Table 3 indicates that the centrifuge test was conducted in 50 g with 8.9 min of consolidation time in model scale in Case B. Here, the time for consolidation is the duration time given to the model to have a normally consolidated condition under specified centrifugal acceleration before shaking.

2.2 Test setup and experimental facilities

The tests were conducted in the geotechnical centrifuge of the Disaster Prevention Research Institute, Kyoto University, Japan, which has an arm length of 2.5 m and is equipped with a shaking table that allows us to expose the models to dynamic excitation in the tangential direction of flight. The instrumentation of the model is shown in Fig. 2. The strong box with inner dimensions of 45 cm by 15 cm (model scale) in width was filled up to an intended height of

Table 3. Test cases with scaling factors, properties of input motion, measured relative density and time for consolidation before shaking

Case	Scaling factors			Target input motion		Initial relative density	Time for consolidation
	1g test	Centrifuge test	Overall	Acceleration	Frequency		
	μ	η	λ=μη	(m/s^2)	(Hz)	(%)	
Prototype	-	-	-	2.5	0.65		
5A50	20	5	100	12.5	30.7	29.5	5.0
10A50	10	10	100	20.85	36.6	24.3	5.0
50A50	2	50	100	104.3	54.7	29.1	5.0
70A50	1.43	70	100	175.1	59.5	32.7	5.0
70A50-2	1.43	70	100	175.1	59.5	32.6	5.0
Prototype	-	-	-	3.1	0.65		
5B50	20	5	100	15.1	30.7	44.3	5.0
5B89	20	5	100	15.1	30.7	43.7	8.9
10B50	10	10	100	31.1	36.6	44.3	5.0
10B75	10	10	100	31.1	36.6	46.9	7.5
50B50	2	50	100	155	54.7	45.7	5.0

25 cm (model scale) corresponding to a 25-m-deep sand deposit in prototype scale.

Acceleration was measured at six different depths of the model (Fig. 2). Also, with depth, five excess pore-water pressure transducers and two earth pressure transducers were installed at the locations specified in Fig. 2. Surface settlements were continuously measured with three laser-displacement transducers attached above the ground surface (Fig. 2). Reflection plates as targets of the laser-displacement transducers were hand-made with the density of the plate adjusted to slightly heavier than that of the mixture of viscous fluid so that it followed the surface settlements (Fig. 2). The height of the ground surface was also manually measured at 18 points before and after shaking.

The temperature of the model ground was monitored by digital thermometers to have the specific viscosity of the pore fluid [Metolose (Shin-Etsu Chemical Co., 1997)], which is known to be highly temperature-dependent.

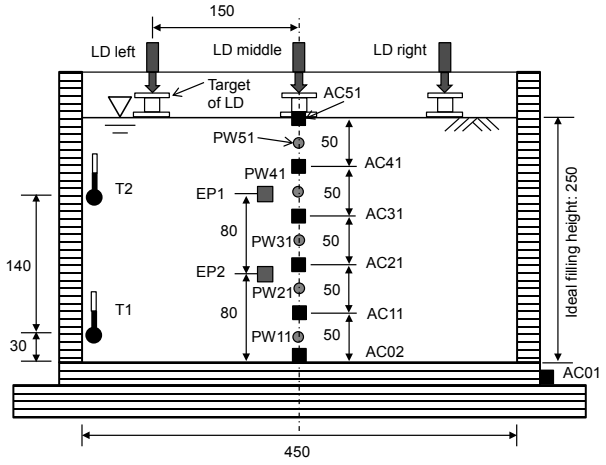


Figure 2. Test setup. LD: Laser displacement transducers. AC: Accelerometers. PW: Pore-water pressure transducers. EP: Earth pressure transducers. T: Thermometers.

2.3 Material of the model ground

The model ground was prepared with the method of water pluviation. Dry silica sand No. 7 was sprinkled slowly into high viscous water from approximately 10 cm (model scale) above water level. The relative density in the models varied between 24% and 33% in Case A, and 44% and 47% in Case B. Although the total weight of sand in the box was kept constant, a slight difference in achieved height of the model ground caused variation of the relative density.

According to the scaling factors in Table 1, the viscosity of the pore fluid has to be scaled with a factor, $\mu^{0.75}\eta$, relative to water. This leads to the use of higher viscous water in all tests than that of usual centrifuge model tests. To produce water with the specific viscosity for each test, the methylcellulose solution (Metolose, SM-100) is employed. The usability of the Metolose to produce high viscous water without changing other significant fluid parameters such as density or surface tension was tested and verified up to 100 mPa s (Dewoolkar et al., 1999; Stewart et al., 1998). As the viscosity of the Metolose solution is highly dependent on the water temperature, it was measured and adjusted by adding water or denser solution before pouring it into the strong box.

3. RESPONSE OF THE MODEL GROUND

3.1 Input and ground acceleration

To fulfill the purpose of the experiments, it is important to give the identical input motions in prototype scale for all of the test cases. Following the scaling relations of acceleration and frequency shown in Table 2, the input amplitude and time scale of acceleration for each test in model scale are determined (Table 3).

At the bottom row of Fig. 3(a), plotted are time histories of input accelerations in model scale. By applying the generalized scaling factors of acceleration and time to those time histories, they are converted into the ones shown in the bottom row of Figure 3(b). As shown in these figures, although amplitudes and durations of shaking of the input acceleration in model scale are different, in prototype scale fairly similar input accelerations are obtained for all of the tests in both cases. This guarantees that nearly identical input

acceleration was given to each model. Note that in the test 10A50 by mistake the frequency of the input motion was a little smaller than the aimed value (34.57 Hz instead of 36.55 Hz). Judging from the figures, the influence should be minor.

In the same way as the input motion mentioned above, time histories of accelerations in the model ground are plotted in Fig. 3 for Cases A. In both cases, accelerations near the ground surface in prototype scale [Figs. 3(b)] show reduction of the amplitude due to liquefaction. The envelope of the time histories in prototype scale are satisfactorily similar to one another, despite the small variation in the relative density of the model ground (Table 3).

3.2 Excess pore-water pressure

Time histories of excess pore-water pressures are compared in Figs. 4 and 5 for Cases A and B, respectively. Figures 4(a) to 4(e) show excess pore-water pressure buildup during shaking, and Figs. 4(f) to 4(j) show those until full dissipation. As shown in Figs. 4(a) to 4(e), agreements are significant for all of the cases, except for case 70A50. In 70A50, by considering that the input and ground accelerations are very similar to the others [Fig. 3(b)], pore-water pressure transducers might be malfunctioning, and possibly they were not perfectly saturated. For Case B in Figs. 5(a) to 5(e), agreements are significant, except for the tests 5B50 and 10B50, in which ceramic filters (5.0 mm thick) whose opening is much smaller than metal mesh (55-μm opening) was attached on the pore-water pressure

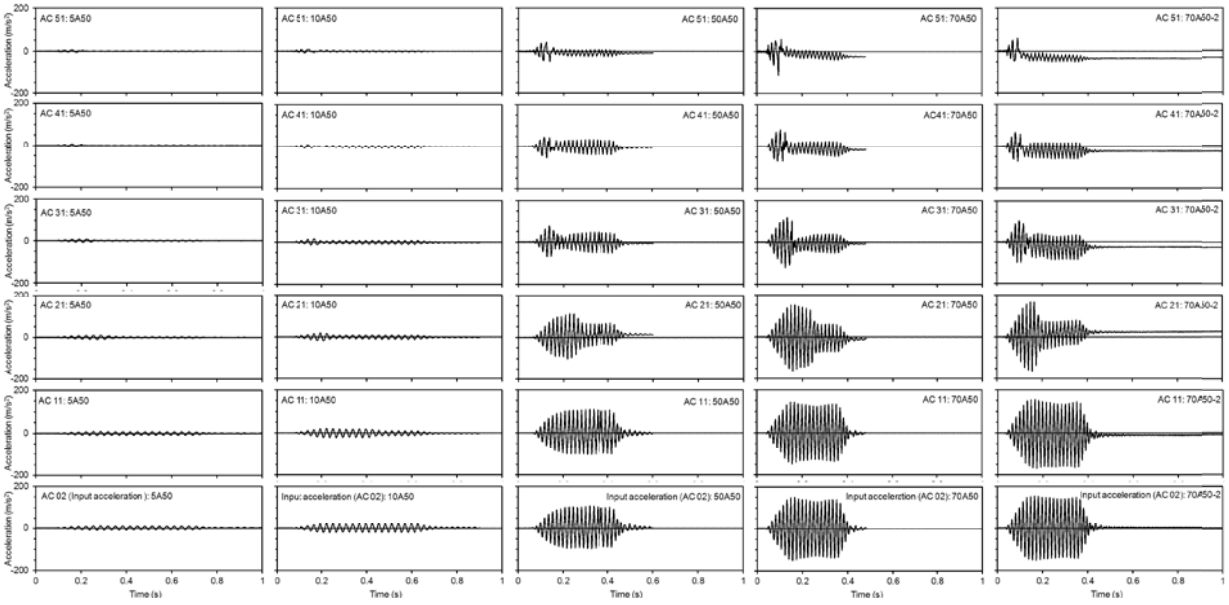


Figure 3(a). Measured time histories of acceleration in model scale for Case A.

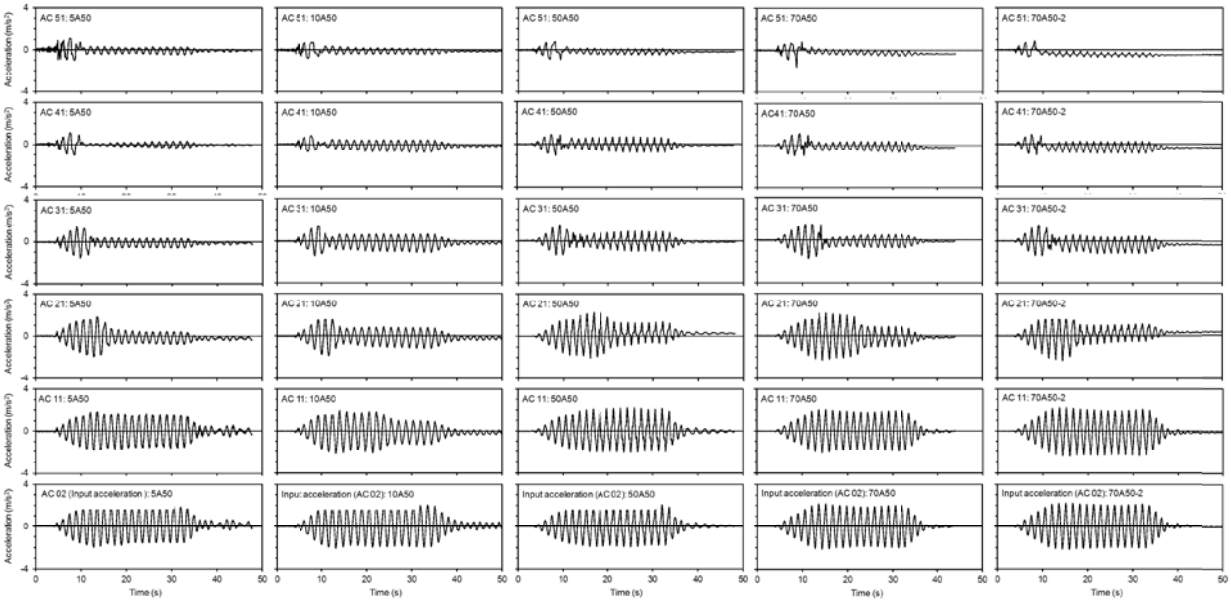


Figure 3(b). Measured time histories of acceleration in prototype scale for Case A.

transducers. Therefore, sensitivity was lost.

As shown in Figs. 4(f) and 4(g) for tests 5A50 and 10A50, the time required for full dissipation is much longer than in the other cases. The same may be said for test 5B50 and 10B50 in Case B, shown in Figs. 5(f) to 5(j), compared with the one shown in Fig. 5(j) for test 50B50. The cause of this will be investigated later.

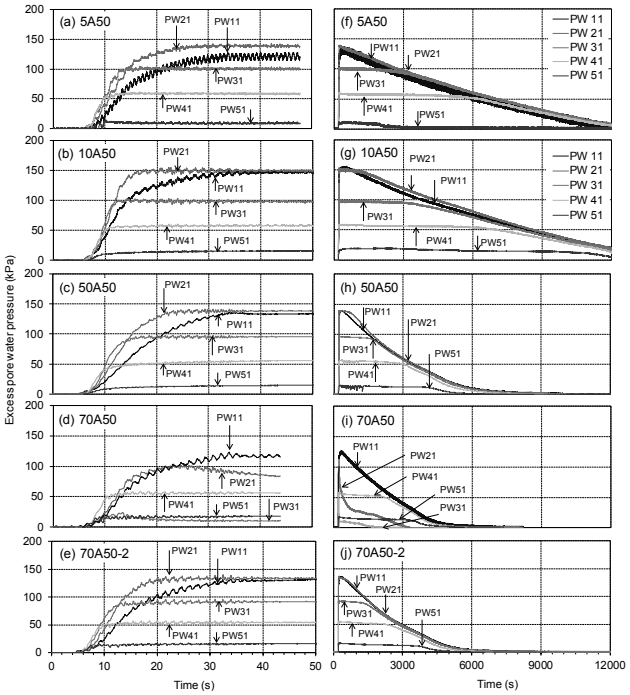


Figure 4. Measured time histories of excess pore-water pressure in prototype scale for Case A: (a) to (e) in the phase of pressure buildup (0–50 s), and (f) to (j) in the phase of dissipation (entire record).

3.3 Ground settlements

For the time range in dynamic excitation, the generalized scaling law can be verified for all reported aspects of soil behavior except for the ground settlements measured with laser displacement transducers which showed a big scatter among the models. Figure 6 shows those for Case A. In these figures, (a) to (c) are the ground settlements during shaking, and figures (d) to (f) are those until nearly complete dissipation of the excess pore-water pressure. The variations seem to be completely random. The variation observed in the ground settlements may be attributed to the device used in the tests and/or large scaling factors for displacement. The target plate of the laser displacement transducer might be influenced by the shaking because of its height, which is 3 cm in model scale (Fig. 2). Another cause may be that the scaling factor of displacement in the generalized scaling law is much larger, i.e., sensitive, compared with other scaling factors (Table 2). Therefore, special care had to be taken in the measurements of ground settlements [e.g., particle image velocimetry (PIV) (White et al., 2003)]. As shown in Fig. 6, the duration of settlements after shaking for tests 5A50 and 10A50 in Case A is much longer than the other cases with higher centrifugal accelerations. A similar trend can be seen in tests 5B50 and 10B50 in Case B—i.e., saturating the model ground with lower centrifugal acceleration tends to take more time for full settlements and give larger residual settlements.

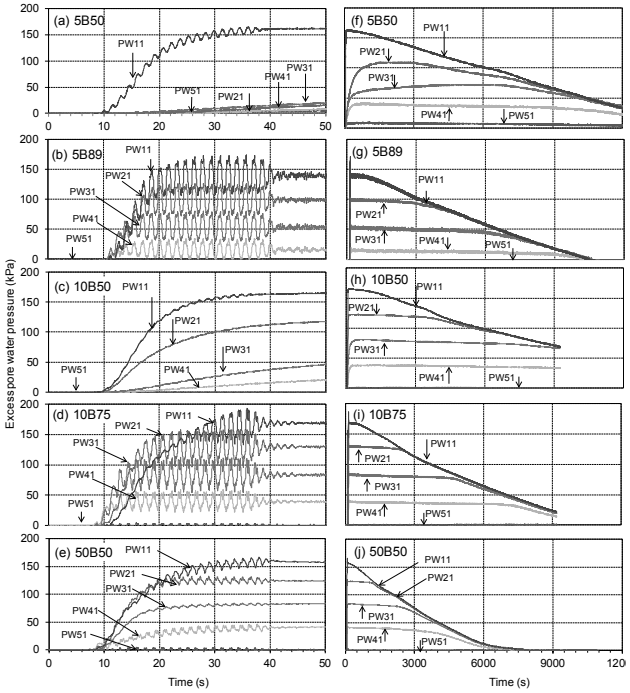


Figure 5. Measured time histories of excess pore-water pressure in prototype scale for Case B: (a) to (e) in the phase of pressure buildup (0–50 s), and (f) to (j) in the phase of dissipation (entire record).

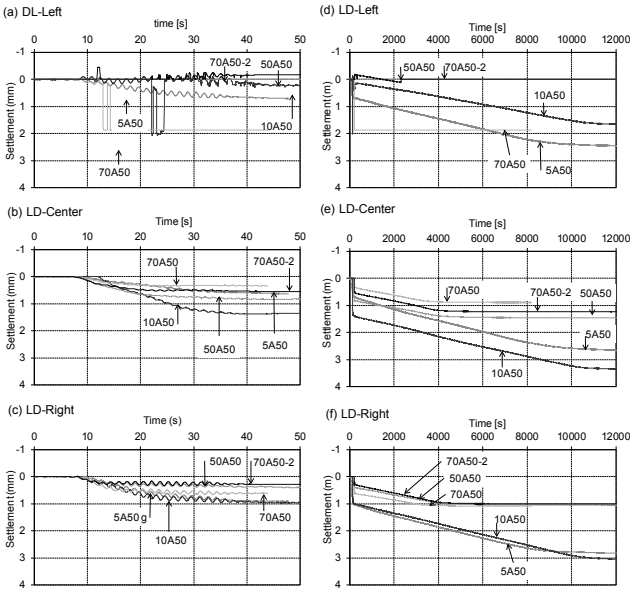


Figure 6. Measured time histories of ground settlements in prototype scale for Case A: (a) to (c) in the phase of shaking (0–50 s), and (d) to (f) in the phase of dissipation (entire record).

4. CAUSES OF DISCREPANCY AT LOW CENTRIFUGAL ACCELERATION

The two cases that were run at 5 g and 10 g showed much larger settlements and a longer duration time for pore-water dissipation in prototype scale than the others with higher centrifugal accelerations. In what follows, investigations are carried out to seek causes of the low rate of dissipation of excess pore-water pressure. Here, the following causes are assumed and examined in detail: (1) effects of duration time for consolidation before shaking, (2) effect of low effective confining stress on the scaling law, and (3) possible change of permeability of the model ground due to adsorption of the Metolose polymers on sand particles.

4.1 Effects of duration time for consolidation before shaking

In the centrifuge experiments, to have a normally consolidated ground under the given centrifugal acceleration, the model ground is consolidated about 5 min before shaking. This 5 min is arbitrarily taken because consolidation of sandy ground is assumed to be quickly achieved. However, with viscous fluid, this assumption may be a mistake. In tests 5B50 and 10B50, fluid viscosities are, respectively, 47.3 mPa s and 56.2 mPa s, and the duration times of consolidation are converted, respectively, to 281 min and 237 min in prototype scale, which is much shorter than that of 50B50—421 min.

In Case B, tests 5B89 and 10B75 are the cases in which the duration time of consolidation is adjusted so that the same duration time with test 50B50 is applied in prototype scale. In tests 5B89 and 10B75, duration times for consolidation were, respectively, 8.9 min and 7.5 min in model scale. As shown in Fig. 5(g) for 5B89 and Fig. 5(i) for 10B75, dissipation of excess pore-water pressure becomes quicker than in the cases of 5B50 and 10B50 and approaches the ones of 50 g's [Fig. 5(j)]. Although the duration time of consolidation is adjusted, a perfect match is not achieved, indicating the existence of other causes on the discrepancy.

4.2 Effect of low effective confining stress on the scaling law

The curves in Figs. 4(f) to 4(j) and Figs. 5(f) to 5(j) indicate that time required for excess pore-water dissipation becomes systematically shorter as the centrifugal acceleration increases. Model behavior in dissipation phase can be explained by the consolidation theory from which the following formula for time for consolidation is derived:

$$t = \frac{T_v d^2 m_v \gamma_w}{k} = \frac{T_v d^2 \gamma_w}{Mk} \tag{1}$$

where T_v: time factor, d: length of longest drainage pass, m_v: volume compressibility (= 1/M), M: constrained modulus of elasticity ($= 2G(1-\nu)/(1-2\nu)$), G: shear modulus, ν : Poisson ratio, γ_w: unit weight of water, and k: permeability. In the experiments under low centrifugal accelerations, the effective confining stress in model scale is low in the dissipation phase, and this may lead to a smaller stiffness of the model ground. From Eq. (1), small elastic stiffness leads to a long period of time for consolidation. Thus, scaling of stiffness might have an influence on the time of the pore-water dissipation.

In what follows, to investigate the scaling of stiffness under low effective confining stress, a scaling factor of strain in the 1-g model test is derived by fitting with experimental results.

The scaling relation of time in general form is expressed from row (4) in Table 1:

$$\lambda_t = \left(\lambda \lambda_\varepsilon / \lambda_g\right)^{0.5} \tag{2}$$

where λ , λ_ε, and λ_g are, respectively, the scaling factor of length, strain, and acceleration. In 1-g model tests, $\lambda_g = 1$, and if the scaling factor of strain is assumed to be $\lambda_\varepsilon = \lambda^{0.5}$ (Iai, 1989), then the scaling factor of time is derived from Eq. (2) as

$$\lambda_t = \lambda^{0.75} \tag{3}$$

For the scaling of centrifuge tests, $\lambda_g = 1/\lambda$, and $\lambda_\varepsilon = 1$, and therefore the scaling of time is derived again from Eq. (2) to be

$$\lambda_t = \lambda \tag{4}$$

When the scaling factor of a 1-g test is μ, and that of a centrifuge test is η, the generalized scaling factor of time is given as a combination of the above two factors (Iai et al., 2005):

$$\lambda_t = \mu^{0.75} \eta \tag{5}$$

In addition to the assumption made for the scaling factor of strains, Iai (1989) showed that when the shear-wave velocity is known, λ_ε can be determined more accurately with the following form:

$$\lambda_\varepsilon = \frac{\lambda}{\left[\left(V_s\right)_p / \left(V_s\right)_m\right]^2} \tag{6}$$

where $(V_s)_p$ and $(V_s)_m$ are, respectively, the shear-wave velocity of the prototype and the model. From Eq. (6), it is evident that the scaling of stain is closely related to shear-wave velocity, which can be readily converted to the shear modulus of the ground.

Now, let us assume that the scaling factor of strain can be expressed with α as

$$\lambda_\varepsilon = \lambda^\alpha \tag{7}$$

Then, from Eq. (2), scaling of time becomes

$$\lambda_t = \lambda^{0.5(1+\alpha)} \tag{8}$$

Scaling of time for the generalized scaling relation is expressed as

$$t_p = \mu^{0.5(1+\alpha)} \eta t_m \tag{9}$$

where t_p and t_m are, respectively, time in the prototype and the model.

Table 4. Parameters for correction of time scaling in the phase of excess pore-pressure dissipation

	Sacling factor of length						Scaling factors			
	1 G	Centrifuge					Time	Displacement		
	μ	η	t_1	t_2	Δt_m	α	$\mu^{\alpha}\eta$	$\mu^{\alpha+1}\eta$	$(V_s)_p/(V_s)_m$	G_p/G_m
5A50	20	5.0	50.0	261.6	211.6	-0.08	20.0	79.8	5.00	2.24
10A50	10	10	44.7	242.8	198.2	-0.39	20.2	40.7	4.96	2.23
50A50	2.0	50	19.5	81.8	62.3	-0.16	66.8	89.2	1.50	1.22
70A50-2	1.4	70	12.1	63.3	51.2	0.50	91.5	119.5	1.09	1.05
5B50	20	5.0	151.5	402.2	250.8	-0.20	16.5	54.3	6.07	2.46
5B89	20	5.0	107.7	216.5	108.7	0.43	42.5	362.0	2.35	1.53
10B50	10	10	139.0	302.8	163.8	-0.19	25.3	63.9	3.96	1.99
10B75	10	10	82.4	194.4	112.0	0.20	39.6	157.1	2.52	1.59
50B50	2.0	50	30.6	82.5	51.9	0.92	97.2	188.8	1.01	1.01

Next, parameter α is fitted with experimental results. Here, the duration time for the excess pore-water dissipation measured at PW31 of test 70A50-2, Δt_p^{70}, in prototype scale, is taken as a reference value to be fitted. Then, by assuming that the duration times for dissipation at PW31 of other tests, Δt_p, in prototype scale, are equal to Δt_p^{70}:

$$\Delta t_p = \Delta t_p^{70} \tag{10}$$

Rewriting Eq. (10) with the generalized scaling factors given in Eq. (9), with time in model scale, Δt_m and Δt_m^{70},

$$\mu^{0.5(1+\alpha)} \times \eta \times \Delta t_m = \mu_{70}^{0.5(1+\alpha)} \times \eta_{70} \times \Delta t_m^{70} \tag{11}$$

where $\mu_{70} = 1.4$ and $\eta_{70} = 70$ are scaling factors, respectively, in the virtual 1-g and 70-g centrifuge model tests. Here, the duration time for dissipation in model scale is defined as,

$$\Delta t_m = t_2 - t_1 \tag{12}$$

where t_1 corresponds to the time when the excess pore-water pressure at PW31 starts to decrease [Figs. 7(a)–(d)] and t_2 is defined at the time when the excess pore-water pressure becomes 5% of the one at time t_1. Solving Eq. (11) for α yields

$$\alpha = 2\left(\log\frac{\eta_{70}\Delta t_m^{70}}{\eta\Delta t_m}\right)\left(\log\frac{\mu}{\mu_{70}}\right)^{-1} - 1 \tag{13}$$

Table 4 shows the computed value of α by substituting Δt_m and Δt_m^{70} into Eq. (13).

In Table 4, the shear-wave ratio is computed by

$$(V_s)_p / (V_s)_m = \mu^{(1-\alpha)/2} \tag{14}$$

and the ratio of shear modulus G_p/G_m is computed by taking the square root of Eq. (14), where G_p and G_m are, respectively, the shear modulus in prototype and model scale.

Figures 7 (a) to 7 (d) show time histories of excess pore-water pressure in model scale. In these figures, duration time for dissipation is indicated by dotted vertical lines. Figures 7(e) to 7(h) are the converted time histories in prototype scale with fitted scaling factors of time listed in Table 4. Here, the scaling for stress—i.e., the magnitude of excess pore-water pressure—is not affected by the fitting procedure.

Ratios of the shear modulus computed with the fitted parameter α in Table 4 show that if the 1-g scaling factor of strain is given as $\lambda_\varepsilon = \mu^{0.5}$ —i.e., $\alpha = 0.5$, then the ratio is assumed to be $G_p/G_m = 0.96$. In this case (70A50-2), it is recognized that the stiffness of the model and the prototype are nearly equal.

For tests with low centrifugal accelerations, 5A50 and 10A50, the values of α are negative, and the ratios are computed to be G_p/G_m(5 g) = 2.24 and G_p/G_m(10 g) = 2.23, which is about two times the one obtained from test 70A50-2, G_p/G_m(70 g) = 1.05 (Table 4). From this computation, if we demand that the shear modulus in prototype scale is constant regardless of the level of centrifugal acceleration, then the shear modulus under low centrifugal acceleration has to be about half of that under high centrifugal acceleration [e.g., G_m(70 g) = 2.1G_m(5 g)]. Thus, in the experiments conducted under low centrifugal acceleration, shear modulus or elastic modulus of the model ground in model scale has to be adjusted smaller than that in high centrifugal accelerations so that an identical duration time of excess pore-water pressure dissipation is achieved in prototype scale.

The fitting for Case B is done by the same procedure by taking the same value of the test 70A50-2 as a reference. In Table 4, the values of parameter α for tests 5B89 and 10B75 are, respectively, 0.43 and 0.20, and the shear modulus ratios are, respectively, G_p/G_m(5 g) = 1.53 and G_p/G_m(10 g) = 1.59, which are smaller than those obtained from tests 5A50 and 10A50 and close to the one in 70A50-2 [G_p/G_m(70 g) = 1.05]. Again, if we demand that shear modulus in prototype scale is identical, we obtain G_m(70 g) = 1.4G_m(5 g) and G_m(70 g) = 1.5G_m(10 g). Thus, to achieve identical duration time for dissipation of excess pore-water pressure with the one under high centrifugal acceleration, the shear modulus in model scale under low centrifugal acceleration has to be larger than that in prototype scale. The discrepancy investigated in this section may be due to the small value of the shear modulus caused by the low confining stress in the model ground under low centrifugal acceleration.

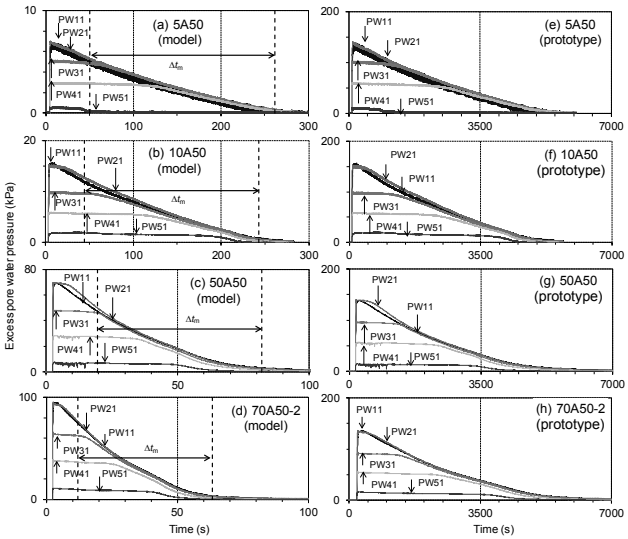


Figure 7. Time histories of excess pore-water pressure build-up for Case A: (a) to (d) model scale, (e) to (h) fitted curves in prototype scale. (h) is shown in Fig. 5(j).

4.3 Possible change of permeability of the model ground due to absorption of the Metolose on sand particles

In the experiment, the Metolose (methylcellulose) was used as a substitute for pore fluid so that scaling for excess pore-water pressure dissipation is satisfied with dynamic conditions (Ko, 1994; Stewart et al., 1998; Dewoolkar et al., 1999). It is known that the viscosity of the methylcellulose is exerted by long chains of micro-fibers (polymers) constituted of cellulose (Stewart et al., 1998). Because of the form of micro-fibers, absorption of the Metolose on sand particles might occur. To investigate the possibility, falling head permeability tests for silica sand No. 7 with a relative density of 40% with water, Metolose solution, and silicone oil were conducted. To conduct the tests, the procedure specified by JIS A 1218:2009 was followed. A metal-mesh net with a 75-μm opening was used as a filter instead of using filter paper in order to prevent clogging of molecular cellulose. Metolose of 2% solution was prepared and adjusted to specific viscosity by adding water. Details of tests can be found elsewhere (Tobita and Iai, 2010, under preparation).

Test results are summarized in Fig. 8. As shown in Fig. 8(a), the permeability of water is kept constant at about 1.0×10^{-2} cm/s. The reduction of permeability after the 11th measurements with water is -4.7%, which can be regarded as no reduction. Meanwhile, as shown in Figs. 8(b) and 8(c), the permeability with the Metolose is consistently decreasing with the number of measurements. For example, the permeability of viscous fluid of 15 mPa s is decreased 44% from 1.46×10^{-3} cm/s to 8.13×10^{-4} cm/s after the 11th measurements. In Fig. 8(d), although the permeability of silicone oil is fluctuating, the permeability is nearly constant for each viscosity.

The reduction in permeability that may be achieved with an increase in pore-fluid viscosity is mostly smaller than the expected values. For example, a reduction in permeability by a factor of 2.4 was recorded for an increase in viscosity of 5 times. This trend has been reported in other research papers (Stewart et al., 1998; Dewoolkar et al., 1999). Stewart et al. (1998) gave possible explanation for this discrepancy that both the Metolose solution and silicone oil may exhibit non-Newtonian behavior, where viscosity is not constant with varying velocity gradients. If this is the case, the reduction ratio of permeability would be different than that of the inverse viscosity ratio.

Based on the permeability test data, the permeability of the model ground during the centrifuge experiments might be slightly decreasing as excess pore-water pressure dissipates with the flow of the viscous fluid. However, no clear trend is found on the permeability change with the magnitude of viscosity. Further investigation is necessary to identify the effect of the absorption on the reduction of permeability.

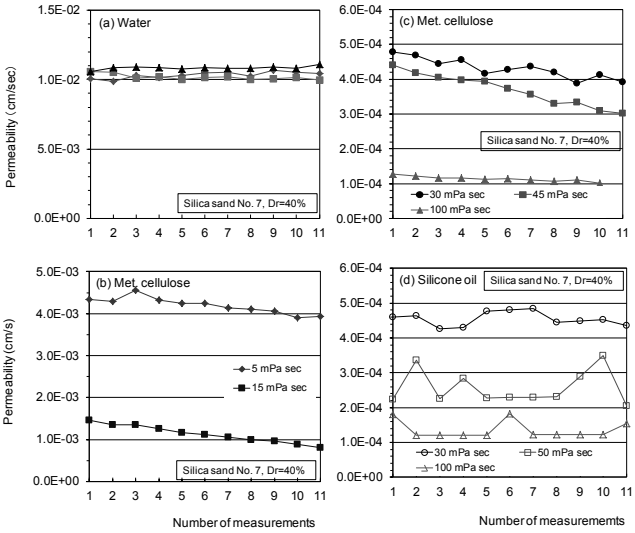


Figure 8. Variation of permeability with the number of measurements: (a) water, (b) methylcellulose of 5 and 15 mPa s, and (c) methylcellulose of 30, 45, and 100 mPa s, and silicone oil of 30, 50, 100 mPa s.

5. CONCLUSIONS

To investigate the applicability of the generalized scaling law in dynamic centrifuge tests on a flat, saturated sand deposit, the modeling-of-models technique was implemented in centrifugal accelerations ranging from 5 to 70 g, and the results were compared in prototype scale. In the tested range of an overall scaling factor of 1/100, the applicability of the generalized scaling law was confirmed for the time range during dynamic excitation. Only the ground settlement in this time range varied among the cases with different centrifugal accelerations. One of the causes might be the target device for the laser displacement transducers, which might not be stable under shaking conditions. Additional care has to be given to measurements of displacement because in the generalized scaling law the scaling factor of displacement tends to be very large, and in turn very sensitive to the measurements.

In the time histories of pore-water dissipation and surface settlements, two cases below 10 g showed much larger duration time for excess pore-water pressure dissipation. Investigations are carried out for (1) the effect of duration time for consolidation before shaking, (2) the effect of low effective confining stress on the scaling law, and (3) possible change of permeability of the model ground due to absorption of methylcellulose polymer on sand particles. A major cause of the discrepancy might be the small value of elastic stiffness due to low confining stress in the model ground under low centrifugal experiments. From results of the permeability tests, use of the Metolose to simulated dissipation behavior is questioned because of the possibility of the absorption on sand particles.

Acknowledgements:
The authors acknowledge that experimental works reported in the present paper are mainly conducted by Ms. Loretta von der Tann (former graduate student at ETH Zurich, Switzerland, visiting research student at Kyoto University, Japan) and Mr. Yuji Yaoi (current graduate student at Kyoto University, Japan.) as part of their graduation thesis.

References:

Craig, W. H. (1984), "Centrifuge modelling for site-specific prototypes. *Proc. Symp. Application of Centrifuge Modelling to Geotechnical Design*," University of Manchester, Balkema, Rotterdam, 473–489.

Dewoolkar, M. M., Ko, H.-Y., Stadler, A. T. and Astaneh, S. M. F. (1999), "A substitute pore fluid for seismic centrifuge modeling. *Geotechnical Testing Journal*," ASTM **22**(3), 196–210.

Einde, V. D., Restrepo, L., Conte, J. P., Luco, E., Seible, F., Filiatrault, A., Clark, A., Johnson, A., Gram, M., Kusner, D. and Thoen, B. (2004), "Development of the George E. Brown Jr. network for earthquake engineering simulation (NEES) large high performance outdoor shake table at the University of California, San Diego." *Proceedings of the 13th World Conference on Earthquake Engineering*, Vancouver, BC, Canada, 1-6 August, Paper No. 3281.

Garnier, J., Gaudin, C., Springman, S. M., Culligan, P. J., Goodings, D., Konig, D., Kutter, B., L., Phillips, R., Randolph, M. F. and Thorel, L. (2007), "Catalogue of scaling laws and similitude questions in geotechnical centrifuge modelling." *International Journal of Physical Modelling in Geotechnics*, 7, No. 3, 1–23.

Gaudin, C., White, D. J., Bezuijen, A., Schaminee, P. E. L. and Garnier, J. (2010), "Physical modelling with industry — overview of practices and benefits," *Physical Modelling in Geotechnics*, Springman, Laue & Seward (eds.). Taylor & Francis Group, London, ISBN 978-0-415-59288-8.

Iai, S. (1989), "Similitude for shaking table tests on soil-structure-fluid model in 1g gravitational field," *Soils and Foundations*, **29**(1), 105–118.

Iai, S., Tobita, T. and Nakahara, T. (2005), "Generalized scaling relations for dynamic centrifuge tests," *Géotechnique*, **55**(5), 355–362.

Ko, H.-Y. (1994), "Modeling seismic problems in centrifuges," *Centrifuge 94*, Leung, Lee & Tan (eds.), Balkema, Rotterdam, ISBN 90 5410 352 3 No. 3-12.

Schofield, A. N. (1980), "Cambridge geotechnical centrifuge operations," *Géotechnique*, **30**(3), 227–268.

Shin-Etsu Chemical Co., L. (1997), "Metolose Brochure," Cellulose Dept., 6-1, Ohtemachi 2-chome, Chiyoda-ku, Tokyo, Japan.

Stewart, D. P., Chen, Y.-R. and Kutter, B. L. (1998), "Experience with the use of Methylcellulose as a viscous pore fluid in centrifuge models," *Geotechnical Testing Journal*, **21**(4), 365–369.

Tann, L. v. d., Tobita, T., and Iai, S. (2010). "Applicability of two stage scaling in dynamic centrifuge tests on saturated sand deposits." *7th International Conference on Physical Modelling in Geotechnics (ICPMG 2010)*, Springman, Laue & Seward (eds), 191-196.

Terashi, M., Katagiri, M. and Ohishi, K. (2004), "Ten years centrifuge operation at a consulting firm," *International Journal of Physical Modelling in Geotechnics*, **4**(1), 1–10.

Tobita, T., Iai, S., and Noda, S. (2009). "Study on generalized scaling law in centrifuge modeling with flat layered media." *Proceedings of the 17th International Conference on Soil Mechanics and Geotechnical Engineering (17th ICSMGE)*, M. Hamza et al. (Eds.), 664-667.

Tobita, T., Iai, S., and Tann, L. v. d. (2010). "Application of the generalized scaling law to saturated ground." Submitted to the *International Journal of Physical Modelling in Geotechnics*.

Tobita, T. and Iai, S. (2010), "Limitation of methylcellulose as a viscous pore fluid in physical model testing," (Under preparation for publication.)

Tokimatsu, K., Suzuki, H., Tabata, K. and Sato, M. (2007), "Three dimensional shaking table tests on soil-pile-structure models using E-Defense facility," *4th International Conference on Earthquake Engineering*, June 25–28, Thessaloniki, Greece.

White, D. J., Take, W. A. and Bolton, M. D. (2003), "Soil deformation measurement using particle image velocimetry (PIV) and photogrammetry," *Géotechnique*, **53**(7), 619–631.

8CUEE CONFERENCE PROCEEDINGS
8th International Conference on Urban Earthquake Engineering
March 7-8, 2011, Tokyo Institute of Technology, Tokyo, Japan

BLAST-INDUCED LIQUEFACTION FOR EARTHQUAKE STUDIES

Michael Eller[1] and Scott A. Ashford[2]

1) Staff Engineer, Geotechnical Engineering, CH2M HILL, Corvallis, Oregon, U.S.A.

2) Professor and Head, School of Civil and Construction Engineering, Oregon State University, Corvallis, Oregon, U.S.A.

michael.eller@ch2m.com, scott.ashford@oregonstate.edu

Abstract: Liquefaction is a critical seismic design issue for geotechnical engineers who are concerned with minimizing damage to lifelines and to maintain performance during and immediately following an earthquake. One developing research tool that may give more insight into liquefaction behavior of soils and structures is through the use of controlled blasting. Initially used as a ground improvement technique, controlled blasting has expanded its applicability to full-scale in-situ liquefaction experiments. In order to promote interest in the emerging topic, this paper aims to provide background into the use of blasting, the mechanics behind the method, existing empirical models to predict soil response, and a presentation on a newly developed empirical model that can be used for blasting studies utilizing multiple blasts.

1. INTRODUCTION

The framework for the understanding of liquefaction began with post-earthquake investigations and laboratory testing. Based upon these observations and results, empirical models were developed that integrate in-situ testing measurements, such as the standard penetration test (SPT), cone penetration test (CPT) or shear-wave velocity measurements, into the liquefaction assessment. Although these models have shown to be applicable for "textbook" liquefiable soils (i.e. loose, saturated clean sands to silty sands), there are some recognized limitations to these methods.

One critical limitation is that these models can become unreliable for gravels, clays, and silts that can be susceptible to strength loss following an earthquake (Bray and Sancio, 2006). Secondly, the laboratory tests that helped form the models may have included uncertainties such as sample disturbance, sample size, misrepresentation of existing conditions of the site, and human error. Therefore, to minimize some of the uncertainties and limitations in performing liquefaction assessments, in-situ testing has been proposed as the supplemental but refining step in the efforts to understand liquefaction, including soil susceptibility and behavior. Testing soil in its in-situ state is highly advantageous as it can minimize effects due to sample disturbance and can account for existing stress conditions.

Current methods emerging as in-situ testing tools include vibroseis and controlled blasting. Vibroseis utilizes a large vibrator applied at the ground surface to induce shear strains at a constant rate to create pore pressure buildup within the soil (Chang et al. 2007). Controlled blasting utilizes detonation of buried explosives, and can generate excess porewater pressures as the shock wave passes through the soil.

2. CONTROLLED BLASTING

2.1 History

Controlled blasting began as a ground improvement to densify loose soils such as embankments and mine tailings (Narin van Court and Mitchell 1994). Prompted by military interest, controlled blasting studies were performed to determine the radius of liquefaction for various types of explosives (Charlie et al. 1988). Recently, blasting has been integrated into seismic studies to initiate liquefaction for several different projects, including a pile behavior (Ashford et al. 2004) and performance of lifelines (Sugano et al. 2002, PARI 2009). Rollins et al. (2004) and Gohl et al (2001) discuss the use of blasting to perform in-situ liquefaction evaluations as a supplement to existing methods.

2.2 Mechanics of Blasting

The effectiveness of blasting is highly influenced on the site conditions, such as soil and rock properties and groundwater conditions, and blasting parameters, including charge weight per unit volume of soil, placement, delay time, and sequence (Charlie 1988). Generally, denser soils require more explosive energy (i.e. charge weight) as they exhibit greater shear strength than looser soils. Also, more explosive energy is required as the distance between the explosive and intended liquefaction area is increased due to attenuation. During blasting, shock waves travel radially from the source throughout the soil as a compression wave. When interfaces are encountered, such as rock-soil boundaries, water table, or ground surface, shear waves and surface waves can be

generated, imparting energy into the blast area. An example of generalized wave paths is shown on Figure 1. A point of interest, as shown in Figure 1, will feel the compression waves first as they travel faster than shear waves. The controlling wave is determined by the distance between the energy source and the point of interest. The compression waves "subject the soil to large and abrupt, albeit short-lived, pressure and strain pulse" (Dowding and Hryciw 1986), but they attenuate much quicker than shear waves. This is observed in earthquakes where the source is tens to hundreds of kilometers away, causing the controlling wave to be shear waves. However, in blasting, the compression waves are the controlling wave due to the short distances separating source to point of interest.

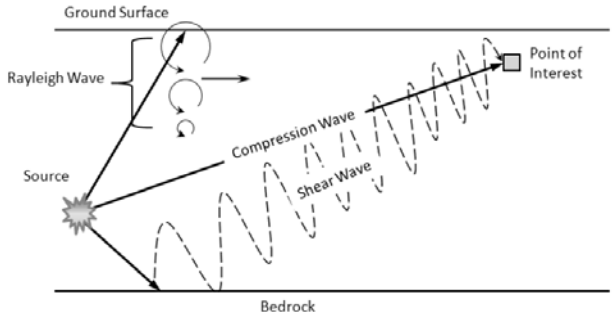


Figure 1 Generalized Wave Paths from an Explosion

Initially, large single explosions were used to liquefy soil. However, it was found that this was ineffective, particularly for ground improvement methods, as it caused cracking in overlying soils and substantial heat loss (Narin van Court and Mitchell 1994). Time-delayed multiple blasts have been used to cyclically load the soil, inducing shear strains in the soil. If the strains are large enough to weaken the soil structure, excess pore pressures can be generated. During undrained conditions, the excess pore pressures lead to a reduction in the effective stress of the soil, leading to a complete loss of shear strength when the excess pore pressure is equal to the initial effective stress. At this state, liquefaction has occurred.

During blasting, a soil will experience three distinct pore pressure response stages: (1) peak, or transient, pore pressure that is attributed to the compression wave, (2) excess (residual) pore pressure, and (3) dissipation of pore pressure. These stages are illustrated in generalized example shown in Figure 2, which show three blasts detonated at time intervals of 1.0 second. The peak pore pressures can exceed the liquefaction level of Ru = 1.0, but they are short-lived. As the excess pore pressures dissipate, the soil transition from their suspended state due to liquefaction and settle, generally rearranging themselves into a denser state than pre-blasting conditions.

2.3 Predicting Pore Pressure Response

Several studies have been conducted to predict pore pressure response with blasting. The general method is to relate excess pore pressure represented by the residual pore pressure ratio, Ru, to the scaled distance, $R/W^{0.33}$, where W is the TNT-equivalent charge size in kilograms, and R is the radial distance between the point of interest and the explosive charge in meters. The inverse of the scaled distance is also used, and is referred to as the Hopkinson's Number (Narin van Court and Mitchell 1994). Other methods predict pore pressure response by peak particle velocity or compressive strain (Charlie 1988, Al-Qasimi et al. 2005).

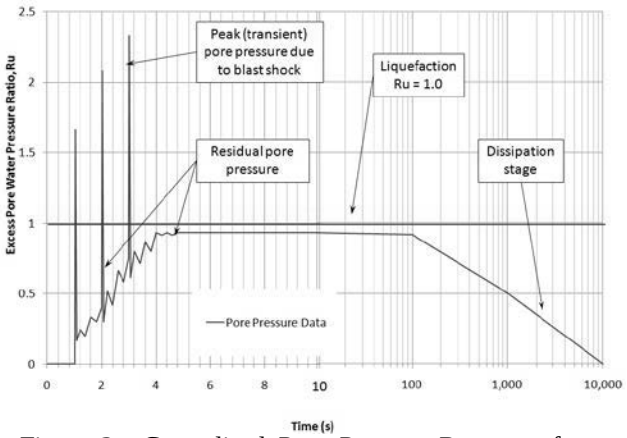


Figure 2 Generalized Pore Pressure Response from an Explosion

Much of the past research in estimating excess pore pressures was centered in saturated sandy soils using single blasts. The first such study observed that liquefaction typically occurred between $R/W^{0.33}$ values of 6 to 8 for a sandy soil with a relative density of 30 to 40% (Ivanov 1967). The most commonly referenced empirical method is the Studer and Kok (1980) relationship developed from a blasting study in Amsterdam Harbor using single blasts. Their method, based on scaled distance, is represented by the following equation and Figure 3:

$$Ru = 1.65 + 0.64 \ln \frac{W^{0.33}}{R} \qquad (1)$$

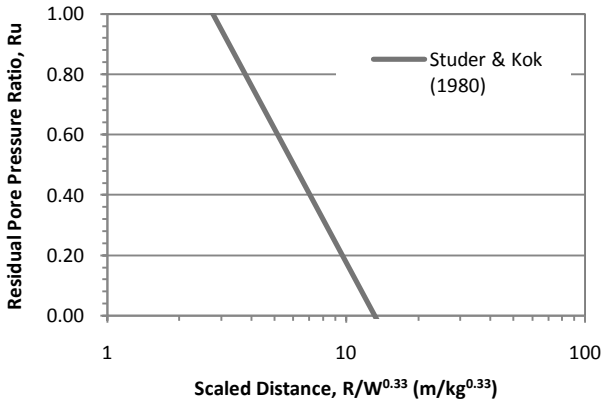


Figure 3 Studer & Kok (1980) Empirical Model predicting residual pore pressure with blasting

2.4 Motivation for Research

In evaluating the current methods used to relate pore pressure buildup with blasting, there are 2 significant limitations associated with these models, particularly the main referenced model by Studer and Kok (1980). The first limitation is that the empirical model does not consider soil conditions when predicting pore pressure response, as it is solely based on charge weight and distance between explosive and point of interest. Generally, denser soils would require more energy to cause contraction and resulting excess pore pressure than loose soils but this is not accounted for or consider with the models.

Secondly, current practice today uses multiple blasts to induce liquefaction rather than the large single blasting program used to develop these models. To induce pore pressure generation within a soil, more energy is required to do it in one blast (i.e. 1 cycle) than in multiple blasts due to cyclic loading. Therefore, an empirical model for single blasts would not be applicable to using multiple blasts for it may underestimate the scaled distance (i.e. representing more energy) for a specific *Ru* value. Therefore, it was deemed that it would be beneficial for the future development of blasting for liquefaction studies to refine the methods used previously to account for multiple blasting and in-situ soil conditions.

3. Development of a Refined Empirical Model

3.1 Accounting for Multiple Blasts

Generally, most of the empirical models relate *Ru* with the scaled distance, $R/W^{0.33}$. The scaled distance is easily calculated for single blasts, but it became unclear how to account for multiple blasts where the distances, weights, and time delays all affect development of *Ru*. Therefore, the following assumptions were made prior to conducting the research:

- The magnitude of pore pressure generated from each sequential blast is influenced by the previous blast and resulting *Ru*. A blast of the same scaled distance will have a different effect on the soil when $Ru = 0$ versus when $Ru = 0.5$.
- Time delays between blast are short enough to minimize significant pore pressure dissipation
- Blasting pattern was not a significant factor in pore pressure generation.

Therefore, from these assumptions, a general method to account for pore pressure generation with multiple blasts was established, and is represented by the following equation:

$$R/W^{0.33} = \frac{\overline{R}}{\Sigma W^{0.33}} = \frac{\left(\frac{R_1+R_2+\ldots R_i}{N_i}\right)}{\Sigma(W_1+W_2+\ldots W_i)^{0.33}} \qquad (2)$$

Where *R* is the radius in meters, *W* is the equivalent charge weight to TNT in kilograms, *N* is the number of blasts, and *1,2,* and *i* denote the associated distance and weight of the charge number.

3.2 Case Histories

After establishing a method to account for multiple blasts, several case histories were selected to development a potential empirical model.

Table 1 – Blast-Induced Liquefaction Case Histories

Test Location/Year	Purpose of Study	Principal References
Ishikari, Hokkaido Island, Japan (2007)	Observe resiliency of airport infrastructure subjected to liquefaction	PARI (2009)
Vancouver, British Columbia., Canada (2004)	Evaluate performance of vertical earthquake drains to mitigate liquefaction	Rollins (2004) Strand (2008)
Maui, Hawaii, USA (2004)	Assess in-situ liquefaction potential of coralline sands	Rollins et al (2004)
Tokachi, Hokkaido Island, Japan (2002)	Performance of piles, pipelines, and quay walls against lateral spreading	Ashford & Juirnarongrit (2004)
Delta, British Columbia., Canada (2004)	In-situ liquefaction evaluation to supplement other data	Gohl et al. (2001)
Treasure Island, San Francisco, California, USA (1998)	Determine lateral load-displacement relationships for piles subjected to liquefaction	Ashford & Rollins (2002) Ashford et al. (2004)
Fort McMurray, Alberta, Canada (1997)	Investigating the potential for blasting as a liquefaction assessment technique	Pathirage (2000)

From the references presented in Table 1, in-situ soil conditions, blasting layout, and pore pressure results were collected. There are several other case histories performed in the past three decades, but these were deemed as being the most useful towards the research due to the available data. Based upon the pore pressure results and blasting layout, and utilizing Eq. (2), *Ru* was plotted against $R/W^{0.33}$ for each case history. The results are shown in Figure 4.

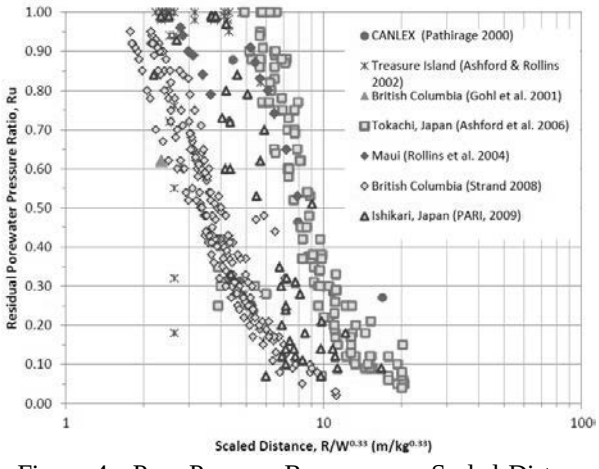


Figure 4 Pore Pressure Response vs. Scaled Distance for Multiple Blasts

Of the case histories analyzed, no two were alike. The tests varied in soil type, density, overlying soils, aging effects, blasting layout, time delays, and many others. However, the goal of the research was to develop an empirical model that could better predict pore pressure generation from blasting.

From Figure 4, it is observed that the pore pressure results all follow a trend of increasing *Ru* with decreasing scaled distance. However, the range of scaled distance for a given *Ru* value, such as 1.0, varies from 2.1 to approximately 7 m/kg$^{0.33}$. In a different view, at a scaled distance of 7 m/kg$^{0.33}$, *Ru* values range from 0.07 to 1.0. This shows that using scaled distance alone to relate to *Ru* is not sufficient. It may be better to account for soil conditions which can affect pore pressure development.

3.3 Regression Analysis

To identify the influence of in-situ soil conditions on predicting blast-induced pore pressure development, several multiple regression analyses were performed. The soil parameters used in the analyses included corrected SPT $(N_1)_{60}$ values, initial relative densities (D_r), corrected shear wave velocities (v_{s1}) initial effective overburden pressure (σ'_{vo}) and the cyclic resistance ratio (*CRR*) as determined from the Youd et al. (2001) method. The scaled distance $R/W^{0.33}$ was used to represent blasting conditions. The results from the analysis, represented by the adjusted correlation scoefficient R^2, are shown below in Table 2. The adjusted correlation coefficient R^2, describes the variability of the predicted data (i.e. *Ru*) as explained by the predictors (i.e. scaled distance, in-situ conditions), and forecasts how well future events are able to be predicted by the model by describing the linear association of the dependent factor to the regressors. A R^2 value of ±1.0 indicates a good fit of the model to the data.

Table 2 – Results from Multiple Regression Analyses

	Blasting Parameters		In-situ Soil Parameters					
Test	Ru	R/W$^{0.33}$ m/kg$^{0.33}$	Relative Density, Dr %	Effective Overburden Stress, σ'v kPa	SPT N-value $(N_1)_{60}$	Cyclic Resistance Ratio, CRR	Shear Wave Velocity, v_{s1} m/s	Adjusted Correlation Coefficient, R^2
1	X	X						0.43
2	X	X	X					0.49
3	X	X		X				0.52
4	X	X			X			0.57
5	X	X				X		0.53
6	X	X					X	0.56
7	X	X		X	X			0.64
8	X	X		X	X	X		0.60
9	X	X		X	X		X	0.62
10	X	X	X	X	X	X	X	0.64
11	X	X			X	X	X	0.62

The regression results shown in Table 2 provide many helpful insights into understanding what has a significant role in predicting blast-induced pore pressure response. When looking at the first test that only considered blasting parameters, the R^2 value of 0.43 confirms that this parameter alone is not a sufficient parameter to estimate blast-induced pore pressure. Test #7, which included SPT $(N_1)_{60}$ values and initial effective overburden pressure (σ'_{vo}) in the analysis, provided the better and most practical model with a R^2 value of 0.64. This is considered the most practical of the models as SPT blowcounts are typically performed in the field prior to testing.

The equation for the empirical model from test #7 provides a logarithmic fit that is consistent with previous models. The equation is as follows:

$$Ru_{multiple-log} = 1.747 - 0.512 \ln\left({}^{R}/_{W^{0.33}}\right) - 0.032(N_1)_{60} - 0.002\sigma'_{v0}\,(kPa) \quad (3)$$

A p-value test was performed to evaluate the reasonableness of including a parameter in the regression analysis. The p-value test indicated that both the SPT $(N_1)_{60}$ value and initial effective overburden pressure (σ'_{vo}) are valid predictors in the analysis. As shown by the equation, the *Ru* value is decreased by increasing SPT $(N_1)_{60}$ values and initial effective overburden pressure (σ'_{vo}). This coincides with the fundamental understanding of inducing pore pressure: denser soils require more energy than looser soils. An example of the model with SPT $(N_1)_{60}$ of 5 and σ'_{vo} of 50 kPa is plotted in Figure 5.

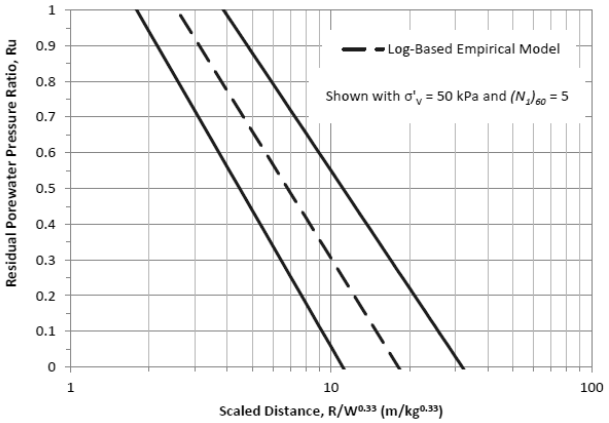


Figure 5 Empirical Model developed for Multiple Blasts (shown with 95% confidence limits)

Although this model can be compared to previous blasting tests, the best and most scrutinizing test would to perform a field blasting experiment. Some uncertainties and limitations that may exist include:

- Consideration of blasting layout. It was observed that simpler layouts (with less than 30 blasts) were better represented by the model than larger, more complex layouts.
- Time delays between blasts may be a factor if significant drainage is occurring within the soil.
- The model was developed for a bounded range of vertical effective overburden stress from 14 to 136 kPa, and SPT $(N_1)_{60}$ values from 1 to 16 blows per 30 cm.

4. CONCLUSIONS

Once used as a ground improvement technique, controlled blasting is developing into a useful research tool to induce excess pore pressures for in-situ liquefaction research. Currently, there are several empirical models to blast-induced pore pressure but to the authors' understanding, they typically do not consider in-situ soil conditions but are solely based on blasting parameters as represented by the scaled distance. Through the use of several controlled blasting case histories, a statistical analysis was performed to identify whether residual pore pressure could be predicted based upon the blasting layout and in-situ soil conditions for multiple blasts.

An empirical model that factors in soil density as represented by SPT $(N_1)_{60}$ values and initial effective overburden pressure (σ'_{vo}) with scaled distance, $R/W^{0.33}$ was developed with a R^2 value of 0.64. This R^2 value indicates that the model does not consider all factors affecting pore pressure development during blasting. However, it is anticipated that the model will provide a better fit than previous models, and is more versatile in that it can be applied to multiple blasts rather than a single blast, and for a variety of soil types.

The true validity test is to perform blasting experiments and compare field measurements to predicted results. If the model is validated, this information can be used in future blasting studies to serve as a tool in developing blasting layout as a function of soil conditions.

Acknowledgements:
The authors would like to thank the engineers and researchers at Japan's Port and Airport Research Institute, particularly Dr. Sugano and Dr. Nakazawa, for their assistance and collaboration in this research. Also, appreciation is shown to Professor Kyle Rollins of BYU for his contributions of his past work to this research.

References:

Al-Qasimi, E.M.A., Charlie, W.A., and Woeller, D.J. (2005). "Canadian Liquefaction Experiment (CANLEX): Blast-Induced Ground Motion and Pore Pressure Experiments." *Geotechnical Testing Journal*, 28(1), January 2005, pp. 9-21.

Ashford, S.A. and Rollins, K.M. (2002). TILT: Treasure Island Liquefaction Test: Final Report. Report SSRP-2001/17, Department of Structural Engineering, University of California, San Diego.

Ashford, S.A., and Juirnarongrit, T. (2004). Performance of Linelines Subjected to Lateral Spreading. Report SSRP-04/18, Department of Structural Engineering, University of California, San Diego.

Ashford, S.A., Rollins, K.M., and Lane, J.D. (2004). "Blast-Induced Liquefaction for Full-Scale Foundation Testing." *Journal of Geotechnical and Geoenvironmental Engineering.* 130(8), August 2004, pp 798 – 806.

Bray, J.D., and Sancio, R.B. (2006). "Assessment of the Liquefaction Susceptibility of Fine-Grained Soils." *Journal of Geotechnical and Geoenvironmental Engineering.* 132(9), September 2006, pp. 1165 – 1177

Chang, W.J., Rathje, E.M., Stokoe II, K.H., and Hazirbaba, K. (2007). "In Situ Pore-Pressure Generation Behavior of Liquefiable Sand." *Journal of Geotechnical and Geoenvironmental Engineering*, 133(8), August 2007, pp. 921 – 931.

Charlie, W.A., Doehring, D.O., Veyera, G.E., and Hassen, H.A. (1988). Blast Induced Liquefaction of Soils: Laboratory and Field Tests. Air Force Office of Scientific Research, Washington D.C., 184 pp.

Dowding, C.H., and Hryciw, R.D. (1986). "A Laboratory Study of Blast Densification of Saturated Sand." *Journal of Geotechnical Engineering*, 112(2), February 1986, pp. 187 – 199.

Eller, J.M. (2010). Predicting Pore Pressure Response in In-Situ Liquefaction Studies using Controlled Blasting. A Thesis in partial fulfillment of the requirement for the degree of Master of Science, Department of Civil and Construction Engineering, Oregon State University, June.

Gohl, W.B., Howie, J.A., and Rea, C.E. (2001). Use of Controlled Detonation of Explosives for Liquefaction Testing. *Proceedings: Fourth International Conference on Recent Advances in Geotechnical Earthquake Engineering and Soil Dynamics and Symposium in Honor of Professor W.D. Liam Finn*, San Diego, March 26 – 31.

Ivanov, P.L. (1967). Compaction of Noncohesive Soils by Explosions (translated from Russian). National Technical Information Service Report No. TT70-57221. U.S. Department of Commerce, Springfield, VA, 211 pp.

Narin Van Court, W.A., and Mitchell, J.K. (1994). Explosive Compaction: Densification of loose, saturated, cohesionless soils by blasting. Geotechnical Engineering Report No. UCB/GT/94-03. May 1994. 116 pp.

Port and Airport Research Institute (PARI), Japan. (2009). Technical Note of the Port and Airport Research Institute: Full-Scale Field Experiment of Airport Facilities during Liquefaction Induced by Controlled Blasting Technique. Independent Administrative Institution, Port and Airport Research Institute, Japan. 338 pp. (in Japanese).

Pathirage, K.S. (2000). *Critical Assessment of the CANLEX Blast Experiment to Facilitate a Development of an In-Situ Liquefaction Methodology Using Explosives*. Thesis in partial fulfillment of the requirements for the Degree of Master of Science, Department of Civil Engineering, The University of British Columbia, December.

Rollins, K.M. (2004). Liquefaction Mitigation Using Vertical Composite Drains: Full Scale Testing. Final Report for Highway IDEA Project 94. Transportation Research Board, February 2004, 105 pp.

Rollins, K.M., Lane, J.D., Nicholson, P.G., and Rollins, R.E. (2004). "Liquefaction Hazard Assessment using Controlled-Blasting Techniques." *Proc. 11th International Conference on Soil Dynamics & Earthquake Engineering.* Vol. 2, 2004, pp. 630 – 637.

Strand, S.R. (2008). *Liquefaction Mitigation using Vertical Composite Drains and Liquefaction-Induced Downdrag on Piles: Implications for Deep Foundation Design.* A Dissertation in partial fulfillment of the requirement for the degree of Doctor of Philosophy, Department of Civil and Environmental Engineering, Brigham Young University, April 2008.

Studer, J. and Kok, L. (1980). Blast-Induced Excess Porewater Pressure and Liquefaction Experience and Application. International Symposium on Soils under Cyclic and Transient Loading, Swansea, UK, January 7 – 11, pp. 581 - 593.

Sugano, T., Kohama, E., Mitoh, M., and Shiozaki, Y. (2002). Seismic Performance of Urban, Reclaimed and Port Areas – Full Scale Experiment at Tokachi Port by Controlled Blasting Technique. The Earthquake Engineering Symposium Proceedings, Vol. 11, pp. 901 – 906.

Youd, T.L., et al.. (2001). "Liquefaction Resistance of Soils: Summary Report from the 1996 NCEER and 1998 NCEER/NSF Workshops on Evaluation of Liquefaction Resistance of Soils." *Journal of Geotechnical and Geoenvironmental Engineering.* ASCE, 127(10), pp. 817-833.

8CUEE CONFERENCE PROCEEDINGS
8th International Conference on Urban Earthquake Engineering
March 7-8, 2011, Tokyo Institute of Technology, Tokyo, Japan

CENTRIFUGE MODELING ON THE SEISMIC RESPONSES OF SANDY DEPOSIT WITH A THIN SILT SEAM

Chung-Jung Lee[1], Yue-Chen Wei[2], Hon-Chen Lien[2], and Hui-Tsyr Chen[1]

1) Professor, Department of Civil Engineering, National Central University, Taiwan
2) Graduate student, Department of Civil Engineering, National Central University, Taiwan
cjleeciv@cc.ncu.edu.tw, ycwei@hotmail.com.tw, chenhtofpadau@seed.net.tw

Abstract: Three dynamic centrifuge model tests were conducted to simulate the seismic responses of sandy soil deposits with a silt seam embedded at various depths. The model sand beds had the same relative density and were saturated with the same viscous pore fluid and then were subjected to the same magnitude of base acceleration. The aim of this study is to investigate the effect of existence of low-permeability silt seam embedded at the different depths for a level ground on the generation and dissipation of excess pore water pressure, the surface settlements and the related liquefaction mechanism in a loose sand deposit. The test results show that (1) the silt seam in the sand deposit can reduce the extent of liquefaction and surface settlement; (3) the magnitude of surface settlement is proportion to the values of the proposed area ratio; (2) liquefaction occurs only beneath the silt layers on the sand bed with a shallow silt seam. However, for the deeper silt intra-layer, liquefaction occurs not only in the sand beneath the thin silt layers but also in the sand near the ground surface.

1. INTRODUCTION

Soil liquefaction or partial loss of soil strength during earthquakes causes severe damage to geotechnical structure systems (e.g., settlement of buildings, pile damage due to lateral spreading of liquefied soils). Natural soil deposit normally consists of sublayers with different permeability, i.e., thin silt or clay layer. In some cases, the thin silt or clay sublayer may not be indentified by a normal geotechnical exploration procedure. If a silt or clay seam is sandwiched in the sand deposit, an upward flow of excess pore water pressure will form a water film beneath the silt seam (Kokusho 1999). Kokusho (2000) also used a simple consolidation theory to simulate the process of water film growth and decay beneath a thin silt seam. This zero strength of thin water film might result that a lateral spread or slope failure in a liquefied ground took place even after ending of shaking. Malvick et al. (2003) performed a centrifuge shake table test to demonstrate formation of water films and void redistribution. The effect of silt seam on the emergency of water film is the major consequence in lateral spreading. In this paper, a series of 1-D centrifuge shaking table tests was performed to investigate the seismic response, pore water pressure generation and post-liquefaction behavior for a sand deposit intra-layered a silt seam at different depths. Two arrays of accelerometers and pore water pressure transducers were used to monitor the time histories of acceleration and the excess pore water pressure along the depths for loose sand subjected to 1-D shaking.

2. GEOTECHNICAL CENTRIFUGE MODELING AND TESTING PROCEDURES

2.1 Testing Equipments

This experimental work was undertaken in the Centrifuge at the National Central University (NCU), Taiwan. The NCU Centrifuge has a nominal radius of 3 m and equips a 1-D servo-hydraulically controlled shaker integrated into a swing basket. The shaker has maximum nominal shaking force 53.4 kN with maximum table displacement of ±6.4 mm and operates at up to 80 g centrifugal acceleration. The nominal operating frequency range is 0 - 250 Hz. The table payload mounting area is 1000 mm x 546 mm x 500mm. A laminar container with inside dimensions of 711 mm x 356 mm x 353 mm is constructed from 38 light-weight aluminum alloy rings arranged in a stack. Each ring is 8.9 mm in height and is separated from those adjacent to it by roller bearings, specially designed to permit translation in the longitudinal direction with minimal frictional resistance. The laminar container is designed for dry or saturated soil models and permits development of stresses and strains associated with one dimensional wave propagation.

2.2 Tested Sand and Preparation of Sand Bed

A fine quartz sand and a silt were used to prepare the sand deposit. The characteristics of the quartz sand and silt are summarized in Table 1. The permeabilities of quartz and silt are 6.8×10^{-5} and 7.4×10^{-6} (m/sec), respectively. The quartz sand was pluviated with a regular path into the container from a hopper at various falling heights and at a constant flow rate for preparing fairly uniform sand deposits

having various relative densities. The pluviation process was interrupted as needed for embedding the transducers at specified elevations. Before placing thin silt layer at the predetermined elevation the prepared sand bed was saturated with a water-metulos solution (MCE) with a viscosity of 70 times the viscosity of water in advance. The surface of pore fluid rose to 10 mm above the prepared sand surface and then the silt was pluviated with a funnel through the pore fluid into the sand surface. The thickness of silt layer was 10 mm. After leveling the silt surface the quartz sand was pluviated as described before until reaching the predetermined thickness of sand bed. Finally the saturation process was conducted again.

An acrylic plate was used to tightly cover the container for the saturation process of sand. Air was then simultaneously and continuously vacuumed out from both the inside of container and the outside of container and at the same time a water-metulos solution was carefully dripped into the container to saturate the sand bed until the water level rose to 2 mm above the sand surface. Multiple saturation processes for the preparation of sand deposit with a thin layer of silt was required to ensure the test model being fully saturated. Then the centrifuge was accelerated at a 10 g per step until it reached the acceleration of 80 g. In each step the model was maintained and lasted for 5 minutes at this g level to ensure the sand bed reaching full consolidation at the current overburden stress. Finally the model was excited with a one-dimensional sinusoid acceleration consisting of 16 cycles having maximum amplitude of 0.1 g and a frequency of 1 Hz in prototype units. Acceleration, pore water pressure and displacement time histories were recorded simultaneously.

Table 1. Characteristics of fine quartz sand and silt.

	G_s	D_{50} in (mm)	D_{10} in (mm)	ρ_{max} (g/cm^3)	ρ_{min} (g/cm^3)	Prototype permeability (m/sec)
Quartz sand	2.65	0.193	0.147	1.66	1.44	6.8×10^{-5}
Silt	2.65	0.025	0.002	1.53	1.29	7.4×10^{-6}

[1]The maximum and minimum densities of the sand were measured in the dry state, according to the method (JSF T 161-1990) specified by the Japanese Geotechnical Society.

2.3 Testing Setup and Testing Conditions

Figure1 presents a sketch of laminar container to show the dimensions of the tested sand bed, the position of silt layer, and the types and the positions of instrumentation used in the models. Figure 2 shows the test package rested on the shaker. The thickness of model sand bed is 30 cm, simulating a 24 m thick and a 56.8 m long sand deposit at a centrifuge acceleration of 80 g. The sand bed is instrumented with seven vertical spaced accelerometers (A#) to record the shear wave propagating from the base to the ground surface as shown in Figure 1. At the same elevations close to the accelerometers six pore water pressure transducers (P#) were instrumented as well. The accelerometers and the pore water pressure transducers were particularly instrumented at the elevations above and beneath the silt layer for examining the changes in the pore water pressure generation and accelerations. Two LVDTs were installed at the top of surface to measure the time history of surface settlement. An attempt was made to locate transducers in similar locations in each test. This comprehensive instrumentation and detailed measurements are necessary to understand the seismic response of the sand deposit with an intra-silt layer and the associated excess pore water pressure generation at various elevations during 1-D shaking. A total of three centrifuge tests were conducted; the test conditions in prototype for each model are listed in Table 2. Model Test1 was the uniform sand deposit, whereas Model Test2 and Model Test3 were the composite deposits with an intra-silt layer emerging at the depths of 4.8-5.7 m and of 9.6-10.4 m, respectively. The test conditions described in Table2 were used to study the major factors contributing to the liquefaction susceptibility of sand deposit with an intra-silt layer at various depths.

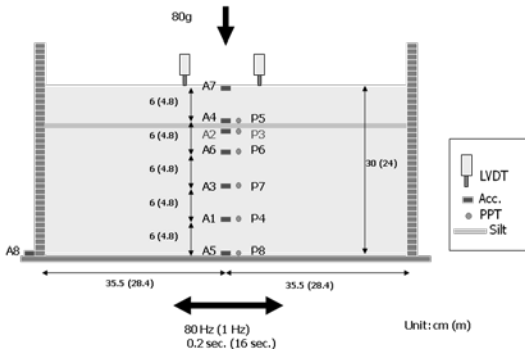


Figure 1 Sketch of laminar container, soil profile and instrumentations used in the models (Test2)

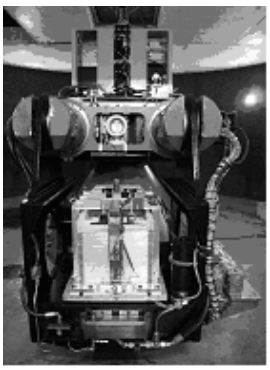


Figure 2 Test package and instrumentations on the shaker

3. TEST RESULTS AND INTERPRETATIONS

3.1 Accelerations on Sand Deposit During Shaking

Figure 3 gives the typical input acceleration time history used in these three tests, in which the maximum input acceleration is around 0.1 g. Figures 4 and 5 presents the comparison of the acceleration time histories measured at different depths for Test1 and Test2 and for Test1 and

Test3, respectively. The long horizontal red bars as shown in Figures 4 and 5 indicate the location of silt layer for Test2 and Test3. The accelerometers of A4 and A2 were located at above and below the silt layer. The attenuation of the acceleration measured at the levels above the depth of 14.4 m is very obvious for Test1. In the case of the silt layer at the depth of 4.8 m (Test2) the high frequency acceleration spikes appear, whereas in the case of the silt layer at the depth of 9.6 m no acceleration spike is observed. The existence of intra-silt layer would greatly modify the seismic responses of the sand deposit above and just beneath the silt layer after comparison of Figures 4 and 5. In addition the embedded depth of silt layer is another factor to influence the seismic response of sand deposit.

Table 2 Summary of testing conditions

Model No.	Dr (%)	Peak input Acc. (g)	Depth of silt layer (m)
Test1	39	0.1	-
Test2	36	0.1	4.8-5.6
Test3	41	0.1	9.6-10.4

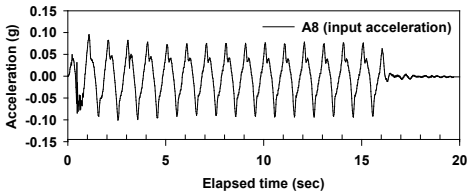


Figure 3 Typical input base acceleration

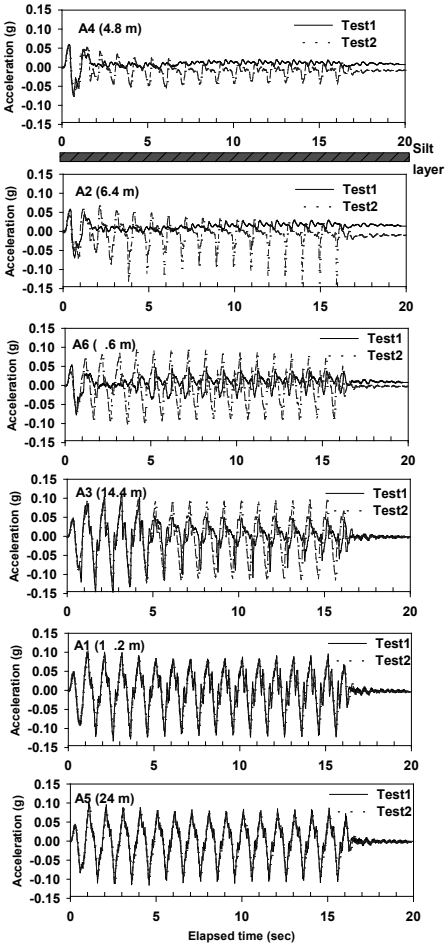


Figure 4 Comparison of acceleration time histories measured at various depths for Test1 and Test2

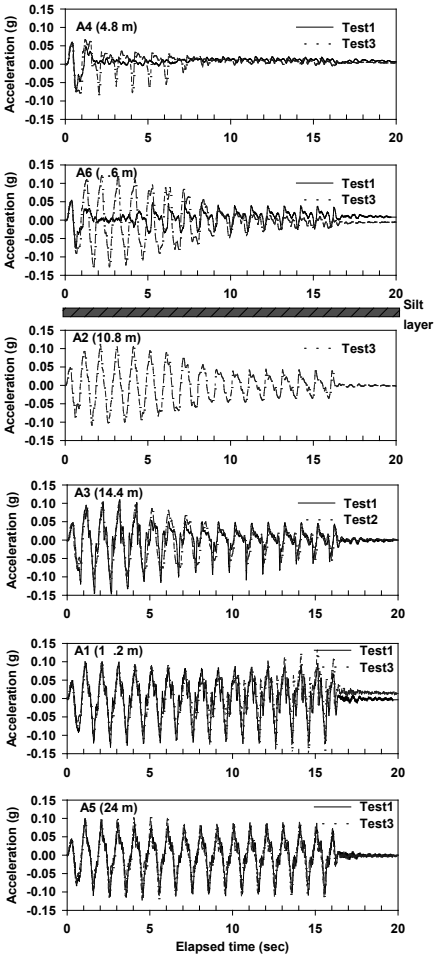


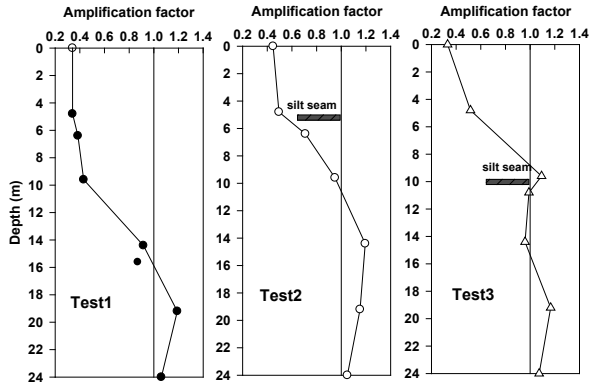
Figure 5 Comparison of acceleration time histories measured at various depths for Test1 and Test3

A single parameter that includes the effects of the amplitude and frequency content of the acceleration time history is the root mean square acceleration (RMS acceleration, a_{rms}), defined as

$$a_{rms} = \sqrt{\frac{1}{T_d}\int_0^{T_d}[a(t)]^2\,dt} \qquad (1)$$

where T_d is the duration of the acceleration and dt is the time interval of the acceleration time history. The larger the RMS acceleration value the higher the energy input to the sand deposit. An acceleration amplification factor is defined as the ratio of the RMS acceleration value measured at different depths to the base RMS acceleration value. Figure

6 presents the RMS acceleration amplification factors, those which were calculated from Test1, Test2, and Test3. The level of the silt seam is also point out with the long red bar in these figures. The amplification factors above the depths of 16 m on the sand deposit without the silt seam (Test1) become less than 1 because of the excess pore water pressure generation. In the deposits sandwiched with the silt seam (Test2 and Test3) the depths at which the amplification factors less than 1 become shallower. The deeper the silt seam embeds the smaller the amplification factor on the ground surface and the less energy input to the ground surface.



(a) (b) (c)

Figure 6 Amplification factors along depths; (a)Test1; (b)Test2; (c)Test3

3.2 Time Histories of Excess Pore Water Pressure in Sand Deposit During And After Shaking

Figures 7, 8 and 9 display the time histories (log scale) of excess pore water pressure ratio, r_u , along the depths for Test1, Test2, and Test3. The excess pore water pressure ratio is defined as the measured excess pore water pressure (Δu) divided by the corresponding effective overburden pressure ($\sigma_v^{'}$).That is:

$$r_u = \frac{\Delta u}{\sigma_v^{'}} \qquad (2)$$

These three figures demonstrate that the patterns of the excess pore water pressure generation and dissipation are quiet different on the sand deposits without and with the silt seam sandwiched at various depths, respectively. For uniform sand deposit the thickness of liquefaction extended from the depth of about 15 m to the surface and liquefaction occurred very early (the 2nd sec) and liquefying lasted for about the 100 seconds (Figure 7). For the sand deposit sandwiched with the shallow silt seam, in contrast, liquefaction only took place beneath the silt seam layer (between 6m to 10 m) and liquefying emerged in the later shaking periods and lasted for the 400 seconds (Figure 8). For the sand deposit sandwiched with the deeper silt seam liquefaction also occurred very early (the 2nd sec) in the top layer but liquefying only lasted for 40 seconds. The liquefaction also appeared beneath the silt seam in the later shaking periods and liquefying lasted for about 100 seconds on the deposit just beneath the silt seam as shown in Figure 9. The time required for the excess pore water fully dissipation on these three sand deposits are different. The required dissipation time is longest for the sand deposit sandwiched with the deeper silt seam and shortest for the sand deposit without silt seam, and in between for sand deposit sandwiched with the shallow silt seam. The existence of the silt seam would lengthen the time of dissipation on the excess pore water pressure.

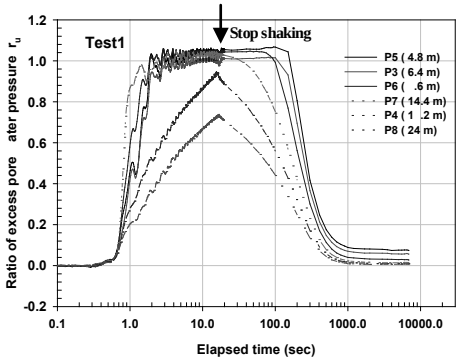


Figure 7 Time histories of r_u at various depths for Test1

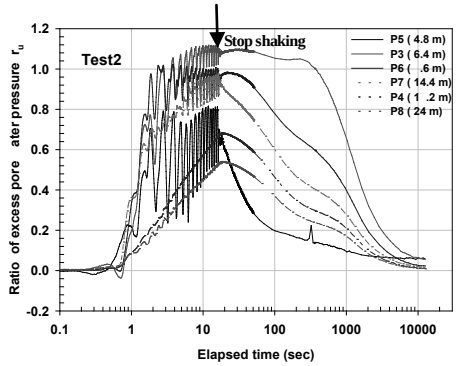


Figure 8 Time histories of r_u at various depths for Test2

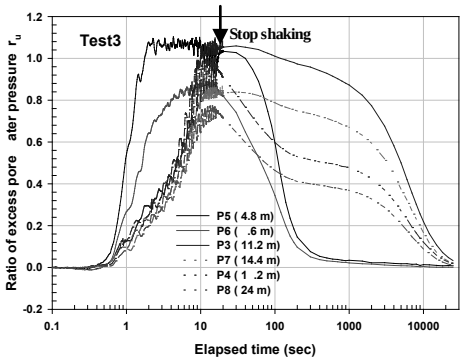
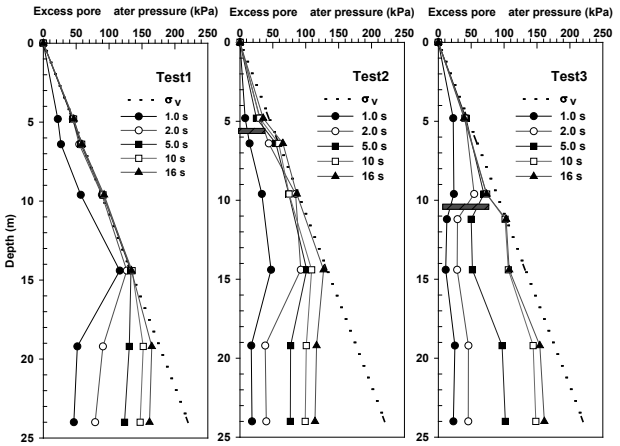


Figure 9 Time histories of r_u at various depths for Test3

Figure 10 demonstrates the excess pore water pressure distribution along the depths at various elapsed times during shaking period for Test1, Test2, and Test3. The horizontal red bars as shown in Figures10 indicate the locations of silt layer for Test2 and Test3. In the case of the uniform sand deposit the largest excess pore water pressure first emerged at the depth of around 15 m in the beginning of shaking and

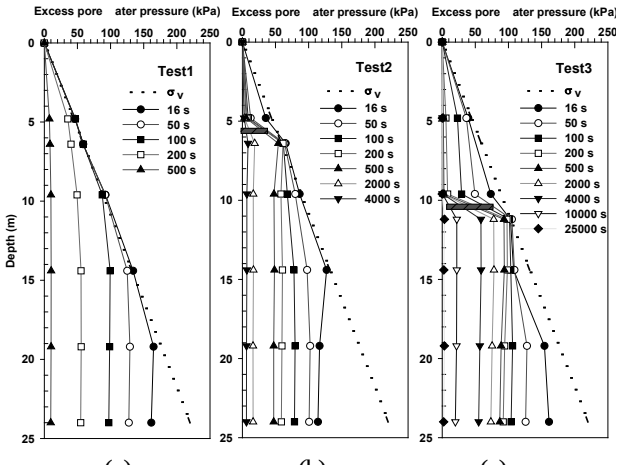
then the excess pore water pressure increased from this elevation both toward the top and the bottom layers. Finally the layer of the top 15 m fully liquefied at the end of shaking. In contrast, in the cases of sand deposit with the silt seam, the excess pore water pressure generation occurred concurrently, both in the upper layer and lower layer. The excess pore water pressure on the top of silt seam was smaller than that below the silt seam for the deposit with the shallow seam, while it was larger in the beginning of shaking for the deposit with deeper silt seam until after 5 seconds.

Figure 11 demonstrates the processes of excess pore water pressure dissipation along the depths at various elapsed times after shaking period for Test1, Test2, and Test3. The elevations of the silt seam on the Test2 and Test4 are also shown in the figure. In the uniform sand deposit the pore water pressure dissipates from the bottom layer to the surface (Figure 11(a)). In contrast, the sand deposits with silt seam, the excess pore water pressure dissipate



(a) (b) (c)

Figure 10 Distribution of excess pore water pressure along depths at various elapsed times during shaking period: (a) Test1; (b) Test2; (c) Test3

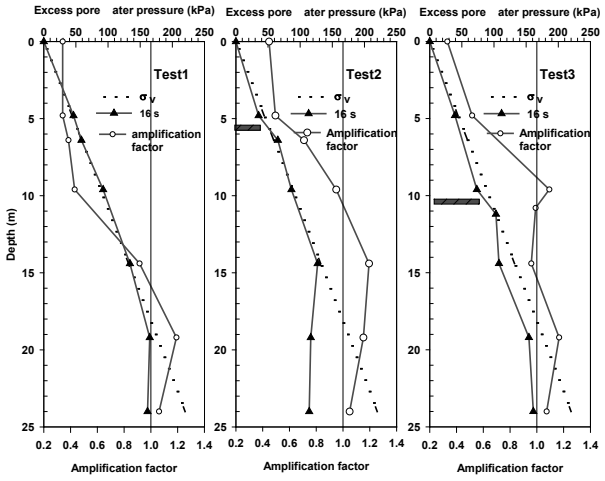


(a) (b) (c)

Figure 11 Distribution of excess pore water pressure along depths at various elapsed times after shaking period: (a) Test1; (b) Test2; (c) Test3

simultaneously, both in the upper and lower layers. The gaps of elevations of silt seam are very obvious and implies that the the excess pore water pressure distribution at the silt seam would experience the seepage flow from the lower layer through the silt seam to the top layer with the higher hydraulic gradient during dissipation period. In addition, the accumulated the excess pore water pressure equal to the effective stress beneath the silt seam lasts for almost 500 seconds. The water film as described by Kokusho (2000) is expected to form beneath the silt seam and lasted for considerable time after shaking.

Figure 12 demonstrates the distribution of excess pore water pressure at the instant of stopping shaking and the amplification factor profiles along the depths for Test1, Test2, and Test3. The greatest amplification factor occurs approximately at the elevation where the effective stress is approximately equal to 0 as shown in Figure 12(a) and 12(b). In the case of sand deposit with deeper silt seam the patterns of excess pore water pressure distribution and of the amplification factor profile in the upper layer are similar to those appeared in lower layer for Test1 and Test2.



(a) (b) (c)

Figure 12 Distribution of excess pore water pressure at stopping shaking and the amplification factor profiles along the depths: (a) Test1; (b) Test2; (c) Test3

3.3 Surface Settlement and Excess Pore Water Pressure in Sand Deposit During And After Shaking

Figure 13 displays the time histories of surface settlement for Test1, Test2, and Test3. There was the largest surface settlement in the uniform sand deposit (Test1) after the excess pore water pressure fully dissipated and the second largest surface settlement in the sand deposit with deeper silt seam (Test3), and the smallest settlement in the sand deposit with the shallower seam in between (Test2). The existence of the silt seam can reduce the extent of liquefaction as shown in figure 10 in the sand deposit and decreases the surface settlement. A concept that the magnitude of surface settlement is proportion to the area ratio, which is defined as the confined area by the excess

pore water pressure profile along the depths divided by the area confined by the effective overburden stress as shown in Figure 10, at the instant of stopping shaking is proposed to evaluate the maximum surface settlement. Figure 14 illustrates the confined area by the excess pore water pressure profile as shown in Figure 10 divided by the area confined by the effective overburden stress. The larger area ratio represents the more great extent of liquefaction in the sand deposit and would cause the larger surface settlement.

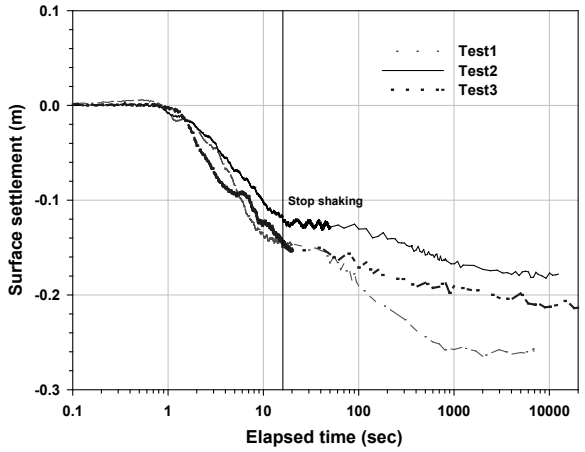


Figure 13 Time histories of ground settlement for Test1, Test2, and Test3

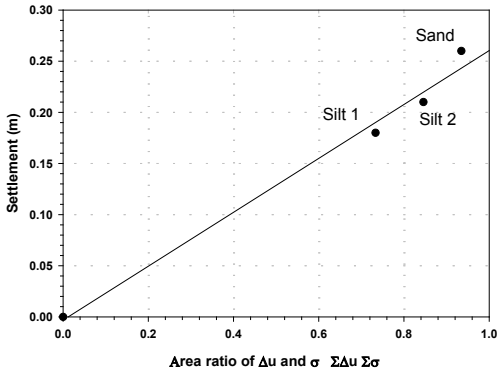


Figure 14 Area ratios of the excess pore water pressure and the effective overburden pressure at the instant of stopping shaking

4. SUMMARY AND CONCLUSIONS

Three dynamic centrifuge model tests were conducted to simulate the seismic responses of sandy soil deposits with the silt seam embedded at various depths. The model sand beds had the same relative density and were saturated with the same viscous pore fluid and then were subjected to the same magnitude of base acceleration. The effect of existence of low-permeability silt seam at the different depths on the generation and dissipation of excess pore water pressure, the surface settlements and the related liquefaction mechanism in a loose sand deposit are investigated in detail. The test results show that (1) the sand deposit without silt seam experienced the largest surface settlement and the silt seam in the sand deposit can reduce the extent of liquefaction and the surface settlement; (2) the concept of area ratio is proposed to evaluate the magnitude of surface settlement; (3) liquefaction occurs only in the sand beneath the thin silt layers for the sand deposit with the shallow silt seam. However, for the deeper thin silt intra-layer, liquefaction occurs not only in the sand beneath the thin silt layers but also in the sand near the surface. (4) the water films are formed beneath the silt seam and would last for amount of time after shaking.

References:

Kokusho T. (1999), "Water film in liquefied sand and its effect on lateral spread," ASCE, Journal of Geotechnical and Geoenvironmental Engineering, **125** (10), pp.817-826.

Kokusho T. (2000), "Mechanism for water film generation and lateral flow in liquefied sand layer," Soils and Foundations, **40**(3), pp.99-111.

Malvick, EJ., Kutter, BL., Boulanger, RW, Feigenbaum ,HP (2003), "Analysis of a void redistribution mechanism in liquefied soil," Proceeding of the 12th Panam. Conference on Soil Mechanism & Geotechnical Engineering, Cambridge, England, pp. 955-961.

8CUEE CONFERENCE PROCEEDINGS
8th International Conference on Urban Earthquake Engineering
March 7-8, 2011, Tokyo Institute of Technology, Tokyo, Japan

PERFORMANCE-BASED POST-LIQUEFACTION SETTLEMENT HAZARD EVALUATION

Steven L. Kramer[1] and Yi-Min Huang[2]

1) Professor, Department of Civil and Environmental Engineering, University of Washington, Seattle, Washington, USA
2) Post-Doctoral Fellow, GIS Research Center, Feng Chia University, Taichung City, Taiwan
kramer@u.washington.edu, niner@gis.tw

Abstract: Advances in the development of performance-based earthquake engineering offer important opportunities for more rational, objective, and consistent evaluation of liquefaction hazards. Performance-based procedures for evaluation of liquefaction potential have been shown to provide more consistent and accurate indications of the actual likelihood of liquefaction in areas of different seismicity than conventional procedures. These procedures can be extended to include effects of liquefaction such as lateral spreading and post-liquefaction settlement. This paper describes a recently developed framework for performance-based liquefaction hazard evaluation. The integration of procedures for estimation of liquefaction susceptibility, potential, and effects are described. The procedures are illustrated with an example of the evaluation of post-liquefaction settlement hazards..

1. INTRODUCTION

Liquefaction hazards are generally assessed by evaluating (a) the susceptibility of a soil deposit to liquefaction, (b) the potential for initiation of liquefaction under some anticipated loading, and (c) the effects of liquefaction. The level of loading considered in the assessment is usually expressed in terms of a ground motion intensity measure at a single return period. In practice, liquefaction susceptibility, potential, and effects are usually evaluated deterministically.

The development of performance-based earthquake engineering concepts allow probabilistic evaluations of susceptibility, initiation, and effects to be combined with a probabilistic evaluation of ground motion hazards to produce more rational and consistent estimates of liquefaction hazards. The purpose of this paper is to show how performance-based concepts can allow uncertainties in susceptibility, initiation, and effects to be incorporated into post-liquefaction settlement hazard assessments.

2. CONVENTIONAL PROCEDURES FOR ASSESSMENT OF LIQUEFACTION HAZARDS

The assessment of liquefaction hazards can be broken down into three primary components (Kramer, 1995) – evaluation of liquefaction susceptibility, evaluation of the potential for initiation of liquefaction, and evaluation of the effects of liquefaction.

2.1 Liquefaction Susceptibility

The primary difficulty in evaluating liquefaction susceptibility at this time lies in the susceptibility of fine-grained soils of marginal plasticity and coarse-grained soils with high fines contents. Following recent observations of liquefaction in fine-grained soils, extensive research on the liquefaction susceptibility of fine-grained soils was undertaken. At this stage, two major studies have proposed criteria for evaluating the liquefaction susceptibility of fine-grained soils. These criteria are consistent for many conditions but differ for others. Both were developed using the results of field observations and laboratory tests by well-respected leaders of the geotechnical engineering profession.

Boulanger and Idriss

Boulanger and Idriss (2005) reviewed case histories and laboratory tests involving cyclic loading of different fine-grained soils. Boulanger and Idriss identified two types of behavior that they described as “sand-like” and “clay-like” on the basis of stress normalization and stress-strain behavior. Soils exhibiting sand-like behavior were considered susceptible to liquefaction and soils exhibiting clay-like behavior were not. Boulanger and Idriss found that soil plasticity characteristics determined whether an individual soil was likely to exhibit sand-like or clay-like behavior, and proposed that the distinction could be made based on plasticity index, *PI*.

To quantify the transitional nature of observed sand-like to clay-like behavior, a numerical relationship can be established. The *PI* transition from clay-like to sand-like behavior from Boulanger and Idriss (2005) can be described using a susceptibility index, defined as

$$S_{BI} = \left[1 + \left(\ln PI / 1.843\right)^{11.483}\right]^{-2.0} \quad (1)$$

which has a value of 0.0 for clay-like (non-susceptible) behavior and 1.0 for sand-like (susceptible) behavior, and varies in a manner consistent with that shown graphically by Boulanger and Idriss (2005).

Bray and Sancio (2006)

Bray and Sancio (2006) investigated fine-grained soils that liquefied during 1994 Northridge, 1999 Kocaeli, and 1999 Chi-Chi earthquakes and proposed new compositional criteria for liquefaction susceptibility evaluation. In addition to plasticity index, Bray and Sancio found the ratio of water content to liquid limit (w_c/LL) to also influence liquefaction susceptibility.

A function similar to that used to approximate the Boulanger and Idriss criterion can be developed to quantify Bray and Sancio's susceptibility criteria. The equation is simply the product of two terms which have same general form as Equation 1, i.e.,

$$S_{BS} = \left[1 + \left(\ln PI / 2.778\right)^{33.077}\right]^{-2.0} \left[1 + \left(4.401 / \ln(w_c / LL)\right)^{360.471}\right]^{-2.0} \quad (2)$$

These equations were determined by assuming the boundary between susceptibility and non-susceptibility to be uniformly distributed within the 'moderately susceptible' zone of Bray and Sancio, and fitting a function that would have the same mean and variance with respect to both *PI* and w_c/LL. As in Equation 1, a value of 0.0 indicates non-susceptibility and 1.0 indicates susceptibility.

2.2 Initiation of Liquefaction

Liquefaction potential is generally evaluated by comparing consistent measures of earthquake loading and liquefaction resistance. It has become common to base the comparison on cyclic shear stress amplitude, usually normalized by initial vertical effective stress and expressed in the form of a cyclic stress ratio, *CSR*, for loading and a cyclic resistance ratio, *CRR*, for resistance. The potential for liquefaction is then described in terms of a factor of safety against liquefaction,

$$FS_L = CRR/CSR \quad (3)$$

Characterization of Earthquake Loading

The cyclic stress ratio is most commonly evaluated using the "simplified method" first described by Seed and Idriss (1971), which can be expressed as

$$CSR = 0.65 \frac{a_{\max}}{g} \cdot \frac{\sigma_{vo}}{\sigma'_{vo}} \cdot \frac{r_d}{MSF} \quad (4)$$

where a_{max} = peak ground surface acceleration, g = acceleration of gravity (in same units as a_{max}), σ_{vo} = initial vertical total stress, σ'_{vo} = initial vertical effective stress, r_d = depth reduction factor, and *MSF* = magnitude scaling factor, which is a function of earthquake magnitude. It should be noted that two pieces of ground motion information, a_{max} and magnitude, are required for estimation of the cyclic stress ratio.

Characterization of Liquefaction Resistance

The cyclic resistance ratio is generally obtained by correlation to insitu test results, principally from standard penetration (SPT), cone penetration (CPT), or shear wave velocity (V_s) tests. Of these, the SPT has been most commonly used and will be used in the remainder of this paper. A number of SPT-based procedures for deterministic (Seed and Idriss, 1971; Seed et al., 1985; Youd et al., 2001, Idriss and Boulanger, 2004) and probabilistic (Liao et al., 1988; Cetin et al., 2004) estimation of liquefaction resistance have been proposed.

3. POST-LIQUEFACTION SETTLEMENT

Damage to structures underlain by liquefiable soils is often affected by settlement of the liquefied soil. The most common form of liquefaction-induced settlement is that which results from the volumetric compression that occurs when excess porewater pressures dissipate under level-ground conditions (i.e., when shearing deformations are insignificant). The contractive nature of sands subjected to vibratory loading has been recognized for many years.

Tokimatsu and Seed (1987) reviewed previous laboratory test data, which showed post-liquefaction volumetric strain to be related to relative density and peak shear strain. They then related relative density to SPT resistance and peak shear strain to cyclic stress ratio to develop curves relating volumetric strain to $(N_1)_{60}$ and *CSR* (Figure 1a). The curves in Figure 1(a) show that post-liquefaction volumetric strain increases with increasing loading and decreasing SPT resistance and suggest that volumetric strains can be as large as 10 percent in extremely loose sands. They also show that, for strong levels of shaking, the soil reaches a limiting volumetric strain. The Tokimatsu and Seed procedure computes ground surface settlement by integrating volumetric strain over the depth of the liquefiable layer, i.e., as

$$\Delta H = \int \varepsilon_v dz \quad (5)$$

Other investigators (Ishihara and Yoshimine, 1992; Shamoto et al., 1998; Wu and Seed, 2004) have proposed similar relationships; that of Wu and Seed (2004) is shown in Figure 1(b). This relationship, like several others, does not suggest the existence of a limiting volumetric strain for moderately dense soils (corrected SPT resistances above about 10).

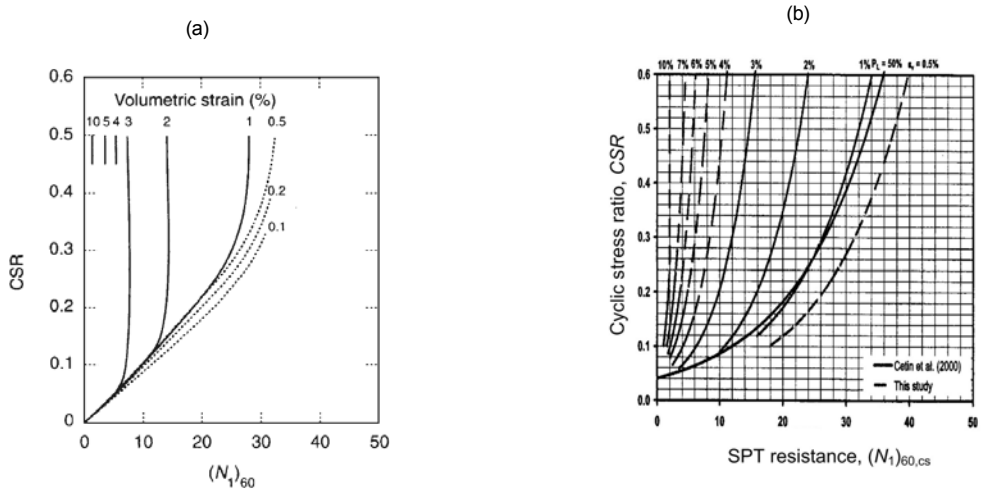


Figure 1 Variation of volumetric strain with corrected SPT resistance and cyclic stress ratio (a) Tokimatsu and Seed (1987), and (b) Wu and Seed (2004).

4. PERFORMANCE-BASED LIQUEFACTION HAZARD ASSESSMENT

Performance-Based Earthquake Engineering (PBEE) is generally formulated in a probabilistic framework to evaluate the risk associated with earthquake shaking at a particular site. The risk can be expressed in terms of economic loss, fatalities, or other measures. Pacific Earthquake Engineering Research (PEER) Center has developed a probabilistic framework for PBEE (Cornell and Krawinkler, 2000; Krawinkler, 2002).

The PEER PBEE framework computes risk as a function of ground shaking through the use of several intermediate variables. The ground motion is characterized by an *Intensity Measure, IM*, which could be any of a number of ground motion parameters. The effects of the *IM* on a system of interest are expressed in terms used primarily by engineers in the form of *Engineering Demand Parameters*, or *EDP*s. For a liquefiable site, the geotechnical engineer's initial contribution to this process for evaluating liquefaction hazards comes primarily in the evaluation of the conditional probability distribution of *EDP* given *IM*. In the PEER framework, the mean annual rate of exceeding some *EDP = edp* is given by

$$\lambda_{EDP}(edp) = \sum_{i=1}^{N_{IM}} P[EDP > edp \mid IM = im_i]\Delta\lambda_{IM}(im_i) \qquad (6)$$

Within the context of the previously described susceptibility/initiation/effects evaluations for liquefaction hazard assessment, the effects of liquefaction (e.g., settlement) would be taken as the *EDP*, and the susceptibility and initiation considerations would need to be addressed as intermediate steps in the evaluation of liquefaction effects. The evaluation of the conditional probability of *EDP* given *IM* would then take the following form

$$P[EDP > edp \mid IM] = P[EDP > edp \mid IM, initiation] \times P[initiation \mid IM, susceptibility]P[susceptbility] \qquad (7)$$

The evaluation of this conditional distribution therefore requires evaluation of the probability that a given element of soil is susceptible to liquefaction, the probability that liquefaction will be triggered by ground motions of various intensities, and the probability that some level of effects will be reached given the intensity level and the fact that liquefaction has been initiated.

4.1 Susceptibility

The susceptibility indices given by Equations 1 and 2 can be interpreted in different ways. Neither were developed in a sufficiently formal manner as to represent probabilities of liquefaction susceptibility. However, they could be interpreted as degrees of belief, or subjective probabilities, that a soil would be susceptible to liquefaction in that they have values of zero for conditions in which Boulanger and Idriss (2005) and Bray and Sancio (2006) indicate non-susceptibility and value of 1.0 where they indicate susceptibility. Differences between the two approaches could be treated as epistemic uncertainty using a logic tree.

4.2 Initiation

As indicated previously, a number of probabilistic liquefaction initiation models have been proposed over the past 20 years. The model of Cetin et al. (2004) provides a good example of such methods. For a soil of a given density, the Cetin et al. (2004) model allows computation of a probability of liquefaction initiation for a liquefaction-susceptible soil as

$$P[initiation|\ IM, susceptbilty] = \Phi\left[-\frac{(N_1)_{60}(1+\theta_1 FC) - \theta_2 \ln CSR_{eq} - \theta_3 \ln M_w - \theta_4 \ln\left(\sigma'_{vo}/p_a\right) + \theta_5 FC + \theta_6}{\sigma_\varepsilon}\right] \quad (8)$$

where Φ is the standard normal cumulative distribution function, $(N_1)_{60}$ = corrected SPT resistance, *FC* = fines content (in percent), CSR_{eq} = cyclic stress ratio (Equation 4 without *MSF*, which serves as the *IM* in this case), M_w = moment magnitude, σ'_{vo} = initial vertical effective stress, p_a is atmospheric pressure (in same units as σ'_{vo}), σ_ε is a measure of the estimated model and parameter uncertainty, and θ_1-θ_6 are model coefficients obtained by regression. In this form, *CSR* and M_w form a vector *IM*.

4.3 Effects

Huang (2008) developed a probabilistic post-liquefaction settlement model based on interpretation of previous laboratory test results presented by Tokimatsu and Seed (1987), Ishihara and Yoshimine (1992), Shamoto et al., (1998), and Wu and Seed (2004). Huang (2008) developed an expression for the median volumetric strain in a liquefiable soils as given by Wu and Seed (2004) as a function of *CSR* and $(N_1)_{60}$. Assuming lognormality, the vertical strain fragility relationship can be expressed as

$$P[\varepsilon_v > \varepsilon_v^* | CSR\ , N] = \Phi\left[\frac{\mu_{\ln \varepsilon v} - \ln \varepsilon_v^*}{\sigma_{\ln \varepsilon_v}}\right] \quad (10)$$

where $\Phi(\cdot)$ is the standard normal cumulative distribution function.

The fact that the Wu and Seed (2004) curves do not become vertical at high *CSR* levels implies that volumetric strain continues to increase without bound with increasing *CSR*. However, considerable experimental evidence suggests that the continued vibration of soil leads to densification only to some limiting void ratio or density. Therefore, there must exist some limiting volumetric strain for a soil of a given initial density. Because the performance-based approach integrates response over all levels of ground motion hazard (Equation 6), extrapolating the Wu and Seed (2004) curves to the very high *CSR* values that can exist in areas of high seismicity can lead to unrealistically high volumetric strain levels. Huang (2008) reviewed data from compaction, minimum void ratio, drained cyclic tests, and consolidation tests following cyclic loading to suggest a tentative relationship between maximum volumetric strain and SPT resistance. The relationship can be approximated by

$$\bar{\varepsilon}_{v,\max}(\%) = 9.765 - 2.427 \ln[(N_1)_{60,cs}] \quad (11)$$

Recognizing the approximate nature of this relationship, Huang (2008) assumed that $\varepsilon_{v,\max}$ was uniformly distributed over a range of 0.5 $\bar{\varepsilon}_{v,\max}$ to 1.5 $\bar{\varepsilon}_{v,\max}$.

Example

To illustrate the performance-based settlement evaluation procedure, a simple, hypothetical site in Seattle, Washington (Figure 2) is assumed. The site consists of 6 m of loose, silty sand with a groundwater level 1 m below the surface. The sand has a corrected clean sand SPT resistance, $(N_1)_{60,cs}$ = 15 and PI = 5.

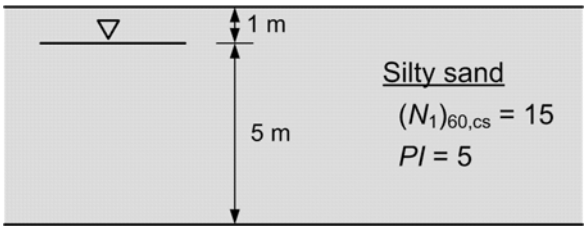


Figure 2. Hypothetical soil profile in Seattle, Washington.

To illustrate the roles of susceptibility, initiation, and maximum volumetric strain, the post-liquefaction settlement hazard for the site is computed for four different cases. Case 1 assumes that P[*susceptibility*] = 1.0, P[*initiation*] = 1.0, and that no maximum volumetric strain exists. For this case, the curves of Wu and Seed (2004) are extrapolated to large *CSR* values. Case 2 is identical to Case 1, except that the distribution of maximum volumetric strain is taken into account. Case 3 is the same as Case 2, except that the probability of initiation of liquefaction is also computed and accounted for. Finally, Case 4 accounts for the probability of liquefaction susceptibility, the probability of initiation, and the existence of a maximum volumetric strain.

The computed settlement hazard curves for all four cases are shown in Figure 3. For Case 1, the settlement hazard curve shows steadily increasing settlement with increasing return period (decreasing mean annual rate of exceedance). At long return periods, the unbounded settlement relationship implies settlement of over 0.5 m, which would correspond to average volumetric strains (over the 5 m saturated thickness) in excess of 10%. This volumetric strain would exceed that which has been observed in laboratory tests. The mean value of $\varepsilon_{v,\max}$ predicted by Equation 11 for such a soil would be approximately 3.2%, so the upper limit according to Huang (2008) would be less than 5%.

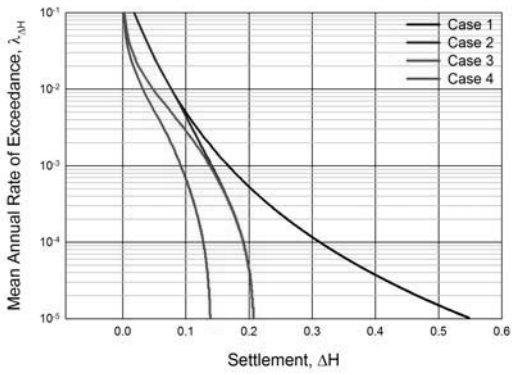


Figure 3. Post-liquefaction settlement hazard curves.

For Case 2, in which the existence of a maximum volumetric strain was considered, the settlement hazard curve matches the Case 1 curve at short return periods where volumetric strains do not approach the maximum value. At return periods beyond about 250 yrs, however, the shaking becomes strong enough that the maximum volumetric strain begins to affect the settlement hazard. At longer return periods, the Case 2 settlement hazard curve drops below the Case 1 curve and eventually becomes asymptotic to a maximum settlement slightly greater than 0.2 m. This settlement would correspond to an average maximum volumetric strain of about 4% under the strongest possible shaking, a value that is consistent with the results of laboratory tests.

The Case 2 curve assumes that liquefaction is initiated at all return periods. For the relatively weak shaking at short return periods, however, the probability of liquefaction may be less than 1.0. The Case 3 curve accounts for the probability of liquefaction initiation, and therefore drops below the Case 2 curve at short return periods. For return periods longer than about 1,000 years, the Case 3 curve converges to the Case 2 curve, as expected.

Finally, the settlement hazard curves for the first three cases all assume that the *PI* = 5 soil is susceptible to liquefaction. This *PI* level, however, would be in the transitional zone identified by Boulanger and Idriss (2005) and would be assigned a value of S_{BI} = 0.68 according to Equation 1. Taking S_{BI} as a subjective probability of susceptibility, the expected value of settlement drops to the Case 4 curve shown in Figure 3.

5. SUMMARY AND CONCLUSIONS

Performance-based concepts can allow objective and consistent evaluation of liquefaction hazards. By properly combining uncertainties in ground motions with uncertainties in liquefaction susceptibility, initiation, and effects, the actual return period for a given level of effects can be computed. The application of these concepts to the problem of post-liquefaction settlement prediction is illustrated in the paper.

The fact that performance-based settlement estimates are based on all levels of ground motion, including very strong levels that may only occur very rarely, requires the consideration of bounding values on volumetric strain. An approximate model for maximum volumetric strain was developed and implemented, and found to have a significant effect on post-liquefaction settlement at long return periods. The implementation of this probabilistic settlement model into a performance-based framework that allows probabilistic characterization of liquefaction susceptibility and the potential for initiation of liquefaction allows the most consistent and objective estimates of post-liquefaction settlement hazards to be evaluated.

Acknowledgements:

The authors acknowledge support from the Washington State Department of Transportation for development of the procedures described in the paper. Many of the basic concepts described in the paper were motivated by the senior author's involvement with the Pacific Earthquake Engineering Research (PEER) Center.

References:

Boulanger, R. W., and Idriss, I. M. (2005). Evaluating cyclic failure in silts and clays. *Proceedings, Geotechnical Earthquake Engineering Satellite Conference on Performance Based Design in Earthquake Geotechnical Engineering: Concepts and Research*. Prepared by TC4 Committee of ICSMGE, Japanese Geotechnical Society, Tokyo, 78-86.

Bray, J.D. and Sancio, R.B. (2006). Assessment of the Liquefaction Susceptibility of Fine-Grained Soils. *Journal of Geotechnical and Geoenvironmental Engineering,* Vol. 132, No. 9, pp. 1165-1177.

Cetin, K.O., Seed, R.B., Der Kiureghian, A., Tokimatsu, K., Harder, L.F., Kayen, R.E., and Moss, R.E.S. (2004). Standard penetration test-based probabilistic and deterministic assessment of seismic soil liquefaction potential, *Journal of Geotechnical and Geoenvironmental Engineering, ASCE*, 130(12), 1314-1340.

Cetin, K.O., Bilge, H.T., Wu, J., Kammerer, A.M., and Seed, R.B. (2004). "Probabilistic model for the assessment of cyclically induced reconsolidation (volumetric) settlements," *Journal of Geotechnical and Geoenvironmental Engineering*, ASCE, 132(3), 387-398.

Cornell, C.A. and Krawinkler, H. (2000). Progress and challenges in seismic performance assessment, *PEER News*, April, 1-3.

Huang, Y. (2008). Performance-Based Design and Evaluation for Liquefaction-Related Seismic Hazard, *PhD Thesis*, University of Washington, Seattle, WA.

Idriss, I.M. and Boulanger, R.W. (2004). Semi empirical procedures for evaluating liquefaction potential during earthquakes, *Proceedings of the 11th International Conference on Soil Dynamics and Earthquake Engineering and 3rd International Conference on Earthquake Geotechnical Engineering*, Vol. I, 32-56.

Kramer, S.L. (1995). *Geotechnical Earthquake Engineering*, Prentice-Hall, Englewood Cliffs, New Jersey, 653 pp.

Krawinkler, H. (2002). A general approach to seismic performance assessment, *Proceedings, International Conference on Advances and New Challenges in Earthquake Engineering Research*, ICANCEER, 2002, Hong Kong.

Liao, S.S.C., Veneziano, D., and Whitman, R.V. (1988). Regression models for evaluating liquefaction probability, *Journal of Geotechnical Engineering, ASCE*, 114(4), 389-409.

Seed, H.B. and Idriss, I.M. (1971). Simplified procedure for evaluating soil liquefaction potential, *Journal of the Soil Mechanics and Foundations Division , ASCE*, 107(SM9), 1249-1274.

Seed, H.B. and Idriss, I.M. (1982). *Ground motions and soil liquefaction during earthquakes*, Earthquake Engineering

Research Institute, Berkeley, California, 134 pp.
Seed, H.B., Tokimatsu, K., Harder, L.F., and Chung, R.M. (1985). Influence of SPT procedures in soil liquefaction resistance evaluations, *Journal of Geotechnical Engineering*, Vol. 111, No. 12, pp.1425-1445.
Tokimatsu, K. and Seed, H.B. (1987). Evaluation of settlements in sand due to earthquake shaking, *Journal of Geotechnical Engineering, ASCE*, Vol. 113, No. 8, pp. 861-878.
Lifeline Facilities and Countermeasures Against Liquefaction, Seattle, Multidisciplinary Center for Earthquake Engineering Research, Buffalo, NY, 69-86.
Wu, J. and Seed, R.B. (2004). Estimation of liquefaction-induced ground settlement (case studies), *Proceedings, Fifth International Conference on Case Histories in Geotechnical Engineering*, New York, pp. 1-8.
Youd, T.L. et al. (2001). Liquefaction resistance of soils: Summary report from the 1996 NCEER and 1998 NCEER/NSF workshops on evaluation of liquefaction resistance of soils, *Journal of Geotechnical and Geoenvironmental Engineering, ASCE*, 127(10), 817-833.

8CUEE CONFERENCE PROCEEDINGS
8th International Conference on Urban Earthquake Engineering
March 7-8, 2011, Tokyo Institute of Technology, Tokyo, Japan

GEOTECHNICAL ASPECTS OF THE 2010 DARFIELD (NEW ZEALAND) EARTHQUAKE

Rolando P Orense[1)], Michael J Pender[2)], Liam M Wotherspoon[3)], and Misko Cubrinovski[4)]

1) Senior Lecturer, Dept. of Civil & Environmental Engineering, University of Auckland, New Zealand
2) Professor, Dept. of Civil & Environmental Engineering, University of Auckland, New Zealand
3) EQC Research Fellow, Dept. of Civil & Environmental Engineering, University of Auckland, New Zealand
4) Associate Professor, Department of Civil & Natural Resources Engineering, University of Canterbury, New Zealand
r.orense@auckland.ac.nz, m.pender@auckland.ac.nz, l.wotherspoon@auckland.ac.nz, misko.cubrinovski@canterbury.ac.nz

Abstract: The 4 September 2010 earthquake in the Canterbury region, New Zealand caused widespread damage to residential buildings and lifeline facilities due to soil liquefaction and the associated ground deformations. Liquefaction occurred in areas which are known to have high potential to liquefaction - former river channels, abandoned meanders, wetlands, and ponds. These areas are characterized by the presence of loose saturated sandy deposits. This paper discusses the results of the post-earthquake damage investigation conducted in the area after the earthquake, with emphasis on liquefaction-induced damage.

1. INTRODUCTION

An earthquake of magnitude (M_w) 7.1 occurred at 4:35am on 4 September 2010 with an epicentre located at Darfield, a town about 40 km west of the city of Christchurch. The earthquake has a focal depth of 10 km and the maximum intensity felt was 8 based on MMI scale (GNS, 2010). Fortunately, the earthquake resulted in no casualties, which is a sort of a miracle considering the magnitude of the earthquake.

According to GNS Science (2010), the earthquake happened in an area that has previously had few earthquakes compared to other parts of the South Island. There are some mapped faults in the region, but the fault rupture occurred along a previously unknown east-west faultline. It is buried under the gravels that were deposited on the plains at the end of the last glaciation, about 16,000 years ago. As the gravels previously showed no sign of having been disturbed, it is likely that the fault that caused the Darfield Earthquake had not moved for at least 16,000 years.

Although damage to buildings due to ground shaking is extensive, especially in the central business district of Christchurch, severe liquefaction has been observed in many areas, notably in Kaiapoi and some of Christchurch's eastern suburbs. Liquefaction caused ground subsidence, tilting and settlement of residential houses while lateral spreading induced cracking of roads, footpaths, grounds and residential buildings. Water and sewer pipes buried underground broke and water from the cracked mains flooded many streets. Sands were ejected under house foundations' ground cracks, covering the houses with thick layers of fine sands and silts. A more comprehensive report of the damage is provided by the NZ-GEER team (2010).

2. GEOLOGICAL AND TECTONIC SETTING

The Canterbury Plains, about 180 km long and of varying width, are New Zealand's largest areas of flat land. They have been formed by the overlapping fans of glacier-fed rivers issuing from the Southern Alps, the mountain range of the South Island. The plains are often described as fertile, but the soils are variable. Most are derived from the greywacke of the mountains or from loess (fine sediment blown from riverbeds). In addition, clay and volcanic rock are present near Christchurch from the Port Hills slopes of Banks Peninsula.

The city of Christchurch is located at the coast of the Canterbury Plains adjacent to an extinct volcanic complex forming Banks Peninsula. Most of the city was mainly swamp, behind beach dune sand, and estuaries and lagoons, which have now been drained (Brown et al., 1995). The landforms in Christchurch and the environs are shown in Figure 1.

Canterbury has abundant water, in the rivers which carry mountain rainfall to the coast, and in aquifers. Beneath the plains, layers of porous gravels are interspersed with impermeable finer sediments. Near Ashburton, bedrock is at a depth of 1,600 metres (Wilson, 2009). Unlike most urban water supplies, Christchurch's water comes from aquifers beneath the city. The aquifers are recharged by rainfall and by river seepage. They have been tapped to irrigate farmland and for town water supplies.

The two main rivers, Avon and Heathcote, which originate from springs in western Christchurch, meander through the city and act as main drainage system. The Waimakariri River with its catchment in the Southern Alps, regularly flooded Christchurch prior to stopbank

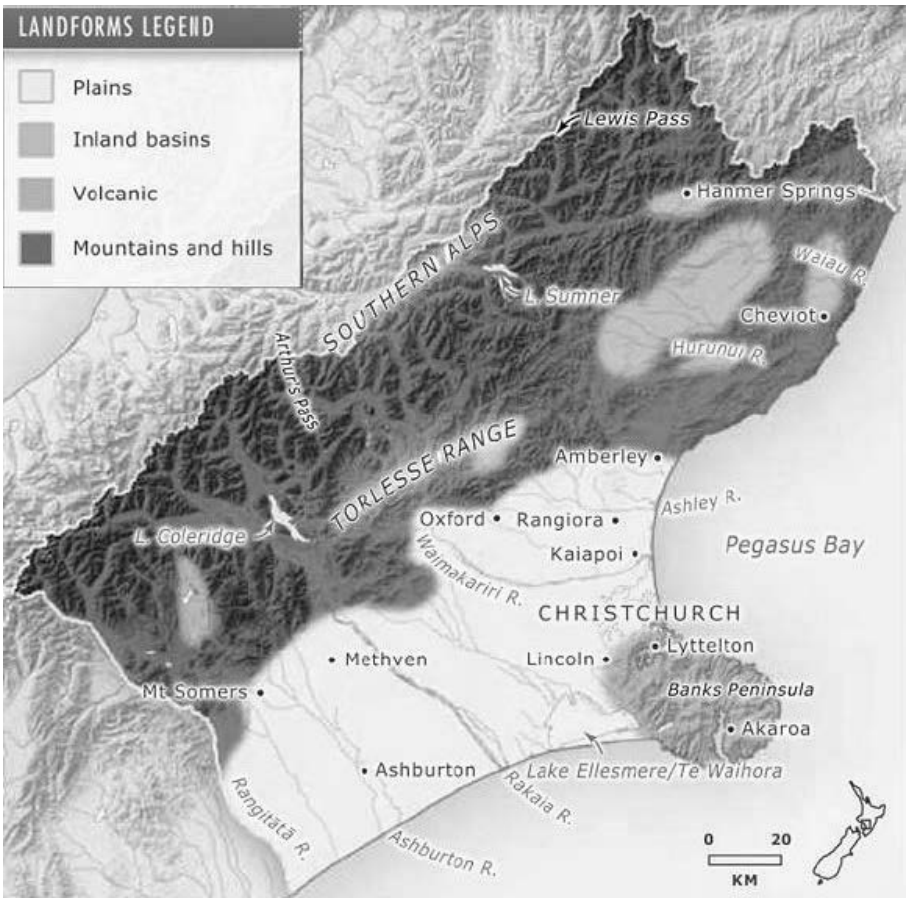


Figure 1. Landforms in and around Canterbury Plains (Source: http://www.teara.govt.nz)

construction and river realignment, which began shortly after the city was established in 1850. Variable foundation conditions as a consequence of a high water table and lateral changes from river floodplain, swamp, and estuarine-lagoonal environments, impose constraints on building design and construction (Brown et al., 1995).

According to studies by Brown et al. (1995), the geology, tectonic setting, and active seismicity of the Christchurch area indicate that future large earthquakes will occur which will have major impact on the city. Based on historical records, the north Canterbury Earthquake of 1888, centred on Amuri, damaged many buildings and caused the top of the spire on Christchurch Cathedral to collapse. In addition, the 1901 earthquake centred near Cheviot caused minor damage in the city while the Arthur's Pass earthquake of 1929 caused significant rockslides in the mountains.

3. STRONG MOTION RECORDS

The New Zealand Earthquake Commission (EQC) has provided funding for the country's real-time seismic hazard monitoring and data collection through GeoNet. The system consists of over 250 strong motion recorders to monitor how structures perform during earthquakes, 46 seismographs to measure accurately the magnitude, location and other characteristics of the earthquakes and another 40 accelerographs in the central south Island operated by the Canterbury strong ground motion network (CanNet) in anticipation of a M8+ rupture of the Alpine fault.

During the 2010 Darfield earthquake, a series of strong motion accelerographs was triggered and motions recorded at several stations. The distribution of maximum horizontal accelerations is shown in Figure 2. Although it can be seen that the maximum recorded acceleration was in the order of 1.25g near the earthquake epicentre, no serious damage was reported in the area. In the city of Christchurch, the recorded accelerations were in the order of 0.2-0.3g. Closer inspection of the ground motion records indicated that the duration of significant shaking was in the order of about 30 sec.

4. LIQUEFACTION-INDUCED DAMAGE

As mentioned above, extensive liquefaction was observed in the town of Kaiapoi and in the eastern suburbs of Christchurch, such as in Dallington and Bexley. In the next sections, typical types of damage observed due to liquefaction are presented based on post-earthquake investigations performed on September 8 and September 10-14. The regions visited are shown in Figure 3. Note that the occurrence of liquefaction was also reported in other areas, aside from those mentioned in this paper; however, these are not discussed herein because of space limitations.

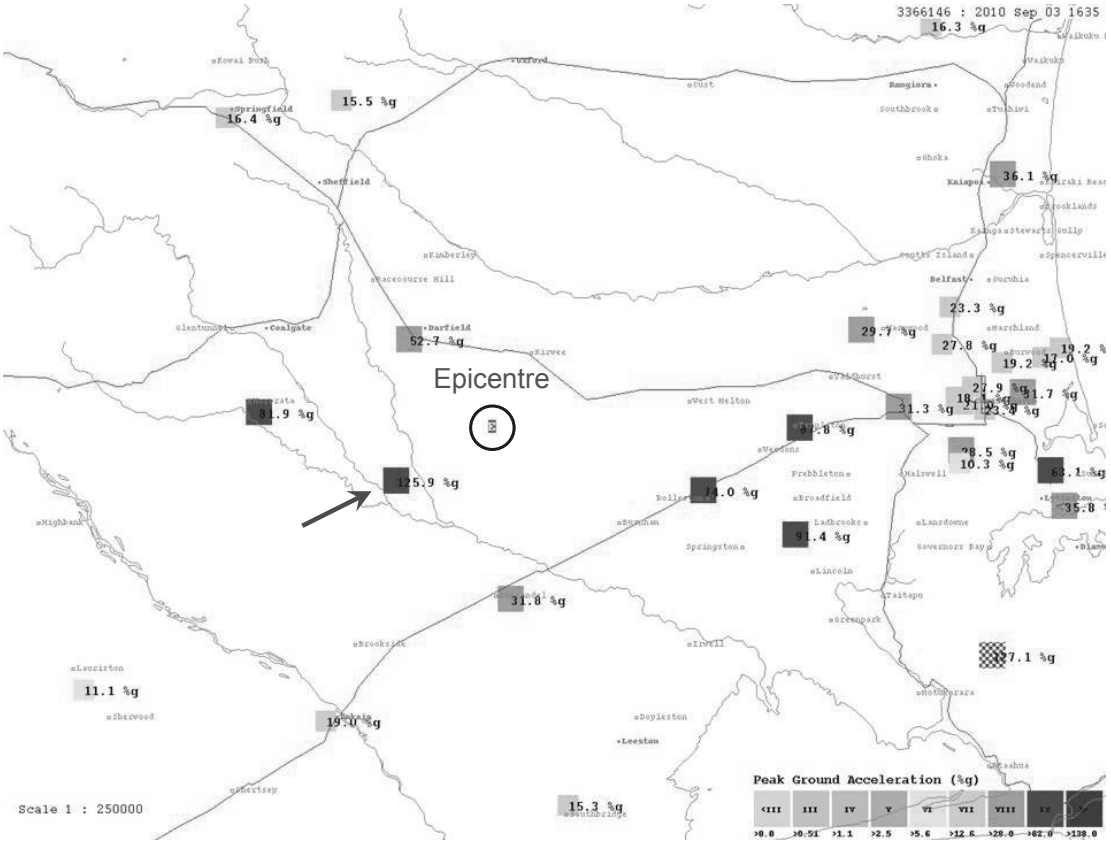


Figure 2. Distribution of maximum horizontal acceleration recorded during the earthquake. E indicates the location of the epicentre (Source: GNS Science website).

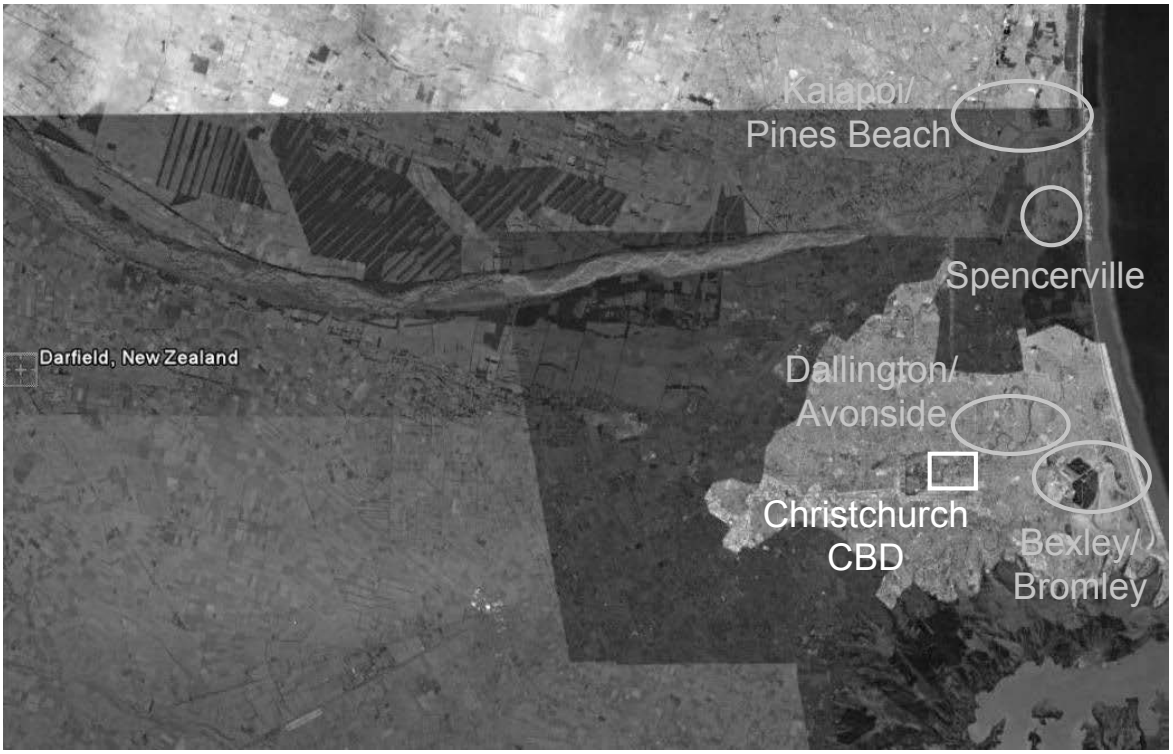


Figure 3. Sites where extensive liquefaction was observed during the 2010 earthquake.

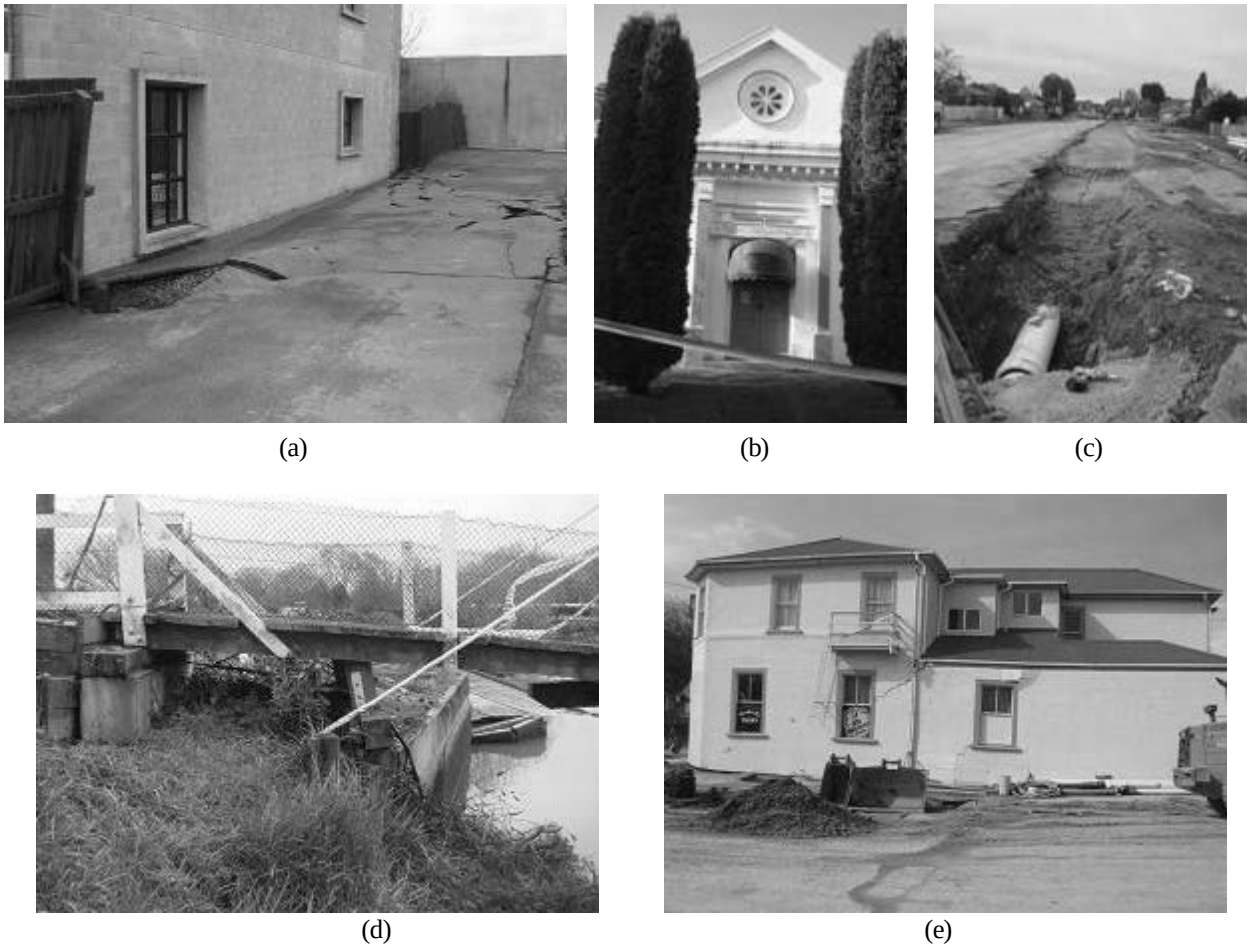


Figure 4. Damage to structures and lifelines in Kaiapoi town.

4.1 Kaiapoi

In terms of liquefaction, the township of Kaiapoi is probably the worst-hit area, with many residential houses, several commercial buildings and other infrastructure facilities suffering damage due to lateral spreading, ground subsidence and differential settlement. Kaiapoi is located in the northeastern end of Canterbury Plains, about 20 km north of Christchurch. The Kaiapoi River, which cuts through the centre of the town, joins the Waimakariri River on the eastern edge of town and flows to the sea.

A reinforced concrete building along Williams St., with 2 storeys in front and 3 storeys at the back, sank and tilted as a result of liquefaction of the foundation ground. Based on the ocular inspection of the site, the building, with a footprint measuring 13m x 20 m, underwent non-uniform settlement, with the southwestern side sinking by as much as 30 cm (Figure 4a), while the northeastern side of the building moving laterally by about 20 cm in the direction of Kaiapoi River. Ground cracks were observed at the back of the building, and sand boils were evident. The pavements in the parking area of the shopping centre located at the back of the said building were also cracked and deformed, with floor slabs of some stores showing large ground cracks. From observation, it appears that the cracks observed were more or less continuous, from the shopping centre cutting through the RC building, passing through Williams St and damaging a house on the opposite side.

Damage was also widespread in other areas north of the river, especially along Charles Street and Sewell Street, which are both parallel to the river. Liquefaction and lateral spreading caused damaged to structures, such as in Southern Cross Lodge (Figure 4b) which tilted and suffered shear cracks on its façade, and was red-tagged (no entry permitted). Sand boils and ground cracks were also observed in the vicinity. Water pipes were broken, and repair works were ongoing during the site visit (Figure 4c).

Berrill et al. (1994) reported that this area underwent liquefaction during the 1901 Cheviot Earthquake. They quoted newspaper reports describing the ejection of sand through cracks and lateral spreading at the east end of Sewell Street. The reports mentioned that cracks can be probed up to a depth of about 2 m. Subsequent field investigation performed at different sites showed cone resistances of about 2-3 MPa throughout layers extending from about 2-6 m, where denser coarse sands and fine gravels were encountered.

The historic Mandeville Swing Bridge, a pedestrian bridge over the Kaiapoi River, buckled (Figure 4d) as a result of liquefaction-induced lateral spreading, which seemed to be more evident on the southern side of the river.



(a) (b)

Figure 5. Damage to a structure and to stop bank along the Kaiapoi river.

Near the abutment, the south bank moved towards the river by about 20 cm, resulting in the deformation of the girders of the bridge. Cracks parallel to the river, as well as sand boils, were observed in the nearby park.

Residential houses and commercial establishments on the south bank of Kaiapoi River underwent settlements in the order of 10-20 cm, and were covered by ejected sands (up to 20 cm thick in some places) immediately after the earthquake. Several houses were structurally damaged due to lateral spreading and uneven settlements (Figures 4e). The railway track near the Fire Station appeared to be damaged as well, as the track was re-ballasted in this area when the visit was made.

The stopbanks confining the flow of Kaiapoi River also suffered damage at various locations. These embankments, measuring about 2.5 m high (from water line) and 2.7 m wide, has slopes of approximately 2H:1V at the riverside and 3H:1V at the landside near the bridge along Williams St. The structure housing the Visitors Information Centre on the north side of the river sank and tilted as a result of liquefaction and lateral spreading (Figure 5a). Ground cracks, as wide as 30 cm and as deep as 100 cm, were observed running parallel to the river. The foundation ground of the structure was laterally displaced towards the river, resulting in settlement and tilting of the structure. The two-storey Waimakariri-Ashley Coastguard building adjacent to the Visitor Centre also suffered the same fate. At some locations east of this building, ground cracks, in the order of 100 cm wide and 150 cm deep, were also observed along the gentler slope of the embankment (Figure 5b), with sand boils scattered all over. Settlement/slumping of foot path on the crest of the banks in the order of 10-30 cm were also noted.

From field investigation, it was observed that liquefaction appears to be extensive in alluvial fan sites adjacent to river channels, such as the Kaiapoi River. Moreover, investigations of old maps by by Wotherspoon et al. (2010) showed that that much of the most significant liquefaction damage in and around Kaiapoi during the Darfield event occurred in areas where river channels had been reclaimed or in old channels that have had flow diverted away. The highly modified nature of the

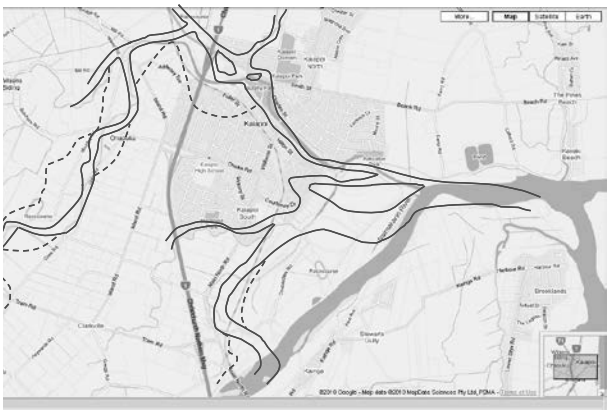


Figure 6. Map of riverbeds in 1865 superposed to the present-day map of Kaiapoi (modified from GoogleMap).

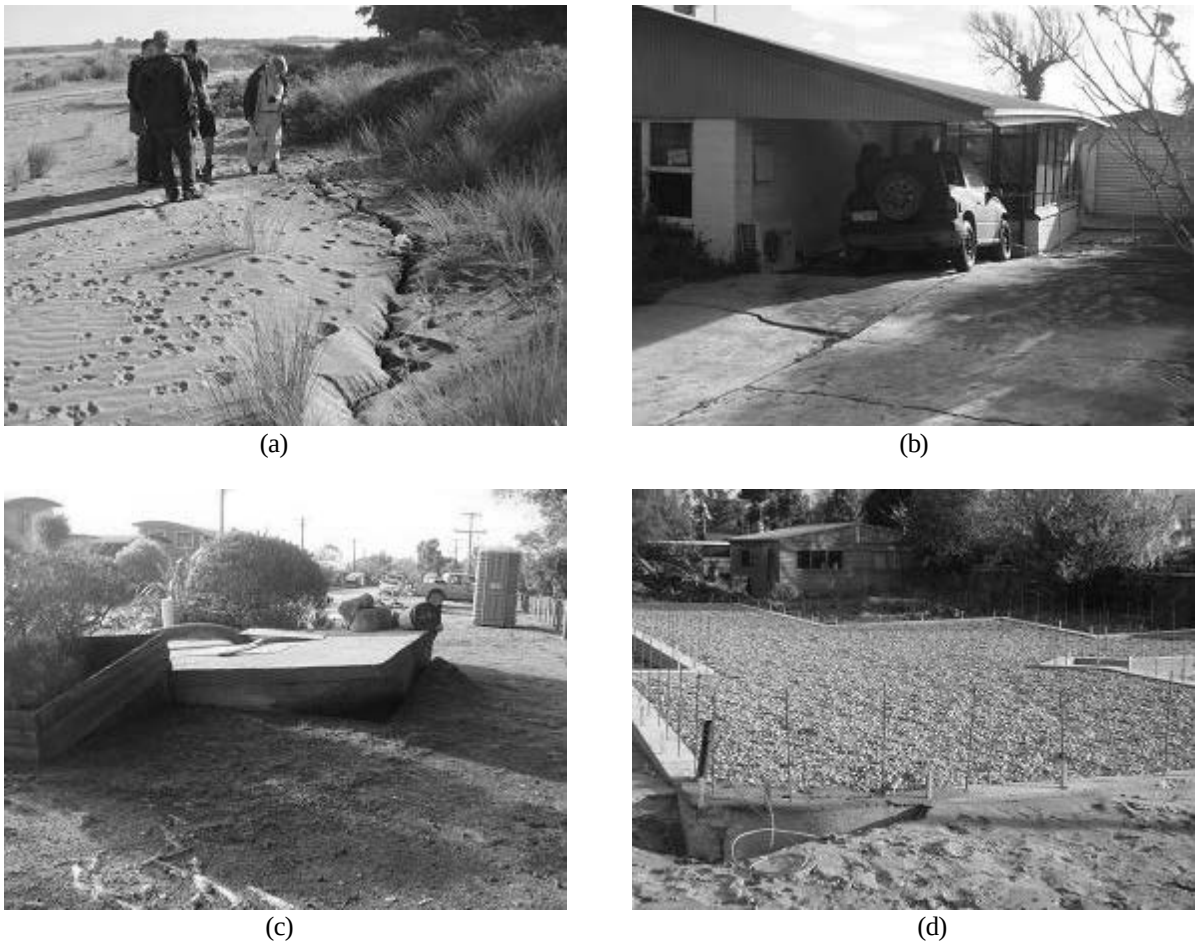
Waimakariri River and its proximity to Kaiapoi meant that some of these areas overlapped areas that have since been developed as the town has grown, as shown in Figure 6.

Thus, what was observed during this earthquake is consistent with the prediction of Christensen (2001) whose studies indicated that the eastern side of Waimakariri District (including Kaiapoi) has high susceptibility to liquefaction and settlements of up to 300 mm may occur for the earthquake scenarios considered in his study.

4.2 Pines Beach

The town of Pines Beach is situated to the east of Kaiapoi. In Kairaki Beach, ground cracks and sand boils were observed, with the cracks oriented parallel to the sea, indicating lateral spreading (Figure 7a). The cracks were as wide as 80 cm and lengths of several tens of meters. Subsequent measurements showed that the beach laterally spread by about 200 cm over a distance of 140 m.

Along Featherstone Avenue, a house settled by about 30 cm (Figure 7b) and sand boils were observed within the property. Interestingly, the ejected sand observed in the area was much less in volume when compared with those observed in most parts of Kaiapoi. The adjacent properties appear to have no damage. Along the same street, a sewer



(a) (b)

(c) (d)

Figure 7. Damage observed in Pines Beach.

tank was uplifted by about 40 cm (Figure 7c). Lots of sand boils were also observed in the nearby Featherstone Park.

In Pine Oval, houses were also damaged due to formation of cracks on the foundation ground. An unfinished house with the foundation exposed was seen in the area, shown in Figure 7d. Sand boils were observed adjacent to the exposed foundation. The perimeter beams, measuring 250 mm x 530 mm, has one D12 reinforcement each at the top and bottom, with concrete cover of about 80 mm. The protruding bars consisted of D10 bars, which will be bent inward and concrete will be poured over the site to form the unreinforced concrete slab. If this was the type of foundation used in many houses in the area, it is clear that these houses do not have enough resistance against uneven settlement or lateral spreading due to liquefaction.

4.3 Spencerville

Some residential houses in Spencerville, located north of Christchurch, were also affected by liquefaction and associated lateral spreading. Spreading was evident in areas along Riverside Lane paralleling the Styx River, where five large and newly constructed houses were severely damaged. These houses appear to be resting on slab foundations and have relatively large footprints (about 200-300m2). Compared to Kaiapoi and other areas affected by the earthquake, little ejected sand was observed but large ground cracks, in the order of 40-50 cm in width, were observed in some places (Figure 8a). The houses underwent minimal settlement, but the laterally spreading ground cut through the houses, destroying slabs and causing structural damage to houses (Figure 8b).

4.4 Bexley

The suburb of Bexley is located southeast of Christchurch CBD. The southern portion of the area was formerly a swamp and formed part of the Bexley wetlands. It has been reclaimed in the late 1990s by filling the area with fill materials and the subdivision was built over it. Interviews with homeowners indicate that the area was fairly new, with some houses built as recent as 5 years ago.

As expected, earthquake shaking triggered liquefaction of the loose swampy deposit, resulting in ground settlement and lateral spreading. Sand boils were observed at the entrance to the Bexley Wetlands Park (Figure 9a), as well as in the swampy areas. Large ground cracks, about 50 cm wide and 60-80 cm deep, were observed at the backyards of some houses and these cracks were oriented parallel to the marshlands (Figure 9b). Ejected sands filled up the whole neighbourhood, as thick as 30 cm in some areas (Figure 9c). Because of liquefaction, houses either tilted (Figure 9d), or were displaced laterally, with some houses showing cracks in the flooring slab. Most of the affected areas were



(a) (b)

Figure 7. Damage induced by lateral spreading in Riverside Lane, Spencerville



(a) (b)

(c) (d)

Figure 8. Observed liquefaction and associated ground deformations in Bexley.

concentrated on the southern portion of Bexley, where houses were built over the uncompacted reclaimed portion of the wetland.

Based on interview with the residents, the design plan for the foundations appear to be similar to those shown in Figure 7d, with perimeter beams and concrete slabs. Because of this, the houses were easily destroyed by the uneven settlement and lateral spreading induced by liquefaction.

When the visit was made, most of the ejected sands have been cleaned up and some home owners were already on the move. Moreover, Bexley Road on the western side of the subdivision was being re-paved and sand boils were also observed in the vicinity of the road.



(a) (b)

Figure 10. Damage to road and pond banks in the oxidation ponds.

4.4 Bromley Sewage Treatment Plant

The Sewage Treatment Plant operated by the Christchurch City Council is situated at Bromley, approximately 6.5 km east of Christchurch CBD and southwest of Bexley subdivision. Here, the domestic and industrial sewage of Christchurch are discharged into this estuary of the Avon and Heathcote Rivers. According to Robb (1974), up to 30 million gallons per day of treated sewage have been discharged since 1962 from a purification installation designed to give primary and secondary treatment, including a period of retention within a series of oxidation ponds.

Dyers Road along State Highway 74 cuts through the oxidation ponds and connects Ferrymead to Bexley. Road pavements were cracked at the site of the oxidation ponds and the road was impassable immediately after the earthquake. According to the engineer interviewed at the site, a 50 cm crack opened near the centreline of the road, although it was already paved during the site visit.

The pond bank separating Ponds 1 & 2 also cracked and slumped as a result of liquefaction (Figure 10a). Boiled sands were evident in many places. A sewage pipe running parallel to the bank was laterally compressed and was seen protruding through the water when the pond water was subsequently drained, as shown in Figure 10b. Note that because of the slumping of the pond banks, engineers decided to drop the pond level. Moreover, sheetpiles were driven into the bund to stabilize them and arrest further movement.

Seismic dilatometer tests were performed in the nearby Bromley Park and the results are shown in Figure 11. It can be seen that the upper 10m of the site consists of sand/silty sand with shear wave velocity less than 200 m/s.

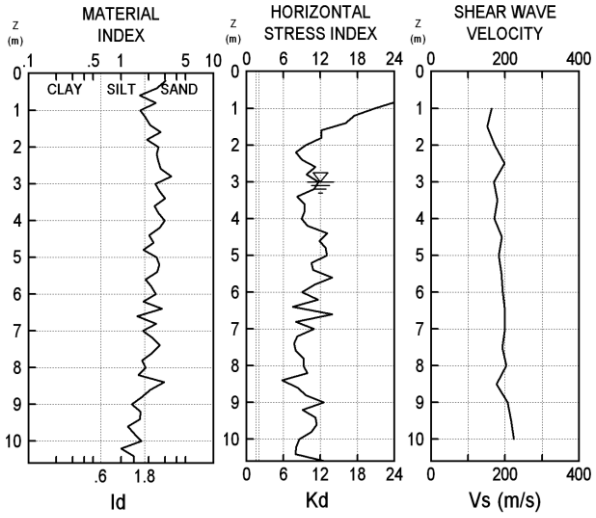


Figure 11. sDMT test results in Bromley Park site.

4.6 Dallington/Avonside

Evidence of liquefaction, such as sand boils and ground cracks, were also seen in many areas adjacent to the Avon River. For example, the hockey field in Porritt Park was destroyed by liquefaction, with boiled sands covering the green artificial cover and cracks and slumps evident underneath (Figure 12a). In the adjacent park, ejected sands and cracks were observed in the grass parallel to the river (Figure 12b). Adjacent to a bridge leading into park, the pavement was cracked, while the adjacent portion of Avon River was filled with mud and peat. From inspection, it appears that the south side of the river had moved towards the north side due to lateral spreading. The excess pore water pressure generated by the shaking could have pushed up the mud into the centre of the river. Note that this area is an abandoned meander of the Avon River, which resulted when the river was straightened for the rowing competition. As a result, it is expected that the ground underneath the park is very loose and prone to liquefaction.

Another area where extensive liquefaction was observed was in Dallington Terrace, located in the inner side of the meandering Avon River. Along Gayhurst Road, sand boils were observed everywhere. The approach to Gayhurst Bridge cracked and settled, rendering the bridge impassable immediately after the earthquake (Figures 13a). Cracks were also observed in the bridge abutments.

St. Paul Church, located also within the bend of Avon River, was damaged as a result of ground cracks induced by lateral spreading toward the river. Sand boils and cracks



(a) (b)

Figure 12. Damage to Horritt Park hockey stadium.



(a) (b)

Figure 13. Damage to Gayhurst Road bridge (courtesy of TV-3 website) and crack in the vicinity of St. Paul Church.

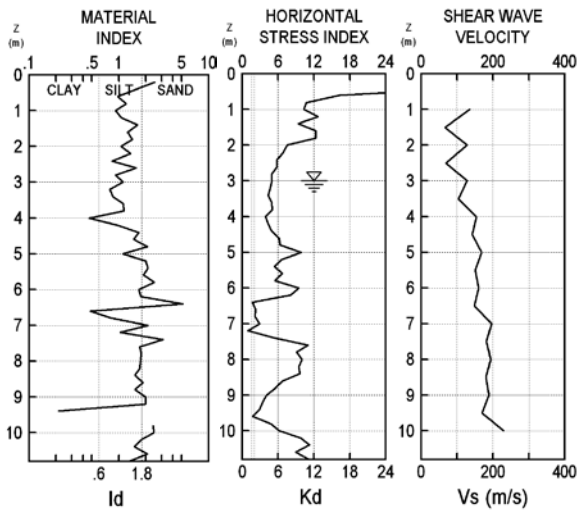


Figure 14. sDMT test results in St. Paul Church.

were observed in the vicinity of the church (Figure 13b). One long crack, about 40 cm wide with vertical offset of 20 cm, cuts through the church and halving it into two, as evident from Figure 18b. The grass adjacent to the church and the parking lots, were all littered by cracks, which were mostly oriented parallel to the river.

Seismic dilatometer tests performed at the back of the church revealed that the upper 10m of the site consists of silty sand materials with shear wave velocity between 100-200 m/sec, indicating that it is susceptible to liquefaction.

Along Locksley Avenue adjacent to Avon River, liquefaction was also evident. The footpath on the west side of Avon River buckled and slumped in several places (Figure 15a), and roads were cracked at several locations (Figure 15b). During the visit, repairs were being made on damaged water pipes. The damaged locations were at the same location as the ground cracks (Figure 15c), suggesting that lateral spreading of the ground induced the damage to underground pipelines.

5 SAND BOILS

In all places visited, the appearance of the ejected sands as a result of liquefaction were very similar, typically grey to dark grey in colour and consisting of very fine sands. Samples were taken at various locations and the grain size distributions were obtained using laser diffraction analysis. Figure 16 shows the grain size distribution curves of soil



(a) (b) (c)

Figure 15. Damage to footpath along Avon River in Locksley Ave.

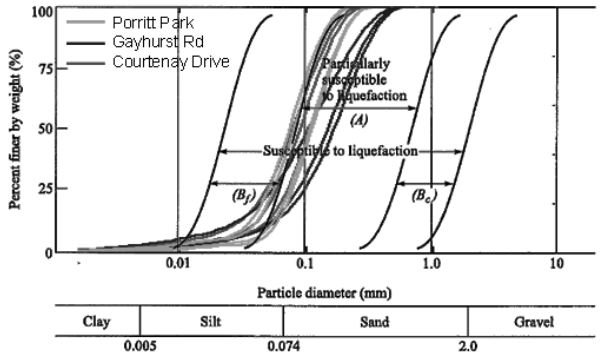


Figure 16. Grain size distribution of ejected sands taken at various locations plotted with respect to distributions observed to be susceptible to liquefaction (Modified from PHRI, 1997).

samples taken at Porritt Park, Gayhurst Road and Courtenay Drive (in Kaiapoi). It can be observed that the distributions of grain sizes were fairly similar, and they plot over a narrow range. The fines contents were low, ranging from 10-25%.

Also shown in the figure are the range of grain size distributions of sands which are deemed to have high possibility of liquefaction (A) and possibility of liquefaction (B). These ranges were obtained from past historical earthquakes in Japan and stipulated in the Japanese design code for port and harbour facilities. Note that there are problems associated with the use of compositional criteria as a measure of liquefaction susceptibility because there are no generally accepted criteria and the difference between natural and reclaimed deposits. Nevertheless, using these criteria, it can be seen that the ejected sands obtained at different locations in Christchurch can be said to be have high potential to liquefy.

6. CONCLUDING REMARKS

Based on the observations derived from the site visits, liquefaction during the 2010 Darfield Earthquake occurred in areas which are known to have high potential to liquefaction - former river channels, abandoned meanders, wetlands, and ponds. These areas are characterized by the presence of loose saturated sandy deposits, which are susceptible to liquefaction. In other words, liquefaction during this earthquake occurred in sites which are expected to liquefy. Liquefaction caused extensive damage to residential houses and other infrastructures through lateral spreading, ground subsidence, and differential settlements.

Acknowledgements:

A part of the post-earthquake investigation work was conducted with the NZ-GEER Reconnaissance Team and the authors would like to acknowledge the assistance of the team members. The seismic dilatometers tests were performed by Ground Investigation Ltd. with the financial support of Hiway Geotechnical Ltd.

References:

Berrill, J.B., Mulqueen, P.C. and Ooi, E.T.C. (1995). "Liquefaction at Kaiapoi in the 1901 Cheviot, New Zealand Earthquake," *Bulletin of the NZSEE*, Vol. 27, No. 3, 178-189.

Brown, L.J., Beetham, R.D., Paterson, B.R. and Weeber, J.H. (1995). "Geology of Christchurch, New Zealand," *Env & Eng Geoscience*, Vol. 1, No. 4, 427-488.

Christensen, A. (2001). "Regional liquefaction study for Waimakariri District," *Proc. NZSEE 2001 Conference*, Paper No. 3.03.01.

GNS Science (2010). *Canterbury Earthquake*, http://www.gns.cri.nz

NZ-GEER Reconnaissance Team (2010). *Geotechnical Reconnaissance of the 2010 Darfield (New Zealand) Earthquake*, 173pp.

Port and Harbour Research Institute (1997). Handbook of Liquefaction Remediation in Reclaimed Lands, Balkema.

Robb, J.A. (1974). "An ecological study of the Bromley oxidation ponds and surrounding environs," *PhD Thesis*, Univ. Canterbury.

Wilson, J. (2009). "Canterbury region – Landscapes," , *Te Ara - the Encyclopedia of New Zealand*, http://www.TeAra.govt.nz/en/canterbury-region/3

Wotherspoon, L.M., Pender, M.J. and Orense, R.P. (2010). "Relationship between observed liquefaction at Kaiapoi following the 2010 Darfield earthquake and old channels of the Waimakariri River," *Engineering Geology* (submitted for publication)

8CUEE CONFERENCE PROCEEDINGS
8th International Conference on Urban Earthquake Engineering
March 7-8, 2011, Tokyo Institute of Technology, Tokyo, Japan

LIQUEFACTION-INDUCED DAMAGE IN CHRISTCHURCH CITY CAUSED BY THE 2010 DARFIELD EARTHQUAKE, NEW ZEALAND

Takashi Kiyota[1)], Mitsu Okamura[2)], Hirofumi Toyota[3)], Misko Cubrinovski[4)], and Rolando P. Orense[5)]

1) Associate Professor, Institute Industrial Science, University of Tokyo, Japan
2) Professor, Department of Civil and Environmental Engineering, Ehime University, Japan
3) Associate Professor, Department of Civil and Environmental Engineering, Nagaoka University of Technology, Japan
4) Associate Professor, Department of Civil and Natural Resources Engineering, University of Canterbury, New Zealand
5) Associate Professor, Department of Civil & Environmental Engineering, University of Auckland, New Zealand
kiyota@iis.u-tokyo.ac.jp, okamura@cee.ehime-u.ac.jp, toyota@vos.nagaokaut.ac.jp, misko.cubrinovski@canterbury.ac.nz, r.orense@auckland.ac.nz

Abstract: On September 4, 2010, the Darfield Earthquake hit around the Canterbury region, New Zealand. This report summarizes results from field investigations in Christchurch city conducted by the Japanese Geotechnical Society survey team. The earthquake-induced liquefaction caused severe damage to residences, buried lifelines and river dikes. High ratio of occurrence of liquefaction was reported in areas which may be linked to the soft subsurface ground, lowland areas, former river channels and reclaimed lands that were constructed on the swamps. By conducting Swedish weight sounding tests, subsurface soil conditions with high ground water table and soft sandy deposits were investigated at several sites where liquefaction occurred in Christchurch city.

1. INTRODUCTION

The Darfield earthquake measuring the moment magnitude Mw of 7.1 (USGS, 2010) occurred at 4:35 local time on Saturday, September 4, 2010 with a focal depth of about 10km. The most affected city was Christchurch, a city about 40km east of the epicenter (Fig. 1). Fortunately, there are no reports of casualties by this earthquake.



Figure 1 Location of epicenter of Darfield earthquake (GeoNet, 2010)

Figure 2 shows the peak ground accelerations that were recorded in the Canterbury region during the earthquake. The ground motion shaking as a result of the main shock was widely felt in the Canterbury region as shown in Fig. 2. Although the recording above 1.0g can be seen in the near epicenter, the most devastated area, Christchurch city, was marked with 100-300gals. According to GNS Science, MMI-VIII was observed in Christchurch city.

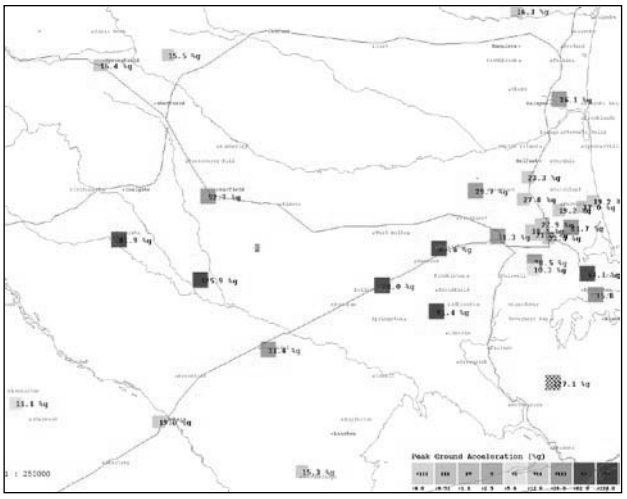


Figure 2 Peak ground accelerations in the Canterbury region during Darfield earthquake (GeoNet, 2010)

Since occurrence of liquefaction-induced damage had been reported by Yasuda (2010), the Japanese Geotechnical Society dispatched a survey team from September 11 to 16 in order to conduct detailed geotechnical investigations. Swedish weight sounding (SWS) device was brought from Japan, and SWS tests were carried out at several sites in Christchurch city. This report summarizes results from the above investigations in Christchurch city.

2. LIQUEFACTION-INDUCED DAMAGE

The business area of Christchurch city is located about 8.5km west of the coast line as shown in Fig. 3. A meandering stream, Avon-river, flows through center part of Christchurch city. Based on the damage aspects found in this survey, Christchurch city can be divided into three areas, business area, Dallington area and Bexley area. The results of the field survey are summarized below for each area.

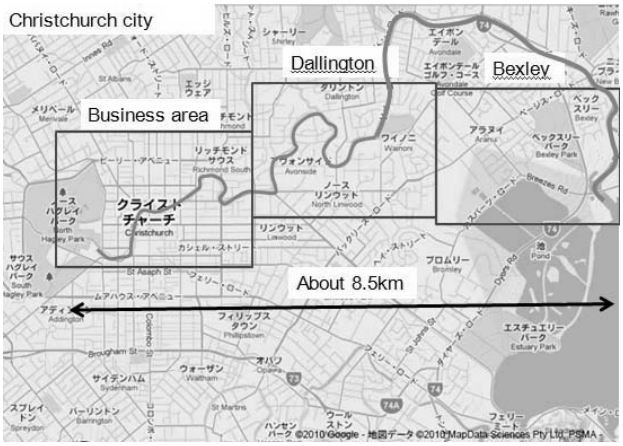


Figure 3 Map of Christchurch city

2.1 Business Area

Figure 4 shows the map of the business area. At site 1 in the park, sand boiling occurred as shown in Photo 1. This suggests that soil deposits in the park have been liquefied. However, in this park, the occurrence of sand boiling was very limited.

No sand boiling could be observed at the center of business are. Although some old buildings including historic sites suffered from cracking and dropping of masonry parts of the building, there was no damage to the symbol of the city, Christchurch cathedral, at site 50 (Photo 2). At site 25, a two stories old brick building was damaged as shown in Photo 3.

At sites 56 (Photo 4), sand boiling was found in residential which clearly indicates occurrence of liquefaction. The boiled sand that was retrieved from this area was fine sand with D_{50} of 0.14 mm and fines content of 17%. At sites 62 and 63, as shown in Photo 5 and 6 respectively, roads and levees along Avon-river suffered from ground deformation, which may be caused by liquefaction of subsoil deposits.

At site 55 about 300m from the Avon river channel, the trace of liquefaction was not observed.

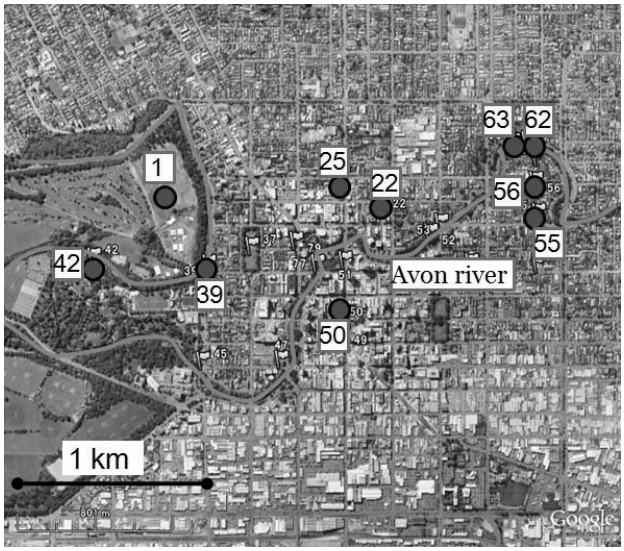


Figure 4 Survey map of business area in Christchurch city


Photo 1 Trace of sand boiling in the park of business area (Site 1 in Fig. 4)


Photo 2 No damage with Christchurch cathedral in business area (Site 50 in Fig. 4)



Photo 3 Brick house suffered damage (Site 25 in Fig. 4)

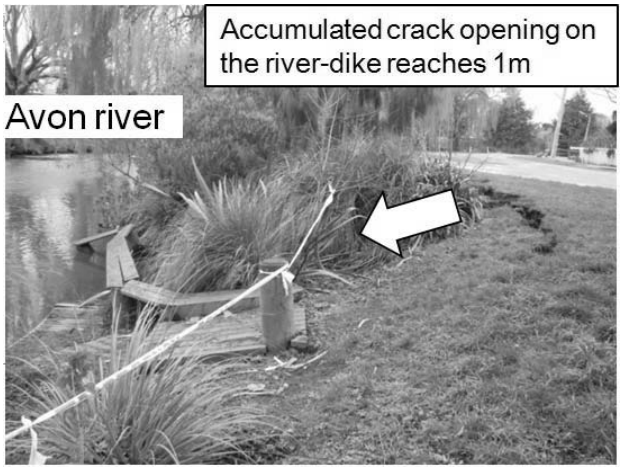


Photo 6 River dike along Avon-river suffered from large crack and lateral deformation (Site 62 in Fig. 4)



Photo 4 Sand boiling occurred at residential district in Business area (Site 56 in Fig. 4)

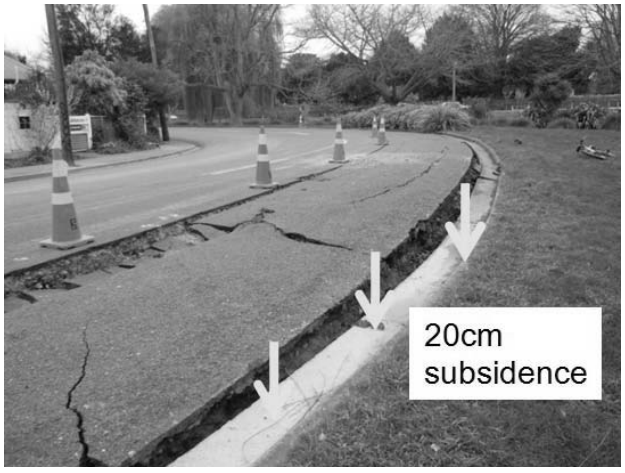


Photo 5 Road on river dike suffered from settlement and cracking (Site 63 in Fig. 4)

2.2 Dallington Area

Since the preceding survey by Yasuda (2010) had reported that extensive damage to houses and roads by liquefaction was concentrated in Dallington district in Christchurch city, attempts were made in the present survey to reveal the soft soil conditions in Dallington district as well as possible effects of liquefaction. The survey map of Dallington area is shown in Fig. 5.

At the time of the earthquake, the areas along Avon-river were inundated with boiled sand and ground water. However, at the time of survey that was conducted in 8 days after the earthquake, no water could be observed on the street, and the sand was placed at the side of the street (Photo 7).

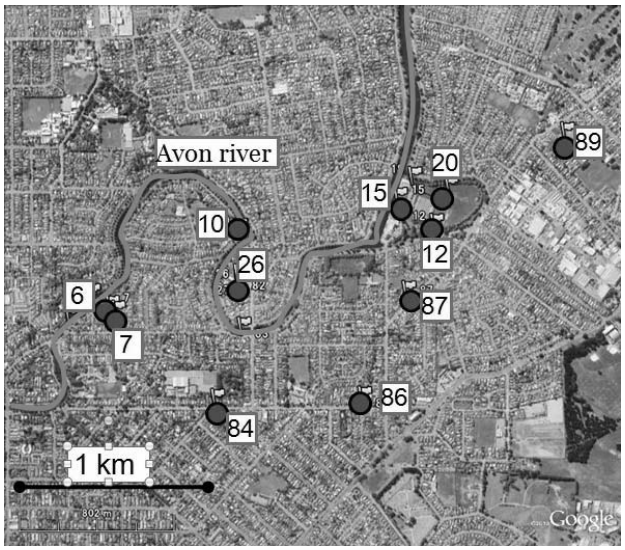


Figure 5 Survey map of Dallington area in Christchurch city



Photo 7 Boiled sand was placed at side of the street. (Site 6 in Fig. 5)

In order to investigate the subsurface soil properties, Swedish weight sounding (SWS) tests were carried out at five sites in Christchurch. Two of them were conducted in Dallington area while the others will be reported next section.

SWS test results conducted at sites 7 and 26 in Dallington district are shown in Fig. 6. Photo 8 shows the implementation of SWS test at site 7. Herein, the measured values of W_{SW} and N_{SW} has been converted into equivalent SPT-N value, N_{SPT}, by using the equation as follows (JIS A 1221).

$$N_{SPT} = 0.002W_{SW} + 0.067N_{SW} \qquad (1)$$

where Wsw is the minimum load required for penetration with 1000N or less than 1000N after starting penetration and N_{SW} is the value of static penetration resistance, which is the number of half rotations per penetration amount of 1m with the load of Wsw=1000N.

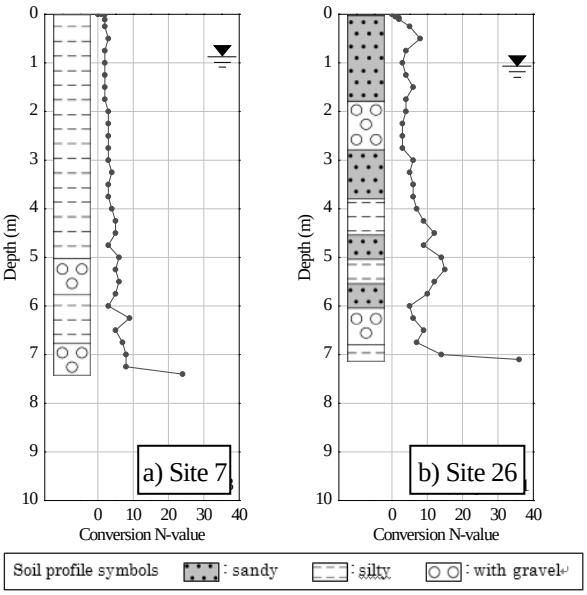


Figure 6 SWS test results (Sites 7 and 26 in Fig. 5)

At site 7, housing floors suffered from cracking that was caused by uneven settlement of the ground, and the boiled sand covered their garden with a thickness of 30cm. As shown in Fig. 6a), the ground water table was shallower than 1m from the ground surface, below which soft soil deposits with N_{SPT} values less than 5 could be found for a thickness of about 5m. It clearly indicates occurrence of liquefaction with this soft layer. The boiled sand that was retrieved at the same location as SWS test was fine sand with D_{50} of 0.12 mm and fines content of 18%.



Photo 8 SWS test (Site 7 in Fig. 5). Behind of experimenters, there is house suffered from cracking.

At site 26, St. Paul's Church that is located near the Avon-river suffered from uneven settlement. As shown in Figure 7, the settlements of 95cm and 109cm were measured at each side of cracking at the center part of the church, and the maximum settlement was measured around the tall structure. The pattern of the settlement of the church could be recognized from the angle of inclination of the wall as shown in Fig. 7. In addition, the pavement around the church also suffered from cracking for a maximum differential settlement of about 50 cm as shown in Photo 9. These damages may have been caused by liquefaction because the extensive sand boiling occurred around the church.

SWS test result conducted at an open space next to the church is shown in Fig. 6b). The ground water level was about 1m from the ground surface, below which soft soil deposits with N_{SPT} values less than 7 could be found for a thickness of about 4m. The boiled sand that was retrieved around the church was fine sand with D_{50} of 0.11mm and fines content of 28% (PI= NP). This suggests that soil deposits around the church may have liquefied significantly.

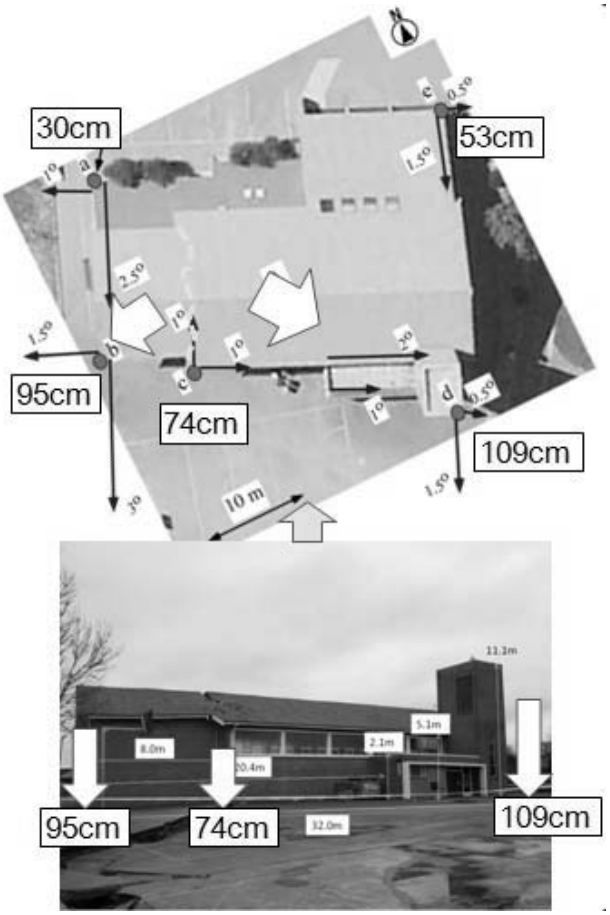


Figure 7 St Paul's church (built in 1956) suffered uneven settlement due to liquefaction (Site 26 in Fig. 5)



Photo 9 Pavement around St Paul's church suffered from large cracking and settlement (Site 26 in Fig. 5)

An unusual aspect of liquefaction observed in this survey is the low height of sand boiling. When liquefaction occurred, splash of both groundwater and liquefied sand to a height of several meters has been frequently observed in past earthquake. Although large amount of boiled sand could be observed throughout the city, there is little evidence of mud marking on the wall which would be resulted by sand boiling. This suggests that liquefied soil deposits may have a wide distribution with homogeneous condition, so that excess pore water pressure at local site became insignificant. In addition, we didn't find any up-lifted manholes and pipes during this survey, which could be frequently observed in past earthquake in Japan.

At site 20 at Porritt Park that is located about 1km east from the St. Paul's Church, sand boiling occurred throughout the park. Although the SWS test was not conducted in this park, the sand deposits were expected to be very soft because this park is surrounded by existing and previous river channels where the loose soil deposit is expected to be. Numerous cracks having a maximum opening width of 70 cm occurred in ground surface (Photo 10). These cracks were caused by liquefaction because almost all crack openings were filled with boiled sand. Since most of these cracks seem to be parallel to the previous river channel, the surface subsoil may have moved to the previous river channel and upraised riverbed as shown in Photo 11.

In the adjacent area (site 15), as show in Photo 12, river levee was damaged due to settlement and cracking, possibly caused by liquefaction of subsoil deposits.



Photo 10 Number of cracking and boiled sand could be observed in Porritt Park (Site 20 in Fig. 5)



Photo 11 Riverbed of previous river is upraised (Site 12 in Fig. 5)

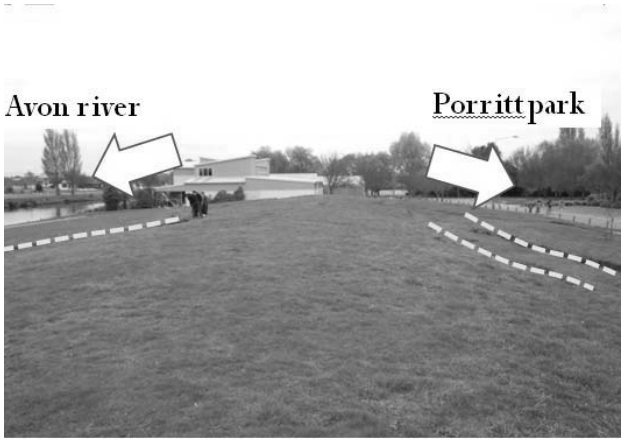


Photo 12 River levee was damaged due to settlement and cracking (Site 15 in Fig. 5)

As mentioned above, damage to the infrastructures due to liquefaction could be observed at many places along Avon-river. However, no sand boiling was observed at sites 84, 86, 87 and 89, about 300-500 m from Avon-river, so that possibility of liquefaction occurrence at these sites seems to be limited.

2.3 Bexley Area

The survey map of Bexley area is shown in Fig. 8. At site 91, about 1 km west from Bexley area as well as Avon river, there was no damage by liquefaction as shown in Photo 13. However, towards the Bexley area, the boiled sand came to be recognized on the street as shown in Photo 14.

Reportedly, the residential area in Bexley had been swamp, which was elevated by soil filling about 5 years ago. The swamp condition may be preserved south of residential area.

High damage ratio of houses was observed along the margins of landfill, and the slope of the filling was damaged due to excessive settlement and cracking (Photo 15). The boiled sand caused by liquefaction of fill material was observed around the damaged area.

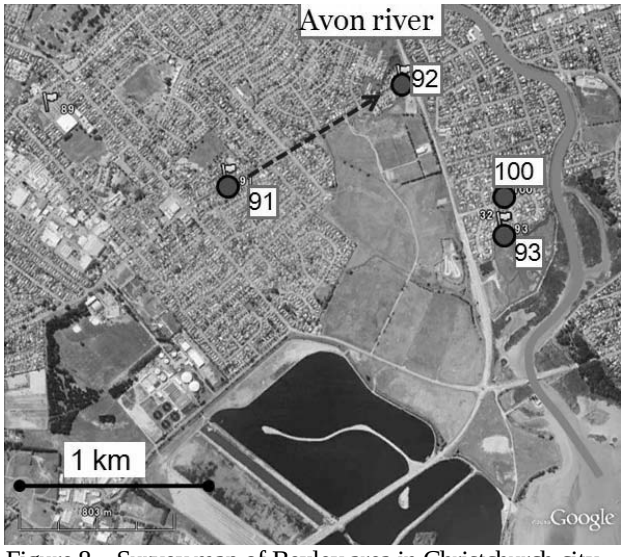


Figure 8 Survey map of Bexley area in Christchurch city



Photo 13 No damage due to liquefaction was observed (Site 91 in Fig. 8)



Photo 14 Street covered with boiled sand (Site 92 in Fig. 8)



Photo 15 Foundation of house suffered from large cracking (Site 93 in Fig. 8)

The result of SWS tests at site 93 that were conducted at the side of damaged house (Photo 15, Fig. 9a)) and the edge of swamp water (Fig. 9b) are shown in Fig. 9. The groundwater level in Fig. 9a) was about 1.5m from the ground surface, below which very soft sandy soil deposits with N_{SPT} values less than 5 could be found for a thickness of about 4m. This suggests that the soil compaction for landfill may not be enough at the time of the construction of

landfill. The boiled sand that was retrieved at the same location of SWS test was fine sand with D50 of 0.13mm and fines content of 12%.

As shown in Fig. 9b), there existed very soft silty soil deposits at the edge of swamp water with N_{SPT} values less than 5 for a thickness of more than 9m.

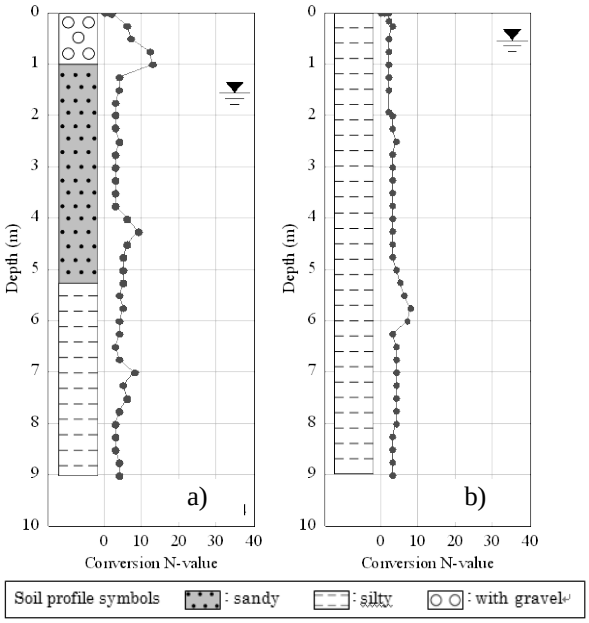


Figure 9 SWS test results (Sites 93 in Fig. 8)

Figure 10 shows the result of SWS test that was conducted on the landfill at site 100, about 300m from the margins of the landfill. The ground water level was shallower than 1.5m from the ground surface, below which soft soil deposits with N_{SPT} values less than 10 could be found for a thickness of about 5m. The N_{SPT} values at this point were slightly higher than those measured at the margins of landfill and the edge of swamp water as shown in Fig. 9. In fact, sand boiling around the site 100 was not significant as compare with other site.

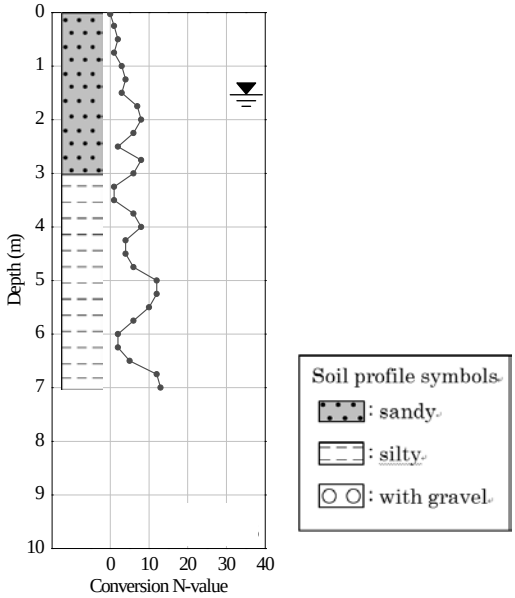


Figure 10 SWS test results (Sites 100 in Fig. 8)

3. SUMMARY

The authors conducted damage survey after the Darfield Earthquake in Christchurch city, New Zealand. The results from the survey can be summarized as follows:

Significant liquefaction occurred in Dallington and Bexley areas, the east part of Christchurch city. It caused severe damage to residences, buried lifelines and levees in Dallington area while the landfill suffered from cracking and deformation in Bexley area. By conducting Swedish weight sounding (SWS) tests, subsurface soil conditions with high groundwater table and soft soil deposits were investigated at several sites in Dallington and Bexley areas. Although sand boiling was seldom observed in business area, some old brick buildings suffered from cracking and dropping of masonry parts of the building.

Based on the survey, the earthquake-induced damages in Christchurch city can be summarized in Fig. 11. The liquefaction-induced damage to the infrastructures including houses could be observed along Avon-river except for business area, while possibility of liquefaction occurrence seems to be limited at the sites that more than 300m from the river.

It should be noted that, as shown in Fig. 11, the classification of damage in Christchurch city has not been completed in every location. Further wide-range of investigations is required.

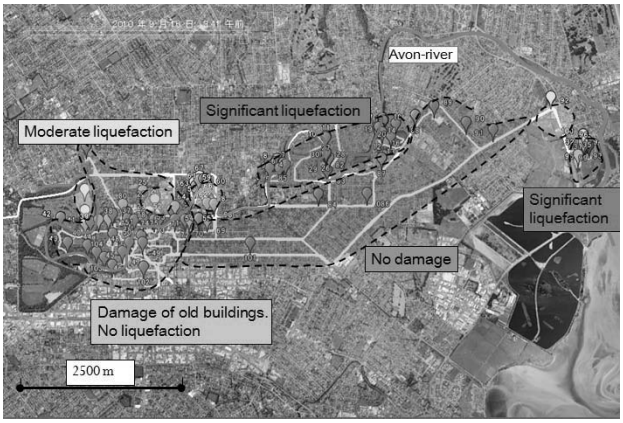


Figure 11 Earthquake-induced damage in Christchurch city on this survey

Acknowledgements:

The authors would like to express their sincere gratitude to Prof. Yasuda (Tokyo Denki University) and Prof. Kiku (Kanto Gakuin University) for provided information and SWS device. The authors also thank to staff and students of Canterbury University for their great help during the experimental work reported here.

References:

Geo-net (2010): http://www.geonet.org.nz/earthquake/quakes/3366146gmaps.html

USGS (2010): http://ehp1-earthquake.cr.usgs.gov/earthquakes/eqinthenews/2010/us2010atbj/

Yasuda (2010): http://yasuda.g.dendai.ac.jp/news100904.html

8CUEE CONFERENCE PROCEEDINGS
8th International Conference on Urban Earthquake Engineering
March 7-8, 2011, Tokyo Institute of Technology, Tokyo, Japan

STRONG GROUND MOTIONS AND SITE EFFECTS OF THE 2010 CHILE EARTHQUAKE

Toru Sekiguchi[1)], Nelson Pulido[2)], Gaku Shoji[3)], Jorge Alba[4)] and Fernando Lázares[5)]

1) Assistant Professor, Dept. of Urban Environment System, Chiba University, Japan
2) Researcher, National Research Institute for Earth Science and Disaster Prevention, Japan
3) Associate Professor, Dept. of Engineering Mechanics and Energy, University of Tsukuba, Japan
4) Professor, Faculty of Civil Engineering, National University of Engineering, Peru
5) Researcher, Japan-Peru Center for Earthquake Engineering and Disaster Mitigation, National University of Engineering, Peru
tsekiguc@faculty.chiba-u.jp, nelson@bosai.go.jp, gshoji@kz.tsukuba.ac.jp, jalvah@terra.com.pe, f_lazares@uni.edu.pe

Abstract: We report on a reconnaissance survey on the seismological and geotechnical aspects of the 27 February, 2010 Maule mega-earthquake, Chile, carried out between April 27 and May 1, 2010. The survey was sponsored by the Japan Science and Technology Agency and JICA (SATREPS). In this study we surveyed the cities of Concepción Viña del Mar and Santiago. We also performed microtremors measurements at strong motion stations that recorded the earthquake. We will give an outline of the fault rupture process and strong motion characteristics of the earthquake and the site effects estimated from microtremor measurement.

1. INTRODUCTION

The 2010/2/27 Maule (Chile) mega-earthquake, the fifth largest earthquake in instrumental history, was located in the subduction of the Nazca plate in Meridional Andes beneath the South American plate. This earthquake fills a well studied seismic gap between the source areas of the largest ever recorded 1960 Great Valdivia earthquake (M 9.5), and the 1985 Valparaiso earthquake (M7.8) (Ruegg et al. 2009). In this study we report on a reconnaissance survey on the seismological and geotechnical aspects of the 27 February, 2010 Maule mega-earthquake, Chile, carried out between April 27 and May 1, 2010. The survey was sponsored by the Japan Science and Technology Agency and JICA (SATREPS), under the framework of a newly launched 5 years SATREPS project entitled "Enhancement of Earthquake and Tsunami Disaster Mitigation Technology in Peru" (Yamazaki et al. 2010). In this study we surveyed the heavily damaged city of Concepción, as well as moderately damaged cities of Viña del Mar and Santiago (Figure1). We performed microtremor measurements at strong motion stations that recorded the earthquake in order to evaluate their site characteristics. We also surveyed the damage to buildings due to tsunami effects in Dichato and Talcahuano among other areas but these results are reported elsewhere (Shoji et al 2010).

2. SOURCE PROCESS OF THE MAULE EARTHQUAKE

The Maule earthquake ruptured a source area of nearly 450 km extending from southern Santiago in the North, down to the Arauco Peninsula south of Concepción city. The intensity distribution obtained from a questionnaire survey soon after the earthquake (Astroza et al 2010), indicates that a region of nearly 350 km above the fault plane experienced an intensity larger than 5 upper in the JMA intensity scale (Figure 2). This earthquake was an inter-plate mega-subduction event with a pure reverse mechanism, and had a seismic moment magnitude of 8.8 (Figure 3). The source rupture model of this earthquake was obtained by inversion of 38 P-wave teleseismic waveforms of the FDSN and GSN global seismic networks and using an inversion technique that incorporates an error component in Green's function calculation and the Akaike's Bayesian Information Criteria (ABIC) (Yagi and Fukuhata 2008). The source process is characterized by two asperities with a peak slip of more than 10 m and a rupture area of approximately 450 by 200 km^2 (Pulido et al. 2010). The first asperity is located at the hypocenter and the second is located approximately 150 km north-east of the hypocenter. The rupture propagated bilaterally starting slightly south of Constitución and with an average rupture velocity of 2.8 km/s, however the main moment release was located towards the North in the Pichilemu region. The source moment function has a total source duration of 150 s and display two sub-events separated by 30s (Figure 3).

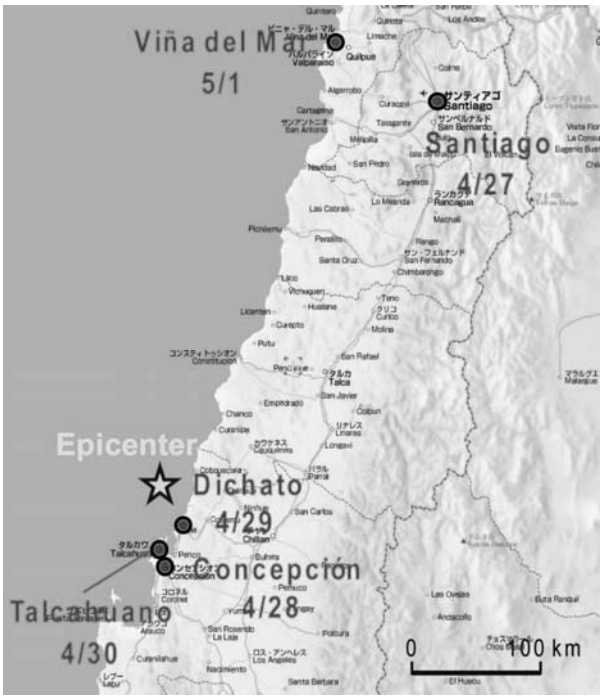


Figure 1 Location of sites for field survey

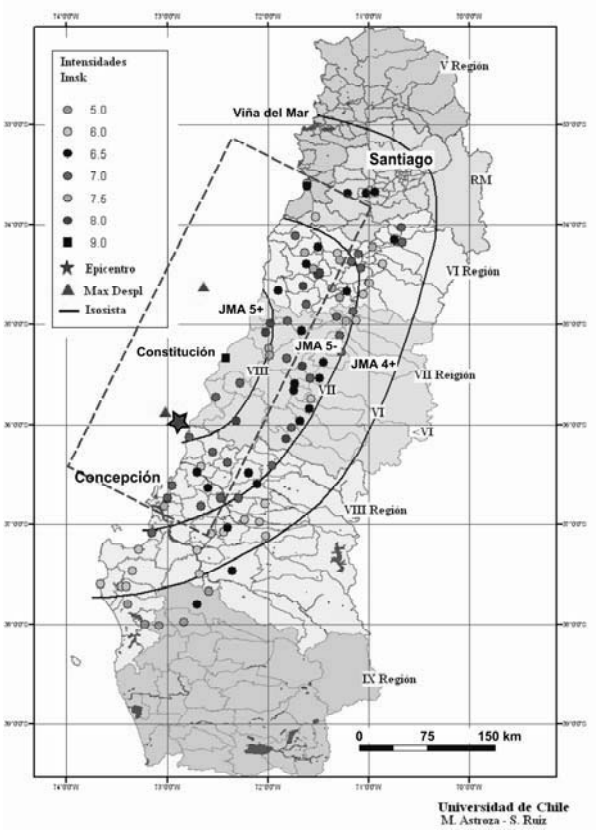


Figure 2 Intensity distribution of the Maule earthquake based on questionnaire survey (Astroza et al. 2010).

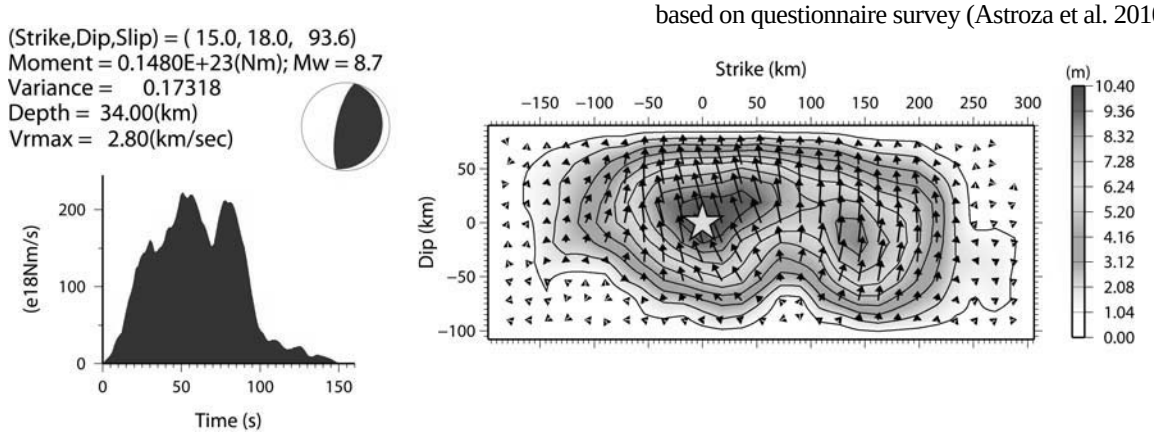


Figure 3. Source model of the 2010/02/27 Maule mega-earthquake (Pulido et al. 2010).

The average rake angle of this earthquake is 93 degrees which approximately corresponds to the oblique convergence of the Nazca plate beneath the South American plate.

3. STRONG MOTION CHARACTERISTICS

The Maule earthquake was recorded by 30 strong motion stations belonging to Universidad de Chile (Servicio Sismológico Nacional SSN, Geophysics department, 10 stations, and Red Nacional de acelerógrafos, RENADIC, Civil Engineering department, 20 stations). Instruments are mostly digital (21), and a large number of them is localized in Santiago (10) (Table 1). Published maximum PGA and PGV values reached 909 cm/s^2 at the Angol station south of Concepción, and 69 cm/s at Constitución (Table 1, Figure 4). Strong ground motions recorded in the northern region of the source area such as Curicó, Santiago and Viña del Mar display two clear sub-events separated by 15s to 30s, which is consistent with a rupture propagation velocity value of 2.8 km/s (Figure 4). Stations towards the central and southern regions of the source area such as Constitución, Concepción and Angol do not diplay distinct sub-events, as the rupture propagation of the northern asperity gradually runs away from southern stations. Angol station displays the largest PGA which indicates the possibility of large slip below the Arauco peninsula (around latitude -37.5 degrees), that is not sufficiently simulated in our current slip model. In fact a recent study indicates that the Arauco peninsula experienced a maximum coseismic uplift of 2.5m along the

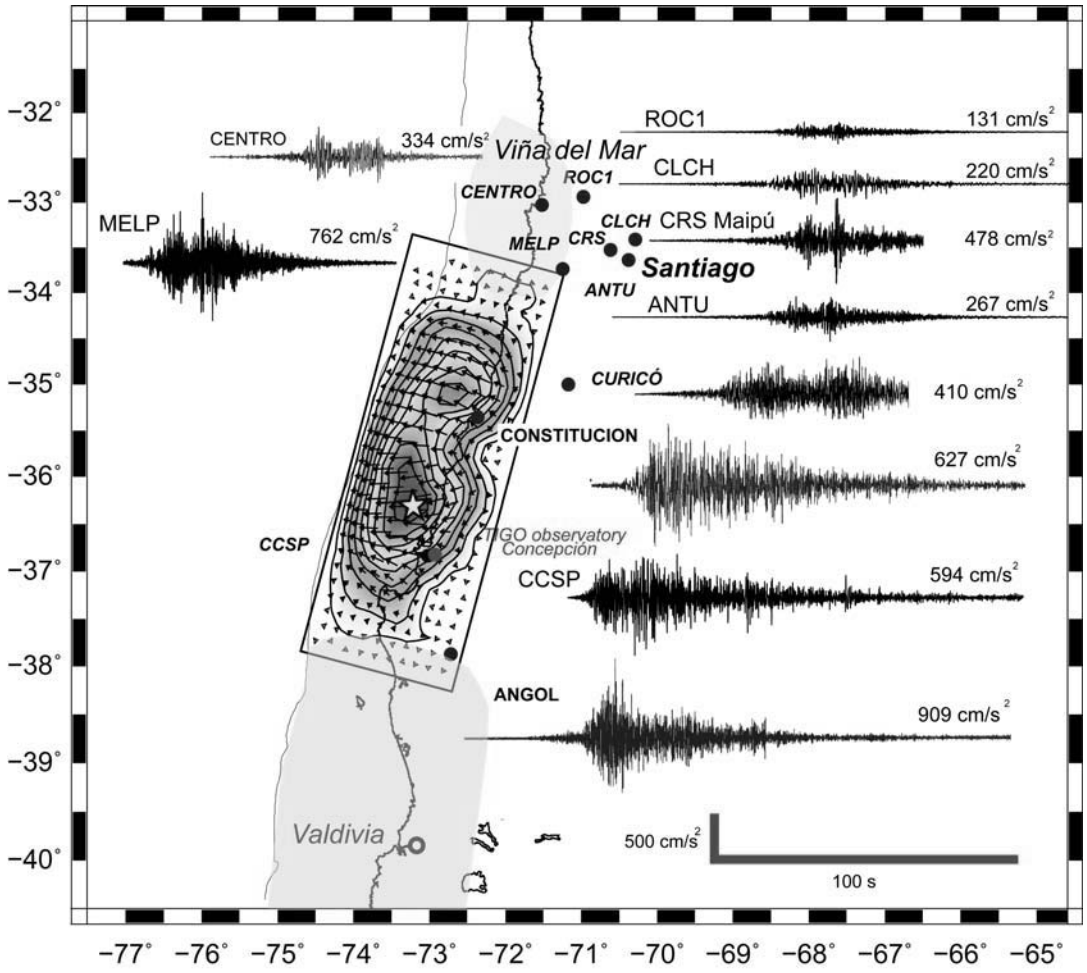


Figure 4. Source model and strong ground motion recordings of the 2010/02/27 Maule mega-earthquake (Pulido et al. 2010).

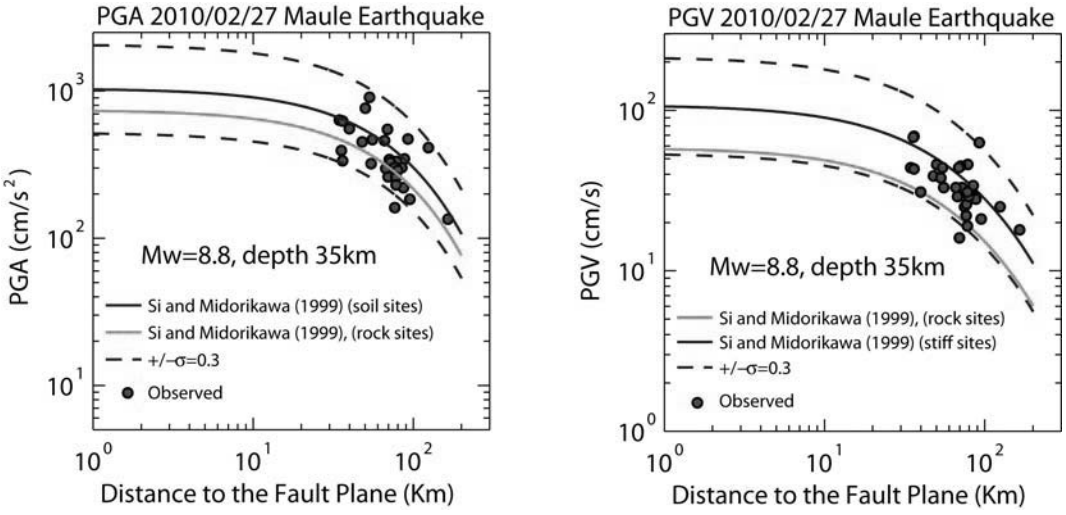


Figure 5. Attenuation of PGA and PGV for observed strong motions Maule mega-earthquake (Chile)

coast, suggesting that the source area could have reached a latitude as far as -38 degrees (Farías et al. 2010), which approximately corresponds the northern end of the 1960 Valdivia earthquake.

In Figure 5 we plotted the PGA and PGV attenuation characteristics of observed strong ground motions of the Maule earthquake, for all the sites described in Table 1. We plot the data together with an empirical relationship of PGA and PGV for inter-plate subduction earthquakes (Mw=8.8, depth 35 km) for soil, stiff soil and rock site conditions (Si and Midorikawa 1999). We may observe that all observed data falls within one sigma (+/-0.3) around the values for a

stiff soil. This result implies that the observed peak ground motions characteristics from the Maule earthquake can be satisfactorily explained by a typical empirical attenuation relationship for inter-plate subduction earthquakes.

Table 1. Strong ground motion stations that recorded the 2010/02/27 Maule mega-earthquake

Station Location	Station	Organization	Instrument	Longitude	Latitude	PGA	PGV
Concepción	CCSP	SSN[2]	ETNA	-73.1087	-36.8443	637	44
Santiago (Campus Antumapu)	ANTU	SSN[2]	Episensor,	-70.6335	-33.5691	267	25
Cerro El Roble	ROC1	SSN[2]	Episensor,	-71.0156	-32.9759	184	21
Santiago (Cerro Galán)	CLCH	SSN[2]	SSA-120SLN,	-70.5369	-33.3961	220	29
Melipilla	MELP	SSN[2]	QDR	-71.2138	-33.6874	762	46
Olmué (10 km West of El Roble)	OLMU	SSN[2]	QDR	-71.1730	-32.9940	347	28
Casablanca, Teatro municipal	CSCH	SSN[2]	QDR	-71.4108	-33.3208	322	44
San José de Maipó[1]	SJCH	SSN[2]	Makalu	-70.3510	-33.6440	471	63
Santiago (Colegio las Américas)	LACH	SSN[2]	Makalu	-70.5308	-33.4518	302	34
Santiago (Cerro Santa Lucía)	STL	SSN[2]	Makalu	-70.6428	-33.4405	332	46
Papudo (V Región)[1]	-	RENADIC[3]	SMA-1	-71.4440	-32.5090	413	25
Viña del Mar Marga-marga (V	-	RENADIC[3]	ETNA	-71.5099	-33.0482	344	45
Viña del Mar Centro (V Región)	-	RENADIC[3]	QDR	-71.5508	-33.0253	327	33
Valparaíso UTFSM (V Región)	-	RENADIC[3]	SMA-1	-71.5956	-33.0346	261	16
Valparaíso Almendral (V Región)[1]	-	RENADIC[3]	SMA-1	-71.6130	-33.0560	298	29
Llolleo (V Región)[1]	-	RENADIC[3]	SMA-1	-71.6150	-33.6130	553	31
Santiago FCFM RM	-	RENADIC[3]	ETNA	-70.6617	-33.4572	162	22
Santiago centro RM (Based Isolated	-	RENADIC[3]	SSA-2	-70.6520	-33.4670	303	26
Santiago Maipú RM (CRS Maipú)	-	RENADIC[3]	QDR	-70.7719	-33.5087	550	44
Santiago Peñalolen RM (Hospital	-	RENADIC[3]	QDR	-70.5792	-33.5006	289	29
Santiago Puente Alto RM (Hospital	-	RENADIC[3]	QDR	-70.5811	-33.5769	260	31
Santiago La Florida RM (Linea 5,	-	RENADIC[3]	K2	-70.6060	-33.5135	231	19
Matanzas (VI Región)	-	RENADIC[3]	SMA-1	-71.8734	-33.9604	335	43
Hualañe (VII Región)	-	RENADIC[3]	SMA-1	-71.8053	-34.9765	452	39
Curico (VII Región)	-	RENADIC[3]	QDR	-71.2364	-34.9808	461	33
Talca (VII Región)	-	RENADIC[3]	SMA-1	-71.6649	-35.4299	467	33
Constitución (VII Región)	-	RENADIC[3]	SMA-1	-72.4057	-35.3401	627	69
Concepción (VIII Región), Colegio	-	RENADIC[3]	SMA-1	-73.0483	-36.8281	394	68
Angol (IX Región)	-	RENADIC[3]	QDR	-72.7081	-37.7947	909	38
Valdivia (XV Región)	-	RENADIC[3]	QDR	-73.2133	-39.8244	135	18

Notes

[1] approximate station coordinates from Google Earth

[2] Servicio Sismológico Nacional, Universidad de Chile

[3] Red Nacional de Acelerógrafos, Universidad de Chile

[4] Most infomation for this table was compiled from [7,8,9,10)]

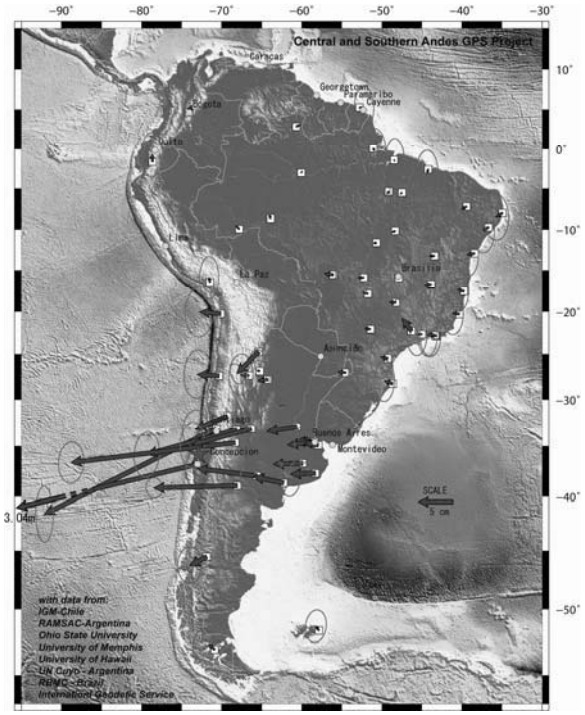


Figure 6. Coseismic displacements at South American GPS stations during the 2010/02/27 Maule mega-earthquake (Chile). Displacements at Concepción are as large as 3 m to the West (Foster and Brooks 2010).

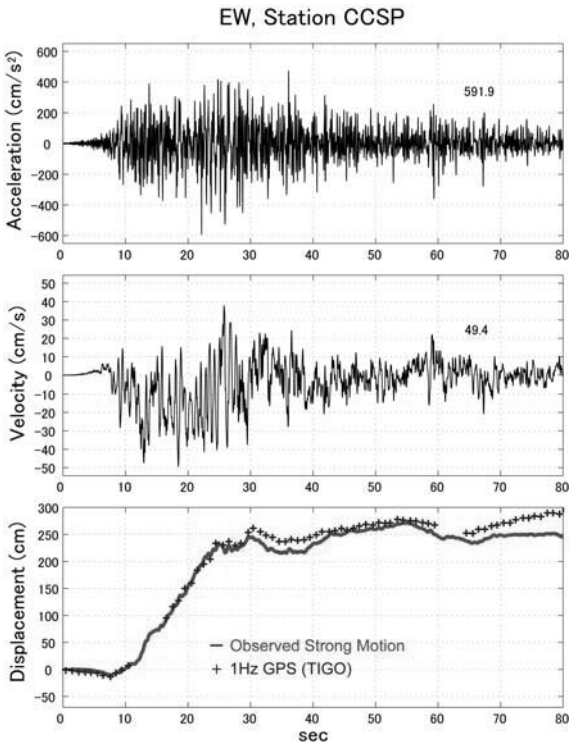


Figure 7. Strong ground motion recording of the 2010/02/27 Maule mega-earthquake (Chile) at the Colegio San Pedro (Concepción), strong motion site. Upper panel shows the unfiltered acceleration, middle panel the unfiltered and de-trended velocity, and the lower panel the calculation of the permanent displacement at this station (Pulido et al. 2010)

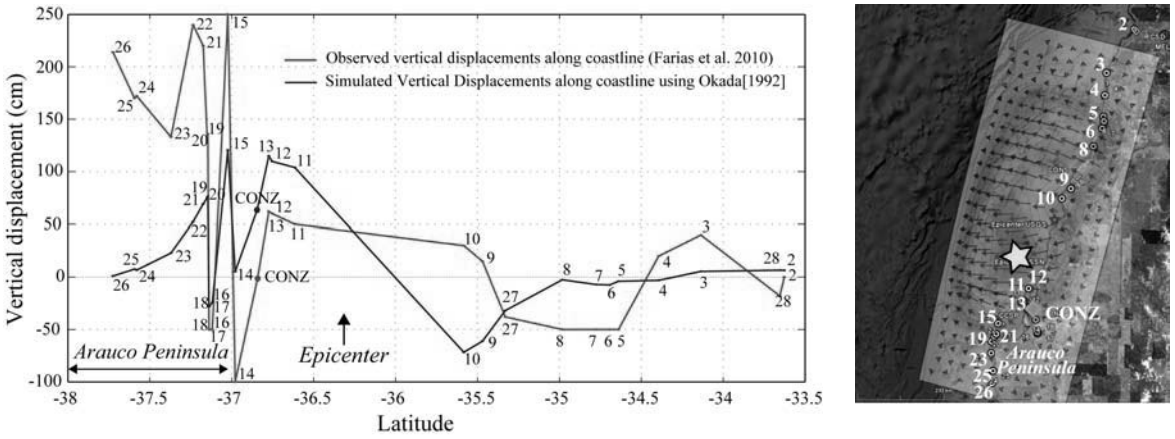


Figure 8. Comparison between observed (red) and simulated (blue) permanent coseismic vertical displacement along the coast during the 2010 Maule earthquake (left figure). Observed vertical uplifts where measured from observation of changes in coral algae along the coast (Farías et al. 2010). Right figure shows the location of vertical displacement measurement points.

4. COSEISMIC PERMANENT DISPLACEMENTS

GPS measurements from the Maule earthquake in South America indicate a coseismic displacement to the West as large as 3m at the CONZ station in Concepción (Figure 6). CONZ is a high sampling GPS (cGPS) station located at the Transportable Integrated Geodetic Observatory (TIGO), which recorded in real time the Maule earthquake (Sierk and Hase 2010). We attempted to calculate the permanent displacement at Con-cepción by using a strong motion recording of the earthquake at the CCSP station, which is closely located to the TIGO observatory. For that purpose we double integrated and de-trended the unfiltered acceleration data. Our results show nearly 3m of permanent displacement to the West, which is in very good agreement with the results by the cGPS recording at TIGO (Figure 7). Displacement time series obtained from this strong ground motion recording are also in close agreement

with the observed cGPS from the arrival of the rupture up the static displacement value.

We also calculated the coseismic vertical displacements along the coastline by using our source model of the Maule earthquake (Figure 3) and analytical expressions for strains and displacements in a half space due to shear dislocations (Okada 1992) (Figure 8). Our simulation results show in general a good agreement with the observed uplift/subsidence values along the coast, estimated from changes in coral algae (Farías et al. 2010) as well as high sampling GPS measurements at the TIGO geodetic observatory [CONZ] (Figure 8). However our simulated vertical displacements underestimate the observed values at the Arauco peninsula, suggestting larger values of coseismic fault slip beneath the Peninsula (Figure 8).

5. MICROTREMORS MEASUREMENS AT STRONG MOTION SITES

In order to estimate the site characteristics at strong motion sites that recorded the mainshock we performed microtremor measurements in Santiago, Concepción and Viña del Mar cities. The microtremor measurements were performed by using a velocity sensor with predominant period of 2 s and a sampling frequency of 200 Hz. Measurement time at each site was set to 300s.

5.1 Santiago City

We surveyed two areas in Santiago city. The first area (MPS) is the RENADIC Santiago Maipú RM strong motion station located in the western region of the city (Figure 9). We found several heavy damaged buildings around this area.

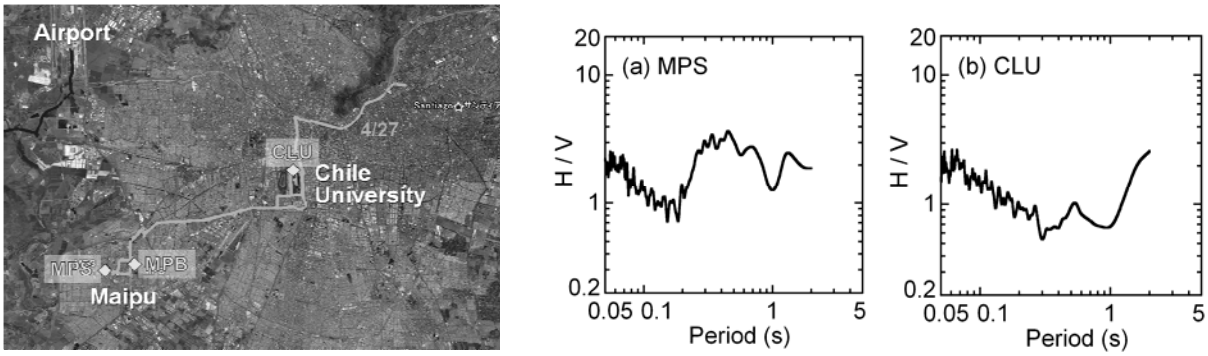


Figure9. H/V of microtremors measurements near strong motion station Maipu [MPS], and Chile university [CLU] in Santiago city

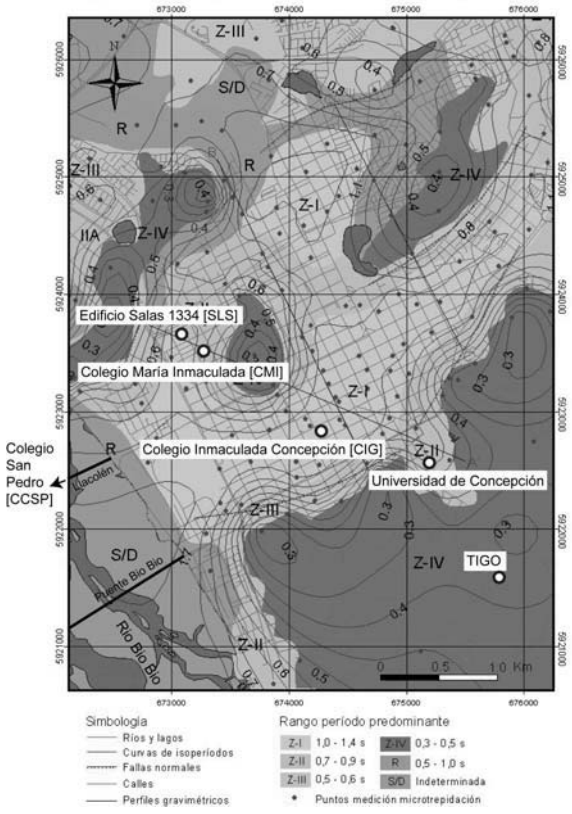


Figure 10. Microzonation map of Concepción city (Ramírez and Vivallos 2009). Survey sites are shown within the figure

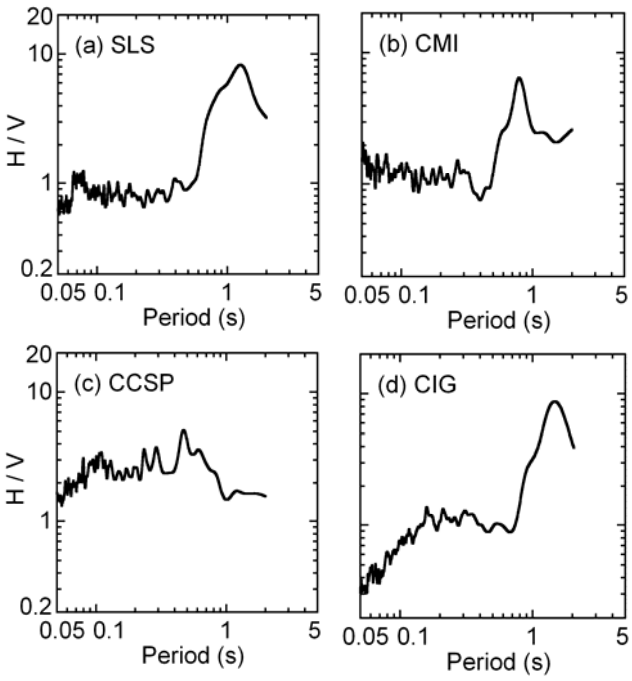


Figure 11. H/V ratios of microtremors in downtown Concepción city

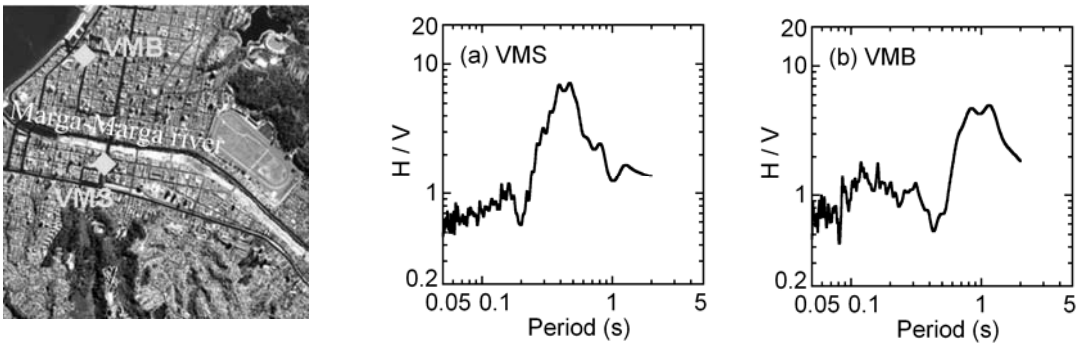


Figure12. H/V of microtremors measurements near strong motion station Viña del Mar Centro [VMS], and within the building damage area [VMB] in Viña del Mar

We also surveyed the area near Chile University in the center of Santiago city (CLU). In this case our survey indicates no building damage around this area. Our H/V measurements at MPS indicate a clear peak around 0.4s. This site experienced a PGA value of 550 cm/s^2 and a PGV of 44 cm/s respectively. On the other hand H/V measurements at CLU don't show a clear peak. These measurements suggest that the site effects may have had a contribution to the building damage near MPS.

5.2 Concepción City

In Figure 10 we show the microtremor measurements sites as well as other survey sites on a microzonation map of Concepción city (Ramírez and Vivallos 2009). This microzonation is based on H/V measurements as well as other geological and geotechnical information. A yellow region on the map (Z-I) corresponds to H/V peaks of 1.0-1.4s. We can observe that the dowtown area is largely characterized by a predominant peak around 1s. On the other hand in the South-West area of downtown runs the Bio-Bio river which suggest that the soil condition in this region might be characterized by thick alluvial deposits. We performed microtremor measurements at four sites including two schools in down-town; Colegio inmaculada Concepción (CIG), Colegio María Inmaculada (CMI), a heavily damaged (to be demolished) 12 stories reinforced concrete building (Edificio Salas 1334, SLS), and another school located in the opposite shore of the Bio-Bio river in a mountain footslope area (Colegio San Pedro) (Figure 10). Our H/V measurements at CIG and SLS show a predominant peak larger than 1s, and a peak of 0.7s at CMI (Figure 11). The heavy damage sustained at SLS might be related with the large H/V peak at this site. The underground floor of the CIG building accomodates a RENADIC analogue acelerograph that recorded a PGA value of 394 cm/s^2 and a PGV of 68 cm/s. This building sustained a moderate damage and according to the shool principal an older section of the school also experienced the 1960 Valdivia earthquake. Our H/V measurements at Colegio San Pedro where located near the CCSP strong motion station within the school premises. This site recorded a PGA value of 637 cm/s^2 and a PGV of 44 cm/s. The school is built on a sandy soil area within a small valley, and the CCSP is located at the egde of the valley near a slope. A 1 story classroom located close to the strong motion station sustained significant damage produced by subsidence of the ground. Although H/V measurements close to the CCSP station do not show significant peaks (Figure 10), another H/V measurement at the school ground in the middle of the valley show a clear peak around 0.3s. This indicates that the CCSP station is located at the edge of the valley sandy soil deposits (Sekiguchi et al. 2010).

5.1 Viña del Mar city

We surveyed two areas in down town Viña del Mar. The first area (VMS) is located in the southern region of the Marga Marga river close to the RENADIC Viña del Mar Centro strong motion station (Figure 12). Our survey indicates no building damage around this area. We also surveyed the area to the north of Marga-Marga river (VMB). In this case we found a heavy concentration of damage to medium rise apartment buildings. Our H/V measurements at VMS indicate a clear peak around 0.4s. This site experienced a PGA value of 327 cm/s^2 and a PGV of 33 cm/s respectively. On the other hand H/V measurements at VMB show a clear peak at 1s. These measurements suggest that the site effects may have had a big contribution to the building damage at VMB, and indicate the ground motion might have been stronger at the Nothern part of Marga-Marga river compared to the Southern area.

6. CONCLUSIONS

We performed a field survey of the 2010 Chile earthquake which included visits to several universities in Santiago, Concepción and Viña del Mar, as well as microtremor measurements near strong motion stations at these cities. Near-source strong ground motions characteristics of the mainshock are largely influenced by complexity in source rupture process. On the other hand ground motion attenuation characteristics of this earthquake can be satisfactorily explained with a typical empirical law for inter-plate subduction earthquakes. Based on a strong motion recording of the mainshock we obtained a 3m

permanent displacement to the west at Concepción city, which is in very good agreement with the results obtained by a 1Hz GPS recording of the earthquake at the TIGO observatory in Concepción. Our theoretical calculations of coseismic displacements along the coast are also in good agreement with the observed data. Our microtremors measurements and field survey indicates a clear relationship between site effects and building damage. Future research work includes the improvement of our source model using constraints from near-source data as well as the strong motion simulation of this earthquake.

Acknowledgements:

We would like to thank Sergio Barrientos, Jaime Campos, Ruben Boroschek as well as other members of Universidad de Chile, Universidad de Concepción, and Universidad de Valparaiso. Strong motion data used in this study belongs to Servicio Sismológico Nacional, Universidad de Chile.

References:

Ruegg, J.C., A. Rudloff, C. Vigny, J.B. de Chabalier, J. Campos, E. Kausel, S. Barrientos, and D. Dimitrov (2009), "Interseismic strain accumulation measured by GPS in the seismic gap between Concepción-Constitución in Chile," Physics of Earth and Planetary Interiors, **175**, 78-85.

Yamazaki, F., Zavala, C., Nakai, S., Koshimura, S., Saito, T. and Midorikawa, S. (2010), "Enhancement of earthquake and tsunami disaster mitigation technology in Peru: A SATREPS project," 7th International Conference on Urban Earthquake Engineering.

Shoji, G., Pulido, N., Sekiguchi, T., Alva, J., Lazares, F., and Saito, T. (2010), "Damage Investigation of The 2010 Chile Earthquake and TSUNAMI – Consideration to The Damage of A Structure Subjected to A Seismic Excitation and A Following TSUNAMI Wave Load," 13th Japan Earthquake Engineering Symposium. (in Japanese)

Astroza, M., Cabezas F., Moroni M., Massone L., Ruiz S., Parra E., Cordero F., and A. Mottadelli (2010), "Intensidades Sismicas en el Area de Daños del Terremoto del 27 de Febrero de 2010," Internal Report Universidad de Chile, Departamento de Ingeniería Civil. (in Spanish)

Yagi, Y. and Fukahata, Y. (2008) "Importance of covariance components in inversion analyses of densely sampled observed data: an application to waveform data inversion for seismic source processes," Geophysical Journal International, **175**, 215–221.

Pulido, N., Yagi, Y., Nishimura, N. and Kumagai, H. (2010), "Source rupture process and strong motion simulation of the Mw8.8, 2010 Chile Mega earthquake," Abstracts of the Fall meeting of the Seismological Society of Japan, B11-07.

Barrientos, S. (2010), "Terremoto Cauquenes 27 Febrero 2010," Servicio Sismológico, Universidad de Chile, Informe Tecnico Actualizado 27 Mayo 2010, 5/2010a. http://ssn.dgf.uchile.cl/informes/INFORME_TECNICO.pdf (in Spanish)

Barrientos, S. (2010), "Acelerogramas del Terremoto del 27 de Febrero 2010 registrados por DGF," Servicio Sismológico, Universidad de Chile, Informe Tecnico Actualizado 27 Mayo 2010, 5/2010b. http://ssn.dgf.uchile.cl/informes/sismogramas.zip

Boroschek, R., P. Soto, and R. Leon (2010), "Report Maule Region Earthquake February 27, 2010 Mw=8.8," Universidad de Chile Facultad de Ciencias Físicas y Matemáticas, Departamento de Ingeniería Civil, Informe RENADIC 10/08, 8/2010a. http://www.cec.uchile.cl/~renadic/red_archivos/RENAMAULE 2010.pdf

Boroschek, R. (2010), "Mapa actualizado de estaciones en la zona del Terremoto del 27 de Febrero 2010," Universidad de Chile Facultad de Ciencias Físicas y Matemáticas, Departamento de Ingeniería Civil, RENADIC, 2010b. http://www.cec.uchile.cl/~renadic/red_archivos/ESTACIONES 20EQ 20CHILE 202010_RBoroschek.kmz

Farías M.,Vargas G., Tassara A., Carretier S., Baize S., Melnick D., and K. Bataille (2010), "Land-Level Changes Produced by the Mw 8.8 2010 Chilean Earthquake," Science, **329**, 916, DOI: 10.1126/science.1192094.

Si, H. and Midorikawa, S. (1999), "Attenuation Relations for Peak Ground Acceleration and Velocity Considering Effects of Fault Type and Site Condition," Journal of Struct. Construct. Eng. (Transactions of AIJ), **523**, 63-70. (in Japanese)

Sierk, B., and Hase, H. (2010), "El terremoto de Chile desde la perspective científica, Transportable Integrated Geodetic Observatory (TIGO)," http://www.tigo.cl/documents/PresDAAD.pdf (in Spanish)

Foster, J., and Brooks, B. (2010), "Science Highlights 2010 - UNAVCO Event Response - Mw=8.8 Chile Earthquake Feb. 27," http://www.unavco.org/research_science/science_highlights/2010/M8.8-Chile.html

Okada, Y. (1992), "Internal deformation due to shear and tensile faults in a half space," Bull. Seismol. Soc. Am., **82**(2), 1018-1040.

Midorikawa, S. (2010), "Earthquake and earthquake motion," Report on the joint survey of the 2010 Chile earthquake. http://www.jaee.gr.jp/disaster/2010/2010chile.html (in Japanese)

Ramírez P. and J. Vivallos (2009), "Microzonificación sísmica de la ciudad de Concepción – Chile," XII Congreso Geológico Chileno, Santiago, 22-26 Noviembre. (in Spanish)

Sekiguchi, T., Pulido, N., Shoji, G., Alva, J., Lázares, F. and Saito, T. (2010), "Damage Investigation of the 2010 Chile Earthquake and Tsunami -Seismic Ground Motion and Site Effects," 13th Japan Earthquake Engineering Symposium. (in Japanese)

8CUEE CONFERENCE PROCEEDINGS
8th International Conference on Urban Earthquake Engineering
March 7-8, 2011, Tokyo Institute of Technology, Tokyo, Japan

SEISMIC RISK PERFORMANCE OF URBAN TRANSPORTATION SYSTEMS CONSIDERING SITE EFFECTS AND INTERACTION WITH THE BUILT ENVIRONMENT

Sotirios Argyroudis[1)] and Kyriazis Pitilakis[2)]

1) Dr Civil Engineer, Dept. of Civil Engineering, Aristotle University of Thessaloniki, Greece
2) Professor, Dept. of Civil Engineering, Aristotle University of Thessaloniki, Greece
sarg@civil.auth.gr, kpitilak@civil.auth.gr

Abstract: Transportation systems play a vital role in urban areas, which is more crucial in an emergency situation such as after a strong seismic event. In areas with high build density and seismicity it is of particular interest to estimate the risk for blockage of roads due to collapsed buildings. A probabilistic framework is described considering the geometrical characteristics of roads and buildings, together with their failure probabilities. The vulnerability of bridges due to ground shaking and the fragility of roads due to soil liquefaction are also estimated based on appropriate fragility curves. The reliability of the network to connect hospitals with residential areas is assessed based on the damage probabilities of the road components. Moreover, the total risk depends on the importance of the network elements, which is classified through a global value analysis, considering different functional and urban criteria. An analysis of this type is performed for the roadway network in the city of Thessaloniki, for scenario seismic events that are based on a detailed microzonation study. Through this approach the role of site effects in the risk assessment of the roadway network is highlighted, while the interconnection between bridges, roads and urban elements (buildings, hospitals, population) is considering.

1. INTRODUCTION

Experience from past earthquakes reveals that road components are quite vulnerable, while their damage could be greatly disruptive due to the lack of redundancy, the lengthy repair time or the rerouting difficulties. For example, the disruption to the road network can strongly affect the emergency efforts immediately after the earthquake or the rebuild and other business activities in the following period.

The complexity and variability of elements at risk, the spatial variability of ground motion, and till recently, the lack of well validated damage and loss data from strong earthquakes, make the vulnerability assessment of each particular component and of the network as a whole, a quite complicated problem. Adding to that the spatial extend of transportation networks, the synergies with the urban system and the inherent uncertainties in seismic hazard estimates, it is obvious that the risk assessment is indeed a complex and challenging issue. Several methodologies have been developed and applied worldwide, which can be assigned to the following three levels:

- Level I is focused on the functioning of the network in terms of pure connectivity (Nuti and Vanzi 1998, Franchin et al. 2006). The considered vulnerable elements are those internal to the network itself, which generally consists of bridges, viaducts, tunnels, retaining structures, etc, and other elements of the surrounding environment, such as buildings or hospitals. These studies focus on one of the services provided by the network, e.g. most typically the rescue function immediately after the earthquake, and may be of interest in identifying portions of the network which are critical with respect to the continued connectivity of the network, while allow the estimation of direct economic loss.

- Level II is further considering the network capacity to accommodate traffic flows (Shinozuka et al. 2003, Kiremidjian et al. 2006, Werner et al. 2006). A first approximation of the indirect loss and travel time delays caused by the earthquake is assessed, sometimes taking into account the repair process.

- Level III is the most general approach, which aims at obtaining a realistic estimate of total loss, inclusive of direct physical damage, network-related loss (increased travel time) and loss due to reduced activity in the economic sectors (industry, services) (Veneziano et al. 2002, Karaca 2005). At this level the relevance and the complexity of the economic models become dominant over that of the transportation network.

In the present paper a level I methodology for the seismic risk assessment of urban road network is described and applied for the city of Thessaloniki, Greece. The expected direct damages of the network are estimated, while the effect of possible building collapses to the functionality of the network is examined. Moreover, the importance of the network components is classified based on a global value system approach and the connectivity between critical origin-destinations of the damaged network is assessed. Representative examples are given for each step of the analysis.

2. METHODOLOGY FOR THE SEISMIC RISK ASSESSMENT OF ROAD NETWORK

The main points of the methodology (Argyroudis 2010) are summarized hereinafter (fig. 1):

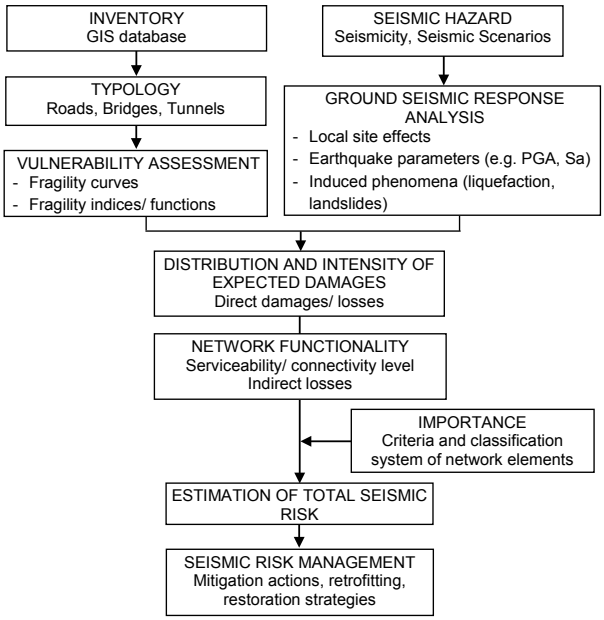


Figure 1 Methodology for the seismic risk assessment of roadway network.

- Inventory is an essential step to identify, characterize and classify all elements of the road network according to their specific typology and their distinctive geometric, structural and functional features. GIS offers the perfect and indispensable platform to implement any inventory inquires.

- Seismic hazard must be specified according to the precise needs for the particular network components as well as the models used to describe vulnerability. The spatial variability of ground motion should consider the effect of local soil conditions, topography etc (Pitilakis et al. 2006).

- The vulnerability of road elements at risk is assessed through appropriate fragility curves or indexes, which are based on analytical, empirical or expert judgment approaches. The earthquake parameter that describes the seismic intensity depends on the typology of the element and the type of seismic hazard. For example when the ground shaking is examined, the best descriptor is a response spectral value at a specific period (i.e. T=1.0sec for bridges) or the peak ground acceleration (i.e. tunnels, bridges). For other components (i.e. embankments, pavements) the permanent ground deformation due to ground failure (i.e. liquefaction, landslide) is used.

- An essential risk for urban roads is the closure due to collapsed buildings. It is assessed based on the fragility of buildings and simplified relationships between the geometry of the buildings and the area of collapse.

- The serviceability of the network for the expected distribution and intensity of damages is assessed based on simplified or more advanced approaches.

- The classification of importance is based on a set of indicators that compose the global value of each element at risk. Such criteria describe the importance and role of each element within the urban system in normal, crisis or recovery periods.

- The total seismic risk is a combination of the vulnerability and importance assessment. The main issues of the system are identified and the priorities for efficient risk mitigation strategies, such as retrofitting actions or restoration works are identified.

Further details of the methodology are given in the following, together with representative examples of the application in the main urban network of Thessaloniki city in Greece.

3. APPLICATION IN THESSALONIKI ROAD NETWORK

The inventory for the roadway network in the metropolitan area of Thessaloniki includes about 600 km of road-lines and 80 bridges. It is rather insufficient, especially in the centre, where the densely built up area creates a complex network, with narrow streets and inadequate parking areas. Roads are classified in freeways, major and secondary arterials, primary and secondary collectives, based on their geometry and functional role in the network. The majority of bridges are in the ring road and the main exits of the city. Their classification is based on the number of spans (single or multiple), the design seismic code level (low or upgraded), the pier type (single or multiple columns) and the span continuity (continuous or simple support). The vulnerability analysis of the network includes the estimation of direct losses such as bridge and road damage due to ground shaking or ground failure, and indirect such as street blockades, due to debris of collapsed buildings.

3.1 Seismic scenarios

The seismic hazard study is based on the seismotectonic environment and the seismicity of the study area. In the framework of the detailed microzonation study of Thessaloniki, three seismic scenarios are considered, with mean return period equal to 100, 475 and 1000 years (Pitilakis et al. 2010). The study is based on the results of a probabilistic seismic hazard analysis using recent data regarding the seismicity, the corresponding seismic zones and the seismic faults in the greater area. A detailed model of the surface geology and geotechnical characteristics, for site effect studies, was generated. The resulted geotechnical map (Anastasiadis et al. 2001) was based on numerous data provided by geotechnical investigations, geophysical surveys, microtremors measurements, classical geotechnical and special soil dynamic tests (Pitilakis et al. 1992, Pitilakis and Anastasiadis 1998, Raptakis et al. 1994a, 1994b, Raptakis 1995, Apostolidis et al. 2004). The dynamic properties of the main soil formations have been defined from an extended laboratory testing including resonant column and cyclic triaxial tests (Pitilakis et al. 1992, Pitilakis and Anastasiadis 1998, Anastasiadis 1994).

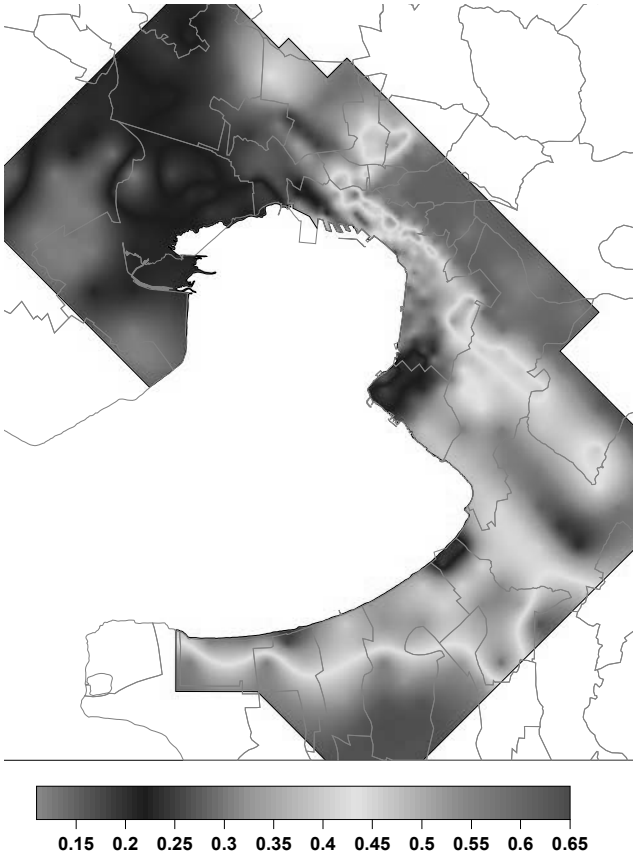


Figure 2. Mean peak acceleration values (g) at the ground surface for the 1000 years seismic scenario.

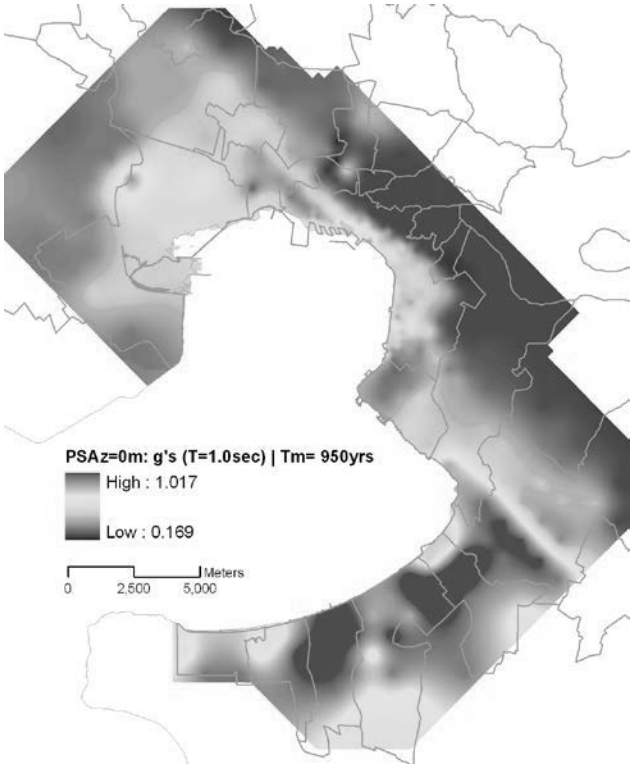


Figure 3. Mean spectral acceleration values at T=1.0sec (g) at the ground surface for the 1000 years seismic scenario.

Site effects due to local soil conditions, are taken into account through 1D linear equivalent response analyses. The analysis is conducted for five different scaled real accelerograms (for bed rock motions), which were selected according to the seismic hazard study, for three scenarios (mean recurrence period of 100, 475 and 1000 years) (Papaioannou 2004). As an example, the characteristics of the calculated seismic ground motions at the free surface, in terms of peak acceleration (PGA) and spectral acceleration (Sa) at T=1.0s are presented in fig. 2 and 3 for the earthquake scenario with mean return period of 1000 years. Similar maps have been generated for all seismic scenarios, and for several other ground motion parameters.

In order to account for the liquefaction-induced phenomena, the evaluation of permanent ground horizontal and vertical displacements (lateral spreading and settlements), has been performed for the three scenarios using empirical and analytical procedures (Ishihara and Yoshimine 1992, Elgamal et al. 2001). Figure 3 illustrates the spatial distribution of permanent ground settlements for the 1000 years scenario, which vary from 5.0 to 30.00cm.

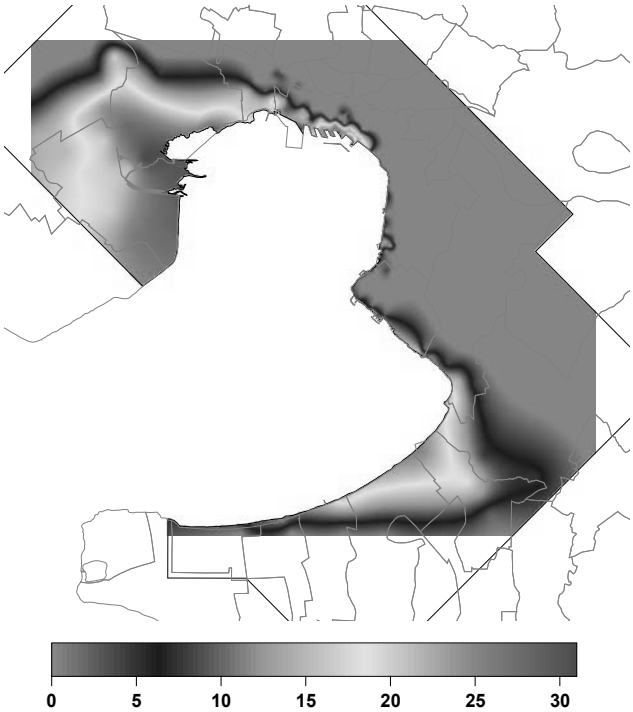


Figure 4. Permanent ground settlements due to liquefaction (cm) for the 1000 years seismic scenario.

3.2 Vulnerability of bridges

The expected level of damages for bridges is assessed based on the fragility curves that are provided in HAZUS (NIBS 2004), for the input earthquake hazard scenario and the estimated mean spectral acceleration at T=1.0sec. The estimated damage state for each bridge for the 1000 years seismic scenario, is presented in fig. 5. The majority of bridges will respond in a satisfactory way, but there are still several bridges, which are expected to sustain serious

damage for the specific seismic hazard scenario. This is due to the higher vulnerability of these bridges (single column, simple support bridges and inadequate seismic design), and the higher values of the expected surface spectral acceleration. The latter is attributed to the local soil conditions and the proximity of the seismic source (e.g. southeast part). For instance, in the west part of the city, deep soft alluvium deposits of sandy-silty clays to clayey sands-silts, with low strength and high compressibility, (category C and D in EC8), present stronger amplification at longer periods.

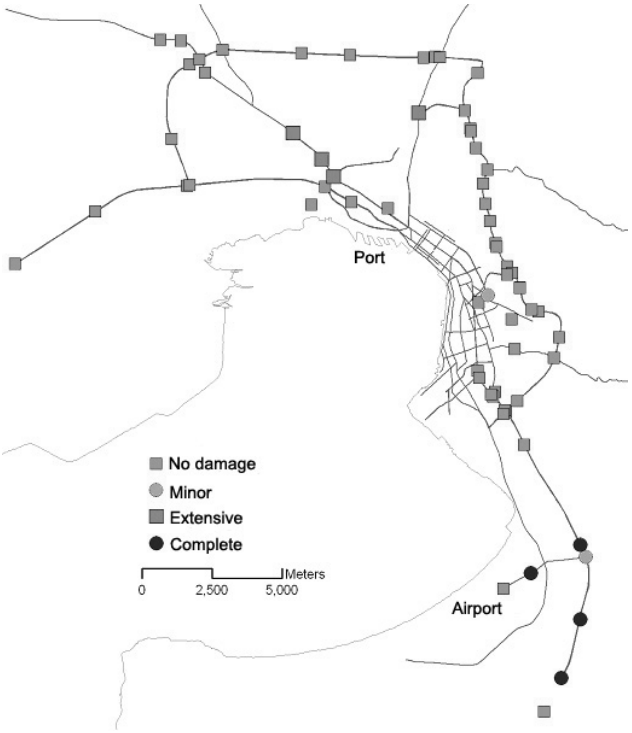


Figure 5 Expected damage states of bridges in Thessaloniki due to ground shaking for the 1000 years seismic scenario.

3.3 Vulnerability of roads due to ground failure

Road pavements are susceptible to damage due to permanent ground displacements which can be induced by liquefaction (settlement or lateral spreading), surface fault rupture and sliding of embankments or slopes. In the present study the vulnerability of the road network due to liquefaction is estimated. The fragility curves that are proposed in HAZUS (NIBS 2004) methodology are applied as they are considered to describe adequately the response of a road pavement due to ground failure. The expected level of damage (none, minor, moderate, extensive/complete) is assessed for the road segments that are lying on liquefiable soils, based on the estimated distribution of the permanent ground deformations (fig. 4). A representative example is shown in figure 6 for the case of the seismic scenario with T=1000 years. Minor damages are expected in few parts of the network, concentrating in susceptible to liquefaction areas, especially near the coastline, where loose sand-silt formations with low plasticity and variable percentage of clay are presented.

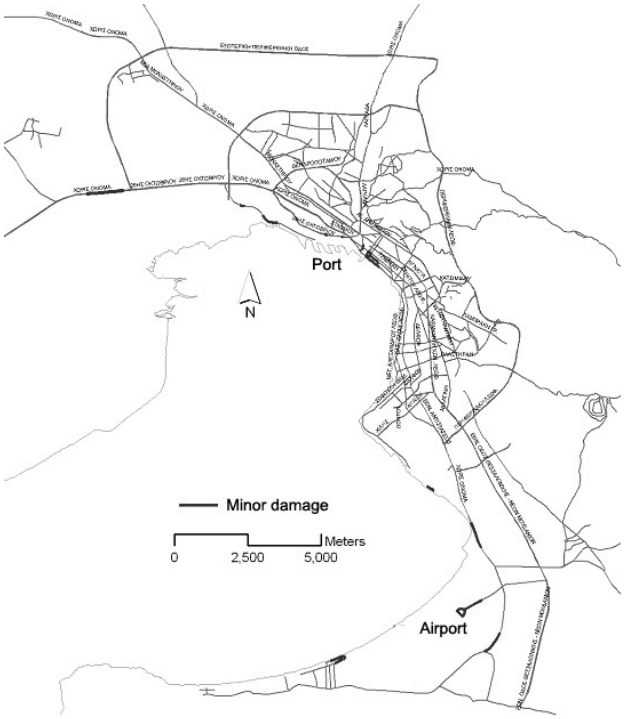


Figure 6 Expected damage state of roads in Thessaloniki due to ground failure for the 1000 years seismic scenario.

3.4 Vulnerability of roads due to building collapses

The impact of collapsed buildings to the functionality of roads just after the earthquake is estimated based on a correlation between building's geometry and width of the induced debris. A Gaussian distribution describes the variation of the debris width, which is a function of the building collapse angle (φ) and the building volume reduction (kv) (fig. 7). This model is used in order to estimate the exceedance probability of certain road function levels (100% open, 50% open, 0% closed or one lane open). The collapse probability of buildings is estimated based on appropriate fragility models which have been developed for the building types commonly presented in Thessaloniki, as a function of the peak ground acceleration (Penelis et al. 2002, Kappos et al. 2006). The spatial distribution of the collapsed or heavily damaged buildings is depending on their typology and the site conditions.

Past experience in Greece reveals that a percentage of collapses ranging between 10 and 20% can have such form and amount of debris, which can result to road closure. The probability of closure due to building collapse is calculated based on the combination of the aforementioned probabilities for each road segment (node to node). Figure 8 illustrates the probability of closure for the main roads in the central city due to building collapses for the scenario with a mean return period 1000 years. The reduction of the road width depends on the distance from the buildings, the width of the road and the induced debris width, while the closure probabilities depends on the concentration of the most vulnerable building type, the length of the road segment and the discrete collapse probabilities related to the local site conditions.

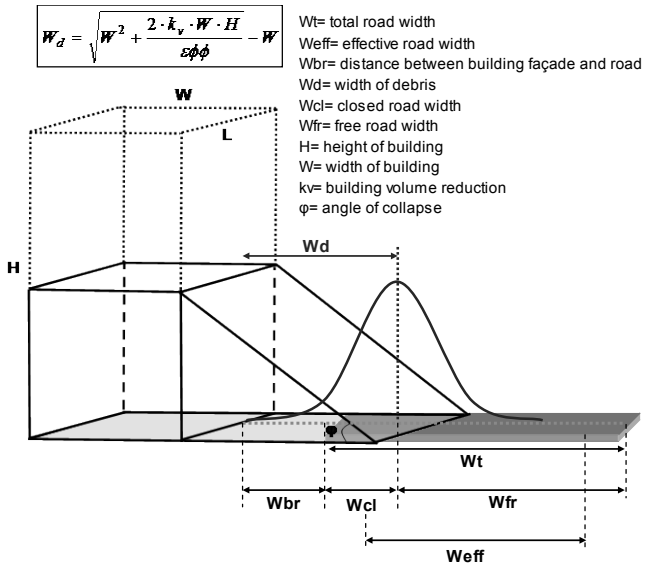


Figure 7. Estimation of debris width and road closure.

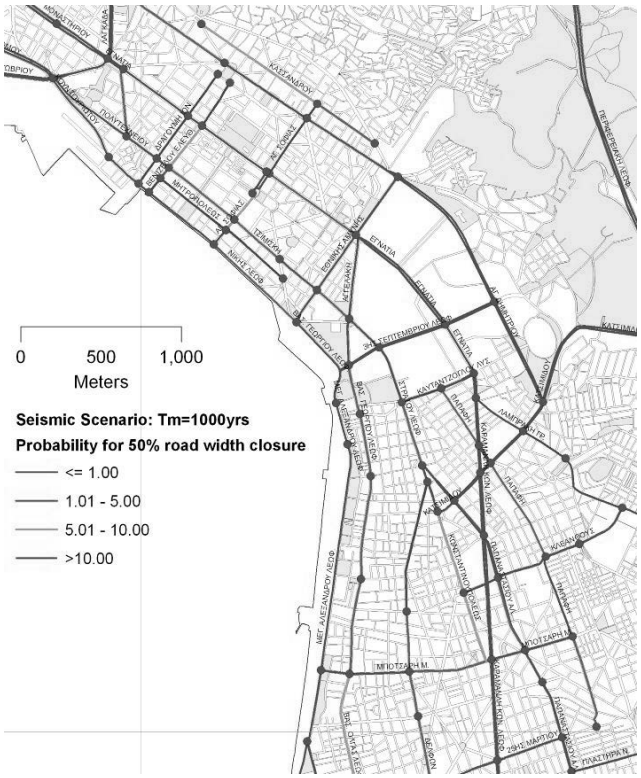


Figure 8. Sample map with probabilities for 50% road width closure of the main road network due to building collapses for the 1000 years seismic scenario.

3.5 Classification of importance-Global value analysis

Within this step, the main issues and relative importance of the road network are identified, through appropriate ranking of the value of the exposed elements (Anastassiadis and Argyroudis 2007, Pitilakis et al. 2010). Various factors and criteria that describe the role of each element in the urban system are used. In that way, the global value of each element at risk depends not only on its direct specific value but also upon its indirect/immaterial value, which is represented by the usefulness and relative role in the whole urban system, at a specific time. Three periods are identified in respect to the occurrence of an earthquake event: normal, crisis and recovery. The criteria for road network include operational attributes, emergency use and urban features (Argyroudis 2010). Qualitative or quantitative indicators and measuring units are defined for each period and the "main", "important" and "secondary" elements are estimated, based on their global value ranking. The indicators used for the classification of the importance of Thessaloniki's road network in each period are described in Table 1, while the relative values of the indicators are given in Table 2. The indicators that describe the interaction of roads with critical services (direct or indirect access) and land uses are ranked based on the classification of importance of these elements. The latter is resulted by applying the global value approach considering different indicators (Anastassiadis and Argyroudis 2007).

Table 1 Indicators and measurement units of global value analysis for urban roads

Indicator	Measurement unit	Period		
		Norm	Crisis	Recov
1. Road hierarchy	Functional classification	✓	✓	✓
2. Traffic capacity	Effective road width	✓	✓	✓
3. Access to critical facilities	Vicinity to critical services (e.g. hospitals, terminal stations, civil protection buildings)	-	✓	✓
4. Emergency use	Importance of road in emergency situation	-	✓	✓
5. Urban factors	a. Population density	✓	✓[1]	-
	b. Trade area density	-	✓[2]	-
	c. Built area density	-	-	✓
1: seismic scenario during non working hours 2: seismic scenario during working hours				

The summation of relative values of each road segment gives its global value, which is used for the classification of importance in the three categories based on appropriate thresholds. A sample map illustrating the definition of main, important and secondary elements at risk is illustrated in fig. 9. Similar approach is followed for the classification of bridges, applying a different set of indicators. The results of this step combined with the outcome of the vulnerability assessment of the exposed elements at risk (roads, bridges, tunnels etc) can contribute to the development of an efficient mitigation and retrofitting strategy and a well-organized emergency planning. In that way, focus will be placed on limiting the necessary recovery period to the least possible extent, in order to provide the related city activities with the optimum feasible operation level.

Table 2 Classification and relative values of measurement units of global value analysis for urban roads

Measurement unit	Description	Relative value
Functional classification	Freeway Main arterial Secondary arterial Primary collective Secondary collective Local	1.00 0.75 0.50 0.25
Effective road width	>15m (>5 lanes) 10-15m (3-5 lanes) 5-10m (2-3 lanes) <=5m (1-2 lanes	1.00 0.75 0.50 0.25
Importance of road access based on the global value classification of the critical services	Main Important Secondary None	1.00 0.75 0.50 0.25
Importance of road in emergency situation	High Low/none	1.00 0.00
Importance of land uses along road axis based on urban indicators (population, trade or built density)	Main Important Secondary None	1.00 0.75 0.50 0.25



Figure 9 Sample map with classification of importance of road network in Thessaloniki for the crisis period (seismic scenario during non working hours)

3.6 Connectivity analysis of road network

The functionality and travel times of the road network could be affected by the direct or indirect damages to road segments or bridges. Moreover, the travel time is important, especially for the transportation of emergency vehicles, after a strong earthquake. A simplified connectivity analysis is performed in the road network of Thessaloniki for specific routes between residential areas and major hospitals, considering the estimated damages of the roadway elements.

A representative example is presented here for two alternative routes (fig. 10) based on the probabilities of road closure due to building collapses and the probabilities of bridge damage along each route. It is presumed that a road is closed when passes over a bridge with at least moderate damage, while the same happens when it passes under a bridge with at least extensive damage. Table 3 describes the alternative routes and travel times, considering an average speed equal to 30km/h for freeways and main arterials, and 25km/h for other road classes. It is observed that the route 1 that is shorter, presents lower reliability (i.e. higher probability of closure) compared to route 2, which is however longer. This is related to the local soil conditions and the higher vulnerability of bridges and buildings along route 1.

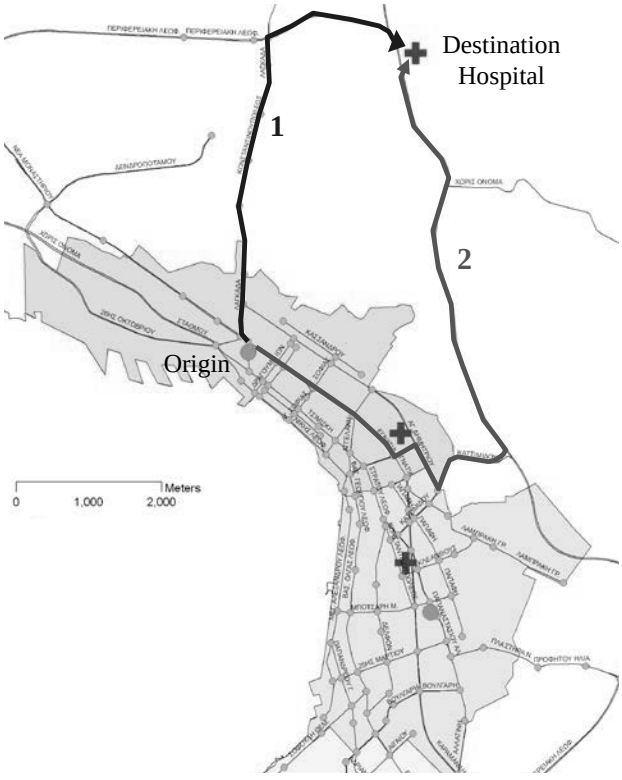


Figure 10 Example of connectivity for the main road network of Thessaloniki, showing two alternative routes between an origin area and a destination hospital.

Through this preliminary approach, the weak areas or points of the network are defined and optimum routes can be proposed. In combination with the classification and hierarchy of importance of the roadway elements it is possible to develop an advanced risk management plan, including efficient pre-earthquake actions and restoration or traffic retour plans.

Table 3 Reliability of alternative routes under study

Route	Length (km)	Travel time (min)	Reliability (probability of non-closure)	
			T=475yrs	T=1000yrs
1	6.90	13.71	0.848	0.780
2	10.50	21.40	0.900	0.717

4. CONCLUSIONS

The seismic risk analysis of transportation network is essential for the efficient seismic risk management and mitigation, especially in urban areas with high seismicity and high population and built densities. A general approach includes the assessment of seismic hazard and seismic ground response for different seismic scenarios, the vulnerability assessment of the exposed elements at risk and the estimation of direct and indirect damages, the classification of their importance and the effects of damages to the functionality of the network.

A short description and an application of a general methodology for the vulnerability assessment and seismic risk management of urban road network are presented. The city of Thessaloniki in Greece is used as test site. The vulnerability and loss estimates of the road network are evaluated on the basis of detailed site specific seismic hazard analysis using available inventory data and adequate fragility relationships. The expected damages of bridges due to ground shaking and of road pavements due to ground failure (liquefaction) are estimated, while the possible road closures due to collapsed buildings are defined. The intensity and spatial variability of the losses are entirely relied on the specific ground response characteristics. Moreover, the connectivity of specific routes to hospitals is examined based on the distribution and intensity of expected damages to the network.

The classification of road elements importance is performed on the basis of a global value analysis, using functional and urban indicators in different periods. In combination with the previous results, this leads in a more efficient prioritization of the pre-earthquake retrofitting actions, and post earthquake restoration efforts. These include upgrading of structural performance of vulnerable elements such as bridges, improvement of existing network performance (road widening, modification to one way or pedestrian roads), planning of traffic retours, implementation of advanced technologies during earthquake emergency (early warning systems, real time damage estimation etc).

References:

Anastasiadis, A. (1994), "Contribution to the Determination of the Dynamic Properties of Natural Greek Soils", *Ph.D. Thesis* (in Greek), Dept. of Civil Engineering, Aristotle University of Thessaloniki, Greece.

Anastasiadis, A., Raptakis, D. and Pitilakis, K. (2001). "Thessaloniki's Detailed Microzoning: Subsurface Structure as basis for Site Response Analysis", *Pure and Applied Geophysics – PAGEOPH*, **158**(12), 2597-2633

Anastassiadis, A. and Argyroudis, S. (2007), "Seismic Vulnerability Analysis in Urban Systems and Road Networks. Application to the City of Thessaloniki, Greece", *International Journal of Sustainable Development and Planning*, **2**(3), 287-301.

Apostolidis, P., Raptakis, D., Roumelioti, Z. and Pitilakis K. (2004), "Determination of S-wave Velocity Structure Using Microtremor and SPAC Method applied in Thessaloniki (Greece)", Journal of Soil Dynamics and Earthquake Engineering, **24**, 49-67.

Argyroudis, S. (2010), "Contribution to Seismic Vulnerability and Risk of Transportation Networks in Urban Environment", *PhD Thesis* (in Greek), Dept. of Civil Engineering, Aristotle University of Thessaloniki, Greece.

Elgamal, A., Yang, Z., and Lu, J. (2006), "Cyclic1D: A Computer Program for Seismic Ground Response", *Report SSRP-06/05*, University of California, San Diego.

Franchin, P., Lupoi, A. and Pinto, P.E. (2006), "On the Role of Road Network in Reducing Human Losses after Earthquakes", *Journal of Earthquake Engineering*, **10**, 195-206.

Ishihara, K. and Yoshimine, M. (1992), "Evaluation of Settlements in Sand Deposits Following Liquefaction during Earthquakes", *Soils and Foundations*, **32**(1), 173-188.

Kappos, A., Panagopoulos, G., Panagiotopoulos, Ch. and Penelis, G. (2006), "A Hybrid Method for the Vulnerability Assessment of R/C and URM Buildings", Bulletin of Earthquake Engineering, **4**, 391-413.

Karaca, E. (2005), "Regional Earthquake Loss Estimation: Role of Transportation Network, Sensitivity and Uncertainty, and Risk Mitigation", *PhD Thesis*, MIT, Cambridge, MA.

Kiremidjian, A., Moore, J., Fan, Y.Y., Basöz, N., Yazali, O., and Williams, M. (2006), "Highway Demonstration Project", *PEER Report 2006/02*, Pacific Earthquake Engineering Research Center, College of Engineering University of California, Berkeley.

National Institute of Building Sciences (NIBS) (2004), "Earthquake Loss Estimation Methodology. HAZUS'99, Technical Manual, vol.1.", Federal Emergency Management Agency, Washington, D.C.

Nuti, C., Vanzi, I. (1998), "Assessment of Post-Earthquake Availability of Hospital System and upgrading Strategies", *Earthquake Engineering and Structural Dynamics*, **27**, 1403-1423.

Papaioannou, Ch. (2004), "Technical Report Research Program SRM-LIFE, Seismic Hazard Scenarios: Probabilistic Analysis of Seismic Hazard", Coord. K.Pitilakis, Thessaloniki.

Penelis, Gr., Kappos, A., Stylianidis, K., and Panagiotopoulos, C. (2002), "2nd Level Analysis and Vulnerability Assessment of URM Buildings", *Proceedings of International Conference on Earthquake Loss Estimation and Risk Reduction*, Bucharest, Romania.

Pitilakis, K. and Anastasiadis, A. (1998), "Soil and Site Characterization for Seismic Response Analysis", *Proceedings of 11th European Conference on Earthquake Engineering*, Paris 6-11 Sept., Inv. Lecture, 65-90.

Pitilakis, K., Anastasiadis, A, and Raptakis, D. (1992), "Field and Laboratory Determination of Dynamic Properties of Natural Soil Deposits", *Proceedings of 10th World Conference on Earthquake Engineering*, Madrid, 5, 1275-1280.

Pitilakis, K., Alexoudi, A., Argyroudis, S., Monge, O., Martin, C., (2006), "Chapter 9: Vulnerability and Risk Assessment of Lifelines", *Assessing and Managing Earthquake Risk*,

Geo-scientific and Engineering Knowledge for Earthquake Risk Mitigation: developments, tools, techniques, Eds. X. Goula, C. S. Oliveira, A. Roca, Springer, ISBN 1-4020-3524-1, 185-211.

Pitilakis, K., Anastasiadis, A., Kakderi, K., Alexoudi M., and Argyroudis, S. (2010), "The Rrole of Soil and Site Conditions in the Vulnerability and Risk Assessment of Lifelines and Infrastructures. The Case of Thessaloniki (Greece)", *Proceedings of the 5th International Conference on Recent Advances in Geotechnical Earthquake Engineering and Soil Dynamics*, San Diego, California, May, 24-29.

Raptakis, D. (1995), "Contribution to the Determination of the Geometry and the Dynamic Characteristics of Soil Formations and their Seismic Response", *Ph.D. Thesis* (in Greek), Dept. of Civil Engineering, Aristotle University of Thessaloniki, Greece.

Raptakis, D., Anastasiadis, A., Pitilakis, K. and Lontzetidis, K. (1994a), "Shear Wave Velocities and Damping of Greek Natural Soils", *Proceedings of 10th European Conference on Earthquake Engineering*, Vienna, Austria, 1, 477-482.

Raptakis, D., Karaolani, E., Pitilakis, K. and Theodulidis, N. (1994b), "Horizontal to Vertical Spectral Ratio and Site Effects: The case of a down-hole array in Thessaloniki (Greece)", *Proceedings of XXIV General Assembly, ESC*, Athens, 3, 1570-1578.

Shinozuka, M., Murachi, Y., Dong, X., Zhou, Y., and Orlikowski, M.J., (2003), "Seismic Performance of Highway Transportation networks", *Proceedings of the China-US Workshop on Protection of Urban Infrastructure and Public Buildings against Earthquakes and Manmade Disasters*, Beijing, China, 21-22 February.

Veneziano, D., Sussman, J., Gupta, U., and Kunnumkal, S.M. (2002), "Earthquake Loss under Limited Transportation Capacity: Assessment, Sensitivity and Remediation," *Proceedings of 7th USNCEE*, Boston, MA, USA.

Werner, S.D., Taylor, C.E., Cho, S., Lavoie, J-P., Huyck, C., Eitzel, C., Chung, H. and Eguchi, R.T. (2006), "REDARS 2 Methodology and Software for Seismic Risk Analysis of Highway Systems", Special Report MCEER-06-SP08, State University of New York, Buffalo.

8CUEE CONFERENCE PROCEEDINGS
8th International Conference on Urban Earthquake Engineering
March 7-8, 2011, Tokyo Institute of Technology, Tokyo, Japan

PIPELINE FAILURE IN EARTHQUAKES: SHOULD ACTIVE FAULT TRACES BE CONSIDERED A SERIOUS HAZARD TO BURIED PIPELINES?

Francesca Draper[1)], William Mahoney[1)], Suresh Dash[2)], and Subhamoy Bhattacharya[3)]

1) Masters Students, Department of Civil Engineering, University of Bristol, United Kingdom
2) Research Assistant, University of Bristol, United Kingdom
3) Senior Lecturer, Department of Civil Engineering, University of Bristol, United Kingdom
fd7504@bristol.ac.uk, wm7830@bristol.ac.uk, suresh.dash@bristol.ac.uk, s.bhattacharya@bristol.ac.uk

Abstract: Design of pipelines is seismic areas requires special attention as these are important lifeline facilities spread over a large area. The seismic hazards that may affect the pipelines can broadly be classified into: (a) fault crossing; (b) locally liquefiable soil zones at shallow depths and/or laterally spreading soils; (c) landslides caused by earthquakes. This paper summarises the observed performance of buried pipelines during the past earthquakes due to various hazards. These failures are further categorised with respect to their various modes of failure. A qualitative study has been carried out to understand the severity of different hazards to refine the seismic design requirements.

1. INTRODUCTION

Pipelines are a vital element of infrastructure in the world today. They support the world's industries, economies and civilisations by transporting precious commodities such as water, gas and oil, wastes and excesses such as sewage and storm water, in a reliable, safe and cost efficient manner. The pipeline industry has grown at a phenomenal rate over the last two centuries (Hopkins, 2007) and continues to grow with hundreds of thousands of kilometres of pipeline proposed in the next decade (Foster, June 2008, August 2008) (Rosner, 2010). Energy analysts predict offshore pipeline installations to increase by 6% annually by 2014 (Infield Energy Analysts, 2009). This development comes alongside considerable increase in risk. Seismic hotspots and faults cannot be avoided, as evidenced by the Trans-Alaskan Pipeline. Worryingly, fault lines may not be identified as in Northridge in 1994 (Yeats et al., 1995) which leads to deficiencies within the design and serious repercussions. It is therefore vital that all hazards are fully understood.

2. OVERVIEW OF PIPELINE HAZARDS

A literature review revealed that currently no comprehensive collation of detailed pipeline failure case studies exists. An attempt at compiling a pipeline failure database was undertaken by Le Val Lund and Anshel Schiff (1992) following the 1989 Loma Prieta earthquake but the records are not in sufficient detail for pipeline failure analysis. This lack of resource precipitated our collation of pipeline failures caused by seismic activity from a wide range of publications, resulting in a total of 30 detailed failures (Table 1). The data was analysed to identify the key hazards affecting pipeline failure (Figure 1) and to locate any pertinent failure trends.

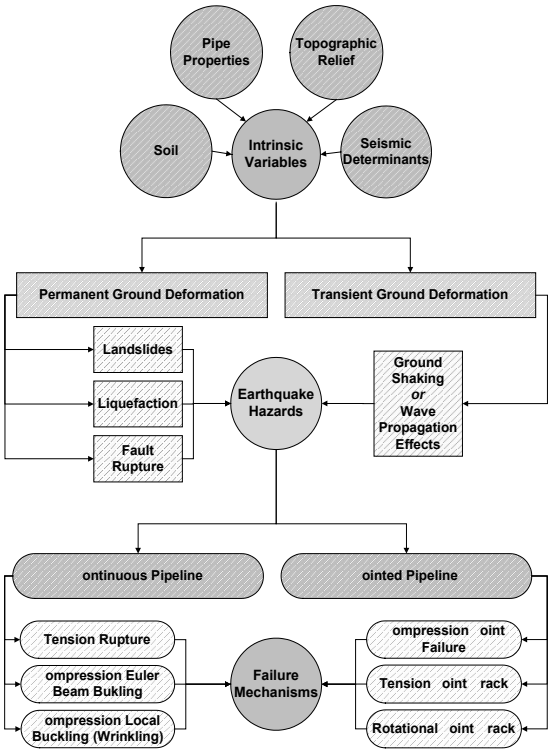


Figure 1 Pipeline Failure Mechanisms as a direct result of seismic activity.

Seismic hazards can principally be divided into two categories – transient ground deformation (TGD) and permanent ground deformation (PGD). Transient Ground Deformation is defined by O'Rourke (1998) as that which "*involves ground waves and soil strains associated with strong shaking*." The principal hazard associated with transient ground deformation is ground shaking or wave propagation. *Ground Shaking or Wave Propagation*

Ground shaking refers to strain and curvature changes generated by seismic wave propagation through the soil. It is rarely solely associated with pipeline failure, with the exception of Michaogan Earthquake in Mexico 1985 (O'Rourke et al., 1990). In this case, the absence of other ground deformations assured the investigators that the pipe wrinkling observed was due to wave propagation alone and is understood to be the only case where a corrosion-free modern steel pipeline has failed in such a way.

On the other hand, O'Rourke (1998) defined Permanent Ground Deformation as that which *"involves the irrecoverable movement of the ground that often is the result of ground failure, but also may result from modest levels of volumetric strain and shear distortion."*These can be categorised into landslides, liquefaction, and fault rupture.

2.1 Landslides

Landslides can typically be generated by earthquakes of 4.0 magnitude and above, where stresses weaken the stability of slopes. The permanent ground deformation tends to be abrupt and concentrated about a specific locale, resulting in severe damage to buried pipelines. The severity of the hazard is reduced by the ease with which it may be predicted from analyses of case history data, as described by Hays (1998). An example of such damage is that caused on the Trans-Ecuador pipeline during 1987 Ecuador Earthquake where landslides were the primary cause of the earthquake losses in the entire region (Bird et al., 2004).



Figure 2 View of valley wall of the Río Malo north-eastern Ecuador, after the 1987 Reventador earthquakes. Similar debris flows were caused throughout the country wreaking havoc. (Photo: *U.S. Geological Survey)*

2.2 Liquefaction

Liquefaction is a permanent ground displacement that results from the increase in pore pressure in a soil reducing its effective stress to zero. This may arise from strong ground shaking in saturated soils, and it is considerably documented by Youd (1978). The most destructive case for buried pipelines is lateral spreading, which involves the horizontal movement of competent soil due to liquefaction on underlying strata. The resulting earth pressures are compressive and tensile, and conducive to damage as noted in the 1994 Northridge Earthquake (O'Rourke et al., 1996).



Figure 3 Tension failure in segmented steel gas pipeline during 1994 Northridge Earthquake. (Photo: Southern Gas Company)

2.3 Fault Rupture

Fault rupture describes the differential movement between two adjoining portions of Earth's crust. The crack or fault within the crust is generally associated with the boundary between the tectonic plates, and when active may generate substantial displacement within a relatively narrow zone. For example the Chelungpu Fault, which flanks the western edge of Taiwan's central mountain range, ruptured over 80km of its length on September 21, 1999 (RMS, 1999). The rupture resulted in scarps 2m-3m high along the southern end, and scarps 4-8m high (EERI, 1999) towards the northern edge despite the lack of previously observed seismicity.



Figure 4 Buckled steel pipe at crossing near Arifiye, during Izmit (Kocaeli) 1999 Earthquake (Photo: Basoz, EERI 1999)

3. PIPELINE DAMAGE DUE TO FAULT RUPTURE

The literature review undertaken focuses primarily on pipeline failure caused by surface fault ruptures in order to appreciate the severity of damage caused. Although the study cannot be considered a quantitive analysis due to lack of consistent documentation of pipeline failure specifics, the 14 cases compiled (Table 1) aid the qualitive understanding of such events. From analysing the incomplete collated data, despite comparing similar

pipeline types, hazards and failure mechanisms, no clear trends were able to be identified. The number of influential variants and the individuality of the conditions at each case make gross comparisons of data in this manner ineffective. This inability to draw any qualitative conclusions suggests that the prediction of failure, and indeed the verification of current Finite Element models should be subject to further scrutiny. However, it can be seen that hazard risk varies principally depending on the character of the fault (types developed bellow) and its relative displacement.

3.1 Strike-Slip Fault

- Movement generated in horizontal plane along fault line.
- High stresses can be safely accommodated by ensuring tension in the pipeline is generated.
- 1968 Meckering Fault generated a maximum dextral movement of 1.5m (Gordon et al., 1980). Goldfields pipe was found shortened by 1.32m as a consequence. The stresses cased brittle failure in the cast iron pipe causing telescoping. Note the pipeline was a surface pipeline, though similar failure may be expected for buried pipes.

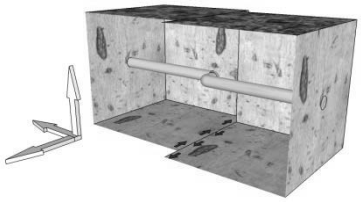


Figure 5 Schematic of buried pipeline subjected to a strike-slip fault.

3.2 Normal Fault

- Movement generated in vertical & horizontal planes perpendicular to fault line.
- Extension of crust commonly generates tensile stresses in the pipeline.
- 1988 Edgecombe Earthquake main shock is believed to have caused the resulting complex series of 7 scarps. The longest scarp being a normal fault 7km long, with 1.5m vertical displacement. Denis (2000) mentions how a gas pipeline crossing the fault was found to have suffered tension yield, though remained functional throughout.

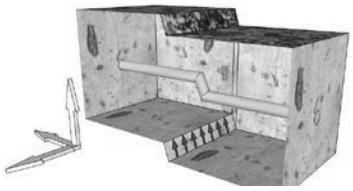


Figure 6 Schematic of buried pipeline subjected to a normal-fault.

3.3 Reverse Fault

- Movement generated in vertical & horizontal planes perpendicular to fault line.
- Shortening of crust commonly generates compressive stresses in the pipeline.
- 2001 Kokoxili earthquake is reportedly the longest documented surface rupture on land. The rural area struck resulted in no casualties, though some damage to temporary houses and telecommunications ensued. Guo et al. (2004) discusses the non-linear finite element analysis conducted on a gas pipeline found during the post-earthquake investigations with Z Shape buckling deformation (compressive failure). The analysis appears consistent with expectations.

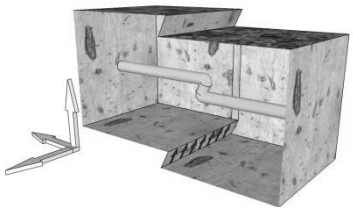


Figure 7 Schematic of a buried pipeline subjected to a reverse fault.

Earthquake reconnaissance also reveals that the typical failure modes that develop for continuous and segmented pipelines during a seismic event are quite distinct. This phenomenon can be understood intuitively; as segmented pipelines typically include joints that are designed to allow for differential movement, these areas are more vulnerable to stress concentrations (bell-and-spigot cast-iron piping system for example). Considerable empirical evidence has been accumulated documenting the structural and stiffness features of ductile iron pipes with push-on rubber gaskets (Singhal, 1984) and other typical pipe joints (Meis et al., 2003). Their findings reveal the importance of cyclic effects amongst other factors, and the latter generated considerable data to be used in modelling. An interesting case is made for the telescoping of a section of segmented pipeline in Meckering Earthquake's Aftershock on the 15th October 1968(Fenton, 2006). The investigator highlights how the Goldfields water pipe must have been severely weakened in the main shock to have resulted in further failure with the subsequent ground surface displacements. The Goldfields water pipeline therefore, can be seen to encapsulate pipelines' performance reliance on not only the primary pipe properties and seismic determinants, but its historic footprint. This makes the task of risk estimation more complex.

4. CASE STUDY (SAP MODELLING)

A failure case of the Gas Line 115 during the 1971 San Fernando Earthquake described by SCGC (1973) and O'Rourke et al., (1996) is now subjected to SAP modelling. This study aimed to investigate the response of a pipeline while subjected to an oblique fault, which includes strike and thrust faulting.

4.1 Modelling details

The considered gas pipeline failed due to the surface faulting of the Sylmar segment of the San Fernando fault zone. Near the Sylmar segment, there were of the order of three compression and ten tensile ruptures of the pipeline. The type of Sylmar fault segment was thrust upward with a dip angle of approximately 15^o to vertical and left lateral oriented 70^o to North. The maximum strike and reverse dip-slip component of fault displacement were 1.9m and 1.5m respectively. The fault zone was ranging between 45m to 106m. In the present analysis the fault displacement was considered at the middle of the fault zone. The pipeline was crossing the fault line at an angle of about 80^o.

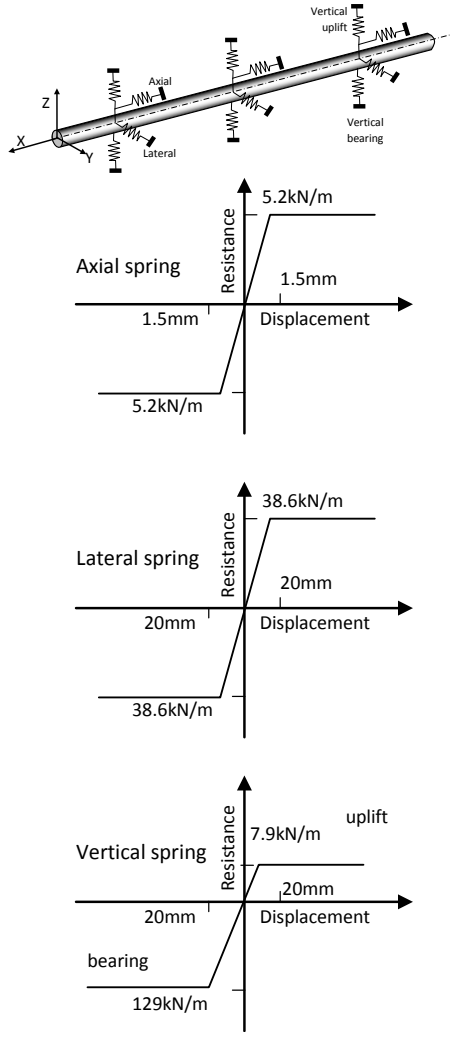


Figure 8 Estimated nonlinear properties of soil springs used in SAP model.

The pipeline was modelled in SAP (CSI, 2010) using a BNWF (Beam on Nonlinear Winkler Foundation) model, where the pipe elements were modelled as beam-column elements, and the soil was modelled as non-linear springs lumped at discrete locations of the pipe. The sectional properties of the pipe were taken as: diameter = 0.4m, wall thickness = 6.5mm. The pipe was buried at an average depth of 80cm from the surface. The pipe elements were discretised with 0.25m segments near the fault zone (for middle 100m) and 5m segments away from fault zone (i.e., 50m away from fault line). The ends of the pipeline were fixed 300m away from the fault line.

The nonlinear properties of soil springs were estimated according to the ASCE guidelines (ALA, 2001). The angle of friction and unit weight of the soil was assumed 30^o and $18kN/m^3$ respectively. Figure 8 shows the estimated values of axial, lateral and vertical soil springs.

The ground displacement due to both strike and thrust fault in the pipeline axis was estimated to be:

- Parallel to longitudinal axis of pipeline = -1.2m
- Lateral to longitudinal axis of pipeline = 1.87m,
- Vertical uplift to longitudinal axis of pipeline = 3.8m.

Figure 9 schematically shows these displacements applied to the ground moved during faulting. The displacements were applied at the fixed ends of the soil springs.

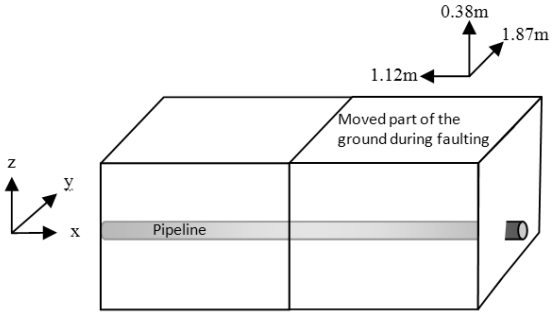


Figure 9 Schematic displaying the displacements applied to modelled ground for fault movement.

4.2 Results and discussion

The deformation pattern of the pipeline due to fault movement in both horizontal and vertical plane is plotted in Figure 10. Most of the deformation is within 10m distance from the fault line in either side for both the planes. The horizontal deformation pattern is symmetric about the fault line. However, the vertical displacement is higher in the stationary section than moving section of the fault model. This is due to the fact that the stationary side of the pipe is pulled upwards and subjected to lower soil resistance in uplift as compared to the opposite half of the pipe, which was pushed into the soil and subjected to higher soil resistance in bearing.

The bending moment of the pipe in both x-z and y-z plane is plotted in Figure 11. The location of maximum bending moment in x-z plane occurs at a distance of about 10m away from the fault line on both sides, where the curvature in the pipe is very high. However, in y-z plane, the bending moment is non uniform with respect to the fault line. The bending moments in both planes are comparable in magnitude. Therefore, while designing pipelines subjected to this kind of oblique fault, it should be designed for biaxial bending moment.

Figure 12 plots the axial compressive force distribution in the pipe. The axial compression in the pipe

was mainly due to the axial shortening of the thrust fault movement. However, the distribution of axial force is more dependent on the end fixity. In this case history, the location of end fixity was not known. However, the maximum axial force occurs near the fault line. Though not very conclusive, this analysis suggests that the pipeline crossing this fault line should have been designed for the expected bending and axial force for a zone of about 25D on either side of the fault line.

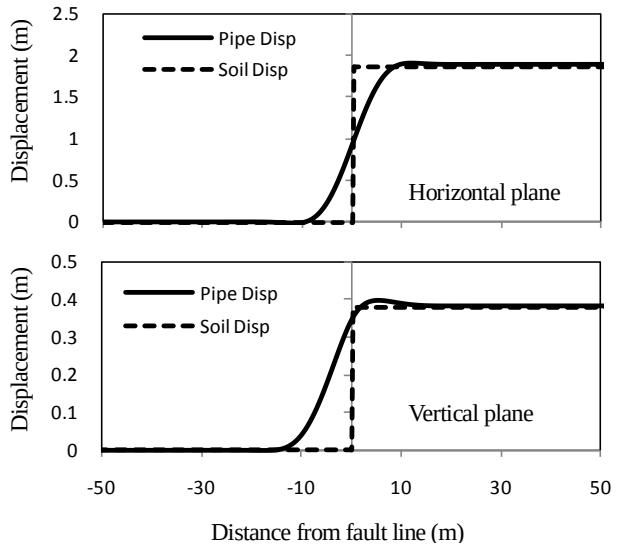


Figure 10: Displacement profile of pipeline due to soil displacement during faulting in both horizontal and vertical plane.

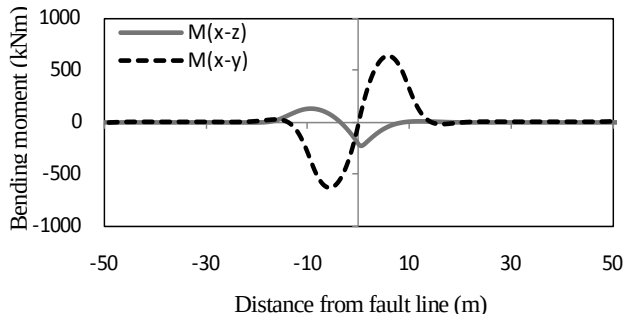


Figure 11: Bending moment in pipeline due to soil displacement during faulting.

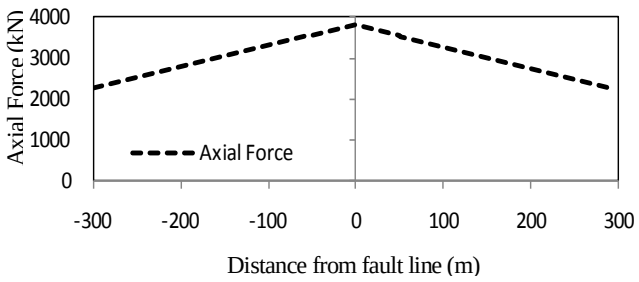


Figure 12: Axial compressive force in pipeline due to soil displacement during faulting.

5. CONCLUSIONS

The literature review shows that seismic fault rupture is a serious hazard to pipeline failure as demonstrated by the impacts associated with the case studies (Table 1). Currently, reporting of these failures are not sufficiently consistent and thorough to allow for conclusions to be drawn and accurate finite element simulation. As the industry expands and sourcing of natural goods becomes more remote, the inevitability of crossing fault lines increases. This industry growth can be expected to drive the need for further understanding in order to reduce associated risks. In order to achieve this, a more detailed earthquake reconnaissance of pipelines will be necessary.

The SAP modelling highlights the elevated nature of the pipeline's stresses close to the fault line during faulting and it is these values that should govern the design. The computer model provides a useful tool for designers but is by no means a guarantor of the field conditions, due to the uncertainties associated with the ground conditions, burial conditions, and loading.

References:

ALA (2001), Guidelines for Design of Buried Steel Pipes, A report by public-private partnership between American Society of Civil Engineers (ASCE) & Federal Emergency Management Agency (FEMA), American Lifelines Alliance (ALA), July 2001.

Bird, J.F. & Bommer, J.J. (2004) Earthquake losses due to ground failure. *Engineering Geology* 75, 147-179.

Ha, D., Abdoun, T. & O'Rourke, M. J. (2008). Soil-Pipeline Interaction Behaviour under Strike-Slip Faulting. *Geot. Earthq. Eng. & Soil Dynamics IV* GSP 181 © 08 ASCE

CSI (2010), SAP 2000: V13.0 - Integrated Software for Structural Analysis and Design. Berkeley, California, USA. Computer and Structures Inc (CSI).

Denis, R. (2000). *Pipeline Technology*. Volume 1. Brugge May 21-20. Elsevier Science BV.

Dong, W., Morrow, G., Tanaka, O., Kagawa, H., Chow, L., Yeh, C., Tsau, Y., Hsu, W., Johnson, L. Von Anne, C., Segawa, S., Wen, K. & Chiang,W., (1999). Event Report, Chi-Chi Taiwan Earthquake. *RMS Reconnaissance Report.*

EERI (1999). The Izmit (Kocaeli), Turkey Earthquake of August 17 1999. *EERI Special Earthquake Report*, October 1999.

EERI (1999). The Chi-Chi, Taiwan Earthquake of September 21, 1999. *EERI Special Earthquake Report*, December 1999.

Fenton, C. (2006). Quantifying surface faulting hazards for lifelines crossing active faults. *IAEG2006 Paper number 236* The Geological Society of London 2006

Foster, J. (2008, June 19). A pipeline through a troubled land: Afghanistan, Canada, and the new great energy game. *Canadian Centre for Policy Alternatives*.

Foster, J. (2008, August 20). Asia's new 'great game' is all about pipelines. *Canadian Centre for Policy Alternatives.*

Gordon, F.P. & Lewis J. D. (1980). The Earthquake and Caligiri Earthquakes of October 1968 and March 1970.

Geological Survey of Western Australia, Bulletin 126. Appendix 1 - Catalogue of Larger Earthquakes recorded in South-western Australia and in National archives ref CA 3539 Mundaring Geophysical Observatory, WA

Guo E., Shao G. & Liu H. (2004). Numerical Study on damage to buried oil pipeline under large fault displacement. *Proceedings of 13th World Conference Earthquake Engineering.*

Hopkins, P. (2007). Pipelines: Past, present and future. *Proceedings of the 5th Asian Pacific IIW International Congress*, Sydney, Australia.

Hays, W.W. (1998). Case histories of damaging earthquakes. *Proceedings of the Fourth International Conference on Case Histories in Geotechnical Engineering*. University of Missouri-Rolla, Rolla, MO, pp. 957–962. Paper No. 8.04.

Infield Energy Analysts (2009). Offshore Pipelines & Control Lines Market Update Report 2009/13 (4th Ed.) & Infield Energy Analysts (2009). Offshore Pipelines & Control Lines Market Update Report to 2014 (5th Ed.).

Lund, Le V.; Schiff, Anshel J. (1992). Earthquake Engineering Online Archive.:TCLEE pipeline failure database. *Technical Council on Lifeline Earthquake Engineering, American Society of Civil Engineers*, 1v (648 L86 1992).

Meis, R. D., Maragakis, E.M. & Siddharthan, R. (2003). Behaviour of Underground Piping Joints due to Static and Dynamic Loading, *Technical Report MCEER*-03-89557.

O'Rourke, M.J. 1 Member, ASCE, Ayala, G. (1990). Seismic Damage to Pipeline: Case Study. (Reviewed by the Pipeline Division) *Journal of Transportation Engineering*, Vol. 116, No. 2, March/April, 1990.

O'Rourke, T.D. & Palmer, M.C. (1994). Earthquake Performance of Gas Transmission Pipelines During the Northridge Earthquake. *NCEER* V._, Number 2, April 1994, pp1-5.

O'Rourke, T. D. & Palmer M.C. (1996). Earthquake Performance of Gas Transmission Pipelines. *Earthquake Spectra*. V. 20, pp. 493-527.

O'Rourke, T.D. (1998). An overview of geotechnical and lifeline earthquake engineering. *Geotechnical Special Publication*, No. 75, ASCE, 2, 1392-1426.

Rosner, K. (2010, January 12). China scored again in energy: Russia & Central Asia. *Journal of Energy Security.*

Schiff, A.J. & Holzer, T.L. (1998). The Lorna Prieta, California, Earthquake of October 17, 1989-Lifelines. *Performance of the Built Env. U.S. Geological Survey Prof Paper* 1552-A.

Singhal, A.C. (1984). Nonlinear behaviour of ductile iron pipeline joints. *Journal of Technical Topics in Civil Engineering, v.*110, no. 1, p. 29-37.

SCGC (1973). Earthquake Effects on Southern California Gas Company Facilities. San Fernando, California Earthquake February 9, 1971, Vol 2, Southern California Gas Company, US Dept. of Commerce, Washington. D.C., pp 59-66.

"Turkey Earthquake Reconnaissance Report" (2000 December). *Earthquake Spectra Kocaeli Supplement A* to Volume 16, Lifelines (pp378-383)

Yeats, R.S. & Huftile, G.J. (1995). The Oak Ridge Fault and 1994 Northridge Earthquake. *Nature* Vol 373, 2 February 1995.

Youd, T.L. (1978). Major Cause of Earthquake Damage is Ground Failure. Civil Engineering ASCE, Volume 48, No.4, pp 47-51.

Table 1 Showing subset of Pipeline Failure Case Studies relevant to Fault crossing

Note Φ indicates lack of available source detail, and *elements in italics* indicate educated guesses.

Earthqu.		Fault Characteristics					Social Impacts		Geology of Area	Pipe Characteristics												Reference
Year	Location	Type	Name	Maximum Displacement H:V (mm)	Length (km)	Magnitude of Accompanying Earthquake	Social Impacts (Fatalities)	Economic	Geology Description	Name	Nature of Content	Diameter (mm)	Material & Condition	Yield Stress (MPa)	Ultimate Tensile Stress (MPa)	Fault Offset (H:V) /m	Width of Fault (m)	Weld / Joint Type	Type of Failure	Other	
1954	Kern County	Left-Lateral Reverse	*White Wolf Fault*	Φ: 1300	60	7.5	12	$50 Million in Property Damage	Separating fundamentally recent quaternary fresh basin deposits, vs. Mesozoic granite rocks.	*PG&E*	*Gas*	864	*Steel (unknown grade)*	*250*	*400*	1.00 : 0.40	Φ	Φ	Beam Buckling	Beam Stress relief resulted in a max. uplift of 720mm and an uncovered length of 170m	(Denis, R. 2001)
1968	Meckering Earthquake	Strike-Slip	Meckering Fault	1500: 2000	40	6.9	0	$5 million (1968 dollars)	Precambrian Shield	Goldfields (above g.)	Water	760	Concrete Line Steel Conduits	Φ	Φ	(1.32 axial Shortng)	*50*	Φ	Telescoping	Note full crustal shortening of 2.11 was housed by both telescoping & arching (0.79m) of the pipe & compression damaging supports.	(Gordon et al., 1980)
1968	Meckering Aftershock (Oct)	Strike-Slip	Meckering Fault	Φ	Φ	3.8	0		Precambrian Shield	Goldfields (above g.)	Water	760	Concrete Line Steel Conduits	Φ	Φ	Φ	Φ	Φ	Telescoping	Note full crustal shortening of 2.11 was housed by both telescoping & arching (0.79m) of the pipe & compression damaging supports.	(Gordon et al., 1980)
1971	San Fernando		Mission Wells Fault Segment	Φ	Φ	6.6	65	$500 Mil.	Alluvial sand and gravel	Line 1001	Gas	300	Steel (unknown grade)	*250*	*400*	Φ	Φ	Φ	Tension Crack	1 break occurred at the crossing, though various breaks along welds in proximity likely to relieve stress of PGD at fault.	(Southern California Gas Company, 1973)
1971	San Fernando	Thrust	Sylmar Fault Segment	2000: Φ	19	6.6	65	$500 Mil.	Alluvial sand and gravel	Line 115	Gas	400	Steel (unknown grade)	*250*	*400*	1.9:1.4	25<w >80	Φ	Local Buck-ling (wrinkling)	3 Compression & 10 tensile Failure of the line close to the fault.	(Southern California Gas Company, 1973)
1971	San Fernando	Thrust	Sylmar Fault Segment	2000: Φ	19	6.6	65	$500 Mil.	Alluvial sand and gravel	Line 115	Gas	400	Steel (unknown grade)	*250*	*400*	1/∞:1.4	25<w >81	Φ	Tension Rupture	3 Compression & 10 tensile Failure of the line close to the fault. Tension width and movement open to interpretation.	(Southern California Gas Company, 1973)

1987	Edgecumbe	Normal Series of 7 faults	Edge-combe. Await	100-1500	Max. Seg. 7km	6.3	0		Z<350mm=Alluvial Plains Ground bellow 14m, marine.	Φ	*Gas*	100	API-5L Steel	448	531	*1.25*	wide	Φ	Tension Yield	No ruptures, just gentle warping caused by tensile force over wide fault.	(Denis, R. 2001)
1988	Tennant Creek	2collinear irregular WNW tending scarps & a shorter ENE tending scarp.	N/A	"2000"	"35"	6.8	0	$2.5 Mil.	Φ	*Near Tennant Creek NT*	*Gas*	350	API X-60 Steel	414	417	Φ	Φ	Φ	Compres-sion deformation	No rupture shown. Replaced as precaution.	(Denis, R. 2001)
1989	Loma Prieta	Reverse-Slip	Cala-veras (San Andreas)		40	6.9	63		Φ	Santa Clara Conduit	Water	2515	Φ	Φ	Φ	Φ	610		Joint failure	2151-Dia pipe separated into 2x 1676-Dia by rubber gasket.Fitted gate prevented major loss of goods & enabled continued supply.	(Schiff et al., 1998)
1989	Loma Prieta	Reverse-Slip	Cala-veras (San Andreas)		40	6.9	63		Φ	Water Main (Hollister)	Water	102	Cast Iron	*130*	*200*	Φ	610	Lead Caulked Joints	Joint failure	Note asbestos-cement pipes were reported to perform better.	(Schiff et al., 1998)
1989	Lorna Prieta	Reverse-Slip	Cala-veras (San Andreas)		40	6.9	63		Φ	Hollister Water Main	Water	102	Asbestos Cement	Φ	Φ	Φ	610	Lead Caulked Joint	Joint failure	Note asbestos-cement pipes were reported to perform better.	(Schiff et al., 1998)
1999	Chi-Chi Taiwan	Reverse-Slip	Chelung-pu Fault	2000: 10000	80	7.6	2400	$10 Billion	Same soil conditions on both sides.	Shigang	Water	2000	Steel	*250*	*400*	6.87 : 3.0 +0.51 Axial Shtg.	Φ	0	Local Buckling	Φ	(Schiff et al., 1998)
1999	Turkey Earthquake-August	Right-Lat strike-slip faults	North Anatolian - Sapanca Segment	3000	110	7.8	17, 439		Soil on one side softer than the other.	Thames Water	Water	2200	Steel	*250*	*400*	1.70 : 0 (1.51 Axial Shortng)	Φ	Butt-welded	Wrinkling pipe	2008, Soil-Pipeline Interaction Behavior	(Da Ha et al., 2008)
1999	Turkey Earthquake-August	Right-Lat strike-slip faults	North Anatolian - Sapanca Segment	3000	110	8.8	17, 439		Φ	Adapazari	Water	700	Asbestos Cement	Φ	Φ	N/A	Φ		Brittle Fracture	Result of both ground softening of alluvial sediments and inherent AC properties.	(Earthquake Spectra, 2000)
2001	Kokoxili	Strike-Slip with Reverse Slip			450	8.1	0		Φ	Oinghai-Xinjiang Border	Oil	170	Steel	Φ	Φ	0.3-3.5m Vs. 0.0-0.8m	Φ	Φ	Z Shape buckling deformation	Φ	(Guo et al., 2004)

8CUEE CONFERENCE PROCEEDINGS
8th International Conference on Urban Earthquake Engineering
March 7-8, 2011, Tokyo Institute of Technology, Tokyo, Japan

ESTIMATION OF SITE EFFECTS BASED ON RECORDED DATA AND THE GROUND MOTION ATTENUATION RELATIONSHIP

H. S. Kuyuk[1], K. Koketsu[2], H. Miyake[3], H. Si[1], Y. Fukushima[4], H. Ghasemi[5], and R. Ibrahim[6]

1) Researcher, Division of Disaster Mitigation Science, Earthquake Research Institute, The University of Tokyo, Japan
2) Professor, Division of Disaster Mitigation Science, Earthquake Research Institute, The University of Tokyo, Japan
3) Assistnat Professor, Division of Disaster Mitigation Science, Earthquake Research Institute, The University of Tokyo, Japan
4) Researcher, ISSC/IAEA, Austria
5) Researcher, Geoscience Australia, Australia
6) Graduate student, Division of Disaster Mitigation Science, Earthquake Research Institute, The University of Tokyo, Japan
kuyuk@eri.u-tokyo.ac.jp, koketsu@eri.u-tokyo.ac.jp, miyake@eri.u-tokyo.ac.jp, shj@eri.u-tokyo.ac.jp, Y.Fukushima@iaea.org, hghasemi@gamil.com, rami@eri.u-tokyo.ac.jp

Abstract: In this study, the site effect on peak ground velocity is investigated for Tottori Region. A frequency dependent correction factor (CF) which is the mean of the summation of the ratio of observed ground motion over a reference attenuation model is employed. We tested the method for 150 stations not just Tottori area but near region through 5988 earthquake records. Totally 46 crustal earthquakes with larger than M_w 4.0 and within 100 km epicentral distance are examined. The correlation between CF and average Vs30 is analyzed. By applying the CF, it is achieved to eliminate site effect an acceptable level for the region. It is found out that there is a good agreement between our results and previously proposed methods in literature. By this method CF can be used as an alternative solution to evaluate site effects where there is no Vs30 in a site of interest if there are adequate recorded events.

1. INTRODUCTION

Accurate prediction of ground motion parameters is an important task which various attenuation relationships proposed for many regions, considering effects of source, site, and path. Site effect is the one that get attention recent years evaluated also in Next Generation Attenuation project initiated by PEER. S velocity in 30 meter of stations is one of the frequently utilized in assessing the effect. On the other hand, Lee and Trifunac (2010) reported that an older site characterization in terms of the soil site parameter proposed by Seed et al. worked better because it included a measure of the thickness of the soil layers to considerably greater depths. While the debates continue, Si et al. (2010) introduced a new and simple method to correct site effects and applied it to well-known 1994 Northridge earthquake. In proposed method, the site effect correction factor for an observation station is defined as the residual between the observational strong motions with that predicted by a reference attenuation model defined on bedrock. Consequently, if a station always shows stronger or weaker motion it will be corrected to show average ones on bedrock. This method is useful for peak ground velocity and longer period components, but may be not enough for peak ground acceleration and shorter period components because of the possible nonlinear behavior. For the latter case, the effect of the nonlinear behavior should be examined when using the proposed method, and if necessary the correction for nonlinear behavior should be performed.

In this study site effect correction factor is investigated and tested in Tottori region, Japan. The peak horizontal ground velocity is adopted as the strong motion parameter since the nonlinear effects can be neglected, and its value on bedrock can be defined by an existing attenuation model developed by Si and Midorikawa (1999). We have compared the results with previous relationship models and have showed that this method can be adopted for evaluation of site effect especially if there is no VS30 information available.

2. METHODOLOGY

The site effect has great influence on strong motion and is important to evaluate in an attenuation relation. The average velocity of shear waves in the top 30 m of soil has become the parameter used by many engineering design codes and most recently by published empirical-scaling equations to estimate the amplitudes of strong ground motion. Si et al (2010) assumed that if seismic source and the path effect can be represented by the reference attenuation model, site effect correction factor can be estimate by performing an average operation using a number of records at the observation station, as shown in Eq. 1

$$R(\omega) = \sum_{i=1}^{n} \left(G(\omega) / G^{'}(\omega) + \varepsilon_i \right) \quad (1)$$

where, i is a specific record from an earthquake, n is the total number of the records used in estimation of the site effects. Since ε_i is a random number, with the increase of records in a station, the term $\Sigma\varepsilon i$ /n will be smaller. This means that R (ω) can represent the site effects if there are sufficient records. R(ω) is defined as site effect correction factor, which to be used to correct the site effect as dividing observation motion to R(ω) to get corrected measures on bedrock.

We compared this method with the previously proposed two relationship equations, Midorikawa et al. (1994) and Fujimoto & Midorikawa(2006). They have described influence of site effect as a function of Vs30 (Eq 2, 3): these equations were derived according to Vs30 however in case of no available information in a station (such as many stations of K-net) they applied a correction to convert Vs20 or Vs12 to Vs30.

$$\log(R) = 1.83 - 0.66 \log(Vs30) \quad (2)$$

$$\log(R) = 2.367 - 0.852 \log(Vs30) \quad (3)$$

46 earthquakes (figure1Figure **1**) with Mjma > 4 were chosen for analysis. The criteria for selecting events were:

(1) events of focal depth less than 30 km within an epicentral distance of 100 km,

(2) stations that recorded less than 10 gal for PGA are not included

(3) the events occurred with a boundary of 33.00N-36.00N latitude and 132.00E-135.00E longitude.

Total 5988 acceleration record is investigated over 150 stations in the area. 0.1-10 Hz butterworth band pass filter is applied before getting PGVs. We used the biggest peak ground velocity of two horizontal records. Because Vs30s are not available for all station in K-net, we calculated them according to procedure develop by Ghasemi H (2009). Also main shock of Tottori earthquake with 7.3 M_{jma} in 2000 is omitted. In order to analyze fitting of method, root mean square error and fundamental statistical analysis of each event is evaluated. Well known attenuation relationship proposed by Si and Midorikawa(1999) is utilized as a reference attenuation model. The model for PGV is defined on engineering bedrock with a shear wave velocity of about 600 m/s. All the earthquakes are used in this study are crustal events. The adopted reference attenuation equation is expressed below

$$\log PGV = 0.58 M_w + 0.0038D - \log(X + 0.0028 \cdot 10^{0.5 Mw}) - 0.002 X - 1.29 \quad (4)$$

where X, M_w, D are fault distance, moment magnitude and focal depth.

This attenuation model is verified with many independent studies and is currently being used national earthquake early warning system for predicting intensities through estimating PGV.

3. RESULTS

Figure1 shows the epicenteral distribution of 46 earthquakes and 150 K-net stations in the investigated region. Red stars shows the epicenters and triangles are the stations. Light grays (total 85 stations) indicate stations that recorded less than three events. Dark gray (36 stations recorded 3, 4 events), blue (17 stations recorded 5 to 9 events), and green triangles (12 stations recorded more than 9 events) are indicated in the Figure. Table 1 gives the origin time of events together with depth, Mw and location. Last column is the number of stations recorded individual event. Most of earthquakes are between 5 to 15 km depths, especially fore- and aftershock of 2000 Tottori Earthquakes.

Relation between moment magnitudes with distance is plotted in Figure 2. M_w less than 4 in the figure and also in tables is due to usage of M_w solution of F-net. We searched for available M_w in F-net database and used them instead of M_{jma}; in case of no information, M_{jma} are directly used in reference attenuation model.

Figure 3 shows the attenuation of two events for PGA and PGV and attenuation curves of Si and Midorikawa, 1999. These are the 13th and 22rd events in table 1 with 4.4 (left two) and 5.1 Mw. Depth is 10 km for both. 10 and 32 stations in the region recorded each event respectively. PGAs for both events are almost in the interval between upper and lower standard deviation of attenuation equation. On the other hand same tendency seen in PGV for the earthquake in 2002 with 5.1 attenuated more rapidly for far distances.

A statistical analysis (Root mean square error, average and standard deviation) is performed for individual event. Observation PGVs are divided to predicted ones which 1.00 means perfect match. Average of RMSE, mean and standard deviation of 46 events are 0.37, 1.02 (with 0.39 std), and 0.57 (with 0.34 std) respectively. Residuals with the variation of hypocentral distance are plotted in figure 4. It is seen here that observed PGVs are smaller than predicted ones in near field due to shorter period components and possible nonlinear behavior. However there is no a general tendency to be mentioned for all records.

According to the proposed method, the accuracy of estimation of site effect depends on the number of records per station. Since the correction factor is derived by the average operation of the residual between observation and prediction. Increasing number of observations per station leads to more accurate estimation. Number of events recorded in each station and their correspondence correction factors are shown in figure 5. Variation of R in stations that recorded only one event is very large (reaches about 10) and also stations recorded only two events decreased to 0.2. Deviation of R is acceptable for stations recorded more than 5 events which indicate average operation is functional and useful for these sites.

Comparisons of the R and the average S-wave velocity of top 30 m are plotted in figure 6. Stations are grouped as same color which defined in Figure 1. Blue line, and black line shows Midorikawa et al. (1994), and Fujimoto and Midorkawa (2006) respectively (refer to equations). There are total 150 correction factor which characterize the factor for relevant station (shown with circles). There is a correlation between Vs30 and R calculated by proposed method. Results also fit with the previous equations. There are four stations that R's are bigger than 4 and eleven stations less than 0.6 which is due to lack of records in these stations. Rest of data especially (green and blue circles) is almost between standard deviation of Midorikawa et al. (1994). Although the number of data used in this study is limited Tottori region, we can conclude that the method proposed in this study is adequate in evaluating the site effects.

4. CONCLUDING REMARKS

We have applied the method proposed by Si et al. (2010) to the area including the western Tottori prefecture. The results show that the estimated site effect is generally consistent with the previous studies. Implicating that the method is effective for estimating site effects.

Acknowledgements:

The strong motion data used in this study are provided by K-NET. The first author would express his sincere gratitude for the financial support from the Earthquake Research Institute, The University of Tokyo.

.

References:

Fujimoto, K., and S. Midorikawa, 2006. Relationship between Average Shear-Wave Velocity and Site Amplification Inferred from Strong Motion Records at Nearby Station Pairs, Journal of JAEE, Vol.6, No.1, pp. 11–22 (in Japanese).

Lee V.W., and Trifunac M.D., "Should averageshear-wavevelocityinthetop30mofsoilbeusedto describe seismicamplification?" Soil Dynamics and Earthquake Engineering 30 (2010) 1250–1258

Ghasemi H (2009), personal cominication

Midorikawa, S., M. Matsuoka and K. Sakugawa, 1994. Site effects on strong-motion records during the 1987 Chiba-ken-toho-oki, Japan Earthquake, Proceedings of the 9th Japan Earthquake Engineering Symposium, pp. 85-90.

Seed HB, Ugas C, Lysmer J. Site-dependent spectra for earthquake-resistant design. Bull Seismol Soc Am 1976;66:221–43.

Si, H., and S. Midorikawa, 1999. New attenuation relationship for peak ground acceleration and velocity considering effects of fault type and site condition, J. Struct. Constr. Eng. AIJ, Vol.523, pp. 63– 70 (in Japanese).

Si, H., and S. Midorikawa, 2000. Attenuation Relationships of Peak Ground Acceleration and Velocity Considering Effects of Fault Type and Site Condition, 12th World Conference on Earthquake Engineering, 532.

Si, H., and S. Midorikawa, 2005. Hanging wall effects on strong motion records during the 2004 Mid Niigata prefecture earthquake and its largest aftershock, Program and abstracts, 2005, Fall meeting, the seismological society of Japan, B081.

Si,H., K. X. Hao, Y. Xu, H. Fujiwara, C. Wu, H. Yamada, and S. Midorikawa, 2008. A Preliminary Study on Attenuation Characteristics of PHA Recorded during the 2008 Wenchuan Earthquake, China, paper presented at Japan Geoscience Union Meeting 2008, JPGU, Makuhari, S152-006.

H. Si, H. Tsutsumi and S. Midorikawa "Valuation of Hanging Wall Effects on Ground Motion Attenuation Relationship Correcting the Site Effects" Proceedings of the 9th U.S. National and 10th Canadian Conference on Earthquake Engineering, July 25-29, 2010, Toronto, Ontario, Canada

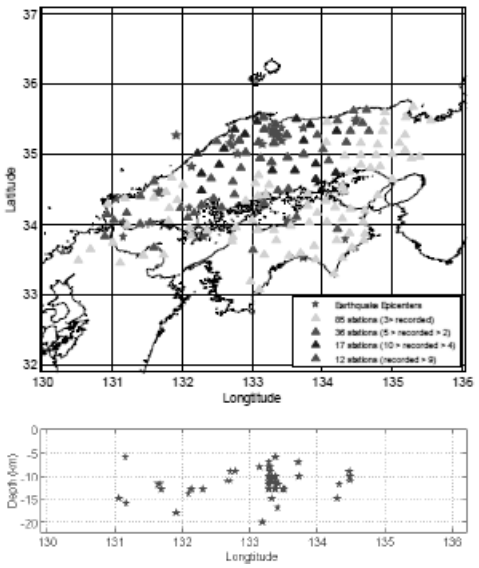


Figure 1. Location of 46 earthquakes and 150 K-net stations in the Tottori region. Red stars shows the epicenters and triangles are the stations. Colors of triangles indicate the number of recorded events in a station. Light grays (total 85 stations recorded 1 or 2 events), dark gray (36 stations recorded 3 or 4 events), blue (17 stations recorded 5 to 9 events), and green triangles (12 stations recorded more than 9 events). Most of earthquakes are between 5 to 15 km depths, especially fore- and aftershock of 2000 Tottori Earthquakes.

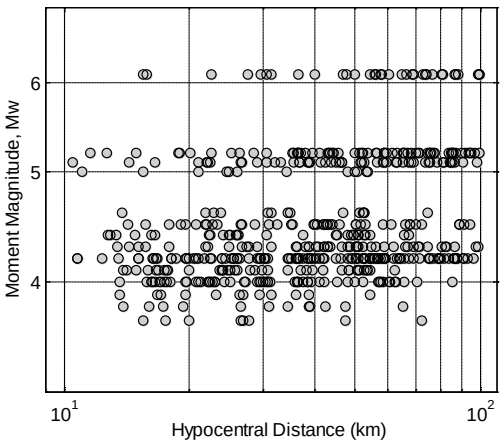


Figure 2 Moment magnitude verses distance distributions. Mw less than 4 is due to usage of Mw solution of F-net. We searched for available Mw in F-net database and used them instead of Mjma; in case of no information, Mjma are directly used in reference attenuation model.

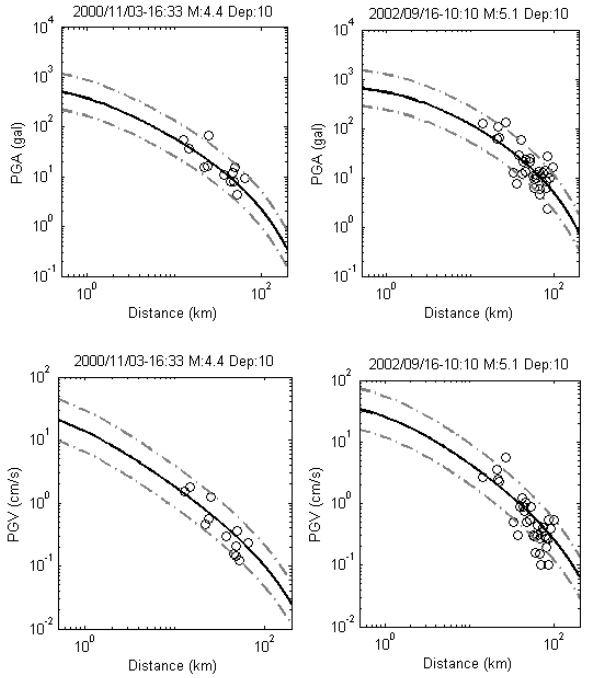


Figure 3 Attenuation curves of Si and Midorikawa, 1999 and observed PGA and PGV for two earthquakes. These are the 13th and 22rd events in Table 1 with 4.4 (left two) and 5.1 Mw. Depth is 10 km for both. 10 and 32 stations recorded each event respectively.

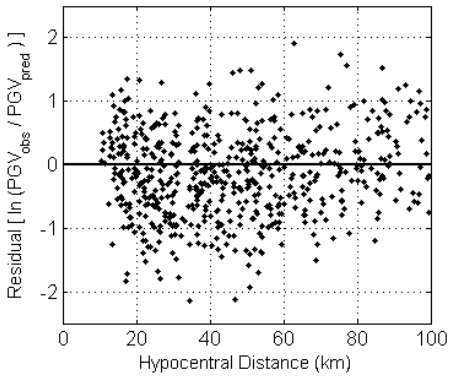


Figure 4 Relationship between residuals and hypocentral distance of all records for PGV.

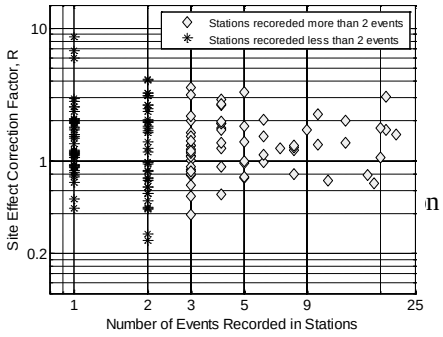


Figure 5 Number of events recorded in each station and their correspondence correction factors. Axes Y is in log scale. Variation of correction factor in stations recorded only one event is very high (reaches about 10) and also stations recorded only two events decreased to 0.2. Deviation of R is acceptable for stations recorded more than 5 events means average operator is functional and useful for this site.

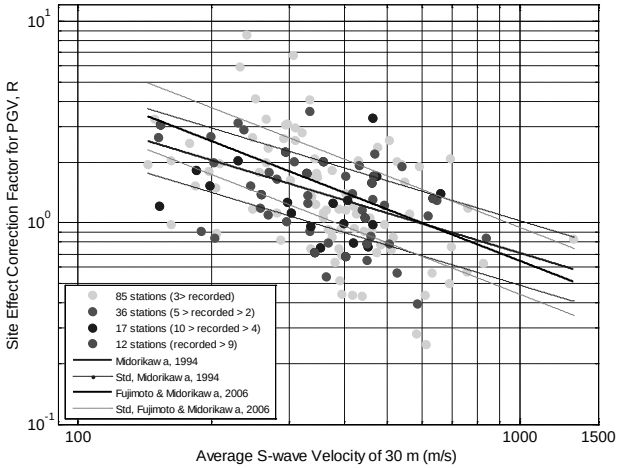


Figure 6 Comparisons of the R and the average S-wave velocity of top 30 m. Stations are grouped as same color which defined in Figure 1. Blue line, and black line shows Midorikawa, 1994, and Fujimoto and Midorkawa 2006 respectively (refer to equations).

Table 1. The events list

No.	Occurance Time	Long (E)	Lat (N)	Depth	Mw	No. of station
1	2000/07/17-08:00	133.419	35.375	17	4	11
2	2000/10/06-14:43	133.319	35.318	11	4.1	3
3	2000/10/06-14:52	133.307	35.361	11	4.4	4
4	2000/10/06-16:21	133.32	35.325	10	4.2	3
5	2000/10/06-23:13	133.287	35.295	8	4.1	3
6	2000/10/07-06:38	133.294	35.361	11	4.2	4
7	2000/10/07-12:03	133.312	35.375	9	4.2	7
8	2000/10/08-06:08	133.294	35.336	7	3.9	2
9	2000/10/08-13:17	133.149	35.14	8	5.1	19
10	2000/10/08-20:51	133.309	35.371	9	5	12
11	2000/10/10-21:58	133.302	35.373	11	4.4	13
12	2000/10/17-22:17	133.425	35.191	12	4.2	13
13	2000/11/03-16:33	133.29	35.36	10	4.4	12
14	2000/12/07-23:09	133.285	35.37	12	4.1	12
15	2000/12/19-06:18	133.294	35.393	13	4.1	8
16	2001/01/12-08:00	134.489	35.466	10	5.2	35
17	2001/01/20-07:24	134.487	35.496	11	4.5	7
18	2001/01/24-00:03	134.482	35.465	9	4.2	12
19	2001/02/11-09:17	133.294	35.421	13	4.3	7
20	2001/10/08-11:23	133.32	35.301	8	3.8	5
21	2002/03/06-07:12	133.33	35.283	15	4.5	20
22	2002/09/16-10:10	133.739	35.37	10	5.1	32
23	2002/10/23-06:22	132.674	35.151	11	3.7	8
24	2003/03/27-13:47	132.137	34.816	13	4.2	3
25	2003/04/02-01:38	132.719	35.12	11	4	8
26	2003/12/13-12:32	134.297	34.558	15	4.3	26
27	2006/05/08-12:45	133.528	34.02	13	3.8	7
28	2006/07/11-03:09	131.167	34.025	16	4	13
29	2007/05/13-08:14	132.792	35.008	9	4.6	14
30	2007/11/10-01:47	131.918	35.267	18	4.3	2
31	2008/05/02-12:23	132.717	35.242	9	4	6
32	2008/05/20-14:41	131.063	34.357	15	4.2	11
33	2010/02/21-11:49	132.307	33.825	13	4.2	14
34	2010/10/06-13:51	133.73	33.527	7	4.2	8
35	1996/06/15-11:10	133.38	35.253	11	4.2	4
36	1996/12/16-01:52	131.165	33.82	6	4	4
37	1997/06/25-18:50	131.665	34.453	12	6.1	34
38	1997/06/25-18:58	131.698	34.453	13	4.1	7
39	1997/08/23-08:35	133.38	35.253	12	4	5
40	1997/09/02-02:07	133.38	35.253	13	4.1	5
41	1997/09/04-05:12	133.38	35.253	10	4.3	13
42	1997/09/04-05:16	133.38	35.27	6	5.2	31
43	1999/02/07-18:15	132.098	34.236	14	4	11
44	1999/07/16-02:59	133.197	34.42	20	4.2	33
45	1999/07/19-05:14	134.33	33.786	12	3.9	10
46	1999/10/30-06:25	133.504	34.051	13	4.5	15

8CUEE CONFERENCE PROCEEDINGS
8th International Conference on Urban Earthquake Engineering
March 7-8, 2011, Tokyo Institute of Technology, Tokyo, Japan

NUMERICAL SIMULATIONS OF A CENTRIFUGE TEST TO STUDY VOID-REDISTRIBUTION AND SHEAR-LOCALIZATION EFFECTS

Ronnie Kamai[1] and Ross W. Boulanger[2]

1) PhD candidate, Dept. of Civil and Environmental Engineering, Univ. of California, Davis, CA
2) Professor, Dept. of Civil and Environmental Engineering, Univ. of California, Davis, CA
rkamai@ucdavis.edu, rwboulanger@ucdavis.ed

Abstract: Numerical simulations are conducted to study the effects of water flow and dissipation patterns on liquefaction-induced ground surface deformations. The numerical approach is validated against a centrifuge test, in which lateral spreading and shear-strain localization at a sand-clay interface were observed and measured. Time histories of acceleration, displacements, and pore-water pressures, as well as displacement profiles are compared and found to be successfully approximated by the simulation results. Volumetric strains tracked by the simulations suggest that a 1-m thick sublayer at the top of the liquefiable sand has significantly loosened from D_R=40% to D_R=30% due to the inflow of water caused by the upward hydraulic gradient following liquefaction. The simulations show that the diffusion of excess pore pressures can lead to shear strain localization in sand below a lower-permeability layer, without reaching critical state or necessarily leading to flow failure.

1. INTRODUCTION

1.1 Void Redistribution

The potential effects of drainage and pore pressure redistribution on liquefaction-related ground-surface deformations have been articulated by Whitman (NRC 1985; Whitman 1985) and have since been demonstrated in shaking table tests, centrifuge model tests, numerical simulations, and inferred from field studies (Kokusho 2003; Kulasingam et al. 2004; Malvick et al. 2006; Seid-Karbasi and Byrne 2007). These studies suggest that pore-water flow, resulting from liquefaction-induced hydraulic gradients, may be impeded by lower-permeability layers which overlay or interbed the liquefiable sand. The impeded flow can lead to loosening and softening of the sand neighboring such permeability-barriers, resulting in strength-loss and excessive deformations.

Liquefaction-induced shear-strain localization has been observed as one of the possible consequences of such dissipation-related softening and strength-loss (Seid-Karbasi and Byrne 2007; Malvick et al. 2008; Kamai and Boulanger 2010). A series of 14 centrifuge tests and accompanying shaking table tests, which involved an embedded silt arc within a liquefiable sand slope, has shown that similar profiles can develop shear strain localization at the sand/silt interface in some cases and uniform strains in others (Kokusho 2003; Kulasingam et al. 2004; Malvick 2005). The occurrence of shear strain localization was found to be dependent on the soil properties (such as density and permeability), layer thickness and geometry (e.g. slope angle), and loading parameters (history, duration, and magnitude).

To better understand the physical mechanisms that tie between pore pressure dissipation, strength-loss, and the eventual localization of shear-strains, a numerical approach is adopted in which boundary conditions can be easily controlled and the problem can be studied under different scales and conditions. In this paper, the numerical approach is validated against a centrifuge-test in which pore-pressure migration, lateral-spreading, and shear-strain localization were observed and measured. The following sections will shortly describe the constitutive model used for the simulations and the centrifuge test configuration, followed by a comparison between simulation and physical test results.

1.2 The Constitutive Model

The constitutive model used for simulating the sand is a bounding surface plasticity model (Boulanger 2010), developed primarily for earthquake engineering applications. It is largely based on the stress-ratio controlled, critical-state compatible, bounding surface plasticity model for sand presented by Dafalias and Manzari (2004). On a p'-q space, the model has a narrow stress-ratio based elastic cone and three other key surfaces – the bounding, dilation and critical-state surfaces (see Figure 1). The locations of the dilation and bounding surfaces are dependent on the relative state of the soil, such that they move towards the critical state surface in a scissor-like movement when the soil is sheared towards critical state, with all three surfaces coinciding when the soil reaches critical state. Modifications to the original model were primarily made to improve its

ability to follow a set of experimentally- and case history based- empirical correlations commonly used in earthquake engineering applications, while remaining relatively user-friendly and easy to calibrate (Boulanger 2010).

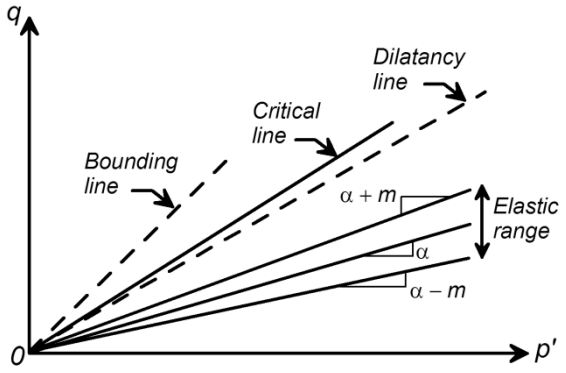


Figure 1 Schematic representation of the *PM4Sand* model, showing the yield, critical, dilation and bounding surfaces.

The constitutive model has 21 input parameters, from which 18 can be left at their default values in case the available experimental data is not sufficient for further calibration. A detailed explanation on the model parameters and their default values is provided in Boulanger (2010). For this study, the three primary parameters – D_R, h_{po}, and G_o (which relates to shear-wave velocity), as well as four additional secondary parameters – h_o, n_b, c_e and z_{max} – were calibrated to obtain the desired response, based on available data from experiments with Nevada Sand. An example response of an undrained DSS, with D_R=40% and σ'_{v0}=100 kPa is presented in Figure 2 and compared with experimental results.

1.3 The Centrifuge Test

The centrifuge test, SSK01, was performed to evaluate the effectiveness of geosynthetic drains for mitigating liquefaction of sands (Kamai et al. 2008; Marinucci et al. 2008). The test was performed in a flexible shear beam container (0.8-m wide, 1.65-m long, 0.5-m deep) on the 9-m radius centrifuge at UC Davis. The test was performed at a centrifugal acceleration of 15 g and the results are presented in equivalent prototype units unless otherwise stated (for description of centrifuge scaling laws see Kutter (1995)).

The soil profile was constructed of two symmetrical sides, sloping at 3˚ towards a central channel. Both had a 5-m thick liquefiable layer of Nevada Sand (D_R=40%) overlain by a 1-m thick layer of clayey-silt (plasticity index, PI=13). Model-scale plastic drains were installed on one side of the centrifuge container prior to pluviation. Close to 100 sensors were placed within the soil and on the surface. The model was saturated under vacuum. The model was subjected to five main shaking events separated from each other by sufficient time for full dissipation of any excess pore water pressures. The five successive shaking events consisted of 20 uniform sinusoidal cycles at 2 Hz with single-amplitudes of 0.01, 0.03, 0.07, 0.11, and 0.3 g. They will be labeled in this paper as “shake 08”, “shake 09”, “shake 10”, “shake 11”, and “shake 12”, respectively (shakes 01-07 had amplitudes less than 0.02 g and did not lead to any significant development of pore pressures).

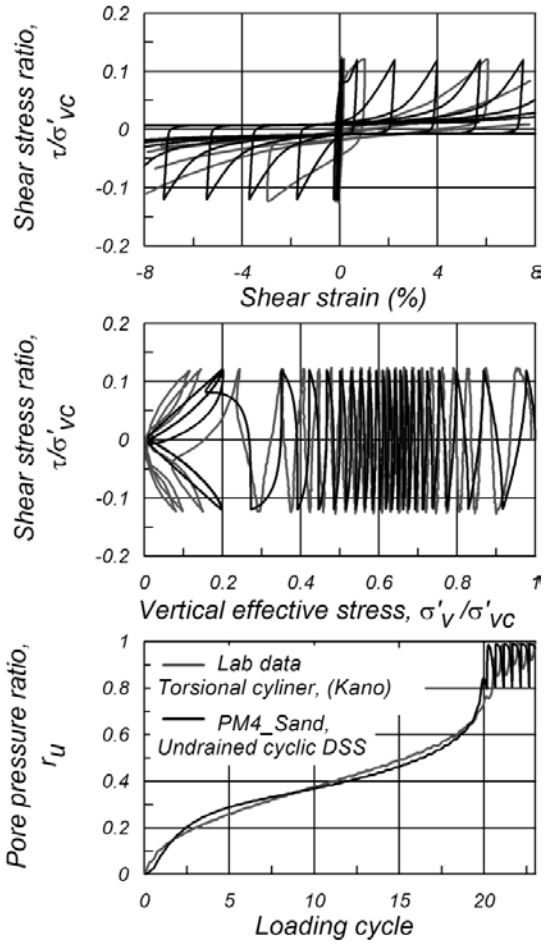


Figure 2 Comparison between simulation results of undrained DSS using *PM4Sand* and lab data of torsional cylinder – Nevada sand, D_R=40%, σ_{v0}' = 100kPa.

2. SIMULATIONS OF A CENTRIFUGE TEST

2.1 Model construction and boundary conditions

The simulations are performed using the commercial finite-difference program FLAC (Itasca 2009), using three different material models, as presented in Figure 3. The aluminum and rubber rings of the container are assigned an elastic material model, following Armstrong (2010). The clayey-silt crust is assigned a Mohr-Coulomb material model with the appropriate properties, as derived from the physical test. The sand layers, both loose (D_R=40%) and dense (D_R=80%), are assigned the user-defined material model *PM4Sand* (Boulanger 2010), which was described earlier.

The prefabricated vertical drains on the drain-treated side are simulated by fixing the pore pressures at vertical columns of nodes (see Figure 3) to their hydrostatic value. This condition is only an approximation of the drainage,

which will produce an over prediction of drainage with comparison to the physical model test, but is sufficient for the purpose of this simulation, which is focused on the response of the non-treated side.

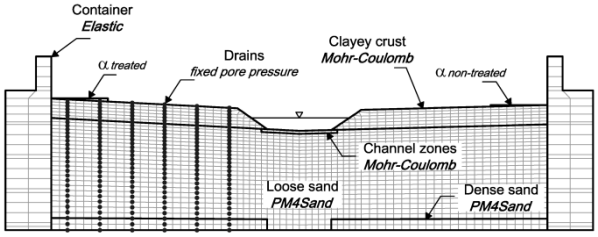


Figure 3 FLAC mesh, showing material models, location of drains and water table height.

The boundary between the soil elements and the container elements is modeled by a frictional interface that allows for relative movement of the soil with respect to the container elements. Vertical displacement of the container is restricted, and container nodes from both sides of the model are slaved to each other in the horizontal direction, to represent the continuation of the container rings in 3D. Pore water is allowed to flow across the top surface of the model, whereas flow across the container boundary is restricted. Water within the central channel is modeled by applying the corresponding pressure to the channel nodes below the water table height. Shaking is applied by subjecting the bottom container nodes to the velocity time history that was measured at the bottom of the container in the centrifuge test. Rayleigh damping is set to 0.5% at a center frequency of 2 Hz, which is the dominant frequency of the input motion.

2.2 Simulation results and comparison with test observations

Simulations of the largest four shaking events were performed (amplitudes of 0.03 - 0.3 g). Two cyclic strengths and two permeability values for sand were compared, to account for scatter in the available data. Simulations were also conducted without 'large deformation' and without 'flow' modes within FLAC, to separate the effects of mesh deformations and of pore water flow within the profile. The full set of results will be presented in an upcoming paper. For purposes of this paper, only one set of results will be presented and discussed. Figures 4 through 6 will show the detailed response of the model to shake 10 (0.07 g) with the higher values of cyclic strength and permeability and with 'flow' and 'large deformations' enabled. Figure 7 will integrate results from four shaking events in a cumulative representation.

The dynamic response of the non-treated soil profile to shake 10 is illustrated in Figure 4. Time histories of crust acceleration, excess pore-pressure in mid-depth of the loose sand layer, surface lateral spreading and vertical settlement at mid-slope for the simulations (in blue) and the centrifuge test (in red) are compared. The numerical prediction is largely successful in capturing the trends and magnitudes of the response. The crust acceleration is slightly overpredicted

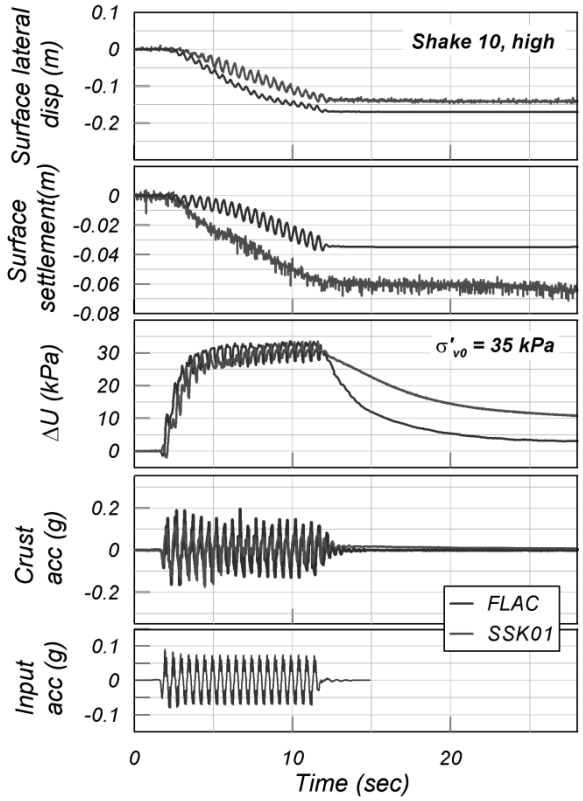


Figure 4 Comparison of centrifuge test and simulation results for shake 10 with high cyclic strength value. Time histories show a reasonable agreement between surface deformations, excess pore pressures, and crust accelerations.

and does not show the same de-amplification as observed in the centrifuge test, but peak magnitudes are similar. Simulations are able to predict the fast accumulation of excess pore pressures and the early triggering of liquefaction throughout the profile, though dissipation rates are faster than in the test. A simulation with 1/3 permeability produces dissipation rates that are in better agreement with measured pore pressure time histories, but over-predict the lateral surface displacements. Figure 4 further shows that the lateral surface displacements in this simulation agree well with the centrifuge test measurements, but that the vertical settlement is under-predicted. This could be a result of slumping and yielding of the crust material itself during the centrifuge test that was not predicted in the simulations. Overall, the dynamic response is in good agreement with the centrifuge test measurements and indicates that the general behavior is achieved in the simulations.

The overall deformation pattern is illustrated by the contour plot in Figure 5. The contours show significantly different deformation patterns in the treated and non-treated sides. On the non-treated side, there is a clear step in displacements across the upper row of sand elements just below the crust, such that the crust deformations are about twice as much as the sand deformations. On the treated side,

there is very little deformation and no concentration of deformations at the interface between the sand and the crust, in agreement with the experimental observations. The large crust displacements result in a gap opening between the non-treated crust and the container wall (only possible with large deformations enabled) and significant flattening of the slope, as also observed in the centrifuge experiment.

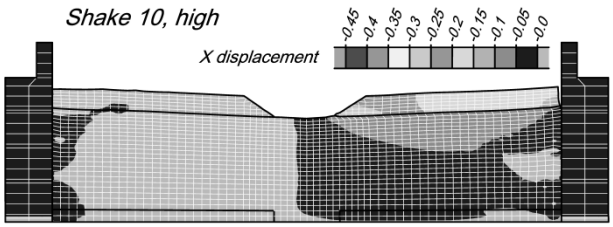


Figure 5 Contour map showing x displacements at the end of shaking. Localization is clearly seen on the non-treated side whereas displacements on the treated side are negligible.

Void-ratio redistribution as a result of the liquefaction-induced hydraulic gradient and upward flow is illustrated by a contour plot of relative-densities at the end of shaking in Figure 6. The top 3-8 sand elements on the non-treated side are loosened by 5-10% relative density, whereas the treated side experiences no loosening, and even some densification towards the container wall. The thickness of the loosening zone is a little less than 1 m, which is in good agreement with previous theoretical and experimental studies (Malvick et al. 2006; Malvick et al. 2008) as well as with the results of inverse analyses of the instrument arrays from this test (Kamai and Boulanger 2010). These other studies had shown zones of dilation at the top of a confined liquefied sand layer that were about 0.6-m to 1.0-m thick, which is much greater than the expected thickness of any eventual localization (i.e., 10 or 20 grain diameters).

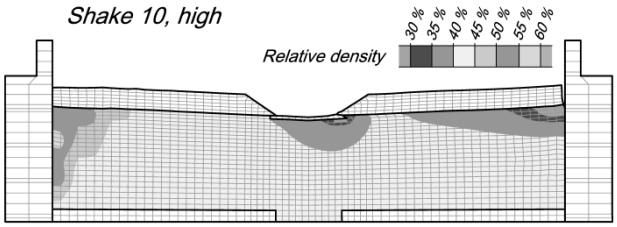


Figure 6 Contour map showing relative density at the end of shaking. On the non-treated side, the upward pore-pressure dissipation which is impeded by the crust layer leads to the loosening of a ~1 m thick sub-layer below the crust.

Cumulative deformation profiles for the non-treated side (approximately at a mid-slope location) at the end of each shaking event are presented in Figure 7. Simulation results (represented by solid lines) are in good agreement with surface measurements from the centrifuge test (represented by open diamonds). The concentration or localization of deformations at the top sand element beneath the crust layer is clearly seen in the simulation results for shakes 10 onwards. The extent of deformations across the physical localization in the centrifuge test could only be measured at the end of the test and is represented by the cross symbols, which are in good agreement with the simulations' cumulative deformation across the top sand element (also called a "localization" for simplicity) at the end of shake 12. No deformation profiles are presented for the drain-treated side, since deformation was very limited, and no localization was observed at the interface, in agreement with observations from the centrifuge test.

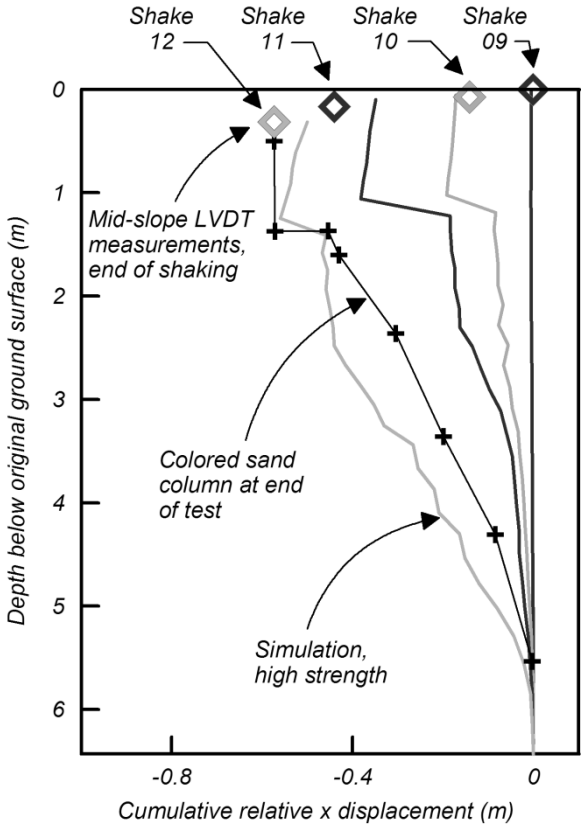


Figure 7 Displaced shape profiles on the non-treated side. Simulation results for shakes 9 through 12 are shown for the high cyclic strength case. The combined lateral and vertical surface displacement, as measured from LVDT's is presented by the open diamonds, and a colored sand column that was measured during excavation of the model at the end of the entire test is shown in the black line with the crosses.

3. DISCUSSION AND CONCLUSIONS

The general trends that were observed in the centrifuge test are successfully captured in the numerical simulations. The predicted surface deformations, pore pressure accumulation and dissipation patterns, and the distribution of strains throughout the profile agree well with the observations and measurements from the test.

The location, initiation, and extent of shear strain localization at the sand/clay interface are consistent with observations from the centrifuge test. This is an indication that the physical mechanism which ties pore-pressure dissipation, void-ratio redistribution, and shear-strain localization is successfully captured by the numerical platform and constitutive model discussed herein. These results were largely independent of element size, within the range of sizes evaluated.

The effective mitigation of surface deformations by liquefaction drains, including the complete prevention of shear-strain localization at the sand/clay interface, is successfully predicted and captured by the numerical simulations. It should be noted, however, that the drains in this study assume drainage walls, so over-prediction of mitigation effectiveness is expected.

Acknowledgements:

Funding for this research was provided the U.S. Geological Survey through Award G09AP00121. Richie Armstrong provided the FLAC model for the centrifuge container. The centrifuge test was performed in collaboration with Ellen Rathje, Antonio Marinucci, Seiji Kano, Carolyn Conlee, and Patricia Gallagher with funding from NSF Award No. CMS-0530478. The above support and assistance is appreciated.

References:

Armstrong, R. J. (2010) "Evaluation of the Performance of Piled Bridge Abutments Affected by Liquefaction-Induced Ground Deformations Through Centrifuge Tests and Numerical Analysis Tools". Ph.D. dissertation, University of California, Davis.

Boulanger, R. W. (2010) "A Sand Plasticity Model for Earthquake Engineering Applications". 2010, Report number: UCD/CGM-10/01.

Dafalias, Y. F. and M. T. Manzari (2004). "Simple plasticity sand model accounting for fabric change effects." *Journal of Engineering Mechanics* **130**(6): 622-634.

Itasca (2009). FLAC - Fast Langrangian Analysis of Continua. Minneapolis, Minnesota, Itasca Consultin Group, Inc.

Kamai, R. and R. Boulanger (2010). Characterizing localization processes during liquefaction using inverse analyses of instrumentation arrays. *Meso-Scale Shear Physics in Earthquake and Landslide Mechanics*. Y. H. Hatzor, J. Sulem and I. Vardoulakis. The Netherlands, CRC Press/.Balkema**:** 219-238.

Kamai, R., S. Kano, et al. (2008) "Evaluation of the effectiveness of prefabricated vertical drains for liquefaction remediation - centrifuge data report for SSK01". 2008, Report number: UCD/CGM-08/01.

Kokusho, T. (2003). "Current state of research on flow failure considering void redistribution in liquefied deposits." *Soil Dynamics and Earthquake Engineering* **23**(7): 585-603.

Kulasingam, R., E. J. Malvick, et al. (2004). "Strength loss and localization of silt interlayers in slopes of liquefied sand." *Journal of Geotechnical and Geoenvironmental Engineering* **130**(11): 1192-1202.

Kutter, B. L. (1995). *Recent Advances in Centrifuge Modeling of Seismic Shaking*. 3rd International Conference on Recent Advances in Geotechnical Earthquake Engineering and Soil Dynamics, University of Missouri-Rolla, Rolla, MO.

Malvick, E. J. (2005) "Void redistribution-induced shear localization and deformation in slopes". PhD dissertation, University of California, Davis.

Malvick, E. J., B. L. Kutter, et al. (2008). "Postshaking shear strain localization in a centrifuge model of a saturated sand slope." *Journal of Geotechnical and Geoenvironmental Engineering* **134**(2): 164-174.

Malvick, E. J., B. L. Kutter, et al. (2006). "Shear localization due to liquefaction-induced void redistribution in a layered infinite slope." *Journal of Geotechnical and Geoenvironmental Engineering* **132**(10): 1293-1303.

Marinucci, A., E. Rathje, et al. (2008). *Centrifuge Testing of Prefabricated Vertical Drains for Liquefaction Remediation*. Geotechnical Earthquake Engineering and Soil Dynamics IV, Sacramento, CA, ASCE.

NRC (1985) "Liquefaction of soils during earthquakes ". National Academy Press, Washington, C.D., 1985, Report.

Seid-Karbasi, M. and P. M. Byrne (2007). "Seismic liquefaction, lateral spreading, and flow slides: a numerical investigation into void redistribution." *Canadian Geotechnical Journal* **44**(7): 873-890.

Whitman, R. V. (1985). *On liquefaction*. 11th Internation Conference on Soil Mechanics and Foundation Engineering, San Francisco, CA., Balkema Rotterdam.

8CUEE CONFERENCE PROCEEDINGS
8th International Conference on Urban Earthquake Engineering
March 7-8, 2011, Tokyo Institute of Technology, Tokyo, Japan

CENTRIFUGE MODELING ON UPLIFT BEHAVIOR OF IMMERSED TUNNEL EMBEDDED IN LIQUEFIED SOILS

Yu-Chen Wei[1)], Wen-Ya Chuang[2)], Wen-Yi Hung[3)], Huei-Tsyr Chen[4)], and Chung-Jung Lee[5)]

1) Ph.D. Candidate, Department of Civil Engineering, National Central University, Taiwan
2) Research Assistant, Department of Civil Engineering, National Central University, Taiwan
3) Associate Technologist, National Center for Research on Earthquake Engineering, Taiwan
4) Professor, Department of Civil Engineering, National Central University, Taiwan
5) Professor, Department of Civil Engineering, National Central University, Taiwan
ycwei@hotmail.com.tw, 973202029@cc.ncu.edu.tw, wyhung@ncree.org.tw, chenht@ncu.edu.tw, cjleeciv@ncu.edu.tw

Abstract: The unit weight of buried structure is inherently lighter than that of surrounding saturated soil, so that the buried structure has high potential to float upward once the surrounding soil liquefies. A series of centrifuge shaking table tests was performed to investigate the uplift mechanism of the immersed railway tunnel during the ambient loose sandy soil liquefied. Different viscous fluid was considered in this study to simulate different types of soil layer. A sinusoid wave with acceleration amplitude of about 250 gal, frequency of 1 Hz (16 cycles) was applied to the base of laminar container in prototype scale. Vertically hydraulic gradient contours were plotted to demonstrate the changes of excess pore water pressure during and after shaking. A severe quick sand condition can be expected beneath the tunnel especially at the lower corner of tunnel. The final uplift displacement of tunnel for Test B was less than that of Test A. The reason of smaller uplift displacement of tunnel in Test B may be due to the apparent cohesion and higher viscous force in the MCE fluid saturated soil specimen. The increasing uplift displacement with increasing FS was observed due to the movement of soil around tunnel during dissipation stage for Test A and Test B.

1. INTRODUCTION

The unit weights of buried structures are inherently lighter than that of ambient saturated soil. The apparent unit weight of a typical immersed tunnel is around 10 kN/m^3, however, the unit weight of the saturated sandy soil is of about 20 kN/m^3. When the sandy soil is completely liquefied, it will make buried structures subjected to upward buoyancy, and squeeze out the buried structure toward ground surface. Therefore the buried structures have high potential to float upward once the surrounding soil liquefied. Uplift failure of buried structures, such as immersed tunnels, manholes and pipeline systems, were observed in the 1964 Niigata earthquake, 1995 Kobe earthquake (Liu and Song, 2005), and 2004 Niigata-ken Chuetsu earthquake (Tobita et al., 2010). Chou et al. (2001) indicated that the Taipei Rapid Transit System (TRTS) tunnel with 17 m buried height in Taipei County can be classified as a light to medium degree of risk for the liquefaction related damage. The related soil profile also shows that the depth of liquefiable soil layer is from 5 meters to 24 meters beneath the ground surface in the interesting site. Thus, the situation could become even worse for a sallow immersed tunnel in Taipei County, and a further research study on the behavior of immersed tunnel in liquefiable soil is needed.

Koseki et al. (1997) performed a series of 1 g shaking table tests to simulate immersed tunnels and manhole uplift behavior due to soil liquefaction. Koseki et al. show that the total tunnel displacement is affected by three different soil-structure interactions: 1) lateral soil deformation of liquefied soil; 2) movement of pore fluid; 3) reconsolidation of soil. Ling et al. (2003) conducted a series of 30 g centrifuge modeling tests to investigate the uplift stability and overburden soil improved strategy of a large-diameter pipe. Sasaki and Tamura (2004) predicted the tunnel uplift displacement based on centrifuge modeling tests results, and the predicted results show a well fit with the measured uplift displacements during shaking.

An existing immersed railway tunnel which is located in the potential liquefaction risk area in Taipei County is considered in this study. A series of dynamic centrifuge modeling tests in a acceleration of 80 g was performed to investigated the seismic response of the immersed railway tunnel with the cross-section of 9.15 m (H) × 18 m (W) embedded in saturated sandy soil. Detail testing setup, test results and discussions present in the following sections.

2. CENTRIFUGE MODELING TESTS

2.1 Equipment and Soil Properties

Centrifuge modeling tests were performed by using the 100g-ton geotechnical centrifuge at National Central University (NCU) in Taiwan. NCU centrifuge has a nominal

radius of 3 m and equips a one dimensional electro-hydraulic servo-controlled shaker integrated within a swing platform. The shaker has maximum nominal shaking force of 53.4 kN, maximum table displacement of ±6.4 mm, and could be operated up to 80 centrifugal acceleration with maximum payload mass of 400 kg. A 38 aluminum rectangular ring formed laminar container with the inside dimensions of 710 mm (L) × 355 mm (W) × 355 mm (H) was conducted in the tests.

Tunnel model was made by an acrylic box in order to control its apparent unit weight as light as existing railway tunnel's. The apparent unit weight of the tunnel model is 9.53 kN/m^3, and is lighter than the unit weight of water. Therefore, the tunnel model has the potential for floating upward in all time even in the static condition. The dimension of the tunnel model is 336 mm (L) × 225 mm (W) × 114 mm (H), can be used to simulate a immersed railway tunnel with inner dimensions of 26.88 m (L) × 18 m (W) × 9.15 m (H). Three pore water pressure transducers were installed inside of the tunnel, and used to measure the pore water pressure distribution at the bottom of the tunnel. Eleven earth pressure transducers were distributed around the tunnel. The picture of the tunnel model shows in Fig. 1.

Fine quartz sand is used to prepare the sand deposit in this study. The characteristics of the quartz sand are summarized in Table 1. The relative density of the tested sand bed was controlled around 55% by air pluviation.

Table 1 Characteristics of Tested Quartz Sand

G_s	2.65
D_{50} (mm)	0.193
D_{10} (mm)	0.147
γ_{max} (kN/m^3)	16.3
γ_{min} (kN/m^3)	13.5
Friction Angel, ϕ (Dr=55%)	35.7°
Permeability, k (mm/sec)	7.7×10^{-4}

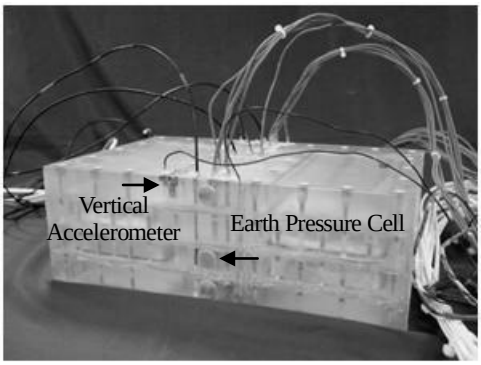


Figure 1 Photo of the Tunnel Model Side View

2.2 Model Preparation and Test Procedures

In the model preparation, the quartz sand was pluviated in a regular path into the container from a hopper at a certain falling height for preparing fairly uniform sand deposits and controlling its relative densities. The pluviation process was interrupted as need for embedding the transducers or tunnel at specified elevations. After completion of the sand bed preparation, the tested model was saturated on the shaker with de-air water or MCE fluid, respectively. The centrifuge was accelerated at an increment of 10 g steps until the centrifugal acceleration field reached to 80 g. A sinusoid wave with acceleration amplitude of about 20 g, frequency of 80 Hz (16 cycles) was applied to the model for duration of 0.2 second. It can simulate an input base ground motion of 250 gal, predominate frequency of 1 Hz and duration of 16 seconds. Various sensors, including accelerometers, pore water pressure transducers and LVDTs, are installed in the model for recording the seismic response of the model during shaking. The configuration of the test setup is shown in Figure 2.Testing conditions are listed in Table 2.

Table 2 Profiles of Testing Conditions

Test No.	Test A	Test B
Viscosity of saturating fluid	1 μ_w	80 μ_w
Input wave amplitude (g)	0.27	0.23
Shaking frequency (Hz)	1	1
Duration (sec.)	16	16
Dr (%)	55.8	55.8
Burial depth (m)	7.68	7.68
Water content (%)	28	28
Saturated soil unit weight γ_{sat} (kN/m^3)	19.1	19.1

* μ_w refers to the water visicosity.

3. TEST RESULTS AND DISCUSSIONS

3.1 Acceleration and Pore Water Pressure Changes

Observed excess pore water pressures (u) in free field were normalized by the corresponding effective vertical stresses (σ'_{vo}) implying the degree of soil liquefaction. In Figure 3, the excess pore water pressure ratio, $r_u = u/\sigma'_{vo}$, presenting the degrees of soil liquefaction in various depths were similar to each other in Test A and B. However, the acceleration response was quite different between Test A and Test B at upper soil layer, see Figure 4. The excess pore water pressure was decreasing during shaking at the depth of 16.8 m (P7) in Test A. It results in the increasing of soil stiffness and the recovery of measured acceleration amplitude at the same depth of tunnel model in the Test A.

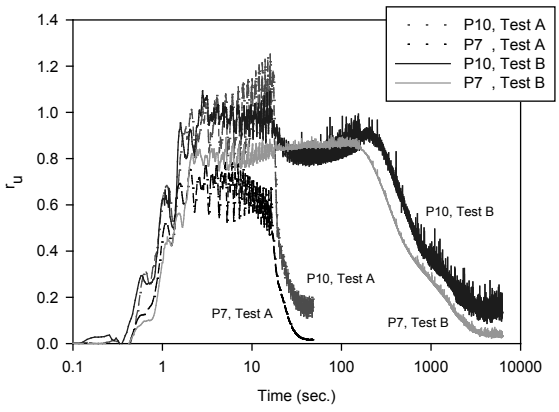


Figure 3 Excess Pore Water Pressure Ratio at Different Depth in Test A and Test B

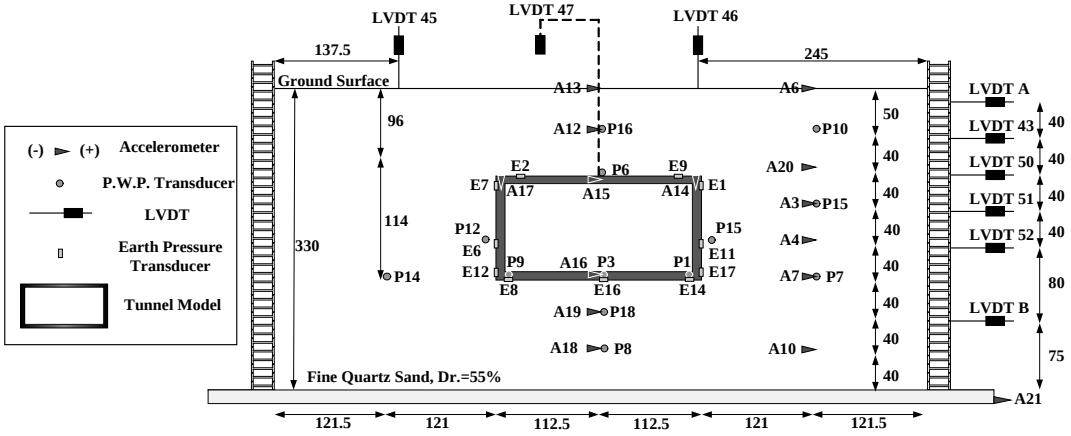


Figure 2 Configuration of Test Setup and Location of Sensors

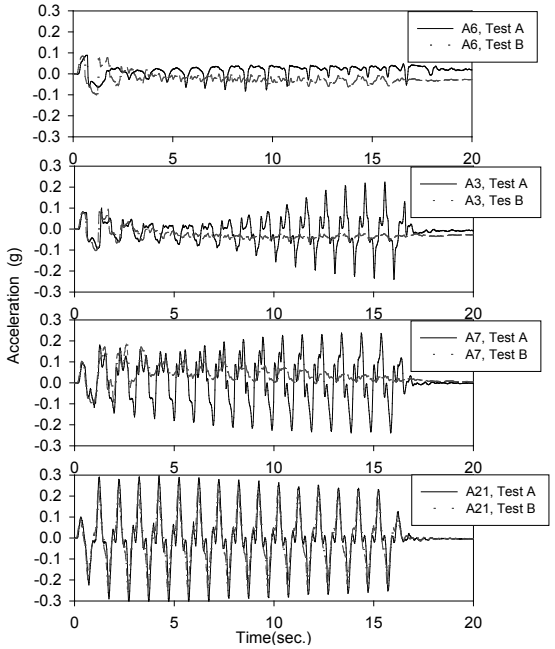


Figure 4 Free Field Acceleration Recordings at Various Depths in Test A and Test B

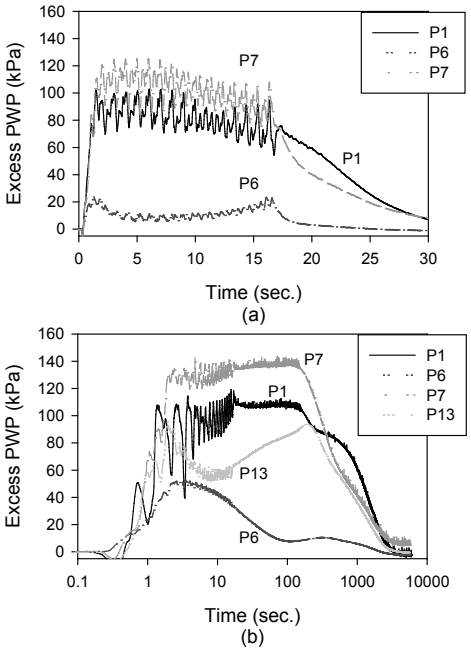


Figure 5 History Recordings for P1, P6, P7 and P13 in (a) Test A ; (b) Test B

In Figure 5, it shows the excess pore water pressure changes measured at the top (P6) and the bottom (P1) surface of tunnel. Measured excess pore water pressure value of P6 was increasing slightly at the beginning of shaking, but it soon decreased during shaking due to the tunnel block effect. It makes the drainage at the upper layer of the tunnel drained toward the ground surface without replenishing from the lower layer of the tunnel. Meanwhile, the drainage generated beneath the tunnel has longer path than that before tunnel existed, and thus the excess pore water pressure may be keeping increase which was discovered in Test B during shaking. The critical hydraulic gradient can be expressed as Eq. (1) :

$$i_c = \frac{G-1}{1+e} \quad \textbf{(1)}$$

where, i_c is the critical hydraulic gradient and e is the void ratio of tested soil.

For the sandy soil used in this study, its critical hydraulic gradient is equal to 0.95. If we took all the pore water pressure transducer recordings into account in Test A and B, the vertically hydraulic gradients were obtained according to Eq. (2).

$$i_v = \frac{\Delta u}{L\gamma_w} \quad \textbf{(2)}$$

where, i_v is the vertically hydraulic gradient, Δu is the difference of adjacent excess pore water pressure readings in vertical direction, γ_w is the unit weight of water and L is the distance between two p.w.p. transducers. The vertically hydraulic gradient is defined as positive as the drainage dissipated toward ground surface. Calculated i_v contour diagram for Test A and Test B was shown in Figure 6. The observed timing was selected at a pair of adjacent local extrema of P1 recordings to investigate the change of vertically hydraulic gradient distribution around tunnel.

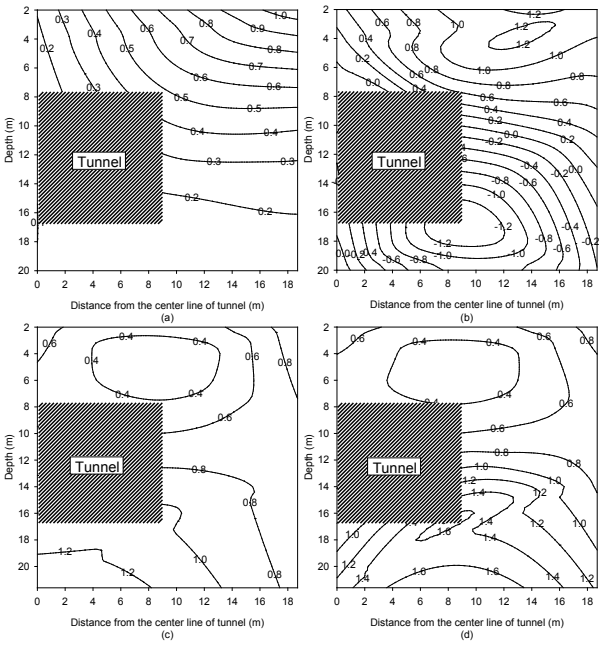


Figure 6 Vertically Hydraulic Gradient Contour Diagram for Test A at (a) 12.768 sec. ; (b) 12.976 sec. ; and for Test B at (c) 7.216 sec. ; (d) 7.712 sec.

While the P1 reading was equal to a local minimum or maximum in Test A, the corresponding vertically hydraulic gradient contour diagrams were shown in Fig. 6 (a) and (b), respectively. In Fig. 6 (a), it was discovered that the maximum vertically hydraulic gradient appeared near the free field ground surface, and its value was greater than the critical hydraulic gradient of tested soil. It is indicated that the quick condition may occur near the ground surface. In Fig. 6 (b), the negative hydraulic gradient distribution region was observed in the right hand side of tunnel. The negative hydraulic gradient distribution may indicate that the ground water flows into the bottom area of the tunnel at this instant, and localized stiffened the soil could be happened due to the increasing effective stresses. The increased soil effective stresses would result in the increase of friction force acted on the side wall of tunnel. While the P1 reading was equal to a local minimum or maximum in Test B, the corresponding vertically hydraulic gradient contour diagrams were shown in Fig. 6 (c) and (d), respectively. It can be found that the value of the hydraulic gradient near the upper corner of the tunnel is relatively smaller than everywhere in the model. In Fig. 6 (d), the hydraulic gradients distributed at the bottom regions of tunnel were greater than the critical hydraulic gradient. A severe quick condition can be expected beneath the tunnel especially near the lower corner of tunnel.

3.2 Uplift Displacement and Earth Pressure Changes

In this study, tunnel uplift displacement was measured by using a wire attached to a pulley LVDT. The measured tunnel uplift displacement and effective earth pressure changes around tunnel in Test A and B were shown in Figure 7 and 8, respectively. The tunnel started to float upward at the beginning of shaking following the increase pore water pressure and the reduction of contacted normal effective

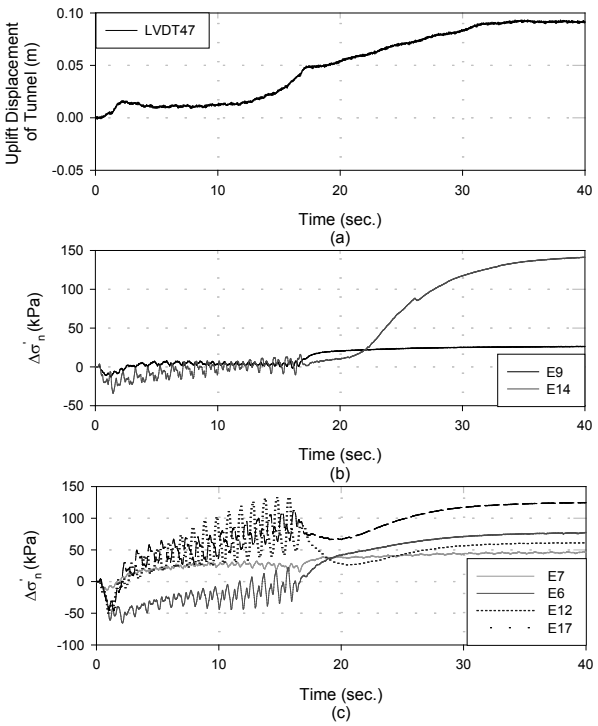


Figure 7 Tunnel Uplift Displacement and Normal Effective Earth Stresses Changes Around Tunnel of Test A

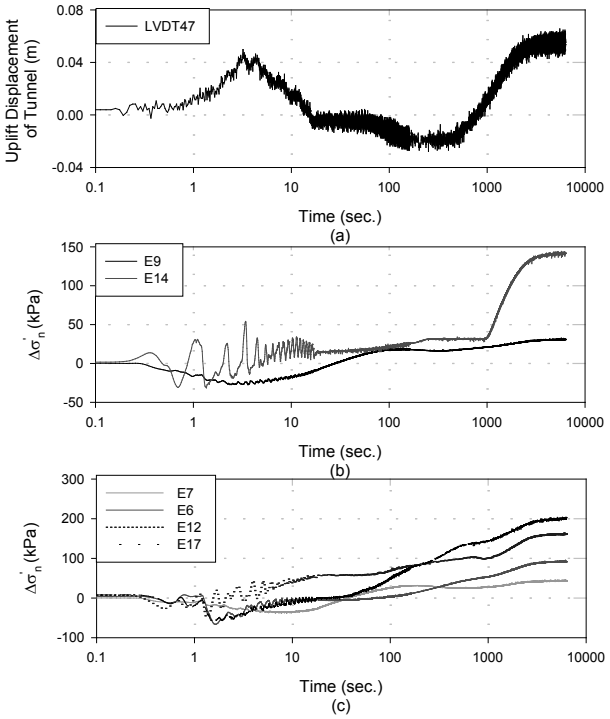


Figure 8 Tunnel Uplift Displacement and Normal Effective Earth Stresses Changes Around Tunnel of Test B

earth stresses (σ'_n). Tunnel uplift displacement variation consists with the change of E9 time history in both tests. However, the tunnel started to settle at 3.1 second of shaking duration in Test B, and began to uplift again in dissipation stage. While the reading of E9 was reducing or increasing,

the tunnel would tend to float upward or to settle downward in both tests. During pore water dissipation, the bottom surface of tunnel would subject to an incremental effective earth pressure, as E14 recording shown, and it may relate to the consolidation and movement of ambient soil. In Test A, a significant earth pressure time history (E12 and E17) oscillation was observed at the lower corner of tunnel, see Fig. 7 (c). For time histories of E12 and E17, it showed a clear out of phase relation, and kept increasing during shaking. Due to the soil lateral compression on the left side of tunnel, the increment of E12 measurement is great than that of E17. The final uplift displacement of tunnel for Test B was equal to 55 mm in prototype, and it was less than that of Test A. The reason of smaller uplift displacement of tunnel in Test B may be due to the apparent cohesion and higher viscous force in the MCE fluid saturated soil specimen. However, an opposite point of view was proposed by Chian et al. (2010). They indicated that the uplift displacement of a large pipe is become greater in the viscous fluid test due to the longer pore water dissipation time. Further investigation on centrifuge modeling test is necessary to clarify the influence of fluid viscosity in such studies.

3.3 Factor of Safety

The safety factor against uplift for the immersed tunnel was defined as Eq. (3):

$$FS = \frac{W_s + W_t + Q_s + Q_t}{U_s + U_d} \quad \textbf{(3)}$$

where W_s is the self weight of soil block above tunnel, W_t is the self weight of tunnel, Q_s is the friction resistance provided of soil block above tunnel, Q_t is the friction force acted on the side wall of tunnel, U_s is the static hydraulic force acted at the bottom surface of tunnel and U_d is the dynamic hydraulic force due to the generation of excess pore water pressure. The relations between *FS* and uplift displacement for Test A and B are shown in Fig. 9 and 10. It can be observed the tunnel uplift displacement would develop until *FS* less than 0.95. However, modeled tunnel would soon start to settle during shaking in Test B. The increasing uplift displacement with increasing FS was observed during dissipation stage for Test A and Test B. While the pore water dissipated toward ground, the volume strain changes and re-distribution of in-situ stress field may result in the movement of soil around tunnel. Therefore,

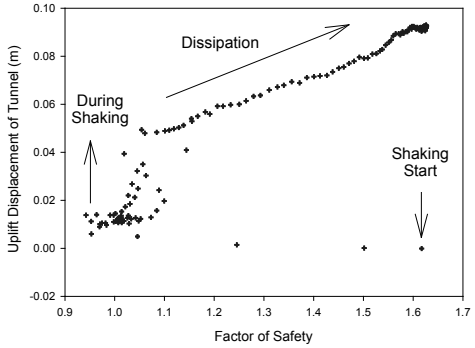


Figure 9 Relation Between Factor of Safety and Uplift Displacement for Test A

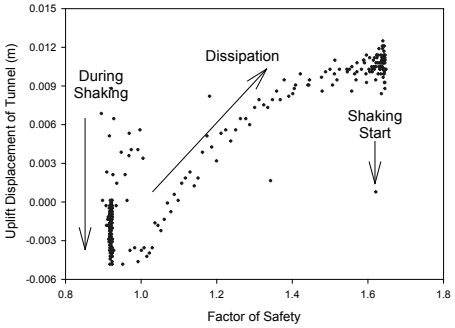


Figure 10 Relation Between Factor of Safety and Uplift Displacement for Test B

significant tunnel uplift displacement supposes to be happened during pore water dissipation.

4. CONCLUSIONS

In this study, a series of centrifuge modeling tests was conducted to investigate the uplift mechanism of immersed railway tunnel which constructed in Taipei County. Acceleration response, pore water pressure variation, earth pressures acted on the model tunnel were observed and discussed. A severe quick sand condition can be expected beneath the tunnel especially at the lower corner of tunnel. The reason of smaller uplift displacement of tunnel in Test B may be due to the apparent cohesion and higher viscous force in the MCE fluid saturated soil specimen. The increasing uplift displacement with increasing FS was observed due to the movement of soil around tunnel during dissipation stage for Test A and Test B.

Acknowledgements:

The authors wish to express their gratitude for the support from CECI Co., Ltd. Taiwan. Without their support, the project would not become possible.

References:

Liu, H. and Song, E. (2005), "Seismic response of large underground structures in liquefiable soils subjected to horizontal and vertical earthquake excitations," *Computers and Geotechnics*, **32**(4), 223-244.

Tobita, T., Kan, G.-C. and Iai, S. (2010), "Uplift Behaviour of Buried Structures Under Strong Shaking," *7th International Conference of Physical Modelling in Geotechnics*, 1439-1444.

Chou, H.S., Yang, C.Y., Hsieh, B.J. and Chang, S.S. (2001), "A Study of Liquefaction Related Damages on Shield Tunnels," *Tunnelling and Underground Space Technology*, **16**(3), 185-193.

Koseki, J., Matsuo, O. and Koga, Y. (1997), "Uplift Behavior of Underground Structures Caused by Liquefaction of Surrounding Soil During Earthquake," *Soils and Foundations*, Japanese Geotechnical Society, **37**(1), 97-108.

Ling, H.I., Mohri, Y., Kawabata, T., Liu, H. and Burke, C., (2003), "Centrifuge Modeling of Seismic Behavior of Large-Diameter Pipe in Liquefiable Soil," *Journal of Geotechnical and Geoenvironmental Engineering*, **129**(12), 1092-1101

Sasaki, T. and Tamura, K., (2004), "Prediction of Liquefaction-Induced Uplift Displacement of Underground Structures," *36th Joint Meeting US-Japan Panel on Wind and Seismic Effects*, 191-198.

Chian, S.C. and Madabhushi, S.P.G., (2010), "Influence of Fluid Viscosity on the Response of Buried Structures in Earthquakes," *7th International Conference of Physical Modelling in Geotechnics*, 111-115.

8CUEE CONFERENCE PROCEEDINGS
8th International Conference on Urban Earthquake Engineering
March 7-8, 2011, Tokyo Institute of Technology, Tokyo, Japan

CENTRIFUGE TESTING OF ROCKING FOUNDATIONS ON SATURATED AND SUBMERGED SAND

Jacquelyn Allmond[1)], Lijun Deng[2)], and Bruce Kutter[3)]

1) M.S. Student Researcher, Department of Civil and Environmental Engineering, University of California, Davis, CA
2) Ph.D. Student Researcher, Department of Civil and Environmental Engineering, University of California, Davis, CA
3) Professor, Department of Civil and Environmental Engineering, University of California, Davis, CA
jdallmond@ucdavis.edu, ljdeng@ucdavis.edu, blkutter@ucdavis.edu

Abstract: Current research has shown the capabilities and improved seismic performance of rocking shallow foundations for bridges, and much work has been done for implementation of such a mechanism in industry. By properly reducing the size of the footing, rocking behavior due to seismic loading can occur about the footing base. It has been shown experimentally that rocking foundations on competent soils can reduce seismic ductility demand on bridge columns and improve bridge performance. One concern of rocking systems is the potential for significant settlement accumulation in poor soil conditions. This research explores soil, footing, and structural responses of similar bridge structures on poor, liquefiable, and saturated soil conditions in addition to the effectiveness and practicality of using unconnected piles as a potential settlement mitigation technique. A centrifuge test series investigated the performance of six individual footing-column-mass structural models in these soil conditions. Although minimal residual rotations were observed, reiterating the tipping stability and recentering mechanism seen in previous testing on competent soil, significant uniform settlements under the footing were also recorded. Results from this research will help define the appropriate applicability range of rocking foundations in seismic design.

1. INTRODUCTION

Many researchers have been studying the rocking shallow foundations for various structures using different experimental tools. Several consecutive series of centrifuge model tests characterized the static and dynamic behavior of rocking shallow foundation for rigid shear walls (Rosebrook 2001, Phalen 2003, Gajan et al. 2005, Ugalde et al. 2010) or for highway bridges (Deng et al. 2010). Additionally, the behavior of rocking foundations has been experimentally investigated using shaking table tests (Sakellaraki et al. 2005, Paolucci et al. 2008) and in-situ model tests (Algie et al. 2010).

Current research has indicated that shallow rocking foundations on competent soils can reduce seismic ductility demand on columns and improve the performance of the system. If the moment capacity of the footing is designed so that is it smaller than the moment capacity of the column, rocking of the structure about the base of the footing will be initiated (Figure 1). In the conventional fixed-base foundation condition, almost all energy must be dissipated through bending of the column. The rocking of the foundation results in a ductility demand transfer from the column to the footing and surrounding soil. This reduces the magnitude of differential displacements imposed along the column for an otherwise fixed foundation.

However, although the beneficial effects of rocking foundation on bridge systems have been widely explored,

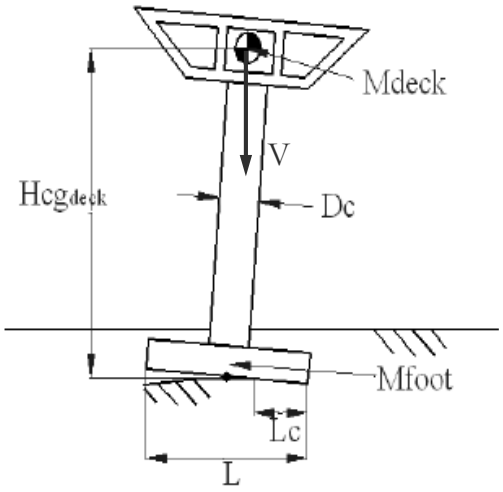


Figure 1: Rocking foundation schematic.

some hurdles impeding the use of rocking shallow foundations in bridge design still exist. One of the hurdles is the excessive displacement and collapse potential due to foundations rocking on poor, liquefiable soils. In responding to this hurdle, one series of centrifuge model test was performed on "single-degree-of-freedom" (SDOF) models that were built upon loose-liquefiable and erosive soil ground. Preliminary results from the model tests will be presented and discussed in this paper.

The overall goals of this research are to (1) delineate the

soil conditions under which rocking foundations would not be acceptable and (2) explore the viability of rocking foundations in poor soil conditions if the foundations are supported on unconnected piles.

2. MECHANISMS

The first centrifuge test aimed at determining potential failure mechanisms due to the interaction of shallow rocking foundations with saturated porous media. It has been analytically and experimentally shown that the introduction of fluid results in settlement associated with traditional shallow foundations in liquefiable conditions (Dashti, 2010a and 2010b). Additionally, other mechanisms may present themselves when coupled with a rocking foundation.

2.1 Suction

A rocking footing in saturated soil has the potential to create high, negative pore pressures at the footing/soil interface. This may cause granular material to move with the uplifting foundation, essentially creating a no-gap condition directly under the footing (Figure 2), resulting in negative settlement or uplift locally around the footing.

2.2 Erosion

The initiation of particle movement is related to the shear stresses imposed on the soil grains from passing fluid. If the fluid velocity and essentially shear stress is high enough, the soil grains will move or erode. This potential is categorized as the threshold of movement and is dependent on fluid imposed shear stress, neighboring particle movement, fluid viscosity, particle density, particle diameter (*see section 2.3 Grain Size*), and gravity (Henderson, 1966). From these values, the dimensionless Reynolds number and Froud number parameters can be determined to categorize the flow regime and the particle's resistance to flow respectively. The study of incipient particle motion was first quantified experimentally by A. Sheilds, who created the Shields diagram for erosion prediction. Using this diagram in combination with the known parameters of the soil bed and fluid, one can generally predict the system's potential for erosion.

In the case of a rocking foundation, fluid is sucked in and pushed out from under the footing during rocking. This creates the potential for particle movement, resulting in significant settlement and soil rounding under the footing.

2.3 Grain Size

The particular soil grain size has an effect on many of these previously mentioned factors (suction, erosion, etc.). This centrifuge test explores this parameter by using two different grain sizes as the surface fill. Since all other parameters described in Section 2.2 are to be held constant for the test, the use of different grain sizes should have some effect in the footing and soil response. As the particle grain size under the footing is increased, the fluid failure mechanisms have the potential to become manageable. This may be one option for site remediation if a larger grain size shows a benefit in the rocking footing response.

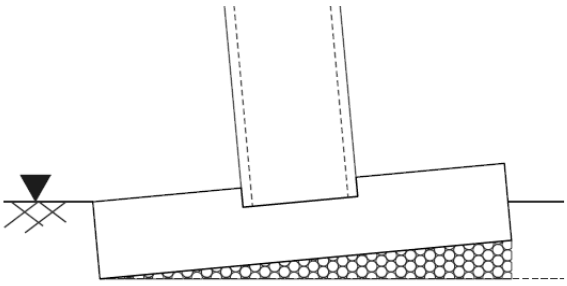
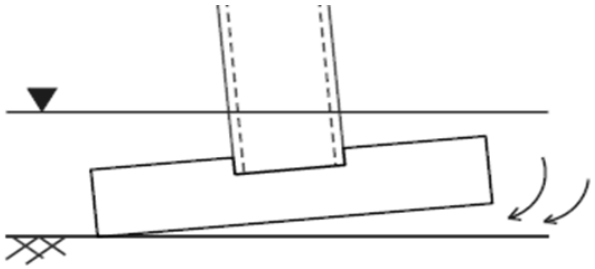
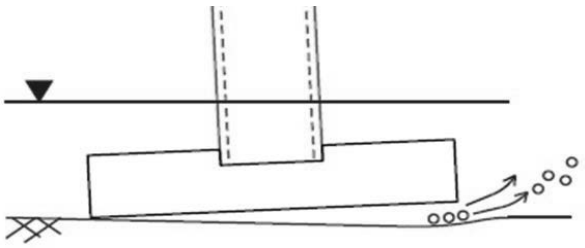


Figure 2: Suction potential in rocking foundations



(a) Water rushes in as foundation uplifts



(b) Soil particles erode as foundation rocks down

Figure 3: Erosion potential in rocking foundations in foundation (a) uplift and (b) gap closing.

2.4 Liquefaction

As previously stated, seismically induced soil liquefaction creates the potential for significant settlement and increased pore pressures. The same holds true in the exploration of failure mechanisms for rocking foundations. However, the dissipation of pore pressure after seismic activity at the liquefiable layer may be significantly affected by the additional pore pressure generation by rocking. This coupling effect needs further investigation.

2.5 Deep Foundations

One goal of this research is to consider the potential benefit of coupling the rocking footing with unconnected deep piles. The purpose of these piles would be to bypass the liquefiable or poor layer of soil to set in a more competent, dense layer. If settlements are in fact

unreasonable, coupling the rocking footing with unconnected piles may reduce excessive settlements. Through the use of unconnected piles, the footings are able to rock freely ensuring the desired self centering effect.

3. CENTRIFUGE TEST CONFIGURATION

The first series of tests (JDA01) was completed at the Center for Geotechnical Modeling Facility at the University of California at Davis on the 9 meter radius centrifuge. The test series was comprised of 11 shakes at a centrifugal acceleration of 54g. A plan and cross-sectional view of the rigid container are presented in Figure 4 and Figure 5 respectively. As shown in Figure 5, the experiment used a flexible laminar container box which could enable the interlayer shear strain. All dimensions referenced in this paper are in prototype units unless noted otherwise.

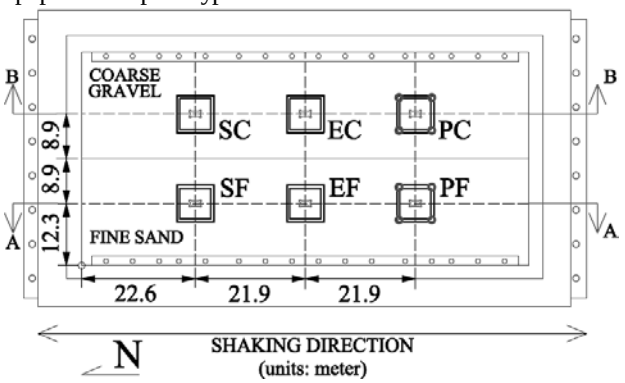
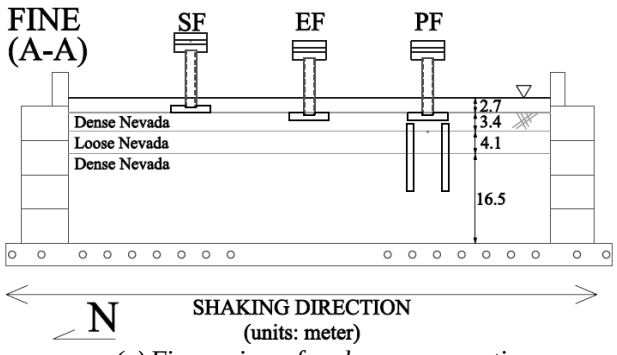
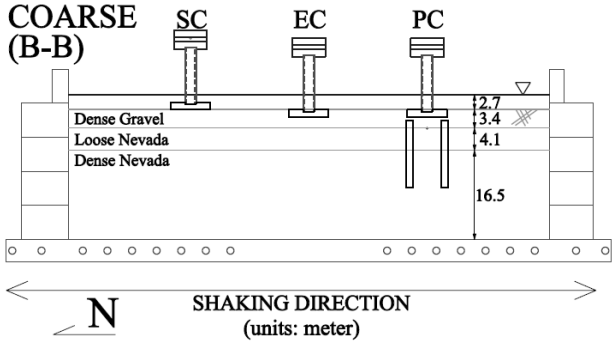


Figure 4: Plan view of JDA01 container



(a) Fine grain surface layer cross section



(b) Coarse grain surface layer cross section

Figure 5: Cross-sectional view of JDA01 container along the (a) Fine grain and (b) Coarse grain surface layer.

3.1 Soil

All soils used in this test were dry pluviated as shown in Figure 5 into the container to ensure consistent relative densities at certain depth intervals. The cross sectional views of the container in Figure 5 show up to 16.5m (304.8 mm model) of Nevada sand was placed at a relative density of 92%. Next, a 4.1m (76.2mm model) layer of "loose" Nevada sand was pluviated at a relative density of 68%. This loose layer was the representative liquefiable layer to be activated during shaking. The remaining 3.4m (50.8mm model) to surface elevation represent the top layer. In this test, two different soil types were used to compare certain response dependencies on grain size.

The "fine" layer consisted of the same Nevada sand (D_{50}=0.17mm) used at depth. The "coarse" layer consisted of Lapis Lustre Medium Aquarium Gravel (D_{50}=1.5mm), also dry pluviated into the container. These two uniformly graded soils were chosen based on particle diameter size. It was determined that the fine grain Nevada sand would erode, while the coarser grain would not, holding all other factors equal (*see section 2.2 and 2.3*). The container was partitioned in two and filled with one type of soil, but with comparable final surface elevation and similar dense relative densities (~90%). Properties for each layer are provided by Allmond (2011).

3.2 Structures

In total, six identical SDOF type models were designed and constructed with an aluminum square 6.1 x 6.1m (114.3 x 114.3mm model) and 3.4m (63.5mm model) high footing, aluminum rectangular tubing column, and aluminum and steel square block deck masses. Each model was labeled with two letters. The first designates footing orientation (S:surface, E:embedded, P:unconnected piles), the second refers to the top layer of soil of which the foundation is seated (F:fine, C:coarse). Therefore, the six structures are identified as follows:

SF	→	footing on **S**urface of **F**ine sand
EF	→	footing **E**mbedded in **F**ine sand
PF	→	footing on **P**iles in **F**ine sand
SC	→	footing on **S**urface of **C**oarse gravel
EC	→	footing **E**mbedded in **C**oarse gravel
PC	→	footing on **P**iles in **C**oarse gravel

The objective of this orientation style was to try and capture the different fluid failure mechanisms previously stated. That is, the surface footings would be susceptible to the rocking induced erosion, the embedded footings to rocking induced suction, and the unconnected pile footings to an improved site condition. The two surface soils were used for comparison purposes, resulting in six different stations of varying footing orientation and grounding. The structures and their respective orientations are also shown in Figure 4 and Figure 5. Summarizes of the period and natural frequency of the fixed case structures can be found in Table 1.

	Natural Period (sec)	
	Longitudinal (Length)	Transverse (width)
Model Scale	0.016	0.026
Prototype Scale	0.871	1.421

Table 1: Natural period of the models.

3.3 Saturation

All soil placed in the container was dry pluviated, which required eventual saturation of the model. Before construction, troughs were placed at both ends of the top container. Tubes were then connected to the base of the troughs, run along the vertical sides of the container, and then fitted with porous stones at the base of the container. After filling it with soil, the container was then placed on the centrifuge arm and prepared for saturation. The container was placed under vacuum, and CO_2 was pumped into the system to fill the voids. The viscous fluid was then pumped to the troughs, saturating the model from base to the surface, and the vacuum was released.

A viscous fluid mixture of water and methyl cellulose was used as the pore fluid in this test. According to scaling laws, the kinematic viscosity of the fluid should be scaled to that of the centrifugal acceleration (54g). However, it has been shown in previous tests and analyses, that the use of a fluid with such a high viscosity dramatically increases the time required for pore pressure dissipation and model saturation (Stewart et al., 1998). The methyl cellulose mixture for this test followed the standards presented in Stewart et al. (1998), resulting in a fluid to water viscosity ratio of eleven.

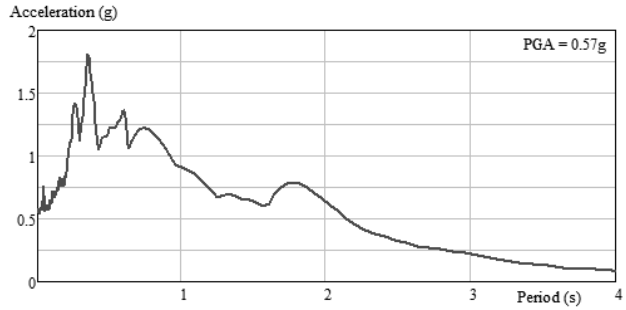


Figure 6: Dry pluviation of Nevada sand.

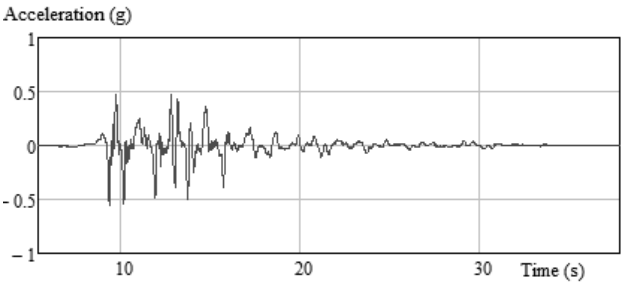
A portion of the test sequence was devoted to analyzing the structural response at different ground water elevations above the soil surface.

3.4 Ground Motions

The model was subjected to 11 events in total in the North-South (longitudinal) direction. These events included several varying amplitudes of a step wave and the Port Island downhole array ground motion recordings of the 1995 Kobe Earthquake. Figure 7 shows the acceleration-time histories as well as the acceleration response spectrum of the largest Port Island event used in this test series.



(a) Acceleration Response Spectrum



(b) Acceleration-time history

Figure 7: Port Island shaking event (PGA = 0.57g) showing (a) Acceleration response spectrum and (b) Acceleration time series.

4. RESULTS AND OBSERVATIONS

Analysis of this test is still ongoing, but preliminary results for the four foundations without piles are provided. All plots shown here after are from one of the large Port Island shakes (PGA = 0.57g) outlined above. The settlement and rotation time series for this shake are shown in Figure 8. The rotation-time series plot shows minimal residual rotations for all the footings, an observation that was consistently seen throughout the testing series. However, the settlement-time plot shows significant amounts of total settlement for the single shake. The moment-rotation curves for these four footings along with the theoretical moment capacity are presented in Figure 9. The data suggests that although significant settlements were observed, the residual rotations after testing were quite minimal. That is, the self centering rocking mechanisms observed in previous testing on competent soil are likewise seen here. Additionally, the moment-rotation curves obtained in this test are much like the trends observed in past testing results, including the fact that the theoretical moment capacity of the

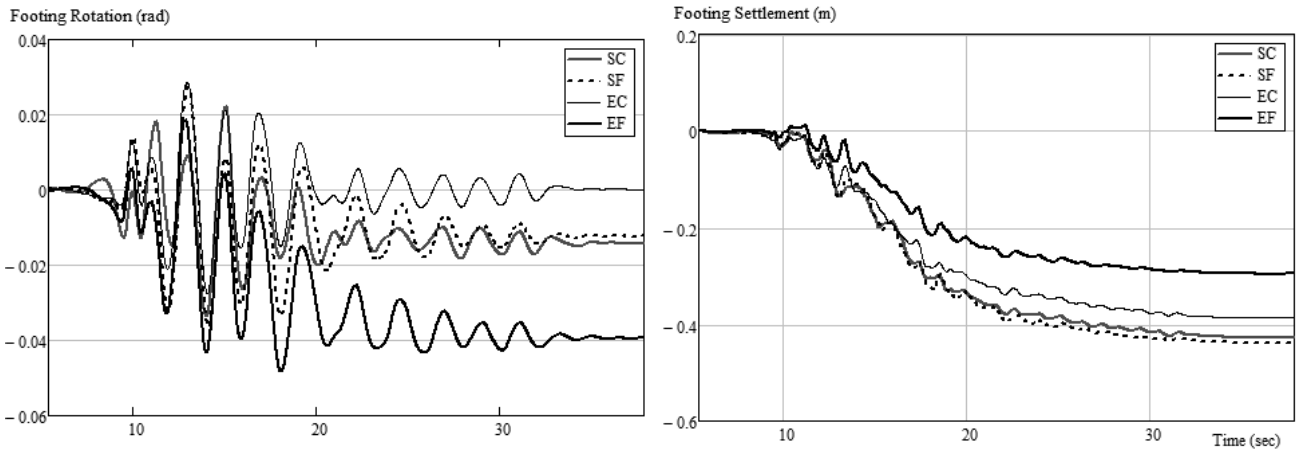


Figure 8: (*Left to Right*) Footing Rotation and Footing Settlement-Time series for the four footings without piles in one of the large Port Island events (PGA = 0.57g).

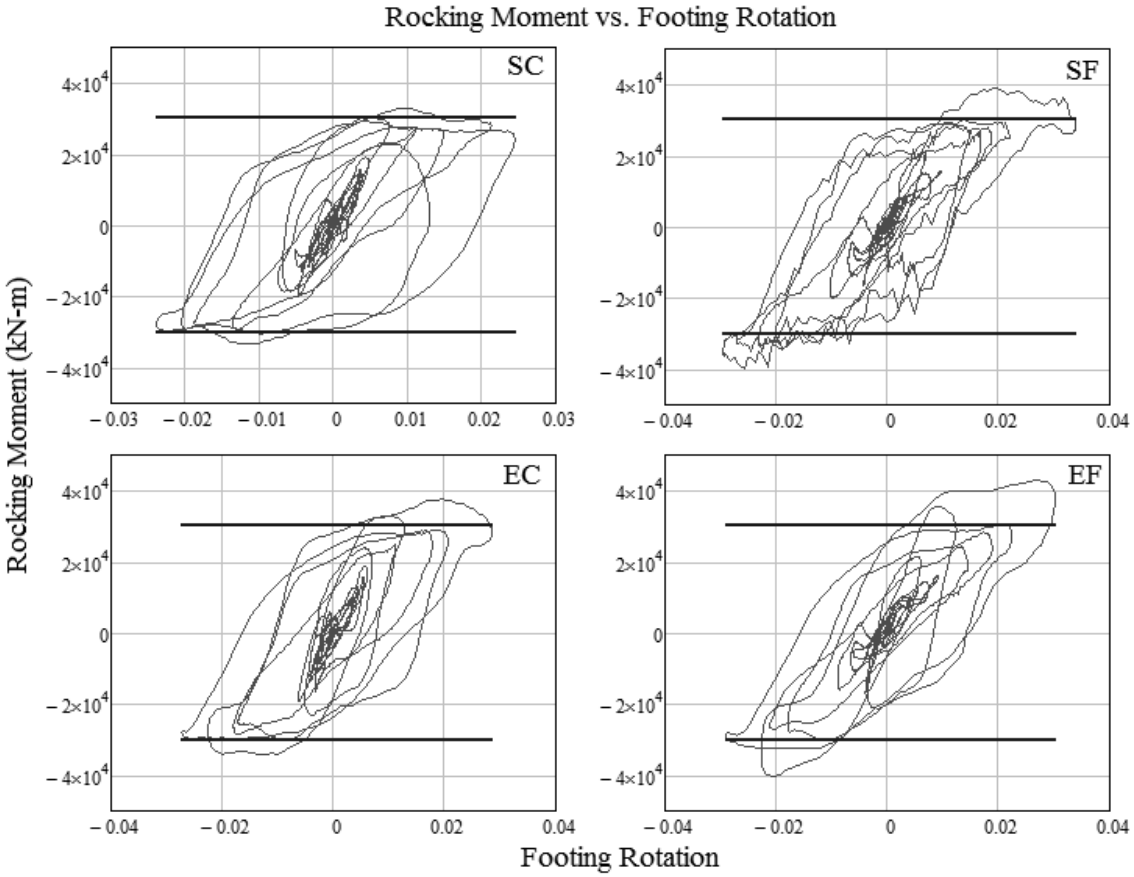


Figure 9: Rocking Moment vs. Footing Rotation curves for (clockwise at upper left corner) Surface on Coarse, Surface on Fine, Embedded on Fine, and Embedded on Coarse foundations with theoretical moment capacity.

footing is still well defined in saturated soil conditions.

Throughout testing, large residual rotations were observed for both structures placed on unconnected piles. During excavation it became clear that the cause of this permanent rotation was due to unseating of the footing from the piles. This result is clearly shown in Figure 10 and the cause of this significant unseating is still unknown. There may have been significant lateral footing displacements from shaking, or the footings may have been not quite centered during model construction. It should be noted that the portion of the footing still placed on the pile after testing experienced much less settlement then those foundations without piles. This leads to the possibility that if the rocking foundation stays centered on the piles, settlements can be minimized in an otherwise settlement prone site. Because of these undetermined factors, the data for the pile foundations has been excluded from this report until further analysis has been completed.

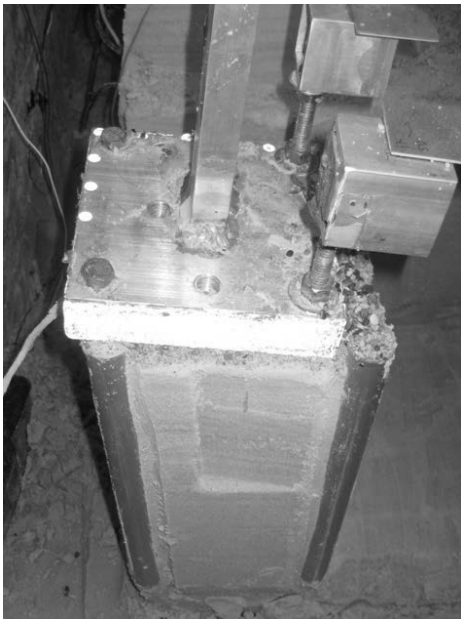


Figure 10: Excavation photo of unseating of unconnected piles.

5. CONCLUSIONS

Previous experimental and analytical research has shown that the rocking foundations could take up most of the ductility demand, rather than the column, from the seismic shear, while still dissipating energy and without imposing significantly increased settlements or residual rotations. Although the system has been analyzed on competent soils, there is a lack of sufficient knowledge of footing and soil response in liquefiable, saturated, and poor conditions. This first centrifuge test results presented here involved different mechanisms one might expect when implementing this design in such poor conditions such as erosion, suction, and liquefaction. Through analysis of the data and observations made during testing and excavation of the model a few conclusions can be drawn. First, although the footings experienced significant settlement during shaking events, the residual rotations were minimal. That is, the recentering mechanism and resistance to tip-over which drive the benefits of the rocking foundation system are still observed in saturated and liquefiable soil conditions. Secondly, the moment-rotation curves obtained in this testing series show similar trends to previous testing data on competent soils, including the capability of defining the moment capacity of the footing. Finally, the unexpected mechanism of unseating of the foundations from the unconnected piles still requires further consideration. However, reduced settlements were observed where the foundation still rested on the pile. This leads to a potential mitigation technique of reducing uniform settlements if the footing stays centered on the piles. Further testing will try to determine a suitable solution to this unseating, while continuing to search for conditions in which rocking foundations are not acceptable. Conclusive results from this research will help determine the limitations of rocking foundations to help guide their implementation and benefit in industry standards.

Acknowledgements:

This work was supported primarily by the Pacific Earthquake Engineering Research Center (PEER) under a project titled *Last Hurdles for the Implementation of Rocking Foundations for Bridges*. The authors would like to acknowledge the suggestions and assistance of Professor Sashi Kunnath of UC Davis, Dan Wilson, Chad Justice, Ray Gerhard, Peter Rojas, Lars Pedersen, and Anatoily Ganchenko of the UC Davis CGM, and UC Davis graduate student Manny Hakhamaneshi. Development of the large centrifuge at UC Davis was supported primarily by the Network of Earthquake Engineering Simulation (NEES), National Science Foundation, NASA, and the University of California.

References:

Algie, T. B., Pender, M. J., Orense, R. P. Wotherspoon, L. M. (2010), "Dynamic field testing of shallow foundations subject to rocking," *Proc. 2010 New Zealand Society for Earthquake Engineering Conference*, March 2010, Wellington, New Zealand, 26-28.

Allmond, J., Kutter, B.L. (2011), "Last Hurdles for the Implementation of Rocking Foundations for Bridges: Centrifuge Data Report for JDA01," University of California, Davis, Center for Geotechnical Modeling, in preparation.

Dashti, S., Bray, J.D., Pestana, J.M., Riemer, M., Wilson, D. (2010a), "Mechanisms of Seismically Induced Settlement of Buildings with Shallow Foundations on Liquefiable Soil," *Journal of Geotechnical and Geoenvironmental Engineering*, ASCE, **136**(1), 151-164.

Dashti, S., Bray, J.D., Pestana, J.M., Riemer, M., Wilson, D. (2010b), "Centrifuge Testing to Evaluate and Mitigate Liquefaction-Induced Building Settlement Mechanisms," *Journal of Geotechnical and Geoenvironmental Engineering*, ASCE, **136**(7), 918-929.

Deng, L., Kutter, B. L., Kunnath, S. (2010b), "Centrifuge modeling of bridge systems designed for rocking foundations," *Journal of Geotechnical and Geoenvironmental Engineering*, ASCE (in review).

Gajan S, Kutter BL, Phalen JD, Hutchinson TC, Martin GR. (2005), "Centrifuge modeling of load-deformation behavior of rocking shallow foundations," *Soil Dynamics and Earthquake Engineering* 2005; 25: 773–783. DOI: 10.1016/j.soildyn.2004.11.019.

Henderson, F.M. (1966), *Open Channel Flow.* Macmillan, New York.

Paolucci, R., Shirato, M., Yilmaz, M. T. (2008), "Seismic behaviour of shallow foundations: Shaking table experiments vs numerical modeling," *Earthquake Engineering and Structural Dynamics*, **37**(4), 577- 595.

Phalen, JD. (2003), "Physical Modeling of the Soil–foundation interaction of spread footings subjected to lateral cyclic loading," MS Thesis, University of California at Davis, School of Engineering.

Rosebrook, K. (2001), "Moment Loading on Shallow Foundations: Centrifuge Test Data Archives," MS Thesis, University of California, Davis.

Sakellaraki D, Watanabe G, Kawashima K. (2005), "Experimental rocking response of direct foundations of bridges," *Second International Conference on Urban Earthquake Engineering*, Tokyo, Japan, 7–8 March 2005, 497–504.

Stewart, D.P., Chen, Y.R., Kutter, B.L. (1998), "Experience with the Use of Methylcellulose as a Viscous Pore Fluid in Centrifuge Models," *Geotechnical Testing Journal*, **21**(4), 365-369.

Ugalde, J., Kutter, B. L., Jeremic, B. (2010), "Rocking Response of Bridges on Shallow," Pacific Earthquake Engineering Research Center Report 2010/101. University of California, Berkeley, California.

8CUEE CONFERENCE PROCEEDINGS
8th International Conference on Urban Earthquake Engineering
March 7-8, 2011, Tokyo Institute of Technology, Tokyo, Japan

FAILURE MECHANISMS OF SHALLOW FOUNDATION UNDER COMBINED LOADINGS

Michael Cocjin[1)], Sakae Seki[2)], and Osamu Kusakabe[3)]

1) PhD student, Department of Civil Engineering, Tokyo Institute of Technology, Japan
2) Laboratory Technician, Department of Civil Engineering, Tokyo Institute of Technology, Japan
3) Professor, Department of Civil Engineering, Tokyo Institute of Technology, Japan
cocjin.m.aa@m.titech.ac.jp, seki@cv.titech.ac.jp, kusakabe@cv.titech.ac.jp

Abstract: The aim of the study is to investigate the interaction of the ground responding to combined loading. Failure loads and corresponding ground deformations of a strip, surface footing overlying dense sand and subjected to different proportions of planar displacements in the vertical, horizontal and rotational directions were investigated. Ground behavior during centrifuge tests was observed using close-range photography and analyzed with particle image velocimetry (PIV). Results revealed that the vertical stress imposed on the footing largely influences the occurrence of horizontal and moment load failure. Conversely, patterns of soil flow at different parts of the loading events were described. Ruptured surface of horizontally and rotationally loaded grounds was seen to have the same geometrical shape at failure.

1. INTRODUCTION

In recent decades, due to the complex nature of multi-directional loading, bearing capacity solutions have been reconstructed in the context of planar component forces. The intent of these reconstructions was to address the gaps of the classical bearing capacity instated by Terzaghi in 1943. In the classical approach, solutions are (still) formulated under the assumption of a predominant vertical load, where complications rendered by horizontal and moment loads are accounted for only by using a series of linear factors as argued by Houlsby and Cassidy (2002). As such, the classical analysis inevitably neglects any consequences for any change in loading conditions because it does not address the issue of plastic strains pre-failure (Gottardi and Butterfield 1993, Houlsby and Cassidy 2002).

In response, analyses founded on elastic-hardening plastic constitutive model for soil were formed (*e.g.* Tan 1990; Martin 1994; Gottardi, et. al. 1999). In these analyses, the bearing capacity problem is addressed directly in terms of planar components forces and corresponding footing displacements (Roscoe and Schofield 1957). It is postulated that after a given footing penetration, a yield surface is established within the vertical, horizontal and moment ($V,H,M/B$) load space (where B is footing breadth), instantaneously defining a failure surface (Houlsby and Cassidy 2002). The footing behavior within this surface is assumed to be elastic and does not provoke failure while the loads that reach the yield surface may instigate elasto-plastic behavior resulting to footing failure for any conjugate displacements (w,u,θ) (Nova and Montrasio 1991).

Past research on this field has generally been involved with developing optimum shapes of failure surface considering particular foundation geometries and soil conditions; for example employing strip footing on loose sand (Nova and Montrasio 1991), strip footing on dense sand (Butterfield and Gottardi 1994), circular footing on dense sand (Gottardi et al. 1999 and Houlsby and Cassidy 2002) and circular spudcan footing on clay (Martin 1994), to name a few. Several numerical studies have also substantially supported these physical experiments (for example Bransby and Randolph 1998, and Bransby and Yun 2009).

Central theme to the abovementioned studies is the description of failure of foundations in the context of failure curves, characteristically limited to the behavior of the footing in isolation. Such approach employs standard solutions that approximate the stiffness of the soil media arbitrated from the forces and displacements experienced by the footing. However, the significance of soil-footing interaction as indivisible phenomena is inadvertently down played by limiting the investigation to only a particular reference load and displacement point about the footing.

In response to this, it is the aim of the present study to extend the investigation of the interaction of the ground responding to combined loading. It is found that only a few studies have been involved with this intent. For instance, in the study of Bransby and Randolph (1998), soil deformation mechanisms at yield were investigated for a strip footing subjected to combined loadings under undrained conditions using two-dimensional finite element and upper-bound plasticity analyses. Taibat and Carter (2000) investigated patterns of soil movement and the development of plastic zones and failure mechanisms for different combinations of loads and moments using finite element analyses of circular

Table 1 Test program

Event	*Test name*	*Swipe name*	*Dr (%)*	V_{max} *(kN)*	V_o *(kN)*
Vertical	VM	-	81.6	10.9	-
	VURa	-	79.6	10.2	-
	VURb	-	83.6	10.6	-
Horizontal swipe	HS1	HS11	84.6	16.1	5.5
		HS12			8.9
		HS13			16.1
	HS2	HS21	82.6	15.7	5.8
		HS22			12.7
	HS3	HS31	84.1	16.6	12.8
Rotational swipe	MS1	MS11	84.6	15.6	5.1
		MS12			10.1
		MS13			15.0
	MS2	MS21	87.5	17.7	5.4
		MS22			10.7
	MS3	MS31	86.5	16.1	8.6

foundations on the surface of homogenous, purely cohesive soil. Bransby and Yun (2009) followed a similar approach to study the influence of skirt geometry on the deformation mechanism of soil under combined loading. However, a few physical models have been done, let alone run in an increased gravitational field. Jumikis (1961), for instance, has extensively studied the geometry of ruptured surfaces post-failure on sand of a strip footing subjected to moment loads using simple setups in 1g. Running on the same manner are the studies of Teh, et al. (2008) on layers of sand and clay and Hossain and Randolph (2010) on clay, both of which were conducted in centrifuge.

Carrying on from the elasto-plasticity based approach of earlier studies, various load states in *VHM* spaces were constructed by conducting several swipe tests. Results of nine (9) model tests of a strip, surface footing overlying dense sand under an increased gravitational field and driven in the vertical, horizontal and rotational directions are presented. Table 1 shows all the test cases performed with obtained relative densities of the ground and the vertical capacity of each test. Ground deformation was observed in-flight using close-range photography. Soil flow was investigated by employing a fully developed displacement field measuring software based on Particle Image Velocimetry (PIV). This software was developed by White and Take (2002) specifically suited to the analysis of geotechnical tests. Characteristics of ground failures are delineated in terms of progressive formation, propagation of soil flow, and orientation of the ruptured surfaces relative to model footing.

2. EXPERIMENTS AND PROCEDURES

2.1 Test set-up and preparations

The test set-up for all the loading tests is shown in Figure 1. All the loading tests were performed under an increased gravitational field (50g) using the Tokyo Tech Mark III Geotechnical Centrifuge (Figure 2).

A dense ground was modeled using standard Toyoura sand with a final height of 230mm and a plan area of 800x150mm shown in Figure 1(a). It was prepared by air pluviation technique. This technique is commonly employed when uniform dry sand is required. It was carried out by pouring the sand on the model container through a hopper suspended from a hoist, maintaining a consistent pouring height relative to the surface of the model ground. After the desired ground height was completely filled up, the soil surface was smoothened using a flat vacuum leveler. Relevant properties of the sand are provided in Table 2.

On the other hand, the model footing (Figure 1(b)) was constructed from hardened steel and is assumed to be rigid. It has a breadth of B=40mm and length of 150mm. Sand paper was glued on the whole span of the footing base to provide a fully rough bottom interface. This footing was modeled as a surface footing in plain-strain condition. The footing itself weighs 304grams.

All the loads applied to the footing were displacement-controlled at a rate of 0.01mm/s. These loads were imposed by means of a sophisticated loading jack in Figure 1(a) which was developed by Puntrattanasin et al. (2003) and was designed specifically for combined loading of foundations. This apparatus has two vertical screw loading jacks (V. jack 1 and V. jack 2) that can independently apply loads at a maximum stroke of 400mm displacement and a horizontal jack (H. jack) with 250mm stroke capacity.

The displacement of the footing base, subsequently called the reference point (RP), in the vertical (w) and horizontal (u) directions as illustrated from Figure 1(c), are given by Equations 1 and 2 as

$$w = 0.5\left(X_1 + X_2\right) + H_t \cos\theta - H_t \quad (1)$$

$$u = X_3 + 0.5\left(L\cos\theta\right) + H_t \sin\theta - 0.5L \quad (2)$$

where X_1, X_2 and X_3 correspond to the displacements directly measured by three long-range Linear Variable Differential Transformers (LVDTs) fixed along V. jack 1, V. jack 2 and H. jack respectively (all in dimensions of *mm*); H_t is the total height of the footing from the load cell to the RP, and L is the span between the two vertical jacks.

The difference in the movement of the two vertical jacks conveniently provides the rotation of the footing θ, and can be expressed as,

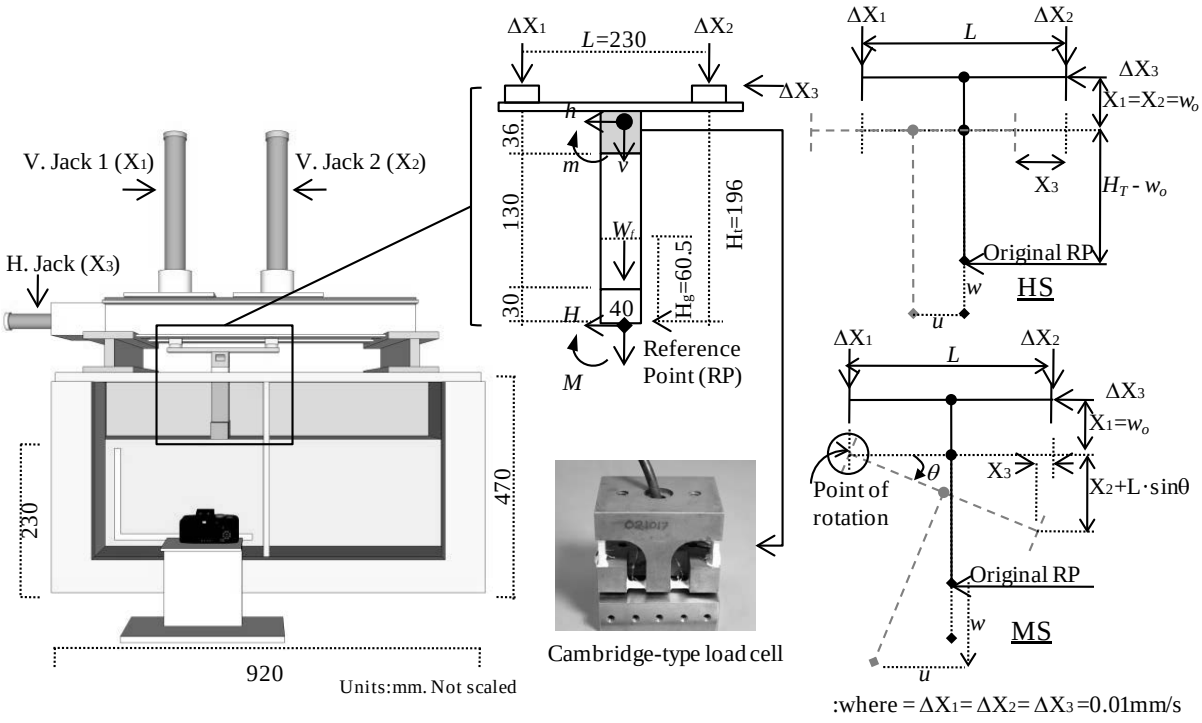
$$\sin\theta = \left(X_2 - X_1\right)/L \quad (3)$$

In the presentation of results, footing displacements w and u were normalized by footing width B and θ is expressed in radian.

On the other hand, the actual loads were quantified

Table 2 Standard Toyoura sand properties

Type	*Values*
Specific gravity	2.645
D_{50} (mm)	0.190
D_{30} (mm)	0.160
D_{10} (mm)	0.140
Coefficient of uniformity	1.620
Coefficient of curvature	1.050
Maximum void ratio, e_{max}	0.973
Minimum void ratio, e_{min}	0.609



(a) (b) (c)

Figure 1 Test set-up: (a) Loading jack with model ground and container and PIV set-up, (b) Schematic drawing of model footing with Cambridge-type load cell, and (c) Loading mechanisms of footing system for HS and MS cases.

using a Cambridge-type load cell bolted between the top of the model footing and the loading arm of the jack shown in Figure 1(b). It is constructed out of hardened-tool steel and is capable of 58.3 kN direct stress load, 8.64 kN shear stress load and 0.505 kN-m moment.

Since footing displacements were interpreted from the RP, loads were subsequently superimposed on the same point. Given that all attachments were well-fixed, the loading arm of the jack and the footing system can be assumed to act as one rigid body during the loading, and that superposition of forces from the load cell to the RP can be convenient.

From Figure 1(b) and (c), superposition of forces gives the vertical, horizontal and moment component forces at the RP as,

$$V = -v - W_f \quad (4)$$

$$\boldsymbol{H} = \boldsymbol{h} \quad (5)$$

$$M/B = -v\cos\theta(H_t) + h\cdot\sin\theta(H_t) - m - W_f\cos\theta\cdot(H_g) \quad (6)$$

where *v*, *h*, *m* are vertical, horizontal and moment loads recorded by the load cell with dimensions of *kN*, *kN* and *kN-mm* respectively; W_f is the weight of the footing; and H_g is the height of the center of gravity of the footing where W_f acts upon.

In the presentation of results, component forces *V*, *H* and *M/B* were normalized by the maximum vertical load, V_{max} experienced in a single model test.

A digital camera (Canon Powershot G7) was mounted about 375mm horizontal distance from the inside window of the container to the level of the model ground to record the soil behavior during the loading tests. The camera was automatically set to obtain images every 100 sec. The captured images were analyzed using the GeoPIV software to obtain displacement vectors of soil flow. The principles of analysis employed in the GeoPIV software are detailed more in the paper of White and Take (2002). Note that the PIV set-up and the PIV analysis which used a patch size of 64 pixels with image-to-scale ratio of 0.14mm/pixel, were found to have a system accuracy 0.45 pixel and a precision of 0.002 pixel for any displacement greater than 10 pixels (Cocjin 2010).

Specifications Tokyo Tech Mark III		
Radius	Platform radius	2.45m
	Effective radius	2.0 - 2.2m
Capacity	Maximum payload	50g.ton
	Maximum number of rotations	300rpm
	Maximum payload at 80-g	600kg

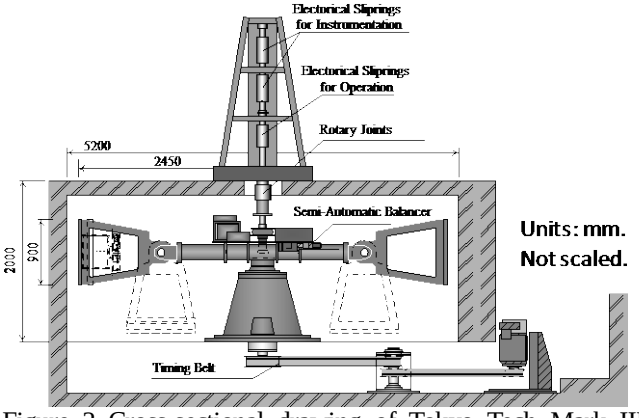


Figure 2 Cross-sectional drawing of Tokyo Tech Mark III centrifuge machine.

2.2 Loading mechanisms

Three cases of pure vertical loading were conducted. A monotonic vertical loading (VM) was carried out as a pilot test. Two cases (VURa and VURb) which involved vertical unloading-reloading excursions were conducted to support the first case, furthermore to investigate the elastic behavior prior to failure. All of the vertical loading events were performed to the full capacity of the loading arm to provide as much data as possible concerning the vertical hardening.

On the other hand, three horizontal swipe model tests (HS) were conducted. In the first two events (HS1 and HS2), multiple horizontal swipes were commenced at various levels of vertical penetration, w_o shown by the dotted footing frame in HS of Figure 1(c). In every horizontal swipe, the vertical displacement was locked (Δw=0) while the footing was translated with constant horizontal displacement Δu until a horizontal peak load was achieved shown by the dashed-line frame in HS of Figure 1(c). After this peak was reached, the footing was driven back horizontally to its original position before further vertical penetration to the next swipe was carried out. After all the swiping events were performed, the footing was loaded vertically until failure to obtain V_{max} of each model test. HS3 provides a case wherein only one horizontal swipe was conducted before the footing was driven vertically to failure. This was so to confirm the similitude of footing behavior for the multiple swipes conducted in the first two horizontal cases. Figure 3(a) shows the normalized displacement trajectories for the HS cases.

Similarly, three (3) rotational swipe events (MS) were also conducted. These tests were performed by penetrating the footing to a particular depth w_o, at which point loading of one of the vertical jacks (V. jack 1) was halted while the other (V. jack 2) was further continued using the same displacement rate. This particular loading mechanism provided a sweep of w which simultaneously increased with footing rotation θ where the point of rotation corresponds to the stagnated location of V.jack 1 before the swiping proceeded (Figure 1(c)). The second vertical jack was loaded continuously until a perceivable peak load can be observed both in the horizontal and moment directions from the data logger; after which, V. jack 2 was retracted to its original position. This mechanism concludes a single rotational swipe event. Multiple swipe events were commenced at different levels of vertical penetration w_o before the footing was vertically loaded to failure. Details of the swiping displacement trajectories (w,θ) for the rotational swipes are given in normalized form in Figure 3(b).

3. RESULTS

3.1 Vertical loads

The normalized vertical load-displacement at the RP for all the loading events is given in Figure 4.

Linear, elastic relationship characterizes the onset of the loading until failure and during unloading-reloading excursions in the cases of purely vertical loading in Figure 4(a). For each case, stress softening was observed at continued penetration shortly after the peak load. A

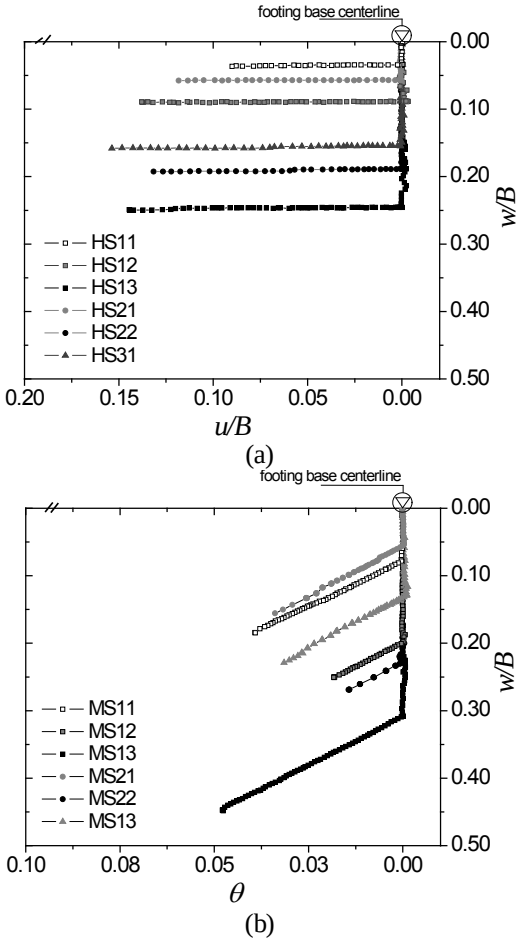


Figure 3 Displacement trajectories for (a) HS and (b) MS.

continued increase in vertical capacity was further seen post-peak, which was also noted in the works of Stuit (1995) in centrifuge involving vertical loading of circular footings on dense sand. He attributed this post-peak hardening to the mobilization of the soil next to the footing which affects a larger area, consequently increasing the recorded bearing capacity.

Conversely, several studies (such as of Nova and Montrasio (1991), Gottardi and Houlsby (1995), and Houlsby and Cassidy (2002)) have proposed expressions called 'hardening laws' which relate the vertical load and plastic vertical penetration of shallow footings. In Figure 4(a), the hardening law expression given by Gottardi and Houlsby (1995) which was derived from set of data tests on a rectangular footing on dense sand, was suitably adjusted and superimposed on the present set of data for comparison. The said expression is given in Equation 7 as,

$$V = \frac{k_p w_p}{1 + \left(\frac{k_p w_{pm}}{V_{\max}} - 2\right)\left(\frac{w_p}{w_{pm}}\right) + \left(\frac{w_p}{w_{pm}}\right)^2} \qquad (7)$$

where V is the vertical load, V_{max} is the vertical capacity equal to unity, w_p is the plastic vertical deformation equivalent to w/B, k_p=5.858 is the initial plastic stiffness derived from the best-fit line, and w_{pm}=0.333 is the value of w_p at V_{max}.

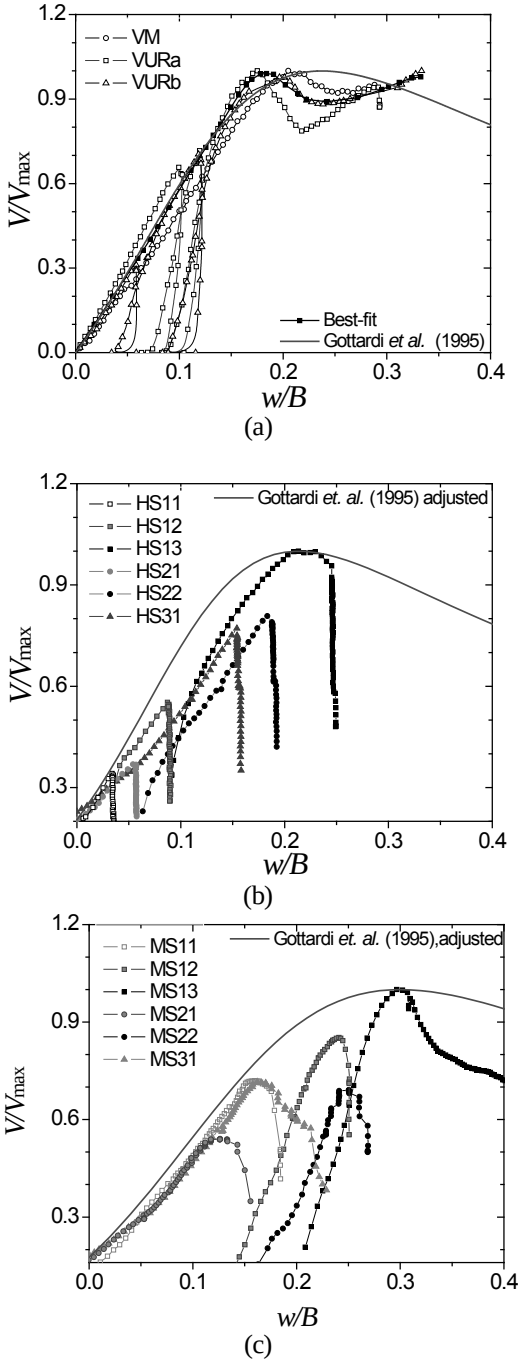


Figure 4 Vertical load-displacement curves of (a) purely vertical loading, (b) HS, and (c) MS.

On the other hand, the behavior of the vertical load during the horizontal and rotational swipes is shown in Figures 4(b) and (c). One swipe event in HS is characterized by a linear increase in vertical load and plastic vertical displacement during the purely vertical loading and an abrupt decrease in vertical stress during swiping at various w_o (Figure 4(b)). In case of HS13, which was loaded to vertical failure before the last swipe, a softening of the vertical stress was observed before it abruptly decreased as the swiping was pursued.

In the case of MS series in Figure 4(c), the rotational displacement was seen to significantly contribute to the increase of the vertical stress level, which increases linearly with vertical penetration, expectedly since footing rotation is largely a function of the vertical displacement (Equation 3). Accordingly, the graph shows that the occurrence of failure in the swiping direction depicts a softening behavior in the vertical stress right after the full mobilization of the vertical footing displacement and components of the footing rotation.

Owing to the type of load cell used in the experiments (Figure 1(b)), purely vertical loading also recorded horizontal and moment load reactions. Figure 5 plots the normalized *V*, *H* and *M/B* generated in the VM, VURa, and VURb cases along with the normalized plastic vertical displacement, *w/B*. In this figure, moment loads were generally seen to increase with vertical loads where *M/B* values at full vertical capacity were in the range of 0.045 to 0.070 of V_{max}. Note however that since the moment load is a function of the footing rotation as given in Equation 6, for an infinitesimal amount of θ during vertical penetration, the vertical load component, *v* directly measured by the load cell diminishes to zero, leaving the generated moment load, *M/B* a function of the moment and horizontal load components, *m* and *h*. In addition, the vertical penetration also generated horizontal loads, *H* in the range of $\pm 0.030 V_{max}$, discriminated solely by the horizontal load component, *h* directly measured by the load cell (Equation 5).

These observations show evidence of appreciable amounts of horizontal and moment loads the footing would experience, which are otherwise ignored in most vertical loading tests. These lateral reactions can be accounted for by the variable effect of soil deformation during the progression of footing penetration. At large embedment, the ground does not only become stiffer but also changes its deformation geometry in order to fully confine the loads imposed on it by the foundation. Such can be deduced from the normalized *wM* plot in Figure 5 where the maximum moment loads were only fully mobilized at footing penetration beyond 15% of the footing width.

3.2 Swipe loads

Six test cases of swipes were conducted, which provided 12 independent displacement trajectories shown in Figure 3. Half of these test cases were carried out by swiping purely in the horizontal direction, and another half was by means of rotating the footing as specified earlier. Each swipe commenced from an arbitrary initial vertical penetration w_o (Figure 1(c)), setting up the corresponding V_o which are provided in Table 1.

Considering the geometry of the model footing and location of the load cell with respect to RP, each swipe case, regardless of displacement trajectory, simultaneously generated both horizontal and moment reactions, which was also shown earlier in the purely vertical cases (Figure 5). In effect, a single swipe provides a defined relationship among the three planar component forces *V*, *H* and *M/B*. However, for convenience in the discussion of swipe loads, all results were grouped according to swiping events and not on directional forces generated, such that a description of footing behavior is specific among all HS only or among all MS only.

Figure 6 shows the normalized vertical and horizontal

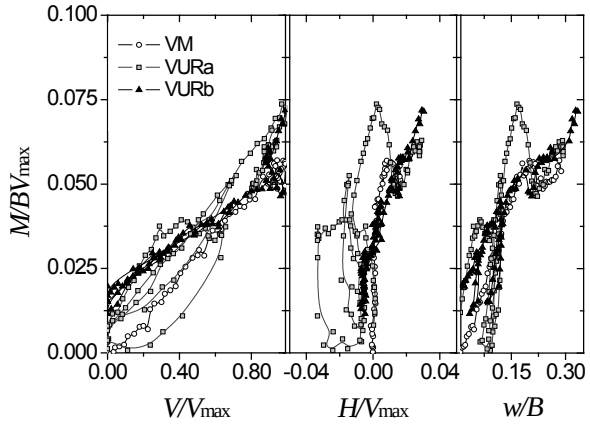


Figure 5 Normalised moment loads with vertical and horizontal loads and vertical penetration of VM, VURa, VURb cases.

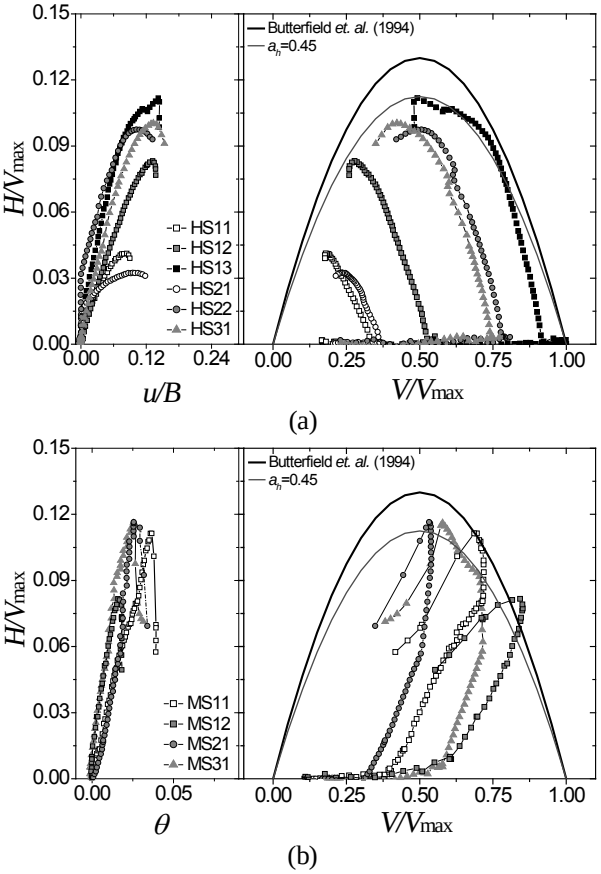


Figure 6 Normalized vertical and horizontal loads with (a) horizontal displacements of HS, and (b) rotational displacements of MS.

loads for HS and MS with respective swiping displacements u/B and θ. From the figures, the horizontal load is seen to increase steeply with horizontal and rotational displacements upon swiping until a maximum horizontal load H_{max} is reached. Horizontal loads consequently dip upon continued horizontal displacement or rotation. This observation clearly manifests the occurrence of plastic footing failure in the horizontal direction on all the swipe cases.

In Figure 6(a), the increase in horizontal loads during the horizontal swiping corresponded to a decrease in vertical loads. The VH load trajectory of HS for a single swipe follows the trajectory of a parabola which commences from V_o until a failure in horizontal direction is reached. Since VH load paths are seen to retract this parabola, it can be said that this parabola bounds the failure zone in the VH load space. Such behavior was observed in several earlier studies such as the numerical simulations of Bransby and Randolph (1998) and Houlsby and Cassidy (2002) and model tests of Nova and Montrasio (1991), Gottardi and Butterfield (1993), Gottardi and Houslby (1995), Gottardi et al. (1999), and Cassidy (2007) on various footing geometries and ground conditions.

Equation 8 provides an approximation to this parabolic shape given in general form as,

$$\left(\frac{H}{V_{\max}}\right) = a_h \frac{V}{V_{\max}}\left(1-\frac{V}{V_{\max}}\right)^{b_h} \qquad (8)$$

where a_h denotes the initial slope of the tangent of the parabola at the origin, and b_h controls the position of the maximum horizontal load for the given V_o, *i.e* the shape of the parabola and is taken equal to 1.

An a_h value of 0.45 fits well in the present set of data. Maximum horizontal capacity, H_{max} occurs at V=0.50·V_{max} where H_{max} is equivalent to 0.11·V_{max}. For purpose of comparison, a parabola with a_h=0.52, as suggested by Butterfield and Gottardi (1994) approximated from results of model tests using rectangular footings over dense sand, was also drawn on the graph. The obvious difference in footing geometry resulted to the observable difference in the sizes of these two parabolas. For instance, in circular footings on dense sand, an a_h value of 0.48 was observed by Gottardi and Butterfield (1993). Circular, spudcans on dense sand pegged an a_h of 0.56 (Dean et al. 1992) on the other hand. Furthermore, some evidence of change in the shape of the parabola can also be seen and is possibly due to the influence of the difference in the vertical hardening experienced prior to each swipe, especially for cases where multiple swipes were conducted.

It can also be deduced from Figure 6(a) that the parabola increases in size with the increase of initial penetration depth w_o, and consequentially of increasing V_o. This observation would suggest that the expansion of the failure surface is dependent on the vertical stress that the footing is carrying before it is subjected to swiping loads.

In contrast, the horizontal loads generated by rotation increase simultaneously with vertical stress commencing from V_o as shown in the VH plot in Figure 6(b). The figure shows that the load path of this particular swipe mechanism radially traverses the VH load space until a point of retraction is reached. In particular, the radial length of the load path from V_o to point of retraction is seen to be dependent on values of V_o, where swipes commencing from smaller V_o take a longer course and those starting from larger V_o take a shorter course. These points of retraction signify that failure in the horizontal direction has been reached. Conclusively, a trace of the two parabolas given earlier in Figure 6(a) following Equation 8 bounded most of these points.

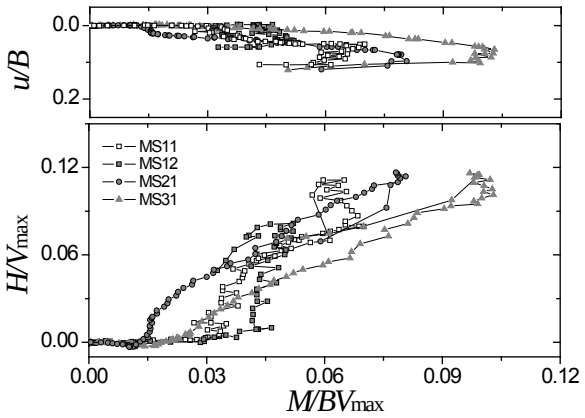


Figure 7 Normalized horizontal and moment loads with horizontal displacement of the RP in MS.

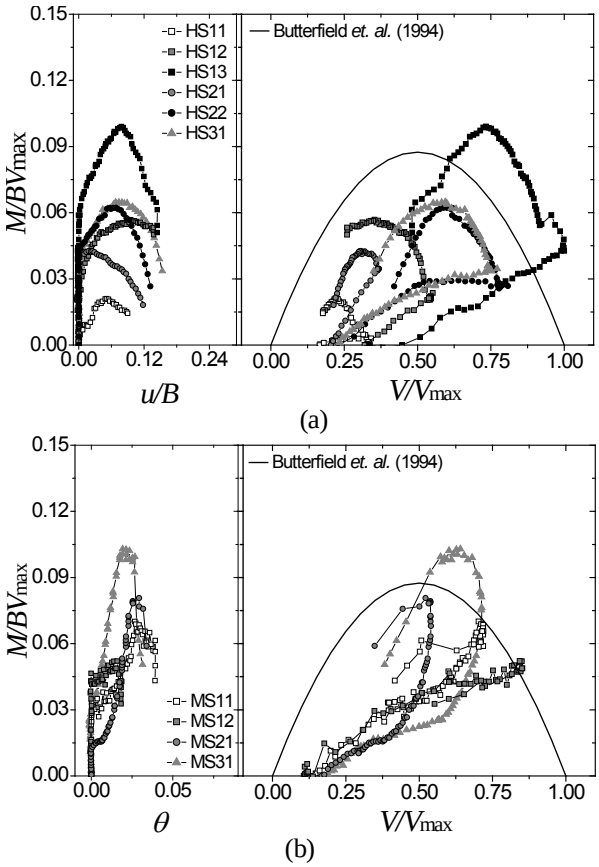


Figure 8 Normalized vertical and moment loads with (a) horizontal displacements of HS, and (b) rotational displacements of MS.

Note that the rotation of the footing also translated the RP horizontally. This horizontal translation of the footing during rotation is plotted in Figure 7 together with the normalized horizontal and moment loads of the MS cases. This graph reveals that large horizontal loads during rotation were experienced at larger horizontal displacements at around $0.10 \cdot B$.

The normalized moment loads for all the swipes are plotted against the normalized vertical loads for HS (Figure 8(a)) with u and MS (Figure 8(b)) with θ.

The amount of moment loads generated during horizontal swipe is seen to be not only generated by the horizontal displacement of the footing. In Figure 8(a), moment loads were already increasing even before the footing was moved horizontally as observed in the *uM* plot. It is revealed in the VM plot of the same figure that this increase in moment corresponded to a linear increase in vertical loads. This brings to light the earlier observation in the vertical loading cases where both horizontal and moment loads were simultaneously generated during vertical penetration (Figure 5). Note, however, that the increase in horizontal load in the HS cases during the footing penetration is found to be insignificant as shown in the abscissa of the VH plot in Figure 6(a). This particular observation would suggest that in the HS case, the increase in moment load, *M/B* during the vertical penetration of the footing is mostly driven by some variables of the vertical load component, which are typically unaccounted for in most vertical loading tests as pointed out earlier. This observation is further supported by Equation 6 where for small values of θ during the vertical penetration, the horizontal component h of the moment load *M/B* subsequently diminishes to zero, leaving the vertical and moment load components, v and m accounting for *M/B*.

Going back to Figure 8(a), it is observed that horizontal translation of the footing increases the moment loads further. However, this increase stops at some point where further horizontal translation only results to a decrease in moment loads. This behavior dictates that plastic moment failure has been reached at these points. The increase in moment loads during horizontal translation corresponded to a decrease in vertical load as observed in the VM plot of the same figure. Since horizontal loads subsequently increase with horizontal displacement (Figure 6(a)), it can be said that the moment loads experienced in the RP is generated simultaneously with horizontal loads. In fact, the generated moment during the horizontal translation is seen to increase linearly with the horizontal load as shown in Figure 9. In this figure, the normalized horizontal and moment loads are plotted with the RP rotation during the horizontal swipe HS. Recalling Equation 6, the calculated moment load at the RP becomes a strong function of the h component even for small amounts of footing rotation which were found to be at around 0.2° (0.0035rad) during the horizontal swipes (Figure 9).

Further comparing Figure 6(a) and Figure 8(a) would tell that all horizontal failure occurred after $0.08 \cdot B$ horizontal displacement while most moment failure have already occurred before this displacement has been reached. This would suggest that for horizontally loaded foundation, moment failure would ensue first before horizontal failure can be reached. This is further exemplified in Figure 9 wherein the horizontal load increases slightly further after the points of retraction of the moment loads, where it eventually goes down with continued decrease in *M/B*. It can then be deduced from these observations that moment failure would govern in the analysis of horizontally loaded foundation.

In Figure 8(b), the moment loads are seen to increase before the footing was set to w_o. When footing rotation was continued further, the moment loads consequently plummeted, signaling the occurrence of plastic footing failure. Considering the VM load paths of the MS cases, it is

seen that moment loads also increase during vertical penetration before swiping, the possible mechanism of which was already explained earlier. This increase in moment is seen linear with the increase in vertical load. The trajectory of the VM load paths changes however once the footing experience rotation. The increase of the VM load path is seen to be stiffer until it reaches moment failure. Upon failure, both moment and vertical loads considerably decrease.

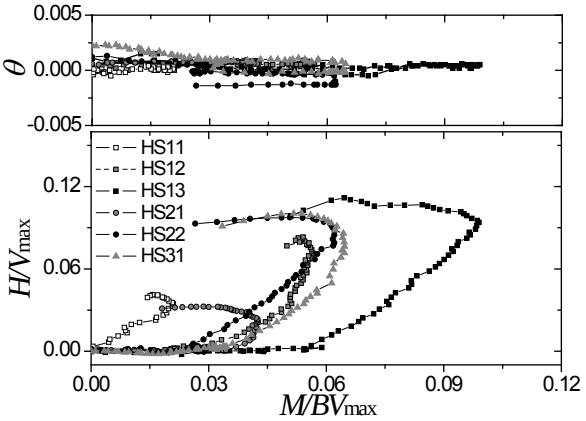


Figure 9 Normalized horizontal and moment loads with rotation of the RP in HS.

In Figure 7, the increase of moment is seen to be linear with the horizontal loads generated during rotation. When failure occurs at maximum rotation, the moment decreases abruptly. Upon closer inspection, it can be observed by comparing the θH in Figure 6(b) and θM in Figure 8(b) that horizontal failures mostly occurred at greater footing rotation for each swipe case. This implies that moment failure occurs first before the footing fails in the horizontal direction during rotation.

In previous studies, the failure defined by VM load paths was mathematically constructed using a parabola. The expression of this particular parabola is given in general form by Equation 9 as,

$$\left(\frac{M}{BV_{\max}}\right) = a_m \frac{V}{V_{\max}}\left(1-\frac{V}{V_{\max}}\right)^{b_m} \qquad (9)$$

where a_m and b_m play the same functions as a_h and b_h given out in Equation 8. The values of a_m for several studies are in the range of 0.35-0.36 (*e.g.* Butterfield and Gottardi (1994) and Gottardi et al. (1999) on rectangular footings on dense sand, and Dean et al. (1992) and Gottardi and Butterfield (1993) on circular footings on dense sand). For comparison, the parabola suggested by Butterfield and Gottardi (1994) with a_m=0.35, was imposed to the VM plots of present set of data in Figure 8. It is found that this particular parabola contains most of the VM load paths of the test cases; however, it provides a conservative approximate to most paths, which can be accounted for by the difference in model footing geometries and loading conditions used in the earlier study.

3.3 Failure mechanisms

Ground behavior was observed in-flight using a digital-camera set up shown in Figure 1(a). Images were captured every 100 secs, which provided the time-lapse for a single analysis in the GeoPIV. Thus, a single analysis only provides the total displacement vector between consecutive images (image *n* and image *n+1*), discriminating potential and actual deformation of earlier analysis observed in earlier images (<image *n*). This was made so in order to more accurately and conveniently superimpose the analysis over the time scale of the loading events thereby giving directly the "current" condition of the soil flow to a particular point in the load plots for a given time frame.

For instance, Figure 10(a) shows the soil flow condition when $V<0.3\cdot V_{max}$ taken from the MS21 case. Conversely, Figure 10(b) reveals the collapse mechanism of the ground after the vertical capacity V_{max} was reached (from VURb case).

In Figure 10(a), the vector values of the soil displacements are defined. It can be observed from the said plot that the region of soil underneath the footing being held in static equilibrium by the vertical load with vector displacements of more than 0.30mm (about 0.75%·*B*) propagates to a maximum span of about 1.0·*B* from the center of the footing, extending to a depth of approximately 1.0·*B* immediately below the RP. The soil flow is generally downward and concentrically in the direction of vertical loading. Eventually, at failure, a ruptured zone develops at both sides of the footing, taking the form of a spitting curved wedge as shown in Figure 10(b). Plastic heaving can be also observed implying that a plastic region was smoothly sheared-off with continued loading. This plastic region can reach to a maximum depth of 2.0·*B* relative to original free surface defined in the figure by the original position of the footing.

Contour plots of the VHM for HS and MS, with VH and VM as corresponding principal axes, are provided in

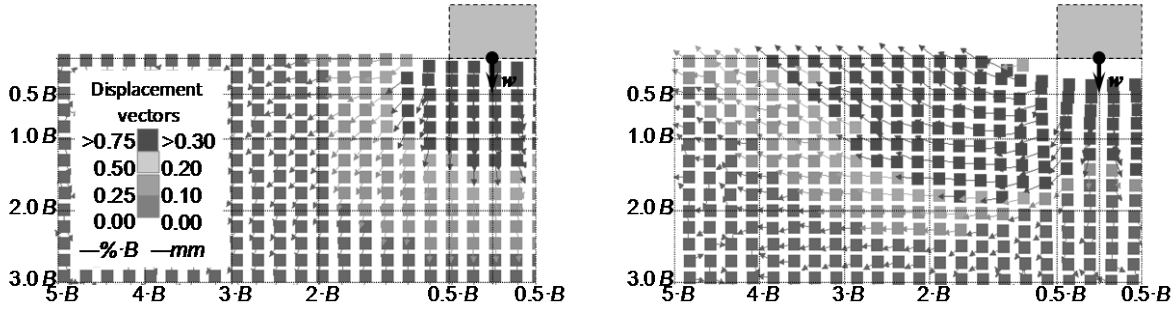


Figure 10 Soil deformation during vertical loading in (a) MS21 for $V<0.3\cdot V_{max}$, before swiping, (b)VURb after vertical failure, V_{max}.

Figures 11(a) and 12(a) respectively. Various points in these load spaces were defined showing specific soil flow conditions, primarily to characterize deformation patterns pre- and post-failure.

Soil deformation before failure in HS is exemplified by points in the HS21 and HS22 swipes in Figures 11(b) and (c).

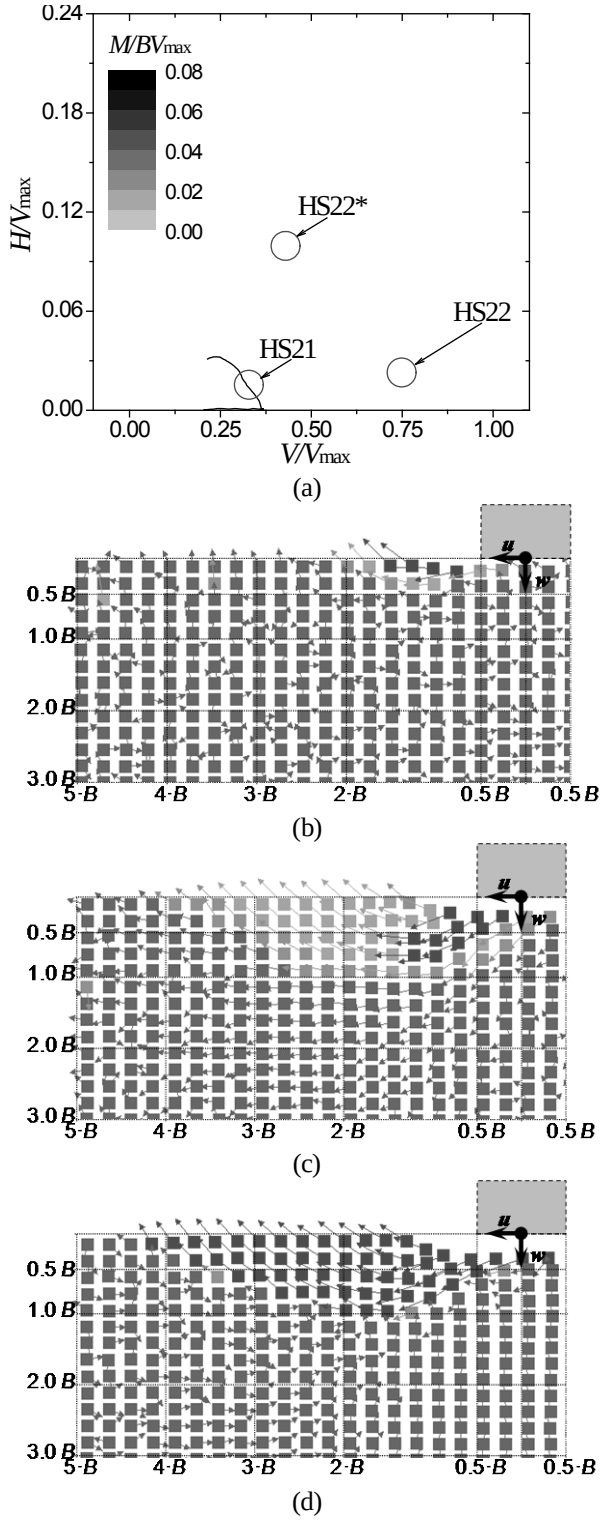


Figure 11 (a) VHM contour plot of HS cases inside parabola a_h=0.45, (b) soil deformation before failure in HS21, (c) soil deformation before failure in HS22, (d) soil deformation after failure in HS22*.

It can be observed that a curved-wedge mass of soil emanating directly below the footing was translated in the direction of the swipe. However, the volume of this translated mass largely depends on the vertical penetration before swipe w_o found to be $0.05 \cdot B$ and $0.2 \cdot B$ for HS21 and HS22 respectively (Figure 4(b)).

A typical failure mechanism for horizontally loaded foundation is shown in Figure 11(d), taken from HS22*. It is seen that the progression of the curved-wedge mass early on in the swipe eventually demarcated the ruptured surface during failure. This ruptured surface has a span of $4 \cdot B$ from the center of the footing, and a maximum depth of $1.0 \cdot B$ relative to free surface wherein further loading will only smoothly translate the mass to the direction of the heave.

Figure 12 shows the ground behavior of rotationally loaded footing. Before failure, the ground is seen to be mobilized by the resulting rotation (Figure 12(b)), wherein a scooping mechanism is exhibited with vector displacements of $0.75\% \cdot B$ expanding until a depth of $1.5 \cdot B$ relative to free surface. However, at failure, the ruptured surface (Figures 12(c) and (d)), takes the shape of a curved-wedge, similar to the horizontally-loaded ruptured surface in Figure 11(d). Similarly, the depth of this wedge is about $1.0 \cdot B$, spanning a distance of $4.0 \cdot B$ from the center of the footing. This observation would suggest that at plastic failure, the ruptured surface of horizontally and rotationally loaded grounds exhibit an almost similar geometry.

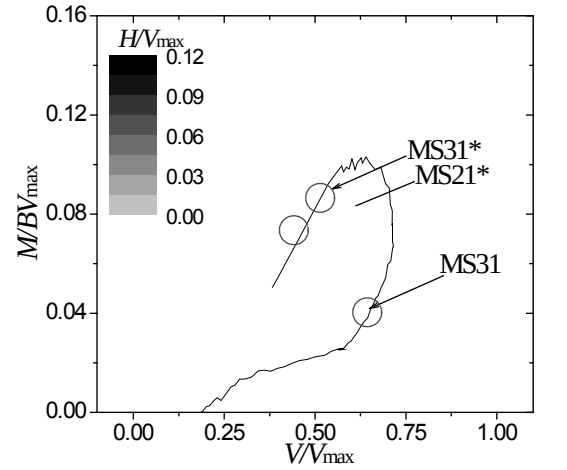
4. CONCLUSIONS

The present study was able to fulfill three major targets: (1) define several independent load paths progressing to failure, (2) define a failure mechanism for the soil-footing system, and (3) superimpose the failure mechanism at different stages of the loading events.

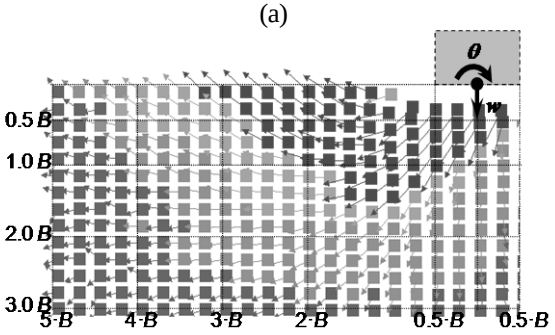
In particular, the study was able to provide evidence of appreciable amounts of horizontal and moment loads which are otherwise ignored in most vertical loading tests. These lateral reactions can be accounted for by the variable effect of soil deformation during the progression of footing penetration, where the ground does not only become stiffer but also changes its deformation geometry in order to fully confine the loads imposed on it by the foundation. This observation imply the substantial effect of footing embedment during vertical penetration beyond $15\% \cdot B$ where at vertical capacity, moment loads in the range of 0.045 to 0.070 of V_{max} and horizontal loads in the range of $\pm 0.030 V_{max}$ were recorded.

It is also found that most horizontal failure occurs at greater plastic displacements compared to moment failure both in the horizontally and rotationally loaded grounds. In particular, maximum moment loads were reached before the horizontal displacement of $0.08 \cdot B$, while horizontal failure occurred at $u > 0.08 \cdot B$. Conversely, the points of maximum moment in the rotation swipe did not correspond to points of maximum horizontal loads. On the contrary, horizontal loads were observed to increase further after a clear moment failure has already been reached. These observations would conclude that moment failure occurs first before the footing fails in the horizontal direction during horizontal and rotational loadings.

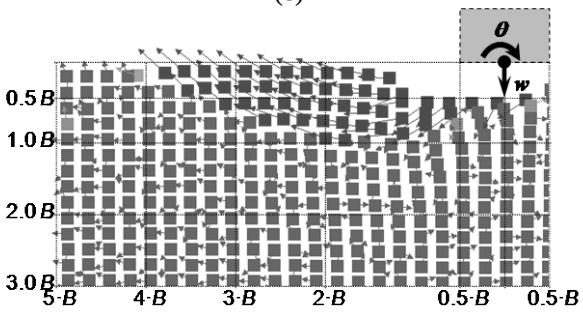
Patters of soil movement before failure seem to vary accordingly with the direction of loading, or the current state of loads. The region of soil underneath the footing being held in static equilibrium by the loads acting on the footing largely depends on the amount of initial vertical penetration w_o. However, at full plastic failure, the ruptured surfaces of horizontally and rotationally loaded grounds exhibit an almost similar size and geometry.



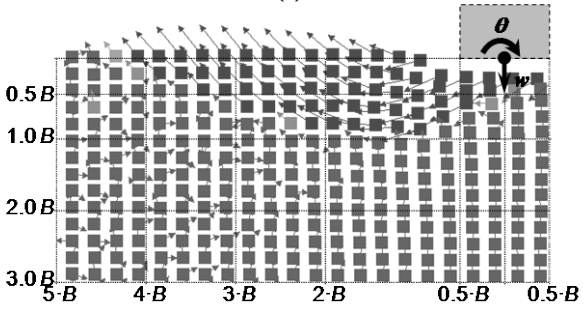
(a)



(b)



(c)



(d)

Figure 12 (a) VHM contour plot of MS cases inside parabola a_m=0.35 after Butterfield et al. (1994), (b) soil deformation before failure in MS31, (c) soil deformation after failure in MS31*, (d) soil deformation after failure in MS21*

References:

Bransby, M. F. and Randolph, M. F. (1998), "Combined loading of skirted foundations," *Géotechnique* **48**, No.5, 637-655.

Bransby, M.F. and Yun, G.J. and (2009), "The undrained capacity of skirted strip foundations under combined loading," *Géotechnique* **59**, No.2, 115-125.

Butterfield, R. and Gottardi, G. (1994), "A complete three-dimensional failure envelope for shallow footings on sand," *Géotechnique* **44**, No.1, 181-184.

Cassidy, M. J. (2007), "Experimental observations of the combined loading behavior of circular footings on loose silica sand," *Géotechnique* **57**, No. 4, 397-401.

Cocjin, M. J. L. (2010), "Development of failure mechanisms of shallow foundations subjected to combined loadings, *MSc thesis*, Tokyo Institute of Technology, Japan.

Dean, E.T.R, James, R.G., Schofield, A.N., Tan, F.S.C. and Tsukamoto, Y. (1992), "The bearing capacity of conical footings on sand in relation to the behavior of spudcan footings of jack-ups," *Predictive Soil Mechanics, Proc. Wroth Mem. Symp.*, Thomas Telford, 230-253.

Gottardi, G. and Houslby, G.T. (1995), "Model tests of circular footings on sand subjected to combined loads," *Report No. 2071/95*, Oxford University Engineering Laboratory.

Gottardi, G., Houlsby, G.T., and Butterfield, R. (1999), "Plastic response of circular footings on sand under general planar loading," *Géotechnique* **49**: 453-469.

Hossain, M. S. and Randolph, M. F. (2010), "Deep-penetrating spudcan foundations on layered clays: centrifuge tests," *Géotechnique* **60**, No. 3, 157-170.

Houlsby, G.T. and Cassidy, M.J. (2002), "A plasticity model for the behavior of footings on sand under combined loading," *Géotechnique* **52**, No. 2, 117-129.

Jumikis, A.R., (1961), "The Shape of Rupture Surface in Sand," *Proceedings of the 5th International Conference on Soil Mechanics and Foundation Engineering*, Vol. 1, 693-696.

Martin, C.M. (1994), "Physical and numerical modeling of offshore foundations under combined loads," *Ph.D. thesis*, University of Oxford, United Kingdom.

Nova, R. and Montrasio, L. (1991), "Settlements of shallow foundations on sand," *Géotechnique* **41**, No.2, 243-256.

Punrattanasin, P., Nishioka, H., Murata, O. and Kusakabe, O. (2003), "Development of combined loading apparatus for centrifuge test," *International Journal of Physical Modeling in Geotechnics*, Vol.4, 1-12.

Roscoe, K. H. and Schofield, A. N. (1957), "The stability of short pier foundations in sand, discussion," *British Welding Journal*, January, 12-18.

Taiebat, H. A. and Carter, J. P. (2000), "Numerical studies of the bearing capacity of shallow foundations on cohesive soil subjected to combined loading," *Géotechnique* **50**, No. 4, 409-418.

Teh, K. L., M. J. Cassidy, C. F. Leung, Y. K. Chow, M. F. Randolph and M. Quah (2008), "Revealing the bearing failure mechanisms of a penetrating spudcan through sand overlaying clay,:" *Géotechnique* **58**, No. 10, 793-804.

White, D. J., and Take, W. A. (2002), "GeoPIV, Particle Image Velocimetery (PIV) software for use in geotechnical testing," *User manual*.

8CUEE CONFERENCE PROCEEDINGS
8th International Conference on Urban Earthquake Engineering
March 7-8, 2011, Tokyo Institute of Technology, Tokyo, Japan

INCLUSION OF AXIAL LOAD ON BENDING RESPONSE OF PILE IN LIQUEFIABLE SOILS

Domenico Lombardi[1)], Suresh R. Dash[2)], and Subhamoy Bhattacharya[3)]

1) Research Scholar, Department of Civil Engineering, University of Bristol, United Kingdom
2) Research Assistant, Department of Civil Engineering, University of Bristol, United Kingdom
3) Senior Lecturer in Dynamics, Department of Civil Engineering, University of Bristol, United Kingdom
Domenico.Lombardi@bristol.ac.uk, Suresh.Dash@bristol.ac.uk, S.Bhattacharya@bristol.ac.uk

Abstract: Collapse or severe damage of structures supported on pile foundations have been observed after many severe earthquakes, especially where the soil conditions consisted of soft deposits characterised by poor mechanical properties (i.e. low values of strength and shear modulus or soil susceptible to liquefaction). The formation of the plastic hinges in the piles at various locations suggest that the bending moments and/or shear forces experienced by them would have exceeded the bending and/or shear capacity of the section. However, many case histories have shown collapses albeit a high margin of safety being effectively applied during design with regard to the classical mechanism of failures, such as the bending and the shear mechanisms. This may suggest that the actual mechanism of failure has not been properly considered. Recently, the buckling instability of piles in liquefiable soils is recognised as a possible failure mechanism. Although the current codes of practice do not explicitly mention this particular issue, the presence of large axial loads may have important consequences, particularly where piles are founded in liquefiable or very soft soils. In such conditions, the axial and lateral loads (from inertia or spreading soil) may also lead to a reduction of the buckling capacity due to the second order non-linear effects, and the piles may fail due to buckling instability. In this paper the role played by the axial loads and its influence on the bending behaviour of piles are investigated.

1. INTRODUCTION

Pile foundations are slender structural elements inserted deep into the ground to support heavily loaded structures such as: bridges, buildings, jetties or oil platforms. Typically, this type of foundations is used when ground is insufficiently strong to support the structure on its own. Often, this condition occurs in seismic-prone zones with loose or medium dense sandy soil. In a saturated condition, these soils are prone to liquefy during medium to strong earthquakes, and undergo significant reduction of their strength and stiffness.

Unfortunately, piles supported structures still collapse and/or show severe damages (see Figure 1 for a case history of bridge collapse in a very recent earthquake), after strong earthquakes, particularly in liquefiable soils. This is despite the fact that large factors of safety are employed in the design. Further discussion in this paper will concentrate on the pile performance in liquefiable soils.

The current understanding of pile failure in liquefiable soils identifies four feasible mechanisms of failure, such as: (a) excessive settlement, (b) bending, (c) shear and (d) buckling. Also combination and the interaction between the above mechanisms can cause failure as well.

Excessive settlements occur when the side friction and the bearing capacity of the pile reduces due to the loss of strength and stiffness of the soil caused by liquefaction. In fact, if the residual bearing capacity is insufficient to carry the vertical load, the foundation may undergo excessive settlement and eventually fail to meet the serviceability criteria. This type of pile failure may not involve any structural damage.

The bending mechanism due to liquefaction induced lateral spreading of the ground is often regarded as the principal cause of pile failure (Hamada 1992, Ishihara 1997, Tokimatsu *et al.* 1998, Goh and O'Rourke 1999, Abdoun and Dobry 2002, Finn and Fujita, 2002).

When the shear capacity of the pile is low, for example for hollow sections, the lateral spreading may cause the pile to fail in shear.

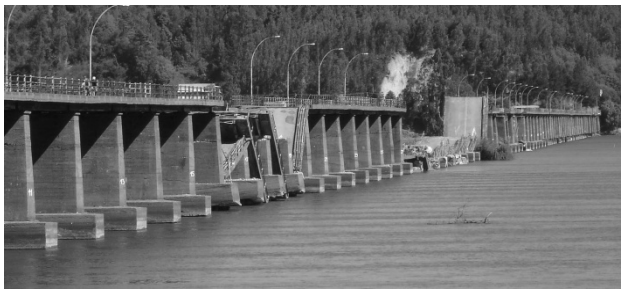


Figure 1. Bio-Bio Bridge damaged during the 2010 Chile earthquake (Courtesy of Daniella Escribano Leiva.).

In contrast to above three failure mechanisms, piles may also fail due to axial instability owing from higher the loss of lateral confinement in liquefied soil (Bhattacharya et al. 2004). This is supported by the fact that many failures of pile foundations in past earthquakes not only occurred in

laterally spreading grounds but also were observed in level grounds where no lateral spreading would be possible.

Buckling mechanism suggests that if the soil liquefies, the pile will lose significant amount of lateral stiffness offered by the surrounding soil and may behave like a long unsupported column with lower buckling capacity, and may buckle due to the presence of axial load from superstructure. While the bending and buckling mechanisms have been studied in detail separately, little has been reported on their interactions (see for example the work done by Dash *et al.* 2009, 2010). It is also important to note that the bending moment in the pile due to lateral loading (e.g., from flow of liquefied soil or inertia) may get amplified in presence of higher axial load. The aim of this paper is to illustrate the effect played by the axial load on the bending response of the pile.

2. CURRENT UNDERSTANDING OF PILE- SOIL INTERACTION

Among four recognised mechanisms of pile failure, two mechanisms generally govern the design of piles in liquefiable soils, which include: bending mechanism and buckling mechanism. The behaviour of pile for these mechanisms is described in detail in the following sections.

2.1 Pile failure based on bending mechanism

In the bending mechanism, piles are considered as beams. The lateral loads on the piles are due to inertial effects from the superstructure and kinematic effects due to ground movement. The pile-soil interaction can be described considering three different phases (Tokimatsu *et al.* 1998), as illustrated in Figure 2.

Phase 1. Prior to the development of pore water pressure, the inertia force from the superstructure may dominate.

Phase 2. Kinematic forces from liquefied soil start acting with increasing pore pressure.

Phase 3. Towards the end of shaking, kinematic forces would dominate and have a significant effect on the pile performance particularly when permanent displacement occurs in laterally spreading soil.

Combination of different phases of loading:

In sloping grounds, the liquefied soil will start to move horizontally, which constrain the pile to deform in the same direction of the slope. It may be assumed that seismic motion has already passed the peak but the shaking may still be persistent with lesser intensity and therefore the inertia force transmitted from the superstructure will be small. Under such loading condition, the maximum bending moment induced by the pile may not occur near the pile head but at a certain depth. Ishihara (1997) noted that during the earthquake, the liquefaction of the soil starts approximately at the time of occurrence of peak ground acceleration. He argues that since the seismic motion has already passed its peak, subsequent shaking will be less intense, so that the lateral inertia force applied by the superstructure will not be significant. Therefore, the effects of inertia of the superstructure on the pile response are considered separately and are not combined with the lateral spreading effects. Hamada (2000) mentioned that permanent displacement of non-liquefied soil overlying the liquefied soil is a governing factor for pile damage. A similar conclusion has also been stated by Berrill *et al.* (2001). Further to this, Tokimatsu et al. (2005) and Tokimatsu and Suzuki (2005) carried out large scale shaking table tests of pile groups in dry and saturated sands and suggested the required conditions and methodology to combine inertial and kinematic loads for piles subjected to seismic loads as follows.

When natural period of structure (T_b) > natural period of ground (T_g):

$$M_p = \sqrt{M_i^2 + M_k^2} \quad (1)$$

When natural period of structure (T_b) < natural period of ground (T_g):

$$M_p = M_i + M_k \quad (2)$$

where, M_p, M_i and M_k are the maximum bending moment, bending moment due to the inertia of the superstructure and bending moment induced by the kinematic interplay (i.e. lateral spreading) respectively.

However, in the literature, it is not clear if the effects due to the inertia and lateral spreading should be analyzed separately or to combine them in order to obtain the maximum bending moment for a field condition.

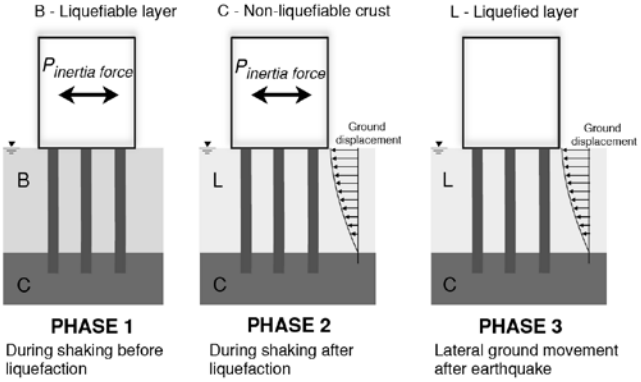


Figure 2. Schematic showing different phases of pile loading based on bending mechanism of pile failure.

2.2 Pile failure based on buckling mechanism

Based on the back-analysis of 14 cases of pile foundation performance and a series of centrifuge tests, Bhattacharya et al. (2004) suggested that the buckling instability may be considered as potential mechanism of pile collapse. As shown in Figure 3, the pile-soil interaction and different phases of loading on pile may be represented by four different stages.

Stage1: Before the earthquake the pile transfers the axial load from superstructure to the supporting soil by 1) shear generated along the surface of the pile due to the soil-pile friction, and 2) point resistance due to the end bearing at the bottom of the pile.

Stage 2: Before the liquefaction the confining pressure around the pile is not expected to decrease substantially. The pile is predominantly loaded by inertia forces generated from the oscillation of the superstructure.

Stage 3: As the shaking continues, in loose to medium dense saturated soils, excess pore pressure develops, and the soil starts to liquefy. With the onset of liquefaction the pile may lose its shaft resistance particularly in the liquefied layer and shed axial loads downwards to mobilize additional base resistance. If the base capacity is exceeded than the axial load demand, settlement failure may occur. If the pile is sufficiently stable at base, it may experience a high slenderness ratio and will be prone to buckling instability.

Stage 4: In sloping ground the pile may also be subjected to additional drag force due to lateral spreading of soil as explained in the previous section, along with the axial load.

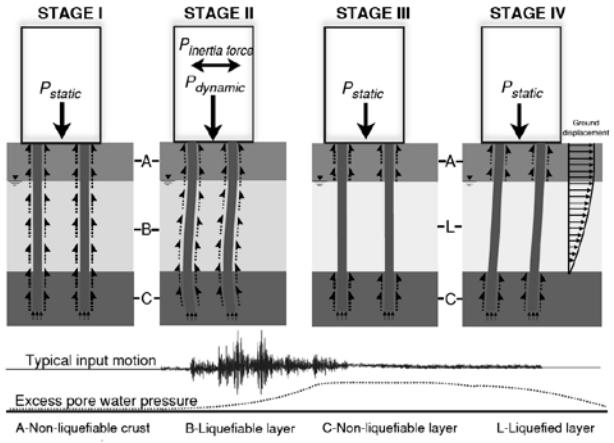


Figure 3. Schematic showing different phases of pile loading based on buckling mechanism of pile failure.

3. EFFECT OF AXIAL LOAD ON BENDING RESPONSE OF THE PILE

In field condition, piles are subjected to both axial and lateral loads during earthquakes, and they should be considered as beam-column elements. During liquefaction the buckling load capacity (P_{cr}) of the pile decreases. Considering the static load of the pile (P) as a constant value throughout, if P_{cr} reaches close to P, the structure can suffer excessive bending due to even a very small amount of lateral loading or imperfection. On the other hand, the lateral deflection or bending moment in pile due to lateral loading is expected to increase with decreasing P_{cr}, (i.e., increasing P/P_{cr} ratio).

The interaction between the axial and lateral load is generally referred to as *P-delta* effect. Stability analysis of elastic column (Timoshenko and Gere, 1961) shows that the lateral deflection (y_0) due to lateral loads is amplified in the presence of axial load (P) producing a final deflection of pile (y) as given in equation (3), which is also plotted in Figure 4.

$$\frac{y}{y_0} = \frac{1}{1-\frac{P}{P_{cr}}} \tag{3}$$

The ratio y/y_0, commonly known as "Buckling Amplification Factor" (BAF), is a function of the critical buckling load, which depends on the boundary conditions of the pile.

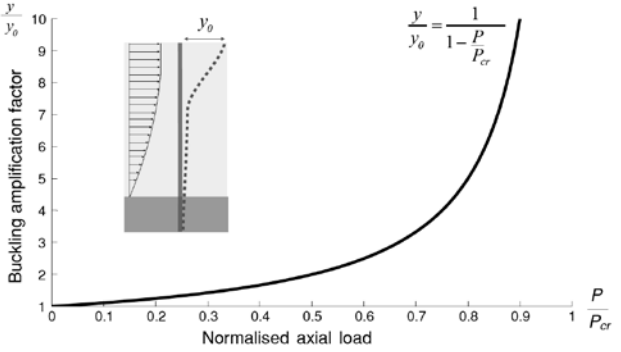


Figure 4. Buckling amplification factor for different ratios of P/P_{cr}.

For piles subjected to lateral spreading the value of y_0, due to the lateral load only, may be assed considering two different methods, namely force and displacement based method. These two approaches are illustrated in more details in the next section, where the effect of axial load is incorporated.

3.1 Numerical model

The inclusion of axial load in bending analysis can be easily implemented in a numerical model, where the lateral and axial loads are considered together. The numerical model for lateral loading of the soil on pile is generally carried out in two different ways such as:

1. force based method
2. displacement based method

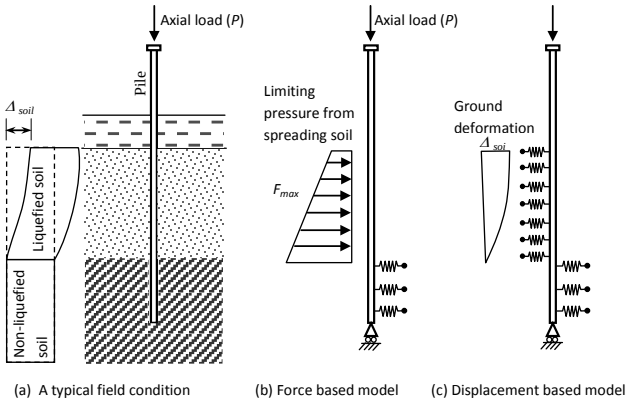


Figure 5. Force and displacement based models of pile-soil interaction in liquefiable soil.

Figure 5 shows these two methods of representing a field condition. In force based method, the force from liquefied soil flow is represented by a limiting pressure (F_{max}) on pile. (see Figure 5b). Figure 5c illustrates displacement based method, where the lateral spreading is modelled by applying

a displacement at the free ends of the soil springs. Typical results of pile response from these two methods with axial load are described in the next section.

3.2 Typical results

Figures 6 shows the effect of the axial load on the bending response of a pile foundation, in terms of normalised pile displacement *y/D* (where *y* is the lateral displacement evaluated considering the effect of axial load) against either Δ_{soil}/D or F/F_{max} depending on the method of analysis (i.e., force based method or displacement based method). Clearly, Figures 6 and 7 show that when the axial load is higher with respect to critical buckling load, the pile head deflection (*y*) and maximum bending moment in pile get larger.

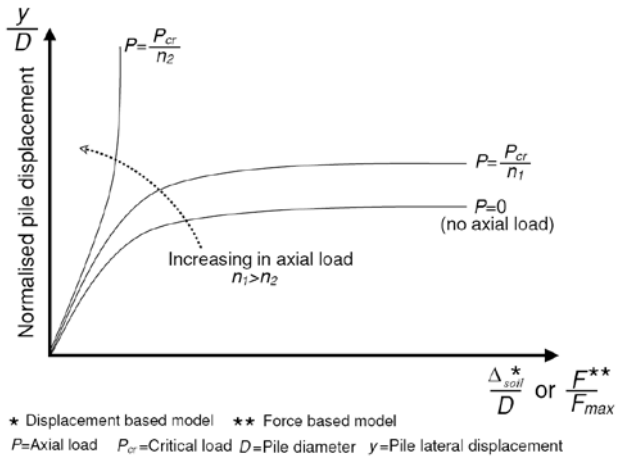


Figure 6. Pile head deflection response due to lateral and axial load.

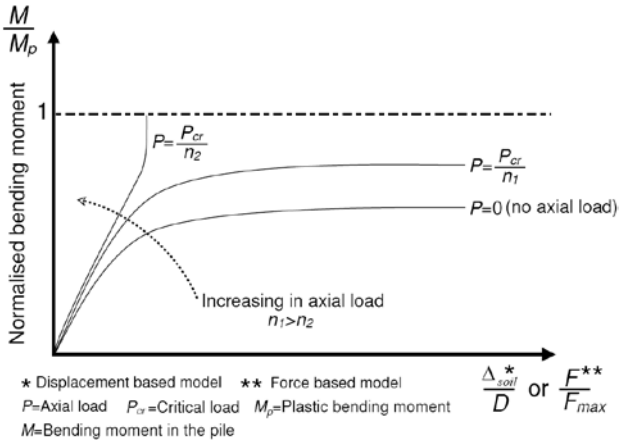


Figure 7. Pile bending moment response due to lateral and axial load.

During liquefaction, as the soil loses its stiffness, the elastic buckling load (P_{cr}) also reduces. Assuming a constant static axial load on pile, this also causes the P/P_{cr} ratio to increase. With the increasing P/P_{cr}, the pile head deflection and bending moment in pile also increase. When this ratio is close to 1, i.e., axial load is close to the buckling load, the bending moment amplification factor becomes very high, which leads the bending moment in pile to reach its plastic moment capacity, M_p, at a lower value of lateral load. The sudden rise in pile head deflection demonstrates the failure of the pile where bending moment reaches M_p and pile continues to deflect without any additional loading. A similar behaviour can also be observed when the axial loaded piles in level liquefied ground subjected to inertia loading.

4. DISCUSSUION ON CURRENT CODES OF PRACTICE

This section reviews the recommendations suggested by the main codes of practice.

- The *Japanese Road Association Guidelines* (JRA, 2002) suggests designing piles against bending failure considering both the inertia and kinematic force due to the lateral spreading. The action of the liquefied soil can be considered as a distribution equals to 30% of the total burden pressure. Figure 8 shows that, if there is also a non-liquefiable crust overlaying the liquefiable layer, its action can be accounted by a passive earth pressure distribution.

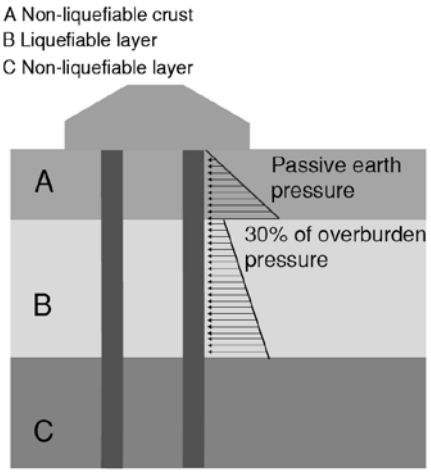


Figure 8. Idealisation of loading for seismic design of pile foundation subjected to lateral spreading as suggested by JRA (2002).

- *Eurocode 8 part 5* (1998) suggests to design considering the bending due to inertia and kinematic loads arising from the deformation of the surrounding soil recommending that piles should be designed to remain elastic. However they admit that the interfaces between layers having different properties should have the capacity to develop plastic hinge. For these calculations the lateral resistance offered by the soil layers susceptible to liquefaction should be ignored.
- Other codes, such as the American code *NEHRP* (2000) and Indian Code *IS-1893* (2000) also focus on the bending mechanism.

5. CONCLUSION

In summary, the current codes of practice treat the piles as beam elements and assumed that the lateral loads from structural inertia and/or soil movement cause bending failure of the piles. In contrast to current practice, present investigation shows that the need of incorporation of axial load can be vital in determining the response of piles in liquefiable soils, and ignoring it during design may be un-conservative.

References:

Abdoun, T. and Dobry, R. (2002), "Evaluation of pile foundation response to lateral spreading". *Soil Dynamics and Earthquake Engineering*, 22, 1051-8.

Berrill, J.B., Christensen, S.A., Keenan, R.P., Okada, W. and Pettinga, J.R. (2001) "Case studies of lateral spreading forces on a piled foundation", *Géotechnique*, Vol.51 No.6, 501-517.

Bhattacharya, S., Madabhushi, S.P.G. and Bolton, M.D. (2004), "An Alternative Mechanism of Pile Failure in Liquefiable Deposits during Earthquake", *Géotechnique*, No.3, 203-213.

Dash, S.R., Govindaraju, L. and Bhattacharya, S. (2009) "A case study of damages of the Kandla Port and Customs Office Tower supported on a mat-pile foundation in liquefied soils under the 2001 Bhuj earthquake", *Soil Dynamics and Earthquake Engineering*, Vol. 29, No. 2, 333-346.

Dash S.R., Bhattacharya, S. and Blakeborough, A. (2010) "Bending-buckling interaction as a failure mechanism of piles in liquefiable soils". *Soil Dynamics and Earthquake Engineering*, 30, 32-39.

Eurocode 8 (Part 5, 1998): "Design provisions for earthquake resistance of structures-foundations, retaining structures and geotechnical aspects", European Committee for Standardization, Brussels

Finn, W.D.L. and Fujita, N. (2002) "Piles in liquefiable soils: seismic analysis and design issues", *Soil Dynamics and Earthquake Engineering*, 22, 731-42.

Goh, S. and O'Rourke, T.D. (1999), "Limited state mode for soil-pile interaction during lateral spread. *Proceedings of the seventh US-Japan workshop on earthquake resistant design of lifeline facilities and countermeasures against soil liquefaction*, Seattle, 1999, 237-260.

Hamada, M. (1992), "Large ground deformations and their effects on lifelines: 1964 Niigata earthquake. Case studies of liquefaction and lifelines performance during past earthquake". Technical Report NCEER-92-0001, National Center for Earthquake Engineering Research, Buffalo, NY.

Hamada M. (2000) "Performances of foundations against liquefaction-induced permanent ground displacements", Paper 1754, *Proceedings of the 12th World Conference on earthquake engineering*, Auckland, New Zealand.

IS 1893 (2002), Indian Code of Practice for Seismic Design.

Ishihara K. (1997) "Terzaghi oration: Geotechnical aspects of the 1995 Kobe earthquake", *Proceedings of ICSMFE*, Hamburg, 2047-2073.

Japan Road Association, JRA (2002) "Specifications for highway bridges", Part V: seismic design, Japan.

National Earthquake Hazards Reduction Program (NEHRP) (2000) Commentary (Federal Emergency Management Agency, USA, 369) for seismic regulations for new buildings and other structures.

Timoshenko, S.P., Gere, J.M. (1961) "Theory of elastic stability", McGraw-Hill book company, New York.

Tokimatsu, K., Oh-oka, H., Satake, K., Shamoto, Y. and Asaka, Y. (1998) "Effects of Lateral ground movements on failure patterns of piles in the 1995 Hyogoken-Nambu earthquake", *Proceedings of a speciality conference, Geotechnical Earthquake Engineering and Soil Dynamics III, ASCE Geotechnical Special publication*, (75), 1175-1186.

Tokimatsu, K. and Suzuki, H. (2005) "Effect of inertial and kinematic interactions on seismic behaviour of pile foundations based on large shaking table tests", *Proceedings of the 2nd CUEE conference on urban earthquake engineering*, Tokyo.

Tokimatsu, K. Suzuki, H. and Sato, M. (2005) "Effects of dynamic soil-pile structure interaction on pile stresses" *Journal of Structural and Construction Engineering, Architectural Institute of Japan*, 587, 125-132.

8CUEE CONFERENCE PROCEEDINGS
8th International Conference on Urban Earthquake Engineering
March 7-8, 2011, Tokyo Institute of Technology, Tokyo, Japan

SIMULATION OF THREE-DIMENSIONAL NONLINEAR BEHAVIOR OF SOIL-PILE-STRUCTURE IN LARGE SHAKING TABLE TESTS

Youhao Zhou[1], Hiroyuki Yoshida[2], Hiroko Suzuki[3], Yasushi Nukui[4], and Kohji Tokimatsu[5]

1) Master Student, Dept. Architecture and Building Engineering, Tokyo Institute of Technology, Japan
2) Chief, Arch Struct. Eng. Operation Center, Tokyo Electric Power Services Co., Ltd., Japan (TITECH)
3) Assistant Professor, Dept. Architecture and Building Engineering, Tokyo Institute of Technology, Japan
4) Group Manager, R&D Center, Tokyo Electric Power Company, Japan
5) Professor, Dept. Architecture and Building Engineering, Tokyo Institute of Technology, Japan
yoshida@tepsco.co.jp, shiyuu.y.aa@m.titech.ac.jp, hsuzuki@arch.titech.ac.jp, nukui.y@tepco.co.jp, kohji@o.cc.titech.ac.jp

Abstract: In order to examine the applicability of the three-dimensional finite element method for evaluating pile foundation behavior while soil shows strong nonlinearity, numerical simulations of two soil-pile-structure models subjected to strong shaking were performed. The tests were conducted using the large-scale shaking table at the E-Defense to investigate the response and failure of a nearly full-scale pile-structure system under multi-dimensional loading. It is shown that the numerical analysis can reproduce the behavior of the piles and superstructure as well as those of soil with a reasonable degree of accuracy, suggesting its applicability to soil-pile-structure system subjected to strong 3-D shaking.

1. INTRODUCTION

Most of Japanese metropolises lie on soft ground near seas and large rivers. For this reason, pile foundations are commonly applied for substructures, representing 70~80% of all buildings. Pile foundation is, however, weak in horizontal direction, thus soil and structures tend to be damaged by both inertial force from superstructures and kinematic force from ground displacement during earthquakes with large-scale horizontal shaking. Despite this fact, mechanism of these damages has not been fully understood, due to the lack of data since no observation has ever been made. Furthermore whether or not the three-dimensional nonlinear behavior of piles during earthquakes can be reproduced by numerical analysis has not been studied sufficiently.

In order to obtain sufficient data to establish a design method for pile foundation with failure of piles taken into account, a series of shaking table tests using soil-pile-structure models were performed (MEXT and NIED, 2006; Suzuki et al., 2008; Tokimatsu et al., 2008). The E-Defense shaking table platform and a cylindrical laminar shear box were used for the tests, and a full-scale pile-structure system was subjected to a series of single- or multi-dimensional loading. In cases where large scale loading was applied, subsidence and residual displacement of footing were observed, and data including pile damage process were obtained.

By performing numerical analysis of the abovementioned shaking table tests using three-dimensional finite element method, this paper verifies the validity of the evaluation method on three-dimensional nonlinear behavior of pile foundation structures during earthquakes.

2. SHAKING TABLE TESTS

The E-Defense shaking table platform has a dimension of 15 m length and 20 m width. Photo 1 and Figure 1 show the test model constructed in a cylindrical laminar box 6.5 m high with an inside diameter of 8.0 m. It consists of forty-one stacked ring frames, enabling two-dimensional shear deformation of the inside soil.

A 3x3 steel pile group was used for the tests. The piles were labeled A1 to C3 according to their locations within the

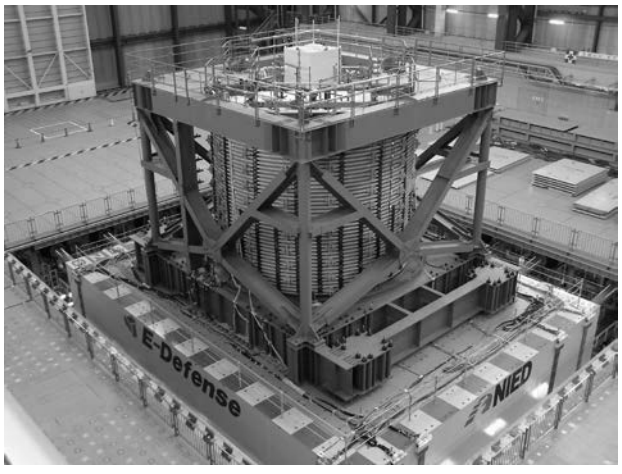


Photo 1 Test Model on Large Shaking Table

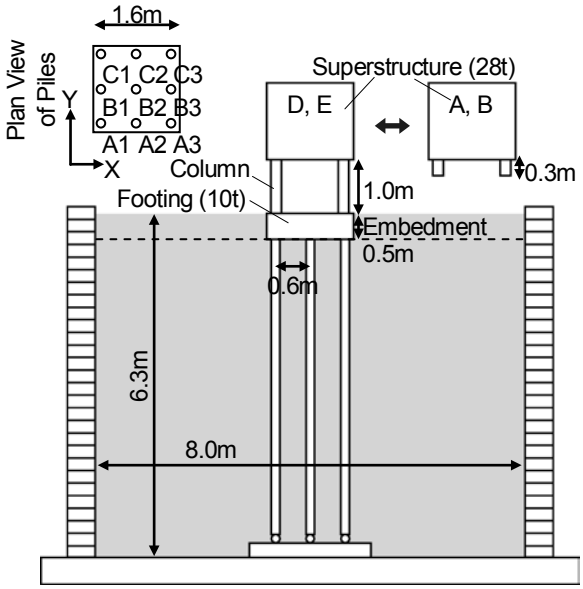


Figure 1 Soil-Pile-Structure Model

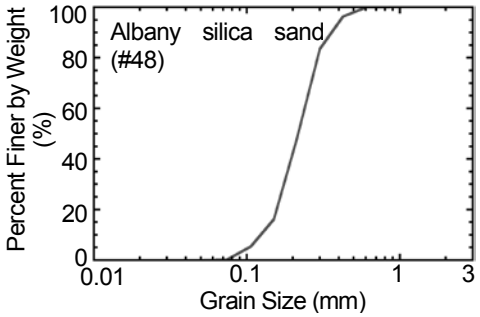


Figure 2 Grain Size Distribution of Albany Sand

pile group, as shown in Figure 1. Each pile had a diameter of 152.4 mm and a wall thickness of 2.0 mm. The piles were set up with a horizontal space of four-pile diameters center to center. Their tips were jointed to the laminar box base with pins and their heads were fixed to the footing of a weight of 10 tons.

Dry Albany sand from Australia was used for preparing the sand deposit. Figure 2 shows the grain size distribution of the sand. The sand had a mean grain size D_{50} of 0.31 mm and a coefficient of uniformity U_c of 2.0. After setting a pile group in the laminar box, the dry sand was air-pluviated and compacted at every 0.275m to a relative density of about 70% to form a uniform sand deposit with a thickness of 6.3m.

As listed in Table 1, a total of five test series named A to E was conducted in alphabetical order, in which the presence of foundation embedment and superstructure, and the natural period of superstructure, as well as the type of input motions, and their component and maximum accelerations were varied.

Table 2 shows the list of shaking conditions of test series. In order to clarify the effect of natural period of superstructure on dynamic behavior of the test model, the tests were conducted under one-, two- or three-dimensional shaking with three types of ground motions, which dominate in different period ranges, with maximum horizontal

Table 1 Test Model Series

	Embedment	Superstructure	Natural period (s)
A	Yes	Yes	0.1
B	Yes	Yes	0.6
C	Yes	No	-
D	Yes	Yes	0.2
E	No	Yes	0.2

Table 2 Shaking Conditions of Test Series

	Maximum input acceleration (m/s^2)			
	JR Takatori		Taft, Tottori	
	XYZ	XY, X, Y	XYZ	XY, X, Y
A	0.3, <u>0.8</u>		0.3, 0.8	-
B	0.3, 0.8			
C	0.3, <u>0.8</u>			
D	0.3, <u>0.8</u>		0.3, 0.8	
E	0.3, <u>0.8</u> 6.0, 8.0	0.3, 0.8	-	

accelerations adjusted to 0.3 m/s^2 and 0.8 m/s^2. Pile strains were within elastic range in all the test series. In addition, in order to investigate the pile destruction process induced by ground motion, additional tests were conducted for series E, under three-dimensional shaking with maximum accelerations at equivalent levels in actual earthquakes. JR Takatori wave was used, with maximum horizontal accelerations at 6.0 m/s^2 and 8.0 m/s^2.

Among the cases conducted with three-dimensional JR Takatori wave, this paper focuses on the ones in test series A, C, D and E with maximum acceleration adjusted to 0.8 m/s^2 (as underlined in Table 2), and reports the results of numerical analysis. None of the piles failed in any of the focused test cases.

3. ANALYTICAL MODEL

Numerical analyses were conducted with a three-dimensional FEM model using analysis code EENA3D developed by TEPCO (Yoshida et al., 2006; Yoshida et al., 2008). Figures 3 and 4 illustrate the analytical model.

The laminar shear box is modeled as solid elements with equivalent mass and adequately small stiffness. The degree of freedom is restrained, so that each ring frame of the shear box may maintain its plane during shear deformation. To take the effect of rocking behavior of the shaking table into account, vertical springs are placed at eight points at the bottom of the box. All analysis cases share the same spring constant.

Figure 4 describes details of piles and footing. Areas of the piles are set as void, and piles are connected to the soil

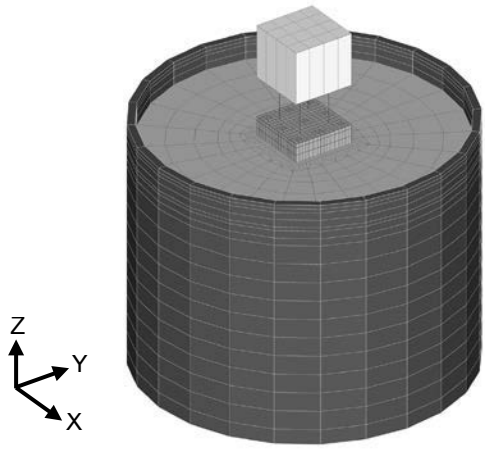


Figure 3 Overview of Analysis Model (Series E)

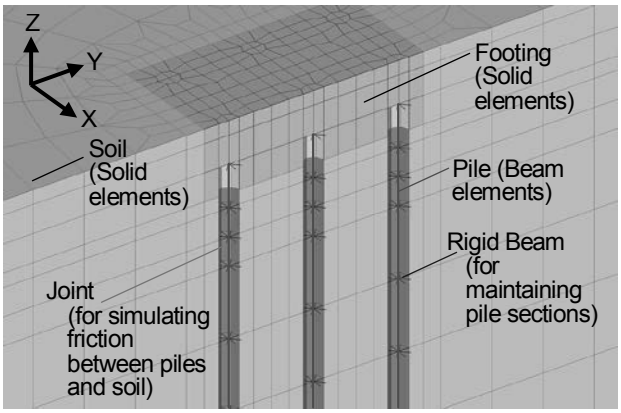


Figure 4 Details of Piles in Analysis Model

Table 3 Specification of Soil

Parameter	Value
Density ρ (t/m^3)	1.71
S wave velocity V_S (m/s)	$85.9\sigma_v'^{0.25}$
P wave velocity V_P (m/s)	$145.9\sigma_v'^{0.25}$
Poisson's ratio ν	0.23
Cohesion c (kPa)	0.0
Internal friction φ (°)	29.5

* σ_v' : Effective overburden pressure (kN/m^2)

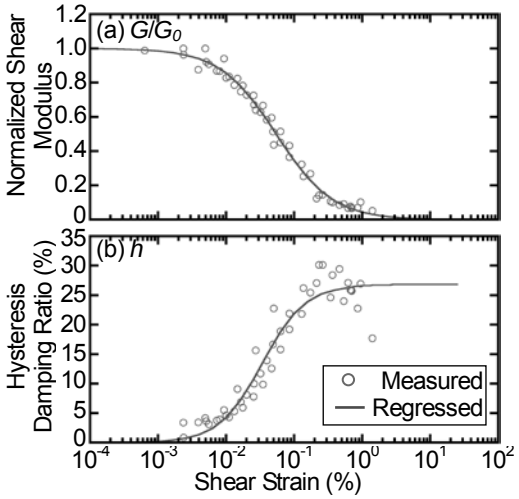


Figure 5 Dynamic Strain Dependency of Soil

with rigid beam elements, maintaining pile sections. Additionally, in order to simulate friction between the piles and the soil, joint elements are inserted between the piles and the soil. Pile head rigidity in the analysis model is 0.86.

Columns are modeled as beam elements. The rigidity of both column ends is set according to footing-superstructure transfer function obtained from the tests.

Specifications and dynamic strain dependency of the soil are explained in Table 3 and Figure 5, respectively. Velocities of P and S waves, V_P and V_S, are obtained by performing regression analysis on the results of PS logging depending on overburden pressure σ'_z. Poisson's ratio ν is calculated from V_P and V_S. As explained in Figure 6, in order not to include engineering judgments in parameter setting, discrete data of G/G_0-γ regression curve shown in Figure 5 are directly inputted to simulate soil's nonlinearity. τ-γ relation is obtained from inputted G/G_0-γdynamic strain dependency curve, also as discrete data. The discrete τ-γ relation is linearly interpolated to define skeleton curve. Cohesion c is set to zero. Internal friction angle φ is obtained from Equation 1;

$$\tau_{max} = \sigma_c \cdot \tan\varphi \tag{1}$$

where σ_c is the consolidation stress; and shear strength τ_{max} is defined by the maximum value of τ-γ skeleton curve. Obtained internal friction angle is used to define the strength of joint elements.

In addition, in this study, the nonlinear model of soil concerning its shear deformation component is defined by

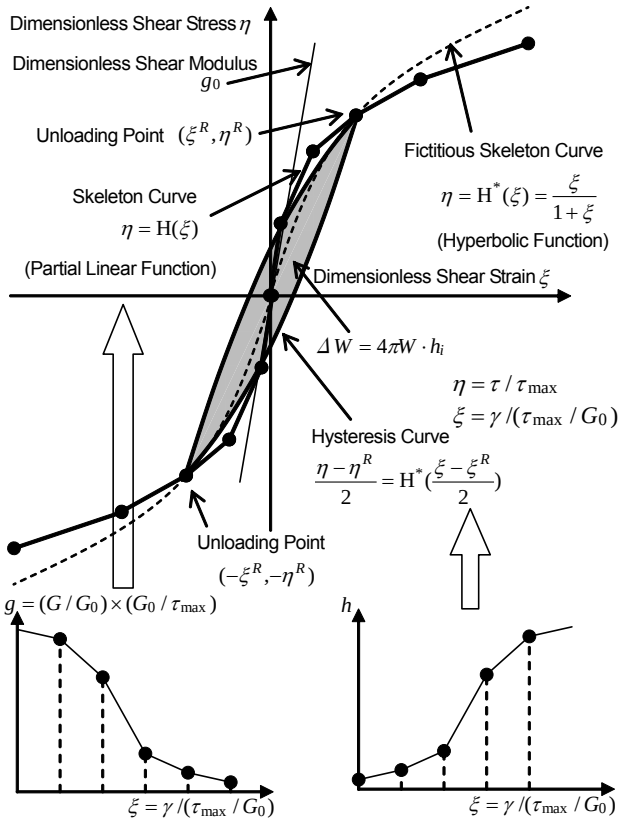


Figure 6 Modeling of Nonlinearity for Shear Strain

the second constant J_2 of deviatoric stress q, based on von Mises' failure criterion. Relation of equivalent stress $\sigma_e(=\sqrt{1/2 \times s_{ij} s_{ij}})$ and equivalent strain $e(=\sqrt{2 \times \varepsilon_{ij} \varepsilon_{ij}})$, which are expressed by root of deviatoric stress q and deviatoric strain ε_s respectively, is defined by stress-strain relation given by Equation 2.

$$\sigma_e = G \cdot e \tag{2}$$

Dynamic strain dependencies (G/G_0-γ, h-γ) are considered in Equation 2. However, since both the equivalent stress σ_e and the equivalent strain e take only positive values, it is impossible to identify whether it is pulsating or alternating. In order to draw hysteresis curve, the radius of yield surface in π plane is given as deviatoric strain e (Yoshida et al., 1993).

Input motion, as shown in Figure 7, is calculated by averaging each component of eight observed records obtained at the bottom of the shear box and the soil. All three components of the input motion are applied simultaneously to the bottom center of the box.

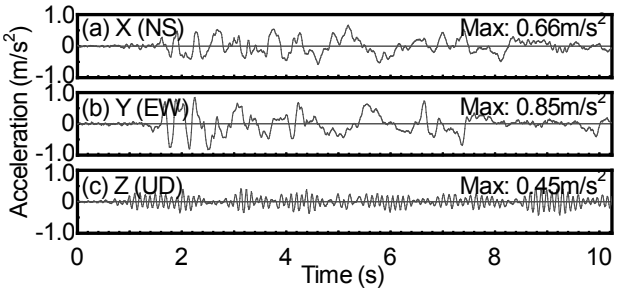


Figure 7 Input Motion (Case E)

4. NUMERICAL ANALYSIS RESULTS

Figures 8-11 show the observed and estimated time histories of accelerations of superstructure, footing and ground surface, as well as time histories of strain of corner pile A1 at pile head (-0.1m) and underground (-1.1m), in all cases. Observed records, as shown in blue lines, show that the accelerations in Y direction tend to be 1.5-2 times larger than those in X direction in all cases.

In Case A, the horizontal acceleration increases in the order of ground surface, footing and superstructure (Figures 8(a)-(c), (f)-(h)). In Case C, which has no superstructure, horizontal accelerations of ground surface and footing have no significant sign of amplification (Figure 9(b)-(c), (g)-(h)). In Cases D and E, the horizontal acceleration increases in the order of footing, ground surface and superstructure. Additionally, the horizontal acceleration of superstructure is larger in Case D, which has embedment in footing portion, rather than in case E, which has no embedment (Figures 10, 11(a)-(c), (f)-(h)). On the other hand, vertical accelerations do not show such a trend of amplification similar to horizontal ones, in any case (Figures 8-11(k)-(m)). Estimated results tend to underestimate slightly the accelerations in Y direction, and underestimate the accelerations in Z direction; however, the overall results are in fairly good agreement with the observed ones.

The bending and axial strains of the piles tend to increase along with the accelerations of upper structures, which suggests that the inertial force has a dominant effect on deforming of piles, and that the axial strains of piles are mainly caused by overturning moment coming from the inertial force (Figures 8-11(d), (e), (i), (j), (n), (o)). In Case C, the inertial force is small and the pile strains are significantly smaller than any other cases (Figure 9(d), (e), (i), (j), (n), (o)). In Cases A and E, bending strains tend to be in opposite phase at pile head and underground (Figures 8, 11(d), (e), (i), (j)), while in Case D, bending strains tend to be in the same phase at pile head and underground (Figure 10(d), (e), (i), (j)). The estimated results from the analyses tend to underestimate the bending strains in Y direction in Case A in comparison with the other cases (Figure 9(i), (j)), and tend to estimate the bending strains at pile head in Case D in the opposite signal (Figure 10(d), (i)); however, the results can reproduce the overall tendencies observed in the tests with a reasonable degree of accuracy.

To discuss the reason of underestimating the vertical accelerations, Figure 12 shows the Fourier amplitudes, calculated from the average of the records obtained at the bottom of the laminar box (Figure 9(a)) and the bottom of the soil (Figure 9(b)), in all cases. The peak value of the Fourier amplitude is significantly larger in soil, which suggests that the vertical input motion level was higher near the center of the test model. This is probably due to elastic deformation of the bottom plate of the laminar box which was caused by the vertical input motion, and such deformation had a considerable effect on the vertical response of the test model, affecting the accuracy of the analyses.

Figures 13-16 show bending strain distributions of three piles, A1, B2 and C3, at the instances when the bending strain takes its peak value at the pile head (cases A, C and E) or underground (case D) in each case. At these instances in all four cases, pile A1 is the leading pile (Figures 13-16(c)) and pile C3 is the trailing pile (Figures 13-16(a)). In Case C, observed bending strain level is low compared to other cases, due to the small inertial force, and has only one peak at pile heads (Figure 14); while in Cases A, D and E, observed bending strain level is high due to the large inertial force, and has a peak underground as well as at pile heads (Figures 13, 15, 16). Case D, compared to Case A, has a taller superstructure, and the rocking mode of the footing is more dominant, so the strain distributions have the same signal at pile heads and underground (Figure 15). Case E, compared to Case D, has no embedment at the footing portion, and the sway mode of the footing is more dominant, so similar to Case A, the strain distributions have opposite signals at pile heads and underground (Figures 13, 16). Additionally, the difference of bending strains between the three piles caused by group pile effect is hardly seen in Case C (Figure 14), while such a difference is significant in Cases A, D and E, where the peak value of bending strain is larger and the depth of inflection point is shallower in the leading

pile than in the trailing pile (Figures 13, 15, 16). Estimated results are in fairly good agreement with observed ones, able to reproduce the difference in bending strains caused by both the difference of model condition and the group pile effect. The analysis has a slightly lower level of accuracy in Case D than other cases, which suggests that the shear mode of pile deforming might have been overestimated in the analyses (Figure 15 (b), (c)).

Overall, it can be confirmed that the estimated results from all cases are able to reproduce the three-dimensional nonlinear behavior of the test models, regardless of the presence and the natural period of the superstructure or the presence of the embedment of the footing.

5. CONCLUSIONS

In order to confirm the applicability of the three-dimensional finite element method for evaluating pile foundation behavior during earthquakes, numerical simulations of four soil-pile-structure models subjected to strong shaking were performed. The tests were conducted using the large-scale shaking table at the E-Defense. It has been shown that the numerical analysis can reproduce the three-dimensional nonlinear behavior of the piles, superstructure and soil with a reasonable degree of accuracy regardless of model condition, as well as the difference in bending strains of piles caused by both the difference of model condition and the group pile effect.

Acknowledgements:

The study described herein was made possible through Special Project for Earthquake Disaster Mitigation in Urban Areas, supported by the Ministry of Education, Culture, Sports, Science and Technology (MEXT). The authors express their sincere thanks to the above organization.

References:

MEXT and NIED (2006), Research Theme No. 2 Annual Report of the fiscal year 2005, Special project for earthquake disaster mitigation in urban area, 831p (in Japanese).

H. Suzuki, K. Tokimatsu, M. Sato and K. Tabata (2008), "Stress distribution within pile group during failure process in large shaking table tests", Proc. of 39th Japan National Conference on Geotechnical Engineering, pp. 1161-1162 (in Japanese).

K. Tokimatsu, H. Suzuki, K. Tabata and M. Sato (2007), "Three-dimensional shaking table tests on soil-pile structure models using E-Defense facility," Proc. of 4th International Conference on Earthquake Geotechnical Engineering, 11 pp.

H. Yoshida, K. Tokimatsu, T. Sugiyama and T. Shiomi (2008), "Practical Three- Dimensional Effective Stress Analysis Considering Cyclic Mobility Behavior," Proc. of 14th World Conference on Earthquake Engineering, Paper_ID 04-01-0061.

H. Yoshida, T. Ishida, T. Shiomi, K. Hijikata, F. Yanagishita, T. Sugiyama, Y. Ohmiya and K. Tokimatsu et al. (2006) "Study on Practicable 3-Dimensional Effective Stress Analysis Using the Ground Survey Result", Summaries of technical papers of Annual Meeting AIJ, p623-626, B-1 (in Japanese).

N. Yoshida and S. Tsujino (1993), "A Simplified Practical Stress-Strain Model for the Multi-Dimensional Analysis under Repeated Loading Part2 Consideration of Dilatancy", Proc. of Annual Conference of the Japan Society of Civil Engineers, pp.1221-1224 (in Japanese).

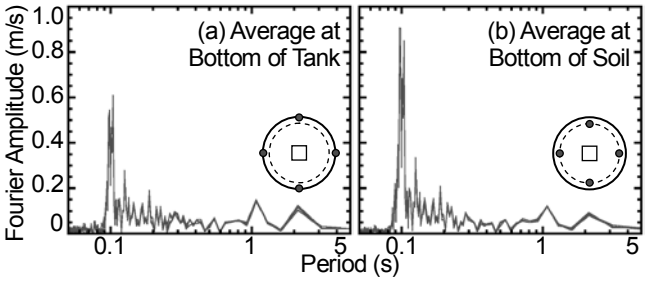


Figure 12 Amplitudes of Vertical Acc. at the Bottom

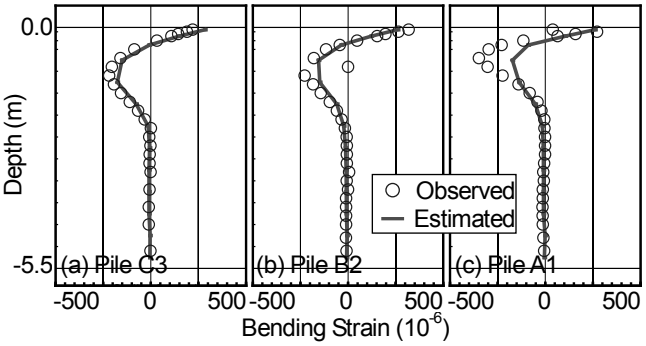


Figure 13 Distributions of Pile Bending Strain (Case A)

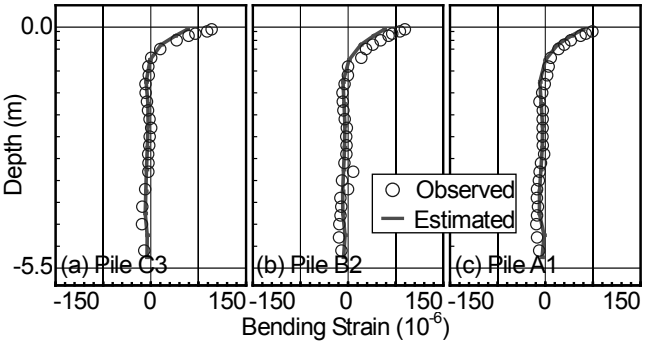


Figure 14 Distributions of Pile Bending Strain (Case C)

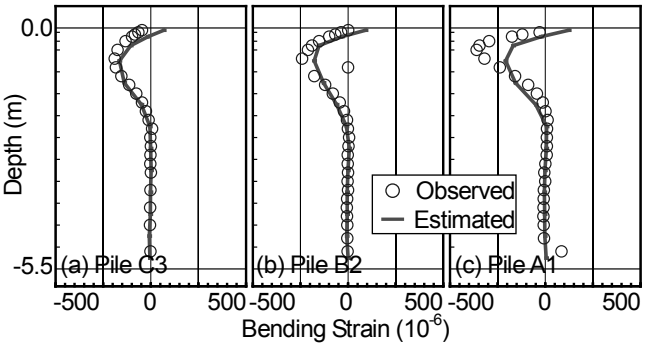


Figure 15 Distributions of Pile Bending Strain (Case D)

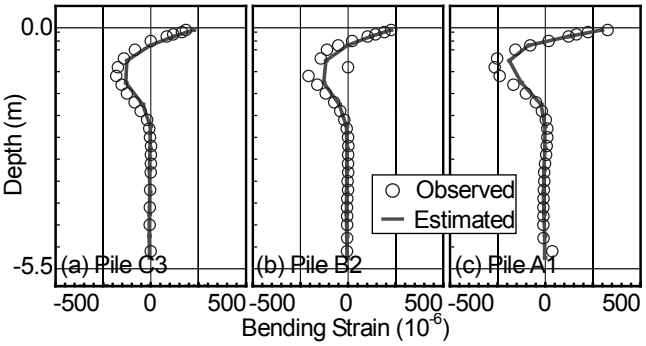


Figure 16 Distributions of Pile Bending Strain (Case E)

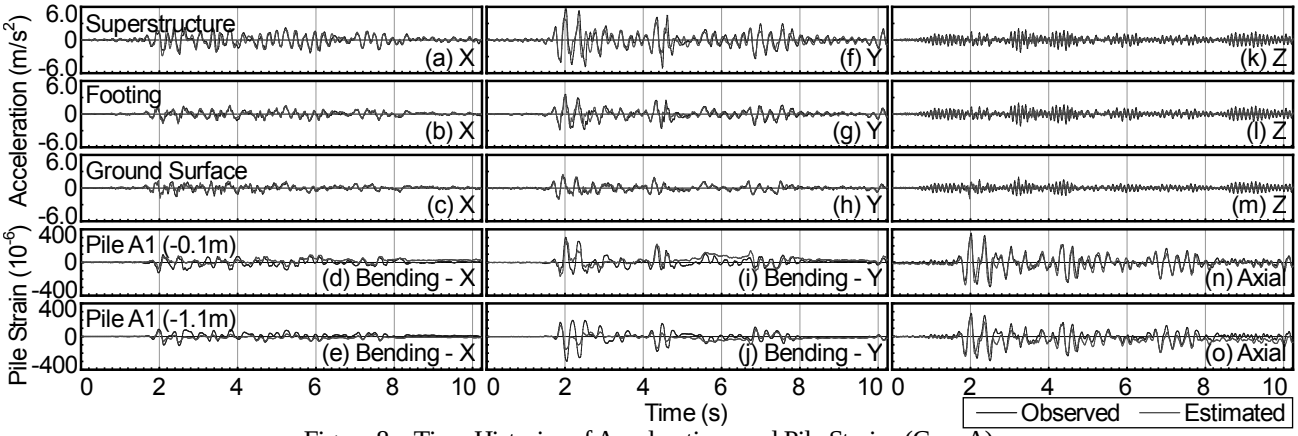


Figure 8 Time Histories of Accelerations and Pile Strains (Case A)

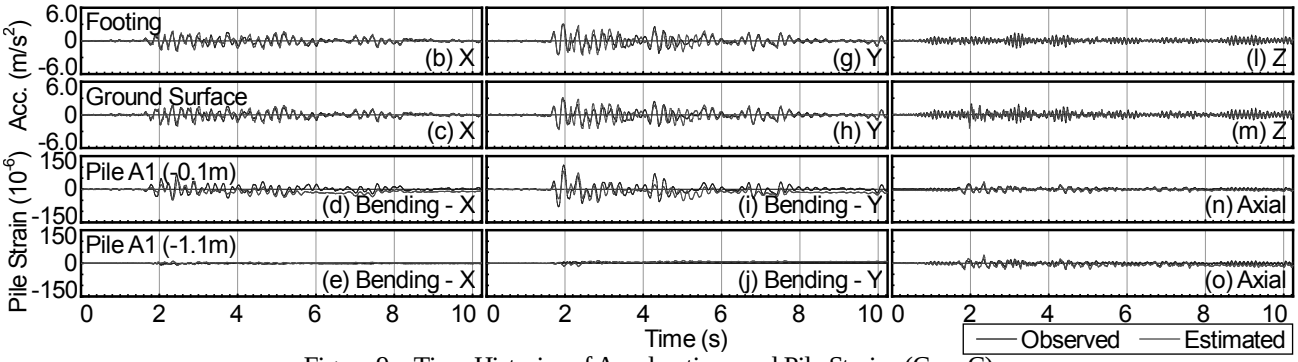


Figure 9 Time Histories of Accelerations and Pile Strains (Case C)

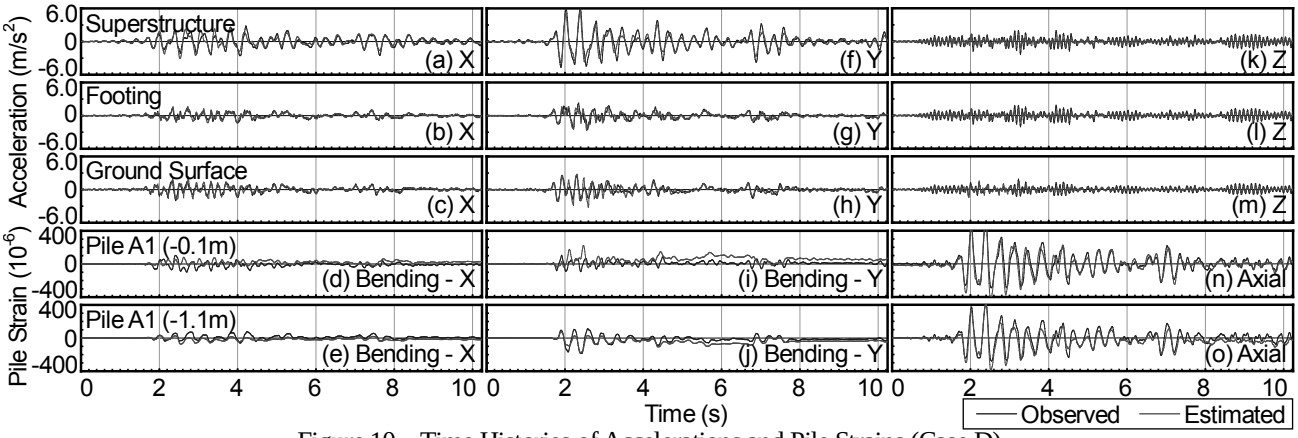


Figure 10 Time Histories of Accelerations and Pile Strains (Case D)

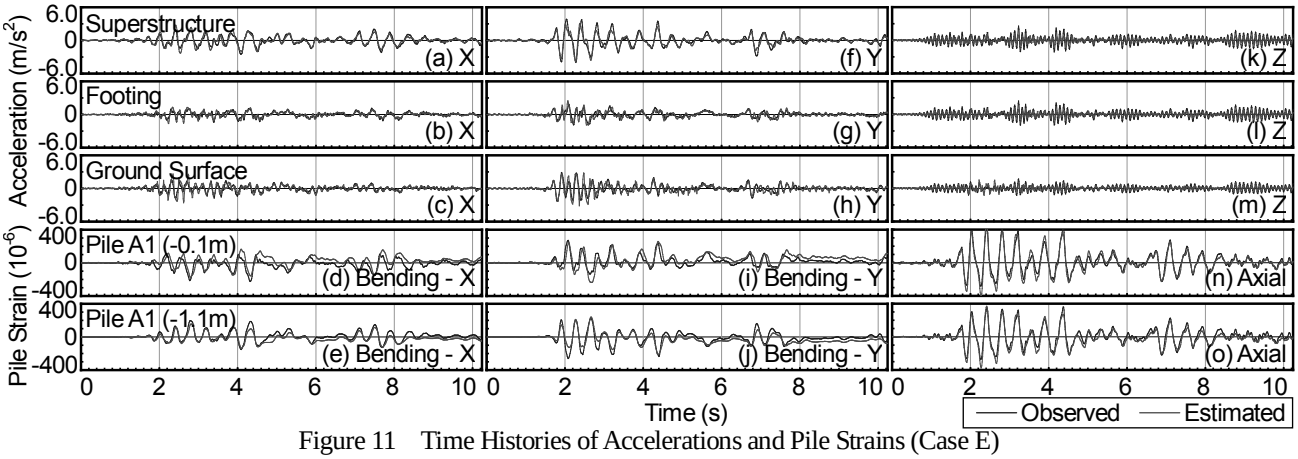


Figure 11 Time Histories of Accelerations and Pile Strains (Case E)

8CUEE CONFERENCE PROCEEDINGS
8th International Conference on Urban Earthquake Engineering
March 7-8, 2011, Tokyo Institute of Technology, Tokyo, Japan

SEISMIC ANALYSIS OF COUPLED SOIL-PILE-STRUCTURE INTERACTION USING FINITE ELEMENTS

Mahmoud N. Hussien[1)], Tetsuo Tobita[2)], and Susumu Iai[3)]

1) PhD student, Department of Civil and Earth Resources Eng., Kyoto University, Japan
2) Assistant professor, Disaster Prevention Research Institute, Kyoto University, Japan
3) Professor, Disaster Prevention Research Institute, Kyoto University, Japan
mnasser2002002@geotech.dpri.kyoto–u.ac.jp, tobita@geotech.dpri.kyoto–u.ac.jp, iai@geotech.dpri.kyoto–u.ac.jp

Abstract: The response of coupled soil-pile-structure systems to seismic loading is studied in the frequency domain using two-dimensional (2D) finite element (FE). The soil-pile interaction in 3D is idealized in 2D type using soil-pile interaction springs with hysteretic load displacement relationships. The soil stratum is meshed with quad plane elements. The length of each element is adequately defined according to the anticipated wavelength propagating in the soil. Bilinear one dimensional beam elements with three degrees of freedom per node are used for modeling the pile and the column. Comparisons of the FE results with established results from the literature suggest that the current model can reasonably capture the essential features of soil, pile, and structural responses.

1. INTRODUCTION

Estimation of the seismic response of piles and piles supporting structures, in highly seismic areas such as Japan, has received large attention in recent years. The available procedures of seismic soil-pile-structure interaction (SSPSI) estimation include those based on simplified interactions models such as the beam on dynamic Winkler Foundation approach (Kagawa and Kraft 1980; Allotey and El Naggar 2008), as well as those based on more rigorous FEM (Cai et al. 1995; Rovithis et al. 2009) or BEM (Kattis et al. 1999; Padrón et al. 2007) formulations. These methods utilize either simplified two-step methods that uncouple the structure and foundation portions (Gazetas 1984; Fan et al. 1991) or a fully coupled SSPSI system in a single step (Kaynia and Mohzooni 1996; Rovithis et al. 2009). The coupled 3D FE approach is most representative of the SSPSI system. However, such this method, even if available, have well-known limitations when used in seismic design. Several investigators attempted to propose procedures to simplify the rigorous 3D FE models. For example, Ozutsumi et al. (2003) proposed a method to idealize soil-pile interaction in 3D into the 2D type using soil-pile interaction springs. While the conventional spring elements used in the analysis of soil-pile interactions are embedded in the same plane of the 2D FE analysis domain, the soil-pile interaction spring proposed by Ozutsumi et al. (2003) is a spring that connect free pile elements to 2D meshes of a soil profile with hysteretic load displacement relationships.

The objective of the current paper is to check the capabilities of the 2D FE model, proposed by Ozutsumi et al. (2003), to the analysis of coupled SSPSI in the frequency domain. A 2D effective stress FE analysis, FLIP (Iai et al. 1992), is employed to this end. Although validation of the model is confirmed in the time domain through comparison of the FE results with recorded centrifuge data (Hussien et al. 2010), verification of the model in the frequency domain is necessary. The verification process has been executed assuming elasto-dynamic behavior of the soil and comparing the free-field, pile head, and structure responses with those found using other established approaches.

2. PROBLEM DEFINITION

The SSPSI examined in this study comprises of an end-bearing single pile supporting a single degree of freedom structure founded on a homogeneous dry sand layer of thickness (L) over rigid rock as shown in figure 1.

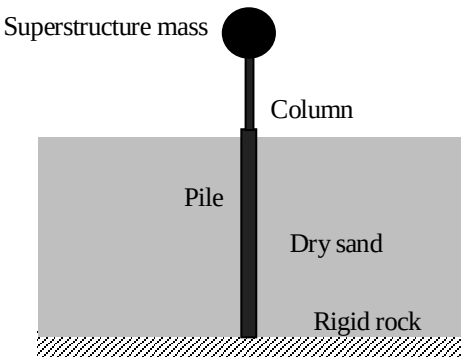


Figure 1 A schematic view of the system under investigation

3. FINITE ELEMENTS AND PARAMETERS IDENTIFICATION

The soil stratum was meshed with quad plane elements. The length of each element was adequately defined according to the anticipated wavelength propagating in the soil. The maximum element size was less than one-fifth to one-eighth the shortest wavelength to ensure accuracy.

The thickness, shear wave velocity, Poisson's ratio, mass density, and hysteretic damping ratio of the dry sand layer are, respectively:

L = 30 m; V_s = 200 m/s; υ_s = 0.4; ρ_s = 1500 kg/m^3; β_s= 5%.

The pile column system was modeled with 20 one dimensional (1D) beam elements. Each node of the pile was connected to the soil mesh with soil-pile spring element. More details on the soil-pile spring could be found in Ozutsumi et al. (2003) . The pile tip is assumed to be pinned and has a circular cross-section of diameter D_p = 1.5 m, length L_p = 30 m (equal to the thickness of the soil stratum L), the pile slendrness ratio (L_p/D_p) = 20, Young's modulus E_p = 65 GPa , Piosson's ratio υ_p = 0.3, and mass density ρ_p = 2500 kg/m^3.

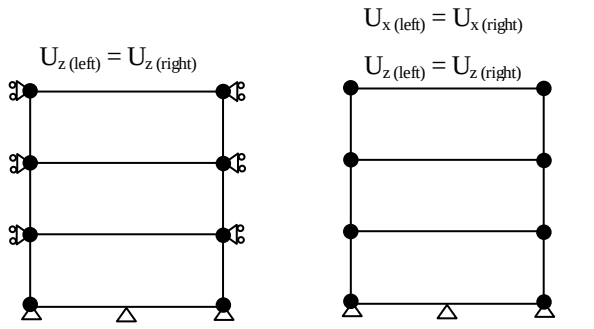
The structural mass (M) and height (H_{st}) were assumed to be equal to 100 Mg and 10 m, respectively and the ratio EI_{st}/EI_p = 0.06 , 0.66, and 1.85 leading to a fundamental frequency $f_{st,fixed}$ = 1.67, 5.0, and 8.4 Hz, respectively. The fixed-base frequency of the structure is equal to the first (f_1), second (f_2), and third (f_3) natural frequencies of the soil layer, respectively.

The wave parameter σ (Veletsos et al. 1974):

$$\sigma = \frac{V_s}{f_{st.fixed}.H_{st}} \qquad (1)$$

which is may be looked upon as a measure of the relative stiffness of the soil and the structure. When V_s and H_{st} are selected to be constants and equal to 200 m/s^2 and 10 m, respectively, σ is inversely proportional to $f_{st.fixed}$. $1/\sigma$ is equal to 0.083, 0.25, and 0.42 corresponding to $f_{st,fixed}$ = 1.67, 5.0, and 8.4 Hz, respectively.

The FE analyses were performed in two steps. In the first step (self-weight analysis), the *in situ* stresses were initialized in the soil due to the own weight of the soil. Properties of pile, pile-soil interaction spring, and structure were set to be zero during this stage of analysis. During the second stage of analysis (seismic response analysis), the actual properties of soil, pile, pile-soil spring, and structure were assigned. Two different boundary conditions were assigned to the model in the two stages of analysis. For the first stage, all nodes on the lateral boundaries are restrained from moving in horizontal direction while vertical displacements of the nodes having the same height were assigned same displacement as shown in Fig. 2(a). For the second stage, not only vertical displacements of nodes having the same height were set to be equal but horizontal displacements were set also as shown in Fig. 2(b) to prevent spurious wave reflections at the boundaries.



(a) Self-weight analysis (b) Seismic response analysis

Figure 2 Boundary condition of the problem model

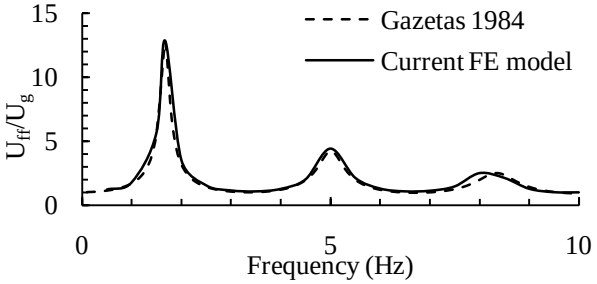


Figure 3 Verification of the free-field amplification

The input motion is specified at bedrock level in the form of a harmonic horizontal displacement $U_g(t) = U_g.\exp(i2\pi ft)$, where U_g = amplitude of the input bedrock displacement; f = frequency of excitation; $i^2 = -1$.

4. FREE FIELD MOTION

Elastic response time histories for free-field are derived at different frequencies of excitations. From these time histories, the amplitude of steady-state response is noted and normalized with respect to the amplitude of input bedrock motion. In figure 3, amplification of the soil stratum obtained using the present 2D FE method is compared with that obtained using a simple 1D free-field analysis (in the frequency domain, Gazetas 1984) at different frequencies of excitation. Amplification for 1D analysis is given by:

$$\frac{U_{ff}}{U_g} = \frac{1}{\cos(qL)} \quad \text{where} \quad q = \frac{2\pi f}{V_s\sqrt{(1+2i\beta_s)}} \qquad (2)$$

where U_{ff} = amplitude of free-field ground displacement. The comparison shows that there is an excellent agreement between the current FE method and free-field analysis conducted by Gazetas 1984 for all frequencies range covered in figure 3.

5. KINEMATIC SOIL-PILE ANALYSIS

A seismic S-wave propagating vertically in a soil layer without any foundation causes only horizontal displacements in the free-field soil. A cylindrical pile tends

to diffract the incident seisnic waves, modifying the free-field soil motion, so that the horizontal displacement of the pile head, U_p, will be different from the free-field surface motion U_{ff}, and a rotation ϕ_p of the pile head will take place. This type of interaction between piles and soils is called kinematic interaction. This kinematic effect is usually asessed in terms of the kinematic interaction factors I_u and I_ϕ, which are defined, respectively, as the maximum translation and rotation of the pile head normalized by the corresponding maximum displacement of the free field soil surface as:

$$I_u = \frac{U_p}{U_{ff}} \quad \text{and} \quad I_\phi = \frac{\phi_p \cdot D_p}{U_{ff}} \tag{3}$$

The kinematic interaction factors obtained by this study were compared to established results from the literature (Fan and Gazetas 1991, Rovithis et al. 2009). The kinematic response of the soil-pile system was examined for the typical pile proprties ($L_p/D_p = 20$, $E_p/E_s = 1000$). Both fixed and free conditions at pile head were considered.

In the particular case of a fixed-head pile, the analytical solution for I_u is given by the expression (Makris and Gazetas 1992):

$$I_u = \Gamma = \frac{k + iwc}{E_p I_p (q^4 + 4\lambda^4)} \tag{4}$$

which was obtained through a properly calibarated dynamic Winkler model. The corresponding kinematic interaction factores for a free head pile are (Nikolaou et al. 2001):

$$I_u = \Gamma\left[1 + \frac{1}{2}\left(\frac{q}{\lambda}\right)^2\right] \tag{5}$$

$$I_\phi = \Gamma \frac{q^2 D_p}{\lambda} \tag{6}$$

in the above equations, (k+iwc) denotes the so-called dynamic impedance of the Winkler bed, with w being the cyclic vibrational frequency and *i* the imaginary unity; $q = w/V_s$ is the wave number of the harmonic SH waves in the soil; λ is the well-known Winkler wave number:

$$\lambda = \left\{\frac{k + iwc - mw^2}{4E_p I_p}\right\}^{\frac{1}{4}} \tag{7}$$

Based on the comparative results shown in figure 4, it is established that the adopted FE model captures well the variation of kinematic pile response in wide range of frequency.

6. KINEMATIC PILE BENDING MOMENT

As well known in linear analysis, all computed stress and strain quantities are proportional to the excitation intensity, expressed by the the amplitude of the bedrock acceleration $\ddot{U}_g = w^2 U_g$. The pile bending moments were normalized to the amplitude of bedrock acceleration (Kavvadas and Gazetas 1993, Rovithis et al. 2009)

$$M_{nor} = \frac{M}{\rho_p D_p^4 \ddot{U}_g} \tag{8}$$

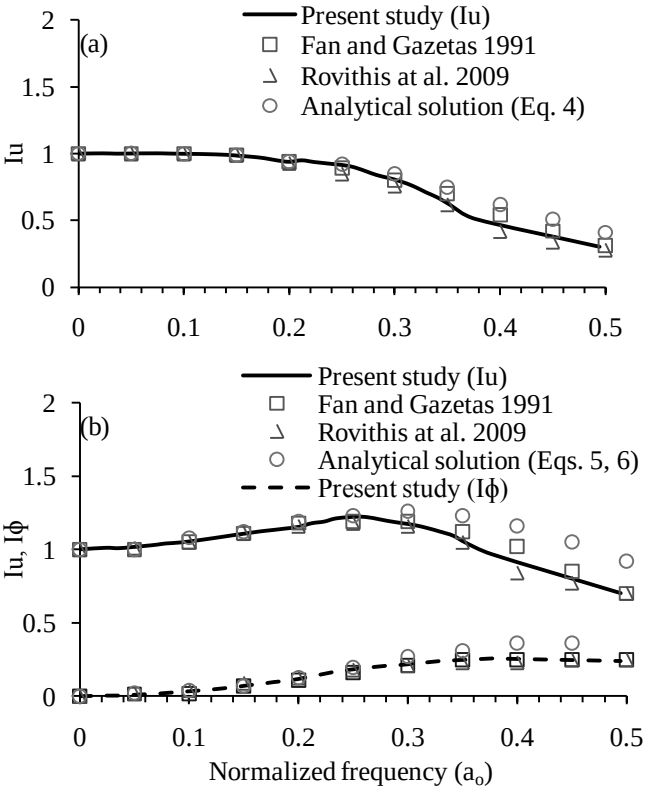


Figure 4 Kinematic soil-pile interaction for : (a) fixed head and (b) free head conditions

Figure 5 presents the distribution of amplitudes of normalized steady state bending moments for the free and fixed pile head conditions at the first two fundamental frequencies of the soil deposit f_1 and f_2 calculated using the present FE method compared to those obtained by Rovithis et al. 2009 (3D FE analysis) with the same soil and pile condtions. Figure 5 implies that the current FE analysis reasonably reproduced normalized pile bending moment agree well previous established ones by Rovithis et al. 2009 for different fundamental frequencies of the soil.

7. DYNAMIC CHARACTERISTICS OF THE SOIL-PILE-STRUCTURE SYSTEM

In this step, a concentrated mass attached to the structural column is introduced to the model. The verification process in this stage focuses on evaluating the effective natural (f_{SSI}). The effective natural frequency (f_{SSI}) of the coupled system is defined, according to Rovithis et al. 2009, as the frequency at which the ratio (U_s/U_{ff}) is maximized, where U_s is the structure mass displacement. Verification was performed by comparing the effective

period of the system (T_{SSI}) calculated using the current FE model at different values of parameter 1/σ with the available analytical solutions as well as 3D FE analysis by Rovithis et al. 2009. The available analytical procedures includes:

- Solution by Veletsos and Meek (1974):

$$T_{SSI} = T_{st,\,fixed}\sqrt{1+\frac{k_{st}}{K_x}\left(1+\frac{K_x H_{st}^2}{K_\theta}\right)} \qquad (9)$$

where $T_{st,\,fixed}$ and K_{st} represent the fixed-base natural period and stiffness of the structure. K_x and K_θ denote the frequency-dependent stiffness in translational and rocking oscillations, respectively.

- Rigorous analytical solution by Maravas et al. (2007):

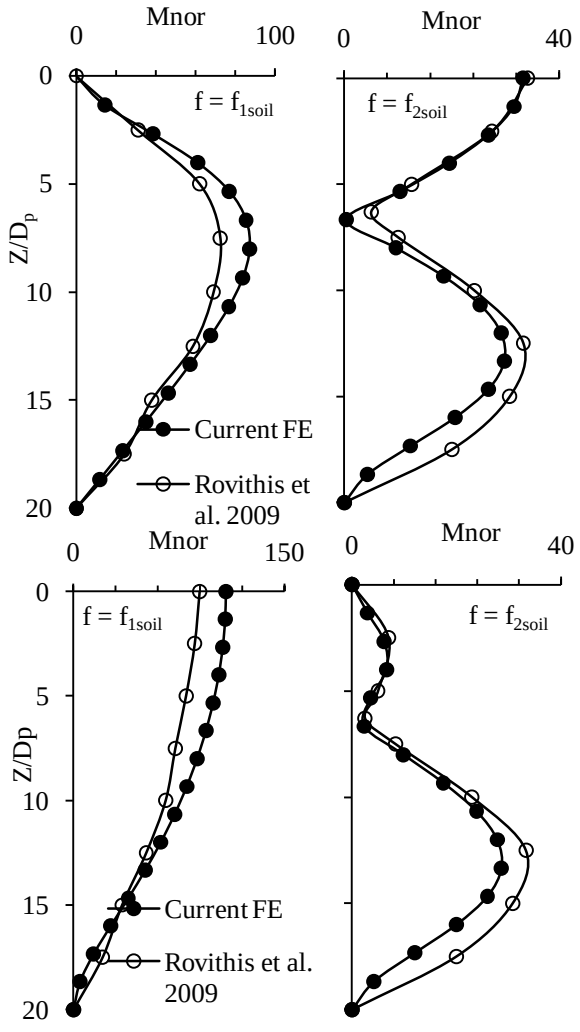


Figure 5 Normalized steady state bending moments at the first two fundamental frequencies of the soil deposits: (a) free head pile; (b) fixed head pile

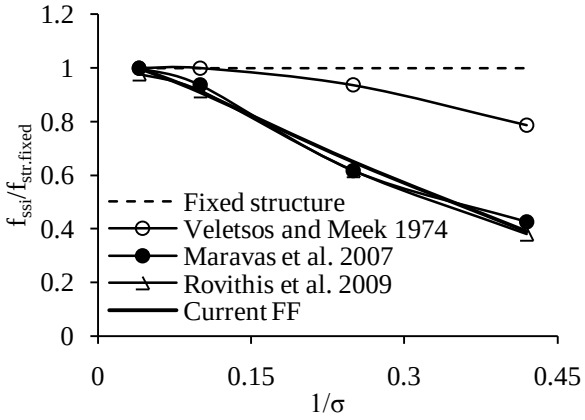


Figure 6 Ratio of the effective natural frequency of the system to the structural fixed-base frequency against parameter 1/σ

$$T_{SSI} = T_{st,\,fixed}\sqrt{\frac{k_{str}}{k_x}\left(\frac{1+4\zeta^2}{1+4\zeta_x^2}\right)+\frac{k_{str}H_{str}^2}{k_\theta}\left(\frac{1+4\zeta^2}{1+4\zeta_\theta^2}\right)+\left(\frac{1+4\zeta^2}{1+4\zeta_{str}^2}\right)} \qquad (10)$$

where ζ_{str} and ζ represent the damping ratio of the fixed-base and flexibly supported structure, respectively, andζ_x, ζ_θ the damping ratios in swaying and rocking of the foundation.

Comparison of the current FE model results against the aforementioned equations as well as results obtained by Rovithis et al. 2009 is illustrated in figure 6, where the ratio of the effective natural frequency of the system to the natural frequency of the fixed-base structure ($f_{SSI}/F_{str.fixed}$) is plotted against the flexibility parameter (1/σ). The very good agreement between the numerical results and both the rigorous analytical solution of Maravas et al. (2007) and the 3D analysis of Rovithis et al. 2009 is evident, confirming the accuracy of the FE model.

8. CONCLUSIONS

In this paper, applicability of the simplified FE model, proposed by Ozutsumi et al. (2003), to the analysis of SSPSI in the frequency domain is examined. The verification process has been executed assuming elasto-dynamic behavior of the soil and comparing the results obtained using the simplified FE model with those found using other established results from the literature. Based on the comparative results in the paper, it is established that It has been shown that this procedure can be used successfully for a provision of the response of a single pile to inertial loading caused by the lateral forces imposed on the over structure and kinematic loading caused by the soil developed during an earthquake.

Acknowledgements:
The first author would like to acknowledge the financial support by Egyptian government.

References:

Kagawa, T. and Kraft, L. (1980), "Seismic P-Y responses of

flexible piles," *Journal of Geotechnical Engineering*, ASCE, 106(8), 899-918.

Allotey, N. and El Naggar, M.H. (2008), "Generalized dynamic Winkler model for nonlinear soil-structure interaction analysis," *Canadian Geotechnical Journal*, 45(4), 560-573.

Cai, Y., Gould, P., Desai, C. (1995), "Numerical implementation of a 3-D nonlinear seismic S-P-S-I methodology, in Seismic Analysis and Design for Soil-Pile-Structure Interactions, *Geotechnical Special Publication*, 70, ASCE, 96-110.

Rovithis, E.N., Pitilakis, K.D., Mylonakis, G.E. (2009), "Seismic analysis of coupled soil-pile-structure systems leading to the definition of a pseudo-natural SSI frequency," *Soil Dynamics and Earthquake Engineering*, 29(6), 1005-1015.

Kattis, S.E., Polyzos, D., Beskos, D.E. (1999), "Vibration isolation by a row of piles using a 3-D frequency domain BEM," *International Journal for Numerical Methods in Engineering*, 64, 713-728.

Padrón, J.A., Aznárez, J.J., Maeso, O. (2007), "BEM–FEM coupling model for the dynamic analysis of piles and pile groups," *Engineering Analysis with Boundary Elements*, 31(6), 473-484.

Gazetas, G. (1984), "Seismic response of end bearing single piles," Soil Dynamics and Earthquake Engineering, 3(2), 82–93.

Fan, K., Gazetas, G., Kaynia, A., Kausel, E., Ahmad, S. (1991), "Kinematic seismic response of single piles and pile groups," *Journal of Geotechnical Engineering*, 117(12), 557–74.

Kaynia, A. M. and Mahzooni, S. (1996), "Forces in pile foundations under seismic loading," *Journal of Engineering Mechanics*, 122(1), 46–53, 1996.

Ozutsumi, O., Tamari, Y., Oka, Y., Ichii, K., Iai, S., Umeki, Y. (2003) "Modeling of soil–pile interaction subjected to soil liquefaction in plane strain analysis," *Proc. of the 38th Japan National Conference on Geotechnical Engineering*, Akita,1899–1900.

Iai, S., Matsunaga, Y., Kameoka, T. (1992), "Strain space plasticity model for cyclic mobility," *Soils and Foundations*, 32(2), 1–15, 1992.

Hussien, M. N., Tobita, T., Iai, S. (2010), "Nonlinear seismic finite element analysis of soil-pile-superstructure interaction," Journal of Applied Mechanics, JSCE, Volume 13, 601-609.

8CUEE CONFERENCE PROCEEDINGS
8th International Conference on Urban Earthquake Engineering
March 7-8, 2011, Tokyo Institute of Technology, Tokyo, Japan

THE EFFECT OF LOADING RATE ON BEARING CAPACITY OF PILE FOUNDATIONS

Koji Watanabe[1] and Osamu Kusakabe[2]

1) Researcher, Geotechnical Engineering Department, Technical Research Institute, Obayashi Corporation, Japan
2) Professor, Dept. of Civil Engineering, Tokyo Institute of Technology, Japan
watanabe.koji.ro@obayashi.co.jp, kusakabe@cv.titech.ac.jp

Abstract: The bearing capacity of pile has been evaluated based on static vertical loading test. However, external forces acting on pile are not only static loads but also dynamic loads such as earthquake loads. In cases of large earthquake, dynamic loads dominate the design considerations. Although loading rate dependency on soil behavior and bearing capacity of pile has been known, there exist little studies and quantitative evaluation methods on bearing capacity of pile considering loading rate have not been proposed yet. The purpose of this study is to investigate the effects of loading rate on sand behavior and bearing capacity of pile for seismic design of pile. The issue to be investigated in this study is the effect of loading rate on sand behavior and bearing capacity of pile. Triaxial compression tests and model loading tests under a centrifuge acceleration field varying loading rate were conducted. The paper summarizes the results of triaxial compression tests and model loading tests.

1. INTRODUCTION

The bearing capacity of pile has been evaluated based on static vertical loading test. However, external forces acting on pile are not only static loads but also dynamic loads like earthquake loads. In cases of large earthquake, dynamic loads dominate the design considerations. Although loading rate dependency on soil behavior and bearing capacity of pile has been known, there exist little studies and quantitative evaluation methods on bearing capacity of pile considering loading rate have not been proposed yet.

Figure 1 illustrates the effects of loading rate on soil behavior, indicating that both soil strength and deformation modulus increase as loading rate increases. Pile loading test such as static loading test is generally used to examine the bearing capacity of piles and soil testing methods such as unconfirmed and triaxial compression tests are used to obtain the soil strength and deformation characteristics. Figure 2 shows typical ranges of loading rate for different loading methods as well as possible maximum vertical velocity during earthquake. The range of maximum velocity during earthquake is almost several kine-several tens kine from observed velocity in the vertical direction as shown in Table 1. Assuming the rocking motion of superstructure during earthquake, the maximum velocity that may occur during rocking motion was calculated as in the order of 20kine. Compared to the possible maximum vertical velocities during earthquake with the loading rates of soil test and investigation method for pile, there is a considerable difference of loading rate. This fact implies that it is necessary to examine the bearing capacity with soil parameters considering loading rate.

From these backgrounds, the purpose of this study is to investigate the effects of loading rate on soil behavior as well as bearing capacity of pile for seismic design of pile.

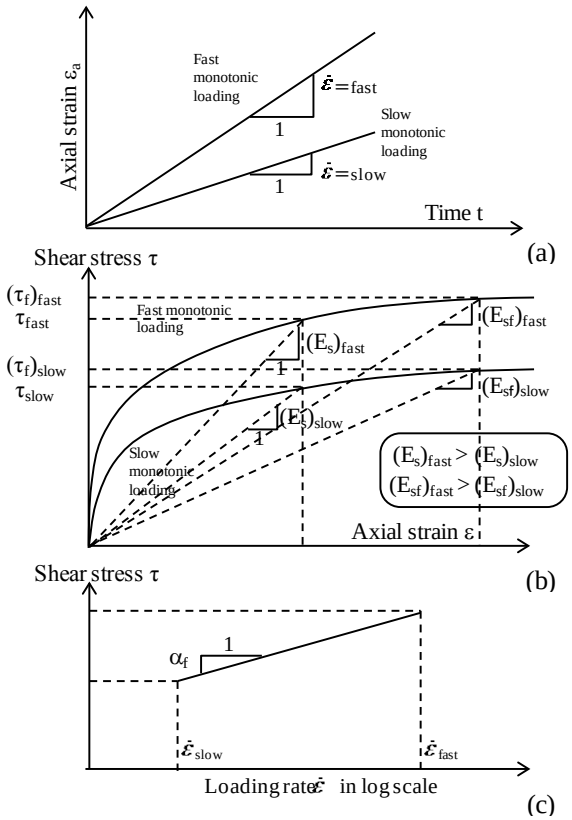


Figure 1 General trend observed in compression test: (a) Axial strain vs. time, (b) Shear stress vs. axial strain, (c) Shear stress vs. loading rate

This paper firstly reviews the effects of loading rate on soil behavior and bearing capacity of foundations, secondly describes the triaxial compression tests with varying loading rate to examine the effect of loading rate on sand behavior, and finally discusses the model loading tests with varying loading rate to confirm the effect of loading rate on bearing capacity of pile.

2. REVIEW OF PREVIOUS STUDY

2.1 Soil Strength and Deformation Characteristics

There are a number of studies using triaxial compression tests. The paper by Casagrande and Shannon (1948) provided the data of strength increase obtained from vacuum triaxial tests on a dry dense sand specimen under a vacuum pressure of 29kPa, showing about 10% increase over the loading rate from 0.00063kine to 63kine with a considerable scatter of maximum principal ratio at failure for higher loading rates. Seed and Lundgren (1954) conducted drained and undrained triaxial compression tests on saturated sand at confining pressures (196kPa) with three loading rates; static tests, slow transient tests and rapid transient tests, of which the time to reach maximum load was 10-15 min (approximately corresponds to 0.002kine), approximately 4 sec (0.375kine) and 0.02 sec(75kine), respectively. They concluded that the strength of dense saturated sand under transient loading conditions is greater than that for normal rates of loading due to (1) the effects of dilatancy combined with lack of drainage and (2) the effects of the rate of deformation.

Pore pressure measurements were made by Whitman and Hearly (1962) who performed undrained traixial tests on saturated sands under a confining pressure of 98kPa and showed the data of pore water pressure change during compression tests. The stress-strain curves for dense saturated sand for two different loading rates (0.003kine and 300kine) showed that in both cases the negative pore water generates with shearing, associated with a sharp increase in deviator stress and no significant effect is observed with respect to loading rate.

Lee et al. (1969) pointed out the significance of confining pressure on the effect of loading rate by performing drained (dry sand) and undrained tests on dense and loose sands at three different confining pressures (98, 588 and 1470kPa) with strain rates varying from 0.00003kine to 25kine. They observed the noticeable greater transient increase of about 20% for dense sands at high confining pressures.

2.2 Loading Rate Effects on Bearing Capacity

Model tests on footings or piles have been also used for the study of the effects of loading rate on bearing capacity of foundations. Vesic et al. (1965) mentioned that their earlier model loading tests performed a series of vertical loading tests for a circular footing on dry or submerged sand using a wide range of loading rates from 0.0002kine to 2kine. The relative density of the model ground is from 75% to 81%. Their results of ultimate bearing capacity with loading rate

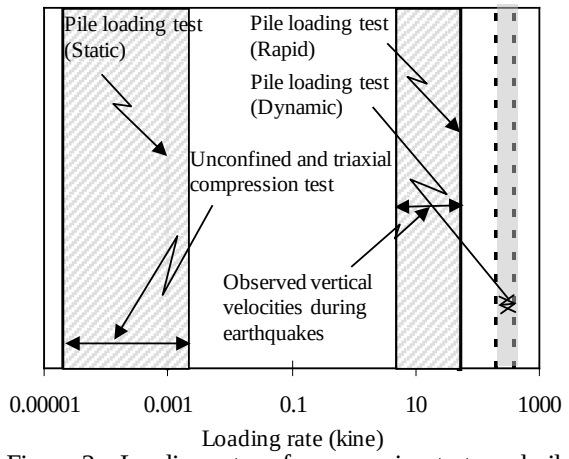


Figure 2 Loading rates of compression tests and pile loading tests

Table 1 Maximum velocities observed in recent earthquakes

Year	Earthquake	Observation point	Maximum velocity (kine)	
			Vertical	Horizontal
1979	Hyogo-ken Nanbu	Kobe marine observatory	51	110
1995	Hyogo-ken Nanbu	JR Takatori	40	90
2004	Niigata Chuetsu	Ojiya	31	98

indicates that the bearing capacity first decreases as loading rate increases up to the loading rate of 0.04kine, but for more rapid loading rate there is a steady increase of bearing capacity. Senanayake (1973) conducted loading tests on shallow circular and square footings on dry dense sand and obtained a steadily increasing trend of bearing capacity with increasing loading rate without any drop. The loading rates are in the ranger of 0.00005kine – 50kine. Konagai et al. (1994) performed model loading tests of a circular surface footing on submerged sand at three different speeds: 0.0017, 0.017, and 0.17kine. Although the trend of variation of bearing capacity seem not conclusive, they stated that their experiments qualitatively confirmed the variation of bearing capacity with loading velocity observed by Vesic et al.

Huy et al. (2005) carried out pile loading tests in unsaturated sand in a calibration chamber, using a CPT cone as a model pile. Model ground was prepared by the cycle of fluidization, vibration and drainage. The loading tests consist of four stages: constant rate test of 2kine, constant rate test of 0.1kine, dynamic test with 25kine and static constant rate test of 0.1kine. The dynamic tests showed an increase in base resistance of 4% and an increase of local shaft resistance of 6%, compared with those of the static test.

Centrifuge cone penetration tests in sand at five European centrifuge centers reported by Bolton et al. (1999) confirmed that small, and generally negligible, effects were observed in dry sand by increasing the penetration rate from 0.25 kine to 2kine. Takemura and Kouda (2000) gathered the similar centrifuge data of cone testing with the penetration rate of 0.017kine to 0.27kine and stated that no apparent difference was observed within this range.

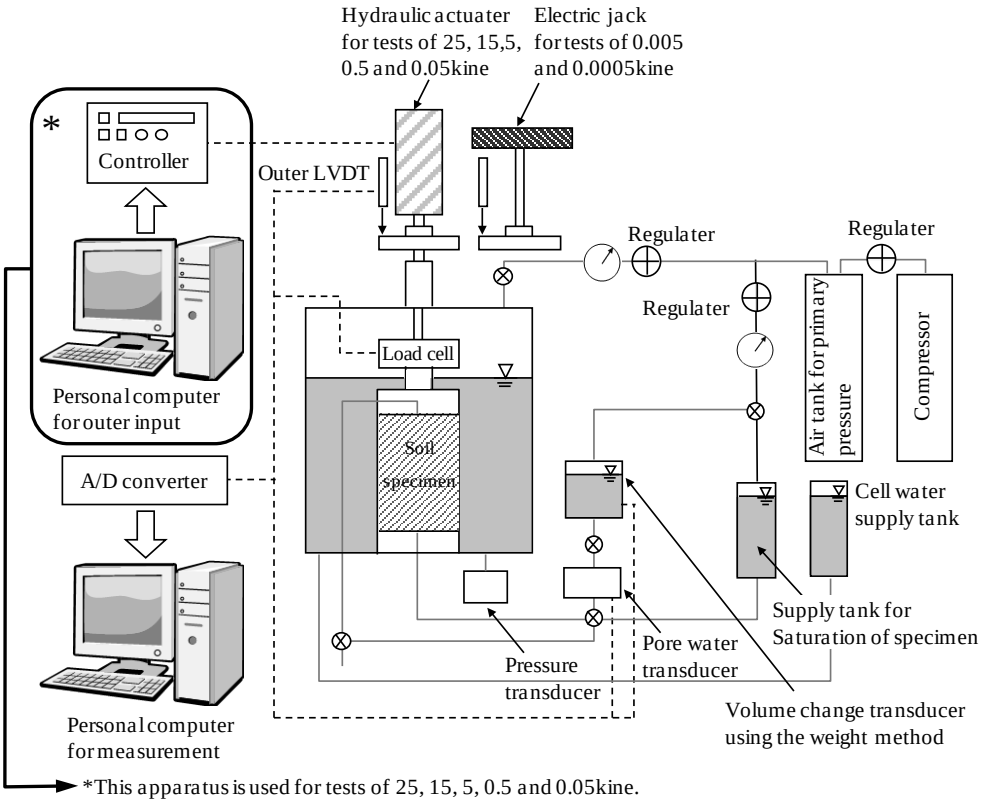


Figure 3 Basic components of triaxial apparatus

3. TRIAXIAL COMPRESSION TESTS

3.1 Test Apparatus, Soils Tested and Test Program

Two different loading systems as shown in Fig. 3 were used in this study to control the loading rate accurately as possible; an electric gear triaxial apparatus for slower loading rate tests and a hydraulic triaxial apparatus for higher loading rate tests. The entire system is closed-loop-controlled by a microcomputer utilizing an analogue-to-digital converter and a stepping motor controller operated by a custom made control program. Load is measured by a load cell, displacement by an LVDT, and cell and pore pressures by pressure transducers mounted on the bottom of the triaxial cell. Drainage is allowed at the top and bottom surfaces of a sand specimen and the pore water pressure measurements are made at the bottom of the specimen. All signals from the instrumentation are conditioned through amplifiers and active filters before entering the microcomputer.

Differential pressure transducers are commonly used for volumetric strain measurement in drained tests with normal loading rates. A newly made volumetric change transducer was used in this study to improve the accuracy of volumetric strain measurement, in particular for higher loading rates. The volumetric change transducer measures the weight of the pore water drained from the specimen,.

The soil used for all tests in this study was Toyoura sand and the material properties are shown in Table 2.

Five series of the tests were performed. Series 1 to 4 used saturated sand specimen and Series 5 dry sand specimen. Specimens with the target relative density of 80% were prepared by air-pluviation method. The coefficient of permeability of the specimen of 80% relative density measured by constant head tests was in the range of 1.0×10^{-2} to 2.0×10^{-2} (cm/sec).

Table 2 Material Properties of Toyoura sand

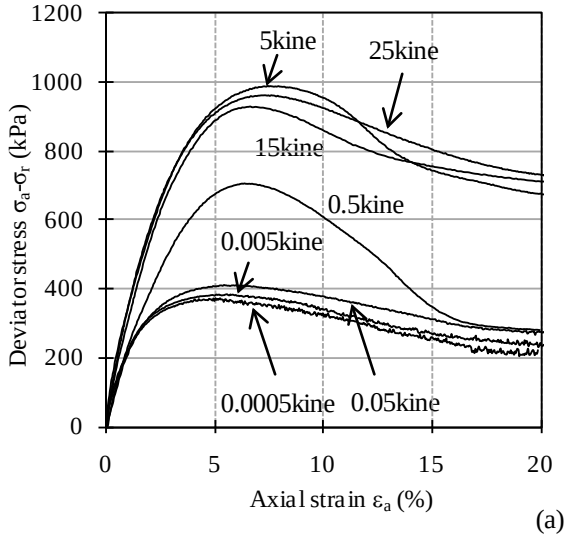
Specific gravity of soil particle: Gs	2.645
Mean grain size: D_{50} (mm)	0.19
30% diameter on the grain size diagram: D_{30}(mm)	0.16
Effective grain size: D_{10} (mm)	0.14
Uniformity coefficient: Uc	1.56
Coefficient of curvature: Uc'	0.95
Maximum void ratio: e_{max}	0.99
Minimum void ratio: e_{min}	0.62

Table 3 Test program

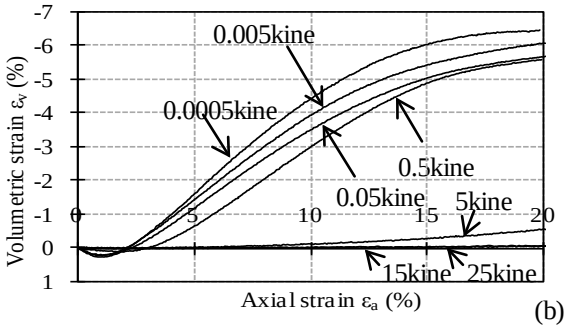
Series	Saturated or dry	Drained condition	Confining pressure (kPa)	Loading rate (kine)	Target relative density (%)
1	Saturated	Drained	100	0.0005,0.005 0.05,5 15,25	80
2			500		
3		Undrained	100		
4			500		
5	Dry	Drained	100		

The specimens were saturated using the CO_2 method for the specimens of Series 1 to 4 and a back pressure of 98kPa was then applied. The B-value was checked for each specimen at a low confining pressure before the test commenced. A minimum value of B=0.95 was obtained to ensure the full saturation of the specimen.

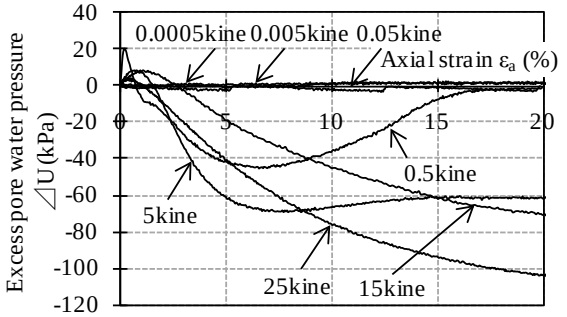
The test program is shown in Table 3. All the tests were



(a)



(b)



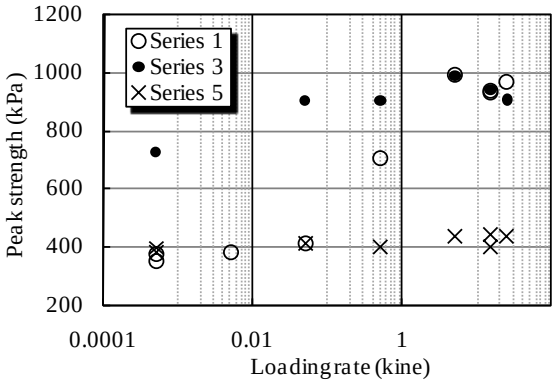
(c)

Figure 4 Results of Series 1:
(a) Deviator stress vs. axial strain
(b) Volumetric strain vs. axial strain
(c) Excess pore water pressure vs. axial strain

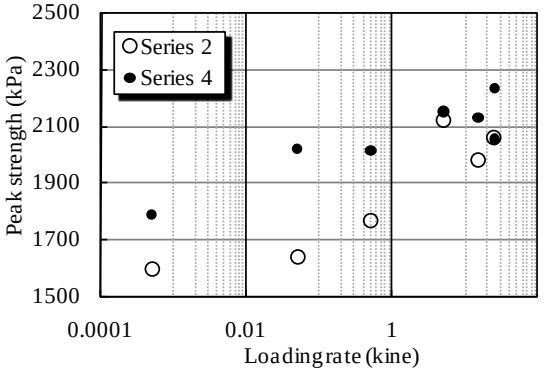
conducted to drained and undrained conditions under the confining pressures of 100 and 500kPa. 'Drained' means here that the valve of drainage line is kept open during the test, which does not ensure that there is no excess pore water pressure within the entire specimen. It may be appropriate therefore to call 'partially drained'.

3.2 Test Results

Figures 4(a), (b) and (c) show the results of Series 1 of partially drained test on saturated sand; deviator stress, volumetric strain and excess pore water pressure vs. axial strain, respectively. Figure 4(a) confirms the findings; sand exhibits stiffer response and higher shear strength when the sand sample is subjected to faster loading rate, and the peak



(a)



(b)

Figure 5 Relationships between maximum deviator stress and loading rate:(a) Series 1, 3 and 5, (b) Series 2 and 4

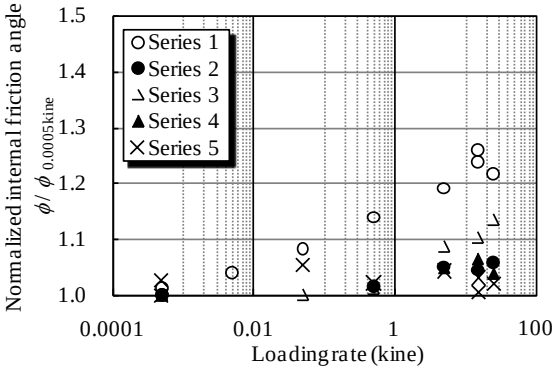


Figure 6 Relationships between normalized internal friction angle at peak stress ratio and loading rate

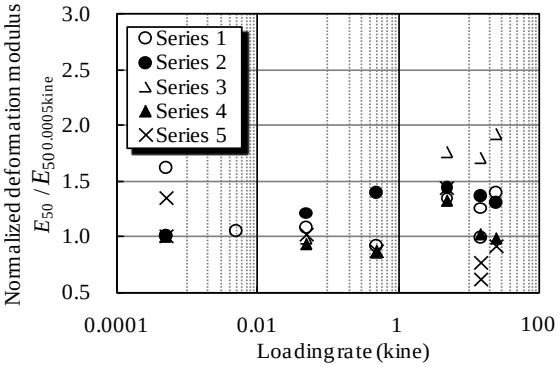


Figure 7 Relationships between normalized deformation modulus and loading rate

strength defined at the deviator stress maximum increases when the loading rate increases. Deviator stress vs. axial

strain relationships in Fig. 4(a) can be classified into two groups; one is the curves of 5kine to 25kine, the other is 0.0005kine to 0.05kine. The curves of 0.5kine lies in between the two groups. Relationships between volumetric strain vs. axial strain in Fig. 4(b) suggests that the first group can be considered as 'undrained' test, since there is no, or negligible volumetric strain throughout the test. The second group can be regarded as fully drained test, since there is no, or negligible excess pore water pressure generation during the test as is seen in Fig. 4(c). The effect of the loading rate on deformation of the specimen is seen in the volumetric strain vs. axial strain curve. It is seen from Fig. 4(b) that the slower the loading rate , the larger the volumetric strain.

The peak strength defined by the maximum deviator stress is plotted against loading rate in logarithmic scale in Fig. 5(a) for Series 1, 3 and 5 with a confining pressure of 100kPa and for Series 2 and 4 with a confining pressure of 500kPa in Fig. 5(b). The rates of increase over the range of 0.05kine to 25kine in terms of one-logarithmic cycle are 5% for Series 5 and 10% for Series 3, respectively. Series 1 of saturated sand under partially drained condition shows a sudden increase of the peak strength from 0.05kine and the peak strength approaches to that under undrained condition at the loading rate of 15kine. This observation is also true for the data of Series 2. This sudden change in peak compressive strength is mainly due to the relative magnitude between the loading rate and the rate of dissipation, and partly due to the change in mode of deformation. The internal friction angle at the maximum stress ratio was calculated by Eq. (1).

$$\phi = \sin^{-1}\left(\frac{\sigma_a - \sigma_r}{\sigma_a + \sigma_r}\right)_{\max} \qquad (1)$$

Plotted in Fig.6 is the internal friction angle at the maximum stress ratio normalized by that at the slowest loading rate of 0.0005kine against the loading rate for various conditions. The figure implies that the mobilized internal friction angle under 25kine is as much as 1.25 times larger than that obtained from triaxial compression tests with the recommended loading rate such as 0.00005kine.

Figure 7 plots deformation modulus E_{50} against loading rate. The deformation modulus E_{50} is normalized by the deformation modulus E_{50} at the loading rate of 0.0005kine. Here, the deformation modulus was estimated using Eq. (2).

$$E_{50} = \frac{(\sigma_a - \sigma_r)_{\max}}{2\varepsilon} \qquad (2)$$

As was illustrated in Fig. 7, the deformation modulus E_{50} becomes larger when the loading rate is higher, except Series 5 of dry sand under partial drained conditions.

3.3 Summary of Triaxial Compression Tests

The purpose of this investigation was to examine the effect of loading rate on sand behavior by conducting a series of triaxial compression tests with a varying loading rate of 0.0005kine to 25kine. The following findings were obtained from triaxial compression tests varying loading rate.

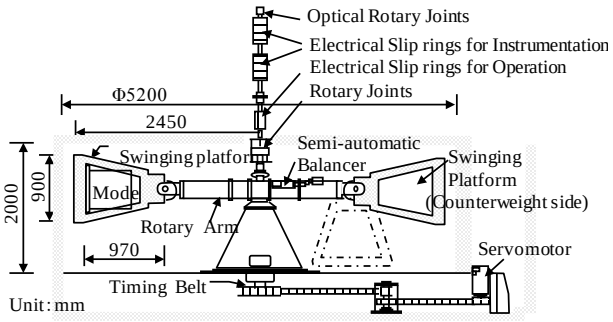


Figure 8 Tokyo Tech Mark 3 Centrifuge apparatus

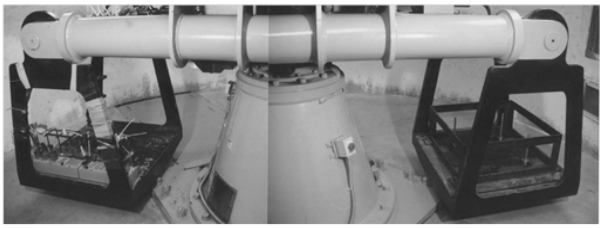


Photo 1 Tokyo Tech Mark 3 Centrifuge apparatus

1) The failure strength and the stiffness of dense sand generally become higher / stiffer when the loading rate is higher.
2) Deviator stress vs. axial strain relationships in partially drained tests were clearly classified into two groups. The soil exhibits undrained behavior when a loading rate is faster than 5kine, while the soil shows no appreciable difference in behavior when the loading rate is slower than 0.05kine.
3) The internal friction angle and the deformation modulus increase with the increase in loading rate. The internal friction angle and the deformation modulus with the loading rate of 25kine may become, respectively, 10-50%, 30-150% larger than those obtained in the compression tests with the recommended loading rate for triaxial tests.

4. CENTRIFUGE MODEL LOAD TESTS

4.1 Test Apparatus, Soil Tested and Test Program

The Tokyo Institute of Technology Mark 3 Centrifuge (Tokyo Tech Mark 3 Centrifuge) was used for the model test described in this paper. This centrifuge is a beam type centrifuge having a pair of parallel arms that hold platforms on which the model container and a weight for counterbalance are mounted as shown in Fig. 8 and Photo 1. Radius of rotation is 2.45m, which is the distance from the rotating shaft to the platform base. The surface of swinging platform is always normal to the resultant acceleration of the centrifuge acceleration, nG, and earth's gravity. Specifications of the centrifuge are summarized in Table 4.

For data acquisitions, two types of signal transmission methods are used. One is classical electrical slip ring. Transducers are connected to the slip rings through a junction box and signals are transferred to amplifiers on the laboratory floor. The other is an optical rotary joint. Transducers are amplified there and then are converted to digital signals by A/D converters. Gains and the other conditions of the signal conditioners can be controlled by a

Table 4 Specifications of the Tokyo Tech Mark 3 Centrifuge apparatus

Radius	Platform radius	2.45	m
	Effective radius	2.0~2.2	m
Platform dimensions	Width	0.9	m
	Depth	0.9	m
	Maximum height	0.97	m
Capacity	Maximum payload	50	G ton
	Maximum number of rotation	300	rpm
	Maximum payload at 80G	600	kg
Electrical slip rings	For instrumentation	72	channels
	For operation	18	channels
Optical rotary joints	Number of ports	4	
Rotary joint	Number of ports for air and water	2	
	Working pressure for air and water	1	Mpa
	Number of ports for oil	2	
	Working pressure for oil	21	Mpa

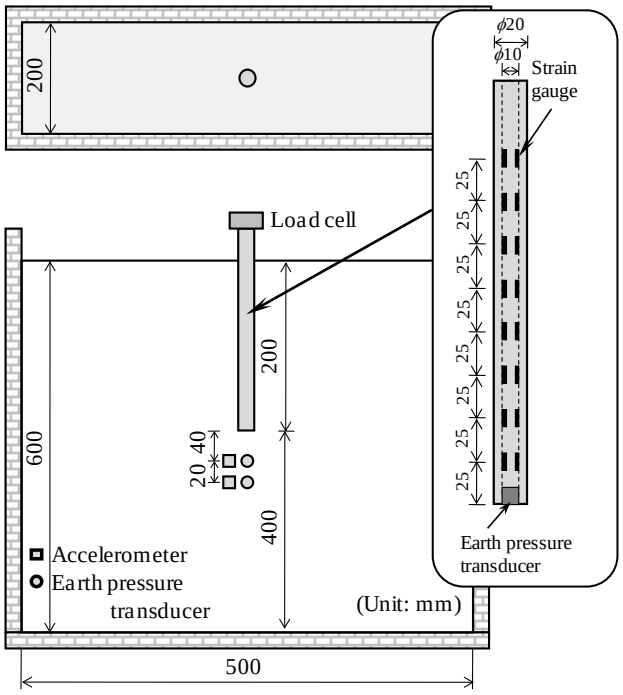


Figure 9 Schematic view of test apparatus

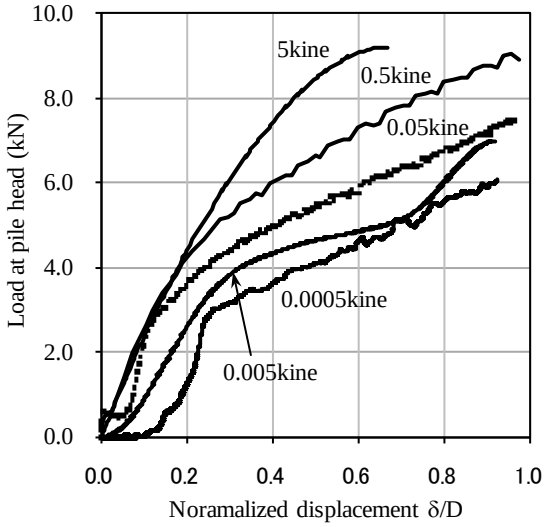


Figure 10 Relationships between load at pile head and normalized displacement δ/D

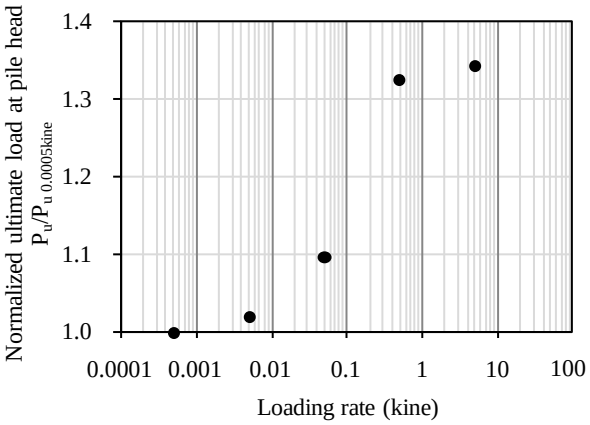


Figure 11 Relationships between normalized ultimate load at pile head and loading rate

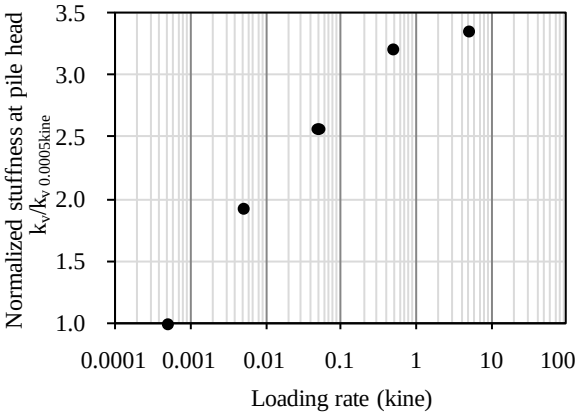


Figure 12 Relationships between normalized stiffness at pile head and loading rate

PC on the laboratory floor. The digital signals are transferred to a PC on the laboratory floor through the optical rotary joint.

The schematic view of test apparatus is shown in Fig. 9. The dimensions of container made by steel were width B=500mm, height h=600mm and length l=200mm. The model pile was steel cylindrical pipe of 20mm in diameter, 200mm in length and 5mm in thickness. The surface of model pile was considered to be smooth. The strain gauges were mounted inside of the model pile to measure the strain of model pile, and the earth pressure transducer was mounted on the tip of model pile to examine the resistance at the pile tip. Earth pressure transducers and accelerometers were embedded in the model ground. The loading was carried out by a hydraulic actuator. The hydraulic actuator was rigidly jointed with the model pile. The ranges of loading rate are 0.0005kine to 25kine by this actuator. The model ground was prepared by air-pluviation method using Toyoura sand to achieve a relative density of Dr=80%. All the tests were conducted under 50 G.

4.2 Test Results

Figure 10 presents the relationships between load at pile head and vertical displacement normalized by the pile diameter, δ/D. These loading tests were carried out in dry

dense sand varying loading rate in the range of 0.0005-5kine. The load at pile head and stiffness generally become higher / stiffer when the loading rate is high.

Figure 11 indicates the relationships between the load at pile head normalized by that at the slowest loading rate and loading rate. The definition of ultimate load at pile head is the measured maximum load at pile head. The data indicates that the load at pile head increases as the loading rate increases. Compared to the results at the slowest loading case and that at the highest loading case, the increment of the load at pile head is almost as large as 30%.

The relationships between the coefficient of subgrade reaction normalized by that at the slowest loading rate and loading rate are plotted in Fig. 12. The coefficient of subgrade reaction is calculated by load increment and displacement increment in the relationships between load and displacement at pile head. The normalized coefficient of subgrade reaction shows the large value when the loading rate is high. Thus, the stiffness at pile head increases as the loading rate is high.

The bearing capacity of pile may be calculated based on the bearing capacity formula as shown Eqs. (3)~(5).

$$Q = Q_s + Q_b \qquad (3)$$

$$Q_b = A_b(cN_c + \gamma DN_q S_q + \gamma BN_\gamma S_\gamma) \qquad (4)$$

$$Q_s = A_s(K_0 \gamma z \tan\phi) \qquad (5)$$

Where,

$N_c = (N_q - 1)$

$N_q = \exp(\pi \tan\phi)\tan^2(45° + \phi/2)$

$N_\gamma \approx 2(N_q + 1)\tan\phi$

S_c, S_q, S_γ: Shape factor, c: Cohesion,
γ: Unit weight of soil, D: Embedded length
B: Pile diameter
K_0: Coefficient of earth pressure at rest, $K_0 = 1 - \sin\phi$
z: Depth measured from the ground surface

The increase in the internal friction angle will directly lead to an increase in the value of the bearing capacity factors for N_q, N_γ used for end bearing capacity, as well as shaft friction. The vertical ultimate bearing capacity of pile was evaluated for the same conditions of model loading test. The internal friction angle ϕ=40deg. obtained from the triaxial compression tests of Series 5 was used for calculation of the ultimate bearing capacity. The relations of the calculated values of bearing capacity normalized by that at the slowest loading rate and loading rate with experimental values are plotted in Fig. 13. Here, the legend of Fig. 13 means that 'Exp.' and 'Cal.' are experimental value and calculated value, respectively. The trend indicates that the normalized calculated ultimate bearing capacity agrees almost with the experimental value. Thus, it is said that the increment of bearing capacity due to the effect of loading rate corresponds with the increment of calculated bearing capacity using bearing capacity formula as shown Eqs. (3)~(5) and the increment of internal friction angle.

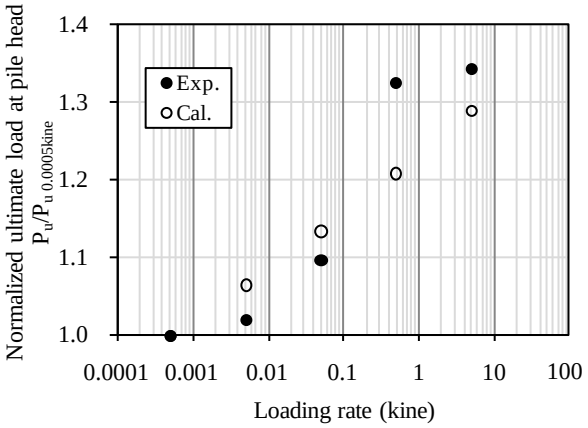


Figure 13 Relationships between normalized ultimate load at pile head by calculation and loading rate with experimental value

4.3 Summary of Model Loading Tests

The purpose of model loading tests is to confirm the effect of loading rate on bearing capacity of pile by conducting a series of centrifuge model tests. The following findings were obtained.

(1) The ultimate bearing capacity and the stiffness at pile head become higher / stiffer when the loading rate is higher.

(2) The ultimate bearing capacity and the coefficient of subgrade reaction at pile head increase as the loading rate increases. The ultimate bearing capacity and the coefficient of subgrade reaction at pile head with the loading rate of 5kine may become, respectively, 35%, 330%, larger than these obtained in the slowest loading cases.

(3) It is concluded that the increment of calculated bearing capacity of pile using bearing capacity formula and the internal friction angle obtained from the results of triaxial compression test on Series 5 agrees almost with the increment of experimental value.

5. CONCLUSIONS

The purposes of this study were to experimentally examine the effect of loading rate on sand behavior by a conducting a series of triaxial compression tests with varying loading rate of 0.0005kine to 25kine and to confirm the effect of loading rate on bearing capacity of pile by conducting a series of model loading tests at centrifuge acceleration field with varying loading rate in the range of 0.0005kine to 5kine. The following findings were obtained;

(1) The effect of loading rate on soil strength and bearing capacity of pile was confirmed clearly. Both soil strength and bearing capacity of pile increase as the loading rate increases.

(2) The effect of loading rate on stiffness of sand and coefficient of subgrade reaction was also examined clearly. Both stiffness of sand and coefficient of subgrade reaction at pile head become higher when the loading rate is high.

Acknowledgements:
The authors would like to thank Mr. Sakae Seki for his

cooperation and advice in carrying out centrifuge model tests.

References:

Casagrande, A. and Shannon, W.L. (1948), "Stress-Deformation and Strength Characteristics of Soils under Dynamic Loads," *Proceedings of the 2nd International Conference on Soil Mechanics and Foundation Engineering*, 29-34.

Seed, H.B. and Lundgren, R. (1954), "Investigation of the Effect of Transient Loading on the Strength and Deformation Characteristics of Saturated Sand," *Proceedings of American Society for Testing and Materials*, 1288-1306.

Whitman, R.V. and Hearly, K.A. (1962), "Shear Strength of Sands during Rapid Loadings," *Journal of the Soil Mechanics and Foundation Division*, American Society for Civil Engineering, **16**(3), 99-132.

Vesic, A.S.,Banks, D.C. and Woodward, J.M. (1969), "An Experimental Study of Dynamic Bearing Capacity of Footing on Sand," *Proceedings of the 6th International Conference on Soil Mechanics and Foundation Engineering*, 209-213.

Lee, K.L., Seed, H.B. and Dunlop, P. (1969), "Effect of Transient Loading on the Strength of Sand," *Proceedings of the 7th International Conference on Soil Mechanics and Foundation Engineering*, 239-247.

Senanayake, K.S. (1973), "Effect of Loading Velocity on the Bearing Capacity and Stress Distribution in a Sandy Soil," *Master Thesis*, Tokyo Institute of Technology

Ranagelow, P., Konagai, K., Namikawa, T. and Katagiri, T. (1994), "An Experimental Study on the Loading Rate Effect on Bearing Capacity of Footing on Saturated Sand," *Proceedings of the 9th Japan Earthquake Symposium*, 307-312.

Bolton, M.D., Gui, M.W., Garnier, J., Corte, J.F., Bagge, G., Laue, J. and Renzi, R. (1999), "Centrifuge Cone Penetration Tests in Sand," *Geotechnique*, **49**(4), 543-552

Takemura, J. and Kouda, M. (2000), "Tests Results and Discussions: Cone Penetration Tests (C2-cone)," *Centrifuge 98 (eds: Kimura Kusakabe and Takemura)*, Tokyo, Japan, Vol. 2, 1109-1116

Huy, N.Q., Dijkstra, J. and van Tol, F. (2005), "Influence of Loading Rate on the Bearing Capacity of Piles in Sand," *Proceedings of the 16th International Conference on Soil Mechanics and Foundation Engineering*, 2125-2128.

8CUEE CONFERENCE PROCEEDINGS
8th International Conference on Urban Earthquake Engineering
March 7-8, 2011, Tokyo Institute of Technology, Tokyo, Japan

EFFECT OF ARCH ACTION ON PSEUDO-STATIC RESPONSE OF URBAN MOUNTAIN TUNNEL AT RELATIVELY SHALLOW DEPTH IN SOFT GROUND

Shuhei Shibayama[1)], Akihiro Takahashi[2)], and Osamu Kusakabe[3)]

1) Doctoral student, Dept. of Civil Engineering, Tokyo Institute of Technology, Japan
2) Associate Professor, Department of Civil Engineering, Tokyo Institute of Technology, Japan
3) Professor, Department of Civil Engineering, Tokyo Institute of Technology, Japan
sh4880@cv.titech.ac.jp, takihiro@cv.titech.ac.jp, kusakabe@cv.titech.ac.jp

Abstract: It is widely accepted that tunnels have high seismic stability because of a confining effect from surrounding ground. However, tunnel structures have experienced serious damages during past huge earthquakes. Although the need for seismic performance of tunnels is emphasized in specifications for tunnels, it is required to understand detailed mechanisms on interaction between the tunnel and the ground. There are many uncertain factors which affect the soil-structure interaction, e.g., arch action of ground, deformation of ground with tunnel and tunnel cover. The arch action of the ground is expected to occur due to stress releasing of the surrounding ground during construction process of the mountain tunnel, and it might be changed by earthquake-induced ground deformation. In order to investigate the pseudo-static response of the urban mountain tunnel in lightly consolidated sandy ground and effect of stress releasing, centrifuge model tests were carried out in this study. In conclusion, following results were obtained. Firstly, due to the arch action, initial bending moments exerted in case with stress releasing are quite small. Secondly, the deterioration of the arch action takes place due to shear deformation of ground. Thirdly, the pseudo-static response before and after deterioration of the arch action are significantly different.

1. INTRODUCTION

Recently, the number of construction of urban tunnels has been increasing because of intensive use of urban areas. In order to reduce construction cost of the urban tunnels, mountain tunnelling methods have extended its application to the urban area in relatively soft ground (e.g. lightly consolidated or unconsolidated sandy ground) at shallow depth.

Underground structures were considered having high seismic stability because of a confining effect from surrounding ground (Kawashima 1994). However, tunnel structures have experienced serious damages in the 1995 Hyogo-Ken Nanbu Earthquake (Asakura et al. 1996), and consequently the design codes for tunnels were revised (e.g. JSCE 1996). The revised specifications recommend taking into account the soil-structure interactions by proper methods, such as the seismic displacement method. This method is a kind of pseudo-static approach in which seismically-induced ground deformation is statically applied to the tunnel structure through the soil springs. This soil-structure interaction is affected by many factors, e.g., stress conditions of soil, tunnel cover depths, deformation of ground together with tunnel structure, surface condition of tunnel and lining structures, thus, there are many uncertainties in the application of the seismic displacement method. Although the need for seismic performance of the urban tunnels is emphasized in JSCE standard specifications for tunnels (JSCE 2008), it is required to understand detailed mechanisms on the soil-structure interaction under various conditions.

Arch action of the ground above the mountain tunnel is expected to occur due to ground deformation during unlined construction process of the moutain tunnel, i.e. stress releasing of the ground is generated, and the earth pressures acting on the tunnel lining are much smaller than that by the shield tunnelling method. According to previous studies (Shibayama et al. 2010), the experimental results showed that the earth pressure acting on tunnel in sand changes due to deterioration of the arch action which is caused by the shear deformation of the ground. However, in the experimental study (Shibayama et al. 2010), at the initial state, actual stress releasing during construction process of the mountain tunnels, are not represented.

In this study, active type shear tests in a centrifuge were carried out to understand the detailed pseudo-static seismic response of the urban mountain tunnel embedded in lightly consolidated sandy ground, and the effect of the stress releasing around the tunnel. In particular, difference of the pseudo-static response of the tunnel structure before and after deterioration of the arch action is discussed.

2. CENTRIFUGE MODEL TEST

2.1 Introduction

Seismic stability of the tunnel structure is usually evaluated by the seismic displacement method. This method evaluates structural forces exerted on the tunnel by applying the shear deformation of surrounding ground to the tunnel structure in a pseudo-static approach, because the effect of inertia force acting to the underground structure can be neglected as compared with superstructures. Figure 1 shows an active type shear box used in this study. The seismic displacement method was experimentally reproduced by using this shear box. Validity of the experimental method for a rectangular tunnel constructed in sand has been confirmed by the previous study (Shibayama et al. 2009). In this study, pseudo-static responses of the urban mountain tunnel were investigated by the experimental simulation of the seismic displacement method using the active type shear box in a centrifuge.

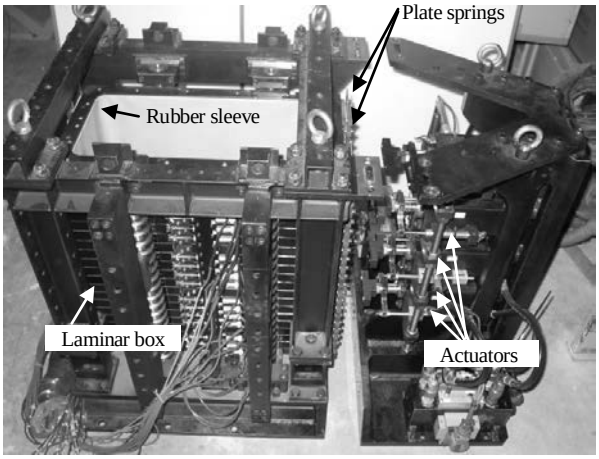


Figure 1 Active type shear box

Table 1 Specifications of active type shear box

Maximum centrifuge acceleration		100g
Actuator	Number	4
	Stroke	±20mm
	Force capacity (20.5MPa oil pressure)	25.8kN (outward) 18.0kN(inward)
	Peak velocity	133mm/sec
Laminar box	Dimensions (inner)	W 452mm B 202mm H 524mm
	Number of laminae	20+fixed one

2.2 Test and model description

The active type shear box comprises two parts; a laminar box and actuators, as shown in Fig. 1. The laminar box consists of 20 stacked 24mm laminae with a roller bearing support and one fixed lamina at the base of the box. The shear deformation of the laminar box was imposed by four hydraulic actuators connected to the four laminae at specific elevations. Horizontal displacements of the other laminae were transmitted through four linked sets of 0.6mm plate springs. A rectangular shape rubber sleeve was placed on the inner wall of the box to prevent the soil particles from getting into the gaps of the laminae. Thin stainless vertical sheets and a horizontal sheet of 0.2mm thickness with rough surface were fixed to both the inner end walls and the base of the box, respectively. These sheets are used for mobilizing the shear stresses on the inner boundary when the box is sheared. The specifications of the active type shear box are summarized in Table 1.

Assuming horseshoe-shaped mountain tunnel in the lightly consolidated sandy ground, an aluminium model tunnel was used for the model tests, as is shown in Figure 2. The model lining has a diameter of 100mm, a height of 75mm and a thickness of 2mm with smooth surface, which approximately corresponds to a 5m diameter tunnel with an unreinforced concrete lining of 300mm thickness in the prototype scale under centrifugal acceleration of 50g.

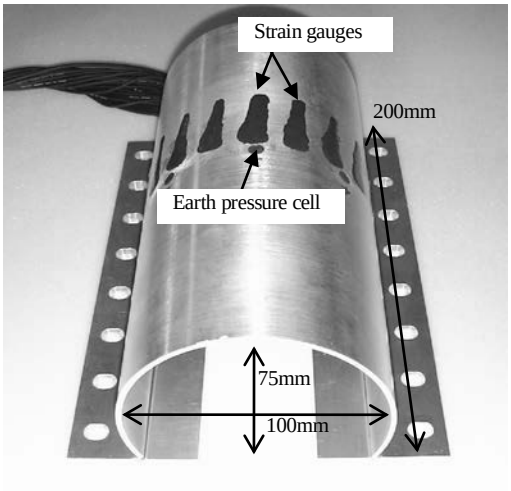


Figure 2 Horseshoe-shaped model tunnel

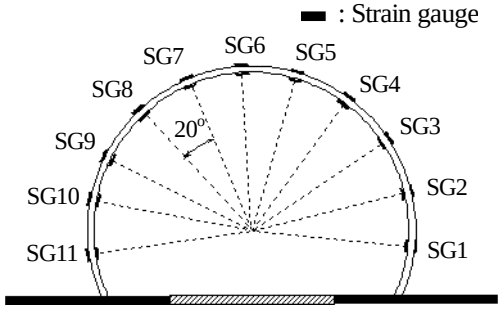


Figure 3 Positions of strain gauges

In total, 22 strain gauges were attached on both outer and inner surface of the model tunnel in pairs to measure sectional forces (especially, bending moment in this paper) exerted on the model tunnel. Figure 3 illustrates the positions of the strain gauges attached to the model tunnel.

Figure 4 illustrates a schematic diagram of model setups for the tests. Assuming lightly consolidated sandy ground, cemented sand was used for the model ground. The cemented sand is comprised of a mixture of silica sand

No. 6 (G_s=2.64, D_{50}=0.51mm, Uc=1.74, e_{max}=0.922, e_{min}=0.565 and ϕ=41deg.), cement, admixtures and water. The material properties of the cemented sand are summarized in Table 2. In order to investigate, an effect of stress releasing on pseudo-static response of the tunnel, two cases of the tests were conducted. In case with the stress releasing (i.e. with SR case), the model ground was constructed to have a certain gap, δ=3mm in radial direction, between tunnel and excavated ground at 1g field as shown in Figure 4. During increasing centrifugal acceleration up to 50g, the excavated ground was deformed by this certain gap. Due to this allowed ground deformation, appropriate initial stress condition, is created. On the other hand, in case without stress releasing (without SR case), there is no gap (i.e. δ=0mm) as shown in Figure 4. According to experimental comparisons between these two cases, the effects of the stress releasing are discussed.

In this kinds of the tests, a tunnel cover (H_c) and diameter (D) ratio is one of important parameter, as the depth controls the stress condition of the tunnel surroundings, including formation of the arch action above the tunnel due to the stress releasing. Generally, depth of the urban tunnels is relatively shallow, it normally has the cover of a several times of the tunnel diameter. Thus, the covers of the model grounds, H_c, were selected to be 300mm which corresponds to a tunnel cover-diameter ratio, H_c/D of 3.

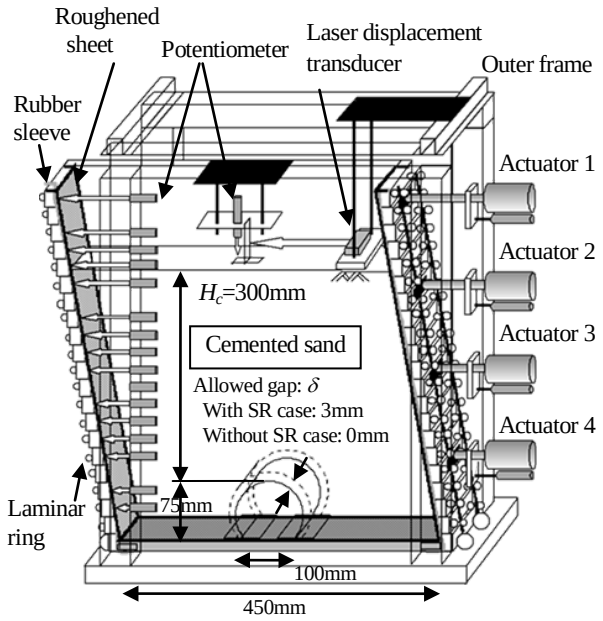


Figure 4 Model setup

Table 2 Material properties of cemented sand

Unconfined compressive strength: q_u (kPa)	50
Young's modulus: E_{50} (kPa)	4600
Water content: w (%)	30
Unit weight: γ(kN/m^3)	18.3

Figure 5 shows typical examples of the input horizontal displacement distributions measured by potentiometers attached to the each laminar ring, when positive and negative certain values of horizontal displacements were applied from the actuators. The measured distributions have almost linear distributions with depth. Thus, input nominal shear strain, γ, is defined by the gradient of the

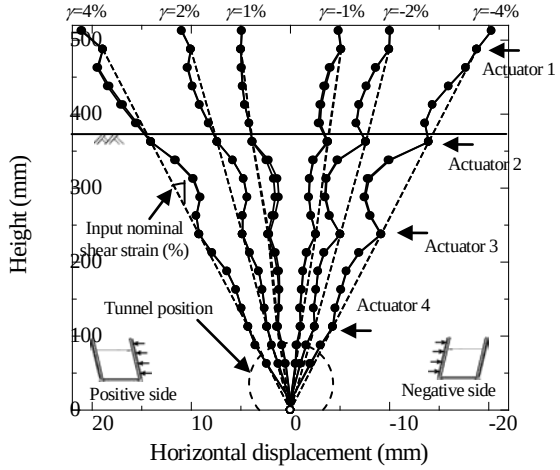


Figure 5 Distributions of horizontal displacement

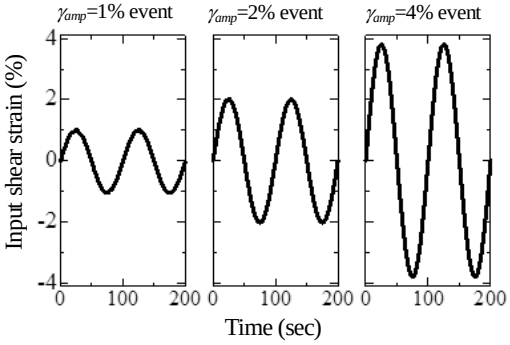


Figure 6 Shear strain history

intended distribution of the input horizontal displacements, as shown in Figure 5.

Time histories the input nominal shear strain are shown in Figure 6. The two cycles sinusoidal nominal shear strain for the amplitudes, γ_{amp}, of 1%, 2% and 4% respectively, were imposed on the model ground continuously under centrifugal acceleration of 50g. An each cycle of the nominal shear strain was applied in 100sec.

3. NUMERICAL CALCULATION

As well as, the centrifuge model tests, FE push over analyses were carried out using the FEM code, PLAXIS 2D Ver. 9.02. Figure 7 illustrates FE mesh configuration and loaded horizontal displacements used in the analyses. As shown in the figure, the calculation mesh has 22.5m wide and 18.75m height in the prototype scale, which is composed by 1450 fifteen-noded triangular two-dimensional plane strain elements and 38 five-noded elastic beam elements. The input horizontal displacements were

statically imposed on the side boundaries of the model ground, which have linear distributions with depth, as shown in Figure 7. The values of the input horizontal displacements at the ground surface are 0.188m, which correspond to the nominal shear strain of 1%. During the whole analyses, displacements were restricted in both direction along the bottom mesh boundary, and horizontal displacements were restricted along the side boundaries, as illustrated in Figure 7. The tunnel structure is modelled as elastic beam elements with appropriate interface elements, and for all analyses it was assumed to behave in a linear elastic manner. The Mohr-Coulomb (MC) model was employed to simulate the soil behaviour in all the FE analyses. The MC model is elasto-plastic model which involves five strength parameters, i.e. Young's modulus, E and Poisson's ratio, ν for soil elasticity; friction angle, ϕ and cohesion, c for soil plasticity and ψ as an angle of dilatancy. Material properties of the tunnel and ground models are summarized in Table 3 and 4, respectively.

When the shear deformation of ground is imposed, considerable static stresses were acting on the tunnel due to overburden pressure and the construction process. Hence, prior to the shear deformation loadings, static analyses of excavated processes were undertaken to establish the initial stresses acting on the tunnel. Starting from a green-field profile, the excavation of the tunnels causes stress relief in the ground. To model this excavation process, concept of the so-called β-method is used. The idea is that the initial stress, p_0, acting around the location where the tunnel is to be constructed is divided into a part (1-β) p_0 that is applied to the unsupported tunnel and a part of βp_0 that is applied to the supported tunnel. Instead of the b value a load contribution ratio (LCR) is used in FE analyses. In fact, when the ground at the tunnel position is excavated, an initial out-of-balance force occurs that is comparable with the initial force, p_0. In the beginning of calculation, this force is fully applied to the ground and it will be stepwise decreased. Then, the calculation has been done until certain value of the LCR is produced, and the out-of-balance force is imposed on tunnel structure. After that, horizontal displacements are imposed on the model ground. As parameter which controls amount of stress releasing, a load contribution ratio (LCR) is used. Varying the parameter, LCR, several cases are calculated. Figure 8 indicates calculated characteristic curve, which is relationship between calculated earth pressure and vertical convergence at the tunnel crown after the static calculations. In the figure, the values of the earth pressures and convergences are normalized by the value of the calculated earth pressure in LCR100% case and the tunnel diameter, respectively. Totally 11 case of the calculation were conducted varying the LCR from 15% to 100%, as shown in Figure 8. In the next section, results of the cases with the LCR 100% and 30% will be discussed, which corresponding the test case without and with stress releasing. As references values, the case with the LRC 15% will also be compared, in which the arch action of the ground almost fully mobilized without the collapse of the surrounding ground.

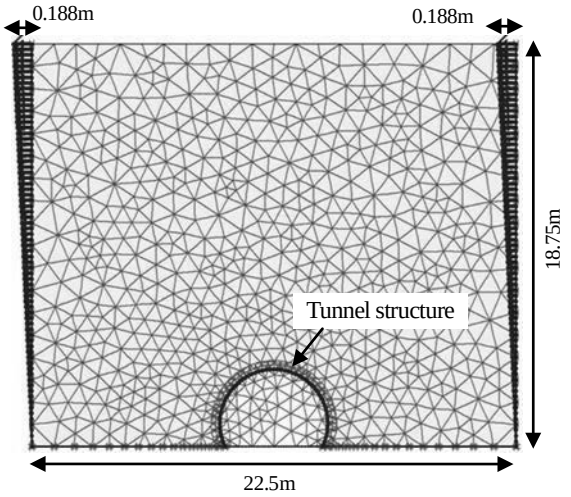


Figure 7 Calculation mesh

Table 3 Material properties of model tunnel in FE analyses

Young's modulus: E	Poisson's ratio: ν	Thickness
70000kPa	0.33	0.10m

Table 4 Material properties of cemented sand in FE analyses

Parameters	**Cemented sand**
Unit weight: γ	18.3kN/m^3
Poisson's ratio: ν	0.333
Young's modulus: E* (at p= 0 and 98kPa)	4600kPa (p=0kPa) 10800kPa (p=0kPa)
Cohesion: c*	27kPa
Friction angle: ϕ*	16deg.
Dilation angle: ψ ($=\phi/3$)	5.33deg.

* obtained by a series of direct shear tests

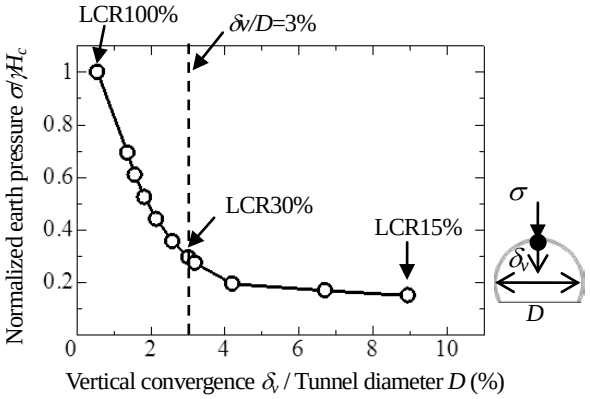


Figure 8 Characteristic curve of calculated results

4. RESULTS AND DISCUSSION

Figure 9 shows initial distributions of measured bending moments for the both with and without stress releasing cases before the shear deformations of the ground were imposed. The cases with and without are indicated by open circles and squares, respectively. In the figure, calculated distributions were also plotted, in which cases with LCR of 100% (as a real line), 30% (a broken line) and 15% (a thin dashed line) are included. The positive bending moment is defined as the case for the inner surface of the tunnel lining suffers tension force. As shown in Figure 9, small amounts of positive and negative bending moments were exerted in the case with stress releasing compared with the without stress releasing, which is probably due to a formation of the arch action of the ground caused by the stress releasing. As mentioned previously, calculated results with LRC of 100% and 30% could be considered as the test cases without and with stress releasing, respectively. And case with LRC=15% is considered as case in which the arch action of the ground is fully mobilized without collapse during the excavation process. As well as the test results, the calculated bending moments of the LCR=30% and 15% are quite small compared with the case of LCR=100% in which the arch action is not considered. Although actual values are slightly different between the measured and calculated results, the calculated bending moment distributions are practically similar to these of the model tests.

Figure 10 shows variations of the bending moment measured at the tunnel crown, the right spring line and mid-part between them in the both tests for with and without stress releasing in the model tests. In Figure 10, solid and broken lines indicate the cases of with and without stress releasing, respectively, and dashed lines show the input shear strain. Cyclic variations of the bending moment at the crown and right spring line are smaller than that at the mid-part. At the crown and spring line, initial values of bending moment of the case of with stress releasing are quite small, as previously mentioned. Then during shearing, the bending moments are increase and approach to these of the case without stress releasing, during shearing.

Figure 11 shows the bending moments measured before and after γ_{amp}=1% shearing event for the both cases with stress releasing and without stress releasing, and Figure 12 shows the bending moments measured before and after γ_{amp}=4% event in the both cases, without stress releasing and with stress releasing. The terms 'before' and 'after' in the figures correspond to the test elapsed time of 0 second and 200 seconds respectively in Figure 6. In these figures, the calculated distributions are also included. In the case of with stress releasing, the bending moments before the first (γ_{amp}=1%) shearing (which has been already introduced in Figure 9 as initial values) are much smaller than those after shearing, and the bending moments at near the crown increase and in side parts decrease after 1% shearing, as shown in Figure 11 (b). Firstly, before γ_{amp}=1% shearing, the measured values are almost the similar to the calculated

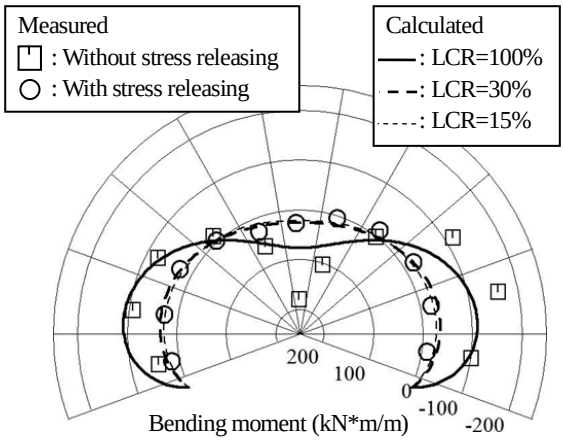


Figure 9 Initial bending moment distributions

distributions with LCR=30% or15%, then after shearing,

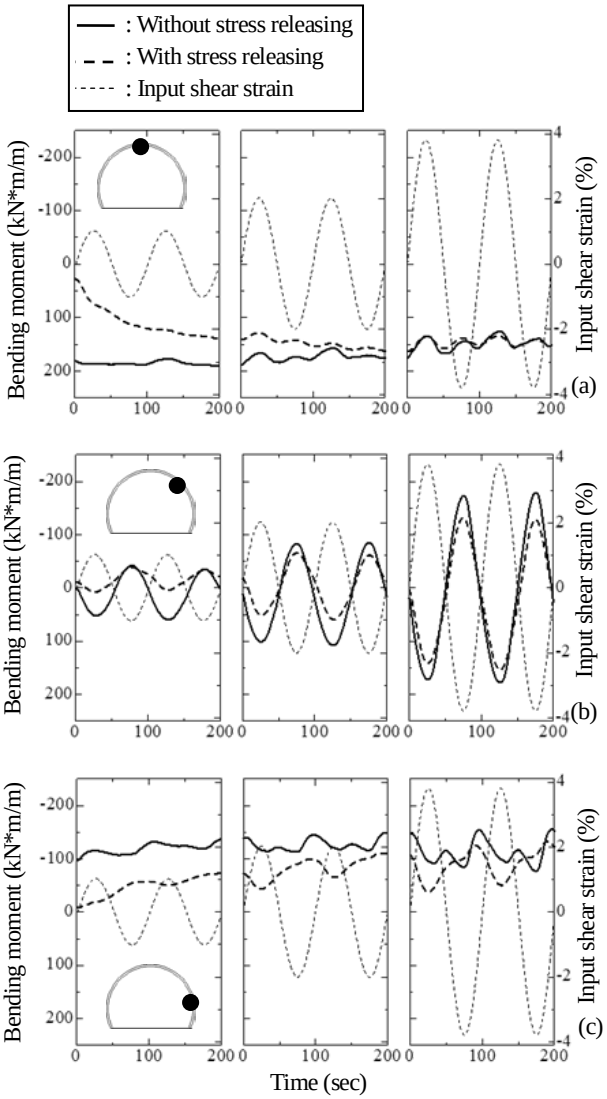


Figure 10 Variation of bending moment (a) at crown (b) at right mid-part and (c) at right spring line

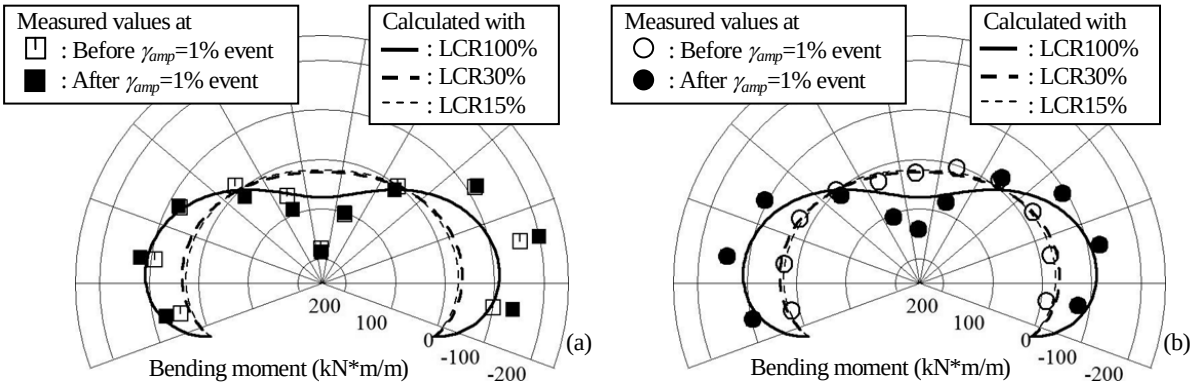


Figure 11 Bending moments measured before and after γ_{amp}=1% event
(a) Without stress releasing and (b) With stress releasing

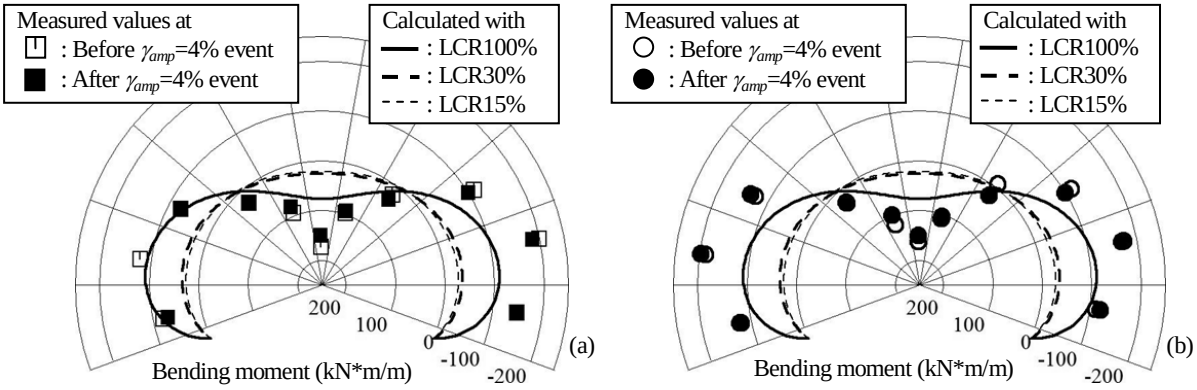


Figure 12 Bending moments measured before and after γ_{amp}=4% event
(a) Without stress releasing and (b) With stress releasing

these are almost the same values of the calculated distribution of LCR=100%. On the other hand, in the case of without stress releasing, 1% shear strain, the moment distributions before and after shearing show almost no change (Figure 11 (a)). Probably, this can be explained by the formation of arch action of the cemented sand above the tunnel with stress releasing during centrifugal acceleration up to 50G, and deterioration of the arch action takes place due to shearing. In Figures 12 (a) and (b), distributions of bending moment before and after 4% shearing show no change in the both cases of with stress releasing and without stress releasing and distributions of the cases of with stress releasing and without stress releasing are almost the same, because the ground of the case with stress releasing has already been subjected to 1% and 2% shear strain cycles and arch action diminished by shearing.

Figure 13 shows comparison between bending moment distributions at after γ_{amp}=4% shearing event of the case without and with stress releasing. In the figure, the calculated distributions were also plotted. As compared with initial values shown in Figure 9, after several shearing event, slightly large amount of bending moments are exerted in the case with stress releasing with respect to the case without stress releasing. This experimental fact might suggest that after the arch action has been deteriorated due to shear deformation of the ground, the larger bending moments exerted in the tunnel with the stress releasing during the excavation process.

In order to understand the effect of the initial condition change on the pseudo-static response of the bending moments due to the shear deformation on the ground, the absolute and incremental values of the bending moments were compared. Figure 14 (a) shows the distributions of the absolute values of the bending moments exerted on the tunnel when the input nominal shear strain γ=1% in the first cycle of the γ_{amp}=1%, 2% and 4% shearing events for the

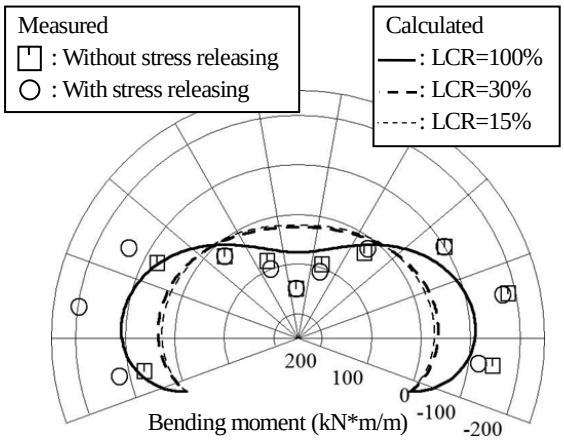


Figure 13 Comparison between bending moment distributions of without and with stress releasing

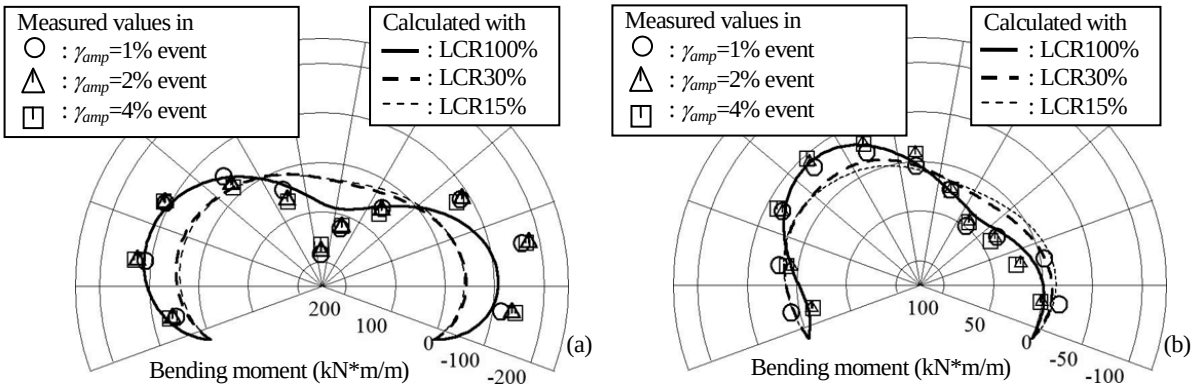


Figure 14 Bending moments measured when γ=1% shear strains imposed for without stress releasing case (a) Absolute values and (b) Incremental values

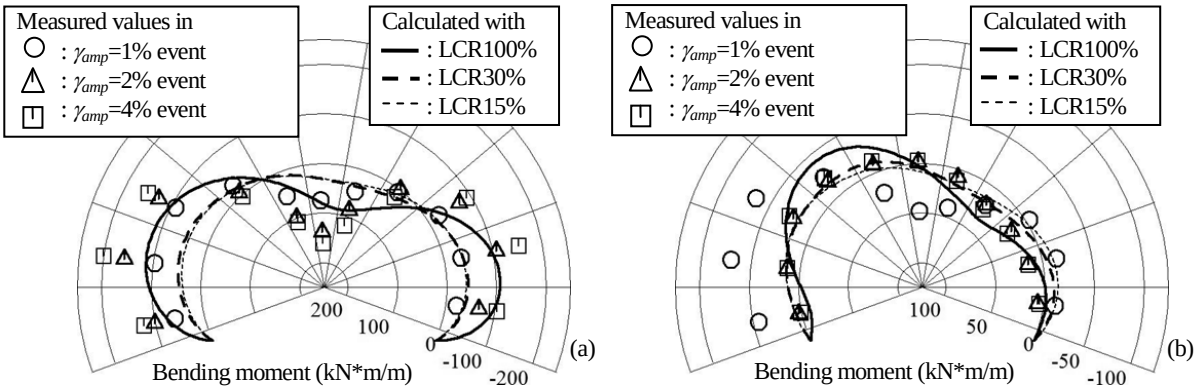


Figure 15 Bending moments measured when γ=1% shear strains imposed for with stress releasing case (a) Absolute values and (b) Incremental values

without stress releasing. Figure 14 (b) indicates distributions of incremental value of the bending moments measured from the beginning of the each shearing events to the same point of Figure 14 (a). In the Figures, the calculated values of the bending moments with the LCR=100%, 30% and 15% were also plotted as a real, a broken and a thin dashed lines, respectively. The previous experiments (Yamada et al. 2002 and Izawa et al. 2006) indicated that sectional forces at the tunnel corners are remarkable when the pseudo-static shear deformation of the ground was imposed on the model tunnel. The present data shown in Figure 14 also support the previous experimental observations. As shown in Figure 14, the absolute and incremental values of pseudo-static responses of bending moments are almost the same. It might be suggested that for the case without stress releasing, if the same values of the ground shear deformations are imposed, the same values of the bending moment responses will be exerted. And it should be noted that the FE analyses well-predict the pseudo-static response for without stress releasing case, because the absolute and incremental experimental values are practically similar to the calculated values. Figure 15 indicates these distributions for the case with stress releasing. As compared with the case without stress releasing, for the with stress releasing, absolute values of the bending moment responses increase from first shearing (γ_{amp}=1%) to final shearing event (γ_{amp}=4%), as shown in Figure 15 (a). This might be explained by the deterioration of the arch action. On the other hand, the larger incremental values of the bending moment are exerted in the γ_{amp}=1% event compared with these in other events, which also related to the deterioration. After the deterioration, the incremental values of γ_{amp}=2% and 4% are almost the same, and practically similar to the calculated results of LCR30%. It can be said that larger values of the bending moment responses will appear after the arch action is deteriorated. After the deterioration, the seismic increments of the bending moments are almost the same if the same values of the ground shear deformations are imposed, however large amount of the absolute bending moments are slightly different after several shear deformation is applied. It might be indicated that prediction of the initial stress condition is quite important.

Figures 16 (a) and (b) show the absolute and incremental values of the bending moments measured when the maximum shear strain was first applied in cyclic shearing 4% in the cases of with and without stress releasing which corresponding to elapsed time of 25 seconds in Figure 6. In Figure 16 (a), for the with stress releasing case, larger values of the bending moments are exerted in left hand side compared with the without stress releasing case. While in Figure 16 (b), incremental values of the bending moments are almost the same between the both with and without stress releasing cases. It might be expected that once the

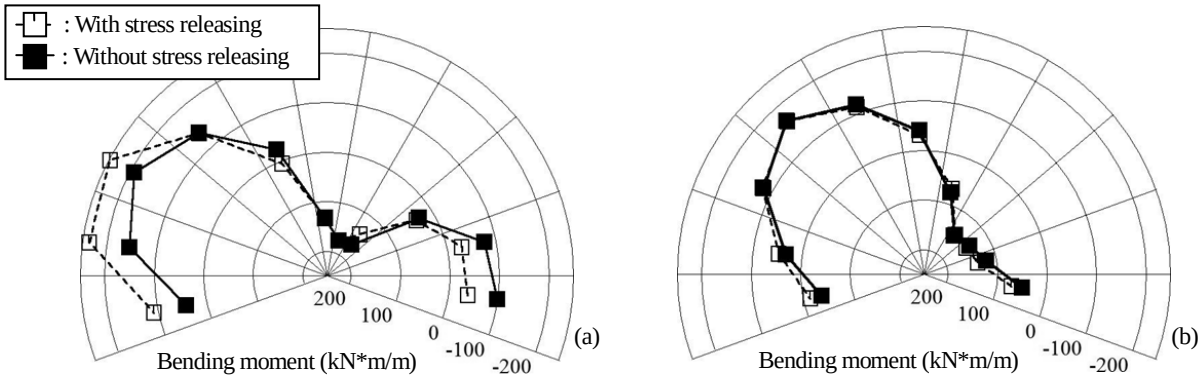


Figure 16 Experimental comparison between bending moments of without and with stress releasing when γ=4% shear strains (a) Absolute values and (b) Incremental values

arch action is deteriorated by the ground shear deformation, larger bending moment exerted in the tunnel.

5. CONCLUSIONS

This paper presented some results of active type shear box tests in a centrifuge by modelling the horse-shoe shaped aluminium tunnel in lightly consolidated sandy ground, as well as FEM analysis, in which construction process of the mountain tunnel is represented. The objective of this study is to investigate, the effects of stress releasing which is expected to occur during the construction process of the tunnel, on pseudo-static response of the tunnel. Following findings are obtained,

1) At initial state, the stress releasing reduces bending moments exerted in the tunnel lining close to zero due to the formation of the arch action of the ground, before shear deformation is imposed.
2) The arch action formed by stress releasing deteriorated by seismically-induced shear deformation of ground. According to the deterioration of the arch action, bending moments exerted in tunnel lining increase.
3) The pseudo-static bending moment responses before and after deterioration of the arch action are different. After the deterioration larger values of bending moments are exerted.
4) After the deterioration, the FE analyses well-predict pseudo-static increment of bending moments. However, to appropriately evaluate seismic performance of tunnel, appropriate initial stress condition due to construction process should be represented.

Acknowledgements:

This research was partially supported by Grant-in-Aid for Scientific Research (A), 2005-2007, No. 17206050, "Seismic stability of the large cross-section urban tunnel with located in relatively shallow depth". The authors gratefully acknowledge the funding for this research from the 21st Century Centre of Excellence (COE) program entitled "Evolution of Urban Earthquake Engineering".

References:

Kawashima, K. (1994), "Seismic Design of Underground Structures," Kajima Publishing Co. Ltd., (In Japanese)

Asakura, T. and Sato, Y. (1996), "Damage to Mountain Tunnels in Hazard Area," *Soils and Foundations Special Issue on Geotechnical Aspects of the January 17 1995 Hyogoken-Nanbu Earthquake*, 301-310.

Japan Society of Civil Engineers (1996), "Standard Specifications for Cut and Cover Tunnels," (in Japanese)

Japan Society of Civil Engineers (2007), "Japanese Standard for Mountain tunnels -2006-,"

Shibayama, S., Izawa, J., Takahashi, A., Takemura, J. and Kusakabe, O. (2010), "Observed Behaviour of a Tunnel in Sand Subjected to Shear Deformation in a Centrifuge," *Soils and Foundations*, **50** (2), 281-294.

Shibayama, S., Izawa, J., Takahashi, A., Takemura, J. and Kusakabe, O. (2009), "A Comparative Study between Dynamic Shake Table Test and Shear Box Test in a Centrifuge," *Int'l. Journal of Physical Modelling in Geotechnics*, **9** (2), 25-32.

Yamada, T., Nagatani, H., Igarashi, H. and Takahashi, A. (2002), "Centrifuge Model Tests on Circular and Rectangular Tunnels Subjected to Large Earthquake-induced Deformation," *Proc. of the 3rd Int'l Symp. on Geotechnical Aspects of Underground Construction in Soft Ground*, 673-678.

Izawa, J., Kusakabe, O., Nagatani, H., Yamada, T. and Ohbo, N. (2006), "Centrifuge Modeling on Seismic Behavior of Rectangular Tunnels," *Physical Modeling in Geotechnics 6th ICPMG*, 1163-1169.

8CUEE CONFERENCE PROCEEDINGS
8th International Conference on Urban Earthquake Engineering
March 7-8, 2011, Tokyo Institute of Technology, Tokyo, Japan

DISPLACEMENT OF TUNNELS IN LIQUEFIED SAND DEPOSITS

Siau Chen Chian[1)] and Santana Phani Gopal Madabhushi[2)]

1) PhD Candidate, Schofield Centre, Dept. of Engineering, University of Cambridge, United Kingdom
2) Reader, Schofield Centre, Dept. of Engineering, University of Cambridge, United Kingdom
scc55@cam.ac.uk, mspg1@eng.cam.ac.uk

Abstract: In an earthquake, tunnels passing through liquefiable soil deposits are susceptible to floatation due to their lower unit weight as compared to the surrounding saturated soil. Centrifuge tests have been carried out to investigate such floatation failure of shallow tunnels. Conventionally, the floatation of a buoyant tunnel in an ideal "viscous" liquefied soil may be deemed to displace vertically up to the surface. However, the presence of a rigid tunnel may lead to a reduction in excess pore pressure due to soil dilation from the soil-structure interaction. This paper presents the cyclic in-plane movement of the floating tunnel derived from instrumentation and the Particle Imaging Velocimetry (PIV) technique. The coupled influence of the cyclic movement of the tunnel on the acceleration and excess pore pressure measured at the springing depth of the tunnel during the floatation process are discussed.

1. INTRODUCTION

Underground infrastructure has been a widespread alternative in redeveloping urban spaces to ease congestion pressure arising from land scarcity. This underground infrastructure has often served as vital lifelines for transport, utility and storage purposes. They include subway train and highway tunnels, gas and water pipelines, and fuel storage tanks. However, in the event of an earthquake, the functionality of these lifelines could be put in question especially in soils susceptible to liquefaction.

Historical earthquake events such as the 1906 San Francisco earthquake (Youd and Hoose, 1976), 1964 Niigata earthquake (Seed, 1970), 1964 Alaska earthquake (Hall and O'Rourke, 1991), 1994 Northridge earthquake (Bardet and Davis, 1999), 1995 Great Hanshin earthquake (Okimura et al., 2006), 2003 Tokachi-oki earthquake (Towhata, 2008), 2004 and 2007 Chuetsu earthquakes (Tobita et al., 2009 and Ghayamghamian et al., 2007), 2009 Padang earthquake (Chian et al., 2010a), and the 2010 Chile earthquake (GEER, 2010) have proven the damage susceptibility of underground structures. In the case of tunnels, they usually serve as transportation facilities which may pose a high degree of risk in terms of human losses should they fail during an earthquake. Blocked or damaged transportation routes may also interfere with the ability of emergency personnel to respond promptly to immediate crisis.

Given the evidence of extensive geotechnical failures of lifelines in many earthquake-hit cities, there exists a need to conduct in-depth research to better understand and mitigate such seismic risk which could bring cities to a standstill following a major earthquake event. Centrifuge tests were conducted to provide a detailed understanding of the seismic response of floating tunnels in liquefied soil deposits.

2. LIQUEFACTION INDUCED FLOATATION OF BURIED STRUCTURES

Buried structures are generally subjected to a buoyant force due to their lower submerged unit weight than the surrounding soil. Conversely, the overlying weight and shear strength of the overlying soil inhibits the floatation. In the event of liquefaction, the soil loses most of its shear strength and the tunnel as shown in Figure 1 may float if the effective buoyant force (F_B) is greater than the combined resisting forces from the overlying soil weight (F_{WS}) and the soil's shear contribution (F_{SP}) as expressed below in Eq. (1):

$$F_B > F_{WS} + F_{SP} \quad (1)$$

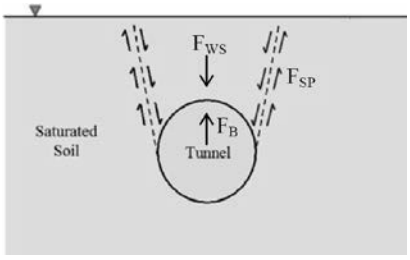


Figure 1 Force components acting on pipe in static condition (Chian and Madabhushi, 2010a)

Schmidt and Hashah (1999) proposed that the floatation of a tunnel requires the following conditions: 1) partial or full liquefaction of the surrounding soil, 2) structure must be buoyant in the liquefied soil mass, 3) nothing holds the structure from floating, and 4) the liquefied material must have mobility and be able to flow as the structure rises. In Figure 2, as the tunnel experiences uplift, the liquefied soil moves underneath the displaced tunnel, further lifting it up

(Hashah et al., 2001). This infers that liquefied soil is free-flowing and capable of filling the void left underneath the displaced tunnel. Based on this assumption, liquefied soil may be deemed as an ideal viscous fluid.

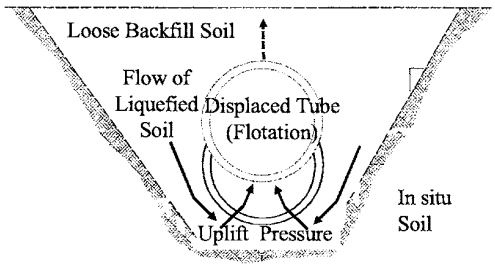


Figure 2 Backfill liquefaction and tube floatation (Schmidt and Hashash, 1999)

This idea of classifying liquefied soil as a viscous fluid have been pursued by many researchers earlier and have concluded that liquefied soil behaves like a viscous non-Newtonian fluid through pulling bar and sinking ball tests at 1g (Kawakami et al., 1994; Miyajima et al., 1995; Hamada and Wakamatsu, 1998; and Hwang et al., 2006).

3. EXPERIMENTAL SETUP

3.1 Centrifuge Modelling

Soil is a highly non-linear material. It is therefore essential to replicate identical stress and strain conditions in laboratory tests as in the prototype scale. Geotechnical centrifuge modelling achieves these conditions with the use of high centrifugal acceleration to scale up the model. A scaled model is made to correspond with the prototype at the pre-determined centrifuge g-level. As a result, a 1:*N* scale model experiences the same stress and strain conditions as the prototype when subjected to a centrifugal acceleration of *N* times earth's gravity A set of scaling laws for other parameters can be derived as shown in Table 1 (Schofield, 1981).

The model tunnel and pipe were buried in sand models prepared to the relative density (D_R) of 65% with the dry pluviation method using the automatic sand pourer and the accompanying design charts by Chian et al. (2010b). The layout of the tunnel, pipe and instruments are illustrated in Figure 3. Mouldable Duxseal was placed on the sides of the container to minimise reflecting incident stress waves (Steedman and Madabhushi, 1991). The material properties of Hostun sand used in the model are described in Table 2.

Based on centrifuge scaling laws, the 75 mm and 21.25 mm diameter model pipes represent a tunnel and a large diameter pipe with diameters of 5m and 1.42m at prototype scale in a 66.7g test respectively. These pipes were buried at a shallow depth of 1.1 times of their diameter to ascertain the difference in their floatation response with respect to their buried depth. A draw-wire potentiometer was attached to the crown of each pipe to measure its uplift response.

After sand pouring was completed, the models were saturated using the computerised system developed by Stringer and Madabhushi (2009). High viscous methyl cellulose fluid (66.7 cSt) prepared with a mixture of Hydroxypropyl methylcellulose (HPMC) powder and water based on the weight concentration by Stewart et al. (1998) was used as pore fluid to satisfy dynamic centrifuge scaling laws as indicated in Table 1. The saturated model was then loaded onto the 10m diameter beam centrifuge for testing. During the test, earthquakes were fired in-flight using the Stored Angular Momentum (SAM) earthquake actuator devised by Madabhushi et al. (1998).

Table 1 Centrifuge scaling laws

Parameter	Model/ Prototype	Units
General (slow events)		
Length	1/N	m
Area	$1/N^2$	m^2
Volume	$1/N^3$	m^3
Mass	$1/N^3$	$Nm^{-1}s$
Stress	1	Nm^{-2}
Strain	1	-
Force	$1/N^2$	N
Bending moment	$1/N^3$	Nm
Work	$1/N^3$	Nm
Energy	$1/N^3$	J
Seepage velocity	1/N	ms^{-1}
Time (consolidation)	$1/N^2$	s
Dynamic events		
Time (dynamic)	1/N	s
Frequency	N	s^{-1}
Displacement	1/N	m
Velocity	1	ms^{-1}
Dynamic Viscosity	N	Nsm^{-2}
Acceleration/acceleration due to gravity (g's)	N	ms^{-2}

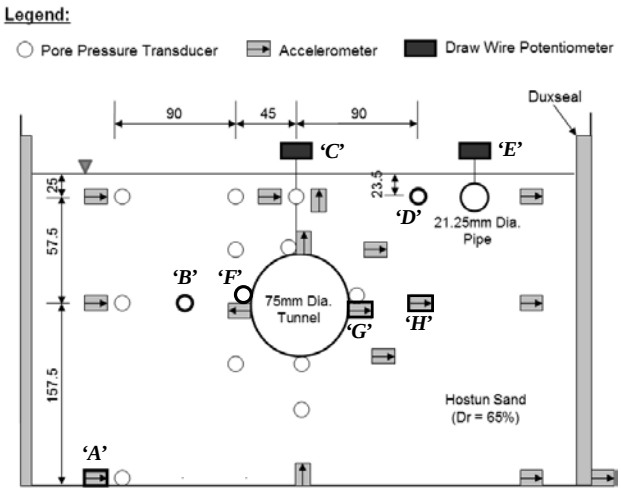


Figure 3 Layout of instruments in centrifuge model, not to scale

Table 2 Material properties of Hostun sands

Properties	Hostun sand
Φ_{crit} *	33° *
D_{10}	0.209 mm
D_{50}	0.335 mm
e_{min} *	0.555 *
e_{max} *	1.01 *
G_s *	2.65 *

* after Mitrani, 2006

3.2 PIV Technique

The Particle Image Velocimetry (PIV) is an optical means to visualise flow dynamics in fluids seeded with tracer particles. It is used to obtain instantaneous velocity measurements and related properties in fluids. This concept was adapted to suit geotechnical applications, using a texture-based image processing technique developed by White et al. (2001) as shown in Figure 4.

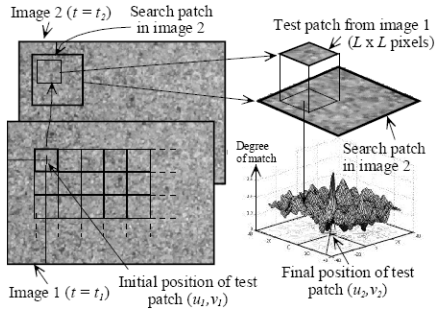


Figure 4 Principles of PIV analysis in geotechnical applications (White et al., 2001)

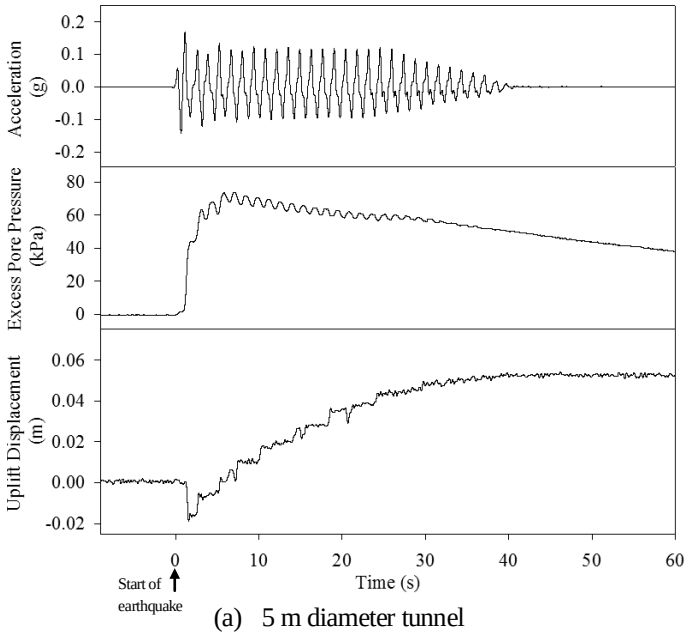
Natural sand has its own texture in the form of different coloured grains. In the case of sands with little texture, the texture can be enhanced with the addition of coloured grains of identical or coarser sand. Based on the unique texture of each patch of soil at the plane of a clear window of Perspex wall of the model box, the deformation of soil can be examined by tracking the movement of these patches from one image to another. Detailed information on the development and performance of the image processing algorithms are described by White et al (2003).

In static tests, the movement of soil grains is slow and progressive. Hence, conventional high resolution cameras were usually used to capture multiple image frames at 3 to 5 second intervals. In the case of earthquake tests, the soil movement is highly influenced by the phase of the earthquake cycle which requires the capturing of large numbers of image frames in each cycle. A typical earthquake of 1 Hz would require a shake frequency of *N* Hz in a dynamic centrifuge test due to scaling law as indicated in Table 1. Hence, a high speed camera is necessary to obtain sufficient image frames to depict the development of soil movement with increasing number of loading cycles. A Phantom v5.0 camera capable of taking 1000 image frames per second was therefore used in these dynamic centrifuge tests.

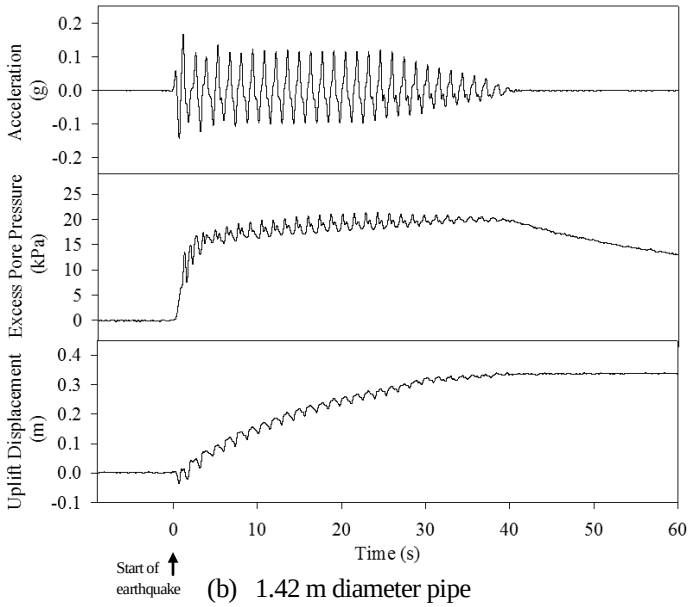
4. BEHAVIOUR OF LIQUEFIED SOIL AROUND A TUNNEL

4.1 Excess Pore Pressure Generation

The uplift of pipe in a liquefied soil may be deemed to be mainly driven by the buoyancy of the pipe. This is accompanied by the loss of shear strength of the soil due to excess pore pressure generation which encourages floatation. Hence, a high degree of liquefaction has to be present to allow the pipe to float easily. Figure 5 shows that significant liquefaction has been achieved at the springing depths of the tunnel and pipe during the earthquake. At this stage, the shear strength of the soil was reduced significantly, resulting in the floatation of tunnel, as evident in the uplift displacement readings shown in the same figure. This is in agreement with the literature in Section 2.



(a) 5 m diameter tunnel



(b) 1.42 m diameter pipe

Figure 5 Plots of acceleration (‘*A*’), excess pore pressure (‘*B*’ and ‘*D*’), and uplift displacement (‘*C*’ and ‘*E*’) of tunnel and pipe, in prototype scale

4.2 Soil Deformation during Tunnel Floatation

PIV analysis in dynamic centrifuge testing has shown to be capable of providing reliable measurements on the progress of soil deformation and uplift displacement of tunnels (Chian and Madabhushi, 2010b). Figure 6 shows the development of the soil deformation mechanism during the floatation of the tunnel, which tends to develop into a circular flow around a circular buried structure, where the soil lifted by the structure gradually replaces the soil which has moved into the displaced void beneath the buoyant structure.

The uplift displacement of the pipe was significantly greater than the tunnel. This is due to the lower confining stress at shallow soil depth, which leads to the high mobility of soil near the surface (Chian and Madabhushi, 2011). This is evident from the large displacement of soil grains near the surface as observed in Figure 6.

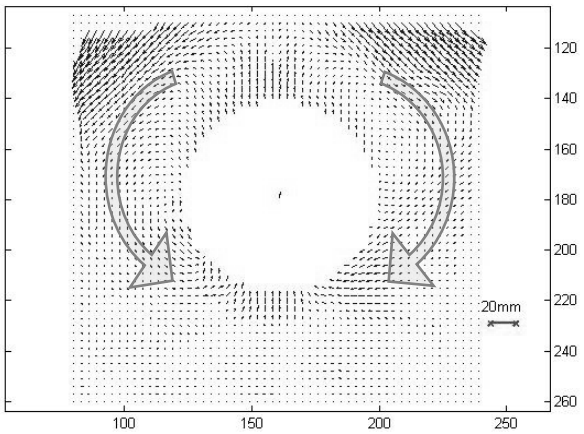


Figure 6 Cumulative displacement vectors of soil and tunnel during the earthquake

4.3 Cyclic Response of Tunnel during Floatation

The hypothetical response of a buoyant object in a viscous fluid is expected to float smoothly towards the soil surface alike to the falling ball viscometer or a sinking ball in liquefied soil test adopted in the measurement of viscosity of liquefied soil. The difference between them is that the former floats rather than sink in the case for the latter. According to Stoke's law as adopted in the sinking ball tests, the viscosity of a fluid can be estimated by the forces of equilibrium acting on a 1-D sinking object as shown in Figure 7 and Eq. (2).

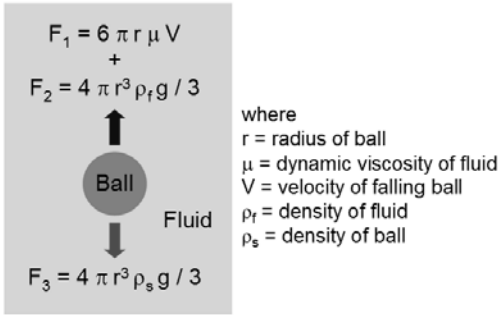


Figure 7 Forces acting on a sinking ball in equilibrium

$$\mu = \frac{2r^2(\rho_s - \rho_f)g}{9V} \quad (2)$$

Detailed movement of the tunnel during the earthquake was investigated with the use of instrumentation attached to the tunnel as well as employing the PIV technique. The vertical movement of the tunnel is obtained from the draw-wire potentiometer or the PIV analysis, while the horizontal movement acquired from the PIV analysis or estimation from the double integration of the acceleration readings from the accelerometers attached on the tunnel. Figure 8 illustrates the cyclic movement of the tunnel during its floatation in prototype scale. The variation between the two sources of measurement is mainly due to the dimensional scaling from model scale to prototype scale. In model scale, the mean differences are merely 0.12mm and 0.22mm in the horizontal and vertical displacements respectively. This indicates the consistency of readings obtained.

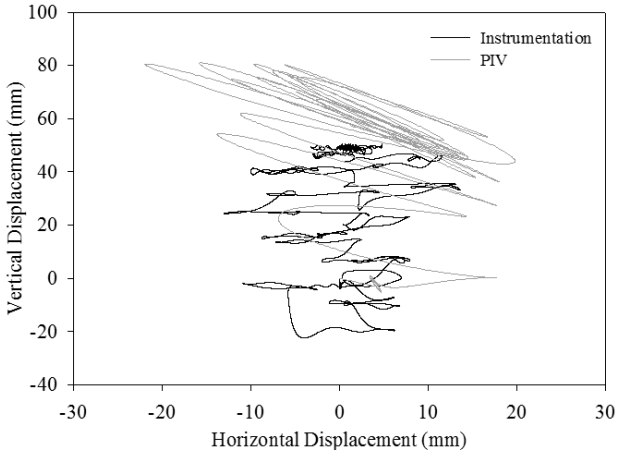


Figure 8 Cyclic movement of tunnel in liquefied soil during floatation, in prototype scale

Centrifuge tests showed the floatation of tunnels in liquefied soil do not follow the same response as the descending sphere in the sinking ball test. Rather than floating directly to the soil surface, the tunnel was observed to also displace horizontally during the earthquake as it floats. This suggests that the liquefied soil may not behave like an ideal viscous fluid in this case due to the interaction between the soil and the oscillating tunnel.

4.4 Soil-Structure Interaction

From the above findings, it is evident that the transition of saturated soil to a liquefied state may cause a buoyant tunnel to float due to the reduction in shear strength and the increased mobility of the liquefied soil. On the other hand, both factors could be altered due to the coupled soil-structure interaction. The liquefied state of the soil influences the buoyant tunnel to float. At the same time, the movement of the tunnel (vertically and horizontally) exerts pressure to the surrounding soil, leading to a partial recovery of the soil's shear strength. This is evident from the reduction in excess

pore pressure as shown in Figure 9. This led to the soil displacing in a wide loop around the tunnel (see Figure 6), unlike the monotonic uplift of structure in upheaval buckling which showed narrow loops of soil movement with high displacement nearer to the structure as shown in Figure 10.

Despite a high excess pore pressure generated, it was observed that the excess pore pressure was dissipating quickly during the earthquake at 3m away from the tunnel face as shown in Figure 9. This indicates that pore fluid is migrating towards the tunnel due to the hydraulic gradient difference as excess pore pressure is relatively lower near the tunnel face at the same soil depth.

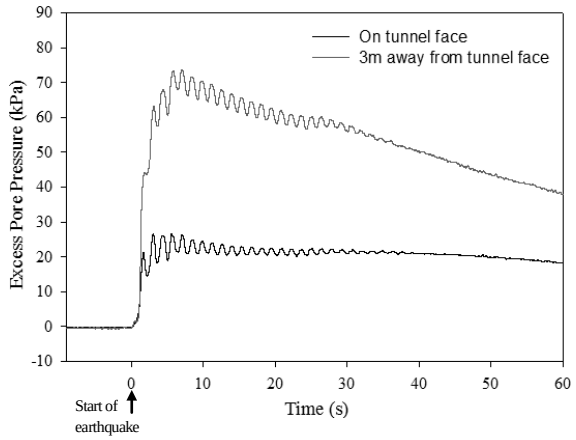


Figure 9 Excess pore pressures at the springing depth of tunnel (*'B'* and *'F'*), in prototype scale

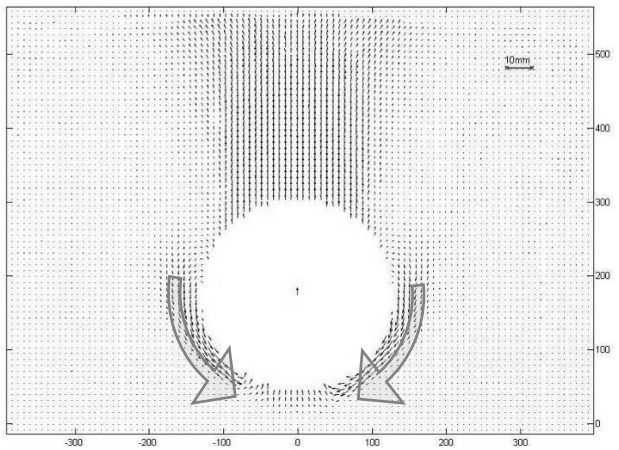


Figure 10 Cumulative displacement vectors of soil and buried structure due to monotonic uplift (Chian et al., 2011)

The accelerations measured on the tunnel face were smaller than those measured 3m from the tunnel face despite being located at the same soil depth as shown in Figure 11. This suggests that the tunnel is getting isolated from earthquake shaking. Pore fluid migration towards the tunnel may be causing a reduction in effective stress locally around the tunnel, thereby isolating it from earthquake shaking. As such, seismic considerations based on free field acceleration may lead to a more conservative analysis on the response of the tunnel.

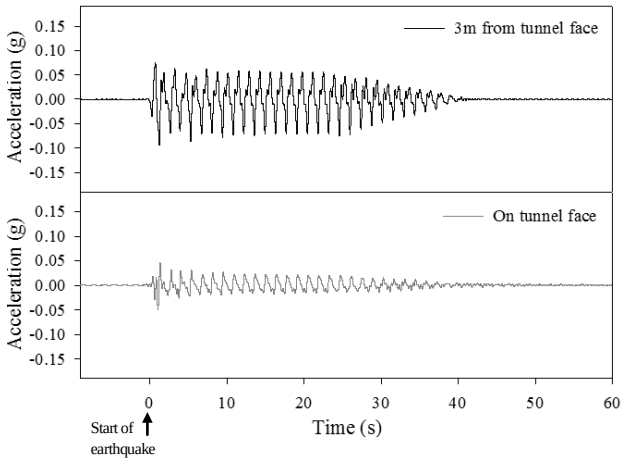


FIGURE 11 Accelerations at the springing depth of tunnel (*'G'* and *'H'*), in prototype scale

5. CONCLUSION

The floatation of tunnel in liquefied soil does not follow the continuous uplift displacement of a typical buoyant object in a viscous fluid. Instead, the tunnel cycles horizontally as it displaces vertically upwards to the soil surface. This indicates that liquefied soil does not behave identical to an ideal viscous fluid in the presence of a rigid tunnel. The cyclic movement of the tunnel, both vertically and horizontally, induces external stresses in the soil around it, thereby leading to partial recovery of shear strength as the soil dilates. This in turn resists floatation of tunnel to occur. The reduction in excess pore pressure near the tunnel also encourages pore fluid migration from the free field. The coupled soil-structure interaction also attenuates the soil's acceleration significantly.

References:

Bardet, J.P. and C.A. Davis (1999), "Responses of Large-Diameter Buried Pipes to Earthquakes," *Proceedings of the 2nd International Conference on Earthquake Geotechnical Engineering*, 973-986.

Chian, S.C. and Madabhushi, S.P.G. (2010a), "Floatation of Tunnels in Liquefiable Soils," *Proceedings of the 5th International Conference on Recent Advances in Geotechnical Earthquake Engineering and Soil Dynamics*, Paper No. 7.04a.

Chian, S.C. and Madabhushi, S.P.G. (2010b), "Use of PIV Analysis for Soil Deformations around a Tunnel in Liquefiable Soils," *Proceedings of the 14th European Conference on Earthquake Engineering*, Paper ID 224.

Chian, S.C. and Madabhushi, S.P.G. (2011), "Tunnel and Pipe Floatation in Liquefied Soils," *Proceedings of the 5th International Conference on Earthquake Geotechnical Engineering*, Paper No. TAPCH.

Chian, S.C., Whittle, J., Mulyani, R., Alarcon, J.E and Wilkinson, S.M. (2010a), "Post Earthquake Field Investigation of the Mw7.6 Padang Earthquake of 30th September 2009",

Proceedings of the 14th European Conference on Earthquake Engineering, Paper ID 1372.

Chian, S.C., Stringer, M.E. and Madabhushi, S.P.G. (2010b), "Use of Automatic Sand Pourer for Loose Sand Models," *Proceedings of the 7th International Conference on Physical Modelling in Geotechnics*, 117-121.

Chian, S.C., Wang, J., Haigh, S.K. and Madabhushi, S.P.G. (2011), "Soil Deformation during Pipe Uplift in Liquefiable Soil," *Submitted to the 21st International Offshore and Polar Engineering Conference*.

Geoengineering Extreme Events Reconnaissance (GEER) Association (2010), "Geo-engineering Reconnaissance of the 2010 Maule, Chile Earthquake," *Report of the NSF Sponsored GEER Association Team*.

Ghayamghamian, M.R., Tobita, T., Iai, S. and Kang, G. C. (2007), "Reconnaissance Report of July 16, 2007 Niigata-Ken Chuetsu-Oki, Japan, Earthquake," *Journal of Seismology and Earthquake Engineering*, Vol. 9, No. 1 and 2.

Hall, W.J. and T.D. O'Rourke (1991), "Seismic Behavior and Vulnerability of Pipelines," *ASCE Lifeline Earthquake Engineering*, 761-773.

Hamada, M. and Wakamatsu, K. (1998), "A Study on Ground Displacement caused by Soil Liquefaction," *Journal of Geotechnical Engineering*, **III-43**(596), 189-208.

Hashash, Y.M.A., Hook, J.J., Schmidt, B. and Yao, J.I. (2001), "Seismic Design and Analysis of Underground Structures," *Tunnelling & Underground Space Technology*, **16**(4), 247-293.

Hwang, J.-I., Kim, C.-Y., Chung, C.-K. and Kim, M.-M. (2006), "Viscous Fluid Characteristics of Liquefied Soils and Behaviour of Piles Subjected to Flow of Liquefied Soils," *Soil Dynamics and Earthquake Engineering*, **26**, 313-323.

Kawakami, T., Suemasa, N., Hamada, M., Sato, H. and Katada, T. (1994), "Experimental Study on Mechanical Properties of Liquefied Sand," *Proceedings of the 5th US-Japan Workshop on Earthquake Resistant Design of Lifeline Facilities and Countermeasures against Soil Liquefaction*, Technical Report NCEER-94-0026, 285-99.

Madabhushi, S.P.G., Schofield, A.N. and Lesley, S. (1998), "A New Stored Angular Momentum Based Earthquake Actuator," *Proceedings of the Centrifuge '98*, Vol. 1, 111-116.

Miyajima, M., Kitaura, M., Koike, T. and Hasegawa, M. (1995), "Experimental Study on Characteristics of Liquefied Ground Flow," *Proceedings of the 1st International Conference on Earthquake Geotechnical Engineering*, Vol. 2, 969-975.

Mitrani, H. (2006), Liquefaction Remediation Techniques for Existing Buildings, PhD Thesis, Cambridge University, U.K.

Okimura, T., Takada, S. and Koid, T.H. (1996), "Outline of the Great Hanshin Earthquake, Japan 1995," *Natural Hazards*, **14**, 39-71.

Schmidt, B. and Hashash, Y.M.A. (1999), "Preventing Tunnel Flotation due to Liquefaction," *Proceedings of the 2nd International Conference on Earthquake Geotechnical Engineering*, 509-512.

Schofield, A.N. (1981), "Cambridge Geotechnical Centrifuge Operations," *Géotechnique*, **25**(4), 743-761.

Seed, H.B. (1970), "Soil Problems and Soil Behaviour," in *Earthquake Engineering*, Chapter 10, Prentice-Hall, New Jersey, 227-252.

Steedman, R.S. and Madabhushi, S.P.G. (1991), "Wave Propagation in Sand Medium," *Proceedings of the International Conference on Seismic Zonation*.

Stewart, D.P., Chen, Y.-R. and Kutter, B.L. (1998), "Experience with the Use of Methylcellulose as a Viscous Pore Fluid in Centrifuge Models," *Geotechnical Testing Journal*, **21**(4), 365-369.

Stringer, M.E. and Madabhushi, S.P.G. (2009), "Novel Computer Controlled Saturation of Dynamic Centrifuge Models using High Viscosity Fluids," *Geotechnical Testing Journal*, **32**(6), 559-564.

Tobita, T., Iai, S., Kang, G. C. and Konishi, Y. (2009), "Observed Damage of Wastewater Pipelines and Estimated Manhole Uplifts during the 2004 Niigataken Chuetsu, Japan, Earthquake," *ASCE Technical Council on Lifeline Earthquake Engineering*, 1-12.

Towhata, I. (2008), "Geotechnical Earthquake Engineering," Springer, Berlin.

White, D.J., Take, W.A. and Bolton, M.D. (2001), "Measuring Soil Deformation in Geotechnical Models using Digital Images and PIV Analysis," *Proceedings of the 10th International Conference on Computer Methods and Advances in Geomechanics*, 997-1002.

White, D.J., Take, W.A. and Bolton, M.D. (2003), "Soil Deformation Measurement using Particle Image Velocimetry (PIV) and Photogrammetry," *Géotechnique*, **53**(7), 619-631.

Youd, T.L. and S.N. Hoose (1976), "Liquefaction during 1906 San Francisco Earthquake," *ASCE Journal of Geotechnical Engineering Division*, **102**(5), 425-439.

8CUEE CONFERENCE PROCEEDINGS
8th International Conference on Urban Earthquake Engineering
March 7-8, 2011, Tokyo Institute of Technology, Tokyo, Japan

STIFFNESS AND POISSON'S RATIO EVALUATION ON GRANULAR MATERIAL BY ELASTIC WAVE MEASUREMENTS ON LABORATORY SPECIMEN

Laxmi Prasad Suwal[1)], Reiko Kuwano[2)], Junichi Koseki[3)] and Takeshi Sato[4)]

1) Graduate Student, Department of Civil Engineering, the University of Tokyo, Japan
2) Associate Professor, Institute of Industrial Science, the University of Tokyo, Japan
3) Professor, Institute of Industrial Science, the University of Tokyo, Japan
4) Technical Director, Integrated Geo-technology Institute Ltd, Japan
suwal@iis.u-tokyo.ac.jp, kuwano@iis.u-tokyo.ac.jp, koseki@iis.u-tokyo.ac.jp, tsato@iis.u-tokyo.ac.jp

Abstract: Elastic wave measurement techniques are becoming reliable methods for studying materials properties. Several methods have been developed in last three decades. Among the various methods of elastic wave measurement techniques in laboratory, recently developed Disk Transducer method and Trigger Accelerometer method are employed in this study. Disk transducer is flat shaped piezo-ceramic transducer installed in the center of the top cap and pedestal on triaxial apparatus which is able to measure both compression and shear wave on a single speciemen.The maximum stiffness moduli (G_{max} or E_{max}) measurement at very small strain level on three granular materials, Toyoura sand, Silica sand and Hime gravel employing Disk Transducer method and Trigger accelerometer method are conducted. The dynamically measured results are compared with the statically measured results applying small strain cyclic loadings. Poisson's ratio (ν) reflects the lateral deformational characteristics. It is one of the prominent characteristics of materials on analysis of deformation behavior. Simultaneous measurements of the compression and shear wave made possible to compute the Poisson's ratio (ν). The Poisson's ratio (ν) derived by wave measurement was computed in each stress levels on previously mentioned three geo-materials. The specimens were prepared by pouring the material through the air with controlling height for all cases and the compression and shear waves were measured from the lower pressure level (50kPa) to the higher pressure level (400kPa). The stiffness moduli are found approximately similar by both elastic wave measurement methods with the statically derived stiffness. The Poison's ratio is evaluated by both methods which are higher than statically determined value and the effect of stress level on Poison's ratio is examined.

1. INTRODUCTION:

Elastic wave measurements for studying the soil properties are being used in laboratory and field extensively during last few decades. The thoroughly studies of the propagated elastic waves are quite informative to investigate the soil properties. Several researchers have attempted to develop a reliable method for propagating elastic waves and its applications on science and engineering fields. One of the prominent applications is to evaluate the maximum stiffness moduli, mainly shear moduli of the geomaterials.The tangent moduli at very small strain level (within strain level 0.001%) is known as the small strain stiffness moduli which is assumed to be elastic, recoverable and independent of strain level and equivalent one determined measuring elastic waves through the material (Richart et al., 1970, Jardine et al., 1986, Burland 1989; Tatsouka and Shibuya 1992, Arroyo et al., 2003). Several laboratory techniques of measuring elastic wave measurements are being used in geotechnical laboratories. It is assumed that the Shirley and Hampton is pioneer, who developed the Bender Element transducer at first (1978). After its invention, it was extensively used in the various testing apparatuses like consolidometer or odometer (Jamiolkowski et at., 1995, Lee et al., 2010), triaxial apparatus (Viggiani and Atkinson, 1995; Jovicic et al., 1996; Hwang et al., 1998), Shear apparatus (Mulmi, S., 2008). Another method of measuring propagated waves in the specimen was proposed in the University of Tokyo around 2000 which is known as Trigger Accelerometer method (Ahn Dan and Koseki, 2002). In this method, a pair of triggers is firmly installed on the top cap which excites according to the function set on the function generator (various types of signal in terms of wavelet form and frequency can be excited as required). A pair of accelerometers (receiver sensors) is fixed on the surface of the specimen with known distance apart which senses the propagating signals in the specimen. Recently, the flat and disk shaped piezo electric transducer "Disk Transducer" has been developed in the Institute of Industrial Science, The University of Tokyo (Suwal and Kuwano, 2010). In spite of huge popularity, Bender element is not applicable to measure both compression and shear wave in a single specimen, where the later both methods are applicable to measure both compression and shear waves in a single specimen. Few researchers tried to measure both elastic waves combining bender element and compression plate on triaxial apparatus (Brignoli at al., 1996, Lee at

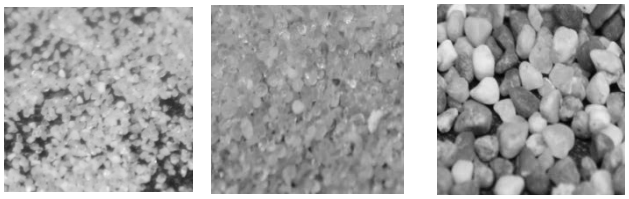
al.,2010,).Recently Bender-extender was developed which is used to measure both compression and Shear waves (Leong et al.,2009, Kumar and Madhusudhan., 2010).

The measurement of both compression and shear waves on single specimen make possible to evaluate the lateral deformation property (poisson's ratio) of the geomaterials dynamically. The effects of relative density and confining pressure on poisson's ratio was investigated in dry sands using Bender –extender and the variability of poisson's ratio was confirmed (Kumar and Madhusudhan., 2010). This study computed the small strain stiffness moduli as well as poisson's ratio by both Trigger accelerometer method and Disk Transducer method including static method on Toyoura sand, silica sand and Hime gravel and the outputs are compared among those methods. The statically derived poisson's ratios for Toyoura sand and Hime gravel are considered as 0.17 and 0.2 (reffering Hoque et al., 1996 and De Silva et al., 2004) in this study.

2. MATERIALS AND TESTING EQUIPMENTS:

2.1. MATERIAL USED:

Three sorts of granular geomaterials, Toyoura sand, Silica sand and Hime gravel, of varying grain size 0.2 mm to 2 mm were tested in study. Toyoura sand is fine-grained, uniformly graded sand, originated from Toyoura Beach area of Yamaguchi prefecture, Japan. Silica sand is one of the popular varieties of sand in the world. Silica sand is produced by degradation of quartz. The quartz crystals are broken down into small grains as Silica sand. The grain size of Silica sand varies from fine to coarse. In this study, Silica sand having mean diameter, D_{50}, 0.45mm was used. Hime gravel is poorly sorted, and the grain shape is angular. It was taken from Hime River, Otari, Kitaazumi, Nagano prefecture, Japan. It is derived from sandstone, chert, granite, sill, quartz etc. The pictures of these materials are shown in Figure 1 (A. Toyoura sand, B. Hime gravel and C. Silica sand). Physical properties including specific gravity, maximum and minimum void ratio, mean diameter and gradation curves are shown in Table 1 and Figure 2 respectively.



a. Toyoura sand b. Silica sand c. Hime gravel

Figure 1. Picture of used materials

2.2 . EQUIPMENTS:

The triaxial apparatus having facility to equip transducers/sensors for wave measurement was employed in this study. Broadly they are categorized as;

A. TRIAXIAL COMPRESSION TESTING MACHINE:

Small size, gear driven and strain controlled triaxial apparatus, as shown in Figure 3 was used for performing experiments. The axial loading system consists of an AC servomotor and a reduction gear system, electro-magnetic clutches and brakes. Stress and strain are precisely controlled by high speed computer.

Table 1. Physical and mechanical properties of tested materials

PHYSICAL AND MECHANICAL PROPERTIES	Toyoura sand	SILICA SAND	Hime gravel
Specific gravity, G_s	2.62	2.64	2.65
Maximum void ratio, e_{max}	0.946	0.787	0.709
Minimum void ratio, e_{min}	0.637	0.538	0.480
Mean Diameter, D_{50} (mm)	0.19	0.45	1.72

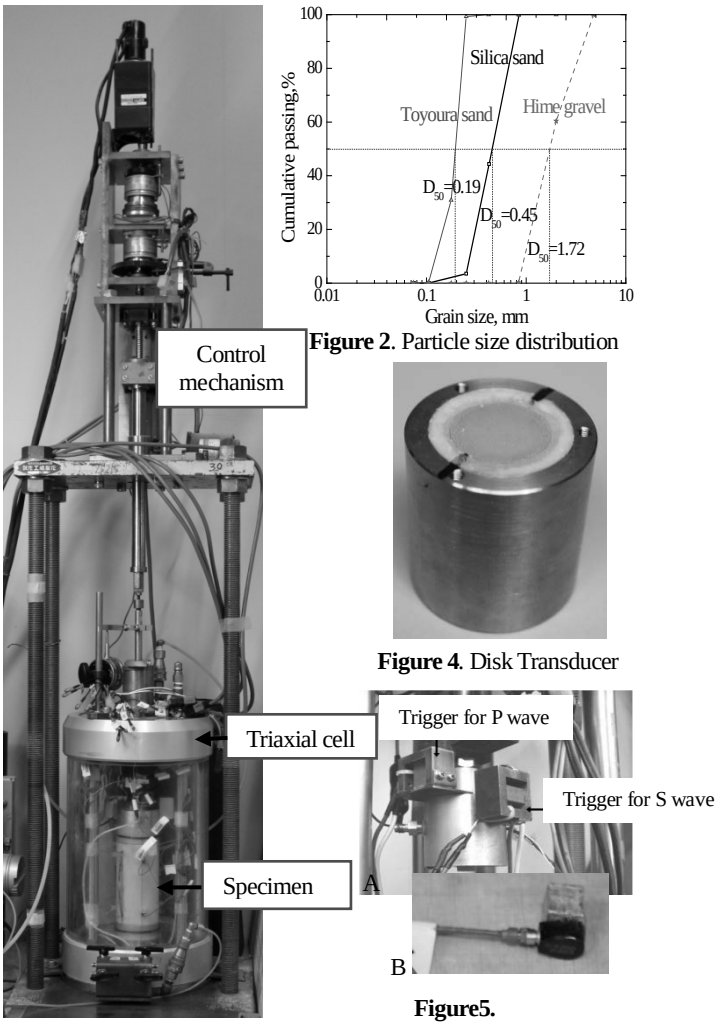


Figure 2. Particle size distribution

Figure 4. Disk Transducer

Figure 3.Triaxial apparatus

Figure5.
A. Triggers B. Accelerometer

B. TRANSDUCERS AND SENSORS:

Two techniques of wave measurement, Disk Transducer method and Trigger Accelerometer method, were applied in this study. The Disk transducer has been recently developed in this study. P-type element and S-type elements are referred for piezo-ceramic element enabling to generate P and S wave on the application of electric voltage. Disk shaped Φ20 mm with thickness 2 mm P-type and thickness 5 mm S-type piezo ceramic elements were used and firmly stuck forming PS-element. Then, it was assembled on metal housing as shown in figure 4 and embedded in top cap and pedestal. The Trigger Accelerometer method was developed

in the University of Tokyo (AnhDan and Kosesi, 2002).The picture of Triggers and Accelerometer are shown in Figure 5.

C. WAVE MEASUREMENT EQUIPMENTS:

Signal for transmitting wave was generated by a digital automatic function generator manufactured by "Tektronix Co. Ltd.". It can produce a maximum peak to peak voltage of 10 V and is capable of producing twelve kinds of different waveforms at frequency ranges of 0.001Hz to 25MHz. An amplifier, NF-HAS 4014 was used to amplify the input signal generated by the function generator before feeding it into the transducer. The oscilloscope HIOKI 8860-50 MEMORY HiCORDER was used to record and display waveforms of the transmitted and received signals.

3. SPECIMEN PREPARATION, TESTING PROCEDUCRES AND ANALYSIS:

3.1 SPECIMEN PREPARATION AND TESTING PROCEDURES:

Specimens of 75 mm in diameter and 150 mm in height were used for all tests. The specimen was prepared by air pluviation technique. The materials were poured through air keeping constant height of pouring to maintain constant density throughout the specimen. Lower pouring height was adopted for erecting loose specimen and higher for dense specimen. In this study, the loose specimens were prepared keeping falling height 20 cm and 80 cm height was maintained while preparing dense specimens. At first, the specimens were set up at an isotropic stress state of 25 kPa, and then the stress was increased to 50, 100, 200 and 400kPa in normally consolidated phase. For over consolidated phase, stress level was descended from 400 kPa to 50 kPa as shown in Figure 6. Specimen was kept in each stress state for sufficient time period to dissipate the creep effect. 11 cyclic loadings with peak to peak strain amplitude of 0.001% were applied in vertical direction and another creep stage was maintained for conducting wave measurement.

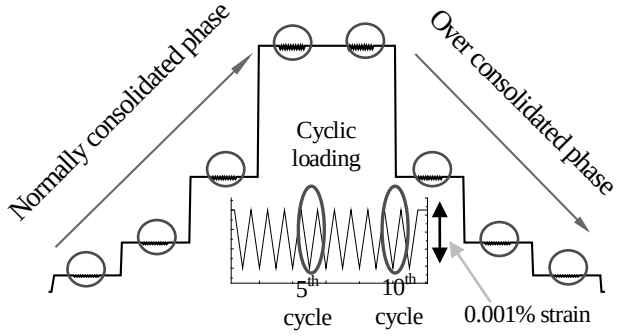


Figure 6. Loading history of experiment

3.2 ANALYSIS PROCEDURES:

Generally, two sorts of analysis were executed namely static and dynamic. Static means result was computed by relation of deformation and stress during small strain cyclic loadings. Deformation was measured by local deformation transducers (LDTs) developed by Goto et al (1991), which can measure local strain in higher accuracy and free from bedding errors. Cyclic (static) Young's modulus (E_{cyc}) was derived by fitting a straight line on the stress-strain plot. The stress-strain relation of 5th cycle and 10th cycle were utilized to evaluate E_{cyc}. The typical plot of stress strain relation is shown in Figure 7. The average results of 0.001% strain amplitude were obtained at each stress state. This stiffness is named as the statically measured stiffness modulus in this study. Stiffness calculated by wave measurement is called as the dynamically measured stiffness modulus. Stiffness was derived by relating stiffness, density and velocity of propagating wave. The Disk Transducers were centrally installed in the top cap and pedestal where as the Accelerometers were fixed on the lateral surface of the specimen. The nature of the wave propagation was schematically shown in figure 8 (a. Disk Transducer method, b. Trigger Accelerometer method). The confining pressure (stress level or cell pressure) employed during experiments varies from 50 kPa to 400 kPa. The cell pressure is applied to simulate (reproduce) the real field condition. It is considered that the cell pressure is working as the confinement in the real field and the propagated waves through the specimen are analyzed as constrained involving no lateral deformation perpendicular to the direction of propagation whether they are measured by centrally installed transducers or sensors fixed at lateral surface. Applying such higher stresses at small specimen (Φ=75mm and 150mm height), the variation on the degree of confinement at center of specimen and surface of specimen is very small and neglected in this study. Constrained vertical modulus (M) could be achieved by Equation (1). The constrained modulus was then converted to the unconstrained modulus using the Equation (2).

$$M = \rho . V_P^2 \tag{1}$$

$$E = \frac{M(1-2\nu)(1+\nu)}{(1-\nu)} \tag{2}$$

$$G = \rho . Vs^2 \tag{3}$$

$$G = \frac{E}{2(1+\nu)} \tag{4}$$

$$\nu = \frac{(0.5V_p^2 - V_s^2)}{V_p^2 - V_s^2} \tag{5}$$

$$f(e) = \frac{(2.17-e)^2}{1+e} \tag{6}$$

[Where, V_p is compression wave velocity, V_s is shear wave velocity, ρ is unit mass of specimen, E is the Young's Modulus ,G is the shear Modulus, e is the void ratio of specimen and ν is the Poisson ratio.]

The dynamically obtained shear moduli are computed measuring shear waves directly as the Equation (3). The relation of Young's modulus and Shear modulus is established by Equation (4) which is used for both static method applying small strain cyclic loadings and wave

measurement methods. One of the benefits of measuring both compression and shear wave in an identical specimen is it permit to evaluate the Poisson's ratio through wave measurement technique directly. Combining the Equations (1), (2) and (3), the Equation of Poisson's ratio in terms of velocity of compression and shear wave is derived (Equation (5)). The densities of specimens were different in tests, so, the void ratio function proposed by Hardin and Richart (1963) was used to eliminate the effects of various densities (void ratio) of specimens. Among the various void ratio functions, Equation (6) proposed for granular materials is used in this study.

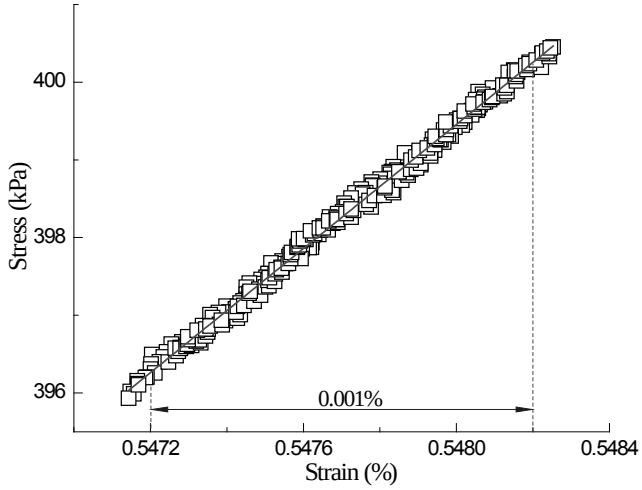


Figure 7. Stress-strain relationship

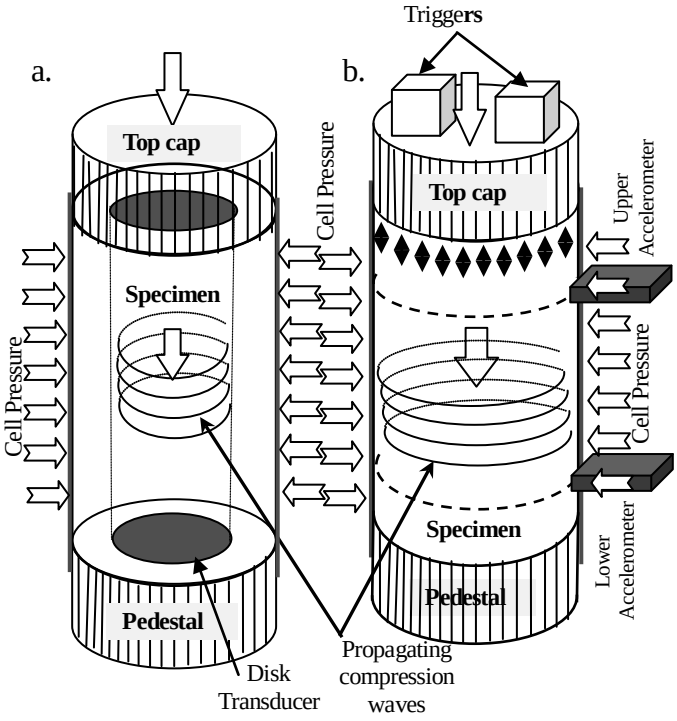


Figure 8 a. Disk Transducer method
b. Trigger Accelerometer method.

a. SIGNAL INTERPRETATIONS:

The output signals generated by receiver transducer are directly fed to the oscilloscope in Disk Transducer method. Any amplifier, signal modifier and filters were not adopted in between receiver transducer and oscilloscope. So, the recorded data were found sometime containing system compliances. It was tried to remove employing Low pass filter. The frequency of the system noise was determined prior to the feeding the signal in the transmitter transducer. The system noises were found to be in the ranges of 22 kHz to 25 kHz. Then the signals were modified as the signals were allowed passing which contains lower frequencies than this. The typical plots of the input, output (recorded) and filtered signals in time series were shown in Figure 9 (P-type) and Figure 10 (S-type) respectively..

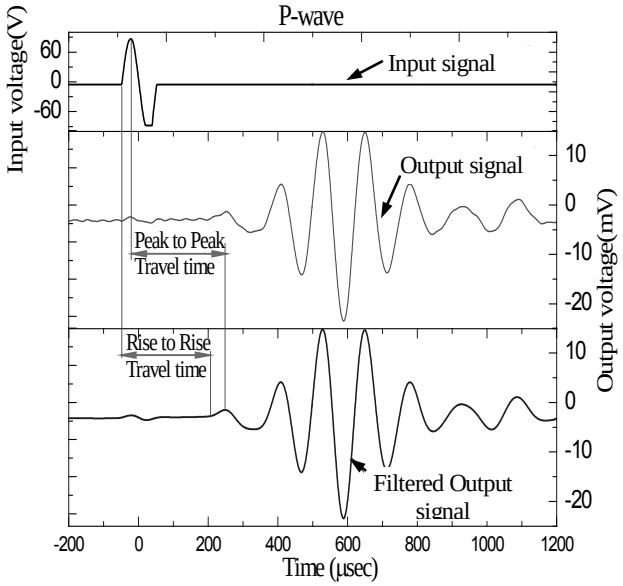


Figure 9: Definition of Travel time for compression wave

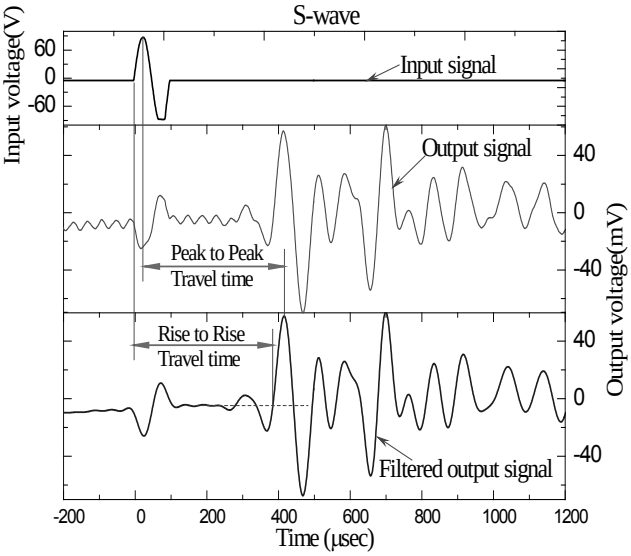


Figure 10:Defination of travel time for shear wave

The compression waves are evaluated as the first sense (deflection) of the signal on time domain series is the real arrival of the compression waves. Figure 9 shows the typical compression wave achieved on this study. The travel time are dealt considering the time gap between the rising of the

input signal to the rising of output signal (T_{rtr}) and the peak of the input signal to the peak of the output signal (T_{ptp}) which are clearly defined on the Figure 9. Interpretation of the shear waves is not still clear and several opinions are presented by various researchers about interpretation techniques. Many studies showed that the first deflection of the shear wave signal may not correspond to the arrival of the shear wave (Mancuso and Vinale, 1988). Disturbances and reflected compression wave travels in the speed of compression wave are arrived at first which create ambiguity on determination of the real shear wave arrival. In single sinusoidal excitation, the rising to rising travel time is defined as the distance from the rising of input signal to the first zero crossing point on the time domain series of the output signal following the recommendation by Jovocic (1996). This zero baseline correction is imposed to minimize the effect of the near field. The criteria employing to determine the travel times based on rise to rise of signals and peak to peak of signals are displayed on Figure 10. The charge amplifier was adopted in Trigger Accelerometer method. So, well informative waveforms are obtained directly. The travel time was determined considering rise of signal at upper Accelerometer to rise of signal at lower Accelerometer

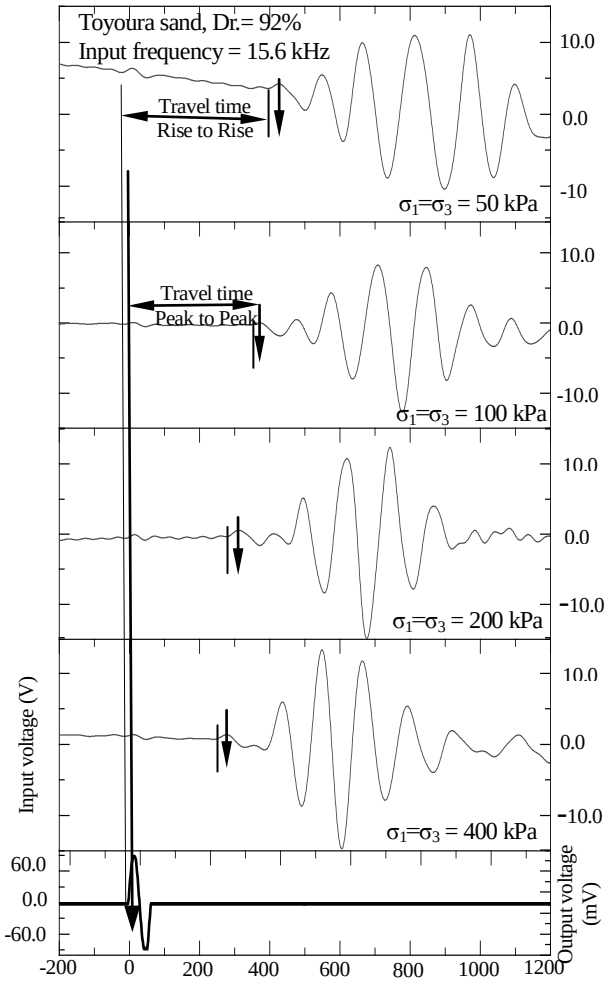


Figure 11. Typical Compression waves obtained on Toyoura sand at various stress level.

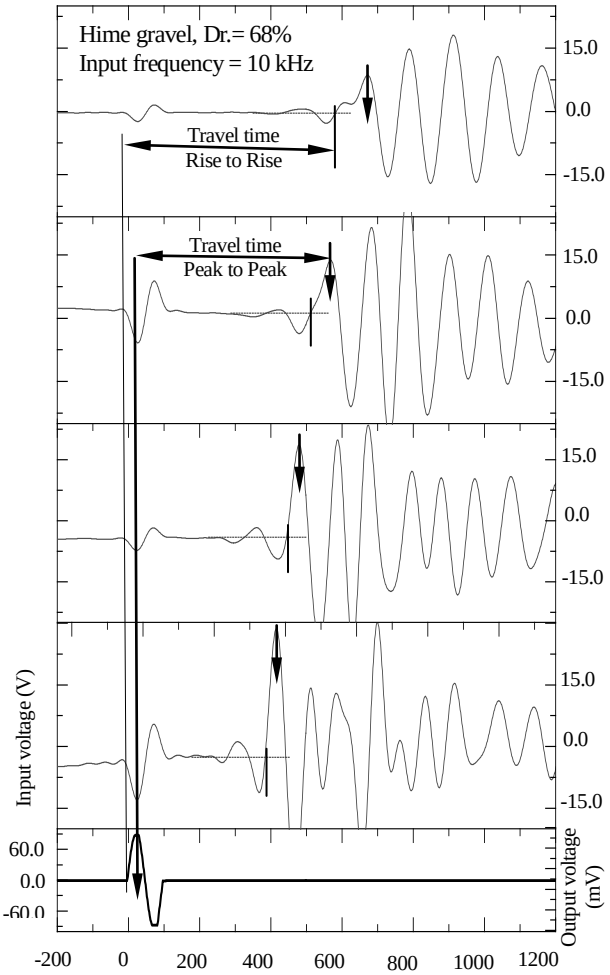


Figure12. Typical shear waves obtained on Hime gravel at various stress level.

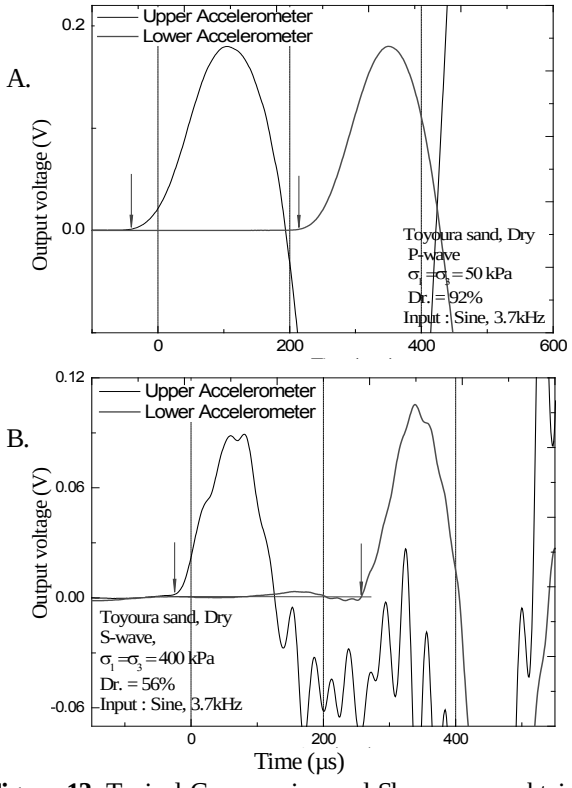


Figure 13. Typical Compression and Shear waves obtained on Toyoura sand at A) lower and B) Higer stress level.

Table 2: List of tests

Test no.	Material	Transducer used	Specimen condition	Relative density (%)	Input Voltage (V)	Input wave	Input frequency range (kHz)
1	Toyoura sand	DT& TA	Dry	56	± 93	sine	2.0 – 30.0
2	Toyoura sand	DT& TA	Dry	92	± 93	sine	2.0 - 30.0
3	Hime gravel	DT& TA	Dry	68	± 93	sine	2.0 – 20.0
4	Hime gravel	DT& TA	Dry	88	± 93	sine	2.0 – 20.0
5	Silica sand	DT& TA	Dry	78	± 93	sine	2.0 – 30.0
6	Silica sand	DT& TA	Dry	99	± 93	sine	2.0 – 30.0

4.0 TEST RESULTS AND DISCUSSIONS

Basically sands are classified according to grain sizes as fine sand (0.125-0.25 mm), medium sand (0.25- 0.5 mm) and coarse sand (0.5-1mm). The material having grain size around 2 mm is called very coarse sand or fine gravel (The international sand collector society, AASTO, USDA, USC). The tested materials, Toyoura sand represents the fine grain material, Silica sand represents the medium grain material and Hime gravel stands for the coarse grain material. The information of the tests is listed on Table 2, in which, the information related to wave measurement is expressed in respect to Disk Transducer method. The wave measurements were conducted inputting the signal of low frequency to higher frequency. Among these frequencies, the waveforms and results of dominant frequency (the frequency at which optimized outputs are achieved) is found out and the analysis is made based on the output of that input frequency.

The tests were performed in loose and dense condition. The input frequency 15.6 kHz was found to be good to propagate elastic waves through Disk Transducers (analyzed by FFT-Fast Fourier Transformation) on toyoura sand specimen. The received signals by P-type receiver while exciting through P-type transmitter elements at various stress level are shown in Figure 11. A single sinusoidal wave of 15.6 kHz was fed through function generator and the received wave was stacked for 100-200 times and the average response was recorded on oscilloscope. The recorded waves were proceeded applying low pass filter and then they are appeared as shown in Figure 11. The waveforms obtained at lower to higher stress levels are displayed from top to bottom and the input signal is shown in lowest of them. In this plot, the signals are plotted in time domain series (microsecond), the input signal is presented in volt and outputs are in milivolt. As discussed in previous, the travel time is determined in each stress level according to rise to rise of signals and peak to peak of signals. Similar waveforms were obtained on the other materials also. The Typical Shear waveforms obtained on Hime gravel are shown in figure 12. The output signals achieved on various stress level are plotted on time domain series which are resulted inputting a single sinusoidal wave of frequency 10.0 kHz. The Waveforms obtained on toyoura sand by Trigger Accelerometer method are shown in figure 13. The Compression waveform at lower stress level and the Shear waveform at higher stress level are shown Figure 13 A. and 13 B. respectively.

4.1 **STIFFNESS MODULI:** The stiffness moludi of the materials are the major parameters used in engineering applications. Currently the facilities of precise measurement of deformation are possible in laboratory. This study employed the LDT for measuring very small scaled deformations. Based on the stress-strain relation during small strain cyclic loadings, statically the young's moduli are calculated and converted into the shear moduli. Dynamically based on wave measurement, the stiffness moduli are determined. The stiffness moduli (Young's and Shear) are determined in both Disk Transducer method and Trigger Accelerometer method. Specimens having lower void and higher void (dense and loose) were tested on this study. The direct comparison of outputs of tests from various density is meaningless due to the outputs are highly influenced by the specimen's density. The stiffness moduli are significantly affected by the density or void ratio of the specimen in granular materials. It needs to nullify for comparing the results of various densities. Many researchers are using the void ratio function specified in Equation (6) for effective nullification of on granular materials with round shape particles, which is also used in this study. The outputs of various modes of measurement are normalized by the Equation (6).The normalized shear moduli are plotted against the normalized statically derived shear moduli in figures 14 – 16 (Figure 14: Results on Toyoura sand, Figure 15: Results on Hime gravel and Figure 16: Results on Silica sand). Both horizontal and vertical axes are expressed in MPa. The stiffness moduli derived by various modes of measurement are found showing approximate equivalency among those modes of wave measurement including static method. In those plots, the direct comparisons of the results amongst different densities as well as the results amongst the several modes of measurement are possible. The degree of scattering of the results in each stress levels reflecting the deficiencies on measurement systems including the reliability of void ratio functions for those materials.

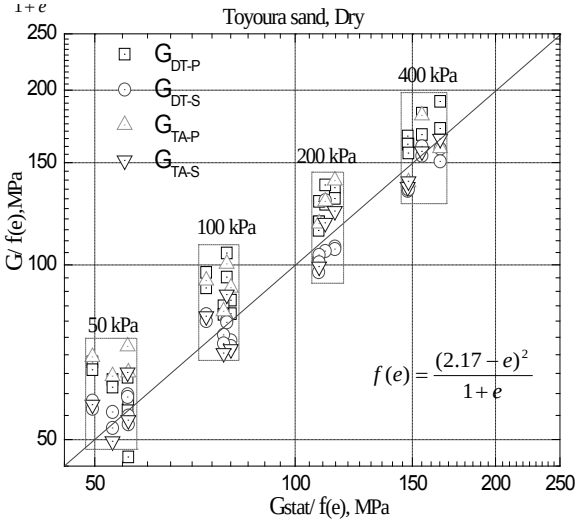


Figure 14 Results on Toyoura sand

These results showed the used void ratio function (equation 6) is effective to nullify the results and the results by both dynamic measurement techniques are equivalent to the static method. The results achieved measuring compression and shear waves are separately displayed in each plot for both Disk transducer and Trigger Accelerometer methods. The results obtained measuring compression waves are found to be higher than measuring shear waves in all stress levels (50kPa to 400kPa).

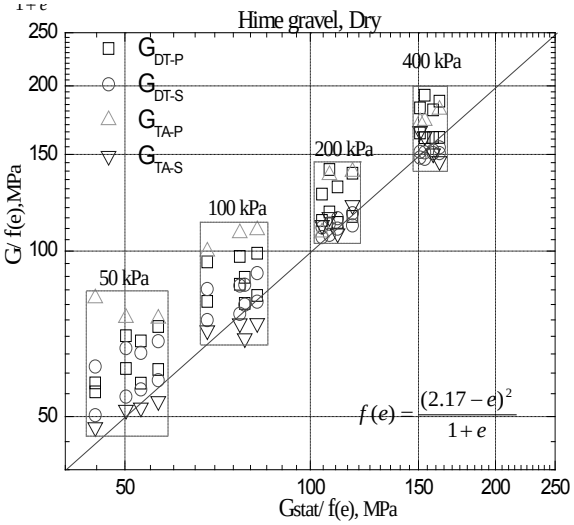


Figure 15 Results on Hime gravel

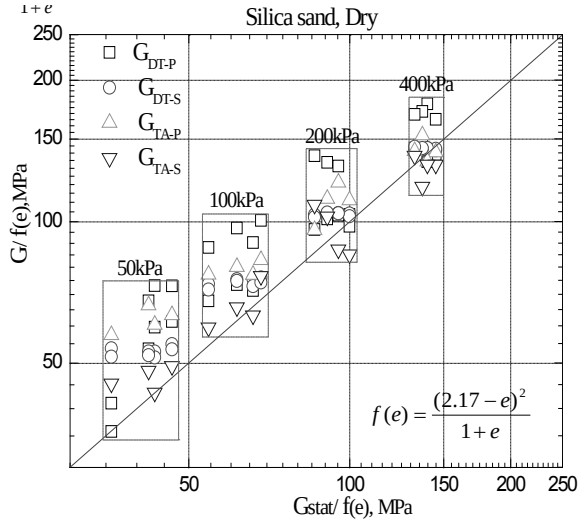


Figure 15 Results on Silica sand

Notations:

G_{stat}: Shear moduli derived applying small strain cyclic loadings.
G_{DT-P}: Shear moduli achieved by P-wave measurement on Disk Transducer method.
G_{DT-S}: Shear moduli achieved by S-wave measurement on Disk Transducer method.
G_{TA-P}: Shear moduli achieved by P-wave measurement on Trigger Accelerometer method.
G_{TA-S}: Shear moduli achieved by S-wave measurement on Trigger Accelerometer method

4.2 **POISSON RATIO**: Poisson's ratio evaluation of the geo-materials in laboratory needs great care and labors. Precise local deformation measuring transducer, LDT was employed to determine vertical and lateral deformations in static method. The success of measuring both compression and shear waves at each stress level in an identical specimen allows calculating the Poisson's ratio in terms of velocity as mentioned in Equation (5). The Poisson ratio is calculated on each test at loose and dense conditions. Figure 15 is the Poisson ratios obtained on Toyoura sand in loose and dense specimen conditions derived by various modes of measurements. The open symbols are representing the results of loose specimen condition and cross symbols are of dense specimen condition. The squares are results obtained by Disk Transducer method and circles are of Trigger Accelerometer method. Similar to Toyoura sand, the results obtained on Hime gravel and Silica Sand are plotted on Figure 16 and 17 respectively (the meaning of symbols also similar).

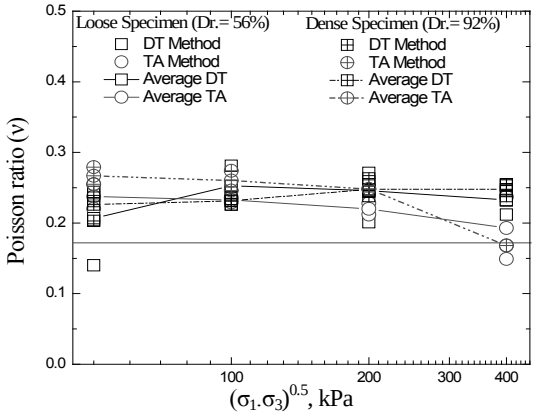


Figure 15 Poisson's ratio obtained on Toyoura sand

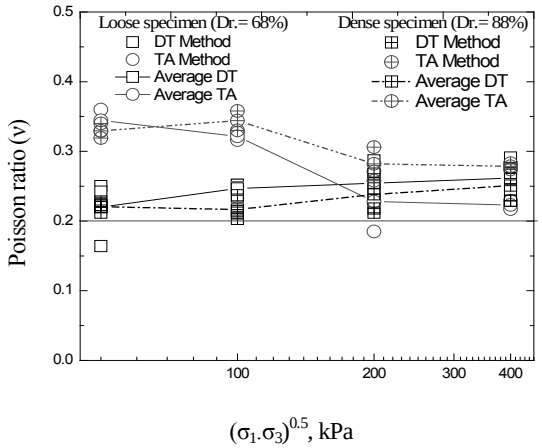


Figure 16 Poisson's ratio obtained on Hime gravel

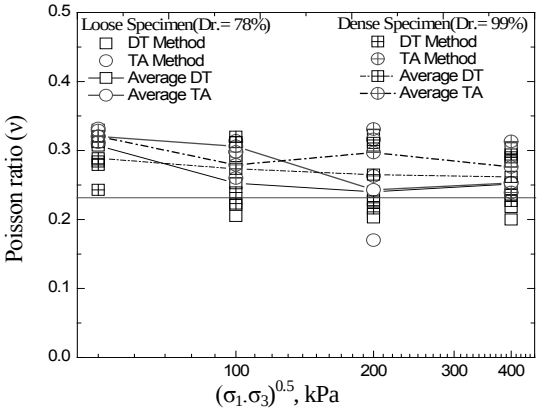


Figure 17 Poisson's ratio obtained on Silica sand

5. CONCLUSIONS:

The small strain stiffness measurement employing the wave measurement techniques were conducted on three granular geo-materials on loose and dense condition at normally and over consolidated stress conditions successfully and results were compared among them. Observing the results, the approximately equivalent stiffness moduli are found through both dynamic methods of measurement and to be comparable with the statically determined results. Poisson ratios are evaluated by both methods of elastic wave measurement at various stress levels which are found to be slightly higher than statically determined value on toyoura sand and Hime gravel. The statically determined results are referred from the previous works by Hoque et al., 1996 and De Silva et al. 2004) for Toyoura sand and Hime gravel respectively.

References:

AnhDan, L. Q., Koseki, J., and Sato, T.,"Comparison of Young's Moduli of Dense Sand and Gravel Measured by Dynamic and Static Methods", *Geotechinical Testing Journal*, ASTM, 2002, Vol. 25, No. 4, pp. 349-368.

Arroyo, M., Wood, D. M., and Greening, P. D., 2003, "Source Near-Field Effects and Pulse Tests in Soil Samples", *Geotechnique*, Vol.53, No. 3, pp. 337-345.

Brignoli, E. G. M., and Stokoe, K. H., II, 1996, "Measurement of shear waves in Laboratory Specimens by Means of Piezoelectric Transducers", *Geotechnical Testing Journal*, Vol. 19, No.4, December, pp. 384-397

Builes, M., 2004, "Dynamic and Static Measurements of Small-strain Stiffness of Geomaterials", *Master thesis*, Department of Civil Engineering, The University of Tokyo, Japan

Burland, J.B and Symes, M., 1982,"A simple axial displacement gauge for use in triaxial apparatus", *Geotechnique*, 32(1), 62-65.

Burland, J. B., 1989, "Ninth Laurits Bjerrum Memorial Lecture: Small is Beautiful-The Stiffness of Soils at Small Strain", *Canadian Geotechnical Journal*, Vol. 26, No. 4, November, pp. 499-516.

De Silva, L.I.N., 2004, "Locally Measured Quasi-Elastic Deformation Properties of Geo-materials under Torsional Shear and Triaxial loadings, "*Master's degree Dissertation*, The University of Tokyo.

Goto, S., Tatsuaka, F., Shibuya, S., Kim, Y-S., and Sato, T. (1991)," A simple Gauge for local small strain Measurements in the laboratory", *Soils and Foundations*, Vol.31, No.1, pp.169-180.

Hardin, B. O., and Richart, F. E., 1963, "Elastic Wave Velocities in Granular Soils", *Journal of Soil Mechanics and Foundations*, ASCE, Vol. 89, No.1, pp. 33-65.

Hoque, E., Tatsuoka, F., and Sato, T., 1996,"Measuring Anisotropic Elastic Properties of Sand Using a Large Triaxial Specimen", *Geotechnical Testing Journal*, Vol. 19, No.4, pp. 411-420.

Hoque, E., 1996,"Elastic deformation of sands in Triaxial tests", *PhD. Thesis*, The University of Tokyo, Japan.

Jardine, R. J., Symes, M. J., and Burland, J. B., 1984, "Measurements of Soil Stiffness in the Triaxial Apparatus", *Geotechnique*, Vol. 34, No. 3, pp. 323-340.

Jiang, G. L., Tatsuoka, F., Flora, A. and Koseki, J., 1997, "Inherent and stress-state induced anisotropy in very small strain stiffness of a sandy gravel, "*Geotechnique*, Vol. 47, No. 3, pp. 509-521.

Jovicic, V., Coop, M. R., and Simic, M., 1996,"Objective Criteria for Determining G_{max} from Bender Element Tests", Technical Note, *Geotechnique*, Vol. 46, No. 22, pp. 357-362.

Kumar, J. and Madhusudhan, B.N. (2010),"Effects of relative density and confining pressure on Poisson ratio from bender and extender elements tests", *Geotechnique* 60, No.7, 561-567.

Kuwano, R., Wicaksono, R.I and Mulmi, S. (2008), "Small strain stiffness of coarse granular materials measured by wave propagation", *Proc. of 4th international symposium on deformation characteristics of geomaterials*, IS-Atlanta 2008, Vol.2, pp.749-756.

Lee, J. S., Sanatamarina, J. C., 2005, "Bender Elements: Performance and Signal Interpretation", *Journal of Geotechnical and Geo-environmental Engineering*, Vol. 131, No. 9, September, pp. 1063-1070.

Leong, C., Yeo, S. H., and Rahardjo, H., 2005, "Measuring Shear wave Velocity Using Bender Elements", *Geotechnical Testing Journal*. Vol. 28, No. 5, pp. 488-498

Leong, E.C., Cahyadi, J.,and Rahardjo, H., 2009, " Measuring shear and compression wave velocities of soil using bender-extender elements", *Canadian Geotechnical Engineering Journal*, Vol. 46, pp. 792-812.

Shirley, D. J., and Hampton, L. D. "Shear-wave Measurements in Laboratory sediments", *Journal of Acoustical Society of America*, 1978, Vol. 63, No. 2, February

Suwal, L. P., and Kuwano, R., 2010 "Development of disc shaped pieze-ceramic plate transducer for elastic wave measurements in laboratory specimens", *Seisan-Kenkyu*, Bimonthly Journal of Institute of Industrial Science, The University of Tokyo, Vol.61,No.6, pp. 123-128

Tatsuoka, F and Kohata, Y (1995) "stiffness of Hard soils and soft rocks in Engineering applications", *keynote Lecture, Proceedings of International Symposium Pre-failure Deformation of Geomaterials* (Shibuya et al., eds), Balkema, 2,pp. 947-1063

Tatsuoka, F., and Shibuya, S., 1992, "Deformation Characteristics of Soils and Rocks from Field and Laboratory Tests", *Proceedings of 9th Asian Regional Conference of SMFE*, Bangkok, Vol.2, pp. 101-170.

Tsutsumi, Y., Builes, M., Sato, T., and Koseki, J., 2006, "Dynamic and Static Measurements of Small Strain Moduli of Toyoura Sand", *Bulletin of ERS*, No. 39, Institute of Industrial Science, The University of Tokyo

Wicaksono, R. I., 2007, "Small Strain Stiffness of Sand and Gravel Based on Dynamic and Static Measurements", *Master Thesis*, Department of Civil Engineering, the University of Tokyo, Japan.

Wicaksono,R.I, and Kuwano,R., 2009, "Small strain shear stiffness of Toyoura sand obtained from various wave measurement techniques", *Bulletin of Earthquake Resistant Structure Research Center*, The university of Tokyo, No.42, pp.107-119.

Woods, R. D., 1991, "Field and Laboratory Determination of Soil Properties at Low and High Strains",*Proceedings of second International Conference on Recent Advances in Geotechnical Earthquake Engineering and Soil Dynamics*, pp. 1727-1741.

8CUEE CONFERENCE PROCEEDINGS
8th International Conference on Urban Earthquake Engineering
March 7-8, 2011, Tokyo Institute of Technology, Tokyo, Japan

EFFECTS OF INITIAL STATIC SHEAR ON SHEAR STRAIN LOCALIZATION CHARACTERISTICS OF SAND IN UNDRAINED CYCLIC TORSIONAL SHEAR TESTS

Gabriele Chiaro[1], Takashi Kiyota[2], and Junichi Koseki[3]

1) Post-doctoral Research Fellow, Institute of Industrial Science, University of Tokyo, Japan
2) Associate Professor, Institute of Industrial Science, University of Tokyo, Japan
3) Professor, Institute of Industrial Science, University of Tokyo, Japan
chiaroga@iis.u-tokyo.ac.jp, kiyota@iis.u-tokyo.ac.jp, koseki@iis.u-tokyo.ac.jp

Abstract: Undrained cyclic torsional shear tests on loose Toyoura sand specimens subjected to single amplitude shear strain exceeding 50% were analyzed to study the effects of initial static shear on the strain localization properties of liquefied sand. Non-uniform specimen deformation was observed at strain levels higher than 20%. The limiting value of half of double amplitude ($\gamma_{DA}/2$) and single amplitude (γ_{SA}) shear strains, at which strain localization began during undrained cyclic loading, were evaluated by looking at the change in the deviator stress response as well as at the change in the strain accumulation properties. In the case of stress-reversal loading tests, it was found that the greater the static shear level the lower $\gamma_{DA}/2$; conversely, γ_{SA} was rather constant. These features suggested that, to define the limiting value of strain to initiate the strain localization of sand with initial static shear, γ_{SA} is a much more appropriate parameter than $\gamma_{DA}/2$. The limiting strain value of γ_{SA} was found to be of 23-28%. As long as the liquefied soil layer remains in uniform deformation, γ_{SA} values may be used in estimating the maximum amount of ground displacement due to liquefaction in natural and artificial slopes of sandy deposits.

1. INTRODUCTION

Following large-magnitude earthquakes (e.g., 1964 Great Alaskan, USA; 1964 Niigata, Japan; 1983 Nihonkai-Chubu, Japan; 1995 Kobe, Japan; etc.) extremely large horizontal ground deformation could be observed either in gentle sloped ground (Hamada et al., 1994; among others) or in level ground behind retaining walls (Ishihara et al., 1996; among others), resulting in severe damage to buildings, infrastructures and lifeline facilities (Hamada et al., 1988).

With the purpose of deeply investigate the large strain properties of liquefied sands, Kiyota et al. (2008) performed a series of undrained cyclic torsional shear tests on Toyoura sand specimens up to a double amplitude shear strain of about 100%. They found that there is a limiting value of double amplitude shear strain to initiate strain localization which increases with a decrease in relative density of the specimen.

Moreover, Kiyota et al. (2010) showed that the limiting value to initiate strain localization observed in torsional shear tests are consistent with the maximum amounts of liquefied-induced ground displacement observed in previous shaking table model tests (Yasuda et al., 1992; etc.) and most of the relevant case studies (Hamada et al., 1996; etc.). These features are reasonable considering the reduction in the mobilized cyclic shear stress in liquefied soils due to degradation of shear resistance.

By employing a torsional shear apparatus capable of achieving large torsional deformation, Chiaro et al. (2011) investigated the role which the static shear play on the large deformation behavior of Toyoura sand during undrained cyclic shear loading by performing a series of undrained cyclic torsional shear tests on loose specimens up to single amplitude shear strain of about 50%. In this paper, the test results presented by Chiaro et al. (2011) are analyzed in order to evaluate the correlation between the extent of initial static shear and the limiting value of both single and half of double amplitude shear strain required to initiate strain localization.

2. DEFORMATION OF SAND SPECIMEN WITH INITIAL STATIC SHEAR

Details of the employed hollow cylindrical torsional shear apparatus and the tested material have been already described by Chiaro et al. (2011). Thus, in this paper only the results from undrained cyclic torsional shear tests on loose saturated Toyoura sand specimens subjected to initial static shear will be briefly shown. It

should be noted that during the process of undrained cyclic torsional loading the vertical displacement of the top cap was prevented with the aim of simulating as much as possible the simple shear condition that ground undergoes during horizontal excitation. In these tests, three types of cyclic loading pattern were employed: stress-reversal, intermediate and non-reversal, as schematically shown in Fig. 1.

Typical test results are presented in Figs. 2 through 4, in terms of effective stress paths and stress-strain relationships. Specimen deformation at several states as numbered 1 through 4 in Fig. 2, Fig. 3 and Fig. 4 are shown in Photos 1, 2 and 3, respectively.

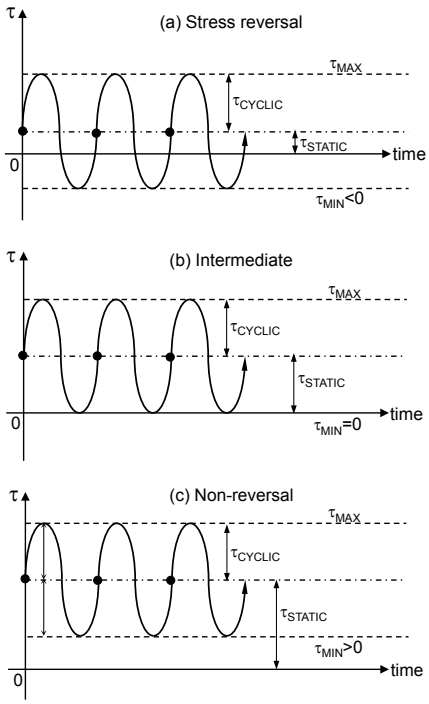


Figure 1. Schematic illustration of cyclic torsional shear loadings (after Chiaro et al., 2011).

2.1 Stress-reversal loading tests

As shown in Fig. 2, in the case of stress-reversal loading test (e.g., Test 3), cyclic mobility was observed in the effective stress path, where the effective stress recovered repeatedly after reaching the state of zero effective stress (i.e., full liquefaction); it was accompanied with a significant development of shear strain as indicated by the stress-strain relationship.

Photo 1 shows specimen deformation observed for this test. At state 1 (γ = 12 %), the deformation was almost uniform except for the regions close to the pedestal and the top cap that are affected by the end restraint; the outer membrane appeared slightly wrinkled. At state 2 (γ = 22 %), the outer membrane was visibly wrinkled; in the regions near the top cap the deformation of the specimen started to localize due probably to water film formation (Kokusho, 1999).

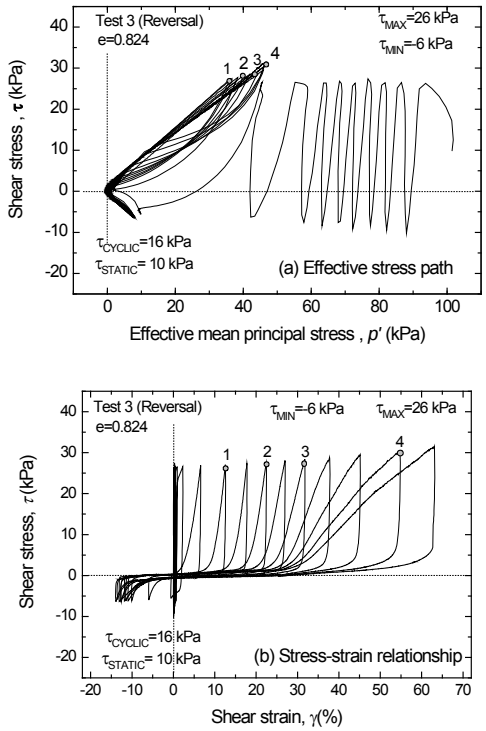


Figure 2. Typical stress-reversal loading test results.

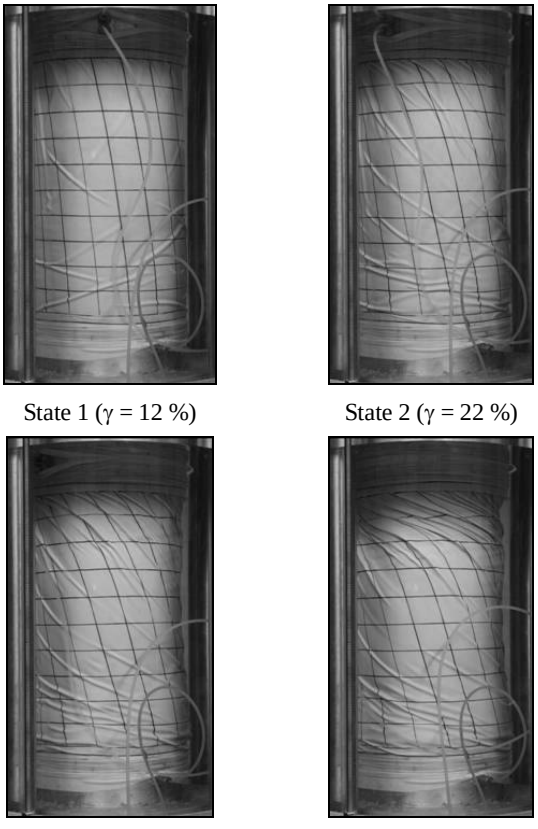


Photo 1. Specimen deformation at states 1 through 4 shown in Fig. 2.

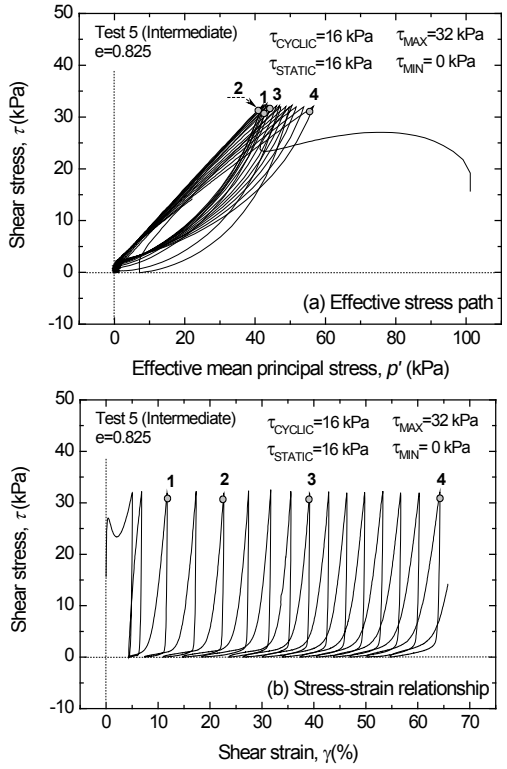


Figure 3. Typical intermediate loading test results.

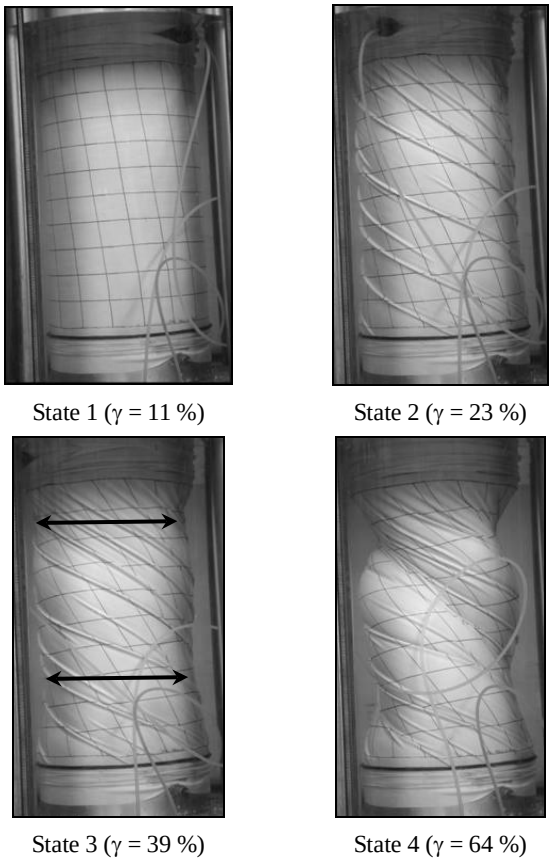


Photo 2. Specimen deformation at states 1 through 4 shown in Fig. 3.

At state 3 (γ = 31 %), the localization of the specimen deformation developed clearly in the upper part of the specimen. On the other hand, in the bottom part the uniformity of the specimen deformation was maintained even many wrinkles appeared. At state 4 (γ = 54 %), the specimen was almost twisted near the top cap.

2.2 Intermediate loading tests

Fig. 3 shows the case of intermediate loading test (e.g., Test 5). This type of test shows behavior that is similar to that of reversal case, in the sense that after reaching a fully liquefied state, progressive large deformation is developed while showing cyclic mobility.

However, it can be distinguished from the reversal one by looking at the specimen deformation as shown in Photo 2. At state 1 (γ = 11 %), the deformation was almost uniform except for the regions close to the pedestal and the top cap that are affected by the end restraint. At state 2 (γ = 23 %), the outer membrane was extensively wrinkled. Yet, it seems that the type of wrinkle observed in this test can have a different meaning with respect to the one observed in the reversal test described above; in fact, in this test, the extent of deformation before and after each wrinkle changed; this behavior suggests that several shear bands were formed in the specimen. At state 3 (γ = 39 %), the specimen reduced its diameter at several locations, as indicated by the arrows, due probably to the formation of shear bands. Finally, at state 4 (γ = 64 %), the specimen was completely twisted.

2.3 Non-reversal loading tests

Fig. 4 illustrates the case of non-reversal loading test (e.g., Test 7). The state of zero effective stress was not achieved even after applying 208 cycles of loading; however, large shear strain exceeding 50% was reached, and the formation of a single spiral shear band could be observed.

Specimen deformation observed for this test is shown in Photo 3. At state 1 (γ = 21 %), the deformation was rather uniform except for the regions close to the pedestal and the top cap that are affected by the end restraint. At state 2 (γ = 25 %), the outer membrane was wrinkled at several locations due to local drainage. At state 3 (γ = 50 %), the outer membrane was extensively wrinkled from the bottom to the top. At state 4 (γ = 0 %, after test), when the zero stress state was recovered while keeping undrained condition, formation of a single spiral shear band could be observed (dotted lines).

3. STRAIN LOCALIZATION DURING CYCLIC LOADING

Tatsuoka et al. (1986) performed drained monotonic torsional shear tests on hollow cylindrical specimens, while keeping the σ_v' and σ_h' constant. They reported that the vertical strain was accumulated on the extension side due to the mobilization of positive dilatancy, and it was

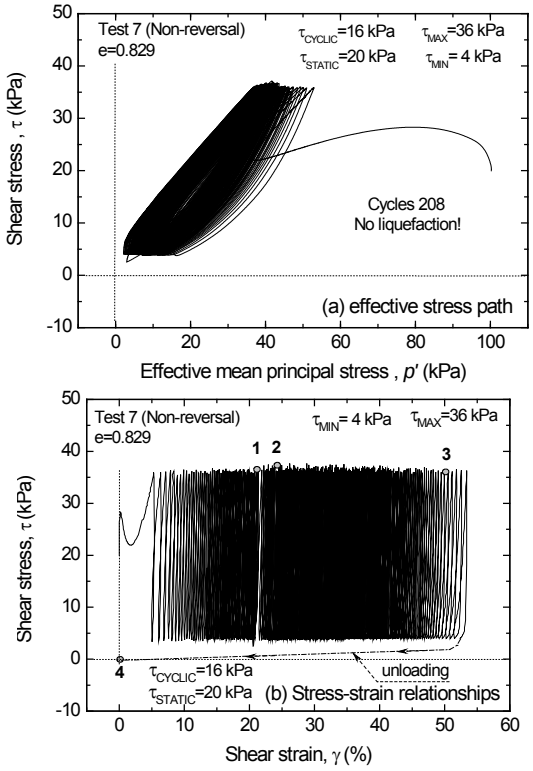
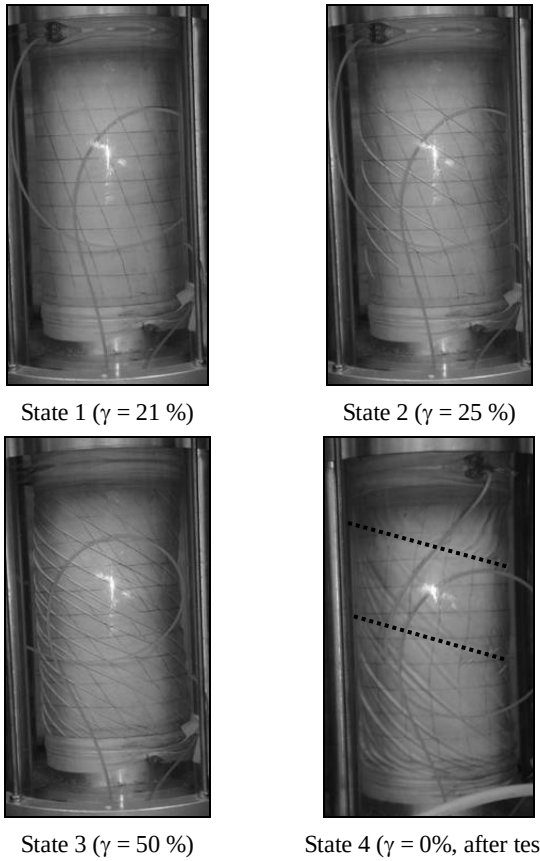


Figure 4. Typical non-reversal loading test results.



State 1 (γ = 21 %) State 2 (γ = 25 %)

State 3 (γ = 50 %) State 4 (γ = 0%, after test)

Photo 3. Specimen deformation at states 1 through 4 shown in Fig. 4.

reduced suddenly when the shear band was formed in the specimen.

Kiyota et al. (2008) performed undrained cyclic torsional shear tests on saturated Toyoura sand, similar to those presented in this study, but without applying any initial static shear. In their tests the initiation of strain localization was defined by looking at the change in the response of the deviator stress q (= σ_v'- σ_h') which was measured during the undrained cyclic torsional shear loading while preventing any vertical displacement of the top cap.

The behavior that was observed during drained monotonic torsional shear tests by Tatsuoka et al. (1986) is consistent with the change in deviator stress observed in undrained torsional shear tests; therefore, Kiyota et al. (2008) considered the state at which the amplitude of q decreases as the limiting state to initiate formation of shear band and thus strain localization. Furthermore, it was accompanied with an increase in the shear increment of single amplitude shear strain ($\Delta\gamma_{SA}$). As a result, these features imply that the stress-strain characteristics of the specimen were changed by the formation of shear band and the initiation of strain localization in the specimen.

In the current study, non-uniform specimen deformations were observed at strain levels higher than 20%. Yet, similarly to Kiyota et al. (2008), the initiation of strain localization could not be clearly defined on the basis of visual observation; hence, to address this issue and evaluate the effects of initial static shear on the specimen deformation behavior, the attempt made by Kiyota et al. (2008) was employed. Consequently, from the analysis of deviator stress responses and stress-strain relationships, as typically shown in Figs. 5 and 6, respectively, the following two states were defined: i) State A: the state at which q suddenly decreases; and ii) State B: the state at which a change in the strain accumulation properties was observed.

The values of shear strain measured at state A and state B, respectively, are shown in Fig. 7 and Fig. 8. They were evaluated in terms of half of double amplitude shear strain ($\gamma_{DA}/2$), as employed by Kiyota et al. (2008), and single amplitude shear strain (γ_{SA}) which Chiaro et al., (2011) used to describe the effects of static shear on the deformation properties of sand.

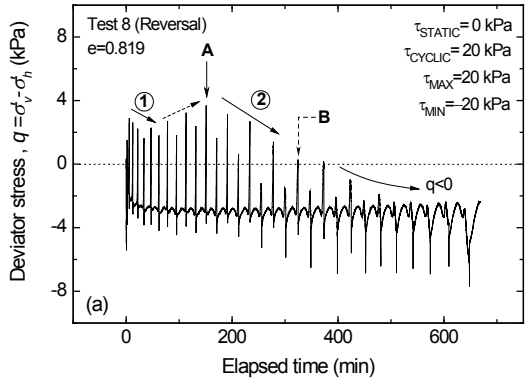


Figure 5. Change in deviator stress response based on the time history of deviator stress.

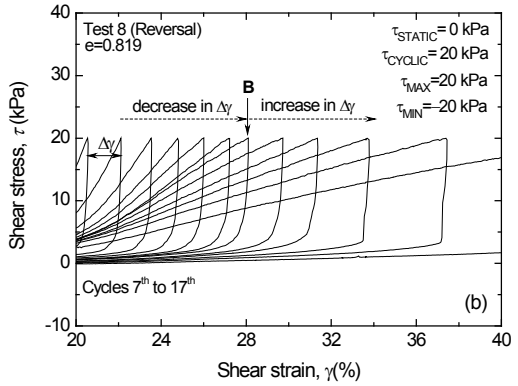


Figure 6. Change in shear strain accumulation during cyclic loading based on the stress-strain relationship.

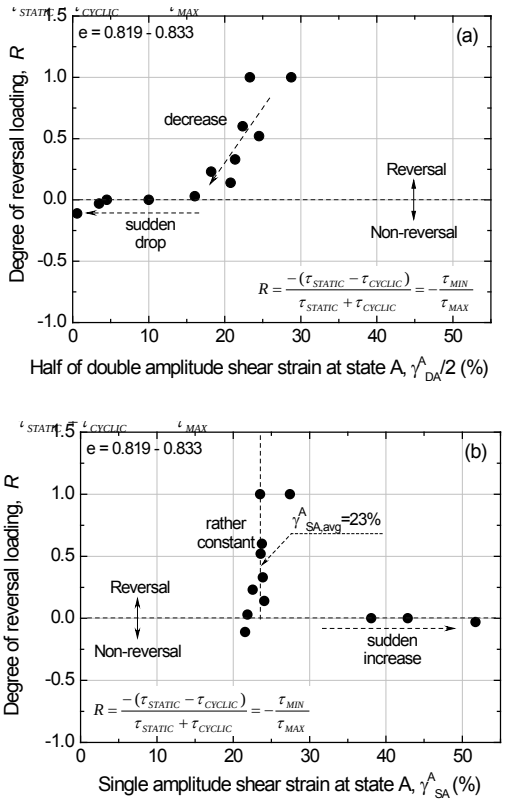


Figure 7. Change in deviator stress response at state A evaluated in terms of: (a) $\gamma_{DA}/2$; and (b) γ_{SA}.

In Fig. 7 and Fig. 8, to consider the combined effects of the initial static shear with the cyclic shear stress, the shear strain is plotted against the degree of reversal loading as defined by Yoshimi and Oh-oka (1975). One can see that in the case of stress-reversal loading tests, the greater the static shear stress (τ_{static}) is, the lower the $\gamma_{DA}/2$ value is; on the other hand, a sudden drop in the value of $\gamma_{DA}/2$ is observed in case of intermediate and non-reversal loading tests. In contrast, the γ_{SA} value is rather constant in the case of stress-reversal loading tests, which sudden increases in the case of intermediate and non-reversal loading tests.

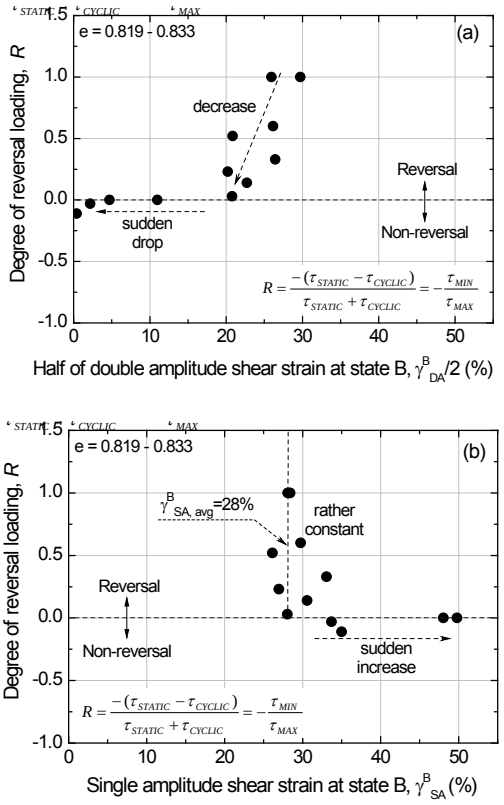


Figure 8. Change in shear strain behavior at state B evaluated in terms of: (a) $\gamma_{DA}/2$; and (b) γ_{SA}.

Based on these considerations, the shear strain required to cause the strain localization of sand specimens subjected to stress-reversal loadings was defined in terms of single amplitude shear strain γ_{SA}. Therefore, it was defined:

(i) $\gamma^A_{SA,avg} \cong 23$ %, which represents the state at which q suddenly decreases (state A);

(ii) $\gamma^B_{SA,avg} \cong 28$ %, which corresponds to the state at which a change in strain accumulation takes place (state B).

As mentioned above, the drop in q implies that the stress-strain characteristics of the specimen were changed by the formation of shear band(s) and the initiation of strain localization in the specimen. Yet, in this study, in several cases, state A was not easy to define (e.g., when the change in the deviator stress amplitude was not unique as shown in Fig. 5 by numbers ① and ②) and thus different evaluations may be given among different researchers. On the contrary, the change in stress accumulation at state B is the direct result of the specimen strain localization (i.e., formation of shear band), and it could be unequivocally evaluated in all the tests. The above observations suggest that, even if slightly over-estimated, the limiting state to initiate the strain localization in the specimen can be defined in terms of γ^B_{SA} which is the direct evidence of formation of shear band(s) and can be clearly determined.

As well, by analyzing the deviator stress responses, it was noted that after achieving state B, the deviator

stress becomes negative ($q < 0$) in the case of reversal loading tests, as typically shown in Fig. 5. This peculiar behavior would be associated with the full development of the shear band into the specimen. The latter behavior was not observed in case of intermediate and non-reversal loading tests.

4. DISCUSSION

As shown in Figs. 7(b) and 8(b), in the case of intermediate and non-reversal loading tests, the limiting values of single amplitude shear strain γ_{SA} evaluated on the basis of a change in deviator stress response or a change in strain accumulation properties, increases drastically up to about 50%, while the visual observation show that non-uniform deformation of specimens appears at shear strain level of about 20-30%. This suggests that the method may be inappropriate in evaluating the limiting value of shear strain to initiate strain localization, either in the case of intermediate or non-reversal stress loading tests. The authors are currently verifying the performance of other methodologies to set in a better and comprehensive understanding this issue.

5. CONCLUSIONS

The purpose of this paper is to investigate the effects of initial static shear stress on the limiting value of shear strain at which strain localization appears during undrained cyclic torsional shear tests. Therefore, a series of undrained cyclic torsional shear tests, carried out on saturated loose Toyoura sand specimens up to reaching a single amplitude shear strain exceeding 50%, was analyzed.

Non-uniform specimen deformation could be observed at higher strain levels; however, the initiation to strain localization could not be defined on the basis of visual observations. The limiting values of half of double amplitude ($\gamma_{DA}/2$) and single amplitude (γ_{SA}) shear strains were evaluated from the test results by looking at the change in the deviator stress response as well as at the change in the strain accumulation properties.

In the case of stress-reversal loading tests, it was found that the greater the static shear level is, the lower the $\gamma_{DA}/2$ value is; on the other hand, the γ_{SA} value is rather constant. These features suggested that to define the limiting value of strain to initiate the strain localization of sand specimens subjected to initial static shear, γ_{SA} is a much more appropriate parameter than $\gamma_{DA}/2$ which usually is employed in previous studies. Finally, the limiting strain value measured in terms of γ_{SA} was evaluated to be in the range of 23-28%. As long as the liquefied soil layer remains in uniform deformation, these limiting values may be used in estimating the maximum amount of ground displacement due to liquefaction in natural and artificial slopes of sandy deposits.

On the other hand, it was recognized that in the case of intermediate and non-reversal loading tests, the limiting value of shear strain to initiate the strain localization cannot be defined on the basis of a change in deviator stress response or a change in strain accumulation properties; therefore alternative methodologies should be explored for a comprehensive understanding on the effects of initial static shear on the shear strain localization characteristics of sands.

References:

Chiaro, G., Sato, T., Kiyota, T. and Koseki, J. (2011): "Effect of initial static shear stress on the undrained cyclic behavior of saturated sand by torsional shear loading", *Proc. of the 5th International Conference on Earthquake Geotechnical Engineering*, Santiago, Chile (to appear).

Hamada, M., Isoyama, R. and Wakamatsu, K. (1996): "Liquefaction-induced ground displacement and its related damage to lifeline facilities", *Soils and Foundations, Special Issue on Geotechnical Aspects of the January 17 1995 Hyogoken-Nambu Earthquake*, 81-97.

Hamada, M., O'Rourke, T. D. and Yoshida, N. (1994): "Liquefaction-induced large ground displacement", *Performance of Ground and Soil Structures during Earthquakes, 13th ICSMFE*, 93-108.

Hamada, M., Yasuda, S. and Wakamatsu, K. (1988): "Case studies on liquefaction-induced permanent ground displacement", *Proc. of the 1st Japan-U.S. Workshop on Liquefaction, Large Ground Deformation and their Effects on Lifeline Facilities*, 3-21.

Ishihara, K., Yasuda, S. and Nagase, H. (1996): "Soil characteristics and ground damage", *Soils and Foundations, Special Issue on Geotechnical Aspects of the January 17 1995 Hyogoken-Nambu Earthquake*, 109-118.

Kiyota, T., Sato, T., Koseki, J., and Mohammad, A. (2008): "Behavior of liquefied sands under extremely large strain levels in cyclic torsional shear tests", *Soils and Foundations*, 48 (5), 727-739.

Kiyota, T., Koseki, J. and Sato (2010): "Comparison of liquefaction-induced ground deformation between results from undrained cyclic torsional shear tests and observations from previous model tests and case studies", *Soils and Foundations*, 50 (3), 421-429.

Kokusho, T. (1999): "Formation of water film in liquefied sand and its effects on lateral spread", *Journal of Geotechnical and Geoenvironmental Engineering*, ASCE, 125 (10), 817-826.

Tatsuoka, F., Sonoda, S., Hara, K., Fukushima, S. and Pradhan, T. B. S. (1986): "Failure and deformation of sand in torsional shear", *Soils and Foundations*, 26 (4), 79-97.

Yasuda, S., Nagase, H., Kiku, H. and Uchida, Y. (1992): "The mechanism and a simplified procedure for the analysis of permanent ground displacement due to liquefaction", *Soils and Foundations*, 32 (1), 149-160.

Yoshimi, Y. and Oh-oka, H. (1975): "Influence of degree of shear stress reversal on the liquefaction potential of saturated sand", *Soils and Foundations*, 15 (3), 27-40.

8CUEE CONFERENCE PROCEEDINGS
8th International Conference on Urban Earthquake Engineering
March 7-8, 2011, Tokyo Institute of Technology, Tokyo, Japan

DYNAMIC CHARACTERISTICS OF THE SURFACE SOILS IN LIMA, PERU

Diana Calderon[1)], Toru Sekiguchi[2)], Zenon Aguilar[3)], Fernando Lazares[4)], and Shoichi Nakai[5)]

1) Doctoral Student, Chiba University, Japan
2) Assistant Professor, Dept. of Urban Environment System, Chiba University, Japan
3) Professor, Fac. of Civil Engineering, National University of Engineering, Peru
4) Researcher, CISMID, National University of Engineering, Peru
5) Professor, Dept. of Urban Environment System, Chiba University, Japan
diana_c@graduate.chiba-u.jp, tsekiguc@faculty.chiba-u.jp, zaguilar@uni.*edu.pe, f_lazares@uni.edu.pe, nakai@faculty.chiba-u.jp*

Abstract: We have obtained dynamic characteristics of the surface soils at eight places in Lima, Peru; specifically we estimated the shear-wave velocity profile. The method we used was the inversion of dispersion curves calculated from array measurements. Small and large arrays of microtremors were carried out, and a new type of sensor was introduced for the large array measurement. Important results are the relative shallow stiff soil layer in the area classified as alluvial gravel deposit, that covers most of the area of Lima city; and the apparently deep soft soil layer in places identified as VSV and CMA. In these last places, it is recommended to complete the analysis with large array measurements.

1. INTRODUCTION

This study is part of the project "Enhancement of Earthquake and Tsunami Disaster Mitigation Technology in Peru", in which Japanese Government represented by Chiba University and the Peruvian government represented by the National University of Engineering (UNI) are working together with the objective to estimate seismic risks, hazards and vulnerabilities in Lima, the capital of Peru, and two other cities of the country. In particular, the results of this study will focus on Lima city only.

Lima is situated in the central coast of Peru, bordered by the Pacific Ocean, in a zone of high seismic activity known as, the Ring of Fire.

Due to the high seismicity of this area and to the rapidly growing urbanization, a study of the soil conditions that characterize areas of low or high probability to be affected by earthquakes is of great importance, specially in places like Lima that have scarce information of deep soil structures.

In this context, this study aims to obtain a primary idea of the Lima's soil structure to the depth extending to the bedrock, which will make possible the analysis of the dynamic characteristics of the surface soils of Lima

To accomplish this objective, microtremor array measurement campaigns were carried out at 8 places of the city; new long-period sensors of microtremor were introduced as part of the technology enhancement politics.

2. AREA OF STUDY

The study was developed over the Lima metropolitan area; where 8 points of measurements were located. Table 1 shows a list of these points with details of their exact location.

Figure 1 shows a map of the Lima's surface soil distribution (estimated in 2005) and the distribution of the microtremor array measurement points.

Table 1. Symbols and location of the measured points in this study

ID	District	Institution	Latitude	Longitude
CMD	Rimac	UNI - CISMID	12.013995°	77.050580°
PQR	Lima cercado	Central Park of Lima	12.071319°	77.033171°
DHN	Callao	Direction of Hydrograph	12.064413°	77.155016°
CMA	Callao	School "Maristas"	12.060734°	77.123570°
VSV	Villa El Salvador	School "6066"	12.213421°	76.938803°
PPI	Puente Piedra	Private House	11.852260°	77.074035°
EMO	La Molina	University La Molina	12.082051°	76.938943°
MOL	La Molina	Municipality	12.077994°	76.917278°

3. SOIL CONDITION AND BORING DATA

As it can be seen from Figure 1, most of Lima area is covered by alluvial gravels that are found at few meter depth,; however, there are concentrated eolian, clays and

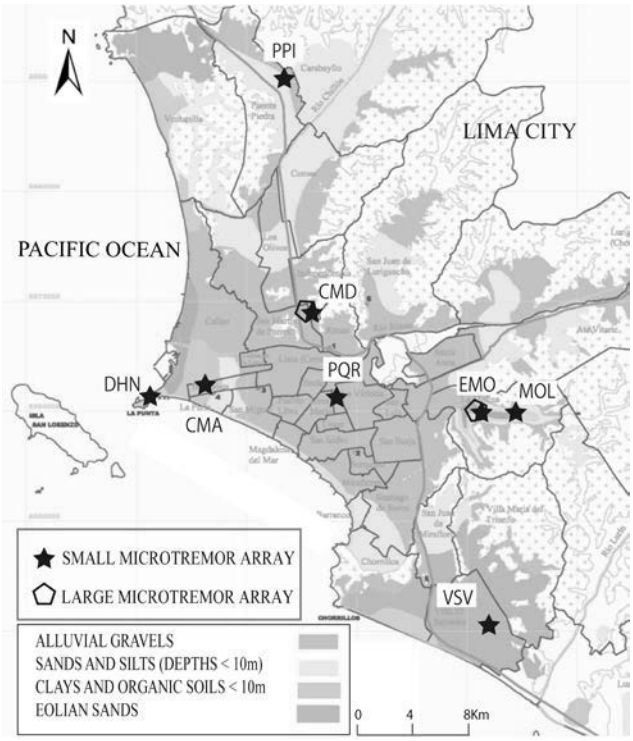


Figure 1. Soil distribution map (CISMID, 2005) and location of microtremor arrays.

silts deposits, of which depths to the base rock are in some cases unknown .

A typical soil profile of the alluvial gravel deposit is shown in Figure 2. The profile corresponds to a soil pit near the array set named CMD. In Lima, soil pits are more popular than SPT explorations because the stiffness of the soils in many areas does not allow the conduction of SPT explorations.

The majority of boring data available in Peru has a similar pattern of profile at CMD, it means the gravel is shallow and the depth of exploration is about 3m.

4. MICROTREMOR ARRAY MEASUREMENTS

One of the reasons to conduct array measurements was the limited depth in the available boring data and the practical way to perform it.

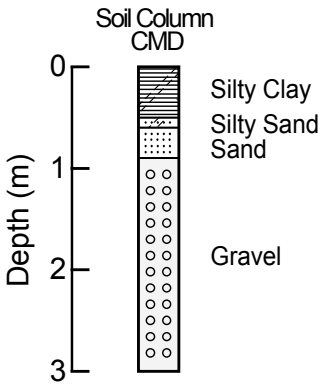


Figure 2. Soil Column CMD (collected data E13 of Rimac district in the study of CISMID, 2005) located at the National University of Engineering.

Two measurement campaigns were carried out, the first consists of 8 sets of small arrays (Figure 1); each set is made of linear arrays of 0.5 and 2m sensor distance, and circular arrays of 10, 20 and 45m radius.

The second campaign consists of 2 sets of large arrays, each set made of circular arrays of 100, 200, 400 and 800m radius.

4.1 Implementation of microtremor sensors

Two types of sensors of microtremors were introduced to Peru through this project. One was the well-known GEODAS sensor (with natural period of 1 second), and the other was a sensor produced by Tokyo Sokushin company with a natural period of 5 seconds.

5. ANALYSIS OF RESULTS

Array set CMD was chosen in this study to be the representative array set; in consequence we will show and comment the detailed procedure to come up with its shear wave velocity profile.

We used two methods to construct the dispersion curve; the high resolution F-k method proposed by Capon in 1979, and the Centerless Circular Array (CCA) proposed by Cho et al in 2006.

5.1 F-k spectrum

The F-k method uses the cross-spectrum between each pair of sensors as a factor to compute the F-k power spectrum. This can be seen with the formula of the F-k spectrum

$$P'(k_x, k_y, f) = \left[\sum_{n,m=1}^{K} q_{mn}(f) \cdot \exp\left\{-i2\pi\left[k_x(x_n - x_m) + k_y(y_n - y_m)\right]\right\} \right]^{-1}$$

where K is the number of channels, k_x is the wave-number in the x-direction, and k_y is the wave-number in the y-direction, and f is the frequency.

$q_{mn}(f)$ is the inverse of a Hermitian matrix whose elements are formed by the cross spectrum between channels m and n. (x_n, y_n) are the coordinates of the sensor n, and (x_m, y_m) are the coordinates of sensor m.

Since the cross spectrum is an important factor in the computation of the F-k spectrum, it is necessary to verify the cross-spectra to see if there is a good correlation between the signals. In general a well correlated cross-spectrum curve is a smooth descending or ascending curve from 0 to 360 degrees or vice verse. If the curve follows this trend the F-k spectrum is verified. Sometimes more than one smooth curve appears, in this case, in the period domain, the curve to verify should be the first at the right side. For example, in Figure 3(a) there are two curves but the one to verify is the curve from 0.025 to 0.07 s, and in Figure 3(b) the curve is from 0.2 to 0.4 s. We will expect that in the dispersion curve for the period ranges mentioned, the curve shows continuity for the array of 10 and 200m respectively.

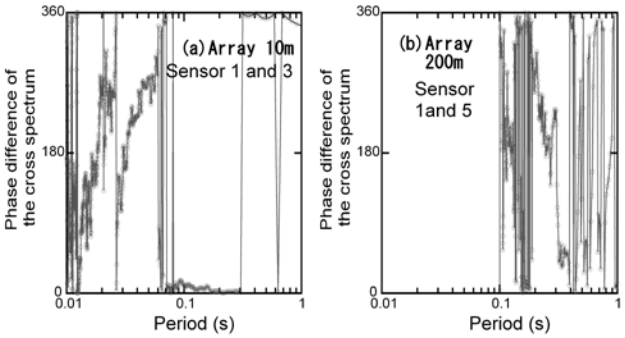


Figure 3. Cross spectra of CMD , (a) For the array of 10m, (b) for the array of 200m.

Figure 4 shows F-k spectra for different array sizes and different periods. It is well-known that a sharp peak develops for ideally noise-free data; from this statement we can conclude that the ratio of noise to signal is low for the periods shown in each F-k spectrum, because in almost all the cases the peak is sharp. This can be used as another way to verify the dispersion curve.

It is also known that the sharp of the peak vary with the coherence value, usually the coherence is high for sharp peak spectra. Another factor that affects the coherence is the number of peaks in the F-k spectrum, when more than one peak appears the coherence decreases. The presence of more than one peak may be due to external noise, in our case we can see that more than one peak occurs specially for the large arrays, which can tend to receive more noise.

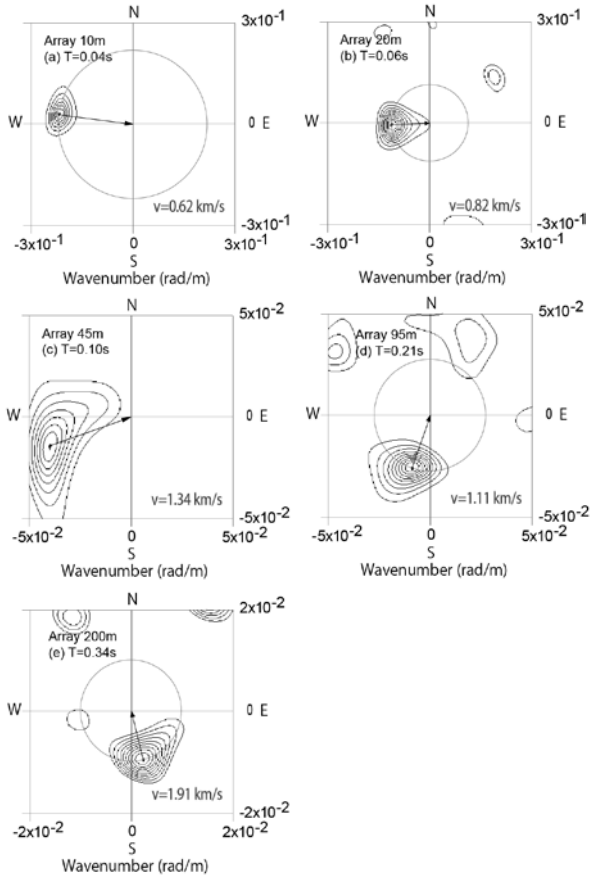


Figure 4. F-k Spectra for CMD arrays

5.2 Dispersion curve

Tokimatsu (1995) mentioned that to obtain reliable results of phase velocities, the effective wavelength range is related with the sensor distance as follows

$$Dmax > \lambda max/3$$
$$Dmin < \lambda min/2$$

which can be written as:

$$2Dmin < \lambda < 3\,Dmax$$

where *Dmax* and *Dmin* is the maximum and the minimum sensor distance respectively, and λ is the wavelength.

This criterion, together with the cross spectrum and the F-k spectrum verification were used to select the points of the dispersion curve when using the F-k method (Figure 5).

However, in the case of the CCA method; Cho et al (2004) found phase velocities at very long wavelength ranges, up to 30 meters the array radius. They stated that it is possible to calculate phase velocities at very long wavelengths when the signal to noise ratio is high, which occurs normally in few meter radius arrays.

In Figure 5 we can observed the continuity between the dispersion curves from array L0.5 (linear array of 0.5m sensor distance) to array C45 (circular array of 45m radius). Nevertheless, arrays C95, C200 and C400 follow another curve. The cause of this difference could be the fact that these large arrays were measured at a place separated about 800m from the place where the small arrays were measured, that is, the surface soil may be different in both places. Small array measurements in the second place are necessary to verify the dispersion curve of the large arrays.

5.3 Inversion of dispersion curves

Several methods of inversion are available, from the conventional least square methods to the genetic algorithm method. The genetic algorithm approach developed by Goldberg (1989) is recently very popular; this method in comparison with the typical least square method has the advantage in which a search can be done for an optimal solution in the local and global space.

In this study we applied the genetic algorithm (GA). To apply this method we input an observed dispersion curve, such as the one in dots in Figure 6(a). Previously we had determined this curve base on the dispersion curve of Figure 5.

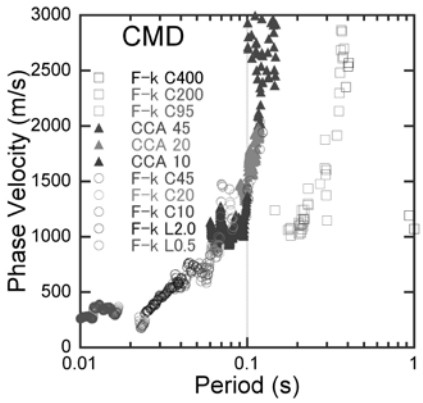


Figure 5. Dispersion curve

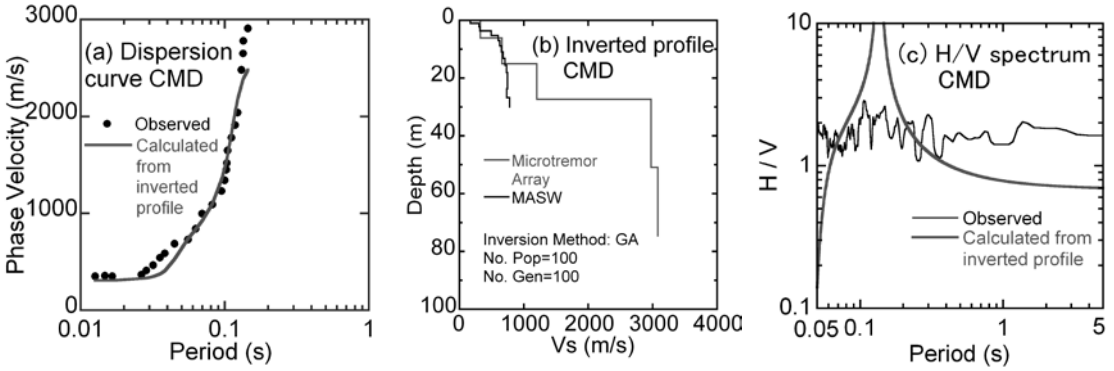


Figure 6. (a) Comparison between the observed and calculated dispersion curve, (b) Comparison between the profiles estimated by inversion of dispersion curves calculated by microtremor arrays and by MASW, (c) Comparison of H/V spectra

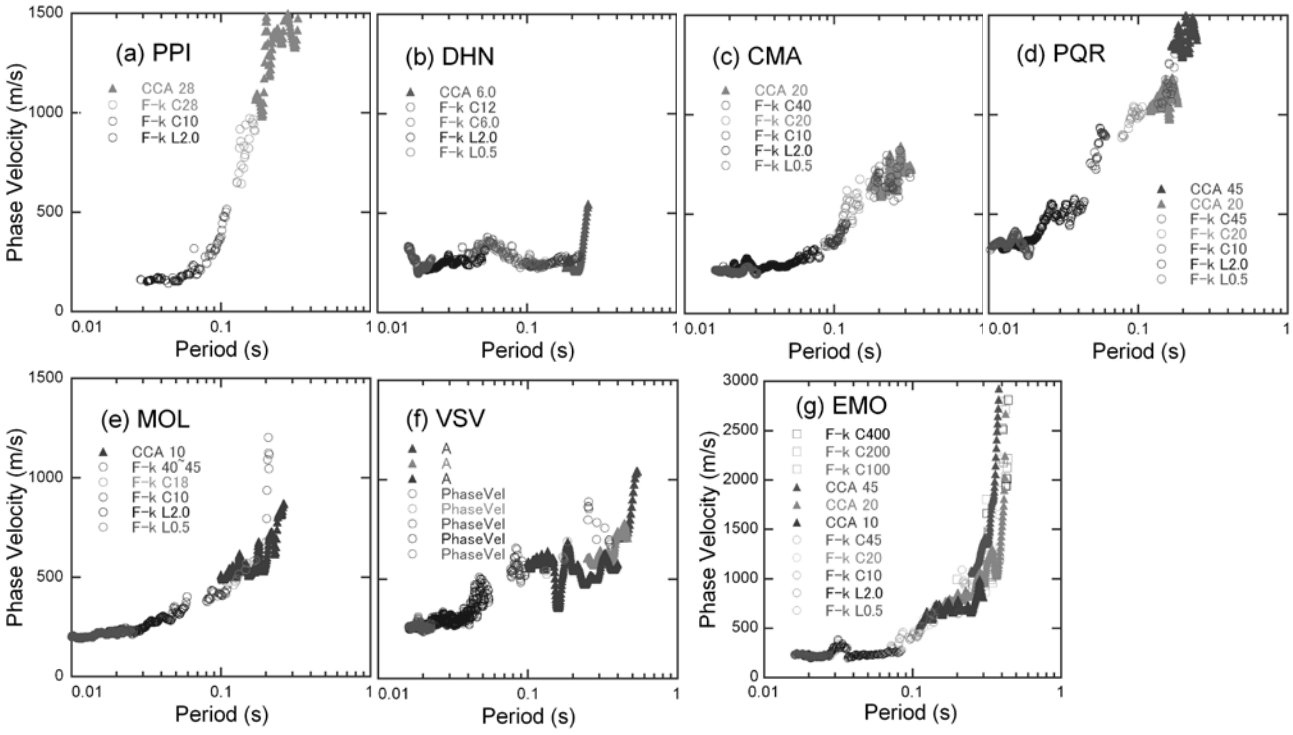


Figure 7. Dispersion curves

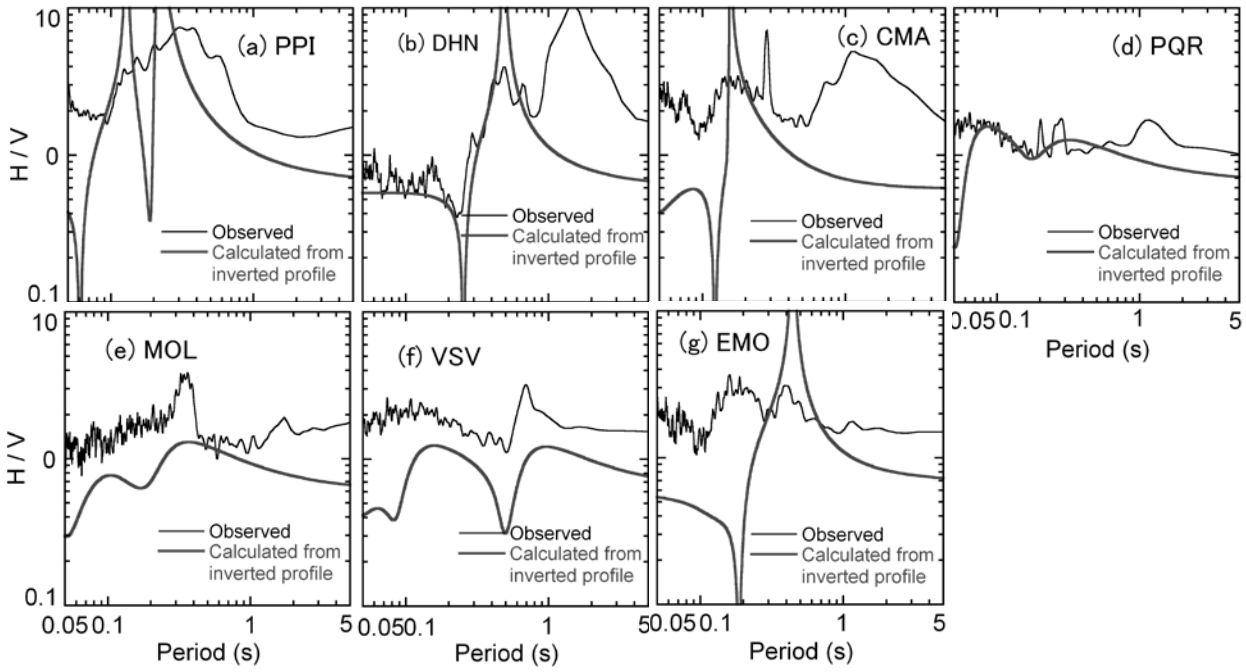


Figure 8. H/V Spectra

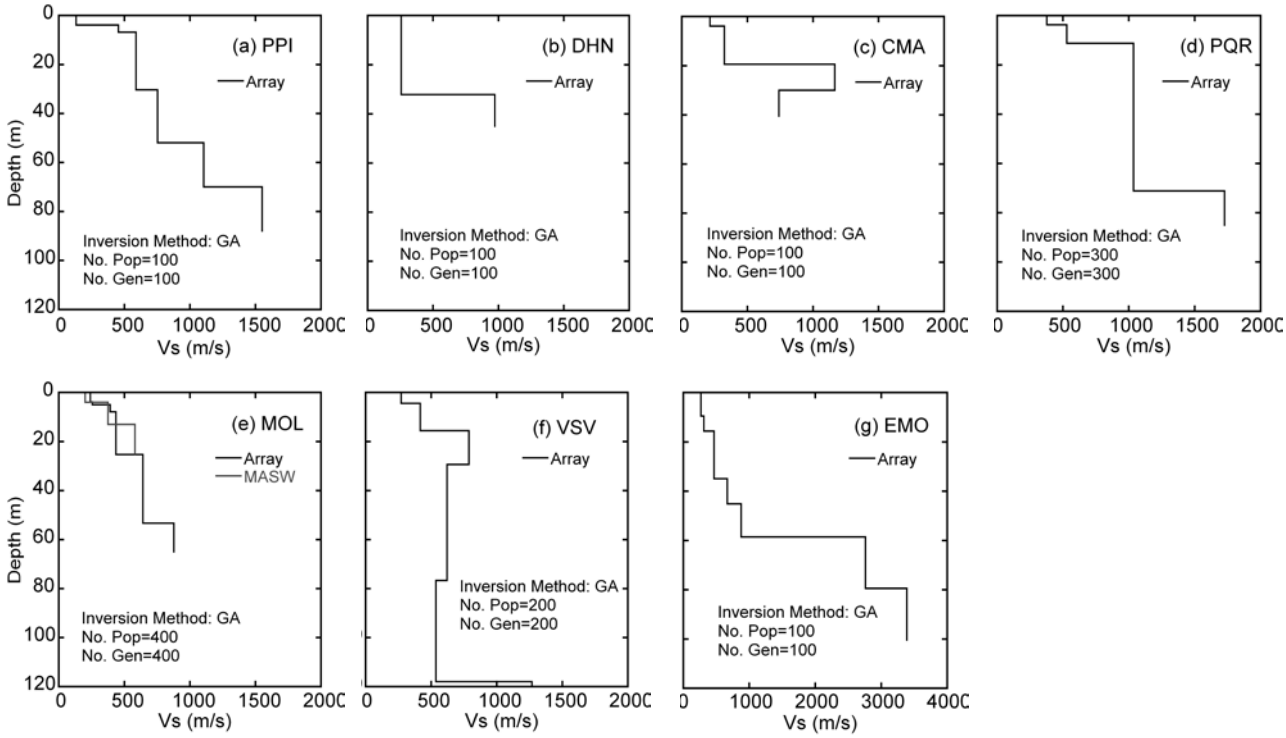


Figure 9. Comparison of Observed and Calculated H/V spectra

This observed curve or target curve, is used to compare all calculation curves obtained in the process of the inversion. The final calculated curve is the one that satisfy the ending criterion, which can be either a limit number of iteration (number of generation) or a minimum fitness value. In this study the first criterion was used, and the value of this limit was up to 100.

Figure 6(b) shows two profiles, one corresponds to the inversion of the dispersion curve calculated from microtremor arrays and the other corresponds to the inversion of the dispersion curve calculated with the MASW method. It is observable that both profiles are in good agreement until the depth of 15m more or less.

Finally to verify the profile obtained with the microtremor array, the H/V spectrum of this profile is calculated and compared with an observed spectrum. Figure 6(c) shows that there is an agreement between both spectra.

5.4 Additional Results

The same procedure taken for the calculation of dispersion curves and estimation of shear-wave velocity profile of study point CMD was used at the other study points.

Figure 7 shows the dispersion curves for the rest of the points of study, Figure 8 shows the the H/V spectra, and Figure 9 shows the shear-wave velocity profiles;

6. DISCUSSION

Looking at the dispersion curves we can see that the CMD place has the most rigid shallow surface soil, it can be explained from the rock formation proximity.

The places with apparent soft deep deposits are DHN, CMA, and VSV.

In the case of CMA, the dispersion curve at long period (array of 45m) does not show a clear curve, and it seems that there is a dip in this part of the curve; it could mean that there is a layer of high velocity overlying one of lower velocity, which is what we found in the inverted profile (Figure 9(c)). Indeed, the H/V spectrum of this place has three clear peaks (Figure 8(c)), one with a period of about 1s, this peak could belong to soft layer mentioned before. To verify this peak we need phase velocities at long period, which can be obtained with large array measurements.

For VSV, the inverted profile (Figure 9 (f)) apparently points out that there is an important contrast down to 100m. The H/V spectrum of the calculated and observed data shows an agreement. However to verify this statement, a large array measurement is necessary.

7. CONCLUSIONS

The results of this study brought the following conclusions:

1. Places located in the area of alluvial gravel of Lima, showed high shear-wave velocities at shallow depths.
2. In the majority of the places studied, the implementation of large array measurements is necessary to estimate the depth to the base-rock.
3. In order to verify the results of array inversion, additional studies, preferably direct exploration test, such as PS logging is of great importance.

Acknowledgements:

The authors acknowledge support from JICA and JST, for providing the tools and facilities that made possible this study. Furthermore, we are grateful to the researches and research assistants at CISMID who helped in the realization of the tests and in the completion of this study.

References:

Capon, J. (1969). "High-resolution frequency-wavenumber spectrum analysis". *Proc. IEEE, Vol. 57, No 8,* 1408-1418.

Cismid (2005). "Study of the Vulnerability and Seismic Risk in 42 districts of Lima and Callao". Japan - Peru Center for Seismic research and Disaster Mitigation, National University of Engineering, Lima, Peru. *(in spanish)*

Cho, I., T.Tada, and Y. Shinozaki (2004). "A new method to determine phase velocities of Rayleigh waves from microseisms", *Geophysics, 69*, 1535-1551.

Goldberg, D.E (1989). "Genetic algorithms in Search, Optimization, and Machine Learning". Addison-Wesley Publishing Company Inc.

Tada, T., I. Cho, and Y. Shinozaki (2010). "Analysis of Love-wave components in microtremors", *Joint Conference Proceedings, 7th International Conference on Urban Earthquake Engineering (7CUEE) & 5th International Conference on Earthquake Engineering (5ICEE), Center for Urban Earthquake Engineering, Tokyo Institute of Technology*, 115-124. BIDO Software downloaded from: http://staff.aist.go.jp/ikuo-chou.

Tokimatsu, K. (1995). "Geotechnical site characterization using surface waves". *The first international conference on earthquake geotechnical engineering IS-Tokyo,* 1333-1368.

8CUEE CONFERENCE PROCEEDINGS
8th International Conference on Urban Earthquake Engineering
March 7-8, 2011, Tokyo Institute of Technology, Tokyo, Japan

SIMULATIONS OF STRONG GROUND MOTIONS RECORDED AT THREE STATIONS IN KASHIWAZAKI CITY DURING THE 2007 NIIGATA-KEN CHUETSU-OKI EARTHQUAKE

Kota Katsumata[1], Kohji Tokimatsu[2], and Hiroshi Arai[3]

1) Graduate Student, Dept. of Architecture and Building Engineering, Tokyo Institute of Technology, Japan
2) Professor, Center for Urban Earthquake Engineering, Tokyo Institute of Technology, Japan
3) Senior Researcher, Building Dept., National Institute for Land and Infrastructure Management, Japan
katsumata.k.aa@m.titech.ac.jp, kohji@o.cc.titech.ac.jp, arai-h92ta@nilim.go.jp

Abstract: The strong ground motions recorded at Kyoshin Network Kashiwazaki (K-NET) and Gas Water Department (GWD) in Kashiwazaki city had strong spiky acceleration time history, while JR Kashiwazaki station (JR) had not such spiky waves. Our previous study showed that the computed ground motion at the K-NET using the bedrock motion deconvoluted from the observed recording at JR site, agreed reasonably well with the observed one. However, the strong motion at GWD site has not been well estimated probably because it contains more and stronger spiky waves than the recorded motion at the K-NET. In this paper, an attempt is further made to examine whether such spiky waves were recorded at both K-NET and GWD stations, using nonlinear dynamic response analysis together with the dynamic soil properties based on borehole investigation and laboratory tests made for the three sites after the earthquake.

1. INTRODUCTION

Niigata-ken Chuetsu-oki Earthquake (Mj=6.8) occurred on July 16, 2007, with an epicenter off the Niigata prefecture. The quake affected the coastal areas of the southwestern Niigata prefecture, including Kashiwazaki city and Kariwa village as well as the Kashiwazaki-Kariwa nuclear power plant of Tokyo Electric Power Company (Tokimatsu, 2008). The earthquake claimed a death toll of fifteen people, with more than 2,340 people injured, as of December 28, 2007. More than forty-one thousand houses were either totally collapsed or were damaged.

The strong ground motions recorded at the Kyoshin Network Kashiwazaki (K-NET) station and those at the Gas and Water Department (GWD) station in Kashiwazaki city had strong spiky acceleration time histories, whereas those at the JR Kashiwazaki station nearby did not show such spiky waves (Yoshida et al, 2007; Tokimatsu, 2008).

Our previous study showed that the computed ground motion at the K-NET using the bedrock motion deconvoluted from the observed recording at JR site, agreed reasonably well with the observed one. However, the strong motion at GWD site has not been well estimated probably because it contains more and stronger spiky waves than the recorded motion at the K-NET.

The objective of this paper is to propose and employ a method for searching reasonable bedrock motion that could simulate the ground surface motions recorded at the three sites during the earthquake, based on numerical analyses using dynamic soil properties obtained from field investigations that were made after the earthquake.

2. GEOLOGICAL SETTINGS

Figure 1 shows a geomorphological map of the central part of Kashiwazaki city (Kashiwazaki city, 1983). The city has been developed in the Kashiwazaki plain that faces the Sea of Japan on the northwest. The Kashiwazaki plain consists mainly of the Holocene alluvial deposit formed by the U and Sabaishi rivers and their tributaries. Running in parallel with and between the coastline of the Sea of Japan and the alluvial deposit is the Arahama sand dune that is trisected by the U and Sabaishi rivers where they flow into the Sea of Japan. It extends from the southwest of the city towards the northeast, with its plateau altitude of about 10 m in the central city of Kashiwazaki.

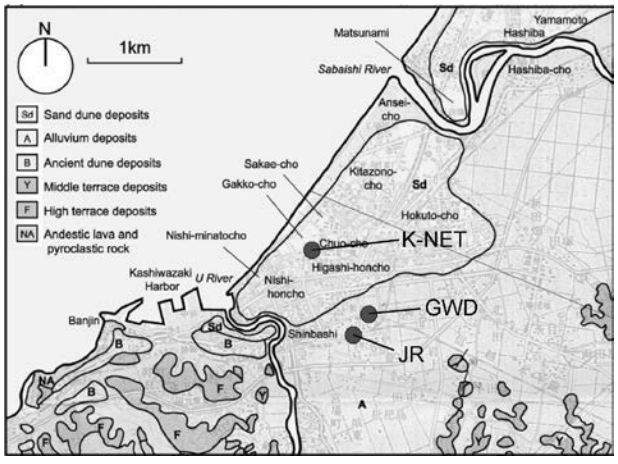


Figure 1 Geomorphological Map of Kashiwazaki City (Kashiwazaki City 1983)

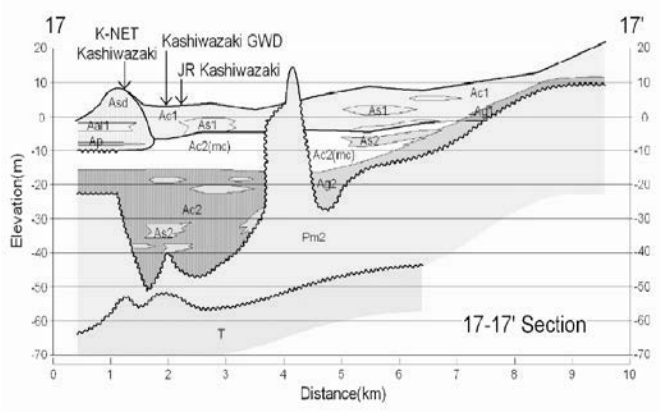


Figure 2 Geological Sections of Kashiwazaki City (ASENP, 2002)

Figure 2 shows a NS geologic section across the city. The Holocene deposit in the lowland consists of the Top, Upper and Lower Kashiwazaki Formations (Ac1/As1, Ac2/As2, and Ac3/As3), with thicknesses varying from 40-70 m along the lower courses of the two rivers, that overlie the Pleistocene and Tertiary Formations (Pm2 and T). The Arahama sand dune about 2 km in width consists of the New Holocene sand dune (Asd) and Pleistocene sand dune called Banjin Formation (Psd) that is underlain by the Kashiwazaki Formations on the south of the Sabaishi River. Typical shear wave velocities of the New Sand Dune, Banjin Formation, Kashiwazaki Formation, Yasuda Formation, and Nishiyama Formation are 100-200 m/s, 200-350 m/s, 100-200 m/s, 350 m/s, and 500-600 m/s, respectively.

The K-NET station is located on the Arahama sand dune, while the GWD and JR stations are on the Holocene deposit about 0.8km and 1.2 km southeast of the K-NET. Geological and geophysical field investigation was made at three stations after the earthquake including laboratory tests to determine dynamic soil properties of the sites.

Figure 3 shows shear wave velocity logs and the geological boring logs for the three sites. The groundwater table was located at a depth of about 5.0 m (K-NET), 1.6m (GWD) and 0.8 m (JR), respectively. The surface soil at the K-NET station to a depth of 13 m is dense sand with SPT N-values ranging from 10 to 40 and Vs from 110-250 m/s, which is underlain by a thick clayey soil with Vs 200-290 m/s. Mudstone with Vs over 500 m/s occurs at a depth of about 65 m. The surface soil at the GWD site to a depth of 0.7 m is sand, which is underlain by a silty clay layer with N-values smaller than 10 to a depth of 3.7 m. Underlain by this layer are alternate layers of sand and clay with N-values less than 10 and Vs of about 100 m/s to a depth of 12.2 m. This is further underlain by clay and silty soils with N-values ranging from 10 to 30 and Vs greater than 200 m/s at a depth of 49 m where an engineering bedrock with Vs larger than 500 m/s occurs. The surface soil at JR station to a depth of 18 m consists of soft silty clay and sandy silt with N-Values of 0-1 and Vs of 70-100 m/s, which overlays alternate sand and clayey silt with N-values of 3-20 and Vs of 190-450 m/s. Mudstone with Vs over 500 m/s occurs at a depth of about 66 m. It seems that the sandy soils at depths between 5-10 m at K-NET and GWD sites might have undergone cyclic mobility and/or liquefaction, although no evidence of soil liquefaction was identified nearby.

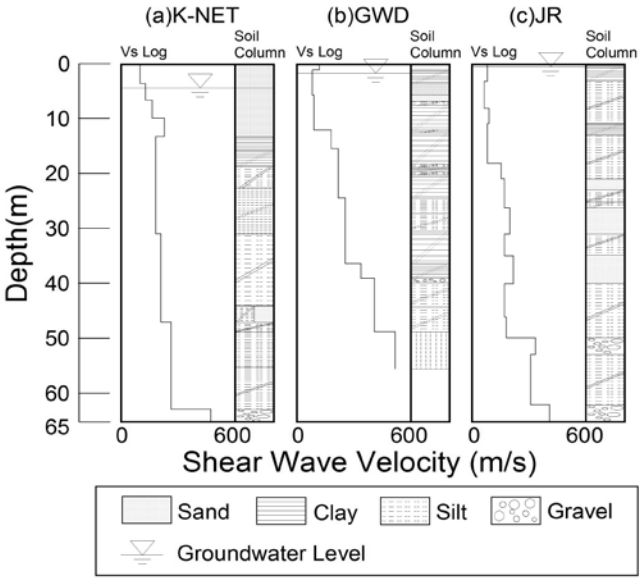


Figure 3 Geological and Geophysical Logs of Three Stations

3. STRONG GROUND MOTION RECORDS

Figure 4 shows acceleration time histories at K-NET, GWD and JR stations during the main shock. The acceleration time histories at all stations have long period components, probably reflecting the thick alluvial deposit underlying the sites. It is interesting to note that the strong motion recording at the K-NET shows strong spiky waves, associated with liquefaction or cyclic mobility of sand, but rapidly decreasing its amplitude with time due probably to cyclic degradation of the sand. The strong motion recording at the GWD shows similar but stronger spiky waves that do not decrease its amplitude with time. Similar spiky waves are not however observed in the acceleration time histories at the JR station.

Some of the strong ground motions recorded at the K-NET and JR stations during other earthquakes are also available, whereas such records are unavailable at the GWD station. Figure 4 shows such acceleration time histories during the aftershock of the Niigata-ken Chuetsu Earthquake that occurred at 18:12 hrs on October 23, 2004. Neither spiky waves nor long period component can be seen in any of the records, contrasting with the strong nonlinear soil behaviour including soil liquefaction and/or cyclic mobility at the K-NET and GWD stations during the main event as shown in Figure 4.

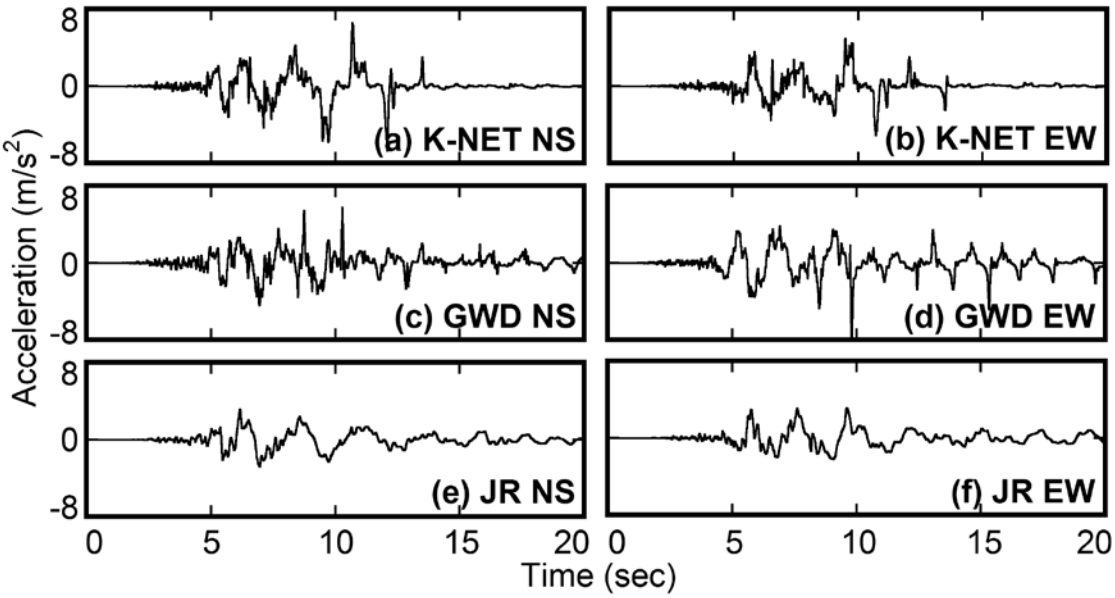


Figure 4 Acceleration Time Histories of K-NET, GWD and JR during the Main Shock

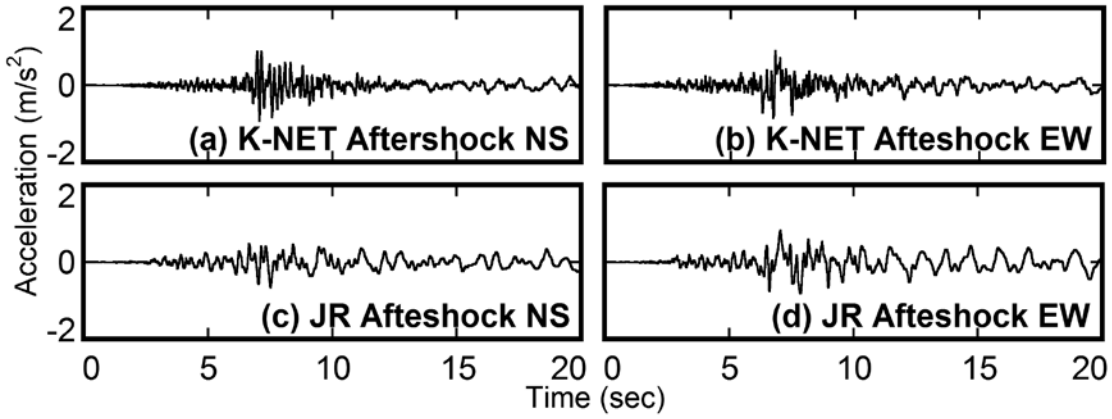


Figure 5 Acceleration Time Histories of K-NET and JR during the Aftershock

4. ANALITYCAL SIMULATION

4.1 Ground Motions during a Moderate-Intensity Earthquake

Figure 6 shows a flowchart to estimate the ground motion recorded at the K-NET and GWD sites from one at JR station. It was assumed that the rock occurring at a depth of 49-66 m of which shear wave velocity is over about 500 m/s is the equivalent rock for the three sites. First, the bedrock motion was estimated, based on the deconvolution analysis using the observed ground motions and soil profile at the JR site. Second, the ground surface motions at the K-NET and GWD stations were estimated, with the back-calculated bedrock motion as input to the bedrock. The programs used for this deconvolution and convolution analyses include the following:

(1) A one-dimensional equivalent-linear response analysis of a deposit subjected to a vertically incident SH waves in which damping ratios of soil depend only on shear strain developed in the soil (hereby called SHAKE 1). The program is exactly the same in concept as the original SHAKE (Schnabel et al, 1972).

(2) An extended version of the equivalent linear response analysis described above in which the damping ratios of the deposit are assumed to be dependent on the Fourier amplitude of shear strain in the frequency domain (e.g., Sugito et al, 1993), which has been developed to improve over-damping nature of the original SHAKE in the short period range during strong shaking (hereby called SHAKE 2)

(3) A nonlinear effective response analysis (Shamoto et al, 1992, hereby called ESA).

The same program was used for both deconvolution and convolution analyses, except for the convolution analysis of ESA for which SHAKE 2 was used for deconvolution analysis.

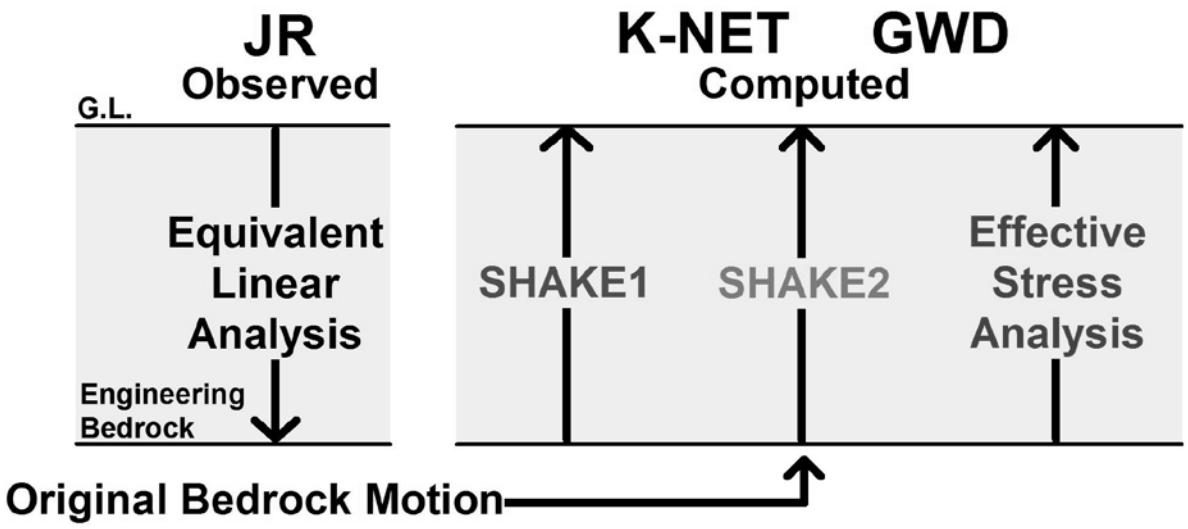


Figure 6 Flowchart to Estimate Ground Motion at K-NET and GWD from Recorded Motion at JR

To confirm the applicability of the deconvolution and convolution analyses shown in Figure 6 for a moderate-intensity earthquake, strong motions recorded at the K-NET and JR stations during the aftershock of the Niigata-ken Chuetsu Earthquake that occurred at 18:12 hrs on October 23, 2004 were used. Similar analysis and confirmation were unable to be performed for the GWD station because of the absence of the strong ground motion at the station during the same earthquake.

Figure 7 shows the time histories computed by the three methods, compared with the recorded ones. There is a good agreement between the observed and computed values, confirming the applicability of any of the deconvolution and convolution analyses for this particular pair of stations subjected to a moderate-intensity earthquake.

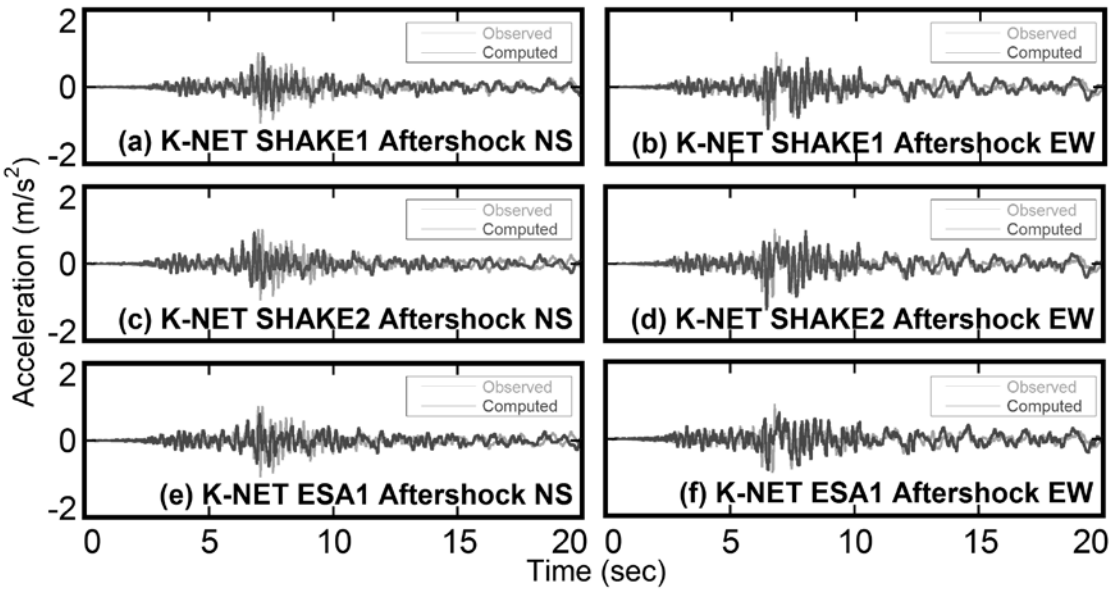


Figure 7 Acceleration Time Histories of Computed Ground Surface Motions, Compared with Those Recorded at K-NET during a Moderate-Intensity Earthquake

4.2 Ground Motions during a Strong-Intensity Earthquake

To study further the applicability and limitation of the three deconvolution and convolution methods for estimating site response during strong-intensity shaking and to examine the cause of the spiky waves observed at the K-NET and GWD stations, the analysis described in Section 4.1 was also performed using the strong ground motions recorded during the 2007 Niigata-ken Chuetsu-oki Earthquake.

Figure 8 shows the acceleration time histories of the deconvoluted bedrock motions using SHAKE2 and the ground surface motions computed from the three methods, compared with those of the recorded motions at the K-NET station. Figure 9 also shows the acceleration time histories computed with the same bedrock motions (Figs. 8(g) and (h)), compared with the observed ground motion at the GWD station. It seems that the computed results from any of the three methods are inconsistent with the recorded motions and are unable to reproduce spiky waves observed in the recorded motions.

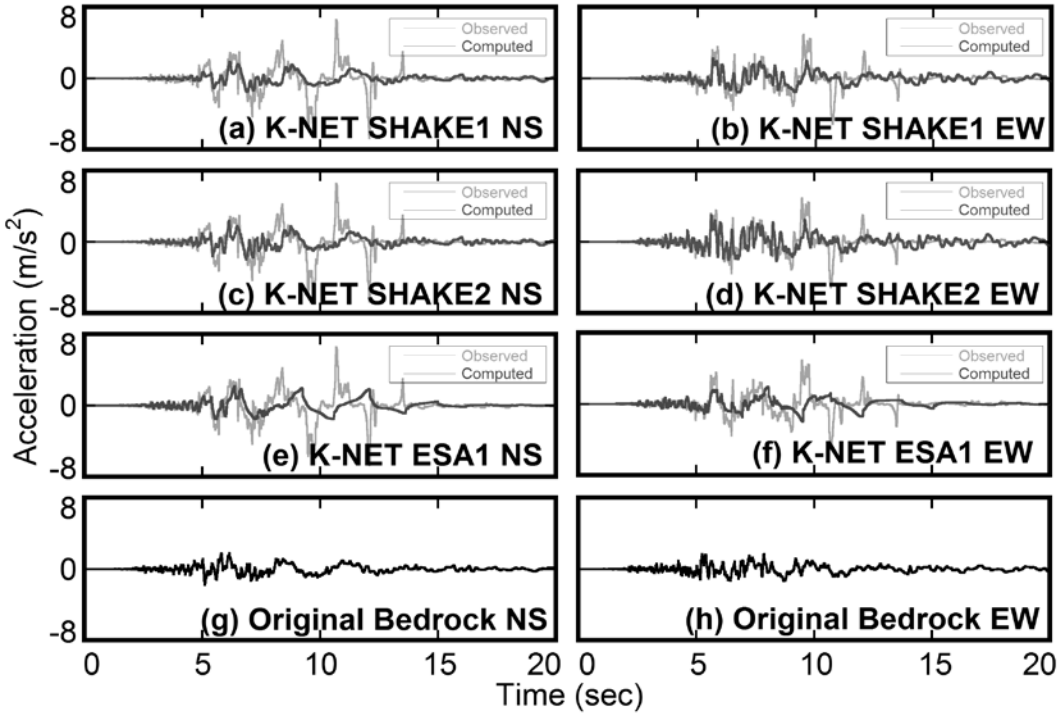


Figure 8 Acceleration Time Histories of Computed Bedrock and Ground Surface Motions, Compared with Those Recorded at K-NET during the 2007 Niigata-ken Chuetsu-oki Earthquake

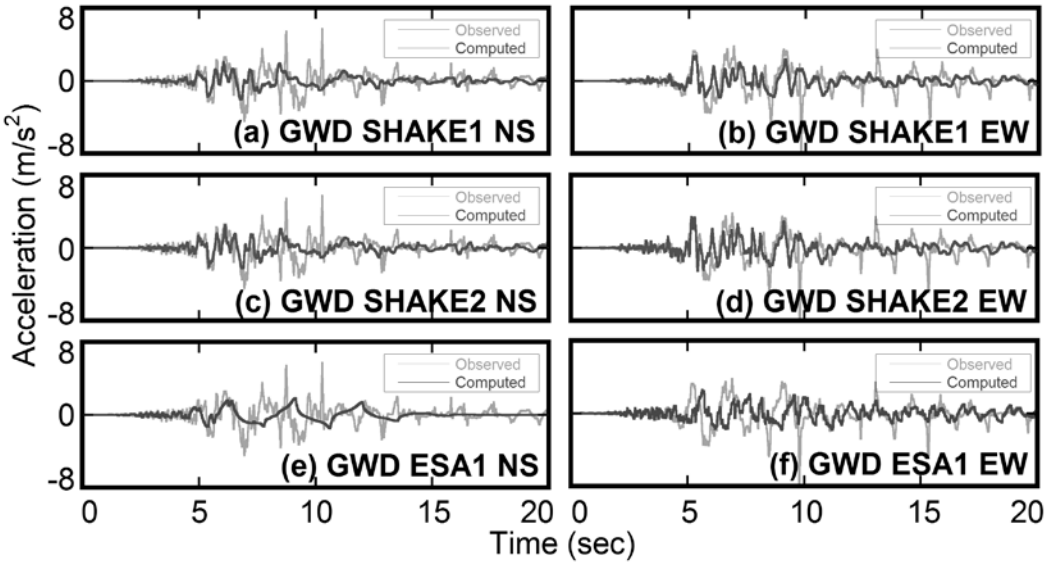


Figure 9 Acceleration Time Histories of Ground Surface Motions, Compared with Those Recorded at GWD during the 2007 Niigata-ken Chuetsu-oki Earthquake

4.3 Searching a Reasonable Bedrock Motion

A close examination of the simulation results further suggests that the computed ground motions shown in Figs. 7 and 8 are smaller in amplitude and more delayed particularly in the later phase than the observed one. This suggests that the actual bedrock motions in the later phase might have been larger and more behind than those deconvoluted by the equivalent linear method.

Based on the above discussions, a preliminary attempt was made to search for more reasonable bedrock motions that could simulate ground motions recorded at the three sites during the main shock. This was made by a trial-and-error method as shown in the flowchart of Figure 10 in which the bedrock motion is updated so that the difference in Fourier spectra between observed and computed ground surface motions can be minimized.

The bedrock motions initially assumed ($2E_{N,1}$) are those determined with the deconvolution analysis of SHAKE2 using the observed ground surface motions ($2E_{1,O}$) at the JR station. The effective stress analysis was then employed to estimate the ground surface motions ($2E_{1,i}$) at the three sites using the deconvoluted bedrock motions.

The bedrock motions ($2E_{N,i+1}$) were updated based on the following equation in such a way that the difference in Fourier spectra between the computed and observed ground surface motions at the three sites becomes small.

$$2E_{N,i+1} = 2E_{N,i} + \alpha \cdot \frac{2E_{N,i}}{2E_{1,o}} \cdot (2E_{1,o} - 2E_{1,i}) \qquad (1)$$

in which E is displacement Fourier spectra; first subscripts *1* and *N* are the ground surface and the bedrock; second subscripts o and I correspond to the observed values and the iteration number of the computed ones and α is a coefficient that is assigned a value greater than zero. This convolution analysis and modification of bedrock motion was repeated until the observed and computed ground surface motions become compatible with each other.

Figure 11 shows the acceleration time histories of the ground surface motions computed with the most updated bedrock motion, compared with the recorded ones. Good agreement exists between the observed and computed values at the K-NET and JR stations, whereas the computed results could not simulate well the observed acceleration time histories including the strong spiky waves.

Figures 12 and 13 show the velocity and displacement time histories of the computed ground surface motions, compared with those of the recorded motions. Again, good agreement exists between the observed and computed values at the K-NET and JR stations. In addition, those of the stronger NS components at the GWD station begin to show a fairly good agreement with those of the observed values, while those of the weaker EW components are still inconsistent with the observed ones.

The good agreement between the computed and observed time histories at the K-NET suggested that the cyclic mobility of the dense sand that occurs at depths of 5-12 m would be the primary cause of the strong spiky waves observed in the acceleration time histories at the site (Tokimatsu et al, 2010). Although similar cyclic mobility of dense sand and/or other unidentified phenomena that induced the stronger spiky waves could have taken place at the GWD station, the present analysis using the dynamic soil properties determined for the site has not identified the possible cause of the spiky waves at this site.

A comparison of the back-calculated bedrock motions between the initial and final trials shown in Figure 11 confirms that the actual bedrock motion in the later phase might have been larger and more behind than the one deconvoluted by the conventional equivalent linear method.

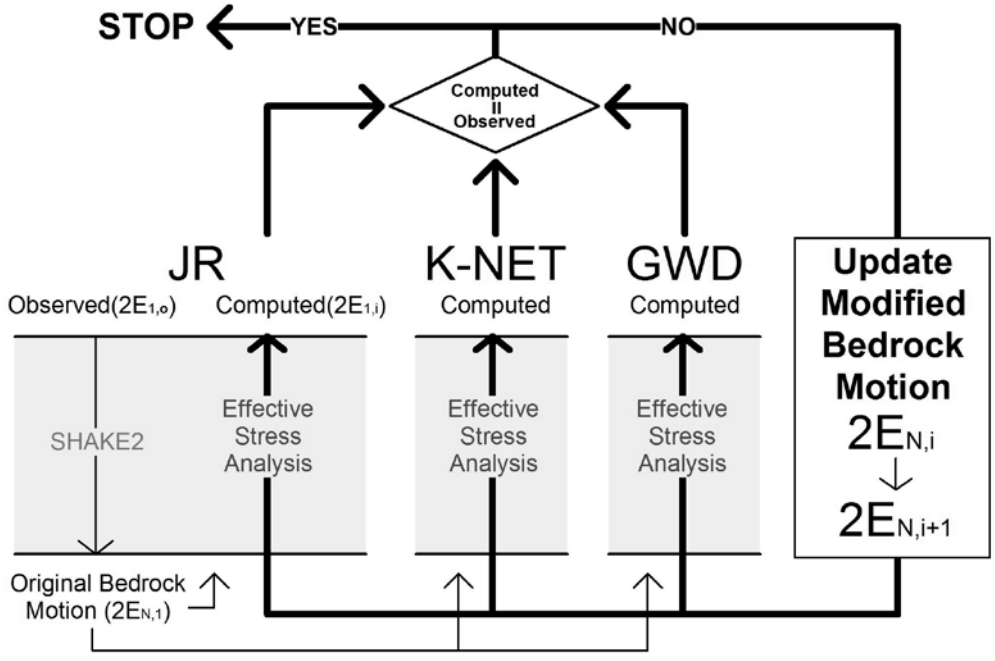


Figure 10 Flowchart to Search Reasonable Bedrock Motion

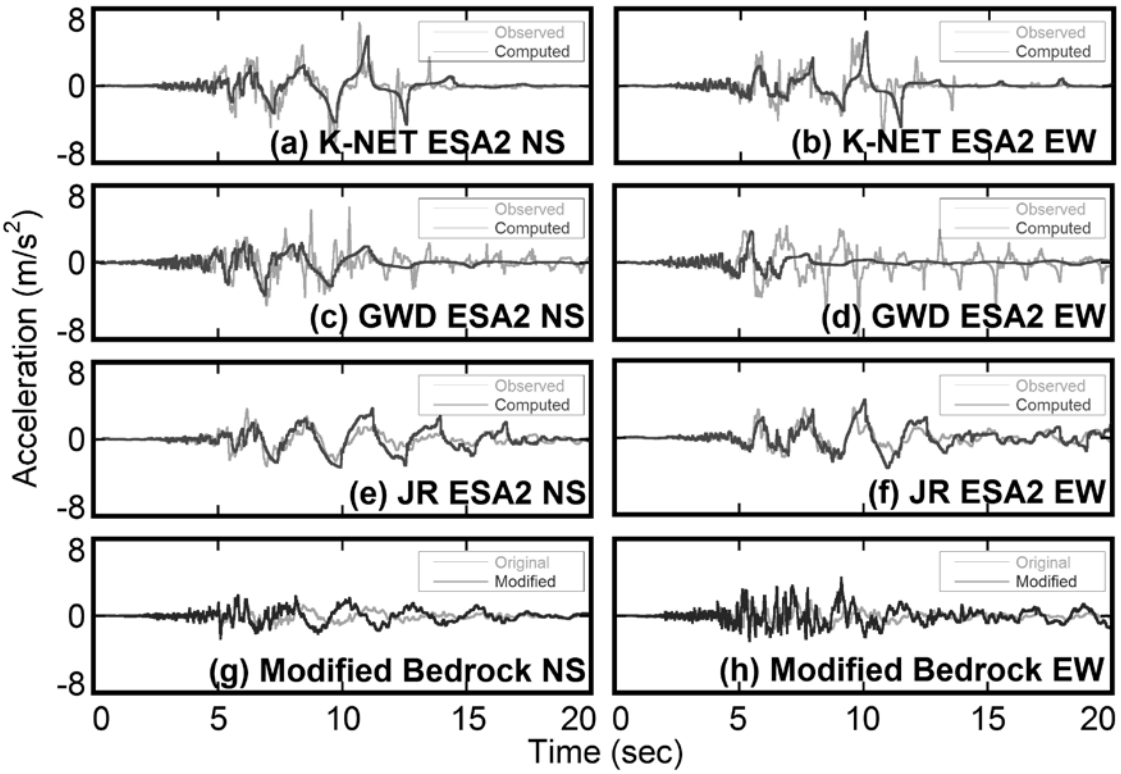


Figure 11 Time Histories of Most Updated Bedrock Motion and Ground Surface Motion, Compared with Those Recorded at K-NET, GWD and JR during the 2007 Niigata-ken Chuetsu-oki Earthquake

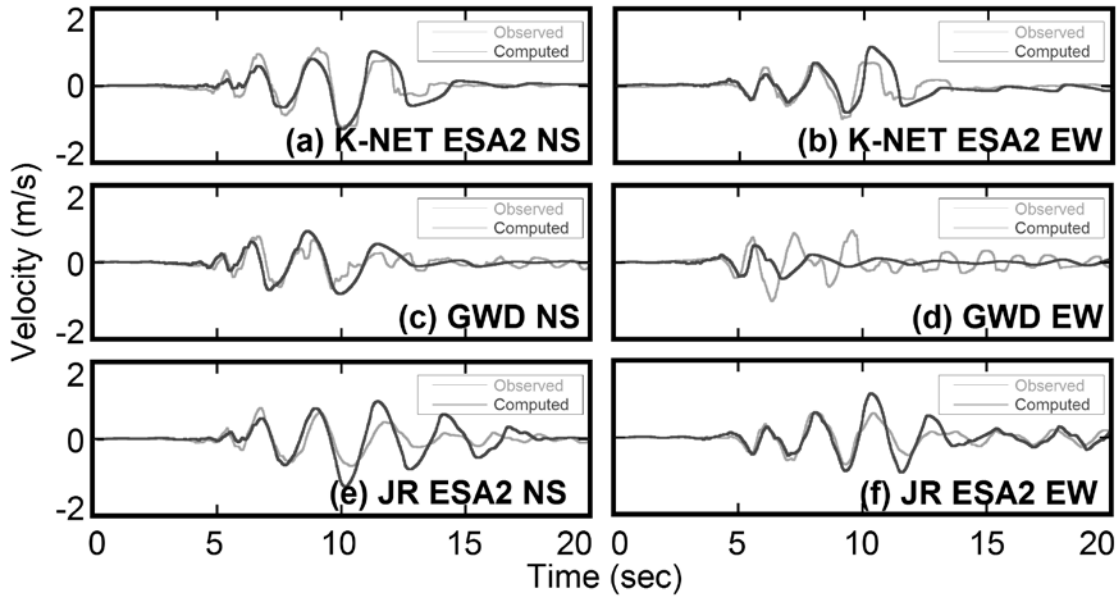


Figure 12 Results of Velocity Compared with Observed Records at the Three Sites

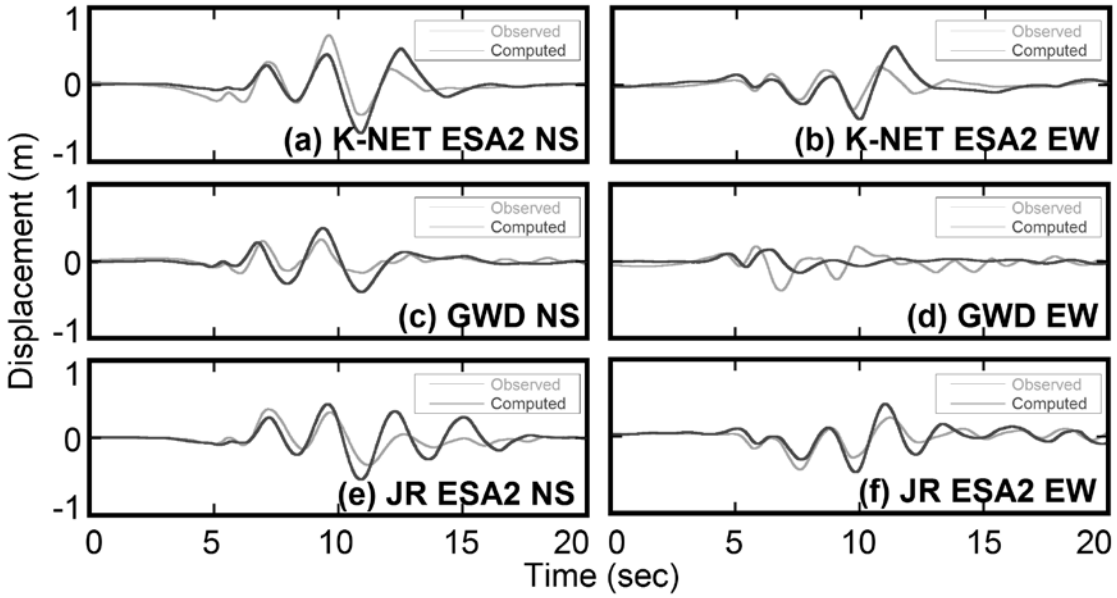


Figure 13 Results of Displacement Compared with Observed Records of the Three Sites

5. CONCLUSION

The strong ground motions recorded at the K-NET and GWD stations in Kashiwazaki city had spiky acceleration time histories, suggesting liquefaction or cyclic mobility of the ground, while those at nearby JR Kashiwazaki did not show such spiky waves. A preliminary attempt has been made to examine why such spiky waves were induced during the main shock and, for this purpose, to propose and employ the method for searching reasonable bedrock motions that could simulate the ground surface motions recorded at the three sites during the main shock. On the basis of the analysis and discussions, the following conclusions have been made:

(1) Conventional deconvolution and convolution analysis using strong motions recording at one site as reference for estimating those at nearby station has been proven effective for a moderate-intensity earthquake, whereas it was ineffective for a strong-intensity shaking which would induce liquefaction of soil deposits under consideration.

(2) The proposed method can reproduce reasonably well the recorded motions including the spiky waves at the K-NET Kashiwazaki and thus could show promise in estimating reasonable bedrock motion from strong ground motions recorded during strong-intensity shaking which would induce liquefaction of soil deposits under consideration.

(3) The proposed method can also reproduce reasonably well the velocity and displacement time hitories of the stronger NS records at the GWD station during the main shock, but cannot simulate the spiky acceleration time histories.

References:

ASENP (2002): Geotechnical Engineering Map of Niigata prefecture, Editorial Committee for geological map of Niigata prefecture, Association of Subsurface Exploration in Niigata Prefecture (ASENP), (in Japanese).

Kashiwazaki city (1983): Historical records of Kashiwazaki city (in Japanese).

Schnabel P.B., J. Lysmer, and H.B. Seed (1972): SHAKE – A computer program for earthquake response analysis of horizontally layered sites, EERC Report, No. 72-12.

Sugito M., Goda H., Masuda T. and Etsunada K. (1993): Equi-linearlized method with frequency-dependent shear modulus and damping, Proc., 28th Japan National Conference on SMFE, pp. 1129-1132 (in Japanese).

Shamoto Y., Tokimatsu K., and Ariizumi K. (1992): Applicability of A One-Dimensional Effective Stress analysis to An Existing Soil Deposit, J. Struct. Constr. Eng., AIJ, 433, 113-119. (in Japanese)

Tokimatsu K. (2008): Geotechnical Problems in the 2007 Niigata-ken Chuetsu-oki Earthquake, Geotechnical Earthquake Engineering and Soil Dynamics (GSP 181), ASCE, Proceedings of the Geotechnical Earthquake Engineering and Soil Dynamics IV Congress 2008, 30pp.

Yoshida N. et al. (2007): Investigation on Record at K-NET Kashiwazaki during the 2007 Niigata-ken Chuetsu-oki earthquake.

Tokimatsu K., Katsumata K. and Arai H. (2011): Simulations of Strong Ground Motions at Kashiwazaki City during the 2007 Niigata-ken Chuetsu-oki Earthquake, Proceedings of 5th ICEGE, 2011

8CUEE CONFERENCE PROCEEDINGS
8th International Conference on Urban Earthquake Engineering
March 7-8, 2011, Tokyo Institute of Technology, Tokyo, Japan

RELIABILITY ASSESSMENT OF TEHRAN PROVINCE GAS DISTRIBUTION PIPELINE SYSTEM DURING LIQUEFACTION

Danesh Nourzadeh[1)], Khosrow Bargi[2)], and Shiro Takada[3)]

1) Graduate Student, School of Civil Engineering, University of Tehran, Iran
2) Professor, School of Civil Engineering, University of Tehran, Iran
3) Adjunct Professor, School of Civil Engineering, University of Tehran, Iran
nourzadeh@ut.ac.ir, kbargi@ut.ac.ir, takada@lifiline-eng.com

Abstract: Although the buried pipelines systems have responded quite satisfying during past earthquakes, in the case of poor ground conditions catastrophic damages have been observed, because of soil instabilities and large deformations. Liquefaction is one of the most destructive side effects of earthquake in loose sandy soils, which induces large permanent ground displacements that could harm underground lifelines. In this paper, system reliability of Tehran gas distribution is challenged by liquefaction. First the probable liquefaction potential pattern is selected based on previous analyzes. After analyzing high and medium pressure buried pipelines as the link portions of the system, by means of simplified equivalent static and also finite element method using beam elements, the global reliability of the distribution system is examined by consideration of lateral spreading and settlement distribution maps in the area. The results show that effect of lateral spreading is negligible for Tehran gas network, but the settlement due to liquefaction in the southeast of Tehran has some major effects on local medium-pressure buried pipelines, that could disrupt the functionality of the system in some parts.

1. INTRODUCTION

Generally, the occurrence of liquefaction due to earthquake in high potential areas can have destructive effects on the buried pipelines. For reduction of the risk of this phenomenon, in the large urban areas, the only way is mitigation of the losses, however, in some isolated locations, the elimination of the hazard could be considered by means of soil rehabilitations or compaction. In order to mitigate the damage of lifelines, real-time monitoring, retrofit and field reconnaissance is needed in addition to seismic analysis and design. Nowadays, major progresses in liquefaction potential assessment and prediction of the complex behavior of buried pipelines are made, that would help to design these structures to resist severe hazards.

Liquefaction could affect the buried pipelines in different ways, reduction in bearing forces of the soil, buoyancy forces due to the submergence of the pipeline in the liquefied soil, ground settlement and lateral spreading as the most hazardous effect. Each of these effects takes place in a specific case, based on the soil characteristics and the location of the buried pipe. In this paper, the potential of liquefaction in Tehran is first reviewed and different effects of liquefaction as discussed above are evaluated. Then the response of Tehran gas pipelines in the high potential area is evaluated by means of simplified methods and also finite element method, and based on the analyses, general quantitative countermeasure plans are suggested.

2. LIQUEFACTION POTENTIAL IN TEHRAN

The evaluation of liquefaction potential is the first step for the risk assessment of the pipelines network. Here, recent researches that evaluated the possibility and potential of liquefaction in different parts of Tehran is reviewed. All of these researches are based on common equations in soil dynamics. A summary of these methods is presented herein.

2.1 Basic Method of Evaluation

Generally, the evaluation is carried out by F_L method in each soil layer, while the liquefaction potential is evaluated by P_L method in the selected point, based on F_L values.

Based on most seismic design guidelines, the FL values are evaluated for sandy soils to the depth of 20 meters in each borehole, where the ground water level is lower than 10 meters from the surface (JRA 2002). The F_L is obtained by the Eq. 1.

$$F_L = R_r / L \quad (1)$$

where, R_r is the cyclic shear resistance, and L is the shear stress ratio, both derived from the specifications of the selected seismic hazard and soil specifications. If the F_L ratio is not less than 1, the soil layer is judged as liquefied.

If for a selected borehole, the F_L values of the layers are greater than 1, liquefaction index (P_L) is derived as below (Iwasaki et al. 1982):

$$P_L = \int_0^{20} F_L W(x) dx \qquad (2)$$

where, W(x) is a prescribed function of x the depth of layer below ground surface in meters. After evaluation of P_L values in a point, the liquefaction potential is assessed based on the Table 1.

Table 1 Liquefaction Potential Judgement Criteria

Liquefaction potential	Criterion
Very high	$P_L > 15$
Relatively high	$5 < P_L < 15$
Relatively low	$0 < P_L < 5$
Very low	$P_L = 0$

2.2. JICA Studies for the Greater Tehran

These studies were carried out in 1999 and 2000 by Japan International Cooperation Agency for Iran as a part of the microzonation studies for the greater Tehran. In this research, the basic evaluation methods summarized above are used, thus the boreholes in the territory in southeast of Tehran, that have a ground water level less than 10 meters are selected for the study. Moreover, the selected earthquake scenario is Ray Fault model which has the largest PGA distribution in the studied area.

This research showed that, in the almost whole area, the liquefaction potential is evaluated as "very low" and "relatively low". A hard cohesive clay soil covers almost the entire area and only in one borehole, the potential is evaluated as "relatively high", while the distribution of the liquefied soil is very limited in the region. The result of this study is presented in the Figure 1 (JICA 2000).

Based on these calculations and results, a distribution map for the horizontal flow of the liquefied soil, known as lateral spreading, is provided as shown in Figure 1 (a), using the flow estimation formula on the slope areas presented in Eq. 3 (JGA 2001).

$$\delta_h = 36c\left\{\sum_{i=1}^{n} \frac{0.5\gamma_i H_i^2 + \sigma_{vi} H_i}{\left(0.5\gamma_i H_i^2 + \sigma_{vi}\right)^{3/2} N_{bi}}\right\}\theta_g \qquad (3)$$

where, δ_h is the amount of lateral flow (m), c is the location correction parameter here equal to 0.5, H_i , γ_i , N_{bi} and σ_{vi} are the properties of the soil layer i, and θ_g is the slope of the area.

Another effect of the liquefaction is the ground settlement, which is assumed to be 5% of the thickness of the liquefied soil, so the values of settlement due to liquefaction were evaluated as shown in Figure 1 (b). As it is understood from Figure 1, lateral spreading effects could be neglected in the analysis of the structures, but the settlement values should be considered as a seismic input on the structures.

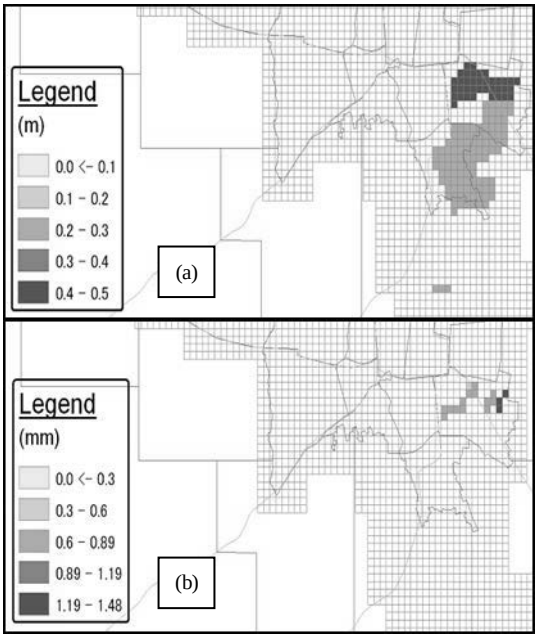


Figure 1 (a) Lateral Spreading, (b) Settlement distribution for Tehran (after JICA 2000)

2.3. IIEES Studies

Different research groups from International Institute of Earthquake Engineering and Seismology (IIEES) have analysed liquefaction potential in Tehran. First in 1993, the occurrence of liquefaction in the southern parts of Tehran was tested in a medium scaled evaluation (Hosseini and Kari 1993). Later, on 1998, the potential of southwest of Tehran was examined using PGA of 0.35g, that showed very low liquefaction potential for liquefaction (Hosseini et al. 1998). One year later in 1999, a joint study by IIEES and the laboratory of Ministry of Roads and Transportation was taken out on 41 boreholes in southeast of Tehran, PGA distribution ranging from 0.2g to 0.4g, locating areas with relatively high liquefaction potentials for 0.3g to 0.4g PGAs (Hosseini 2002). Finally, in 2002, a large scaled study was carried out on the southeast area of Tehran using site specifications and seismic hazard analysis which is discussed in the following (Askari and Kasaei 2002).

In this study, the selected area in the southeast of Tehran as shown in Figure 2 (a), was divided into the 1km by 1km blocks, and in each block PGA according to the calculated Maximum Credible Earthquake (MCE) was assumed, and based on the F_L and P_L method described above, the liquefaction potential of he selected area was evaluated. The P_L values for every block are shown in the Figure 2 (b).

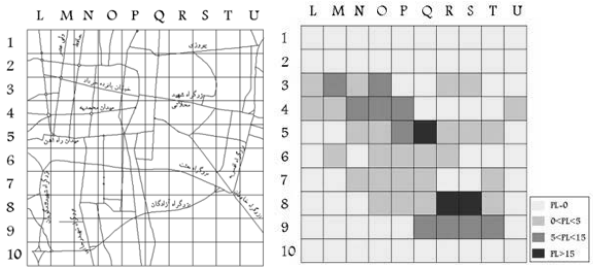


Figure 2 (a) Location and discretization of the analyzed area, (b) F_L values distributions in the blocks (after Askari and Kasaei 2002).

3. SELECTED AREA FOR THE STUDY

According to the previous studies discussed above, the area for analysis of liquefaction effects on the gas pipelines is the southeast of Tehran. For the purpose of analysis, a region which includes all the risky areas in the previous analyses was selected as shown in Figure 3 (a). The buried pipelines of 250 psi and 60 psi gas distribution networks in this region are shown in Figure 3 (b) and (c) respectively.



Figure 3 (a) Location and discretization of the analyzed area, (b) High pressure gas pipelines, (c) Medium pressure pipelines in the area.

4. ANALYTICAL MODELS FOR BURIED PIPELINES

In this section, the numerical analysis of buried gas pipelines which were located in the selected are in the southeast of Tehran is discussed. For determination of the response of these lifelines under the probable liquefaction hazard, first the two different pipelines network was analysed using equivalent static method based on major seismic design codes for lifelines (JGA 2001, ALA 2001, and JGA 2003), and then a more detailed finite element analysis was conducted. The pipelines are considered as continuous welded pipelines. Moreover, as it was discussed earlier, the effect of lateral spreading and buoyancy is negligible and the only considerable effect of liquefaction is the settlement, which two levels of settlement hazards based on JICA studies are selected as the major loading and are included in the cases. In the table below, Ks is the soil stiffness coefficient obtained from the seismic design references.

4.1. Equivalent Static Model

The approach for design and analysis of high pressure and low or medium pressure pipelines differ in the codes because of different functions and post-earthquake performance demands. So for the analysis of response of Tehran gas pipelines, these two types were separated.

4.1.1. High pressure pipelines

In the seismic design codes (JGA 2003), there are formulas for determination of the distortion angle of high pressure pipelines buried in the liquefiable areas. These formulas are different for straight, curved and T-portions of pipes. Hence, since there is no bending or curves in the pipeline length in the planes of the settlement loading (vertical), all the pipelines in the area could be assumed to deform like straight pipes, and the effect of curves and elbows could be neglected in the studies. Thus the bending angle of the straight pipes due to the liquefaction deformations of the ground could be obtained from Eq. 4 (JGA 2001).

$$\omega_s = \frac{180}{\pi} \cdot 127 \cdot D_i \cdot \sqrt{\frac{P_1 \cdot \gamma_\delta \cdot \delta_h}{EI}} \quad \text{for} \quad P_1 = D_i \cdot \gamma_k \cdot \sigma_c \qquad (4)$$

where ω_s is the bending angle in degrees, D_i is the pipe diameter in meters, γ_δ and γ_k are the partial safety coefficients taken 1.0 and 1.1 respectively, δ_h is the soil displacement in centimeters, EI is the bending stiffness of the pipe in N.cm^2, and σ_c is the yielding stress of the soil in the direction of the loading.

Also the bending capacity of the straight pipelines in the liquefaction could be obtained from the formulation below (JGA 2001).

$$\varpi_{sc} = \left\{ 0.44 \frac{t_s}{D_i} \left(8k - \frac{2k^2}{3} \right) + \frac{3.44}{\sqrt{\frac{2D_i}{t_s}}} \left(1 + \frac{\varepsilon_f}{2} \right) \right\} \cdot \frac{180}{\pi} \qquad (5)$$

where t_s is the wall thickness of the pipe, k is assumed to be 3.2, and ε_f is the ultimate strain of the pipelines suggested to be taken 0.35.

These two demand and capacity values are calculated and shown in the Table 2. As it is carried out by this method, the capacity of Tehran gas distribution pipelines in the selected region in southeast is more than the probable liquefaction hazard by a large safe margin.

Table 2 Results of ESM Analysis of High Pressure Pipelines

Case	D_i	δ_h (mm)	Material	ω_s	ω_{sc}
1	6"	300	Steel- GrB	1.35	57.39
2	8"	300	Steel- GrB	1.18	51.99
3	10"	300	Steel- GrB	1.07	48.66
4	12"	300	Steel- X42	1.04	43.66
5	16"	300	Steel- X42	0.96	36.10
6	22"	300	Steel- X42	0.90	29.39
7	24"	300	Steel- X42	0.88	27.81
8	30"	300	Steel- X42	0.84	24.18
9	6"	500	Steel- GrB	1.74	57.39
10	8"	500	Steel- GrB	1.52	51.99
11	10"	500	Steel- GrB	1.38	48.66
12	12"	500	Steel- X42	1.34	43.66
13	16"	500	Steel- X42	1.24	36.10
14	22"	500	Steel- X42	1.16	29.39
15	24"	500	Steel- X42	1.13	27.81
16	30"	500	Steel- X42	1.08	24.18

4.1.2. Medium pressure pipelines

For analysis and design of medium and low pressure pipelines, the codes suggest evaluating the response displacement of the pipeline and checking it with the demands, which are mostly assumed as amplitude of 5cm displacement in each direction for design purposes (JGA 2003). However, in the case of risk analysis, the displacement capacity is compared with the selected hazard level. Thus, in this study the relations to calculate the vertical displacement capacity of the straight medium pressure pipelines such as shown in the Eq. 6 and 7 are used and the results are compared with 30cm and 50cm values of settlement induced by liquefaction.

$$\Delta v = \frac{2\sqrt{2}e^{\frac{\pi}{4}}}{D_i} \sqrt{\frac{4EI}{k_s D_i}} \varepsilon_0 \quad \text{(cm) for free ended pipes} \qquad (6)$$

$$\Delta v = \frac{1}{D_i} \sqrt{\frac{4EI}{k_s D_i}} \varepsilon_0 \quad \text{(cm) for clamped pipes} \qquad (7)$$

where Δv is the vertical capacity of pipelines, and ε_0 is the critical strain of the pipe material, assumed 0.03 for steel pipes and PE pipes.

As it could be obtained from the Table 3, the capacities of some pipes that are highlighted are not sufficient for this level of liquefaction settlements, and a more detailed study should be done.

Table 3 Results of ESM analysis of medium pressure pipelines

Case	D_i	Material	δ (cm)	ΔV (cm)	ΔV (cm) (clamped)
1	4"	Steel-GrB	30	73.05	11.78
2	6"	Steel-GrB	30	96.31	15.52
3	8"	Steel-GrB	30	116.38	18.76
4	10"	Steel-GrB	30	135.53	21.85
13	63 mm	PE100	30	5.83	0.94
14	90 mm	PE100	30	7.94	1.28
15	125 mm	PE100	30	10.58	1.71
16	4"	Steel-GrB	50	73.05	11.78
17	6"	Steel-GrB	50	96.31	15.52
18	8"	Steel-GrB	50	116.38	18.76
19	10"	Steel-GrB	50	135.53	21.85
28	63 mm	PE100	50	5.83	0.94
29	90 mm	PE101	50	7.94	1.28
30	125 mm	PE102	50	10.58	1.71

4.2. Finite Element Model

Although the previous analyses suggested no damages in high pressure pipelines, here multiple cases for both high and medium pressure pipelines were selected to be analysed by FEM. In this analysis, PIPE type elements (BEAM elements enabling the internal pressure effects) were used in

the FE code ABAQUS v.6.9, and also surrounding soil was modelled as nonlinear Winkler vertical and axial springs (JGA 2001, ALA 2001). Moreover, the loadings included internal pressure and also soil pressure on the pipes, and the liquefaction settlement was inserted to the end of the soil springs, and quasi-static analysis was carried out. The outline of this FE modelling is shown in the Figure 4.

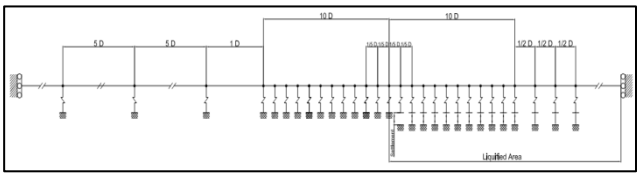


Figure 4 Schematic model of FE analysis and meshes

Different lengths for the liquefied area was tested ranging from 100m to 2km, and also the effect of curves along the pipelines were tested by using elbow elements, but as it was predicted it was negligible. Also the material nonlinearities were modelled as the basic nonlinear curves (Pezeshki, et al 2004). The results of this analysis are shown in Table 4. In this table, every value for the strains represents the maximum of numerous test results including 45 and 90 degree bended pipes, different assumed dimensions for liquefied area, and different boundary conditions for pipelines. As it is understood from the table, small diameters of PE pipes could have troubles to resist the amount of liquefaction settlements, as it is highlighted.

5. CONCLUSION AND COUNTERMEASURES

1. As it is shown in the results of the analyses, high pressure pipelines of Tehran would not encounter any major risks during the possible liquefaction occurrence in the southeast of Tehran. Although these types of gas pipelines could maintain their integrity and functionality, they may experience some plastic which implies the need for inspections after the earthquake occurrence.
2. This problem for 60psi pipeline network is more sever. These pipelines could experience large deformations in the southeast of Tehran, and also Polyethylene pipelines with diameters smaller than 125mm, could lose their functionality after the liquefaction.
3. The places in the region which was selected in this study should be marked for urgent post-earthquake measures to check the safety of the pipelines and using shut-off valves for medium pressure pipelines especially PE pipes could be a good retrofit plan.
4. As far as there is no real-time monitoring for Tehran gas network, the urgent post-earthquake planning is necessary to shut the flow and diagnose the disruptions. However, the necessity of establishing a monitoring system such as SCADA, for all types of lifeline systems in Tehran is felt. The SCADA should be synchronized with a dense array of seismographs for real-time monitoring and immediate measures in the cases of earthquake occurrence.

Table 4 Results of FE analysis of pipelines

Case	D	δ (mm)	Material	Internal Pressure (PSI)	Max. Principal Strain	Allowable Max. Strain	Min. Principal Strain	Allowable Min. Strain
1	6"	500	Steel- GrB	60	1.54E-02	3E-02	-7.21E-03	-4.10E-02
2	10"	500	Steel- GrB	60	1.14E-02	3E-02	-5.23E-03	-3.22E-02
3	6"	500	Steel- GrB	250	1.52E-02	3E-01	-6.49E-03	-4.10E-02
4	10"	500	Steel- GrB	250	1.12E-02	3E-01	-4.55E-03	-3.22E-02
5	16"	500	Steel- X42	250	7.72E-04	3E-01	-5.24E-05	-2.06E-02
6	22"	500	Steel- X42	250	3.61E-04	3E-01	-1.03E-05	-1.50E-02
7	30"	500	Steel- X42	250	3.41E-04	3E-01	-1.63E-05	-1.10E-02
8	63 mm	500	PE 100	60	3.9E+00	2E-01	-1.76E+00	-8.10E-02
9	90 mm	500	PE 100	60	2.5E+00	2E-01	-1.07E+00	-8.02E-02
10	125 mm	500	PE 100	60	6.00E-02	2E-01	-2.81E-02	-8.03E-02
11	63 mm	300	PE 100	60	2.0E+00	2E-01	-8.76E-01	-8.10E-02
12	90 mm	300	PE 100	60	8.28E-01	2E-01	-3.60E-01	-8.02E-02

6. ACKNOWLWDGEMENT

This paper was a part of a project funded by Tehran Province Gas Company. The authors would like to acknowledge the research and technology department head and members for their intimate supports during the project.

References:

Japan Road Association, (2002), "Specifications for Highway Bridges", Part V: Seismic Design.

Iwasaki, T., Tokida K., Tatsuoka F., Watanabe S., Yasuda S., and Sato H., (1982), "Microzonation for Soil Liquefaction Potential Using Simplified Methods", *Proceedings of 3rd International Earthquake Microzonation Conference*, Seattle.

Japan International Cooperations Agency, (2000), "The Study on Seismic Microzoning of the Greater Tehran Area in the Islamic Republic of Iran", Main Report to Tehran Municipality.

Japan Gas Association, (2001), "Seismic Design Guideline for Liquefaction for High Pressure Gas Pipeline", JGA-207-01. (Written in Japanese)

Mirmohammad Hosseini M., Kari M, (1993), "Preliminary Microzoning of Areas Prone to Liquefaction in Tehran", *Proceedings of 2nd International Conference on Seismology and Earthquake Engineering*, Iran.

Mirmohammad Hosseini M., et al (1998), "Microzonation of Southeast of Tehran for Liquefaction", IIEES, Iran.

Mirmohammad Hosseini M, (2002), "Microzonation of Southeast of Tehran for Liquefaction", National Research Program in IIEES, Iran.

Askari F., Kasaei M, (2002), "Analysis of Liquefaction Potential in Some Parts of Southeast Tehran". *Journal of Faculty of Engineering*, University of Tehran, Iran.

American Lifeline Alliances, (2001), "Guideline for Design of Buried Steel Pipe", ASCE, USA.

Japan Gas Association, (2003), "Seismic Design Guideline for Middle and Low Pressure Gas Pipelines". (Written in Japanese)

Pezeshki H., Ueno J. and Takada S, (2004), "Performance and allowable fault dislocation for steel and polyethylene pipelines crossing faults", *Memoirs of Construction Engineering Research Institute no.46*, pp. 152-163.

8CUEE CONFERENCE PROCEEDINGS
8th International Conference on Urban Earthquake Engineering
March 7-8, 2011, Tokyo Institute of Technology, Tokyo, Japan

SEISMIC PERFORMANCE OF A SYSTEM OF INTERDEPENDENT LIFELINE AND INFRASTRUCTURE COMPONENTS

Jacopo Selva[1], Kalliopi Kakderi[2], Maria Alexoudi[3], and Kyriazis Pitilakis[4]

1) Istituto Nazionale di Geofisica e Vulcanologia, Sezione di Bologna, Italy
2) Civil Engineer, MSc, Dept. of Civil Engineering, Aristotle University of Thessaloniki, Greece
3) Civil Engineer, MSc, PhD, Dept. of Civil Engineering, Aristotle University of Thessaloniki, Greece
4) Professor, Dept. of Civil Engineering, Aristotle University of Thessaloniki, Greece
selva@bo.ingv.it, kakderi@civil.auth.gr, alexoudi@civil.auth.gr, kpitilak@civil.auth.gr

Abstract: The aim of this research is to develop a generic procedure for the assessment of the serviceability of a system (single system or system of systems) if one or more interacting components of the system are damaged by an earthquake. The system serviceability (functionality) is evaluated starting from the expected degree of damage of the single components (direct physical damage estimated using appropriate fragility functions) and accounting for their functional interaction (functional system architecture and single or by-directional interactions among components). Through the evaluation of the components' non-functionality, the overall serviceability of the system is assessed, possibly in the form of a "system serviceability curve", for different levels of seismic input intensity. Aleatory and epistemic uncertainties are treated using a Bayesian inference. The applicability of the proposed approach is established through an illustrative example. It is shown that the methodology is quite general and applicable to real systems with diverse degrees of complexity and knowledge of system and components details.

1. INTRODUCTION

In the framework of a comprehensive risk analysis and management of interacting lifeline and infrastructure systems, their seismic performance should be considered in a rigorous and unified way. This could only be achieved through the assessment of the systems' functionality, considering the complexity of structures and the interdependencies among systems and their components.

Several approaches are available to help describe the relations existing between system's components. Some of these are: Graph theory, Fault-tree analysis (FTA), Event-tree analysis (ETA), Series system in parallel (SSP), Agent-based models and Complex Adaptive Systems (Amin 2001, Little 2002, Brown et al. 2004, Bernhardt and McNeil 2004, Tolone et al. 2004). The probabilistic evaluation of the performance of the system (PNET) can be carried out employing the methods of System Reliability Analysis. These include expansion methods, such as FORM/SORM or the response surface technique (Ditlevsen and Madsen 1996), as well as the Monte Carlo simulation methods (Rubinstein 1981). Depending on the nature of uncertainty and the aptitude to determine them, the probabilistic approach may be replaced or enhanced by possibilistic approaches based on Fuzzy Logics, so-called Fuzzy Networks. Also, non-simulation methods have recently seen interesting advances, e.g. in the form of Matrix System Reliability Analysis (Song and Der Kiureghian 2003, Der Kiureghian and Song 2008).

Moving to a higher level, several researchers have proposed different types of interdependency (interactions between different critical infrastructures) simulation models (Kameda 2000, Giannini and Vanzi 2000, Rinaldi et al. 2001, Peerendoom et al. 2001, Amin 2001, Haimes and Jiang 2001, Little 2002, Li and He 2002, Tang et al. 2004, Yao et al. 2004, Brown et al. 2004, Bernhardt and McNeil 2004, Santos and Haimes 2004). Only few methodologies have incorporated interdependencies in the seismic risk analysis of lifelines (Nojima and Kameda 1991, Scawthorn 1992, Eidinger 1993, Shinozuka et al. 1993, Shinozuka and Tanaka 1996, Menoni 2001, Duenas-Osorio et al. 2007, Tang and Wen 2008).

Furthermore, very few studies can be found in the literature dealing with the highest level problem of multiple systems interaction in the case of seismic vulnerability and loss estimates (Duenas-Osorio et al. 2007, Kim et al. 2007). They have still an exploratory character and are based on rather extreme simplifications, being limited to the analysis of at most two systems. Network analysis and graph theory are usually adopted. The Bayesian approach is often used for network analysis. The systems' serviceability is also analyzed using flow or connectivity analysis. Some recent studies have been focused on the proposal of a methodology to evaluate the associated losses of interacting lifeline elements for various strong motion intensities and the estimation of complex fragility curves of interdependent components (Kakderi et al. 2007, Kakderi et al. 2008, Alexoudi et al. 2008a, b).

There is a need for the development of a rigorous methodology for the assessment of systems functionality, considering the complexity of structures and the interdependencies among systems and their components. The ultimate goal is the formulation of a system function that allows the evaluation of the state of the system as a function of the states of its components. The availability of such a function is a prerequisite for the evaluation of the system performance.

Herein, a generic procedure is developed for the assessment of the serviceability of a system, if one or more interacting components of the system are damaged by an earthquake. With the word system, we consider either a single system composed by many interacting components (e.g., one lifeline) or a system of systems (e.g., a set of lifelines and infrastructures), where interaction among components and systems are accounted for. The various types of uncertainties (aleatory and epistemic) are treated with the use a Bayesian inference.

The method introduces a formal and schematic way to account for several innovations in the systemic vulnerability field, such as, different levels of damages, their uncertain link to different levels of functionality, the uncertain configuration of each sub-system, the epistemic uncertainties related to each probability value, the summarization of single functionalities through a normalized performance index of the whole system. All these issues are developed in a generic and coherent framework. However, given the modularity of the methodology, each one of such innovations may be adapted to be applied as single module in the previously presented methodology. In any case, the proposed methodology is quite general and it is applicable, eventually with several further assumptions and/or simplifications, to real systems with diverse degrees of complexity and knowledge of system and components details.

2. SERVICEABILITY MODEL – UNCERTAINTIES AND INTERDEPENDENCIES

The modular procedure to assess the system serviceability proposed by Selva et al. (2011) is adopted. The procedure starts from the Physical Damages (PD) of each component of the system, as assessed through its specific fragility curves. Then, the PDs of all components are translated into their Physical Non-Functionality (PNF), that is, the impossibility of the component to provide its service (supply) to the other components of the system due to the experienced damages. Interactions among the functionality of the components, i.e., their interdependencies, are accounted for assessing the Actual Non-Functionality (ANF) of components and/or sub-systems, i.e., the impossibility to provide services not only because of physical damages (PNF), but also because of the lack of external supplies that are necessary to it. Note that the ANF can be referred to either single "physical" components or "sub-systems", for which a global ANF is modeled starting from the PNF of the "representative" components. Finally, the overall Serviceability of the System (Ss) is assessed, by analyzing the ANF of the "real components" and/or of the "representative sub-systems" that provide the system's final service(s).

The procedure is schematically reported in Figure 1, and it can be summarized as following:

- STEP 0: FC (Fragility curve of a component) → PD (Physical Damages of the component).
- STEP 1: PD → PNF (Physical Non-Functionality of the component due to physical damages).
- STEP 2: PNFs → ANF (Actual Non-Functionality of a component or a sub-system, given the interaction among components).
- STEP 3: ANFs → Ss (overall Serviceability of a System).

The method aims at accounting for all the uncertainties involved in the serviceability assessment. In particular, it explicitly deals with (i) the epistemic uncertainties related to all probability assessments (e.g. Woo 1999), (ii) the uncertainties related to loss estimation and quantitative risk probability assessment [uncertainty related to seismic hazard, response and vulnerability of structures, probability of damage or collapse and the damage/ collapse to loss relationships (e.g. Spence 2007)], and (iii) the problems related to the partial knowledge of systems, in particular regarding missing components and/or links (e.g. Pitilakis et al. 2005). This goal is achieved by combining several strategies.

First, the process is schematized in several consequent events, making the model more readable (and testable) and allowing the use of conditional probabilities (Marzocchi et al. 2010, Grezio et al. 2009). Second, all parameters and values of the model (including probability estimations) are evaluated in a Bayesian perspective, that is, through probability density functions (pdf) (e.g. Gelman et al. 1995). All the probability density functions are then combined together by the extensive use of Monte Carlo simulations. Third, since several "sub-systems" (e.g., networks) cannot be completely known and/or change quickly through time, they are modeled starting from their general characteristics, without assuming specific configurations. In this case, groups of "representative" components are modeled jointly, so that the range of applicability of the method is by far increased, but also the sensibility of the results to missing or not known elements/ links is minimized.

Other important aspects of this model are the fact that it allows (i) to account for the interdependency among different components of the same system (e.g. Kakderi et al. 2007, Duenas-Osorio et al. 2007, Alexoudi et al. 2008 a or b) (ii) to assess and merge the different levels of both "physical damage" and "non-functionality" that each component may experience (Kim et al. 2007, Menoni et al. 2002), (iii) to circularly apply the procedure from single systems to higher level system of systems.

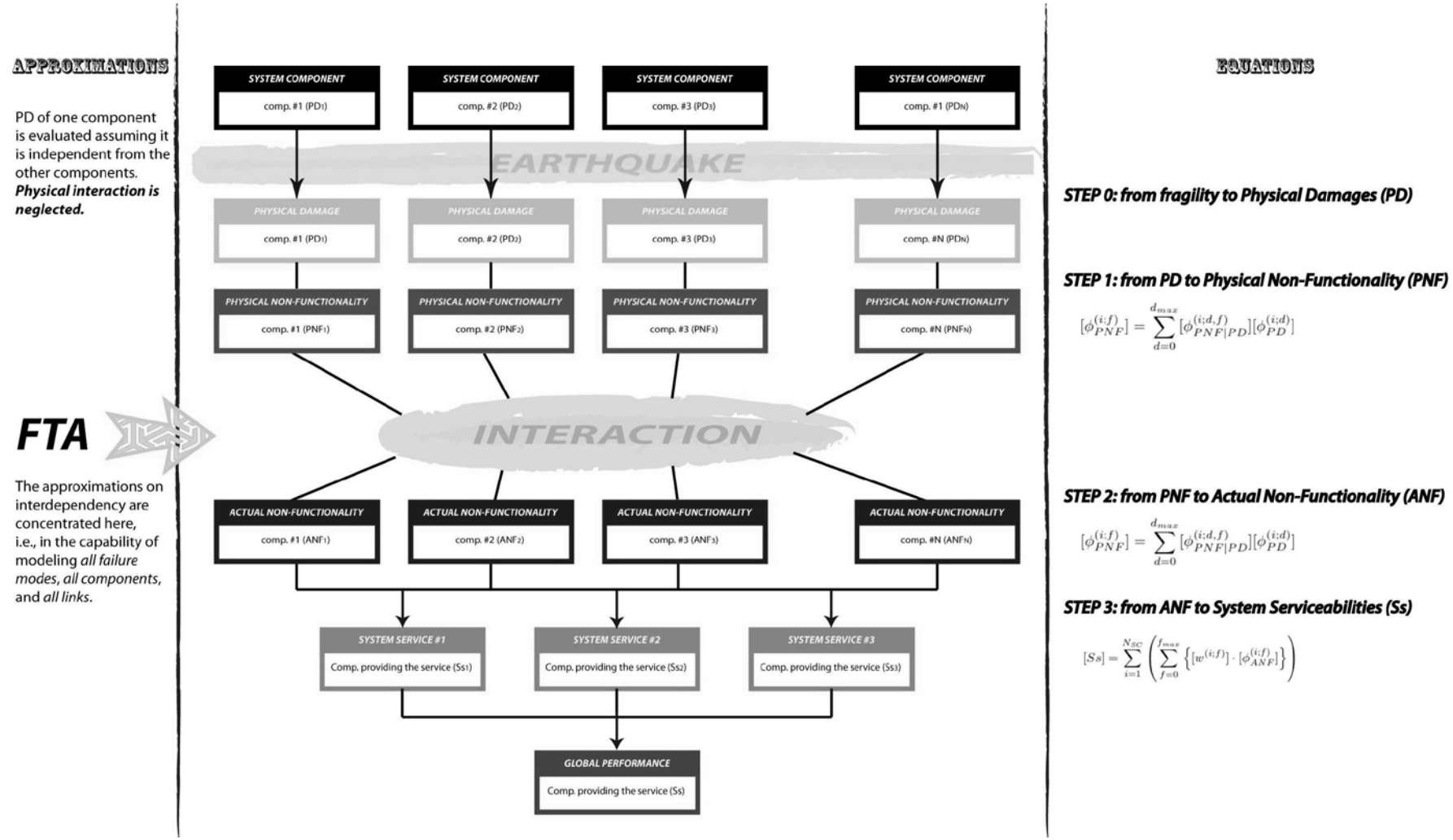


Figure 1. Framework of the proposed methodology (Selva et al. 2011).

3. ILLUSTRATIVE EXAMPLE

The goal of this application is to show a possible implementation of the model described above at various levels of seismic intensity, by considering the elements that contribute to provide service, accounting also for interaction with other infrastructure systems. Herein, two lifelines are examined, the water and electric power supply systems, with the final demand being the supply of potable water to the end users. The final serviceability is evaluated at two levels a) for all end users and b) for emergency use. The system is essentially divisible into three inter-dependent sub-systems: the electric power supply, the pumping and the pipe network sub-systems.

The whole system is assumed only partially known, and it is simulated through its main characteristics. The various sources of uncertainties are modeled following the Bayesian approach, so that all the uncertain parameters (including probabilities) are modeled through appropriate statistical distributions.

The seismic input is expressed in terms of PGA and it is made vary from 0 to 1 g. At each PGA level, the actual input for all elements is randomly sampled from a uniform distribution centered on the level and with a width 0.1 g. The analysis is then performed with 50 different sampled inputs, which simulate the variability of the seismic intensity at a local scale.

Three levels of application are performed, in order to capture all possible modes of inter and intra-dependencies and assess the altering mode of systems serviceability with an increasing level of induced interactions among components and systems. The three cases examined are the following:

Case 1: Water supply system comprised only of pipeline elements (study of interactions between the same components of one system). The Actual Non-Functionality (ANF) of the Pipeline Network (PN) depends only on its Physical Non-Functionality (PNF) (Figure 2A), as assessed through global properties of network (see below).

Case 2: Water supply system comprised of pipeline elements and one pumping station (study of interactions between different components in the same system). The Actual Non-Functionality (ANF) of the Pipeline Network (PN) depends on its PNF and the Actual Non-Functionality (ANF) of the Pumping Station (PST). In a row, the ANF of PST depends only on its PNF (Figure 2B).

Case 3: Water supply (pipelines and pumping station) and electric power system (electric substation) (study of interactions between systems). The Physical Non-Functionality (PNF) of the Pipeline Network (PN) depends on its PNF and the Actual Non-Functionality (ANF) of the Pumping Station (PST), as in Case 2. However, in this case the ANF of the PST depends on its PNF and the ANF of the Distribution Network (DS). Finally, the ANF of the DS depends on its PNF that depends on the PNF of the ETMS and a probability of transition that models the not perfect knowledge of the network (Figure 2C).

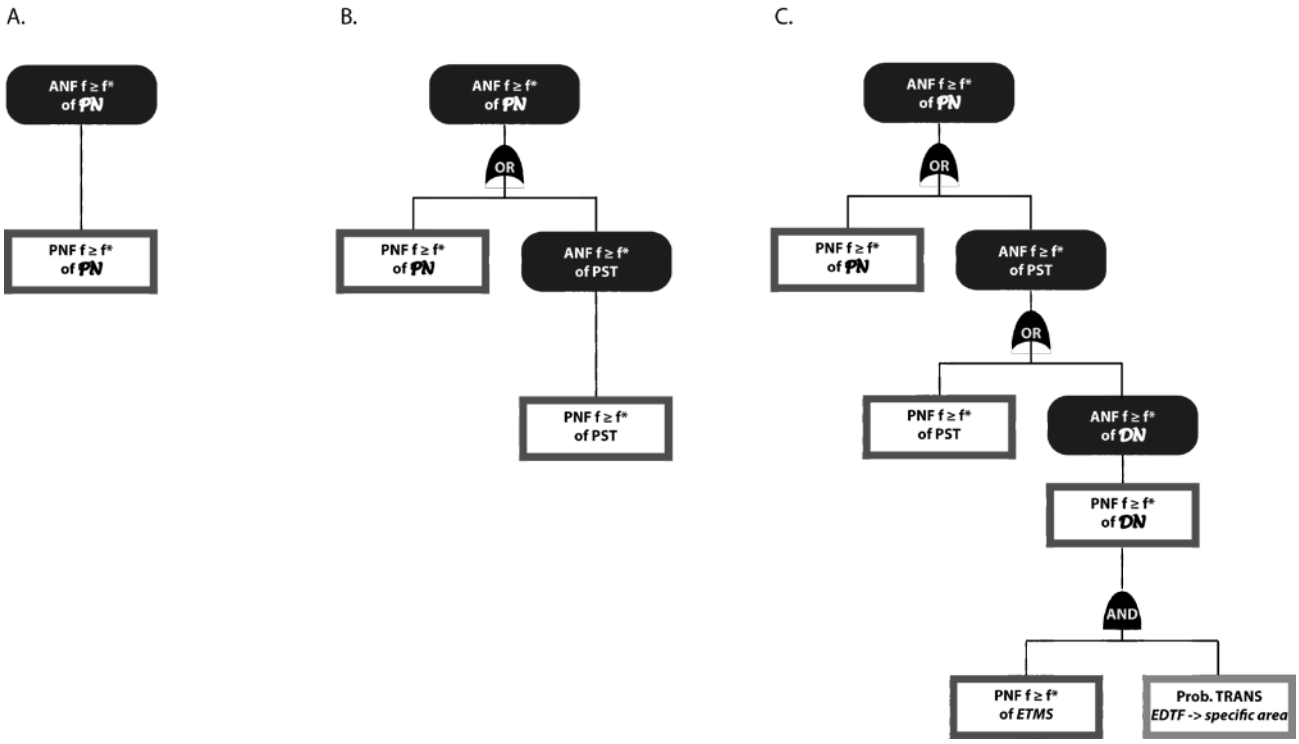


Figure 2. (A) FTA for Case 1 (water supply system- pipeline elements), (B) FTA for Case 2 (water supply system- pipeline elements and pumping station), and (C) FTA for Case 3 (water supply and electric power systems).

The Physical Non-Functionality of the Electric Substation (ETMS) and the Pumping Station (PST) is defined based on the 5 damage states fragility functions proposed in HAZUS (NIBS 2004) for medium voltage substations with anchored subcomponents and for medium /large pumping stations with anchored subcomponents respectively. A 5-d Dirichlet distribution is used to model the uncertainty with a quite high level of confidence (equivalent number of data Λ is set in both cases to 50). The best guess values at all degrees of functionality (f) for the Electric Substation and the Pumping Station are reported in Table 1. Since the Electric Substation (ETMS) is a representative element of the electric supply system (its non-functionality does not necessarily leads to the non-functionality the entire system) a "probability of transition" equal to 0.3 is considered in order to simulate the possibility that the failure of the ETMS is compensated by the rest of the network.

Table 1. Best guess values at all degrees of functionality (f) for the Electric Substation (ETMS) and the Pumping Station (PST).

	0 – complete functionality	1 - partial non-functionality	2 - complete non-functionality
0 (no damages)	1	0	0
1 (minor damages)	0.9	0.1	0
2 (moderate damages)	0	0.65	0.35
3 (extensive damages)	0	0	1
4 (complete damages)	0	0	1

The Pipeline Network sub-system (PN) is a complicated network of different types of pipe, subject to spatially varying seismic input. Their functionality is evaluated at the network level, instead of at the level of single elements based on the statistics of the Repair Rate per pipeline length (RR/km) of each one of the element. For the estimation of the RR/km, O'Rourke and Ayala fragility function is used as proposed in HAZUS (NIBS 2004) for wave propagation. A network composed by 1000 pipeline elements, nominally with a length of 30 m, with a total length of 30 km is considered herein. Each one of them is characterized by its RR/km and the population mean for the entire network (μ_r) is computed. The mean μ_r, normally distributed for central limit theorem, is then compared with appropriate values of the thresholds of μ_r (t_1 and t_2) separating the (non)-functionality states. In practice, the probability of complete functionality is the probability of $\mu_r<t_1$, the one of partial non-functionality the probability of $t_1<\mu_r<t_2$, and the one of complete non-functionality the probability of $\mu_r>t_2$. The thresholds are chosen according to the age and the connectivity degree of the system, the physical and the actual non-functionality of the network are estimated. The uncertainty is modeled using a 3-d Dirichlet distribution. For this application, a new and moderately connected network is considered. The uncertainty on thresholds t_1 and t_2 is modeled through uniform distribution, that is $t_1 \sim$ Unif (0.28, 0.33) and $t_2 \sim$ Unif (0.50, 0.55). By applying the method above, the means of the Dirichlet distribution of the Physical Non-Functionality (PNF) for the Pipeline Network are set, while Λ is subjectively set to 10 (quite low confidence).

Note that for the case of pipelines the seismic intensity to be considered is Peak Ground Velocity (PGV) which presents a better correlation with damages. Also, only ground shaking and not ground failure is examined. For simplicity, we assume uniform stiff soil conditions in the area and hence, PGV may be assessed starting from PGA using simplified empirical relationships (Seed and Idriss 1982). Each sampled PGA_i is translated in terms of PGV_i through an empirical linear relationship. The constant of proportionality is chosen for stiff soils, and it is sampled from a uniform distribution between 90 and 190 cm/sec (due to the variability on source magnitude M_w from 6.5 to 8.5 and source-site distance from 0 to 100 km) to simulate the uncertainties. Also, for reasons of simplicity, PGA values (and thus PGV) are treated as completely spatially uncorrelated. In real applications however, some level of correlation should be taken into consideration, as well as the dependence of the spatial variability of PGV on the specific site effects, which in turn, will be also influenced by the seismic magnitude, source and azimuth effects. However, the correlation given by spatial proximity cannot affect the results since we do not assume any specific spatial configuration for the sub-system.

4. RESULTS

The Physical Non-Functionality (PNF) and the Actual Non-Functionality (ANF) of the three sub-systems, Electric Substation (ETMS), Pumping Station (PST) and Pipeline Network (PN) are presented in Figure 3 for Case 1 (PN independent), Case 2 (PN dependent on PST) and Case 3 (PN dependent on both PST and ETMS). The results of all the elements are given at all PGA levels (0-1.0 g). For Case 1 and for the Pipeline Network the Physical and Actual Non-Functionality are plotted in respect to PGV values, to facilitate the critical consideration of the results also in respect to available fragility relations and real earthquake damage records. By comparing out the Physical Non-Functionality (PNF, dots) and the Actual Non-Functionality (ANF, continuous lines) curves the effect of interaction on each component of the system becomes evident. If, for one component, the PNF and ANF are not significantly different, the component is substantially independent from the other ones, since its functionality depends essentially only on its physical state. On the contrary, great differences in PNF and ANF indicate strong levels of interdependency.

The model seems to capture well the anticipated behavior of the system for all three cases. In case of the independent Pipeline Network (Case 1) the probability of Physical Non-Functionality for both the Electric Substation

(ETMS) and the Pumping Station (PST) seems to increase with PGA, but the probability of Actual Non-Functionality to the supply of water (final system service) is zero since the two systems are not connected with the Pipeline Network considered as the final supply point to the end users. The same is true for the ETMS in Case 2. Another observation is that both the Pumping Station (PST) in Case 2 and the Electric Substation (ETMS) in Case 3 are completely independent from the other elements, i.e., their PNF and ANF are equal.

The effect of interaction is obvious in the alteration of the Actual Non-Functionality of the dependent sub-systems in Cases 2 and 3. The complete non- functionality state seems to be more affected compared to partial non-functionality. The effect of the interaction between the Pumping Station (PST) and the Pipeline Network (PN) is more predominant compared to the interaction with the Electric Substation (ETMS) and always in respect to the level of final supply of water. This could be attributed to the quite "soft" connection assumed between the ETMS and PST with the "probability of transition" equal to 0.3.

Finally, the effect of interaction is obvious in the functionality curves of the final supply point, i.e. the Pipeline Network (PN). Moving from Case 1 to 3 with increasing level of interaction, the functionality curves become more spread (less steep) and move towards greater values of seismic intensity. Even for the case of independent network (Case 1) the probability of both states of non-functionality (partial and complete) seem to be in line with existing fragility functions and experience from past earthquakes. For example given a PGV equal to 80-90 cm/sec, the probability of complete non-functionality is almost 100%, while for PGV values around 60 cm/sec, the partial non- functionality of the network is almost certain. The quite steep shape of the functionality curves of the Pipeline Network (PN) could be attributed to the very stable average RR/km with very small errors. This sudden change in functionality for the PN can be understood when plotting the average RR/km, as a function of both PGA and PGV (Figure 4 for Case 1).

In Figure 5, the results regarding the serviceability of the system are reported. In particular, the probability of serviceability of the system for end-users and emergency operators are reported along with the respective realizations of serviceability. The determinant role of the Pumping Station (PST) is thus identified; a fact of major importance in possible future risk management and mitigation studies.

5. CONCLUSIONS

A generic, modular procedure for the assessment of the serviceability of a system (a single system or a system of systems), if one or more interacting components of the system are damaged by an earthquake is developed. The serviceability (functionality) of each single system, as well as of the entire system of systems, is evaluated, starting from the expected degree of damage (physical damage) of the single components and accounting for their functional interaction. The serviceability is then expressed as the expected (normalized) performance of the system(s) in terms of the service provided to final user(s).

The proposed methodology is quite general and it is developed in a way in order to be applicable to real systems with diverse degrees of complexity and knowledge of system and components details (engineering sound simplifications and assumptions are always necessary). This is established through an illustrative example given for 3 different cases: a single system comprised of the same components (Pipeline Network; Case 1); a simple system (water system) composed by two main interacting components (Pipeline Network and Pumping Station; Case 2) and a system of systems which includes two main water system components (Pipeline Network, Pumping Station) that interact with a main component (Electric Substation) of another lifeline (electric power system). The method presented briefly herein, through the three representative illustrative examples, gives the basis to account for the interdependency among different components of the same system, to assess and merge the different levels of both "physical damage" and "non-functionality" that each component may experience and to circularly apply the procedure from single systems to higher-level system of systems, accounting for the significant uncertainties at each of these steps. The analysis of (aleatory and epistemic) uncertainties plays a central role in the developed methodology, allowing a full treatment of the different sources of uncertainty.

The proposed approach can straightforwardly be applicable to any set of interacting systems, as for example modern urban regions, where the existence of strong dependence between lifeline systems and infrastructures makes the assessment of their functionality a very challenging issue. The quite high level of complexity inherent in such cases can be encountered for, providing not exactly "precise" but, what is most important, "reliable" and "accurate" estimates of the system(s) serviceability after the occurrence of earthquakes with variable levels of seismic intensity. On the other hand, the identification of the more uncertain steps allows concentrating future research efforts on these specific topics.

Incorporating infrastructure dependences in the analysis of post-seismic serviceability of complex systems can lead to a more rigorous assessment of lifeline seismic vulnerability and system reliability. Finally the identification of possible weak points and/or components/ systems with larger influence on the whole performance of the integrated "urban lifeline network", also allows the definition and implementation of effective risk mitigation actions.

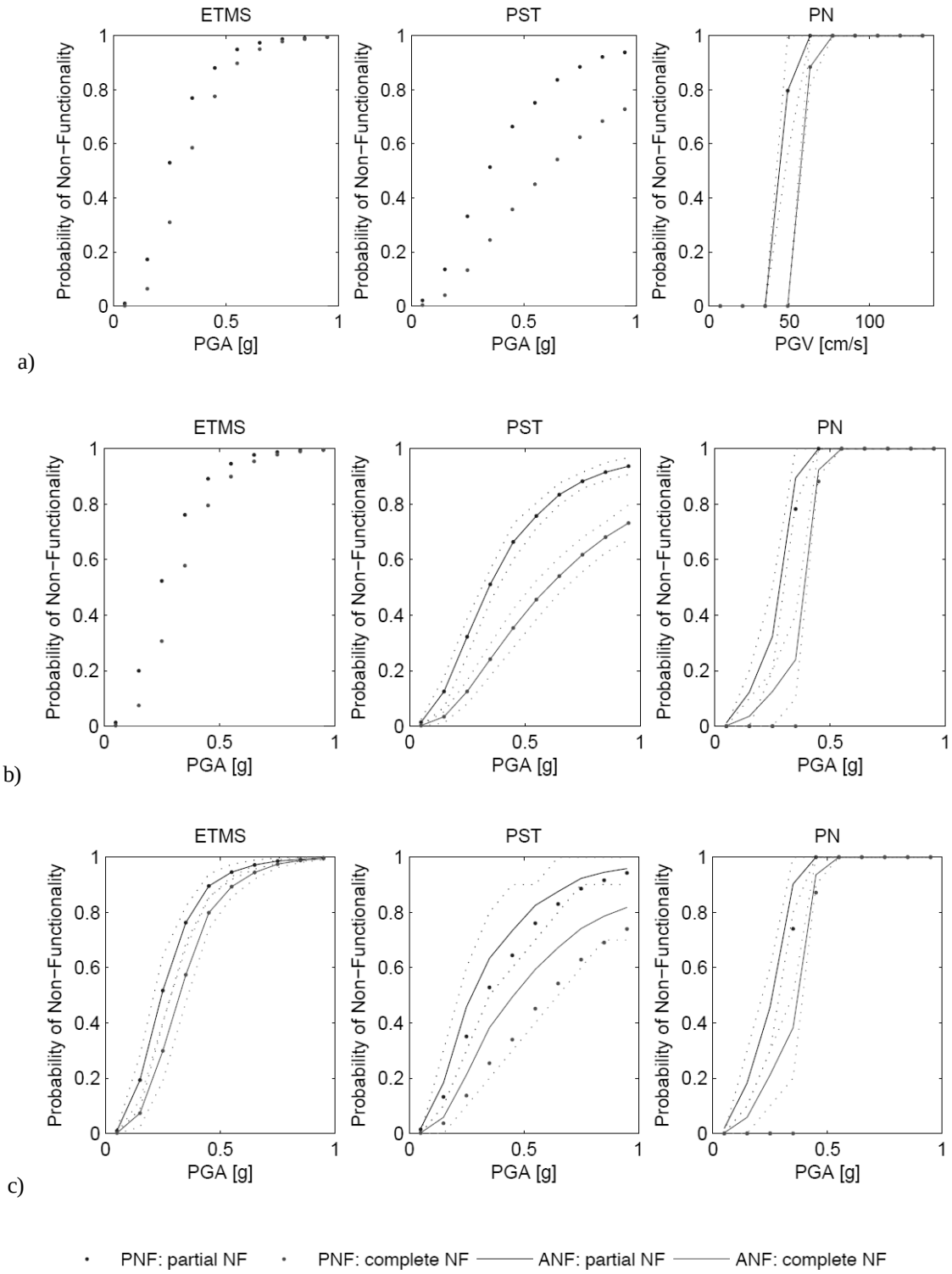


Figure 3. Physical Non-Functionality (PNF), illustrated with dots, and Actual Non-Functionality (ANF), illustrated with lines, for the Electric Substation (ETMS), Pumping Station (PST) and Pipeline Network (PN) and for the three Cases; a) Case 1/ PN independent, b) Case 2/ PN dependent on PST and c) Case 3/ PN dependent on both PST and ETMS. In blue is reported the partial functionality degree (f = 1)) and in red the complete non-functionality degree (f = 2).

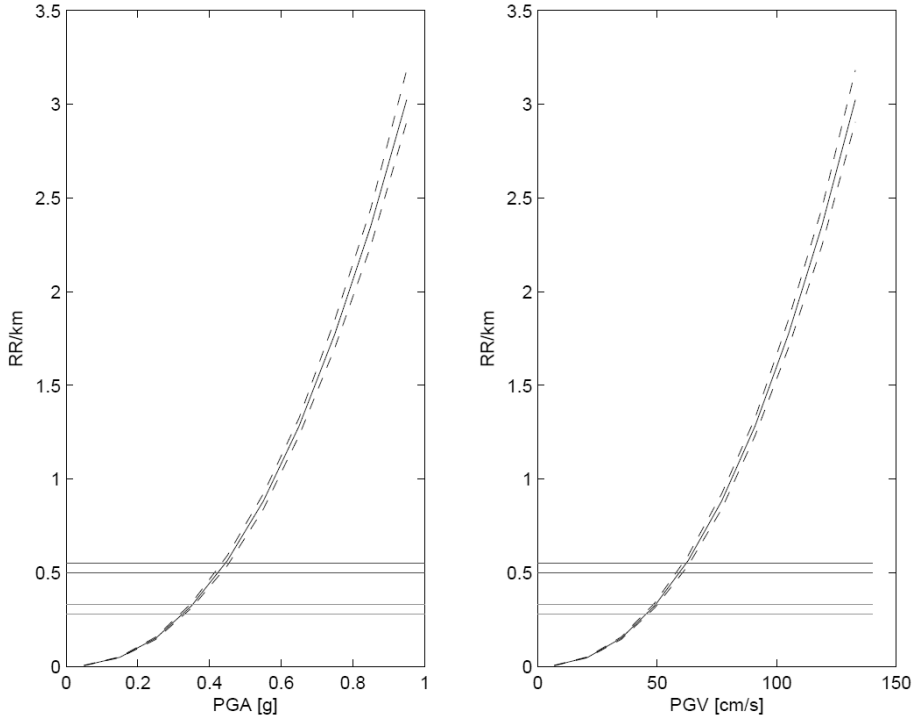


Figure 4. Average Repair Rate/km (RR/km) as a function of both PGA and PGV for Case 1(Pipeline Network independent).

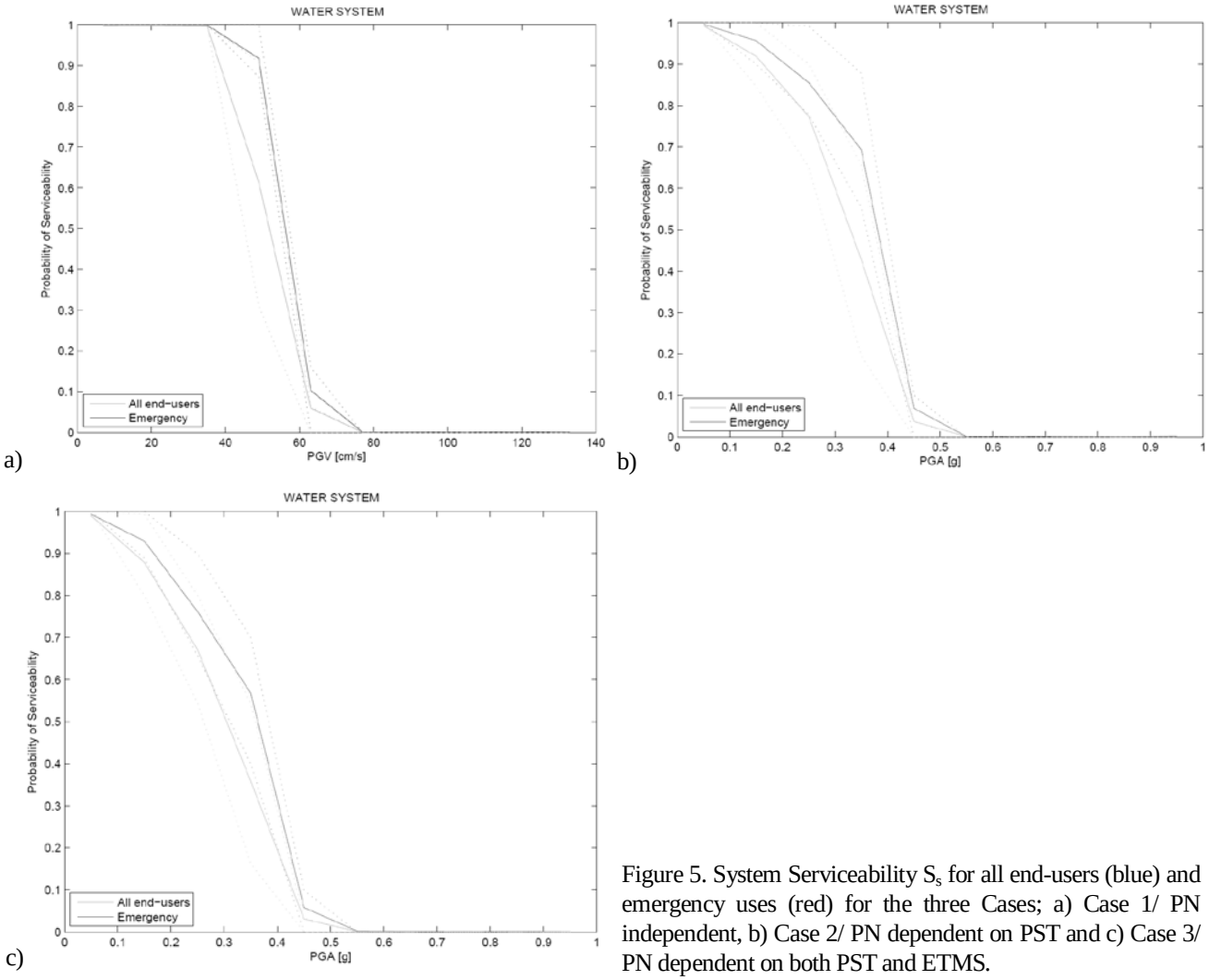


Figure 5. System Serviceability S_s for all end-users (blue) and emergency uses (red) for the three Cases; a) Case 1/ PN independent, b) Case 2/ PN dependent on PST and c) Case 3/ PN dependent on both PST and ETMS.

References:

Alexoudi, M., Kakderi, K., and Pitilakis, K. (2008a), "Seismic risk of interdependent lifeline system using fuzzy reasoning," *Proceedings of the 14th World Conference on Earthquake Engineering*, Beijing, China, Paper No. 06-0122.

Alexoudi, M., Kakderi, K., and Pitilakis, K. (2008b), "Advanced fragility curves of interdependent lifelines using decision making process," *Proceedings of the 1st International Symposium on Life-Cycle Civil Engineering*, Varenna, Lake Como, Italy, Paper No. 129.

Amin, M. (2001), "Toward Self-Healing Energy Infrastructure Systems", *IEEE Computer. Applications in Power*, **14**(1), 20-28.

Bernhardt, K.L.S., and McNeil, S. (2004), "An Agent Based Approach to Modeling the Behavior of Civil Infrastructure Systems," Engineering Systems Symposium, Tang Center, MIT.

Brown, Th., Beyeler, W., and Barton, D. (2004), "Assessing Infrastructure Interdependencies: the Challenge of Risk Analysis for Complex Adaptive Systems," *International Journal of Critical Infrastructures*, **1**(1), 108-117.

Der Kiureghian, A., and Song, J. (2008), "Multi-scale Reliability Analysis and Updating of Complex Systems by use of Linear Programming," *Reliability Engineering & System Safety*, **93**(2), 288-297.

Ditlevsen, O., and Madsen, H.O (1996), "Structural Reliability Methods," John Wiley & Sons Ltd, Chichester.

Dueñas-Osorio, L., Craig, J.I., and Goodno, B.J. (2007), "Seismic Response of Critical Interdependent Networks," *Earthquake Engineering & Structural Dynamics*, Special Issue on Earthquake Engineering for Electric Power Equipment and Lifeline Systems, **36**(2), 285-306.

Eidinger, J. (1993), "Fire conflagration and post-earthquake response of power and water lifelines," *Proceedings of the 4th DOE of Energy Natural Phenomena Hazards Mitigation Conference*, Atlanta, GA.

Gelman, A., Carlin, J., Stern, H., and Rubin, D. (1995), "Bayesian Data Analysis," Chapman and Hall/CRC.

Giannini, R., and Vanzi, A. (2000), "Seismic Reliability of Electric Networks and Interaction with other Damage Indicators," *Proceedings of the 12th World Conference on Earthquake Engineering*.

Giannini, R., and Vanzi, A. (2000), "Seismic Reliability of Electric Networks and Interaction with other Damage Indicators," *Proceedings of the 12th World Conference on Earthquake Engineering*.

Haimes, Y.Y., and Jiang, P. (2001), "Leontief-based Model of Risk in Complex Interconnected Infrastructures," *Journal of Infrastructure Systems*, **7**(1), 1-12.

Kakderi, K., Alexoudi, M., and Pitilakis, K. (2007), "Seismic Risk Analysis of Interdependent Lifeline systems," *Proceedings of the 4th International Conference on Earthquake Geotechnical Engineering*, Thessaloniki, Greece, Paper No. 1578.

Kakderi, K., Alexoudi, M., and Pitilakis, K. (2008), "Seismic Risk Analysis of Interdependent Lifeline Systems," *Proceedings of the 3rd Greek Conference on Earthquake Engineering and Engineering Seismology*, Athens, Greece, Paper No. 1940 [in Greek].

Kameda, H. (2000), "Engineering management of lifeline systems under earthquake risk," *Proceedings of the 12th World Conference on Earthquake Engineering*.

Kim, Y.S., Spencer, B.F., Song, J., Elnashai, A.S., and Stokes, T. (2007), "Seismic Performance Assessment of Interdependent Lifeline Systems," MAEC Report, Mid America Earthq. Research Center, Univ. of Illinois, Urbana-Champaign, CD Release 07-16.

Li, J., and He, J. (2002), "A Recursive Decomposition Algorithm for Network Seismic Reliability Evaluation," *Journal of Earthquake Engineering and Structural Dynamics*, **31**(8), 1525-1539.

Little, R. (2002), "Controlling cascading failure: Understanding the vulnerabilities of interconnected infrastructures," *Journal of Urban Technology*, **9**(1), 109–123.

Marzocchi, W., Sandri, L., Gasparini, P., Newhall, C., and Boschi, E. (2004), "Quantifying probabilities of volcanic events: the example of volcanic hazard at Mount Vesuvius," *Journal of Geophysical Research*, **109**(B11201), doi:10.1029/2004JB003155.

Menoni, S. (2001), "Chains of damages and failures in a metropolitan environment: some observations on the Kobe earthquake in 1995," *Journal of Hazardous Materials*, **86**(1), 101–119.

Menoni, S., Pergalani, F., Boni, M. and Petrini, V. (2002), "Lifelines earthquake vulnerability assessment: a systemic approach," *Soil Dynamics and Earthquake Engineering*, **22**(12), 1199–1208.

National Institute of Building Sciences (NIBS), (2004), "Earthquake loss estimation methodology. HAZUS'04", Technical manual, vol.1, Federal Emergency Management Agency, Washington, D.C.

Nojima, N., and Kameda, H. (1991), "Cross impact analysis for lifeline interactions," *Proceedings of the 3rd US Conference on Lifeline Earthquake Engineering*, edited by M. Cassaro, **4**, 629–638, TCLEE/ASCE, Los Angeles, California.

O'Rourke, M., and Ayala, G. (1993), "Pipeline damage due to wave propagation", *Journal of Geotechnical Engineering*, ASCE, **119**(9), 1490–1498.

Peerenboom, J., Fisher, R., and Whitfield, R. (2001), "Recovering from Disruptions of Interdependent Critical Infrastructures," *Proceedings of the Workshop on Mitigating the Vulnerability of Critical Infrastructures to Catastrophic Failures*, Lyceum, Alexandria, Virginia.

Pitilakis K., Alexoudi, M., Kakderi, K., Manou, D., Batum, E., and Raptakis D. (2005), "Vulnerability Analysis of Water Supply Systems in Strong Earthquakes. The case of Lefkas (Greece) and Duzce (Turkey)," *Proceedings of the International Symposium on the Geodynamics of Eastern Mediterranean*.

Rinaldi, S., Peerendoom, P., and Kelly, T. (2001), "Identifying, understanding, and analyzing critical infrastructure interdependencies," *IEEE Control Systems Magazine*, **21**(6), 11–25.

Rubinstein, R.Y. (1981), "Simulation and Monte Carlo Method," Wiley, New York.

Santos, J.R., and Haimes, Y.Y. (2004), "Modeling the Demand Reduction Input-Output (I-O) Inoperability Due to Terrorism of Interconnected Infrastructures," *Risk Analysis*, **24**(6), 1437-1451.

Scawthorn, C. (1992), "Lifeline interaction and post- earthquake functionality," *Proceedings of the 5th U.S- Japan Workshop on Earthquake Disaster Prevention for Lifeline Systems*, pp. 441–450.

Seed, H., and Idriss, I. (1982), "Ground Motions and Soil Liquefaction During Earthquakes", Berkeley, California, Earthquake Engineering Research Institute.

Selva, J., Kakderi, K., Alexoudi, M., and Pitilakis, K. (2011), "Serviceability of a system of interdependent components," in preparation.

Shinozuka, M., and Tanaka, S. (1996), "Effects of lifeline interaction under seismic conditions," *Proceedings of the 11th World Conference on Earthquake Engineering*.

Shinozuka, M., Hwang, H., and Tanaka, S. (1993), "Gis - based assessment of the seismic performance of water delivery system," *Proceedings of the 5th U.S- Japan Workshop on Earthquake Disaster Prevention for Lifeline Systems*, edited by K. Kawashima, H. Sugita, and T. Nakajima, 233–249, PWRI 3198, Public Works Research Institute, Tsukuba, Japan.

Song, J., and Der Kiureghian, A. (2003), "Bounds on system reliability by linear programming," *Journal of Engineering Mechanics*, ASCE, **129**(6), 627-636.

Spence, R. Ed (2007), "Earthquake disaster scenario predictions and loss modelling for urban areas," LESSLOSS Report 7, IUSS Press, Pavia, Italy.

Tang, A., and Wen, A. (2008), "An intelligent simulation system for

earthquake disaster assessment," *Computers and Geosciences*, doi:10.1016/j.cageo.2008.03.003.

Tang, A., Jinping Wen Aihua, O. and Xiaxin, T. (2004), "Lifeline systems interaction and their seismic performance assessment," *Proceedings of the 13th World Conference on Earthquake Engineering*, Vancouver, B.C., Canada.

Tolone, W.J., Wilson, D., Raja, A., Xiang, W.-N., Hao, H., Phelps, S., and Johnson E.W. (2004), "Critical Infrastructure Integration Modeling and Simulation," *Proceedings of the 2nd Symposium in Intelligence and Security Informatics*, Tucson, Arizona.

Woo, G. (1999), "The Mathematics of Natural Catastrophes," Imperial College Press, London.

Yao, B., Xie, L., and Huo, E. (2004), "Study Effect on Lifeline Interaction under Seismic Conditions", *Proceedings of the 13th World Conference on Earthquake Engineering*, Vancouver, B.C., Canada.

8CUEE CONFERENCE PROCEEDINGS
8th International Conference on Urban Earthquake Engineering
March 7-8, 2011, Tokyo Institute of Technology, Tokyo, Japan

STUDY OF GROUND RESPONSE OF THREE CITIES OF KATHMANDU VALLEY OF NEPAL USING MICROTREMOR OBSERVATIONS

Youb Raj Paudyal[1)], Ryuichi Yatabe[2)], and Netra Prakash Bhandary[3)]

1) Graduate Student, Graduate School of Science and Engineering, Ehime University, Bunkyo-3, Matsuyama, Japan
2) Professor, Graduate School of Science and Engineering, Ehime University, Bunkyo-3, Matsuyama, Japan
3) Assistant Professor, Graduate School of Science and Engineering, Ehime University, Bunkyo-3, Matsuyama, Japan
yrpaudyal@gmail.com, yatabe@cee.ehime-u.ac.jp, netra@cee.ehime-u.ac.jp

Abstract: In this paper an attempt was made to evaluate the site specific ground response of overburden soil using microtremor observations of three major cities - Kathmandu, Lalitpur and Bhaktapur of Kathmandu Valley Nepal. Kathmandu Valley cities are built on the former bed of a drained lake over soft soil deposition of lacustrine origin. The thickness and properties of these sediments vary from one place to other and hence the behavior of the seismic waves might be different from one place to others. It is therefore imperative to conduct a detailed site specific hazard assessment, which can assist in systematic earthquake mitigation program. The predominant time periods of the ground were determined from the horizontal to vertical spectral ratio technique. A map showing the distribution of site predominant periods was developed and the related results in relation with the building vulnerability were done. The time periods showed good agreement with period obtained from the borehole data analysis and distribution of the soil in three cites of Kathmandu Valley. The study shows that there is a longer period ground vibration in an area towards the center of Kathmandu city in compared to other two cities.

1. INTRODUCTION

It has been known for many years that buildings supported on different types of soils suffer different levels of damage from earthquake shaking. It is also well known that the major damage arise at resonance, when the natural period of structure is equal or very close to the dominant period of the site. Therefore, the ground response analysis of an area is an important component in the correct evaluation of site dominant period which is widely used by the geotechnical experts, engineers and/or city planners for the design of buildings and infrastructures.

Numerous ground response studies in earthquakes during the last few decades showed large concentration on damage in specific area overlain by soft sediments. The 1934 Great Bihar Nepal earthquake (Pandey and Molnar, 1988) and the 1985 Michochan Earthquake, Mexico (Estrellav and Gonzalez, 2002) have demonstrated the significant contribution of local geology which controls the intensity of ground shaking. The 1985 Michochan Earthquake is well known for heavy damages in buildings in the Mexico city. Although this city was located at 390 km from the fault area, the capital city suffered an unexpectedly significant damage. The devastation caused in Mexico city was due to the strong amplification of the ground motion by the soft deposit of soil in the city. From this earthquake and damage condition, it can be understood that the natural period of ground depends not only on the stiffness of soil but also on the thickness of soil. The response of earthquake is thereby site specific.

Kathmandu Valley, the capital of Nepal, consists of three major cities – Kathmandu, Lalitpur and Bhaktapur. Historically and archeologically these cities are famous for ancient cities of fine arts and crafts and cities of devotees. These cities are seismically most vulnerable because of their seismicity, population density, building condition and geological setting. They are laying on thick unconsolidated lacustrine soil deposits which vary from one area to other (max upto 550 m). Many observers have likened the soil condition of Kathmandu to those of Mexico city which is notorious for its susceptibility to damage during the earthquake.

Nepal has experienced several devastating earthquakes in the past resulting in huge amount of property damage and large number of human deaths. In each and every earthquake, Kathmandu Valley's cities have been heavily devastated. In 1934, an earthquake of M 8.4, epicenter located about 240 km towards east of

Kathmandu Valley, produced strong shaking in Kathmandu Valley and destroyed 19% and damaged 38% of valley`s building stock (Pandey and Molnar 1988). In Kathmandu itself, one quarter of all homes were destroyed. The destruction was most complete at Bhaktapur and neighboring villages in the eastern part of the valley.

Devastation of these three cities of Kathmandu Valley from historical earthquakes, the M8.4 Bihar-Nepal Great Earthquake of 1934 in particular, suggest that spectral ground amplification due to unconsolidated quaternary sediments is playing the major role in the intensification of ground motion. The intensity distribution in the valley by this earthquake varies from VIII to X MMI within different sedimentary facial domains of unconsolidated sediments. From the evidence of Kathmandu basin, it can be understood that the unconsolidated sediments in the three cities of Kathmandu basin shows far most complex picture with considerable local variation over short distances and this composition of subsurface structure makes its susceptible to intensification of incoming seismic waves and hence damage to the structures. The actual behavior of soil to the incoming seismic waves could be different from one area to others within the city as sediment properties and thickness change. No in depth studies have been carried out for ground response study of these cites to date. So it is urgent and necessary to analyze the ground response in various areas of these cities so that the site dominant period of the ground can be evaluated correctly in different areas of these three major cities of Nepal.

Study of subsoil condition has great importance in civil engineering and is usually performed by drill holes. However, this method has different limitations when applied in urbanized and densely populated area mainly because of its cost, time and environmental impact (use of drilling). Methods based on the analysis of strong motion records are straight forward for determining the site response. However, availability of ground motion record is limited to very few countries and possibility of data recording in required station is almost impossible in developing countries like Nepal because of urbanization and economic feasibility. So, this method is not suitable for the site response analysis of urban areas. In this context, the method based on ambient noise recording became more and more popular over the last decades and it offers a convenient practical and low cost tool to be used in urbanized area and has become the most appealing approach for site response studies.

A technique horizontal-to-vertical spectral ratio (H/V) of microtremors was first proposed by Nogoshi and Igarashi (1971) where they relate the H/V ratio of microtremors with a measure of ellipticity of Rayleigh waves, as an indicator of the fundamental resonance frequency of structure. Nakamura (1989) modified microtremor analysis by proposing a new understanding, generally referred to as the Nakamura or H/V method. He indicated that the horizontal-to-vertical (H/V) spectral ratio at a site roughly equals to the S-wave transfer function between the ground surface and basement layer at the site. This means that the H/V predominant period and the peak value at the period themselves correspond to the natural period and peak amplification factor of the site, respectively. He proposed this new technique, based on his understanding of microtremors and demonstration of consistency between actually observed damage distributions by the earthquakes and microtremor measurement results by this technique. This method does not require any borehole and is, hence, more convenient and inexpensive compared to the traditional borehole method. As a result, this technique for microtremor studies has gained much popularity over the past years due to its inherent advantages of the ease of microtremor recording with a single station and ability to provide reliable information related to site response (Nakamura, 1989, 1997, 2000, 2008; Bard and Chavez-Garcia, 1993; Field and Jacob, 1993; Lermo and Chavez-Garcia, 1993, 1994; Theodulidis and Bard 1995; Theodulidis et al., 1996, 2005; Field et al., 1995; Bour et al., 1998; Teves-Costa et al., 1996, 2001; Hung and Teng, 1999; Delgado et al., 2000; Zaslavsky et al., 2000; Fäh et al., 2000; Diagourtas et al., 2001; Estrella and Gonzalez, 2002; Huang, 2002; Parolai et al., 2004; Carniel et al. 2005; Hung et al., 2005; Bonnefoy-Claudet et al., 2006; Hasancebi and Ulnsay, 2006; Gosar, 2007; Gueguen et al., 2007; Herak, 2007; Birgören et al., 2008). Although his theoretical explanation remains questionable to many scientists, this method is now widely used for microtremor observations. Different experimental data analysis supported that the H/V ratios are stable and on soft soils they exhibit a clear peak which is well correlated with the fundamental resonant frequency of the sites. Among several proposed microtremor methods, the H/V method has proven to be one of the most convenient techniques to estimate the fundamental frequency of soft deposits (Fäh et al., 2008). Nowadays this method has extremely been used for evaluation of seismic characteristics of many areas of the world situated within the thick soil deposit, where devastation is expected due to future earthquakes.

In this study, microtremor measurements were performed in the core area of three cities in Kathmandu Valley of Nepal and subsequent analysis and interpretation of result will be done to assess the geotechnical condition of subsurface structure of these three cities. The objectives of field investigation in the cities were to measure the microtremors in many locations especially in the core area of cities and to analyze and interpret them by the H/V method in order to find out the dominant period of the different locations.

2. GEOLOGY AND SEISMICITY OF THE STUDY AREA

2.1. Study area and geotechnical setting.

The Kathmandu Valley lies in central part of Nepal. The valley's maximum width is approximately 25 km

from east to west and 20 km from north to south and it has average elevation of around 1340 m. Its three districts- Kathmandu, Lalitpur and Bhaktapur- cover an area of 899 square kilometers, out of which the valley covers 665 square kilometers. The cities of Kathmandu and Lalitpur are separated by the Bagmati River and, due to the expansion of the urban areas in both the cities, the boundary between the two now has only historical, political and administrative importance. Likewise, the spatial separation between Bhaktapur and the other two cities is rapidly becoming less and less conspicuous. The location map of three cities and microtremor observation area are shown in Figure 1.

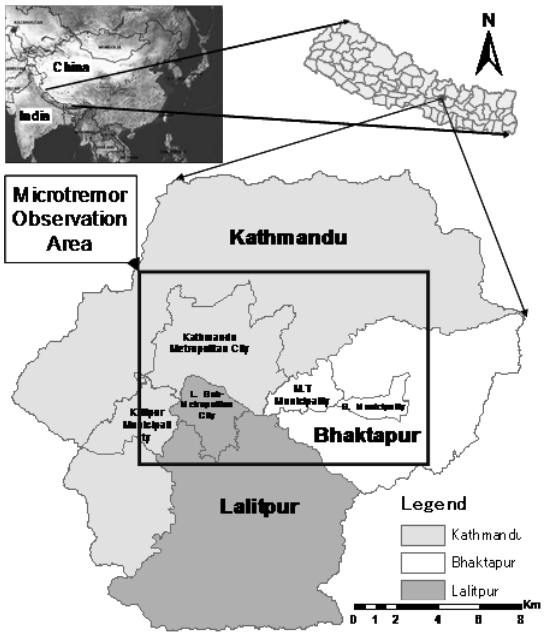


Figure 1 Location map of study area

surrounded by the Mahabharat Mountains in the south and the Shivapuri Mountain in the north. The evolution of the basin started in neogene - quarternary time as a consequence of higher rate of uplift in the south in relation to north as a response to evolving Himalaya thrust tectonics. The southward flowing valley drainage stopped because of this uplift and formed a lake and the subsequent deposition of layers of rivers and lake sediments (Sakai, H. et al., 2001).

The basin is filled with thick sediments composed of unconsolidated clay, silt, sand and gravel ranging in the age from the late Pliocene to the present and all are derived from the Shivapuri and Mahabharat mountains around the valley (Dongol, 1985; Sakai, H. et al., 2001). The unconsolidated clay of the valley varies widely in composition and is divided into three groups (Sakai, H., 2001). The northern part of the valley consists of marginal fluvio-deltaic facies (typical riverbed layered deposits of clays, silts, sand and gravels) while those in the southern part mainly alluvial fan facies (lake deposits of clays and silts, usually sandwiched between thin layers of coarse sediments) and the central part of the basin consists of open lacustrine facies (a thick organic mud, the black (kalimati) clay). Based on the gravity measurement in the Kathmandu Valley, Moribayashi and Maruo (1980) estimated the maximum thickness of the basin-fill sediments to be 650 m. A number of drill well data prove that more than 300 m thick mud and sands are extensively distributed under the Kathmandu Basin (Moribayashi and Maruo, 1980; Katel et al., 1996; Sakai, H. et al., 2001). Figure 3 shows the fence diagram of subsurface structure of the Kathmandu basin prepared by Katel et al., 1996 which indicates extensive distribution of black clay sediments of lacustrine origin, rich in organic matter. From the above discussion, it is clear that the sediment in Kathmandu basin shows far more

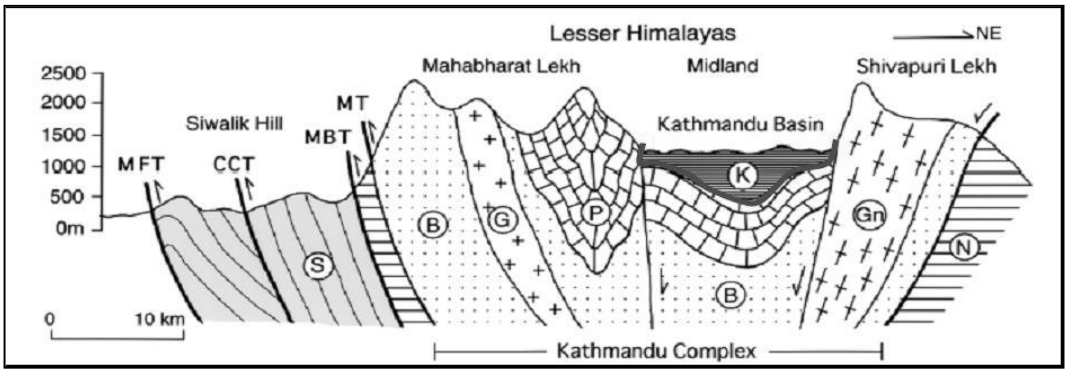


Figure 2 A schematic cross section in the Central Nepal Himalayas based on Sakai, H. et al. (2002) (modified after Stocklin and Bhattari, 1981). S: Shivalik group, P: Phulchauki group, N: Nuwakot complexes, G: Granite, Gn: Gneiss complex, K: Kathmandu complex, MFT: Main Frontal Thrust, CCT: Central Churia Thrust, MBT: Main Boundary Thrust (Main Central Thrust: MCT)

Kathmandu basin has been evolving as a tectonic intramontaine, bowl shape, basin in Lesser Himalaya of Central Nepal since the neogene - quaternary period (Yoshida and Igarashi, 1984; Katel et al., 1996; Sakai H. et al., 2002) as shown in Figure 2. The basin is complex picture with considerable local variation over short distances. Such a composition of the valley subsurface makes it susceptible to promoting damage during an earthquake.

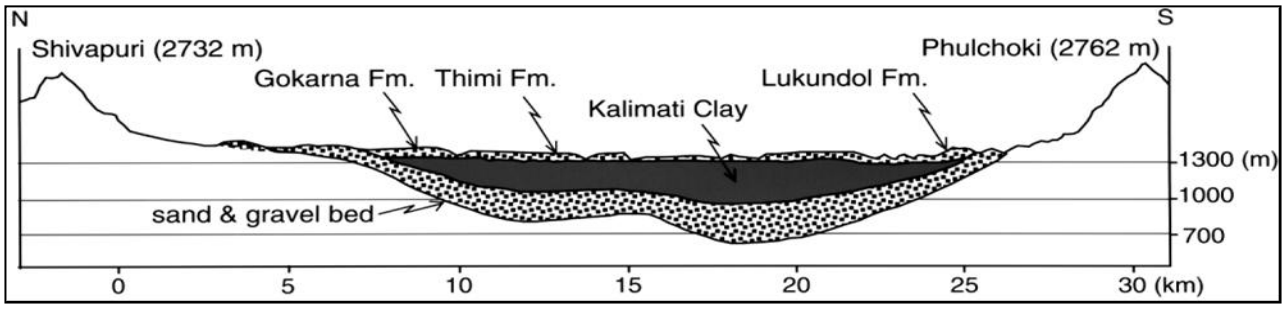


Figure 3 A schematic geological cross-section of the Kathmandu basin, showing sediment distribution in north-south direction through center of the Kathmandu Valley (Katel et al., 1996)

2.2. Seismicity

Geologically, Nepal and the Himalayan range that forms its northern border with China were formed as a result of the collision of the Indian Plate with the Eurasian Plate about 55 million years ago (Molnar, 1986). The collision was followed by subduction of the Indian plate underneath Tibet, which continues today at an estimated rate of about 2 cm per year (Bilham et al., 1995). This makes Nepal and the entire Himalayan range one of the seismically active spots on the earth.

The major fault systems are parallel to the Himalayan arc formed by the collision and subduction of these two plates. The fault systems in the Himalayan arc are divided into four major systems:

- Main Frontal Thrust (MFT)
- Main Boundary Thrust (MBT)
- Main Central Thrust (MCT)
- South Tibetan Detachment system (STDS)

The subduction results in tectonic stresses along these fault systems and the movement of these major fault systems and their branches creates the earthquakes in the region. Numerous earthquakes have occurred in this region, including four major ones of magnitude greater than M8 within the last 100 years and resulted in huge amount of economic loss and large number of casualties (Molnar, 1984; Bilham et al., 1995).

During the development of Nepal National Building Code in 1994, five active faults have been identified (UNDP 1994) within KV. Most of the faults are dip-slip and some of them are strike-sip also and lie within 5 to 8 km from the center of KV. These faults are believed to be capable of generating a maximum of 6.6 Richter magnitude events. However there has not been any detailed study carried out to quantify these faults and their activity. There are other faults which are within the distance of 20 to 50 km from KV. These faults are believed to be capable of generating a maximum of 6.9 to 7.1 Richter magnitude events and hence any major earthquakes along these faults definitely affect the Kathmandu Valley.

Moreover, during the study of earthquake risk management in KV in 2002, Japan International Cooperation Agency (JICA) has developed a four scenario earthquake for KV based on the historical earthquake catalogue, recent seismicity, and tectonic aspects in and around Nepal and the KV and prepared earthquake intensity map of each scenario for KV. Out of them, Mid Nepal earthquake scenario is considered to be the most severe scenario for KV in which earthquake with a magnitude of 8 has been included considering the seismic gap in the middle of Nepal. Several researchers have pointed out that a huge earthquake may occur in near future in this gap. The Kathmandu Valley would experience peak ground acceleration of about 200 to 300 gal (JICA, 2002).

From the review of the past study and historical seismicity in Nepal, it is found that there is a high possibility of occurrence of huge earthquake in mid Nepal and the condition of Kathmandu Valley in terms of geology, building, building code enforcement, urban planning is so poor that it would suffer very heavily if this earthquake strikes at any time in this region.

3. MATERIALS AND METHOD

Microtremors are continuous small amplitude vibrations of ground originating from unknown sources, which have amplitude varying between 0.01 – 0.001 mm and period of 0.01 – 20 seconds. Sources of microtremors can be natural, like ocean waves or wind, and/or artificial due to human activity such as traffic, industrial noise, etc.

The most common procedure of microtremors analysis is to divide the Fourier amplitude spectrum of ground motions observed on soft soil site by that observed at nearby reference site on bedrock. The ratio thus obtained can be considered as transfer function between the bedrock and the free surface of the site for estimating the site response, provided that the two recordings are of the same source, the same path effects, and that the reference site has a negligible site effect. Nakamura (1989) introduced a new method to estimate the dynamic characteristics of surface layers by measuring solely the microtremors at the surface of the ground. He assumed that components of ground motion are equal in all directions at the bed rock and there is no amplification in vertical ground motion components. According to him only horizontal microtremors are influenced by soil and that source spectral characteristics

are maintained in vertical as well as in horizontal microtremors. It was confirmed by many observational results that the transfer function can be obtained solely from the motion of microtremors at surface which obviously makes it easier to estimate the characteristics of ground motion.

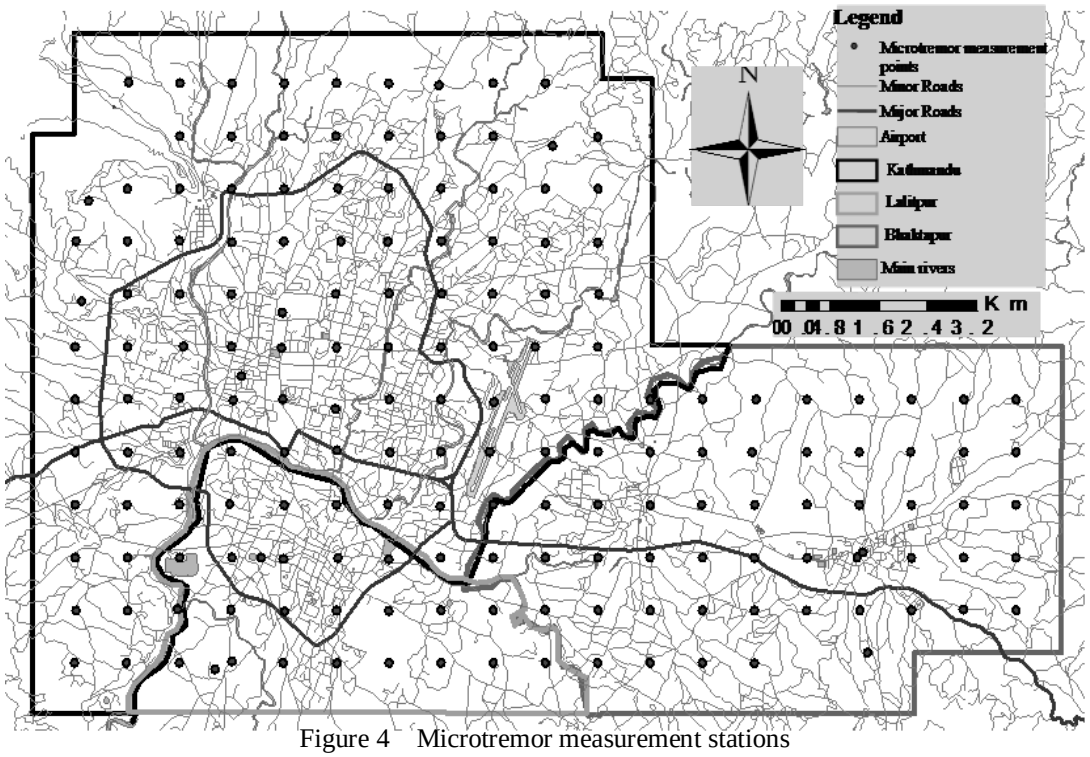


Figure 4 Microtremor measurement stations

The microtremor observation was carried out in January and February 2010 covering the densely populated urban area of Kathmandu, Lalitpur and Bhaktapur City of Kathmandu Valley of Nepal. The main rationale of this study is to evaluate the characteristic site period of ground of these cities. For this purpose, city core areas were divided into different zone by 1 km grid along east-west and north-south direction respectively as shown in Figure 4. Latitude and longitude of the sites were taken from Geographic Information System (GIS). To accurately identify the sites for microtremor survey, site maps were prepared. Then, site map and GIS coordinates were used to accurately set up microtremor measurement instrument set in a site. Microtremor observations were performed using portable microtremor equipment. Sensor for New PIC made by System and Data Research (SDR) Co. Ltd. Japan was used for the data acquisition. The sampling frequency for all measurements was set at 100 Hz. The velocity sensor used can measure three components of vibration: two horizontal along east-west and north-south and one along vertical direction. A global positioning system (GPS) was used for recording the coordinate of observation sites.

The microtremor instrument was set up in each grid points and measurements were carried out at each point along the grid as shown in Figure 4 at a distance interval of 1 km. Microtremor recordings were carried out in regular grid as far as possible. A single recording was enough if there was not any influence on recorded data by traffic and human activity, but more than one time of recording were conducted when the recorded data was unsatisfactory. The microtremors sensor are very sensitive one, even a small disturbance or vibration caused by human foot steps nearby or vibration caused by heavy vehicles far away from the measurement station is recorded during measurement. These unwanted recorded vibrations may affect the results of the analysis and output might not represent the actual condition of the sites. So, these unwanted recorded vibrations data such as the vibration from the heavy traffic especially large vehicles and nearby pedestrians must be removed before the data analysis.

Microtremor data measurements were done at more than 100, 30 and 57 sites in Kathmandu, Lalitpur and Bhaktapur city areas, respectively. At each site, data was recorded for 300 seconds (i.e. 30,000 data points at the sampling rate of 100 Hz). The recorded data was extracted from the data acquisition system. The time history graph of all recorded data was drawn. The recorded time series data were divided into 15 segments each of 20.48 s duration. For each site, as many as possible (generally 8 – 12) segments of the data were chosen from 15 segments, omitting the segments that are influenced by nearby heavy noise sources, for the calculations. The Fourier analysis of the selected segments was carried out using the Fast Fourier Transform (FFT) computer program and the Fourier spectrum and H/V ratio of all segments were obtained and then smoothened using a Parzen window of bandwidth 0.5 Hz. The average spectral ratio of the

horizontal-to-vertical components was calculated according to:

$$H/V = \sqrt{[(F_{NS}^2 + F_{EW}^2) \Big/ (2F_{UD}^2)]}$$

Where, F_{NS}, F_{EW} and F_{UD} are the Fourier amplitude spectra in the north-south (NS), east-west (EW) and up-down (UD) direction, respectively.

This procedure was repeated with the remaining segments. After obtaining the H/V spectra for all the segments, the average of the spectra was obtained as the H/V spectrum for a particular site. The frequency corresponding to the maximum amplitude of H/V spectrum plot shows the predominant frequency of the site. So, measuring the three components of background noise at a site, site specific resonance frequency will be calculated.

4. RESULTS AND DISCUSSION

Data analysis of all measurement sites of three cities were performed by H/V method and the predominant time period of all sites were obtained. The predominate time period in the case of Kathmandu city were found in the range from 0.11 to 2.05 sec while Lalitpur and Bhaktapur city predominant time period were found in the range from 0.166 to 1.428 sec and 0.263 to 1.28 sec respectively. The results showed that the range of time period in the case of Kathmandu city is longer than that of other two cities and also the maximum time period of Kathamndu city is higher than that of other two cities. In the case of Kathmandu city the maximum time period was found 2.05 sec while 1.42 sec and 1.28 sec were found for Lalitpur and Bhaktapur city respectively. The variations of time periods in three cities are shown in Figure 8, Figure 9 and Figure 10.

From the result of microtremor observation in three cites of Nepal, it can be observed that the predominant time period of ground increases towards the center of Kathmandu city whereas such increasing pattern is not seen in the case of other two cities. In the case of Kathmandu city, especially in the center part, variation of time periods were found from 1.2 to 2.05 s as shown in Figure 8 but in the case of Lalitpur and Bhaktapur city such large variations were not seen. Most of the densely populated core area of Kathmandu city have time period in the range from 0.8 to 2.05 sec while area outer side of the core city area have time period in the range of 0.11 to 0.8 s as shown in Figure. 8. Similarly most of the area of Lalitpur city have time period in the range of 0.7 to 1.2 sec while most of the area of Bhaktapur city have time period in the range from 0.5 to 1.0 sec as shown in Figure 9 and Figure 10. Moreover, the average time period in the case of Bhaktapur city is found lower than that of the other two cities. Figure 5 shows the H/V spectral ratio of microtremor for sites within the densely populated core city area the Kathmandu city. Similarly Figure 6 and Figure 7 show the H/V spectral ratio of microtremor for Lalitpur and Bhaktapur city area in which most of the sites were with in the range of time period as mentioned in Figure 6 and Figure 7.

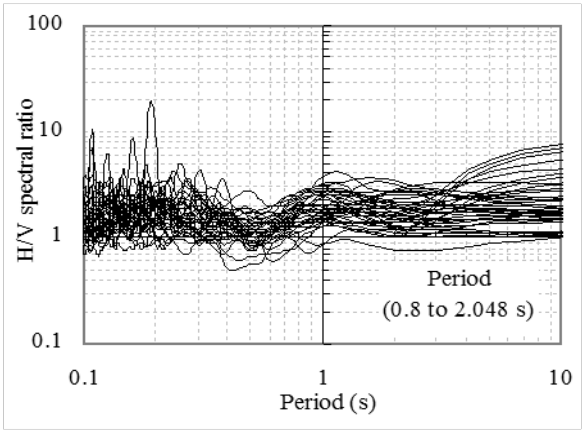


Figure 5 H/V spectral ratio of microtremor for Kathmandu city having time period 0.8 to 2.05 s (core city area)

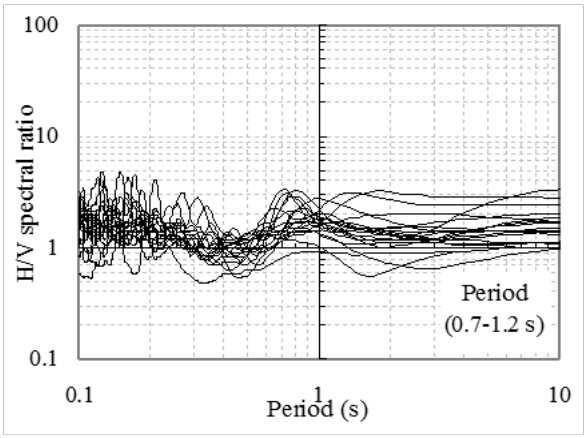


Figure 6 H/V spectral ratio of microtremor for Lalitpur city having timet period 0.7 to 1.2 s (covering most of the city area)

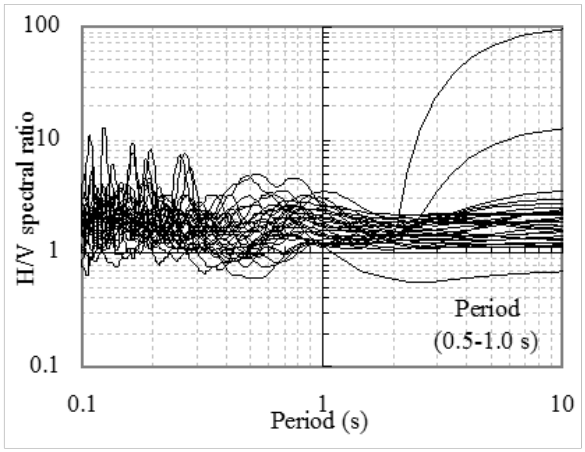


Figure 7 H/V spectral ratio of microtremor for Bhaktapur city having time period 0.5 to 1.0 s (covering most of the area of city)

The profile as shown in Figure 11 drawn along the center of Kathmandu Valley along north to south direction based on predominant time period obtained by the H/V method shows good correlation with the variation of the sediment thickness of the Kathmandu basin proposed by Katel et al. (1996) as shown in Figure 3.

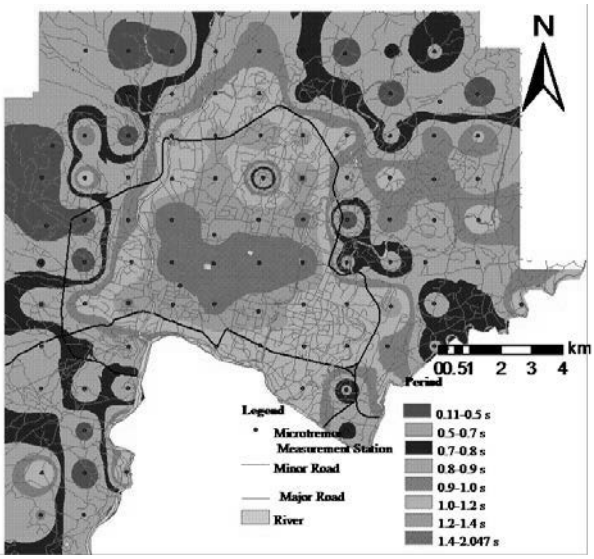


Figure 8 Microzonation of Kathmandu city based on the predominant time period

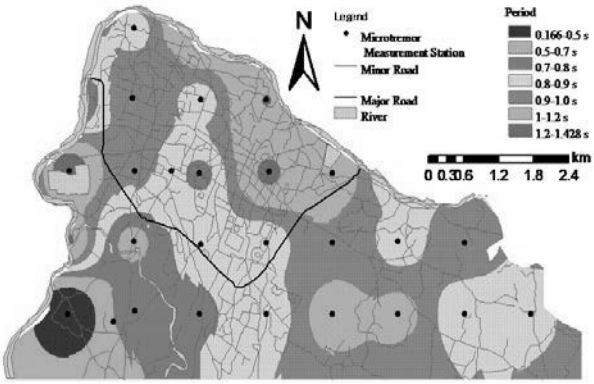


Figure 9 Microzonation of Lalitpur city based on the predominate time period

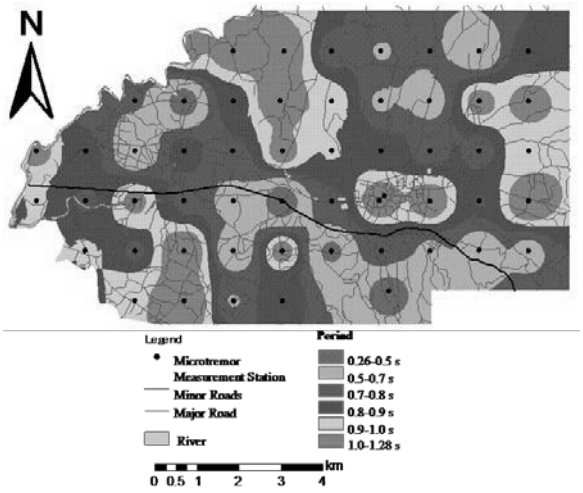


Figure 10 Microzonation of Bhaktapur city based on the predominant time period

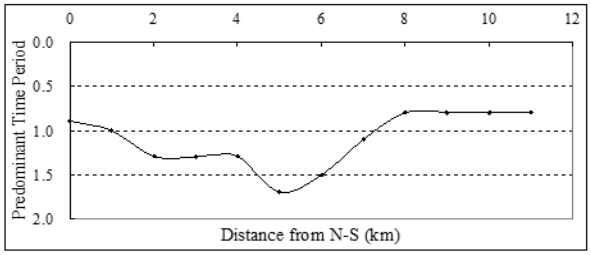


Figure 11 Profile of time period along north to south direction through center of Kathmandu Valley

5. CONCLUSIONS

In this study, microtremor measurements were carried out at more than 100 sites in Kathmandu city, 30 sites in Lalitpur city and 57 sites in Bhaktapur city, especially in densely populated urban areas. Predominant time periods of the ground were obtained using the horizontal and vertical spectral ratio (H/V) technique. Based on the H/V ratios of the microtremors, the predominant periods in the core city areas of Kathmandu were found higher than the Lalitpur and Bhaktapur city area as the sediment thickness is higher in center of Kathmandu city.

The classification into areas of different hazard level was done based on the dominant time period of the ground in different areas of three cities. Since the predominate time period of ground, which depends on the soil thickness, plays a very important role in the resonance effect with seismic waves and structures, it will be useful from hazard estimation point of view.

The time period obtained with H/V method shows good correlation with the variation of the sediment thickness of the Kathmandu basin carried out by Katel et al. (1996). With in the center part of Kathmandu city, the predominant time period were found maximum where the basin attains the maximum thickness and gradually decreases in the predominant time period towards the periphery of the basin, as the sediment thickness decreases, confirming the structure of the basin.

This study shows that the predominant time period of ground is different in different area of cities, which may affect structures having period according to the period of ground. Hence special attention should be given towards seismically design and construction of such structures.

References:

Bard, P.Y., Chavez-Garcia, F.J. (1993), "On the decoupling of surficial sediments form surrounding geology at Mexico City," *Bulletin of the Seismological Society of America* 83, 1979-1991.

Bilham, R., Bodin, P., and Jackson, M. (1995), "Entertaining a Great Earthquake in western Nepal: historic inactivity and geodetic tests for the present state of strain," *Journal of Nepal Geological Society*, vol. 11 (1) 73-78, 1995.

Birgören G., Ozel, O., and Siyahi, B. (2008), "Bedrock depth mapping of the Coast South of Istunbul: comparison of analytical and experimental analyses," *Turkish Journal of Earth Sciences (Turkish J. Earth Sci.)*, Col. 18, 2009, pp. 315-329.

Bonnefoy-Claudet, S., Cotton, F., Bard P.Y. (2006), "The nature of noise wave field and its applications for site effects studies: A literature review," *Earth-Science Reviews*, 79 (2006) 205-227.

Bonnefoy – Claudet, S., Cornou, C., Bard, P.Y., Cotton, F., Moczo, P., Kristek, J., and Fäh, D. (2006), "H/V ratio: a tool for site effects evaluation. Results from 1-D noise simulations," *Geophys. J. Int*. (2006) 167, 827-837.

Bour, M., Fouissac, D., Dominique, P. & Martin, C. (1998), "One the use of microtremor recordings in seismic microzonation," *Soil Dynamics and Earthquake Engineering* 17 (1998) 465-474.

Dongol, G.M.S. (1985), "Geology of the Kathmandu fluvial lacustrine sediments in the light of new vertebrate fossil occurrences," *Journal of Nepal Geological Society*, 3, 43-57.

Delgado, J., Casado, C.L., Lopez, Giner, J., Estevez, A., Cuenca, A. and Molina, S. (2000), "Microtremors as a Geophysical Exploration Tool: Applications and Limitations," *Pure and Applied Geophysics*, 157 (2000) 1445-1462.

Diagourtas, D., Tzanis, A. and Makropoulos, K. (2001), "Comparative study of microtremor analysis methods," Pure *and Applied Geophysics*.

Estrella, H.F. and Gonzalez, J. A. (2002), "SPAC: An alternative method to estimate earthquake site effects in Mexico City," *Geofisica Internacional* (2003), vol. 42, Num.2, pp.227-236.

Fäh, D., Kind, F. and Giardini D. (2000), "A theoretical investigation of average H/V ratios," Geophys. *J. Int.* (2001) 145, 535-549.

Fäh, D., Stamm, G., and Havenith, H.-B. (2008), "Analysis of three-component ambient vibration array measurements," *Geophys. J. Int.* (2008) 172, 199–213.

Field, E., Jacob, K. (1993), "The theoretical response of sedimentary layers to ambient seismic Noise," *Geophysical Research Letters*, Vol. 20, no. 24, pp. 2925-2928.

Field, E.H.,Clement, A.C., Jacob, K.H., Aharonian, V., Hough, S.E., Friberg, P.A., Babaian, T.O., Karapetian, S.S., Hovanessian, S.M., Abramian, H.A. (1995), "Earthquake site-response study in Giuari (formerly Leninakan), Armenia, using ambient noise observations," *Bulletian of the Seismological Society of America* 85 (1), 349-353.

Gosar, A. (2007), "Microtremor HVSR study for assessing site effects in the Bovec basin (NW Slovenia) related to 1998 Mw 5.6 and 2004 Mw5.2 earthquakes," *Engineering Geology* 91 (2007) 178 – 193.

Gueguen, P., Cornou, C., Garambois, S. And Banton, J. (2007), "On the Limitation of the H/V Spectral Ratio Using Seismic Noise as an Exploration Tool: Application to the Grenoble Valley (France), a Small Apex Ratio Basin," *Pure appl. geophys*. 164 (2007) 115–134.

Herak, M. (2007), "Model HVSR—A Matlab tool to model horizontal-to-vertical spectral ratio of ambient noise," *Computers & Geosciences* 34 (2008) 1514–1526.

Hasancebi, N. and Ulusay, R. (2006), "Evaluation of site amplification and site period using different methods for an earthquake-prone settlement in Western Turkey," *Engineering Geology* 87 (2006) 85–104

Huang, H.C, and Teng, T.L. (1999), "An evaluation on H/V Ratio vs. Spectral Ratio for Site-response estimation using the 1994 Northridge Earthquake Sequences," *Pure and applied geophysics* 156 (1999) 631-649.

Huang, H.C., Huang, S.W and Chiu, H.C. (2005), "Observed Evolution of Linear and Nonlinear Effects at the Dahan Downhole Array, Taiwan: Analysis of the September 21, 1999 M 7.3 Chi-Chi Earthquake Sequence," *Pure appl. geophys.* 162 (2005) 1–20.

Huang, H.C., Yang, Y.T., and Chiu, H.C. (2002), "Site Response Evaluation Using the H/V Ratio at the Yan-Liau Station in Hualien, Taiwan," *Pure appl. geophys.* 159 (2002) 2715–2731.

JICA, (2002), "The Study on earthquake disaster mitigation in the Kathmandu Valley Kingdom of Nepal," Japan International Cooperation Agency (JICA) and Ministry of Home Affairs, His Majesty's Government of Nepal, volume I, Summary, 110+p, volume III, Main Report 2/2, Earthquake Disaster Assessment and Data Base System, 76+p.

Katel, T.P., Upreti, B.N. and Pokharel, G.S. (1996), "Engineering properties of fine grained soils of Kathmandu Valley, Nepal," *Journal of Nepal Geological Society*, 13, 121-138.

Lermo, J., Chavaz-Garcia, F.J. (1993), "Site effect evaluation using spectral ratios with only one station," *Bulletin of the Seismological Society of America* 83:1574-1594.

Lermo, J., Chavaz-Garcia, F.J. (1994), "Are microtremors useful in site response evaluation?," *Bulletin of the Seismological Society of America*, 84 (5), 1350-1364.

Molnar, P (1984), "Structure and tectonics of the Himalaya: Constraints and implications of geophysical data," *Ann. Rev. Earth Planet. Science*, 1984, 12:489-518.

Molnar, P. (1986), "The geologic history and structure of the Himalaya," *America Science Geology-Himalaya.*

Moribayashi, S. and Maruo, Y. (1980), "Basement topography of the Kathmandu Valley, Nepal- an application of the gravitational method to the survey of a tectonic basin in the Himalaya," *Journal of Japan Society of Engineering Geology*, vol. 21, pp. 30-37.

Nogoshi, M., Igarashi, T. (1971), "On the amplitude characteristics of microtremor (Part 2)," *Journal of Seismological Society of Japan* 24, 26-40 (in Japanese with English abstract).

Nakamura, Y. (1989), "A method for dynamic characteristics estimation of subsurface using microtremor on the ground surface," *Quarterly Report of the Railway Technical Research Institute* 30 (1), 25-33.

Nakamura, Y. (1997), "Seismic vulnerability indices for ground and structures using microtremor," *World Congress on Railway Research*, Florence.

Nakamura, Y. (2000), "Clear identification of fundamental idea of Nakamura's Technique and its applications," *Proceedings of 12th World Conference in Earthquake Engineering, Auckland, NZ*, 2656.

Nakamura, Y., Sato, T. and Nishinaga, M. (2000), "Local site effect of Kobe based on microtremor measurement," *Proceedings of the Sixth International Conference on Seismic Zonation* (6ISCZ), EERI, November 12-15, 2000/ Plam Springs. California.

Nakamura, Y. (2008), "On the H/V spectrum," *The 14th World Conference on Earthquake Engineering*, October 12-17, 2008, Beijing, China.

Nakamura, Y., Gurler, E.D., Saita, J., Rovelli, A., Donati, S. (2000), "Vulnerability investigation of roman colosseum using microtremor," *Prepared for 12th WCEE 2000*, Auckland, NZ.

Pandey, M. R. and Molnar, P. (1988), "The distribution of intensity of the Bihar-Nepal earthquake 15 January 1934 and bounds of the extent of the rupture zone," *Journal of Nepal Geological Society*, vol. 5 No. 1, 22-44.

Sakai, H., Fujii, R., Kuwahara, Y. (2002), "Changes in the depositional system of the Paleo-Kathmandu Lake caused by uplift of the Nepal Lesser Himalayas," *Journal of Asian Earth Sciences* 20 (2002) 267-276

Sakai, H., Fujii, R., Kuwahara, Y., Upreti, B.N., and Shrestha, S.D. (2001), "Core drilling of the basin-fill sediments in the Kathmandu Valley for palaeocliatic study: preliminary results," *Journal of Nepal Geological Society*, 2001, Vol. 25 (Sp. Issue) pp. 9-18.

Sakai, H. (2001), "Stratigraphic division and sedimentary facies of the Kathmandu Basin Group, central Nepal," Journal of Nepal Geological Society, 2001, Vol. 25 (Sp. Issue) pp. 19-32.

Sakai, H. and Fujii, R. (2002), "Paleoclimatic changes during the last 2.5 myr recorded in the Kathmandu Basin, Central Nepal Himalayas," *Journal of Asian Earth Sciences*, 20 (2002) 255-266.

Teves-Costa, P., Matias, L., and Bard, P.Y. (1996), "Seismic behavior estimation of thin alluvium layers using microtremor recordings," *Soil Dynamics and Earthquake Engineering*, 15 (1996) 201-209.

Teves-Costa, P., Almeida, I.M., and Silva, P.L. (2001), "Microzonaton of Lisbon: 1-D Theoretical Approach," *Pure and Applied Geophysics* 158 (2001) 2579-2596.

Theodulidis, N., Panou, A.A., Hatzidimitriou, P., Stylianidis, K., Papazachos, C.B. (2005), "Ambient noise horizontal-to-vertical spectral ratio in site effects estimation and correlation with seismic damage distribution in urban environment: the case of the city of Thessaloniki (Northern Greece)," *Soil Dynamics and Earthquake Engineering* 25 (2005) 261–274.

Theodulidis, N., Bard, P.Y. (1995), "Horizontal to vertical spectral ratio and geological conditions: an analysis of strong motion data from Greece and Taiwan (SMART-1)," *Soil Dynamics and Earthquake Engineering*, 14(1995) 177-197.

Theodulidis, N., Bard, P.Y., Archuleta, R., Bouchon, M. (1996), "Horizontal-to-vertical spectral ratio and geological conditions: the case of Garner Valley downhole array in southern California," *Bulletin of Seismological Society of America*, vol. 86, no. 2, pp. 306-319, April 1996.

UNDP (1994), "Seismic hazard mapping and risk assessment for Nepal," His Majesty's Government of Nepal, Ministry of Housing and Physical Planning, UNDP/UNCHS(Habitat) Subproject NEP/88/054/21.03.

Yoshida, M. and Igarashi, Y. (1984), "Neogene to Quaternary lacustrine sediments in the Kathmandu Valley, Nepal," *Journal of Nepal Geological Society*, 4, 73-100.

Zaslavsky, Y., Shapira, A., Arzi, A.A. (2000), "Amplification effects from earthquakes and ambient noise in the Dead Sea rift (Israel)," *Soil Dynamics and Earthquake Engineering*, 20 (2000), 187-207.

8CUEE CONFERENCE PROCEEDINGS
8th International Conference on Urban Earthquake Engineering
March 7-8, 2011, Tokyo Institute of Technology, Tokyo, Japan

NUMERICAL STUDY ON SCOUR PROBLEM INDUCED BY TSUNAMI FLOOD

Tso-Ren Wu[1], Chung-Yue Wang[2], Meng-Zhi Chen[3], Ray Shyan Wu[2], and Yuan-Fan Tsai [4]

1) Assistant Professor, Graduate Institute of Hydrological and Oceanic Sciences, National Central University, Taiwan
2) Professor, Dept. of Civil Engineering, National Central University, Taiwan
3) Master Student, Graduate Institute of Hydrological and Oceanic Sciences, National Central University, Taiwan
4) Professor, Dept. of Social and Regional Development, National Taipei University of Education, Taiwan
tsoren@ncu.edu.tw, cywang@ncu.edu.tw, 976206005@cc.ncu.edu.tw, raywu@ncu.edu.tw, tyf@tea.ntue.edu.tw

Abstract: Local scour induced by tsunami floods or rover floods is the major problem that causes the failure of a structure. However, due to the difficulty on describing the sediment transport mechanism, engineers deeply rely on empirical or semi-empirical formulae which are mostly derived from steady and equilibrium conditions. Unfortunately, the structure failure usually occurred in the event of extreme flood which deviates tremendously from the assumption mentioned above. In this paper, we propose a 3D numerical scouring model based on the Bingham rheological theory. The bed load, suspended load, and laminated load in the conventional sediment transport theory are converted into a clear water area, mixed area, and plug area in the Bingham model. The model is validated by the analytical solution of a Bingham flow in a channel with excellent agreement. This model is further used to simulate the submerged jet-scour problem. The multi-fluid flow, including air-water and water-sediment, is described by the Volume-of-Fluid (VOF) method. The profile of the scouring bed is compared with the laboratory experiment. Both the maximum scouring depth and location can be well predicted. At the end, this model is used to simulate the failure of Shuan-Yuan Bridge in the event of 2009 Typhoon Morakot. The computed scouring depth is compared with the field measurement with good agreement. The profile of the riverbed around the bridge piers after scouring is presented.

1. INTRODUCTION

Local scour is the removal of the streambed material from bridge foundations due to the flooding water, and is the most common cause of bridge failures during the typhoon events in Taiwan. To minimize the future bridge damage, an accurate estimation or simulation on the scouring depth is the key. However, very few studies have been developed for evaluating bridge scour under extreme weather. In the past few decays, the estimation of scour depth relayed on the empirical formula. One example is the Lacey's formula (1930). In Lacey's formula, the scour depth was related to the discharge, sediment particle size, as well as some local empirical parameters. Followed by Lacey's formula, many efforts have been made to evaluate the local scour depth around bridge piers. A number of prediction methods are available (Melville 1997; Rahman and Haque, 2002, and many others). Most of the formulae are empirical or semi-empirical which can be applied at a limited range of hydraulic condition. In other words, the variability of natural rivers often exceeds the limitations of these formulae, not to say under the extreme weather condition.

In order to predict the local scour around the bridge piles more accurately, efforts are made to couple the sediment transport theory with the flow solver. Mao (1986) applied a modified potential flow theory and sediment continuity equation to simulate scour below a long cylinder on a sandy bottom subject to a mean current. An empirical sediment transport formula is adopted. Li and Cheng (2000) solved the Navier-Stokes (NS) equations with Smagorinsky sub-grid scale (SGS) closure. They calculated the equilibrium scour pit size by assuming that the shear stress on the seabed is close to the far-field shear stress when an equilibrium state is reached. Their model was able to predict the upstream portion of the scour hole with reasonable accuracy. Brørs (1999) utilized a finite element method to solve the RANS equation with k−ε closure. In his study, the sediment transport model is solved simultaneously which included both the bed-load and suspended-load transports. Liang et al. (2005) utilized the similar approach to simulate the scouring around pipelines. In order to avoid the appearance of unrealistically sharp irregular scour profiles and numerical instabilities, a special smoothing technique was employed. Later on, many models were developed based on the sediment transport theory in the frame work of Navier-Stokes equations. In order to avoid using the purely empirical sediment transport formulae, two-phase formulations are developed based on more fundamental concepts. Zhao and Frenando (2007) developed an Eulerian two-phase model embedded in FLUENT software to simulate scour around pipelines. The flow-particle interaction and particle-particle interactions are considered in the model formulation. Good agreement with the laboratory measurement can be seen in terms of the

development of the scouring profiles.

However, the free-surface effect was neglected in most of the studies mentioned above. This is valid only if the free-surface does not change too much along the channel. For rapidly changing water surface, this assumption will introduce nonphysical errors. In the scour problem, the bed deformation needs to be coupled with the flow field. Liu and García (2008) developed a 3D VOF model with k−ε closure. The behavior of the water-sediment interface is captured with a moving-mesh method, which is a Lagrangian approach. The bed-load and suspended load were considered in the bed morphology model. They demonstrated the model performance on the 2D turbulent wall jet flow and the scour hold. Very good agreement can be seen. A 3D wave scour around large vertical circular cylinder was simulated with reasonably good results. However, their model adopted the moving-mesh method which increased difficulty on simulating complex geometry, and only one sediment material can be simulated. In the practical scouring problem, the field measurement always shows complex combination with stratified layers. Also, using the conventional sediment transport theory requires calibration and validation on many model parameters. Such as Shields number, critical Shields numbers, bed-load transport coefficient, suspended-load coefficient, and more. These coefficients have to be determined prior, and the simulation results are sensitive to some of the empirical coefficient. The validation on the empirical coefficients impedes the application on solving the real case with nature riverbed.

In this study, we intend to avoid using the conventional transport model. Instead, adopting the Bingham model coupled with the VOF-NS model to simulate the local scour problem under the situation of violent flood. The Bingham model has been widely used to study the nature phenomena, such as the mudflows, landslides, lava flows in formation of depth-integrated method. The characteristic stress-strain relationship of a Bingham fluid is that the applied shear stress must exceed a threshold value, referred as yield stress, to liquefy the fluid from a solid material. Once the yield stress reaches, the liquefied material behaviors just like the Newton fluid. This Bingham characteristic is very close to the sediment transport on the river bed. However, implementation of Bingham model with 3D NS equation is rare. One of the reasons is that NS equation cannot be used to describe the solid motion. To overcome this problem, the solid part of the Bingham is simulated as the high viscous fluid. An extreme high viscous is set to the plug area and the Bingham model is transformed to the "bi-viscous" model. Assier-Rzadkiewicz et al. (1997) proposed this method on simulating 2D landslide generated waves. However, due to the stability constrain, large value of viscosity will significantly reduce the time marching step if the explicit scheme is adopted. The small time step impedes the implementations to the physical cases. To overcome this problem, the implicit viscous solved is adopted in this study.

2. ALGORITHM

2.1 Rheological Model of Dense Part

Many materials such as river mud, river sediment, snow, volcanic lava, and even the toothpaste behave like a non-Newtonian fluid. Some of them are called viscoplastic materials with a critical value of shear stress. The critical shear stress represents the plasticity of the material. This critical value is called the yield stress, or the Bingham yield. Below this yield stress, the material behaves like a rigid body, and the cohesion is important. Above this critical value, the material behaves like a Newtonian fluid. There are many rheological models to simulate this viscoplastic behavior. However, the Bingham plastic model is the simplest and best-known one. As described in the Bingham model, there is no deformation takes place until a specified shear stress is applied. By combining the yield stress τ_0 and the plastic dynamic viscosity μ_B (Liu and Mei, 1989), this model is able to describe the rheological behavior of these fluids. The nonlinear stress-strain relation between the shear stress and the strain rate can be expressed by $\tau = 2\mu\bar{D}$, in which τ is the deviatoric part of the stress tensor. $\bar{D}$ is the strain rate. $\mu = \mu(\bar{D})$ can be expressed as

$$\begin{aligned} &\mu\left(\bar{D}\right) = \mu_B + {\tau_0}\Big/{2\sqrt{\tfrac{1}{2}\bar{D}:\bar{D}}}, \text{ if } \frac{1}{2}\tau:\tau > \tau_0^2; \\ &\mu\left(\bar{D}\right) = \mu_\infty \text{ and } \bar{D} = 0, \text{ if } \frac{1}{2}\tau:\tau \le \tau_0^2 \end{aligned} \tag{1}$$

where μ_∞ is a large number indicating the solid behavior. This nonlinear relation leads to two distinct zones in the flow, a shear zone and a plug zone. In this study, μ_∞ is set to $10^5 \sim 10^{12}$ Pa·s which is much greater than water viscosity at 10^{-3} Pa·s.

2.2 Fluid Solver: 3D VOF model

The complete scouring model is a coupling between sediments and free-surface flow. The open-source code, "Truchas", developed by Los Alamos National Lab (LANL) is utilized and modified. The Eulerian code, Truchas, solves the 3D complete incompressible NS equations for multi-fluid flow based on the VOF method. The details of the algorithm can be found in Liu et al. (2005).

In this study, the Bingham material is treated as one of the multiple fluids. A fixed Cartesian grid is adopted for simulating each fluid. No grid deformation technique is required. The mixture concept is adopted for calculating the effective viscosity in a numerical cell: $\mu_{eff} = \sum f_m \mu_m$, in which f_m is the volume fraction of the m^{th} fluid. μ_m is the viscosity of the m^{th} material.

Based on the mixture concept, the conventional sediment transport theory can be transferred into the Bingham model. The Shields number is close to the Bingham yield. The fixed water bed is represented as the plug area. The bed load, laminated load, and suspended load

are the mixture of water, air, and Bingham fluids with different concentrations.

3. MODEL VALIDATION

3.1 Comparison with Analytical Solution

To validate the scouring model, the numerical simulations and analytical solutions are compared for a Bingham flow between two fixed parallel plates. The analytical solutions were derived by Bird et al. (1983). A Bingham fluid between two parallel plates of length L and width 2B is being driven in the x direction by a pressure gradient. The problem is stationary and the velocity profile can be derived with no-slip boundary conditions applied along the plates. Two zones are distinguished inside the fluid. In the simulation, the length L is 10 m. The half width is 1m. $P_0 = 10$ Pa and $P_L = 0$ Pa. The plastic viscosity $\mu_B = 5.0\ \text{Pa}\cdot\text{s}$. The yield stress is $\tau_0 = 0.5$ Pa. $\mu_\infty = 1e6\ \text{Pa}\cdot\text{s}$

Figure 1 shows the comparison between computed and analytical velocity profile for Bingham Flow.

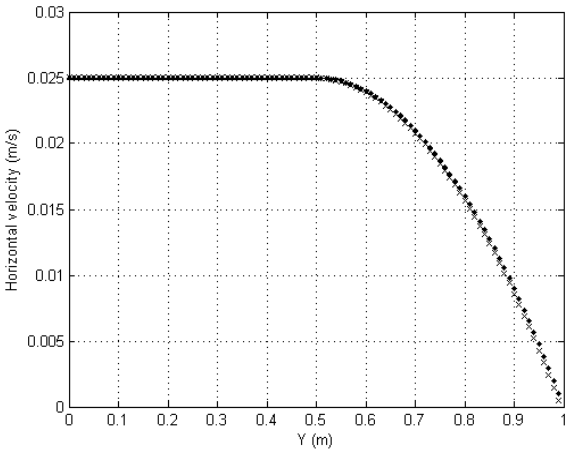


Figure 1 Comparison of the Velocity Profiles for Bingham Fluid. Diamond: Computed. Cross: Analytical.

3.2 Model Validation – Submerged Horizontal Jet

After validating with the analytical Bingham flow solution, the model is then utilized to study the benchmark problem of the submerged horizontal jet (Chatterjee et al., 1994). In their experiment, water entered the flume through a narrow slit of 2 cm in openness under water pressure. The inlet velocity was measured to be 1.56 m/s. The resulting 2D sheet of water flowed over a solid apron with 66 cm in length, and contacted a packed bed of sand bed 300 cm in length and 25 cm deep. The averaged density of sediment bed was measured to be 1709 kg/m^3. However, the Bingham yield τ_0, Bingham dynamic viscosity μ_B, and the maximum viscosity μ_∞ were not reported. In the numerical simulation, the μ_∞ is set to be $10^5\ \text{Pa}\cdot\text{s}$. From the numerical tests, we found that the final results is not sensitive to μ_∞ as long as μ_∞ is greater then $10^5\ \text{Pa}\cdot\text{s}$. The only parameter needs to be determined are τ_0 and μ_B. After trial and error method, the Bingham yield is found to be $150\ \text{N/m}^2$ and the Bingham viscosity $\mu_B = 0.08\ \text{Pa}\cdot\text{s}$. Figure 2 shows the experimentally observed bed profile and the simulation result from this study. The shape and the maximum scour depth of the predicted bed profiles compare very well to the experimentally observed sand bed. However, the downstream accumulation height is slight under predicted. This might require further fine tuning on the Bingham parameters.

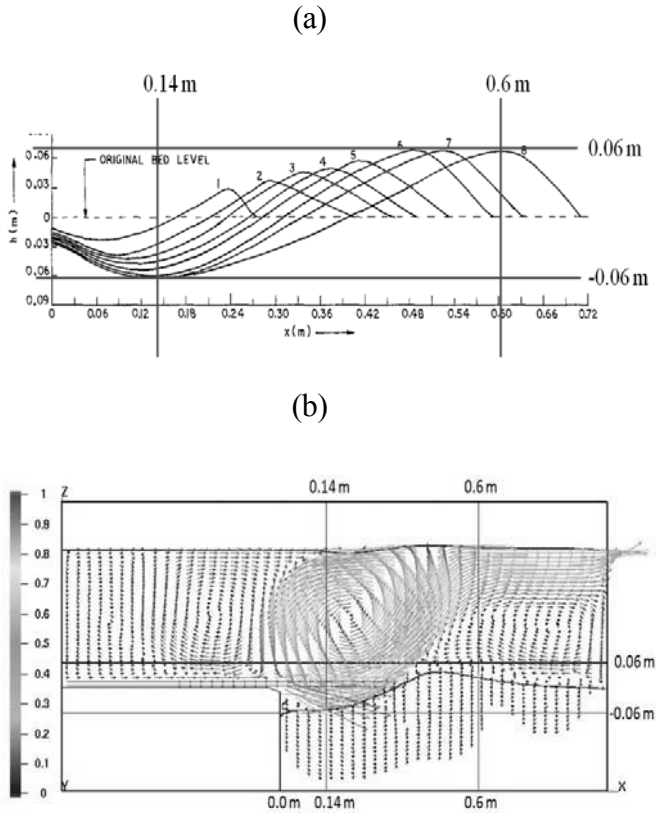


Figure 2 Comparison between computed and experimental scour profiles. (a) Experimental, (b) Numerical.

4. CASE STUDY – THE FAILURE OF SHUAN-YUAN BRIDGE

The validated scouring model is utilized to study the failure of Shuan-Yuan Bridge in the event of 2009 Typhoon Morakot. In this event, the flooding velocity was estimated and measured to be 8 m/s in the upstream direction of the bridge piles. The field measure also indicated that a 21 m scour depth right in front of the bridge piles might be the major cause to the bridge failure. The filed measure also indicated that a 15 m scour depth was measured 30 m away in the upstream direction. In this study, we shall simulate the 3D scour hole under the bridge pile. The Bingham parameters used in this case are $\tau_0 = 1600\ \text{N/m}^2$, $\mu_B = 10.0\ \text{Pa}\cdot\text{s}$, and $\mu_\infty = 1e6\ \text{Pa}\cdot\text{s}$. Figure 3(a) shows the over view of the setup and simulation results at

the quasi-steady state including the scour profile and free-surface. Figure 3(b) shows the local scour hole. The maximum scour depth is about 20.5 m which is very close the field measurement. The scour depth 30 m away from the bridge piles in the upstream direction is about 16 m which is close to the field measurement, too. Figure 3(c) shows the stream lines on the vertical cross-section. The stream lines shows that the flood causes the strong local scour right beneath the front row of the bridge piles. Figure 3(d) shows the overview of the local scour profile and the stream lines. Scouring mechanism can be seen clearly.

4. CONCLUSIONS

In this study, we proposed a new scour model by coupling the Bingham Rheological Model and the VOF-NS model. The plug area in the Bingham model is model as a high-viscous fluid. The viscosity is extremely high that makes the fluid behaves like a solid material. The implicit viscous solver is adopted to reduce the computational time. The newly developed scour model has no limitation on the number of Bingham materials, and is very suitable for simulating the field cases. This model is also suitable for simulating scouring problems under the strong floods in which the free-surface effect cannot be ignored. Because the Bingham model is used, only Bingham yield and Bingham viscosity are needed. Doesn't like the conventional sediment transport theory, the present model doesn't require other empirical or semi-empirical coefficients.

The model is validated with the analytical solution, 2D submerged jet problem, and 3D Shuan-Yuan Bridge scouring problem. Very good agreement can be seen while comparing the numerical solution to the analytical solution, experiment measurement, and field survey, respectively. The good results show the feasibility of using Bingham model on the scouring problems.

Acknowledgements:

The organizers wish to express their gratitude for the support from the CECI and Center for Bridge Engineering Research, College of Engineering, and Dept. of Civil Engineering of the National Central University. Without their support, the symposium would not become possible.

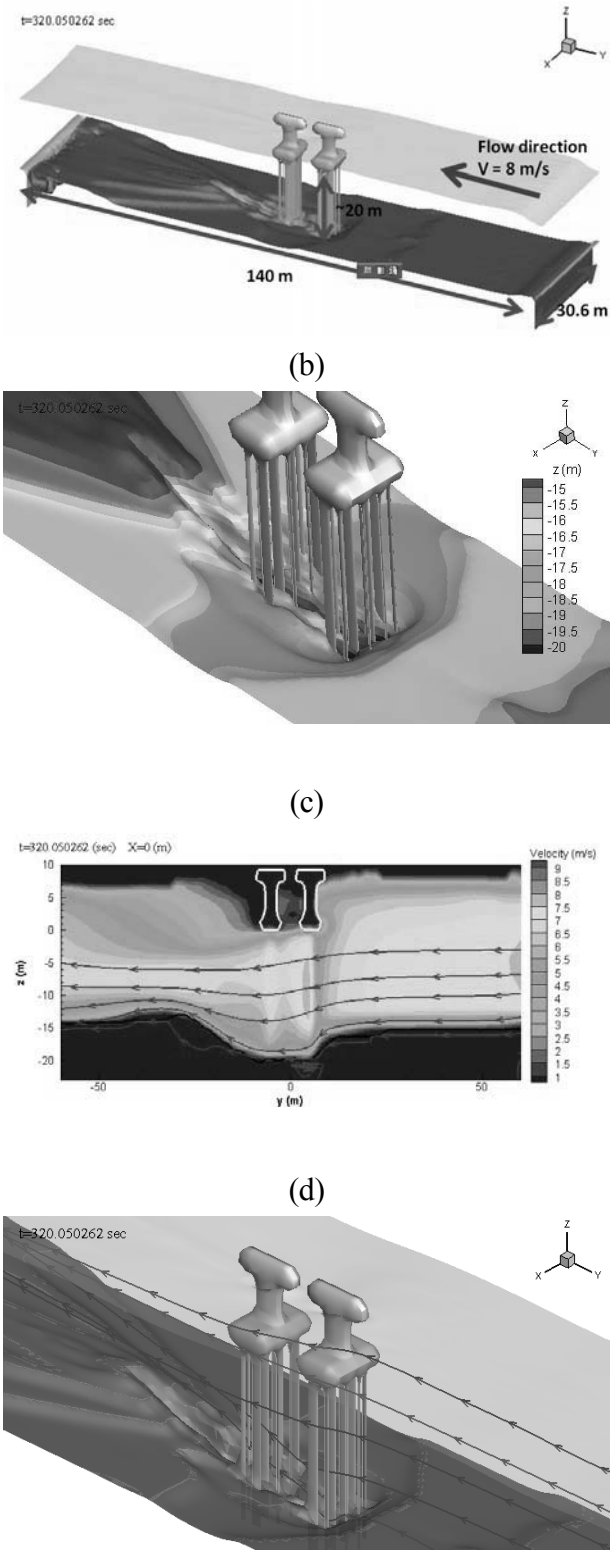


Figure 3 Computed Scour Profile of Shuan-Yuan Bridge. (a) Setup and Overview (b) Profile of Local Scouring Hole. (c) Vertical Cross-Section of Velocity and Streamlines. (d) Overview of Scour Profile and Streamlines.

(a)

References:

Assier-Rzadkiewicz, S, Mariotti, C, and Heinrich, P (1997). "Numerical Simulation of Submarine Landslides and their Hydraulic Effects," *Journal of Waterway, Port, Coastal, and Ocean Engineering, ASCE*, **123**(4), 149-157.

Bird, R. B., Dai, G. C., and Yarusso, B. J. (1983), "The rheology and flow of viscoplastic materials," *Rev. of Chemical Engrg*., **1**(1), 1-70.

Brørs B (1999), "Numerical modeling of flow and scour at pipelines," *J. Hydr. Eng*. **125,** 511–523.

Chatterjee,, S. S., Ghosh, S. N., and Chatterjee, M.., (1994), "Local scour due to submerged horizontal jet," *J. Hydraulic Engineering*, **120**(8), pp. 973-992.

Lacey, G. (1930), "Stable channels in alluvium," *Paper 4736, Minutes of the Proc., Institution of civil Engineers*, William Clowes and Sons Ltd., London, Great Britain, **229**, 259-92.

Li F, Cheng L (2000), "Numerical simulation of pipeline local scour with lee-wake effects," *Int. J.Offshore Polar Eng.* **10**, 195–199

Liang D, Cheng L, Li F (2005), "Numerical modeling flow and scour below a pipeline in currents. Part II. Scour simulation.," *Coastal Eng*. **52**, 43–62.

Liu, P.L.-F., Wu, T.-R., Raichlen, F., Synolakis, C., and Borrero, J., (2005), "Runup and rundown from three-dimensional sliding masses," *Journal of Fluid Mechanics*, **536**, 107-144.

Liu, K. F., and Mei, C. C. (1989). "Slow spreading of a sheet of Bingham fluid on an inclined plane," *J. Fluid Mech., Cambridge, U.K*., **207**, 505-529.

Liu, X., García, M.H., (2008) , "A three-dimensional numerical model with free water surface and mesh deformation for local sediment scour," *Journal of Waterway, Port, Coastal, and Ocean Engineering*, **134**(4), 203-217.

Mao Y (1986), "The interaction between a pipeline and an erodible bed," *PhD thesis, Institute of Hydrodynamics and Hydraulic Engineering, Technical University of Denmark, Lyngby*, Denmark.

Melville, B.W. (1992), "Local scour at bridge abutments," *J. Hydraulic Division, ASCE*, **118**(4), 615-631.

Rahman, M.M. and Haque, A. (2002), "Flow field and the maximum local scour depth around piers and abutments," *Journal of Indian Water Resources Society*, **22**(3), 117-124.

Zhao Z., Fernando H.J.S. (2007), "Numerical simulation of scour around pipelines using an Euler-Euler coupled two phase model," *Env. Fluid Dyn*., **7** (2), 121-142.

8CUEE CONFERENCE PROCEEDINGS
8th International Conference on Urban Earthquake Engineering
March 7-8, 2011, Tokyo Institute of Technology, Tokyo, Japan

THE SEISMIC MITIGATION ASSESSMENT OF LNG TANK BY 3D NUMERICAL SIMULATION

Ruifu Zhang[1)], Dagen Weng[2)], and Weibo Ni[3)]

1) Ph.D. candidate, State Key Laboratory for Disaster Reduction in Civil Engineering, Tongji University, Shanghai, China
2) Professor, State Key Laboratory for Disaster Reduction in Civil Engineering, Tongji University, Shanghai, China
3) M.S candidate, State Key Laboratory for Disaster Reduction in Civil Engineering, Tongji University, Shanghai, China
zhangruifu@gmail.com , wdg@tongji.edu.cn, niweibo1985@hotmail.com

Abstract: The seismic mitigation effectiveness of insulation layer of LNG storage tank has been investigated through 3D finite element numerical models. LNG tanks are important facilities which are used to supply natural gas. Inner tank is much more sensitive to seismic effects and the design requirements of pile are fairly stringent. However, it is not considered that inner tank is protected by insulation layer and outer tank generally, and there are some thresholds beyond which the tank may not operate normally. The 3D finite element models are built for LNG tank with insulation layer and isolation bearings. A comparison between considering and without considering insulation layer has also been performed. Data reported and statistically sorted include tank wall stress, pile shear, global overturning moment, and wave height in the tank. The seismic mitigation effect is judged by these date. A common insulating material of LNG tank is used to evaluate influence of dynamic interaction. The results show that the insulation layer may not be neglected in the seismic design of LNG tank.

1. INTRODUCTION

LNG tanks are considered to be lifeline engineering due to the liquefied natural gas that they store. The volumes of these tanks are very large and have capacities about 160,000 m^3. LNG tank consists of inner steel tank, which contains the LNG, and outer concrete tank encasing and protecting the inner tank, with insulation placed between the two tank walls (Figure 1).

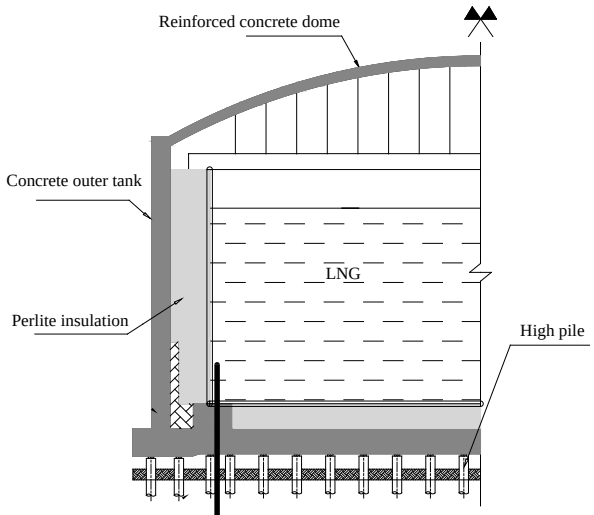


Figure 1 Schematic view of a modern LNG tank

The tanks could be damaged easily in the earthquake, which had been proved in many cases in last years. Typical damages of tanks during past earthquakes such as 1989 Loma Prieta, 1994 Northridge, Ji-Ji Taiwan and 1999 Kocaeli, were in the form of cracking at the corner of the bottom plate and compression buckling of tank wall (elephant foot buckling) due to uplift, sliding of the base, anchorage failure, sloshing damage around the roof, failure of piping systems and plastic deformation of base plate (Abali and Uckan 2009; Chalhoub and Kelly 1990). Originally, Housner (1957) developed a mathematical model in which the mass of liquid portion that accelerates with the tank wall together is called as the impulsive and the mass of liquid portion that causes sloshing motion of the free surface near the tank roof is called as the convective. A different approach to the analysis of flexible containers was developed by Veletsos (1974). He presented a simple procedure for evaluating hydrodynamic forces induced in flexible liquid filled tanks. Later, Veletsos and Yang (1976) estimated maximum base overturning moment induced by a horizontal earthquake motion by modifying Housner's model to consider the first cantilever mode of the tank. They presented simplified formulas to obtain the fundamental natural frequencies of liquid filled shells by the Rayleigh-Ritz energy method. Haroun and Housner (1980; 1981; 1983) modified the Housner's model and took into account the flexibility of the tank wall in the seismic analysis. In 2000, Malhotra et al. (2000) modified the mechanical analog proposed by Veletsos and Yang using only one convective mode. The procedure takes into account impulsive and convective (sloshing) actions of the liquid in flexible steel or concrete tanks fixed to rigid foundations.

A new approach developed by various researchers

proposes to use the isolation bearings to decrease the seismic response of tanks. Chalhoub and Kelly (1990) determined favorable effects of base isolation of liquid storage tanks through shake table tests on isolated and non-isolated tanks. In 2000, Bachmann and Wenk (2000) applied seismic isolation system to a liquid storage tank supported by short columns. They named this rehabilitation scheme as softening. As part of this "softening" approach, 26 high-damping bearings were incorporated into the structural system. Shrimali and Jangid (2002) investigated the seismic response of the liquid storage tanks isolated by lead-rubber bearings (LRB) for bi-directional earthquake excitation.

One of the original researches on seismic response of a base isolated LNG tank was conducted by Tsopelas et al. (1994). Seismic analysis of base-isolated LNG tank using the BE-FE-BE coupling technique was conducted by Kim et al. (2002). A project was investigated by Boduroğlu et al. (2006) to learn the dynamic behavior and weaknesses of these structures by site and laboratory tests and response analysis. To achieve these goals a study program including in-situ dynamic tests, shaking table tests and analytical analysis was followed. The results obtained showed that this type of structures is vulnerable to earthquake effects and the use of base isolation system is very effective in minimizing the earthquake effects. Christovasilis et al. (2008) study the utility of the simplified analogs for the analysis and design of liquid storage tanks constructed using conventional and protective systems. The Finite Element Method (FEM) is utilized to model the tank, as well as the contained liquid. Seismic isolation is implemented by introducing horizontal inelastic beam elements between the base and the ground. Zhang et al. (2010) present a LNG tank isolation system which is composed of annular damper reaction wall, viscous dampers, and lead rubber bearings mounted on the top of the piles in order to decrease pile shear and isolation displacement. The annular damper reaction wall which is not connected with the piles is embedded into the ground independently. However, dynamic interaction between the inner tank and outer tanks was neglected in these studies.

A simplified finite element model presented by Malhotra is used to judge the periods of inner tank. Data reported and statistically sorted include pile shear, Von Mises stress, wave height, and overturning moment. 3D finite element models are built for LNG tank with insulation layer and isolation bearings. The comparison between considering and without considering insulation layer is performed. Data reported and statistically sorted include tank wall stress, pile shear, isolation displacement, global overturning moment, and wave height in the tank. The seismic mitigation effect is judged by these date.

2. STRUCTURAL MODEL OF TANK

2.1 Malhotra Mechanical Model

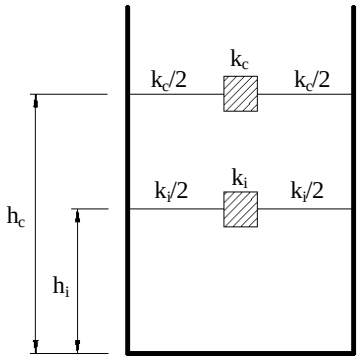


Figure 2 Mechanical analog proposed by Malhotra et al.

The procedure was based on the work of Veletsos and co-workers with certain modifications that included:

Combining the higher impulsive modal mass with the first impulsive mode and the higher convective modal mass with the first convective mode.

Modifying modal heights to account for the contribution of higher modes to the base overturning moment.

Generalizing the formula for the impulsive period so that it could be applied to steel and concrete tanks of various wall thicknesses.

The values proposed by Malhotra for the properties of the analog are presented in Table 1 and Eqs. 1 ~ 2, where t_s is the equivalent uniform thickness of the tank wall, E_s is the modulus of elasticity of the inner tank wall material, ρ_l is the mass density of the liquid, T_i and T_c are the periods of the impulsive and convective modes, m_i and m_c are masses of the impulsive and convective, m_l is the total liquid mass, and C_i and C_C are dimensionless factors, H is the height of liquid in the tank, r is the inner tank radius, and h_i and h_c are the heights of the centroids of the impulsive and convective hydrodynamic wall pressures.

$$T_i = C_i \frac{H\sqrt{\rho_l}}{\sqrt{t_s / r} \times \sqrt{E_s}} \tag{1}$$

$$T_c = C_C \sqrt{r} \tag{2}$$

Table 1 Properties of the mechanical analog (Malhotra 2000)

H/r	C_i	C_c	m_i/m_l	m_c/m_l	h_i/H	h_c/H
0.3	9.28	2.09	0.176	0.824	0.4	0.521
0.5	7.74	1.74	0.3	0.7	0.4	0.543
0.7	6.97	1.6	0.414	0.586	0.401	0.571
1	6.36	1.52	0.548	0.452	0.419	0.616
1.5	6.06	1.48	0.686	0.314	0.439	0.69
2	6.21	1.48	0.763	0.237	0.448	0.751
2.5	6.56	1.48	0.81	0.19	0.452	0.794
3	7.03	1.48	0.842	0.158	0.453	0.825

2.2 Governing Equations of Motion

The governing equations of motion of LNG tank may be expressed as:

$$m_c\left(\ddot{u}_c + \ddot{u}_b\right) + c_c\dot{u}_c + k_c u_c = -m_c\ddot{u}_g \tag{3}$$

$$m_i\left(\ddot{u}_i + \ddot{u}_b\right) + c_i\dot{u}_i + k_i u_i = -m_i\ddot{u}_g \tag{4}$$

$$m_{ot}\left(\ddot{u}_{ot}+\ddot{u}_b\right)+c_{ot}\dot{u}_{ot}+k_{ot}u_{ot}=-m_{ot}\ddot{u}_g \quad (5)$$

$$m_{it}\ddot{u}_b+c_e\dot{u}_b-c_c\dot{u}_c-c_i\dot{u}_i-c_{ot}\dot{u}_{ot}+k_eu_b -k_cu_c-k_iu_i-k_{ot}u_{ot}=-m_{it}\ddot{u}_g \quad (6)$$

$$m_{it}=m_{iw}+m_b \quad (7)$$

where u_c is the displacement of the convective mass relative to bearing displacement in horizontal direction, u_i is the displacement of the impulsive mass relative to bearing displacement in the horizontal direction, u_{ot} is the displacement of the outer tank mass relative to bearing displacement in the horizontal direction, u_b is the displacement of the bearings relative to ground in the horizontal direction, c_c is the damping of the convective mass, c_i is the damping of the impulsive mass, c_{ot} is the damping of the outer tank mass, c_e is the equivalent damping of the isolation devices, k_c is the stiffness of the convective mass, k_i is the stiffness of the impulsive mass, k_{ot} is the stiffness of the outer tank mass, k_e is the equivalent stiffness of the isolation devices, $\ddot{u}_g$ is the earthquake ground acceleration, m_{iw} is the mass of the inner tank wall, m_{ot} is the total mass of the outer tank, m_b is the mass of the bottom plate and foam glass, m_{it} is the total mass of the inner tank and bottom plate.

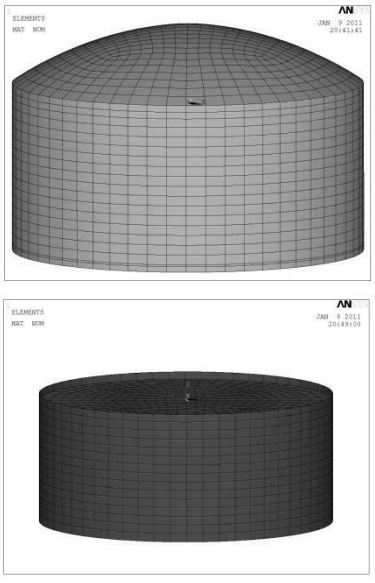
2.3 Behavior of Lead Rubber Bearing

Nonlinear inverse force of the lead rubber bearing can be modeled with the bilinear hysteretic model. Here the Bouc-Wen model is used to facilitate the calculation.

The Bouc-Wen model has been extensively used to describe nonlinear hysteretic behaviors, particularly, in seismic isolation devices (Wen 1976).

3. NUMERICAL MODELS OF THE LNG TANK

3.1 Dimensions of the LNG tank



(a)

(b)

Figure 3 Finite element model of LNG tank: (a) outer tank, and (b) inner tank

A steel inner tank with a radius r of 40m and total height of 35 m is fully anchored to a concrete slab. The tank is filled with liquid to a height H of 33 m. The density of LNG in the inner tank ρ_l is 480 kg/m^3. The tank wall is made of three courses, and 10 m, 10m and 15m high. The lower course is 25mm thick, the middle course is 18mm and the upper course is 12mm thick. For steel, $E_s = 2\times10^{11}$N/m^2, $\rho = 7.9\times10^3$ kg/m^3.

The height of the outer tank wall L is 40m, the medium radius of the outer tank D_c is 41.45 m, the thickness of the outer tank wall t_c is 0.9 m, the density of the wall concrete ρ_c is 2500 kg/m^3, the modulus of elasticity of the wall concrete E_c is 3×10^{10} Pa, the poison's ratio of the wall concrete υ_c is 0.3.

The parameters of LRBs selected in SC_3 and SC_4 are shown in Table 2.

Damping is defined through a Rayleigh global damping matrix. The damping ratio for the impulsive mode is typically considered to be 2% of critical for a steel tank responding in the linear elastic range. The damping ratio for the sloshing mode is assumed to be 0.5% of critical (Haroun and Housner 1981; Veletsos 1984) per industry practice.

Scheme 1 (SC-1) is the LNG storage tank without considering insulation, and Scheme 2 (SC-2) is the LNG storage tank with perlite insulation. Scheme 3 (SC-3) is the isolated LNG storage tank without considering insulation, and Scheme 4 (SC-4) is the isolated LNG storage tank with perlite insulation. There are 360 piles are arranged under LNG storage tank. The flat and elevation diagrams of tank with isolators are plotted in Figure 4 and 5.

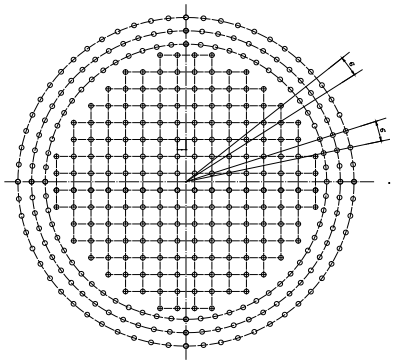


Figure 4 Flat diagram of tank with high piles

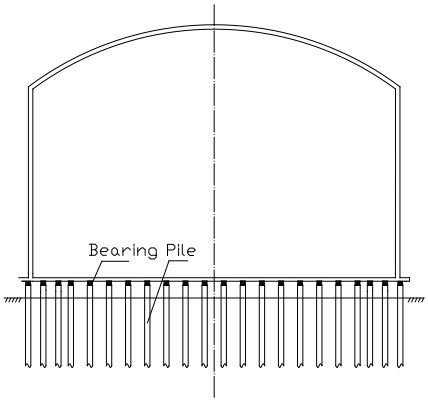


Figure 5 Profile diagram of tank with bearings

Table 2 Parameters of lead rubber bearings

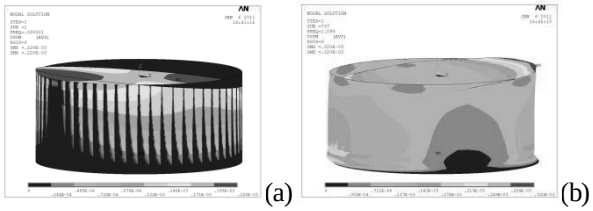
type	Design capacity	yield force	Pre-yield stiffness	Post-yield stiffness	Equivalent stiffness	number
	kN	kN	kN/mm	kN/mm	kN/mm	
LRB600	4000	96.1	4.64	0.58	1.62	240
LRB650	5000	79.2	5.28	0.66	1.53	120

Notes: LRB650s are mounted on top of the outer piles and LRB600s are mounted on top of inner piles.

Modal analysis was performed in ANSYS using reduced method. Table 3 summarizes the eigenvalues obtained from Housner method and FE model, and Figure 6 illustrates the convective and impulsive modes of FE model for the inner tank. The convective mode shapes involve sloshing of the contained liquid. The natural periods predicted by the simplified model are very close to those predicted by ANSYS.

Table 3 Modes information of the inner tank

Modes	Period[s]	
	simplified model	FE model
convective period	9.91	10.07
impulsive period	0.50	0.52



(a) (b)

Figure 6 Vibration Modes of LNG inner tank: (a) Convective Mode, and (b) Impulsive Mode

3.2 Seismic input

A LNG terminal project is located in the circum-Pacific seismic belt. The seismic acceleration of the operating basis earthquake (OBE) design is 0.16g and the seismic acceleration of the safe shutdown earthquake (SSE) is 0.30g. Artificial seismic waves are generated by design response spectrum which is suitable for the local field condition. Two of six simulated seismic waves are plotted in Figure 7 and 8 and design response spectrum curves are plotted in Figure 9 and 10. The parameters of seismic spectrum are shown in Eq. 10 and Table 4. Where β is spectral amplification factor, T is structural vibration period, γ is attenuation index, and $A_{\max}$ is acceleration amplitude.

$$\beta = \begin{cases} 1 & T \le 0.04s \\ 1+(\beta_{\max}-1)\dfrac{T-0.04}{T_1-0.04} & 0.04s < T \le T_1 \\ \beta_{\max} & T_1 < T \le T_2 \\ \beta_{\max}(T_2/T)^{\gamma} & T_2 < T \le 8.0s \end{cases} \quad (8)$$

Table 4 Parametric of seismic response spectra

Level	$A_{\max}$ [gal]	T_1 [s]	T_2 [s]	$\beta_{\max}$	γ
OBE	160	0.2	0.55	2.5	1.1
SSE	300	0.2	0.7	2.5	1.1

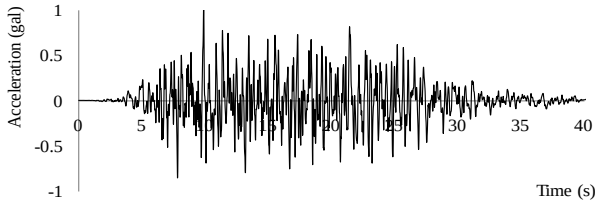


Figure 7 OBE1-XIN artificial time history curve

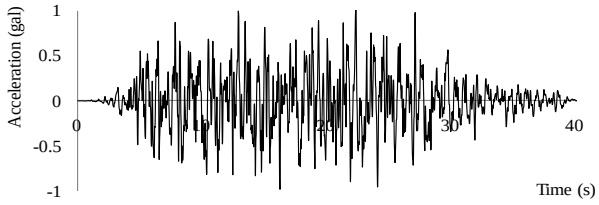


Figure 8 SSE1-XIN artificial time history curve

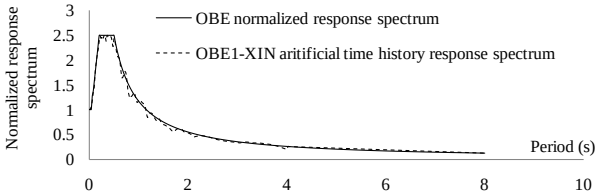


Figure 9 OBE1-XIN response spectrum curve

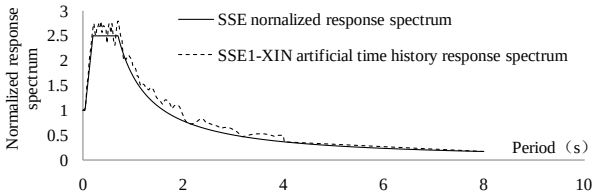


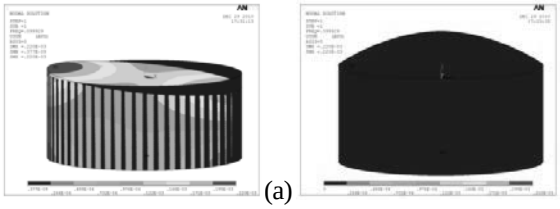
Figure 10 SSE1-XIN response spectrum curve

3.3 Modal analysis results

According to seismic design specification, LNG storage tank is analyzed by time history curves in the four schemes. The model information are listed in Table 5 and Figure 11 ～ 18.

Table 5 The modes information

Modes	Period[s]			
	SC-1	SC-2	SC-3	SC-4
convective period	10.01	9.99	10.15	10.14
coupled period	0.49	0.29	2.76	2.77



(a) (b)

Figure 11 Convective modes of LNG tank in SC_1: (a) inner tank, and (b) outer tank

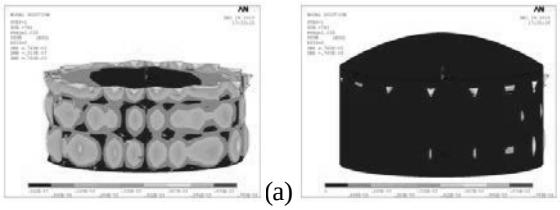


Figure 12 Impulsive modes of LNG tank in SC_1: (a) inner tank, and (b) outer tank

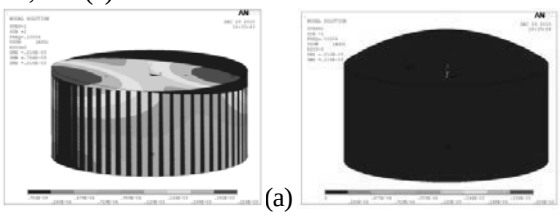


Figure 13 Convective modes of LNG tank in SC_2: (a) inner tank, and (b) outer tank

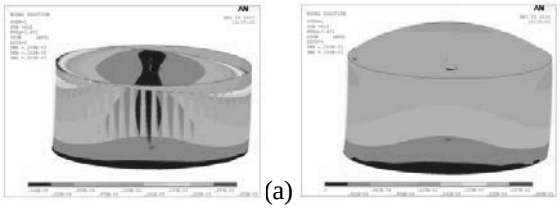


Figure 14 Impulsive modes of LNG tank in SC_2: (a) inner tank, and (b) outer tank

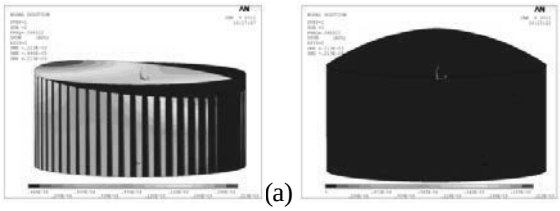


Figure 15 Convective modes of LNG tank in SC_3: (a) inner tank, and (b) outer tank

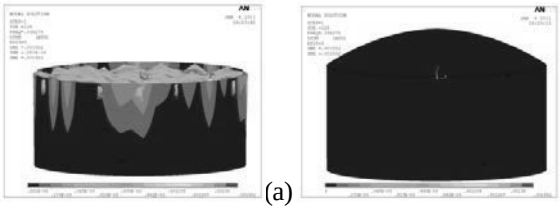


Figure 16 Impulsive modes of LNG tank in SC_3: (a) inner tank, and (b) outer tank

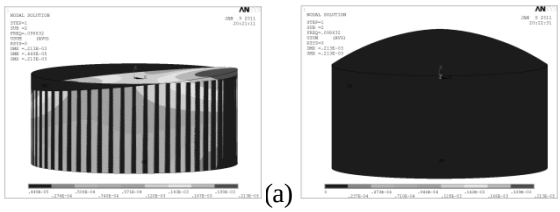


Figure 17 Convective modes of LNG tank in SC_4: (a) inner tank, and (b) outer tank

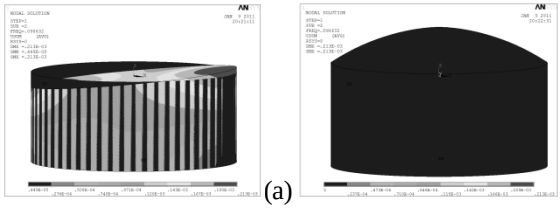


Figure 18 Impulsive modes of LNG tank in SC_4: (a) inner tank, and (b) outer tank

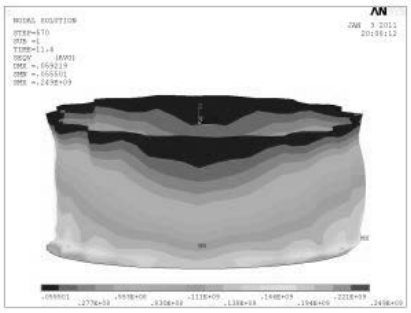
The maximum mean value of dynamic response is presented in Table 6 and 8. The differences between the mean values of maximum responses are listed in Table 7 and 9. And maximum Von Mises stresses are shown in Figure 19 and 20.

Table 6 Time history analysis results for SC-1 and SC-2

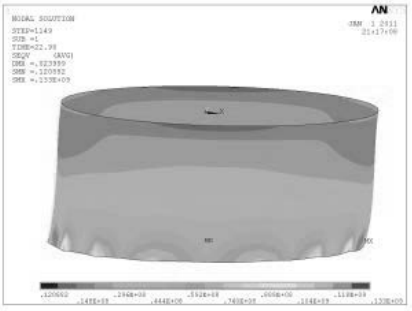
Case	Technique indicator	Units	SC-1	SC-2
OBE1	Single pile shear	[kN]	621	718
	Overturning moment	[kN-m]	7.78E+06	8.98E+06
	Von Mises stress	[Pa]	1.27E+08	5.08E+07
	Wave height	[mm]	237	237
OBE2	Single pile shear	[kN]	667	806
	Overturning moment	[kN-m]	8.35E+06	1.01E+07
	Von Mises stress	[Pa]	1.01E+08	5.67E+07
	Wave height	[mm]	223	213
OBE3	Single pile shear	[kN]	638	820
	Overturning moment	[kN-m]	7.99E+06	1.03E+07
	Von Mises stress	[Pa]	1.49E+08	5.39E+07
	Wave height	[mm]	305	275
SSE1	Single pile shear	[kN]	1503	1880
	Overturning moment	[kN-m]	1.88E+07	2.35E+07
	Von Mises stress	[Pa]	2.12E+08	1.33E+08
	Wave height	[mm]	397	385
SSE2	Single pile shear	[kN]	1408	1591
	Overturning moment	[kN-m]	1.76E+07	1.99E+07
	Von Mises stress	[Pa]	2.49E+08	1.05E+08
	Wave height	[mm]	846	780
SSE3	Single pile shear	[kN]	1354	1699
	Overturning moment	[kN-m]	1.69E+07	2.13E+07
	Von Mises stress	[Pa]	1.52E+08	1.16E+08
	Wave height	[mm]	1246	1206

Table 7 Mean values of dynamic analysis results for SC-1 and SC-2

Case	Technique indicator	Mean value			Difference (%)
		Units	SC-1	SC-2	
OBE	Single pile shear	[kN]	642	781	22%
	Overturning moment	[kN-m]	8.04E+06	9.79E+06	22%
	Von Mises stress	[Pa]	1.26E+08	5.38E+07	-57%
	Wave height	[mm]	255	242	-5%
SSE	Single pile shear	[kN]	1422	1723	21%
	Overturning moment	[kN-m]	1.78E+07	2.16E+07	21%
	Von Mises stress	[Pa]	2.04E+08	1.18E+08	-42%
	Wave height	[mm]	830	790	-5%

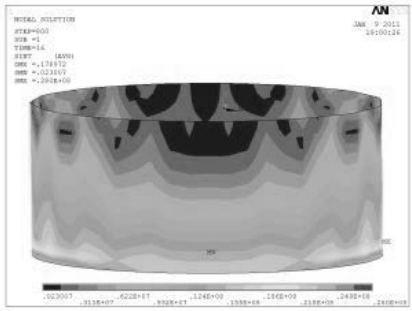


(a)

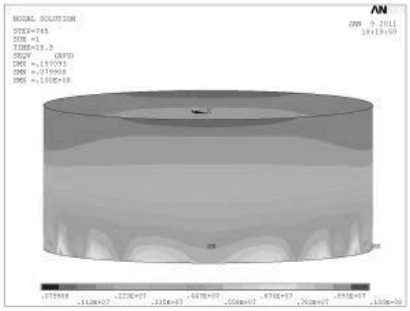


(b)

Figure 19 Von Mises stresses for steel shell walls at the time step of maximum base shear under SSE: (a) SC-1), (b) SC-2



(a)



(b)

Figure 20 Von Mises stresses for steel shell walls at the time step of maximum base shear under SSE: (a) SC-3, (b) SC-4

Table 8 Time history analysis results for SC-3 and SC-4

Case	Technique indicator	Units	SC-3	SC-4
OBE1	Single Pile shear	[kN]	131	132
	Overturning moment	[kN-m]	1.64E+06	1.65E+06
	Von Mises stress	[Pa]	1.91E+07	6.40E+06
	Wave height	[mm]	267	266
OBE2	Single pile shear	[kN]	134	135
	Overturning moment	[kN-m]	1.68E+06	1.68E+06
	Von Mises stress	[Pa]	1.83E+07	5.58E+06
	Wave height	[mm]	303	296
OBE3	Single pile shear	[kN]	123	123
	Overturning moment	[kN-m]	1.54E+06	1.54E+06
	Von Mises stress	[Pa]	1.65E+07	6.18E+06
	Wave height	[mm]	328	326
SSE1	Single pile shear	[kN]	212	211
	Overturning moment	[kN-m]	2.65E+06	2.64E+06
	Von Mises stress	[Pa]	2.64E+07	1.00E+07
	Wave height	[mm]	478	483
SSE2	Single pile shear	[kN]	216	221
	Overturning moment	[kN-m]	2.70E+06	2.76E+06
	Von Mises stress	[Pa]	2.52E+07	9.86E+06
	Wave height	[mm]	821	821
SSE3	Single pile shear	[kN]	196	198
	Overturning moment	[kN-m]	2.45E+06	2.48E+06
	Von Mises stress	[Pa]	2.80E+07	9.40E+06
	Wave height	[mm]	1243	1247

Table 9 Mean values of dynamic analysis results for SC-3 and SC-4

Case	Technique indicator	Mean value			Difference (%)
		Units	SC-3	SC-4	
OBE	Single pile shear	[kN]	129	130	1%
	Overturning moment	[kN-m]	1.62E+06	1.62E+06	0%
	Von Mises stresses	[Pa]	1.80E+07	6.05E+06	-66%
	Wave height	[mm]	299	296	-1%
SSE	Single pile shear	[kN]	208	210	1%
	Overturning moment	[kN-m]	2.60E+06	2.63E+06	1%
	Von Mises stress	[Pa]	2.65E+07	9.75E+06	-63%
	Wave height	[mm]	847	850	0%

The comparison of the indicators above Table 6 ～ 9 are represented in the bar charts (see Figure 21～24)

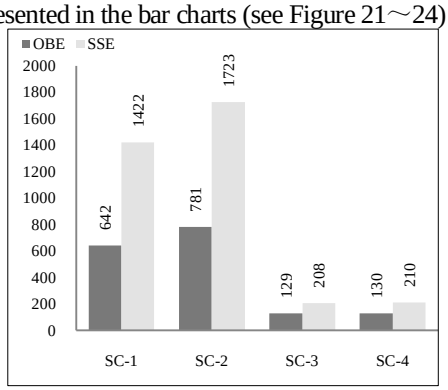


Figure 21 Single pile shear

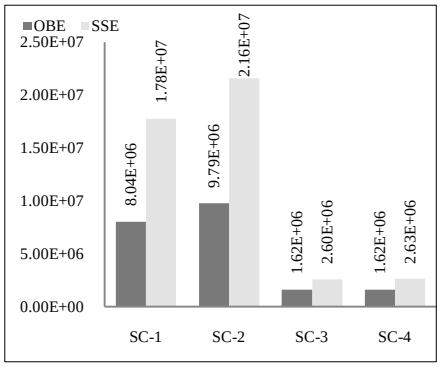


Figure 22 Overturning moment

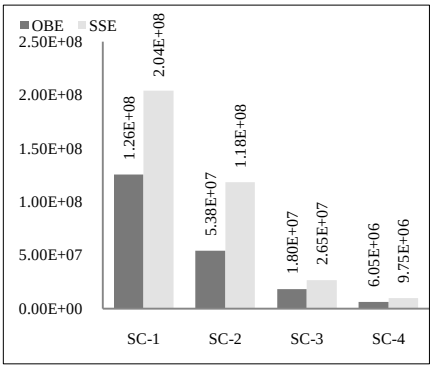


Figure 23 Von Mises stress

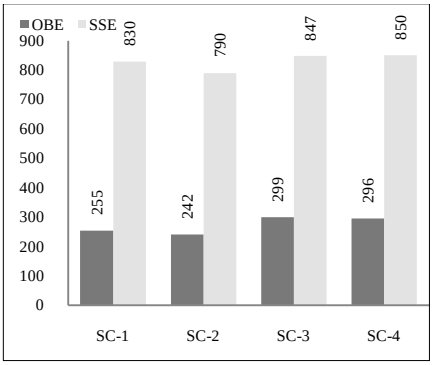


Figure 24 Wave height

The maximum responses of the numerical models for the 6 earthquake ground motions, scaled for both OBE and SSE shaking. Since the models are elastic, the SSE responses are about twice the OBE responses.

Contrast to the SC_1 and SC_2, indicators such as the shearing force of single pile and overturning moment are increased by SC-2 by considering the insulation. However, Von Mises stress and wave height is decreased by SC-2, especially Von Mises stress.

For the isolated LNG tank, the influence of insulation layer is limited except Von Mises stresses in the SC-3 and SC-4, but the seismic performance of the LNG tank is improved by seismic-isolated scheme.

4. CONCLUSIONS

A study has been made of the dynamic response of the LNG tank using four different schemes, when subjected to lateral seismic motion. A common insulating material of LNG tank is used to evaluate influence of dynamic interaction. Four schemes of LNG tank are anchorage tank without insulation layer (SC_1), with insulation layer (SC_2), and isolated tank without insulations (SC-3), with insulations (SC-4). Some key indicators are used to judge mitigation effect of different solutions. The following conclusions can be drawn from this study.

1. For four different schemes, it can be found that the maximum response of the tank always happen in the anchorage LNG tank.

2. Compare to SC_1, Von Mises stress of SC_2 can be decreased obviously. But some indicators such as the single pile shear and overturning moment are increased by SC-2, which means the shear and moment of the tank may be underestimated if not considering insulation layer for the anchorage tank.

3. Because isolators are mounted on the top of the high piles in the SC-3 and SC-4, the influence of insulation layer to the structural is limited except the Von Mises stress. So it is feasible for the design of the isolated LNG tank neglecting the insulation layer, which is conventional method.

Acknowledgements:

This work is supported by Foundation of State Key Laboratory for Disaster Reduction of China in Civil Engineering under Grant No. SLDRCE10-D-01. The authors acknowledge also support from the Urban Earthquake Engineering (CUEE) in Tokyo Institute of Technology for the conference.

References:

Abali, E., and Uckan, E. (2009). "Parametric analysis of liquid storage tanks base isolated by curved surface sliding bearings." *Soil Dynamics and Earthquake Engineering*, 30(1-2), 21-31.

Bachmann, H., and Wenk, T. (2000). "Softening instead of strengthening for seismic rehabilitation." *International Structural Engineering*, 10(1), 61-65.

Boduroğlu, M. H., Timur, T., and Timur, S. Ç. (2006). "Evaluation of seismic safety of liquid storage tanks and application of base isolation system." *İÇTAG – I587/MAK(102I054)*, OCAK, İstanbul.

Chalhoub, M. S., and Kelly, J. M. (1990). "Shake table test of cylindrical water tanks in base-isolated structures." *Journal of Engineering Mechanics*, 116(7), 1451-1472.

Christovasilis, I. P., and Whittaker, A. S. (2008). "Seismic analysis of conventional and isolated LNG tanks using mechanical analogs." *Earthquake Spectra*, 24(3), 599-616.

Haroun, M. A. (1980). "Dynamic analyses of liquid storage tanks." *EERL 80-04*, California Institute of Technology, Pasadena, California.

Haroun, M. A., and Housner, G. W. (1981). "Dynamic interaction of liquid storage tanks and foundation soil." Proceedings of 2nd ASCE Engineering Mechanical Specialty Conf. on the Dynamic Response of Structures, New York, 346-360.

Haroun, M. A., and Housner, G. W. (1983). "Vibration studies and tests of liquid storage tanks." *Earthquake Engineering and Structural Dynamics*, 11(2), 179-206.

Housner, G. W. (1957). "Dynamic pressure on accelerated fluid containers. Bulletin Seism." *Soc. America*, 47(1), 15-35.

Kim, M. K., Lim, Y. M., Cho, S. Y., Cho, K. H., and Lee, K. W. (2002). "Seismic analysis of base-isolated liquid storage tanks using the BE-FE-BE coupling technique." *Soil Dynamics and Earthquake Engineering*, 22(9-12), 1151-1158.

Malhotra, P. K., Wenk, T., and Wieland, M. (2000). "Simple procedure for seismic analysis of liquid-storage tanks." *Structural Engineering International*, 10(3), 197-201.

Shrimali, M. K., and Jangid, R. S. (2002). "Non-linear seismic response of base-isolated liquid storage tanks to bi-directional excitation." *Nuclear Engineering and Design*, 217(1-2), 1-20.

Tsopelas, P., Constantinou, M. C., and Reinhorn, A. M. (1994). "3D-BASIS-ME: Computer program for nonlinear dynamic analysis of seismically isolated single and multiple structures

and liquid storage tanks." *NCEER 94-0010*, National Center for Earthquake Engineering Research, State Univ. of New York, Buffalo, NY.

Veletsos, A. S. (1974). "Seismic effects in flexible liquid storage tanks." Proceedings of the 5th World Conference on Earthquake Engineering, Rome, Italy, 255-370, 442-461.

Veletsos, A. S. (1984). "Seismic response and design of liquid storage tanks." *Guidelines for the Seismic Design of Oil and Gas Pipeline Systems*, 255-370.

Veletsos, A. S., and Yang, J. Y. (1976). "Dynamics of fixed base liquid storage tanks." Proceedings of U.S.-Japan seminar on earthquake engineering research with emphasis on lifeline systems, Japan society for promotion of earthquake engineering, Tokyo, Japan, 317-341.

Wen, Y. (1976). "Method for random vibration of hysteretic systems." *Journal of the Engineering Mechanics Division*, 102(2), 249-263.

Zhang, R. F., Weng, D. G., and Ni, W. B. (2010). "Application of annular damper reaction wall in seismic isolated LNG tank." Proceedings of the ASME 2010 Pressure Vessels & Piping Division / K-PVP Conference, Bellevue, Washington, USA.

8CUEE CONFERENCE PROCEEDINGS
8th International Conference on Urban Earthquake Engineering
March 7-8, 2011, Tokyo Institute of Technology, Tokyo, Japan

BEHAVIOR OF FRP-CONFINED CAPSULE-SHAPED RC COLUMNS UNDER LATERAL LOADING

Kiang Hwee Tan[1], Tamali Bhowmik[2], and T. Balendra[3]

1) Professor, Department of Civil & Environmental Engineering, National University of Singapore, Singapore
2) PhD Candidate, Dept. of Civil & Environmental Engineering, National University of Singapore, Singapore
3) Professor, Department of Civil & Environmental Engineering, National University of Singapore, Singapore
cvetankh@nus.edu.sg, g0600987@nus.edu.sg, cvebalen@nus.edu.sg

Abstract: The use of externally bonded carbon fiber-reinforced polymer (FRP) systems in enhancing the behavior of gravity-load-designed building columns under lateral loading that may result from seismic actions was investigated in this study. The columns had a rectangular cross section with a high aspect ratio of 3.65. To improve the effectiveness of the FRP systems, the columns were enlarged at the short ends by circular segments, forming capsule-shaped sections, before they were bonded with FRP sheets. Seven half-scale column specimens, with concrete strength of 30 MPa, longitudinal steel ratio of 2%, and normal transverse steel reinforcement, were subjected to a constant axial load, and tested to failure under lateral loading. Test results indicated that the lateral load-carrying capacity increased with the provision of the circular segments, while the ductility of the columns increased with the number of ply of transverse FRP sheets in particular. The mode of failure changed from shear-compression to flexure with FRP rupture with the section enlargement and bonded FRP system. The test results are compared with analytical predictions based on conventional flexural and shear theories, which in turn could be compared with seismic demand capacity to determine the survivability of the columns under seismic actions.

1. INTRODUCTION

Inadequate lateral reinforcement and improper splicing of longitudinal reinforcement in the plastic hinge zone of columns have been featured as some of the main causes of building collapse during recent earthquakes. To enhance the axial load and shear capacities, as well as to increase the ductility and energy dissipation capacities, reinforced concrete columns could be confined using transverse fiber-reinforced polymer (FRP) systems. Recent studies have indicated that FRP confined square or rectangular columns with a cross-sectional aspect ratio of up to 1.5 exhibited significantly improved performance under cyclic or pushover loading.

In reality, many building columns are rectangular in shape with an aspect ratio of more than 1.5, and as large as 7, which may well be termed "wall-like" columns. The confinement effect of transverse FRP reinforcement on such rectangular columns is known to be insignificant. To increase the confinement effect, it is proposed that the short ends of the rectangular section be rounded off by adding circular concrete segments and thus forming a capsule-shaped section before applying the transverse FRP reinforcement.

The present study was therefore carried out to examine the behavior of FRP-confined capsule-shaped reinforced concrete columns under lateral push-over loading, with focus on the effect of section geometry and the number of ply of transverse FRP sheets.

2. TEST PROGRAM

A total of seven half-scale column specimens were prepared and tested to failure under a constant axial load and a monotonically increasing lateral load.

2.1 Specimen details

The columns were designated as "L-*x*-*y*" where 'L' stands for laterally loaded specimens; '*x*' denotes the shape parameter, $\Delta h/b$, where Δh is the ratio of thickness of the cap at the two short sides and b is the width of column as shown in Figure 1; and '*y*' represents the number of ply of transverse carbon FRP (CFRP) sheets.

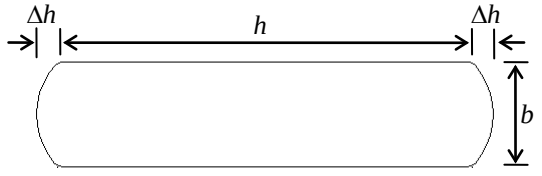


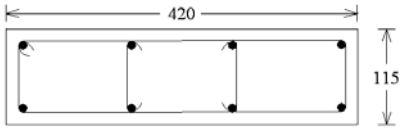
Figure 1 Capsule-shaped column

The seven columns were classified into three groups. Group A consisted of one specimen which had a

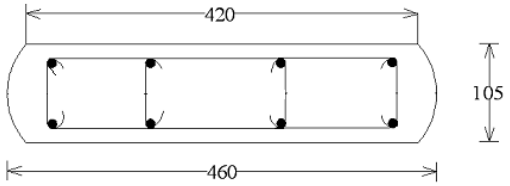
rectangular cross-section measuring 115 mm by 420 mm, with an aspect ratio of 3.65. Group B comprised three capsule-shaped columns with an overall dimension of 105 mm by 460 mm; while Group C included three other capsule-shaped columns with an overall dimension of 105 mm by 525 mm, as shown in Figure 2.

The height of the column specimens corresponded to the distance from the section of maximum moment to the point of contraflexure under lateral loading, and was taken as 940 mm.

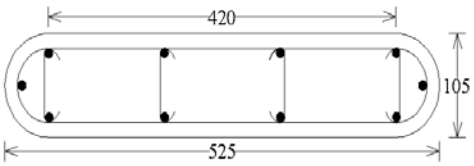
For FRP-confined columns, the first ply was applied over the full height whereas the second ply was applied over the lower half of the column.



Group 'A' Column (L-0-1)
Area, A_g = 48,300 mm^2
Long. steel area = 1062 mm^2 (= 2.2%A_g)



Group 'B' Columns (L-0.19-0, 1, 2)
Area, A_g = 46,989 mm^2
Long. steel area = 1062 mm^2 (= 2.26%A_g)



Group 'C' Columns (L-0.5-0, 1, 2)
Area, A_g = 52,759 mm^2
Long. steel area = 1327 mm^2 (= 2.5%A_g)

Figure 2 Details of specimens (*all dimensions in mm.*)

2.2 Concrete

Ordinary Portland cement, natural sand (fine aggregate), crushed granite of 10-mm maximum size (coarse aggregate) and water were used in the proportion of 1 : 3.08 : 3.14 : 0.79 by weight for the concrete mix. The target cube compressive strength at 28 days was 30 MPa.

2.3 Internal steel reinforcement

The reinforcing cages were made using three types of reinforcing steel. Longitudinal reinforcement consisted of eight 13-mm diameter deformed bars in Group A and B columns, and ten 13-mm diameter deformed bars in Group B columns. The longitudinal steel ratio was thus maintained at between 2.2 to 2.5%.

The transverse steel reinforcement consisted of rectangular or capsule-shaped closed links and ties as shown in Figure 2. They were made of 6-mm diameter mild steel bars and spaced at 100 mm spacing in the longitudinal direction, which corresponded to nominal transverse reinforcement in gravity-load-designed building columns.

The average yield strength of 13-mm diameter high-yield deformed bars and 6-mm mild steel round bars was 460 MPa and 300 MPa respectively.

2.4 FRP system

Carbon FRP (CFRP) sheets were used. The primary properties as provided by the manufacturer are shown in the Table 1. A three-part resin was used to bond the FRP sheets on to the specimens and the mix proportion of the resin is shown in Table 2.

Table 1 Properties of Carbon FRP Sheet

Design Thickness (per ply)	0.176 mm
Fibre weight	300 g/m^2
Elastic modulus	240 kN/mm^2
Tensile strength	3800 N/mm^2
Elongation at rupture (%)	1.55

Table 2 Mix proportion of resin

Components	Weight (per m^2 of CFRP sheet)
Main	600g/m^2
Hardener	300g/m^2
Powder	600g/m^2

2.5 Fabrication of specimens and test set-up

The reinforcement cage for the column and the column base, which measured 350 mm by 1000 mm on plan and 300 mm in thickness, was assembled and placed in the formwork. Holes were provided through the thickness of the base to facilitate the anchoring of specimen to the strong floor using long anchor bolts. The specimen was cast and formwork was removed after one day. The specimens were then cured by covering with damp gunny sacks for a week. They were then left in the laboratory under ambient conditions. Accompanying cubes for the determination of concrete compressive strength were cast and cured in the same manner.

About three weeks after casting, all specimens

except L-0.19-0 and L-0.5-0 were bonded with carbon FRP systems. A week after this, the specimens were placed and anchored to the workshop floor via a strong beam as shown in Figure 3.

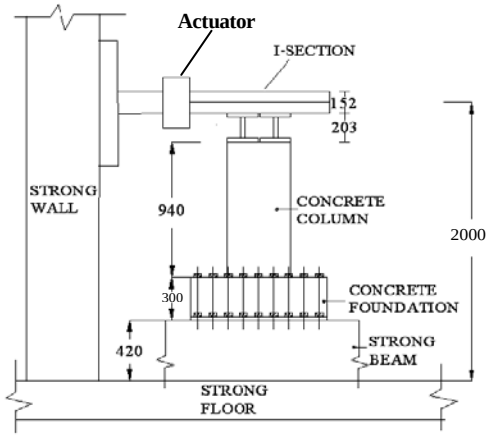


Figure 3 Test set-up

Two cross-beams were placed on top of the column specimen, which was then loaded axially using prestressing strands placed through and anchored on the cross-beams at the top and the strong beam at the bottom, to simulate the axial force from the upper stories. A total of eight seven-wire strands were used. Each strand had a diameter of 12.9 mm, nominal cross-sectional area of 100 mm^2, breaking load of 130 kN and Young's modulus of 195 GPa. For all columns, the axial load ratio ($N_u / f'_c A_g$) was 0.3.

Another I-beam was bolted to the cross-beams, and a 65-ton capacity actuator fixed on a strong wall was used to apply the lateral load on the beam assembly on top of the specimen.

2.6 Test procedure

The columns were subjected to monotonically increasing lateral pushover load after applying the axial load. The strains in the strands were monitored to ensure no significant drop in preload. The specimens were also instrumented for lateral deflection measurements at the top end, and strain development in the transverse and longitudinal steel reinforcement as well as in the externally bonded CFRP system.

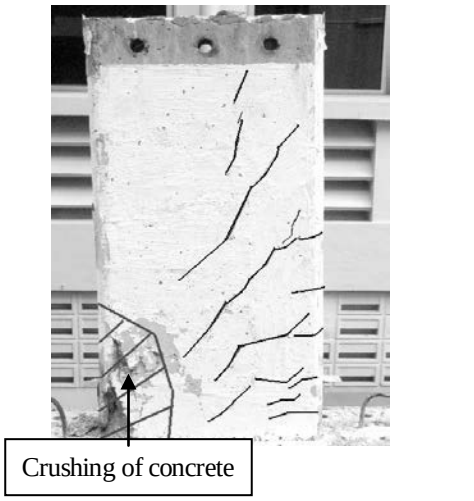
The lateral load was applied using displacement control method. The initial rate of loading was 0.15 mm/min. After first yielding of the internal longitudinal steel, the loading rate was increased to 0.3mm/min and kept constant up to the failure of column.

3 TEST RESULTS

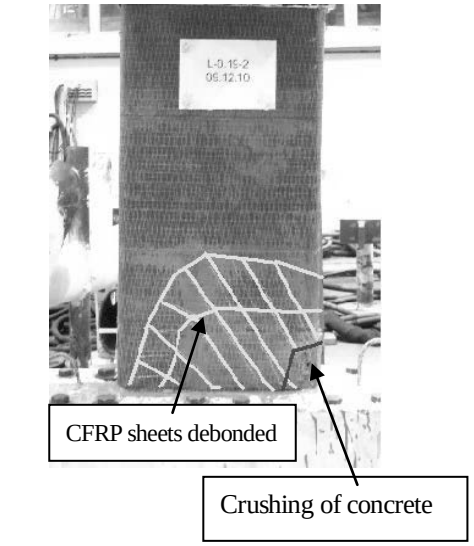
3.1 Behavior and mode of failure

In unconfined specimens L-0.19-0 and L-0.5-0, fine cracks were observed near the base (foundation) on the tensile side of the column at a load of 40 to 50 kN. The first horizontal flexural cracks were observed to propagate from the tension side of the column at a height of 150 mm from the base at 70 kN and 80 kN for L-0.19-0 and L-0.5-0 respectively; and successive flexural cracks were formed at intervals of about 150 mm up to a height of 600 mm.

Inclined shear cracks started to form in the columns near the top of the column at 90 to 100 kN. The number and widths of inclined cracks increased gradually and the cracks propagated in a converging manner towards the compression face of column at the base as shown in Figure 4(a). The outermost longitudinal steel bars first yielded in tension at a load of 97 kN and 116 kN, respectively, for L-0.19-0 and L-0.5-0.



(a) Unconfined column



(b) Confined column

Figure 4 Typical failure patterns

Final failure occurred in unconfined columns due to concrete crushing on the compression side. The load at which the load started to drop and concrete crushed simultaneously was taken as the ultimate lateral load. The corresponding displacement was noted as the ultimate

displacement. The test results are shown in Tables 3 and 4.

Cracks could not be observed in the case of confined columns due to the presence of FRP system. However, a change in color in the FRP system was observed within the plastic hinge zone, which indicated the separation of fiber sheets from the concrete surface as crushing of concrete started. This was confirmed by tapping on the FRP systems using a metal rod or a coin.

Near the failure load, sounds of breaking of the hardened epoxy within the plastic hinge zone were increasingly heard, and final failure occurred with the rupture of CFRP sheets and crushing of concrete at the compression face of column near the base as shown in Figure 4(b).

Table 3 Ultimate lateral load

Speci-men	f'_{co} (MPa)	$P_{u\text{-}pred}$ (kN)		$P_{u,test}$ (kN)	$\frac{P_{u,test}}{P_{u,pred}}$*
		$P_{u,sh}$	$P_{u,fl}$		
L-0-1	24.2	254	96	116	1.21
L-0.19-0	25.2	108	100	122	1.22
L-0.19-1	25.6	263	121	142	1.16
L-0.19-2	24.6	418	133	147	1.10
L-0.5-0	26.6	129	136	142	1.04
L-0.5-1	23.9	306	156	178	1.14
L-0.5-2	27.2	484	180	203	1.12

Note: f'_{co} = cylinder strength; $P_{u,pred}$ * = Predicted ultimate lateral load = smaller of ($P_{u,sh}$, $P_{u,fl}$) ; $P_{u,sh}$= Predicted ultimate lateral load based on shear capacity; $P_{u,fl}$ = Predicted ult. lateral load based on flexural capacity; $P_{u,test}$ = Maximum observed lateral load.

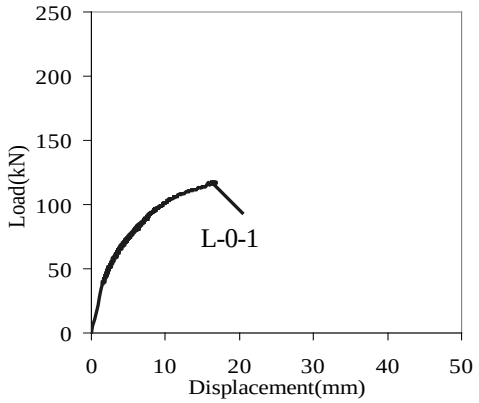
Table 4 Displacement ductility and drift ratio

Specimen	Δ_y (mm)	Δ_u (mm)	μ_Δ	Δ_u / L (%)
L-0-1	5.9	16.0	2.7	1.7
L-0.19-0	9.1	20.3	2.2	2.1
L-0.19-1	8.2	26.9	3.3	2.9
L-0.19-2	7.6	42.3	5.6	4.5
L-0.5-0	6.4	14.0	2.2	1.5
L-0.5-1	6.3	22.1	2.9	2.3
L-0.5-2	6.3	31.7	4.9	3.4

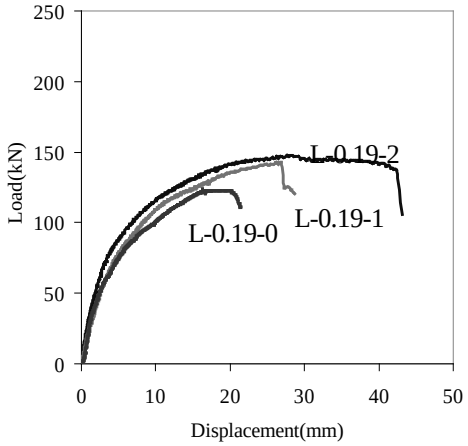
Note: Δ_y = Yield displacement; Δ_u = Maximum lateral displacement; μ_Δ = Displacement ductility factor; L = Height of column; Δ_u / L = Drift ratio.

3.2 Load-displacement response

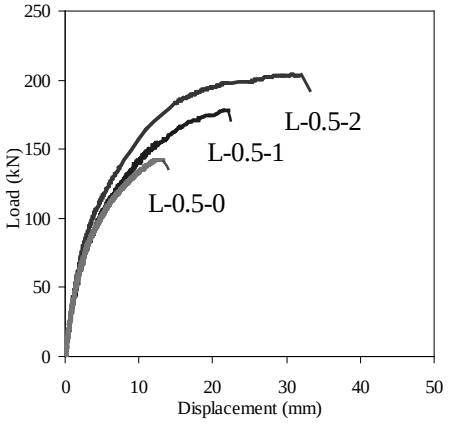
Figure 5 shows the load vs. lateral displacement characteristics of all specimens. For Group A column, the yield and maximum lateral displacement were observed as 5.9 mm (at 80 kN) and 16 mm (at 116 kN). The displacement ductility, defined as the ratio of maximum lateral displacement to the yield displacement, was thus 2.7.



(a) Group A specimen



(b) Group B specimens



(c) Group C specimens

Figure 5 Load-displacement characteristics

For Group B specimens, the yield loads were 97 kN, 100 kN and 104 kN for columns L-0.19-0, L-0.19-1 and

L-0.19-2, and the corresponding displacements were 9.1 mm, 8.2 mm and 7.6 mm respectively. The ultimate lateral displacements at which the load began to drop significantly were 20.3 mm (at 122 kN), 26.9 mm (at 142 kN) and 42.3 mm (at 137 kN), respectively.

The displacement ductility was calculated as 2.2, 3.3 and 5.6 for L-0.19-0, L-0.19-1 and L-0.19-2 respectively which showed that the ductility was increased by 50% and 154% with 1 ply and 2 plies of transverse CFRP sheets. Also, it may be noted that the lateral load capacities of L-0.19-1 and L-0.19-2 were 16% and 20% higher than L-0.19-0.

The yield displacements of L-0.5-0, L-0.5-1 and L-0.5-2 (Group C specimens) were 6.4 mm (at 116 kN), 6.3 mm (at 122 kN) and 6.3 mm (at 125 kN) respectively. The ultimate lateral displacement were on the other hand 14.0 mm (at 142 kN), 22.1 mm (at 178 kN) and 31.7 mm (at 203 kN) respectively. Thus, the displacement ductility was calculated as 2.2, 2.9 and 4.9 for L-0.5-0, L-0.5-1 and L-0.5-2 respectively. The lateral load capacity of L-0.5-1 and L-0.5-2 was 25% and 43% higher than L-0.5-0.

To evaluate the effect of effect of section geometry, the load-displacement characteristics of L-0-1, L-0.19-1 and L-0.5-1 are compared in Figure 6. Both the ultimate lateral load capacity and the ultimate lateral displacement increased with the shape factor $\Delta h/b$. The ultimate lateral load increased from 116 kN to 142 kN and 178 kN as the shape factor increased from zero to 0.19 and 5 respectively, as shown in Table 3. This was partly due to the enlarged concrete areas which led to an increase in shear and flexural resistance.

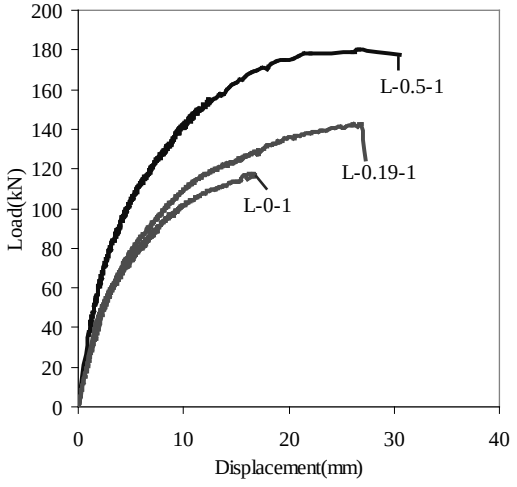


Figure 6 Effect of section geometry

On the other hand, however, the displacement ductility increased from 2.7 to 3.3 and 2.9 respectively as the shape factor increased from zero to 0.19 and 0.5 respectively. Similarly, the drift ratio increased from 1.7 to 2.9 and 2.3 percent respectively. It therefore appeared that Group B specimens with a shape factor of 0.19 were more efficient in terms of ductility.

4. THEORETICAL PREDICTIONS

The ultimate lateral load capacity was determined as the smaller of the lateral load that would result in shear or flexural failure of the column.

4.1 Shear Capacity

The theoretical calculation of shear capacity of FRP confined columns is based on the consideration that there should not be large dilation strains in loading direction; because a large dilation strain implies the degradation of aggregate interlock action which is the most essential component to protect the column in case of unexpected overload during earthquake. Hence, the maximum permissible dilation strain has been proposed as 0.004 by Seible et al. (1997).

The shear capacity of confined columns (V_{shear}) in this study was therefore calculated using the following equation as proposed in the work by Seible et al. (1997):

$$V_{shear} = V_c + V_s + V_{CFRP} = \left(1 + \frac{N_u}{14A_g}\right)\frac{\sqrt{f'_c}}{6} b_w d + \frac{A_v f_{yv} d}{s} + 2t_{CFRP} D\left(0.004 E_{CFRP}\right) \quad (1)$$

where V_c, V_s and V_{CFRP} = contribution to shear capacity from concrete, transverse steel stirrups and CFRP sheets, respectively; N_u, A_g, f'_c, b_w, d are the applied axial load, gross cross-sectional area of column, unconfined cylinder compressive strength of concrete, and width and effective depth of column respectively; A_v, f_{yv} and s are the cross-sectional area, yield strength and spacing of stirrup respectively; t_{CFRP}, E_{CFRP} and D = thickness of CFRP sheets, modulus of CFRP, and column dimension in the loading direction, respectively. For capsule- shaped columns, the term $b_w d$ was taken as equal to the area up to the outermost tensile longitudinal steel bar.

The predicted shear capacities of the test columns are given in Table 3. It can be seen that the CFRP sheets led to significant increase in the shear capacity of rectangular and capsule-shaped columns.

4.2 Flexural Capacity

The externally bonded transverse CFRP sheets confine the plastic hinge region of columns by restraining the lateral expansion of the concrete, thereby retaining the integrity of the core concrete and facilitating higher compressive stresses and strains to be sustained by the compression zone of column section before rupture of CFRP sheets occurs. By equating the strain energy capacity of the transversely wrapped CFRP systems as it is strained to peak stress to the increase in energy absorbed by concrete resulting from confinement, the ultimate confined compressive strain was determined by Priestley et al. (1996) as

$$\varepsilon_{cu} = 0.004 + 2.5\frac{\rho_{CFRP} f_{uj} \varepsilon_{uj}}{f'_{cc}} \quad (2)$$

where ε_{uj} is the hoop strain of FRP at failure, ρ_{CFRP} is the volumetric ratio of confining CFRP systems, f_{uj} is the tensile strength of CFRP systems and f'_{cc} is the confined compressive strength of concrete.

Initially, Equation (2) was proposed for circular columns only. For rectangular columns with a cross-section aspect ratio of 1.5, an effectiveness factor of 0.5 was proposed based on test results by Priestley et al. (1996).

In the present study, Equation (3) was used with the effective hoop strain ε_{uj} equal to 0.004, which correspond to 0.26 times the rupture strain of the CFRP system (ε_{fu}) which is 0.004. Thus, the modified ultimate confined compressive strain is given by

$$\varepsilon_{cu} = 0.004\left[1 + 2.5\frac{\rho_{CFRP} f_{uj}}{f'_{cc}}\right] \quad (3)$$

The maximum flexural capacity of capsule-shaped column was calculated by section analysis using Equation (3) and the following stress-strain model for FRP-confined concrete (ACI 440 2008):

$$f_c = E_c\varepsilon_c - \frac{(E_c - E_2)^2}{4f'_{co}}\varepsilon_c^2 \quad (\text{for } 0 \le \varepsilon_c \le \varepsilon'_t) \quad (4)$$

$$f_c = f'_{co} + E_2\varepsilon_c \quad (\text{for } \varepsilon'_t \le \varepsilon_c \le \varepsilon_{cu}) \quad (5)$$

$$E_2 = \frac{f'_{cc} - f'_{co}}{\varepsilon_{cu}} \quad (6)$$

$$\varepsilon'_t = \frac{2f'_{co}}{E_c - E_2} \quad (7)$$

where f_c and ε_c are the stress and strain, respectively; E_c is the elastic modulus of concrete; f'_{cc} and f'_{co} are the confined and unconfined concrete strength respectively.

Also, the confined concrete strength f'_{cc} was obtained from:

$$\frac{f'_{cc}}{f'_{co}} = 1 + k_1\varepsilon_{fe}\frac{f^*_l}{f'_{co}} \quad (8)$$

$$f^*_l = k_e\left(\frac{b+h}{bh}\right)E_{FRP}t_j \quad (9)$$

in which the value of $k_1\varepsilon_{fe}$ was taken as 0.0379 and k_e assumed to be equal to 0.7, based on a separate study on the confinement effectiveness of CFRP systems in capsule-shaped columns.

The predicted lateral load capacity based on the flexural moment capacity of the critical base section for the test columns in this study is given in Table 3. A nominal increase in the ultimate load capacity is noted.

4.3 Comparison with test results

The predicted ultimate lateral load capacity of the columns and failure mode corresponded to that which gave the lower ultimate load. Table 3 shows that all specimens except L-0.5-0 would fail in flexure while L-0.5-0 would fail in shear. This is in agreement with experimental observation except for L-0.19-0 which failed in shear-compression instead of flexure. This was because the predicted values were close to each other for L-0.19-0. The observed ultimate load capacities were between 4 and 22% higher than the predicted values.

5. CONCLUSION

The behavior of axially loaded FRP-confined capsule-shaped RC columns under lateral pushover loading was investigated. Test results indicated that the lateral load-carrying capacity of rectangular columns increased with the enlargement of the sections at the short ends using circular segments. The ultimate lateral displacement of such capsule-shaped columns increased with the application of transverse carbon FRP sheets. The displacement ductility and drift ratio was found to be largest in columns with an intermediate shape parameter value of 0.19.

Also, an analytical model to predict the lateral load-carrying capacity based on shear and flexural capacities was proposed and found to agree with the observed test results reasonably well.

Acknowledgements:

The authors thank the S & P Clever Reinforcement Company for supplying the CFRP system for the study.

References:

ACI Committee 440 (2008) "Guide for the Design and Construction of Externally Bonded FRP Systems for Strengthening Concrete Structures", ACI 440.2R-08, American Concrete Institute, Detroit.

Priestly, M. J. N., Seible, F., and Calvi, G. M. (1996), "Seismic Design and Retrofit of Bridges", Wiley, New York.

Seible F. et al. (1997), "Seismic Retrofit of RC columns with Continuous Carbon Fiber Jackets", *J. of Composites for Construction*, **1**(2), 52-62.

8CUEE CONFERENCE PROCEEDINGS
8th International Conference on Urban Earthquake Engineering
March 7-8, 2011, Tokyo Institute of Technology, Tokyo, Japan

SEISMIC PERFORMANCE OF A COUPLED WALL WITH HIGH PERFORMANCE FIBER REINFORCED CONCRETE

Chung-Chan Hung

Assistant Professor, Dept. of Civil Engineering, National Central University, Taiwan
cchung@ncu.edu.tw

Abstract: High performance fiber reinforced concrete (HPFRC) possesses a unique strain hardening behavior in tension that translates into enhanced shear and bending behavior at the structural level. This paper investigates the seismic performance of an 18-story coupled wall system in which HPFRC is used to replace the traditional reinforced concrete (RC) in coupling beams and the plastic hinge regions in shear walls. System performance is evaluated using various parameters, such as deflection curves, inter-story drifts, maximum response, and shear deformation. The effectiveness of using HPFRC in the coupled wall system to enhance the seismic performance of the system is discussed in light of the results from nonlinear dynamic analysis.

1. INTRODUCTION

High performance fiber reinforced concrete (HPFRC) is a class of materials that have properties that are attractive to structural engineers. These materials are characterized by pseudo-ductile tensile strain hardening behavior after first cracking accompanied by multiple cracks and large energy absorption prior to crack localization (Hung and El-Tawil 2010; Li 2003; Naaman 2006). HPFRC has the potential to serve as highly damage tolerant and energy absorbing materials under severe loading conditions, especially seismic loading. This paper numerically studies and compares the performance of a traditional 18-story RC coupled wall system with another similar system in which the coupling beams and plastic hinge regions are HPFRC instead of RC.

2. SYSTEM DESIGN

The theme system considered herein consists of a 94 ft (28.7 m) by 78.5 ft (23.9 m) (in plan) steel moment resisting frame surrounding a 47 ft (14.3 m) by 31.5 ft (9.6 m) (in plan) core wall system. The plan view of the prototype structure is given in Figure 1. The total height of the structure is 219 ft (66.7 m). The first floor's height is 15 ft (4.6 m) and typical floors are 12 ft (3.7 m) high. The thickness of the wall is 20 in (508 mm) and the total structure's weight is 20,831 kips (9449 tons). Two different prototype wall systems are designed. The first is a traditional RC system. The second prototype has HPFRC coupling beams. In addition, HPFRC is used in the first four floors of the wall piers.

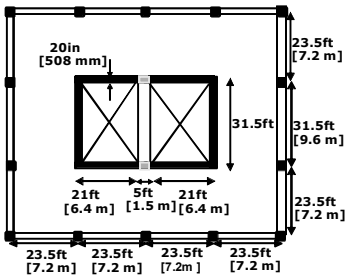
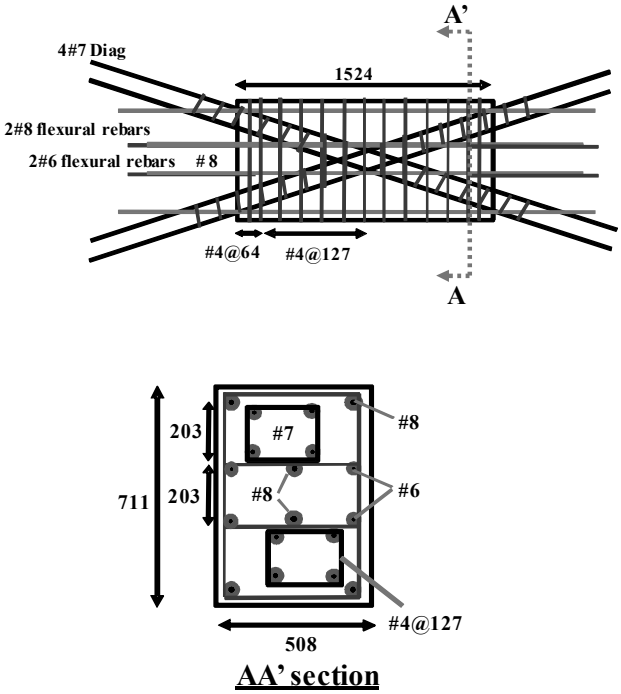


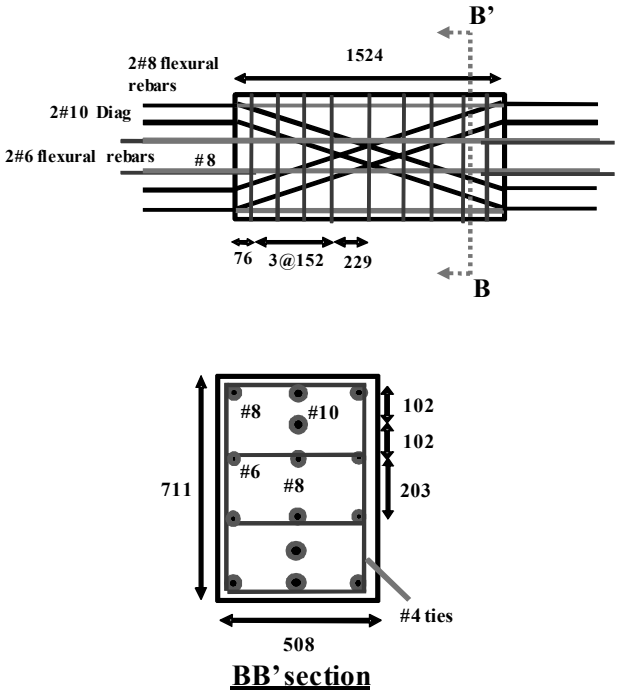
Figure 1. Plan view of prototype structural system.

Detail of the reinforcement design for RC coupling beams is shown in Figure 2(a), in which diagonal reinforcement cages with dense confining reinforcement are used. For the HPFRC coupling beams, reinforcement detailing design suggested by Canbolat et al. (2005) is used here that results in a single layer of diagonal reinforcement consisting of 2 #10 bars without confining reinforcement. The dimension and the amount of vertical reinforcement for the HPFRC beams are the same as that for the RC beams, while the horizontal reinforcement is reduced for the HPFRC coupling beams as shown in Figure 2.

The RC wall design details are compliant with (ACI 318 2008) and are shown in Figure 3, Table 1, and Table 2; where tw is the thickness of the wall, and Lbe is the length of boundary zone. The flexural and horizontal reinforcement of the HPFRC walls is reduced from that of the RC walls to take into account the additional tensile and shear capacity that HPFRC can provide.



(a) RC coupling beam (unit: mm).



(b) HPFRC coupling beam (unit: mm).

Figure 2. Reinforcement layout for the coupling beams.

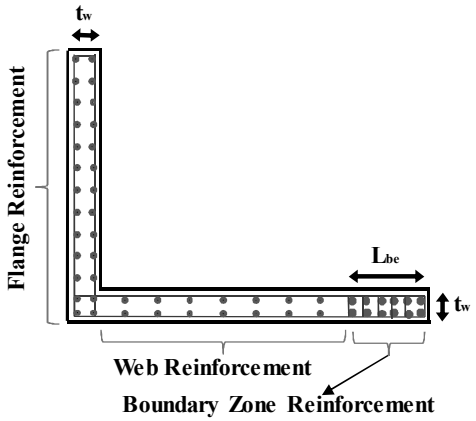


Figure 3. Shear wall cross section detail.

Table 1. Reinforcement details of HPFRC walls [unit:mm].

			Flange	
System	**Floors**	**L_{be}**	**Horiz.**	**Vert.**
HPFRC Walls	**17-18**	0	#4@305	#4@305
	15-16	610	#4@305	#4@305
	13-14	813	#4@203	#5@305
	11-12	813	#4@203	#6@305
	9-10	1016	#5@203	#6@203
	7-8	1016	#5@203	#7@203
	5-6	1219	#5@203	#8@203
	3-4	1219	#6@203	#7@203
	1-2	1219	#6@203	#7@203

	Web		Boundary Zone	
Floors	**Horiz.**	**Vert.**	**Horiz.**	**Vert.**
17-18	#4@305	#5@203	-	-
15-16	#4@305	#5@203	#4@305	12#7
13-14	#4@203	#5@203	#4@203	16#9
11-12	#4@203	#5@203	#4@203	16#9
9-10	#5@203	#6@203	#4@203	20#9
7-8	#5@203	#6@203	#5@203	20#10
5-6	#5@203	#7@203	#5@203	24#10
3-4	#6@203	#7@203	#5@203	24#10
1-2	#6@203	#7@203	#5@203	24#10

Table 2. Reinforcement details of RC walls [unit:mm].

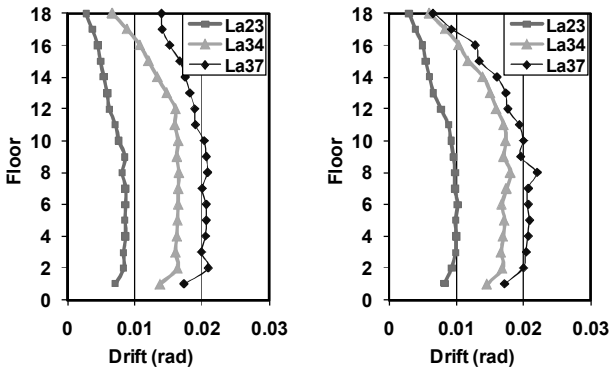
			Flange	
	Floors	**L_{be}**	**Horiz.**	**Vert.**
RC Walls	**17-18**	0	#4@305	#4@305
	15-16	610	#4@305	#4@305
	13-14	813	#4@203	#5@305
	11-12	813	#4@203	#6@305
	9-10	1016	#5@203	#6@203
	7-8	1016	#5@203	#7@203
	5-6	1219	#5@203	#8@203
	3-4	1219	#6@203	#8@203
	1-2	1219	#6@203	#8@203

	Web		Boundary Zone	
Floors	**Horiz.**	**Vert.**	**Horiz.**	**Vert.**
17-18	#4@305	#5@203	-	-
15-16	#4@305	#5@203	#4@305	12#7
13-14	#4@203	#5@203	#4@203	16#9
11-12	#4@203	#5@203	#4@203	16#9
9-10	#5@203	#6@203	#4@203	20#9
7-8	#5@203	#6@203	#5@203	20#10
5-6	#5@203	#7@203	#5@203	24#10
3-4	#6@203	#7@203	#5@102	24#11
1-2	#6@203	#7@203	#5@102	24#11

3. ANALYSIS RESULTS

Performance of the systems is evaluated using nonlinear dynamic time history analysis. Three simulated time history ground motion records, LA23, LA34, and LA37 representing the seismic hazard level with probability of exceedance of 2% in 50 years (2/50) are used. The ground motions, which were developed by the SAC (Acronym for *Structural Engineers Association of California* 'SEAOC', *Applied Technology Council* 'ATC' and *California University for Research* in Earthquake Engineering 'CUREe') steel project, have a PGA of 0.42g, 0.68g, and 0.71g for LA23, LA34, and LA37, respectively. To reduce the computational effort, only the strong motion duration of the ground motion record is adopted for seismic excitation. The strong motion duration is defined as the time segment in which 90 percent of the seismic energy is delivered (Hassan 2005).

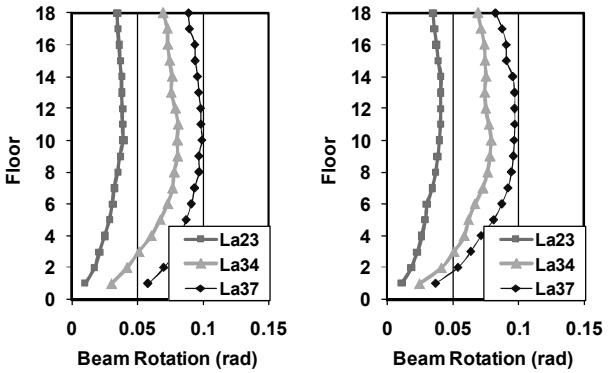
Details of component responses, drawn at the time corresponding to the occurrence of maximum system response (as determined by roof drift) during each earthquake, are plotted in Figures 4-6. Figure 4 shows the story drift of the two systems under each prescribed motion. The figure indicates that the story drifts of both systems are approximately the same along the building height. The drift limits in (ASCE 7 2002) imply that a maximum interstory drift of 2% shall not be exceeded at the Lift Safety performance level, while this criterion does not need to be observed at Collapse Prevention level. Nevertheless, the maximum interstory drifts of both prototype structures are around 2% during the 2/50 events, implying that the two systems can deliver similarly good performance.



(a) RC system (b) HPFRC system

Figure 4. Interstory drift of the systems

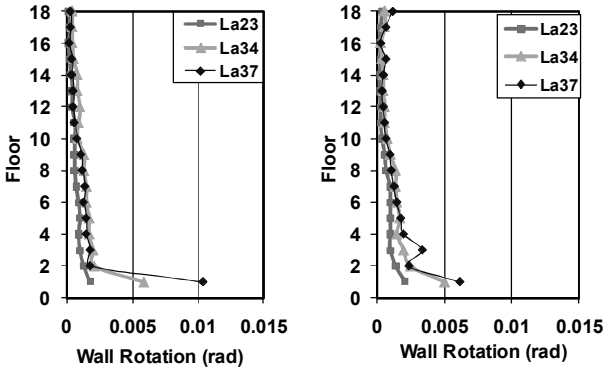
Coupling beam rotations in both systems are plotted in Figure 5. Clearly both systems have similar coupling beam rotation demands in spite of the reduced reinforcement amount and detailing in the HPFRC system.



(a) RC system (b) HPFRC system

Figure 5. Beam rotation levels at peak drift.

Wall rotations are plotted in Figure 6. It is clear that plastic hinges forms at the base of both systems when the peak displacement is reached. While both systems yield similar wall rotations along the height of the building under LA23 and LA34, LA37 results in a maximum wall base rotation of 0.01 for the RC system, which is about two times larger than the maximum response of the HPFRC system. This is taken to imply that the HPFRC system is capable of providing improved flexural behavior compared to conventional RC systems.



(a) RC system (b) HPFRC system

Figure 6. Wall rotation levels at peak drift.

4. CONCLUSIONS

The effectiveness of using HPFRC material to replace conventional RC material in the critical portions of an 18-story coupled wall system was discussed. Two coupled wall systems were considered: the first was a traditional RC design, while the second was a modified design in which HPFRC was used in the plastic hinge regions of the wall piers and in the coupling beams. The latter system was designed with less steel and relaxed detailing than the former in recognition of the beneficial effects of HPFRC. The responses of both systems subjected to strong seismic events with a 2% probability of exceedance in 50 years were then

compared. Comparisons of seismic response were made using story drift, wall rotation, and rotation of the coupling beams. The performance parameters studied suggested that both systems deliver similar performance in spite of the reduced reinforcement quantity and relaxed detailing in the HPFRC system compared to the RC system. This study was conducted using 3 seismic events with probability of exceedance of 2% in 50 years. The authors are currently expanding the study to investigate system responses in a stochastic manner, using a battery of seismic inputs representing various hazard levels.

References:

ACI (American Concrete Institute) Committee 318. (2008). "ACI 318 Building Code Requirements for Structural Concrete (318-08)" ACI-318, Farmington Hills, Mich.

ASCE (American Society of Civil Engineers). (2002). "SEI/ASCE 7-02: Minimum Design Loads for Buildings and Other Structures" American Society of Civil Engineers, Reston, VA.

Canbolat, B. A., Parra-Montesinos, G. J., and Wight, J. K. (2005). "Experimental Study on Seismic Behavior of High-Performance Fiber-Reinforced Cement Composite Coupling Beams" ACI Structural Journal 102(1), 159-166.

Hassan, M. (2004). "Inelastic Dynamic Behavior and Design of Hybrid Coupled Wall Systems" Ph.D. Thesis, Department of Civil and Environmental Engineering, University of Central Florida Orlando, Florida.

Hung, C.-C. and El-Tawil, S. (2010). "Hybrid Rotating/Fixed-crack Model for High Performance Fiber Reinforced Cementitious Composistes" ACI Materials Journal, 107(6), 569-577.

Li, V. C. (2003). "On Engineered Cementitious Composites (ECC) – A Review of the Material and Its Applications" Journal of Advanced Concrete Technology 1(3), 215-230.

Naaman, A. E., and Reinhardt, H. W. (2006). "Proposed Classification of HPFRC Composites Based On Their Tensile Response" Materials and Structures 39, 547-555.

8CUEE CONFERENCE PROCEEDINGS
8th International Conference on Urban Earthquake Engineering
March 7-8, 2011, Tokyo Institute of Technology, Tokyo, Japan

RAPID RECOVERY TECHNIQUE BY USING FIBER REINFORCED COMPOSITE FOR DAMAGED RC COLUMN UNDER SEISMIC LOADING

Minoru Kunieda[1)], Yasushi Umeda[2)], Naoshi Ueda[3)], and Hikaru Nakamura[4)]

1) Associate Professor, Dept. of Civil Engineering, Nagoya University, Japan
2) Graduate Student, Dept. of Civil Engineering, Nagoya University, Japan
3) Assistant Professor, Dept. of Civil Engineering, Nagoya University, Japan
4) Professor, Dept. of Civil Engineering, Nagoya University, Japan
kunieda@nagoya-u.jp, umeda.yasushi@b.mbox.nagoya-u.ac.jp, n.ueda@nagoya-u.jp, hikaru@nagoya-u.jp

Abstract: This paper introduces a rapid recovery technique using UHP-SHCC for damaged RC column, which involves only spraying of UHP-SHCC. Any formwork and additional reinforcement are not required. It might be helpful to reduce a construction process that is corresponding to reduction of cost. Cyclic loading tests were conducted for the column specimens repaired by UHP-SHCC and ordinary polymer cement mortar. It was confirmed experimentally that the developed technique using UHP-SHCC improve not only ultimate load but also ductility of recovered specimen. It seems that the prevention of buckling of longitudinal reinforcement, which was constrained by UHP-SHCC, imparts the mechanical improvement to the column specimens.

1. INTRODUCTION

For concrete structures such as super structures in highway, development of rapid recovery method[1)] is a very important issue and required in terms of business continuity plan (BCP).

Ishibashi[2)] has investigated recovery method on damaged RC column under cyclic loading. In the case of severe damage having spalling of cover concrete and buckling of longitudinal reinforcement, both crack injection and patching repairs were effective to recover the mechanical performance of the column. The thickness of patch repaired layer was larger than cover concrete thickness, and it means nominal cross sectional area of the column was increased.

There are a wide variety of methods such as jacketing with steel plate, continuous fibers and RC. However, these methods involve many construction processes such as manufacture of parts in steel jacketing, formwork and arrangement of steel reinforcement in RC jacketing. The many construction process gives longer downtime of the infrastructure.

Ultra High Performance-Strain Hardening Cementitious Composites (UHP-SHCC)[3)] is one of the fiber reinforced composites and has high strength in both compression and tension, high strain capacity in tension with pseudo strain hardening behavior. And spraying technique with UHP-SHCC has been also developed[4)].

This paper presents the experimental investigation on the developed rapid recovery technique using UHP-SHCC for damaged RC subjected to seismic loading. The column specimen repaired by UHP-SHCC was tested, and load carrying capacity and ductility were evaluated comparing to the specimen repaired by ordinary Polymer Cement Mortar (PCM).

2. CONCEPTUAL IDEA ON RAPID RECOVERY TECHNIQUE AND ITS ADVANTAGES

As shown in Fig. 1, UHP-SHCC is sprayed to a damaged part without any additional reinforcement. Both the novel material properties (i.e. high strength and high strain capacity) and spraying technique enable to develop the rapid recovery technique, and followings are feature of the developed technique including its advantages.

- A damaged structure for this recovery has buckling of longitudinal reinforcement with spalling of cover concrete.
- Load carrying capacity including ductility after the recovery is as well as that before the repair.
- Cross sectional shape after the recovery is the same as that before recovery. It means that the damaged concrete corresponding to cover concrete is replaced by the repair material (UHP-SHCC). It is possible to apply the other strengthening (e.g. steel plate jacketing) later.
- No additional reinforcement is utilized in the recovery.

- No formwork is required because of spraying technique.

3. OUTLINE OF EXPERIMENTAL PROGRAM

3.1 Procedure of Experiment

Outline of this experiment is summarized in Fig. 2. In this study, a cyclic loading was carried out in order to induce initial damage for column specimen (namely initial loading). After that, repair of the damaged column was conducted using two kinds of repair materials; one was ordinary PCM, and the other was UHP-SHCC. After the curing of the repaired specimens for 7days, a cyclic loading was conducted again (second loading).

3.2 Specimens

Shape of column specimens and reinforcement arrangement in the specimens are shown in Fig. 3. Sixteen longitudinal reinforcements (D13, SD345, f_y=368MPa) were used, and hoop reinforcement (D13, SD295A, f_y=360MPa) were also arranged at intervals of 80mm. Reinforcement ratio of longitudinal tensile reinforcement was 0.44%. In order to measure the strain of reinforcement and concrete, strain gages having the gauge length of 2mm and 30mm were attached, as shown in Fig. 3. Two specimens were prepared in this study, because different repair materials were adopted.

Material properties of concrete at the age of 28days and reinforcements are tabulated in Tables 1 and 2, respectively.

3.3 Loading Manner

As mentioned above, a cyclic loading was adopted to the column specimens in both initial loading and second one. Axial load of 160kN (nominal axial stress: 1MPa) was adopted. Displacement at yielding of reinforcement (δ_y) was 6.9mm in initial loading. The loading was terminated, when the load was decreased up to yielding load after the peak.

4. INITIAL LOADING TO INDUCE DAMAGE

4.1 Relationship between Load and Displacement

Figure 4 shows the relationship between load and displacement of the specimen in initial loading. Yielding of longitudinal reinforcement was occurred at load of 160kN and displacement of 6.9mm (δy). Horizontal load was significantly increased until 2δy. However, the curve represents plateau after 2δy. The peak load of the first specimen was 205kN at the displacement of 41.4mm (6δy), and the peak load of the second specimen was 200kN at displacement of 48.3mm (7δ_y). Note that, the first and second specimens were used for the repair using PCM and UHP-SHCC, respectively. After that, softening behavior was observed in both specimens, and loading was terminated when the load was same as yielding load

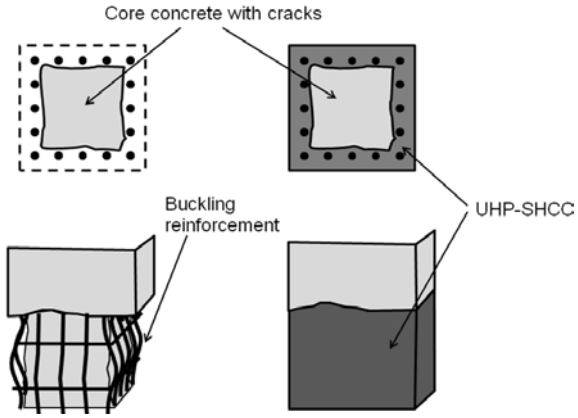


Figure 1 Construction Procedure of Developed Technique: (a) Damaged Column, and (b) Repaired Column

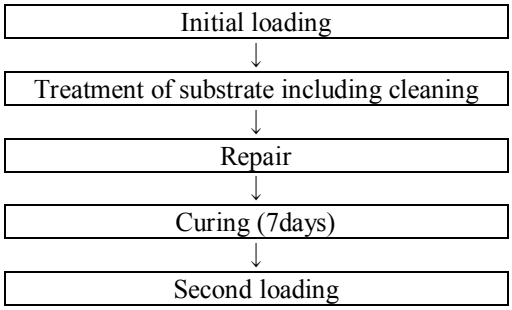


Figure 2 Experimental Procedure

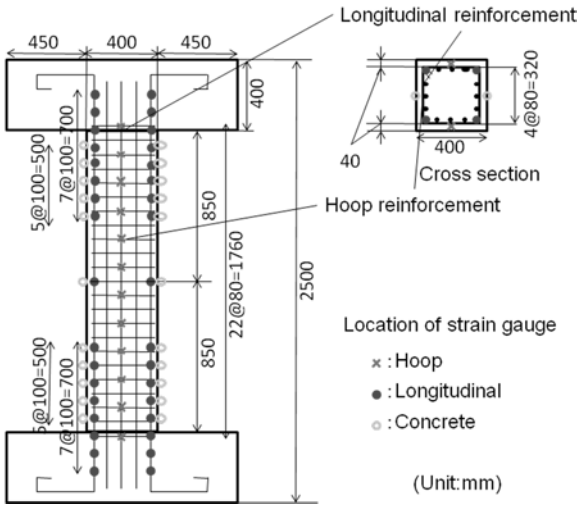


Figure 3 Specimen and Reinforcement Arrangement

Table 1 Material Properties of Concrete (28days)

Compressive strength (MPa)	Young's modulus (GPa)
29.3	32

Table 2 Material Properties of Reinforcement

Longitudinal		Hoop	
Yield strength (MPa)	Young's modulus (GPa)	Yield strength (MPa)	Young's modulus (GPa)
368	186	360	190

(164kN). Eventually, both specimens exhibited similar load-displacement response, as shown in Fig. 4.

4.2 Induced Damage

Crack patterns during initial loading tests are given in Fig. 5. Flexural cracks occurred and propagated at hinge part of the column specimens mainly, and the number of cracks increased until the displacement corresponding to 1δy. After that, the number of crack was not increased, however, each crack opened wider.

On the side face of the column specimens, shear cracks occurred within 1D height (D: effective depth) from footing. And spalling of cover concrete was observed partially. Finally, buckling of longitudinal reinforcement was observed after spalling of cover concrete. In addition, fracture of core concrete was also obtained.

4.3 Strain Distribution

Figure 6(a) shows strain distribution of longitudinal reinforcement (left side of the column specimen) at each loading level, and Fig. 6(b) shows that of hoop reinforcement. Note that the loading direction was plus direction, as shown in Fig. 6.

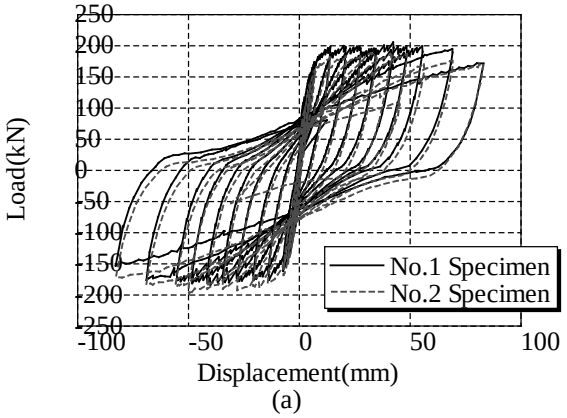
Regarding the longitudinal reinforcement, strain value at hinge part of column specimen was increased with increasing of loading cycles up to displacement of 20.7mm (3δy), the higher strain region was corresponding to the damaged area mentioned in previous section. In the bottom of the column specimen, tensile strain was measured at final stage. It seems that elongation of the longitudinal reinforcement due to plastic strain was increased.

For the hoop reinforcement, the strain value became higher with increasing of loading cycles, and the higher strain region also agreed with the damaged area having a spalling of cover concrete. However, yielding of hoop reinforcement was not observed.

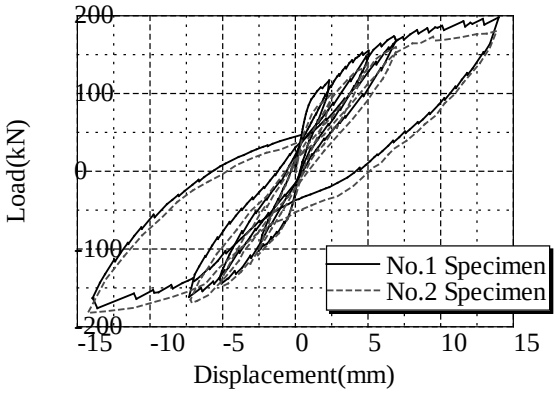
5. APPLICATION OF RECOVERY TECHNIQUE

5.1 Repair Materials

As described in Section 3.1, two kinds of cement

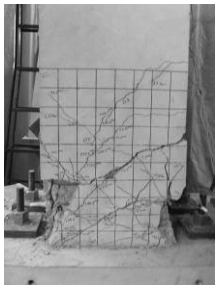


(a)



(b)

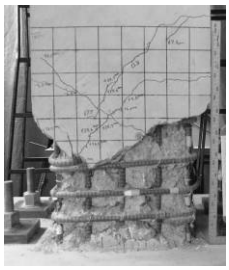
Figure 4 Load-displacement Curves of Initial Loading: (a) Overall, and (b) Zoom Up



(a)



(b)



(c)



(d)

Figure 5 Photo of Damaged Specimens: (a) Front View (Final), (b) Side View (Final), (c) Front View (After Removing Cover Concrete), and (d) Side View (After Removing Cover Concrete)

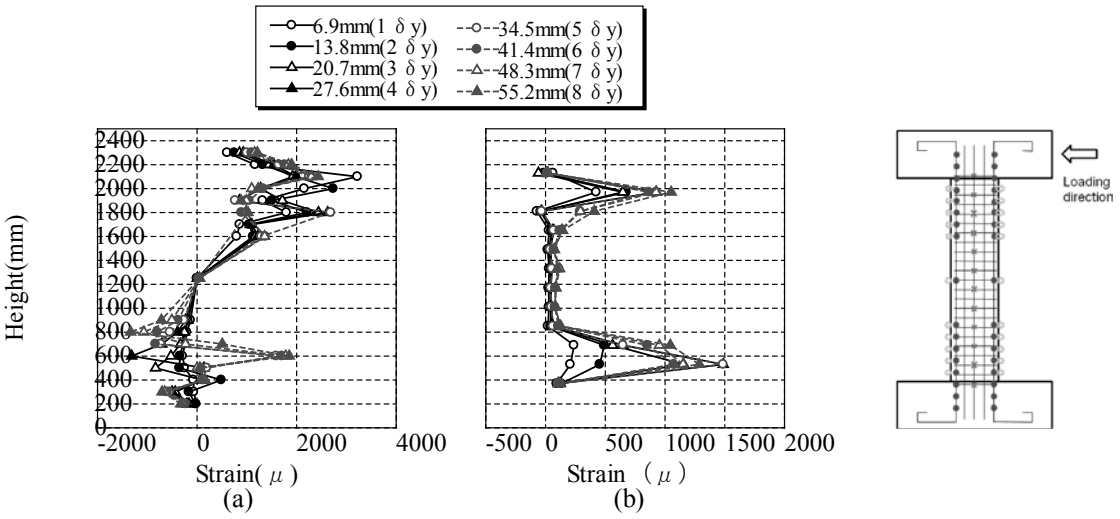


Figure 6 Strain Distribution of Reinforcement: (a) Longitudinal, and (b) Hoop

Table 3 Material Properties of Repair Materials (7days)

PCM		UHP-SHCC			
Compressive strength (MPa)	Young's modulus (GPa)	Compressive strength (MPa)	Young's modulus (GPa)	Tensile strength (MPa	Strain at tensile strength (%)
23.2	19.2	79.7	23.7	7.7	1.22

based materials were used in this study; one was ordinary PCM (premixed type) for plastering, and the other was UHP-SHCC for spraying. Where used PCM is not for this usage generally (i.e. no reinforcement is used).

Table 3 tabulates the material properties of each repair material at the age of 7days, which is corresponding to the loading age of second loading. Compressive strengths of PCM and UHP-SHCC were 23.2MPa and 79.7MPa, respectively. The compressive strength was obtained from the cylindrical specimens having the size of 50mm in diameter and 100mm in length. Figure 7 illustrates the tensile test results of UHP-SHCC dumbbell shaped specimens (5specimens), which were made by spraying. Note that tested cross section was 30x13mm. Averaged tensile strength of UHP-SHCC was 7.7MPa, and pseudo strain hardening and multiple fine cracking were observed, in addition to higher strain capacity over 1%.

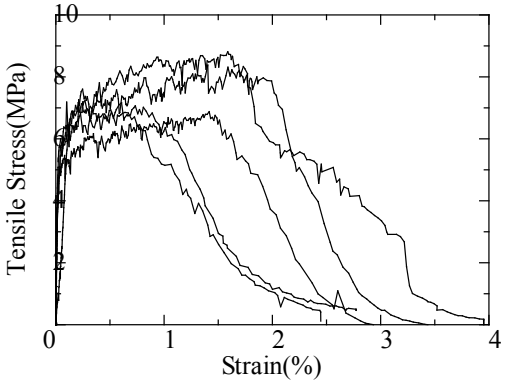


Figure 7 Tensile Stress-strain Curves of UHP-SHCC

5.2 Repair Method

The target of recovery was the damaged column specimens that were brought to the original position (residual displacement: 0mm). The damaged cover concrete was removed by using a hammer. And water spraying was also applied to prevent the water absorption of repair material itself.

PCM was applied by using plaster finishing. Note that the finished cross section was almost the same with un-damaged one (i.e. 400mm x 400mm).

Regarding UHP-SHCC, it was only sprayed to the damaged part, as shown in Fig. 8.

After the repair, curing was conducted for 7days,



Figure 8 Spraying of UHP-SHCC

and cyclic loading was carried out again for repaired specimens.

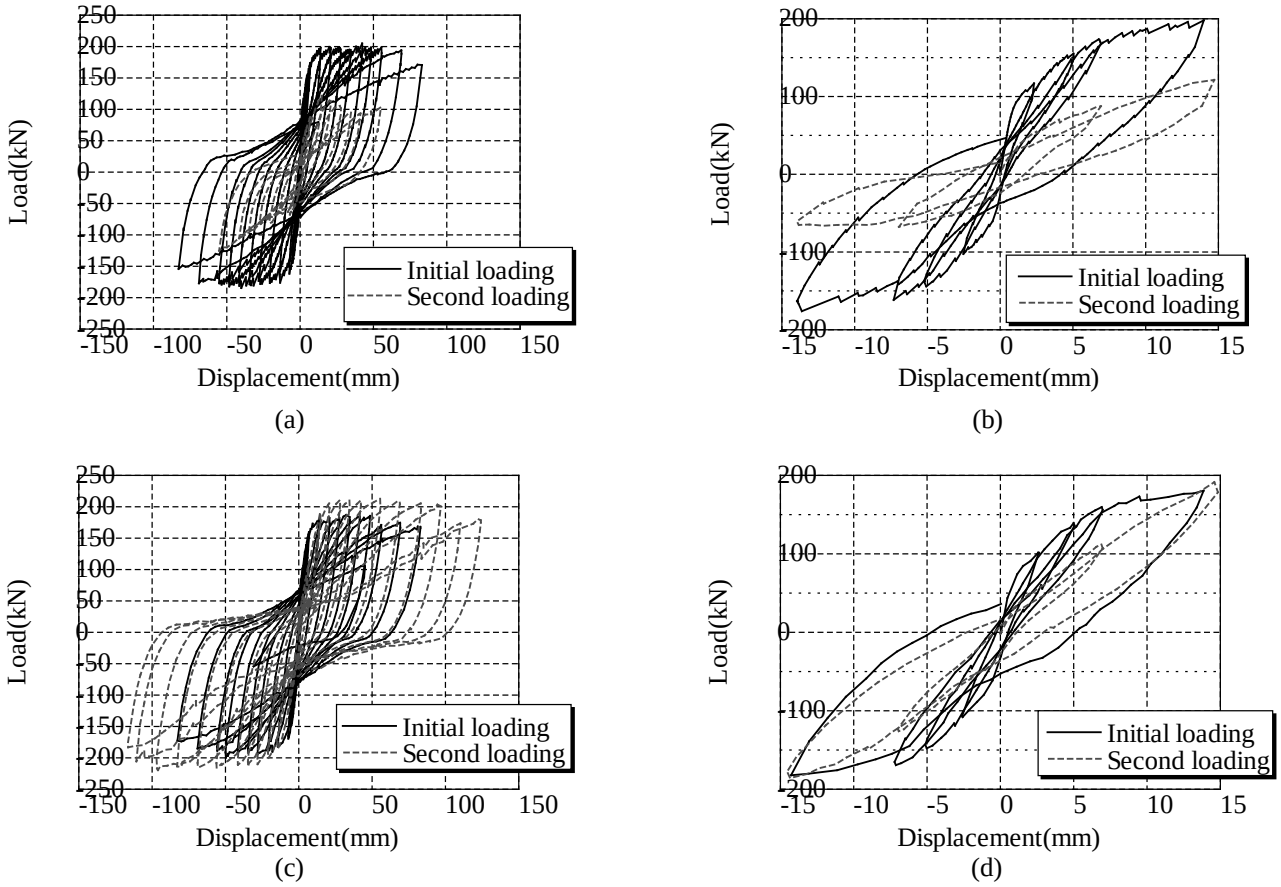


Figure 9 Load-displacement Curves of Each Repaired Specimens: (a) PCM (Overall), (b) PCM (Zoom Up), (c) UHP-SHCC (Overall), and (d) UHP-SHCC (Zoom Up)

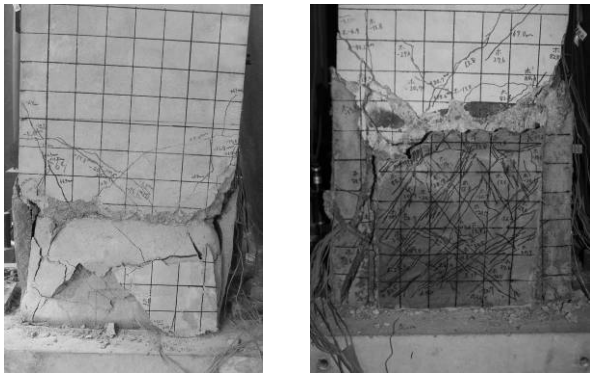
6. SECOND LOADING FOR REPAIRED SPECIMENS

6.1 Load-displacement Curves and Failure Behavior

Figures 9 (a) and (b) show the load-displacement curves of the specimens repaired by PCM and its zoom up one, respectively. Maximum load was about 120kN and it was dramatically decreased comparing to that of initial loading. Ductility of the specimen was also decreased significantly. In the initial loading stage (up to 2δy), splitting cracks occurred adjacent to longitudinal reinforcement of tensile side, and the cracks induced the buckling of reinforcement under compressive stress.

Figures 9 (c) and (d) illustrate the load-displacement curves of the specimens repaired by UHP-SHCC and its zoom up one, respectively. Maximum load was about 210kN, and it was higher than that of initial loading. Load was significantly decreased at 12δy, and ductility of the specimen was increased comparing to that of initial loading, eventually. As indicated in Fig. 9(d), initial stiffness was not recovered because of the crack located at the joint between column and footing.

Photos of the damaged part of the specimen with PCM and UHP-SHCC are shown in Figs. 10(a) and (b), respectively. In the case of specimen with PCM, splitting cracks were observed along longitudinal reinforcement,



(a) (b)

Figure 10 Photo of Damaged Specimen in Second Loading (Front View): (a) PCM, and (b) UHP-SHCC

and repaired part was crushed and spalling. Regarding the specimen with UHP-SHCC, however, diagonal multiple cracking was observed in the front side. No crashing of the UHP-SHCC was observed. However, concrete just above the interface between UHP-SHCC and concrete was damaged finally.

Regarding the side surface that is perpendicular to loading direction, although multiple cracking was expected, no crack was observed.

6.2 Relationship between Vertical and Horizontal Displacement

Figure 11 shows relationship between vertical and horizontal displacement of the columns repaired by PCM and UHP-SHCC. In the case of PCM, it was indicated that vertical displacement of second loading was decreased with increasing of loading cycles, because buckling of longitudinal reinforcement progressed. It seems that PCM could not resist against buckling of the longitudinal reinforcement.

Regarding the specimen with UHP-SHCC, vertical displacement was increased with increasing of loading cycles. It means that UHP-SHCC imparts higher resistance against buckling of the longitudinal reinforcement to the column specimen.

6.3 Energy Absorption Capacity

Figure 12 shows the relationship between loading cycle and energy absorption. In the case of specimen with UHP-SHCC, although energy absorption was slightly lower than that of initial loading in early stage, it became larger than that of initial loading finally. In the case of specimen with PCM, energy absorption was dramatically decreased comparing to other cases.

7. CONCLUSIONS

The rapid recovery technique using UHP-SHCC for damaged RC column was developed, and cyclic loading tests were conducted. Following conclusions were obtained;

(1) The rapid recovery technique involves only spraying of UHP-SHCC. Any formwork and additional reinforcement are not required. It might be helpful to reduce a construction process that is corresponding to reduction of cost.

(2) It was confirmed experimentally that the developed technique using UHP-SHCC improve not only ultimate load but also ductility of recovered specimen. It seems that the prevention of buckling of longitudinal reinforcement, which was constrained by UHP-SHCC, imparts the mechanical improvement to the column specimens.

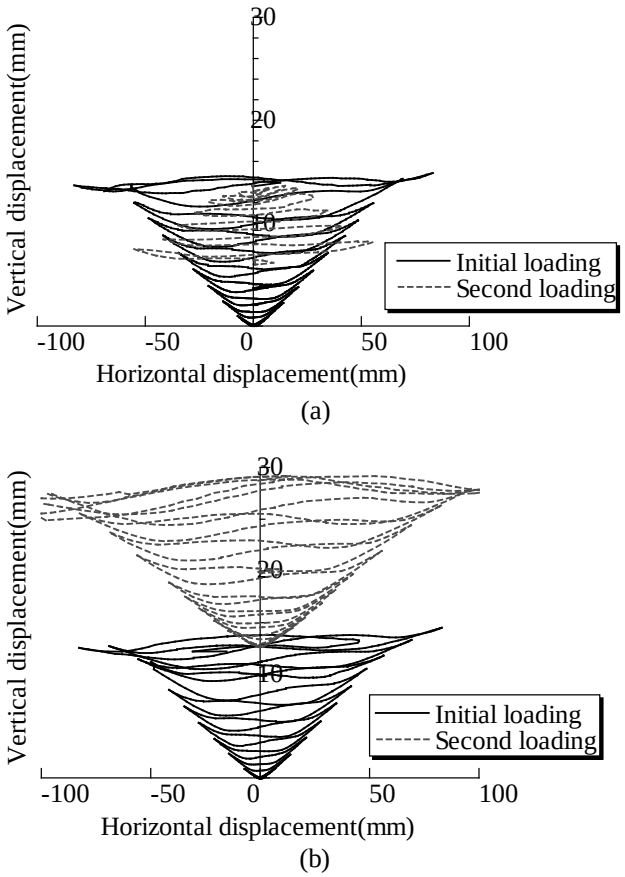


Figure 11 Vertical Displacement: (a) PCM, and (b) UHP-SHCC

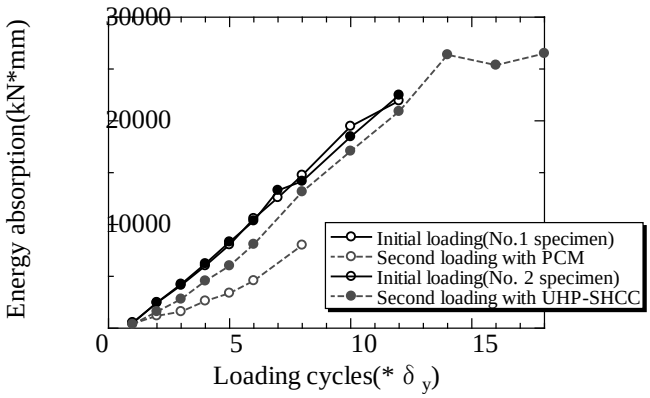


Figure 12 Energy Absorption of Each Specimen

Acknowledgement:
A part of this research was supported by Committee on Advanced Road Technology in established by Road Bureau of Ministry of Land, Infrastructure, Transport and Tourism. The authors would like to express their sincere thanks to their financial support.

References:

1) Inaguma, H. and Seki, M. (2005), "Study on Restoration Work Method of Steel Jacketing Retrofit Column of Railway Viaduct," Proc. of the Japan Concrete Institute, 27(2), 1057-1062. (in Japanese)

2) Ishibashi, T., Tsuyoshi, T., Kobayashi, K., Kobayashi, M. (2000), "An experimental study on damage levels and repairing effects of reinforced concrete columns subjected to reversal cyclic loading with large deformations," JSCE Journal of Materials, Concrete Structures and Pavements, V-47(648), 55-69. (in Japanese)

3) Kunieda, M., Denarié, E., Brühwiler, E. and Nakamura, H. (2007), "Challenges for Strain Hardening Cementitious Composites – Deformability Versus Matrix Density," Proc. of the fifth International RILEM Workshop on HPFRCC, 31-38.

4) Kunieda, M., Ueda, N., Nakamura, H., Tamakoshi, T. (2009), "Development of Spraying Technique for UHP-SHCC," Proc. of the Concrete Structure Scenarios, 9, 349-354. (in Japanese)

8CUEE CONFERENCE PROCEEDINGS
8th International Conference on Urban Earthquake Engineering
March 7-8, 2011, Tokyo Institute of Technology, Tokyo, Japan

STRUCTURAL BEHAVIOR OF DEEP BEAM WITH DETERIORATED ANCHORAGE OF MAIN REINFORCEMENT

Akira Hosoda[1)], Hiroshi Kaneko[2)], and Misato Yuzurio[3)]

1) Associate Professor, Graduate School of Environment and Information Sciences, Yokohama National University, Japan
2) East Japan Railway Company, Japan
3) Daiwa House Industry Co., Ltd., Japan
concrete@ynu.ac.jp

Abstract: Deterioration of anchorage of reinforcement in RC structures can be caused by ASR or chloride ion induced corrosion. In this study, structural behaviors of deep beams with deteriorated anchorage of main reinforcement were investigated by experimental work. With bond deterioration of main reinforcement near the supports, the stiffness after the generation of diagonal cracks was remarkably reduced and the maximum load was also remarkably reduced. In experimental work, the effects of stirrups were investigated. When stirrups with small diameter were distributed, the stiffness after diagonal cracking was improved, and the maximum load was increased. Experimental results were numerically simulated by 3D FEM. Deterioration of bond was modeled by joint element, and experimental results were simulated well when appropriate shear strength of joint element was determined. Verification of analysis was conducted through load-displacement relationship, deformation, and strain distribution of main reinforcement.

1. INTRODUCTION

Due to the rupture of bending portion of re-bars by Alkali Silica Reaction , and due to the corrosion of re-bars at the ends of girders by de-icing agent, the deterioration of anchorage can be caused in actual concrete structures. The corrosion of re-bars by chloride ion will induce longitudinal cracking along re-bars which will cause bond deterioration. The deterioration of anchorage and bond can cause catastrophic failure of members.

The deterioration of bond near the anchorage of main re-bars adversely affects structural behaviors especially in deep beams. However, many past researches examined the effects of bond deterioration without the existence of stirrups.

In this research, the reinforcing effects of stirrups will be investigated in deep beam with initial deterioration of bond near the anchorage of main re-bars. Static loading of deep beams will be conducted where the adverse effects of bond deterioration and the reinforcing effects of stirrups with different arrangement will be investigated. 3 dimensional FEM simulation was conducted to understand the mechanism.

2. EXPERIMENTAL PROGRAM

2.1 Details of Specimens

The section and the shape of the specimens are shown in Figure 1. The width is 200mm and the height is 300mm. The effective depth is 260mm and the shear span is 450mm, and therefore a/d is 1.73. The length from the support to the bent portion of hook of the main re-bar was made long enough as 310mm. To obtain shear failure of the beams, the ratio of shear capacity to the shear force at flexural capacity was made lower than 1.0. Niwa's equation (JSCE, 2007) was used to calculate shear capacity.

Information about the specimens is summarized in Table 1. The properties of re-bars are shown in Table 2. Two specimens were made for all the cases to check reproducibility. As main re-bars, three D22 bars were arranged. When the effect of initial bond deterioration was examined in specimens N, ST6, ST13, the bond of main re-bars was removed in the range of 460mm from the bending portion of the hook. To remove bond, wax was filled in between the ribs of re-bars and the surface was made flat, and furthermore, the surface of that bond deterioration area was coated by grease and polyvinyl tape.

ST6 and ST13 specimens had stirrups, and in both cases the stirrup ratio was 0.422%. This satisfies the minimum reinforcement ratio in JSCE code and is almost equal to the reinforcement ratio of normal beams of road bridge piers. In ST6 specimens, stirrups of D6 were distributed with the spacing of 75mm. In ST13 specimens, D13 stirrups were coarsely arranged with the spacing of 300mm. D13 stirrups were arranged to cross the arch to connect the loading plate and the support as shown in Figure 1. For ST6 and ST13 specimens, compressive re-bars of D6 were arranged and stirrups were anchored to them.

Tabel 1 Details of Specimens and Experimental Results

Specimen	Main re-bar	Stirrup			f'_c (MPa)	Diagonal Cracking Load (kN)	Maximum Load (kN)	Failure Pattern
	Bond deterioration length (mm)	Re-bar	Spacing (mm)	Reinforcement Ratio (%)				
H-1	0	-	-	-	28.5	159.4	381.3	Shear Compression
H-2						166.5	397.6	Shear Compression
N-1	460	-	-	-	36.4	92	262.1	Bond Failure of Main Re-bars
N-2						105.2	175.3	Shear Compression
ST6-1		D6	75	0.422		85.9	259.4	Shear Compression
ST6-2						76.3	304.2	Shear Compression
ST13-1		D13	300	0.422		89.4	148.1	Shear Compression
ST13-2						88.5	192.8	Shear Compression

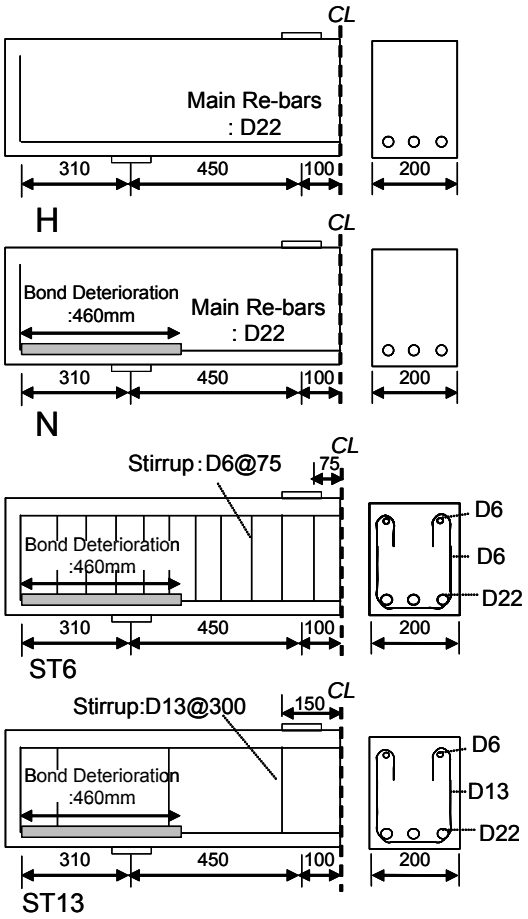


Figure 1 Arrangement of Re-bars

2.2 Loading Method and Measurement of Displacement and Strain

2 points monotonic loading was statically applied. Steel plates with 100mm width were used for loading plates and supports. Up to diagonal cracking, loading was conducted in load control with 10kN step. After diagonal cracking, displacement control was used. The vertical displacement at the center of the span and the strains of main re-bars and stirrups were measured.

Table 2 Properties of Re-bars

Re-bar	Yielding Stress (MPa)	Tensile Strength (MPa)	Young's Modulus (MPa)
D22 for H	389	570	192
D22 for N, ST6, ST13	381	553	185
D6	303	509	187
D13	350	489	189

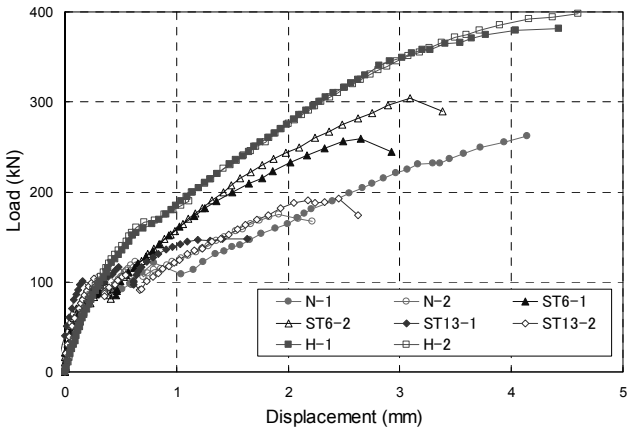


Figure 2 Load – Displacement Relationships

3. EXPERIMENTAL RESULTS

3.1 Stiffness after Diagonal Cracking

Figure 2 shows the relationships between load and the displacement at the center of the span. The beams H without initial bond deterioration show apparently higher diagonal cracking load and higher stiffness after diagonal cracking.

ST6 specimens with distributed stirrups showed higher stiffness after diagonal cracking and higher maximum load than N specimens without stirrups. Just after diagonal cracking, crack width was visually investigated. Diagonal crack width of ST6 was apparently restrained compared to that of N, which was caused by stirrups in the shear span.

ST13 specimens with coarse arrangement of stirrups showed almost the same behavior with N specimens. In terms of stiffness and failure pattern, the reinforcing effects

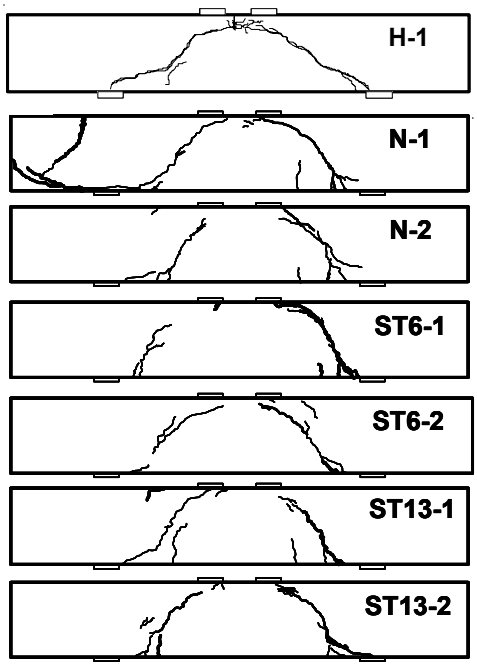


Figure 3 Crack Conditions

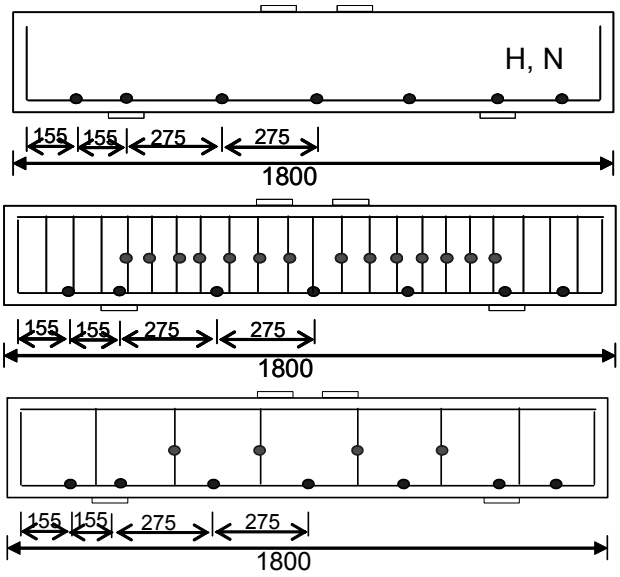


Figure 4 Locations to Measure Strain of Re-bars

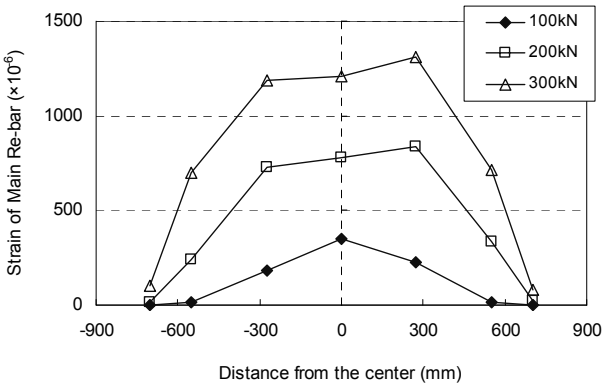


Figure 5 Strain Distribution of Main Re-bar (H-1)

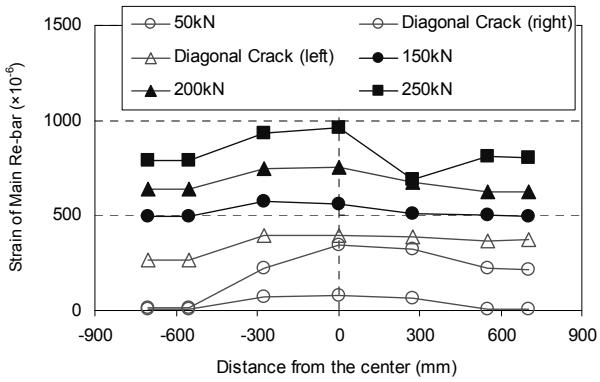


Figure 6 Strain Distribution of Main Re-bar (N-1)

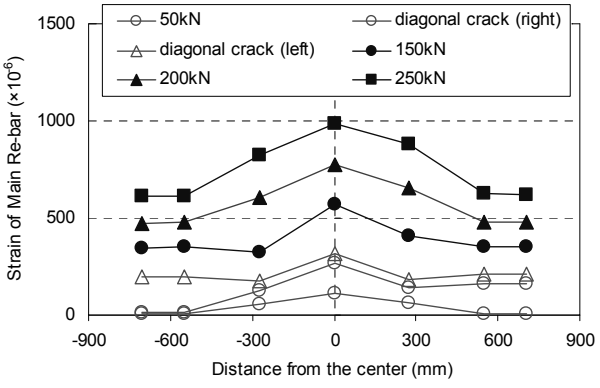


Figure 7 Strain Distribution of Main Re-bar (ST6-1)

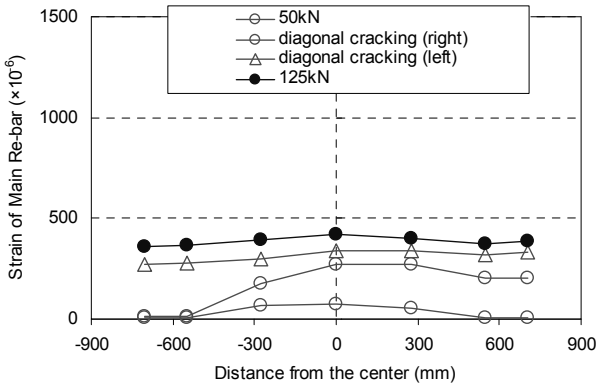


Figure 8 Strain Distribution of Main Re-bar (ST13-1)

of stirrups were not observed.

3.2 Crack Pattern and Failure Mode

Figure 3 shows the conditions of diagonal cracks after loading. In all the specimens with initial bond deterioration, diagonal crack developed from around the end of bond deterioration zone (460mm from the bending portion of hook of main re-bar). The origin of diagonal crack was the bending crack that was generated at the end of bond deterioration zone.

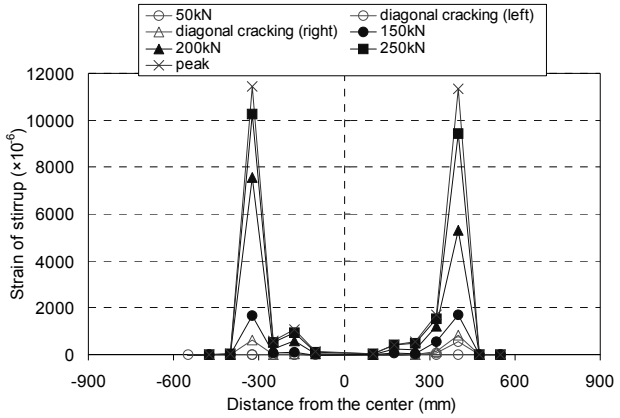


Figure 9 Strain Distribution of Stirrups (ST6-1)

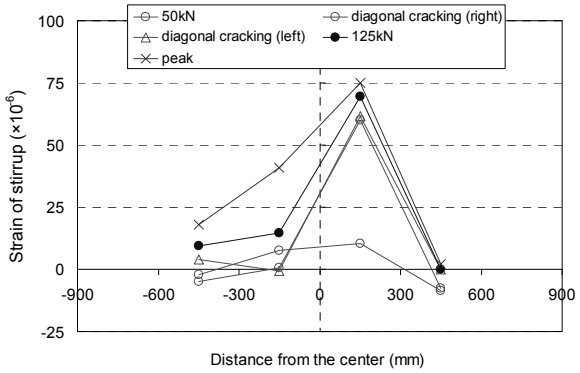


Figure 10 Strain Distribution of Stirrups (ST13-1)

In the case of H specimens, load increased after diagonal cracking, and diagonal cracks developed to go under the loading plates, and then finally failed with crushing of concrete in the bending compressive zone.

In the case of N-2 specimen, diagonal crack penetrated to the upper end of the beam beside the loading plate, and then showed shear compression failure. On the other hand, N-1 specimen carried larger force because diagonal cracks developed under the loading plates. N-1 specimen finally showed anchorage failure due to the slip of main re-bars with the appearance of vertical cracks at the upper portion of the beam.

ST6 specimens showed small distributed cracks near diagonal cracks which were not observed in H nor N specimens. This was due to bond effect of stirrups.

In ST13 specimens, diagonal cracks which developed from around the ends of bond deterioration zone crossed only small parts of stirrups coarsely arranged in the shear span.

The maximum loads in this experiment were varied a lot depending on the location of diagonal cracks, etc. When diagonal cracks penetrated to the upper end without going under the loading plates, maximum loads were relatively lower resulting in apparent shear failure with clear failure sound. In the next section, investigation by FEM simulation will be conducted where the stiffness after diagonal cracking rather than maximum load will be focused on.

3.3 Strain Distribution of Re-bars

Figure 4 shows the location to measure the strain of re-bars. Figures 5-8 show the strain distributions of main re-bars measured at 7 points along the longitudinal direction. Figures 9-10 show the strain distributions of stirrups.

From Figures 6-8, it can be seen that in all the specimens with bond deterioration, after diagonal cracking, strain of main re-bars in the bond deterioration area was started to increase.

In the case of N specimens, the strains of main re-bars at 7 points became almost uniform after diagonal cracking. This means that main re-bars from the bending portion of hooks to the center of the re-bars became uniform tension ties of arch mechanism. The beam load carrying mechanism before diagonal cracking shifted to arch mechanism where main re-bars carry almost uniform tensile force along the longitudinal direction.

In the case of ST13 specimens, the strain distributions of main re-bars had almost the same shape as that of N specimens. Judging from this result, the reinforcing effect of stirrups in ST13 was hardly achieved.

In the case of ST6 specimens, the strains of main re-bars near the center of the beam was increased after diagonal cracking, which was different from N specimens. Looking at Figure 9, the stirrups in the center of the shear span showed considerably large strain and got yielded. Stirrups carried shear force, and the strain of main re-bars was restrained, which resulted in larger stiffness after diagonal cracking than that of N specimens. This mechanism will be further investigated in the next section.

Before conducting this experiment, the authors expected that the slip of main re-bars might be restrained by friction caused by the stirrups surrounding main re-bars with bond deterioration. However, ST13 specimens showed almost no reinforcing effect, therefore we concluded that such kind of confining effect of stirrups was not observed.

4. FEM SIMULATION OF EXPERIMENTAL RESULTS

4.1 Outline of FEM Simulation

In this research, FEM program, "COM3" (Maekawa et al. 2003) was used which adopted constitutive laws based basically on smeared crack model. Simulation was conducted with axis-symmetric model as shown in Figure 11 (the model for specimen N). COM3 categorizes concrete elements into two types, such as RC elements and PL(Plain Concrete) elements (Maekawa et al. 2003). In RC elements, bond effect to distribute cracks is considered, and in PL elements a crack is localized without bond effect. In this research, main reinforcing bars were modeled as pure reinforcing bars without concrete, because joint elements were inserted between concrete elements and re-bar elements to express slipping due to bond deterioration by assuming appropriate shear stiffness of joint elements (Figure 14).

Main re-bars were modeled with pure re-bar model, and bond effective area was modeled as RC element. The

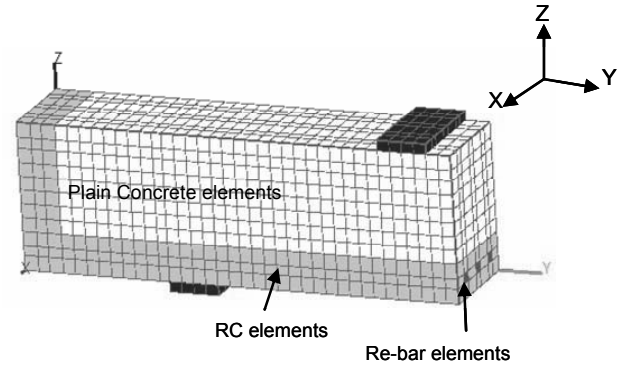


Figure 11 Analytical Model (N)

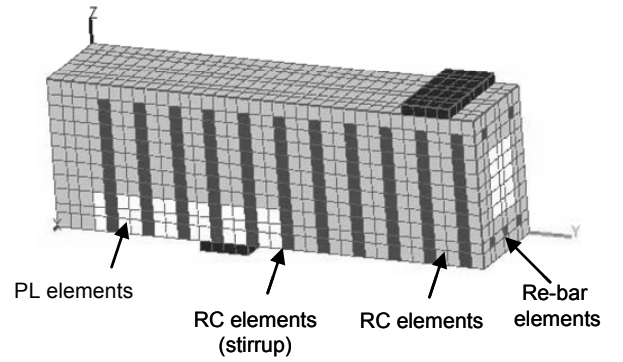


Figure 12 Analytical Model (ST6)

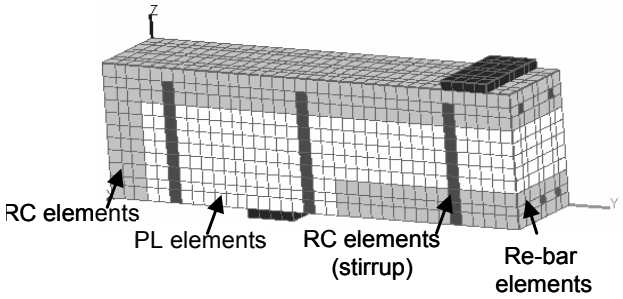


Figure 13 Analytical Model (ST13)

models for ST6 and ST13 were shown in Figures 12 and 13. In the case of ST6, considering the dense arrangement of stirrups, the width of RC zone was set as twice of cover thickness in X direction (Tsuchiya et al. 2001), and was set as the spacing of stirrups in Y direction. In the case of ST13, considering the coarse arrangement of stirrups, the width of an element including a stirrup was set as 25mm, and only that element with a stirrup was set as RC zone both in X and Y directions. In RC zones, the tension softening factor was set as 0.4 both for X and Y directions. In PL zones, the tension softening factor was decided considering fracture energy (Maekawa et al. 2003).

Bond deterioration of main re-bars was modeled using joint elements around pure re-bar elements. The length of bond deterioration and material properties of joint elements such as shear stiffness and opening/closing stiffness were set as shown in Figure 14 and Table 3 referring bond deterioration range by Okamura et al.(1991).

The bond property in non-deteriorated healthy area

Table 3 Material Properties of Joint Element

Healthy Bond Area		Bond Deterioration Area	
Shear Stiffness	Opening/Closing Stiffness	Shear Stiffness	Opening/Closing Stiffness
$N/mm^2/mm$	$kN/mm^2/mm$	$N/mm^2/mm$	$kN/mm^2/mm$
25	100	0	0

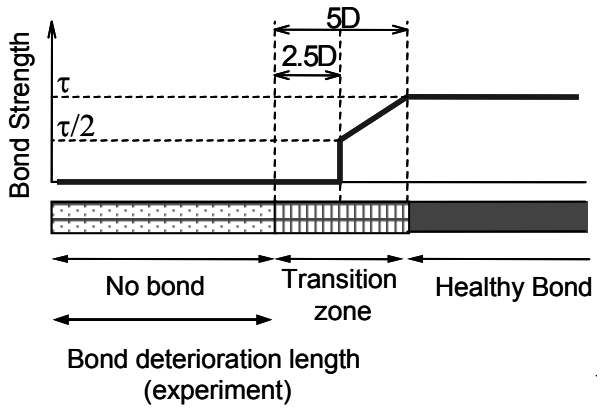


Figure 14 Modeling of Bond deterioration

were identified by the results of comparisons of numerical simulation and uni-axial tension tests by Tamai et al. (1987). The shear stiffness of joint elements of non-deteriorated area was decided to obtain almost the same behavior as the behavior of uni-axial tension tests. The behavior of reinforced concrete around tensile main re-bars is similar to that of uni-axial tension test. The same shear stiffness $25N/mm^2/mm$ was set for joint elements regardless of the location along healthy main re-bars. That value seems reasonable referring the value shown by Suzuki et al.(2005).

4.2 Results of FEM Simulation

The results of FEM simulation were shown in Figures 15 to 18. Figure 15 shows the relationships between load and displacement at the center of the span. Figure 16 shows the strain distribution of main re-bars. Figure 17 shows the strain distribution of stirrups. Figure 18 shows the contour of stress.

Regarding N specimens, the load at the generation of diagonal crack and the stiffness after diagonal cracking was evaluated appropriately. Looking at the strain distribution of main re-bars in Figure 16, the strain distribution was flat in the bond deterioration area, which was observed in N specimens as shown in Figure 6. This flat distribution leads to larger slip near the anchorage, and compressive stress tends to flow from the loading plate to the bending portion of anchorage of main re-bars (Figure 18). This will be the reason of lower stiffness after diagonal cracking than that of healthy deep beam.

Regarding ST6, the load – displacement relationship was predicted with sufficient accuracy including the stiffness after diagonal cracking. As shown in Figure 16, the strain of main re-bars of ST6 specimens was lower than that of N specimens at the same load. The shape of strain distribution of ST6 was sharp compared to flat distribution of N

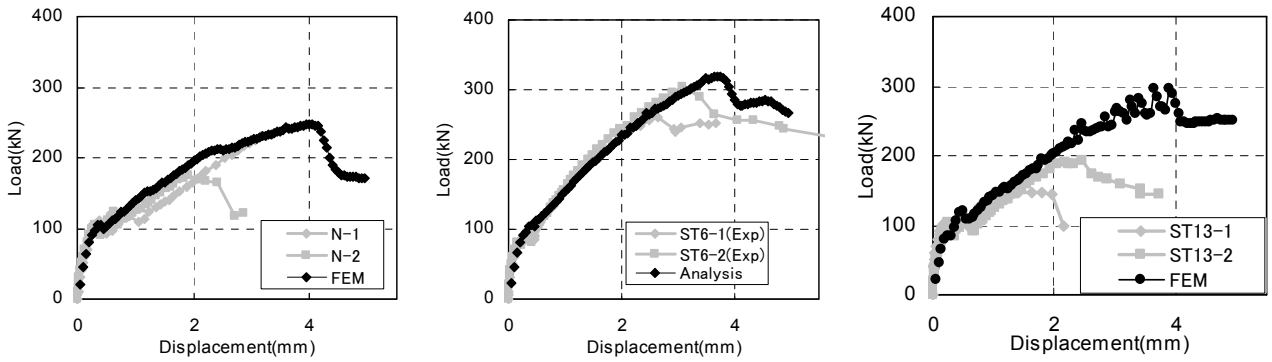


Figure 15 Load – Displacement Relationships (FEM)

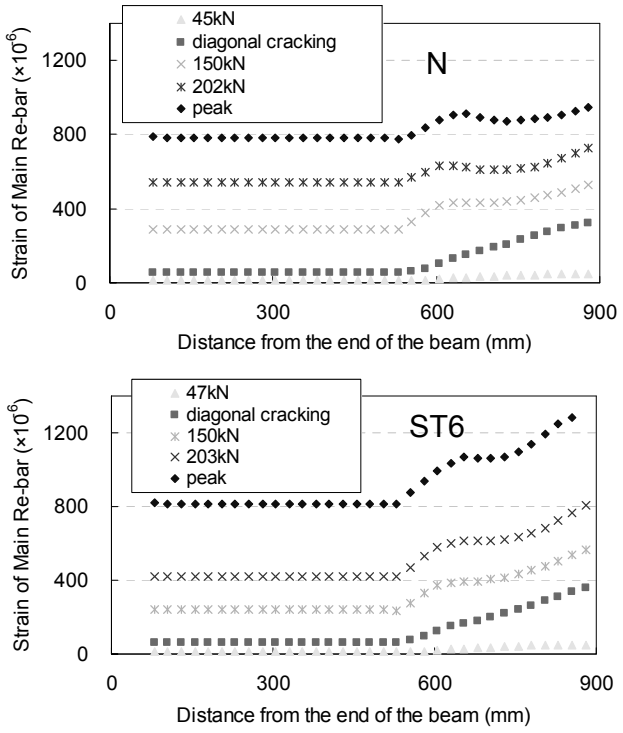


Figure 16 Strain Distribution of Main Rebar (FEM)

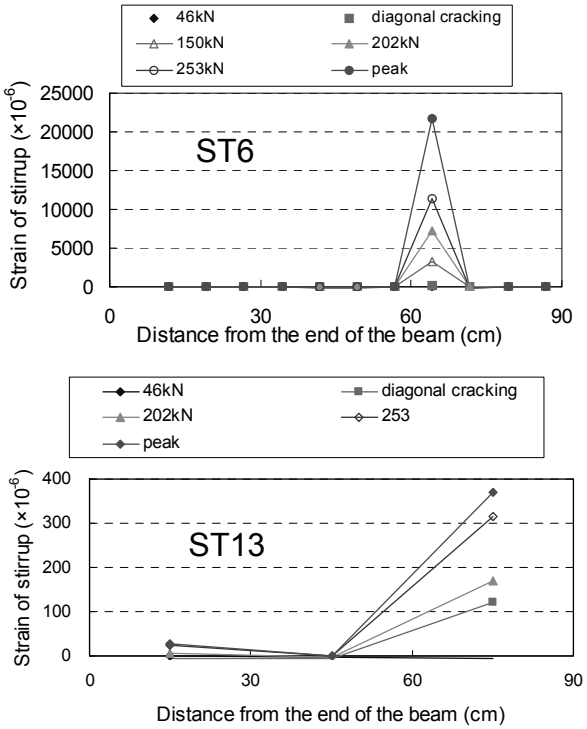


Figure 17 Strain Distribution of Stirrups (FEM)



Figure 18 Contour of Stress (FEM)

specimens. These were caused by the effect of stirrups.

The authors think that the effects of stirrups are to carry shear force, to improve shear transfer by restraining diagonal crack width, to distribute compressive stress in the strut by confinement effect, and to increase dowel action of main re-bars. From Figure 17, it is clear that the stirrups carry sufficient shear force in ST6. Figure 18 shows that compressive stress in diagonal direction is more distributed in ST6.

N and ST6 specimens show clear difference in the stiffness after diagonal cracking, which must be caused by the effects of stirrups. In the case of N, after diagonal cracking, the slip in the bond deterioration area caused further opening of diagonal crack, which led to lower stiffness than the beams without initial bond deterioration. On the other hand, in the case of ST6, due to the effects of stirrups, the opening of diagonal crack and the slip in the bond deterioration area were restrained, which led to increasing the stiffness of tied arch.

Regarding ST13, the maximum load in simulation was much higher than the experimental results. The reason is clearly shown in Figure 17, which shows the carrying of shear force by stirrups different from experiment. The simulation in this research could not reproduce a localized behavior, winding away of diagonal crack from a stirrup

near the loading plate, which was caused by the coarse arrangement of stirrups. The stiffness of ST13 after diagonal cracking was simulated well, because in the simulation only the stirrup just under the loading plate carried shear force and therefore diagonal crack width in the shear span was not restrained.

5. CONCLUSIONS

The adverse effects of bond deterioration of main re-bars and the reinforcing effects of stirrups were investigated in RC deep beam. The following results were obtained from experiment and 3D FEM simulation.

1) Due to bond deterioration near the anchorage of main re-bars, the load of diagonal cracking, the stiffness after diagonal cracking, and the maximum load were apparently reduced.

2) Distributed stirrups improved the stiffness after diagonal cracking in deep beam with initial bond deterioration. Due to the existence of distributed stirrups, the width of diagonal crack was restrained and the slip of main re-bars in the range of bond deterioration was restrained.

3) Coarsely arranged stirrups did not show reinforcing effect in deep beam with initial bond deterioration. Diagonal crack did not cross stirrups in the shear span, which could not be simulated well by 3D FEM.

4) Initial bond deterioration was appropriately modeled in FEM using joint elements around re-bar elements. The structural behaviors of deep beam with initial bond deterioration of main re-bars were simulated with sufficient accuracy. The effects of distributed stirrups were also well simulated.

Acknowledgements:

The authors acknowledge valuable comments from Dr. Yasushi Tanaka, Nagaoka University of Technology.

References:

JSCE (2007), "Standard Specifications for Concrete Structures," [Design].

Okamura, H., and Maekawa, K. (1991), "Nonlinear Analysis and Constitutive Models of Reinforced Concrete", Gihodo.

Maekawa,K., Pimanmas, A., and Okamura, H. (2003), "Nonlinear Mechanics of Reinforced Concrete", Spon Press.

Tamai, S., Shima, H., Izumo, J., and Okamura, H. (1987), "Average stress - average strain relationship of steel in uniaxial tension member in post - yield range", *Jounal of Materials, Concrete Structures and Pavements*, **378**/V-6, 165-174.

Tsuchiya, S., Nakahama, S., and Maekawa, K. (2001), "The effects of lateral reinforcement on shear capacity and 3 dimensional distribution of diagonal crack of RC beam", *Proceedings of JCI*, **23**(3), 997-1002, .

Suzuki, N., Miki, T., and Niwa, J. (2005), "Lattice Model Analysis of RC Members Considering the Deterioration of Re-bar Corrosion", *Proceedings of JCI*, **27**(2), 97-102

8CUEE CONFERENCE PROCEEDINGS
8th International Conference on Urban Earthquake Engineering
March 7-8, 2011, Tokyo Institute of Technology, Tokyo, Japan

EVALUATION OF SHEAR RESISTING MECHANISM OF PARTIALLY CORRODED RC BEAMS

Tomohiro Miki[1)] and Yasuhito Takeuchi[2)]

1) Associate Professor, Department of Civil Engineering, Kobe University, Japan
2) Graduate Student, Department of Civil Engineering, Kobe University, Japan
mikitomo@port.kobe-u.ac.jp

Abstract: This research includes an experimental investigation to evaluate the residual structural performance of RC beams having partially corroded longitudinal reinforcing bars. The acceleration corrosion was applied to the RC beams which were subsequently used in the loading test. From measurement instruments embedded in the web concrete of RC beams, the minimum principle strain which is calculated by measured strain in the concrete is significant along with the diagonal crack in the shear span. Finally, the experiment results for the failure mode of RC beams can be classified according to the location, range and degree of the steel corrosion of the longitudinal reinforcement in the RC beams.

1. INTRODUCTION

An appropriate method for the maintenance of existing structures has been required to keep the structures having their initial required performance. Deteriorations such as steel corrosion due to the permeation of chloride ions should be considered as one of the durability problems of reinforced concrete (RC) structures. With the deteriorated RC structures, it is required to evaluate the residual performance of the structures in a maintenance system, and hence an analytical tool to evaluate the performance of the structures is keenly needed. In the analysis for these structures, not only the material deteriorations itself but the interaction between concrete and steel reinforcement will be considered. This is because of that both the cross-section of the reinforcement and the bond property due to the expansion pressure by the corrosion products decrease when the steel corrosion occurs in the RC structures. Consequently the safety and serviceability of the structures is affected by the corrosion of steel reinforcement.

Since the shear failure suddenly occurs without any notice and results in a complete loss of structural capacity, it is certainly important to assess the shear carrying capacity of RC structural members accurately. However, it is difficult to formulate a phenomenon of RC behavior in shear which depends on variables, including the bond property between concrete and longitudinal reinforcement. Ikeda and Uji (1980) have been proposed a unified concept for the influence of bond on the shear behavior of RC beams based on their experiment and analysis. Matsuo et al. (2004) conducted the loading tests on the RC beams with or without stirrups having corrosion of reinforcements. The acceleration corrosion procedure by means of applying electric current was used to make corrosion in the steel reinforcement. The RC beams had longitudinal reinforcements with somewhat uniform condition in the shear span as compared to that observed in actual structures. It should note that the corrosion conditions of reinforcement in the actual structures may vary spatially since the surface condition of concrete structures and the environmental actions subjected to the structures depend on the site.

The final goal of this research framework is to establish a method to evaluate the performance of the RC structures using given information for the deterioration due to steel corrosion (Miki and Takeuchi 2010). To achieve this goal, the aim of this study is to evaluate the residual performance of RC beams having partially corroded longitudinal reinforcement by means of the experimental research. In the experiment, a developed measurement instrument embedded in the web concrete of RC beams is used to obtain the internal strain distribution in the concrete being affected by the corrosion condition of reinforcement.

2. TEST PROGRAMS

2.1 Specimens

The test program consisted in a total number of six RC beams. Details of the beam geometry and reinforcement layout are presented in Figure 1 and Table 1. Two series of the beam size is used in the experiment. As it can be seen from the figure, there are no stirrups in the shear span. The reason for such a reinforcement layout is that we want to evaluate the shear carrying capacity of the concrete itself without the help of shear reinforcement. For each concrete mix in Table 2 beams with the dimensions of length, 1200

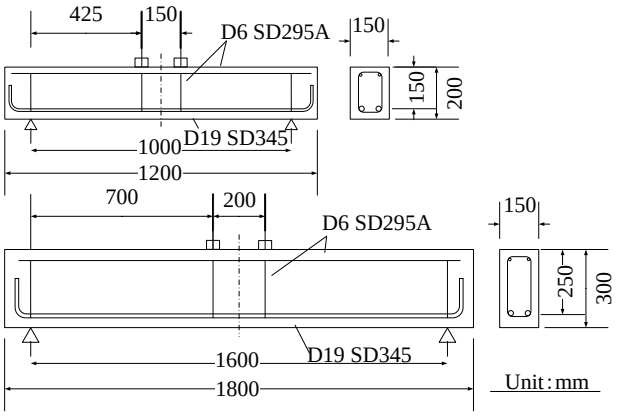


Figure 1 Details of tested beams

Table 1 Outlines of tested beams

Specimen ID	No.1-5	No.6
Cross-sectional width, b (mm)	150	150
Shear span, a (mm)	425	700
Effective depth, d (mm)	150	250
a/d	2.83	2.80
Concrete cover, side (mm)	30	36
Concrete cover, bottom (mm)	40.5	40.5
Cross-section of main bar A_s (mm^2)	573	573
$p_t = A_s/(b*d)$	1.91%	1.53%

Table 2 Mixture properties

G_{max} (mm)	W/C (%)	s/a (%)	W	C	S	G	AE
			(kg/m^3)				(ml/m^3)
20	64.9	45.0	179	276	886	945	414

mm or 1800 mm and a cross-section of 200 × 150 mm have been cast. In this study, a concrete with a designed compressive strength of 30 N/mm^2, obtained from uniaxial compression tests at 14 days, was considered. Maximum size of coarse aggregate was 20 mm. Early-strength Portland cement was used with an air entraining agent in the concrete mixes.

A series of test specimens are summarized in Table 3 and illustrated in Figure 2 except specimen No.6. The experimental parameters were set to be a location, range and degree of the steel corrosion in longitudinal reinforcements. The accelerated corrosion area was located at the middle of shear spans (No.2, No.5 and No.6), ranged from the middle of a shear span to the beam end (No.3 and No.4), as shown in Figure 2. As for the specimen No.4, in the anchorage zone from the support to the beams end, the current was applied additionally. The specimen No.5 had initial simulant cracks at the middle of shear spans where the accelerated corrosion was locally applied. These cracks were formed by means of thin stainless plates which are set there before concrete casting of the beam and removes after the removal of forms. The crack width was 0.2 mm. The specimen No.6 has similar to specimen No.2 with respect to the condition of the steel corrosion in the longitudinal reinforcement but different size of the beam.

2.2 Accelerated Corrosion Tests

Accelerated corrosion tests have been used successfully to determine the susceptibility of steel reinforcement to corrosion. The accelerated corrosion setup used in this investigation consisted of a DC power supply, plastic tanks, electrolytic solution (3% sodium chloride, NaCl by the weight of water) and stainless plates in each tank, as shown in Figure 3. The RC beam soffit was partially attached with a plastic sponge of which other side is immersed in the electrolytic solution of NaCl. The range and location of corrosion in the longitudinal reinforcement was controlled by the ones where the plastic sponge was attached with the soffit of the beams. During the accelerated corrosion test, the cumulative current per unit corrosion area ($A*day/m^2$) applying with a current which is set from 0.7 to 1.7 A was controlled to induce the expected corrosion degree.

2.3 Loading Tests

To obtain the shear carrying capacity of the RC beams, a four point loading test was carried out. A 2000kN universal test machine was used. During the loading test, the load, displacements at both supports and midspan, steel strain of longitudinal reinforcement, and strain in the web concrete

Table 3 Series of experiment

Specimen	Corrosion conditions (mm)
No.1	Reference
No.2	Middle of shear span, 100
No.3	Ranged from the middle of shear span to the beam end, 312.5
No.4	Ranged from the middle of shear span to the beam end, 312.5; Additional corrosion at the anchorage zone, 100
No.5	Middle of shear span, 100 with initial cracks, CMO = 0.2
No.6	Middle of shear span, 165

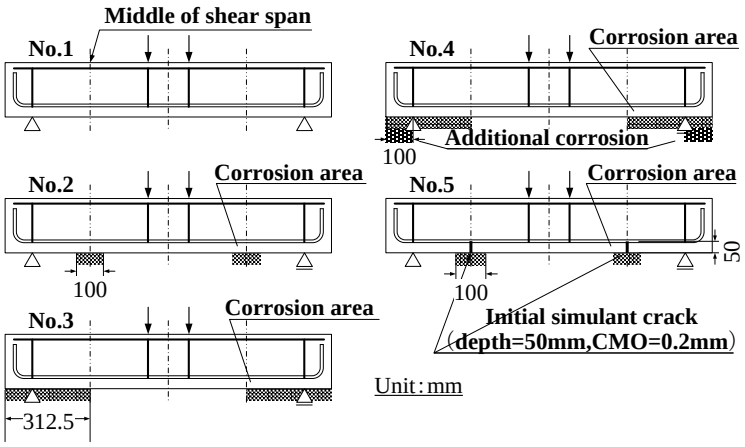


Figure 2 Corrosion condition in the tested beams

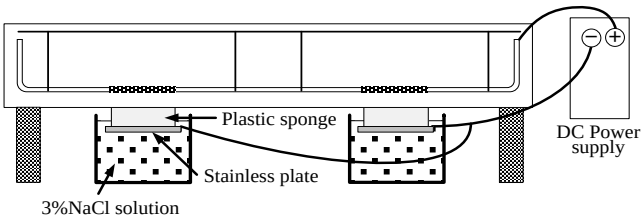


Figure 3 Arrangement for accelerated corrosion test

explained detail in following section were measured. For the purpose of the friction reduction at each support, a set of Teflon sheets lubricated with grease was used.

2.4 Measurement of Strain in the Web Concrete

The internal strain in the web concrete within the shear span of a RC beam was measured during loading tests. Six triaxial rosette strain gages attached on an acryl plate (Tadokoro et al., 2005, Miki and Takeuchi 2010) which was formed and fabricated to firmly behave with surrounded concrete were embedded in the beam. This instrument with strain gages was fixed to the reinforcements for the preparation of concrete casting. For the specimens No.3 to No.5, two fabricated acryl gages, so that 12 measuring points was set were used in the both shear spans of the RC beams. In the specimen No.6, two layers of the fabricated acryl gage was installed to measure the distribution of strain in the height direction. Figures 4 and 5 illustrates details of the acryl attached strain gages and their location set in the specimen No.6, respectively. The material properties of the acryl used in the test are summarized here; a density of 1.18 g/cm3, a tensile strength of 60 MPa, a yield strain of 4.5% and a Young's modulus in tension of 3000 MPa.

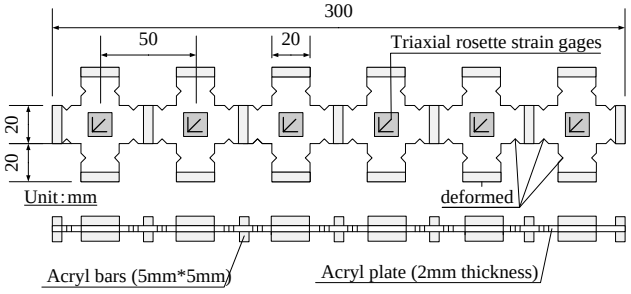


Figure 4 Details of a fabricated acryl gage

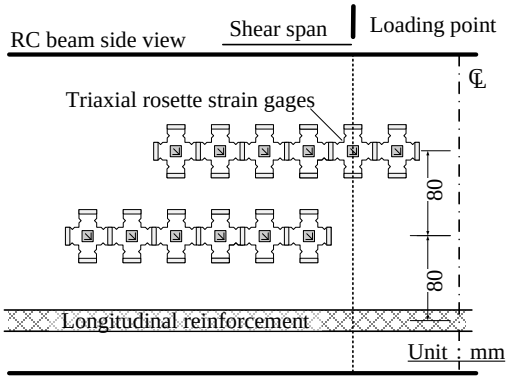


Figure 5 Location of the gages in specimen No.6

2.5 Procedure to Determine the Degree of Corrosion

The degree of corrosion was determined by the weight reduction of the steel reinforcement. In this study, the ratio of cross-sectional loss of reinforcing bar due to corrosion is defined as a ratio of the weight-loss of corroded reinforcing bar from its initial weight to that of non-corroded reinforcing bar. Tensile reinforcement was taken from the demolished RC beams after loading tests. To remove the rust on the steel reinforcement, the reinforcing bars were immersed in the 10% solution of diammonium hydrogen citrate at room temperature for 3 days. Then all reinforcing bars were divided into samples with the length of 50 mm. The ratios of cross-sectional loss were measured for each sample, and the distributions of the ratios of cross-sectional loss of reinforcing bar were measured. Therefore, the amount of corrosion can be estimated by using Eq. (1) as follows;

$$C = \frac{\Delta w}{w} \times 100 \tag{1}$$

where, Δw: weight difference between the samples of non-corroded and corroded reinforcing bars (g/mm), w: weight of non-corroded reinforcing bar (g/mm)

3. TEST RESULTS AND DISCUSSION

3.1 Load-Displacement Relationships

The load-displacement relationships of all specimens are shown in Figure 6. In addition, the results of loading test are summarized in Table 4. It should be mentioned that all specimens showed no yielding of longitudinal reinforcement during the loading test. The stiffness of all beams so that the inclination of the load-displacement curve decreased at 30 kN corresponding the flexural cracking load. The stiffness of the specimens having the corroded reinforcement is similar to the control specimen No.1 until 70 kN at which diagonal crack occurs except the specimens No.3 and No.6.

As for the behavior after diagonal cracking, clear difference between corroded and non-corroded specimens can be exhibited. The specimen No.1 indicated a diagonal tension failure so that the beam failed in brittle immediately after a decisive diagonal crack widely opened. On the other hand, the load of the specimens No.2 to No.6, which are the beams having the corroded longitudinal reinforcement, increased after the diagonal crack occurred, then the failure mode does not become brittle. From the results it can be expected that the failure mode changes with varying the condition of corrosion of the longitudinal reinforcement in the RC beams.

3.2 Crack Patterns of Tested Beams

The crack patterns of all beams after the loading tests are shown in Figure 7. In the figure an inclination angle of the decisive diagonal crack is also shown. Here, this

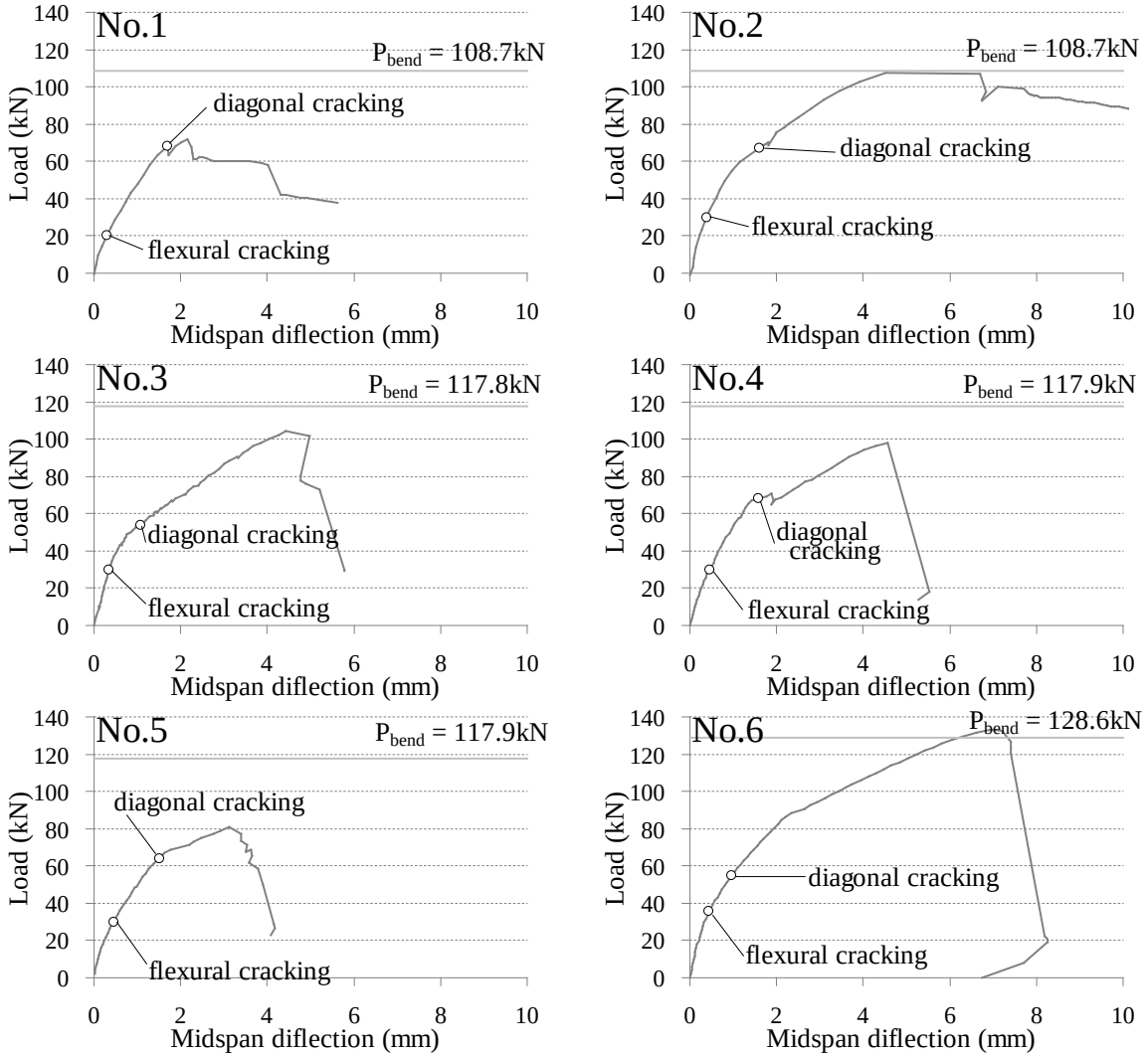


Figure 6 Load-displacement relationships

inclination angle is defined as that of a linear approximation between the loading point and a crossing point of the diagonal crack to the longitudinal reinforcement, as referred the previous study (Tsunoda et al., 2008). The values of θ in Figure 7 are mean values of the inclinations estimated in the shear spans of the beams.

The decisive diagonal crack in the specimen No.1 seems to be located along with a line connecting the support and loading point. On the other hand, the specimens having the corroded reinforcement have the steeper decisive diagonal crack than in the control specimen. With the specimens No.2 and No.6, diagonal cracks initially developed from the corrosion crack at an angle of around 33° and 39°, respectively to the horizontal axis. With further loading, it was observed that the existing corrosion crack had opened at the middle of the shear span. The final failure of the beam is caused by a crushing of the compression zone over the diagonal crack, as referred to a shear compression failure.

The specimens No.3 and No.4 had diagonal cracks propagated from the corrosion crack. This behavior is similar to one of the specimen No.2. The experiment for specimens No.3 and No.4 showed that in these beams the anchorage failure along with the end of the longitudinal reinforcement seemed to occur simultaneously with the crushing of concrete over the diagonal crack that is the vicinity of the loading point.

The specimen No.5 was able to carry additional load

Table 4 Results of loading tests

Beam ID	f_c' (MPa)	Diagonal cracking load (kN)	Max. load (kN)	Failure mode
No.1	23.3	68	71.9	Diagonal tens.
No.2	23.3	67	107.7	Shear comp.
No.3	33.2	54	104.1	Shear comp./ Shear tens.
No.4	33.4	68	98.1	Shear comp./ Shear tens.
No.5	33.4	64	80.9	Diagonal tens.
No.6	34.7	55	133.3	Shear comp.

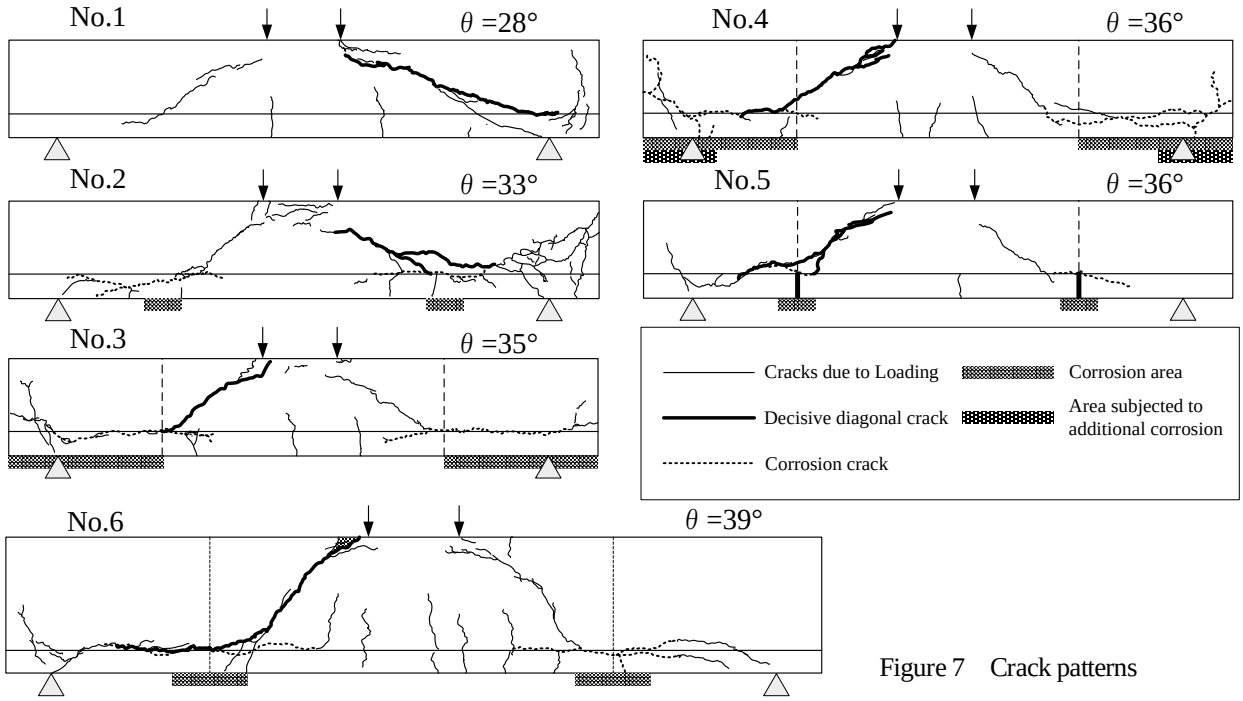


Figure 7 Crack patterns

after developing the diagonal crack at an angle of around 36°. This diagonal crack had propagated from the present corrosion crack at the middle of shear span. At ultimate stage the other crack whose angle was smaller than the former subsequently occurred. This crack propagated and opened gradually and consequently resulted in a diagonal tension failure.

3.3 Concrete Strain in the Web Concrete

As mentioned previously the internal strain in the web concrete within the shear span of a RC beam was measured during loading tests. Figure 8 indicates one of the results for the distribution of maximum and minimum principle strains in the specimen No.6. The results shown here were measured at the loads at the diagonal cracking (84.6kN) to the load carrying capacity (133.3kN) of RC beams, respectively. The length of lines in the figure corresponds to the magnitude of the maximum and minimum principle strains and its inclination indicates the direction of the principle strains. The measured location of the strain gages corresponds to a center point of this line. In the legend symbol, the length of the lines is corresponding to the strain value of $250*10^{-6}$. As can be seen in the figure, the minimum principle strain measured near the diagonal crack significantly increased until the maximum load after the diagonal cracking. This strain is the state of compression. In addition, the direction of the minimum principle strain corresponds to that of the decisive diagonal crack in the shear span. This behavior implies that the formation of the tied arch mechanism in the beam can be predicted. Moreover, the strut of concrete in the tied arch mechanism is formed along with the diagonal crack on its upper region.

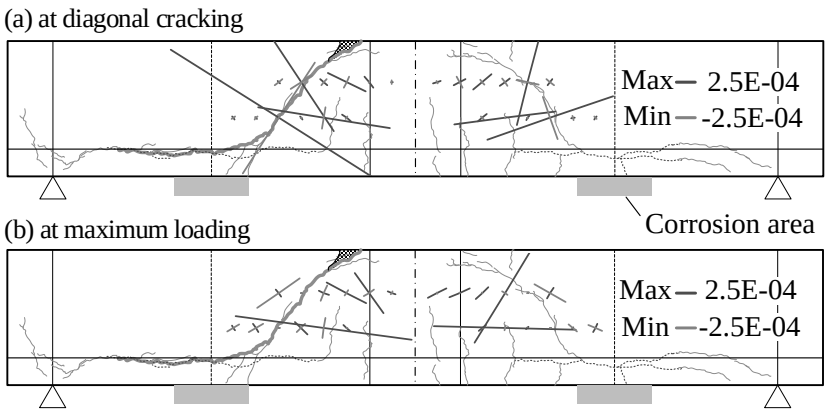


Figure 8 Distribution of maximum and minimum principle strains in the web concrete within the shear span of specimen No.6

3.4 Classification of the Failure Mode of RC Beams According to the Corrosion Condition in the Beams

The control RC beam (No.1) indicates the diagonal tension failure in which the beam failed in brittle immediately after a decisive diagonal crack widely opened. On the other hand, the load of the beams corroded in the longitudinal reinforcement increases after the diagonal crack occurs. The direction of diagonal crack of the corroded RC beams is steeper than that of the control beam. From the experiment, the failure behavior of these corroded RC beams can be classified as follows:

For the RC beams having the corrosion of longitudinal reinforcement in the anchorage zone (No.3, No.4), the diagonal crack propagated from the corrosion crack was observed. At the ultimate stage of these beams, the anchorage failure along with the end of the longitudinal reinforcement occurs simultaneously with the crushing of concrete over the diagonal crack that is the vicinity of the loading point.

On the other hands, the RC beams having the corrosion of longitudinal reinforcement in the shear span (No.2, No.6) suffers after the diagonal crack occurs. With further loading, the existing corrosion crack opens at the middle of the shear span. The failure of the beam is caused by a crushing of the compression zone over the diagonal crack, as referred to the shear compression failure. On the other hands, the RC beam corroded in the shear span but the rage of the crack due to corrosion products is localized because of the presence of a flexural crack shows different failure mode (No.5). The diagonal crack of this beam is propagated from the existing corrosion crack at the middle of shear span. At ultimate stage the other crack whose angle is smaller than the former subsequently occurs. This crack propagates and opens gradually and consequently results in the diagonal tension failure.

4. CONCLUSIONS

In this study the accelerated corrosion tests and loading tests was carried out for six RC beams with and without the corroded longitudinal reinforcement. A control RC beam with a shear span ratio a/d = 2.8 designed failed in shear. Using beams with same dimension to the control, loading test was carried out in order to evaluate the influence of the range and location of corrosion in the longitudinal reinforcement on the shear resisting mechanism of damaged RC beams. The conclusions obtained in the present study are as follows:

1) The carrying capacity of the RC beams having partially corroded longitudinal reinforcement increases compared to a non-corroded beam.
2) The experiment shows the influence of corrosion cracks that are locally observed in the shear span and occurred along with the longitudinal reinforcement on the initiation and propagation of the decisive diagonal crack due to the further loading.
3) Using the measurement instrument embedded in the web concrete, the maximum and minimum principle strains which are calculated by measured strain can be obtained. The distribution of the minimum principle strain indicates the formation of the tied arch mechanism in the beam. In addition, the strut of concrete in the tied arch mechanism is formed along with the diagonal crack on its upper region.
4) The failure mode of partially corroded RC beams can be classified according to the location, range and degree of the steel corrosion of the longitudinal reinforcement.

Acknowledgements:

This research was partially supported from the Ministry of Education, Culture, Sports, Science and Technology (MEXT), Grant-in-Aid for Young Scientists (B), 20760304.

References:

Ikeda, S. and Uji, K. (1980), "Studies on the Effect of Bond on the Shear Behavior of Reinforced Concrete Beams," *Journal of Materials, Concrete Structures and Pavement*, **293**, 101-109.

Matsuo, T., Sakai, M., Matsumura, T. and Kanazu, T. (2004), "An Experimental Study on Shear Resisting Mechanism of RC Beams with Corroded Reinforcement," *Concrete Research and Technology*, **15**(2), 69-77.

Miki and Takeuchi, Y. (2010), "Shear Carrying Capacity of RC Beams Having Partially Corroded Longitudinal Reinforcement," *Proceedings of 7th International Conference on Urban Earthquake Engineering*, 2109-2114.

Tadokoro, (2005), "Effects of Shear Span Ratio on Shear Strength of RC Members with Circular Section," *Journal of Japan Concrete Institute*, **27**(2), 811-816.

Tsunoda, M., Watanabe, K., Miki, T. and Niwa, J. (2008), "Shear Behavior of RC Beams with Locally Corroded Reinforcement," *Journal of Japan Concrete Institute*, **30**(3), 1705-1710.

8CUEE CONFERENCE PROCEEDINGS
8th International Conference on Urban Earthquake Engineering
March 7-8, 2011, Tokyo Institute of Technology, Tokyo, Japan

EVALUATION METHOD FOR LOAD-CARRYING CAPACITY OF INCOMPLETELY-GROUTED PC GIRDERS WITH BROKEN TENDONS

Ken Watanabe[1)], Toshiya Tadokoro[1)], and Yukihiro Tanimura[2)]

1) Assistant Senior Researcher, Structures Technology Division, Railway Technical Research Institute, Japan
2) Laboratory Head, Structures Technology Division, Railway Technical Research Institute, Japan
wataken@rtri.or.jp, tadokoro@rtri.or.jp, tanimura@rtri.or.jp

Abstract: Since low-grade material had been used for grouting of sheath in PC girder, some PC girders initially constructed in 1950s include sheaths being not fully filled by grout. The exposure of PC tendon in the sheath will corrode and break PC tendons, and reduce the load capacity of PC girders. This research focused on the interface bond between PC tendons and grout in sheath through the loading test and FEM analysis in order to explain the loading capacity of deteriorated PC girders.

1. INTRODUCTION

After the construction of first Daidogawa-bridge in 1954: the first post-tension prestressed concrete (PC) girder in Japan, more than 10,000 of post-tension PC girders have been constructed and used for Japanese railway. In such PC girders, the inside of sheaths should be filled with the grout to prevent the PC tendons from corrosion. The grout, however, does not completely fill inside the sheath by various reasons. (Mutsuyoshi 2006) As a results, the corrosion and broken of tendons have been reported. (Ishibashi, T. 2003) PC tendons in the post tension PC-girder are anchored at both ends in order to ensure the enough amount of the stress installed by tendons. Therefore, the corrosion of tendons will drastically change the mechanical performance of the PC girder and reduce the serviceability and the safety of the structure. Therefore, the mechanical performance of incompletely-grouted PC girders with broken tendons should be evaluated to execute the repairing and reinforcing according to it. (Coronelli et al. 2009)

If the grout is partially filled inside the sheath, the stress will transmit from tendons to concrete because the bond exists between tendons and grout after cutting the tendons. This means that the bond between the grout and tendons as well as the residual stress of the PC girder will be a key to evaluate the mechanical performance of the PC girder reasonably. There are several reports of the pull-out test of PC tendon from concrete by referring to the test for the reinforcing bar. (Korenaga and Watanabe 1999) The method, however, cannot duplicate the strain condition of broken-tendon.

The non-destructive evaluation system for understanding the existence the grout inside the sheath is now developing. The corrosion process of PC tendon also has been reported in the world. Integration of these research with the evaluation of the residual stress has a potential to evaluate the mechanical performance of the PC girder immediately.

The objective of this paper is to evaluate the bond between PC tendon and the grout inside the sheath, and the flexural load capacity of incompletely-grouted PC girder with broken tendons. In order to overcome the objective, we conducted a series of rupture tests of PC tendon by using the uni-axially prestressed specimens, and the bond characteristic of the PC tendon was assumed as a function of the PC-tendon type and the grout strength. Finally, the paper proposed the flexural load capacity of incompletely-grouted PC girder with broken tendons with the verification by the experimental results.

2. EVALUATION OF RESIDUAL PRESTRESS OF PC-GIRDERS WITH BROKEN TENDONS

2.1 Rupture Test of PC-Tendon in Uni-axial Specimen

Figure 1 indicates the outline of specimen. The specimen had a rectangular cross-section with 250×250 mm or 400×400 mm, and the hole was located at the edge of specimen in order to cut the PC tendon before loading. The

target compressive strength of concrete was 50 N/mm^2.

The grout was filled enough in the steel sheath, and four longitudinal re-bars were arranged in surrounding of the sheath, and stirrups with the nominal diameter of 13 mm were provided with an interval of 100 mm. In addition, the deformed re-bars having a series of strain gauges were installed along the sheath of the specimen.

Table 1 lists the parameter of nine specimens used in this study: the compressive strength of the grout (grout strength) and the type of PC-tendon. According to Korenaga and Watanabe (1999), both affect the bond characteristic between tendons and the grout. The age of installing the prestress force was 10 days, and the tendon was cut at 30 days after the casting.

2.2 Residual Stress Ratio

The magnitude of residual stress after cutting the PC tendon was measured by using the gauge arranged on the re-bars. Figure 3 shows the residual stress ratio, which can be calculated by comparing the strain measured before and after cutting the tendon.

Figure 3(a) compares the influence of the grout

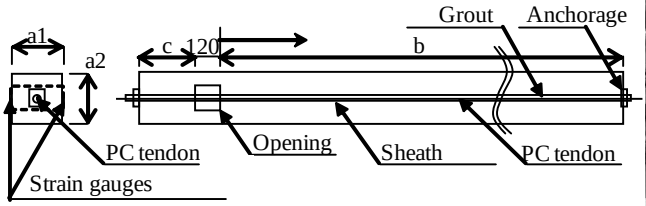


Fig. 1 Outline of specimen

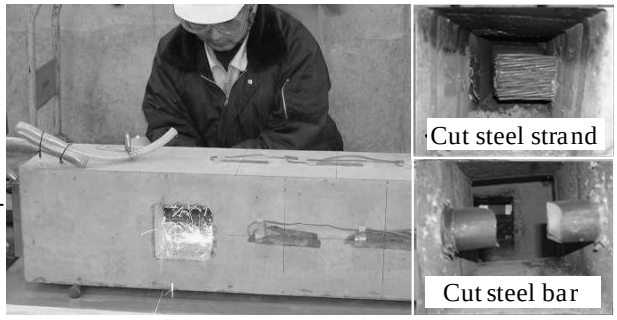
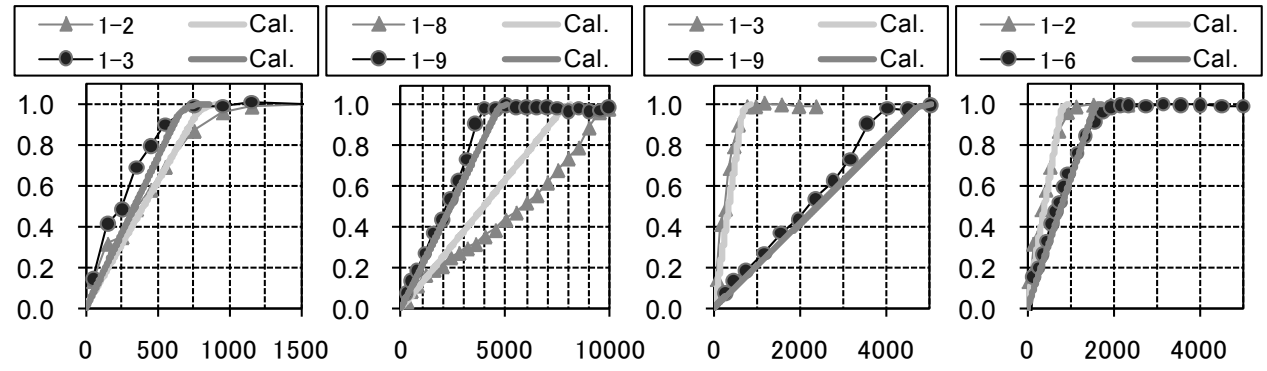


Fig.2 Cutting of PC tendon

Table 1 Specimen detail

No.	Dimension					PC tendon			Grout		Concrete		Effective prestress force (kN)
	a1 (mm)	*a2* (mm)	*b* (mm)	*c* (mm)	Sheath (mm)	Type	#-ϕ (mm)	f_y (N/mm^2)	f'_g (N/mm^2)	E_g (kN/mm^2)	f'_c (N/mm^2)	E_c (kN/mm^2)	
1-1	250	250	3000	280	38	Steel strand SWPR7AL SWPR7BL	1T9.3	1683	48.8	15.4	53.6	32.0	58
1-2							1T12.7	1824	30.3	12.7			108
1-3									48.8	15.4			114
1-4									67.0	16.8			106
1-5							1T15.2	1875	48.8	15.4			192
1-6	400	400	10000	450	65		12T12.7	1883	26.8	10.9	54.5	40.0	1192
1-7									44.6	15.5	54.5	39.0	1193
1-8	250	250		280	38	Round bar SBPR 930/1080	ϕ 32	813	26.8	10.9	54.5	40.0	558
1-9									44.6	15.5	54.5	39.0	561

ϕ: diameter of round bar, f_y: yield strength of PC tendon, f'_g: compressive strength of grout, E_g: Young's modulus of grout, f'_c: compressive strength of concrete, E_c: Young's modulus of concrete



(a) Effect of grout strength (Steel strand) (b) Effect of grout strength (round bar) (c) Effect of PC tendon type (d) Effect of number of strand

Fig. 3 Residual ratio of stress after cutting PC tendon

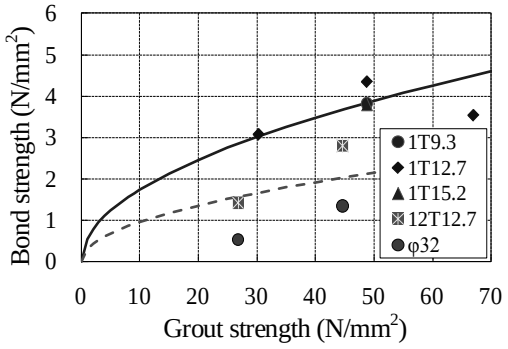


Fig. 4 Bond strength of specimen (see Table 1)

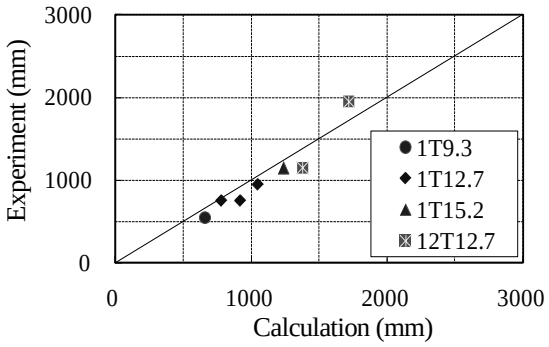
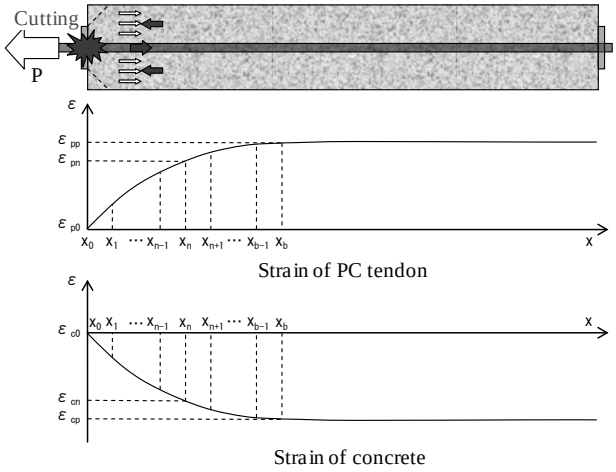


Fig. 5 Length of the stress-decreasing region



where,
P: effective prestress force (N),
ε_p: strain of PC tendon,
ε_c: strain of concrete,
s: slip displacement (mm),
x: distance from cut-point $\Delta x=x_n-x_{n-1}$ (mm),
A_p: cross sectional area of re-bars (mm^2),
E_p: Young's modulus of PC tendon (kN/mm^2),
D: nominal diameter of re-bar (mm),
A_c: cross sectional area of concrete (mm^2),
E_c: Young's modulus of concrete (kN/mm^2).

(Boundary condition)
Cut-point: $x_0=0$, $\varepsilon_{p0}=0$, $\varepsilon_{c0}=0$, $\varepsilon_{pp}=P/(E_p*A_p)$, $\varepsilon_{cp}=-P/(E_c*A_c)$, $s_b=0$, $\tau_{pb}=0$, $\tau_{cb}=0$.

Fig. 6 Calculation of residual stress in concrete and strain at PC tendon after cutting the tendon

strength on the residual stress ratio between experimental results of 1-2 and 1-3. The figure indicates that the bond strength between tendons and the grout increased with the increase in the grout strength, and the stress-decreasing region where the ratio indicate less than 1.0 became small.

Figure 3(b): the result of 1-8 and 1-9, shows the influence of the grout strength on the length of stress-decreasing region became large when the PC tendon was a round re-bar. In addition, Fig. 3(c), which compares the result of 1-9 using the round re-bar and 1-3 using strands as for PC tendon, informs that the length of stress-decreasing region also changed strongly depending on the type of

tendons.

Figure 3(d) indicates the PC tendon that consisted of two or more strands increased the length of stress-decreasing region because these strands contacting each other cannot attach to the grout.

2.3 Calculation of Residual Stress

Figure 3 implied that the relationship between the residual stress and the distance from the breaking position of PC tendon showed a linear in the stress-decreasing region. This means that inclination seems to be a linear relationship, so the bond stress was constant in the stress-decreasing region. This study calculated the bond strength with dividing the effective stress by the surface area of the PC tendon.

Based on the experimental results, Fig. 4 plots the bond strength as the function of the grout strength, of which tendency that the bond strength increases as the grout strength increases. This study assumed the relationship can be as a function of grout strength (f_g') by referring to Korenaga and Watanabe (1999).

The phenomenon of this research is the generation of bond force according to the stress releasing of PC tendon, on the other hands, Korenaga and Watanabe (1999) focused on the bond-slip displacement based on the pull-out test of PC tendon from concrete. Even these two phenomena will be different in the point of bond characteristic with grout according to the extension or the shrinkage of PC tendon, this study followed the function form of Korenaga and Watanabe (1999) in the range of this study.

In addition, Fig. 3(d) confirmed that the length of the stress-decreasing region was different between the specimens having one strand wire and two or more strand wires. Therefore, the bond strength of grout and PC tendon was provided respectively as a function of f_g' as Eqs. (1) and (2) according to the number of the strand wire. The calculation by Eqs. (1) and (2) are plotted in Fig. 4 to compare with the experimental results.

$$\tau_1 = 0.55\sqrt{f_g'} : \text{single strand} \tag{1}$$

$$\tau_2 = 0.30\sqrt{f_g'} : \text{malch strands} \tag{2}$$

The bond-slip relationship was expressed as bi-linear based on the bond strength by Eqs. (1) or (2).

Figure 5 shows the pattern diagrams of the strain distribution of concrete and PC tendon after the tendon is broken in the PC beam. The force balance in a certain section: the accumulation of bond force between PC tendon and grout is equals to the decreased force in the tendon in the section, derived the following Eqs. (3) to (6).

$$s_{n-1} = s_n + \left(\varepsilon_{pp} - \frac{\varepsilon_{pn} + \varepsilon_{pn-1}}{2}\right)\Delta x - \left(\varepsilon_{cp} - \frac{\varepsilon_{cn} + \varepsilon_{cn-1}}{2}\right)\Delta x \tag{3}$$

$$\tau_{cn-1} = \frac{E_c\left(\varepsilon_{cn-1} - \varepsilon_{cn}\right)A_c}{\pi D \Delta x} \tag{4}$$

Table 2 Specimen detail

Specimen detail					Experiment and calculation results					
No.	Concrete		Effective prestress force (kN)	Cutting ratio (%)	Load at PC-tendon yielded			Flexural capacity		
	f'_c (N/mm^2)	E_c (kN/mm^2)			P_y (N)	P_{y1} (N)	P_y/P_{y1}	P_{max} (N)	P_{mu} (N)	P_{max}/P_{mu}
2-1	58.1	39.5	1213	0	448	439	1.02	714	675	1.06
2-2			1268	50	381	401	0.95	698	594	1.18
2-3	57.0	40.1	1174	75	355	276	1.28	600	430	1.40
2-4			1217	0～67	-	356	-	615	544	1.13

f'_c: compressive strength of concrete, E_c: Young's modulus of concrete, P_y: load at longitudinal re-bars yielding, P_{y1}: load corresponding to yielding moment (M_{y1}) acting on failed cross-section, P_{max}: experimental value of flexural load capacity, P_{mu}: load corresponding to maximum moment (M_u) acting on failed cross-section, P_{max}: experimental value of flexural load capacity.

$$\tau_{pn-1} = \frac{E_p(\varepsilon_{pn} - \varepsilon_{pn-1})A_c}{\pi D \Delta x} \quad (5)$$

$$\tau_{cn} = \tau_{pn} \quad (6)$$

The residual stress ratio of the specimen was calculated according to Eqs. (3) to (6), and plotted in Fig.3. Figure 6 indicates the stress-decreasing region based on experiment and calculation results. It confirmed that the calculation value can reproduce the test results. The stress-decreasing region and the magnitude of stress were calculated by the developed bond-slip relationship (t-s) and Eqs. (3) to (6).

3. EVALUATION FOR FLEXURAL LOAD CAPACITY OF INCOMPLETELY-GROUTED PC GIRDERS WITH BROKEN TENDONS

3.1 Bending Test of PC Girders with Broken Tendons

Table 2 lists the parameter of the specimen test and the material used in this study, Fig.7 shows the outline of the specimen. The PC tendon was a single strand (SWPR7BL: 12T12.7) with yield strength (f_{py}) of 1849 N/mm^2, the tensile strength of 2020 N/mm^2, and Young's modulus (E_p) of 194 N/mm^2. The longitudinal re-bar has the nominal diameter of 12.7 mm, the tensile yield strength (f_{sy}) of 370 N/mm^2, and Young's modulus (E_s) of 194 kN/mm^2. Stirrups has the nominal diameter of 15.9 mm, the tensile yield strength (f_{sy}) of 345 N/mm^2, and Young's modulus (E_s) of 194 kN/mm^2.

Steel sheath with the diameter of 65 mm was used. The inside of the sheath were filled by grout (the compressive strength of 34.1 N/mm^2). The bond between PC tendon and the grout had been removed in the range of 1000 mm from one-support of the beam by wrapping the tape around the tendon. Four specimens were prepared: 2-1 with no-broken tendon and 2-2 to 2-4 with 50 to 75 % of tendons being broken. PC tendons in 2-2 and 2-3 were cut before the loading test, and the tendon of 2-4 was gradually cut with applying the load of 620 kN.

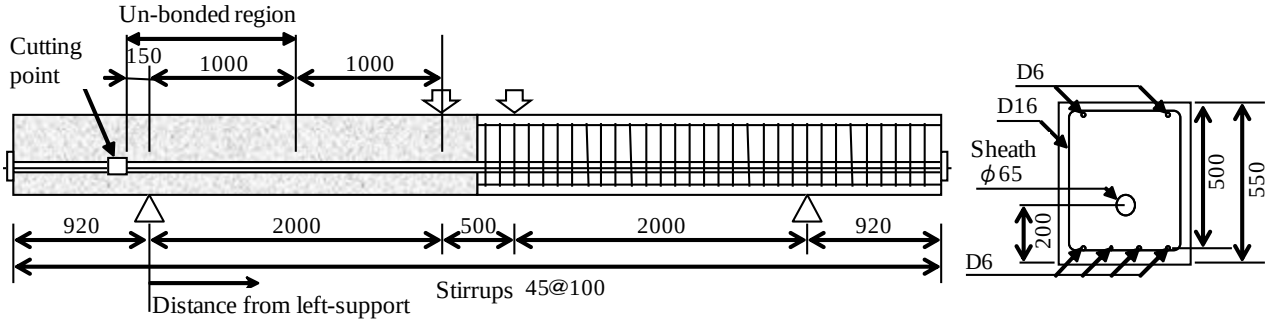


Fig.7 Specimen detail

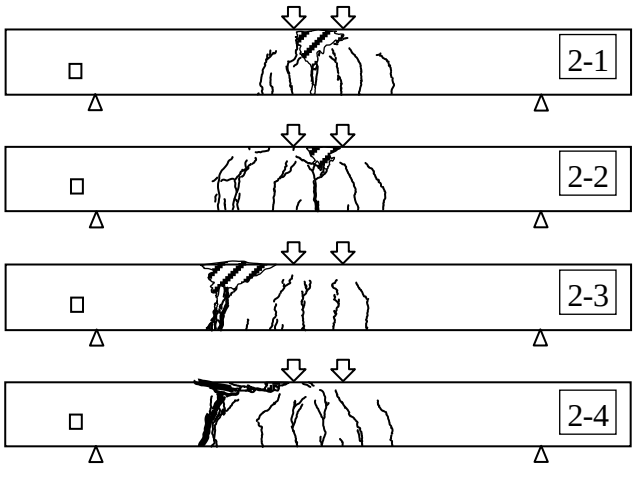


Fig.8 Failed specimens

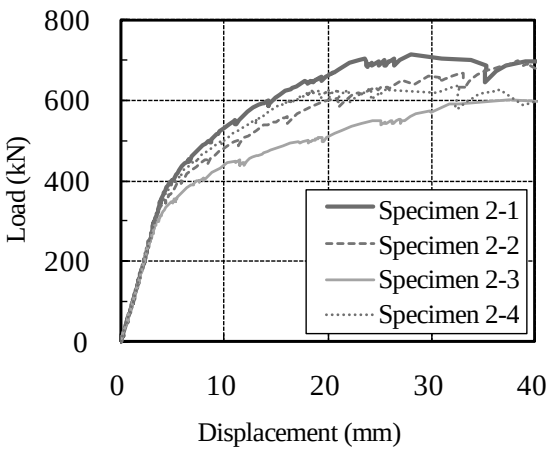
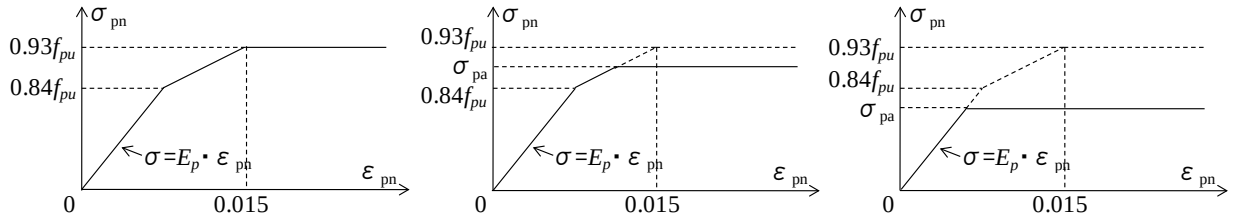


Fig.9 Comparison of load-displacement relationship



(a)No-damaged PC (b) Broken PC tendon, $\sigma_{pa} < 0.93f_{pu}$ (c) Broken PC tendon, $\sigma_{pa} < 0.84f_{pu} = f_{py}$

where, σ_{pa} : stress in PC tendon when the tendon slips (N/mm^2), $\sigma_{pa}=\tau_1 * \phi * \pi * L_a/A_{pn}$
L_a : Distance between failed cross-section and cutting point of PC tendon. (mm)

Fig. 10 Stress-strain relationship of PC tendon

Figure 8 shows the crack distribution of tested specimens. All specimens were failed in flexural with crashing the concrete at the top-edge. Table 2 summarizes the experiment and calculation results. The flexural crack generated at the load of 252 to 346 kN. The number of the crack increased with the increase in the amount of cutting the PC tendon.

According to the crack distribution of 2-2, some flexural cracks were observed in left side, and concrete at the middle span of specimen was crashed. This crashing position was transferred to the left side: 1300 mm from left support in the specimen 2-3. The number of flexural crack in the left span of 2-4 was increased as the PC tendon cutting, then concrete between 1200 to 1800 mm from left support.

Figure 9 compares the load-displacement relationship of all specimens. The load-carrying capacity and stiffness were depending on the number of tendon. Specimen 2-4 was not able to hold the load 620 kN when 67 % of wires were broken.

3.2 Evaluation of Flexural Load Capacity

The flexural capacity of PC beams with broken tendons was calculated according to the assumption of plane stress remained plane, and the balance force in the section as (RTRI 2004):

$$C' = \int_0^x \sigma'_c(u) \cdot b(u) du \quad (7)$$

$$T_p = \sum A_{pn} \cdot \sigma_{pn} \quad (8)$$

$$T_s = A_s \cdot \sigma_s \quad (9)$$

where, C' : compressive force carried by concrete (kN), T_p : tensile force carried by PC tendon (kN), T_s : tensile force carried by longitudinal re-bars (kN), σ'_c(u): compressive stress carried by concrete at the height (u) from neutral axis (N/mm^2), b(u): width of cross-section at the height (u) from neutral axis (mm), A_{pn}: cross-section area of PC-tendon at n (mm^2), σ_{pn}: stress of PC-tendon at n (N/mm^2), A_s: cross-section area of tensile re-bars (mm^2), and σ_s: tensile stress at centroid of longitudinal re-bars (N/mm^2).

The flexural capacity M_u was calculated by Eqs. (10) to (12) as:

$$N'_d = C' - T_s - T_p \quad (10)$$

$$M_u = C'(d_s - e_s - \beta_x) + T_s \cdot e_s + \sum A_{pn} \cdot \sigma_{pn} \cdot e_{pn} \quad (11)$$

$$\beta_x = x - \frac{\int_0^x \sigma'_c(u) \cdot b(u) \cdot u \cdot du}{C'} \quad (12)$$

where, N'_d: force in longitudinal direction (kN), M_u: maximum moment (kNm), d_s: distance from compressive edge to the centroid of tensile longitudinal bars (mm), e_s: distance between centroids of tensile longitudinal bars and cross-section (mm), e_{pn}: distance between between centroids of PC tendon at n and cross-section (mm), and x: distance between compressive flange and neutral axis (mm).

The tensile force carried by broken PC tendon was calculated by the tensile strain (ε_{pn}) estimated by considering the bond of PC tendon as Fig. 10.

3.3 Verification of Calculations by Comparing with Experimental Results

The flexural capacity of partially prestressed concrete beams was calculated by verifying the balance between the action and the resistance moments in all cross-section of the specimen. The checking position is corresponding to the position of failed cross-section section in the experiment.

Table 2 compares the maximum load capacity in the experiment and the calculation according to section 3.2. Based on the result of 2-4, the load-capacity of the specimen was assumed to be 620 kN when 67 % of the tendon was broken. The calculated results seem to be a similar to the experimental values. The ratios between both were 1.13 to 1.40; that became larger by cutting the PC tendon.

One of the reasons for the experimental values being larger than the calculation was considered as the influence of the moment action on the bond behavior. Even so, the proposed method in this study can evaluate the flexural load capacity of incompletely-grouted PC girders with broken tendons, and enable more reasonable method for repairing and reinforcing the deteriorated PC girders.

4. CONCLUSIONS

The influence of grout strength and a type of PC tendon on the length of stress-decreasing region was examined, and proposed the method for getting the residual stress in PC girders. Finally the method for evaluating the flexural load capacity of incompletely-grouted PC girders with broken tendons was proposed.

This research has been supported by the subsidy from Ministry of Land, Infrastructure, Transport and Tourism.

References:

Coronelli, D., Castel, A., Anh Vu, N., and Francois, R., (2009) "Corroded Post-tensioned Beams with Bonded Tendons and Wire Failure," *Engineering Structures*, 31, 1687-1697.

Ishibashi, T. (2003), "Deterioration and Countermeasures of PC Railway Strictures," *J. of Prestressed Concrete*, 45(1), pp.72-75.

Korenaga T., Watanabe H. (1999), "Medol of the Bond Characteristics between Prestressing Strand and Grout Mortar, *Proc. of Architectural Institute of Japan*, pp.1083-1084.

Mutsuyoshi, H. (2006), "Present Situation and Problems on PC Grouting," *J. of Prestressed Concrete*, 48(2), pp.22-25.

Railway Technical Research Institute (2004), "Design Standards for Railway Structures and Commentary (Concrete Structures)" Maruzen.

8CUEE CONFERENCE PROCEEDINGS
8th International Conference on Urban Earthquake Engineering
March 7-8, 2011, Tokyo Institute of Technology, Tokyo, Japan

DEFORMABILITY MODELS FOR SHEAR CRITICAL REINFORCED CONCRETE MEMBERS

Sung-Gul Hong

Professor, Dept of Architecture, Seoul National University, Korea
sglhong@snu.ac.kr

Abstract: This paper presents how to estimate deformability of shear critical reinforced concrete members. This study focuses on ductility of reinforced concrete members which mostly depends on ultimate strain of concrete in compression. For ductile behavior of systems seismic design practices rely on formation of plastic hinge an intended region of flexural members. To guarantee and increase deformability of concrete in compression appropriate reinforcement details for confinement have been focused on. Most design provisions are supposed to suppress premature shear strength dependent on deformation cannot be avoided such as in deep coupling beams and beam-column joints even after flexural yielding for stable energy dissipation. Since most of ductility of limited ductility concepts have been introduced for flexural shear failure of columns and shear strength of walls of low aspect ratios. This study shows the utilization of failure mechanisms of strut-and-tie models for deformability. Crushing of compressive struts and bond strength degradation can be extended to the estimation of deformability of other shear critical members.

1. INTRODUCTION

Structural concrete in disturbed regions (D-regions) is characterized by geometric discontinuities, adjacency to holes, abrupt changes in the cross-section or direction, or statical discontinuities, which are regions near concentrated loads and reactions. Strut-and-tie models (STM) have been successfully used to detail structural concrete in D-regions, as these models illustrate the explicable force flows within D-regions (Marti 1985-1, Marti 1985-2, Muttoni 1997, Schlaich et al. 1987, MaGregor 1988, Schlaich et al. 1991). Inelastic deformations of shear-dominated walls, potential plastic hinges at the bases of columns, and coupling beams in such D-regions are associated with limited ductility and shear strength reduction (Paulay et al. 1992). In practical designs, it has been recommended that the contribution of the concrete to the shear strength is reduced for such shear critical members of limited ductility. Furthermore, when designing the squat wall according to the provision of NZS 3101(Standard Association of New Zealand 1982), the dependable displacement ductility capacity in the squat wall is assumed to be affected by the aspect ratio. However, questions remain as to why most shear transfer members that rely on diagonal struts and/or diagonal compression fields show brittle behavior or limited ductility even after the yielding of longitudinal reinforcements while under-reinforced flexural members show larger ductility.

Many researchers have analyzed the load-deformation curves and deformation capacity of structural concrete in continuity regions using compression field theory or the modified compression field theory in terms of the average stress and strain (Collins 1978, Vecchio 1986). The cracked membrane model (Kaufmann 1998, Kaufmann et al. 1998) further combines the basic concept of the modified compression field theory and the tension chord model that adopts a stepped, rigid-perfectly plastic bond stress-slip relationship to investigate problems related to the deformation capacity of both non-prestressed and prestressed concrete members. Subsequently, the tension chord model (Marti et al. 1998) was attempted to apply, along with the discontinuous stress field in disturbed regions, to determine the rotation capacity of plastic hinge regions and to evaluate the permissible moment redistribution in continuous members. Similarly, the deformation capacity of interior beam-column joints with plastic hinges at beams was proposed by the consideration of change in nodal zones and shear force transfer within joints (Hong et al. 2011-1). For practical reasons, however, the development of a more efficient method is needed to estimate the deformation capacity of structural concrete in a simple and direct manner without recourse to an iterative and incremental analysis using the modified compression field theory or the cracked membrane model.

One of the methods to estimate the deformation capacity of structural systems is a mechanism-based approach which considers admissible geometric configurations at the ultimate state. A mechanism-based approach (Paulay 1998, Paulay 2002) which considers admissible geometric configurations at the ultimate state was developed as a way to estimate the deformation capacity of structural systems (e.g., torsional behavior of asymmetric shear wall systems). The mechanism-based approach is a clear, rational method

for estimating system ductility taking into account the maximum deformation of critical components; that is, the ductility limit of the system depends on given ductility limits of the components of a static system. This study shows how this concept is extended to the estimation of the maximum deformation of structural concrete, which is controlled by the deformation capacity of compression struts, critical components that govern the failure mechanisms (Hong et al. 2011-2).

The objective of this paper is to introduce a simple, clear, and rational model to estimate the deformation capacity of structural concrete in D-regions in terms of direct shear transfer and indirect shear transfer. Failure mechanisms that are compatible with STMs are considered to determine the governing deformation patterns of the struts and bond failure. The proposed model addresses the effects of the aspect ratio, reinforcing degree, and ultimate compressive strain of concrete on the deformation capacity. The proposed model can serve as a deformation estimation tool for the D-regions of limited ductility such as joints, coupling beams and walls that are dominated by shear.

2. FUNDAMENTALS

2.1 Classification of Load Transfer for Shear

Shear force transfer has been explained by direct transfer via diagonal struts and indirect transfer via transverse reinforcement in a beam as shown in **Fig. 1**. In other words, direct transfer by strut action and/or arch action and indirect transfer by truss actions. Arch action relies on compressive strength of concrete and slope of struts while truss action on transverse ties with bond.

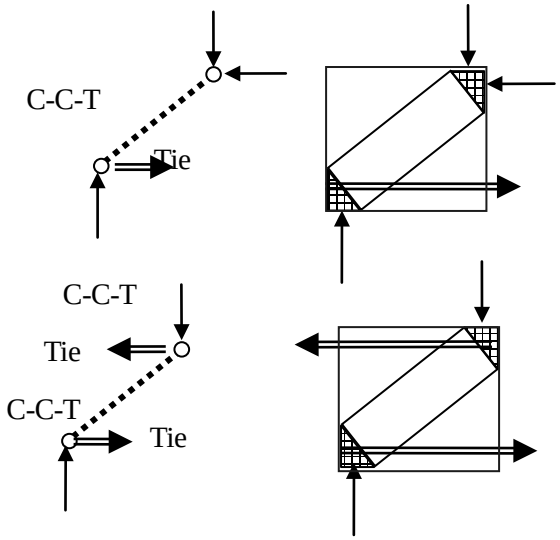


Fig. 1 Direct Shear Transfer

Typical indirect shear transfer can be explained by a uniform or smoothly varying stress fields (B-regions) such as in shallow beams in shear and it has been so-called truss action. The total shear strength relies on diagonal strut and fan or diagonal compression fields. Selection of fan or diagonal compression fields for indirect shear transfers depends on ways of shear acting on boundaries. For a concentrated load the diagonal strut is combined with fans while for distributed shear applied along the boundary the diagonal strut is combined with diagonal compression field as shown in **Fig. 2**. In case of distributed shear along the boundaries the maximum shear strength is developed by sum of diagonal strut action and truss action.

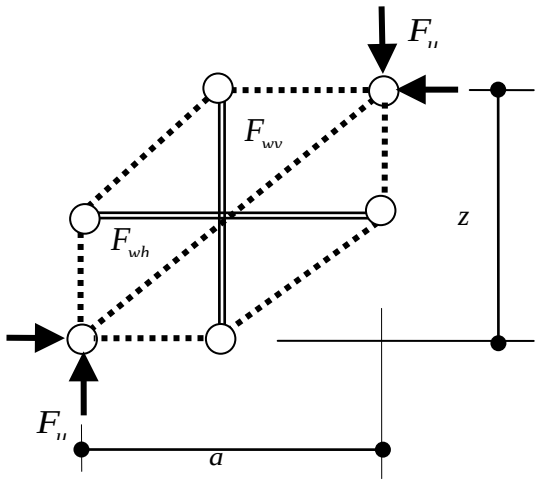


Fig. 2 Indirect Shear Transfer

2.2 Yield Condition and Assumption

The square yield locus with a zero tension cut-off in **Fig. 3** is used for the yield condition for concrete in this study. A reinforcing bar is assumed to resist in the axial direction only, and dowel action is neglected (**Fig. 3**). The effectiveness factors and for reinforcing steel and concrete relate the yield strengths of the idealized plastic material to the properties of the actual material and the factors generally depend on the strain environment.

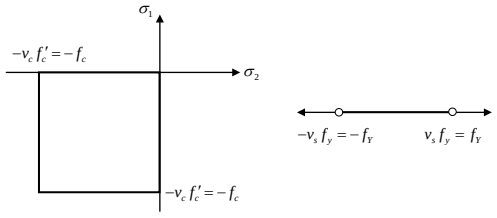


Fig. 3 Yield Conditions for Concrete and Steel

The change in geometry of the structure that occurs at the limit load is assumed to be negligible. The geometric description of the structure due to failure mechanism remains unchanged, so as to allow the formulation of displacement sets based on the original configuration. It is assumed that the displacements induced by the failure mechanisms equal the total deformations of limiting values as indicated in **Fig. 4**.

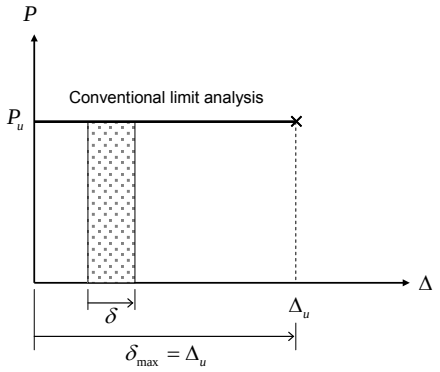


Fig. 4 Rigid-plastic Behavior

3. DEFORMABILITY FOR DIRECT TRANSFER OF SHEAR

3.1 Stress Fields and Failure Mechanisms

In order to understand direct load transfer for shear, consider a simple case where one concentrated force at the top in the right of half of deep beam is supposed to be transferred the support located at the left bottom of beam.

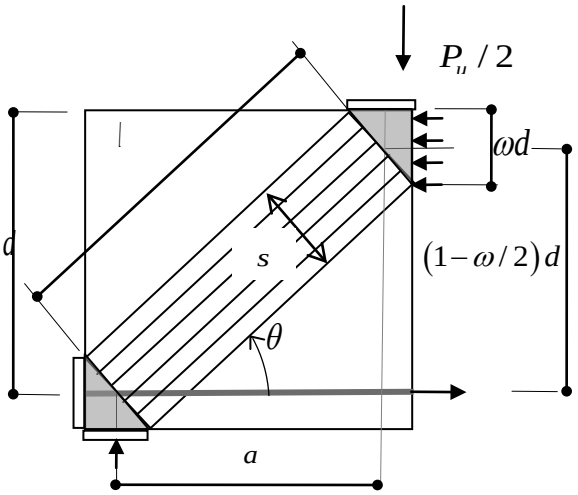


Fig. 5 Stress Field for Half of Simply Supported Deep Beam

The distances between the two points are *z* and *a* in the vertical and horizontal directions, respectively. A simple stress field for half of the deep beam of depth *d* and width *b* under two vertical loads on the top is considered, as shown in **Fig. 5**. The stress field consists of a strut of uniform width, a horizontal tie, and two bi-axially compressed nodal zones at the left loading point and the support. At the ultimate condition, the yielding of the tie provides the width of the strut *s* as

$$s = \omega d / \cos\theta \qquad (1)$$

where ω is defined as the reinforcement degree $(A_s f_Y)/(bdf_c)$, A_s is the sectional area of the longitudinal reinforcement, f_c is the effective compressive strength of the concrete, and θ is the inclination angle of the strut with respect to the horizontal axis.

The selection of possible failure mechanisms for this stress field depends on whether or not the chosen failure mechanism requires the yielding of a horizontal tie. Three well-known failure mechanisms for the crushing of a strut involve bending, translational, and rotational mechanisms involving a hyperbolic failure curve (Marti et al 1982, Ashour et al. 1996). The deformation of each failure mechanism is assumed to be limited by the ultimate compressive strain in the struts.

3.2 Deformation Capacity Models

The bending mechanism in **Fig. 6** involves the elongation of the horizontal tie and the rotation of the strut. The strut is assumed to rotate about the bottom corner of the bi-axially compressed nodal zone at the loading point.

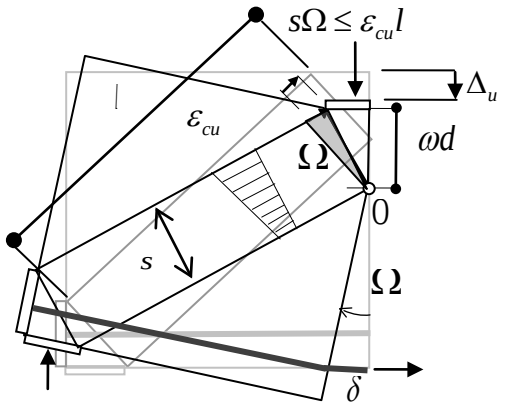


Fig. 6 Bending Mechanism

The deformation limit in this bending mechanism is expressed in terms of mechanical reinforcement ratio, *a/d*, and ultimate compressive strain of concrete.

$$\frac{\Delta_u}{a} \le \left[\frac{1}{\omega}\frac{a}{d} + \frac{(1-\omega/2)}{2}\frac{d}{a}\right]\varepsilon_{cu} \qquad (2)$$

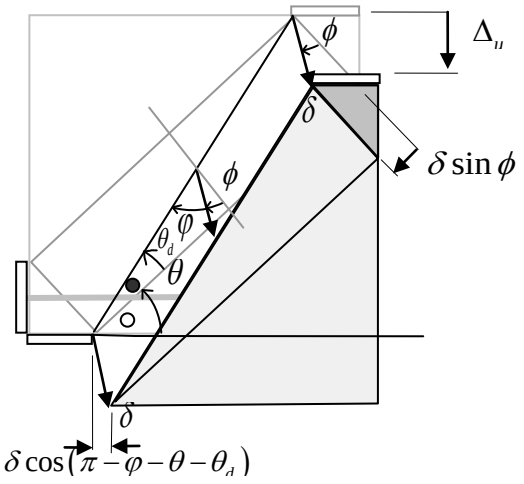


Fig. 7 Translational Mechanism

Next, consider a translational failure mechanism involving the straight diagonal failure crack in the strut as shown in **Fig. 7**. This translational mechanism for the deep beam accompanies the yielding of the horizontal tie depending on whether the horizontal displacement component of the horizontal tie across the diagonal failure crack occurs or not. Since the strut's shortening should be equal to the absolute difference of the movement of its ends, the translational displacement δ along the diagonal in the strut results in the shortening of strut.

$$\frac{\Delta_u}{a} \le \frac{1}{(1-\omega/2)}\left[\frac{a}{d}+\frac{d}{a}(1-\omega/2)^2\right]\varepsilon_{cu} \qquad (3)$$

Finally, consider the so-called hyperbolic failure mechanism, in which failure crack occurs along a hyperbolic curve within a strut as shown in **Fig. 8**. Due to this rotational mechanism, two rigid bodies are separated along a hyperbolic curve passing through two corner points of strut. In this case, the bottom rigid body is assumed to rotate about an instantaneous center of rotation located at any point along the diagonal of the strut. This failure mechanism results in a sliding surface that causes crushing of concrete in the strut.

To describe the hyperbolic curve and the corresponding displacement field, it is convenient to introduce a local *x*-*y* coordinate system with the origin at an instantaneous center of rotation to describe the hyperbolic curve and the corresponding displacement field. The *x*-axis runs parallel to the axis of strut.

This failure mechanism involves non-yielding of the horizontal tie, when the instantaneous center of rotation is located at the intersection point of the diagonal of strut and an extended line of the tie. On the other hand, when the instantaneous center of rotation is located at any other point along the diagonal, the crushing of the strut is combined with the yielding of the horizontal tie because the elongation of the tie due to the mechanism occurs as shown in Fig. 8.

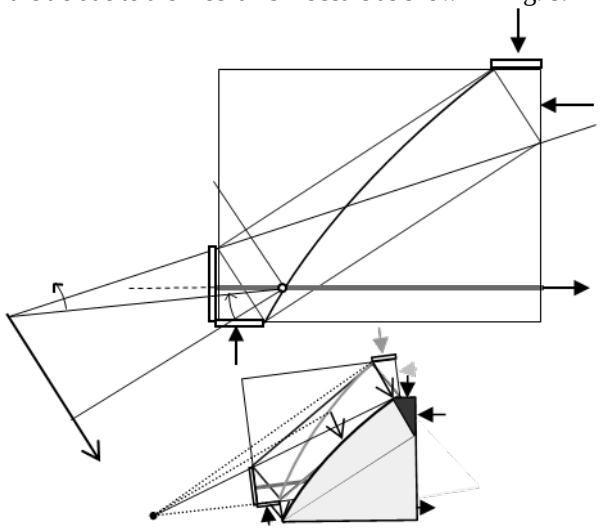


Fig. 8 Rotation Mechanism Involving Hyperbolic Curve

$$\frac{\Delta_u}{a} \le \left(1-\cos^2\theta+\cot\phi_b\sin\theta\cos\theta\right)\frac{1}{\sin\theta\cos\theta}\varepsilon_{cu} \qquad (4)$$

4. DEFORMABILITY OF INDIRECT SHEAR TRANSFER

4.1 Stress Fields and Failure Mechanisms

Shear transfer in a deep beam with stirrups has been treated as indeterminate strut-and-tie models in terms of arch action and truss action which is so called indirect load transfer for shear.

Distribution between arch action and truss action is assumed or can be determined using stiffness ratio, strength ratio, and the energy based methods. For example, the strength ratio gives a possible distribution between direct and indirect load transfer of shear. As **Fig. 2** indicates, the equilibrium conditions at nodes and strengths of vertical and horizontal reinforcement result in the ratio of shear strength by diagonal strut to the total shear strength F_u as

$$\zeta_0 = 1-\frac{F_{wv}}{F_u}-\frac{F_{wh}}{F_u}\frac{z}{a} \qquad (5)$$

where z denotes the arm length of flexural compression to the tension tie and a shear span length. The strength of intermediate vertical and horizontal ties denotes F_v and F_h, respectively.

We may consider two fan-shaped stress fields with diagonal strut for example of indirect load transfer as shown in **Fig. 9**, when the stress fields for combination of direct and indirect load transfer are constructed at onset of yielding of flexural reinforcements or partial loss of bond near the location of the maximum moment. After yielding or partial loss of bond along the longitudinal bar, the load transfer in deep beams begins to change due to the yield penetration or the loss of bond of longitudinal bar so that the stress fields are necessary to be modified.

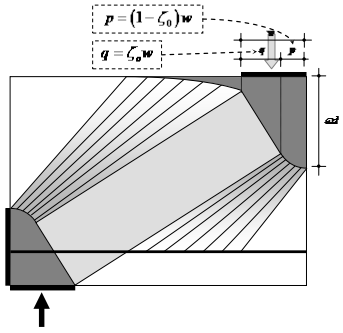


Fig. 9 Stress Field for Indirect Shear Transfer in a Simply Supported Deep Beam

The ultimate state of a STM involving direct transfer and indirect transfer is explained by yielding of one component

of each STM. The yielding of the horizontal tie induces the system to fail in flexural failure mode without yielding of other remaining components. If the yielding of the horizontal tie is combined with the yielding of the shear transfer components such as a diagonal strut and vertical ties, it is called flexural-shear failure.

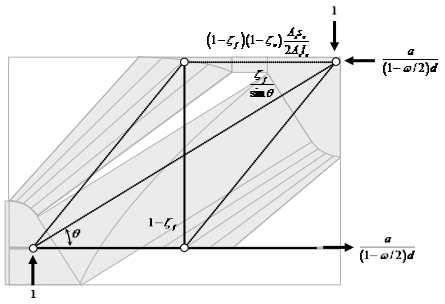


Fig. 10 Stress Field for Indirect Shear Transfer

In the post yield stage a partial yield penetration of longitudinal bars is developed accompanying the loss of bond along the bottom chord. The loss of bond results in no resistance of transverse ties in the segment of yield penetration of the bottom chord. Thereby, it is necessary to modify the initial strut-and-tie model for the maximum shear strength for flexural-shear failure as new one. As a result of the loss of bond along the bottom chord a horizontal strut along the top chord is developed as shown in **Fig.10**. The reduced shear resistance by transverse ties is compensated with diagonal strut.

Among possible failure mechanisms for deformability of limited ductility of a simply supported deep beam, we may select a rotational mechanism involving hyperbolic curve in the diagonal strut as shown in **Fig. 11**. If the center of rotation is selected at the intersection of diagonal with the extended line of longitudinal tie, this mechanism can exclude the extension of longitudinal tie anymore after yielding and consider the partial loss of bond. This failure mechanism enables us to explain the shear failure before or after the flexural failure.

4.2 Deformability Models

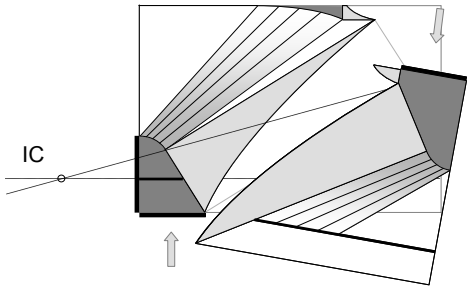


Fig. 11 Possible Failure Mechanism for Indirect Shear Transfer in a Deep Beam

In order to estimate the deformability of the simply supported deep beam with vertical ties, we need to consider possible failure mechanisms as displacement sets. One of displacement sets under the ultimate strength is considered as the rotational mechanism involving a hyperbolic curve as discussed for the deformability of a diagonal strut.

The main components contributing to the estimation of deformability is composed of the rotation of diagonal strut, horizontal strut, and the yielding of vertical tie. The displacement of each component is limited by the maximum rotation angle at which the crushing of diagonal strut is occurred.

For a deep beam with stirrups, the longitudinal reinforcement near the point at which the hyperbolic curve meets does not yield. Thereby, the instantaneous center of rotation is located at the intersection point of extended line of diagonal line GF and the extended line of longitudinal tie as shown in **Fig. 12**. The lower rigid body separated by the hyperbolic curve is assumed to rotate about O by Ω without elongation of longitudinal tie. It is convenience to introduce *x*-*y* coordinate system with the origin at the instantaneous center of rotation. The *x*-axis runs parallel with the direction along the diagonal strut and the *y*-axis is perpendicular to *x*-axis downwards.

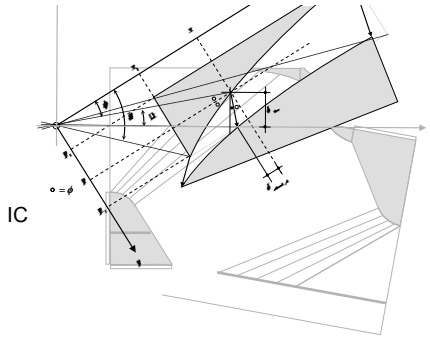


Fig. 12 Displacement Field for Diagonal Strut by Rotational Mechanism involving Hyperbolic Curves

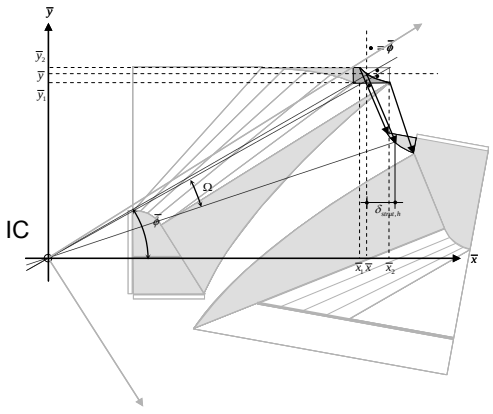


Fig. 13 Description of Displacement Field for Horizontal Strut

The horizontal strut shares the instantaneous center and the maximum rotation angle with the diagonal strut. It is convenience to introduce $\bar{x}$ - $\bar{y}$ coordinate system with the origin at the instantaneous center of rotation. The $\bar{x}$ -axis runs parallel with the direction along the longitudinal tie and the $\bar{y}$ -axis is perpendicular to $\bar{x}$ -axis upwards.

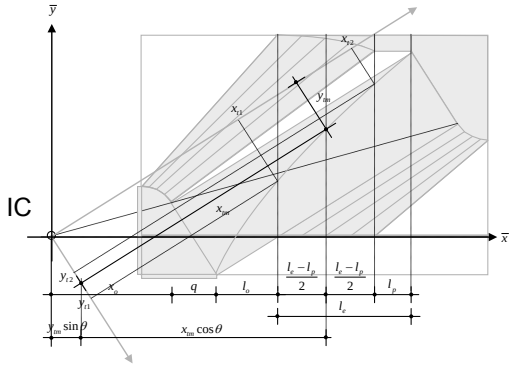


Fig. 14 Displacement Field for Vertical Stirrups

The equilibrium set under unit load and the displacement set by failure mechanism under ultimate load provides the deformability of deep beams with stirrups by virtual works. **Figs. 12**, **13**, and **14** illustrate the displacement set for the horizontal and diagonal struts and vertical ties. Application of the virtual work method for the equilibrium set and the displacement set based on the mechanism results in the deformability l expressed by equation (6) in terms of various parameters such as the length of plastic hinge, span-to-depth ratio, the ratio of flexural reinforcement, and the ratio of shear reinforcement.

$$\Delta_u \le \left(\frac{1}{2}(1-\zeta_o)(1-\zeta_f)\frac{\rho_h}{\rho_v}\frac{d}{l_e},\quad \frac{\zeta_f}{\sin\theta},\quad 1-\zeta_f \right) * \begin{pmatrix} \frac{1}{2}(2d-s) \\ \frac{1}{2}\left(2\frac{x_o}{\sin\phi_o}\sin(\theta-\phi_o)+\frac{r}{\cos\theta} \right) \\ \left(x_o+q+l_o+\frac{1}{2}(l_e-l_p) \right) \end{pmatrix} \Omega_{\max} \quad (6)$$

As the length of plastic hinge, the ratio of flexural and shear reinforcement increase, the ultimate deformation increase. The large shear span-to-depth ratio enlarges the deformability.

The deformability of deep beams with stirrups is mainly affected by the length of plastic hinge and the shear span-to-depth ratio. These are related to the geometry of the stress-fields which determine the width of the diagonal strut. The effects of the ratio of flexural and shear reinforcement is less than the other factors. Hence, the factors closely connected with the depth of diagonal struts influence on the ultimate deformation significantly.

4.2 Deformability of Truss Action

In this section, the deformation capacity models for diagonal compression fields are discussed. Consider a simply supported beam with shear span length *a*, internal lever arm length *jd*, width b_w as show in **Fig. 15**. The angle θ of inclination can be obtained by the energy methods. **Fig. 16** shows the failure mechanism. The maximum displacement is obtained as in Eq. (7).

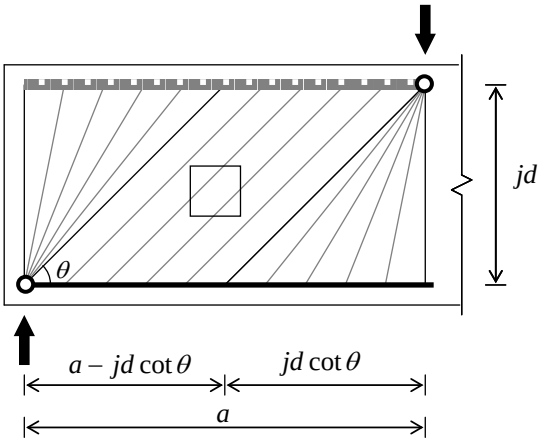


Fig. 15 Diagonal Compression Field between Fans

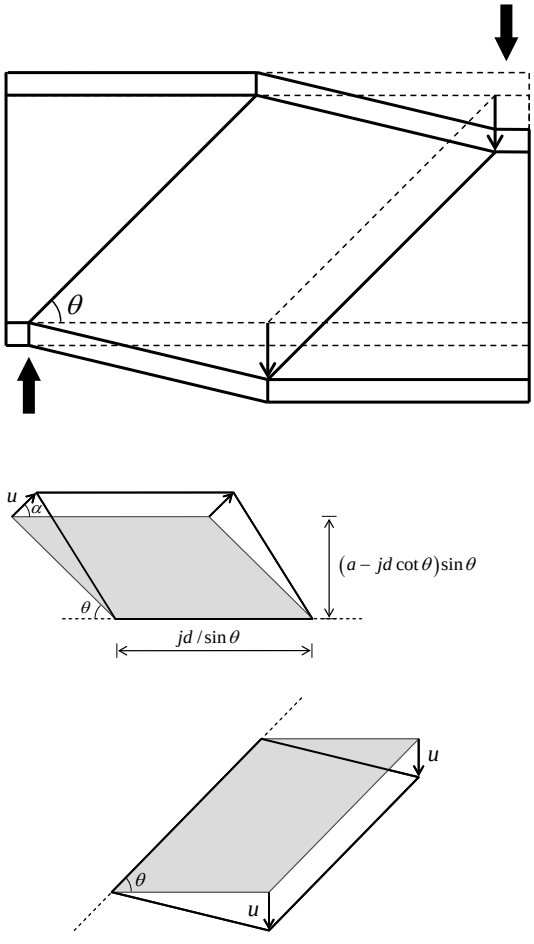


Fig. 15 Displacement Field for Vertical Stirrups

$$\frac{u_{\max}}{a} = -\frac{2}{(1-\cos\theta)}\left(\sin\theta - \cos\theta\frac{jd}{a}\right)\varepsilon_{cu} \qquad (7)$$

5. COUPLING BEAMS

The proposed concepts with along the procedure for a simply supported deep beam may be extended to the case of a coupling beam. After flexural yielding of a coupling beam, we need horizontal struts as in case of a simply supported beam. The dimensions of nodal zones can be determined by the equilibrium and ultimate stress states. The vertical dimension of top nodal zone is described by assuming that compression stresses reach compressive strength of concrete. We may have two different stress fields depending on force distribution along the longitudinal ties. The first one consists of horizontal struts after yield penetration (**Fig. 16**) and the second one is developed by bond along the fans (**Fig. 17**).

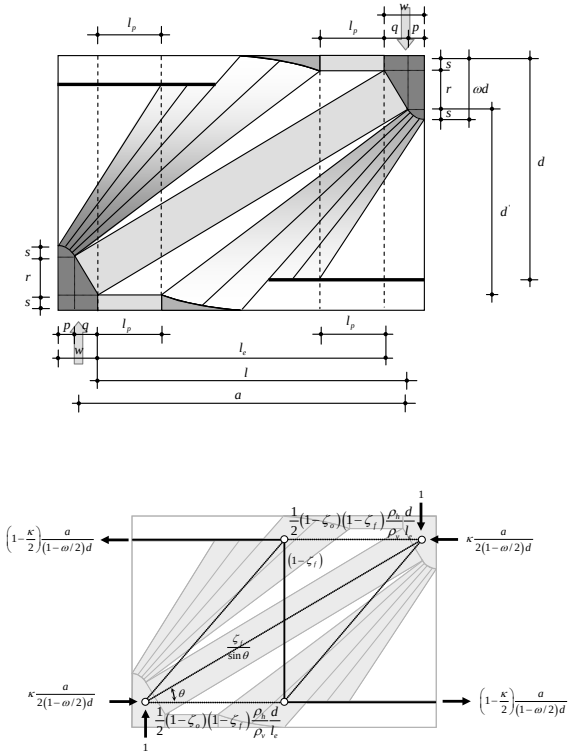


Fig. 16 Stress Field and Equilibrium System under a Unit Load with Yield Penetration along Longitudinal Bar

The stress fields including horizontal struts are considered with translational mechanism (Type I). The stress fields with longitudinal tie along entire length consider the bending mechanism (Type II) and translational mechanism (Type III).

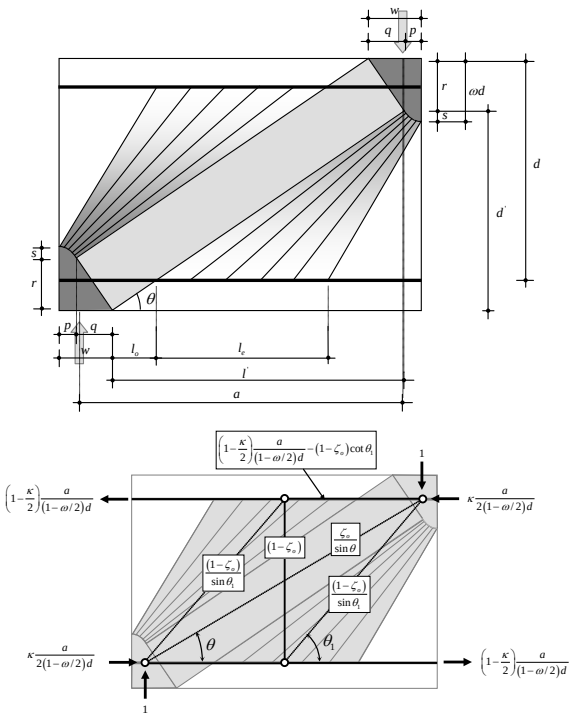


Fig. 17 Stress Field and Equilibrium System under a Unit Load Relying on Bond

5.1 Translational Failure Mechanism involving Horizontal Struts

After the stress fields which take the length of yield penetration into account is constructed, the possible failure mechanisms compatible with stress fields are considered. The stress fields including the horizontal strut and diagonal strut allows the translational failure mechanism as shown in **Fig. 18**. It is associated with the crushing of the horizontal struts in company with diagonal strut and the extension of the vertical ties. The horizontal struts share the displacement vector with the diagonal strut. The direction of displacement vector is defined by the normality rule satisfying in translational mechanism for horizontal and diagonal strut simultaneously.

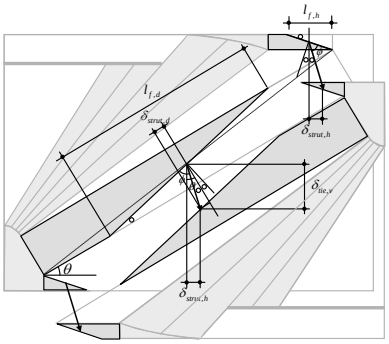


Fig. 18 Translational Mechanism for Coupling Beam with Diagonal and Horizontal Struts

$$\Delta_u \le \left(2\times\frac{1}{2}(1-\zeta_o)(1-\zeta_f)\frac{\rho_h}{\rho_v}\frac{d}{l_e} \quad \frac{\zeta_f}{\sin\theta} \quad 1-\zeta_f \right) * \begin{pmatrix} \sin\left(\theta+\frac{\phi}{2}-\frac{\pi}{4}\right) \\ \sin\left(\frac{\pi}{4}-\frac{\phi}{2}\right) \\ \cos\left(\theta+\frac{\phi}{2}-\frac{\pi}{4}\right) \end{pmatrix} \delta_{\max} \quad (8)$$

Using the same concept, we have the deformability for translational mechanism by Eq (8).

5.2 Translational Failure Mechanism

The fan-shaped stress fields have variable stresses in longitudinal reinforcements. In order to satisfy this stress fields, the diagonal strut must translate in the direction of perpendicular to longitudinal reinforcement. If diagonal strut moves in other direction, the longitudinal reinforcements yield near the strut and have uniform stress in the whole length.

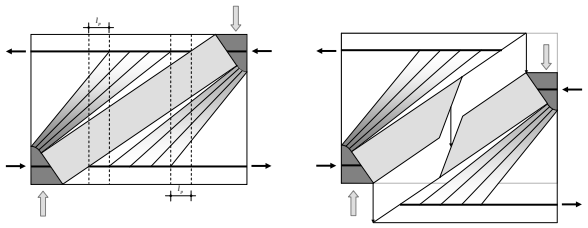


Fig. 19 Translational Mechanism for Coupling Beam with Diagonal Strut

Application of the procedure as discussed to the translational mechanism shown in **Fig. 19** results in

$$\Delta_u \le \left(\frac{\zeta_f}{\sin\theta} \quad 1-\zeta_f \right) \begin{pmatrix} \sin\theta \\ 1 \end{pmatrix} \delta_{\max} \quad (9)$$

where $\delta_{\max} = \frac{r}{\sin^2\theta}\varepsilon_{cu}$

5.3 Bending Failure Mechanism

In bending mechanism as shown in **Fig. 20**, the rotation of diagonal strut about point O by Ω makes the longitudinal reinforcement yield at point A. Bending mechanism consider only the shortening of the diagonal strut and the extension of the longitudinal reinforcement. The limit of deformation according to bending mechanism is determined by the crushing of diagonal strut

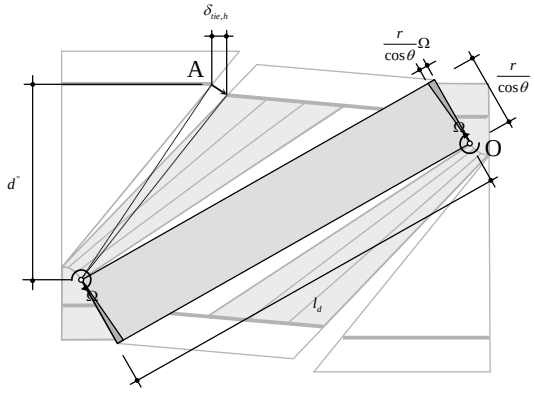


Fig. 20 Bending Mechanism for Coupling Beam with Diagonal Strut

$$\Delta_u \le 2\left(\left(1-\frac{\kappa}{2}\right)\frac{a}{(1-\omega/2)d} \quad \frac{\zeta_f}{\sin\theta}\frac{1}{2}\frac{r}{\cos\theta} \right) * \begin{pmatrix} d-r \\ 1 \end{pmatrix} \Omega_{\max} \quad (10)$$

6. APPLICATIONS

A squat shear wall under the horizontal shear is known as to have limited ductility. To construct shear and-flexural strength model, we need to set up stress fields such as arch action with tension and compression chords for flexure. Pure shear failure mode requires translational failure mechanism in the diagonal strut only while flexural failure mode requires crushing in compression chord with bending mechanism in the diagonal strut.

6.1 Deformability Models for Squat Walls

Consider a squat shear wall under the horizontal shear as shown in **Fig. 21**. To construct shear- flexural interaction curve, we need to set up stress fields such as arch action with tension and compression chords for flexure. Pure shear failure mode is considered as translational failure mechanism in the diagonal strut only and flexural-shear failure mode may be explained by crushing in compression chord with bending mechanism in the diagonal strut.
The deformability of squat wall subject to the horizontal shear is estimated by the translational mechanism. It is assumed that the main diagonal cracking from the top corner to the bottom corner of wall controls deformation capacity of wall in this study.

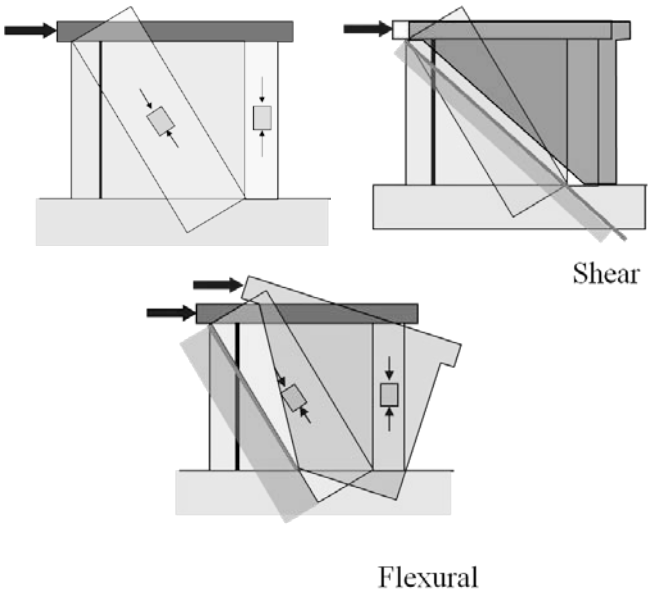


Fig. 21 Failure Mechanisms of Squat Walls

As a result of the horizontal displacement, the compressive strain in compression field of the inclination angle develops the ultimate compressive strain as shown in **Fig. 22**. The maximum displacement is limited by the ultimate strain of concrete in compression.

$$\frac{\Delta\cos(\alpha-\theta)}{\sqrt{l_w^2+h_w^2}} \le \varepsilon_{cu} \tag{11}$$

Based on the deformation models the maximum shear angle of wall is limited by

$$\frac{\Delta}{h_w} \le \frac{\varepsilon_{cu}\sqrt{(l_w/h_w)^2+1}}{\cos(\alpha-\theta)} \tag{12}$$

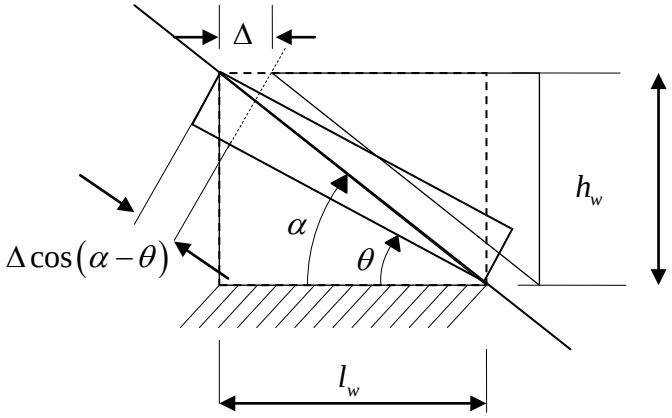


Fig. 22 Deformation Capacity of Squat Wall in Translational Mechanism

Traditionally, strength interaction curves have been constructed by lower bound approach, in which equilibrium conditions and yield conditions for components must be satisfied. Flexural-shear interaction curve for beams needs a truss action in web and relationship between slope angle of diagonal stress field and forces in top and bottom chords.

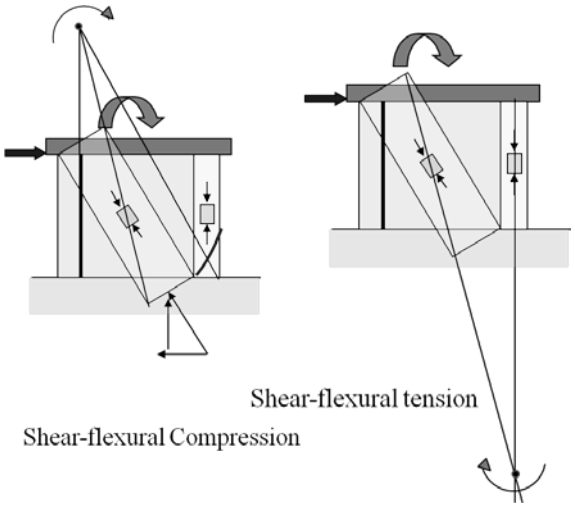


Fig. 23 Shear-flexural failure mechanism by rotational mechanism for diagonal strut

Instead of bending mechanism for the diagonal strut, rotational mechanism for the diagonal strut is applied to shear-flexural compression failure as well as shear-flexural tension. For an equilibrium system and failure mode by failure mechanism, we apply the virtual work method for derivation of interaction curves.

6.2 Deformability Models for Joints

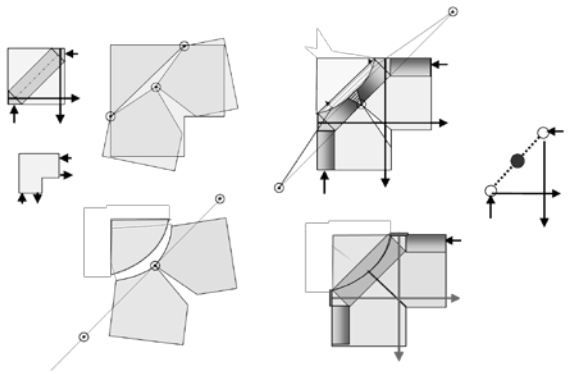


Fig. 24 Deformability of Opening Joint

The concept is extended to estimate the deformation of beam-column joints. Consider an opening joint as shown in **Fig. 24**. If the diagonal crack within the joint controls the ultimate state of the joint, the crushing failure of the diagonal strut is expected. The rotational mechanism involving hyperbolic curves and new flexural type failure mechanism may explain the failure mechanism with estimation of deformation in terms of ration angle of joint.

6.3 Verification

In order to verify the proposed deformability models, experimental data from literature and experimental program were compared with the theoretical results. The experimental data involve those from shear test of simply supported deep beams and coupling beams. The comparison showed good agreement with the calculation using the proposed models. Especially, the deformation limit of shear walls has been explained by the translational mechanism showing 0.6 % drift ratio in case of shear failure mode.

7. CONCLUSIONS

In order to estimate the deformation capacity of a typical structural concrete failure mechanisms compatible with their corresponding STM have been considered on the basis of basic concepts of limit analysis. The bending, translational, and rotational failure mechanisms of struts in crushing failure mode have been investigated as governing deformation patterns of STMs in D-regions. On the basis of this investigation the following main conclusion may be drawn:

1) The proposed models show the deformation capacity depending on whether each failure mechanism involves yielding of longitudinal tie or not. Both the bending and the translational mechanisms with yielding of longitudinal ties show larger deformation capacity than those by the other failure mechanism with non-yielding of longitudinal ties in the range of moderate mechanical reinforcement degree.

2) When deformation limits of struts in failure mechanisms alone are considered to control deformation capacity of structural concrete, the deformation capacity is expressed in terms of shear span to beam depth ratios, reinforcement degree of longitudinal ties and transverse ties, and an ultimate compressive strain of concrete. According to the proposed equation, the deformation capacity is directly proportional to an ultimate or limiting strain of concrete in compression.

3) The proposed model based on STM relying on a diagonal strut alone has predicted smaller deformation capacity than experimental results. Larger deformation capacity due to the web reinforcement is explained by the deformability models for indirect shear transfer.

Acknowledgements:

This work was supported in part by the Korea Science & Engineering Foundation (KOSEF) through the Korea Earthquake Engineering Research Center at Seoul National University and in part by Interdisciplinary Research Grants R01-2004-000-10290-0**.** Opinions, findings, conclusions, and recommendations in this paper are those of writer, and do not necessarily represent those of the sponsors.

References:

Ashour, A. F. and Morley, C. T. (1996), "Effectiveness Factor of Concrete in Continuous Deep Beams," Journal of Structural Engineering, ASCE, Vol.122, No.1, pp.169-178.

Collins, M. P. (1978), "Towards a Rational Theory for RC Members in Shear," Journal of the Structural Division, ASCE, Vol. 104, No. ST4, pp. 649-666

Hong, S-G., Hong, N. K., and Jang, S-K. (2011) "Deformation Capacity of Structural Concrete in Disturbed Regions," ACI Structural Journal, ACI (in Press)

Hong, S-G., Lee, S-G., Kang, T. H-K. (2011), "Deformation-Based Strut-and-Tie Models for Interior Beam-Column Joint of Frames subject to Load Reversal," ACI Structural Journal, ACI (in Press)

Kaufmann, W. (1998), "Strength and Deformation of Structural Concrete Subjected to In-plane Shear and Normal Forces," ETH, Zurich, Bericht Nr. 234, 147pp

Kaufmann, W., and Marti, P. (1998), "Structural Concrete: Cracked Membrane Model," Journal of Structural Engineering, ASCE, Vol. 124, No. 12, pp. 1467-1475

MacGregor, J. G. (1988), "REINFORCED CONCRETE: Mechanics and Design," Prentice-Hall, Englewood, New Jersey, 799pp.

Marti, P. (1985), "Basic Tools of Reinforced Concrete Beam Design," ACI Journal, pp.46-56.

Marti, P. (1985), "Truss models in Detailing," Concrete international, V. 7, No. 12, Dec., 1985, pp.66-73.

Marti, P., Alvarez, M., Kaufmann, W., and Sigrist, V., (1998) "Tension Chord Model for Structural Concrete," Structural Engineering International, IABSE, Vol. 8, No. 4, pp. 287-298

Marti, P. and Clyde, D. H. (1982), "Discussion: An Upper-bound Rigid-plastic Solution for the Shear Failure of Concrete Beams without Shear Reinforcement," Magazine of Concrete Research, Vol. 34, No. 119, p.96

Muttoni, A., Schwartz, J., and Thürlimann, B. (1997), "Design of Concretes with Stress Fields," Birkhäuser, Boston, 143pp.

Standard Association of New Zealand (1982), New Zealand Standard Code of Practice for the Design of Concrete Structures, NZS 3101: Part1, 127pp; Commentary NZS 3101: Part 2, 156pp; Wellington, New Zealand

Paulay, T. and Priestley, M.J.N. (1992), "Seismic Design of Reinforced Concrete and Masonry Buildings," John Wiley & Sons, New York, 744pp

Paulay, T. (1998), "Torsional Mechanisms in Ductile Building Systems," Earthquake Engineering and Structural Dynamics, 27, pp.1101-1121

Paulay, T. (2002), "An Estimation of Displacement Limits for Ductile Systems," Earthquake Engineering and Structural Dynamics, Vol. 31, pp.583-599

Schlaich, J., Schäfer, K., and Jennewein, M. (1987), "Toward a Consistent Design of Structural Concrete," PCI J. Vol.32, No.3, pp.74-150.

Schlaich, J. and Schafer, K. (1991), "Design and detailing of Structural Concrete using Strut-Tie Models," The Structural Engineer, Vol.69, No.6, pp.113-125

Sigrist, V., Alvarez, M., and Kaufmann, W. (1995), "Shear and Flexure in Structural Concrete Beams," CEB Bulletin No 223, pp.7-49

Vecchio, F. J. and Collins, M. P. (1986), "The Modified Compression Field Theory for Reinforced Concrete Elements Subjected to Shear," ACI Journal, Vol. 83, No. 2., pp. 219-231

8CUEE CONFERENCE PROCEEDINGS
8th International Conference on Urban Earthquake Engineering
March 7-8, 2011, Tokyo Institute of Technology, Tokyo, Japan

EFFECT OF CRACK CONFIGURATION, AXIAL LOAD, AND SHEAR REINFORCEMENT UPON HYSTERESIS CHARACTERISTICS OF HIGH-STRENGTH RC COLUMNS

Yasuji Shinohara[1] and Shizuo Hayashi[2]

1) Associate Professor, Structural Engineering Research Center, Tokyo Institute of Technology, Japan
2) Professor, Secure Materials Center, Tokyo Institute of Technology, Japan
yshinoha@serc.titech.ac.jp, hayashi.s.ac@m.titech.ac.jp

Abstract: The configuration of a crack in high-strength concrete that has a strength that exceeds 100 N/mm^2 is much smoother than that in normal-strength concrete (under 45 N/mm^2), and results in a loss of shear-transfer ability across the crack. Tests were performed on reinforced concrete (RC) columns having concrete strengths of 40 N/mm^2 to 120 N/mm^2, axial load ratios of 0.1 to 0.28, and shear reinforcement ratios of 0.39% to 0.78% in order to study the influence of crack configuration, axial load, and shear reinforcement upon the hysteresis characteristics of the columns under cyclic shear loading. With an increase in axial load and a decrease in shear reinforcement, the shear slide in a closed smooth crack in high-strength concrete increases, and the solidity as an RC member is compromised. As a result, the hysteresis curves of high-strength concrete columns with higher axial load and less shear reinforcement show an asymmetric response between positive and negative loading as a result of large slippage in a closed shear crack. Finite element method analyses are carried out to examine the effect of the coefficient of friction when closing shear cracks.

1. INTRODUCTION

In recent years, the construction of super-high-rise apartment buildings has proceeded on a large scale in urban areas. As these apartment buildings require a structural rigidity that will resist strong winds and microtremors, as well as a degree of sound insulation to afford living comfort, they are typically built using a reinforced concrete (RC), for economic reasons. Furthermore, the design of the latest super-high-rise apartment buildings also requires that the cross-section of columns be reduced and the spacing among columns be increased to accommodate the idea of free planning to enable the use of the buildings for more than one generation, in addition to providing long-term durability. Therefore, high-strength concrete is absolutely indispensable for the construction of the columns of the lower stories that will support huge axial loads, and it is expected that there will be continuing demands for higher-strength concretes.

Concrete having a strength of more than 60 N/mm^2, which is outside the scope of the calculation criterion and the guidelines in the Architectural Institute of Japan (AIJ) standards, is used for the columns of the lower stories of super-high-rise apartment buildings. However, some problems have been pointed out with regard to the hysteresis characteristics of RC members that use high-strength concrete (Teraoka *et al*. 2003). For example, in the hysteresis characteristics of an ultra-high-strength concrete column, there is a tendency for the shear force under negative loading to be less than the shear force under positive loading. The reason is probably that the solidity (rigidity) of a member is degraded by a slide in a smooth crack surface, although a crack generated under positive loading is closed under negative loading.

We have investigated the shear transfer mechanism of smooth crack surfaces in ultra-high-strength concrete having a compressive strength in excess of 100 N/mm^2 (Hasegawa *et al*. 2004). In addition, we have carried out flexure-shear experiments and analyses of RC members using an ultra-high-strength concrete to study the effect of a smooth crack surface on the shear behavior of an RC member after shear-cracking (Shinohara *et al*. 2007). However, as a flexural yield precedence-type specimen that does not introduce an axial load was adopted, the hysteresis characteristics that destroy the symmetrical response under positive and negative loading could not be reproduced. This asymmetrical hysteresis characteristic is one of the problems of RC members made of ultra-high-strength concrete.

In this paper, a flexure-shear experiment is conducted on shear failure precedence-type RC columns to examine how crack surface behavior and an axial load influence hysteresis characteristics from the occurrence of shear-crack to the maximum shear strength. For this reason, this crack behavior is recorded under positive and negative loading, and we examine the asymmetry of hysteresis characteristics based on crack behavior. Moreover, finite element method (FEM) analysis taking account of the aggregate interlocking and shear friction in a crack surface is conducted, and the coefficient of friction of a smooth crack surface of an RC column that uses high-strength concrete is proposed.

2. OVERVIEW OF EXPERIMENTS

2.1 Details of Test Specimens

The specimen used in this study is about one-fourth the size of an actual column. The specimen configuration and the rebar arrangement are shown in Fig. 1. Common factors are the cross-sectional dimensions (200 mm × 254 mm), the shear-span ratio (1.2) and the main reinforcement (8-D16, σ_y = 1030 N/mm^2). The variable factors are the concrete strengths of two levels (Fc120, Fc30), the axial load ratios of two levels (0.10, 0.28), and the shear reinforcement ratios of two levels (0.39%, 0.78%). Specimen details are shown in Table 1. The specimen designation is expressed by the concrete strength (H, N), the shear reinforcement ratio (%), and the axial load ratio. The shear reinforcement consisted of four bars [four bars (legs) constitute one set of shear reinforcement (see Fig. 1).] (5.0 mm or 7.0 mm in diameter) positioned at intervals of 100 mm. All RC column specimens were designed to reach shear failure before the longitudinal reinforcement yield. For this reason, a high-strength steel reinforcement was used for the main reinforcement, and the ends were welded to an anchor plate. Moreover, additional rebars (D13) were fitted between shear reinforcements to prevent the columns from splitting as a result of bond failure. The stub concrete was widened by 10 mm on the right and left so that the edge of the steel stubs would not damage the specimens. The concrete was laterally poured in the specimen mould. After pouring and curing, the specimen was connected to the steel stubs using high-strength steel bolts embedded in the upper and lower stubs. The mix proportions of the concrete are shown in Table 2. Silica-fume cement is used for the high-strength concrete, and an air-entraining and high-range water-reducing admixture is added to it. Ordinary portland cement and an air-entraining and water-reducing admixture are used for normal-strength concrete. As the interlocking effect of the aggregate in a crack surface is the purpose of our research, the concrete is mixed so that the amount of coarse aggregates in high-strength concrete is the same as that in normal-strength concrete. The coarse aggregate is a land gravel that has a maximum diameter of 25 mm, a specific gravity of 2.61, and a water absorption of 1.1%. For high-strength concrete, the air content was 1.1% to 2.6%, and the slump flow was 50 cm to 63 cm. For normal-strength concrete, the air content was 4.1% to 4.3%, and the slump value was 19 cm to 20 cm.

Table 1 List of test specimens

Test designation	η_0	σ_B N/mm^2	E_c N/mm^2	Shear Rebar	p_w (%)	$_w\sigma_y$ N/mm^2
HRC-0.39-0.10	0.10	98.0	3.98x10^4	Φ5.0	0.39	1430
HRC-0.39-0.28	0.28	121	4.15 x10^4	Φ5.0	0.39	1430
HRC-0.39L-0.28	0.28	109	4.02 x10^4	Φ5.0	0.39	596
HRC-0.78-0.10	0.10	98.0	4.00 x10^4	Φ7.0	0.78	1340
HRC-0.78-0.28	0.28	122	4.27 x10^4	Φ7.0	0.78	1340
NRC-0.39-0.28	0.28	36.8	2.78 x10^4	Φ5.0	0.39	912
NRC-0.39L-0.28	0.28	43.0	2.99 x10^4	Φ5.0	0.39	596
NRC-0.78-0.28	0.28	43.9	3.23 x10^4	Φ7.0	0.78	809

$\eta_0 = N/(bD\sigma_B)$ axial load ratio, N = axial load, bD=sectional area of column, σ_B = compressive strength of concrete, E_c = elastic modulus of concrete, p_w = shear reinforcement ratio, $_w\sigma_y$ = yield strength of shear reinforcement

Table 2 Mix proportion (Unit: kg/m^3)

Nominal Strength	W / C	Water	Cement	Sand	Aggregate	Super-plasticizer
Fc120	0.20	150	750	658	864	7.28
Fc30	0.40	200	500	742	864	1.25

2.2 Loading and Measuring Method

The loading device used in the experiments is shown in Fig. 2. The lower stub of the specimen was fixed to the loading main frame, and a loading beam was connected to the upper stub. Then, channel steel was attached to the upper stub to restrain any out-of-plane deformation. After introducing a predetermined axial load to the specimen using a 2000 kN hydraulic jack, a constant axial load was maintained using the controller until the completion of the test. Cyclic horizontal loading was applied by controlling 1000 kN and 500 kN hydraulic jacks with a controller so that the upper end of the specimen did not rotate, so that an antisymmetric flexural would occur in the specimen. The horizontal force was decreased when the rotation angle of

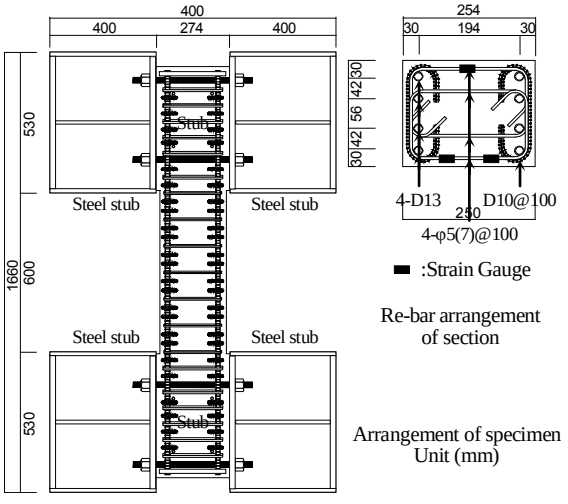


Figure 1 Appearance of specimen and re-bar arrangement

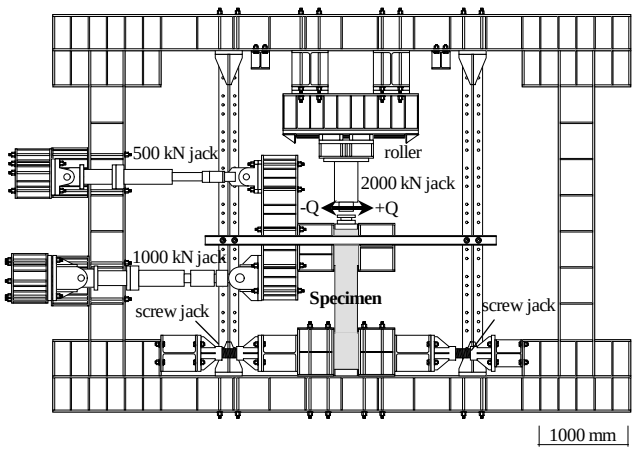


Figure 2 Loading apparatus

the column amounted to ±1/400, ±1/200, ±1/133, ±1/100, and ±1/67, until the peak load was reached. The relative displacement (horizontal and vertical) between the stubs was measured using a displacement-measuring jig attached to the upper and lower concrete stub. Strain on the main reinforcement was measured at the ends of the test section to ascertain the flexural yielding of the main reinforcement. To examine the correspondence to shear-crack behavior, the strain on the shear reinforcement was measured by attaching two strain gauges on the front bar and one gauge on the back bar of all reinforcements.

All shear-crack behavior was measured at peak and unloading in each cycle using a digital microscope with a resolution of 0.01 mm. After shear cracking, the displacements in the direction of depth (x axis) and height (y axis) of a specimen, and the angle (θ) between a shear crack and the x axis were measured at the intersection point of a shear crack and a line drawn every 50 mm symmetrically on the specimen facade (Fig. 3). The crack width, w, perpendicular and the crack sliding, δ, parallel to a crack surface were computed based on the above-mentioned measured value. Measurement of the shear crack was performed at all measuring points up to a rotation angle of R = 1/100 rad., in which crack damage by repeated loading does not influence measurement. For some main cracks, crack behavior in the loading progress was measured in the rotation angle of R = ±1/400 rad., ±1/200 rad., ±1/133 rad., and ±1/100 rad.

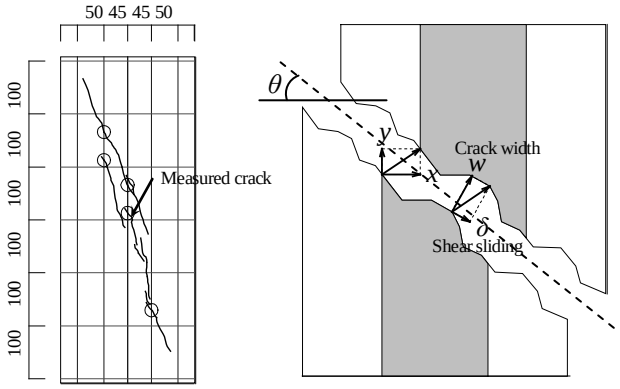


Figure 3 Definitions of crack displacements

3. EXPERIMENTAL RESULTS

3.1 Shear Force and Rotation Angle Curves

Figure 4 shows the shear force Q versus rotation angle R curves obtained from the experiments, where ◊ and ○ indicate the shear-crack strength and ultimate shear strength, respectively. In the case of specimens that use a high-strength shear reinforcement, the reinforcement did not yield to the maximum shear force, but the shear force declined as a result of the collapse of the concrete in the compression zone of a member end. In the case of specimens (HRC-0.39L-0.28 and NRC-0.39L-0.28), which permitted yielding of the shear reinforcement, the shear force declined by widening the shear crack in R = 1/100 cycles after the yielding of a part of the reinforcements (Fig. 4). As none of the main reinforcements yielded until they reached maximum strength, it was judged that all specimens caused shear failure. In the ultra-high-strength concrete specimens (HRC-0.39-0.28 and HRC-0.39L-0.28) that have few shear reinforcements and on which a high axial load acts, the positive and negative hysteresis characteristics differed greatly, and the strength difference increased after shear cracking. The HRC-0.39L-0.28 specimen reached maximum strength under positive loading in the first cycle of R = +1/133, after that, the shear crack occurred in the first cycle of R = −1/133, in the second cycle of R = +1/133, another crack caused by positive loading occurred, which might be derived from the crack generated under the negative loading just imposed. Although the crack strength and the shear

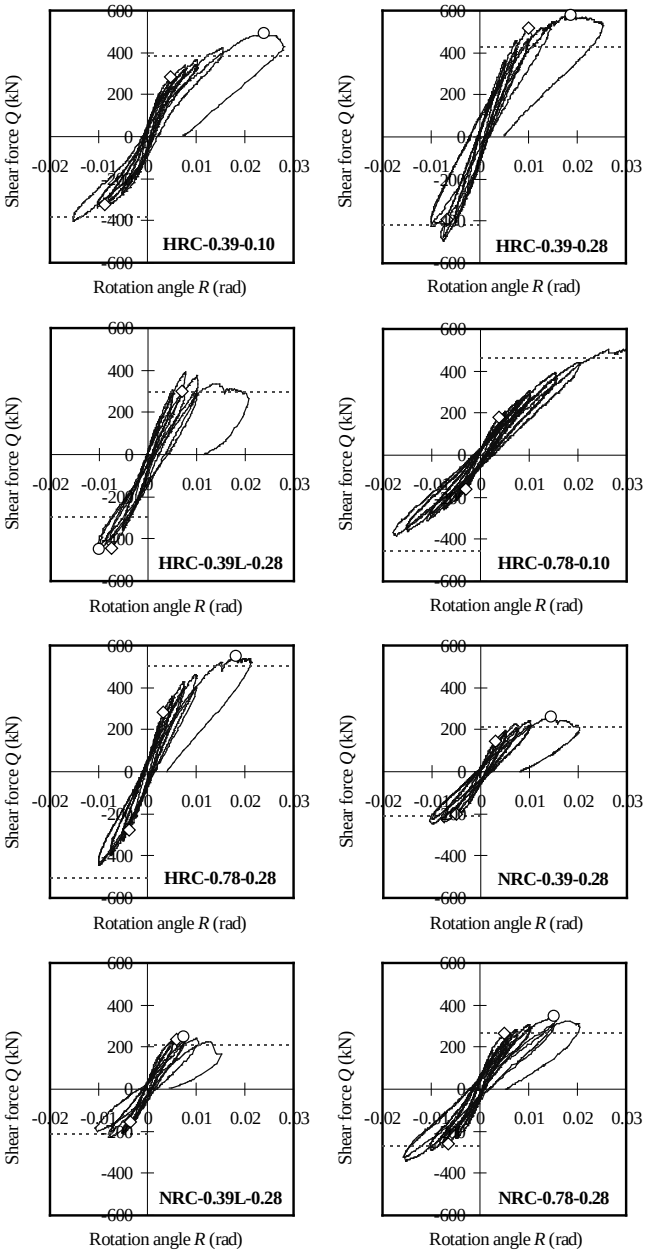


Figure 4 Q-R curves obtained from experiment

stiffness generally showed a tendency to decrease when the ratio of the axial load became low, the crack strength and the shear stiffness of the HRC-0.78-0.10 specimen are smaller than those of the HRC-0.39-0.10 specimen having the same concrete strength and axial load. This seems to be the influence of the crack caused by shrinkage before loading.

The envelope curves of positive loading and negative loading are compared and shown in Fig. 5 for specimens that have a ratio of axial load, a shear reinforcement ratio, and a concrete strength different from the HRC-0.39-0.28 specimen that exhibits asymmetrical hysteresis characteristics after shear cracking under a positive loading. Compared with the HRC-0.39-0.28 specimen in which the strength decreased by a little more than 20% in the negative loading cycle after shear cracking, a strength decrease in the specimens of a low ratio of axial load (HRC-0.39-0.10), a double shear-reinforcement ratio (HRC-0.78-0.28), and a normal concrete strength (NRC-0.39-0.28) is less than 10%. In high-strength concrete, the asymmetry of the hysteresis characteristics appears notably in the HRC-0.39-0.28 specimen that has a high ratio of axial load and low shear-reinforcement ratios. Moreover, comparing the HRC-0.39-0.10 and NRC-0.39-0.28 specimens with approximately the same axial load, the asymmetric hysteresis characteristics appear more clearly in high-strength concrete having a smoother crack surface. This indicates that the axial load, the amount of shear-reinforcement, and the crack surface configuration affect the asymmetry of the hysteresis characteristics of an RC column.

Table 3 shows the shear-crack strength, ultimate shear strength, bond splitting strength, and bending strength obtained from the calculation according to design guidelines (AIJ 1997) and the experiments. Plus and minus in an experimental value indicates positive and negative loading, respectively. The ultimate shear strength by experiment exceeds the calculated value for all the specimens. In the case of the HRC-0.39-0.28 and HRC-0.39L-0.28 specimens, which have high axial loads and few shear reinforcements, the shear crack occurred at a higher shear force than the ultimate strength determined by calculation. For this reason, the shear transferred by the arch mechanism before cracking increased greatly, and the ultimate shear strength by experiment exceeded the calculated value by 40% to 50%.

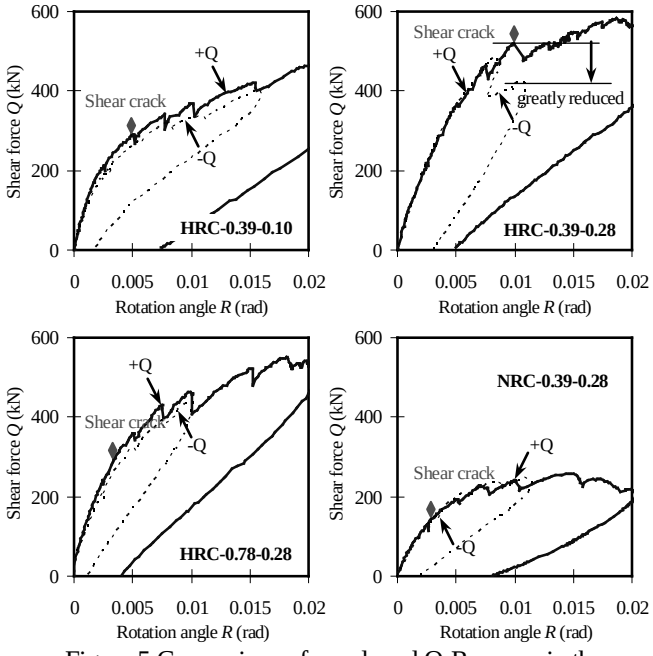


Figure 5 Comparison of enveloped Q-R curves in the positive and negative shear loading cycle

Table 3 Shear crack strength and ultimate shear strength

Test designation	${}_{cal}Q_{sc}$ (kN)	${}_{cal}Q_{su}$ (kN)	${}_{cal}Q_{bu}$ (kN)	${}_{cal}Q_{mu}$ (kN)	${}_{exp}Q_{sc}$ (kN)	${}_{exp}Q_{sc}$ (kN)	${}_{exp}Q_{max}$ (kN)
HRC-0.39-0.10	221	379	425	697	284	-323	491
HRC-0.39-0.28	394	423	457	718	513	-391	577
HRC-0.39L-0.28	365	295	440	718	302	-444	-447
HRC-0.78-0.10	221	456	473	697	181	-160	514
HRC-0.78-0.28	399	504	508	718	284	-275	547
NRC-0.39-0.28	168	208	319	323	142	-199	258
NRC-0.39L-0.28	188	205	380	323	236	-154	248
NRC-0.78-0.28	191	266	331	323	264	-260	349

${}_{cal}Q_{sc}$ = shear crack strength by AIJ Code, ${}_{cal}Q_{su}$ = ultimate shear strength by AIJ Code, ${}_{cal}Q_{bu}$ = bond splitting strength by AIJ Code, ${}_{cal}Q_{mu}$ = ultimate flexural strength by AIJ Code, ${}_{exp}Q_{sc}$ = shear crack strength by experiment, ${}_{exp}Q_{max}$ = ultimate strength by experiment

3.2 Shear Crack Behavior

The crack pattern at the maximum shear load of each specimen is shown in Fig. 6. In the figure, ○ and ◊ show the point that measured the crack under positive loading and negative loading, respectively, while ● indicates a main crack measured at a rotation angle of ±1/400, ±1/200, ±1/133, and ±1/100 in addition to at the peak load and the unloading of each cycle in order to study the progress of crack behavior. In the case of the HRC-0.39-0.28 and HRC-0.39L-0.28 specimens having few shear reinforcements and a high axial load, the shear crack occurred in an instant at a rotation angle of +1/100 under positive loading and at a rotation angle of −1/133 under negative loading, respectively, in the diagonal direction of a specimen with a loud splitting sound. As these two specimens decrease in strength in reverse-direction loading as described in the previous section, there were comparatively few cracks caused by reverse-direction loading, and the shear crack generated first behaved dominantly. Other specimens showed an increase in the number of cracks with an increase in shear force, and the cracks were localized as the amounts of shear reinforcement decreased and as the axial load increased. The average strain distribution of three gauges attached to the shear reinforcements with a close relation to shear-crack width is shown in Fig. 7 (Shinohara, *et al*. 2005). The strain on the reinforcement is large in the mid-height of a specimen not restrained laterally by a stub. If specimens having the same ratio of axial load are compared, the strain decreases and the crack width is controlled as the amount of shear reinforcement increases. Moreover, if specimens with the

same shear reinforcement ratio are compared, the strain increases with an increase in axial load, but as it is related to the shear slide of a crack, this is discussed in the next section. The maximum crack width was less than 1 mm except for the NRC-0.39L-0.28 specimen until a rotation angle of 1/100.

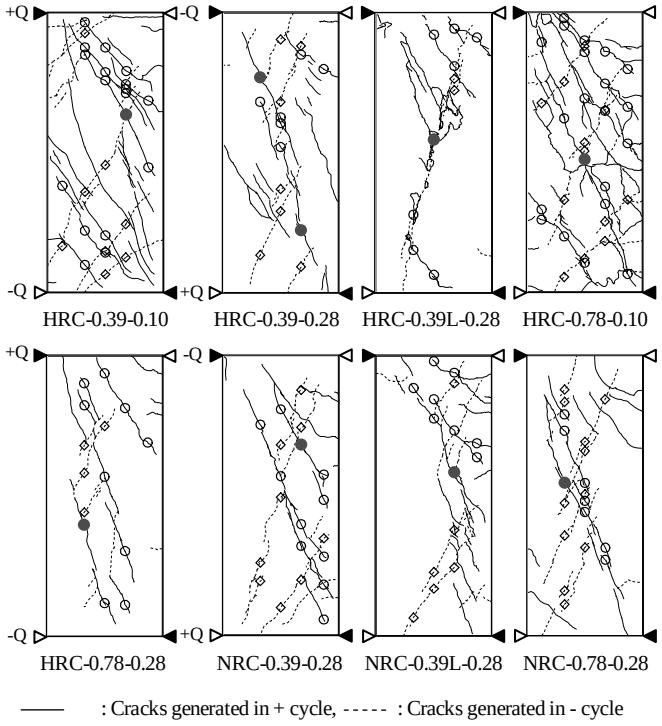


Figure 6 Final crack patterns and measured points

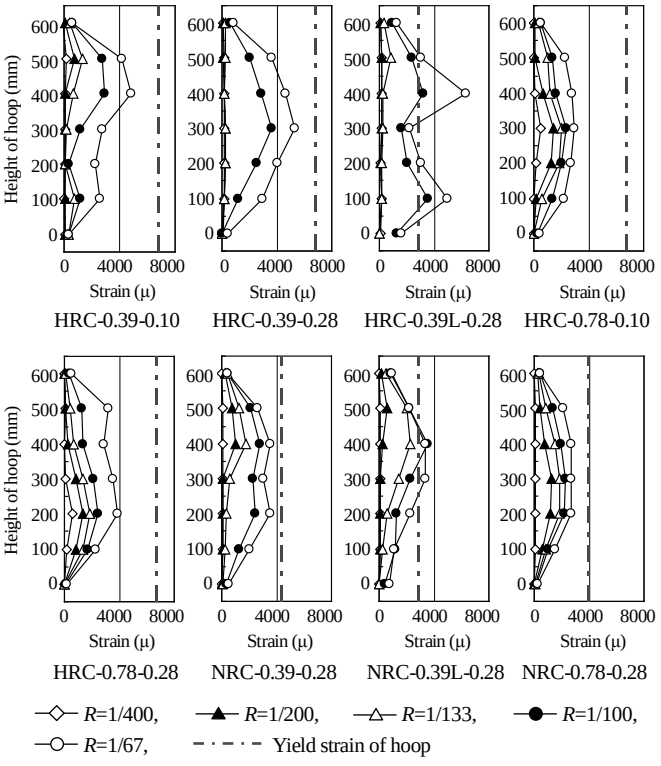


Figure 7 Strain distribution of shear reinforcement

4. SHEAR CRACK BEHAVIOR AND HYSTERESIS CHARACTERISTICS

A crack generated and opened in a certain direction of a loading is closed by a reverse-direction loading. To examine the effect of crack behavior on the hysteresis characteristics of an RC column, each crack is differentiated as an "opening crack" or a "closed crack" in this study. Figure 8 shows the relation between crack width and shear slide from the shear-crack generating until the cycle of R = 1/100 for a high-strength concrete column, where opening cracks are shown on the left and closed cracks on the right. A shear slide is displaced below in a load cycle from a peak to an unloading and a reverse-direction loading, as shown later in Fig. 10. All shear sliding displacements in Fig. 8 are shown by absolute value in order to study the relation between crack width and shear sliding displacement. In the figure, "●" and "×" indicate a shear crack generated under positive and negative loading, respectively. For the opening crack in the experiment on a high-strength concrete member that does not introduce an axial load, both the shear-crack width and the shear slide have been controlled by providing many shear reinforcements (Shinohara *et al*. 2007). When introducing an axial load, if specimens having the same ratio of axial load are compared, the shear-crack width tends to decrease as the amount of shear reinforcements increases, but if specimens having the same amount of shear reinforcements are compared, the crack width decreases as the axial load increases. Generally, if the shear reinforcement is doubled, the strain of reinforcement and the crack width is decreased by half (Shinohara, *et al*. 2009), but in the crack behavior of the HRC-0.78-0.10 specimen and the HRC-0.39-0.10 specimen, even if the amount of shear reinforcements is doubled, the crack width does not decrease as much as in the strain distribution of the shear reinforcement shown in Fig. 7. The reason is probably that the shrinkage crack before loading exerted an influence, as described in the Q-R relation shown in Fig. 5. Most shear slides of an opening crack are 0.2 mm or less, and a significant difference was not seen in a comparison with cases in which the amount of reinforcements was approximately doubled. On the other hand, a shear slide of closed cracks increases as the ratio of axial load increases and the amount of shear reinforcements decreases. In particular, the HRC-0.39-0.28 and HRC-0.39L-0.28 specimens, in which the strength difference of the positive and negative loadings was large, produced a shear slide of 0.6 mm or more at the reverse-direction loading peak. Although the width of an opening crack is small in specimens having a high axial load, the strain of a shear reinforcement is large because of the large amount of sliding in a closed crack. Thus, shear reinforcement functions to control not only shear-crack width but also shear slide (Shinohara, *et al*. 2009).

In the five high-strength concrete specimens and the NRC-0.38-0.28 specimen, the ratio of negative to positive shear force (the first drawing), the maximum shear sliding displacement in a closed crack (the second drawing), and an

axial displacement (the third drawing) are shown in Fig. 9 for the 1st cycle of each rotation angle. A shear sliding displacement is negative when displaced below, and an axial displacement is negative when contracted. Although a variation in the experimental result appears in the small rotation angle before shear cracking, the ratio, −Qp/+Qp, of the shear force of a positive and negative loading tends to

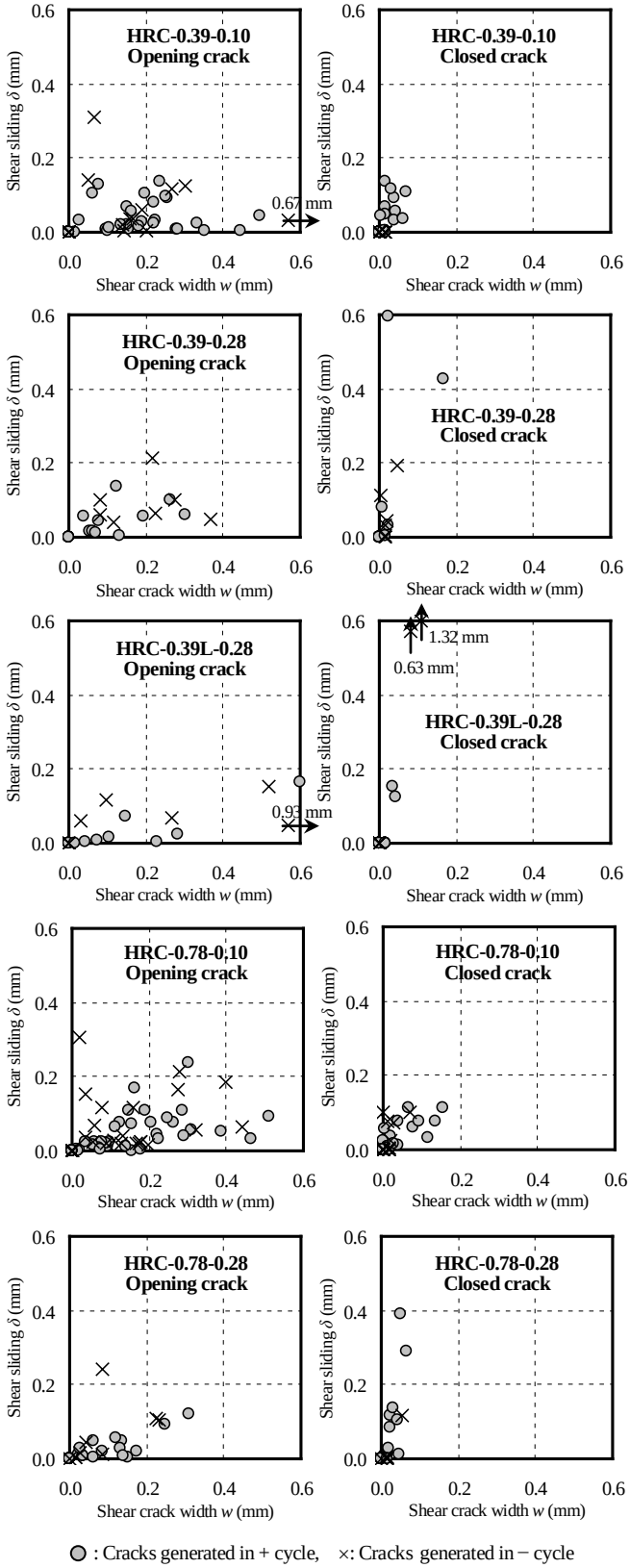


Figure 8 Relation between shear crack width and shear sliding at peak load in each cycle

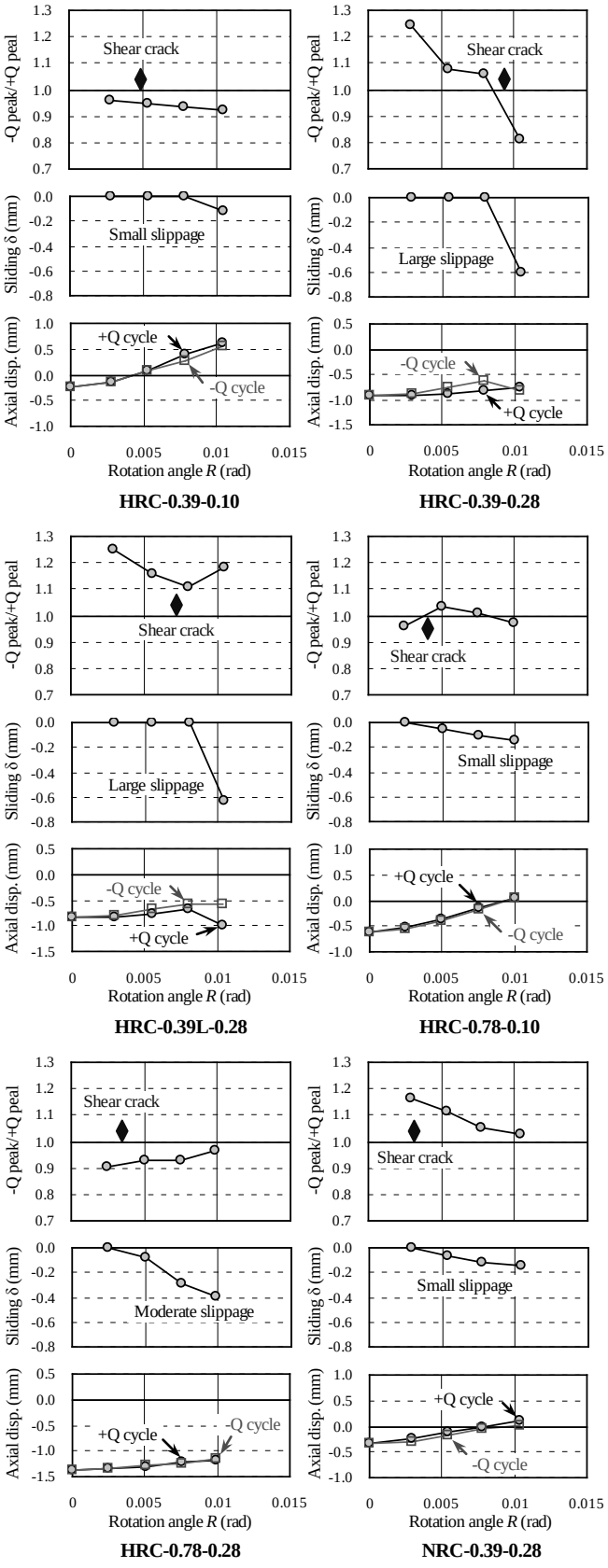


Figure 9 Relation between rotation angle and –Q peak/+Q peak ratio, sliding in shear crack, axial displacement

decrease as the shear slide increases. In the case of the HRC-0.39L-0.28 specimen, as the shear force of the positive loading decreases by sliding in a shear crack generated under negative loading, the ratio of −Qp/+Qp increases after shear cracking. In particular, in the case of the HRC-0.39-0.28 and HRC-0.39L-0.28 specimens showing a significant asymmetry of the skeleton curve, when a crack that is generated with a loud splitting sound closes during reverse-direction loading, the shear slide increases along with axial contraction, and its solidity (rigidity) as a member is degraded. The ratio of the negative to the positive shear force, −Qp/+Qp, changes sharply as a result of the deteriorating shear stiffness of RC members. In contrast to the above-mentioned specimen, a specimen having a small ratio of axial load and/or thicker shear reinforcements has a shear slide of less than 0.2 mm (HRC-0.78-0.28 specimen less than 0.4 mm), the variation of −Qp/+Qp and the axial

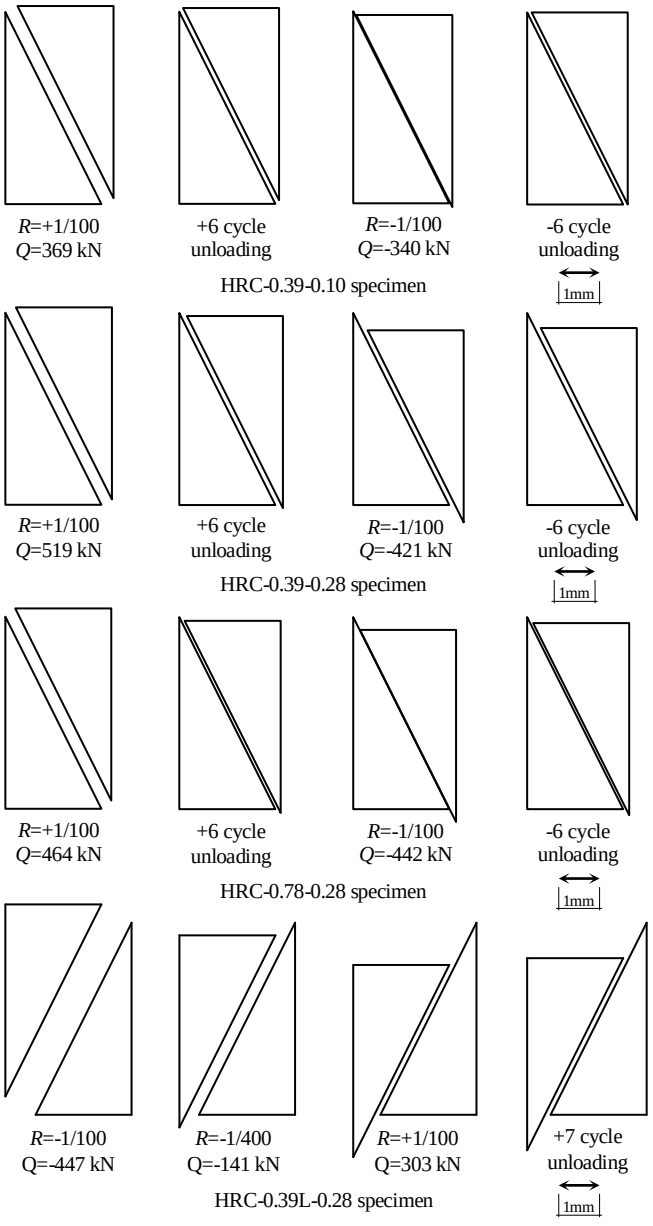


Figure 10 Comparison of crack behaviors between specimens with different axial load and shear reinforcement

contraction after shear cracking reduces, and the hysteresis characteristics under positive and negative loading becomes symmetric. A normal-strength concrete specimen also has symmetrical hysteresis characteristics under positive and negative loading provided the shear reinforcement does not yield.

The crack behavior from the +6 cycle (the first cycle of R = +1/100) to −6 cycle (the first cycle of R = −1/100) in the measuring point (● symbols in Fig. 6) that recorded maximum displacement is expanded and shown in Fig. 10 using the same multiplying factor. However, the crack behavior of the HRC-0.39L-0.28 specimen that the shear crack generated under negative loading is shown from the −6 cycle to the +7 cycle (the second cycle of R = 1/100). Here, "unloading" means Q = 0 kN of each cycle. Although the crack width exceeds 0.3 mm at the peak of R = +1/100 cycles in the HRC-0.39-0.10 specimen, its opening is mostly closed and the shear slide is small during the process of subsequent unloading and negative loading, so that the shear force of the peak load of R = −1/100 cycles is hardly reduced. On the other hand, although the crack behavior at the peak of R = +1/100 cycles in the HRC-0.39-0.28 specimen having a high axial load is almost the same as that of the HRC-0.39-0.10 specimen, the shear slide to the slanting lower part caused by a high axial load during the progress of unloading and negative loading increases substantially. As a result, the shear force of the peak load of R = −1/100 cycles is reduced by 20%, and the majority of shear slides remain even after unloading. Moreover, in the case of the HRC-0.39L-0.28 specimen, as the shear reinforcement yields in part in R = −1/100 cycles (Fig. 7), the crack width approaches 1 mm and the shear slide in subsequent unloading progress also increases remarkably. As the +7 cycle is the second cycle of R = +1/100, the peak shear force declines 30% or more, the residual shear slide exceeds 1 mm, and the solidity as a member is degraded greatly.

5. COEFFICIENT OF FRICTION OF CRACK SURFACE OBTAINED FROM ANALYSIS

To examine the coefficient of friction in the smooth crack surface of an RC column made of high-strength concrete, FEM analysis incorporating the aggregate interlocking and shear friction in a crack surface was carried out. Although the analysis included a stub part, the FEM of a test section only is shown in Fig. 11. The opening crack and closed crack were modeled with an interface element with an X shape, and the Li and Maekawa model (Li *et al.* 1989) and the Coulomb friction model (Chen 1982) were applied to each interface. As splitting of the aggregate was observed in high-strength concrete, the aggregate dimension in an opening-crack model was set to 10 mm. On the other hand, for a closed crack with reference to the friction model applied to high-strength concrete in a previous paper (Shinohara 2007-2), the cohesion was set to 0, the expansion coefficient was set to 0.2, and the coefficient of friction

assumed values from 0.9 (F0.9) to infinity (F∞), which does not permit a shear slide. The concrete was modeled with an isoparametric plane-stress element that has an intermediate node. A trilinear bond-slip relation by the Hayashi model (Hayashi *et al.* 1985) based on an experiment on a member was applied to the bond behavior of the main reinforcement. The shear reinforcement was modeled with a two-node truss element, and the bond was not taken into consideration. As the vertical displacements of the nodes on the upper stub are changed uniformly to restrain rotation, an antisymmetric flexural is obtained as in the experiment. After introducing a predetermined axial load in 10 steps, the shear force was imparted by a compulsive displacement of 0.1 mm increments.

In the analysis, the strengths of high-strength concrete specimens having a low axial load and a high axial load were set to 98 N/mm^2 and 119 N/mm^2, respectively, that of a normal-strength concrete specimen was set to 40 N/mm^2 (see Table 1), and the strength of the cover concrete was reduced to 85%. A Drucker–Prager criterion (Chen 1982) having a 10-degree internal friction angle as a state of plane stress was adopted for the compressive failure of concrete, and linear softening behavior was assumed after maximum strength. The softening slope of the core concrete was set up, in consideration of the confining effect by shear reinforcement, more gently than that of the cover concrete (Fig. 12). Multidirectional crack models having a threshold value of 60 degrees were used for concretes other than the interface of the X shape, and the decrease in shear stiffness accompanying the increase in crack width was taken into consideration (Shinohara *et al*. 1999). The analytical models and mechanical properties of concrete are shown in Fig. 12. The reinforcement was modeled as perfect plasticity without strain hardening after yield strength.

Figure 13 shows the relation of the shear force and rotation angle obtained from the analysis, together with the envelope curve of the positive loading and the negative

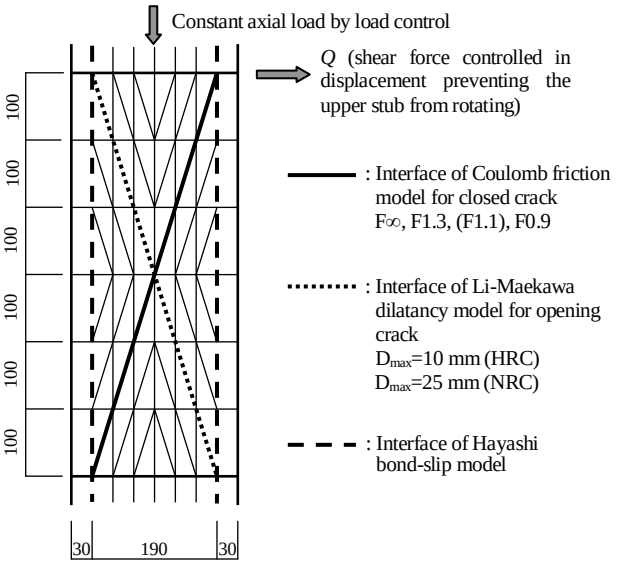
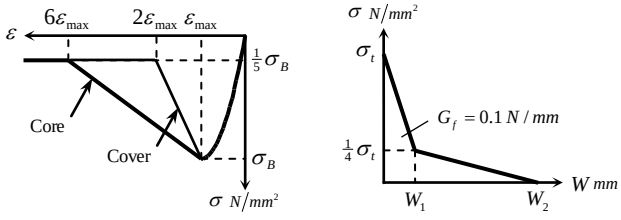


Figure 11 Finite element mesh and assumed models



Compressive stress strain curve Tensile stress crack-width curve

Concrete	σ_B N/mm^2	ε_{max}	E_c N/mm^2	σ_t N/mm^2	W_1 mm	W_2 mm	ν
HRC-0.10	98	-0.0028	40000	3.6	0.025	0.13	0.2
HRC-0.28	119	-0.0030	40000	3.6	0.025	0.13	0.2
NRC	40	-0.0018	30000	2.7	0.035	0.17	0.2

ν: Poisson's ratio

Figure 12 Mechanical properties and analytical model

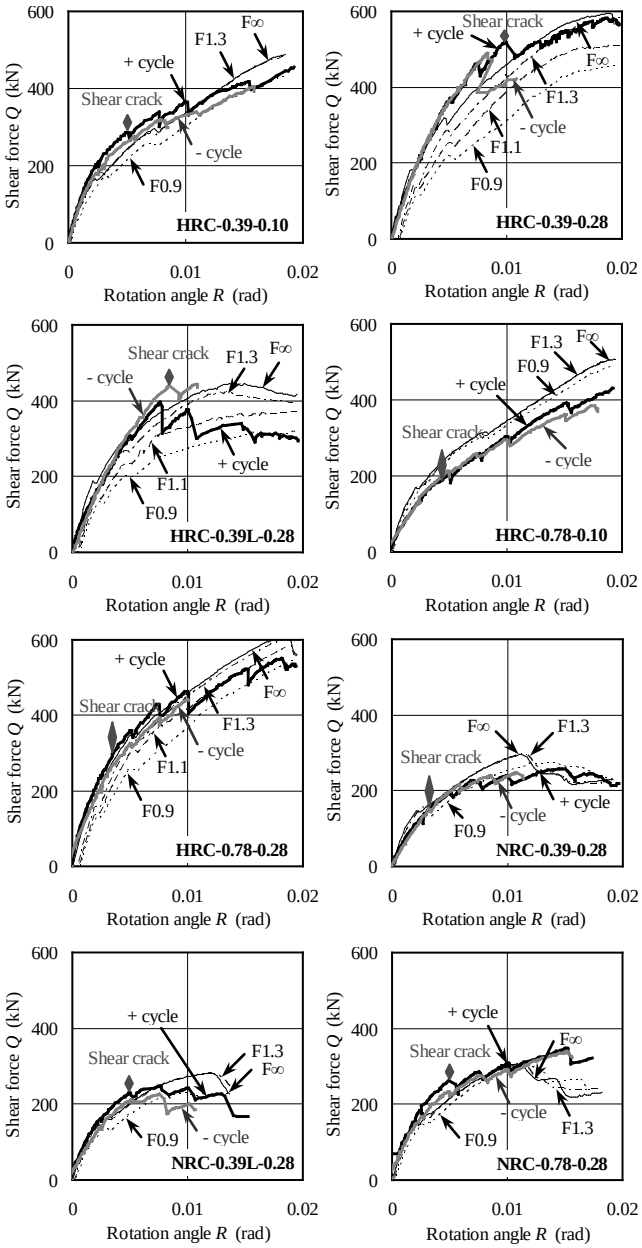


Figure 13 Comparison of Q-R curves obtained experimentally and analytically for different coefficient of friction

loading obtained from the experiment. The analysis of F∞ assumes a case of no shear slide in a closed crack. As shear reinforcement carries the majority of shear forces after shear cracking, and the interlocking effect of an aggregate decreases with an increase of an axial load, as shown in our previous paper (Shinohara *et al*. 2009), the same Li and Maekawa model was applied for all cases. In the experiment, a shear slide is produced in a closed-crack surface in reverse-direction loading after cracking (Figs. 8–10), and rigidity is reduced. On the other hand, in an analysis, as a crack interface is incorporated from the 1st stage, a shear slide grows in a friction interface during the axial-load introduction stage, the shear slide increases further in a subsequent shear loading progress, and rigidity is reduced. In the experiments, the envelope curve under positive and negative loading is almost the same until a shear crack occurs, and the analytical result of F∞, which does not permit the shear slide of a friction surface, exhibits behavior similar to the experimental result. As for a specimen with a high axial load and few shear reinforcements, the shear stiffness decreases after shear cracking in the experiment, and similarly, the effect of the coefficient of friction is remarkable also in the analysis. Especially, the shear stiffness of the HRC-0.39-0.28 and HRC-0.39L-0.28 specimens decreases greatly after shear cracking, and approaches the analysis result for coefficients of friction of 0.9 and 1.1, respectively. For high-strength concrete specimens having a small axial load and normal-strength concrete specimens, a distinct difference in the envelope curve under positive and negative loading was not seen in the experiment, even after shear cracking. Consequently, the effect of the coefficient of friction is negligible also in the analyses. The axial load introduced to these specimens is 500 kN to 600 kN, and is about one-third that of high-strength concrete columns having a ratio of axial load of 0.28. Moreover, although in the NRC-0.39L-0.28 specimen made of normal-strength concrete the shear-crack width exceeded 1 mm after the yield of shear reinforcement, the shear slide of the crack surface increased, and the shear force decreased in a negative loading. From the above, the shear slide of the closed crack related to the solidity of a member is greatly influenced by the amount of axial load and the yield of shear reinforcement. In addition, if the axial load increases and the amount of shear reinforcements decreases, it can be seen that the effect of the crack surface configuration (coefficient of friction) becomes remarkable.

In the case of the HRC-0.39L-0.28 specimen in which a shear crack occurs under negative loading and a large shear slide is produced under positive loading, the deformations after introducing the axial load, at a rotation angle of R = 1/300, R = 1/150, and R = 1/100 are expanded 30 times, as is shown in Fig. 14. In the case of a coefficient of friction of F∞, the shear slide was not produced in the friction surface, but the opening of an opening crack increased with the shear loading, and, in particular, it increased rapidly between R = 1/150 and R = 1/100 when the shear reinforcement yielded. If the coefficient of friction is reduced, the shear slide in a closed crack and the axial contraction increase, and the crack width of an opening crack decreases, that is, the phenomenon seen in the experiment reappears in the analysis.

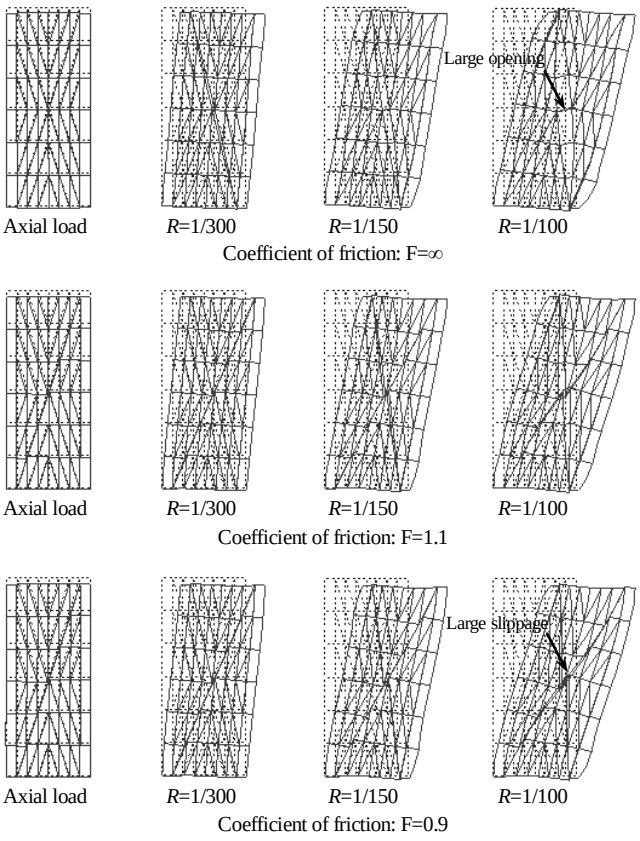


Figure 14 Comparison of transformation for HRC-0.39L-0.28 with different coefficient of friction

6. CONCLUSIONS

A flexure-shear experiment was conducted and the effect of the crack surface configuration, axial load, and shear reinforcement on the hysteresis characteristics of high-strength RC columns was studied. Furthermore, FEM analysis in consideration of shear friction was conducted, and the coefficient of friction of a smooth crack surface was examined. The main conclusions are as follows:

1) The asymmetry of the hysteresis characteristics of a high-strength concrete column originates in an increasing slide in a smooth crack surface closed by a reverse loading.
2) If the shear force currently carried in the concrete can be transmitted by shear reinforcement after shear cracking, an opening crack will have little influence on the hysteresis characteristics.
3) Although shear slide in a closed crack increases with an increase in axial load and with a decrease in the roughness of a crack surface, it can be controlled by proving a large amount of shear reinforcements.
4) The strain of shear reinforcement increases with the increase in crack width and/or a shear slide. Thus, the

shear reinforcement functions to control not only the shear-crack width but also shear slide.

5) In the case of a specimen that has a high axial load and a small amount of shear reinforcements, the shear slide of a closed crack is greatly dependent on the coefficient of friction, and the coefficient of friction of the crack surface of high-strength concrete is 0.9 to 1.1 according to the analytical results.

References:

Teraoka, M. *et al*. (2003), 'Some Questions for Seismic Design and Performance Evaluation on Members of Reinforced Concrete Framed Structures',*Concrete Journal*, Vol.41 , No.4 , pp.37-46.

Hasegawa, R. *et al*. (2004), 'Shear Transfer Mechanism on the Crack Surface in High Strength Concrete', *Proceedings of the Japan Concrete Institute*, Vol.26, No.2, pp.91-96.

Shinohara, Y. *et al*. (2007), 'Shear Transfer Mechanism in Smooth Cracks of Ultra-High-Strength Reinforced Concrete Members', *J. Struct. Const. Eng.*, AIJ, [618], pp.183-190.

Architectural Institute of Japan (1997), 'Design Guidelines for Earthquake Resistant Reinforced Concrete Buildings Based on Inelastic Displacement Concept', AIJ.

Shinohara, Y. *et al*. (2005), 'Active Confining Effect and Shear Crack Behavior for RC Columns Prestressed Laterally', *J. Struct. Const. Eng*., AIJ, [587], pp.147-153.

Shinohara, Y. *et al*. (2009), 'Effect of Axial Load on Shear Transfer Mechanism during Shear Damage Progress in RC Columns', *J. Struct. Const. Eng.*, AIJ, [639], pp.897-905.

Li, B. Maekawa, K. and Okamura, H. (1989) : Contact Density Model for Stress Transfer across Cracks in Concrete, *J. of the faculty of eng., The university of Tokyo*, Vol. XXXX, No.1, pp.9-52

Chen, W. F., (1982), 'Plasticity in Reinforced Concrete', McGraw-Hill Book Company

Shinohara, Y. (2007-2), 'Stress Transfer Mechanism in Shear Cracks of Reinforced Concrete', *J. Struct. Const. Eng.*, AIJ, [620], pp.109-116.

Hayashi S. *et al*. (1985), 'The Bond Behavior of Reinforcing Bars through the Interior of the Beam Column Joint', *J. Struct. Const. Eng*., AIJ, [357], pp.101-111.

Shinohara, Y. *et al*. (1999), 'Compressive Shear Behavior in Fracture Process Zone of Concrete', *J. Struct. Const. Eng*., AIJ, [525], pp.1-6.

8CUEE CONFERENCE PROCEEDINGS
8th International Conference on Urban Earthquake Engineering
March 7-8, 2011, Tokyo Institute of Technology, Tokyo, Japan

A SIMPLIFIED NUMERICAL APPROACH TO CUMULATED DAMAGE EFFECTS ON SEISMIC PERFORMANCE OF EXISTING RC FRAME STRUCTURES

Jiang Qian[1)], Wei Huang[2)], and Binbin Zhuang[2)]

1) Professor, State Key Laboratory of Disaster Reduction in Civil Engineering, Tongji University, P. R. China
2) Graduate Student, State Key Laboratory of Disaster Reduction in Civil Engineering, Tongji University, P. R. China
jqian@tongji.edu.cn, 2008huangwei@tongji.edu.cn

Abstract: Seismic performance capacity of a real in service building structure may differ from what it was expected in its design stage because of damage accumulation from long term withstanding to service loads, previous earthquakes or degeneration in material properties caused by serious environment. In view that for most commonly used material models cumulated damage in a structure can only be measured by residual strain, a two step pushover analysis procedure has been proposed herein. First response analysis of the structure to a cyclic loading of certain intensity was performed, and then a static pushover analysis was carried out in consequence with residual strain taken into account, which represents the damage accumulation in structures caused by previous loading history. A number of numerical examples are presented. It is shown that structures constructed in different time or designed according to different standard may suffer from cumulated damage in an obvious different manner. It seems that buildings designed following old version standard are more sensitive to cumulated damage.

1. INTRODUCTION

Recent earthquakes have shown that research in earthquake engineering has to be focused on the assessment of vulnerability of existing constructions. It is not only for their lacking appropriate seismic resisting characteristics but also for their capacity degeneration due to long term withstanding to service loads, serious environment or previous earthquakes (Rizzano and Tolone 2009, Ou and Wu 1993 and 1994). In fact, older buildings, designed and constructed before 1990's, without considering earthquake provisions, constitute a significant hazard in 2008 Sichuan earthquake (Wang 2008).

The structure's ability to survive an earthquake may be measured in terms of the expected state of damage of the structure after the earthquake. There are several ways to define the damage state of the structure. Empirical and theoretical approaches have been applied to yield various estimates of structural damage. The empirical damage models are based on statistics of observed structural damage following earthquakes and thus may be subjective. They provide useful qualitative information on the overall seismic performance of structural system. However, the empirical evaluation does not lend itself well to rationally prediction the strength reserve and response characteristics of a structure with a specified degree of damage. The analytical damage models may involve various degrees of complexity as they account for the characteristics of the structure and its seismic response. They can be generally divided into two classes: (1) strength-based damage indices; and (2) response-based damage indices. Strength-based damage indices are simple and do not require response analysis. However, it must be calibrated against observed damage using a large database. If field observations of damaged structures due to seismic loads are not available, the damage index may be calibrated based on damage prediction using nonlinear dynamic analysis.

The seismic performance of structures is commonly related to the capacity to undergo inelastic deformations, defined as the ratio of peak inelastic response to the corresponding yield response or ductility. Experimental studies show that failure of brittle systems is caused by excessive deformation while failure of ideal ductile systems is initiated by repeated inelastic deformations. The problem is that for existing building damages are usually already undertaken in someway and to a certain extent. Seismic performance capacity of a real in service building structure must take this into account. Ghobarah et al. (1999), after an extensive reviewing and evaluating the available response-based damage models, proposed a new approach for damage assessment of structures. The approach is to perform pushover analysis for the structure twice; once before subjecting the structure to the earthquake and once after subjecting the structure to the ground motion. Before performing the second pushover analysis, the structure is returned to the unloaded static state. It is believed that the difference in initial stiffness before and after subjecting the structure to an earthquake shows damage accumulation. In view that for most commonly used material models cumulated damage in a structure can only be measured by

residual strain, the full dynamic response analysis can be replaced by a cyclic loading procedure for computational efficiency.

In this context, the two-step pushover analysis procedure has been proposed. First response analysis of the structure to a cyclic loading of certain intensity was performed, and then a static pushover analysis was carried out in consequence with residual strain taken into account, which represents the damage accumulation in structures caused by previous loading history. A number of numerical examples are presented. It is shown that structures constructed in different time or designed according to different standard may suffer from cumulated damage in an obvious different manner. It seems that buildings designed following old version standard are more sensitive to cumulated damage.

2. STRUCTURAL DETAILS OF THE BUILDING AND FE MODELING

As examples, the damage analysis is performed for a simple low-rise three story concrete frame building with different reinforcement, named as Frame A, B and C, as shown in Figure 1. Frame A is designed according to GB50011-2010, the current code, Frame B according to earlier code GBJ11-89, while Frame C without any reinforcement, which may represent a serious rusty in steel

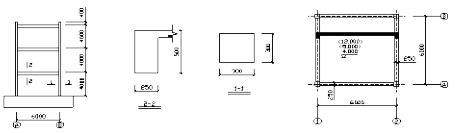
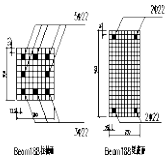
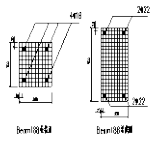


Figure 1 Dimensions of the Three-Story Frame Building



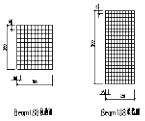
Column Section Beam Section

(A) Frame A



Column Section Beam Section

(A) Frame B

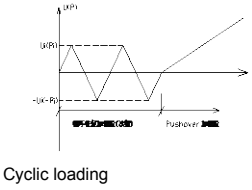


Column Section Beam Section

(A) Frame C

Figure 2 Reinforcement Details in Beams and Columns

reinforcement. Section dimensions for the columns and beams and the reinforcement are also shown in Figure 1



Cyclic loading

Figure 3 Loading Pattern in Two-Step Pushover Analysis

A finite element model for the frame has been established by using ANSYS package, in which concrete beams and columns were modeled by elements with fiber-like section discretization, as shown in Figure 2. The elasto-plastic material model with bilinear isotropic hardening is adopted.

The loading program is designed as that: before pushover analysis, two cyclic loading with specified intensity was applied to the structure first, as shown in Figure 3. The intensity of the cyclic loading depends on target design base shear. The design base shear for the frame at different earthquake intensity is list in Table 1.

Table 1 Design Base Shear (kN)

Modal No.	Frame A	Frame B	Frame C
Frequent, intensity Ⅷ	71	70	68
Rare, intensity Ⅶ	196	189	174
Rare, intensity Ⅷ	389	372	344

3. NUMERICAL RESULTS

3.1 Results of Modal Analysis

The first six vibration modes were computed and modal frequencies are listed in Table 2. There are slight differences in modal frequencies for the three frames because of difference in reinforcement.

Table 2 Modal Frequencies (Hz)

Modal No.	Frame A	Frame B	Frame C
1	1.24	1.19	1.08
2	1.24	1.19	1.08
3	1.75	1.69	1.55
4	3.71	3.54	3.24
5	3.71	3.54	3.24
6	5.27	5.04	4.63

3.2 Pushover Analysis

First, a conventional pushover analysis was conducted using an inverted triangular load. The base shear-displacement curves at top floor are shown in Figure 4. It can seen that initial slops of the base shear-top deflection of the three frames are almost the same while ultimate loading capacities are 616kN, 397kN and 179kN for Frame A, B and C, respectively.

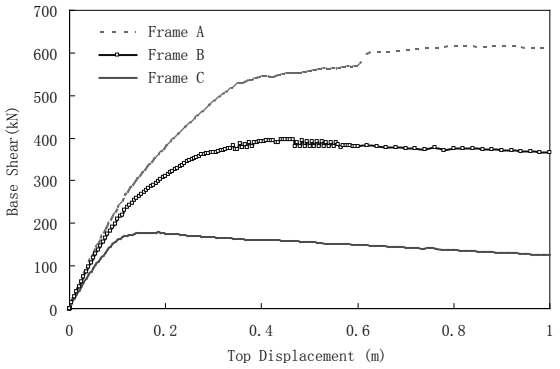


Figure 4 Base shear-displacement curves

3.3 Pushover Analysis to Frames with cumulated damage

Then, the two-step pushover analysis was carried out. In this analysis, response analysis of the structure to a cyclic loading with base shear intensity of three levels listed in Table 1 was performed first. And then, a static pushover analysis was conducted in consequence with residual strain taken into account, which represents the damage accumulation in structures caused by previous cyclic loading.

Numerical results are given in Figure 5, 6 and 7 for Frame A, B and C, respectively. It can be seen that structures with damage accumulation will exhibit an obvious initial slop decrease in response curves. Structure designed following old version standard that is Frame B, seems more sensitive to cumulated damage. For Frame C, the structure without any reinforcement or a structure with its steel reinforcement in serious rusty, it may even crash in the first cyclic loading step of high intensity.

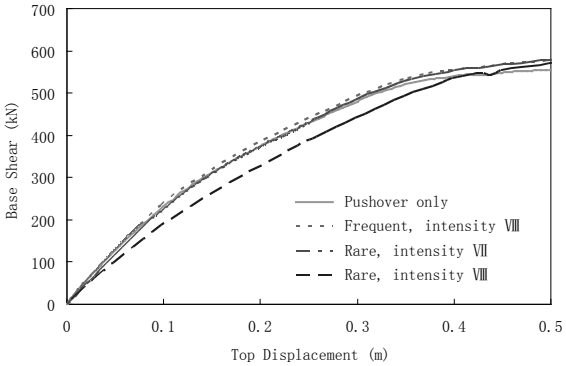


Figure 5 Pushover analyses with different level of damage accumulation for Frame A

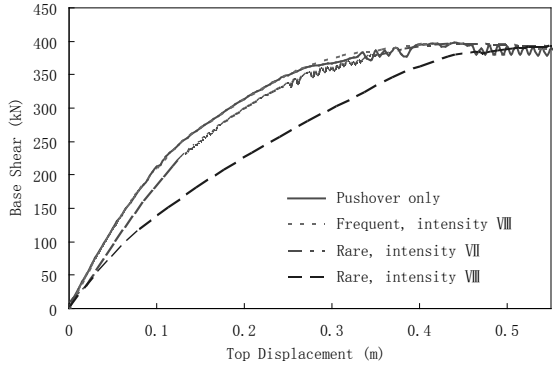


Figure 6 Pushover analyses with different level of damage accumulation for Frame B

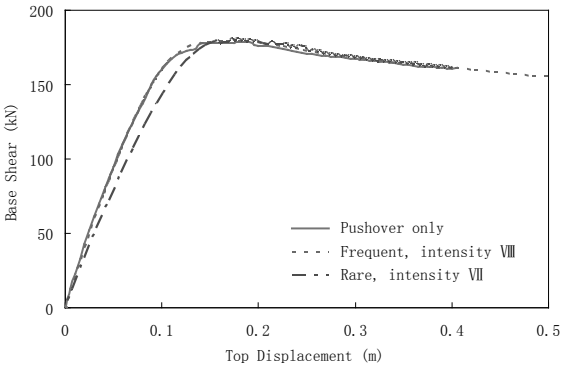


Figure 7 Pushover analyses with different level of damage accumulation for Frame C

4. CONCLUSIONS

A simplified numerical approach to cumulated damage effects on seismic performance of existing RC frame structures has been proposed. It is a two-step pushover analysis procedure. Response analysis of the structure to a cyclic loading of certain intensity was first performed to produce designed damage in the structure, and then a static pushover analysis was carried out in consequence with residual strain taken into account. Numerical examples show that structures constructed in different time or designed

according to different standard may suffer from cumulated damage in an obvious different manner. It seems that buildings designed following old version standard are more sensitive to cumulated damage.

Acknowledgements:

The authors acknowledge with thanks support from (a) the National Natural Science Foundation of China under grant No. 90815029 and No. 51021140006, (b) the National Basic Research Program of China under the Grant No. 2007CB714202, and (c) the Ministry of Science and Technology of China through the Research Grant under grant No. SLDRCE10-B-07.

References:

Rizzano, G and Tolone, I, (2009), "Seismic Assessment of Existing RC Frames: Probabilistic Approach", Journal of Structural Engineering, ASCE, 135(7), 836-852.

Ou, J.P. and Wu, B., (1993), "Probabilistic Cumulated Damage Analysis of RC Structures Under Earthquake Having Aftershock", Shanghai Journal of Mechanics, 14(4), 63-70.

Ou, J.P. and Wu, B., (1994), "Test Research on the Cumulative Damage of Compression-Flexure Members under Main-shock and Aftershocks", Earthquake Engineering and Engineering Vibration, 14(3), 20-29.

Wang Yayong, (2008), "Lessons learnt from building damages in the Wenchuan earthquake - seismic concept design of buildings", Journal of Building Structures 29(4), 20-25.

Ghobarah, A., Abou-Elfath, H. and Biddah, A., (1999), "Response Based Damage Assessment of Structures", Earthquake Engineering and Structural Dyanmics, 28(1), 79-104.

GB50011-2010, (2010), "Code for seismic design of buildings", China Architecture and Building Press.

GBJ11-89, (1989), "Code for seismic design of buildings", China Architecture and Building Press.

8CUEE CONFERENCE PROCEEDINGS
8th International Conference on Urban Earthquake Engineering
March 7-8, 2011, Tokyo Institute of Technology, Tokyo, Japan

NON-LINEAR FE ANALYSIS OF POST-TENSIONED PRECAST CONCRETE WALL

Ohmura Tetsuya[1] and Gregory G. Deierlein[2]

1) Lecturer, Department of Architecture, Tokyo City University, Japan
2) Professor, Engineering Department of Civil & Environmental Engineering, Stanford University, USA
tohmura@tcu.ac.jp, ggd@stanford.edu

Abstract: Vertical post-tensioning has been proposed as a cost effective technique to improve concrete shear wall performance by improving shear resistance and minimizing residual deformations following large earthquakes. Monotonic loading response of finite element models for precast concrete reinforced walls are compared to published test data, showing good agreement.

1. INTRODUCTION

Reinforced concrete walls are effective lateral systems for seismic design in buildings. However concrete walls have potential problems for severe cracking and residual deformations from extreme earthquakes that are difficult and costly to repair. Vertical post-tensioning has been proposed as a cost effective technique to improve concrete shear wall performance by improving shear resistance and minimizing residual deformations following large earthquakes.

While the basic principles of vertical post-tensioning are straightforward, details of the shear wall response, including the interaction of flexure and shear and self-centering characteristics are not well understood.

We have analyzed conventional wall and post-tensioned concrete wall to evaluate these ultimate flexural moments and residual drift angles. And we have verified our modeling method and analyses[1].

This paper examines the behavior of post-tensioned precast concrete walls through detailed finite element modeling. Monotonic loading response of finite element models for precast concrete reinforced walls is compared to published test data.

2. FE ANALYSIS

2.1 Specimen in published test data

Figures 1 and 2 show the specimen in published data[2]. The specimen consists of precast concrete wall and foundation. The wall has a total height of 3,658mm, total length of 2,438mm and a thickness of 158.8mm. Four #6 bars and two 13mm unbounded tendons are located in the center of the wall. The concrete at the wall toe are confined by hoop of #3 and reinforced by wire mesh.

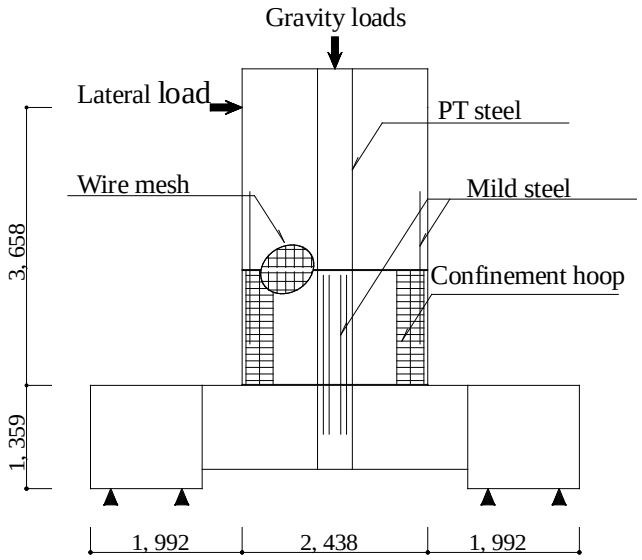


Figure 1 Specimen (unit : mm)

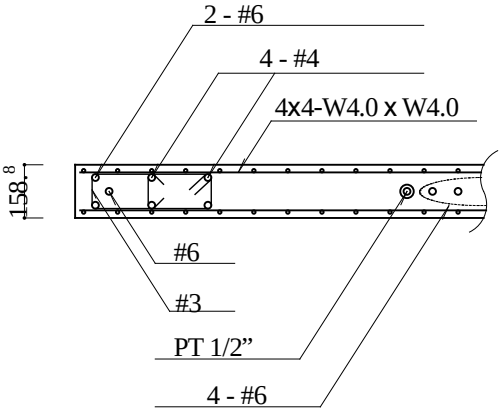


Figure 2 Section of wall (unit : mm)

Table 1 Property of material

	Steel grade		Measured area(mm^2)	Perimeter(mm)	Measured yeild strength(N/mm^2)
#3	ASTM A706 STEEL	Grade60	71	30	517
#4			129	40	517
#6			284	60	445
PT 1/2"	ASTM A 416-06	Grade270	96.1		1675
WIRE MESH	4x4-W4.0xW4.0	Grade60	254mm^2/m		420

Concrete Strength 33N/mm^2

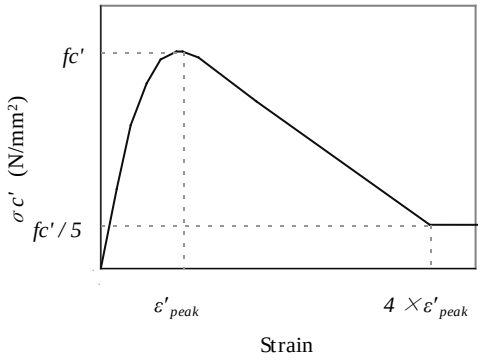


Figure 3 Compressive stress – stress history (concrete)

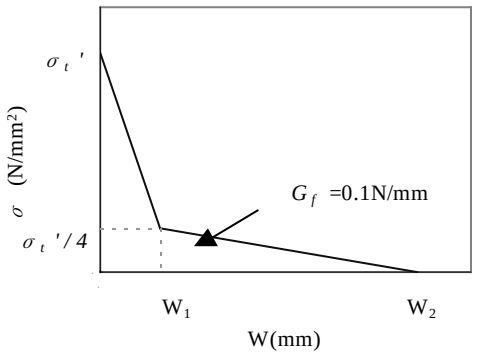


Figure 4 Tensile stress – crack width history

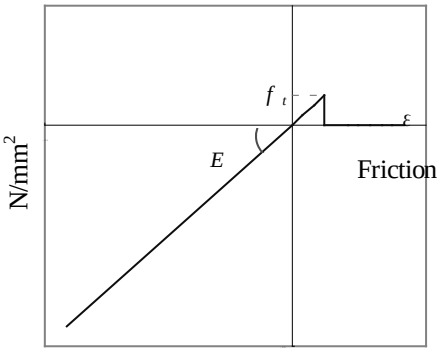
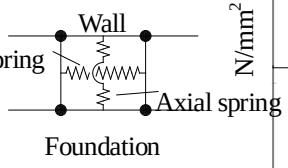


Figure 5 Axial stress – strain history at the concrete joint



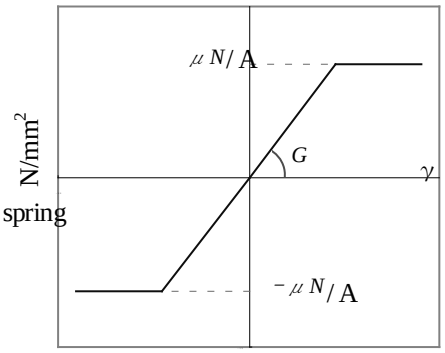


Figure 6 Friction – slip history at the concrete joint

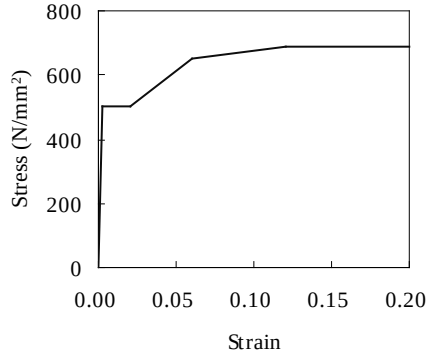


Figure 7 Stress – strain history (bar)

Table 1 shows the property of the materials. All bars except PT steel tendons are mild steel and concrete strength was 33N/mm^2.

A downward axial load of about 325kN was applied at the centerline of the wall. The average initial stress in the tendons was 1,024N/mm^2. A reversed-cyclic lateral displacement history was used during the test, with three fully repeated cycles at each displacement increment.

2.2 Modeling

To simulate the behavior of the specimen, a nonlinear finite element analysis applying monotonic loading is conducted under plane stress conditions. The four-node iso-parametric shell elements were used for the concrete, and the bar elements included hoops for reinforcements were layered on the shell elements as truss considered bond slip. Wire mesh was embedded. PT steel was unbounded and modeled as bi-linear. Bond between mild steels and concrete was considered just as the published paper[1].

Concrete was modeled as shown in Figures 3 and 4 considered strain softening. The joint between foundation and wall was modeled as shown in Figure 5 and 6, where the friction coefficient is 0.4; however they have enough stiffness and strength just as proven in the test result. Strain hardening was considered for mild steels located in the center of the wall as shown in Figure 7.

2.3 Solution

At first, the post tension force was given and axial load was applied at the top of the center of the wall. Next, the lateral load was applied at the wall. By applying the Newton method, the number of load steps required to minimize the work done by the unbalanced forces was determined. The number of iterations in each loading step was placed less than 50.

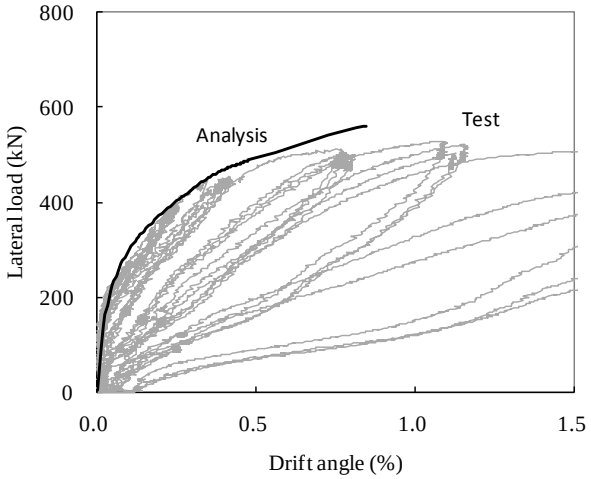


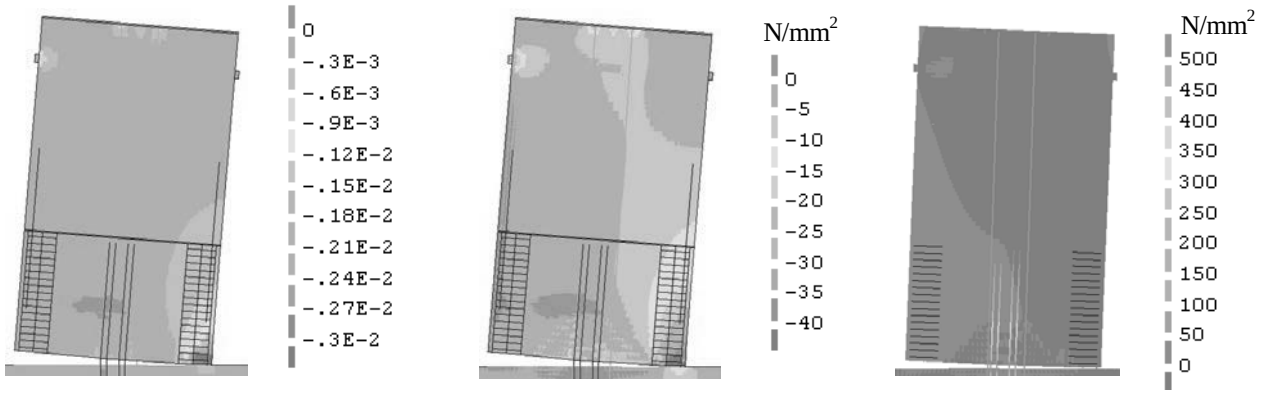
Figure 8 Hysteresis curve

3. ANALYSIS RESULT

3.1 Hysteresis curve

Figure 8 shows hysteresis curve. The grey line represents the test result and the black line represents the analysis result. The analysis was stopped because of large unbalance energy.

According to the test result, the residual drift angle is eliminated to under 0.2% due to post tension tendons, even though peak drift angle is over 1%. Stiffness and lateral load in the test and analysis are almost suited up to 0.5% drift angle. Maximum lateral load in the analysis 561kN was larger than in the test result 527kN. Good agreement was shown between the test result and analysis result up to 0.85% drift angle.



(a) Concrete strain (b) Concrete stress (c) Longitudinal bar stress

Figure 9 Stress and strain distribution at the final step

3.2 Concrete compressive strain and stress

Figure 9(a) shows concrete compressive strain distribution. Large compressive strain is observed at the bottom right of the wall. Hoops are effectively located at the toe of the wall.

Figure 9(b) shows concrete compressive stress distribution. Large compressive stress is observed at the bottom right of the wall as well as the concrete compressive strain distribution. In addition, large compressive stress is concentrated and developed at the local area. Concrete compressive strut is diagonally formed which resist lateral load. This analysis is useful to observe concrete stress distribution.

3.3 Longitudinal bar stress

Figure 9(c) shows longitudinal bar stress. Four mild steels #6 located in the center of the wall are yield but two PT steels are not. PT steel stress distribution is constant because they are unbounded. This result is as well as the test result.

Bonded mild steels are effective to absorb energy during large earthquake. PT steels are effective to eliminate residual drift angle, because they are almost elastic. It is important to examine the amount of PT steels and PT force, not to be yield.

3.4 Hoop and wire mesh stress

Figure 10(a) shows hoop stress distribution. The stress is developed to be yield at the bottom right corner of the wall. Hoops are partially effective to confined concrete at the toe of the wall, therefore they should be located as this specimen, because strain softening is improved by its' confined effect.

Figure 10(b) shows wire mesh stress distribution. The stress is developed to be yield at the bottom right corner of the wall as well as the hoop. It is easy to be yield, because the diameter of the wire mesh is smaller than that of the hoop. The wire mesh is not so expected to resist such a lateral load, but it is partially effective.

3.5 Displacement distribution

Figure 10(c) shows displacement distribution. The gap between the foundation and wall is developed, because this specimen consists of precast concrete having concrete joint there. The gap is easily opened and developed, so it was grouted by non-shrinkage mortar and longitudinal bars are located around the center of the wall. Damage is concentrated at the gap, so there is little damage on the wall except for the bottom right corner.

4. CONCLUSION

We have verified our modeling and analyses in the published paper[1)], and studied on the behavior of the post-tensioned precast concrete wall applied lateral force using finite element analysis. Hysteresis curve in the analysis was suited to that in the test up to about 0.85% drift angle, hoops and wire mesh at the toe of the wall were effective. Ultimate flexural moment can be estimated by our model and analysis.

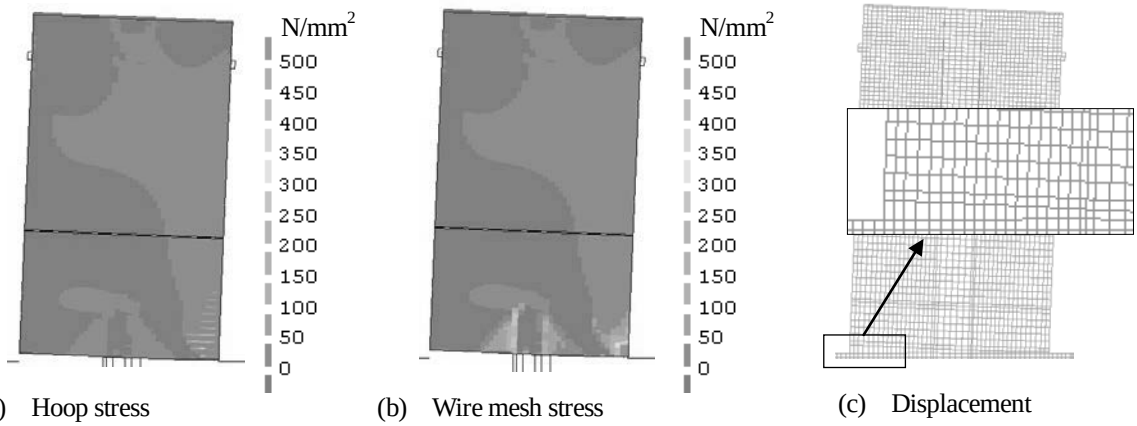
Acknowledgements:

Professor Yahya C. Kurama is thanked for sending test data, his support and many helpful comments in the course of this study. The support of JIP Techno Science staff is deeply appreciated.

References:

1) Tetsuya Ohmura and Gregory G. Deierlein, "NONLINEAR ANALYSIS OF POST-TENSIONED CONCRETE WALLS THAT MINIMIZE RESIDUAL DRIFTS UNDER SEISMIC LOADING", *3rd fib International Congress*, CD-ROM , May 2010

2) Smith, B. and Kurama, Y., "Seismic Behavior of a Hybrid Precast Concrete Wall Specimen: Measured Response versus Design Predictions," *9th U.S. National and 10th Canadian Conference on Earthquake Engineering*, Toronto, ON, Canada, 2010, 10 pp.



(a) Hoop stress (b) Wire mesh stress (c) Displacement

Figure 10 Stress and displacement at the final step

8CUEE CONFERENCE PROCEEDINGS
8th International Conference on Urban Earthquake Engineering
March 7-8, 2011, Tokyo Institute of Technology, Tokyo, Japan

SEISMIC BEHAVIOR OF L-SHAPED CORE-WALLS

Susumu Kono[1], Kohei Sakamoto[2], Kazuma Inada[3], and Masanobu Sakashita[4]

1) Associate Professor, Dept. of Architecture and Architectural Engineering, Kyoto University, Japan
2) Graduate Student, Dept. of Architecture and Architectural Engineering, Kyoto University, Japan
3) Structural Engineer, JR West, Japan
4) Assistant Professor, Dept. of Architecture and Architectural Engineering, Kyoto University, Japan
kono@archi.kyoto-u.ac.jp, sakashita@archi.kyoto-u.ac.jp

Abstract: This paper addresses the seismic performance of core-walls with L-shaped cross sections based on an experiment and numerical analysis on three reinforced concrete specimens with 1/4.5 scale. The specimens had large amount of vertical reinforcement in wall panels and boundary columns, and the concrete compressive strength of 80 MPa so that the core-walls behaved as a major seismic resisting component in tall buildings. Test variables included section configurations and loading directions. Axial load was varied up to 12MN or 31% of axial load capacity as a linear function of the lateral load intensity. The lateral load-drift relations were recorded with local deformation and damage focusing on the yield of reinforcement and crushing of concrete. Damage of boundary columns was severe and indicated the importance of good confinement at the end of wall sections. A simple fiber model simulated the lateral load - drift angle relations by considering pullout of longitudinal reinforcement. It was concluded that the pullout of longitudinal reinforcement and local crushing of concrete had a significant influence on the behavior of core-walls.

This paper was reprinted from the 3rd International FIB Congress PaperID #613[1] after making minor changes.

1 INTRODUCTION

Maffei and Yuen[2] addressed the advantage of core-wall buildings in their article as follows. "*In recent years, a new type of tall buildings is being constructed. They use reinforced concrete core-walls without supplemental moment resisting frames in the seismic force resisting system. RC core-walls offer advantages of open and flexible architecture. By eliminating the need for moment resisting frames, smaller framing members or flat slabs can be used for the building floors, and the framing depth of floors can be reduced. In a core-wall building, resistance to seismic forces is provided by a reinforced concrete core that surrounds the elevator banks. A core-wall building eventually realizes lower costs and faster construction.*"

Adebar et al.[3] summarized previous tests on concrete structural walls with height-to-length ratios greater than 2.0. The cross section of those specimens were mainly rectangular, flanged, and barbell. Total vertical reinforcement, as ratio of gross area of wall cross section, was 2.62 and the axial compression level was 20% at maximum. In Japan, a large seismic demand requires larger core-walls with heavy vertical reinforcement and higher concrete strength. Since late 1990's, behaviors of large scale core-walls have been studied extensively in Japan [4] and [5]. Konishi et al.[6] reported that the confinement of concrete at the corner or the end of the section increased the deformation capability. They simulated the load-displacement relation with good accuracy with a fiber model adapting the plane-sections-remain-plane assumption. Maruta[7] proposed a method to determine the amount of shear reinforcement at the boundary column region to confine the crushed concrete based on Konishi's work. However, Nakachi[8] reported that the plane-sections-remain-plane assumption cannot be applied to a core-wall after the formation of flexure-shear cracks.

Recently, additional experiments have been conducted on core-walls with different types of cross sections in some Japanese research institutes. In Kyoto University, a seismic behavior of core-walls was studied using three 1/4.5 scaled specimens with L-shape cross sections. The specimens had well confined boundary columns, a large amount of vertical reinforcement, and high strength concrete of 80 MPa. The vertical load up to 12MN or 31% of axial load capacity was applied to simulate the variation of axial load conditions of tall buildings. The damage process was recorded and the load-displacement relation was simulated with a fiber model.

2 TEST SETUPS

Figure 1 shows configuration and reinforcement arrangement of three specimens (L00A, L45A and L45B). The cross section of L45A and L00A were equilateral and that of L45B was inequilateral. The 1/4.5 scaled core-walls with L-shaped cross sections represented three lowest stories

of a prototype 40-story reinforced concrete office building. All wall panels had same thickness of 200mm and height of 2480mm. In this study, a square area of 200mm by 200mm at either end of the wall section was treated as a boundary column. The boundary columns were confined with large amount of longitudinal and shear reinforcement as shown in Table 1. Two types of test variables are section configuration and loading direction as shown in Table 2. It is noted that high strength concrete with the compressive strength of 80 MPa was used as shown in Table 3.

Table 1 Types of reinforcement

Member (Section size)	Reinforcement		Steel ratio (%)
Column (200x200mm)	Longitudina	16-D13	5.07
	Transverse	4-D6@80	0.79
Wall (200 mm	Vertical	3-D13@63	3.02
	Horizontal	2-D10@80	0.89

Table 2 Test variables

Specimen	Section configuration	Loading direction angle to the wall (degree)
L00A	Equilateral	0
L45A	Equilateral	45
L45B	Inequilateral	45

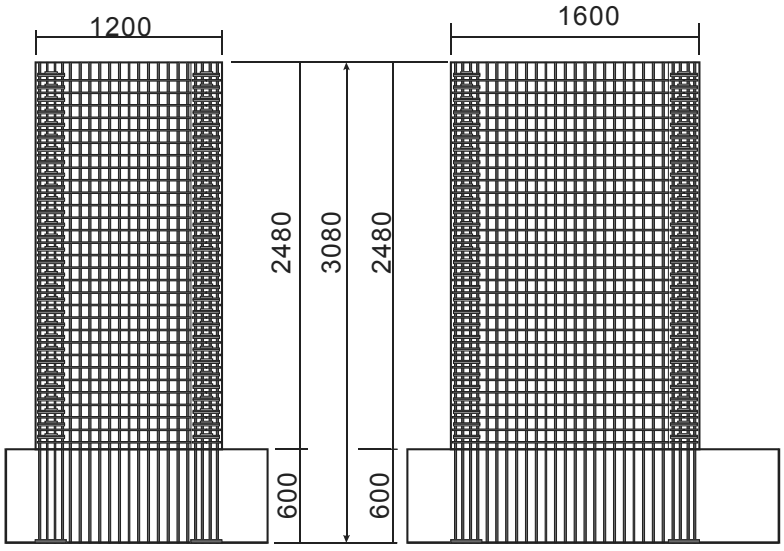
Table 3 Mechanical properties of materials

(a) Concrete

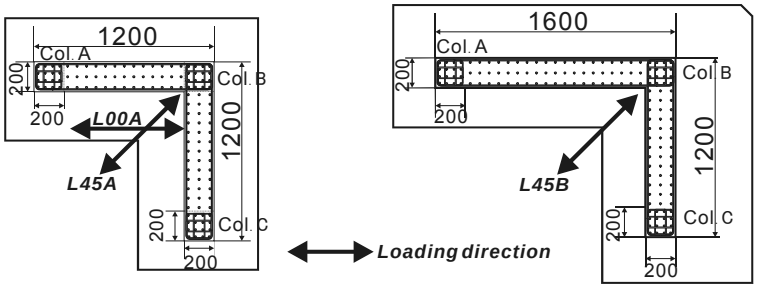
Specimen	Compressive strength (MPa)	Young's modulus (GPa)	Splitting strength (MPa)
L00A	88.6	39.1	6.35
L45A	76.4	40.4	5.00
L45B	89.1	39.6	5.56

(b) Reinforcement

Type	Yield strength (MPa)	Tensile strength (MPa)	Young's modulus (GPa)
D13	444	611	187
D10	443	607	180
D6	425	539	198



(a) Elevation (L00A, L45A) (b) Elevation (L45B)



(c) Plan view (L00A, L45A) (d) Plan view (L45B)

Figure 1 Configuration and reinforcement arrangement (Unit: mm)

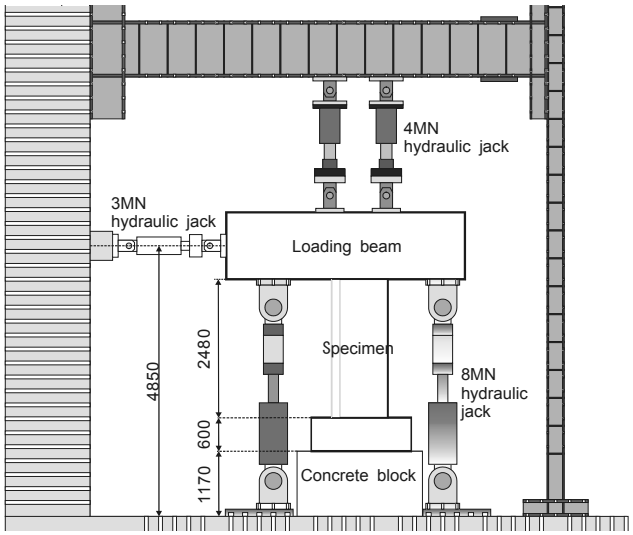


Figure 2 Loading system (Unit: mm)

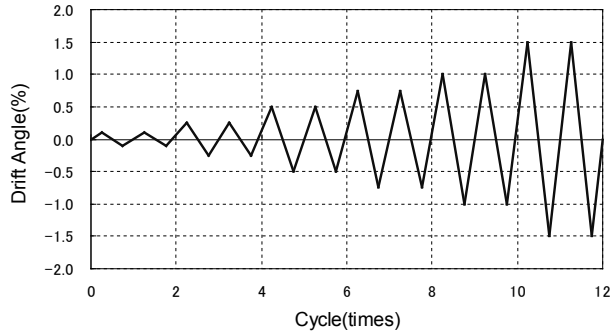


Figure 3 Loading protocol

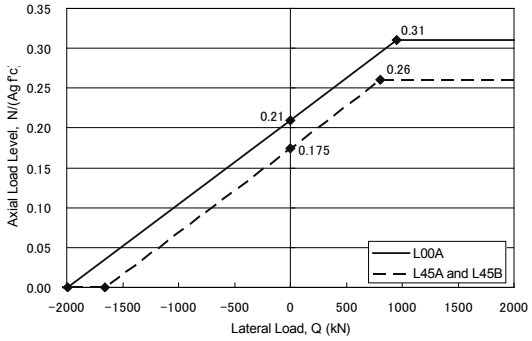


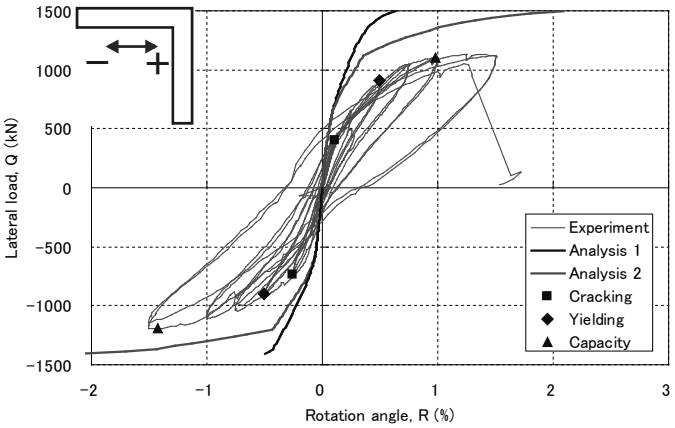
Figure 4 Loading path on the axial load level - lateral load relation space

Figure 2 shows the loading system. In addition to 3MN hydraulic jack for the lateral load, four hydraulic jacks were used to control the vertical load. Additional three 1 MN hydraulic jacks, which are behind the loading beam and not shown in the figure, were used to prevent the out-of-plane movement of the loading beam. Loading protocol of lateral displacement is shown in Figure 3. The drift is defined as the horizontal displacement of the centroid of the section at 2130 mm above the upper surface of the stub where 2130 mm is the height of the sixth floor level of the prototype building. The drift angle was computed by dividing the drift by 2130 mm. Four vertical hydraulic jacks were adjusted so that the height of contraflexure point remained a constant value of 4260 mm above the upper surface of the stub. In addition, the long term vertical load, N, was set $0.21A_gf'_c$ for L00A and 0.175 $A_gf'_c$ for L45A and L45B where A_g is the gross section area of the core-wall. The vertical load was varied as the linear function of the lateral load as shown in Figure 4. Loading direction was either parallel to or 45 degrees angle to the wall panel as shown in Figure 1(c) and (d).

3 TEST RESULTS

Figure 5 shows the lateral load (Q) – drift angle (R) relations and damage at the ultimate loading stage. L00A had the initial flexural cracks at drift angle (R hereafter), R=+0.1%. Longitudinal reinforcement in Columns B and C (Naming of boundary columns is shown in Figure 1) yielded in compression at R=+0.25% and that in Column A yielded in tension at R=+0.5%. Concrete in compression region showed no damage until R=+1.0%, at which the peak load was reached. After the peak, the damage of concrete in compression region progressed rapidly. The final failure occurred at the base of the wall between Columns B and C when the concrete failed in shear suddenly as shown in Figure 5 (b). In negative loading, the damage progress was similar to that in positive loading until R=-0.5%. However, the crushing of concrete at Column A occurred at R=-0.5%. The concrete crushing took place much earlier than that in positive loading because a large amount of tensile reinforcement carried large tensile force and compressive strength of concrete was not sufficient to balance it.

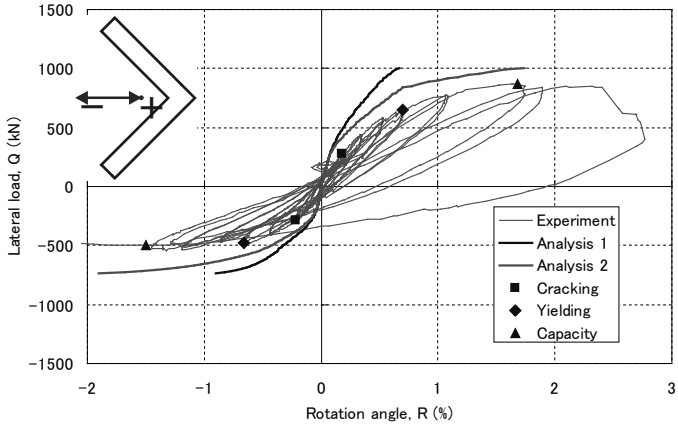
L45A had the initial flexural cracks at R=+0.16%. Longitudinal reinforcement in Column B yielded under compression at R=+0.34%, and the concrete at the base of Column B started to crush at R=+0.5%. The peak load was reached at R=+1.5% but the deformation progressed without losing too much load carrying capacity until R=+2.5%. The final failure occurred at R=+2.5% when the concrete at Column B crushed under compression. In the negative loading, the initial flexural cracks were found at R=-0.34% at Column B, the reinforcement in Columns A and C yielded in compression and that in Column B yielded in tension at R=-0.5%. The crushing of concrete at Columns A and C happened at R=-1.5%. The damage under negative direction was less severe than that under positive direction at the same drift ratio because the axial load is lower on the negative side. When the loading was reversed at R=+2.5% to the negative direction, the shear sliding failure occurred near the base of the wall.



(a) Q-R relation of L00A



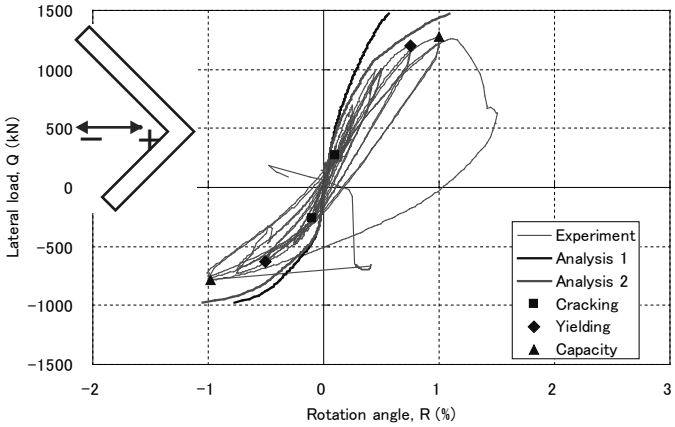
(b) Failure mode of L00A



(c) Q-R relation of L45A



(d) Failure mode of L45A



(e)Q-R relation of L45B



(f) Failure mode of L45B

Figure 5　Lateral load – drift angle relations and failure modes

L45B showed a similar damage progress to L45A until the positive peak load. The peak load was reached at R=+1.0%. The load carrying capacity degraded gradually till the concrete completely crushed at R=+1.5%. In the negative loading, the shorter side suffered severer damage than the longer side.

Figure 6 shows strain distributions of the vertical reinforcement along the section, which is 60mm above the wall base, of L45A. X-axis represents the distance of strain gages from the corner as shown in a small diagram in the figure. For drift angle less than R=+0.34%, the strain distribution was nearly linear. However, when the drift angle exceeded R=+0.5%, the strain of compression region progressed rapidly and the strain distribution was not linear anymore as can be seen in Figure 6(a). In negative loading in Figure 6(b), the strain distribution was nearly linear until the end of the loading. Two other specimens showed similar strain distributions. This shows that the plane-sections-remain-plane assumption is not valid after the concrete started to crush.

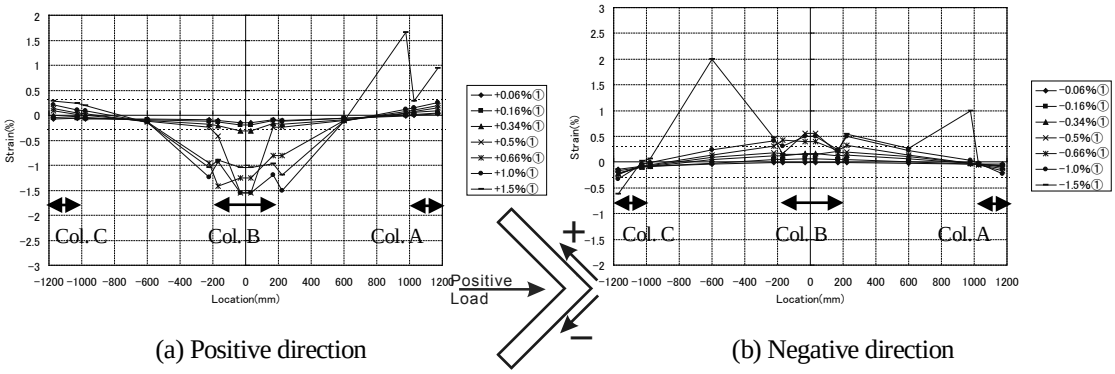
Figure 7 shows the strain distribution of longitudinal bars along the axis of Columns A and C of L45A. After R=1.0%, the strains became greater than 0.5% at the columns base. The figure indicates the effect of pullout of longitudinal reinforcement from the stub and columns on the drift of the core-wall as follows. Defining that $\varepsilon_r(x)$ is the strain of reinforcement and $\varepsilon_c(x)$ is the strain of concrete along the reinforcement at gage height, x, the elongation of reinforcement, δ_r, and that of concrete, δ_c, are expressed as Eqs. (1) and (2), respectively. Then, the pullout of reinforcement, $\delta_{pullout}$, can be obtained as Eq. (3). Assuming the total pullout appears at the interface between the stub and columns, the drift angle due to pullout of reinforcement, $R_{pullout}$, can be computed based on the distance between the reinforcement and the neutral axis, d_n, where d_n was obtained from the section analysis. In numerical computation, Figure 7 was used for $\varepsilon_r(x)$ and a section analysis was used for $\varepsilon_c(x)$.

$$\delta_r = \int_{x=-600}^{x=+2480} \varepsilon_r(x)dx \tag{1}$$

$$\delta_c = \int_{x=-600}^{x=+2480} \varepsilon_c(x)dx \tag{2}$$

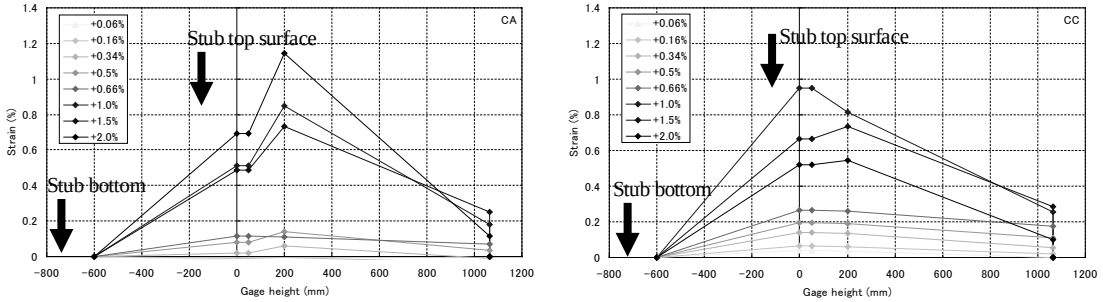
$$\delta_{pullout} = \delta_r - \delta_c \tag{3}$$

$$R_{pullout} = \frac{\delta_{pullout}}{d_n} \tag{4}$$



(a) Positive direction (b) Negative direction

Figure 6 Distributions of vertical strain at 60 mm above the stub surface in L45A



(a) Column A (b) Column C

Figure 7 Strain distributions of longitudinal reinforcement under positive loading in L45A

The drift angle due to pullout of reinforcement, $R_{pullout}$, was computed separately using strains of Columns A and C. The results are shown in terms of total drift angel, R, in Figure 8. The figure also have a solid line (Model A) representing $R_{pullout}$, using the proposed model in Ref. 9). It can be seen that a large amount of drift is attributed to the pullout of reinforcement from the stub and column. It should be noted that the longitudinal reinforcement of columns were welded to anchor plates at the base of the stub and the rotation due to the pullout of reinforcement was not attributed to incomplete anchorage.

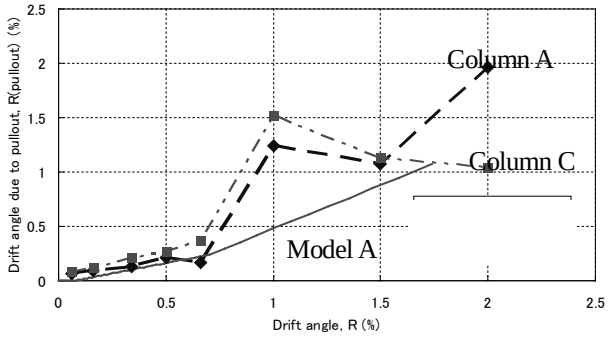


Figure 8 $R_{pullout}$ and R relation in L45A

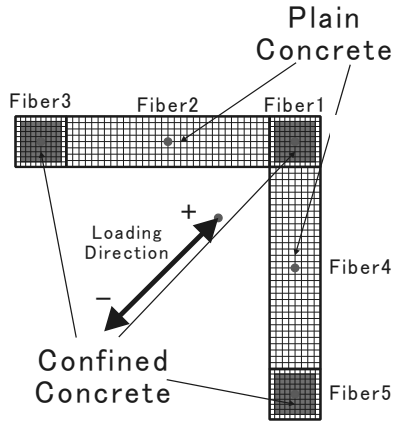


Figure 9 Fiber model mesh in a numerical simulation

4 NUMERICAL SIMULATION

The lateral load – drift angle relation of a core-wall was simulated using a fiber model. The specimen was divided into eight layers vertically and each layer was subdivided into 704 fibers as shown in Figure 9. Fibers were categorized into three material groups; plain concrete, confined concrete and longitudinal steel. Hoshikuma's model[10] was used for plain concrete, and Sun and Sakino's model[11] was used for confined concrete, and the elastic-perfectly plastic model was used for longitudinal steel, respectively. The numerical results are compared with the experimental results in Figure 5. Analysis 1 is a fiber model without considering pullout and Analysis 2 is a combination of a fiber model and pullout expressed in Eq. (4).

Figures 5(a), (c) and (e) show that the pullout of longitudinal reinforcement had a significant influence to predict the drift of the core walls by comparing Analyses 1 and 2. Analysis 2 simulates the experimental results relatively well for both L45A and L45B although the precision is not so good for L00A. The larger stiffness and maximum lateral load of L45B compared to L45A due to larger section size was simulated by Analysis 2. However, the stiffness of Analysis 2 is still smaller than the experimental results. Especially the large drift increment after the yielding of the longitudinal reinforcement in three specimens was not explained by the current model. It is considered that the effect of concrete crushing should be included to further increase the precision in displacement. The predicted lateral load capacities in the positive direction for both Analyses 1 and 2 are higher than the experimental results by 27% for L00A, 14% for L45A and 13% for L45B. This may be attributed to the immature concrete crushing due to buckling of the wall panel. However, it is not conclusive at this moment and the further study is under way.

5 CONCLUSIONS

Three reinforced concrete model specimens of an L-shaped core-wall were constructed with 1/4.5 scale and statically loaded to study the effect of loading direction and the section configuration on the seismic behavior of core-walls.

- Three specimens showed large deformation capability until the peak load. The peak load was reached at drift angle of 1.0% in positive direction when the vertical load was about 30% of the axial load capacity. The failure was caused by the crushing of concrete at the compression zone. The failed region in L45A and L45B covered a relatively larger area than predicted by a section analysis and that of L00A covered the whole flange section. It is recommended to provide good confinement to a relatively larger region of concrete to secure higher ductility.
- The deformation followed the 'plane sections remain plane' assumption until the drift ratio of +0.34%. After +0.5%, the deformation of concrete under compression progressed faster than the deformation of other region and the assumption was not valid any more.
- A simple fiber model simulated the lateral load - drift angle relation if the pullout of reinforcement was properly modeled.

Acknowledgements:

This research was conducted as the collaborative research project between Asanuma Corporation (PI: N. Fukumoto) and Kyoto Univ. (PI: S. Kono). The authors appreciate N. Fukumoto, S. Inoue, T. Nakasawa, Y. Tobita,

and T. Yamauchi for their technical and financial supports to the experimental and analytical works.

References:

1) Kono, S. Inada, K. Sakashita, M. Sato H. (2010): Lateral Load Resistance of L-Shaped Core-Walls for Tall Buildings, 3rd International FIB Congress, Washington DC, USA, PaperID #613.
2) Maffei, J. and Yuen, N. (2007). Seismic Performance and Design Requirements for High-Rise Building. Structure Magazine, National Council of Engineers Associations, April, pp. 28-32.
3) Adebar, P., Ibrahim, A. M. M., and Bryson, M., (2007) "Test of High-Rise Core Wall: Effective Stiffness for Seismic Analysis," ACI Structural Journal, V. 104, No. 5, Sept.-Oct., pp. 549-559.
4) H. Kumagai, H., Tozawa, M., and Kuruse, Y., (2005), "Study on 3-dimensional RC Structural Wall Under Flexural Compression (in Japanese)," Journal of Japan Concrete Institute, V.16, No. 3, pp. 59-68.
5) Funaki, H. et al. (2007), "Experimental Study on Structural Performance of RC Shear Walls with L Shaped Section (in Japanese)," Summaries of technical papers of Annual Meeting Architectural Institute of Japan. C-2, Structures IV, pp. 699-704.
6) Konishi, S., Maruta, M., Suzuki, N., and Besho, S., (1997), "Experimental Study on RC L-shaped Core Structural Wall (in Japanese)," Proceedings of the Japan Concrete Institute, V. 19, No. 2, pp. 1083-1088.
7) Maruta, M., Suzuki, N., and Besho, S., (1999),"Structural capacities of open-section r/c core walls (in Japanese)," Journal of Structural and Construction Engineering, Architectural Institute of Japan, pp. 109-116.
8) Nakachi, T. (2007), "FEM Analysis of Reinforced Concrete Core Walls (in Japanese)," Proceedings of the Japan Concrete Institute, V. 19, No. 3, pp. 319-324.
9) Architectural Institute of Japan, "Guidelines for Performance Evaluation of Earthquake Resistant Reinforced Concrete Buildings (Draft), explanation on $R_{u,pj}$ and $R_{u,b}$ (In Japanese)" AIJ, 2004, pp. 148-149.
10) Hoshikuma, J., Kawashima, K., Nagaya, K. and Taylor, A. W. (1997). Stress-Strain Model for Confined Reinforced Concrete in Bridge Piers. Journal of Structural Eng., ASCE V. 123, No. 5, pp. 624-633.
11) Sun, Y. and Sakino, K. (1993). Experimental Study on improvement of ductility of RC columns with high performance Materials (in Japanese). Proceedings of the Japan Concrete Institute, V. 15, No. 2, pp. 719-724.

8CUEE CONFERENCE PROCEEDINGS
8th International Conference on Urban Earthquake Engineering
March 7-8, 2011, Tokyo Institute of Technology, Tokyo, Japan

DEVELOPMENT OF AN ENERGY DISSIPATION DEVICE FOR PRESTRESSED CONCRETE MEMBERS

Yasushi Sanada[1)], Yuta Sashima[2)], and Hiroki Sugiura[3)]

1) Associate Professor, Department of Architecture and Civil Engineering, Toyohashi University of Technology, Japan
2) Graduate Student, Department of Architecture and Civil Engineering, Toyohashi University of Technology, Japan
3) Graduate Student, Department of Architecture and Civil Engineering, Toyohashi University of Technology, Japan
sanada@ace.tut.ac.jp, sashima.yuta@rc.ace.tut.ac.jp, sugiura.hiroki@rc.ace.tut.ac.jp

Abstract: Structural damage due to earthquakes can be reduced in prestressed concrete (PC) buildings by their self-centering characteristics, comparing to reinforced concrete (RC) buildings. However, seismic energy dissipation of PC buildings is much lower than that of RC buildings. Therefore, this paper proposes a new energy dissipation device to be attached to PC members to improve their energy dissipation capacity. A friction damper was developed and its performance was verified in preliminary tests. Repeated loads were applied to the damper to measure its frictional forces. As a result, friction increased with a higher compression on the damper, which also indicated that the frictional coefficient was approximately 0.27. A typical PC beam specimen was prepared to quantitatively evaluate the contributions of the developed damper to the seismic performance of specimen. Cyclic loading tests of the specimen were carried out with and without the damper. As a result, 1) the energy dissipation of the specimen increased significantly when the damper was attached to it. 2) Although residual deformations also increased in this case, they could be canceled by releasing frictional forces of the damper. 3) The damper contributions were asymmetric in each loading direction, which was clarified theoretically.

1. INTRODUCTION

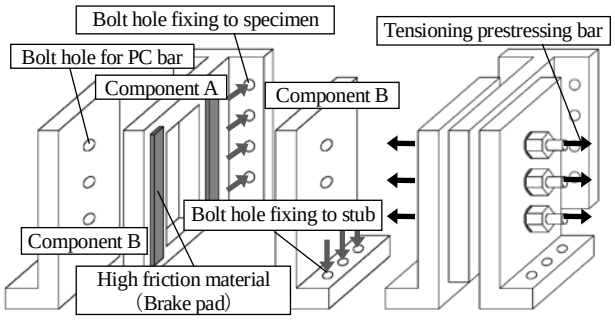
Structural damage due to earthquakes can be reduced in prestressed concrete (PC) buildings by their self-centering characteristics, comparing to reinforced concrete (RC) buildings. However, seismic energy dissipation of PC buildings is much lower than that of RC buildings.

A method to improve the energy dissipation capacity of PC buildings using a friction damper was proposed in the past study (Morgen and Kurama 2004). It is effective to improve the seismic performance of PC buildings using this kind of damper because the damper performance can be controlled by compression applied to it. In this study, it was applied to the upper and lower surfaces of beam members. However, it seems more convenient to be attached only to the lower surface for practical application.

Therefore, this paper proposes a new energy dissipation device for PC members to improve their energy dissipation capacity. Several structural tests were conducted to evaluate the performance of the proposed device and to verify its contributions to the seismic performance of a PC beam.

2. FRICTION DAMPER

A friction damper was designed and manufactured, as shown in Figure 1. The damper consisted of the A and B components in the figure. Brake pads were welded to the A component. Compressive forces were acted between A and B by tensioning prestressing bars. Frictional forces were generated when relative displacements were caused between A and B.



(a) (b)

Figure 1 Friction Damper: (a) Components, and (b) Introducing Prestressing Force

Repeated loads were applied to the damper to measure its frictional forces under tension forces, T_0 of 300 to 1800 kN every 300 kN using the compression testing machine, as shown in Figure 2. As a result, friction increased with a higher compression on the damper, as shown in Figure 3. These results also indicated that the frictional coefficient was approximately 0.27.

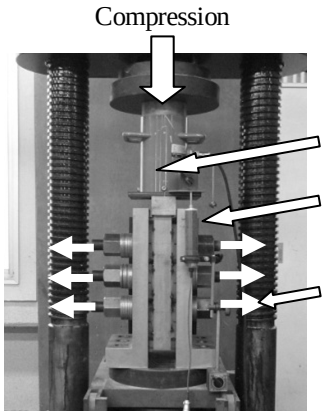


Figure 2 Performance Test of Damper

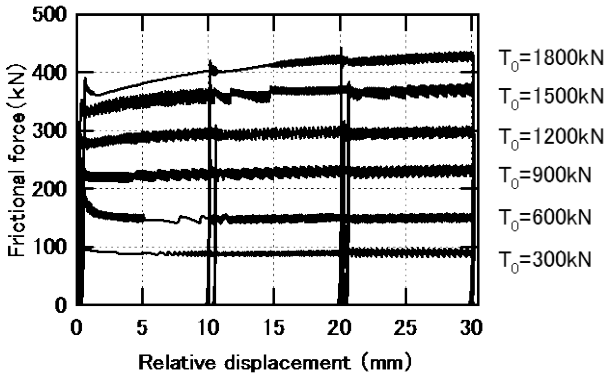
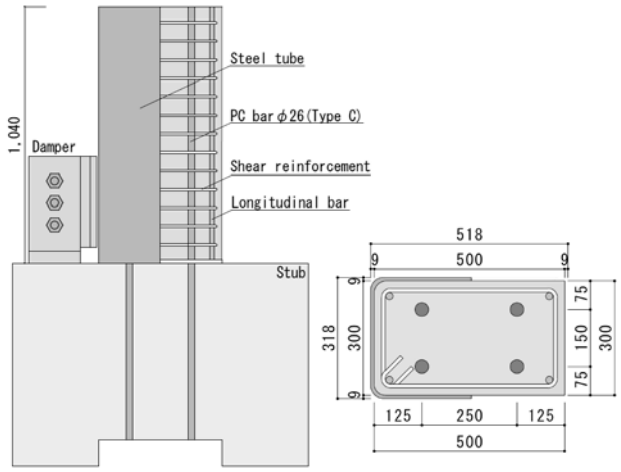


Figure 3 Damper Performance



Unit: mm

Figure 4 Details of PC Beam Specimen

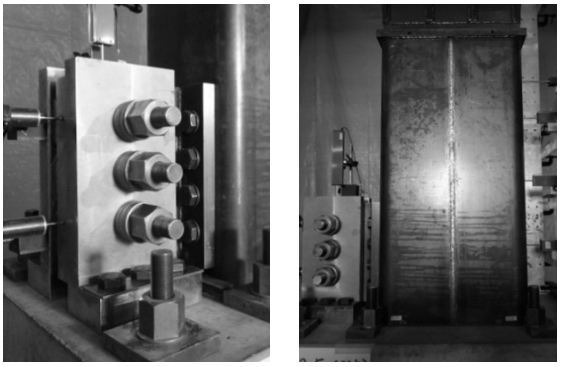


Figure 5 Specimen with Developed Damper

3. DAMPER APPLICATION

3.1 PC Beam Specimen

An unbonded PC beam specimen was prepared to apply the friction damper developed as above. Figure 4 illustrates the details of specimen. Steel jacketing was applied to the specimen to reduce damage because it was repeatedly subjected to cyclic loads under several levels of damper forces, as mentioned below. Table 1 summarizes the specimen including material properties. The damper was attached to the end of beam by high tension bolts, as shown in Figure 5.

Table 1 Structural Details of Specimen

Beam	B x D	300 x 500 mm
	Design compressive strength	50 N/mm^2
	Longitudinal bars	SD345, 4-D19
	Shear reinforcements	SD345, D10@75
PC bar	Prestressing bars	4-ϕ26
	Initial prestressing force, P_N	400 kN
	Yield strength, P_y (P_N/P_y)	650kN (0.62)
Steel tube	Material	SS400
	Bending radius	30 mm
	Thickness	9 mm
Concrete	Material age	76 days
	Compressive strength	53.6 N/mm^2
	Tensile strength	3.5 N/mm^2

3.2 Loading Program and Measurement

The schematic representation of experimental set-up is shown in Figure 6. The specimen was vertically placed and fixed at the upper and lower stubs to the loading frames. Reversed cyclic loads were applied to the specimen using the horizontal jack under no axial load. Lateral loading program is shown in Table 2. Tension force applied to the damper, T_0 was varied during the test.

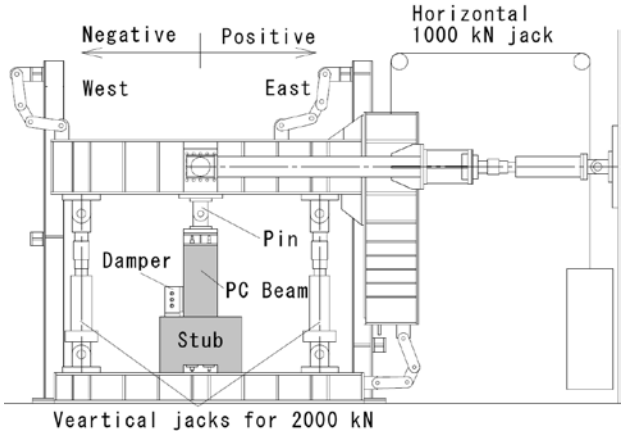
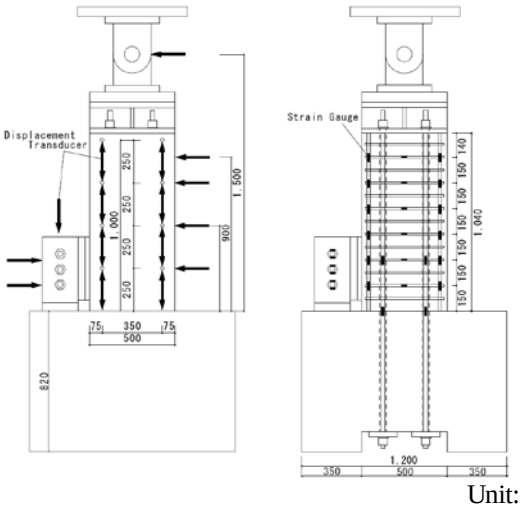


Figure 6 Schematic View of Test Set-up

Table 2 Lateral Loading Program

N	R (rad.)	T_0 (kN)	C	N	R (rad.)	T_0 (kN)	C
1	1/800	0	(1)	6	1/50	0	(1) (2)
2	1/400	0	(1)			300	(3)
3	1/200	0	(1) (2)			600	(4)
		300	(3)			1200	(5)
		600	(4)			0	(6)
		1200	(5)	7	1/33	0	(1) (2)
		0	(6)			300	(3)
4	1/100	0	(1) (2)			600	(4)
		300	(3)			1200	(5)
		600	(4)			0	(6)
		1200	(5)	8	1/25	0	(1) (2)
		0	(6)			300	(3)
5	1/67	0	(1) (2)			600	(4)
		300	(3)			1200	(5)
		600	(4)			0	(6)
		1200	(5)	9	1/20	0	(1) (2)
		0	(6)			300	(3)
N: order of lateral loading R: drift ratio T_0: initial tension force C: order of loading cycle						600	(4)
						1200	(5)
						0	(6)

The horizontal absolute displacements and vertical relative displacements of the specimen were measured with transducers. The applied loads were also monitored throughout the test. Figure 7 shows the set-up of transducers and arrangement of strain gauges.



Unit: mm

Figure 7 Set-up of Transducers and Arrangement of Strain Gauges

3.3 Behavior of PC Beam without Damper

Figure 8 gives the relationship between lateral force and drift ratio of the specimen without the damper (T_0=0 in Table 2). The initial stiffness degraded at the circle in the figure during the cycle to R=1/200, then initial yielding of a prestressing bar was observed at the triangle during the cycle to R=1/33. The specimen exhibited stable hysteresis loops up to the final cycle to R=1/20.

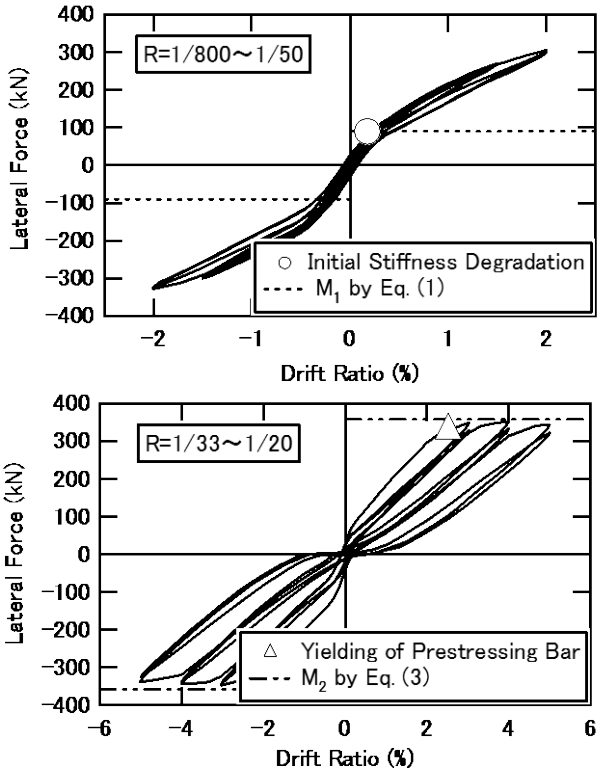


Figure 8 Lateral Force and Drift Ratio Relationship of Specimen without Damper

The circle in Figure 8 represents an initial separation between the beam end and stub. Therefore, the strength, M_1 can be evaluated by Eq. (1).

$$M_1 = \frac{\Sigma P_N}{A_e} Z_e \tag{1}$$

where, ΣP_N: prestressing force, A_e: equivalent cross-sectional area, Z_e: equivalent section modulus.

On the other hand, the triangle in Figure 8 means the flexural yielding of specimen. The flexural strength, M_2 was evaluated as follows:

1. Calculating an initial strain of each component (ε_{pc0}, ε_{c0} in Figure 9) of the beam after tensioning prestressing bars.
2. Assuming strain distributions at yielding of the prestressing bar (ε_y in Figure 9) based on Navier's hypothesis, as shown in Figure 9.
3. Determining strains (ε_{pcp}, ε_c, ε_s in Figure 9) and forces (N_y, N_{pcp}, N_c, N_s in Figure 9) of all components assuming a distance from the compressive edge to the axis with concrete strain of ε_{c0}, x_r.
4. Evaluating x_r and M_2 from Eqs. (2) and (3), respectively.

$$N_y + N_{pcp} + N_c + N_s = 0 \tag{2}$$

$$M_2 = N_y L_1 + N_{pcp} L_2 + N_c L_3 + N_s L_4 \tag{3}$$

where, N_y: yield strength of prestressing bars on the tensile side, N_{pcp}: axial force of prestressing bars on the compressive side, N_c: compressive force of concrete, N_s: compressive force of steel jacket, L_1, L_2, L_3, and L_4: refer to Figure 9.

The lateral strengths converted from M_1 and M_2 are also indicated in Figure 8, which had good agreements with the test results.

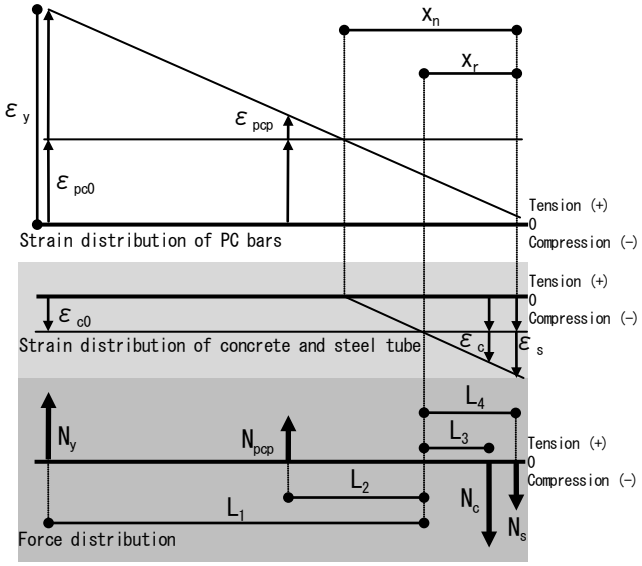


Figure 9 Strain Distributions at Flexural Yielding

3.4 Contributions of Damper to the Seismic Performance of PC Beam

Figure 10 compares the relationships between lateral force and drift ratio observed during the cycles to R=1/200 and 1/20 among the cases of T_0=0 (the second cycle in Table 2), 600, 1200 kN. Applying the damper to the beam specimen, the maximum strength, hysteresis loop, and residual drift increased, and the incremental ratios were higher with higher T_0 values. However, the damper contributions were asymmetric in the positive and negative loading. Figure 11 shows the equivalent damping factors (h_{eq} defined in Figure 12) throughout the test. The values were evaluated as an average observed in both the loading directions because of the asymmetric damper contribution, and plotted in the figure. In the case of T_0=0, h_{eq} of the

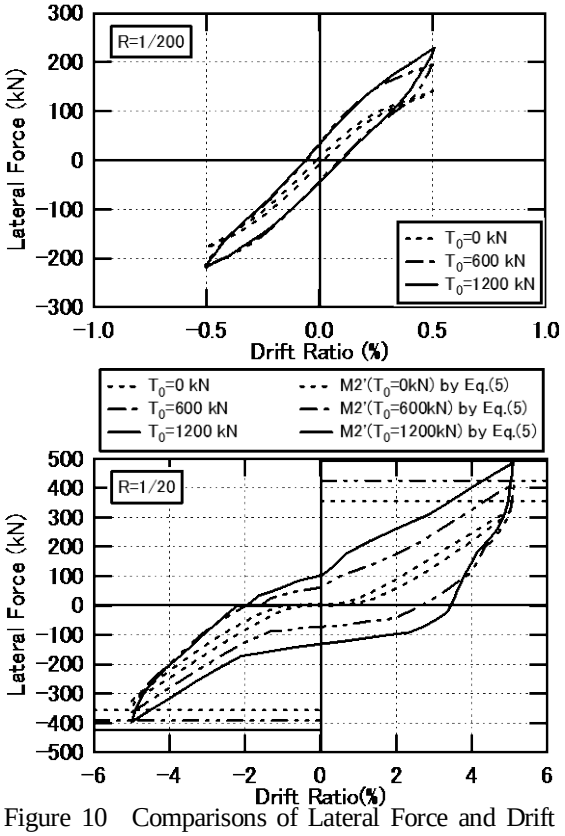
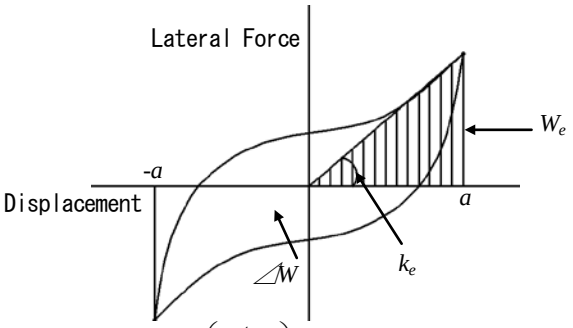


Figure 10 Comparisons of Lateral Force and Drift Ratio Relationships of Specimen with/without Damper



$$h_{eq} = \frac{1}{4\pi}\left(\frac{\Delta W}{W_e}\right)$$

ΔW= area of hysteresis loop

W_e= equivalent potential energy

$$= \frac{1}{2} k_e a^2$$

Figure 12 Equivalent Damping Factor

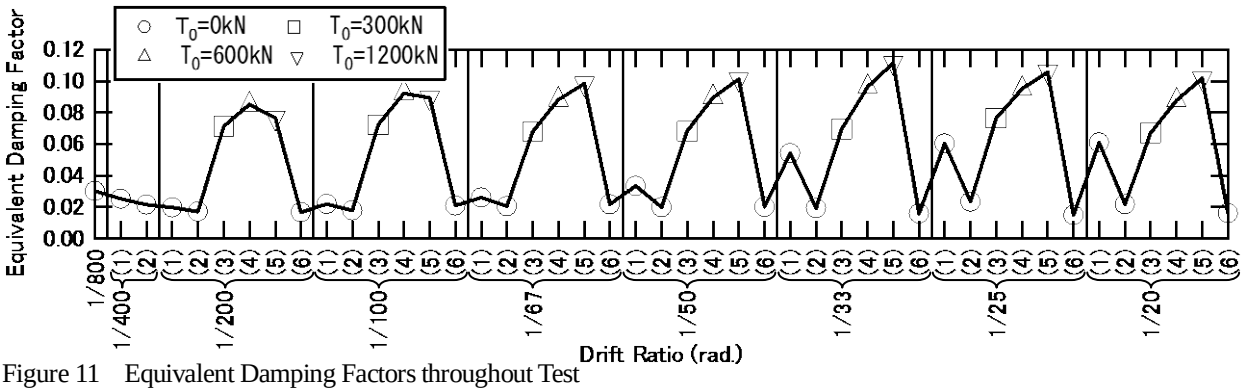


Figure 11 Equivalent Damping Factors throughout Test

second cycles decreased compared to those of the first cycles. However, little differences were observed between the second and sixth cycles, which means that the beam specimen did not degrade after the second cycle. On the other hand, h_{eq} of the specimen with the damper was generally higher in the case of higher T_0 values.

The damper contributions to the strength of specimen were asymmetric in the positive and negative loading, as mentioned above. It seemed to be caused as follows.

Figure 13 gives the distributions of curvatures along the member length, which were evaluated from outputs of vertical transducers in Figure 7. The specimen approximately exhibited a locking behavior, and hence the damper behaved as shown in Figure 14. Therefore, the damper contributions were different in the positive and negative directions because of different distances between the axis of rotation and the center of damper. The maximum strengths of the specimen with the damper were evaluated by Eqs. (4) and (5) considering a damper term in Eqs. (2) and (3), respectively, and plotted in Figure 10. Good agreements were observed between the experimental and calculated values.

$$N_y + N_{pcp} + N_c + N_s + N_d \cos\theta = 0 \qquad (4)$$

$$M_2' = N_y L_1 + N_{pcp} L_2 + N_c L_3 + N_s L_4 + N_d L_d \qquad (5)$$

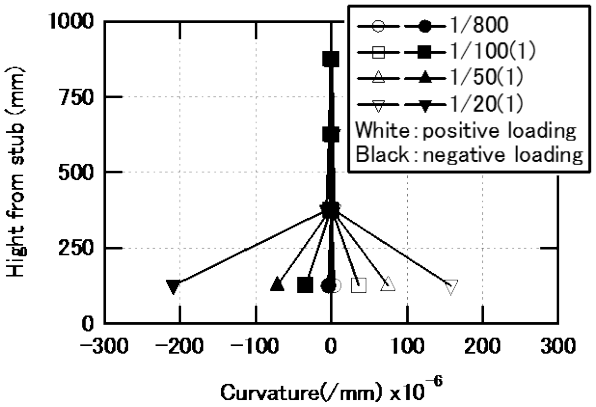


Figure 13 Distributions of Curvatures along Length

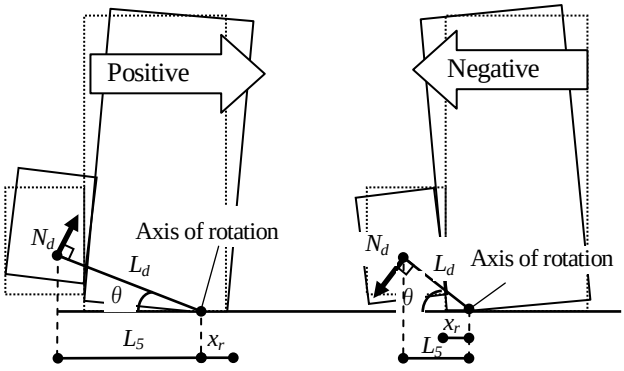


Figure 14 Behavior of Specimen with Damper

where, N_d: frictional force of damper, θ and L_d: refer to Figure 14.

Finally, larger residual displacements were focused when the damper was attached to the specimen. Figure 15 shows the behavior when releasing friction of the damper after the fifth cycle to R=1/20 (T_0=1200). It was found that the residual displacement under T_0=1200 was restored to that without the damper observed after the second cycle. This means that the residual displacement can be restored to that of PC members without the damper by releasing tension forces of the prestressing bars in Figure 1, even if large residual displacements were caused under severe seismic loads.

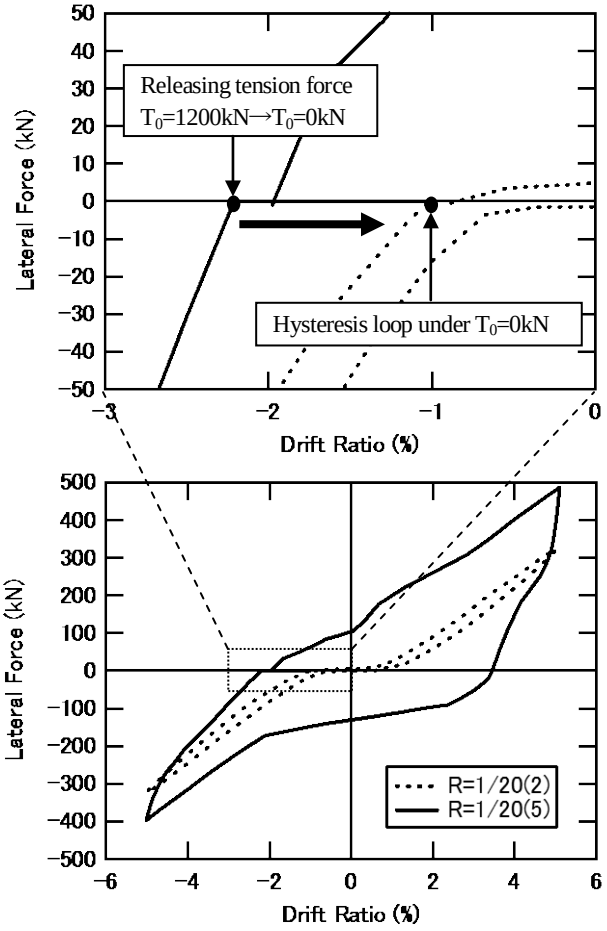


Figure 15 Behavior when Releasing Friction of Damper

4. CONCLUSIONS

A friction damper was developed to improve the seismic performance of PC buildings. Major findings of this study are as follows:

1. Performance evaluation test of the damper was conducted using the compression testing machine. The frictional coefficient was approximately 0.27.
2. The damper was applied to an unbounded PC beam specimen. It increased the overall strength and energy dissipation capacity. However, asymmetric contributions

were observed in each loading direction.

3. The asymmetric contributions were caused by different axes of rotation in both the loading direction. Therefore, the damper contributions could be evaluated by determining the distance between the axis of rotation and the center of damper.

4. The damper also increased residual deformations after unloading, however, which could be canceled by releasing compression acting on the damper.

References:

Morgen, B. G. and Kurama, Y. C. (2004), "A Friction Damper for Post-Tensioned Precast Concrete Moment Frames," *PCI Journal*, **49**(4), 112-133.

8CUEE CONFERENCE PROCEEDINGS
8th International Conference on Urban Earthquake Engineering
March 7-8, 2011, Tokyo Institute of Technology, Tokyo, Japan

RESPONSE OF HIGH PERFORMANCE FIBER REINFORCED CONCRETE INFILL PANELS RETROFITTING STEEL MOMENT-RESISTING FRAMES

Sarah L. Billington[1)], Dimitrios G. Lignos[2)], Joan V. Hanson[3)], and Daniel Moreno-Luna[4)]

1) Associate Professor, Department of Civil & Environmental Engineering, Stanford University, USA
2) Assistant Professor, Department of Civil Engineering & Applied Mechanics, McGill University, Canada
3) Structural Engineer, Austin, Texas, USA
4) Graduate Research Assistant, Department of Civil & Environmental Engineering, Stanford University, USA
billington@stanford.edu, dimitrios.lignos@mcgill.ca, joan.hanson@gmail.com, danielm3@stanford.edu

Abstract: The cyclic and pseudo-dynamic performance of a new infill panel system made of precast, high-performance fiber reinforced concrete to retrofit existing steel moment-resisting frames has recently been investigated. The infill system is used to protect a structural system under an extreme seismic event and secondarily provide protection to non-structural components. The panels are bolted to each other and into existing steel moment-frames with pre-tensioned, slip-critical connections to add stiffness, strength, and energy dissipation to the structure. The effectiveness of the proposed seismic retrofit system has been evaluated with component testing as well as state-of-the-art hybrid simulation of a 2-story steel moment resisting frame designed in the United States in the 1980s and tested at the Network for Earthquake Engineering Simulation facility at Berkeley. Infill panel performance from cyclic testing and from hybrid simulation are presented and compared. It was found that the SC-HPFRC panels performed similarly in the component and hybrid simulation experiments with the exception of the degree of multiple cracking. In both cases the primary mode of panel failure was flexural and the SC-HPFRC was robust against spalling and bearing loads. Damage of the infill panels in the hybrid experiment was well distributed as designed.

1 INTRODUCTION

Ductile, fiber-reinforced cement-based materials are being investigated for many structural-scale applications. These materials exhibit fine, multiple cracking in direct tension, reaching strains of 0.5 to 3 percent and generally exhibit little to no spalling in compression. The materials are often referred to as high performance fiber-reinforced concrete (HPFRC) or high performance, fiber-reinforced, cement-based composites (HPFRCC) if they contain no coarse aggregate. The term high performance is used when the fiber volume fraction is relatively low (2% or less) and the tensile properties are either high strength (e.g. increase in tensile strength after first cracking) or high ductility (e.g. >3% strain while maintaining full tensile carrying capacity).

An infill panel system using a self-compacting HPFRC (SC-HPFRC, Liao *et al.,* 2006) has been proposed to retrofit fracture-critical steel frames for seismic loading (Olsen & Billington, 2009) (Figure 1). The infill panels are precast, and intended to be both easily installed and rapidly replaced after an earthquake, if damaged. Three series of testing have been carried out to investigate the performance of the infill panels to cyclic

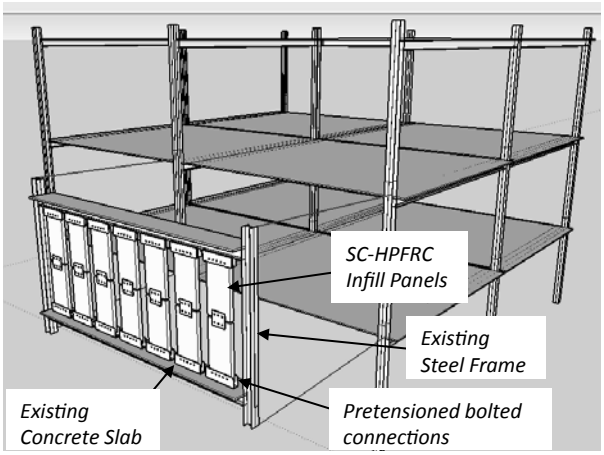


Figure 1 Ductile fiber-reinforced concrete infill panel system proposed for seismic retrofitting of steel frame structures.

loading and the performance of a retrofitted steel frame to simulated earthquake loading using hybrid simulation. In the first test series, seven single panel specimens were tested with a fixed base and loaded laterally at the top, where the point of inflection would be for a double panel system under lateral load in a frame (i.e. half of one of the seven double-height panels shown in Figure 1). The results of this test series are summarized in Olsen & Billington (2011). In the second test series, four double-height panel sets were tested under quasi-static cyclic lateral load within a 4-pinned steel frame (Hanson, 2008). In the third test series, a single-bay, two-story steel frame with 5 sets of double height infill panels in each story was tested using hybrid simulation (see Lignos *et al.,* 2011). Two phases of simulated earthquake loading were conducted in order to evaluate the seismic performance of the retrofitted test frame.

This paper focuses on the response of the SC-HPFRC infill panels to cyclic loading in the 2nd test series and Phase I of the 3rd (i.e. hybrid simulation) test series.

2 DOUBLE-HEIGHT PANEL EXPERIMENTS

Four full-story double panel components were designed and tested under quasi-static cyclic loading. A proposed center connection between top and bottom panels, the top panel-to-frame connection and the double panel interaction including out-of-plane response were of particular interest to evaluate during this series of tests. A brief overview of the panel designs and experimental results are presented here with details given in Hanson & Billington (2011).

The experiments consisted of a set of double panels connected to steel beam sections at the top and bottom and fixed in a four-pin testing frame. Lateral load was applied at the center of the top of the testing frame. The panel set up was approximately 2/3-scale. The double panel experiments included the SC-HPFRC panels, the connections of these to each other and to the top and bottom representative steel frame members, and the representative steel frame members' connections to the test frame (Figure 2). It is noted that the boundary condition at the top was fixed rather than allowed to rotate as would be the case in an actual moment-resisting frame where beams typically deform in double curvature.

The details of the three primary connections of the double panel system are shown in Figures 2 and 3. They are: a top connection where the top panel is connected to the upper floor beam, the center connection where the top and bottom panels are joined, and the bottom connection where the bottom panel connects to the base beam (test frame).

Four different panel designs were investigated (one per test for a total of four tests). Only one design, for Test 3, is discussed in detail here. The design for Test 3 was referred to as "P-bar with Interior bar" in Hanson (2008) and the reinforcement layout and geometry are

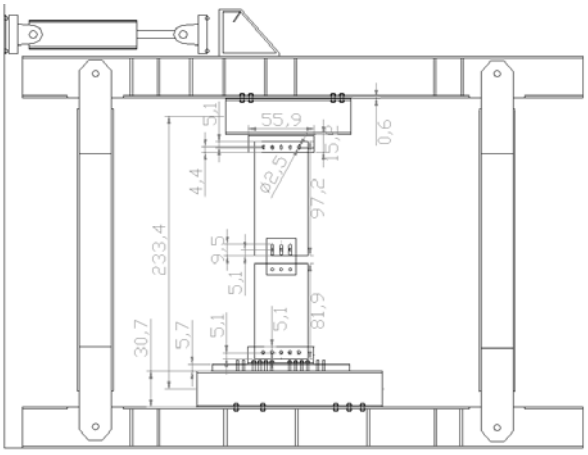


Figure 2 Double-height panel test set-up in a four-pin frame (dimensions in cm).

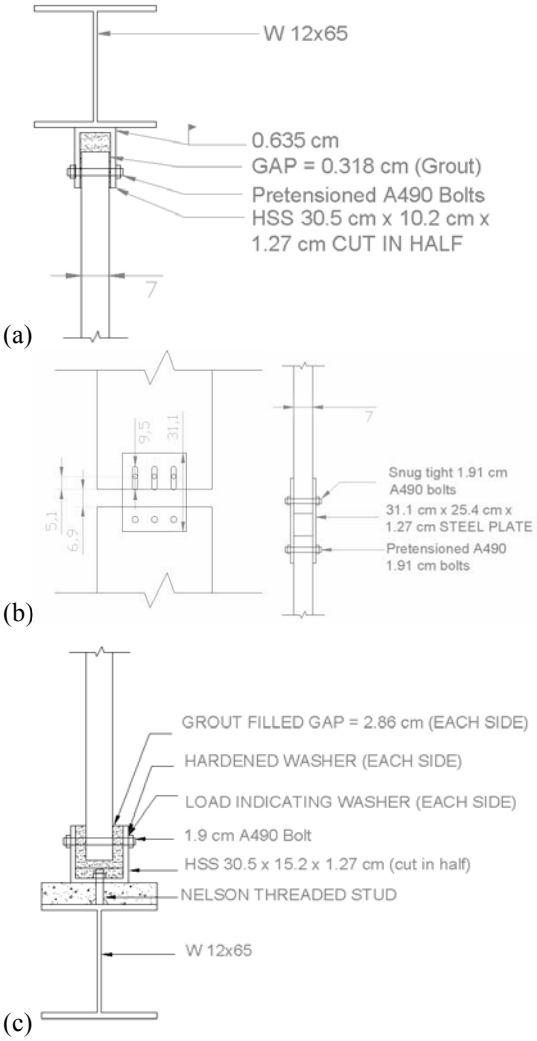


Figure 3 Details of the (a) top connection, (b) center connection, and (c) bottom connection (used for tests 2, 3 and 4). Dimensions in cm.

shown in Figure 4. The perimeter and U-shaped bars were US No. 3 (diameter 9.5mm) bars and the mesh reinforcement was a 10-gauge welded wire fabric with a

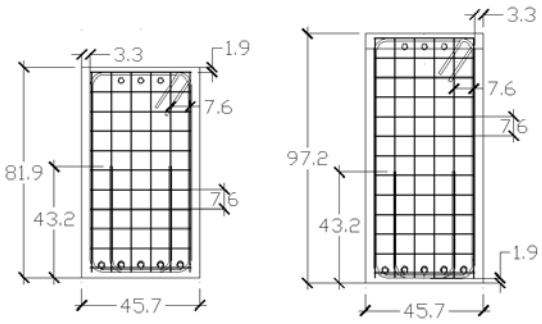


Figure 4 Panel design for Test 3 from Hanson & Billington (2011). Dimensions in cm.

diameter of 2.6mm. The proportions of the SC-HPFRC mixture by weight were; Type III Portland cement (1), Class C Fly ash (2.2), Silica sand #16 (2.2), Crushed limestone with 12mm maximum sized aggregate (1.2), water (0.8), high range water reducing admixture (0.005), viscosity modifying agent (0.038), and high strength steel fibers (0.315).

The panels were tested under quasi-static cyclic displacement control. Three reverse cycles at drift levels of positive/negative, 0.25%, 0.375%, 0.5%, and 0.75% were followed by two reverse cycles at drift levels of positive/negative 1%, 1.25%, 1.5%, 1.75%, 2%, 2.5%, 3%, 3.5%, 4%, 4.5%, and 5%. The story drift represented the drift of the scale model frame, calculated as the displacement at the top of the test frame divided by the centerline story height (234 cm).

2.1 Hysteretic Response of Double Panel System

The load vs. drift response of Test 3 is shown in Figure 5. Drift was measured as the displacement of the testing frame divided by the center-to-center distance of the W-sections to which the panel retrofit system was attached (i.e. the "story drift"). At peak load in the positive direction damage localized in a flexure-shear crack slightly below the top of the interior bar. The crack widened, the welded wire mesh reinforcement fractured, fiber pullout in the SC-HPFRC was observed, and the interior bar pulled out. Multiple cracking was observed along the length of the bars near the failure zone in tension. In compression, the SC-HPFRC spalled along the tensile cracking lines from the opposite direction of loading and the material was no longer confining the reinforcement, which then buckled. A large section of the perimeter bar was exposed, essentially unbonded. Due to this large unbonded segment, the steel was able to continue to deform, as the SC-HPFRC carried compression in the center portion (Figure 6a). This reduced "moment arm" is apparent in the residual capacity of the panel system observed in the hysteretic response (Figure 5), which was 25% of the peak capacity in the positive direction and 45% of the peak capacity in the negative direction.

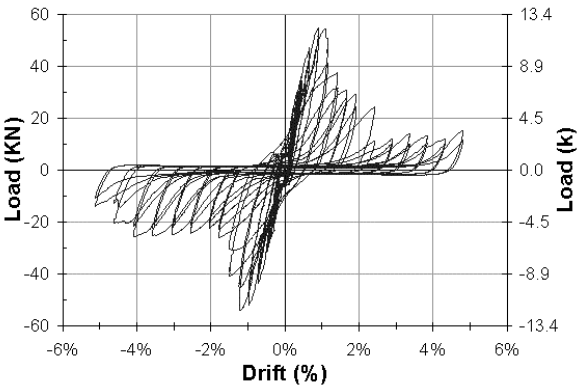
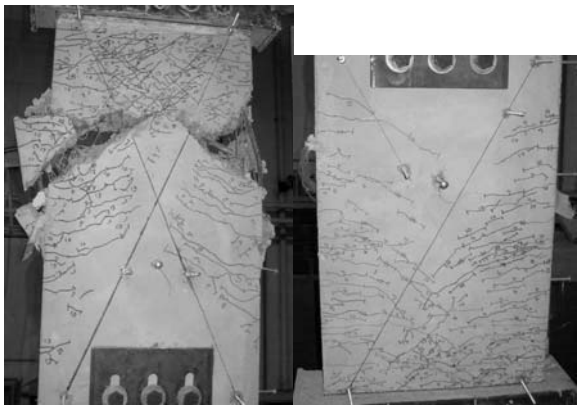


Figure 5 Hysteretic response of Test 3.



(a) Top panel (b) Bottom panel

Figure 6 Final appearance of Test 3 panels after testing

2.2 Representative Cracking Response

The cracking pattern up to failure is illustrated in Figure 7. Considerable distributed cracking was observed particularly in the bottom 2/3 of the panels (where "bottom" refers to the fixed end). As the cracking moved towards the center connection it remained well distributed, and as expected, flexure-shear cracks began to form. Some cracking was observed in both

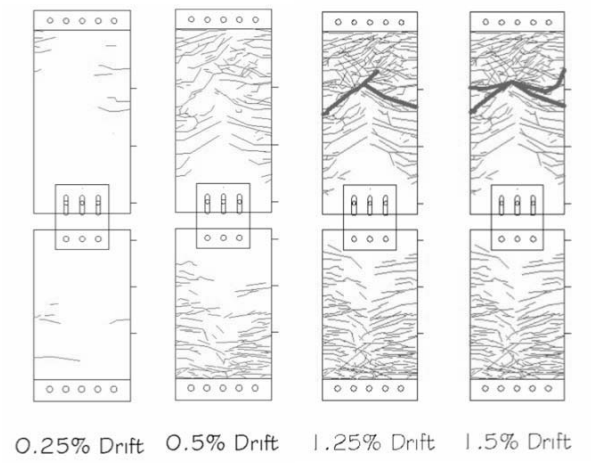


Figure 7 Crack progression up to failure

panels towards the center connection, with cracking stopping about 3" above the bolt line in the center connection in the top panel, and going all the way up to the bolt line of the center connection in the bottom panel. In both cases cracking was stopping roughly equidistant to the point of inflection of the double panel system.

3 INFILLED FRAME EXPERIMENTS: HYBRID SIMULATION

Large-scale hybrid (pseudo-dynamic) testing of the infill panels installed in a two-story steel frame has recently been completed as the third of three test series on the retrofit system. The testing included a physical subassembly of a one bay two-story sub-frame with five sets of SC-HPFRC panels per story, and a numerical subassembly to represent the remainder of the moment resisting frame and modeled in the Open System for Earthquake Engineering Simulation (OpenSees, 2009) platform. A schematic representation of the hybrid model is shown in Figure 8 (Lignos and Billington, 2010). This moment resisting frame was part of the lateral system of a 2-story office building designed in California in 1980s. The building did not meet the retrofit objectives based on ASCE41/07. This prototype building had a period of 0.75sec in the longitudinal direction of interest. The hybrid model of the moment resisting frame was scaled based on similitude laws that are summarized in Moncarz and Krawinkler (1981). The exterior columns of the test subassembly shown in Figure 8 were W10x45 and the first and second floor beams were W14x26 and W10x30, respectively.

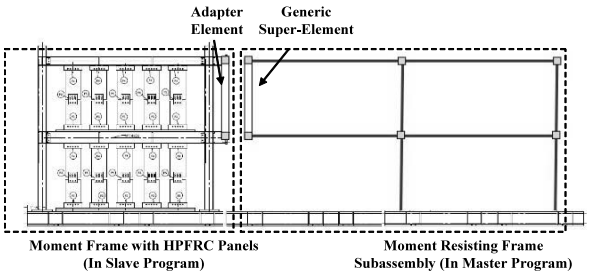


Figure 8 Hybrid simulation set up with physical model (left) and numerical model (right).

Two horizontal translational degrees of freedom at each one of the floor levels of the experimental subassembly were controlled during the hybrid test. Two phases of testing were performed with the loading for Phase 1 described in Table 1. A detailed description of the hybrid simulation testing and seismic response of the hybrid model is given in Lignos *et al.* (2011). This section focuses on the infill panel response from the Phase I testing and is compared with the quasi-static cyclic loading response presented in Section 2.

A picture of the physical subassembly is shown in Figure 9. Connection details of the panels were the same as those shown in Figure 3. Although the prototype frame was designed based on pre-Northridge seismic provisions, the four steel moment connections in the physical subassembly were designed as standard welded, unreinforced flange-bolted web connections per FEMA-350 (2000) provisions to avoid any control instability of actuators during testing due to beam-column joint fracture. Fracture was simulated in the numerical portion of the hybrid model though recognizing the possibility of having fracture(s) at design level earthquake events.



Figure 9 Physical test set-up prior to Phase 1 testing

Table 1. Hybrid Testing Experimental Program

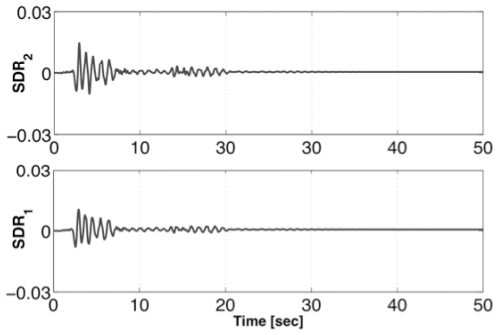
Phase I			
Level of Intensity	**Notation**	**Gr. Motion Intensity**	**Earthquake Record**
Service Level	SLE	30%	Petrolia (Cape Mendocino, 1992)
Design Level	DLE-I	70%	Petrolia (Cape Mendocino, 1992)
Design Level	DLE-II	100%	Canoga Park (Northridge, 1994)

During hybrid testing the two horizontal translational degrees of freedom were the control quantities and the physical subassembly was connected with a link that was designed to behave elastically. Two 975-kN dynamic actuators imposed the computed displacements and also measured the force and displacement quantities from the physical subassembly.

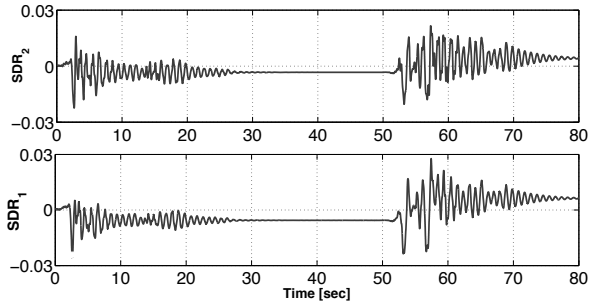
The 2-dimensional test frame was modeled in OpenSees with elastic beam-column elements that had concentrated plasticity springs at their ends. The hysteretic response of these springs was bilinear. The springs simulated component deterioration based on the modified Ibarra-Krawinkler model (Lignos and Krawinkler, 2009, 2011). Deterioration parameters of the components were determined from relationships for deterioration modeling that were derived from a recently developed database of steel components for deterioration modeling (Lignos and Krawinkler, 2007, 2009, 2011).

3.1 Global Response of Hybrid Model (Phase 1)

The hybrid model reached a peak story drift ratio of 1.9% and a residual story drift ratio of less than 0.5% after the first design level earthquake loading (DLE-I, 70% Petrolia, Table 1). The maximum story drift ratio was 3% in the first story when subjected to the second design level earthquake (DLE-II, Table 1, unscaled Canoga Park) (Figure 10), which corresponds to a lateral displacement of 67mm. The maximum story drift ratios in the infilled frame were reduced by roughly 10% and 25% in the first and second stories, respectively, relative to the expected peak drift ratios in the bare frame (Lignos *et al.,* 2011). The residual story drift ratios after the completion of DLE-II were about 0.6% for both stories of the test frame, which corresponds to a roughly 50% reduction of residual drift ratios compared to the bare frame.



(a)



(b)

Figure 10 Story drift ratio (SDR) time histories for the (a) SLE, and (b) DLE-I and DLE-II loadings.

3.2 Infill Panel Response to Phase I Hybrid Testing

The damage to the panels after the DLE-I and DLE-II ground motions is shown schematically in Figure 11. Details of typically observed cracking and damage are shown in Figure 12. Flexural cracking was observed but to less of an extent than appeared in the component testing, i.e. the second test series (Section 2). The less cracking in the hybrid simulation experiment is attributed primarily to the boundary conditions of the test frame relative to that of the four-pin frame, which provided a fixed end condition to the component tests. Additional reasons for differences in cracking response are the differing loading protocols (earthquake vs. symmetric loading protocol), with fewer large cycles in the hybrid simulation relative to multiple symmetric cycles in the component tests, as well as the ductility of the SC-HPFRC material. The SC-HPFRC material in the hybrid simulation experiment was older and had an average compressive strength of 7400psi. The material in the component tests had an average compressive strength of 5860 ksi. Assuming a correspondingly larger tensile strength in the hybrid simulation experiment panels, it could be expected to see less multiple cracking due to

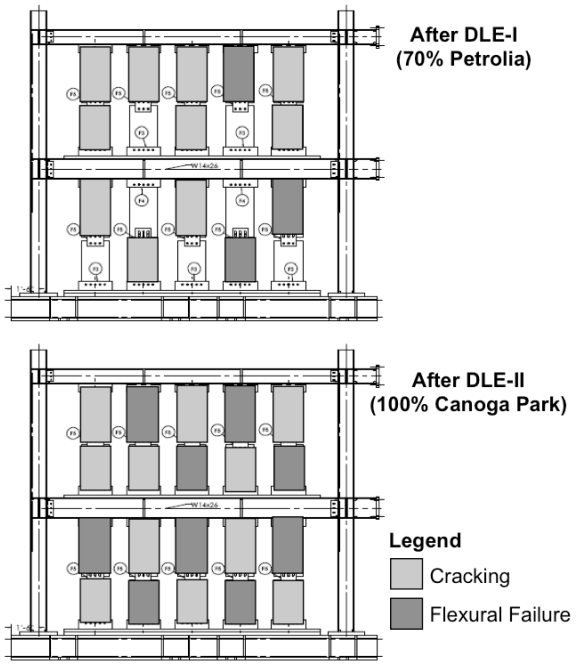


Figure 11 Schematic of cracking and damage in panels after the DLE loadings in Phase I testing.

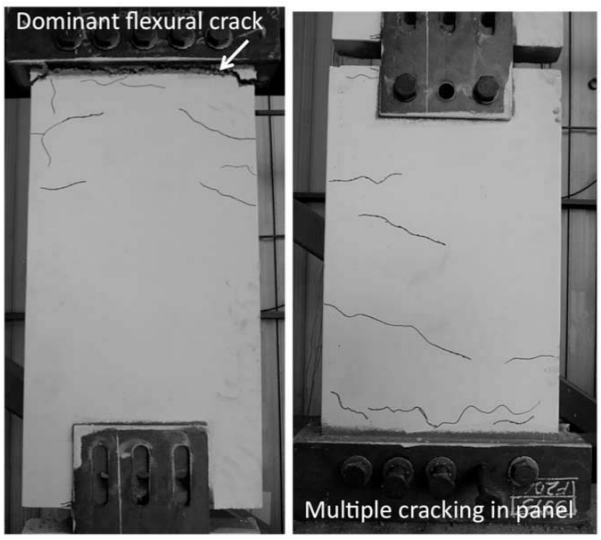


Figure 12 Tyipcal cracking and damage in panels observed in Phase I testing.

more rapid crack localization with higher forces required to open cracks.

For the panels that failed in flexure, the damage was localized at the base of the panel (top of the top panels or bottom of the bottom panels) where a dominant crack had formed and the reinforcement was observed to have fractured. After such failures, the panels were able to rock in a rigid body motion.

In addition to flexural cracking, some minor cracking was observed near the center connection where there appeared to be bearing of the bolts at this connection on the panel holes (Figure 13). It was later determined that the pre-tensioning force used in the center connection was considerably less than intended and the connection was therefore not acting as a pre-tensioned, slip-critical connection. Despite this fabrication error, the ductile nature of the material proved to be robust and allow for bearing without failure. In Phase II testing (Lignos *et al.,* 2011), adequate pre-tensioning was applied and no center connection slippage was observed.

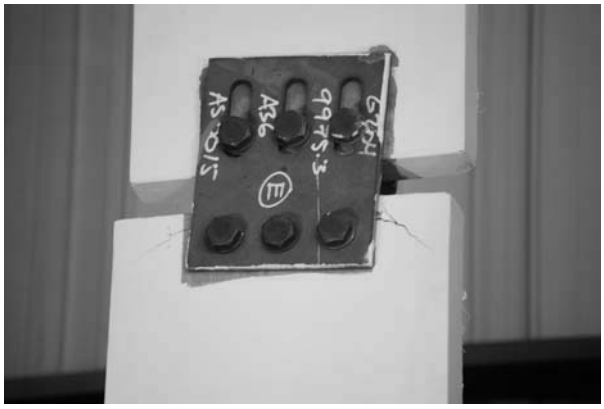


Figure 13 Cracking at center connection due to bearing (panels are 457mm wide).

Panel deformations are investigated in detail for the SLE loading here. Figure 14 shows the panel displacement time histories for displacements due to flexural deformation, as determined from the strain gage data of the top and bottom panels in the top right corner of the hybrid simulation experiment. The strain gages did not capture deformation beyond ~5 sec. most likely because they were not located exactly where cracking occurred. Shear deformations were also measured on the back face of the same panels during testing. The flexural displacement was estimated by assuming a linear shape for the curvature along the panel height with a localized curvature at the base of the panel. During the SLE loading, the peak displacement due to flexure and shear were determined to be 5mm and 0.2mm, respectively for the top panel and 12mm and 0mm, respectively for the bottom panel. The peak second story deformation at this point was in the negative direction and was measured to be 33mm during the SLE loading (compared with 17.2mm from pure panel deformations). The difference is assumed to be primarily due to panel rotation (rigid body) due to frame beam rotations. There is also a small contribution to displacement from the oversized holes and it is possible that curvature was underestimated from the data from the strain gages, which were not at the exact location of yielding of the reinforcing bar.

Figure 15 shows the estimated panel forces during the DLE-I loading after subtracting the 2nd story shear forces of the steel columns from the total 2nd story shear force history during DLE-I and equally distributing the remaining story shear force to the five sets of panels. For this estimate, it is assumed that each panel set carries the same amount of shear as individual force measurements during the test were not feasible. From Figure 15 it can be seen that the peak story shear in one panel set is roughly 45kN. Under the SLE loading the forces were slightly lower. At these peaks, the panel deformations computed from the instrumentation as described above corresponded to a relative panel deformation (from channel connection to channel connection) of ~1%. In the component tests (e.g. the test presented in Section 2), these levels of shear (lateral) force in the panels were

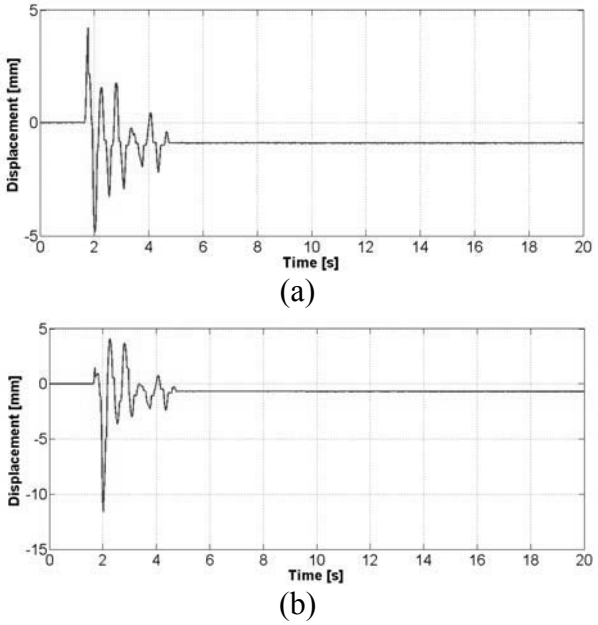


Figure 14 Displacement histories due to flexural deformations for SLE (a) Top Panel (b) Bottom Panel

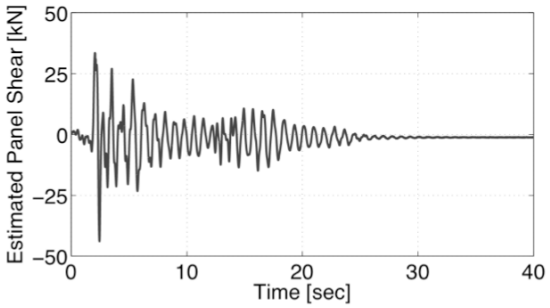


Figure 15 Estimated shear force in each panel set on the second story during the DLE-I loading.

reached at approximately the same amount of relative panel deformation (note Figure 5 shows story deformation, not relative panel deformation), indicating that the hysteretic response of the panels was similar in both sets of experiments (cyclic static and hybrid simulation tests). It is noted that the panels in the two sets of experiments were of slightly different design. The impacts of these variations are currently under investigation.

4 CONCLUSIONS

The experimental response of Self-Compacting, High Performance Fiber Reinforced Concrete (SC-HPFRC) infill panels retrofitting steel frames in two different experimental configurations has been presented. In the first configuration, a double-height panel system tested with fixed-end conditions in a four-pin frame under quasi-static cyclic loading was presented. In the second, the experimental response of SC-HPFRC infill panels in a two-story, single-bay frame with five sets of panels per story subjected to seismic loading through a hybrid simulation set up has been presented. The main conclusions from comparing the experimental responses of these two testing configurations are:

1. Infill panels in the hybrid simulation experiments behaved similarly to component panel tests with the exception of the degree of multiple cracking. Less cracking in the panels from the hybrid testing is attributed to the fewer load cycles, the boundary conditions in the frame that are able to rotate, and slightly higher SC-HPFRC strength.
2. Damage to the panels in the hybrid simulation experiments was well-distributed among panels as intended.
3. The SC-HPFRC material proved to be exceptionally robust in the base of center connection slippage, where bearing was well controlled by the tough SC-HPFRC material.
4. Panel deformation for the set of panels studied here was found to be primarily flexural based on instrumentation data. All cracking and deformation appeared to be flexural based on observation.

The data from the hybrid simulation experiments is currently being analyzed in greater detail.

5 ACKNOWLEDGEMENTS

Financial support provided by the National Science Foundation (CMS-0530383), the Blume Center for Earthquake Engineering and the School of Engineering at Stanford University, and the National Consortium for Graduate Degrees for Minorities in Engineering and Science (GEM). In addition the considerable support for the double-height panel testing, by faculty and staff in structural engineering at The University of Michigan at Ann Arbor as well as for the hybrid simulation testing by the staff at NEES@Berkeley is gratefully acknowledged. Generous donations from the Herrick Steel Corporation and Mid-State Precast as well as the University of Michigan, Williams Form Engineering, and Sika Corporation are also gratefully acknowledged. The opinions expressed in this paper do not reflect those of the financial sponsors.

6 REFERENCES

ASCE (2007). "Seismic Rehabilitation of Existing Buildings," *ASCE Standard ASCE/SEI 41-06,* American Society of Civil Engineers/Structural Engineering Institute, Reston, VA.

Federal Emergency Management Agency–FEMA 350 (2000). Recommended seismic design criteria for new steel moment frame buildings, Washington, DC, July.

Federal Emergency Management Agency–FEMA 351 (2000). Recommended seismic evaluation and upgrade criteria for existing welded steel moment-frame buildings, Washington, DC: Federal Emergency Management Agency, July.

Hanson, J.V. and S.L. Billington. (2011). Cyclic testing of a ductile fiber-reinforced concrete infill panel system for seismic retrofitting of steel frames, *Report TR. 173*, John Blume Earthquake Engineering Center, Stanford, CA.

Liao, W.-C., Chao, S.-H., Park, S.-Y., and A.E. Naaman (2006). "Self-Consolidating High Performance Fiber Reinforced Concrete (SCHPFRC) - Preliminary Investigation," Report UMCEE 06-02, Dept. of Civil & Environmental Engineering, University of Michigan, Ann Arbor, MI, 76 pp.

Lignos, D.G., Hunt, C.M., Krebs, A.D., and S.L. Billington. (2009). Comparison of retrofitting techniques for existing steel moment resisting frames, Proceedings ATC/SEI Conference, San Francisco, CA, December.

Lignos, D.G., and H. Krawinkler. (2007). A database in support of modeling of component deterioration for collapse prediction of steel frame structures, ASCE Structures Congress, Long Beach CA, SEI.

Lignos, D.G., and H. Krawinkler. (2009). Sidesway collapse of deteriorating structural systems under seismic excitations, *Report TR 172*, *John A. Blume Earthquake Eng. Center,* Stanford U., Stanford, CA.

Lignos, D.G., and Billington, S. L. (2010). Hybrid Testing of a Retrofitted Steel Moment Resisting Frame with High Performance Fiber Reinforced Concrete Infill Panels, *9th US National & 10th Canadian Conf. on Earthquake Eng.,* Toronto, Canada, July.

Lignos, D.G., Moreno-Luna, D.M., and S.L. Billington (2011). "Experimental and Analytical Validation of a Seismic Retrofit Systems for Existing Steel Moment-Resisting Frames," *Proc. 8th International Conference on Urban Earthquake Engineering*, Tokyo Institute of Technology, Tokyo, Japan, March.

Lignos, D. G., and Krawinkler, H. (2011). "Deterioration Modeling of Steel Components in Support of Collapse

Prediction of Steel Moment Frames under Earthquake Loading", *J. Structural Engineering,* ASCE, in press

Moncarz, P.D. and Krawinkler, H., (1981). "Theory and application of experimental model analysis in earthquake engineering," *Report No. 50, John A. Blume Earthquake Eng. Center*, Stanford U., Stanford, CA.

Olsen, E.C. and Billington, S.L. (2011). "Cyclic behavior of precast, self-compacting ductile concrete infill panels for seismic retrofit of steel frame buildings," *ACI Structural Journal*, **108**(1):51-60.

Olsen, E.C., and Billington, S.L. (2009). "Evaluation of precast, high-performance fiber-reinforced concrete infill panels for seismic retrofit of steel frame building: Phase 1-cyclic testing of single panel components," *Report No. TR 158, John A Blume Earthquake Engineering Center*, Stanford University, Stanford CA.

OpenSees. (2009). "Open System for Earthquake Engineering Simulation," Pacific Earthquake Eng. Research Center (PEER), http://opensees.berkeley.edu

8CUEE CONFERENCE PROCEEDINGS
8th International Conference on Urban Earthquake Engineering
March 7-8, 2011, Tokyo Institute of Technology, Tokyo, Japan

DAMAGE INVESTIGATION OF REINFORCED CONCRETE BUILDINGS AT THE 2010 CHILE EARTHQUAKE

Taiki Saito[1)], Susumu Kono[2)], Koichi Kusunoki[3)], Yousok Kim[4)], Tomoya Matsui[5)], Masanori Tani[6)], Yo Hibino[7)], Carlos Zavala[8)], and Patricia Gibu[8)]

1) Chief Research Engineer, IISEE, Building Research Institute, Japan
2) Associate Professor, Kyoto University, Japan
3) Associate Professor, Yokohama National University, Japan
4) Research Associate, Earthquake Research Institute, The University of Tokyo, Japan
5) Research Associate, Toyohashi University of Technology, Japan
6) Research Associate, Kobe University, Japan
7) Research Associate, Materials and Structures Laboratory, Tokyo Institute of Technology, Japan
8) Japan-Peru Center for Earthquake Engineering and Disaster Mitigation, National University of Engineering, Peru
tsaito@kenken.go.jp, kono@archi.kyoto-u.ac.jp, kusunoki@ynu.ac.jp,yskim@eri.u-tokyo.ac.jp,matsui@ace.tut.ac.jp
mtani@port.kobe-u.ac.jp, hibino@serc.titech.ac.jp, czavala@uni.edu.pe, pgibu@uni.edu.pe

Abstract: A great earthquake of magnitude 8.8 struck on the Pacific coast of Chile, at 3:34a.m. local time on February 27, 2010, and the earthquake and Tsunami caused widespread damage in Chile. The group of Japanese and Peruvian researchers conducted disaster investigation especially for buildings from 26 April to 3 May, 2010.

1. INTRODUCTION

A great earthquake of Mw8.8 occurred at 3:34 A.M. on February 27, 2010 local time with the Pacific coast of Chile as the hypocenter. This earthquake collapsed or destroyed more than 810,000 buildings etc., resulting in more than 1.8 million victims including 432 deaths (as of March 27). When the earthquake occurred, in Peru, which a neighboring country of Chile, the Japan-Peru international joint research project, "Project for Enhancement of Earthquake and Tsunami Disaster Mitigation Technology in Peru" (JST-JICA Science and Technology Research Partnership for Sustainable Development Project, representative researcher: Fumio Yamazaki, professor at Chiba University, 2009-2014) was under way. Given that Peru and Chile are closely related to each other in terms of the seismotectonic and natural/social environments, and hence the findings obtained from the study on the great earthquake of Chile are expected to be mostly applied to Peru, with considerable ripple effects on other Latin-American countries, it was decided to perform investigation and information gathering on the damage caused by the earthquake and Tsunami that hit Chile, jointly with the counterpart from Peru. In addition, it was also decided that the second investigation team (team leader: Susumu Kawano) would be dispatched from the Architectural Institute of Japan to the site around the same period to perform a joint investigation.

The investigation was performed from April 26 to May 3, approximately two months after the earthquake. Given the JICA Study Team (March 13 to 23) and a joint study team comprised of four societies (Japan Association for Earthquake Engineering, Japan Society of Civil Engineers, Japanese Geotechnical Society, and Architectural Institute of Japan) (March 27 to April 8) already dispatched from Japan and the limited investigation days, this investigation was devoted chiefly to performing on-the-spot inspection of disaster-stricken buildings, acquisition of design documents, hearing with relevant parties, and so on, with the objective of elaborately investigating reinforced concrete buildings. While our activities included the investigation of buildings equipped with a base isolation or seismic control structures, we would like to report in this paper our investigation results on the damage to reinforced concrete structures.

2. OUTLINE OF INVESTIGATION

The investigation was performed chiefly in principal cities (Santiago, Concepcion, and Viña del Mar) of Chile and the surroundings. Figure 1 was the investigation points and the locations of faults. Table 1 shows the list of the investigated buildings. The results of our detailed investigation on the underlined buildings of those listed in the table are as follows:

3. RESULTS OF BUILDING DAMAGE

2.1 Damaged buildings in Santiago City

a) B4. Sol Oriente 1 and 2

It is an apartment complex constructed of box-frame-type reinforced concrete in 2007 with 18 stories above ground (2 stories underground) (Photo 1). The building was damaged particularly on the first basement level of the underground self parking lot (Photos 2, 3). The structural features and the summary of damage are follows:

- Multi-story shear wall structure connected by flat slabs.
- Flexural tension failure occurred in three structure planes out of five 4-span ones on the first basement. An end main reinforcement ruptured.

The height of the north side multi-story shear wall on the basement is shorter by 1200 mm than on higher floors. In addition, only the northern end of the north side multi-story shear wall lacks an orthogonal wall (Figures 2, 3). Accordingly, the flexural strength of the north side multi-story shear wall is low on the first basement, likely resulting in the flexural tension failure in the south direction on the north side multi-story shear wall.

2.1 Damaged buildings in Concepcion City

Concepcion City is a city located approximately 105 km away from the hypocenter with a population of approximately 900 thousand. The earthquake brought eight buildings into serious damage, of which one was completely collapsed. We could obtain entry permits to and design documents of several buildings thanks to the cooperation of the Urban Development Bureau and the Police Bureau of Concepcion City.

a) B11. LINCOYAN 440 (Torre Livertad)

It is an RC wall flat slab structure constructed in 1973. The building has 17 stories above ground and one basement (with no underground car park), of which the three lower floors are occupied by commercial tenants and the fourth and above floors are used for housing (Photo 4). The machine room on the first basement was hardly damaged. The non-structural brick wall collapsed more seriously on upper floors. The walls on the first and second floors failed in flexural tension with the wall-end main reinforcement fractured or buckled (Photo 5). While the building was damaged particularly on the walls in the northeast and southwest directions, little damage was observed on the walls in the orthogonal direction. The damage concentrated on the wall footing is likely attributable to the lack of flexural strength of the T section web resulting from the respective bending deformation of two multi-story shear walls arranged in parallel due to the limited floor slab area in the staircase (Figures 4, 5, 6).

b) B13. Alto Rio

It is a reinforced concrete apartment complex constructed in 2008 with 15 stories above ground and two stories underground (parking lot). The building completely fell down from the base on the first floor (Photo 6, 7). Photo 7 shows the appearance of all the reinforcing bars on the first floor having been pulled out or cut down from the wall pillars and load-bearing walls on the first floor during the overturning of the building. Conversely, little damage was observed on the underground end plane walls. As shown in the plan view of Figure 7, the walls on the first floor and the basements (parking lot) are smaller than those on the second and above floors in both length and volume. This fact may have resulted in the damage particularly on the wall footing on the basements.

c) B14. SALAS 1343

It is an apartment complex constructed in 2007 with 13 stories above ground and an underground car park provided beside the building. It consists of two buildings arranged in L shape and connected with an expansion joint (Photo 8, Figure 8). It is constructed with a middle corridor in planar shape with more wall volume in the ridge direction. While the south side building was seriously damaged, the north side building was slightly damaged. The south side building seems to have suffered torsional vibration caused by stiffness eccentricity resulting from the many walls in the surrounding of elevators and staircases.

2.3 Damaged buildings in Viña del Mar City

Viña del Mar City is a city with a population of approximately 300 thousand. The 1985 Chile Earthquake (magnitude 7.8, 150 deaths) damaged many high-rise RC buildings within the city.

a) B21. Building Festival

It is an apartment complex (wall-type flat slab structure) with 14 stories above ground and one basement. It was severely damaged (Photo 9). The building had undergone seismic retrofitting such as the placement of additional concrete for walls and beams and the additional installation of walls in response to the earthquake in 1985, but suffered damage in the recent earthquake such as flexural tension failure and separation of concrete- added walls in the wall footing (Photo 10, Figure 9).

4. SUMMARY

The characteristics of the damaged buildings are as summarized below:

- Many of the damaged buildings are flat slab structures with no beam or frame column on the wall.
- The standard size of wall reinforcement is D10@250.
- At the wall end, confinement steel (or supplementary cross ties) is installed as well as bending reinforcement.
- The wall pillars, which are provided in place of pillars, are arranged longitudinally in the span direction for reasons of the layout of the parking lot. This fact may result in lower flexural strength and stiffness in the ridge direction.
- The length of a multi-story shear wall may be reduced in the underground parking lot space for the sake of vehicular traffic.
- A parking lot in the underground of the building may be

constructed in a shape protruded in one direction. In this case, the parking lot is enclosed only by the three-side retaining walls immediately below the building, with the other side of wall set back in the ridge direction.

- Some walls or wall pillars in the span direction are not connected to orthogonal walls. Such walls include a wall extending in the span direction on the side without a retaining wall and a piloti-type wall pillar (ground parking lot). They were damaged probably due to the low flexural strength when the tensile load was exerted to the side with no orthogonal wall.
- The buildings have a relatively large number of stories and a high slenderness ratio. As a result, the walls of such buildings mostly underwent flexural tension failure. In addition, lack of enough strength to bear the story shear force on the compression side may result in collapse of the building.

Most of the severely damaged or collapsed buildings were high-rise constructions with 13 or more stories and damage concentrated on the footing of the multi-story shear wall observed as a common characteristic. Conversely, most buildings in cities appeared to be sound and few buildings suffered intermediate damage, e.g. slight or medium damage. This may be a characteristic of damage to box frame constructions without plastic deformability. The damage can be considered generally minor, in view of the great magnitude of the recent earthquake at 8.8. While elaborate analysis is still required as to the extent of the seismic force applied to the buildings, given the fact that the damage remained so modest after the great earthquake, the Chilean Seismic Code seems to have functioned extremely well. One of the factors behind the major lack of damage to buildings in the recent earthquake was the positive introduction of the load-bearing wall.

The Chilean Seismic Code includes a provision likely encouraging the positive introduction of the load-bearing wall such as a strict restriction of deformation and reduction of the design seismic force according to the load ratio of the load-bearing wall. In Japan, the height of wall-type rigid-frame structures is limited to 15 stories. Given the modest damage to buildings in the recent Chile Earthquake and the continuous usability of post-earthquake buildings, Japan may also need to recognize anew the benefits of box frame constructions.

From the research perspective, a design method needs to be established to prevent such brittle failure after flexural yielding as observed in the recent seismic damage. Structural testing on flexural failure of load-bearing walls is not common in Japan and future research and development is awaited.

Acknowledgements:

This damage investigation was performed as a part of the international joint research project "Project for Enhancement of Earthquake and Tsunami Disaster Mitigation Technology in Peru" (JST-JICA Science and Technology Research Partnership for Sustainable Development Project, representative researcher: Fumio Yamazaki, professor at Chiba University, 2009-2014) and an earthquake disaster investigation of the Architectural Institute of Japan. In conducting this investigation, we obtained cooperation from many people including Professor Boroschek and Mr. Tomas of the University of Chile; Professor Cruz of the Pontifical Catholic University; an ex-trainee, Mr. Raul; and the JICA Chile Office. We wish to express our gratitude to them.

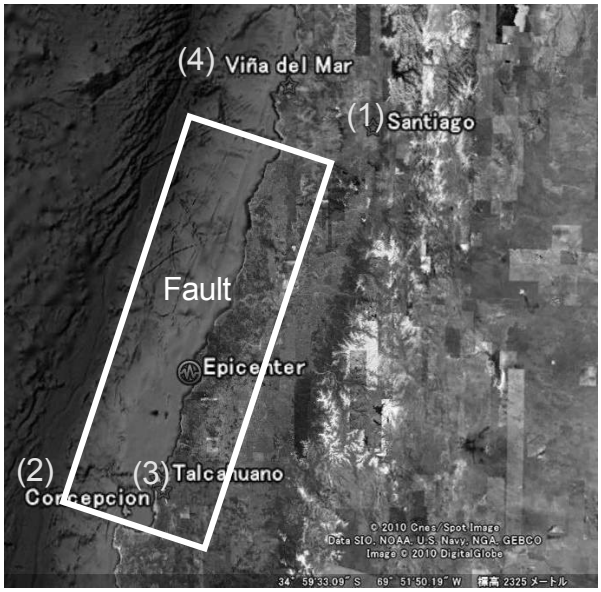
References:

A study team from the Japan Association for Earthquake Engineering and the Architectural Institute of Japan: Damage Investigation Report for Maule, Chile, Earthquake of 27 February 2010 dated May 2010.

Hiroto Kato, Seitarou Tajiri, Tomohisa Mukai (2010), " 2010 Chile Earthquake Field Survey Report (Flash Report), Building Research Institute

"Learning from Earthquake, The Mw 8.8 Chile Earthquake of February 27, 2010," EERI Special Earthquake Report, 2010.6.

Riddle, R., Wood, S.L. and De La Liera, J.C. (1987), "The 1985 Chile Earthquake," A Report to the National Science Foundation, Research Grants ECE 86—03789, Univ. of Illinois



4/27	(1)	Santiago
4/28	(1)	Santiago
4/29	(2)	Concepcion
4/30	(2)	Concepcion, (3) Talcahuano
5/1	(4)	Viña Del Mar

Figure 1 Investigation points and locations of fault

Table 1 List of investigated buildings

(Santiago)
B1. Torre Titanium (vibration control)
B2. Ciudad Empresarial
B3. Edificio Leones 1300
B4. Sol Oriente 1 and 2
B5. Edificio Don Luis
B6. Edificio Don Tristan
B7. Edificio Don Luis
B8. Hall Arnoldo Hax (Catolica Univ., seismic isolation)
B9. Comunidad Andalucia (seismic isolation)

(Concepcion)
B10. Torre O'Higgins 241
B11. LINCOYAN 440 (Torre Livertad)
B12. CAUPOLICAN 518
B13. Alto Rio
B14. SALAS 1343
B15. LOS CARRERAS 1535
B16. ROZAS 1145 (Edificio Don Feodra)
B17. FREIRE 1965 (Edificio Centro Mayor)
B18. Plaza Mayor
B19. BARROS ARANA 272

(Talcahuano)
B20.Edificio de Biblioteca Municipal de Talcahuano

(Viña del Mar)
B21. Building Festival
B22. ACHS (Asociacion Chilena de Seguridad) (seismic isolation)
B23. Efidicio Rio Petrohue



Photo 1 Appearance of the building



Photo 2 Underground parking lot



Photo 3 Shear wall in B1F

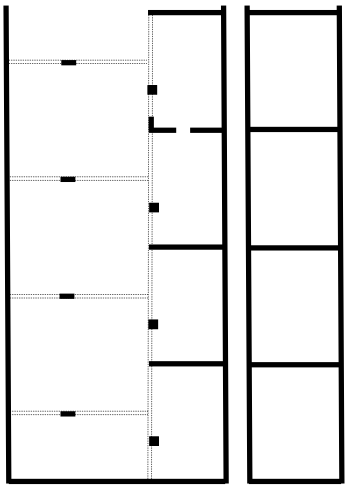


Figure 2 Basement plan view

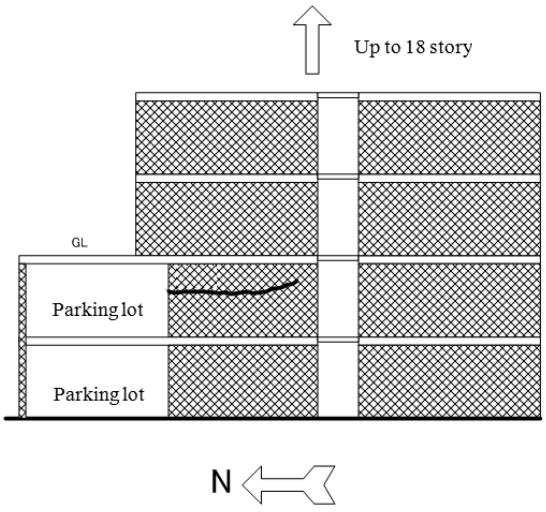


Figure 3 Building section view (sketch)



Photo 4 Appearance of the building

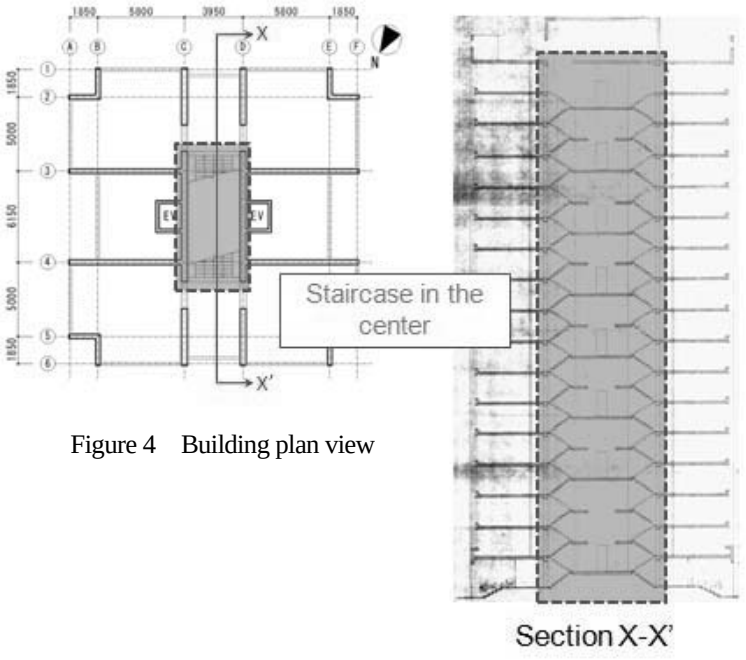


Figure 4 Building plan view

Figure 5 X-X' section view

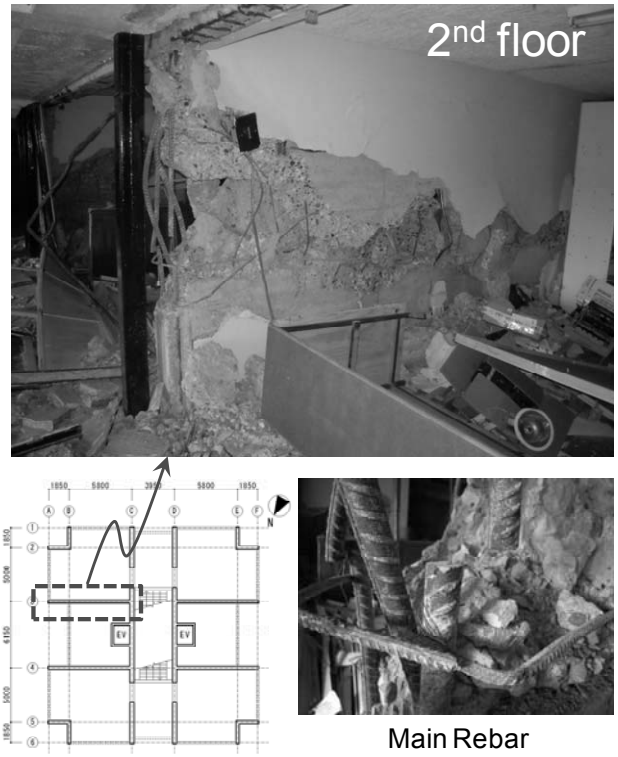


Photo 5 Wall fracture

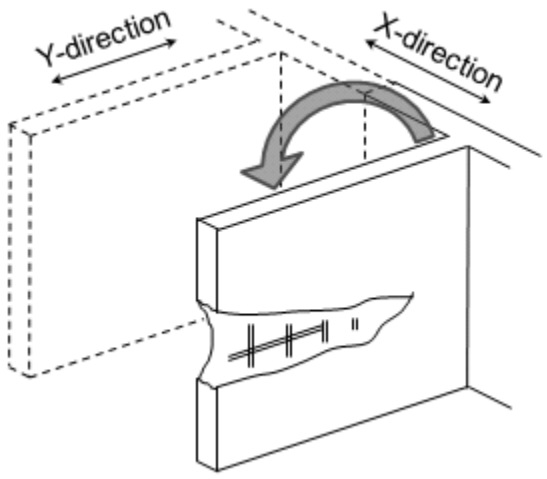


Figure 6 Failure mechanism of T-shaped section wall



Photo 6 Photo of the building before collapsed (excerpted from the Web Page)



Photo 7 Collapsed building

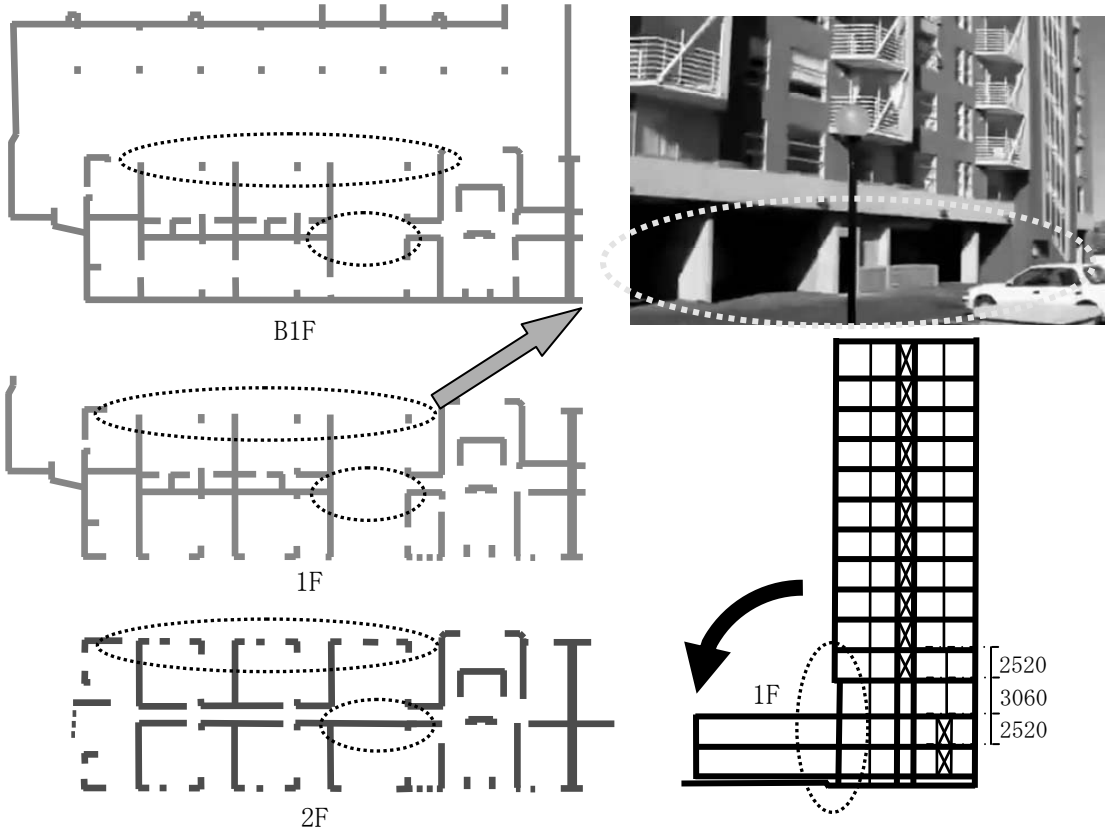


Figure 7 Difference in wall volume and layout among basement, first floor, and second floor

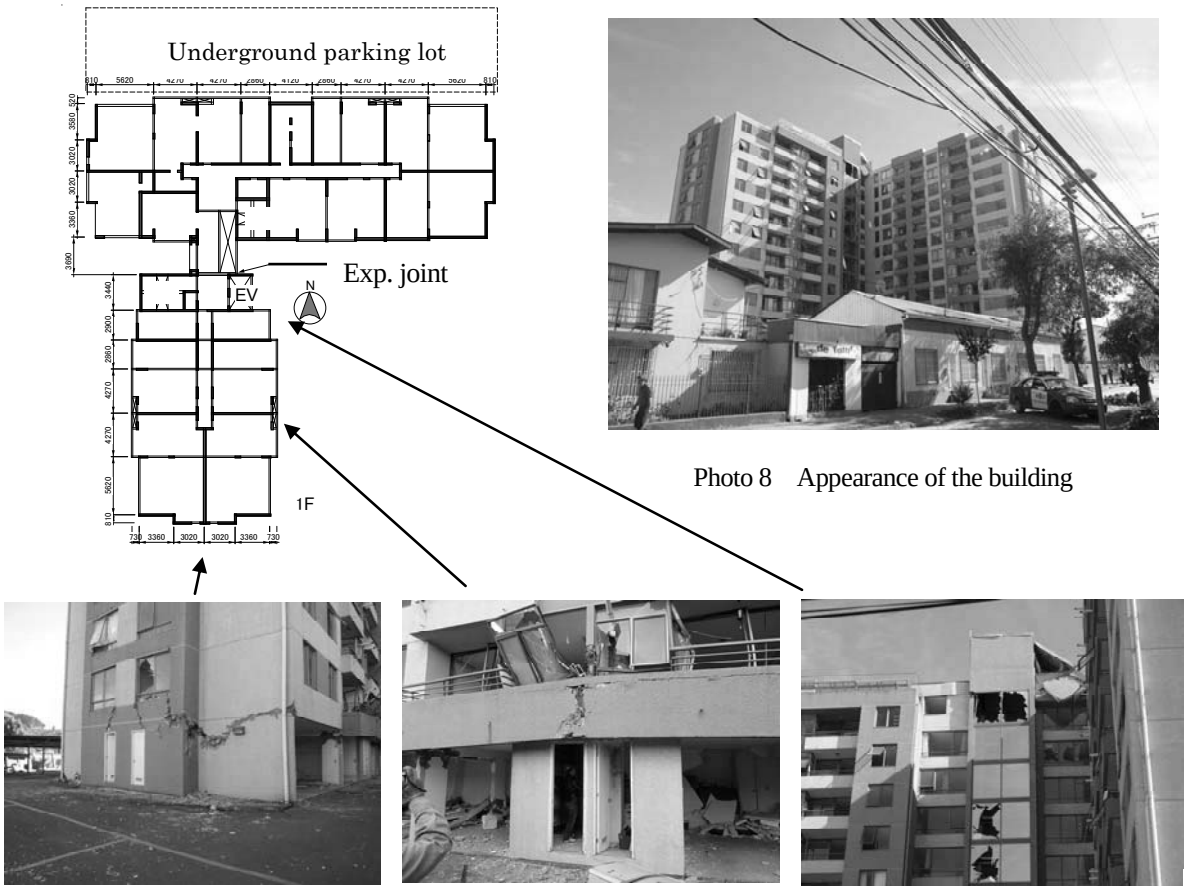


Photo 8 Appearance of the building

Figure 8 Plan view and damage



Photo 9 Appearance of the building



Photo 10 Appearance of the building

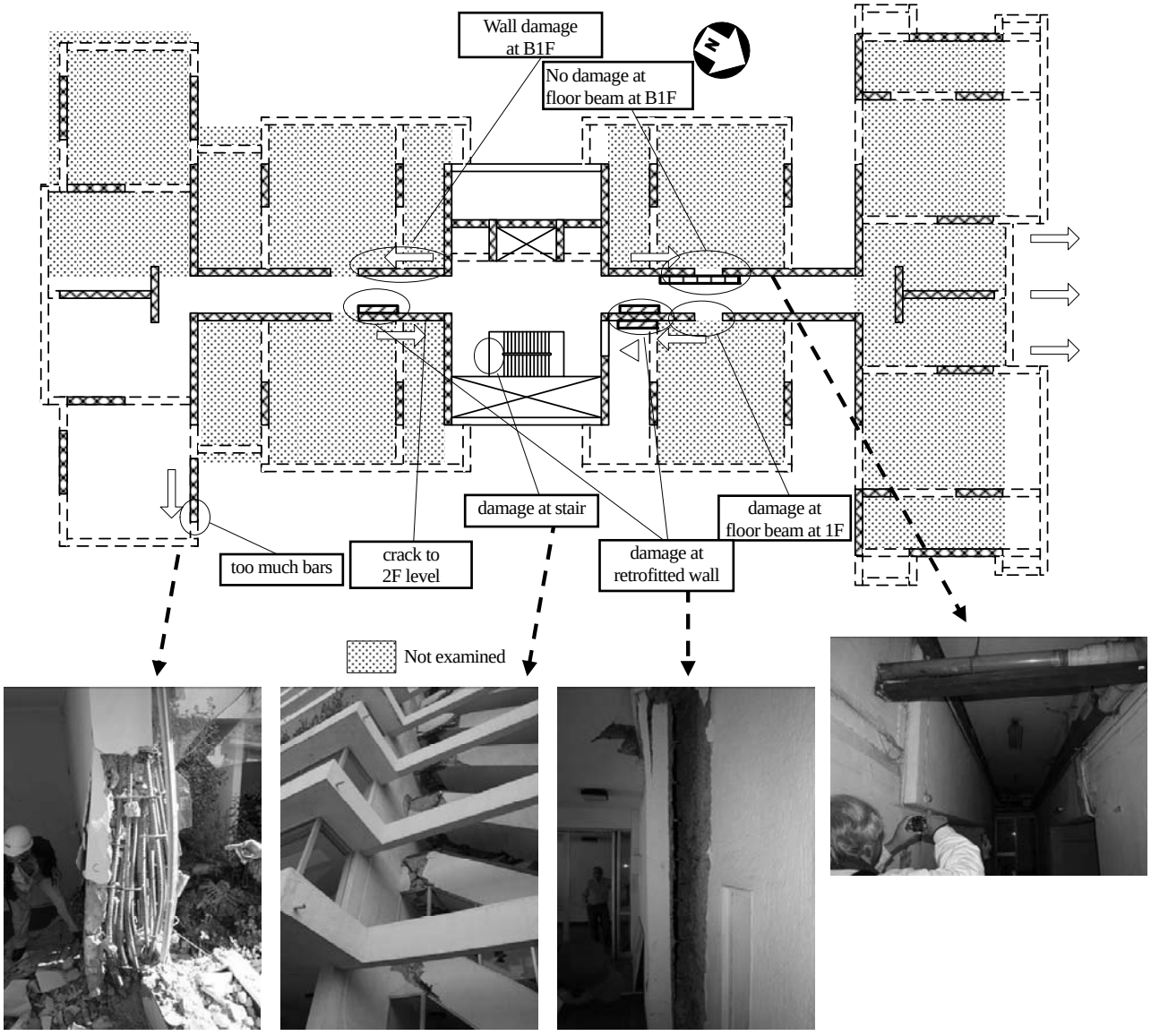


Figure 9 Plan view and damage

8CUEE CONFERENCE PROCEEDINGS
8th International Conference on Urban Earthquake Engineering
March 7-8, 2011, Tokyo Institute of Technology, Tokyo, Japan

SEISMIC FRAGILITY ANALYSIS OF RC FRAME STRUCTURES

Huanjun Jiang[1)], Junjie Mao[2)], Xilin Lu[1)], and Linzhi Chen[3)]

1) Professor, Research Institute of Structural Engineering and Disaster Reduction, Tongji University, P.R. China
2) Graduate student, Research Institute of Structural Engineering and Disaster Reduction, Tongji University, P.R. China
3) Engineer, China Southeast Architecture Design Institute Co., Ltd., P.R. China
jhj73@tongji.edu.cn, maojunjie125407815@126.com, lxlst@tongji.edu.cn, wchen120@gmail.com

Abstract: Seismic fragility analysis is performed for RC frame building structures that are designed in line with the current Chinese seismic design code for buildings, considering the uncertainty of structural performance and earthquake ground motions. Site soil type, number of stories, and seismic fortification intensity are taken as the main variables of design parameter of reference structures. The global seismic damage index and the maximum inter-story drift ratio, which have close relationship with seismic damage of structural and non-structural components, are employed as the damage identifiers. Four damage levels, i.e. fully operational, operational, repairable, and collapse prevention, are considered in this study. For each frame structure, the probability exceeding each damage level under the earthquakes with each specified PGA is obtained by conducting nonlinear time history analysis with the aid of OpenSees. The fragility curves of each damage level are obtained by regression analysis using nonlinear least-squares method. The seismic fragility analysis results indicate that the required seismic performance objectives could be realized for RC frames structures designed by using the current Chinese seismic design code.

1. INTRODUCTION

Reliable earthquake risk evaluation requires a good analysis of seismic vulnerability of structures through appropriate seismic damage indicators. Seismic fragility is a measure of how vulnerable a building is to the damage under a given severity of earthquake. Generally, seismic fragility can be formulated by fragility curves or damage probability matrices. Fragility curves describe the conditional probability of attainment or exceedance of a certain damage state for a given intensity of ground excitation. The conditional probability is defined as

$$P_{ik} = P[D \geq d_i \mid Y = y_k] \tag{1}$$

where P_{ik} is the conditional probability of attainment or exceedance of the damage state d_i for a given intensity of ground excitation y_k; D is the variable that reflects the damage; and Y is the variable that reflects the intensity of ground excitation.

Different types of approaches have been proposed by the researchers to build fragility relationships, which could be classified into four categories (Rossetto and Elnashai 2003): (1) Empirical Method. This method, as the most practical way, is based on the statistical analysis on post-earthquake survey data of damage (Orsini 1999); (2) Judgmental Method. This method depends on expert experience and opinion; (3) Analytical Method. This method utilizes numerical analysis to simulate the behavior of structures under earthquakes. A variety of analysis procedures have been followed, ranging from elastic analysis (Mosalam et al. 1997), adaptive pushover analysis (Rossetto and Elnashai 2005), to nonlinear time history analysis (Seyedi et al. 2010). (4) Hybrid Method. This method is formed by the combination of more than one of the former three methods. The comprehensive review on the four types of approaches could be found in the literature (Rossetto and Elnashai 2003).

There is very limited information available about the seismic vulnerability of building structures designed according to the current seismic design code. In this study the seismic fragility analysis is conducted on RC frame building structures designed in accordance with current Chinese seismic design code by means of analytical method. The fragility curves corresponding to four damage levels quantified by the global seismic damage index and the maximum inter-story drift ratio are generated on the basis of regression analysis on the results of a large number of nonlinear time history analyses of numerical models. The global damage index proposed by the authors, different from those in the literature, takes the contribution of the individual structural member into account. The appropriateness of the current Chinese seismic design code is verified by the results of this work.

2. SEISMIC DAMAGE LEVELS

2.1 Seismic Damage Index

One of the best known and most widely used seismic

damage models for structural members is the Park-Ang model (Park and Ang 1985). A modification as follows is proposed by the authors for the Park-Ang damage model, eliminating its non-convergence problem at upper and lower limits:

$$D = (1-\beta)\cdot\frac{\delta_m - \delta_c}{\delta_u - \delta_c} + \beta\cdot\frac{\int dE}{F_y(\delta_u - \delta_y)} \tag{2}$$

where D is the damage index of the structural member; δ_c, δ_y, and δ_u, are the deformations at cracking, yielding, and ultimate limit state under monotonic loading, respectively; δ_m is the maximum deformation experienced during the loading history; F_y is the yielding strength; β is the combination coefficient; and $\int dE$ is the total dissipated energy during the loading history. The bigger one of the two ends is taken as the damage index of the structural member.

The damage index of a story in a building is derived based on the weighted average of damage scores of all the relevant members as follows:

$$D_i = \sum_{j=1}^{n} \lambda_j D_j^{(i)} \tag{3}$$

$$\lambda_j = \frac{D_j^{(i)}}{\sum_{k=1}^{n} D_k^{(i)}} \tag{4}$$

where D_i is the damage index of the ith story; $D_j^{(i)}$ is the damage index of the jth member at the ith story; and λ_j is the importance factor of the jth member. The global damage index of the entire building structure is taken as the maximum of the damage index of all stories, expressed as

$$D_G = \{D_1, \quad D_2, \cdots, D_i, \cdots, D_N\}_{\max} \tag{5}$$

2.2 Limit Values of Damage Parameters

Four damage levels, i.e. fully operational, operational, repairable, and collapse prevention, are considered. The global seismic damage index and the maximum inter-story drift ratio, which correlate well with seismic damage of structural and non-structural components respectively, are used as the damage indicators in this study. The seismic performance objectives for ordinary buildings, expressed as the coupling of expected damage levels with expected levels of earthquake ground motions, and the limit values of the two damage parameters corresponding to the attainment of each damage level are given in Table1. The return periods of the four intensity levels of earthquakes are 50, 475, 975, and 2475 years respectively, and the corresponding exceeding probability in 50 years are 63.2%, 10%, 5%, and 2%.

Table 1 Seismic Performance Objectives and Limit Values of Damage Parameters

Earthquake design level	Damage level	Global damage index	Maximum Inter-story drift ratio
Frequent earthquake	Fully operational	0.05	1/550
Occasional earthquake	Operational	0.20	1/250
Rare earthquake	Repairable	0.40	1/100
Extremely rare earthquake	Collapse prevention	0.80	1/50

3. ANALYTICAL MODEL

Site soil type, number of stories, and seismic fortification intensity are considered as the main variables of design parameter of reference building structures in this study. Three numbers of stories, 3, 6, 10, representing low-rise, mid-rise, and high-rise building respectively, are taken. Two seismic fortification intensities, intensity 7 and 8, are selected since most of the areas in China belong to the zone of intensity 7 and 8. In Chinese seismic design code there are four categories of site soil condition ranging from stiff to soft soil, i.e. Class I, II, III, and IV, each of which is further classified into three design groups according to the characteristic period of the earthquake. The design group reflects the influence of the epicentral distance. All the 12 types of site soil are taken into account here. Therefore, in total 72 frame structures are designed in accordance with Chinese seismic design code. The typical plan layout of reference building structures is shown in Figure 1. The material strengths are chosen as follows: standard yielding strength of steel reinforcement is 335 MPa, and standard concrete cubic compressive strength is 30 MPa.

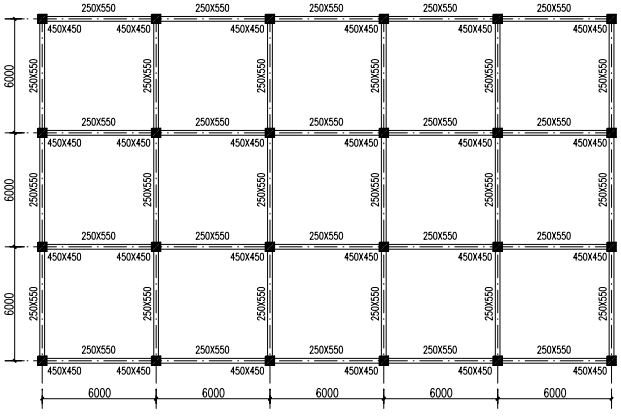


Figure 1 Typical Structural Plan Layout (unit: mm)

The analytical model is constructed with the aid of the program OpenSees. The flexibility-based fiber model is applied. The modified Kent-Park model for confined and unconfined concrete, proposed by Scott et al. (1982), is

employed for the core concrete and cover concrete respectively. The constitutive model proposed by Filippou et al. (1983) is employed for steel reinforcement. The rigid zone at the member joint is considered in line with the Chinese design code for RC tall buildings.

4. UNCERTENTY MODELING

According to Eq.(1), the seismic fragility assessment results are mainly affected by the uncertainty existing in the demand of earthquake response and the capacity of the structural system. The demand and capacity depend significantly on the earthquake ground motions and the properties of the structure. It has been found that one of the main sources of uncertainty of an RC structure is the inherent variability of material strengths (Ji et al. 2009).

4.1 Variability of Material Strength

In this study the compressive strength of concrete and yielding strength of steel reinforcement are chosen as the principal random variables. As the randomness of compressive strength of concrete is concerned, normal distribution is assumed for convenience according to the statistical survey of the test results in different areas in China. The coefficient of variance is taken as 14%. Similarly, normal distribution is assumed for steel reinforcement, and the coefficient of variance is taken as 5%.

To reduce the computation efforts effectively, the advanced sampling method, Latin Hypercube Sampling proposed by Mckay et al. (1979), is utilized for the combination of the properties of two constituent materials. The distribution of sampling material strength is shown in Figure 2. The abscissa represents the compressive strength of concrete, and the ordinate represents the yielding strength of steel reinforcement.

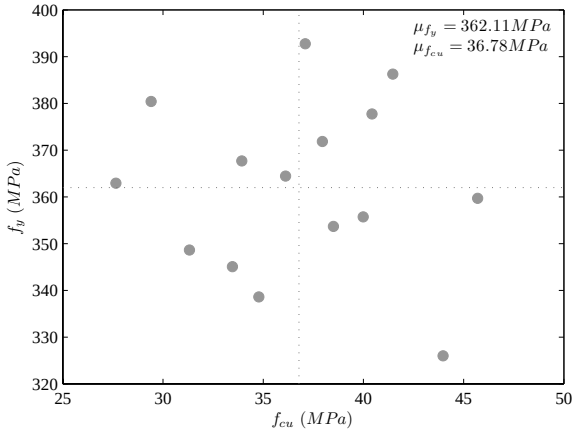


Figure 2 Material Strength of Sample

4.2 Earthquake Ground Motions

The main source of uncertainty exists in the seismic demand due to the uncertainty of earthquake ground motions resulted by the complexity of source mechanism, path attenuation, and site effects. In this study the natural earthquake ground motion records are carefully selected in line with the design acceleration spectra specified in Chinese seismic design code. There are 641 pairs of natural earthquake ground motions collected by the authors' laboratory. All the ground motions are classified into 12 groups in accordance with Chinese seismic design code. In each group 10 pairs of ground motions whose elastic acceleration spectra agree best with the design spectra specified in the code are picked out from the database. In total 120 pairs of ground motions are used as the input motions in the time history analysis. The comparison between the mean acceleration spectrum of the selected ground motions and design spectrum for four groups is shown in Figure 3, which shows good agreement.

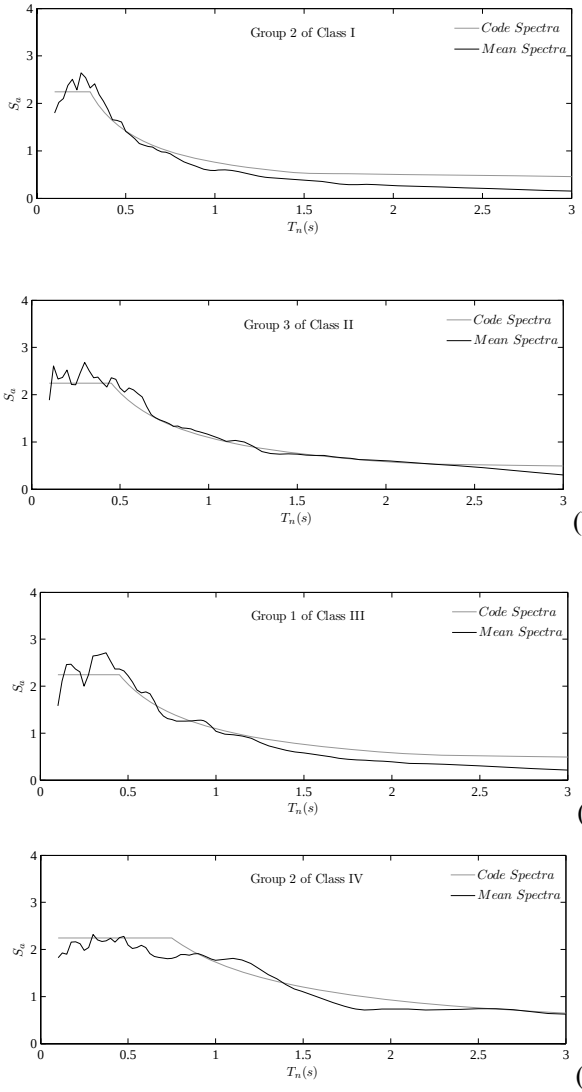


Figure 3 Comparison of Acceleration Spectrum: (a) Design Group 2 of Class I, (b) Design Group 3 of Class II, (c) Design Group 1 of Class III, and (d) Design Group 2 of Class IV

For each frame structure, one group with 10 pairs of selected ground motions covering the uncertainty aspects, which is in line with the design group of site soil for determining the strength and steel reinforcement of the structure, is used as the input motions.

There are several commonly used intensity measures

for seismic fragility assessment, such as peak ground acceleration (PGA), spectral acceleration, and spectral displacement. In this study PGA is taken as the only parameter of intensity measure. The accelerations of input motions are scaled according to the required PGA. Five discrete PGA values, 0.5m/s^2, 1.0m/s^2, 1.5m/s^2, 2.0m/s^2, and 2.5m/s^2, are set for the structure designed with the fortification intensity of 7. Six discrete PGA values, 0.5m/s^2, 1.0m/s^2, 1.5m/s^2, 2.0m/s^2, 3.0m/s^2, and 4.0m/s^2, are set for that of intensity 8.

5. FRAGILITY CURVES

5.1 Derivation of Fragility Curves

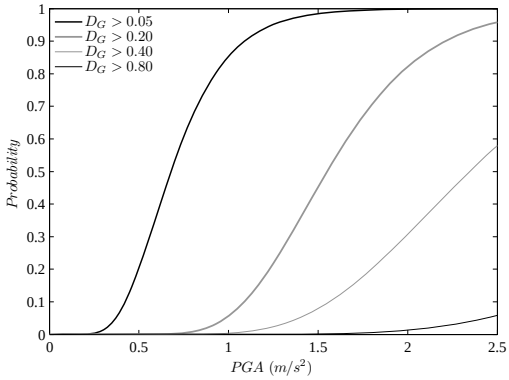
In total there are 59400 numerical simulations of time history analysis for 72 reference building structures. A MATLAB code is written to control the execution of analysis including modification of the input data, running OpenSees, and post-processing the simulation results. The probability of exceeding the limit of global damage index and maximum inter-story drift ratio specified for each damage level under a given intensity of ground excitation is obtained by using Eq.(1). Lognormal distribution as follows is assumed for regression of the fragility relationship according to the work (Sucuoglu et al. 1998):

$$P_i = \Phi\left[\frac{\ln Y - \lambda}{\zeta}\right] \tag{6}$$

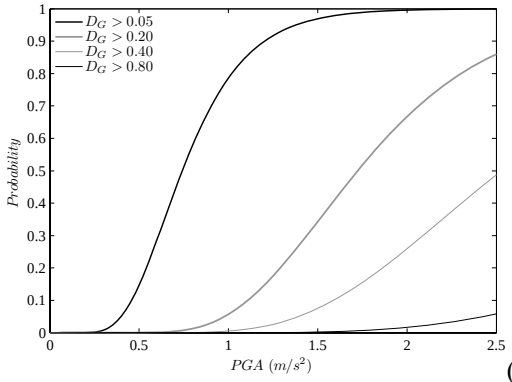
where Φ is the standard normal accumulative distribution function; Y is the intensity measure of ground motions, and here it is PGA; and λ and ζ are function parameters, indicating the mean and standard deviation of $\ln Y$. Nonlinear curve-fitting techniques are used to optimize the two function parameters. Accordingly, the fragility curves are derived.

5.2 Parameter Analysis

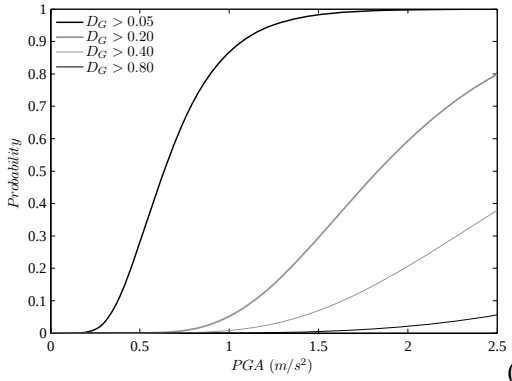
The derived fragility curves of frame structures with same fortification intensity and different stories are shown in Figures 4~7. The variation of exceeding probability with number of stories is not distinct. Generally, the slope of curve gets steeper for slighter damage level.



(a)

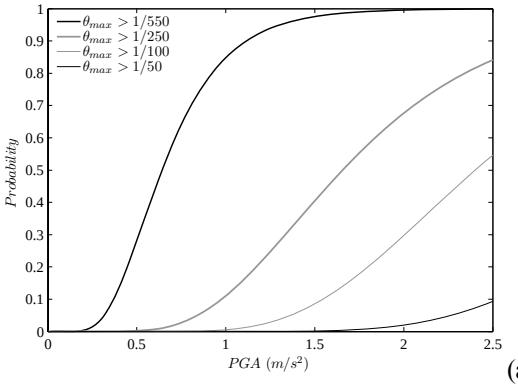


(b)

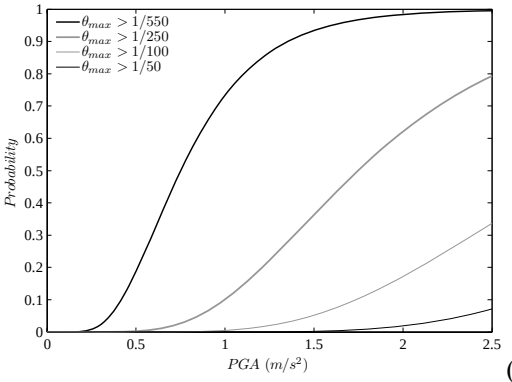


(c)

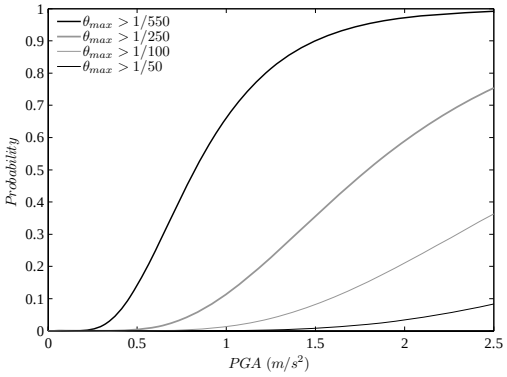
Figure 4 Fragility Curves of Global Damage Index with Intensity 7: (a) 3 Stories, (b) 6 Stories, and (c) 10 Stories



(a)

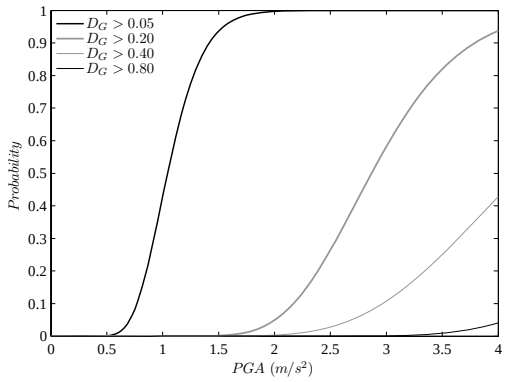


(b)

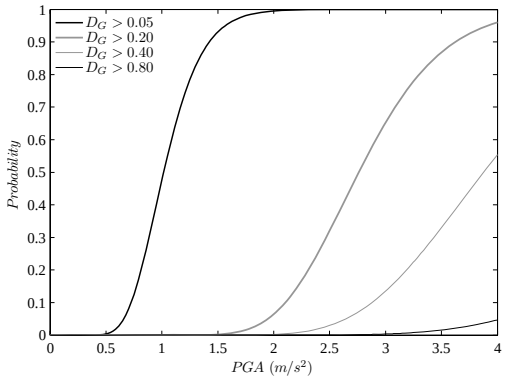


(c)

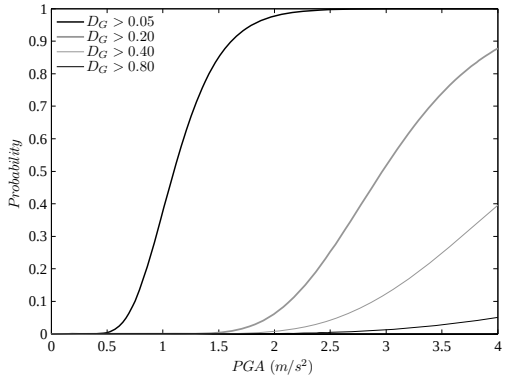
Figure 5 Fragility Curves of Maximum Inter-story Drift Ratio with Intensity 7: (a) 3 Stories, (b) 6 Stories, and (c) 10 Stories



(a)

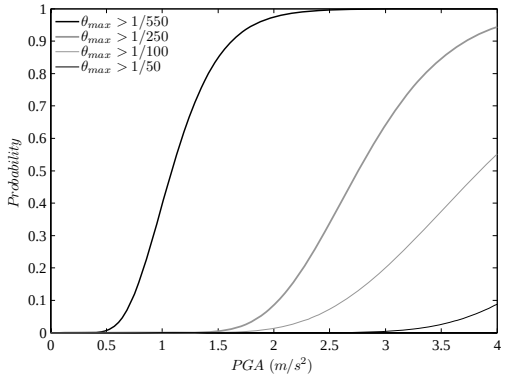


(b)

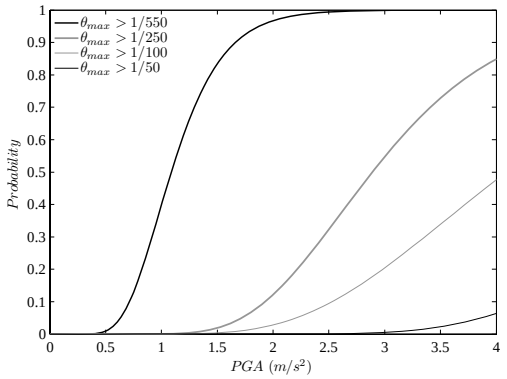


(c)

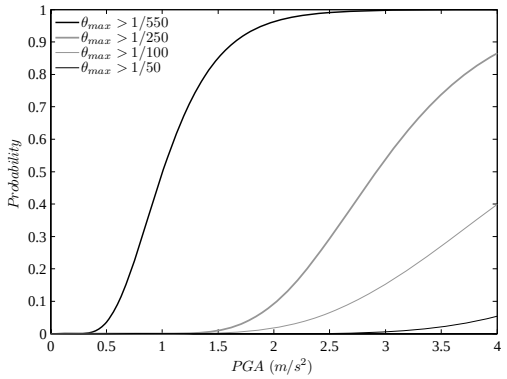
Figure 6 Fragility Curves of Global Damage Index with Intensity 8: (a) 3 Stories, (b) 6 Stories, and (c) 10 Stories



(a)



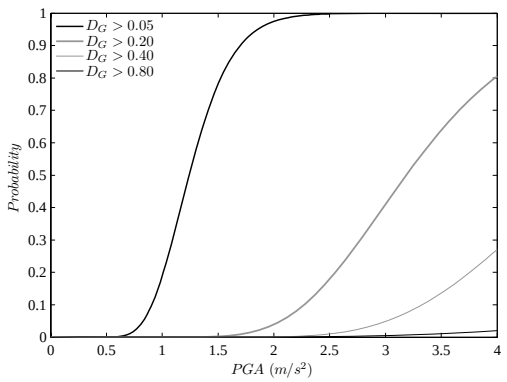
(b)



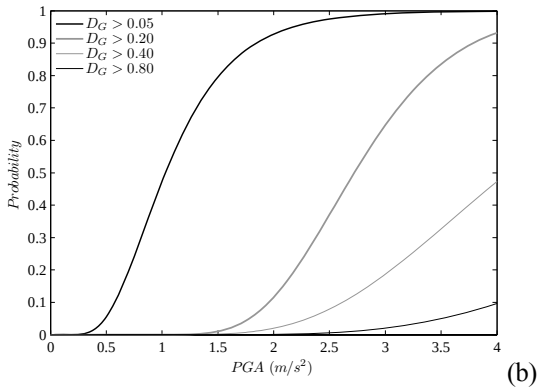
(c)

Figure 7 Fragility Curves of Maximum Inter-story Drift Ratio with Intensity 8: (a) 3 Stories, (b) 6 Stories, and (c) 10 Stories

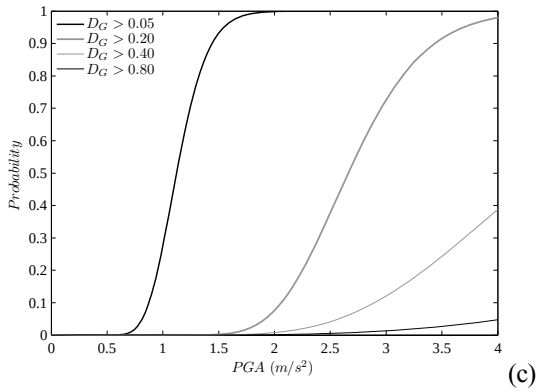
The effect of site soil class and design group on fragility curves is significant, as shown in Figures 8 and 9. In general, the exceeding probability tends to increase when the site soil gets softer.



(a)

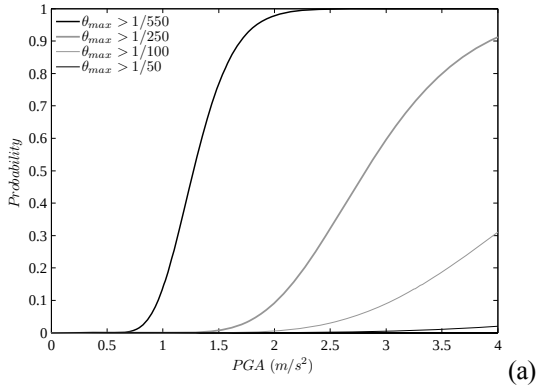


(b)

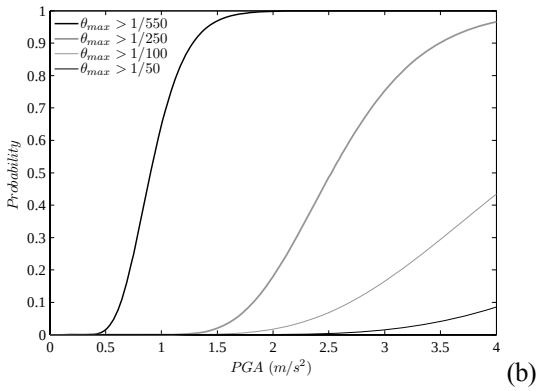


(c)

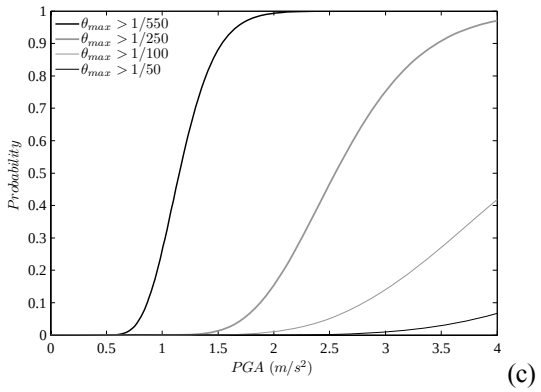
Figure 8 Fragility Curves of Global Damage Index of 6-Story Structures with Intensity 8: (a) Design Group 1 of Site Soil Class II, (b) Design Group 1 of Site Soil Class IV, and (c) Design Group 3 of Site Soil Class II



(a)



(b)



(c)

Figure 9 Fragility Curves of Maximum Inter-story Drift Ratio of 6-Story Structures with Intensity 8: (a) Design Group 1 of Site Soil Class II, (b) Design Group 1 of Site Soil Class IV, and (c) Design Group 3 of Site Soil Class II

5.3 Verification of Seismic Performance Objectives

Based on the fragility curves derived above, the average probability of exceeding each damage level at each specified earthquake design level is obtained to verify the seismic performance objectives listed in Table 1. The results are shown in Tables 2 and 3. In general the exceeding probability of maximum inter-story drift ratio is a little larger than that of global damage index. All the exceeding probabilities are less than 10%. The multiple seismic performance objectives could be realized with high reliability for the buildings structures designed in line with the current Chinese seismic design code.

Table 2 Average Exceeding Probability of Global Damage Index (unit: %)

Design earthquake level	Fully operational	Operational	Repairable	Collapse prevention
Frequent earthquake	5.17	0	0	0
Occasional earthquake	90.17	4.88	0.50	0.04
Rare earthquake	97.78	28.51	4.63	0.26
Extremely rare earthquake	99.94	83.98	37.73	3.84

Table 3 Average Exceeding Probability of Maximum Inter-story Drift Ratio (unit: %)

Design earthquake level	Fully operational	Operational	Repairable	Collapse prevention
Frequent earthquake	8.46	0.01	0	0
Occasional earthquake	84.86	9.42	1.21	0.01
Rare earthquake	94.72	33.47	7.19	0.15
Extremely rare earthquake	99.51	79.60	38.87	5.55

6. CONCLUSIONS

The seismic fragility relationships of RC frame building structures designed in accordance with current Chinese seismic design code are derived from the results of a large number of nonlinear time history analysis, which take the uncertainty of structural performance and earthquake ground motions into account. The main variables of design parameter of frame structure include site soil type, number of stories, and seismic fortification intensity. Fragility curves are obtained for four damage levels, i.e. fully operational, operational, repairable, and collapse prevention, using global seismic damage index and maximum inter-story drift ratio as damage identifiers. The reliability of multiple seismic performance objectives predefined for ordinary buildings are checked in terms of exceeding probability. The results indicate that the performance objectives of the structures designed according to Chinese seismic design code could be implemented appropriately.

Acknowledgements:

The authors acknowledge the support from National Natural Science Foundation of China under grant No. 51021140006 and 51078272, and Key Project of Chinese National Program for Fundamental Research and Development under grant No. 2007CB714202.

References:

Filippou F.C., Popov E.P., and Bertero V.V. (1983), "Effects of Bond Deterioration on Hysteretic Behavior of Reinforced Concrete Joints," EERC Report 83-19, Earthquake Engineering Research Center, Berkeley.

Ji J., Elnashai A.S., and Kuchma D.A. (2009), "Seismic Fragility Relationships of Reinforced Concrete High-rise Buildings," *The Structural Design of Tall and Special Buildings*, **18**(3), 259-277.

Mckay M.D., Beckman R.J., and Conover W.J. (1979), "Comparison of 3 Methods for Selecting Values of Input Variables in the Analysis of Output from a Computer Code," *Technometrics*, **21**(2), 239-245.

Mosalam K., Ayala G., White R., and Roth C. (1997), "Seismic Fragility of LRC Frames with and without Masonry Infill Walls," *Journal of Earthquake Engineering*, **1**(4), 693-720.

Orsini G. (1999), "Model for Buildings' Vulnerability Assessment Using the Parameterless Scale of Seismic Intensity (PSI)," *Earthquake Spectra*, **15**(3), 463-483.

Park Y.J. and Ang A.H.S. (1985), "Mechanistic Seismic Damage Model for Reinforced Concrete," *Journal of Structural Engineering*, **111**(4), 722-739.

Rossetto T. and Elnashai A. (2003), "Derivation of Vulnerability Functions for European-type RC Structures Based on Observational Data," *Engineering Structures*, **25**(10), 1241-1263.

Rossetto T. and Elnashai A. (2005), "A New Analytical Procedure for the Derivation of Displacement-based Vulnerability Curves for Populations of RC Structures," *Engineering Structures*, **27**(3), 397-409.

Scott B.D., Park R., Priestley M.J.N. (1982), "Stress-strain Behavior of Concrete Confined by Overlapping Hoops at Low and High-strain Rates," *Journal of the American Concrete Institute*, **79**(1), 13-27.

Seyedi D.M., Gehl P., Douglas J. et al. (2010), "Development of Seismic Fragility Surfaces for Reinforced Concrete Buildings by Means of Nonlinear Time-history Analysis," *Earthquake Engineering and Structural Dynamics*, **39**(1), 91-108.

Sucuoglu H., Yucemen S., Gezer A., and Erberik A. (1998), "Statistical Evaluation of the Damage Potential of Earthquake Ground Motions," *Structural Safety*, **20**(4), 357-378.

8CUEE CONFERENCE PROCEEDINGS
8th International Conference on Urban Earthquake Engineering
March 7-8, 2011, Tokyo Institute of Technology, Tokyo, Japan

STUDY ON INFLUENCES OF CONSTRUCTION JOINTS AND MULTI-LAYERED LONGITUDINAL BARS ON RESTORING FORCE CHARACTERISTICS IN R/C CANTILEVER BEAMS

Koshiro Nishimura

Assistant Professor, Dept. of Architecture and Building Engineering, Tokyo Institute of Technology, Japan
nishimura.k.ac@m.titech.ac.jp

Abstract: It is important to estimate stiffness of R/C beams accurate enough. However, studies on influence of multi-layered longitudinal bars and construction joints are limited. It is necessary to make clear those influences in view of the development in the design methods in these days. In this study, the influences of the construction joints and multi-layered longitudinal bars upon flexural strength, stiffness, cracks and damages were examine. R/C cantilever specimens were subjected to cyclic lateral loads. Parameters in this experiment were arrangement of longitudinal bars, place of the construction joints, and condition of joint surfaces. As results, the construction joint degraded initial cracking strengths, but there were no remarkable difference in yield strength and stiffness between with and without the joints. And then, stiffness up to flexural yielding was considered based on the test results.

1. INTRODUCTION

It is important to estimate stiffness of R/C beams accurate enough. However, studies on influence of multi-layered longitudinal bars and construction joints are limited. Moreover, strengths and stiffness in R/C members are often calculated as there are no construction joints in seismic design. It is necessary to make clear those influences in view of the development in the design methods in these days.

In this study, the influences of the construction joints and multi-layered longitudinal bars upon flexural strength, stiffness, cracks and damages were examine. R/C cantilever specimens were subjected to cyclic lateral loads. Parameters in this experiment were arrangement of longitudinal bars, place of the construction joints, and condition of joint surfaces.

2. EXPERIMENTAL PROGRAM

2.1 Specimens

Eight cantilever beam specimens were prepared for the tests. Three of them had construction joints on beam sections, which had four D10 of longitudinal bars in single layer on each top and bottom side. The other five specimens had no construction joints. Parameters for those five specimens were diameter, which were D6 and D10, respectively, and numbers of layer for longitudinal bars, which were single layer, double layer, and single with center layers. Figure 1 shows detail of specimens. The longitudinal bars were welded on steel anchor plates at the top and bottom. Table 1 and Table 2 show the parameters of specimens and material properties for concrete, and properties for deformed bar, respectively. Deformed bars D4 were used for transverse bars, which the beams were designed not to fail in shear. And Figure 2 shows condition for construction joints. The construction joint in B-D10-4, named normal joint, were roughen by wire brush next day to concrete placing in order to remove laitance on the surface. The smooth joints were formed by lumber board.

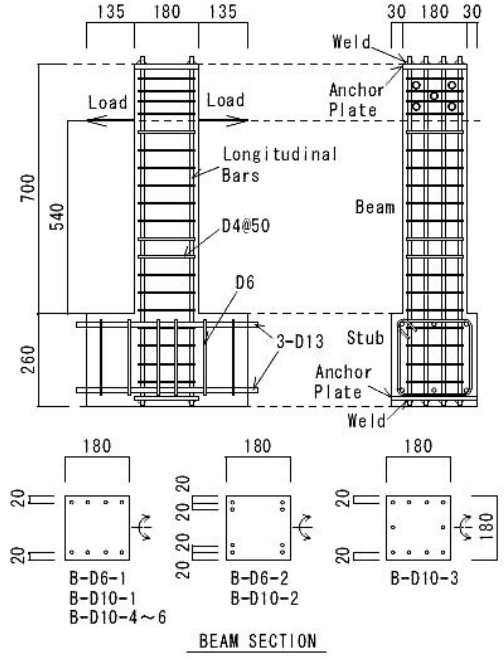


Figure 1 Details of Specimens

Table 1 List of Specimens and Material Properties for Concrete

Name of Specimens	Longitudinal Bars (p_g: total area of bars/section area)	Construction Joint	Concrete		
			Compressive Strength [N/mm^2]	Splitting Tensile Strength [N/mm^2]	1/3 Secant Modulus [N/mm^2]
B-D6-1	4-D6, 4-D6: (0.78 %)	no joint	39	3.0	26 x 10^3
B-D6-2	4-D6, 4-D6: double-layer: (0.78 %)				
B-D10-1	4-D10, 4-D10: (1.8 %)		36	3.3	27 x 10^3
B-D10-2	4-D10, 4-D10: double-layer: (1.8 %)		39	3.0	26 x 10^3
B-D10-3	4-D10, 2-D10, 4-D10: (2.2 %)		41	3.3	29 x 10^3
B-D10-4	4-D10, 4-D10: (1.8 %)	normal joint at the end	36 (41 in stub)	3.3 (3.3 in stub)	27 x 10^3 (29 x 10^3 in stub)
B-D10-5		smooth joint at the end			
B-D10-6		smooth joint at offset section			

Table 2 Material Properties for Deformed Bars

Name of Deformed Bar	D4	D6	D10
Nominal Diameter [mm]	4	6	10
Nominal Section Area [mm^2]	14.05	31.67	71.33
Yield Strength [N/mm^2]	359*	448	351
Tensile Strength [N/mm^2]	533	617	497
Yong's Modulus [kN/mm^2]	184	204	190

*: 0.2% offset method

2.2 Loading Setup and Measurement System

The cantilever beam specimens were subjected to cyclic loading as shown in Figure 3. Two hydraulic jacks attached to the specimen applied only tension load in this test. Steel plates were attached on the top of specimens in order to make bending moment distribution linear in shear span of 540 mm. The Figure 3 also shows measurement setup that lateral displacements and rotation on top and bottom of the beams were measured. Deformations in this study were defined as shown in a right figure of Figure 3. A rotation of beam, R_X, are given by dividing δ_X by initial shear span of 540 mm, and a rotation θ_X are given by subtracting rotation on bottom from that on top those were measured as shown in the left figure of Figure 3.

3. TEST RESULTS AND CONSIDERATION

3.1 Outline of Test Results

Figure 4 shows a test result of specimen B-D10-1. As shown in this figure, the beam yielded in flexural. Axial deformation grew tensile side after yielding and was almost constant under unloading. Therefore the axial deformation accumulated to tensile side. As Shown in the P_X-R_X curve, good loops were observed because longitudinal bars contributed to energy dissipation. Those were caused by no restraint in axial direction and easier bond condition than anti- symmetric bending or hooked anchorage of longitudinal bars at the end. These tendencies were observed in all the specimens in this study.

3.2 Influence of Multi-Layered Longitudinal Bars

In Figure 5, the test result of beams with double layered longitudinal were compared with that of single layered one, where left one shows results for D6 of longitudinal bars and right one shows results for D10. Three tendencies were observed in this figure; double layered one had almost the same yield strength as single layered one in initial loading direction, double layered one had lower yield strength than single layered one in the opposite direction, and

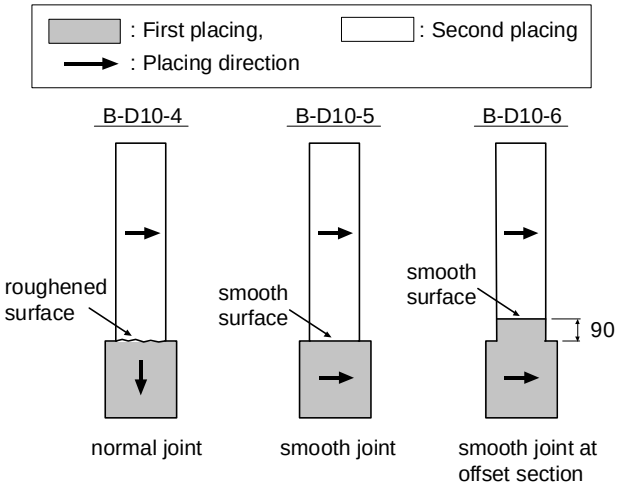


Figure 2 Construction Joints

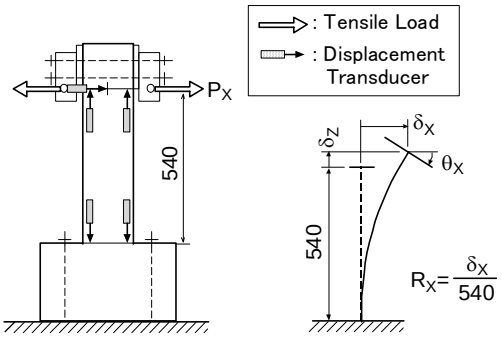


Figure 3 Loading Setup and Deformations

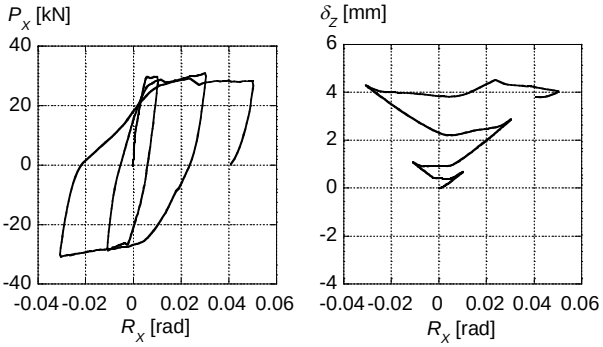


Figure 4 Test Result of Specimen B-D10-1

displacement for yielding in double layered one was larger than that in single layered one. The second tendency must be due to stress in longitudinal bars in interior layer of compressive side in the double layered beam, which was tensile stress under initial loading and compressive stress under the opposite side loading. It was considered that the third tendency depended on yielding in longitudinal bars in interior layer of tensile side in the double layered beams. In this test, rigidities must be obviously degraded after yielding in the longitudinal bars in interior layer of tensile side. Figure 6 shows photos of the specimens after the cyclic loading test. As shown in this figure, cracks in the double layered beam were more dispersed than those in single layered beam.

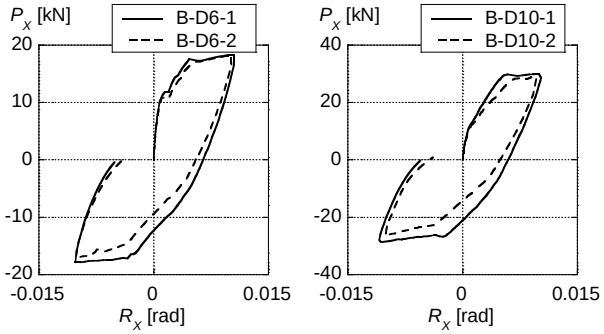
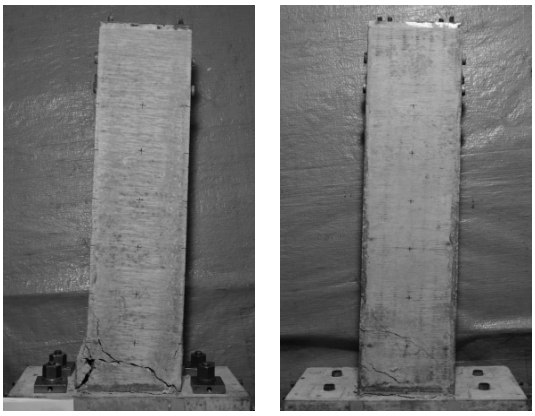


Figure 5 Comparison between Beams with Single and Double Layered longitudinal bars

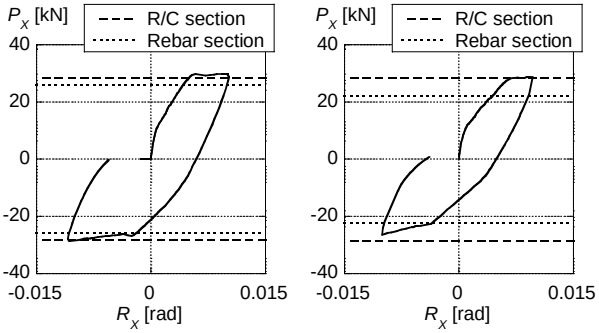


B-D10-1 B-D10-2

Figure 6 Photos of specimens after the tests

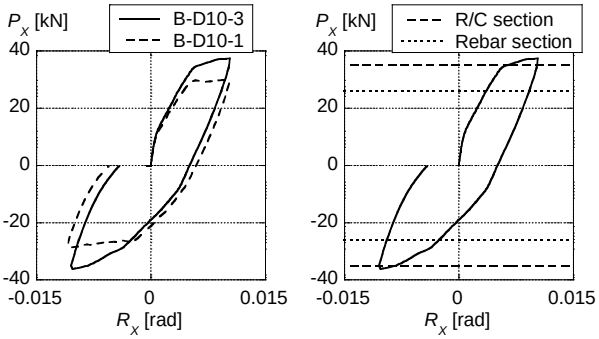
Two Calculations for yield strengths are shown in Figure 7 those are R/C section and longitudinal bars section without concrete. The yield bending moment were calculated with assumptions of rigid-perfectly plastic body in materials, which yield strengths of concrete and deformed bars were compressive strength in Table 1 and yield strength in Table 2, respectively. As shown in Figure 7, the yield strength under initial loading showed good agreement with R/C section strength of calculation, however, in the opposite direction, the strength of test results agreed with longitudinal bars section strength. This is because, as mentioned above, concrete resisted very low stress due to axial tensile deformation.

Figure 8 shows strength and deformation for yielding in B-D10-3. As shown in a left figure, longitudinal bars at the center of beam depth were contributed to yield strength and yield deformation was almost the same as B-D10-1. The yield deformation seemed to depend on yielding in longitudinal bars of exterior layer of tensile side. As shown in a right figure of Figure 8, the yield strength under initial loading showed good agreement with calculated R/C section strength, however there was no clear yielding up to -0.01 rad in the opposite direction.



B-D10-1 B-D10-2

Figure 7 Yield Strength for B-D10-1 and B-D10-2



B-D10-3

Figure 8 Strength and Deformation for Yielding in B-D10-3

3.3 Influence of Construction Joints

A left figure in Figure 9 shows difference due to condition in construction joist. B-D10-4, B-D10-5, and B-D10-6 had normal joint at the end of beam, smooth joint at the end of beam and at the section of 90 mm apart from the end, respectively. Figure 10 shows photos of the specimens after the tests those had normal joint and smooth joint apart from the end of beam, respectively. As shown in a left figure in Figure 9, B-D10-4 and B-D10-5 had almost the same curves. B-D10-6, which had offset jointed section, had a little larger yield strength than the other two specimens in initial loading direction, and obvious lower strength in the opposite side loading because of damages at the offset construction joint, as shown in Figure 10.

In a right figure of Figure 9, the test result of B-D10-4, which had normal joint, is compared with that of B-D10-1 that had no construction joint. These two curves were almost the same. In the detail, B-D10-1 showed a little larger yield strength than B-D10-4 that could be seen in comparison between B-D-10-4 and B-D10-6. It can be said from these

comparison that the specimens without joint at the end of beam showed larger yield strength than the specimens with construction joint at the end of beam. It can be considered this difference is due to tensile stress in concrete at the end section of the beam. As shown in Figure 11, it was observed that bending crack in the beam without joint grew toward inside of stub as against bending crack with joint grew along the joint. Therefore, tensile resistance in concrete at the end of beam without the joint must be larger than that with the joint.

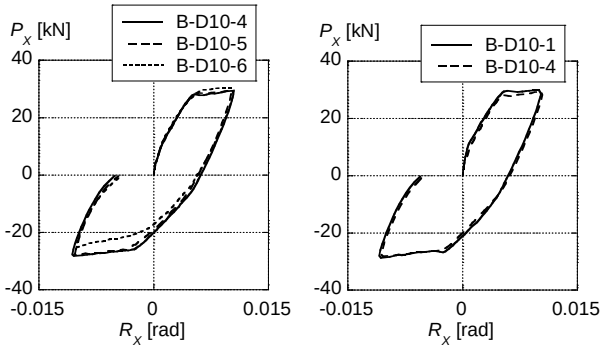
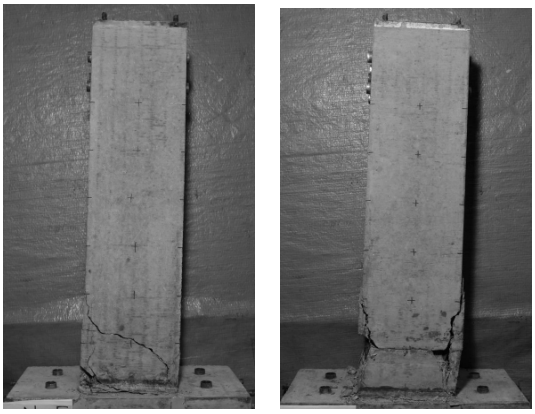
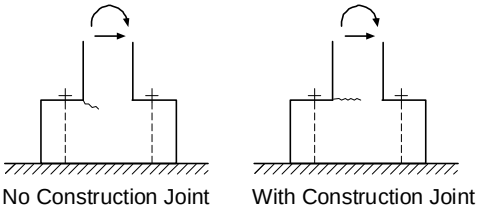


Figure 9 Difference due to Condition in Construction Joint



B-D10-4 B-D10-6

Figure 10 Photos of specimens after the tests



No Construction Joint With Construction Joint

Figure 11 Cracking at the End of Beam

Figure 12 shows initial stiffness in detail. In this figure, initial P_X-R_X curves and R_X-θ_X curves of test results were compared with calculation. In calculation, contribution of longitudinal bars and shear deformation of concrete were considered, where poisson's ratio and coefficient concerning relationship between mean shear stress and shear deformation for concrete were assumed as 0.2 and 1.2, respectively. A clear span of beam is assumed as 540 mm, as shown in Figure 1. In Figure 12, solid lines are results for specimens without construction joint, and broken lines are for specimens with construction joints. Those curves were normalized by dividing test results by bending strength and deformation at initial cracking, which the bending strength for initial cracking was calculated as following equation (Architectural Institute of Japan, 1999).

$$M_c = 0.56\sqrt{f_C}Z_e + ND/6 \quad \text{(N mm)} \quad (1)$$

In above equation, f_C, Z_e, N, and D are compressive concrete strength, section modulus including contribution of longitudinal bars, axial load, and depth of the member, respectively. As shown in a left figure of Figure 12, loads in the specimens with construction joints were lower than that without joint. On the other hand, as shown in a right figure, normalized R_X-θ_X curves were almost the same. These means influence of construction joints could be seen in tensile resistance of concrete at the end of beams and the other effects like a deformation could be neglected in this test.

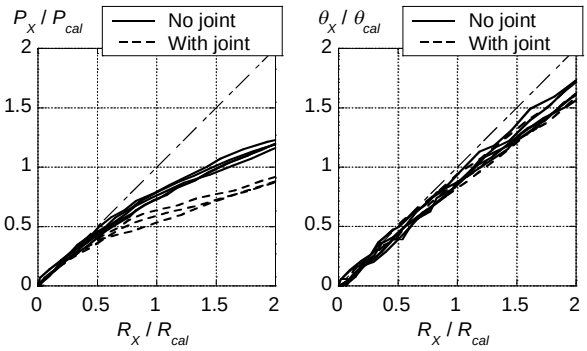


Figure 12 Initial Stiffness and Initial Rotation

3.4 Comparison with Tri-Linear Model

The restoring force characteristics of R/C members are often modeled in tri-linear curves, which two points of changing rigidities are initial cracking and yielding against bending, and third rigidity is very small or zero. Here, the test results are compared with the calculated tri-linear model.

The calculation for initial stiffness, bending moment of initial cracking, and yield strength were mentioned above. Therefore, the tri-linear model was completed if yield deformation can be estimated. In AIJ standard (Architectural Institute of Japan, 1999), the following equation is shown as degrading ratio of yield point secant stiffness, α_y.

$$\alpha_y = \left(0.043 + 1.64np_t + 0.043a/D + 0.33\eta_0\right)\left(\frac{d}{D}\right)^2 \quad (2)$$

α_y is based on more than 200 experimental data, which parameters were with in p_t=0.4 to 2.8 %, a/D=2.0 to 5.0, and η_0=0 to 0.55. The yield point secant stiffness is given by multiplying α_y and initial bending stiffness of concrete section with no longitudinal bars and no shear deformation. In Eq.(2), n is a ratio for young's modulus of deformed bar to concrete; p_t is a ratio for area of tensile longitudinal bar to total section; a is a shear span; η_0 is a ratio for axial force to maximum force of concrete section; and d is effectiveness depth of member concerning tensile longitudinal bars. α_y is basically used to R/C section with single layered

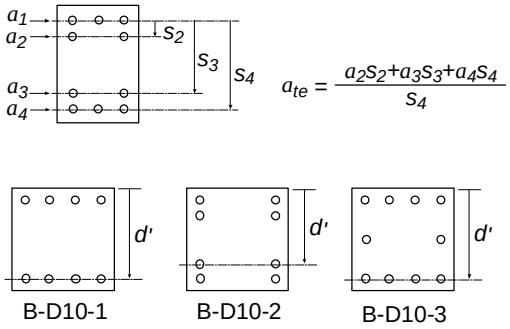


Figure 13 Equivalent Coefficient a_t and d in Eq.(2)

longitudinal bars, therefore some kind of modeling is needed for adopting to R/C section with multi-layered longitudinal bars. The multi-layered longitudinal bars were usually converted into single layer, but this method didn't adapt to the test result of B-D10-3 due to longitudinal bars at the center of depth. In this paper, p_{te} is assumed as the following equation, and is substituted for p_t in Eq.(2).

$$p_{te} = \frac{a_{te}}{A} = \left(\sum_{i}^{n} a_i s_i \right) \Big/ \left(A s_n \right) \tag{3}$$

In above equation, A is total section area, a_i is a sum of section areas of longitudinal bars in the same layer, s_i is a distance from an exterior layer in compressive side, and a subscript i is a number of order for the layer from the exterior layer so that subscript n means an exterior layer in tensile side. An example for a_{te} is shown in an upper figure of Figure 13. In this example, a_{te} is the same as sum of a_3 and a_4 if $a_2 = a_3$ and $s_2 + s_3 = s_4$. Regarding d in Eq.(2), d' shown in a lower figures of Figure 13 were adopted those were decided as a distance from compressive edge to a layer of longitudinal bars that was suggested to yield at the yield point of R/C beam. In the other word, a person who calculates α_y needs to judge d'. Figure 13 shows comparison between the test results and the tri-linear model. As shown in these figures, tri-linear models show good agreements with the test results. It is noticed that the methods of calculating yield deformation shown here need to examine with more experimental data including data of beams and columns with high strength material.

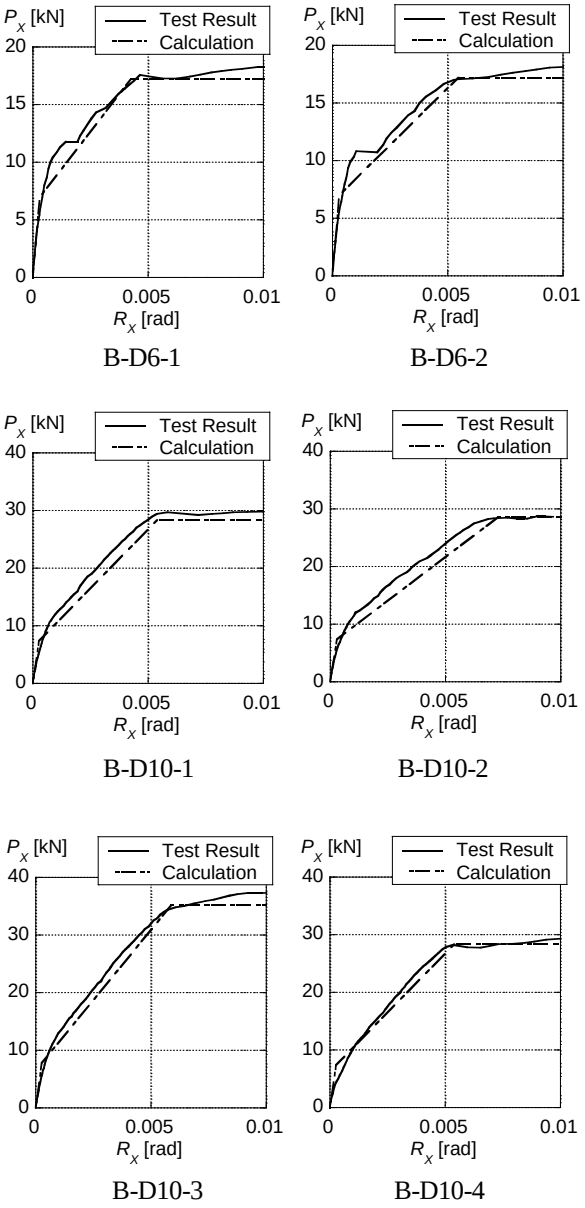


Figure 14 Comparison with Tri-Linear Models

4. CONCLUSIONS

In this study, eight cantilever beam specimens were prepared for cyclic loading tests, and the influences of the construction joints and multi-layered longitudinal bars upon flexural strength, stiffness, cracks and damages were examine. As results, the following conclusions could be found.

1. Though the construction joints at the end of the beam degraded initial stiffness, cracking strength, and yield strength because of lower resistance against tensile stress in concrete at the joints, there were no significant differences in load- displacement curves between beams with and without the joints.
2. The construction joint apart from the beam end, which is the same distance as a half beam depth, caused obvious loss of strength in cyclic loading.
3. The beams with double layered longitudinal bars showed larger yield deformation, and lower yield strength in the opposite directional loading against first loading, than the beams with single layered longitudinal bars.
4. A Tri-linear model written in AIJ standard (Architectural Institute of Japan, 1999) showed good agreement with the test results.

References:

Architectural Institute of Japan. (2010), "AIJ Standard for Structural Calculation of Reinforced Concrete Structures, revised 2010", Architectural Institute of Japan, (in Japanese).

8CUEE CONFERENCE PROCEEDINGS
8th International Conference on Urban Earthquake Engineering
March 7-8, 2011, Tokyo Institute of Technology, Tokyo, Japan

EXPERIMENTAL STUDY ON BONDING ACTION WITH NEUTRON DIFFRACTION TECHNIQUE:

Koichi Kusunoki[1)], Kenji Kabayama[2)], Tomohisa Mukai[3)], Yuichi Hatanaka[4)], Hiroshi Suzuki[5)], and Akira Tasai[6)]

1) Associate Professor, Dept. of Architecture and Building Science, Yokohama National University, Japan
2) Associate Professor, Dept. of Architecture, Shibaura Institute of Technology, Japan
3) Senior Researcher, International Institute of Seismology and Earthquake Engineering, Building Research Institute, Japan
4) Technical Staff, Dept. of Architecture and Building Science, Yokohama National University, Japan
5) Researcher, Quantum Beam Science Directorate, Japan Atomic Energy Agency, Japan
6) Professor, Dept. of Architecture and Building Science, Yokohama National University, Japan
kusunoki@ynu.ac.jp, kaba@sic.shibaura-it.ac.jp, t_mukai@kenken.go.jp,
hatanaka@ynu.ac.jp, suzuki.hiroshi07@jaea.go.jp, tasai@ynu.ac.jp

Abstract: Bonding action between concrete and rebar plays one of the most important roles for reinforced concrete structure. Investigation on the bonding action is, however, very difficult since strain gauges are usually used to measure the strain distribution of the rebar and they can disturb the bonding action itself. In this research, Neutron diffraction technique was applied to measure the strain distribution on a rebar in a concrete. Normal concrete does not have enough permeability because of hydrogen contained in the concrete. Therefore, concrete was dried absolutely to get high permeability. The pull-out test with the rebar with the diameter of 10mm embedded in the reinforced concrete specimen was conducted and the strain distribution was measured with the neutron diffraction technique. Results showed the accuracy of the measuring system with the Neutron and non-linearity of the bonding action.

1. INTRODUCTION

Bonding action between concrete and rebar plays one of the most important roles for reinforced concrete structure. If the bonding strength is not strong enough or the anchorage length of rebar is not enough, the rebar is pulled out before yielding under tensile stress. Its failure mechanism is called 'bonding failure'. If the bonding failure occurs, the structure cannot keep its unity. Therefore the bonding failure is classified as 'brittle failure'. Investigation on the bonding action is, however, very difficult since strain gauges are usually used to measure the strain distribution of the rebar and they can disturb the bonding action itself.

In this research, neutron diffraction technique, which does not need any sensor to paste on rebar, was applied to measure the strain distribution on a rebar in a concrete. Elastic Strain of rebar embedded in concrete can be measured from outside of the concrete by measuring diffraction angle of neutron. The engineering diffractometer for stress analysis, RESA-1 **(Suzuki et al. 2008)**, in the Japan Research Reactor No. 3 (JRR-3) at the Japan Atomic Energy Agency was utilized for the test. Normal concrete, however, does not have enough permeability because of hydrogen contained in the concrete. Therefore, concrete was dried absolutely to get high permeability. In this paper, a pull-out test was conducted under moment and shear forces with various tensile force levels. The same test with same tensile force levels were also conducted with a specimen of which rebar has strain gauges to measure strain. The comparison of test results from RESA and strain gauges is also discussed.

2. OUTLINE OF NEUTRON DIFFRACTION TECHNIQUE

The engineering diffractometer for stress analysis, RESA-1 is located in the Tokai Research Area of Japan Atomic Energy Agency. The outline of the RESA-1 is shown in Photo 1. Monochromatic neutron beam is obtained from the Japan Research Reactor No.3 (JRR-3), and irradiated to the specimen at the angle of θ. The diffracted neutron is detected by the detector. The diffracted angle becomes slightly different from θ according to the intermolecular distance. The number of neutrons diffracted at each angle is measured by the detector. The relationship between diffracted angle and number of neutrons follows Gaussian distribution as shown in Figure 2 if there is no error contained. The average strain of the specimen at hatched area in Figure 1 is calculated as Equation (1).

$$\varepsilon = -\frac{2\theta - 2\theta_0}{2} \frac{1}{\tan(2\theta_0/2)} \quad (1)$$

Where; θ is diffraction angle at the peak intensity, and θ_0 is the diffraction angle without stress (initial angle).

Since the measured strain, ε, is calculated according to the intermolecular distance, ε is elastic strain. Therefore, stress can be obtained by multiplying Young's modulus to ε.

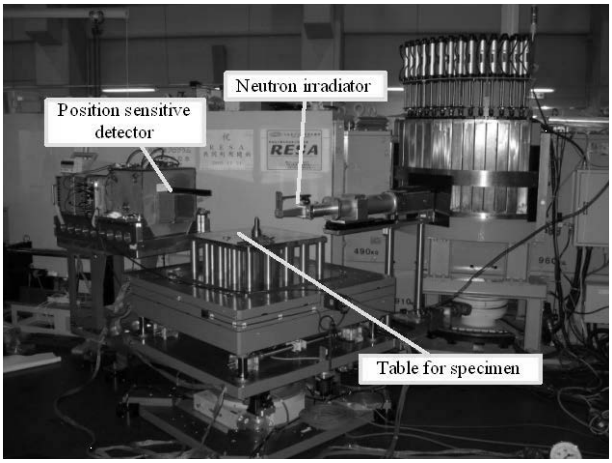


Photo 1 Outline of RESA

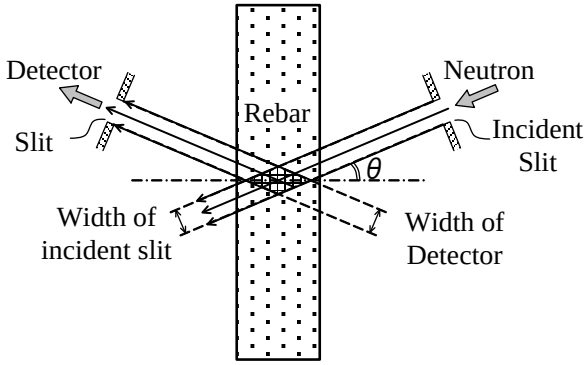


Figure 1 Outline of Measurement

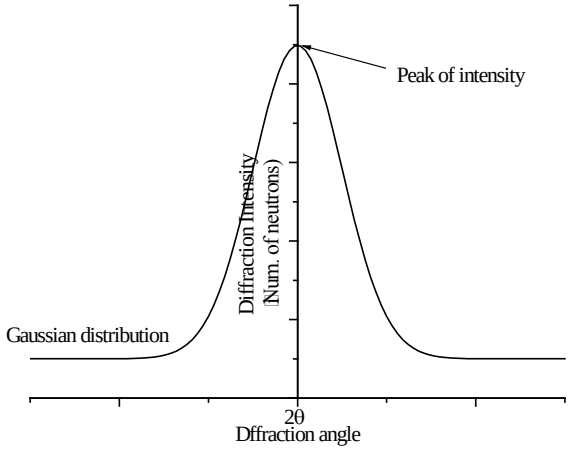


Figure 2 Diffraction Profile

2. OUTLINE OF LOADING SYSTEM

Applied loading system is shown in Figure 3. Tensile force was applied by the center hole jack, which was measured by the load cell. A steel spring was also used to maintain the applied force constant. The shear force and moment distributions in the specimen are shown in Figure 4. The loading system reproduces the shear and moment distributions as beam and column.

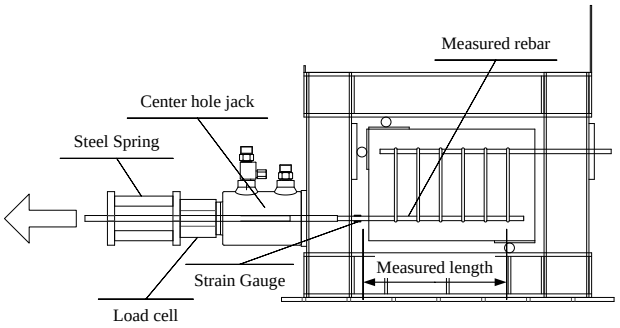


Figure 3 Loading System

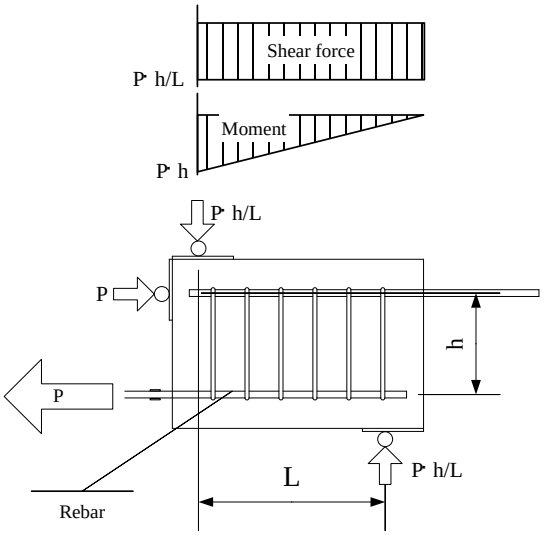


Figure 4 Shear force and moment distribution

2. OUTLINE OF SPECIMEN

2.1 Dimensions of Specimen

Dimensions of the specimen are shown in Figure 5. The rebar measured by RESA-1 is D10, deformed bar with the diameter of 10mm, which is embedded to the concrete with the length of 370mm. Specimen has D6 stirrups with the pitch of 50mm. The embedded length was decided so that the rebar yields at outside of the concrete and bonding failure does not occur. Two strain gauges were pasted to the

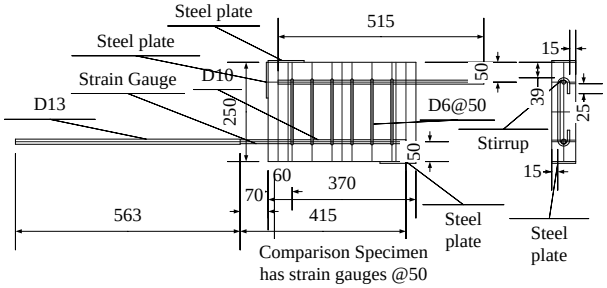


Figure 5 Dimensions of the Specimen

rebar outside of the concrete to measure the strain of the rebar. Two specimens were constructed. One of them had strain gauges inside of the concrete. The location of the gauges were 30mm, 80mm, 135mm, 185mm, 235mm and 285mm from the surface of the specimen as shown in Figure 5.

2.2 Material Properties

Design strength of concrete was 24 N/mm^2. Maximum size of rough aggregates was 20mm. Water-cement ratio was 59.4% and fine aggregate ratio was 47.7%. Material test was conducted at 42 days old. The average compression strength was 33.4N/mm^2 and tensile strength was 2.8N/mm^2. The specimens were moved into an absolute dry oven in Building Research Institute at 16 days old for 2 weeks with the temperature of 105 Celsius. Then the temperature in the oven was cooled down to 10 Celsius in 24 hours. The weight of the specimen reduced from 14306.4g to 13539.9g. From the concrete cylinder test, which was with the specimen in the oven, the compression strength was 26.9N/mm^2 and tensile strength was 2.0N/mm^2 at 31 days old.

Steel bar of D10 was also tested to find the yield strength and Young's modulus. The yield strength was 357N/mm^2 and Young's modulus was 184,826N/mm^2.

3. TEST RESULTS WITH RESA-1

3.1 Loading History

Tensile force was induced to the rebar with the loading system shown in Figure 3. The load levels of 20N/mm^2、145N/mm^2、270N/mm^2、145N/mm^2、270N/mm^2、20N/mm^2 were applied in order.

3.2 Outline of Measurement

The grid strain of Fe atom was measured by RESA-1. The wavelength of neutron beam was 2.0 A, and the diffraction angle 2θ was about 58.5 deg. The dimensions of the neutron beam was 5mm in width and 10mm in height. The neutron beam path is shown in Figure 6. The average strain in the hatched region in Figure 6 is measured by RESA-1.

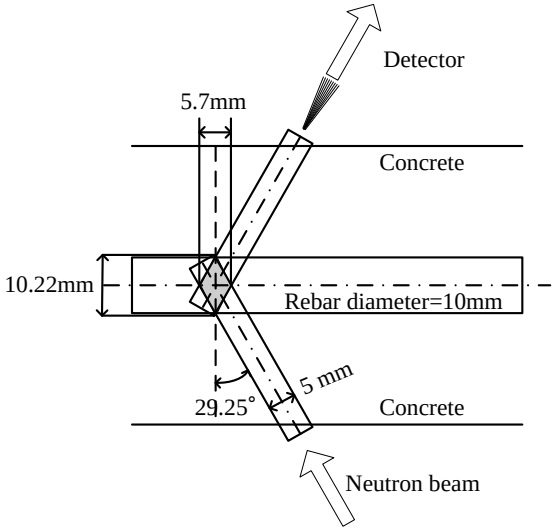


Figure 6 Neutron Beam Path

From the preliminary measurement, the neutron beam was irradiated for 30 minutes at each point to get better diffraction profile. Every 5mm to 10mm point was measured. The measured points were limited due to the time limitation of the RESA-1 machine time (96 hours in total).

3.3 Test Results

Figure 7 shows the Gaussian distribution approximation error at each force level along with the rebar. The errors at most of all points were less than 0.003, but the error becomes larger at every 50mm. It shows the location of the stirrups.

The strain at each point was calculated with Equation (1) from the measured diffraction angle profiles. The diffraction angle measured at 300mm from the surface at the second 22 N/mm^2 tensile force was applied as $2\theta_0$. The strain along with the rebar at each force level is shown in Figure 8. Note that the calculated strain is the absolute elastic strain. The strain distributions also show disturbed at every 50mm as Figure 7.

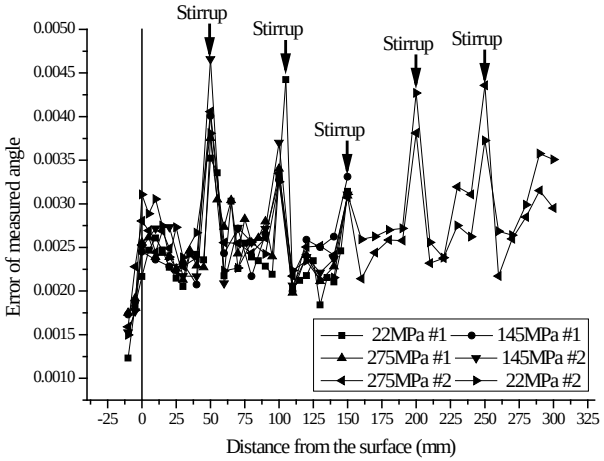


Figure 7 Gaussian Distribution Approximation Error

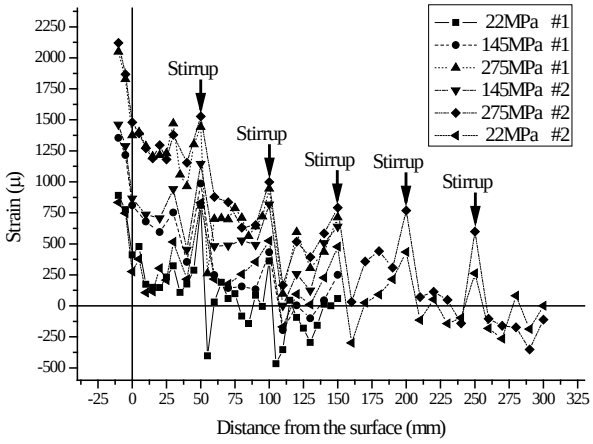


Figure 8 Strain Distributions Measured by RESA-1

The stress distributions along with the rebar at 275N/mm^2 tensile force are shown in Figure 9. The stress at

each point is calculated by multiplying the strain shown in Figure 8 by the Young's modulus of 2.24×10^5 N/mm^2.

The stress distributions at the first and second loadings were almost the same and the effect of unloading was not observed.

The stress distributions along with the rebar at 145 N/mm^2 and 22 N/mm^2 tensile forces are also shown in Figure 10 and Figure 11, respectively. Different from Figure 9, the slope of the stress distribution at the second loading is gentler than the first time. At the second loading of 145 N/mm^2 loading, the specimen suffered 275 N/mm^2 loading once, and the second time of 22 N/mm2 loadings suffered 275 N/mm^2 − 145N/mm^2 − 275N/mm^2 loadings. It can be said that the nonlinearity due to higher load causes the change of the slope.

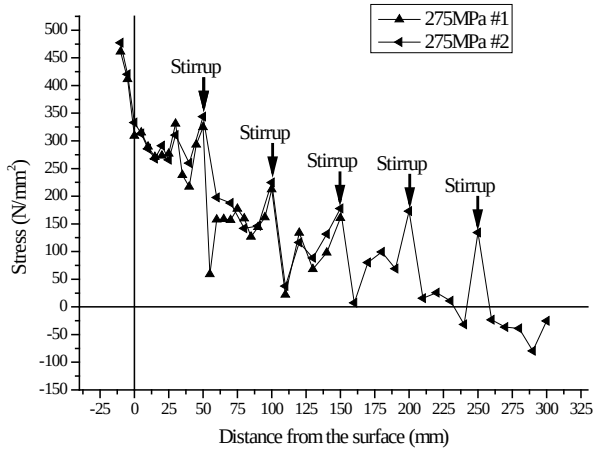


Figure 9 Stress Distribution Measured by RESA-1 (275N/mm^2)

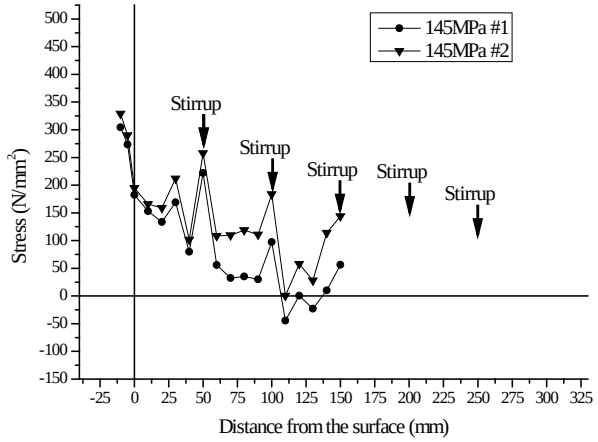


Figure 10 Stress Distribution Measured by RESA-1 (145N/mm^2)

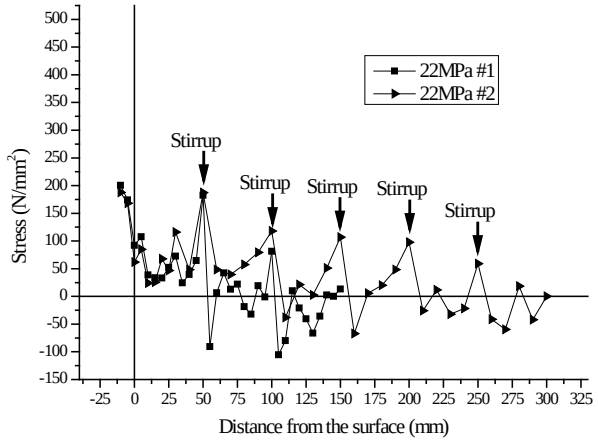


Figure 11 Stress Distribution Measured by RESA-1 (22N/mm^2)

In Figure 9 to 10, the stresses outside of the concrete (shown as the "minus" distance in the figures) must be the same as applied force, but they are not. One of the reason is that the stress along with the rebar was calculated based on the $2\theta_0$ of the diffraction angle measured at 300mm from the surface at the second 22N/mm^2. The result shows that $2\theta_0$ at each point can be different. In order to neglect the effect of $2\theta_0$, the relative stress distributions at each force level to the distribution at the second time of 22 N/mm^2 are calculated and shown in Figure 12. The stress distributions becomes clear. It can be said that the stress distribution at the second time of 145 N/mm^2 is almost constant until the stress distribution curve reaches that of 275 N/mm^2.

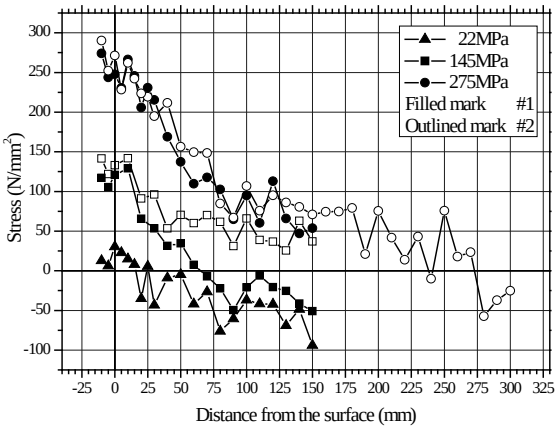


Figure 12 Stress Distribution Measured by RESA-1 (Relative to the Distribution at 22N/mm^2 #2)

3. TEST RESULTS WITH STRAIN GAUGES

The specimen with strain gauges was loaded with the loading history shown in Figure 13, which is the same as the loading history for RESA-1. The initial values of strain gauges were measured just before starting the loading. Therefore, the measured strain does not contain initial strain due to shrinkage. The cables of strain gauges were arranged perpendicular to the rebar to reduce the effect of the cable on the bonding action.

The relationships between the applied tensile force and strains measured by strain gauges are shown in Figure 14. The stress-strain relationship at the outside of the concrete is linear, since the applied force is less than the yield strength of the rebar. On the other hand, the stress-strain relationships at the inside of the concrete show nonlinearity. Unloading stiffness is, however, as

high as the initial stiffness.

Figure 15 shows the measured stress distributions at the tensile force levels that are close to the levels applied for the RESA-1 specimen. The stress distributions at 275 N/mm^2 at the first and second loadings are almost same. On the other hand, the stress distribution at the second 145 N/mm^2 level showed constant stress distribution from the surface of the specimen to the point where the stress meets the slope of 275 N/mm^2, though the stress distribution at the first 145 N/mm^2 level showed constant descending. The nonlinearity of the bonding action shown in Figure 14 can be one of the reasons. The internal tensile stress was measured at the second 22 N/mm^2 loading.

4. COMPARISON OF THE TEST RESULTS

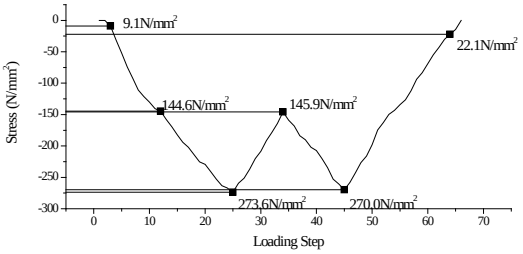


Figure 13 Loading History

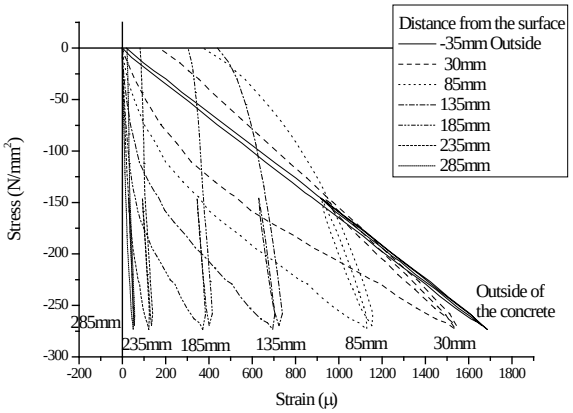


Figure 14 Relationships between Applied Tensile Force and Measured Strains by Strain Gauge

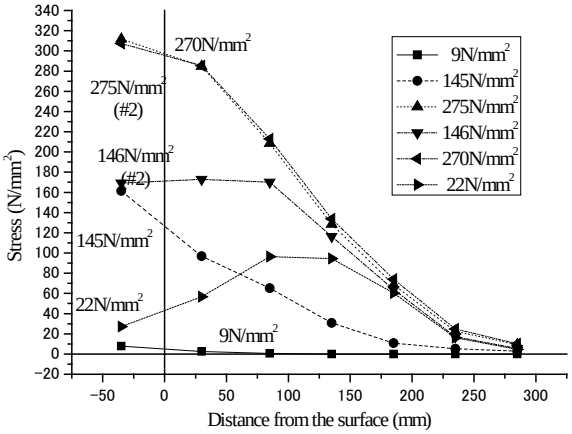


Figure 15 Stress Distribution Measured by Strain Gauges

Since strain measured by strain gauges cannot consider the initial strain due to shrinkage, and the same value of the diffraction angle is used for $2\theta_0$ for the whole rebar, direct comparison of the stress distributions measured by RESA-1 and strain gauges is not appropriate. Therefore, relative stress distributions to the final measurement at the second 22 N/mm^2 level are compared. The result is shown in Figure 16. The tendency of the stress distribution measured by RESA-1 and strain gauges coincide well each other.

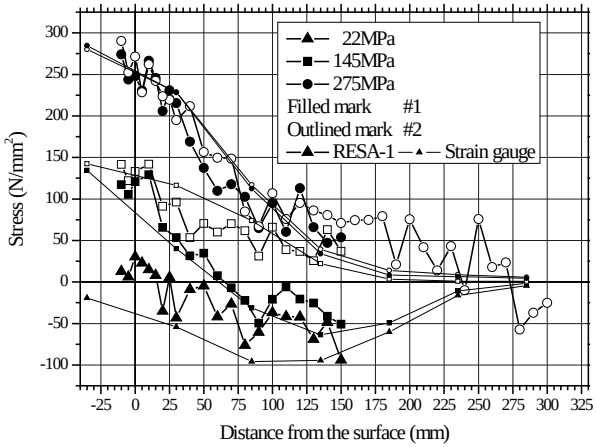


Figure 16 Comparison of Stress Distributions Measured by RESA-1 and Strain Gauges (Relative to the Distribution at 22N/mm^2 #2)

3. CONCLUSIONS

Results obtained from the research can be summarized as follows;

1. Neutron beam can go through dried concrete.
2. Stress distribution of rebar can be measured from outside of the concrete with neutron diffraction technique.
3. The stress distribution measured by carefully arranged strain gauges agreed well with the distribution measured by RESA-1
4. Bonding action shows nonlinearity if it experiences higher loading.

Acknowledgements:

This work was performed under the Common-Use Facility Program of JAEA

References:

Suzuki H.; Machiya S.; Saito T.; Moriai A; Morii Y., Abstract of MECASENS-IV, 2008.

Koichi KUSUNOKI, et Al., "Experimental study on the anchorage length of rebar measured with the neutron deflection technique", annual meeting of Japan Concrete Institute, CD-ROM, 2008.

Koichi KUSUNOKI, et Al., "Experimental study on the anchorage length of rebar with neutralized concrete measured with the neutron deflection technique", annual meeting of Japan Concrete Institute, CD-ROM, 2009.

8CUEE CONFERENCE PROCEEDINGS
8th International Conference on Urban Earthquake Engineering
March 7-8, 2011, Tokyo Institute of Technology, Tokyo, Japan

VIBRATION CHARACTERISTICS OF TRADITIONAL ADOBE-QUINCHA BUILDINGS LOCATED AT LIMA HISTORIC CENTRE

C. Cuadra[1)], C. Zavala[2)], A. Abe[3)], T. Saito[4)], and S. Sugano[5)]

1) Associate Professor, Dept. of Architecture and Environment Systems, Akita Prefectural University, Japan
2) Professor, Faculty of Civil Engineering, National University of Engineering, Lima, Peru
3) Director, Tokyo Soil Research Co. Ltd, Japan
4) Chief Research Engineer, IISEE, Building Research Institute, Japan
5) Guest Researcher and Lecturer, Building Research Institute, Japan
carlos@akita-pu.ac.jp, czavala@amauta.rcp.net.pe

Abstract: The historic centre of Lima city was declared as World Heritage site in the year 1988 for its originality and high concentration of historic monuments constructed in the time of the Colonial period and at the beginning of the Republican era. The architecture of the buildings corresponds in general to typical Hispano-American baroque of the 17th and 18th centuries. Together with churches and palaces there are particular buildings constructed of traditional adobe-quincha materials. These buildings consist of a first floor made of adobe or sun-dried bricks and upper floors made of wooden frame or panels which support a mesh of cane to receive a finishing plaster of mud and gypsum. In this paper a preliminary study of the dynamic characteristics of these traditional buildings is presented. Microtremor measurements have been performed in one typical building to obtain its vibration characteristics. Although light weight of the upper stories could signify a better seismic behavior, deterioration and lack of repair and maintenance make critical the vulnerability of these buildings. This study is part of a more general SATREPS project on Enhancement of Earthquake and Tsunami Disaster Mitigation Technology in Peru supported by JST/JICA.

1. INTRODUCTION

The city of Lima, the capital of Peru, was founded by Spanish conquistador Francisco Pizarro on January 18, 1535 and given the name City of the Kings. Lima played a leading role in the history of the New World from 1542, when Carlos V establish the vice royalty of Peru, until the middle of the 18th century. In 1988, UNESCO declared the historic center of Lima a World Heritage Site for its originality and high concentration of historic monuments constructed in the time of Spanish presence and at the beginning of the Republican era. The architecture of the buildings corresponds in general to typical Hispano-American baroque of the 17th and 18th centuries. Since its foundation the city has suffered the action of many earthquakes that have severely affected historical buildings and reconstruction works have been done keeping the originality of the buildings. However due to the age of buildings studies for retrofitting or strengthening are necessary. In this study attention is focused on one type of traditional construction called adobe-quincha. A difference than churches and palaces this type of construction was widely used to construct residences or houses. At present this old big houses in some cases had been converted into slum dwellings. These buildings consist of a first floor made of adobe or sun-dried bricks and upper floors made of wooden frame or panels which support a mesh of cane to receive a finishing plaster of mud and gypsum. This system of wooden frame with cane and plaster is called as quincha. In this paper a preliminary study of the dynamic characteristics of these traditional buildings is presented. Apparently, from experiences of past earthquakes that strike Lima city, a second floor or upper floors made of light material provided better seismic behavior. However since the basic material is earth (earthen constructions) is obvious that appropriate maintenance and conservation task are necessary. Therefore, in this research, a preliminary evaluation of structural condition of these kinds of buildings is presented. As example a building that correspond to an old hotel is presented where ambient vibration measurements were performed to estimate the period of vibration. The building presents some partial collapse of interior walls and serious deterioration of the quincha walls. Although light weight of the upper stories could signify a better seismic behavior, deterioration and lack of repair and maintenance make critical the vulnerability of these buildings.

At present the adobe-quincha system is investigated in Peru as an alternative for low cost housing in towns and rural areas. In those zones buildings are mostly adobe masonry structures and due to the increasing need of housing in populated areas and the low cost of construction, two story adobe dwellings are often built in cities and small

towns in the interior regions where adobe is sometimes the only material available. However, two story adobe masonry structures have shown poor behavior during earthquakes, due, mainly, to the large weight of the walls. One alternative, to these two-story adobe buildings is to employ a lightweight second story. However the main problem became the connection and continuity between the first story made of adobe and the second story made of a lightweight material.

2. THE ADOBE QUINCHA SYSTEM

To explain the characteristics of the adobe quincha system the model employed by Miranda et al. (2000) are used. This model is shown in Figure 1.

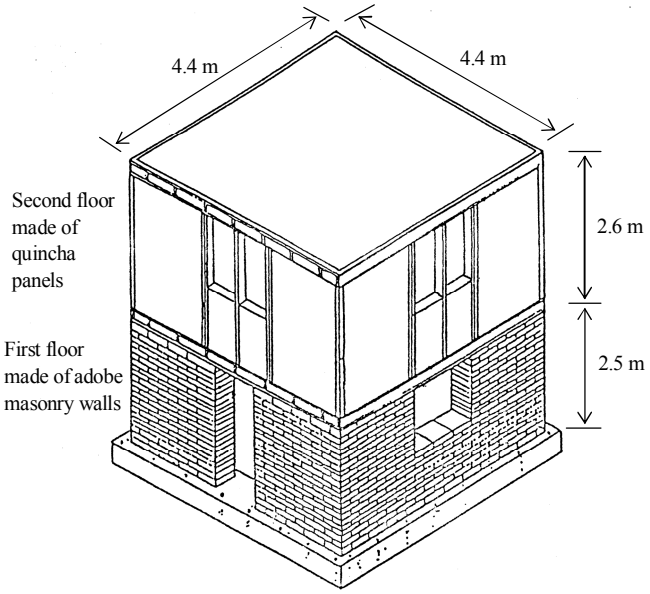


Figure 1 Prototype of the adobe-quincha system

The quincha system of construction consists, basically of wood panels with a kind of bamboo mesh and a plaster made of mud and gypsum. The construction of this full-scale model permitted to solve some constructive problems in relation to the inter-story floor and the connection between the adobe walls and the quincha panels of the second floor. As it is observed, the first floor is made of adobe masonry and the second floor consists of wood panels with finishing plaster of mud and gypsum. The thickness of the walls of the first floor is 40 cm, while the second floor walls are of 10 cm of thickness. In order to connect appropriately the first floor and the second floor, eucalyptus rods of 7.5 cm of diameter were fixed in the foundation to act as columns. These rod columns are embedded in the adobe wall and are located at the corners and distributed along the wall with 1.2 m of spacing. To permit the inclusion of the rod columns in the walls, the adobe masonry units have an especial shape as is shown in Figure 2. The adobe masonry units have a modular dimension of 40 × 40 cm and 10 cm of height with semicircular incisions of 10 cm of diameter in two opposite sides. Also there are adobe units which are half units to permit the appropriate fabric of the masonry. The incisions of the adobe masonry units permit to form the cylindrical space to allocate the eucalyptus rod columns.

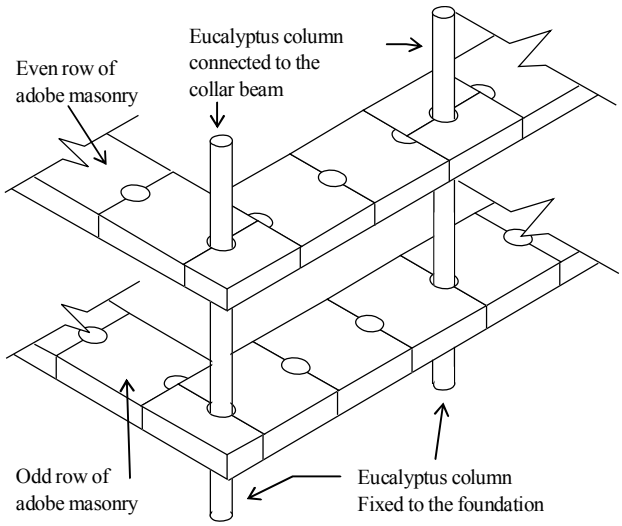


Figure 2 Detail of the adobe masonry and eucalyptus columns

These rod columns permit to fix the collar beam in the upper perimeter of the adobe walls. In this way the adobe masonry wall is confined and the collar beam on the top of the masonry wall permit an efficient connection with the quincha panels as is shown in Figure 3. These rods also contribute to take the tension stress produced by the lateral load during earthquakes. The inter-story floor is supported by the floor beams, which rest on the collar beam, transmitting the load to the walls of the first floor. Also these beams receive the load transmitted by the quincha panels. The quincha panels are fixed to the inter-story floor beams with nailed connections.

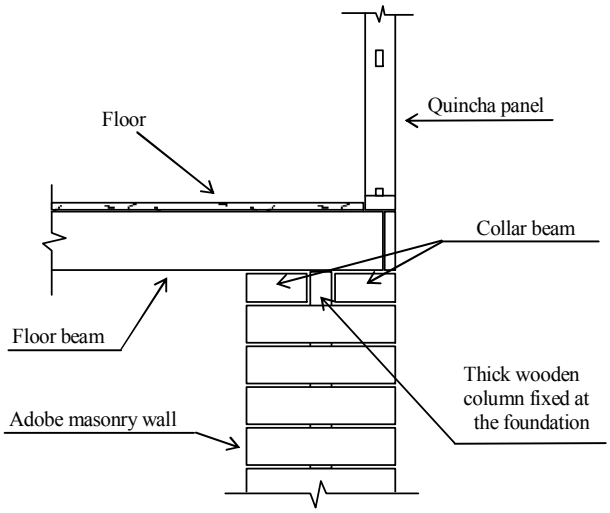


Figure 3 Detail of the connection between adobe wall and quincha panel

In the case of old traditional constructions that are

found in Lima Centre, the dimensions of the walls and inter-story heights are quite large. The adobe walls of the first floor have a thickness that varies from 60 cm. to 100 cm. The height of the first floor reaches sometimes 5 m. or more. The thickness of the upper floors ranges from 20 cm to 50 cm. In general the wooden frames were constructed in-situ and the connection between elements presents different patterns like insertions of beam ends into the columns, nailed joints, joints fixed with ties made of animal fur or leather, etc. The mesh of cane is made of very thin canes called "carrizo", and "caña brava". These canes are fixed to the wooden structure by means of cords or ropes made also of vegetal material. To fix the quincha system to the adobe walls the bottom part of the wooden frame is constraint by means of heavy materials like adobe itself or clay bricks as can be observed in Figure 4.



Figure 4 Typical quincha wall at Lima centre

3. VIBRATION CHARACTERISTICS

3.1 Pseudo dynamic test

A series of pseudo-dynamic tests were performed on prototype described in the previous section to verify the dynamic behavior of this system. The pseudo-dynamic test method uses on-line computers to monitor and control a test specimen closely resemble those that would occur if the test specimen were tested dynamically. Pseudo-dynamic tests combine analytical and experimental techniques. Experimental measurements are made of the restoring forces during the test. These measured forces are used by the computer, together with a set of mathematical equations which, ideally, describe the dynamic responses of the structure, to determine changes in the structural displacements that should be imposed on the specimen as a consequence of the given ground acceleration. The structural restoring forces are experimentally measured rather that computed from a mathematical model, and physical force actuators are used to cause the displacements of the test specimen to equal the computed structural displacements.

Two degree of freedom systems with lumped masses at floor level were adopted to model the specimens. The degrees of freedom were associated to the horizontal displacements at the center of each floor since perfect symmetry was assumed.

In order to obtain initial flexibility matrices of the specimens, a load was applied at one of the floor level while the other floor level was free. The fundamental period computed from these preliminary tests was 0.12 s.

Viscous damping was considered in the form of a matrix proportional to initial stiffness, with 2% of critical damping for the first mode and remained unchanged during the test.

The specimen was tested with a ground acceleration corresponding to the N08E component of the Lima earthquake of October 10, 1966, (IGP66-NE). A portion from 18.25 to 22.25 seconds, which contains the peak acceleration of 293.6 Gal, was selected for this test program. The record was scaled to have maximum ground acceleration of 100, 200, 400 and 600 Gal. The specimen was tested with these earthquake motions. The average duration of each test was 6 hours.

Time history responses for story displacements were obtained for the test sequence. Figure 5 shows the time history responses for displacements of the first and second floor when specimens were tested with the ground acceleration scaled to 400 Gal. Solid line plots the displacement of the first floor while dashed line plots the top displacement of the second floor.

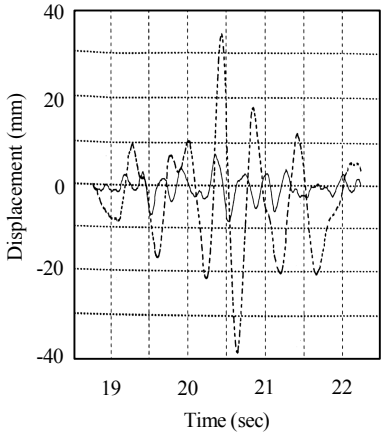


Figure 5 Time history displacement response (IGP-66, 400 Gal)

Figure 6 shows the load-displacement curves obtained for the input motion scaled to 400 Gal. It can be observed that the shape of the hysteretic loop shows large energy dissipation. These pattern were observed in all test performed with 100 Gal, 200 Gal, 400 Gal and 600 Gal respectively.

The failure of the specimen was by shear in the walls of the first floor. The adobe-quincha model resisted the 400 Gal earthquake and even the 600 Gal earthquake. However, very large displacement was observed in the second floor with considerable lost of stiffness. This excessive displacement produced during large earthquakes requires additional research to control and keep the lateral displacement of the second floor below a reasonable value.

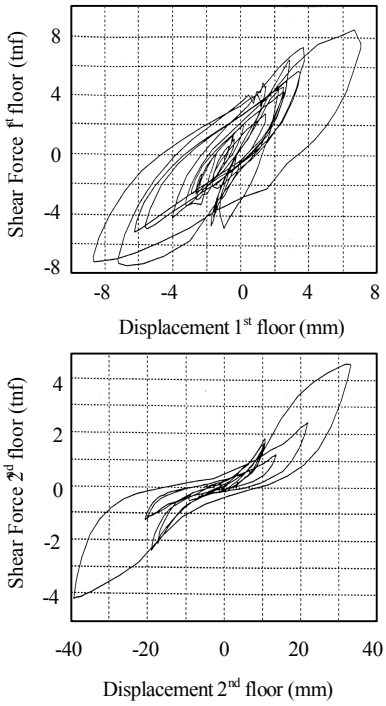


Figure 6 Load-displacement curves (IGP-66, 400 Gal)

The maximum values of shear forces and shear stress that were observed during the tests are presented in Table 1. It can be observed that even for 600 gal earthquake the maximum shear stress in the walls of the first floor was 0.3 kg/cm^2 that is slightly larger than the allowable design shear stress specified in the current Peruvian code on adobe constructions.

Table 1. Maximum shear forces and shear stress

Input Motion	Shear force (tonf)	Shear stress (kg/cm^2)
IGP-66-100 gal	6.13	0.21
IGP-66-200 gal	7.42	0.26
IGP-66-400 gal	8.47	0.29
IGP-66-600 gal	8.75	0.30

Maximum relative displacements that were observed in each run are presented in Table 2. It can be observed that the adobe-quincha model is very flexible, specially the second floor reaching a displacement of 50.56 mm when the model was subjected to the input motion of 600 Gal. of maximum acceleration. This displacement represents a drift angle of 1/50 approximately, which could be excessive for this type of constructions, although the specimen has not collapsed.
These results have permitted to analyze the general behavior of the typical traditional constructions of two-story in Peru, and show that the appropriate use of a lightweight material in the upper story could be an appropriate solution to get a better behavior of these buildings during earthquakes. However the excessive relative displacement of the upper floors could be a problem during earthquake occurrence.

Table 2. Maximum displacements observed during tests

Input Motion	1st floor (mm)	2nd floor (mm)
IGP-66-100 gal	2.32	9.40
IGP-66-200 gal	3.68	20.12
IGP-66-400 gal	8.70	39.17
IGP-66-600 gal	12.54	50.56

3.2 Ambient vibration measurements

As example a building that correspond to an old hotel is presented where ambient vibration measurements were performed to estimate its period of vibration. This building can be observed in Figure 7. The walls of the upper stories (second and third floors) are made of quincha and the first story is made of adobe walls. The building presents some partial collapse of interior walls and serious deterioration of the quincha walls.



Figure 7 Adobe-quincha building at historic centre of Lima

Results of ambient vibration show a predominant frequency of the order of 3.3 Hz. Figure 8 shows the predominant frequencies for NS and EW directions respectively. The NS direction was taken as the direction parallel to the façade and the predominant frequency is 3.37 Hz. In the EW direction that is perpendicular to the façade the predominant frequency is 3.21 Hz. These frequencies represent reasonable values for a building of 12 m of height however more detailed measurement are necessary to detect the local vibration of portions of the building that could indicate the condition of deterioration.

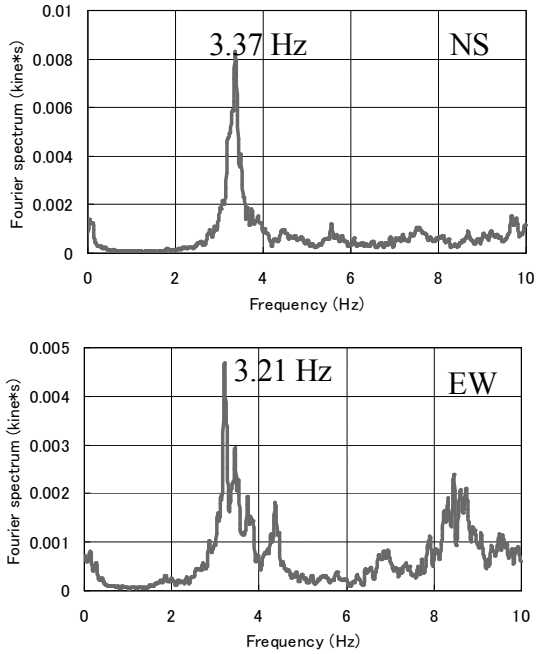


Figure 8 Predominant frequency of selected historical building of centre of Lima

3. CONCLUSIONS

Vibration characteristics of heritage architecture made of traditional adobe-quincha system that is located in Lima city were discussed. Since the heritage architecture is exposed to the action of earthquakes, the understanding of the dynamic properties of these constructions is very important as a first step for future recommendations in relation to conservation, repair and maintenance works. The adobe-quincha heritage architecture is mostly in a state of disrepair and therefore the seismic risk and other kind of risks are particularly acute.

The mixed adobe-quincha system could represents a suitable alternative for two-story traditional constructions in Peru since the lightweight second floor reduces the base shear force during earthquake motions having a better seismic behavior than heavy two-story adobe buildings. However the large displacement that can occur at the upper floor needs more research to be controlled appropriately.

Microtremor measurements at typical adobe-quincha construction have permitted to determine the predominant period of vibration of this building which falls in a reasonable value considering the building height. This value could be used to construct and calibrate analytical models for future analysis on seismic behavior of this kind of buildings.

Acknowledgements:

The authors acknowledge JST/JICA, SATREPS for the support of the research for Enhancement of Earthquake and Tsunami Disaster Mitigation Technology in Peru, under which this surver was conducted. The authors would like to thank also to the National Institute of Culture of Peru (INC) in the person of Architect Maria del Carmen Corrales for permit the measurements in historic building at centre of Lima.

References:

Cardenas, L. & Zavala, C. (2008) "Estudio de Vulnerabilidad Estructural del Hotel Comercio" (Study on Structural Vulnerability of Hotel Comercio), CISMID-UNI Report (in Spanish).

Cuadra, C., Sato, Y., Tokeshi, J. C., Kanno, H., Ogawa, J., Karkee, M. B. & Rojas, J. (2005) "Evaluation of the dynamic characteristics of typical Inca heritage structures in Machupicchu". *Ninth International Conference on Structural Studies, Repairs and Maintenance of Heritage Architecture, STREMAH IX*, Malta, Jun. 2005, pp. 237-244.

M. B. Karkee, C. Cuadra, & L. Sunuwar. The challenges of protecting heritage architecture in developing countries from earthqauke disasters. *Ninth International Conference on Structural Studies, Repairs and Maintenance of Heritage Architecture, STREMAH IX*, Malta, Jun. 2005, pp. 407-419.

C. Cuadra, M.B. Karkee, J. Ogawa, and J. Rojas. An evaluation of earthquake risk to Inca's historical constructions. *Proceedings of the 13th World Conference on Earthquake Engineering*, Vancouver, B.C., Canada, August 1-6, 2004, CD-ROM Paper No. 150.

Sudhir R. Shrestha, Madan B. Karkee, Carlos H. Cuadra, Juan C. Tokeshi and S. N. Miller. Preliminary study for evaluation of earthquake risk to the historical structures in Kathmandu valley (Nepal). *Proceedings of the 13th World Conference on Earthquake Engineering*, Vancouver, B.C., Canada, August 1-6, 2004, CD-ROM Paper No. 172.

J. Ogawa, C. Cuadra, M.B. Karkee, and J. Rojas. A study on seismic vulnerability of Inca's constructions. *Proceedings of the 4th International Conference on Computer Simulation in Risk Analysis and Hazard Mitigation. Risk Analysis IV*, Rhodes, Greece 2004, pp 3-12.

C. Cuadra, M.B. Karkee, J. Ogawa, and J. Rojas. Preliminary investigation of earthquake risk to Inca's architectural heritage. *Proceedings of the Fourth International Conference of Earthquake Resistant Engineering Structures,* Ancona, Italy 2003, pp. 167-176.

K. R. Wright and A. Valencia. *Machu Picchu: A Civil Engineering Marvel*. American Society of Civil Engineers ASCE PRESS, Reston Virginia, 2000.

Sunuwar, L., Karkee, M., Tokeshi, J., and Cuadra, C. Applications of GIS in Probabilistic Seismic Hazard Analysis of Urban Areas. *Proc. Of the Fourth International Conference of Earthquake Engineering and Seismology,* Tehran, Iran, 2003.

Thiel, C. Earthquake Damageability Criteria for Due Diligence Investigations. *The Structural Design of Tall Buildings,* 11, pp 233-263.

Miranda, O., Gallardo, J., Cuadra, C. & Ogawa, J. (2000) "Reduction of seismic damage in Peruvian traditional constructions" 2nd International Conference on Computer Simulation in Risk Analysis and Hazard Mitigation. Risk Analysis II, Bologna, Italy, Oct. 2000, pp389-396

8CUEE CONFERENCE PROCEEDINGS
8th International Conference on Urban Earthquake Engineering
March 7-8, 2011, Tokyo Institute of Technology, Tokyo, Japan

EXPERIMENTAL SHEAR STRENGTH OF SQUAT MASONRY SHEAR WALLS

Mohamed A. ElGawady[1] and Jamal Elmapruk[2]

1) Visiting Associate Professor, Department of Civil Engineering, Tokyo Institute of Technology, Japan
2) Former Graduate Student, Civil and Environmental Engineering Dept., Washington State University, USA
elgawady.m.aa@m.titech.ac.jp, elmapruk@wsu.edu

Abstract: Partially grouted masonry shear walls are common structural systems in North America. This research examines the shear behavior of six partially grouted masonry shear walls. The walls have an aspect ratio of 0.58, vertical reinforcement ratio of 0.33% and axial force of 49 kN (11 kips). They were subjected to in-plane lateral cyclic loading in a displacement control. The walls had grout horizontal spacing of 610, 813, and 1219 mm (24, 32, and 48 in., respectively). Horizontal reinforcement ratios ranging from 0.127% to 0.254% were investigated as well. The test results showed that the shear strength of the walls significantly depends on the grout horizontal spacing. In addition, there seems to be a threshold horizontal reinforcement ratio beyond which any increase in the reinforcement ratio does not result in increase in the shear strength of partially grouted shear walls. The measured shear strengths of the test specimens were compared to those predicted shear strengths using MSJC (2008) shear design equations. The comparisons showed that the MSJC overestimated the shear strength of partially grouted walls having grout horizontal spacing greater than 610 mm (24 in.).

1. SHEAR STRENGTH OF PARTIALLY GROUTED MASONRY WALLS

Partially grouted masonry wall (PG-MW) is a common form of construction throughout the Unites States, including seismic zones. Most of the currently available test results on PG-MWs are credited to Matsumura (1986) who tested 51 PG-MWs and developed empirical expressions to calculate the shear strength of both fully grouted and partially grouted masonry shear walls. These equations assumed that the contribution of horizontal shear reinforcement and masonry to shear strength of PG-MWs is approximately 60% of those of fully grouted walls.

Very few studies have been carried out in the United States to address the in-plane shear strength of PG-MWs. Yancey and Scribner (1989) tested ten PG-MWs under cyclic loading. Horizontal reinforcement ratio (ρ_h) ranging from 0 to 0.215% and different distributions of horizontal shear reinforcement were investigated. Fattal (1993a) investigated available literature and experimental results on PG-MW and showed that Matsumura's equations predicted lateral strengths that varied from 23% to 180% of the measured strengths of the test specimens with a coefficient of variation of approximately 33%. Fattal (1993a) improved Matsumura's equations and assumed that the contribution of the horizontal shear reinforcement and masonry to the shear strength of PG-MWs are approximately 64% and 80% of those of fully grouted walls, respectively. Using this new set of equations the predicted shear strengths ranged from 41% to 146% of the measured shear strengths with a coefficient of variation of approximately 22%. In another study, Fattal (1993b) analyzed the test data of PG-MWs available in the literature and found that the lateral strengths of PG-MWs increased with increasing horizontal reinforcement ratio, but there is a threshold horizontal reinforcement ratio of 0.2%, beyond which additional horizontal reinforcement did not appear to be as effective in increasing the lateral strength. Ghanem et al. (1992 and 1993) investigated six one-third scale partially grouted shear walls under in-plane monotonic loading. The effects of reinforcement distribution and applied axial load on shear strength were investigated. All the specimens had a constant horizontal and vertical reinforcement ratio of 0.12%. The distribution of horizontal and vertical reinforcement as well as the level of the applied axial force had significant effects on the mode of failure, strength, and displacement ductility. As the vertical and horizontal reinforcement were more uniformly distributed, both the strength and ductility of the walls improved. Schultz (1996) and Schultz et al. (1998) tested twelve PG-MWs, having aspect ratios of 0.5, 0.7, and 1.0, to examine the effects of distribution and ratio of horizontal reinforcement. It was shown that increasing the aspect ratio from 0.5 to 0.7 significantly increased the ultimate shear stresses. However, increasing the aspect ratio from 0.7 to 1.0 had a negligible effect on the ultimate shear stresses. In addition, increasing the shear reinforcement ratio was found to increase the ultimate strength of slender walls but decrease those of the squat walls. Finally, it was concluded that the failure mechanism of PG-MWs differs from that of fully grouted shear walls. PG-MWs behaved similar to masonry infilled reinforced concrete frames. Recently, four partially grouted masonry shear walls have been tested (Minaie et al. 2010). It was found that the MSJC (2008) shear design

equations overestimated the shear strengths of the four test specimens by a factor of approximately two.

Maleki (2008) tested five PG-MWs built according to the Canadian Standard (CSA 2004). Out of them, four walls failed in shear while the fifth wall failed in flexure. All the walls had a ρ_h of 0.05% and vertical reinforcement ratio of 0.18%. The horizontal distance between the vertical grouted cells ranged from 0.56 m to 1.70 m. The constructed walls had two aspect ratios (height/width), 1.0 and 0.5, and were tested under zero normal force. The MSJC (2008) shear design provisions provided a good prediction of the shear strengths of the test specimens.

2. SHEAR STRENGTH PROVISIONS OF MSJC (2008)

The MSJC (2008) provisions use expressions 1 through 5 for calculating the nominal shear strength of masonry shear walls (V_n). These expressions recognize the contribution of masonry (V_m) and horizontal shear reinforcement (V_S). Unlike Matsumura's and Fattal's expressions, the MSJC shear provisions do not distinguish between PG-MW and fully grouted masonry walls.

$$V_n = V_s + V_m \tag{1}$$

$$V_m = (4 - 1.75\frac{M}{Vd})A_n\sqrt{f'_m} + 0.25P \tag{2}$$

$$V_s = 0.5\frac{A_{sh}}{s}d_v f_{yh} \tag{3}$$

$$V_n \leq 6A_n\sqrt{f'_m} \qquad for\ {}^{M}/_{Vd} \leq 0.25 \tag{4}$$

$$V_n \leq 4A_n\sqrt{f'_m} \qquad for\ {}^{M}/_{Vd} \leq 1.00 \tag{5}$$

Where M/Vd = effective moment to shear ratio, A_n = net cross sectional area, f'_m= specified compressive strength of masonry, P = applied axial load, A_{sh} = cross sectional area of shear reinforcement, and f_{yh} = yield strength of horizontal shear reinforcement.

3. TEST SPECIMENS

A total of six masonry shear walls were tested. To achieve shear dominated behavior an aspect ratio of approximately 0.58 was selected for the test specimens. The aspect ratio is defined as the height between point of application of the lateral loading and the wall base divided by the wall length. The wall length was selected based on the available testing facilities at the Wood Materials and Engineering Laboratory at Washington State University. In addition, the wall length was selected to allow for symmetrical distribution of vertical reinforcement with maximum horizontal spacing between vertical grouted cells of 1219 mm (48 in.). This resulted in wall length of 2642 mm (104 in.) and height of 1626 mm (64 in.). Each wall consisted of 8 courses high, and 6½ blocks long. In addition, two more courses were added above course No. 8 to act as a cap beam that uniformly distributes the applied axial and lateral loads. The test specimens were built by experienced bricklaying crew in a running bond pattern with 203 mm (8 in.) hollow concrete masonry units using face shell mortar bedding. Standard 406 mm x 203 mm x 203 mm (16 in. x 8 in. x 8 in.) for full units and 203 mm x 203 mm x 203 mm (8 in. x 8 in. x 8 in.) for half-unit concrete masonry units (CMUs) were used for the construction of the test specimens. Knockout units were used in the 4th and 8th to 10th masonry courses to form bond beams where the shear reinforcement was fully embedded in grout.

Every specimen was assigned a name in the form of PG (partially grouted) followed by XXX-SP where XXX is the horizontal reinforcement ratio (ρ_h) multiplied by 100000, followed by the horizontal grout spacing in inches. For example, specimen PG127-48 was a partially grouted specimen reinforced using a horizontal reinforcement ratio of 0.00127 and a horizontal grout spacing of 1219 mm (48 in.).

The specimens were reinforced horizontally and grouted at courses No. 4, 8, 9, and 10. Each one of these courses included a single leg D 16 (No. 5) rebar, except for specimens PG180-48 and PG254-48, where a single D 19 (No. 6) and 2 D 16 (No. 5) were used, respectively. This resulted in a horizontal reinforcement ratio (ρ_h) of 0.127% for all specimens except specimens PG180-48 and PG254-48, where ρ_h of 0.180% and 0.254% were used, respectively. The horizontal reinforcement ratio was calculated as the cross sectional area of the shear reinforcement in a bond beam divided by (203 mm x 1219 mm) i.e. the wall thickness and distance between the bond beams.

The horizontal reinforcements were hooked according to MSJC (2008) using a 180^o hook around the outermost vertical rebar located at 102 mm from the ends of each wall (Figure 1). The walls were reinforced vertically using identical reinforcement ratio of 0.33% at horizontal spacing of 610 mm (24 in.), 813 mm (32 in.), and 1219 mm (48 in.). As shown in Figure 2, all specimens except specimens PG127-32 and PG127-24 were reinforced using 2#6 at 1219mm (48 in.). Specimens PG127-32 and PG127-24 were reinforced using 2#6 in each outermost cell. The inner cells were reinforced using either 1# 6 @ 813 mm (32 in.) or 1# 5 @ 610 mm (24 in.) in the case of specimen PG127-32, and PG127-24, respectively. Each cell containing vertical reinforcement was grouted.

Each wall was constructed on over-designed reinforced concrete foundation. The vertical flexural reinforcement rebar were extended from the foundation completely through the full



Figure 1 The 180^o hook as used in the specimens

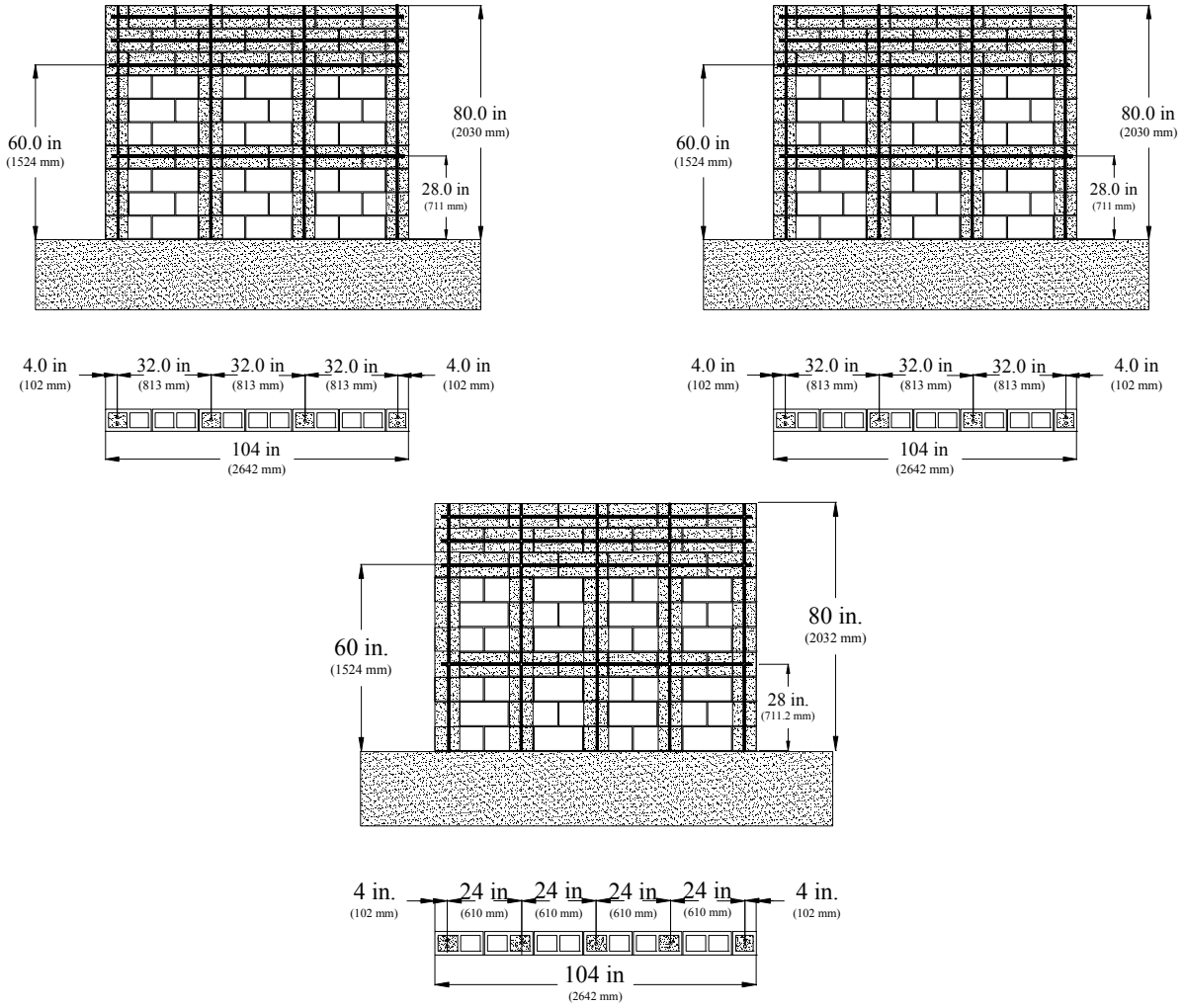


Figure 2 Typical dimensions of test specimens

height of the wall without lap splice to avoid strength degradation due to splice rupture. The wall longitudinal rebar were hooked around the longitudinal rebar of the foundation using a 90° hook.

2.1 Construction Material Properties

A high slump fine grout was mixed and used to grout the reinforced cells and bond beams of the walls. Four grout-prisms 102 x 102 x 203 mm (4 x 4 x 8 in.) were prepared and tested according to ASTM C1019-07. The grout had an average compressive stress of 35.85 MPa (5200psi) with a standard deviation of 3.5 MPa (511 psi).

The specimens were built using Portland cement lime type S mortar. Five 51 mm (2 in.) diameter by 102 mm (4 in.) high mortar cylinders were casted and tested according to ASTM C780 (2090). The mortar had an average compressive strength of 14.89 MPa (2160 psi) and standard deviation of 1.3 MPa (185 psi).

Five grouted and five un-grouted two-block high single-block long prisms were tested according to ASTM C1314-07 to determine the masonry compressive stress (f'_m). The tested ungrouted prisms had an average f'_m of 17.44 MPa (2530 psi) with standard deviation of 2.0 MPa (290 psi). The tested grouted prisms had an average f'_m greater than 24.40 MPa (3540 psi) since the compression machine reached its ultimate capacity without rupture of the grouted prisms (Table 1).

The steel rebar used in the walls construction were Grade 60 for both vertical and horizontal reinforcement and had measured yield stresses of 452 MPa (65.6 ksi) and 427 MPa (61.9 ksi) for #5 and #6, respectively.

3. TEST SETUP AND LOADING SYSTEM

The RC footing of each wall was post-tensioned to the laboratory strong floor using eight high strength steel bars (Figure 30. A superimposed gravity load of approximately 49.4 kN (11.1 kips) was applied to the specimen using two jacks operated by a manual hydraulic pump. To uniformly distribute the applied axial load, the actuators were connected at their

bottoms to stiff hollow square steel section that was mounted on top of the wall, i.e. at the 10th masonry course.



Figure 3 Test Setup

Table 1 Prism test results

Type	Sample No.	Load (Ib)	Area (in^2)	(f'_m) (psi)	Corrected (f'_m) (psi)	Avg. of corrected f'_m psi (MPa)
Ungrouted	1	193,300	67.04	2883.3	2874.6	2530 (17.44)
	2	151,940	67.04	2266.4	2259.6	
	3	147,911	67.04	2206.3	2199.7	
	4	179872	67.04	2683.1	2675	
	5	178392	67.04	2661	2653	
Grouted	1*	425752	119.15	3573.2	3562.5	3540 (24.40)
	2*	424255	119.15	3560.7	3550	
	3*	424342	119.15	3561.4	3551	
	4*	424198	119.15	3560.2	3549	
	5	414872	119.15	3482	3471.5	

Correction factor =0.997

* Sample reached the machine's maximum load without rupture.

The tops of the hydraulic jacks were connected to the main cross beam of the strong steel frame using a slippery plate to allow lateral movement of the actuator while applying the axial load. The applied normal force corresponds to a stress of 0.10 MPa (14 psi).

As described earlier courses No. 8, 9, and 10 in each wall were grouted and reinforced to act as a stiff cab beam. The lateral load was applied through a 1000 kN (225 kip) capacity hydraulic actuator with its centerline aligned at the middle of the 8th masonry course as shown in Figure 2. The actuator was fixed from one end to the steel strong frame and from the other end to two stiff C-shaped built-up steel sections which were bolted at the 8th masonry course to both sides of each wall. The C sections were bolted using 19 mm (¾ in.) diameter shear studs passing through the thickness of each masonry wall. The holes for these studs were drilled after the walls had grouted and cured for approximately 7 days. A high strength anchorage epoxy was used to fill any tolerance between the bolts and holes.

In order to eliminate any sliding in the concrete base during the cyclic loading, the concrete base was braced using two stiff built-up steel angles bolted to the laboratory strong floor, as shown in Figure 3.

Each specimen was subjected to the displacement-controlled reversed cyclic loading shown in Figure 4. The typical cyclic loading sequence adopted for the tests consisted of three cycles at lateral displacement levels of ± 0.5 Δ_y, ± 1.0 Δ_y, ± 1.5 Δ_y, ± 2.0 Δ_y, ± 2.5 Δ_y, ± 3.0 Δ_y, ± 3.5 Δ_y, ± 4.0 Δ_y, ± 5.0 Δ_y, ± 6.0 Δ_y, ± 6.0 Δ_y, ± 8.0 Δ_y, and ± 10.0 Δ_y, etc. Δ_y is the theoretical yield displacement and was determined as 1.27 mm (0.05 in.) using Equation 6 (Priestley et al. 2007):

$$\Delta_y = 0.6\varepsilon_y h_e \frac{h_e}{L_W} \quad (6)$$

Where h_e= height of wall = 1524 mm (60 in.), L_w = wall length = 2631 mm (103.6 in.), ε_y = yield strain of the flexural steel = 0.00207 for grade 60. The loading rate was 4.76 mm/min (0.1875 in/min). In this experimental program, failure of a specimen was defined as the point on the loading curve where the wall strength reduced to 80% of the peak strength of this specimen.

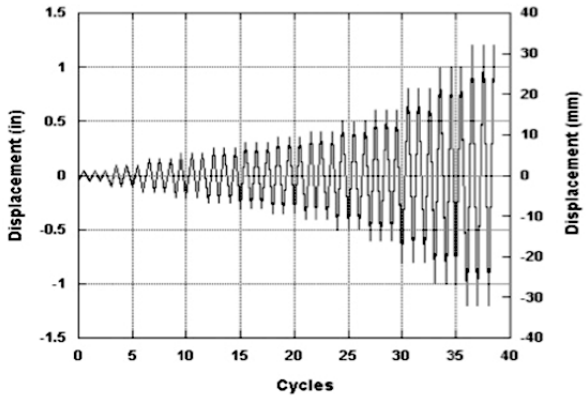


Figure 4 Loading protocol

3.1 Instrumentations

The specimens were instrumented with several devices. The lateral displacement at masonry course No. 8 was measured using string potentiometers. The applied lateral forces were measured using the load cell of the actuator.

4. EXPERIMENTAL RESULTS

4.1 Specimens PG127-48 and PG-127-48I

PG127-48 and PG-127-48I are identical specimens having grouted vertical cells at horizontal spacing of 1219 mm (48 in). Each wall was reinforced horizontally using 1 No. 5 (D 16) in courses No. 4, and 8 to 10 (ρ_h= 0.127%). The first crack was a diagonal crack in the form of stair-step cracks passing through mortar bed and head-joints along the bottom three brick courses. The crack appeared at lateral loads of 178 kN (39.9 kips) and 164 kN (36.8 kips) for specimens PG127-48 and PG127-48I, respectively. These loads correspond to lateral drift angle of approximately 0.09%. More stepped cracks occurred while the applied lateral displacement was increased. Specimen PG127-48 reached its peak strength of 253 kN (56.84 kips) at a drift angle of 0.22%. At this drift angle, 45° cracks occurred through the masonry units at the 2nd and 3rd masonry courses of the vertical grouted cells at the wall mid-length. Beyond that drift angle, more 45° cracks passing through the masonry units at the specimen's toes occurred. These diagonal cracks were initiated by diagonal tension splitting of masonry in the compression struts. At a lateral drift angle of 0.51% and lateral load of 203kN (45.72 kips), vertical splitting cracks occurred at the middle bond beam on the outer grouted cells in both load directions (Figure 5). Testing continued and spalling of CMU and mortar occurred. By a drift angle of 1.1% and lateral load of 158 kN (35.5 kips), the vertical splitting crack width significantly increased and led to spalling of the masonry end shells of the end blocks at the third and fourth masonry courses as shown in Figure 6. At this damage level, the test was stopped and the lateral strength of the specimen dropped by 45% of the measured specimen's peak strength.

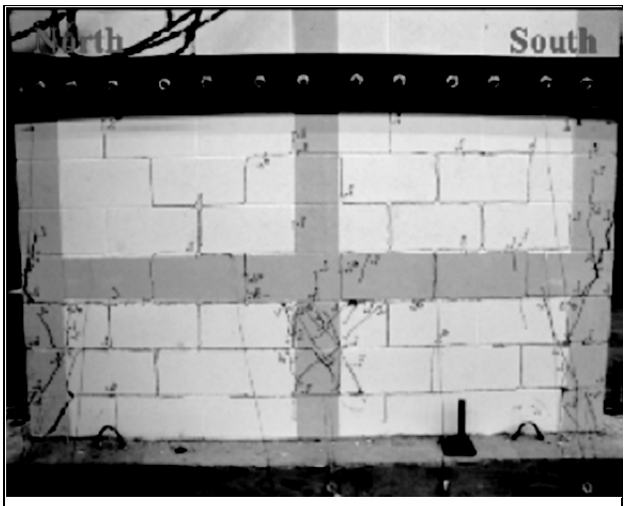


Figure 5 Specimen PG127-48 at drift angle of 0.51% during testing

Specimen PG127-48I behaved similar to specimen PG127-48 with a peak strength of 231 kN (51.9 kips) at lateral drift angle of 0.3%. At drift angle of 0.88%, vertical cracks were observed at the outermost blocks in the 3rd through the 5th masonry courses leading to a reduction in the lateral strength of the specimen by approximately 35% and the specimen reached a lateral strength of 170 kN (38.17 kips).

4.2 Specimens PG180-48

Specimen PG180-48 had grouted vertical cells at horizontal spacing of 1219 mm (48 in). The wall was reinforced horizontally using 1 D 19 (No. 6) in courses No. 4, and 8 (ρ_h= 0.180%). Courses No. 9 and 10 were also reinforced using 1 D 19 (No. 6), each, to act as rigid beam where the axial and the

lateral loads were applied. The first crack was stepped crack in the bottom masonry panel and it occurred at a drift angle of

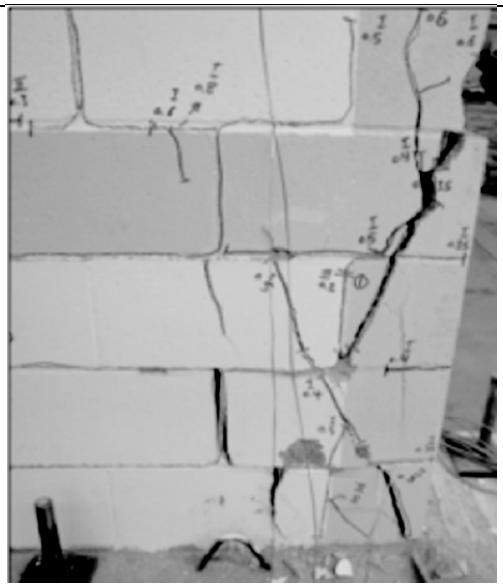


Figure 6 Toe crushing of specimen PG127-48 at drift angle of 1.1%

0.09% and lateral load of 188 kN (42.3 kips). Stepped cracks continued to occur by increasing the applied lateral drift. At a drift angle of 0.36% and lateral load of 266 kN (59.1 kips), diagonal cracks appeared in the CMUs at the toes of the wall. At a drift angle of 0.42% and a lateral load of 289 kN (65.03 kips), the specimen reached its ultimate strength. At a drift angle of 0.58% and a lateral load of 279 kN (62.8 kips), a significant diagonal crack approximately 2-block high passing through the bond beam and outermost grouted cells appeared through the 4th and 5th masonry courses. Cycling continued and vertical cracks 3-block high appeared in the outermost grouted cells in the north and south directions. Face shells spalling of the masonry blocks surrounding the toes of the wall occurred at a drift angle of 0.88% and a lateral load of 252kN (56.7 kips) (Figure 8). By a drift angle of 0.91%, the lateral resistance of the specimen dropped by 40% and the test was stopped.

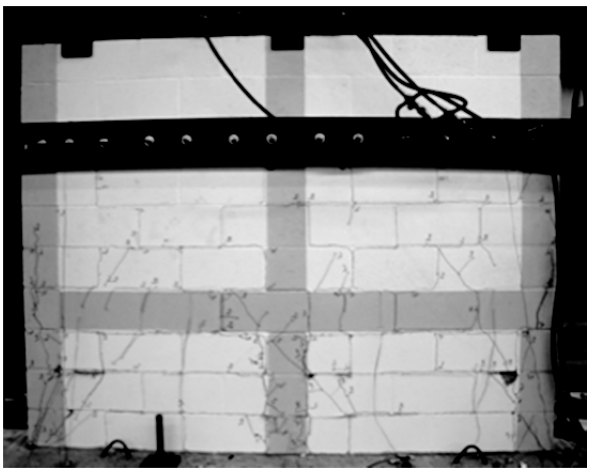


Figure 7 Specimen PG127-48I at drift angle of 0.88%

4.3 Specimens PG253-48

Specimen PG253-48 had grouted vertical cells at horizontal spacing of 1219 mm (48 in). The wall was reinforced horizontally using 2 D 16 (No. 5) in courses No. 4, and 8 (ρ_h= 0.253%). Courses No. 9 and 10 were also reinforced using 2 D 16 (No. 5), each. The first crack was stepped crack occurred in the top and bottom masonry panels and it occurred at a drift angle of 0.06% and lateral load of 186 kN (41.75 kips). Stepped cracks continued to occur by increasing the applied lateral drift. At a drift angle of 0.30% and lateral load of 271 kN (61.0 kips), diagonal cracks appeared in the CMUs at the toes of the wall. At a drift angle of 0.42% and a lateral load of 291 kN (65.50 kips), the specimen reached its ultimate strength. Cycling continued and vertical cracks 5-block high appeared in the outermost grouted cells in the north and south directions (Figure 9). By a drift angle of 0.80%, the lateral resistance of the specimen dropped by 47% and the test was stopped.



Figure 8 Specimen PG180-48 at drift angle of 0.88%

4.4 Specimen PG127-32

Specimen PG127-32 had grouted vertical cells at horizontal spacing of 813 mm (32 in). The wall was reinforced horizontally using 1 D 16 (No. 5) in courses No. 4, and 8 (ρ_h= 0.127%). Courses No. 9 and 10 were also reinforced using 1 D 16 (No. 5), each. The first observed crack was a stepped crack passing through mortar joints in the top middle masonry panel and it occurred at drift angle of 0.08% and lateral load of 219 kN (49.26 kips). While pulling the specimen to a drift angle of 0.25% and lateral load of 315 kN (70.9 kips), diagonal cracks occurred in the wall toes. At a drift angle of 0.47% and lateral load 357 kN (80.2 kips), the specimen reached its peak strength. Beyond that the strength of the specimen started to degrade due to substantial widening of exiting diagonal cracks. At a drift angle of 0.85% and lateral load of 347kN (77.5 kips), new vertical cracks appeared in the outermost cells in the 4th and 5th masonry course (Figure 10). Finally, at a drift angle of 1.29%, the resistance of the specimen dropped by 28% of its peak

resistance and the test was stopped.

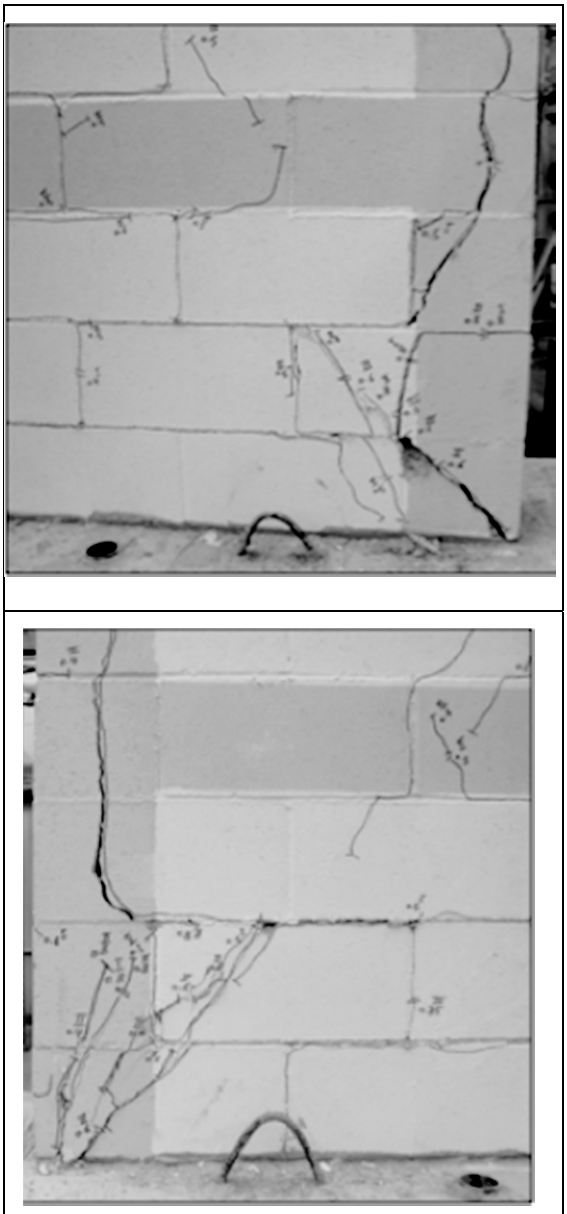


Figure 9 Vertical and diagonal cracks at drift angle of 0.70% in the toes of specimen PG253-48

4.4 Specimen PG127-24

Specimen PG127-24 had grouted vertical cells at horizontal spacing of 610 mm (24 in). The wall was reinforced horizontally using 1 D 16 (No. 5) in courses No. 4, and 8 (ρh= 0.127%). Courses No. 9 and 10 were also reinforced using 1 D 16 (No. 5), each.

Specimen PG135-24 behaved similar to the rest of the other specimens and had a dominant shear response, as indicated by diagonal stepped cracks. The first crack was a diagonal stepped crack occurred at the top masonry panels while loading the specimen to a drift angle of 0.12% and a lateral load of 254 kN (57.2 kips). While pulling the specimen to a drift angle of 0.23% and lateral load of 309 kN (69.5 kips), a diagonal crack passing through the CMUs in the bottom four courses of the

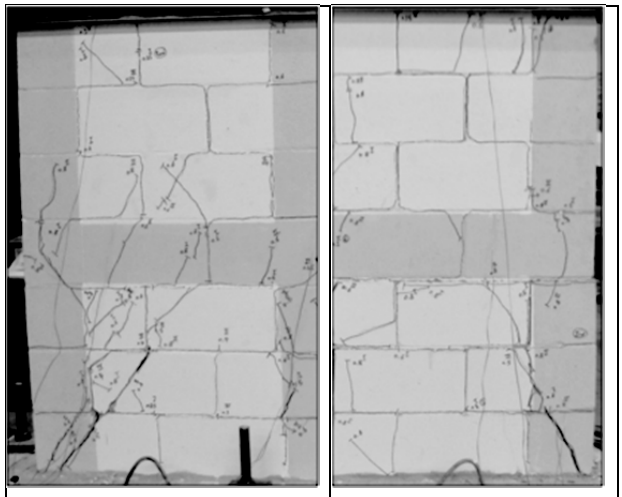


Figure 10 Damage of the toes of specimen PG127-32 at drift angle of 0.85%

northern masonry panel occurred. By a drift angle of 0.71%, diagonal cracks passing through CMUs were everywhere in the specimen and the specimen reached its ultimate strength of 430 kN (96.8 kips). By a drift angle of 1.00% and load of 299 kN (67.3 kips), substantial vertical cracks appeared in the outermost grouted cells and the toes were significantly damaged as well as the lateral strength of the wall dropped by 30% of its peak strength. (Figure 11).

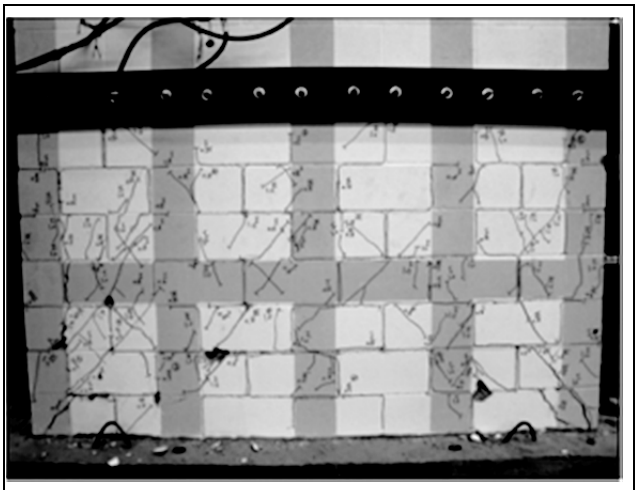


Figure 11 Specimen PG127-24 at drift angle 1.00%

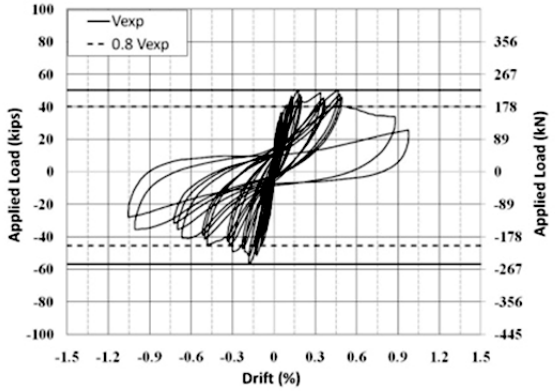
5. DISCUSSION

The shear strength of each shear wall was calculated using the shear provisions of the current MSJC (2008). The MSJC (2008) predicts the nominal shear strength (V_n) of partially grouted masonry shear walls (PGMW) using Equations 1 to 5. V_n is calculated as the summation of the nominal shear strength provided by shear reinforcement (V_{ns}) and masonry panel (V_{nm}). The only distinction between partially and fully grouted

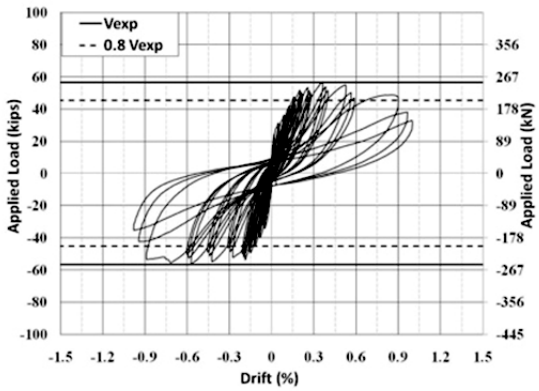
masonry walls is that, in the case of partially grouted walls the MSJC (2008) uses the net grouted area (A_n) instead of the gross cross sectional area (A_g), as in the case of fully grouted masonry walls.

Table 2 presents the parameters used to calculate the shear strength for the tested specimens. It is worth noting that the net cross sectional area was calculated using the sum of the areas of the face shells and the grouted cells for each specimen. In addition, Table 2 shows the calculated and measured strength values. Finally, the hysteretic loops of the test specimens as well as the calculated values for V_n and V_n times the shear strength reduction factor $\phi = 0.8$ are also presented on Figure 12. As shown in the figure and the table, the MSJC (2008) shear design equations are highly un-conservative and over-estimated the shear strength capacity for the tested walls. The measured shear strengths ranged from 60% to 91% of the predicted values.

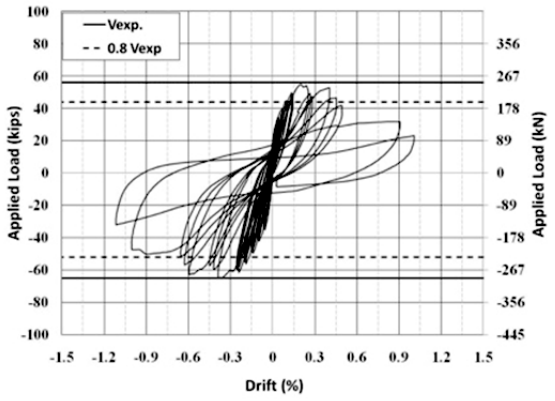
Figure 13 shows the relationship between the horizontal reinforcement ratio and V_{exp}/V_n which represents the ratio between the measured and the predicted nominal shear strength. As shown in the figure, the error in predicting the nominal shear strength slightly decreased with increasing the provided shear reinforcement. For specimens having reinforcement ratio of 0.127% (i.e. specimens PG127-48 and PG127-48I), the error was approximately 38%. Doubling the reinforcement ratio to 0.254% (i.e. specimen PG254-48), decreased the error in the prediction of V_n to 30%.



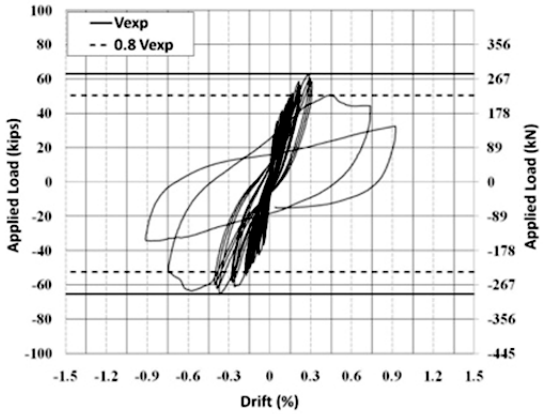
(a) PG127-48



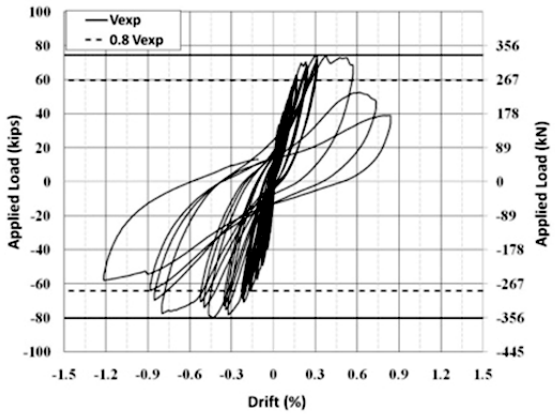
(b) PG127-48I



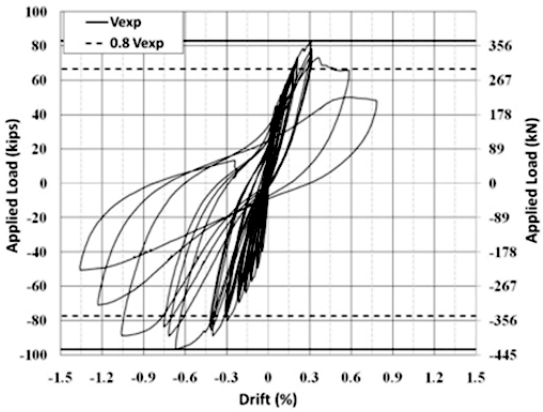
(c) PG180-48



(d) PG254-48



(e) PG127-32



(f) PG127-24

Figure 12 Load- displacement hysteresis loops

Table 1 Parameters used for MSJC (2008) shear calculations

Wall ID	PG127-48	PG127-48I	PG180-48	PG254-48	PG127-32	PG127-24	Units
A_n	356 (229,677)	356 (229,677)	356 (229,677)	356 (229,677)	388 (250,322)	421 (271,612)	in^2 (mm^2)
A_v	0.31 (200)	0.31 (200)	0.44 (284)	0.62 (400)	0.31 (200)	0.31 (200)	in^2 (mm^2)
V_{nm}	56.2 (250)	56.2 (250)	56.2 (250)	56.2 (250)	61 (271)	66 (294)	kips (kN)
V_{ns}	32.9 (146)	32.9 (146)	44 (196)	65.8 (293)	32.9 (146)	32.9 (146)	kips (kN)
V_n	89.1 (396)	89.1 (396)	100.2 (446)	122 (543)	93.8 (424)	99 (440)	kips (kN)
$V^*_{n\ final}$	89.1 (396)	89.1 (396)	91.7 (408)	91.7 (408)	93.8 (424)	99 (440)	kips (kN)
f_y	61.5 (424)	61.5 (424)	65.6 (452)	61.5 (424)	61.5 (424)	61.5 (424)	ksi (MPa)
Measured strength (V_{exp})	53.5 kips (238) kN	56.7 kips (252) kN	59.8 kips (246) kN	64.2 kips (286) kN	77.3 kips (344) kN	89.9 kips (400) kN	kips (kN)
V_{exp}/V_n	60%	63%	65%	70%	82%	91%	

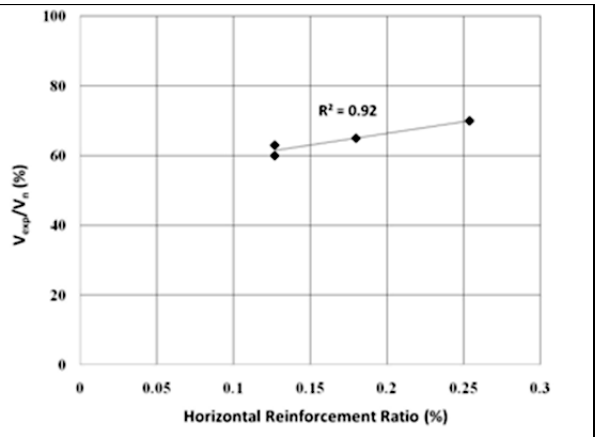


Figure 13 Effect of horizontal reinforcement on the predictions using MSJC (2008) shear equation for specimens with grout horizontal spacing of 1219 mm (48 in.)

Specimens PG127-48, PG127-48I, PG127-32, and PG127-24 have constant horizontal reinforcement ratio of 0.127%, but different grout horizontal spacings of 1219 mm (48 in.), 813 mm (32 in.), and 610 mm (24 in.), respectively. Figure 14 shows the relationship between the net cross sectional area and the measured shear strengths. Also, the figure shows predictions using MSJC (2008) shear design equations. As shown in the figure, by decreasing the grouted cross sectional area, the differences between the predicted values using MSJC (2008) shear design equations and the measured shear strengths increased. This finding indicates the need to modify the shear strength of partially grouted masonry shear walls with respect to grout horizontal spacing and net cross sectional area.

6. CONCLUSIONS

The experimental work presented in this thesis revealed that:

- There seems to be a threshold horizontal reinforcement ratio beyond which any increase in the shear reinforcement does not yield any increase in the strength of the shear walls since failure occurred due to compression strut failure.
- Decreasing the grout horizontal spacing significantly improved the strength of the investigated shear walls.
- The current MSJC (2008) shear design equation for partially grouted masonry shear walls is highly un-conservative and over-estimated the shear strength capacity for the tested walls. The over-estimation in the predicted shear strengths using the current MSJC (2008) ranged from 60 to 91%.

The experimental work presented in this thesis revealed that:

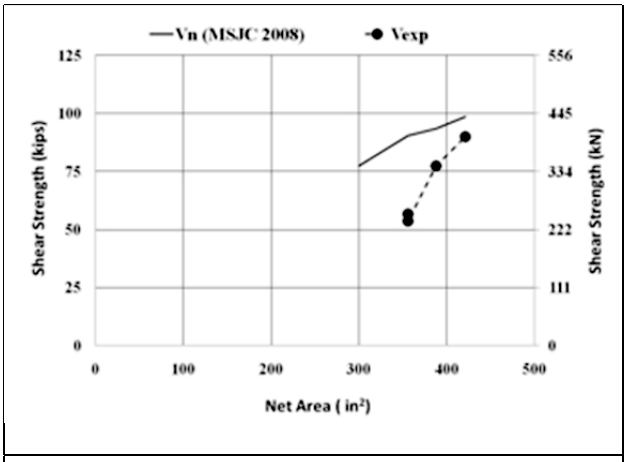


Figure 14 Net area vs. V_{exp} and V_n for specimens having horizontal reinforcement of 0.127%

Acknowledgements:

Thanks are also due to National Concrete Masonry Association, the Northwest Concrete Masonry Association, and the Eastern Washington Masonry Promotion Group for partial funding. Deep thanks to Bob Duncan and Scott Lewis at the Composite Materials and Engineering Center and Miles Pepper at the Engineering shop center for their help during the experimental part of the project. At the last but not the least, I would like to thank the higher minister of education in Libya for giving me this opportunity to pursue my M.Sc. degree in the USA.

References:

American Concrete Institute: 2005, Building Code Requirements for Structural Concrete (ACI 318-05) and Commentary (ACI 318R-05), Farmington Hills, MI.

ASTM Standard C 140, "Standard Test Methods for Sampling and Testing Concrete Masonry Units and Related Units," ASTM International, West Conshohocken, PA, www.astm.org

ASTM Standard C 270, "Standard Specification for Mortar for Unit Masonry," ASTM International, West Conshohocken, PA, www.astm.org

ASTM Standard C 476, "Standard Specification for Grout for Masonry," ASTM International, West Conshohocken, PA, www.astm.org

Brandow, G.E., Ekwueme, C.G., Hart G.C., 2006 Design of Reinforced Masonry Structures, Concrete Masonry Association of California and Nevada, Citrus Heights, CA, 2007.

Davis, C.L. "Evaluation of design provisions for in-plane shear in masonry walls", Washington State University, Masters Thesis, Dec 2008.

Maleki, Majid "Behaviour of Partially Grouted Reinforced Masonry Shear Walls Under Cyclic Reversed Loading" University of McMaster, PhD Thesis, June 2008.

Masonry Standards Joint Committee: 2008, Building Code Requirements for Masonry Structures, TMS 402-08, The Masonry Society, Boulder, CO, ACI 530-08, American Concrete Institute, Farmington Hills, MI, ASCE 5-08, American Society of Civil Engineers, Reston, VA.

Matsumura, A. (1985) "Effect of Shear Reinforcement in Concrete Masonry Walls," First Joint Technical Coordinating Committee on Masonry Research, U.S.-Japan Coordinated Earthquake Research Program, Tokyo, Japan, August 26 - 27, 1985

Matsumura, A. (1986) "Shear strength of reinforced hollow unit masonry walls," Second Meeting of the U.S.-Japan Joint Technical Coordinating Committee on Masonry Research, Keystone, Colorado

Minaie, Ehsan 'Behavior and Vulnerability of Reinforced Masonry Shear Walls' Drexel University, PhD Thesis, August 2009.

New Zealand Standard 4230:2004, Design of Reinforced Concrete Masonry Structures, Standards Association of New Zealand, Wellington.

Nolph, Shown 'In-plane shear performance of partially grouted masonry shear walls" Washington State University, M.Sc. Thesis, August 2010.

Priestley, M.J.N., Calvi, G.M., Kowalsky, M.J., Displacement-Based Seismic Design of Structures, IUSS Press, Italy, 978-88-6198-000-6, 2007.

Priestley, M.J.N., Seible, F., Calvi, G.M., Seismic Design and Retrofit of Bridges, Wiley, New York, NY, 0-471-57998-X, 1996.

Voon, K.C. and Ingham J. M. (2006) "Experimental In-Plane Shear Strength Investigation of Reinforced Concrete Masonry Walls", Journal of Structural Engineering, Vol. 132, No. 3, pp. 400-408

Voon, K.C. "In-Plane Seismic Design of Concrete Masonry Structures", University of Auckland, PhD Thesis, June 2007.

Wight, G.D., Kowalsky, M.J., Ingham, J.M., "Direct Displacement-Based Seismic Design of Unbonded Post-Tensioned Masonry Walls." ACI Structural Journal, Sept-Oct 2007, pp560-569.

Fattal, S. G. (1993a) "Strength of partially-grouted masonry shear walls under lateral loads," NISTIR 93-5147, Gaithersburg, MD.

Fattal, S. G. (1993b) "The effect of critical parameters on the behavior of partially grouted masonry shear walls under lateral loads," NISTIR 93-5147, Gaithersburg, MD

FEMA 356: Prestandard and Commentary for the Seismic Rehabilitation of Buildings, Federal Emergency Management Agency, Washington, D.C., Nov 2000

Elmapruk, J.H., ElGawady, M.A., "Evaluation of the MSJC 2008 Shear Strength Equations For Partially Grouted Masonry Shear Walls." 11th Canadian Masonry Symposium, Toronto, Ontario, May 31-June 3, 2009.

8CUEE CONFERENCE PROCEEDINGS
8th International Conference on Urban Earthquake Engineering
March 7-8, 2011, Tokyo Institute of Technology, Tokyo, Japan

SHEAR STRENGTHENING FOR REINFORCED CONCRETE BEAMS USING ECC PANELS

Koji Matsumoto[1)], Asami Yamamoto[2)], and Junichiro Niwa[3)]

1) Assistant Professor, Department of Civil Engineering, Tokyo Institute of Technology, Japan
2) East Nippon Expressway Company Ltd., Japan
3) Professor, Department of Civil Engineering, Tokyo Institute of Technology, Japan
matsumoto.k.ar@m.titech.ac.jp, a.yamamoto.ae@e-nexco.co.jp, jniwa@cv.titech.ac.jp

Abstract: This paper presents shear strengthening method for reinforced concrete (RC) beams using Engineered Cementitious Composite (ECC) panels. ECC is one of the cementitious materials which are known as its pseudo strain hardening behavior and crack dispersibility. ECC panels were attached on both sides of RC beam specimen by stainless anchor bolts. Experimental parameters were presence of shear keys at the interface between panels and steel mesh inside of the panels. Non-strengthened RC beam was also prepared as a reference specimen. The specimens were subjected to 4-point loading. As a result of the experiment, ECC panels could considerably increase shear capacity of RC beams. Especially shear capacity of the beam strengthened by ECC panels with providing shear keys was increased up to 150% of that of non-strengthened specimen. This is because shear keys enable to transfer stress in perpendicular direction of member axis, and hence diagonal compression forces were formed across the interface between the panels.

1. INTRODUCTION

In the Great Hanshin (Kobe) earthquake 1995 Japan, shear failure of reinforced concrete (RC) structure occurred and a lot of human lives were lost because of its brittle behavior. Another problem of shear failure is its difficulty for rehabilitation. In the Great Hanshin earthquake, RC piers of highway bridge were collapsed and it took long time to restore. It inhibited rescue activities for the disaster victims. Shear capacity of RC structures is therefore one of the most important issues to mitigate seismic risk of urban cities.

To reduce social damage in the next coming great earthquake, Japan Society of Civil Engineers (JSCE) and Architectural Institute of Japan (AIJ) have revised their design specification for shear of RC members. Thus, newly-constructed structures satisfy safer structural performance, however, more practical problem is repairing and strengthening of existing structures because of the financial situation in Japan and other countries.

As methods for repairing and strengthening of RC members, surface treatment, resin injection for cracks, patch repair, steel plate attachment, FRP sheet attachment, and external cable prestressing have been proposed and started to be used. However, these methods have some problems such as corrosion and heavy weight of steel plate and brittle failure of FRP material. On the other hand, Engineered Cement Composite (ECC) is an advanced cementitious material which is known as its pseudo strain hardening behavior and crack dispersibility (Li 1998). Yamamoto et al. (2010) conducted uni-axial tensile loading tests and resonant frequency tests of damaged early-age ECC after wet-dry cycles. They reported that self-healing of pre-induced cracks was observed and tensile strength and resonant frequency were recovered. Thus, ECC has a possibility to enhance not only mechanical performance but also durability of structures.

Because of the above point of view, this study explored shear strengthening method for RC beams using ECC panels. ECC was cast in panel shape, and then attached on both sides of RC beams by anchor bolts. Four-point bending tests of strengthened beams were carried out. Strengthening effect and shear resisting mechanism of ECC panels were investigated.

2. EXPERIMENTAL PROGRAM

2.1 Materials

Table 1 shows mix proportion of ECC used in this study. The pre-mix binder contained ordinary Portland cement, limestone powder, fly ash and expansion agent. Properties of the used polypropylene fiber were length = 12 mm, density = 0.91 g/cm^3, tensile strength = 482 N/mm^2, and elastic modulus = 5000 N/mm^2, respectively.

Table 2 shows mix proportion of concrete. Early strength cement was used. Water to cement ratio (*W/C*) and

Table 1 Mix proportion of ECC

W/P [%]	V_f [Vol. %]	Unit quantity [kg/m^3]		
		W	*PM*	*Ad*
27	3.0	371	1400	7

W: Water
V_f: Volume fraction of Polypropylene fiber
W/P: Water to powder ratio
PM: Premixed material (Including ordinary Portland cement, Fly Ash, Limestone powder and Expansion agent)
Ad: Flow aid

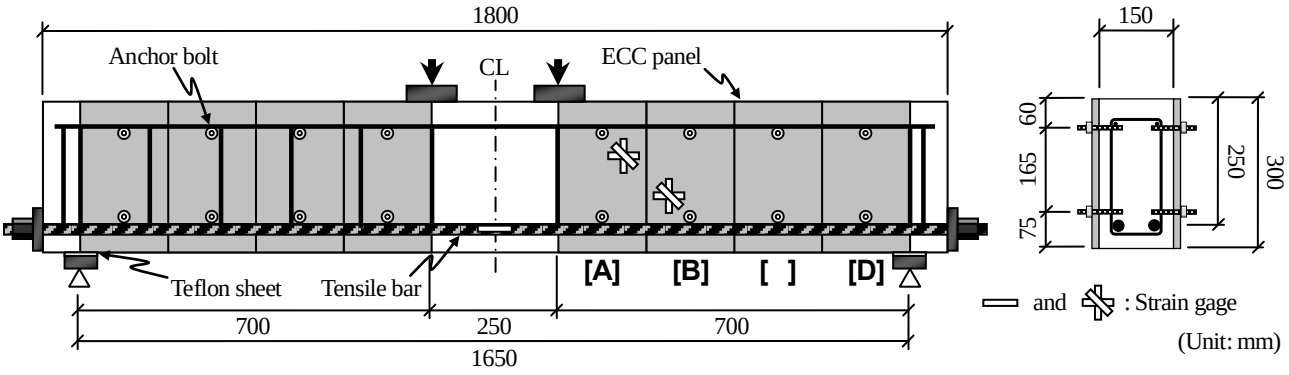


Figure 1 Dimension, reinforcing bar arrangement and panel location of the specimen.

Table 2 Mix proportion of concrete

G_{max} [mm]	W/C [%]	S/a	Unit quantity [kg/m^3]				
			W	C	S	G	AE
20	60	45	177	296	838	967	0.443

G_{max}: Maximum aggregate size
C: Early strength cement
S: Sand
G: Gravel
AE: Air entraining and water reducing agent

Table 3 Specification of the specimen.

Item	Symbol	Unit	Value
Reinforcement ratio	p_w	%	2.06
Width	b_w	mm	150
Shear span	a	mm	700
Effective depth	d	mm	250
Shear span to effective depth ratio	a/d	-	2.8
Design shear capacity	V_{cal}	kN	52.5

Table 4 Material properties of reinforcing bars.

Use	Type	Nominal cross section [mm^2]	Yielding strength [N/mm^2]
Tensile bars	Deformed	387.1	1046
Compression bars	Plain	28.3	308
Stirrups	Deformed	31.7	339

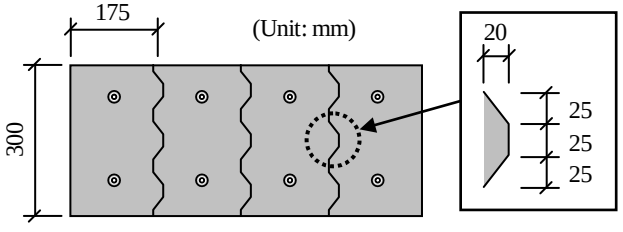


Figure 2 Size of the ECC panels and shear leys.

maximum size of coarse aggregate (G_{max}) were 0.6 and 20 mm, respectively.

2.2 Specimens

Figure 1 shows dimension and reinforcing bar arrangement of RC beams and location of the ECC panels. The shear span and the effective depth were 700 mm and 250 mm, respectively. The concrete mentioned in section **2.1** was used and the specimen was cured during 1 week. Tables 3 and 4 list specification of the RC beam and material properties of the reinforcing bars, respectively. For all specimens, failure side was controlled in the right span with putting stirrups into the left span. Stirrups were not provided in the test span.

Figure 2 shows dimension of the ECC panels. Totally 16 pieces of ECC panels whose size is 175 mm in width, 300 mm in height and 14 mm in thickness were attached on both sides of the both shear spans by using stainless anchor bolts. In this paper, the ECC panels attached on the test span are called panel [A], [B], [C] and [D], depending on the attached location. Presence of shear keys provided between the ECC panels and steel mesh at the inside of the ECC panels were the experimental parameters. Shape of the shear keys were trapezoid with 20 mm in height, 25 mm in upper base and 75 mm in lower base. Figure 3 illustrates arrangement of the steel mesh.

2.3 Experimental Cases

Table 5 lists the experimental cases in this study. Totally 5 RC beams were prepared. Two of them are the specimen tested in the authors' previous study (Matsumoto et al. 2010). REF is the reference specimen which ECC panels were not provided. NK-WM is the specimen in which shear keys were not provided but the steel mesh was used. WK-NM is the specimen in which shear keys were provided but the steel mesh was not used. WK-WM is the specimen in which both shear keys and the steel mesh were provided. NK-NM(UFC) is the other reference specimen conducted in the authors' previous study in which panels made of Ultra High Strength Fiber Reinforced Concrete (UFC) were attached.

2.4 Loading method

Load was applied by 2000 kN Amsler type loading machine. As illustrated in Fig. 1, the specimen was subjected to 2-point loading under simply supported condition. To satisfy simple supporting condition, steel plate whose width is 65 mm was put on the pin hinge supports and antifriction pad, which is consisted of two layers Teflon sheet and grease,

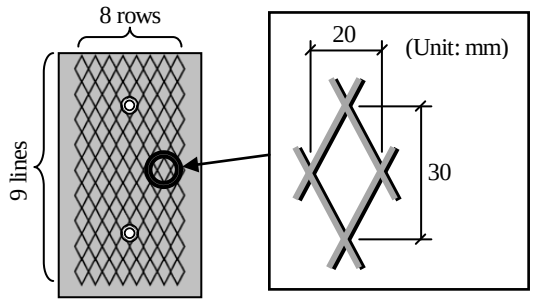


Figure 3 Dimension and arrangement of the steel mesh.

Table 5 Experimental cases.

Specimen name	Strengthening	Shear keys	Steel mesh
REF	None	-	-
NK-WM	ECC panels	N	Y
WK-NM		Y	N
WK-WM		Y	Y
NK-NM(UFC)	UFC panels	N	N

*WK and NK means with and without shear keys, respectively.
*WM and NM means with and without steel mesh, respectively.

Table 6 Mechanical properties of concrete, UFC and ECC and results of loading test.

Specimen name	Mechanical properties of concrete			Mechanical properties of UFC or ECC		Shear capacity		
	f'_c	f_t	E_c	f_{panel}	E_{panel}	V_u	V_{REF}	n
	[N/mm^2]		[kN/mm^2]	[N/mm^2]	[kN/mm^2]	[kN]		[%]
REF	33.2	2.1	28.4	-	-	52.8	-	-
NK-WM	41.7	3.1	29.8	26.3	16.4	52.7	57.0	-7.5
WK-NM	34.3	3.1	28.4	33.9	15.8	82.2	53.4	53.9
WK-WM	36.4	2.7	28.7	28.7	18.5	75.8	54.4	39.3
NK-NM(UFC)	32.3	2.2	29.5	211.9	50.1	64.6	52.3	23.5

f'_c is compressive strength of concrete, f_t is tensile strength of concrete, E_c is elastic modulus of concrete, f_{panel} is compressive strength of UFC or ECC, E_{panel} is elastic modulus of UFC or ECC, V_u is shear capacity, V_{REF} is Shear capacity of non-strengthened specimen considering the variation of compressive strength of concrete, and n is ratio of shear capacity increase to the shear capacity of non-strengthened specimen.

was inserted between the steel plate and the specimen. On the top surface of the specimen, gypsum was applied at the loading points, and loading plates whose width is 100 mm, steel rollers and load distribution beam were set.

2.5 Measuring Items

Measuring items were applied load, displacements at the mid span and supporting points, strain of tensile reinforcing bar at mid span and strain of the ECC panels. Displacements were measured by displacement transducers. Strain of tensile reinforcing bar at the mid span was measured by strain gauge whose length was 2 mm. In addition, for the ECC panels having shear keys, tri-axial strain gauges were attached to measure the principal strain and its direction.

3. RESULT OF THE EXPERIMENT

3.1 Increase Rate of Shear Capacity

Table 6 tabulates the material property of concrete and ECC and the results of loading tests. The ratio of shear capacity increase to the shear capacity of non-strengthened specimen n was calculated by Eq. (1).

$$n = \frac{V_u - V_{REF}}{V_{REF}} \times 100 \quad (1)$$

In Eq. (1), V_{REF} is the value expressed by the Eq. (2) which eliminates the effect of variation of compressive strength of concrete among the RC beams.

$$V_{REF} = \left(\frac{f'_c}{f'_{c_REF}} \right)^{\frac{1}{3}} \times V'_{REF} \quad (2)$$

where, f'_{c_REF} is the compressive strength of concrete used in the non-strengthened specimen (=33.2 N/mm^2), and V'_{REF} is the shear capacity of the non-strengthened specimen obtained in the loading test (=52.8 kN).

From Table 6, the specimens can be arranged as WK-NM, WK-WN, NK-NM(UFC) and NK-WM in order of increase in n. That is, the shear strengthening effect was prominent in specimens with providing shear keys to the panels (WK series). The noteworthy point is that the shear capacities of WK-NM and WK-WM were higher than that of the specimen strengthened by UFC which has much higher strength and modulus of elasticity. In addition, WK-NM showed the higher shear capacity than WK-WM which had the steel mesh for strengthening. The construction of anchor bolts could be the reason as discussed in detail later.

3.2 Load-Deflection Relationships and Crack Patterns

Figure 4 shows the relationship between applied load and the mid-span deflection. Figure 5 illustrates the crack patterns after the loading tests. The bold lines seen in each RC beam represent the most distinguished crack. The fracture process in each specimen will be discussed below.

(1) NK-WM

After the initiation of the flexural crack, the load reached the maximum value, 105.4 kN. No cracks were observed in ECC panels as seen in Fig. 5(a-1).

From Fig. 5(a-2), it is seen that cracks were connecting the holes for anchor bolts. In addition, crack penetration from the upper hole for panel [B] to the compression fiber was confirmed. This is because micro cracks were induced during the making holes. Regarding the following specimens, the embedded length of anchor bolts was shortened from 70 mm to 60 mm in order to prevent micro crack formation while making holes.

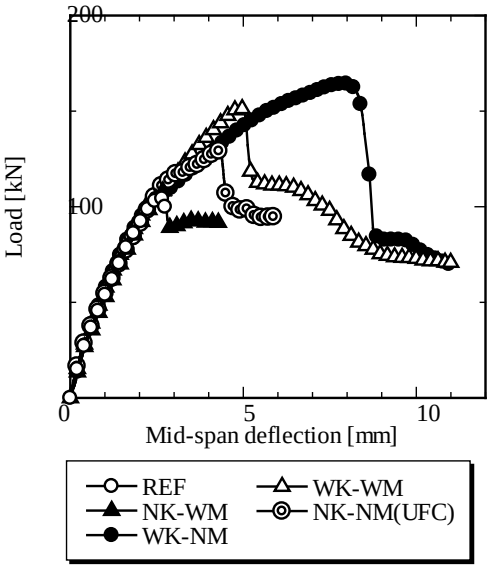


Figure 4 Load-deflection relationships.

(2) WK-WM

After the initiation of the flexural crack, the diagonal crack occurred in the RC beam when the applied load reached 107.0 kN. The load continuously increased up to 151.6 kN. As seen in Fig. 5(b-1), no cracks were observed in the ECC panels. After the loading test, some anchor bolts were pulled out.

(3) WK-NM

After the initiation of the flexural crack, the diagonal crack occurred in the RC beam at 107.0 kN. The load continuously increased to 164.4 kN. As seen in Fig. 16(c-1), some cracks were observed in panel [A]. After the loading tests, some anchor bolts were pulled out as well as observed in WK-WM.

4. SHEAR RESISTING MECHANISM

4.1 Strengthening Effect due to the Strain-Hardening Property

Figure 6 shows the maximum and minimum principal strain in panel [A] and panel [B] of WK-WM

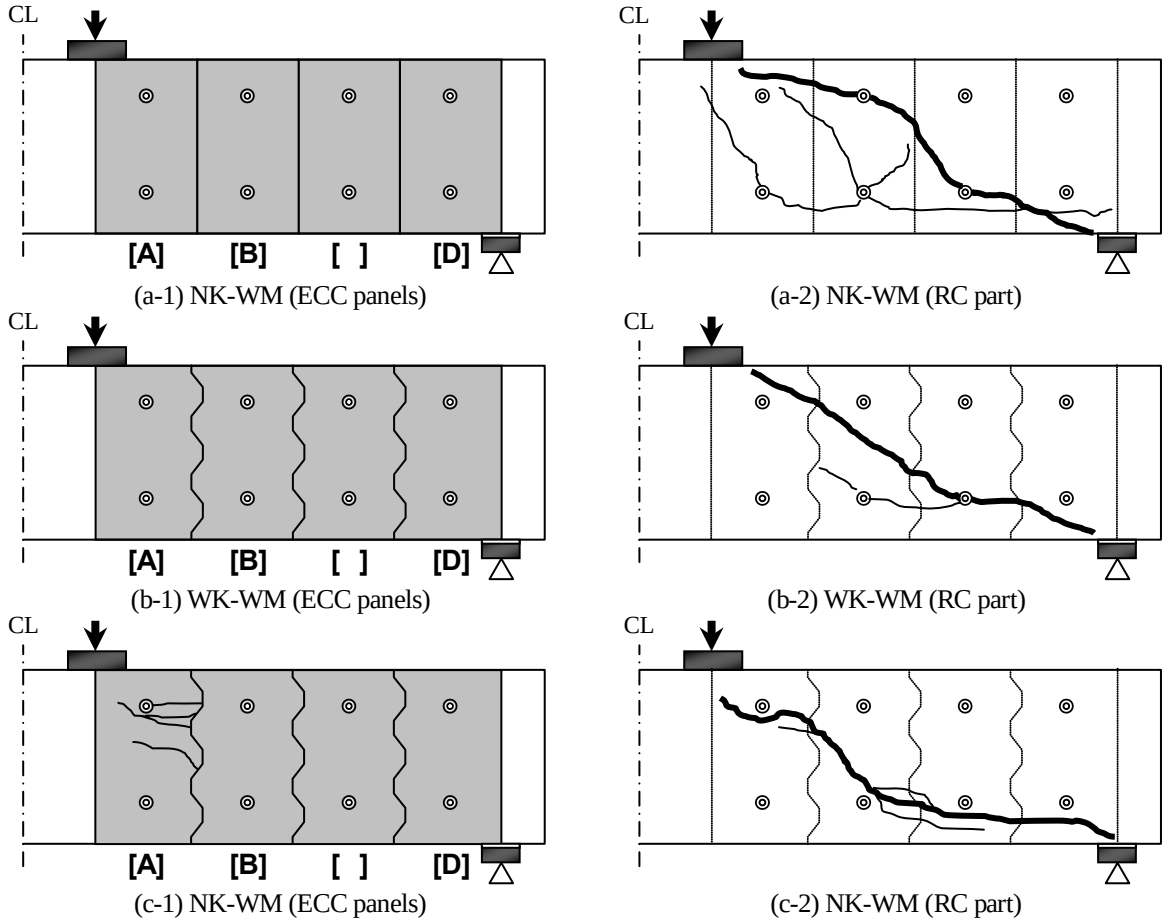


Figure 5 Crack patterns after the loading tests.

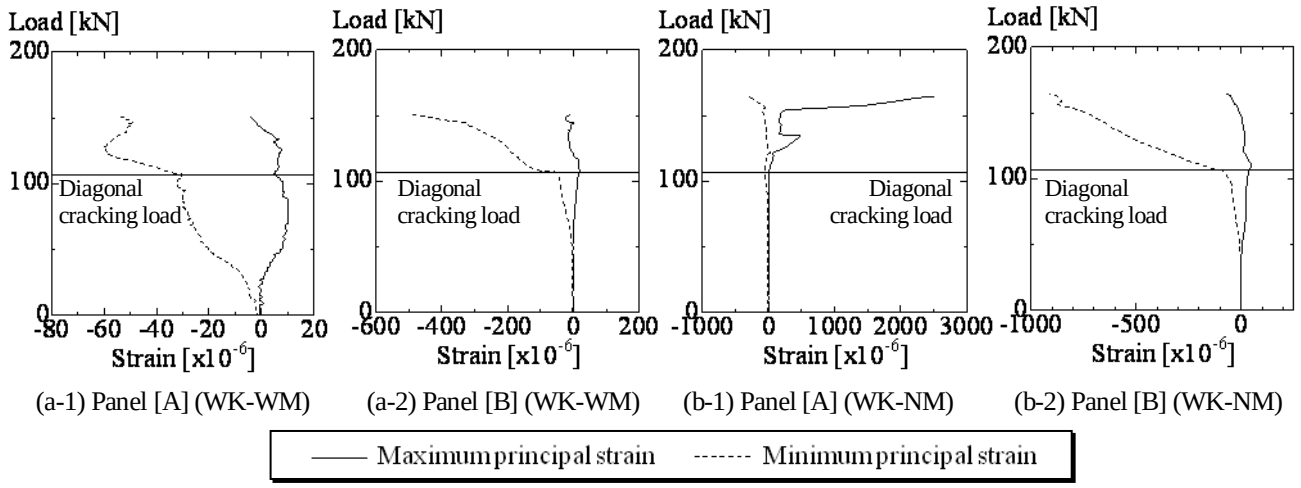


Figure 6 Principal strain in the specimens strengthened by ECC panels with shear keys.

Table 7 Angle of principal strain.

Specimen name	Panel	Angle of maximum principal strain, θ_{max} [degs]	Angle of minimum principal strain, θ_{max} [degs]
WK-WM	[A]	171	81
	[B]	179	89
WK-NM	[A]	28	118
	[B]	3	93

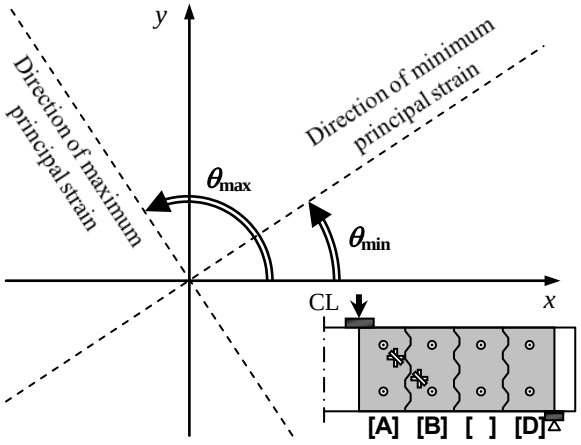


Figure 7 Definition of angle of principal strain.

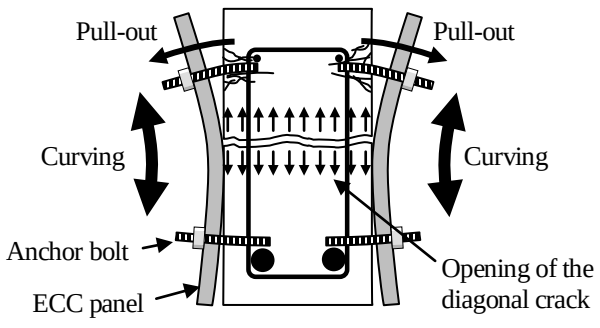


Figure 8 Pull-out of anchor bolts and panel curving.

and WK-NM. Here, the tensile strain is shown as positive value and the graphs are drawn until the load reached the maximum value. The angle of the principal strain at the maximum load is summarized in Table 7. The angle of the principal strain is the rotation angle from the horizontal direction of a specimen in a counterclockwise direction as shown in Fig. 7.

From Fig. 6(a-2) and (b-2), it can be seen that the minimum principal strain changed to the compressive direction in panel [B] of both WK-WM and WK-NM after the diagonal crack occurred. From Table 7, it is also seen that the direction of the minimum principal strain in panel [B] is almost vertical to the beam axis. In addition, significant peeling was observed between panel [B] and RC part in both WK-WM and WK-NM.

Considering the above points, the failure mechanism shown in Fig. 8 could occur in panel [B] of both specimens. Due to the initiation and widening of the diagonal crack in a RC part, the forces, which push out the two anchor bolts connecting the panel [B], occur. Due to these forces, the two anchor bolts are yielded or surrounding concrete is crushed. As a result, pull-out failure of the anchor bolts is caused. ECC panels are curved due to the pull-out failure of the anchor bolts. This panel curving results the wide opening between the RC part and ECC panels. In addition, no crack occurrence on the surface of ECC panels is also ascribable to this panel curving because the compression stress is induced on the outer surface of the panels.

On the other hand, given the increase in shear capacity of RC beams due to the contribution of ECC panels, it can be thought that the tensile force in the vertical direction also acted to the ECC panels. In other words, tensile force as the contribution to the increase in the shear capacity and bending moment as shown in Fig. 8 acted at the same time. Consequently, there is a possibility that cracks occurred in the back side of a panel which was the attached surface to the RC beam. The fiber bridging at these cracks could transfer the load and contribute to the increase in the shear capacity.

Next, the behavior of panel [A] in WK-NM is focused.

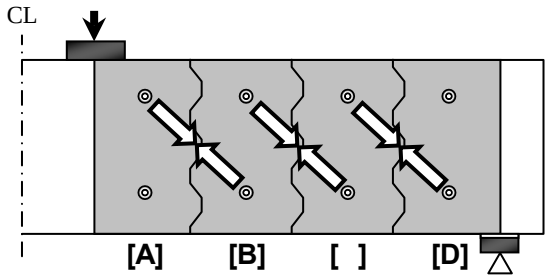


Figure 9 Flow of the diagonal compression force.

From Fig. 6(b-1), only a small amount of principal strain is seen before the diagonal crack occurred in RC part. However, the maximum principal strain started to increase in the tensile direction at the load of 122.0 kN. Afterward, the maximum principal strain showed the sharp decrease at the load of 135.0 kN. The cause of this decrease can be explained that the cracking in the back side of the ECC panel as discussed above temporary reduces the vertical force of panels. The maximum principal strain continued to increase at the load of 154.0 kN. This is caused by the cracking on the surface of the panel. It is inferable that there is less curving in panel [A] of WK-NM and therefore cracks on the surface of panel happened.

4.2 Role of the Shear Keys

From Fig. 6(b-1), it can be confirmed that the minimum principal strain in panel [A] of WK-NM increased in compression at the load of 157.0 kN. In addition, as seen in Table 7, the angle of the minimum principal strain was different from that of the other panels.

This is because the interlock of shear keys provided the diagonal compression force. The diagonal crack in RC part was widened as the loading test proceeded. With the widening of the diagonal crack, ECC panels moved up or down and the adjacent ECC panels were interlocked each other. This helped the diagonal compression force could be transferred. As a result, the flow of the compression force is formed from the upper and lower anchor bolts in the adjacent ECC panels as shown in Fig. 9.

5. CONCLUSIONS

In this study, shear behavior of RC beams strengthened by ECC panels was investigated. Loading tests of RC beams with attaching ECC panels on both sides by using anchor bolts were carried out. Presence of shear keys between panels and steel mesh inside the panels were the experimental parameter. Strengthening effect was verified by comparing to non-strengthened beam and the beam strengthened by UFC panels. As a result, following conclusions were obtained.

1) Shear capacity of the RC beams strengthened by ECC panels with shear keys drastically increased compared to the non-strengthened beam. Even though the material strength of UFC is much higher than that of ECC, the shear capacity was larger than that of the beam strengthened by UFC.
2) Curving of the ECC panels and pull-out of the anchor bolts lead to the failure of the RC beams strengthened by ECC panels with shear keys. The cause of panel curving and pull-out of anchor bolts was the force generated due to the occurrence and widening of the diagonal crack. The force acted vertically to push out the anchor bolts and resulted the yielding of anchor bolts or crushing of surrounding concrete. It caused the pull-out force of the anchor bolts.
3) When shear keys were provided between the ECC panels, the principal strain of the ECC panel increased in compression after the occurrence of the diagonal crack. In addition, direction of the compressive principal strain was inclined. It indicates that the formation of diagonal compressive force caused by interlocking of shear keys contributed to the shear resisting mechanism.

References:

Li, V.C. (1998), "Engineered Cementitious Composite (ECC) – Tailored Composites through Micromechanical Modeling," *Presented and the Future edited by Banthia et al., CSCE, Montreal*.

Yamamoto, A., Watanabe, K., Li, V.C. and Niwa, J. (2010), "Effect of Wet-Dry Condition on Self-healing Property of Eary-age ECC," *Proceedings of Japan Concrete Institute*, **32**(1), 251-256.

Matsumoto, K., Shibata, K. and Niwa, J. (2010), "Shear Retrofitting Method for RC Beam Using UFC Panels," *Joint Conference Proceedings of 7 CUEE and 5ICEE*, 1887-1893.

8CUEE CONFERENCE PROCEEDINGS
8th International Conference on Urban Earthquake Engineering
March 7-8, 2011, Tokyo Institute of Technology, Tokyo, Japan

APPLICABILITY OF TENSION SOFTENING CURVES FOR THE CONTRIBUTION OF STEEL FIBERS TO SHEAR RESISTANCE OF RSF BEAMS

Pitcha Jongvivatsakul[1], Ken Watanabe[2], Koji Matsumoto[3], and Junichiro Niwa[4]

1) Graduate Student, Department of Civil Engineering, Tokyo Institute of Technology, Japan
2) Assistant Senior Researcher, Concrete Structures, Railway Technical Research Institute, Japan
3) Assistant Professor, Department of Civil Engineering, Tokyo Institute of Technology, Japan
4) Professor, Department of Civil Engineering, Tokyo Institute of Technology, Japan
jongvivatsakul.p.aa@m.titech.ac.jp, wataken@rtri.or.jp, matsumoto.k.ar@m.titech.ac.jp, jniwa@cv.titech.ac.jp

Abstract: Shear failure in reinforced concrete (RC) beams is well known as the brittle behavior happening without any warnings. This failure can be prevented by improving the shear capacity of the structures. The use of steel fibers as a shear reinforcement is one of the alternatives to enhance the shear resistance and ductility of the structures and this type of structures is called reinforced concrete with steel fibers (RSF). However, the current equation of Japan Society of Civil Engineers (JSCE) design guidelines for RSF members has not considered the post cracking behavior of reinforced concrete with steel fibers in details. The objective of this paper is to evaluate the contribution of steel fibers to shear resistance of RSF beams using the tension softening curves. Eight RSF beams with various steel fiber volume fraction and stirrup ratio were tested. The crack surface displacement was investigated from the image analyzing system. Length of the diagonal crack was measured for computing the area of stress transfer. The tension softening curves were used to calculate the stress transferred across the diagonal crack. Finally, the shear carried by steel fibers was investigated.

1. INTRODUCTION

The standards specifications of Japan Society of Civil Engineers (JSCE) for seismic design of reinforced concrete structures (2002) have been revised after the 1995 Hyogoken-Nambu earthquake resulting in high requirement for steel bars in the structures. This leads congestion of steel bars; thus, it is difficult to fill concrete during the construction. The use of steel fibers is one of the solutions for this problem. Many researchers (Narayanan and Darwish 1987 and Watanabe et al. 2009) have reported that the addition of steel fibers can improve the shear resistance and the ductility of reinforced concrete (RC) beams. Steel fibers enhance the energy dissipation capacity. Hence, reinforced concrete with steel fibers (RSF) beams provide higher seismic performance than ordinary RC beams.

In JSCE design guidelines for RSF members (1999), the increment of the shear strength by steel fibers has been expressed as a value κ, which is defined as a ratio of the shear carried by steel fibers to the shear carried by concrete and κ is considered as 1.0. However, the current equation underestimated the shear capacity of RSF beams. Watanabe et al. (2009) concluded that the values of κ observed in the experiment were more than 1.0. In addition, there was an optimized combination of steel fibers volume fraction (SF) and the stirrup ratio (r_w) to increase the value of κ. It was suggested that the optimized combination would be related to the crack surface displacement and the length of the diagonal crack. Nevertheless, there was no verification for the influence of crack surface displacement and length of the diagonal crack on the shear carried by steel fibers of RSF beams.

The purpose of this research is to evaluate the shear carried by steel fibers of RSF beams. Eight RSF beams with different SF and r_w were tested. The crack surface displacement (u), which was the displacement of crack in the direction of crack's movement, was evaluated by using the displacements of targets obtained through the image analyzing system. The tension softening curve, which was one of the fracture parameters, was used to explain the shear resistance mechanism of RSF beams. The tensile stress transferring at the diagonal crack surfaces was calculated from measured crack surface displacement by using the relationship of the tension softening curves. The shear carried by steel fibers was evaluated. The comparison between the experimental values and the calculated values was presented for the validation of the proposed method.

2. TENSION SOFTENING CURVES

In order to estimate the tension softening curves, the bending tests of notched beams were conducted according to the standard of Japan Concrete Institute (JCI) (2003). The tension softening curve represents the relationship between tensile stress and crack opening displacement in the fracture

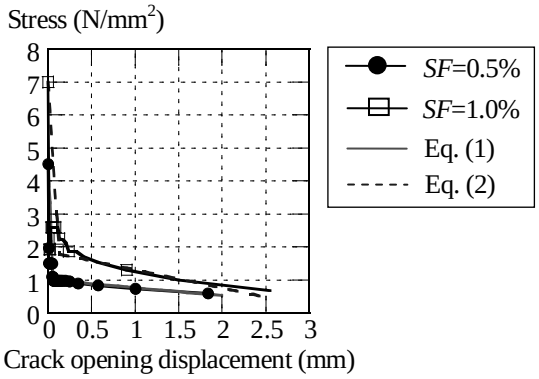


Figure 1 Tension Softening Curves

zone. The tension softening curves of fiber reinforced concrete having SF = 0.5% and 1.0% of concrete full volume were examined as shown in Figure 1. The compressive strength of concrete was 59.6 and 56.5 N/mm^2; in addition, the fracture energy of concrete was 2.03 and 3.26 N/mm when SF = 0.5 and 1.0%, respectively. From the tension softening curves, the relationships between the crack surface displacement (u) and tensile stress of concrete (σ) can be obtained by the regression analysis. The bilinear curves for $\sigma(u)$ of 0.5 and 1.0% of steel fiber volume fraction are given by Eqs. (1) and (2), respectively.

$$\sigma = \begin{cases} 4.5 - 58.6u & \text{for } u < 0.06\,\text{mm} \\ 1.0 - 0.24u & \text{for } u \geq 0.06\,\text{mm} \end{cases} \quad (1)$$

$$\sigma = \begin{cases} 7.0 - 40.2u & \text{for } u < 0.13\,\text{mm} \\ 1.85 - 0.55u & \text{for } u \geq 0.13\,\text{mm} \end{cases} \quad (2)$$

3. EXPERIMENTAL PROGRAM

3.1 Test Specimens

The test program consisted of eight RSF beams with different SF and r_w. SF was 0.5 and 1.0% of concrete volume. r_w was varied (i.e. r_w=0.00, 0.12, 0.18, 0.24, and 0.30%). The detail of a RSF beam is illustrated in Figure 2. The shear span (a) was 700 mm and effective depth (d) was 250 mm. The shear span to effective depth ratio (a/d) was 2.8. The longitudinal reinforcement ratio (p_w) was 2.7%. The number of stirrups used in each specimen was changed corresponding to the stirrup ratio. The specimen cases are summarized in Table 1. Specimens were named according to SF and r_w; e.g. SF10-r18 corresponded to the specimen with SF=1.0% and r_w=0.18%.

3.2 Material

The detail of mix proportion of concrete is summarized in Table 2. The concrete was designed with average 7-day age strength of 50 N/mm^2. The steel fibers used in this research had hook-ends. The length was 30 mm, the diameter was 0.62 mm, the aspect ratio was 48, the yield strength was 1050 N/mm^2, the density was 7850 kg/m^3, and

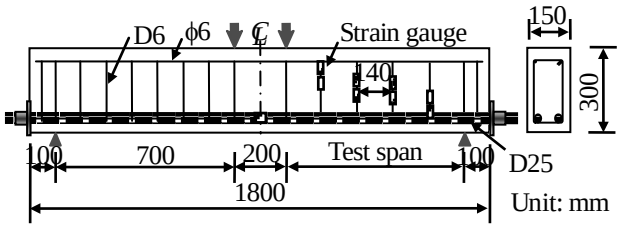


Figure 2 Outline of a RSF Beam

Table 1 Experimental Cases

Case	Steel fiber volume fraction (%)	Stirrup ratio (%)
SF05-r00	0.5	0.00
SF05-r18		0.18
SF05-r30		0.30
SF10-r00	1.0	0.00
SF10-r12		0.12
SF10-r18		0.18
SF10-r24		0.24
SF10-r30		0.30

the elastic modulus was 210 kN/mm^2. The longitudinal reinforcing bars were deformed steel with 25.4 mm of the nominal diameter. The yield strength was 1016 N/mm^2. The stirrups with deformed steel of 6 mm in the diameter were arranged as the shear reinforcement. The yield strength was 336 N/mm^2. Two round bars with the diameter of 6 mm were used as compression bars. The yield strength was 293 N/mm^2.

3.3 Loading Method and Measurement Items

Specimens were subjected to a four-point bending. Locations of loading and supporting points are illustrated in Figure 2. Specimens were placed on the roller supports.

During the loading test, the applied load was measured. Mid-span deflection was measured using four transducers. The strain gauges were used for measuring strain of longitudinal steel bars at mid-span. Besides, the strains of stirrups were measured at the locations that diagonal crack was expected to occur as shown in Figure 2.

3.4 Image Analysis and Crack Surface Displacement

The image analyzing system developed by Higashi et al. (2009) was conducted in order to measure the crack surface displacements of specimens. Red targets with diameter of 5 mm were attached on the specimen surface with an interval of 20 mm. The white light-emitting diodes (LED) were used to increase accuracy of the image analysis. During the loading test, photos of the specimen were taken by every 5 kN of the shear force by using three digital cameras fixed on tripods. A picture of loading test is shown in Figure 3. The coordinates of targets were investigated by the image analysis.

Crack surface displacement (u) is defined as the relative displacement of targets on the principal tensile strain direction, which is the direction of crack's movement. The calculation procedure of u is shown in Figure 4. First, the

Table 2 Mix Proportion of Concrete

Maximum size of coarse aggregate (mm)	Water-cement ratio *W/C* (%)	Sand-aggregate ratio *s/a* (%)	Unit weight (kg/m^3)				
			Water	Cement	Fine aggregate	Coarse aggregate	Superplasticizer
20	35	53.1	165	471	917	790	5.2

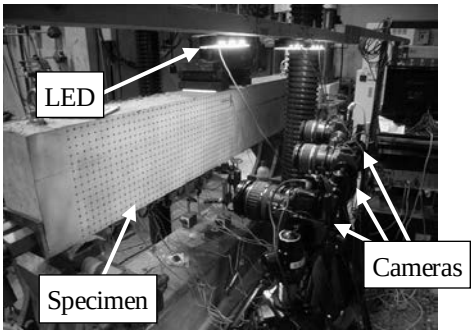


Figure 3 Loading Test

displacements of targets in x and y directions are examined. The displacements of targets are the difference of coordinate of targets between first photo and any photos. Second, the relative displacement between two targets that the crack passed (Δx, Δy) (Figure 4 (a)) is calculated using Eq. (3). Third, the angle of principal tensile strain (θ) is calculated at the center of square that the crack passed (Figure 4 (b)) by using Eq. (4). Finally, crack surface displacement, u, is determined by Eq. (5) as shown in Figure 4 (c).

$$\Delta x = \Delta x_1 - \Delta x_2\,, \quad \Delta y = \Delta y_1 - \Delta y_2 \tag{3}$$

$$\theta = 0.5\tan^{-1}\left\{\frac{\gamma_{xy}}{(\varepsilon_x - \varepsilon_y)}\right\} \tag{4}$$

$$u = \Delta x \cdot \cos\theta + \Delta y \cdot \sin\theta \tag{5}$$

where, Δx is the relative displacement in x direction, Δy is the relative displacement in y direction, (Δx_1, Δx_2) is the displacement of targets in x direction, (Δy_1, Δy_2) is the displacement of targets in y direction, θ is the angle of principal tensile strain, γ_{xy} is the shear strain, ε_x is the strain of x-axis, and ε_y is the strain of y-axis.

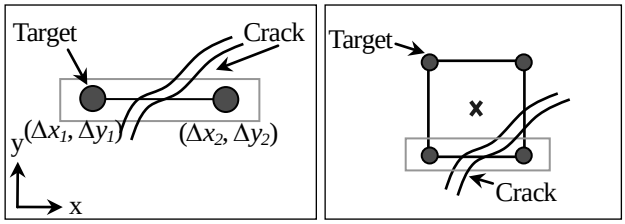
3.5 Measurements of Length and Angle of Diagonal Crack

The length and angle of diagonal crack were measured from the visible diagonal crack at the peak load by using the image processing software. The images taken for measuring the crack surface displacements were also used to measure the diagonal crack length and angle of diagonal crack.

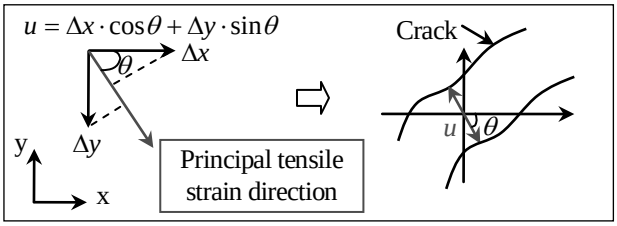
4. EXPERIMENTAL RESULTS

4.1 Load-Deflection Relationship of RSF Beams

The load-mid span deflection relationships of RSF beams are presented in Figure 5. These diagrams show



(a) Targets that Crack Passed (b) Square that Crack Passed



(c) Crack Surface Displacement

Figure 4 Calculation of Crack Surface Displacement

clearly that the shapes of the load-deflection curve of the corresponding beams were basically similar in all specimens. All the beams exhibited similar linear behavior from the initial loading up to the first flexural crack. After the first flexural crack, the curve still increased linearly until the initiation of a diagonal crack occurred in a shear span. The diagonal crack was observed around the middle height of the specimen. After the initiation of a diagonal crack, the diagonal crack propagated to supports and to the top of specimens. In addition, the appearance of the diagonal crack reduced the slope of load-deflection curves of RSF beams. All of the stirrups, which the diagonal crack passed, showed the yielding strain in this stage. The propagation of the diagonal crack length stopped when the diagonal crack reached to the compression zone. From this stage, the rate of load increment became slight and the load-deflection curves showed nonlinear behavior. Then, the load reached to the peak and suddenly dropped due to the crushing of the concrete in compression zone. Similar process of shear failure was observed in all beams.

4.2 Diagonal Cracking Behaviour

One critical diagonal crack was remarkable in each specimen. This study focuses on the tensile force along this diagonal crack. Specimens were divided to 15 elements with a height of 20 mm corresponding to the interval of targets of the image analysis as shown in Figure 6. Crack surface displacement (u_i), length (L_i), angle of principal tensile strain (θ_i), and angle of a diagonal crack (β_i) of each element were investigated based on the pictures taken at peak load.

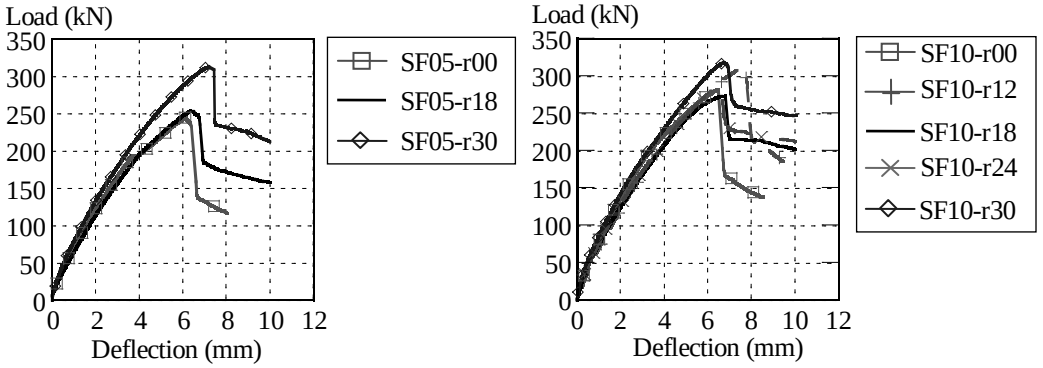
1. *Crack surface displacement (u)*

The value of u along the height of specimens at the maximum load is shown in Figure 7. Unlike the flexure

Table 3 Summary of the Experimental Results

Specimen	Concrete properties		Diagonal crack				Experimental results					Calculation	
	f_c' (N/mm^2)	f_t (N/mm^2)	u_{avg} (mm)	L (mm)	θ_{avg} (°)	β_{avg} (°)	V_{exp} (kN)	V_c (kN)	V_s (kN)	V_{fexp} (kN)	κ_{exp}	V_{fcal} (kN)	V_{fexp} /V_{fcal}
SF05-r00	54.1	2.81	1.40	660.1	64.4	29.7	122.4	55.9	0.0	66.5	1.19	60.2	1.11
SF05-r18	45.0	2.59	0.69	487.9	63.2	35.8	126.9	52.6	21.3	53.1	1.01	51.2	1.04
SF05-r30	59.3	3.17	1.25	582.0	63.9	33.0	156.5	57.6	42.5	56.4	0.98	56.1	1.00
SF10-r00	64.9	3.90	1.54	539.0	66.9	27.9	141.1	59.4	0.0	81.7	1.38	73.5	1.11
SF10-r12	53.0	3.91	1.12	493.2	62.5	33.4	155.5	55.5	20.6	79.5	1.43	83.5	0.95
SF10-r18	46.6	3.45	1.10	422.1	62.4	35.1	136.8	53.2	20.6	63.1	1.19	63.4	1.00
SF10-r24	48.3	3.26	0.94	438.6	63.1	34.0	143.1	53.8	21.5	67.8	1.26	71.6	0.95
SF10-r30	55.3	3.05	0.67	387.3	63.3	34.0	158.8	56.3	40.3	62.1	1.10	72.6	0.86

f_c': compressive strength, f_t: tensile strength, u_{avg}: average crack surface displacement at the peak, L: total crack length at the peak, θ_{avg}: average angle of principal tensile strain at the peak, β_{avg}: average angle of diagonal crack at the peak



(a) SF = 0.5% (b) SF = 1.0%

Figure 5 Load-Deflection Curves

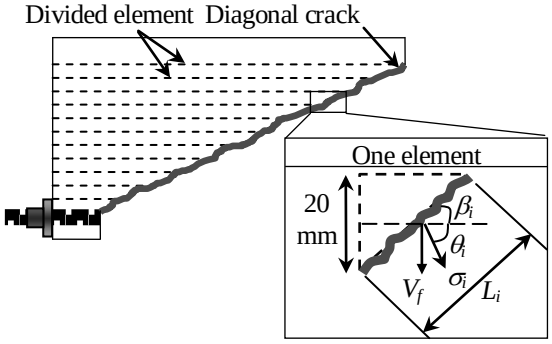


Figure 6 Free Body Diagram

crack, the diagonal crack surface displacement was larger at around the middle height of specimens compared with the u at the top and the bottom of specimens because there was compression zone at top of specimens and restraint by longitudinal reinforcing bars at the bottom fiber. Table 3 shows the average value of crack surface displacement (u_{avg}) of diagonal crack in the region of interest. The region of interest is from the height below the compression zone until the tip of the diagonal crack in the tension zone, which is the same position with the location of tensile bars in specimens having SF=1.0%. In specimens which SF=0.5%, the diagonal crack propagated into the concrete cover zone and stopped at 30 mm from the bottom fiber because of the less shear reinforcement. The compression zone is the height of specimens from the top fiber to the location of neutral axis. The neutral axis was calculated from the displacements of targets obtained through the image analysis. The region of interest is shown in Figure 7. The results showed that u_{avg} increased with the increase in the steel fiber volume fraction and decreased with the increase in the stirrup ratio.

2. *Diagonal crack length (L)*

The crack length (L) is the length of a diagonal crack in the region of interest. L decreased with the increase in SF and r_w as shown in Table 3.

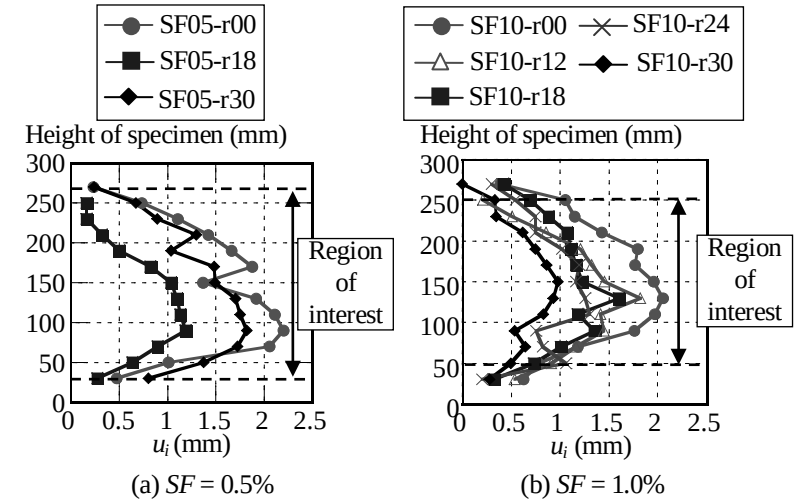
3. *Angles of principal tensile strain (θ) and diagonal crack (β)*

The angles of principal tensile strain (θ) and diagonal crack (β) were measured at the same position with the crack surface displacement. Table 3 presents the average value of these angles in the region of interest. θ_{avg} and β_{avg} did not change significantly among these specimens.

5. SHEAR FORCES

5.1 Calculation Method and Experimental Values of Shear Forces

According to JSCE design guidelines (1999), the shear capacity of RSF members (V_{cal}) and the shear carried by concrete (V_c) can be calculated from Eqs. (6) and (7). The



(a) SF = 0.5% (b) SF = 1.0%

Figure 7 Distribution of Crack Surface Displacement at Peak Load

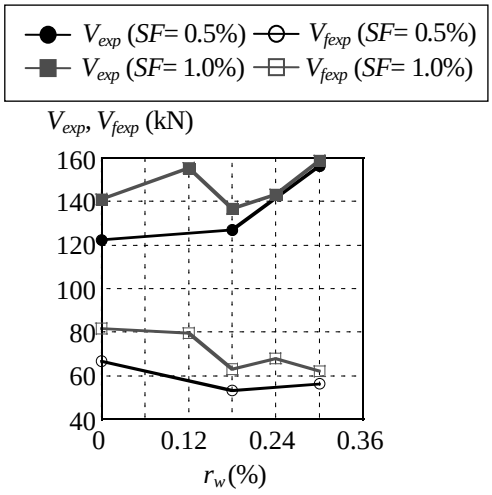
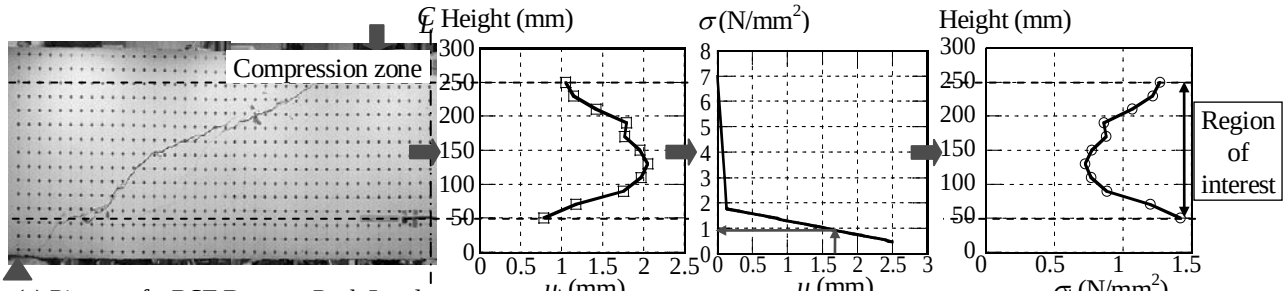


Figure 8 Effect of SF and r_w on V_{exp} and V_{fexp}



(a) Picture of a RSF Beam at Peak Load (SF10-r00) (b) u Distribution (c) Tension Softening Curve (d) Stress Distribution

Figure 9 Investigation Procedures of Tensile Stress Transferred across the Diagonal Crack

shear carried by stirrups (V_s) was calculated from the yielding stress of stirrups that diagonal crack passed as shown in Eq. (8). The experimental value of shear carried by steel fibers (V_{fexp}) was investigated by Eq. (9) while experimental value of κ was calculated by using Eq. (10).

$$V_{cal} = (1+\kappa)\cdot V_c + V_s \quad (6)$$

$$V_c = 0.2\cdot\sqrt[3]{f_c'}\cdot\sqrt[4]{1000/d}\cdot\sqrt[3]{100\,p_w}\cdot b_w\cdot d \quad (7)$$

$$V_s = \sum A_w f_{wy} \quad (8)$$

$$V_{f\,exp} = V_{exp} - V_c - V_s \quad (9)$$

$$\kappa_{exp} = V_{f\,exp}/V_c \quad (10)$$

where, κ is coefficient representing the effect of fibers (κ=1.0), f_c' is compressive strength of concrete (N/mm^2), d is effective depth (mm), p_w is longitudinal reinforcement ratio (%), b_w is web thickness (mm), A_w is cross section area of stirrups (mm^2), and f_{wy} is yield strength of stirrups (N/mm^2).

The shear forces from experimental results are listed in Table 3. The shear capacity of RSF beams (V_{exp}) was higher than the calculated value obtained from Eq. (6). κ_{exp} was more than 1.0 except SF05-r30. The values of V_{exp} and V_{fexp} varied depending on SF and r_w.

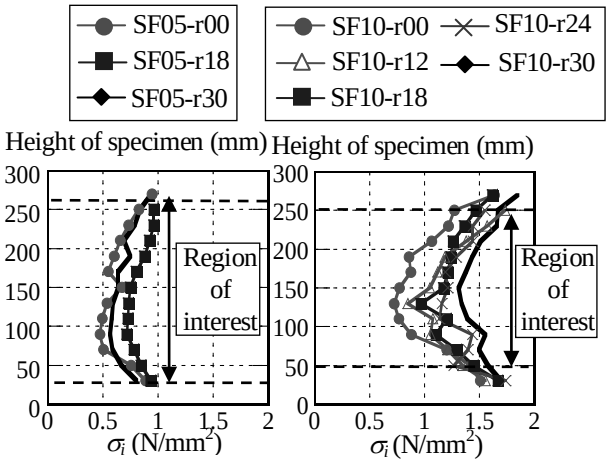
5.2 Influences of Steel Fiber Volume Fraction and Stirrup Ratio

The effect of SF and r_w on V_{exp} and V_{fexp} of RSF beams is shown in Figure 8. V_{exp} showed the maximum value in SF10-r30, while the maximum value of V_{fexp} was SF10-r00. By comparing V_{exp} and V_{fexp} of specimens with the same r_w, it was found that the increase in the SF from 0.5 to 1.0% enhanced the values of V_{exp} and V_{fexp}. However, the improvement of V_{exp} and V_{fexp} due to the effect of SF became less significant with the increase in r_w. This implies that the effect of steel fibers as the shear reinforcement is dominant in case of smaller r_w.

On the other hand, beams with the same SF but different in r_w showed another tendency. That is, the value of V_{exp} in RSF beams will not necessarily increase with the increase in r_w as shown in Figure 8. This is because of the reduction of V_{fexp} in specimens with high r_w. This result confirms that there is a combination effect of stirrups and steel fibers to increase the value of V_{fexp}.

6. EVALUATION OF SHEAR CARRIED BY STEEL FIBERS

The shear carried by steel fibers was investigated using tension softening curves. Calculation procedures of the shear carried by steel fibers in this study are shown in Figure 9. The crack surface displacement of each element was



(a) SF = 0.5% (b) SF = 1.0%

Figure 10 Stress Distribution along the Diagonal Crack

converted to the tensile stress transferring along the diagonal crack by using the relationship of tension softening curves (Eqs. (1) and (2)). The results of tensile stress along the height of diagonal crack at peak load are shown in Figure 10. The larger stress could be resisted at top and bottom parts of specimens due to the smaller crack surface displacement.

By considering the force acting at a diagonal crack in a RSF beam due to the effect of steel fibers (Figure 6), the tensile force along the diagonal crack of each element can be obtained by multiplying σ_i with the area of crack surface normal to the direction of σ_i. The shear force was calculated for element by element. The vertical component of the force with the consideration of θ_i is the shear carried by steel fibers. According to Figure 6, the force along the diagonal crack is obtained from the portion below the compression zone to the tip of diagonal crack in the tension zone. The numbers of elements in the region of interest were 13 elements for specimens having SF=0.5% and 11 elements for specimens having SF=1.0%. The shear carried by steel fibers (V_{fcal}) can be expressed as Eq. (11).

$$V_{fcal} = \sum_{i=1}^{n} \left(\sigma_i \cdot b_w \cdot L_i \cdot \cos\left(\theta_i + \beta_i - 90\right) \cdot \sin\theta_i\right) \qquad (11)$$

where, n is number of elements in the region of interest, σ_i is the tensile stress of element i (N/mm^2), L_i is the length of diagonal crack of element i (mm), θ_i is the angle of principal tensile strain of element i (degree), and β_i is the angle of diagonal crack of element i (degree).

The result of calculated shear carried by steel fibers (V_{fcal}) using Eq. (11) and the experimental value (V_{fexp}) given by Eq. (9) is summarized in Table 3. Figure 11 presents the comparison of the experimental results and calculated values. A total of eight specimens were used to validate the proposed method. The mean value of the experimental value to calculated value of the shear carried by steel fibers was 1.00 with the coefficient of variation (*C.V.*) of 8.5%. The comparison demonstrates that V_{fcal} corresponded with V_{fexp}. This finding implies that the shear carried by steel fibers can be evaluated by using the tension softening curves.

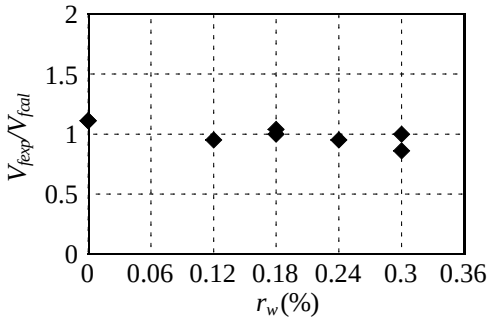


Figure 11 Comparison of V_{fexp} and V_{fcal}

7. CONCLUSIONS

The following conclusions were drawn from the study on the contribution of steel fiber to the shear capacity of reinforced concrete beams with steel fibers by considering the steel fiber volume fraction and the stirrup ratio.

(1) The crack surface displacement of diagonal crack around the middle height of specimens was larger than those at top and bottom fibers because there was the compression zone at the top fiber and restraint by the longitudinal steel bars at the bottom fibers.

(2) The crack surface displacement increased with the increase in the steel fiber volume fraction and decreased with the increase in the stirrup ratio.

(3) The length of diagonal crack decreased when the steel fiber volume fraction and the stirrup ratio increased.

(4) By comparing with the tensile stress around the middle of specimens, the tensile stress transferred across the diagonal crack was higher in top and bottom fibers due to the smaller crack surface displacement.

(5) The shear carried by steel fibers calculated by using the crack surface displacement, the diagonal crack length and the relationship of the tension softening curves corresponded with experimental values.

Acknowledgements:

The authors acknowledge the support from the Grant-in-Aid for Scientific Research (A: No.19206050) from JSPS and the Maeda Engineering Foundation.

References:

Higashi, H., Watanabe, K., and Niwa, J. (2009), "Image Analysis for Failure Mode of RC Beams with Fractured Longitudinal Reinforcement", *Proceedings of the Japan Concrete Institute*, Japan Concrete Institute, **31**(2), 727-732. (in Japanese)

Japan Concrete Institute (JCI) (2003), "Method of Test for Fracture Energy of Concrete by Use of Notched Beams", JCI Standard.

Japan Society of Civil Engineers (JSCE) (1999), "Guidelines of Design for RSF Piers", Concrete Library 97. (in Japanese)

Japan Society of Civil Engineers (JSCE) (2002), "Standard Specifications for Concrete Structures (Structural Performance Verification)".

Narayanan, R. and Darwish, I. Y. S. (1987), "Use of Steel Fibers as Shear Reinforcements", *ACI Structural Journal*, American Concrete Institute, **84**(3), 216-227.

Watanabe, K., Kimura, T., Kodama, T., Kita, S., Odera, I., and Niwa, J. (2009), "Shear Reinforcement for RC Linear Members by a Combination of Steel Fibers and Shear Reinforcing Bars", *Journal of Materials, Concrete Structures and Pavements*, Japan Society of Civil Engineers, **65**(3), 322-331. (in Japanese)

8CUEE CONFERENCE PROCEEDINGS
8th International Conference on Urban Earthquake Engineering
March 7-8, 2011, Tokyo Institute of Technology, Tokyo, Japan

EXPERIMENTAL STUDY ON DIAGONAL COMPRESSIVE CAPACITY OF REINFORCED CONCRETE BEAMS USING HIGH STRENGTH MATERIALS

Patarapol Tantipidok[1)], Koji Matsumoto[2)], Ken Watanabe[3)], and Junichiro Niwa[4)]

1) Ph.D. Candidate, Dept. of Civil Engineering, Tokyo Institute of Technology, Japan
2) Assistant Professor, Dept. of Civil Engineering, Tokyo Institute of Technology, Japan
3) Assistant Senior Researcher, Railway Technical Research Institute, Japan
4) Professor, Department of Civil Engineering, Tokyo Institute of Technology, Japan
tantipidok.p.aa@m.titech.ac.jp, matsumoto.k.ar@m.titech.ac.jp, wataken@rtri.or.jp, jniwa@cv.titech.ac.jp

Abstract: The utilization of recently developed high strength materials can satisfy the need for improving seismic performance of infrastructures. However, in case of reinforced concrete (RC) beams, the combination of thin web T- or I-shaped cross section and high strength shear reinforcing bars will lead to an uncommon type of shear failure known as the diagonal compression failure. This research aims to investigate the influence of various parameters on diagonal compressive capacity of RC beams using high strength materials. Eight I-beams were tested by three-point bending. Verification of the effect of compressive strength of concrete, stirrup spacing, flange width to web width ratio and effective depth was performed. As a result, the effect of compressive strength of concrete and stirrup spacing were interrelated while the effect of the other factors cannot be observed. Finally, the accuracy of the existing equations for the diagonal compressive capacity was revealed.

1. INTRODUCTION

The improvement of seismic performance of infrastructures is required in order to mitigate the seismic risk and build a safe society. This demand can be satisfied by the utilization of the recently developed high strength materials, e.g. high strength concrete with the compressive strength (f'_c) greater than 100 N/mm^2 and high strength reinforcing bars with the yield strength (f_y) greater than 685 N/mm^2. Because of their high strength properties, cross-sectional area of bridge girders can be reduced which resulting in the reduction of dead load transferred into substructure. However, in case of reinforced concrete (RC) beams, the combination of thin web T- or I-shaped cross section and high strength shear reinforcing bars will lead to an uncommon type of shear failure known as the diagonal compression failure. It is caused by the crushing of web concrete prior to the yielding of stirrups. This type of failure is hazardous because of its brittle behavior.

The research on the mechanism of diagonal compression failure is insufficient since it is usually avoided. On top of that, there are some concerns regarding the applicability of the existing predictive equation for diagonal compressive capacity to high strength concrete since most of them were based on experimental results of beam specimens with normal strength concrete. The design equation for the diagonal compressive capacity of RC beams in the current Japan Society of Civil Engineers (JSCE) standard specifications for concrete structures (2002) only considers the effect of compressive strength and limits the applicability to concrete with f'_c up to 50 N/mm^2.

Besides, there are limited studies on diagonal compression failure in high strength RC beams except for Kobayashi et al. (2009). They reported that the factors affecting the diagonal compressive capacity are the compressive strength (f'_c), the stirrup ratio (r_w) and the shear-span to effective depth ratio (a/d). However, in regard to some factors, e.g. f'_c and r_w, there is a lack of experimental data especially in both $f'_c > 100$ N/mm^2 and $r_w < 2\%$. As well, the effect of the flange width to web width rato (b_f/b_w) and effective depth (d) or size effect on the diagonal compressive capacity has not been clarified yet. From these reasons, further study is required.

The main objectives of this research are to investigate the mechanism of the diagonal compression failure of thin web RC beams using high strength materials. In this study, eight I-shaped RC beams were tested by three-point bending. The effect of f'_c, r_w, b_f/b_w and d on the diagonal compressive capacity was evaluated. Finally, the accuracy of the existing equations was verified.

2. REVIEW OF THE EXISTING EQUATIONS FOR DIAGONAL COMPRESSIVE CAPACITY

2.1 The equation by Placas and Regan

Placas and Regan (1971) proposed an empirical

equation for evaluating the diagonal compressive capacity as the following:

$$V_{Placas} = (1.04 + 0.21 r_w)\sqrt{f'_c}\, b_w d \qquad (1)$$

Factors involving the diagonal compressive capacity in this equation are f'_c and the stirrup ratio, r_w (%). Although there is no upper limit of f'_c stated in this equation, the experimental evidences used to derive this equation approximate 35 N/mm^2.

2.2 JSCE Standard Specifications

In JSCE standard specifications (2002), only f'_c is considered as the influential parameter of diagonal compressive capacity. Therefore, this equation is quite conservative and only valid for concrete with f'_c not exceeding 50 N/mm^2.

$$V_{JSCE} = 1.25\sqrt{f'_c}\, b_w d \qquad (2)$$

2.3 Eurocode2 1992-1-1:2004

In Eurocode 2 (2004), the strut inclination method based on a truss model was used to design members with shear reinforcement. Designers can select the values of angle of concrete strut (θ) freely from 21.8 to 45 degrees. In this paper, to study the most extreme cases, θ was assumed to be 45 degrees. Hence, the maximum shear capacity which can be sustained by the member, limited by crushing of the compression struts, becomes the following:

$$V_{EC2} = 0.45 \nu f'_c\, b_w d \qquad (3)$$

where; ν is a coefficient that takes into account the increase of fragility and the reduction of shear transfer by the aggregate interlock with the increase of f'_c. It may be taken to be 0.6 for $f'_c \leq 60$ N/mm^2 and the minimum between 0.9-(f'_c/200) and 0.5 for $f'_c > 60$ N/mm^2.

3. EXPERIMENTAL PROGRAM

3.1 Specimen details

The experimental program prepared eight RC beams with I-shaped cross section. Three-point bending tests were conducted by a 2000kN capacity hydraulic testing machine. The summary of experimental cases and details of specimens are provided in Table 1 and Figure 1. The specimens were designed based on the study of Kobayashi et al. (2009) in order to discuss and compare with their results. The web width (b_w) and effective depth (d) of all specimens were 40 mm and 220 mm, except for U-s100L which has b_w=58 mm and d=319mm. The main parameters were f'_c, r_w, s, b_f/b_w and d. The experimental cases can be classified into four series. Series I is the effect of r_w and s in high strength concrete beams with various diameters of stirrups. Series II is the effect of s with different f'_c. Series III is the effect of b_f/b_w by varying the flange width. Series IV is the effect of d or size effect.

All specimens were designed to be symmetric. The combination of thin web cross section and high strength shear and tensile reinforcements (f_y, f_{wy} > 930 N/mm^2) will cause specimens to exhibit the diagonal compression failure. In order to avoid the local failure, the web width outside support was increased to that of the bottom flange. Anchor plates and nuts were used to ensure the sufficient anchorage of the tensile bars and prevent the anchorage failure.

3.2 Instrumentation and test procedures

For all specimens, the applied load, mid-span deflections and strains of concrete, tensile bars and stirrups were measured. Strain gauges were attached at the mid span to measure the strain of longitudinal bars whereas at the distance of d/2 from the top fiber for all stirrups in the shear spans. The additional strain gauges

Table 1 List of experimental cases

Specimen	f'_c [N/mm^2]	b_f *1 [mm]	b_w [mm]	d [mm]	a/d	b_f/b_w	p_w *2 [%]	D *3 [mm]	f_y [N/mm^2]	r_w *4 [%]	ϕ_d *5 [mm]	s *6 [mm]	f_{wy} *7 [N/mm^2]
U1.2-s150	100	250	40	220	3.0	6.25	8.8	22.2	1204	1.8	10	100	953
U1.5-s120										1.5		120	
U1.8-s100										1.2		150	
SU-s90	130								930	3.5	13	90	955
SU-s160										2.0		160	
SU-f150		150				3.75			1204	3.0	10	60	967
SU-f500		500				12.5				3.0	10		
U-s100L	100	343	58	319		6.25	8.6	31.8	1187	2.2	13	100	931

*1 upper flange width, *2 longitudinal reinforcement ratio (=100A_s/($b_w d$)), *3 nominal diameter of longitudinal bar, *4 stirrup ratio (=100A_w/($b_w s$)), *5 diameter of stirrups, *6 spacing of stirrups, *7 yield strength of stirrup.

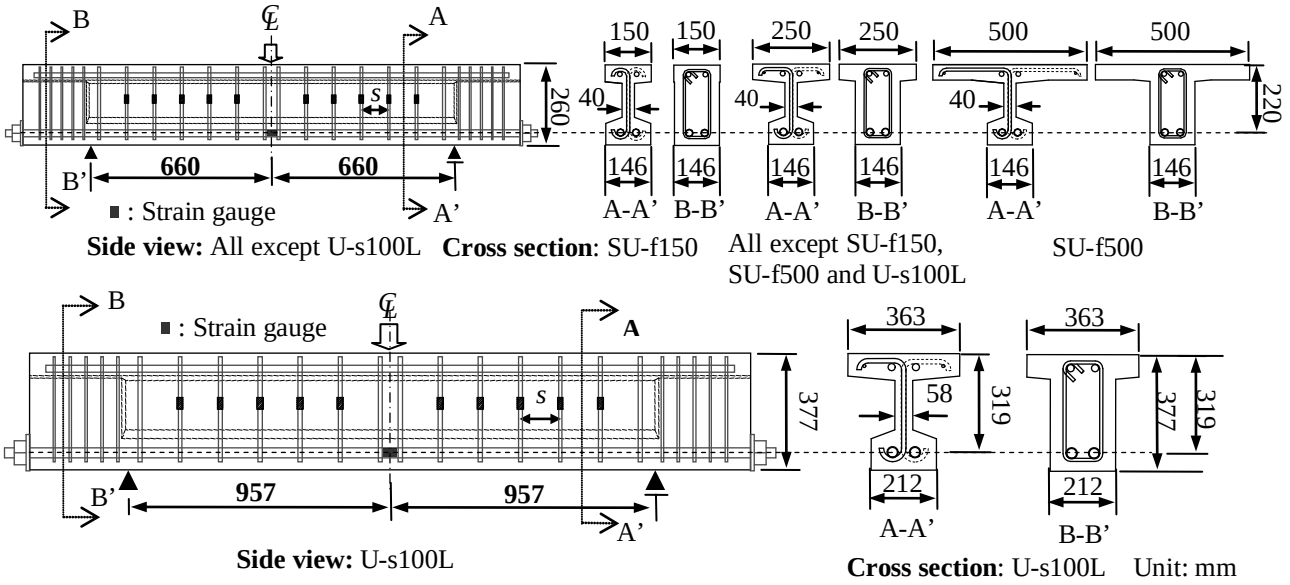


Figure 1 Dimensions and re-bar layout of specimens

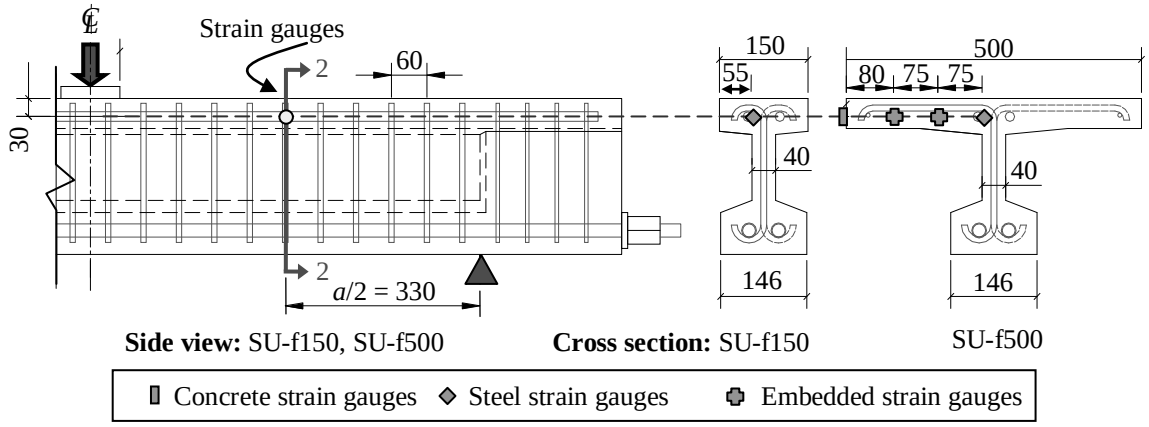


Figure 2 Location of the strain gauges of SU-f150 and SU-f500

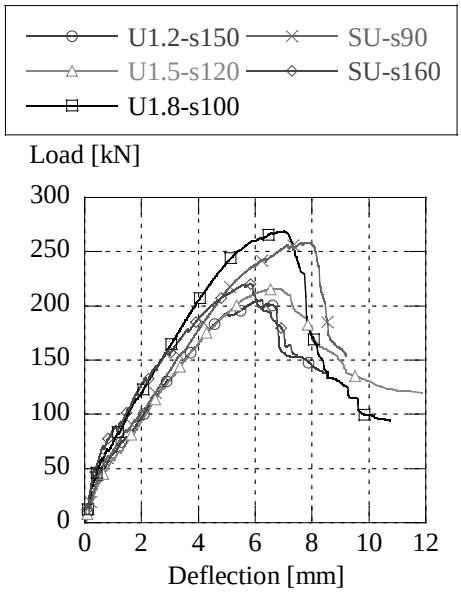


Figure 3 Load-deflection curves of series I and II

were provided in SU-f150 and SU-f500 as shown in Figure 2. As for SU-f500, embedded strain gauges were installed inside the concrete in the flange portion to measure the strain distribution in the flange. Besides, both surfaces of all specimens were painted by white color to ease the drawing and observation of crack during the experiments. The load at first flexural crack (P_{cr}), the average horizontal crack spacing at the peak load ($s_{c,avg}$) as well as the average crack angle (β_{avg}) were measured at the middle height of the web.

4. EXPERIMENTAL RESULTS

4.1 Load-deflection relationship

Load-deflection relationships of series I and II are illustrated in Figure 3. Firstly, specimens behaved in elastic manner until the first flexural crack occurred in the bottom flange near the mid span, which is reflected in the graph as a rate of inclination decreases. After the first flexural crack, the load-deflection curve remains to advance linearly with the initiation of diagonal cracks at the web concrete in the order from the loading point to the support. In the pre-peak region, the deflection

Table 2 Experimental results

Specimen	f'_c [N/mm^2]	r_w [%]	s [mm]	a/d	b_f/b_w	f_y [N/mm^2]	$\sigma_{s,max}$ [*1] [N/mm^2]	f_{wy} [N/mm^2]	$\sigma_{w,max}$ [*2] [N/mm^2]	$s_{c,avg}$ [*3] [mm]	β_{avg} [*4] [°]	P_{cr} [*5] [kN]	V_{exp} [*6] [kN]
U1.2-s150	105	1.2	100	3.0	6.25	1204	401.4	953	550.8	91.0	40.8	26	102.7
U1.5-s120	101	1.5	120				454.2		403.4	99.0	40.6	26	108.0
U1.8-s100	107	1.8	150				613.2		549.6	92.5	38.6	38	134.3
SU-s90	131	3.5	90			930	594.4	955	363.4	73.2	39.0	36	129.3
SU-s160	128	2.0	160				402.0		377.8	111.3	40.2	50	110.1
SU-f150	130	3.0	60		3.75	1204	665.8	967	359.4	53.0	43.1	37	159.9
SU-f500	135				12.5		583.2		508.2	49.0	43.0	40	161.4
U-s100L	108	2.2	100		6.25	1187	641.6	931	627.2	128.4	43.0	40	288.7

[*1] maximum stress in longitudinal bars, [*2] maximum stress in stirrups, [*3] average horizontal crack spacing at peak load, [*4] average crack angle at peak load, [*5] load at first flexure crack, [*6] diagonal compressive capacity.

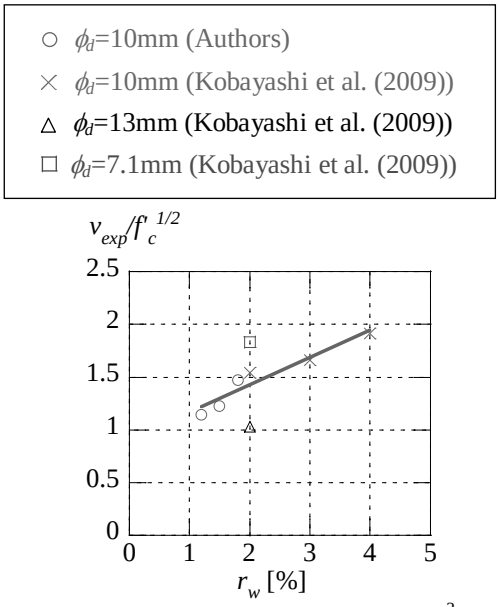


Figure 4 Effect of r_w (f'_c=100N/mm^2)

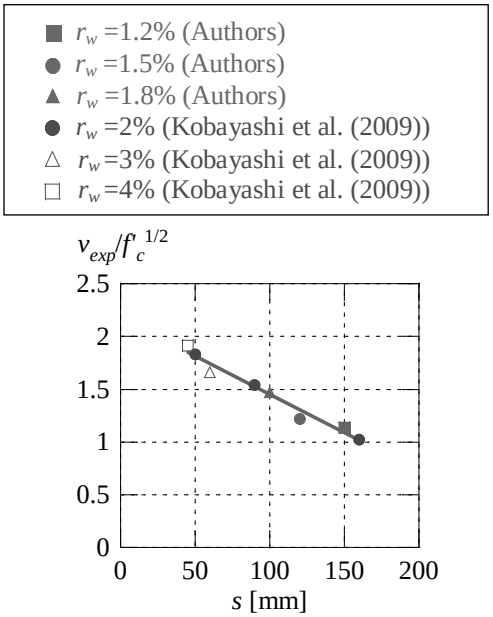


Figure 5 Effect of s (f'_c=100N/mm^2)

increased with a relatively small increase in applied load until the web concrete began to crush. Afterwards, the applied load reached to the peak. The experimental results are summarized in Table 2. Data of the strains of longitudinal bars and stirrups revealed no yielding and the values were much less than their yield strength. It implies that the failure mode was neither flexure failure nor diagonal tension failure. As concrete crushing occurred, the failure mode of all specimens was diagonal compression failure. After the peak load, applied load rapidly decreased. From Table 2, it is revealed that small variation of β_{avg} can be observed in all specimens.

4.2 Effect of stirrup ratio with different diameters

Kobayashi et al. (2009) adapted a method to eliminate the effect of f'_c by normalizing the obtained shear capacities by $f'_c{}^{1/2}$ which is used in the design equation of JSCE (2002) and the predictive equations by Placas et al. (1971). This method is also applied in this study. The relationships between r_w and $v_{exp}/f'_c{}^{1/2}$ for the specimens with f'_c = 100 N/mm^2 are demonstrated in Figure 4, where v_{exp} is the shear strength ($=V_{exp}/b_w d$). With the increase in r_w, the diagonal compressive capacity increases when using diameter of stirrups (ϕ_d) = 10 mm. A linear relationship agrees well with the test results. However, in the case of constant value of r_w = 2% with different ϕ_d and s, $v_{exp}/f'_c{}^{1/2}$ differs significantly. From Table 2, $s_{c,avg}$ among these three specimens is also different. With the increase in stirrup spacing, $s_{c,avg}$ also increases. Furthermore, the results of the same set of data are plotted against s despite of r_w in Figure 5. Notwithstanding ϕ_d and r_w are different, the diagonal compressive capacities are distributed along the same linear line. It means that the diagonal compressive capacity can be represented by not r_w but s. Therefore, the diagonal compressive capacity will be discussed by s

in the following section.

The difference in the diagonal compressive capacity with the change in s can be explained by two mechanisms (Kobayashi et al. 2009). One is the increase of confinement effect on cracks by providing closer shear reinforcements. It results in smaller diagonal crack width (w); therefore, the critical average stress in web concrete (σ_{2max}) would be greater because w affected the diagonal compressive capacity as reported by Schäfer et al. (1990) and Reineck (1989). The other is the localization of compressive strut. Figure 6 explains the model of compressive strut formation under different stirrup spacing proposed by Kobayashi et al. (2009). Figure 6(a) demonstrates that the diagonal stress generates uniformly along the beam with close-spacing stirrups. While in Figure 6(b), the diagonal stress is concentrated in a local portion of the beam with wide-spacing stirrups. This stress concentration causes early crushing in the web concrete; hence the diagonal compressive capacity decreases.

This mechanism can be observed in this study as well. The $s_{c,avg}$ shows decreasing trend with closer stirrup spacing. It implies that the failure localization occurred in U1.2-s150 and SU-s160 as higher $s_{c,avg}$ were observed. Since the confinement effect of stirrups helps the stress to transfer across a crack after the crack initiation, the stress can distribute along the beam. Therefore, the localization of compressive strut was induced by a lack of the confinement effect. However, further study by some analytical approach is required to clarify the actual stress flow.

4.3 Effect of stirrup spacing with different compressive strength

Figure 7 shows $v_{exp}/f'_c{}^{1/2}$ as a function of s for specimens with different f'_c. It is confirmed that the effect of s depends on f'_c. There is slight variation in $v_{exp}/f'_c{}^{1/2}$ by the change in s when using normal strength concrete while the greater effect of s can be observed in high strength concrete beams. As for beams with f'_c > 65 N/mm^2, the diagonal compressive capacity reduces as s increases in linear relationship. With higher f'_c, the inclination of trend line increases with a limitation when f'_c approximates 100 N/mm^2. It can be explained by considering that the diagonal compressive capacity depends on not only f'_c but also the width of compressive strut. If the width of compressive strut becomes smaller with higher f'_c, the area loss of the struts reduces the diagonal compressive capacity. Thus the diagonal compressive capacity is limited.

Figure 8 plots the shear strength v_{exp} as a function of f'_c. Since there is slight effect of s when using f'_c = 30 N/mm^2, the specimen NH3 (Kobayashi et al. 2009) is used as a representative of specimen with f'_c = 30 N/mm^2 and s = 60 mm in this figure. It can be observed that v_{exp} increases with the increase in f'_c with different incremental rate depending on s.

4.4 Effect of flange width to web width ratio

Series III comprises of three specimens SU-f150, UH3 (Kobayashi et al. 2009) and SU-f500. The web width was designed to be constant and b_f/b_w was varied by increasing the upper flange width. From Table 2, slight differences in $s_{c,avg}$ and β_{avg} can be noticed. $v_{exp}/f'_c{}^{1/2}$ against b_f/b_w is drawn in Figure 9. It can be seen that $v_{exp}/f'_c{}^{1/2}$ shows nearly constant value with the increasing of b_f/b_w. Hence, there is no effect of b_f/b_w on the diagonal compressive capacity of RC I-beams. It can be explained by that the increase in the upper flange width becomes ineffective. The strain distribution at mid span (see Figure 3) in the upper flange at different load level of SU-f500 is shown in Figure 10. The positive

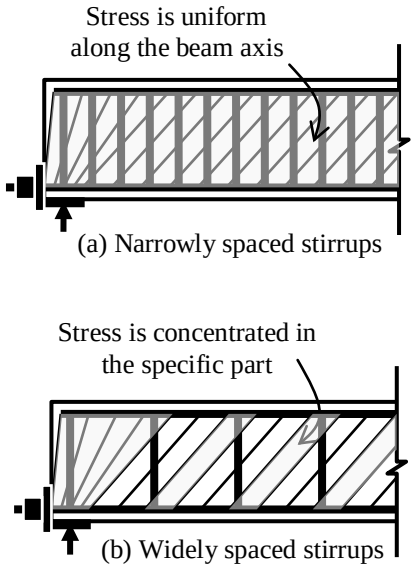


Figure 6 Effect of spacing of stirrups (Kobayashi et al. (2009))

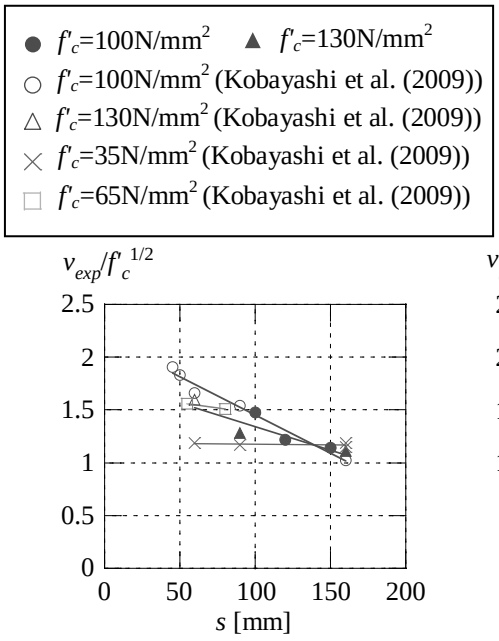


Fig. 7: Effect of s with different f'_c

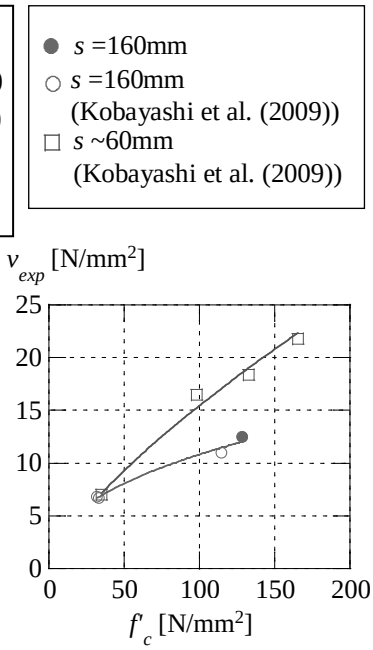


Figure 8 Effect of f'_c (v_{exp}-f'_c)

value indicates tensile strain. The strain concentration can be observed at the zone near center of the beam. This tensile strain is resulted from the development of high diagonal compressive stress in the web. As the distance from the beam center increases, the strain decreases and becomes comparatively small at some distance. Thus the outside flange portion resists less stress and can be considered as an ineffective area.

4.5 Effect of effective depth

Size effect was examined by comparing between U1.8-s100 and U-s100L. Size of U-s100L was magnified by 1.45 scale factors in three dimensions. The f'_c, p_w, a/d, b_f/b_w as well as s in this series were designed to be constant. As a result of series I, s was chosen to be constant, rather than r_w. From Table 2, $s_{c,avg}$ is wider in larger specimen and approximate 1.45 times larger. Figure 11 plots the shear strength v_{exp} as a function of d. It exhibits slight variation of the shear strength with the change of d. Therefore, the effect of d from 220 to 319 mm on the diagonal compressive capacity cannot be observed.

5. ACCURACY OF THE EXISTING EQUATIONS

The shear capacity from the experimental results of the total of 41 beams including Kobayashi et al. (2009), Placas et al. (1971), Reineck (1989), Rangan (1991), and Leonhardt et al. (1963) was used to illustrate the accuracy of the existing equations. All specimens were reported to fail in diagonal compression failure. The ratio between the shear capacity from experiments and results obtained by the existing equations were calculated. The average of these ratios (*avg.*) with a coefficient of variation (*C.V.*) is presented in Figure 12.

Figure 12(a) compares the diagonal compressive capacity from test results with those obtained by the equation by Placas et al. (1971). The average of V_{exp}/V_{Placas} = 0.98 with a *C.V.* of 18.3%. It implies that Placas equation can evaluate an average value of the diagonal compressive capacity including the case of f'_c > 100 N/mm^2. In contrary, this equation exhibits quite large variation as *C.V.* = 18.3%.

JSCE standard specifications (2002) demonstrate the average of V_{exp}/V_{JSCE} = 1.18. Figure 12(b) indicates that JSCE equation underestimates the capacity in almost all specimens. The specifications may be conservative

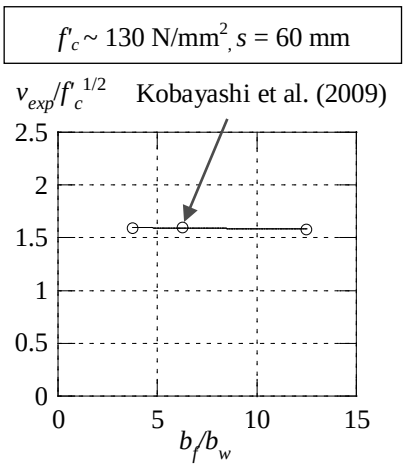


Figure 9 Effect of b_f/b_w

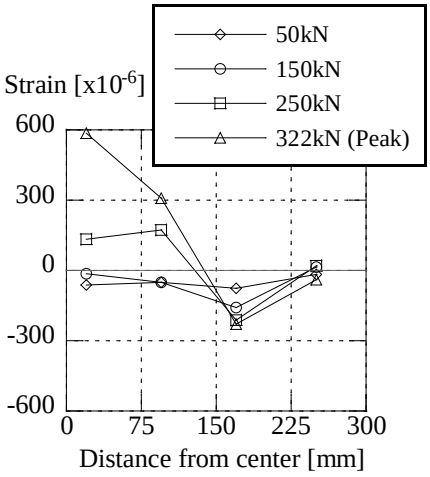


Figure 10 Strain distributions in upper flange

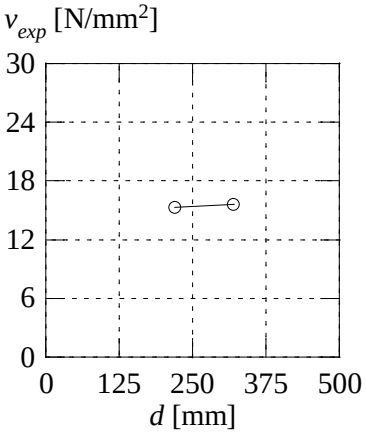
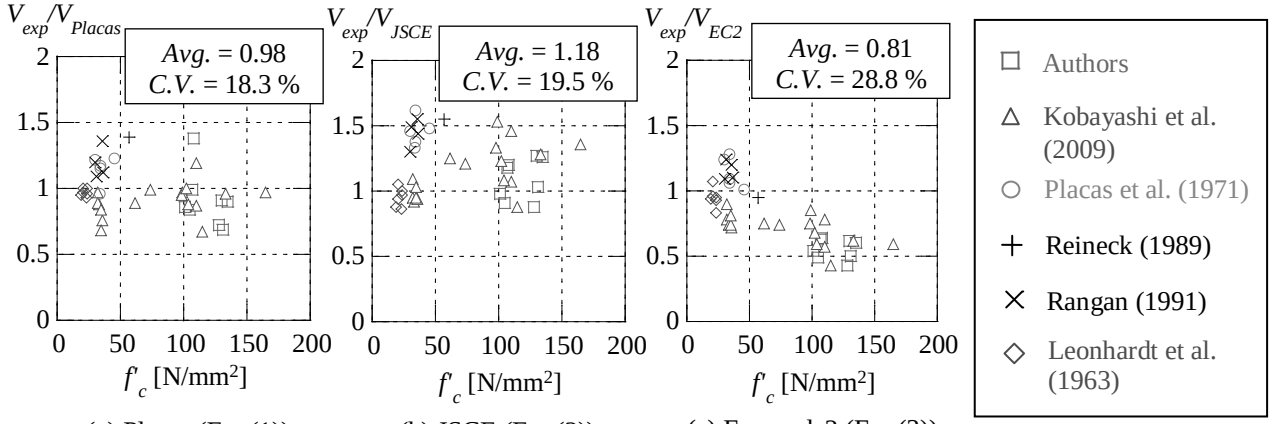


Figure 11 Effect of d



(a) Placas (Eq. (1)) (b) JSCE (Eq. (2)) (c) Eurocode2 (Eq. (3))

Figure 12 Accuracy of the existing equations

for safety reason. Similar as Placas equation, JSCE standard specifications shows large variation as *C.V.* = 19.5%.

The accuracy of the Eurocode 2 (2004) is shown in Fig. 12(c). The average of V_{exp}/V_{EC2} is 0.81 with a *C.V.* of 28.8 %. The Eurocode 2 severely overestimates the capacity in case of high strength concrete. Likewise, the Eurocode 2 does not consider the presence of stirrups. Thus it shows huge scattering.

From the reasons mentioned above, the current equations are not accurate enough to evaluate the diagonal compressive capacity of RC beams, especially in high strength concrete. Besides, the evaluation for r_w in the existing equation is not appropriate as explained in section 4.2.

5. CONCLUSIONS

(1) Stirrup spacing is prominent, not stirrup ratio, for evaluating diagonal compressive capacity of RC beams because of the localization of compressive stress in a strut.
(2) The effect of compressive strength and stirrup spacing on the diagonal compressive capacity of RC beams is interrelated. The greater effect of stirrup spacing is observed in high strength concrete.
(3) The diagonal compressive capacity increases as compressive strength of concrete increases with different increment ratio depending on stirrup spacing.
(4) The ratio of flange width to web width from 3.75 to 12.5 has almost no influence on the diagonal compressive capacity because the addition flange portion is not effective.
(5) The effect of effective depth on the diagonal compressive capacity cannot be observed in the range from 220 mm to 319 mm.
(6) The existing equations are not accurate enough to predict the diagonal compressive capacity, especially in high strength concrete.

References:

Japan Society of Civil Engineers (2002), "Standard Specifications for Concrete Structures-2002 [Structural Performance Verification]," 78-83.

Kobayashi, C., Watanabe, K., and Niwa, J. (2009), "Evaluation for Diagonal Compressive Capacity of RC Beams," *Proceedings of the Japan Concrete Institute*, **31**(2), 557-582. (In Japanese)

Placas, A., and Regan, P.E. (1971), "Shear Failure of Reinforced Concrete Beams," *Journal of the American Concrete Institute*, American Concrete Institute, **68**(10), 763-774.

European Committee for Standardization (2004), "Eurocode 2 Design of Concrete Structures, Part 1, General Rules and Rules for Buildings, EN 1992-1-1:2004", 84-90.

Schäfer, K., Schelling, G., and Kuchler, T. (1990), "Compression and Transverse Tension in Reinforced Concrete Elements," *Deutscher Ausschuss für Stahlbeton*, **408**, 85. (In German)

Reineck, K.H. (1989), "Theoretical Considerations and Experimental Evidence on Web Compression Failures of High Strength Concrete Beams," *CEB Bulletin D'Information*, fédération internationale du béton, **193**, 59-74.

Rangan, B.V. (1991), "Web crushing Strength of Reinforced and Prestressed Concrete Beams," *ACI Structural Journal*, American Concrete Institute, **88**, 12-16.

Leonhardt, F. and Walther, R. (1963), "Shear Tests on T-Beam with Varying Shear Reinforcement," *Deutscher Ausschuss für Stahlbeton*, **156**, 84. (In German)

8CUEE CONFERENCE PROCEEDINGS
8th International Conference on Urban Earthquake Engineering
March 7-8, 2011, Tokyo Institute of Technology, Tokyo, Japan

EXPERIMENTAL RESPONSE OF STEEL FIBER REINFORCED CONCRETE KNEE JOINTS OF RIGID-FRAMED RAILWAY BRIDGES UNDER CYCLIC LOADING

Kabir Shakya[1)], Koji Matsumoto[2)], and Junichiro Niwa[3)]

1) Ph.D. Student, Department of Civil Engineering, Tokyo Institute of Technology, Japan
2) Assistant Professor, Department of Civil Engineering, Tokyo Institute of Technology, Japan
3) Professor, Department of Civil Engineering, Tokyo Institute of Technology, Japan
shakya.k.aa@m.titech.ac.jp, matsumoto.k.ar@m.titech.ac.jp, jniwa@cv.titech.ac.jp

Abstract: The experimental results of three one-sixth scaled knee joints of a railway bridge are presented in this paper. Following the design and detailings of the existing railway bridge in Japan, the first specimen was prepared. In other two specimens, the amount of steel reinforcements was reduced and 1.5% of hooked end steel fibers were added. The tests were performed under the displacement controlled quasi-static cyclic loading. Observing the crack patterns, yielding of rebars, buckling and rupture of rebars, the failure mode of the specimens were decided. The load-displacement curves and energy dissipation capacities of the specimens were also compared and found that the strength deficit caused by the reduction of steel reinforcements can be restored by using steel fibers.

1. INTRODUCTION

Beam-column joints have been recognized as one of the important structural elements to effectively transfer load between the connecting members, beams and columns. The integrity of beam-column joints highly governs the overall performance of the structures. After experiencing severe damages to the structures during past major earthquakes, many researches were conducted for retrofitting, strengthening of existing structures and to propose design guidelines for new structures to withstand the probable big earthquakes. Many countries around the world revised the seismic codes and raised the level for the structural design requirements of new structures. Accordingly, amount of steel reinforcements were increased in beams and columns due to which mainly at the beam-column joints congestion of steel reinforcements occurred. The congestion at the joints resulted in the poor workability and poor performance of joints during earthquakes. To some extent, the hooks provided at the end of steel rebars also contribute in congestion. The provision of hooks can be eliminated by using headed steel rebars, however, the headed rebars cannot improve the strength of the joints. Also, headed rebars cannot address the congestions caused by longitudinal and shear reinforcements in the joints. Use of steel fiber reinforced concrete (SFRC) can be promising in reducing longitudinal and shear reinforcements, as it is capable of enhancing the flexural and shear capacities. In addition, steel fibers can improve ductility and energy dissipation capacity of concrete along with improvement of bond between concrete and steel reinforcements.

A large portion of railway bridges in Japan have been constructed as framed bridges (Figure 1) in which dense reinforcement are provided at the beam-column joints. Hence, to reduce the amount of steel reinforcement for the avoidance of congestion at the knee joints of railway bridges, this research is conducted. Three one-sixth scale specimens were prepared. One of which was constructed based on the existing railway bridge in Japan and in other two specimens steel reinforcements were reduced and 1.5% of hooked-end steel fiber were added. The tests were conducted under displacement controlled quasi-static cyclic loading. The performances of different specimens were compared in terms of crack patterns, load-deflection relationship and energy dissipation.

2. RELATED RESEARCH

The conventional beam-column joints without joint reinforcements are vulnerable to shear. With variation in

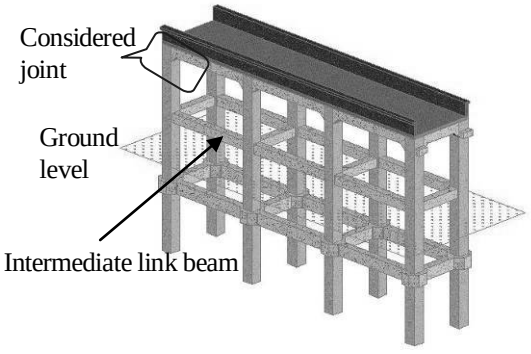
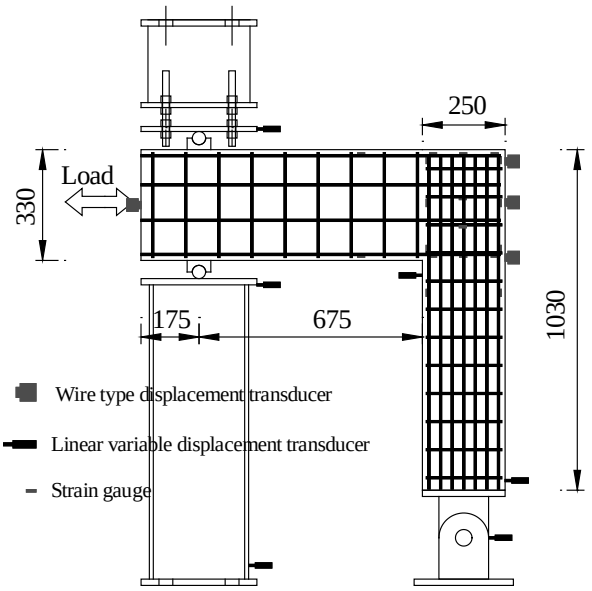


Figure 1 Rigid-framed railway bridge

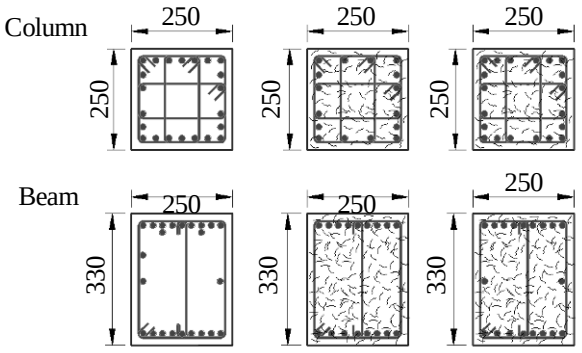
Table 1 Material properties and amount of steel reinforcements

Specimen	f_c' (N/mm^2)	Steel fiber (%)	Longitudinal rebar size	Stirrup size	Hoop size	Yield strength (N/mm^2)	Tensile strength (N/mm^2)	Percentage of steel (%)			
								Column		Beam	
								Longitudinal reinforcement	Hoop	Longitudinal reinforcement	Stirrup
Prototype structure	30.0	0	D32	D16	D16	*	*	0.99	0.57	0.92	0.28
KJ-ED	33.2	0	D6	D6	D6	325	470	1.11	0.60	0.97	0.29
KJ-1.5	28.9	1.5	D6	D6	D6	325	470	0.81	0.46	0.72	0.21
MKJ-1.5	30.1	1.5	D6	D6	D6	325	470	1.01	0.42	0.80	0.20

steel reinforcement arrangement at beam-column joint causes different mechanisms of shear transfer in knee and T-joints (Priestley et al. (1996)). During seismic events high shear forces are subjected to the joints. Hence, beam-column joints should withstand such shear forces. Since, steel fibers are capable of increasing the shear strength of concrete through the bridging action across the cracks, use of steel fibers can be a possible alternative to conventional confining reinforcements to provide adequate ductility (Filiatrault et al. (1995)). Also, it can enable the increase of the spacing of closely spaced. In addition to shear, the bond between concrete and steel reinforcements and anchorage can highly influence the performance of beam-column joints. Conducting experiments on numerous beam-column connections, Hamad et al. (2011) investigated the effects of steel fibers in the performance hooked bars embedded in normal strength concrete specimens and reported the significant improvement in bond performance and the ductility of failure mode. Although efforts have been made to reduce the longitudinal reinforcements in beams by using steel fibers, no study has been conducted regarding the reduction of longitudinal steel reinforcements in beam-column joints. Based on the experiments performed on the beams, Oh (1992) stated that on neglecting the contribution of steel fibers, the flexural capacity of fiber-reinforced concrete beams are considerably underestimated. To estimate the flexural capacity of doubly reinforced concrete beams containing steel fibers, an analytical method was also proposed. It is also shown that when 2% of steel fibers were added, about 60% increase of the flexural strength could be achieved.



(a) Bar arrangement and measurement system



(b) Cross section of columns and beams

Unit: mm

Figure 2 Specimen details

3. EXPERIMENTAL SETUP AND MEASUREMENT SYSTEM

3.1 Material properties

The material properties were chosen based on the existing railway bridges in Japan. The considered existing bridge was designed following the Japanese Code, "Design Standards for Railway Structures and Commentary (Concrete Structures)", April, 2004, and is referred as a prototype structure. The compressive strength of concrete used in the prototype structure was 30 N/mm^2 and accordingly the mix proportion of concrete were designed. The average compressive strength of concrete used in the specimens are shown in Table 1. Three numbers of 100 mm × 200 mm were cast and cured for compressive strength test. The maximum size of the coarse aggregate was 10 mm. D6 bars having nominal diameter of 6.35 mm were used for both longitudinal and shear reinforcements. From tensile strength test of rebars, the yield strength and ultimate strength were found to be 325 N/mm^2 and 470 N/mm^2, respectively. The steel fibers, a cold drawn wire fiber glued in bundle, with hooked ends were used. The aspect ratio was

Table 2 Percentage reduction of steel rebars

Specimen	KJ-ED	KJ-1.5	MKJ-1.5
Column longitudinal rebar	Existing design	27.3%	9.1%
Hoops	Existing design	15.0%	29.2%
Beam longitudinal rebar	Existing design	26.1%	17.4%
Stirrups	Existing design	26.0%	31.25%

48. The length and diameter of steel fibers were 30 mm and 0.62 mm respectively. The tensile strength of steel fibers were 1050 N/mm^2.

3.2 Test specimens

Figure 2 shows one-sixth scaled knee joint specimen. Considering a half of the column height and a half of the beam span of a rigid-framed railway bridge, the height of a column and the length of a beam from column face for the specimens were chosen as 1030 mm and 850 mm, respectively. The cross-sectional size of column was 250 mm × 250 mm and that of beam was 250 mm × 330 mm. All together three specimens, KJ-ED, KJ-1.5 and MKJ-1.5, were casted. Here, KJ, ED, 1.5 and MKJ stand for Knee Joint, Existing Design, percentage of steel fibers by volume and Modified Knee Joint, respectively. In the control specimen, KJ-ED, the amount of steel rebars in beam and column including rebar detailings were provided analogous to the considered existing railway bridge. In KJ-1.5, the amount of rebars were reduced but the rebar detailings were kept unchanged. However, along with reduction of steel rebars, the hook length of bottom beam rebars were modified in MKJ-1.5. The amount of steel rebars and its properties are tabulated in Table 1. The reduced amount of steel rebars were different in KJ-1.5 and MKJ-1.5. The reduction of steel rebars in KJ-1.5 was made based on authors' previous study on T-joints of a railway bridge (Shakya et al. (2010)) and in MKJ-1.5, the steel in beam and column were reduced in such a way that the flexural capacity of beam and column are equal. In both KJ-1.5 and MKJ-1.5, 1.5% of hooked end steel fibers by volume were added. The percentage reduction of steel rebars in KJ-1.5 and MKJ-1.5 compared to KJ-ED are tabulated in Table 2.

In KJ-ED, 22 numbers of rebars in column, 11 numbers of top beam rebars, 9 numbers of bottom beam rebars and 3 numbers of side face rebars were provided. The column rebars were reduced to 16 numbers in KJ-1.5. In addition, all the side face rebars were removed. Only 9 numbers of top beam rebars and 8 numbers of bottom beam rebars were provided. In MKJ-1.5, 20 numbers of column rebars, 9 numbers of top beam rebars, 8 numbers of bottom beam rebars and 2 numbers of side face reinforcements were provided. In all the column rebars 180° hook were provided at the end of rebars. In top beam rebars of KJ-ED, out of 11 rebars, 3 rebars with 180° hook, 3 rebars with 90° hook having hook length 35ϕ (ϕ is rebar diameter), 3 rebars with 90° hook having hook length 15ϕ and 2 rebars without hook

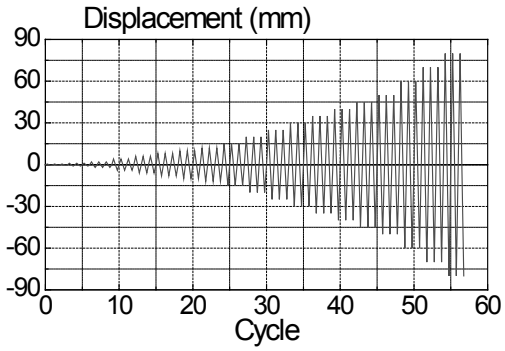


Figure 3 Applied displacement cycle

were provided. All the 9 numbers of rebars in bottom of beam were provided with 90° hook having hook length of 3ϕ. No hooks were provided in the side face rebars. All the hooks and hook lengths were decided as per reinforcement detailing of the existing railway bridge. In comparison to KJ-ED, 2 top beam rebars without hook and 1 bottom beam rebars were removed in. KJ-1.5 and MKJ-1.5. In MKJ-1.5, the hook length of bottom beam rebars were increased to 12ϕ, which is minimum hook length required by JSCE standard. The spacing of hoops in KJ-ED, KJ-1.5 and MKJ-1.5 were 85 mm, 100 mm and 120 mm, respectively. Similarly, the stirrups were spaced at 110 mm, 150 mm and 160 mm in KJ-ED, KJ-1.5 and MKJ-1.5, respectively.

3.3 Loading and instrumentation

Using displacement controlled 200 kN capacity actuator, a cyclic horizontal quasi-static load was applied at the end of beam (Figure 2). The displacement amplitude was varied from 0.5 mm to 80 mm (Figure 3) and each displacement amplitude was exerted for 3 cycles. Displacement transducers and strain gauges were attached at various locations of the specimens to record displacements and strains so that the structural behavior could be understand. Transducers were also attached in the steel column and hinge support, so that the displacement of supports can be monitored and if supports were displaced, correction in displacement at other locations could be made.

4. EXPERIMENTAL RESULTS AND DISCUSSIONS

4.1 Crack pattern and failure mode

The observed crack patterns in the specimens by the end of the tests are shown in Figure 4. In all the specimens, the first flexural crack (FFC) was observed during application of 2nd loading cycle of 4 mm displacement amplitude. On further loading, the number of cracks increased rapidly until peak load was observed. After 40 mm displacement amplitude, no cracks were generated in all the specimens, however, only opening and closing of cracks were noticed. As indicated in the Figure 4, wider cracks were observed throughout the beam and the column of KJ-ED and KJ-1.5. The cracks were propagated throughout the column at first and then crack propagation took place

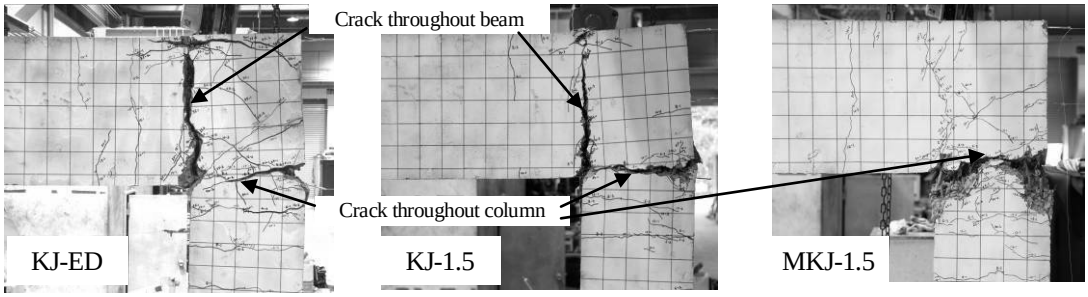


Figure 4 Crack patterns after the loading test

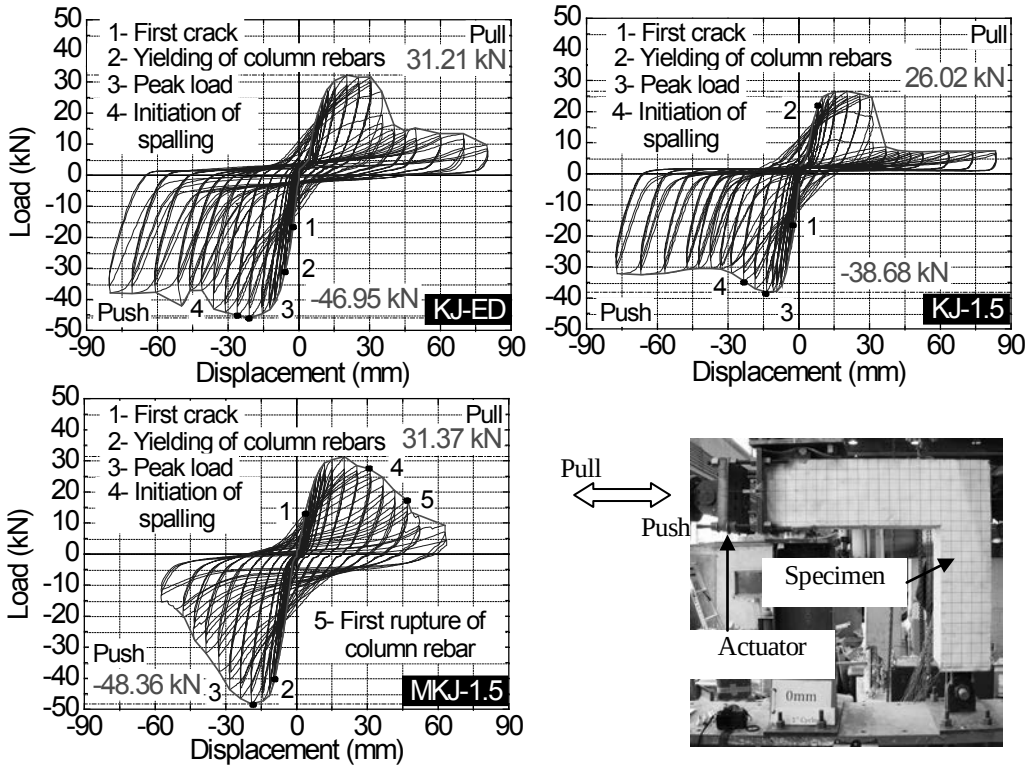


Figure 5 Load-displacement curve

throughout the beam of both KJ-ED and KJ-1.5. The bond deterioration and anchorage failure due to insufficient hook lengths were the main cause of formation and widening of crack along the column. The presence of side face rebars in the beam delayed the crack opening in the beam in KJ-ED compared to that in KJ-1.5. Significant shear cracks were also observed within the beam-column joint of KJ-ED. Although the amount of steel rebars were reduced in KJ-1.5, the number of cracks were significantly reduced due to addition of 1.5% of steel fibers. Also, no shear cracks were observed in the beam-column joint. However, the absence of side face rebars caused the rapid propagation and widening of cracks in the beam. The anchorage failure was prevented in MKJ-1.5 after increasing the hook length of beam bottom rebars and adding 1.5% of steel fibers. However, bond failure between concrete and beam bottom rebars could not be prevented due to which longitudinal crack along the beam bottom rebars within the column section was generated. Also, the number of shear cracks in the beam-column joints were reduced compared to those in KJ-ED. The application of repeated cyclic load resulted in crumbling of concrete at the junction of beam and column. The absence of concrete at the junction and further loading caused the buckling of column rebars and finally column rebars were ruptured. Hence, the failure mode of MKJ-1.5 was depicted as the flexural failure.

4.2 Load-displacement relationships

In Figure 5., the relationship between applied displacement at the end of beam and corresponding load recorded during the quasi-static cyclic load is expressed in terms of load-displacement curve. The displacement was considered as positive when the specimen was pulled towards the actuator and vice-versa. The envelope curves along with some important points are also presented. The experimental results of all the specimens are summarized in Table 3.

In all the specimens, the FFCs were formed during 2nd cycle of 4 mm displacement, however, the magnitudes of

Table 3 Comparison of experimental results

	KJ-ED	KJ-1.5	MKJ-1.5
First cracking displacement cycle	4 mm – 2nd cycle	4 mm – 2nd cycle	4 mm – 2nd cycle
First cracking load	-17.25 kN	-17.47 kN	13.68 kN
Yield displacement of column rebars	12 mm	10 mm	10 mm
Yield load	-37.57 kN	22.99 kN	-40.65 kN
Peak load	-46.95 kN	-38.68 kN	-48.36 kN
Displacement at concrete spalling at column face	25 mm	25 mm	30 mm
Pull out of rebars in beam	All bottom rebars	All bottom rebars	No pull out
Column rebar rupture	No rupture	No rupture	10 out of 20 rebars
Failure mode	Anchorage	Anchorage	Flexural

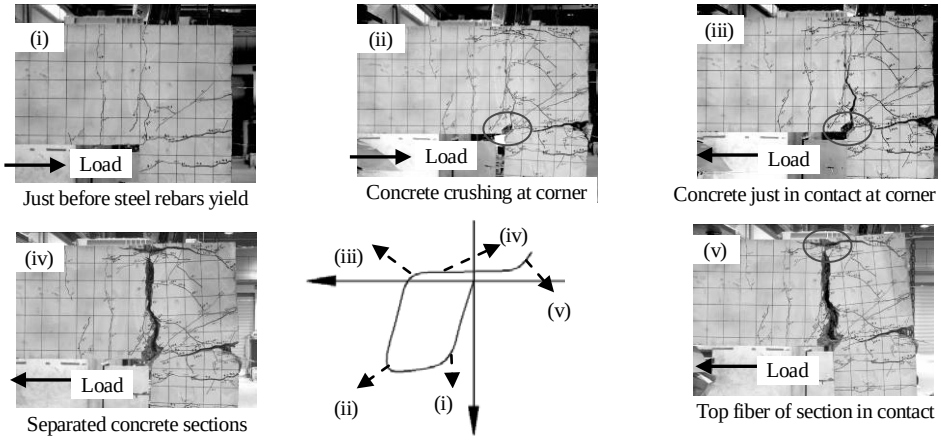


Figure 6 Post yield behavior

cracking load were different. On increasing the displacement amplitude to 12 mm, the column rebars at the junction of beam and column yielded in KJ-ED whereas yielding of column rebars took place in KJ-1.5 and MKJ-1.5 when the applied displacement was 10 mm. The lowest yield load was observed in KJ-1.5 as the provided amount of steel rebars was the least. Although the amount of steel rebars in MKJ-1.5 were less compared to KJ-ED, the largest yield load of 40.65 kN was observed by the virtue of addition of steel fibers. It indicates that the addition of steel fibers in concrete was capable of improving the flexural capacity of concrete. Moreover, the largest peak load of 48.36 kN was also observed in MKJ-1.5. Due to inappropriate amount of reduction of steel rebars, the load capacity of KJ-1.5 was less than that of KJ-ED although 1.5% of steel fibers were added. In the post peak region, sharp decrease in load capacities were noticed in KJ-ED and KJ-1.5, due to the anchorage failure at the displacement of 30 mm and 35 mm. The anchorage failure was of brittle nature and are not desirable in structures. The addition of steel fibers along with increase in hook length of beam bottom rebars prevented the anchorage failure in MKJ-1.5. Instead buckling of column rebars were observed. The first column rebar ruptured when 45 mm displacement amplitude was applied. Finally 10 out of 20 column rebars were ruptured by the end of 60 mm displacement amplitude. Due to significant loss in load capacity, the test on MKJ-1.5 was terminated once 3 cycles of 60 mm displacement was exerted.

When the positive displacement was applied in the specimen, an axial tensile force was induced in the column due to which micro flexural cracks were formed at the lower amplitude of applied displacement. At the higher amplitude of displacement, the wider cracks were formed at the junction of beam and column. Due to these reasons, the load capacity of the specimens in the positive loading cycles were lesser than that in negative loading cycles. Also, on comparing the load-displacement curves in Figure 5, it can be clearly seen that the post yield behavior of KJ-ED and KJ-1.5 are quite similar. The behavior in the post yield region can be clarified through Figure 6 where the crack patterns including situation of concrete and steel rebars in KJ-ED during different stage of loading are shown. In this region, big opening of cracks, crushing of concrete, plastic deformation of rebars, buckling and rupture of rebars can be expected. The load displacement relationship is linear (phase i) before the rebars yield. On increasing the displacement, the column rebars yield and due to excessive compression, the concrete at the junction of beam and column starts crushing resulting in deterioration of bond between bottom beam rebars and concrete. Only marginal increase in load capacity can be observed (phase ii) in this phase and also this phase is responsible for the formation of plateau in the load-displacement curve. Upon reversing the loading direction, the linear unloading curve can be observed till the instance when the concrete in the beam and the column are just in contact (phase iii). Once, the contact between concrete of beam and column vanishes, all the applied load is resisted only by steel rebars. During this phase almost horizontal load displacement curve can be observed (phase iv). On further increasing the displacement, the top fiber of

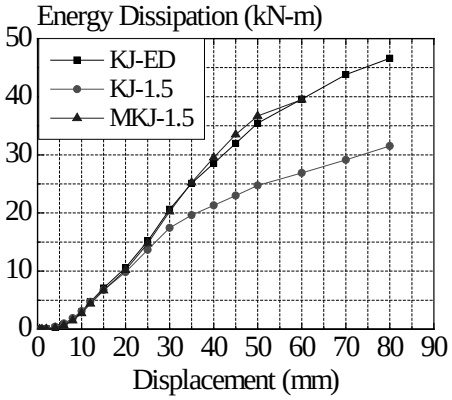


Figure 7 Energy dissipation

beam and column came into contact and again load starts increasing. In KJ-ED and KJ-1.5, all of these five phases were observed. The crushing of concrete at the junction of beam and column resulted the plateau in both positive and negative loading cycles of the load-displacement curves. However, in MKJ-1.5, due to buckling of column rebars, the plateau could not be observed. The buckling and rupture of rebars caused the gradual decrease in load capacity after the peak load.

4.3 Energy dissipation

On subjecting large cyclic displacements to a specimen, the concrete components in the beam-column joint experiences significant degradation of strength and stiffness. Reinforcing rebars also undergo inelastic deformations. The inelastic behavior of rebars is the primary source of energy dissipation. Hence, energy dissipation occurs due to induced damage in the specimens and depends on concrete cracking, yielding and buckling of rebars. The energy dissipation capacity of each specimen can be obtained by computing external work, W_e which refers to the area enclosed by the load-displacement curve and is given by

$$W_e = \int P\,dx \tag{1}$$

where, P is a load and x is an applied lateral displacement. The relationship between cumulative energy dissipation and applied displacement is shown in Figure 7. Among all the specimens, the energy dissipated by KJ-1.5 was the least. Nevertheless, the energy dissipated by KJ-ED and MKJ-1.5 were almost equal. Therefore, the performance of MKJ-1.5 in terms of energy dissipation was also satisfactory. The comparable energy dissipation capacity also justifies that the certain amount of steel rebars in knee joints can be reduced if steel fibers are used.

5. CONCLUSIONS

Displacement controlled cyclic quasi-static loading test were conducted on three one-sixth scaled knee joint specimens. One of the specimens was analogous to the existing railway bridge in terms of section properties, concrete strength, amount of steel reinforcements and its detailings. While in other two specimens, amount of longitudinal and shear reinforcements were reduced and steel fibers were added. Based on the experimental results following conclusions are drawn:

(1) Due to the insufficient hook length in the beam bottom rebars, the specimen designed and detailed based on the existing railway bridge and the specimen with 1.5% steel fibers but without modification in hook length failed in anchorage.
(2) The delay in anchorage failure and spalling of concrete show the enhancement in anchorage and bond between concrete and steel rebar upon using steel fibers.
(3) Flexural failure was observed on using 1.5% volume fraction of steel fibers and providing steel rebars in beam and column such that the flexural capacities of beam and column were equal.
(4) The shear capacity of the concrete was enhanced as the shear cracks were reduced in the beam-column joints after providing steel fibers in concrete.
(5) SFRC can contribute in enhancing flexural capacity, and energy dissipation capacity.

Hence, based on obtained results, it is concluded that the use of steel fibers is effective in restoring the capacity without compromising the overall performance of structures even after reducing certain amount of longitudinal and shear reinforcements in beam and column of knee joints.

Acknowledgements:

The authors are very grateful to Center for Urban Earthquake Engineering (CUEE), Tokyo Institute of Technology, for providing research fund.

References:

Oh, B. H. (1992), "Flexural Analysis of Reinforced Concrete Beams Containing Steel Fibers," *Journal of Structural Engineering*, American Society of Civil Engineers, **118**(10), 2821-2836.

Filiatrault, A., Pineau, S. and Houde, J. (1995), "Seismic Behavior of Steel-Fiber Reinforced Concrete Interior Beam-Column Joints," *ACI Structural Journal*, **92**(5), 1-10.

Priestley, M. J. N., Seible, F. and Calvi, G. M., (1996), "Seismic Design and Retrofit of Bridges," John Wiley and Sons, Inc.

Railway Technical Research Institute (2004), "Design standards for railway structures and commentary," (Concrete Structures).

Shakya, K., Matsumoto, K., Watanabe, K. and Niwa, J., (2010), "Influence of Steel Fibers on Cyclic Behavior of Beam-Column Joints in Rigid-Framed Railway Bridges," *Proceedings of the 4th ACF International Conference*, Paper No. S1. 3-01.

Hamad, B. S., Haidar, E. Y. A., and Harajli, M. H., (2011), "Effect of Steel Fibers on Bond Strength of Hooked Bars in Normal-Strength Concrete," *ACI Structural Journal*, **108**(1), 42-50.

8CUEE CONFERENCE PROCEEDINGS
8th International Conference on Urban Earthquake Engineering
March 7-8, 2011, Tokyo Institute of Technology, Tokyo, Japan

SEISMIC VULNERABILITY AND STRUCTURAL RETROFITTING OF MUNICIPAL THEATRE OF LAMA, PERU

R. Proaño[1)], L. Quiroz[2)], and C. Zavala[2)]

1) Associated Researcher, Seismic Department, Japan-Perú Earthquake Engineering and Disaster Mitigation Center, Faculty of Civil Engineering, National University of Engineering, Lima Perú
2) Researcher, Japan-Perú Earthquake Engineering and Disaster Mitigation Center, Faculty of Civil Engineering, National University of Engineering, Lima Perú
rproano@uni.edu.pe

Abstract: The building of Municipal Theatre of Lima started in 1920. Since then, the structure has experienced at least four major earthquakes and a fire in 1998 had damaged roof of the building. Since 2008 a restoration project that includes a structural retrofitting have been carried out. The Lima´s municipal theatre has a plan area of 1190m^2. It is a concrete structure constructed with a theatre purposes. It has a Hall and a Reception salon in front and a Pit area and stage. This five story building has a 17m high. The roof structure was made of steel in area of 396m^2. The total weight of the structure is about 5,940 metric tons. This paper presents results of the seismic vulnerability study for the old and the retrofitted structure carried out in the Japan-Perú Earthquake Engineering Research and Disaster Mitigation Center (CISMID) of the National University of Engineering of Perú. The most vulnerable components of the old structure were front wall in the upper part and the lateral concrete frames with infill blocks of plaster masonry existing in the second and third floor. Some parts of the concrete frames structure show damage in steel bars due to humidity and poor maintenance. The old roof steel structure was severity affected due to fire. Numerical simulations on the old building show irregularities that affect its seismic response. The retrofitting carried out on the building pretend to correct these irregularities trying to enhance its seismic behavior.

1. INTRODUCTION

The lot assigned to the Municipal Theatre of Lima was built with theatre purposes in the early 1920´s. It is a five story concrete building. Since then, at least four major earthquakes and a fire occurred 1998 have affected the roof of the structure. After 1998 the building is closed because the fire badly damages the steel roof structure and the stage.

Before the retrofitting the concrete structure presented cracks and exposed steel bars in the third floor of the gallery for the audience. There is also some damage due to past earthquakes and structural deficiencies which were never completely corrected. The whole structure seems to be rigid whereas the concrete elements were not accorded with the quantities of steel recommended in ours actual seismic standards. Also there is some deterioration mainly as a result of environmental effects, humidity and poor maintenance.

The roof structure of the theatre were composed by five steel truss that were severe badly damage due to the fire. Above this structure were two wood stories that had been removed. Numerical simulations on the old building show irregularities that affect its seismic response. The retrofitting carried out on the building pretend to correct these irregularities trying to enhance its seismic behavior.

Development of an effective methodology for future repairs and strengthening of upon important historical constructions require an integration of knowledge at least in the areas of seismology, geotechnics, structural engineering, material science, architecture, art as well as social, cultural and economic aspects. This paper presents the results of the earthquake response analysis for the original building and the retrofitted one. Some details in the retrofitting process will be discussed.

2. ABOUT THE THEATRE

The building of the theatre was built under the influence of French later neoclassic style. It has two important main areas: In front, the span of the three levels with the entrance, the principal hall and cafeteria (basement); inside the building, the five's levels gallery for the audience with a common shape plan view of horse-shoe. The imperial ladder is a singular element that connects both main areas. Architectonically, the main chamber presents a great number of blaster ornaments cover with gold sheets.

The structural configuration of the theatre is irregular in plan and elevation. It is made on reinforced concrete frames and concrete walls in the first two floors. In the third and fourth floor of the auditorium presents a concrete frame system with some masonry infill walls made of plaster and clay blocks. The density of concrete walls on the first floor

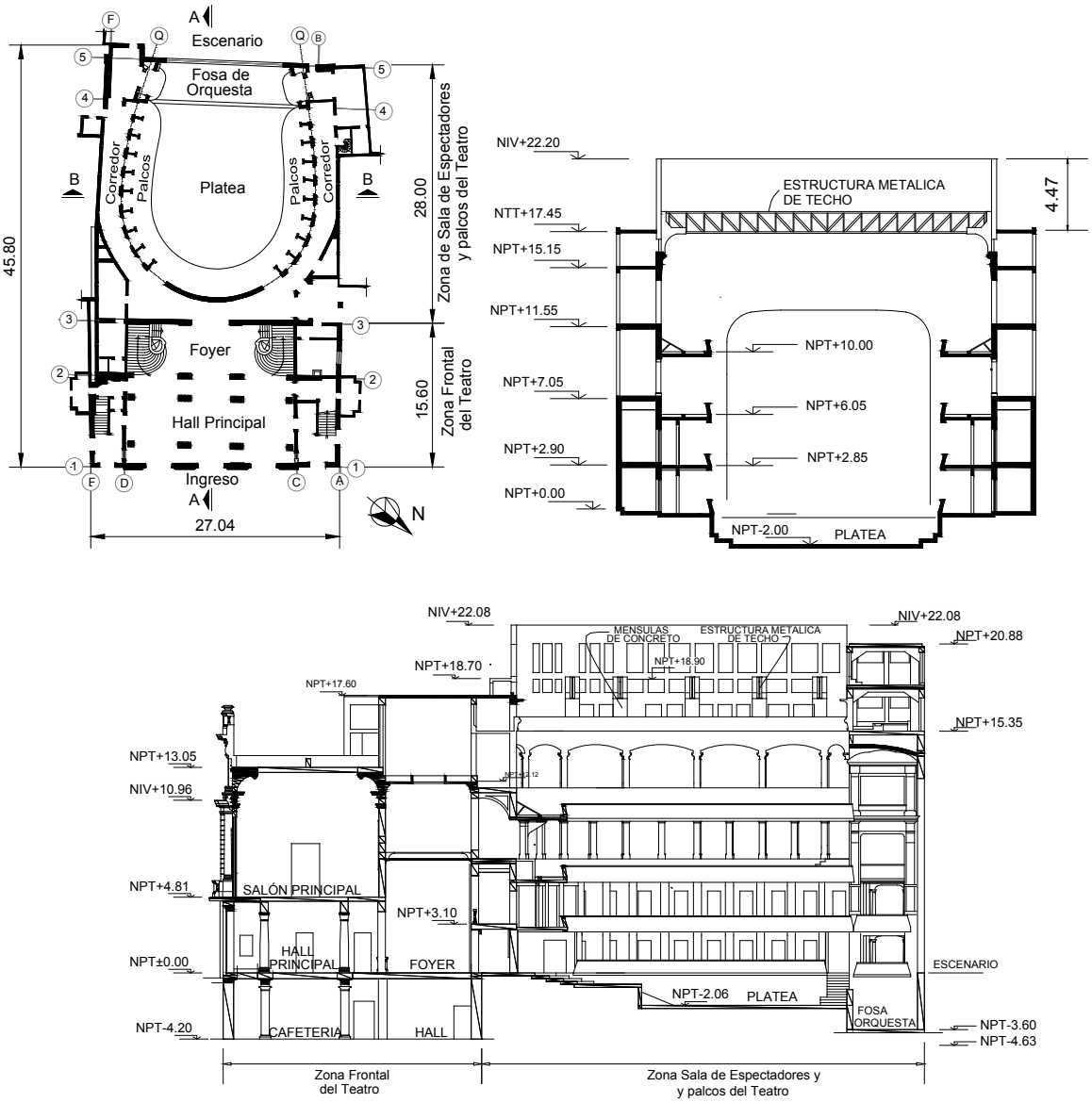


Figure 1 a) Plan view of the structure, b) elevation of the building, c) Lateral elevation of the building.

of the building is about 9%.

The main entrance hall is 4.65m height and structurally consists of walls of concrete, masonry and 12 circular columns; the roof slab is supported on reinforced concrete beams. The second floor reference area for the reception hall is 8.3m height and has walls of concrete and masonry, the roof slab is supported by inverted beams. On the other hand, auditorium zone of the building have five levels. Each level has an area of corridors and flown slabs corresponding private rooms (first and second floors) and area galleries (third and fourth floor). The old roof structure of the theatre was composed by five 20.0m steel truss. This steel truss was simply supported at the ends.

3. STATE OF THE STRUCTURE

The structure of the theater shows structural damage in specific areas of it. The steel structure of the roof of the auditorium has obvious structural damage by fire (see photo 2 (i)).

The front area of the building area is better preserved and the one with less damage, however, the 4m height no confined front masonry wall above the upper story presents little horizontal cracks at the bottom showing its seismic vulnerability

The frames of the axes A and F of the second, third & fourth floor have 10cm infill walls made of brick units of plaster. Some of the beams and columns of these frames have exposed reinforcing steel and an advanced grade of corrosion. (see photo 2 (e) and (f)).

Some columns located at the third and fourth floor of the auditorium area presents shear reinforcement distribution (stirrups) does not reach the standards for concrete in seismic regions (see photo 2c).

The 20cm concrete shear wall have a steel ratio of about 0.12%, which is much smaller than specified in current codes of reinforced concrete (see photo 2 (g)).



(a)



(b)



(c)



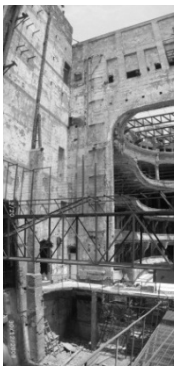
(d)



(e)



(f)



(g)



(h)



(i)

Figure 2 a) Internal view of the building. b) Principal Hall c) Third floor column, d) Floor system of fourth level of galleries e) y f) Lateral views of building, g) view of the concrete wall at the back of the building. h) Back view of the building i) Old steel roof structure of the building.

Defects such as cracks and material deterioration due to steel corrosion were often repaired aiming only at aesthetics, rather than correcting the structural causes of damage. It is then important to make an exhaustive review of the structural elements and contrast this information with the analysis results. There is no evidence of differential settlement in the walls. There is no evidence of humidity.

4. SOIL CONDITIONS

The theatre stands on firm soil formed from well graded sediments like gravel, sands and pebbles of alluvial nature, coming from resistant rocks like granodiorite, gabbrodiorite, diorite and granite. The thickness of this dry and compacted material is estimated as several hundred of meters. For the purpose of the seismic analysis the soil profile is qualified as rigid, with a characteristic period less than 0.4s.

5. MATERIAL PROPERTIES

Most structural elements in the building were made of reinforced concrete. In order to quantify the strength and stiffness of concrete, compression tests were performed in CISMID. The maximum compressive strength of concrete were 9.07MPa (99kgf/cm^2) in 1st floor plate, 11.82MPa (113kgf/cm^2) in the 2nd floor plate, 25.1MPa (256kgf/cm^2) on the 2nd floor beams, 12.06MPa (123kgf/cm^2) on the 3rd floor beams, 6.96MPa (71kgf/cm^2) and 13.04MPa (133kgf/cm^2) in the columns of the 3rd and 4th floor, and 18.73MPa (191kgf/cm^2) in the columns of the structure above portal of the stage.

The steels bar used in the building has a modulus of elasticity of 2.0 x 109 MPa (2.1x1010 kgf/cm^2) and the yield stress is 274MPa (2800kgf/cm^2).

6. MICROTREMOR MEASUREMENTS

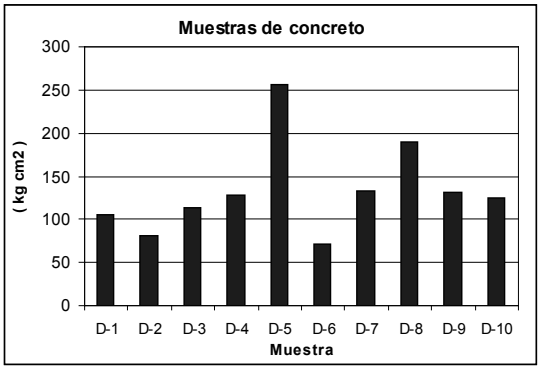
We performed a study of environmental microtremors purpose of obtaining fundamental modes of vibration of the structure at various points and levels of the building. The Fourier transforms obtained from measurements in the building have peaks at 3.3 – 3.5 Hertz (0.28s). This value of fundamental period has been the basis for calibration of the period of vibration of corroborating mathematical model of mass and stiffness ratios referred to in it.



Figure 3: Left: concrete simple from concrete Wall in 1st floor. Center: 4th column sample. Right: inverted concrete beam of 4th floor.

Table 1. Results of concrete sample in compression test

Identificaci n	Elemento	bicaci n	Resistencia (Kg cm2)
D-1	Muro	1º piso	105
D-2	Muro	1º piso	81
D-3	Muro	2º piso	113
D-4	Viga	3º piso	129
D-5	Viga	2º piso	256
D-6	Columna	3º piso	71
D-7	Columna	4º piso	133
D-8	Columna	5° piso	191
D-9	Muro	1º piso	132
D-10	Viga	4º piso	124





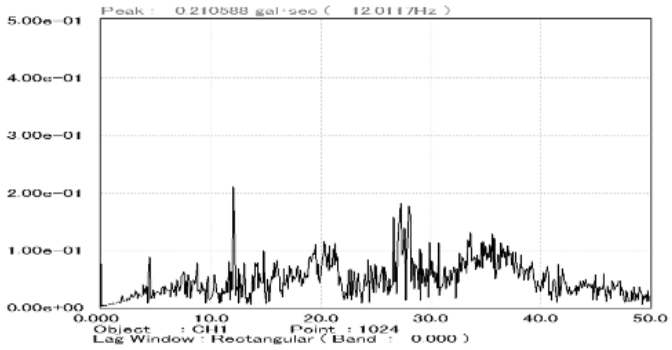


Figure 4 Left: Microtremor test of building. Right: Fourier transform from measurements

7. STRUCTURAL MODEL

A special effort was made for the development of an appropriate mathematical model for the analysis of this building of complex geometry. The building mainly consists of walls of concrete and masonry, and concrete frames. A linear elastic analysis was considered a reasonable tool for the structural investigation, providing at least a basic understanding of the existing building response.

Figure 5 depicts the mathematical model for the analysis. 5,808 frame elements were used to represent beams and columns. The walls and the roof covers were modeled with 26,197 two dimensional shell elements.

The structural walls of the building are composed of at least two materials: brick and cement mortar. Although they are strictly non-homogeneous and anisotropic, they were modeled as homogeneous and isotropic, with equivalent linear properties based on tests. The walls were supposed fixed at their base. This is consistent with the observation that; even for extreme conditions, there are not vertical tensile stresses at the base of the walls

The plaster masonry walls of the third and four floors were no performed in the present analysis due to its architectonic more than structural nature.

The adequacy of the model was corroborated by its ability to predict not only the results of the microtremor tests but also to identify the portions of the structure which may be more severely stressed by earthquake loads, which are in agreement with the damage observed in past events.

8. NUMERICAL ANALYSIS AND RESULTS

An elastic analysis of the building was carried out for dead and live loads and earthquake effects. Wind loading is not important in this case. The analysis provided essential information about stress distributions and an estimate of the seismic response of the structure, helping to identify the most vulnerable zones in the building and to interpret the existent damage. The seismic analysis was based on a seudo acceleration spectrum as defined in the Peruvian seismic code, with the following parameters: Z=0.4 (zone factor), U=1.3 (importance factor), S=1.0 (soil factor), C=2.5Tp/T 2.5 (dynamic amplification factor), R=3/4*(4) (for reduction factor).

The fundamental periods obtained for the structure ware 0.36seg having coupled masses in both directions. The maximum displacements in the top of the building were 9.13cm in x direction analysis and 8.0cm; both of displacements occurred near to the stage of the theatre. In the front of the building the displacements were 2.6cm, greatly reduced due to the wall density and less story levels. The drift in the fifth level were 5.8/1000 at the back of the building and correspond to an intermediate damage level due to the low ductility of the structural elements.

Most of the concrete walls of the building have earthquake shear stresses which are well below their allowable capacity. However, there are some exceptions, described in what follows: the shear stress of the laterals walls in the first and second floor reaches 1.47MPa (15kgf/cm^2) and 1.079MPa (11kgf/cm^2) for the second floor.

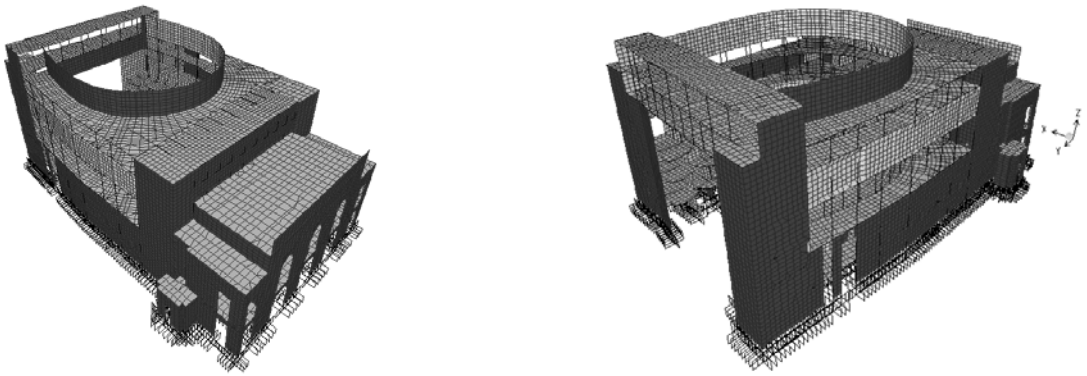


Figure 5 Mathematical model of theatre structure

The shear capacity of wall in axis 5 results below than the seismic demand.

Some shear concrete shear walls form first and second floors have levels of stress because of earthquake effects that were over its capacity due to the low compressive strength of existing concrete with a poor reinforcement.

The flexural and shear capacity of the third floor columns in the area of audience no reach the seismic demand because of the less shear reinforced and poor concrete quality.

The front non confined masonry wall in the upper part of the building have a displacement that reach 4.5cm out of the plane and have no capacity to resist out of plane excitations.

9. STRUCTURAL RETROFITTING

The process of retrofitting the building pass over the correct the deficiencies found in the analysis of seismic vulnerability considering the building with a new roof steel structure at the top of the building described in what follows:

a) External retrofitting of concrete existing columns: to enhance the capacity of the columns it has been added external steel plates.

b) External retrofitting of existing concrete shear walls: It has been added steel mesh to the shear walls.

c) Addition of new infill concrete shear walls in existing concrete frames in building in Y direction.

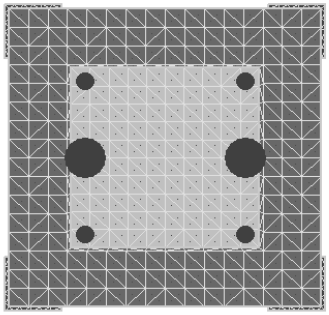
d) Union of some floor slabs in the building

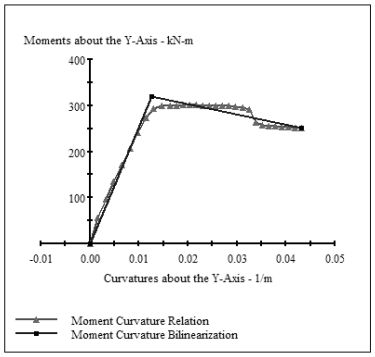
e) Reinforcement of front wall of the building

10. CONCLUSIONS

Structural analysis showed that the former theater building had some deficiencies in seismic behavior due to their configuration and poor maintenance. A deficiency is in concrete frames of the third and fourth floors parallel Y direction on the axes A and F which in some cases have exposed reinforcing the presence of moisture. The no confined front wall above last level is vulnerable to earthquakes by large out of plane displacements. The columns inside audience room in third and four floors present seismic deficiencies in shear and bending demand. Some existing concrete walls in first and second floors of the building have poor steel ratios that not agree with nowadays standard requirements. The fire damage occurred in 1998 full coverage of the former steel, but not concrete structures.

The strengthening over the building tries to introduce some capacity to supply its earthquake deficiencies. The concrete walls of the first and second floors have more steel ratio. The columns of the third and fourth floor have been reinforced by external steel plates. Also, there have been some concrete walls between the frames fill perimeter in the





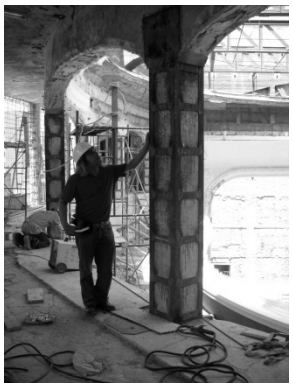


Figure 6(a) External retrofitting of concrete existing columns: to enhance the capacity of the columns it has been added external steel plates



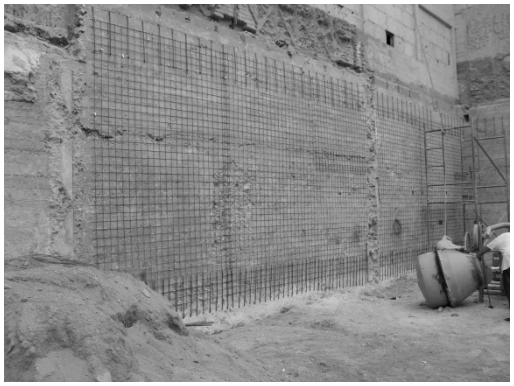


Figure 6(b) External retrofitting of existing concrete shear walls: It has been added steel mesh to the shear walls



Figure 6(c) Addition of new infill concrete shear walls in existing concrete frames in building in Y direction



Figure 6(d) Union of some floor slabs in the building

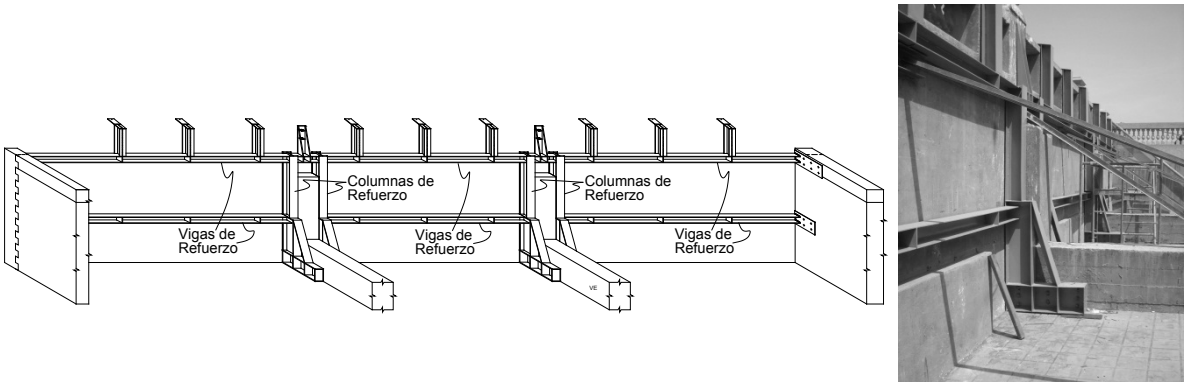


Figure 6(e) Reinforcement of front wall of the building

third and fourth floors. It has also reinforced the front wall by a steel structure attached to it. The old steel roof has been replaced by a new one.

The reinforcement has tried to correct the major structural deficiencies found in the building and does not imply no need for further structural located intervention in case of an earthquake. However, adequate monitoring and maintenance of the structures could ensure the continued operation of the theater for many years, safeguarding the lives of people and historical value that holds the building.

References:

San Cristóbal, A. (1999). Arquitectura Virreinal Peruana. Instituto General de Investigación, Facultad de Arquitectura, Urbanismo y Artes. Universidad Nacional de Ingeniería.

Silgado, E. (1978). Historia de los Sismos más Notables Ocurridos en el Perú. Geodinámica e Ingeniería Geológica. Boletín Nº3, serie C. Instituto Geológico y Minero, Lima Perú.

Ballardini, R., Gavarini, C. (1992) Seismic Protection of Monumental Buildings in Italy, Proceedings of the tenth World Conference on Earthquake Engineering, Madrid, Spain A. A. Balkema, Rotterdam

Meli, R. (1998). Ingeniería Estructural de los Edificios Históricos. Fundación Ica A.C. México.

Meli, R. Y Sanchez-Ramirez, R. (1993). Studies for the Rehabilitation of the Mexico City Cathedral. Structural Preservation of the Architectural Heritage, IABSE Symposium, Rome, Italy.

8CUEE CONFERENCE PROCEEDINGS
8th International Conference on Urban Earthquake Engineering
March 7-8, 2011, Tokyo Institute of Technology, Tokyo, Japan

DYNAMIC IDENTIFICATION OF REHABILITATED MASONRY BUILDING BY AMBIENT AND FORCED VIBRATION TESTS

Rafik Taleb[1)], Farid Bouriche[2)], Mehdi Boukri[3)], and Fouad Kehila[4)]

1) Researcher, National Center for Applied Research on Earthquake Engineering, Algeria
2) Researcher, National Center for Applied Research on Earthquake Engineering, Algeria
3) Researcher, National Center for Applied Research on Earthquake Engineering, Algeria
4) Researcher, National Center for Applied Research on Earthquake Engineering, Algeria
taleb_rafik@yahoo.fr, bourichefarid2002@yahoo.f, boukri_mehdi@yahoo.fr, fouad.kehila@gmail.com

Abstract: The aim of the paper is to investigate the capability of dynamic identification procedures, usually applied to reinforced concrete or steel buildings, in the estimation of the dynamic characteristics of unreinforced masonry buildings. For this purpose, the dynamic characteristics of a two story stone masonry building retrofitted by DC-90 dampers for seismic safety were evaluated by ambient and forced vibration techniques. Ambient vibrations were measured before and after retrofitting. A series of low amplitude steady state harmonic forced vibration tests were conducted after strengthening using eccentric mass shaker. The resonant frequency curves, mode shapes and damping coefficients as well as stress distribution in the steel braces of the DC-90 dampers have been investigated and could be defined. It was shown that the dynamic behaviour of the masonry building, even if not regular and with deformable floors, can be effectively represented. It can be concluded that the retrofitting of the building does not change the dynamic properties of the building due to the fact of low amplitude excitation which do not activate the dampers.

1. INTRODUCTION

Unreinforced masonry buildings have long been recognized to perform poorly under earthquake excitation. This deficient performance was clearly demonstrated in several past major earthquakes in Algeria such as the 1994 Beni-Chougrane earthquake (Naili 1996) and the 2003 Boumerdes earthquake (Oussalem et al. 2003) or over the word such as the 1989 Loma Prieta earthquake (Bruneau 1994) earthquake. In accordance with their poor performance in earthquakes, an understanding of the dynamic behaviour of unreinforced masonry buildings when subjected to seismic excitation is of major interest in many seismically active countries such as Algeria.

In Algeria, masonry buildings are a typical residential constructions type found in most Algerian urban centres. This construction, built mostly before the 1950s by French contractors, is no longer practiced (Farsi et al. 2002). Buildings of this type are typically 2 to 6 stories high. The slabs are wooden structures or shallow arches supported by steel beams, filled with earth materials. Masonry walls, usually 400 to 600 mm thick, have adequate gravity load-bearing capacity; however, their lateral load resistance is very low. As a result, these buildings are considered to be highly vulnerable to seismic hazard.

While ambient and forced vibration tests are usual applied techniques for reinforced concrete or steel buildings to understand and identify their dynamic behavior, less is known about masonry buildings. The dynamic behaviour of old masonry buildings differs from that of concrete or steel buildings, due to the historic construction typology, leading to walls and floors not rigidly attached to each other. Hence, local modes are more evident with respect to frame buildings (De Sortis et al. 2005). For the same reason, usually the dynamic forced response depends on the shaker location and applied force amplitude. Therefore, it is essential to determine dynamic parameters such as natural frequencies, damping factors and mode shapes, which are typically obtained using modal identification techniques by conducting ambient or forced vibration tests (Abdul Karim et al. 2008).

Ambient vibration can be from sources such as wind, waves, pedestrian or vehicles, with the vibration not controlled but instead considered as a stationary random process. Thus, the response data from the structure alone is used to estimate the dynamic parameters (Shabbir 2008). In contrast, forced vibration testing provides a known input force over the frequency bands of interest, which can be achieved by the excitation input motions. Thus, the dynamic characteristics of structures can be explicitly recognized.

The objectives of the testing for our masonry building were first, to investigate the change of natural frequencies of the building before and after strengthening by ambient vibration test and second, to investigate the dynamic behavior of the building after strengthening at resonant conditions (harmonic forced vibration) by forced vibration test. Based on forced vibration techniques, the resonant frequency curves, mode shapes and damping coefficients as well as stress distribution at strengthening system could be defined. These parameters are strongly related to prediction of dynamic behaviour of the structure under earthquake excitation.

2. DESCRIPTION OF THE BUILDING AND THE RETROFITTING SYSTEM

The aimed building was constructed in 1908 during the French colonization period, and now is used as a residential building. The building has an irregular shape consisting of basement, ground floor, two floors and tower, representing a part of third floor. The in plane dimensions of the building are of length 22m and 17.75m. The structural system is composed by masonry bearing walls, with mean thickness of 50cm. The floors were built with hollow clay elements supported by steel beams interspaced at 50cm. The steel beams are simply supported by the bearing walls. A main view of the building before strengthening is shown in figure 1.



Figure 1 View of the building before retrofitting (S-W façade)

There were some visible cracks, which happened during the past 2003 Boumerdes earthquake. It was obviously that some repairing and strengthening solution should be applied. The retrofitting system DC-90 consists of several steel elements such as anchors, prestressing bars, diagonal bracings and yielding type dampers (Skuber et al. 2006). Figure 2 shows details for the connection of the damper, diagonal brace and vertical bar. The appearance of the building after retrofitting is presented in figure 3.



Figure 2 View of the a connection detail for DC-90 system



(a) (b)

Figure 3 View of the building after retrofitting:
(a) N-E façade, and (b) S-W façade

3. TEST EQUIPMENT AND MEASUREMENT METHODOLOGY

The building dynamic behaviour has been monitored by three different types of instrumentation: seismometers for ambient vibration measurements, accelerometers for forced vibration measurements and strain gauges for recording the strains (stress) in steel bracings of the DC-90 system.

3.1 Ambient Vibration Test

The ambient vibration testing methodology is based on ambient excitation such as wind. The very sensitive seismometers are capable to catch the produced micro-tremors which is a random type of signal, consisting of excitation frequencies in broad frequency range, enough to excite several modes of structural vibration. The measurements performed in selected 15 points at level III, as shown in figure 4, give some general information about natural frequencies of the building after retrofitting. The ambient vibration equipment consists of City Shark I station (digital recorder) coupled by Lennartz seismometers type LE-3D. One by one, fifteen points have been measured in two orthogonal directions at level III. The objective was to give a first estimation of

the natural frequencies before retrofitting of the building, and to estimate the position of the centre of torsion where the shaker will be placed for forced vibration test.

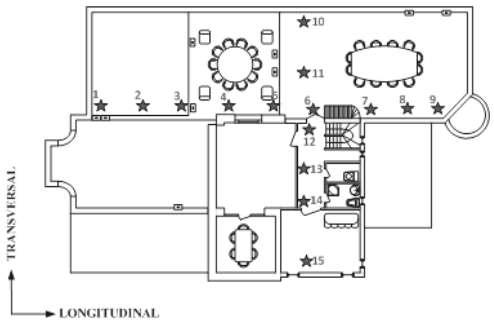


Figure 4 Measurement points position on level III for ambient vibration test.

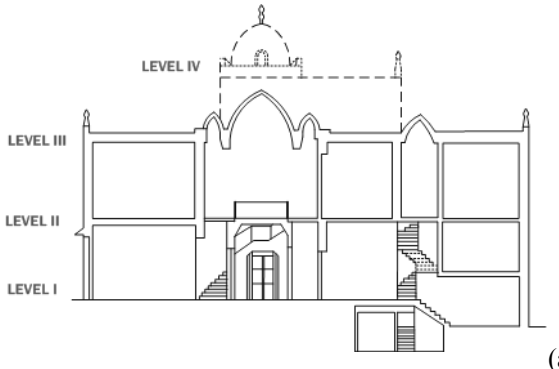
3.2 Forced Vibration Test

The forced vibration testing methodology is based on resonant concept. By the application of a dynamic harmonic force on the top of the building, it is possible to excite the resonant frequencies of the building, if the frequency of the force is equal to one of the natural frequencies of the building. The frequency of the force can be gradually changed in small steps within the range of 0.5-16.0 Hz. The resonant state is reached when the acceleration response at the measurement point become maximum and then decrease even the frequency of the force still increase. On this manner, frequency response curves can be obtained for each orthogonal direction and torsion.

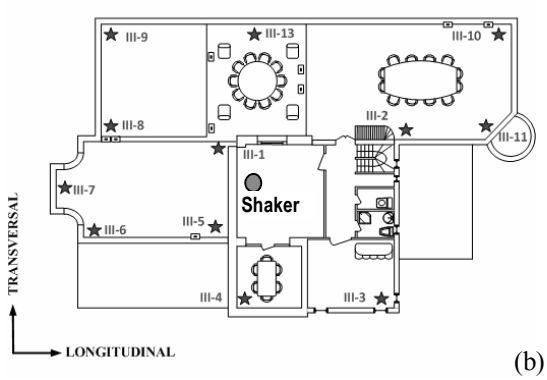
The forced vibration equipment consists of an eccentric mass shaker for excitation with a harmonic sinusoidal force within the frequency range 1-15 Hz (Shenk-Germany) as well as signal recording equipment: data acquisition system 16 channels - National Instruments-USA, Kistler accelerometers 5g, and signal amplifier- Kistler-USA, for accelerometers (8 channels), signal amplifier-Kyowa, for Kyowa strain-gauges KFC-5 (8 channels). A labtop computer was used to process the digitised data. The shaker is shown in figure 5, while the measurement points position for level III and level IV is shown in figure 6.



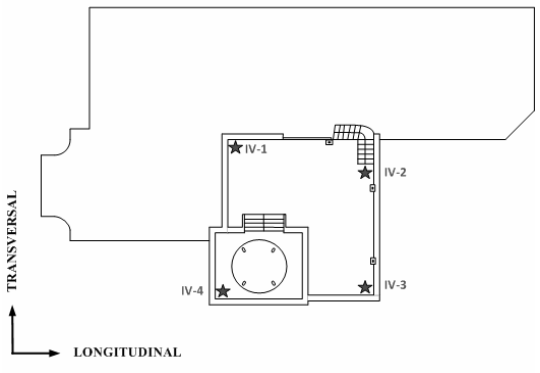
Figure 5 Eccentric mass shaker for excitation of harmonic force



(a)



(b)



(c)

Figure 6 Measurement points position for forced vibration test: (a) Elevation view, (b) Level III, and (c) Level IV.

4. AMBIENT VIBRATION TEST RESULTS

Fourier amplitude spectra recorded in measurement point 4 before retrofitting is shown in figure 7 for longitudinal and transversal directions, while thus recorded after retrofitting by DC-90 System is shown in figure 8. Comparative presentation of the frequencies is given on Table 1. The comparison between natural frequencies given by ambient vibration test before and after retrofitting shows that they become higher after retrofitting for about 5%.

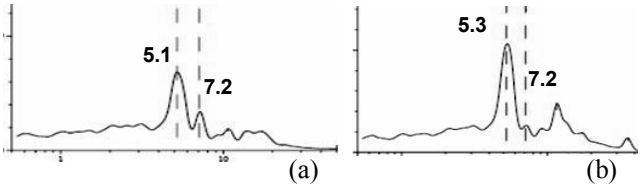


Figure 7 Fourier amplitude spectra before retrofitting: (a) Transversal direction, and (b) Longitudinal direction

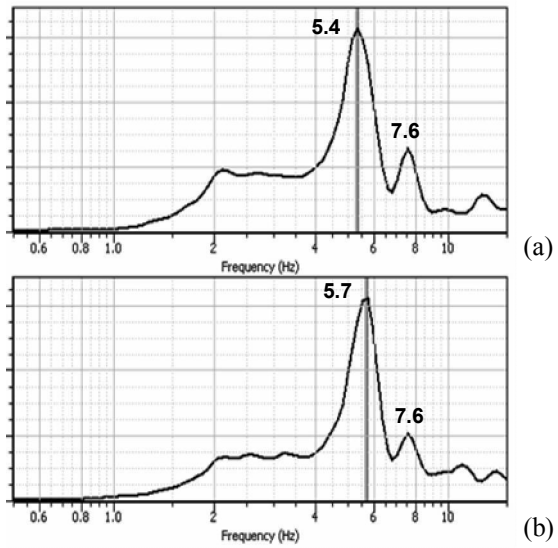


Figure 8 Fourier amplitude spectra before retrofitting: (a) Transversal direction, and (b) Longitudinal direction

Table 1 Natural frequencies of the building before and after retrofitting

Direction	Natural Frequency (Hz)	
	Before retrofitting	After retrofitting
Transversal	5.1	5.4
Longitudinal	5.3	5.7
Torsion	7.2	7.6

5. FORCED VIBRATION TEST RESULTS

5.1. Frequency response curves

Frequency response curves are obtained by recording the acceleration response at particular points on level III and IV in two orthogonal directions (Longitudinal and transversal directions). The frequency response curves for some recording points are given in figures 9 through figure 12.

The resonant frequencies defined by force vibration method as can be seen from resonant frequency curves, are smaller than the ambient frequencies for about 3-5 %, which is close to the original state before retrofitting (Table 2). It can be concluded that the retrofitting of the building does not change the dynamic properties of the building. This is mainly due to the high stiffness of the masonry walls, in which, the inserted steel bars do not change their stiffness.

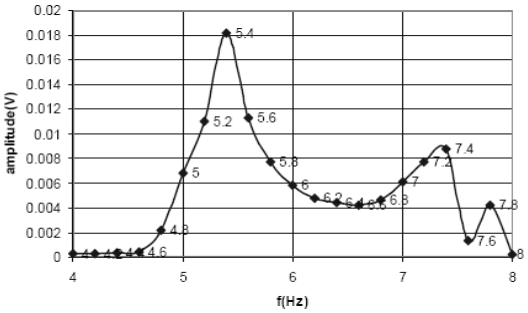


Figure 9 Frequency Response Curve for transversal excitation - point III-1

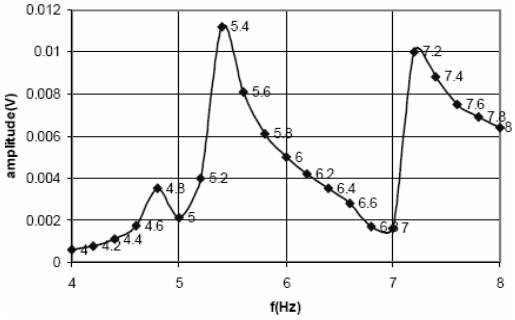


Figure 10 Frequency Response Curve for transversal excitation - point III-10

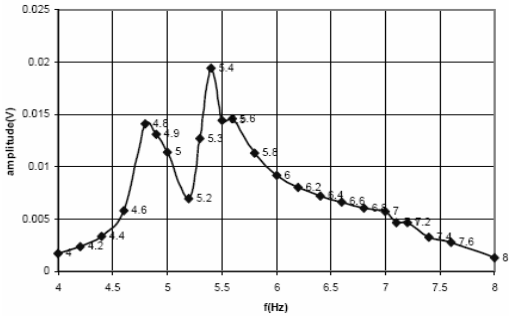


Figure 11 Frequency Response Curve for longitudinal excitation - point III-10

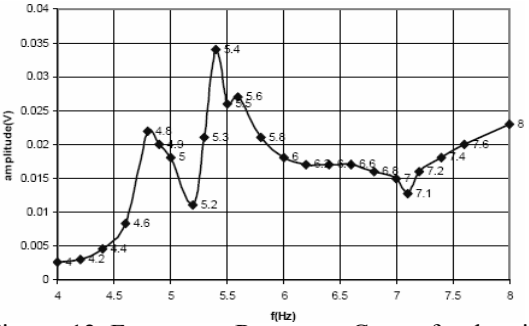


Figure 12 Frequency Response Curve for longitudinal excitation - point III-1

Table 2 Natural frequencies of the building by ambient and forced vibration tests

Direction	Natural frequency (Hz)		
	Ambient vibration		Forced vibration
	Before retrofitting	After retrofitting	After retrofitting
Transversal	5.1	5.4	4.8
Longitudinal	5.3	5.7	5.4
Torsion	7.2	7.6	7.2

5.2. Damping coefficients

As far as damping coefficients concerns, they are defined from frequency response curves based on half power method. Table 3 shows the damping ratios as a percentage of critical damping corresponding to some measured points. The damping ratios are ranging between 2.7-5.8 %. This is rather high damping, which is good for dissipation of the energy during earthquake. These values should be much higher when DC-90 dampers become active when lateral displacements reach 1-5mm during earthquake. For this low level of excitation by force vibration activation of the dampers is not expected.

Table 3 Damping coefficients

Excitation direction	Freq. (Hz)	Damping at particular points (%)					
		III-10		IV-1		IV-4	
		T	L	T	L	T	L
Transversal	4.8	3.5	3.0	3.5	/	/	/
	5.4	3.1	2.7	3.1	3.1	/	/
	7.2	/	3.5	/	/	/	/
Longitudinal	4.8	/	3.1	/	3.1	/	4.2
	5.4	2.9	2.8	5.5	2.8	5.8	3.7
	7.2	3.0	3.5	/	/	/	3.6

/ No measured values at that point

5.3. Stress distribution at steel bracings of DC-90 system

Stress distribution at the steel bracings was investigated by recording the strains at 14 selected points at the level I (ground floor). The disposition of the strain gauges is given in Figure 13. The stresses, given on Table 4 for some measurement locations, are calculated based on measured strains following the Hook's low. The maximum value is obtained at point 14d for excitation in longitudinal direction with σ= 4.06 Mpa corresponding to peak strain of about 20 μstr. Considering the obtained values, it is obvious that level of dynamic excitation is very low (about 0.95 %g peak response) comparing to a real earthquake strong motion level.

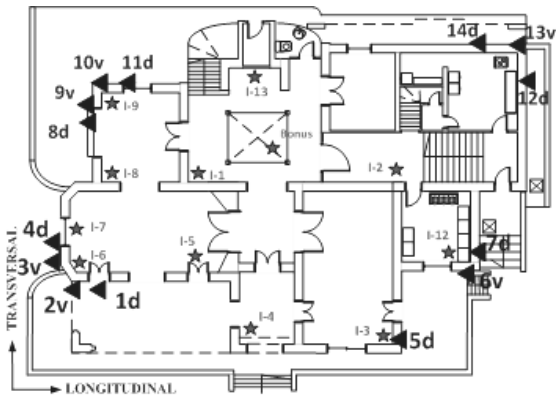


Figure 13 Disposition of the strain gauges at bracings (Level I). v: vertical bar, d: diagonal brace

Table 4: Calculated peak stresses at vertical bars and diagonal bracings

Dir.	Freq (Hz)	Calculated peak stresses (MPa)					
		1d	2v	6v	7d	13v	14d
Trans.	4.8	0.12	0.12	0.36	0.34	0.62	2.16
	5.4	0.22	0.14	0.42	0.48	0.46	2.10
	7.2	0.20	0.16	0.46	0.54	1.08	3.02
Long.	4.8	1.00	0.50	0.66	0.62	1.00	2.62
	5.4	0.86	0.44	0.62	0.58	0.78	3.16
	7.2	0.98	0.40	1.40	1.40	2.04	4.06

5.4. Vibration mode shapes

The main objectives of forced vibration test were to define the resonant frequencies, damping coefficients and mode shapes of vibration of the building under resonant conditions. Having in mind the irregular shape of the building (unsymmetrical in plane), the torsional effects have been expected. To record such effects, two orthogonal horizontal components at each measuring point have been measured: one in direction of excitation and other in direction transversal to excitation force. The spatial shape of vibration was estimated by application of ARTeMIS software (svibs, 2001).
Figures 14-16 show the spatial mode shapes for three defined resonant frequencies. It is obvious that torsional effect is present more-less in all three mode shapes which means that the modes are coupled i.e. for any excitation direction and frequency near resonant, the structure will vibrate torsionally. The most intensive vibration appears under the frequency 5.4Hz. It is visible from the frequency response curves and peak acceleration recorded at characteristic points of the building.



Figure 14 Vibration shape of the building at resonant frequency f=4.8Hz by excitation in the transversal direction.

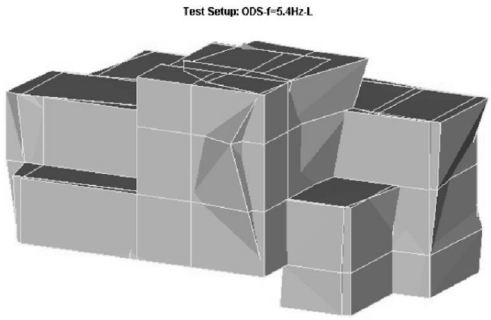


Figure 15 Vibration shape of the building at resonant frequency f=5.4Hz by excitation in the longitudinal direction.

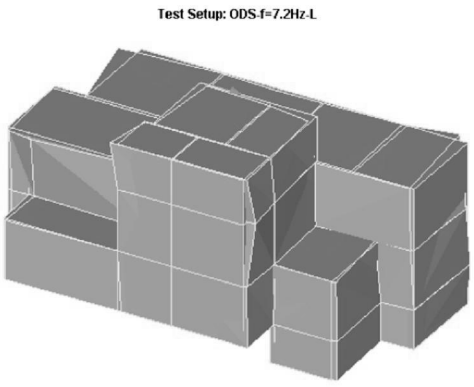


Figure 16 Vibration shape of the building at resonant frequency f= 7.2 Hz by excitation in longitudinal direction

6. CONCLUSIONS

Based on experimental testing of the masonry building by ambient and forced vibration methods, the following summarized results are obtained:

The first set of fundamental frequencies of the building is: transversal direction f1= 4.8Hz, longitudinal direction: f2=5.4 Hz and torsion: 7.2 Hz. The vibration of the building at resonance condition is of the same intensity in longitudinal and transversal directions. For both excitation directions, all three frequencies are excited i.e. the building vibrate torsionally with coupling effect between the modes.

The vibration effect produced by forced vibration test was rather small comparing to real earthquake excitation conditions. Namely, the peak acceleration on the top of the building was about 0.01g, peak displacement about 0.1 mm, peak stress at point 14d was about 4.0 Mpa and peak strain about 20 μstr, The capacity of the shaker was much bigger than it was used, but because of safety precaution, higher excitation force was not applied. The measured values at 14 points on vertical and diagonal bracings at ground floor show the distribution of the stress. If we analyze the data from Table 6, it can be concluded that the diagonal bracing at point 14d is more stressed than the others (2-5 times) and that stresses at longitudinal excitation are about two times higher then in transversal for corresponding points. This is probably because the irregular shape of the structure as well as non-uniform distribution of the inertial forces in both directions.

The damping of the structure obtained from frequency response curve based on half-power method ranges between: 3-6 % of critical damping even under low amplitude vibration level. For realistic earthquake conditions it could reach much higher level considering the presence of the DC-90 dampers. At the excited level of vibration (1%g) the dampers have not been activated.

References:

Abdul Karim A. R., C. Oyarzo-Vera, N. M.Sa'don, and J. M. Ingham (2008) "Forced Vibration Response of Small Scale URM House with Flexible Timber Diaphragm", *Australian Earthquake Engineering Conference AEES2008*, Ballarat, Victoria, 21-23 November 2008.

Bouriche F., Taleb R., Ramas A. Boukri M., Razkallah H., Kehila F. (2007) « Rapport des essais de vibrations ambiantes et forcées Résidence de l'Ambassade de Finlande –Alger », *National Centre for Applied Research on Earthquake Engineering*, Internal report, April 2007. (In french)

Bruneau M. (1994) "State-of-the-art report on seismic performance of unreinforced masonry buildings" *Journal of Structural Engineering*, 120(1), 230-251.

De Sortis A., Antonacci E. Vestroni F. (2005), "Dynamic identification of a masonry building using forced vibration tests", *Engineering Structures*, 27 (2005) 155–165.

Farsi M. N., Lazzali F., Ait-Meziane Y. (2002), "Housing Report: Stone masonry apartment building in Algeria", *World Housing Encyclopedia*, Report N°75, EERI & IAEE.

Naili M. (1996), « Le séisme des Béni-Chougrane (Algérie, 18/08/94) », *Association fran aise de génie parasismique*, Cahier technique N° 12 (in french).

Ousalem, H., Bechtoula, H. (2003) "Report on the damage investigation and post-seismic compaign of the 2003 Zemmouri earthquake in Algeria", *University of Tokyo & Kyoto university*, Personal Report, Auguest 2003.

Shabbir F., and Omenzetter P. (2008). "Forced vibration testing of a thirteen storey concrete building." *2008 NZSEE Conference*, Taupo, New Zealand.

Skuber P., Beg, D., Sinur, F. (2006) “Experimental analysis of DC90 energy absorber device”, *PROHITECH WP7 internal report*.

Structural Vibration Solutions ApS (2001), ARTeMIS Extractor, Aalborg, Denmark, www.svibs.com

Tashkov L., and Krstevska L. (2007) “Evaluation of dynamic behaviour of Finland Embassy at Algiers based on forced vibration tests after strengthening by DC-90 system”, *Institute of Earthquake Engineering and Engineering Seismology University " Ss. Cyril and Methodius"*, Report IZIIS 2007-15.

8CUEE CONFERENCE PROCEEDINGS
8th International Conference on Urban Earthquake Engineering
March 7-8, 2011, Tokyo Institute of Technology, Tokyo, Japan

A STUDY ON FAILURE MECHANISM OF RC STRUCTURES WITH SPECIALLY SHAPED COLUMNS WITH CONSIDERATION OF DIAPHRAGM USING PUSHOVER ANALYSIS

Pu Yang[1)2)], Xiaoliang Wang[3)], Hongliu Xia[1)], Yi Liu[1)], Wei Wei[1)], and Akira Wada[4)]

1) Associate Professor, College of Civil Engineering, Chongqing University, Chongqing, China
2) Key Laboratory of New Technology for Construction of Cities in Mountain Area (Chongqing Univ.), Ministry of Education, China
3) Engineer, Strategy Architectural Design Co. Ltd, Beijing, China
4) Professor, Center for Urban Earthquake Engineering, Tokyo Institute of Technology, Japan
yangpu@cqu.edu.cn, wangxl1025@hotmail.com, xiahongliu@cqu.edu.cn, liuyicg@cqu.edu.cn, wweeiiz@cqu.edu.cn, wada@serc.titech.ac.jp

Abstract: Although failure mechanism of strong column-weak beam is expected by Chinese Seismic Code, several collapses of RC frames occurred due to damages of columns during Wenchuan earthquake. This caused heated debate among many scholars and engineers all over the world. Investigations and researches illustrated that seismic design without consideration of diaphragm was one of the main reasons. In this paper, with flexibility-based fiber model, the seismic behaviors of RC structures with specially shaped columns which are designed according to the current Chinese codes or technical specification are analyzed under unidirectional rare earthquakes using PushOver analysis method. The beam strength is calculated with or without consideration of the diaphragm and its reinforcement. The results are compared and conclusion has been drawn that the bending capacity of beams would be increased due to the effect of diaphragm and its reinforcement, and which would change the failure mechanism of RC frames under rare earthquake, especially in high intensity areas. Therefore, the influence of the diaphragm should be considered in the seismic design of this type of structure and corresponding design code should been improved.

1. INTRODUCTION

Although failure mechanism of strong column-weak beam is expected by seismic design codes for RC frames, plastic hinges at the beam ends were rarely developed during Wenchuan earthquake occurred in China on May 12th 2008 while lots of plastic hinges formed at the end of columns of RC frames. Among those buildings, many were designed strictly following the Chinese Code for Seismic Design of buildings (2001version). This phenomenon has caused much attention of the committees of Chinese Codes and many engineers. A great deal of research works were carried out to analyze the causes of this typical failure mechanism. According to the investigations of the earthquake hazard and the latest studies by the authors (Ye Lieping 2008, Wang Yayong 2008, Su Youpo 2009 and Huo Linsheng 2009 etc.), one of the important reasons is that the effect of the floor diaphragm is usually neglected in seismic design. The ratio of stiffness and strength of beam to column in the same joint would be changed because of the diaphragm and its reinforcement, i.e. the yield state and order of beams and columns would be changed, and thus the failure mechanism of strong column-weak beam might not be realized. Because the RC frames with specially shaped columns are seldom constructed in Wenchuan, their seismic behaviors have not been proved by actual strong earthquake. Meanwhile the achievements about the failure mechanism of the typical structures all over the world are very little. It is still uncertain for researchers and designers whether the failure mechanism with beams' hinges would be taken place after strong earthquakes. So it is necessary to analyze the failure mechanism of the type of RC frames affected by the floor diaphragm and evaluate the efficiency of the current Chinese codes.

In this paper, with the flexibility-based fiber model, the seismic behaviors of RC structures with specially shaped columns, designed according to the Chinese current codes including Code for Seismic Design of buildings and Technical Specification for Concrete Structures with Specially Shaped columns, are analyzed using nonlinear dynamic analysis method and PushOver analysis method. The beam strength is calculated with or without consideration of the diaphragm and its reinforcement. The results are compared and conclusion has been obtained.

2. STRUCTURAL MODEL AND CORRESPONDING PARAMETERS

Two RC model structures with specially shaped columns, which were named S-015g and S-020g respectively, were designed according to the Chinese

Technical Specification for Concrete Structures with Specially Shaped columns (JGJ149-2006) in this paper. The Site Classification is Class II. The Earthquake Group Classification which represents the fault distance is Group 1. The layout of the structure is illustrated in Figure 1. The corresponding parameters of two structures are given in Table 1.

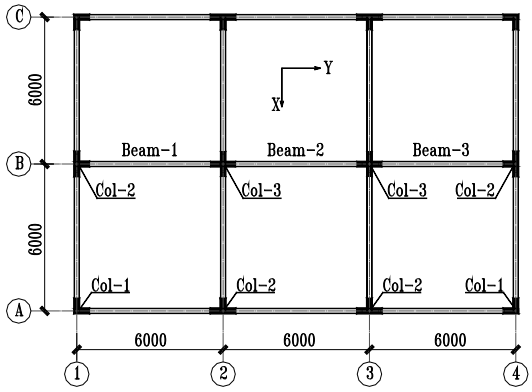
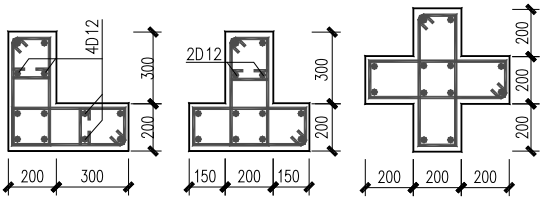


Figure 1 Layout of Model Structure

Table 1 Main Parameters of the Model Structures

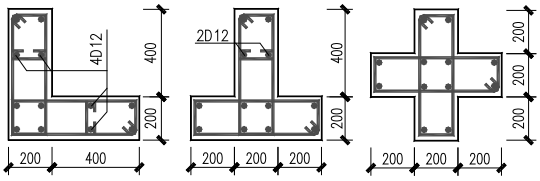
Model Structure	Seismic Design Intensity	Structural Height /m	Seismic Class	Fundamental Period /s
S-015g	0.15g	18 (6 floors)	Class 3	0.93
S-020g	0.20g	12 (4 floors)	Class 2	0.55

The concrete compressive design strength is assumed to be 30MPa. The internal forces and reinforcement of structures are determined using the Chinese Business Software SATWE and CRSC. And the minimum ratio of reinforcement for columns and beams, axial compression ratio of column and elastic story drift of structures under frequent earthquake met the requirements of Chinese Codes. The thickness of floor diaphragm is 120mm and its bottom bi-directional reinforcement is φ^R10@180 (the design yield strength, fy, is 400N/mm^2) while at the top is φ^R10@100 closing to beams. The bottom bi-directional reinforcement of roof diaphragm is φ^R10@150.



(a) Col-1 (b) Col-2 (c) Col-3

Figure 2 Dimensions and Reinforcement Type of Columns of Model Structure S-015g



(a) Col-1 (b) Col-2 (c) Col-3

Figure 3 Dimensions and Reinforcement Type of Columns of Model Structure S-020g

The sectional dimensions and type of reinforcements of specially shaped columns of the two model structures are given in figure 2 and figure 3 (units: mm).

The longitudinal reinforcement of specially shaped columns corresponding to the two model structures is shown in Table 2. In the Table, "D" means the diameter of longitudinal reinforcement. For instance, "8D16" represents 8 pieces of longitudinal reinforcement whose diameter is 16mm and its designed yield strength is 300N/mm^2. The diameter of hoop reinforcement is 8mm for Col-1 and Col-2 and 10mm for Col-3. The spacing of hoop reinforcement was 100mm for all columns.

Table 2 Details of longitudinal reinforcement of columns

Columns	Floor	Model Structure	
		S-015g	S-020g
Col-1	1st floor	8D16+4D12	8D22+4D12
	others		8D16+4D12
Col-2	1st floor	10D18+2D12	10D22+2D12
	others	10D16+2D12	10D16+2D12
Col-3	All floors	12D16	12D16

3. NONLINEAR ANALYSIS OF THE MODEL STRUCTURES

The fiber model is used to simulate the behavior of the specially shaped column. The effectiveness of fiber model in simulating the behavior of RC columns had been verified by comparing the analysis results with the experimental results obtained under cyclic loading in previous research by authors (Yang Pu 2006). Fiber division of beams considering the effect of floor diaphragm is shown in Figure 4. The effective flange width of beam is assumed to be the width of beam plus six times the depth of diaphragm at each side of beam according to the work by Zheng Shiju (2009), Wu Yong (2009) and ACI 318-08. And fiber division of specially shaped columns is shown in Figure 5.

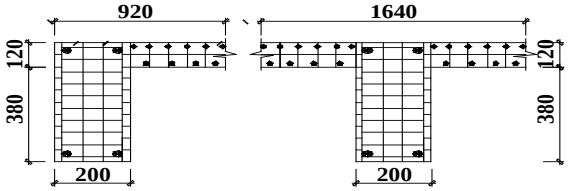
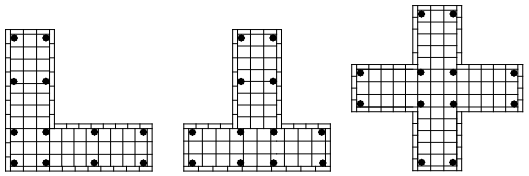


Figure 4 Fiber Division of Beams Considering Effect of Floor Diaphragm



(a) Col-1 b) Col-2 (c) Col-3

Figure 5 Fiber Division of Columns

Monegotto-Pinto model which accounts for strain hardening is adopted to represent the stress-strain relationship of steel reinforcement fiber in single direction. The modified Kent-Park model is adopted to illustrate the

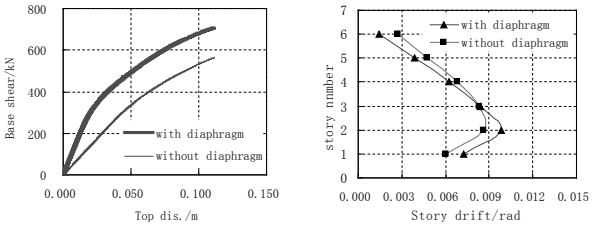
stress-strain relationship of concrete fiber in which relative slip between steel bars and concrete is not taken into account but the confinement of concrete by hoop reinforcement is considered.

The dynamic analysis was carried out by selecting three actual earthquake waves and one artificial earthquake wave. The results of dynamic analysis were different due to the difference of waves. Therefore this paper focused on the results of PushOver analysis in order to eliminate the effect of input waves and compared with results of dynamic analysis.

Because of symmetry of mass and stiffness of the two model structures, the lateral load was applied only in the direction of Y axis and the pattern of load was assumed as inversed triangle. And the target top displacement of structures was assigned the average value plus one time variance of the maximum top displacement under four earthquake waves using dynamic analysis method without considering the effect of the diaphragm.

3.1 Nonlinear Analysis Results of the Model Structure S-015g

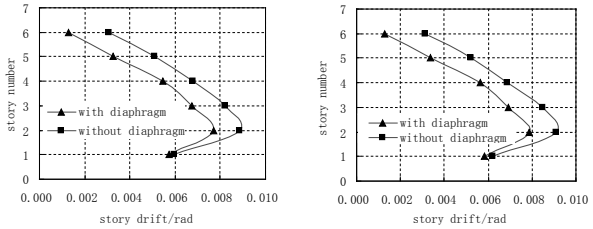
The capacity spectrum, curve of base shear vs. top displacement, of model structure S-015g were obtained and shown in Figure 6(a) using PushOver analysis method. It is obvious that the base shear is higher taking account of effect of the diaphragm than one without considering the diaphragm at the same top displacement. In other words, the diaphragm and its reinforcement increased the structural stiffness if its effect was considered.



(a) capacity spectrum (b) story drift

Figure 6 PushOver Analysis Results of Model Structure S-015g

The story drift of model Structure S-015g along its height is shown in Figure 6(b). It can be found that the maximum story drift is at the second story whether or not consider the effects of the diaphragm and its reinforcement. Thus the weak story of the model structure is obviously the second story.

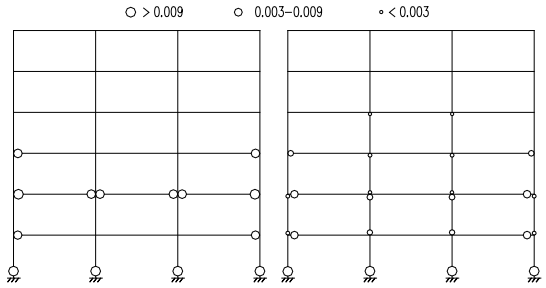


(a) USA0021 (b) USA002755

Figure 7 Story Drift of Model Structure S-015g Using Dynamic Analysis Method

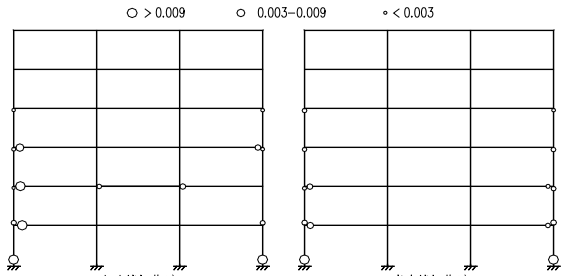
The maximum story drift is larger considering the diaphragm than not considering at the same target top displacement and the story drift is more even along the height. This phenomenon is not the same as the one using dynamic analysis shown in Figure 7 due to two possible reasons. The first one may be load pattern which may not comply with the distribution of inertia force along the height of structure under actual earthquake. Another one is the target top displacement may not equal because of effect of the diaphragm. After all, it can be concluded that the diaphragm would affect significantly the behavior of structure.

The distributions of plastic hinges of the frame on axis B of the model structure S-015g under rare earthquake by PushOver analysis and dynamic analysis under earthquake wave USA002152 with and without consideration of the effect of the diaphragm are shown in Figure 8 and 9.



(a) without diaphragm (b) with diaphragm

Figure 8 Distribution of Plastic Hinges under Rare Earthquake by PushOver Analysis Method



(a) without diaphragm (b) with diaphragm

Figure 9 Distribution of Plastic Hinges under Rare Earthquake Using Dynamic Analysis (USA002152)

Several conclusions can be obtained from the above results:

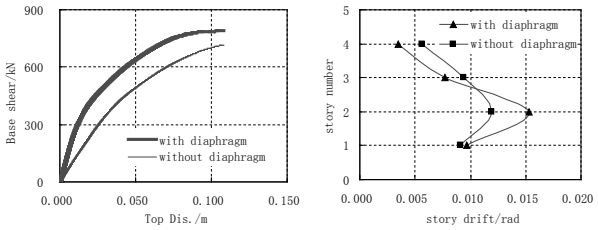
1) When the effect of the diaphragm is considered, the number of plastic hinges at the end of beams is decreased while the one at the end of columns is increased. And the angle of plastic hinges of beams is decreased while the one of columns was increased. The reason is the increase of strength of beams due to the floor diaphragm and its reinforcement.

2) According to the calculated results, the equal longitudinal reinforcement at top of beams would almost double if reinforcement of the diaphragm is considered. Therefore the plastic hinge at end of beam formed at the bottom of beam because the bottom reinforcement reached the design yield strength, while the plastic hinge at end of beam usually forms at the top of beam because the top

reinforcement reaches design yield strength if not considering the diaphragm and its reinforcement. This has not been studied in-depth by researchers in their previous studies.

3.2 Nonlinear Analysis Results of the Model Structure S-020g

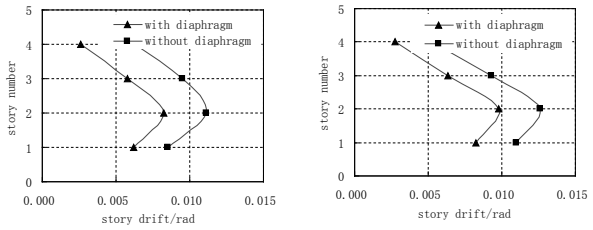
The capacity spectrum and curve of base shear vs. top displacement, of model Structure S-020g were obtained and shown in Figure 10(a) using PushOver analysis method. It is obvious that the base shear is higher taking account of effect of the diaphragm than one without taking account of the diaphragm at the same top displacement. The reason is the same as the model Structure S-015g.



(a) capacity spectrum (b) story drift

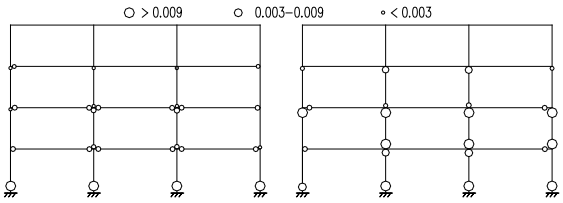
Figure 10 PushOver Analysis Results of Structure S-020g

The story drift of Structure S-020g along its height is shown in Figure 10b. It can be found that the maximum story drift is at the second story whether or not considering the effect of the diaphragm and its reinforcement, so the weak story of structure is obviously the second story. And the maximum story drift is larger considering the diaphragm than not considering at the same target top displacement and the story drift is more even along the height. This phenomenon is not same as the one using dynamic analysis shown in Figure 11. The reasons are the same as the Structure S-015g.



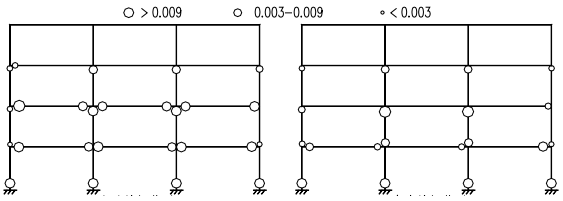
(a) USA000535 (b) USA002551

Figure 11 Story Drift of Structure S-020g Using Dynamic Analysis Method



(a) without diaphragm (b) with diaphragm

Figure 12 Distribution of Plastic Hinges under Rare Earthquake by PushOver Analysis Method



(a) without diaphragm (b) with diaphragm

Figure 13 Distribution of Plastic Hinges under Rare Earthquake by Dynamic Analysis (USA002551)

The distribution of plastic hinges of frame in axis B of structure S-020g under rare earthquake by PushOver analysis and dynamic analysis under earthquake wave USA002551 whether or not considering the effect of the diaphragm is shown in Figure 12 and 13.

From the above figures, several conclusions can be obtained:

1) As the effect of the diaphragm is considered, the number of plastic hinges at the end of beams is decreased while the one of plastic hinges at the end of columns is increased. And the angle of plastic hinges of beams is decreased while the one of plastic hinges of columns is increased. The plastic hinges are occurred at the end of almost all columns at the second story and this is severe for seismic design. The reason, similar to the structure S-015g, is the promotion of strength of beams due to the diaphragm and its reinforcement.

2) When the reinforcement of diaphragm is considered, the plastic hinge at beam end forms at the bottom of beam because the bottom reinforcement reaches yield strength. while the plastic hinge at end of beam is usually occurred at the top of beam because the top reinforcement is up to design yield strength if not considering the diaphragm and its reinforcement.

3) Compared with structure S-015g, there are more plastic hinges at the end of columns of structure S-020g. The reason may be that the longitudinal reinforcement of columns in higher seismic design intensity areas is controlled by the internal force of combination of vertical load and earthquake action while the one in lower seismic design intensity areas is controlled by detailing requirements instead of the internal force. Therefore, the structures in higher seismic design intensity areas should be more strictly required by the codes to improve their seismic behavior.

4. CONCLUSIONS

In the paper, with flexibility-based fiber model, the seismic behaviors of RC structures with specially shaped columns are analyzed under unidirectional rare earthquakes using PushOver analysis method. The beam strength is calculated with or without consideration of the diaphragm and its reinforcement. The results of analysis considering the diaphragm were compared with the one without considering the diaphragm and several conclusions are drawn as follows:

1) The floor diaphragm is one of the most important

factors that affect the seismic behavior and failure mechanism of RC frames with specially shaped column. Therefore its effect should not be neglected in seismic design.

2) As the effect of diaphragm is considered, the number of plastic hinges at the end of beams is decreased while the one at the end of columns is increased. And the rotation angle of plastic hinges of beams is also decreased while the one of columns is increased. The reason is the diaphragm and its reinforcement would increase the strength of beams.

3) Although two structures are all designed complying with Chinese Codes, there are more plastic hinges at the end of columns of structure in higher seismic design intensity areas than one in lower seismic design intensity areas under rare earthquake. Thus the structures in higher seismic design intensity areas should be more strictly regulated by the codes.

Acknowledgements:

This research was sponsored by the Chinese National Key Research Program (Project No. 2009BAJ28B03).

References:

Ye Lieping, Qu Zhe, Ma Qianli (2008). "Study on ensuring the strong column-weak beam mechanism for RC frames based on the damage analysis in the Wenchuan earthquake," *Building structure*, **38**(11), 52-59 (In Chinese)

Wang Yayong (2008), "Lessons learnt from building damages in the Wenchuan earthquake−seismic concept design of buildings," *Journal of Building Structures*, **29**(4), 20-22 (In Chinese)

Su Youpo, Zhang Yumin, Wang Shaojie (2009), "The necessary and feasibility of enhancing seismic design of structures based on the Wenchuan Earthquake," *China Civil Engineering Journal*, **42**(5), 25-32 (In Chinese)

Huo Linsheng, Li Hongnan, Xiao Shiyun (2009),."Earthquake damage investigation and analysis of reinforced concrete frame structures in Wenchuan earthquake," *Journal of Dalian University of Technology*, **49**(5), 718-723 (In Chinese)

French C.W. and Moehle J.P (1991), "Effect of Floor Slab on Behavior of Slab-Beam-Column Connections," Design of Beam-Column Joints for Seismic Resistance, SP-123, American Concrete Institute, Farmington Hills, Mich., 225-258

F.C.Filippou, E.P.Popov, V.V.Bertero (1983), "Effects of bond deterioration on hysteretic behavior of reinforced concrete joints", EERC report, University of California at Berkeley

Lau C Y, Chan S L, So A K W (1993), "Biaxial bending design of arbitrarily shaped reinforced concrete column," *ACI Structural Journal*, **90** (3), 269- 278

Zheng Shiju, Jiang Lixue, Zhang Weiping (2009), "Experimental research and analysis of effective flange width of beam end section in cast-situ concrete frames," *Structural Engineers*, **25**(2), 134-140 (In Chinese)

Wang Suguo, Han Xiaolei, Ji Jing (2009), "The effect slabs on the failure mode of reinforced concrete frame structures," *Journal of Civil, Architectural & Environmental Engineering*, **31**(1), 66-70 (In Chinese)

Wu Yong, Lei Jichuan, Yang Hong (2009), "Discussion on negative flexural strength of beam including slabs," *Journal of Chongqing Jianzhu University*, **24**(3): 33-37 (In Chinese)

JGJ149-2006, "Technical specification for concrete structures with specially shaped columns". Beijing: China Architecture & Building Press (In Chinese)

Yang Pu, Tang Jing, Huang Zongming (2006), "Study on seismic performance of regular RC frame with special -shaped columns," *Earthquake Engineering and Engineering Vibration*, **26**(3), 145-147 (In Chinese)

Guan Minsheng, Du Hongbiao (2005), "Pushover analysis of effect of casting slab on RC frame structure," *Earthquake Engineering and Engineering Vibration*, **25**(5), 117-123 (In Chinese)

Pantazopoulou S J, French C W (2001), "Slab participation in practical earthquake design of reinforced concrete frame," *ACI Structural Journal*, 98(4), 479-489

Cardone D (2007), "Nonlinear static methods vs. experimental shaking table test results," *Journal of Earthquake Engineering*, **11**(6), 847-875

ACI 318-08 (2007), "Building code requirements for structural concrete and commentary," Farmington Hills, Michigan, USA; American Concrete Institute

8CUEE CONFERENCE PROCEEDINGS
8th International Conference on Urban Earthquake Engineering
March 7-8, 2011, Tokyo Institute of Technology, Tokyo, Japan

ATTEMPTS AT SIMULATING MEMBRANE EFFECTS IN SLABS USING FINITE ELEMENT ANALYSIS

Saurabh Prasad[1] and Tara C. Hutchinson[2]

1) Graduate Student, Department of Structural Engineering, University of California, San Diego, USA
2) Professor, Department of Structural Engineering, University of California, San Diego, USA
saprasad@ucsd.edu, tara@ucsd.edu

Abstract: It is well known that the ultimate load capacity of a reinforced concrete slab can be much larger than that predicted by Johansen's Yield Line Theory (YLT). This increase in load capacity can largely be attributed to the ability of the slab to act as a membrane, allowing it to carry vertical loads through compression and tension struts rather than simple flexure. This paper discusses several attempts at capturing membrane effects in reinforced concrete slabs, varying in complexity from simple grillage to 3D finite element models. The grillage model, which is often used for bridge deck analysis, is implemented within the OpenSEES platform, using non-linear beam elements arrayed orthogonally across the slab. In parallel, a model is developed in LS-DYNA using composite shell and solid elements with embedded bar elements representing the reinforcing steel. Evaluation of the numerical model is undertaken using two series of classical experimental datasets, namely those of (i) Hung and Nawy (1971), whereby two-way square slabs with different edge conditions are tested and (ii) those of Park (1971), whereby a 2 slab panel is tested. The paper concludes by providing general suggestions regarding modeling strategies to most reasonably capture the vertical response of reinforced concrete slabs considering membrane action.

1. INTRODUCTION

1.1 Background

Reinforced Concrete (RC) slabs are an integral part of a structure and are required to transfer gravity loads to columns/shear walls. As per ACI-318, slabs are designed to carry gravity and lateral loads through flexure and shear. During analysis of a structure, it is generally assumed that the slab behaves as a rigid diaphragm and its effect on the dynamic performance of the structure is ignored. However, past experimental research (e.g. Malik and Bertero, 1976; Hwang and Moehle, 1993) has clearly demonstrated that slabs acts with other structural components and therefore considering their behavior is important to characterizing the response of an entire structure. Similarly, numerical simulations of 3D structures (e.g. Kang, 1993), whereby slab flexibility is included, indicate that although the initial elastic stiffness may not be greatly affected, slab flexibility will have a noteworthy effect on the first significant yield of the structure. The inelastic behavior of slab also contributes to the difference in base shear between internal and external columns.

In practice, the ultimate strength of slabs is often estimated using Johansen's Yield Line Theory (1962) (YLT). YLT assumes that the slabs plastic deformation is localized along predefined yield lines. Past research however has clearly shown that YLT underestimates the ultimate load carrying capacity of slab (e.g. Hopkins, 1969; Park 1970; Christiansen and Frederiksen, 1983; Vecchio and Tang, 1990). Hopkins (1969) for example, upon testing a 1/4th scale beam-slab model, finds that the ultimate strength attained by the 3x3 test slab is twice that predicted by YLT.

This enhancement in slab performance is attributed to membrane forces within the slab which develop at large vertical deformations, and can be further enhanced with any increased restrained provided to the slab. Figure 1 illustrates the compressive and tensile membrane action that occurs in plates.

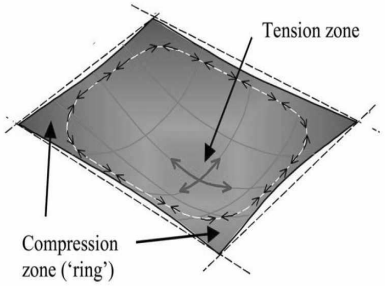


Figure 1. Membrane Forces in a Rectangular Panel (from Bailey 2004).

1.2 Scope of the Study

It is clear from previous research that it is important to include the effect of the slab when modeling a larger structure to improve accuracy of the system level response estimation. Herein, we focus on exercising potential modeling strategies related to modeling the slab itself, utilizing a pair of well-documented experimental datasets.

2. TEST PROGRAMS SELECTED FOR MODELING

2.1 Specific Details

Of the experiments conducted on slabs and beam-slab-column sub-assemblies, two notable and well documented experiments were selected. The first test program was conducted by Hung and Nawy (1971) and involved 29 isotropically reinforced, single panel slabs loaded under uniform loading. In the second test by Park (1971), a 2-panel slab with beams was loaded vertically. The effect of restraint provided by adjacent panels is mimicked in the test program by thickening the edge beams.

In the experiments conducted by Hung and Nawy (1971), all slabs are isotropically reinforced, top and bottom, using either deformed welded wire fabric or Grade 40 #3 bars (f_y = 287 MPa, 9.52 mm diameter). Of the 29 tests performed, two slabs are selected herein. These two slabs are selected for the study, as they only differ in boundary condition on one edge. Both slabs have a 1.524 m × 1.524 m clear span with a total depth of 63.5 mm. The average effective depth, i.e. the distance from the exterior concrete face to the center of the reinforcing steel, is 50.8 mm. One of the slabs has all four edges restrained against translation and rotation. The second slab considered for this study is fully restrained on three edges and hinged on one edge. The loading configuration adopted in these tests is shown in Figure 2. Both of the slabs are constructed with normal strength concrete with a mean compressive strength of 39 MPa and reinforced with #3 bars top and bottom, resulting in a reinforcing ratio of 0.58%. The slabs are able to carry 67% and 122%, respectively, more than predicted by YLT and this additional capacity is attributed to development of membrane action (Hung and Nawy, 1971).

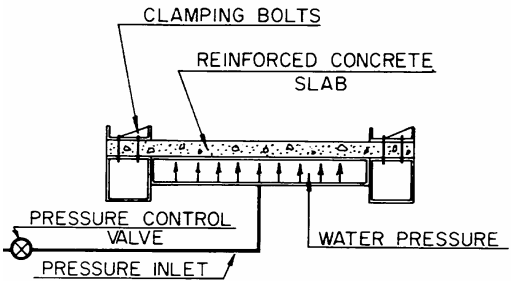


Figure 2 Test Setup of Hung and Nawy (1971), Single Panel Slab Experiment.

In the experiment conducted by Park (1971), a 1/4th scale slab-beam system is designed adopting yield line theory for the slab and assuming a collapse mechanism for the beam. The test specimen is 3.05 m × 3.12 m in plan dimension and simulates two slab panels with beams on each side. The effect of adjacent panels is simulated in the experiment by stiffening the beams in one direction. Figure 3 shows the general layout and dimensions of the beam-panel system. The slab model is restrained vertically at twelve locations, spaced 1.524 m from each other.

Slab panels are reinforced using 3.18 mm bars top and bottom resulting in a reinforcing ratio of approximately 0.2%. The beams are 7.6 cm × 11.2 cm in cross-sectional dimension, reinforced with 6.4 and 9.5 mm bars, resulting in a reinforcement ratio of approximately 0.3%. Stirrups are provided in the beam adjacent to the panels using 3.18 mm bars, with the stirrup spacing ranging from 34.0 to 76.2 mm.

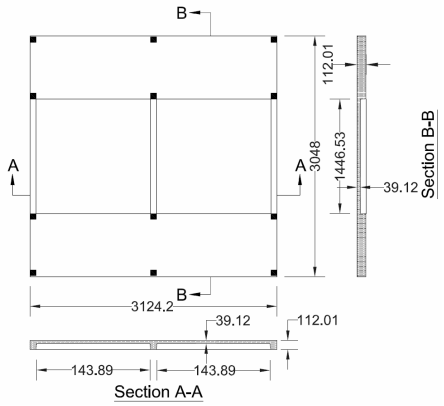


Figure 3 Dimensions of the beam-slab system tested by Park (1971), dimensions in mm, supports are shown in black

The load is applied in on the slab panel in two phases. In the first phase, a load amplitude slightly greater than the service load of the designed panel is applied and subsequently it is unloaded. In the second phase, the load continually increased until the panel fails. Deflections are recorded at the beam mid-span and at the center of the panels. The author concludes that the slab is able to take 64% to 88% greater load than the ultimate load as estimated with YLT.

2.2 Estimation of ultimate load for the Hung and Nawy slab Using YLT

Yield line theory assumes that the deformation in the slab is concentrated along *yield lines*, that is lines along which hinging occurs, while the remainder of the slab behaves as rigid body. As the load is increased, new yield lines will form, resulting to a plastic mechanism, until the slab can no longer carry additional load, yet will only continue to deform. Using the method of virtual work, YLT provides a strategy for predicting the ultimate load carrying capacity for different edge and loading conditions for slabs.

McGregor (1988) shows that for an orthogonally reinforced slab, if the yield line forms at an angle θ with the 'x' direction reinforcing bars, the bending and the twisting moment per unit length of the yield line can be calculated using Equations 1 and 2.

$$m_b = m_x \sin^2\theta + m_y \cos^2\theta \quad (1)$$

$$m_t = \left(\frac{m_x - m_y}{2} \right) \sin 2\theta \quad (2)$$

where m_x and m_y are the flexure capacity in the X and Y direction, m_b is the flexure capacity along the yield line, and m_t is the twisting moment. For isotropically reinforced slabs,

$$m_X = m_y \tag{3}$$

$$m_b = m_x = m_y \text{; therefore } m_t = 0 \tag{4}$$

Using the yield lines suggested by Johansen (1972) for rectangular slabs, and considering the symmetry for a square slab with all edge restrained the yield lines are shown in Figure 4. Assuming a unit deflection at the center of the slab, to calculate the internal work done along the hinge lines, the rotation of each hinge line needs to be calculated. Figure 5 articulates the deformation for each yield line.

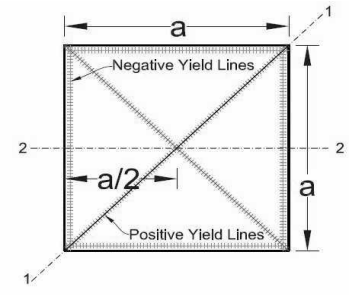
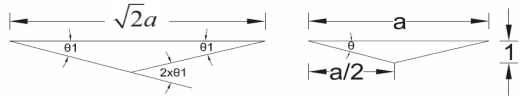


Figure 4 Location of yield lines in a square slab restrained on all sides



(a) (b)

Figure 5 Deflection and plastic hinge rotation along the yield lines, (a) Section 1-1 and (b) Section 2-2

Under a unit deflection, the external work done by a uniform surface load *q* is given by Equation 6.

$$W_{Ext} = q \times \frac{1}{3} a^2 \times 1 \tag{5}$$

One may also calculate the rotation along the positive and negative yield lines for the assumed deflection as:

$$2 \times \theta_1 = 2 \times \frac{\sqrt{2}}{a}, \quad \theta = 1 \times \frac{2}{a} \tag{6}$$

Therefore, the internal work along the yield lines is:

$$W_{Int} = 4 \times \left(m_{+ve} \times \frac{a}{\sqrt{2}} \times 2 \times \theta_1 + m_{-ve} \times a \times \theta \right) \tag{7}$$

where m_{+ve} and m_{-ve} are the yield moments in the positive and negative directions. From Equations 7 and 8 and substituting the values of $2\theta_1$ and θ:

$$W_{Int} = 4 \times \left(m_{+ve} \times \frac{a}{\sqrt{2}} \times 2 \frac{\sqrt{2}}{a} + m_{-ve} \times a \times \frac{2}{a} \right) \tag{8}$$

$$W_{Int} = 4 \times \left(m_{+ve} \times 2 + m_{-ve} \times 2 \right) \tag{9}$$

$$q \times \frac{1}{3} a^2 \times 1 = 4 \times \left(m_{+ve} \times 2 + m_{-ve} \times 2 \right) \tag{10}$$

For the square slab tested by Hung and Nawy (1971), $m_{+ve} = m_{-ve}$. Figure 6 presents the idealized and actual moment-curvature response for the 1m section of the slab (Hung and Nawy 1971), as obtained from an OpenSees (Mazzoni et al. 2005) analysis. The idealized yield moment of a unit of the slab section is calculated as 4.57 kN-m/m. Using Equation 10, the ultimate load carrying capacity of the slab is calculated as 94.4 kPa. This calculated load is 2% less than the ultimate load calculation done by Hung and Nawy (1971) using YLT.

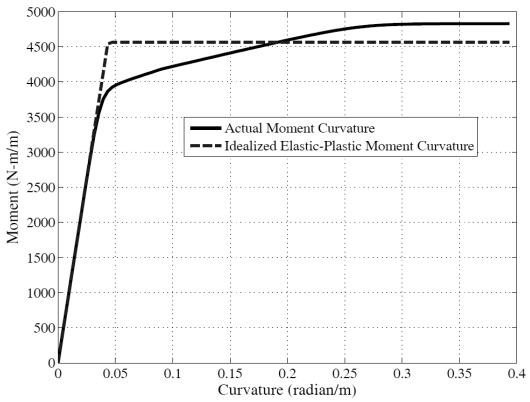


Figure 6 Moment curvature analysis of a unit cross section of the slab tested by – Hung and Nawy (1971) – actual estimated using OpenSees and idealized estimated using YLT.

3. NUMERICAL MODELING: HUNG AND NAWY SPECIMENS

3.1 Grillage model in OpenSees

Grillage models have been widely used in bridge deck analysis (e.g. O'Brien and Keogh,1999). A grillage model decouples the slab system into a grid of beam elements placed in orthogonal directions. In this fashion a 3-dimensional analysis can be undertaken using simple beam elements. In work done by Elghazouli et al. (2000), for example, a grillage model is used for the analysis of a slab deck under thermal loading. Figure 7 shows a simple grillage developed for modeling the slab system tested by Hung and Nawy (1971). In this model, each element is defined as a non-linear beam-column element with its cross

section defined by fibers made of uni-axial concrete and steel material. Each element has 6 degrees of freedom per each node, 3 translational and 3 rotational.

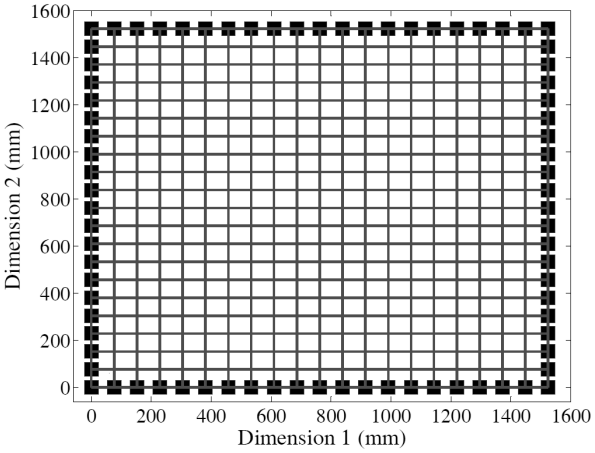


Figure 7. Grillage model (developed in OpenSees) of the slab tested by Hung and Nawy (1971) - grid size of 76.3 mm. Fixed boundary condition is shown in black square.

Concrete is modeled using the backbone for compression as proposed by Popovics (1973), with degraded linear unloading and reloading stiffness according to the work of Karsan and Jirsa (1969). Tension is assumed to following a linear secant stiffness path (*Concrete04*). The reinforcing steel is modeled using the *reinforcingSteel* material built in OpenSees. This material exhibits elastic behavior until yield, followed by a plateau region and eventually strain hardening.

A parametric study is undertaken to compare the numerical results from the OpenSees grillage model to the experimental results obtained by Hung and Nawy (1971). The parameters studied include (i) the effective width of the concrete section in flexure, (ii) the mesh size, and (iii) the torsional stiffness of the section. The effective width of the concrete section is a manifestation of the assumption inherent in grillage models, namely, since the response in two orthogonal directions is decoupled and represented by separate elements, an effective width to account for this decoupling of flexure must be defined. With regard to the torsional stiffness, it should be noted that OpenSees does not calculate the torsional properties of the section automatically. Torsional properties of the cross-section are defined by the analyst within the flexural properties of the section using *section-aggregate* command. Herein, the section is assumed to have elastic-perfectly plastic torsional behavior. For a section with no shear reinforcement, it is assumed that the section behaves elastically until cracking occurs. The cracking torsional resistance is estimated using the recommendations of ACI-318 (2008). The torsion properties are calculated assuming a rectangular concrete section as shown in Equations 11 - 13:

$$T_{cr} = 4\lambda\sqrt{f_c'}\left(\frac{A_{cp}^2}{p_{cp}}\right) \tag{11}$$

$$K_T = \frac{CG}{L} \tag{12}$$

$$C = \beta a b^3 \tag{13}$$

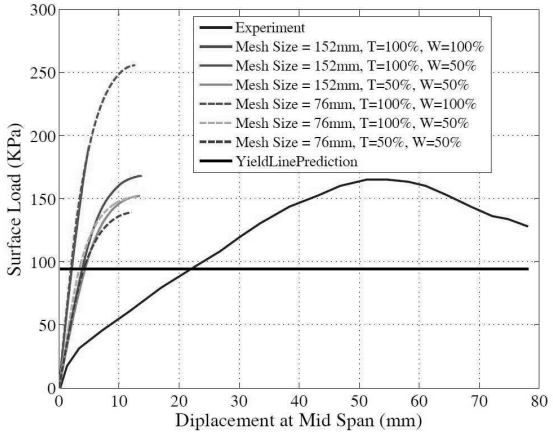
where T_{cr} is the cracking torsional strength, f'_c is the compressive strength of concrete, A_{cp} is the area of the concrete section, p_{cp} is the perimeter of the section, K_T is the torsional stiffness, G is the shear modulus, L is the length of the element, C is the torsional constant of the section of size a × b (a>b) and β is a constant depending on the ratio a/b.

In the grillage model, concentrated loads are applied at the node locations, equal to, the uniform load × tributary area of each node. A non-linear, iterative, implicit analysis is performed to go from one load step to another.

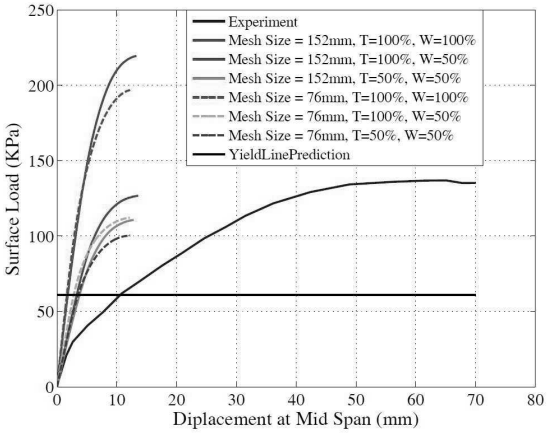
3.2 Numerical-experimental response comparison

Figure 8 presents the load versus displacement response of the two slabs modeled in OpenSees, considering variations in mesh size, effective width (W) and torsional stiffness (T). As observed in Figure 8, for all analyses, the grillage model appears to respond in a much stiffer fashion than the experimental specimen. However, concentrating on the effects of parameter variation, one may observe that varying the mesh size from 76.2 mm to 152 mm results in a difference of 10-15% in ultimate load, when other parameters are fixed. For both specimens (part a and b) it is clear that the width and torsional stiffness must be reduced, as 100% of initial estimates grossly overestimate the strength and stiffness of the section. When the effectiveness factor in flexure is decreased to 50%, the numerical simulation predicts the ultimate load with some degree of accuracy, though the low deformation stiffness is still overestimated. With 50% torsional stiffness of the original cross section, the calculated ultimate load decreases by approximately 10% for both the slabs. From these analyses, it appears reasonable, when seeking to capture the ultimate load, to use 50% of the effective width for flexure and 100% for torsion.

In all cases, the initial stiffness of the slab under vertical load is greater than that measured during the experiment. One reason for the larger stiffness is the assumption of perfect bond between the steel and the concrete, as adopted in the numerical simulation. A secondary reason may be the inability to accurately model the boundary conditions of such an experiment. Currently in the model, a perfect fixed boundary condition is applied at the individual nodes on the edge, while in the experiment this fixity at the boundary is applied via clamping a portion of the slab with through bolts. The boundary applied during the experiment may allow for small deformations, unlike the simulation, which assumes the boundaries to be perfectly fixed.



(a)



(b)

Figure 8 Load-displacement response comparison between the numerical grillage model in OpenSees and the experiments of Hung and Nawy, specimen with: (a) all edges fixed, (b) one hinged edge.

Figure 9 shows the location of yielding, when the ultimate load is achieved in the OpenSees model, for the slab restrained on all edges. In comparison with visual and measured strain data obtained during the experiment, OpenSees correctly predicts the yielding at the fixed edges in negative moment (shown in blue) and in positive moment at the center (shown in red). Although perfect agreement between the experiment and numerical model is not achieved throughout the deformation history of the specimen, the simple grillage model is shown to be effective in capturing salient features such as ultimate strength and strain distribution.

4. NUMERICAL MODELING: PARK SPECIMEN

This section describes the Park (1971) slab numerical modeling. This test specimen is modeled using similar grillage model concepts previously described, as well as adaptation of a 3-dimensional model in the platform LS-DYNA. Observations from the prior analyses indicate an effectiveness factor of 50% and 100%, for effective width in flexure and torsion respectively, are reasonable when adopting the grillage model concept, therefore these values are implemented in the analysis of the Park specimen.

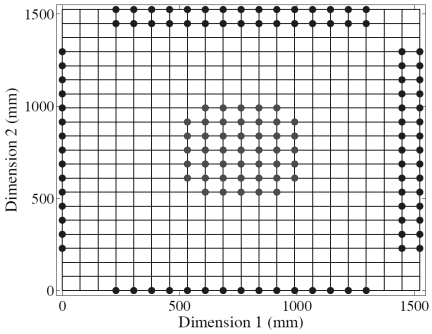


Figure 9 Location of yielding as predicted by the OpenSees grillage model; *Red* - yielding in positive direction and *Blue* - yielding in negative direction – Hung and Nawy slab specimen fixed on all edges.

4.1 Grillage model in OpenSees

A grid size of 152 mm is chosen for this analysis (span/10), based on the suggestion of Hambly (1999), who recommends at-least 10-12 elements along the span. The supports are fixed in the vertical direction using single point constraints. Figure 10 shows the grid and the support locations for the simulation in OpenSees.

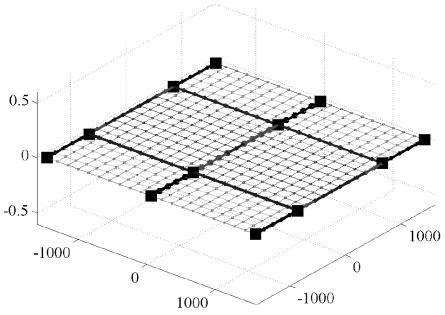


Figure 10 Grillage model of the Park (1971) experiment. The twelve supports are shown by the black squares. The color of the grillage elements represent different beam cross section

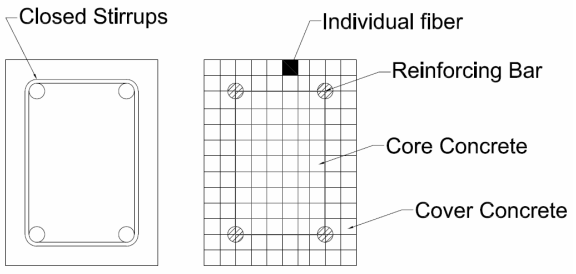


Figure 11 Reinforced concrete cross section of the beam model for the Park specimen, including its representation in OpenSees.

Due to presence of stirrups in the beam along the center span of the specimen, the beams in this region are modeled considering the effect of confining pressure. The method proposed by Mander et al. (1988) is used to calculate the effective confining pressure and the increase in the concrete compressive strength due to this confinement. A typical beam cross section used in the OpenSees analysis is shown in Figure 11. In this figure, the core and cover concrete materials are denoted.

4.2 3-Dimensional model in LS-DYNA

LS-DYNA is a commercial 3-dimensional, finite element software, developed by Livermore Software Technology Corporation (LSTC), widely used in the automobile industry for simulating automobile crash (Hallquist, 2006). It has a built-in material library for concrete materials, most of which are defined for solid elements. Select concrete materials are also defined for 4-noded shell and 2-noded beam elements. For the purpose of this study, the shell element material (MAT_172), is used to model the reinforced concrete slab and the 8 node solid element material (MAT_159) is used when modeling the reinforced beams.

The material 159 (Continuous Surface Cap Model) uses three failure surfaces to define the behavior of concrete. This material has the option of defining all the parameters effecting concrete behavior or the user can use a parameter generation option which only requires the concrete compressive strength and size of aggregate. Extensive tests have been done using this material and evaluated against experimental results (Murray, 2007; Murray et al., 2007).

For reinforcing steel, modeled by 2-node beam elements, a piecewise elastic-plastic material is used. To define this material, an analyst must define the steel elastic modulus, yield strength, Poisson's ratio and hardening modulus.

For beam and solid elements to work as a system, they need to be coupled. Sharing the solid nodes with beam nodes, wherever present is a straight forward way of coupling the two elements together. However, this does not account for slip between the concrete and rebar. Alternatively, coupling the beam and solid element can be incorporated in LS-DYNA using a 1-D contact algorithm. This algorithm requires the beam and solid element nodes to be along the same line, however, they do not need to be co-incident. The bond-slip relationship is defined using the radius of the rebar, the strength of concrete and the bond shear modulus between the rebar and concrete. Both of these methods require alignment between the beam and solid nodes, which is not always feasible. The third option available in LS-DYNA does not require the beam nodes to be aligned with the solid element nodes and constrains the beam nodes to move relative to the solid elements. Due to its simplicity and ease of input this later method is used herein to couple beam and solid elements.

Since a slab resembles a thin walled structure, with one dimension small compared to its span, shell elements are used to model the slab in LS-DYNA using material 172. Material 172 (MAT_CONCRETE_EC2) can be used to model plain concrete, plain steel or a mix of the two by defining a steel ratio for each case in both directions. When using this material, concrete is treated as a composite material formed by layer(s) of steel sandwiched between concrete. The exact position of steel and concrete is defined by specifying an integration rule for the shell elements. When defining the integration rule, the depth of each layer is defined in the iso-parametric coordinate system (i.e. $-1 \leq \xi \leq 1$) with the weight of each layer equal to the ratio of the thickness of the layer to the total thickness of the composite. For example, if a 2mm steel layer is present in a composite of total thickness 20mm, the weight corresponding to the steel layer is 2/20 = 0.1.

Material 172, used to model the slab panels, is not capable of accounting for vertical reinforcement and its effect on beam behavior in shear and torsion. To include the confined concrete behavior in LS-DYNA, the beams are modeled with 8-noded solid elements, while the beam reinforcement is modeled using 2-noded beam elements. The stiffened slab and the center slab panel are modeled using shell elements as they do not have any shear reinforcement present in them.

The average mesh size for this model is 17mm. This number is derived from the fact that at-least 4 elements are required in any direction to model beam bending with acceptable accuracy when using reduced integration solid elements. The 8-node single point integration solid elements do not have any rotational degrees of freedom. For moment transfer it is necessary that the slab rotates with the beam as a single system. Shell nodes are therefore constrained with the adjacent solid nodes for rotational compatibility. Figure 12 presents the wire-frame mesh of LS-DYNA model.

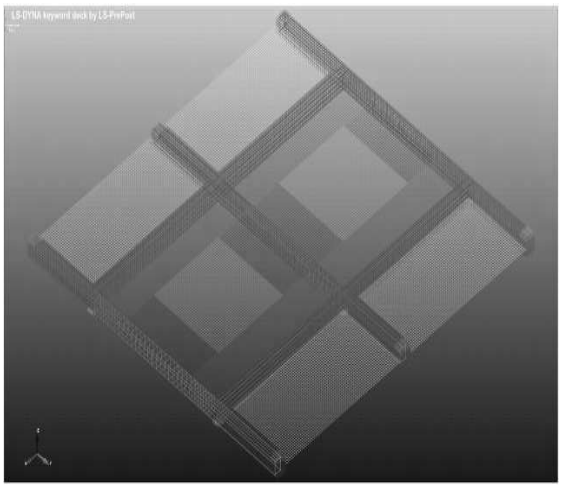


Figure 12 Wire-frame view of the Park (1972) LS-Dyna model.

Supports are modeled using rigid elements, which are restrained in the vertical direction only. To avoid local failure at the contact between the support and concrete beams, some elements are defined as elastic elements, with Young's Modulus and density of concrete.

A constant surface load is applied on the shell elements depicting dead load of the slab. A surface load is then applied to the center slab panel representing the load applied during the experiment.

4.3 Numerical-experimental response comparison

Figure 13 presents the load versus deflection response comparison between the numerical grillage and LS-Dyna models to the experiments. As can be seen, the numerical analysis with OpenSees is able to predict the ultimate load however, fails to predict the deflections correctly. It should be noted however that these analyses are performed under load control, therefore attainment of displacement response up to ultimate load, and not beyond, is anticipated. In this case the grillage model results in a slightly softer response when compared to the experimental results. Figure 14 shows the deflection profile of the beam-slab assembly as predicted by the grillage model at ultimate load. The deflected profile clearly articulates the extra restraint provided by the exterior and interior beams. The stiffened section of the slab, simulating adjacent slabs, do not deform considerably, compared to the center of the slab panel.

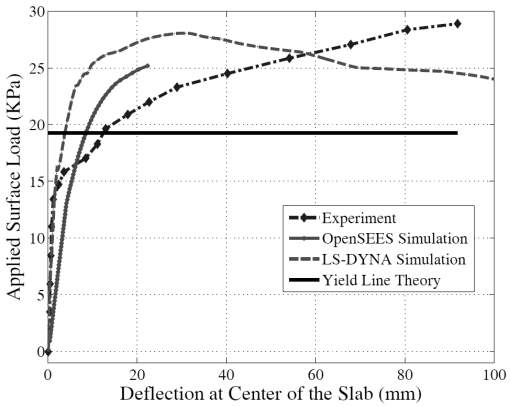


Figure 13 Comparison of slab center deflection as measured during the experiment to the grillage and 3-D modeling approaches.

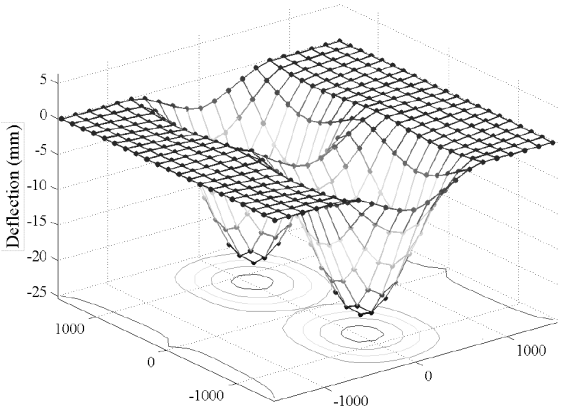


Figure 14 Deflection profile of the system under uniform loading as predicted with the OpenSees grillage model.

Comparing the numerical results from LS-DYNA with the experimental data, LS-DYNA is able to capture the initial stiffness of the system with reasonable accuracy. The results differ from the experimental data once the deflection is greater than 3-4 mm as shown in Figure 13, however overall the load versus deflection behavior is quite reasonably captured with LS-Dyna. Figure 15 presents the plastic strain development just prior to slab failure. The 'X – shaped' yield lines form in the slab where as the RC beams, modeled using solid and beam elements, articulate plastic regions at the supports and mid-span of the beam. These strain distributions are consistent with observations during the experiment.

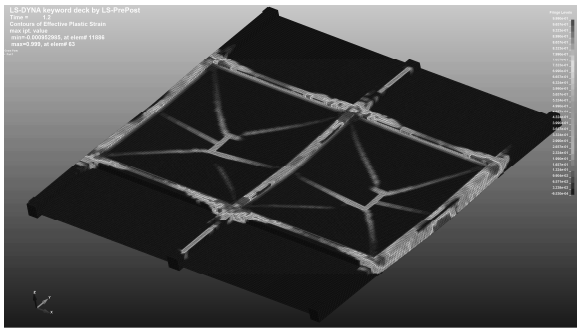


Figure 15 Plastic strains in the slab at ultimate load.

5. CONCLUSIONS

Numerical modeling of a series of slab test specimens is undertaken to investigate strategies for capturing membrane action in slab subsystems. Two finite element approaches are endeavored, namely, a simplified grillage model and a more complex 3-dimensional model using the platforms of OpenSees and LS-DYNA, respectively. The grillage model uncouples the behavior of the slab in two orthogonal directions. Though not accurate through a deformation history, this model does present reasonable results when comparing ultimate load and strain distribution at ultimate, thus it can be used to include the inelastic response of a slab into larger structural models. A grid dimension of clear-span/10 is recommended when using this method in bridge deck analysis (Hambly, 1991) and is shown to be reasonable for the numerical analyses cases discussed in this paper. This study also shows that since the response in two orthogonal directions are decoupled, it is advisable to decrease the flexural effectiveness of the section in each direction by reducing the width of each section by 50%. In the numerical analyses discussed in this paper the grillage model in OpenSees is capable of providing better results at low levels of inelastic behavior, and unfortunately at high levels convergence issues are observed.

LS-DYNA performs better when compared with the OpenSees grillage model. Moreover, an analyst has more liberty with materials and element types available to model reinforced concrete structures. LS-DYNA is able to model complex boundary conditions with ease. An analyst can

choose to model the structure using solid or shell elements depending on the expected behavior.

Both methods discussed herein do have their drawbacks. The grillage model analysis, though easier to perform and less computationally demanding, does not perform very well in predicting the vertical stiffness of the slab subsystem. The 3-D model on other hand, although it presents better results is much more computationally intensive. Depending on the complexity of the problem and level of inelasticity expected in the slab, either of the two numerical methods could be suitable for analysis.

Acknowledgements:

This study is supported through the NEESR project entitled: Mitigation of Collapse Risk in Vulnerable Concrete Buildings, where Prof Jack Moehle is the PI. Funding is provided through NSF grant number: CMMI-0618804. Opinions and findings of this study are of the authors and do not necessarily reflect those of the sponsor.

References:

ACI 318 (2008). "Building Code Requirements for Structural Concrete and Commentary (ACI 318-08)." *American Concrete Institute*, Farmington Hills, Michigan.

Bailey, C. G. (2004). "Membrane action of slab/beam composite floor systems in fire." *Engineering Structures*, 26(12), 1691-1703

Christiansen, K. P., Frederiksen, V. T. (2006), "Experimental investigation of rectangular concrete slabs with horizontal restraints", *Material and Structures*, 16(3), 179-192.

Elghazouli, A. Y., Izzuddin, B. A., and Richardson, A. J. (2000). "Numerical modelling of the structural fire behavior of composite buildings." *Fire Safety Journal*, 35(4), 279-297.

Hallquist, J. O. (2006). "LS-DYNA Theoretical Manual", Livermore Software Technology Corporation, March 2006.

Hambly, E. C., 1991. "Bridge Deck Analysis.", Spon Press, Routledge, U.K.

Hopkins, D.C. (1969), " Effects of Membrane Action on the Ultimate Strength of Reinforced Concrete Slabs." University of Canterbury, Christchurch, New Zealand, PhD Thesis,.

Hung, T. Y., Nawy, E. G. (1971). "Limit strength and serviceability factors in uniformly loaded, isotropically reinforced two-way slabs." *American Concrete Institute*, SP-30, Detroit, 301-24

Hwang, S. J., Moehle, J. P. (1993). "An experimental study of flat-plate structures under vertical and lateral loads." University of California, Berkeley, Report No. EERC 93-03, EERC, February 1993.

Johansen, K. W. (1962). "Yield-line theory", *Cement and Concrete Association*, London, 181 pp.

Johansen, K. W. (1972). "Yield-line formulae for slabs", *Cement and Concrete Association*, London, 106 pp.

Kang, S. B. (1993). "Inelastic Seismic Response Analysis of 3-D Reinforced Concrete Structures Considering Effect of Diaphragm Flexibility." Lehigh University, Pennsylvania. Doctor of Philosophy in Civil Engineering.

Karsan, I. D., and Jirsa, J. O. (1969). "Behavior of concrete under compressive loading." *Journal of Structural Division ASCE*, 95(ST12).

MacGregor, J. G. (1988). "Reinforced Concrete, Mechanics and Design," Prentice Hall, New Jersey.

Malik, L. E., Bertero, V. V. (1976). "Contribution of a floor system to the dynamic characterstics of reinforced concrete buildings." University of California, Berkeley, Report No. EERC 76-30, EERC, December 1976.

Mander, J. B., Priestley, M. J. N., Park, R. (1988). "Theoretical Stress-Strain Model for Confined Concrete." *ASCE Journal of Structural Engineering*, 114(8), 1804-1826

Mazzoni, S., McKenna, F., and Fenves, G. L. (2005). " Opensees command language manual." Technical Rep., http://opensees.berkeley.edu/, Pacific Earthquake Engineering Research (PEER).

Murray, Y.D. (2007), "Users Manual for LS-DYNA Concrete Material Model 159." Report No. FHWA-HRT-05-062, *Federal Highway Administration*, McLean, Virginia

Murray, Y. D., Abu-Odeh, A., and Bligh R. (2007), "Evaluation of Concrete Material Model 159." Report No. FHWA-HRT-05-062, *Federal Highway Administration*, McLean, Virginia

O'Brien, E. J. and Keogh, D. (1999). " Bridge Deck Analysis.", Spon Press, Routledge, U.K.

Park, R. (1970), "The behavior of a model slab and beam floor designed by limit design." *Civil Engineering Transactions*, Institution of Engineers, Australia, 12(1), 1-6.

Park, R. (1971), "Further test on a reinforced concrete floor designed by limit procedures." *American Concrete Institute*, SP -30, 251(70).

Popovics, S. (1973). "A numerical approach to the complete stress strain curve for concrete." *Cement and concrete research*, 3(5), 583-599.

Vecchio, F. J. and Tang, K. (1990), "Membrane action in reinforced concrete slabs." *Canadian Journal of Civil Engineering*, 17(5) 686–697

8CUEE CONFERENCE PROCEEDINGS
8th International Conference on Urban Earthquake Engineering
March 7-8, 2011, Tokyo Institute of Technology, Tokyo, Japan

REINFORCED CONCRETE BEAM-COLUMN JOINT STRENGTHENED BY FERROCEMENT

B. Li[1] and Eddie S.S. Lam[2]

1) Research Student, Dept. of Civil and Structural Engineering, The Hong Kong Polytechnic University, Hong Kong
2) Associate Professor, Dept. of Civil and Structural Engineering, The Hong Kong Polytechnic University, Hong Kong
cse.libo@polyu.edu.hk, cesslam@polyu.edu.hk

Abstract: When subjected to seismic action, beam-column joints designed without seismic provisions (i.e. based on gravity load only) have been proved to be the vulnerable component in the moment resisting frames. The situation is particular devastating in old buildings with possible deterioration of concrete and reinforcements. The above urges for immediate attention and repair. In this study, a strengthening method using ferrocement and diagonal reinforcements is proposed to reduce the seismic risk and to possibly extend the life span of old buildings. Two specimens, including a control specimen and a specimen strengthened by the proposed strengthening method, were constructed and tested under cyclic loading. The specimens were designed to represent non-ductile beam-column joints. Horizontal cyclic displacement was applied at the upper column after high axial load was imposed on the column. Seismic performance of the specimens was evaluated in terms of strength, stiffness, energy dissipation and ductility. The test results have indicated that the proposed strengthening method is effective for enhancing the shear capacity of the joint. In addition, condition of the joint is significantly improved due to the reduction of joint shear force. The main parameters considered in further studies are mechanical properties of ferrocement and bonding behavior between ferrocement and the joint.

1. INTRODUCTION

In Hong Kong, more than 18,000 buildings were constructed in over 30 years ago, and pressingly, most of them are facing different degrees of degradation. For instance, Buildings Department of the HKSAR Government received roughly 7,300 dangerous building reports annually during the past decade (Law et al. 2010). In the next ten years, more than 500 buildings will reach their design life. As deign life of a building is around 50 years, proper maintenance and repair is necessary if we want to extend the usable life of buildings in particular those constructed in or before 1960s. The collapse of a 55 years old 5-story building on 29th January 2010 in Hong Kong, has raised further concern by the public urging proper repair/restoration of the old buildings. In addition, Hong Kong has been recognized as an area with moderate seismic risk but buildings in Hong Kong have been traditionally designed without seismic provisions (Lam et al. 2002). Thus, strengthening of old buildings is necessary and it requires means both to extend the life span and to improve the seismic behavior.

In terms of strengthening a reinforced concrete framed structures, beam-column joint has been recognized as a key member that affects the overall behavior of buildings under seismic action. Evidence from previous earthquakes has shown that failure of beam-column joints may cause the collapse of buildings (EERI 1999, Huo et al. 2009, EERI 2010). Figure 1 shows some damaged beam-column joints in Wenchuan earthquake. As a result, particular attentions have been paid on strengthening beam-column joints in the last forty years. Hakuto et al. (2000) and Pampanin et al. (2002) illustrated poor performance of typical interior beam-column joints designed without transverse reinforcement in the joint core (i.e. designed to gravity action only similar to those commonly found in Hong Kong). As such, strengthening of beam-column joints in existing buildings is inevitable.



Figure 1 Damaged beam-column joints in Wenchuan earthquake (Huo et al. 2009)

There exist various existing methods for strengthening beam-column joints. Concrete jacketing, one of the earliest and common methods, has been used for strengthening beam-column joints for many years. Hakuto et al. (2000) strengthened the interior and exterior beam-column joints by concrete jacketing of which was identified as an effective method for enhancing stiffness, strength and ductility. Recently, reinforced concrete jacketing with no joint shear hoops and no anchors installed into the joints was successfully applied to strengthen non-ductile interior beam-column joints (Wang and Hsu 2009). Unfortunately, concrete jacketing is labor intensive and space limitative.

Alternatively, steel jacketing was applied. Ghobarah et al. (1997) conducted experimental studies and verified the effectiveness of using steel jacketing for upgrading strength and ductility. Apart from potentially vulnerable to corrosion, steel jacketing is difficult to install and has poor performance under fire. Ghobarah and Said (2002), Pantelides et al. (2008) and Lee et al. (2010) proposed strengthening beam-column joint subassemblages with FRP. Enhancement on strength and ductility was observed; even through in some cases, debonding of FRP occurred at final stage of the tests. However, similar deficiency under fire condition has also been found in FRP. Bisby et al. (2005) illustrated that mechanical properties of FRP were substantially reduced during fire, with or without proper fire insulation. This has undermined its excellent performance in easy application, high ratio of strength to weight, corrosion resistance, etc. With the limitations on high cost and poor fire resistance of the above-mentioned methods, researchers have strived to develop alternative materials for strengthening. For example, Izi (2008) proposed steel-reinforced polymer composites for strengthening shear-deficient exterior joints. In the study, a new approach using ferrocement and diagonal reinforcement was proposed to strengthen beam-column joints. In previous research, Ho and Lam (2010) strengthened full-scale columns using high performance ferrocement. Effect of variation of mesh density and mortar strength to confinement action was investigated. Test results have shown that ferrocement is effective to enhance the axial load carrying capacity of columns.

Aim of this study is to investigate the behavior of beam-column joints strengthened by the proposed method. Main parameters affecting efficiency of the proposed method are discussed, such as mechanical properties of ferrocement and bonding conditions of interface between ferrocement and the joint.

2. FERROCEMENT FOR STRENGTHENING

Ferrocement is defined by ACI committee 549 in the report on ferrocement as “a type of thin wall reinforced concrete commonly constructed of hydraulic cement mortar reinforced with closely spaced layers of continuous and relatively small size wire mesh. The mesh may be made of metallic or other suitable materials” (ACI 1997). Ferrocement exhibits a number of mechanical characteristics different from concrete, such as high strength to weight ratio, crack resistance, durability, impact resistance and ductility. Furthermore, ferrocement is able to achieve these properties through a thin panel reinforced in two directions to protect the reinforcements. Thus, ferrocement is an ideal material for strengthening structural members. In addition, it has favorable fire resistance as compared with steel or FRP jacketing. Eltegaway (2009) illustrated that ferrocement panel, when subjected to 700℃ for 30 minutes, can still resist fire and reduce crack propagation. Nedwell (2010) indicated ductility and shock resistance of ferrocement have not been fully utilized. Kumer and Rao (2006) revealed large energy absorption capacity of ferrocement. Other advantages include ease of construction and requiring no special technique making it user friendly.

On the basis of the excellent behavior of ferrocement, it has been successfully used for strengthening various types of structural members. Shannag (2009) strengthened plain concrete cylinders by high strength ferrocement laminates and considered it a promising material for structural strengthening. Abdullah and Takiguchi (2003) investigated the behavior of column strengthened with ferrocement jacketing for confinement action. Lim et al. (2000) strengthened flexural strength of beams by incorporating ferrocement reinforced with longitude bars onto the soffits. Cao et al. (2008) strengthened beam-column joints by mortar reinforced with high strength wire. In the application field of ferrocement for strengthening, Wang et al. (2006) strengthened Zheng Chenggong memorial by ferrocement in Xiamen. The above have demonstrated ferrocement is a promising alterative material for strengthening structural members.

3. EXPERIMENTAL PRGRAM

3.1 Specimens

Two 2/3 scale interior beam-column joints were constructed and tested under cyclic loading. The first one is the control specimen, namely C1, which is based on typical reinforcement detail used in the existing buildings in Hong Kong. The other is the strengthened specimen, namely S1, which is strengthened by ferrocement and diagonal reinforcements. Both specimens have the same dimension and reinforcement arrangement as shown in Figure 2.

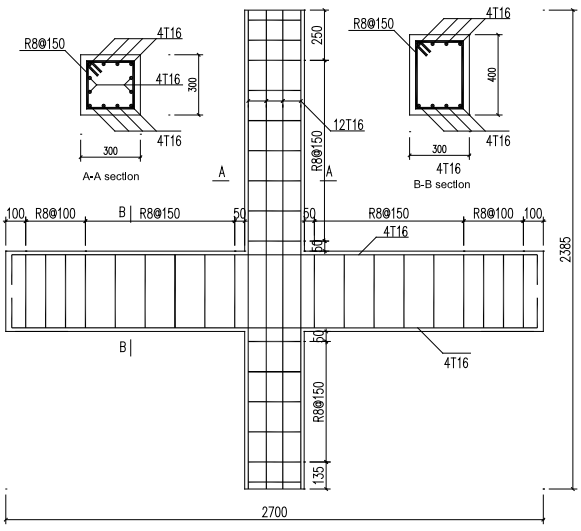


Figure 2 Details of specimen

Both specimens replicate lower stories of a building. Ends of the specimens coincide with the mid-span and mid-height of the actual frame structure. Columns are 2,385mm height and 300mm by 300mm in cross-section.

Main reinforcements comprise 12T16 (or 2.7% main reinforcement ratio). Beams are 2,700mm long and 300mm by 400mm in cross-section. Transverse reinforcements comprise R8 rectangular ties at 150mm spacing. Same reinforcements (4T16) are provided as top and bottom steel (or 1.35% main reinforcement ratio). The joints have no transverse reinforcements and are prone to shear failure when subjected to cyclic loading.

As stated in the above, the ratio of column depth to diameter of main reinforcements in beams is h_c/d_b=300/16=18.75, which does not satisfy the ratio of 20 as recommended by ACI-ASCE 352. Moreover, the beams have larger moment capacity as compared with the columns, which is also not in accordance with the current code of practice. The above are typical joint details in frame structures in Hong Kong. In addition, the concrete used in the specimens had measured cube strength on the day of test of 46.1MPa. Mix proportion of concrete is shown in Table 1. Measured yield strength of main reinforcement and transverse reinforcement are 540MPa and 410MPa respectively.

Table 1 Mix proportion of concrete

Component	Content
Cement (kg/m^3)	340
Coarse aggregate (kg/m^3)	880
Fine aggregate (kg/m^3)	875
Water (kg/m^3)	226
Super plasticizer (kg/m^3)	3.06

3.2 Test Setup and Loading Routine

The test setup is shown in Figure 3. The specimens are tested by a displacement control multi-purpose testing system with a maximum loading capacity of 10,000kN. The bottom column is fixed by a hinge, so that the bottom column is constrained in lateral displacement but allowed to rotate. Both ends of the beam are supported by rollers to enable ends of the beams free to move horizontally but not vertically.

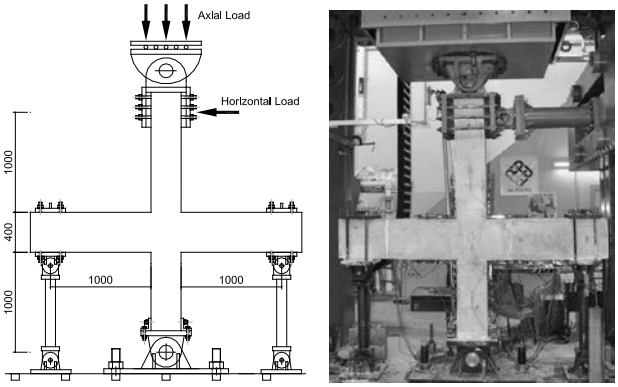


Figure 3 Test setup for beam-column joint

Axial load is applied at top of the top column and is kept constant throughout the loading test. Afterwards, cycles of horizontal displacement are applied from the top of the upper column based on displacement control. First of all, the yield displacement Δ_y is determinate as follows. The specimen is subjected to progressive increase in the horizontal load up to 75% of the nominal moment capacity of the columns. The corresponding tip displacement at the top is recorded and extrapolated to determine the yield displacement of column Δ_y. Afterwards, displacement ductility factor μ (ratio of actual displacement to yielding displacement) is used to control the loading cycles.

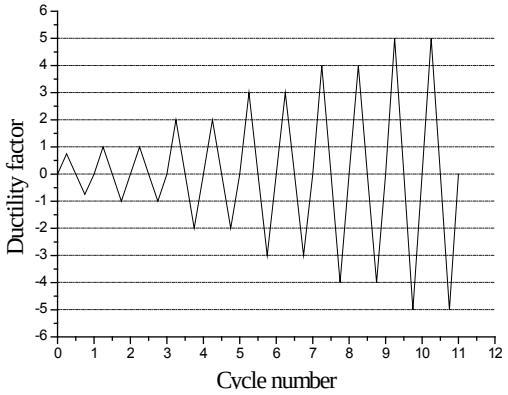


Figure 4 Loading routine

Each loading cycle is repeated twice until the horizontal load dropped to 85% of its maximum value. Loading routine is shown in Figure 4. It is to be noted that axial load reaches $0.6f_c'A_g$ which is consistent with the common range of axial load from 0.5 to 0.7 due to high main reinforcement ratio in the columns (Lam et al. 2000).

3.3 Strengthening Scheme

Strengthening of a beam-column joint is achieved by ferrocement and diagonal reinforcements as shown in Figure 5. The proposed strengthening scheme can be divided in two parts. Firstly, ferrocement with the wire mesh properly folded along the dotted lines and cut along solid lines is installed to replace the concrete cover in the beam-column joint region (Figure 5(a)). It enhances shear capacity and provides confinement. In this study, two layers of wire mesh were installed in the joint region. Welded square mesh is adopted in this study. The mesh has averaged wire diameter of 1.45mm and width of spacing at 13.23mm in both directions. Cement-based mortar of averaged 7-day cube strength of 33MPa is used. The ratio of binder over sand is 1:2.5 by weight, and 15% of cement was replaced by PFA. Although PFA retards the early strength, it improves workability. Secondly, two diagonal reinforcements of 10mm diameter are installed in the joint and effectively anchored to the main reinforcements of the beams to reduce the force transferred to the joint. Its yield stress is about 800MPa.

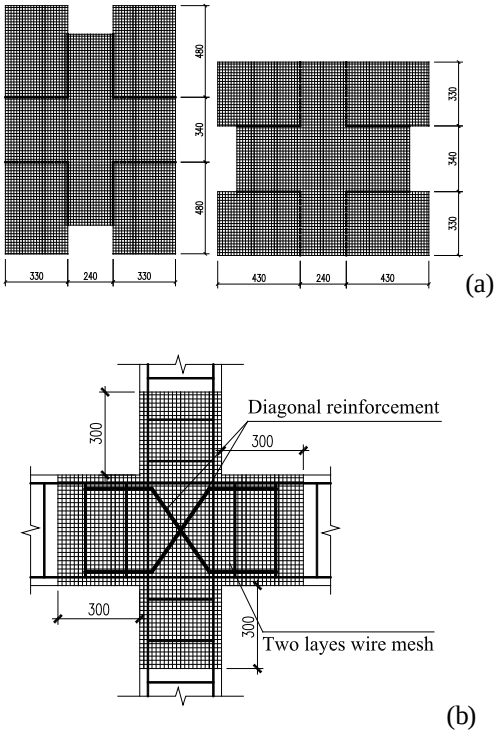


Figure 5 Strengthening scheme

Strengthening process is consisted of four steps. Firstly, concrete cover is removed and surface of the joint region is roughed. Secondly, holes are drilled for installation of diagonal reinforcements. Diagonal reinforcements are welded to main reinforcements of the beams and the holes are subsequently grouted with mortar. Thirdly, wire mesh is installed to beam-column joints. Wire mesh is cut to size and folded to warp around beams and columns. Lapping between wire mesh is at least 100mm. Lastly, mortar is applied to specified thickness of 30mm after bonding agency is brushed. Main procedures of the strengthening process are as shown in Figure 6.



Unstrengthened specimen | Prepare surface & Drill hole | Weld diagonal reinforcements



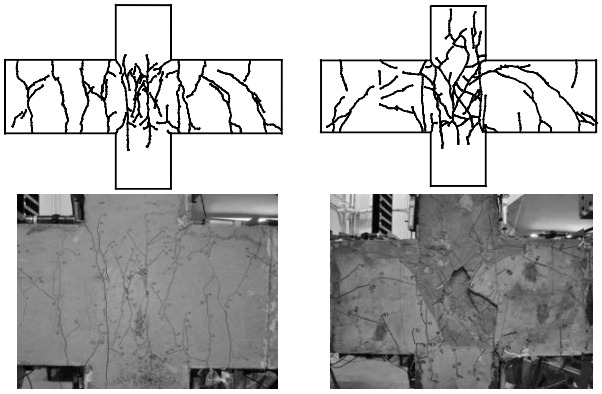
Install wire mesh | Apply of bond & rendering material | Strengthened specimen

Figure 6 Strengthening procedure

4. EXPERIMENTAL RESULTS

4.1 General Behavior and Failure Modes

For the control specimen C1, one vertical crack in the joint and several flexural cracks in the beams were observed after applying the axial load. When the displacement at the column tip reached 17.4mm, second vertical crack was observed. Occurrence of vertical cracks in the joint is attributed to the deformation of the main reinforcements of the column without shear hoops under high level of axial load. This is also supported by phenomenon of bulging in the joint. Meanwhile, diagonal cracks appeared at the corner of the joint at the same displacement of 17.4mm. As the horizontal displacement increased, diagonal cracks propagated due to diagonal tension. Moreover, obvious diagonal cracks were observed on both sides of the joint. With opening and closing of diagonal cracks under the cyclic loading, spalling of concrete in the joint along the diagonal direction occurred. Although moment capacity of the columns is smaller than that of the beams, crack was not observed on the column. This is attributed to the high level of axial load in the columns that reduces tensile strain in the columns. Final crack pattern was consisted of two vertical cracks along the main reinforcements of the columns, diagonal cracks in the joint and flexural cracks in the beams as shown in Figure 7.



(a) (b)

Figure 7 Crack patterns of (a) specimen C1, and (b) specimen S1

Formation of cracks in strengthened specimen S1 was improved due to better ability on crack control offered by ferrocement. However, once the ultimate tensile strain of ferrocement was attained, cracks propagated. When horizontal displacement reached its fourth cycle of 8.7mm, an obvious diagonal crack was observed. In the next cycle of 17.4mm, diagonal cracks formed in the other diagonal direction, and several inclined cracks occurred in the column. Subsequently, the cracks propagated to the overall joint region. At the displacement of 26.1mm, spalling of mortar was observed outside the wire mesh in the upper column. This was probably caused by inconsistent deformation between the parent substrate and ferrocement under high

axial load. Diagonal cracks of strengthened specimen also appeared earlier than that of the control specimen. This may be attributed to the low strength of mortar. It is worth noticing that delamination of ferrocement and bulging of the main reinforcements of column occurred as shown in Figure 8. Main reinforcement buckled due to inadequate confinement. Nevertheless, ferrocement offers some degree of confinement to the joint, though ferrocement in the joint region spalled off at the advanced stage of loading. Another apparent observation is that cracks were distributed more uniformly in the case of specimen S1 and serves to demonstrate that ferrocement has good ability of crack control.

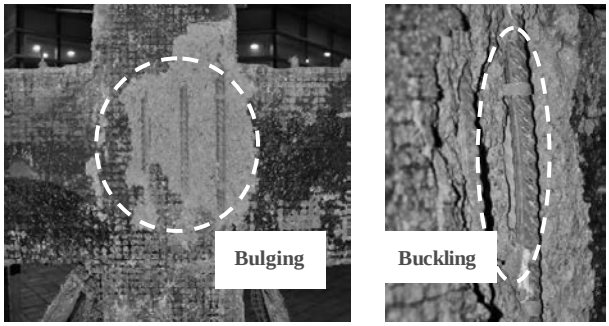


Figure 8 Failure of beam-column joints

Failure modes of both specimens are generally similar and are due to insufficient shear strength in the joint and buckling of main reinforcement of the columns. For specimen S1, delamination of ferrocement occurred at the joint.

4.2 Hysteretic Behavior

The horizontal load-displacement relationship of the column tip for control specimen C1 and strengthened specimen S1 are shown in Figure 9. It is noticed that the ultimate load of specimen S1 is higher than that of control specimen C1. Specimen S1 reaches its ultimate load of 92.4kN at the displacement of 23.20mm and -90.1kN at the displacement of -17.40mm, while specimen C1 attained its ultimate load of 84.3kN at the displacement of 25.4mm and -84.7kN at the displacement of -25.35mm. Here positive and negative displacement represent pull and push direction respectively. Ultimate strength is enhanced by 9.6% in pull direction and 6.4% in push direction. This is attributed to the strengthening scheme, which enhanced the capacity of the joint. Obviously, the enhanced strength is limited due to the spalling of mortar during the tests. Furthermore, comparison of drift capacity between control specimen and strengthened specimen indicates that the proposed strengthening method may increase the drift capacity.

Envelopes of lateral load-displacements for control specimen and strengthened specimen are shown in Figure 10. Horizontal load of specimen C1 is smaller than that of specimen S1 except at horizontal displacement of -26.4mm (a minus represents push direction). This is due to failure of ferrocement at this loading stage.

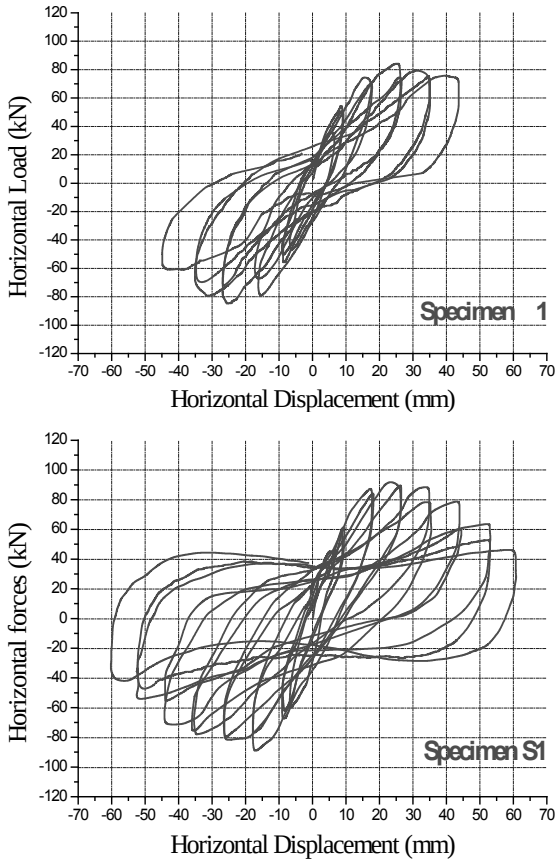


Figure 9 Column tip load-displacement relationship

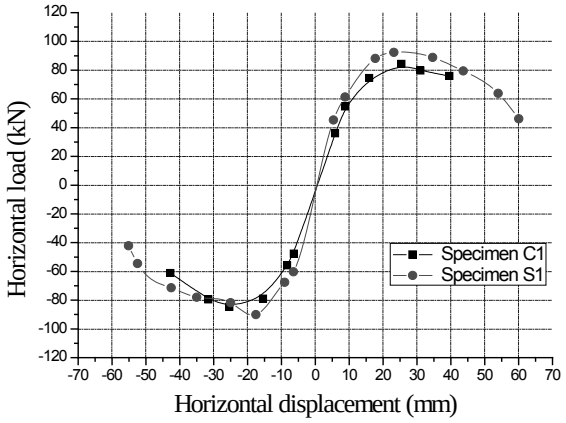


Figure 10 Relationship between envelope of horizontal load and horizontal displacement

4.3 Energy Dissipation

Energy dissipation of both specimens under cyclic loading is calculated from the area of lateral load-displacement loops at different cycles of horizontal displacement. Energy dissipated at each cycle and cumulative energy dissipation are shown in Figure 11(a) and Figure 11(b) respectively. Energy dissipation capacity is enhanced at higher loading stage. In other words, if the same energy dissipation is required during an earthquake, specimen S1 will have smaller horizontal displacement as compared with specimen C1. At higher loading, energy

dissipation of specimen S1 is larger than that of specimen C1. Specimen S1 sustains a larger increase in energy dissipation as the horizontal displacement cycle increases. At horizontal displacement cycle of 10, energy dissipation and cumulative energy dissipation for specimen S1 are enhanced by 14.7% and 19.6% respectively as compared with specimen C1.

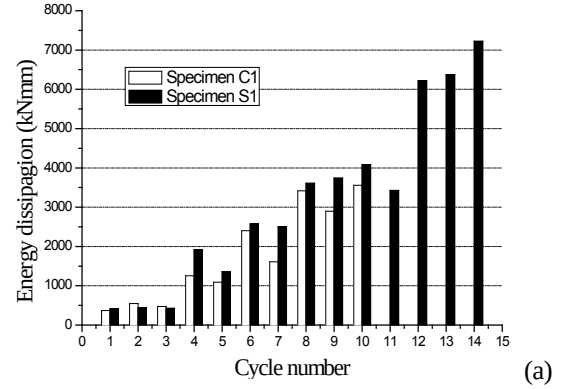


Figure 11 Energy dissipation of (a) Each cycle, and (b) Cumulative at each cycle

4.4 Stiffness Degradation

Stiffness of a specimen is determined by secant slope of line passes origin to the point interested at each loading cycle. It represents resistance of structural member to deformation. The results are plotted in Figure 12. Initial stiffness of specimen S1 is significantly higher than that of control specimen C1. This can be attributed to the use of ferrocement and diagonal reinforcements in the joint region. However, stiffness of specimen S1 decreases rapidly as the horizontal displacement increases due to delamination of ferrocement. In addition, at the later stage of loading, stiffnesses of both specimens degenerate similarly. In general, stiffness of specimen S1 is greater than that of specimen C1.

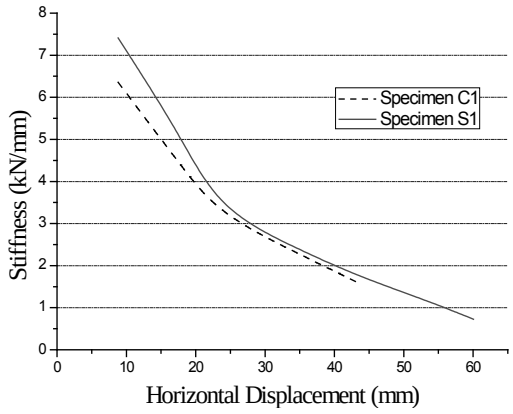


Figure 12 Relationship between stiffness degradation and horizontal displacement

4.5 Curvature

Curvatures are calculated from measured values obtained from a pair of LVTDs installed at both sides of a beam (as shown in Figure 13). The averaged curvature at each cross section can be calculated as follows:

$$\frac{1}{\rho} = \frac{\Delta_{Li} - \Delta'_{Li}}{L_i h} \quad (1)$$

Where Δ_{Li} and Δ'_{Li} are the readings of the ith pair of LVDTs installed at the top and bottom of beam respectively, L_i is the length between the measurements and h is the center-to-center distance between top and bottom LVDTs. In this study, L_i=100mm and h=430mm.

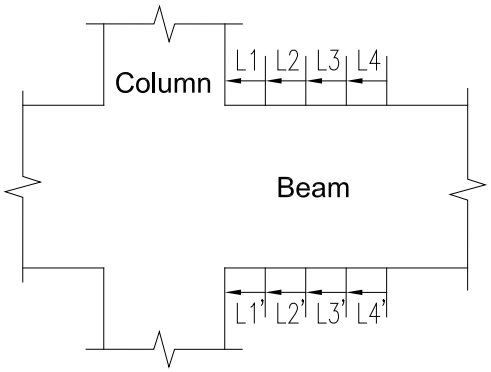


Figure 13 Arrangement of LVDTs on beam

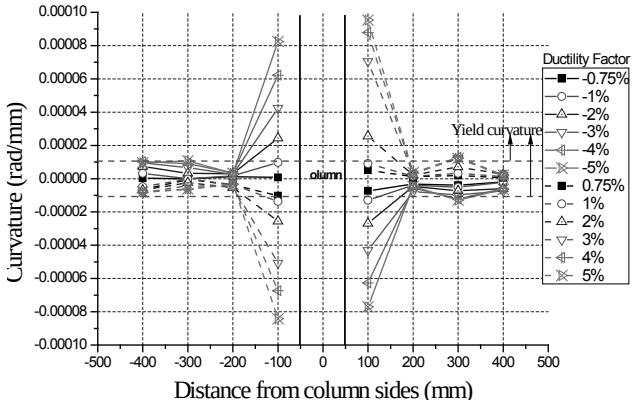
Figure 14(a) and Figure 14(b) show the beam curvature profiles of specimens at each displacement ductility factor. Both specimens show high curvature values within the distance of 100mm from the column face. This is attributed to the large bending moment in this region and wider crack width as observed during the test. With the contribution of the ferrocement applied at the sides of beams, curvature of specimen S1 at the same displacement ductility was smaller than that of specimen C1. As the displacement ductility increased, curvature increased. Since deformation ability was weakened by deterioration of mortar. It is apparent that ferrocement is effective to strengthen beams close to the column face if high strength ferrocement is applied.

Theoretically, curvature can be calculated by equation (2) based on linear elastic method.

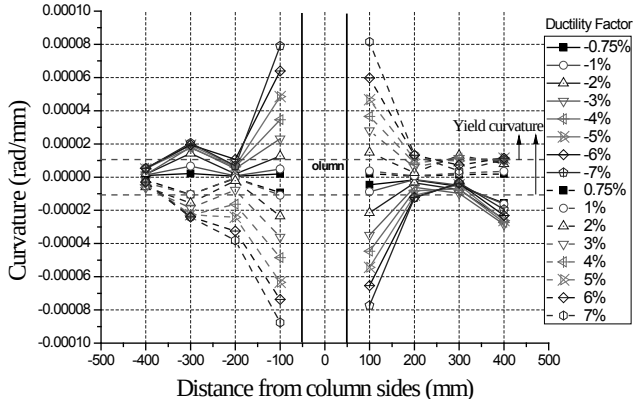
$$\frac{1}{\rho} = \frac{M}{EI} \quad (2)$$

Where ρ is radius of curvature, E is elastic modulus, I is moment of inertia of cross section, and M is bending moment. Reinforced concrete members exhibit nonlinear relationship between bending moment and curvature as stiffness EI changes. In the initial stage, reinforced concrete showed almost elastic behavior before cracking. Due to cracking of members, the increase in curvature was caused by yielding of reinforcements in the beams. Curvatures of reinforced concrete members were taken into account through using equivalent cross section according to ACI 318.

Beam curvature is at or above 1.1×10^{-5}mm^{-1} when the reinforcement yields. The yield curvature is shown in Figure 14 in dotted lines. For specimen C1, yielding of beam began at the interface of 100mm away from column face when the horizontal ductility factor reached 1. As the horizontal displacement increased, yielding was extended away from interface at final stage of loading. For specimen S1, yielding was first observed in the cross section away from column face of 400mm. The plastic hinge zone of specimen S1 was larger than that of specimen C1.



(a)



(b)

Figure 14 Curvature profile of beam for (a) Specimen C1, and (b) Specimen S1

4.6 Joint Shear Stress

Joint shear stress is estimated by shear force V_{jh} divided by effective joint area A_j. The shear force acted on the joint is calculated using equation (3) (Pauley and Priestly 1992) in the form of,

$$V_{jh} = T + C_c + C_s - V_{col} \tag{3}$$

By approximating $T'=C_c+C_s$, the joint shear force is simplified to

$$V_{jh} = T + T' - V_{col} \tag{4}$$

Where T and T' are tension force acting at opposite column faces, C_c and C_s are compression forces acting on the joint by concrete and reinforcements respectively, and V_{col} is the column joint shear force. Thus, joint shear force is obtained based on the tensile force of reinforcements acting at both column faces and shear force of the column. Tensile force of reinforcement is estimated from measured strains of reinforcement at column faces, which represents the force transferred to joint core. Shear force of column is the applied horizontal force. The effective joint area is calculated by considering $A_j=b_jh_c$ (ACI-ASCE 352). Where b_j is the effective joint width and is whichever the smallest of $(b_b+b_c)/2$, $b_b+\Sigma mh_c/2$ and b_c (h_c is the depth of column). Based on the above, joint shear stresses are 11.45MPa and 8.10MPa for specimen C1 and Specimen S1 respectively as shown in Table 2.

Joint shear stress has significant effect on the performance of the joint, especially the bonding condition and stiffness of the joint. Thus, several design codes have specified that the nominal shear stress of joint depends on the strength of concrete and other parameters. ACI code suggests a nominal shear stress of $\sqrt{f_c'}$MPa. New Zealand Standard specifies $0.2f_c'$ as the lower limit of joint shear strength. EN code restrains the joint shear strength through the following equation,

$$v_{jh} \le \eta f_c' \sqrt{1 - v_d / \eta} \tag{5}$$

Where $\eta=0.6(1-f_c'/250)$ denotes the reduction factor on compressive strength of concrete due to tensile strain in the transverse direction. v_d is normalized axial force ratio on column. Different from the other two codes, EN code incorporates the effect of axial load ratio on shear stress. The limiting shear stress decreases as the axial load ratio increases. Shear stresses suggested by ACI, NZS and EN codes and measured shear stress of specimens are shown in Table 2.

From the table, it is obvious that both specimens do not satisfy the limiting value of joint shear stress, though the joint shear stress in specimen S1 is reduced by 30%. One reason for reduction on shear stress is due to the use of diagonal reinforcements that can effectively reduce the forces transferred to the joint from the beams. The other contributor for reduction of shear stress is due to ferrocement in the joint that resists part of the shear stress.

Table 2 Joint shear stresses suggested by ACI, NZS and EN codes and measured values obtained from specimen C1 and specimen S1

	ACI	NZS	EN code*	Specimen C1	Specimen S1
Shear stress# (MPa)	5.88	6.92	N/A	11.45	8.10

Based on the averaged value of maximum shear stress in both loading directions.
* High axial load ratio is not included in EN code for shear stress in interior joint.

5. FURTHER STUDIES

It is necessary to improve performance of the proposed strengthening method. Firstly, mode of failure of specimen S1 is primarily due to shear and this is not desirable. Secondly, there is limited enhancement on strength. Based on the observations and experimental results, high performance mortar will be used and varying layers of wire mesh will be applied in further studies. Moreover, bonding behavior between ferrocement and the joint will be improved by incorporating shear studs.

In a previous study, Lam et al. (2009) demonstrated that fiber reinforced concrete is a sustainable construction material. Adding fibers to the mortar have the advantage of crack control at the stage of hardening and avoidance of spalling under fire condition. Moreover, as fiber reinforced mortar possesses higher tensile strength due to bridging of fibers, ferrocement can contribute more shear resistance in the joint. Hence, mortar mixed with fibers will be used in further studies. To achieve the above, mechanical properties of ferrocement and bonding conditions will be estimated. Direct tensile test at room temperature and elevated temperature as well as direct shear test will be conducting on high performance ferrocement. Direct tensile test will be used to determine the ultimate strength and modulus at differential temperatures. Direct shear test will be used to assess shear behavior at ideal pure shear state. Figure 15 shows the test setup of direct tensile test and shear test.



(a) (b)

Figure 15 Test setup for (a) direct tensile test, and (b) direct shear test

6. CONCLUSIONS

An experimental program was conducted to evaluate the effectiveness of revitalizing interior beam-column joint subassemblages using ferrocement and diagonal reinforcements. Based on the observations and experimental results of two interior beam-column joint subassemblages, the following are concluded.

(I). Seismic performance of interior beam-column subassemblages is improved by the proposed strengthening method with enhancement on ultimate strength, energy dissipation, stiffness and drift.

(II). Significant reduction on joint shear stress was obtained in the strengthened specimen. This is attributed to diagonal reinforcements which balance part of force and ferrocement which resists part of the shear stress.

(III). Modes of failure of both specimens are due to buckling of main reinforcements in the columns accompanied by shear failure in the beam-column joint subassemblages. Improved confinement to main reinforcements in the joint will have to be provided.

(IV). Although both specimens fail in unexpected modes, strengthened specimen S1 is able to sustain its load carrying capacity after cracking due to confinement action provided by ferrocement. Improvement on the proposed strengthening method will be carried out through using high performance mortar, applying varying layers of wire mesh and improving the bond behavior between ferrocement and the joint.

Acknowledgements:

The authors are grateful to the financial support from The Hong Kong Polytechnic University and the Research Grants Council of Hong Kong (RGC No: PolyU 5206/08E). The authors would like to thank for the technical assistance provided by the Heavy Structural Laboratory of the Hong Kong Polytechnic University.

References:

Abdullah, and Takiguchi, K. (2003), "An investigation into the behavior and strength of reinforced concrete columns strengthened with ferrocement jackets", *Cement and Concrete Composites*, Vol. 25, Issue 2, pp. 233-242.

ACI 318-08, "Building Code Requirements for Structural Concrete and Commentary", ACI Committee 318, 2008.

ACI 549R-97, "Report on Ferrocement", ACI Committee 549, 1997.

ACI-ASCE 352, "Recommendations for design if beam-column connections in monolithic reinforced concrete structures", Joint ACI-ASCE Committee 352, 2002, Farmington Hills, Mich.

Bisby, L.A., Green, M.F. and Kodur, K.R. (2005), "Response to fire of concrete structures that incorporate FRP", *Progress in Structural Engineering and Materials*, Vol. 7, Issue 3, pp 136-149.

Cao, Z., Li, A., Wang, Y.Y., Zhang, W. and Yao, Q. (2007), "Experimental study on RC space beam-column joints strengthened with high strength steel wire mesh and polymer mortar", *Journal of Southeast University (Natural Science Edition)*, Vol. 37, No. 2, pp 235-239. (In Chinese)

Earthquake Engineering Research Institute (EERI) (1999)

"Learning from earthquake The Chi-Chi, Taiwan Earthquake of September 21, 1999", *EERI Special Earthquake report*, 12P.

Earthquake Engineering Research Institute (EERI) (2010) "EERI preliminary report on the 2010, M7.2 EL Mayor-Cucapah earthquake", Editor: Jorge Meneses, 125P.

Eltehawy, E. (2009), "Effect of using ferrocement on the mechanical properties of reinforced concrete slabs subjected to dynamic loads", 13th international conference on Aerospace Sciences and Aviation Technology, 26-28 May 2009, Cairo, Egypt.

Ghobarah, A., Aziz, T.S. and Biddah, A. (1997), "Rehabilitation of reinforced concrete frame connections using corrugated steel jacketing", *ACI Structural Journal*, Vol. 94, No. 2, May-June 1997, pp 283-293.

Ghobarah, A. and Said, A. (2002), "Shear strengthening of beam-column joints", *Engineering Structures*, Vol. 24, Issue 7, pp. 881-888.

Hakuto, S., Park, R. and Tanaka, H. (2000), "Seismic load tests on interior and exterior beam-column joints with substandard reinforcing details", *ACI Structural Journal*, Vol. 97, No. 1, pp. 11-25.

Ho, I.F.Y. and Lam, S.S.E. (2010), "Strengthening Reinforced Concrete Columns by High Performance Ferrocement", *Proc. Joint Conf. of 7th Int. Conf. on Urban Earthquake Engng. & 5th Int. Conf. on Earthquake Engng.*, March 3-5, 2010, Tokyo Institute of Technology, Tokyo, Japan.

Huo, L., Li, H., Xiao, S. and Wang, D. (2009), "Earthquake damage investigation and analysis of reinforced concrete frame structures in Wenchuan earthquake", *Journal of Dalian University of Technology*, Vol. 49, No. 5, pp. 718-723. (In Chinese)

Izi, R., Elbadry, M. and Ibrahim, H. (2008), "Steel Reinforced Polymers Enhance Strength and Ductility of Beam-Column Joints under Seismic Loads", *Structures 2008: Crossing Borders*, *ASCE*.

Kumar, P.R. and Rao, C.B.K. (2006), "Constitutive behavior of high-performance ferrocement under axial compression", Magazine of Concrete Research, Vol. 58, No. 10, pp. 647-656.

Lam, S.S.E, Wu, B., Wong, Y.L., Chau, K.T. Chen, A. and Li, C.S (2000), "Ultimate drift of rectangular reinforced concrete columns in Hong Kong when subjected to earthquake action", Seismic study for Hong Kong, Construction Industry Development Studies and Research Center, 48P.

Lam, S.S.E., Xu, Y.L., Chau, K.T., Wong, Y.L., and Ko, J.M. (2002), "Progress in earthquake resistant design of buildings in Hong Kong", Structural Engineering World Congress, Oct 9-12, 2002, Yokohama, Japan.

Lam, S.S.E., Chan, S.T., Fung, K.M., Ho, J., Li, B. and Ho, I.F.Y. (2009), "Fiber reinforced concrete as a sustainable construction material", Proceeding of Materials Science and Technology in Engineering Conference, 3-4 Dec. 2009, City University of Hong Kong.

Law, C.K., Chui, E.W.T., Wong, Y.C. and Ho, L.S. (2010), "The Achievements and Challenges of Urban Renewal in Hong Kong", Study Report, March, 2010.

Lee, W.T., Chiou, Y.J. and Shih, M.H. (2010), "Reinforced concrete beam–column joint strengthened with carbon fiber reinforced polymer", *Composite Structures*, Vol. 92, issue 1, pp. 48-60.

Lim, C.T.E., Ong, K.C.G. and Paramasivam, P. (2000), "Ferrocement repaired reinforced concrete beams subjected to quasi-static and cyclic loadings", *proceedings of fourth international conference on Repair, Rehabilitation, and Maintenance of concrete structures, and innovations in design and construction*, Seoul, Korea, pp. 887-907.

Nedwell, P.J. (2010), "The use of ferrocement", *Concrete*, August 2010, pp. 52-54.

Pampanin, S., Calvi, G.M. and Moratti, M. (2002), "Seismic behavior of RC beam-column joints designed for gravity loads", *12th European Conference on Earthquake Engineering*, Paper Reference 726.

Pantelides, C.P., Okahashi, Y. and Reaveley, L.D. (2008), "Seismic rehabilitation of reinforced concrete frame interior beam-column joints with FRP composites", *Journal of composites for construction*, ASCE, July/August 2008, pp. 435-445.

Shannag, M.J. (2009), "High strength ferrocement laminates for structural repair", *Proceedings of the international conference on concrete solutions*, Padua, Italy, 22-25 June 2009.

Paulay, T. and Priestley, M.J.N. (1992), "Seismic Design of Reinforced Concrete and Masonry Buildings", John Wiley & Sons, Inc.

Wang, Y.C. and Hsu, K. (2009), "Shear Strength of RC Jacketed Interior Beam-Column Joints without Horizontal Shear Reinforcement", *ACI Structural Journal*, March-April 2009, pp. 222-232.

Wang, Y.Y., Yao, Q.L., Gong, Z.G., Chen, Y.M., Xie, Y.R. and Chen, Z.M. (2005), "Application of Strengthened Technology by composite cover combined with high strength wire cable mesh and polymeric Mortar in Zheng Chenggong Memorial Strengthened Engineering", *Building Structures*, Vol. 35, No. 8, pp. 40-42. (In Chinese)

8CUEE CONFERENCE PROCEEDINGS
8th International Conference on Urban Earthquake Engineering
March 7-8, 2011, Tokyo Institute of Technology, Tokyo, Japan

EVALUATION OF THE DAMAGE OBSERVED IN A REINFORCED CONCRETE WALL BUILDING DURING THE FEBRUARY 27, 2010 CHILE EARTHQUAKE

Fabian Rojas[1)], James Anderson[2)]

1) PhD Student, Department of Civil and Environmental Engineering, University of Southern California, USA
2) Professor, Department of Civil and Environmental Engineering, University of Southern California, USA
rojasbar@usc.edu, jamesa@usc.edu

Abstract: The most common structural system used in the design of mid- to high-rise residential buildings in Chile is shear wall construction. The 2010 Chilean Earthquake, Magnitude 8.8 created a unique opportunity for the evaluation of the performance of wall and frame wall buildings designed according to modern building codes that are similar to those used in the USA and Japan. Due to the extent of the rupture area during the earthquake, many large cities of Chile were affected with different levels of intensity and PGA. In effect, it created a full-scale laboratory that can be used to study the interrelation of the different elements in a wall system during strong ground motions, and also the design provisions for wall buildings that are currently in buildings codes of seismically active countries. A study of the damage observed in a typical building is conducted, and an elastic 3D model of the building is used to study the distribution of the stress in the different resistant axis and their influence in the damages observed.

1. INTRODUCTION

The most common structural system used in the design of mid- to high-rise residential buildings (over 3 stories) in Chile is shear wall construction with a story height around 2.5 [m] with typically wall thicknesses of 15 [cm], 20 [cm] 25 [cm]. The structural walls are located in the interior and on the perimeter of the building for the two principal direction of the building.

Guendelman et al. (1997) used mainly two parameters to characterize the Chilean buildings; the first parameter is the ratio of the building height, H, to the fundamental period of the building, T, or H/T. In a recent study also made by Guendelman et al. (2000) results gave an average value for H/T of around 40 to 70 meters/second for buildings in Chile. Using this parameter, a lower value would indicate a more flexible building and a higher value would indicate a more stiff building. The second parameter used by Guendelman et al. (1997) is the density of walls in the buildings. The density of wall is calculated as the wall area in one direction divided by the total area of the floor. The value of this parameter has remained relatively constant, around 3%, in the last few years. However, it is important to note that this parameter does not reflect the fact that the heights of the buildings in Chile have been increasing in the past few years.

The Chilean's buildings are designed under the code and standards created by the National Institute of Normalization (INN) and approved by the authorities of the country (Ministry of Housing). Typically, the Chilean codes are based in the International Codes and the national codes used in other seismically active countries like USA, Japan and New Zealand. The Official Seismic Chilean Code is the NCh433 Of. 96 on Earthquake Resistant Design of Building, this code was written and developed by the Asociación Chilena de Sismología e Ingeniería Antisísmica (ACHISINA).

The basic objectives and principles used for the seismic design of buildings in Chile are established in the Section 5, which in the subsection 5.5.1 (NCh433of96) states "*..this code applied together with the specific design code for each of the materials named in paragraph 5.3, aims to produce structures that:*

- *Resist moderate intensity seismic actions without damages*
- *Limit damage to non-structural elements during earthquakes of regular intensity*
- *Prevent collapse during earthquakes of exceptionally severe intensity, even though they show some damage"*

These principles are very similar to the philosophy that is described in the Recommended Lateral Force Requirements and Commentary of the Structural Engineers Association of California (2009) known as the "SEAOC Blue Book." (Rojas et al. 2010a)

In addition, the Chile Earthquake, February 27, 2010 provided a unique opportunity to study the behavior of all kind of structures and, in particular, the behavior of mid- to high-rise buildings that were designed with a recent building code and subjected to strong and long duration ground motions. The most common type of damage experienced by the buildings in Chile during the earthquake are located at or near the ground level due to compression and tension

effects in the walls. This caused the crushing of the concrete due to heavy compression at the end of the elements and the buckling and fracture of the steel bars in the boundaries of the walls. The long duration of the ground motions apparently caused cyclical fatigue during the strong shaking, and the buckling of the vertical reinforcing steel was almost ubiquitous, as was reported by the Reconnaissance Team of Los Angeles Tall Building Structural Design Council (Naeim et al. 2010, Carpenter et al. 2010, Rojas et al. 2010b} and other teams (Moehle et al 2010). The lack of confinement of the boundary elements in the walls, seismic hooks and cross ties were also observed, this happened because the Chilean code (Nch433 OF 96 - Section B.2.2) allows the requirements for boundary elements in structural walls from the ACI 318-95 to be disregarded.

In this paper a preliminary study of a 20 story building located in the Concepcion Area that suffered severe damage during the Magnitude 8.8 Chile Earthquake will be discussed. First, the building and the damages observed during the earthquake are described in detail, and following an elastic 3D model of the building using Etabs software (CSI) is analyzed the behavior that the structures suffered during the earthquake.

2. CASE OF STUDY

2.1 Description of Building

The building study is a 20-story reinforced concrete wall building for residential used with one basement. It is located between Concepcion and Coronel in Concepcion Province, Octava Region (Figure 1). This is the second building of a complex of eight buildings that is under development in the same location, until now only two building have been built. The studied building has a rectangular shape in plan view, with the long direction oriented in the north-south direction, and the narrow direction pointing east-west, view Figure 1. The design was finished in 2006, and the construction was finished in 2008.



Figure 1: Location of the Building (Google Map, 2010)



(a) (b)

Figure 2 Exterior view of the Building:
(a) Front (Facing Inland) (b) Back (Facing Ocean)

The main lateral resisting system is a wall system, with wall placed in the interior and on the perimeter of the building as shown in Figure 3 and Figure 4. The typical size of the wall used is 20 [cm]. The main walls for the long direction are located along axis K, L, Figure 3, in the corridor area, and for the short direction the walls that take the lateral loads are distributed over all the length of the building at difference of the long direction. The story heights are presented in the Table 1. The Building is regular and constant between floors 2nd and 18th, with some small differences in the 15th, 16th and 17th floors. The 19 and 20 floors correspond to a reduced floor where the Gym, swimming pool and the elevator mechanical room are located. In the first floor are presented some modifications in main direction to close the building in the first floor and also to make room for the entrance. The basement is only under the center portion of the building. The slab thickness is 15 [cm], which provided the rigid diaphragm at each floor, the slab only has large openings at the elevator location and stairs. The stairs are connected directly to the walls. Most of the beams are located in the perimeter of the building to create the balcony, and support for the slab, with typical dimension of 20 [cm] wide and depths of 29.5, 67.5, 112.5 and 152.5 [cm]. The vertical load is carried by the slab to the same walls that form the resisting lateral system and from there to the foundations.

Table 1 Story Height Building

Floor	Height [cm]
Basement	255
1st Floor	320
2nd to 19th Floor	255
Gym Floor	350

The Concrete used for all elements of the building had a compressive stress of fc' = 250 [kg/cm^2] (H-30), and an

A63-42H steel was used for the steel bars used for the reinforcement of the concrete, which had a fy = 4200 [kg/cm^2]. The longitudinal steel used in the walls varies between a minimum of 8 [mm] diameter bars with a spacing of 20 [cm] (steel ratio of 0.625%) to 22 [mm] diameter bars with a spacing of 20 [cm] (steel ratio of 2.37%), and the transversal reinforcement used in the building varies between a minimum of 8 [mm] diameter bars with a spacing of 20 [cm] (steel ratio of 0.625%) to a 16 [mm] diameter bars with a spacing of 13 [cm] (steel ratio of 1.93%). At the edges of the wall only the last two lines of reinforcement at each face of the wall are confined with typically 12 [mm] diameter bars at 20 [cm] spacing (Youssef et al. 2010).

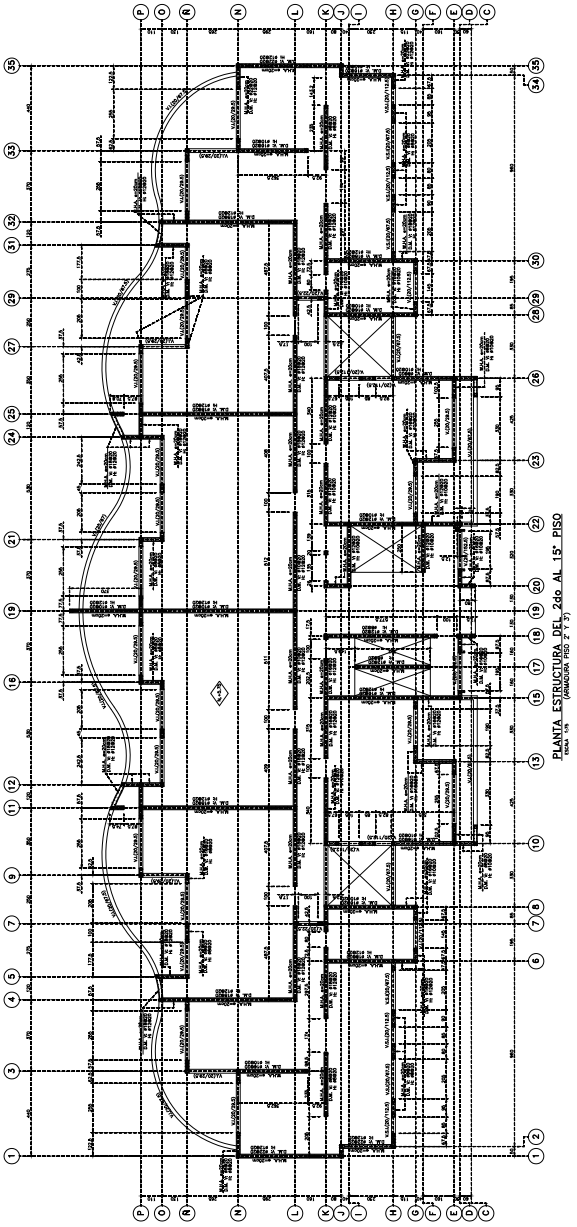


Figure 3: Typical Floor Plan of the Building

The Region of Concepcion, where the building is located, has a variable ground condition, as was reported by Rojas et al (2010b), because the influence of the Bio - Bio River in the North - West Side of the location of the Building, which has produced a large area of the soil of San Pedro city is formed with unconsolidated recent deposits, which come from unconsolidated sand from fluvial origin, clays and fine sediment from the water in swamps, and river deltas (Galli et al. 1963). However, in the east side of the building we have the influence of the marine deposition. In conclusion, the area of the building can be described as a main thick layer of sand with areas with superficial thin layer of artificial deposit (unconsolidated clays, silts and sands). This type of soil when the sand is dense is classified as Soil Type III under the NCh433 OF 96, which is the case of the building studied. The foundation used for the building consists in a mat foundation with a thickness of 120 [cm].

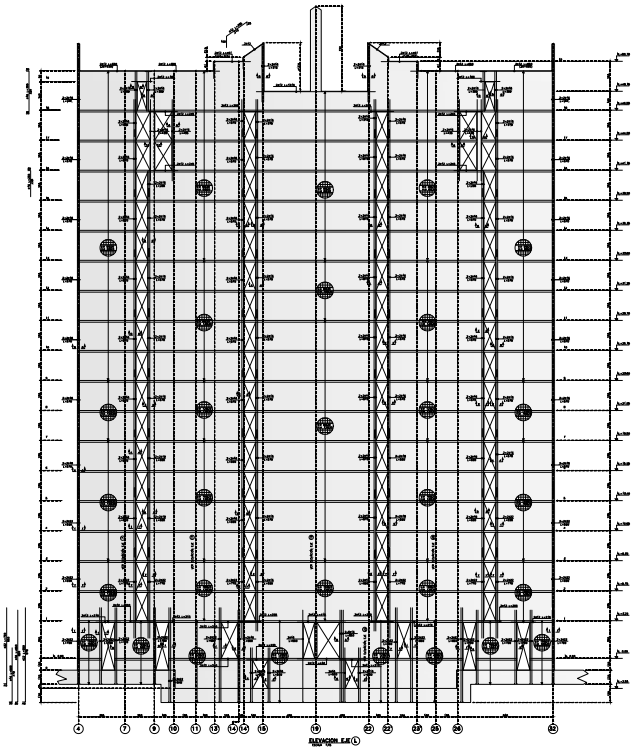


Figure 4: Elevation L

The Building was designed according to the Chile codes and standards, using the load shown in the Table 2, and a soil capacity of σ_{adm}=2.5 [kg/cm^2] in the static case and of σ_{adm}=3.0 [kg/cm^2] for the seismic case, this was informed by the designers, and because the structure is located in a seismic zone 3, with a soil type III, the elastic response spectra used for the modal analysis is shown in Figure 6. For more information of the code requirements and equations used for the construction of the response spectra, the reader is reference to Rojas et al. (2010a).

Table 2 Load used in the design of the Building

Load Case	[kg/m^2]
Additional Dead Load	50
Live Load	200
Live Load Roof	100

2.2 February 27, 2010 Magnitude 8.8 Chile Earthquake

The Magnitude 8.8 Chile earthquake occurred at 3:34 am local time in the central area of Chile, the rupture started at 36° 12' 28" S and 72° 57' 46" W at a depth estimated of 47 [Km], the area of the total rupture was 450 [Km] of length by 130 [km] wide. Concepcion is located 105 [Km] from the epicenter of the earthquake (Seismological Service, Univ. of Chile 2010). An effect of cascade due to the length of the rupture produced a buildup of pulses that created strong ground motion that was felt over all the center and south part of Chile, in San Pedro city the total shaking time was roughly 3 min.

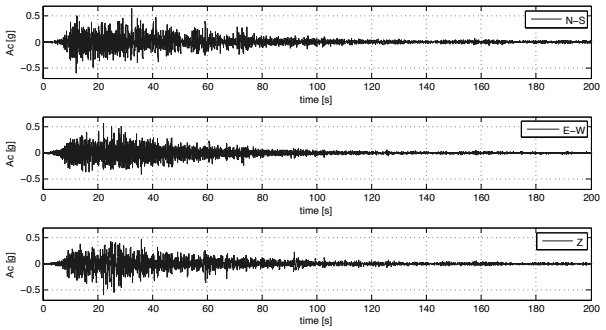


Figure 5 Acceleration Record at San Pedro High School, Concepction (02/27/2010 – Recorded by Seismological Service, Univ. of Chile)

Two accelerometers were working at the moment of the earthquake in the area of Concepcion, each instrument recorded 3 components (N-S, E-W and Vertical). One instrument was located in the downtown of Concepcion, however, this record has not been yet released to the public domain. The other instrument was in San Pedro High School , located in the San Pedro City , at roughly 3 miles from the Downtown of Concepcion and on the other side of the Bio-Bio River (S.S. Univ. of Chile, 2010). The second instrument, shown in the Figure 1, measured an acceleration of 0.65g in the N-S direction, 0.58 g in the E-W direction and 0.6 g in the vertical direction (S.S. Univ. of Chile 2010), and the duration of the record is approximately 3 min with almost 60 second of strong ground motion. This is the nearest recorded data available for the Building studied, which is around 3 miles away.

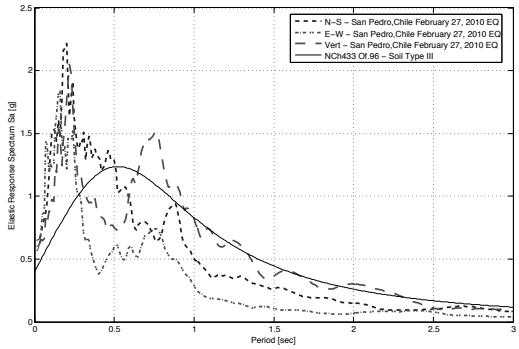


Figure 6 Comparison Elastic Response Spectra Seismic Zone 3 - Soil Type III vs recorded Acc obtained in San Pedro HS during the February 17, 2010 Chile Earthquake

In addition, A GPS station located in the Transportable Integrated Geodesic Observatory (TIGO) at the University of Concepcion, about 8 [km] from building studied, measure and recorded the event showing a displacement at Concepcion of roughly 3 [m] in the west direction (GEO's Chile Event Supersite Website, 2010).

2.3 Damage Observed

The principal type of damage detected in the reinforced concrete wall buildings in Chile after the February 27, 2010 Chile Earthquake are located in the ground level, due to compression and tension effects in the walls, causing the crushing of the concrete due to a heavy compression at the end of the elements and the buckling and fracture of the steel bars in the boundary elements of the walls due to cyclic fatigue during the shaking. Also, in some cases, buckling of the bars in the vertical reinforced steel bars through the wall was observed. Also, at other areas in Chile, the confinement of the boundary zone of the walls was not observed in the construction that suffer failure; this is consequence that the Chilean code (Nch433 of 96 - Section B.2.2) allows one to ignore these requirements that are present in the ACI318. Also a lack of seismic hooks and cross ties in the wall elements was observed. This was reported by the Reconnaissance Team of Los Angeles Tall Building Structural Design Council (Naeim et al. 2010, Carpenter et al. 2010, Rojas et al. 2010b} and other teams (Moehle et al 2010).

A continuation is detailed the damage observed in the building during the two visit done by the author of this paper when participated as a member of the Reconnaissance Team of Los Angeles Tall Building Structural Design Council (LATBSDC) for the February 27, 2010 Chile Earthquake. In addition, also are shown part of the study of the building done by the team after the earthquake (Youssef et al. 2010) and additional remarks.

As is shown in the areal view Figure 1, two building are presented in the site, rectangular shape building, which is the studied building that suffer considerable damage, and a V shape building. This second structure, a 13-story Building, suffered only minor damage. The difference of response could be attributed to the shape and orientation of the building with respect to the ground motion, assuming that do to the proximity of the two building, they have similar soil condition, and felt similar ground motions, this may indicate a important role of the directionality of the earthquake in the behavior of the building, as it was also noted by Youssef et al. (2010)

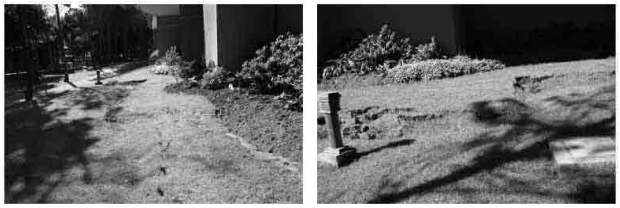


Figure 7 Damage in the soil around the Building

In an inspection of the exterior of the building different

types of damages were detected. In the soil around the building, and specially in the back of the building, large settlement of the ground Figure 7, which can be attributed to poor backfill compaction of the soil after construction, because no indication of foundation or settlement of the foundation were observed. In the structure, some short column failures, Figure 8a, shear failure of short beam; Figure 8b, shear wall failure, Figure 8c, crushing of the concrete, Figure 8c, and flexural-compression crushing of concrete and the steel in walls Figure 8d were observed. All the severe damage observed in the exterior is located at the first floor level.

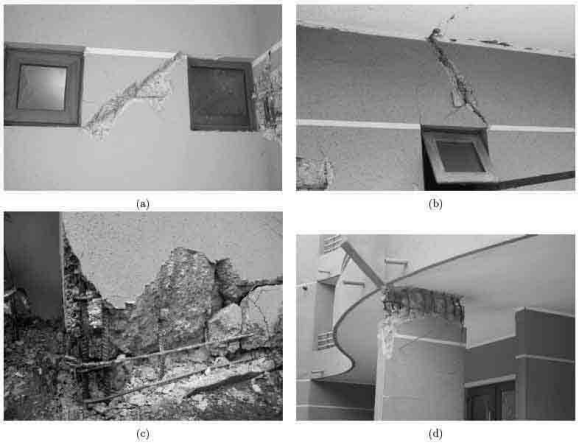


Figure 8 Damage in the Exterior of the Building: (a) Short Column Failure; (b) Shear Beam Failure; (c) Concrete Crush; (d) Compression - Tension Failure

The two main shear wall failures in the exterior of the building are concentrated in the two walls that are in the entrance of the building. These walls spans along the 15 and 22 gridline between the gridline K and D Figure 3, above the first floor, in the first floor theses walls are extended out of the building to form the entrance, which create a vertical discontinuity and an outrigger effect. In the elevation of the gridline 15 shown a opening just under the diagonal cracking, and also is noted that one side under the opening is connected to the mat foundation, and the other side is founded on another. In conclusion, the opening produced an extended part of the first floor that attracted large demand; there was not enough area at the end of the opening for the load to travel producing a crushing at the end of the diagonal Figure 9, as it was also reported by Youssef et al. (2010).

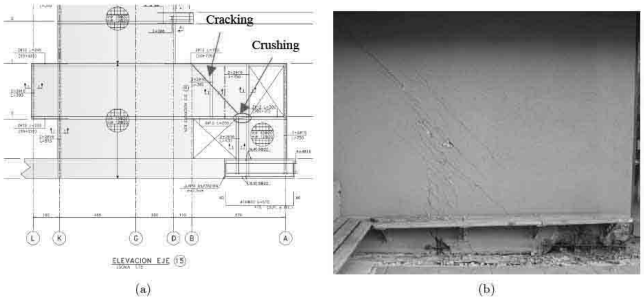


Figure 9 Damage in the Elevation 15: (a) Elevation 15 (Youssef et al 2010); (b)Shear Damage and Concrete Crushing

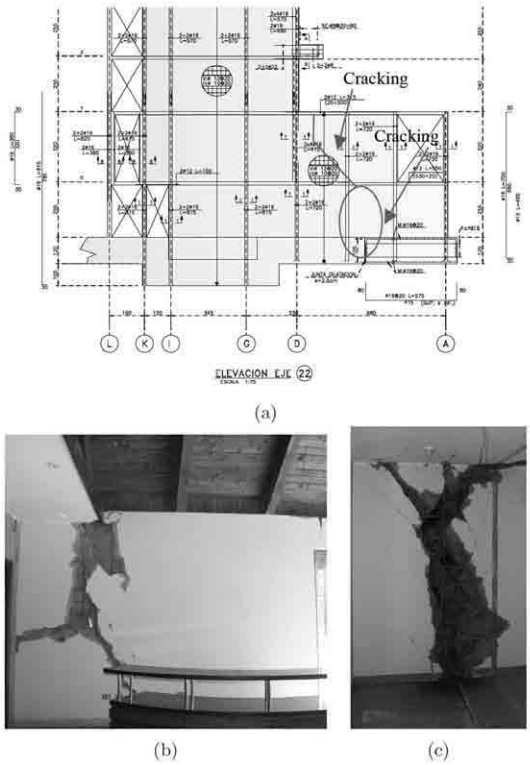


Figure 10 Damage in the Elevation 22: (a) Elevation 22; (b) Crack 1st Floor; (c) Cracked Basement

Instead, in the gridline 22, the wall is extended even more in the basement. No opening is observed at the first floor, Figure 10. However the wall is founded one part over the mat foundation, and the other portion over a different foundation, which could have produced some differential deformation in the wall due to the overturning moment of the building which produce a failure in the wall at the level of the basement Figure 10.

The damage of the thin walls produced by the coupling of flexural and compression demand that caused the crushing of the poorly confined or even unconfined boundary element part of the walls, which crack and propagate through the section, it was reported almost in all the building review and visited by the different Reconnaissance teams (Youssef et al 2010, Naeim et al. 2010, Carpenter et al. 2010, Rojas et al. 2010b, Moehle et al. 2010), and was mainly observed what happened in the walls that presented vertical discontinuities at the first floor and form the so call ``Flag Wall''. In the ocean facing exterior of the Building studied is observed the failure of a wall due to flexural crushing, in the wall at the end of the gridline 19. The wall in this gridline span between the balconies beams and the gridline L Figure 3 without openings between the 2nd and 19th floor, and only at first floor two openings appear, the smaller for architectural reasons, and the other to locate the door for a room at the entrance level Figure 11. In addition, the exterior edge of the wall is set back a few inches in the first floor. This could have caused the end wall to be submitted to large compression and tension demand for the overturning moment due to the wall in the above floors.

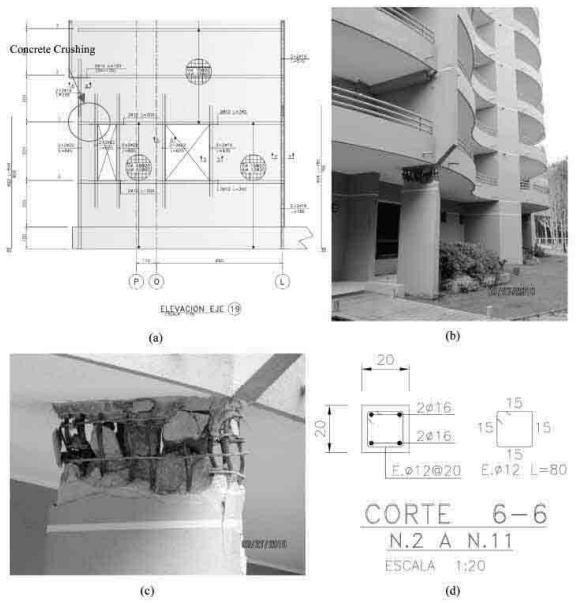


Figure 11 (a) Elevation of lower floors along line 19; (b) concrete crushing along line 19; (c) closer view of crushing at top of wall; (d) boundary confinement details at line 19 (Youssef et al 2010)

In the Interior of the building the damage is concentrated mainly in the center part of the building along gridline L. In the first Floor the damage in gridline L is centered around gridline 22 Figure 12, the large crack turns horizontal at the end of the wall, with crushing of the concrete at the boundary element, and buckling and fracture of some of the longitudinal steel bars. Looking the elevation of the gridline L at that position is observed that the damage could be the result of the discontinuity of the wall above in combination of the thin wall and poor confinement of the boundary elements, Figure 12, and also the crushing in the top the wall at first floor could be caused by the flexural over turning of the two different walls from above (Youssef et al. 2010).

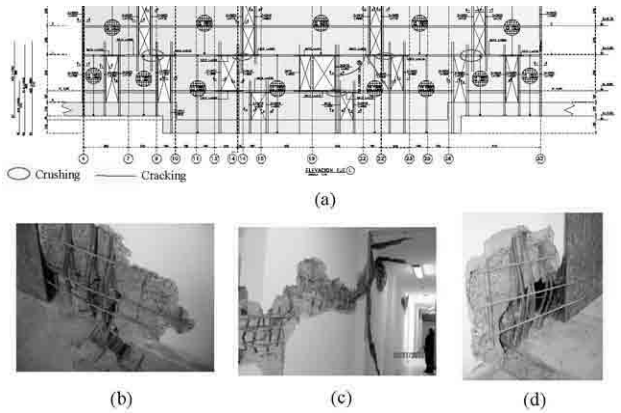


Figure 12 Damage in the elevation L in the interior of the Building at the 1st and 2nd Level: (a) Elevation with damage location (b) damage at left size; (c) damage at center of elevation (d) damage at right size

In addition, the elevation L presented some crushing of the wall at the end of the 2nd floor around gridlines 6 - 8 and 28 - 30 Figure 12a, these failures can also be attributed to the discontinuity in the walls. In this case two walls at each edge of the elevation, which are separate over all the height of the building, were connected at the first floor, and also included some openings, which produce a reduction of the section of the walls. Trying to compensate this reduction, an increase of the wall at the first floor is observed. However the area for the transition of the load at the second level was not enough to produce the crush of the concrete and the buckling of the steel bars Figure 12 b,d.

In the rest of the stories the damage is concentrated mainly in the floor, showing a severe damage of the floor when acted as a coupling beams along the walls in the gridline L and K Figure 13 (a) and (b), show the deterioration of the floors at the position of the door openings, because the crushing of the concrete, and diagonal crack between the doors openings in opposite side of the corridor. No special detailing for steel reinforcement is observed for the bars parallels to gridline L, K for the area of the slab located in the door openings that connect the walls along gridline L and K, it is typically found 8 [mm] diameter bars at 20 [cm] spacing (Youssef et al. 2010). In addition, it is interesting to note that the slab between the gridline L and K also acts as a coupling beam in the perpendicular direction to the corridor between the gridline L and K for the wall in the short direction of the building, this is shown for the parallels crack observed in the celling along the the wall in the gridline L and K Figure 13 (c) and (d). This type of damage was observed almost in all the building visited by the different by the different Reconnaissance teams (Naeim et al. 2010, Carpenter et al. 2010, Rojas et al. 2010b, Moehle et al. 2010)



Figure 13 Damage observed in the slabs at different levels: (a) and (b) damage of the slab between walls; (c) and (d) parallels cracks to walls in the slabs at the corridor area

The final severe damage observed in a wall in the building is located in the top of the building in the gymnasium area, and is a shear wall failure. This failure also happened for a vertical discontinuity of the wall in the gridline 15, which caused the connection in the last floor of

the wall along K and L, producing a large shearing demand over that section of the wall. This is traduced in the failure observed, which was also noted by Youssef et al. (2010).

2.4 3D Elastic Model

A 3D elastic model of the building is developed using Etabs software V9.7 (CSI, 2010), Figure 14, as an initial approach to study the behavior of the building during of the Magnitude 8.8 Chile Earthquake February, 27 2010. The modal analysis of the model indicates that the 1st and 3rd modes are a coupling of the longitudinal direction and torsional, which is expected due to the distribution of the resistant walls in the x direction (See Figure 3), and the 2nd mode is in the transversal direction.

Table 3 Modal Participation Factor of the Building

Mode	Period [sec]	Mxx	Myy	Mzz
1	0.71	27.90	0.37	41.02
2	0.69	0.14	67.42	0.26
3	0.57	43.95	0.00	26.93



Figure 14 3D Elastic Model

In the Table 4 is presented the weight for square meter used in the model for each floor, that come from account for the 100% of the dead load and a 25% of the live load. The other parameter shown is the density of wall area in each direction for each floor. The values obtain for this building are typical for residential Chilean building, which are 1 Ton/m^2 and above 3 % of wall area for each direction. However, the H/T ratio gave 79.9 m/sec for the longitudinal direction, and 96.8 m/sec in the transversal direction, which indicates a more stiff building.

A response spectra analysis is used to analyze the distribution of stresses inside the building. The elastic response spectra with 5% damping used is obtained from the accelerograms recorded during the earthquake (Figure 6). The N-S record is applied to the longitudinal direction (Long direction) and the W-E record is applied to the transversal direction (short direction).

Table 4 Properties for Floor

Story	H	Weight/Area Floor [Ton/m^2]	% Density of Wall in X	% Density of Wall in Y
19	2.55	1	3.46	4.76
18	2.55	1.18	3.19	4.85
17	2.55	0.99	2.67	4.12
16	2.55	0.97	2.72	3.44
2 - 15	2.55	0.97	2.7	3.31
1	3.2	1.11	3.34	3.59

To account for the inelastic behavior of the structure in the response spectrum is used the reduction factor defined in the Chilean Seismic Code (NCh433 of 96) (Figure 15) for Wall system building

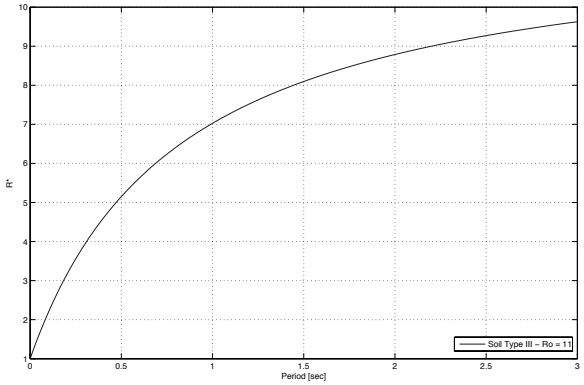


Figure 15 Reduction Factor

The Shear and Moment over the structure in the two principal directions are shown in Figure 16. The shear in the N-S direction corresponds to an 11.3 % of the total weight of the building and a 9.4 % of the total weight in the W-E direction (Short Direction)

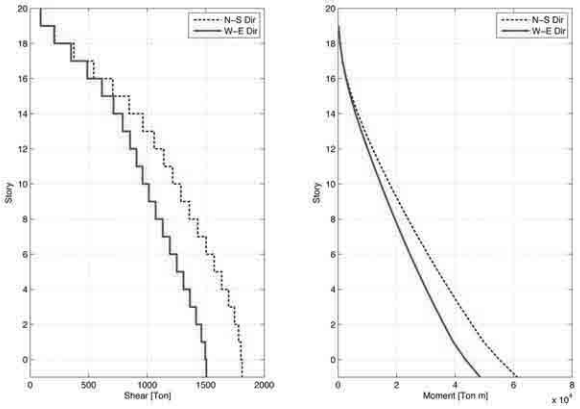
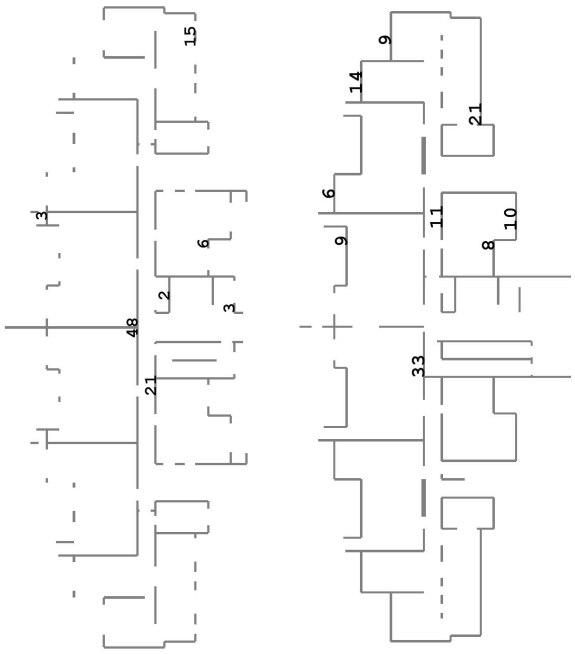


Figure 16 Reduction Factor

In addition, it is studied the distribution of shear in each direction inside of the building. It is observed that for the long direction between the 2nd and 16th floor the axis L and K take around a 70 % of the total shear of the floor (Figure

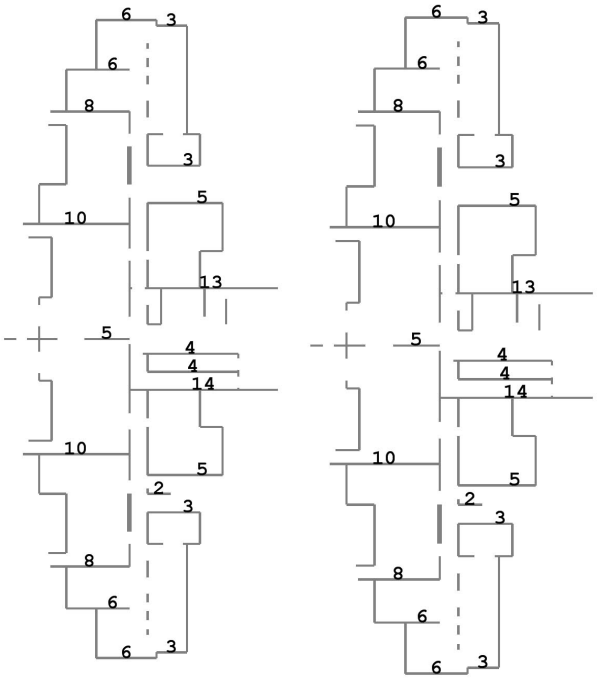
17a), and at level of the first floor some of this shear is released to the exterior wall that appears only at that floor (Figure 17b), which can cause the failure of the short column and short beam in the first floor at this new walls (Figure 8)



(a) (b)

Figure 17 Distribution of % Shear in the Long Direction
(a) Typical Floor (b)1st Floor

In the other direction the shear is distributed more uniformly over the different resistant axis (Figure 18). In addition this axis help to resist the torsion form for the separation between the center of gravity and the center of rigidity in the short direction.



(a) (b)

Figure 18 Distribution of % of Shear in Short Direction
(a) Typical Floor (b)1st Floor

The damage in line 19, it is attributed to the action of the overturning and the combination of the axial load when the wall is divided to accommodate a door and an architectural feature, that cause an over compression stress of the head of the wall at the first level. This type of failure was very common in the all the Chilean building. Also the damage in the slab at the level of the corridor it is observed in the model for a concentration of stress at zone of the perpendicular wall that corroborate the assumption that the slab is acting as a coupling beam in the structure. The damage in line 15 and 22 are corroborate for the model to observed a increase in the shear demand at that lines at the level of the first floor (Figure 18)

The internal damage observed in the axis L, like in the Figure 12a and 12b, are attributed by a excessive compression stress due to the transference of forces at that strangulation, that produce an increase in the shear and compression demand, which is shown in the result of the model. In addition the overturning along that resistant axis produce an additional component that contribute to the failure.

3. CONCLUSIONS

The Chile Earthquake provided a unique opportunity to study the behavior of reinforced concrete wall buildings. The Building study is one of the examples available to study and compare analytical model with real response. In fact, these buildings are real laboratory test cases, that need large studies to understand better the interrelation of the different elements of the structures when are subjected to strong ground motion, and use these studies to improve the codes and stander available for seismic design.

This particular building was selected because of the amount of data that is available on hand, such us recorded accelerogram of near field, drawings, building specifications, and damage information. Also, this building has the characteristic of having severe damage and many different types of damage. An initial study of the damage and comparison of the damage and elastic model was presented in this paper to evaluate the damage of a shear wall building during a Magnitude 8.8 earthquake. Even if an elastic model is used for analysis of the structure, the model is able to represent where the concentration of stresses were during the earthquake and evaluate theses critical points in the structure. A more comprehensive model it is need to study in more depth the actual value in each area and study how was the evolution of the damage in the structure and how the interrelation of the different components of the structure, such as wall, slab and beam, interacted during the earthquake.

References:

Carpenter, L. D., Naeim, F., Lew, M., Youssef, N. F., Rojas, F., Saragoni, G. R. and Adaros, M. S. (2010), "Performance of tall buildings in Viña del Mar in the 27 February 2010 offshore Maule, Chile earthquake," *The Structural Design of Tall and Special Buildings*, n/a. doi: 10.1002/tal.672

Etabs V9.7 (CSI, 2010), Structural Analysis Software. CSI. Computer & structures, inc http://www.csiberkeley.com, 2010

Galli, C. and Sanchez, J. (1963), "Effects of the earthquake of May 1960 in Concepcion and Vicinity," *Bulletin of the Seismological Society of America*, **53**(6), 1281-1297.

GEO's Chile Event Supersite Website, (2010). *Group on Earth Observation*, Retrieved June, 2010. Website: http://supersites.unavco.org/chile.php

Guendelman, T., Guendelman, M., and Lindenberg, J. (1997), "Perfil Bio-Sismico de Edificios," *VII Jornadas Chilenas de Sismologia e Ingenieria Antisismica y Primer Congreso Iberoamericano de Ingeniria Sismica*, La Serena, Chile. (Spanish)

Institute of the Cement and Concrete of Chile (ICH) (2002)), "Chilean Buildings of Reinforced Concrete," *Commission of Structural Design in Concrete and Masonry,* Camara Chilena de la Construcción e Instituto del Cemento y del Hormigon, 1st Edition (Spanish)

Guendelman, T., Guendelman, M., and Lindenberg, J. (1997), "Chapter 11: Perfil Bio-Sismico de Edificios," *I.E.C. Inenieria S.A.*, Santiago, Chile. (Spanish)

Moehle, J., Wallace, J., Maffei, C., Sempere, C., Celestino, A., Besa, J. J., Dragovich, J., Westenenk, B., Millan, A., Frings, C., and Herranz, J. P. (2010)," February 27, 2010 chile earthquake reconnaissance team investigation: Reinforced concrete buildings". *Reconnaissance report*, EERI, 2010.

Naeim, F., Lew, M., Carpenter, L. D., Youssef, N. F., Rojas, F., Saragoni, G. R. and Adaros, M. S. (2010), "Performance of tall buildings in Santiago, Chile during the 27 February 2010 offshore Maule, Chile earthquake," *The Structural Design of Tall and Special Buildings*, n/a. doi: 10.1002/tal.675

NCh433of96. (1996), "Earthqauke Resistant Design of Building, Official Chilean Code NCh433.Of96" *National Institute of Normalization*

Rojas, F., Lew, M., and Naeim, F. (2010a), "An overview of building codes and standards in Chile at the time of the 27 february 2010 offshore maule, Chile earthquake,"*The Structural Design of Tall and Special Buildings*, **19**(8), 853-865.

Rojas, F., Naeim, F., Lew, M., Carpenter, L. D., Youssef, N. F., Saragoni, G. R. and Adaros, M. S. (2010b), "Performance of tall buildings in Concepción during the 27 February 2010 moment magnitude 8.8 offshore Maule, Chile earthquake," *The Structural Design of Tall and Special Buildings*, n/a. doi: 10.1002/tal.674

Youssef, N. F., Tunick, D., Naeim, F., Lew, M., Carpenter, L. D., Rojas, F., Saragoni, G. R. and Adaros, M. S. (2010), "Performance of the Torre Bosquemar and Olas buildings in San Pedro de la Paz and the Pedro de Valdivia building in Concepción in the 27 February 2010 offshore Maule, Chile earthquake," *The Structural Design of Tall and Special Buildings*, n/a. doi: 10.1002/tal.670

Seismological Service, Univ of Chile (2010), "Technical Report: Cauquenes Earthquake: February 27, 2010," *Technical Report*, Seismological Service, Univ of Chile, April 3, 2010. Chile. (Spanish)

8CUEE CONFERENCE PROCEEDINGS
8th International Conference on Urban Earthquake Engineering
March 7-8, 2011, Tokyo Institute of Technology, Tokyo, Japan

PRELIMINARY COLLAPSE ASSESSMENT OF THE TORRE ALTO RIO BUILDING IN THE MW = 8.8 FEBRUARY 27, 2010 CHILE EARTHQUAKE

Zeynep Tuna[1] and John W. Wallace[2]

1) Ph.D. Candidate, Dept. of Civil and Environmental Engineering, University of California, Los Angeles
2) Professor, Dept. of Civil and Environmental Engineering, University of California, Los Angeles
zynptna@ucla.edu, wallacej@ucla.edu

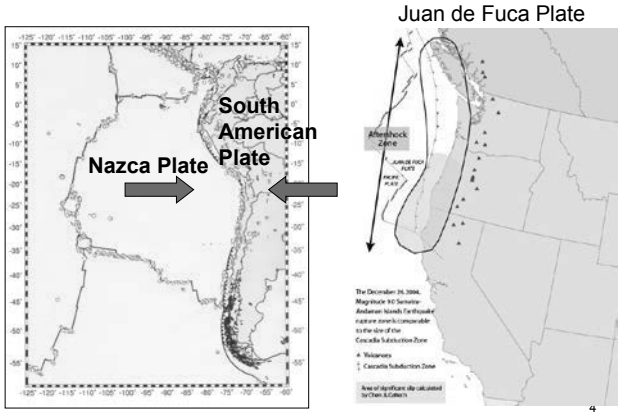
Abstract: Reinforced concrete shear wall buildings are by far the most common lateral force resisting system used to resist ground shaking that occurs in the frequent large earthquakes that occur in Chile. Since the Chilean building code is based on ACI 318-95, with only a few exceptions, the performance of buildings in Chile to the very strong shaking that occurred in the Mw = 8.8 February 27, 2010 earthquake provides an excellent opportunity to evaluate the behavior of taller RC buildings (>10 stories). The 15-story, residential, Torre Alto Rio building was one of the few, modern RC buildings over ten stories to collapse. Studies of reasons for the collapse were conducted using post-earthquake observed damage, structural drawings, and preliminary analyses (e.g., section analyses and two-dimensional nonlinear analyses). The preliminary studies indicate that collapse was likely influenced by discontinuous walls on the east side of the building, wall layout and configuration, and the location of splices of wall vertical reinforcement.

1. INTRODUCTION

Reinforced concrete shear wall buildings are the predominant lateral force resisting systems used to resist ground shaking that occurs in the frequent large earthquakes that occur in Chile. Detailed studies of a number of Chilean buildings were conducted following the March 3, 1985 M7.8 earthquake (Wallace and Moehle, 1989; 1993; Wood, 1991). These studies indicated that the overall good performance of the modern RC buildings in Chile resulted due to the use of a large percentage of wall area to floor plan area, as well as limited wall axial stress.

The building codes in Chile are similar to building codes used in the United States. Chile's reinforced concrete design specifications are based on ACI 318 Building Code requirements. An important variation between ACI 318 in the Chilean code (NCh 433.Of96) involves an exception which allows shear walls in Chile to be constructed without special boundary elements and significant boundary transverse reinforcement. Preliminary reports (EERI, June 2010; Wallace, 2011) indicate that the lack of boundary transverse reinforcement, thin walls, and relatively high levels of axial stress likely led to greater damage to buildings in 2010 than was observed in 1985.

The recent and past earthquakes in Chile provide an excellent opportunity to evaluate the behavior of taller (more than 10 stories) reinforced concrete buildings subjected to strong, long duration, ground motions. Moreover, it is noted that the subduction zone in Chile is similar to that in the US Pacific Northwest, where the Juan de Fuca plate subducts under the North American plate (Figure 1-1).



http://upload.wikimedia.org/wikipedia/commons/3/38/Cascadia_subduction_zone_USGS.png

Figure 1-1 Subduction zones

1.1 The February 27, 2010 Chile Earthquake- A Brief Overview

The 2010 Chilean earthquake occurred off the coast of the Maule Region of Chile on February 27, 2010, with Mw = 8.8 for shaking lasting about two minutes. The epicenter of the earthquake was located at 335 km (210 miles) SW of Chile's capital city, Santiago, and 105 km (65 miles) NNE of Chile's second largest city, Concepcion. Displacement spectra with 5% damping is shown in Figure 1-2.

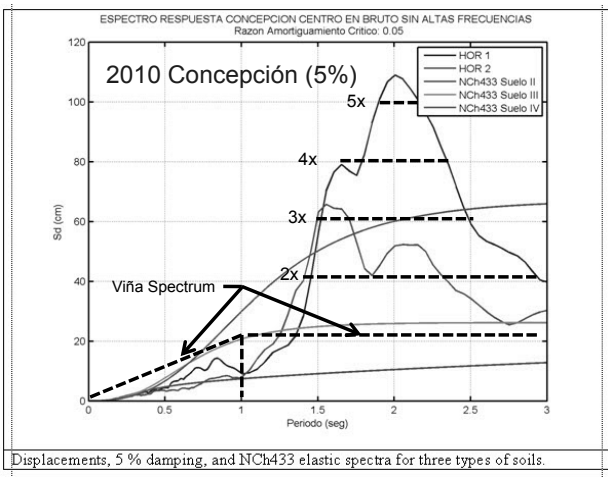


Figure 1-2 Displacement Spectra with 5% damping

2. OBSERVED DAMAGE

The 15-story residential building Torre Alto Rio, constructed in 2008, collapsed in the main shock and led to the majority of deaths reported in modern reinforced concrete buildings (EERI Newsletter, June 2010). Photos of the collapsed building are provided in Figures 2-1 and 2-2.



Figure 2-1 Collapsed building: Torre Alto Rio [The Associated Press]



Figure 2-2 Collapsed building view from the base

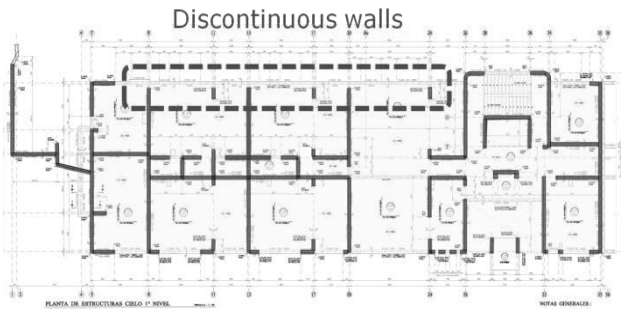


Figure 2-3 Plan view [Moehle,9th US NCEE, Toronto]

Shear wall layout can be clearly seen in the plan view (Figure 2-3), with primary lateral strength direction provided by walls with T-shaped cross sections, with flanges formed by the corridor walls (Figure 2-4). Therefore, when loaded, one of the T-shaped walls has flange in compression (Figure 2-5 (a)), the other one (Figure 2-5 (b)) has flange in tension.

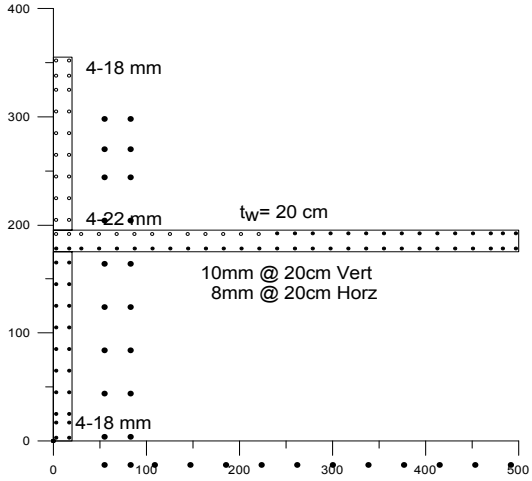


Figure 2-4 Cross-sectional view of the T-shaped wall highlighted in Figure 2-4

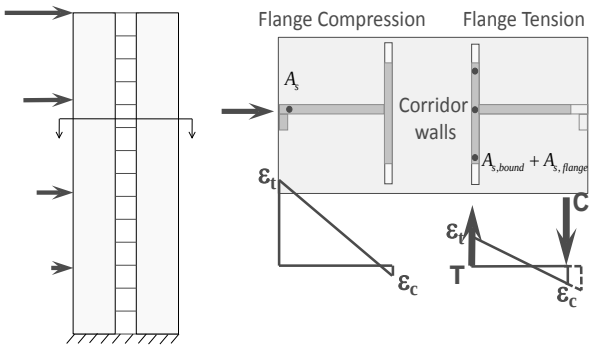


Figure 2-5 Schematic plan view

In case (a), large tensile strains are developed at the wall boundaries at the building edge (east and west faces).

The very wide compression zone formed by the corridor wall results in a very small depth of the compression zone due to the small quantity of tension reinforcement used at the east edge of the wall. The large tensile strains make the boundary longitudinal reinforcement susceptible to fracture. Some of the wall vertical reinforcement fractured at the building edge and rebar splice failures were observed along the tension web. [EERI Special Earthquake Report- June 2010] (Figure 2-6). On the other hand, in case (b), large web-compression forces occur in T-shaped walls (corridor walls in tension) and results in buckling of the vertical reinforcement and concrete crushing at the building edges. The latter case can be clearly seen in Figure 2-7 which presents the behavior of a T-shaped wall with flange under tension, from an experimental study of reinforced concrete structural walls with rectangular and T-shaped cross-sections (Thomsen and Wallace, 1995; 2004). These issues are discussed in more detail and similar post-earthquake and experimental damage photos are presented by Wallace (2011).

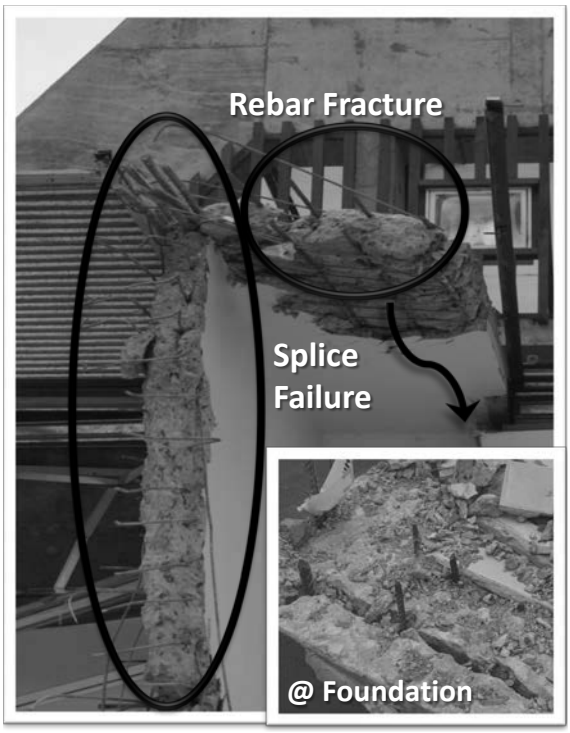


Figure 2-6 Splice failure and rebar fracture

To understand the reasons for collapse, curvature demand is compared with curvature capacity of the T-shaped wall. Curvature demand is calculated as 0.00012/cm using displacement-based design methodology (Eq. (1)), where spectral displacement is obtained from Figure 1-2 as 12 cm by estimating fundamental period of the building as 1 sec. In the equation, plastic hinge length is taken as two times the wall thickness (i.e., α=2) based on results presented by Wallace (2011). Curvature capacity is obtained using moment-curvature analysis and compared with curvature demand in Figure 2-8. The red solid line represents the behavior with axial load based on tributary gravity load, whereas the blue dashed lines display the curvature demand and indicate that concrete crushing is expected (along with rebar buckling). Once the wall web crushes/buckles, (type (b)), the wall shortens and causing the building to rotate/lean. Post-earthquake observations indicate that crushing/buckling of wall webs was very common for T-shaped walls, particularly when there is setback at the web boundary (Figures 2-9, 2-10). Rotation in the building is likely to produce large tension on the opposite wall (type (a)). Due to the large tensile force, longitudinal reinforcement fracture and splice failure are likely. This sequence is illustrated in Figure 2-11.

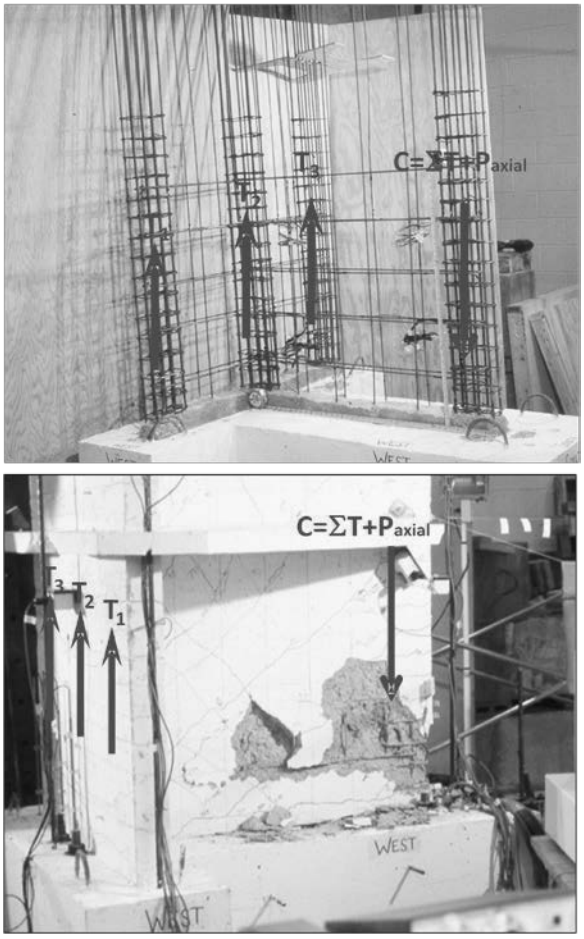


Figure 2.7 Specimen TW1 [Thomsen and Wallace, 2004]

$$
\begin{aligned}
S_d(T = N/15 = 1\text{sec}) &= 12cm \\
\frac{\delta_u}{h_w} &= \frac{1.5S_d}{39m} = 0.0046 \\
\phi_{demand} &= \left(\frac{\delta_u}{h_w}\right)\left(\frac{1}{l_p = \alpha t_w}\right) \\
\phi_{demand} &= (0.0046)(1/2*20cm) \\
\phi_{demand} &= 0.00012/cm
\end{aligned}
\tag{1}
$$

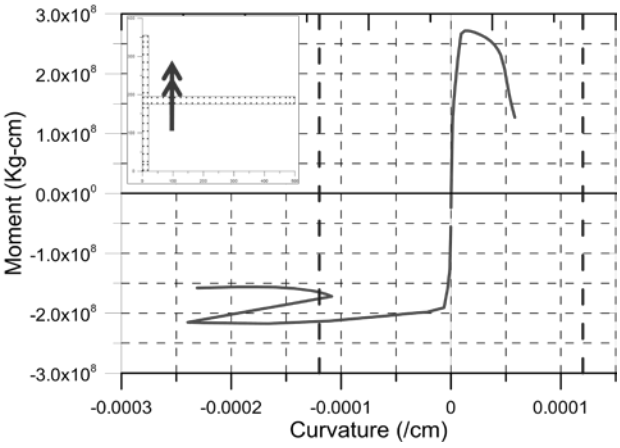


Figure 2.8 Moment-curvature relation of the T-section (Figure 2-4)



Figure 2.9 Example for wall crushing (Macul, Santiago) [Wallace, 2010]

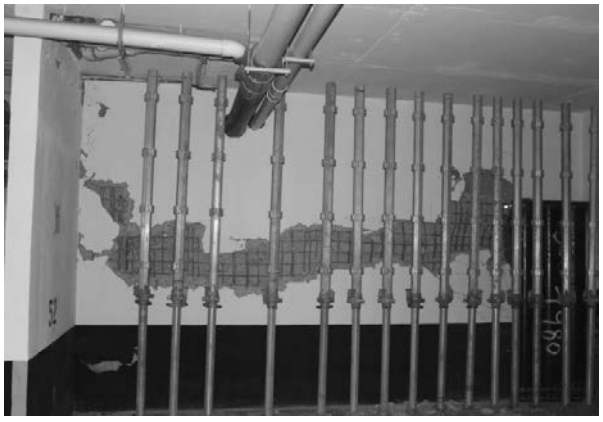


Figure 2.10 Example for wall crushing (Santiago) [Moehle, 2010]

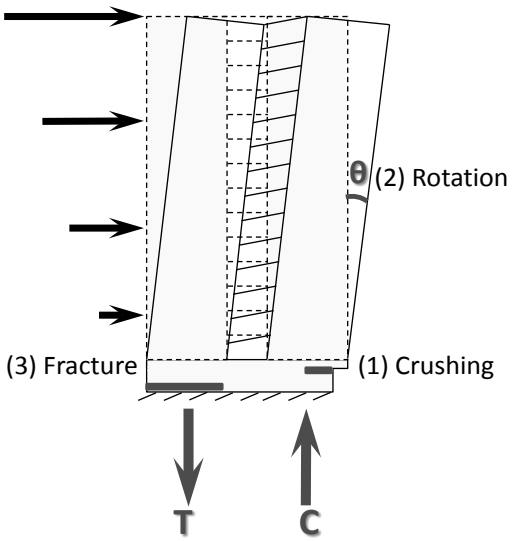


Figure 2.11 Assumed collapse mechanism

Vertical wall discontinuity, on the other hand, can be clearly seen in the schematic elevation view of the building (Figure 2-12). Shear walls below the ground level were setback to provide for parking spaces. As discussed above, when the corridor wall (flange) is in tension, larger wall shear and web-boundary compression forces develop. The large compression, along with the vertical wall discontinuities, were important factors leading to the observed building performance (collapse).

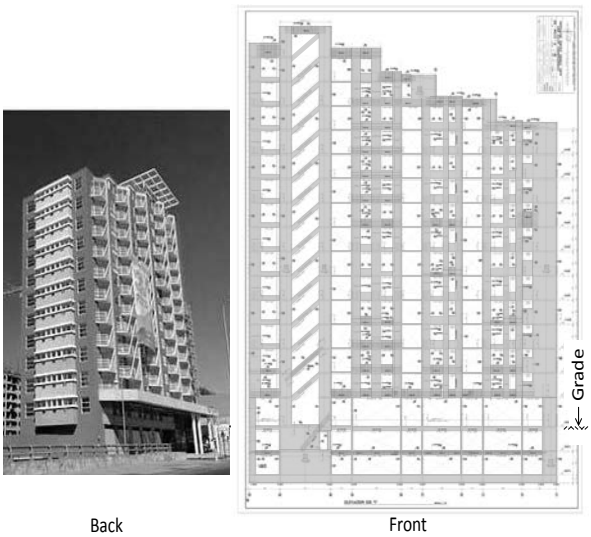


Figure 2.12 Elevation view of the building [Moehle, 9th US NCEE, Toronto]

3. CONCLUSIONS

Reinforced concrete shear wall buildings are the predominant lateral force resisting systems used to resist ground shaking that occurs in the frequent large earthquakes that occur in Chile. Since the building code in Chile is based on ACI 318-95 and the subduction zone in Chile is similar to that in the US Pacific Northwest, the performance of buildings in Chile that are subjected to the very strong shaking in the February 27, 2010 earthquake provides an excellent opportunity to evaluate the behavior of taller reinforced concrete buildings. The Torre Alto Rio; a 15 story, residential, modern reinforced concrete building collapsed in February 27, 2010 earthquake. Reasons for the collapse were studied using post-earthquake observed damage, structural drawings, and moment-curvature analysis. The preliminary studies show that collapse was most likely affected by:

- wall layout (T-shaped walls),
- discontinuity and setback in the east-side basement walls to provide space for parking, and
- lack of sufficient transverse reinforcement at wall web boundaries.

Acknowledgements:

The authors acknowledge support from the Japan Ministry of Education, Culture, Sport, Science, and Technology (MEXT) for establishing the Center for Urban Earthquake Engineering (CUEE) in Tokyo Institute of Technology. This support makes possible the forthcoming international conference, as well as international joint research projects and exchange programs with overseas universities. Travel support for the second author to visit Chile was provided by NEEScomm. The authors' appreciate the input provided by the EERI Chile reconnaissance team members and the large number of individuals in Chile who assisted the reconnaissance effort. In particular, we wish to acknowledge EERI team member leader Professor Jack Moehle (UC Berkeley), who also is a member of the first author's Ph.D. committee, EERI team member Alvaro Celestino (Degenkolb Engineers), who visited the building with the second author, and Professor Patricio Bonelli and graduate student Arturo Millán (Federico Santa Maria Technical University), who provided valuable input and logistical support in Chile. Opinions, findings, conclusions, and recommendations in this paper are those of the author, and do not necessarily represent those of the sponsor or others mentioned.

References:

ACI 318-95, *Building Code Requirements for Structural Concrete and Commentary,* American Concrete Institute Committee 318, 1995.

Earthquake Engineering Research Institute, 2010, "EERI Special Earthquake Report- June 2010: The Mw 8.8 Chile Earthquake of February 27, 2010," Oakland, CA.

Thomsen, J. H., and Wallace, J. W., "Displacement-Based Design of Reinforced Concrete Structural Walls: An Experimental Investigation of Walls with Rectangular and T-Shaped Cross-Sections," Report No. CU/CEE-95/06, Department of Civil Engineering Clarkson University, Postdam, N.Y., 1995, 353 pp.

Thomsen IV, J. H., and Wallace, J. W., "Experimental Verification of Displacement-Based Design Procedures for Slender Reinforced Concrete Structural Walls," Journal of Structural Engineering, ASCE, V. 130, No. 4, 2004, pp. 618-630.

Wallace, J. W., Moehle, J. P., "An Evaluation of Ductility and Detailing Requirements of Bearing Wall Buildings Using Structural Walls," Journal of Structural Engineering, 1993; 121(1).

Wallace, J. W., Moehle, J. P., "The 1985 Chile Earthquake: An Evaluation of Structural Requirements for Bearing Wall Buildings," Report N° UCB/EERC-89-05, July 1989.

Wallace, J. W. (2011), "February 27, 2010 Chile Earthquake: Preliminary Observations on Structural Performance and Implications for U.S. Building Codes and Standards," ASCE Structures Congress, Las Vegas, April 14-16, 2011, Paper 1159.

Wood, S. (1991), "Performance of Reinforced Concrete Buildings during the 1985 Chile Earthquake: Implications for the Design of Structural Walls," *Earthquake Spectra 7*, 607.

8CUEE CONFERENCE PROCEEDINGS
8th International Conference on Urban Earthquake Engineering
March 7-8, 2011, Tokyo Institute of Technology, Tokyo, Japan

DEVELOPMENT OF PARTIALLY TUBE-CONFINED REINFORCED CONCRETE DUCTILE MOMENT FRAME

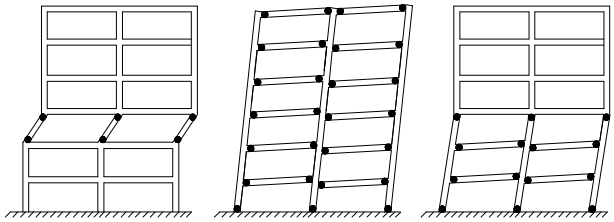
Yuntian Wu[1), 3), 4)], Yan Xiao[4), 5)], Yingmin Li[2), 3)], Shuyan Ji[1), 3)] and Akira Wada[6)]

1) Associate Professor, College of Civil Engineering, Chongqing Univ., China
2) Professor, College of Civil Engineering, Chongqing Univ., China
3) Key Lab of New Technology for Construction of Cities in Mountain Area (Chongqing Univ.), Ministry of Education, China
4) Key Lab of Building Safety and Efficiency (Hunan Univ.), Ministry of Education, China
5) Professor, Dept. of Civil and Environmental Engineering, Univ. of Southern California, USA;
6) Professor, Structural Engineering Research Center, Tokyo Institute of Technology, Japan
yuntianw@cqu.edu.cn, yanxiao@usc.edu, liyingmin@cqu.edu.cn, jishuyan@cqu.edu.cn, wada@ serc.titech.ac.jp

Abstract: In design of ductile RC moment frames, more hoops than needed for shear resistance are required at ends of beams and columns both to confine the concrete and restrain the buckling of longitudinal reinforcement. However, disadvantages of using hoops for confinement are inherent. Hoops can only confine the concrete core, which usually results in the spalling off of concrete cover during large inelastic deformation reversals. Amount of hoops for yield regions is usually dictated by code specified maximum spacing instead of by a rational design. In addition, closely spaced hoops and supplementary bars at yield regions require more construction time and efforts, not to mention the miscellaneous stringent detailing requirements. In order to achieve improved constructability, better confining effect and better post-earthquake reparability, new types of ductile RC moment frames were proposed where yield regions of columns are wrapped with external tube confinement instead of using extra transverse reinforcement. This paper focuses on the development of a rational design procedure that aims to relate the characteristics of tube confined concrete to the overall system behavior.

1. INTRODUCTION

The ductile reinforced concrete moment frames have been widely constructed in regions of highest seismicity in most of the world. According to the seismic design method used in many countries, the ductile inelastic response of a RC frame during strong earthquake ground shaking can be achieved if the following design goals are satisfactorily met: 1) strong column-weak beam mechanism; 2) adequate shear strength; 3) sufficient transverse confinement at yield regions of members; and 4) avoidance of anchorage and/or splice failure. It can be seen that the transverse hoops plays a significant role in ensuring the expected ductile inelastic response in traditional RC frames. In current seismic design codes transverse hoops have three main functions: 1) provide shear strength; 2) prevent buckling of longitudinal rebars; and 3) confine the core concrete of yield regions for better deformability. The current transverse hoop design is based on the work of Richart et al. (1929) and was developed so that the compressive strength of the confined core of a column after spalling should be equal to the strength of the gross section of the column before spalling. However, the disadvantages of using transverse hoops for confinement are inherent. Firstly, transverse hoops can only confine the core concrete and leave the concrete covet neither confined nor reinforced. Under large inelastic deformation reversals, the concrete cover will spall off, causing bond stress loss of longitudinal reinforcement and loss of stiffness and strength of the member due to the reduction of sectional area. Secondly, the current confinement reinforcement design leads to extra construction cost and efforts in that closely spaced hoops will concentrate within the lengths of yield regions and thus increase the construction time of steel cage and the difficulty in pouring and vibrating concrete, not to mention the stringent detailing requirements for the supplementary cross ties. Thirdly, although the strong column and weak beam mechanism is intended to restrain the local damage at beam ends and then to avoid the story mechanism due to the existence of weak columns, as shown in Figure 1(a), column yielding is inevitable due to the limiting column-beam strength ratios. Kuntz and Browning have suggested that only when column-to-beam strength ratio is relatively high (on the order of four) can the most preferred full structural mechanism, as shown in Figure 1(b), be developed. ACI 318 adopted a relatively low while very practical value of 1.2 as the column-to-beam strength ratio, leading to the intermediate mechanism as shown in Figure 1(c). This intermediate mechanism is associated with stringent detailing requirements on hoops at yield regions, resulting increased construction cost.



(a) (b) (c)

Figure 1 Failure patterns of ductile RC frames (a) story mechanism (b) beam mechanism and (c) intermediate mechanism

It is believed by the authors that the traditional way of using transverse hoops as confinement reinforcement in ductile RC moment frame is inherently inefficient to ensure the strong column-weak beam mechanism and to provide confinement at yield regions of members. Using hoops at yield regions for confinement requires extra construction efforts in steel cage fabrication, concrete pouring and vibrating, and quality control. In order to enhance the confinement effect at yield regions and improve the constructability of ductile RC frames, a new type of ductile RC frame where transverse hoops are only for shear resistance and the yields regions are confined with steel tubes is proposed in this paper.

2. REARCH BACKGROUND

A great deal of research work has been carried out to investigate the behavior of retrofitted deficient RC bridge columns. Those existing RC bridge columns designed following old codes needed retrofitting in that previous earthquakes had revealed their inherent deficiencies in strength, ductility and energy dissipation capacity (Fung et al, 1971; Priestley, 1988; Lew, 1990). Various retrofitting methods were developed by researchers around the world, mainly in U.S. and Japan. It has been widely accepted that using steel jacket to encase the potential plastic hinge regions of circular and rectangular bridge columns can result in the increase in ultimate compressive strain, strength and ductility (Sakino and Ishibashi, 1985; Tomii et al, 1987; Xiao, 2001; Zelinski, 1990; Priestley et al, 1992; Priestley, et al. 1994a and b). Carbon fiber reinforced plastic has attracted a great deal of attention from researchers due to its superior mechanical properties. Using CFRP wrap to enhance the flexural strength and ductility of deficient bridge columns has been accepted as an effective way of retrofitting. Using post-tensioning straps for strengthening was different from the above-mentioned methods in that the straps actively prestressed the column laterally. Therefore, it was more efficient in terms of material use and confining effect. Hassan et al. has conducted experimental studies on the behavior of columns confined by external prestressed metal straps and obtained satisfactory results.

One of the most interesting conclusions drawn from previous research was that the confinement could reach best effects on circular column section while for square or rectangular column section the confinement would be less effective compared with circular columns. However, it is obvious that if this issue could not be resolved satisfactorily, the use of externally confined concrete in new building structures would be very limited since most of the columns in building structures are square or rectangular. Therefore, it is worthwhile to further investigate the external confining methods for non-circular columns.

Although a lot of research programs have been carried out on the behavior and modeling of confined concrete, only few of them focused on the confined concrete for new buildings. Thus the design method of the confinement steel, especially the external confinement was empirical instead of rational. Furthermore, previous research only focused on the behavior of a structural member while rarely studied the confined concrete at the system level. This lack of systematic study on confined concrete has limited its application in newly built structures. This research aims to conduct some preliminary studies on the externally confined concrete as part of a structural system.

3. PROPOSED PARTIALLY TUBE-CONFINED RC DUCTILE FRAME

In order to improve the constructability and meanwhile enhance the seismic performance, several partially external tube-confined structural columns were conceived by the authors. It is proposed herein to develop new types of RC ductile frames with partially tube-confined columns where yield regions are confined using external encasement instead of transverse reinforcement.

The proposed partially tube-confined ductile RC moment frame is depicted in Figure 2. Deviating from the conventional ductile RC moment frames, transverse hoops in partially tube-confined ductile RC frames are only for shear resistance, resulting in the uniform distribution of hoops along the full height of the column except for the joint regions. At the ends of columns, tubes are provided to confine the entire column sections of potential yield lengths. The construction procedure of the partially tube-confined RC frame is very similar to that of traditional RC frame. The only difference is that the confining tube is installed after the column concrete has been cured. The confining tube can be fabricated by welding steel shells that form an enclosure to the column sections at potential yield regions. The external encasement is terminated slightly short of the connecting member or footing (e.g. 5 mm gap) to ensure that the tube provides confinement only.

2.1. Type-1: RC Columns Partially Confined by Steel Tubes

The use of rectilinear steel tubes for confining square or rectangular columns has been proved experimentally to be very effective provided that the steel shell has sufficient out of plane flexural stiffness. The beam action will be relied on to develop efficient lateral confinement to the concrete sections. The construction of the steel tube is depicted in Figure 3(a). The steel shells can be field welded to form the encasement of the column section. A thin layer of cement grout is filled between the column surface and the steel encasement.

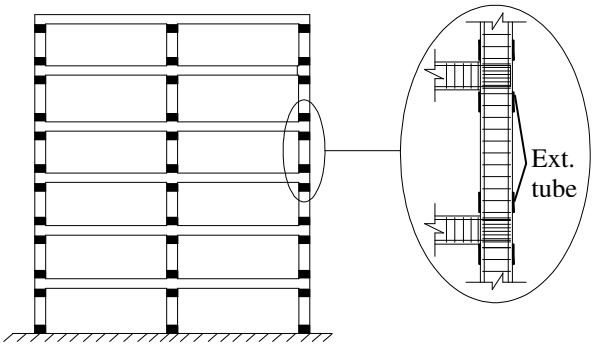


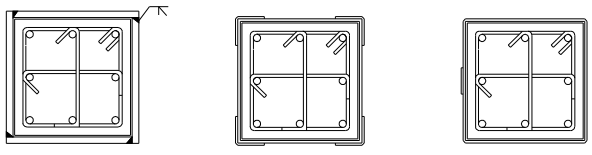
Figure 2 Partially tube-confined RC frame

2.2. Type-2: RC Columns Partially Confined by Carbon Fiber Reinforced Plastic (CFRP) tubes

Figure 3(b) illustrates the proposed CFRP tube details. The corners of the CFRP tube are strengthened by adding extra layers locally. Due to the substantially varied distribution of the confining pressure for square and rectangular column sections, much higher pressures are developed at corners as compared to the pressure developed at the midpoints between corners. Therefore, without special strengthening measures taken, the CFRP confining tubes will most likely fracture at the corners, resulting in relatively poor confinement effects compared with circular columns. Therefore local strengthening at corners of the CFRP confining tube can enhance the confining effect.

2.3. Type-3: RC Columns Partially Confined by Post-tensioning Metal Straps

Post-tensioning metal straps



(a) (b) (c)

Figure 3 Details of proposed external tube confinement: (a) steel tube; (b) CFRP tube; (c) post-tensioned metal strips

4. RESEARCH OBJECTIVES AND SCOPE

This research program is to investigate the seismic performance and to develop guidelines for design of RC ductile moment frames where yield regions of columns are confined using external tube encasement instead of traditional transverse reinforcement. The followings are the detailed objectives of this program:

i. To define and to provide constructable details of the external tube confinement at column ends using different materials;

ii. To develop and to evaluate design methods for the partially tube-confined RC columns;

iii. To develop and evaluate the design method for the RC ductile frame system consisting of partially tube-confined columns and regular beams;

iv. To evaluate the effectiveness of the currently available constitutive models for confined concrete;

v. To compare the effectiveness of different partial confinement schemes using different materials.

5. PROPOSED DESIGN APPROACH FOR PARTIALLY TUBE-CONFINED COLUMN

A performance design approach is proposed to design the partially tube-confined RC ductile frame. The approach includes the following major steps:

i) Select a controlling sway mechanism of the preliminary proportioned frame using limit analysis;

ii) Estimate the required column-girder flexural strength ratios from the results of step i;

iii) Estimate the required drift demand;

iv) Design column and confinement to satisfy strength and deformation demand obtained from steps ii and iii;

v. Conduct a refined analysis and check the strength and deformation adequacy.

Four possible failure patterns of the partially tube-confined column were identified, including shear failure, flexural failure at critical confined section at column ends, flexural failure at critical section of unconfined column section and failure of confining steel tube. In order to ensure the ductile inelastic response of the column, shear failure should be avoided before the development of the flexural mechanism strength at selected locations. As shown in Figure 3, section A represents the critical section of the confined yield regions. Section B is the critical section of the unconfined segment of the column. Although the flexural failures of the critical sections of both confined and unconfined column segments are ductile, more benefits can be expected if choosing the external confining steel tube as the structural component where ductile failure occurs first. Since the confining tube exists externally, it would be very convenient to remove the failed tube and replace with a new one after experiencing rare earthquake events. In other words, choosing the yielding of the external confinement as the failure mechanism of the system can result in superior reparability compared to other mechanisms. Furthermore, the strengths of the column would be sustained even if the external confinement fails. Thus the collapse of building can be

prevented.

5.1 Confining Tube Design

In design of the confining tube, the equivalent confinement pressure is estimated first corresponding to the moment when the nominal flexural strength of the confined section. A simple way of estimating such an equivalent confinement pressure can be established based on the ACI 318 code (2008). To ensure the rotational deformability of the potential plastic hinges near column ends, ACIT 318 code requires the transverse reinforcement be

$$A_{sh} \geq 0.3 \frac{sh_c f_c^{'}}{f_{yh}} (\frac{A_g}{A_{ch}} - 1) \quad (1)$$

$$A_{sh} \geq 0.09 sh_c \frac{f_c^{'}}{f_{yh}} \quad (2)$$

Where A_{sh} is the total transverse steel cross-sectional area within spacing s; h_c is the cross-sectional dimension of column core measured center-to-center of the outermost peripheral hoops; f_c' is the specified compressive strength of concrete; f_{yh} is the specified yield strength of the transverse reinforcement; A_g is the gross area of section; and A_{ch} is the cross-sectional area of the column measured out-to-out of transverse reinforcement. Eqs. (1) and (2) can be used to define an equivalent lateral pressure f_{eq}. Since f_{eq} is corresponding to the development of nominal flexural strength of the confined section, the concrete compressive strength f_c' can be substituted by the compressive strength of confined concrete f_{cc}'. Thus, f_{eq} can be expressed as

$$f_{eq} = \frac{A_{sh} f_{yh}}{sh_c} \geq 0.3 f_{cc}^{'} (\frac{A_g}{A_{ch}} - 1) \quad (3)$$

$$f_{eq} = \frac{A_{sh} f_{yh}}{sh_c} \geq 0.09 f_{cc}^{'} \quad (4)$$

It can be seen that for externally confined column sections Eqs. (1) and (3) are automatically satisfied. Thus Eqs. (2) and (4) govern the design. The design of the confining tube is based on a limit state where an appropriate yield mechanism is formed. For steel tube confinement, the limit state can be the beam action with plastic hinges formed at middle and corner sections along each side. For CFRP tube, the mechanism can be the failure at corners. For post-tensioning straps, the mechanism can be the yielding at corners. The length of the tube encasement is chosen to ensure that the moment demand immediately beyond the tube will not exceed 75% of the original flexural capacity.

5.2 Flexural Strength Check at Critical Column Sections

The required flexural strength for the critical section at the confined segment is determined based on the mechanism flexural strength at beam end multiplied by a column-to-beam strength ratio. Since the confined concrete effect is considered, a moment-curvature sectional analysis may be necessary to estimate the flexural strength of the critical confined section based on the stress-strain relationship of confined concrete. The flexural strength demand at the critical unconfined concrete can be estimated by assuming the inflection point is located at the mid height.

5.2 Shear Design

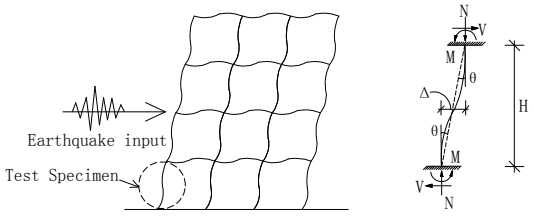
The shear demands of the columns should be calculated based on the plastic moments at column ends considering confined concrete effect. The transverse reinforcement can then be determined based on the shear demand following relevant shear design provisions in ACI 318 code. The spacing of transverse reinforcement is uniform along the clear column height.

5.3 Joint Check

Due to the consideration of confined concrete effect at column ends, the shear demand may increase and result in the development of shear cracks. The joint reinforcement is then of great significance to ensure the strong column-weak beam mechanism.

6. EXPERIMENTAL PROGRAM

A comprehensive experimental program is under development at the structural laboratory of Chongqing University. The experimental program consists of two phases of testing. At phase one, short square columns with proposed external confinement will be tested under axial compression to examine the effectiveness of the additional measures that aim to compensate for the reduction of confining effect due to non-circular column section. The stress-strain relationships of confined concrete as well as the stress state of the confining tube will also be studied.



(a (b)

Figure 4 (a) Prototype structure; (b) loading condition

At phase two, the model column specimens simulating the behavior of frame columns will be tested subjected to cyclic lateral loading under constant axial load. The prototype building and the loading conditions of the specimens are depicted in Figure 4. by assuming the infinity of the floor slab stiffness, the column ends are treated as fixed. Under constant axial load N and cyclic lateral shear force V, the specimen will deform as shown in Figure 4(b) with double curvature. It is

believed this loading condition can satisfactorily simulate the frame column behavior during earthquake event.

7. SUMMARY

Partially external tube-confined RC ductile moment frames are proposed along with three different confining schemes. Using external confinement can overcome the inherent disadvantages of traditional transverse reinforcement and provide additional benefits such as the improved reparability after earthquake. A design procedure is also suggested to design the system including the partially confined column. The forthcoming experimental program was briefly outlined.

Acknowledgements

The research project described in this paper is currently undergoing and is supported by the Fundamental Research Funds for the Central Universities and project of Ministry of Education Key Laboratory of Building Safety and Energy Efficiency, Hunan University. The authors would like to appreciate the supports of various sponsoring agencies.

References:

Richart, F.E., Brandtzaeg, A. and Brown, R.L. (1929). "The failure of plain and spirally reinforced concrete in compression." Bulletin No. 190, Univ. of Illinois Engrg. Experimental Station, Urbanna, Ill.

Kuntz, G.L., Browning, J., (2003). "Reduction of column yielding during earthquakes for reinforced concrete columns." *ACI Structural J.,* 100(5), 573-580.

Fung, G.G. et al. 1971. Field investigation of bridge damage in the San Fernando Earthquake. Technical report, Bridge Department, Caltrans, California.

Lew, H.S. (editor) 1990. Perofrmance of structures during the Loma Prieta Earthquake of October 17, 1989. National Institute of Standards and Technology SP 778.

Priestley, M.J.N 1988. Damage of the I-5/I-605 Separator in the Whittier Earthquake of October 1987. *Earthquake Spectra*, 492), 389-405.

Zelinski, R. 1990. California highway bridge retrofit strategy and details. In Final Proceeding Second Workshop on Bridge Engineering Research in Progress, Civil Engineering Dept., Univ. of Nevada, Reno, Oct. 29-30.

Tomii, M.,Sakino, K.,Watanabe, K. and Xiao Y., 1985a, Lateral load capacity of reinforced concrete short columns confined by steel tube – experimental results of preliminary research, Proceedings of the International Speciality Conference on Concrete Filled Steel Tubular Structures, Harbin, China, pp.19-26, August;

Tomii, M., Sakino, K., Xiao Y. and Watanabe, K., 1985b, Earthquake-resisting hysteretic behaviorof reinforced concrete short columns confined by steel tube – experimental results of preliminary research, Proceedings of the International Speciality Conference on Concrete Filled Steel Tubular Structures, Harbin, China, pp.119-125, August;

Sakino,K. and Ishibashi, H., Experimental studies on concrete filled square steel tubular short columns subjected to cyclic shearing force and constant axial force, Journal of Structural and Construction Engineering, Transactions of AIJ, No. 353, July, 1985, pp.87-89;

Tomii, M., Sakino, K., Xiao, Y. (1987). "Ultimate moment of reinforced concrete short columns confined in steel tube." Proc. Pacific Conf. on Earthquake Engineering, Vol. 2, New Zealand, August 5-8, 11-22;

Sakino, K., Sun, Y.P., and Aklan, A. (1996). "Effects of wall thickness of steel tube on the behavior of square tubed R/C columns." 11th World Conf. on Earthquake Engrg.;

Aboutaha, R.S., Machado, R.I., Seismic resistance of steel tubed high-strength reinforced concrete columns. J. Struct. Engrg. ASCE, 1999,125(5),485-494;

Priestley M J N, Seible F., Calvi, M. (1996). Seismic design and retrofit of bridges. John Wiley & Sons, 686;

Xiao, Y., Wu, H. (2003). "Retrofit of reinforced concrete columns using partially stiffened steel jackets." J. Struct. Engr. ASCE, 129(6), 725-732;

Asadollah Esmaeily-Gh and Xiao Yan, Seismic behavior of bridge columns subjected to various loading patterns, Pacific Earthquake Engineering Research Center, 2002;

Moghaddam H., Pilakoutas K., Samadi, M., Mohebbi, S. 2008 Behavior and modeling of concrete columns confined by external post-tensioned straps. ASCE Structure Congress 2008: Crossing borders

8CUEE CONFERENCE PROCEEDINGS
8th International Conference on Urban Earthquake Engineering
March 7-8, 2011, Tokyo Institute of Technology, Tokyo, Japan

ESTIMATION OF PEAK IMPACT FORCE DUE TO IMPACT OF TSUNAMI WATER-BORNE SHIPPING CONTAINERS ON RC COLUMNS

M. A. K. M. Madurapperuma[1] and Anil C. Wijeyewickrema[2]

1) Graduate Student, Department of Civil and Environmental Engineering, Tokyo Institute of Technology, Japan
2) Associate Professor, Department of Civil and Environmental Engineering, Tokyo Institute of Technology, Japan
ma.k.aa@m.titech.ac.jp, wijeyewickrema.a.aa@m.titech.ac.jp

Abstract: This paper reports the results of the numerical investigation of reinforced concrete (RC) columns subjected to impact loads from tsunami water-borne shipping containers. High-fidelity numerical simulation of the shipping container-column impact is carried out using the nonlinear finite element code LS-DYNA. A series of RC columns with square and circular cross-sections is considered to investigate effects of transverse reinforcement ratio, longitudinal reinforcement ratio, column section size, and axial load ratio on peak impact force. Based on the numerical results, formulae to estimate peak impact force on RC columns are obtained in terms of column cross-section size and kinetic energy of the container.

1. INTRODUCTION

Indian Ocean tsunami of December 2004 resulted in massive destruction to coastal communities particularly with a higher death toll compared to all other tsunamis that have occurred in the past. Post tsunami reconnaissance surveys have reported that light-framed wood and unreinforced masonry residential buildings were severely damaged or completely collapsed due to impact of water-borne massive objects such as boats and heavy vehicles (Ghobarah et al. 2006, Inoue et al. 2007, Kaushik and Jain 2007). Similar damage was reported due to recent tsunamis of September 2009 in Samoa and February 2010 in Chile, where many water-borne shipping containers impacted on buildings and port facilities as the area became inundated (Robertson et al. 2010ab). An example of damage to an RC building due to impact of a shipping container during the Samoa tsunami is shown in Fig. 1. Several RC columns collapsed and beams in the impacted region sustained severe damage due to the container impact.

Madurapperuma and Wijeyewickrema (2011) considered the impact of a water-borne shipping container on an RC building, where the impact force-time histories were first obtained from a high-fidelity finite element analysis using LS-DYNA (2007) and next the impact analysis of the entire building was carried out using OpenSees (2009), an analysis framework that uses beam-column elements with fiber-based descretization. In the present study, the numerical simulation carried out using detailed finite element models facilitates a more comprehensive analysis of the shipping container-column impact scenario. The impact analysis is carried out using the nonlinear finite element code LS-DYNA (2007). Prior



(a) (b)

Fig. 1. (a) Damage to an RC building due to impact of a shipping container during the Samoa tsunami and (b) close-up view of the damage (Robertson et al. 2010a).

to numerical simulation, formulae to estimate the peak impact force given in current design guidelines such as ASCE 7-10 (ASCE 2010) and FEMA P646 (FEMA 2008) are critically reviewed. Next, details of finite element models and numerical results for the container-column impact are presented. A series of RC columns with square and circular cross-sections is considered to investigate effects of transverse reinforcement ratio, longitudinal reinforcement ratio, column section size, and axial load ratio on peak impact force. Based on numerical results, formulae to estimate the peak impact force on RC columns are obtained. The present study can be considered as a very comprehensive investigation of container-column impact.

2. EXISTING METHODS TO ESTIMATE PEAK IMPACT FORCE

In this section the current design guidelines (ASCE 2010, FEMA 2008) which refer to impact force due to water-borne objects are reviewed.

The peak force F_p due to impact of a water-borne massive object given in ASCE 7-10 (ASCE 2010) is

$$F_p = \frac{\pi m v}{2\Delta t}, \tag{1}$$

where m is mass of the object, v is velocity of the object before impact, and Δt is time to decrease object velocity to zero in the compression phase. Equation (1) is based on the principle of impulse and momentum, and assumes a half-sine pulse for the impact force-time history where the force increases from zero to the peak value F_p in time Δt, then decreases to zero in the restitution phase. Although the value of Δt would vary with the stiffness characteristics of the impacting objects a single value of $\Delta t = 0.03$ has been recommended in ASCE 7-10 (ASCE 2010).

In the case of FEMA P646 (FEMA 2008) the peak impact force is given by

$$F_p = C_m v \sqrt{k_{eff} m}, \tag{2}$$

where C_m is added mass coefficient and k_{eff} is effective contact stiffness i.e., $1/k_{eff} = 1/k_{obj} + 1/k_{str}$; in which k_{obj} and k_{str} are contact stiffness of the impacting object and the structural member, respectively. Equation (2) is based on an undamped single-degree-of-freedom (SDOF) system and can be obtained by considering energy conservation and a linear force-deformation relation i.e., $F(x) = k_{eff} x$ where x is deformation in the contact region. Although this approach is rational compared to the impulse-momentum consideration given in ASCE 7-10 (ASCE 2010) as it incorporates stiffness properties of impacting objects, the estimation of k_{eff} is not always straightforward in practical applications. The mass and effective stiffness values are provided in FEMA P646 for a few types of water-borne massive objects.

For example, consider a $20'$ shipping container with a tare weight of 2200 kg for velocities ranging from 0-10 m/s (Yeom et al. 2009) impacting on a structure. Using $k_{eff} = 1.5 \times 10^9$ N/m (FEMA 2008), the estimated peak impact forces obtained from Eqs. (1) and (2) are compared in Fig. 2. It is seen that, for instance, at a container velocity of 6 m/s the estimated peak impact force is 691 kN from ASCE 7-10 and 10,900 kN from FEMA P646 without considering added mass effect. This indicates that the above formulae are not consistent in the estimation of peak impact force and further investigations are warranted. In the present study, formulae to estimate peak forces on RC columns due to impact of shipping containers are obtained based on a series of numerical analyses.

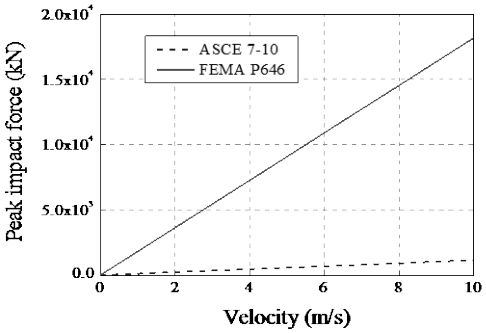


Fig. 2. Comparison of estimated peak impact force for $20'$ shipping container.

3. FINITE ELEMENT MODELING OF SHIPPING CONTAINER-COLUMN IMPACT

In the impact problem under consideration the finite element simulation takes into account the following critical modeling issues: (a) appropriate inelastic material models, (b) strain rate effects of the container and the RC column, (c) reinforcement slip in the column and (d) accurate modeling of contact. The explicit Lagrangian finite element code LS-DYNA (2007), used extensively for impact problems, is used in the present study.

3.1 Shipping Container

In the present study, A $20'$ (20 foot) standard shipping container which has a length of 6.06 m $(20')$, width of 2.44 m $(8')$, and height of 2.59 m $(8'6'')$ is considered (Maersk Line 2010, Magellan 2010). The different parts of the container which include corrugated panels, corner posts, top side rails, bottom side rails and cross members (see Fig. 3a) are modeled using 4-node Belytschko-Lin-Tsay shell elements (Belytschko et al. 2000). A finer mesh is used at

critical locations of the container which enhances the accuracy of the inelastic deformations of these parts. A coarse mesh is sufficient in non-critical locations where the container does not experience much of deformation during the impact (Figs. 3b and c). Hence, the 20′ container model consists of 64,608 nodes and 41,537 elements.

The material model MAT_PIECEWISE_LINEAR_PLASTICITY (MAT_024) with strain rate effects is used to represent material behavior of the container (LS-DYNA 2007). Previous studies have shown that this material model is computationally efficient for use with shell elements for impact simulations (Wu and Thomson 2007). The material properties density 7850 kg/m^3, Young's modulus 200 GPa, Poisson's ratio 0.3, yield strength 343 MPa, tensile strength 481 MPa and strain at fracture in tension 22%, and details of section sizes are given in container specifications (Maersk Line 2010, Magellan 2010).

3.2 RC Columns

Square and circular columns that are commonly used in buildings are considered for the impact simulation. The columns were designed and detailed only for gravity loads according to the requirement in ACI 318-08 (ACI 2008) considering a 3-story, 2-bay by 2-bay RC building, supporting $6\text{ m} \times 6\text{ m}$ slabs at each floor which carries uniformly distributed loads of 4.8 kN/m^2 representing live load on a typical office building, school or building for public assembly (ASCE 2010). The compressive strength of concrete f_c' is taken as 37 MPa. The axial load on the center column of the periphery which will be considered for the impact simulations is 340 kN. For comparison purposes, circular columns are chosen to have nearly the same cross-sectional area as the square columns.

The constant stress 8-node solid elements with one-point quadrature and the Hughes-Liu beam elements are used to represent concrete and reinforcing steel, respectively (Fig. 4a). Each concrete element in the square column is a 25 mm cube, and the element length of 25 mm is used in the circular column in axial direction. The longitudinal and transverse reinforcement are modeled using 25 mm long beam elements. The material models MAT_CONCRETE_DAMAGE_REL3 (MAT_072R3) and MAT_PLASTIC_KINEMATIC (MAT_003) are used for concrete and reinforcement, respectively (LS-DYNA 2007). More details of the RC column model which incorporates strain rate effect and bond slip and associated validation are given in Madurapperuma and Wijeyewickrema (2010).

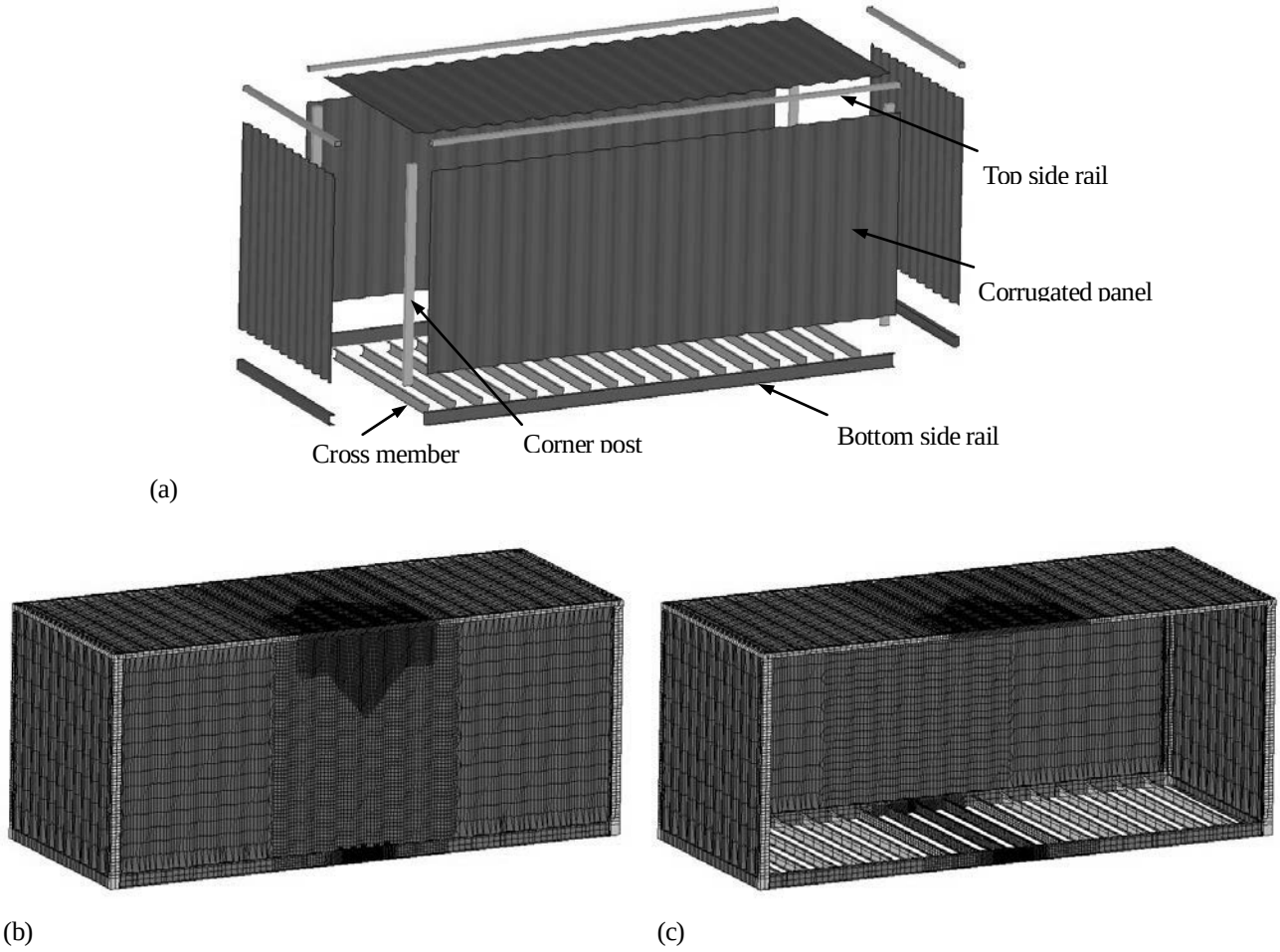
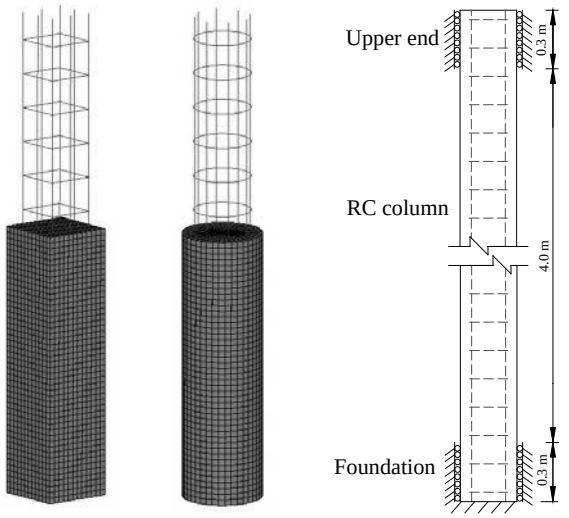


Fig. 3. (a) Different parts of the shipping container, (b) exterior view and (c) interior view.

The constraints provided by foundation and the upper end at the beam-column joint were included in the model as shown in Fig. 4(b).



(a) (b)

Fig. 4. (a) RC column models and (b) constraint conditions.

4. FORMULAE FOR PEAK IMPACT FORCE

Formulae to estimate peak impact forces on RC columns are obtained in terms of significant parameters using a series of container-column impact analyses. The parameters considered in the present study are transverse reinforcement ratio ρ_s, longitudinal reinforcement ratio ρ, column section size (width b or diameter d), and axial load ratio $P_N / f_c' A_g$ in which P_N is axial load, f_c' is compressive strength of concrete, and A_g is cross-sectional area of the column. In each analysis, the container height above ground level is 0.05 m and the container impacts with the column in the transverse direction (Fig. 5).

First, gravity loads acting on the column are applied as an axial load. This axial load is applied gradually to minimize inertia effects since the analysis is explicit dynamic. Next, container impacts the axially loaded column and the peak impact force on the column is obtained. The effect of each parameter on peak impact force is shown in Figs. 6-9. In these figures horizontal axis represent kinetic energy of the container before impact. The container mass is 2200 kg and the velocity varies from 1-10 m/s, and the corresponding kinetic energy varies from 1 to 110 kJ.

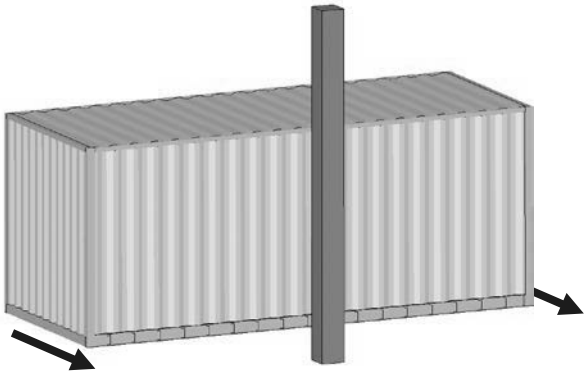
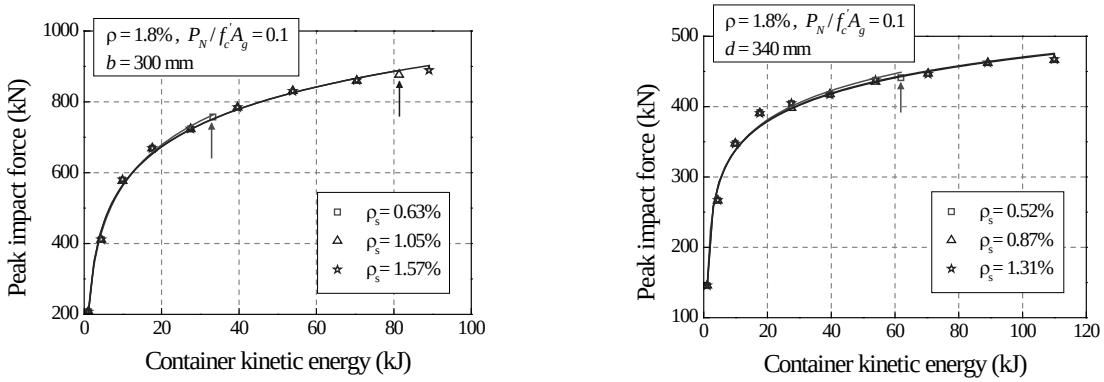
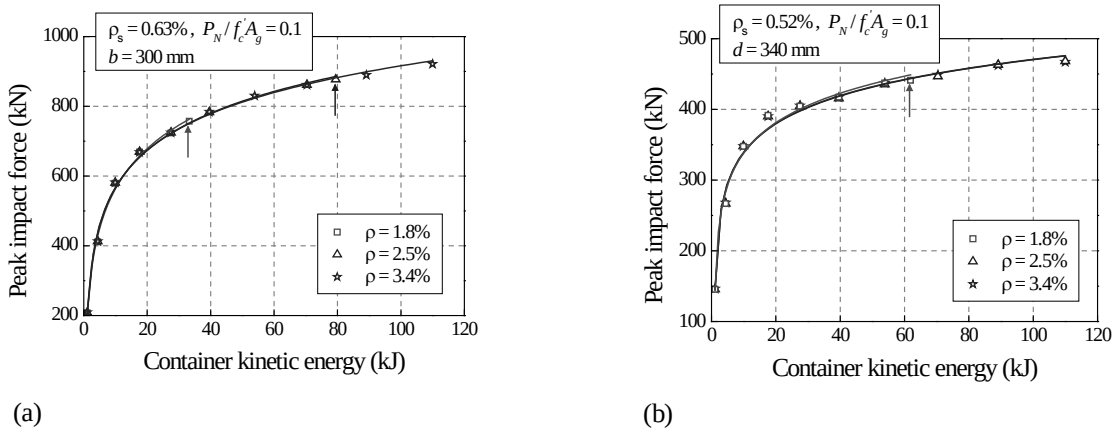


Fig. 5. Transverse impact configuration.



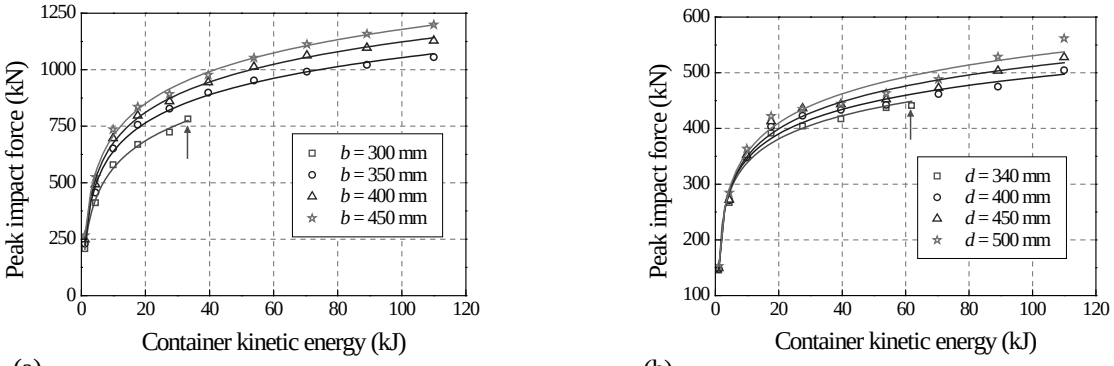
(a) (b)

Fig. 6. Effect of transverse reinforcement ratio on peak impact force: (a) square columns and (b) circular columns. The arrow indicates that for container kinetic energy beyond this that the column would collapse.



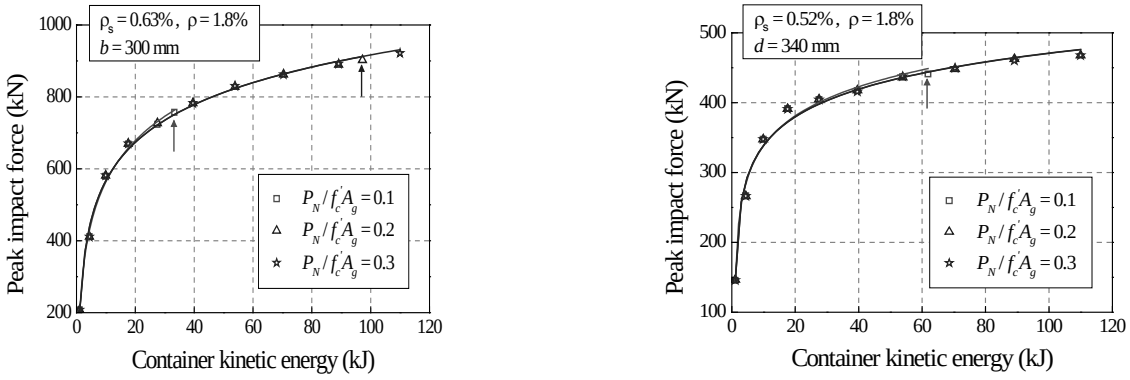
(a) (b)

Fig. 7. Effect of longitudinal reinforcement ratio on peak impact force: (a) square columns and (b) circular columns. The arrow indicates that for container kinetic energy beyond this that the column would collapse.



(a) (b)

Fig. 8. Effect of column section size (width or diameter) on peak impact force: (a) square columns and (b) circular columns. The arrow indicates that for container kinetic energy beyond this that the column would collapse.



(a) (b)

Fig. 9. Effect of axial load ratio on peak impact force: (a) square columns and (b) circular columns. The arrow indicates that for container kinetic energy beyond this that the column would collapse.

As shown in Figs. 6-9, the peak impact force increases with container kinetic energy but its rate of increase tends to decrease due to rapid degradation of container stiffness in the vicinity of contact. The numerical results revealed that the most significant parameter that affects the peak impact force is the column section size (width or diameter). The increase in the width (or diameter) of a column increases the number of cross members that simultaneously resist deformation, hence characterizing the sensitivity of force magnitude to column width (or diameter) as shown in Fig. 8.

Since, the peak force usually occurs early during an impact event and the column has no time to respond to the rapid change of loading, the effects of either reinforcement ratio or axial load ratio on the peak impact force are not significant. It is noted that several columns tend to collapse when the container kinetic energy is less than 110 kJ, i.e., equivalent to the kinetic energy of a container with mass of 2200 kg and velocity of 10 m/s, and indicated by an arrow in these figures.

Formulae to estimate the peak impact force are obtained in terms of column section size (width or diameter) and container kinetic energy using nonlinear regression analysis. For square columns, the corresponding formula is

$$F_p^{sq} = 117.8 + 261.6\, b + (70.6 + 306.9\, b)\ln(E_i), \quad (3)$$

where b is column width and E_i is kinetic energy of the container before impact. For circular columns, the formula is

$$F_p^{cir} = 175.9 - 27.9\, d + (40.9 + 79.8\, d)\ln(E_i), \quad (4)$$

where d is column diameter. In Eqs. (3) and (4) F_p^{sq} and F_p^{cir} are in kN, b and d are in m, and E_i is in kJ. It is noted that the proposed formulae are obtained by considering a container mass of 2200 kg and velocities ranging from 1 to 10 m/s, and the corresponding kinetic energy varies from 1 to 110 kJ. In the case of fully loaded container with a mass of 30,480 kg, the impacting kinetic energy typically varies within the considered range as the velocity of a water-borne container tends to decrease significantly with the increase of container mass (FEMA 2008). Hence, the range of kinetic energy considered is typical for impact of a tsunami water-borne shipping container.

The comparison of estimated peak forces from the proposed formulae with the numerical results is shown in Figs. 10 and 11. The solid lines in each plot denote curves obtained from the proposed formulae, and the dashed line denotes the curve obtained from the formula given by ASCE 7-10. The curves obtained from the above formulae for different column widths and diameters correlate very well with the numerical results. As shown in Fig. 10, for the square columns, ASCE 7-10 underestimates the peak impact force for kinetic energy $E_i < 60$ kJ. For the circular columns (see Fig. 11), the peak impact forces estimated by the proposed formula are less than those estimated by ASCE 7-10 when the kinetic energy $E_i > 8$ kJ. As noted in Section 2, the peak impact forces estimated by FEMA P646 are extremely conservative and differ by an order of magnitude and are not shown in Figs. 10 and 11.

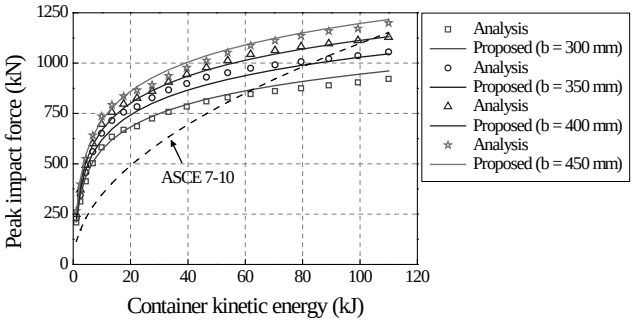


Fig. 10. Comparison of numerical results, proposed curves, and ASCE 7-10 estimate for peak impact force for square columns.

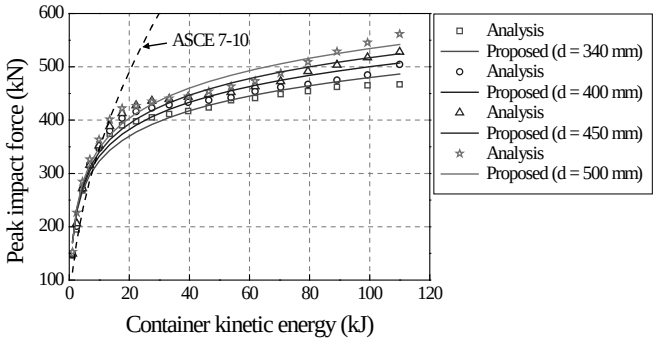


Fig. 11. Comparison of numerical results, proposed curves, and ASCE 7-10 estimate for peak impact force for circular columns.

5. CONCLUSIONS

Impact of tsunami water-borne shipping containers on RC columns was investigated using a detailed finite element model of the 20′ container which is a general purpose standard shipping container and a series of RC columns with square and circular cross-sections.

Formulae to estimate peak impact forces on RC columns are obtained in terms of column cross-section size and kinetic energy of the shipping container. The peak impact forces obtained from the proposed formulae compare well with the numerical results.

For the square columns, ASCE 7-10 underestimates the peak impact force when the kinetic energy is less than 60 kJ. For the circular columns, the peak impact forces estimated by the proposed formula are significantly less than those estimated by ASCE 7-10 when the kinetic energy is greater than 8 kJ. On the other hand, the peak impact forces estimated by FEMA P646 are extremely conservative and differ by an order of magnitude for both square and circular columns.

Acknowledgements:
The authors are very grateful to Professor Kohji Tokimatsu, GCOE Program Leader of Center for Urban Earthquake Engineering

(CUEE), Tokyo Institute of Technology, for his advice and support. Financial support from CUEE is gratefully acknowledged.

References:

ASCE. (2010), "Minimum design loads for buildings and other structures", Standard ASCE/SEI 7-10, American Society of Civil Engineers, Reston (VA).

ACI. (2008), "Building code requirements for structural concrete (ACI 318-08) and commentary", ACI Committee 318, American Concrete Institute, Farmington Hills (MI).

Belytschko, T., Liu, W.K. and Moran, B. (2000), "Nonlinear Finite Elements for Continua and Structures", Wiley, New York.

FEMA. (2008), "Guidelines for design of structures for vertical evacuation from tsunamis", Report FEMA P646, Federal Emergency Management Agency, Washington (DC).

Ghobarah, A., Saatcioglu, M. and Nistor, I. (2006), "The impact of the 26 December 2004 earthquake and tsunami on structures and infrastructure", *Engineering Structures*, **28**(2), 312-326.

Inoue, S., Wijeyewickrema, A.C., Matsumoto, H., Miura, H., Gunaratna, P., Madurapperuma, M.A.K.M. and Sekiguchi, T. (2007), "Field survey of tsunami effects in Sri Lanka due to the Sumatra-Andaman earthquake of December 26, 2004", *Pure and Applied Geophysics*, **164**(2-3), 395-411.

Kaushik, H.B. and Jain, S.K. (2007), "Impact of great December 26, 2004 Sumatra earthquake and tsunami on structures in Port Blair", *Journal of Performance of Constructed Facilities*, American Society of Civil Engineers, **21**(2): 128-142.

LS-DYNA. (2007), "Keyword user's manual", Livermore Software Technology Corporation, California.

Madurapperuma, M.A.K.M. and Wijeyewickrema, A.C., (2010), "Nonlinear behavior of reinforced concrete columns impacted by a tsunami water-borne shipping container", *Proc. of the Seventh International Conference on Urban Earthquake Engineering (7CUEE) and Fifth International Conference on Earthquake Engineering (5ICEE)*, Tokyo, Japan, p. 1795-1804.

Madurapperuma, M.A.K.M. and Wijeyewickrema, A.C. (2011), "Inelastic dynamic analysis of an RC building impacted by a tsunami water-borne shipping container", *Journal of Earthquake and Tsunami*, (accepted for publication).

Maersk Line. (2010), "Container equipment guide", Maersk Group. <http://www.maerskline.com/>.

Magellan. (2010), "Technical specification for a typical steel dry cargo container", Magellan Maritime Services GmbH. <http://www.magellan-maritime.de/cms/mdb/7/299.pdf>.

OpenSees. (2009), "Open system for earthquake engineering simulation", Pacific Earthquake Engineering Research Center, Berkeley (CA).

Robertson, I.N., Carden, L., Riggs, H.R., Yim, S., Young, Y.L., Paczkowski, K. and Witt, D. (2010a), "Reconnaissance following the September 29, 2009 tsunami in Samoa", Research report UHM/CEE/10-01, Department of Civil and Environmental Engineering, University of Hawaii at Manoa, Honolulu, Hawaii.

Robertson, I.N., Chock, G. and Morla, J. (2010b), "Tsunami effects of the February 27, 2010 Chile earthquake", EERI preliminary reports, Earthquake Engineering Research Institute, Oakland, California.

Wu, W. and Thomson, R. (2007), "A study of the interaction between a guardrail post and soil during quasi-static and dynamic loading", *International Journal of Impact Engineering*, **34**(5), 883-898.

Yeom, G-S., Nakamura, T. and Mizutani, N. (2009), "Collision analysis of container drifted by runup tsunami using drift collision coupled model", *Journal of Disaster Research*, **4**(6), 441-449.

8CUEE CONFERENCE PROCEEDINGS
8th International Conference on Urban Earthquake Engineering
March 7-8, 2011, Tokyo Institute of Technology, Tokyo, Japan

FLEXURAL BEHAVIOR OF BELLED PILE WITH HIGH-STRENGTH LONGITUDINAL REINFORCEMENT

Yo Hibino[1], Yasuji Shinohara[2], and Shizuo Hayashi[3]

1) Assistant Professor, Secure Materials Center, Tokyo Institute of Technology, Japan
2) Associate Professor, Structural Engineering Research Center, Tokyo Institute of Technology, Japan
3) Professor, Secure Materials Center, Tokyo Institute of Technology, Japan
hibino@serc.titech.ac.jp, yshinoha@serc.titech.ac.jp, hayashi.s.ac@m.titech.ac.jp

Abstract: A series of belled piles with high-strength longitudinal reinforcement were tested to investigate seismic performance focusing flexural behavior. In comparison with large diameter and small diameter piles with high-strength reinforcement, this paper presented that the flexural behavior of belled pile with high-strength longitudinal reinforcement was equivalent to the pile with normal-strength one; however, large splitting out of reinforcement and large rotation was occurred.

1. INTRODUCTION

The belled pile has been used for mid-rise or high-rise reinforced concrete buildings. Regarding design of the piles, the calculation of ultimate strength of belled pile is not required under AIJ guideline (1999) and ACI guideline (2008); however, the ultimate strength of belled pile after flexural yielding becomes major topic to ensure sufficient seismic capacity of buildings recently. To obtain enough capacity for large ductility, large flexural strength and shear strength is offered. Hence, large amount of reinforcement is offered, too.

Nagae et al. (2000) carried out experimental test of belled piles with high-strength transverse reinforcement and presented that the pile have large flexural capacity and longitudinal reinforcement tends to be overstuffed.

Then this paper presents flexural behavior of belled pile with high-strength longitudinal reinforcement to develop an ultimate strength design of that. The experimental tests were carried out to investigate the behavior of belled pile after flexural yielding.

2. EXPERIMENTAL TEST PROGRAM

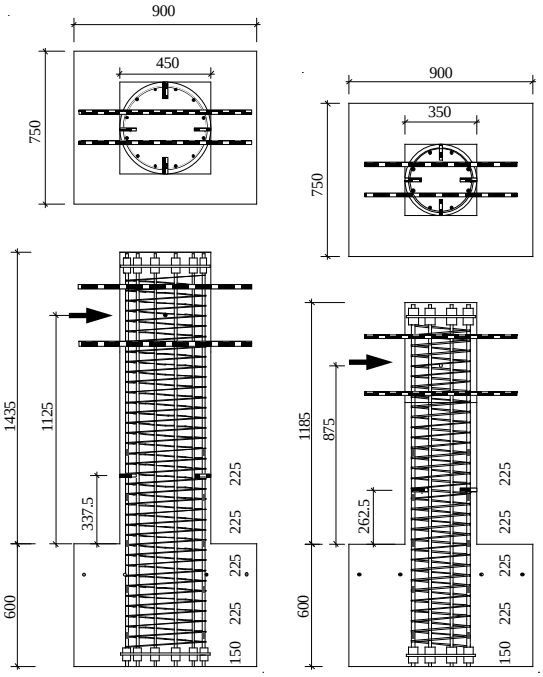
2.1 Test Specimens

A series of piles with high-strength longitudinal reinforcement were tested to investigate seismic performance focusing flexural behavior. A summary of the main properties of the specimens is shown in Table 1. The specimens were fabricated as 1/5-scale pile assuming the pile in mid-story reinforced concrete building and different diameters and different strength of longitudinal reinforcements were used to compare effect of those on flexural capacity. The prototype pile, L1 presented in Fig. 1(a) has 450 mm diameter with normal-strength longitudinal reinforcements, otherwise, the pile L2 has 450 mm diameter with normal-strength longitudinal reinforcements. The S

Table 1 Properties of test specimens

Specimen	D, mm	Longitudinal reinforcement			Transverse reinforcement			Axial Force, kN	σ_0, MPa	Concrete type	σ_0/f_c'
		Reinforcing bar	ρ_s, %	Strength	Reinforcing bar	ρ_w, %	Strength				
L1	450	12-D13	1.0	390	ϕ3.2@50 mm	0.08	1275	407.4	2.57	Fc25	0.1
L2	450	6-D16	0.8	685	ϕ3.2@50 mm	0.08	1275	407.4	2.57	Fc25	0.1
S1	350	8-D16	1.7	685	ϕ5.5@50 mm	0.31	1275	407.4	4.24	Fc25	0.17
S2	350	8-D16	1.7	685	ϕ5.5@50 mm	0.31	1275	407.4	4.24	Fc45	0.09
S3	350	8-D13	1.1	980	ϕ5.5@50 mm	0.31	1275	407.4	4.24	Fc25	0.17
S4	350	8-D13	1.1	980	ϕ5.5@50 mm	0.31	1275	407.4	4.24	Fc45	0.09

Note: D is pile diameter; M/VD is shear span-to-depth ratio; ρ_s and ρ_w is reinforcement ratio; σ_0 is effective stress on section.



(a) L1 (b) S2

Fig. 1 Geometric properties of test specimens (unit: mm)

Table 2 Concrete characteristics

Type	f_c' MPa	E_c MPa
Fc25	25.0	27000
Fc45	51.7	34700

Table 3 Steel characteristics

Type		f_y	E_s	f_{su}
No.	Strength	MPa	MPa	MPa
D13	390	422	584	185000
D16	685	708	832	179000
D13	980	987	1022	172000
ϕ3.2	1275	1677	1910	202000
ϕ5.5	1275	1535	1828	227000

series specimens have 350 mm diameter with high-strength longitudinal reinforcements. Fig. 1(b) shows the geometric properties of the pile S1. The amount of longitudinal reinforcements of each pile was determined by fiber analysis of section so that the flexural strengths of those were the same. The axial load was assumed as 407.4 kN considering dead load of mid-rise reinforced concrete building by the calculation provided by AIJ guideline (1999). The shear span-to-depth ratio, M/VD=2.5 was constant for all the specimens, which was assumed by Chang method whose N value is 3 in condition that a pile head was fixed. The compressive strengths of concrete were targeted as 25 MPa and 45 MPa. The 25 MPa was assumed as the same as generally used strength for belled pile and the 45 MPa was assumed to obtain fully yielding condition of longitudinal reinforcement (Suzuki et al., 1998). The material properties of steel, and concrete were shown in Table 2 and Table 3.

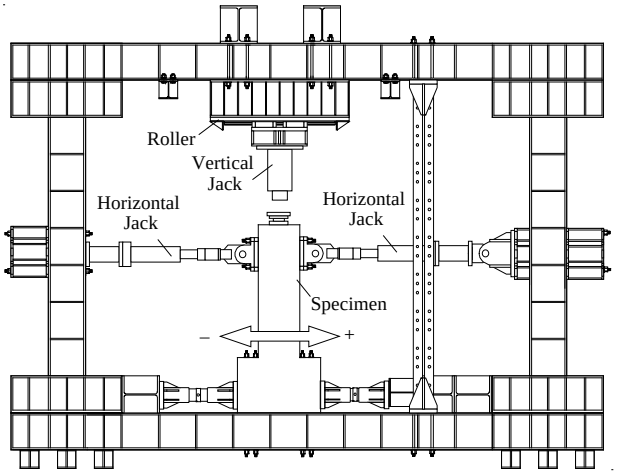


Fig. 2 Test setup

2.2 Test Setup

Bi-directional cyclic loading tests were conducted using the test rig shown in Fig. 2. The cyclic lateral load applied by cantilever system with two horizontal jacks who are installed on each side of the frame. A vertical jack is installed in the middle of the frame to apply a constant axial load at the top of the pile. A roller is placed between a vertical jack and the frame to free horizontal movement of the pile during lateral cycling loading while maintaining the vertical load. The plus and minus beside arrow symbol shows the loading direction. The tests were controlled by deflection angle, R obtained from the horizontal displacement divided by shear span length. The loading history was as follows: R=±1/400×1, R=±1/200×2, R=±1/100×2, R=±1/67×2, R=±1/50×2, R=±1/33×2 and R=±1/25×1.

2.3 Test Results

Comparisons between the measured lateral load versus deflection ratio for L1, L2, S1, S2, S3 and S4 are shown in Fig. 3(a) to (f), respectively. The broken-line on the figure indicates the predictions by AIJ guideline (1999). Square, diamond and circle symbols are drawn at the points where concrete crushing at the boundary surface, flexural yielding of longitudinal reinforcements and peak shear strength, respectively. The observed and predicted shear strength for the piles are summarized in Table 4.

The cyclic loading of all the specimens showed that large flexural capacity still after the deflection angle of 0.02 rad. Small strength degradation is observed when the defection angle was 0.04 rad. The prediction of the specimens S1 to S4 was a little smaller than the peak shear strength point, otherwise the predictions of the piles L1 and L2 are vice versa. The cyclic loading of the specimen with high-strength reinforcements shows larger stiffness while unloading, which makes hysteresis curves close to origin-oriented hysteresis. The effect of difference from diameter on flexural behaviors was not observed by comparing the pile between L2 and S1. The peak shear strength of the pile S2 and S4 were 20 % larger than that of the pile S1 and S3, respectively, which indicates that increasing of peak shear strength was attributed to the

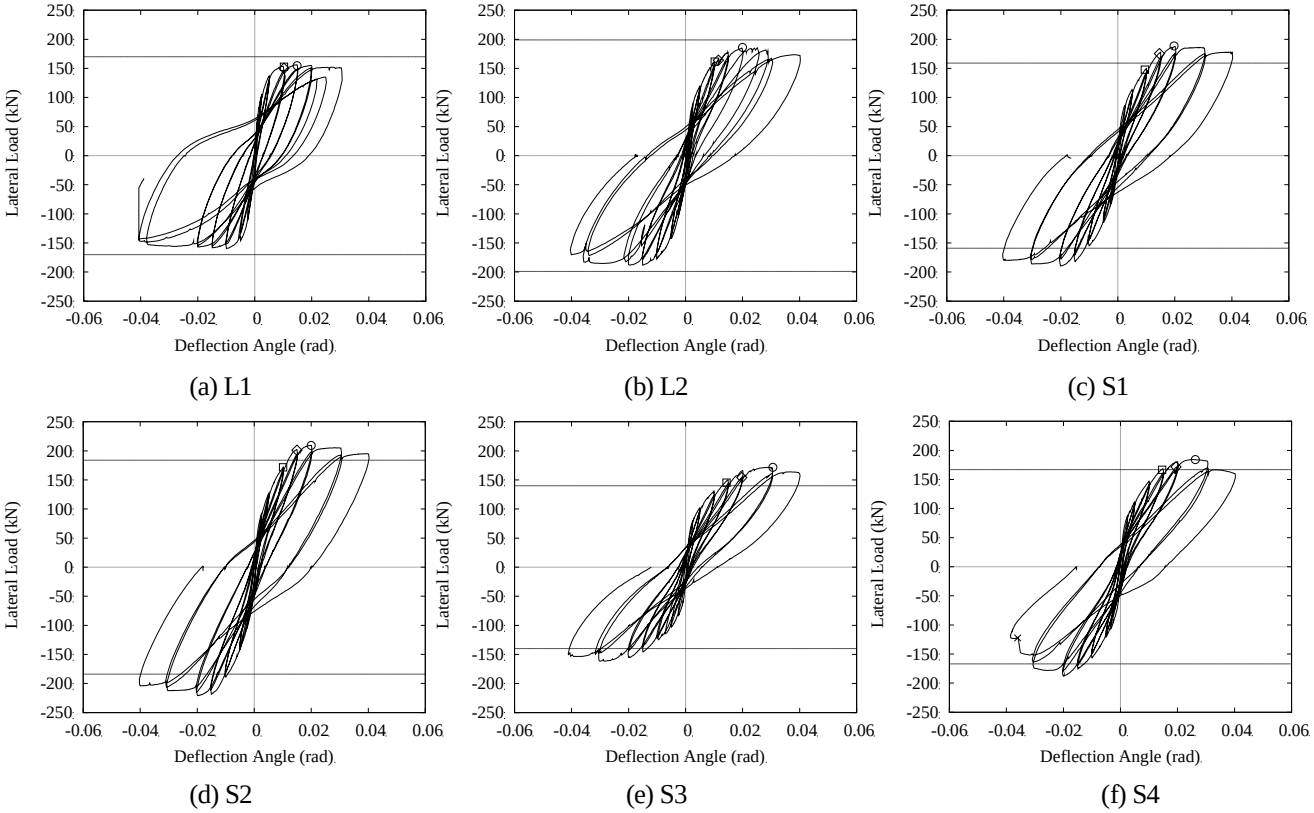


Fig. 3 Experimental lateral load-displacement relationship

Table 4 Summary of test results

Specimen	V_p kN	V_{exp} kN		V_{exp}/V_p
		Positive direction	Negative direction	
L1	170	156	160	0.94
L2	199	185	188	0.94
S1	159	188	190	1.19
S2	184	209	221	1.20
S3	140	172	161	1.23
S4	167	184	188	1.13

V_p is prediction; V_{exp} is peak strength.

Table 5 Comparison of post yielding stiffness

Specimen	R_y	V_y kN	Post yielding stiffness MPa	Ratio
L1	0.005	117	23000	1
L2	0.015	176	10700	0.47
S1	0.017	178	12200	0.53
S2	0.014	197	16600	0.72
S3	0.018	140	8780	0.38
S4	0.019	163	9940	0.43

concrete strength. Additionally, a fracture of reinforcement was observed only on the pile S4 where the point illustrated by x symbol on Fig. 3(f) with large strength degradation.

Comparison of obtained post yielding stiffness was shown in Table 5. The R_y and K_y represent the deflection angle at the flexural yielding and post yielding stiffness,

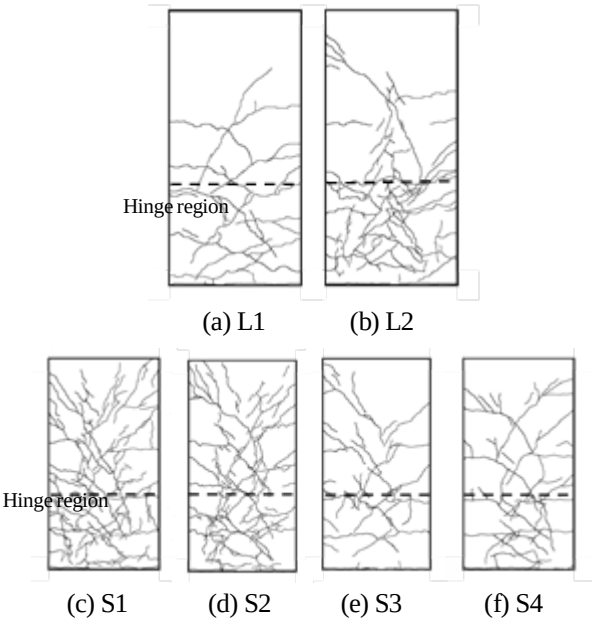


Fig. 4 Crack patterns of the piles after failure

respectively. The K_y was a stiffness obtained by a diagonal line connecting between origin and yielding point on relationship lateral load versus deflection.

The post yielding stiffnesses of the pile with high strength reinforcements were smaller than that of the pile L1; however, for the piles, S2 and S4, it was 10 % larger than that of the piles, S1 and S3, respectively.

The observed crack drawings are shown in Fig. 4. The blue, red and broken line represent the cracks at positive

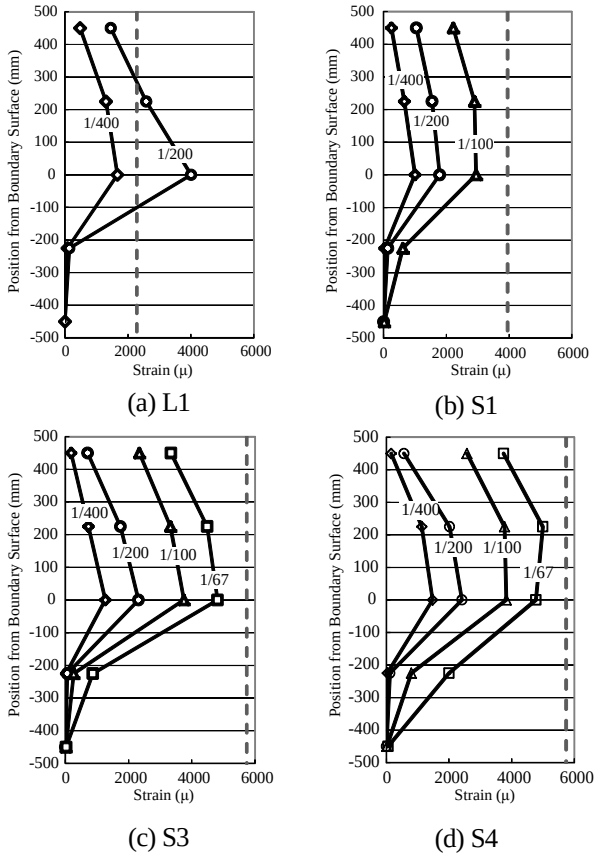


Fig. 5 Distribution of strain of longitudinal reinforcement

direction's loading, negative ones and height of the hinge region which was 0.85*D* height from the boundary surface, respectively.

The first bending cracks were observed at the boundary surface of pile. Then, the cracks were distributed toward to the top of piles as increasing shear force. After that, the shear cracks were observed as increasing the yielding of reinforcements. Distribution of shear cracks of the piles with normal-strength reinforcements was wider than that of the one with high-strength reinforcements, which indicates the rotation of the hinge region was distinguished.

2.4 Distribution of reinforcements' strain

Measured strain of longitudinal reinforcements for each cycle's loading: *R*=1/400, *R*=1/200 and *R*=1/100, is shown in Fig. 5 The y axis represents measured position from boundary surface. The positions of strain gage were illustrated in Fig. 1 with red rectangles. The broken line drawn in figure indicates the yield strain of reinforcements.

The strain of reinforcements at 0 mm was largest in all the piles till *R*=1/200; however, the strains of the piles S1, S3 and S4 were constantly increased after *R*=1/100 at the range between 0 mm and 225 mm where is inside of hinge region. The strain of the pile S4 is larger than that of the pile S3 when the deflection angle is *R*=1/67, which indicates that high-strength reinforcement of the piles with 45 MPa concrete is worked effectively for increasing flexural capacity.

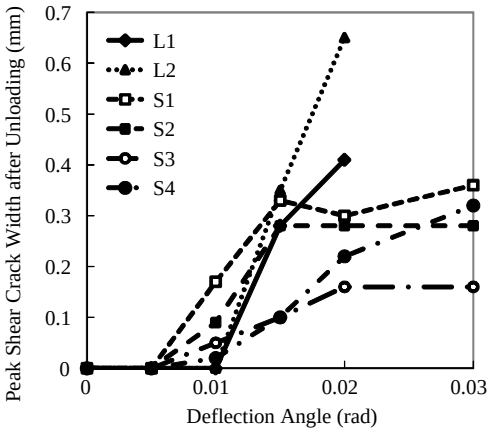


Fig. 6 Comparison of shear crack width and deflection angle

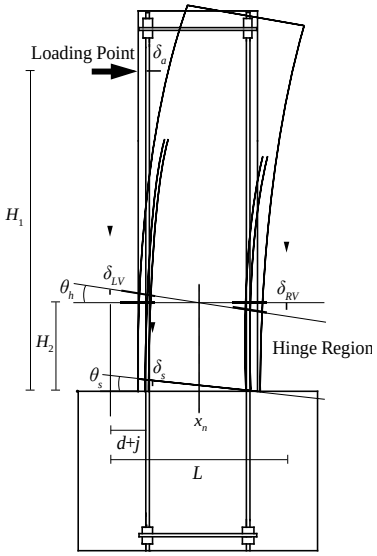


Fig. 7 Schematic of deflection measurement

2.5 Comparison of shear crack width and deflection angle

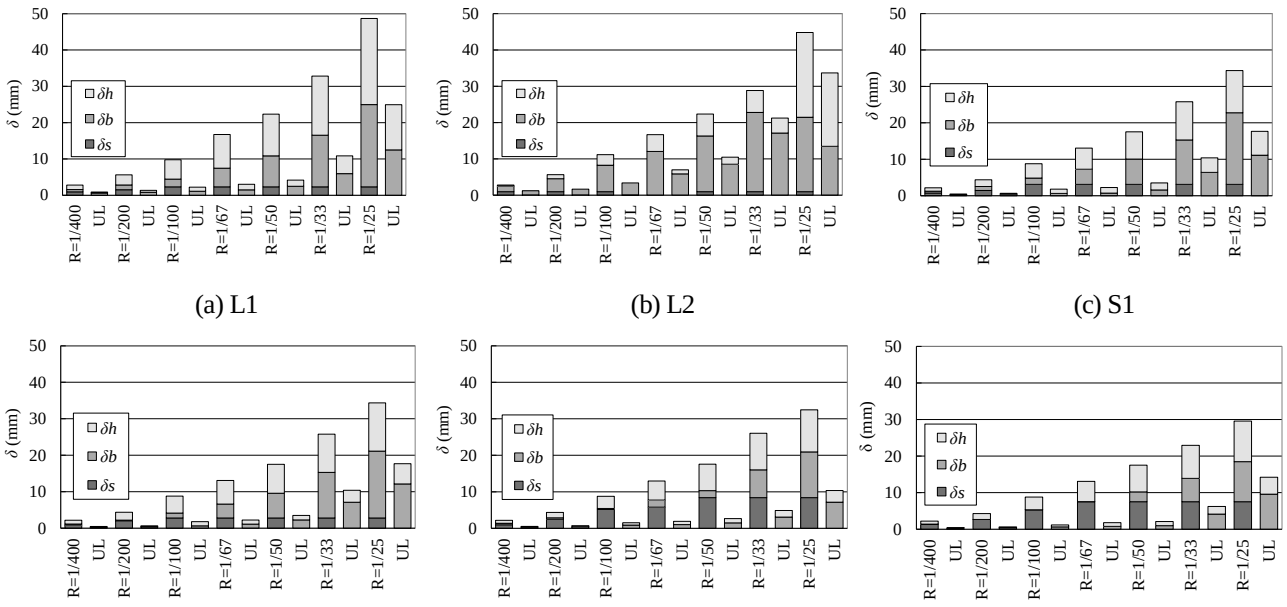
Relationship between shear crack width and deflection angle is shown in Fig. 6. The shear crack width was measured in a direction perpendicular to a crack and the diagonal crack which was extended from a bending crack was taken into account too. A digital microscope which has 0.01 mm limit of resolution was used for measurement.

Fig. 6 shows that cracks are the smaller when deflection angle is *R*=1/100, the larger the reinforcements' strength and concrete strength are. The cracks of the S series piles caused smaller cracks in ultimate state than that of the L series piles because of large transverse reinforcement ratio and large axial force. The piles with high-strength longitudinal reinforcement are effective for large earthquake to minimize damage in ultimate state.

2.6 Ratio of amount of deflection

To study a damage contribution of parts of the pile for total deflection, a ratio of amount of parts' deflection was calculated using measured displacement the parts.

The total horizontal displacement, δ_a is measured



(a) L1 (b) L2 (c) S1

(d) S2 (e) S3 (f) S4

Fig. 8 Ratio of amount of deflection

deflection by strain gauge-type transduces at the loading position's height. The rotation angle at hinge position, θ_h was assumed by following equation using vertical displacement measured by transducers installed on both side of the specimen which is shown in Fig. 7.

$$\theta_h = \frac{\delta_{LV} - \delta_{RV}}{L} \tag{1}$$

where δ_{LV} and δ_{RV} are vertical displacement of left and right, respectively; L is distance between δ_{LV} and δ_{RV}.

Herein, deflection caused by the pile's rotation at hinge region, δ_h is given by following equation using θ_h.

$$\delta_h = \theta_h \left(H_1 - H_2 \right) \tag{2}$$

where H_1 is shear span length; H_2 is height of hinge region.

The rotation angle at boundary surface is given by following equation on assumption that a neutral axis position, x_n at boundary surface is the same as that at hinge height. Note that the x_n was calculated by δ_{LV} and δ_{RV}.

$$\theta_s = \frac{l_s}{x_n - \left(d + j \right)} \tag{3}$$

where l_s is calculated length of slipping out of longitudinal reinforcement by integrating of measured strain placed in foundation (see Fig. 1); d is distance between tensile edge and rebar's position; j is distance from vertical transducer's position to the pile surface (see Fig. 7).

The deflection due to the hinge region's rotation occurred by slipping out of longitudinal reinforcement, δ_s is obtained by Eq. (4) and deflection due to bending of the pile, δ_b is given by Eq. (5). The deflection, δ_s is considered till before a cycle when reinforcement is yielded and after the cycle, the displacement was assumed as constant. Note that if the deflection, δ_s is larger than the deflection, δ_h, the deflection, δ_s is assumed to be equal to δ_h.

$$\delta_s = \theta_s \cdot H_1 \tag{4}$$

$$\delta_b = \delta_a - \delta_h \tag{5}$$

The ratio of amount of deflection at each cycle's loading and unloading is shown in Fig. 8. The UL of x axis represents unloading.

The deflection, δ_s of the pile L1 are smaller than the others at each cycle and that of the pile L2 is much smaller because of lesser numbers of reinforcement (see Fig. 9(a), 9(b)). For the pile L2, large residual deflection was observed at every cycle which indicates that the rotation due to a splitting out of reinforcements was distinguished. The displacement, δ_b of the pile S1 is larger than that of the others till R=1/33 cycle when a stiffness degradation was occurred (see Fig. 9(c)). Regarding of comparison between Fig. 9(c) and (e), the deflection, δ_s is the larger, the larger the strength of reinforcement is. For the pile S3, the deflection, δ_s is constant between R=1/400 and R=1/50; and after R=1/50, the bending deflection, δ_b was increased whereas the deflection due to splitting out of reinforcement, δ_s was decreased (see Fig. 9(e)). Therefore, large splitting out of longitudinal reinforcement and large rotation were attributed to large stain and large stress of high-strength reinforcements which makes a hysteresis similar to origin-oriented hysteresis (see Fig. 3). The effect of difference of concrete strength on flexural behavior could not be observed from the comparison of amount of deflections.

3. CONCLUSIONS

This paper focuces on the flexural behavior of belled piles with high-strength reinforcement. The bi-directional experimental tests of specimens were carried out. In

comparison with large diameter and small diameter piles with high-strength reinforcement, the following conclusions were obtained:

1. The flexural behavior of the pile with small high-strength reinforcement is almost equivalent to the pile with large normal-strength reinforcement.
2. Large splitting out of reinforcement occurred in the pile with high-strength reinforcement which causes large rotation and low post yielding stiffness; however, small shear cracks occurred.
3. Increasing of concrete strength does not affect the ultimate deformation capacity and causes ductile failure due to a fracture of longitudinal reinforcement; however, increase the post yielding stiffness.

Acknowledgements:

The authors wish to acknowledgement the supplier of the reinforcement; Neturen Co. Ltd., Tokyotekko Co. Ltd.

References:

American Concrete Institute (2008), Building Code Requirements for Structural Concrete (ACI 318-08) and Commentary, Michigan, USA.

Architectural Institute of Japan (1999), *AIJ Standard for Structural Calculation of Reinforced concrete Structures –Based on Allowable Stress Concept-*, Tokyo, Japan. (in Japanese)

Nagae, T., Wang, J., Katori, K., and Hayashi, S. (2000), "Shear Crack and Failure Process of Slip Reinforced Concrete Pile", *Concrete Journal*, Japan Concrete Institute, **22**(3), 619-624. (in Japanese)

Suzuki, K., Mishima, T., Sato, T., and Watanabe, T. (1998), "Experimental Test on Evaluation of Deformation Capacity of Reinforced Concrete Column Using High Strength Material", *Concrete Journal*, Japan Concrete Institute, **20**(3), 265-270. (in Japanese)

8CUEE CONFERENCE PROCEEDINGS
8th International Conference on Urban Earthquake Engineering
March 7-8, 2011, Tokyo Institute of Technology, Tokyo, Japan

SEISMIC DAMAGE MECHANISM CONTROL OF RC DUCTILE FRAMES FROM A STIFFNESS POINT OF VIEW

Zhe Qu[1], Lieping Ye[2] and Akira Wada[3]

1) Postdoctoral research fellow, Center for Urban Earthquake Engineering, Tokyo Institute of Technology, Japan
2) Professor, Department of Civil Engineering, Tsinghua University, China
3) Professor, Structural Engineering Research Center, Tokyo Institute of Technology, Japan
m.quzhe@gmail.com, ylp@tsinghua.edu.cn, wada@serc.titech.ac.jp

Abstract: Devastating earthquakes have shown the difficulty in preventing weak story failure in ductile moment resisting frames. Rather than relying on the strength hierarchy between columns and beams, it is attempted to handle this problem by providing additional continuous stiffness to the frame. The effect of continuous stiffness on the story drift concentration of frame structures is evaluated through nonlinear dynamic analysis. Preliminary equation of estimating the continuous stiffness demand is obtained. A rocking wall-frame system to implement continuous stiffness in concrete structures is then introduced. The effectiveness of rocking walls to control the deformation pattern of reinforced concrete frames is demonstrated through numerical simulations of an example rocking wall-frame structure.

1. INTRODUCTION

The difficulty in suppressing the unintended weak story failure in frame structures is evident from building damages in devastating earthquakes (Villeverda 1991; AIJ, 1991; Ye, 2009). As a well-known effort to control the failure mechanism of concrete structures, the capacity design methodology developed by Paulay and Priestley (1980, 1992) has lead to a widely accepted concept of strong column-weak beam for seismic design of ductile moment-resisting frames. Some amplification factor is applied to the flexural strength demands for columns as stipulated in major seismic codes in the world for decades in the hope of better ensuring the global failure mechanism (SNZ, 2004; ACI, 2005; GB50011, 2001). Such kind of design measures have, however, been frequently questioned by the professions in view of the many unintended weak story failures that actually happened in strong earthquakes (Bondy, 1996; Villaverde, 1997; Ye, 2009).

Strong column-weak beam type global failure mechanism should not be the ultimate goal of seismic design. Rather, it's only one of the ideas to control the deformation pattern in ductile frames and to prevent weak story failure. Rather than the strength hierarchy between beams and columns, MacRae *et al* (2004) revealed that continuous columns (e.g. gravity columns) in concentrically braced frames can reduce the story drift concentration. This effect was also examined by Ji *et al* (2010) in a more analytical manner. Tagawa (2005) extends this effort to moment-resisting steel frames. The appreciation of the global effect of continuous stiffness over the height of the structure may lead to another and more promising solution for the prevention of weak-story mechanism. In what follows, the relationship between continuous stiffness and inter-story drift concentration is examined. Rocking wall-frame system for multi-story reinforced concrete structure is introduced and its efficiency is demonstrated through numerical analysis.

2. EFFECT OF CONTINUOUS STIFFNESS

2.1 Numerical model

Lumped-mass shear model with continuous column is adopted herein to evaluate the effect of continuous stiffness on the story drift concentration, where the shear model represents the ductile moment-resisting frame. The continuous column is connected to the lumped mass by ideal horizontal links. The shear springs have peak-oriented hysteresis and continuous column is assumed linearly elastic and pinned at the bottom. Each lumped mass has only 1 DOF in the horizontal direction. The effect of vertical loads is not considered.

9, 6 and 3-story models are considered. It is assumed for all the models that the story stiffness and mass is identical for every story in the moment frame and the fundamental period of the frame is tuned to be 0.1*N*, where *N* is the number of story. The shear strengths of each story are proportioned in accordance with the Chinese seismic code (GB50011, 2001).

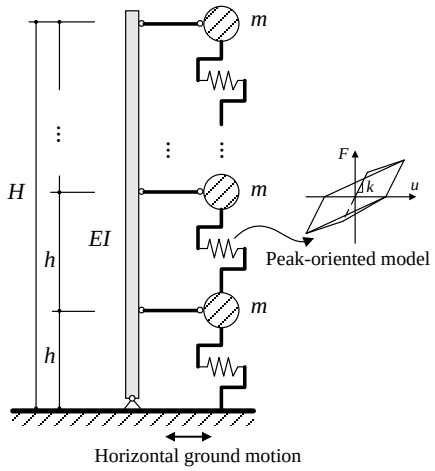


Figure 1 Lumped mass model with continuous column

As suggested by MacRae *et al* (2004), stiffness ratio α as defined in Equation 1 is used herein as a dimensionless measure of the continuous stiffness.

$$\alpha = \frac{EI}{kh^3} \tag{1}$$

where EI is the sectional bending stiffness of the continuous column, h is story height and k is story stiffness of the frame.

In the following discussion, α varies in the range of 0.001 to 10 by proportioning the cross section of the continuous column.

The models are subjected to a suite of 22 ground motion records selected from the PEER/NGA strong motion database as well as the China Strong Motion Network Center (CSMNC) database of the 2008 Wenchuan earthquake. All the ground motions are scaled so that the spectral acceleration at the structure's fundamental period $S_a(T_1)$ equals $\alpha_1 g$, where α_1 is the base shear coefficient in the seismic code and g is the acceleration of gravity.

2.2 Relationship of drift concentration-stiffness ratio

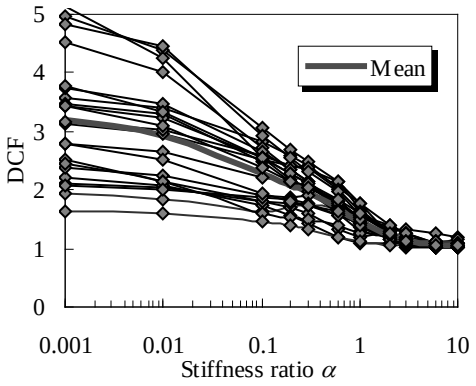
Nonlinear dynamic analysis is carried out and the drift concentration factor (DCF) results are shown in Figure 2. DCF is defined in Equation 2.

$$\mathrm{DCF} = \frac{\mathrm{IDR}_{\max}}{u_r / H} \tag{2}$$

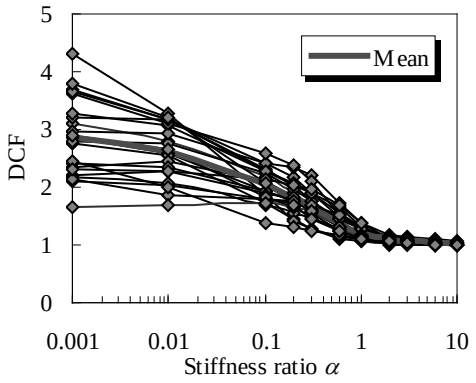
where $\mathrm{IDR}_{\max}$ is the maximum inter-story drift ratio among stories. u_r is the roof displacement and H is the total height of the structure.

DCF is considered as a measure of uniformity of the deformation pattern over the height of the structure. It is observed that DCF decreases rapidly with the increase of stiffness ratio α, suggesting that the continuous stiffness is very effective in reducing the inter-story drift concentration.

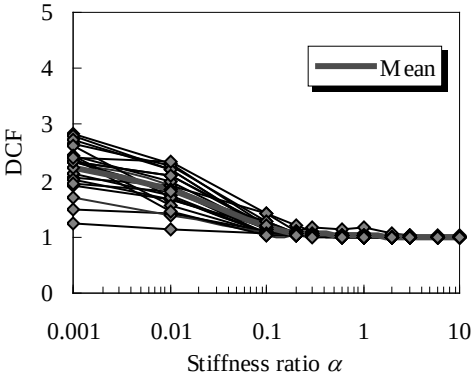
Besides, DCFs in higher structures are larger until α is large enough to produce a unity DCF, in which cases the continuous columns behaves almost like a rigid body rotating around the base pin.



(a) 9 story



(b) 6 story



(c) 3 story

Figure 2 Relationship between drift concentration factor (DCF) and stiffness ratio α

2.3 Continuous stiffness demand

Controlling target of DCF needs to be carefully chosen so that it can ensure high probability that weak story failure mechanism can be suppressed. It's considered not practical and also not necessary to require the DCF to be unity since unreasonably large continuous

stiffness would be required. Here the DCF of the 1st mode vibration of the structure is simply selected as the controlling target. The required α (denoted as α_{dem}) can be collected from the average curve of the above results for structures with different numbers of stories (Figure 3a). When plotted against the number of stories, α_{dem} shows an almost linear relationship with the number of storiy (Figure 3b).

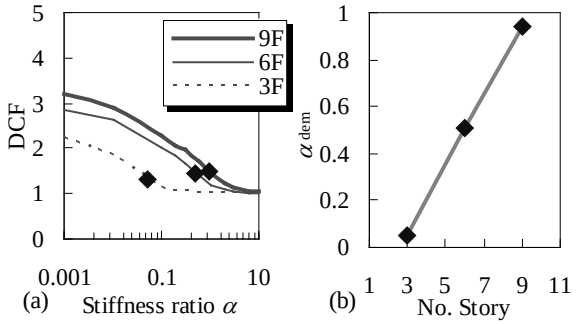


Figure 3 Relationship of number of story and demand stiffness ratio α_{dem}

Quantitative relation between α_{dem} and number of story N can then be found by linear regression as shown in Equation 3. With this equation, the required continuous stiffness can be readily estimated only from the number of story, based on which the cross sections of the continuous components can be checked and determined.

$$\alpha_{dem} = 0.148N - 0.368 \quad (3)$$

In what follows, this equation is used to estimate the required stiffness of rocking wall in order to prevent weak story failure in reinforced concrete moment frames.

3. CONTINUOUS STIFFNESS IN RC FRAME

3.1 Introduction to rocking walls

In steel frames, gravity columns serve as the continuous components that provide continuous stiffness to mitigate the risk of weak story collapse. In reinforced concrete frames, however, it's not easy to construct such gravity columns. Instead, concrete walls often provide strong resistance to weak story failure if shear failure in the wall can be successfully prevented. An innovative solution is provided and demonstrated by the retrofit project of G3 Building on the Suzukakedai campus of Tokyo Tech, in which post-tensioned continuous concrete walls with pin bearing at the bottom (so-called "rocking walls") are attached to the existing steel reinforced concrete frame (Wada *et al*, 2009).

To verify the effectiveness of rocking walls in controlling the deformation pattern, reinforced concrete (RC) moment frame as shown in Figure 4a is enhanced by replacing the middle column with a piece of rocking wall (Figure 4b). Their responses to strong ground motions are evaluated through nonlinear dynamic analysis.

The original RC frame is 8-story high and is seismically designed in accordance with the Chinese seismic code (GB50011, 2001). In the lower 4 stories, column cross section is 600❹800mm and beam cross section is 350❹700mm. In the upper 4 stories, the cross sections are reduced to 600❹600mm for columns and 300❹700mm for beams.

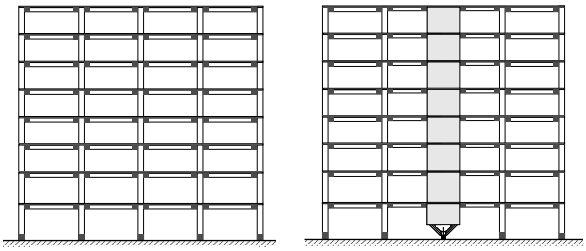


Figure 4 Pure frame and rocking wall-frame

In the rocking wall-frame structure (Figure 4b), the cross section dimensions of the rocking wall are determined based on the required continuous stiffness *EI* calculated from Equation 3. However, an amplification factor of 2.0 is imposed to consider the stiffness loss due to cracking of the rocking wall. The resulting cross section of the rocking wall is 3600❹300mm. The reinforcement of the rocking wall is shown in Figure 5. The rocking wall is supported by steel pin-bearing at the bottom which can resist large shear force while providing little rotational constraint.

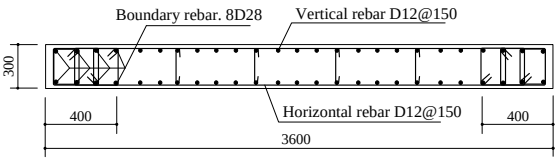


Figure 5 Reinforcement of rocking wall

3.2 Numerical assessment of damage mechanism

The above pure frame (F) and the rocking wall-frame (RWF) are modeled by fiber-based beam element in ABAQUS 6.8 with user-defined material models for concrete and steel fibers. Details of the user-defined material models can be found in Qu (2009). A set of 10 ground motion records are used as earthquake input, which is a subset of the above mentioned 22 ground motions used to evaluate the relationship between DCF and stiffness ratio α. In order to provide an identical earthquake scenario, the ground motions are scaled by non-structure-specific intensity measure PGV, rather than $S_a(T_1)$ as previously did. All the records are scaled to PGV=50cm/s.

3.3 Results and discussions

Inter-story drift ratio (IDR) responses of the rocking wall-frame (RWF) to the ground motion set are shown in Figure 6, where the mean and one deviation responses are compared with those of the pure frame (F). It is obvious that the maximum inter-story drift of the rocking wall-frame is much smaller than that of the pure frame. Most importantly, deformation in the rocking wall-frame is more uniformly distribution over the height of the structure compared to the pure frame. The drift concentration factors (DCF) of rocking wall-frame under various ground motions are much smaller than those of the pure frame (Figure 7).

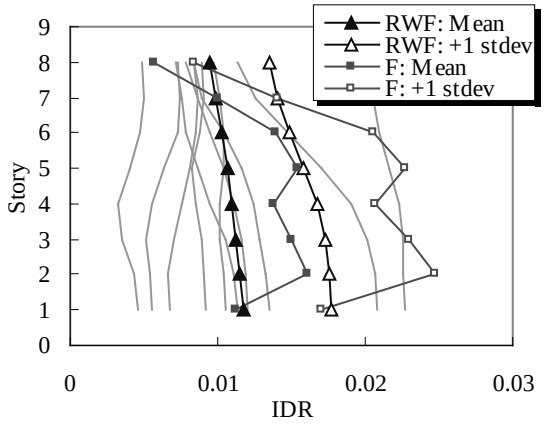


Figure 6 Inter-story drift ratios (IDR) of rocking wall-frame

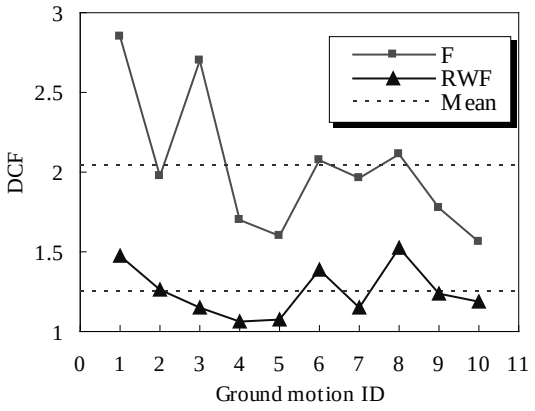
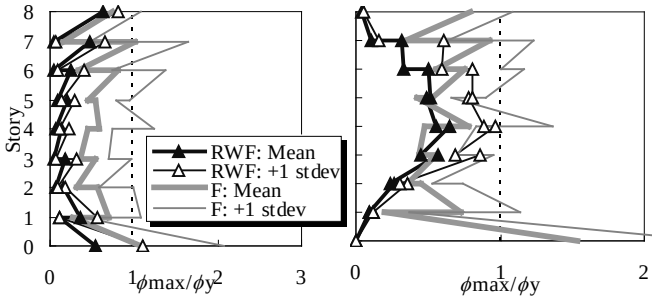


Figure 7 Drift concentration factors (DCF) of rocking wall-frame and pure frame

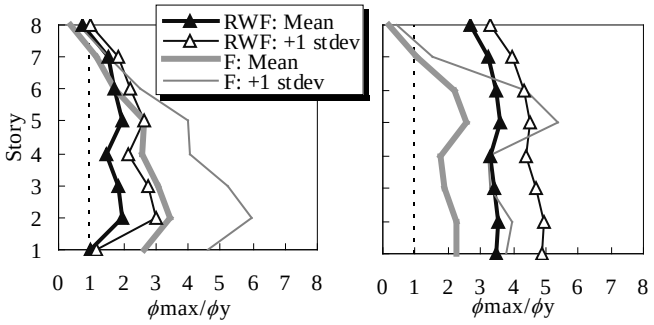
In terms of curvature ductility ϕ_{max}/ϕ_y, Figure 8 and 9 compare the damage mechanism of the rocking wall-frame and pure frame. There's only marginal damage in the rocking wall and columns in the rocking-wall frame structure as the mean and one deviation ductility are almost below 1.0 (Figure 8). On the other hand, damages to the beam ends in the middle span of the rocking wall-frame are increased and more uniformly distributed (Figure 9). They concentrate the energy dissipation of the whole structure.

From these results, the effectiveness of the rocking wall to control the deformation patter and damage mechanism is demonstrated.



(a) Side column (b) Rocking wall

Figure 8 Curvature ductility (ϕ_{max}/ϕ_y) in columns and rocking wall



(a) Beam in the side span (b) Beam in the middle span

Figure 9 Curvature ductility (ϕ_{max}/ϕ_y) in beams

4. CONCLUSIONS

An attempt is made to control the seismic damage mechanism and to prevent weak-story failure in ductile moment frames by continuous stiffness. The effect of continuous stiffness on the drift concentration of frame structures are evaluated through simple numerical models and preliminary equation of estimating the required stiffness ratio α is obtained assuming the controlling target to be the DCF of the 1st mode vibration. Rocking wall-frame system is introduced as a manner to increase the continuous stiffness for reinforced concrete frame. A case study of an 8-story ductile RC frame is provided which demonstrated the effectiveness of the rocking wall to control the seismic damage mechanism.

Acknowledgements:

The authors acknowledge support from National Natural Science Foundation of China (Major program No. 90815025), Ph.D. Programs Foundation of Ministry of Education of China (No. 200800030001) and Special program fund of Ministry of Construction of China.

References:

ACI 318M-05 (2005), "Building code requirements for structural concrete and commentary". Farmington Hills, Michigan, US: American Concrete Institute.

AIJ (1997), "Report on the Hanshin-Awaji earthquake disaster-Building series volume 1: Structural damage to reinforced concrete building". AIJ. (in Japanese)

GB50011 (2001), “Code for seismic design of buildings”. Ministry of Construction of China, Beijing.

Ji, X.D., Kata, M., Wang, T. et al. (2009), “Effect of gravity columns on mitigation of drift concentration for braced frames”. *Journal of Constructional Steel Research*, **65**(12), 2148-2156.

MacRae, G.A., Kimura, Y., Roeder, C. (2004), “Effect of column stiffness on braced frame seismic behavior”. *Journal of Structural Engineering, ASCE*, 130(3), 381-391.

Paulay, T. (1983), “Deterministic design procedures for ductile frames in seismic areas”. *ACI publication*, **SP-63**, 357-381.

Paulay, T., Priestley, M.J.N. (1992), “Seismic design of reinforced concrete and masonry buildings.” New York: John Wiley & Sons, Inc.

Qu, Z. (2010), “Study on seismic damage mechanism control and design of rocking wall-frame structures.” Beijing: Doctor thesis, Tsinghua University. (in Chinese)

SNZ (2004), “Concrete structures standard (NZS 3101.1).” Standards New Zealand, Wellington, New Zealand.

Tagawa, H. (2005), “Towards an understanding of seismic response of 3D structures - stability & reliability”. Doctor Thesis, Washington: University of Washington.

Villaverde, R. (1991), “Explanation for the numerous upper floor collapses during the 1985 Mexico City earthquake.” *Earthquake Engineering & Structural Dynamics*, **20**(3), 223-241.

Villaverde, R. (1997), “Discussion of ‘A more rational approach to capacity design of seismic moment frame columns’ By K. Dirk Bondy.” *Earthquake Spectra*, **13**(2), 321-322.

Ye, L.P., Lu, X.Z., Zhao, S.C., et al. (2009), “Seismic collapse resistance of RC frame structures.” *Journal of Building Structures*, **30**(6), 67-76. (in Chinese)

Wada, A., Qu, Z., Ito, H., et al. (2009) “Seismic retrofit using rocking walls and steel dampers”. Proc. ATC/SEI Conference on Improving The Seismic Performance of Existing Buildings and Other Structures, San Francisco, CA, U.S., Dec. 2009

8CUEE CONFERENCE PROCEEDINGS
8th International Conference on Urban Earthquake Engineering
March 7-8, 2011, Tokyo Institute of Technology, Tokyo, Japan

SEISMIC ANALYSIS OF RC STRUCTURE UNDER MULTIPLE EARTHQUAKES

Bin Wang[1)], Huanjun Jiang[2)], and Xilin Lu[2)]

1) Ph.D. Candidate, State Key laboratory of Disaster Reduction in Civil Engineering, Tongji University, Shanghai, P.R.China
2) Professor, State Key laboratory of Disaster Reduction in Civil Engineering, Tongji University, Shanghai, P.R.China
2008wangbin@tongji.edu.cn, jhj73@tongji.edu.cn, lxlst@tongji.edu.cn

Abstract: Structures during their service life time may be attacked by one or more aftershocks within a short period following the occurrence of mainshock or different earthquakes occurring at different time. Multiple earthquakes may have the potential to cause more extensive structural damage and property loss due to accumulated effect. Most of previous research focused on the responses of structures due to single earthquake. In this study, reinforced concrete (RC) structure under multiple earthquakes is investigated based on the concept of accumulated damage, and damage accumulation is analyzed in terms of maximum inter-storey drift and damage development. The results demonstrate that the responses of the structures subjected to multiple earthquakes may lead to more structural damage. Under multiple earthquakes in different sequence, the subsequent damage evolution is not consistent.

1. INTRODUCTION

Around the world, there are many areas where earthquakes occur as a series shocks. After an earthquake of large magnitude (referred to as mainshock), many induced multiple earthquakes or aftershocks (hereafter referred to as the general name of aftershocks) will occur due to the reason that the fault rupture does not usually relieve all accumulated energy at once (Figure 1). Earthquake aftershocks may have the potential to cause more extensive structural damage and property loss due to accumulated effect. Occasionally, they can result in building collapse. This risk of collapse is very high for previously damaged buildings. These buildings in 2008 Wenchuan, China, are generally unstable and may collapse in an aftershock (Figure 2). The study of aftershocks will be one of branches of the more familiar study of modern Performance-based Earthquake Engineering (PBEE).



Figure 1 Aftershock distribution for the 2010 Haiti earthquake through 21 January 2010 (from USGS)



Figure 2 Damaged buildings in Wenchuan earthquake

Most of previous research focused on the response of structures due to single earthquake, which neglected two main points: (1) the development of accumulated damage of overall structure and its components; and (2) the change of structural dynamic properties. It should be noted that related research about buildings under multiple earthquakes have risen recently (Lee and Foutch 2004, Luco et al. 2004, Li and Ellingwood 2007, Yeo and Cornell 2009, Abdelnabi and Elnashai 2009), however, the focuses of these studies were different. The following section presents the information from the literatures.

It should be pointed out that the earthquake damage survey and shaking table tests are the more direct assessment approaches to evaluate the effect of accumulated damage. However, it is still very hard to grasp the development of the damage accumulation in detail by using these methods. Meanwhile, most of these studies were limited to the specific structures, and there are no the generally conclusions.

In this study, a reinforced concrete (RC) structure under multiple earthquakes based on the concept of accumulated damage is investigated, and damage accumulation is analyzed in terms of maximum inter-storey drift and damage development. Numerical models are established using commercial nonlinear structural analysis program. Ground motions are input using multiple earthquakes concept.

2. RELATED RESEARCH

The related research presented here focused on the responses of structures based on multiple earthquakes or using the concept of residual capacity to account for accumulated damage in structures.

In the previous cited paper by Lee and Foutch (2004), the performance of damaged buildings subjected to a sets of ground motions representing different hazard levels were conducted. Mainshock-aftershock sequences were modeled by back to back identical accelerograms, which is a conservative (unlikely) occurrence.

In 2004, Luco et al. (2004) put forward a static approach for computing the median residual capacity of a mainshock-damaged building in term of the aftershock ground motions. The static approach based on the result of back to back mainshock-aftershock nonlinear dynamic analyses of case-study building models. Such study involved the use of residual capacity (residual roof drift) regarding the effect of aftershock.

Li and Ellingwood (2007) explored the relationship between the mainshock and aftershock in term of their respective intensities, and stochastic structural response and damage patterns were calculated based on two steel moment frames.

A parametric study was conducted by Yeo and Cornell (2009) based on specific case examples to illustrate the effect of ground motion intensity, duration, elapsed time from mainshock, mainshock magnitude, site location and structure periods on aftershock hazard. Such research results are useful for how to quantify the aftershock when considering its effect.

Abdelnabi and Elnashai (2009) made a study of response of RC buildings under multiple earthquakes, and also pointed out the previous research shortcomings. However, the substantial conclusions were absent owing to lack of numerical analysis.

Therefore, this study focuses on the damage accumulation and the change of structural dynamic properties based on a 12-storey RC moment frame subjected reasonable multiple earthquakes.

3. ANALYSIS METHODOLOGY

Computing the effect of multiple earthquakes by numerical simulation, elapsed time from mainshock should be considered. In most cases, we can assume that the structure is under a "static" state before the following earthquakes. In such a "static" state, there are no acceleration, speed and inertia on structure, but there may be residual deformation. In this case, to consider the structure under accumulated damage, the damaged performance will be inherited including structural strength and stiffness degradation, residual deformation and change of damping ratio.

4. SIMULATION OF RC MOMENT FRAME

4.1 Description of the Structure

The elevation and plan of the 12-storey RC building, as well as the typical reinforcement of columns and beams, are shown in Figure 3. The columns have dimensions: 600mm×600mm. The two exceptions are columns B (Figure 3), which have dimensions: 700mm×700mm. All the beams have rectangular cross-sections, with the width of 350mm and height of 500mm. The slabs have a thickness of 100mm. To simplify the analysis, the component dimension does not change in overall building.

The structure was designed according to Code for Seismic Design of Buildings (GB50011-2001) for a fortification intensity of 7, soil type Ⅳ. A permanent load of 8kN/m^2 was assumed, and a live load of 2kN/m^2 was adopted in the design of the structure. The only exception is the roof, which have a permanent load of 9 kN/m^2 and a live load of 0.5kN/m^2. Concrete with quality C30 and Q335 longitudinal reinforcement (yield strength of normalized value amounts to 335MPa) were used for the construction of described building. The transverse reinforcement type is Q235, whose yield strength of normalized value is 235MPa.

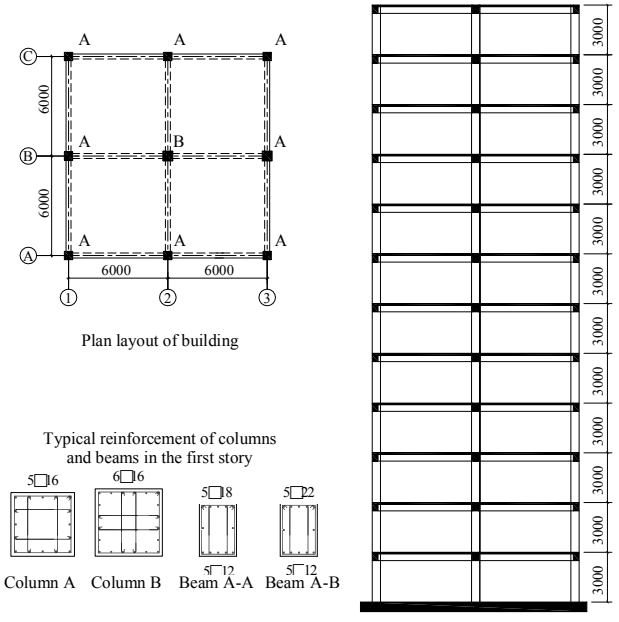


Figure 3 The 12-storey RC moment resistant frame building

4.2 Nonlinear Model for Dynamic Analyses

Nonlinear dynamic analyses were conducted for the 12-storey frame with different ground motions. The computer software for three dimensional nonlinear and dynamic structural analysis CANNY (Li 2009) was selected for the analyses. The mass of each floor was lumped at the column joints according to the tributary areas.

The beams were modeled as linear elastic elements

with two inelastic single-component flexure rotation springs located at the ends of the member. Columns were simulated by multi-axial spring model (called MS model), which was developed to reproduce the behavior of flexure and axial deformation of column element. The MS model has a line element and two multi-axial spring element at the column ends. Meanwhile, the multi-shear-spring model, which was arranged at equal angle in the section at column middle span, was intended to simulate the biaxial shear behavior of column element subjected to bi-directional lateral loads. The frame joints were assumed to be rigid and rigid zones were applied at the ends of each member (although this assumption does not conform to reality). Figure 4 shows the idealization of different members of the studied frames.

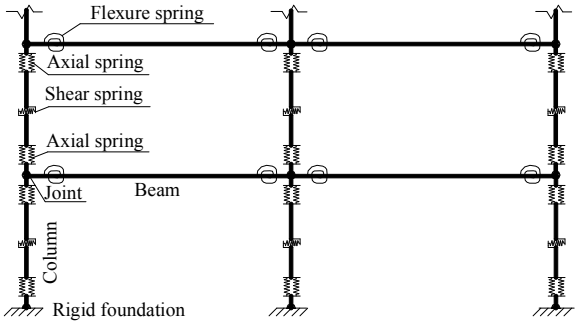


Figure 4 Analytical model of the studied frame

Unlike linear analysis, where the elastic stiffness and percentage of critical modal damping remain constant, in nonlinear analysis the stiffness matrix softens due to inelastic effects, and the relative significance of damping can change dramatically during the analysis. For example, consider a case where the damping matrix is defined based on the initial elastic stiffness and the fundamental period of vibration. If the damping matrix is fixed during the analysis, then as the structure softens and the effective first-mode period elongates, the percentage of damping in the elongated fundamental mode will tend to increase. The relative significance of the damping matrix would increase as the stiffness matrix softens. Considering the structure under multiple earthquakes, such a change of damping ratio ought to be adopted in our study. In the paper, the approach of renew damping at stiffness change is conducted, so it make the program extract mode and re-evaluate the damping coefficients for stiffness matrix proportional damping in the occurrence of stiffness changes.

4.3 Properties of the Selected Ground Motions

The selection of appropriate ground motions for a given structure from available records represents a crucial task in earthquake engineering. The selection of records for the site is generally based on the magnitude, the site-source distance and the local soil condition. Although many aftershock accelerations were recorded in past research, to obtain some general conclusions, some certain ground motions were selected.

Select a representative set of three ground motions were applied as input accelerations based on the site condition, without regard to the fault mechanism, magnitude and attenuation relationships. Quantifying these uncertainties is beyond the scope of this paper.

The selected ground motions included two natural records and one artificial wave. Figure 5 shows the comparison of response spectrum of input seismic waves and design spectrum in GB50011-2001 Code.

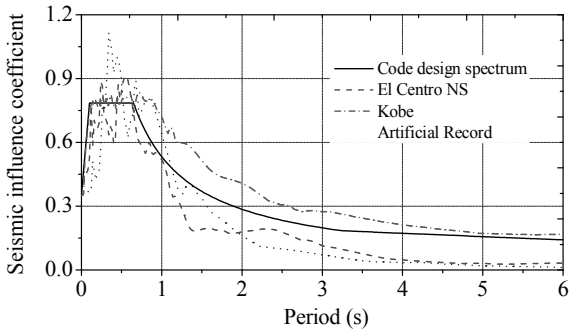


Figure 5 Comparison of response spectrum between code design spectrum and selected ground motions

4.4 Analytical Procedures

Researchers have to agree that the characteristics between a mainshock and its following aftershock is related on many factors, including intensity or magnitude, the effect of duration, elapsed time from mainshock and site location, all of which exhibit some stochastic effects. Identifying all such information is a complex task that beyond the scope of this paper.

Referring to the research approach adopted by Lee and Foutch (2004), the mainshock and aftershock accelerograms were repeated in this study with appropriately scaled intensity for simplicity. This is a deterministic and extreme condition procedure. The hazard levels were considered by the following way: 2% and 63% probability of exceedance in 50 years.

In the proposed methodology, same ground motion was selected with different intensity as its aftershock under the assumption that some certain degree of correlation in aftershock locations is potentially to be expected given that they are induced by the mainshock.

5. ANALYSIS RESULTS

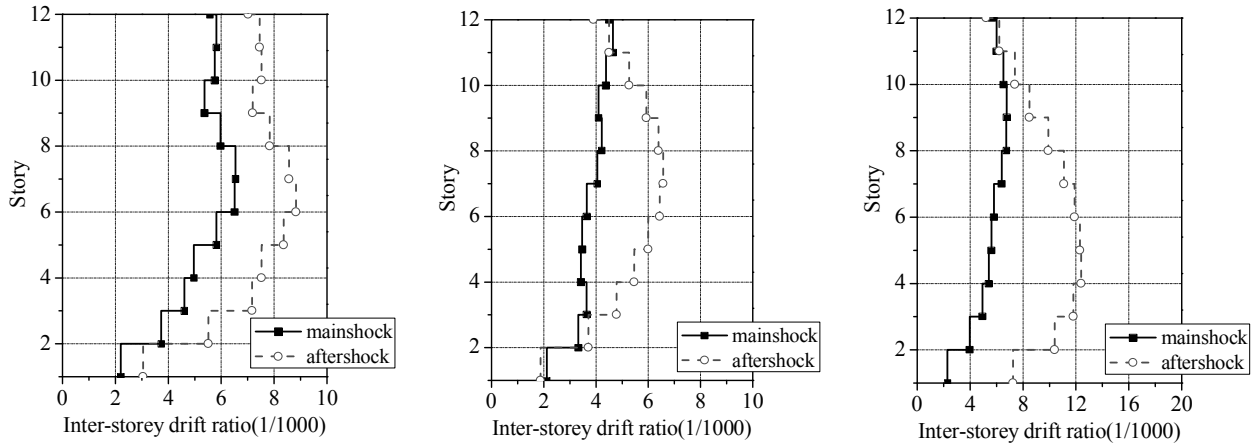
5.1 Damage Development under Different Hazards

Assuming that the structure did not experience a local and global collapse, the damage states of the building were recorded under different intensity ground motions, which simulated the effect of aftershock.

To simplify the outcome, some typical components, including three columns and two beams at Floor 1, were selected to show the damage development. Table 1 indicates the damage pattern that subjected to different hazard levels.

Table 1 Comparison between damage of multiple earthquakes to some typical components

Component	El Centro		Kobe		Artificial wave	
	2%/50	63%/50	2%/50	63%/50	2%/50	63%/50
C1 (X1-Y1 1F)	50.0% concrete tension crack at bottom ends	67.5% concrete tension crack at bottom ends	60.8% concrete tension crack at bottom ends	60.8% concrete tension crack at bottom ends	68.1% concrete tension crack at bottom ends	component yield
C2 (X2-Y1 1F)	39.1% concrete tension crack at bottom ends	56.6% concrete tension crack at bottom ends	50.1% concrete tension crack at bottom ends	60.8% concrete tension crack at bottom ends	60.1% concrete tension crack at bottom ends	component yield
C3 (X2-Y2 1F)	50.0% concrete tension crack at bottom ends	77.1% concrete tension crack at bottom ends	61.7% concrete tension crack at bottom ends	61.7% concrete tension crack at bottom ends, 5.7% concrete tension crack at top ends	61.7% concrete tension crack at bottom ends	61.8% concrete tension crack at bottom ends
B1 (X1-X2 Y1 1F)	Concrete of two ends cracks	Concrete of two ends cracks	Concrete of two ends cracks	Concrete of two ends cracks	Concrete of left ends cracks	Concrete of two ends cracks
B2 (X1-X2 Y2 1F)	Concrete of two ends cracks	Concrete of two ends cracks	Concrete of two ends cracks	Concrete of two ends cracks	Concrete of left ends cracks	Concrete of two ends cracks



(a) El Centro (b) Kobe (c) Artificial wave

Figure 6 Comparison of inter-storey drift between mainshock and aftershock

An amount of additional damage occurred for the aftershock analysis. Significant differences of damage development were observed between different ground motions.

5.2 Inter-storey Drift Analysis

The second input of 63%/50 accelerograms resulted in the inter-storey drift of overall structure further increased. Results for the building are shown in Figure 6.

Compared to El Centro and Kobe, the second input of artificial wave leads to the inter-storey drift increase obviously. This is consistent with the damage development results shown in Table 1, which indicates that more damage develops under artificial input.

5.3 Change of Natural Period of Vibration

The change of natural period of vibration is a good indicator to performance evaluation. Previous study had rarely focused on such point. According to the change of nature period, the degradation of structural stiffness could be obtained quickly.

Table 2 Natural period of vibration before and after different ground motions

Input	Undamaged (s)	After 2%/50 Input (s)	After 63%/50 Input (s)
El Centro	1.304	3.34	3.40
Kobe	1.304	3.37	3.50
Artificial	1.304	3.73	4.37

The natural period of building before and after each ground motion input is given table 2.

6. SUMMARY AND CONCLUSIONS

This study focused on the potential effect of multiple earthquakes, which might cause more extensive structural damage and change the dynamic property of the structure. The research about structure under multiple earthquakes has risen recently. However, the focuses of these studies are different.

Three ground motions were selected to evaluate the effect of back-to-back earthquakes on different hazard levels. The results demonstrate that, the second input could cause structural damage and inter-storey drift also increased. It should be pointed out that the purpose of this paper is to describe the effect of multiple earthquakes. However, different ground motions input may produce different results.

The following aftershock is related on many factors, including intensity or magnitude, the effect of duration, elapsed time from mainshock and site location, all of which exhibit some stochastic effects. Accordingly, studies are needed to ascertain these factors in the further research.

Acknowledgements:

The authors acknowledge support from the Center for Urban Earthquake Engineering (CUEE). The financial supports provided by key project of Beijing science and technology program D09050600370000 and key project of Chinese national program for fundamental research and development 2007CB714202 are gratefully acknowledged.

References:

Lee, K. and Foutch, D.A. (2004), Performance evaluation of damaged steel frame building to seismic loads. *Journal of Structural Engineering*, 130 (4): 588-599.

Luco, N., Bazzurro, P. and Cornell, C.A. (2004), Dynamic versus static computation of the residual capacity of a mainshock-damaged building to withstand an aftershock. *Proceeding of the 13WCEE*, Vancouver, Canada. Paper No.2405.

Li, Q.W. and Ellingwood, B,R. (2007), Performance evaluation and damage assessment of steel frame buildings under main shock-aftershock earthquake sequences. *Earthquake engineering and structural dynamics*, 36: 405-427.

Yeo, G.L. and Cornell, C.A. (2009), A probabilistic framework for quantification of aftershock ground-notion hazard in California: methodology and parametric study. *Earthquake engineering and structural dynamics*, 38: 45-60.

Abdelnabi, A.E. and Elnashai, A,S.(2009), Response of RC buildings under multiple earthquakes. Proceeding 7th International Conference on Urban Earthquake Engineering (7CUEE) and 5th International Conference on Earthquake Engineering (5ICEE), Tokyo, Japan.

Li, K.N. (2009), Canny for 3D nonlinear static/dynamic structural analysis computer program.

GB50011-2001(2008), Code for seismic design of building (2008 version). Beijing: China Architecture and Building Press.

8CUEE CONFERENCE PROCEEDINGS
8th International Conference on Urban Earthquake Engineering
March 7-8, 2011, Tokyo Institute of Technology, Tokyo, Japan

ANALYTICAL INVESTIGATION ON SEISMIC BEHAVIOR OF CONNECTIONS BETWEEN PRECAST RC COLUMNS AND STEEL BEAMS

Qiyun Zhu[1] and Xilin Lu[2]

1) Ph.D. Candidate, Research Institute of Structural Engineering and Disaster Reduction, Tongji University, Shanghai, China
2) Professor, Research Institute of Structural Engineering and Disaster Reduction, Tongji University, Shanghai, China
kerryzqy@hotmail.com, lxlst@tongji.edu.cn

Abstract: While hybrid structures that consist of reinforced concrete columns and steel beams exhibit advantages from both structural and constructional viewpoints, they are expected to provide repairable performance for post-seismic immediate occupancy. This paper introduces a new type of RC column-steel beam connection for this purpose. The joint region is composed of face plates, stiffening web with holes and connecting bolts. Based on the experimental study, nonlinear finite element analysis is carried out to investigate the mechanical behavior of such connection. A detailed three-dimensional finite element model is developed, which takes into consideration the nonlinear material behavior of steel and concrete, as well as the surface-to-surface contact problem. The finite element model is validated using the pseudo-static test results of precast RC column-steel beam subassemblies previously obtained. Stress fields in the steel components and concrete obtained from the analytical study are presented to determine the internal mechanisms of the joint region. Experimental and analytical results show that such connection form offers a reliable connecting quality. Stiffening web inside joint contribute to the shear resistance capacity of such hybrid connection. Concrete diagonal strut is observed between the horizontal stiffeners in the analytical results.

1. INTRODUCTION

Hybrid frames that consist of reinforced concrete (RC) columns and steel (S) beams have gained increasingly concern due to its widely accepted advantages. The effective combination of such two kinds of structural members enables long span floor framing and reduces significantly the weight of the building. While such hybrid structures exhibit advantages from both structural and constructional viewpoints, they are expected to provide repairable performance for post-seismic immediate occupancy.

Prefabricated RCS frames system can be developed as a main alternative for this purpose. The reinforced concrete columns and composite floor system can be produced in factory and fabricated at the construction site, instead of conventional cast-in-site construction method. Such industrialized construction method of buildings offer significant advantages, such as shortened construction time, less construction site waste, less environmental emissions, and reduction of energy and water consumption. Furthermore, structural members can be replaced easily when suffering from earthquake, and the damaged members can also be reused for other purposes, resulting in material cost savings. Therefore, prefabricated RCS frames offer a substantial opportunity to provide repairable performance for post-seismic immediate occupancy and promote the sustainable development of structural engineering.

Connection technologies have significant influence on the repairable performance and seismic behavior of such RCS frames. Numerous joint details have been developed in the recent decades to make the RCS frame systems practical. The through-beam-type RCS hybrid joint in which steel beams running continuously through column panel zones has been studied in previous work by the authors (Shiekh et al. 1989, Parra-Montesinos and Weight 2000, Liang and Parra-Montesinos 2004). Extensive research work has focused on the development of RCS connection details and seismic behavior of RCS hybrid connection. However, joint details in such connection are considered complicated, so that some operation difficulties still exist in concrete placement, as well as longitudinal bars passing through flanges and stirrups passing through webs, especially when beams are framing into the joint region from more than one direction. In addition, connection behavior varies with different joint details such as face bearing plates, steel band plates, and so on. Through-column-type has been studied, as shown in the work by Kuramoto and Nishiyama (2004). Another connection is so-called “end-plate bolted connection”, in which bi-directional bolts holes in the joint region largely weaken shear capacity of concrete in the joint region, such connection has been researched in

previous work by the author(Ma. 2003). The engineering application of RCS hybrid frame systems has been limited due to the existence of problems in such RCS hybrid connection. Therefore, advanced research work for developing a new type of RCS hybrid connection is needed.

Based on the research of above RCS hybrid connections, a new type of RCS connection was proposed. The joint region is composed of inside stiffening web, steel cover plates, horizontal stiffeners and connecting bolts. The concrete in the joint region is encased by face plates and embedded with stiffening webs, which can largely enhance the shear resistance capacity of joint. Drilling holes or welding studs on stiffening webs can be adopted to provide shear transferring capacity between the stiffening webs and the surrounding concrete in the joint region. End-plate bolted connection between steel beam and RC column is adopted, thus the steel beams can be replaced when it suffers severe seismic damage.

An experimental program involved RC column-steel beam subassemblies has been conducted under low cyclic reversed loading to investigate the seismic behavior of prefabricated RCS subassemblies and the efficiency of the new type of joint detail. In order to further clarify the mechanical characteristic of the new type of RCS connection, nonlinear numerical simulation of two RC column-steel beam connections under monotonic loading was carried out using ANSYS program.

2. EXPERIMENTAL PROGRAM

2.1 Description of Test Specimens

Half scale RC column-steel beam subassemblies were designed following a strong column-weak beam philosophy, which simulated interior joint for RCS frames. The cross-sections of the columns were 250mm ×250mm, and the cross-sections of the beams were 248mm × 124mm × 5mm × 8mm, which were Q235 grade. Eight HRB400 grade longitudinal bars which diameter was 16 mm were arranged symmetrically, and 6mm–diameter stirrups with 100 mm spacing were used in each column, as shown in Figure 1. Concrete grade of the column was C40.

Details of steel components of the connection are shown in Figure 2. Steel components composed of stiffening webs, face plates, batten plates and horizontal stiffeners were welded as a steel assembly. The thickness of the stiffening webs with holes was 8mm for specimen 1 and 6mm for specimen 2. Three batten plates were welded to the face plates in order to observe the concrete cracking, and there were no stirrups in the joint region. The thickness of the face plates was 20mm, while the thickness of the batten plates was 6mm. The depth of the face places was 440mm.

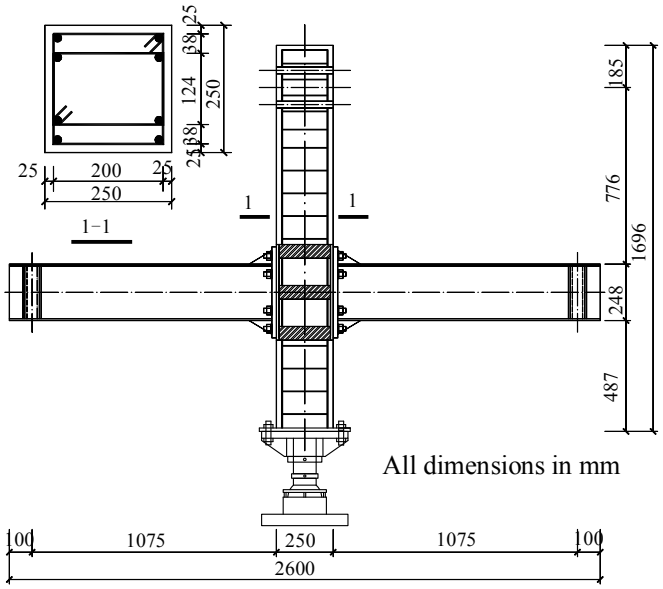


Figure 1 Details of Specimens

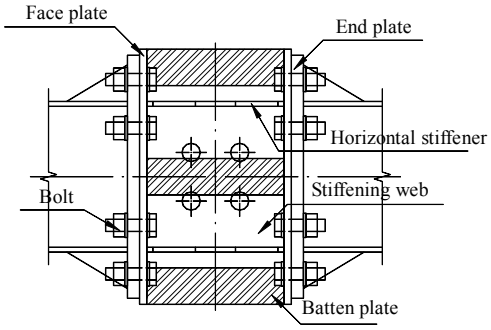




Figure 2 Connection Details

Steel beams and steel components in the joint region were shaped in the factory, gas shielded welding was applied in the steel welding work to ensure welding quality. High strength bolts (grade 10.9M20) were adopted in the connection. During the preparation of

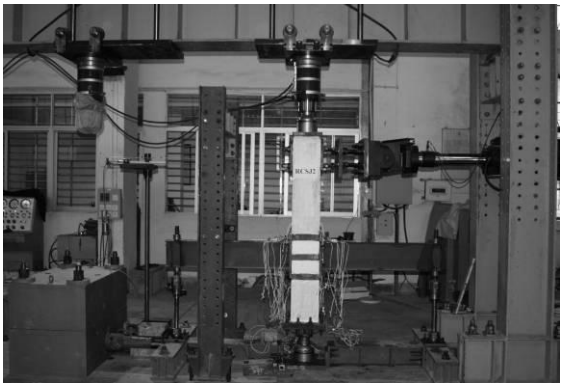


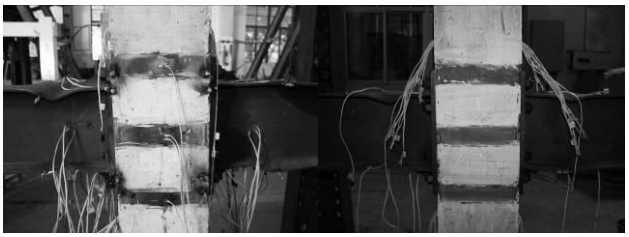
Figure 3 Test Set-up

specimens, steel assembly was installed into the column reinforcement before placing concrete. The bolts were fixed on the face plates by welding. After the columns were shaped, steel beams were installed on the precast columns.

The test setup used for the experimental program is shown in Figure 3. During the test, the constant axial compressive load was held at the top of the column by a hydraulic jack. The lateral cyclic reversed loading was applied at the top of the column. The lateral load was reversed once starting from 60kN and increase by 20kN for each cycle, lateral displacement was repeated in three cycles after specimens yielding, each at the story drift angles of 1/50, 1/35, 1/25.

2.2 Test Results

Visual observation revealed that specimens performed similarly with plastic hinges formed at the beam ends near the end-plates, where local buckling took place at the beam flanges and webs, and shear failure of the concrete panel were not observed even at the final stage of loading, only minor damage such as some diagonal cracks were observed in the joint region, as shown in Figure 4. In addition, the end-plate bolted connection behaved well during the entire test.



(a) Specimen 1 (b) Specimen 2

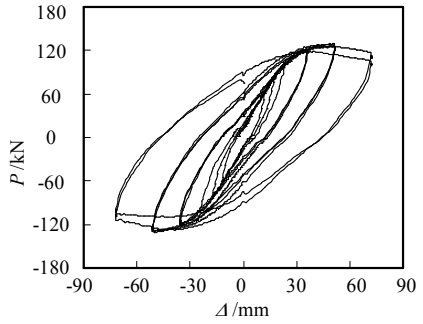
Figure 4 Failure Mode

As shown in Figure 5, shuttle-shaped hysteretic responses of lateral load versus story drift for each specimen were observed. At large displacement cycles, during which flexural plastic deformations occurred at the beam ends, plump hysteretic loops were noticed, At 1/35 drift, the specimens reached their peak strength, and large residual deformation were observed. The specimens exhibited stable responses with only minor decay in strength and stiffness during repeated cycles at the same drift level, retaining more than 85% of their peak strength at the end of the tests.

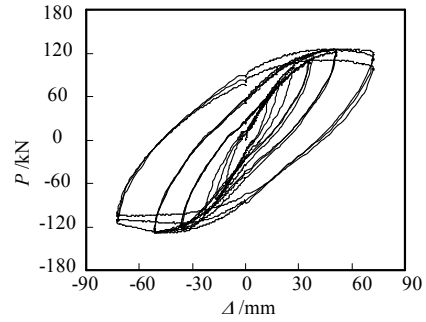
3. ANALYTICAL MODELING

3.1 Element type

Several kinds of element were adopted in the finite element models. Solid65 element was used to model the concrete of column. This type of element is defined by eight nodes having three degrees of freedom at each node, which is capable of cracking in tension and crushing in compression. A value of zero was entered for all real



(a) Specimen 1



(b) Specimen 2

Figure 5 Load versus Story Drift Hysteretic Curves

constants which turned the smeared reinforcement capability of Solid65 element off. Steel beams and all steel plates were modeled using Solid45 element, which has plasticity, stress stiffening capabilities. No real constant set exists for the Solid45 element.

Longitudinal bars and stirrups in the column were modeled using Link8 element, which is a uniaxial tension-compression element with three degrees of freedom at each node. In order to avoid large amount of elements and shorten the computation time, high strength bolts were simplified using Beam4 element, which is a uniaxial element with tension, compression, and bending capabilities.

The interface between the end-plates of beams and the face plates of the joint region was simulated by defining contact pairs with the 3-D target surface element Target170 and the surface-to-surface contact element Contact174. The face plates of the joint region were chosen as the target surface, and the end-plates were chosen as contact surface. The target surface is paired with its associated contact surface via a shared real constant set. The coefficient of friction for the steel contact surfaces was taken as 0.45.

3.2 Material Properties

The uniaxial stress-strain relationship for concrete in compression was simulated with multi-linear isotropic model. Since the axial compression ratio applied on the column is so small that the effect of stirrup confinement is not obviously, Saenz concrete constitutive material model was used, which can be expressed as follows:

$$\sigma = \frac{E_c \varepsilon}{1 + \left(\frac{E_c}{E_c'} - 2\right)\frac{\varepsilon}{\varepsilon_0} + \left(\frac{\varepsilon}{\varepsilon_0}\right)^2} \quad (1)$$

Where E_c is the elastic modulus of the concrete, and E_c' is the secant modulus corresponding to peak stress of stress-strain curve. ε_0 is the strain corresponding to the peak stress of stress-strain curve. The nonlinear compressive stress-strain curve for concrete is shown in Figure 6.

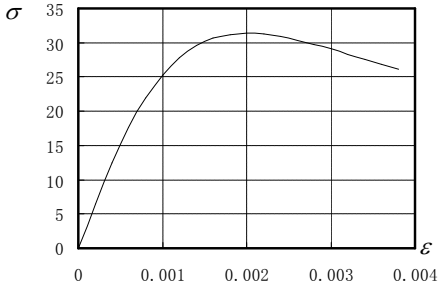


Figure 6 Stress-Strain Curve of Concrete

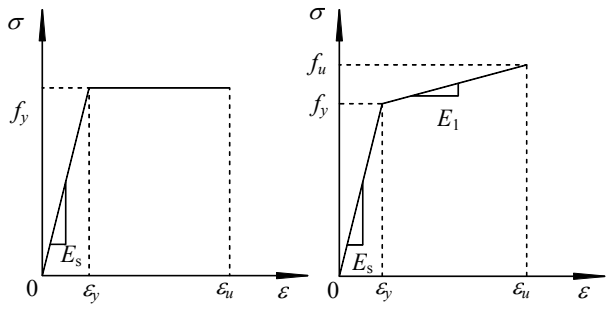
In addition, Willam-Warnke failure model was used as the failure criterion for concrete, where several coefficients are required to input. Additional concrete material data, such as the shear transfer coefficient β_t for open cracks and β_c for closed cracks are also needed. The shear transfer coefficients β_t and β_c control the amount of shear transfer across the cracks. The values of 0.35 and 0.8 were used in the model for β_t and β_c, respectively. The Poisson's ratio was assumed to be 0.2 for concrete. The elastic modulus of concrete, uniaxial compressive and tensile strength was calculated as follows:

$$E_c = \frac{10^5}{2.2 + \frac{34.7}{f_{cu,k}}} \quad (2)$$

$$f_{ck} = 0.76 f_{cu,k} \quad (3)$$

$$f_{tk} = 0.26 f_{cu,k}^{2/3} \quad (4)$$

Where $f_{cu,k}$ is the cube compressive strength of concrete, f_{ck} is the uniaxial compressive strength, f_{tk} is the uniaxial tensile strength.



(a) (b)

Figure 7 Stress-Strain Curves of Steel

The Von Mises yielding criterion with kinematic hardening rule was adopted for all steel materials in the finite element analysis. Elastic-perfectly plastic model was adopted to simulate the stress-strain relationship of all steel plates, as well as flanges and webs of beams, as shown in Figure 7(a). The bilinear stress-strain relationship was used to model the longitudinal bars and stirrups of the columns as shown in Figure 7(b), where E_1=0.01E_s. The elastic modulus E_s and yielding strength f_y were obtained from the testing of material properties, as listed in Table 1. Poisson's ratio was assumed to be 0.3 for steel materials in this analysis.

Table 1 Input Parameters of Steel

Type	f_y (MPa)	E_s (MPa)	E_1 (MPa)
Flange	270.7	1.91×10^5	-
Web	301.9	2.05×10^5	-
Plate (t=6mm)	350.4	1.89×10^5	-
Plate (t=8mm)	339.2	1.94×10^5	-
Longitudinal bar (d=16mm)	490.0	2.19×10^5	2.19×10^3
Stirrup (d=6mm)	428.3	1.95×10^5	1.95×10^3

3.3 Finite Element Mesh

Simplification was made in the modeling so as to avoid detailed modeling and shorten the computation time. The solid model was established according to the geometrical configuration and dimensions of the test specimens. Boolean operations including Glue and Overlap were applied in the solid modeling. The model was segmented by work plane at the location of steel plates or reinforcement in order to facilitate the mesh. Mapped meshing of solid was conducted after the element types and material properties were attributed to the corresponding parts. The meshing of the reinforcement is a special case compared to the volumes. The nodes of reinforcement element were created in the meshing of the concrete volume. The interface between the steel plates and concrete was assumed to have a full bond condition, and the slip between the bars and concrete was also neglected in the analysis. A general view of the three-dimensional finite element model is shown in Figure 8.

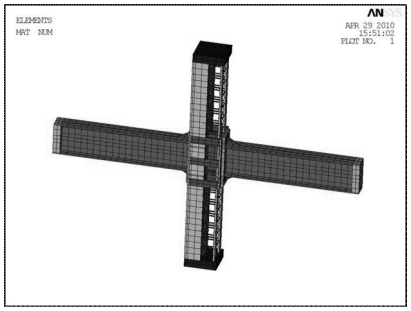


Figure 8 Finite Element Model

3.4 Boundary Condition and Solution

The boundary conditions of the analytical model were created to be similar to those of the test specimens, as shown in Figure 9. The nodes of the middle line at the bottom of the column were restrained in three translational degrees of freedom, and the nodes located at the beam ends were restrained in the vertical y direction and lateral z direction to enable the horizontal movement of beams. Elastic blocks were placed both at the top and bottom of the column, as well as the beam ends, such operation can avoid stress concentration at the restrained area and achieve convergence better.

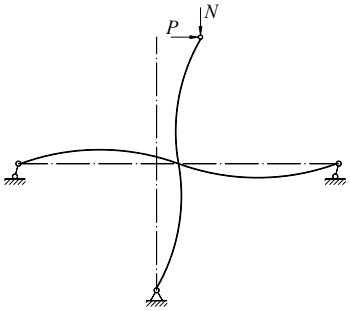


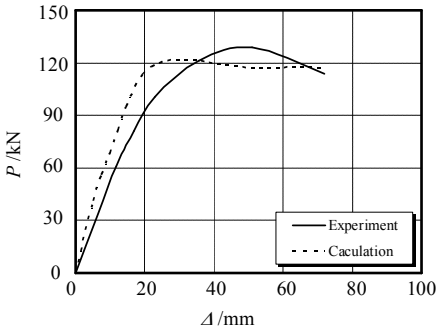
Figure 9 Boundary Condition

Loading process can be divided into three steps. Temperature load was applied to the bolts to generate the pretension of bolts and the compressive effect between the plates, and then the axial load was applied to the top face of the column. Before displacement was applied to the column, all nodes located at the top face of the column were coupled in the horizontal x direction to ensure all nodes move together, thus, horizontal displacement was applied to the main node. The applied displacement was divided into a series of increments called load steps and load substeps. To predict and control load step size increments, the options of automatic time stepping, linear searching and freedom predicting were turned on in the analysis in order to achieve convergence of the operation. Full Newton-Raphson equilibrium iteration method was adopted in the solution process of nonlinear analysis.

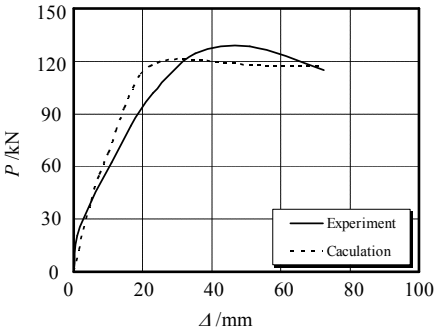
4. ANALYSIS RESULTS AND DISCUSSION

4.1 Comparison of Numerical and Experimental Results

Lateral load versus story drift curves of the analytical results under monotonic loading are compared with experimental load-displacement skeleton curves, as show in Figure 10. In general, load versus displacement response obtained from the numerical analysis showed good agreement with the skeleton curves of experimental results. Difference of the two curves may caused by the existence of frictional force and some initial gap in the test set-up. It is observed that the analytical curve decline earlier than the experimental one, it is due to the fact that elastic-perfectly plastic model is adopted for the steel beam, and the strain hardening is neglected.



(a) Specimen 1



(b) Specimen 2

Figure 10 Comparison of Numerical and Test Results of P-Δ curves

The yield strength and maximum strength of the connections are shown in table 2. The yield strength was obtained by energy equivalent method. It can be seen from Table 2 that the finite element analysis results show fairly good agreement with the experimental ones in terms of yield and maximum strength for each connection.

Table 2 Comparison of Numerical and Test Results

Specimen	Yield Strength(kN)		Maximum Strength(kN)	
	$P_{y,c}$	$P_{y,t}$	$P_{max,c}$	$P_{max,t}$
1	106.15	101.63	121.98	129.10
2	110.70	98.62	121.31	128.42

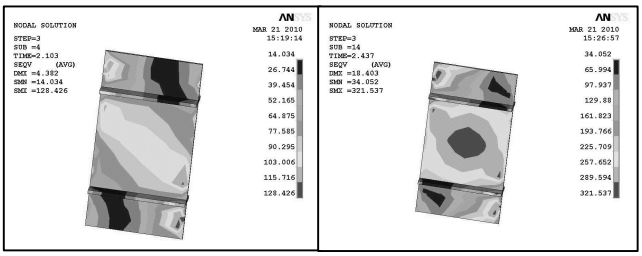
Note: The subscript c and t represent the calculation and experimental results, respectively

4.2 Stress Distribution of Numerical Results

The numerical simulation also provides some extra valuable results which were hard to measure during the testing, including the stress distribution of steel components and concrete in the joint region.

The Von Mises stress distribution of inside stiffening web for specimen 2 is shown in Figure 11. It can be noticed that diagonal principal stress flow of stiffening web formed between the horizontal stiffeners before yielding, and then yielding area expand gradually with the load increasing. It is indicated that stiffening

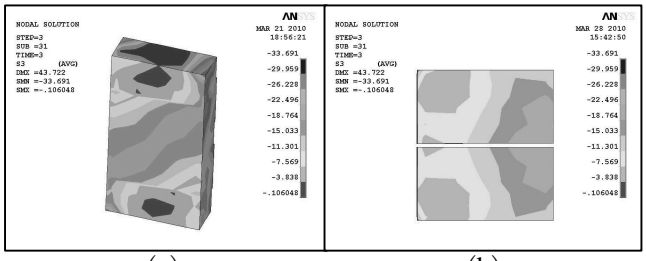
web contributes to the shear resistance capacity of such connection.



(a) (b)

Figure 11 Stress Distribution of Stiffening Web

The stress distribution of the concrete in the panel zone of specimen 2 at the ultimate stage is shown in Figure.12. It can be seen that a diagonal strut is formed in the concrete between the horizontal stiffeners to resist the shear force of the panel zone. Therefore, the diagonal strut model can be used in the shear capacity analysis for concrete in the panel zone. It can be also observed that the effect of diagonal strut decrease outward.



(a) (b)

Figure 12 Stress Distribution of Concrete

The stress distribution of the batten plates is shown in Figure 13. It can be noted that the stress of batten plates is small, which is consistent to the experimental observation of strain value. Figure 14 shows the stress distribution of the face plates, which indicates that there are somewhat stress concentrated at the location of tensile bolts.

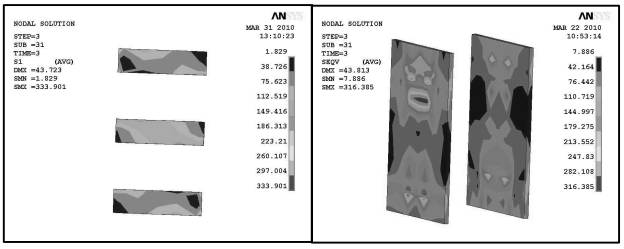


Figure 13 Batten plates

Figure 14 Face Plates

5. CONCLUSION

This paper introduces a new type of RCS connection. Based on the experimental results of connections composed of reinforced concrete columns and steel beams, three-dimensional nonlinear finite element model was established using ANSYS program with appropriate modeling methodology. Finite element analysis was conducted under monotonic loading to analyze the mechanical characteristic of such type of connection. The main results can be summarized as follows:

(1) The lateral load-displacement curves obtained from the finite element analyses are in good agreement with those of the tests. The overall behavior of RCS connection of this type can be efficiently simulated, which allows for further parametric analysis of the new type of RCS connection.

(2) The existence of stiffening web inside joint region is effective for the shear resistance capacity of such connection. Concrete diagonal strut is formed between the horizontal stiffeners in the analytical results, which provide a basis for the theoretical analysis of the shear resistance capacity for the new type of RCS connection.

(3) Both analytical and experimental results indicate that end-plate bolted connection composed of reinforced concrete columns and steel beams is feasible and offers a reliable connecting quality, which facilitates the replacement of steel beams when they suffered from earthquake damage.

Acknowledgements:

This research is a part of the research program on "a new type of connection for RC column-steel beam frame". The authors gratefully acknowledge the financial support provided by the Excellent Talent of New Century for Education Ministry of China (Grant No.NCET-06-0571). The assistance of Prof. Guo during the experimental study at Huaqiao University was particularly appreciated.

References:

Shiekh, T.M., Deierlein, G.G., and Yura, J.A. (1989), "beam-column moment connection for composite frames: Part1," *Journal of Structural Engineering*, American Society of Civil Engineers, 115(11), 2858-2875.

Parra-Montesinos, G.J. and Weight, J.K. (2000), "Seismic Response of Exterior RC Column-to-Steel Beam Connections," *Journal of Structural Engineering*, American Society of Civil Engineers, 126(10), 1113-1121.

Liang, X.M. and Parra-Montesinos, G.J. (2004), "Seismic Behavior of Reinforced Concrete Column-Steel Beam Subassemblies," *Journal of Structural Engineering*, American Society of Civil Engineers, 130(2), 310-319.

Kuramoto, H. and Nishiyama, I. (2004), "Seismic Performance and Stress Transferring Mechanism of Through-Column-Type Joints for Composite Reinforced Concrete and Steel Frames," *Journal of Structural Engineering*, American Society of Civil Engineers, 130(2), 352-360.

Ma, H.W. (2003), "Study on the Joints of Composite Beam and Continuous Compound Spiral Hoop Reinforced Concrete Column," Ph.D. dissertation, Xi'an University of Architecture & Technology.

8CUEE CONFERENCE PROCEEDINGS
8th International Conference on Urban Earthquake Engineering
March 7-8, 2011, Tokyo Institute of Technology, Tokyo, Japan

A FUNDAMENTAL STUDY ON STRUCTURAL PERFORMANCE OF CES SHEAR WALL WITH DIFFERENT ANCHORAGE CONDITION OF WALL REINFORCEMENT

Tomoya Matsui[1)], Suguru Suzuki[2)], and Hiroshi Kuramoto[3)]

1) Assistant Professor, Dept. of Architectural and Civil Engineering, Toyohashi University of Technology, Japan
2) Graduate School of Eng., Toyohashi University of Technology, Japan
3) Professor, Dept. of Architectural Engineering, Osaka University, Suita, Japan
matsui@ace.tut.ac.jp, suzuki.suguru@rc.ace.tut.ac.jp, kuramoto@arch.eng.osaka-u.ac.jp

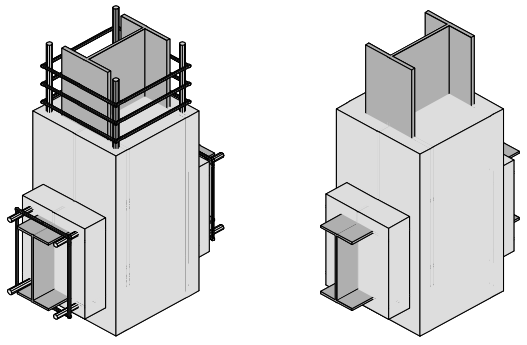
Abstract: Composite Concrete Encased Steel (CES) structures composed of steel and fiber reinforced concrete (FRC) have been continuously studied by the authors. In this study, static loading tests of CES shear wall whose anchoring method to connect CES frame with FRC wall panel was simplified were carried out, and the basic structural performance, strength, deformability and failure mechanism of the CES shear wall were investigated. Variables investigated are the anchorage conditions between CES beams and FRC wall panels and the failure mode of the shear walls, the anchorage conditions tested were two types in which longitudinal wall reinforcing bars are connected to CES boundary beams or not, while the failure modes selected are the flexural failure and shear failure of the shear walls. In this paper, structural performance of CES shear wall obtained from the tests are described. The results show that the effect of the anchorage condition of wall longitudinal reinforcement on both shear and flexural strengths of CES shear wall is not significant. The deformability of CES shear wall is slightly improved by omitting anchorage of wall longitudinal reinforcement because the damage area of concrete in wall panel is reduced with increasing slip deformation between walls and boundary beams.

1. INTRODUCTION

Steel Reinforced Concrete (SRC) Structures developed in Japan have good structural performance for resisting lateral forces imposed by wind and earthquakes, and have been adopted for medium-rise, high-rise, and super high-rise buildings. However, the number of SRC buildings constructed has decreased since the 1990s. Although the decrease might be caused by the development of a new structural engineering system called the High-strength concrete structure or Concrete-Filled Steel Tube (CFT) structure, the main reason seems to be the construction problems that increase construction costs and lengthen construction schedules. Even so, it could be important that SRC structures provide better seismic performance in comparison with other structural systems. So, the authors aim to develop a structural system with as good seismic performance as SRC structures and good workability, and have conducted a continuing development study on composite Concrete Encased Steel (CES) structures composed of steel and fiber reinforced concrete (FRC) as shown in Figure 1.

In the experimental study on CES columns, CES beam-column joints and two-bay two-story CES frame, it was confirmed that CES structural system showed stable restoring force characteristics and good seismic performance.

On the other hand, shear wall which is main earthquake resistant member is effective in increasing stiffness and strength for also CES structural system. However, it will be difficult to arrange reinforcement bars in CES structure which have encased steel in beam and column. In recently, there are some researches about method of joint of frame and wall panel on SRC shear wall, it is an important problem to improve workability of joint of frame and wall panel in CES structure.



(a) SRC structure (b) CES structure

Figure 1 Composite Concrete Encased Steel structural system

In this study, Static loading test of CES shear wall whose anchorage method of CES frame and FRC wall panel is simplified was carried out, and basic structural performance, strength, deformability and failure mechanism of the CES shear wall are investigate.

2. OUTLINE OF CES COLUMN TEST

2.1 Description of Specimens

The specimens are designed to simulate the lower two story of multi-story shear wall in medium-high-rise building and scaled to one-third of the prototype walls. Four specimens were prepared in this test.

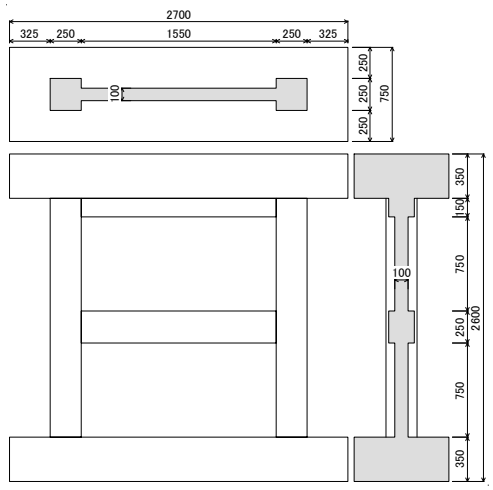


Figure 2 Test specimens

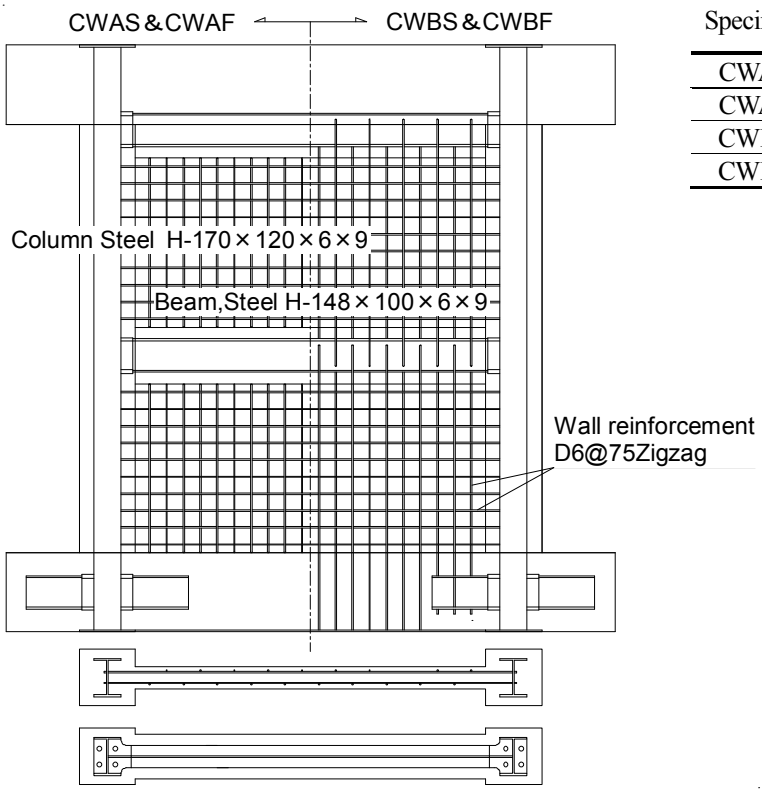


Figure 3 Bar arrangement

Configuration and bar arrangement of specimens are shown Figure 2, Figure 3 and Figure 4. Detail of the section is shown in Table 1. The column has 250 mm square section, the beam has the section of 200 mm×250 mm. The column span length is 1800mm and thickness of wall is 100 mm. Experimental variables are the shear-span ratio and anchorage condition of longitudinal wall reinforcement as shown Table 2. Shear span ratio are 1.1 of specimen CWAS and CWBS, and 1.65 of specimen CWAF and CWBF. Specimen CWAS and CWBS expected to be shear failure. Specimen CWAF and CWBF expected to be flexural failure. Longitudinal wall reinforcement of Specimen CWAS and CWAF is bent in wall panel. On the other hand, longitudinal wall reinforcement of Specimen CWBS and CWBF is anchored to beam or stub as shown in Figure 4. Horizontal wall reinforcement bars in all specimens are securely fixed by welding to steel web of column.

Table 1 Specification of section

Column	BxD (mm)	250×250
	Steel	H-170×120×6×9 ($_{s}p$=4.9%)
Beam	BxD (mm)	200×250
	Steel	H-148×100×6×9 ($_{s}p$=5.2%)
Wall	Thickness (mm)	100
	Longitudinal bar	D6@75 zigzag ($_{w}p$=0.42%)
	Transverse bar	

Table 2 Experimental variable

Specimen	Shear span ratio	Anchorage of longitudinal wall reinforcement
CWAS	1.10	Nonexistence
CWAF	1.65	
CWBS	1.10	180° hook in beam
CWBF	1.65	

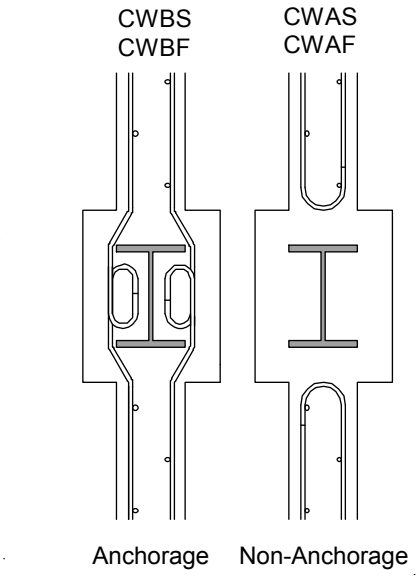


Figure 4 Bar arrangement in the beam

Mechanical properties of concrete and steel used are shown in Tables 2 and 3. Vinylon fibers with a diameter of 0.66 mm and a length of 30 mm were used for FRC. The volumetric ratio of the fibers was 1.0% and the water-cement ratio was 60%.

2.2 Loading Procedure

Figure 5 shows the loading apparatus used. The wall specimens were loaded with horizontal cyclic shear forces by a hydraulic jack of 2,000 kN capacity with applying constant axial force of 1260kN (N/N_0=0.2, N: axial load, N_0: axial load capacity including steel of columns) by two vertical manual jacks of 2,000kN capacity for each. During the testing, the additional moment was also applied to the top of specimens using vertical jacks to keep the prescribed shear-span ratio of 1.1 or 1.65 as the following equations.

Table 2 Material properties of concrete

Specimen		σ_B (MPa)	E_c (GPa)	ε_{c0} (μ)	Age (day)
CWAS	1 story	38.6	24.8	2814	91
	2 story	36.4	26.7	2550	86
CWBS	1 story	42.0	25.7	2587	94
	2 story	30.6	29.5	2558	89
CWAF	1 story	41.2	25.5	2457	100
	2 story	38.6	27.6	2423	95
CWBF	1 story	40.1	24.9	2765	105
	2 story	35.9	24.8	4160	100

σ_B: Compressive strength, E_c: Elastic modulus,
ε_{c0}: Strain at compressive strength

Table 3 Material properties of steel

	Yield strength (MPa)	Tensile strength (MPa)	Elastic modulus (GPa)
PL-6 (SS400)	260	409	190
PL-9 (SS400)	282	418	197
D6 (SD295A)	345	501	190

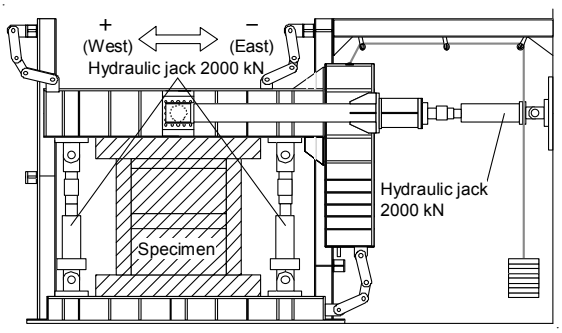


Figure 5 Loading apparatus

$$N_e = \frac{N_c}{2} - \frac{Q}{l}(h-a), \quad N_w = \frac{N_c}{2} + \frac{Q}{l}(h-a) \qquad (1)$$

Where, N_e: axial force of east side jack, N_w: axial force of west side jack, N_c: constant axial force (1260kN), Q: Shear force, l: distance between two vertical jack, h: assumed height of applying shear force, a: actual height of applying shear force.

The loading was conducted by controlling the relative wall drift angle, R, given by the ratio of the height of corresponding to the measuring point of horizontal displacement at the top of the specimen, h (2,050mm), to the horizontal deformation, δ, i.e. R=δ/ h. The horizontal load sequence consisted of two cycles to each story drift angle as shown Table 4.

2.3 Measuring method

Measuring plans of displacement and strains of bars and steel are shown in Figure 6. Measured points of

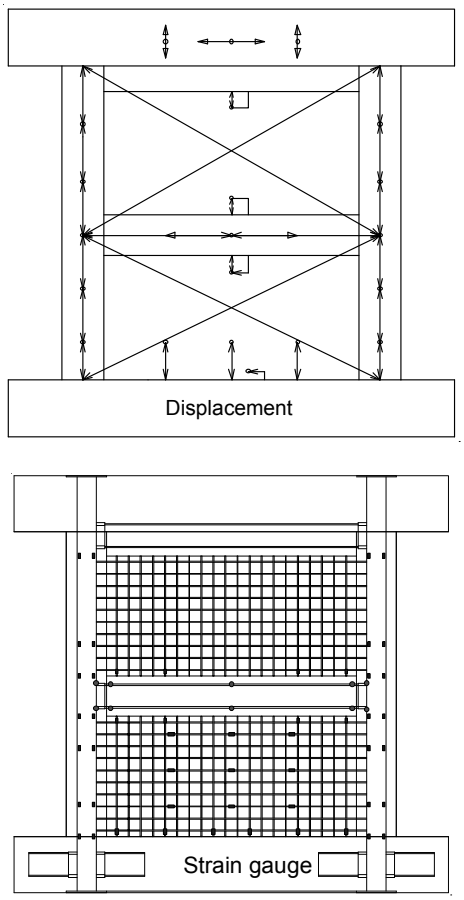


Figure 6 Measured points

Table 4 Loading cycle

R ($x10^{-2}$)	0.0625	0.125	0.25	0.5	0.75	1.0	1.5	2.0	3.0	4.0
δ (mm)	1.28	2.56	5.13	10.3	15.4	20.5	30.8	41.0	61.5	82.0
Cycle	1	2	2	2	2	2	2	2	1	1

displacement are horizontal displacement, longitudinal deformation of column and partial deformation of wall panel. The strain of steel of column and beam, longitudinal bar and horizontal bar of wall are measured by strain gages. Additionally, widths of crack are measured with crack scale after each loading cycle.

3. TEST RESULTS

3.1 Failure Mode and Hysteretic Characteristics

Figure 7 shows the shear force versus drift angle relationships for all specimens. Figure 8 shows cracking pattern of each specimen after load cycle of 0.0075 and 0.03rad..

Results of Specimen CWAS and CWBS which are

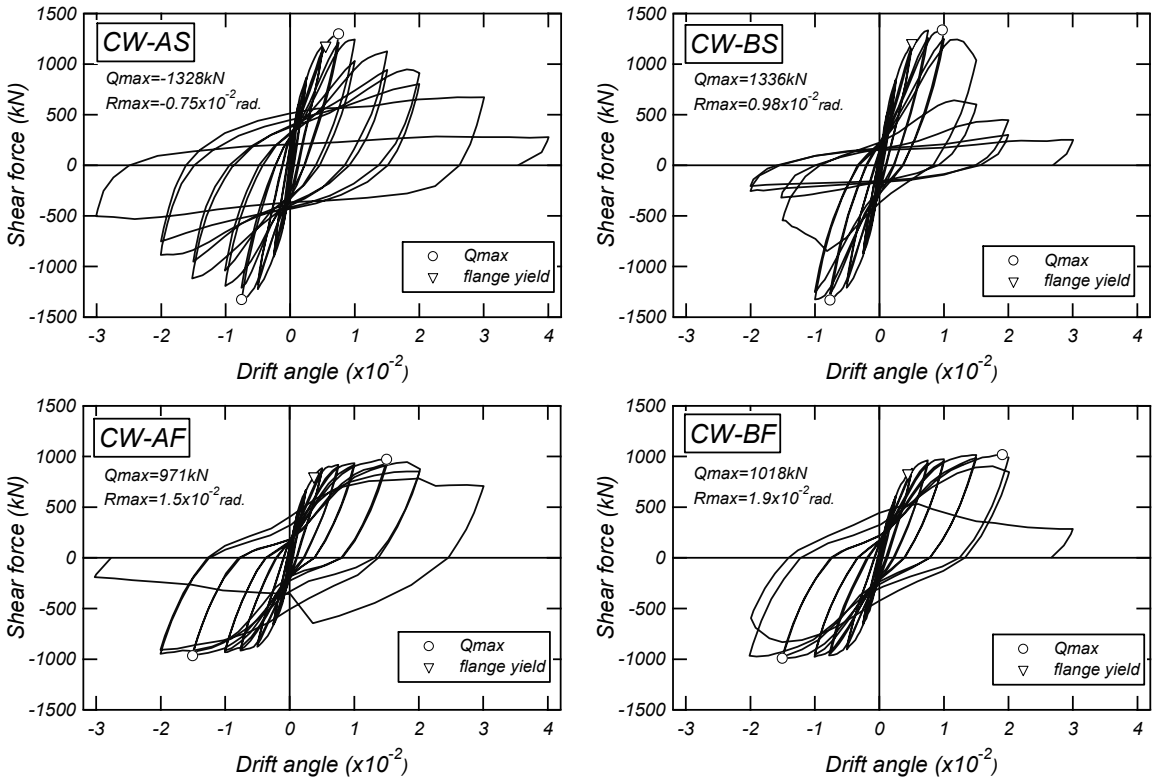
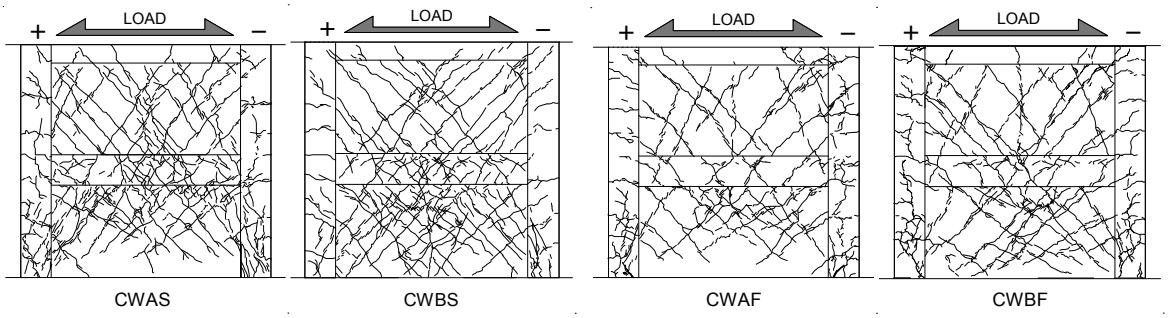
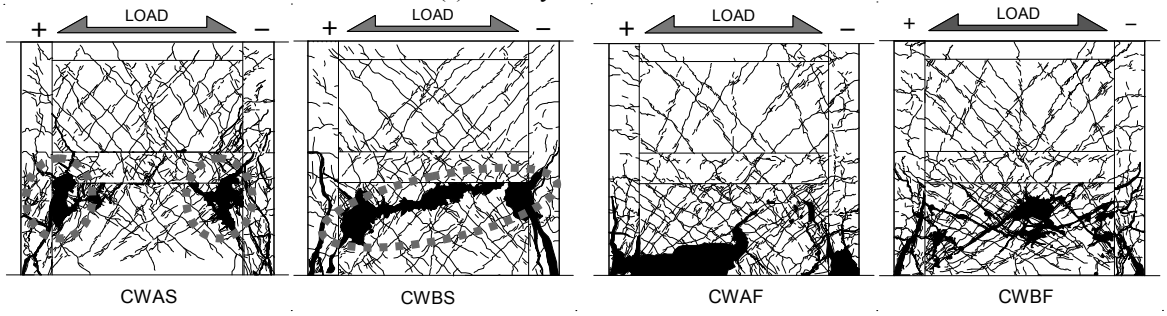


Figure 7 Shear force versus drift angle relationships



(a) After cycle of 0.0075 rad.



(b) After cycle of 0.03 rad.

Figure 8 Cracking patterns

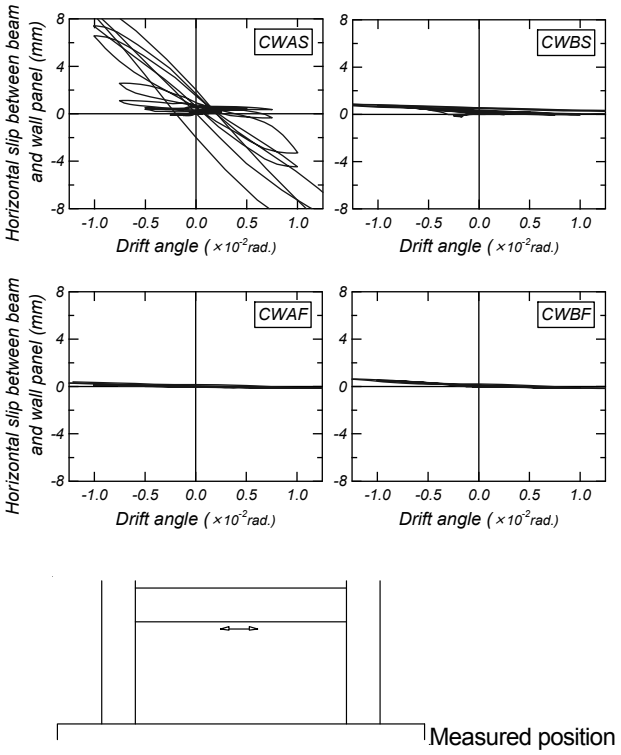


Figure 9 Horizontal slip between beam and wall panel

shear failure type are shown. As to Specimen CWAS without anchorage of wall reinforcement, steel flange of column yielded in the cycle of 0.0075 rad., and then maximum shear force reached 1328kN. As to Specimen CWBS with anchorage of wall reinforcement, steel flange of column yielded in the cycle of 0.005 rad., and then maximum shear force reached 1336kN in the cycle of 0.01rad.. Maximum shear forces of both specimens are almost same. However, deformability between Specimen CWAS and CWBS is different. After peak, shear forces of Specimen CWAS decreased slowly. But shear forces of Specimen CWBS decreased steeply in the cycle of 0.015rad..

Seeing cracking pattern shown in Figure 8, it is found that Shear failure occurred across the first-story wall in Specimen CWBS in final load cycle. On the other hand, Specimen CWAS showed much shear cracks at the upper corner of first-story wall in the cycle of 0.0075rad, and damage of concrete of Specimen CWAS concentrate at the upper corner of first-story wall in the cycle of 0.03rad., and it is shown that final damage condition is also different between Specimen CWAS and CWBS.

Figure 9 shows horizontal slip between boundary beam and wall panel. In Specimen CWAS, the slip increase in the cycle of 0.01rad. after reaching maximum shear force. But the slip hardly occurs in Specimen CWBS. Therefore, , it is thought that discrepancy is shown in deformability between Specimen CWAS and CWBS, because damage area of concrete of wall panel in Specimen CWAS is reduced by occurring slip under the beam after reaching maximum shear force due to without anchorage of wall reinforcement.

Results of Specimen CWAF and CWBF which are flexural failure type are shown. In Specimen CWAF without anchorage of wall reinforcement, steel flange of column yielded in the cycle of 0.005 rad., and then maximum shear force reached 971kN in cycle of 0.015ra.. In Specimen CWBF with anchorage of wall reinforcement, steel flange of column yielded in the cycle of 0.005 rad., and then maximum shear force reached 1018kN in the cycle of 0.02rad.. Maximum shear forces of both specimens are almost same with or without anchorage of wall reinforcement. Specimen CWAF showed steep strength deterioration in the positive direction loading of 0.03rad. and Specimen CWBF showed steel strength deterioration in the negative direction loading of 0.03rad. as shown in Figure 7. It is found that deformability of Specimen CWBF with anchorage of wall reinforcement is slightly poor.

As the results of these tests, it is though that the effect of anchorage condition of wall longitudinal reinforcement on shear strength and flexural strength of CES shear wall is small. And deformability of CES shear wall slightly improves by omitting anchorage of wall vertical reinforcement.

3.2 Stress of Reinforcement Bars and Steel

Figure 10 shows stress of horizontal wall reinforcement bars and steel flange of beam of Specimen CWAS and CWBS which exhibited shear failure until load cycle of 0.01 rad. On the assumption that the hysteresis characteristic of a steel bar is bilinear, the stress was calculated using strain measured by the strain gauge. And dashed line in these figures is yield stress shown in table 3. Data which can not be measured is not plotted in these figures. Stress at the five position are shown, upper flange and under flange of beam, upper section, mid section and under section of wall panel.

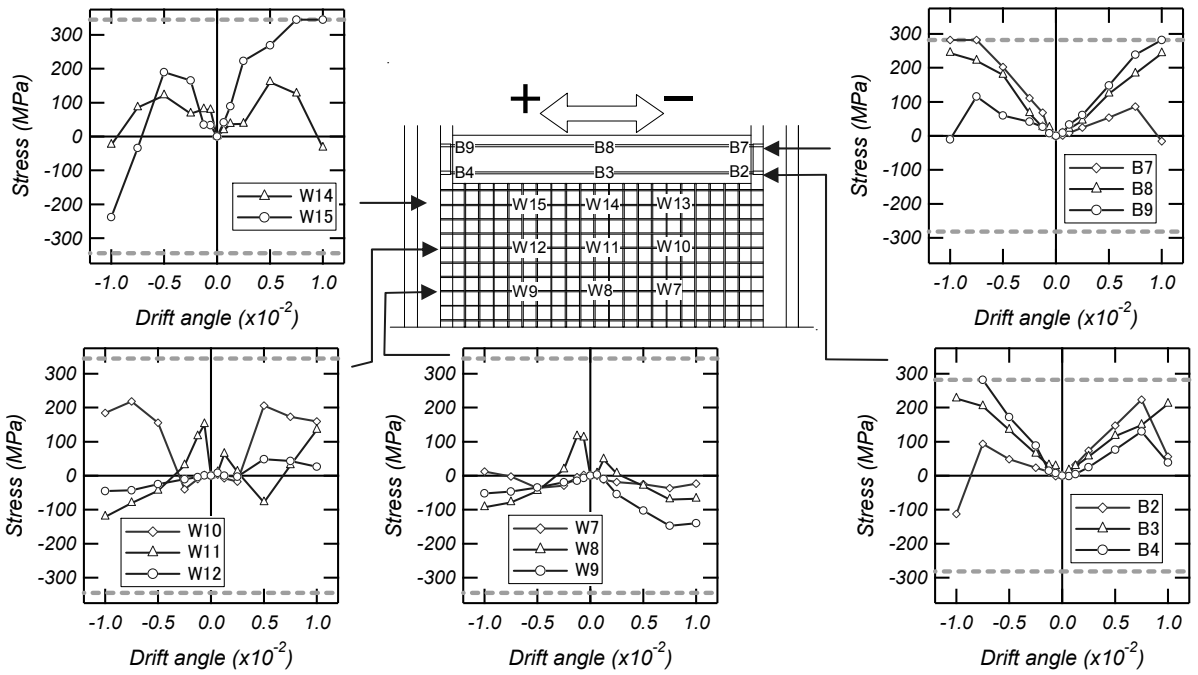
As for Specimen CWAS, Horizontal wall reinforcement at upper section yielded at drift angle of 0.0075 rad. when reached maximum shear force. As for Specimen CWBS, Horizontal wall reinforcement at upper and mid section yielded until drift angle of 0.0075 rad. when reached maximum shear force. And stresses of the wall reinforcement at under section are low. These situations correspond to observed damage situation of concrete as shown in Figure 7 of cracking pattern.

Seeing stresses of steel of beam, steel of beam was subjected to tensile force during the load. And either upper flange or under flange of steel beam approximately reach yield stress. It is confirmed that steel of beam work to resist against shear force effectively.

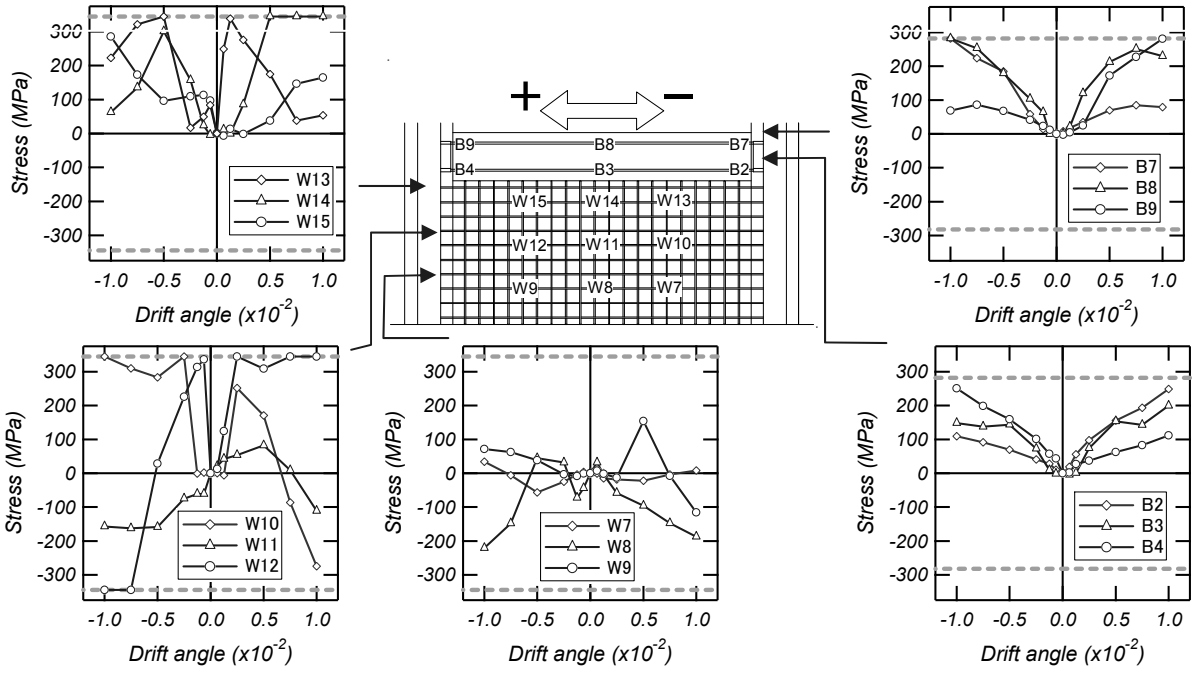
3.3 Curvature of Steel of Column and Beam

Figure 11 shows curvature distribution of encased steel of CES frame of Specimen CWAS which exhibited shear failure. the curvatures were calculated using strain measured by the strain gauge.

In the steel of boundary beam, it is confirmed that reversely symmetric moment occur corresponding to the curvature distribution. In view of side columns, although the effect of boundary beam is seen in west side column, curvature distribution shows almost linear shape at the small



a) CWAS



a) CWBS

Figure 10 Yield situations of horizontal wall reinforcement bars and steel flange of beam
(Dashed line is yield stress of material)

displacement (R=0.0625×10^{-2}rad.) .

Then, curvature distributions are more visible in the at the R of 0.75×10^{-2}rad. when Specimen CWAS reached maximum shear force. When steel of column of first-story is shown, it is confirmed that curvatures in position of circle in the graphs are increase, and moment distribution is estimated from the shape of this curvature distribution as shown in Figure 12. This means the forces dominantly act to side column in external direction. Moreover, it is thought that diagonal compressive force acts in the concrete wall panel surrounded by CES frame and CES frame exhibit the constraint effect on diagonal compressive force.

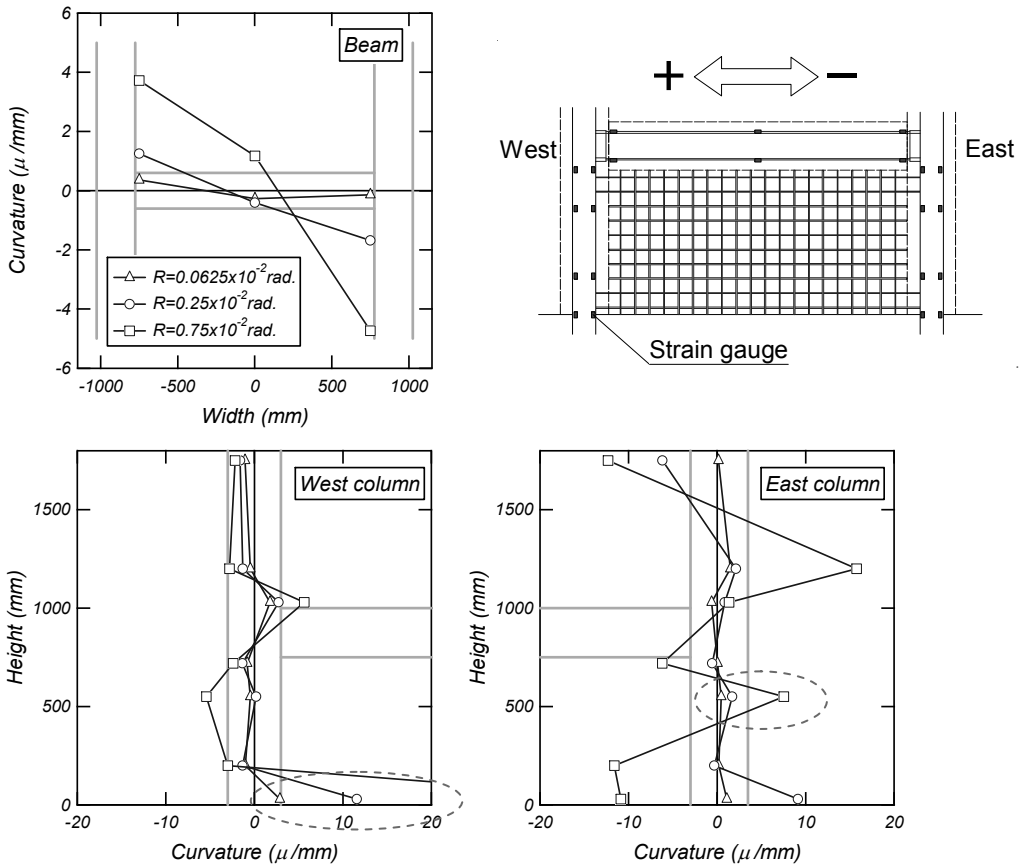


Figure 11 Curvature of steel of CES frame

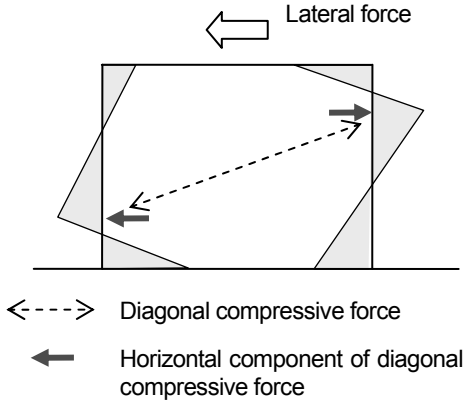


Figure 12 Moment acting to side column at the first-story

4. CONCLUSIONS

Static loading test of CES shear wall whose anchorage method of CES frame and FRC wall panel is simplified was conducted in which the test variables are anchorage condition of longitudinal wall reinforcement and the shear-span ratio. The Failure mode, lateral load carrying capacity and deformability of CES columns were examined. The following conclusions can be drawn.

The specimen CWBS with anchorage of wall reinforcement showed shear failure across the first-story wall panel, the specimen CWAS without anchorage of wall reinforcement showed shear failure at the region of upper corner of first-story wall panel. It is found that fracture region of concrete is different.

It is confirmed that the effect of anchorage condition of wall longitudinal reinforcement on shear strength and flexural strength of CES shear wall is small.

The deformability of CES shear wall slightly improves by omitting anchorage of wall longitudinal reinforcement, It is because that damage area of concrete of wall panel is reduced by occurring slip under the beam after reaching maximum shear force due to without anchorage of wall reinforcement.

It is thought that CES frame exhibit the constraint effect on diagonal compressive force acting in the concrete wall panel surrounded by CES frame.

References:

Adachi T. and Kuramoto H., (2003), "Study on structural performance of composite CES columns using FRC under high axial compression", Proceedings of the Japan Concrete Institute, Vol.25, No. 2, 289-294. (in Japanese)

Haruyama S., Onozato N., Tozawa T., (2006), "Study on anchored method of reinforcing bars utilized for SRC framed shear walls" Summaries of technical papers of Annual meeting architectural institute of Japan, C-1, 1147-1148. (in Japanese)

Kuramoto H., Matsui T., Imamura T., Taguchi T., (2007), "Structural performance of a plane frame for composite CES structural system", Journal of structural and construction engineering, No.629, 1103-1110.(in Japanese)

Matsui T., Kuramoto H., (2009), "Static loading test on CES columns with H-shaped steel under different axial force levels and shear-span ratio", Proceedings of The Eleventh Taiwan-Korea-Japan Joint Seminar on Earthquake Engineering for Building Structures, 189-197.

Matsui T., Kuramoto H., (2008), "Stress Transferring Mechanism of Beam-Column Joints for Composite CES Structural System Subjected to Seismic Load", 14thWCEE, PaperNo.05-06-0081

Nagata S., Matsui T., and Kuramoto H., (2006), "A fundamental study on structural performance of CES beam-column joints", Proceedings of the Japan Concrete Institute, Vol.28, No. 2, 1279-1284. (in Japanese)

Shibayama Y., Kuramoto H., Nagata S., Kawasaki K., (2005) "A study on restoring force characteristic of CES columns covered by FRC panels", Proceedings of the Japan Concrete Institute, Vol.27, No. 2, 241-246. (in Japanese)

Takahashi H., Maeda M., and Kuramoto H. (2000), "Test on hysteresis characteristics of steel concrete columns using ductile cement composite" Proceedings of the Japan Concrete Institute, Vol.22, No. 3, 1075-1080. (in Japanese)

Taguchi T., Nagata S., Matsui T., and Kuramot H. (2006), "Structural characteristics of CES columns with H-shaped steel", Proceedings of the Japan Concrete Institute, Vol.28, No. 2, 1273-1278. (in Japanese)

8CUEE CONFERENCE PROCEEDINGS
8th International Conference on Urban Earthquake Engineering
March 7-8, 2011, Tokyo Institute of Technology, Tokyo, Japan

BRACED FRAMES FOR SEISMIC DESIGN IN URBAN AREAS

Charles W. Roeder[1)], Dawn E. Lehman[2)], Po-Chien Hsiao[3)], and Keith Palmer[3)]

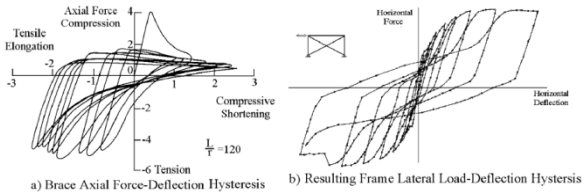
1) Professor, Dept. of Civil Engineering, University of Washington, Seattle, WA 98195 USA
2) Associate Professor, , Dept. of Civil Engineering, University of Washington, Seattle, WA 98195 USA
3) Graduate Student, Dept. of Civil Engineering, University of Washington, Seattle, WA 98195 USA
croeder@u.washington.edu, delehman@u.washington.edu, pchsiao@u.washington.edu, palme278@u.washington.edu

Abstract: Braced frames are stiff, strong systems, and they are desirable and economical earthquake resistant structural systems in urban areas. However, the design procedures used for braced frames varies from country to country, and their inelastic seismic behavior is not easily evaluated. With concentrically braced frames, seismic behavior is dominated by tensile yield and post-buckling deformation, and this behavior is not well-understood and viewed with distrust. Buckling restrained braced frames are used, but the design requirements and perceived ductility demands vary widely. Recent experimental and analytical research to better understand and evaluate braced frame behavior is summarized. These research results are discussed to provide a better understanding of the seismic performance of different braced frame systems. Methods for improving the seismic performance of braced frames are described, and potential weaknesses or deficiencies of various braced frame systems are noted. In particular it will be noted that the connections used to form the braced frame and the geometry of the bracing system play major roles in defining the seismic performance. The results of recent nonlinear dynamic analyses will be summarized to show the importance of accurate modeling of system nonlinear behavior, and the impact of potential design changes to current US design procedures will be noted.

1. INTRODUCTION

In the US, buildings are designed to remain elastic for small, frequent earthquakes to assure serviceability, but cyclic, inelastic deformation assures that the structure retains its integrity, minimizes loss of life, and prevents collapse during large infrequent events. Special concentrically braced frames (SCBFs) are stiff, strong structures that meet serviceability limits states and provide economical seismic design. During inelastic deformation, the brace buckles in compression, yields in tension, and sustains inelastic post-buckling deformation. Plastic hinges form in the brace due to P-δ moments, and this yielding contributes to the post-buckling yield behavior. SCBFs have special seismic design requirements to insure good inelastic performance. These effects lead to the one-sided axial force-deflection behavior of a braced bay seen in Fig. 1a. SCBFs braces are placed in opposing pairs, and the resulting system has inelastic hysteretic behavior illustrated in Fig. 1b. The braces are attached to the beams and columns by gusset plate connections such as illustrated in Fig. 2. The brace end rotation associated with brace buckling, causes large rotation demands on the gusset plate connection during these larger earthquakes.

Engineers recognize the complex inelastic behavior of SCBFs, and buckling restrained braces (BRBs) have been developed as an alternative system. BRBs are patented structural items where the brace is a small core element encased in a stiff outer casing as illustrated in Fig. 3. The core element is not bonded to the encasing material, and it is free to slip and strain independently of the casing. Therefore, no stress is transferred between the casing and core element. The resulting brace theoretically yields in tension and compression and can tolerate large inelastic axial deformations. As a result, BRBs are highly regarded by engineers and have been used with increasing frequency in recent years. A significant body of research has been completed on their performance, but this research has primarily focused on axial load and the deformation capacities of isolated braces. In the US, BRBs also employ gusset plate connections, but they alleviate the gusset plate rotation required for brace buckling. Nevertheless, BRBs sustain large seismic deformations during severe earthquake loading, and these large frame deformations are the focus of this research.



a) Brace Axial Force-Deflection Hysteresis b) Resulting Frame Lateral Load-Deflection Hystersis

Figure 1 Behavior of Special Concentrically Braced Frames

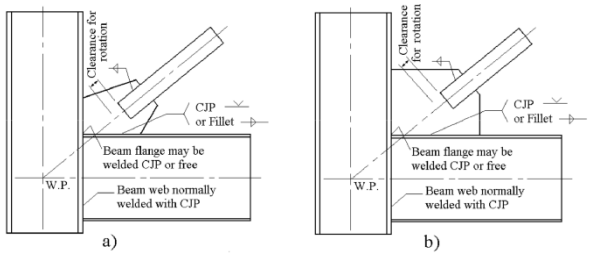


Figure 2. Schematic of Typical Gusset Plate

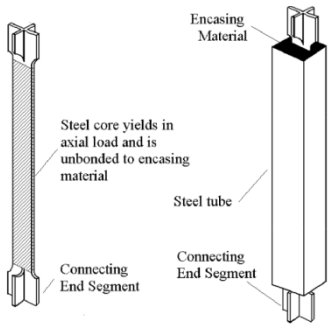


Figure 3. Schematic of Buckling Restrained Brace

2. GUSSET PLATE CONNECTIONS

While gusset plate connections are used for both the SCBF and BRBF systems, there are some differences in their gusset plate connection designs. AISC Seismic Provisions have numerous SCBF and BRBF design requirements, which are intended to assure good inelastic performance (AISC 2005a). For SCBFs, brace slenderness limits are applied to assure that the frame provides adequate ductility during post-buckling deformation, and additional framing system requirements balance the lateral resistance between tensile and compressive braces and control yielding in the beam due to unbalanced brace forces in V- or Inverted V-braced systems. Gusset plate connections are designed by variations of the AISC Uniform Force Method (UFM) (Thornton, 1991; AISC, 2005b), which was originally developed for wind load design. The UFM is adapted to seismic applications by designing the connection to resist the expected tensile ($R_y A_g F_y$) and compressive ($R_y A_g F_{cr}$) resistance of the brace. The expected brace resistances are much larger than the factored design loads. Rectangular high strength steel tubes are commonly used for the brace, and the tube is slit to slip over the gusset plate for the brace-to-gusset interface.

Net section fracture of the brace may occur at the end of the slit, and net section reinforcement is often required. The tubes are normally joined to the gusset plate with fillet welds sized to develop the expected tensile resistance of the brace, and block shear must also be checked for this interface joint. The Whitmore width (Whitmore, 1950) of the gusset plate is defined at the end of the brace-to-gusset interface by projecting a 30^o angle from the start to the end of the bolted or welded joint, and the area associated with this Whitmore width is used to define the area resisting the compressive buckling, tensile yield, and fracture capacities of the gusset. The Thornton method is commonly used for evaluation of this gusset plate buckling, and it uses the Whitmore width with an average effective buckling length of the plate over this width. The effective length coefficient is typically 0.65 for corner gusset plates and 1.2 to 1.4 for midspan gusset plates. The gusset plate must accommodate end rotation due to brace buckling, and this is normally accomplished by the $2t_p$ linear clearance model illustrated in Fig. 2. This requirement commonly results in large gusset plate dimensions and consequently thicker gusset plates. Once the gusset plate geometry and thickness are defined, the bolts or welds joining the gusset plate to the beam and column are sized by the equilibrium forces associated with the UFM. Welds are often fillet welds on both sides of the plate, but complete joint penetration welds may also be employed.

The beam-column connection also affects SCBF performance. Forces that are transferred by the brace to the beam or column or by drag struts to the braced bay frequently must be transferred through this beam-column connection. Some engineers use CJP welds between the beam and column flanges to assure full force transfer (see Fig. 2). Other engineers think that this welding is costly and unneeded, and they may use only web attachments. These combined requirements and practices result in wide variations in gusset plate connection design.

BRBFs have similar gusset plate design requirements, but there are also distinct differences in their design. The connection design utilizes the expected capacity of the brace, but the expected capacity of a BRB includes the strain hardening in tension and compression expected during inelastic deformation. These result in very large connection design forces, especially for the brace in compression. Since BRBs are designed to avoid brace buckling, end rotation due to buckling of the brace is not expected. As a result, the 2tp clearance zone illustrated in Fig. 2 is not required, and the gusset plates are more compact than those used for SCBF systems. The large expected forces lead to thick, stiff gusset plates.

The use of the expected brace forces for connection design is a rational design concept, but it sometimes leads to the mistaken perception that a bigger, stronger gusset plate makes a better connection. As a result, gusset plate connections are generally relative stiff and strong for both SCBF and BRBF systems.

3. RESEARCH PROGRAM

A comprehensive research study addressing the seismic behavior of SCBF and BRBF braced frames has been initiated. The research includes both analytical and experimental investigations. Thirty-six full scale SCBFs and 7 full scale BRBFs have been tested. These tests realistically simulated the demands, capacities, and performance of the braced frames and the gusset plate connections. Figure 4 shows the test setup used for most test specimens. The specimens were subjected to a cyclic

inelastic deformation history based on the ATC-24 testing protocol, although a few tests employed a near-fault deformation history. The experimental results were used to develop, calibrate and verify analytical models that were used to extend the experimental results.

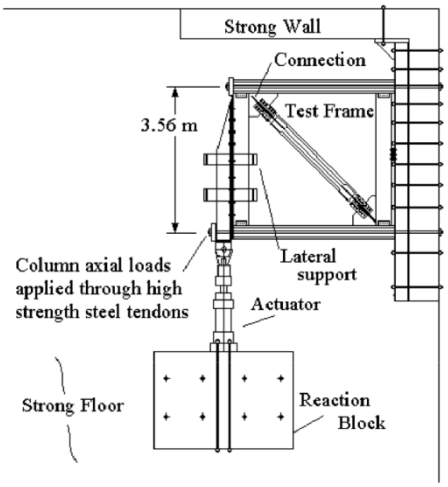


Figure 4. Typical Test Setup

4. SUMMARY OF SCBF RESULTS

The SCBF experimental results are too comprehensive for complete description here, but Fig. 5 illustrates the results from 4 different tests (Johnson 2005, Herman 2006, Kotulka 2007, Clark 2009, Powell 2010, Lumpkin 2009, Lehman et al. 2007). The frame geometry, beams, columns, and braces were identical for these 4 specimens, but the connections were different. Comparison of the 4 plots in Fig. 5 shows that there are dramatic differences in performance with these seemingly similar braced frames. The maximum inelastic deformation capacity shown in Fig. 5b is more than 2.5 times the maximum capacity of the specimens shown in Figs. 5a and 5d. The maximum resistance for the test specimen shown in Fig. 5d is approximately 40% larger that achieved with other specimens. This simple comparison clearly shows that the gusset plate design plays a major role in the inelastic performance of the SCBF system.

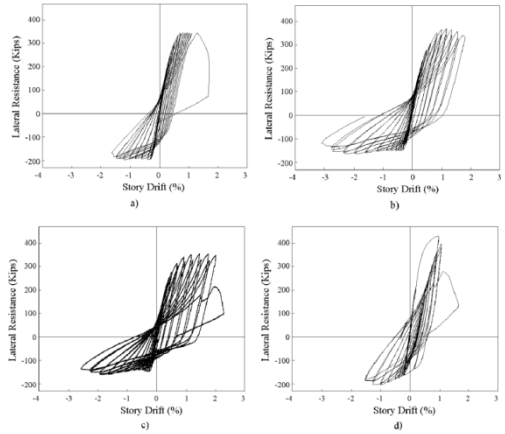


Figure 5. Typical SCBF Results

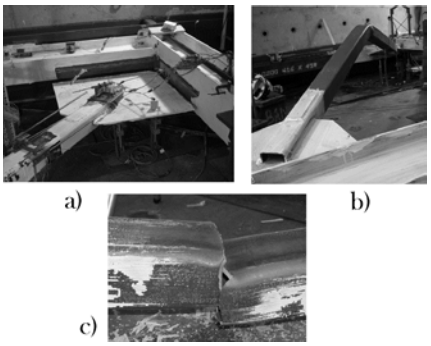


Figure 6. Photos of SCBF Tests

A wide range of behaviors were observed in these tests. More ductile specimens developed brace buckling with large out-of-plane deformations as shown in Fig. 6b. Ultimately these braces developed localization of yielding and brace tearing and fracture as shown in Fig. 6c. However, the deformation achieved before brace fracture was highly dependent upon gusset plate design. Extensive yielding and limited weld cracking was noted in the gusset plates, and this yield occurred regardless of the connection design. Weld cracking was generally controlled by the use of demand critical weld metal, but the tests clearly showed that the welds must be designed to develop the plastic capacity of the gusset plate rather than the UFM. Specimens with stiffer and stronger gussets also noted extensive yielding in the beams and columns and the reentrant corners of the gusset.

A number of observations were made from the experimental research, and a few key conclusions are noted here. These include:

1) Welds joining the gusset plate to the beam and column must be designed to achieve the plastic capacity of the gusset plate rather than the expected plastic capacity of the brace and the UFM.
2) The $8t_p$ elliptical clearance model significantly increases the inelastic deformation capacity of rectangular gusset plates. It permits smaller, more compact gusset plates, which reduce the size of the relatively rigid connection zone, and as a consequence reduce damage to the welds, beams and columns adjacent to the gusset plate. The vertical 6tp clearance zone provides similar performance for midspan gusset plates.
3) Yielding in the Whitmore width of the gusset plate is a desirable yield mechanism if it starts after initiation of yielding and buckling of the brace. This yielding minimizes damage to the welds and reduces local buckling and yield deformation in the beams and columns.
4) The strength and stiffness of the gusset plate must be adequate to assure that the brace develops it full resistance and inelastic deformation capacity, but it should not be excessively stiff or strong, because this causes early brace fracture.
5) The effective length of the brace should be taken as the true brace length when these rules are employed.
6) Tapered gusset plates may provide good end rotational capacity for the brace, but they may result in thicker gussets or greater inelastic demands on the gusset plate and the welds.

To incorporate these conclusions a balanced design procedure was proposed (Roeder et al. 2005, 2012). This balanced design method utilizes the $8t_p$ elliptical clearance model for corner gusset plates and a $6t_p$ vertical clearance band for midspan gusset plates. These clearance models establish the basic size and geometry of the connection. Plate thickness, weld size, and other gusset requirements are determined from yield mechanisms and failure modes, but these failure modes are evaluated with balance factors (β factors) rather than the resistance factors commonly used in design. The proposed procedure is similar to current design methods in that the framing elements are designed to resist the factored loads, and the connection design utilizes the expected tensile yield ($R_yF_yA_g$) and compressive buckling ($R_yF_{cr}A_g$) capacities of the brace for design. A balanced design procedure is used to evaluate the resistance associated with each yield mechanism and failure mode for the frame and the connection. The consequence of this method is a 46% increase in the resulting inelastic deformation of the system prior to initial failure over that achieved with the current SCBF design method.

The inelastic deformation capacity achieved with SCBFs varied depending upon the brace type and the gusset plate connection design procedure. SCBFs with HSS rectangular tube braces achieve somewhat less inelastic deformation capacity than SCBFs with wide flange braces. Frames designed by current procedures with rectangular tubes achieved total inelastic deformation ranges between approximately 1.5% and 5.6% prior to initial failure with an average value of approximately 3.5%. SCBFs with HSS rectangular tubes but designed with enhanced balanced design procedure noted above achieved total inelastic deformation ranges of between approximately 3.9% and 5.4%, with an average value approximately 46% larger than that achieved by current design method. Frames designed by this enhanced method on average had significantly less inelastic deformation and damage to the beams and columns. SCBFs designed by the enhanced gusset plate design procedure with wide flange braces achieved total inelastic deformation ranges between 5.5% and 6%..

5. SUMMARY OF BRBF RESULTS

Severn BRBFs were tested. Six of the specimens were single-story frames with bolted connections (Christopulos 2005). These frames were tested in the apparatus as illustrated in Fig. 4. BRBF5 was a single-story specimen designed with a rectangular gusset with slip critical bolts and the core plate of the BRB was oriented in the plane of the braced frame. This specimen was designed to simulate current design practice for bolted BRBF gusset plate connections. The AISC Uniform Force method was used to design the gusset after considering the strain hardening of the brace in tension and compression. Typical strain hardening factors of 1.5 to 1.55 were used for tension and compression in the connection design. The bolts were designed as slip critical bolts considering the brace load capacity after strain hardening of the brace. The gusset plate and rib plate thicknesses match the BRB core thickness (19 mm) according to usual practice. The plate was quite stiff and the nominal design stress in the plate based upon the Whitmore width was quite small. The rib plate was extended to within 25mm of the face of the beam flange.

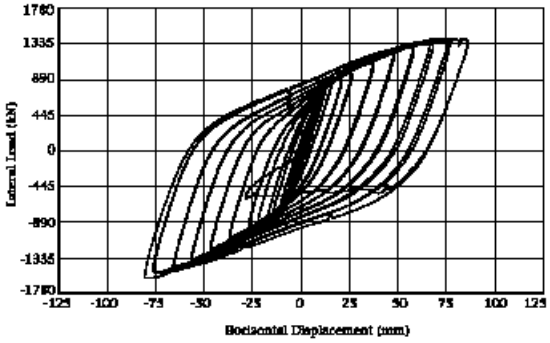


Figure 7. Force-Deflection Behavior of Reference Specimen.

Figure 7 shows the resulting story shear force-deflection plot for this test specimen. The hysteresis curves are full with substantial energy dissipation. However, the frame reached moderate story drift angles of 2.5% and -2.4%. This resulted in a total story drift range of approximately 4.9%. The frame experienced large deformations and yielding in the beams and columns adjacent to the gusset plates at this deformation as illustrated in Fig. 8. This beam yield deformation led to out-of-plane rotation of the beam flange and web and nearly rigid body rotation of the gusset plate. The gusset connection rotation produced an eccentricity in the BRB, and this resulted in large out-of-plane deformation demands on the BRB. This caused the ultimate out-of-plane plastic deformation failure of the brace shown in Fig. 9.

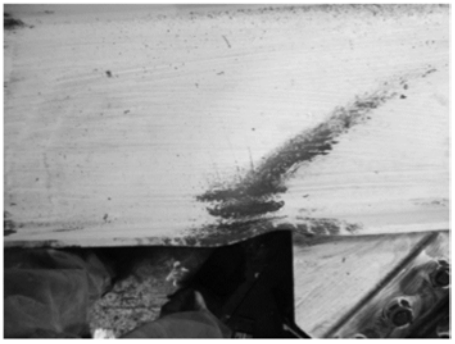


Figure 8. Local Yielding in the Beam Adjacent to Gusset



Figure 9. Out-of-Plane Plastic Deformation of BRB

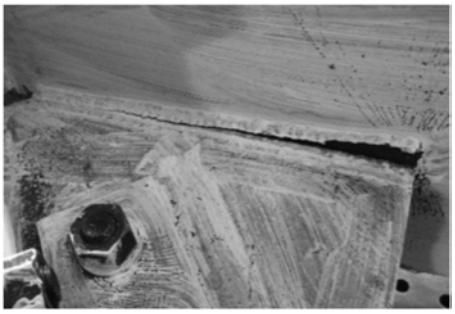


Figure 10. Crack Initiation and Ductile Tearing of Welds.

Significant inelastic deformation damage to the beams and columns in the region of the gusset plate connections occurred. Local yielding initiated at drift levels less than 1%, and the severity and extent of yielding increased as the deformation of the frame increased. Figure 8 is a photo showing the extent of yielding in the beam at the corner of the gusset plate at the end of the test. Welds attaching the gusset plate to the beams and columns initiated cracking at drifts slightly less than 2%, and the crack length grew in a ductile manner through increasing inelastic deformations. At the end of the test, the weld crack adjacent to the gusset had grown to a significant length as shown in the photo of Fig. 10.

Other variations of the single-story bolted connection specimens were tested, and some variations achieved story drift ranges up to 5.4%. However, all specimens had extensive yielding in the beams and columns, and some dramatic failure modes were noted. Figure 11 shows a beam flange fracture at the edge of the gusset plate for specimen BRBF1. This fracture occurred after extensive yielding of the beam, and it limited the total inelastic deformation range to 4.2%.

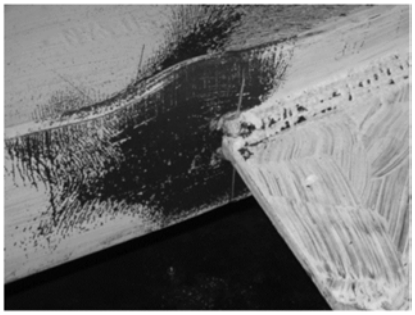


Figure 11. Beam flange fracture noted with BRBF1.

Specimen BRB6 was also a single-story bolted connection, it was manufactured in a different lot. It ultimately developed weld fracture of the gusset as shown in Fig. 12. Current gusset plate design procedure designs the gussets for the maximum expected axial load in the BRB, but the actual stresses in the gusset are much larger than the design stresses because of the frame deformation, and these stresses and the deformations associated with the local yielding place increased demands on the welds.

Hysteretic curves for the bolted single-story BRB test frames were full with good energy dissipation. The accumulated plastic strains observed in the BRBs of this test program where comparable and consistent with those observed in other past research. However, the total inelastic deformation capacity of the frames was disappointing. Past tests on BRBs suggest that larger deformations of the brace are possible. The maximum story drifts achieved in these tests were larger than those normally expected with small or moderate seismic events, but they were smaller than commonly expected for extreme, infrequent seismic events such as required in US practice. The observed limitation in the frame deformation capacity frequently was caused by the gusset plate connection and the inelastic damage induced in the beam and column by the connection rigidity. The BRBs provide good inelastic behavior in that they did not cause the ultimate failure.



Figure 12. Gusset weld fracture for specimen BRBF6.

A 3-dimensional 2 story BRBF with pin-ended braces was tested at the University of Minnesota MAST facility. Results of this test are not fully analyzed, and conclusions are somewhat limited. Because of the pinned end BRBs, the gussets were more compact than those required for the bolted gussets, but they were still relatively thick and stiff. Significant inelastic deformation in the framing members was also noted in this frame. Figure 13 shows weld cracking at the gussets because of the extensive yielding in the connection area. Figure 14 shows the extensive column yielding at the gusset location. While results are preliminary, the inelastic deformation was somewhat larger than noted with the bolted connection tests, since the total inelastic deformation range was approximately 7% before failure of the BRB.



Figure 13. Weld cracking of gusset plate



Figure 14. Yield damage and deformation to column

6. CONCLUSIONS

A comprehensive study of the inelastic seismic performance of SCBF and BRBF systems has been completed. The study includes a wide range of experiments and inelastic analyses. Little discussion of the inelastic analysis is provided here due to space limitations. The research shows that inelastic deformation capacity of both BRBFs and SCBFs is highly dependent upon their connection to the other framing members. A balanced design procedure, which significantly increases the inelastic deformation capacity of the SCBF system, was developed, and this procedure significantly increases the deformation capacity achievable from a given system. This procedure results in lighter more compact gusset plates and it reduces the inelastic deformation in the framing members. BRBs are very ductile with large deformation capacity when loaded under axial load. However, when employed in a frame structure, they cause significant local yielding in the beams and columns and this yielding may ultimately reduce the deformation capacity achieved by the BRBF system.

Acknowledgements:

The National Science Foundation under grants CMS-0301792, Performance-Based Design of Concentrically Braced Frames and CMS-0619161, NEESR-SG International Hybrid Simulation of Tomorrow's Braced Frames funded this research. Supplemental funding was provided by AISC. The Nippon Steel and Star Seismic Corporations donated the BRBs. International testing, fabrication and collaboration was conducted at the NCREE Laboratory in Taiwan with Dr. Keh-Chyuan Tsai, Laboratory Director. Testing was also completed at the University of Minnesota, MAST Laboratory with Prof. Carol Shield coordinating. Frequent advice and guidance was provided through the research Advisory Group, composed of Tom Schlafly (AISC), Tim Fraser (CANRON), Walterio Lopez (Rutherford and Chekene), Larry Muir (CIVES) and Rafael Sabelli (Walter P. Moore). The advice and financial support of these individuals and institutions is greatly appreciated.

References:

AISC, (2005a). "Seismic Provisions for Structural Steel Buildings," American Institute of Steel Construction, Chicago, IL

AISC (2005b). "*Steel construction manual*," 13th Ed., 2005, American Institute of Steel Construction, Chicago, IL

Christopulos, A. (2005) "Improved Seismic Performance of Buckling Restrained Braced Frames," a thesis submitted in partial fulfillment of the requirements for the degree of MSCE, University of Washington, Seattle, WA.

Clark, K.A. (2009) "Experimental performance of multi-story X-brace systems," *a thesis submitted in partial fulfillment of the MS degree*, 2009, University of Washington, Seattle

Herman, D. (2007) "Further improvements on and understanding of SCBF systems," a thesis submitted in partial fulfillment of the Master of Science Degree at the University of Washington, Seattle, WA.

Johnson, S. (2005) "Improved seismic performance of concentrically braced frames," a thesis submitted in partial fulfillment of the Master of Science Degree at the University of Washington, Seattle, WA

Kotulka, B. (2007) "Analysis for a design guide on gusset plates used in special concentrically braced frames," a thesis submitted in partial fulfillment of the Master of Science Degree at the University of Washington, Seattle, WA.

Lehman, D.E., Roeder, C.W., Herman, D., Johnson, S., and Kotulka, B., (2007) "Improved Seismic Performance of Gusset Plate Connections," submitted for publication review, ASCE, *Journal of Structural Engineering*, Reston, VA.

Lumpkin, E.J. (2009) "Enhanced seismic performance of multi-story special concentrically brace frames using a balanced design procedure," *a thesis submitted in partial fulfillment of the MS degree*, 2009, University of Washington, Seattle.

Powell, J.A. (2010) "Evaluation of special concentrically braced frames for improved seismic performance and constructability," *a thesis submitted in partial fulfillment of the MS degree*, 2010, University of Washington, Seattle.

Roeder, C.W., Lehman, D.E., and Yoo, J.H., (2005) "Improved Seismic Design of Steel Frame Connections," *International Journal of Steel Structures*, Korean Society of Steel Construction, Seoul, Korea, Vol. 5, No. 2, pgs 141-53

Roeder, C.W., Lumpkin, E.J., and Lehman, D.E. (2012) "Balanced Design Procedure for Special Concentrically Braced Frame Connections," submitted for publication review, *Journal of Constructional Steel Research*, Elsevier.

Thornton, W.A., (1991) "On the Analysis and Design of Bracing Connections," AISC, *Proceedings of National Steel Construction Conference*, Section 26, pgs 1-33.

Whitmore, R.E., (1950) "Experimental Investigation of Stresses in Gusset Plates," a thesis submitted in partial fulfillment of the Master of Science Degree at the University of Tennessee, Knoxville, Tennessee.

8CUEE CONFERENCE PROCEEDINGS
8th International Conference on Urban Earthquake Engineering
March 7-8, 2011, Tokyo Institute of Technology, Tokyo, Japan

SEISMIC DESIGN OF RECENT PROJECTS ON TOKYO TECH O-OKAYAMA CAMPUS

Toru Takeuchi

Professor, Dept. of Arch. & Build. Eng., Tokyo Institute of Technology, Japan

Abstract: This paper briefly reports the seismic design concepts of recent projects realized on Tokyo Tech O-okayama campus. We first describe the superstructure of the new library named the Glass House. The discussion includes the structural design and its seismic performance. We then describe the seismic retrofit design of the Secretariat 1st Building originally built in 1967. New energy-dissipating diagonal louvers are adopted for this retrofit deign; they are developed from the integrated façade concept used in the retrofit of the Midorigaoka-1st building.

1. INTRODUCTION

The 8th International Conference on Urban Earthquake Engineering will be held in March 7-8, 2011, at the O-okayama Campus of the Tokyo Institute of Technology. By March, several construction projects near the conference venue will be completed, and some of them are notable from the viewpoint of seismic design. This paper briefly describes the design of two projects recently carried out on the Tokyo Tech O-okayama campus.

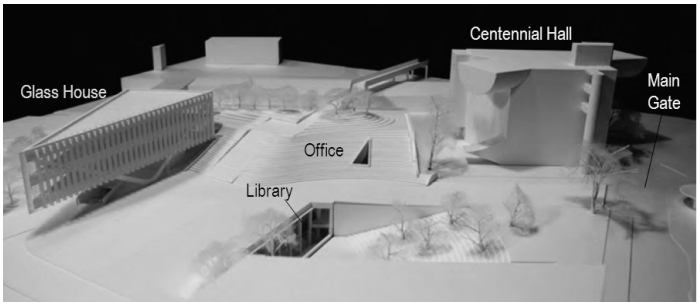


Figure 1 New Library, Tokyo Institute of Technology

2. THE NEW LIBRARY

2.1 Project Outline

The existing library at Tokyo Tech was built in 1970, and in recent evaluations, it was found to have insufficient seismic performance. Several retrofit designs were considered, but they were not adopted because of the deterioration of the concrete materials. They also would have required additional frames in the interior spaces which reducing the functionality of the library. Thus, the university decided to build a new library as part of its 130th anniversary celebrations. The authors proposed an underground library to maintain an unobstructed view along the axis from the main gate to the main building and to keep valuable documents away from sunlight. However, a small above-ground building was added to the design; it is intended for students' study and discussions and is a symbol of the library. This building has been named as Glass House. Figures 1 to 3 show the expected view, a sectional view, and the plan of the B1 level. The library facility consists of the underground library, service office under an artificial hill, and the Glass House. The library is spread over two levels, B1 and B2, and the main entrance is located under the Glass House. Dry pits are distributed around the underground library, to supply the natural lights to the floors.

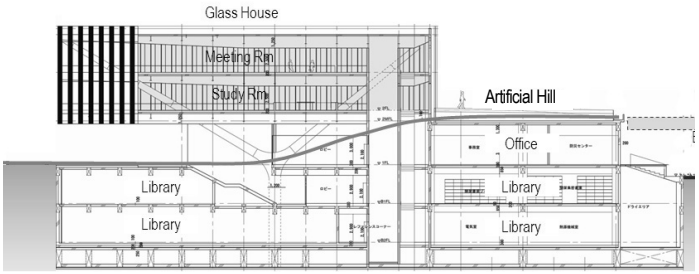


Figure 2 Section of New Library

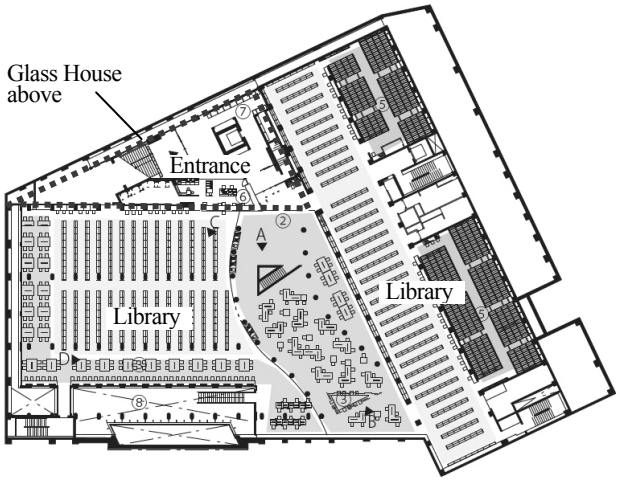


Figure 3 Basement Plan of new Library

2.2 Glass House Structure

The structural system of the Glass House is shown in Figure 4. This building has three triangular stories. Each floor is supported by three sets of V-shaped diagonal columns, and perimeter beams to connect them each other. Perimeter frames composed of perimeter beams and plate columns in second and third floors form a Vierendeel truss. The toe of the plan is a 15 m cantilever, supported by a pair of diagonal columns. The overturning moment of the whole structure is anchored by the back diagonals. The EV shaft composed of truss frames with concrete walls receive about 50% of the horizontal force. The EV shaft and perimeter frames are connected by steel floor beams and concrete slabs.

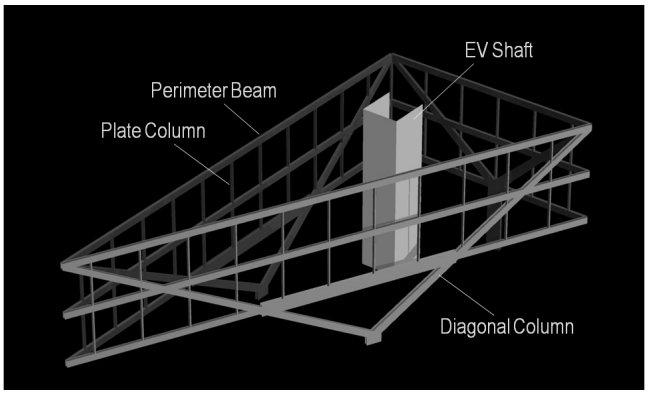


Figure 4 Structural System of Glass House

Figure 5 shows the details of the steel structure. All the diagonal columns, perimeter beams, and plate columns are designed with double-plate sections connected with thin stiffeners. The axial force and bending moment are transferred through the double plate only, and connections at the stiffeners are not required. This system simplifies the connection between the diagonal columns and perimeter beams and is also effective for easy site-welding. These systems are already sketched in the preliminary design stages as shown in Figure 6(a).

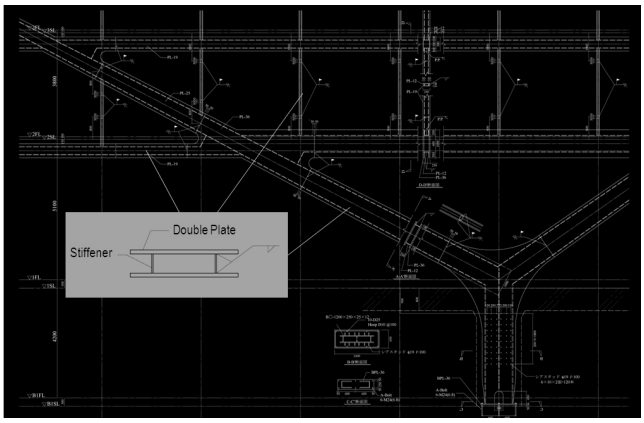


Figure 5 Details of Glass House Structure

Figure 6(b) also shows alternative structural systems considered at the preliminary design stage. Options included the as truss option or parabola option, but the simplest system directly supporting the toe was selected. There were also discussions whether vertical strut and diagonal damper member should be attached around the supporting diagonal columns as in Figure 6(c). However neither was employed to avoid the obstruction around the entrance.

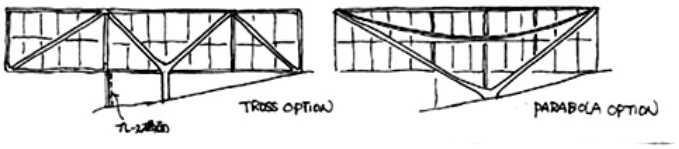


Figure 6(b) Alternative Structural System at Early Stage

2.3 Seismic Performance of Structure

Figure 7 shows the bending-moment distributions under vertical loads. Because the vertical strut has been omitted, bending moments appear for the second floor perimeter beam between the two diagonal columns. To withstand this

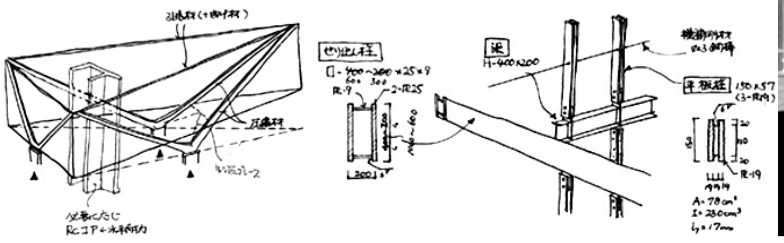


Figure 6(a) Structural Sketches at Early Stage

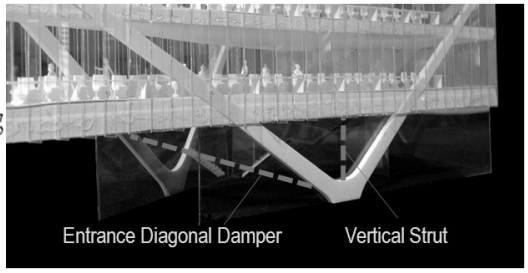


Figure 6(c) Additional Members Considered

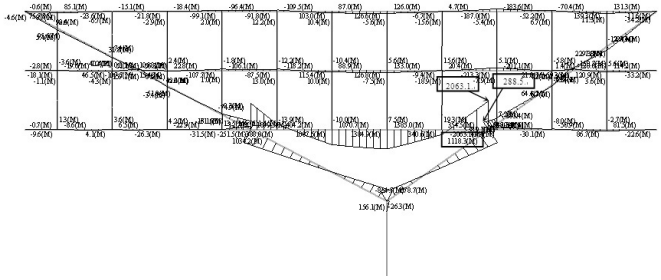


Figure 7 Bending Moments under Vertical Load

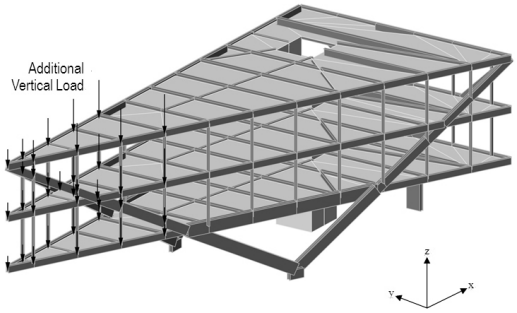


Figure 8 Vertical Seismic Loads in Cantilever Zone

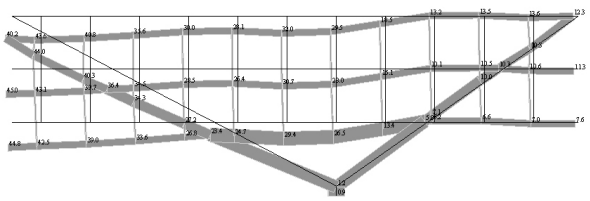


Figure 9 Deflections under Vertical and Seismic Loads

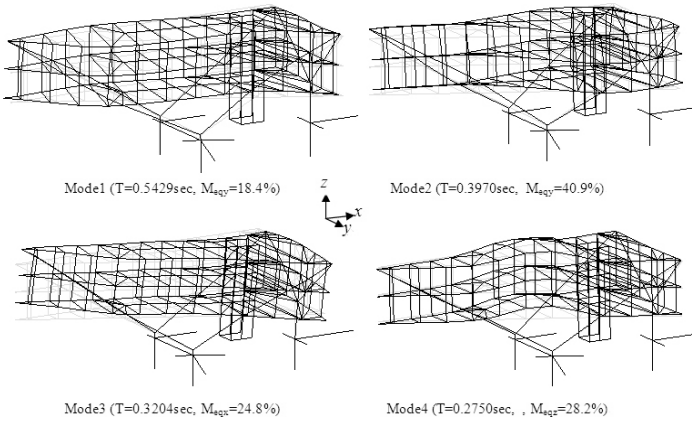


Figure 10 Vibration Eigenmodes

bending moment, the depths of the perimeter beams in this zone were increased from 500 mm to 1000 mm. Thus, the structural system of this building is not a pure axial system, but include partial bending elements.

In the seismic design, a static seismic force of base-shear C_0=0.2 was considered for the allowable stress design, and a base-shear of C_0=0.4 was considered for the ultimate strength design. A vertical seismic force of 1.0 times the self -weight was also considered, as shown in Figure 8, to estimate the vertical response excitation. Figure 9 shows the deflection distribution under vertical and seismic loads. The maximum vertical deflection at the toe is estimated to be around 45 mm.

To analyze the dynamic characteristics, eigenvalue analyses were carried out. Figure 10 shows the vibration modes and natural periods obtained. Because the entrance diagonal damper has been omitted, the twisting modes first appear as the forsta and second modes, which dominate the vibration in the y- (transverse) direction. The natural periods of these modes are 0.54 and 0.40 sec, respectively. The third vibration mode excites vibrations in x- (longitudinal) direction and vertical vibrations in the toe zone, the natural period of which is 0.32 sec. the fourth mode is vibration of the Vierendeel truss in the z- (vertical) direction around the bending zones between the diagonal columns, the natural period of which is 0.28 sec. All these vibration modes have similar natural periods, and the seismic response of this structure is expected to include the combination of these modes. The measured vertical natural period at the toe zone in the construction site was about 0.23 sec. which generally meets the analyses considering the effect of the live loads and the stiffness of the curtain walls.

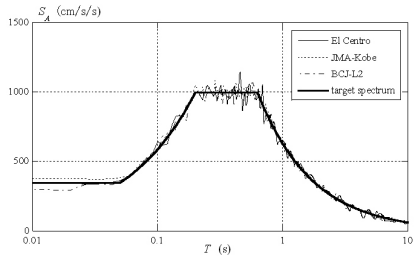


Figure 11 Acceleration Response Spectrum for Applied Seismic Input

Table 1: Maximum Deflections at Toe

Static Analysis (C_0=0.4+Vertical 1.0)			(mm)
mm	2nd Floor	3rd Floor	Roof
X-dir.	6.1	13.8	19.5
Y-dir.	27.1	33.2	28.9
Z-dir.	52.4	52.0	46.1
Time-history Analysis			(mm)
X-dir.	16.5	22.6	25.1
Y-dir.	88.6	77.9	61.8
Z-dir.	35.8	35.7	32.6

Table 2: Maximum Story Drift Angle

Static Analysis (C_0=0.4+Vertical 1.0)			(%)
mm	1st Floor	2nd Floor	3rd Floor
X-dir.	0.11	0.15	0.15
Y-dir.	0.11	0.24	0.28
Time-history Analysis			(%)
X-dir.	0.10	0.17	0.21
Y-dir.	0.39	0.31	0.46

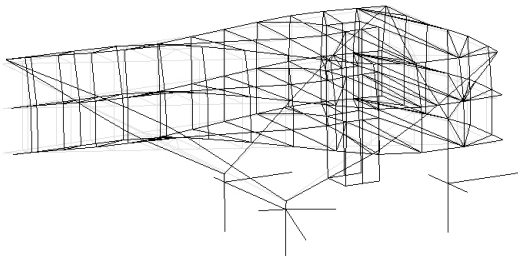


Figure 12 Maximum Deflection in Time-History Analysis



Figure 13 Completion of Steel Structure

The seismic performance of the structure is also evaluated by time-history analyses. The acceleration response spectrum of the seismic input is shown in Figure 11.Because the dominant natural periods are around 0.3 to 0.5 sec., about 1000 cm/sec^2 of acceleration is expected to be excited. In the analyses, all members are assumed to be elastic, and the damping is set as $h = 0.02$ for the first mode. The results are compared with static analyses in Tables 1 and 2. Table 1 indicates the maximum deflections of the toe in each direction. In the x - and y - directions, the maximum values obtained by the time-history analyses are two to three times of the static ultimate loads. In the z - direction, the values under static loads exceed the results from the time-history analyses, because of the additional vertical seismic loads shown in Figure 8. Table 2 shows the maximum story drift under both estimations. Again, the values of the time-history analyses are around two to three times the static results, and both satisfying required drift limit of 1/200=0.5%. The maximum vertical acceleration calculated at the toe is about 1900 cm/ sec^2, but the displacement amplitudes are relatively smaller than the static evaluations.

In these conditions, all the members remain within the ultimate strength. This means that the structure of the Glass House generally stays within the overall elastic limit for seismic input shown in Figure 11.

Construction work started April 2009, and is expected to be completed in February 2011. Figure 13 shows a view of the construction site in November 2010, the steel structure of the Glass House has been completed.

3. SEISMIC RETROFIT OF SECRETARIAT BUILDING

3.1 Project Outline

The secretariat 1st building (Figure 14) on O-okayama campus, located just beside the main building, was constructed in 1967 and designed by the famous architect, Professor Kiyoshi Seike. In a 2007 evaluation, the seismic performance of this building was judged to be insufficient, and was decided that the retrofit is necessary.

The building has a unique front façade composed of the president's office with vertical concrete louvers supported by pilotis columns. As shown in Figure 15, four stories of office floors are attached behind the front block. The evaluated seismic indexes are plotted in Figure 16. The required level is Is = 0.7. The x - (longitudinal) direction frame has enough strength except for the first floor, but the y - (transverse) direction frame is insufficient for the first to third floors. The concrete strength satisfied the designed strength and the chemical neutrality of the concrete was not progressed. To reinforce the longitudinal frames, additional concrete walls or braces along the windows of the office blocks and between the front pilotis columns were considered. However, this concept had problems:

1) To prevent alteration of the building's appearance, additional braces between the front columns should be avoided.
2) In the office floors, the spaces between the columns are occupied by various facilities, so additional braces



Figure 14 Secretariat 1st Building

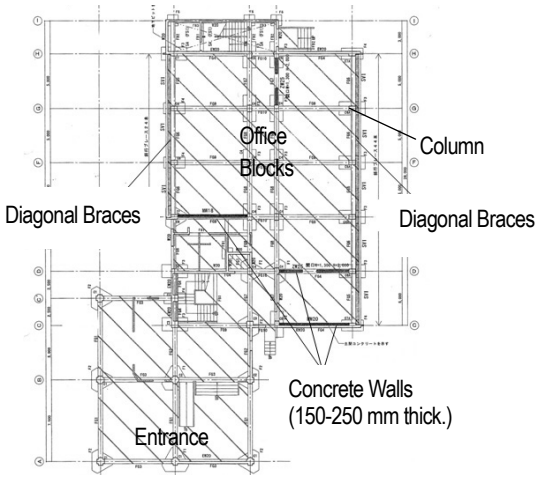


Figure 15 Ground Floor Plan of Secretariat 1st Building

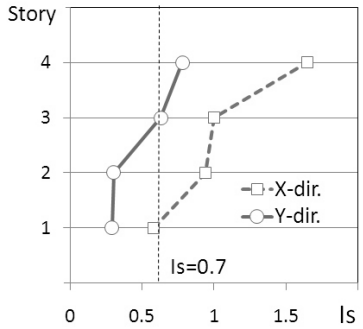


Figure 16 Seismic Index Before Retrofit



(a)Before Retrofit



(b) After Retrofit

Figure 17 Midorigaoka 1st Building Retrofit



(a) Conventional Retrofit



(b) Diagonal Energy-Dissipation Louver

Figure 18 Diagonal Energy-dissipation Louver Concept



Figure 19 Diagonal Louver Mock-ups

between the columns are not desirable. Concrete walls that block the windows are not acceptable.

3.2 Retrofit Concept

The integrated façade concept is applicable to this situation. This concept aims to design a new façade that simultaneously improves the architectural features, the seismic performance, and the energy efficiency. The concept was first applied to the seismic retrofit of Midorigaoka-1st building in 2006; as in Figures 17(a) and 17(b). (Takeuchi et al.2006) The new façade is composed of seismic energy dissipation braces, horizontal louvers, and glasses. Because hysteretic dampers are used as energy dissipation braces, the seismic performance retains the elasticity of the main frame up to a Level-2 earthquake. The authors also developed diagonal energy-dissipating louvers with the diagonal parallel louvers acting as buckling-restrained braces. Diagonal parallel louvers in the east and west walls of buildings are known to be effective for controlling sunshine.

The buckling-restrained braces have small sections as 80mm x 150mm, providing 300kN of yield strength. Sections of each louver are designed to reflect the sunshine into the room. Figures 18 show images of the conventional steel-brace retrofit (Figure 18(a)) and the diagonal energy-dissipating louver concept (Figure 18(b)). In the proposed method, the obstruction of the inner space is minimized and the interior appearance is improved. The efficiency of this system is confirmed by a mock-up test (Figure 19) and an element structural test (Figure 20). The figure indicates the presence of stable hysteresis loops up to 2% axial strain ratio, which is equivalent to 1% story drift.

3.3 Retrofit Design

For the secretariat 1st building, the above concept was considered. However, it is not desirable to attach the new louver to the outside, because the original office block façade has sophisticated site-casting walls and is one of the masterpieces characterizing this building. Therefore, we proposed distributing the diagonal louvers inside between the wall and columns, as shown in Figure 21. This treatment decreases the thermal control, but still reduces the direct sunshine effectively. Each diagonal brace has 300kN of yield force and stable hysteresis for dissipating the seismic energy after the yielding. Because this type of buckling-restrained braces has complete symmetrical hysteresis between compression and tension, a one-way diagonal layout provides

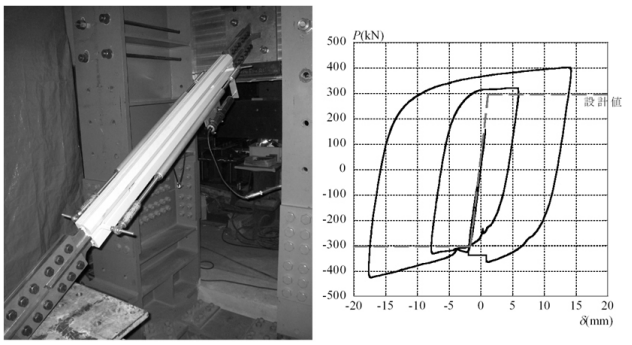


Figure 20 Structural Test of Diagonal Louver

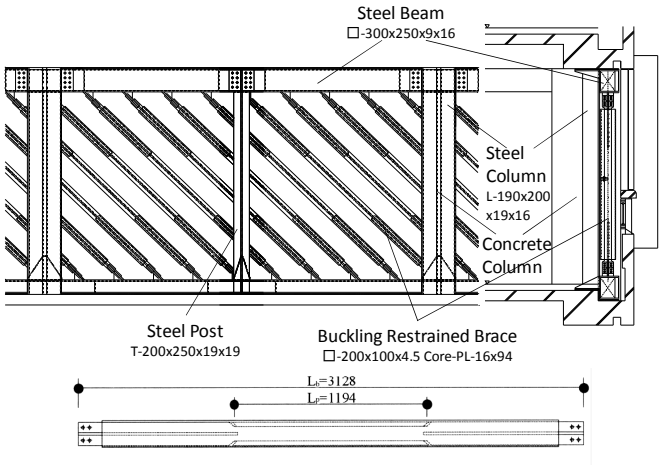


Figure 21 Layouts of Diagonal Braces

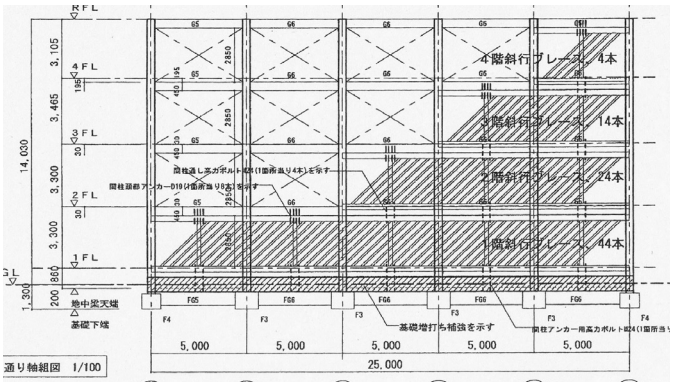


Figure 22 Layouts of Diagonal Braces in South Facade

the same performance in both directions. Ten diagonal braces are distributed in one bay between column-to-column which consist 2000kN strength of shearwall, which is equivalent to ordinary steel-brace reinforcement. Each brace has a section of 100mm x 200mm with the conventional composition of buckling-restrained braces. As in Figure 21, the length of the plastic zone in each brace is set to about 1/3 of the total length, to obtain a small yield deflection for dissipating energy from a small story-drift angle.

To transfer the seismic force to these braces, an outer frame composed of box beams and L- or T- section columns is provided and attached to the existing concrete columns. These frames are attached in the perimeter zone between the columns and outer walls, and they are fixed by anchor bolts and epoxy resin. The diagonal brace layout in the south façade is shown in Figure 22. The braces are fully distributed on the first floor; they are decreased on upper floors, because the required additional shear strength is less. The figure shows that the diagonal braces form large triangular elements.

The additional braced frames are placed on the existing frames with eccentricity, and the elastic deformation of the outer frames decreases the effect of hysteretic damping. To confirm these effects, we carried out FEM analyses as shown in Figure 23. In the FEM analyses the outer frames and core plates of the diagonal buckling restrained braces are modeled with shell elements, and shear forces equivalent to the yield forces of the braces are applied to the outer surface of the existing columns. The deflection distributions of the frame are shown in Figure 23(a). The maximum horizontal deformation was about 9.4 mm, which is equivalent to a story drift angle of 0.28%. (about 1/350). The existing fame is considered to start deteriorating from 0.4% rad. (1/250) story drift, and the brace is expected to dissipate energy between these story drifts. The stress distributions of the frame are shown in Figure 23(b). At the brace yielding point, the frame is fully within the elastic range. The effects of these energy dissipation braces are discussed below.

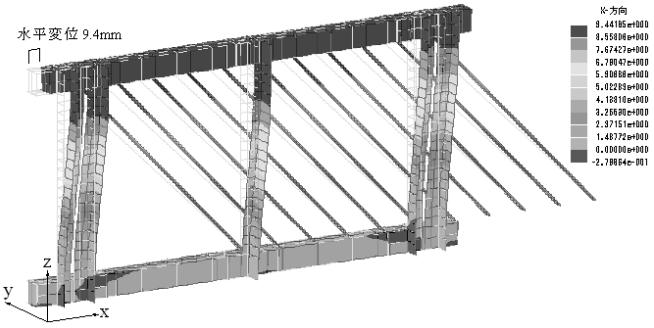
3.4 Seismic Performance of the Structure

The current Japanese seismic retrofit design recommendations use the seismic index defined as;

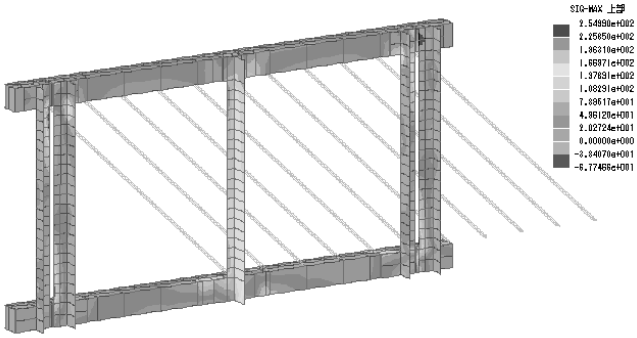
$$I_{Si} = F_i \cdot C_i = \frac{Q_{Ei}}{Q_{ui}} \cdot \frac{Q_{ui}}{\left(F_{esi} \cdot Z \cdot R_t \cdot A_i \cdot \sum W_i\right)} = \frac{Q_{Ei}}{\left(F_{esi} \cdot Z \cdot R_t \cdot A_i \cdot \sum W_i\right)} \qquad (1)$$

where, Q_{Ei} is the elastic response shear force in the i^{-th}-story, Q_{ui} is the ultimate shear strength of i^{-th}-story, F_{esi} is the multiplier for stiffness ratio and eccentricity ratio, Z is the site effect, R_t is the acceleration spectrum index, C_i is the shear strength coefficient in the i^{-th}-story, F_i is the ductility factor in the i^{-th}-story, W_i is the Weight in the i^{-th} -story, A_i is the height multiplier reflecting the first vibration mode.

Eq.(1) indicates the seismic index defined by the product of the shear strength coefficient and the ductility factor based on the property of energy conservation. When this concept is applied to damper-added structures, Kuramoto et al. (2002), Takeuchi et al. (2010) propose introducing D_h factor to evaluate the response reduction by equivalent damping, as follows;



(a) Deflection Distribution



(b) Stress Distribution

Figure 23 FEM analyses for Braced Frame

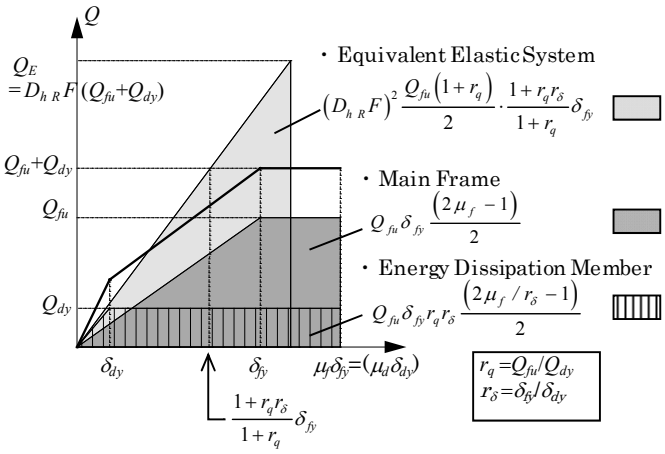


Figure 24 Seismic Index with Energy Dissipation Members

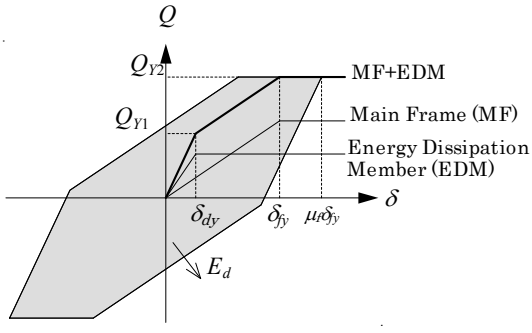


Figure 25 Equivalent Damping Ratios

$$ {}_R F = F / D_h \tag{2} $$

$$ D_h = C_{ec}\sqrt{\left(1+\alpha h_0\right)/\left(1+\alpha h_{eq}\right)} \qquad \left(\alpha = 25, h_0 = 0.02\right) \tag{3} $$

$$ C_{ec} = 1/\left(1 - 0.025\ K_d / K_f\right) \tag{4} $$

where, h_0 is the original damping ratio, h_{eq} is the equivalent damping ratio considering effect of energy-dissipation elements, C_{ec} is the reduction factor for hysteresis bias.
Introducing Eq.(2)-(4), Eq.(1) becomes

$$ I_S = \left(C_f + C_d\right)\cdot {}_R F = \frac{\left(C_f + C_d\right)\cdot F}{D_h} = \frac{C_f \cdot F_f + C_d \cdot F_d}{D_h} \tag{5} $$

Where, the shear strength coefficient of the existing frame is

$$ C_f = Q_{fu} / \left(F_{es} \cdot Z \cdot R_t \cdot A_i \cdot \sum W_i\right) \tag{6} $$

and the shear strength coefficient of the additional damper is

$$ C_d = Q_{du} / \left(F_{es} \cdot Z \cdot R_t \cdot A_i \cdot \sum W_i\right) \tag{7} $$

Figure 23 indicates the proposed relationship between the *Is* index and the hysteresis of the frame and dampers. In this relationship, D_h F can be calculated from the following equation.

$$ D_h\ {}_R F = \sqrt{\frac{2\mu_f - 1 + \left(2\mu_f - r_\delta\right) r_q}{1 + r_q r_\delta}} \tag{8} $$

where r_q and r_d are the shear strength ratio and yield deflection ratio between the existing frame and dampers. When F_f is 1.0-1.3, the equivalent F_d is distributed above 3.0, and this value is used in the following.

To estimate D_h, the equivalent damping ratio h_{eq} is required. When the existing frame is at elastic limit (μ_f= 1.0 in Figure 24), the equivalent damping ratio h_{eq} can be estimated by the following equation.

$$ h_{eq} = h_0 + \frac{1.6}{\pi} \times \left\{ \frac{\delta_{dy}}{\delta_{fy}} \frac{\left(K_d / K_f\right)\left(\delta_{fy} - \delta_{dy}\right)}{\left(K_d / K_f\right)\delta_{dy} + \delta_{fy}} \right\} \tag{9} $$

In this project, the stiffness ratios of the braces to the existing frames K_d/K_f range from 2.0 in the first floor to 0.5 in the fourth floor, and the yield ratios are estimated to be δ_{dy}=9.3 mm and δ_{fy}=13 mm. The estimated seismic index in the x-direction after the retrofit is shown in Figure 26. The numbers of braces are distributed so as to satisfy *Is* > 0.7 with their yield shear strength (labeled "After" in the plot). The plot labeled "Substantial" contain the values derived from Eqs.(5) and (9). The substantial indexes are distributed around *Is*=1.0, which means that the retrofitted structure will generally withstand an earthquake with a response of 1000cm/sec^2 up to the elastic limit of the existing frames.
The retrofit construction began in July 2008 and completed in March 2009. Figure 27 shows the attachment of the frames and braces. All works was carried out using only chain-blocks and human power. Each component was divided into pieces of less than 100 kg connected by friction bolts and site welding. The completed interior view is shown in Figure 28(a) and an exterior view is shown in Figure 28(b). The additional braces do not affect the interior space, and the effect on the existing façade is considered to be minimal.

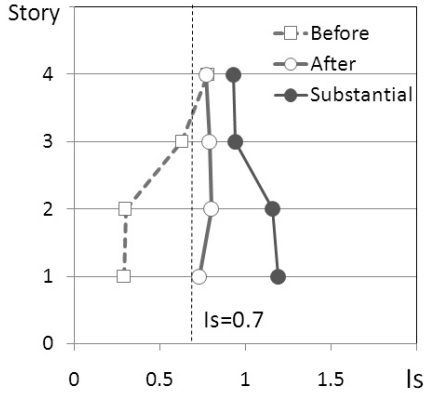


Figure 26 Seismic Index after Retrofit (x-direction)


Figure 27 Attachment of Braced Frames


(a) Interior View


(b) Exterior View

Figure 28 Completion Views after Retrofit

4. CONCLUDING REMARKS

We have presented the project outlines for the superstructure of the new library building and the secretariat building retrofit, and discussed their seismic performances. Generally the structures are designed to withstand level-2 earthquake with maximum acceleration response of 1000cm/sec^2 at their elastic limit. They are expected to be usable after such an earthquake. Another new building, the environment and energy innovation center is also under construction. This building is covered by solar panels and has buckling -restrained braces at the perimeter frames, as shown in Figure 29(a) and (b), and designed to retain similar seismic performance. Their locations of the projects on O-okayama campus are indicated in Figure 30.

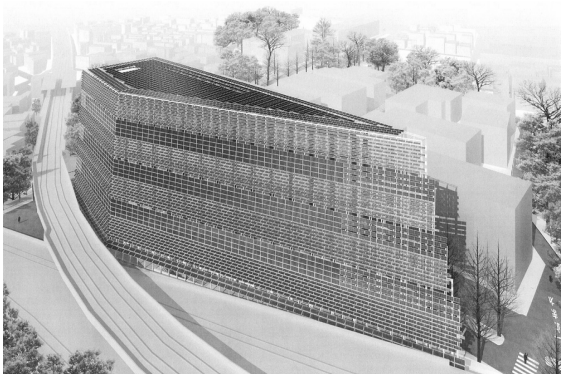
Acknowledgements
The credit for each project is as follows;
New Library: Architectural design by Koichi Yasuda Lab. and Sato-sogo Associates, structural design by Toru Takeuchi Lab. and Sato-sogo Associates, project management by facility management division of Tokyo Institute of Technology.
Secretariat Building Retrofit: Design by Sowa giken, Toru Takeuchi Lab. and project management by facility management division of T Tokyo Institute of Technology.

References

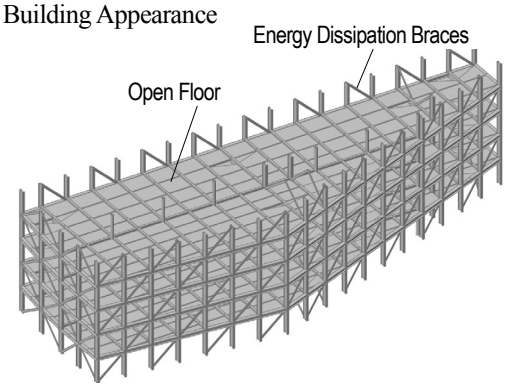
Kuramoto, H., Iiba, M., Wada, A., (2002), "A Seismic Evaluation Method for Existing Reinforced Concrete Buildings Retrofitted by Response Controlling Technics", *Journal of Struct. Constr:Eng.*, A.I. J, No.559, 189-195.(in Japanese)

Takeuchi, T., Yasuda, K., Iwata, M., (2006), "Studies on Integrated Building Facade Engineering with High-Performance Structural Elements", IABSE int. conf. (Budapest)

Takeuchi, T., Tsutsumi, Y., Kumagai, T., Ogawa, T., (2010),"Seismic Retrofit of Steel-Structure School Gymnasia with Energy Dissipation Devices and Their Effects" *Journal of Struct. Constr:Eng.*, A.I. J, Vol.75 No.656, 1891-1900.(in Japanese)



(a) Building Appearance



(b)Structural System

Figure 29 Environment & Energy Innovation Center

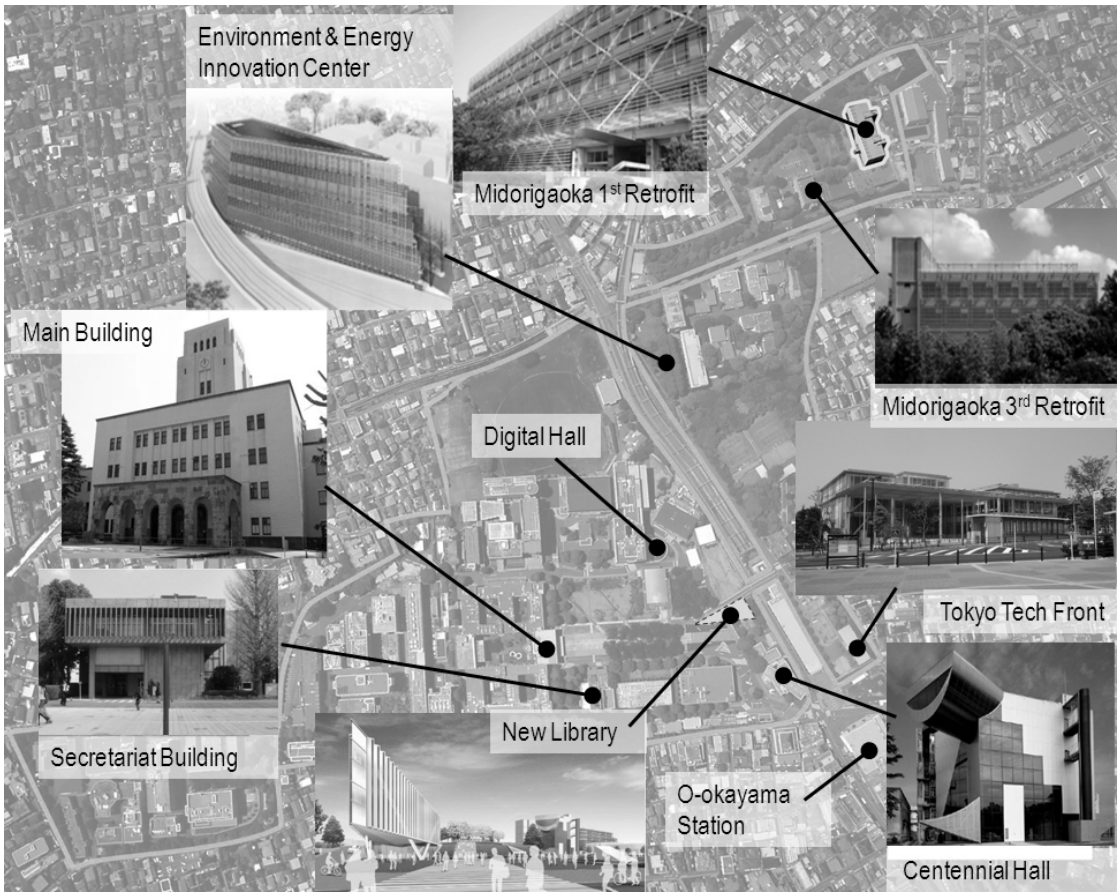


Figure 30 Locations of Projects on O-okayama Campus

8CUEE CONFERENCE PROCEEDINGS
8th International Conference on Urban Earthquake Engineering
March 7-8, 2011, Tokyo Institute of Technology, Tokyo, Japan

EXPERIMENTAL AND ANALYTICAL VALIDATION OF A SEISMIC RETROFIT SYSTEM FOR EXISTING STEEL MOMENT-RESISTING FRAMES

Dimitrios G. Lignos[1)], Daniel M. Moreno-Luna[2)], and Sarah L. Billington[3)]

1) Assistant Professor, Civil Engineering and Applied Mechanics, McGill University, Canada
2) PhD Student, Dept. of Civil and Environmental Engineering, Stanford University, United States of America
3) Associate Professor, Dept. of Civil and Environmental Engineering, Stanford University, United States of America
dimitrios.lignos@mcgill.ca, damielm3@stanford.edu, billington@stanford.edu

Abstract: Recent breakthroughs in fiber reinforced concrete technology have made it possible to utilize High Performance Fiber Reinforced Cementitious (HPFRC) materials for structural applications including seismic retrofit. For this purpose, an innovative retrofit system that consists of HPFRC infill panels that are acting as energy dissipation fuses has been developed. The seismic performance evaluation of the infill panel retrofit system was validated through large scale hybrid simulation testing series of a 2-story steel moment-resisting frame, designed based on older seismic provisions in California. These tests were conducted at the NEES facility at University of California at Berkeley. The proposed retrofit system was proven to be able to reduce maximum story drift ratios and residual deformations of the retrofitted steel moment resisting frame relative to bare frame performance. This paper summarizes the experimental validation of the proposed HPFRC retrofit system. The available experimental data is also utilized for the development of phenomenological analytical models that are implemented in the OpenSees simulation platform and permit the seismic assessment of retrofitted steel moment resisting frames in a Performance Based Earthquake Engineering context.

1. INTRODUCTION

Recent earthquakes around the world have demonstrated that steel moment frame structures designed based on older seismic provisions (UBC 1994) might be seismically deficient due to premature fracture of beam-to-column connections at fused zone or column flange often noted as "divot" zone (FEMA 351). Further, important facilities such as hospitals that have been designed in the 1980s and it is likely that their seismic vulnerability is high, should remain operational to minimize human casualties and economic losses after a major earthquake. Seismic retrofit is an economic solution to upgrade existing infrastructure.

In 1990s the Federal Emergency Management Agency (FEMA) and the State of California developed a program for seismic rehabilitation strategies summarized in FEMA 356 (2000). The main strategies of these rehabilitation techniques in the United States typically involve (1) global modification of the structural system and (2) local modifications of isolated components of the structural and nonstructural system (e.g. steel, fiber reinforced composite jackets, beam-to-column connection modification improvements). The emphasis is on global modification techniques that involve: (a) the use of reduced steel thickness shear walls (Bruneau 2005) that allow shear buckling and act as an energy dissipation mechanism; (b) ductile fuse elements that move plastic deformation ways from beam-to-column connections (Leelataviwat et al. 1998); (c) self-centering systems (Ricles et al. 2001, Christopoulos et al. 2002, 2008, Tremblay et al. 2008); (d) buckling restraint braces that primarily enhance the strength of the structural system (Clark et al. 1999, Wada et al. 1998, Lopez et al. 2002, Uang and Kiggins 2003); (e) passive energy dissipation devices including various types of dampers (Constantinou and Symans 1992, Soong and Spencer 2002, Kasai et al. 2010).

Recently, infill panels have become popular for structural applications including seismic retrofitting. Jung and Aref (2005) using polymer matrix composite (PMC) infill panels showed that damping as well as lateral resistance of existing steel frames can be increased. Using recent breakthroughs in fiber reinforced concrete technology, Kesner and Billington (2005) utilized High Performance Fiber-Reinforced cementitious (HPFRC) composites to seismically retrofit vulnerable steel moment frame structures. This system was redesigned and evaluated extensively through an experimental program that included a large number of infill panel component tests (see Olsen and Billington 2009, Hanson and Billington 2009) and a series of large-scale hybrid simulation tests of a 2-story steel moment frame designed in 1980s in California. These tests were conducted at the Network for Earthquake Engineering Simulation (NEES) facility at University of California at Berkeley. This paper discusses the experimental and analytical validation of the proposed retrofit system for existing steel moment frame structures subjected to earthquakes.

2. PROPOSED SEISMIC RETROFIT SYSTEM

The proposed infill panel system for seismic retrofit of existing steel frame structures is based on an HPFRC mix originally developed by Naaman (2003). Its 28 day compressive strength f_c' is in the range of 5ksi to 7ksi and its ultimate tensile strength is higher than its first cracking strength accompanied by multiple cracking during inelastic deformation of HPFRC components. An example of the monotonic response of a standard ASTM beam from a 4-point bending strength is shown in Figure 1. From this figure it can be seen that prior to strength deterioration the HPFRC beam has a plastic deformation capacity of about 0.04 inches (i.e. a ductility of about 0.06/0.02 = 3.0).

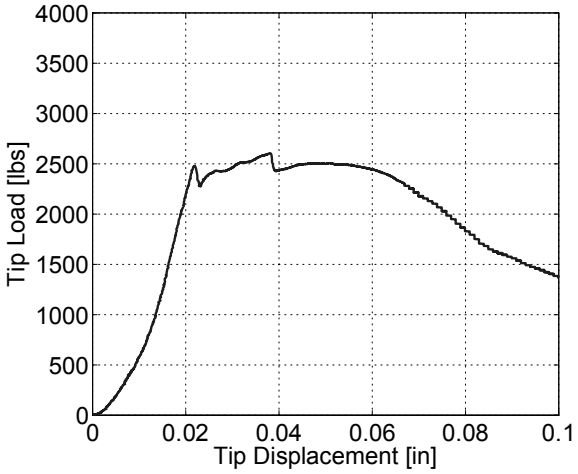
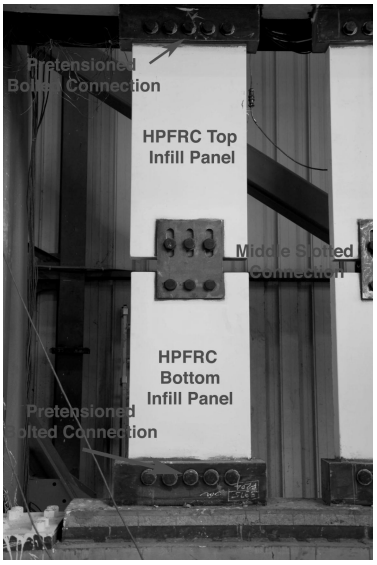


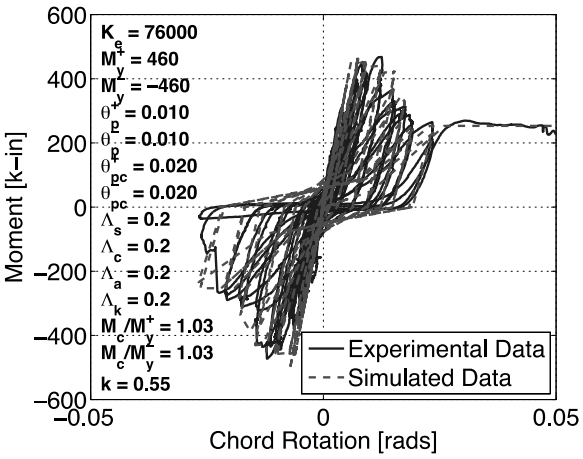
Figure 1 Monotonic load-displacement curve of ASTM HPFRC beam based on a 4-point bending test

The system shown in Figure 2a consists of two precast HPFRC infill panels. These panels utilize welded wire fabric (WWF) and Grade 60 steel reinforcement. The two panels are hand-bolted together at story mid-height with a slotted steel connection that is shown in the same figure. This connection guarantees that the point of inflection of the infill panel system stays at mid-height when one or both infill panels experience inelastic deformations during an earthquake. The same connection also prevents any out of plane movement due to axial load that may build up in the panel system because of lateral and vertical loads. The bottom panel is pre-tensioned with a steel channel that is installed at the top of the floor slab with a regular technique. The top HPRFC infill panel is also pre-tensioned with a steel channel that is welded at the bottom flange of the upper floor steel beam with fillet weld on the site.

Olsen and Billington (2009) and Hanson and Billington (2009) tested experimentally alternative infill panel configurations. They evaluated the cyclic performance of HPFRC panels with different reinforcement ratios and geometries (tapered versus rectangular panels). These tests illustrated that the infill panel system has a pinched hysteretic response (see Figure 2b) and is able to dissipate energy at least up to 5% story drift ratios.



(a)



(b)

Figure 2 HPFRC infill panel system; (a) basic description; (b) example of calibrated hysteretic response

3. PROTOTYPE STEEL STRUCTURE

In order to evaluate the effectiveness of the proposed HPFRC infill panel system discussed in Section 2 of this paper as a seismic retrofit, a prototype steel structure designed in 1980s is utilized. This structure is a 2-story by 3–bay office building with 90ft x 90ft rectangular plan view. Its structural system consists of perimeter moment resisting frames (MRFs). The geometric properties of the steel sections of the perimeter moment resisting frames are shown in Figure 3. The predominant period of the building is 0.75sec in the loading direction of interest (east-west). The building does not meet the retrofit objectives specified in ASCE 41 (2007). Thus, it is retrofitted with the HPFRC infill panel system discussed in Section 2. Five individual HPFRC infill panel systems are installed in the first bay of the steel moment frame shown in Figure 3. The period of the

retrofitted prototype frame is 0.39sec. A 2/3-scale model of the retrofitted steel moment frame was tested at the Network for Earthquake Engineering Simulation (NEES) facility at University of California at Berkeley. The test specimen and experimental program is discussed in detail in the next section.

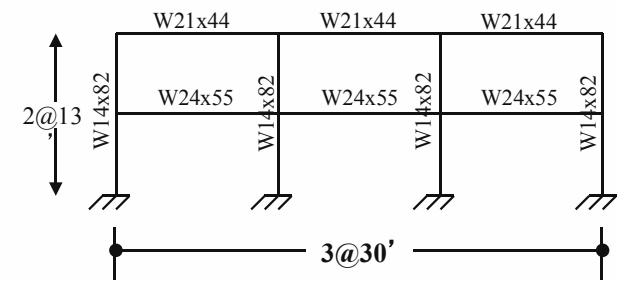


Figure 3 Steel moment frame designed based on 1980s

4. TEST SPECIMEN & EXPERIMENTAL PROGRAM

The 2/3-scale frame of the prototype steel moment frame discussed in Section 3 is scaled based on similitude laws summarized in Moncarz and Krawinkler (1981) for strength and stiffness. The steel sections were selected such that the web and flange slenderness ratios h_f/t_f, $b_f/2t_f$ are almost the same with the original sections of the prototype moment resisting frame in order to achieve the same component deterioration parameters and minimize scale effects. Details related to the testing procedure, test setup, and the testing protocol are discussed in this section.

4.1 Hybrid Simulation

The state-of-the art hybrid simulation technique is utilized for the test series discussed later in Section 4.4. This technique allows testing of the retrofitted part of the moment resisting frame (1-bay frame) only and the rest of the steel moment frame is modeled numerically in the OpenSees (2009) analysis platform. The Open-source Framework for Experimental Setup and Control (OpenFresco) is used to conduct the hybrid simulations (Takahashi and Fenves 2006, Schellenberg 2008). The explicit Newmark integration algorithm with fixed number of 10 iterations is used for the integration of equations of motions. This is a direct integration scheme. The selection of the integrator was based on extensive number of numerical studies that were conducted prior to the testing program and were based on coupled simulation (Lignos and Billington 2010) through a generic adapter element approach implemented in OpenFresco (Schellenberg et al. 2007). For these simulations the HPFRC infill panel system was modeled with a pinching hysteretic response that follows the modified Ibarra-Krawinkler model degradation rules (Lignos and Krawinkler 2009). An example calibration of the hysteretic response of this model against component tests is shown in Figure 2b. The initial 2x2 stiffness matrix needed to conduct the hybrid simulations was determined based on pull-back tests prior to the testing sequence discussed in Section 4.3 of this paper. In this paper, the hybrid model refers to the physically subassembly tested in the lab and the numerical model that is carried in the OpenSees simulation platform.

4.2 Test Setup and Test Frame Description

The 2/3-scale model of the prototype steel MRF consists of W10x45 steel columns. The first and second floor beams are W14x26 and W10x30, respectively. All the sections are made of A995 Gr. 50 steel. The test frame together with the test setup is shown in Figure 4. The test frame is welded on a W14x311 steel beam in order to guarantee "fixed" conditions at the base of the steel columns.

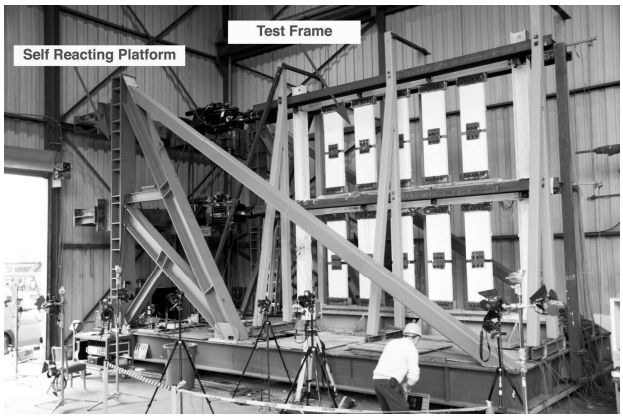


Figure 4 Test frame after completion of the test setup

Although the beam-to-column connections of the prototype steel MRF were pre-Northridge connections, the four moment resisting connections of the test frame were designed as standard welded unreinforced flange (WUF) connections in accordance with FEMA 350 (see Figure 5). This was decided for safety reasons in order to avoid any control instability of the two actuators because of connection fracture during testing. However, fracture is modeled in the numerical portion of the hybrid model based on the modified Ibarra-Krawinkler model (Lignos and Krawinkler 2011).

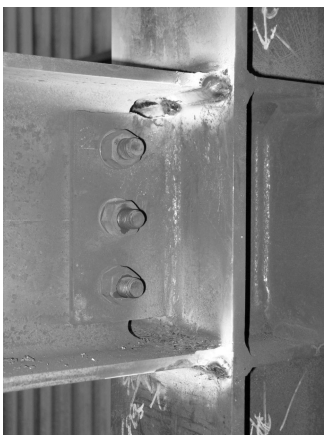


Figure 5 Typical WUF connection of the test frame

A concrete slab was fabricated to realistically simulate the connection between the steel channels with the concrete slab. Figure 6 shows the formwork for this slab after pouring the concrete.

The test frame is built on a self-reacting platform shown in Figure 4 that was designed to eliminate deflections for the maximum expected base shear of the test frame during the two testing phases. In order to eliminate out of plane deformations of the test frame, a lateral support system is designed that consists of longitudinal beams that allow sliding of the test frame through slotted sliders that are greased to eliminate friction. The friction force between the test frame and the lateral support system was practically zero based on the measurements of the instrumented diagonal elements that are bolted on the self-reacting platform and provide lateral resistance to the lateral support system.



Figure 6 Slab details of the test frame after the pouring of concrete

Two 250kips dynamic actuators are connected with the test frame at each floor level with a specially designed beam extension that was stiffened to avoid shear buckling of the beam web. In total, 170 channels were used to instrument the test specimen. Most of them were strain gages. A laser scanner was also utilized that scanned the bottom story right column and exterior infill panel. The scans were synchronized with the data acquisition system.

4.3 Numerical Modeling

The numerical portion of the hybrid model (highlighted 2-bay frame shown in Figure 3) was modeled with elastic beam – column elements and concentrated plasticity springs at their ends. These springs follow a bilinear hysteretic response including component deterioration based on the modified Ibarra Krawinkler model implemented in OpenSees (Lignos and Krawinkler 2011). The model was also able to simulate fracture of beam-to-column connections. Deterioration parameters for the steel beams and columns of the numerical subassembly were extracted from a recently developed steel component database that includes information for more than 300 steel beams (Lignos and Krawinkler 2009, 2011). P-Delta effects were modeled with a leaning column that was connected with axially rigid links with the steel MRF. More details about modeling of the numerical portion of the hybrid model can be found in Lignos and Billington (2010).

4.4 Testing Protocol

Two testing phases are designed for verification of the effectiveness of the proposed seismic retrofit system with the infill panel system. During the first phase, the test frame was subjected to 3 ground motions sequentially. The first ground motion was 30% of the fault normal Petrolia record (1992, Cape Mendocino). This motion represents a Service Level Earthquake (SLE) with 50% probability of exccedence in 50 years at the first mode period of the retrofitted steel MRF. The test frame was then subjected to two Design Level Earthquakes (DLE). The first one was the 70% of the unscaled Petrolia record (noted as DLE-I) and the second one is the unscaled Canoga Park record from the 1994 Northridge earthquake. Figure 7 shows the unscaled acceleration spectra of these two ground motions.

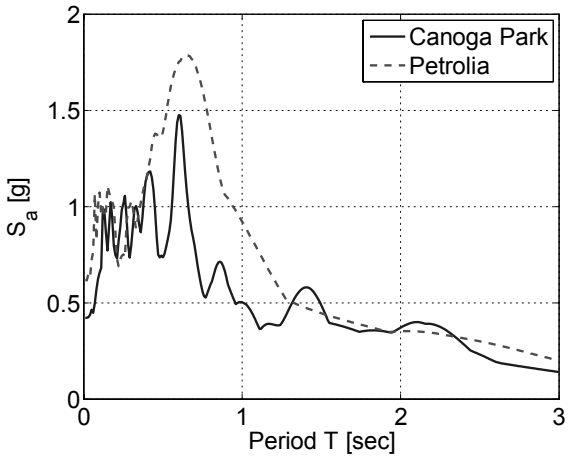


Figure 7 Unscaled acceleration spectra of Petrolia and Canoga Park ground motions

After completion of testing phase I, all the HPFRC panels were replaced with a new set with nominally identical material properties with the first set of panels. Testing phase II included the same SLE motion with Phase I for comparison purposes, followed by a Maximum Considered Earthquake (MCE), which was the 100% of the Petrolia record. For exploratory purposes, after the completion of Phase II, the hybrid model with the severally damaged infill panels was subjected to the 70% of the unscaled JR Takatori record. Due to brevity, information related to this ground motion is not part of this paper.

5. EXPERIMENTAL RESULTS AND DISCUSSION

5.1 Global Response During Testing Phase I

During the first testing phase, the retrofitted test specimen reached about 1% maximum story drift ratios (SDR) at both

stories during SLE. There was partial energy dissipation through micro cracking of the HPFRC infill panels. This can be seen from Figure 8 that shows the base shear versus first story drift of the hybrid model. The base shear in this plot is normalized with respect to the seismic weight of the test specimen.

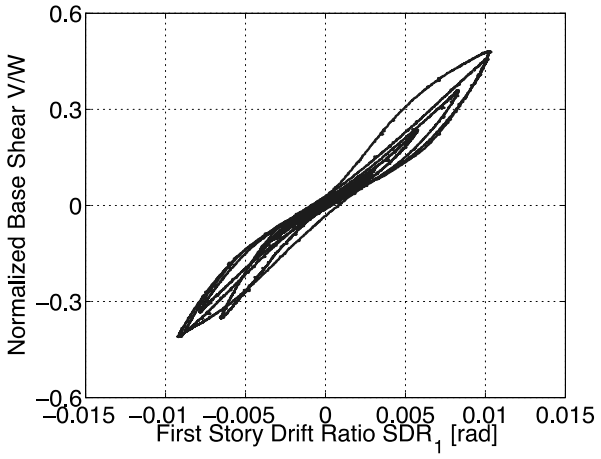


Figure 8 Normalized base shear versus first story drift ratio during SLE ground motion (testing Phase I)

During the DLE-I (70% Petrolia) the hybrid model did not exceed more than 1.9% maximum SDR. After the completion of this ground motion the residual SDRs in both stories was less than 0.5%. Similarly, when the hybrid model was subjected to the unscaled Canoga Park record (DLE-II) the maximum SDRs that the specimen experienced were in the order of 3% in the first story. This can be seen from Figure 9 that shows the story drift ratio histories for the first and second story of the test specimen for test phase I.

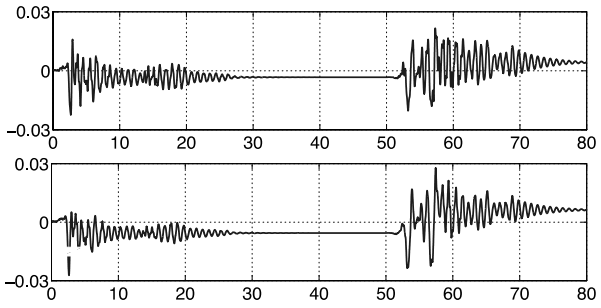
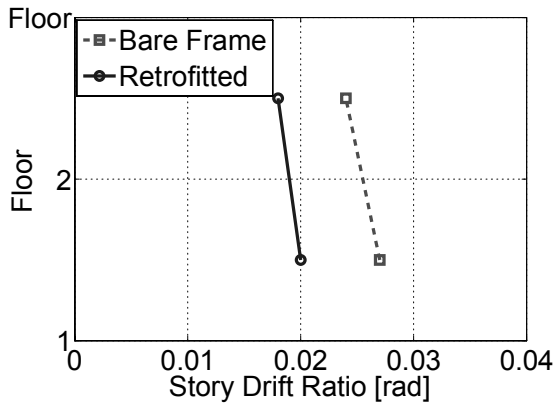
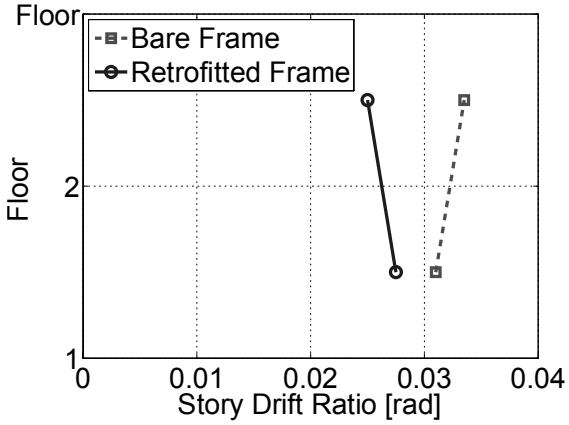


Figure 9 Story drift ratio histories of the hybrid model during testing Phase I (DLE-I, DLE-II)

Comparing the maximum story drift ratios for DLE-I and DLE-II with the ones of the bare frame response it can be seen that in both cases the seismic retrofit system meets the retrofit objectives by means of maximum story drift ratios. This can be seen in Figures 10a and 10b that show a comparison of maximum SDRs of the retrofitted frame with respect to the bare frame performance for DLE-I and DLE-II, respectively.



(a)



(b)

Figure 10 Comparison of maximum story drift ratios of retrofitted and bare frame for testing Phase I; (a) DLE-I; (b) DLE-II

5.2 Observations for Infill Panels During Phase I

After DLE-I ground motion a typical damage pattern of the infill panel system is shown in Figure 11a. Few flexural cracks are evident but not as much as one would expect considering the component tests. More distributed cracking was observed to the infill panels that were adjacent to the steel columns and the set that was located at the center of the span. The main reason for this damage pattern is that the boundary conditions of the top and bottom part of the infill panels are not fixed since the beams deform in double curvature. Another reason is the effect of loading history on the panel response (symmetric cycles versus few cycles and monotonic push during an earthquake). An HPFRC infill panel typically failed completely at the base connection with the steel channel due to rigid body motion (see Figure 11b). After this failure the panels were rocking. This failure mode was observed to 3 panels only during DLE-I. There were no damage observations for the rest of the panels. This implies that after one design level earthquake the infill panel system does not need to be replaced and the steel moment frame is fully operational. However, after DLE-II all the panels were severally damaged and were fully replaced.



(a)



(b)

Figure 11 Infill panel damage patterns after testing Phase I

5.3 Structural Damage Observations After Completion of Testing Phase I

The retrofitted steel moment frame after the completion of Phase I did not have any notable structural damage. The steel beam-to-column connections at the first and second floor slightly yielded as it can be seen from Figure 12 that shows the first floor beam. Note that there was no indication of local buckling in any of the steel beams.



Figure 12 Structural damage after completion of testing Phase I at the first floor beam

Similarly, the two columns at the base yielded as shown in Figure 13 that shows the base of the first story column. This agrees with the hysteretic response of the analytical model.



Figure 13 Structural damage after completion of testing Phase I at the first story column at the base

5.4 Global Response During Testing Phase II

After completion of testing Phase I all the HPFRC infill panels were replaced with a new set. The 2x2 initial stiffness matrix of the retrofitted specimen used in testing Phase II was almost identical with the one obtained prior to testing Phase I. The reason was that there was no lateral torsional buckling in testing Phase I in any of the steel beams (i.e. no unloading stiffness deterioration). Thus, the response of the retrofitted specimen during SLE in Phase II was almost identical with the one during Phase I for the same level of intensity. During the MCE (unscaled Petrolia record) the hybrid model exhibited 3.5% SDR in the first story, as can be seen in Figure 14 that shows the story drift ratio histories during SLE and MCE ground motions for testing Phase II.

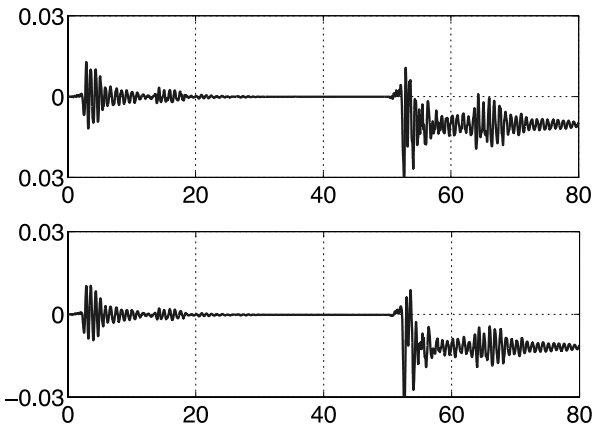


Figure 14 Story drift histories of hybrid model during testing Phase II for SLE and MCE ground motions

A comparison between the maximum story drift ratios of the retrofitted and bare frame during testing Phase II can be seen in Figure 15. From this figure, it is evident that the HPFRC infill panel system is effective as a seismic retrofit system for existing steel moment frame structures designed based on older seismic provisions. The same can be concluded by looking at the residual drifts in both stories of the hybrid model.

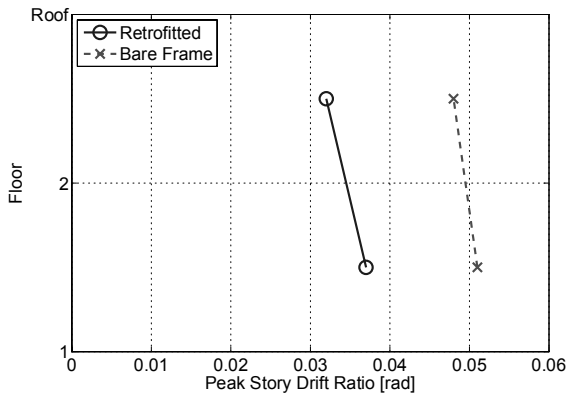


Figure 15 Comparison of maximum story drift ratios of retrofitted and bare frame for MCE during testing Phase II

5.5 Observations for Infill Panels During Phase II

A typical damage pattern of the infill panel system after MCE is shown in Figure 16. Flexural cracks were evident compared to Phase I. Similarly with testing Phase I, more distributed cracking was observed to the infill panels that were adjacent to the columns and the center of the span. The general observation is that all the infill panels were severally damaged during MCE and the failure at the bottom (or top) of the connection line with the steel channel was consistent.



Figure 16 Infill panel damage patterns after the completion of MCE ground motion

5.6 Structural Damage Observations After Completion of Maximum Considered Earthquake

Most of the inelastic behavior of the test specimen during the MCE ground motion occurred in the HPFRC infill panels. Even if the specimen exhibited 3.5% rad SDR in the first story, there was no indication of local buckling in any of the beam-to-column connections of the physical subassembly. This can be seen in Figure 17 that shows the first floor beam at the major peak of the unscaled Petrolia record. Yielding was only observed through the flacking of the white paint that was used for damage observations prior to testing Phase II. More over, none of the connections modeled numerically deteriorated in strength (i.e. local buckling did not occur). An interesting observation was that the bottom flange of the first and second floor beams yielded in between the steel channels during the MCE ground motion. This happened due to shear distribution of the infill panels that resulted to additional bending in the steel beams as shown in Figure 17.



Figure 17 First floor beam at peak of MCE ground motion

6. SUMMARY AND CONCLUSIONS

This paper summarizes the experimental validation of a recently developed infill panel system made of High Performance Fiber Reinforced Cementitious (HPFRC) material for seismic retrofit applications of existing steel moment frame structures. The effectiveness of the HPFRC infill panel system as a seismic retrofit was validated through a two-phase large-scale hybrid simulation testing series that was conducted at the NEES facility of University of California at Berkeley. A 2/3 scale of a 2-story steel moment frame was subjected to a sequence of Design level and Maximum Considered earthquake events. The main conclusions from the testing program are summarized as follows:

1. Inelastic response in terms of peak story drift ratios and residual deformations of the retrofitted moment frame are reduced compared the bare frame performance for both DLE and MCE events.
2. The HPFRC infill panel system was proven to work effectively for a sequence of design level earthquakes

without having to be replaced in between design level ground motions.

3. No indication of severe structural damage was observed for both DLE and MCE in any of the structural components (beams and columns) of the test frame, including the numerical model.

Acknowledgements:

This study is based on work supported by the United States National Science Foundation (NSF) under Grant No. CMS-0530383 within the George E. Brown, Jr. Network for Earthquake Engineering Simulation (NEES) Consortium Operations. The steel frame and associated parts of the test setup, including erection, was generously donated by Herrick Corporation in Stockton. Midstate Precast generously donated the fabrication of the HPFRC infill panels. The financial support of NSF, Herrick and Midstate Precast is gratefully acknowledged. The authors also thank the undergraduate students A. Cantu, D. Ouyang, E. Flores, J. Dory, K. Morales, S. Vanderboll, William Tressler, M.S. (Stanford University), Dr. Andreas Schellenberg, Dr. Selim Gunay, Dr. Shakhzod Tachirov and the rest of the technical staff at the NEES facility at the University of California at Berkeley for their assistance with many aspects of the hybrid simulation testing program. The authors would also like to thank Mr. Ron Hamburger, Mr. David Mar and Dr. Greg Luth for their valuable input regarding the proposed testing phases for the experimental program. Any opinions, findings, and conclusions expressed in this paper are those of the authors and do not necessarily reflect the views of the sponsors.

References:

ASCE (2007). "Seismic Rehabilitation of Existing Buildings," *ASCE Standard ASCE/SEI 41-06,* American Society of Civil Engineers/Structural Engineering Institute, Reston, VA.

Bruneau, M. (2005). "Seismic Retrofit of Steel Structures," *Proceeedings of the 1st Canadian Conference on Effective Design of Structures, McMaster University, Hamilton, Ontario, Canada, July 10-13, 2005.*

Christopoulos, C., Filiatrault, A., Uang, C. M. (2002), "Self-Centering Post-Tensioned Energy Dissipating (PTED) Steel Frames for Seismic Regions," *Structural Systems Research Project Report No. SSRP-2002/06*. Department of Structural Engineering, University of California, San Diego, La Jolla, CA, 292p.

Christopoulos, C., Tremblay, R., Kim, H.-J., Lacente, M. (2008). "Self-Centering Energy Dissipative Bracing System for the Seismic Resistance of Structures: Development and Validation", Journal of Structural Engineering, ASCE, **134** (1), 96-107.

Clark, P., Aiken, I., Kasai, K., Ko, E., Kimura, I. (1999). "Design Procedures for Buildings Incorporating Hysteretic Damping Devices," *Proceedings of the 68th Annual Convention Structural Engineers Association of California, Sacramento*, pp. 355-371.

Constantinou, M.C, Symans, M.D. (1992). "Experimental and Analytical Investigation of Seismic Response of Structures With Supplemental Fluid Viscous Dampers," *Report NCEER-92-0032*, State University of New York, Buffalo.

FEMA 350 (2000). "Recommended Seismic Design Criteria for New Steel Moment Frame Buildings," Washington, DC: Federal Emergency Management Agency.

FEMA 351 (2000). "Recommended Seismic Evaluation and Upgrade Criteria for Existing Welded Steel Moment-Frame Buildings," Washington, DC: Federal Emergency Management Agency.

FEMA 356 (2000). "Prestandard and Commentary for the Seismic Rehabilitation of Buildings," Washington, DC: Federal Emergency Management Agency.

Hanson, J., Billington, S. L. (2009). Cyclic Testing of a Ductile Fiber-Reinforced Concrete Infill Panel System for Seismic Retrofitting of Steel Frames," *Report TR. 173*, John Blume Earthquake Engineering Center, Stanford, CA, 2009.

Jung, W.Y., Aref, A.J. (2005). "Analytical and Numerical Studies of Polymer Matrix Composite Sandwich Infill Panels", *Journal of Composite Structures*, **68**, 359-370.

Kasai, K., Ito, H., Ooki, Y., Hikino, T., Kajiwara, K., Motorui, S., Ozaki, H., Ishii, M. (2010). "Full-Scale Shake Table Tests of 5-Story Steel Building With Various Dampers", *Proceedings 7th International Conference on Urban Earthquake Engineering (7CUEE), March 3-5, 2010, Tokyo Institute of Technology, Tokyo, Japan.*

Kesner, K.E., Billington, S.L. (2005). "Investigation of Infill Panels Made From Engineered Cementitious Composites for Seismic Strengthening and Retrofit," *Journal Structural Engineering,* ASCE, **131** (11), 1712-1720.

Leelataviwat, S, Goel, S. C., Stojadinovic, B. (1998). "Drift and Yield Mechanism Based Seismic Design and Upgrading of Steel Moment Frames," *Research Report No. UMCEE 98-29*, Department of Civil & Environmental Engineering, The University of Michigan, Ann Arbor, MI, August.

Lignos, D. G., Krawinkler, H. (2009). "Sidesway Collapse of Deteriorating Structural Systems Under Seismic Excitations," *Report TR 172*, John A. Blume Earthquake Engineering Center, Stanford CA.

Lignos, D. G., Billington, S. L. (2010). "Hybrid Testing of a Retrofitted Steel Moment Resisting Frame with High Performance Fiber Reinforced Concrete Infill Panels," *Proceedings 9th US National and 10th Canadian Conference on Earthquake Engineering: Reaching Beyond Borders, July 25th -29th*, Toronto, Canada, 2010.

Lignos, D. G., Krawinkler, H. (2011). "Deterioration Modeling of Steel Components in Support of Collapse Prediction of Steel Moment Frames under Earthquake Loading", *Journal of Structural Engineering,* ASCE, (accepted for publication).

López, W.A., Gwie, D.S., Saunders, C.M., Lauck, T.W. (2002). "Lessons Learned From Large-Scale Tests of Unbonded Braced Frame Subassemblages," *Proceedings of the 71st Annual Convention Structural Engineers Association of California, Sacramento*, 171-183,

Moncarz, P.D., Krawinkler, H., (1981). "Theory and Application of Experimental Model Analysis in Earthquake Engineering," *Report No. 50*, John A. Blume Earthquake Engineering Center, Department of Civil Engineering, Stanford University.

Naaman, A. (2003). "Strain Hardening and Deflection Hardening Fiber Reinforced Cement Composites: HPFRCC," Rilem Publications, France.

Olsen, C., Billington, S. L. (2009). "Evaluation of Precast, High-Performance Fiber- Reinforced Concrete Infill Panels for Seismic Retrofit of Steel Frame Building: Phase 1- Cyclic Testing of Single Panel Components," *Report No. TR 158,* John A Blume Earthquake Engineering Center, Stanford CA.

OpenSees. (2009). "Open System for Earthquake Engineering Simulation," Pacific Earthquake Engineering Research Center (PEER), (http://opensees.berkeley.edu).

Ricles, J. M., Sause, R., Garlock, M., and Zhao, C. (2001). "Posttensioned Seismic-Resistant Connections for Steel Frames," *Journal of Structural Engineering*, ASCE, **127** (2), 113–121.

Schellenberg, A., Mahin, S., Fenves, G. (2007). "Software Framework for Hybrid Simulation of Large Structural Systems," *Proceedings, Structures Congress, ASCE, Long Beach, CA*, United States.

Schellenberg, A. H. (2008). "Advanced Implementation of Hybrid Simulation," *PhD Dissertation*, Civil and Environmental Engineering, University of California, Berkeley.

Soong, T.T, Spencer, B.F. (2002). "Supplemental Energy Dissipation: State-of- the-Art and State-of-the Practice," *Journal*

Engineering Structures, **24** (3), 243–259.
Uang, C. M., Kiggins, S. (2003). "Reducing Residual Drift of Buckling-Restrained Braced Frames as a Dual System," *Proceedings of International Workshop on Steel and Concrete Composite Construction (IWSCCC-2003*), Report No. NCREE-03-026, *National Center for Research on Earthquake Engineering*, Taipei, 189-198.
Tremblay, R., Lacerte, M., Christopoulos, C., (2008). "Seismic Response of Multi-Storey Buildings with Self-Centering Energy Dissipative Steel Braces," *Journal of Structural Engineering*, ASCE, 134 (1), 108–120.
Uniform Building Code (1994). "Uniform Building Code," Vol 2: Structural Engineering Design Provisions.
Wada, A., Saeki, E., Takeuchi, T., Watanabe, A. (1998). "Development of Unbonded Brace," *Report Nippon Steel's Unbonded Braces* (promotional document), pp. 1-16, Nippon Steel Corporation Building Construction and Urban Development Division, Tokyo.

8CUEE CONFERENCE PROCEEDINGS
8th International Conference on Urban Earthquake Engineering
March 7-8, 2011, Tokyo Institute of Technology, Tokyo, Japan

FACTORS INFLUENCING THE PROGRESSIVE COLLAPSE OF FRAME STRUCTURES AND SENSITIVITY OF THE COLLAPSE TO THESE FACTORS

Liping Liu[1)2)], Pei Cao[1)2)], Yingmin Li[1)2)], Akira Wada[3)], Mingkui Xiao[1)2)], and Yangbing Liu[1)2)]

1) College of Civil Engineering, Chongqing University, Chongqing, 400045, China
2) Key Laboratory of New Technology for Construction of Cities in Mountain Area (Chongqing University), Ministry of Education, Chongqing 400045, China
3) Center for Urban Earthquake Engineering, Tokyo Institute of Technology, Yokohama, 226-8503, Japan
liuliping@cqu.edu.cn

Abstract: The ability of a structure to resist progressive collapse is affected by a number of factors and the main factors are the storey number, span length, span number and floor area. The factors influencing the progressive collapse and the sensitivity of the collapse to these factors are important in structural design. Currently, studies of these factors are mainly based on elastic static theoretical analysis. However, the collapse mechanism is highly nonlinear in behavior. Therefore, a more sophisticated model should be used to find the factors influencing progressive collapse. In this study, the factors influencing progressive collapse of frame structures will be determined through theoretical analysis and numerical simulation. The numerical simulation method will take into account of the material and geometrical nonlinear properties. The alternate path method will be used in design examples to determine how the factors influencing progressive collapse. Finally, a design method for progressive collapse resistance of frame structures will be proposed.

1. INTRODUCTION

The collapse of WTC buildings in New York City has not only been paid extensive attentions since the "9.11" event, but also reminds that researchers and technicians in structural engineering should deeply reflect on the issues of structural safety due to emergent event. Emergent events are unpredictable as one kind of accidental event, and normally cause direct failures of local components, which possibly induce farther losses of total structure. Such failure mode of progressive collapse reveals the weakness of structure systems to resist initial and progressive failure with great potential of dangers.

Redundancy is a key design feature for the prevention of progressive collapse. Redundancy tends to promote an overall more robust structure and helps to ensure that alternate load paths are available in the case of a structure element failure. Three evaluation criterions are given in the literature (Working groups on concepts and techniques, safety evaluation, design and optimization and code implementation 1990) for the redundancy properties: 1) degree of statical indeterminacy, 2) the ratio of system failure probability to partial unit failure probability, 3) the additional bearing capacity not required for structure design. Visible, redundancy properties are endowed with broader implications.

Redundancy properties of structure firstly depend on the type of structural system. For the no-bracing reinforced concrete (RC) frames involve in this paper, they mainly depend on the stiffness of beam-column connection, storey number, bay number and so on. This paper designs 9 RC frames according to the Chinese Seismic Design Code GB50011-2001 (National standard of PRC 2001a), which have different storey number, bay number, span length and earthquake intensity. Then, the alternate path (AP) method will be used to obtain their progressive collapse properties.

2. PROGRESSIVE COLLAPSE ANALYSIS BASED ON AP METHOD

2.1 The Choice of The Analysis Methods

In order to do the progressive collapse design of building structures, many countries have published the relevant codes one after another. Some of them are very representative, such as "Progressive Collapse Analysis and Design Guidelines for New Federal Office Buildings and Major Modernization Projects" (GSA2003) and "Design of Buildings to Resist Progressive Collapse" (DoD2009) in the United States. The guidelines above recommend the AP method as the basis analysis method for progressive collapse analysis.

Currently the following four procedures are generally recommended to operate the AP method for progressive collapse analysis: linear elastic static (LS) analysis, linear elastic dynamic (LD) analysis, nonlinear static (NS) analysis

and nonlinear dynamic (ND) analysis. Advantages and disadvantages of these approaches have been discussed by Marjanishvili and Agnew (2006).

The progressive collapse of structures is a complex nonlinear dynamic process, so the material and geometrical nonlinear properties should be considered. Nonlinear static analysis and nonlinear dynamic analysis are the main analysis method used in this paper.

2.2 Applied Loads for Static and Dynamic Analyses

In this paper, the load combination of the GSA2003 is selected for the progressive collapse analysis. The GSA2003 proposes the amplification factor of 2 for the static analysis to account for dynamic redistribution of forces. The load combination of the GSA2003 for the nonlinear static analysis is 2(Dead Load+0.25Live Load). This amplified load is applied only in the spans in which a column is removed while unamplified load is applied in the other spans (Fig. 1). The load combination for the nonlinear dynamic analysis is (Dead Load+0.25Live Load).

In this study, the nonlinear static analysis or vertical pushover analysis is applied by increasing the vertical displacement in the location of the removed column to investigate the resistance of the structure against such deformation. Since the vertical pushover method is displacement controlled, the analysis is carried out by increasing displacement to an arbitrary level. In the analysis, vertical load is imposed on all beams with its original loading pattern (Fig. 1) unchanged. At every step during the vertical pushover analysis, i.e., at each level of the vertical displacement, the amount of equivalent load corresponding to the displacement level is determined. The amount of the load is referred to as "load factor", which is the ratio of the equivalent load to the full vertical load.

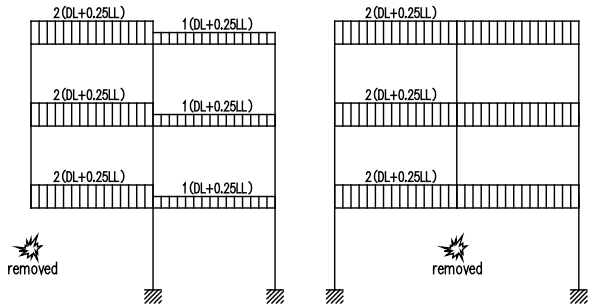


Fig. 1. Applied Load for Static Analysis

For dynamic analysis the guidelines do not recommend to use the dynamic amplification factor. To carry out dynamic analysis, the joint force acting on a column is computed before it is removed. Then the column is replaced by joint loads equivalent of its member forces as shown in Fig. 2. To simulate the phenomenon that the column is abruptly removed, the vertical supporting element should be removed over a time period that is 1/10 of the period associated with the structural response mode for the vertical element removal (GSA2003).

2.3 Loss Scenario

For progressive collapse analysis, the guidelines mandate several loss scenarios. However, only one element removal is required at a time. The cause of element failure is not considered. Statistically (Ellingwood B R et al 2007), the progressive collapse of the public buildings is mainly because the vehicle collisions and car-bomb attack. So the columns of the ground floor are more likely to be damaged than the columns of upper floors; the perimeter columns are more likely to be damaged than the interior columns. So we have considered the loss scenarios of the perimeter columns of the ground floor in this paper.

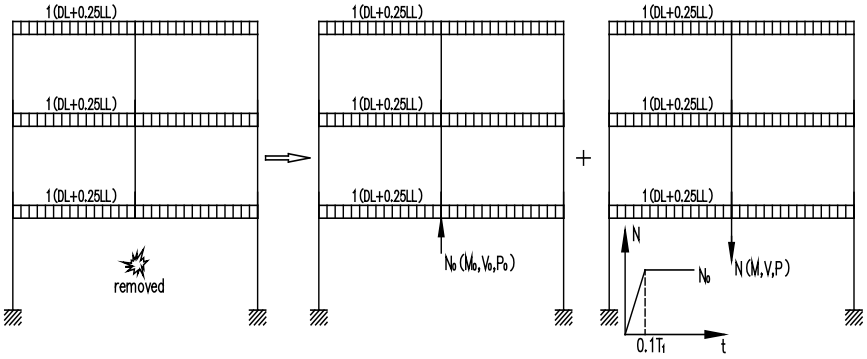


Fig. 2. Applied Load for Dynamic Analysis

2.4 Analysis Program and Evaluation Criterion

Using the commercially available structural analysis software SAP2000, the three-dimensional models of RC buildings are developed. Bernoulli beam elements with localized plastic hinges are used to model material nonlinearity in beams and columns. Geometric nonlinearity is also considered. Plastic hinges are modeled based on the FEMA356 guidelines (Federal Emergency Management Agency 2000). Different performance levels are shown in Fig. 3.

There are different evaluation criterions for the performance of the structure to resist progressive collapse, like strength criterion, deformation criterion and energy

criterion. Since the purpose of this article is to determine how the factors influencing progressive collapse properties, the finite element models have taken some measures to simplify. So deformation criterion and strength criterion are used in this paper.

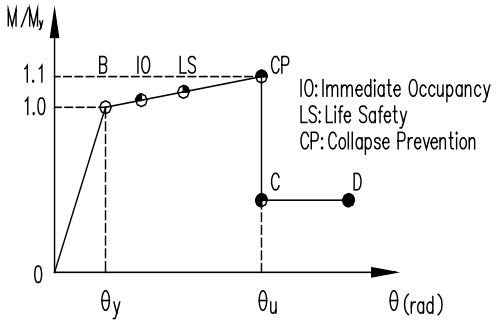


Fig. 3. The plastic hinge model

3. STRUCTURAL MODELS AND PARAMETERS

9 RC frames, of which each has the equal spans and storey heights, in different seismic fortification zone are designed according to the Chinese Seismic Design Code GB50011-2001 with PKPM software. The concrete strengths of beams and columns are C30. The longitudinal reinforcements of beams and columns are HRB400 rebar (fy=360 MPa) while the stirrups are HPB235 rebar (fy=235 MPa). The dead load (DL) on the roof is 8.5 kN/m^2 while the other floors are 6.5 kN/m^2 (including the dead weight of the slab). The live loads (LL) are 2 kN/m^2 on both the roof and other floors. The storey height is 3.6m for all the storeies. The major parameters of the 9 frames are shown in Table 1. Influences of storey number, bay number, span length and earthquake intensity to progressive collapse resistance of RC frames are mainly considered.

Table 1. Parameters of Structural Models

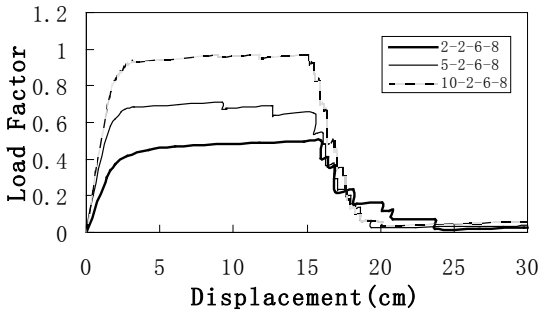
Model name	Storey number	bay number	Span length (m)	Seismic fortification intensity(degree)	Section size of column (mm×mm)	Section size of beam (mm×mm)
2-2-6-8	2	2	6	8	400×400	200×500
5-2-6-8	5	2	6	8	550×550	300×550
10-2-6-8	10	2	6	8	700×700	300×650
5-2-7.5-8	5	2	7.5	8	650×650	300×650
5-2-9-8	5	2	9	8	750×750	350×750
5-4-6-8	5	4	6	8	600×600	300×550
5-6-6-8	5	6	6	8	700×700	300×550
5-2-6-6	5	2	6	6	400×400	200×450
5-2-6-7	5	2	6	7	500×500	250×500

4. CALCULATION RESULTS AND DISCUSSIONS

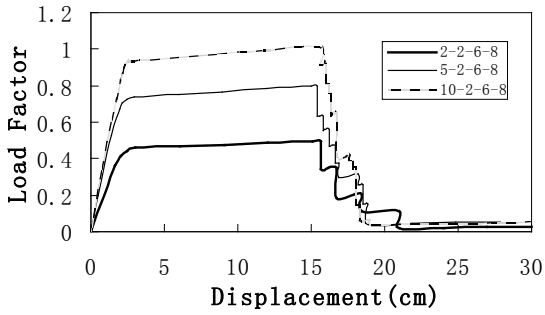
4.1 Explanation for The Curves

In seismic pushover analysis the relationship between the base shear and the story drift is observed to estimate the seismic load resisting capacity. In this study of vertical pushover analysis, the vertical displacement and the sum of the vertical loads corresponding to the vertical displacement are plotted for various parameters such as span length, number of stories, number of bays and earthquake intensities. Since the vertical load varies with the dimension of the plan and the elevation, the ratio of the vertical load at each step to the specified total vertical load shown in Fig. 1 is plotted in the figures as dimensionless loading parameter.

To confirm the result obtained from the vertical pushover analysis, the ND analysis is conducted with the same model structures. The ND analysis result depicts the vertical deflection of the joint from which a column is removed.

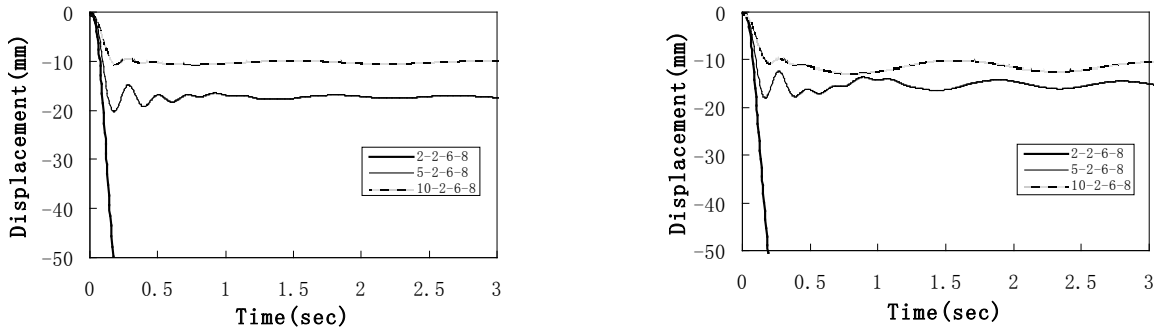


(a) Removal of Center Column



(b) Removal of Corner Column

Fig. 4. Load-Displacement Curves for The Comparison of Different Storey Number



(a) Removal of Center Column (b) Removal of Corner Column

Fig. 5. Displacement Time History Curves for The Comparison of Different Storey Number

4.2 Comparison for Different Storey Number

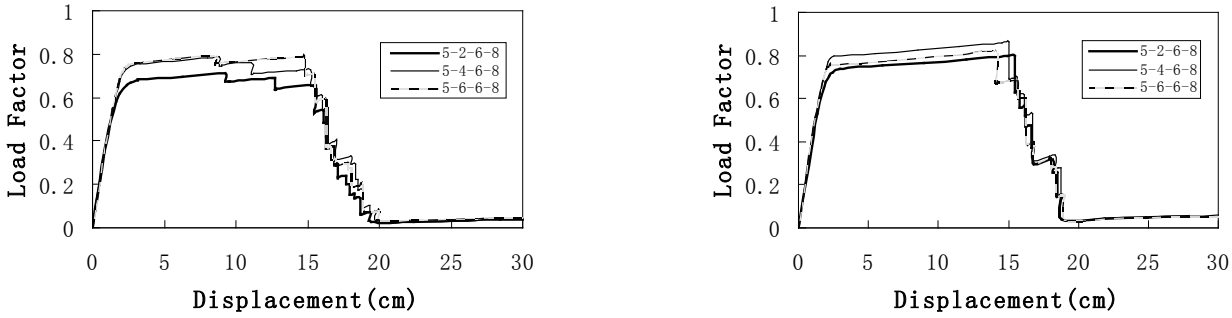
In Fig. 4, it can be observed that as the number of stories increases both the stiffness and the ultimate strength of model structures increase as well. In Fig. 5, it can be observed that the maximum displacements decrease as the number of stories increases.

This seems to be reasonable considering that as the number of stories increases the number of structural members involved in the load transfer also increases and so do the redundancy and the resistance to progressive collapse.

4.3 Comparison for Different Bay Number

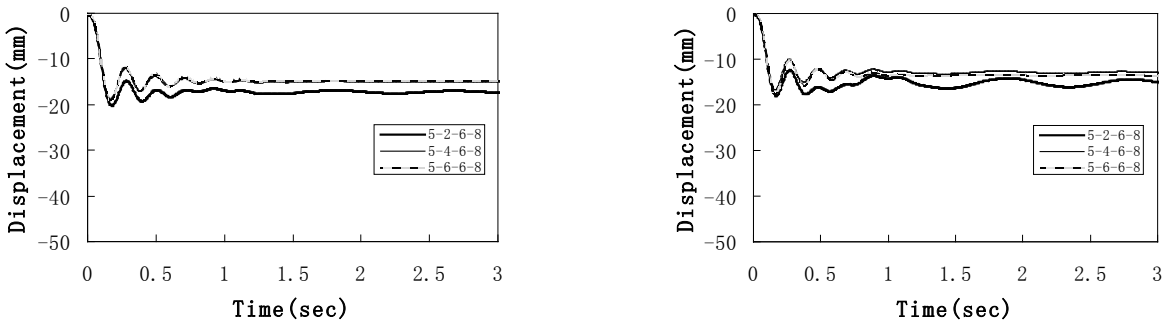
Fig. 6 shows the results of the model structures with 2, 4, and 6 bays. It can be observed that the strength of model structures increases as the number of bays increase from 2 to 4. But this law becomes not obvious when the number of bays continue to increase from 4 to 6. The similar phenomena can be obtained from the displacement time history curves in Fig. 7.

Although the increase of bay numbers will increase the redundancy of the structures, this does not means that the progressive collapse resistance of structures will also be continued increasing as the increase of bay numbers. The analysis results show that only the increasing bays adjacent to the bay in which a column is removed will increase the progressive collapse resistance of the model structures effectively. The increasing bays which are far away from the bay in which a column is removed have little effect to increase the progressive collapse resistance of the RC frames.



(a) Removal of Center Column (b) Removal of Corner Column

Fig. 6. Load-Displacement Curves for The Comparison of Different Bay Number



(a) Removal of Center Column (b) Removal of Corner Column

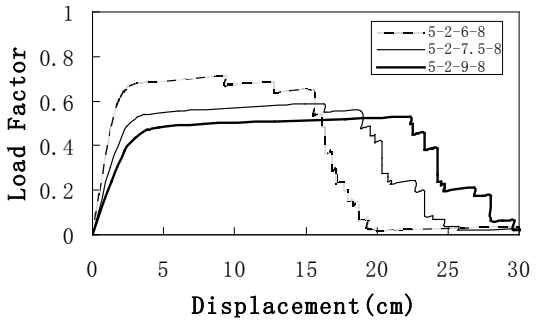
Fig. 7. Displacement Time History Curves for The Comparison of Different Bay Number

4.4 Comparison for Different Span Length

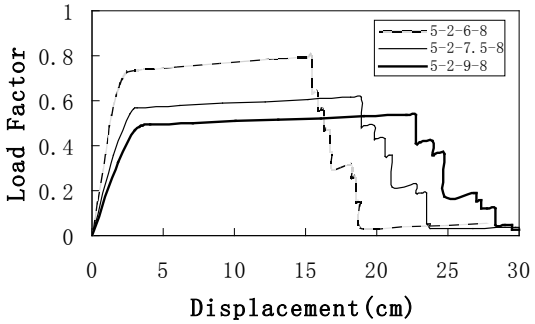
In Fig. 8, it can be found that both the stiffness and the ultimate strength of model structures decrease as the span length increases. It also can be noticed that the maximum displacements at the limit state of failure increase with the span length.

In Fig. 9, it can be observed that the maximum displacements of model structures increase as the span length increase. This phenomenon is more obvious for the removal of center column.

The reason is that the increase of span leads to the increase of total gravity loads, which results in larger axial compression. It can be found that the collapse possibility becomes larger as span increases.

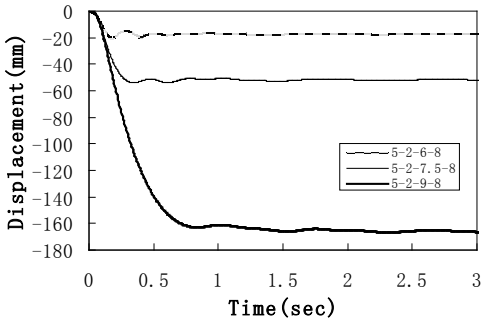


(a) Removal of Center Column

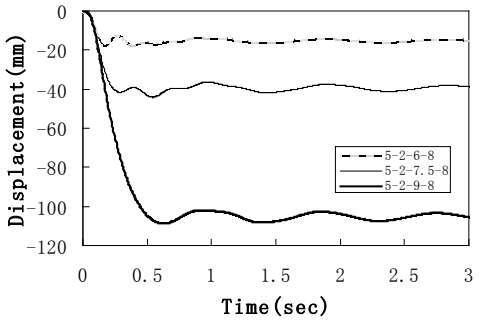


(b) Removal of Corner Column

Fig. 8. Load-Displacement Curves for The Comparison of Different Span Length



(a) Removal of Center Column

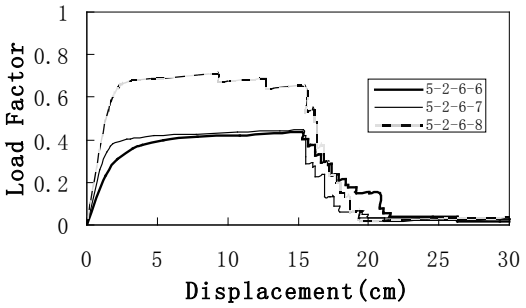


(b) Removal of Corner Column

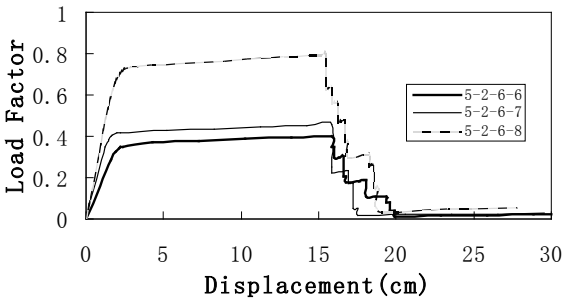
Fig. 9. Displacement Time History Curves for The Comparison of Different Span Length

4.5 Comparison for Different Earthquake Intensity

In Fig. 10-11, the load resisting capability of the structures designed for 8-degree seismic fortification zone according to the Chinese Seismic Design Code increase as compared with those of structures designed for 6 and 7-degree seismic fortification zone. This is reasonable since the members are designed with bigger lateral loads. However, the structures designed for 6 and 7-degree seismic fortification zone have little difference. This is due to the fact that the contribution of gravity load is greater than the seismic load in 6 and 7-degree seismic fortification zones.

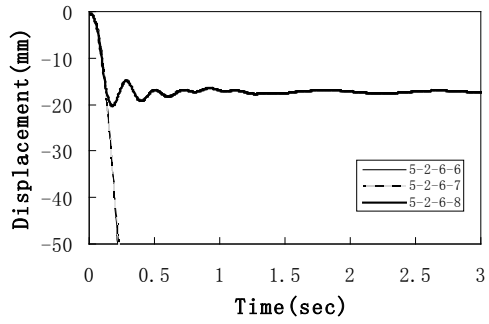


(a) Removal of Center Column

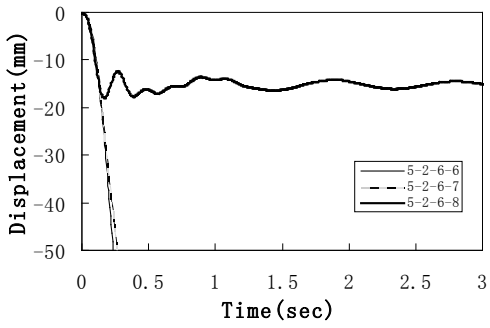


(b) Removal of Corner Column

Fig. 10. Load-Displacement Curves for The Comparison of Different Earthquake Intensity



(a) Removal of Center Column



(b) Removal of Corner Column

Fig. 11. Displacement Time History Curves for The Comparison of Different Earthquake Intensity

5. CONCLUSIONS

This paper analyzes progressive collapse resistances of 9 RC frames which have different storey number, bay number, span length and earthquake intensity, designed according to the Chinese Seismic Design Code. The results show that the progressive collapse resisting capacity of the RC frames increases as the number of stories increases and the span length decreases. The increasing bays adjacent to the bay in which a column is removed will increase the progressive collapse resistance of the RC frames slightly. In the highly seismic area, when the contribution of the seismic load is greater than gravity load, the progressive collapse resistance will increases as the earthquake intensity increases.

6. ACKNOWLEDGE

The paper are supported by Natural Science Foundation Project of CQ CSTC (2009BB4202), and National Key Technology R&D Program of China(2009BAJ28B01-2).

References:

Working groups on concepts and techniques, safety evaluation, design and optimization and code implementation (1990). "Research needs in structural reliability." *Structural Safety*, 7:299-309.

National standard of PRC 2001a. *Code for seismic design of buildings GB50011-2001. Beijing: China Architecture and Building Pres.*

U.S. General Service Administration (GSA), 2003. *Progressive collapse analysis and design guidelines for new federal office buildings and major modernization projects, Washington D. C.*

Unified Facilities Criteria-department of Defense (UFC-DOD). (2009). *Design of structures to resist progressive collapse, Washington D. C.*

Marjanishvili, S. and E. Agnew (2006). "Comparison of Various Procedures for Progressive Collapse Analysis." *Journal of Performance of Constructed Facilities* 20(4): 365-374.

Ellingwood B R, Smilowitz R, Dusenberry D O, et al (2007). "Best practices for reducing the potential for progressive collapse in buildings." *National Institute of Standards and Technology*, NISTIR 7396:216.

SAP2000 software. *Computers and structures-Inc. Berkeley, CA.*

Federal Emergency Management Agency (FEMA 356), 2000. *Prestandard and Commentary for the Seismic Rehabilitation of Buildings. Washington D. C.*

Dusenberry D O. (2002) "Review of existing guidelines and provisions related to progressive collapse." *Washington D. C.: NIBS. http://www.nibs.org.*

Ellingwood B R. (2005) "Building design for abnormal loads and progressive collapse." *Computer-Aided Civil and Infrastructure Engineering*, 20(3):194-205.

8CUEE CONFERENCE PROCEEDINGS
8th International Conference on Urban Earthquake Engineering
March 7-8, 2011, Tokyo Institute of Technology, Tokyo, Japan

COLLAPSE BEHAVIOR AND ULTIMATE EARTHQUAKE RESISTANCE OF WEAK COLUMN TYPE MULTI STORY STEEL FRAME UNDER BI-AXIAL GROUND MOTION

Satoshi Yamada[1] and Yuko Shimada[2]

1) Associate Professor, Structural Engineering Research Center, Tokyo Institute of Technology, Japan
2) Assistant Professor, Faculty of Engineering, Chiba University, Chiba, Japan
naniwa@serc.titech.ac.jp, yshimada@faculty.chiba-u.jp

Abstract: In seismic design, moment resisting frame is designed to form the overall sway mechanism under severe earthquake. However, it is possible to form the weak column mechanism with the rise of strength of beams and panel zone due to strain hardening. The causes to collapse the weak column type frame are strong bi-axial seismic force, P-Δ effect and deterioration of restoring force. In this study, a series of response analyses of weak column type multi story steel frames under bi-axial ground motion are carried out. In the analysis, realistic hysteresis model of story including deteriorating range is used. From analytical results, collapse behavior and ultimate earthquake resistance of steel frames governed by deterioration of columns are evaluated.

1. INTRODUCTION

In seismic design, moment resisting frame is designed to form the overall sway mechanism under severe earthquake. However, it is possible to form the weak column mechanism with the rise of strength of beams and panel zone due to strain hardening. In the full scale shaking table test of 4 story steel moment frame conducted at E-defense in 2007, Yamada et. al. (2008) and Suita et. al. (2008), specimen building made sway mechanism under design level earthquake. However under extremely strong ground motion, mechanism changed to weak story type and specimen building completely collapsed. The causes to collapse the weak column type frame are strong bi-axial seismic force, P-Δ effect and deterioration of restoring force caused by local buckling in column. Many studies focused on the influence of P-Δ effect to earthquake resistance of moment frame were carried out. But most of them dose not consider the realistic deterioration behavior of column.

In this study, a series of response analyses of weak column type multi-story steel frames under bi-axial ground motion are carried out. Hysteresis model used in analysis based on the realistic behavior of column including the deteriorating range governed by local buckling. From analytical results, collapse behavior and ultimate earthquake resistance of weak column type steel frame under bi-axial excitation is clarified.

2. OUTLINE OF ANALYSIS

2.1 MSS Model

In this study, MSS (Multiple Shear Spring) model, Wada et. al. (1989), shown in Fig.1 is used. In the MSS model, behavior of the story is expressed by the equal shear springs which placed at an equal angle. Analytical model of multi story shear system which placed MSS between each mass has degree of freedom of two horizontal directions in each story. The reason to use this model is that rectangular hollow section steel tube which frequently used as column of steel building structures in Japan has small directionality of the structural characteristics. In addition, behaviors of the columns govern the collapse behavior of structure that forms weak story mechanism. By consideration of accuracy, number of shear springs in a story is 16. P-Δ effect is considerd as negative stiffness, Akiyama (1984).

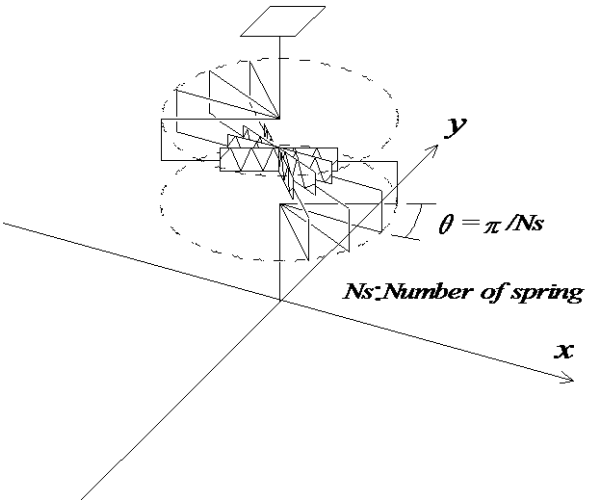


Fig.1: MSS (Multiple Shear Spring) model

2.2 Hysteresis model of the story based on the realistic behavior of column

Hysteresis model used in this analysis consists with skeleton curve which corresponds to the load-deflection relationship under monotonic loading, Bauschinger part, and elastically unloading part, as shown in Fig.2, Akiyama et. al. (1990). Based on the calculated load-deformation relationship of RHS column under monotonic loading including deteriorating behavior governed by local buckling , Yamada et. al (1993), skeleton curve of the story is modeled. In this study, two types of cold-formed RHS column are used. One has section with D/t ratio of 20 which represents columns with enough ductility; the other has section with D/t ratio of 30 which represents columns with poor ductility. Fig. 3 shows the analytical result. In the analysis, axial force ratio set 0.2.

Skeleton curve of the story and load deformation relationship of column corresponds under following assumptions. (1) Yield rotation angle of column is 1/3 of yield story drift angle. (2) Yield story shear corresponds to full plastic moment of column. (3) Beams and panel-zones yield simultaneously with columns. (5) About second modulus of the story, two types of model set. In Model 1, second modulus of story has 1/2 of the second modulus of column. In Model 2, second modulus of story has 1/3 of the second modulus of column. The ratio of the plastic deformation of the column in the plastic deformation of the story becomes 1/2 and 1/3 in the Model 1 and Model 2 respectively. (6) In the deteriorating range, stiffness of the story set same with stiffness of column. Fig. 4 shows the skeleton curve of the story. In the analysis, the skeleton curve of the story divided to the element springs in the MSS.

As the Bauschinger part, Akiyama and Takahashi's model, Akiyama et. al. (1990). is applied.

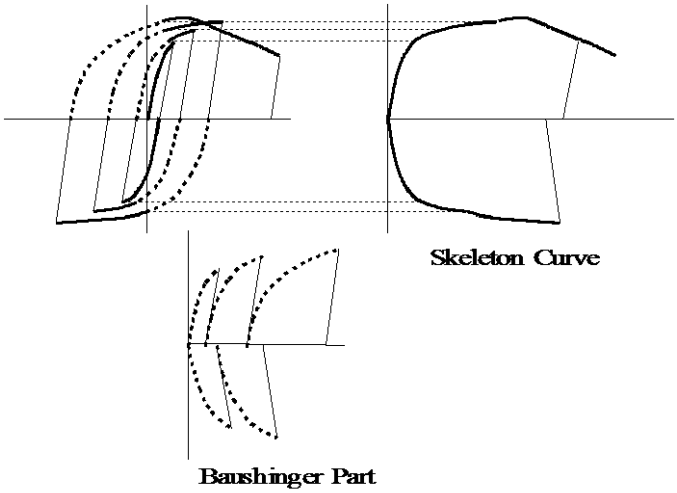


Fig.2: Decomposition of the hysteresis loop

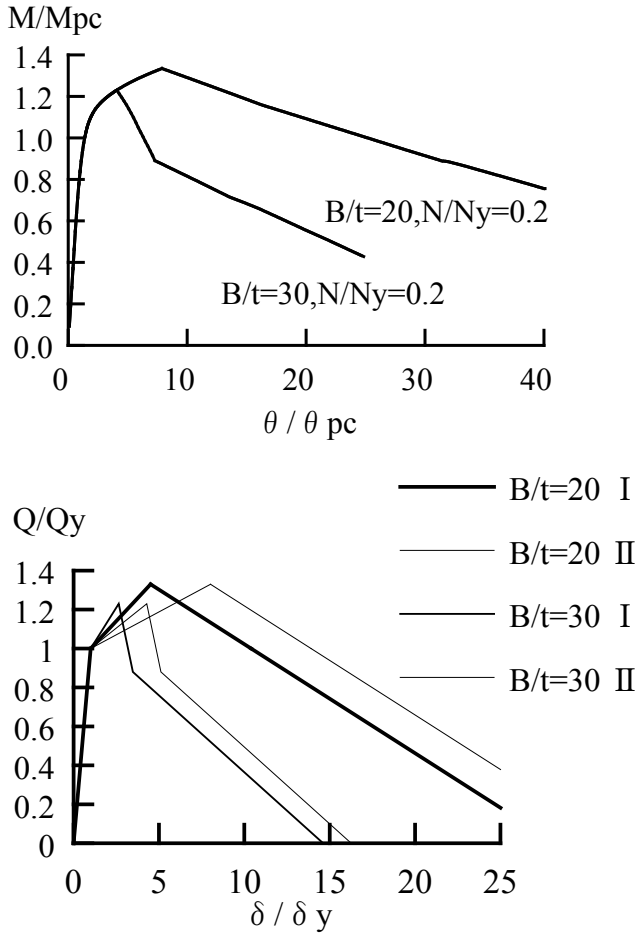
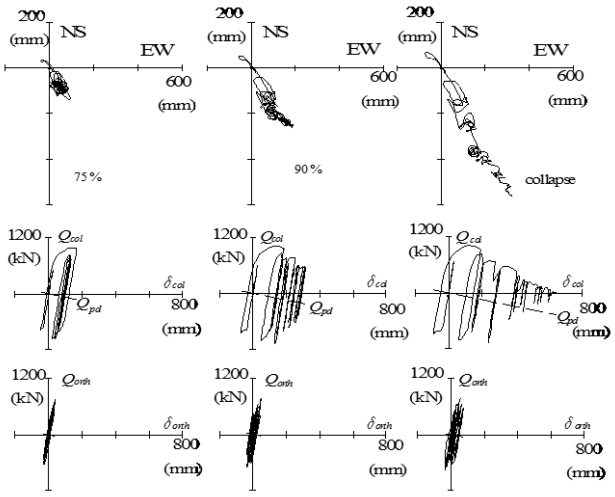


Fig.4: Skeleton curve of the story

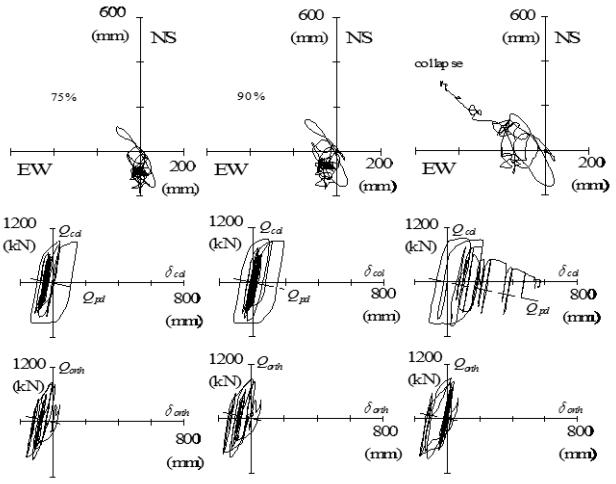
2.3 Parameter

Analytical models are multi-story shear model. Standard model set with number of the story (N) of 3, story shear coefficient of the 1st story (α 1) of 0.3 and yield story drift angle (θ y) of 0.01. Difference of the collapse behavior of multi story steel frame with four kinds of restoring force characteristics set in the former part is examined by using standard model. The influences of other parameters of frame, i.e. number of the story, story shear coefficient of 1st story and yield story drift angle, are examined by changing one parameter from standard model with hysteresis Model 1 of D/t=20. Examined parameters are story number of 9, story shear coefficient of 1st story of 0.5 and yield story drift angle of 0.005. In all models, weight of each story is 1000kN, height of each story is 4m, and distribution of stiffness corresponds to the optimum story shear coefficient distribution. And in order to make weak 1st story mechanism, except 1st story are kept in elastic range.

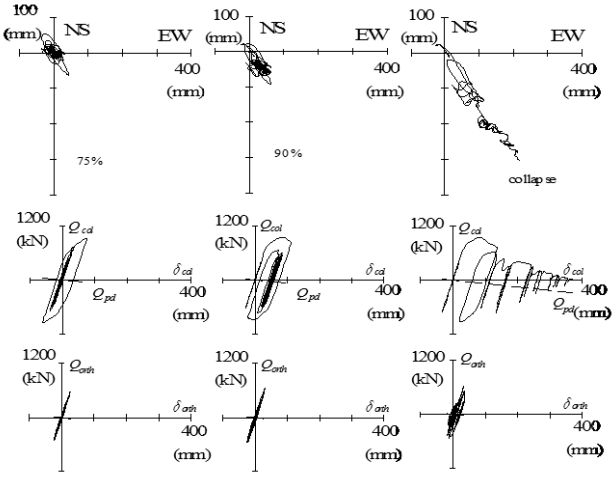
As input waves, JMA Kobe record, El-Centro record, Hachinohe record and Taft record are used. In the analysis, amplification factor is multiplied to the acceleration record in order to change input level up to collapse.



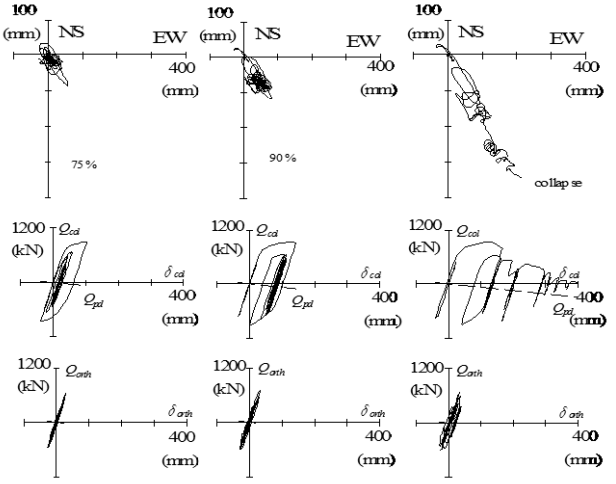
(1) N=3, α_1=0.3, θ_y =0.01, D/t=20 Model 1



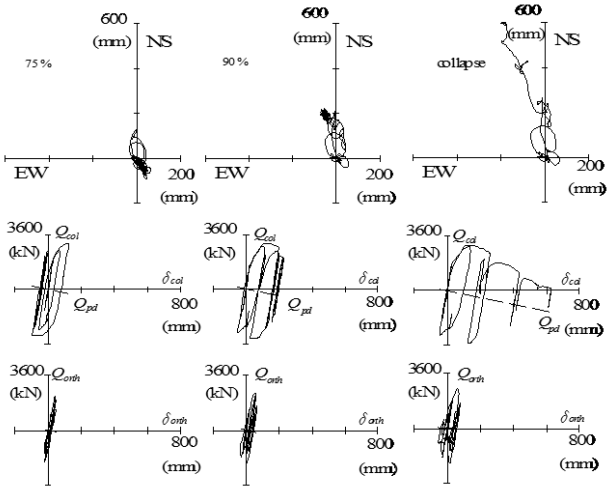
(2) N=3, α_1=0.3, θ_y =0.01, D/t=20 Model 2



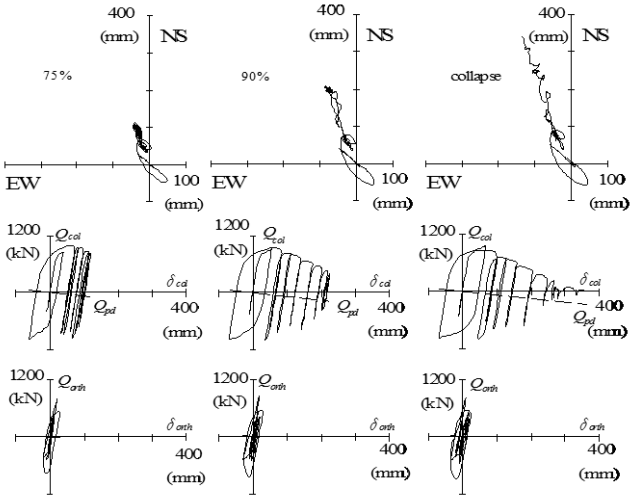
(3) N=3, α_1=0.3, θ_y=0.01, D/t=30 Model 1



(4) N=3, α_1=0.3, θ_y=0.01, D/t=30 Model 2



(5) N=9, α_1=0.3, θ_y=0.01, D/t=20 Model 1



(6) N=3, α_1=0.3, θ_y=0.005, D/t=20 Model 1

Fig.5: Orbit and hysteresis of 1st story under JMA-Kobe record

3. COLLAPSE BEHAVIOR AND ULTIMATE EARTHQUAKE RESISTANCE OF WEAK STORY TYPE MULTI STORY FRAMES UNDER BI-AXIAL GROUND MOTION

Orbit and hysteresis of 1st story under JMA-Kobe record are shown in Fig.5. Hystereses are in collapsed and its orthogonal directions respectively. In the figure, analytical result of collapse level, 90% of collapse level and 75% of collapse level are compared. In any case, displacement progresses to one direction when the story stiffness becomes negative according to deterioration though bias of the displacement are small until story reaches its maximum strength. Comparing the hysteresis of each model in collapsed direction, in case of Model 2 with D/t=20 even in the collapse level excitation stable behavior is appeared until story reaches its maximum strength. On the other hand, in cases of models with less ductility, displacement progresses to one direction without obvious cyclic behavior under collapse level excitation.

Hysteretic dissipated energy in the collapse direction of collapsed case is shown in Fig.6 divided by the dissipated energy under monotonic loading. Ratios of dissipated energy in the collapse direction to the dissipated energy under monotonic loading are around 1.0 except cases with enough ductility. Even if model has enough ductility、lowest value of the ratio is 1.3. When weak story type steel frame collapse under bi axial ground motion, hysteretic dissipated energy in the collapse direction can be evaluated as approximately same with the hysteretic dissipated energy under monotonic loading.

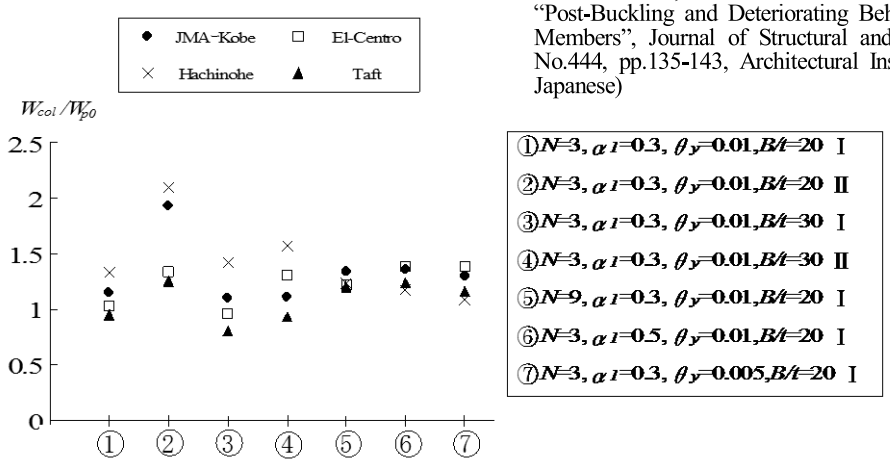


Fig.6: Hysteretic dissipated energy in the collapse direction

4. CONCLUSIONS

A series of response analyses of weak column type multi-story steel frames under bi-axial ground motion are carried out. Hysteresis model used in analysis is based on the realistic behavior of column including the deterioration range governed by local buckling. From analytical results, following conclusions are obtained.

1. Focusing on orbit of the 1st story, displacement progresses to one direction when the story stiffness becomes negative according to deterioration though bias of the displacement are small until story reaches its maximum strength.
2. When weak story type steel frame collapse under bi axial ground motion, hysteretic dissipated energy in the collapse direction can be evaluated as approximately same with the hysteretic dissipated energy under monotonic loading.

References:

YAMADA S., SUITA K., TADA M., KASAI K.,MATSUOKA Y. and SHIMADA Y.(2008), " Collapse Experiment on 4-Story Steel Moment Frame, Part 1 Outline of Test Results", Proc. of 14WCEE, DVD, 2008.10

SUITA K., YAMADA S., TADA M., KASAI K., MATSUOKA Y. and SHIMADA Y.(2008); Collapse Experiment on 4-Story Steel Moment Frame, Part 2 Detail of Collapse Behavior, Proc. of 14WCEE, DVD, 2008.10

WADA A., HIROSE K.(1989), "Elasto-Plastic Behaviors of the Building Frames Subjected to Bi-Directional Earthquake Motion", Journal of Structural and Construction Engineering, No.399, pp.37-47, Architectural Institute of Japan, 1989.5 (in Japanese)

AKIYAMA H.(1984), "P-Δ Effect on Energy Absorption Capacity of Steel Framed Structures Subjected to Earthquakes, Transaction of the Architectural Institute of Japan, No.340, pp.11-16, 1984.6 (in Japanese)

AKIYAMA H. and TAKAHASHI M.(1990) "Influence of Bauschinger Effect on Seismic Resistance of Steel Structures", Journal of Structural and Construction Engineering, No.418, pp.49-57, Architectural Institute of Japan, 1990.12 (in Japanese)

YAMADA S., AKIYAMA H. and KUAMURA H.(1993) "Post-Buckling and Deteriorating Behavior of Box-Section Steel Members", Journal of Structural and Construction Engineering, No.444, pp.135-143, Architectural Institute of Japan, 1993.2 (in Japanese)

8CUEE CONFERENCE PROCEEDINGS
8th International Conference on Urban Earthquake Engineering
March 7-8, 2011, Tokyo Institute of Technology, Tokyo, Japan

EFFECT OF YIELDING OF ROOF MEMBERS ON SEISMIC RESPONSE BEHAVIOR OF DOUBLE LAYER LATTICE DOMES

Tomohiko Kumagai[1], Toru Takeuchi[2], and Toshiyuki Ogawa[2]

1) Assistant Professor, Dept. of Architecture and Building Engineering, Tokyo Institute of Technology, Japan
2) Professor, Dept. of Architecture and Building Engineering, Tokyo Institute of Technology, Japan
kuma@arch.titech.ac.jp, ttoru@arch.titech.ac.jp, togawa@arch.titech.ac.jp

Abstract: In this study, a medium scale double layer lattice domes with substructure whose natural period is equal to the natural period of roof structure are made an object of investigation, the effects of yielding of roof members on seismic response behavior of lattice domes are examined by elasto-plastic dynamic response analysis which takes into account the geometrical nonlinearity. In addition, the simplified evaluation method for reductions of seismic response accelerations and displacements at roof members yielding is proposed. The strain energy produced to the upper structure of equivalent double-mass system based on dome model is used for this evaluation method.

1. INTRODUCTION

On seismic responses of lattice domes, when roof structure resonates with substructure large response accelerations occur at roof structure as shown in the work by Takeuchi et al. (2007). As a result, there is a possibility that the members of roof structure yield. In this study, the double layer lattice domes with substructure whose natural period is equal to the natural period of roof structure are made an object of investigation, the effects of yielding of roof members on seismic response behavior of lattice domes are examined by elasto-plastic dynamic response analyses. In addition, the simplified evaluation method for reductions of seismic response accelerations and displacements by roof members yielding is proposed. The strain energy produced to the upper structure of equivalent double-mass system based on dome model is used for this evaluation method.

2. ANALYSIS MODELS AND NUMERICAL ANALYSIS METHODS

2.1 Analysis Models

The analysis model for this study is a medium scale double layer lattice dome with 6000cm span as shown in Figs.1 and 2. Table 1 shows the dimensions of dome. The half subtended angle of the dome is 30 degrees. The member properties for roof structure are shown in Table 2. The members of dome roof are steel tubular sections and these are designed so that combined stresses (compressive or tensile stress and bending stress) of the members under the dead load of the dome will be uniform. The members of substructure are designed so that the story deformation angle under horizontal load with base shear coefficient 0.3 will be less than 1/200. The horizontal stiffness of substructure is set so that the ratio of natural period R_T is adjusted to 1.0. Here, the natural period ratio R_T is the ratio of natural period of substructure with rigid roof to that antisymmetrical 1 wave mode of roof structure without substructure. The stress-strain relationship is assumed to be a bi-linear type for dome roof members and a linear type for the other members. The joints between the tension ring of dome roof and the top of column of the substructure are pin joints. For the boundary condition, the bases of columns are pin supported. The dead load is assumed to be 1.18kN/m^2 for the dome roof in consideration of the structural material weight and finishing material weight, etc.

2.2 Numerical Analysis Methods and Input Seismic Waves

The method of analyses are a time history response analysis and a static buckling analysis those takes into account the geometrical and material nonlinearities. A numerical integration scheme for time history response analysis is the Newmark β = 1/4 method. The time increment Δt is 0.005sec. Rayleigh damping is applied to the dome damping. The damping factor h is 2% for 1st and 2nd (or 3rd) modes. The input seismic waves are two observed earthquake motions El Centro NS (1940) and JMA Kobe NS (1995). The input direction of seismic waves is horizontal x direction.

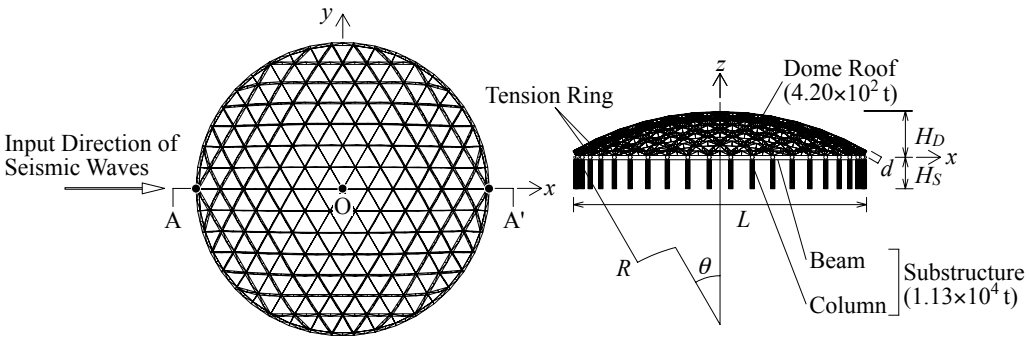


Figure 1 Analysis Model (Double Layer Lattice Dome)

Table 1 Dimensions of Dome

Half Subtended Angle θ (deg.)	30
Span of Dome L (cm)	6000
Radius of Dome R (cm)	6000
Dome Rise H_D (cm)	909
Column Higtht H_S (cm)	600
Ridge Member Length l (cm)	523
Depth d (cm)	113

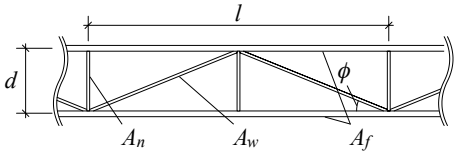


Figure 2 Detail of Roof Member

Table 2 Member Properties for Dome Roof (on Line AOA')

A_f (cm^2)	10.0-18.2
A_w, A_n (cm^2)	8.42-14.9
ϕ (deg.)	23.4
Young's Modulus E (N/mm^2)	2.06×10^5
Modulus of Strain Hardening E_t (N/mm^2)	2.06×10^3
Yield Stress σ_y (N/mm^2)	294

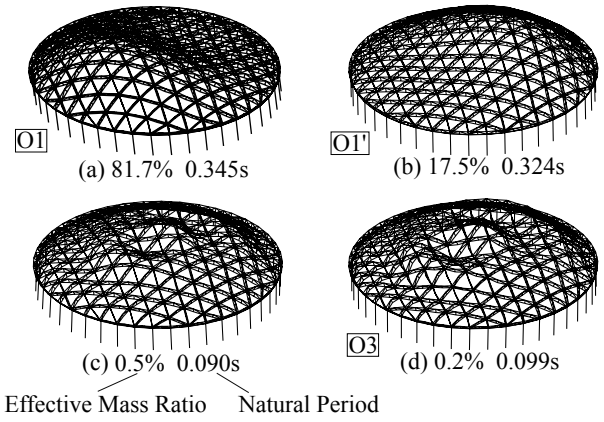


Figure 3 Natural Vibrational Characteristics (in Elastic Range)

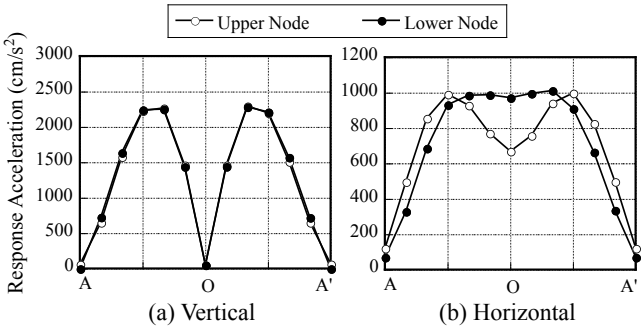


Figure 4 Distributions of Maximum Response Accelerations on line AOA'
(El Centro NS 25cm/s Input, Elastic Response)

3. ELASTIC RESPONSE BEHAVIOR

Fig.3 shows the natural vibrational characteristics at elastic range. The shape of mode with maximum effective mass ratio is the antisymmetrical one wave mode (O1 mode). The effective mass ratio of this mode is 81.7%.

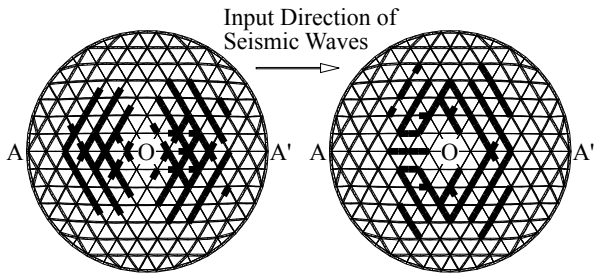
The distributions of maximum response accelerations on line AOA' at elastic range are shown in Fig.4. The response accelerations are the relative values between the responses of roof structure and those at top of column of substructure. The distribution shapes of vertical acceleration are the antisymmetrical shape, the influence of O1 mode appear. In horizontal direction, the difference of responses of upper nodes and lower ones is found. This difference occurs because of the rigid body rotation of chord members.

4. EFFECT OF YIELDING OF ROOF MEMBERS ON RESPONSE BEHAVIOR

4.1 Elasto-plastic Response Behavior

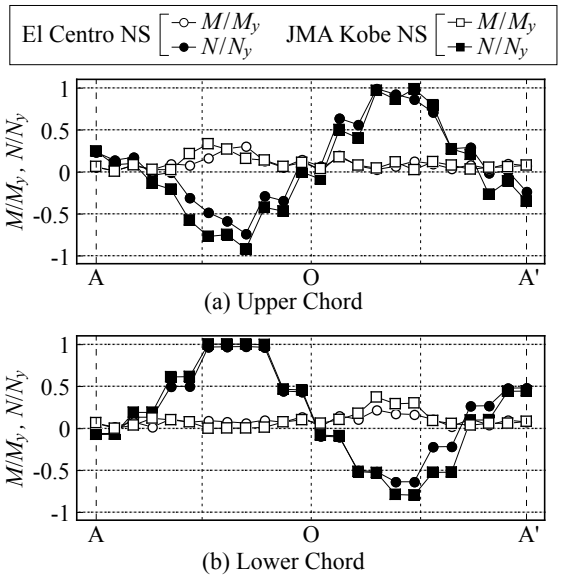
At first the responses of dome roof subjected to seismic waves with maximum velocity of 75cm/s are investigated. Fig.5 shows the distributions of yielding roof members when number of yielding members is a maximum. The members yielding occurs in the vicinity of antinode of antisymmetrical one wave mode with maximum effective mass ratio. There is a difference between the distribution of yielding members of upper layer and that of lower layer due to the difference of horizontal responses

between upper nodes and lower ones. Fig.6 shows the distributions of axial forces and bending moments on line AOA' at the same time as Figure 5. N_y is the yield axial force, M_y is the yield moment. The axial forces are dominant compared with the bending moments regardless of the layer. The shape of distribution of axial forces is the antisymmetrical one wave shape.



(a) Upper Chord (b) Lower Chord

Figure 5 Distributions of Yielding Members of Dome Roof (at Time of Maximum Number of Yielding members, 75cm/s Input)



(a) Upper Chord

(b) Lower Chord

Figure 6 Distributions of Axial Forces and Bending Moments on line AOA' (at Time of Maximum Number of Yielding members, 75cm/s Input)

Next, the effects of maximum velocity of input seismic wave on elasto-plastic response behavior of dome are examined. The maximum velocities of input seismic waves are 25~100cm/s (at intervals of 25cm/s). Fig.7 shows the relationships between maximum number of yielding members and input velocity of seismic waves. The number of yielding members increases with increase in input velocity. The distributions of maximum response acceleration amplification factors on line AOA' are shown in Fig.8. The maximum response acceleration amplification factors F_{AV} and F_{AH} are defined as Eqs. (1) and (2).

$$F_{AV} = A_V / A_{eq} \quad (1)$$

$$F_{AH} = A_H / A_{eq} \quad (2)$$

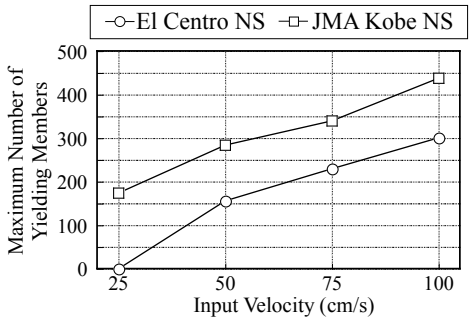
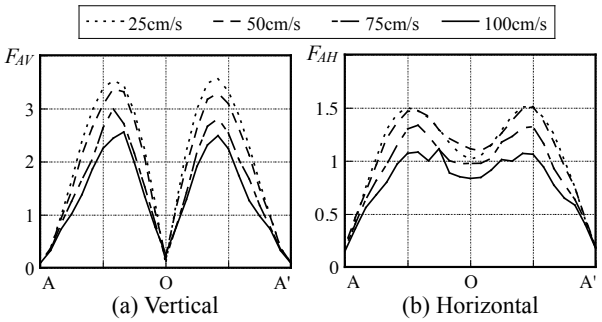


Figure 7 Relationships between Maximum Number of Yielding Members and Input Velocity of Seismic Waves



(a) Vertical (b) Horizontal

Figure 8 Distributions of Maximum Response Acceleration Amplification Factors on line AOA' (Upper Layer, El Centro NS)

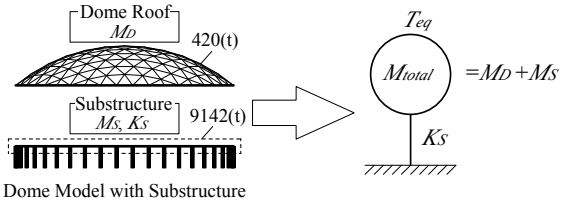


Figure 9 Conversion to Equivalent Single-mass System

where A_V and A_H are the maximum vertical and horizontal response accelerations respectively, A_{eq} is the maximum response acceleration of equivalent single-mass system shown in Fig.9.

As the number of yielding members increase, the response amplification factors decrease uniformly in any node.

4.2 Examination of Reduction of Response Amplification Factor due to Plasticity of Roof Members

In this section, the reason of reduction of response amplification factors due to plasticity of roof members is investigated. At first, the change of natural vibrational characteristics due to plasticity of members is examined. Fig.10 shows the natural vibrational characteristics in elasto-plastic range. Input Seismic wave is El Centro NS with maximum velocity 100cm/s. The vibrational characteristics at the time when the maximum vertical response acceleration occurs are indicated. The natural period of mode with maximum effective mass ratio does not change because of the plasticity of roof members. One of the reasons for this is that the mass of substructure which is assumed to be in elastic state is larger than that

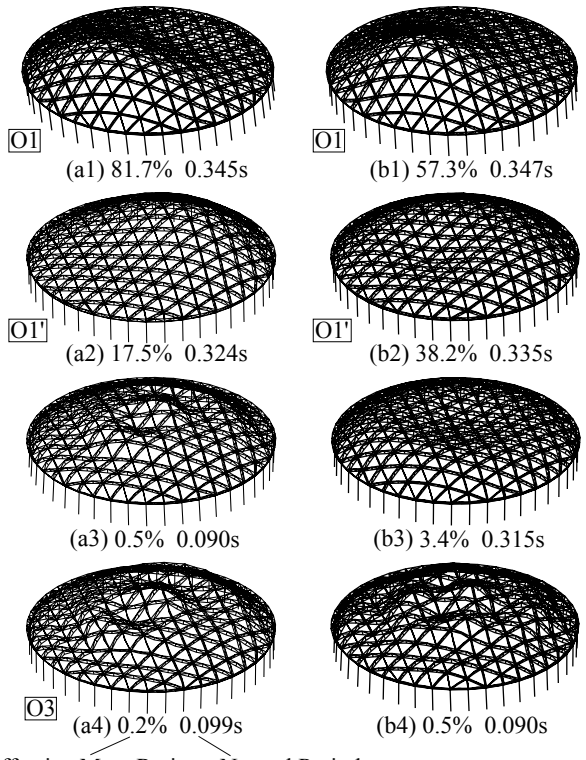


Figure 10 Comparison of Natural Vibrational Characteristics in Elastic Range with Those in Elasto-plastic Range
(Elasto-plastic Range: El Centro NS, 100cm/s Input)

of dome roof. Consequently, the effect of the change of vibrational mode due to the plasticity of roof members on response behavior is small.

Next, we take note of the strain energy produced to the whole dome roof when the maximum response occurs. Fig.11 shows the time histories of strain energy produced to the dome roof. The cumulative plastic strain energy increases every half of natural period of O1 mode. Then the response reduction ratios D_h^{dome} are evaluated from Eqs. (3)~(5)[Kasai et al. (2003)] by using this cumulative plastic strain energy W_P and elastic strain energy W_E.

$$h_{eq} = 0.8\frac{1}{4\pi}\frac{W_P}{W_E} \quad (3)$$

$$h = h_{eq} + h_0 \quad (h_0 = 0.02) \quad (4)$$

$$D_h^{dome} = \sqrt{\frac{1+\alpha h_0}{1+\alpha h}} \quad (\alpha = 25) \quad (5)\text{[Kasai et al. (2003)]}$$

Fig. 12 shows the response reduction ratios D_h^{dome} and D_r^{dome}. D_r^{dome} those are calculated from Eqs. (6)~(9) using the maximum response amplification factors are the response reduction ratios in analysis results.

$$D_{rAV}^{dome} = F_{AV}/F_{eAV} \quad (6) \qquad D_{rAH}^{dome} = F_{AH}/F_{eAH} \quad (7)$$

$$D_{rDV}^{dome} = F_{DV}/F_{eDV} \quad (8) \qquad D_{rDH}^{dome} = F_{DH}/F_{eDH} \quad (9)$$

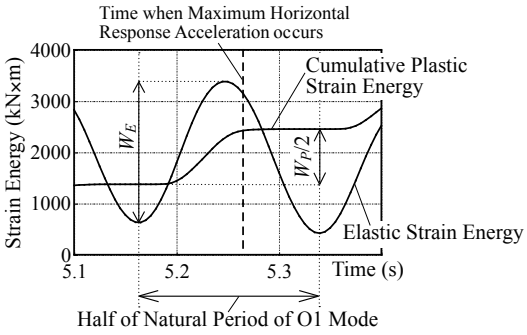
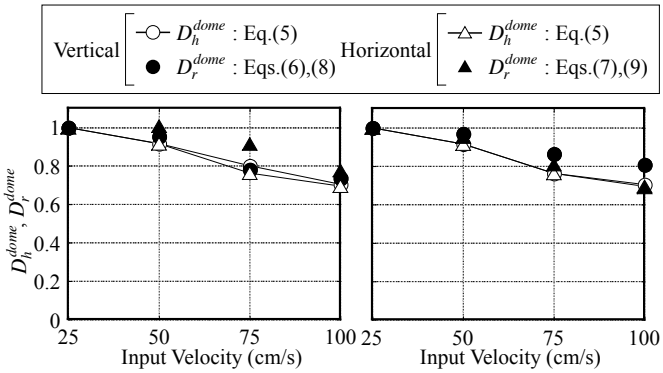


Figure 11 Time Histories of Strain Energy
(El Centro NS, 75cm/s Input)



(a) Response Acceleration (b) Response Displacement

Figure 12 Relationships between Response Reduction Ratios and Input Velocity of Seismic Waves
(El Centro NS)

where F_{AV}, F_{AH}, F_{DV} and F_{DH} are the maximum response amplification factors for acceleration (A) and displacement (D), and for vertical direction (V) and horizontal direction (H) respectively. F_e are the maximum response amplification factors in elastic response.
The estimated response reduction ratios D_h^{dome} agree approximately with the analysis results D_r^{dome}. From the above, the reduction of maximum response amplification factors due to plasticity of members can be explained by the response reduction ratios estimated from the strain energy produced to the whole dome roof.

5. EVALUATION METHOD FOR RESPONSE REDUCTION DUE TO PLASTICITY OF MEMBERS

The response reductions are attempted to evaluate by estimating the strain energy produced to the dome roof from the time history responses of equivalent double-mass system. The equivalent double-mass system is made based on the vibration characteristic of O1 mode. The procedure of making of equivalent double-mass system is shown in Fig.13.

1) The effective mass of O1 mode M_e is computed by eigenvalue analysis (Fig. 13(1)).
2) The stiffness of substructure K_{Se} is determined so that the natural period of single-mass system with

mass M_e shown in Fig.13(2) agrees with that of equivalent single-mass system shown in Fig.9.

3) The stiffness of roof structure K_{De} is determined so that the natural period of equivalent double-mass system shown in Fig.13(3) agrees with the period of O1 mode. The effective mass is apportioned to the upper and lower structures of double-mass system according to the ratio of mass of dome roof to that of substructure.

The mechanical characteristics of double-mass system are the bi-linear type for roof structure and the linear type for substructure. The second gradient of roof structure of double-mass system is determined as half of initial stiffness based on the relationship between horizontal load and horizontal average displacement of dome model by static buckling analysis shown in Fig.14. The initial yield loads of dome model and double-mass system are equal.

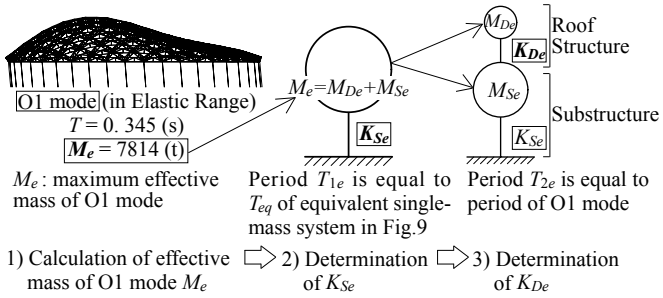


Figure 13 Procedure of Making of Equivalent Double-mass System

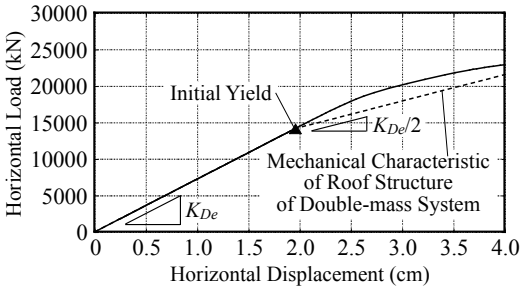


Figure 14 Relationships between Horizontal Load and Horizontal Displacement

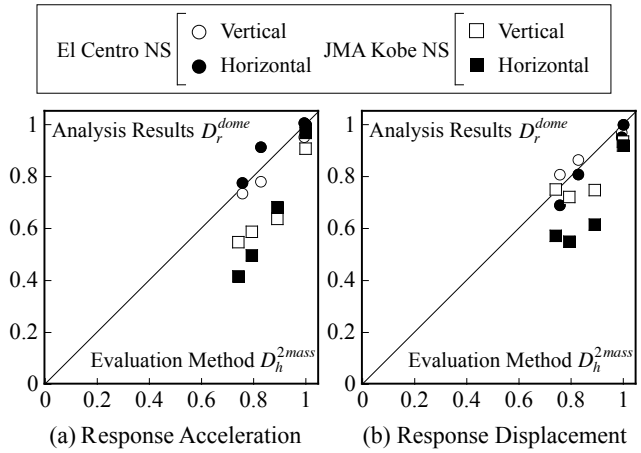


Figure 15 Accuracies of Proposed Evaluation Method for Response Reduction Ratio using Strain Energy of Equivalent Double-mass System

The response reduction ratios of equivalent double-mass system D_h^{2mass} are evaluated by substituting the strain energy of double-mass system W_P^{2mass}, W_E^{2mass} for Eqs. (3)~(5). Fig.15 shows the accuracies of proposed evaluation method for response reduction ratio using the strain energy of equivalent double-mass system. The evaluated response reduction ratios D_h^{2mass} agree approximately with the analysis results D_r^{dome}. Therefore it is possible to evaluate the response reduction ratio of double layer lattice dome by using the equivalent double-mass system.

However, there are several cases those the evaluated values D_h^{2mass} are larger than the analysis results D_r^{dome} because it is impossible to express the pulsating in vertical response displacement of lattice dome subjected to JMA Kobe NS by the response of double-mass system.

6. CONCLUSIONS

It is concluded as follows, from the results of above numerical analyses.

1) The yielding of members of dome roof subjected to seismic waves with maximum velocity 75cm/s occurs in the vicinity of antinode of natural vibration mode with maximum effective mass ratio in the case of the roof structure resonating with the substructure.
2) The maximum response amplification factors of dome roof reduce uniformly in any node without the change of distribution shapes due to plasticity of members of dome roof.
3) It is possible to evaluate the response reduction ratio of double layer lattice dome by using the strain energy produced to the upper structure of equivalent double-mass system based on the vibration characteristic of mode with maximum effective mass ratio of dome model.

Acknowledgements:

I would like to thank Hidetoshi Takayama for his great cooperation through his master's thesis. The present paper was supported in part by a grant from Grant-in-Aid for Young Scientists (B) (Research No.21760427) and Grant-in-Aid for Scientific Research (B) (Research No.19360247) by Japan Society for the Promotion of Science (JSPS).

References:

Takeuchi, T., Kumagai, T., Shirabe, H. and Ogawa, T. (2007), "Seismic Response Evaluation of Lattice Shell Roofs Supported by Multistory Structures," *Journal of Structural and Construction Engineering (Transaction of AIJ)*, No.**619**, 97-104 (in Japanese).

Kasai, K., Ito, H. and Watanabe, A. (2003), "Peak Response Prediction Rule for a SDOF Elasto-plastic System Based on Equivalent Linearization Technique," *Journal of Structural and Construction Engineering (Transaction of AIJ)*, No.**571**, 53-62 (in Japanese).

8CUEE CONFERENCE PROCEEDINGS
8th International Conference on Urban Earthquake Engineering
March 7-8, 2011, Tokyo Institute of Technology, Tokyo, Japan

THE AISC 2010 SEISMIC PROVISIONS FOR COMPOSITE STRUCTURES: TOWARDS AN APPLICATION OF PBD PRINCIPLES FOR INNOVATIVE CONNECTIONS

Roberto T. Leon[1] and Jong Wan Hu[2]

1) Professor, School of Civil and Environmental Engineering, Georgia Tech, Atlanta, USA
2) Associate Research Fellow, Korea Institute of S&T Evaluation and Planning, Seoul, Korea
Rl58@ce.gatech.edu, jongp24@kistep.re.kr

Abstract: The 2010 AISC Seismic Design provisions represent a major change for composite structures for at least two reasons. First, the provisions for composite structures have been folded into a single document with those for steel; the net result, at least superficially, is that composite construction is considered equivalent to steel in quality and performance. Second, the provisions for composite members and structural systems have become more prescriptive in an attempt to ensure a minimum level of performance. An unintended consequence of this latter item is that some freedom in the introduction of innovative composite connections has been removed. In this paper, a short review of the AISC composite provisions will be given, and a case study on the development of an innovative connection to be used in composite (steel-concrete) moment frames will be described. The innovative aspects of this connection are in the use of partial restraint connections between steel beams and concrete-filled tube columns that utilize a combination of low-carbon steel and shape memory alloy components. A refined finite element model with sophisticated three dimensional solid elements was developed to conduct numerical experiments on the proposed joints to obtain the global behavior of the connection and develop simplified models. Very good agreement was found between the simple and sophisticated models for strength, stiffness and energy dissipation capacity, verifying the robustness of the approach. The paper argues that careful analytical studies can replace the requirement for physical testing present in current steel codes.

1. BACKGROUND

Seismic design provisions for buildings have a long history in the USA, dating back to the Uniform Building Code of 1927. These provisions were steadily but slowly improved until the Applied Technology Council (ATC) issued a comprehensive set of seismic design provisions following the 1971 San Fernando Valley Earthquake (ATC 3-06, 1978). This effort has continued through the issuance of updated provisions by the National Earthquake Hazard Reduction Program (NEHRP). These provisions are developed through the Provisions Update Committee of the Building Seismic Safety Council (PUC/BSSC) (NIBS 2010). They were originally intended to serve as a model and resource code, but were adopted *in toto* into the 2000 version of the International Building Code, the first unified building code in the USA (IBC 2010).

Currently seismic loading provisions have been consolidated into ASCE 7-10 (ASCE 7 2010), while provisions for design of members, connections and structural systems have been remanded to material organizations. Provisions for steel structures began to be developed by the American Institute of Steel Construction (AISC) in the mid 1990s in an effort to provide a single set of consistent specifications for seismic design of metal structures. At that time PUC/BSSC has a small working group on composite structures which had produced a short draft on seismic design of a number of composite members and structural systems (NEHRP 1994). AISC decided to incorporate these provisions for composite structures as Part II of its first seismic design specification (AISC 1997). The structure of the AISC Seismic Specification remained unchanged until its last edition (AISC Seismic 2010), with Part I being a comprehensive and prescriptive set of rules for steel structures and Part II being a less complete and more performance-based document for composite members and structural systems.

Another important development in seismic design over the last 5 years has been the introduction of performance-based design (PBD) requirements for tall buildings. This development took place essentially because designers did not think that a number of the conventional provisions, particularly those requiring a backup structural system with a capacity to resist 25% of the design base shear, made sense structurally and economically for tall buildings. In the very hot property market that preceded the economic collapse of 2007, there were several dozen tall buildings being planned for high seismic cities such as San Francisco and Los Angeles. Designers for these structures proposed a series of innovative structural systems and connections that were not contemplated by the prescriptive provisions of existing codes. To attempt to provide some basic guidance as to how to demonstrate the validity of these systems, both the cities of San Francisco

and Los Angeles issued guidelines on how to use performance-based design and similar concepts to justify innovative designs (LA 2005, SF 2009).

This paper briefly proposes how the 2010 AISC Specification can be used, in conjunction with existing PBD guidelines, to permit the use of innovative connections without the need to perform extensive full-scale connection qualification tests

2. THE 2010 AISC SEISMIC SPECIFICATION

2.1 Major Changes

As usual with new versions of any specification, the AISC 2010 Seismic Provisions (AISC Seismic 2010) contains a number of new and evolutionary design requirements that reflect the latest in seismic research and practice. In addition, however, there have been two major changes. The first change, which can be considered editorial in nature, is that wherever possible, the provisions now have a consistent set of subsections for all seismic structural systems. These subsections include scope, basis for design, analysis requirements, structural system requirements, member design, and connection provisions. This new organization considerably simplifies the design process and makes possible quick comparisons between alternative structural solutions.

The second change, which is more philosophical in nature, is that the old Part I (Steel Construction) and Part II (Composite Construction) have been completely merged into a single document. For composite structures, this has had two major consequences. First, this approach makes composite design essentially equivalent to traditional steel insofar as expected performance is concerned. This is an important result because composite construction is not considered a viable option in the USA except for tall structures. It is hoped that its inclusion into a single design document with steel structures will make more designers consider composite systems for low- and mid-rise construction. The second consequence is that the old Part II provisions, which were intentionally nebulous in handling many design details, needed to be updated and rendered far more prescriptive in nature. The original NEHRP composite provisions, issued by NEHRP in 1994, were developed as enabling legislation for composite systems, and permitted the use of systems that had neither been tested nor built at the time.

The 2010 AISC main specification for steel structures (AISC 2010) provides much of the background to the seismic provisions and, as its predecessors, contains two important additional statements that are relevant to this paper. First, in its Preface it states that: "*The intention is to provide design criteria for routine use and not to provide specific criteria for infrequently encountered problems, which occur in the full range of structural design."* Second, in its Scope, it states that: *"Where conditions are not covered by the Specification, designs are permitted to be based on tests or analysis, subject to the approval of the authority having jurisdiction. Alternative methods of analysis and design are permitted, provided such alternative methods or criteria are acceptable to the authority having jurisdiction."* (AISC 2010)

Taken together, these two statements provide an escape route for designers wishing to circumvent prescriptive design procedures, but leave the responsibility to accept such approaches to the building officials. The PBD documents from the cities of SFO and LA cited previously aim at providing designers with some guidance on how to fulfill these requirements.

2.2 Member and Connection Design

General requirements for member and connection design are covered in Section D of the new AISC 2010 Specification.

Insofar as member design is concerned (Section D1), the most important change in the new edition is the explicit recognition, and associated requirements, for three types of seismic member categories: conventional, moderately ductile and highly ductile. Conventional members need only comply with the requirements of the main specification (AISC 2010), while the seismic specification gives detailed requirements for moderately and highly ductile members primarily in terms of width-to-thickness ratios, bracing, and protected zone provisions.

Insofar as this paper is concerned, the most important provisions regarding connection design are given in both the general section on connections (Section D2) and on Section E3 (Special Moment Frames). The majority of the important details for this paper are given in Section E3. Connections in special moment frames are required to provide deformation capacity through yielding of beams and panel zone deformations. For steel connections, it is required that (a) the connection shall be capable of accommodating a story drift angle of at least 0.04 rad., and (b) the measured flexural resistance of the connection, determined at the column face, shall equal at least 0.80Mp of the connected beam at a story drift angle of 0.04 rad. Compliance with these requirements can come from:

1. Use of connection prequalified as per AISC 358 (2005). AISC 358 currently prequalifies 7 types of connections based on extensive testing and analysis, primarily from results of the SAC research program (FEMA 2000).
2. Testing as per Appendices K1 and K2 of the seismic specification, which require at least two full-scale connections tests under a stringent displacement history.

It is worthwhile to notice that AISC requires physical testing, and that the testing needs to be supplemented by advanced analyses.

3. PBD GUIDELINES

As noted earlier, there have been two initiatives aimed at promoting the use of performance-based design approaches to seismic design. They include the recommendations of (a) a committee of the Structural Engineers of Northern California, which resulted in a

building ordinance for the city of San Francisco entitled *Requirements and Guidelines for the Seismic Design and Review of New Tall Buildings using Non-Prescriptive Seismic-Design Procedures* (SFO 2007), and (b) the Los Angeles Tall Building Design Council which resulted in a design guideline entitled *An Alternative Procedure for Seismic Analysis and Design of Tall Buildings Located in the Los Angeles Region* (LA 2005).

Only the LA document is truly a PBD document as it states clearly in its scope that its approach "*is based on capacity design principles followed by a series of state-of-the-art performance based design evaluations"* that aims to provide serviceable behavior under frequent events (43 year return period, or 50% probability of exceedance in 30 years) and very low probability of collapse under extreme events (2475 year return period, or 2% probability of exceedance in 50 years). The document provides analyses requirements in terms both of the model and load histories to be used. It focuses on the demand side and as a default, suggests using the member capacities established by ASC 41 (ASCE 41) to check performance. Iit adds an exception that "larger deformation capacities may be used only if substantiated by appropriate laboratory tests and approved by the Peer Review Panel and the Building Official."

The SFO document also utilizes the same two-level approach as the LA one, but intentionally avoids the use of PBD terminology and contains a mix of mandatory and non-mandatory provisions. It focuses on the demand side and is silent on the need for testing to justify the strength and deformation capacity of members and connections.

4.0 INNOVATIVE CONNECTIONS

The previous sections describe the current state of seismic design codes for composite structures in the USA. The rest of this paper describes the how development of an innovative connection can fit within these frameworks without having to carry out extensive physical testing.

The connection under consideration combines the robustness and structural efficiency of concrete-filled tube (CFT) columns with the ductility and recentering capabilities of a partially restrained (PR) connection (Fig. 1). The key innovative part of the connection is the use of a combination of mild steel and shape memory alloy (SMA) through rods as the connecting elements. The mild steel rods provide energy dissipation, while the SMA rods provide recentering capability (Hu and Leon 2010).

This type of connection is applicable in special and intermediate composite moment-resisting frames up to about 10 stories, and combines a number of the advantages associated with composite systems. For CFT columns, these advantages include the fact that the concrete prevents local buckling of the steel tube wall and the confinement action of the steel tube extends the usable strain of the concrete. CFT beam-columns and panel zones provide enhanced ductility and reduced rates of degradation under cycling at large drifts when compared to conventional steel or RC columns.

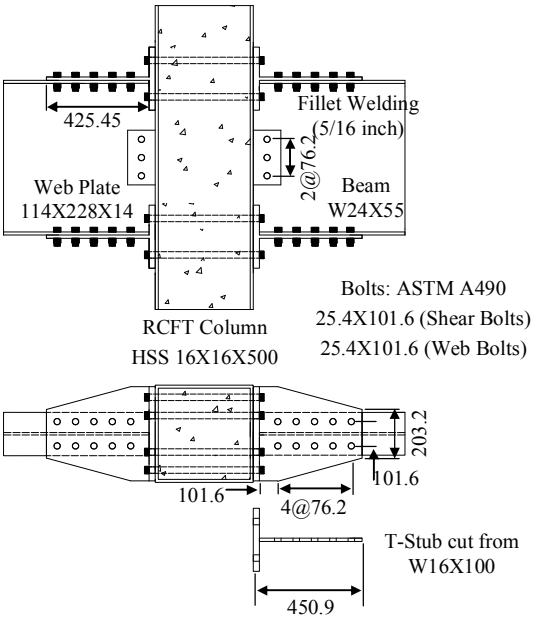


Figure 1 – PR composite connection

In order to utilize these connections in an actual structure, several obstacles need to be overcome as follows:

- The currently available PBD guidelines (see Section 3) will need to be extended to low-rise construction, as currently they are applicable only to structures over 49m in height. As the requirements for taller structures are more restrictive than those for lower ones, acceptance of this approach by progressive building officials is possible.
- The current requirement for full-scale physical testing of composite connections (see Section 2) will need to be waived and replaced by extensive advanced analytical studies. The rest of this paper looks at how this issue can be justified and the level of effort required.
- The use and scope of peer review panels need to be expanded as they need to become the main deciders, as opposed to building coded officials, of the technical merits of an innovative structural solution.

4.1 Connection Modeling and Calibration

The first step in justifying this approach is linked to the development of a simplified connection model whose components' cyclic behavior is well understood. In the case of the connection shown in Fig.1, these components are: (a) the steel beam; (b) the bolted T-stubs that provide the connections to the flanges; (c) the fin plate connection that provides shear transfer; (d) the mild steel and SMA rods that provide axial restraint; (e) the composite panel zone; and (f) the composite CFT column.

Fig. 2 shows a simplified generic model that is suitable to model this connection. In this model, springs C1 and C2 represent the T-stubs in tension and bearing, springs B1 through B4 represent the steel and SMA bars in tension and compression, springs D represent the joint shear deformation, and spring E the shear connection to the beam. Each of these springs can have its own backbone load-deformation

curve, which can represent many forms of deformation. For example, spring C1 includes the deformations due to slippage of the bolts between the beam and T-stub, the axial deformation of the T-stub stem, the flexural and shear deformation of the T-stub flanges, and the ovalization of the bolt holes in bearing. In addition, the cyclic behavior and degradation rules for each spring can be set independently. These models can easily be implemented into a number of existing platforms; OPenSEES was used in this study (Mazzone et al. 2006)

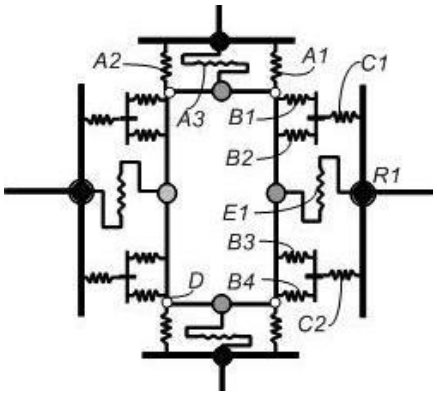


Figure 2 Simplified model of proposed connection

The key question becomes whether the behavior of all of these springs can be accurately predicted. The answer, for this connection, is yes as the individual behavior of (a) T-stubs, including slip, bearing, and ovalization (Swanson 1999,), (b) composite panel zones (Wu et. al. 2007), and (c) SMA materials (Tami and Kitagawa 2002, Song et al. 2006) is well established.. In addition, behavior of both SMA in large connections (Leon et al. 2001, Ocel 2002, Penar 2005) and CFT columns member and panel (Hu et al. 2005, 2007) has been verified by a number of research efforts.

Nevertheless, extensive calibration of the simplified model shown in Fig. 2 to advanced 3D FE models, such as that shown in Fig. 3, is a must. These models need to be very carefully developed to ensure proper meshing and boundary conditions. In addition, smaller detailed models of areas of stress concentrations (Fig. 4) also need to be examined to ensure that no possible failure modes are ignored. ABAQUS (2006) was the FE coded used herein.

The work requires that calibration of each individual mode of deformation be made to well-documented tests. Figs. 5 and 6 show comparisons for the axial deformations of the T-stub stem and slippage of the bolts for a T-stub specimen tested by Swanson (1999). These two deformation modes are built into spring C1 in Fig. 3. The models are capable of reproducing not only the behavior of components but also of entire connections. Fig. 7 shows a comparison between plastic rotations vs. moment for a connection tested by Swanson (1999) and a simplified model in OpenSEES. The model matches well all the observed test behavior both qualitatively and quantitatively.

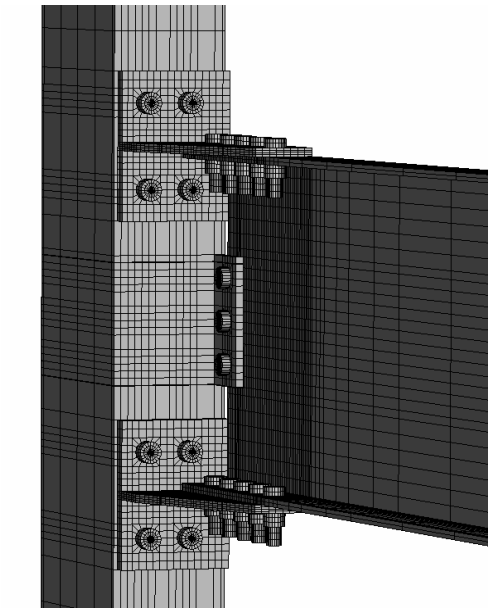


Figure 3 - 3D FE model of proposed connection

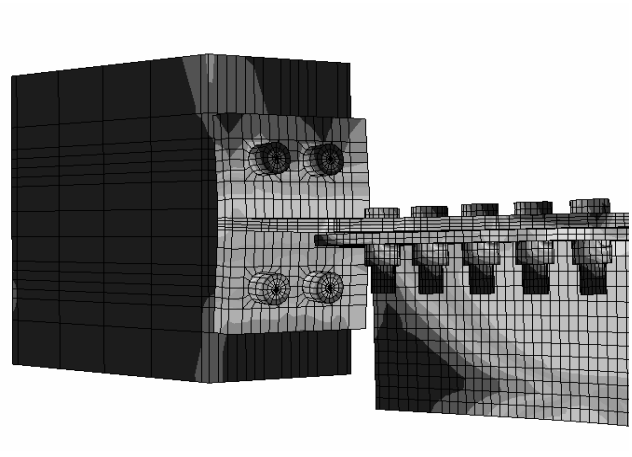


Figure 4 Detailed FE model of critical connection region

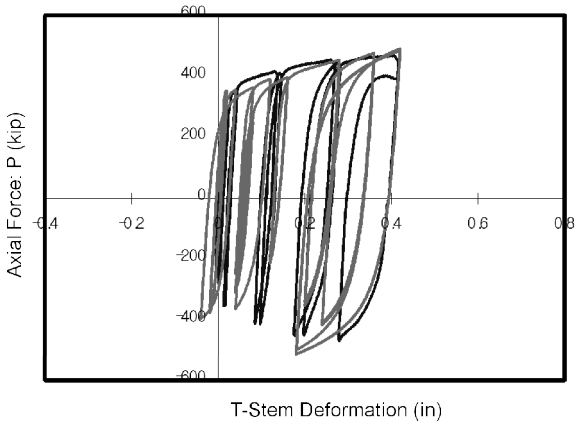


Figure 5 Comparison of T-stub stem deformation from tests and simplified model

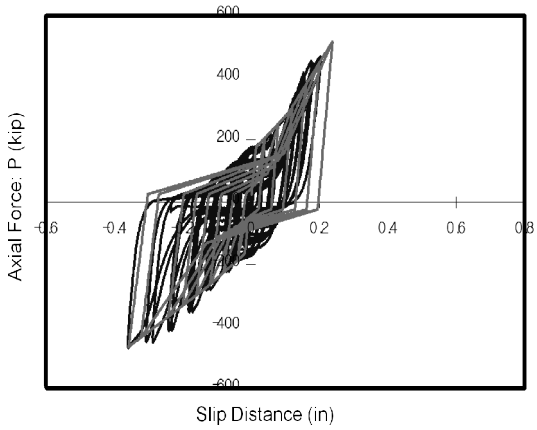


Figure 6 Comparison of T-stub slip from tests and simplified model

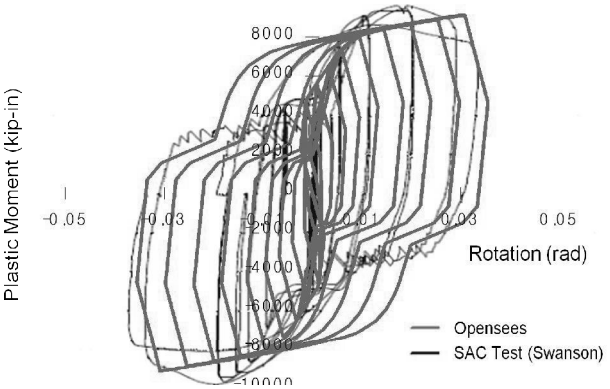


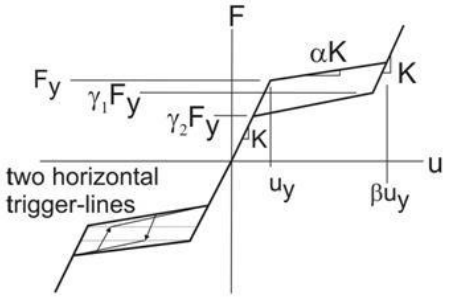
Figure 7 Comparison of measured and predicted moment vs. plastic rotations for a full-scale T-stub connection.

For these connections another complicating factor is the modeling of the shape memory effect, as shown in Fig. 8. Ideally, the material shows a flag-shaped behavior as shown in Fig. 8(a), with a number of break points and trigger lines related to the heat treatment of the material. However, actual data for one quadrant shows (Fig. 8(b)) that these lines and points are not easy to characterize.

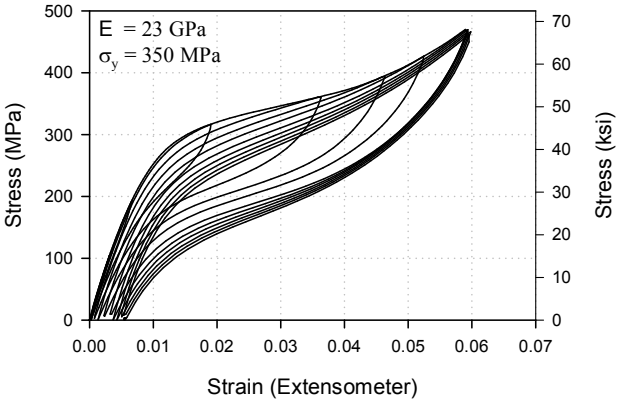
4.2 Connection Design Issues

The connection models described in the previous section have only been calibrated to a relatively small number of tests, so it is important that the limitations of the approach be understood. The first important limitation is that the simplified model basically does not consider interactions between failure modes. From the design standpoint this means that failure modes must be carefully separated and that a large number of yielding mechanisms must occur before any fractures or similar failures can take place. This can be accomplished by a well-thought out capacity design approach that clearly recognizes sources of over- and under-strength in the connection. For the connection in Fig. 1, this means that slippage of the bolts will occur first (clearly evident at about 1/3 of the connection strength in Fig. 7, with hole ovalization leading to larger deformations with cycling).

This initial deformation mechanism should be followed by yielding of the beam, tensile yielding of the SMA and mild steel through rods, yielding of the T-stub stem in tension, flexural yielding of the T-stub flanges, and yielding of the panel zone in shear, roughly in that order. These failure modes should provide all the required ductility (on the order of 0.03 to 0.05 rad. of plastic deformation), with local buckling and local crushing of the concrete providing additional deformation capacity should plastic large rotations in excess of 0.05 rad. occurs. Under no circumstance should fracture of the through rods in tension or bolts in shear be permitted at loads less than 150% of those creating yielding mechanisms.



(a) Idealized shape memory behavior



(b) Actual behavior

Figure 8 Comparison of idealized and actual SMA behavior

A second important limitation is that models such as those discussed here can only capture very limited strength and stiffness degradation. In particular, test results such as those shown in Fig. 7 indicate that, at large deformations, there is a gradual reduction of strength and stiffness due to local buckling in the beam flanges. Including this behavior in the connection model will require additional springs and the occurrence of negative stiffnesses from several degrading spring can lead to significant numerical problems for the entire spring assembly. A nice feature of this connection is that the through rods actually behave like buckling restrained braces as they are embedded in a plastic sheath with a diameter slightly larger than the bars itself, and thus their performance in compression is very similar to that

in tension. This is true for the mild steel bars; there is some difference in tension and compression behavior of the SMA that is a function of the material processing. From the design standpoint degradation issues due to local buckling should be dealt with by specifying very compact sections for the beam flange and web, as well as for all other components subjected to yielding in compression. It should be noted that the large amounts of local buckling observed near the end of physical tests are more a creature of the boundary conditions from the test frame (i.e., lack of axial restraint in the beams) than a reflection of actual behavior.

A third important limitation of this approach is that it ignores the effect of the floor slab in redistributing stresses in the connection area. This issue has often been overlooked in seismic codes, but based on the work of Leon et al. (1998) and others, the latest AISC seismic specification explicitly requires that designers either account for this effect in their analysis and design or provide a small opening around in the slab around the column to limit those effects.

An important fourth limitation is the need to arbitrarily impose some strain (or deformation) limitations on the load-deformation curves for the individual springs. Although a large number of tests have been carried out on individual components and these can serve as a basis for establishing such limits, there is little or no statistical work related to the potential for failure when several components show large deformations simultaneously. In a connection such as that under study, where a very large number of deformation mechanism are expected to contribute to the overall connection ductility, this effect may be important.

A final problem that has not received much attention is the robustness of the analytical tools as very large deformations, and consequently very low stiffnesses, are reached. In most cases, it is impossible to ascertain the reasonableness of the results without detailed investigation of the quantitative contribution of each mechanism.

While these limitations are important, it should be recognized that they are not unique to the type of connections of interest here. In general, designers tend to dismiss them as either too difficult to handle in everyday design or as not significant to their design.

The design approach proposed here is based on establishing a prescribed series of yielding mechanisms and capacity design principles. The yielding of the through rods provides an ideal deformation mechanism, as the free length of the rods (around 40cm to 50cm in many cases) provides very large local deformations at reasonable low average strains. However, compliance with this approach is not simple as only a small number of fixed geometries are available for T-stubs cut from rolled sections. More recently, work on T-stubs made from welded plates has considerably eased that problem, and it is expected that in the very near future AISC 358 will sanction this approach.

4.3 Frame Performance

The last step in this design process is to evaluate the seismic performance of the overall structure through both pushover and non-linear dynamic analyses of a set of archetypical frames. This evaluation requires that comparisons be made to similarly designed, all-steel frames that comply with all the requirements present in applicable design codes. Details of these studies have been recently published (Hu and Leon 2010). Figure 8 shows a comparison of the pushover analyses for a 6-story, 5-bay frame for a welded, all-steel special moment frame (6TSU-C7) and two frames using the connections shown in Fig. 1 (6TSU-C1 and C4). Based on initial stiffnesses, the innovative frames fall in the PR category. The welded frame shows less ductility because of weld fractures, which begin around 4% story drift. The frames with innovative connections show almost unlimited ductility and little sensitivity to P-D effects. Both frames show a substantial overstrengthwith respect to the design base shear because these frames are controlled by drift.

The frames were also subjected to the suite of SAC ground motions (SAC 2005). Fig. 9 shows typical results for the LA21 (Kobe 1995) ground motion. The welded frames show very significant residual deformations and a possible collapse at 12 sec. due to fractures in the first story connections. This conclusion is supported by the very large interstory drifts in the first floor at the maximum base shear (Fig. 10(b)). The frames with welded connection show significantly higher drifts, and likely collapses as the drifts exceed 0.1. The average and 84^{TH} percentile interstory drifts for the frame with the innovative connections (Fig. 11), on the other hand, show large but contained deformations.

A large number of frames were designed and studied using data similar to that in Figs. 9 through 11. The results indicate that:

- Overall, the initial stiffness of the frames with welded connections was larger than that of those of the frames with PR connections. However, the strength of welded frames deteriorated very rapidly because the welded connections were susceptible to brittle failure and P-Δ effects. In contrast, the use of flexible tension bars in the innovative connections provided extra deformation capacity, so the composite frames with PR connections showed more gradual strength degradation. As expected, the strength of the taller frames deteriorated more rapidly than that of the shorter frame because of the large P-D effect due to the heavier gravity loads.
- Composite moment frames with PR connections showed smaller residual displacements than those with welded connections due to the recentering effect of the SMA barst. In addition, composite frames with PR connections showed a more gradual strength degradation. For the PR composite frames, the envelope of the cyclic curves corresponded to that of the monotonic curves when the same models were compared.
- Composite moment frames with welded connections showed the largest roof displacements. The outstanding energy dissipation properties of the PR connections resulted in lower drifts.

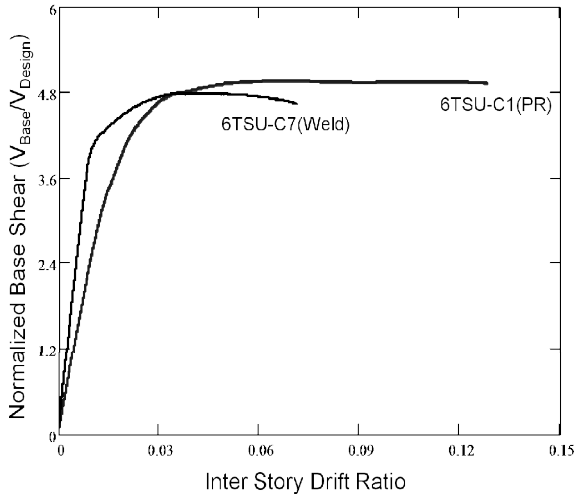
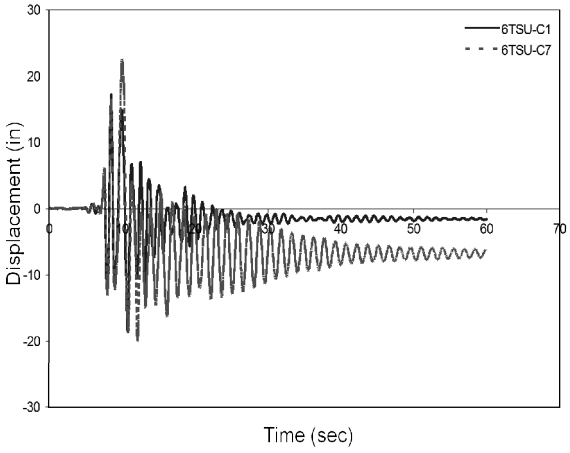
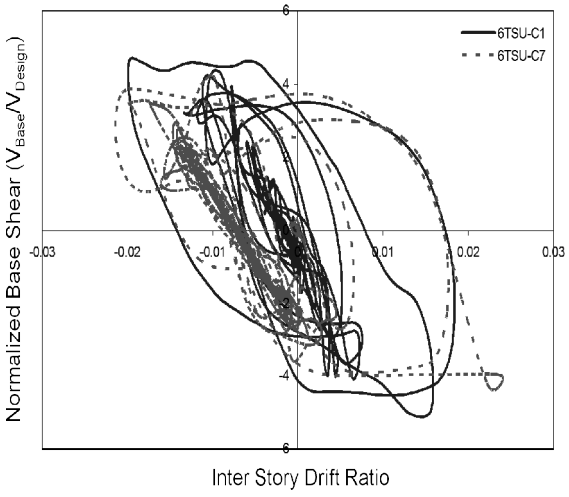


Figure 8 Comparison of pushover behavior between frames with welded and innovative connections

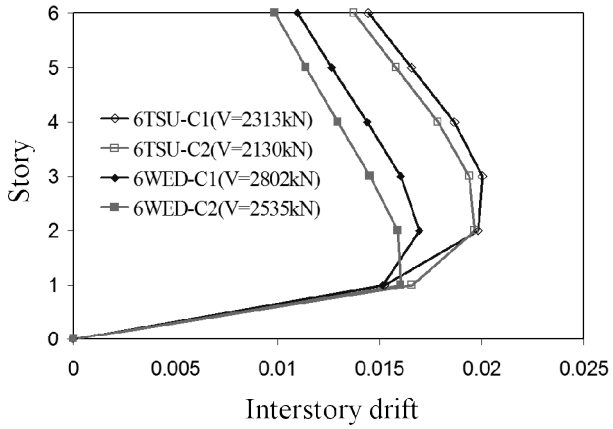


(a) Roof displacement vs. time

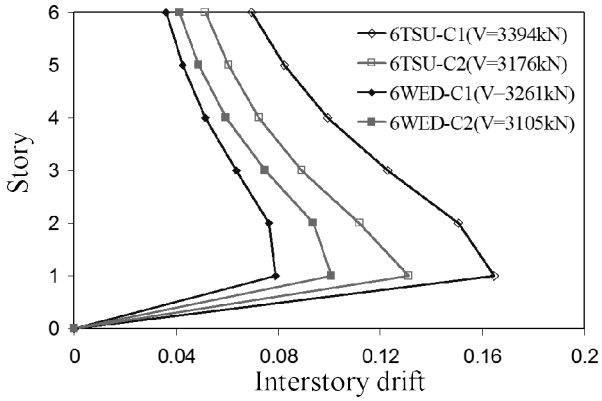


(b) Base shear vs. average interstory drift

Figure 9 – Response of welded and innovative frames to the LA 21 ground motion



(a) At initial yield



(b) At ultimate

Figure 10 – Comparison of drifts for welded and innovative frames.

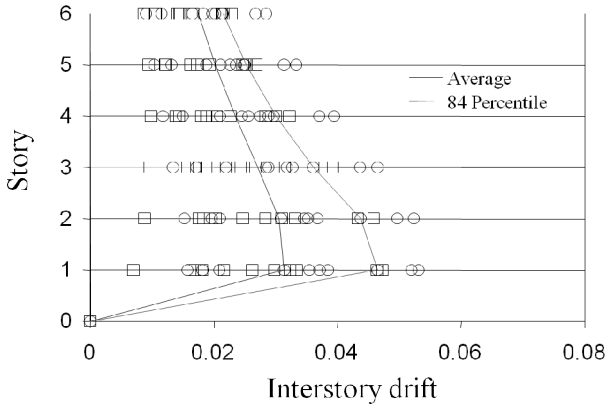


Figure 11 Range of interstory drifts for an innovative frame subjected to a large suite of ground motions.

- Overall, maximum displacement, velocity, and pseudo-acceleration occurred at the roof. The occurrence time for each peak value subjected to the same ground motion was slightly different and trailed the occurrence of the peak ground acceleration (PGA).

- Statistical distributions of the peak interstory drifts were obtained from the dynamic analyses. The peak interstory drifts occurred at the first story level and decreased rapidly as one moved up the structure.

Both the analyses of individual connections and multi-story frames show that these innovative PR frames will display excellent performance when properly designed.

3. CLOSING REMARKS

This paper began with a description of some of the 2010 AISC seismic provisions for composite structures and of the LA and SFO PBD guidelines for tall buildings. It then described the detailed analyses carried out for the development of an innovative PR connection that utilizes a mix of steel and SMA rods as the main yielding mechanism. These analyses were intended to provide enough supporting evidence to convince building officials to waive the requirement for physical testing of full-scale connections present in current codes. The authors believe that careful application of the most advanced analytical tools available coupled with characterization of system response based on a large suite of ground motions provides equal or better justification than physical tests. It should be noted that physical tests have significant shortcomings at the very least with respect to the fact that (a) only two specimens are required (a statistical insignificant number); (b) only a slowly increasing set of deformation cycles are used (very different from what areal earthquake will produce); and (c) boundary conditions are highly idealized and do not correspond to actual designs (slabs and 3D effects are completely ignored in most tests) (Leon and Deierlein 1997). The authors are thus comfortable in concluding that one of the original purposes of the Network for Earthquake Engineering Simulation (NEES), the migration from pure physical testing to full-scale simulation, is well underway and succeeding.

Acknowledgements:

This work was partially carried out under NSF Grant 0324542 to Georgia Tech. The opinions given and results described herein are the exclusive responsibility of the senior author and do not reflect the views of any of the universities involved, nor the National Science Foundation. The second author gratefully acknowledges KOSEF (M06-2003-000-10009-0) for its support as a graduate scholarship student.

Reference

ABAQUS 2006. Theory and User's Manual, Hibbit, Karlsson & Sorensen, Inc., Pawtucket, RI.

AISC 1995, *Seismic Provisions for Structural Steel Buildings*, American Institute of Steel Construction, Chicago, IL.

AISC 2010. *Specification for Structural Steel Buildings, (ANSI/AISC 360-10),* American Institute of Steel Construction, Chicago, IL.

AISC-358 2005. *Prequalified Connections for Special and Intermediate Steel Moment Frames for Seismic Applications* (*ANSI/AISC 358-05*), American Institute of Steel Construction, Chicago, IL.

AISC Seismic 2010, *Seismic Provisions for Structural Steel Buildings*, *(ANSI/AISC 341-10),* American Institute of Steel Construction, Chicago, IL.

ASCE-7 2010, *Minimum Design Loads for Buildings and Other Structures*, ASCE 7-10, American Society of Civil Engineers (ASCE), Reston, VA.

ATC 3-06 1978. *Tentative Provisions for the Development of Seismic Regulations for Buildings*, Applied Technology Council, Redwood Ciy.

FEMA, 2000. State of the Art Report on Systems Performance of Steel Moment Frames Subjected to Earthquake Ground Shaking, *FEMA-355C (SAC Joint Venture),* Washington, D.C.

Hu, T., Huang, C. S. and Chen, Z. L., 2005. Finite Element Analysis of CFT columns subjected to an axial compressive force and bending moment in combination, *J of Constructional Steel Research*, v. 62, pp 1692-1712

IBC 2010. http://www.iccsafe.org/CS/Pages/default.aspx

LA 2005. *An Alternative Procedure for Seismic Analysis and Design of Tall Buildings Located in the Los Angeles Region*, Los Angeles Tall Building Design Council, Los Angeles, CA

Leon, R. T .and Deierlein, G.G., 1996. Considerations for the Use of Quasi-Static Testing, *Earthquake Spectra*, Vol. 12, No.1, pp. 87-110.

Leon, R. T., 1997. Seismic Performance of Bolted and Riveted Connections, Background Reports, FEMA Publication No.288, Federal Emergency Management Association, Washington D.C., March.

Leon, R. T., DesRoches, R., Ocel, J. Hess, G., 2001. Innovative Beam Column using Shape Memory Alloys, *Proceedings of SPIE*, 4330, pp. 227-237

Leon, R.T., Hajjar, J.F., and Gustafson, M.A., 1998. Seismic Response of Composite Moment-Resisting Connections. I: Performance, *JSE,* ASCE, v. 124, pp. 868-876

Mazzoni, S., Mckenna, F., Fenves, G. L., 2006. Opensees Command Language Manual, Department of Civil Environmental Engineering, University of California, Berkley.

NEHRP 1994. *NEHRP Recommended Provisions for Seismic Regulations for New Buildings and Other Structures*, FEMA 222A and 223A, Federal Emergency Management Agency, Washington, D.C.

NIBS 2010. http://www.nibs.org/index.php/bssc/projects/

Ocel, J. M., 2002. Cyclic Behavior of Steel Beam-Column Connections with Shape Memory Alloy Connection Elements, Master's thesis, Georgia Institute of Technology.

Penar, B. W., 2005. Recentering Beam-Column Connections using Shape Memory Alloys, Master's thesis, Georgia Institute of Technology.

SAC 2005. http://nisee.berkeley.edu/data/strong_motion/sacsteel/

SFO 2007. *Requirements and Guidelines for the Seismic Design and Review of New Tall Buildings using Non-Prescriptive Seismic-Design Procedures,* ABO83, Department of Building Inspection, San Francisco, CA

Song, G., Ma, N., Li, N. H., 2006. Application of Shape Memory Alloys in Civil Structures*, Engineering Structures*, v.28, pp 1266-1274

Swanson, J., 1999. Characterization of the Strength, Stiffness, and Ductility Behavior of T-stun Connection. Ph.D Dissertation, Georgia Institute of Technology, Atlanta, GA.

Tami, H. and Kitagawa, Y., 2002. Pseudoelastic behavior of Shape Memory Alloy Wires and its Application to Seismic Resistance Member for Building, Computational Material Science, v. 25, pp 218-227

Wu, L. Y., Chung, L. L, Tsai, S. F., Lu, C. F. and Huang, G. L., 2005. Seismic Behavior of Bolted Beam to Column Connections for Concrete Filled Steel Tube, *Journal of Constructional Steel Research*, v. 61, pp 1387-1410

Wu, L. Y., Chung, L. L, Tsai, S. F., Lu, C. F. and Huang, G. L., 2007. Seismic Behavior of Bidirectional Bolted Connections for CFT Columns and H-Beams, *Engineering Structures*, v.29, pp. 395-407

8CUEE CONFERENCE PROCEEDINGS
8th International Conference on Urban Earthquake Engineering
March 7-8, 2011, Tokyo Institute of Technology, Tokyo, Japan

EXPERIMENTAL EVALUATION OF COMPOSITE EFFECTS ON STRUCTURAL BEHAVIOR OF PANEL ZONE

Shoichi Kishiki[1] and Satoshi Yamada[2]

1) Assistant Professor, Structural Engineering Research Center, Tokyo Institute of Technology, Japan
2) Associate Professor, Structural Engineering Research Center, Tokyo Institute of Technology, Japan
kishiki@serc.titech.ac.jp, naniwa@serc.titech.ac.jp

Abstract: In the 1994 Northridge and the 1995 Kobe earthquake, brittle fractures had been occurred at the beam-bottom-flange of welded beam-ends. After these earthquakes, a remarkable number of studies have been made on welded beam-to-column connections. From the research results, plastic rotation capacity of the steel beam ended in the beam-bottom-flange ductile fracture is affected by the presence of a concrete slab. On the other hand, it is known that composite effects of concrete slab have been observed in not only steel beams but also steel panel zones. In Japanese low- and medium-rise steel buildings, columns are designed to have more strength than that of beams to realize beam-yield mechanism. However, the strength of both beams and panel zones is increased by the presence of the concrete slab. Therefore these effects might lead to damage to column to cause story-collapse mechanism. It is very important to consider the composite effects on elasto-plastic behavior of steel beams and panel zones at the stage of seismic design.
Composite effects on elasto-plastic behavior of panel zone are discussed in this paper. Based on equilibrium condition of forces around a panel zone, evaluation models for the composite effects on initial elastic stiffness and yield strength of panel zone were established. And then, cyclic loading tests of four beam-column subassemblies with a concrete slab were carried out. From the test results, composite effects on structural behavior of panel-zone were investigated. Finally, the composite effects obtained from the tests were proven by evaluation models.

1. INTRODUCTION

In the 1994 Northridge and the 1995 Kobe earthquake, brittle fractures had been occurred at the beam-bottom-flange of welded beam-ends. After these earthquakes, a remarkable number of studies have been made on welded beam-to-column connections. From these research results, plastic rotation capacity of the steel beam ended in the beam-bottom-flange ductile fracture is affected by ductility of material, welding condition, geometrical discontinuity (weld access holes), and the presence of a concrete slab. Since most of the fractures were observed at the bottom beam-flange, it was found out that strain concentration caused by a concrete slab was very severe. However, these effects by a concrete slab have been hardly clear in the previous studies.

On the other hand, it is known that composite effects of concrete slab have been observed in not only steel beams but also steel panel zones (Naka et al., 1972, 1973, 1979, Nakao and Osano, 1987, 1988; Kawano et al., 1993; Yamada et al., 2009). In Japanese low- and medium-rise steel buildings, columns are designed to have more strength than that of beams to realize beam-yield mechanism. However, the strength of both beams and panel zones is increased by the presence of the concrete slab. Therefore these effects might lead to damage to column to cause story-collapse mechanism. It is very important to consider the composite effects on elasto-plastic behavior of steel beams and panel zones at the stage of seismic design.

In this paper, composite effects on elasto-plastic behavior of panel zone are discussed. Based on equilibrium condition of forces around a panel zone, evaluation models for the composite effects on initial elastic stiffness and yield strength of panel zone are established. And then, cyclic loading tests of four beam-column subassemblies with a concrete slab are carried out to investigate composite effects on panel-zone.

2. STRUCTURAL BEHAVIOR OF PANEL ZONE CONSIDERING THE PRESENCE OF CONCRETE SLAB

2.1 Evaluation Equation of Composite Effects on Panel Zone based on Equilibrium Condition of Forces

At first, composite effects on structural behavior of panel zone are discussed here. Equilibrium condition of forces around a panel zone without or with a concrete slab is expressed in Figure 1. In case of bare steel structures, as shown in Figure 1(a), bending moments ${}_bM_R$ and ${}_bM_L$ at the both beam-ends divided by effective beam depth d_b are lateral forces at the panel zone. Therefore, column shear force H subtracted from the forces $({}_bM_R + {}_bM_L) / d_b$ is shear force Q at the panel zone. Eq.(1) shows the shear force Q. Note, in Japanese conventional seismic design, the shear

force Q at the panel zone is expressed as panel moment by multiplying beam effective depth d_b.

$$Q = \frac{{}_bM_R - {}_bM_L}{d_b} - H \tag{1}$$

On the other hand, in case of composite structures, the right bending moment ${}_bM_R$ is affected by the presence of a concrete slab. ${}_bM_R$ is decomposed into bending moment ${}_bm_R$ at the bare steel beam section and bending moment $N \cdot z$ caused by axial force N at the concrete slab. z is a length between effective center positions of both a concrete slab and bare steel beam section. ${}_bm_R$ and N at the bare steel beam section are transmitted to panel zone by both upper and lower beam-flanges. Especially in Japan, the Rectangular Hollow Section (RHS) is used for column, and bending moment at the beam-web is decreased by out-of-plane deformation at the RHS column. Bending moment at a concrete slab is neglected in this equation, although a cross section of a concrete slab is thinner than that of bare steel beam. Eq.(2) shows the shear force Q*.

$$Q^* = \frac{{}_bm_R - {}_bM_L}{d_b} - H + \frac{N}{2} \tag{2}$$

Here, parameter α is defined as the ratio between bending moment $N \cdot z$ and the right bending moment ${}_bM_R$. And parameter β is defined as the ratio between the left bending moment ${}_bM_L$ and the right bending moment ${}_bM_R$. Eq.(3), (4) express these parameters.

$$\alpha = \frac{N \cdot z}{{}_bM_R} \tag{3}$$

$$\beta = \frac{{}_bM_L}{{}_bM_R} \tag{4}$$

Column shear force H is obtained from the assumptions: (a)structures have infinite same shapes with beam span l and story height h; (b)increase of story shear between upper and lower story is negligible, and is expressed as Eq.(5).

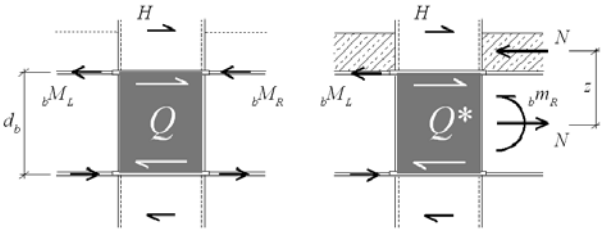
$$H = \frac{{}_bM_R - {}_bM_L}{h'} \tag{5}$$

Here, h' is effective height of structures and defined as Eq. (6).

$$h' = (1 - \frac{D_c}{l}) \cdot h \tag{6}$$

where, D_c : width of column.

Shear force Q expressed as Eq.(1) is shear force at the panel zone without a concrete slab. On the other hand, shear force Q* expressed as Eq.(2) is "true" shear force at the panel zone considering effects of a concrete slab. Therefore,



(a) (b)

Figure 1 Shear force to panel zone: (a)bare steel structures; (b)considering concrete slab

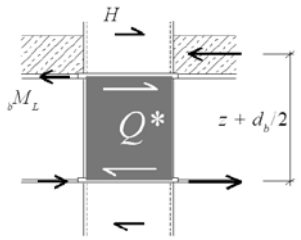


Figure 2 Simple evaluation model for composite effects on structural behavior of panel zone (Nakao and Osano, 1987, 1988; Kawano et al., 1993; Yamada et al., 2009)

increase of stiffness and strength caused by the presence of a concrete slab is expressed as subtraction between Q* and Q. Shear force Q or panel moment $Q \cdot d_b$ is a useful index for seismic design. In other words, increase Q*– Q caused by the presence of a concrete slab is easily applied to current seismic design procedure.

$$Q^* - Q = \left(1 - \frac{d_b}{2\,z}\right) \cdot \alpha \cdot \frac{{}_bM_R}{d_b} \tag{7}$$

z is a length between effective center positions of both a concrete slab and bare steel beam section, and is larger than half of effective beam depth d_b. It indicates that Eq.(7) is always positive. Therefore, shear force Q is underestimation, although panel zone is affected by the presence of a concrete slab.

Here, composite effect is expressed as the ratio between Q and Q* to evaluate parameter effects on the increase of stiffness and strength. Composite effect Q / Q* is expressed as Eq.(8).

$$\frac{Q}{Q^*} = \frac{(1+\beta)(1-\frac{d_b}{h'})}{(1+\beta)(1-\frac{d_b}{h'}) - (1-\frac{d_b}{2\,z})\alpha} \tag{8}$$

On the other hand, the past researches (Nakao and Osano, 1987, 1988; Kawano et al., 1993; Yamada et al., 2009) on composite effects on panel zone presented simple evaluation model, as illustrated in Figure 2. This model considers composite effects of the right beam as increase of

effective beam depth d_b. Mentioned above, the upper beam-flange transmitted ${}_bM/d_b$ and $-N/2$ to panel zone, based on evaluation model in Figure 1. The past model has the assumptions that lateral force at the upper beam-flange is negligible. "True" shear force Q* established by the past researches is expressed as Eq.(9).

$$Q^* = \frac{{}_bM_R}{z + \frac{d_b}{2}} - \frac{{}_bM_L}{d_b} - H \tag{9}$$

And then, Composite effect Q/Q* is expressed as Eq.(10).

$$\frac{Q}{Q^*} = \frac{(1+\beta)(1-\frac{d_b}{h'})}{(1+\beta)(1-\frac{d_b}{h'}) - (1-\frac{d_b}{2z})(1+\frac{d_b}{2z})^{-1}} \tag{9}$$

2.2 Parameter Study on Composite Effects

Parameter study on indexes α, β, and $d_b/2z$ affecting increase of stiffness and strength is conducted by using evaluation Q / Q* expressed as Eq.(8) and Eq.(10).

First parameter study with variable index β, the ratio between the left bending moment ${}_bM_L$ and the right bending moment ${}_bM_R$, is showed in Figure 3. Parameter α, the ratio between bending moment $N{\cdot}z$ and the right bending moment ${}_bM_R$, is plotted on the X-axis, and calculated composite effect Q / Q* by $d_b/2z$ (=0.71) of test specimens in Chapter 3 is plotted on the Y-axis.

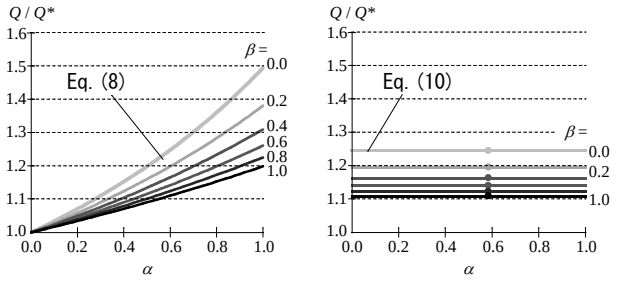
Increase of parameter α is lead to increase of composite effects Q / Q*, based on evaluation of Eq.(8). Parameter β is calculated from 0.0 (external column) and 1.0. Change of composite effects Q / Q* is strongly affected by parameter α, when parameter β equals to 0.0 (external column). Parameter β is the ratio of bending moment between bare steel beam and composite beam, and composite effects on beam lead increase of stiffness and strength to panel zone. In the previous test (Yamada et al., 2009), elasto-plastic behavior of panel zone in beam to external column with a concrete slab was investigated, and the strong effects caused by the presence of a concrete slab were observed. Evaluation value of composite effects shows the similar trend of the previous test of external column.

On the other hand, composite effects Q / Q* are hardly affected by increase of parameter α, based on evaluation of Eq.(10). Comparing both equations, $1/(1+d_b/2z)$ works as parameter α in Eq.(10). It indicates that parameter α is given as the constant value by geometrical condition d_b and z in Eq.(10), since this simple evaluation model considers composite effects of the right beam as increase of effective beam depth d_b. In case of parameter study shown in Figure 3., parameter α (=$1/(1+d_b/2z)$) equal to 0.58, the cross points of both Figure 3.(a) and (b).

Parameter study with variable index $d_b/2$ is showed in Figure 4. Parameter α is plotted on the X-axis, and calculated composite effect Q / Q* by β (=0.5) of test results in Chapter 3 is plotted on the Y-axis.

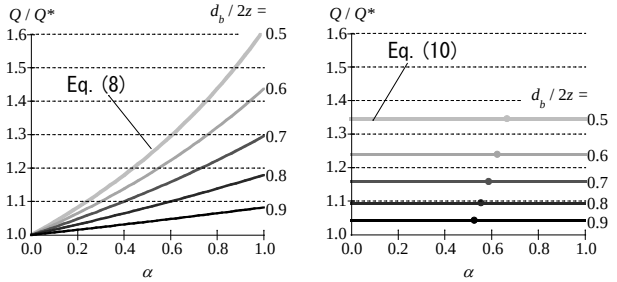
Increase of parameter α is lead to increase of composite effects Q / Q*, based on evaluation of Eq.(8). Parameter $d_b/2z$ is calculated from 0.5 and 0.9. Comparing Figure 3 and 4, change of composite effects Q / Q* is more strongly affected by parameter $d_b/2z$, and more than parameter α.

On the other hand, composite effects Q / Q* are hardly affected by increase of parameter α, based on evaluation of Eq.(10). Effects on change of Q / Q* caused by parameter $d_b/2z$ are larger than that of parameter α. It is because that increase of parameter $d_b/2z$ is lead to both α and $d_b/2z$.



(a) (b)

Figure 3 Parameter Q/Q* study(variable index β): (a) Eq.(8); (b) Eq.(10)



(a) (b)

Figure 4 Parameter Q/Q* study(variable index $d_b/2z$): (a) Eq.(8); (b) Eq.(10)

3. TEST OF BEAM-COLUMN SUBASSEMBLIES WITH A CONCRETE SLAB

3.1 Test Plan

A constant comparison was used for all specimens to investigate structural behavior of beam-column subassemblies affected by the presence of a concrete slab. Capacity limitations of the testing equipment, as well as constraints on the overall size of the test specimen, dictated that the specimens were approximately half of the actual building bay width and story height. The specimen was cut from the frame with a bay width of 3.5m and a story height of 2.35m. The test set-up is illustrated in Figure 5.

Two series of specimen were tested. In the first series named (F), a rectangular flat section was used for a concrete slab. On the other hand, flat section with deck plates was used for a concrete slab in the second series named (D). Added to this, the first subassemblies (F) was designed as weak panel zone frame by using 9mm of column thickness

and SM490A steel grade for beams. While, the second (D) was designed as weak beam frame by using 12mm of column thickness and SN400B steel grade for beams. Overall details are complied in Table 1.

A detail of the test specimen is shown in Figure 6.

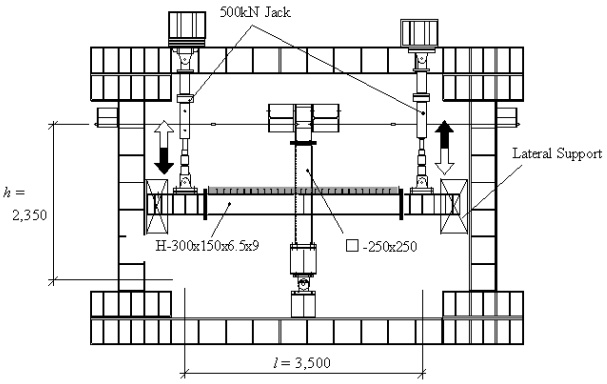


Figure 5 Test setup

Table 1 Overall details of test specimen

	Specimen	Column & Panel Zone	Beam	Concrete Slab
F	F_FULL	□-250x250x9 (BCR295)	H-300x150x6.5x9 (SM490A)	110x1,500x2,800
	F_MINI			110x400x850
D	D_LS	□-250x250x12 (BCR295)	H-300x150x6.5x9 (SN400B)	110x1,500x2,800 (+Deck Plate)
	D_SS			

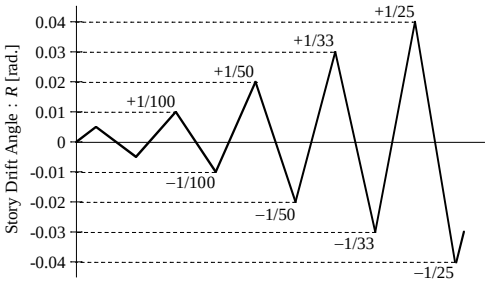


Figure 7 Loading Program

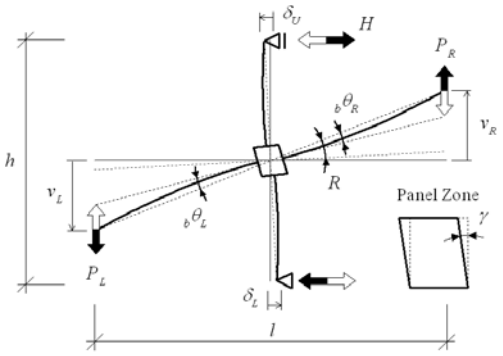


Figure 8 Loading Program

Quasi-static loading was carried out following to a simple loading program shown in Figure 7. The loading program was based on story drift angles *R* of the specimen, which were 1/200, 1/100, 1/50, 1/33, and 1/25 radian. The beam-column subassemblies had a height *h* from the top and bottom pin joints. The total tip deflection was due to elastic

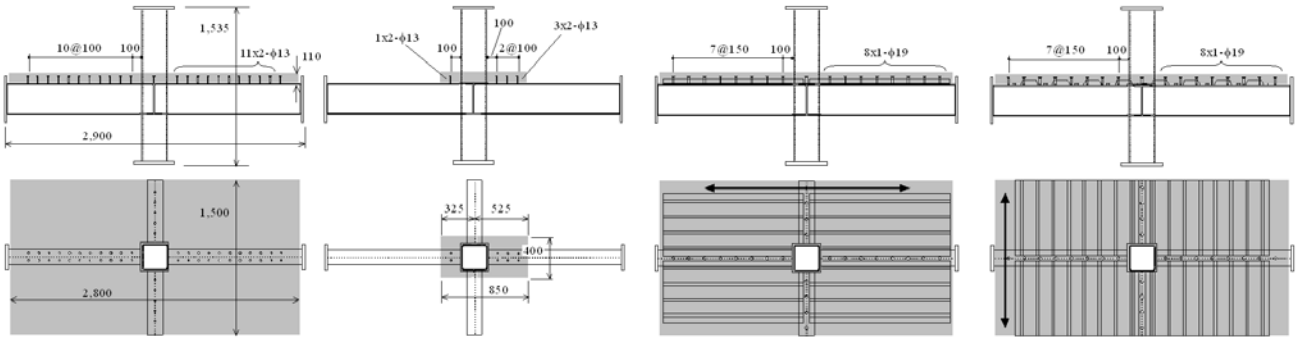


Figure 6 Detail of test specimen:
(a) F_FULL; (b) F_MINI; (c) D_LS; (d) D_LL

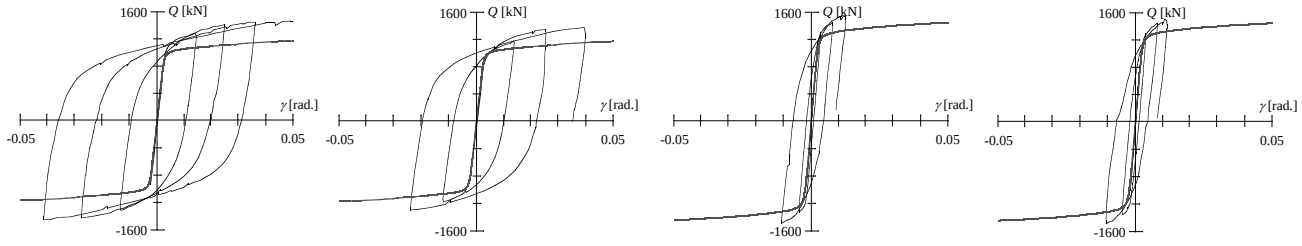


Figure 9 Elasto-plastic behavior of panel zone obtained from test
(a) F_FULL; (b) F_MINI; (c) D_LS; (d) D_LL

and plastic flexural deformation of the column and beams, and shear deformation of panel zone. A story drift angle R of test specimen can be found out by dividing the total tip deformation by h. Definitions of deformations and loads in this test are illustrated in Figure 8.

3.2 Test Results

Relation between shear force Q and shear deformation angle γ of each specimen are shown in Figure 9. Monotonic behavior of bare panel zone expressed in red line is calculated based on coupon test of steel used for column panel zone.

Test specimen shows stable hysteresis loop and sufficient plastic deformation capacity until 5%. The increases of stiffness and yield strength are as follows: Specimen F_FULL: 10 to 20% increase in stiffness and 10 to 15% increase in yield strength is observed, respectively. F_MINI: 5% increases in stiffness and yield strength are observed. D_LS: 15 to 25% increase in stiffness and 10% increase in yield strength is observed, respectively. D_LL: 15% increase in stiffness and 10% increase in yield strength is observed, respectively.

Quasi-static loading was carried out following to a simple loading program shown in Figure 7. The loading program was based

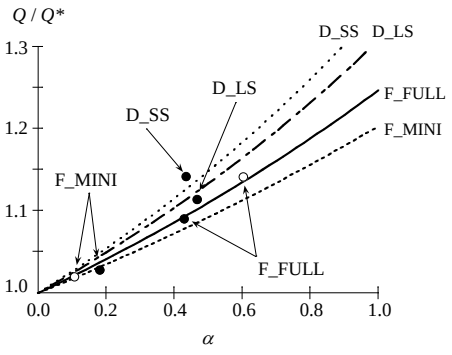
3.3 Evaluation of Composite Effects

Experimental values of composite effects on increase of stiffness and yield strength of panel zone are plotted in Figure 10. The experimental values are defined as a position in X-axis, with evaluation of parameter α from the test results. And four lines shows calculated values of composite effects Q / Q* obtained from Eq.(8) and Eq.(10). Geometrical conditions d_b and z are based on test specimen, and parameters α and β are obtained from the test results.

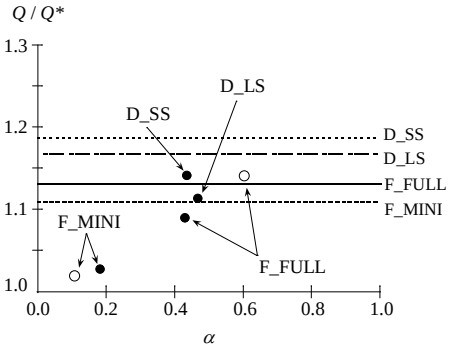
Calculated values by Eq.(8) shows good corresponding with experimental values of increase in stiffness and yield strength. Meanwhile, calculated values by Eq.(10) shows overestimation to experimental values. It is indicating that parameter α, the ratio between bending moment $N{\cdot}z$ and the right bending moment ${}_bM_R$, is important index for evaluating composite effects on panel zone.

4. CONCLUSIONS

It is known that composite effects of concrete slab have been observed in not only steel beams but also steel panel zones. Though effects might lead to damage to column to cause story-collapse mechanism, it is very important to consider the composite effects on steel beams and panel zones at the stage of seismic design. In this paper, composite effects on elasto-plastic behavior of panel zone were discussed. Based on equilibrium condition of forces around a panel zone, evaluation models for the composite effects on initial elastic stiffness and yield strength of panel zone were established. And then, cyclic loading tests of four beam-column subassemblies with a concrete slab were carried out to investigate composite effects on panel-zone. Finally, the composite effects obtained from the tests were proven by evaluation models.



(a)



(b)

Figure 10 Definitions of deformations and loads: (a) evaluated by Eq.(8); (b) evaluated by Eq.(10)

Acknowledgements:

This work was supported by KAKENHI(No.19686034), Japanese Society for the Promotion of Science(JSPS), Grant-in-Aid for Young Scientists (A). Mr. Daisuke KADONO worked this project as a graduate student at Tokyo Institute of Technology. Prof. Keiichi SATSUKAWA, associate professor of Aichi Sangyo University, worked this project as special adviser. The support is gratefully acknowledged.

References:

Naka, T., Umino, S., Nakao, M., and Osano, H. (1972) Connection Composed of H-shaped Column and Composite Beams –Report1–, Summaries of technical papers of Annual Meeting Architectural Institute of Japan, pp.1869-1870, (1973) –Report2–, pp.1259-1260, (1973) –Report3–, pp.1565-1566 (in Japanese).

Nakao, H. and Osano, H. (1987) Influence of Concrete Slab on the Restoring Force Characteristics of Steel Beam-to-Column Connections –Report1–, Summaries of technical papers of Annual Meeting Architectural Institute of Japan, pp.905-906, (1988) □–Report2–, pp.905-906 (in Japanese)

Kawano, A., Asega, H., and Hasebe. H. (1993) An Experimental Study on Ductility of Wide-Flange Steel Frame with Composite Beam including Weak Joint Panel in Different Collapse Modes, Journal of structural and construction engineering, Transactions of AIJ, No.452, pp.109-119 (in Japanese)

Yamada, S., Satsukawa, K., Kishiki, S., Shimada, Y., Matsuoka, Y., and Suita, K.(2009) Elasto-Plastic Behavior of Panel Zone in Beam to External Column Connection with Concrete Slab, Journal of structural and construction engineering, Transactions of AIJ, No.644, pp.1841-1849 (in Japanese)

8CUEE CONFERENCE PROCEEDINGS
8th International Conference on Urban Earthquake Engineering
March 7-8, 2011, Tokyo Institute of Technology, Tokyo, Japan

CYCLIC BEHAVIOR OF STEEL TUBE-REINFORCED CONCRETE COMPOSITE WALLS WITH HIGH AXIAL FORCE RATIO

Xiaodong Ji[1], Jiaru Qian[2], and Zao Jiang[3]

1) Department of Civil Engineering, Tsinghua University, Beijing, P.R. China
2) Department of Civil Engineering, Tsinghua University, Beijing, P.R. China
3) Architectural Design and Research Institute, Tsinghua University, Beijing, P.R. China
jixd@mail.tsinghua.edu.cn, qianjr@mail.tsinghua.edu.cn, jiang-z05@mails.tsinghua.edu.cn

Abstract: Reinforced concrete (RC) shear walls have been widely used as the major lateral force-resistant member in high-rise buildings. However, the RC walls with high axial force ratios are less ductile. This paper proposed an innovative composite wall, named the steel tube-reinforced concrete (ST-RC) composite wall. Steel tubes were embedded at the wall's boundary elements and fully anchored within the foundation, which could enhance the seismic performance of the wall. A series of quasi-static tests were conducted to examine the proposed walls subjected to high axial force and lateral cyclic loads. The effects of the area ratio of steel tubes/CFSTs, axial force ratio, and cross-sectional shape of wall were investigated. The test results indicated that the ST-RC composite walls had both larger load-carrying and deformation capacities than the RC walls. The deformation capacity of the composite walls increased with an increase in the area ratio of steel tubes/CFSTs and decreased with an increase in the axial force ratio. The barbell-shaped composite wall had remarkably larger deformation and energy dissipation capacities than the rectangular-shaped composite walls. Simplified formulation was proposed for evaluating the strength of the composite walls, and some recommendations were proposed for seismic design of the composite walls.

1. INTRODUCTION

Reinforced concrete (RC) shear walls have been widely used as the major lateral force-resistant components in high-rise buildings because of their large lateral stiffness and strength. However, RC walls are less ductile when subjected to both considerable large axial forces exerted from gravity loads and cyclic lateral seismic loads (Paulay and Priestly 1992, Qian et al. 1999). Such poor performance is reflected in seismic codes (for example, UBC 1997, EuroCode8 2003, GB 50011-2001, ACI 318-05 and NZS 3101:2006), which specify the upper limits of the axial force ratio. As a result of the code requirements, the RC walls in lower stories of earthquake-resistant high-rise buildings are often assigned with rather thick sections, occupying usable floor areas. On the other hand, these codes require the amount of transverse reinforcements in the confined boundary element. To satisfy the code provisions, dense stirrups are assigned at the wall boundaries, causing serious difficulties in construction. It is thus crucial to develop innovative shear walls with excellent earthquake-resistant performance even under a high axial force ratio and with less transverse reinforcement at the wall boundary elements.

In recent years, a variety of steel-concrete composite walls have been developed (for example, Hajjar 2002, Hossain and Wright 2004, Zhao and Abolhassan 2004, Qian et al. 2008, and Eom et al. 2009). These walls combine the beauty of two construction materials, steel and concrete, and provide a promising alternative to conventional RC walls. In this paper, an innovative shear wall called steel tube-reinforced concrete (ST-RC) composite wall is proposed by embedding circular steel tubes at the wall boundary elements. The steel tubes are fully anchored within the foundation. The embedded steel tubes act compositely with their concrete cores to form concrete-filled steel tubes (CFSTs), which can enhance both strength and deformation capacities of the wall. In addition, the proposed composite wall takes advantages of ease of construction, since no special elements (e.g., shear studs) are needed for the connection between the embedded steel tubes and their surrounding concrete.

This paper presents a series of quasi-static tests of the ST-RC composite walls under high axial force ratios and cyclic lateral loading conditions, and examines their seismic behavior (i.e., failure mode, lateral load-carrying capacity, deformation capacity, and energy dissipation). The effects of the area ratio of steel tubes/CFSTs, the axial force ratio, and the cross-sectional shape of wall on the seismic behavior are investigated, and the possibility of loosening the code requirements on the axial force ratio and the amount of transverse reinforcement at the boundary elements which are adopted for RC walls is explored. Based on test observations and data analysis, some recommendations are proposed for seismic design of the

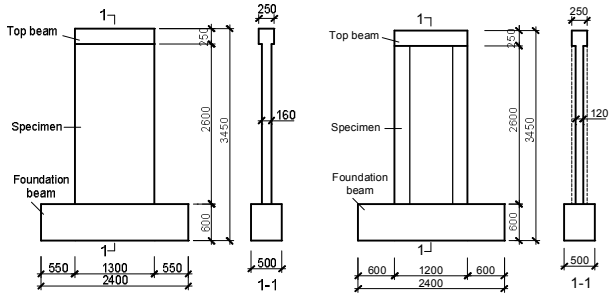
ST-RC composite walls.

2. EXPERIMENTAL PROGRAM

2.1 Test Specimens

2.1.1 Specimens Design

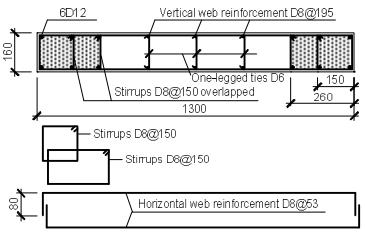
The test specimens were designed to represent the lower stories of structural walls in high-rise buildings, and were fabricated at approximately 1/3 scale. Seven walls labeled Specimens SW1 to SW7 were examined. Specimen SW1 was a RC wall, and the others were ST-RC composite walls. The overall geometries of the specimens are shown in Fig. 1. A foundation beam and a top beam were cast together with the wall. The wall was 2600 mm tall, and had an aspect ratio (height-to-width ratio) of around 2.0.



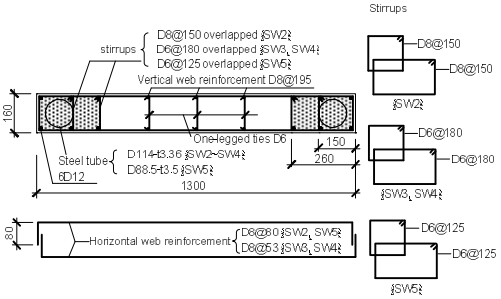
(a) (b)

Figure 1. Elevation view of shear wall specimens (Unit: mm): (a) SW1 through SW6, and (b) SW7

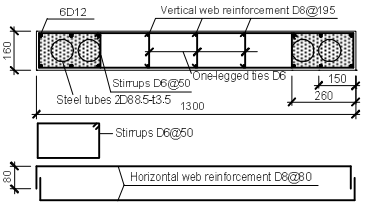
Fig.2 shows the sectional dimensions of the specimens. Specimens SW1 through SW6 had a rectangular-shaped cross section. They were classified into three pairs. The first pair consisted of Specimens SW1 and SW2, where the former was a RC wall and the latter was a ST-RC composite wall. The second pair included Specimens SW3 and SW4, which were different only at the applied axial force during tests. The third pair involved Specimens SW5 and SW6, where one had an embedded steel tube at each boundary element and the other had two tubes. Specimen SW7 was a ST-RC composite wall with a barbell-shaped cross section which included a wall web and two square edge columns.



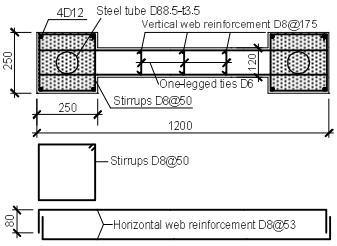
(a)



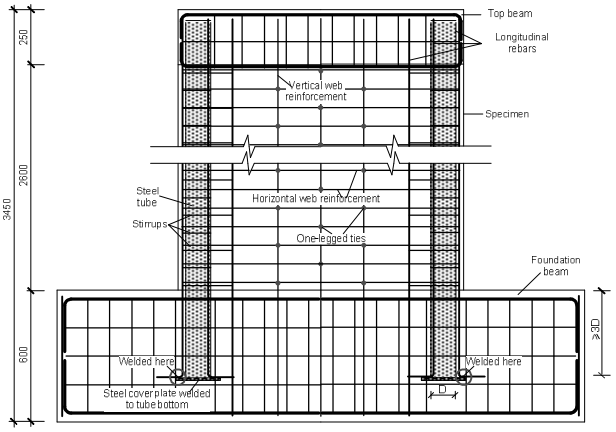
(b)



(c)



(d)



(e)

Figure 2. Section dimensions and reinforcing details (Unit: mm): (a) SW1, (b) SW2 through SW5, (c) SW6, (d) SW7, and (e) Elevation drawing of steel tubes and reinforcement for SW2

Fig. 2 shows the confined boundary elements by shadowing. The boundary elements were determined according to the Chinese code for seismic design of buildings (GB 50011-2001), which stipulates that the extent of the confined boundary element for the walls constructed at severe earthquake-prone regions (seismic fortification intensity of 8, PGA=0.2 g) shall be not less than 0.2 times the wall's sectional depth for the rectangular-shaped walls and not less than the edge column depth for the

barbell-shaped walls.

Fig. 2 also presents the reinforcing details of the specimens. Note that the assignment of reinforcing bars could secure the "strong shear and weak bending" mechanism of the specimens. All walls were designated with D8 (Diameter=8 mm) vertical and horizontal web reinforcement. Six D12 (Diameter=12 mm) steel rebars were placed as the vertical reinforcement at the boundary elements for Specimens SW1 through SW6, which corresponded to a 1.63% reinforcement ratio (i.e., the ratio of cross-sectional areas between the vertical rebars and the boundary element). Four D12 vertical rebars were placed in each edge column for Specimen SW7, which corresponded to a reinforcement ratio of 0.72%. The transverse reinforcement at the confined boundary elements was made in the form of rectangular hoops. Further details on the transverse reinforcement at the boundary elements are described in Subsection 2.1.3.

Fig. 2(e) shows an elevation drawing of steel tubes and reinforcement for Specimen SW2. The steel tubes and vertical reinforcement were extended into the foundation beam and top beam to achieve the full anchorage. The anchorage depth of the steel tubes within the foundation beams was not less than three times the tube's diameter. In addition, a steel cover plate was welded at the tube bottom, which could also contribute to the secure anchorage. Note that no special elements (e.g., shear studs) were used for the bond between the steel tubes and their surrounding concrete.

2.1.2 Material Properties

The walls were constructed with the concrete that had a strength grade of C40 (the nominal cubic compressive strength, $f_{cu,d}$=40 MPa, and the design value of axial compressive strength, $f_{c,d}$=19.1 MPa). The means values of the measured cubic compressive strengths $f_{cu,t}$ of the wall concrete at the time of testing were 40.2, 44.3, 40.5, 40.1, 46.7, 49.8 and 47.3 MPa for Specimens SW1 through SW7, respectively. The tested cubes had the dimension of 150 mm×150 mm×150 mm. The higher strength grade concrete, C50 (the nominal cubic compressive strength, $f_{cu,d}$=50 MPa, and the design value of axial compressive strength, $f_{c,d}$=23.1 MPa), was used to fill in steel tubes. The measured cubic compressive strength $f_{cu,t}$ was 57.5 MPa. Note that the actual value of axial compressive strength of concrete $f_{c,t}$ was taken as $0.76f_{cu,t}$ according to the Chinese code for design of concrete structures (GB 50010-2002).

The steel grade of D12 rebar was HRB335 (the nominal yield stress, f_y=335 MPa) and the other rebars were HPB235 (f_y=235 MPa). The measured yield strengths of steel were 382, 344 and 409 MPa for the rebars D12, D8 and D6, respectively. Steel tubes were fabricated by Grade Q235 steel (fy=235 MPa). The yield strengths of steel measured by coupon tests were 369 and 356 MPa for the steel tubes with the diameter of 114 and 88.5 mm, respectively.

2.1.3 Transverse reinforcement at boundary elements

The transverse reinforcement at wall boundary elements is essential for confining concrete when the compressive strain exceeds a critical value (Thomsen and Wallace 2004). The amount of transverse reinforcement is expressed in terms of the volumetric transverse reinforcement ratio ρ_v (i.e., the ratio of volumes between the stirrups and the concrete core confined by stirrups) or the stirrup characteristic value ($\lambda = \rho_v f_{yv} / f_c$,where f_{yv} and f_c denote the yield strength of transverse reinforcement and the axial compressive strength of concrete, respectively).

A discrepancy exists in the treatment of transverse reinforcement at the confined boundary elements among different codes. In the codes of United States and elsewhere, a uniform amount of transverse reinforcement is adopted for the entire confined boundary element. In Chinese codes, the boundary element is divided into two regions, as shown in Fig. 3. Varying amounts of transverse reinforcement are allowed for different regions. Region I is specified to have double the amount of transverse reinforcement as Region II, which is attributed to larger compressive strains developing in Region I by the combination of actions of the axial compression and bending. Region I had an extent of 150 mm from the wall edge for the tested rectangular-shaped walls. The Chinese seismic design code requires that the stirrup characteristic value for Region I should be no less than 0.2 for the walls used in severe earthquake-prone regions (GB 50011-2001).

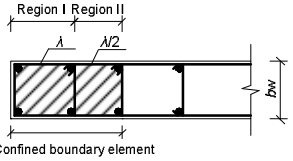


Figure 3. Chinese code requirement on transverse reinforcement at confined boundary element

Table 1 Transverse reinforcement at confined boundary elements

Specimen no.	Stirrup		ρ_v/%	λ
	Region I	Region II		
SW1	D8@75	D8@150	1.86	0.21
SW2	D8@75	D8@150	3.88	0.43
SW3	D6@90	D6@180	1.83	0.20
SW4	D6@90	D6@180	1.83	0.20
SW5	D6@63	D6@125	1.86	0.20
SW6	D6@50	D6@50	1.91	0.21
SW7	D8@50		1.91	0.21

Notes: ρ_v and λ in Table above indicate the amount of transverse reinforcement in Region I for the rectangular wall specimens and in the edge column for Specimen SW7.

The transverse reinforcement at the confined boundary elements of the test specimens is summarized in Table 1. When calculating the volumetric transverse reinforcement ratio and the corresponding stirrup characteristic value, the CFST volume was excluded in calculating the volume of concrete confined by stirrups, since the concrete core of CFST could be well confined by a steel tube. The stirrup

characteristic value of each specimen was no less than 0.2, which satisfied the code provision. Table 1 indicates that the stirrup characteristic value of each specimen was no less than 0.2, which satisfied the code provision. Note that the stirrup characteristic values shown in Table 1 were calculated through the use of the design value of material strengths.

2.2 Primary variables

Three primary variables were considered in the tests: the area ratio of steel tubes/CFSTs, the axial force ratio, and the cross-sectional shape of wall. As shown in Fig. 2, two types of wall cross sections (i.e. the rectangle-shaped and barbell-shaped sections) were considered in the tests. Details of other two variables are described as follows.

2.2.1 Area ratio of steel tubes/CFSTs

Two sizes of circular steel tubes were included, of which one was used for Specimens SW2 through SW4 and the other for Specimens SW5 through SW7. The former steel tube was denoted as ST-114-3.36 and the latter was denoted as ST-88.5-3.5. In the nomenclature for identifying steel tubes, the first number represented the outer diameter and the second number represented the thickness in mm. ST-114-3.36 had a diameter-to-thickness ratio of 31.7, and ST-88.5-3.5 had a smaller diameter-to-thickness ratio of 25.3. Only one steel tube was encased at each boundary element for ST-RC composite wall specimens except Specimen SW6 which had two steel tubes embedded at each boundary element. The steel tube and concrete core acted compositely as a CFST. CFST-114-3.36 and CFST-88.5-3.5 were used to represent the CFSTs that consisted of the corresponding steel tubes.

In order to investigate the effect of steel tubes and CFSTs, two indices were defined: the steel tube ratio and CFST ratio. The steel tube ratio, ρ, represents the ratio of the cross-sectional areas between the steel tube and the boundary element. The CFST ratio, ξ, represents the ratio of the cross-sectional areas between the CFST and the boundary element. Fig. 4 shows these indices for all test specimens. Specimen SW6 had the highest steel tube ratio and CFST ratio, whereas Specimen SW7 had the lowest steel tube ratio and CFST ratio because of its larger cross-sectional area covered by the edge column.

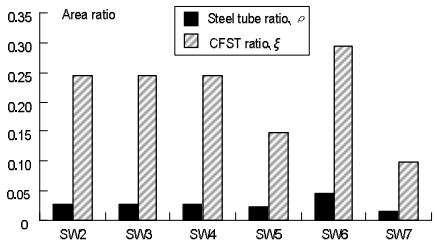


Figure 4. Area ratios of steel tubes and of CFSTs

2.2.2 Axial force ratio

The increase of the axial compressive force increases the depth of the compression zone and consequently decreases the ultimate deformation capacity for the lateral force-resistant elements (Paulay and Priestly 1992). The axial force ratio was thus considered as one of the critical concerns for the design of ductile structural walls. For ST-RC composite walls, the axial force ratio was defined as follows:

$$n_{\mathrm{d}} = \frac{N_{\mathrm{d}}}{f_{\mathrm{c,d}}(A - A_{\mathrm{CFST}}) + f_{\mathrm{cc,d}} A_{\mathrm{CFST}}} \tag{1-a}$$

$$n_{\mathrm{t}} = \frac{N_{\mathrm{t}}}{f_{\mathrm{c,t}}(A - A_{\mathrm{CFST}}) + f_{\mathrm{cc,t}} A_{\mathrm{CFST}}} \tag{1-b}$$

in which, n denotes the axial force ratio; N denotes the axial load applied on the specimen; f_{c} and f_{cc} denote the axial compressive strength of wall concrete and core concrete in the steel tube, respectively; A represents the gross cross-sectional area of the wall; A_{CFST} represents the gross cross-sectional area of the CFSTs; and subscripts d and t represent the design and test values, respectively. In the code GB 50011-2001, the design axial load is defined as N_{d}=1.2(D+0.5L), where D and L represent the dead and live loads, respectively. The specified load factor is taken as 1.2, and the live load has a reduction factor of 0.5. Thus, the design value of axial loads of the walls was 1.2 times the test value of axial loads applied on the specimens. The Chinese design code specifies that the design value of the axial compressive strength of concrete is equal to its test value of the strength multiplied by the reduction factor, to allow for the under-strength probability due to material variations and reliability. For instance, the design and test values of the axial compressive strength of concrete C40 were equal to 19.1 and 30.4 MPa, respectively, which corresponded to a material strength reduction factor of 0.63. An overall ratio between the design and the test values of the axial force ratios combines the load factor and material strength reduction factor, which accordingly equals to 1.2/0.63=1.9, rounded up to 2.

Table 2 shows the axial loads applied in the test specimens and the corresponding axial force ratios. The first pair, Specimens SW1 and SW2, had the same design axial force ratio of 0.55. For the second pair, Specimen SW3 was assigned a design axial force ratio of 0.60, while Specimen SW4 had a higher ratio of 0.72. The third pair, Specimens SW5 and SW6, had a design axial force ratio of approximately 0.70. Specimen SW7 had the largest design axial force ratio of 0.76. Note that the design axial force ratios for the specimens were larger than 0.5, i.e., the limit value for the ductile RC walls specified in the Chinese seismic design code.

Table 2 Applied axial force and axial force ratio

Specimen no.	Axial force N_t (kN)	Axial force ratio n	
		n_d	n_t
SW1	1821	0.55	0.29
SW2	1873	0.55	0.26
SW3	2042	0.60	0.31
SW4	2462	0.72	0.38
SW5	2346	0.70	0.32
SW6	2495	0.73	0.31
SW7	2570	0.76	0.34

2.3 Test setup and loading program

The test specimen was placed in a loading frame, as shown in Fig. 5. A vertical load was initially applied to the specimen by the vertical jack and it was maintained constantly for the duration of the test. Afterwards, cyclic lateral loads were applied quasi-statically by the actuator mounted horizontally to the reaction wall. The horizontal loading point was 2690 mm high above the wall bottom. The shear span ratios were 2.1 for Specimens SW1 through SW6, and 2.3 for Specimen SW7.

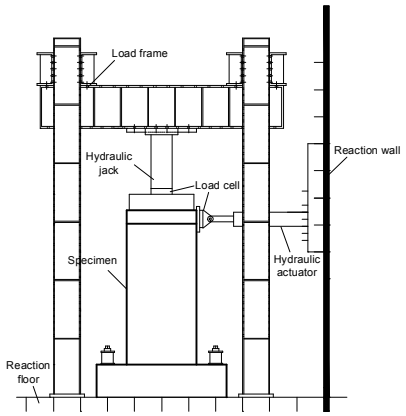


Figure 5. Test setup

Fig. 6 shows the loading history for the tests. Before the specimen yielded, the lateral loading was force-controlled and a cycle was performed at each force level. Four levels were considered in this phase: 0.25, 0.5, 0.75, and 1.0 times the predicted yield load. The loading was changed to displacement control after the specimen yielded. The displacement was expressed in terms of the drift ratio θ, which was defined as the ratio of the lateral displacement at the loading point over the height of the loading point from the wall bottom. The drift ratios increased in sequence of 1/200, 1/150, 1/100, 1/75 and 1/50, and two cycles were repeated at each drift level. In each cycle, a push was exerted and then followed by a pull, where the push was defined as the positive loading and the pull as the negative loading. The test was terminated at a complete failure due to concrete crushing developed at the wall bottom.

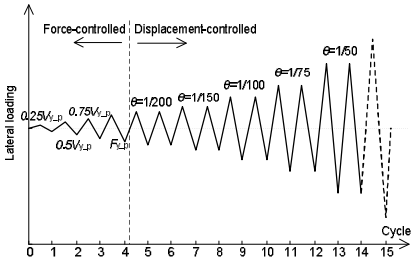


Figure 6. Loading history

2.4 Instrumentation

Instrumentation was used to measure loads, displacements and strains for each specimen. Load cells measured the vertical and lateral loads applied to the specimen. Five linear variable differential transformers (LVDTs) were mounted to measure the lateral displacements at 520 mm intervals over the wall height. A LVDT was mounted horizontally on the foundation beam to monitor any horizontal slip of the foundation beam along the reaction floor. The strains in the reinforcing steel were measured through the use of strain gauges. The strains of the vertical boundary steel rebars and vertical web steel rebars were monitored. The longitudinal and hoop strains of the steel tubes were measured. All gauges were located approximately 20 mm above the wall bottom. All measurements were recorded by a computer data acquisition system. During the tests, cracks and failures were observed carefully and were recorded by hand.

3. EXPERIMENTAL RESULTS

3.1 Damage and failure mode

The walls behaved in a similar manner for each test. Specimen SW5 was selected to show a typical envelope curve of the measured lateral force versus the top displacement in Fig. 7. In general, the damage of the specimen could be characterized into three stages: initial cracking stage, crack developing and yield stage, and failure stage. These stages correspond to Points A, B and C in Fig. 7, respectively. Fig. 8 shows the concrete cracking and crushing patterns for Specimens SW1 and SW5 after the tests. The cracking and crushing patterns for other composite walls were similar to that for Specimen SW5. The damage observed at each stage is summarized as follows.

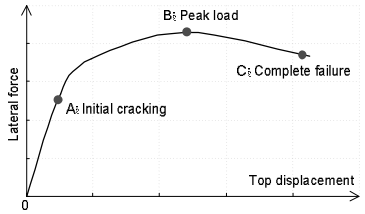


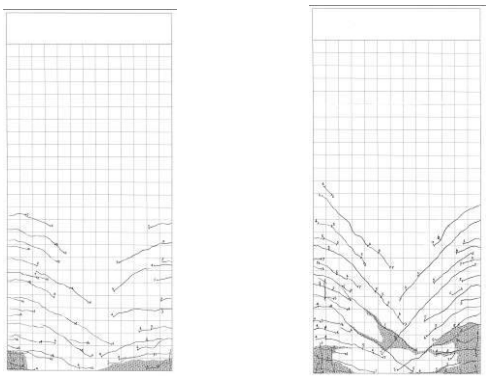
Figure 7. Typical envelope curve of lateral force versus top displacement

Initial cracking stage: This stage began from the onset

of testing to the occurrence of the initial crack. When the drift ratio reached 0.14% on the average (varied from 0.11% to 0.16% for different specimens), a horizontal flexure crack was observed initially at the wall bottom. A higher axial force ratio could delay the onset of flexure cracking. For instance, Specimen SW3 (n_d=0.60) cracked initially at a 0.13% drift ratio, whereas Specimen SW4 (n_d=0.72) cracked initially at a 0.16% drift ratio. On the other hand, a higher axial force ratio could expedite the compressive yield of vertical boundary reinforcement. For Specimen SW4 (i.e., the one subjected to the highest actual axial force ratio), the vertical boundary rebars yielded in compression nearly at the same time as the initial cracking. For other Specimens, the vertical boundary rebars experienced compressive yield after the cracks developed horizontally along the wall bottom. The specimens behaved almost linearly before cracking, and the initial cracking caused an obvious loss of stiffness as indicated in Fig. 7.

Crack developing and yield stage: This stage began from the initial cracking to the point when the specimen reached its peak load. Following the initial cracking, both the occurrences of new cracks and the extension and widening of existing cracks were observed upon further loading. The cracks were distributed in the region from the wall bottom up to an approximate height equal to the wall's sectional depth. The horizontal cracks extended from the boundary elements to the wall web, and then developed along the diagonal directions. The diagonal cracks were at an approximately 45° angle. Fig. 8 shows that the cracks in the RC wall were sparser and wider relative to those developed in the ST-RC composite walls. The measured strains indicated that the reinforcing bars and steel tubes sustained compressive yielding at an average drift ratio of 0.23%, and then experienced tensile yielding at an average drift ratio of 0.44%. Following the rapid development of the post-yield strains in rebars and steel tubes, the specimen reached the peak load at an average drift ratio of 0.58%.

Failure stage: This stage started from the peak load point to a complete failure of the specimen. After the lateral peak load was attained, vertical cracks caused by extremely large compressive strain occurred at the bottom corners of the wall. Concrete spalling and crushing occurred at further cycles, along with gradual strength deterioration. In the end, concrete crushing significantly reduced the wall's vertical load-carrying capacity, and consequently resulted in a complete failure. Concrete crushing was concentrated in the region from the wall bottom up to above 400 mm height. At the end of the tests, significant local buckling was observed at the bottom of CFSTs after removing the loose concrete.

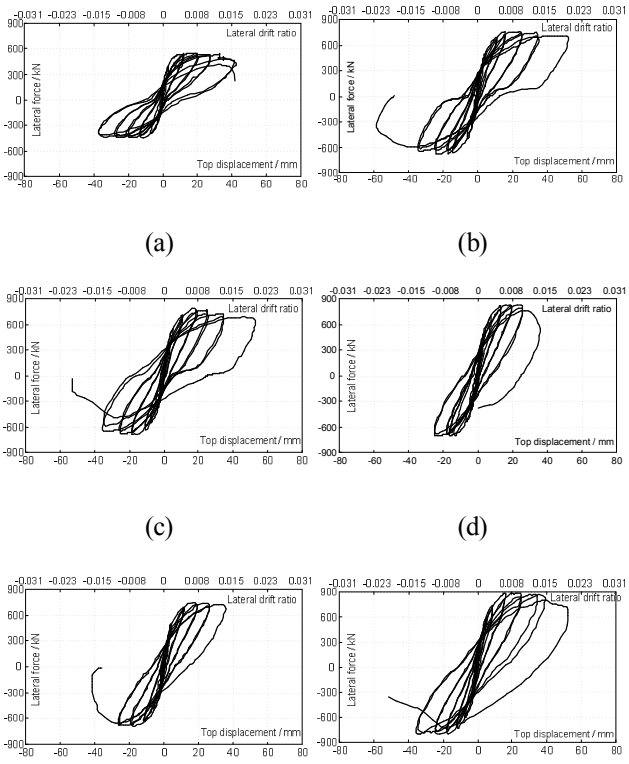


(a) (b)

Figure 8. Cracking and crushing patterns after tests: (a) SW1, and (b) SW5.

3.2 Force-Displacement Relationship

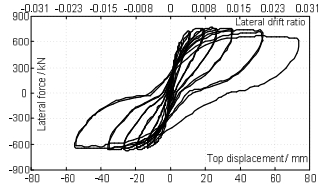
Fig. 9 shows the measured lateral force versus top displacement relationships for all seven specimens. In view of the hysteretic loops, the following observations were evident. The hysteresis loops of all specimens were fat and not significantly pinched, showing the characteristics of the flexure failure mode. When loading and unloading within a small drift (prior to the concrete cracking), the hysteretic curves cycled almost linearly with no residual displacement. After cracking, the stiffness clearly degraded and the strength steadily increased. Residual deformation was observed in unloading. After the peak load, the hysteretic curves showed a pinching effect, and the residual deformation became noticeable.



(a) (b)

(c) (d)

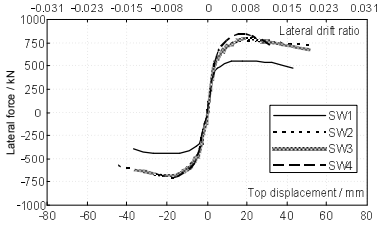
(e) (f)



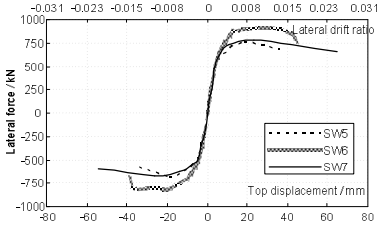
(g)

Figure 9. Hysteretic loops of lateral force versus top displacement relationships of specimens: (a) SW1, (b) SW2, (c) SW3, (d) SW4, (e) SW5, (f) SW6, and (g) SW7.

Fig. 10 plots the envelope curves of the lateral force versus top displacement relationships. All specimens had nearly identical initial stiffness. For the first pair of specimens, Specimen SW2 exhibited both larger lateral load-carrying and deformation capacities than Specimen SW1, due to the contribution of embedded CFSTs. Note that Specimen SW1 was over-loaded in the positive loading at its last loading cycle with the drift ratio θ=1/75 (i.e., 1.33%) due to loading error, which could affect its measured maximum deformation. For the second pair, Specimens SW3 and SW4 showed similar strengths, while Specimen SW4, which was under a higher axial force ratio, had a far smaller ultimate deformation than Specimen SW3. For the third pair, Specimens SW6, which had larger steel tube and CFST ratios, exhibited both larger lateral load-carrying and deformation capacities relative to Specimen SW5. Specimen SW7, the barbell-shaped wall, had the largest deformation capacity among all specimens due to the enhancement of edge columns. Quantitative discussions on the load-carrying and deformation capacities of the specimens are stated in the following subsections.



(a)



(b)

Figure 10. Envelope curves of lateral force versus top displacement of specimens: (a) SW1 through SW4, and (b) SW5 through SW7

3.3 Lateral load-Carrying Capacity

Table 3 illustrates the measured crack load V_{cr_m}, yield load V_{y_m} and peak load V_{p_m} of the specimens. The crack load V_{cr_m} corresponded to the load measured at initial cracking. The values of crack load and corresponding crack displacement could have some degree of uncertainty, since the naked-eye observation of cracks was affected by inspectors. The yield load V_{y_m} was defined by using the concept of equal plastic energy (Choi and Park 2008) so that the area enclosed by the idealized elastic-perfectly plastic envelope curve was the same as the measured envelope curve. The comparison between Specimen SW1 and SW2 indicated that the presence of CFSTs at the boundary elements evidently increased the crack load and yield load, and enlarged the peak load by 44%. The peak load of Specimen SW6 was 18% greater than Specimen SW5, indicating that larger steel tube/CFST ratios could improve the lateral load-carrying capacity.

Table 3 Lateral load-carrying capacity of specimens

Specimen no.	V_{cr_m} (kN)	V_{y_m} (kN)	Peak load		
			V_{p_m}(kN)	V_{p_e}(kN)	V_{p_m}/V_{p_e}
SW1	335	422	503	424.8	1.18
SW2	410	601	718	639.2	1.12
SW3	445	617	738	642.8	1.15
SW4	515	647	771	669.4	1.15
SW5	445	598	719	636.8	1.13
SW6	490	697	851	771.6	1.10
SW7	475	602	721	663.5	1.09

Since the specimens displayed a flexure-dominated behavior, the lateral load-carrying capacity could be estimated from the flexural strength at the wall bottom section. The following assumptions were made in assessing flexural strength. (1) Initially plane sections remained plane after bending. (2) The unconfined compression strengths of concrete f_c were utilized, ignoring the increased influence of compression strengths of the concrete that was confined by steel tubes and by stirrups at the boundary elements. Tension strength of concrete was ignored. (3) The steel's stress-strain relationship was idealized by an elastic-perfectly plastic approximation, ignoring the strain hardening and the effect of buckling of steel tubes and rebars. (4) The internal compression force of concrete were calculated by using the equivalent rectangular stress block of average stress αf_c and of the extent x from the extreme compression fiber. (5) The steel tubes were conservatively treated as vertical steel rebars. The steel tubes and vertical rebars in the boundary elements of two edges yielded in tension and in compression, respectively, which was evidenced by the measured strain data. (6) The contribution of the vertical web rebars that were placed within the extent of 1.5x from the extreme compression fiber were neglected, since they were close to the neural axis and their stress did not developed fully. Whereas the other vertical web rebars were assumed to yield in tension (JGJ 3−2002). Fig. 11 illustrates the mechanism principle of simplified evaluation for the flexure strength of wall section.

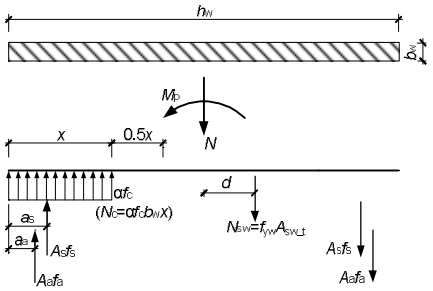


Figure 11. Flexure strength evaluation of wall cross section

According to the force equilibrium and moment equilibrium with respected to the wall's centroid, the following equations were derived:

$$N = N_c - N_{sw} \tag{2-a}$$

$$M_p = 0.5N_c\left(h_w - x\right) + A_s f_y\left(h_w - 2a_s\right) + A_a f_a\left(h_w - 2a_a\right) + N_{sw} d \tag{2-b}$$

$$N_c = \alpha f_c b_w x \tag{2-c}$$

$$N_{sw} = f_{yw} A_{sw_t} \tag{2-d}$$

where N denotes the axial load applied at the top of the wall; M_p denotes the flexure strength at the wall bottom section under the axial compressive force N; N_c and N_{sw} denote the reaction forces provided by the concrete in compression and by the vertical web rebars in tension, respectively; h_w and b_w denote the depth and thickness of the wall section, respectively; A_s and A_a denote the gross cross-sectional areas of the vertical rebars and steel tubes in one boundary element, respectively; A_{sw_t} denotes the gross cross-sectional areas of the vertical web rebars that were in tension; f_y, f_a, and f_{yw} represent the yield strengths of the vertical boundary rebars, steel tubes and vertical web rebars, respectively; f_c represents the axial compressive strength of concrete; a_s and a_a represent the distances of the vertical boundary rebar centroid and of steel tube centroid to the nearest wall edge, respectively; d denotes the distance between the centroid of the vertical web rebars that were in tension and the centroid of the wall section; x represents the extent of the equivalent rectangular stress block; and αf_c denotes the average stress of equivalent rectangular stress block, and the value for α factor is taken to be 1.0 for the concrete of which the cubic compressive strength is not higher than C50 (JGJ 3−2002). Note that the strength variety of the concretes inside and outside steel tubes were considered in the evaluation.

After assessing the flexural strength at the wall bottom section, M_p, the lateral load-carrying capacity was calculated by Equation (3) which included the P-Δ effect (Park and Eom 2007).

$$V_{p_e} = \frac{M_p - N\Delta_p}{H} \tag{3}$$

Where V_{p_e} denotes the evaluated lateral load-carrying capacity, Δ_p denotes the measured lateral displacement of the lateral loading point at the peak load, and H denotes the height of the lateral loading point relative to the wall base. Table 3 shows the values of V_{p_e} for all specimens and the comparison with the measured peak lateral load V_{p_m} in the tests. The evaluated results for ST-RC composite walls correlated well with the corresponding test results, with no more than 15% errors.

3.4 Deformation Capacity

Table 4 presents the crack displacement Δ_{cr}, yield displacement Δ_y, ultimate displacement Δ_u, displacement ductility ratio μ_Δ, and ultimate drift ratio θ_u of the specimens. The yield displacement Δ_y was the displacement at the yield load V_{y_m}. The ultimate displacement Δ_u was defined as the post-peak displacement at the instant when the lateral load decreased to 85% of the peak lateral load. If the lateral load did not drop to 85%, then the maximum displacement at the last loading cycle was taken as the ultimate displacement. Note that the displacement in the push direction was considered for analyzing the deformation capacity because the pull displacement at failure could not exceed the displacement at the previous cycle due to significant damage caused by prior push loading. The displacement ductility ratio μ_Δ was calculated as $\mu_\Delta = \Delta_u/\Delta_y$, and the ultimate drift ratio was calculated as $\theta_u = \Delta_u/H$.

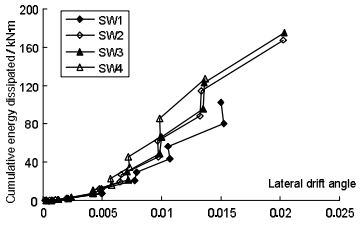
Table 4 Deformation capacity and ductility ratio of specimens

Specimen no.	Δ_{cr} (mm)	Δ_y (mm)	Δ_u (mm)	μ_Δ	θ_u
SW1	3.23	5.24	42.70	8.15	0.016
SW2	3.09	8.36	51.93	6.21	0.020
SW3	3.43	8.16	51.60	6.32	0.020
SW4	4.22	7.49	31.90	4.26	0.012
SW5	3.62	7.89	35.73	4.53	0.014
SW6	3.65	8.79	44.96	5.11	0.017
SW7	3.72	6.88	64.61	9.39	0.025

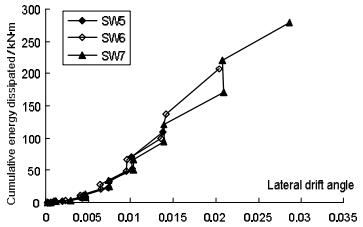
Table 4 indicates the following observations. The ultimate drift ratio of Specimen SW2 was 22% greater than the corresponding RC wall, Specimen SW1. For the two identical walls, Specimens SW3 and SW4, the ultimate drift ratio decreased to 60% when the test axial force ratio increased from 0.31 to 0.38. The ultimate drift ratio of Specimen SW6 was 26% greater than Specimen SW5, which indicated that having larger steel tube/CFST ratios could improve the ultimate deformation capacity. Specimen SW7, the barbell-shaped wall, exhibited a much larger deformation capacity relative to the rectangular-shaped walls, with an ultimate drift ratio of 0.025. It should be pointed out that because the presence of CFSTs at the boundary elements increased both the yield displacement and ultimate displacement, the displacement ductility ratio of ST-RC composite walls was smaller than the corresponding RC wall.

3.5 Energy Dissipation Capacity

Fig. 12 shows the energy dissipation curves for the specimens. The energy dissipation capacity of rectangular walls increased with an increase in steel tube/CFST ratios, and decreased with an increase in the axial force ratio. The total energy dissipated by Specimen SW2 was 63% greater than the corresponding RC wall, Specimen SW1. Due to the presence of edge columns, Specimen SW7 exhibited the largest energy dissipation capacity. It is notable that the ST-RC composite walls under design axial force ratios of up to 0.7 (e.g., Specimens SW4 through SW6) showed greater hysteretic energy dissipation capacities than the RC shear wall under a design axial force ratio of 0.55.



(a)



(b)

Figure 12. Energy dissipation curves for specimens: (a) SW1 through SW4, and (b) SW5 through SW7

4 CONCLUSIONS AND RECOMMENDATIONS

This paper presented an innovative composite wall, named the ST-RC composite wall. A series of quasi-static tests were conducted to investigate the lateral load-carrying capacity, deformation capacity, and energy dissipation of the walls under the condition of high axial force ratios and cyclic lateral loading. The primary test variables included the steel tubes/CFSTs ratios, the axial force ratio, and the cross-sectional shape of wall. Key observations obtained from this study were as follows:

(1) The ST-RC composite wall specimens showed a flexure failure mode, characterized by tensile yield of the vertical reinforcement and steel tubes in the boundary elements and compressive crushing of concrete at the wall bottom.

(2) With the addition of embedded steel tubes, the ST-RC composite walls showed a larger crack load, yield load, peak load, and ultimate deformation capacity relative to the RC wall. The deformation capacities of the ST-RC composite walls increased with an increase in the steel tube/CFST ratios, and decreased with an increase in the axial force ratio.

(3) The barbell-shaped ST-RC composite wall that was configured with edge columns showed remarkably larger deformation and energy dissipation capacities relative to the rectangular-shaped composite walls.

(4) Simplified formulation was developed to evaluate the lateral load-carrying capacity of the composite walls, in which the steel tubes were taken as vertical steel rebars. The evaluated results for the ST-RC composite walls showed no more than 15% errors compared with the corresponding test results.

Based on tests observation and data analysis, the following recommendations were proposed for seismic design of the ST-RC composite walls.

(1) Under the design axial force ratio of 0.73 and the confined boundary element's stirrup characteristic value of 0.20, the rectangular-shaped ST-RC wall had an ultimate drift ratio of 0.012, which was larger than the story drift requirement (i.e., 1/120=0.0083 drift ratio) for RC wall structures under the action of maximum considered earthquakes specified in the Chinese code for seismic design of buildings (GB 50011-2001). Considering the reliability of the design, rectangular-shaped ST-RC composite walls that were adopted in severe earthquake-prone regions were suggested under a design axial force ratio no greater than 0.65 and a confined boundary element's stirrup characteristic value no less than 0.2. Note that the CFST volume could be excluded from the concrete volume when calculating the volumetric transverse reinforcement ratio of the boundary elements.

(2) The barbell-shaped ST-RC composite wall that was configured with edge columns had an ultimate drift ratio of 0.025 under the design axial force ratio of up to 0.76 and an edge column's stirrup characteristic value of approximately 0.2. The barbell-shaped ST-RC composite walls used in severe earthquake-prone regions were suggested under a design axial force ratio no greater than 0.70 and an edge column's stirrup characteristic value no less than 0.2. Similarly, the CFST volume could be excluded from the concrete volume when calculating the volumetric transverse reinforcement ratio of the boundary elements.

Acknowledgements:

This work presented herein was supported by a research grant (90815025) sponsored by the National Natural Science Foundation of China. The writers wish to express their sincere gratitude to the sponsor.

References:

ACI (2005), "Building Code Requirements for Structural Concrete and Commentary (ACI 318-05)," American Concrete Institute, Farmington Hills.

CEN (2003), "Final Draft of EuroCode 8: Design Provisions for Earthquake Resistance-Part 1: General Rules, Seismic Actions and Rules for Buildings," European Committee for Standardization, Bruxelles.

Choi, I. and Park, H. (2008) "Ductility and energy dissipation capacity of shear-dominated steel plate walls," *Journal of Structural Engineering*, American Society of Civil Engineers, **134**(9): 1495-1507.

CMC (2001), "Code for Seismic Design of Buildings (GB 50011-2001)," China Ministry of Construction, Beijing, (in

Chinese).
CMC (2002), "Code for Design of Concrete Structures (GB 50010-2002)," China Ministry of Construction, Beijing (in Chinese).
CMC (2002), "Technical specification for concrete structures of tall building (JGJ 3−2002)," China Ministry of Construction, Beijing (in Chinese).
Eom, T.S., Park, H.G., Lee, C.H., Kim, J.H. and Chang, I.H. (2009), "Behavior of double skin composite wall subjected to in-plane cyclic loading," *Journal of Structural Engineering*, American Society of Civil Engineers, **135**(10): 1239-1249.
Hajjar, J.F. (2002), "Composite steel and concrete structural systems for seismic engineering," *Journal of Constructional Steel Research*, **58**(5-8): 703-723.
Hossain, K.M.A. and Wright, H.D. (2004), "Experimental and theoretical behaviour of double skin composite walls under in-plane shear," *Journal of Constructional Steel Research*, **60**(1): 59-83.
ICBO (1997), "Uniform Building Code," International Conference of Building Officials, Whittier.
Park, H. and Eom, T. (2007) "Truss model for nonlinear analysis of RC members subject to cyclic loading," *Journal of Structural Engineering*, American Society of Civil Engineers, **133**(10): 1351-1363.
Paulay, T. and Priestley, M.J.N. (1992), "Seismic Design of Reinforced Concrete and Masonry Buildings," Wiley Interscience Publication, New York.
Qian J.R., Lu W., and Fang E.H. (1999), "Displacement ductility-based aseismic design for shear walls," *Journal of Building Structures*, **20**(3): 42-49 (in Chinese).
Qian, J.R., Wei, Y., Zhao, Z.Z., Cai, Y.Y., Yu, Y.Q., Shen, L. (2008), "Experimental study on seismic behavior of SRC shear walls with high axial force ratio," *Journal of Building Structures*, **29**(2): 43-50 (in Chinese).
SNZ (2006), "Concrete Structure Standard (NZS 3101:2006)," Standard New Zealand, Wellington.
Thomsen, IV. J.H. and Wallace, J.W. (2004) "Displacement-based design of slender reinforced concrete structural walls-Experimental verification," *Journal of Structural Engineering*, American Society of Civil Engineers, **130**(4): 618-630.
Zhao, Q.H. and Abolhassan, A.A. (2004), "Cyclic behavior of traditional and innovative composite shear wall," *Journal of Structural Engineering*, American Society of Civil Engineers, **130**(2): 271-285.

8CUEE CONFERENCE PROCEEDINGS
8th International Conference on Urban Earthquake Engineering
March 7-8, 2011, Tokyo Institute of Technology, Tokyo, Japan

EXPERIMENTAL STUDY ON THE DEVELOPMENT OF A TUBULAR DAMPER FOR USE IN BOLT JOINTS

Seiji MUKAIDE[1)], Daiki IMOTO[2)], Nobuhiro NAGAYAMA[2)], and Motohide TADA [3)]

1) Asst. Professor, Div. of Global Architecture, Graduate School of Engineering, Osaka University, Japan
2) Graduate Student, Div. of Global Architecture, Graduate School of Engineering, Osaka University, Japan
3) Professor, Div. of Global Architecture, Graduate School of Engineering, Osaka University, Japan
mukaide@arch.eng.osaka-u.ac.jp, imoto_daiki@arch.eng.osaka-u.ac.jp,
nagayama_nobuhiro@arch.eng.osaka-u.ac.jp, tada@arch.eng.osaka-u.ac.jp

Abstract: In order to adapt to anchor bolts of exposed bases in steel moment frames, we have devised a hysteretic damper of tubular shaped steel for use in a bolt joint. The damper is expected to deform stably over a large plastic deformation range after local buckling occurs in the tubular part. The present paper describes basic experiments conducted during the development of the. Cyclic axial loading tests of the damper are conducted in order to investigate the deformation capacity of the damper. The length and diameter-thickness ratio of the damper are adopted as the experiment parameters. The test results reveal that the local buckling mode and the deformation capacity depend on the length and the diameter-to-thickness ratio.

1. INTRODUCTION

A variety of seismic dampers are used to reduce the structural response to seismic loading. Although viscoelastic or hysteretic dampers can reduce structural and nonstructural damage from seismic events, it is difficult to design a steel moment frame that will not be damaged at column bottoms of the first story by a severe earthquake. In order to adapt to the anchor bolts of exposed-type column bases in steel moment frames, we have devised a hysteretic damper of tubular shaped steel for use in a bolt joint, as shown in Fig. 1 (Mukaide). In the proposed device, one end of the damper is in contact with the nut, and the other is in contact with the base plate. When the column bottom is subjected to a large bending moment, the damper is expected to ensure that the other parts remain elastic by absorbing seismic input energy.

The proposed device consists of a bolt joint and a tubular damper. In this device, one end of the damper is in contact with the nut, and the other is in contact with the base plate. Figure 2 shows examples of the configuration detail. The welded damper in Fig. 2(a) is welded to the nut via the flange and the base plate. The screw-on damper in Fig. 2(b) is machined from extremely thick tube, and the ends of the damper have external screws on the outer circumferences. The damper is screwed onto the base plate and the lock nut. Thus, the

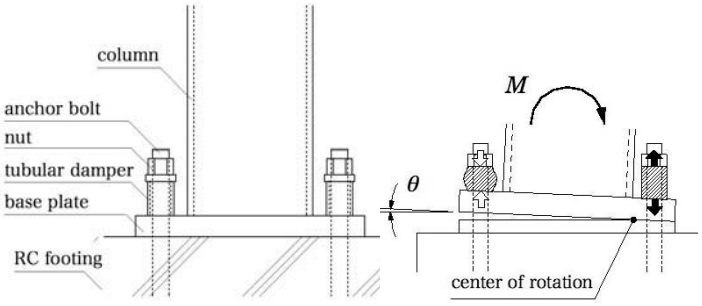


Fig. 1 Proposed device

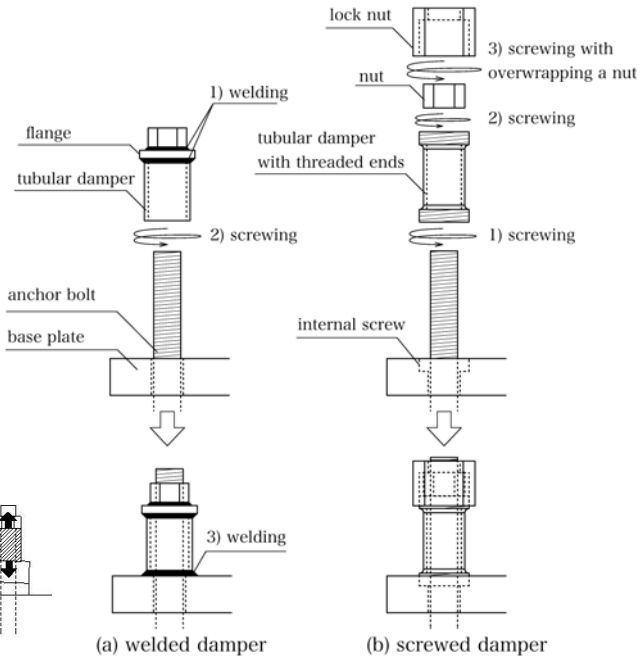
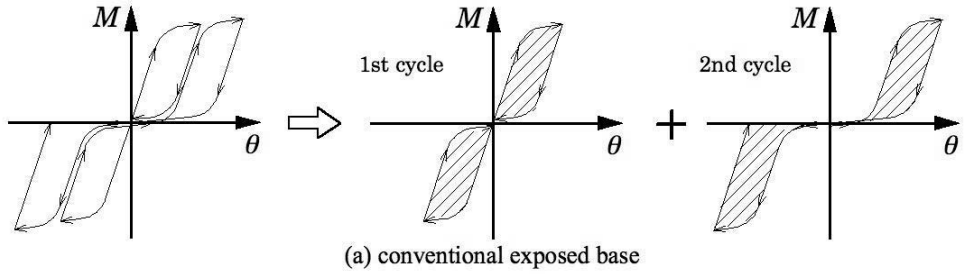
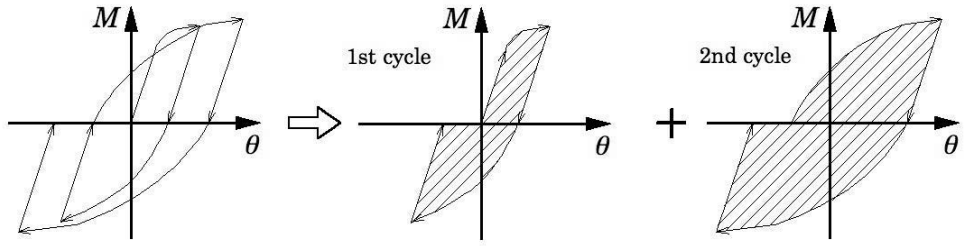


Fig. 2 Damper configuration



(a) conventional exposed base



(b) exposed base with the proposed device

Fig. 3 Hysteresis loops

damper is subjected to not only compressive stress but also tensile stress.

Since the center of rotation of the base is generally near the compressive flange of the column, the axial deformation of the damper is much larger in the compressive direction than in the tensile direction. Therefore, the damper must deform stably over a large plastic deformation range after local buckling occurs in the tubular part.

Figure 3(a) shows the hysteretic behavior of a conventional exposed base, in which the anchor bolts yield first. The restoring force characteristics shift to a slip-type behavior after the anchor bolts yield. The area of the hysteresis loops is much smaller than spindle-shaped hysteresis loops. However, in the proposed device, the exposed base is predicted to exhibit a pattern of a roughly spindle-shaped hysteresis loops, as shown in Fig. 3(b). Therefore, the proposed device will be able to absorb seismic input energy as a hysteretic damper.

A number of the present authors have conducted monotonic and cyclic loading tests during the development of the proposed system (Mukaide). Monotonic tests revealed high deformation performance of steel tubes with low diameter-to-thickness ratios, and cyclic loading tests of the welded damper (Fig. 2(a)) revealed that the deformation capacity was low because of fracturing at welded joints.

The present paper reports the data obtained in our latest fundamental tests. In these tests, screw-on dampers (Fig. 2(b)) are considered with the hope of improving deformation capacity. The purpose of the present study is to clarify the potential performance of the proposed system.

2. EXPERIMENT

For the case in which the damper is applied to exposed-type column bases, an axial load acts dominantly on the damper. In order to investigate the deformation capacities, cyclic axial loading tests of the dampers are conducted.

The tubular damper must fracture over a large deformation range with local buckling so that the damper may absorb a great deal of energy. Therefore, the diameter-to-thickness ratio and the length of the damper are used as experimental parameters because these factors may influence the local buckling characteristics.

A schematic diagram of the specimens is shown in Fig. 4. Table 1 lists the dimensions and materials of the specimens. The specimens are characterized by low diameter-to-thickness ratios *D/t*. The specimens are constructed from carbon steel tubes for machine structural purposes (JIS STKM13A). The mechanical properties obtained by a tension test are shown in Table 2.

The loading set-up is shown in Fig. 5. The joints of specimens are connected to loading plates by screws. One end of the specimen is fixed, and the other is connected to an oil-jack. The center of rotation of an exposed base is generally near the compressive flange of

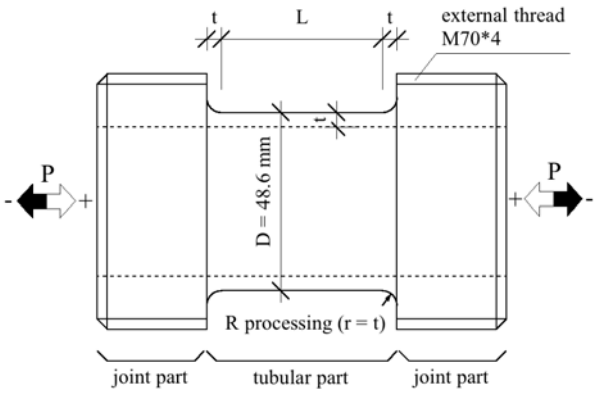


Fig. 4 Schematic diagram of the specimens

the column. Assuming that ratio of compressive deformation to tensile deformation is 8, the specimens are loaded cyclically according to the history shown in Fig. 6. The calculated length of one local buckling, ${}_cl$ is used as the reference value of the target deformation. Based on the classical theory (Timoshenko), ${}_cl$ is expressed by

$$ {}_cl = 2\pi \cdot \sqrt[4]{\frac{(D \cdot t)^2}{48(1-\nu^2)}} \qquad (1) $$

3. EXPERIMENTAL RESULTS

3.1 Axial Strength

The test results and some of the hysteresis curves are shown in Table 1 and Fig. 7, respectively. The yield strength is calculated based on the tensile test results.

The greater the diameter-thickness ratio *D/t* of the damper, the greater the maximum strength. The maximum strengths of the damper with *D/t* = 16.8 (G15 series) and D/t = 8.1 (G8 series) are increased approximately 1.7- and 2.1-fold, respectively. The maximum strength of the damper with *D/t* = 8.1 (G8 series) is increased approximately 2.1-fold.

The maximum strength tends to decrease slightly as the tubular part becomes longer, although there the length did not significantly affect the hysteresis curve (shown in Fig. 7). This strength decrease is influenced by the local buckling mode explained later.

Table 2 Material properties

specimen	YS (N/mm^2)	TS (N/mm^2)	EL (%)
G15-0.75,G15-1.0,G15-1.25,G12-1.3	269	430	40
others	275	456	40
minimum value of standard	215	370	30

YS: yield strength, TS: tensile strength, EL: breaking elongation

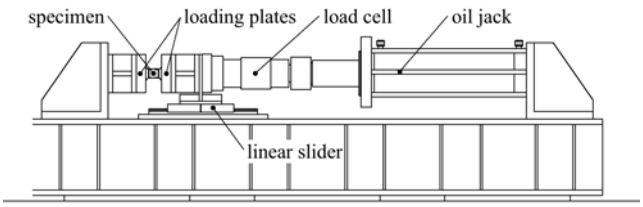


Fig. 5 Set-up of the cyclic loading test

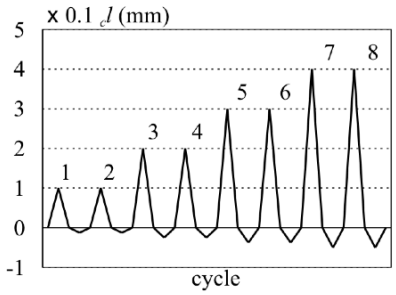


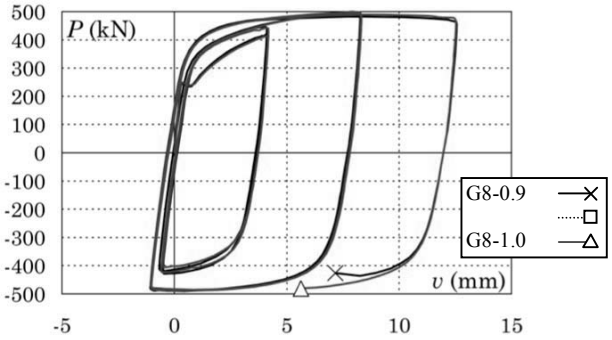
Fig. 6 Loading history

Table 1 Test matrix

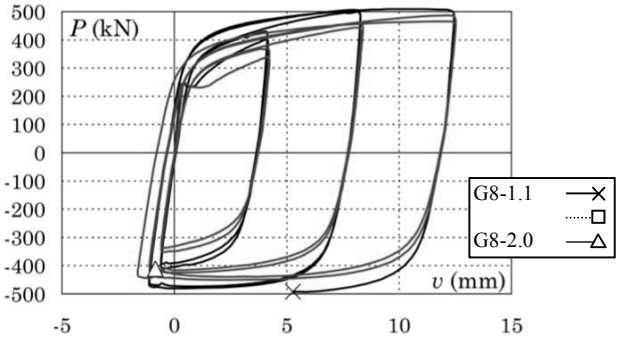
specimen	section Dxt (*D/t*)	length *L*	*L / D*
G15-0.75	ϕ48.6x2.9 (16.8)	36 mm	0.73
G15-1.0		49 mm	1.00
G15-1.25		61 mm	1.24
G12-0.6	ϕ48.6x4.0 (12.2)	29 mm	0.59
G12-0.7		34 mm	0.69
G12-0.8		39 mm	0.80
G12-0.9		44 mm	0.90
G12-1.0		49 mm	1.00
G12-1.1		54 mm	1.10
G12-1.2		59 mm	1.20
G10-0.7	ϕ48.6x4.9 (9.9)	34 mm	0.69
G10-0.8		39 mm	0.80
G10-0.9		44 mm	0.90
G10-1.0		49 mm	1.00
G10-1.1		54 mm	1.10
G10-1.2		59 mm	1.20
G10-1.3		63 mm	1.29
G8-0.8	ϕ48.6x6.0 (8.1)	39 mm	0.80
G8-0.9		44 mm	0.90
G8-1.0		49 mm	1.00
G8-1.1		54 mm	1.10
G8-1.2		59 mm	1.20
G8-1.4		69 mm	1.41
G8-1.6		78 mm	1.59
G8-1.8		88 mm	1.80
G8-2.0		98 mm	2.00
G8-2.2		108 mm	2.20

Table 3 Test results

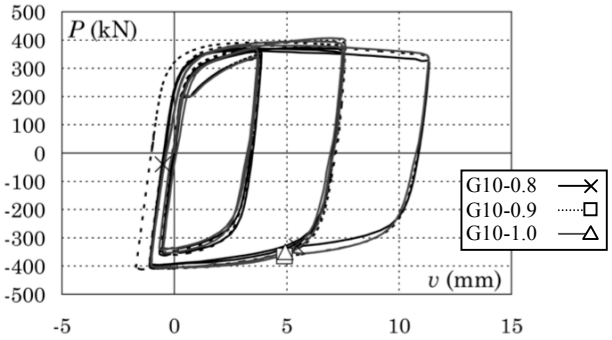
specimens	calculated value			test results				
	$\frac{L}{{}_cl}$	${}_cP_y$ (kN)	${}_cP_{max}$ (kN)	${}_eP_{max}$ (kN)	${}_eP_{min}$ (kN)	local buckling mode	v_{max} (mm) [loading cycle at fracture]	$\frac{\Sigma E}{P_y}$ (mm)
G15-0.75	1.24	114	187	197	-230	mode-Is	9.2 [5]	75
G15-1.00	1.69			194	-215	mode-II	9.2 [5]	71
G15-1.25	2.10			195	-213	mode-II	9.2 [5]	76
G12-0.6	0.85	151	294	294	-333	mode-Is	6.8 [4]	66
G12-0.7	1.00			301	-337	mode-Is	6.8 [4]	70
G12-0.8	1.14			303	-336	mode-Is	10.2 [5]	102
G12-0.9	1.29			315	-333	mode-Ia	10.2 [5]	103
G12-1.0	1.44			313	-314	mode-II	10.2 [5]	98
G12-1.1	1.58			307	-309	mode-II	10.2 [5]	94
G12-1.2	1.73			301	-305	mode-II	10.2 [5]	99
G10-0.7	0.90	181	395	376	-405	mode-Is	7.5 [4]	74
G10-0.8	1.03			372	-397	mode-Is	11.3 [5]	111
G10-0.9	1.17			396	-412	mode-Is	11.3 [5]	121
G10-1.0	1.30			407	-407	mode-Ia	11.3 [5]	113
G10-1.1	1.43			417	-401	mode-Ia	11.3 [5]	111
G10-1.2	1.56			386	-373	mode-II	11.3 [5]	107
G10-1.3	1.67			382	-371	mode-II	11.3 [5]	110
G8-0.8	0.93	216	532	469	-472	mode-Is	8.3 [4]	86
G8-0.9	1.05			491	-490	mode-Is	12.5 [5]	126
G8-1.0	1.17			500	-489	mode-Is	12.5 [5]	130
G8-1.1	1.29			509	-493	mode-Ia	12.5 [5]	128
G8-1.2	1.41			499	-450	mode-II	12.5 [5]	116
G8-1.4	1.65			460	-443	mode-II	12.5 [5]	120
G8-1.6	1.87			454	-442	mode-II	12.5 [6]	161
G8-1.8	2.11			453	-433	mode-II	12.5 [6]	165
G8-2.0	2.35			486	-450	mode-II	12.5 [6]	174
G8-2.2	2.59			448	-413	mode-II	16.7 [7]	200



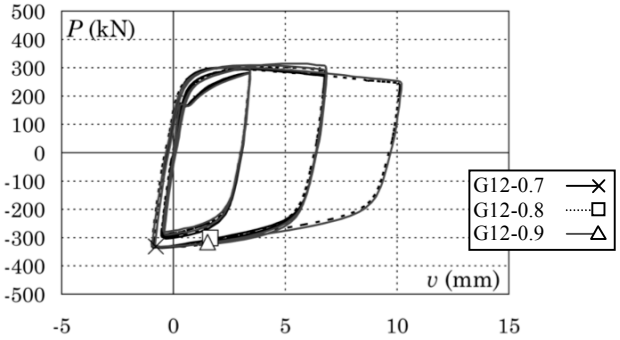
(a) G8 series (G8-0.9 and G10-1.0)



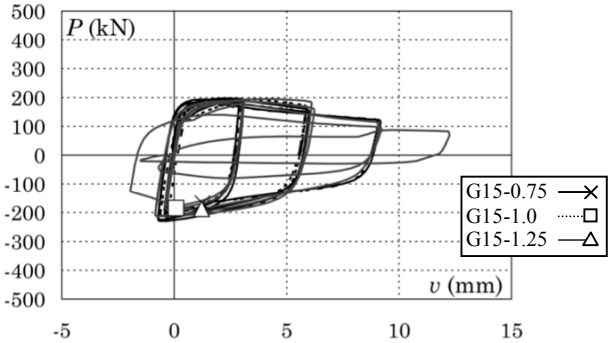
(b) G8 series (G8-1.1 and G10-2.0)



(c) G10 series (G10-0.8, G10-0.9, and G10-1.0)



(d) G12 series (G12-0.7, G12-0.8, and G12-0.9)



(e) G15 series (G8-0.9 and G10-1.0)

Fig. 7 Hysteresis curves

In Table 3, ${}_cP_{max}$ is the maximum strength, which is expressed as

$$ {}_cP_{max} = {}_cP_y \left(0.0163 \frac{E \cdot t}{\sigma_{yc} \cdot D} + 0.929 \right) \qquad (2) $$

where E is Young's modulus and σ_{yc} is the compressive yield stress (tensile yield stress is used in the present paper). The strength ${}_eP_{max}$ must be calculated in order to design the other parts so that they will remain elastic. Equation (2) is an empirical formula based on the monotonic compressive loading test (Suzuki) with a thinner tube (for which D/t is from 20 to 80) than the specimens in this test. Although this test is out of the applicable range of the formula, ${}_cP_{max}$ is in good agreement with ${}_eP_{max}$, except for G8 series.

After the maximum strengths, the restoring forces of the G15 series degrade rapidly. Hence, tubes thinner than the G15 series appear to be in appropriate for hysteretic dampers.

3.2 Local Buckling Mode

Examples of the deformation state after loading are shown in Photo. 1. Even for the same diameter-to-thickness ratio, these results are grouped roughly into three local buckling modes according to $L/{}_cl$. These three modes, as shown in Fig. 8, are a mode with a buckling wave at the center of the tubular part (mode-Is), a mode with an asymmetrical buckling (mode-Ia), and a mode with two buckling waves (mode-II) in ascending order of length. Table 3 indicates that the boundary of $L/{}_cl$ between mode-Is and mode-Ia is somewhere between 1.2 and 1.3 and that the boundary of $L/{}_cl$ between mode-Ia and mode-II is somewhere between 1.4 and 1.6.

3.3 Deformation Capacity

The deformation capacity to fracture is



Photo. 1 Deformation state after loading

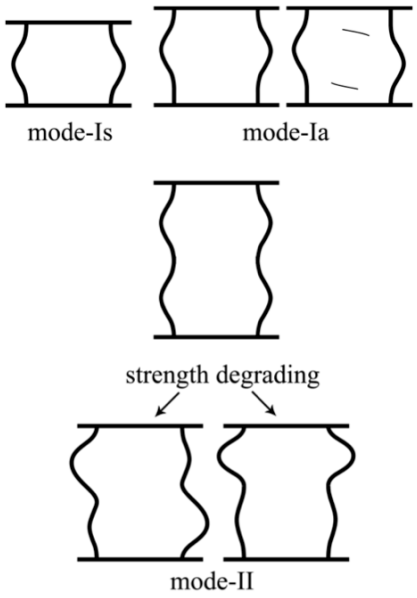


Fig.8 Local buckling modes

evaluated based on v_{max} and $\Sigma E/P_y$ in Table 3. The deformation capacities of respective local buckling modes exhibit different trends.

In the case of mode-Is and mode-Ia, specimens for which length L is shorter than ${}_cl$ fracture during the fourth loading cycle, whereas specimens for which L is longer than ${}_cl$ fracture during the fifth loading cycle. The shorter specimens have shorter buckling waves. Therefore, the premature fracturing of the shorter specimens is caused by larger out-of-plane bending deformation. The longer specimens have subequal buckling wavelengths and similar deformation capacities.

In the case of mode-II, specimens of the G10, G12, and G15 series have comparable deformation capacities to the mode-Is and mode-Ia specimens. This is because only one of the two local buckling waves deforms and the other is unloaded after the strength degrades. On the other hand, the specimens of the G8 series have a higher deformation capacity. Both of the local buckling waves deform significantly because these specimens maintain their ultimate strength without degradation until fracture. The longer specimens of mode-II have higher deformation capacities than the shorter specimens, which is also the case for mode-Is and mode-Ia.

Compared with the welded dampers, the screw-on dampers, which have the same form, exhibit a 1.2- to 3.1-fold increase in $\Sigma E/P_y$. This is because the fractures occurred in the base rather than ay the weld.

In the case of the proposed dampers, design decisions such as the section size of the column and the layout of anchor bolts affect the deformation capacity of the exposed base. Assuming that distance from the dampers to the center of rotation of the base is 400 mm, the maximum rotation angle to fracture for specimen G8-2.2 exceeds 0.04 rad. This is believed to be sufficient for hysteretic dampers.

4. CONCLUSIONS

In order to develop a new hysteretic damper for bolted joints, we have investigated experimentally the fundamental properties of a damper under axial load. The main conclusions are summarized as follows:

1) The local buckling mode of the tubular part varies

according to the diameter-to-thickness ratio and the length.

2) The specimens exhibiting mode-Ia or mode-Is buckling have similar deformation capacities (v_{max} = 0.3 $_{c}l$). The specimens of the G8 series exhibiting mode-II buckling have good performance. These results suggest the efficacy of the dampers when they are adapted to the anchor bolts of exposed-type column bases.

In the next series of experiments, the exposed base with the proposed dampers will be loaded in order to investigate the deformation capacities

Acknowledgements:

This work was supported by a Grant-in-Aid for Young Scientists (B), 20760374.

References:

Mukaide, S., Asamitsu, T., Tada, M., and Kohzu, I. "Basic Experiments for Developing Tubular Dampers Applied to Bolt Joints", The 10th Japan-Korea-Taiwan Joint Seminar on Earthquake Engineering for Building Structures (SEEBUS 2008), pp.171-176, 2008.10

Suzuki, T., Ogawa, T., Kato, M., and Kurimoto, T. (1972), "A Study of Inelastic Buckling of High-Strength Steel Pipes under Axial Compression," Journal of Structural and Construction Engineering, AIJ, Vol. 321, 28-37. (in Japanese)

Timoshenko, S. P., Gere J. M. (1963), "Theory of Elastic Stability," Mac Graw-Hill Company

8CUEE CONFERENCE PROCEEDINGS
8th International Conference on Urban Earthquake Engineering
March 7-8, 2011, Tokyo Institute of Technology, Tokyo, Japan

A SENSITIVITY STUDY OF BOLT TENSION EFFECT ON SEISMIC RESPONSE OF SPECIAL BOLTED MOMENT FRAMES

Atsushi Sato[1] and Chia-Ming Uang[2]

1) Associate Professor, Department of Scientific and Engineering Simulation, Nagoya Institute of Technology, Japan
2) Professor, Department of Structural Engineering, University of California, San Diego, United States of America
sato.atsushi@nitech.ac.jp, cmu@ucsd.edu

Abstract: High-strength bolts used in Special Bolted Moment Frame (SBMF) are in snug-tight conditions. AISI S110 Standard provides a design table with values that are based on 75.6 kN bolt tension force for 25.4 mm diameter high-strength bolts with a slip coefficient 0.19. To evaluate the effect of bolt over-tightening or under-tightening on the seismic response of SBMF including story drift ratio and maximum moment in the bolted connection, a sensitivity study was conducted. Additionally, the effect of the variation of bolt tension on the collapse margin was evaluated per the FEMA P695 Methodology. It was concluded that the over-tightening or over-tightening of the bolts is not a major concern.

1. INTRODUCTION

The American Iron and Steel Institute (AISI) recently published S110 "*Standard for Seismic Design of Cold-Formed Steel Structural Systems–Special Bolted Moment Frames*" (AISI 2007). Special Bolted Moment Frame (SBMF) is intended for use as free-standing light storage mezzanines, elevated office support platforms, equivalent support platform, and small buildings in all seismic areas. It is composed of cold-formed Hollow Structural Sections (HSS) columns and double C-section beams connected by snug-tight high-strength bolts (see Figure 1). If needed, bearing plate can be welded to the connection region to increase the bearing strength of the bolted moment connection. Based on the cyclic test results of 9 full-scale beam-column subassemblies (Hong and Uang 2004), it was shown that using a 75.6 kN bolt tension for 25.4 mm diameter high-strength bolts with a slip coefficient k=0.19 would provide a satisfactory correlation of the test results in the slip range (Uang et al. 2010). Therefore, this bolt tension force and slip coefficient were adopted in the AISI S110 Standard (2009) to compute the slip resistance of the bolt group.

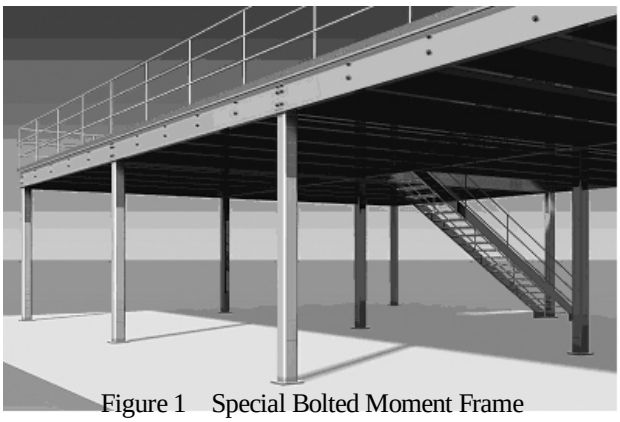


Figure 1 Special Bolted Moment Frame

Since bolts are to be tensioned to a snug-tight condition (RCSC 2004), a concern was raised on whether over-tightening or under-tightening will affect the maximum moment that can be developed in the bolted connection. Since the inelastic action in a SBMF is to be developed in the bolted moment connection during a seismic event, a high moment in the bolted connection may over-load the beams and columns and cause the frame to failure in a non-ductile manner.

To evaluate the effect of bolt over-tightening or under-tightening on the seismic response of SBMF, a sensitivity study was conducted. A series of nonlinear time-history analyses of sample SBMFs by using a suite of 44 earthquake ground motions were conducted to evaluate statistically effect of the variation of bolt tension on the seismic response including the story drift and the maximum moment in the bolted connection. The effect of the variation of bolt tension on the collapse margin was also evaluated per FEMA P695 Methodology (2009).

2. STRUCTURAL MODEL

2.1 Archetype Structural Design

Figure 2 shows the two-dimensional frame geometry that was used to model the one-story SBMF structures; Table 1 shows the design data of each archetype design. The archetypes were designed for Site Class D condition (soft soil) with S_{DS} = 1.0g as well as S_{D1} = 0.6g. The

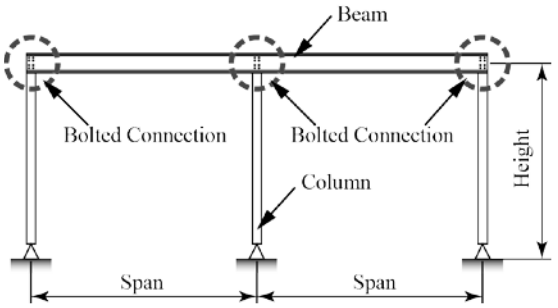


Figure 2 Archetype Analysis Model for SBMF

corresponding Maximum Considered Earthquake (MCE) hazard spectral values were equal to 1.5 times of these design spectral values (ASCE 2005). Following the P695 Methodology, the archetype models were designed based on the following seismic load combinations:

$$(1.2 + 0.2S_{DS})D + \rho Q_E + L \quad (1)$$

$$(0.9 - 0.2S_{DS})D + \rho Q_E \quad (2)$$

where D is the structural self-weight and superimposed dead loads, and L is the design live load (see Table 2). Q_E is the effect of horizontal seismic forces resulting from the base shear, V. Following P695, the redundancy factor, ρ, was conservatively assumed to be 1.0 in all cases.

The structural design was in accordance with S110; Response Modification Coefficient, R, is equal to 3.5. The beams were specified to be ASTM A653 galvanized cold-formed steel C-section members with nominal yield stress (F_y) and ultimate strength (F_u) of 345 and 483 N/mm^2, respectively. ASTM A500 Grade B HSS members with F_y and F_u values of 317 and 483 N/mm^2, respectively, were used for the columns. Tables 2 and 3 summarize the member and connection designs based on the seismic load combinations in Eqs. 1 and 2.

2.2 Development of Nonlinear Structural Model

The nonlinear analyses were performed by using the software OpenSees (PEER 2006). The model shown in Figure 2 included beam and column elements as well as a zero-length rotational spring to simulate the nonlinear behavior of the bolted beam-to-column connections (Uang et al. 2010). Fiber element was used to model the yielding of the beams and columns; no buckling was considered in the analysis.

The expected yield stress (= R_yF_y) was used to compute the strength for the beam and column, where R_y is equal to 1.1 and 1.4 for the beam and column, respectively (AISI 2007). To model the hardening range of the bolted moment connection response, the bearing strength at bolt holes is a function of the expected tensile strength (= R_tF_u). The following R_t values were used: 1.1 for the beam and 1.3 for the column (AISI 2007).

For either nonlinear static or dynamic analysis, P695 requires that the following gravity loads be imposed to the model structure:

Table 1 Archetype Structural Design Parameters

ID	No. of Span	Span (m)	Bay (m)	Height (m)	T (sec)	$S_{MT}(T)$ (g)
1	2	6.52	6.10	3.12	0.51	1.50
2	2	6.52	3.66	9.14	1.36	0.66
3	1	6.10	4.88	4.88	0.73	1.24
4	2	6.52	4.27	7.32	1.08	0.84

T : Natural Period, S_{MT} (T) : Maximum Considered Earthquake intensity at Natural Period, T.

Table 2 Archetype Structure Model Sizes

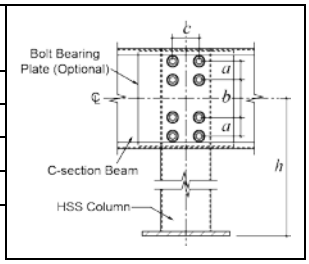
ID	Beam (mm)	Column* (mm)	Live Load L (N/m^2)	Dead Load D (N/m^2)
1	406CS89×3.4	HSS203×6.4	2394	575
2	508CS89×3.4	HSS305×6.4	5985	575
3	406CS89×3.4	HSS254×6.4	5985	575
4	508CS89×3.4	HSS305×6.4	5985	575

* Columns are square HSS.

Table 3 Bolt Configurations

ID	a (mm)	b (mm)	c (mm)
1	76	152	108
2	76	254	210
3	76	152	159
4	76	254	210

25.4mm diameter snug-tight high strength bolts are used.



$$1.05D + 0.25L \quad (3)$$

A 5% damping ratio was assumed for the models. The P-Delta effect was also included in the analysis.

For each archetype, 3 models were considered. The "Standard" (ST) model assumes that the bolts were properly tightened to the snug-tight condition such that the bolt tension is the same as that assumed (T = 75.6 kN). The "over-tightened" (OT) model assumes that all the bolts were over-tightened such that the bolt tension is 50% larger (i.e., T = 133 kN). The "under-tightened" (UT) model assumes that the bolt tension is 70% of that assumed in the standard model (i.e., T = 52.9 kN).

3. ANALYSES RESULTS

3.1 Static Pushover Analysis

A comparison of the static pushover results can be made in Figure 3. The variation in the bolt tension mainly affects the response in the slip range, but not too much in the bearing range.

3.2 Dynamic Analysis at DBE Level

A sample comparison of the global responses of Archetype 3 for three bolt tension models at Design Basis Earthquake (DBE) Level is shown in Figure 4. Figure 5 summarizes the maximum story drift ratio produced by all

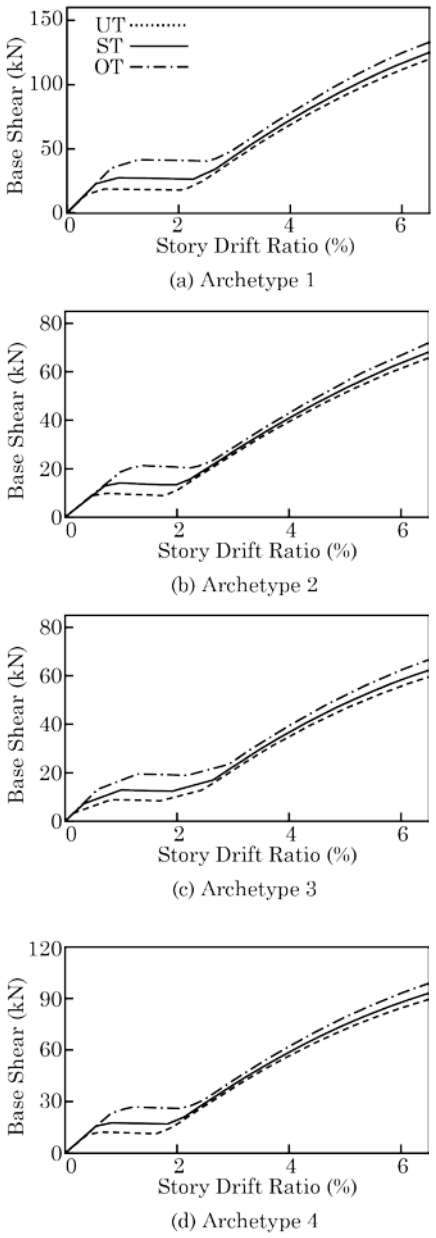


Figure 3 Sensitivity of Bolt Tension on Pushover Analysis

44 ground motions per P695. Figure 6 shows a summary of the based shear. (The maximum moment in a bolted connection is proportional to the base shear). The average value and the standard deviation of both the story drift and base shear are summarized in Table 4.

Even with the assumption that the bolt tension would be increased by 50% due to over-tightening, it is observed from Table 4 that both the story drift ratio and base shear (or moment in the bolted connection) are not very sensitive to the variation of bolt tension. In this case, over-tightening reduces the story drift by 2.7% to 3.4%, although the maximum moment in the bolted connection is increased by 4.4% to 18%. If the bolt tension was reduced by 30% due to under-tightening, it is also observed from Table 4 that both the story drift ratio and base shear are not very sensitive to the variation of bolt tension. In this case, under-tightening

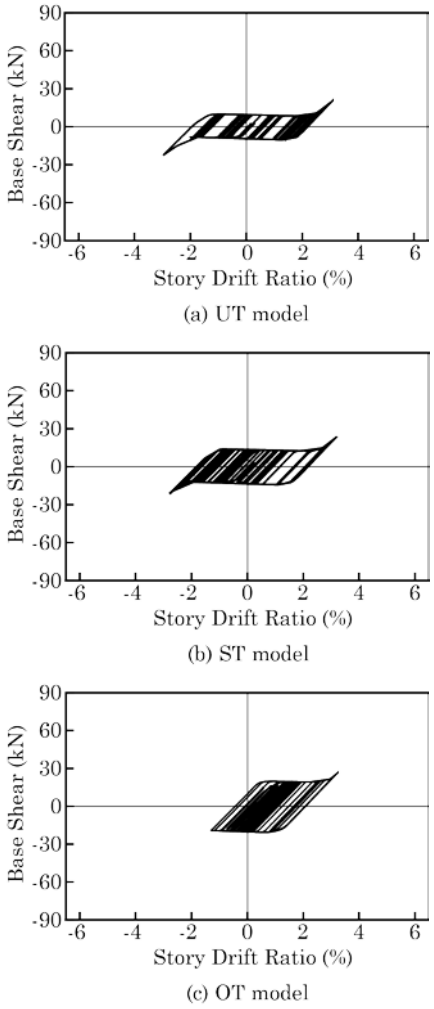


Figure 4 Global Response of Archetype 3 at DBE Level (GM: 1979 Imperial Valley, IMPVAL/H-DLT262)

Table 4 Bolt Tension Effect on the Maximum Base Shear and Story Drift

ID	Height (m)	Bolt Tension*	Maximum Base Shear (kN)	Maximum Story Drift (%)
1	3.12	UT	48.9 [27.1]	3.2 [1.2]
		ST	48.9 [23.1]	2.9 [1.2]
		OT	54.7 [18.2]	2.7 [1.2]
2	9.14	UT	23.6 [11.1]	2.8 [0.97]
		ST	24.5 [9.3]	2.7 [0.92]
		OT	28.9 [10.2]	2.7 [1.0]
3	4.88	UT	23.1 [13.3]	3.2 [1.1]
		ST	24.5 [12.9]	3.0 [1.2]
		OT	28.0 [10.7]	2.9 [1.1]
4	7.32	UT	37.8 [20.0]	3.0 [1.1]
		ST	39.1 [19.1]	2.9 [1.2]
		OT	40.9 [16.1]	2.8 [1.1]

* UT: Under tightened T = 52.9 kN, ST: Standard T = 75.6 kN, OT: Over tightened T = 113 kN, [ ]: Standard Deviation.

increases the story drift by 3.3% to 10%, and maximum moment in the bolted connection is reduced by up to 5.7%. Therefore, this sensitivity study concludes that the over-tightening or under-tightening is not a major concern.

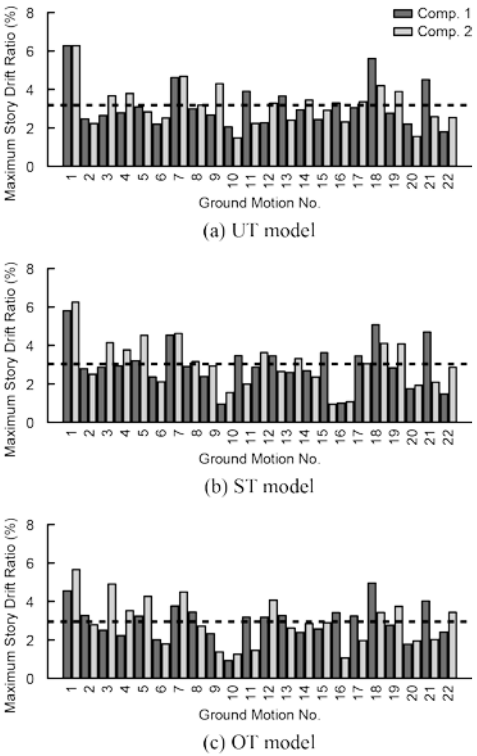


Figure 5 Maximum Story Drift at DBE Level (Archetype 3)

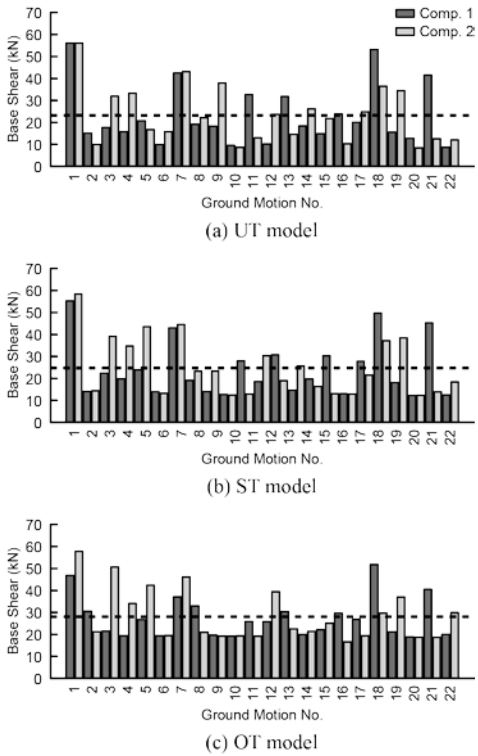


Figure 6 Maximum Base Shear at DBE Level (Archetype 3)

3.3 Evaluation of Collapse Margin

For each archetype model, the spectral acceleration at collapse, S_{CT}, was computed for each of the 44 ground motion, from which the median collapse intensity, $\hat{S}_{CT}$, was computed. $\hat{S}_{CT}$ was obtained by scaling all the records in the record set to the MCE intensity, S_{MT}, and then by increasing the intensity until one-half of the scaled ground motion records caused collapse. The ration between the median collapse intensity, $\hat{S}_{CT}$, and MCE intensity, S_{MT}, is the Collapse Margin Ratio (*CMR*).

$$CMR = \hat{S}_{CT} / S_{MT} \tag{4}$$

The value of $\hat{S}_{CT}$ depends on how the collapse is defined. Using a very large story drift ratio to define $\hat{S}_{CT}$ gives a nonconservative estimation of *CMR*. On the other hand, using the code specified story drift limits (ASCE 2005) to define $\hat{S}_{CT}$ is too conservative because the actual story drift capacity is generally higher. Since the beam and column of all the archetypes satisfied the S110 seismic compactness requirements, it is judged that a story drift capacity of 0.06 radians was a reasonable value to define the lower bound collapse limit state (Uang et al. 2010). Figure 7 shows the Incremental Dynamic Analysis (IDA) results for calculating the lower bound $\hat{S}_{CT}$ and *CMR* values for "Standard" (ST) model of Archetype 3. Figure 8 shows the collapse probability obtained from the IDA with bolt tensions varied, i.e., Standard (ST), over-tightened (OT), and under-tightened (UT). The lower bound $\hat{S}_{CT}$ and *CMR* values for all archetypes are summarized in Table 5.

According to P695, Spectral Shape Factor, *SSF*, is considered to remove the conservatism from using the

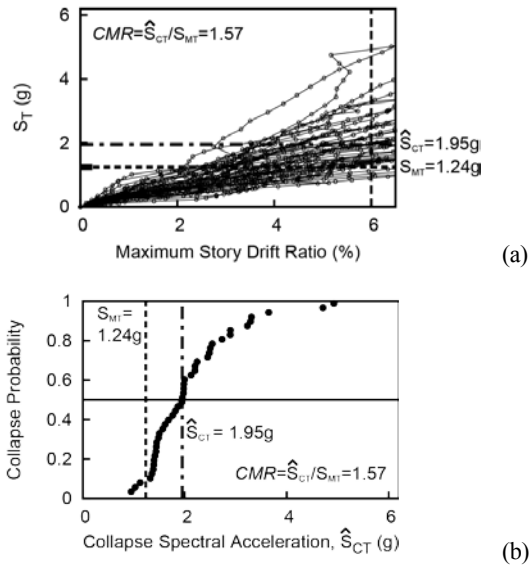


Figure 7 Sample IDA results and Collapse Probability (Archetype 3)

ground motion record set and the Adjusted Collapse Margin Ratio, *ACMR*, is used to compare with the acceptable values.

$$ACMR = SSF \times CMR \tag{5}$$

The Acceptable *ACMR* values are also provided in P695. For each archetype, the following criterion has to be satisfied.

$$ACMR_i \geq ACMR_{20\%} \tag{6}$$

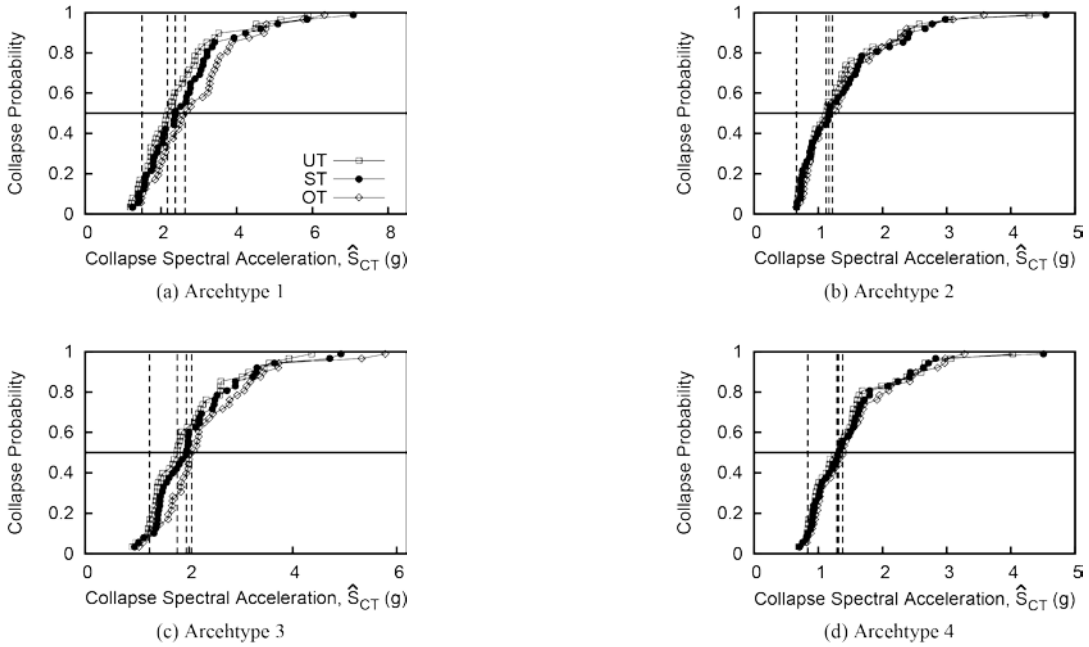


Figure 8 Sensitivity of Bolt Tension on Collapse Probability

$ACRM_{20\%}$ is the acceptable value with a collapse probability of 20%. This value is a function of the total system collapse uncertainty, β_{TOT}. This parameter reflects the fact that systems that have more robust design requirements, more comprehensive test data, and more detailed nonlinear analysis models, have less collapse uncertainty. In this study, a value of 0.60 for β_{TOT} is used per P695. As the result, a value of 1.66 is used for $ACRM_{20\%}$. A comparison of the calculated and acceptable *ACMR* values in Table 5 shows that Eq. (6) is satisfied. These results also showed that bolt tension force is not a major concern and a sufficient margin against collapse due to Maximum Considered Earthquake ground motions is provided.

4. CONCLUSIONS

A sensitivity study of the bolt tension force on the story drift ratio, maximum moment in the bolted connection, and the collapse margins of Special Bolted Moment Frame (SBMF) was presented in this paper. Over-tightening of the bolts reduced the story drift ratio by up to 3.4%, although the maximum moment in the bolted connection was increased by 4.4% to 18%. On the other hand, under-tightening of the bolts increased the story drift ratio by 3.3% to 10%, and the maximum moment in the bolted connection was reduced by up to 5.7%. Evaluating the collapse margin, the effect of bolt tension was not significant and the acceptance criteria provided by FEMA P695 were met. Therefore, it can be concluded that over-tightening or under-tightening of the bolts in SBMF is not a major concern.

Acknowledgements:

Funding for this project was provided by the American Iron and Steel Institute. The authors would like to acknowledge Mr. Ken Wood for designing the archetypes.

References:

American Iron and Steel Institute (2007), "Standard for Seismic Design of Cold-Formed Steel Structural Systems–Special Bolted Moment Frames," *AISI S110*, Washington, D.C.

American Iron and Steel Institute (2009), "Standard for Seismic Design of Cold-Formed Steel Structural Systems–Special Bolted Moment Frames with Supplement No.1," *AISI S110-07-S1-09*, Washington, D.C.

American Society of Civil Engineering (2005), "Minimum Design Loads for Buildings and Other Structures," *ASCE/SEI 7-05*, Reston, VA.

Federal Emergency Management Agency (2009), "Qualification of Building Seismic Performance Factors," *FEMA P695*, Washington, D.C.

Hong, J. K., and Uang, C. M. (2004), "Cyclic Testing of Cold-Formed Steel Moment Connection for Pre-Fabricated Mezzanines," *Report No. TR-04/03*, Department of Structural Engineering, University of California, San Diego, La Jolla, CA.

Pacific Earthquake Engineering Center (2006), "Open System for Earthquake Engineering Simulation (OpenSees)," University of California, Berkeley, CA.

Research Council of Structural Connections (2004), "Specification for Structural Joints Using ASTM A325 or A490 Bolts,", Chicago, IL.

Uang, C. M., Sato, A., Hong, J. K., and Wood, K. (2010), "Cyclic Testing and Modeling of Cold-Formed Steel Special Bolted Moment Frame Connections," *Journal of Structural Engineering*, **136(8)**, 953-960.

Table 5 Summary of Collapse Results for Archetype Design, Final Collapse Margins and Acceptance Criteria

ID	Bolt Tension*	IDA Results			Computed Collapse Margin		Acceptance Check	
		S_{MT} (g)	$\hat{S}_{CT}$ (g)	*CMR*	*SSF*	*ACMR*	$ACMR_{20\%}$	Pass/ Fail
1	UT	1.50	2.17	1.45	1.35	1.96	1.66	Pass
	ST		2.38	1.59	1.35	2.15		Pass
	OT		2.64	1.76	1.31	2.31		Pass
2	UT	0.66	1.12	1.70	1.58	2.69		Pass
	ST		1.77	1.77	1.58	2.80		Pass
	OT		1.22	1.85	1.46	2.70		Pass
3	UT	1.24	1.77	1.43	1.40	2.00		Pass
	ST		1.95	1.57	1.40	2.20		Pass
	OT		2.05	1.65	1.37	2.26		Pass
4	UT	0.84	1.29	1.54	1.49	2.29		Pass
	ST		1.31	1.56	1.49	2.32		Pass
	OT		1.38	1.64	1.41	2.31		Pass

* UT: Under tightened T = 52.9 kN, ST: Standard T = 75.6 kN, OT: Over tightened T = 113 kN

8CUEE CONFERENCE PROCEEDINGS
8th International Conference on Urban Earthquake Engineering
March 7-8, 2011, Tokyo Institute of Technology, Tokyo, Japan

WHICH SPECTRAL SHAPE REALLY MATTER TO PREDICT NONLINEAR STRUCTURAL RESPONSE: APPLICATION TO STEEL FRAMES

Edén Bojórquez[1)], Iunio Iervolino[2)], and Alfredo Reyes-Salazar[1)]

1) Professor, Faculty of Engineering, Universidad Autonoma de Sinaloa, Culiacan, Sinaloa, México
2) Professor, Dept. of Structural Engineering, University of Naples, Naples, Italy
ebojorq@uas.uasnet.mx, iunio.iervolino@unina.it, reyes@uas.uasnet.mx

Abstract: In this paper, several vector-valued ground motion intensity measures based on a parameter to characterize the spectral shape named N_p are analyzed. The parameter N_p is commonly used to represent the spectral acceleration response spectra in a range of periods, and in the present study this parameters was used to discuss which spectral shape is more related with a specific performance parameter corresponding to maximum and energy demands. For this aim, vector-valued ground motion intensity measures based on N_p through different type of response spectra such as: pseudo-acceleration, pseudo-velocity and input energy are analyzed. The efficiency of the vectors to predict the nonlinear response of several steel frames subjected to narrow-band motions from the soft soil of Mexico City is compared. Finally, an approach to predict the nonlinear response of structures dominated by higher modes of vibrations is proposed.

1. INTRODUCTION

In the last years, parameters to represent the ground motion potential of an earthquake named intensity measures (IMs) have been proposed (Housner 1952, Arias 1970, Von-Thun et al. 1988, Cordova et al. 2001, Baker and Cornell 2005, Tothong and Luco 2007, Baker and Cornell 2008, Bojórquez and Iervolino 2010). One of the desirable features of an IM must be the ability to predict the response of structures subjected to earthquakes (small variability of structural response given the IM). This ability is known as *efficiency* (Bazzurro 1998, Shome 1999, Luco 2002). The efficiency is crucial in records selection for nonlinear structural response with seismic design purposes as well as for reliability-based analysis. Due to this, many efforts have been oriented to propose ground motion intensity measures. Most of these parameters have the peculiar characteristic of representing the spectral shape in a range of periods, which is strongly related with the structural response as suggested in many studies (Cordova et al. 2001, Baker and Cornell 2005, Tothong and Luco 2007, Baker and Cornell 2008, Bojórquez and Iervolino 2010). In particular, vector and scalar ground motion intensity measures based on N_p which is representative of the spectral shape have resulted very well correlated with the nonlinear structural response (Bojórquez and Iervolino 2010, Bojórquez et al. 2010a). However, the studies regarding the parameter N_p have been developed considering only the spectral pseudo-acceleration shape, and it is important to observe which spectral shape is more related with a specific performance parameters as in the case of maximum interstory drift, hysteretic energy, etc. It is the main objective of this paper to analyze the efficiency of several vector-valued ground motion intensity measures, based on N_p and considering different types of response spectra, to predict the structural response of steel frames.

2. THE PARAMETER N_p

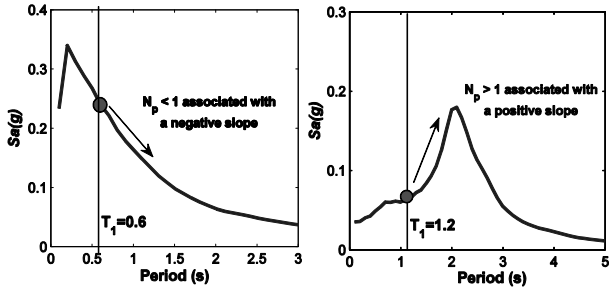
2.1 Definition

It has been mentioned that IMs often try to capture the structural response via the spectral shape with different degrees of accuracy. For example, $Sa(T_1)$, is the perfect predictor for the response of elastic single degree of freedom systems, and a good predictor for elastic multi-degree of freedom systems dominated by the first mode of vibration (associated to the T_1 period). Moreover, studies have found the sufficiency of $Sa(T_1)$ with respect to magnitude and distance (Shome 1999, Iervolino and Cornell 2005). Nevertheless, $Sa(T_1)$ does not provide information about the spectral shape in other regions of the spectrum, which may be important for the nonlinear behavior (beyond T_1) or for structures dominated by higher modes (before T_1). In the case of structures with nonlinear behavior, the structural response may be sensitive to different spectral values associated to the whole range of periods, from the fundamental period until a specific period of the structure beyond of T_1 to account for nonlinear behavior here named T_N. This calls for intensity measures providing information

about the spectral shape in different regions of the spectrum (Baker and Cornell 2008). The parameter N_p is inspired and focused in the featuring of the spectral acceleration shape and it can be obtained by the ratio between the geometrical mean in the range of periods from T_1 until T_N $Sa_{avg}(T_1,...,T_N)$ divided by $Sa(T_1)$. It is mathematically represented as:

$$Np = \frac{Sa_{avg}(T_1,...,T_N)}{Sa(T_1)} \quad (1)$$

According to this equation, if we have one or *n* records with a mean N_p value close to one, it is expected that the average spectrum be about flat in the range of periods between T_1 and T_N. For a N_p value lower than one, an average spectrum with negative slope is expected. As an example, the mean value of N_p for a group of ordinary records in the period T_1 = 0.6s is 0.39. In Figure 1a, the average spectrum of this set is illustrated. In the case of N_p values larger than one, the spectra tend to increase beyond T_1. As it can be appreciated for a set of narrow-band records, where the mean value of N_p=1.9 for T_1=1.2s, the average spectrum shows an increasing accelerations zone (see Figure 1b). Finally, the normalization of $Sa(T_1)$ let N_p be independent of the scaling level of the records based on $Sa(T_1)$, but most importantly it helps to improve the knowledge of the path of the spectrum from period T_1 until T_N, which is related with the nonlinear structural response. In the present study, for all the cases analyzed T_N equals to 2.2 times T_1 was used, as suggested by Bojórquez and Iervolino (2010).



(a) (b)

Figure 1 Mean elastic response spectra for a set of records with: (a) N_p=0.39, and (b) N_p=1.9

3. FEATURING DIFFERENT TYPES OF SPECTRAL SHAPE, AND VECTOR-VALUED GROUND MOTION IMs CONSIDERED

The efficiency to predict the nonlinear response of moment-resisting steel frames subjected to ground motion records is compared by means of different alternatives vector-valued ground motion intensity measures IMs with two parameters. An efficient IM can help to considerably reduce the number of analyses required to estimate the response of structures subjected to earthquakes with accuracy. Because most of the seismic hazard maps around the world were developed for the spectral acceleration at first mode of vibration $Sa(T_1)$, all the vectors here considered are based in $Sa(T_1)$ as the first parameter; however, other parameters as pseudo-velocity or nonlinear parameters can be used. In the second parameter of the vector, N_p was considered but using different types of response spectra. In total three different response spectra were considered to feature N_p as the second parameter. The first vector considered is $<Sa(T_1),N_{pSa}>$ which originally was proposed by Bojórquez and Iervolino (2010). It can be obtained by using Equation 1. The second vector is $<Sa(T_1),N_{pSv}>$, where N_{pSv} is obtained from Equation 1, but using the pseudo-velocity response spectrum instead of the pseudo-acceleration response spectrum. Finally, the last vector-valued ground motion intensity measure considered was $<Sa(T_1), N_{pEI}>$, where N_{pEI} is based on the input energy response spectrum. The input energy can be defined from the equation of motion of a single degree of freedom system as follows:

$$m\,\ddot{x}(t) + c\,\dot{x}(t) + f_s(x,\dot{x}) = -m\ddot{x}_g(t) \quad (2)$$

In equation 2, m is the mass of the system; c, the viscous damping coefficient; $f_s(x,\dot{x})$, the non-linear force; $\ddot{x}$, the ground acceleration; and x, the displacement with respect to the base of the system. A dot above x indicates a derivative with respect to time. In case of an elastic linear system, $f_s(x,\dot{x}) = k\,x$, where k is the stiffness of the system.

Integrating each member of Equation 2 with respects to x, yields:

$$\int m\,\ddot{x}(t)\,dx + \int c\,\dot{x}(t)\,dx + \int f_s(x,\dot{x})\,dx = -\int m\,\ddot{x}_g(t)\,dx \quad (3)$$

Equation 3 can be written as energy balanced equation as follows:

$$E_K + E_D + E_S + E_H = E_I \quad (4)$$

where E_K, E_D, E_S and E_H represent the kinetic (k), viscous damping (D), deformation (S) and dissipated hysteretic (H) energies, respectively; and E_I is the relative input energy, which will be used to obtain the vector $<Sa(T_1), N_{pEI}>$. Note that all the vectors were selected to represent maximum and cumulative potential of a ground motion shaking.

4. STRUCTURAL STEEL FRAME MODELS, SEISMIC RECORDS AND PERFORMANCE PARAMETERS

4.1 Structural steel frame models

Four moment-resisting steel frames having 4, 6, 8 and 10 stories, were considered for the studies reported herein. The frames are denoted as F4, F6, F8 and F10, respectively. As shown in Figure 2, the frames, designed according to the Mexico City Building Code (MCBC), have three eight-meter bays and inter-story heights of 3.5 meters. Each frame was provided with ductile detailing and its lateral strength was established according to the MCBC. A36 steel was used for the beams and columns of the frames. Relevant characteristics for each frame, such as the fundamental period of vibration (T_1), and the seismic coefficient and

displacement at yielding (*Cy* and *Dy*) are shown in Table 1 (the latter two values were established from static nonlinear analyses).

A two dimensional, lumped plasticity nonlinear model of each frame was prepared and analyzed. For this purpose, an elasto-plastic model with 3% strain-hardening was used to represent the cyclic behavior (in terms of bending moment and rotation) of the transverse sections located at both ends of the steel beams and columns. As discussed by Bojórquez and Rivera (2008), this model provides a good approximation to the actual hysteretic behavior of steel members. The frames were analyzed considering 3% of critical damping.

Table 1 Relevant characteristics of the steel frames

Frame	Number of Stories	T_1 (s)	C_y	D_y (m)
F4	4	0.90	0.45	0.136
F6	6	1.07	0.42	0.174
F8	8	1.20	0.38	0.192
F10	10	1.37	0.36	0.226

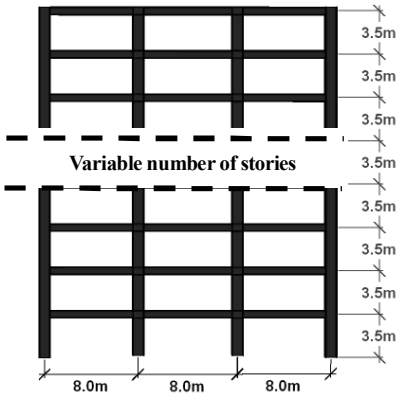


Figure 2 Geometrical characteristics of the steel frames considered

4.2 Seismic records

A set of 30 narrow-banded ground motions recorded at Lake Zone sites of Mexico City was considered. Particularly, all motions were recorded at sites having soil periods of two seconds, during seismic events with magnitudes near of seven or larger and having epicenters located at distances of 300 km or more from Mexico City. Some important characteristics of the records are summarized in Table 2. In this table, *PGA* and *PGV* denote the peak ground acceleration and velocity, respectively. It should be mentioned that sites having soil periods of two seconds are fairly common within the Lake Zone, and that the higher levels of shaking (in terms of peak ground acceleration) have been consistently observed at these sites.

4.3 Performance parameters

Two performance parameters were considered. The maximum interstory drift ratio, due to its relevance for design purposes, and the normalized dissipated hysteretic energy (E_N) by yielding displacement (D_y) and strength (F_y), see Equation 5. E_N was selected here as a performance parameter because its direct relationship with the cumulative demands (Iervolino et al. 2006). In fact, currently various damage indexes have been proposed based on hysteretic energy (Terán and Jirsa 2005, Rodriguez and Padilla 2008, Bojórquez et al. 2010b). It is important to say, that F_y and D_y were obtained from a push-over analysis, and E_H corresponds to the total plastic energy dissipated by the structure (the plastic energy dissipated by all the elements).

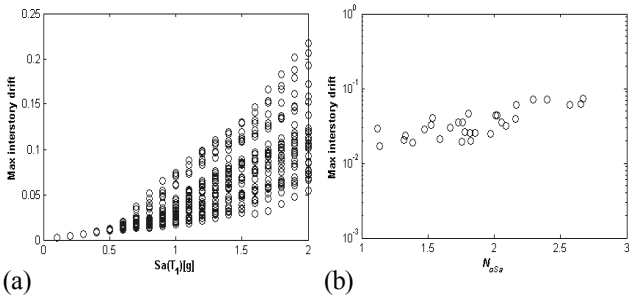
$$N_{EH} = \frac{E_H}{F_y D_y} \tag{5}$$

Table 2 Ground motion records

Record	Date	Magnitude	PGA (cm/s²)	PGV (cm/s)
1	19/09/1985	8.1	178.0	59.5
2	21/09/1985	7.6	48.7	14.6
3	25/04/1989	6.9	45.0	15.6
4	25/04/1989	6.9	68.0	21.5
5	25/04/1989	6.9	44.9	12.8
6	25/04/1989	6.9	45.1	15.3
7	25/04/1989	6.9	52.9	17.3
8	25/04/1989	6.9	49.5	17.3
9	14/09/1995	7.3	39.3	12.2
10	14/09/1995	7.3	39.1	10.6
11	14/09/1995	7.3	30.1	9.62
12	14/09/1995	7.3	33.5	9.37
13	14/09/1995	7.3	34.3	12.5
14	14/09/1995	7.3	27.5	7.8
15	14/09/1995	7.3	27.2	7.4
16	09/10/1995	7.5	14.4	4.6
17	09/10/1995	7.5	15.8	5.1
18	09/10/1995	7.5	15.7	4.8
19	09/10/1995	7.5	24.9	8.6
20	09/10/1995	7.5	17.6	6.3
21	09/10/1995	7.5	19.2	7.9
22	09/10/1995	7.5	13.7	5.3
23	09/10/1995	7.5	17.9	7.18
24	11/01/1997	6.9	16.2	5.9
25	11/01/1997	6.9	16.3	5.5
26	11/01/1997	6.9	18.7	6.9
27	11/01/1997	6.9	22.2	8.6
28	11/01/1997	6.9	21.0	7.76
29	11/01/1997	6.9	20.4	7.1
30	11/01/1997	6.9	16.0	7.2

5 RELATION BETWEEN VECTOR-VALUED IMs AND THE STRUCTURAL DEMAND OF STEEL FRAMES

Baker and Cornell (2005) and Bojórquez and Iervolino (2010) showed the advantages of using vector-valued ground motion intensity measures instead of scalars. The main advantage is the increment in the efficiency to predict the structural response. Herein with the aim to obtain the relation between the structural response of steel frames and the vectors selected; nonlinear incremental dynamic analysis of the frames subjected to the 30 records by using the first parameter of the vector, in this case $Sa(T_1)$ was perform, and then the relation between the structural response of the steel frames and the second parameter of the vector based on N_p is obtained. Note that it must be developed for a specific level of spectral acceleration and for all the intensity levels considered. While Figure 3a shows and example of the incremental dynamic analysis for $Sa(T_1)$, Figure 3b illustrates the relation obtained for $<Sa(T_1),N_{pSa}>$ and the maximum interstory drift demand when $Sa(T_1)$=1g. Note the good relation between N_{pSa} and the maximum interstory drift reflecting the advantage of the vector-valued ground motion intensity measure.

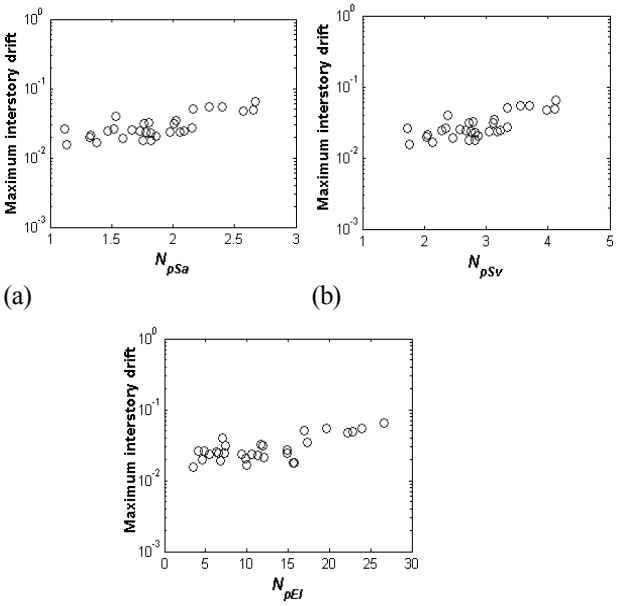


(a) (b)

Figure 3 (a) incremental dynamic analysis scaling for $Sa(T_1)$; (b) relation between N_{pSa} and the maximum interstory drift for $Sa(T_1)$=1g

5.1 Prediction of maximum interstory drift and normalized hysteretic energy via vector-valued ground motion intensity measures: Analyses results

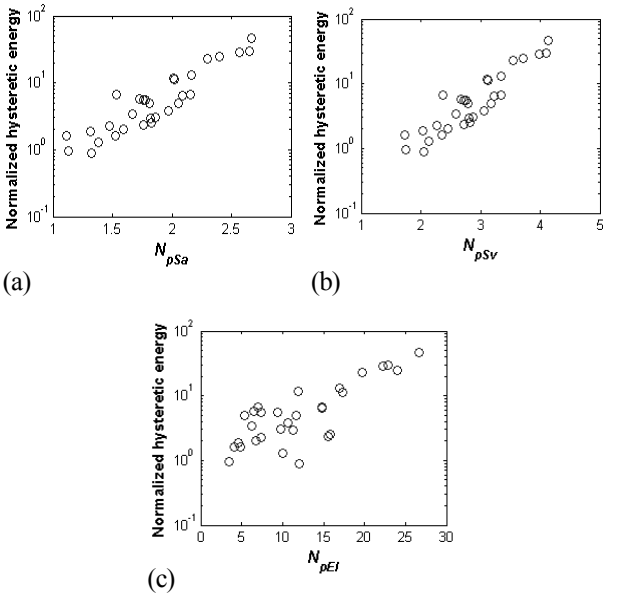
The relation between maximum interstory drift and normalized hysteretic energy demand of the frames analyzed is discussed. Figure 4 compares N_{pSa}, N_{pSv} and N_{pEI} with the maximum interstoy drift for frame F6, and for the records scaled at $Sa(T_1)$=0.9g. This scaling level corresponds to the point where the median value of the maximum interstory drift achieves 0.03 (structural collapse according to the MCBC). However, other scaling levels are considered as will be illustrated below. A good correlation can be observed between maximum interstory drift and all the parameters based on the spectral shape considered. This observation is valid also to predict the normalized hysteretic energy, see Figure 5; except that in this case, the parameter based on the input energy spectral shape is less effectiveness to predict normalized hysteretic energy demands, which is an important observation since this vector take into account structural damage potential. All these conclusions are valid also for the other frames under considerations. An important issue fall in the fact that the variation of the N_p based on spectral acceleration is in the range from 1 to 3 while in the other cases this variation is larger; particularly for the input energy the interval is between 0 and 30 which is quite large. Finally, the trend observed for the N_p based on pseudo-acceleration and pseudo-velocity response spectra is very similar due to the dependence of these parameters through the circular frequency.



(a) (b)

(c)

Figure 4 Maximum interstory drift prediction for the steel frame F6 with T_1=1.07s ($Sa(T_1)$=0.9g) for: (a) N_{pSa}, (b) N_{pSv} and (c) N_{pEI}



(a) (b)

(c)

Figure 5 Normalized hysteretic energy prediction for the steel frame F6 with T_1=1.07s (Sa=0.9g) for: (a) N_{pSa}; (b) N_{pSv} and (c) N_{pEI}

To demonstrate that all the conclusions obtained before are valid for a wider range of intensity levels. Figure 6 compares the standard deviation of the natural logarithm of maximum interstory drift for frame F4 and for all the IMs: $Sa(T_1)$ and the vectors $<Sa,N_{pSa}>$, $<Sa, N_{pSv}>$ and $<Sa,N_{pEI}>$. As Figure 6 suggests, the vector-valued ground motion intensity measures results in less dispersion for all the scaling level of the records compared with the scaling criteria based on spectral acceleration. Note that the vectors based on pseudo-acceleration and pseudo-velocity results in similar standard deviation. As it has been mentioned before, this is due to the relationship between both parameters, which suggest that there is no significant difference when using spectral acceleration shape or pseudo-velocity spectral shape as the type of vector here presented. The same conclusion is valid for frame F6 illustrated in Figure 7.

The results for normalized dissipated hysteretic energy and all the frames under consideration are presented in Figure 8. It is observed that, the vectors $<Sa,N_{pSa}>$ and $<Sa, N_{pSv}>$ are similar for frames F4 and F6, but in the case of frames F8 and F10 they results with minimum difference. The figure suggests that $<Sa,N_{pSa}>$ is the best correlated with nonlinear structural response of the steel frames subjected to narrow-band motions, and for this reason, it suggests that the spectral acceleration shape is a good indicator to predict maximum and cumulative demands. Regarding the question of which spectral shape really matter to predict nonlinear structural response?, the study conclude that both pseudo-acceleration and pseudo-velocity response spectra really matter; in particular, the spectral pseudo-acceleration shape.

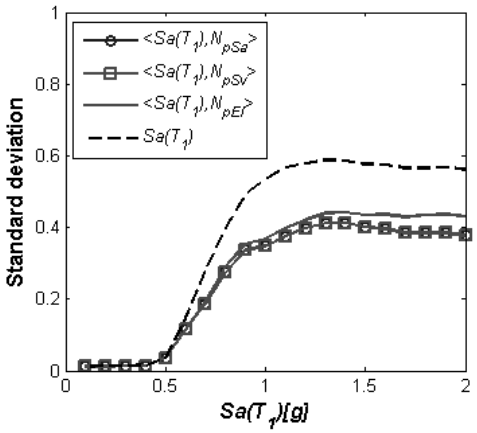


Figure 6 Standard deviation of the natural logarithm of maximum interstory drift given $S_a(T_1)$ and the vectors $<Sa, N_{pSa}>$, $<Sa,N_{pSv}>$ and $<Sa,N_{pEI}>$ at different intensity levels for frame F4

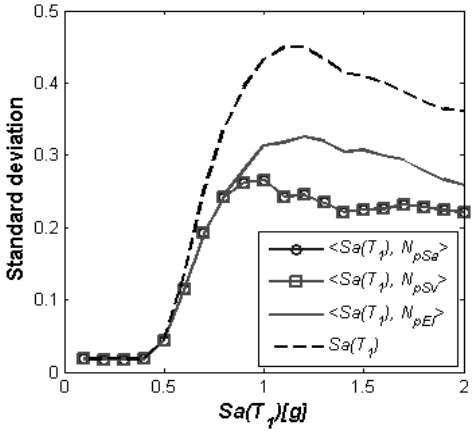


Figure 7 Standard deviation of the natural logarithm of maximum interstory drift given $S_a(T_1)$ and the vectors $<Sa, N_{pSa}>$, $<Sa,N_{pSv}>$ and $<Sa,N_{pEI}>$ at different intensity levels for frame F6

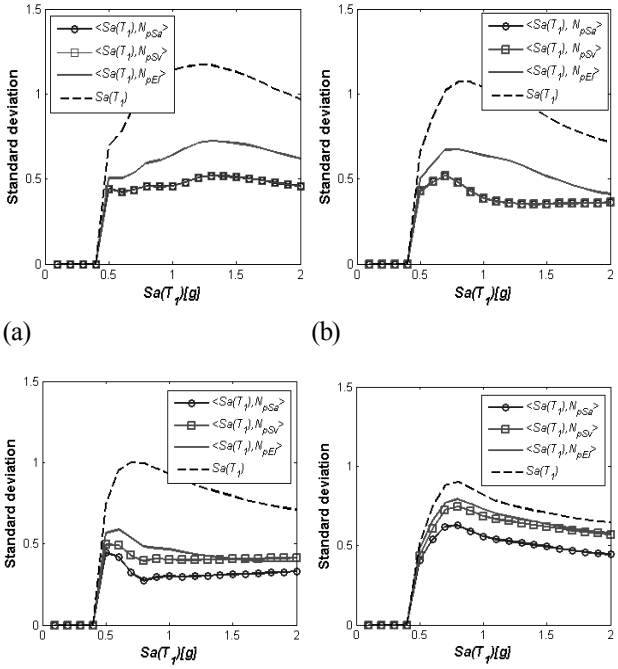


Figure 8 Standard deviation of the natural logarithm of normalized hysteretic energy given $S_a(T_1)$ and the vectors $<Sa, N_{pSa}>$, $<Sa,N_{pSv}>$ and $<Sa,N_{pEI}>$ at different intensity levels for frames (a) F4, (b) F6, (c) F8 and (d) F10

6. INCORPORING THE EFFECT OF HIGHER MODES OF VIBRATION AND FUTURE STUDIES

The work presented here was limited to predict the nonlinear seismic response of structural steel frames. Nevertheless, an efficient ground motion intensity measure should also be able to predict the nonlinear seismic response of structures dominated by higher modes as in the case of tall buildings. This is out of the scope of this paper; however,

some ideas to incorporate the effect of higher modes are given herein.

The influence of higher modes of vibration in structural response can be developed through a simple modification in the intervals of periods delimiting the parameter N_p. This is, instead assessing N_p between the range of T_1 (initial period) and T_N (final period), one possibility is to evaluate this parameter from the period of the interest mode (e.g. T_{2modo}) until T_N. Note that seismic ground motions selection in FEMA is based on a very similar approach. Moreover, the N_p parameter can be an alternative in record selection for nonlinear dynamic analysis. Furthermore, the inclusion of higher modes can be realized via vector with three parameters, as example: $<Sa, R_{T1,T2}, R_{T1,T2modo}>$, $<Sa, N_{pT1,TN}, R_{T1,T2modo}>$ or, $<Sa, N_{pT1,TN}, N_{pT1,T2modo}>$ (where $R_{T1,T2}$ proposed by Cordoba et al. 2001, is the ratio of the spectral acceleration at period T_2 and the spectral acceleration at period T_1; T_2 represents a period longer than T_1, the same is valid for other modes).

Another alternative is by giving a specific weighted to the contribution of the elastic response, nonlinear response or that dominated by higher modes of vibrations.

It would be of interest to develop a similar study but evaluating N_p non as the relation between the geometrical means divided by $Sa(T_1)$, if not by the relation of the weighted geometrical mean divided by $Sa(T_1)$. This can improve considerably the efficiency of the vectors here proposed. As can be observed, there are an ample possible alternatives to be incorporated in similar studies with the aim of increasing the efficiency of ground motion intensity measures to predict the seismic response of structures under earthquakes. Further, although it is necessary to compare other ground motion intensity measure commonly used with no dependence of the spectral shape, a recent study developed by Bojórquez et al. (2010a) showed that fragility assessment of steel buildings results more benefic if spectral shape ground motion intensity measure are used, compared with the traditional IMs as Arias intensity (Arias 1970), peak ground acceleration, peak ground velocity, ground motions durations an others.

7. CONCLUSIONS

A study to observe which spectral shape is more related with the structural response was developed. The study considers spectral shape ground motion intensity measures based on maximum and cumulative damage potential of an earthquake. The results suggest that the use of vector-valued ground motion IMs considerably predict with better approximation the structural response compared with the most commonly scalar IM (spectral acceleration at first mode of vibration). The study concludes that spectral shape ground motion IMs based on the pseudo-acceleration or pseudo-velocity spectra are more effective than those based on input energy; either to predict maximum interstory drift of steel frames under narrow-band motions, or hysteretic energy demands. In general, the work here presented recommends the use of the vector $<Sa, N_{pSa}>$ for prediction of nonlinear seismic response of structures.

Acknowledgements:

The support given by la Secretaría de Educación Pública under PROMEP and La Universidad Autónoma de Sinaloa under grant PROFAPI 2010/018 is appreciated.

References:

Housner, G.W. (1952), "Spectrum intensities of strong motion earthquakes," *Proceedings, Symposium on Earthquake and Blast Effects on Structures*, Earthquake Engineering Research Institute, 1952.

Arias, A. (1970), "A measure of earthquake intensity," *Seismic Design for Nuclear Power Plants*, edited by R. J. Hansen, MIT Press, Cambridge, MA, 438-483.

Von-Thun, J.L., Rochin, L.H., Scott, G.A. and Wilson, J.A. (1988), "Earthquake ground motions for design and analysis of dams, in: Earthquake Engineering and Soil Dynamics II – Recent Advance in Ground-Motion Evaluation," *Geotechnical Special Publication 20 ASCE*, New York, 463-481.

Cordova, P.P., Dierlein, G.G., Mehanny, S.S.F. and Cornell, C.A. (2001), "Development of a two parameter seismic intensity measure and probabilistic assessment procedure," *The second U.S.-Japan Workshop on Performance-Based Earthquake Engineering Methodology for Reinforce Concrete Building Structures*, Sapporo, Hokkaido, 187-206.

Baker, J.W. and Cornell, C.A. (2005), "A vector-valued ground motion intensity measure consisting of spectral acceleration and epsilon," *Earthquake Engineering and Structural Dynamics*, **34**, 1193-1217.

Tothong, P. and Luco, N. (2007), "Probabilistic seismic demand analysis using advanced ground motion intensity measures," *Earthquake Engineering and Structural Dynamics*, **36**, 1837-1860.

Baker, J.W. and Cornell, C.A. (2008), "Vector-valued intensity measures incorporating spectral shape for prediction of structural response," *Journal of Earthquake Engineering*, **12**(4), 534-554.

Bojórquez, E. and Iervolino I. (2010), "Spectral shape proxies and nonlinear structural response," Under review for *Soil Dynamics and Earthquake Engineering*.

Bojórquez, E., Reyes-Salazar, A., Rodriguez, H.E., Velázquez-Dimas J.I.. and Iervolino, I. (2010a), "Evaluation of seismic fragility of steel frames using vector-valued IM," *14th European Conference on Earthquake Engineering*, Ohrid, Macedonia.

Bazzurro, P. (1998), "Probabilistic seismic demand analysis", *Ph.D. Thesis*, Stanford University.

Shome, N. (1999), "Probabilistic seismic demand analysis of nonlinear structures," *Ph.D. Thesis*, Stanford University.

Luco, N. (2002), "Probabilistic seismic demand analysis, SMRF connection fractures, and near-source effects," *Ph.D. Thesis*, Stanford University.

Iervolino, I. and Cornell C.A. (2005), "Records selection for nonlinear seismic analysis of structures," *Earthquake Spectra*, **21**(3), 685-713.

Bojórquez, E. and Rivera, J.L. (2008), "Effects of degrading models for ductility and dissipated hysteretic energy in uniform annual failure rate spectra," *The 14th World Conference on Earthquake Engineering*, Beijing, China.

Terán-Gilmore, A. and Jirsa, J.O. (2005), "A damage model for practical seismic design that accounts for low cycle fatigue," *Earthquake Spectra*, **21**(3), 803-832.

Rodríguez, M.E. and Padilla, C. (2008), "A damage index for the seismic analysis of reinforced concrete members," *Journal of Earthquake Engineering*, **13**(3), 364-383.

Bojórquez, E., Reyes-Salazar A., Terán-Gilmore A. and Ruiz S.E. (2010b), "Energy-based damage index for steel structures," *Journal of Steel and Composite Structures,* **10**(4), 343-360.

8CUEE CONFERENCE PROCEEDINGS
8th International Conference on Urban Earthquake Engineering
March 7-8, 2011, Tokyo Institute of Technology, Tokyo, Japan

PLASTIC DEFORMATION CAPACITY OF STRUCTURAL STEEL UNDER VARIOUS AXIAL STRAIN HISTORIES

Yu Jiao[1], Satoshi Yamada[2], and Shoichi Kishiki[3]

1) Graduate student, Department of Environmental Science and Technology, Tokyo Institute of Technology, Japan
2) Associate Professor, Structural Engineering Research Center, Tokyo Institute of Technology, Japan
3) Assistant Professor, Structural Engineering Research Center, Tokyo Institute of Technology, Japan
jiao.y.aa@m.titech.ac.jp, yamada.s.ad@m.titech.ac.jp, kishiki.s.aa@m.titech.ac.jp

Abstract: In the field of energy based seismic design, the structural performance of steel structures is determined by the energy dissipation capacity, which depends greatly on the plastic deformation capacity of the structural components that form the whole system. The plastic strain capacity of the structural steel is one of the primary factors that determine the components' plastic deformation capacity. Most of the cyclic loadings employed in the structural steel tests are the recommended standard (typically incremental or constant amplitude) loading protocols, which is insufficient to study the deformation capacity under random loadings such as earthquake effects. This paper focuses on the evaluation of the plastic strain capacity of structural steel under various axial strain histories till ductile fracture. A series of element specimens made of SS400 and SN400 steel were tested under diverse cyclic axial strain loadings. The deformation capacity of the structural steel under cyclic axial loading till fracture was evaluated by studying the experimental strain capacity/energy dissipation capacity of the skeleton curve and the Bauschinger part. The error range of this method was proved smaller than that of the Miner's rules.

1. INTRODUCTION

In energy-based seismic design, the seismic performances of buildings which are subjected to random lateral loading histories such as earthquakes are evaluated by regarding the energy input to the structures as the seismic demand and the energy dissipation capacity of structures as the structural seismic performance (Akiyama 1985). In this design method, it is necessary to accurately reflect the energy dissipation capacity, i.e., the ultimate cumulative plastic deformation capacity, of the structural components constituting the whole system.

Seismic effects applied on the steel components during earthquakes depend on the configuration, strength, stiffness, etc. of the structure. Fracture is one of the typical ultimate states of steel components under earthquakes. Many researchers have been paying attention to the plastic deformation capacity of steel components till fracture. In case of component fracture, it is also important to clarify the relationship between the local strain history at the fracture area and the plastic strain capacity of the material (structural steel). Consequently, in addition to the evaluation of plastic deformation capacity of different structural components, it is necessary to carry out fundamental research focusing on the plastic strain capacity of structural steel under various loading (strain) histories. Moreover, it is also important to clarify the relationship between the energy dissipation capacity of steel components and the material. Unfortunately, this kind of work has not been fully understood.

There are several conventional evaluation methods of the plastic deformation capacity of structural steel suffering ductile fracture under axial strain histories, such as the experimental Manson-Coffin relation (fatigue life) of structural steel under constant amplitude cyclic strain histories. Among them, the most popular method is the combination of Manson-Coffin relation (Manson 1954, Coffin et al 1954) and Miner's rule (Miner et al1945). However, it is reported when the structures are subjected to seismic effects, the amplitudes of the strain history at the fracture area are usually quite large and the material fracture under several cycles. In these cases, the above mentioned method always gives obvious error which should not be neglected.

Other than the Manson-Coffin & Miner method, it is possible to evaluate the plastic deformation capacity of steel components or material through the plastic deformation capacity of the skeleton curves, which can be extracted from the hysteresis curves. This method is developed based on empirical law (Kato 1970) of the stress-strain relation of steel material under cyclic loadings, which has been employed to evaluate the plastic deformation capacity of steel components. The analytical results of Yamada et al (Yamada et al 2006) indicate that there is a correspondence between the skeleton curve of the steel components and the structural steel. It is possible to obtain the relationship between the plastic deformation capacities of steel

components and structural steel as long as the deformation capacity of steel is known.

Therefore, in this study, a series of plate element specimens made of SS400 and SN400 steel were tested under diverse cyclic axial strain loadings. The hysteresis loops of the specimens are divided into the skeleton curves and Bauschinger parts. The plastic strain capacity of structural steel SS400 and SN400 under cyclic axial strain histories is evaluated by studying the plastic deformation capacity of each parts of the hysteresis loops

2. CYCLIC LOADING TESTS OF STEEL PLATE ELEMENTS

2.1 Details of the Specimens

The shape of the steel plate specimen is shown in Figure 1. The parameters of this experiment are the different lots of steel and the strain histories, the details of which are shown in Table 1. Twenty-eight specimens were made from 4 different steel/lots (1~4) of SS400 steel and eighteen specimens were made from the same steel/lot (5) of SN400 steel. The size of the testing part is 40mm 100mm (the lengths of specimens FF01, 02 and 03 are 80mm). In order to avoid stress concentration, both sides of the testing part are designed to have a corner R. Here, R=10mm for SS400 steel 1~4 while R=20mm for SN400 steel 5.

Tensile coupon test was conducted using the JIS-1A standard coupon. The results of the tensile test (material stress-strain relation) are shown in Figure 2.

2.2 Test Setup

Figure 3 shows the setup details of the experiment. A testing machine with its loading capacity of 500kN was

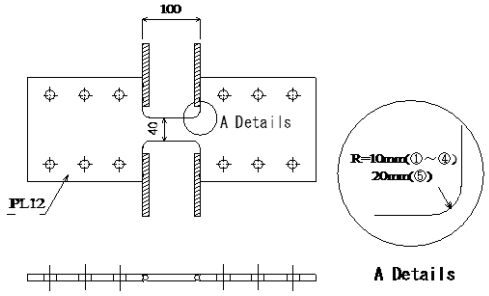


Figure 1 Shape of the specimen

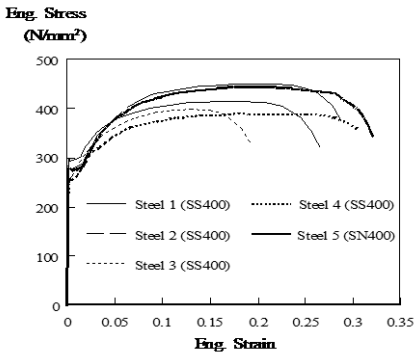


Figure 2 Results of the coupon tests (Engineering values)

employed to offer axial load. In order to prevent buckling, several buckling restraining jigs were set around the specimen. Teflon sheets were attached to the jigs to avoid the friction between the jigs and the specimen. The load was recorded by the load cell of the testing machine. Four displacement transducers were set to the end of the testing area. The deformation of the specimens was calculated through the results of these four transducers.

2.3 Strain histories

The main parameter of this experiment is the strain histories. The details of each strain history in this study are listed in Table 1. Six basic patterns of loading histories were applied to the specimens during testing (Figure 4).

1) Constant amplitude cyclic loading till fracture (Con. Amp.)

2) Constant amplitude cyclic loading followed by tension till fracture (Con. Amp.→Ten.)

3) Incremental amplitude cyclic loading followed by tension till fracture (Inc. Amp.→Ten.)

4) Constant amplitude cyclic loading followed by same constant amplitude cyclic loading with the neutral axis offset to tension side till fracture (Off.)

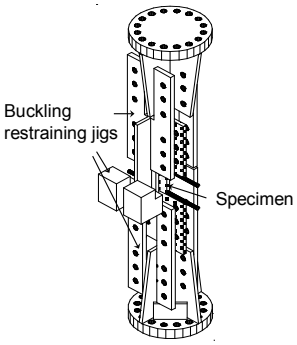


Figure 3 Test setup

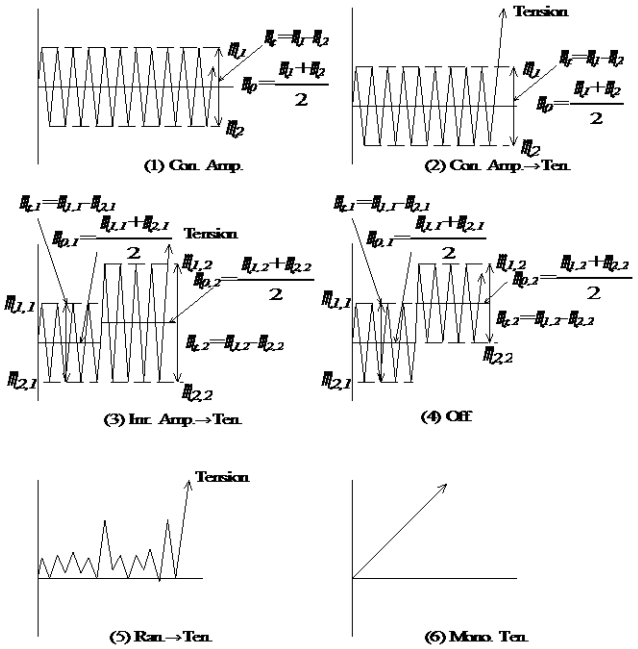


Figure 4 Basic loading pattern

Table 1　List of specimens and testing results

Name	Type	Steel	Yield point	Loading pattern	Strain histories	$\square_s^+$	$\square_s^-$	$\square_B^+$	$\square_B^-$
B01	SS400	1	291.4	Con. Amp.→Ten.	6%(0%)×10→Ten.	163.3	49.1	351.6	328.0
B05				Inr. Amp.→Ten.	6%(0%)×5→7%(0.5%)×5→8%(1%)×5→Ten.	141.3	61.6	624.1	582.4
B06				Con. Amp.	6%(0%)×57.5	51.4	53.2	2096.9	2057.4
B07				Con. Amp.→Ten.	6%(0%)×50→Ten.	114.2	53.5	1848.3	1805.6
B08				Con. Amp.→Ten.	6%(0%)×40→Ten.	129.9	48.6	1469.4	1436.6
B09				Inr. Amp.→Ten.	6%(0%)×5→7%(0.5%)×5→8%(1%)×5→9%(1.5%)×5→Ten.	146.0	78.5	903.6	853.8
B10				Inr. Amp.→Ten.	6%(0%)×5→7%(0.5%)×5→8%(1%)×5→9%(1.5%)×5→10%(2%)×5→Ten.	82.7	80.4	1220.3	1148.0
B15				Ran.→Ten.	Ran.×1→Ten.	145.1	13.6	47.5	26.4
B18				Ran.→Ten.	Ran.×2→Ten.	139.6	16.7	101.1	59.7
B20				Con. Amp.	4.2%(0%)×143.5	43.1	42.0	3762.7	3758.9
B49				Mono. Ten.		143.8	–	–	–
D1	SS400	2	304.7	Mono. Ten.		123.4	–	–	–
D20				Con. Amp.→Ten.	2.5%(1.25%)×1→Ten.	128.5	16.0	12.2	0.0
D22				Con. Amp.→Ten.	5%(2.5%)×1→Ten.	136.1	32.6	25.0	0.0
D29				Con. Amp.→Ten.	7.5%(3.75%)×1→Ten.	127.1	46.9	35.9	0.0
D34				Con. Amp.→Ten.	5%(0%)×3→Ten.	132.2	43.0	70.1	54.5
D58				Con. Amp.→Ten.	10%(0%)×3→Ten.	96.8	76.7	133.6	103.8
D62				Con. Amp.→Ten.	2.4%(0%)×3→Ten.	130.9	17.5	17.2	14.9
E01	SS400	3	245.2	Mono. Ten.		143.0	–	–	–
E02				Con. Amp.→Ten.	6.4%(0%)×10→Ten.	126.8	50.5	435.1	402.3
E05				Inr. Amp.→Ten.	6.4%(0%)×5→7.4%(0.5%)×5→8.4%(1%)×5→Ten.	144.9	75.1	801.4	757.7
F01	SS400	4	242.6	Mono. Ten.		183.7	–	–	–
F02				Con. Amp.	4.2%(0%)×180.5	50.4	49.6	5616.1	5615.1
F03				Con. Amp.→Ten.	6.2%(0%)×41→Ten.	128.8	55.5	1865.6	1904.6
F04				Con. Amp.	4.2%(0%)×123.5	51.7	40.0	3875.7	3873.8
FF01				Mono. Ten.		183.7	–	–	–
FF02				Off.	3.9%(9.55%)×141.5	83.1	28.8	4136.0	4095.9
FF03				Off.	5.7%(9.65%)×41→Ten.	92.9	45.5	1861.2	1749.5
S20	SN400	5	276.1	Mono. Ten.		120.1	–	–	–
S21				Con. Amp.	5.6%(0%)×48.5	67.7	63.3	1703.8	1698.7
S23				Con. Amp.	3.6%(0%)×126.5	39.0	43.5	2851.9	2852.9
S24				Con. Amp.	1.6%(0%)×532.5	20.4	19.2	4479.5	4508.1
S25				Con. Amp.	2.6%(0%)×234.5	30.3	30.0	3765.9	3765.9
S26				Off.	1.8%(1.9%)×449.5	23.0	19.0	4603.1	4625.7
S27				Off.	3.8%(1%)×109.5	40.7	39.4	2498.6	2487.2
S28				Off.	3.5%(4.8%)×97.5	47.3	28.2	2225.0	2198.4
S29				Off.	3.6%(-1.1%)×106.5	37.5	39.4	2413.6	2401.3
S30				Off.	3.6%(0%)×10→3.6%(1%)×10→3.6%(2%)×10→3.6%(3%)×10→3.5%(4%)×10→3.5%(5%)×10→3.5%(6%)×10→3.5%(7%)×10→3.5%(8%)×6.5	51.3	40.0	1995.3	1935.5
S31				Off.	3.5%(7.7%)×92.5	67.4	22.9	2071.6	2056.3
S32				Off.	3.7%(0%)×6→3.6%(1%)×4→3.6%(2%)×5→3.6%(3%)×5→3.5%(4%)×4→3.5%(5%)×5→3.5%(6%)×6→3.5%(7%)×4→3.5%(8%)×5→3.4%(9%)×5→3.4%(10%)×6→3.4%(11%)×4→4.1%(11.5%)×5→4.7%(12%)×6→4%(14%)×5→4%(15%)×4→4%(16%)×4.5	58.6	46.7	2056.0	1966.4
S33				Off.	3%(0%)×5→3%(0.3%)×5→3%(0.6%)×5→3%(0.9%)×5→3%(1.2%)×4→3%(1.5%)×5→2.9%(1.8%)×5→2.9%(2.1%)×5→2.9%(2.4%)×5→2.9%(2.7%)×5→2.9%(3%)×6→2.9%(3.3%)×6→2.9%(3.6%)×5→2.9%(3.9%)×5→2.9%(4.2%)×5→2.9%(4.5%)×5→2.9%(4.8%)×5→2.8%(5.1%)×5→2.8%(5.4%)×5→2.8%(5.7%)×5→2.8%(6%)×5→2.8%(6.3%)×5→2.8%(6.6%)×5→2.8%(6.9%)×5→2.8%(7.2%)×5→2.8%(7.5%)×5→2.7%(7.8%)×5→2.7%(8.1%)×5→3%(8.4%)×5→3%(8.6%)×5→3%(8.9%)×5→3%(9.2%)×5→3%(9.5%)×5→2.8%(9.8%)×5→2.7%(10%)×5→2.7%(10.2%)×5→2.7%(10.5%)×5→2.7%(10.8%)×5→2.7%(11.1%)×5→2.7%(11.4%)×5→2.7%(11.7%)×6→2.7%(12%)×5→2.7%(12.3%)×4→2.7%(12.6%)×6→2.7%(12.9%)×5→2.7%(13.2%)×3.5	39.2	29.2	3761.6	3710.8
S34				Off.	3%(0%)×5→3%(0.28%)×5→3%(0.6%)×5→3%(0.9%)×5→3%(1.2%)×5→3%(1.5%)×5→2.9%(1.8%)×5→2.9%(2.1%)×5→2.9%(2.4%)×5→2.9%(2.7%)×5→2.9%(2.9%)×5→2.9%(3.2%)×5→2.9%(3.5%)×5→2.9%(3.8%)×5→2.9%(4.1%)×5→2.9%(4.4%)×5→2.9%(4.7%)×5→2.8%(5.0%)×5→2.8%(5.2%)×5→2.8%(5.5%)×5→2.8%(5.8%)×5→2.8%(6.1%)×5→2.8%(6.4%)×5→2.8%(6.6%)×5→2.8%(6.9%)×5→2.8%(7.2%)×5→2.8%(7.5%)×5→2.8%(7.8%)×5→2.8%(8.0%)×5→2.8%(8.3%)×5→2.7%(8.6%)×5→2.7%(8.9%)×5→2.7%(9.2%)×5→2.7%(9.4%)×5→2.7%(9.7%)×5→2.7%(10.0%)×5→2.7%(10.3%)×5→2.7%(10.5%)×5→2.7%(10.8%)×5→2.7%(11.0%)×5→2.7%(11.3%)×5→2.7%(11.6%)×5→2.7%(11.8%)×5→2.7%(12.1%)×5→2.7%(12.4%)×5→2.6%(12.6%)×5→2.6%(12.9%)×5→2.6%(13.1%)×5→2.6%(13.4%)×5→2.6%(13.7%)×4.5	36.9	27.4	3867.6	3772.6
S35				Off.	2.6%(13.5%)×151.5	104.0	13.7	2191.4	2232.3
S36				Con. Amp.	2.6%(0%)×251.5	32.2	31.8	3998.2	3986.3
S37				Off.	2.3%(15.8%)×143.5	116.6	12.8	1995.0	1993.1
S39				Off.	3.6%(0%)×5→3.6%(0.5%)×5→3.6%(1%)×5→3.6%(1.5%)×5→3.5%(1.9%)×5→3.5%(2.4%)×5→3.6%(2.9%)×5→3.5%(3.4%)×5→3.5%(3.9%)×5→3.5%(4.4%)×5→3.5%(4.8%)×5→3.4%(5.3%)×5→3.4%(5.8%)×5→3.4%(6.3%)×5→3.4%(6.7%)×5→3.4%(7.2%)×5→3.4%(7.7%)×5→3.3%(8.1%)×5→3.3%(8.6%)×5→3.3%(9%)×5→3.3%(9.5%)×5→3.3%(10%)×5→3.3%(10.4%)×3.5	49.3	39.5	2534.1	2483.7

Note: 1) In this table, the loading histories are expressed as
"Full amplitude ε_t (Neutral axis ε_0)"×Number of cycles N

5) Random strain histories followed by tension till fracture (Ran.→Ten.)
6) Monotonic tension loading till fracture (Mono. Ten.)

2.4 Experimental results

The experimental results are shown in Table 1. The engineering stress-strain relations were obtained during testing. This study focuses on the fracture of structural steel, therefore, the true stress-true strain relations (${}_t\sigma_t\varepsilon$) were calculated from the direct engineering stress-strain results (${}_n\sigma_n\varepsilon$). Under the assumption of constant volume of the testing area, the following equations can be used for conversion.

$$ {}_t\sigma = (1+{}_n\varepsilon)\cdot {}_n\sigma \quad (1) $$

$$ {}_t\varepsilon = \ln(1+{}_n\varepsilon) \quad (2) $$

Note that in this study, fracture point is defined as the point when the slope of the true stress-strain turns from positive to negative. It is reasonable to use this definition, in other word, to study the deformation behavior of steel till its uniform elongation, when discussing the relation between components and material from a macro perspective.

Some typical true stress-strain relations of each loading pattern are shown in Figure 5 as examples. The true stress-strain hysteresis loops of this experiment were divided in to 3 parts of the skeleton curve, Bauschinger part as well as the elastic unloading part, as shown in Figure 6. The skeleton curve is obtained by connecting parts of the true stress-strain relation of both tension and compression sides sequentially, when the steel experienced its highest loading for the first time. The cumulative plastic strain of both tension and compression side in the skeleton curve and

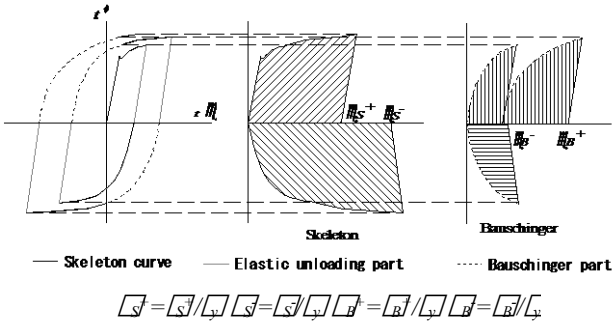


Figure 6 Decomposition of the hysteresis loops

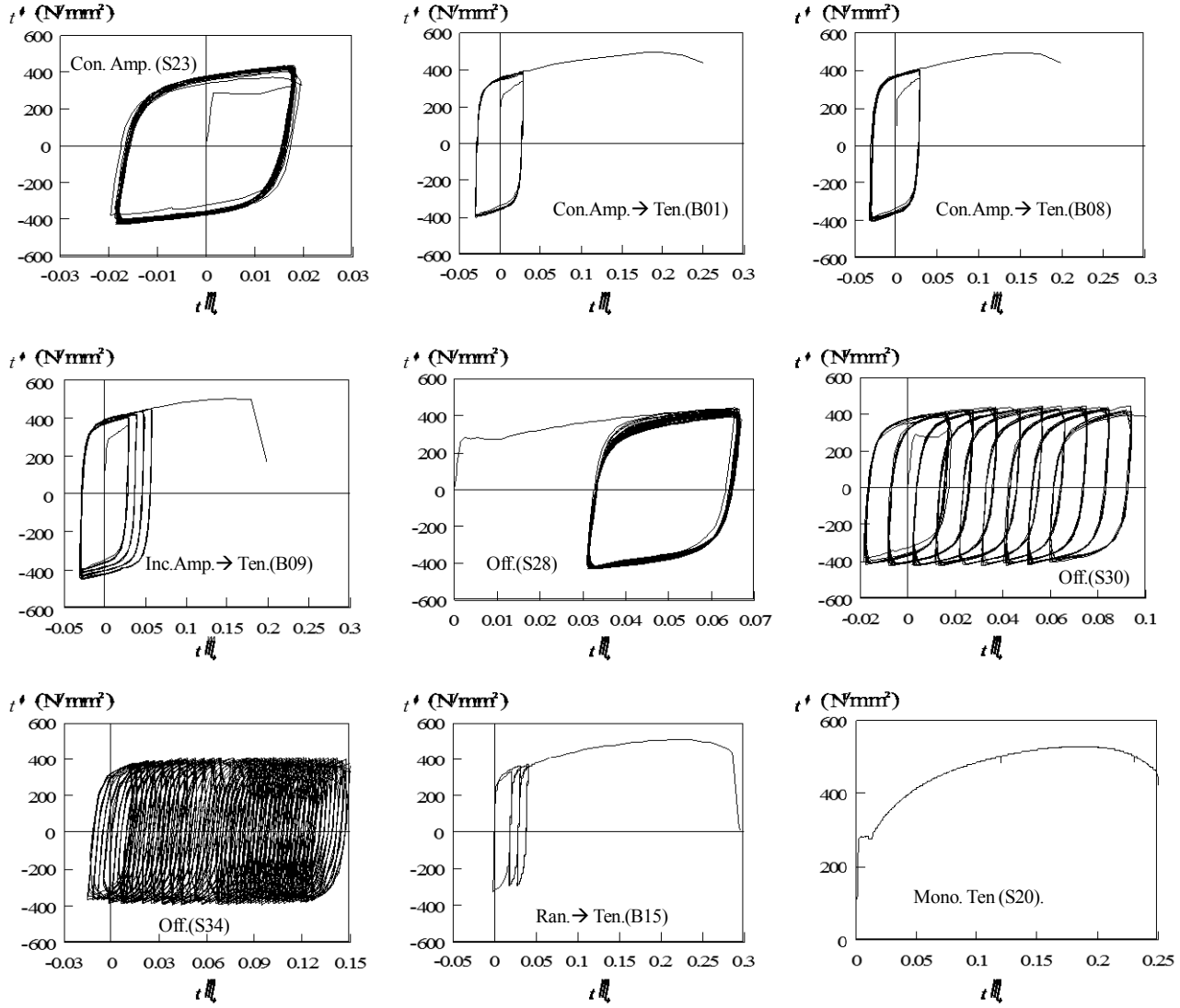


Figure 5 True stress-true strain relation (examples)

Bauschinger part is expressed as ($\varepsilon_S^+, \varepsilon_S^-, \varepsilon_B^+, \varepsilon_B^-$) respectively. The cumulative plastic strain ratio ($\eta_S^+, \eta_S^-, \eta_B^+, \eta_B^-$) is defined as ($\varepsilon_S^+, \varepsilon_S^-, \varepsilon_B^+, \varepsilon_B^-$) divided by yield strain ε_y (refer to the equations in Figure 6). The cumulative plastic strain ratio is the index that evaluates the plastic strain capacity of the steel. The $\eta_S^+, \eta_S^-, \eta_B^+, \eta_B^-$ of all specimens were calculated and shown in Table 1.

3. EVALUATION OF THE PLASTIC DEFORMATION CAPACITY OF STRUCTURAL STEEL THROUGH THE SKELETON METHOD

In this section, the plastic deformation capacity of steel suffering ductile fracture is evaluated by studying the cumulative plastic strain ratio ($\eta_S^+, \eta_S^-, \eta_B^+, \eta_B^-$) of the specimen. This method is called skeleton method in short from now on. The total plastic deformation capacity is the sum of that obtained from each part of the hysteresis loops, which can be written as $\eta_T = \eta_S^+ + \eta_S^- + \eta_B^+ + \eta_B^-$. The relation between η_T and η_S^+ of all specimens are plotted in Figure 7. Here, all the values are normalized by dividing η_0, which is the cumulative plastic strain ratio, in order to eliminate the effect of different material. A linear relation can be seen in Figure 7. Equation 3 can be used to express this linear relationship.

$$\eta_T / \eta_0 = 70 \cdot (1 - \eta_S^+ / \eta_0) + 1 \qquad (3)$$
$$(0.17 \le \eta_T / \eta_0 \le 1.0)$$

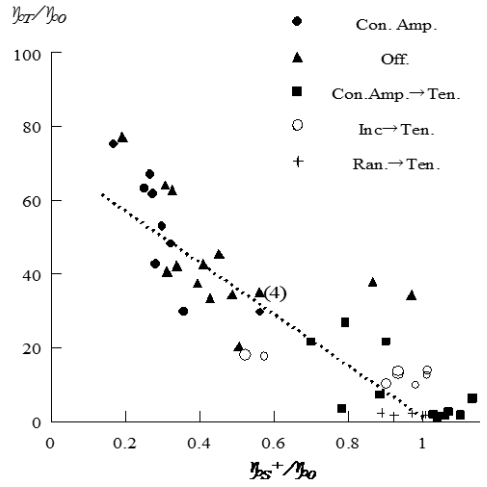


Figure 7 Relation between η_T / η_0 and η_S^+ / η_0

4. EVALUATION OF THE PLASTIC DEFORMATION CAPACITY OF STRUCTURAL STEEL THROUGH THE M-M METHOD

The combination of Manson-Coffin relation and the Miner's rule (M-M method in short) is commonly used to predict the fatigue life of steel. Manson-Coffin relation is the relation between S (amplitude) and N (number of loading cycles till fracture) of steel subjected to constant amplitude cyclic loading history, which is also the foundation of using the Miner's.

The Manson coffin relation of the steel in this research (SS400 and SN400) can be obtained through the experimental results of the specimens subjected to constant amplitude loadings. Equation 4 and Figure 8 show the Manson-Coffin relation of these specimens.

$$\Delta\varepsilon_P = 0.6 \cdot N_f^{-0.57} \qquad (4)$$

The Miner's rule is often used in the evaluation of the accumulated damage of steel under various amplitude cyclic loadings, shown in Equation 5. The material fractures when D equals to 1.

$$D = \sum (n_i / N_i) \qquad (5)$$

where n_i is the number of loading cycles under a certain loading amplitude A, and N_i is the number of loading cycles till fracture if the material is subject to the constant amplitude A cyclic loading.

Using the M-M method, the accumulated damage of all specimens was calculated. The results are shown in Figure 9. Here, the rainflow counting algorithm (Endo et al 1974) was introduced into the study to count the number of loading cycles.

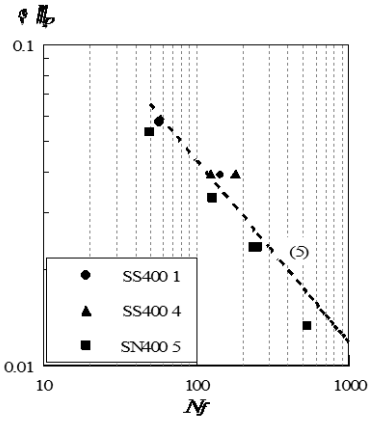


Figure 8 Manson-Coffin relation obtained from the specimens subjected to Con. Amp. loadings

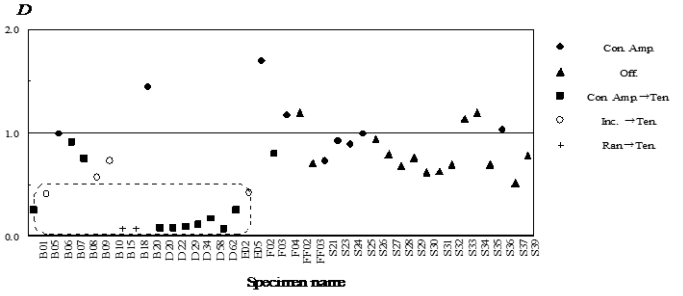


Figure 9 Evaluation of accumulative damage through the Miner's rule

Using the M-M method, the accumulated damage of all specimens was calculated. The results are shown in Figure 9. Here, the rainflow counting algorithm (Endo et al 1974) was introduced into the study to count the number of loading cycles. It is observed that the M-M method tends to give too small evaluation to those specimens that fractured within fewer loading cycles (especially the specimens in the dash square). According to the characteristics of seismic effects and the steel structures, structural steel is very likely to be subjected to the cyclic loadings with relatively large amplitudes, and fractures after several loading cycles.

5. COMPARISON OF THE EVALUATION METHODS

In this section, the evaluation method explained in Section 3 which focuses on the skeleton curve is compared to the evaluation method based on the Manson-Coffin equation and Miner's Rule in Section 4. As the error in the skeleton method is expressed by the accumulated plastic strain, and the error in the method based on the Mason-Coffin relation and Minor's Rule is expressed as the accumulated damage, these two cannot be compared directly. Therefore, in this research, in order to do the comparison, the errors was converted in to a same index—the number of loading cycles under a certain amplitude. The plastic strain amplitude of 2% was chose in this study.

First, in the skeleton evaluation method, the experimental error ${}_{err}\eta_T$ of cumulative plastic strain ratio can be obtained from equation 4. Then ${}_{err}\eta_T \cdot \varepsilon_y$ is the cumulative plastic strain error, where ε_y is the yield strain. Consequently the error in form of the number of loading cycles with plastic amplitude of 2% can be expressed as follow:

$$ {}_{err}N_{skl} = {}_{err}\eta_T \cdot \varepsilon_y / (2 \cdot 0.02) \qquad (6) $$

On the other hand, the error ${}_{err}N_{mcm}$ for the evaluation method based on the Mason-Coffin relation and Miner's Rule was obtained through the following steps: The error of the accumulated damage can be obtained through Equation 5. This value times the number of loading cycles that the specimen would fracture under the constant amplitude loading of 2% is the ${}_{err}N_{mcm}$.

The comparison of these two evaluation methods is illustrated in Figure 10. The errors of the skeleton method are plotted on Y-axis and those of the M-M method are plotted on X-axis. It is obvious that the error level of the skeleton method is smaller than that of the other's. Moreover, the M-M method tends to give smaller evaluation than the real value, while the skeleton method appears to have symmetric errors.

The M-M method is valid from the fatigue region to the low cycle fatigue region, while the skeleton method can only

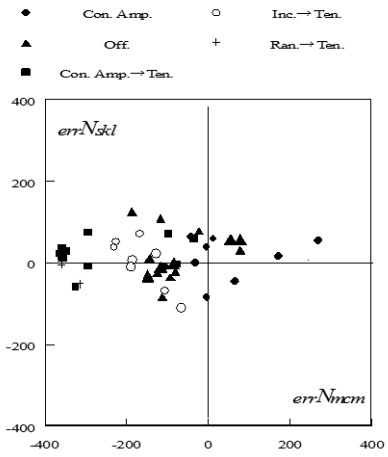


Figure 10 Comparison of two evaluation methods

be used in the low cycle fatigue region since the condition of using this method is the plastification of the material. However, the advantage of the skeleton method is its accuracy when evaluating the plastic deformation capacity of the steel subjected to relatively large amplitude loadings, which is close to the seismic effects.

6. CONCLUSIONS

In order to evaluate the plastic strain capacity of structural steel under various axial strain histories till ductile fracture, a series of element specimens made of SS400 and SN400 steel were tested under diverse cyclic axial strain loadings. The deformation capacity of the structural steel under cyclic axial loading till fracture was evaluated by studying the experimental strain capacity of the skeleton curve and the Bauschinger part. The error range of this method was proved smaller than that of the Miner's rules.

References:

Akiyama H. (1985), Earthquake-resistant limit-state design for buildings, Tokyo: University of Tokyo Press.

Manson S.S.(1954), Behavior of materials under conditions of thermal stress, NASA TND, 2933

Coffin L.F. JR., Schenectady N.Y. (1954), A study of the effect of cyclic thermal stresses on a ductile metal, Transactions of the ASME,pp.931-950

Miner M. A., Monica S. (1945), Cumulative Damage in Fatigue, Journal of Applied Mechanics, pp. A159-A164, 1945.9

Kato B., Aoki H. and Yamanouchi H. (1970). Experimental research of the behavior of steel subjected to cyclic loading. (In Japanese) Summaries of technical papers of annual meeting of AIJ Vol.49: 689-690

Yamada S., Chung K.S., Kishiki S. (2006), Relationships of damage between steel member and material subjected to cyclic loading (In Japanese), Transactions of the AIJ; No 603: pp.139-146

Endo T, Matsuishi M, Mitsunaga K, Kobayashi K, Takahashi K. (1974) Rainflow method, the proposal and the applications (In Japanese). Bulletin of the Kyushu Institute of Technology, Science and Technology; No. 28: pp.33-62.

8CUEE CONFERENCE PROCEEDINGS
8th International Conference on Urban Earthquake Engineering
March 7-8, 2011, Tokyo Institute of Technology, Tokyo, Japan

ELASTO-PLASTIC BEHAVIOR OF RHS COLUMNS UNDER BI-AXIAL BENDING MOMENTS

Yuko Shimada[1] and Satoshi Yamada[2]

1) Assistant Professor, School of Engineering, Chiba University, Japan
2) Associate Professor, Structural Engineering Research Center, Tokyo Institute of Technology, Japan
yshimada@faculty.chiba-u.jp, naniwa@serc.titech.ac.jp

Abstract: This paper describes elasto-plastic behavior of RHS columns under bi-axial bending moments. First, the monotonic loading test of RHS columns by a simple beam-style without an axial force was conducted in order to obtain the strength, stiffness, and deteriorate behaviors. Secondly, shear stress distribution in RHS columns with a bi-axial bending moment was expressed based on the proposed equations from previous studies which have only considered mono-axial bending moments. From these examinations, the fundamental performance in RHS columns affected by both a bi-axial bending moment and the axial force is clarified.

1. INTRODUCTION

RHS columns are usually used in steel buildings in Japan because it has no distinction between its strong axis and its weak axis. Because this feature and its closed section undergo, RHS columns hardly twist. Under earthquake motions, the structures receive three-dimensional forces and the columns experience not only an axial force but also a bi-axial bending moment. A lot of studies of RHS columns under mono-axial bending moments have been conducted, from the elastic region to the elasto-plastic region. Viewing previous studies, it has been pointed out that strength under bi-axial bending moments decreases faster than under mono-axial bending moments. However, there are very few of these studies, and enough researches were not done. Also, very few studies about the deterioration region of RHS columns with local buckling, therefore, how RHS columns under bi-axial bending moment deteriorate, compared to under mono-axial bending moments, is unclear.

In order to clarify the elasto-plastic behavior of RHS columns under bi-axial bending moment, experiment on RHS columns were conducted and evaluations of stress were made. First, the strength, stiffness, and deteriorate behavior under monotonic loading without the axial force were obtained by the simple beam-style test. Secondly, shear stress distribution in RHS columns considering bi-axial bending moment was expressed based on the proposed equations from previous studies. From these examinations, the fundamental performance in RHS columns, affected by both bi-axial bending moments and an axial force is clarified.

2. EXPERIMENT PROCEDURE

2.1 Specimen and Setup

Specimens are four type of simple-beam as shown in Figure 1. All specimen consists of RHS column; □-200×8 (BCR295) and a steel plate; PL28 (SN400). Parameter is angle between loading direction and RHS column surface α; 0[deg], 15[deg], 30[deg], 45[deg]. Each specimen has made with different angle.

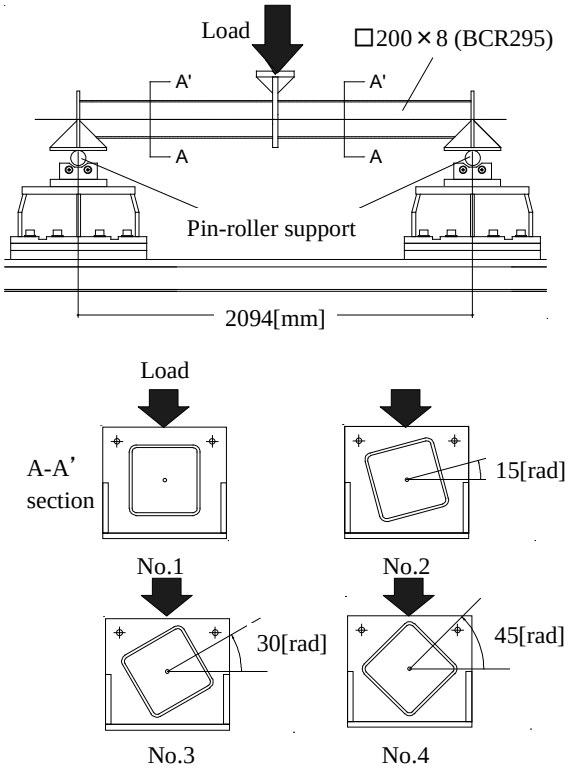


Figure 1 Specimen and Setup

Setup is also shows in Figure 1. Both edges of specimen support by pin-roller systems. Monotonic Load added at the center of specimen by knife-edge which is attached to the testing machine.

Table 1 shows results of coupon test by JIS-1A type test piece.

Table 1 Steel Characteristics

σ_y [N/mm^2]	σ_u [N/mm^2]	yield ratio [%]
374	443	84

2.2 Measurement

Rotation angles and bending moments around the center of each specimen calculated by measured values of displacement transducers as shown in Figure 2. Displacement transducers are settled at both sides above specimen, each measured value is average of displacement at both sides. The equations show below based on displacements as shown in Figure 2 and 3.

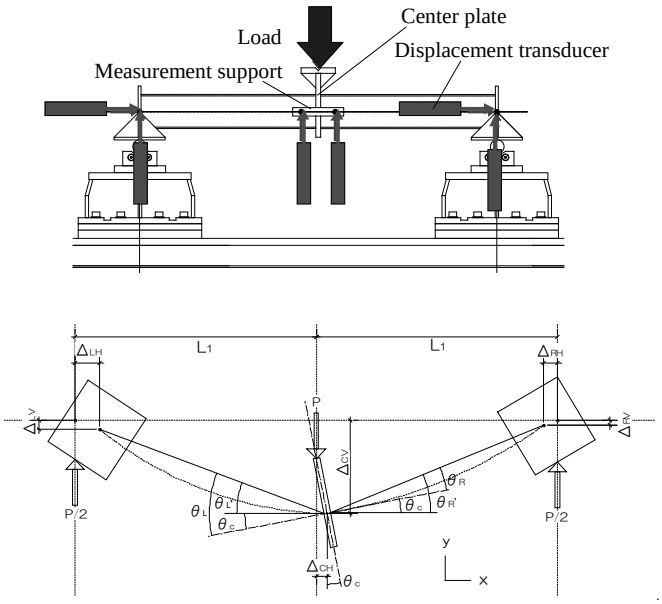


Figure 2 Measurement system

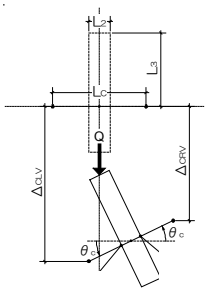


Figure 3 Measurement system (close-up)

$$\theta_C = \tan^{-1}\frac{\Delta_{CLv}-\Delta_{CRv}}{\sqrt{{L_C}^2-\left(\Delta_{CLv}-\Delta_{CRv}\right)^2}}$$

$$\Delta_{Cv}=\frac{\Delta_{CLv}+\Delta_{CRv}}{2} \qquad \Delta_{Ch}=-L_3\cdot\sin\theta_c$$

$$\theta_L{}'=\tan^{-1}\frac{-\Delta_{Cv}+\Delta_{Lv}+\frac{1}{2}L_2\cdot\sin\theta_c}{L_1+\Delta_{Ch}-\Delta_{Lh}-\frac{1}{2}L_2\cdot\cos\theta_c} \qquad \theta_L=\theta_L{}'-\theta_C$$

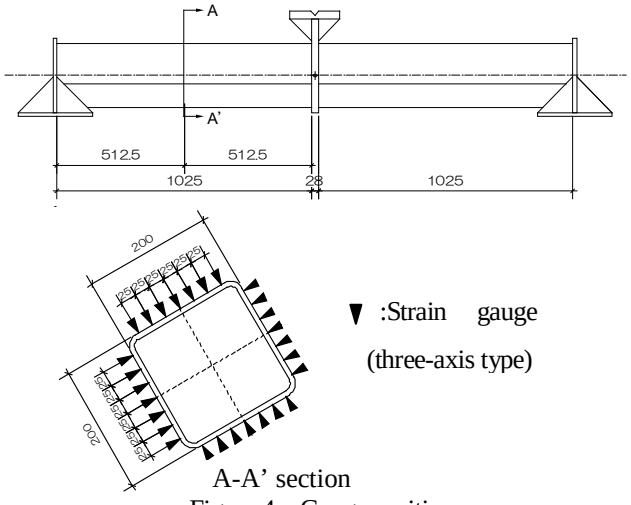
$$\theta_R{}'=\tan^{-1}\frac{\Delta_{Cv}-\Delta_{Rv}-\frac{1}{2}L_2\cdot\sin\theta_c}{L_1-\Delta_{Ch}+\Delta_{Rh}-\frac{1}{2}L_2\cdot\cos\theta_c} \qquad \theta_R=\theta_R{}'-\theta_C$$

$$M_L=\frac{1}{2}P\left(L_1+\Delta_{Ch}-\frac{1}{2}L_2\cdot\cos\theta_c\right)$$

$$M_R=-\frac{1}{2}P\left(L_1-\Delta_{Ch}-\frac{1}{2}L_2\cdot\cos\theta_c\right)$$

Where, θ_C is rotation angle of the center plate, Δ_{Cv} is vertical displacement in the center, Δ_{Ch} is horizontal displacement in the center, Δ_{CLv} is vertical displacement in the center (left side of the center plate), Δ_{CRv} is vertical displacement in the center (right side of the center plate), L_3 is height between the top of the center plate and measurement support, $\theta_L{}'$ is angle between RHS column and measurement support (left side of the center plate), θ_L is rotation angle of RHS column (left side of the center plate), $\theta_R{}'$ is angle between RHS column and measurement support (right side of the center plate), θ_R is rotation angle of RHS column (right side of the center plate), L_2 is thickness of the center plate, L_1 is length of the RHS column.

In order to measure the distinction of shear stress of RHS member, strain gauges (three-axis type) glued at the section shown in Figure 4.



A-A' section

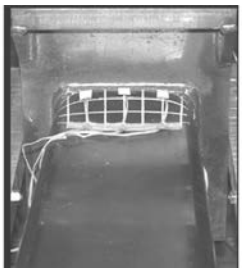
Figure 4 Gauge position

3. EXPRIMENTAL RESULTS

Figure 5 shows the local buckling after the loading ended. Table 2 shows bending moments and rotation angles at the half span which occurred local buckling in each specimen. Figure 6 is bending moment versus rotation angle relationship of each specimen and these four relationships gathered and shows in Figure 7.

The bending moment at the time which local buckling occurred slightly decrease accompanying that the angle between loading direction and RHS surface increased step by step from 0[deg] to 45[deg]. Whereas, the rotation angle at the same time increased. This difference in bending moments and rotation angle is considered as the effect that each specimen has different from bending stress distribution. It is based that elastic buckling of a plate element is affected by stress distribution. The bending stress distribution of each specimen under bi-axial bending moment shows in Figure 8. Therefore, this method is applied to the buckling at elasto-plastic region.

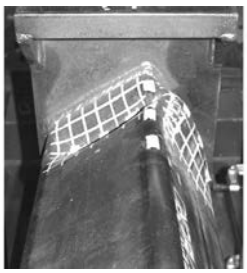
The maximum values of bending moment slightly decrease accompanied byθload increased step by step from 0[deg] to 45[deg]. Whereas, the rotation angle at the time of the maximum values of bending moment occurred is increased. As shown in Figure 7, bending moment versus rotation angle relationship before it reached the maximum values of bending moment in each specimen is observed almost same hysteresis.



(a) No.1 (α =0 [rad])



(b) No.2 (α =15 [rad])



(c) No.3 (α =30 [rad])



(d) No.4 (α =45 [rad])

Figure 5 Local buckling after loading finished

Table 2 List of experimental results

	θ_{lb} [rad]	θ_{lb}/θ_p	M_{lb} [kNm]	M_{lb}/M_p	θ_u [rad]	θ_u/θ_p	M_u [kNm]	M_u/M_p
No.1	0.032	4.03	203.34	1.23	0.035	4.4	204.77	1.24
No.2	0.036	4.53	206.40	1.25	0.044	5.53	208.62	1.26
No.3	0.050	6.29	202.47	1.22	0.049	6.16	203.30	1.23
No.4	0.049	6.16	201.95	1.22	0.052	6.54	202.86	1.23

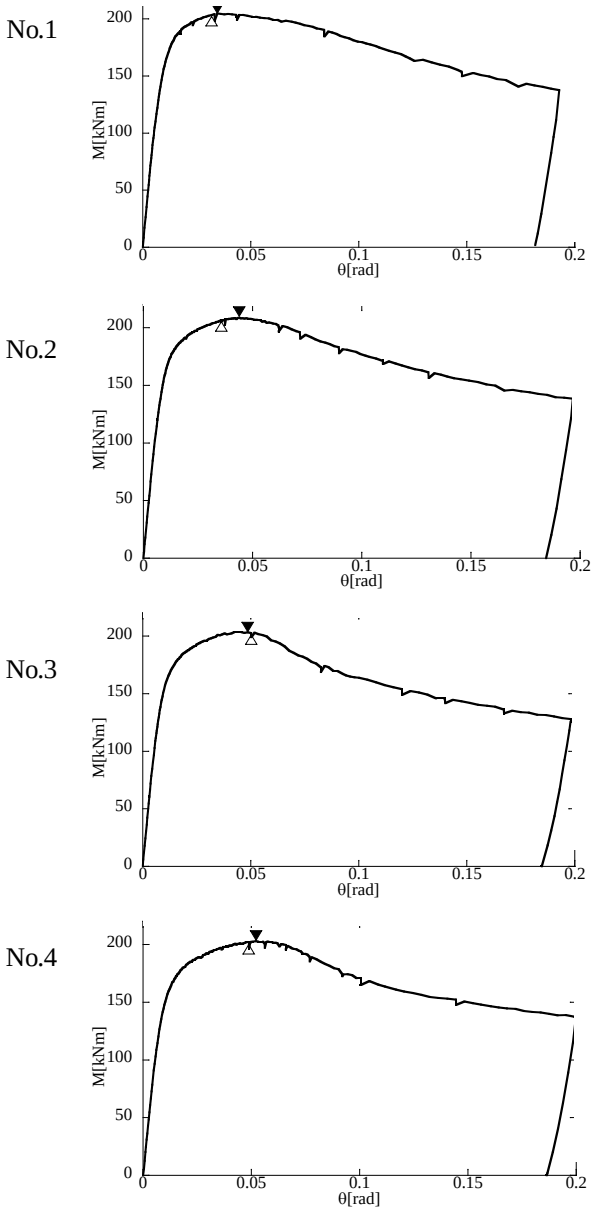


Figure 6 Bending moment - rotation angle relationship

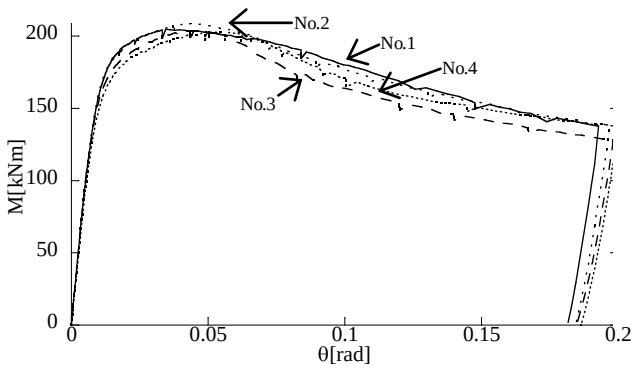
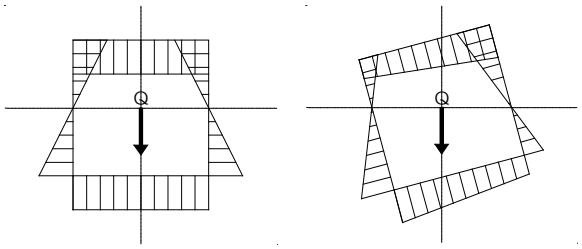
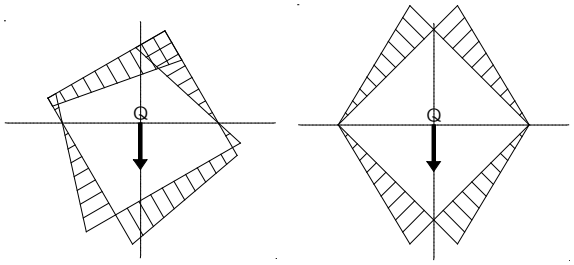


Figure 7 Comparison of Bending moment - rotation angle relationship in all specimen



(a) No.1 (α =0 [rad]) (b) No.2 (α =15 [rad])



(c) No.3 (α =30 [rad]) (d) No.4 (α =45 [rad])

Figure 8 The bending stress distribution in elastic region under bi-axial bending moment

4. SHEAR STRESS DISTRIBUTION

The shear flow theory has proposed as shear stress distribution in the cross section consists of some thin plates. In this theory, shear stress in the direction for thickness of plate is supposed zero, therefore, shear stress can be expressed as shown below;

$$\tau = \frac{Q}{I_x t_1} \cdot \int_0^s ytds$$

For example, shear stress distributions of opened section and closed symmetrical section based on the shear flow theory are shown in Figure 9. Based on the theory, all force in the section balances if shear force loads at the end of the opened section or the center of the closed symmetry section. However, the cross section of RHS member under bi-axial bending is closed nonsymmetrical. In case of closed nonsymmetrical section, all force in the section doesn't balance if shear force loads the center of the section and equations have not proposed.

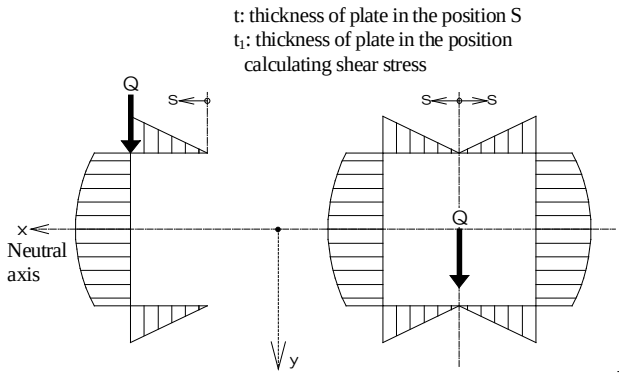


Figure 9 Shear stress distribution of symmetrical section

In this study, the equations which calculate shear stress distribution present based on the shear flow theory to closed nonsymmetrical section as shown below equation (1)~(4). Figure 10 shows the diagram to obtain the shear stress distribution. As shown this figure, cross section is replaced to wires and all corners are neglected roundness.

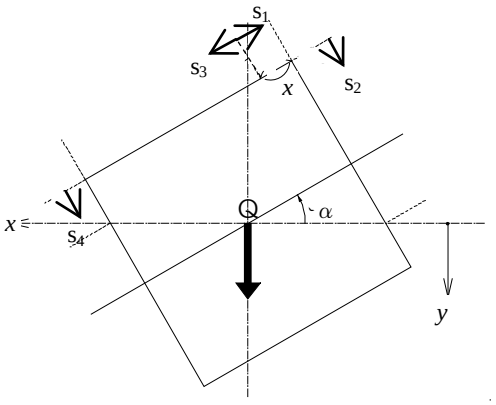


Figure 10 The diagram to obtain shear stress distribution

Where;

$$x = \frac{d(\cos\alpha + \sin\alpha) - d\sqrt{1 + 2\sin^2\alpha}}{2\sin\alpha}$$

In case of $0 \le s_1 \le x$,

$$\tau_1 = \frac{Q}{I_x}\left[\left\{\frac{\sqrt{2}}{2}d\sin(45° + \alpha) - x\sin\alpha\right\}s_1 + \frac{1}{2}s_1^2\sin\alpha\right] \quad (1)$$

In case of $0 \le s_2 \le \left\{\sqrt{2}d\sin(45° + \alpha)\right\}/2\cos\alpha$

$$\tau_2 = \frac{Q}{I_x}\left\{\frac{\sqrt{2}}{2}dx\sin(45° + \alpha) - \frac{1}{2}x^2\sin\alpha + \frac{\sqrt{2}}{2}ds_2\sin(45° + \alpha) - \frac{1}{2}s_2^2\cos\alpha\right\} \quad (2)$$

In case of $0 \le s_3 \le d - x$

$$\tau_3 = \frac{Q}{I_x}\left[\left\{\frac{\sqrt{2}}{2}d\sin(45° + \alpha) - x\sin\alpha\right\}s_3 - \frac{1}{2}s_3^2\sin\alpha\right] \quad (3)$$

In case of $0 \le s_4 \le \left\{\sqrt{2}d\sin(45° - \alpha)\right\}/2\cos\alpha$

$$\tau_4 = \frac{Q}{I_x}\left\{-\frac{1}{2}dx(\sin\alpha + \cos\alpha) + \frac{1}{2}x^2\sin\alpha + \frac{\sqrt{2}}{2}ds_4\sin(45° - \alpha) - \frac{1}{2}s_4^2\cos\alpha\right\} \quad (4)$$

Figure 11 shows the comparisons of the shear stress distributions between obtained by equation (1)~(4) and obtained by experiment results at the time that the maximum values of bending moment occurred. As shown in this figure, equations presented this study and experiment results almost correspond.

5. SUMMARY

In this study, the fundamental consideration is conducted about elasto-plastic behavior of RHS column under bi-axial bending.

The important findings are follows;

1. The strength of the RHS-column under bi-axial bending moment without any axial force slightly decreased than under mono-axial bending moment.

2. M- θ relationships before RHS-column yielded are similar in all specimens.

3. The hysterisys after local buckling occurred changes as the angle α increases.

4. The formulas used to calculate shear stress distribution in a closed nonsymmetrical section, such as the RHS-column under the bi-axial bending moment, were shown to be true.

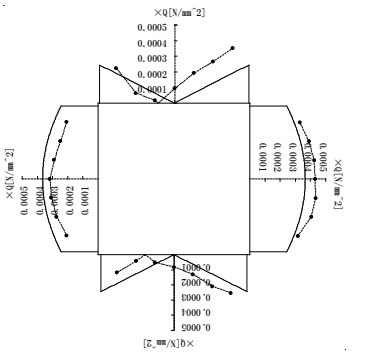
References:

Matsui C., Morino S., Tsuda K., and Ohya K. (1981) Post Local-Buckling Behavior of Box Steel Beam-Columns : Part 3 Behavior under Monotonic Bending and Bi-axial Bending [in Japanese], *Summaries of Technical Papers of Annual Meeting Architectural Institute of Japan* : Structures, pp. 2093-2094.

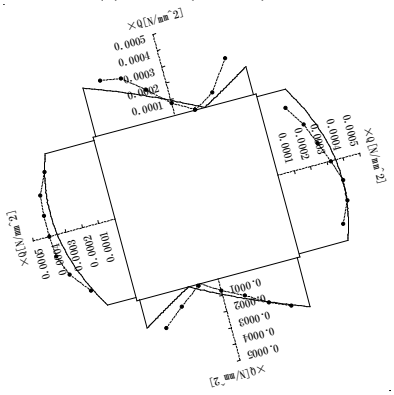
Matsui C., Morino S., Tsuda K., and Ohya K. (1981) Post Local-Buckling Behavior of Box Steel Beam-Columns : Part 4 Consideration of structural design equation [in Japanese], *Summaries of Technical Papers of Annual Meeting Architectural Institute of Japan* : Structures, pp. 2095-2096.

Timoshenko S.P. (1964) Theory of Elastic Stability, McGraw-Hill College

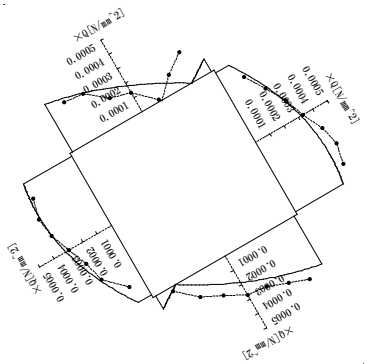
Kuwamura H. (2001), Dynamics of architecture – Plastic Theory and the application [in Japanese], Inouesyoin Corp.



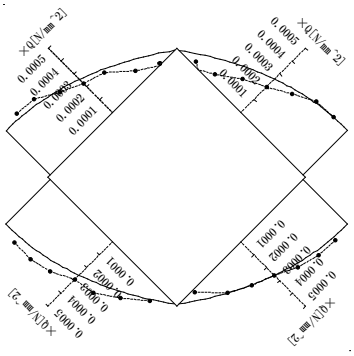
(a) No.1 (0 [rad])



(b) No.2 (15 [rad])



(c) No.3 (30 [rad])



(d) No.4 (45 [rad])

Figure 11 Comparison of shear stress distribution (Loading test versus shear flow theory)

8CUEE CONFERENCE PROCEEDINGS
8th International Conference on Urban Earthquake Engineering
March 7-8, 2011, Tokyo Institute of Technology, Tokyo, Japan

INVESTIGATION OF CYCLIC DETERIORATION BEHAVIOR OF RHS-COLUMNS

Takanori Ishida[1], Yuko Shimada[2], and Satoshi Yamada[3]

1) Graduate Student, Tokyo Institute of Technology, Japan
2) Assistant Professor, School of Engineering, Chiba University, Japan
3) Associate Professor, Structural Engineering Research Center, Tokyo Institute of Technology, Japan
ishida.t.ae@m.titech.ac.jp, yshimada@faculty.chiba-u.jp, naniwa@serc.titech.ac.jp

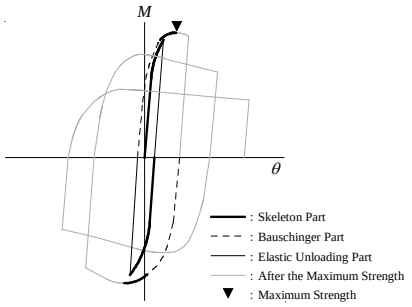
Abstract: In Japan, RHS (Rectangular Hollow Section)-columns are generally used in steel building structures. In the evaluation of earthquake-resistant limit-state capacity of building structures, it is important to clarify the ultimate behavior of columns. In this paper, the post-buckling and deterioration behavior of RHS-columns under cyclic loadings are investigated based on the database built from previous cyclic loading test results.

1. INTRODUCTION

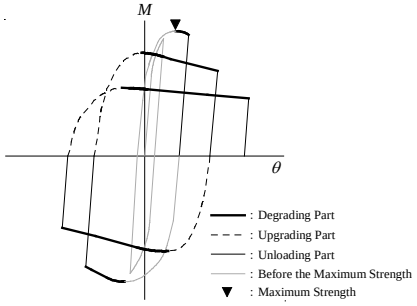
In Japan, RHS-columns are generally used in steel building structures. In the evaluation of earthquake-resistant limit-state capacity of building structures, it is important to clarify the ultimate behavior of columns. According to the previous studies, under cyclic loading, before the steel member reaches its maximum strength, the hysteresis loop can be decomposed into the skeleton part, Bauschinger part and the elastic unloading part. Moreover, it is also known that the skeleton part corresponds to the load-deformation relation of steel member under monotonic loading and the Bauschinger part can be modeled through the bilinear model [1]. On the other hand, the post-buckling and deterioration behavior of RHS-columns were studied analytically under monotonic loading [2]. Nevertheless, although many experiments focusing on the deterioration behavior of RHS-columns under cyclic loadings have been carried out, the general restoring force characteristics including the deterioration behavior of RHS-columns have not been modelled yet. In this paper, the post-buckling and deterioration behavior of RHS-columns under cyclic loadings are investigated based on the database built from previous cyclic loading test results.

2. DECOMPOSITION OF HYSTERESIS LOOP

Before the steel member reaches its maximum strength, the load-deformation relation under cyclic loading (hysteresis loop) can be decomposed into three parts: skeleton curve, Bauschinger part and the elastic unloading part (Figure 1(a)). The load-deformation relation of both positive and negative loading directions in the post-buckling and deterioration range can also be divided into three parts, which are defined as degrading part, upgrading part and



(a) Until the Maximum Strength



(b) After the Maximum Strength

Figure 1 Restoring Force Characteristics of Steel Columns under Cyclic Loading

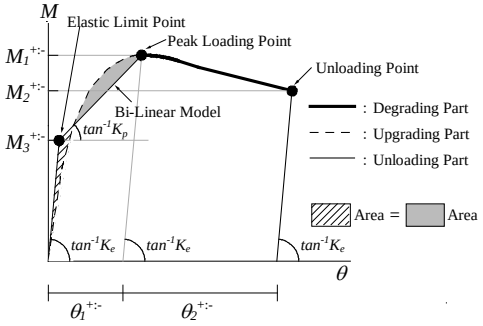


Figure 2 Load-Deformation Relations of Half Cycles

unloading part (Figure 1(b)). The degrading part can be assumed as skeleton part, and the upgrading part as Bauschinger part. A half cycle of the hysteresis loop in the deterioration range is shown in Figure 2. The degrading part is from the peak loading point to the unloading point, while the unloading part is from the unloading point to the point that the load reaches 0. The segment left is the upgrading part. Furthermore, the upgrading part is simplified to a bilinear model which dissipates equivalent amount of plastic energy as the original one does. Here, $M_1^{+,-}$ is the moment of peak loading point, $M_2^{+,-}$ and $M_3^{+,-}$ are the moment of unloading point and the elastic limit point respectively. $\theta_1^{+,-}$ is the maximum deformation of upgrading part, and $\theta_2^{+,-}$ is the deformation of degrading part. K_e and K_p are the elastic and inelastic stiffness. Superscript + and – denote the positive and negative loading domains.

3. INVESTIGATION OF CYCLIC DETERIORATION BEHAVIOR BASED ON THE DATABASE

3.1 Extraction of the Parameters

In order to clarify the post-bucking and deterioration behavior of RHS-columns under cyclic loadings, the database is built based on previous cyclic loading test results.

The load-deformation relations of previous test results are normalized to the dimensionless moment-rotation relations (M/M_p-θ/θ_p relations) so that $M_1^{+,-}$, $\theta_1^{+,-}$, $M_2^{+,-}$, $\theta_2^{+,-}$, and $M_3^{+,-}$ can be obtained. These parameters ($M_1^{+,-}$, $\theta_1^{+,-}$, $M_2^{+,-}$, $\theta_2^{+,-}$, and $M_3^{+,-}$) are the characteristics of the hysteresis loops in the deterioration range, as shown in Figure 1, where M_p is the full-plastic moment of each specimen, and θ_p is the elastic rotation corresponding to M_p. However, in case of the half cycles where the specimens were unloaded within the upgrading part, the data of these half cycles are eliminated from the database. As for the elastic stiffness K_e, the calculated value is used ($K_e = M_p/\theta_p$). If the experimental elastic stiffness of the specimen shows bad correspondence to the calculated value, the unloading stiffness of the first cycle is used as elastic stiffness.

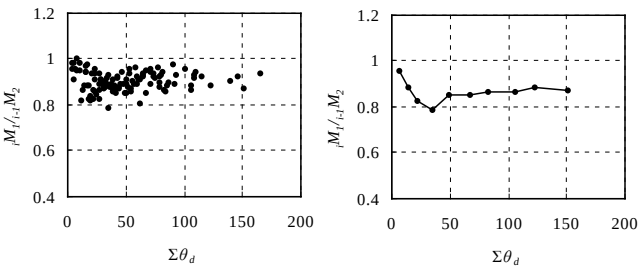
3.2 Strength Restoration Ratio

In both positive and negative loading directions, it is possible to obtain the ratio of the peak load of arbitrary cycle ($_iM_1^+$, $_iM_1^-$) to the load of unloading point in the previous cycle ($_{i-1}M_2^+$, $_{i-1}M_2^-$) $_iM_1^+/_{i-1}M_2^+$ and $_iM_1^-/_{i-1}M_2^-$, which are defined as the strength restoration ratio $_iM_1/_{i-1}M_2$, where the subscript i is the number of cycles. Furthermore, the cumulative plastic deformation $\Sigma\theta_d$ ($\Sigma\theta_d = \Sigma\theta_d^+ + \Sigma|\theta_d^-|$) is obtained by eliminating the elastic deformation from the cumulative deformation after reaching the maximum strength. The relations between the strength restoration ratios $_iM_1/_{i-1}M_2$ and the cumulative plastic deformation $\Sigma\theta_d$ from every half cycle of each specimen are shown in Figure 3. The results of one specimen of each axial force ratio are also exemplified in Figure 3. The strength restoration ratio is almost a constant despite the increase of cumulative plastic deformation after the maximum strength. This trend has been seen in all specimens. Consequently, it is reasonable to study the relation between the average values of strength restoration ratio and the multiplicative inverse of normalized equivalent width to thickness ratio $1/\alpha_e$, which is shown in Figure 4. Here, the normalized equivalent width to thickness ratio α_e, which governs the post-buckling and deterioration behavior of RHS members, is obtained by equation (1) [2]. The strength restoration ratio is almost a constant 0.9.

$$\alpha_e = \frac{(1+k^2)}{2}\frac{\sigma_y}{E}(B/t)^2 \qquad (1)$$

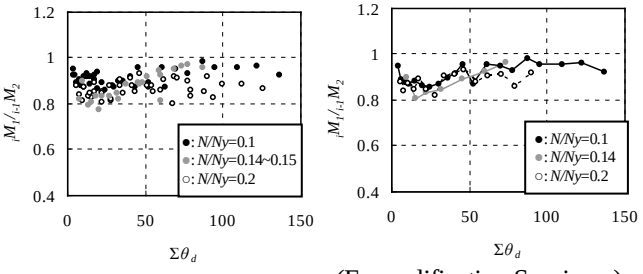
Where

E: Young's modulus, σ_y: Yield stress, B: Width, t: Thickness, k: The area ratio of the web subjected to compression force at the full-plastic state



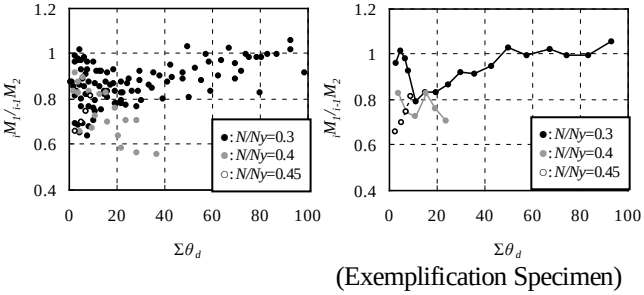
(Exemplification Specimen)

(a) N/N_y=0



(Exemplification Specimen)

(b) N/N_y=0.1~0.2



(Exemplification Specimen)

(c) N/N_y=0.3~0.45

Figure 3 $_iM_1/_{i-1}M_2$ vs. $\Sigma\theta_d$

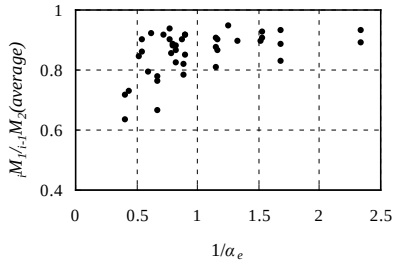
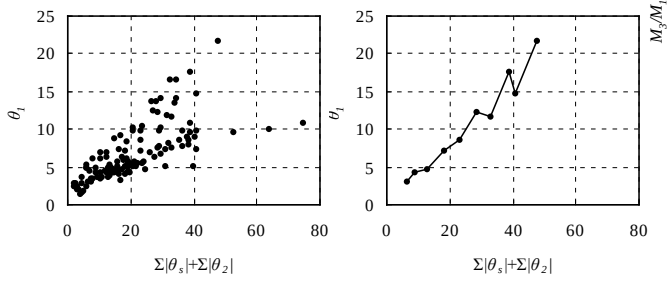


Figure 4 $_iM_1/_{i-1}M_2$(average) vs. $1/\alpha_e$

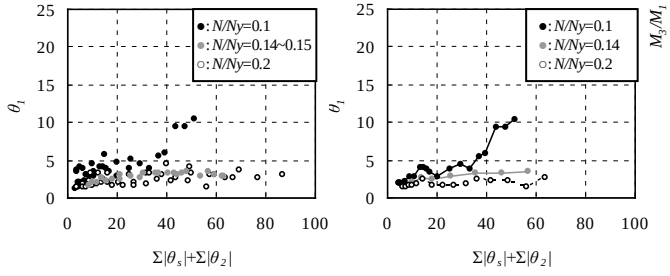
3.3 Maximum Deformation of Upgrading Part

The maximum deformations of the upgrading parts that correspond to Bauschinger parts, $\theta_1^+$and $|\theta_1^-|$, are expressed by θ_1. The cumulative plastic deformation of skeleton part is denoted by $\Sigma|\theta_s|$. The cumulative plastic deformation of the degrading part that corresponds to the skeleton part is denoted by $\Sigma|\theta_2|$. The relation between θ_1 and $\Sigma|\theta_s|+\Sigma|\theta_2|$ of each specimen is shown in Figure 5. The results of one specimen of each axial force ratio are also exemplified in Figure 5. The maximum deformation of upgrading part becomes smaller as axial force ratio increase.



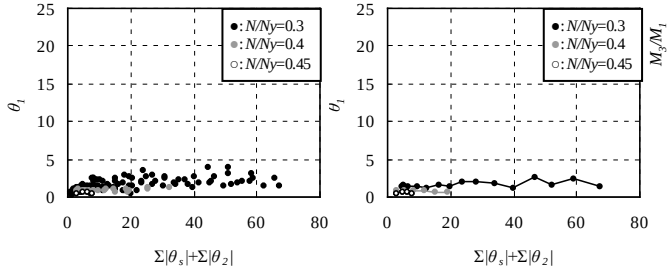
(Exemplification Specimen)

(a) N/N_y=0



(Exemplification Specimen)

(b) N/N_y=0.1~0.2



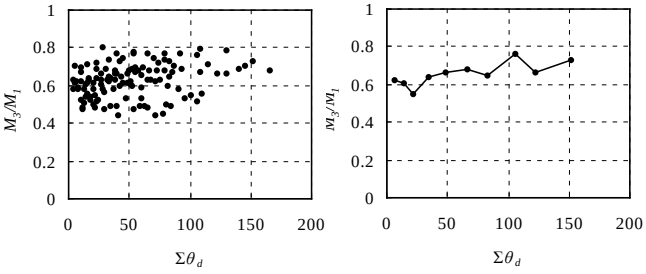
(Exemplification Specimen)

(c) N/N_y=0.3~0.45

Figure 5 θ_1 vs. $\Sigma|\theta_s|+\Sigma|\theta_2|$

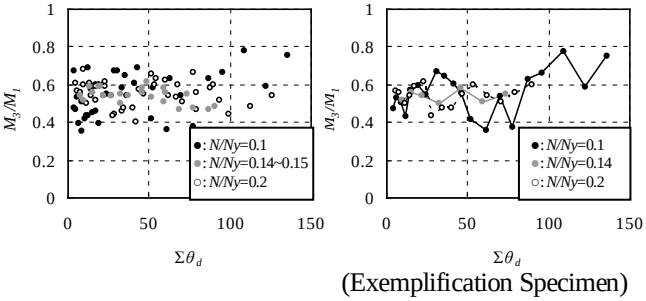
3.4 Elastic Limit Point of Upgrading Part

The ratio of the load of elastic limit point M_3^+, M_3^- and the load of peak loading point M_1^+, M_1^- in each half cycle, M_3^+/M_1^+ and M_3^-/M_1^- are denoted by M_3/M_1. The relations between the ratio M_3/M_1 of each specimen from each half cycle and the cumulative plastic deformation $\Sigma\theta_d$ after reaching the maximum strength are shown in Figure 6. The results of one specimen of each axial force ratio are also exemplified in Figure 6. The ratio M_3/M_1 is approximately constant in spite of the increase of the cumulative plastic deformation after the peak loading point. This trend has been seen in all specimens. Therefore, the average M_3/M_1 of each specimen is calculated. The relation between average M_3/M_1 of each specimen and $1/\alpha_e$ is shown in Figure 7. M_3/M_1 and $1/\alpha_e$ has an approximately linear relation.



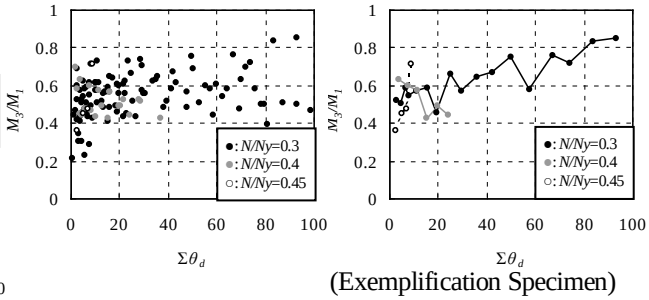
(Exemplification Specimen)

(a) N/N_y=0



(Exemplification Specimen)

(b) N/N_y=0.1~0.2



(Exemplification Specimen)

(c) N/N_y=0.3~0.45

Figure 6 M_3/M_1 vs. $\Sigma\theta_d$

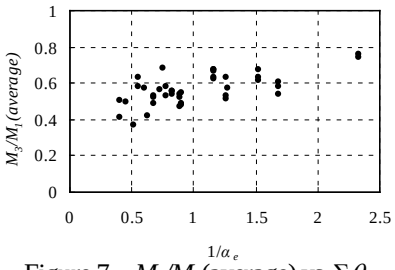


Figure 7 M_3/M_1(average) vs. $\Sigma\theta_d$

3.5 Envelope Curve of Deterioration Range

Based on the observation from section 3.2-3.4, the bilinear model of the upgrading part can be modeled by formulating the strength restoration ratio, the maximum deformation of upgrading part, and elastic limit point. Therefore, the restoring force characteristics in the deterioration range under cyclic loading can be modeled by clarifying the slope of load degrading part. The envelope curve of the steel member in the deterioration range is obtained by connecting hysteresis loops in each cycle of positive or negative loading direction sequentially. Empirical rule shows that the envelope curve corresponds to the load-deformation relation under monotonic loading [14]. The slope of the degrading part is denoted by K_d, and the slope of the segment between the peak loading point of a certain cycle and the unloading point of the previous cycle is denoted by K_d', as shown in Figure 8. The relation of K_d-$\Sigma\theta_d$ is shown in Figure 9, the relation of K_d'-$\Sigma\theta_d$ is also shown in Figure 9. Notice here, the specimens with their calculated elastic stiffness different from the experimental results were eliminated from the database. It is noted that K_d almost corresponds to K_d'. Therefore, the envelope curve is approximately continuous.

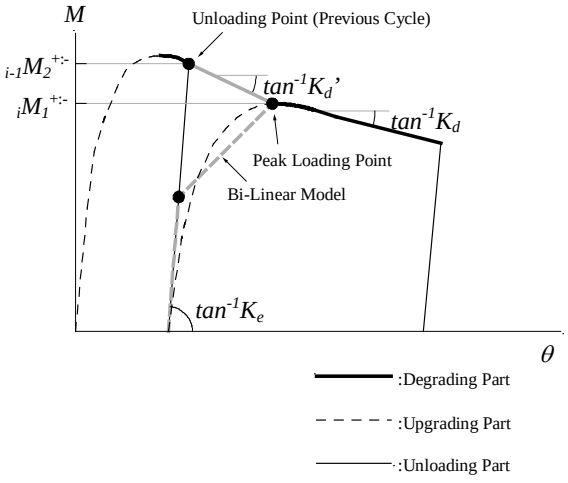
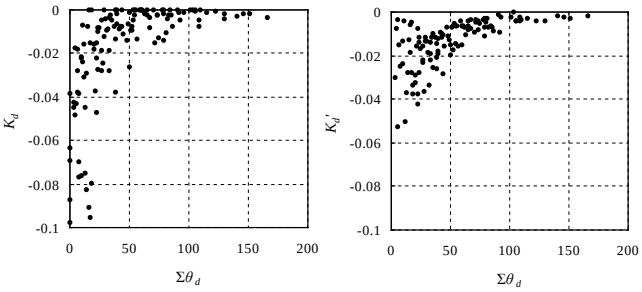
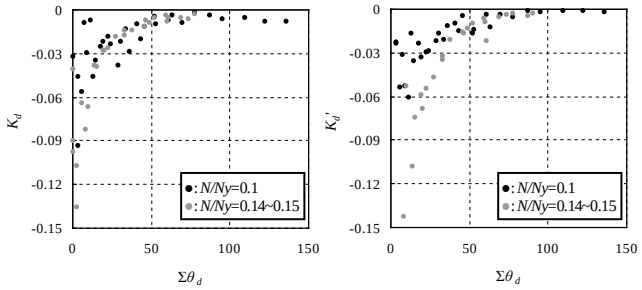


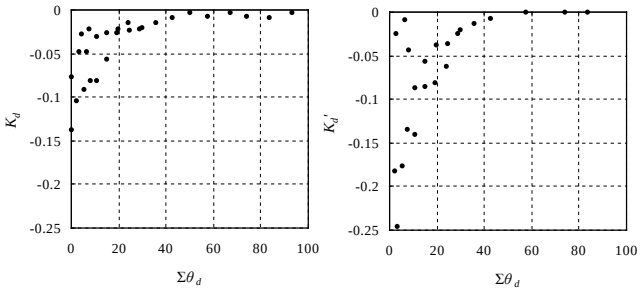
Figure 8 Envelope Curve of Deterioration Range



(a) N/N_y=0



(b) N/N_y=0.1~0.15



(c) N/N_y=0.3

Figure 9 K_d vs. $\Sigma\theta_d$, K_d' vs. $\Sigma\theta_d$

4. CONCLUSIONS

Post-buckling and deterioration behavior of the RHS-columns under cyclic loading was investigated based on the database built based on previous cyclic loading test results. In this paper, the hysteresis loop of deterioration range is decomposed into three parts: the degrading part that corresponds to skeleton part, the upgrading part that corresponds to Bauschinger part and the elastic unloading part. Main conclusions can be drawn as follows:

1) The strength restoration ratio is almost constant despite the increase of the cumulative plastic deformation after reaching the maximum strength. Moreover, the relation between the average strength restoration ratio of each specimen and the multiplicative inverse of normalized equivalent width to thickness ratio shows that the average of strength restoration ratio of each specimen is approximate 0.9.

2) Although within the axial force ratio range of 0~0.1, the maximum deformation of upgrading part increases linearly

with the increase of $\Sigma|\theta_s| + \Sigma|\theta_2|$. In case of axial force ratio more than 0.14, the maximum deformation of upgrading part is almost constant. In summary, the maximum deformation of upgrading part becomes smaller as axial force ratio increase.

3) The ratio M_3/M_1 is approximately constant in spite of the changing cumulative plastic deformation after reaching the maximum strength. The relation between the average M_3/M_1 in each specimen and $1/\alpha_e$ shows an approximately liner relation.

4) It is noted that K_d almost corresponds to K_d'. Therefore, the envelope curve is approximately continuous.

References:

[1] AKIYAMA H., and TAKAHASHI M., "*Influence of Bauschinger Effect on Seismic Resistance of Steel Structures*", Trans. of AIJ, No. 418, 1990, p. 49-57. (in Japanese)

[2] YAMADA S., AKIYAMA H., and KUWAMURA H., "*Post-buckling and Deteriorating Behavior of Box-section Steel Members*", Trans. of AIJ, No. 444, 1993, p. 135-143. (in Japanese)

[3] ISHIDA T., JIAO Y., SHIMADA Y., and YAMADA S., "*Post-buckling and Deteriorating Behavior of RHS-columns under Cyclic Loading (Part. 1)*", Proceedings of Architectural Research Meetings, AIJ Kanto Branch, 2010, p. 457-460. (in Japanese)

[4] AKAZAWA M., ITO Y., SHIMADA Y., MATSUOKA Y., YAMADA S., and SUITA K., "*Dynamic Collapse Test of Full-scale 4-story Steel Building (Part. 3)*", Proceedings of the 5th Annual Meeting of Japan Association for Earthquake Engineering, JAEE, 2007, p. 220-221. (in Japanese)

[5] YAMADA S., and SHIMADA Y., "*Cyclic Loading Test of RHS-columns under Bi-axial Bending*", Proceedings of The 13th Japan earthquake Engineering Symposium, 2010 (in Japanese)

[6] KITA Y., and TSUJI B., "*Elastic Plastic Behavior of Beam-columns with Square Hollow Section*", Summaries of Technical Papers of Annual Meeting, AIJ, 1991, p. 1305-1306. (in Japanese)

[7] IGARASHI S., TSUJIOKA S., YAJIMA S., and SUGIYAMA S., "*Experimental Investigation of Bending Behavior of Cold-formed Rectangular Hollow Structural Sections (Part. 2)*", Summaries of Technical Papers of Annual Meeting, AIJ, 1984, p. 1351-1352. (in Japanese)

[8] SHIMADA Y., AKAZAWA M., ITO Y., MATSUOKA Y., YAMADA S., and SUITA K., "*Shaking Table Test on Collapse Behavior of Small-scale Steel Frame Structure*", Trans. of AIJ, No. 620, 2007, p. 125-132. (in Japanese)

[9] KURATA M., NAKASHIMA M., and SUITA K., "*Test on Large Cyclic Deformation of Steel Tube Columns Having Fixed Column Bases*", Trans. of AIJ, No. 598, 2005, p. 149-154. (in Japanese)

[10] ZHU D., IYAMA J., TAKADA K., and KUWAMURA H., "*鋼部材の繰返し履歴曲線と単調載荷曲線の関係 その 2 座屈する場合*", Proceedings of Architectural Research Meetings, AIJ Kanto Branch, 1997, p. 89-92. (in Japanese)

[11] TSUDA K., and MATSUI C., "*Strength of Square Steel Tubular Beam-columns under Constant Vertical and Horizontal Loads*", Trans. of AIJ, No. 512, 1998, p. 149-156. (in Japanese)

[12] YAMADA M., KAWAMURA H., TANI A., and YAMANAKA K., "*Elasto-plastic Deformation and Fracture Behavior of Steel Box Columns Subjected to Double Curvature Cyclic Bending under Constant Axial Load (Part. 2)*", Summaries of Technical Papers of Annual Meeting, AIJ, 1984, p. 1347-1348. (in Japanese)/ (Part. 4), Summaries of Technical Papers of Annual Meeting, AIJ, 1985, p. 679-680. (in Japanese)/ (Part. 5), Proceedings of Architectural Research Meetings, AIJ Kinki Branch, 1986, p. 409-412. (in Japanese)

[13] ISHIDA T., SHIMADA Y., and YAMADA S., "*Post-buckling and Deteriorating Behavior of RHS-columns under Cyclic Loading*" Proceedings of The 13th Japan earthquake Engineering Symposium, 2010 (in Japanese)

[14] KATO B., AKIYAMA H., and OBI Y., "*Deformation Characteristics of H-shaped Steel Members Influenced by Local Buckling*", Trans. of AIJ, No. 257, 1977, p. 49-58. (in Japanese)

8CUEE CONFERENCE PROCEEDINGS
8th International Conference on Urban Earthquake Engineering
March 7-8, 2011, Tokyo Institute of Technology, Tokyo, Japan

Proposal of an Elastic Buckling Strength Formula for Columns in Steel Moment Frames Considering Anti-Symmetric Axial Forces Generated by Horizontal Loads

Akinobu Takada[1], Motohide Tada[2], Seiji Mukaide[3], Yoshikazu Araki[4]

1)Graduate Student, Graduate School of Engineering, Osaka University, Japan
2)Professor, Graduate School of Engineering, Osaka University, Japan
3)Assistant Professor, Graduate School of Engineering, Osaka University, Japan
4)Associate Professor, Graduate School of Engineering, Kyoto University, Japan
takada_akinobu@arch.eng.osaka-u.ac.jp, tada@arch.eng.osaka-u.ac.jp
mukaide@arch.eng.osaka-u.ac.jp, araki@archi.kyoto-u.ac.jp

Abstract: The elastic buckling strength of columns in steel moment resisting frames had been investigated extensively for regular vertical loads. However, in Japan, where seismic loads are significant, the axial forces corresponding to the overturning moment due to seismic loads should be considered in design. Under such load conditions, a column that is subjected to a larger compressive force can be supported laterally by other columns, which sustain moderate or tensile axial forces. This present paper proposes a method by which to estimate the elastic buckling strength of columns in moment resisting frames under anti-symmetric vertical loads on beam-to-column nodes. The accuracy of estimation is confirmed through comparison to the results of obtained by geometrical non-linear analyses or eigenvalue analyses for portal frames.

1. INTRODUCTION

In the design of a steel structural building, it is necessary to consider the flexural buckling of the column. The calculation method used to determine the buckling length of the column in a regular moment frame in which the lateral displacement is not restrained is given in, for example, the "Design Standard for Steel Structures" (AIJ, 2002) etc. Moreover, Mitani et al. (2002) and Morino et al. (1993) reported the accuracy of applying the calculation method to irregular frames. In addition, an improved method was proposed by Tsuda (2001, 2003) and Shibata (2003). The above studies investigated vertical loads. However, in Japan, where seismic loads are predominant, it is also necessary to consider the column-buckling by the compressive force generated by the overturning moment due to the horizontal load (Figure 1). In this case, the column that receives a larger compressive force is laterally restrained by other columns which receive smaller compressive or tensile forces. Therefore, the buckling length is thought to be shorter than the case in which vertical loads act on the column.

The present paper proposes formulas by which to estimate the elastic buckling strength of columns under arbitrary boundary conditions. The proposed formulas are explicit expressions in which numerical analyses are not necessary. The calculation results confirm the results of the eigenvalue analysis and the increment analysis of the equilibrium path for the entire frame, and the error margins are small. The proposed formulas assume anti-symmetry vertical loads on the beam-to-column nodes (Figure 2). This load assumes an axial force distribution in the column due to the horizontal loads.

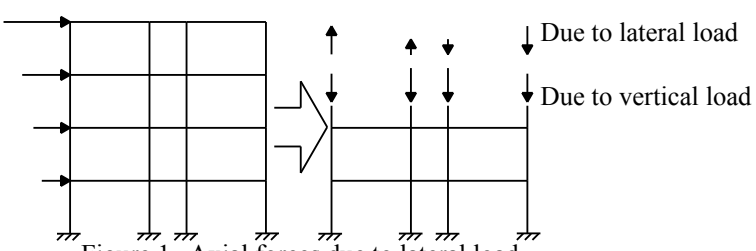
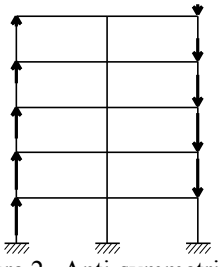


Figure 1. Axial forces due to lateral load


Figure 2. Anti-symmetric load

2. PROPOSED FORMULA

2.1 Previous Study

Inoue and Tada (2007) proposed simple formulas of elastic buckling strength of columns in a moment frame by considering the lateral restraint of adjacent columns. They first modeled the column as shown in Figure 3 and then divided the model into two models according to the buckling mode, as shown in Figures 4(a) and 4(b). Each model was applied according to the magnitude of rigidity of the horizontal spring, K_H. The respective buckling strengths were formulated as follows:

Mode 1 : $$ {}_1P_{cr} = \frac{\pi^2 EI_c}{h^2} \quad (1) $$

Mode 2 : $$ {}_2P_{cr} = K_H h \quad (2) $$

In the present study, two buckling modes are assumed also as shown by Inoue and Tada (2007). The mode in which the capital does not sway, as shown in Figure 5(a), is referred to as the *member-buckling* mode, and the mode in which the capital sways laterally, as shown in Figure 5(b), is referred to as the *sway buckling* mode. In the following sections, the mechanical model shown in Figure 3 will be used.

2.2 Member-buckling mode

The formula for elastic buckling strength for an arbitrary supported column corresponding to the *member-buckling* mode will be derived in this section. As shown in Figure 5(a), the horizontal spring at the capital elongates only slightly in this mode. The postulated conditions are illustrated in Figure 6(a), and they are as follows. The lateral displacement of the capital is ignored. The deflection of the column is approximated by two cubic functions for the upper part u_2 and the lower part u_1, respectively. The boundary conditions are expressed by the following nine equations:

$$ u_1(0) = 0, \quad \left.\frac{du_1}{dz}\right|_{z=0} = \theta_B, \quad u_1\left(\frac{h}{2}\right) = u_2\left(\frac{h}{2}\right) $$

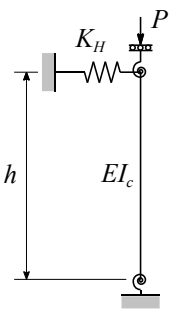
$$ u_2(h) = 0, \quad \left.\frac{du_2}{dz}\right|_{z=h} = -\theta_T, \quad \left.\frac{du_1}{dz}\right|_{z=\frac{h}{2}} = \left.\frac{du_2}{dz}\right|_{z=\frac{h}{2}} $$

$$ \left.\frac{d^2u_1}{dz^2}\right|_{z=0} = \frac{K_{rB}\theta_B}{EI_c} = k_{rB}\theta_B\frac{1}{h} $$

$$ \left.\frac{d^2u_2}{dz^2}\right|_{z=h} = \frac{K_{rT}\theta_T}{EI_c} = k_{rT}\theta_T\frac{1}{h} $$

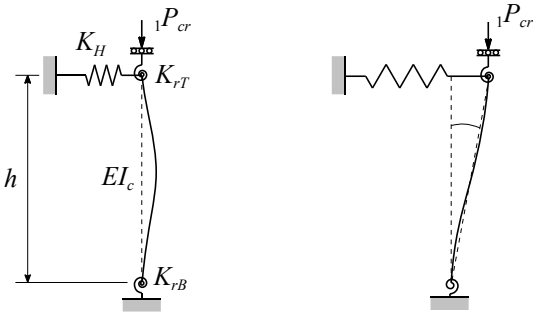
$$ -EI_c\left.\frac{d^3u_1}{dz^3}\right|_{z=0} = -EI_c\left.\frac{d^3u_2}{dz^3}\right|_{z=h} \quad (3a \sim i) $$

Based on these boundary conditions, deflections u_1 and u_2 are derived as follows:



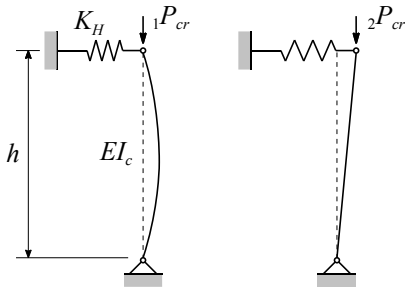
E	: Young's Modulus
I_c	: Geometric moment of inertia
K_H	: Horizontal spring stiffness
h	: Length of column
K_{rT}, K_{rB}	: Rotational spring stiffness
${}_1P_{cr}$, ${}_2P_{cr}$	: Buckling strength
M_T, M_B	: Reaction moment at ends
Q_T, Q_B	: Reaction force (shear) at ends
θ_T, θ_B	: Nodal rotation at ends
R	: Column out-of-plumbness
u, z	: Axes of coordinate

Figure 3. Column model



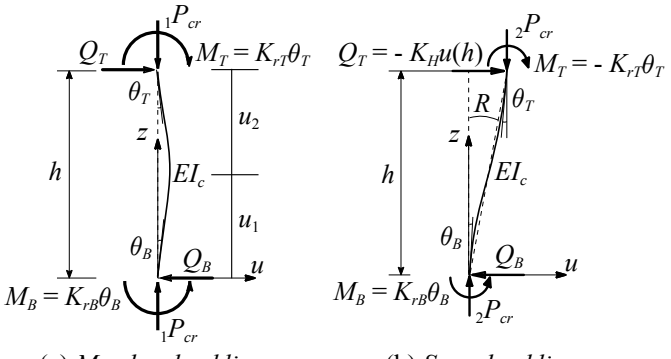
(a) *Member-buckling* (b) *Sway buckling*

Figure 5. The two buckling modes



(a) Mode 1 (b) Mode 2

Figure 4. Simplified model and buckling modes



(a) *Member-buckling* (b) *Sway buckling*

Figure 6. Boundary conditions

$$u_1 = \left\{ -\frac{\xi}{3}\frac{z^3}{h^2} + \frac{\mu k_{rT}\eta}{2}\frac{z^2}{h} + \eta z \right\}\theta_T \quad (4)$$

$$u_2 = \left\{ \frac{\xi}{3}\frac{(z-h)^3}{h^2} + \frac{k_{rT}}{2}\frac{(z-h)^2}{h} - (z-h)z \right\}\theta_T \quad (5)$$

Here,

$$\xi = \frac{2\{(\mu k_{rT}+3)(k_{rT}+3)-1\}}{\mu k_{rT}+4}, \quad \eta = \frac{\theta_B}{\theta_T} = \frac{k_{rT}+4}{\mu k_{rT}+4}$$

$$\mu = \frac{K_{rB}}{K_{rT}}, \quad k_{rT} = \frac{K_{rT}}{EI_c/h}, \quad k_{rB} = \frac{K_{rB}}{EI_c/h} \quad (6a \sim e)$$

Then, virtual displacement Δw is assumed at the top of the column and Δw can be approximated by following equation:

$$\Delta w = \int_0^h \theta \Delta\theta dz = \int_0^h \frac{du}{dz}\frac{d\Delta u}{dz} dz \quad (7)$$

Hence, external virtual work ΔW_{ex} can be expressed as follows:

$$\Delta W_{ex} = {}_1P_{cr}\Delta w = {}_1P_{cr}\left(\int_0^{h/2} \frac{du_1}{dz}\frac{d\Delta u_1}{dz} dz + \int_{h/2}^h \frac{du_2}{dz}\frac{d\Delta u_2}{dz} dz \right) \quad (8)$$

In the above equation, Δu_1 and Δu_2 are obtained by replacing θ_T with $\Delta\theta_T$ in Equations 4 and 5, where $\Delta\theta_T$ is the virtual increment of the nodal rotation angle at the top of the column. On the other hand, internal virtual work ΔW_{in} can be expressed as follows:

$$\Delta W_{in} = \int_0^h M\Delta\phi dz + (K_{rT}\theta_T)\Delta\theta_T + (K_{rB}\theta_B)\Delta\theta_B = EI_c\int_0^{h/2} \frac{d^2u_1}{dz^2}\frac{d^2\Delta u_1}{dz^2} dz + EI_c\int_{h/2}^h \frac{d^2u_2}{dz^2}\frac{d^2\Delta u_2}{dz^2} dz + K_{rT}\theta_T\Delta\theta_T + K_{rB}\theta_B\Delta\theta_B \quad (9)$$

where, M is the sectional moment, ϕ is the curvature, and $\Delta\theta_B$ is a virtual increment of the nodal rotation angle at the bottom of the column. By equating external and internal virtual work, the buckling strength for the *member-buckling* mode can be derived as follows:

$${}_1P_{cr} = \frac{\Delta W_{in}}{\Delta w} \quad (10)$$

By combining Equations 4 trough 10, the general formula for the *member-buckling* strength under an arbitrary boundary condition can be derived as Equation 22 in Table 1. Moreover, the formulas under specific conditions are shown in Equations 18, 20, and 24.

2.2 Sway buckling

Here, the induction process of the *sway buckling* strength formula for a column of arbitrary boundary conditions is shown. As shown in Figure 5(b), the *sway buckling* mode is a phenomenon whereby the topside horizontal spring expands and becomes unstable before *member-buckling* occurs. The boundary condition is shown in Figure 6(b). The deflection curve is approximated as a cubic curve u. The boundary conditions are expressed by the following five equations:

$$u(0) = 0, \quad \left.\frac{du}{dz}\right|_{z=0} = \theta_B, \quad \left.\frac{du}{dz}\right|_{z=h} = \theta_T$$

$$\left.\frac{d^2u}{dz^2}\right|_{z=0} = \frac{K_{rB}\theta_B}{EI_c} = k_{rB}\theta_B\frac{1}{h}$$

$$\left.\frac{d^2u}{dz^2}\right|_{z=h} = \frac{-K_{rT}\theta_T}{EI_c} = -k_{rT}\theta_T\frac{1}{h} \quad (11a \sim e)$$

Based on these boundary conditions, u is given as follows:

$$u = \left\{ -\frac{\xi}{3}\frac{z^3}{h^2} + \frac{\mu k_{rT}\eta}{2}\frac{z^2}{h} + \eta z \right\}\theta_T \quad (12)$$

where,

$$\xi = \frac{k_{rT} + \mu k_{rT} + \mu k_{rT}^2}{\mu k_{rT}+2}, \quad \eta = \frac{\theta_B}{\theta_T} = \frac{k_{rT}+2}{\mu k_{rT}+2} \quad (13a, b)$$

Then, in Figure 6(b), virtual displacement Δw is assumed at the top of the column. The virtual increment of external work ΔW_{ex} by Δw is given as follows:

$$\Delta W_{ex} = {}_2P_{cr}\Delta w = {}_2P_{cr}\int_0^h \frac{du}{dz}\frac{d\Delta u}{dz} dz \quad (14)$$

where, Δu is obtained by replacing θ_T with $\Delta\theta_T$ in Equation 12. On the other hand, the virtual increment of internal work ΔW_{in} becomes.

$$\Delta W_{in} = \int_0^h M\Delta\phi dz + (K_{rT}\theta_T)\Delta\theta_T + (K_{rB}\theta_B)\Delta\theta_B + (K_H u(h))\Delta u(h) = EI_c\int_0^h \frac{d^2u}{dz^2}\frac{d^2\Delta u}{dz^2} dz + K_{rT}\theta_T\Delta\theta_T + K_{rB}\theta_B\Delta\theta_B + K_H u(h)\Delta u(h) \quad (15)$$

Since the virtual increments of external work and internal work are equal, the *sway buckling* strength can be calculated as follows:

$$ {}_2P_{cr} = \frac{\Delta W_{in}}{\Delta w} \tag{16} $$

Based on Equations 12 through 16, the *sway buckling* strength formula for an arbitrary boundary conditions is given by Equation 23 in Table 1. Moreover, the formulas for specific conditions are given as Equation 19, 21, and 25. Here, k_H is defined as follows:

$$ k_H = \frac{K_H}{12EI_c/h^3} \tag{17} $$

Table 2 shows the elastic buckling strength formula for an arbitrary boundary condition obtained using the buckling-slope-deflection method. The induction process of the equations are shown at the end of the present paper.

3. Application of the proposed formula to portal frames

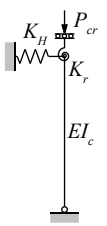
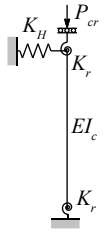
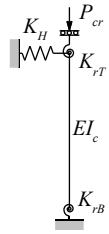
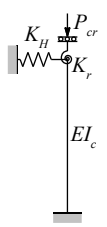
This section compares the computer analysis and the proposed formula, shown in Table 1 obtained using portal frames having fixed column bases and verifies the validity the proposed formula. The proposed formula assumes that the frames receive an anti-symmetric load. However, the computer analysis and the proposed formula are also compared for other load conditions.

3.1 Calculation of spring stiffness

(1) Rotational springs

In order to calculate the buckling strength using the proposed formula, it is necessary to calculate the stiffness of each spring shown in Figure 5. Here, the calculation of the stiffness for portal frames is shown. First, the calculation method of the rotational spring stiffness is

Table 1. Proposed formulas

Support condition	Buckling mode	Proposed formula
Spr.-Pin 	*Member -buckling*	${}_1P_{cr} = \frac{3k_r^2 + 18k_r + 32}{11k_r^2 + 92k_r + 256} \cdot \frac{80EI_c}{h^2}$ (18)
	Sway buckling	${}_2P_{cr} = \frac{k_r(k_r+3) + 4k_H(k_r+3)^2}{2k_r^2 + 10k_r + 15} \cdot \frac{5EI_c}{h^2}$ (19)
SameSpr. 	*Member -buckling*	${}_1P_{cr} = \frac{k_r^2 + 10k_r + 16}{k_r^2 + 14k_r + 64} \cdot \frac{40EI_c}{h^2}$ (20)
	Sway buckling	${}_2P_{cr} = \frac{k_r(k_r+6) + k_H(k_r+6)^2}{k_r^2 + 10k_r + 30} \cdot \frac{10EI_c}{h^2}$ (21)
Arbitrary 	*Member -buckling*	${}_1P_{cr} = \frac{\xi^2 - 3\xi\mu k_{rT}\eta + 3\mu^2 k_{rT}^2\eta^2 + \xi^2 - 3\xi k_{rT} + 3k_{rT}^2 + 6k_{rT}(1+\mu\eta^2)}{3\xi^2 - 5\xi(3\mu k_{rT}+8)\eta + 20(\mu^2 k_{rT}^2 + 6\mu k_{rT} + 12)\eta^2 + 3\xi^2 - 5\xi(3k_{rT}+8) + 20(k_{rT}^2 + 6k_{rT} + 12)} \cdot \frac{80EI_c}{h^2}$ (22) $\xi = \frac{2\{(\mu k_{rT}+3)(k_{rT}+3) - 1\}}{\mu k_{rT} + 4} \qquad \eta = \frac{k_{rT}+4}{\mu k_{rT}+4}$
	Sway buckling	${}_2P_{cr} = \frac{4\xi^2 - 6\xi\mu k_{rT}\eta + 3\mu^2 k_{rT}^2\eta^2 + k_H\{-2\xi + 3(\mu k_{rT}+2)\eta\}^2 + 3k_{rT}(1+\mu\eta^2)}{6\xi^2 - 5\xi(3\mu k_{rT}+4)\eta + 10(\mu^2 k_{rT}^2 + 3\mu k_{rT} + 3)\eta^2} \cdot \frac{10EI_c}{h^2}$ (23) $\xi = \frac{k_{rT} + \mu k_{rT} + \mu k_{rT}^2}{\mu k_T + 2} \qquad \eta = \frac{k_{rT}+2}{\mu k_{rT}+2}$
Spr.-Fix. 	*Member -buckling*	${}_1P_{cr} = \frac{k_r^2 + 9k_r + 24}{k_r^2 + 11k_r + 44} \cdot \frac{40EI_c}{h^2}$ (24)
	Sway buckling	${}_2P_{cr} = \frac{(k_r+1)(k_r+4) + k_H(k_r+4)^2}{k_r^2 + 7k_r + 16} \cdot \frac{10EI_c}{h^2}$ (25)

$k_r = \frac{K_r}{EI_c/h}$ $\quad k_{rB} = \frac{K_{rB}}{EI_c/h}$ $\quad k_{rT} = \frac{K_{rT}}{EI_c/h}$ $\quad \mu = \frac{K_{rB}}{K_{rT}}$ $\quad k_H = \frac{K_H}{12EI_c/h^3}$

Table 2. *Member-buckling* strength formulas obtained by buckling-slope-deflection method

Support condition	*Member-buckling* strength formula	
Spring - Pin	$-k_r = s(1-c^2)$	(26)
Same spring on each end	$-k_r^2 = s\{s(1-c^2)+2k_r\}$	(27)
Arbitrary boundary condition	$-\mu k_{rT}^2 = s\{s(1-c^2)+k_{rT}(1+\mu)\}$	(28)
Spring - Fix	$-k_r = s$	(29)

$$s = \frac{\{\sin(\gamma)-\gamma\cos(\gamma)\}\gamma}{2\{1-\cos(\gamma)\}-\gamma\sin(\gamma)} \qquad c = \frac{\gamma-\sin(\gamma)}{\sin(\gamma)-\gamma\cos(\gamma)}$$

$$\gamma = \pi\sqrt{\frac{{}_{SD}P_{cr}}{N_E}} \qquad N_E = \frac{\pi^2 EI_c}{h^2} \qquad (30a \sim d)$$

${}_{SD}P_{cr}$: *Member-buckling* strength obtained by buckling-slope-dflection method

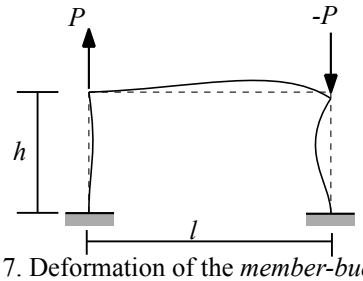


Figure 7. Deformation of the *member-buckling* mode

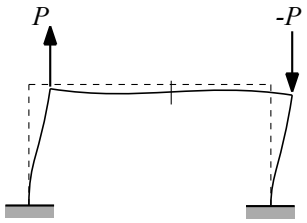


Figure 8. Deformation of the *sway buckling* mode

shown. The portal frame exhibits the deformation shown in Figure 7 when *member-buckling* occurs. In Figure 7, the point of contrary flexure of the beam is between the top of left-hand column and the center of the beam. Hence, the topside rotational spring stiffness is approximated by Equation 31. This is equivalent to the flexure rigidity of a simply supported beam, where the bending moment is received at one end of the beam.

$$K_r = \frac{3EI_b}{l} \qquad (31)$$

Moreover, the portal frame is assumed to exhibit the deformation shown in Figure 8 when *sway buckling* occurs. The topside rotational spring stiffness can be approximated by Equation 32, if it is assumed that the point of contrary flexure is at the center of the beam. This is equivalent to the flexure rigidity of a simply supported beam, where the anti-symmetric bending moment is received.

$$K_r = \frac{6EI_b}{l} \qquad (32)$$

In any case, the column base is fixed.

(2) Horizontal spring

It is necessary to calculate the horizontal spring stiffness of the top of the column only when the *sway buckling* strength is calculated. If a point of contrary flexure is assumed to exist in the center of the beam when *sway buckling* occurs (shown in Figure 8), then it is assumed that the L-shaped frame, which is to the left of the point of contrary flexure, restrains the right-hand column from moving laterally due to the buckling. Therefore, horizontal spring stiffness K_H is defined by the following equation:

$$K_H = K_{H0} + P / h \qquad (33)$$

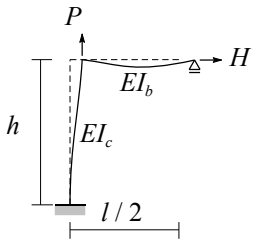
The first term is the horizontal rigidity K_{H0} of the L-shaped frame that does not consider axial force, and the second term is the geometric stiffness provided by *P*-Δ *effect* through the tensile force. In order to verify the validity of Equation 33, computer analysis using tensile force P as the parameter is performed. This computer analysis is an elastic increment analysis that considers geometric non-linear using CLAP.f (Ogawa and Tada, 1994). The analysis frame is shown in Figure 9, in which each member is divided into 10 segments, and the cross sections are solid boxes.

Figure 10 shows the results of the computer analysis and the value of Equation 33. The vertical axis is the non-dimensional lateral rigidity against lateral force H, and the horizontal axis is tensile force P divided by N_E. The solid line is obtained by dividing Equation 33 by N_E, and the solid squares show the results of the computer analysis. The error margin is small although the value of Equation 33 becomes smaller than in the computer analysis.

3.2 Calculation of buckling strength and comparison

(1) Analysis frame and analytical conditions

The portal frame to which column bases are fixed is shown in Figure 11. In Figure 11, the load condition is an anti-symmetric load if $\lambda = 1$ and is a symmetric vertical load if $\lambda = -1$. In the proposed formula, since the right-hand column is modeled as shown in Figure 3, the rotational and horizontal spring stiffnesses are calculated by the method described in the previous section. In the computer analysis, an elastic increment analysis that considers geometrical non-linear using CLAP.f and eigenvalue analysis are performed. The analysis using CLAP.f is run until the vertical displacement of the top of



Young's Modulus	: E = 205,000 (N / mm^2)
Column Area	: A_c = 90,000 (mm^2)
Column Geometric Moment of Inertia	: I_c = 675,000,000 (mm^4)
Beam Area	: A_b = 102,600 (mm^2)
Beam Geometric Moment of Inertia	: I_b = 877,500,000 (mm^4)
Column Length	: h = 4 (m)
Beam Length	: l = 6 (m)
Flexure Rigidity Ratio	: (I_b / l) / (I_c / h) = 0.867
L-shape Frame Story Stiffness	: K_{H0} = 17,490,000 (N / m)

Figure 9. L-shaped frame (for verification of Equation 33)

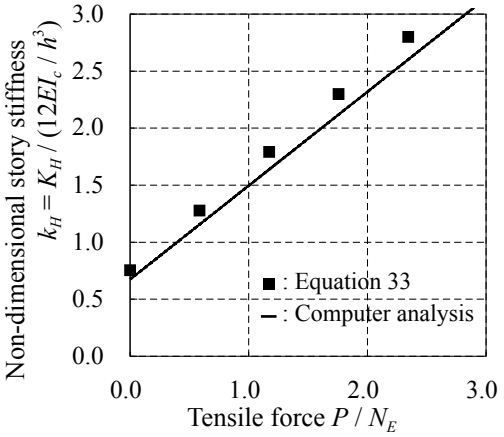
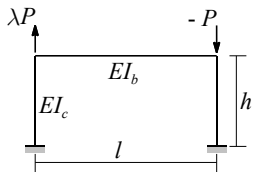


Figure 10. Verification of Equation 33



h = 4 (m)
l = 8 (m)
E = 205,000 (N/mm^2)
$\alpha = l/h$ = 2.0
$\beta = I_b/I_c$ = 0.4,1.3
β/α = 0.2, 0.65

Figure 11. Analysis portal frame

the right-hand column becomes δ_z = - 400 (mm).

The cross section is designed such that the relative story displacement becomes 1/200 (rad) for lateral load (seismic load) Q (story shear force coefficient C_0 = 0.2), as established in the *Order for Enforcement of the Building Standard Act* (In Japanese), in elastic increment analysis that does not consider geometric non-linear. The long-term load (dead load and live load) is assumed to be a uniformly distributed load q = 50,000 (N/m) on the beam. Therefore, the seismic load for the section design is Q = 0.2 x 50,000 x 8 = 80,000 (N). The cross sections are solid boxes, and each member is divided into 10 segments.

When buckling analysis is performed, columns are inclined to 1/20,000 (rad) as an initial imperfection and are then modeled. The proportional load shown in Figure 11 is made to act after long-term load P_L is made to act. The long-term load P_L uses the symmetric load on the beam-to-column nodes calculated from uniformly distributed load q on the beam. Therefore, P_L = 50,000 x 8/2 = 200,000 (N).

(2) Parameters

The analysis parameters are β and λ, where β is the ratio of the geometric moments of inertia between the beam and the column, and values of 0.4 and 1.3 are used in the present study. Hence, a frame having a flexure rigidity ratio between the beam and the column of β/α = 0.4/2.0 = 0.2 (α is the aspect ratio $\alpha = l/h$ = 8/4 = 2) is denoted as A20B04 and a frame with β/α = 1.3/2.0 = 0.65 is denoted as A20B13. On the other hand, λ is a coefficient shown in Figure 11, for A20B04, λ = -1, 0, 0.5, 0.7, 0.8, 1.0, 1.2, 1.5, 2, and 5, and for A20B13, λ = - 1, 0, 0.5, 0.7, 1, 1.1, 1.5, and 2. Table 3 lists various characteristics of these frames.

(3) Calculation of buckling load by the proposed formula

The process of calculating the buckling strength using the proposed formula, shown in Table 1, is described in the following. First, Equation 31 is used to calculate rotational spring stiffness K_r when the *member-buckling* strength ${}_1P_{cr}$ is calculated, and Equation 32 is used when the *sway buckling* strength is calculated. The following equation is obtained from these two equations and Equation 6d:

$$\textit{member}: \quad k_r = K_r/(EI_c/h)$$
$$= 3\,(I_b/I_c)/(l/h) = 3\beta/\alpha = 0.6,\ 1.95 \qquad (34)$$
$$\textit{sway}: \quad k_r = 6\beta/\alpha = 1.2,\ 3.9 \qquad (35)$$

Table 3. Cross section specifications

name	I_b / I_c	I_c (mm^4)	A_c (mm^2)	I_b (mm^4)	A_b (mm^2)	N_E (N)
A20B04	0.4	123,000,000	38,420	49,200,000	24,300	15,550,000
A20B13	1.3	83,890,000	31,730	109,100,000	36,180	10,610,000

A_c: Column area A_b: Beam area
I_c: Column geometric moment of inertia I_b: Beam geometric moment of inertia $N_E = \pi^2 EI_c/h^2$

Moreover, the following equation is obtained when P is replaced with ($\lambda_2 P_{cr}$ - P_L) in Equation 33 and the resulting equation is substituted into Equation 17:

$$k_H = \frac{h^3}{12EI_c}\left(K_{H0} + \frac{\lambda_2 P_{cr} - P_L}{h}\right) \qquad (36)$$

However, it is assumed that $k_H = 0$ for $\lambda = -1$. Here, since the cross section is designed such that the relative story displacement becomes 1/200 (rad) for a lateral load of Q = 80,000 (N), K_{H0} is given as:

$$K_{H0} = \{80{,}000/(4/200)\}/2 = 2{,}000{,}000 \text{ (N/m)} \qquad (37)$$

Therefore, ${}_1P_{cr}$ is obtained when Equation 34 is substituted for Equation 24, and ${}_2P_{cr}$ is obtained when Equations 35 and 36 are substituted for Equation 25. Then, the smaller of both ${}_1P_{cr}$ and ${}_2P_{cr}$ is the buckling load of the right-hand column of the portal frame shown in Figure 11.

(4) Results

Figures 12 through 20 show the results of the computer analysis and the proposed formula. Figures 12 through 15 and 20(a) show the results for A20B04 ($\alpha = l/h = 2.0$, $\beta = I_b/I_c = 0.4$), and Figures 16 through 19 and 20(b) show the results for A20B13 ($\alpha = l/h = 2.0$, $\beta = I_b/I_c = 1.3$). Figures 12(a) through 19(a) are graphs of the non-dimensional load-displacement curves obtained by CLAP. f. The vertical axes show the perpendicular reaction force N_1 in the base of the right-hand column divided by N_E. The horizontal axes show the vertical and horizontal displacements, δ_z and δ_x, of the top of the right-hand column divided by the frame height h. The positive δ_z direction is upward, and the positive δ_x direction is to the right. The dashed-dotted lines indicate the buckling load of the right-hand column obtained by the proposed formula P_{cr}, and the chain double-dashed lines shows the buckling load of the right-hand column obtained by eigenvalue analysis V_{cr}. Figures 12(a) through 19(a) are the deformation diagrams when the computer analysis by CLAP.f finalizes, and Figures 12(c) througth 19(c) show the buckling modes obtained by eigenvalue analysis. In Figure 20, the vertical axes show the buckling loads divided by N_E, and the horizontal axes shows λ. The two solid lines (or curves) are given by the proposed formulas, and the dashed lines are given by Equation 29, which was obtained by the buckling-slope-deflection method. The cross symbols indicate the results of the eigenvalue analysis.

(5) Comparison

Based on Figures 12(a) and 16(a), when the frame receives a symmetric perpendicular load ($\lambda = -1$), the buckling load becomes less than N_E which means that the buckling length is longer than the floor height h. On the other hand, when the frame receives an anti-symmetric load ($\lambda = 1$, Figures 14(a) and 19(a)), the buckling load exceeds N_E. This means that the buckling length is shorter than the floor height h.

For the frame A20B04, as shown in Figure 20(a), the error between the value of the proposed formula and the results of the eigenvalue analysis is largest at the intersection of the two solid (proposed formula) lines. (The largest is +26% at $\lambda = 0.7$) It is thought that the reason for this error margin is that the proposed formula does not consider the intermediate buckling mode between *member-buckling* and *sway buckling*. The buckling mode changes continuously in the computer analysis, as indicated by Figures 12(b) through 15(b). For frame A20B13, as shown in Figure 20(b), the error between the value of the proposed formula and the results of the eigenvalue analysis is not so large. The largest error is +5.2% at $\lambda = 0.5$. The comparison of frames A20B04 and A20B13 indicates that the error between the proposed formula and the computer analysis decreases as the flexure rigidity ratio increases.

4. Conclusion

In the present paper, we proposed an elastic buckling strength formula for a column under an arbitrary boundary condition. The proposed formula targets the loads shown in Figure 2, which correspond to the column axis forces generated by the overturning moment of the lateral loads, and two buckling modes of *member-buckling* and *sway buckling* were assumed.

Moreover, using portal frames, the value obtained by the proposed formula was compared with the results of computer analysis, and the following conclusions were drawn.

(1) When the frame receives a symmetric perpendicular load, the buckling load becomes less than N_E. On the other hand, when the frame receives an anti-symmetric load, the buckling load exceeds N_E which means that the buckling length is shorter than the column length.

(2) For frame A20B04, the flexure rigidity ratio of which is 0.2, the error between value obtained by the proposed formula and the results of an eigenvalue analysis was greatest at the intersection of the two proposed formula lines. (The largest error is +26%). It is thought that the reason for this error is that the proposed formula does not consider the intermediate buckling mode between *member-buckling* and *sway buckling*.

(3) For frame A20B13, the flexure rigidity ratio of which is 0.65, the error between the value obtained by the proposed formula and the results of the eigenvalue analysis was not so large. The largest error was +5.2%.

(4) The error of the proposed formula and the computer analysis becomes smaller as the flexure rigidity ratio increases.

NEXT PAGE

δ_x, δ_z : Vertical and horizontal displacements at the top of the right-hand column

P_{cr} : Buckling load of the right-hand column obtained using the proposed formula

N_1 : Reaction axial force at the base of the right-hand column

V_{cr} : Buckling load of the right-hand column obtained by the eigenvalue analysis

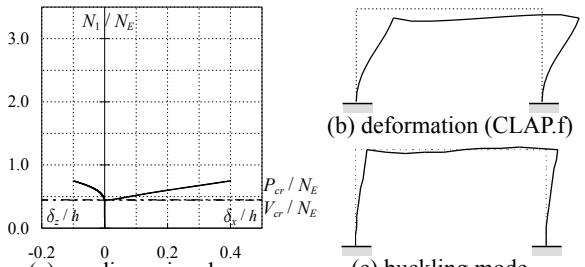


Figure 12. λ = - 1 (A20B04)

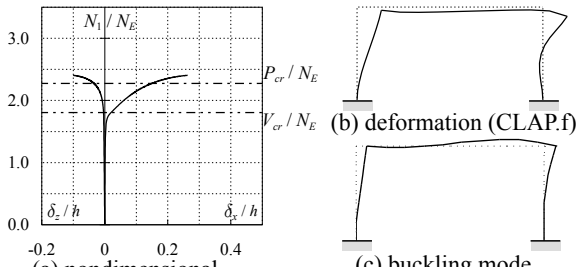


Figure 13. λ = 0.7 (A20B04)

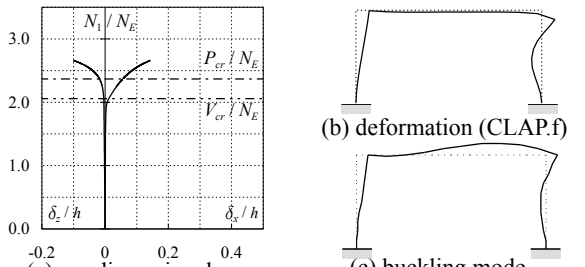


Figure 14. λ = 1 (A20B04)

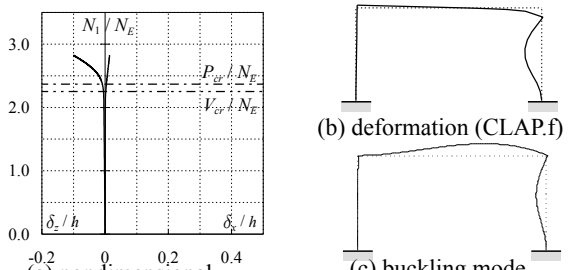


Figure 15. λ = 5 (A20B04)

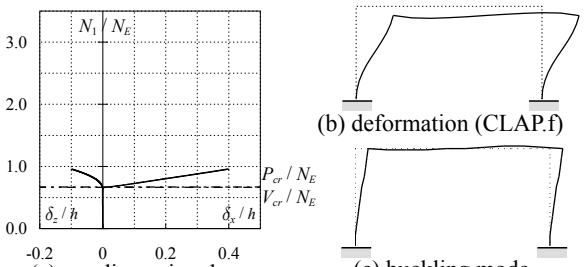


Figure 16. λ = - 1 (A20B13)

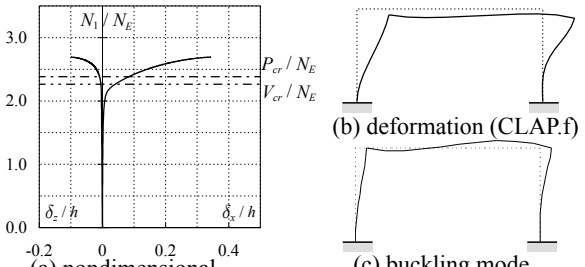


Figure 17. λ = 0.5 (A20B13)

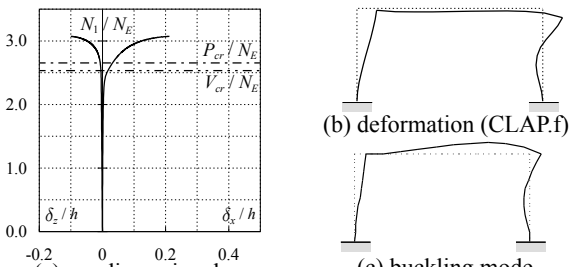


Figure 18. λ = 0.7 (A20B13)

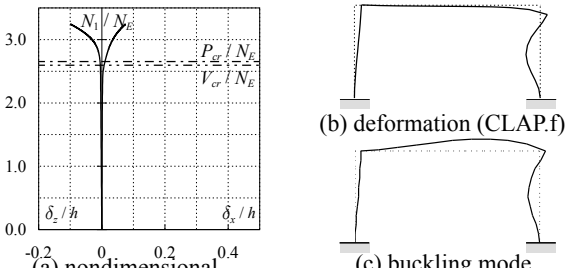


Figure 19. λ = 1 (A20B13)

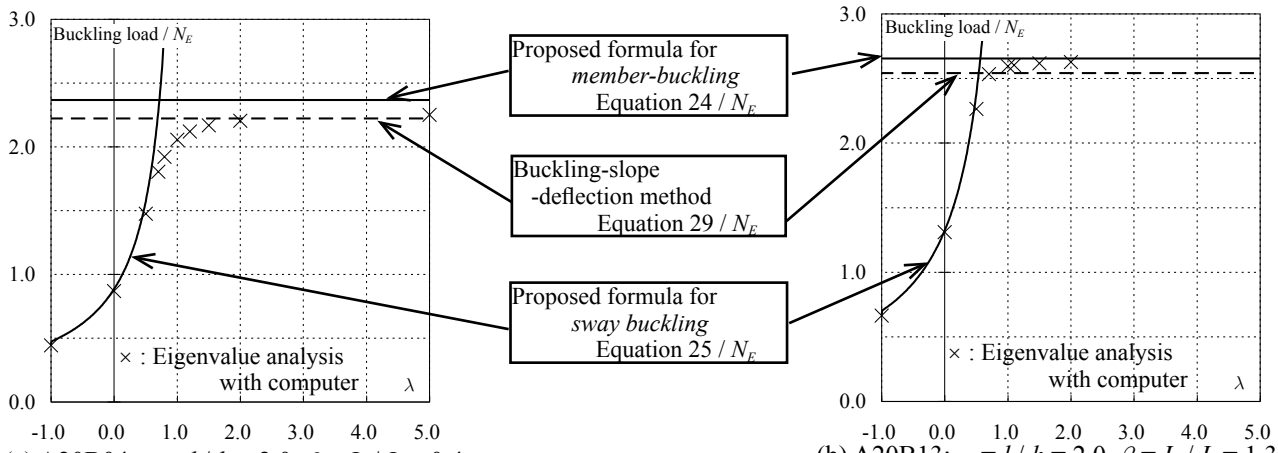


Figure 20. Comparison of the proposed formula with computer analysis

Acknowledgements:

The present study was supported through the Project of Research and Education for Steel Construction (KOKOZO KENKYU-KYOIKU JOSEI JIGYO) by the Japan Iron and Steel Federation. The authors would like to thank Prof. Inoue K. of Okayama University of Science for his valuable comments.

Reference:

Araki Y., Takagi J., Uetani K. (2005), "Stability Design of Plane Steel Frames Using Linearized Buckling Analysis –Part 2 Formulation for Earthquake Loading and Application to A Braced Frame-", Journal of Structural and Construction Engineering, No.590, 129-136. (In Japanese)

Architectural Institute of Japan (2002), Design Standard for Steel Structure, 65-66 (In Japanese)

Architectural Institute of Japan (2009), Recommendations for Stability Design of Steel Structure, 260-270 (In Japanese)

Architectural Institute of Japan (1998), Recommendation for Limit State Design of Steel Structure, 78-80 (In Japanese)

Architectural Institute of Japan (2002), Recommendations for the Plastic Design of Steel Structure, 112-117 (In Japanese)

Inoue K., Tada M. (2007), "On The Buckling Length of Steel Column", Proceedings of Annual Research Meeting Kinki Chapter, No.47(Structure), 193-196. (In Japanese)

Mitani I., Katahira T., Ohtani Y., and Hayashihara K. (2002), "Buckling Load of Rigid Frame with Slender Columns," Journal of Structural and Construction Engineering, No.557, 161-166. (In Japanese)

Mitani I., Katahira T., and Ohtani Y. (2002), "Inelastic Buckling Load of Unbraced Frame Dominated by Single Buckling of Column," Journal of Structural and Construction Engineering, No.562, 167-173. (In Japanese)

Mitani I., and Katahira T. (2002), "A Study on Buckling Design Method of Unbraced Frame with Slender Columns," Journal of Constructional Steel, Vol. 10, 479-484. (In Japanese)

Ogawa K., Tada M. (1994), "Computer Program for Static and Dynamic Analysis of Steel Frames Considering The Deformation of Joint Panel", Proceedings of The 17th Symposium on Computer Technology of Information, System and Applications, 79-84. (In Japanese)

Shibata M. (2003), "Effective Length of A Long Column in The Well", Journal of Structural and Construction Engineering, No.567, 133-139. (In Japanese)

Suzuki H., Morino S., and Kawaguchi J. (1993), "Approximate Method of Elastic Buckling Load Analysis for Irregular Rectangular Frames," Journal of Constructional Steel, Vol. 1, 257-264. (In Japanese)

Tsuda K. (2001), "Simplified Design Formula for Effective Length of Column in Unbraced Frame", Journal of Structural and Construction Engineering, No.545, 151-155. (in Japanese)

Tsuda K. (2002), "Simplified Design Formula for Effective Length of Column in Braced Frame", Journal of Structural and Construction Engineering, No.553, 129-134. (In Japanese)

Appendix:

This appendix derives the *member-buckling* strength formula listed in Table 2 with the buckling-slope-deflection method.

Here, the induction process of Equation 28 is shown. The other equations (Equations 26, 27, and 29) are specific cases of Equation 28. Figure 6(a) indicated that there is no horizontal displacement at the top of the column, in the *member buckling* mode. The essential formulas of the buckling-slope-deflection method are as follows:

$$M_{TB} = \frac{EI_c}{h}(s\theta_T + sc\theta_B) = -K_{rT}\theta_T \tag{38}$$

$$M_{BT} = \frac{EI_c}{h}(s\theta_B + sc\theta_T) = -K_{rB}\theta_B \tag{39}$$

where M_{TB} and M_{BT} are the end node bending moments. The above two equations can be rewitten in matrix form as follows:

$$\begin{bmatrix} s + k_{rT} & sc \\ sc & s + k_{rB} \end{bmatrix} \begin{pmatrix} \theta_T \\ \theta_B \end{pmatrix} = \begin{pmatrix} 0 \\ 0 \end{pmatrix} \tag{40}$$

If $(\theta_T \ \theta_B)^{\mathrm{T}} \neq 0$, then buckling occurs. Therefore, the buckling conditional equation is given by the following equation:

$$(s + k_{rT})(s + k_{rB}) - s^2c^2 = 0 \tag{41}$$

Equation 28 is obtained by deforming Equation 41.

8CUEE CONFERENCE PROCEEDINGS
8th International Conference on Urban Earthquake Engineering
March 7-8, 2011, Tokyo Institute of Technology, Tokyo, Japan

SHEAR RESISTANCE OF EXPOSED COLUMN BASES IN STEEL BRACED FRAMES

Hayato Asada[1)], Shoichi Kishiki[2)], and Satoshi Yamada[3)]

1) Graduate Student, Structural Engineering Research Center, Tokyo Institute of Technology, Japan
2) Assistant Professor, Structural Engineering Research Center, Tokyo Institute of Technology, Japan
3) Associate Professor, Structural Engineering Research Center, Tokyo Institute of Technology, Japan
asada@serc.titech.ac.jp, kishiki@serc.titech.ac.jp, naniwa@serc.titech.ac.jp

Abstract: Cyclic loading tests of column base in braced frames were conducted. Based on the test results, shear resistances governed by concrete edge failure of column base with various anchor spacing and reinforcement patterns were evaluated. Post-concrete edge failure behavior was also discussed to evaluate ultimate shear resistant mechanism considering the contribution of reinforcements around anchor bolts.

1. INTRODUCTION

Exposed-type column bases are widely employed in not only low or middle-rise steel moment-resisting frame but also braced frame to fasten the base plate of steel column to reinforced concrete foundation in Japan. For steel braced frame, these type column base connections requires sufficient lateral stiffness and strength to transmit large shear due to the brace force to concrete foundation as smoothly as possible thorough anchor bolts and/or with friction resistance between base plate and concrete foundation.

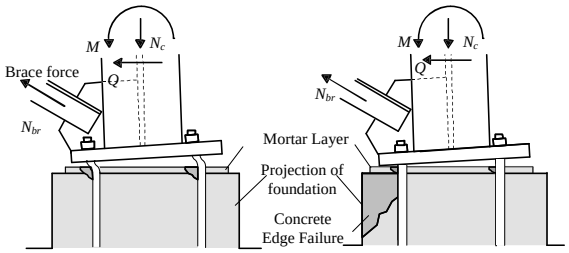
significant damages due to the brace force which are not only anchor steel failure (Fig. 1(a)) but also concrete edge failure of anchor bolts embedded near the free edges (Fig. 1(b)) were observed in steel braced building during recent earthquakes (BRI, 2003). These facts indicate that it is necessary to investigate the seismic performance of column base in braced frame subjected to large shear force. In addition, brittle failure such as concrete edge failure as well as early anchor bolt failure must be eliminated to ensure sufficient ductility. Although Concrete failure of a single or multiple anchor bolts under pure shear or combined tension and shear have been examined extensively, (Klingner, R. et al. 1982, Fuchs, W. et al. 1995, Kawano, H., et al. 2003) Shear resistance behavior of column base connection considering the shear transfer mechanism has not been discussed.

This paper presents the experimental investigation of shear resistance of exposed-type column base in braced frame governed by concrete failure.

2. TEST PROGRAM

2.1 Test Specimens

The test specimens were designed to simulate the exposed column base connections in the braced frames of low- to medium-rise buildings. The objective of this test is to investigate the shear resistance governed by the edge failure of the concrete foundation beam. The effect of the arrangement of anchor bolts and the reinforcement around the anchor bolts on the shear resistance were investigated. Moreover, the different failure modes of column base caused by the anchor bolts were investigated. There are six specimens, which were designed according to the survey of the column base connections in existing braced steel gymnasium (Asada et al. 2011), as shown in Table 1. The material properties of steel and concrete are shown in Table 2 and 3, respectively.



(a) Anchor steel yielding (b) Concrete edge failure

Figure 1 Failure Modes of Exposed Type Column Base on Projection of Foundation

Figure 2 shows the configuration of specimen and the arrangement of reinforcement. The specimen consists of the column, base plate (B.PL in the follows), gusset plate (G.PL), and the reinforced concrete foundation beam, in which the projection of foundation was designed. The column section was RH-200x200x8x12. The gusset plate was connected with the web of the column on the weak axis and a stiffener was welded on the other side of the web to resist the out-of-plane deformation. The base plate size is 350 mm in width, 420 mm in depth, and 40 mm in thickness. Four bolts were arranged at each corner of the base plate.

To investigate the edge failure of the RC foundation beam,

the failure of mortar layer was excluded by removing the mortar layer under the base plate for the specimens.

Generally, the shear resistance of the exposed column base is provided by a combination the friction along the contact area between the base plate and RC foundation beam and the bending and shear of anchor bolts. To investigate the contribution of the shear resistance of the anchor bolt, a Teflon sheet was inserted between the base plate and RC foundation beam to reduce the friction resistance in this study.

Figure 3 shows the embedment of the anchor bolt. In this study, the embedded length of anchor bolt (l_e) was 400 mm, two types diameters of anchor bolt (d), 20 mm and 23 mm, were used. The ratios of embedded length to diameter of anchor bolt were 20 and 17, respectively. The bottom end of the anchor bolt was fixed with the φ60×22 nut by welding. The Steel PC bar with the diameter of 23 mm was used for the anchor bolts of the specimens failed in RC foundation beam to promise the concrete edge failure before the significant yield of the anchor bolts. To avoid the slip of the base plate at the initial loading, the clearance between anchor bolts and bolt holes of base plate was filled by grout.

The dimensions of the RC foundation beam were the same for all the specimens, as shown in Fig. 2 (b). The distance from the anchor bolt to the free edge of the projection of foundation beam along the loading direction, c_1, which is the most critical parameter to the shear resistance governed by concrete edge failure of the RC foundation beam, was 160mm. The distance from the anchor bolt to the free edge perpendicular to the loading direction, c_2, was 1.5 times c_1 (240 mm) to exclude the effect of the free edge to the shear resistance of the concrete edge failure (Asada et al., 2010). The spacing of anchor bolts perpendicular to the loading direction, s_2, was twice of c_1 (320 mm). The spacing of anchor bolts along the loading direction, s_1, was chosen as the parameters. According to the survey of the existing steel gymnasium (Asada et al. 2011), three values were chosen as follows:s_1/c_1=0.75(s_1=120mm),1.0(s_1=160mm),1.5(s_1=240mm).

The reinforcement configurations of the foundation beam are shown in Fig. 2. Three types of reinforcement of the projection of foundation beam were adopted in this study. The main reinforcing bars of 10-D19 and hoops of D10@100 were used as the basic reinforcement for the projection of foundation beam, as shown in Fig. 2 (a). The mechanical anchors were used to avoid the overlap of the reinforcements. To investigate the contribution of the reinforcement along the loading direction of the projection of foundation beam, the hoops were removed and the main reinforcing bars were changed to 5-D19 for one specimen (unreinforced specimen). To investigate the effect of the reinforcement around the anchor bolts, the hairpin reinforcement was designed for one specimen (strengthen specimen), as shown in Figure 4.

The projection of foundation beam is 800 mm width perpendicular to the loading direction and 300 mm in height.

Table 1 List of Test Specimens

Specimens	Edge Distance and Anchor spacings				Reinforcment pattern
	c_1 [mm]	c_2 [mm]	s_1 [mm]	s_2 [mm]	
T-1.0	160	240	160	320	Reinforced*2
T-1.5			240		
T-0.75			120		
T-1.0_S.R.			160		with Hairpin
T-1.0_U.R.					Unreinforced*3

*2: See Figure 2(a), *3: See Figure 2(b)

2.2 Test Setup and loading program

The test specimen was placed in the loading frame shown in Figure 5. The foundation beam was connected with the loading frame by PC bars and screw jacks. The column top was clamped to two hydraulic jacks, one in the horizontal direction and the other in the vertical direction. The gusset plate was clamped to one jack to simulate the brace load N_{br}. The specimen was subjected to a constant vertical force with the axial force ratio of 0.05. A displacement-controlled load was applied in the horizontal direction. The displacement was expressed in terms of the drift angle R. The brace load N_{br} was controlled by the applied horizontal displacement of the top of column. The brace force behavior is described as shown in Fig. 7, the brace yielded at the drift angle R of 1/400 with the yield brace load of 200 kN in tension and the brace does not resist compressive load. For the specimens failed in RC foundation beam, one cycle of the drift angles of 1/400 and 1/100 rad and the monotonic loading to the horizontal displacement of the column base ${}_{cb}\delta_h$ of 20 mm after unloading were adopted.

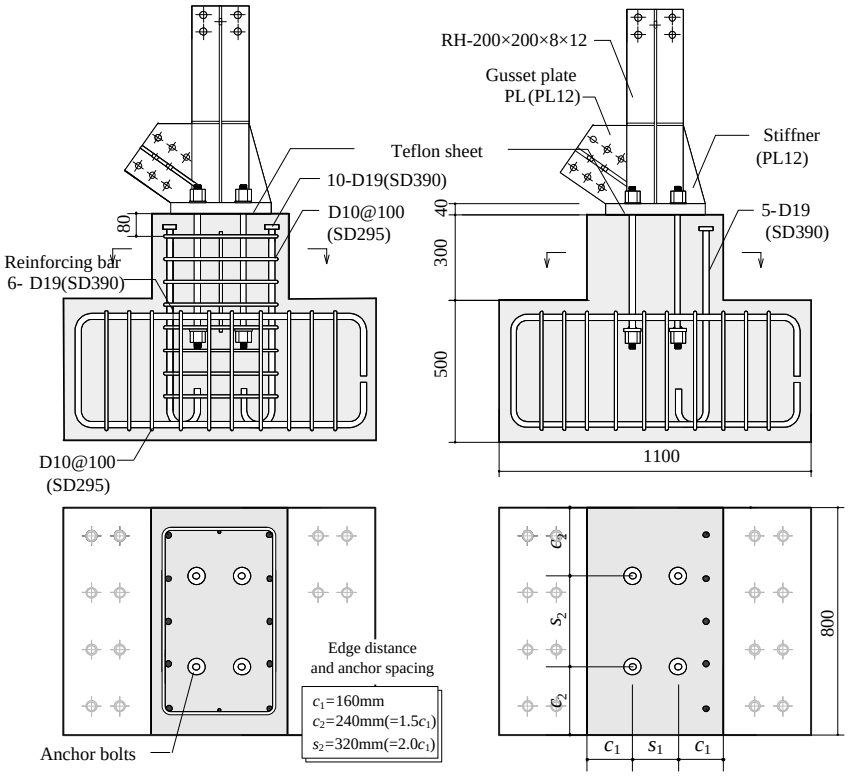
Table 2 Material Properties (a) Steel, and (b) Concrete

(a)

		Yield strength [N/mm^2]	Tensile Strength [N/mm^2]
Base Plate		285	434
Column	Web	288	437
	Frange	285	438
Hoop reinforcement	D10	344	497
Hairpin reinforcement	D13	357	527
Main reinforcement	D19	393	554

(b)

Spliting strength [N/mm^2]	Compressive Strength [N/mm^2]	Young's Modulus [N/mm^2]
2.45	32.2	2.43×10^4



(a) Reinforced Specimen (b) Unreinforced Specimen

Figure 2 Configurations of Test Specimens

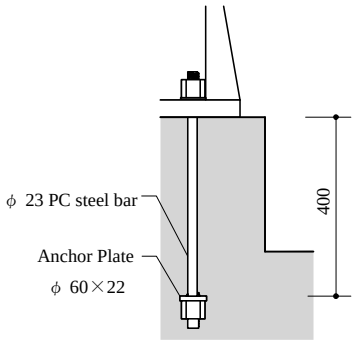


Figure 3 Embedment of Anchor bolts

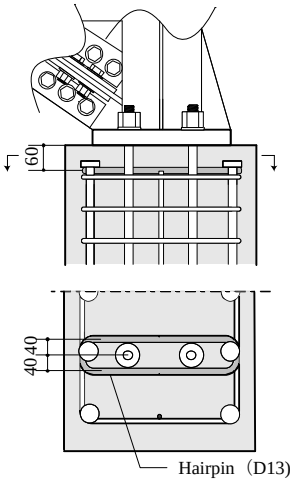


Figure 4 Arrangement of Hairpin Reinforcements

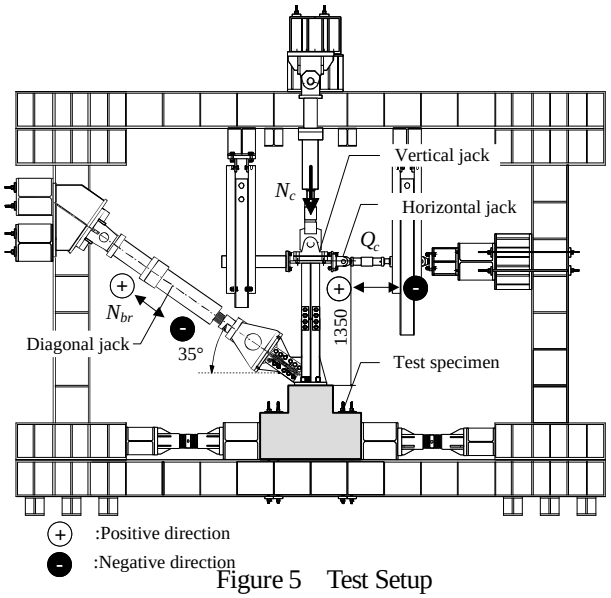


Figure 5 Test Setup

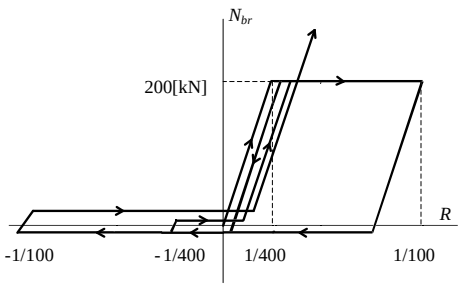


Figure 6 Brace Force Control

2.3 Measurement system

The deformation of the specimen was described in Figure 8. All the measured displacements were the relative displacement from the foundation beam. The story drift angle R is calculated as follows:

$$R = \frac{{}_t\delta_h - {}_{cb}\delta_h}{l_h - {}_t\delta_v - {}_{cb}\delta_v} \quad (1)$$

As shown in Figure 8, the rotation of the column base ${}_{cb}\theta$ is calculated as the vertical displacements measured from the base plate and the horizontal displacement of column base is measured from the front surface of the base plate. The incline of the jack was considered to calculate the resistance of the specimen.

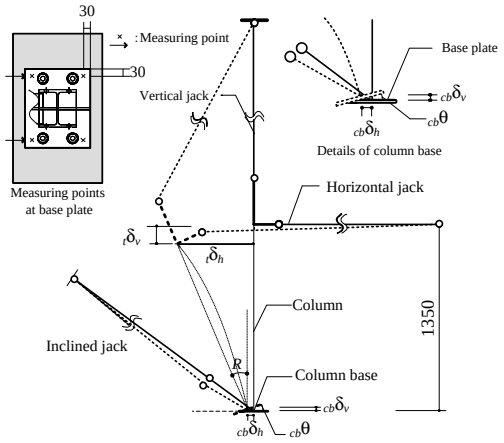
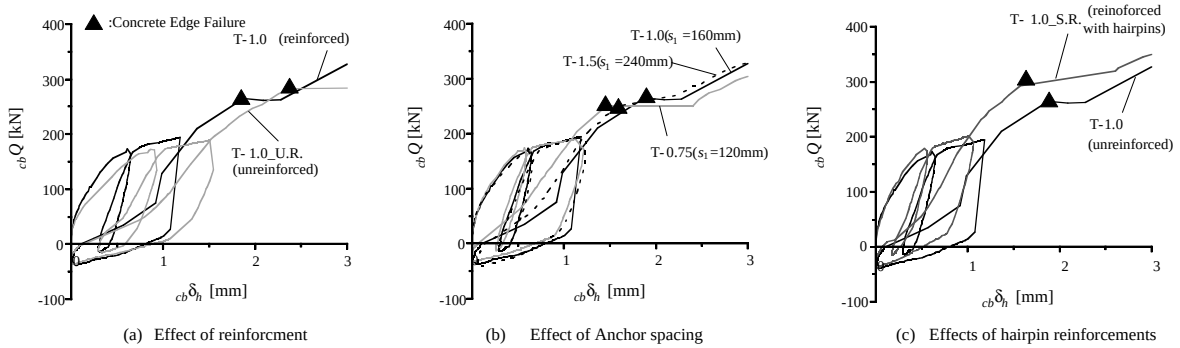


Figure 7 Measurement System



(a) Effect of reinforcment (b) Effect of Anchor spacing (c) Effects of hairpin reinforcements

Figure 8 Shear Resistance of Column Base till Concrete Edge Failure occurred

3. Test Results

3.1 Shear resistance behavior till concrete edge failure occurred

As observed from the test, the edge failure occurred at the column base horizontal displacement $_{cb}\delta_h$ of 3 mm. The relationships of shear resistance of column base $_{cb}Q$ and column base horizontal displacement $_{cb}\delta_h$ up to the concrete edge failure are shown in Figure 8. The shear resistance of column base $_{cb}Q$ is calculated as the combination of the shear force of column and the horizontal component of brace force. The cracking patterns of specimens at the column base horizontal displacement of 3mm and after testing are shown in Fig. 9.

As indicated in Figure 9, the concrete edge failure occurred at the column base horizontal displacement around 2 mm. When the concrete edge failure occurred, the diagonal cracks propagated from the anchor bolts at the upstream of the loading direction were observed for all the specimens. And the cracks caused by bending at the bottom of the projection of foundation beam were observed, too. For the specimens with the anchor bolts spacing s_1 not larger than the edge distance c_1, specimens "T-1.0", "T-1.0_U.R.", and "T-0.75", the diagonal cracks developed from the anchor bolts at the downstream (back A.B.) of the loading direction directly after the propagation of the diagonal cracks at the upstream anchor bolts (front A.B.). For the specimen with the anchor bolts spacing s_1 is 1.5 times the edge distance c_1, specimen "T-1.5", the diagonal cracks from the back anchor bolts developed when the shear resistance was 290 kN, after the propagation of the cracks from the front anchor bolts. The strength deterioration caused by the edge failure was not observed for all the specimens even for the unreinforced specimen, specimen "T-1.0_U.R". The reason will be discussed in the following section. In comparison with the unreinforced specimen, the initial stiffness of the reinforced specimens was larger. The initial stiffness was further increased because of the presence of the hairpin reinforcement around the anchor bolts.

As shown in Figure 9, the edge failure resistance of the reinforced specimen ("T-1.0") is slightly smaller than that of the unreinforced specimen ("T-1.0_U.R."). It is the same as observed in the previous study (Asada et al. 2010). The reduction of the strength is caused by the reduction of the effective concrete surface in the failure region, since the

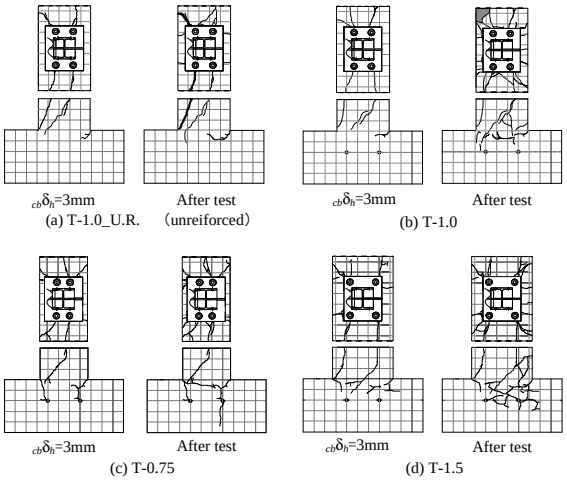


Figure 9 Cracking Patterns of Concrete Foundations

reinforcing bars occupied the part where the concrete was. Therefore, the increment of the edge failure resistance of the strength specimen ("T-1.0_S.R.") is slight compared with the unreinforced specimen ("T-1.0_U.R.").

3.2 Evaluation of the edge failure resistance

Two methods, the AIJ design guideline (AIJ, 2006) based on the 45 degree concrete cone method and CCD method (Hofmann, 2004), are adopted in this study to evaluate the edge failure resistance of the anchor bolts in shear. For the calculation, it is assumed that the four anchor bolts transferred the shear force evenly and the shear force when the edge failure caused by the front two anchor bolts occurred is the sum of the shear force transferred by the four anchor bolts. The evaluations based on AIJ design Recommendation (AIJ, 2010) and CCD method (Hofmann, 2004) are as follows.

$$_{AIJ_c}Q_{ce} = 2\times 0.31\sqrt{\sigma_B}\cdot A_c \qquad (2)$$

where, A_c is the projected areas for a group of anchor bolts, as shown in Figure 11(a).

$$_{CCD_c}Q_{ce} = 2\times\frac{A_{cc}}{A_{cc0}}\cdot\Psi_s\cdot\Psi_h\cdot Q_0 \qquad (3)$$

where,

$$Q_0 = 3.0\cdot d^{\alpha}\cdot l_e^{\beta}\sqrt{\sigma_B}\cdot c_1^{1.5} \qquad (4)$$

$$\alpha = 0.1\cdot\left(\frac{l_e}{c_1}\right)^{0.5} \qquad (5) \qquad\qquad \beta = 0.1\cdot\left(\frac{d}{c_1}\right)^{0.2} \qquad (6)$$

$$\Psi_s = 0.7 + 0.3 \cdot c_2 / (1.5 \cdot c_1) \le 1 \quad (7)$$

$$\Psi_h = (1.5 \cdot c_1 / h)^{1.5} \ge 1 \quad (8)$$

where, l_e is the embedded length of anchor bolt, d is the diameter of anchor bolt, A_{cc0} is the projected area for a single anchor bolt without the effect of the edge distance and group effect ($=4.5c_1^2$), h is the height of the projection of foundation, and A_{cc} is the projected area for anchor bolts considering the effect of edge distance and group effect, as shown in Figure 10-(b).

The calculated strengths are compared with the experimental results in Table 3. The calculated edge failure resistances using AIJ method and CCD method agree with the experimental results well. The calculated strengths of unreinforced specimen "T-1.0_U.R." and strengthen specimen "T-1.0_S.R" are smaller than the experimental results within 10% difference, which is conservative for design, while, the calculated strengths of reinforced specimens are slightly larger than the experimental results around 12% difference.

In this study, the edge distance along the loading direction c_1 is relatively small, the edge distance perpendicular to the loading direction c_2 and the anchor bolt spacing perpendicular to the loading direction s_2 are sufficient. Therefore, both the AIJ and CCD method are able to evaluate the resistance reasonably within an acceptable accuracy. However, the AIJ method is not able to trace the size effect of the edge distance along the loading direction c_1 and the reduction of resistance caused by the reduction of the edge distance perpendicular to the loading direction c_2.

3.3 Shear resistance after the edge failure

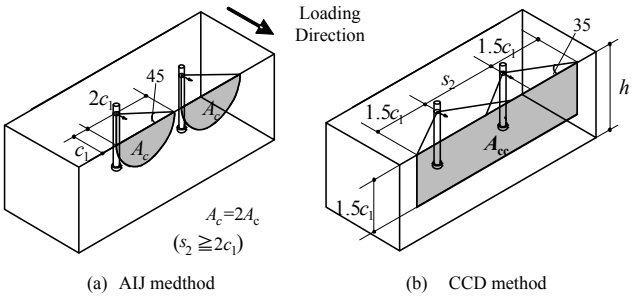
The relationships of shear resistance of column base ${}_{cb}Q$ and column base horizontal displacement ${}_{cb}\delta_h$ till the end of loading, when the horizontal displacement ${}_{cb}\delta_h$ was 20mm, are shown in Figure 11. As show in Figure 11, The shear resistances of the column base connections including unreiforced specimen "T-1.0_UR were increased steadily even after concrete edge failure occur. It is primarily because the shear resistance of the back anchor bolts (in tension side), is much larger than that of front anchor bolts (in compression side) governed by concrete edge failure. In addition, based on the crack patterns shown in Fig. 10, it is speculated that back anchor bolts resist to the shear force by forming of strut between the back anchor bolts and the main reinforcement of the foundation beam described in Figure 12.

Therefore, if the shear resistance of the back anchor bolts is larger than the concrete edge failure resistance, the shear resistance of the column base connections is governed by that of the back anchor bolts

Using the evaluation of shear resistance of studs with large enough edge distance in loading direction recommended by AIJ (AIJ 2010) the maximum shear resistance of the unreinforced specimen "T-1.0_UR" governed by back anchor resistance is calculated as follows;

$${}_cQ_{cu} = 0.5 \cdot {}_t n \cdot {}_b A \sqrt{\sigma_B \cdot E_c} \quad (9)$$

in which, ${}_tn$ is the number of the anchor bolts in tension side, ${}_bA$ is the section area of on anchor bolt, ${}_cE_c$ is the young Modulus of concrete, and σ_B is the compressive stress of concrete. As shown in Figure 11, the calculated shear resistance governed by the back anchor bolts using Eq. (9) agreed with the measured maximum shear resistance of the unreinforced specimen "T-1.0_U.R." well. After the loading, it is observed that the concrete bearing the back anchor bolts was crushed as shown in Photo 1. Such failure indicated that



(a) AIJ medthod (b) CCD method

Figure 10 Idealized Concrete Failure Body Assumed in AIJ and CCD Medhods

Table 3 Comparison between Calculated and Experimental Concrete Edge Failure Load

Specimens	${}_eQ_{ce}$ [kN]	${}_{AIJ_c}Q_{ce}$ [kN]	${}_{CCD_c}Q_{ce}$ [kN]	${}_eQ_{ce}/{}_{AIJ_c}Q_{ce}$	${}_eQ_{ce}/{}_{CCD_c}Q_{ce}$
T-1.0	265.23	283.11	282.95	0.94	0.94
T-1.5	264.45			0.93	0.93
T-0.75	249.90			0.88	0.88
T-1.0_S.R.	292.20	267.59	258.98	1.09	1.13
T-1.0_U.R.	283.16	283.11	282.95	1.00	1.00

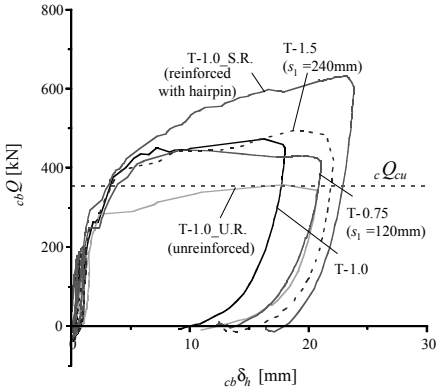


Figure 11 Shear Resistance of Column Base after Concrete Edge Failure occurred

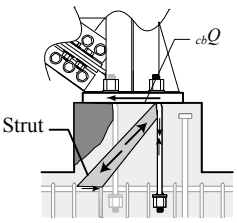


Figure 12 Shear Resistance by Forming of Strut



Photo 1 Bearing Failure of Back Anchor Bolt Observed in T-1.0_U.R.

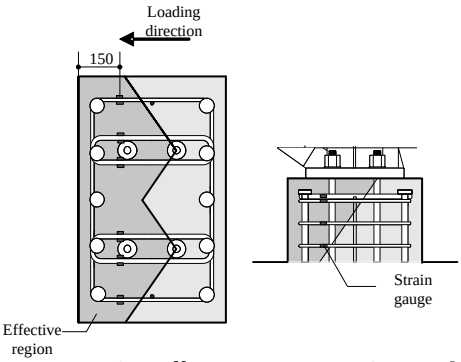


Figure 13 Effective Resistance Area and Arrangement of Strain Gauges

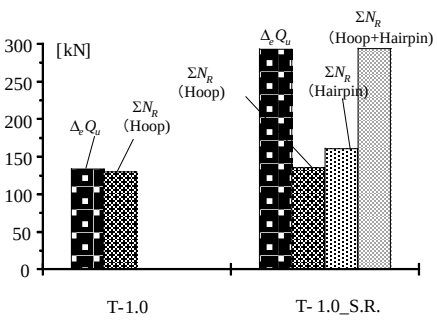


Figure 14 Contributions of Reinforcements around Anchor Bolts

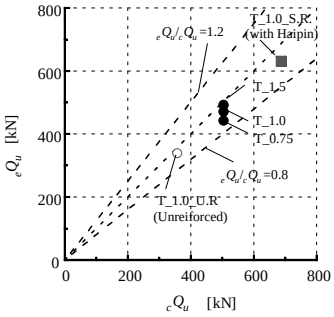


Figure 15 Comparison of Calculated and Experimental Maximum Shear resistance

the shear strength was mainly transferred by the strut mechanism between the back anchor bolts and the foundation beam after the concrete edge failure.

Note that, to form the strut for the shear resistance, the shear failure strength of the back anchor bolts is required to be larger than the concrete edge failure resistance. And the anchor bolts are needed to be embedded in the foundation beam with enough anchorage. Moreover, according to the crack patterns observed in this study, the edge distance of the back anchor bolts along the loading direction c_1+s_1 should not be smaller than the height of the projection of the foundation beam to ensure the strut develop sufficient width. However, there is few available test data on the strut mechanism. Further study is needed to quantify the conditions for the strut mechanism.

As shown in Figure 12, the maximum shear resistances of the reinforced specimens are larger than that of the unreinforced specimen. And the increments were nearly the constant regardless of the variation of the anchor bolts spacing s_1. The maximum shear resistance of the strengthen specimen "T-1.0_S.R" was further increased compared with the reinforced specimens, because of the presence of the hairpin reinforcement.

The contribution of the reinforcement to the shear resistance is discussed using the measured axial strain of the reinforcement. The arrangement of the strain gauges is shown in Figure 13 The strain gauges were attached on the reinforcements along the loading direction within the effective region (Asada et al. 2010), which is the same as the failure area of the CCD method.

The increment of the maximum shear resistance of the reinforced specimen "T-1.0" and the specimen reinforced with hairpin "T-1.0_S.R." from that of the unreinforced specimen "T-1.0_U.R." $\Delta_e Q_u$ is compared with the total axial force of reinforcement in the effective region at the maximum shear resistance ΣN_R in Figure 14. It is noted that the contribution of the reinforcement in the effective region is nearly the same as the increments of the maximum shear resistance for both specimens.

Based on the observations, the maximum shear resistance of the reinforced specimen is the combination of the tension resistance of the horizontal reinforcement in the effective region and the shear resistance of the back anchor bolts, Eq. 10.

$$_cQ_u = {}_cQ_{cu} + {}_cQ_{ru} = \min\left\{{}_cQ_{cu1}, {}_cQ_{cu2}\right\} + \sum {}_r a \cdot {}_r\sigma_y \quad (10)$$

in which, $\Sigma\, {}_r a \cdot {}_r\sigma_y$ is the yield strength of the reinforcement s in the effective region.

The comparison between the calculated and experimental maximum shear strength of the specimens, $_cQ_u$ and $_eQ_u$, after the concrete edge failure occurred is shown in Figure 15. The calculated strength agreed with the measured strength well. According to the test results, it is clarified that the shear resistance of the column base is improved by the presence of the horizontal reinforcement within the effective region.

4. CONCLUSIONS

Cyclic loading tests were conducted to investigate the shear resistance governed by concrete failure of exposed-type column base in steel braced frame. Form the experimental results, It is conformed that applicability of existing evaluation methods of concrete edge failure and maximum shear resistance of anchor bolts with high strength after concrete edge failure.

References:

Building Research Institute (2004), "A Survey Report for Bullding Damages Due to The 2006 Niigata-ken Chuetsu Earthquake" (in Japanese)

Klingner, R. et al. (1982), "Shear Capacity of Short Anchor Bolts and Welded Studs : Literature Review," *ACI Journal*, Vol.79, No.4, 270-279

Fuchs, W. et al. (1995), "Concrete Capacity Design (CCD) Approach for Fastening to Concrete," *ACI Structural Journal*, V.92, No.1, 73-94

Kawano, H., et al. (2003), "Experimental Study on Shear Resistance of anchor bolts in Exposed-type of Steel Column Bases," *Journal of Structural and Construction Engineering*, AIJ, No.567, 141-148 (in Japanese)

Asada H., Kishiki S., and Yamada S. (2010), "Shear Resistance of Anchor Bolt with Small Free Edges in Exposed Type Steel Column Base," *Journal of Structural and Construction Engineering (Transactions of AIJ)*, No.654, 1517-1525. (in Japanese).

AIJ (2010), "Design Recommendations for Composite Construstions"

Hofmann J. (2004), "Tragverhalten und Bemessung von Befestigungen unter beliebiger Querbelastung in ungerissenem Beton," (in German)

8CUEE CONFERENCE PROCEEDINGS
8th International Conference on Urban Earthquake Engineering
March 7-8, 2011, Tokyo Institute of Technology, Tokyo, Japan

STRENGTH EVALUATION OF INTERFACE WELD OF GUSSET PLATE CONNECTIONS

Yao Cui[1], Hayato Asada[2], Shoichi Kishiki[3], and Satoshi Yamada[4]

1) G-COE Fellow, Center for Urban Earthquake Engineering, Tokyo Institute of Technology, Japan
2) Graduate Student, JSPS Research Fellow, Tokyo Institute of Technology, Japan
3) Assistant Professor, Structural Engineering Research Center, Tokyo Institute of Technology, Japan
4) Associate Professor, Structural Engineering Research Center, Tokyo Institute of Technology, Japan
cui.y.aa@m.titech.ac.jp, asada@serc.titech.ac.jp, kishiki@serc.titech.ac.jp, naniwa@serc.titech.ac.jp

Abstract: Braced frames are commonly used lateral-load resisting systems in seismic design. In braced frames the braces are connected to the beams and columns by gusset plate connection. And fillet welds are commonly used to connect the gusset plate to frame. The ultimate strength of the weld between gusset plate and frame components is determined by the weld effective length, size and stress. However, there is not a standard design method for the interface weld in Japan. Experimental study was conducted and showed that the Whitmore effective region concept works well. To improve the understanding and design of the ultimate strength of welded gusset plate connections, a series of analytical study was undertaken. The verified numerical model was used to evaluate the ultimate strength of the welded gusset plate connection and interface forces at the gusset-to-beam/column. A parametric study was conducted to examine the influence of he gusset plate size, brace angles, and eccentricity of brace on the connection interface forces. Based on the results, an evaluation of the effective length was suggested.

1. INTRODUCTION

Braced frames are widely used for steel constructions in seismic regions. In general, the axial load from the brace is transferred to the beam and column through the gusset plate, which is normally bolted or welded to the brace and connected to the column and beam by welds. Gusset plate should have sufficient strength and stiffness to transfer the applied forces. Fracture of a gusset plate connection will result in considerable loss of strength and stiffness of the brace. The seismic performance of the braced frame will be thereby reduced. Many experimental and analytical studies have conducted to investigate the behavior of gusset plate connections. And the design provisions were updated based on the studies (AISC, 2005).

Fillet welds are widely used to connect the gusset plate to beams and columns. The fracture of weld between gusset plate and beams and columns is the brittle failure and should be avoided during the design (Astaneh-Asl, 1998 and Roeder et al. 2005). However, few studies have done yet on the interface weld of gusset plate connection (Thornton, 1991, Richard, 1986, and Gross, 1990). Although the welds were sized to develop the expected tensile yield capacity of the brace following the design provisions, the fracture of interface welds of gusset plate was observed in previous studies (Yoo et al. 2008) and earthquakes (Elnashai and Samo, 2008).

There are various design practices to evaluate the resistance capacity of interface welds of the gusset plate connection in Japan. However the adequacy of the methods of design with respect to safety and economy of construction has not been confirmed. In this paper, the current design practices of the interface welds of gusset plate connections in Japan are discussed with previous experimental study (Asada et al. 2011) and a series numerical analytical parametric study.

2. CURRENT DESIGN PRACTICE IN JAPAN

In Japan, three design methods of the interface weld of gusset plate connections are commonly used. The differences of the three design methods are the effective length of the interface weld and the direction of the interface force. The details of the three design methods are introduced as follows.

1. Method I -- AIJ method (AIJ, 2006)

This method is recommended by Architectural Institute of Japan (AIJ, 2006). The effective weld length and interface force direction were considered. As shown in Fig. 1, the effective weld length ($_{AIJ}l$) is nominally the shortest length between entire interface weld length and the length controlled by the 30-degrees effective region. If the end returns is not used, the effective length should subtract two times the nominal fillet weld size (S) for the calculation. In the following discussion, the influence of the end of weld is

neglected by assuming the end returns were used. The resistance of interface weld is assumed parallel to the brace. The resistance capacity of the interface weld is calculated as Eq. 1.

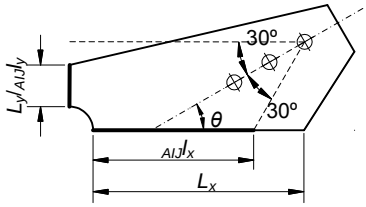


Fig. 1 Effective length of interface weld

$$N_{u,I} = 2_{AIJ}\, l_x (1+0.4\sin\theta) a \frac{{}_c F_u}{\sqrt{3}} + 2_{AIJ}\, l_y (1+0.4\cos\theta) a \frac{{}_c F_u}{\sqrt{3}} \quad (1)$$

where, θ is the brace angle; ${}_cF_u$ is the tensile stress of base material, and a is the throat size of weld.

2. Method II -- Practical method (BCJ, 2007)

Method II is the most commonly used in Japan for the interface weld design. The entire interface weld length is counted. And the direction of interface weld is not considered, by assuming the interface weld failed by pure shear. The resistance capacity of the interface force is calculated as Eq. 2.

$$N_{u,II} = 2(L_x + L_y) a \frac{{}_c F_u}{\sqrt{3}} \quad (2)$$

where, L_x and L_y are the entire interface weld lengths in beam and column side, respectively.

3. Method III -- Simple method (JSSC, 2009)

This is a simplest design method. It is simple with respect to calculations but it yields very conservative designs. As with Method II, the entire interface weld length is counted for the design. In this method, the entire horizontal and vertical brace component were assumed be transferred by the beam and column side, respectively. This method is similar to the Special Case 1 of the Uniform Force Method (UFM) (AISC, 2005).

$$N_{u,III} = \min(N_B, N_C) \quad (3)$$

$$N_B = 2 \cdot L_x \cdot a \cdot \frac{{}_c F_u}{\sqrt{3}} / \cos\theta \quad (3a)$$

$$N_C = 2 \cdot L_y \cdot a \cdot \frac{{}_c F_u}{\sqrt{3}} / \sin\theta \quad (3b)$$

The experimental research at Tokyo Institute of Technology (Asada et al. 2011) provided a basis of the analytical research and design methods. The test specimens were full-scale as illustrated in Fig.3. Each specimen consisted of two end plates (PL-26x200x269 and PL-26x200x258) and one gusset plate (t_p=12 mm). All specimens were fabricated by SM490 steel. The bracing angle of 30 degrees was used. Tapered gusset plates were used for all specimens. The parameter of the specimens was the geometry size of the gusset plate. Fillet welds were used to connect the gusset plates to the endplates. The designation of the specimen indicated the studied parameter and its value, e.g., Specimen B135-C45 is the specimen with the gusset plate having 135 mm and 45 mm interface weld along beam and column side, respectively.

All specimens were loaded monotonically till the failure of either gusset plate or interface weld. Linear variable displacement transducers (LVDTs) were used to monitor the displacements of the gusset plate specimens and the test frame assembly. In order to measure the strain distribution in the gusset plate, strain gages were placed on each specimen, on one side of the gusset plate.

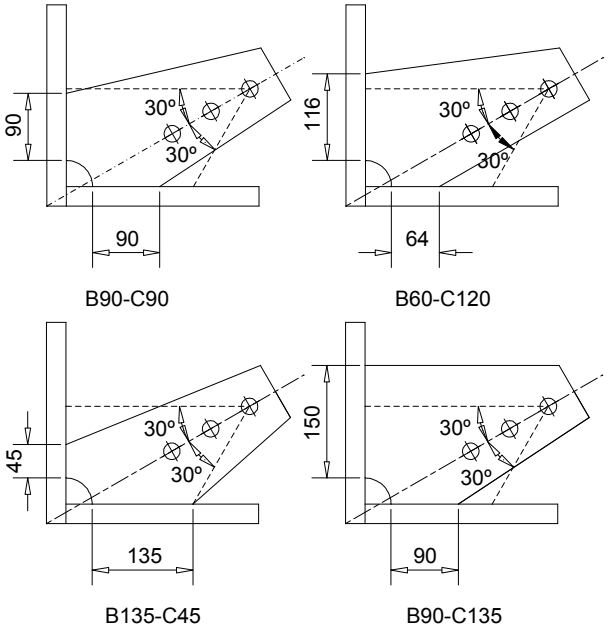


Fig.2 Gusset plate connection specimen

Four specimens failed in two different failure modes. Specimen B135-C45 failed by fracture of interface weld (Fig. 4 (b)). Specimens B90-C90, B60-B120, and B90-C150 failed by fracture of net area of gusset plate through the last bolt of brace-to-gusset connection (Fig. 4 (c)). The measured maximum axial forces transferred by the specimens are listed in Table 2.

The measured ultimate strength was used to assess the accuracy of weld size prediction of the three models introduced. As illustrated in Table 1, the Method III[8] provided the largest and most conservative weld size in comparison with the other two methods. The weld sized by Method I[6] is the closest to the measured from the experimental specimens.

It is noted that the interface weld could be designed reasonably if the contribution of the interface welds in both beam and column side are considered in the design. However, the consideration of the effective length and the interface angle is not clear. In the following sections, such

issues are explored using finite element method analysis. A numerical model is developed to simulate the gusset plate behavior till the fracture of interface weld. A series of parametric studies are conducted to investigate the effect of the gusset plate size and brace angle on the effective length and resistance capacity of interface weld.

Table 1 Experimental results

Specimen	$_{exp}P_{br,u}$ (kN)	Failure Mode	Weld size, S (mm)			
			Measured	Design		
				S_I	S_{II}	S_{III}
B90-C90	679	GP	5.5	7	9	15
B60- C120	608	GP	5.6	7	8	22
B135- C45	695	W	5.6	7	9	18
B90- C150	696	GP	5.7	7	7	18

* GP indicated the fracture of gusset plate; W indicates the fracture of weld

3. VERIFICATION OF NUMERICAL MODELING

A comprehensive series of nonlinear, inelastic FE analyses were performed to simulate the response of the test specimens using the ABAQUS 6.9 (ABAQSU, 2009). Figure 3 shows a typical FE model of a gusset plate connection specimen. The gusset plate at the intersection between beam and column was partitioned into 5 mm height slice to represent the weld. The FE model was constructed using 3D solid element for all of the members. 8-node linear brick, reduced integration element (C3D8R) was used for the gusset plate and two endplates. The equivalent region of weld on the gusset plate was modeled by 8-node linear brick element (C3D8). A mesh refinement study was conducted to determine the mesh size required to ensure convergence and accuracy of the FE solution and simultaneously minimizing the execution time. On the basis of this study, a fine mesh (5 mm) was used for the gusset plate, and finer mesh (2.5 mm) was used for the weld part. A coarser mesh was used for endplate due to the elastic behavior observed in the experiments.

Elastic-plastic and isotropic strain hardening material models were assigned to gusset plate based on measured stress-strain relationships obtained from the experimental research, as shown in Fig. 3 (b). Elastic material with the modulus of elasticity of 205000 MPa was assigned to the endplates. Elastic-plastic material with a maximum stress of 575 MPa and stress reduction to 100 MPa at strain of 0.1 was assigned to the weld region on the gusset plate, as shown in Fig. 3 (b).

The translational degrees of freedom at the nodes along the bolt holes of the two endplates were fully restrained. The load was applied through the nodes along the front half side bolt holes considering the bearing interaction between bolts and gusset plate. Monotonic in-plane displacement was loaded along the brace direction in tension, as shown in Fig. 3 (c).

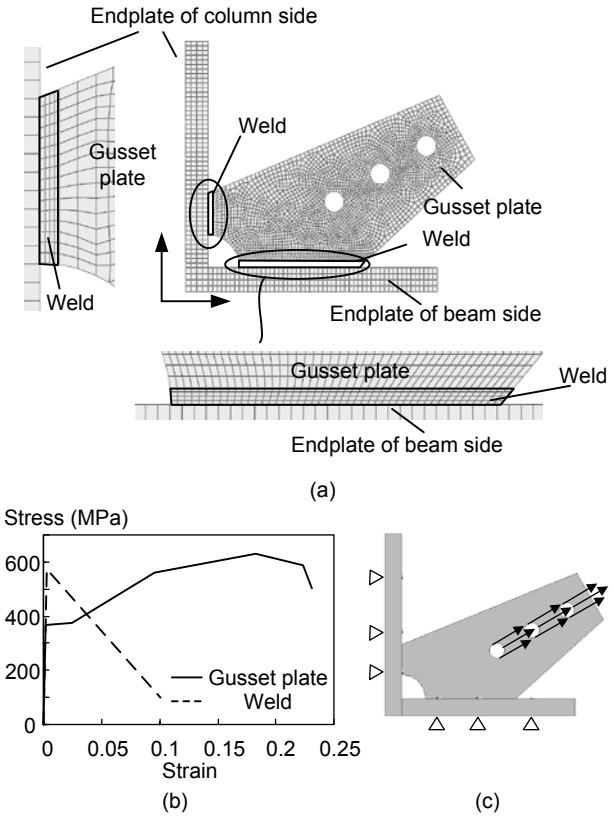


Fig. 3 Model of test specimen: (a) FE model; (b) material properties; (c) boundary condition

Specimens B135-C45 and B90-C90, which failed in different failure modes, were chosen to verify the FE model. The experimental and analytical relations between the axial load and the displacement for Specimens B135-C45 and B90-C90 are shown in Fig. 4. The FEM model closely approximated all aspects of the measured response. The difference between experimental and analytical maximum strength is 3% and 14% for specimens B135-C45 and B90-C90, respectively.

The analytical model also simulated the local behavior well. Figure 4 (b) and (c) show observed (experiment) and simulated (FE model) failure pattern. The failure portion of the analyzed specimen is indicated by the contours of the maximum principal plastic strain (PE) distribution. The failure regions are marked in white, where the tensile strain reached to the critical levels, i.e., the strain is larger than 10% and 20% for weld and gusset plate, respectively. As indicated in the strain contours, few portion of the gusset plate along the last bolt of the brace-to-gusset plate connection reached the critical strain level; however, the entire interface weld on column side reached the strain level far larger than the critical strain level for specimen B135-C45. For specimen B90-C90, the net section through the last bolt of the brace-to-gusset plate connection reached the critical strain level while the other portion was still in low strain level. The failure region shown by the critical strain level agreed with observed failure mode well.

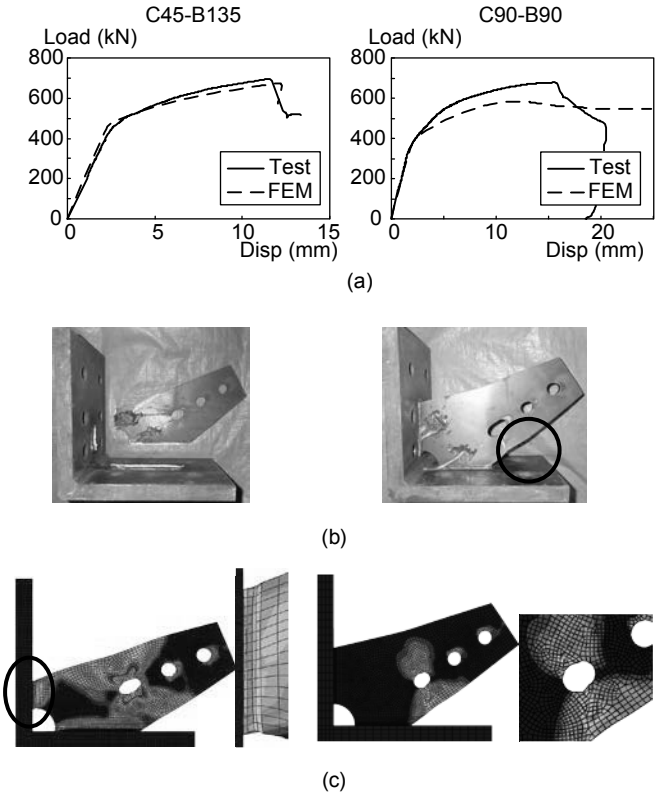


Fig. 4 Comparison between test and FE analysis: (a) load-displacement, (b) failure mode of experimental specimens, and (c) failure mode of analytical specimens

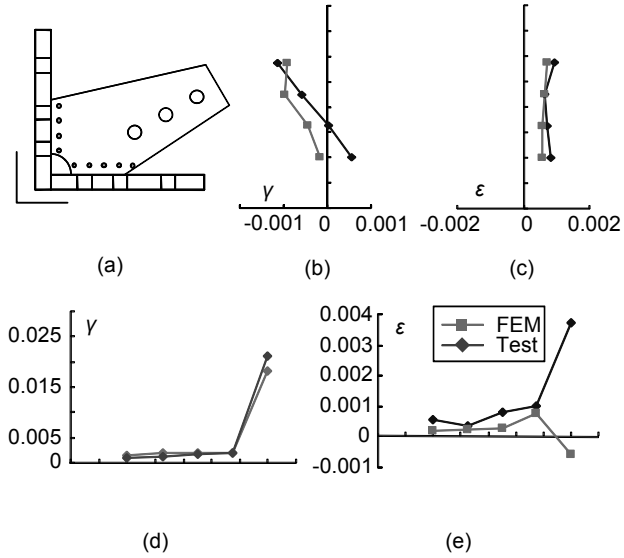


Fig. 5 Comparison of strain distribution of specimen B90-C90 between test and FE analysis: (a) strain gauge location; (b) shear stress on column side; (c) normal stress on column side; (d) shear stress on beam side; (d) normal stress on beam side

The strain distributions along the region close to the interface weld (Fig. 5 (a)) were measured in the experiments. The simulated strains distributions were compared with the experimental strains distribution at the maximum axial brace force in Fig. 5 (b-e). It is noted that the analytical normal and shear strain distribution agreed with the experimental results well. On the basis of these investigations, it can be concluded that the FE model simulated the local behaviors quite well.

It is noted in Fig. 4(b) of Part I that the gusset plate of Specimen B135-C45 yield around the blot holes when the maximum brace force was reached because of the interface weld fracture. Such damage in the gusset plate lowered the resistance of the gusset plate connection and the resistance demand of the interface weld was reduced. Therefore, to investigate the maximum resistance capacity of the interface weld, the elastic material property was assigned to the gusset plate. The load-displacements of Specimen B135-C45 with elastic and elastic-plastic material property were compared in Fig. 6 (a). The maximum strength transferred by gusset plate was significant increased with the elastic gusset plate. The Von-Mises stress distributions along weld of beam and column side are compared in Fig. 6 (b). The mises stress reached the maximum stress of weld and distributed uniformly along the interface weld for the model with elastic gusset plate in comparison with the one with plastic gusset plate. The capacity of the interface weld was fully developed with elastic gusset plate. The elastic gusset plate was used for the following parametric study.

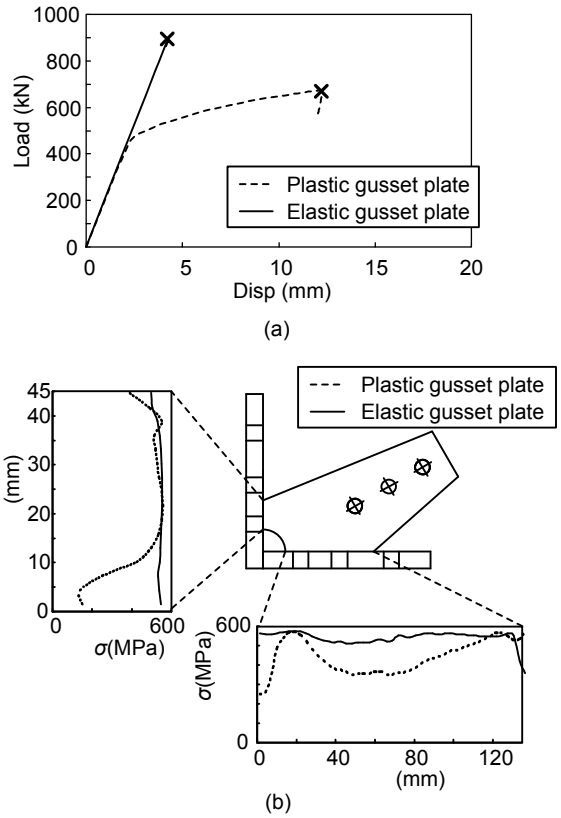


Fig.6 Comparison of results between plastic gusset plate and elastic gusset plate: (a) load-displacement response; (b) von Mises stress distribution along weld

4. PARAMETRIC ANALYSIS

4.1 Overview of analytical parameter study

The parameters include the geometry of the gusset plate (L_x, L_y), brace angle (θ), and eccentricity of the brace along beam side (e_x), as shown in Fig. 7. The brace angle (θ) is defined as the angle that the bracing member makes with the beam. Gusset plate size was varied based on the Whitmore effective region and the rectangular shape. Four types interface weld length were chosen for beam and column side, respectively. They are half the Whitmore effective length (0.5 $_{30}l$), the Whitmore effective length ($_{30}l$), the length between Whitmore effective length and rectangular length (0.5 ($_{30}l$+ $_{rect}l$)), and the rectangular length ($_{rect}l$). Brace angle was 30 and 45 degrees. Eccentricity along beam side is controlled by the offset ratio β (see Eq. (4)). In this study, the offset ratio of 0.25 and 0.33 were used.

$$\beta = \frac{e_x}{r_x + L_x} \tag{4}$$

where, r_x is the size of the weld access hole on beam side , e_x is the offset distance of the brace along the beam side.

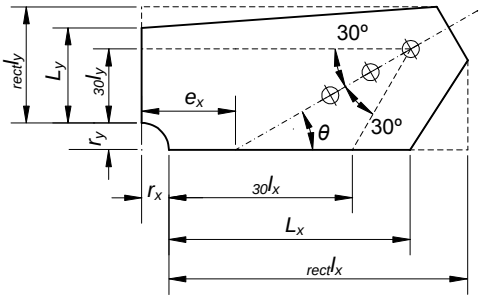


Fig.7 Gusset plate geometry details

The parameters groupings and specific values for individual specimens that were analyzed within each group are identified in Table 2 (shaded cells indicate the prototype models for the models with brace eccentricity). Analytical specimen B135-C45 indicates the gusset plate with the length of 135 mm and 45 mm in beam and column side, respectively. For the specimens with brace eccentricity, specimen B135-C90-033E indicates the gusset plate B135-C90 with the brace offset ratio of 0.33, the name in brackets indicates the size of the specimen.

Table 2 Model List

a) θ=30º, No eccentricity

L_y (mm)	L_x (mm)			
	60	135	200	265
45	B60-C45	B135-C45	B200-C45	B265-C45
90	B60-C90	B135-C90	B200-C90	B265-C90
120	B60-C120	B135-C120	B200-C120	B265-C120
150	B60-C150	B135-C150	B200-C150	B265-C150

b) θ=45º, No eccentricity

L_y (mm)	L_x (mm)			
	60	108	165	217
60	B60-C60	B108-C60	B165-C60	B217-C60
108	--	B108-C108	B165-C108	B217-C108
165	--	--	B165-C165	B217-C165
217	--	--	--	B217-C217

c) θ=30º, Eccentricity

α	0.25	0.33
B60-C45	B60-C45-025E (B92-C45)	B60-C45-033E (B105-C45)
B135-C90	B135-C90-025E (B190-C90)	B135-C90-033E (B220-C90)
B200-C120	B200-C120-025E (B280-C120)	B200-C120-033E (B315-C120)
B265-C150	B265-C150-025E (B365-C150)	B265-C150-033E (B410-C150)

d) θ=45º, Eccentricity

α	0.25	0.33
B60-C60	B60-C60-025E (B92-C60)	B60-C60-033E (B150-C60)
B108-C108	B108-C108-025E (B155-C108)	B108-C108-033E (B180-C108)
B165-C165	B165-C165-025E (B230-C165)	B165-C165-033E (B265-C165)
B217-C217	B217-C217-025E (B300-C217)	B217-C217-033E (B340-C217)

4.2 Results

4.2.1 Interface stress distribution

Typical von-Mises stress distributions along interface weld at the ultimate strength were shown in Fig. 8, in which the dash line showed the AIJ effective length ($_{AIJ}l$). The analytical specimens B135-C45 and B108-C108 (Fig. 8 (a and b)), whose gusset plate size are within the Whitmore effective region, showed the uniform stress distribution of interface weld along both beam and column side. And the stress of interface weld reached the ultimate weld stress. For the analytical specimen B217-C217, whose gusset plate size is larger than the Whitmore effective region, the stress of the interface weld reached the ultimate weld stress and uniformly distributed within the Whitmore effective region. And the weld stress gradually reduced along the interface weld in the part out of the Whitmore effective region.

Figure8 (d) showed the stress distribution of the analytical specimen B135-C90, in which the column side interface weld length increased from 45 mm to 90 mm compared with the specimen B135-C45 (Fig. 8 (a)). In this specimen, the weld stress reached the ultimate stress and uniformly distributed along beam side, while the stress of interface weld on column side did not reach the ultimate weld stress. The same behavior was observed for the analytical specimen B108-C60 (Fig. 8 (e)), in which the column side interface weld length reduced from 108 mm to 60 mm compared with the specimen B108-C108 (Fig. 8 (b)).

The stress distribution of the analytical specimen B217-C217-033E (B300-C217), in which the brace axis is offset by 121 mm from the gusset plate corner, is shown in Fig. 8 (f). It is noted the weld stress uniformly reached the ultimate weld stress along beam side within the Whitmore effective region. However, the weld stress of column side did not reach the ultimate weld stress and uniformly stress distribution was not observed, even the interface weld along

column side is longer than the AIJ effective length.

As observed from the analytical results, the entire interface weld did not contribute to the resistance for all the size of gusset plate. The stress distribution of the interface weld is affected by the gusset plate size and brace angle.

4.2.2 Effective length

To quantify the resistance region of the interface weld, the effective length ($_{FEM}l$) is calculated using Eq.5. As illustrated in Fig. 9 (a), the weld stress is assumed to reach the ultimate stress and uniformly distributed along the interface weld within the effective length ($_{FEM}l$).

$$_{FEM}l = \frac{\sum L_i \cdot \sigma_i}{\sigma_{u,weld}} \quad (5)$$

Where, $_{FEM}l$ is the effective length calculated from the analytical results, L_i is the distance between each measured node, σ_i is the von-Mises stress at the measured node, $\sigma_{u,weld}$ (=575MPa) is the ultimate stress of the weld.

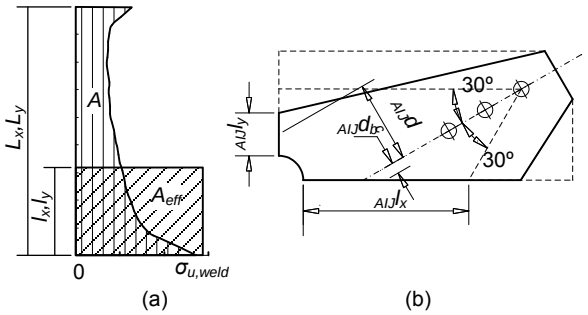


Figure 9 (a) Effective length from numerical results; (b) effective length of AIJ evaluation

The effective length evaluated based on the numerical results ($_{FEM}l$) are compared with the AIJ effective length ($_{AIJ}l$) in Fig. 10. It is noted that the effective length of interface weld is evaluated well by AIJ method ($_{FEM}l_y/_{AIJ}l_y \approx 1.0$) when the gusset plate size is within the Whitmore effective region and the distance from each interface weld to brace axis is nearly the same ($_{AIJ}d_b/_{AIJ}d_c \approx 1.0$). The effective length of interface weld on column side is underestimated by AIJ method ($_{FEM}l_y/_{AIJ}l_y < 1.0$) when the beam side distance is smaller than the column side ($_{AIJ}d_b/_{AIJ}d_c < 1.0$). And the effective length of interface weld on beam side is

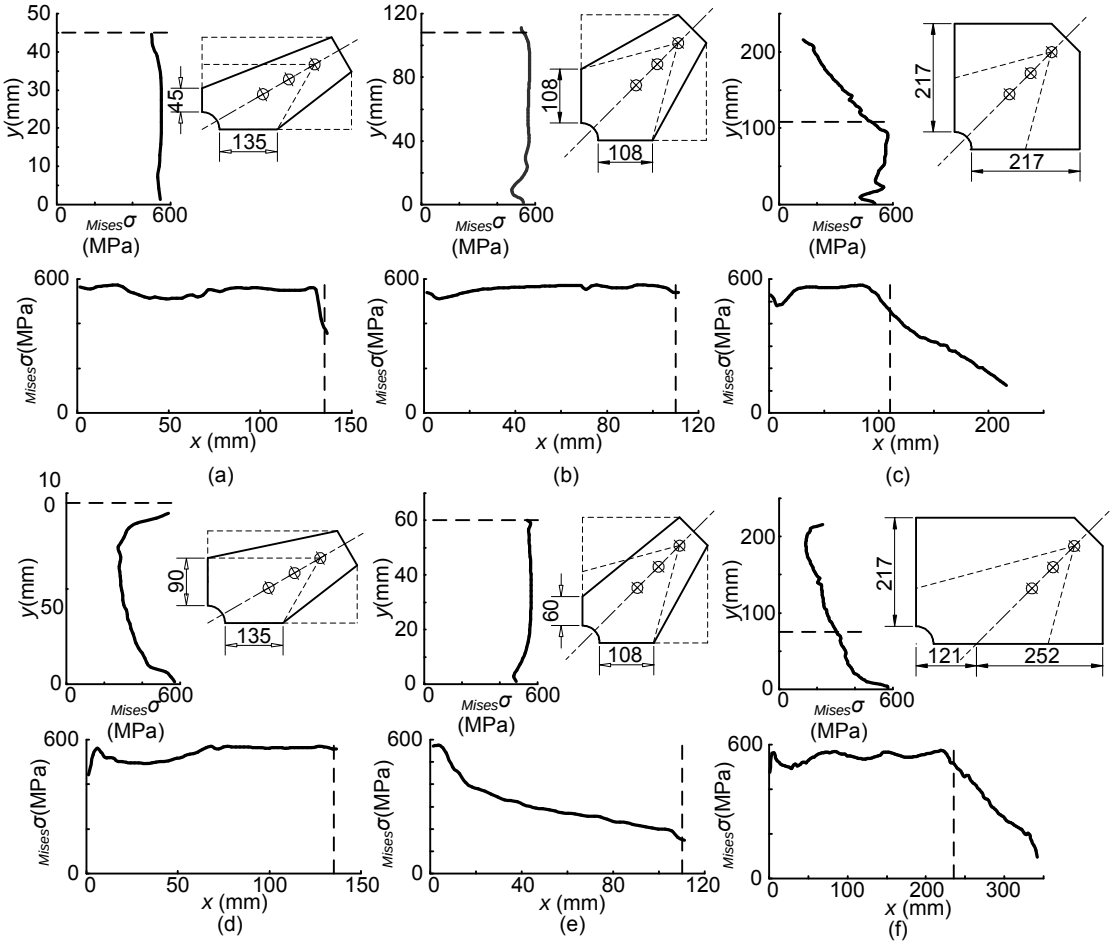
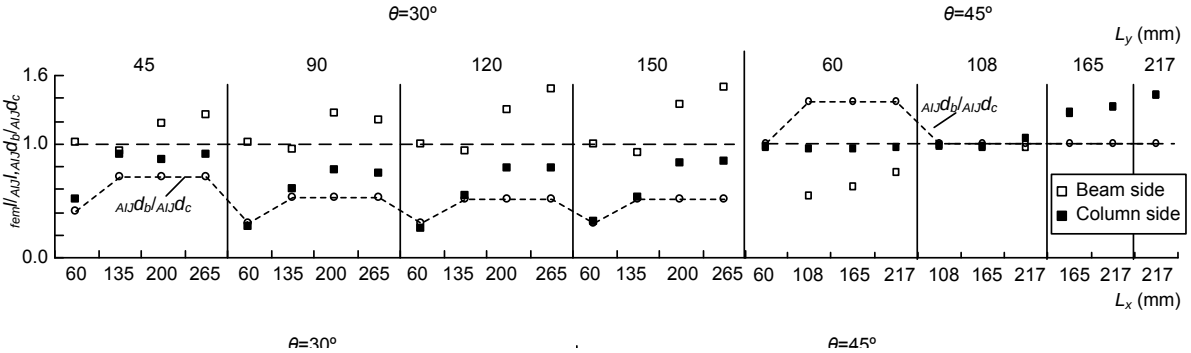


Figure 8 VonMises stress distribution along interface weld: (a) B135-C45; (b) B108-C108; (c) B217-C217; (d) B135-C90; (e) B108-C60; (f) B217-C217-033E (B340-C217)



underestimated by AIJ method ($_{FEM}l_x/_{AIJ}l_x$<1.0) when the beam side distance is larger than the column side ($_{AIJ}d_b/_{AIJ}d_c$>1.0).

When the gusset plate size is larger than the Whitmore effective region, the AIJ effective length ($_{AIJ}l$) tended to underestimate the effective length. It is primarily because the contribution of the stress distributed beyond the Whitmore effective region, as shown in Fig. 8 (c) and (f), is not counted by AIJ effective length. As the brace eccentricity along beam side increased, the effective length on column side was overestimated and the effective length on beam side was underestimated by AIJ effective length. And the beam side distance was reduced and the column side distance was increased as the brace eccentricity increased, the ratio of the beam and column side distance was thereby reduced.

5. CONCLUSIONS AND RECOMMENDATIONS FOR FUTURE WORK

As observed from experimental study, AIJ effective length provide more accurate evaluation of interface weld effective length among the current design methods. A series of parametric study was conducted to investigate the effect of gusset plate size, brace angle, and brace eccentricity on the stress distribution of interface weld and resultant force distribution of gusset plate. It is observed that AIJ effective length method is not able to consider the interaction between beam and column side interface length and the effect of brace angle. A revised evaluation based on AIJ effective length was proposed in this study based analytical results.

The evaluation of effective length and ultimate strength of weld is developed based on the numerical results. Experimental study is required to verify the proposed evaluation. In addition, more parameters should be considered, such as the connection between brace and gusset plate and the effect of gusset plate plastic behavior.

Acknowledgements:

The authors acknowledge support from the Japan Ministry of Land, Infrastructure, Transport and Tourism for the Grants of Promotion of Development of Building Code 2010.

References:

ABAQUS/ Standard user's manual , version 6.9. (2009), Hibbitt, Karlson and Sorensen, Inc.

American Institute of Steel Construction (AISC). (2005). "Steel Construction Mnual, 13th Ed.," Chicago.

Architectural Institute of Japan (AIJ). Recommendations for Design of Connections in Steel Structures, Tokyo, 2006. (in Japanese).

Asada H., Yamada S., Kishiki S., and Minowada S. (2011), "Investigation of tension brace connections in existing steel gymnasium and evaluation on ultimate strength of fillet welded gusset plate connection," *Journal of Structural and Construction Engineering (Transactions of AIJ)*, Vol.76, No.659, 185-193. (in Japanese).

Astaneh-Asl, H. (1998). "Seismic behavior and design of gusset plates", Steel Tips, Structural Steel Education Council, Moraga, Calif.

The Building Center of Japan (BCJ). (2007), "Commentary of structure design provisions for buildings 2007," Government Publications Service Center, Tokyo. (in Japanese).

Bjorhovde, R and Chakrabarti, S. K. (1985), "Tests of Full-size Gusset Plate Connections", *Journal of Structural Engineering*, ASCE, Vol. 111, No. 3, March, 667-684.

Elnashai AS, Sarno LD. (2008), "Fundamentals of earthquake engineering," John Wiley & Sons, Ltd, London.

Gross, J. L. (1990). "Experimental study of gusseted connections", *Engineering Journal, Am. Inst. Of Steel Constr.*, v27 n3 3rd Quarter , p89-97.

Japanese Society of Steel Construction (JSSC). (2009), "Fundamentals of steel structure design (4th Edition), Gihodoshuppan, Tokyo. (in Japanse).

Lehman DE, Roeder CW, Herman D, Johnson S, Kotulka B. (2008), "Improved seismic performance of gusset plate connection," *Journal of Structural Engineering*, ASCE, **134**(6),890-901.

Richard, R. (1986), "Analysis of Large Bracing Connection Designs for Heavy Construction", *Proceedings of the 1986 National Engineering Conference*, AISC, Nashville

Roeder C, Lehman D, and Yoo, J.H. (2005), "Improved design of steel frame connections". *International Journal of Steel Structures*,141-53.

Thornton, W. A. (1991), "On the analysis and design of bracing connections". *Proc. 1991 AISC National Steel Construction Conf.*, Washington, DC, June, pp. 26-1-33.

Yoo J.H., Roeder C.W., and Lehman D.E. (2008), "Analytical performance simulation of special concentrically braced frames," *Journal of Structural Engineering*, ASCE, **134**(6), 881-889.

8CUEE CONFERENCE PROCEEDINGS
8th International Conference on Urban Earthquake Engineering
March 7-8, 2011, Tokyo Institute of Technology, Tokyo, Japan

SEISMIC DAMPING CONTROLLED SHEAR WALL SYSTEM AND ITS DESIGN METHODOLOGY

Chao Pan[1] and Dagen Weng[2]

1) PhD. Candidate, State Key Laboratory of Disaster Reduction in Civil Engineering, Tongji University, China
2) Professor, State Key Laboratory of Disaster Reduction in Civil Engineering, Tongji University, China
pcabaqus@gmail.com, wdg@tongji.edu.cn

Abstract: The design philosophy of regarding shear walls as seismic damping controlled elements (by meliorating the constructional details of the wall or installing damping devices in it) has been proved to be an efficient approach to enhance the seismic performance of structures with shear walls. This paper summarized and illustrated the conception of structural system with seismic damping controlled shear walls (DSW) based on the existing relevant research findings. The walls are controlled using various deformation types of the walls to activate the damping devices, such as vertical dislocation between adjacent walls, base rotation or shear deformation of walls, etc. The performance-based design methodology of structural system with DSW, including design principles, structural performance indices and design method, was proposed on account of vertical damping mechanism. An example of DSW structure was designed utilizing the proposed methodology of which the feasibility was verified by nonlinear dynamic analysis.

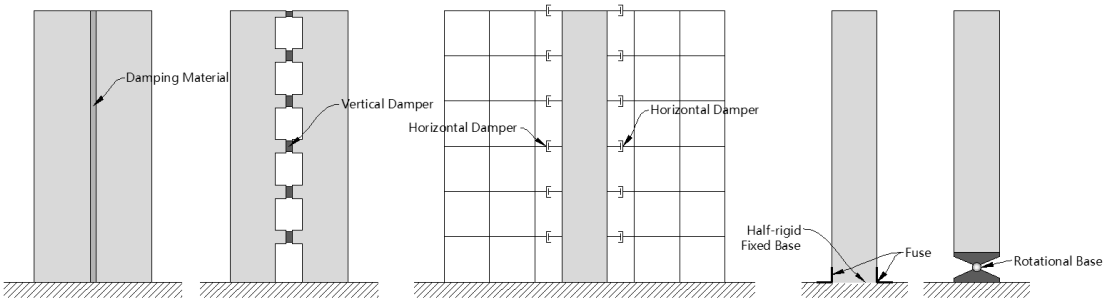
1. THE CONCEPT OF DAMPING CONTROLLED SHEAR WALL SYSTEM

The R/C shear wall is always regard as the first defence system of a high-rise building because of its great stiffness and strength, however, the lack of deform ductility make the shear wall less reliable during earthquakes. Lots of methods have been proposed based on the concept of structural control to enhanced the seismic performance of R/C shear walls, such as slit shear wall #, damped coupling beam (Chung et al. 2009), composite in-filled damping wall (Zhao 2004), rocking wall (Wada et al. 2009), etc. With better performance in seismic ductility and energy absorption capability, these damping controlled walls become more and more concerned in the field of earthquake engineering.

Damping controlled shear wall system, DSW for short, is an improved shear wall structure system (i.e., structure with R/C walls, e.g., shear wall structure, frame-shear wall structure, frame-tube structure, etc.) with detail-changed and damping-controlled walls, of which the controlling measures include setting slits in the wall, appending energy dissipative devices (EDD), and so on. Well-designed DSW can show better seismic performance than traditional R/C wall system. The damping mechanism and expected performance of the damping-controlled wall which is mainly composed of the wall and EDDs, are defined below based on different earthquake precaution levels: Under small earthquakes, the wall and EDDs keep elastic, providing enough lateral stiffness and well serviceability, meanwhile, the dynamic properties of the wall can be adjusted by changing the parameters of EDDs; as for moderate or strong earthquakes, the EDDs would yield, resulting in the reduction of the wall's stiffness and the earthquake action, simultaneously the yielding EDDs would also dissipate earthquake energy instead of the structure by means of reciprocating elastoplastic deformation or interfacial friction, therefore, the failure mode of the wall is changed with higher ductility and severe damage can be avoided. Essentially, the DSW is a compromise between stiffness and ductility, that is, the wall is weaken in stiffness in order to get a controllable failure mode with enhanced ductility and equipped with EDDs to absorb earthquake energy and attenuate the dynamic response.

2. CLASSIFICATION OF DAMPING CONTROLLED SHEAR WALL SYSTEM

Damping effect of the DSW is mainly depend on the following two ingredient: the type (viz mechanism) and location of EDDs. A favorable type of EDD should be provided with stable hysteresis character, excellent low-cycle fatigue performance, perfect adaptability to the environment and temperature, and satisfactory durability, while an agreeable location of EDDs should be able to supply the EDDs with deformation large enough to dissipate energy efficiently and the structure should not be excessively damaged when EDDs reach the predicted maximum deformation. According to the existing research findings related to DSW, types/mechanisms of EDDs used in DSW are interfacial friction, mild steel damper, rubber and so on,



(a) Vertical coupled (b) Horizontal coupled (c) Base-released rocking wall

Figure 1 Classification of Damping Controlled Shear Wall System

and locations of EDDs are preset horizontal or vertical slits, structural joints, wall base, etc. Location of EDDs decides the mechanical mechanism, and then determines the analytical model, therefore, from the view of analysis and design, the DSWs can be classified as follows (Figure 1): (i) vertical coupled DSW, (ii) horizontal coupled DSW, and (iii) rocking-base DSW. The aforesaid three types of DSW can be combined in various forms in order to gain a satisfactory damping effect. This paper focuses on the seismic design methodology of DSW (VDSW for short).

3. PARAMETER STUDY OF VDSW

3.1 Analysis of VDSW Using Continuous Medium Method

Continuous medium method is a common used simplified method to analyze coupled shear walls, and the method is adopted herein to evaluate the mechanical property of VDSW, of which the dampers (i.e., EDDs), together with the R/C coupling beams, are considered as the equivalent coupling beams. As shown in Figure 2, the deflection δ of the equivalent coupling beam due to shear force V_d is

$$\delta = \delta_f + \delta_s + \delta_d = \frac{V_d l_b^3}{3EI_{cb}} + \frac{\mu V_d l_b}{GA_{cb}} + \frac{V_d}{2k_d}$$

Where $k_d = \dfrac{\partial F_d}{\partial u_d}$ is the stiffness of dampers.

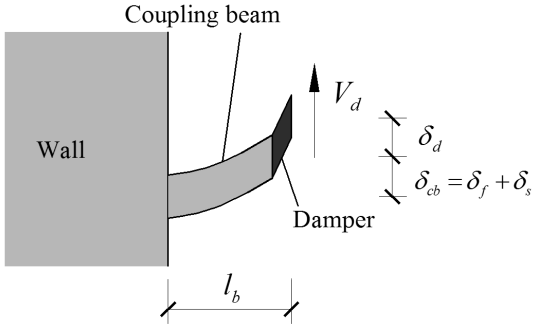


Figure 2 Deformation of coupling beams and damper (semi-structure)

Then we can get the stiffness of the equivalent coupling beam

$$K_{cb} = \frac{V_d}{\delta_{cb}} = \left(\frac{l_b^3}{3EI_{cb}} + \frac{\mu l_b}{GA_{cb}} + \frac{1}{2k_d} \right)^{-1} = \frac{3E\tilde{I}_{cb}}{l_b^3}$$

Where $\tilde{I}_{cb} = \dfrac{I_{cb}}{1 + \dfrac{3\mu EI_{cb}}{GA_{cb} l_b^2} + \dfrac{3EI_{cb}}{2k_d l_b^3}}$ is the converted moment of inertia of the equivalent coupling beam regarding the shear deformation of the beam and damper. Based on the derivation above, a factor is defined to reflect the magnitude of the Dampers' deformation with regard to the beams, that is

$$\lambda = \frac{K_{cb}}{2k_d} = \frac{3E\tilde{I}_{cb}}{2k_d l_b^3} \quad (1)$$

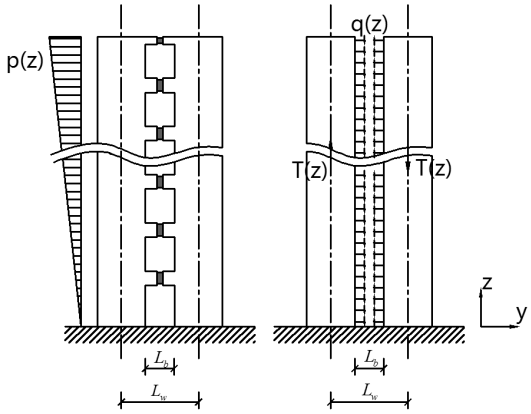


Figure 3 Continuous medium method for coupled wall

In the light of Figure 3, the differential equation of VDSW exerted by lateral load $p(z)$ based on the continuous medium method proposed by Rosman (Rosman 1964):

$$T''(z) - (\alpha k)^2 T(z) + \beta M(z) = 0 \quad (2)$$

If expressed with the variable of lateral deflection of the wall $y(z)$, the equation can rewrite as below:

$$\frac{d^4 y}{dz^4} - (k\alpha)^2 \frac{d^2 y}{dz^2} - \frac{1}{EI}\left[p(z) - \alpha^2 \left(k^2 - 1\right) M(z) \right] = 0 \quad (3)$$

Where $\alpha^2 = \frac{(GA)}{\sum EI_i} = \frac{12\tilde{I}_{cb}L_w^2}{L_b^3 h\sum I_i}$ (4)

($\alpha^2 = \frac{L_w k_d}{\sum I_i}$ When the coupling beam's stiffness can be regarded as infinite),

$\beta = \frac{\alpha^2}{L_w}$, $k^2 = 1 + \frac{\sum I_i}{\sum A_i c_i^2}$, $M(z) = \int_z^H p(\tilde{z})(\tilde{z} - z)d\tilde{z}$

is the overturning moment induced by lateral load $p(z)$.

Actually, equation (3) has a more generalized meaning, i.e., it can also describe the structural behavior of frame structures or frame-wall structures, but the expressions of α^2 and k^2 would be different (Smith et al. 1984). The analytical solutions of equation (3) were given by Bryan et al. under several typical loads (Bryan and Alex 1991). The solutions also can be achieved with the benefit of mathematical calculation software, such as MATLAB etc.

According to D'Alembert's principle, lateral $p(z)$ could be replaced by $-m\frac{\partial^2 y}{\partial t^2}$ when the wall is vibrated freely and the governing equation for undamped free vibration of the wall becomes:

$$\frac{\partial^4 y}{\partial z^4} - (k\alpha)^2 \frac{\partial^2 y}{\partial z^2} + \frac{m}{EI}\left[1 - \alpha^2\left(k^2 - 1\right)\frac{z^2}{2}\right]\frac{\partial^2 y}{\partial t^2} = 0 \quad (5)$$

An approximate solution of natural vibration period was given as follows (Heidebrecht and Smith 1973) :

$$T_n = \frac{2\pi}{\lambda_n^2}\sqrt{\frac{m}{E\sum I_i}} \approx \left(\frac{k^2 - 1}{\lambda_{fn}^4} + \frac{1}{\lambda_{sfn}^4}\right)\frac{2\pi}{k}\sqrt{\frac{m}{E\sum I_i}} \quad (6)$$

For the basic period

$$T_1 \approx \frac{H^4}{1.875^4}\left(k^2 - \frac{k\alpha H}{1.875 + k\alpha H}\right)\frac{2\pi}{k}\sqrt{\frac{m}{E\sum I_i}} \quad (7)$$

3.2 Evaluation of Dampers' deformation and VDSW's equivalent damping ratio

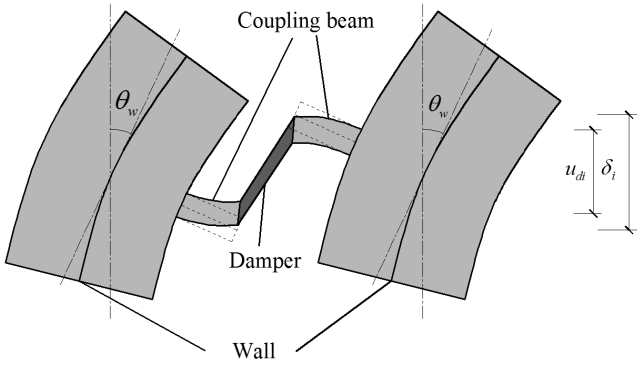


Figure 4 Geometrical Relationship Between δ_i and θ_w

The geometrical relationship between the dislocation of the coupling beam in the mid span δ_i and the rotational angel of the wall θ_w at the height of $z = h_i$ (i.e., the *i*-th floor) is shown in Figure 4, and it can be derived from the figure that

$$\delta_i \approx l_w\theta_w = l_w\frac{dy}{dz}\Big|_{z=h_i} \quad (8)$$

So the deformation of the damper is

$$u_{d,i} = \lambda\delta_i = \lambda l_w\frac{dy}{dz}\Big|_{z=h_i} \quad (9)$$

The equivalent damping ratio of VDSW can be expressed as $\xi_s = \xi_0 + \xi_d$, where ξ_0 stands for the damping ratio of original structure and ξ_d for the damping ratio provided by EDDs, which can be calculated as

$$\xi_d = \frac{W_d}{4\pi W_s} \quad (10)$$

Where, W_d, the energy consumed by EDDs, (together with the equivalent stiffness of damper in the *i*-th floor $k_{de,i}$) can be evaluated by:

$$W_d = 4\sum_i F_{dy,i}(1 - \eta_i)\left(u_{d,i} - \frac{F_{dy,i}}{k_{0,i}}\right) \quad (11)$$

$$k_{de,i} = \frac{F_{y,i} + \eta_i\left(k_{d0,i}u_{d,i} - F_{y,i}\right)}{u_{d,i}} \quad (12)$$

Where, $F_{dy,i}, u_{d,i}, \eta_i$ respectively stand for the damper's yielding force, maximum deformation, post-yielding, and stiffness ratio at the *i*-th floor.

W_s in equation (10) means the elastic potential energy of the structure, which is usually expressed as

$$W_s = \frac{1}{2}\sum F_i u_i \quad (13)$$

W_d, W_s can be evaluated using continuous medium method referred above in the initial stage of design, and the expressions turn out to be:

$$W_d = 4\sum_i F_{dy,i}(1 - \eta_i)\left(\lambda l_w\frac{dy}{dz}\Big|_{z=h_i} - \frac{F_{dy,i}}{k_{0,i}}\right) \quad (14)$$

$$W_s = \int_0^H \frac{1}{2}p(z)y(z)dz \quad (15)$$

Where, $y(z)$ is the solution of equation (3) using dampers' equivalent stiffness.

Besides, the distribution mode of dampers' mechanical parameters is one of the key issues in the design procedure of VDSW, for a proper distribution could bring EDDs' function into full play with relatively less dampers. There are two key parameters for displacement-type EDDs adopted herein: the initial stiffness k_{d0} and the yielding force F_{dy} (for ideal friction damper, only F_{dy} should be considered). When designing, the distribution of parameters can be assumed to be uniform, and after a pilot analysis the distribution mode should be adjusted in accordance with the deformation and shear force response of the coupling beams, while the adjustment should be carried out based on the principle of conservation of total dissipated energy.

3.2 Performance Indices

3.2.1 Coupling Ratio

Coupling ratio (*CR*), of which the definition is shown in equation (16), is chosen to be one of controlling indices for preliminary design. It has been proved that (Harries et al. 2004) *CR* is the key factor reflecting the mechanical performance of coupled shear walls, in detail, that is the coupling degree provided by coupling beams to the adjacent wall piers under lateral loads, that is to say, *CR* is essentially the synthesized representation of both the structural ingredient and load ingredient. Shear walls with an extremely large or small value of *CR* would resulting in poor structural performance, thus *CR* can be regarded as design index of coupled shear wall as well as performance evaluation index.

$$CR = \frac{L_w \sum V_{beam}}{L_w \sum V_{beam} + \sum m_i} = \frac{L_w \sum V_{beam}}{OTM} \tag{16}$$

Where OTM is the overturning moment induced by lateral loading.

As for the determination of a proper value of *CR*, M. J. N., Priestley (2005) pointed out that the value of *CR* that will induce tension force in the walls should be avoided; Harries (2001) gave the upper limit of CR, 66%, for a uniformly distributed coupling beams; El-Tawil (2010) indicated that 30%~45% may be an appropriate range of CR for design.

CR of VDSW referred in this paper subjected to triangularly distributed loading can be evaluated using the following equation (Chaallal and Nollet 1997):

$$CR = \frac{3}{k^2(k\alpha H)^2}\left\{\frac{(k\alpha H)^2}{3} - \cosh(k\alpha H) + \tanh(k\alpha H)\left[\sinh(k\alpha H) - \frac{k\alpha H}{2} + \frac{1}{k\alpha H}\right]\right\} \tag{17}$$

As for the elastoplastic stage of VDSW with yielding EDDs and wall bases, the expression of CR is given as follows:

$$CR = \frac{L_w \sum F_{dy}}{L_w \sum F_{dy} + \sum M_y} \tag{18}$$

Where $\sum F_{dy}$ is the sum of the dampers' yielding force and $\sum M_y$ is the sum of the walls' yielding moment at the base section.

3.2.2 Common Used Indices

The limit values of story drift angle, base rotation, and so forth, are commonly used indices to assess shear wall structures for performance based design of structures. The indices are divided into two types in the paper for different design purposes, i.e., absolute indices $[R]$ and relative indices γ, of which absolute indices is the limit values specified by design codes and relative indices referred herein means the variation (reduction for most cases) ratio of maximum structural response of unimproved/uncontrolled structures vs. absolute performance indices, that is:

$$\gamma = [R] / R_{\max} \tag{19}$$

For newly built traditional structures, it would be best to use absolute indices during design, but for structures to be retrofitted or damping controlled, relative indices may provide a more effective and purposive design procedure. The relative indices may need to be adjusted during iterative analyses after every pilot calculation.

4. DESIGN PROCEDURE OF VDSW

The basic framework of VDSWs' design methodology is proposed in the paper referring to the concept of seismic performance-based design and Chinese codes for design. The flowchart of the design procedure is drawn in Figure 5. According to the previous discussion on the expected performance of DSW under different earthquake precaution levels, the design procedure is divided into two stages, that is, the (I) elastic stage and (II) elastoplastic stage, which are described below in detail:

(I) Elastic stage: Firstly, perform the preliminary design of the uncontrolled structure in accord with traditional design method; then determine a proper period of the structure or a proper value of *CR* in order to obtain the initial stiffness of uniform dampers k_{d0}. Specific execution steps are as follows:

Step 1: Preliminary Design of uncontrolled structure. Referring to the specification of codes and design experiences, the profile of structural members is determined elementarily and then basic parameters of the structure referred before, such as $k\alpha H, T, CR$, etc., also should be calculated to get the knowledge of the initially designed structure.

Step 2: Determination of k_{d0}. The value of k_{d0} can be determined by equation (7) or (17) with a pre-selected basic period T_1 or coupling ratio CR. An alternative method to choose a proper value of T_1 is provided as follows referring to the displacement-based design method: With a preset value of α and deformation mode of the wall, such as the deformation shape under triangular loading or the first mode of free vibration, the structure is transformed into a SDOF system, and then the basic period of the equivalent SDOF system $T_{1,0}$ in line with the performance indices and displacement spectrum under frequently-occurred earthquakes, and with a updated α a new value of the period $T_{1,1}$ is got by the method above, then repeat the procedure until $T_{1,i} \approx T_{1,i-1}$, at that time, it can be regarded that $T_1 = T_{1,i}$. The determination of CR should be based on the design experiences, a rational range of CR would be 0.3~0.66 (El-Tawil et al. 2010).

Step 3: Performance Check. Check the structure response with the performance indices under frequently-occurred earthquakes by taking the value of k_{d0}

obtained in *Step 2*, and adjust k_{d0} if not satisfied.

The elastic stage can be carried out by design softwares for analysis and design to reduce the calculation and get a better accuracy. Dampers can be modeled as link elements in software or simply considered by reducing the stiffness of the coupling beams based on equation (1).

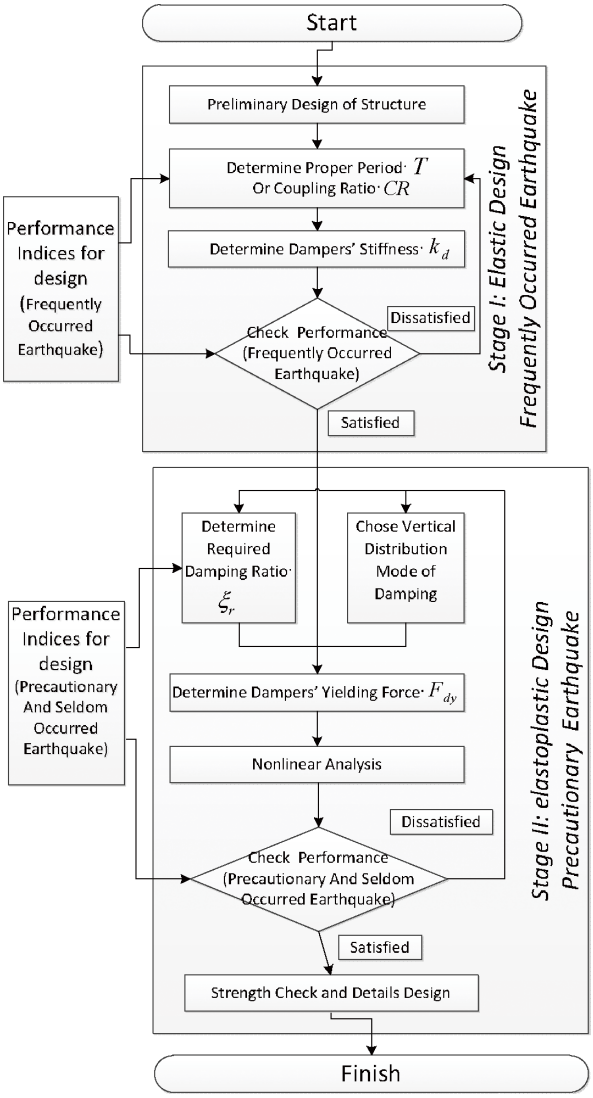


Figure 5 Design flowchart for vertical damping controlled shear wall

(II) Elastoplastic stage: Decide the required damping ratio ξ_r, and then the yielding force of the damper at every floor $F_{dy,i}$ can be obtained in combination with a proper distribution mode of the damping and the determined k_{d0}. Then exert the force capacity check and the adjustment of the reinforcement of the members' sections, and so does the detail design for the joints between the dampers and the coupling beams or wall piers.

Step 1: Determination of demand damping ratio ξ_r. ξ_r is decided in the step according to performance indices to the specification of codes and design experiences, and then the damping ratio provided by dampers $\xi_d = \xi_r - \xi_s$. Methods to find out ξ_r is discussed as follows: (i) Displacement based design method using absolute indices, i.e., the method involved equivalent SDOF system converting and displacement spectra, since the deformation mode would change due to the plastic condition of the dampers, so the equivalent stiffness of dampers k_{de} (approximately as $0.4k_{d0} \sim 0.6k_{d0}$ on experiences) should be adopted, and the calculation may needs some iterations. (ii) The method adopted in the paper based on relative performance indices. Analyze the structure with dampers' stiffness as k_{de} under precautionary earthquake and relative performance indices can be worked out according to equation (19) base on the analytical response. Thus ξ_r can be evaluated by comparison of multi spectra curves with various damping ratios.

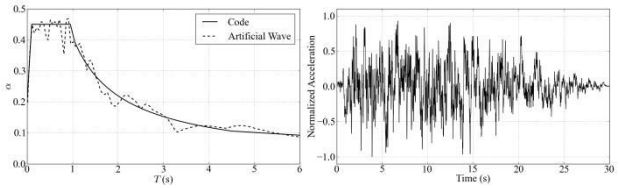
Step 2: Determination of $F_{dy,i}$. The yielding force of the damper at every floor $F_{dy,i}$ can be worked out by equation (11) in combination with a proper distribution mode of the damping and the previously chosen k_{d0}. Then nonlinear dynamic analysis has better be executed in order to accommodate the distribution mode of the damping, to be exactly, the distribution of $F_{dy,i}$, a feasible redistribution of $F_{dy,i}$ is based on the response deformation of dampers with a constant $\sum F_{dy,i}$, i.e., $F'_{dy,i} = \dfrac{u_{di}}{\sum u_{di}} \sum F_{dy,i}$.

Step 3: Performance Check. With the selected parameters, performance check of the system under precautionary and seldom occurred earthquakes is carried out to find whether the system meets the predestinate performance demands. Several pilot calculation may be required to get a satisfactory damping effect, and after the iterative processes, the design procedure would be pulled back to the traditional routine, i.e., strength checking, reinforcement adjustment, and the like. So far, the design of VDSW would come to an end.

5. DESIGN EXAMPLE

A design example of a planer coupled shear wall reformed by vertical EDDs was carried out using the method mentioned above, and the design procedure is shown below, besides, the calculation is both conducted by the equations above and the FEM software named OpenSees in order to check the accuracy of the equations.

Earthquake Parameters and Performance Indices for design. Seismic precautionary intensity of the wall is 8 with the characteristic period of 0.90s, and then we could get the design spectrum in light of the code and an artificial earthquake wave in alignment with the spectrum, which are drawn in Figure 6. Story drift angle is chosen as the index for performance check, and limit values of story drift angle $[\theta]$ for shear wall structures are shown in Table 1.



(a) Spectrum (b) Artificial earthquake wave

Figure 6 Design Spectrum and earthquake wave

Table 1 Limit values of story drift angle for shear wall structures

Earthquake Precaution Level	Frequently Occurred	Precautionary	Seldom Occurred
$[\theta]$	1/1000	1/400	1/120

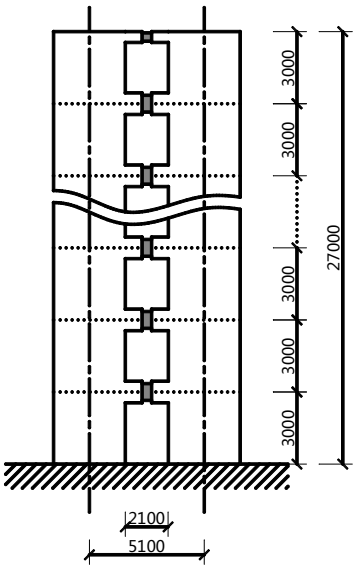


Figure 7 Profile of The Wall

(I) Elastic Stage

General Information of the original wall. The is demonstrated in , which is a ten-story planar coupling shear wall with the height of 27m. The thickness of wall piers is 250mm and the width is 3000mm, while the span of coupling beams is 2100mm and the section height is 1200mm. C40 concrete and HRB 335 steel bars are used for the construction of the wall. Seismic precautionary intensity of the wall is 7 with site IV. According to equation (7) and (17) we can work out that $k\alpha H = 13.502$, $T_1 = 0.545$ s, $CR = 0.798$, while the results calculated by the software are $T_1 = 0.575$ s, $CR = 0.792$.

Determination of k_{d0}. We use the *CR* method to determine the uniform stiffness of the damper k_{d0} for convenience. The initially assumed *CR* equals 0.66, and then it can be achieved that $k\alpha H = 5.300$, after that, based on equation (4), k_{d0} would be calculated out to be $k_{d0} = 102$ kN/mm , and the resulting basic period $T_1 = 0.694$ s by equation (17) and $T_1 = 0.704$ s by software.

Performance Check. The FEM model of the wall is set up to check the performance of the preliminarily designed VDSW under frequently occurred earthquake. After analysis, peak response of story drift angle is $1/1422 < 1/1000$, i.e., the performance is satisfied.

(II) Elastoplastic Stage.

Determination of ξ_r. The structure is analyzed with dampers' stiffness as $k_{de} = 0.7k_{d0}$ under precautionary earthquake and the resulting peak value of story drift angle is $\theta_{\max} = 1/303 > 1/400$, so relative performance indices is $\gamma = 303/400 = 0.758$, thus it can be evaluated by design spectra that $\xi_r = 11.34\%$, so $\xi_d = \xi_r - \xi_s = 6.34\%$.

Determination of $F_{dy,i}$. Assuming that $F_{dy,i}$ is uniformly distributed, we can work out the value of $F_{dy,i}$ with known k_{d0} and ξ_d, that is $F_{dy,i} = 85$ kN. Then the distribution mode of $F_{dy,i}$ is adjusted by the analytical response of dampers' deformation (Figure 8). Story drift angle response with different damping settings is shown in Figure 9. From the figure it can be found that the adjusted distribution of damping shows a better controlling effect. The analytical damping ratio provided by dampers is $\xi_d = 6.40\% \approx 6.34\%$.

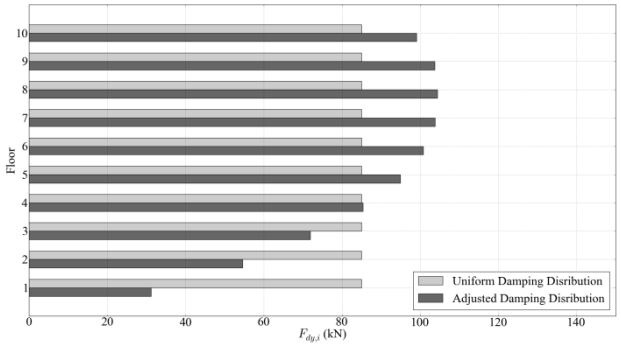


Figure 8 Distribution Modes of $F_{dy,i}$

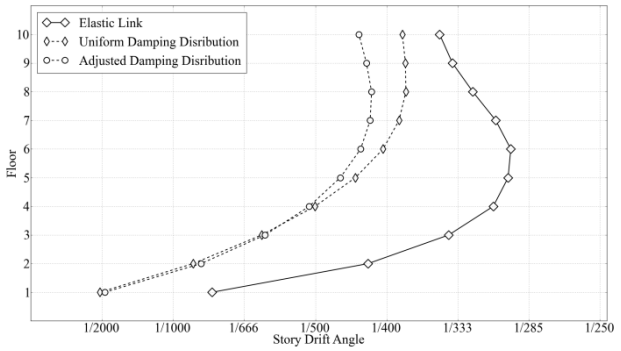


Figure 9 Story Drift Angle Response (Precautionary Earthquake)

Performance Check. Figure 9 exhibits that the peak response of story drift is $\theta_{\max} = 1/418 < 1/400$ under precautionary earthquake and the analysis of the designed

VDSW under seldom occurred earthquake was also performed, yielding the response of Story drift angle is $\theta_{\max} = 1/147 < 1/120$. The hysteretic curves of the damper with maximum deformation under different earthquake levels are shown in Figure 10 and the stable, plump curves prove that dampers are efficiency in energy dissipation. The analytical results mean that the performance demand is satisfied thus the selected parameters of dampers are agreeable. Since the paper is mainly focusing on the design of the dampers, the succeeding design steps are omitted.

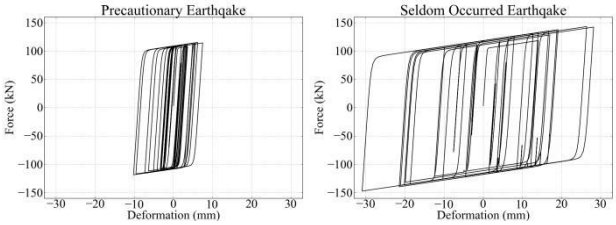


Figure 10 Hysteretic Curves of Dampers

6. CONCLUSIONS

The paper has summarized and represented the concept, brief profile, and classification of damping controlled shear wall system. The design methodology of vertical coupled DSW is proposed based on the simplified analysis of the structure system and a design example is performed to verify the feasibility of the method. Though it is of efficiency, the method should be improved in order to avoid interactive calculations.

References:

Rosman, Riko. (1964). "Approximate Analysis of Shear Walls subject to Lateral Loads." *ACI Journal, Proceedings*, 61(6), 717-734.

Heidebrecht, Arthur C., and Smith, Bryan Stafford. (1973). "APPROXIMATE ANALYSIS OF TALL WALL-FRAME STRUCTURES.", 99(ST2), 199-221.

Smith, Bryan Stafford, Kuster, M., and Hoenderkainp, Johannes Christinus Dorotheas. (1984). "Generalized Method for Estimating Drift in High-Rise Structures." *Journal of Structural Engineering*, 110(7), 1549-1562.

Bryan, Stafford Smith, and Alex, Coull. (1991). *Tall Building Structures: Analysis and Design*, John Wiley & Sons, Inc.

Chaallal, O., and Nollet, M. J. (1997). "Upgrading the degree of coupling of coupled shear walls." *Canadian Journal of Civil Engineering*, 24(6), 986-995.

Kent A. Harries, MEERI. (2001). "Ductility and deformability of coupling beams in reinforced concrete coupled walls." *Earthquake Spectra*, 17, 457.

Harries, Kent A., Moulton, J. Dan'l, and Clemson, Robert L. (2004). "Parametric Study of Coupled Wall Behavior---Implications for the Design of Coupling Beams." *Journal of Structural Engineering*, 130(3), 480-488.

Zhao, Q. (2004). "Cyclic behavior of traditional and innovative composite shear walls." *Journal of Structural Engineering*, 130, 271.

M. J. N., Priestley, G. M., Calvi, and M. J., Kowalsky. (2005). *Displacement-Based Seismic Design of Structures*, IUSS Press, Pavia.

Chung, H. S., Moon, B. W., Lee, S. K., Park, J. H., and Min, K. W. (2009). "Seismic performance of friction dampers using flexure of RC shear wall system." *The Structural Design of Tall and Special Buildings*, 18(7), 807-822.

Wada, A., Qu, Z., Ito, H., Motoyui, S., Sakata, H., and Kasai, K. "Seismic Retrofit Using Rocking Walls and Steel Dampers." *Proceedings of the 2009 ATC&SEI Conference on Improving the Seismic Performance of Existing Buildings and Other Structures*, San Francisco, California, 92-92.

El-Tawil, Sherif, Harries, Kent A., Fortney, Patrick J., Shahrooz, Bahram M., and Kurama, Yahya. (2010). "Seismic Design of Hybrid Coupled Wall Systems: State of the Art." *Journal of Structural Engineering*, 136(7), 755-769.

8CUEE CONFERENCE PROCEEDINGS
8th International Conference on Urban Earthquake Engineering
March 7-8, 2011, Tokyo Institute of Technology, Tokyo, Japan

DEVELOPMENT OF A SELF-CENTERING STEEL PLATE SHEAR WALL

Patricia M. Clayton[1], Jeffrey W. Berman[2], Tyler Winkley[3], and Laura N. Lowes[4]

1) Graduate Student, Dept. of Civil and Environmental Engineering, University of Washington, Seattle, WA, USA
2) Assistant Professor, Dept. of Civil and Environmental Engineering, University of Washington, Seattle, WA, USA
3) Graduate Student, Dept. of Civil and Environmental Engineering, University of Washington, Seattle, WA, USA
4) Associate Professor, Dept. of Civil and Environmental Engineering, University of Washington, Seattle, WA, USA
claytp@u.washington.edu, jwberman@u.washington.edu, tdubs88@u.washington.edu, lowes@u.washington.edu

Abstract: The self-centering steel plate shear wall (SC-SPSW) system has been developed to combine the lateral load resisting benefits of the SPSW with the self-centering capabilities of post-tensioned connections by replacing the typical moment resisting connections of a conventional SPSW with post-tensioned (PT) beam-to-column connections. This system resists the lateral load and dissipated energy through development of tension field action and yielding in the thin steel infill panel, known as the web plate, while the PT beam-to-column connections reduce the potential for damage in the beams, and provide system recentering and post-earthquake functionality. In the event that yielded or damaged web plates require repair or replacement following an earthquake, the building is designed to return to a recentered and functional state while the relatively quick and easy repair of the plates takes place, greatly reducing the downtime associated with costly beam and column repairs. A performance-based design procedure has been developed for the SC-SPSW, and analytical and experimental studies show that the system is capable of meeting proposed performance objectives.

1. INTRODUCTION

Steel plate shear walls (SPSWs) have been used as the primary lateral load resisting system of buildings in high seismic areas (Selie and Hooper 2005, Sabelli and Bruneau 2007). When SPSWs are subjected to severe earthquakes, the thin steel infill plates, referred to as the web plates, buckle in shear and resist lateral load through the development of tension field action. Energy dissipation is provided primarily through yielding in the diagonal tension field. The moment-resisting (MR) beam-to-column connections in conventional SPSWs can develop plastic axial-flexural hinges due to the forces imposed by the web plate during sever earthquakes, which can lead to significant residual deformations and costly repairs of the horizontal and vertical boundary elements (HBEs and VBEs).

In an attempt to reduce post-event repair and loss of functionality, the SPSW has been combined with the self-centering capabilities of post-tensioned (PT) beam-to-column connections to create a self-centering SPSW (SC-SPSW) system. In a SC-SPSW (Fig. 1a), the typical MR HBE-to-VBE connections are replaced with PT connections (Fig. 1b) that allow the connection to rock about the HBE flanges and form a gap, θ_r (Fig. 1c). The formation of this gap, referred to as decompression, causes the PT strands in the connection to elongate elastically, which provides the forces necessary to recenter the building, and prevents damage at the HBE ends. Unlike other self-centering frame systems (Garlock et al. 2007, Kim and Christopoulos 2008) where the lateral strength of the system is primarily provided by the strength of the PT connection and its components, the lateral strength of the SC-SPSW is primarily provided by the web plate, which also serves as the replaceable energy dissipating fuse of the system, while the PT connections primarily serve to recenter the building after an earthquake.

This paper presents an overview of the mechanics and behavior of the SC-SPSW system. An outline of a proposed performance-based design procedure for the SC-SPSW system and a description of current SC-SPSW subassembly experimental studies are also presented.

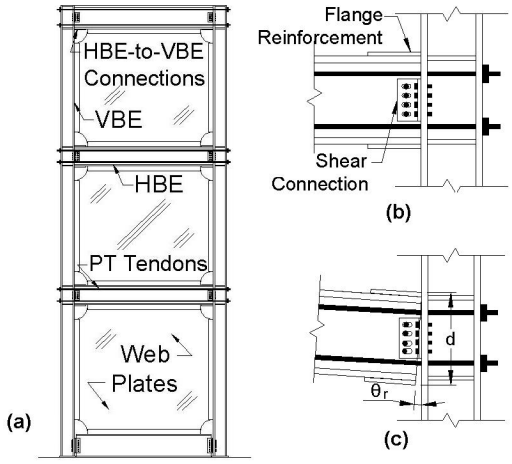


Figure 1: Elevation of (a) SC-SPSW, (b) PT connection, and (c) PT connection after gap formation

2. SC-SPSW BEHAVIOR

2.1 HBE Forces

The HBE is a key component in the SC-SPSW system. Understanding the mechanics of the HBE and the interaction of the web plate and PT connection forces acting on the HBE is important in understanding the behavior of the system and SC-SPSW design concepts.

Fig. 2 shows a free-body diagram of an intermediate HBE after connection decompression, where $\omega_{b(i)}$ and $\omega_{b(i+1)}$ are the distributed forces from the yielded web plate below and above the HBE acting in the direction of the diagonal tension field, T_{PT} is the total force of the PT strands acting on opposite flanges at the ends of the HBE, referred to as the connection rocking points, $P_{HBE(VBE)}$ is the compressive force acting at the HBE rocking points that is due to the distributed web plate forces pulling in the VBEs, $P_{HBE(web)}$ is the reaction force at the ends of the HBE due to the net axial distributed load acting on the HBE when the web plates above and below the HBE are of different strength or thickness, and V_L and V_R are the shear reactions at the left and right ends of the HBE, respectively. Expressions for $P_{HBE(VBE)}$ and $P_{HBE(web)}$ can be found in Sabelli and Bruneau (2007), and expressions for the shear forces and total PT force, including losses due to HBE shortening, can be found in Dowden et al. (2011). Although in construction, radial corner cutouts (as shown in Fig. 1a) would be necessary to prevent localized damage to the web plate during connection decompression, for the purpose of simplicity in this paper, the corner cutouts are ignored, and the web plate is assumed to extend over the entire length of the HBE, L.

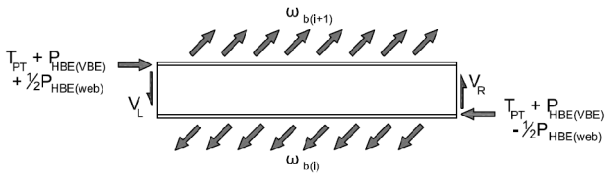


Figure 2: Free-body diagram of intermediate HBE

For design of the HBE, a moment diagram must be developed from the free-body diagram in Fig. 2 to better understand the interaction between the PT and web plate forces acting on the HBE. As shown in Fig. 3, the HBE moment diagram can be separated into components. Fig. 3a shows the linear moment diagram component due to the compressive forces from the total PT and VBE pull-in forces acting at the rocking points. The magnitude of the moment at the end of the HBE due to this component is the compressive reaction force from these components, T_{PT} + $P_{HBE(VBE)}$, times the lever arm of $d/2$, where d is the depth of the HBE. Fig. 3b shows the parabolic moment diagram component due to the vertical components of the net distributed web plate force acting on the HBE, $\Delta\omega_{yb}$. Fig. 3c

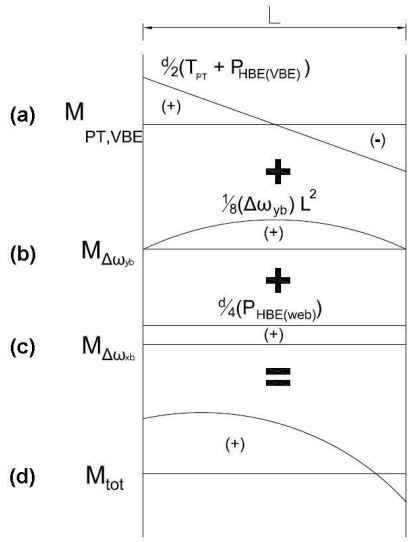


Figure 3: (a) Compression flange reaction component, (b) net vertical web plate component, (c) net horizontal web plate component, and (d) combined moment diagram of intermediate HBE

shows the constant moment diagram component due to the net horizontal distributed web plate forces acting on the HBE. The magnitude of this component is the end reaction due to the net horizontal web plate loading, $\frac{1}{2}P_{HBE(web)}$, times the lever arm of $d/2$. Each of these components can be superimposed onto one another to determine the total moment diagram shown in Fig. 3d. More details on the moment, shear, and axial force diagrams of an intermediate HBE in a SC-SPSW can be found in Dowden et al. (2011).

It is important to note in Fig. 3d that it is possible for the maximum moment to be along the length of the HBE. This condition makes the HBE susceptible to the occurrence of in-span flexural hinging, which can affect development of the tension field and can lead to a reduction of lateral load resistance in the SPSW (Purba and Bruneau 2010). In-span hinging can be avoided if the linear component of the moment diagram (i.e. the PT and VBE pull-in force contributions) is sufficiently large to force the maximum moment to occur at the end of the HBE. Since the PT force is dependent on the amount of gap opening, which is related to the column drift, the PT can be design in such a way to ensure that the maximum moment occurs at the end of the HBE at a specified drift level before the onset of HBE yielding (Dowden et al. 2011), which will prevent the detrimental occurrence of in-span hinging in the HBE.

2.2 SC-SPSW Cyclic Behavior

The cyclic behavior of the SC-SPSW can be determined by combing the behaviors of the individual system components: the SPSW and the PT frame responses, as shown in Fig. 4.

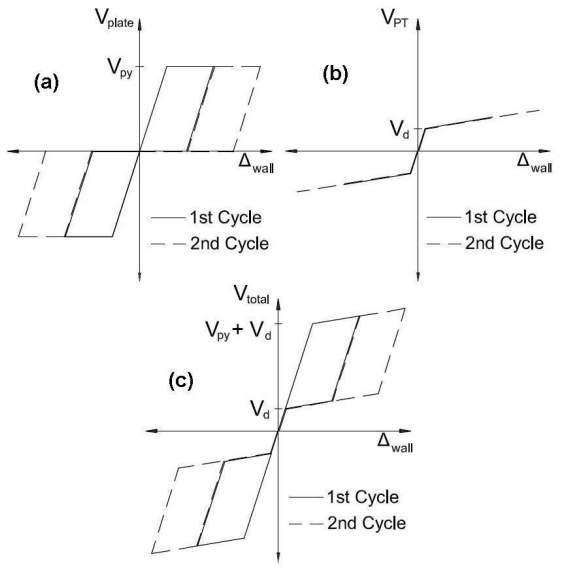


Figure 4: Idealized system-force-displacement response of (a) SPSW, (b) PT frame, and (c) SC-SPSW

The idealized SPSW behavior (Fig. 4a) is characterized by a large initial stiffness due to the lateral force resistance provided by the tension field, followed by yielding of the plate at a load V_{py} in the direction of the tension field. The pinched hysteresis is due to the thin web plate buckling in compression under reverse cyclic loading. As a result, the low SPSW stiffness after web plate unloading requires smaller restoring forces in order to recenter the system, a benefit of SPSWs that is leveraged when combined with the recentering capabilities of the PT connections. Note that in the idealized behavior shown in Fig 4a, the entire web plate is assumed to yield simultaneously and behave in an elastic-perfectly-plastic manner, and the buckling strength of the web plate in shear is ignored. Also, the idealized SPSW is assumed to not resist any loading until it reaches its previous peak plastic strain, after which point it resists additional load with its initial stiffness. As will be discussed later, SPSW behavior is more complex than this, but these idealizations are made to facilitate an understanding of general SPSW cyclic behavior.

The PT frame behavior is characterized by a bilinear elastic behavior. The initial stiffness is equivalent to that of a welded moment resisting frame. After decompression at a load V_d, the frame stiffness is reduced due to the formation of the gap in the connection. Assuming that the PT and frame elements remain elastic, the PT frame system follows the same force-displacement path upon uploading, resulting in no energy dissipation contribution from the PT frame alone.

Combination of the two systems to form the SC-SPSW results in a flag-shaped hysteresis that is typical of self-centering systems, where the primary strength of the system is provided by the SPSW and the recentering capability is provided PT frame after the web plate is fully unloaded, returning the building to zero displacement.

2.3 PT Connection Behavior

The PT connection behavior is best characterized by a plot of the moment at the connection, M_{conn}, versus gap rotation, θ_r. Fig. 5 shows a schematic of the idealized SC-SPSW connection response with the same simplifying assumptions of web plate behavior that were made in Fig. 4. Before connection decompression, the gap rotation is zero. The moment at the end of the HBE at the time of decompression, M_d, is determined by the HBE depth, d, and the initial force in the PT, T_o.

$$M_d = T_0 \, d/2 \tag{1}$$

For purposes of simplification, the connection shown in Fig. 5 is assumed to decompress before the web plate develops any significant forces.

After decompression, the connection strength increases due to the increase in axial load at the ends of the HBE caused by the increase in web plate forces. As shown previously, the connection moment is determined by the total compressive force at the end of the HBE acting with a lever arm of $d/2$. Also note that in Fig. 5, it is possible for the ultimate connection capacity under positive and negative loading to be different. This is due to the $\pm \frac{1}{2}P_{HBE(web)}$ term in the end reaction force in Fig. 2. For example, for a SC-SPSW being loading to the right in Fig. 2, if the plate thickness below the HBE is larger than the thickness above, then the left connection will have a higher capacity than the right due to the net leftward force from the distributed web plate forces.

Assuming elastic-perfectly-plastic yielding of the web plate, after web plate yielding, the connection strength increases at a rate of k_d^{θ} (Garlock 2002), which primarily depends on the HEB depth, d, and the total PT axial stiffness. Upon unloading, the connection initially looses strength due to the loss of effective post-tensioning provided by the web plates as they unload. Once the web plates are fully unloaded, the connection recompresses at a stiffness of k_d^{θ}.

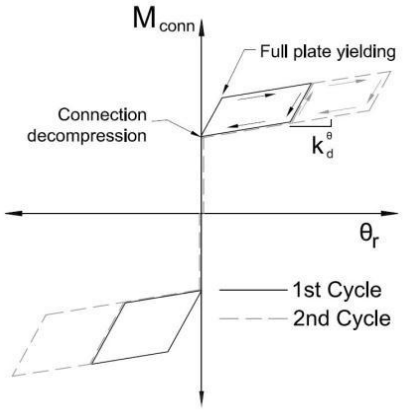


Figure 5: SC-SPSW PT connection response

3. PERFORMANCE-BASED DESIGN APPROACH

The behavior characteristics of the SC-SPSW allow for the system components to be designed to meet a specified performance level under a specified seismic input level. The seismic hazard levels considered in the proposed SC-SPSW performance-based design (PBD) approach are earthquakes with a 50%, 10%, and 2% probability of exceedence in 50 years (denoted as 50/50, 10/50, 2/50, respectively). These earthquake hazard levels are approximations of the frequent, design, and maximum credible earthquakes, respectively.

3.1 Performance Objectives

The PBD procedure for the SC-SPSW was developed to achieve the following performance objectives:

1. *No connection decompression under wind or gravity loading.*
2. *System recenters and no repair required under frequent* (50/50) *earthquake demands.* Recentering is assessed using a residual drift limit of 0.2%%, corresponding to out-of-plumb limits in construction. The no repair limit state requires that the web plate remain essentially elastic and is assessed using a peak story drift limit of 0.5%, the median drift at which web plate repair is required in conventional SPSW experimental studies (Baldvins et al. 2010).
3. *System recenters and only web plate repair required under design* (10/50) *earthquake demands.* The web plate may have significant yielding; however, the boundary frame and PT elements should remain elastic and the system should recenter. The damaged web plate can be replaced relatively quickly and simply, resulting in a more rapid return to occupancy following an earthquake (Qu et al. 2008). The story drift at this hazard level should be less than the 2% code-based drift limit for design level earthquakes.
4. *Collapse prevention for the maximum credible earthquake* (2/10). Residual drifts and minor frame yielding may occur; however, soft-story mechanisms and significant PT and frame yielding should be avoided. A target drift limit of this performance objective was assumed to be 4%, based on engineering judgment and the drift at which significant strength loss was observed in conventional SPSW experimental studies (Baldvins et al. 2010).

Since designing for elastic (no repair) behavior under frequent earthquake demands may not be feasible or economical in some locations with significantly large 50/50 earthquake accelerations. For this reason, Performance Objective 2 (the no repair performance objective) is considered an optional objective.

3.2 PBD Procedure

The following procedure was developed to meet the previously described performance objectives:

1. Make initial assumptions about SC-SPSW geometry and number of walls in the building.
2. Determine the seismic loads and lateral load distribution. Here a modified load distribution as developed by Chao et al. (2007) was used to account for higher-mode effects, as SC-SPSWs and other self-centering PT systems (Garlock 2002) designed using typical code-based load distributions have exhibited larger drift demands and damage in the upper stories due to these higher-mode effects.
3. Design the web plates to remain elastic under 50% in 50 year loads. If the optional "no repair" performance objective is not being considered, then design the web plates for code-based design forces (approximated here as the 10/50 shear forces reduced by a response modification factor, R).
4. Design the PT connection to have sufficient stiffness to ensure recentering under the influence of P-Delta effects (Clayton 2010).
5. Capacity design the PT and HBE to remain elastic and prevent in-span hinging at a target drift of 4%, corresponding to the 2/50 earthquake demands. (Dowden et al. 2011)
6. Capacity design the VBE to remain elastic up to 5% drift (Berman and Bruneau 2008).
7. Check that design meets code-based drift limits and that the required amount of PT can fit reasonably within the depth of the HBE.
8. Iterate as needed until a final design is converged upon.

3.3 Evaluation of Design Procedure

To assess the adequacy of the proposed design procedure, seven different 3- and 9-story SC-SPSW buildings were designed according to the previously described procedure. These buildings were based on the SAC building located in the Los Angeles, California area (Gupta and Krawinkler 1999). Variations in the prototype buildings were inclusion of the optional "no repair" performance objective and variation in the number of SC-SPSWs in the building. Details of these designs can be found in Clayton (2010).

To determine if the buildings designed according to the proposed procedure were able to meet the intended performance objectives, a numerical model of each SC-SPSW was subjected to a suite of 60 ground motions representing the three seismic hazards considered in the design (Clayton 2010). The performance of these models was evaluated by a series of response parameters, including the peak story drift, the residual story drift, the occurrence of PT yielding, and the occurrence of HBE and VBE yielding as evaluated by the interaction equation per Eqn. H1-1 (AISC 2005).

As an example, the median and 84th percentile peak

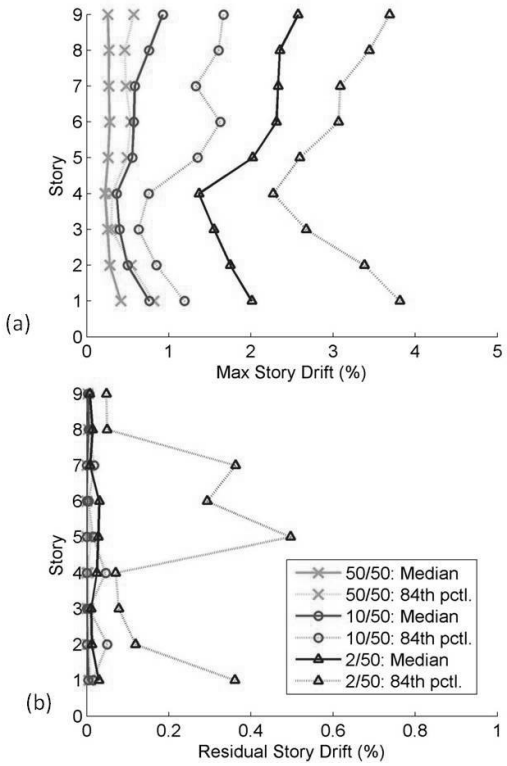


Figure 6: Example of median and 84th percentile (a) peak story drift sand (b) residual story drifts at each hazard level for a 9-story SC-SPSW.

story drift and residual story drift under each hazard level for a typical 9-story SC-SPSW for which the no repair performance objective was considered optional is shown in Fig. 6. Fig. 6b shows that the SC-SPW was able to recenter (residual story drift less than 0.2%, as described previously) at the 10/50 hazard level as was intended in Performance Objective 3. Fig. 6a shows that the peak story drifts were less than the 2% code-based drift limit at the 10/50 hazard level (Performance Objective 3). This figure also shows that peak story drifts were less than the 4% drift limit assumed for design at the 2/50 hazard level, meaning that there were little to no occurrences of PT or frame yielding at this hazard level, thus meeting Performance Objective 4. Additional results for the other buildings showed that the SC-SPSWs designed according to the proposed PBD procedure were capable of meeting the intended performance objectives with little or no modification to the design procedure (Clayton 2010).

4. EXPERIMENTAL STUDY

Experimental investigation of the SC-SPSW system is currently taking place at the University of Washington. The initial experimental testing of a SC-SPSW subassembly is aimed at capturing the effects of the interaction of the PT and web plate forces acting on an intermediate HBE and to validate numerical modeling methods.

4.1 Test Setup

A schematic of the test setup is shown in Fig. 7. The 2-story configuration of the setup was used to simulate the boundary conditions for an intermediate HBE (middle HBE in Fig. 7), where the web plates above and below the HBE induce an effective post-tensioning in the HBE due to pull-in of the VBEs ($P_{HBE(VBE)}$). The SC-SPSW subassembly measures 3235 mm wide (centerline VBE dimension), with story heights (HBE centerline dimensions) of 1724 mm.

Due to the HBE rocking about its flanges, as a gap forms in the connection, the VBEs spread apart (Garlock et al. 2007). This beam growth is accommodated in the physical model with a roller under the left VBE, allowing the frame to expand horizontally without imposing additional compressive forces on the middle HBE due to VBE restraint at its base. For similar purposes, the top and bottom anchor HBEs also have PT HBE-to-VBE connections, such that the gap opening, and thus the beam growth, at these levels are similar to the middle HBE.

Shear forces at the PT HBE-to-VBE connections are transferred through slotted shear tab connections. Long slotted bolt holes are used in the shear tab to allow for connection rotation. The HBE flanges at the connections are also reinforced to protect against local damage due to the large compressive forces acting on the flanges after decompression. Also, corner cutouts are provided in the web plates to prevent localized damage in the plate as a gap forms in the connection.

The boundary frame elements are of A992 steel and are designed to remain elastic during testing so that they can be reused for multiple tests. The PT strands are 13 mm diameter Grade 270 seven-wire strand with reusable 3-wedge barrel anchors at each end. The PT strands are all placed symmetrically about the centerline of the HBE within the depth of its flanges and are also designed to remain elastic during testing. The web plates are of ASTM A1008 steel with a yield strength of approximately 190 MPa and are connected to the boundary elements via a bolted fishplate connection. The bolted web plate-to-fishplate connection allows for the yielded web plates to be easily removed and

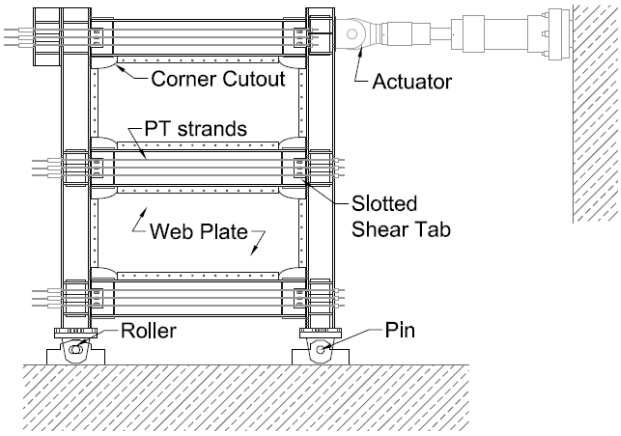


Figure 7: Schematic of test setup.

replaced following each test.

The test matrix includes variations in the web plate thicknesses, HBE depth, initial PT force, and number of PT strands in the connection to study the effects of web plate and PT connection strengths and stiffnesses.

4.2 Instrumentation and Displacement History

Instrumentation was installed on the specimen to measure applied loads, global displacements, gap rotations, PT forces, and HBE and VBE strains. The cyclic displacement history for the tests are a modification of ATC-24 (ATC 1992), similar to the history used in previous SPSW experiments by Vian et al. (2009), with 3 cycles at each increment of 0.25 of the estimated yield displacement, δ_y, up to δ_y. After this point, the peak displacements were incremented in multiples of δ_y up to approximately 2% drift, after which, the peak displacements were increased in increments of 0.5% drift up to 4%. Three cycles were done at each displacement increment up to approximately 1% drift, and only two cycles were done at each subsequent drift level.

4.3 Experimental Results and Observations

The results presented here are for a test with W18x106 HBEs with 6 PT strands at each HBE, where each strand was post-tensioned to an initial force of 55.6 kN. The web plates in this test were 20 Gage (0.9mm thick). Fig. 8 shows the force-displacement response of the test specimen up to 4% drift.

In comparing the hysteretic response of the system with that of a general idealized SC-SPSW system (Fig.4c), notice that the test specimen exhibits the expected flag-shape hysteresis with recentering (residual drift < 0.2%) at zero-loading. As noted previously, the web plate hysteretic behavior is more complex than the idealized assumptions made in Fig. 4. For example, the web plate in the specimen is capable of resisting a portion of lateral load with a reduced stiffness before it reaches its previous peak plastic strain, as seen by the reloading stiffness in repeated cycles in Fig. 8.

The reduction of strength at larger drift levels was due to tearing of the web plate that was first observed at 2.5% drift. The web plate tearing was typically observed along the edge of the fish plate, and was most likely due to out-of-plane deformation of the web plate being restricted by the edges of the fishplate that is welded to the HBE. At 4% drift, the tears in the web plate propagated through the entire panel, causing a large reduction in lateral load capacity of the SC-SPSW; however, at this drift level, no damage was observed in the boundary frame and PT elements. This web plate damage, and ultimate failure, is believed to be a result of the bolted fishplate connection that was used to facilitate rapid replacement of the web plates for multiple tests; therefore, future tests will be done with a welded web plate-to-fishplate connection detail that would typically be used in practice to determine how the progression of web plate damage depends on the type of web plate connection detail.

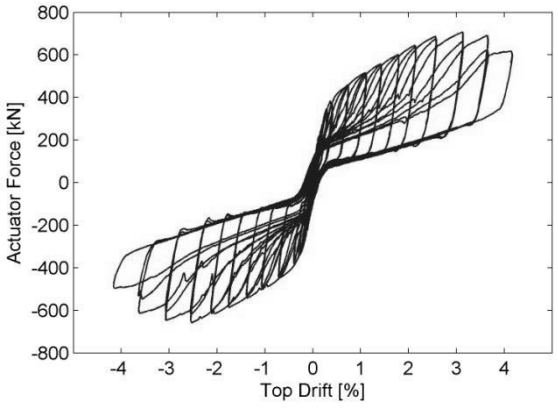


Figure 8: Force-displacement response of specimen.

5. CONCLUSIONS

The fundamental behavior of the SC-SPSW was presented through a description of the web plate and PT force interaction in the HBEs and by developing an understanding of the cyclic behavior of the SPSW and PT frame components of the SC-SPSW system. The fundamental SC-SPSW behavior was used to develop a set of performance objectives to be used in a performance-based design (PBD) procedure for the system. A summary of analytical results showed that the proposed PBD procedure was capable of producing 3- and 9-story SC-SPSWs that could meet the proposed performance objectives at three different seismic hazard levels.

The experimental investigation of a SC-SPSW subassembly was introduced. The force-displacement response for a single specimen was presented. The overall behavior of the specimen matched relatively well with the general idealized behavior assumed in the aforementioned description of cyclic SC-SPSW behavior, with the exception of the complex web plate behavior that was neglected in the idealization. The test specimen was able to recenter when loaded up to 4% drift with no damage to the frame and PT members. Strength loss in the system was due to tearing in the web plates along the bolted web plate-to-fishplate connection. This damage is believed to be due to the bolted connection detail that was used for repeatable testing of the specimen; however, future tests will be conducted to evaluate whether similar web plate damage is observed when a more conventional welded web plate-to-fishplate connection detail is employed. These experimental results, along with others, will later be used to validate numerical SC-SPSW models and determine the methods for SC-SPSW construction.

Acknowledgements:

The authors acknowledge support from the National Science Foundation (Award number CMMI-0830294) and the Valle Scholarship Foundation. Any opinions, findings, conclusions, and recommendation presented in this paper are those of the authors and do not necessarily reflect the views of the sponsors.

References:

AISC (2005). *Specification for Structural Steel Buildings*, *ANSI/AISC 341-05*. American Institute of Steel Construction, Chicago, IL.

Applied Technology Council (ATC), (1992), "Guidelines for seismic testing of components of steel structures." *Rep. No. 24*, ATC, Redwood City, Calif.

Baldvins, N., Berman, J.W., Lowes, L.N., and Janes, T. (2010), "Development of damage prediction models for steel plate shear walls." *Earthquake Spectra*, (submitted).

Berman, J. Bruneau, M., (2008). "Capacity Design of Vertical Boundary Elements in Steel Plate Shear Walls." *Engineering Journal*, First Quarter 57-71.

Chao, S.-H., Goel, S.C., Lee, S.-S. (2007), "A seismic design lateral force distribution based on inelastic state of structures." *Earthquake Spectra*, 23(3), 547-569.

Clayton, P.M. (2010), "Self-Centering Steel Plate Shear Walls: Development of Design Procedure and Evaluation of Seismic Performance," Master's thesis, Civil and Env. Eng. Dept., Univ. of Washington, Seattle, WA.

Dowden, D.M., Purba, R., and Bruneau, M. (2011), "Behavior of self-centering steel plate shear walls and design consideration", Submitted for review and possible publication to the ASCE Journal of Structural Engineering.

Garlock, M. (2002), "Design, Analysis, and Experimental Behavior of Seismic Resistant Post-Tensioned Steel Moment Resisting Frames," Ph.D. dissertation, Civil and Env. Eng. Dept., Lehigh University.

Garlock, M.M., Sause, R., Ricles, J.M. (2007), "Behavior and design of posttensioned steel frame systems." *Journal of Structural Engineering*, 133(3), 389-399.

Gupta, A. and Krawinkler, H. (1999). Seismic Demands for Performance Evaluation of Steel Moment Resisting Frame Structures, *Report No. 132*, John A. Blume Earthquake Engineering Center, Stanford University, Stanford, CA.

Kin, H.-J., and Christopoulos, C. (2008), "Seismic design procedure and seismic response of post-tensioned self-centering steel frames." *Earthquake Engineering and Structural Dynamics*, 38, 355-376.

Purba, R. and Bruneau, M. (2010), "Impact of Horizontal Boundary Elements Design on Seismic Behavior of Steel Plate Shear Walls," *Tech. Rep. MCEER-10-0007*, Multidisciplinary Center for Earthquake Engineering Research, SUNY-Buffalo, Buffalo, NY.

Qu, B., Bruneau, M., Lin, C.H., and Tsai, K.C. (2008), "Testing of Full Scale Two-Story Steel Plate Shear Walls with Reduced Beam Section Connections and Composite Floors." Journal of Structural Eng., ASCE, 134(3), 3364-373.

Sabelli, R. and Bruneau, M. (2007), *Design Guide 20: Steel Plate Shear Walls*. American Inst. Of Steel Construction, Chicago, IL.

Seilie, I.F. and Hooper, J.D. (2005), "Steel Plate Shear Walls: Practical Design and Construction," *AISC Modern Steel Construction*, April.

Vian, D., Vruneau, M., Tsai, K.C., Lin, Y.-C. (2009), "Special Perforated Steel Plate Shear Walls with Reduced Beam Section Anchor Beams. I: Experimental Investigation." Journal of Struct. Eng., ASCE, 135(3), 211-220.

8CUEE CONFERENCE PROCEEDINGS
8th International Conference on Urban Earthquake Engineering
March 7-8, 2011, Tokyo Institute of Technology, Tokyo, Japan

NONLINEAR SEISMIC RESPONSE OF STEEL CONCENTRICALLY BRACED FRAMES USING ENDURANCE TIME METHOD

M. A. Hariri Ardebili[1)], Y. Zarringhalam[2)], M. Yahyai[3)], and M. Mirtaheri[4)]

1,2) Graduate Students, Department of Civil Engineering, K. N. Toosi University of Technology, Tehran, Iran
3) Associate Professor, Department of Civil Engineering, K. N. Toosi University of Technology, Tehran, Iran
4) Assistant Professor, Department of Civil Engineering, K. N. Toosi University of Technology, Tehran, Iran
amin_hariri@sina.kntu.ac.ir, zaringhalam@sina.kntu.ac.ir, yahyai@kntu.ac.ir, mmirtaheri@kntu.ac.ir

Abstract: In present paper Endurance Time (ET) method which is a new time-history based dynamic pushover procedure is introduced and application of this method in seismic analysis of steel concentrically braced frames is studied. In this method structure is subjected to a set of predesigned increasing acceleration functions and various responses of the structure are recorded during synthetic seismic excitation. The averages of maximum values for various responses in nonlinear time-history (NTH) analyses extracted from real ground motions are expected to be close to those obtained from ET method up to equivalent target time. For this purpose a set of 9, 11, 13 and 15 stories steel frames were designed and plastic hinge method was selected as source of nonlinearity in all cases. Results were compared based on maximum story displacement, interstory drift ratio and story shear obtained from two methods. Results show satisfactory consistency between two methods. Finally, it was concluded that the ET method can be used as alternative method for seismic analysis of concentrically braced steel frames.

1. INTRODUCTION

Because of the simplicity, reality and accuracy of performance-based earthquake engineering (PBEE), many of structural codes are moving towards using this concept in their design guidelines (Hamburger, 1998). In PBEE, structures should be capable of satisfying various performance levels, under a spectrum of design ground motions which are extending from minor to severe excitation levels. Recent developments in computational technology lead to the application of numerically intensive analysis methods in the field of earthquake engineering and reduce the amount of uncertainties in PBEE.

Quest to find new analysis methods which can estimate actual seismic performance of engineering structures under various excitation levels, always was one of important concerns of earthquake engineers. Endurance Time (ET) method which is introduced by Estekanchi et al. (2004) is basically a simple dynamic pushover test that tries to predict various responses of structures at different excitation levels by subjecting them to some predesigned intensifying dynamic excitations which are called Endurance Time Acceleration Functions (ETAFs) (Riahi et al., 2009). Because of the increasing demand of the ETAFs, structures gradually go through elastic to yielding and nonlinear inelastic phases, finally leading to global dynamic instability.

Application of ET method in linear seismic analysis of structures has been studied before (Estekanchi et al., 2007). In this study, a-series of ETAFs have been applied to various moment resisting and braced steel frames which were designed based on Iranian National Building Code (INBC) and the results of analysis were compared with conventional equivalent static and response spectrum seismic analysis procedures. It was found that story drifts and internal forces from ET method are consistent with response spectrum analysis and static analysis results within acceptable tolerances. In another case, Estekanchi et al. (2008) were used damage indexes in ET method as the endurance criteria. In this investigation, correlation between the values of various damage indexes obtained from Nonlinear Time-History (NTH) analysis of steel moment frames subjected to scaled earthquakes were compared with those from ET method at the same level of spectral acceleration. It was found that the average value of various damage indexes can be estimated from ET analysis results. Application of ET method in nonlinear analysis of SDOF system was investigated by Riahi et al. (2009) as well. In this study they compared the results of ET analyses with real ground motions analysis results in different strength ratio, ductility and damping ratios. Also they considered the effects of stiffness degeneration and strength deterioration in studies. They showed that the results of ET method are in good agreement with the exact response history results of the similar ground motions.

In another study, Riahi et al. (2009) were investigated the accuracy of the ET method in estimating average deformation demands of low and medium rise steel frames using f-series of ETAFs. In their study an

elastic-perfectly-plastic model and also a bilinear material model were considered. It was shown that, although the results of the ET analysis are not exactly consistent with the results of ground motions analysis, the ET method can clearly identify the structure with a better performance even in the case of structures with a relatively complicated nonlinear behavior.

In present paper, the concept of ET method is first described and brief review is done on characteristics of second generation of ETAFs which used in this study. Compliance and level of accuracy of this method in nonlinear seismic analysis of mid-rise and high-rise steel concentrically braced frames (SCBF) is investigated. The accuracy of ET method in prediction of the response in SCBFs is investigated by using a set of 9, 11, 13 and 15 stories frames with three bays. In addition, plastic hinge method is used as source of material nonlinearity behavior in present study. It is shown that ET analysis estimates the results of NTH analysis with reasonable accuracy.

2. CONCEPT OF ENDURANCE TIME METHOD

ET method is a time-history based dynamic pushover procedure used in seismic analysis and performance evaluation of structures by measuring their resilience when they are subjected to ETAFs (Riahi et al., 2009). In this method, numerical or experimental model of structures are subjected to intensifying ETAFs and structural responses, such as drifts and shears are recorded during the analysis up to the point where the structure collapses or the analysis is terminated. Then behavior of the structure can be observed at target time which is calculated using design response spectrum.

If this test is utilized for two frames with unknown properties, the longer endurance time, which is time duration from start of the test or analysis to collapse or target point, is interpreted as better performance of that frame (Estekanchi et al., 2008). In this method after design of frames based on appropriate codes, the system is excited using a set of ETAFs and equivalent target time is calculated by suitable method for each structure respectively. Various responses of the frames at equivalent target time describe behavior of the frame in a certain performance level. In the next step, the maximum results obtained from ET method up to equivalent target time are compared with those obtained from NTH analysis of real ground motions.

3. SPECIFICATION OF SCBFs, GROUND MOTIONs and ETAFs

A set of SCBFs with different number of stories were selected as case studies. This set consists of 2D regular frames with 9, 11, 13 and 15 stories and three bays which lead to categorize of them as mid-rise and high-rise frames. These frames are designed according to the UBC-97 design code (1997). All considered frames are classify in group 4 of occupancy category based on UBC-97 and therefore seismic importance coefficient is set to one in these frames. The main purpose in design of such structures is to minimize loss of life under earthquake ground motions with 475-year return period (10% probability of occurrence in 50 year). It means that based on FEMA356 (2000) life safety (LS) performance level should be satisfied in this condition.

It is not worthy that in order to considering the stiffness effects of infilled frames and also non-structural components of structure, stronger sections were considered in present analyses rather than designed sections so that the first mode period of the simulated model be close to analytical period in code. The section properties of all frames and also characteristics of them are described in table 1.

Table 1 Characteristics of frames and fundamental period of 1st mode

NO OF STORIES									
	15	IPB 360	2L100×10/10/						
	14	IPB 360	2L100×10/10/						
	13	IPB 360	2L100×15/10/	IPB 360	2L100×10/10/				
	12	IPB 360	2L100×15/10/	IPB 360	2L100×10/10/				
	11	IPB 360	2L100×10/10/	IPB 360	2L100×10/10/	IPB 360	2L100×10/10/		
	10	IPB 400	2L100×10/10/	IPB 360	2L100×10/10/	IPB 360	2L100×10/10/		
	9	IPB 400	2L120×12/10/	IPB 360	2L100×10/10/	IPB 360	2L100×10/10/	IPB 360	2L100×10/10/
	8	IPB 450	2L120×12/10/	IPB 400	2L100×10/10/	IPB 360	2L100×10/10/	IPB 360	2L100×10/10/
	7	IPB 450	2L120×12/10/	IPB 400	2L120×12/10/	IPB 360	2L100×10/10/	IPB 360	2L100×10/10/
	6	IPB 550	2L120×12/10/	IPB 450	2L120×12/10/	IPB 400	2L100×10/10/	IPB 360	2L100×10/10/
	5	IPB 600	2L120×12/10/	IPB 450	2L120×12/10/	IPB 400	2L120×12/10/	IPB 360	2L100×10/10/
	4	IPB 600	2L120×12/10/	IPB 550	2L120×12/10/	IPB 450	2L120×12/10/	IPB 400	2L100×10/10/
	3	IPB 700	2L150×15/10/	IPB 600	2L120×12/10/	IPB 450	2L120×12/10/	IPB 400	2L120×12/10/
	2	IPB 800	2L150×15/10/	IPB 600	2L120×12/10/	IPB 550	2L120×12/10/	IPB 450	2L120×12/10/
	1	IPB 900	2L150×15/10/	IPB 700	2L150×15/10/	IPB 600	2L120×12/10/	IPB 450	2L120×12/10/
Models and Abbreviations		**Column**	**Brace**	**Column**	**Brace**	**Column**	**Brace**	**Column**	**Brace**
		SCBF15@3		**SCBF13@3**		**SCBF11@3**		**SCBF09@3**	
Fundamental Period (sec)		1.299		1.076		0.865		0.661	

The tri-linear material model with a post-yield stiffness equal to 3% of the initial elastic stiffness and considering effects of strength degeneration were used to study the nonlinear behavior of the frames. This model has been used widely in previous investigations and therefore represents a benchmark to study the effect of hysteretic behavior. Furthermore, recent studies have shown that this is a reasonable hysteretic model for steel beams (Foutch and Shi, 1998). For more realistic nonlinear behavior, the chord rotation model is also used in this study. This model is the easiest to use and FEMA-356 gives specific guidelines for this model. To apply these material models in the analysis, the PERFORM software was used (PERFORM user manual, 2010). Only one (horizontal) component of the ground motion has been considered, while dynamic soil-structure interaction is neglected. P-Δ effects have been included in the analysis. A viscous damping of 5%, as customary for these types of frame, has been applied in the analyses. This value of damping is consistent with the value used for generating codified response spectra and ET acceleration functions.

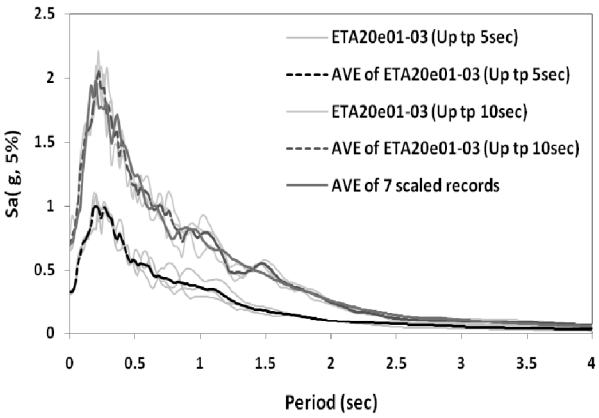


Figure 1 Acceleration response spectrum of ETA20e at various times for ξ=5%

For analysis of frames based on ET method e- and f-series of ETAFs which are shown as ETA20e01-03 and ETA20f01-03 are used in present study. These sets were generated using the average of scaled response spectrum of seven ground motions called as GM1 set which were selected be Valamanesh et al. (2010). These accelerograms which are recorded on site class C and used in FEMA 440 are presented in table 2. The smoothed spectrum of GM1 is target spectrum in generating e- and f-series. As it is clear in figure 1, the response spectrum of a window of ETAFs from t_0=0 to t_1=10 matches reasonably well with the average response spectrum of the seven ground motion records. It is important to note that the ET response spectra remain proportional to the target spectra from seven ground motions at all times. For example, response spectrum in t=10s is twice of spectrum in t=5s. Acceleration, velocity and displacement functions of ETA20e01, as a sample, are shown in figure 2.

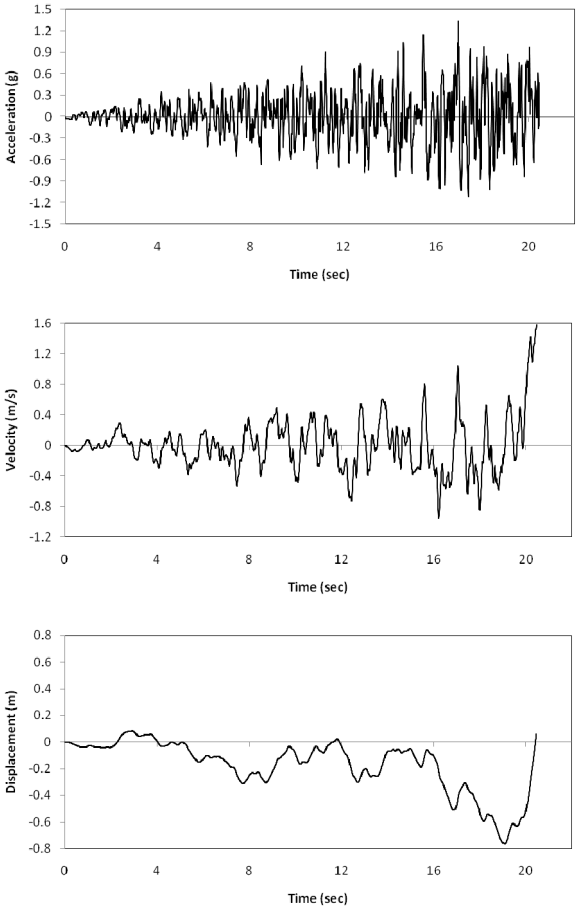


Figure 2 Acceleration, velocity and displacement functions of ETA20e01

Table 2 Characteristics of GM1 set of ground motions used for generation of e- and f-series of ETAFs

Abbreviation	Earthquake name and date	Station No.	Selected component	Magnitude (M_s)	PGA (cm/s^2)
LADSP000	Landers (06/28/1992)	12149	0	7.5	167.8
LPSTG000	Loma Prieta (10/17/1989)	58065	0	7.1	494.5
LPGIL067	Loma Prieta (10/17/1989)	47006	67	7.1	349.1
LPLOB000	Loma Prieta (10/17/1989)	58135	360	7.1	433.1
LPAND270	Loma Prieta (10/17/1989)	1652	270	7.1	239.4
MHG06090	Morgan Hill (04/24/1984)	57383	90	6.1	280.4
NRORR360	North-Ridge (01/17/1994)	24278	360	6.8	504.2

In present paper, to compare the results of ET analysis with real earthquakes, GM1 set is used. To be consistent with the seismic codes, the GM1 set of ground motions should be scaled. Considering that in the present study only single horizontal component of ground motions are used to analysis of frames, records are scaled individually. For this purpose it is suppose that the average of 5% damped linear response spectra does not fall below the design spectrum for the period range $0.2T_i$ to $1.5T_i$ where T_i is the fundamental period of vibration of each frame modeled as a linear system. Here, scale factors are obtained in a way that the ground motion spectrum matches the UBC-97 (1997) spectrum in the mentioned range. Scale factors obtained by this method for the GM1 set are shown in table 3 for each frame.

Table 3 Scale factors of GM1 set and equivalent target time for SCBFs

	Frames			
	SCBF 15@3	**SCBF 13@3**	**SCBF 11@3**	**SCBF 09@3**
LADSP000	4.678	4.011	4.215	4.093
LPSTG000	1.562	1.339	1.408	1.367
LPGIL067	2.241	1.921	2.019	1.961
LPLOB000	1.776	1.522	1.6	1.554
LPAND270	3.277	2.81	2.954	2.868
MHG06090	2.739	2.349	2.468	2.397
NRORR360	1.555	1.333	1.401	1.361
Equivalent Target Time (sec)	13.31	10.68	11.55	11.00

Because of increasing nature of ETAFs, it is questionable that how the results of two methods can be compared with each other. As it is clear, in this method the time is correlated with intensity and different responses of structure are calculated for various values of dynamic load intensity in an ET analysis. To establish a relation between the results of the ET and NTH methods, the intensity value of the NTH analysis should be found in the ET analysis. Therefore, a procedure should be defined to find an equivalent target time in the ET analysis in which the intensity values of the two methods have equal values.

Various quantities can be used to characterize the intensity of a ground motion record, i.e. Peak Ground Acceleration (PGA), Peak Ground Velocity (PGV) and Spectral Acceleration at the structure's first-mode period ($S_a(T_1)$). In present research, $S_a(T_1)$ is used as dynamic load intensity to obtain the equivalent target time.

The equivalent target time can be calculated for a single record or a set of records. In the proposed technique at the current study, 10^{th} second of ETAFs is selected as base target time and therefore, the average response spectrum resulted up to the 10^{th} second of ETAFs is interpreted as base response spectrum (which is corresponding with base target response spectrum for generation of ETAFs). Consequently, equivalent target time is calculated by multiplying ψ factor, called as spectrum ratio, in constant 10 as shown in Eq.1:

$$t_{eq}(T_R) = \psi(T_R, T_{eff}) \times 10 \tag{1}$$

in which $t_{eq}(T_R)$ is equivalent target time for the desired performance level with return period T_R and $\psi(T_R, T_{eff})$ is spectrum ratio with return period T_R and for effective period interval equal to T_{eff}. In the present study spectrum ratio is calculated as follow:

$$\psi(T_R, T_{eff}) = \frac{S_a^{T_R, T_n}}{S_a^{ET, T_n}} \tag{2}$$

where $S_a^{T_R, T_n}$ is average of the spectral acceleration of the seven ground motions at the first-mode period (fundamental period) and S_a^{ET, T_n} is the value of the smooth response spectrum used for the generation of ETAFs at the first-mode period. The calculated equivalent target times for each frame are tabulated in last row of table 3. Based on table 3, the equivalent target time for SCBF15@3 is 13.31s. It means that the results obtained from average of ET analyses up to 13.31s should have the same or close values to the average maximum values resulted from TH analyses from seven ground motions. This rule is indefeasible in other frames.

4. RESULTS AND DISCUSSION

In the following subsections, ability of ET method in estimating various parameters such as displacement, story shear and interstory drift ratio is considered.

4.1 Story Displacement

In this subsection, displacements obtained from ET method at equivalent target time and NTH analyses are compared with each other along stories of frames. Figure 3 shows non-concurrent envelopes of displacement for different frames extracted from NTH analyses and ET method. As shown in this figure dispersion of results between ETAFs are very less than seven ground motions. Although, using three or six ETAFs can reduce percentages of errors between average of ET and NTH analyses, its effect is negligible especially for mid-rise frames. It means that in SCBFs using only e- or f-series of ETAFs for estimation of NTH results is enough. Maximum of average displacements estimated by e- and f-series and also GM1 set for SCBF09@3 are 127mm, 128mm and 132mm. As it is clear both e- and f-series have very excellent estimation of exact displacement in this frame. The percentage of errors between ET and NTH analyses are only -3.8% for e-series and -3.0% for f-series. The sign (-) indicates that ET method estimates

lower results in comparison with NTH method. Roof displacements for SCBF11@3 based on e-, f-series and GM1 set are 190mm, 187mm and 184mm respectively which lead to about +3.2% errors in e-series and +1.6% errors in f-series for this frame. For SCBF13@3 maximum displacement for mentioned dynamic loads are obtained as 227mm, 237mm and 229mm. Errors based on e- or f-series of ETAFs are +0.4% and +3.4%. In SCBR15@3 the results of displacement based on e-, f-series and GM1 set are obtained as 285mm, 273mm and 285mm which lead to error about -4.2% in f-series while results obtained from e-series and NTH are exactly same. Except of roof displacement which has been estimated by ET method in high accuracy, total trend of maximum displacements in each story are very close in ET and NTH methods.

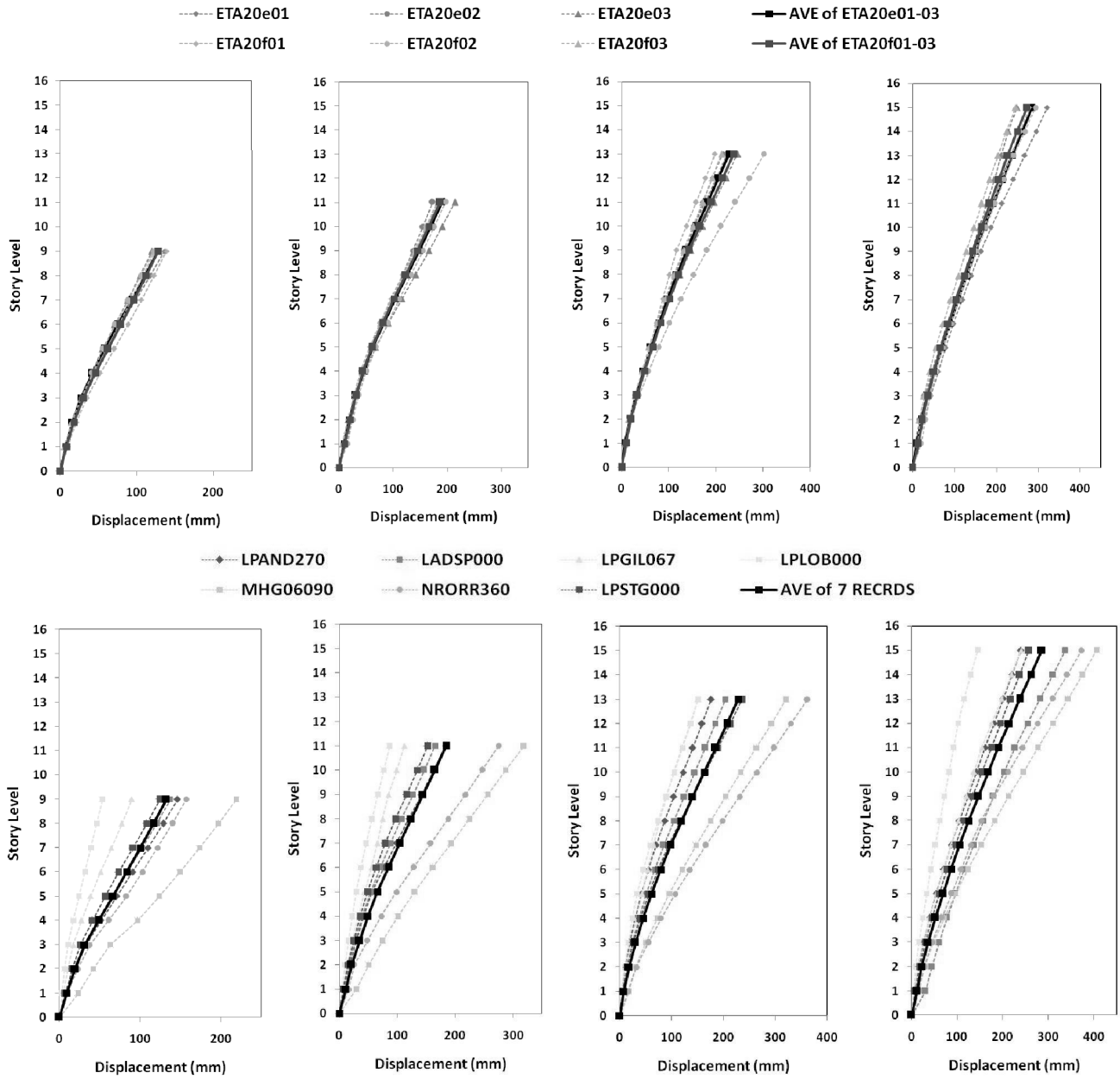


Figure 3 Non-concurrent envelope of story displacement resulted from ET and NTH analysis

4.2 Story Shear

Figure 4 shows non-concurrent envelopes of story shear for different frames extracted from NTH analyses and ET method. Generally there is good consistency between the results of two methods. Like displacement, in this response dispersion of results are very limit in ET rather than NTH method. It is not worthy that dispersion of results obtained from NTH method for shear is less than displacement. Moreover the average results of e- and f-series of ETAFs are very close together but their

consistency is less than displacement. The value of base shear for SCBF09@3, SCBF11@3, SCBF13@3 and SCBF15@3 resulted from average of GM1 set are 2509KN, 2351KN, 2546KN and 2485KN respectively. The corresponding values extracted from e-series are 2880KN, 2770KN, 2781KN and 2644KN. Values of base shear from f-series for mentioned frames are 2823KN, 2993KN, 2788KN and finally 2854KN. So the percentage of errors between ET and NTH methods based on using e- or f-series are about +14.7% and +12.5% for SCBF09@3, +17.8% and +27.3% for SCBF11@3, +9.2% and +9.5% for SCBF13@3 and finally +6.3% and +14.8% for SCBF15@3. As it is clear all errors have positive sign and it means that ET method overestimates results of NTH method.

On the other hand ET has better estimation of shear in last story in each frame. Average errors between e- and f-series of ETAFs with NTH method are +12.1% and +4.9% for SCBF09@3, +22.4% and +17% for SCBF11@3, +3.7% and -0.1% for SCBF13@3 and finally +10.5% and +4.9% for SCBF15@3.

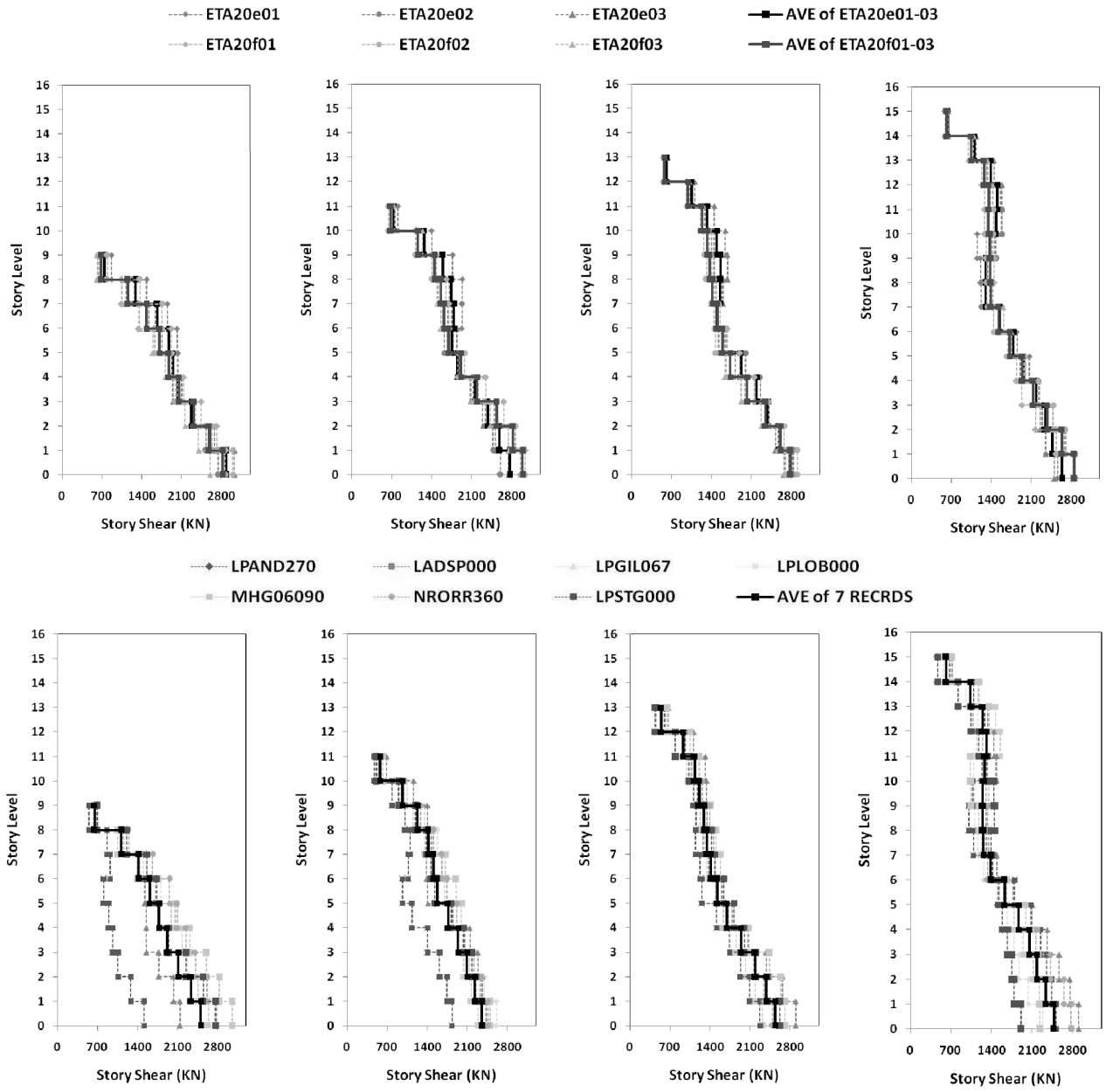


Figure 4 Non-concurrent envelope of story shear resulted from ET and NTH analysis

4.3 Interstory Drift Ratio

Figure 5 shows maximum interstory drift ratio for different frames extracted from NTH analyses and ET method. As can be seen in this figure, in all cases the average of interstory drift ratio extracted from e-, f-series and GM1 set satisfy LS performance level (in all cases θ_{max} are below the 1.2%). Maximum interstory drift ratio for all frames in upper stories is more than lower ones. This effect is significant especially for high-rise frames. Although dispersion of results in real ground motions are meaningful, they are close together in ET method. Results of θ_{max} by using e- or f-series of ETAFs are very close in SCBF09@3, while increasing height of frames lead to some differences between e- and f-series. θ_{max} for the SCBF09@3, SCBF11@3, SCBF13@3 and SCBF15@3 resulted from average of GM1 set are 0.62%, 0.72%, 0.77% and 0.83%. The corresponding values extracted from e-series are 0.63%, 0.75%, 0.81% and 0.93% and the values of θ_{max} from f-series for mentioned frames are 0.60%, 0.72%, 0.75% and finally 0.84%. Therefore the percentage of errors between ET and NTH methods based on using e- or f-series are about +1.6% and -3.2% for SCBF09@3, +4.1% and 0.0% for SCBF11@3, 1.3% and -2.6% for SCBF13@3 and +12% and +1.2% for SCBF15@3. As it is clear by using three ETAFs as ET analyses all percentage of errors except SCBF15@3 are very low. It is not worthy that using six ETAFs (combination of e- and f-series) lead to decrease percentage of errors to about +6.6% for SCBF15@3.

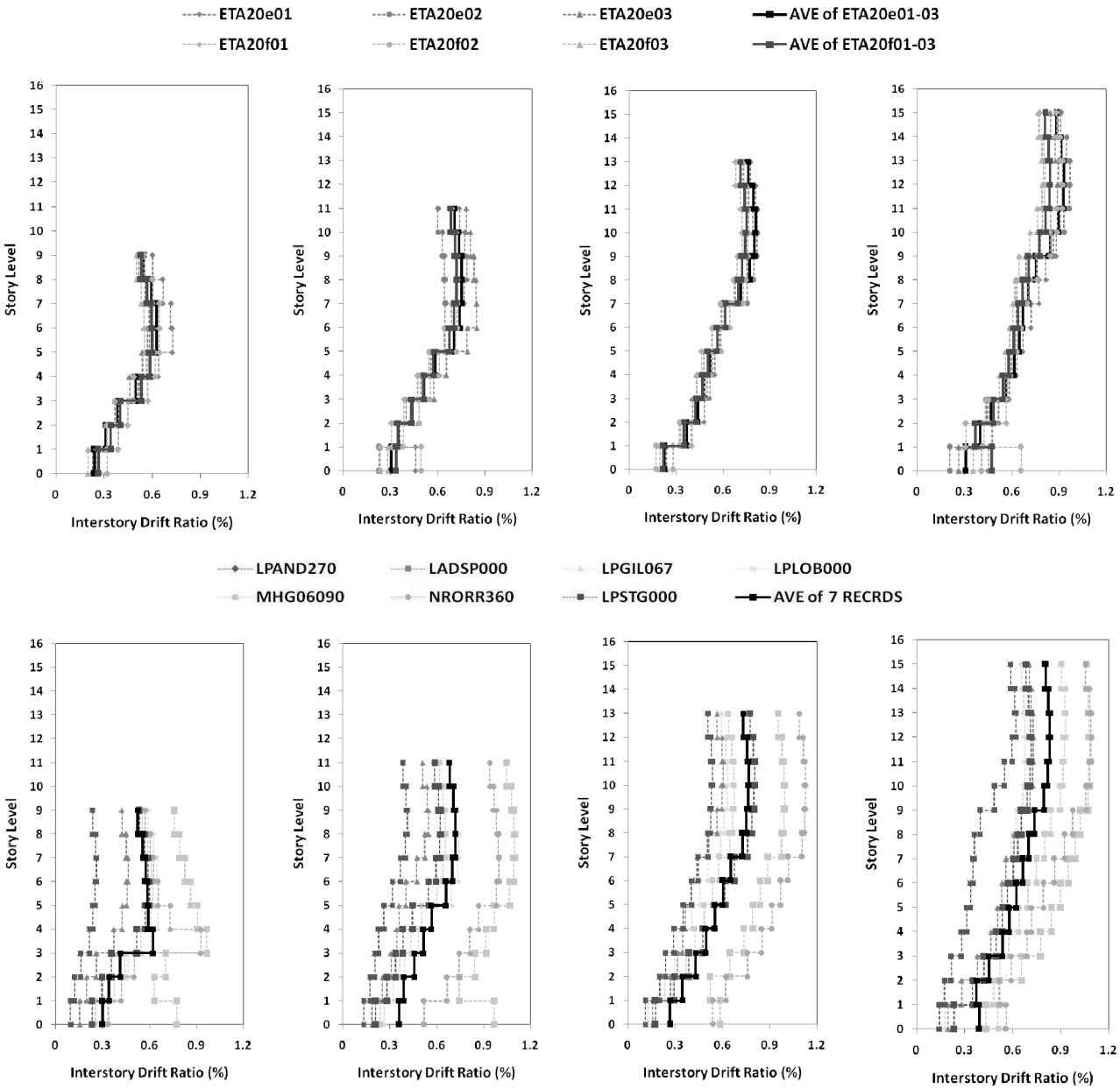


Figure 5 Maximum interstory drift ratio resulted from ET and NTH analyses

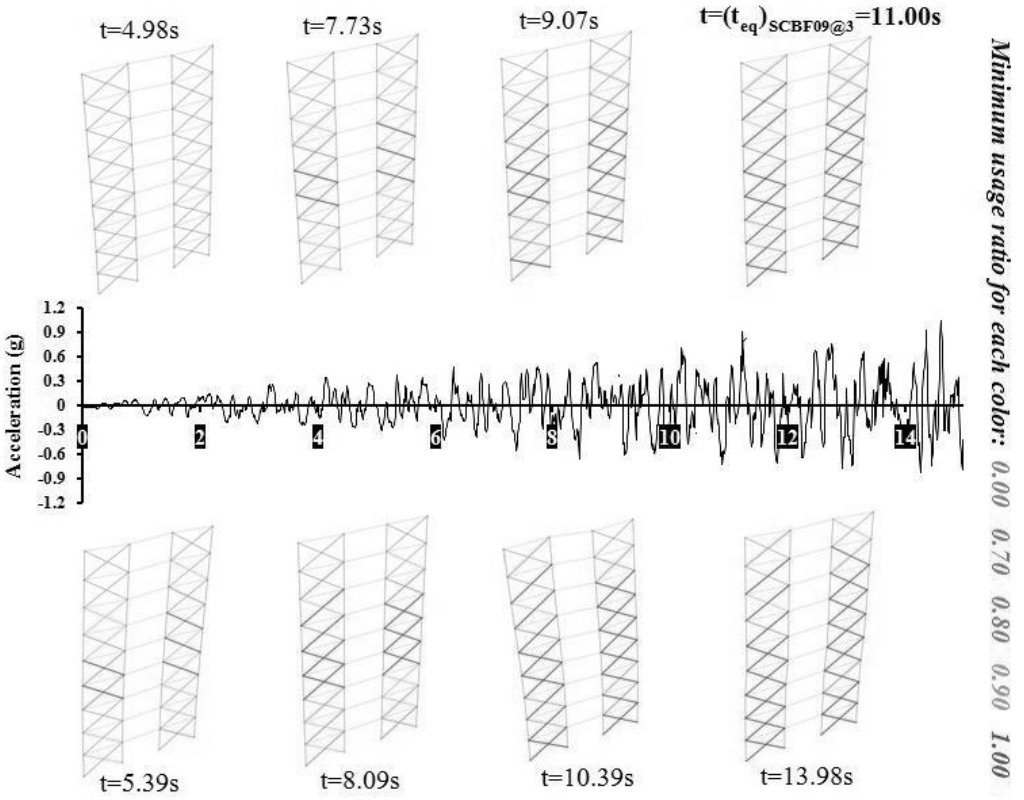


Figure 6 Strain ratio in braces of SCBF09@3 under ETA20e01 at various times

4.4 Maximum Strain Ratio in Braces

Figure 6 shows strain ratio in braces of SCBF09@3, as a sample, at various times under ETA20e01 acceleration function using appropriate colored contours. As can be seen with time passing, the structure experience higher PGA and energy and therefore number of braces which exceed certain criteria increase. For example, based on this figure, it is clear that none of braces exceed ratio=1 in t=4.98s and all of them in safe rang, but one of each concentrically braces in 3rd floor have potential for exceed ratio=1 with little increases in time (increases in input energy consequently). This happens when ETA20e01 apply to frame up to t=5.39s. In this time some of braces in 3rd, 4th and 5th floors exceed ratio=1. Monitoring behavior of frame at various times under an ETAF gives appropriate information about both location and extension of overstrain areas in frame and is effective way to find weakest elements in system and retrofit of them. Finally figure 6 presents status of frame at t=11.00s (which is equivalent target time for SCBF09@3). Based on previous results about estimation of responses by ET method at equivalent target time, it is not worthy that this figure (at t=11.00s) is an average of status of braces under real ground motions (GM1 set). It shows that almost all braces except braces in floor 9 and some braces in floor 8 exceed ratio=1. It is important to remember that because of random nature of ETAFs, it is better to use at least three of them and taking their average for reducing uncertainties in analyses.

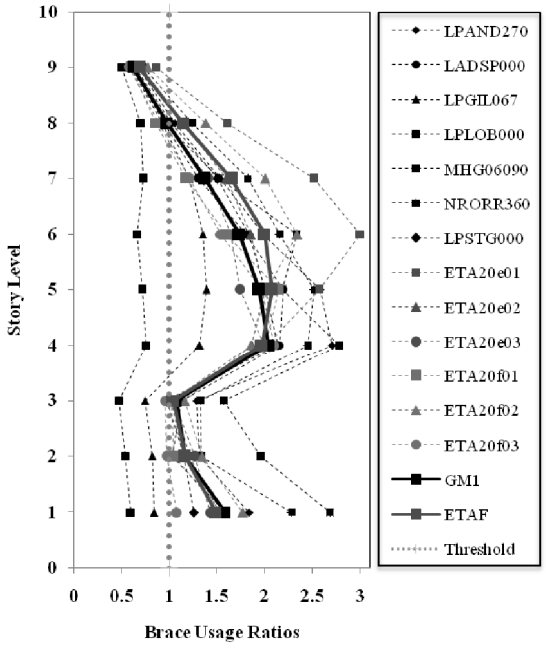


Figure 7 Maximum strain ratio in braces of SCBF09@3 extracted from NTH and ET methods

To investigate accuracy of figure 6 in estimation of maximum train ratio, total behavior of mentioned frame (SCBF09@3) under seven ground motions (GM1 set) and also six ETAFs (e- and f-series) are studied. Figure 7 represents maximum strain ratios for braces in each story of frame under total time of real ground motions and up to t=11.00s (equivalent target time) based on ETAFs. As can be seen except LPLOB000 which is not exceed ratio=1 and LPGIL067 which is not exceed ratio=1 in lower stories, all other five ground motions and also all six ETAFs exceed ratio=1 in almost all stories except 9th floor and in some cases 8th floor. So the results of figure 6 are satisfied by complete review of responses in figure 7.

5. CONCLUSIONS

In the present paper, Endurance Time method as a new time-history based dynamic pushover procedure was introduced and its application in estimation of various structural responses in concentrically braced steel frames was investigated. A set of mid-rise and high-rise frames were designed as 2D frames for this purpose. In addition, the results of Endurance Time analysis were compared with average results of real ground motions. Results show that Endurance time method estimate total displacements of stories with high accuracy. Maximum percentage of error between nonlinear time-history method and Endurance Time analysis for this response is only 4.2%. For interstory drift ratio, Endurance time method has very good estimation of nonlinear time-history method for all frames except 15-story frames. In all cases maximum percentage of errors are limit to 4.1%, but in 15-story frame percentage of error rise to 12% by using e-series of acceleration function. In this frame combination of e- and f-series of acceleration functions, decrease errors to about 6.6%. Although Endurance Time method gives very good estimation of displacements and interstory drifts, the percentage of errors are increases for shear. Total percentage of errors between average of GM1 set and six ETAFs for base shear are 13.6% for SCBF09@3, 22.5% for SCBF11@3, 9.3% for SCBF13@3 and 10.5% for SCBF15@3. As can be seen errors decrease for high-rise frames in comparison with mid-rise ones. Finally the most interesting ability of Endurance Time method is analysis of structural system and estimation of various responses with less number of analyses. This characteristic is important when it is required to analyze of system in different intensities, where Endurance Time method can gives useful information about responses in various intensities just be single analysis. Also this method is capable to detect weakest elements and parts in system when they are subjected to seismic inputs and can be used for retrofit of weak and under-designed systems.

Acknowledgements:

The authors would like to thank the scientific supports of Dr. H.E. Estekanchi in Sharif University of Technology in providing basic data during this research.

References:

Hamburger, R.O. (1998), "A Reliability Basis for Design Performance Objectives," Structural Engineering World Wide, Elsevier Science Ltd., Oxford, England, T166-1.

Estekanchi, H.E., Vafai, A. and Sadeghazar, M. (2004), "Endurance Time Method for Seismic Analysis and Design of Structures," Scientia Iranica, **11**(4), 361-370.

Riahi, H.T., Estekanchi, H.E. and Vafai, A. (2009), "Endurance Time method-Application in nonlinear seismic analysis of single degree of freedom systems," Journal of Applied Sciences, **9**(10), 1817-1832.

Estekanchi, H.E., Valamanesh, V. and Vafai, A. (2007), "Application of Endurance Time Method in Linear Seismic Analysis," Engineering Structures, **29**(10), 2551-2562.

Estekanchi, H.E., Arjomandi, K. and Vafai, A. (2008), "Estimating Structural Damage of Steel Moment Frames by Endurance Time Method," Journal of Constructional Steel Research, **64**(2), 145-155.

Riahi, H.T., Estekanchi, H.E. and Vafai, A. (2009), "Estimates of Average Inelastic Deformation Demands for Regular Steel Frames by the Endurance Time Method," Scientia Iranica, **16**(5), 388-402.

Uniform Building Code, (1997), International Code Council.

Federal Emergency Management Agency, (2000), "FEMA-356, Pre-standard and commentary for the seismic rehabilitation of buildings," Washington, D.C., USA.

Foutch, D.A. and Shi, S. (1998), "Effects of hysteresis type on the seismic response of buildings," Proceedings of 6th U.S. National Conference on Earthquake Engineering, Washington, Earthquake Engineering Research Institute, Oakland, California.

Perform 3D, Version 4.0.1., (2006), "Element Descriptions".

Valamanesh, V., Estekanchi, H.E. and Vafai, A. (2010), "Characteristics of Second Generation Endurance Time Acceleration Functions," Scientia Iranica, **17**(1), 53-61.

8CUEE CONFERENCE PROCEEDINGS
8th International Conference on Urban Earthquake Engineering
March 7-8, 2011, Tokyo Institute of Technology, Tokyo, Japan

A METHOD TO DETECT STRUCTURAL DAMAGE USING HIGH-FREQUENCY SEISMOGRAMS

Vanessa M. Heckman[1], Monica D. Kohler[2], and Thomas H. Heaton[3]

1) Graduate Student, Department of Mechanical and Civil Engineering, California Institute of Technology, USA
2) Professional Researcher, Center for Embedded Networked Sensing, University of California at Los Angeles, USA
3) Professor of Engineering Seismology, Department of Mechanical and Civil Engineering, California Institute of Technology, USA
heckman@caltech.edu, kohler@ess.ucla.edu, heaton@caltech.edu

Abstract: A numerical study is performed to gain insight into applying a novel method to detect high-frequency dynamic failure in buildings. The method relies on prerecorded catalog of Green's functions for instrumented buildings. Structural failure during a seismic event is detected by screening continuous data for the presence of waveform similarities to each of the cataloged building responses. In the first part of this numerical study, an impulse-like force is applied to a beam column connection in a linear elastic steel frame. A time-reversed reciprocal method is used to demonstrate that the resulting simulated displacements can be used to determine the absolute time and location of the applied force. In the second part of the study, a steel frame's response to two loading cases, an impulse-like force and an opening crack tensile stress, is computed on a temporal scale of microseconds. Results indicate that the velocity waveform generated by a tensile crack can be approximated by the velocity waveform generated by an impulse-like force load applied at the proper location. These results support the idea of using a nondestructive impulse-like force (e.g. hammer blow) to characterize the building response to high-frequency dynamic failure (e.g. weld fracture).

1. INTRODUCTION

There has been recent interest in using acoustic techniques to detect damage in instrumented civil structures. An automated damage detection method that analyzes recorded data has application to building types that are susceptible to a signature type of failure, where locations of potential structural damage are known a priori. Such a method would be valuable if it could be used to detect types of damage that are otherwise difficult and costly to detect. In particular, this method has application to the detection of brittle failure of welded beam-column connections in steel moment resisting frames (MRFs). The 1994 Northridge earthquake exposed this type of damage, which can occur without accompanying damage to architectural finishes and cladding; in some cases, detection requires intrusive inspections that can be costly and time-consuming (Rodgers et al. 2007). An automated damage detection method could be used to located areas of probable damage to guide post-earthquake building inspection.

Acoustic damage detection methods rely on the comparison of a recent signal to an archived baseline response function, known as a template. The template is recorded at a time when the structure is undamaged. The sensor network must have a high sampling rate to capture the propagation of waves throughout the structure. Acoustic techniques have been explored experimentally and numerically for thin plates and beams (Park et al. 2007, Wang and Rose 2003, Wang et al. 2004), which serve as waveguides that effectively carry information from the location of structural damage to a receiver. This information, namely differences in waveform and amplitude between the current signal and the template, are used to diagnose damage.

Acoustic methods can be passive or active, and sensor networks can be permanently installed or temporary. Giurgiutiu (2005) reviews current techniques, including embedded ultrasonic non-destructive evaluation (NDE), which uses a transmitter to interrogate the structure while a receiver records the structural response.

1) *Pitch-catch*: A pulse is emitted by a transmitter and travels through the material to a receiver. Differences in guided wave shape, phase, and amplitude are used to detect damage in the medium between the transmitter and receiver.
2) *Pulse-echo*: A pulse is emitted by a transmitter, which also acts as a receiver to detect damage in the form of additional echoes.
3) *Time-reversal*: A signal sent by a transmitter arrives at a receiver, where the signal is time-reversed and reemitted. Structural damage that causes linear reciprocity to break down leads to discrepancy between the original signal and the final signal received by the transmitter.
4) *Migration*: Recorded waves are back-propagated through the material by systematically solving the wave equation to image reflectors in the medium.

In this paper, a complementary acoustic method is

presented, that makes use of a prerecorded catalog of Green's functions and a matched filter method to passively detect the original failure event. This technique is different from existing acoustic methods as it is designed to recognize seismic waves radiated by the original brittle failure event. The matched filter method has been successfully used in other fields (Gibbons and Ringdal 2006, Anstey 1964), but the method has yet to be explored in the context of acoustic damage detection of civil structures.

The proposed method is described in greater detail in the following section. Two numerical studies are performed; the first compares our method to a similar time-reversed reciprocal method, and the second provides a waveform comparison between a non-destructive event and a failure event.

2. MATCHED FILTER METHOD

The proposed method would make use of a prerecorded catalog of Green's functions for an instrumented building to detect structural damage during a later seismic event. Continuous data collected on a passive network is screened for the presence of waveform similarity to one of the Green's function templates. The method is outlined below.

1) Identify probable points of failure in an instrumented building before structural damage has occurred. As pre-Northridge steel MRFs are susceptible to the brittle failure of welded beam-column connections, these would be the locations of probable failure for this type of building.

2) At each labeled location, apply a short-duration high-frequency pulse (e.g. using a force transducer hammer). The response of the building at each instrument site is the Green's function specific to that source location-receiver pair. The Green's functions are archived in the catalog of templates to be used later to screen the high-frequency seismogram for a damage signal.

3) For each possible source location k, perform a running cross-correlation between the Green's function templates for that source location and a moving window of the seismogram that recorded the shaking event, stacking over the receivers. Cross-correlation between the k^{th} Green's function template x_i^k recorded by the i^{th} receiver and the seismogram x_i recorded by the i^{th} receiver is given by

$$C_i^k(t) = \frac{\int_0^T x_i^k(\tau) x_i(t+\tau) d\tau}{\left(\int_0^T \left(x_i^k(\tau)\right)^2 d\tau \int_0^T \left(x_i(t+\tau)\right)^2 d\tau \right)^{1/2}}. \quad (1)$$

Time T is the duration of the template, and the cross-correlation is normalized by the autocorrelation values for the given time window.

Compute the stacked cross-correlation function by summing over the R receiver locations to obtain

$$C^k(t) = \frac{1}{R} \sum_{i=1}^{R} C_i^k(t). \quad (2)$$

4) If damage occurred at or near the k^{th} source location, the stacked cross-correlation function given by Eq. (2) should peak at a value close to one at the correct time of the structural damage event. In the case of multiple locations of damage, then the stacked cross-correlation functions should each peak at a value close to one at the corresponding times, provided the correct Green's function templates are used. This procedure could be extended to the three-dimensional case.

The proposed method makes some assumptions. The first is that the signal due to the failure event will be observable over the predominant building response to seismic loading. Rodgers et al. (2007) carried out experimentation on a one-third scale model steel moment frame and found that "high-frequency high-amplitude transient accelerations" were observable over the structural response to shaking and could be attributed to connection fracture. They further analyzed building records from the 1994 Northridge earthquake by identifying transient signals and classifying the possible causes, and they were able to determine with a 67% success rate whether each building had undergone connection fracture.

A second assumption is that the template will not change significantly over time. However, it has been shown that changes in environmental conditions as well as moderately large local earthquakes can lead to observed changes in a building's natural frequency (Clinton et al. 2006). This has not been extended to observed changes in wave propagation through the structural components of the building. A similar matched filter method has been successfully employed by Gibbons and Ringdal (2006) to detect similar low-magnitude seismic events by cross-correlating a waveform template with successive time segments of incoming data and stacking over the seismic array.

A third assumption is that the sensor network will be able to capture waves propagating away from the damage location throughout the structure. Kohler et al. (2009) have carried out preliminary experimentation on the UCLA Factor building using hammer blows to generate Green's function templates. The structural response to the hammer blow was observable well above ambient noise, and the signal could be seen to propagate away from the source location at a downsampled rate of 200 sps, achieved by filtering the 500 sps accelerometer array data for frequencies between 10 and 95 Hz.

A fourth assumption is that the Green's function template will be similar to the damage signal. This assumption is addressed in Section 4.

3. A TIME-REVERSED RECIPROCAL NUMERICAL EXPERIMENT

A time-reversed reciprocal method is applied to demonstrate that the location of a nondestructive

impulse-like force can be determined by using the numerically computed displacement records to time-reverse and retransmit the signal. First, the response of a two-story one-bay steel frame to an impulse-like force applied to a beam-column connection is computed. A cross section of the three-dimensional steel model is shown in Figure 1 below. Each beam and column has a square cross section of length 0.5 m. The model parameters are governed by linear elastic material properties of A36 structural steel (E = 200 GPa, μ = 80 GPa, ρ = 7850 kg/m^3), which correspond to seismic velocities of c_s = 3.2 km/s and c_p = 5.6 km/s. The hex 8 mesh elements have a discretization length of 2.5 cm; the total time is 4 ms with a time step of 2 μs. CUBIT is used for mesh generation, PyLith for physics code, and ParaView for visualization (Aagaard 2008).

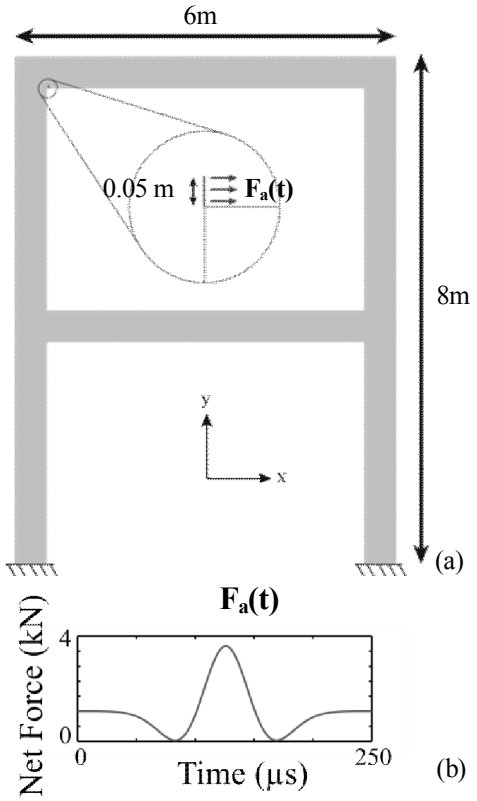


Figure 1 Numerical Setup for Steel Frame: (a) Impulse-like force is applied at beam-column connection in a direction parallel to the x-axis (b) Ricker wavelet is used for time-force history.

3.1 Forward Simulation

The response of the steel frame to an impulse-like force applied to a beam-column connection is computed. As shown in Figure 1 above, the force is applied along the positive x-axis to the close-up section of the connection. The total force is distributed proportionally over nodes according to the amount of surface area contained by each node. The force-time history is a Ricker wavelet.

Waves propagate away from the location of the source, reflecting off the edges of the frame, as shown in Figure 2 below. Resulting displacements are recorded at the twelve receiver locations approximately evenly spaced along the central cross section of the frame. A representative sample of displacements is provided in Figure 3(a) below.

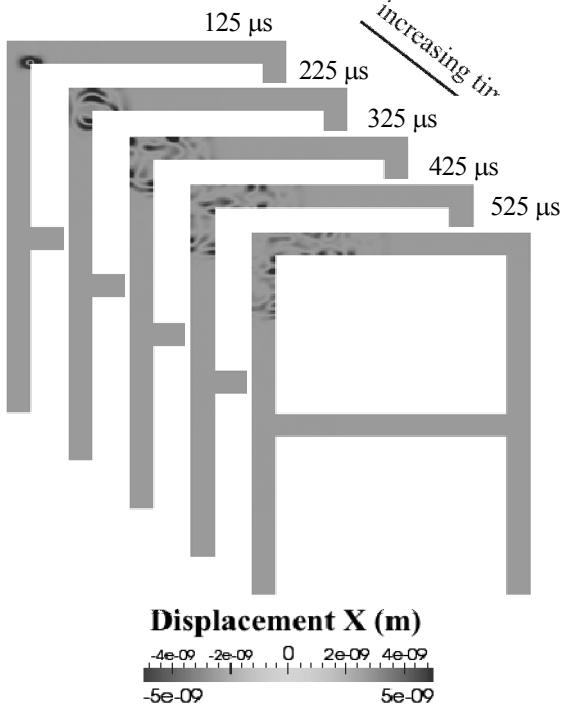


Figure 2 Response of Steel Frame to Nondestructive Impulse-like Force Applied to Beam-Column Connection.

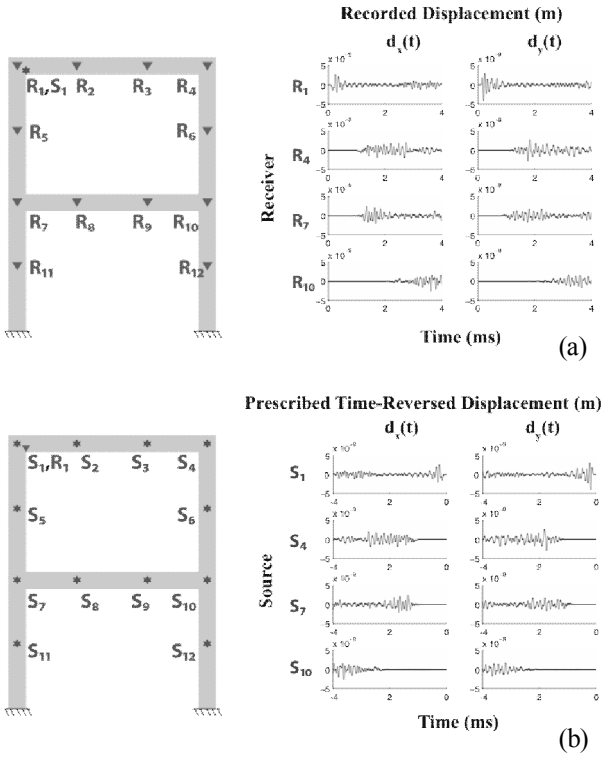


Figure 3 Receivers, Sources, and Displacements: (a) Receiver locations and examples of recorded displacements for forward simulation. (b) Source locations and corresponding prescribed time-reverse displacements for reverse simulation. Due to symmetry, $d_z(t) = 0$.

3.2 Reverse Simulation

Following the time-reversed reciprocal method, the receiver and source locations are interchanged, and each of the displacement records is time-reversed and applied at the respective new source location as prescribed Dirichlet conditions, as shown in Figure 3(b) above. The retransmitted signal propagates through the frame, and the waves generated by the twelve new source locations interfere constructively to focus at the original source location $\mathbf{S_1}$, where the nondestructive load was applied, and at the correct time. To simplify timing, the reverse simulation begins at -4 ms and ends at 0 ms, with waves focusing on the beam-column connection at the correct time of -125 μs, demonstrated in Figure 4 below. Thus, by using a time-reversed reciprocal method, the recorded displacements are used to determine the absolute time and location of the original applied force.

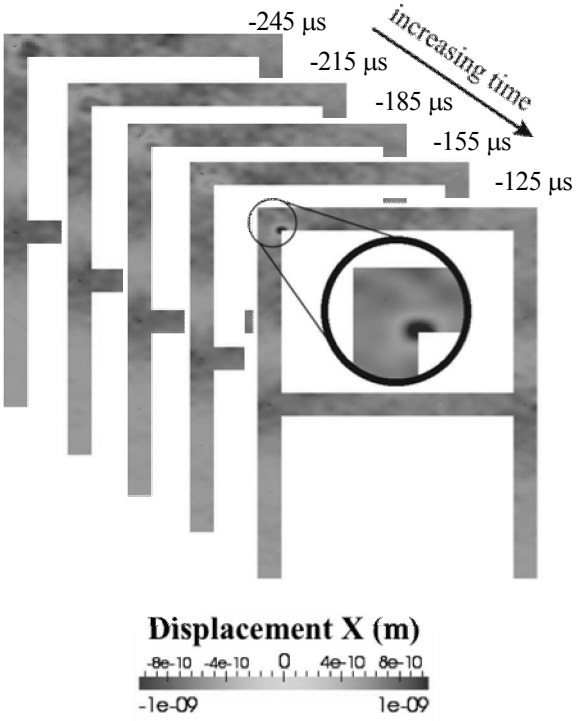


Figure 4 Response of Steel Frame to Prescribed Time-Reversed Displacements. Waves generated at each of the twelve source locations converge at the correct location at the correct time.

4. NUMERICAL APPLICATION OF MATCHED FILTER METHOD

A time-reversed reciprocal method as presented in the previous section is not application-realistic, as the location of the receiver may not coincide with the location of damage, and thus, the focusing of the transmitted time-reversed signal could go undetected. The purpose of this section is to investigate numerically an alternative yet similar approach that makes use of Green's functions, waveform similarity, and wave propagation reciprocity. The matched filter method is used to screen data recorded by a passive seismic network for waveform similarities to an archived template, ultimately relying on experimental, not simulated, building response. To validate the feasibility of the proposed method, it is first necessary to provide justification for using the structural response to an impulse-like force to approximate the structural response to an opening crack tensile stress.

4.1 Comparison of Structural Response to Two Different Source Conditions

The response of a steel frame to two different loading cases, an impulse-like force and an opening crack tensile stress, both shown in Figure 5, is compared to determine whether the waveform generated by a nondestructive source can be used to approximate the waveform generated by a structurally damaging source. The same material properties and dimensions as in Section 3 are used. A square notch is introduced in the opening crack tensile stress case, to simulate crack initiation at the beam-column connection. The square notch has a length of 0.05 m, consistent with the dimensions used for the unnotched frame.

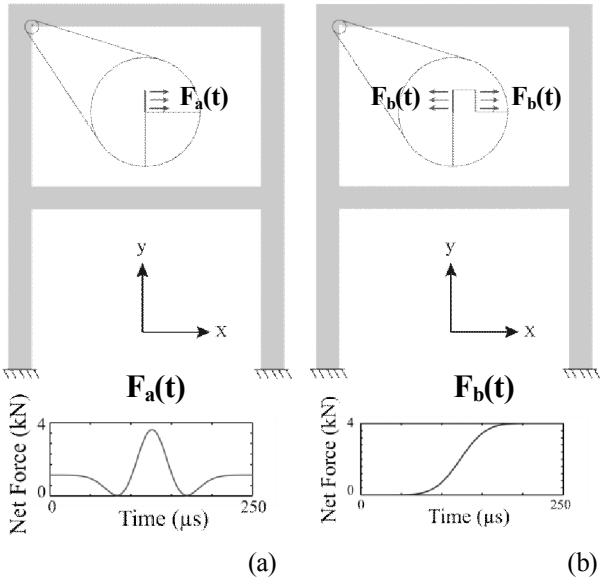


Figure 5 Numerical Setup: (a) Impulse-like force using Ricker wavelet force-time history applied to top left beam-column connection in an unnotched frame, and (b) Opening crack tensile stress using error function force-time history applied to the same connection in a notched frame.

Resulting displacements and velocities are recorded at four receivers located along the central cross section of the frame, shown in Figure 6 below. The simulation is repeated at each of the four source locations for both a force impulse and a tensile crack.

The displacement records, provided in Figure 7 below, generated by using the nondestructive source differ significantly between the displacement records generated by using the structurally damaging sources, primarily due to the static offset across the notch. The two sets of velocity

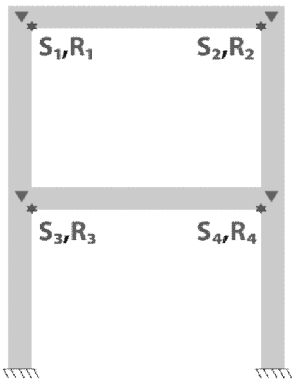
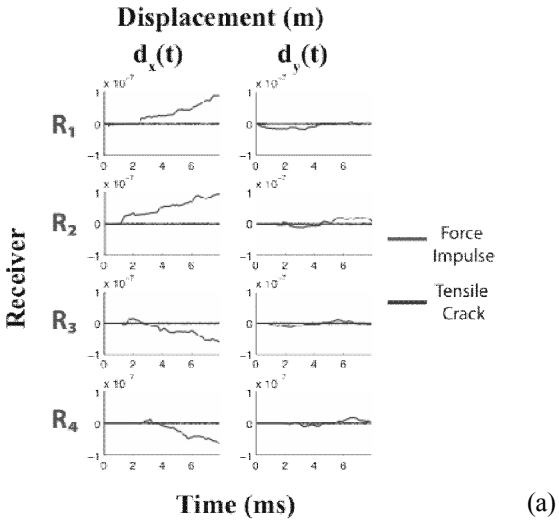
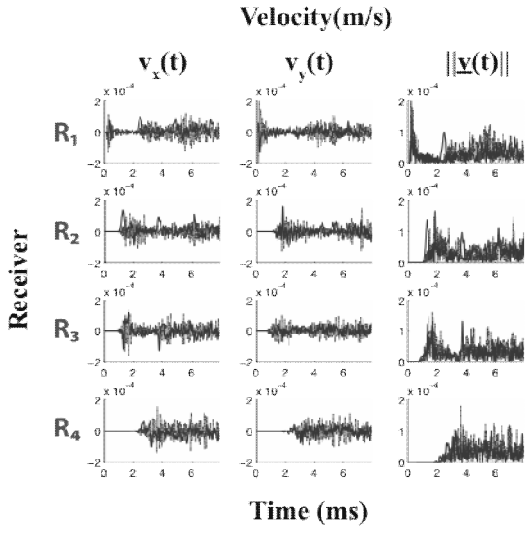


Figure 6 Source and Receiver Locations.



(a)



(b)

Figure 7 High-Frequency Seismograms Using Source Location S_1: (a) Displacements differ significantly between the impulse-like force (red) and opening crack tensile stress (blue) case. (b) Velocities provide a better agreement, and polarity differences are improved by taking the absolute value or magnitude of the record. Due to symmetry, $d_z=v_z=0$.

records are more similar to each other than are the two sets of displacement records. The similarities between force impulse and tensile crack velocity waveforms underscore the fact that, for traveling elastic waves, the strains are proportional to their associated particle velocities, regardless of the source mechanism. Thus, the template is created using the velocity record.

4.2 Stacked Cross-Correlation Values

A stacked cross-correlation method is used to determine the similarity of velocity waveforms generated by a force impulse at source location S_k and a tensile crack at source location S_l. The summarized method follows:

1) A set of velocities $\{\underline{v}_1^k(t), \underline{v}_2^k(t), \underline{v}_3^k(t), \underline{v}_4^k(t)\}$ are recorded for a force impulse applied at source location S_k, where $\underline{v}_i^k(t)$ is the three-component velocity vector recorded at the i^{th} receiver. Due to symmetry and the fact that the receivers are located along the central cross section of the frame, the z-component of the velocity vector is zero.

2) The set of envelopes $\{\underline{e}_1^k(t), \underline{e}_2^k(t), \underline{e}_3^k(t), \underline{e}_4^k(t)\}$ is computed using the velocities. The magnitude of each 3-component envelope is passed through a low-pass filter to produce a set of scalar functions of time $\{e_1^k(t), e_2^k(t), e_3^k(t), e_4^k(t)\}$. These records are archived as our template signals for damage caused at the k^{th} source location. The duration of our template is time T.

3) Similarly, a set of scalar filtered envelopes for a tensile crack at the l^{th} source location S_l are computed:
$\{\tilde{e}_1^l(t),\tilde{e}_2^l(t),\tilde{e}_3^l(t),\tilde{e}_4^l(t)\}$

4) For simplicity, pad each record $\{\tilde{e}_1^l(t),\tilde{e}_2^l(t),\tilde{e}_3^l(t),\tilde{e}_4^l(t)\}$ with a duration of T zeros at both the beginning and end, and compute the cross-correlation value for each receiver location as given by

$$C_i^{kl} = \frac{\max\limits_{t\in(-T,2T)}\left(\int_0^T e_i^k(\tau)\tilde{e}_i^l(t+\tau)d\tau\right)}{\left(\int_0^T \left(e_i^k(\tau)\right)^2 d\tau \int_0^T \left(\tilde{e}_i^l(\tau)\right)^2 d\tau\right)^{1/2}}. \quad (3)$$

5) Compute the stacked cross-correlation value by summing over all four receiver locations to obtain

$$C^{kl} = \frac{1}{4}\sum_{i=1}^{4} C_i^{kl}. \quad (4)$$

The maximum value of C^{kl} occurs near time $t = 0$, and is recorded in the k^{th} row and l^{th} column in Table 1 below. Correlation values are highest when the location of the tensile crack and the location of the force impulse are the same.

Table 1 Stacked Cross-Correlation Values.

Force Impulse Source Location \ Tensile Crack Source Location	S_1	S_2	S_3	S_4
S_1	**0.92**	0.78	0.79	0.84
S_2	0.78	**0.92**	0.84	0.79
S_3	0.77	0.92	**0.91**	0.81
S_4	0.88	0.77	0.81	**0.91**

5. CONCLUSIONS

By applying a time-reversed reciprocal method to a two-story one-bay steel frame, the location and application time of an impulse-like force can be determined.

The velocity waveform of a tensile crack can be approximated by the velocity waveform of an impulse-like force applied at the same beam-column connection of a steel frame.

The results support the use of waveform cross-correlation using a pre-event catalog of Green's function templates to determine the location and time of occurrence of a subsequent fracture recorded on a network of vibration sensors.

Acknowledgements:

The authors acknowledge support from the Hartley Foundation. The authors thank Brad Aagaard for the significant time and effort invested in making PyLith available.

References:

Aagaard, B., Williams, C., and Knepley, M. (2008), "PyLith: A finite-element code for modeling quasi-static and dynamic crustal deformation," *Eos Transactions*, *Fall Meeting Supplement*, American Geophysical Union, **89**(53), Abstract T41A-192.

Anstey, N.A. (1964) "Correlation Techniques – A Review," *Geophysical Prospecting,* **12**(4), 355-382.

Clinton, J.F., Bradford, S.C., Heaton, T.H., and Favela, J. (2006) "The Observed Wander of the Natural Frequencies in a Structure," Bulletin of the Seismological Society of America, **96**(1), 237-257.

Gibbons, S.J. and Ringdal, F. (2005), "The detection of low magnitude seismic events using array-based waveform correlation," *Geophysical Journal International*, **165**(1), 149-166.

Giurgiutiu, V. and Cuc, A. (2005), "Embedded Non-destructive Evaluation for Structural Health Monitoring, Damage Detection, and Failure Prevention," *Shock and Vibration Digest*, **37**(2), 83-105.

Kohler, M.D., Heaton, T.H., and Heckman V.M. (2009) "A Time-Revered Reciprocal Method for Detecting High-Frequency Events in Civil Structures with Accelerometer Arrays," *Proceedings of the Fifth International Workshop on Advanced Smart Materials and Smart Structures Technology*.

Park, H.W., Sohn, H., Law, K.H., and Farrar, C.R. (2007) "Time reversal active sensing for health monitoring of a composite plate," *Journal of Sound and Vibration* **302**(1-2), 50-66.

Rodgers, J.E., Mahin, S.A., and Celebi, M. (2007) "Proposed Approaches to Fracture Damage Detection for Sparsely Instrumented Steel Moment-framed Buildings," *International Journal of Steel Structures*, **7**(1), 1-10.

Wang, C.H., Rose, J.T., and Chang, F.K. (2004) "A synthetic time-reversal imaging method for structural health monitoring," *Smart Materials and Structures*, **13**(2), 415-423.

Wang, C.H., and Rose, L.R.F. (2003) "Wave reflection and transmission in beams containing delamination and inhomogeneity," *Journal of Sound and Vibration*, **264**(4), 851-872.

8CUEE CONFERENCE PROCEEDINGS
8th International Conference on Urban Earthquake Engineering
March 7-8, 2011, Tokyo Institute of Technology, Tokyo, Japan

DYNAMIC ANALYSIS OF A FULL-SCALE FOUR-STORY STEEL BUILDING EXPERIMENTED TO COLLAPSE BY STRONG GROUND MOTIONS

Tran Tuan Nam[1] and Kazuhiko Kasai[2]

1) Graduate Student, Department of Built Environment, Tokyo Institute of Technology, Japan
2) Professor, Structural Engineering Research Center, Tokyo Institute of Technology, Japan
tuanam.t.aa@m.titech.ac.jp, kasai@serc.titech.ac.jp

Abstract: This paper presents the dynamic collapse analysis of a full-scale four-story steel building which was experimented to collapse at the E-Defense, in Miki, Japan, in 2007, using the ground acceleration histories recorded at the JR Takatori station during the 1995 Hyogo-ken Nanbu earthquake. Deterioration of columns on the first story level due to local buckling is thought to be one of major reasons for the building collapse. Fiber method approach is adopted in the analysis to simulate local buckling at the column ends. Hypothetical analyses estimate the collapse capacity of the building specimen at approximately 0.9 times Takatori ground motion level. The collapse capacity of the building specimen under various propagating directions of the 1.0 times Takatori ground motion is also investigated, showing that the building likely collapses under any propagating direction of the ground motion.

1. INTRODUCTION

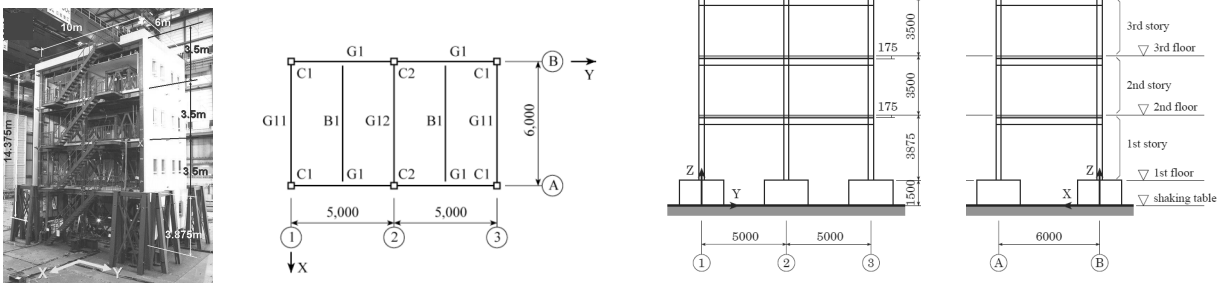
In September 2007, a full-scale four-story steel building was experimented to collapse on the E-Defense which is the world's largest three-dimensional shake-table located in Miki City, Hyogo Prefecture, Japan. The ground acceleration histories recorded at the JR Takatori station during the 1995 Hyogo-ken Nanbu earthquake were used as the input for the shake-table experiments under various scales. Experimental result shows that collapse occurred under the 100% Takatori motion, due to local buckling leading to deterioration of columns in the first story level.

Collapse behavior of the building in this experiment has attracted a lot of researchers to study and establish an effective model for simulating the collapse manner. However, behavior of the specimen involving yielding and local buckling of columns is still very difficult to simulate. The study deals with establishing a simple analytical model of the building specimen addressing that key point.

Fiber method approach was adopted to simulate local buckling behavior of column members. The analytical model consists of both structural and non-structural components. Dynamic responses of the frame model subjected to the same input ground motions as those adopted in the test are analyzed and compared to experimental data. Collapse mechanism is analytically interpreted, and hypothetical analyses for evaluating collapse capacity of the building specimen are also carried out.

2. BUILDING SPECIMEN

The building specimen is a full-scale 4-story steel moment frame with concrete slabs and autoclaved aerated concrete panels for exterior walls. The plan dimension is 6 m × 10 m, and the total height from the upper surface of stiff foundation is about 14 m (Fig. 1).



PLAN ELEVATION

Figure 1 Building Specimen

Table 1 Sections and Materials of the Steel Frame

	Beam (SN400B)			Column (BCR295)
Story	G1	G11	G12	C1,C2
4	H-346×174×6×9	H-346×174×6×9	H-346×174×6×9	RHS-300×9
3	H-350×175×7×11	H-350×175×7×11	H-350×175×9×14	RHS-300×9
2	H-396×199×7×11	H-400×200×8×13	H-400×200×8×13	RHS-300×9
1	H-400×200×8×13	H-400×200×8×13	H-390×200×10×16	RHS-300×9

Wide-flange sections are used for beams and hollow square sections are used for columns. Steel material type is SN400B for beams and BCR295 for columns. Section shapes are given in Table 1.

3. MODELING FEATURES

3.1 General modeling

The building specimen is numerically simulated by PC-ANSR analysis program, using a three-dimensional model composed of various frame members, such as beams, columns, beam-to-column panel zones, column base plates, and others (Fig. 2). Slab diaphragm is adopted by using truss bars, thus in-plane displacements of all nodes at the same floor level are equal. Composite action of the steel beam and concrete slab is taken into account. Column-base is modeled as elastic rotational spring.

The beam-to-column panel zone tends to deform in shape of parallelogram where one diagonal direction is in tension and the other is in compression; besides, right angles at the joints between beam/column-end and panel remains right angles (Fig. 3). Shear strain causes the panel to rotate at certain angle; thus the panel can be considered to work as a rotational spring.

3.2 Modeling of column hinges

3.2.1 Fiber method approach

Fiber method approach was employed in this study, where the column end is modeled as a 'fiber hinge' composed of two rigid plates connected by fibers distributed over the cross section (Fig. 4). The hinge zone is modeled to have a zero length, which means its two end nodes must have the same coordinates. Its rotation characteristic is defined by considering finite length of buckling zone.

The nonlinear stress-strain properties of 'fiber element' which are based on this finite length is illustrated in Fig. 5, where σ_y^+ and σ_y^- represent nominal yield stress due to tension and nominal buckling stress due to compression, respectively; ε_1, ε_2, ε_3 are negative strains associated with each gradually reduced buckling stiffness of the element; and α, β, γ are factors used to define the stresses corresponding to some control points on the curve.

The first zone O-A is associated with the initial loading of the element which approaches the critical buckling stress (assumed to be equal to yield stress) at point A. Zone A-B is characterized by a decreasing load accompanied by element shortening and buckling.

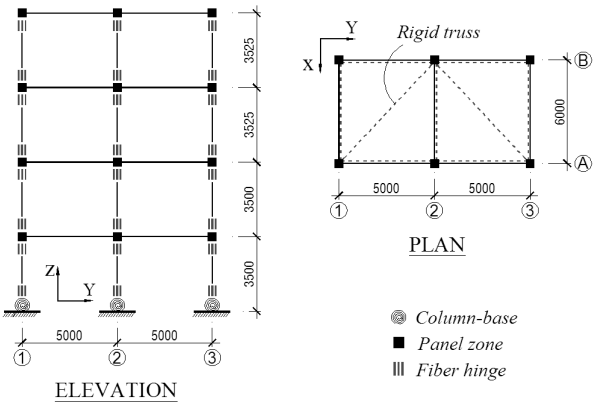


Figure 2 Three-Dimensional Analytical Model

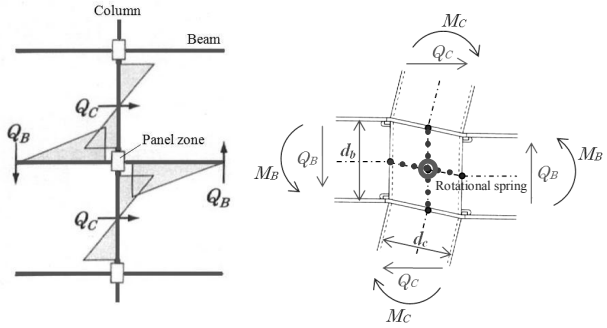


Figure 3 Beam-to-Column Panel Zone Model

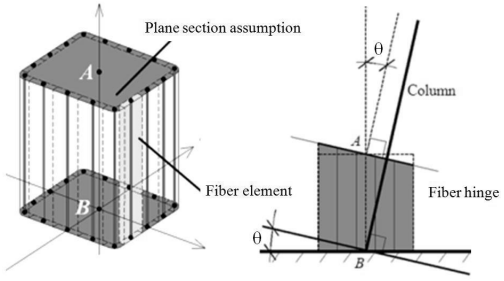


Figure 4 Column Hinge Modeled by Fiber Elements

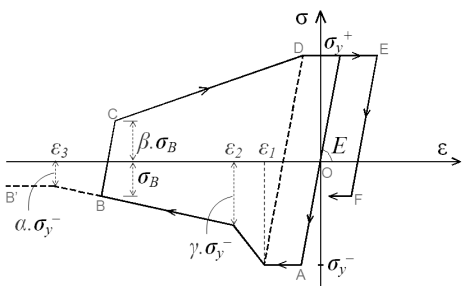


Figure 5 Hysteretic Behavior of Fiber Elements

Zone B-C-D is the compression unloading and tensile loading of the fiber element. Subsequent hysteretic loops have the same characteristic except that the consecutive peak compressive stresses are reduced due to deterioration caused by the previous inelastic cycling of the material. Hence, the compressive yield stress at point F, where the element begins to yield in compression, is set equal to the value of compressive stress at point B. Point B is named for the reversal location of the curve when the element shortening stops. This location changes per load cycle. Accordingly, the curve continues to approach point B and thereafter along zone B-B'.

3.2.2 Influence of fiber hinges on column stiffness

Fiber hinges are added at both top and bottom ends of every column. At each floor level, columns are considered to work as the model shown in Fig. 6, where both column ends are ideally restrained from rotation but top end allowed to translate. In such manner, the column (length *L*) is supposed to consist of two cantilever column portions joining at the inflection point which generally locates at the mid-height of the column.

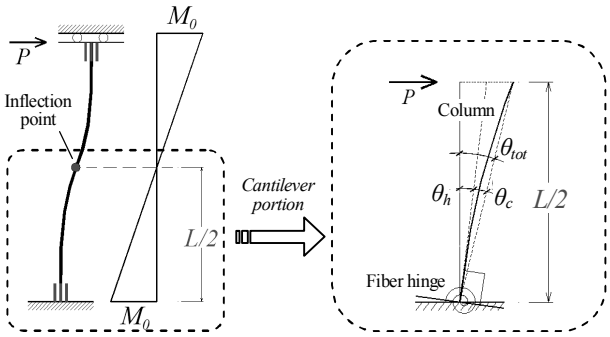


Figure 6 Column Modeling

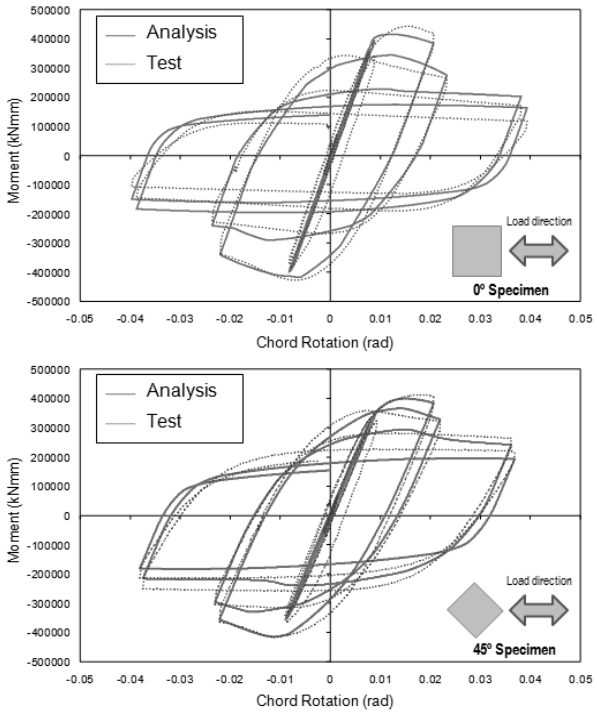


Figure 7 Cantilever Column M-θ Curves

Finite length *l* of the hinge evidently changes column bending stiffness. Thus, the column needs to be stiffened in order to eliminate the additional flexibility due to fiber hinges. By equating the deflection of the cantilever portion (length *L/2*) induced by both hinge rotation and column elastic rotation with theoretical value, the following formula which is used to stiffen the column by increasing its Young's modulus of elasticity to a fictitious value, *E',* is obtained, where *E* is original Young's modulus, *L* is the full column length and *l* is the finite length of fiber element. The effect of this stiffness modification is shown up on the moment vs. chord rotation relationship of the cantilever column (Fig. 7). The analytical results almost match the experimental data.

$$E' = E.\frac{L/2}{L/2 - 3l} = E.\frac{L}{L - 6l} \quad (1)$$

Moreover, the base plate also affects stiffness of the columns in the first story. To evaluate the effect of base plate on column flexibility, the following check is carried out. A base plate with rotational stiffness of α times column stiffness (EI/L) is added to bottom end of the column (Fig. 8-a). Location of the inflection point in terms of α is plotted in Fig. 8-b, indicating that the error of the model created by assuming inflection point at mid-height of column is insignificant as long as the rotational stiffness of the base plate is much larger than column stiffness, as the actual model. This also indicates that fiber method approach can be used as long as the inflection point is close to the middle.

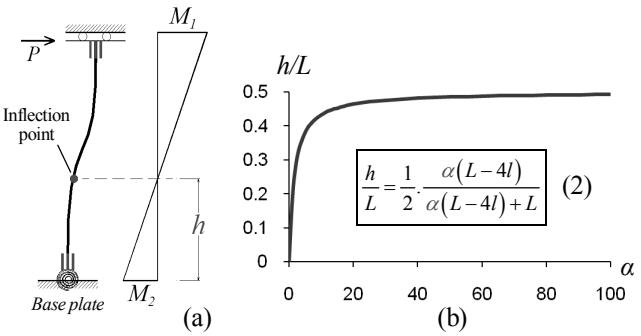


Figure 8 Influence of Fiber Hinges on Column

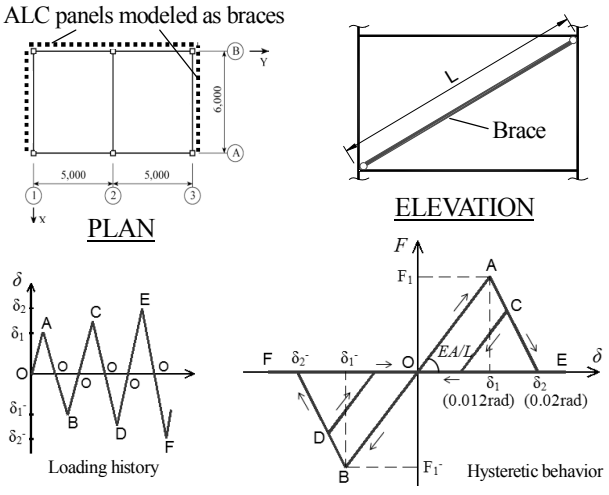


Figure 9 Modeling of Non-Structural Components

3.3 Modeling of non-structural components

Non-structural components are simulated using braces added on three external frames of the building, with slip behavior so as to degrade resistant capacity after the story drift angle overpassed 0.012 rad and be completely damaged under the story drift angle of 0.02 rad, as shown in Fig. 9. These components contribute about 10% lateral stiffness at each story. Elastic stiffness of non-structural components on each story which is determined by the subtraction of frame stiffness from stiffness of the whole building is then distributed to each brace.

4. TIME-HISTORY ANALYSES

Rayleigh damping is considered in the analyses, and damping ratio of 2% is assigned to cover the first two fundamental modes in both X and Y directions. It is noteworthy that due to counting for stiffness of nonstructural components, the obtained vibration periods (shown in Table 2) are consistent with those from the free vibration test of the building specimen which are 0.80 sec in X direction and 0.76 sec in Y direction.

Table 2 Fundamental Periods [sec]

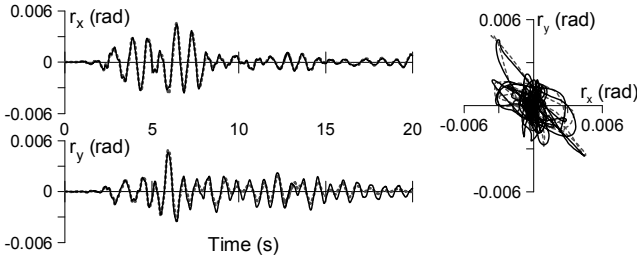
Mode	X-dir.	Y-dir.
1	0.79	0.76
2	0.25	0.24

Actual acceleration records measured on the shaking table during the test are adopted as the input acceleration in the analyses. EW, NS and UD components are used for the X, Y and Z directions, respectively. Three analysis cases of excitation levels, including 20%, 60% and 100% Takatori ground motions, are presented.

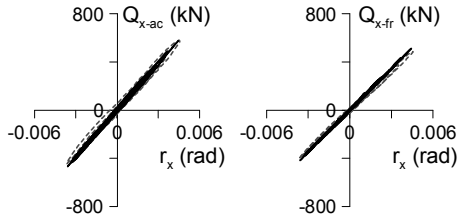
Subjected to the motion of 20% Takatori record, the building has worked elastically. The ground motion which is equal to Level-1 design earthquake is not strong enough to separate the base plate away from the stiff foundation. There is hence little likelihood that pre-tension force of anchor bolts is overcome. Thus, the column base under this elastic load case is considered to be very stiff. By using such manner, the analysis output almost agrees with that recorded in the experiment, as shown in Fig. 10.

Fig. 10-a shows the time-history curves of story drift angle in the first story level in X and Y directions, respectively. Fig. 10-b,c shows the story shear (Q) vs. story drift angle (r) relation of the first story. In those plots, solid lines stand for the analytical results, and broken lines show the experimental records provided by the Building Collapse Simulation Working Group. Those figures show good agreement between the analytical results and experimental records.

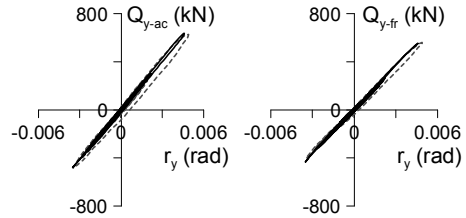
Under the 60% Takatori ground motion which is 1.5 times larger than the Japanese Level-2 design earthquake (i.e. peak ground velocity at 0.75 m/s), the building performed inelastic behavior. The recorded maximum elongation of anchor bolts reaches up to 0.85 mm, large enough for the



(a) Story Drift Angle Time-History & Orbit

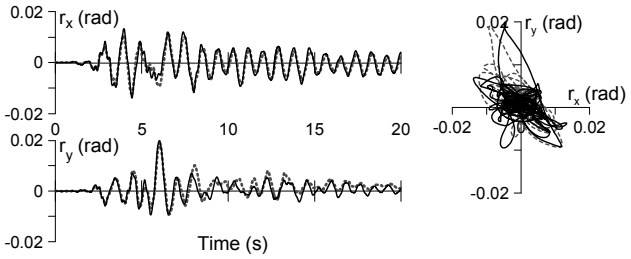


(b) Story Shear vs. Story Drift Angle, X-dir.

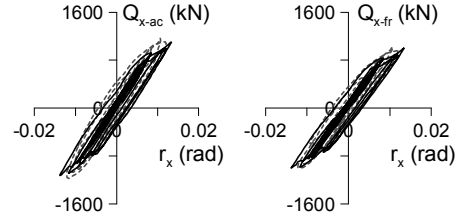


(c) Story Shear vs. Story Drift Angle, Y-dir.

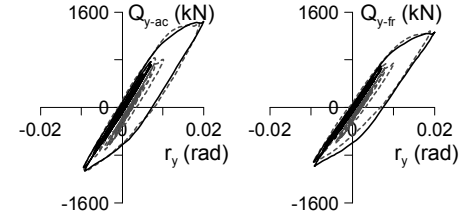
Figure 10 Analysis Results (20% Takatori, 1st Story)



(a) Story Drift Angle Time-History & Orbit

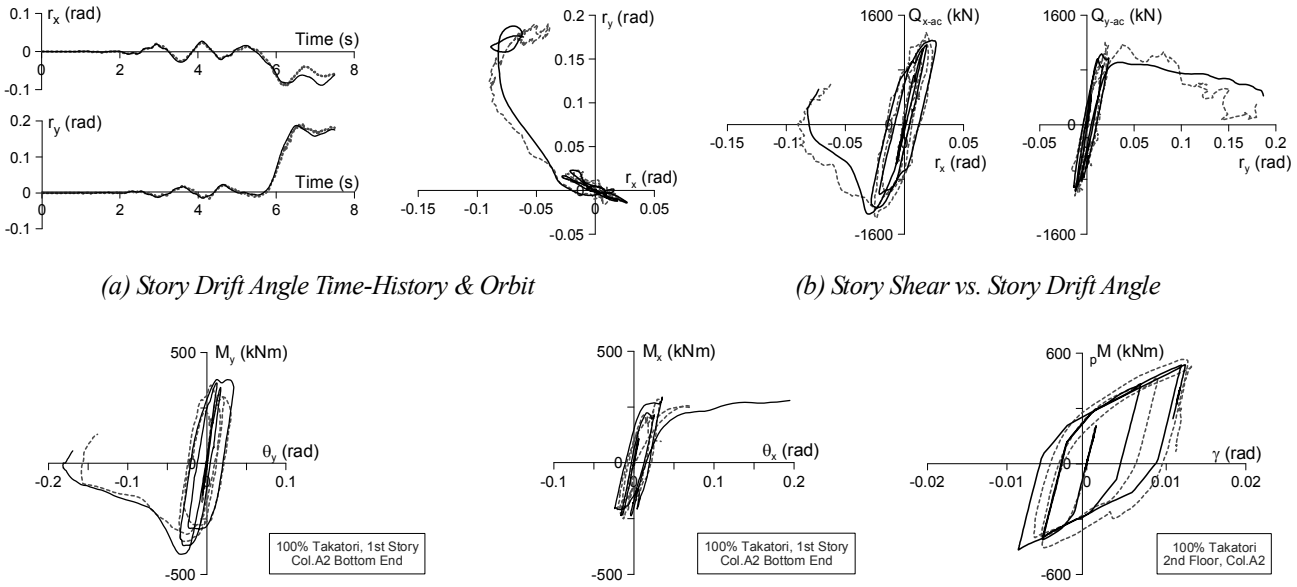


(b) Story Shear vs. Story Drift Angle, X-dir.



(c) Story Shear vs. Story Drift Angle, Y-dir.

Figure 11 Analysis Results (60% Takatori, 1st Story)



(a) Story Drift Angle Time-History & Orbit *(b) Story Shear vs. Story Drift Angle*

(c) Column Moment vs. Rotation, X-dir. *(d) Column Moment vs. Rotation, Y-dir.* *(e) Panel Moment vs. Rotation, Y-dir.*

Figure 12 Time-History Analysis Results (100% Takatori Excitation Level, 1st Story)

separation of base plate to occur. Hence, elastic rotational stiffness is assigned for column base plate when analyzing this case. Fig. 11 shows good correspondence between the analytical results and experimental records.

Since non-structural components are taken into account in this study, the analytical model is capable of capturing the difference between the *acceleration-based story shear* (Q_{ac}) obtained from story acceleration times story mass and the *frame-based story shear* (Q_{fr}) obtained from summation of column restoring forces, demonstrating the certain contribution of non-structural components in lateral stiffness of the building. The effect of non-structural components in carrying lateral forces shows up evidently, in which, for instance, the peak Q_{ac} in Y direction is much larger than peak Q_{fr}.

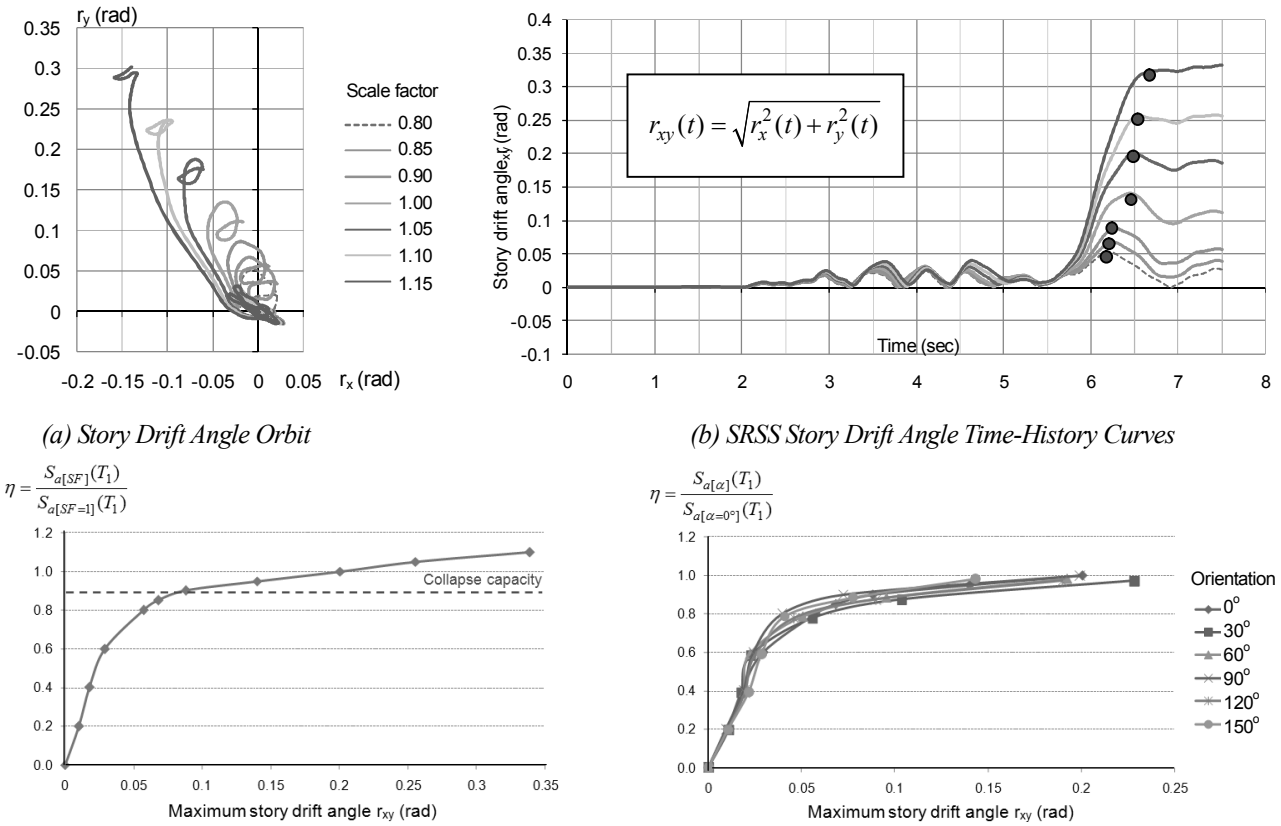
The collapse occurred when the building was subjected to the 100% Takatori ground motion which is 2.5 times larger than Level-2 design earthquake (i.e. peak ground velocity at 1.28 m/s). Fig. 12-a,b shows the analytical results for the collapse excitation level in the same arrangement as those of 60% Takatori presented above. Fig. 12-c,d shows the moment (M) vs. rotation (θ) relation of the column at the A-2 row in the first story. Fig. 12-e shows the moment ($_pM$) - shear angle (γ) relation of the beam-to-column panel in Y direction at the A-2 row in the second floor. The model shows good accuracy of story drift angle time-history curves in comparison with experimental data. Target collapse story drift angle of the first story in either X or Y direction is almost achieved, which is 0.080 rad and 0.186 rad, respectively. Deterioration of column strength due to local buckling characterized by negative slope in the plot of story shear vs. story drift angle relation (Fig. 12-a) also shows up significantly, leading the specimen to collapse.

5. COLLAPSE CAPACITY

Having recently emerged as a powerful means to study the collapse behavior of structures, 'Incremental Dynamic Analysis' involves performing a series of nonlinear dynamic analyses in which the intensity of the ground motion selected for the collapse investigation is incrementally increased until the global collapse capacity of the structure is attained. It also involves plotting a measure of the ground motion intensity (e.g. spectral acceleration at the fundamental natural period of the structure) against a response parameter (e.g. peak story drift ratio), namely Incremental Dynamic Analysis (IDA) curve.

Incremental dynamic analysis is carried out to the analytical model. Peak story drift angle per scale factor is marked by red circles in Fig. 13-a,b. The IDA curve is shown in Fig. 13-c, in which the abscissa indicates peak story drift ratio that normally obtained from the first story, and the ordinate stands for normalized spectral acceleration at fundamental natural period $S_a(T_1)$ (also equal to scale factor), which is the ratio of $S_{a[SF]}(T_1)$ in case of scaled ground motion to $S_{a[SF=1]}(T_1)$ in case of non-scaled motion.

The global collapse capacity is considered reached when the curve in this plot becomes flat. That is, when a small increase in the ground motion intensity generates a large increase in the structural response. However, since infinity is not a possible numerical result, FEMA 350 (2000) suggested the 20% tangent slope approach, in which the last point on the curve with a tangent slope equal to 20% of the slope in the elastic region is defined to be the capacity point. Using the 20% tangent slope approach, the collapse capacity is estimated to be corresponding to the scale factor of approximately 0.90, where the tangent slope of the IDA



(a) Story Drift Angle Orbit

(b) SRSS Story Drift Angle Time-History Curves

(c) IDA Curve (Original Case)

(d) IDA Curves (Varied Cases of Orientations)

Figure 13 Incremental Dynamic Analysis Results

curve is five times smaller than its elastic slope.

The collapse capacity of the building specimen under various propagating directions of the 1.0×Takatori ground motion is also investigated. The EW and NS components of the Takatori record which are used previously for X and Y directions are rotated at an angle of α with respect to the original ones. SRSS story drift angle (r_{xy}) and SRSS spectral acceleration are adopted, in which SRSS stands for square root of sum of squares of the parameters in X and Y directions at specific time. The IDA curves for those cases are shown in Fig. 13-d, in which the normalized spectral acceleration is the ratio of spectral acceleration obtained from the direction-rotated ground motion to spectral acceleration estimated from the original ground motion. Results from the curves show that collapse capacity of the building specimen under various load cases is almost equivalent to the original case (i.e. α = 0). It thus can be concluded that the building likely collapses under any direction of the 1.0×Takatori ground motion.

6. CONCLUSIONS

Numerical simulation and collapse dynamic analysis of the E-Defense four-story steel building were summarized in this paper. Followings are some concluding remarks:

(1) Fiber element based method which is adopted in the study is a simple approach but takes effect in modeling local buckling at the column ends, one of the major reasons of building collapse.

(2) The analytical model is successful in simulating dynamic inelastic response and collapse manner of the building which is supposed to be the deterioration of column strength due to local buckling.

(3) Collapse capacity of the building specimen is estimated at approximately 0.9 times the original Takatori ground motion.

Acknowledgements:

The authors acknowledge Dr. Bruce F. Maison (California, USA), Dr. Troy A. Morgan (TIT, Japan) and Prof. Tada Motohide (Osaka University, Japan) for their enthusiastic technical supports.

References:

Yamada, S., Suita, K., Tada, M., Kasai, K., Matsuoka, Y., and Shimada, Y. (2008), "Collapse Experiment on 4-Story Steel Moment Frame: Part 1 Outline of Test Results", *Proceedings of the 14th World Conference on Earthquake Engineering.*

Suita, K., Yamada, S., Tada, M., Kasai, K., Matsuoka, Y., and Shimada, Y. (2008), "Collapse Experiment on 4-Story Steel Moment Frame: Part 2 Details of Collapse Behavior", *Proceedings of the 14th World Conference on Earthquake Engineering.*

Tada, M., Tamai, H., Ohgami, K., Kuwahara, S., and Horimoto. A. (2008), "Analytical Simulation Utilizing Collaborative Structural Analysis System", *Proceedings of the 14th World Conference on Earthquake Engineering*.

FEMA (2000), Recommended Seismic Design Criteria for New Steel Moment-Frame Buildings, Publ. No. 350, American Society of Civil Engineers.

8CUEE CONFERENCE PROCEEDINGS
8th International Conference on Urban Earthquake Engineering
March 7-8, 2011, Tokyo Institute of Technology, Tokyo, Japan

PERFORMANCE OF STEEL SELF-CENTERING BRACED FRAME SYSTEM DURING INTENSE EARTHQUAKE AND AFTERSHOCK GROUND MOTIONS

Nathan Brent Chancellor[1], David A. Roke[2], Richard Sause[3], James M. Ricles[4], and Nathaniel P. Gonner[5]

1) Ph.D Student, ATLSS Engineering Research Center, Lehigh University, Bethlehem, Pennsylvania, USA
2) Assistant Professor, Dept. of Civil Engineering, University of Akron, Akron, Ohio, USA
3) Professor, Dept. of Civil and Environmental Engineering, Lehigh University, Bethlehem, Pennsylvania, USA
4) Professor, Dept. of Civil and Environmental Engineering, Lehigh University, Bethlehem, Pennsylvania, USA
5) Structural Designer, Skidmore, Owings, and Merrill
nbc208@lehigh.edu, roke@uakron.edu, rs0c@lehigh.edu, jmr5@lehigh.edu

Abstract: A steel concentrically braced frame (CBF) is an efficient, stiff building system. However, CBFs may exhibit limited ductility and poor seismic behavior due to brace buckling and low cycle fatigue. An alternative building frame system known as a Self-Centering CBF (SC-CBF) has been extensively tested at the Lehigh University NEES Equipment Site. The SC-CBF increases the ductility capacity of the CBF system by allowing the frame to rock on its base. Post-tensioning bars run vertically along the height of the SC-CBF to self-center the structure leaving no residual drift. The SC-CBF building system is designed using a performance based design procedure that limits the yielding of the post-tensioning (PT) bars under the design basis earthquake but permits significant yielding of the PT bars under intense ground motion such as the maximum considered earthquake in the US (with about a 2500 year return period). Because aftershocks may occur before repairs can be completed it is also desirable to know how the SC-CBF with yielded PT bars will perform. Experimental results show the SC-CBF system performs well in intense earthquake ground motions at the maximum considered earthquake demand level. Results also indicate that the SC-CBF system performs well after the PT bars yield when subjected to a strong aftershock at the design basis earthquake level (475 year return period).

1. INTRODUCTION

Steel concentrically braced frames (CBFs) are an efficient, stiff building frame system which may have limited ductility capacity and poor seismic behavior due to brace buckling and low cycle fatigue. An alternative building frame system (Roke et al., 2006) that retains the high stiffness of a CBF at low levels of lateral load but has significantly increased ductility capacity is being developed at Lehigh University. This new system is called the Self-Centering Concentrically Braced Frame (SC-CBF). The SC-CBF increases the ductility capacity of the building system through rocking of the braced frame on its base. Post-tensioning (PT) bars run vertically along the height of the SC-CBF to self-center the structure leaving little or no residual drift. A schematic of this system is shown in Figure 1 and a typical cyclic hysteresis plot is shown in Figure 2.

A 4 story 0.6 scale SC-CBF was tested using the hybrid simulation technique at the Lehigh University NEES Equipment Site. The SC-CBF was subjected to a total of 31 ground motions at the design basis earthquake (DBE) and maximum considered earthquake (MCE) demand levels. The DBE and MCE are defined by FEMA 450 (FEMA 2003). The DBE corresponds to an event with an approximately 475 year return period while the MCE corresponds to an event with an approximately 2500 year return period. A ground motion record from the 1995 Kobe earthquake at 0.9 scale was used in simulations. The SC-CBF frame was also subjected to "aftershock" earthquake ground motions. An aftershock ground motion record was run twice after yielding the PT bars. Yielding of the PT bars reduced the initial PT force below the design PT bar force. This paper gives a description of the SC-CBF building system and system behavior, describes the laboratory test structure, and presents laboratory testing results from the MCE and aftershock hybrid simulations.

2. SC-CBF BUILDING SYSTEM

2.1 System Behavior

The behavior of the SC-CBF system for the configuration discussed in this paper is shown schematically in Figure 3. Other configurations have been studied and are discussed by Roke et al. (2006, 2009, 2010), Eatherton et al. (2010), and Ma et al. (2010). As shown in Figure 3a gravity loads from each floor are carried by gravity columns

located adjacent to the SC-CBF frame columns. Lateral loads are transferred to the SC-CBF frame through friction lateral load bearings.

The initial lateral load resisting behavior of the SC-CBF frame is similar to a conventional CBF. At low levels of lateral force the frame deforms elastically as shown in Figure 3(b). At higher levels of lateral load the "tension" column decompresses or lifts up and the SC-CBF rotates about the base of the "compression" column. This rocking behavior is shown in Figure 3(c). The initial overturning moment resistance is provided by the prestress force in the vertical PT bars, the friction lateral load bearings, and the weight of the SC-CBF.

The post-decompression lateral translation behavior is largely rigid body rotation. Once the lateral load is removed the force in the PT bars acts as a restoring overturning moment to self-center the SC-CBF. The rocking action of the SC-CBF (and yielding of the PT bars if the seismic demands are high enough) limits the internal frame forces that develop due to earthquake loading. The post-decompression stiffness of the frame is controlled by the amount and location of the PT bars. A distribution strut may be used in the top story to spread out the PT force over multiple stories.

2.2 Limit States and Performance Based Design

There are four primary limit states for the SC-CBF system: (1) decompression, (2) PT bar yielding, (3) significant frame member yielding and (4) frame member failure. Decompression is controlled by the initial prestress force in the PT steel. The occurrence of PT bar yielding is affected by the initial PT prestress force and the deformation demands imposed by a seismic event. Frame member yielding and failure are primarily controlled by member strength and ductility capacity.

In performance based design there are two levels of seismic demand that are considered, the DBE and the MCE. The performance objective for the DBE is immediate occupancy (IO) while the performance objective for the MCE is collapse prevention (CP). The four primary limits states are reconsidered in light of these performance objectives. The performance objectives and primary limit states are summarized in Figure 4. Decompression and uplift of the SC-CBF columns does not cause structural damage if the column base is detailed properly and friction lateral load bearings are used. Therefore the decompression limit state does not affect IO. Yielding of the PT steel reduces the initial prestress force and affects the performance of the structure in aftershocks. While this damage should be repaired by replacing or restressing the PT bars, PT bar yielding does not compromise the safety of the structure and is considered acceptable for IO. It should be noted that the consequence of PT yielding is determined by the PT steel used. Some PT strand and anchorage systems may not be ductile. Some high strength PT bar and anchorage systems have large ductility (Perez et al. 2003). The PT steel used in this study of the SC-CBF system was a PT bar system that can develop ductile behavior.

Small amount of yielding in the frame members (beams, braces, columns, and struts) may not have a significant effect on self-centering behavior of the structure but significant yielding of the frame members may affect IO. Significant yielding of frame members may require repair or the structure may be condemned due to residual drift. Significant member yielding should not occur under the DBE. Yielding of the frame members can be controlled by allowing the PT steel to act as a fuse to limit the amount of force that can be transmitted to the frame members. The performance based design approach for the SC-CBF system uses capacity design principles to keep the frame members essentially elastic at lateral load levels that cause PT bar yielding. See Roke et al. (2010) for more details on the SC-CBF performance based design procedure.

Failure of the frame members by fracture or buckling indicates the onset of collapse of the SC-CBF and should not occur except in very rare seismic events well beyond the MCE. This limit state can be controlled through yielding of the PT bars and the ductility capacity available in the members.

3. LABORATORY HYBRID SIMULATIONS

3.1 Design of Prototype Test Structure

The SC-CBF system and performance based design procedure (Roke et al., 2010) was evaluated through hybrid simulation of a scaled prototype structure. The scale factor was chosen as 0.6 to meet laboratory constraints. This prototype structure, shown in Figure 5, is 6 bays in length and width. Each bay is 5.49 m wide. There are four stories above grade and one basement story. The story heights above grade are 2.74 m for the first story and 2.29 m for the upper three stories. There are four SC-CBFs in each orthogonal direction. Each of these four SC-CBFs carries $1/4^{th}$ of the seismic mass of the test structure due to symmetry.

The prototype structure was assumed to be located at a stiff soil site in Van Nuys, California for the purpose of seismic design and analysis. Since $1/4^{th}$ of the mass of the prototype structure is tributary to each SC-CBF only one frame with two adjacent gravity columns was physically placed in the laboratory. The rest of the prototype structure was modeled numerically. The physical response of the SC-CBF and numerical response of the prototype structure are combined using the well known hybrid simulation technique ("*Hybrid Simulation*", 2008).

The laboratory test substructure consisted of one SC-CBF frame with an adjacent gravity column on each side and six high-strength vertical post-tensioning bars. The SC-CBF will carry $1/4^{th}$ of the seismic mass of the prototype structure. The seismic masses for $1/4^{th}$ of the prototype structure (lumped at each floor) are 135900 kg, 134800 kg, 134800 kg, and 142200 kg from the first floor to the roof, respectively. The total gravity loads carried by $1/4^{th}$ of the gravity load system for the structure are, from the first floor to the roof, 1495 kN, 1484 kN, 1484 kN, and 1556 kN.

The members of the laboratory substructure were designed using the performance based design procedure described in Roke et al. (2010). The members were fabricated from A992 steel and the AISC section sizes are: W10x112 SC-CBF columns, W12x50 beams, W8x67 gravity columns, W8x48 braces for the first, second and third stories, and W8x58 for the fourth story. The distribution strut at the fourth story was a W8x48 and the strut at the base of the frame between the SC-CBF columns was a W8x67, both made of A992 steel. The PT steel was six, 25.4 mm diameter bars. The ultimate strength of each bar, published by the manufacturer, was 567 kN. The yield strength for the PT steel was taken as 454 kN. The initial prestress force in each PT bar for the MCE tests varied from approximately 178-200 kN. The initial PT force for the aftershock tests was substantially less.

The friction lateral load bearings (shown in Figure 6) are located at each floor and are comprised of a brass wearing plate on the SC-CBF column side and a hot-rolled steel "knuckle" on the gravity column side. There is a small gap between the two elements of the friction lateral load bearing. The design value for the coefficient of friction for the friction lateral load bearings was 0.45.

3.2 Maximum Considered Earthquakes

Five different MCE level ground motions were selected to examine the performance of the prototype SC-CBF structure. Ground motions at the DBE level were also used but they are not included in this paper. See Roke et al. (2010) and Sause et al., (2010) for more information on the performance of the prototype SC-CBF structure subjected to DBE level ground motions. Hybrid simulation of the five MCE ground motions was used to couple the response of the laboratory substructure and the rest of the prototype structure. Raleigh damping was used in the hybrid simulation with 2% in the first mode and 5% in the second mode, respectively. A summary of the records used is shown in Table 1. The laboratory testing results for the five MCE records are shown in Tables 2-5.

In addition to the five MCE ground motions a record from the 1995 Kobe, Japan earthquake was included in the hybrid simulations. This record is identified as tak090 and produces a roof drift response well above the mean roof drift response. See Roke et al. (2010) for more details on the mean roof drift response of the prototype structure. The record was scaled by 0.9 because of laboratory constraints. The results of this tak090 hybrid simulation are included in Tables 2-6. The roof drift time-history response is shown in Figure 7 while Figure 8 shows the overturning moment versus the roof drift and the overturning moment versus the gap that develops at the column base.

As shown in Table 2 the MCE ground motions produce a roof drift response greater than 1%. The tak090 produced a significantly greater roof drift response (3.85%). Only records cap000 and tak090 caused yielding of the PT bars. The time history plot of the PT bar force for tak090 is shown in Figure 9. The base shear (V_b) response for all of the MCE records is greater than or equal to 2.9 times the design base shear (V_D). The base shear response to the tak090 record is 4.3 times the design base shear. The overturning moment (OM) varies from 10275 kN-m to 19857 kN-m. The two records that cause yielding in the PT bars (cap000 and tak090) both had maximum overturning moments greater than 14000 kN-m.

The maximum interstory drift for each story and MCE ground motion record is shown in Table 3. All of the stories had an interstory drift greater than 1%, where tak090 had the largest interstory drift at 3.88%.

Normalized brace, and distribution strut forces are given in Tables 4 and 5. The maximum absolute value of the member force was normalized by the factored axial force design demand (see Roke et al. (2010) for more information on this calculation). Three braces exceeded the factored design demand for the tak090 ground motion. The normalized fourth story distribution strut ratio exceeds 1.0 for tak090 only. No yielding of the braces or distribution strut was observed throughout testing.

3.3 Aftershock Earthquakes

Intense earthquakes, such as a MCE, may yield the PT bars. If the PT bars yield then some or all of the initial prestress force may be lost. Yielding of the PT bars and loss of prestress force will affect the performance of the SC-CBF during an aftershock.

There were two aftershock hybrid simulation tests done at Lehigh University. The first aftershock test followed a partial simulation of tak090 that was aborted before completing the test. The PT bars yielded during the aborted tak090 simulation and the total prestress force was reduced to 60-65% of the design prestress force. The SC-CBF was then subjected to an aftershock hybrid simulation. After the first aftershock simulation the prestress force in the PT bars was reduced much further by yielding the PR bars even more. This time yielding of the PT bars was achieved by displacing the frame to a large roof drift in a controlled manner. The prestress force in each bar was reduced to a small value. Some bars were completely slack with a small gap (a few millimeters or less) between the anchor plate and the foundation anchorage. This was followed by the second aftershock simulation.

The ground motion record for the aftershocks was a DBE ground motion record from the 1994 Northridge earthquake (Santa Susana station, 090 component). The scale factor for this ground motion was 2.49 and a plot of the pseudo-acceleration response spectra can be seen in Figure 10.

Hybrid simulations were completed for the two aftershock cases (ReducedPT force and SmallPT force) and the results compared with testing results from a case where the prestess force in the PT bars was near the design value. These results are summarized in Tables 6-9.

The maximum roof drift (shown in Table 6) increased only slightly to 0.79% in the ReducedPT case when compared with the DesignPT. The SmallPT case, however, increased to 0.99% drift when compared to the DesignPT case. This is a 27% increase in roof drift compared with

the DesignPT case even though the total roof drift is not significant (<1%). The maximum base shear went up for the ReducedPT case by 5.4% compared to the DesignPT, but the base shear for the SmallPT case stayed about the same. The overturning moment decreased by 10% for the ReducedPT case when compared with the DesignPT and the SmallPT case decreased by 34.8% compared with the DesignPT case.

The maximum interstory drift shown in Table 7 increases for the ReducedPT case by 0.04-0.08% for each story when compared with the DesignPT case and by 0.12-0.29% for each story for the SmallPT case when compared with the DesignPT case.

Normalized brace and distribution strut forces can be found in Tables 8 and 9. The maximum absolute value of the member force was normalized by the factored axial force design demand (see Roke et al. (2010) for more information on this calculation). The maximum normalized brace forces increased for stories 1 and 3 but decreased for stories 2 and 4 for the ReducedPT case when compared with the DesignPT case. The SmallPT normalized brace forces decreased for all stories when compared with the DesignPT case. Normalized distribution strut forces decreased for the ReducedPT case and even more for the SmallPT case when compared to the DesignPT case. This is expected as the force in the distribution strut is primarily influenced by the force in the PT bars.

4. SUMMARY AND CONCLUSIONS

The SC-CBF system performed well during laboratory hybrid simulations at the MCE seismic demand level with only two ground motion records (cap000, tak090) yielding the PT bars. Yielding of the PT bars results in a loss of prestress force. Significant aftershock ground motions may follow a MCE level earthquake. The aftershock performance of the SC-CBF system was studied in laboratory hybrid simulations after yielding of the PT bars reduced the total initial prestress force to 60-65% of the design prestress force and then later additional yielding reduced the initial prestress force in the PT bars to a small value. The "damaged" frame was subjected to a DBE level aftershock ground motion at each reduced level of PT prestress force. The SC-CBF system performed well in the hybrid aftershock simulations. The test data indicates that the aftershock performance of a damaged SC-CBF is adequate, but more studies should be done. The study documented here was limited and does not address all possible outcomes. Further studies of the aftershock performance of a SC-CBF system could lead to recommendations on how quickly a SC-CBF structure should be repaired after an earthquake and what precautions should be taken regarding immediate occupancy.

Acknowledgements:

The SC-CBF building system mentioned in this paper was tested at Lehigh University in the NEES Real-Time Multi-Directional (RTMD) Earthquake Simulation Facility in the ATLSS Research Center. This research is supported by the National Science Foundation under Award No. CMS-0420974, within the George E. Brown, Jr. Network for Earthquake Engineering Simulation Research (NEESR) program and Award No. CMS-0402490 in the NEES Consortium Operation. The research reported in this paper is also based upon work supported by grants from the Pennsylvania Department of Community and Economic Development through the Pennsylvania Infrastructure Technology Alliance in addition to the American Institute of Steel Construction. Any opinions, findings, and conclusions or recommendations expressed in this material are those of the authors and do not necessarily reflect the views of the National Science Foundation.

References:

Eatherton, M.; Hajjar, J.; Ma, X.; Krawinkler, H.; and Deierlein, G. (2010). "Seismic Design and Behavior of Steel Frames with Controlled Rocking – Part I: Concepts and Quasi-Static Subassembly Testing." *Proceedings, ASCE Structures Congress*, Orlando, May.

FEMA. (2003), NEHRP Recommended Provisions for Seismic Regulations for New Buildings and Other Structures. Part 1 – Provisions and Part 2 – Commentary, FEMA 450, Federal Emergency Management Agency, Washington, D.C.

Hybrid Simulation: Theory, Implementation and Applications, Edited by Victor Saouma and Siva Mettupalayam, Francis and Taylor Publishers, London, England, 2008.

Ma, X.; Eatherton, M.; Hajjar, J.; Krawinkler, H.; and Deierlein, G. (2010). "Seismic Design and Behavior of Steel Frames with Controlled Rocking – Part II: Large Scale Shake Table Testing and System Collapse Analysis." *Proceedings, ASCE Structures Congress*, Orlando, May.

Perez, F.J.; Pessiki, S.; Sause, R.; and Lu, L.-W. (2003). "Lateral load tests of unbonded post-tensioned precast concrete walls." *Large-Scale Structural Testing*, ACI SP-211, 161-182.

Roke, D.; Sause, R.; Ricles, J.M.; Seo, C.-Y.; and Lee, K.S.(2006). "Self-centering seismic-resistant steel concentrically-braced frames." *Proceedings, Eighth U.S. National Conference on Earthquake Engineering*, San Francisco, April, EERI.

Roke, D.; Sause, R.; Ricles, J.M.; and Gonner, N. (2009). "Damage-free seismic-resistant self-centering steel concentrically-braced frames." STESSA 2009, *Proceedings of the 6th International Conference on Behavior of Steel Structures in Seismic Areas*, Philadelphia, August.

Roke, D.; Sause, R.; Ricles, J.M.; and Chancellor, N.B. (2010). "Damage-Free Seismic-Resistant Self-Centering Concentrically-Braced Frames." *ATLSS Report 10-09*, Lehigh University, Bethlehem, PA.

Sause, R.; Ricles, J.M., Roke, D.A.; Chancellor, N.B.; and Gonner, N.P. (2010a). "Large-Scale Experimental Studies of Damage-Free Self-Centering Concentrically-Braced Frame under Seismic Loading." *Proceedings, ASCE Structures Congress*, Orlando, May.

Table 1 MCE ground motion records used in the hybrid simulation testing of SC-CBF test frame

Event	Identifier	Station	Component	Magnitude	Distance (km)	Scale Factor
1994 Northridge	stn110	LA-Saturn St	110	6.69	27.01	1.98
1976 Friuli, Italy	a-tmz270	Tolmezzo	270	6.50	15.82	2.55
1989 Loma, Prieta	lp-hda255	Hollister Diff Array	255	6.93	15.19	2.24
1989 Loma, Prieta	cap000	Capitola	000	6.93	15.23	1.45
1989 Imperial Valley	h-cpe237	Cerro Prieto	237	6.53	15.19	3.85
1995 Kobe	tak090	Takatori	090	6.90	19.15	0.9

Table 2 Maximum roof drift, normalized base shear, and overturning moment for SC-CBF test frame response to MCE level ground motions

EQ Record	Max. Roof Drift (%)	Max. V_b/V_D	Max. OM (kN-m)
a-tmz-270	1.12	2.93	10275
cap000	1.87	3.43	14499
h-cpe237	1.64	3.22	11537
lp-hda255	1.41	3.54	10588
stn110	1.55	2.88	11957
tak090	3.85	4.32	19857

Table 3 Maximum interstory drift for SC-CBF test frame response to MCE level ground motions (%)

	Story 1	Story 2	Story 3	Story 4
a-tmz-270	1.05	1.11	1.19	1.23
cap000	1.96	1.91	1.86	1.86
h-cpe237	1.71	1.69	1.66	1.67
lp-hda255	1.55	1.41	1.49	1.53
stn110	1.62	1.58	1.72	1.60
tak090	3.88	3.87	3.86	3.79

Table 4 Maximum normalized brace forces for SC-CBF test frame response to MCE level ground motions

	Story 1	Story 2	Story 3	Story 4
a-tmz-270	0.80	0.84	0.88	0.67
cap000	0.88	1.09	0.82	0.68
h-cpe237	0.87	0.95	0.83	0.69
lp-hda255	0.96	1.02	0.86	0.73
stn110	0.75	0.94	1.07	0.76
tak090	1.14	1.52	1.13	0.83

Table 5 Maximum normalized distribution strut forces for SC-CBF test frame response to MCE level ground motions

	Story 4
a-tmz-270	0.69
cap000	0.88
h-cpe237	0.82
lp-hda255	0.80
stn110	0.84
tak090	1.06

Table 6 Maximum roof drift, normalized base shear, and overturning moment for SC-CBF test frame response during aftershock testing

	Max. Roof Drift (%)	Max. V_b/V_D	Max. OM (kN-m)
DesignPT	0.78	2.3	8240
ReducedPT	0.79	2.5	7415
SmallPT	0.99	2.3	5374

Table 7 Maximum interstory drift for SC-CBF test frame during aftershock testing (%)

	Story 1	Story 2	Story 3	Story 4
DesignPT	0.91	0.81	0.85	0.81
ReducedPT	0.98	0.85	0.93	0.88
SmallPT	1.03	1.08	1.14	1.09

Table 8 Maximum normalized brace forces for SC-CBF test frame during aftershock testing

	Story 1	Story 2	Story 3	Story 4
DesignPT	0.83	0.78	0.74	0.62
ReducedPT	0.85	0.69	0.82	0.58
SmallPT	0.68	0.65	0.66	0.59

Table 9 Maximum normalized distribution strut forces for SC-CBF test frame during aftershock testing

	Story 4
DesignPT	0.61
ReducedPT	0.50
SmallPT	0.34

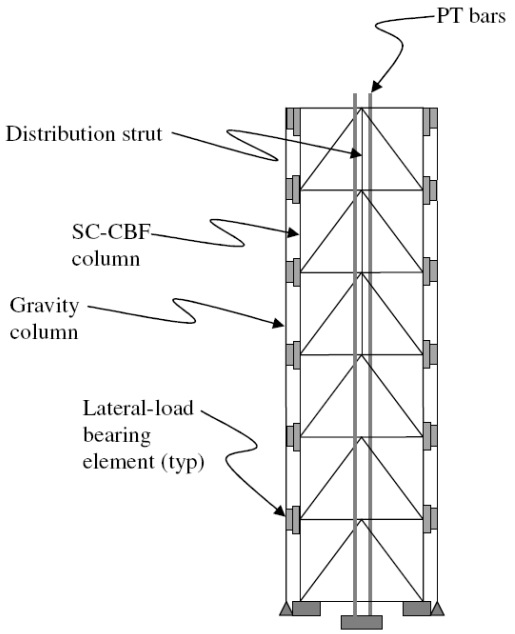


Figure 1 Schematic of SC-CBF system

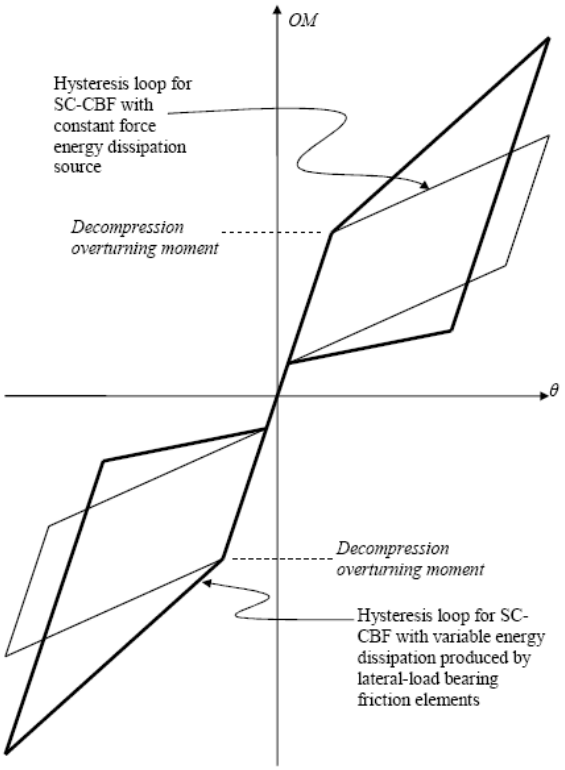


Figure 2 Typical plot of SC-CBF system hysteretic behavior

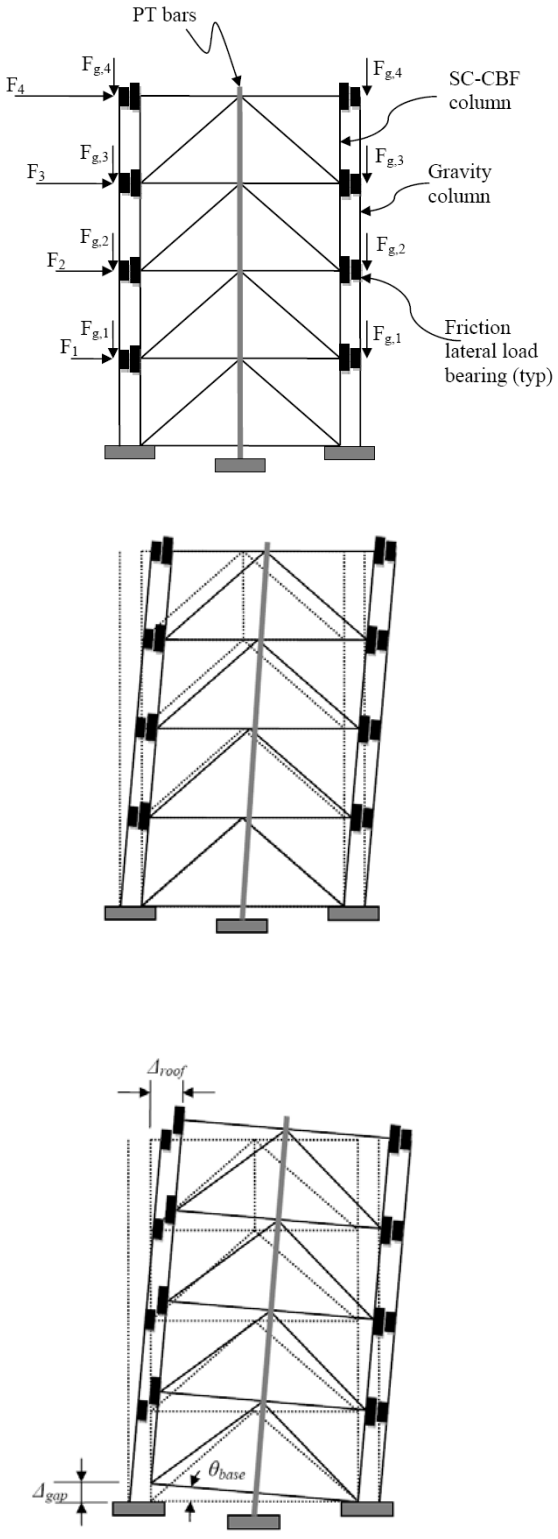


Figure 3 Behavior of SC-CBF under lateral loads: (a)Vertical gravity and lateral seismic forces; (b) elastic response of SC-CBF frame before frame column lifts up; (c) rigid body rocking of frame about column base

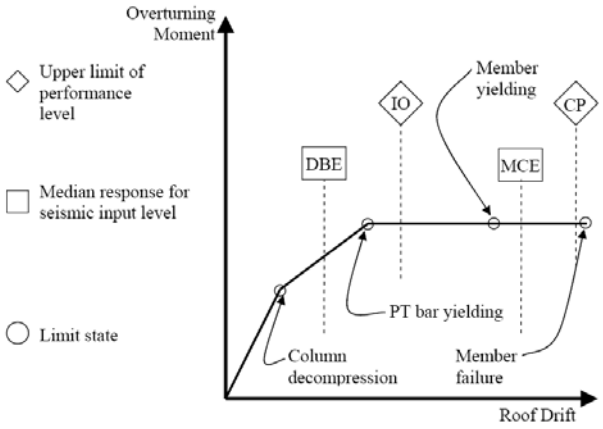
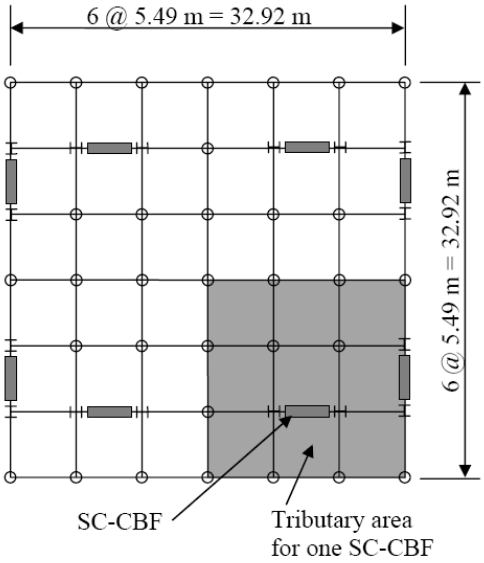
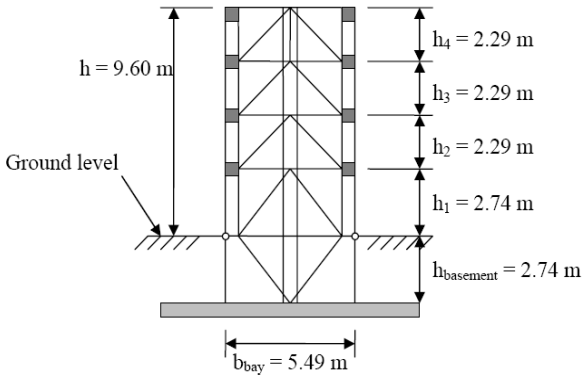


Figure 4 SC-CBF performance based design criteria summary

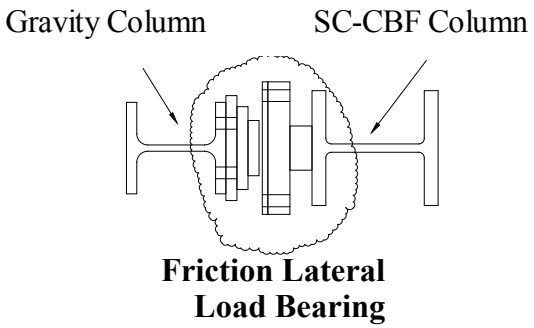


(a)

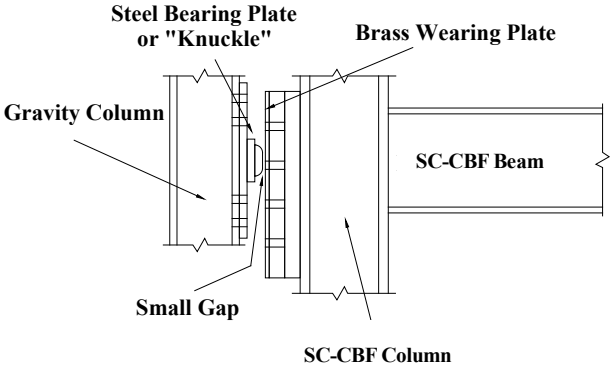


(b)

Figure 5 Plan and elevation views of prototype structure: (a) plan view; (b) elevation view



(a)



(b)

Figure 6 Friction lateral load bearing detail: (a) plan view; (b) elevation view

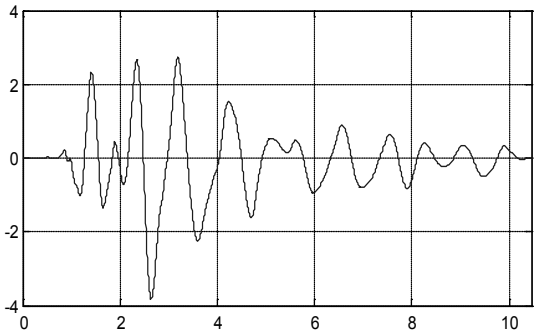


Figure 7 Roof drift response history of SC-CBF test frame to 1995 Kobe ground motion (tak090 at 0.9 scale)

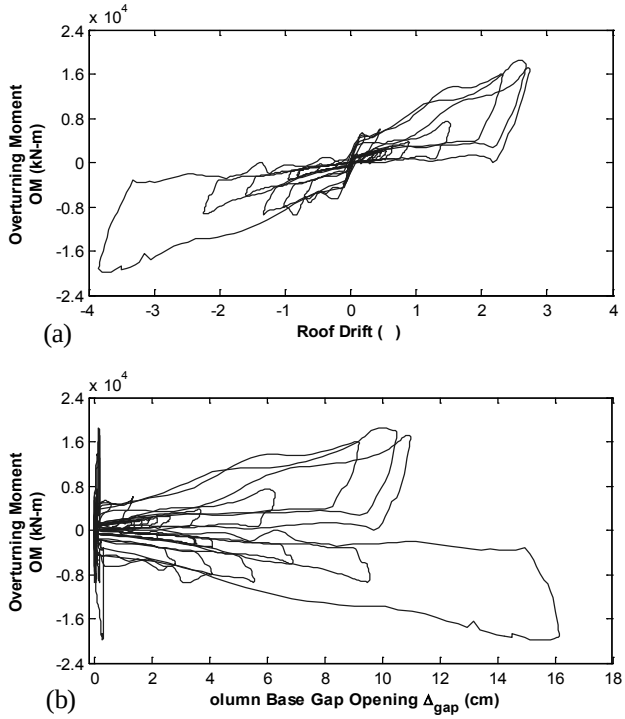


Figure 8 Response of SC-CBF test frame to 1995 Kobe ground motion (tak090 at 0.9 scale): (a) overturning moment versus roof drift; (b) column base gap opening for

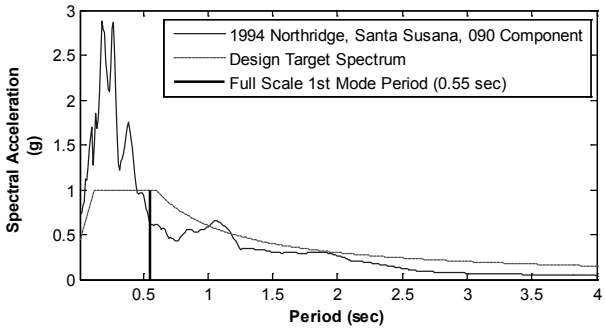


Figure 10 Pseuso-acceleration response spectra for ground motion used in aftershock testing of SC-CBF test frame

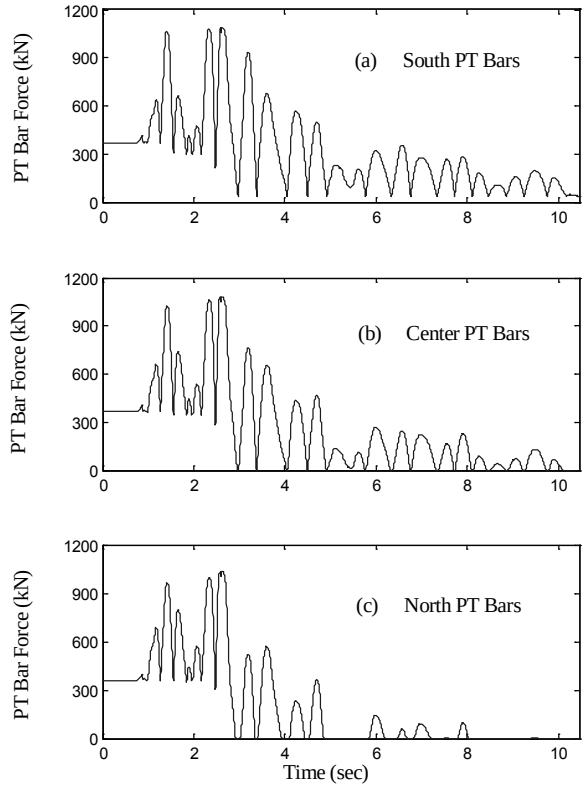


Figure 9 PT bar response history of SC-CBF test frame to 1995 Kobe ground motion (tak090 at 0.9 scale)

8CUEE CONFERENCE PROCEEDINGS
8th International Conference on Urban Earthquake Engineering
March 7-8, 2011, Tokyo Institute of Technology, Tokyo, Japan

COMPUTER MODELING OF SPECIAL CONCENTRICALLY BRACED FRAME STRUCTURAL SYSTEMS

Po-Chien Hsiao[1], Dawn E. Lehman[2], and Charles W. Roeder[3]

1) Ph.D student, Department of Civil Engineering, University of Washington, Seattle, WA
2) Associate Professor, Department of Civil Engineering, University of Washington, Seattle, WA
3) Professor, Department of Civil Engineering, University of Washington, Seattle, WA
pchsiao@uw.edu, delehman@u.washington.edu, croeder@u.washington.edu

Abstract: Special Concentrically Braced Frames are used for seismic design. During small frequent events, their strength and stiffness assure serviceable performance, but inelastic tensile yield and post-buckling compressive deformations of the brace dominate performance during large seismic events. Inelastic deformations of the brace place significant secondary inelastic deformation demands on beams, columns, and connections, which significantly affect the seismic performance. Performance based concepts which require accurate prediction of elastic and inelastic deformations as well as yield mechanisms and failure modes of the system are sometimes used. However. computer models commonly used in practice seldom capture the full range of SCBF behavior. An improved model for the OpenSees computer program is developed to accurately predict seismic performance. This proposed model is somewhat more complex than models currently used in design practice, but it is relatively simple and is suitable for a wide range of practical applications. The model is based upon prior experimental research and is used for both nonlinear pushover and dynamic analyses. The model parameters are based upon the member sizes, properties and connection designs. The model is compared to experimental results and computer predictions commonly used in practice. Errors in theoretical predictions from the various models are compared to experimental data. The proposed model provides accurate simulation of global behavior, while retaining simplicity and providing reasonable predictions for many local behaviors.

1. INTRODUCTION

Special concentrically braced frames (SCBFs) are widely used for lateral-load resistance of buildings. They provide the strength and stiffness needed for an economical system that easily meets serviceability limit states for performance based seismic design (PBSD). During large, infrequent earthquakes, SCBFs must assure life safety and collapse prevention PBSD limit states, and this requires prediction of the inelastic behavior. As a result, theoretical models for PBSD must reliably predict both elastic and inelastic performance. However, current modeling methods seldom accurately predict these full behavior, yield mechanisms, and failure modes.

The inelastic seismic response of SCBFs is dominated by compressive buckling, tensile yielding and post-buckling behavior of the braces [Popov et al. 1976]. The braces are typically connected to beams and columns through gusset plate connections, which must tolerate large inelastic deformations and end rotations associated with brace buckling, while sustaining the full axial resistance of the brace. Gusset plate connections and beam and column framing members provide boundary conditions to the brace, and therefore influence its resistance and deformation capacity. Proper design of the connections may significantly improve the response and deformation capacity of the frames [Lehman and Roeder 2008]. However, in many analyses for structural design, the gusset plate connection is simulated as pinned or rigid joints. These approximations may limit the accuracy of the stiffness and resistance predicted by the computer simulation, and they commonly lead to erroneous predictions of the deformation capacity and failure modes of the system.

Since the seismic behavior of SCBFs is quite complex, some very detailed computer models have been developed to accurately predict their performance [Huang and Mahin 2010, Shaw etal. 2010, Yoo 2006, Yoo et al. 2008-2009]. These models have invariability employed a relatively fine mesh of nonlinear shell or 3-dimensional brick elements. Some analyses modeled only braces or their connections [Huang and Mahin 2010, Shaw etal. 2010], while others evaluated individual braced bays or multi-story single-bay CBFs [Yoo 2006, Yoo et al. 2008-2009]. Accurate models must include large deformation theory for simulation of both local and global buckling, and some studies extended the models to include consideration of initiation of cracking and fracture based upon the strains, components of strains, or stress-strain history computed in the analyses [Huang and Mahin 2010, Shaw etal. 2010, Yoo et al. 2008-2009]. The effort required to develop these models is substantial, since some had more than 20,000 shell elements and a much larger number of degrees of freedom. Nonlinear analyses

of these complex models required considerable computing time with the analyses required several days to complete a cyclic load history. Nevertheless, these complex models provide accurate representation of global and local behavior of the system, and numerous comparisons are made between local and global behavior in analysis and experiments. However, these complex models are too time consuming and expensive for typical professional practice, and further they are not suitable for completing nonlinear static and dynamic analysis for PBD of larger braced frame systems.

Simpler methods are needed for nonlinear dynamic analysis and practical evaluation of the nonlinear performance of large structural systems. Unfortunately, most simple models result in significant loss in accuracy in predictions of SCBF performance. A simplified but relatively accurate nonlinear method is developed for the OpenSees computer program and evaluated in this paper. It utilizes basic concepts of engineering mechanics to provide properties of key components of the analytical model, and these concepts are based upon observed performance of braced frames in past experimental research. The accuracy of the proposed model is verified by comparison to past experimental results, and comparisons are made with other common computer models to show that the proposed model provides improves accuracy over current methods and permits reliable prediction of seismic performance of SCBF systems.

2. Observed Behavior from Experimental Research

The proposed model is based upon behavior observed in prior experiments, and therefore a brief review of prior experimental research is required. A number of experiments have been performed on braces, gusset plate connections and other components of SCBFs. However, research shows that component tests do not accurately reflect SCBF system behavior due to the complex interactions of the brace with connections and other framing members during cyclic inelastic deformation [Lehman and Roeder 2008]. A more limited base of test data is available for SCBF system tests. A series of single-story and multi-story braced frame tests, which focus on the influence of the gusset plate design on the overall cyclic lateral response of SCBFs, were conducted at University of Washington (UW) and National Center for Research on Earthquake Engineering (NCREE) in Taipei, Taiwan.

Thirty single-story frame specimens such as illustrated in Fig. 1a were tested at the UW. These steel frames had no slab and had somewhat idealized boundary conditions, but they were tested with a wide range of gusset plate configurations, design strategies, brace types and configurations. Three 2-story and three 3-story SCBFs as illustrated in Figs. 2b and 2c were tested at the NCREE Laboratory in Taiwan. These frames included composite floor slabs with realistic test boundary conditions. Several variations of connection design and brace type were tested, but a major goal of these multi-story tests were to provide confirmation of analytical models and design methods that could not be obtained from the single-story single-bay tests. An extensive body of local and global data is available from these tests, and this data was used for development, calibration and verification of the proposed model.

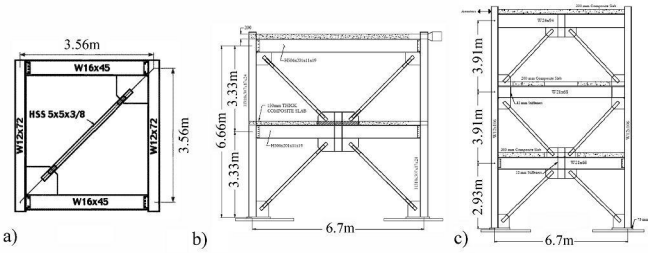


Figure 1. Typical Test Specimens; a) Single-Story Single Bay SCBF, b) Two-Story Single-Bay SCBF, and c) Three-Story Single-Bay SCBF

A number of important observations were made from this experimental research, and a number of important recommendations and observations can be noted. These include:

- Extensive local yielding must be expected in the beam and column adjacent to the gusset plate.
- Extensive inelastic deformation of the gusset plate must be expected, but it should occur after initial yielding and buckling of the brace to maximize SCBF inelastic deformation capacity. Gusset plate yielding reduces local buckling, deformation in the beams and columns adjacent to the gusset plate, and damage to the welds. Different methods are available for permitting and accommodating gusset plate deformation. The 2tp linear clearance shown in Fig. 2a works well with tapered gusset plate connections, but if often leads to larger, thicker gusset plates, which may significantly reduce the inelastic deformation capacity of the system. The 8tp elliptical clearance model shown in Fig. 2b often permits smaller, more compact gusset plates, which provides increased inelastic deformation capacity and reduces the size of the relatively rigid connection stiffness zone and the damage to welds, beams and columns adjacent to the gusset. This 6tp horizontal clearance zone shown in Fig. 2c works better than alternatives at the midspan gusset, because the bottom flange of the beam provides less restrain to the gusset than that provided when two edges are restrained by the beam and column at corner gusset connections.
- The strength and stiffness of the gusset plate connection must be adequate to develop the expected resistance of the brace, but excess strength and stiffness concentrates the inelastic deformation into a short length of the brace and causes early brace fracture.
- Tapered gusset plates behave a bit differently than rectangular gussets. They may provide good end rotational capacity for the brace, but they also result in thicker gussets or greater inelastic demands on the gusset plate and the welds.
- Wide flange braces achieve larger inelastic deformations

than HSS tubes, but they do this at the cost of increased deformation demands on the gusset plate connection.

These observations all affect the inelastic response of SCBF system, and the proposed computer model or any other model that accurately predicts SCBF performance must be capable of incorporating these and other behaviors.

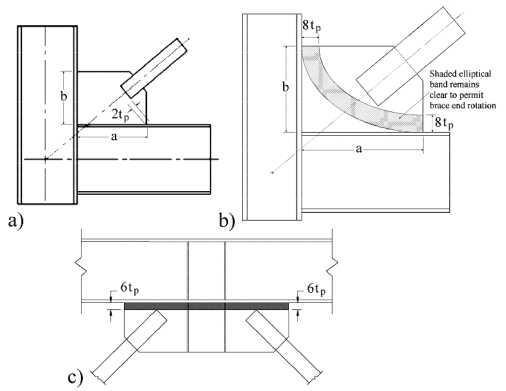


Figure 2. Variations in Gusset Plate Connections; a) Current 2tp Linear Clearance, b) Elliptical Clearance, and c) Horizontal Clearance for Midspan Gussets

A wide range of analyses including the full nonlinear shell element analyses as well as the simplified analyses described in this paper were performed on each of the 36 test specimens. The specimens cover a wide range of analytical parameters, and a group of 14 specimens, which reflect the full range of observed performance, were selected to demonstrate the effect of all parameters on the accuracy and viability of the various computer models. The analyses will include and verify the important observations from the experimental study for these 14 SCBF frames, and critical data for these specimens is defined in Figs 3a to 3c and Tables 1 and 2.

The 14 specimens included 9 single-story single-bay frames (HSS1, HSS2, HSS5, HSS7, HSS10, HSS11, HSS12, HSS17 and WF23) as described in Table 1. HSS 5x5x3/8 brace tube were adopted for all of the HSS specimens. HSS1 and HSS12 were included because they used the current AISC design practice. They employed the 2tp linear clearance, and as a result had larger gusset plates. The two specimens had different failure modes, and the size and thickness of gusset plates strongly influence system performance. HSS2 and HSS5 were specimens designed with thinner more compact gusset plates by the elliptical clearance method, but different clearance values were employed. HSS10 and HSS17 had a tapered gusset plate, which clearly have different behavior than rectangular gussets. HSS7 and HSS11 employed the elliptical clearance model but the gusset plate was thicker than the minimum required, and HSS11 also had heavier beams than required. Strength and stiffness of the connection and framing members strongly influences SCBF performance. WF23 had a wide flange brace, and wide flange braces can sustain larger inelastic deformations and place greater inelastic demands on the connections than HSS tubes. These parameters address key conclusions noted from the experimental research [Johnson 2005, Herman 2006, Kotulka 2007, Powell 2009]. The ability of computer models to capture these differences is important.

Three 2-story single bay frames (TCBF1-HSS, -WF and -TG) and two 3-story single-bay frames (TCBF2-HSS and -WF) were included in the analytical study as shown in Table 2. These multi-story frame tests permit evaluation of more variation in braces and connections, composite floor slabs, different boundary conditions, and the ability to predict multi-story effects. Specimens TCBF1-HSS, -WF and -TG were tested by using a single set of framing using Taiwanese hot rolled shapes, H506x201x11x9 for beams and H318x307x17x24 for columns as shown in Fig. 2b. Two different types of braces, HSS- and WF-sections, with gussets designed by the 8-tp elliptical clearance model, were evaluated in TCBF1-HSS and -WF tests. TCBF1-TG had tapered gusset plates with 2-tp linear clearance. Specimens TCBF2-HSS and –WF employed another set of beam and column framing with US shapes as shown in Fig 1c, and it had mid-span gusset connections with the 6-tp horizontal clearance (Figure 2b). The braces and gusset plates were replaced between the tests for all multi-story frames. Lateral cyclic loads were only applied at the top level of concrete slab through the load beams, and the framing members were reused through entire phase. Only the braces and gusset plates were replaced between the tests. Additional details of the test setup and dimensions may be found elsewhere [Clark 2009, Lumpkin 2009].

Table 1. Dimensions and material properties of gusset plates of the test specimens

Specimen	Gusset Plate				Clearance	
	a in	b in	t (actual) in	Fy ksi	Type	N (t)
HSS1	34.00	30.00	0.503	119.0	Linear	2
HSS2	25.00	21.00	0.489	65.9	Elliptical	6
HSS5	25.00	21.00	0.375	65.8	Elliptical	8
HSS7	28.50	24.50	0.867	59.0	Elliptical	6
HSS10*	18.69	16.50	0.500	68.6	Elliptical	6
HSS11	28.50	24.50	0.886	63.1	Elliptical	6
HSS12	34.00	30.00	0.500	32.2	Linear	2
HSS17*	20.69	16.25	0.375	41.9	Elliptical	6
WF23#	21.88	20.00	0.375	41.9	Elliptical	8

*: using tapered gusset plate; #: using wide-flange brace (W6x25)

Table 2. Dimensions and material properties of braces and gussets of the test specimens

Specimen	Brace			Gusset Plate		
	Section	Fy ksi	Shape	Clearance	t mm	Fy ksi
Phase I - Two-story frames						
TCBF1-HSS	HSS125x125x9 (mm)	65.3	Rectangular#	8-tp elliptical	10	59.0
TCBF1-WF	H175x175x7.5x11 (mm)	46.8	Rectangular#	8-tp elliptical	10	59.4
TCBF1-TG	HSS125x125x9 (mm)	64.6	Tapered	2-tp linear	20	50.7
Phase II - Three-story frames						
TCBF2-HSS	HSS5x5x3/8 (in.)	46.0	Rectangular	8-tp elli. (at corner) 6-tp lin. (mid-span)	10	57.9
TCBF2-WF	H175x175x7.5x11 (mm)	49.7	Rectangular	8-tp elli. (at corner) 6-tp lin. (mid-span)	10	56.0

#: using edge stiffeners at the mid-span gussets

3. Computer modeling of SCBFs

Tensile yielding, buckling and post-buckling behavior of the brace are highly nonlinear and key elements in the seismic response of the SCBF system. Significant deformation and yielding are also required in the gusset plate connections, and local yielding of the beams and columns adjacent to the gusset plate are invariably noted in experiments. To simulate these complex behaviors, the typical continuum finite element analysis such as the detail nonlinear shell element model described earlier has been used. However, these complex finite element simulations are always computational costly and time consuming. Further, large structural systems would require so many elements and degrees of frame, that analysis this complex modeling impractical for nonlinear dynamic analysis of complete systems. A proposed model of the concentrically braced frame was developed in OpenSees framework [OpenSees], which was a simplified discrete model that enabled accurate representation of SCBF behavior. Similar OpenSees models have been used in other recent research, however different models of connection performance were employed [Uriz and Mahin 2008]. The force-based nonlinear beam-column element with four integration points was the primary element in the proposed model. The sections were created using fiber sections, which enable the creation of the various steel cross sections with an assumption of the plane remains plane. The Giuffre-Menegotto-Pinto model with the Steel02 material was the nonlinear constitutive law used for all members. The OpenSees model also was used to evaluate nonlinear models with pinned or rigid joints at the brace-beam-column connections.

3.1 Simulation of Brace buckling behavior

Modeling the cyclic inelastic behavior of braces, including buckling in compression, yielding in tension and post-buckling behavior, must be included in the analysis of SCBF system performance. The proposed OpenSees model in this analytical research built upon the modeling approach developed by Gunnarson in a prior analytical study [Gunnarsson 2004]. This prior work showed that accurate simulation of brace buckling behavior is achieved with ten or more nonlinear beam-column elements using fiber sections along the length of the brace. The fiber sections consisted of several quadrilateral patches provided in the OpenSees program that allow for variability of the cross-section. The mesh of fibers within each quadrilateral patch is defined by the number of subdivisions (fibers) in both directions of each patch. Prior study also showed that accurate predictions of AISC buckling capacity are achieved with initial imperfection of 1/500 of the length of the brace in the shape of sine function, and verified the approach for different cross-sections and end conditions [Gunnarsson 2004, AISC 2005].

The required number of the fibers through the cross-section of the brace was investigated, and 4-by-4 fibers for each of eight quadrilateral patches to form the tube section, as shown in Fig. 3a, were found to converge accurately on brace performance. For wide-flange braces, the 2-by-10 fibers were used for each flange and web, and the finer mesh of fibers was arranged in the buckling direction of the cross-section as shown in Fig. 3b. The material properties were based upon measured properties noted for each test specimen, and 1% strain hardening was used for the brace elements. The brace was invariably stiffer and stronger at each end due to the overlap length of the gusset and net section reinforcement commonly required at the gusset. This increased local strength and stiffness was modeled, and reduced deformation with little local yielding occurred in this portion of the brace. To represent the complex cross-section at these locations, an increased strength element was used at each end of the brace. To accomplish this, the yield stress and initial stiffness of the steel in this local area were multiplied by 3 to assure that the local region remaining elastic. This ratio was deemed to be appropriate because the Whitmore width of the gusset should have somewhat more area than the brace, and net section reinforced further increased the local strength and stiffness. To capture large deformations of the SCBF system, the structural analysis used the co-rotational coordinate transformation, which performs an exact geometric transformation of element stiffness and resisting force from the local coordinate system into the global coordinate system.

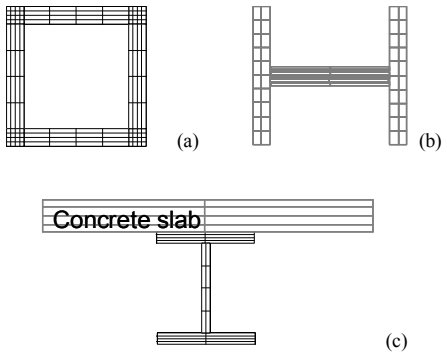


Figure 3. Fiber sections of brace and composite beam members; a) HSS tube brace, b) Wide-flange brace, and c) composite beam.

3.2 Modeling of framing components

Significant local yielding in beam and column members adjacent to gusset plate connections occur in SCBF experiments. As a result, the nonlinear behavior of all beam and column members also employed beam-column elements combined with fiber sections using 2-by-4 fibers for each flange and web. More fibers were arranged in the bending direction in the cross-section as depicted in Fig. 5. The single-story single-bay frames and columns of multi-story frames were steel members without composite action. However, the beams in the multi-story test frames were composite member. To consider the composite effect of the concrete slabs in the simulation of the multi-story frame specimens, 2 by 4 fibers representing concrete behavior

were used in the fiber section of the composite beam as illustrated in Fig. 3c. The true dimensions of the slab in the specimens were used in the model, and an elastic material model, which did not develop tensile stress, was used for representing the concrete behavior.

3.3 Beam-Column Connections.

Beam column connections were commonly shear plate or shear tab connections for beam-column joints without gusset plates attached. Shear tab connections were bare-steel in the single-story single-bay test specimens and with slabs in multi-story specimens. A zero-length nonlinear spring element using the moment-rotation model developed by Liu [2000] was useded to estimate the initial rotational stiffness and the maximum positive and negative moment capacity for the shear tab connections with and without slabs. This model considers composite action for shear tabs with composite slabs bearing against the face of the column. Beam-column connections at beam-column-brace connections were usually welded-flange welded-web connections. As a resulted, they were treated as fully restrained connections with the simplified pinned or fixed connection models. The brace was either pinned or rigidly fixed to the beam-column joint with the simplified pinned or fixed connection models, since these assumptions are common in practice.

3.4 Proposed model of gusset plate connections

Gusset plate connections in the real structures are neither pinned nor fixed joints, and these connections have a significant effect on the stiffness, resistance and inelastic deformation capacity of the SCBF system. Hence, accurate simulation of these connections is required. A wide of alternatives were considered in developing an accurate simulation. To simulate the nonlinear out-of-plane rotational behavior of the gusset plate connections, single and multiple springs along the brace axial direction at and beyond the end of the brace were considered and investigated. Various initial rotational spring stiffness, from pinned to rigid joints, and with different yield strength of the nonlinear springs were evaluated. It was found that increased initial spring stiffness increased the predicted buckling capacity of the brace. Hence, the correct estimate of the gusset plate stiffness is required to accurately predicting the buckling capacity of the brace.

The results showed that the multiple spring model provided similar analytical responses with the single nonlinear spring model but frequently caused convergence problems. Ultimately, simplified single-spring models which were placed at the ends of the brace were selected. Rigid links from the work point of the connection to the spring at the end of the brace and to the partial dimensions of the gusset were employed because of the relative in-plane rigidity of the gusset and the limited deformation occurring at the beam and the column attached to the gusset plate. Figure 4 shows a schematic of the proposed model for the connections. The stiffness of the zero-length nonlinear rotational spring element at the end of the brace simulated the out-of-plane deformational stiffness of the connection. Therefore the stiffness of this rotational spring was based upon the geometry and properties of the gusset plate. This initial out-of-plane rotational stiffness of the nonlinear rotational springs is a rational estimate of gusset stiffness and it is based upon a prior continuum finite element study by Yoo [2006].

$$K_{cal}^{rotational} = \frac{E}{L_{ave}}\left(\frac{W_w t^3}{12}\right) \qquad \text{(Eq. 1)}$$

where E is Young's modulus of steel, Ww is the Whitmore width defined by a 45° projection angle, Lave is the average of L1, L2 and L3 as shown in Figure 4, and t is the thickness of the gusset plate. The analyses showed that using the plastic moment capacity of the Whitmore cross-section with a 45° projection angle as the yield resistance for the rotational spring model led to the best prediction of the post-buckling compressive resisting strength of the frame.

These parameters are somewhat empirical terms, but they are also consistent with basic engineering mechanics. Gusset plates are designed for stress levels averaged over the Whitmore width of the gusset, and so this width represents the portion of the gusset that is considered effective in resisting the loads and deformations of the brace. The rotational stiffness in Eq. 1 is effectively the EI/L of the gusset, and EI/L is the rotational stiffness of a cantilever beam with the properties of the gusset. The stiffness is affected by the thickness and properties of the gusset, and the Whitmore width will be affected by tapered gusset plates, since the actual width of a tapered gusset is used if the actual width is smaller than the Whitmore width.

The gusset plate is relatively rigid against in-plane deformation, and therefore rigid links are used to simulate this rigidity in the proposed improved model. The rigid zone extends from the work point of the connection to the physical end of the brace and the physical end of the gusset as it extends up the column. However, it only extends out to 75% of the dimension "a" on the beam (see Fig. 2a and 2b) to permit some limited deformation within the "rigid" zone. The adopted rigid link at the ends of the brace makes the brace length identical to the specimens, and provides the most accurate estimate of brace buckling resistance. Experiments show that some in-plane deformation of the gusset occurs due to diagonal stresses and deformation, and therefore the ideal rigid zone is somewhat smaller than the full size of gusset, since this permits more beam and column deformation. The analytical results of the study showed that using smaller rigid zone on the beams and columns results in smaller compressive resisting strength of the frame in the post-buckling level, and the adopted size of rigid zone on the beams and columns defined above was the size found to best represent the experimental behavior for all test specimens. Tapered gussets have smaller dimensions "a" and "b" than rectangular gussets, and hence greater deformation is permitted. The analytical results also confirmed that the fiber elements joining to the rigid links on

the beams and columns permit yielding that reflects the local yielding observed in experiments. The combined effect of these modeling attributes led to significant improvements in the predicted performance of the SCBF systems.

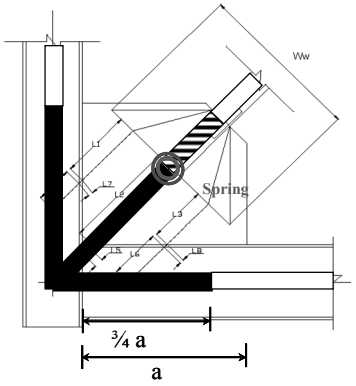


Figure 4. A schematic of the gusset plate connection model

3.5 Alternate models

While the proposed improved model is simpler than the complex shell element models described earlier, they are a bit more complex that models commonly used in engineering practice. In most cases, shear plate connections are analyzed as pin connections for practical analytical studies. Beam-column connections may be modeled as rigid connections for beam-column connections at gusset plate connections or fully restrained beam-column joints. Brace buckling may be modeled through nonlinear elements, but the ends of the brace are either pinned or fixed to be work point of the beam column joint. Two alternate connections with these simplified assumptions are depicted in the top of Table 3. The two alternate connections reflect the variation that is expected in practice, and they are compared to theoretical predictions with the proposed improved model to demonstrate the effect of variations in analytical model on the accuracy of the predicted results. The OpenSees beam and column modeling was similar for all analytical models. While the pinned and fixed models included in the study use simplified assumptions of the connections, they continue to employ the full benefits of nonlinear modeling and analysis provided by OpenSees, even though many commonly used computer programs has significantly less capabilities for simulating material and geometric nonlinearities.

4. Simulation results

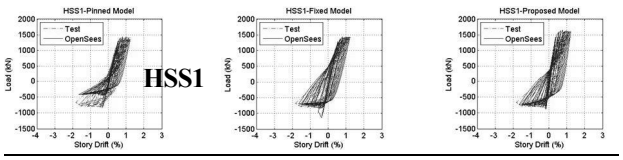
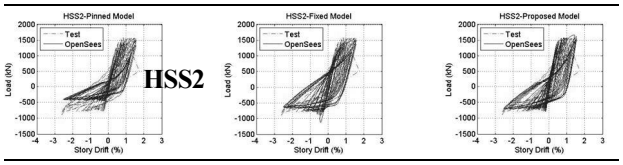
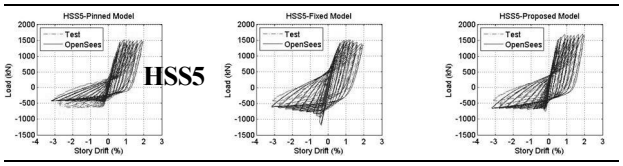
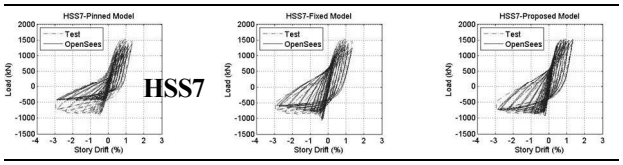
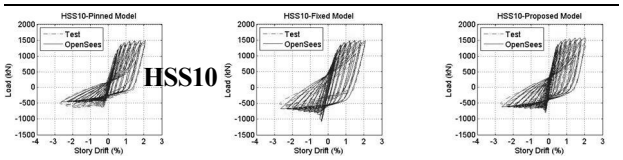
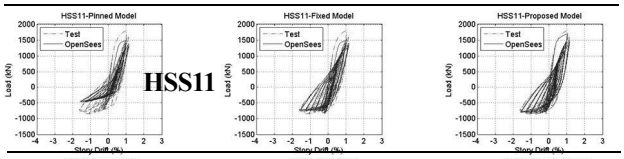
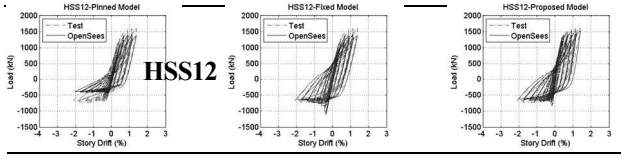
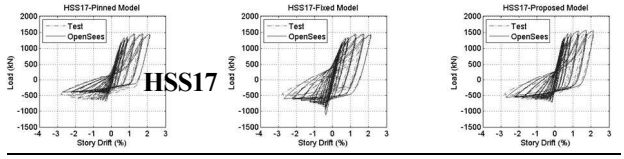
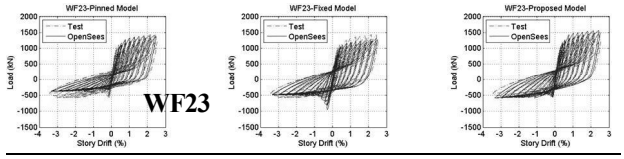
The proposed models was compare to the test results of the 14 experiments and to the analytical results obtained with pinned brace joint and fixed brace joint models to demonstrate the relative accuracy of the different theoretical predictions.

4.1 Single story frames

The 9 single-story single-bay frames were analyzed with the proposed improved model as well as nonlinear models with pinned and fixed brace joints, and the results of the global response are given in Table 3. The pinned model always significantly underestimated the buckling capacity of the brace. The fixed model always significantly overestimated the brace buckling capacity, and it also predicted more dramatic loss of resistance during post-buckling deformation. The proposed model consistently provided a more accurate prediction of the buckling capacity of the brace due to using the real length of the brace and proper modeling of the gusset plate connection. It should be emphasized that the basic frame modeling was the same for the different analytical models. Moreover, the proposed model simulates the post-buckling behavior with reasonable accuracy for all specimens due to both of the appropriate modeling of the brace and rigid links on the beams and columns adjacent to the gusset plate connections. All models provided similar predictions of tensile resistance and stiffness of the frame. They overestimated or underestimated the tensile resistance with similar errors and frequency.

A number of individual differences and comparisons are noted. HSS1 was designed by the 2tp linear clearance method with current design provisions and had a relatively large gusset plate and rigid-length effect. The improved proposed model slightly overestimated the initial stiffness and tensile strength of the frame. The pinned and fixed joint models, which excluded the rigid off-set, better captured the initial stiffness and the tensile strength of the frame, but had significant error in the compressive resistance. HSS2 was designed with the elliptical-clearance model and had smaller gusset plates comparing with HSS1. This resulted in more accurate estimates of stiffness and compressive and tensile resistance than the pinned or fixed joint models. HSS5 had thin gusset plates with 8tp-elliptical-clearance gusset plates, which provided greater ductility and deformation capacity than other specimens. The proposed model slightly overestimated the initial stiffness and the tensile strength compared to the traditional models. HSS7 and HSS 11 had thick gusset plates of 7/8 inches and the proposed improved model provided consistently better estimates of stiffness and resistance. HSS10 had tapered gusset plates that led to shorter rigid lengths on the beams and columns, and the proposed model had better estimates of compressive behavior than pinned and fixed joint models. The tensile resistance was again overestimated by a modest amount. HSS12 had exactly the same dimensions of specimen HSS1 but using the CJP welding at the gusset to beam and column connections, but avoided the early weld fracture noted with HSS1. As a result, the proposed model more accurately predict the behavior of the specimen. HSS17 had thin and tapered gusset plates, and the proposed model again predicted the overall behavior of the frame more accurately than other models. WF23 had wide-flange brace with thin gusset plate designed by the 8tp elliptical clearance model. The proposed model accurately predicted the buckling capacity and the post-buckling behavior of the brace, but overestimated the strength with the brace in tension.

Table 3. Analytical and experimental responses of the single-story frames

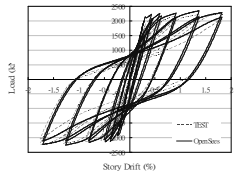
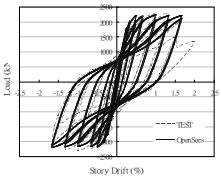
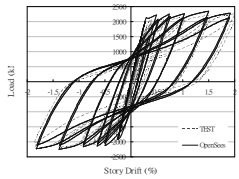
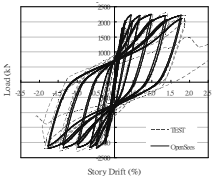
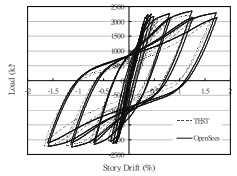
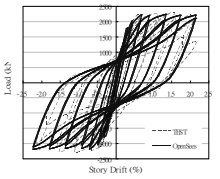
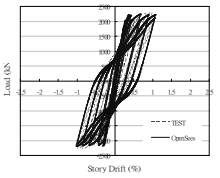
Pinned	Fixed	Proposed model
		
HSS1		
		
HSS2		
		
HSS5		
		
HSS7		
		
HSS10		
		
HSS11		
		
HSS12		
		
HSS17		
		
WF23		

4.2 Multi-story frames

After the development of the proposed model, the multi-story frames were tested, and they were used to further verify the proposed model. The composite effect of the concrete slab was included in the model except the block-out regions which was used for the installation of the gusset plate connections due to the reuse of the framing system, as shown in Fig. 1. The global and individual story hysteretic responses were compared with test results in Tables 4.

TCBF1-HSS was a two-story with rectangular HSS braces. Table 4 shows that the proposed model accurately predicted the hysteretic behavior of the specimens not only at the roof level but also the individual story responses. The proposed model accurately estimated the stiffness distribution of the multi-story specimen, as shown in Table 4. The 3-story single-bay frames were also analyzed and comparisons. TCBF2-HSS was tested first, and the proposed model accurately represented the initial stiffness, lateral resistance and the distribution of stiffness and deformation over the height of the frame, as shown in Table 4. The comparisons of other multi-story specimens, TCBF1-WF, TCBF1-TG and TCBF2-WF, had similar trend, which are not shown in this paper due to the length limit of the conference paper.

Table 4. Analytical and experimental responses of the multi-story frames

Story	TCBF1-HSS	TCBF2-HSS
Global		
1st-story		
2nd-story		
3rd-story	--	

The errors in prediction of the overall energy dissipation, maximum lateral resistance and buckling capacity of the frames were calculated to further demonstrate the relative accuracy of the various models. These comparisons are shown in Table 5. The energy dissipation of the analytical and experimental cyclic responses was calculated by integrating and accumulating the areas of every hysteretic cycles of the frames. The analyses and experiments were displacement controlled, and so the applied story drift was identical between the experimental and analytical responses. As a result, the errors of the energy dissipation reflect the accumulated errors of the predicted resistance of the frames. Through all

specimens, the average errors of the energy dissipation were around 13% by using the proposed model, and 42% and 20% by using pinned and fixed model, respectively. In terms of the maximum resistance of the frames, the proposed model consistently provided a better estimate than the pinned and fixed joint models. The pinned joint consistently underestimated the compressive resistance, while the fixed joint model consistently overestimated the compressive resistance. The proposed model slightly overestimated the resistance with the frame having very thin gusset plates. Moreover, the proposed model provided significantly better estimates of buckling and post-buckling behavior than the pinned and fixed joint models for the single-story frames. For multi-story frames, the pinned joint models provided relatively poor estimates, while the proposed model and the fixed joint model were relatively comparable. In general, the proposed model best represented the experimental response for all single-story to multi-story frames.

Table 5. Errors of energy dissipation and maximum resisting forces of the simulations

Specimen		Errors of Energy Dissipation (%)			Errors of Maximum Resisting Force (%)			Errors of Buckling CapacityForce (%)		
		Propose	Pinned	Fixed	Propose	Pinned	Fixed	Propose	Pinned	Fixed
HSS1(1/2", AISC)		24.2+	50.2-	18.2+	15.3+	1.6-	0.5-	7.7+	45.5-	36.3+
HSS2 (1/2")		3.7-	48.6-	8.2+	6.7+	2.0-	3.2-	10.1-	48.9-	27.1+
HSS5 (3/8")		14.1+	29.8-	44.6+	11.7+	0.3-	1.3-	12.8+	28.1-	82.8+
HSS7 (7/8")		11.1+	46.6-	15.8+	1.2-	11.3-	12.0-	3.5+	49.2-	17.5+
HSS10 (1/2",tapered)		28.6+	23.6-	48.5+	5.8+	0.1+	0.3-	23.4+	24.7-	67.1+
HSS11(7/8", large beam)		12.1+	52.6-	6.1+	4.8-	15.8-	15.8-	0.3+	44.1-	0.9-
HSS12(1/2", CJP welding)		11.7+	39.7-	29.6+	2.4-	13.5-	14.1-	4.2-	40.2-	47.1+
HSS17(3/8",tapered)		24.5+	24.7-	52.8+	3.4+	4.4-	5.1-	4.1+	35.3-	59.9+
WF23 (3/8")		4.6+	38.0-	3.3+	9.7+	0.7-	8.2-	1.8+	33.9-	63.3+
TCBF1-HSS (10mm)	Average	6.3+	47.8-	8.3-	4.6+	13.6-	3.2-	-	-	-
	1st-story	6.9+	57.6-	23.0-						
	2nd-story	5.5+	35.6-	9.9+						
TCBF1-WF (10mm)	Average	16.4+	42.0-	7.2+	2.0-	18.2-	0.0+	-	-	-
	1st-story	13.6+	51.4-	13.8-						
	2nd-story	20.1+	29.6-	34.9+						
TCBF1-TG (20mm, AISC)	Average	8.3-	41.3-	8.4+	10.2+	1.1-	13.5+	-	-	-
	1st-story	14.7-	54.0-	13.3-						
	2nd-story	0.4+	24.2-	37.7+						
TCBF2-1 (10mm, HSS)	Average	2.0+	47.5-	2.7-	2.2-	15.2-	4.0+	-	-	-
	1st-story	9.2-	60.3-	16.1-						
	2nd-story	21.1+	38.8-	25.7+						
	3rd-story	10.0-	38.6-	27.7-						
TCBF2-2 (10mm,WF)	Average	0.6+	60.0-	22.2+	3.4-	19.3-	0.1+	-	-	-
	1st-story	7.3-	67.5-	12.7+						
	2nd-story	2.9-	62.2-	17.7+						
	3rd-story	37.0+	33.3-	66.6+						

+ Overestimated, - Underestimated

5. Local Comparison

The ability to predict local behaviors is another important test of finite element analysis. The complex nonlinear shell element analyses provide accurate predictions of local behavior including local yield and local buckling and distortions. OpenSees analyses clearly are not capable of capturing some of these local effects, because the plane-sections-remain-plane constraint effective restrains deformations so that most local buckling and distortion cannot occur. However, local yielding is observed in the beams and columns adjacent to the gusset plate, and the extent of the computed yielding is clearly approximately proportional to that observed in the tests.

Midspan out-of-plane deflection of the brace is a key element of the local responses of the SCBF systems, and it is more easily captured and documented in the OpenSees analysis. This out-of-plane deformation is an important parameter, because it is closely related to the fracture potential of the brace. The OpenSees models employ the assumption that plane-sections-remain-plane, and therefore, they cannot capture the local buckling behavior observed at the midspan of the brace during experiments. Therefore OpenSees models would be expected to always slightly underestimate the amount of the midspan deflections measured during the test. Table 6 provides comparisons of the maximum analytical and experimental out-of-plane displacement of the within the single-story one-bay tests. The story drift for the experiment and analysis are identical for all models at this comparison point. The basic model with fixed joints always predicted smaller out-of-plane deformations than the pinned joint model and the proposed model, due to the more rigid boundary condition of the braces. The proposed model and the pinned joint model were relatively comparable. However, the proposed model having real brace length in the analysis would predict closer deformed shapes of the out-of-plane deflection along the braces. Through the series of the single-story one-bay tests, the proposed model enabled to accurately predict the out-of-plane deformations for the specimens with normal rectangular gussets, while have relatively larger errors for the specimens having tapered gusset plates, HSS10 and HSS17, and that having larger beam, HSS11.

Table 6. Experimental and analytical mid-span out-of-plane deflections of the braces

Specimens	Exp. Def. (m)	Proposed Model		Pinned Model		Fixed Model	
		Def. (m)	Error (%)	Def. (m)	Error (%)	Def. (m)	Error (%)
HSS5	0.432	0.427	1.2-	0.378	12.5-	0.340	21.2-
HSS7	0.385	0.368	4.4-	0.346	9.9-	0.293	23.9-
HSS10	0.437	0.381	12.9-	0.385	12.0-	0.374	14.3-
HSS11	0.384	0.274	28.7-	0.280	27.3-	0.246	36.1-
HSS12	0.311	0.301	3.2-	0.325	4.5+	0.285	8.3-
HSS17	0.490	0.399	18.6-	0.387	21.0-	0.368	24.9-
WF23	0.506	0.472	6.8-	0.539	6.4+	0.493	2.6-

+: Overestimated, -: Underestimated

6. Summary and Conclusions

This paper has addressed the nonlinear finite element analysis of the seismic performance of the the SCBF system. A simplified improved model was proposed and the computed results were compared to experimental results and the computed for nonlinear models more commonly used in analysis. The proposed model consisted of beam-column, rigid-length and spring-type elements, and they enabled accurate simulation of the cyclic behavior of the braced frames with minimal computing cost and time. The model includes the effects of buckling, post-buckling and tensile-yielding behaviors of the frames, and it was verified through a great number of specimens using various types of braces and gusset plates.

The computed analytical results varied significantly with different models. Pinned and fixed end brace models are commonly used in practice for simulation of braced frame performance. However, both of these models resulted in significantly different and inaccurate analytical responses comparing with experimental results through a great number of specimens. The fixed end brace model significantly overestimated the compressive resistance of the brace and the deterioration of resistance in post-buckling deformation, but it underestimated some local deformations such as the out-of-plane deformation of the brace. The pinned end brace models significantly underestimated the compressive resistance of the brace, and sometimes overestimated local deformations such as the out-of-plane deformation of the brace. All models provided good but similar variability in accuracy in predicting stiffness and tensile resistance.

The proposed improved model provided significantly more accurate estimates of compressive capacity of the brace and post buckling deformation. It provided good estimate of the distribution of deformation between stories of multi-story frames. It consistently provided reasonable accuracy through the wide range of parameters considered in the experimental program.

Using real length of the brace and appropriate boundary conditions helped the proposed model accurately estimate the buckling capacity of the brace in the structures. Moreover, modeling the proper rigid off-set on the beams and columns at the gusset plate connections significantly affected the simulations of the tensile strength and post-buckling behavior of the frame. Based on the analytical investigation, besides the buckling capacity of the braces, the post-buckling behavior of the frames was also accurately predicted by the proposed model due to the proper rigid off-set of beams and columns. In terms of the tensile strength, the frames with thick gusset plates were accurately predicted by the proposed model, while that with thin gusset plate, 3/8-inche plate, were slightly overestimated. In the comparisons of energy dissipation and lateral resisting forces, the traditional model with pin-ended braces had poorest accuracy. In terms of comparisons of the midspan out-of-plane deflections of the brace, the basic model with fixed brace joints had poorest accuracy. In general, the proposed improved model always gave the consistently highest-accuracy and more reliable predictions in both of the global and local response levels.

Acknowledgements:

This research was funded by the National Science Foundation under grants CMS-0301792, Performance-Based Design of Concentrically Braced Frames and CMS-0619161, NEESR-SG International Hybrid Simulation of Tomorrow's Braced Frames. Supplemental funding was provided by AISC. International testing, fabrication and collaboration was conducted at the NCREE Laboratory in Taiwan with Dr. Keh-Chyuan Tsai, Laboratory Director. Frequent advice and guidance was provided through the research Advisory Group, composed of Tom Schlafly (AISC), Tim Fraser (CANRON), Walterio Lopez (Rutherford and Chekene), Larry Muir (CIVES) and Rafael Sabelli (Walter P. Moore). The advice and financial support of these individuals and institutions is greatly appreciated.

References:

Popov, E.P., Takanashi, K., Roeder, C.W. (1976), "Structural steel bracing systems," *EERC Report 76-17*, University of California, Berkeley.

Lehman, D.E., Roeder, C.W. (2008), "Improved seismic design of concentrically braced frames and gusset plate connections, " *ASCE.*

Huang, Y., Mahin, S.A. (2010), "Simulating the Inelastic Seismic Behavior of Steel Braced Frames Including the Effects of Low-Cycle Fatigue," *PEER Report 10/104*, Pacific Earthquake Engineering Research Center, University of California, Berkeley, CA.

Shaw, S.M., Kanvinde, A.M., Fell, B.V. (2010), "Earthquake-induced net-section fracture in brace connections - experiments and simulations," *Journal of Constructional Steel Research*, Elsevier; 66(12), 1492-1501.

Yoo, J.H. (2006), "Analytical investigation on the seismic performance of special concentrically braced frames," a thesis submitted in partial fulfillment of the Ph.D., University of Washington, Seattle.

Yoo, J.H., Roeder, C.W., Lehman, D.E. (2008), "FEM Simulation and Failure Analysis of Special Concentrically Braced Frame Tests," ASCE, *Journal of Structural Engineering*, Vol.134, No. 6, Reston, VA;, p. 881-89.

Yoo, J.H., Roeder, C.W., Lehman, D.E. (2009), "Simulated behavior of multi-story X-braced frames," Engineering Structures; Vol. 31, Issue 1, p.182-197.

Yoo, J.H., Lehman, D.E., Roeder, C.W. (2008), "Influence of Connection Design Parameters on the Seismic Performance of Braced Frames," *Journal of Constructional Steel Research*, Elsevier; Vol. 64, p. 607-623.

Johnson, S. (2005), "Improved seismic performance of special concentrically braced frames," a thesis submitted in partial fulfillment of the MSCE, University of Washington, Seattle.

Herman, D. (2006), "Further improvements on and understanding of SCBF systems," a thesis submitted in partial fulfillment of the MSCE, University of Washington, Seattle.

Kotulka, B.A. (2007), "Analysis for a design guide on gusset plates used in special concentrically braced frames," a thesis submitted in partial fulfillment of the MSCE, University of Washington, Seattle.

Powell, J. (2009), "Evaluation of special concentrically braced frames for improved seismic performance and constructability," a thesis submitted in partial fulfillment of the MSCE, University of Washington, Seattle.

Clark, K.A. (2009), "Experimental Performance of Multi-Story X-Brace Systems," a thesis submitted in partial fulfillment of the MSCE, University of Washington, Seattle.

Lumpkin, E.J. (2009), "Enhanced seismic performance of multi-Story special concentrically braced frames using a balanced design," Master thesis, University of Washington, Seattle.

Open System for Earthquake Engineering Simulation (OpenSees), http:// opensees.berkeley.edu, accessed December 2010.

Uriz, P., Mahin, S. (2008), "Toward Earthquake Design of Concentrically Braced Steel Frame Structures," *PEER Report 08/08*, Pacific Earthquake Engineering Research Center, University of California, Berkeley, CA.

Gunnarsson, I..R. (2004), "Numerical performance evaluation of braced frame systems," a thesis submitted in partial fulfillment of the MSCE, University of Washington, Seattle.

American Institute of Steel Construction (AISC) (2005), *Manual of steel construction*, Chicago, IL.

Liu, J., Astaneh-Asl, A. (2000), "Cyclic testing of simple connections including effects of slab," *Journal of structural engineering*; Vol.126, No. 1.

8CUEE CONFERENCE PROCEEDINGS
8th International Conference on Urban Earthquake Engineering
March 7-8, 2011, Tokyo Institute of Technology, Tokyo, Japan

THREE-DIMENSIONAL TESTS OF TWO-STORY, ONE-BAY BY ONE-BAY, STEEL CONCENTRIC BRACED FRAMES

Keith Palmer[1], Charles Roeder[2], Taichiro Okazaki[3], Carol Sheiled[4], and Dawn Lehman[2]

1) Graduate Research Assistant, Dept. of Civil Engineering, University of Washington, Seattle, WA 98195
2) Professor, Dept. of Civil Engineering, University of Washington, Seattle, WA 98195
3) Professor, Faculty and Graduate School of Engineering, Hokkaido University, Sapporo, Japan
4) Professor, Dept. of Civil Engineering, University of Minnesota, Minneapolis, MN 55455
palme278@u.washington.edu, croeder@u.washington.edu, tokazaki@eng.hokudai.ac.jp, ckshield@umn.edu, delehman@u.washington.edu

Abstract: Steel concentric braced frames (CBFs) are widely used as systems to resist lateral loads induced from wind and seismic loading. Recent research on full-scale CBF subassemblages has shown that current design provisions fall short of the design intent. Additionally, the effect of imposed out-of-plane deformation on the system has never been evaluated experimentally in this manner. This paper describes the design, test setup and experimental results of two tests performed on a two-story, one-bay by one-bay CBFs, an HSS buckling-brace system in a single-story X-configuration, and a buckling-restrained braced frame (BRBF) in a single-diagonal configuration. The design of the gusset plates for the HSS braces followed a balanced design procedure with an elliptical clearance to permit out-of-plane rotation due to brace buckling. The HSS braces fractured at 2% story drift. The BRBF gusset plate design followed current U.S. design standards, and the BRB cores fractured at 3.5% story drift prior to any instability.

1. INTRODUCTION

Concentric braced frames (CBFs) are widely used as systems to resist lateral loads induced from seismic loading. In high seismic regions, special concentric braced frames (SCBFs) are used. Recent research on full-scale CBF subassemblages has shown that current design provisions fall short of the design intent (Chen et al. 2004, Mahin et al. 2004). Subsequent research has evaluated improvements to the connection design (Yoo et al. 2008). The results have been used to develop a design methodology to balance the multiple yield mechanisms of the frame, most importantly the brace and the gusset plate, to maximize the drift capacity. The process further evaluates all potential failure modes to ensure the desired mechanism occurs and all others are suppressed. This research has resulted in more rational design and detailing rules for SCBFs.

Prior tests performed on braced frames were planar, single and multi-story specimens. The current paper focuses on the full, three-dimensional response of a two-story, one-bay by one-bay large-scale CBF structure that was tested using the MAST laboratory at the University of Minnesota as part of the NSF-funded project entitled "International Hybrid Simulation of Tomorrow's Braced Frame Systems" through the NEES research program. The test specimen simulated the corner bay of a two-story building system braced in two orthogonal directions. The first test used conventional HSS diagonal braces in a single-story X-configuration in each story. The second test used buckling restrained braces (BRBs) in a single diagonal configuration.

The objectives of the test were: (1) to examine the large-displacement, bi-directional behavior of CBFs and BRBFs, (2) to examine the applicability of the latest design and detailing rules for these systems, (3) to examine the behavior of columns shared by two orthogonal braces, (4) to examine the effect of gusset plates framing into the column web, and (5) to examine the effect of composite concrete slabs on the behavior of CBFs and BRBFs.

2. EXPERIMENTAL PROGRAM

2.1 Specimen Description

Two specimens were tested in this research program. Both were nearly full-scale, one-bay by one-bay, two-story frames with braces in two orthogonal bays and framing into a "shared" column. Buckling HSS braces were used in the first test while the second test used BRBs. Fig. 1(a) and 1(b) show the second and third floor plan, respectively, of both test specimens. The braced frames occur along grid lines A and 1 as indicated by the dashed lines near the girders. Note that column A-1 is the "shared" column as the two orthogonal braced bents frame into this column. The second floor deck consists of 51 mm thick ribbed metal deck topped by 83 mm of normal weight concrete for a total depth of 135

mm as in typical steel buildings. The third floor slab will be used to transfer the load from the loading beam into the test specimen and as such, required a 254 mm thick concrete slab.

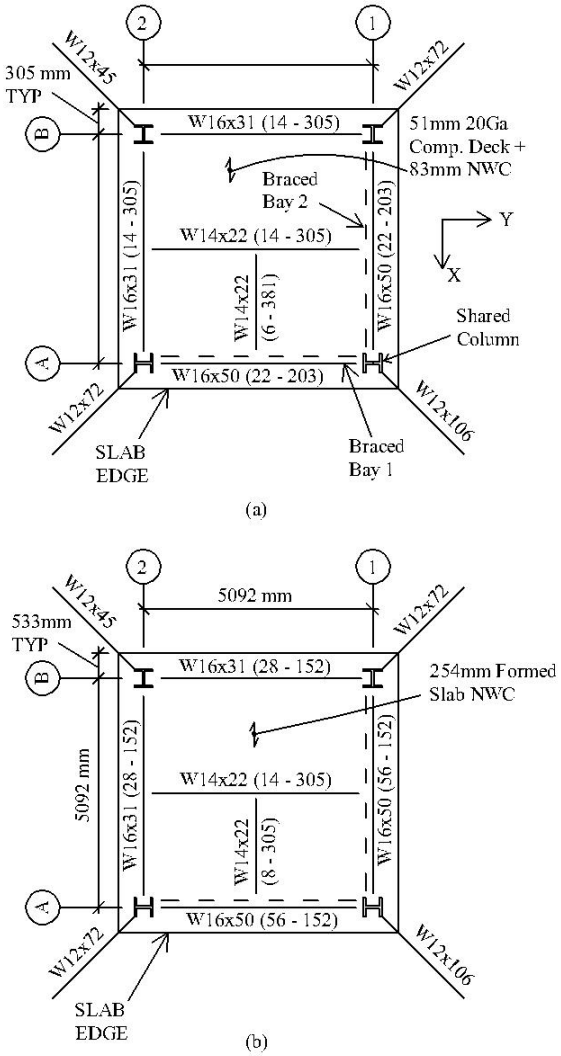


Figure 1. Test specimen floor plans: (a) second floor; (b) third floor plan.

The braced frame elevations for the buckling brace frame and the BRBF are shown in Fig. 2(a) and 2(b), respectively. The beam connections in each braced bay are welded flange – welded web (WFWW) connections with demand-critical welds, while those in the other two bays are simple shear connections. The buckling braces were A500B HSS3x3x1/4 while the BRB cores were 300 MPa steel with a design maximum adjusted brace force of 979 kN at 3% story drift. A photo of the test setup showing the strongwalls, crosshead and the first specimen is shown in Fig. 3.

2.2 Specimen Design

The sizes of the HSS buckling braces and BRBs in the test specimen were determined based on the capacity of the MAST lab strongfloor and force actuator system while ensuring that sizes which are typical of current construction could be used. The size of the braces chosen is typical of the upper stories in a mid to high-rise building or the lower stories of a low-rise building. The design of the test frame members followed current design practice based on the AISC Seismic Provisions (AISC 2005b), ASCE 7 (ASCE 2005), and a procedure shown by Lopez and Sabelli (2004).

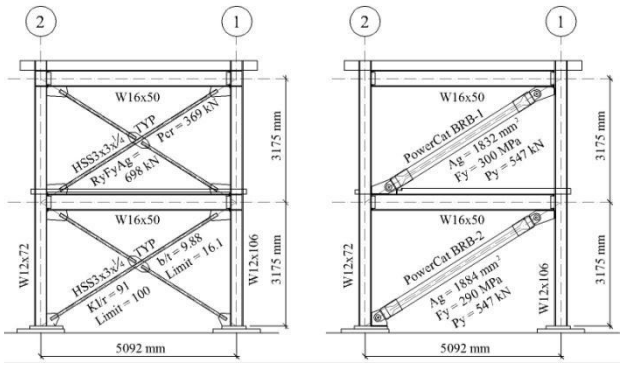


Figure 2. Braced frame elevations: (a) buckling brace frame; (b) buckling-restrained braced frame.

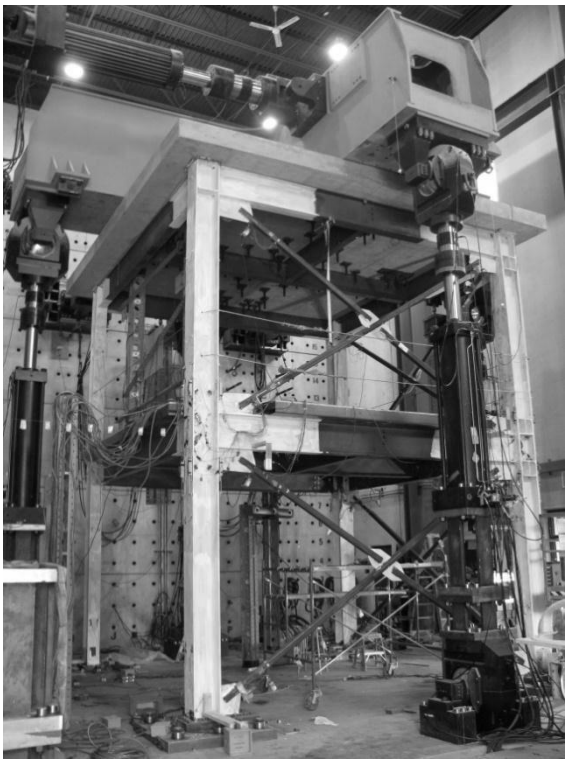


Figure 3. Photo of first test specimen in MAST lab

The beams and columns were designed to resist the maximum expected BRB force at $2.0\Delta_{bm}$, where Δ_{bm} is the brace axial deformation corresponding to the design story drift, in combination with the gravity load using the applicable load combinations. The frame beams and columns conform to the strong-column weak-beam philosophy. The demand on the shared column was found assuming 100% of the brace and beam capacities were realized in one direction while 30% of the capacities of these

elements were realized in the orthogonal direction.

2.3 Gusset Plate Design

2.3.1 Buckling brace test specimen gusset design

Current seismic design rules (AISC 2005b) require the bracing connection to develop the strength of the brace while accommodating the rotation associated with out-of-plane brace buckling. As shown in Fig. 4(a), accommodation of the rotational capacity is generally accomplished through a linear clearance model, whereby the brace is terminated a distance $2t_p$ before the line of restraint, where t_p is the thickness of the gusset plate. This requirement can result in large buckling lengths of the gusset plate, and consequently, lead to heavy and overly stiff connections that have a detrimental effect on the behavior of the system (Roeder and Lehman 2009).

Based on tests at the University of Washington (UW) of over 30 one-bay, one-story planar CBFs, a new clearance model has been developed that when combined with the proposed balanced design procedure (Roeder et. al. 2005), results in thinner and smaller gusset plates. These thinner gusset plates have been shown to reliably accommodate large out-of-plane gusset rotations at the brace ends and sustain the tensile strength of the brace. This clearance model, called the elliptical clearance model, is shown in Fig. 4(b). A clearance of $8t_p$ has been shown to be the most efficient.

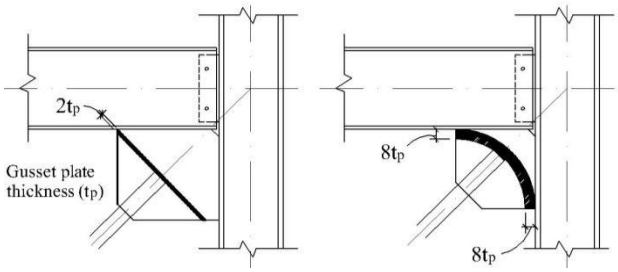


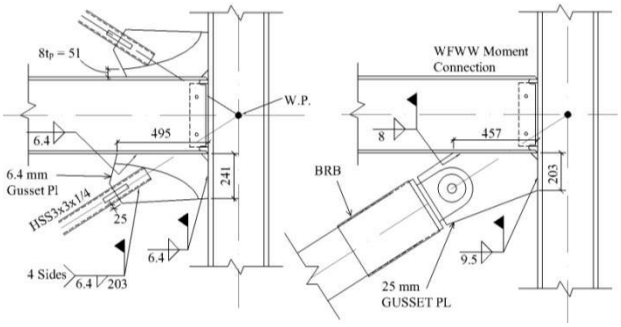
Figure 4. Clearance models: (a) currently used clearance, per AISC, $2t_p$ and (b) proposed 8tp elliptical clearance model.

The balance factors in the balanced design method are used in a similar manner to the AISC resistance factors except that they are used to achieve ductility and inelastic deformation capacity rather than strength. Smaller balance factors indicate that the exceedance of the considered limit state would cause significant deterioration of strength, stiffness and ductility, and/or that the capacity prediction is less reliable.

An example of a typical gusset design for the buckling brace frame is shown in Figure 5(a). It should be noted that the welds connecting the gusset plate to the beams and columns are sized to resist the strength of the gusset plate and not the forces that result from application of the Uniform Force Method (UFM). The buckling lengths of the gusset plates were computed as the average centroidal length and the two lengths at the extreme points of the Whitmore width. An effective length factor, K, of 0.65 was used.

2.3.2 BRBF gusset design

Because BRBs are generally not expected to deform out-of-plane, the clearance model for CBFs does not apply to BRBFs. Given that much less research has been performed on gusset plates for this system, it was decided that the gusset plates in the BRBF specimen would be designed according to the current standards using the uniform force method and the limit states outlined in AISC (2005a) instead of the balanced design approach. Figure 5(b) shows a typical gusset detail used in the BRBF test specimen.



(a) (b)

Figure 5. Gusset plate details: (a) buckling brace test specimen; (b) BRBF test specimen

2.4 Loading Protocol

Cyclic displacements were applied in each horizontal direction at the top floor while rotation of the crosshead about the vertical axis was maintained at zero to prevent torsional deformation from occurring. Free rotation about both horizontal axes was permitted. To limit the differences between the uni-directional tests performed at UW and those performed here, the same uni-directional displacement histories was used in the current tests that were used in the tests at UW.

The determination of the bi-directional qualities of the bi-directional loading protocol was facilitated by nonlinear time-history analyses of prototype braced frame buildings. Three and 6-story single diagonal BRBF buildings were designed and simultaneously subjected to the X and Y-component of 10 ground motions from the SAC program.

Using rainflow cycle counting, the ratio of the frame damage (cumulative plastic deformation) in X and Y was found for each case and a ratio of 1.5 was chosen. The final displacement-controlled protocol is shown in Figure 6.

3. EXPERIMENTAL RESULTS

3.1 Buckling Brace Test Results

As discussed earlier, the test specimen was loaded according to Figure 6, where the Y-direction corresponds to that shown in the floor plans in Figure 1. Figure 7 shows the story shear – story drift ratio response for the second floor of each orthogonal braced bent. The top discontinuous brace at the 2nd story fractured during the first negative drift excursion at approximately 2% story drift following the first positive excursion. This drift ratio at fracture is consistent

with that observed in two previous tests of a similar single-story X-configuration at UW and those tested by Tremblay et al (2003). After fracture, the test specimen was unloaded in this frame's direction and uni-directional loading was applied to the specimen in the other direction continuing from the drift at which fracture occurred. The test proceeded until the top discontinuous brace in Braced Bay 2 was deemed close to fracture at approximately 1.7% story drift. The test was stopped prior to brace fracture in this bent to prevent damage to the frame as this frame was to be used again for the BRBF test.

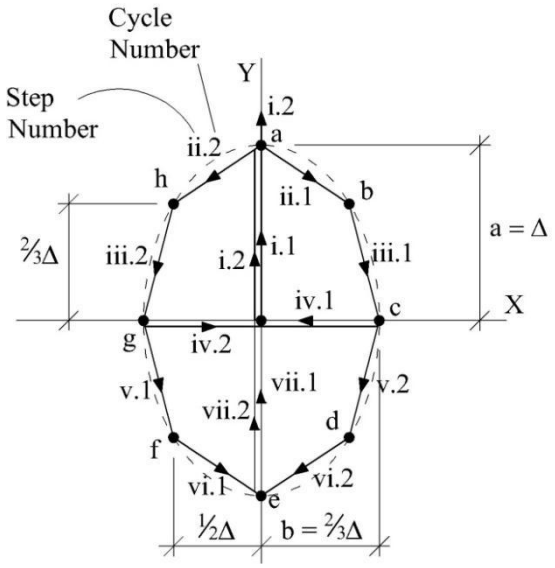
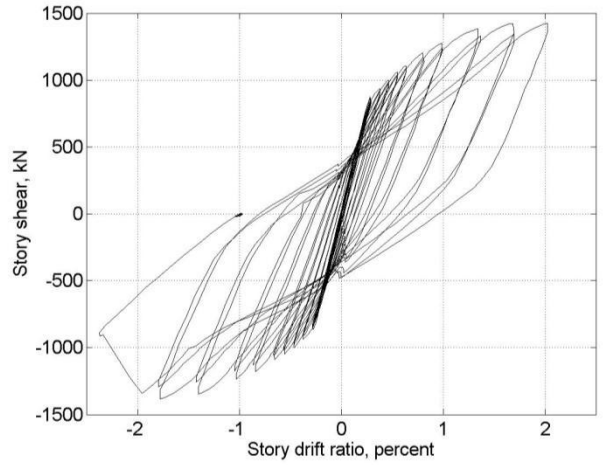


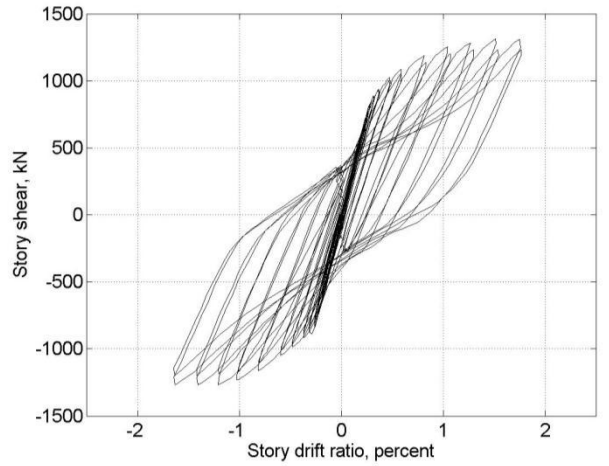
Figure 6. Bi-directional loading protocol "cloverleaf"

Based on brace strain gauge data, and global and local force-deformation curves, brace buckling occurred simultaneously in the discontinuous braces in the 1st and 2nd story of Braced Bay 1 at 0.25% story drift. Yielding of the braces occurred at 0.37% story drift. In the orthogonal direction, brace buckling occurred at 0.22% story drift and yielding at 0.36% story drift. Due to a number of factors including brace end connection stiffness and initial imperfections, brace buckling and subsequent brace damage occurred in only one half of the discontinuous brace while the continuous brace buckled in reverse curvature with the tension brace acting as a lateral support.

Prior to brace fracture there was extensive yielding in the gusset plates due to brace axial force and gusset plate bending due to brace buckling. This type of behavior was intended as part of the balanced design philosophy of maximizing energy dissipation and encouraging other yielding mechanisms beyond brace yielding. Slight gusset plate yielding was visually observed (flaking of whitewash) at approximately 0.23% story drift in the corner gussets just prior to brace buckling. Figure 8 shows a typical gusset yielding pattern in the corner gusset plates at 2% story drift. This pattern was typical of these joints. Additionally, frame action (opening and closing of the joint) cause additional yielding and deformation in the gusset as seen in the diagonal yield pattern originating at the intersection of the bottom beam flange and column flange shown in Figure 8.



(a)



(b)

Figure 7. Buckling brace test 2nd story hysteretic curves: (a) Braced Bay 1 (Y-direction); (b) Braced Bay 2 (X-direction)

Column yielding initiated at the base of the three braced frame columns at approximately 0.46% story drift and continued to spread at the bases as the story drift increased. Figure 9 shows the yielding at the base of the column in Braced Bay 1 at 2% story drift. Additionally, the web of the beam on the second floor of Braced Bay 1 at the shared column side yielded and deformed at the instant of brace fracture. Up to that point, only limited yielding was observed at this location.

3.1 BRBF Test Results

The BBRB followed the same loading protocol as the first test with the exception of the principal loading direction. Based on the beam web damage described previously, it was decided to make Braced Bay 2 the principal loading direction. Additionally, a web doubler plate with the same thickness as the beam web was attached to the damaged beam web to ensure that would not be the weak link in the BRBF test. It should also be noted that there were initial lateral frame deformations of 50 mm in the Y direction and

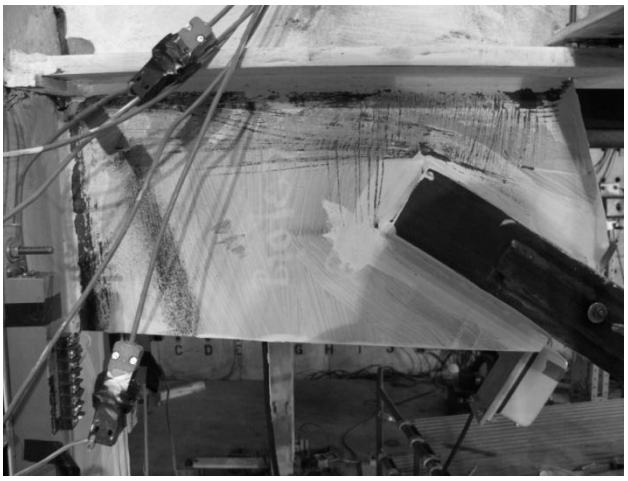


Figure 8. Gusset plate yielding, buckling brace test, 2% story drift



Figure 9. Column and gusset plate yielding at base, buckling brace test, 2% story drift

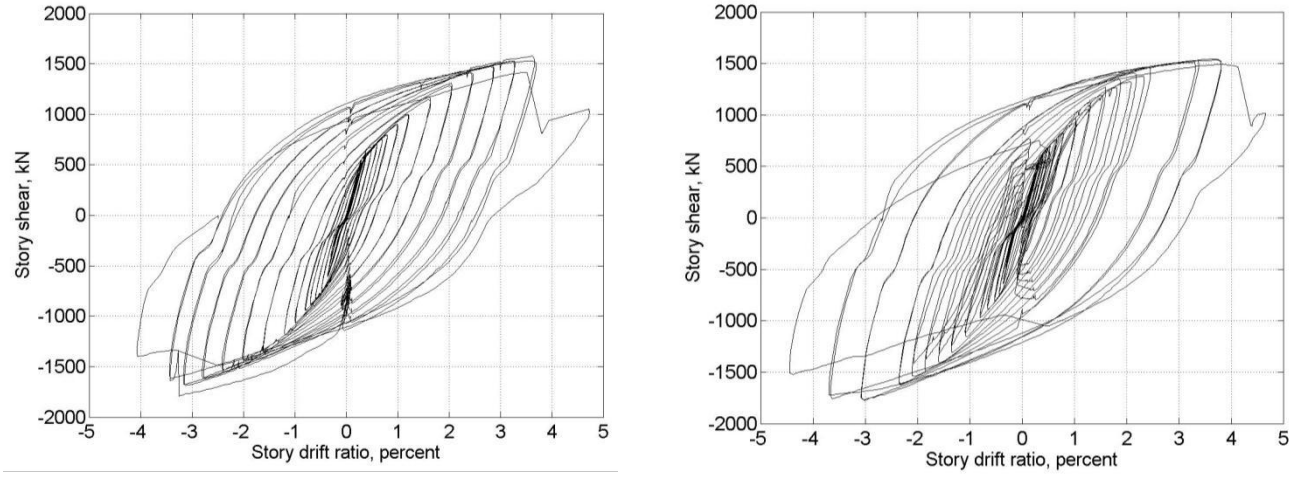
25 mm in the X direction due to the permanent frame deformation from the first test. The drifts reported below are relative to the initial permanent deformation.

Figure 10 shows the story shear – story drift ratio response for the second floor of each orthogonal braced bent. Yielding of the BRB cores occurred at approximately 0.33% story drift ration in each direction. In the Y-direction, the BRB core fractured at approximately 3.5% average roof drift ratio (RDR) while in the X-direction, the BRB core fractured at 4.1% RDR. The BRBs in the first story did not fracture as the first story columns resisted a larger amount of the story shear than the second story columns due to the base fixity. After core fracture, the load resisted by each frame was reduced by approximately 40%. The test was continued after core fracture and the frame stiffness remained the same due to the stiffness of the moment frame and the fact that the stiffness of the BRBs at this point was practically zero due to yielding of the BRB core.

At -3.2% RDR, the bottom flange in the second floor beam attached to the shared column in Braced Bay 2 (X-direction) fractured suddenly just outside of the CJP as shown in Figure 11. This occurred after the web at this location exhibited ductile tearing that extended through more than half of the beam web. This tearing was initiated at the erection bolt holes at the beam splice three feet away from the centerline of the column.

As shown in Figure 13, the web and bottom flange of the third floor beam at the shared column side in Braced Bay 1 also exhibited considerable yielding, local buckling and ductile tearing. The tear occurred at the edge of the gusset plate and extended completely through the bottom flange up to approximately ¾ of the beam depth. The braced frame columns yielded considerably at the base and above and below the second and third floor joints. Additionally, local buckling occurred at the base of the two frame columns that the BRBs framed into. This occurred on the side opposite of the gusset plates as shown in Figure 12(b). Column flange and web yielding can also be seen in this photo.

Limited gusset plate yielding was observed and was confined to a localized area approximately one inch square near the gusset-column reentrant corner. Weld tearing occurred in the second and third floor gusset plates at the gusset-column weld. These tears propagated through the total length of the weld and were due to frame action as they initiated when the brace was in compression and the joint

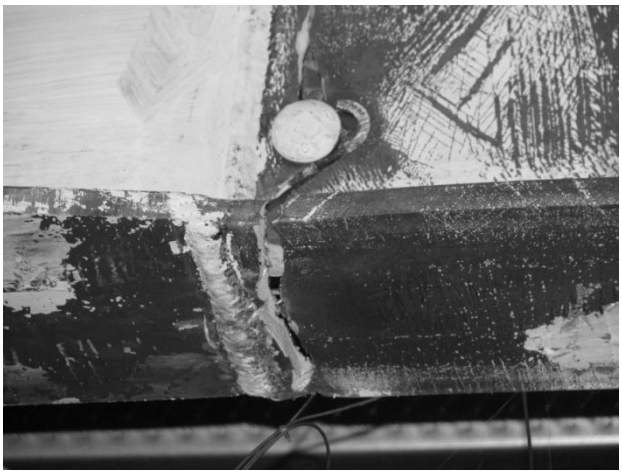


(a) (b)

Figure 10. BRBF test 2nd story hysteretic curves: (a) Braced Bay 1 (Y-direction); (b) Braced Bay 2 (X-direction).



(a)



(b)

Figure 11. BRBF test photos, -3.2% story drift: (a) beam web and flange tear outside of beam splice; (b) close-up of fracture at bottom flange





(a) (b)

Figure 12. BRBF test photos, -3.2% story drift: (a) gusset weld tear at column; (b) column local buckling and yielding

was opening. Preliminary analysis indicates that this tearing had limited effect on the overall frame behavior but further analysis is required to fully quantify this.

The BRBs were connected to the gusset plates with pins which limited the amount of moment transferred between these two elements. As a result of fabrication and fit-up tolerances, which require the hole to be slightly larger than the pin, and yielding of the pin and steel in the vicinity of the pinhole, there was a reduction in frame stiffness as the BRBs underwent a change in the sign of the axial force. This can be seen clearly in the hysteretic curves shown in Figure 10. Additional damage occurring in the frame included panel zone yielding in the columns, tearing at the bolt holes that connected the gravity beams to the braced frame columns, and beam web yielding near the end of the gusset plates. Second floor composite slab damage was limited to hairline cracks around the braced frame columns but were more indicative of shrinkage cracks than flexural cracks.



Figure 13. BRBF test photos, -3.6% story drift: beam web and bottom flange tear at edge of gusset plate

4. CONCLUSIONS AND FUTURE WORK

The out-of-plane loading appeared to have negligible effect on the frame behavior. The HSS braces fractured at 2% story drift which is consistent with previous tests performed on a similar frame loaded uni-directionally at UW. There was considerable gusset plate yielding in the first test which was expected as gusset plate yielding was specifically designed for and deemed a desirable secondary yielding mechanism. Additionally, the elliptical clearance method provided adequate rotation capability of the gusset plates while providing a much more compact design than the $2t_p$ linear offset method most commonly used in practice today.

Similar to the first test, the out-of-plane deformation appeared to have minimal effect on the BRBF behavior. The BRB cores fractured at 3.5 and 4% story drift and no instabilities occurred in the BRB prior to fracture. As BRBs are proprietary and are detailed differently, especially at the ends, this type of behavior may not be typical of all BRBs. Indeed, instabilities have been shown to occur at the end of the BRBs in previous tests that have not been subjected to out-of-plane deformation (Mahin et al. 2004). Frame action, as opposed to brace action, had a dominating effect on the demands on the gusset-frame welds. Approximately half of the gusset to column welds tore completely through along their lengths as a result of the joint opening.

Work is ongoing to further analyze the test results with

the goals of better quantification of the effect of out-of-plane deformation on the system, the effect of the concrete floor slab, and the demands on the shared column due to bi-directional effects. To aid in this work, 3D finite element models will be developed and calibrated to the test results and parametric studies shall be performed.

Acknowledgements:

This is a continuing research project funded by the National Science Foundation through Grant CMS-619161, "NEESR-SG: International Hybrid Simulation of Tomorrow's Braced Frame Systems." Dr. Joy Pauschke is the Program Officer for this research. Structural steel has been provided by the American Institute of Steel Construction with Mr. Tom Schlafly providing the oversight and technical contact. The authors would like to thank the MAST lab staff for their expertise and hard work.

References:

AISC, (2005a), *Steel Construction Manual, 13th Edition*, American Institute of Steel Construction, Chicago, IL.

AISC, (2005b), *Seismic Provisions for Structural Steel Buildings*, American Institute of Steel Construction, Chicago, IL.

ASCE, (2005), *ASCE 7-05 – Minimum Design Loads for Buildings and Other Structures*, American Society of Civil Engineers

Chen, C.H., Hsiao, P.C., Lai, J.W., Lin, M.L., Weng, Y.T. and Tsai, K.C. (2004), "Pseudo-Dynamic Test of a Full-Scale CFT/BRB Frame: Part 2 – Construction and Testing," *13th World Conference on Earthquake Engineering*, Vancouver, B.C., Canada, Paper No. 2175.

Lopez, W. A., Sabelli, R., 2004. "Seismic Design of Buckling-Restrained Braced Frames", *SteelTips*, Structural Steel Educational Council.

Mahin, S., Uriz, P., Aiken, I., Field, C., Ko, E., 2004. "Seismic Performance of Buckling-Restrained Braced Frame Systems", *13th World Conference on Earthquake Engineering*, Vancouver, B.C, Canada, Paper No. 1681.

Roeder, C.W., Lehman, D.E., You, J.H., 2005. "Improved Seismic Design of Steel Frame Connections", *International Journal of Steel Structures*, Korean Society of Steel Construction, Seoul, Korea, 5 (2), 141-153.

Roeder, C.W, Lehman, D.E., 2009. "Performance and Behavior of Gusset Plate Connections", *2009 NASCC Conference Proceedings*, Phoenix, AZ, USA.

Trembaly, R., Archambault, M.-H., Filiatrault, A. 2003. "Seismic response of Concentrically Braced Steel Frames Made with Rectangular Hollow Bracing Members", *Journal of Structural Engineering*, 129 (12), 1626-1636.

Yoo, J., Lehman, D.E., Roeder, C.W., 2008. "Influence of connection design parameters on the seismic perform ance of braced frames", *Journal of Constructional Steel Research*, 64, 607-623.

8CUEE CONFERENCE PROCEEDINGS
8th International Conference on Urban Earthquake Engineering
March 7-8, 2011, Tokyo Institute of Technology, Tokyo, Japan

A METHOD FOR THE DAMAGE ASSESSMENT OF SINGLE-LAYER LATTICED SHELLS BY PERFORMING STATIC STABILITY ANALYSIS TWICE

Dabin Yang[1], Yigang Zhang[2], and Jinzhi Wu[3]

1) Ph.D. Candidate, Spatial Structures Research Center, Beijing University of Technology, China
2) Professor, Spatial Structures Research Center, Beijing University of Technology, China
3) Associate Professor, Spatial Structures Research Center, Beijing University of Technology, China
yangdabin@126.com, zyg@bjut.edu.cn, kongjian@ bjut.edu.cn

Abstract: The static stability capacity is the main index to measure the whole mechanical performance of single-layer latticed shells. A new damage assessment method of single-layer latticed shells was presented by performing static stability analysis once before and once after subjecting the shell to earthquakes, and the damage index is calculated from a perspective of the static stability capacity degradation incurred by earthquakes. The method has a solid theoretical basis and can be easily implemented. Compared with other methods to assess the damage of single-layer latticed shells, the examples show that the method has a high precision especially when the shells near collapse.

1. INTRODUCTION

The damage assessment has been one of the key and difficult problems in the earthquake engineering. The state of structural damage is usually described by a damage index D because of its simplicity and effectiveness. A rational damage index should be in the range of [0,1], and a value of zero represents no damage while a damage index value of one corresponds to collapse. The damage indices can be broadly divided into two classes (Ghobarah et al. 1999): strength-based damage indices; and response-based damage indices. The latter has been widely used, which can also be divided into two types according to the calculating method: (1) The damage indices are calculated by the damage parameters such as stresses, displacements and energy, etc. The well-known Park-Ang damage model (Park and Ang, 1985) is a typical example of this approach. (2) The damage indices are calculated from a perspective of the degradation of structural performance such as stiffness and frequency. One of the typical example is the method presented by the authors (Ghobarah et al. 1999), the basic procedure of which is to perform pushover analysis for the structure before and after subjecting the structure to the earthquake, then the damage index is calculated according to the stiffness degradation:

$$D=1-(K_{final}/K_{initial}) \quad (1)$$

where $K_{initial}$ is the initial slope of the base shear-top deflection relationship resulting from the pushover analysis of the structure before subjecting it to the earthquake and K_{final} is the initial slope of the same relationship but after subjecting the frame to the earthquake. This method and the modified version have been widely used in the damage assessment of frame structures.

Most of the damage assessment methods are about the multi-story structures. In the research of the damage assessment of single-layer latticed shells, the authors (Zhi et al. 2007)presented a fitted damage index with the span, strains, nodal displacements and yielded members ratio as the damage parameters. The authors (Du et al. 2007) evaluated the damage of single-layer latticed domes with the Park-Ang damage index. The authors (Kato and Nakazawa 2010) presented discrete damage values of a single-layer latticed dome and the substructure with the maximum displacement and acceleration as the damage parameters. It can be seen that all the available methods are of the first kind of response-based damage assessment methods, and there are no assessment methods of the second kind. A new damage assessment method of single-layer latticed shells was presented in the paper by performing static stability analysis twice: once before and once after subjecting the shell to earthquakes, and the damage index is calculated in this method from a perspective of the static stability capacity degradation incurred by earthquakes.

2. BASIC PRINCIPLES

2.1 Word Processing

The design of the most single-layer latticed shells are controlled by the static stability capacity, so the static stability capacity is the main index to measure the whole

mechanical performance of single-layer latticed shells. It is rational and effective to calculate the damage index from a perspective of the static stability capacity degradation incurred by earthquakes. Similar to the method presented by Ghobarah, the method is to perform static stability analysis for the shell twice: once before subjecting the shell to the earthquake and once after subjecting the shell to the earthquake. The load-displacement curves are shown in Fig.1, where P_i and P_f are the static stability capacities of the shell under dead load P_0 before and after the earthquake. Unlike the method presented by Ghobarah, if the shell does not collapse after the earthquake, then the static stability capacity will at least be the self weight P_0 (including the self weight of members and the super dead load) of the shell, so the influence of P_0 should be removed when the damage index is calculated by the method. Similar to Equation 1, the damage index D can be calculated as follows:

$$D=1-(P_f-P_0)/(P_i-P_0)=(P_i-P_f)/(P_i-P_0) \quad (2)$$

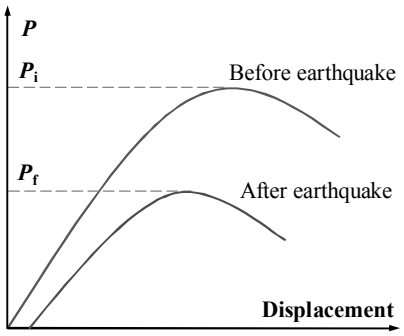


Figure 1 Load vs. Displacement Curve

If the load P is expressed by the load factor F , i.e., introducing the equations $P_i = P_0F_i$ and $P_f = P_0F_f$ into the equation above, a new form of it is:

$$D=(F_i-F_f)/(F_i-1) \quad (3)$$

3. APPLICATION IN SINGLE-LAYER SPHERICAL DOME

3.1 Model

A single-layer latticed dome shown in Fig.2 is taken as the numerical example, and the span and height of the dome are 40m and 8m, respectively. All the periphery nodes are pin-supported, and the material is the ideal elasto-plastic model with the yield stress of 235MPa and Young's modulus of 2.06e5MPa.

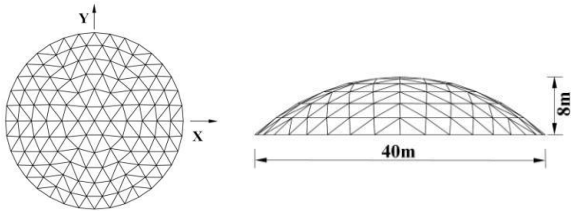


Figure 2 Single-Layer Latticed Dome

The members section arrangement has a great influence on the static stability performance of the single-layer latticed shells, and a rational section arrangement should make sure most members work together to bear the loads, thus a relatively high static stability capacity will be achieved. After comparison of the static stability performance of some domes with different section arrangements, the radial and hoop members section are determined as Ø114×4mm and the others are determined as Ø108×3.5mm. The basic eigenvalue buckling mode is taken as initial geometry imperfection applied to the dome, and the maximum imperfection value is taken as 1/300 of the span. Both geometric and material nonlinearity are included in the analysis. The static buckling shape of the dome before earthquake is shown in Fig.3, in which the yielded members are depicted with blue lines and the red dot denotes the node with maximum vertical displacement in the buckling shape.

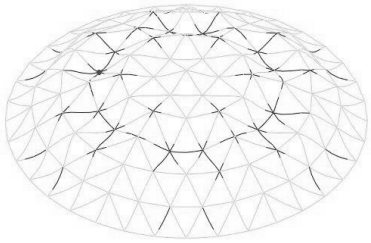


Figure 3 Static Buckling Shape and Yielded Members (scale 30)

The load factor-vertical displacement curve of the node is depicted in Fig.4, from which the static stability capacity factor can be drawn as 6.831.

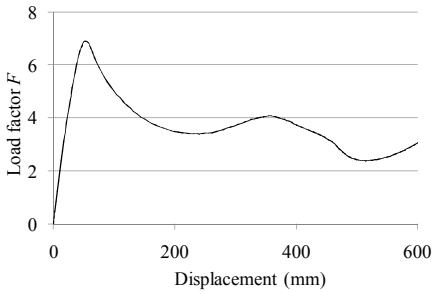


Figure 4 Load Factor vs.Vertical Displacement Curve

3.2 Seismic Time History Analysis and Static Stability Analysis

The FEA software ABAQUS 6.9-1 is used to do the time history and static stability analysis, and Both geometric and material nonlinearity are considered in the analysis. All the members are meshed with 4 beam elements-B31 with the section type of PIPE. The Riks arc-length method is used to do the static stability analysis, and restart technology is used to do the static stability analysis after earthquake in order to import the damage state into the beginning of the second static stability analysis. The default Hilber-Hughes-Taylor implicit integration algorithm in ABAQUS/Standard is used to do the time history analysis. Self weight of members is automatically considered by the

software, and super dead load of 0.5kN/m^2 is converted to nodal masses. Rayleigh damping ratio is taken as 0.02 and the damping coefficients are computed by the WLS method presented by the authors (Yang et al. 2010).

To learn the yield extent of the members, plastic strains of eight member section points are outputted, which is shown in Fig.5, and 1P is used to denote the members in which at least one section point enter into plastic stage, and 8P denote the members in which all the eight section points enter into plastic stage.

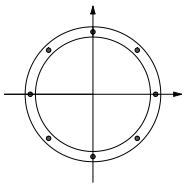


Figure 5 Section Points

Three dimensional El-Centro and Taft earthquake acceleration records are selected as the input excitations. The accelerations are scaled to different PGA in order to learn damage states of the dome under the earthquakes with different intensities. The dome is unloaded after the earthquake, then the second static stability analysis is performed.

3.3 Analyses Result

The maximum nodal vertical displacement DS_{max} during the time histories are shown in Fig.6.

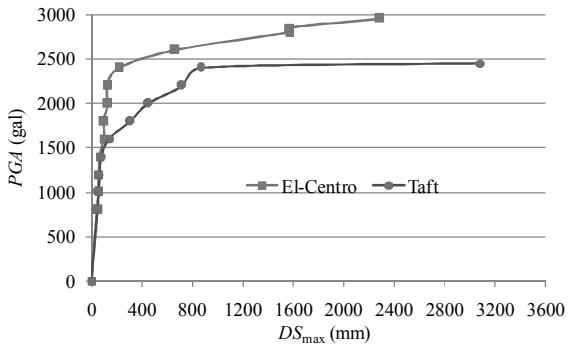
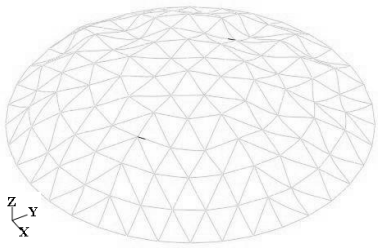
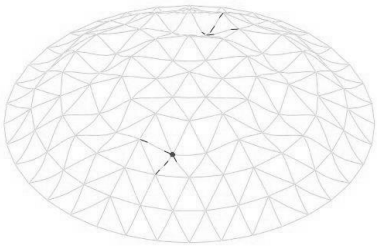
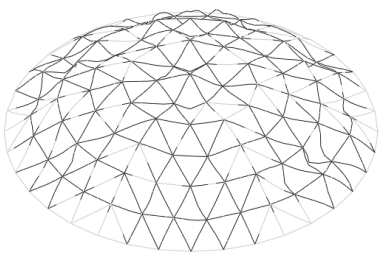
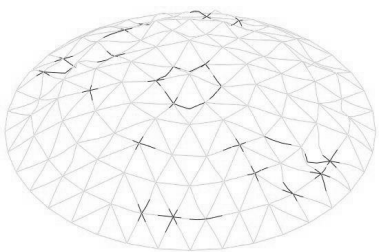
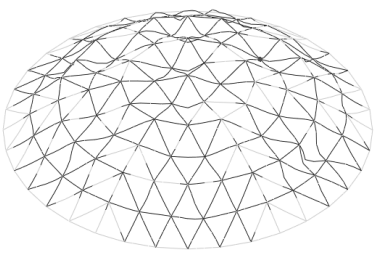


Figure 6 PGA vs. DS_{max} Curves

To learn damage states of the dome clearly, the shape and the second buckling shape coupled with the yielded members distribution after the El-Centro and Taft earthquakes with different PGA are shown in Table.1 and Table.2, in which the red dots denote the nodes with maximum vertical displacements in the buckling shape, and the numbers under each deformed shape denote the scaled times of the displacements. The 1P and 8P members are depicted with blue lines in the figures, and there are no 8P members after both earthquakes with the PGA as 800gal, so the figures are vacant in the corresponding grids. All the deformed shape have the same axis as the one depicted in the first figure.

Table 1 Dome Damage under El-Centro Earthquake and Second Buckling State

PGA (gal)	Shape and 1P members distribution(blue lines)	Shape and 8P members distribution(blue lines)	Buckling shape and 1P members distribution(blue lines)
800	 80	No 8P members	 30
1600	 30	 30	 20

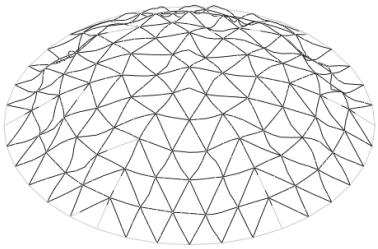
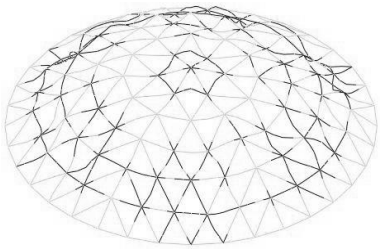
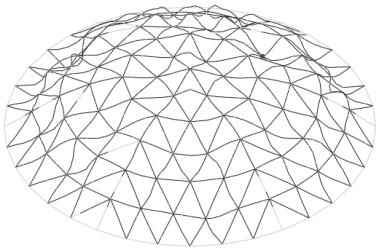
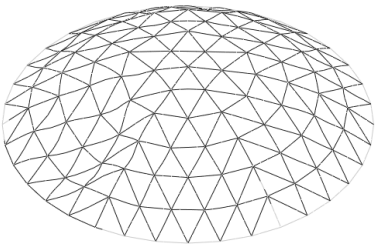
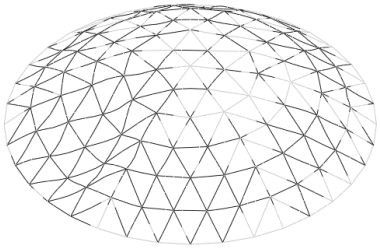
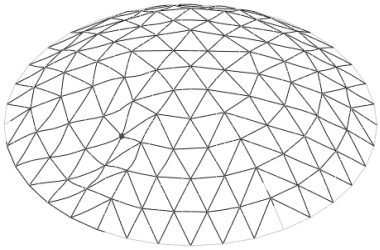
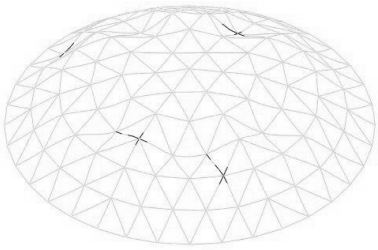
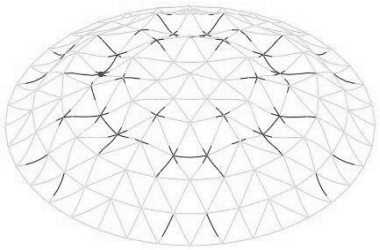
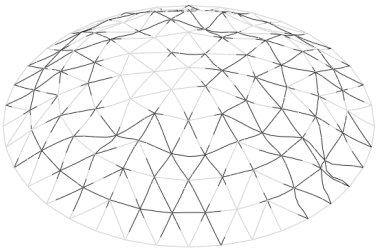
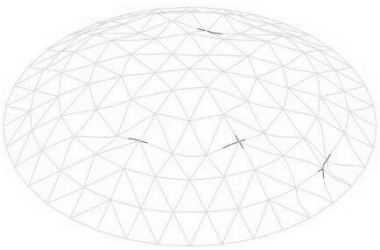
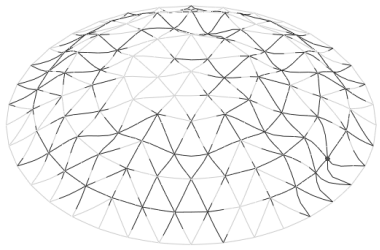
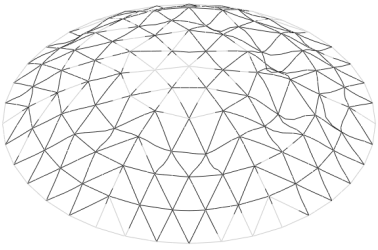
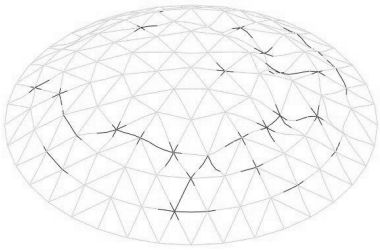
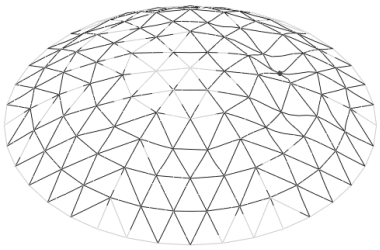
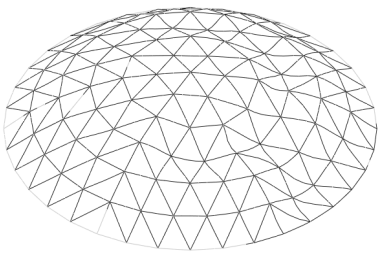
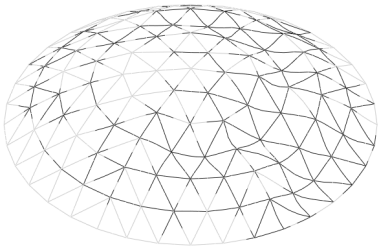
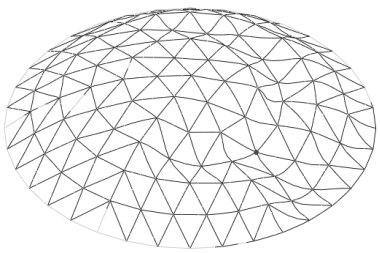
2400	 10	 10	 5
2950	 1	 1	 1

Table 2 Dome Damage under Taft Earthquake and Second Buckling State

PGA (gal)	Shape and 1P members distribution(blue lines)	Shape and 8P members distribution(blue lines)	Buckling shape and 1P members distribution(blue lines)
800	 80	No 8P members	 30
1400	 80	 80	 25
1800	 10	 10	 3

2450			
	1	1	1

The static stability load factor vs. displacement curves before and after earthquakes with different PGA are depicted in Fig.7 and Fig.8, in which PGA=0 denotes the first static stability curve before earthquakes. Fig.9 shows the static stability capacity factors after earthquakes with different PGA.

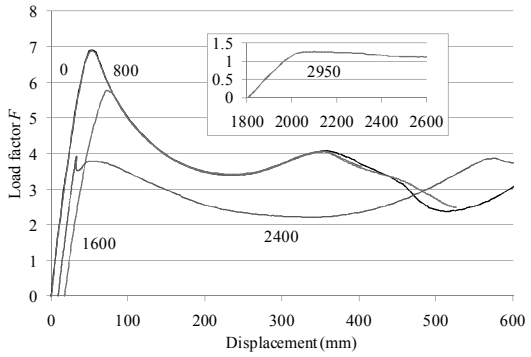


Figure 7 F vs. Displacement Curves (El-Centro)

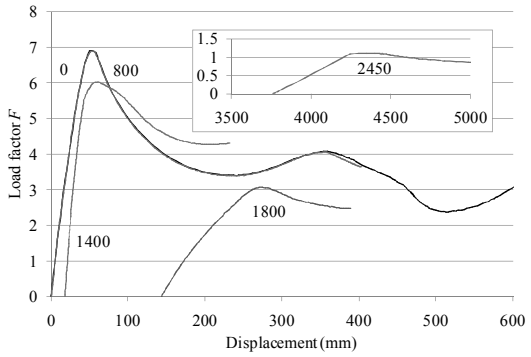


Figure 8 F vs. Displacement Curves (Taft)

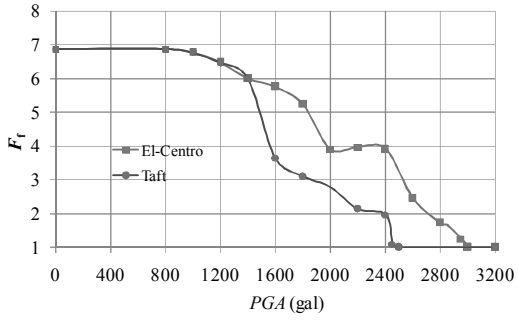


Figure 9 F_f vs. PGA Curves

PGA_y and PGA_c are used to denote the PGA when the dome yields and collapses, respectively. The PGA_y for both El-Centro and Taft earthquakes are 800gal, and the PGA_c are 3000gal and 2500gal, respectively. It can be seen from the figures above that when PGA is less than PGA_y, the dome remains elastic after the earthquakes and the static stability capacity will not reduce; and when PGA is equal to PGA_y, only a few members of the dome yield after the earthquakes, so F_f almost equals F_i; and when PGA is greater than PGA_y and less than PGA_c, the DS_{max}, the quantity of 1P and 8P members increase gradually on the whole with the increase of PGA, while F_f almost decrease gradually with the increase of PGA, and when PGA is close to PGA_c, almost all the dome members yield and the quantity ratio of 8P members to all the members is also high; when PGA is equal to or greater than PGA_c, the dome collapse. It can also be seen that the shape after the earthquakes is similar to the static buckling shape after the earthquakes, which shows that buckling of the dome follow the shape and damage state incurred by the earthquakes. Through comparing the figures in the last row of the two tables, it can be seen that the severe damaged area after the earthquake and the buckling area of the dome under the El-Centro motion are larger than those under the Taft motion, which shows that different ground motions may inflict more or less damage areas on the dome.

There is a hardening phenomenon (Vamvatsikos and Cornell 2002) that need to be noted in Fig.6 and Fig.9 with the El-Centro earthquake. The DS_{max} and F_f curves deviate from the original developing trend when PGA reaches 1100gal, thus making the DS_{max} and the F_f non-monotonic functions of the PGA. This is called hardening which is a frequent phenomenon in the incremental dynamic analysis(IDA) of frame structures (Vamvatsikos and Cornell 2002) and spatial structures (Yang et al. 2010), whereas it needs further research about whether there is a correlation between the reverse of maximum displacement and that of static stability capacity when domes harden.

3.4 Damage Assessment of the Dome

By Substituting F_f in Fig.9 and F_i=6.887 into the Equation 3, the damage index D under El-Centro and Taft earthquakes can be calculated, which is shown in Fig.10.

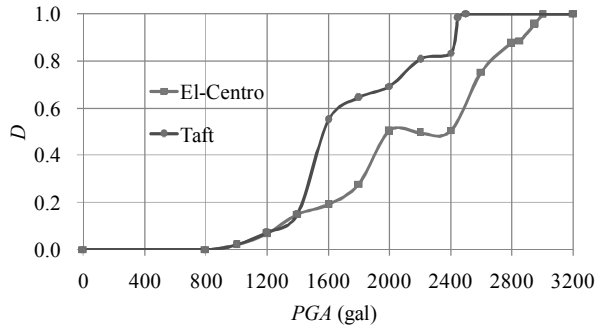


Figure 10 *D* vs. PGA Curves

When PGA is less than PGA_y, the dome remains elastic after the earthquakes and *D* equals zero; and when PGA is equal to or greater than PGA_y and less than PGA_c, *D* increases on the whole with the increase of PGA except the occasional hardening of the dome, and *D* converges to one when the PGA approaches PGA_c; and when PGA is equal to or greater than PGA_c, the dome collapse, so *D* is taken as one. Therefore, compared with the other damage assessment methods of single-layer latticed domes, the most advantage of the method is the high precision especially when the dome nears collapse.

3.5 Damage Assessment of the Dome under Other Ground Motions

The damage assessment of the dome under other ground motions in Table.3 is presented in Fig.11.

Table 3 Ground Motions

ID	name	M	Year	Recording Station
1	Northridge	6.7	1994	Beverly Hills-Mulhol
2	Northridge	6.7	1994	Canyon Country-WLC
3	Imperial Valley	6.5	1979	El Centro Array #11
4	Kobe, Japan	6.9	1995	Nishi-Akashi
5	San Fernando	6.6	1971	LA-Hollywood Stor

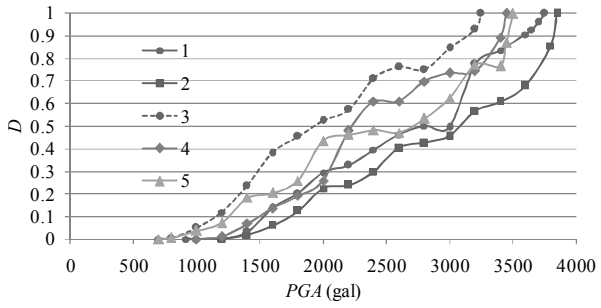


Figure 11 *D* vs. PGA Curves

4. APPLICATION IN SINGLE-LAYER CYLINDRICAL SHELL

4.1 Model

The geometry of the single-layer cylindrical latticed shell is shown in Fig.12, where the length *L*, span *B* and height *f* of the shell are 40m, 20m and 5m, respectively.

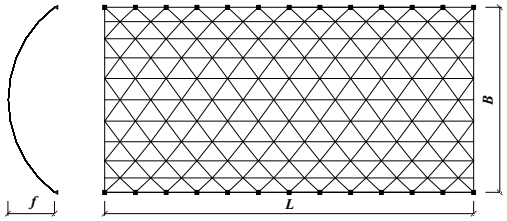


Figure 12 Single-Layer Cylindrical Latticed Shell

All the longitudinal edge nodes are pin-supported, and the diagonal members are of the section Ø159×5,while other members Ø89×4. The material is the same as the one for the spherical dome. Fig.13 shows the basic eigenvalue buckling mode of the shell, which is applied to the shell as initial geometry imperfection with the maximum value as *B*/300.

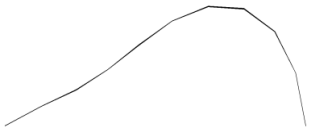


Figure 13 Basic Eigenvalue Buckling Mode

4.2 Analyses Result

The three dimensional Northridge ground motions is selected as the input excitations. The analysis procedure is the same as presented above. Fig.14 shows the maximum nodal vertical displacement DS_{max} during the time history with different PGA.

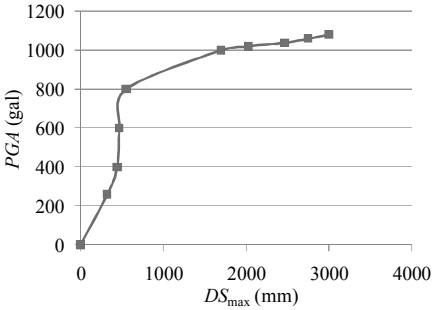
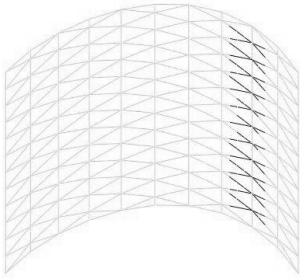
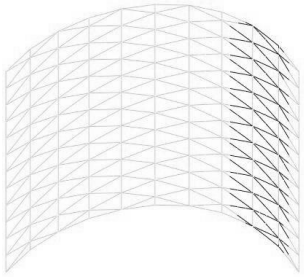
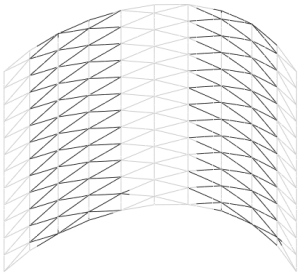
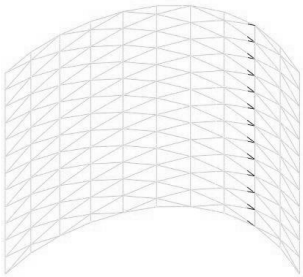
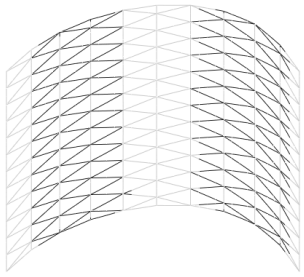
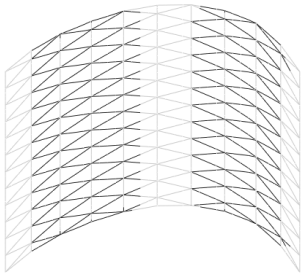
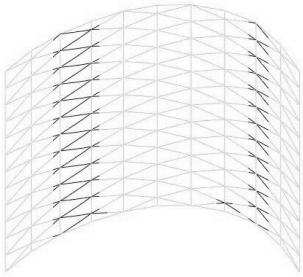
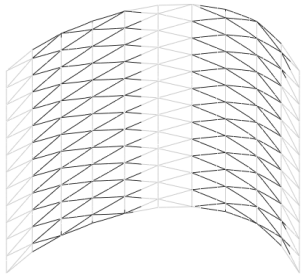
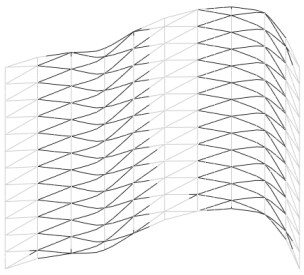
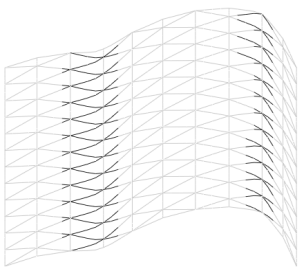
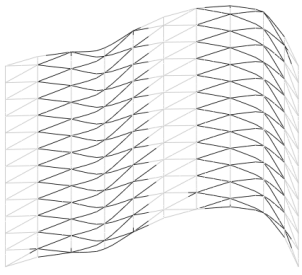


Figure 14 PGA vs. DS_{max} Curve

Table.4 presents the damage states of the shell after Northridge earthquake and the second buckling shapes and yielded members.

Table 4 Shell Damage under Northridge Earthquake and Second Buckling State

PGA (gal)	Shape and 1P members distribution(blue lines)	Shape and 8P members distribution(blue lines)	Buckling shape and 1P members distribution(blue lines)
260		No 8P members	
600			
800			
1080			

The figures in Table.4 show that the longitudinal supported single-layer cylindrical shell has a very distinct one way mechanical characteristics, and with the span direction as the main force bearing direction, the damages are almost the same along the longitudinal direction. The same damage feature of the shell can also be observed under other ground motions.

Fig.15 shows the static stability load factor F vs. displacement curves before and after Northridge earthquake with different PGA.

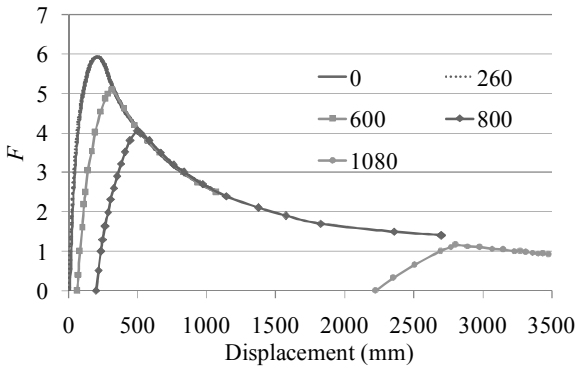


Figure 15 F vs. Displacement Curves

4.3 Damage Assessment of the Shell

Fig.16 shows the damage index under Northridge earthquake with different PGA.

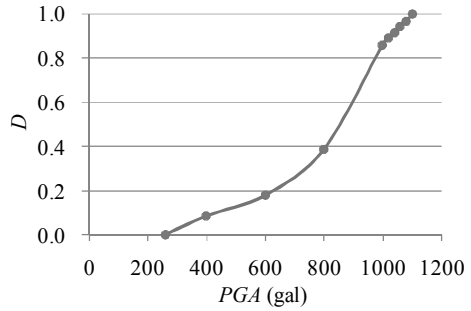


Figure 16 *D* vs. PGA Curve

4.4 Damage Assessment of the Shell under Other Ground Motions

The damage assessment of the shell under other 4 ground motions in Table.5 is presented in Fig.17.

Table 5 Ground Motions

ID	name	M	Year	Recording Station
1	Kocaeli, Turkey	7.5	1999	Yarimca
2	Chi-Chi, Taiwan	7.6	1999	TCU065
3	Imperial Valley-06	6.5	1979	Chihuahua
4	Kocaeli, Turkey	7.5	1999	Izmit

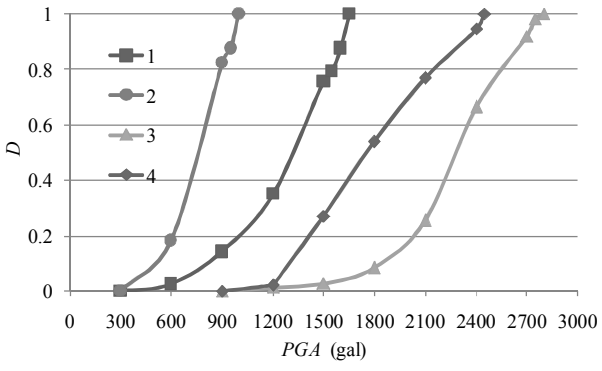


Figure 17 *D* vs. PGA Curves

Compared with the damage state of the spherical domes under earthquakes, the damage index D vs. PGA curves of cylindrical shells are more straightforward with less backward curves, which is mainly due to the simple and one way mechanical characteristics of the longitudinal supported cylindrical shell.

5. SUMMARY OF THE METHOD

The general formula of the method is as follows:

$$D=\begin{cases}0, & PGA<PGA_{\mathrm{y}}\\ \left(F_{\mathrm{i}}-F_{\mathrm{f}}\right)/\left(F_{\mathrm{i}}-1\right), & PGA_{\mathrm{y}}\le PGA<PGA_{c}\\ 1, & PGA\ge PGA_{c}\end{cases} \quad (4)$$

The method is of the second kind of response-based damage assessment methods, and it avoids the calculation of damage parameters and only needs static stability analysis before and after the earthquake, so it is easily implemented and the calculation is simple.

6. CONCLUSIONS

A new damage assessment method of single-layer latticed shells was presented by performing static stability analysis twice. The method has a solid theoretical basis and can be easily implemented. Compared with the other methods to assess the damage of single-layer latticed shells, the example shows that the method has a high precision especially when the shell near collapse.

References:

Ghobarah, A., Abou-Elfath, H., and Biddah, A. (1999), "Response-based damage assessment of structures," *Earthquake Engineering and Structural Dynamics*, 28(1), 79-104.

Park, Y. J., and Ang, A. H. S. (1985), "Mechanistic seismic damage model for reinforced concrete," *Journal of Structural Engineering*, 111(4), 722-739.

Zhi, X. D., Fan, F., and Shen, S. Z. (2007), "Failure mechanisms of single-layer reticulated domes subjected to earthquakes," *Journal of the International Association for Shell and Spatial Structures*, 48(153), 29-44.

Du, W. F., Gao, B. Q., and Dong, S. L. (2007), "Double-control criterion of dynamical strength failure for single layer latticed shells," *Journal of Zhejiang University(Engineering Science)*, 41(11), 1916-1920.(in Chinese)

Kato, S., and Nakazawa, S. (2010), "A trial for seismic fragility evaluation of a large lattice dome supported by buckling restrained braces," *International Journal of Space Structures*, 25(2), 125-134.

Yang, D. B., Zhang, Y. G., and Wu, J. Z. (2010), "Computation of Rayleigh damping coefficients in seismic time-history analysis of spatial structures," *Journal of the International Association for Shell and Spatial Structures,* 51(2), 125-135.

Vamvatsikos, D., and Cornell, C. A.(2002), "Incremental dynamic analysis, Earthquake Engineering and Structural Dynamics," 31(3), 491-514.

Yang, D. B., Zhang, Y. G., and Wu, J. Z. (2010), "Application of incremental dynamic analysis in the collapse evaluation of single-layer latticed dome," *Space Structures*, 16(3), 91-96.(in Chinese)

8CUEE CONFERENCE PROCEEDINGS
8th International Conference on Urban Earthquake Engineering
March 7-8, 2011, Tokyo Institute of Technology, Tokyo, Japan

EFFECT OF BRACE FRACTURE ON SEISMIC PERFORMANCE OF BRACED FRAME

Ryota Matsui[1] and Toru Takeuchi[2]

1) Graduate Student, Dept of Architecture and Building Engineering, Tokyo Institute of Technology, Japan
2) Professor, Dept of Architecture and Building Engineering, Tokyo Institute of Technology, Japan
matsui.r.aa@m.titech.ac.jp, ttoru@arch.titech.ac.jp

Abstract: A moment frame with bracing elements is one of efficient seismic-resistant structural system used in elastic design. However, when the seismic input is larger than the buckling strength of the braces, the braces first undergo overall buckling and subsequent local buckling; further, concentration of plastic strain in the local buckling zone leads to brace fracture. The authors have previously proposed a brace fracture prediction method. In this study, they carry out time-history response analyses for braced frames using the proposed method and investigate the fatigue distribution in different types of frames, by taking into account the effect of brace fracture.

1. INTRODUCTION

In elastic design, a building structure with a braced frame is considered to be an efficient and economical system. However, in elasto-plastic design, under large earthquake the brace causes buckling and their hysteresis are unstable. In this case, the strength of the structure is commonly evaluated by ductility index or time-history response analysis. Including post-buckling many researchers have proposed the use of a hysteresis model for simulating the brace behavior; for instance, the method proposed by Shibata and Wakabayashi (1982) have been used to develop a hysteresis model for the accurate simulation of buckling behavior.

Goel (1989) and Takeuchi (2006) et al. indicated that once braces undergo overall buckling and subsequent local buckling, a large plastic strain is induced to the limited position, and this leads to brace fracture. Since the abovementioned Shibata and Wakabayashi hysteresis model does not take into account this fracture phenomenon, it cannot be used for the accurate simulation of brace behavior. Kanvinde and Deierlein (2007) reported that brace fracture can be assessed by micro-finite element analysis. This analysis, however, is not suitable for large-scale structures because it consumes long time and the result depends on the finite division method. Kanao and Nakashima et al. (2004) reported the dynamic response of the braced frame considering the brace fracture condition determined by the maximum response. However, brace fracture is not unambiguous determined by the maximum response, the results are evaluated under a hypothetical theory. Mukaide and Tada et al. (2010) investigated the seismic response of a tubular braced frame using a collaborative pseudo dynamic test. The results of this investigation increase the reliability of the brace fracture estimation. However, this proposed method can only simulate an experimented particular braced frame. On the other hand, the authors have proposed a brace fracture prediction method by taking into account a strain concentration ratio in the local buckling zone which is an increasing index between the entire strain and the local strain, without carrying out micro-finite element analysis. However, their accuracy was reported not necessarily precise (Mukaide and Tada et al. 2010).

In this study, the equation of strain concentration ratio is re-constructed and to improve the brace fracture prediction accuracy. Time history analysis program is constituted using the improved strain concentration ratio. The proposed analysis algorithm is applied to predict the dynamic response behavior and energy dissipation performance of six types of braced frames considering brace fracture.

2. BRACE FRACTURE PREDICTION METHOD

In the case of circular-tube braces, after local buckling, the local strain in the buckling zone becomes markedly higher than that in the other zones, and this leads to fracture. In this study, we develop a practical model for predicting the local strain transition and fracture in circular-tube braces on the basis of fatigue curves, by postulating a simplified hinge zone model. In this model, the plastic hinge is assumed to occupy the center of the circular-tube brace during overall buckling, as shown in Figure 1. The length of the plastic zone, L_h, is calculated using Eq. (1):

$$L_h = L\left(1-\left(\frac{S}{Z}\right)\right) \tag{1}$$

where L is the total length of the circular brace; S, the section modulus of the circular-tube; and Z, the plastic section modulus of the circular-tube. The hinge angle, θ_h, is calculated using Eq. (2), and the normalized deformation amplitude for the braces, $\Delta\varepsilon_n$, on the compression side is assessed by using Eq. (3), which includes a term for the maximum normalized tensile deformation, ε_{ntm}, observed before compression.

$$\theta_h = \cos^{-1}\left(1-\Delta\varepsilon_n\right) \tag{2}$$

$$\Delta\varepsilon_n = \varepsilon_{ntm} - \varepsilon_n \tag{3}$$

Here, the normalized deformation, ε_n, is defined as the ratio of the longitudinal displacement, δ, to the total length of the brace, L, as shown in Eq. (4).

$$\varepsilon_n = \delta / L \tag{4}$$

The local strain in the hinge zone, ε_h, is calculated by the average approximation shown in Eq. (5):

$$\varepsilon_h = \frac{\theta_h D}{L_h} = \frac{\theta_h D}{L\left(1-\left(\frac{S}{Z}\right)\right)} \fallingdotseq \frac{\theta_h D}{L\left(1-\frac{\pi}{4}\right)} \tag{5}$$

where D is the circular-tube diameter. The deformation of the circular-tube after local buckling is modeled in Figure 2. The relation in Eq. (6) defines the normalized deformation initiated by local buckling, ε_{lb}, according to previously reported experimental data (Ogawa et al. 1995). The hinge angle corresponding to local buckling θ_{lb} is calculated using Eq. (7), which is identical to Eq. (2).

$$\varepsilon_{lb} = 0.0683\varepsilon_y^{-0.39}\left(\frac{D}{t}\right)^{-1.39} \tag{6}$$

$$\theta_{lb} = \cos^{-1}\left(1-\varepsilon_{lb}\right) \tag{7}$$

where ε_y, the yield strain, and t, the circular-tube thickness. The hinge angle increment $\Delta\theta_h$ in the local buckling zone can be calculated using Eq. (8):

$$\Delta\theta_h = \theta_h - \theta_{lb} \qquad (\theta_h > \theta_{lb}) \tag{8}$$

The angle in the local buckling zone φ_h itself is calculated from Eq. (9) by using $\Delta\theta_h$ at which local buckling occurs, as shown in Figure 2:

$$\varphi_h = \cos^{-1}\left(\cos\Delta\theta_h - \frac{D\sin\Delta\theta_h}{l_p}\right) \tag{9}$$

where l_p is the half-amplitude of the local buckling wave; all the other variables have been defined previously. l_p is derived on the basis of the classical theory of buckling using Eq. (10) (Timoshenko et al. 1963), where ν_p is the plastic Poisson's ratio with a value of 0.5.

$$l_p = \pi\sqrt[4]{\frac{D^2t^2}{48\left(1-\nu_p^2\right)}} = \pi\sqrt{\frac{Dt}{6}} \tag{10}$$

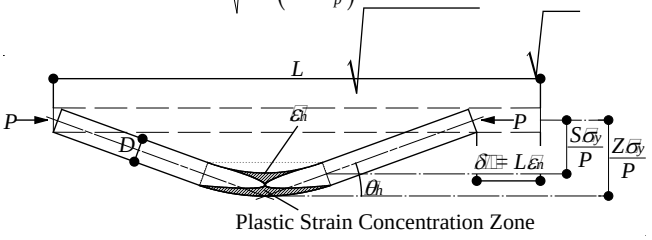


Figure 1 Overall Buckling of Circular-tube Brace

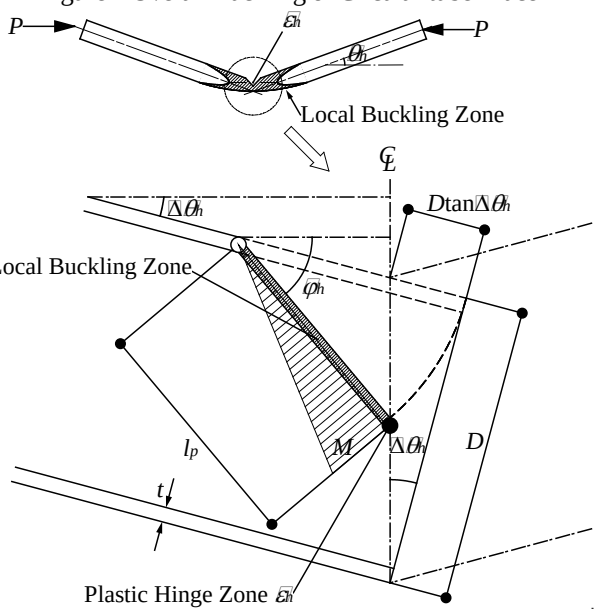


Figure 2 Local Buckling of Circular-tube Brace

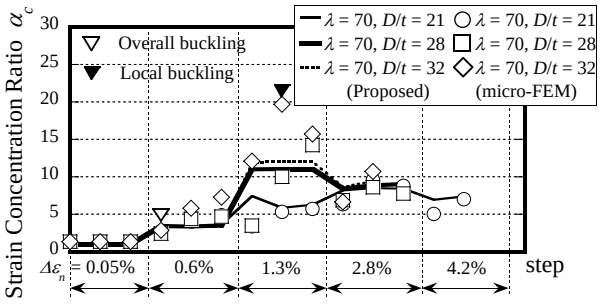


Figure 3 Strain Concentration Ratio

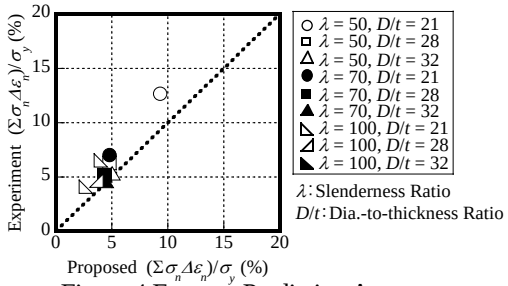


Figure 4 Fracture Prediction Accuracy

The strain in the hinge zone ε_h is expressed as the sum of overall and local buckling, as shown in Eq. (11):

$$\varepsilon_h = \frac{\varphi_h t}{2l_p\left(1-\frac{S_l}{Z_l}\right)} + \frac{\theta_{lb} D}{L\left(1-\frac{S}{Z}\right)} = \frac{3\sqrt{6}\varphi_h}{2\pi\sqrt{\frac{D}{t}}} + \frac{\theta_{lb} D}{L\left(1-\frac{\pi}{4}\right)} \quad (11)$$

where S_l and Z_l are the section modulus and plastic section modulus in the local buckling zone, respectively. Here, the local buckling zone is assumed to be rectangular, and the ratio of the abovementioned section moduli (S_l/Z_l) is 2/3. Thus, we assess the local strain in the local buckling zone before and during overall buckling, as well as that during the local buckling process. Therefore, the strain concentration ratio, α_c, is defined as shown in Eq. (12) at the bottom of this page. Here, ε_{cr} (= σ_{cr}/E) is the normalized axial deformation corresponding to overall buckling; σ_{cr}, the overall buckling stress; and E, the elastic modulus of steel. All the other variables used in this equation have been defined previously. Eq. (12) can be employed to calculate the local strain in the plastic hinge zone on the basis of the total normalized deformation. The strain concentration ratios increase drastically after local buckling and are large for specimens with a large diameter-to-thickness ratio; this trend is consistent with that observed in the experimental results. Figure 3 shows the plots drawn using the values calculated from Eq. (12) in accordance with the proposed method. These plots are in good agreement with those obtained by reconstituted micro-FEM analysis results as similar as Takeuchi and Suzuki et al. (2006) reported. By making use of this strain concentration ratio, the local strain transition can be evaluated from the ε_n value determined from Eqs. (3) and (4), and the instant of fracture can be determined by comparing the cumulative local plastic strain $\Sigma\Delta\varepsilon_{hp}$ and average plastic strain amplitude $\Delta\varepsilon_{hp}$ with the experimental fatigue curve as Eq. (13) (Saeki et al. 1995).

Table 1 Frame Type

Frame Type \ Brace Type	BRB	Ordinary Brace
SB Type (Strong, Beam-Yield Type)	Medium Damage	Medium Damage
SC Type (Strong, Column-Yield Type)	Medium Damage	Major Damage
WB Type (Weak, Beam-Yield Type)	Medium Damage	Major Damage
WC Type (Weak, Column-Yield Type)	Major Damage	Major Damage

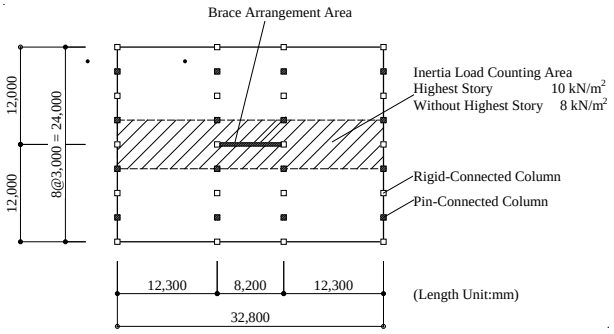


Figure 5 Typical Floor Plan of the Assumed Building

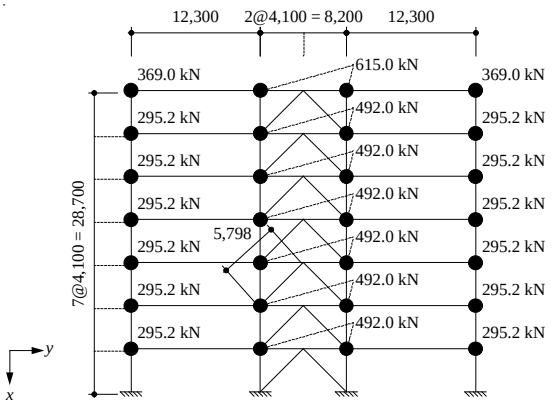


Figure 6 Assumed Inertia Load and Member Size

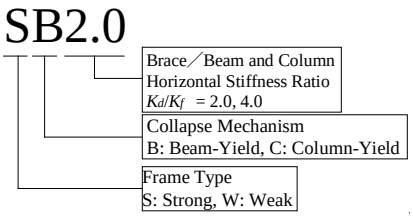


Figure 7 Frame Type Label

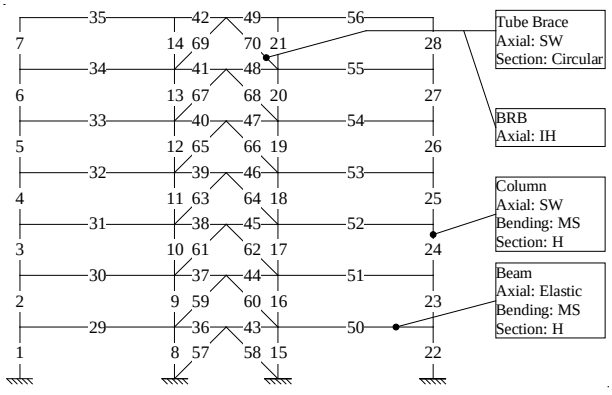


Figure 8 Frame-Member Number and Model

$$\alpha_c = \frac{\Delta\varepsilon_h}{\Delta\varepsilon_n} = \begin{cases} 1.0 & (\Delta\varepsilon_n < \varepsilon_{cr}, \text{ Prebuckling stage and tensile stage}) \\ \dfrac{\theta_h D}{L\left(1-\frac{\pi}{4}\right)\Delta\varepsilon_n} & (\varepsilon_{cr} < \Delta\varepsilon_n < \varepsilon_{lb}, \text{ Overall buckling stage}) \\ \dfrac{3\sqrt{6}\varphi_h}{2\pi\sqrt{\frac{D}{t}}\Delta\varepsilon_n} + \dfrac{\theta_{lb} D}{L\left(1-\frac{\pi}{4}\right)\Delta\varepsilon_n} & (\varepsilon_{lb} < \Delta\varepsilon_n, \text{ Local buckling stage}) \end{cases} \quad (12)$$

$$\sum \Delta\varepsilon_{hp} = 3857\overline{\Delta\varepsilon_{hp}}^{-1.13} \quad (13)$$

In Figure 4, the cumulative dissipation energy $\Sigma(\sigma_n \Delta\varepsilon_n/\sigma_y)$ determined from the proposed method is compared with the experimentally determined value. The estimates obtained by the proposed method are by and large consistent with the experimental results, and hence, this method is considered suitable for fracture prediction.

3. ANALYSIS MODEL OF BRACED FRAME

Figures 5 and 6 show a plane-frame model of a seven-story building with a rigid frame that includes braces. The black mark column in Figure 5 represents a pin-ended column that can support only the dead load, while the white mark column can withstand the dead load and the lateral seismic force; the plans of all the seven stories are designed to be similar. Thus, a dead load equivalent to that in one-half of the shaded area and an inertial mass equivalent to that in the shaded area are applied to the plane frame. The different types of models used in this study are listed in Table 1. The models are designated as SB, SC, WB, and WC; here, S, W, B, and C stand for high-strength frame, low-strength frame, beam-yield type, and column-yield type, respectively. The member size of the S-type frames is decided on the basis of the data available for normal buildings in Japan, while that of the W-type frames is decided from the data available for buildings in the United States. The plastic section modulus ratio, Z_{bp}/Z_{cp}, for the B-type frames is lesser than 1.0, while that for the C-type frames is greater than 1.0. Table 2 shows the frame parameters; the plastic section modulus of the S- and W-frames is set to 0.8 for the beam-yield type and 2.0 for the column-yield type. The lateral stiffness ratio between the brace and the frame, K_d/K_f, is set to 2.0 and 4.0 for the S- and W-type frames, respectively. Figure 7 shows the building types, and Table 3 lists the mechanical properties of steel. The natural period is in the range 0.72–1.08 s (0.025*H*–0.038*H*) for the S-type frame and 0.90–1.71 s (0.03*H*–0.06*H*) for the W-type frame (*H* denotes the building height in meters) as shown in Table 4. A circular-tube brace and a buckling-restrained brace (BRB) are used for the analysis. Here, the strength of a BRB pair is

Table 3 Mechanical Properties of Steel

Young's Modulus E (N/mm^2)	Strain-hardening Tangent Modulus E_t (N/mm^2)	Yield Stress σ_y (N/mm^2)
205000	205	258.5

Table 4 Natural Period of the Frames

Frame Type	Natural Period (sec)	
	Circular-tube	BRB
SB2.0	0.72	0.83
SC2.0	0.93	1.08
WB2.0	1.05	1.23
WC2.0	1.46	1.71
WB4.0	0.90	1.05
WC4.0	1.21	1.46

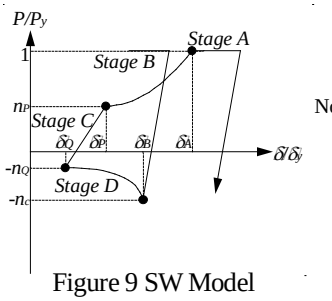


Figure 9 SW Model

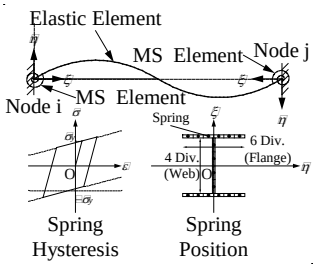


Figure 10 MS Model

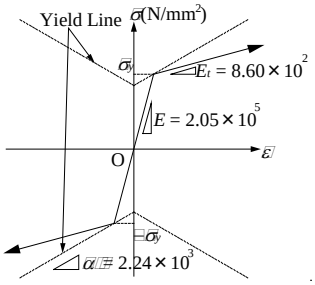


Figure 11 IH Model

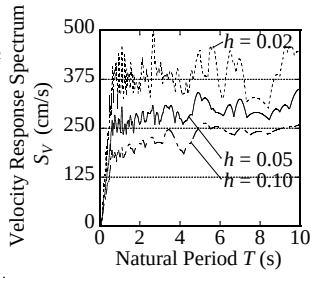


Figure 12 BCJ-L2 (2.5 times)

Table 2 Frame Parameters (Length Unit: mm)

Frame Type	Assumed Plastic Section Modulus Ratio Z_{bp}/Z_{cp}	Assumed Stiffness Ratio K_{di}/K_{fi}	Story	Beam	Column	Plastic Section Modulus Ratio Z_{bp}/Z_{cp}	Circular-tube Brace	Stiffness Ratio (Circular-tube Brace) K_{di}/K_{fi}	Sectional Area of BRB (mm^2)	Stiffness Ratio (BRB) K_{di}/K_{fi}
SB2.0	0.8	2.0	7-2	H-900 × 350 × 16 × 22	H-600 × 600 × 19 × 32	0.79	φ216.3 × 10.0	1.80-2.01	2994.3	0.83-0.93
			1				φ216.3 × 20.0	2.04	6481.1	1.07
SC2.0	2.0	2.0	7-2		H-450 × 450 × 16 × 22	1.98	φ216.3 × 6.0	1.90-1.99	1878.0	0.90-0.94
			1				φ216.3 × 8.0	1.97	2798.6	0.99
WB2.0	0.8	2.0	7-2	H-700 × 250 × 16 × 22	H-450 × 450 × 19 × 32	0.81	φ216.3 × 4.2	1.82-1.99	1346.5	0.88-0.96
			1				φ216.3 × 8.0	2.06	2667.8	1.05
WC2.0	2.0	2.0	7-2		H-300 × 300 × 16 × 32	1.95	φ216.3 × 2.0	1.88-1.94	676.4	0.95-0.98
			1				φ216.3 × 2.8	2.04	1012.2	1.10
WB4.0	0.8	4.0	7-2		H-450 × 450 × 19 × 32	0.81	φ216.3 × 8.5	3.61-3.94	2798.6	1.82-1.99
			1				φ216.3 × 16.0	3.96	5235.1	2.06
WC4.0	2.0	4.0	7-2		H-300 × 300 × 16 × 32	1.95	φ216.3 × 4.2	3.91-4.04	1346.5	1.88-1.94
			1				φ216.3 × 6.0	4.30	1878.0	2.04

equivalent to that of a circular-tube brace on the tensile side, and the instant of fracture for the BRB is defined on the basis of the method developed by Takeuchi and Ida et al (2008).

The member index and element type model for each frame are shown in Figure 8. A multi-spring element is added to both ends of the beam and column members, and the axial stiffness of all the members is defined on the basis of the numerical model proposed by Shibata and Wakabayashi (SW Model) as Figure 9; these members undergo fracture at the point where the cumulative value and average value of local strain calculated from Eq. (12) meets the fatigue curve of Eq. (13). After a given member is fractured, its stiffness decreases to 1/1000 of the original value and the stress reduces to 0. The multi-spring model (MS Model) is modeled from 16 elasto-plastic springs as Figure 10, and it plays the role of a plastic hinge when the spring at the end of the web undergoes plastic deformation, and the post-yield tangent modulus is approximately 1/60 of strain-hardening tangent modulus provided in Table 3. The hysteresis curve for the BRB is simulated by using the isotropic hardening model (IH Model) as Figure 11. Assuming the earthquake magnitude as 7, the input seismic acceleration is 2.5 times that of an artificial seismic wave BCJ-L2 developed by Building Center of Japan, as shown in Figure 12. The structural damping factor h has a value of 0.02 taking into account 1st and 2nd vibration mode as Rayleigh damping.

4. RESPONSE OF BRACED FRAME TAKING INTO ACCOUNT BRACE FRACTURE

4.1 Effect of Brace Fracture

The response behavior of the braced frame determined from the time-history response analysis (discussed in Section 3) is compared with that determined on the basis of a no

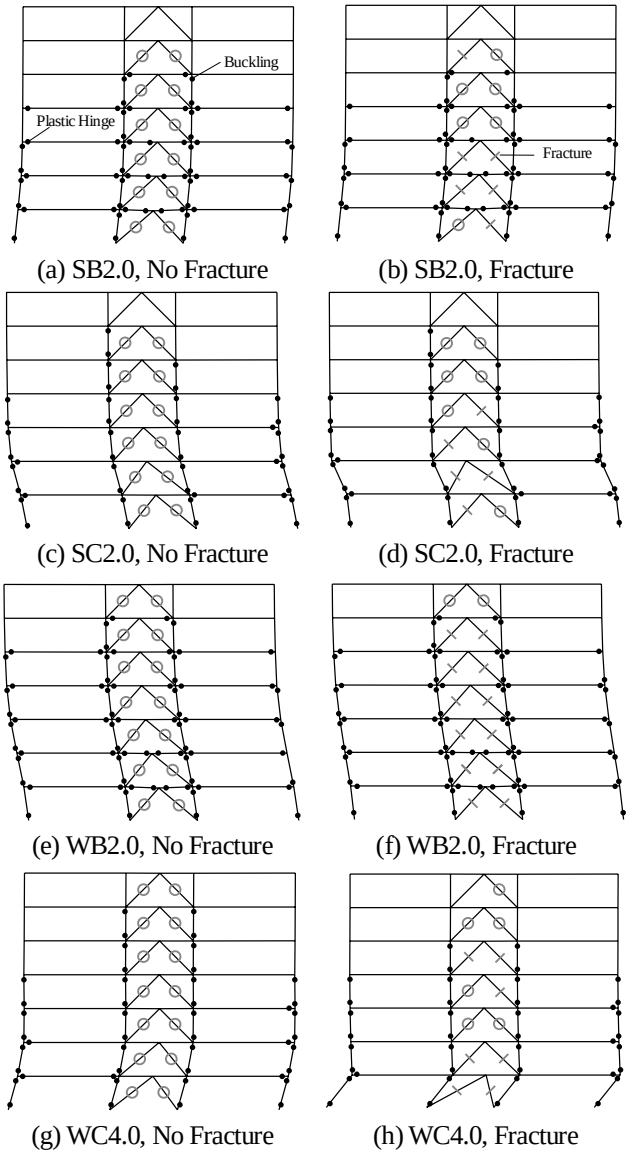


Figure 13 Collapse Mechanism

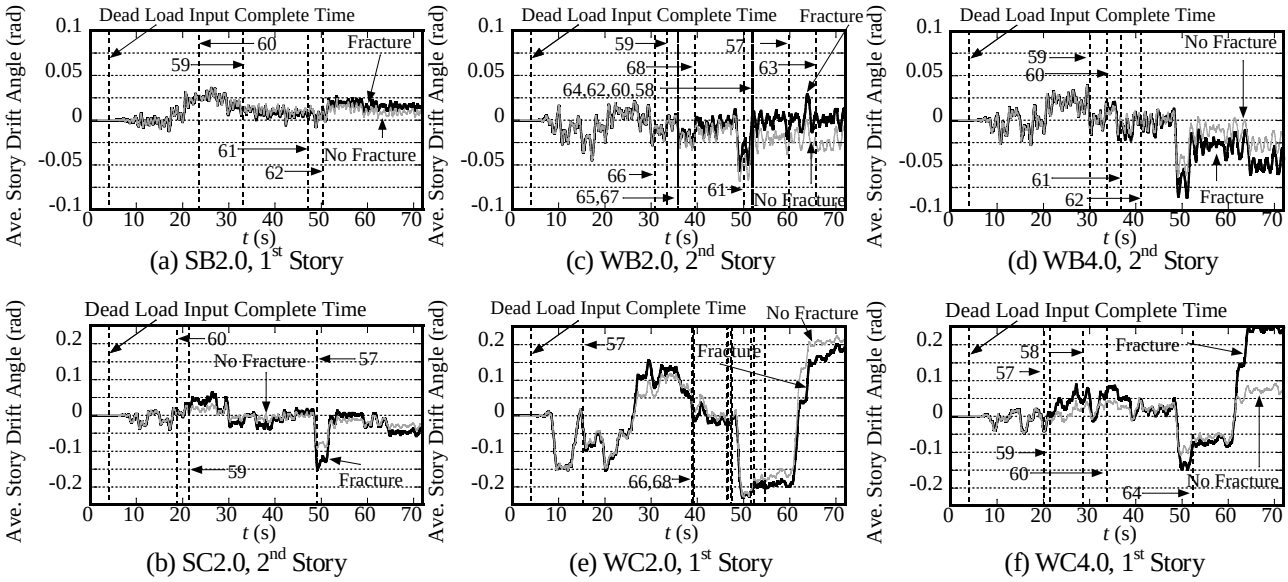


Figure 14 Average Story Drift Angle

fracture analysis, in which the effect of brace fracture is ignored. Figures 13 (a)–(h) show the models for the yielding mechanism, displacement response, and buckling and fracture braces. In this figure, the black points represent the plastic hinge, and the circles at the midpoint of the brace indicate buckling; further, the slash marks indicate the areas of fracture. Figure 14 shows that the time-history of the average story drift angle. SB2.0, which is shown in Figures 13(a) and (b), indicates that buckling occurs in 12 braces up to the first six stories and that six braces suffer fracture. However, there is no significant difference between the average story drift angle determined by the no fracture analysis and the fracture analysis. The collapse mode in SB2.0 is of the beam-yield type. The collapse mode of SB2.0 is dominated by the beam-yield since plastic hinge formation is initiated first at the beam ends and then at the column end. SC2.0 shown in Figures 13(c) and (d) indicates that the member number of the fracture brace is smaller than that of SB2.0. The average story drift angle in the second story is larger in the fracture analysis than in the no fracture analysis, and thus, the damage is concentrated in this story. The collapse mode of SC2.0 is dominated by the column-yield, and the main frame is almost elastic. The collapse mode of WC2.0 is dominated by the beam-yield, as in the case of SB2.0. The fracture-member number for WC2.0 is greater than that for SB2.0 and SC2.0. On the other hand, the difference between the average story drift angle determined by the no fracture and fracture analyses in this case is less significant than that in the case of SB2.0 and SC2.0. Figures 13(g) and (h) show the results obtained for WC4.0: all braces except for the 69th member undergo buckling, and seven braces up to the fifth story undergo fracture. The number of fracture braces in WC4.0 is greater than that in SC2.0. The average story drift angle in the fracture analysis is considerably larger than that in the no fracture analysis; further, according to the fracture analysis, the first story collapses. From the abovementioned observations, it is apparent that there is a significant difference between the behavior of the column-yield-type frames in the no fracture and fracture analyses and that the damage concentrates in a certain story.

4.2 Effect on Maximum Story Drift Angle

Models in which circular-tube braces are replaced with BRBs are studied. Figure 15 shows the maximum story drift angle in each case. The difference between the drift angle in the no fracture and fracture analyses is small in the case of SB2.0, as shown in Figure 15(a), and the maximum story drift angle of SB2.0 using BRB distributes more uniformly. In the case of SC2.0, the maximum story drift angle at the second story is 1.6 times higher in the fracture analysis than in the no fracture analysis, as shown in Figure 15(b). On the other hand, when a BRB is used for SC2.0, the damage at second story is reduced. The difference between the maximum story drift angle in the fracture and no fracture analyses is not very significant in the case of WB2.0, as shown in Figure 15(c), and the use of BRB for WB2.0 does not prevent damage concentration. However, the energy distribution determined by the fracture method differs significantly from that determined by the no fracture analysis. The difference between the maximum story drift angle in the case of WC2.0 is similar to that in the case of SC2.0, as shown in Figure 15(d). The difference between the maximum story drift angle determined by the no fracture and fracture analyses is more significant in the case of WB4.0 than in the case of WB2.0, as shown in Figure 15(e). In the case of WC4.0, the maximum story drift angle at the first story is dramatically higher in the fracture analysis than in the no fracture analysis, as shown in Figure 15(f).

4.3 Hysteresis in Each Member

Figure 16 shows the normalized force-deformation curves for the circular-tube brace and the BRB in a given story; these curves indicate a significant difference between the results of the no fracture and fracture analyses. Here, the normalized force is the value obtained when the force is divided by the initial section area. Brace energy dissipation

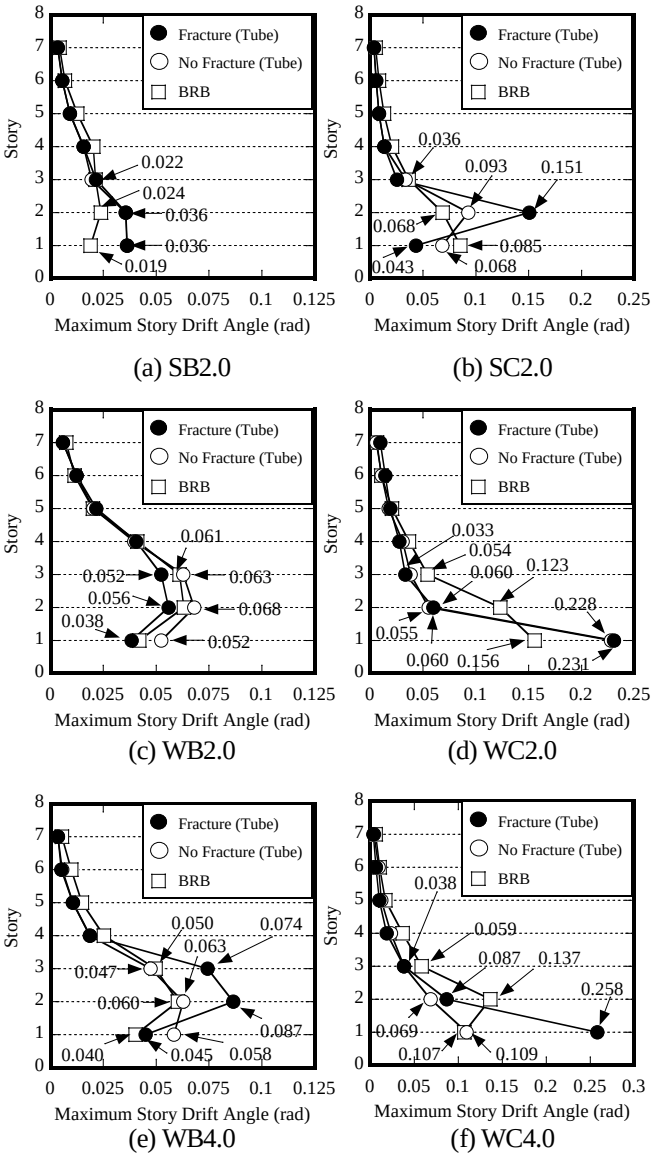


Figure 15 Maximum Story Drift Angle

ceases after the instant of fracture, as shown in Figures 16(a)–(d). Among these four cases, the difference between the results of the no fracture and fracture analyses is the most prominent for SC2.0, as shown in Figure 16(b). On the other hand, the hysteresis curve for the BRB represented in Figures 16(e) and (f) indicates the isotropic hardening behavior of SB2.0 and SC2.0; energy dissipation in the BRBs in these models is greater than that for the circular-tube brace. In addition, fracture does not occur in any of the BRBs in the models considered in this study.

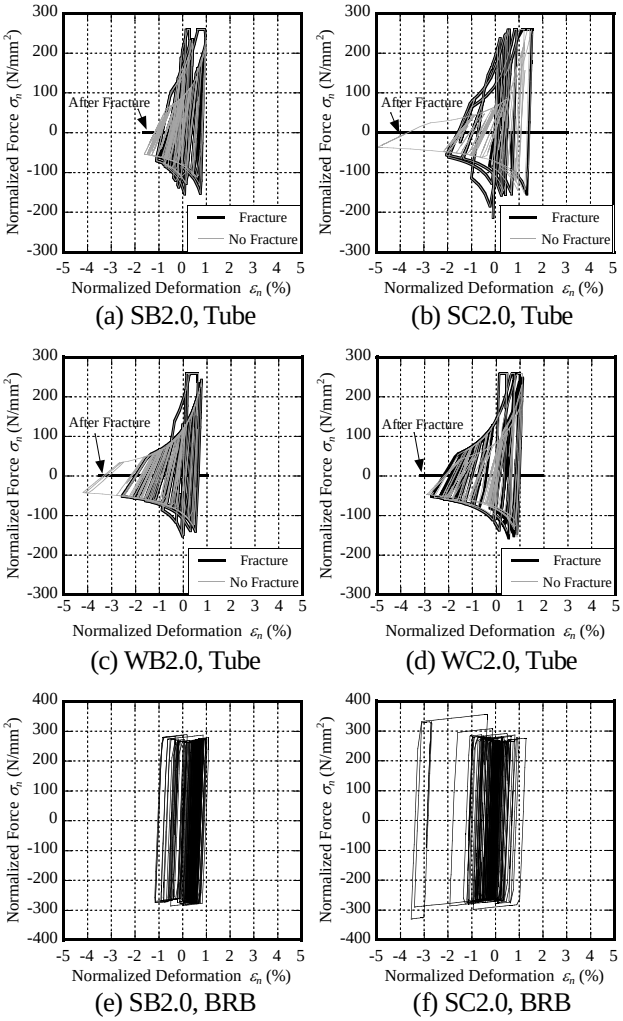
Figure 17 shows the relationship between the non-dimensional bending moment and the relative rotational angle for SB2.0, WC2.0, and WC4.0. The average bending moment M_{ave} and the relative rotational angle θ_{eq} are defined as shown in Eq. (14).

$$\begin{cases} M_{ave} = \dfrac{M_j + M_i}{2} \\ \theta_{eq} = \dfrac{\left(v_j - v_i\right)}{L} + \dfrac{\theta_j + \theta_i}{2} \end{cases} \tag{14}$$

Here, M_i and M_j are the bending moments; v_i and v_j, the transverse displacements; and θ_i and θ_j, the rotational angles at each end of the member. M_p is the plastic bending moment, which is defined as the product of the plastic section modulus and the yield stress. Since SB2.0 is of the beam-yield type, the energy dissipation in the beam is greater than that in the column, and the difference between the results of the no fracture and fracture analyses of the circular-tube braced frame is not significant as shown in Figures 17(a) and (b). On the other hand, since WC2.0 and WC4.0 are of the column-yield type, the energy dissipation in the column is considerably greater than that in the beam, as shown in Figures 17(c)–(f). From the calculation results, we come to the following conclusion: if the braced frame is of the column-yield type and the brace strength is high, the difference between the results of the no fracture and fracture analyses is significant.

5. EVALUATION OF ENERGY DISSIPATION PERFORMANCE OF BRACED FRAME ON THE BASIS OF BRACE FRACTURE

In this section, we describe the evaluation of the energy dissipation (CED) performance for each analysis case. The

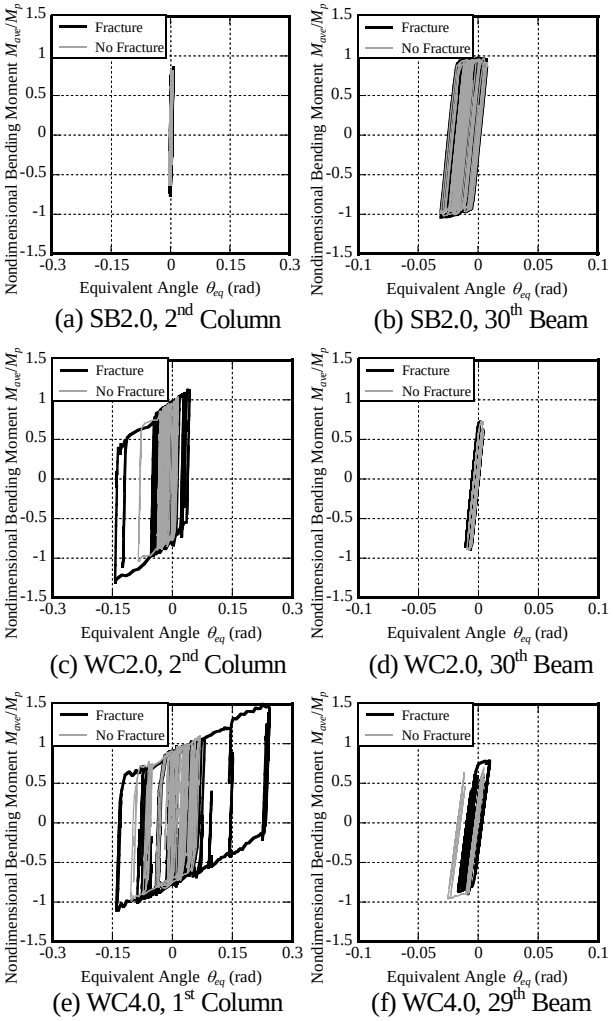


(a) SB2.0, Tube (b) SC2.0, Tube

(c) WB2.0, Tube (d) WC2.0, Tube

(e) SB2.0, BRB (f) SC2.0, BRB

Figure 16 Hysteresis Curve for Brace Number 59



(a) SB2.0, 2nd Column (b) SB2.0, 30th Beam

(c) WC2.0, 2nd Column (d) WC2.0, 30th Beam

(e) WC4.0, 1st Column (f) WC4.0, 29th Beam

Figure 17 Beam and Column Hysteresis Curve

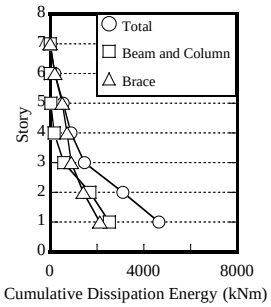
CED of the beam and column, W_{pf}, and that of the brace, W_{pb}, are defined as follows.

$$\begin{cases} W_{pf} = \int M_{ave}\theta_{eq}d\theta \\ W_{pb} = \int_V \sigma_{eq}\varepsilon_{eq}d\varepsilon_{eq} \end{cases} \quad (15)$$

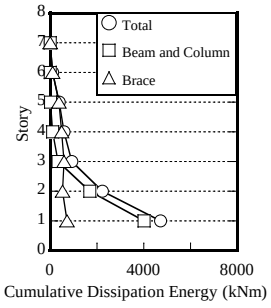
The total CED is evaluated as the sum of W_{pf} and W_{pb}. Figures 18(a)–(c) show the effect of brace fracture on the CED in the case of WC4.0. Because the CED in the brace ceases after the instant of fracture, as shown in Figure 18(b), the CED for the beam and column determined by the fracture analysis is greater than that determined by the no fracture analysis, as shown in Figure 18(a). In contrast, the CED in the BRB is greater than that in the beam and column, and the CED distribution ratio for the beam and column is much lesser than that for the circular-tube braced frame. There is no notable difference between the total CED in the BRB frame at each story and that in the circular-tube braced frame; however, the energy dissipation in the BRB frame is more uniform than that in the circular-tube frame.

The CED distribution in the beam and column and that in the brace are shown in Figures 19(a)–(i). The CED distribution in the brace is not more than 30–40% of that in the circular-tube braced frame, as shown in Figures 19(a)–(f). In particular, in the case of WC4.0, the CED distribution estimated by the fracture analysis is markedly smaller than that determined by the no fracture analysis, indicating the collapse of the first or second story. In this case, the CED distribution in the beam and column determined by the fracture analysis increases and becomes 70–90% of that determined by the no fracture analysis.

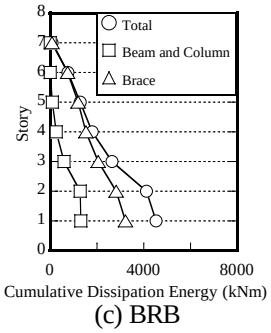
The fatigue characteristic at the point of intersection of the beam and column indicate that an increase in the CED distribution in the beam and column may lead to fracture at the point of intersection and a consequent degradation of the seismic performance of the braced frame. On the other hand, the CED distribution in the brace is higher than that in the beam and column in the case of the BRB frame, and hence, very less damage is caused to the beam and column. The CED distribution in each frame is more uniform in the case



(a) No Fracture

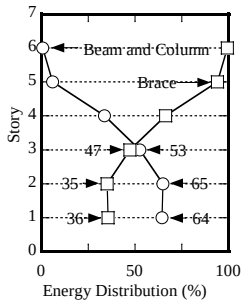


(b) Fracture

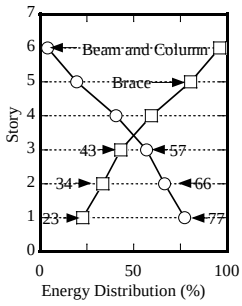


(c) BRB

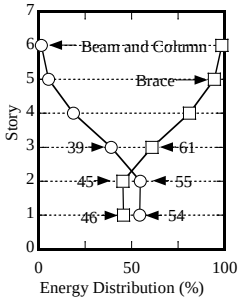
Figure 18 CED (WC4.0)



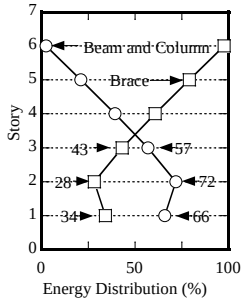
(a) WB2.0, No Fracture



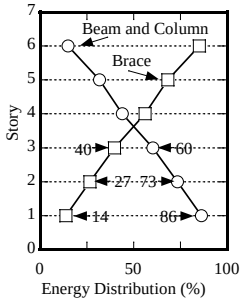
(b) WC2.0, No Fracture



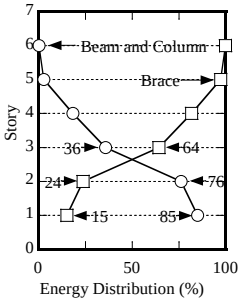
(c) WC4.0, No Fracture



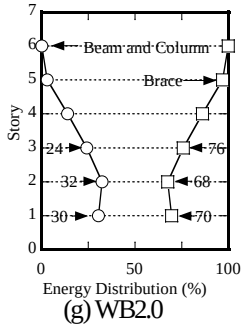
(d) WB2.0, Fracture



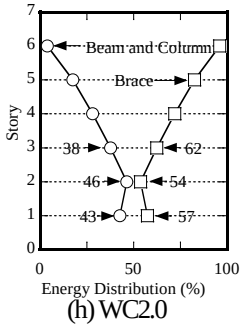
(e) WC2.0,Fracture



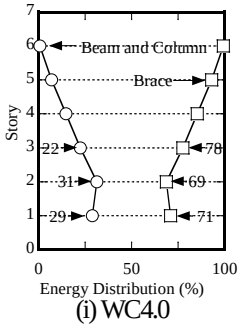
(f) WC4.0, Fracture



(g) WB2.0

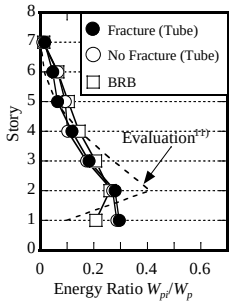


(h) WC2.0

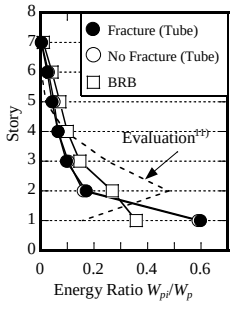


(i) WC4.0

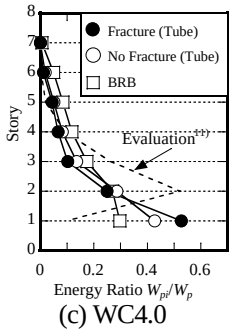
Figure 19 CED Distribution of Tube ((a)-(f)) and BRB ((g)-(i))



(a) WB2.0



(b) WC2.0



(c) WC4.0

Figure 20 CED Ratio

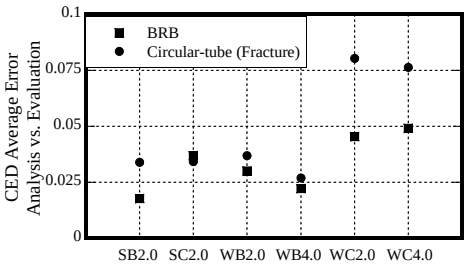


Figure 21 CED Average Errors
(Analysis vs Evaluation)

of WB2.0 and WC4.0 than in the case of WC2.0, at each story. There is no significant difference between the maximum story drift angle for the circular-tube braced frame and the BRB frame in the case of WB2.0; however, there is a significant difference between the CED distribution in the column and beam and that in the brace.

The damage distribution at each story is related to the CED. Akiyama (1999) proposed a method to predict the CED distribution. In the present study, the plastic level exceeds the allowable limit predicted on the basis of Akiyama's method.

For trial, we applied Akiyama's method to the frame result by taking into account the brace fracture. The CED distribution at each story is defined as shown in Eq. (16).

$$\frac{W_{pi}}{W_p} = \frac{s_i p_i^{-n}}{\sum_{j=1}^{N} s_j p_j^{-n}} \tag{16}$$

Here, W_{pi} is the CED at the i^{th} story, and W_p is the total CED of all the stories. n denotes the damage concentration index, whose value is 4 for the beam-yield type and 8 for the column-yield type. The values of s_i and p_i are calculated using Eq. (17).

$$\begin{cases} s_i = \left(\sum_{j=i}^{N} m_i \Big/ M \right) A_i \left(k_1 / k_i \right) \\ p_i = \left(\alpha_i / \alpha_1 A_i \right) \end{cases} \tag{17}$$

Here, M is the total mass; m_i, mass of the i^{th} story, α_i, the yield shear force coefficient; A_i, the shear force coefficient ratio; and k_i, the horizontal stiffness of the frame at each story.

The evaluated CED ratio values are plotted in Figure 20 (dashed line) along with the values calculated by the time-history response analysis. In the assumed building models, the damage is normally concentrated at the second story. In all the models, the evaluated CED ratio is smaller than that determined by the response analysis, and the accuracy of the evaluated value decreases up to the third story. This is because the stiffness and strength defined on the basis of the elastic situation are used for the evaluation. The CED average errors between the evaluated value and the response analysis value are compared, as shown in Figure 21. The CED average errors for the BRB frame are closer to 1.0 than is the value for the circular-tube braced frame, and thus, it apparent that the accuracy between the evaluated and response-analysis value is stronger for the BRB frame than for the ordinary braced frame. The accuracy for the column-yield-type frames is weaker than that for the beam-yield-type frames.

6. CONCLUSIONS

In this study, we carried out the time-history response analysis to determine the instant of brace fracture, on the basis of the strain concentration ratio, and investigate the dynamic behavior and energy response behavior of braced frames. Following are the conclusions of this study.

1) If the braced frame is of the column-yield type and the brace stiffness and strength are high, the damage concentrates at a certain story, and the maximum story drift angle response evaluated from the time-history analysis by taking into account brace fracture is significant higher than that in the no fracture case. Generally, the damage concentration is reduced when circular-tube braces are replaced with BRBs; however, in column-yield types, the use of BRBs does not guarantee damage mitigation. In this study, the braced frame is highly robust to damage when the strength of the beam and column is high and the braced-frame collapse is of the beam-yield type.

2) The maximum story drift angle for some BRBs is almost equal to that of a circular-tube braced frame. However, there is a significant difference between the energy dissipation distribution in the beam and column and that in the brace; as a result, the damage in the beam and column is mitigated.

3) The energy dissipation distribution in the assumed braced frames is evaluated by Akiyama's method; the estimation accuracy decreases owing to the effect of buckling and fracture. This is because the stiffness and strength are significantly different from those in the initial condition. On the other hand, the estimation accuracy for the BRB frames is lower than that for the circular-tube braced frame, and the evaluated value is effective in case of the beam-yield-type frames at a certain level.

4) The ultimate strength of a braced frame subjected to an extremely large earthquake can be assessed and compared with that determined by the proposed time-history analysis program.

Acknowledgements:

This research was supported by the Japan Society for the Promotion of Science (No: 08J09406). The authors thank Professor Toshiyuki Ogawa and Assistant Professor Tomohiko Kumagai of Tokyo Institute of Technology for their contribution to the constitution of the numerical analysis program.

References:

Shibata, M. and Wakabayashi, M. (1982), "Mathematical Expression of Hysteretic Behavior of Braces –Part 2 Application to dynamic response analysis-," *Journal of Structural Construction Engineering*, Architectural Institute of Japan, **320**(10), 29-35 (in Japanese)

Tang, X. and Goel, S. C (1989), "Brace Fractures and Analysis of Phase I Structure." *Journal of Structural Engineering*, American Society of Civil Engineers, **115** (8), 1960-1976

Takeuchi, T., Suzuki, K., Matsui, R. and Ogawa, T. (2006), "Cumulative Cyclic Deformation Capacity of Tubular Braces with Local Buckling," *Journal of Structural Construction Engineering*, Architectural Institute of Japan, **608**(10), 143-150 (in Japanese)

Takeuchi, T., Kang, Q. and Matsui, R. (2008), "Cumulative Cyclic Deformation Capacity of H-section Braces with Local Buckling," *Journal of Structural Construction Engineering*, Architectural Institute of Japan, **632**(10), 1875-1882 (in Japanese)

Kanvinde, A. M. and Deierlein, G. G. (2007), "Cyclic Void Growth Model to Assess Ductile Fracture Initiation in Structural Steels due to Ultra Low Cycle Fatigue," *Journal of Engineering Mechanics*, American Society of Civil Engineers, **133**(6), 701-712

Kanao, I., Nakashima, M. and Takehara, S. (2004), "Braced Frame Model Considering Buckling and Fracture and Its Responses under Near Fault Strong Motions," *Journal of Structural Construction Engineering*, Architectural Institute of Japan, **577**(3), 117-122 (in Japanese)

Mukaide, S., Kataoka, M. and Tada, M. (2010), "Seismic Response of Steel Structures Including Fractures at Tubular Braces Using Collaborative Pseudo Dynamic Test," *Journal of Structural Construction Engineering*, Transactions of Architectural Institute of Japan, **652**(6), 1139-1147 (in Japanese)

Ogawa, K., Kurobane, T. and Maeda, T. (1995), "Post-buckling Behavior of Circular Tubular Struts," *Journal of Structural Construction Engineering*, Architectural Institute of Japan, **475**(9), 133-144 (in Japanese)

Saeki, E., Sugisawa, M., Yamaguchi, T., Mochizuki, H., and Wada, A. (1995), "A Study on Hysteresis and Hysteresis Energy Characteristics of Low Yield Strength Steel," *Journal of Structural Construction Engineering*, Architectural Institute of Japan, **473**(7), 159-168 (in Japanese)

Timoshenko, S. P. and Gere, J. M.: Theory of Elastic Stability, Second Edition, Mc-GRAWHILL, 1963

Takeuchi, T., Ida., M., Yamada, S. and Suzuki, K. (2008), "Estimation of Cumulative Deformation Capacity of Buckling Restrained Braces," *Journal of Structural Engineering*, American Society of Civil Engineers, **134**(5), 822-831

Ishii, M., Saitoh, Y., Asano, M. and Horii, M. (1997), "Characteristics of Multi-spring Model: Part1. Characteristics of Member Stiffness," *Summarized of Technical Papers of Annual Meeting Architectural Institute of Japan B-1*, Architectural Institute of Japan, 383-384 (in Japanese)

Akiyama, H. (1999), "Earthquake-Resistant Design Method for Building Based on Energy Balance," Gihodo Shuppan (in Japanaese)

8CUEE CONFERENCE PROCEEDINGS
8th International Conference on Urban Earthquake Engineering
March 7-8, 2011, Tokyo Institute of Technology, Tokyo, Japan

COMPARISON STUDY ON DAMAGE POTENTIAL OF SYNTHETIC AND RECORDED GROUND MOTIONS

Shiling Pei[1)], John W. van de Lindt[2)], Stephen Hartzell[3)], and Nicolas Luco[4)]

1) Assistant Professor, Dept. of Civil and Environmental Engineering, South Dakota State University, U.S.A.
2) Professor and Garry Neil Drummond Endowed Chair in Civil Engineering, Department of Civil, Construction, and Environmental Engineering, The University of Alabama, U.S.A.
3) United States Geological Survey, National Earthquake Information Center, Golden, U.S.A.
4) United States Geological Survey, National Earthquake Information Center, Golden, U.S.A.
shiling.pei@sdstate.edu, jwvandelindt@eng.ua.edu, shartzell@usgs.gov, nluco@usgs.gov

Abstract: Synthetic earthquake ground motions are commonly used tools in earthquake engineering and hazard mapping. These ground motions are often generated to match the characteristics of recorded ground motions. In this paper, the effectiveness of multiple synthetic ground motions was evaluated based their similarity to recorded motions in inducing structure damage. Using a calibrated damage potential indicator, the damage potential of synthetic ground motions generated using four different physical models was compared to the historically recorded ground motions at corresponding sites. It was concluded that synthetic ground motions are able to produce damage to North American light frame wood buildings similar to that produced by their recorded counterparts; but the damage prediction potential varies with the generating model, target structural type, ground motion intensity, and site parameters.

1. INTRODUCTION

For a particular structure, the damage induced by an earthquake is a function of the ground motion, the building site, and the properties of the building system. One of the simplest indicators that combine ground motion intensities and building response characteristics is spectral acceleration at a building's natural period. Despite its wide use in design codes and simplified seismic calculations, spectral acceleration is most accurate for linear systems since it is developed using a linear oscillator and is not the best candidate for damage prediction of nonlinear systems (e.g. Elenas and Meskouris, 2001). Many past research studies have realized that in order to capture the damage to buildings caused by a given earthquake ground motion, nonlinear characteristics of the building should be taken into account (Krawinkler and Nassar, 1990, Atkinson and Goda, 2010, Sunasaka et al., 2003). Work by Bazzurro and Luco (2003) investigated non-stationary characteristics of seismic ground motion and concluded that a damage indicator that incorporates both ground motion and nonlinear building properties is desirable for quantifying the damage potential of ground motions.

Synthetic ground motion generation is an important component in seismic risk research, including seismic hazard mapping, because it supplements the relatively sparse worldwide database of strong ground motions. Recent mapping studies are moving beyond simply providing some measure of seismic intensity, and toward predicting building performance (e.g. Atkinson and Goda, 2010, Hall et al. 1995). Therefore it is important from an applicability standpoint that synthetic ground motions induce similar levels of damage to the built environment as do comparable recorded ground motions. A number of studies on generating synthetic ground motion have focused on characteristics of the generated ground motions themselves, essentially comparing waveforms and spectral acceleration (e.g. Hartzell et al., 2005, Frankel 2009, Liu et al. 2004, and Zeng et al. 1994). There have been studies that applied both synthetic and recorded ground motions in analysis of building structures (e.g. Jalayer et al. 2004), but to date there have been few direct comparisons of the damage caused to a particular building type as the result of recorded versus synthetic ground motions (e.g. Bazzurro et al. 2004). This relative absence provided the impetus for this study.

2. SYNTHETIC GROUND MOTION MODELS

Four synthetic ground motion models were investigated in this study. For simplicity, these models were named in this study after their authors as "Artf" for Frankel (2009), "Hart" for Hartzell et al. (2005), "Pliu" for Liu et al. (2004), and "Zeng" for Zeng et al. (1994). Detailed information about and suitable applications of these models can be found in the publications of the original studies. A brief comparison of the characteristics and properties of these models is presented in Table 1.

Table 1 Synthetic ground motion models

Synthetic motion model	Artf	Hart	Pliu	Zeng
Green's functions	Plane layered full wave theory at low frequencies; stochastic at high frequencies	Plane layered full wave theory	Plane layered full wave theory	Plane layered full wave theory
Source Distribution	Uniform size distribution; non-overlapping sources	Fractal size distribution; non-overlapping sources	Uniform size distribution; non-overlapping sources	Fractal size distribution; overlapping sources
Slip Distribution	k^{-2}, with x and y correlation lengths	k^{-2}, with variable corner wavelength	k^{-2}, with x and y correlation lengths and Cauchy amplitude distribution	Based on fractal size distribution and Brune (1970) model
Subevent Source Time Function	Brune (1970)	Brune (1970)	Functional form from dynamic models	Brune (1970)
Rupture Velocity	Secant rupture velocity with randomness	Secant rupture velocity with random subevent initiation points	Secant rupture velocity correlated with slip amplitude	Secant rupture velocity with random subevent initiation points
Local site and soil nonlinearity	DESRA2[b]	NOAHW[a]	NOAHW[a]	DESRA2[b]

Note: Local site and soil nonlinearity for each model was based on early works by (a) Bonilla et al. (1998), Hartzell et al. (2004), and (b) Lee et al. (1978) respectively.

Each of the models listed in Table 1 was used to generate ground motions at a series of earthquake recording stations for three earthquakes, including 17 stations for the 1999 Izmit earthquake in Turkey, 42 stations for the 1994 Northridge earthquake in California, USA, and 83 stations for the 1989 Loma Prieta earthquake in California, USA. Table 2 lists the basic properties of these earthquake events. The availability of historically recorded ground motions at these stations enabled a comparison between the generated and recorded motions. A total of 142 biaxial synthetic ground motion records were generated from each model. The vertical components were not considered in this study since horizontal components contribute to the majority of the lateral responses of civil engineering structures, which in turn leads to the majority of the damage.

Table 2 Earthquakes investigated in this study

Earthquake	Northridge	Loma Prieta	Izmit
	1994	1898	1999
Moment Magnitude	6.7	6.9	7.5
Recording stations	42	83	17
Strike	122	128	90
Dip	40	70	90
Rake	90	144	180
Fault Length (km)	20	40	160
Fault Width (km)	24	20	17
Depth of Hypocenter (km)	17.5	18	15.9

3. DAMAGE POTENTIAL INDICATOR

In this study, the equivalent oscillator for a building is defined as a Sdof elasto-plastic oscillator with unit mass and initial natural period equal to T from equation (1). The yielding force for the oscillator is the weight of the unit mass times Cs from equation (2). The damping ratio of 5% was used for all simulation. The benefit of using the seismic design parameters to construct equivalent oscillators is two-fold. Firstly, only minimal information related to the details of the building is required. Secondly, these parameters are relatively easy to estimate for existing and new buildings. An equivalent oscillator can be constructed as long as the building's structural type, height, and design ground motion information are known. Once the equivalent oscillator for the building type of interest was obtained, numerical integration was performed using the synthetic and recorded ground motions to find key Sdof oscillator responses. Adopting a format similar to the concrete damage index developed by Park and Ang (1985), the proposed damage potential indicator (DPI) can be written as

$$DPI = c_1 \frac{\Delta_m - \Delta_y}{(\mu - 1)\Delta_y} + c_2 \frac{E}{4F_y \mu \Delta_y} \quad \text{and} \quad 0 \le DPI \le 1 \qquad (1)$$

where Δ_m is the maximum displacement of the Sdof oscillator; Δ_y is the elastic displacement limit (yielding displacement); μ is the designated displacement ductility capacity for the structure type, defined as a ratio of a failure deformation to an elastic deformation limit. Note that although the equivalent Sdof oscillator does not incorporate ductility of the system it represents, the influence of system ductility in DPI calculation is accounted for through parameter μ; E is the total hysteresis energy dissipated by the Sdof oscillator; F_y is the yielding force for the Sdof oscillator; and c_1 and c_2 are the calibration coefficients for the DPI, which are determined (later in this paper) by comparing observed damage of a building and the DPI calculated using the corresponding equivalent Sdof oscillator.

The variability of ground motions, structural configurations, and quantification of observed damage makes it unrealistic to achieve a one-to-one mapping between a DPI and observed damage. However, it is reasonable to expect the proposed DPI to provide a consistent and strong correlation to observed structural damage. This can be achieved by calibrating the DPI coefficients (c_1 and c_2) using realistic structural damage data. In this study, the DPI calibration was focused on light-frame wood buildings through a verified damage index from an earlier study. That damage index was developed using data from tests of a full-scale, two-story light-frame wood townhouse building that took place at the University at Buffalo shake table (Filiatrault et al, 2010) as part of the NEESWood research project in 2006. The damage observed during the tests was recorded in detail following each shake and later a Park-Ang damage index model for the building and components was calibrated by Park and van de Lindt (2009). This damage index model was used in this study to generate damage indices of the townhouse building under a suite of earthquake ground motions. Then DPI for the same

suite of motions were calculated using equation (1) with varying c_1 and c_2 until maximum correlation between DPI and damage index was achieved. In the case of this wood frame building, based on the observation of the trend of correlation coefficient against varying calibration coefficients, eliminating the term associated with c_1 maximized the correlation. The DPI was then normalized by a constant so that the DPI's for all ground motion records that cause building collapse in the numerical analyses were greater than 1.0. Finally, the calibrated DPI in this study was:

$$DPI = 1.44\frac{E}{4F_y\mu\Delta_y} \quad \text{and} \quad 0 \le DPI \le 1 \qquad (2)$$

4. DPI FOR RECORDED AND SYNTHETIC GROUND MOTIONS

4.1 Delta-DPI Contour

Authors In order to identify the performance of the synthetic ground motions over a wide range of design configurations, DPI's were generated for various combinations of design base shear capacity (Cs) and natural period (Tn) over a structural "design space" (shown in Figure 1) to form a "DPI surface." It is expected that the same earthquake ground motion can have a significantly different damage potential for different design configurations. Although it would be ideal if the DPI for every point on the design space were calculated using a formula calibrated for that design configuration, this was not done here due to the lack of full-scale structural damage data (e.g. from shake table tests) for other types of building configurations. Thus Equation (2) was used to generate DPI's over the entire design space. The DPI surface was constructed for all synthetic and recorded ground motions.

Figure 1 shows the DPI surface for one of the recorded Northridge earthquake ground motions in this study. Inspection of Figure 1 shows that there is a failure plateau near the lower left corner where the design configuration is weak (low base shear capacity) and stiff (short period). The upper right corner represents strong and flexible designs (e.g. high-rise buildings), which had essentially no damage. In between, there is a band in the design space that experiences moderate damage. In this study, the projection of the DPI surface onto the Cs-Tn plane is termed the "DPI contour," as shown in Figure 1. Figure 2 shows the DPI contours for the synthetically-generated ground motions at the same site. Comparing the DPI contours for the recorded and synthetic motions, one can see that the performance of the synthetic models can be quite different depending on the location within the design space. For example, at point Tn=0.2, Cs=0.5 on the plot, the Artf model resulted in numerical failure of the structure, the Hart model produced virtually no damage, and the corresponding recorded ground motion produced moderate damage. However, because of the uncertain nature of seismic loading, the evaluation of synthetic ground motions should not be conducted based on only one ground motion, but rather should be (and will be) performed in a statistical sense using a suite of ground motions.

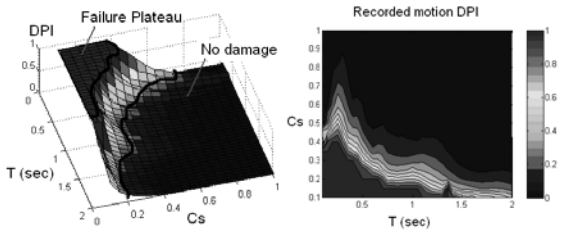


Figure 1 DPI surface and contour developed from a single recorded earthquake ground motion

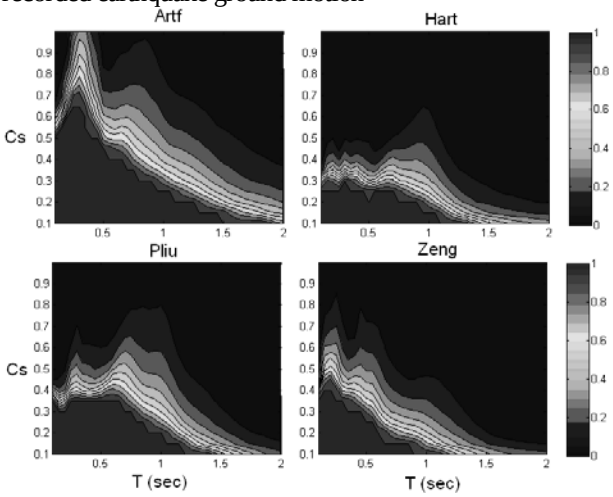


Figure 2 DPI contours for corresponding synthetic ground motion models

Using the recorded ground motions as the basis, the difference between the synthetic motion DPI and recorded motion DPI over the design space can be calculated. This value ranges from -1 to 1 and is termed herein the "Delta-DPI." Delta-DPI can be used as a measure of damage prediction accuracy for the synthetic ground motion generation models, with the damage induced by recorded ground motion as the reference point. If a model has a positive Delta-DPI, it suggests that the model would elicit more damage to the building than its recorded counterpart. On the other hand, a negative Delta-DPI indicates that the synthetic ground motion model would cause less damage to the structure than the corresponding recorded ground motion. The Delta-DPI was obtained and plotted for each of the four synthetic ground motion models in Figure 3 for one Northridge site using the data presented earlier in Figures 1 and 2.

With Delta-DPI as an indicator of a synthetic model's ability to induce damage to a building that is comparable to recorded ground motions, the effectiveness of the model may be assessed through a statistical evaluation of Delta-DPI for all sites investigated in this study. The mean and standard deviation of Delta-DPI for all 284 ground motion records is presented in Figures 4 and 5. The point P on the design space corresponds to the light-frame wood building used to calibrate DPI in this study.

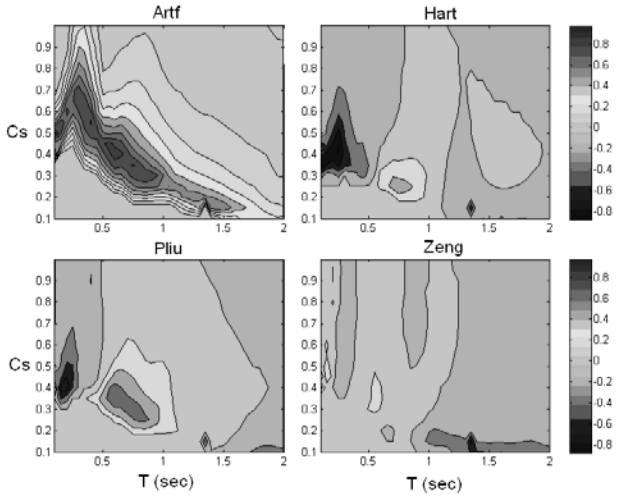


Figure 3 Delta-DPI contours for synthetic ground motion models

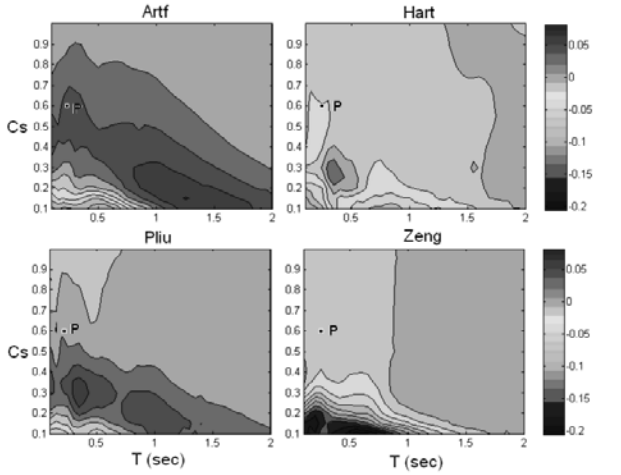


Figure 4 Mean of Delta-DPI for synthetic ground motion models (Point P represents NEESWood Benchmark building)

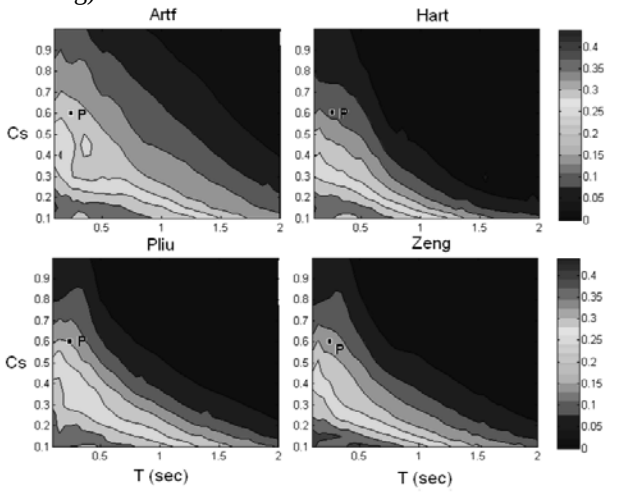


Figure 5 Standard Deviation of Delta-DPI for synthetic ground motion models (Point P represents NEESWood Benchmark building)

One can see from the Figures 7 and 8 that, on average, all the synthetic ground motions have Delta-DPI's that were fairly close to zero for most design combinations. Over-prediction was seen in limited regions of the design space for the Artf and Pliu models. The Zeng model was more likely than the other models to under-estimate damage for weak structural configurations. The variation, i.e. standard deviation, of Delta-DPI showed a constantly increasing trend as the design configuration moved towards weak and stiff (small Cs and natural period values) systems. For very weak buildings, the dispersion is close to 0.5. This indicates the building is so sensitive to the differences between ground motions that the induced damage can be quite different if the synthetic ground motion does not exactly match the actual ground motion. This is in fact not unexpected for these structural systems. Thus, it may be very difficult to use individual synthetic ground motion to reliably replicate damage to such structures from recorded ground motion.

4.2 Sensitivity to Wood Building Damage

Since the DPI used here was well calibrated for wood frame buildings, the performance of the synthetic ground motions for this building type was investigated in more detail. The purpose was to find out the accuracy of each synthetic generation model in reproducing recorded ground motion damage. Thus the Delta-DPI value for each ground motion was plotted against site or motion characteristics to identify impact of these characteristics to synthetic motion damage reproducing accuracy. Keep in mind that negative Delta-DPI indicates under-predicting real damage, positive values indicate over-predicting, and accurate damage prediction yields Delta-DPI equals to zero.

The relationship between Delta-DPI and source distance is shown in Figure 6 with scatter plots for the four synthetic ground motion models. One can see from the figure that model accuracy and distance are closely related. For ground motion sites over 30 km from the source, there is no difference between the DPI for the synthetic and recorded ground motions. For ground motions closer to the source, there is no clear trend of any specific model over- or under-predicting damage.

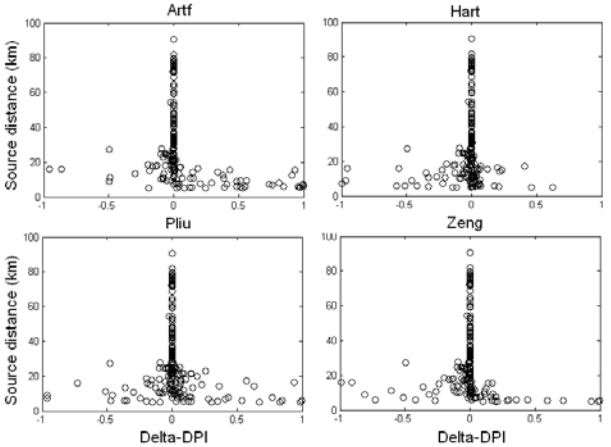


Figure 6 Relationship between Delta-DPI and source distance

Each ground motion site was assumed to be of a certain NEHRP site class as designated by the shear-wave velocity in the top 30 meters during the simulations of synthetic

ground motions. Overall, there are five site classes, namely B through E. In the scatter plots of site class versus Delta-DPI shown in Figure 7, each site class was assigned a number, with B equal to 2 and E equal to 5. The site class boundaries such as BC or DE were assigned numbers in between, i.e. 2.5 or 4.5.

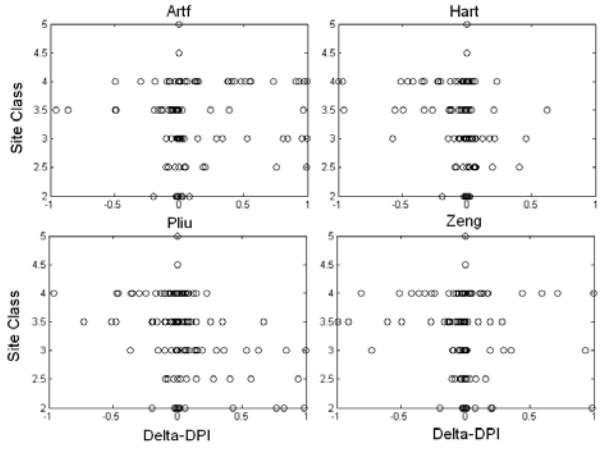


Figure 7 Relationship between Delta-DPI and site class

One can see from Figure 7 that some of the synthetic ground motion models perform differently across site conditions. The Hart and Pliu models in particular seem to show a higher possibility of over-predicting damage for site classes BC and C (2.5 and 3), but appear to under-predict for site classes CD and D (3.5 and 4). All of the models perform quite well for site class B. Although Figure 13 does not show significant dispersion in Delta-DPI for site classes DE and E, the number of such sites is too small to formulate a reliable conclusion.

A similar comparison was conducted for the level of spectral acceleration (Sa) at the building period (0.2 seconds, 5% damping). Note that the Sa values used here are from the recorded ground motions. Figure 8 shows the relationship between the site Sa and Delta-DPI. It can be seen that the stronger the ground motion, the more difficult it is to accurately replicate damage using the synthetic ground motions. It is interesting to see that all of the synthetic models over-predict damage when Sa is between 0.5 and 1.0 g. As the spectral acceleration increases above 1.0g, almost all of the models under-predict damage.

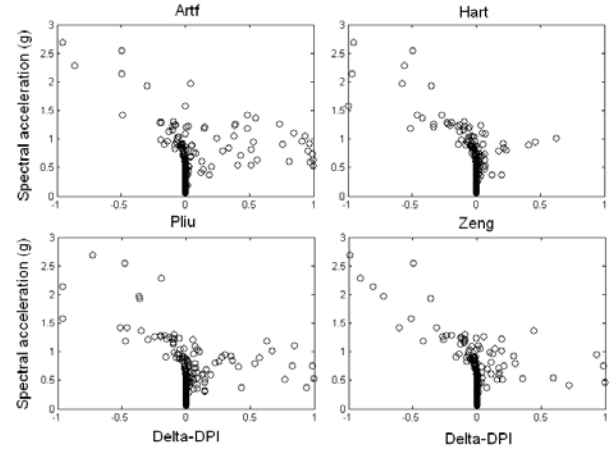


Figure 8 Relationship between Delta-DPI and Sa level

Another investigation related to the spectral acceleration parameter was conducted in this study by focusing on the ground motion sites at which the synthetic models accurately replicated (synthetic ground motion Sa within 15% of the recorded Sa value) the recorded Sa at the building period (0.2 sec). Only the ground motions with a Sa value greater than 0.5 g were considered here in order to eliminate the cases that would not cause any damage. By looking at Delta-DPI for the cases having Sa values close to those of the recorded ground motions, one can evaluate if matching the spectral acceleration at the building period will be sufficient produce synthetic ground motions with similar damage potential to recorded motions, albeit reasoning this with a single case. Figure 9 shows the CDF of the Delta-DPI for each model at the sites that have records generated with Sa values that were within 15% of the recorded motions. One can see that for most sites considered, the Delta-DPI for all models were close to zero, indicating good damage prediction accuracy especially for the Hart and Pliu models. However, some ground motions generated with model Artf and Zeng did not reproduce damage with reasonable accuracy even when the Sa at building period was matched quite well (within 15%) with their recorded counterparts. The reason for this difference was not investigated here due to the scope of the study.

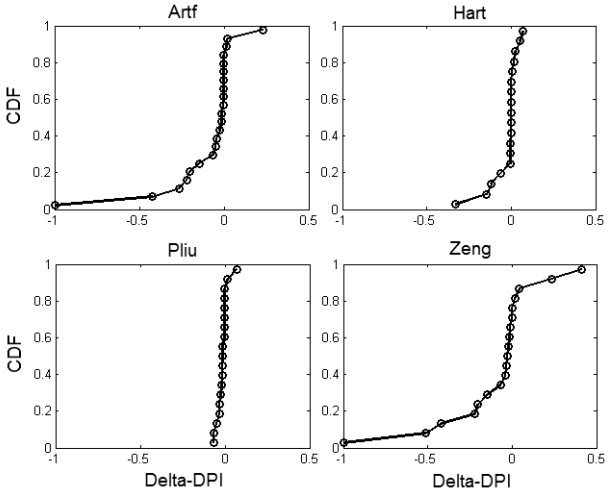


Figure 9 Distribution of Delta-DPI for synthetic motions with accurate Sa value at building period

3. CONCLUSIONS

Synthetic ground motions generated using four different models for three historical earthquakes were compared in this study based on their potential to induce damage in buildings. A damage potential indicator (DPI) that combines ground motion and building category characteristics was proposed and calibrated using damage observations from a shake table test of a full-scale wood frame structure. The proposed DPI utilizes structural parameters that are from widely adopted seismic design and evaluation standards, making the DPI a suitable candidate for general ground motion damage potential evaluation for various types of buildings. The DPI contours presented here provide a

comprehensive measure of damage potential for ground motions over a wide range of building types. Although the calibration of the proposed DPI to observed damage was limited to wood frame structures in this study, more representative DPI contours could be generated by following the same procedure using damage data for other structure types. Based on the DPI contours presented in this study, the following conclusions can be drawn related to the ability of the synthetic ground motion models to imitate the damage potential of their recorded counterparts:

Damage prediction using the synthetic ground motions is more accurate for buildings designed for significant lateral strength demands that thereby experience less ductility demand. Synthetic ground motions did not reliably predict damage to weak buildings; i.e. a high level of dispersion in the prediction was observed for such buildings.

For the three earthquake events simulated in this study, the performance of the four synthetic ground motion models was similar in that they all accurately predicted the damage potential for the majority of the sites, as compared to the recorded ground motions. However, the ability of each model to accurately predict damage at a particular site differs from model to model, especially for sites with higher ground motion intensities. At some sites (the overlapping sites in Groups A and C), the difficulty in predicting the damage potential is common to all the synthetic ground motion models investigated here, and appears to be related to the complexity and variability of ground motion close to faults.

Site-to-source distance is an important factor in the performance of the synthetic ground motions. Primarily due to ground motion attenuation and an escape from near-fault complexities, all of the models accurately predicted the damage potential for sites with distances greater than 30km. Site class seems to affect synthetic motion performance as well. More variability in synthetic motion accuracy was found for site classes C to E. This may be caused by the one-dimensional shear wave velocity models used in generating the synthetic motions, which may not account for distinct wave propagation effects at those sites, such as enclosed sedimentary basins. For all the synthetic models investigated in this study, the damage potential for sites with recorded spectral acceleration smaller than 0.5g was generally well predicted. The damage potential for sites in the approximate range of 0.5g<Sa<1.25g was over-predicted by the synthetic models and sites with Sa greater than 1.25g were typically under-predicted. Finally, matching synthetic motion spectral acceleration at the target building period with recorded ground motion appears to help achieve more accurate damage predictions for the synthetic motions. However, matching of Sa at the building period should not be used as the only procedure to achieve accurate damage prediction because some synthetic motions can produce significantly different damage even with a closely matched Sa to the recorded motions.

None of the synthetic ground motion models investigated in this study replicated the damage potential of the recorded ground motion completely. However, depending on the structure type and seismic design level of interest, some models did appear to perform better than others in certain circumstances. The proposed procedure provided another way to evaluate the effectiveness of synthetic ground motion models once details for their application was provided.

Acknowledgements:

The authors gratefully acknowledge the National Earthquake Hazards Reduction Program, External Research Grant No. G09AP00011. Support for SAPWood programming was provided through U.S. NSF Grant CMMI-0529903. The opinions expressed in this document are solely those of the authors and do not represent the view of the sponsors.

References:

ASCE, (2006) "Minimum design loads for buildings and other structures" American Society of Civil Engineers.

Atkinson G.M. and Goda K. (2010) "Inelastic Seismic Demand of Real versus Simulated Ground-Motion Records for Cascadia Subduction Earthquakes" Bulletin of the Seismological Society of America, 100(1): 102–115

Bazzurro P. and Luco N. (2003) "Parameterization of non-stationary acceleration time histories" Report for Pacific Earthquake Engineering Research Center (PEER) Lifelines Program Project 1G00, Berkeley, CA.

Bazzurro P., Sjoberg B., and Luco N. (2004) "Post-Elastic Response of Structures to Synthetic Ground Motions" Report for Pacific Earthquake Engineering Research Center (PEER) Lifelines Program Project 1G00 Addenda, Berkeley, CA.Bonilla, L., D. Lavallee, and R. Archuleta (1998). Nonlinear site response: Laboratory modeling as a constraint for modeling accelerograms, in Proc. The Effects of Surface Geology on Seismic Motion, Yokohama, Japan, vol. 2, 793-800.

Elenas A. and Meskouris K. (2001) "Correlation study between seismic acceleration parameters and damage indices of structures" Engineering Structures, 23: 698–704

Frankel, A. (2009). A constant stress-drop model for producing broadband synthetic seismograms: comparison with the next generation attenuation relations, Bull. Seism. Soc. Am. 99, 664-680.

Hall, J. F., T. H. Heaton, M. W. Halling, and D. J. Wald (1995). Near-source ground motion and its effects on flexible buildings, Earthquake Spectra 11, 569-605.

Haluk S. Semih Y., Alper G., and Altug E., (1998) "Statistical evaluation of the damage potential of earthquake ground motions" Structural Safety 20: 357-378

Hartzell S., Guatteri M., P. Martin Mai, Liu P., and Fisk M., (2005) "Calculation of Broadband Time Histories of Ground Motion, Part II:Kinematic and Dynamic Modeling Using Theoretical Green's Functionsand Comparison with the 1994 Northridge Earthquake" Bulletin of the Seismological Society of America, 95(2): 614–645

Hartzell, S., L. F. Bonilla, and R. A. Williams (2004). Prediction of nonlinear soil effects, Bull. Seism. Soc. Am. 94, 1609-1629.

International Code Council, (2006). International Building Code. International Code Council, Washington DC.

Jalayer F., Beck J.L., Porter K.A., and Hall J.F. (2004) "Effects of ground motion uncertainty on predicting the response of an existing RC frame structure" 13th World Conference on Earthquake Engineering, Vancouver, B.C., Canada.

Krawinkler H. and Nassar A., (1990) " Damage potential of earthquake ground motions" Proceedings of fourth U.S. national conference on earthquake engineering, Palm Springs CA

Lee, M. K. W., and W. D. L. Finn (1978). DESRA-2, dynamic effective stress response analysis of soil deposits with energy transmitting boundary including assessment of liquefaction potential, Soil Mechanics Series No. 38, Dept. of Civil

Engineering, University of British Columbia, Vancouver, B. C.
Liu, P., R. J. Archuleta, and S. Hartzell (2006). Prediction of broadband ground-motion time histories: hybrid low/high-frequency method with correlated random source parameters, Bull. Seism. Soc, Am. 96, 2118-2130.
Norio H. and Norio I. (2002) "Damaging properties of ground motions and prediction of maximum response of structures based on momentary energy response" Earthquake Engng Struct. Dyn. 31:1657–1679
Park S. and van de Lindt J.W. (2009) "Formulation of seismic fragilities for a wood-frame building based on visually determined damage indexes" Journal of Performance of Constructed Facilities, 23(5): 346-352.
Park Y.J., Ang A.H.S. (1985) "Mechanistic seismic damage model for reinforced concrete." Journal of Structural Engineering, 111(4):722–739.
Pei S. and van de Lindt J.W. (2010) "Seismic Analysis Package for Woodframe Structures: User's manual" NEESWood report: SAPWood User's manual, Fort Collins CO.
Sunasaka Y, Toki K. and Kiremidjian A.S. (2003) "Evaluation of damage potential of ground motions during great earthquakes" Earthquake Spectra, 19(3) 713-730
van de Lindt J.W., Pei S., Liu H., and Filiatrault A. (2010) "Three-dimensional seismic response of a full-scale light-frame wood building: Numerical study" Journal of Structural Engineering, 136(1): 56-65.
Zeng, Y., J. Anderson, and G. Yu (1994). A composite source model for computing realistic synthetic strong ground motions, Geophys. Res. Lett. 21, 725-728.

8CUEE CONFERENCE PROCEEDINGS
8th International Conference on Urban Earthquake Engineering
March 7-8, 2011, Tokyo Institute of Technology, Tokyo, Japan

SEISMIC DESIGN OF HIGHWAY BRIDGES IN CALIFORNIA

Lian Duan

Senior Bridge Engineer, California Department of Transportation, Sacramento, California, USA
lian_duan@dot.ca.gov

Abstract: This paper presents an overview of the *Seismic Design Criteria* (SDC) and the *Guide Specifications for Seismic Design of Steel Bridges* (Guides) developed by California Department of Transportation (Caltrans). Caltrans SDC and Guides are based on required seismic performance criteria, displacement-based approach and capacity design concept. All ordinary standard bridges designed in accordance with SDC and Guides are expected to remain standing but may suffer significant damage requiring closure during the design earthquake. Important and nonstandard bridges are designed in accordance with project-specific design criteria. Structural components are classified as *Ductile* and *Capacity-protected*. Inelastic deformations are generally expected in substructure components which are identified and detailed for ductile response. Inelastic behavior in the form of controlled flexural damage may be permitted in some of the steel superstructure components such as end cross frames, shear keys and bearings to prevent damage in other parts of structures. Capacity-protected components are designed to resist the force demands determined from the overstrength capacity of ductile components connected. Details such as seat width, bearing assemblies, beam-joints and connections, reinforcement confinements, end cross frames, limiting slenderness ratios, are properly designed to ensure continuity of load path during earthquake and to ensure the design objectives are achieved.

1. INTRODUCTION

Prior to the 1989 Loma Prieta earthquake, highway bridges in California were typically designed using a single-level force-based design approach based on a "no-collapse" design philosophy. Seismic loads were determined based on a set of soil conditions and a suite of four site-based standard Acceleration Response Spectra (ARS). Structures were analyzed using the three-dimensional elastic dynamic multi-modal response spectrum method. Structural components were designed by using a reduction *Z*-factor to reduce seismic forces for ductility and risk. Minimum transverse reinforcement confinements were required.

Since 1989, the design criteria specified in California Department of Transportation (Caltrans) Bridge Design Specifications (Caltrans, 1990) and several design manuals (Caltrans, 2010a and 2010b) have been updated continuously to reflect recent research findings and development in the field of seismic bridge design. Caltrans has been shifting toward a displacement-based design approach. ATC (1996) published the improved seismic design criteria recommendations for California bridges in 1996. Caltrans published the performance and displacement-based Seismic Design Criteria (SDC), which focuses mainly on concrete bridges in 1999 (Caltrans 1999a), with the current version 1.6 (Caltrans, 2010c). The Caltrans Guide Specifications for Seismic Design of Steel Bridge (Caltrans 2001) was published in 2001. Significant advances in earthquake engineering have been made during the last 20 years.

This paper first presents seismic bridge design philosophies and concepts in general, and then presents effective details for seismic design of highway bridges used in Caltrans practice.

2. SEISMIC PERFORMANCE AND DESIGN PHOLISOPHY

Caltrans seismic performance criteria (Caltrans 2010a) shown in Table 1 includes bridge category, post earthquake damage and service levels for two seismic hazard levels.

A bridge is classified as "**Important**" when it meets one of the following:

- Required to provide post earthquake life safety; such as access to emergency facilities.
- Time for restoration of functionality after closure would create a major economic impact.
- Formally designated as critical by a local emergency plan.

A bridge is classified as "**Ordinary**" when it is not classified as an important bridge.

For Standard "Ordinary" bridges, the displacement-based one-level safety-evaluation design ("no-collapsed" design) is only required in the Caltrans SDC (Caltrans, 2010c). For non-standard "Ordinary" bridges featuring irregular geometry and framing (multi-level, variable width, bifurcating, or highly horizontally curved

superstructures, different structure types, outriggers, unbalanced mass and/or stiffness, high skew) and unusual geologic conditions (soft soil, moderate to high liquefaction potential and proximity to an earthquake fault), project specific criteria need to be developed and approved to address their non-standard features.

For "Important" bridges, the performance-based project-specific criteria are required to be developed. The performance-based criteria usually require two-level design. The first level of design is to ensure the performance (service) of a bridge in earthquake events that have relatively small magnitude but may occur several times during the life of the bridge. The second level of design is to achieve the performance (no collapse) of a bridge under the severe earthquakes that have only a small probability of occurring during the useful life of the bridge. The performance-based criteria shall include guidelines for development of site-specific ground motion estimates, capacity design to preclude brittle failure modes, rational procedures for joint shear design in concrete and the definition of limit states for various performance objectives. Several criteria (Caltrans 1997, 1999b, IAI 1995) have been developed and implemented for the design and retrofitting of important bridges by California bridge engineers.

Table 1 Caltrans Seismic Performance Criteria

Bridge Category	Seismic Hazard Evaluation Level	Post Earthquake Damage Level	Post Earthquake Service Level
Important	Functional	*Minimum*	*Immediate*
	Safety	*Repairable*	*Limited*
Ordinary	Safety	*Significant*	*No Collapse*

Functional Level Evaluation: A project specific hazard level will be developed in consultation with the Seismic Safety Peer Review Panel as defined in MTD 20-16. Ordinary Bridges are not designed for Functional Evaluation Seismic Hazards.

Safety Level Evaluation: For Ordinary Bridges, this is the "Design Earthquake" as defined below. For Important Bridges, the safety evaluation ground motion has a return period of approximately 1000-2000 years.

Design Earthquake is the collection of seismic hazards at the bridge site used in the design of bridges. The Design Earthquake" consists of the Design Spectrum as design in the SDC Version 1.5 Appendix B and may include other seismic hazards such as in liquefaction, lateral spreading, surface faulting and tsunami.

Damage Levels:

- *Minimal:* Essentially elastic performance.
- *Repairable:* Damage that can be repaired with a minimum risk of losing functionality.

Significant: A minimum risk of collapse, but damage that could require closure to repair.

Service Levels:

- *Immediate:* Full access to normal traffic is available almost immediately following the earthquake.
- *Limited:* Limited access (e.g. reduced lanes, light emergency traffic) is possible with days of the earthquake. Full service is restorable within months.
- *No Collapse:* There may be no access following the earthquake.

3. SEISMIC LOADS

For Ordinary Bridges, Safety-Evaluation ground motion is presented by the Design Response Spectrum, the envelope of a deterministic and probabilistic spectrum Figure 1 shows a set of the horizontal Design Response Spectrum. When the bridge site peak rock acceleration is 0.6g or greater, an equivalent static vertical uniform load equal to 25% of the dead load shall be applied upward and downward to the superstructure to estimate the effects of vertical acceleration.

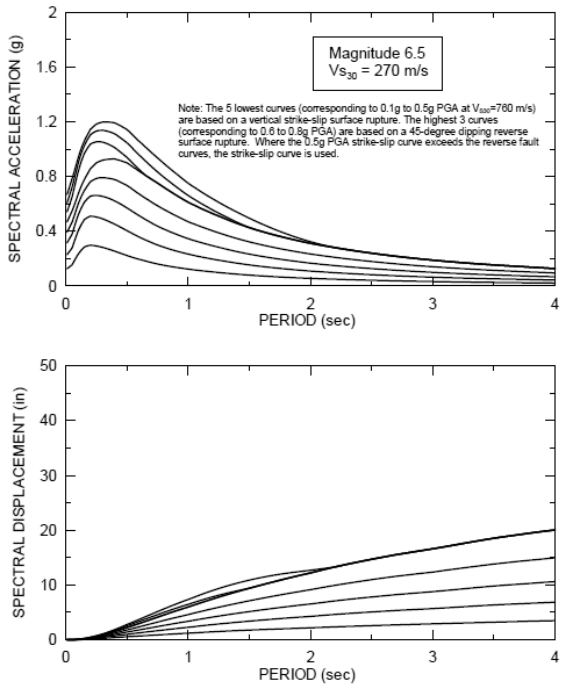


Figure 1. Spectral Accelration and Displacement for V_{30} = 270 m/s (M = 6.5)

For structures within 25 km from an active fault, the spectral ordinates of the appropriate standard Response Spectrum curves shall be modified by a near-fault adjustment factor as shown in Figure 2.

4. GENERAL SEISMIC PROVISIONS

For Ordinary bridges, structural members are identified as either ductile or capacity-protected members. A ductile member is a member that is intentionally well designed to deform inelastically for several cycles without significant degradation of strength or stiffness under the design earthquake. On the other hand, a capacity-protected member is a member that is expected to behave essentially elastic. The preferable ductile members on most bridges shall be limited to pre-determined locations within the bridge that can be easily inspected and repaired following an earthquake and may include columns, pier walls, backwalls, wingwalls,

seismic isolation and damping devices, bearings, shear keys and steel end diaphragms.

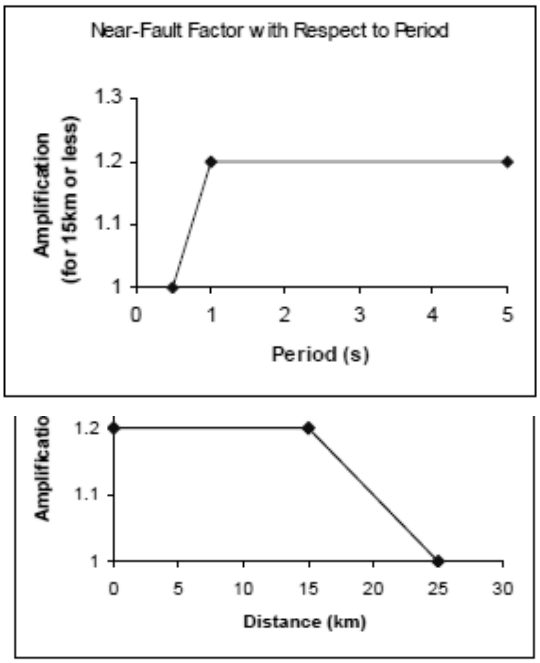


Figure 2. Near-Fault Adjustment Factor

The displacement-based design approach is used to ensure that the structural system and its individual members have enough displacement capacities to withstand the deformation imposed by the design earthquake. The capacity design concept is used to ensure all other elements not explicitly designed as ductile or sacrificial to be capacity protected such that they remain essentially elastic. This procedure has been used widely in seismic bridge design in California since 1994. Figure 3 shows the design flowchart for the ordinary standard bridges.

4.1 Global Displacement

The displacements of the global bridge system and the frame shall satisfy the following requirement:

$$\Delta_D \leq \Delta_C \quad (1)$$

where Δ_D is displacement demand determined by the global analysis, the stand alone analysis, or the larger of the two if both types of analyses are necessary; Δ_C is displacement capacity when any plastic hinge capacity reaches its ultimate capacity.

4.2 Local Displacement Ductility Capacity

To ensure the dependable ductile behavior of all columns regardless of seismic demand, a minimum local displacement ductility capacity of $\mu_c = \Delta_c/\Delta_Y \geq 3$ is required, and target local ductility of $\mu_c \geq 4$ is recommended. The local displacement ductility capacity shall be calculated for an equivalent member that approximates a fixed base cantilever element.

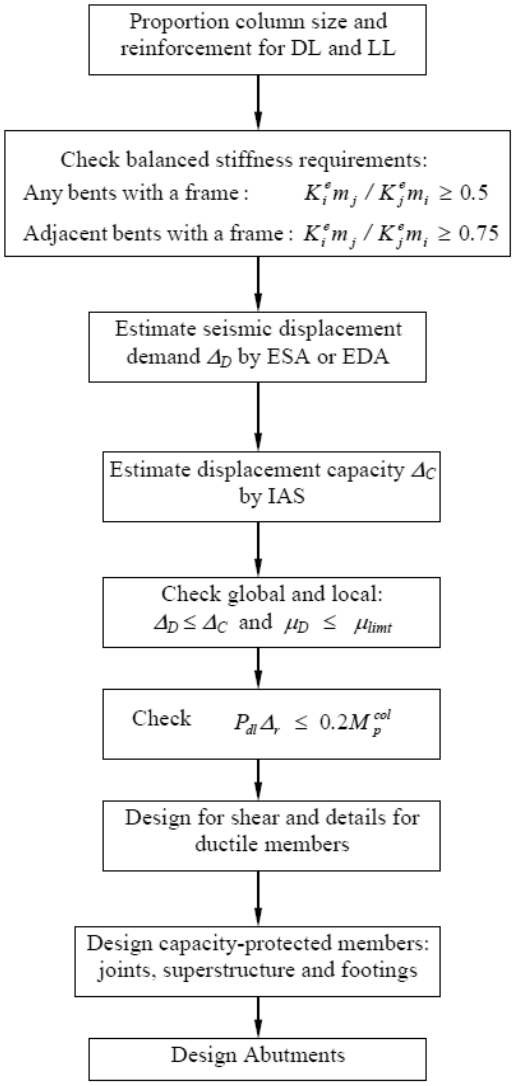


Figure 3. Caltrans Seismic Design Procedure for Ordinary Standard Bridges

4.3 Target Displacement Ductility Demand

The engineers are encouraged to limit displacement ductility demands, defined as $\mu_D = \Delta_D/\Delta_Y$ to the following limits which were calibrated to laboratory tests:

- Single Column Bents supported on fixed foundation $\mu_D \leq 4$
- Multi-Column Bents supported on fixed or pinned footings $\mu_D \leq 5$
- Pier Walls (weak direction) supported on fixed or pinned footings $\mu_D \leq 5$
- Pier walls (strong direction) supported on fixed or pinned footings $\mu_D \leq 1$

4.4 Force

The forces in a capacity-protected member shall satisfy the following requirement:

$$F_D \leq F_C \quad (2)$$

where F_D is force demand determined by determined by the

joint-force equilibrium considering plastic hinging capacity of the ductile component multiplied by 1.2 of an overstrength factor; F_C is force capacity limit specified in SDC (Caltrans 2010c) for concrete members and Guides (Caltrans 2001) for steel members.

4.5 *P-Δ Effects*

The *P-Δ* effects tend to increase the displacement and decrease lateral load-carrying capacity of a bridge column. These effects can typically be ignored if the moment ($P_{dl}\Delta_r$) is less than or equal to 20% of the column plastic moment, i.e.

$$P_{dl}\Delta_r \le 0.2\, M_p^{col} \tag{3}$$

where Δ_r is the relative offset between the point of contra-flexure and the base of plastic hinge and P_{dl} is the tributary dead load applied at the center gravity of the bridge column.

4.6 Minimum Lateral Strength

Although providing ductile detailing is essential for achieving the expected performance requirements, each column shall be designed to have a minimum lateral flexural capacity to resist a lateral force of $0.1P_{dl}$ where P_{dl} is the tributary dead load applied at the center gravity of the superstructure.

5. SEISMIC ANALYSIS METHODS FOR DEMAND

For Ordinary Standard Bridges, the following methods are recommended to estimate the displacement demands.

5.1 Equivalent Static Analysis (ESA)

The ESA method specified in Caltrans SDC (Caltrans 2010c) can be used to estimate the displacement demands for simpler structures which have balanced spans, similar bent stiffness, and low skew and seismic response is primarily captured by the fundamental mode of vibration. In the ESA method, the fundamental period is determined using tributary mass and stiffness at each bent. The applied seismic force is the product of the period dependent ARS coefficient and the tributary weight.

5.2 Elastic Dynamic Analysis (EDA)

The EDA is linear elastic multi-mode spectral analysis with the appropriate response spectrum and with an adequate number of modes considered to capture a minimum of 90% mass participation. A minimum of three elements per column and four elements per superstructure span shall be used. The complete quadratic combination (CQC) method is recommended to combine EDA modal results.

5.3 Global and Stand-Alone Analysis

The global analysis specified in Caltrans SDC (Caltrans 2010c) is an elastic dynamic analysis with considering the entire bridge modeled from abutment to abutment. It is often used to determine displacement demands on multi-frame structures. The stand-alone analysis is an elastic dynamic analysis with considering only one individual frame. To avoid having individual frames dependent on the strength and stiffness of adjacent frames, the separate stand-alone model for each frame must meet all requirements of the SDC.

5.4 Effective Stiffness

In both ESA and EDA methods, effective stiffness of the components shall be used in order to obtain realistic evaluation for the structure's period and displacement demands. The effective stiffness of ductile components shall represent the component's actual secant stiffness near yield. The effective stiffness shall include the effects of concrete cracking, reinforcement and axial load for concrete components; residual stresses, out-of-straightness and axial load for steel components; the restraints of the surrounding soil for pile.

For ductile concrete column members, effective moments of inertia, I_{eff} shall be based on cracked section properties and can be determined from the initial slope of the M-ϕ curve between the origin and the point designating first yield of tensile reinforcement. The torsional moment of inertia of concrete column J_{eff} may be taken as 0.2 time J_{gross}. For capacity-protected concrete members, I_{eff} shall be based on their level of cracking. For conventionally reinforced concrete box girder superstructure, I_{eff} can be estimated between 0.5-0.75 times I_{gross}, moment of inertia of a gross section. For pretsressed concrete superstructures, I_{eff} is assumed the same as I_{gross} because prestressing steel limits the cracking of concrete superstructures.

For built-up steel members, effective section properties developed by Duan, Reno and Lynch (2000) may be used.

6. SEISMIC ANALYSIS METHODS FOR CAPACITY

6.1 Inelastic Static Analysis (ISA) – Push Over Analysis

Inelastic Static Analysis (ISA), commonly referred to as the "push over analysis", shall be used to determine the displacement capacity of a bridge. The expected material properties shall be used to model structural members. IAS is a static, nonlinear procedure in which the magnitude of lateral loading is incrementally increased with a certain predefined pattern, until the potential collapse mechanism is achieved.

The simplest method, elastic-plastic hinge analysis, may be used to obtain an upper bound solution. The most accurate method, distributed plasticity analysis, can be used to obtain a better solution. Refined plastic hinge analysis is an alternative that can reasonably achieve both computational efficiency and accuracy.

A pushover analysis example (Akkari and Duan 2000) of a typical reinforced concrete bridge bent frame consisting of a bent cap beam and two circular columns supported on pile foundations is shown in Figure 4. Due to lack of adequate column transverse reinforcement, the columns are retrofitted with 12.7 mm thick steel jacket. Figure 5 shows an

analytical push-over model for the example bridge bent. Figure 6 shows the lateral load vs. displacement response.

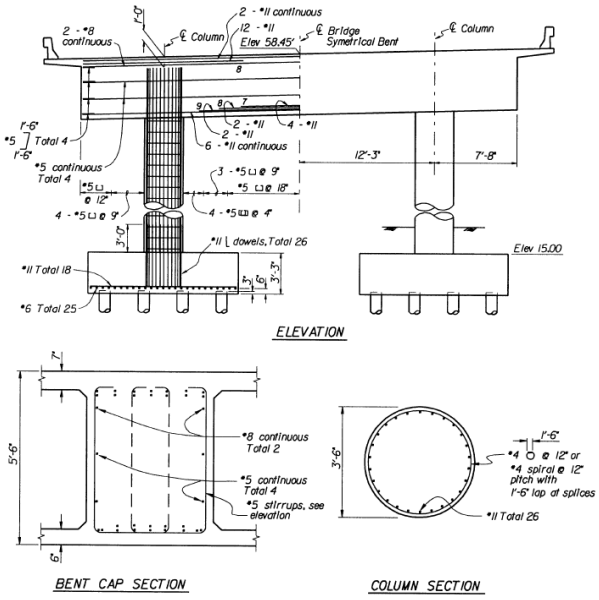


Figure 4. A Typical Reinforced Concrete Bridge Bent

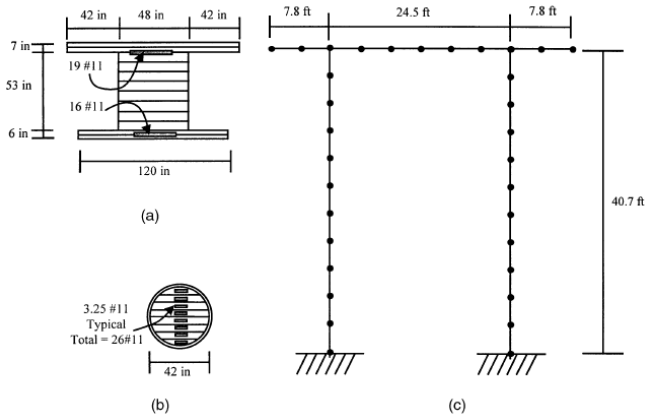


Figure 5. Analytical Model for Example Bridge Bent

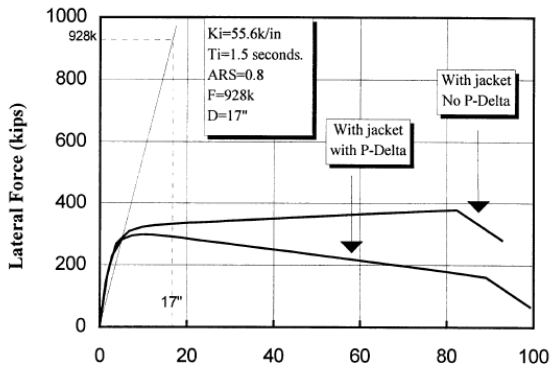


Figure 6. Lateral Load - Displacement Response

6.2 Moment-Curvature Analysis

The main purpose of moment-curvature analysis is to study the section behavior and to provide basic input data for the pushover analysis.

For a reinforced concrete member, the cross section is divided into a proper number of concrete and steel layers or filaments representing the concrete and reinforcing steel. Each concrete and steel layer or filament is assigned its corresponding stress-strain relationships. Confined and un-confined stress-strain relationships are used for the core concrete and for cover concrete, respectively.

For a structural steel member, the section is divided into steel layers or filaments and a typical steel stress-strain relationship is used for tension and compact compression elements, and an equivalent stress-strain relationship with reduced yield stress and strain can be used for a non-compact compression element.

7. SEISMIC DETAILING REQUIREMENTS

7.1 Minimum Seat Width

To prevent unseating of superstructures at hinges, piers and abutments, the seat width shall be available to accommodate the anticipated thermal movement, prestressing shortening, concrete creep and shrinkage, and the relative longitudinal earthquake displacement, and shall not exceed the following minimum seat requirements (Caltrans 2010a):

$$N_{\min} = \text{larger of} \begin{cases} \Delta_{ps} + \Delta_{cr+sh} + \Delta_{temp} + \Delta_{eq} + 100\,(\text{mm}) \\ 600\ \text{mm}\,(\text{For seat width at hinges}) \\ 760\ \text{mm}\,(\text{For seat width at Abutments}) \end{cases} \tag{4}$$

where Δ_{ps}, Δ_{cr+sh}, Δ_{temp} *and* Δ_{eq} are relative displacement due to prestressing, concrete creep and shrinkage, temperature and earthquake, respectively (mm).

7.2 Structural Steel

7.2.1 Limiting Width-to-Thickness Ratios

For capacity-protected components, the width-thickness ratios of compression elements shall not exceed the limiting value λ_r as specified in Caltrans Guide Specification (Caltrans 2001). For ductile components, width-thickness ratios shall not exceed the λ_p as specified in Table 19.13. Welds located in the expected inelastic region of ductile components are preferably complete penetration welds. Partial penetration groove welds are not recommended in these regions. If the fillet welds are only practical solution for an inelastic region, Quality Control (QC) and Quality Assurance (QA) inspection procedures for the Fracture Critical Members shall be followed.

7.2.2 Limiting Slenderness Ratio

The slenderness parameter λ_c for compression members,

and λ_b for flexural members shall not exceed the limiting values, λ_{cp} and λ_{bp}, as specified in the Guide Specifications (Caltrans 2001), respectively.

7.2.3 Limiting Axial Load Ratio

High axial load in column usually results in the early deterioration of strength and ductility.
The ratio of factored axial compression due to seismic load and permanent loads to yield strength (A_gF_y) for columns in ductile moment-resisting frames and single column structures shall not exceed 0.3.

7.2.4 Shear Connectors

Shear connectors shall be provided on the flanges of girders, end cross frames or diaphragms to transfer seismic loads from the concrete deck to the abutments or pier supports. The cross frames or diaphragms at the end of each span are the main components to transfer the lateral seismic loads from the deck down to the bearing locations.

7.3 Concrete

7.3.1 Limiting Longitudinal Reinforcement Ratios

The ratio of longitudinal reinforcement to the gross cross-section of the compression members shall not be less than 0.01 and 0.005 for columns and pier walls, respectively, and more than 0.04.

7.3.2 Plastic Hinge Region

The plastic hinge region for ductile members is defined as the larger of the following:

- 1.5(the cross sectional dimension in the direction of bending)
- Region where the moment exceeds 75% of maximum plastic moment, M_p^{col}
- 0.25(Length of column form the point of maximum moment to the point of contra-flexure).

7.3.2 Transverse Reinforcement in Plastic Hinge Regions

For confinement in plastic hinge regions, in term of the volumetric ratio, ρ_s for columns with circular and interlocking core sections, $\rho_s = 4A_{bh} / D's$, shall be designed to ensure members meet the performance requirements.

The maximum spacing (s) for lateral reinforcement in the plastic end regions shall not exceed the smallest of (1) 20% of the least dimension of the cross-section for columns and one-half of the least cross-section dimension of piers, (2) Six times the nominal diameter of the longitudinal reinforcement and (3) 200 mm.

7.3.3 Joint Proportion and Reinforcement

- Moment-resisting integral connections shall be designed to resist the overstregnth capacity M_p^{col} and associated shear.
- The principal tension stress p_t and compression stress p_c shall not exceed $1.0\sqrt{f_c'}$ (Mpa) and $0.25\, f_c'$, respectively. The bent cap width required for the join shear transfer shall not less than the cross section dimension of the column in the direction of bending plus 600 mm.
- When the principal tension stress $p_t \le 0.29\sqrt{f_c'}$ (MPa), for circular columns, or columns with intersecting spirals, the volumetric ratio of transverse reinforcement in the form of spirals or hoops to be continued into the cap or footing ρ_s shall not less than $0.29\sqrt{f_c'} / f_{yh}$.
- When the principal tension stress $p_t > 0.29\sqrt{f_c'}$ the additional reinforcement shall be provided and well distributed within D/2 from the face of column as specified in Caltrans SDC (Caltrans 2010c).

Figure 7 shows 3-D representation of knee joint shear reinforcement layout.

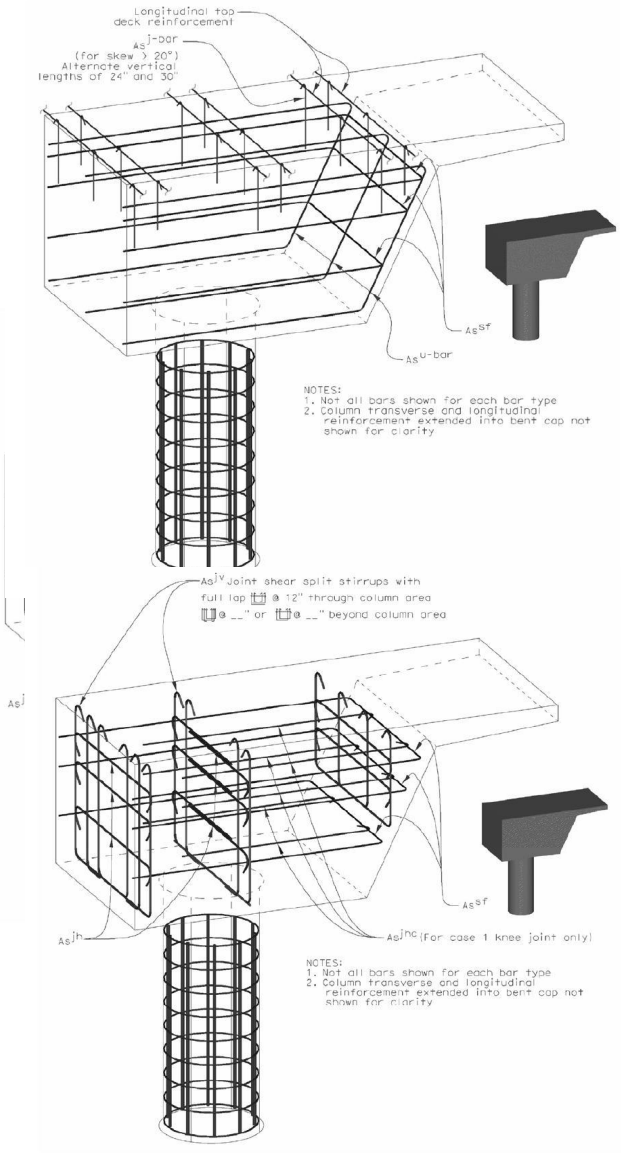


Figure 7. Knee Joint Shear Reinforcement Layout

8. CONCLUSIONS

Caltrans has been using displacement-based design approach for seismic design of highway bridges to ensure that the structural system and its individual members have enough displacement capacities to withstand the deformation imposed by the design earthquake since 1994. Structural components are classified as *Ductile* and *Capacity-protected.* Inelastic deformations are generally expected in substructure components which are pre-identified and well detailed for ductile response. Inelastic behavior in the form of controlled flexural damage may be permitted in some of the steel superstructure components such as end cross frames, shear keys and bearings to prevent damage in other parts of structures. The capacity design concept is used to ensure all other elements not explicitly designed as ductile or sacrificial to be capacity protected such that they remain essentially elastic. Capacity-protected components are designed to resist the force demands determined from the overstrength capacity of ductile components connected. Details such as seat width, bearing assemblies, beam-joints and connections, reinforcement confinements, end cross frames, limiting slenderness ratios, are properly designed to ensure continuity of load path during earthquake and to ensure the design objectives are achieved.

References:

Akkari, M. and Duan, L. (2000), "Chapter 36: Nonlinear Analysis of Bridge Structures," Bridge Engineering Handbook, Ed., W.F. Chen and L. Duan, CRC Press, Baca Raton, FL.

ATC, (1996), *Improved Seismic Design Criteria for California Bridges: Provisional Recommendations*, Report No. ATC-32, Applied Technology Council, Redwood City, CA.

Caltrans, (2010a), *Bridge Memo to Designers (20-1) - Seismic Design Methodology*, California Department of Transportation, Sacramento, CA.

Caltrans, (2010b), *Bridge Memo to Designers (20-4) – Seismic Retrofit Guidelines for Bridges in California.* California Department of Transportation, Sacramento, CA.

Caltrans, (2010c), *Seismic Design Criteria, Version 1.6*, California Department of Transportation, Sacramento, CA.

Caltrans, (2001), *Guide Specifications for Seismic Design of Steel Bridges, First Edition,* California Department of Transportation, Sacramento, CA.

Caltrans, (1999a), *Seismic Design Criteria, Version 1.1*, California Department of Transportation, Sacramento, CA.

Caltrans, (1999b), *San Francisco-Oakland Bay Bridge East Span Seismic Safety Project Design Criteria, Version 7*, Prepared by TY Lin/Moffatt & Nichol Engineers, California Department of Transportation, Sacramento, CA.

Caltrans, (1997), *San Francisco - Oakland Bay Bridge West Spans Seismic Retrofit Design Criteria*, Edited by Duan, L., California Department of Transportation, Sacramento, CA.

Caltrans, (1990), *Bridge Design Specifications*, California Department of Transportation, Sacramento, CA.

Duan, L., Reno, M. and Lynch J. (2000), "Section Properties for Latticed Members of San Francisco-Oakland Bay Bridge," *Journal of Bridge Engineering,* ASCE **5**(2), 156-164.

IAI, (1995), *Benicia-Martinez Bridge Seismic Retrofit - Main Truss Spans Final Retrofit Strategy Report*, Imbsen and Association, Inc., Sacramento, CA.

8CUEE CONFERENCE PROCEEDINGS
8th International Conference on Urban Earthquake Engineering
March 7-8, 2011, Tokyo Institute of Technology, Tokyo, Japan

SEISMIC BEHAVIOR OF CURVED STEEL-GIRDER HIGHWAY BRIDGES

Ian G. Buckle[1)], Eric V. Monzon[2)], and Ahmad M. Itani[1)]

1) Professor, Department of Civil and Environmental Engineering, University of Nevada, Reno, USA
2) Research Assistant, Department of Civil and Environmental Engineering, University of Nevada, Reno, USA
igbuckle@unr.edu, emonzon@unr.edu, itani@unr.edu

Abstract: A common assumption in the seismic analysis of curved highway bridges is to ignore the curvature and analyze these structures as if they are straight. But this approach may seriously underestimate the forces in the components of the superstructure as shown in this paper for continuous, steel plate, I-girder superstructures supported by bearings on conventional concrete substructures. The load path in a curved superstructure is highly dependent on the degree of curvature because the inherent torsional moments in the superstructure increases with increasing values for the subtended angle. This leads to high cross-frame forces and a distribution of bearing loads that are significantly different from those found in straight bridges. This paper discusses this effect as well as the effect of various modeling techniques on the seismic response of a highly curved, steel I-girder bridge to be tested at University of Nevada, Reno, in Summer 2011.

1 INTRODUCTION

The influence of bridge irregularity is one of the important lessons learned from bridge performance in previous earthquakes. Bridge spans have collapsed or been severely damaged due to non-uniform distributions of stiffness and weight caused by irregular geometry. This irregularity exists in many different forms including variation of span length and weight, column height, presence of skew, and curvature.

Despite the prevalence of curved bridges in urban areas, their seismic behavior is poorly understood. Current U.S and Japanese bridge design specifications provide little guidance on their seismic analysis and design.

A common assumption in the analysis of curved highway bridges is to ignore the curvature and analyze these structures as if they are straight. But for bridges with considerable amount of curvature, this approach may underestimate the forces in the superstructure. Under gravity loads, curved steel I-girder superstructures are subjected to internal torsion which is distributed to the girders through the cross-frames (or diaphragms). The outer girders take more load than the inner girders causing each girder to deflect differently.

The AASHTO LRFD Bridge Design Specifications (AASHTO 2008) permits curved I-girders to be analyzed as a straight girder for determining the major-axis bending moments and shears due to dead and live loads, provided the girders are concentric, the bearing lines are not skewed more than 10^o from the radial direction, all of the girders are about the same stiffness, and the subtended angle of the span is less than 4^o. For bridges with larger curvature, where the lateral flange bending moment can be substantial, the V-load method (United States Steel 1984) is recommended for use in design. In this method, the individual girders are analyzed first as straight to determine the primary major-axis bending moments and shears. These moments and shears are then adjusted using the V-loads, which are a set of self-equilibrating shears between the adjacent girders. The lateral bending moment M_{lat} in the flanges is then approximated using the equation:

$$M_{lat} = \frac{Ml^2}{NRD} \tag{1}$$

where M is the major-axis bending moment, l is the girder unbraced length, R is the girder radius, D is the web depth, and N is a constant taken as either 10 or 12 depending on the desired level of conservatism.

For seismic analysis, the AASHTO LRFD Specifications (AASHTO 2008) and the Guide Specifications for LRFD Seismic Bridge Design (AASHTO 2009) permit curved bridges to be analyzed as if they were straight when the subtended angle is less than 90^o and the bridge has otherwise 'regular' properties, as defined in these specifications.

The Japanese Seismic Specifications for Seismic Design of Highway Bridges (JRA 1996) has language for prevention of unseating of curved bridges during seismic events but provides little information on modeling and seismic analysis of these structures.

In curved steel I-girder bridges, the consideration of geometry is as important as selection of the method of analysis. In general there are three modeling techniques for the analysis of steel I-girder bridges: stick (or spine) model, grillage model, and finite element model. The AASHTO Specifications permit the use of curved stick models for superstructures that do not distort or warp significantly under torsion. For superstructures with multiple girder-lines this distortion may however be large (depending on the cross-frame spacing) and such bridges should be analyzed as grids or continuums. In each case, it is usual to assume the longitudinal beams are straight between nodes.

This paper discusses the results of using different analytical models for calculating response to static lateral loads, and the determination of dynamic modal properties. It also discusses the effect of curvature on response, and the influence of various superstructure components on the seismic load path in horizontally curved steel I-girder bridges.

2 3-SPAN HORIZONTALLY CURVED STEEL I-GIRDER BRIDGE

The geometry and section properties of the bridges used in the analyses presented in this paper, are based on a 3-span, curved, steel I-girder bridge with high degree of curvature (subtended angle is 104^o (1.8 radians)). A 0.4-scale model of this bridge will be tested using the NEES multiple shake tables in the Large-Scale Structures Laboratory at the University of Nevada, Reno in Summer 2011.

The geometry of the prototype and model is summarized in Table 1. The superstructure consists of a reinforced concrete (R/C) deck that is composite with three steel I-girders. The girders are built-up sections consisting of 16 mm by 229 mm flange plates and 10 mm by 660 mm web plate. The R/C deck is 83 mm thick with 19 mm haunch. The piers are single columns with a drop cap.

The model will be used to experimentally study the seismic performance of this bridge in a variety of different configurations including:

- conventional superstructure, columns and bearings without live load (benchmark bridge) and with live load (Figure 1)
- fully isolated superstructure on conventional columns
- partially isolated superstructure with ductile cross-frames on conventional columns (hybrid protective system)
- conventional superstructure on rocking columns, and
- conventional superstructure and columns with abutment interaction and simulated backfill.

The findings of these experimental studies, coupled with analytical investigations, will be used to develop a set of seismic design guidelines for horizontally curved steel bridges.

Table 1 Properties of the 3-Span Curved Bridge

	Prototype	Model
Total length (m)	110.5	44.2
Span lengths (m)	32-46.5-32	12.8-18.6-12.8
Centerline radius (m)	61	24.4
Total width (m)	9.15	3.66
Girder spacing (m)	3.4	1.37
Column height (m)	6.1	2.44
Column diameter (m)	1.52	0.61

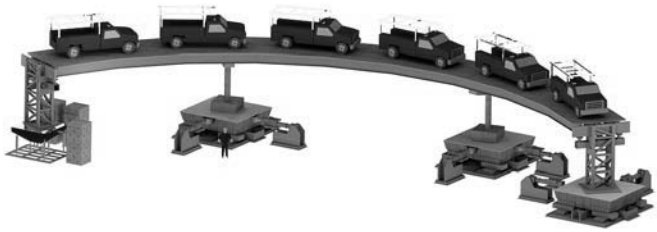


Figure 1 3D Rendering of the 0.4-Scale Curved Bridge Model with Simulated Truck Loading

3 MODELING OF HORIZONTALLY CURVED STEEL PLATE GIRDER BRIDGES

The AASHTO/NSBA Guidelines for the Analysis of Steel Girder Bridges (AASHTO/NSBA 2010) provides a detailed discussion of analysis methods for steel girder bridges including guidance on modeling the superstructure from construction to completion.

In general, three modeling techniques are recommended for the analysis of steel girder bridges:

- Stick beam (also called 'spine' beam)
- Grillage
- 3D Finite Element Assemblage

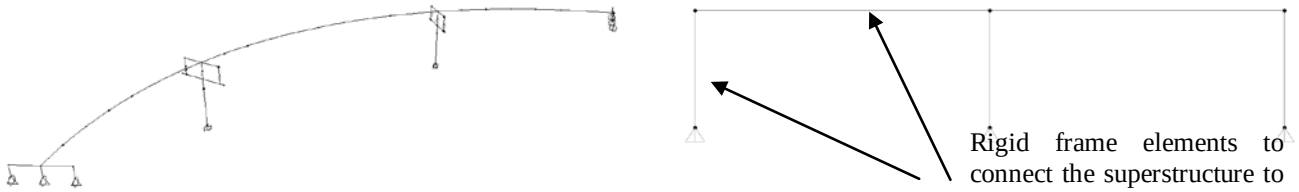
In a stick model (Figure 2a), the superstructure is modeled as a single beam element with equivalent section properties. However stick models created by many computer programs may not include the rotational mass inertia of the superstructure about its longitudinal axis and this should be added to the nodes of the beam, particularly for curved bridges. This model can capture the global response of the bridge with reasonable accuracy including column forces and moments but it does not give good results for local behavior in the superstructure such as torsional rotation, cross-frame and bearing forces. In curved steel bridges, due to geometry, internal torsion is created in the superstructure resulting in an uneven distribution of loads between the girders. The girder on the outside of the curve receives more load and thus has larger deflections than the adjacent girders. Because of this, the deflections obtained from stick models should not be used to determine the camber in the girders. In addition, the effect of cross-frames on the overall structural system is neglected. These frames provide resistance to the torsional moments in the

superstructure and may be subjected to large forces depending on the bridge curvature.

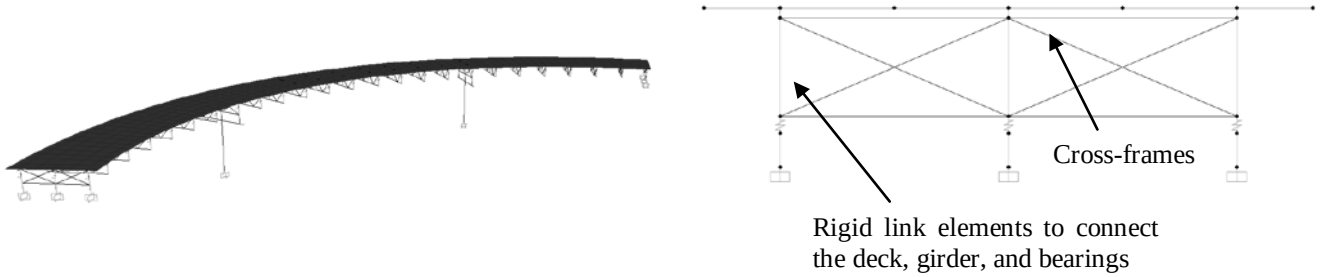
In the grillage model, the individual girders are modeled and are connected transversely by beam elements representing the deck and/or the cross-frames. This modeling technique provides a better representation of the mass across and along the superstructure and thus rotational inertia is implicitly included in this model. However, since the grid elements are located in the same plane, the cross-frames connecting the adjacent girders are modeled using beam elements that have either flexural or shear stiffness. This approach may not be able to capture the actual behavior of cross-frames when subjected to various loadings and it does not provide the cross-frame forces directly. Because the grid elements are located in the same plane, the actual location of bearing supports, which are at the bottom of the girder, may not be modeled correctly. It is noted that horizontal bearing reactions create moments in the superstructure because they are acting at some distance from the superstructure neutral axis. These errors, however, can be lessened through a variation of the grillage model, called the plate-and-beam model.

In the plate-and-beam model (Figure 2b), the deck is modeled as plate or shell elements while the girders are modeled as beam elements. The deck flexibility is modeled accurately and there is better distribution of mass than in the traditional grillage model. The beam element may be placed at the girder center-of-gravity and then connected to the deck and bearings by link elements. Since the superstructure model has "depth", the actual geometry of the cross-frames can be modeled and the bearings can be placed at their correct location.

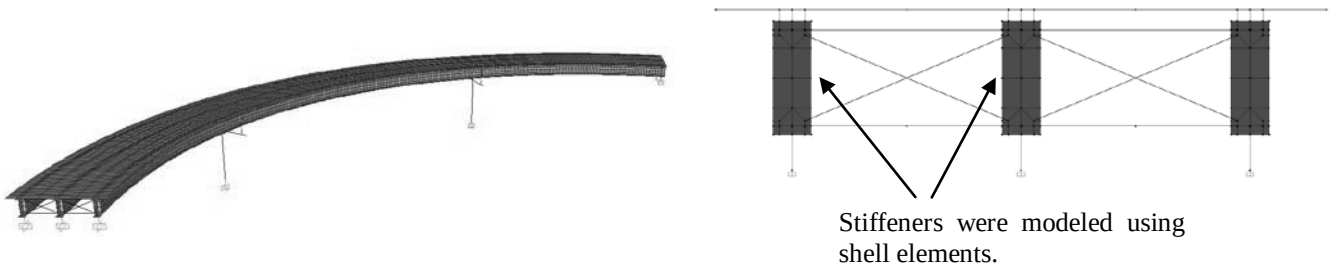
The 3D Finite Element (FE) model (Figure 2c) is the most rigorous of all the modeling techniques and is regarded as the most accurate. The deck is modeled as shell elements while the girders are modeled by either shell elements for the web and flanges or by combination of shell elements for the web and beam elements for the flanges. Because the superstructure is modeled in detail, information about the stress state of the components is provided. However, this technique can be time-consuming and complicated. Additionally, post-processing is required since the output is in terms of stresses and not moments, shears, and axial loads that are typically used in design calculations.



(a) Stick model: 3D view (left) and section at abutments and piers (right)



(b) Plate-and-beam model: 3D view (left) and section at abutments and piers (right)



(c) Finite Element model: 3D view (left) and section at abutments and piers (right)

Figure 2 Structural Models for a Curved Bridge

4 EFFECT OF MODELING

Depending on the complexity and desired level of accuracy, a bridge can be modeled using any of the above techniques. Two cases are given below to illustrate the results given by these modeling techniques for the seismic response of curved girder bridges.

4.1 Static Load Case

Stick, plate-and-beam, and finite element (FE) models of the curved bridge model described in Section 2 were developed in order to compare their response under lateral loading. The assumed boundary conditions are:

a) guided bearings at the abutments that allow translation in the tangential direction but restrain translation in the radial direction
b) pin connection between the girders and pier cap (rotation permitted, translation restrained)

A distributed lateral load (totaling 1,000 kN) was applied to the superstructure of each model in the transverse direction, i.e., normal to the chord joining the two abutments. In the stick model, the distributed load was applied uniformly along the superstructure beam, while in the plate-and-beam and FE models, the loads were distributed equally to each node in the deck. The bearing reactions were then determined and compared as shown in Figure 3.

Using the results of FE model as the baseline, the stick model overestimates the total shear at the abutment by 15%. This overestimation of shear is attributed to the use of rigid frame elements between the superstructure and bearings (see Figure 2a) which stiffens the abutments causing it to attract more load. The most remarkable observation, however, is the difference in vertical reactions at the bearings where the stick model underestimates the reactions by about 50%. This underestimation can have a significant effect on the design of the bearings and other components such as uplift restrainers.

The results from the plate-and-beam model compare well with the FE model although the distribution of radial shears among the bearings varies as much as 9%. This is attributed to the stiffening of the superstructure due to the rigid link elements used to connect the deck, girders and bearings. This suggests that the rigid links should be used with caution because, depending on the stiffness of the cross-frames, the seismic load path might be altered.

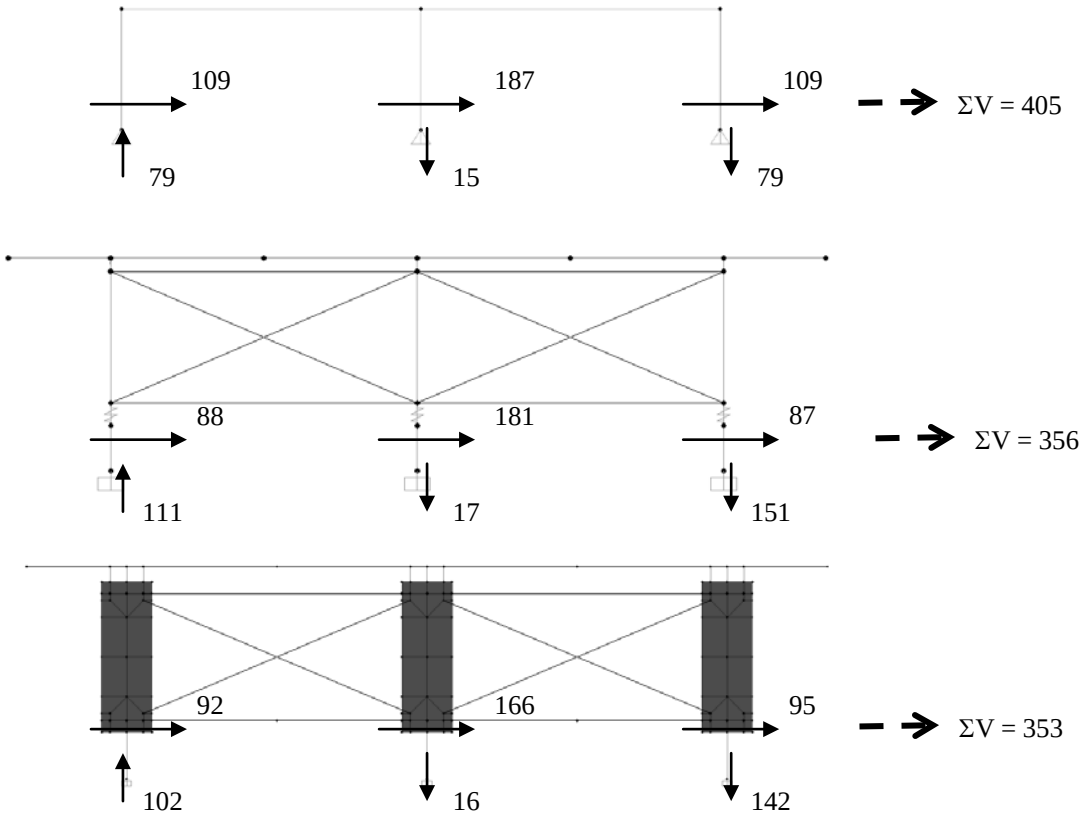


Figure 3 Radial and Vertical Reactions at Abutment due to 1,000 kN Transverse Load on the Superstructure: Stick Model (top), Plate-and-Beam Model (center), Finite Element Model (bottom)

4.2 Dynamic Load Case

To determine how well the three models capture the vibration properties of the curved bridge described in Section 2, modal analyses were performed using each model in turn. The modal periods and modal mass participation ratios of the first five modes of each model are shown in Tables 2 to 4.

The plate-and-beam model compares well with the FE model although it is consistently stiffer than the FE model. Again, this is attributed to the use of rigid link elements between the deck and girders which creates unnecessary stiffening of the superstructure.

The stick model is even stiffer than the plate-and-beam model except for the transverse modes (Modes 2 and 3). Both of these modes are translation in the transverse direction coupled with superstructure flexure and rotation, which is different to the transverse mode of the plate-and-beam and FE models.

These results show that the seismic response provided by the stick model can be significantly in error. The response provided by the plate-and-beam model is reasonable and can be further improved, possibly by using link elements with equivalent girder stiffness between the deck, girders, and bearings.

Table 2 Modal Periods and Mass Participation Ratios: Stick Model

Mode	**Period**	**Mass Participation Ratios**		
No.	sec	X	Y	Z
1	0.749	0.757	0.000	0.000
2	0.607	0.000	0.375	0.010
3	0.564	0.000	0.528	0.001
4	0.268	0.001	0.000	0.000
5	0.175	0.000	0.003	0.597

Table 3 Modal Periods and Mass Participation Ratios: Beam-and-Plate Model

Mode	**Period**	**Mass Participating Ratios**		
No.	Sec	X	Y	Z
1	0.775	0.681	0.000	0.000
2	0.512	0.000	0.795	0.000
3	0.316	0.000	0.004	0.046
4	0.159	0.001	0.000	0.000
5	0.145	0.149	0.000	0.000
6	0.135	0.000	0.002	0.564

5 EFFECT OF CURVATURE

The AASHTO Specifications (2008) specify the conditions when a curved bridge may be analyzed as if it were straight. Depending on various parameters such as boundary conditions, curvature, skew, and other geometric irregularities, the straight bridge assumption might be able to capture some of the global response. However, this assumption could either underestimate or overestimate the response of local components such as the bearings and cross-frame forces. Bearing forces obtained from a curved bridge can be significantly different than from the corresponding straight bridge due to the difference in boundary conditions, frame action between the piers and abutments, and inherent superstructure torsion. Cross-frame forces must be determined accurately and designed accordingly since they are primary load-carrying members in a curved bridge.

Table 4 Modal Periods and Mass ParticipationRatios: FE Model

Mode	**Period**	**Mass Participating Ratios**		
No.	Sec	X	Y	Z
1	0.795	0.771	0.000	0.000
2	0.532	0.000	0.871	0.001
3	0.350	0.000	0.012	0.039
4	0.172	0.007	0.000	0.000
5	0.150	0.161	0.000	0.000

To determine the effect of curvature, an FE model of a straight bridge with the same properties as the curved bridge model was developed. The cross-frame forces in the two models under dead and seismic loadings were then compared. There are 25 sets of cross-frames in the bridge in Section 2, spaced about 1.83 m apart. The seismic loading was based on a response spectrum defined by a PGA of 0.472g, S_s of 1.135g, and S_1 of 0.41g. This loading was applied in the transverse direction only. The multi-mode spectral analysis method was used to determine the response of the bridge .

Figure 4 shows the comparison of axial forces in one of the diagonal members of the cross-frames under dead load. As shown, the cross-frame forces in a curved bridge can be twice those in the corresponding straight bridge. This discrepancy is most pronounced at the midspan of the center span (cross-frame number 13) and at the piers (cross-frame numbers 8 and 18). The torsional deformations in a curved bridge are largest at the midspan causing axial forces in the nearby cross-frames which are not generated in straight bridges.

Since a curved bridge tends to twist towards the outside of the curve, more load is shifted to the outside bearings at the piers. The pier cap then will have a larger displacement at one end (on the outside of the curve) and smaller displacement at the other end (on the inside of curve). These differential displacements generate forces in the cross-frames. In a straight bridge, cross-frame forces are also generated due to bent cap flexibility but they are smaller because of relatively uniform distribution of bearing forces. At the abutments, the cross-frames forces are small or zero

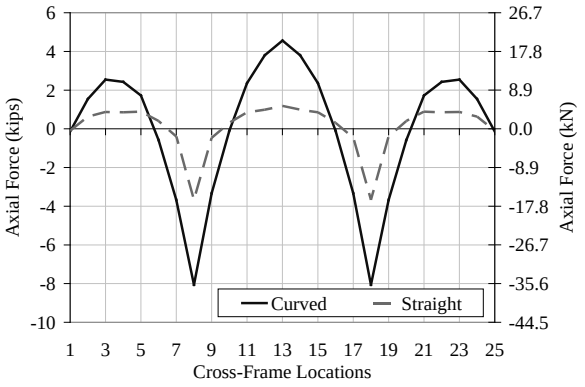


Figure 4 Comparison of Cross-Frame Forces (Diagonal Member) in Curved and Straight Bridge due to Dead Load

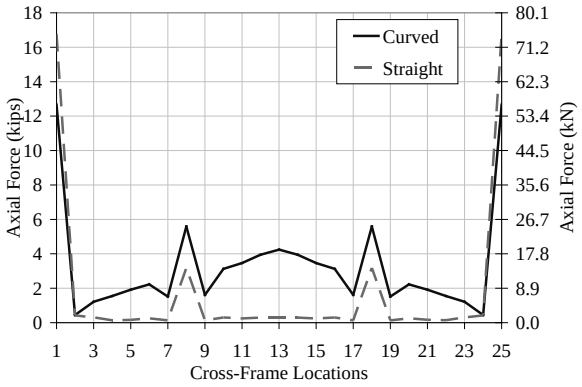


Figure 5 Comparison of Cross-Frame Forces (Diagonal Member) in Curved and Straight Bridge due to Earthquake Loading

because of the near-rigid support provided by the abutment.

Figure 5 shows the comparison of axial forces in one of the diagonal members of the cross-frames under seismic loading. Similar to the observation made under dead load, the discrepancy in the cross-frame forces is largest at midpsan of the center span. Seismic loading in the transverse direction creates frame action in curved bridges due to the offset between the abutments and piers. This frame action results in seismic axial forces in the columns and vertical reactions in the abutment bearings which must be resisted by superstructure torsion (Priestley et al. 1996). This torsion is then resisted by the cross-frames. When added to the dead load effects, this further increases the cross-frame forces in a curved bridge.

However, at the abutments, the cross-frame forces in the straight bridge are larger than those in the curved bridge. This is due to the difference in the boundary conditions in the transverse direction. Since the guided bearings in the curved bridge allow translation in the tangential direction but restrain the radial direction, the transverse direction is only partially restrained. However, in the straight bridge, the abutments are fully restrained in the transverse direction as the guided bearings allow translation in the longitudinal direction only.

As mentioned above, frame action occurs in a curved bridge when subjected to lateral loading in the transverse direction. The transverse lateral loading creates axial forces in the columns due to the offset between the abutments and piers. Depending on the magnitude of seismic force and the amount of offset between the abutments and piers, the columns may be subjected to large fluctuation in axial forces.

6 SEISMIC LOAD PATH

The seismic load path in a straight steel I-girder bridge has been described by Itani et al. (2010). The majority of the inertia loads are generated in the deck slab since the slab and barriers typically account for 80% of the bridge weight.

In the transverse direction, earthquake loading causes transverse bending of the superstructure resulting in transverse reactions at the abutments and piers. Numerical analyses have shown that seismic forces are largely distributed through the deck slab to the ends of the span (Carden et al. 2005a; 2005b; Bahrami et al. 2009) and thus the intermediate cross-frames take very little load. The forces at the ends of the span are then distributed vertically through the abutment and bent cross-frames (Itani 1995; Itani and Rimal 1996; Zahrai and Bruneau 1998) where they are then transmitted to the bearings and shear keys. Since the primary function of the bearings and shear keys is to allow the bridge to expand and contract longitudinally due to temperature variation, the abutments are usually restrained from translation in the transverse direction.

Under longitudinal loading, the load path is from the deck slab to the shear connectors, to the girders, and then to the bearings. This load may be assumed to be distributed uniformly to the shear connectors since they run parallel to the direction of loading and the superstructure is virtually rigid in this direction. If seat-type abutments are used these forces are resisted by the columns alone until the abutment backwall is engaged.

In a curved bridge, the load path is basically the same as that of a straight bridge. However, unlike a straight bridge, the intermediate cross-frames are primary members since they provide torsional rigidity to the superstructure.

Understanding the load path is important particularly in seismic design because it identifies the components that can be designed and detailed to provide energy dissipation during seismic excitation. In straight, steel I-girder bridges, the end cross-frames or diaphragms have been identified analytically (Itani and Rimal 1996; Astaneh-Asl and Donikian 1995; Zahrai and Bruneau 1998) and experimentally (Zahrai

and Bruneau 1999; Carden et al. 2005a; Bahrami et al. 2009) as critical components in the transverse seismic load path. Thus, these components can be designed as ductile members and thereby reduce the forces in a bridge during a transverse earthquake. The cross-frames in a straight bridge have a secondary role during normal operation and can be easily inspected and replaced after an earthquake. It is not clear at this time whether cross-frames in a curved bridge can be designed to play a similar role.

7 EFFECT OF COMPONENT FLEXIBILITIES

As discussed above, the cross-frames, girders, shear connectors, and deck slab are major components in the seismic load path. A parametric study has been conducted to determine the relative importance of these components on the seismic response. Results are briefly described in this section.

7.1 Cross-frames and Girders

Previous research has established that the end cross-frames are an essential component of the seismic load path. Accordingly, a parametric analysis was performed using the FE model of both the curved and straight bridges to determine the effectiveness of the end cross-frames in transferring the seismic forces to the bearings.

This effectiveness was quantified based on the percentage of seismic force transmitted through the end cross-frames. This was accomplished by calculating the ratio of the sum of the horizontal components of cross-frame forces, F_x, to the sum of abutment bearing shears, V_r. In the curved bridge, V_r corresponds to the total abutment radial shear since translation in the tangential direction is free while the radial direction is restrained. In the straight bridge, V_r corresponds to the total abutment transverse shear since translation in the longitudinal direction is free while the transverse direction is restrained.

The lateral loads are applied in the transverse direction and distributed equally among the deck nodes. The ratio F_x / V_r is then plotted as a function of the cross-frame-to-girder lateral stiffness ratio which is defined below.

The cross-frame lateral stiffness is calculated based on the properties of the braces (diagonal members) and is given by:

$$k = \frac{AE}{L}\cos^2(\theta) \tag{2}$$

where, A is the cross-sectional area, E is the modulus of elasticity, L is the brace length, and θ is the angle of the brace measured from the horizontal. Eq. (2) is then multiplied by four to determine the total lateral stiffness since there are four diagonal members in the example bridge.

At the supports, assuming the girder top flange is rigidly connected to the deck and the bottom flange is restrained from translation but free in rotation (i.e. a pin support), the girder deforms by rotation about its longitudinal axis. Then, assuming the girder is fixed against rotation at the location of first intermediate cross-frame due to the restraint provided by the cross-frame, the girder lateral stiffness is given by Carden et al. (2005a) as follows:

$$k_{t\theta} = \frac{k_{\theta g}}{d_{gf}^2} \tag{3}$$

where, $k_{\theta g}$ is the torsional stiffness of the girder between the end and first intermediate cross-frame and is given by Brockenbrough and Johnston (1968) as follows:

$$k_{\theta g} = \frac{J_g G}{a}\frac{1}{\frac{L_1}{a} - \tanh\left(\frac{L_1}{a}\right)} \tag{4}$$

$$a = \frac{d_{gf}}{2}\sqrt{\frac{EI_{gy}}{J_g G}} \tag{5}$$

$$J_g = \sum\left(\frac{bt^3}{3} - 0.21t^4\right) \tag{6}$$

where, L_1 is the length of the girder between the end and first intermediate cross-frames, E is the modulus of elasticity of steel, G is the shear modulus of steel, d_{gf} is the depth of the girder between the center of the flanges, I_{gy} is the moment of inertia of the girder about its weak axis, and b and t are the width and thickness of the plates in the built-up girder.

However, as shown below, it is the flexural stiffness of the bearing stiffeners that has the significant impact on the girder lateral stiffness. Based on the assumption that the top flange is rigidly connected to the deck and a pinned connection to the bottom flange, the flexural stiffness of the bearing stiffener is given by:

$$k_{tb} = \frac{3EI_{ws}}{d_{gf}^3} \tag{7}$$

where, I_{ws} is the moment of inertia of the bearing stiffener.

$$I_{ws} = \frac{t_s b_s^3}{12} \tag{8}$$

where, t_s is the thickness of the bearing stiffener and b_s is the total width of the bearing stiffener including the girder web thickness.

Therefore, the total lateral stiffness of the girder at the supports is given by:

$$K_t = k_{t\theta} + k_{tb} \tag{9}$$

For the bridges used in this parametric study, the lateral stiffness due to girder rotation is 0.88 kN/mm (5 kips/in). This is only 4% of the lateral stiffness provided by the bearing stiffener which is 24.52 kN/mm (140 kips/in). Since there are three girders in the bridge, the total lateral stiffness is 76.18

kN/mm (435 kips/in). Analysis of the FE model without end cross-frames and assuming a rigid deck (similar to the assumption used in developing the above equations) showed that the lateral stiffness is 79.50 kN/mm (454 kips/in), which is close to the calculated stiffness.

Figure 6 shows the relationship between the F_x / V_r ratio and cross-frame-to-girder stiffness ratio. As shown, the percentage of seismic forces transmitted by the end cross-frames increases with increasing stiffness ratio. Since the trend is about the same for both curved and straight bridges, this plot may be used to determine the level of seismic force that the cross-frames should be designed when the base shear is known. One application, for instance, is in capacity-protected design. Suppose the cross-frame-to-girder stiffness ratio is equal to 1.0, the cross-frames will carry about 80% of the base shear and the girders the remaining 20%. Now suppose that, in order to protect the foundation piles from damage, the abutment shear is limited to 1,000kN. In this case the cross-frames must be designed to yield at 800kN of lateral force. Designing the cross-frames to yield at, say, 1,000kN will overload the foundation and potentially damage the supporting piles.

Figure 6 indicates that for stiffness ratios less than 1.0, the girders are carrying most of the lateral load to the supports. This condition could be undesirable since the girders will be subjected to lateral bending. The most desirable condition occurs when the stiffness ratio is of the order of 3.0 since, at this point, the F_x / V_r ratio is almost 1.0 and all of the the seismic load is transferred to the abutments through the cross-frames and the girders carry negligible loads. At stiffness ratios greater than 3.0, the cross-frame forces are higher than the abutment shear. This means that an opposing force develops in the girders, which is transmitted away from the abutments to the piers. This condition could also be undesirable since not only will the girders be subjected to lateral bending but also the column forces will increase.

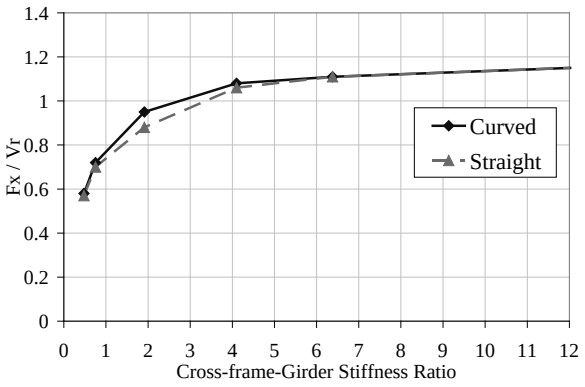


Figure 6 Relationship Between Cross-Frame Forces and Cross-Frame-to-Girder Stiffness Ratio

7.2 Shear Connectors

The primary function of the shear connectors (studs) in steel I-girder bridges is to provide composite action between the deck slab and the girders. As mentioned previously, the shear connectors are one of the main components in the load path in both the transverse and longitudinal directions. Failure of the studs near the supports causes the entire load path to be altered such that the intermediate cross-frames will be subjected to large seismic forces and the girders will be sustain large lateral bending.

A common assumption in analytical modeling of steel I-girder bridges is that the studs are rigid. Thus, a parametric analysis was performed to determine if the flexibility of the studs affects the distribution of seismic forces. As in the previous section, this effect is quantified in terms of the F_x / V_r ratio.

The stud transverse stiffness is determined for each of three conditions:

(a) First, the stud is assumed free to bend along its entire length which means the deck is fully cracked. This represents a lower bound on the stud stiffness.

$$k_b = \frac{12EI}{L^3} \tag{10}$$

where, E is the stud modulus of elasticity, I is the stud moment of inertia, and L is the effective length.

(b) Second, the stud is assumed free to bend along its half length only. This assumption is based on the fact that the stud is unconfined along the haunch thickness and cracking is usually observed at this location. This cracking can extend up to the half length of the stud. The equivalent transverse stiffness including shear deformation is:

$$k = \frac{1}{1/k_b + 1/k_s} \tag{11}$$

where, k_s is the shear stiffness given by Eq. (12).

(c) Third, as an upper bound on stud stiffness, it is assumed that the stud is restrained against bending along its entire length but can deform in shear. The shear stiffness is given by:

$$k_s = \frac{GA}{L} \tag{12}$$

where, G is the stud shear modulus, A is the area of the stud.

The studs used in the bridge model are 10 mm (3/8 in.) with an effective total length of 70 mm (2-3/4 in.). Using the above equations, the stud stiffness for each condition is (a) 2.84 kN/mm (16.24 kips/in) per stud, (b) 19.88 kN/mm (113.5 kips/in) per stud, and (c) 78.10 kN/mm (446 kips/in) per stud. There are three studs per row in each girder.

Figure 7 shows the relationship between the F_x / V_r ratio and stud stiffness. It is seen that stud stiffness has negligible effect on the distribution of seismic loads among the cross-frames and girders. It is also

seen that this observation is independent of the assumption about deck flexibility. However deck flexibility can have a significant effect on the distribution of seismic loads, as discussed in the next section.

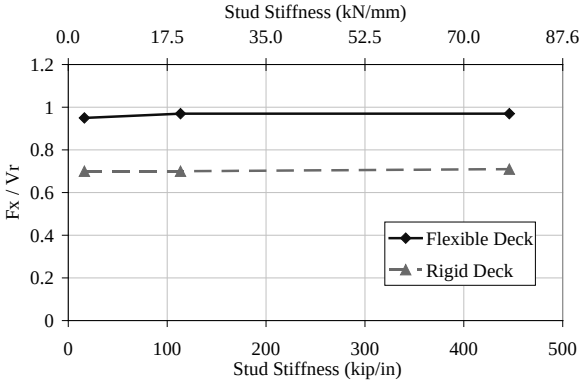


Figure 7 Effect of Shear Connector Stiffness on F_x/V_r

7.3 Deck Slab

The effect of deck flexibility on the distribution of seismic loads among the components is investigated by varying the ratio of the in-plane flexural rigidity (EI) of the deck slab to the transverse rigidity (EI) of the girders. In this study, the girder EI was kept constant while the deck slab EI was varied. The effect on the load distribution was then quantified in terms of the F_x / V_r ratio as before. Figure 8 shows that as the deck-girder stiffness ratio increases, the amount of seismic load transferred by the cross-frames decreases. For a rigid deck, the cross-frames transmit only 70% of the seismic load.

It should be noted that the above observations also apply to straight I-girder bridges.

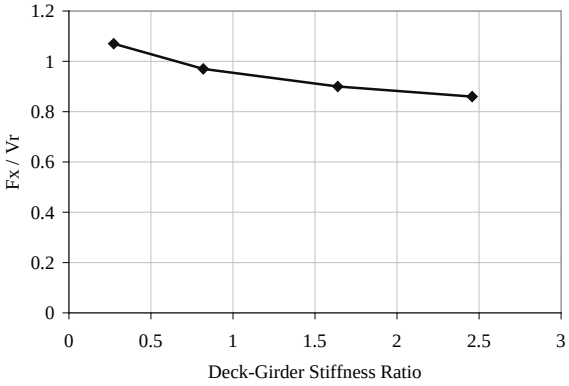


Figure 8 Effect of Deck Stiffness on F_x/V_r

8 CONCLUSIONS

Different modeling techniques used in the analysis of curved steel I-girder bridges have been discussed in this paper. The effect of modeling on response was determined by comparing the seismic response of stick, grillage (plate-and-beam), and finite element models. It has been shown that the seismic response of the stick model can be significantly in error, whereas the response of plate-and-beam model is comparable to that of FE model.

The effect of curvature was determined by comparing the response of straight and curved bridges under dead and seismic loads. It has been shown that the straight bridge assumption can lead to significant underestimation of local component response.

A parametric study was conducted to determine the influence of the relative stiffness of the cross-frames, girders, shear connectors, and deck slab on the distribution of seismic loads (i.e., the seismic load path). The following conclusions were made:

- The cross-frames are most effective in transferring the seismic forces to the bearings when the cross-frame-to-girder stiffness ratio is equal to 3.0.
- Modeling of the shear connectors has negligible effect on the distribution of seismic forces among the cross-frames and girders.
- The seismic forces transmitted by the cross-frames to the bearings decreases as the deck stiffness increases.

The relationships established may be used to proportion the components along the load path for optimal seismic response.

Acknowledgements:

This project is principally funded by the Federal Highway Administration of the U.S. Department of Transportation. Other sponsors include the California Department of Transportation (live load studies) and the National Science Foundation for use of the NEES Shake Tables at UNR under a Shared-Use Agreement with NEEScomm at Purdue University.

References:

American Association of State Highway and Transportation Officials (AASHTO). (2008), *AASHTO LRFD Bridge Design Specifications*, AASHTO, Washington D.C.

American Association of State Highway and Transportation Officials (AASHTO). (2009), *Guide Specifications for LRFD Seismic Bridge Design*, AASHTO, Washington D.C.

American Association of State Highway and Transportation Officials/National Steel Bridge Alliance Steel Bridge Collaboration (AASHTO/NSBA). (2010), *Guidelines for the Analysis of Steel Girder Bridges*, Chicago, IL.

Astaneh-Asl, A. and Donikian, R. (1995), *Seismic Behavior and Design of Steel Bridges, Volume I – Response Modification Factor Based Design*, American Iron and Steel Institute, Washinton D.C.

Bahrami, H., Itani, A.M., and Buckle, I.G. (2009), "Guidelines for the Seismic Design of Ductile End Cross-Frames and Diaphragms in Steel Girder Bridge Superstructures," *Report CCEER 09-04*, University of Nevada, Reno, NV.

Brockenbrough, R.L. and Johnston, B.G. (1968), *Steel Design Manual*, United States Steel Corporation, Pittsburgh, PA.

Carden, L.P., Itani, A.M., and Buckle, I.G. (2005a), "Seismic Load Path in Steel Girder Bridge Superstructures," *Report CCEER 05-03*, University of Nevada, Reno, NV.

Carden, L.P., Itani, A.M., and Buckle, I.G. (2005b), "Seismic Performance of Steel Girder Bridge Superstructures with Ductile End Cross Frames and Seismic Isolation," *Report CCEER 05-04*, University of Nevada, Reno, NV.

Japan Road Association (JRA). (1996), *Specifications for Highway Bridges: Part V Seismic Design*, JRA, Japan.

Itani, A.M. (1995), "Cross Frames Effect on the Seismic Behavior of Steel Plate Girders Bridges," *Structural Stability Research Council*, 27-28 March, 1995, Kansas City, MO, 73-82.

Itani, A.M., Grubb, M.A., and Monzon, E.V. (2010), "Proposed Seismic Provisions and Commentary for Steel Plate Girder Superstructure," *Report CCEER 10-03*, University of Nevada, Reno, NV.

Itani, A.M. and Rimal, P.P. (1996), "Seismic Analysis and Design of Modern Steel Highway Connectors," *Earthquake Spectra*, 12(2), 275-296.

Priestley, M.J.N., Seible, F., and Calvi, G.M. (1996). *Seismic Design and Retrofit of Bridges*, John Wiley and Sons, Inc. New York, NY.

Unites States Steel (1984), "V-Load Analysis," *USS Highway Structures Design Handbook*, I(12).

Zahrai, S.M. and Bruneau, M. (1998), "Impact of Diaphragms on Seismic Response of Slab-on-Girder Steel Bridges," *Journal of Structural Engineering*, American Society of Civil Engineers, 124(8), 938-947.

Zahrai, S.M. and Bruneau, M. (1999), "Cyclic testing of Ductile End-Diaphragms for Slab-on-Girder Steel Bridges," *Journal of Structural Engineering*, American Society of Civil Engineers, 125(9), 987-996.

8CUEE CONFERENCE PROCEEDINGS
8th International Conference on Urban Earthquake Engineering
March 7-8, 2011, Tokyo Institute of Technology, Tokyo, Japan

SEISMIC PERFORMANCE OF TWIN-CELL HOLLOW COMPOSITE MEMBERS

H.-L. Hsu[1] and R.-Z. Lee[2]

1) Professor, Dept. of Civil Engineering, National Central University, Taiwan
2) M.S., formerly Graduate student, Dept. of Civil Engineering, National Central University, Taiwan
t3200178@ncu.edu.tw

Abstract: This study focused on the performance evaluation of twin-cell hollow composite members subjected to combined cyclic loads. A series of composite members with various sectional aspect ratios were tested under bending, torsion and their combinations. It was observed that the deterioration in strength was lower for member with higher aspect ratio when the member was subjected to combined bending and torsion. It is also found from the test results that the energy dissipation capacities for members with larger aspect ratios were higher when they were subjected to the combined loads. Finally, an empirical expression for strength evaluation of members subjected to combined bending and torsion was proposed for engineering practice purpose.

1. INTRODUCTION

Steel-concrete composite members possess high strength and sufficient ductility thus are suitable structural forms for earthquake-resistant design for bridge constructions [El-Tawil and Deierlein 1999, Inai et al. 2004]. For bridge piers designed for extreme loads, the structural members with excessive dimensions and weight are usually required to sustain the applied loads. This hampers the competitiveness of the designs, and thus should be resolved with modified details. In this regard, the use of hollow sections is a remedy, as lower structural weight could be achieved to reduce the earthquake-induced lateral force and to alleviate the design demands [Bernardo and Lopes 2009, Lopes and Bernardo 2009, Taylor et al. 1995].

In general, the design of composite hollow bridge piers with excessive dimensions will incur concerns on the adequateness of the sectional detailing. For example, the width/thickness ratios of the sectional walls would be large if the light structural weight requirement is to be sustained. In such cases, the achievable strength of the member will be reduced as premature failure would occur in the section's thin walls. In order to mitigate the risk of premature failure in those regions, the sectional stability must be improved. For this purpose, a twin-cell composite section, as shown in Figure 1, is proposed in this study to possibly enhance the member performance.
For bridge piers designed for earthquake-resistant purposes, the structural performance must be validated under general loads induced by the earthquake, particularly torsion and combined loads coupled with torsion, because concrete is vulnerable to the torsion-induced shear. Therefore, this study focused on the performance evaluation of the twin-cell hollow composite members under combined bending and torsion. A series of cyclic loading tests on composite members with various sectional compositions were conducted. Test results were used to investigate the relationship between the member performance and the sectional configurations, and to establish design reference for engineering practice.

2. EXPERIMENTAL PROGRAM

Twelve twin-cell hollow composite specimens, as described in Figure 2, with different aspect ratios were fabricated for testing. The specimens were divided into three categories: 150, 250, and 350 series according to the dimensions of the steel tubes: 150×150×6mm, 250×150×6mm, and 350×150×6mm, respectively. Concrete thickness of all specimens was 100mm. Therefore, the aspect ratios (B/D; width/depth) of the three test series were 1.714, 2.286 and 2.857, respectively. The reinforced concrete was composed of #6 longitudinal bars and #3 stirrups. Stirrup spacings in the confined and unconfined zones were 70mm and 150 mm, respectively. The bottom of the member was clamped by a pair of stiffened platforms so that a rigid boundary condition

could be achieved. A pair of stiffened loading beams were attached to the member tops for load transmission. In order to evaluate the member performance, four load combinations were adopted for testing. These loads included bending, pure torsion, bending and smaller torsion, and bending with larger torsion, respectively. Specimens were labels according to their cross-sections and the applied load combinations, and were listed in Table 1.

For bending tests, a hydraulic actuator was placed at the center of the loading beam and driven by a set of increasing displacement commands, as shown is Figure 3. For the pure torsion tests, the actuator was moved to one end and a stiffened strut with hinged ends was placed at the center of the loading beam. Torsion was generated via the couple action of the actuator and the strut. Combined bending and torsion was generated by the actuator that was eccentrically placed and driven by the same displacement commands as those in the bending tests. The test set-up is shown in Figure 4.

3. FAILURE PATTERNS

Failure of members subjected to bending was initiated by the crack formation at the member bottoms. Concrete spalling was observed during the cyclic loading process. Buckling of the longitudinal bars was observed when members were subjected to large deformation. Plastic hinges were formed when the cover concrete crushed. For members subjected to pure torsion, failure was found to be concentrated at the center portions of the members. Crack widened and spread as twist angles were increased. Concrete spalling due to squeezing of cracked concrete blocks was observed at large distortion. The member's torsional strength deteriorated after the member reached the maximum strength.

For members subjected to lateral load with smaller eccentricity, the damage zone was closer to the bottom of the members. However, when the magnitude of applied torsion increased, the damaged region was shifted to the center portions of the members. The member performance was thus susceptible as less confinement was arranged in those areas. This phenomenon validated the importance of torsional effect on the design of composite members. Typical failure modes of members subjected to various loads are shown in Figure 5.

4. COMPARISONS OF TEST RESULTS

4.1 Strength

Figure 6 shows the typical hysteretic relationships for members subjected to different load combinations. The backbone curves for the members are also compared in Figure 7. It can be found from the figure that the deterioration rates in strength was smaller for member with larger steel strength ratio. This phenomenon can be explained by the effective flexural rigidity of the steel tube because the tube strength contributed major portion of the member strength when the concrete was damaged at large deformation. Therefore, members with larger steel strength ratio could sustain higher member strength.

In order to define the relationship between aspect ratio and the member performance, the achievable strength of members subjected to combined bending and torsion was further evaluated. Figure 8 shows the relationship between normalized bending and torsional strength. It can be found from the figure that member's flexural strength decreased when the torsion magnitude was increased. The relationships can be linearly approximated with adequate accuracy, and expressed as follows:

$$\frac{M}{M_u} + \alpha \cdot (\frac{T}{T_u}) = 1 \qquad (1)$$

in which M and T are the achievable flexural and torsional strength when the members are under combined loading, M_u and T_u are the bending and torsional strength of the section, α is a reduction factor accounting for the torsional effect. The relationships for the three test series were

150 series (B/D=1.714),

$$\frac{M}{M_u} + 0.43942 \cdot (\frac{T}{T_u}) = 1 \qquad (2)$$

250 series (B/D=2.286),

$$\frac{M}{M_u} + 0.32201 \cdot (\frac{T}{T_u}) = 1 \qquad (3)$$

350 series (B/D=2.857),

$$\frac{M}{M_u} + 0.25361 \cdot (\frac{T}{T_u}) = 1 \qquad (4)$$

It can be found from the above equations that the reduction factor α is related to the sectional aspect ratio (B/D), as shown in Figure 9. Therefore, the member strength under combined bending and torsion can be further refined as follows:

$$\frac{M}{M_u} + (0.7119 - 0.16257 \frac{B}{D}) \cdot (\frac{T}{T_u}) = 1 \qquad (5)$$

4.2 Energy Dissipation

Energy dissipation was evaluated using the cumulative area of the hysteretic curve. Figure 10 shows the relationship between the strength and the cumulative energy dissipation for the three test series. In order to investigate the members' performance, the achievable cumulative energy when members reached the failure state, defined by the state at which the member strength dropped to 85% of the member's bending strength, was compared. It can be observed from the comparison that member's energy dissipation capacity was significantly reduced when torsion was presented. It can also be found

from the figure that members with larger sectional aspect ratio maintained sufficient energy dissipation capacity no matter the member were under small eccentric load or large eccentric load. However, for members with smaller sectional aspect ratios, e.g. 150 series and 250 series, the members' energy dissipation could be susceptible when loads coupling with torsion was applied. These phenomena validated the importance of the cross-sectional aspect ratio on the seismic performance of twin-cell hollow composite members.

5. CONCLUSIONS

This study evaluated the performance of twin-cell hollow composite members subjected to combined cyclic loads. A series of composite members with various sectional aspect ratios were tested under bending, torsion and their combinations. It was observed that the deterioration in strength was lower for member with higher aspect ratio when the member was subjected to combined bending and torsion. It is also found from the test results that the energy dissipation capacities for members with larger aspect ratios were higher when they were subjected to the combined loads. Finally, an empirical expression for strength evaluation of members subjected to combined bending and torsion was proposed for engineering practice purpose.

References

EI-Tawil, S. and Deierlein, G. (1999), "Strength and ductility of concrete encased composite columns", *Journal of Structural Engineering*, ASCE, 125(9), 1009-1019.

Inai, E., Mukai, A., Kai, M., Tokinoya, H., Fukumoto, T. and Mori, K. (2004),"Behavior of concrete-filled steel tube beam columns", *Journal of Structural Engineering,* ASCE, 130(2), 189-202.

Bernardo, L. and Lopes, S. (2009), "Torsion in high-strength concrete hollow beams: strength and ductility analysis", *ACI Structural Journal*, 106(1), 39-48.

Lopes, S. and Bernardo, L. (2009), "Twist behavior of high-strength concrete hollow beams – formation of plastic hinges along the length", *Engineering Structures*, 31(1), 138-149.

Taylor, A., Rowell, R. and Breen, J. (1995), "Behavior of thin-walled concrete box piers", *ACI Structural Journal*, 92(3), 319-333.

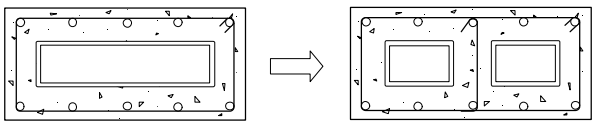


Figure 1 Design Concepts for Twin-cell Hollow Composite Members

Table 1 Specimen Details

Series	Specimen Label	(b_s×d_s×t) (mm)	Aspect Ratio (B/D)	Load Combination
150	M-C-150	150x150x6	1.714	Bending
	SE-150			Bending + smaller torsion
	LE-150			Bending + larger torsion
	T-150			Pure torsion
250	M-C-250	250x150x6	2.286	Bending
	SE-250			Bending + smaller torsion
	LE-250			Bending + larger torsion
	T-250			Pure torsion
350	M-C-350	350x150x6	2.857	Bending
	SE-350			Bending + smaller torsion
	LE-350			Bending + larger torsion
	T-350			Pure torsion

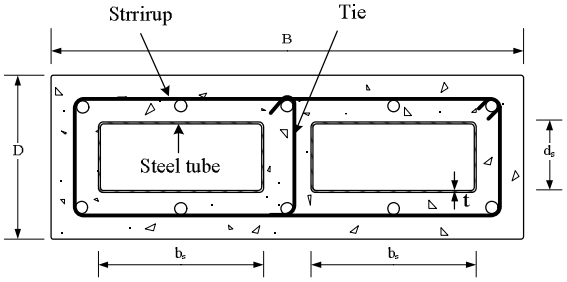


Figure 2 Cross-Sectional Details

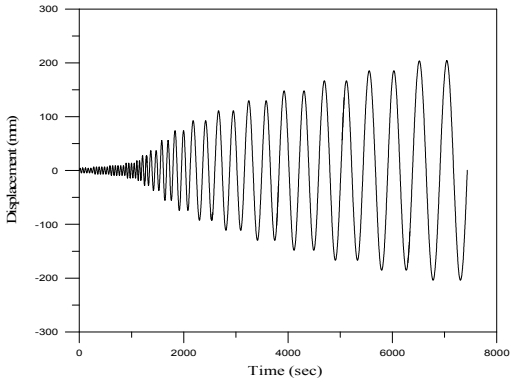


Figure 3 Displacement Commands

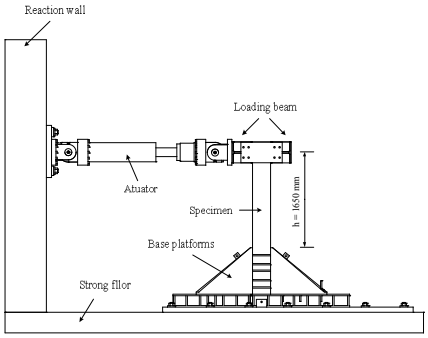
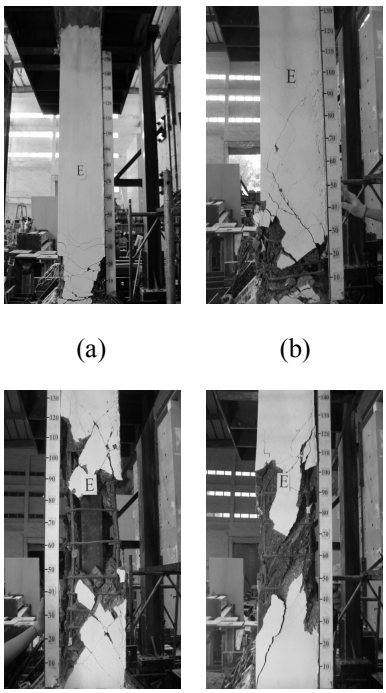


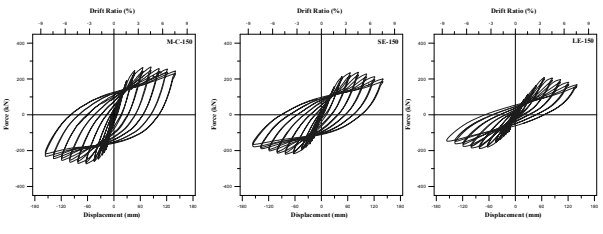
Figure 4 Test Set-up



(a) (b)

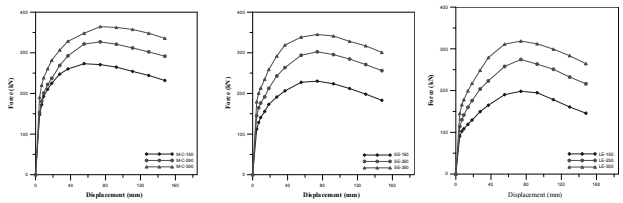
(c) (d)

Figure 5 Typical Failure Modes of Members Subjected to Various Loads: (a) Bending; (b) Bending with Smaller Torsion; (c)Bending with Larger Torsion; (d)Torsion



(a) (b) (c)

Figure 6 Typical Hysteretic Relationships for Members Subjected to Different Load Combinations: (a) Bending; (b) Bending with Smaller Torsion; (c) Bending with Larger Torsion.



(a) (b) (c)

Figure 7 Backbone Curves for Members Subjected to Different Load Combinations: (a) Bending; (b) Bending with Smaller Torsion; (c) Bending with Larger Torsion.

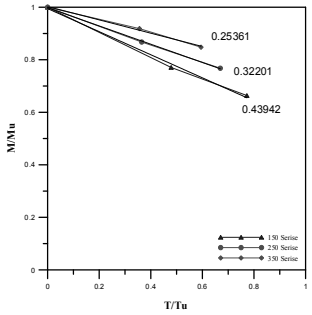


Figure 8 Relationship Between Normalized Bending and Torsional Strength.

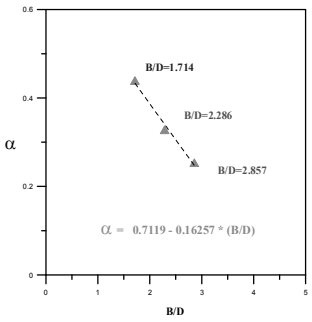
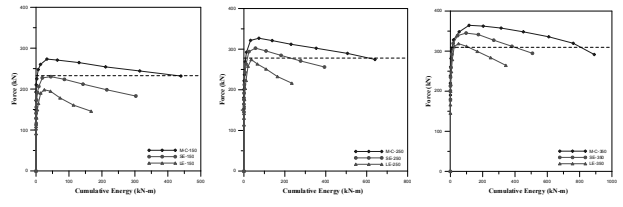


Figure 9 Relationship Between Reduction Factor and Aspect Ratios



(a) (b) (c)

Figure 10 Relationship Between the Strength and the Cumulative Energy Dissipation: (a) 150 Series; (b) 250 Series; (c) 350 Series.

8CUEE CONFERENCE PROCEEDINGS
8th International Conference on Urban Earthquake Engineering
March 7-8, 2011, Tokyo Institute of Technology, Tokyo, Japan

SCALE EFFECTS OF REINFORCED CONCRETE COLUMNS UNDER SHAKE TABLE TESTING: PHASE I – FULL SCALE TEST RESULTS

José I. Restrepo[1)], Matthew J. Schoettler[2)], Gabrielle Guerrini[3)], David E. Duck[3)], and Francesco Carrea[4)]

1) Professor, Department of Structural Engineering, University of California, San Diego, United States
2) Post-doctoral researcher, Department of Structural Engineering, University of California, San Diego, United States
3) Graduate student researcher, Department of Structural Engineering, University of California, San Diego, United States
4) Graduate student researcher, Department of Structural Engineering, University of Bologna, Italy
jrestrepo@ucsd.edu, mschoett@ucsd.edu, gguerrin@ucsd.edu, dduck@ucsd.edu, francesco_carrea@hotmail.it

Abstract: Seismic design procedures for reinforced concrete bridges columns in the United States are based on theoretical models that have been calibrated against results from numerous cyclic load tests and shake table experiments. Most if not all of the shake table experiments were performed on scaled specimens due to prior limitations of shake tables. The investigation of the modes of failure of columns built at full-scale and tested under simulated earthquake loading is a critical link to evaluate the basis for the seismic design procedure. To study potential scale effects, full-scale dynamic testing is necessary. For this stipulation, shake table test results of a 1.22-m diameter reinforced concrete bridge column was conducted. This was the first shake table test of a full-scale bridge column detailed with current Caltrans design practices. The objective of testing was to induce nonlinear deformation demands and monitor the dynamic response for comparison with a small-scale shake table test to be conducted at the University of California, Berkeley.

1. INTRODUCTION

Results from the first shake table test of a full-scale bridge column detailed with current Caltrans design practices are presented. For the investigation of scale effects, a 1.22-m diameter reinforced concrete bridge column was tested under simulated historical earthquakes. The column, whose height to diameter aspect ratio was six, was expected to have a flexurally dominated response. To mobilize the column's capacity, a concrete mass weighing 2.32 MN was placed on top of the 7.32-m column.

The objective of testing was to induce nonlinear deformation demands and monitor the dynamic response for comparison with a small-scale shake table test to be conducted at the University of California, Berkeley. Validation of current design practices and analysis methods were of primary interest in this project and can be assessed from the achieved objective.

The test specimen was densely instrumented to obtain high quality response measurements under various earthquake ground motions. A total of ten earthquake simulations were conducted with the larger intensity simulations producing large inelastic response. Tests were conducted over two days on the NEES shake table at the University of California, San Diego's Englekirk Structural Engineering Center between September 20th and 21st, 2010.

2. TEST SETUP

The test specimen included a cantilevered reinforced concrete column, footing, and superstructure mass, see Figure 1. The column represented a full scale bridge column designed to current Caltrans design guidelines, but was not modeled after an existing prototype bridge column. The column's footing was secured to the shake table with post-tensioning to prevent decompression under maximum expected overturning moment and provide shear transfer without sliding. The superstructure mass provided the appropriate column axial load and mass necessary to generate the forces inducing nonlinear response.

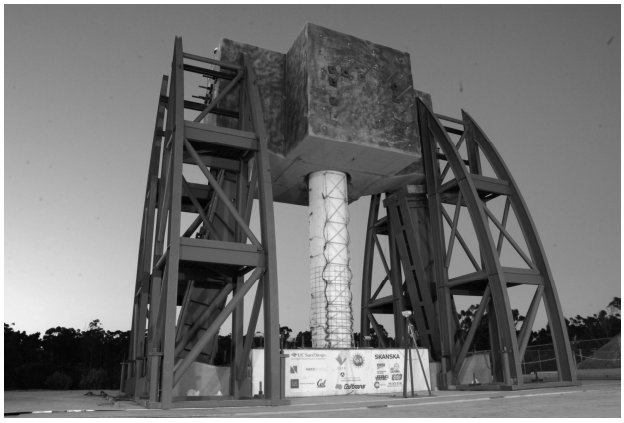


Figure 1 Test setup

The column was designed according to Caltrans Seismic Design Criteria (Caltrans, 2006) and Bridge Design Specifications (Caltrans, 2004). The 1.22-m diameter cantilever column spanned 7.31 m above the footing. The longitudinal reinforcement consisted of eighteen #11 (35.8-mm diameter) bars evenly spaced around the column perimeter. Butt-welded, double #5 (15.9-mm diameter) hoops, spaced at 152 mm on-center were used as transverse reinforcement. The term "double" refers to two hoops bundled together at each 152 mm spacing. Clear cover to the hoops was 51 mm. Column reinforcement layout and the test specimen's geometry are provided in Figure 2.

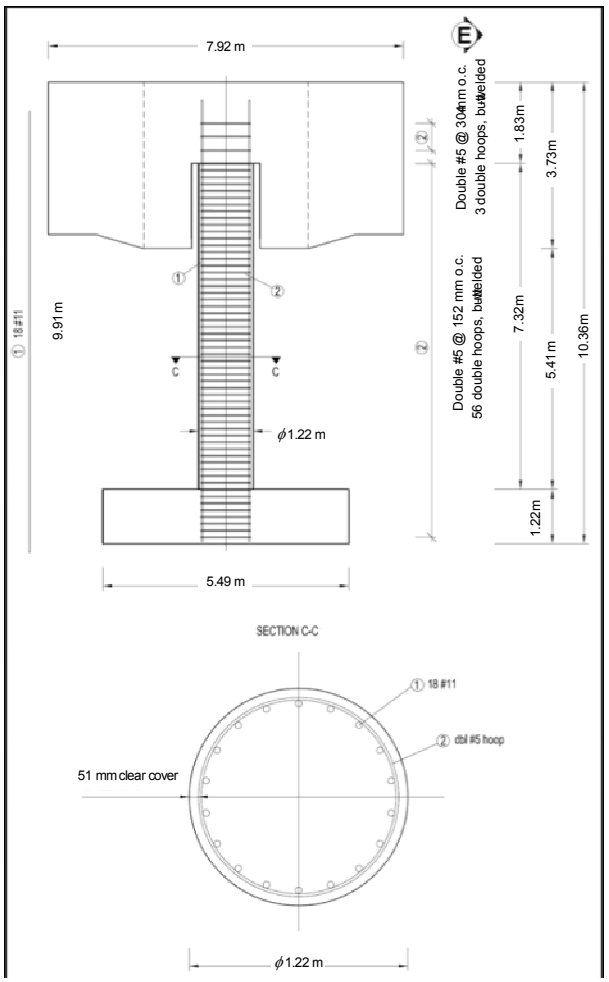


Figure 2 Reinforcing details of the test specimen

A longitudinal reinforcement ratio, ρ_l, of 1.55%, typical of current practice, was provided for the column. The transverse reinforcement provided a volumetric confining ratio, ρ_s, of 0.953%. Reinforcement complied with minimum and maximum requirements (Caltrans, 2004 and Caltrans, 2006).

The estimated axial load at the column base was 2.53 MN. Accounting for the measured concrete strength at day one of testing, this axial load produced an axial load ratio of 5.34%.

The superstructure block's geometry was designed so its center of mass was located at the top of the column. To ensure an unencumbered column height of 7.32 m, a blockout was provided between the column and the block for the bottom 1.91 m of the block. A 1.52-m diameter corrugated pipe embedded in the block resulted in a 152.4-mm gap between the block and the column. The corrugated pipe was utilized as stay-in-place formwork.

Safety restraints, secured to the shake table, surrounded the test specimen to provide protection to site personnel and equipment. To preclude out-of-plane motion, the safety restraints located at the corners of the specimen were fitted with guides. Pairs of steel tubes were aligned in the direction of shaking and welded to the arched safety towers. A clear 6.4 mm gap between the guides and concrete blocks was greased to reduce friction should contact initiate between the blocks and the restraint towers.

To limit the column displacement to a 10% drift ratio and prevent a gravity load collapse, inclined safety columns were placed on either side of the column in the direction of shaking. Large timbers secured to the safety columns were incorporated to dissipate energy at impact between the superstructure mass and the columns.

3. MATERIAL PROPERTIES

The specified concrete strength of the column was 27.6 MPa. Maximum aggregate size was 25.4 mm. At the time of casting, 152.4-mm diameter by 304.8-mm high concrete test cylinders were taken. These provided an average concrete unit weight of 23.58 kN/m3. Cylinders were tested under monotonic compression in sets of three samples at twenty-nine, forty-two, and forty-three days. Commencement of shake table testing corresponded to an age of forty-two days in the column concrete. The forty-three day age corresponded to the second day of shake table testing. Of the three samples in a set, two samples were taken from the first batch of concrete delivered to the site and one sample was from the second batch of concrete. This gave emphasis to the concrete strength in the plastic hinge region. Table 1 summarizes the results of these compression tests.

Table 1 Column concrete strength

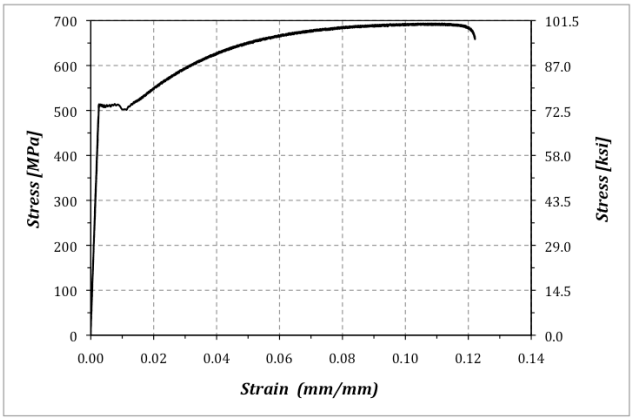
Age	f'_c
(Days)	(MPa)
29	40.3 *
42	40.9 +
43	42.0 ‡

* Average of three samples
+ Average of five samples
‡ Average of six samples

Column longitudinal and transverse reinforcement was specified as Grade 60 (414 MPa) steel conforming to ASTM A706. The #11 (35.8-mm diameter) longitudinal reinforcement had a yield strength of 518.5 MPa and an

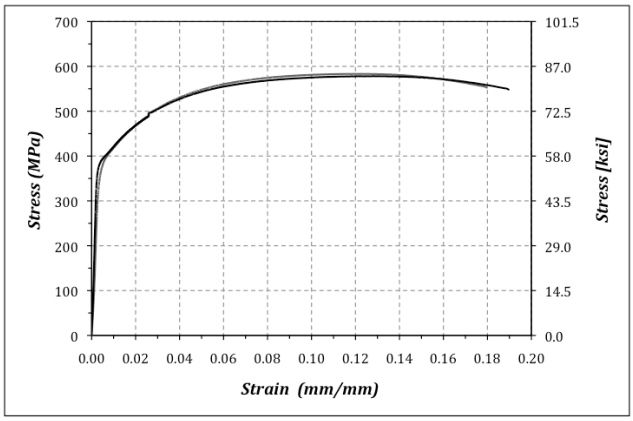
ultimate strength of 706.7 MPa. These strengths were obtained from monotonic tension tests. A complete stress-strain curve for this reinforcement is provided in Figure 3.

Figure 3 Column longitudinal reinforcement stress-strain relationship



Samples taken from the #5 (15.9-mm diameter) transverse hoops tested under monotonic tension did not exhibit a yield plateau. The peak stress was 592.2 MPa. A full stress-strain relationship of two samples is provided in Figure 4. These samples were cut from three bent hoops outside of the weld-affected region. The butt welds of the three sample hoops were also tested and all failed outside of the weld. Yield strength based on the mill cert of the straight #5 bars was expected to be 454 MPa and the ultimate tensile strength was expected to be 600 MPa.

Figure 4 Column transverse hoop reinforcement stress-strain relationship



4. LOADING PROTOCOL

A total of ten earthquake simulation tests were conducted. The intended loading protocol consisted of six simulated earthquake tests. Four historical earthquake recordings were selected as shake table input motions. A site of San Francisco, California, was considered for the seismic hazard. Therefore, earthquake recordings from a strike slip fault mechanism were given preference. Three input motions were selected from the 1989 Loma Prieta earthquake. The fourth record was sourced from the Takatori station during the 1995 Kobe earthquake. These records are identified in Table 2. Each of the recordings was obtained from the PEER's strong motion database (PEER, 2007).

Table 2 Ground motion selections

Test	Target displacement ductility	Scale factor	Table PGA (g)
EQ1	1.0	1.0	-0.199
EQ2	2.0	1.0	0.409
EQ3	4.0	1.0	0.526
EQ4	2.0	1.0	0.454
EQ5	8.0	-0.8	-0.533
EQ6	4.0	1.0	-0.512
EQ7	Not applicable	1.0	0.646
EQ8	Not applicable	-1.2	-0.829
EQ9	Not applicable	1.2	0.819
EQ10	Not applicable	1.2	0.851

Input motions were selected based on their ability to produce a target displacement, in terms of displacement ductility, in the test specimen without scaling. The target drifts were anticipated from linear elastic displacement response spectra and nonlinear dynamic time history analyses using a lumped plasticity column model. Based on the nonlinear analytical demands, the Takatori record for EQ5 was scaled down to 80% of the original record to produce the targeted displacement in the analytical model. The polarity of this record was inverted based on analytically predicted residual drifts. The targeted displacement ductility, scale factor, and resulting peak ground acceleration (PGA) are identified with the test name in Table 3.

Table 3 Ground motion scale factors

Test	Earthquake	Station	Comp-onent
EQ1	Loma Prieta	Agnew State Hospital	090
EQ2	Loma Prieta	Corralitos	090
EQ3	Loma Prieta	LGPC	000
EQ4	Loma Prieta	Corralitos	090
EQ5	Kobe	Takatori	000
EQ6	Loma Prieta	LGPC	000
EQ7	Kobe	Takatori	000
EQ8	Kobe	Takatori	000
EQ9	Kobe	Takatori	000
EQ10	Kobe	Takatori	000

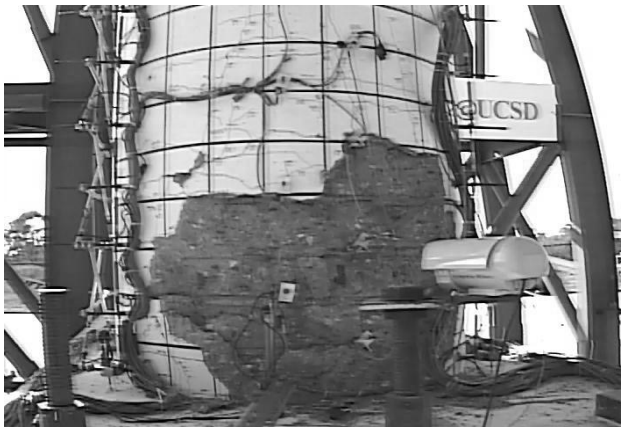
Before the first earthquake simulation, two white noise table motions were conducted. A white noise table motion with a 0.03-g root mean square amplitude was used to check the instrumentation for quality control assurance. The same input motion was repeated before testing commenced and then repeated between subsequent

earthquake tests. This was implemented to observe the period shift and mode shape changes caused by damage accumulation.

5. RESULTS

The results summarized pertain to the extended scope of testing. This includes the last four tests referred to as EQ7 through EQ10. As a result of the prior six earthquake simulations, the column was damaged and had a fully developed plastic hinge. Concrete had spalled at the base of the column, and cracks extended the visible height of the column. Figure # is a view of the East face of the column's base post-EQ6 test. The residual displacement caused by the preceding tests was 50 mm or 0.68% residual drift ratio.

Figure 3 Column base post-EQ6



The objective of extended testing was to initiate failure and bring the column to a near-collapse condition. This was implemented with the Takatori record of the 1995 Kobe earthquake at various scaled amplitudes.

5.1 Test EQ7

In test EQ7, the Takatori motion was utilized at 100% of the original record. This resulted in a peak drift ratio of 7.56%. A residual drift ratio of -1.98%, or -145 mm column displacement, remained post-test.

A post-test view of the East face of the column base is shown in Figure 4. Although not visible in this figure, further spalling was produced and more of the longitudinal bars were exposed as the spalling penetrated deeper into the face of the column.

The peak column base moment was 7,378 kN-m, see Figure 5. This was the maximum overturning moment obtained in any of the tests. The peak shear force was 817 kN, the second largest shear force obtained in any of the tests. The lateral shear force and displacement response is shown in Figure 6.

Figure 4 Column base post-EQ7

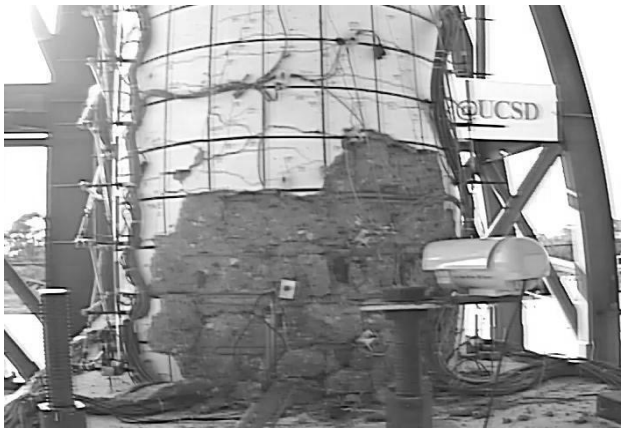


Figure 5 EQ7 moment-curvature relationship

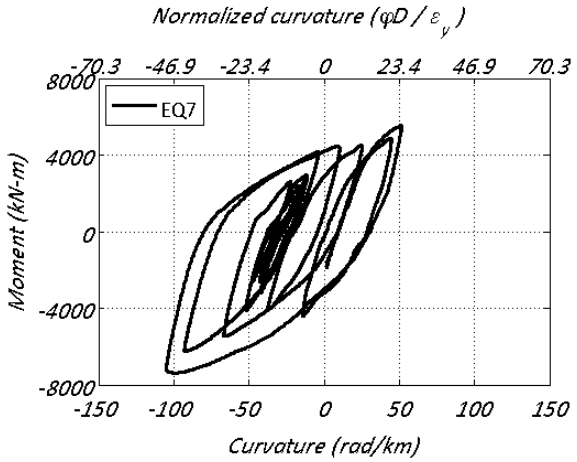
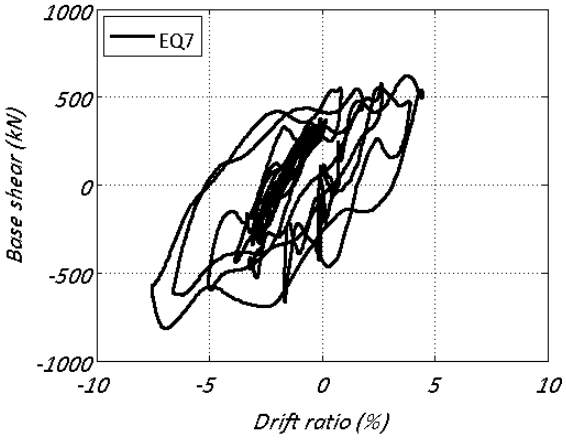


Figure 6 EQ7 shear-drift ratio relationship



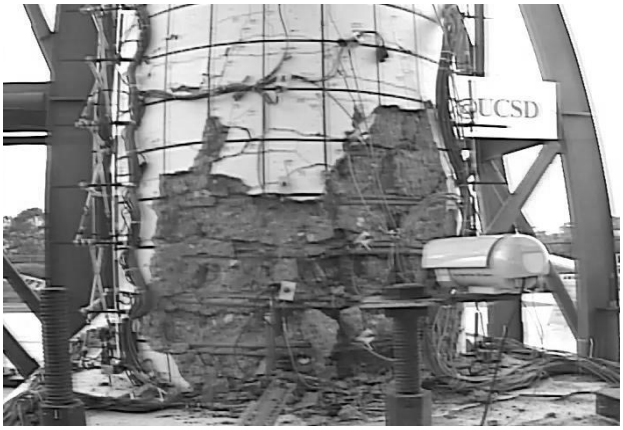
5.2 Test EQ8

A scale factor of -1.2 was used with the original Takatori record in test EQ8. This imposed a 606 mm column displacement. The corresponding drift ratio was 8.28%. The residual displacement was 97 mm at the top of the column, which normalizes to 1.33% residual drift ratio.

A post-test view of the East face of the column base is shown in Figure 7. In this figure, the two exposed longitudinal reinforcing bars on the right side of the column

centerline have fractured. Neither the fracture nor the bar's buckled shape are apparent in this figure. This was the first damage beyond concrete cracking and spalling induced in the test specimen.

Figure 7 Column base post-EQ8



The peak column base moment was 7,117 kN-m see Figure 8. The peak shear force was 745 kN, see Figure 9.

Figure 8 EQ8 moment-curvature relationship

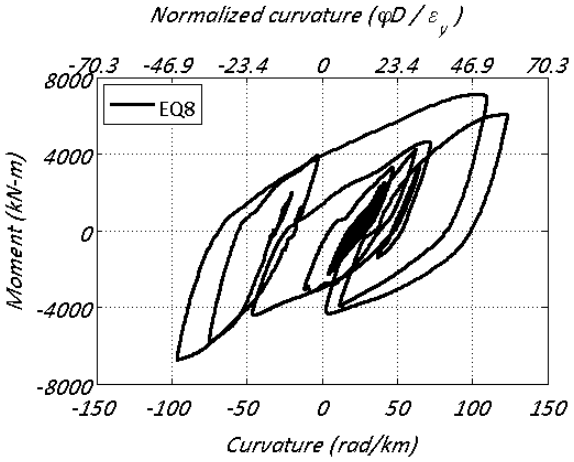
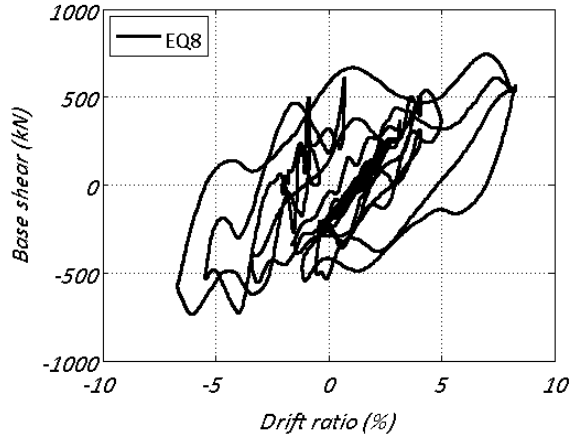


Figure 9 EQ8 shear-drift ratio relationship



5.3 Test EQ9

Reversing the polarity of the previous test, a scale factor of 1.2 was used with the original Takatori record for test EQ9. Early in the time history, a third longitudinal reinforcing bar fractured on the East face of the column. A post-test view of the East face of the column base is shown in Figure 10, but the fractures are not apparent. Two reinforcing bars fractured on the West face during this test. This is evident as a drop in moment capacity at about 110 rad/km in the moment-curvature relationship of Figure 11.

Figure 10 Column base post-EQ9



The peak column displacement was 635 mm corresponding to a drift ratio of 8.69%. A residual displacement of 225 mm, or 3.07% residual drift ratio, remained post-test.

The peak column base moment was 6,111 kN-m. This is 83% of the peak moment achieved in test EQ7. Stiffness degradation is apparent in the moment-curvature response, see Figure 11. The peak shear force was 742 kN. The lateral shear force-displacement response is shown in Figure 12.

Figure 11 EQ9 moment-curvature relationship

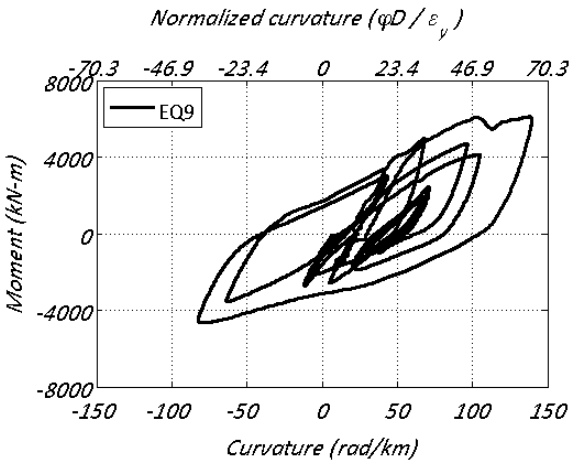
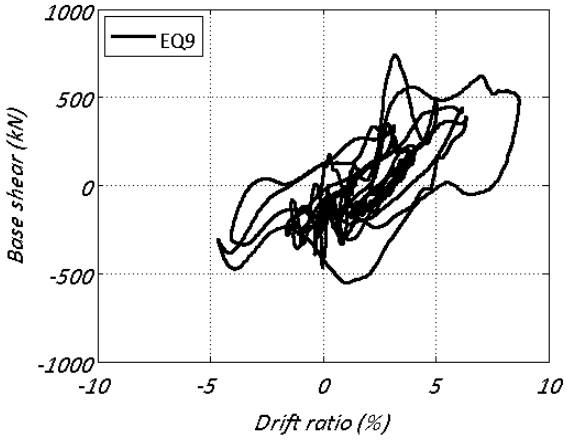


Figure 12 EQ9 shear-drift ratio relationship

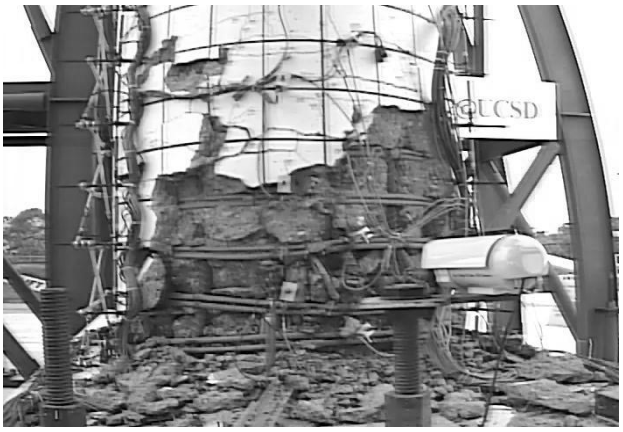


5.4 Test EQ10

The same scale factor of 1.2 was utilized with the Takatori record as in test EQ9. Prior tests resulted in a reduced column capacity caused by the fracture of five longitudinal bars. A sixth longitudinal reinforcing bar fractured during this test. This was the fourth bar to fracture on the East face of the column. However, the superstructure mass impacted the East safety column before this fracture occurred. During impact, the column displaced 757 mm. The drift ratio at impact was 10.34%.

A post-test view of the East face of the column base is shown in Figure 13. Vertical offset of the transverse hoops caused by the buckled longitudinal reinforcement is evident in this figure. However, the transverse reinforcement did not fracture.

Figure 13 Column base post-EQ10



The derived moment and shear force are heavily influenced at impact, and are therefore not reported. These peak moment and shear force are also omitted for this reason from Table 4, which contains a summary of several response quantities for each test. The drift ratio, longitudinal strain, base moment, base shear, and average base curvature are provided in terms of peak demand.

Table 4 Peak response quantities

Test	Peak drift ratio	Peak longitudinal strain	Peak moment	Peak shear	Peak curvature
	(%)	(mm/mm)	(MN-m)	(kN)	(rad/km)
EQ1	0.85	0.0022	3.93	500	6.8
EQ2	1.82	0.0132	5.87	698	15.6
EQ3	4.93	0.0298	6.60	887	60.8
EQ4	2.33	0.0144	3.70	399	25.1
EQ5	7.78	0.0466	7.21	813	105.3
EQ6	6.69	0.0423	6.51	766	91.6
EQ7	7.56	0.0428	7.38	817	104.9
EQ8	8.28	0.0584	7.12	745	123.3
EQ9	8.69	0.0638	6.11	742	139.6
EQ10*	10.34	0.0116	-	-	214.2

* Impacted the East safety column at peak displacement.

3. CONCLUSIONS

Ten earthquake simulations were conducted on a full-scale bridge column built to current Caltrans design specifications. Damage occurred in a concentrated plastic hinge at the base of the column. The response was dominated by a flexural plastic hinge, and shear capacity was maintained throughout testing.

Column cracks extended the accessible height of the column by testing completion. However, concrete spalling, longitudinal bar buckling, and longitudinal bar fracture were located within 1.22-m, or one column diameter, of the base of the column. Four longitudinal bars on the East face of the column fractured. Two longitudinal bars on the West face fractured and an additional two bars developed cracks which did not propagate through the bar diameter. All of the exposed longitudinal bars exhibited buckling deformation. Transverse hoops did not fracture and the concrete core remained largely intact.

To further the investigation on scale effects of reinforced concrete bridge columns, a scaled replica will be constructed and tested at University of California, Berkeley. This direct comparison of failure modes is a critical link to assess the consequence or validity of relying on small-scale tests for the development of seismic design procedures of reinforced concrete columns.

Acknowledgements:

This project was sponsored by the Pacific Earthquake Engineering Research Center's Program of Applied Earthquake Engineering Research of Lifelines Systems supported by the California Energy Commission, California Department of Transportation, and the Pacific Gas and Electric Company. Additional support was provided from the Federal Highway Administration contract DTFH61-07-C-00031.

This work made use of the Earthquake Engineering Research Centers Shared Facilities supported by the National Science Foundation, under award number EEC-9701568 through the Pacific Earthquake Engineering Research Center (PEER).

Any opinions, findings, and conclusions or recommendations expressed in this material are those of the authors and do not

necessarily reflect those of the National Science Foundation or the Federal Highway Administration.

References:

Caltrans, (2004), Bridge Design Specifications, California Department of Transportation, Sacramento, CA.

Caltrans (2006), Seismic Design Criteria, California Department of Transportation, Sacramento, CA.

PEER (2007), "PEER Strong Motion Database: Introduction." <http://peer.berkeley.edu/smcat/> (July, 2010).

8CUEE CONFERENCE PROCEEDINGS
8th International Conference on Urban Earthquake Engineering
March 7-8, 2011, Tokyo Institute of Technology, Tokyo, Japan

RESPONSE OF BRIDGE UNDER SEISMIC LOAD INCLUDING COLLISIONS

Eiki Yamaguchi[1] and Keita Yamada[2]

1) Professor, Department of Civil Engineering, Kyushu Institute of Technology, Japan
2) Graduate Student, Department of Civil Engineering, Kyushu Institute of Technology, Japan
yamaguch@civil.kyutech.ac.jp

Abstract: In the Mid Niigata Prefecture Earthquake in 2004, the damage of a bridge pier was found mitigated by the collision between the girder and the abutment. In the seismic response analysis, it is thus important to include the effect of collision. A simple and practical method of simulating collision in the numerical analysis is the introduction of a spring where the collision occurs. However, the constant of such a collision spring is yet to be formulated well. In this study, an appropriate collision-spring constant is investigated for simulating the collisions between girders and between a girder and an abutment. A small collision-spring constant tends to cause the large overlap of colliding bodies while a large collision-spring constant tends to cause many fictitious collisions during the real collision. Various girder-girder-collision and abutment-girder-collision models are analyzed, based on which formulas for the collision-spring constants are proposed. The response analysis of a bridge under seismic loading is then conducted to see the effect of the collision.

1. INTRODUCTION

Collision between bridge girders and/or between an abutment and a bridge girder may take place during earthquake. In the Mid Niigata Prefecture Earthquake in 2004, collision between an abutment and a bridge girder occurred indeed in a PC girder bridge (Photo 1) and a study revealed that the damage could have been much worse if not for the collision (Kosa et al. 2005). The collision can thus play an important role in the behavior of a bridge during earthquake: without including the effect of the collision, the analysis of a bridge behavior during earthquake can be quite misleading.

A simple and practical method of simulating collision in the numerical analysis is the introduction of a spring where the collision occurs. Nevertheless, not much research on the appropriate collision-spring constant has been conducted. To the best of the authors' knowledge, Kawashima (1981) is the only one who has proposed a formula for the collision-spring constant. The application of the formula is however limited to the case in which the colliding bodies are identical and modeled by the finite elements of equal length.

The colliding girders of a bridge are not always identical; an abutment and a girder are very different structures; and the size of a finite element used for modeling a girder usually varies along the girder axis. Therefore, the formula proposed by Kawashima (1981) may not be always applicable in practice. In such cases, an appropriate collision-spring constant is not known at the current stage of development.

Against the background of the above information, an appropriate value of the collision-spring constant between colliding bodies that have different stiffnesses is investigated in the present study. To be specific, the collisions between two girders and between a girder and an abutment are considered first. The response analysis of a bridge under seismic loading is then conducted. In all the analyses, the finite element software Y-FIBER3D (Yamato 2000) is used.



Photo 1 Collision between Abutment and Girder

2. ANALYSIS MODELS

The behavior of the collision spring is illustrated in Figure 1. The relative displacement is the distance between the two bodies, the relative displacement equal to zero corresponding to the initial state that has some gap (initial gap) between the bodies; the initial gap is introduced in bridge design to avoid contact due to temperature rise etc.

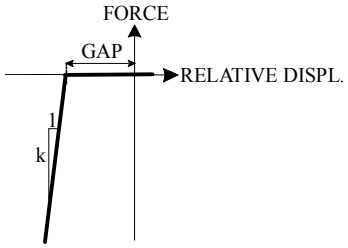


Figure 1 Characteristics of Collision Spring

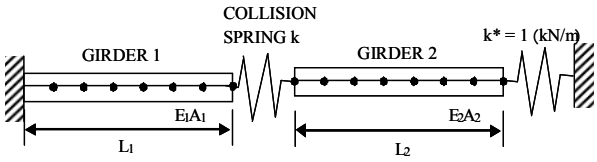


Figure 2 Girder-Girder Analysis Model

The relative displacement is positive when the gap becomes longer than that in the initial state while it is negative when the gap shortens. Only when the gap is closed completely, the two bodies are in actual contact. Figure 1 shows these characteristics of the collision spring. The slope k shown in Figure 1 is the collision-spring constant to be studied in the present study.

Kawashima's formula (Kawashima1981) for the spring constant is given by

$$k = \frac{nEA}{L} \tag{1}$$

where n is the number of finite elements, E is Young's modulus, A is the cross-sectional area and L is the girder length. The formula indicates that the collision-spring constant can be set equal to the axial stiffness of the finite element. The present study is to utilize the axial stiffness of the element as well and the analysis models are set up from this viewpoint.

The simulation of the collision by a spring is practical, yet it is quite an approximation of the behavior so that the overlap of the two bodies and the repetitive short collisions during the real collision period of time are unavoidable. The overlap becomes larger as the collision-spring constant is smaller; and more small collisions occur as the collision-spring constant is larger. The collision-spring constant that does not evoke those fictitious phenomena excessively is considered appropriate (Kawashima 1981).

By conducting seismic response analysis with various collision-spring constants, formulas for appropriate collision-spring constants are to be investigated herein. To this end, a simple triangular seismic wave is applied in the girder-axial direction in the response analysis. Time increment of 1/50000 sec is employed throughout this study.

2.1 Girder-Girder Collision

Figure 2 shows the analysis model to study collision between two girders. The girders are modeled by two-node beam elements, and a collision spring is placed between the girders. The spring with a very small spring constant at the right end of the right girder is introduced to prevent the free movement of the girder in the dynamic analysis. In this analysis model, Young's moduli of the two girders, E_1 and E_2, are both 2×10^5 N/mm^2, their girder lengths, L_1 and L_2, are both 50 m and the initial gap between the two girders is 0.15 m and the Rayleigh damping constant is 0.02.

The axial stiffness of a bridge girder usually falls in the range from 5.0×10^5 to 5.0×10^6 kN/m. Based on this observation, three values of 5.0×10^5, 1.0×10^6 and 5.0×10^6 kN/m are employed in the present study. In addition, three different values are used for the axial stiffness of an element in the vicinity of collision. The combination of them yields 9 analysis models as shown in Table 1. The element length Le in Table 1 is applied to those elements located in the region within 5 m from the collision point in Model GG1-GG3 and 6 m from the collision point in the other models. In the remaining region, the lengths of the elements are all 1 m.

As realized in Table 1, in Models GG1-GG3, the two girders have the same axial stiffness of the girder and the same axial stiffness of the element; in Models GG4-GG7, only either the axial stiffness of the girder or the axial stiffness of the element is the same; and in Models GG8 and GG9, neither the axial stiffness of the girder nor the axial stiffness of the element is the same.

2.2 Abutment-Girder Collision

Figure 3 is the abutment-girder collision model. The girder assumes the same material and structural characteristics as those of the girder-girder collision model. The spring with a very small spring constant at the right end of the girder is also used in the abutment-girder collision model.

For the axial stiffness of the girder, the same values as those of the girder-girder collision model, 5.0×10^5, 1.0×10^6, and 5.0×10^6 kN/m, are utilized. The abutment is modeled by a spring, as is often the case with the models in existing studies. Four values of the spring constant k_A are assumed for the abutment: 1.0×10^5, 1.0×10^6, 1.0×10^7 and 3.0×10^8 kN/m.

The combination gives 12 abutment-girder collision analysis models. In all these models, the element length of 0.5 m is used in the region within 5 m from the collision point and the element length of 1 m is employed for the remaining region.

3. PROPOSED FORMULA

3.1 Girder-Girder Collision

Figure 4 shows the variation of the maximum relative displacement (absolute value) on the negative side with the

Table 1 Girder-Girder Analysis Models

Model	Girder 1			Girder 2		
	EA/L (kN/m)	EA/L^e (kN/m)	L^e (m)	EA/L (kN/m)	EA/L^e (kN/m)	L^e (m)
GG1	5.0×10^5	5.0×10^7	0.5	5.0×10^5	5.0×10^7	0.5
GG2	1.0×10^6	1.0×10^8	0.5	1.0×10^6	1.0×10^8	0.5
GG3	5.0×10^6	5.0×10^8	0.5	5.0×10^6	5.0×10^8	0.5
GG4	1.0×10^6	1.0×10^8	0.5	1.0×10^6	2.0×10^8	0.25
GG5	1.0×10^6	1.0×10^8	0.5	1.0×10^6	6.67×10^7	0.75
GG6	1.0×10^6	2.0×10^8	0.25	1.0×10^6	6.67×10^7	0.75
GG7	5.0×10^5	1.0×10^8	0.25	1.0×10^6	1.0×10^8	0.5
GG8	5.0×10^5	5.0×10^7	0.5	5.0×10^6	5.0×10^8	0.5
GG9	1.0×10^6	1.0×10^8	0.5	5.0×10^6	1.0×10^9	0.25

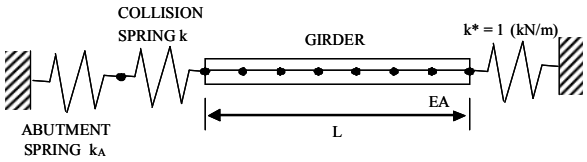


Figure 3 Abutment-Girder Analysis Model

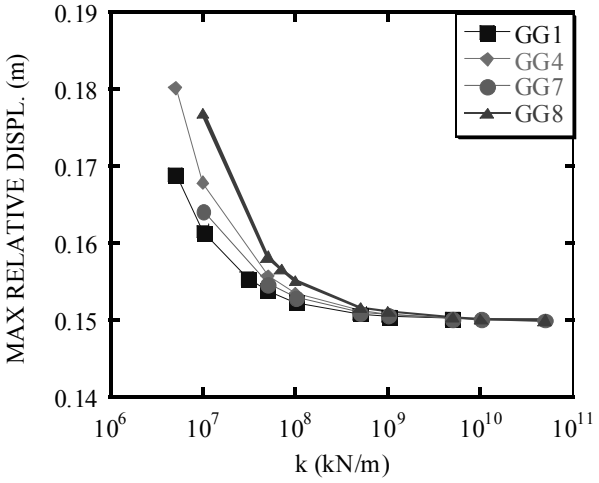


Figure 4 Variation of Maximum Relative Displacement with Collision-Spring Constant

collision-spring constant. As the collision-spring constant becomes lager, the maximum relative displacement decreases. For the sake of clarity, the results of only four models are given in Figure 4, but the others yield the same tendency.

To determine the allowable relative displacement, the

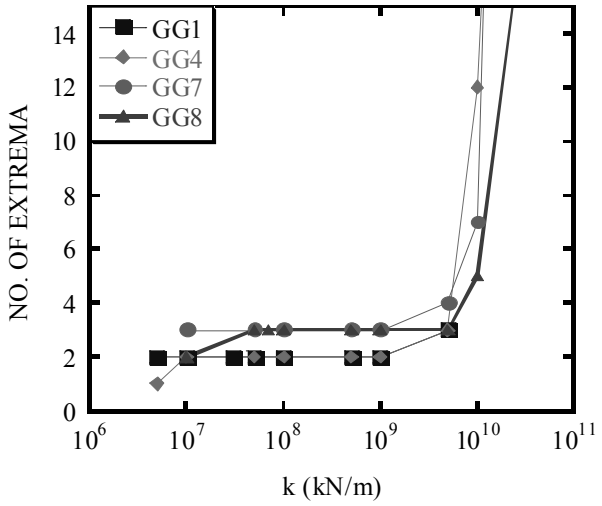


Figure 5 Relationships between Number of Extrema of Relative Velocity and Collision-Spring Constant

girder-girder analysis models to which Eq. (1) is applicable are set up additionally. These models are basically the same as GG2 and GG3, but the two girder models are discretized by the beam elements of equal length entirely.

The maximum relative displacement in the seismic response analysis of the additional analysis models is found 0.157 m. In the present study, 0.157 m is then employed for the allowable relative displacement. That is, the collision-spring constant that gives the maximum relative displacement less than 0.157 m is to be judged appropriate. As Figure 4 indicates, this criterion gives the lower bound of the collision-spring constant.

To investigate the phenomenon of the repetitive short collisions during the real collision period of time, the extrema in the variation of the relative velocity with time during the collision is counted. Figure 5 shows the relationships between the number of extrema thus obtained

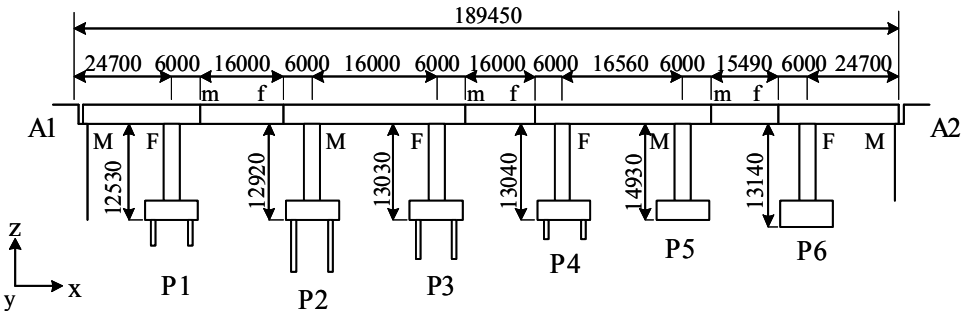


Figure 6 Bridge Model (Units: mm)

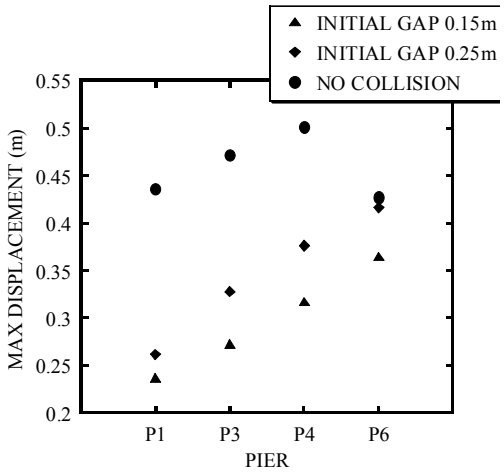


Figure 7 Maximum Horizontal Displacement of Piers

and the collision-spring constant. A tendency for the number of extrema to increase with the collision-spring constant is recognized. For the sake of clarity, the results of only four models are given in Figure 5, but the others yield the same tendency.

The analysis of the additional models shows threeextrema in the relative velocity, so that three extrema are considered allowable. As Figure 5 indicates, the criterion gives the upper bound of the collision-spring constant.

Based on the results of the seismic response analysis of the 9 models in Table 1, the following formula is proposed for the collision-spring constant that satisfies the criteria mentioned above:

$$k = \frac{2k_1k_2}{k_1 + k_2} \tag{2}$$

Where

$$k_1 = \frac{E_1A_1}{L_1^e}, \quad k_2 = \frac{E_2A_2}{L_2^e} \tag{3}$$

It is noted that Eq. (2) becomes Eq. (1) when the two girders are identical.

3.2 Abutment-Girder Collision

The abutment-girder collision is studied similarly, and the same tendencies as those in the girder-girder collision are recognized. The criteria employed to derive Eq. (2) are used also for the abutment-girder collision, and the following formula for the collision-spring constant is obtained:

$$\log_{10} k = 4.8 - 0.6 \times \log_{10}\left(\frac{k_A + k_G}{k_A k_G}\right) \tag{4}$$

where k_G is the axial stiffness of the element having the collision point.

4. RESPONSE ANALYSIS OF GIRDER BRIDGE

A bridge model is constructed based on an existing bridge and analyzed. Figure 6 shows the schematic of the bridge: it is a 7-span cantilever girder bridge and the length is 189.45 m. In the figure, M, F, m and f stand for a movable bearing support, a fixed bearing support, a movable hinge and a fixed hinge, respectively. An abutment is assumed at each end of the bridge.

The superstructure is a composite girder with four steel I-shaped girders and a concrete deck. The bridge piers are made of concrete, having the rectangular cross section of 2.2 m × 10.6 m at the top and 3.6 m × 13.6 m at the bottom. The nonlinear material behaviors of steel and concrete are assumed with the yield stress of steel σ_y and the compressive strength of concrete σ_{ck} equal to 360 N/mm^2 and 21 N/mm^2, respectively. The behavior of the foundation is modeled by springs whose constants are given by Design Specifications of Highway Bridges (Japan Road Association 2002). The collision-spring constants are determined by the formulas proposed above.

The seismic wave in the form of acceleration recorded during the Mid Niigata Prefecture Earthquake in 2004 is used for the analysis. Two initial gaps are assumed: 0.15 m and 0.25 m. The analysis that ignores the collision effect is also conducted.

Figure 7 summarize the results of the maximum horizontal displacements of four piers (P1, P3, P4 and P6). It is clearly observed in this figure that the collisions suppress the movement of the bridge, possibly mitigating the

damages of the piers.

5. CONCLUDING REMARKS

To include the effect of the collisions in the finite element analysis, the collision spring is often used. Yet an appropriate constant of the collision spring is not available in the literature except when two colliding bodies are identical. The present study tackled this issue and, through numerical study, it proposed the formulas for acceptable collision-spring constants between girders and between a girder and an abutment, respectively. The dynamic response analysis of a girder bridge was then conducted and the significant effect of the collisions was indeed observed, clearly showing the importance of the collision effect.

References:

Kawashima, K. (1981), "An Analytical Model of Contact and Impact in Dynamic Response Analysis," Technical Note, *Journal of JSCE*, 308, 123-126.

Kosa, K., Yamaguchi, E., Inokuma, Y., Tasaki, K. (2005), "Investigation and Analysis of Bridges and Other Structures Damaged during the Mid Niigata Prefecture Earthquake in 2004," *Proceedings of the 8th Symposium on Ductility Design Method for Bridges*, 35-40.

Japan Road Association (2002), "Design Specifications of Highway Bridges: Part V Seismic Design," Maruzen, Japan.

Yamato Design Co., Ltd. (2000), "User's Manual for Y-FIBER3D."

8CUEE CONFERENCE PROCEEDINGS
8th International Conference on Urban Earthquake Engineering
March 7-8, 2011, Tokyo Institute of Technology, Tokyo, Japan

PERFORMANCE-BASED SEISMIC ASSESSMENT OF SKEWED BRIDGES

Farzin Zareian[1)], Ertugrul Taciroglu[2)], Peyman Kaviani[3)], Curt B. Haselton[4)], and Pere Pla-Junca[5)]

1) Assistant Professor, Dept. of Civil and Environmental Engineering, University of California – Irvine, Irvine, United States
2) Associate Professor, Dept. of Civil and Environmental Engineering, University of California – Los Angeles, Los Angeles, United States
3) Graduate Student Researcher, Dept. of Civil and Environmental Engineering, University of California – Irvine, Irvine, United States
4) Assistant Professor, Dept. of Civil and Environmental Engineering, Calif. State University - Chico, Chico, United States
5) Graduate Student Researcher, Dept. of Civil and Environmental Engineering, University of California – Irvine, Irvine, United States
zareian@uci.edu, etacir@ucla.edu, pkaviani@uci.edu, chaselton@csuchico.edu, pplajunc@uci.edu

Abstract: This paper summarizes the analyses of the sensitivity of a two-span single column bridge in California to variations in structural and ground motion properties. A similar study has been conducted for other bridge configurations as part of a comprehensive study of performance-based assessment of skewed bridges, starting from seismic excitation modeling to modeling techniques that best represent the skewed abutment response for such bridges. Recent earthquakes have shown that skewed bridges tend to rotate about their vertical axes under seismic excitation and that this motion can cause excessive column hinging and unseating of the deck. In this study, we explore modeling techniques that capture the essence of skewed bridge response. By using these models, we quantify the sensitivity of response to variations in the bridge's geometric parameters and the type of seismic excitation. We also gauge state-of-the-art ground motion selection and scaling methodologies for assessing the response of such bridges in comparison to a "high-end prediction" that is based on a large number of simulations. The over-arching aim in this study is to reach to a set of practical guidelines for design of skewed bridges in high seismic regions, which when followed minimizes the damages that result in downtime losses usually deemed as the most important type of loss in highway network systems.

1. INTRODUCTION

Skewed bridges are required when the alignment of crossing roadways are not a right angle. Current state of practice for design of such bridges (Caltrans SDC 2006) comprises using a seat-type abutment to lessen demand on foundation and allows more movement of the superstructure during seismic excitation. Despite having a fair amount knowledge of their performance under service conditions, seismic performance of skewed bridges during past earthquakes were not well predicted. Transversely, the exterior shear keys are designed as a fuse and break off under intense impact. Similarly, under longitudinal excitation, the backwall is designed to break off and allow the generation of passive pressures on the backfill soil. The demand imposed on seat-type abutment's foundation is less than that for a diaphragm abutment, due to freedom of movement of the superstructure in different directions.

Much research has been conducted on seismic response of regular or non-skewed bridges (see, for example, Aviram et al. 2008, Johnson et al. 2009, Kotsoglou and Pantazopoulou 2010, Mackie and Stojadinovic 2007, Paraskeva et al. 2006). Observations from past earthquakes indicate that the unseating of the bridge deck due to in-plane rotation is the primary mode of failure in skewed bridges (Jennings 1971, Ghobarah and Tso 1974, Wakefield et al. 1991, Meng and Lui 2000). This rotational response is exacerbated once the bridge is subjected to near field motions (Shamsabadi et al. 2006). However, there still remains significant uncertainty in models that can predict this mode of failure. Understanding the seismic behavior of skewed bridges and improving the modeling and design guidelines for this type of bridge are the main objectives of this research.

This paper summarizes an attempt for bracketing the skew bridge response through a performance-based assessment methodology. The particular performance-based methodology adopted herein is that proposed by the Pacific Earthquake Engineering Research (PEER) Center, with specific extensions we have devised for bridges. Through this approach, the sensitivity of skewed bridge response to variations in bridge geometric parameters and type of seismic excitation is quantified. The primary focus is on the ground motion selection/scaling and structural modeling techniques.

Nonlinear structural response is often highly sensitive to the selection and modification (e.g., scaling) of input ground motions and, not surprisingly, many ground motion selection and modification methods have been proposed to date. Nevertheless, there is no systematic study that provides impartial guidance to engineers and delineates appropriate methods for use in a specific application. This is problematic because the predicted structural response can

vary dramatically depending on the prescribed ground motion. The engineer's choice of ground motion selection and modification method can lead to an over-designed, or worse, unsafe structure.

2. PERFORMANCE-BASED SEISMIC ASSESSMENT

Performance-Based (seismic) Assessment, PBA, has been the focus of much research in the past decade (e.g., Cornell and Krawinkler 2000, Krawinkler and Miranda 2004, Mackie and Stojadinovic 2007). Researchers have faced up to challenges such as: identifying performance objectives that are quantifiable and meaningful for engineers and stakeholders alike, identifying representations of ground motion intensity that well relate to seismic hazard at the site and the global bridge response characteristics, and many other advances whose enumeration does not fit into this brief introduction. The new challenge facing researchers is to transfer these sophisticated developments to the practicing engineers through relatively simple but comprehensive procedures that facilitate implementation.

Researchers at the Pacific Earthquake Engineering Research (PEER) Center have developed a sophisticated PBA methodology, which utilizes a chain of four random variables: Intensity Measure (*IM*), Engineering Demand Parameter (*EDP*), Damage Measure (*DM*), and Decision Variable (*DV*). *IM* is a scalar or vector (Baker and Cornell, 2006) quantity that represents the intensity of a ground motion. Traditionally, the elastic spectral acceleration at the first mode period of the structural system, $Sa(T_1)$, is used as an *IM*. However, recent studies show that using a vector valued *IM* in which the shape of the ground motion spectrum is considered in the ground motion selection and scaling process can lead to better estimation of the structural response. *EDP* is a bridge response parameter (e.g., maximum deck rotation, column drift ratio) and is estimated through nonlinear response analysis of the bridge model subjected to a ground motion. *DM* is the representation of damage (e.g., cracks in columns) and is determined based on repair strategy and many other considerations. Ultimately, *DV* is a measure of performance, with a focus on three major loss categories: direct ($) losses, downtime losses, and life losses. The PEER PBA methodology is completed by following a flow from *IM* to *DV* according to Equation (1) (the PEER framework equation):

$$\lambda(DV) = \iiint G(DV \mid DM) \cdot dG(DM \mid EDP) \cdot dG(EDP \mid IM) \cdot d\lambda(IM) \quad (1)$$

In Equation (1), $\lambda(DV)$ is the desired realization of the *DV* (e.g., mean annual frequency of exceedance) and the *G* functions represent complementary cumulative distribution functions. For instance, for downtime performance (i.e., average annual downtime for a given bridge) one can complete the PBA methodology as follows: intensity measures, *IM*s, (e.g., spectral acceleration at the first mode period of the structure, $Sa(T_1)$), are determined from seismic hazard analysis; relevant engineering demand parameters, EDPs, (e.g., deck rotation, column drift ratio) are predicted from structural analysis for given values of *IM*s (and representative ground motions); component/system damage states are developed from repair strategies and *DM*s fragility curves are developed for each component/system; and finally, predictions are made on *DV*s (i.e., total amount of downtime losses of the bridge).

This paper briefly goes through two important aspects of the PBA for bridges. First, the sensitivity of bridge response to variation in ground motion and structural properties, and second, the accuracy of various ground motion selection and scaling processes by which a more accurate estimate of bridge is obtained.

3. GROUND MOTIONS

Nonlinear dynamic analysis of structures is becoming increasingly prevalent in code and regulatory documents prescribing design and analysis. A recurring challenge for both practicing engineers and developers of these documents is the selection and modification of ground motions for these nonlinear dynamic analyses. Our investigation in addressing the effects ground motion model on bridge response is focused on two issues. First, we investigate the sensitivity of bridge response to standardized sets of ground motions each representing a typical geotechnical system located in an active seismic region like California. Second, we focus on ground motion selection and scaling procedures to identify the superior procedure by which a small subset (e.g., seven) of ground motions can provide an acceptable estimate of median bridge response.

To investigate the sensitivity of bridge response to typical ground motions in California sites, three sets of ground motions were selected by the PEER Transportation Research Program (Jayaram et al. 2010). Theses sets are denoted as "Soil," "Rock," and "Pulse," each of which comprise forty ground motions. Figures 1, 2, and 3, show the fault-normal and fault-parallel spectra for these ground motion sets, respectively. These ground motions are not location specific and rather are standardized to accommodate comparative evaluations. These ground motions are selected from a subset of the PEER NGA Project ground motion library (PEER 2010) with ground motions from mid- to large-magnitude earthquakes at close distances. Selected ground motions have a variety of spectral shapes, durations, and directivity periods. For each set, the mean and variance of the natural logarithm of spectral acceleration match $M_w = 7$ and $R = 10$km generic scenario in California.

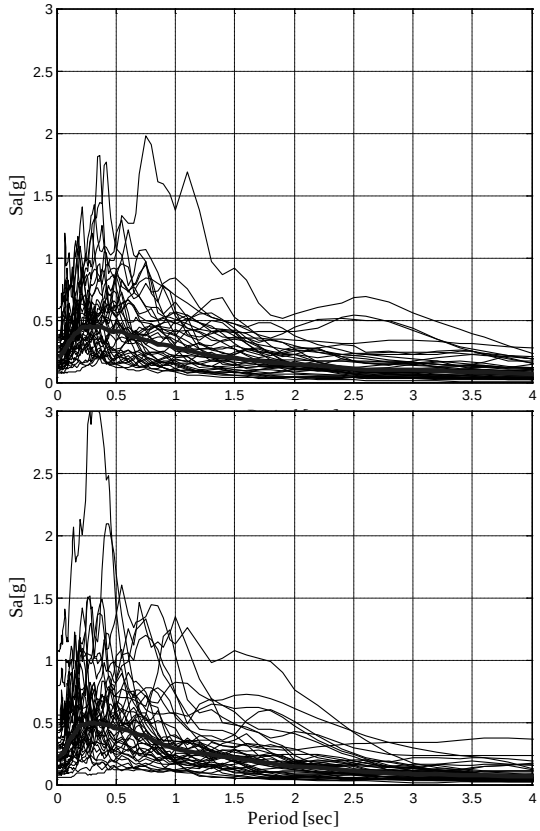


Figure 1 Response spectra of selected ground motions for soil sites. (a) Fault normal comp., (b) fault parallel comp.

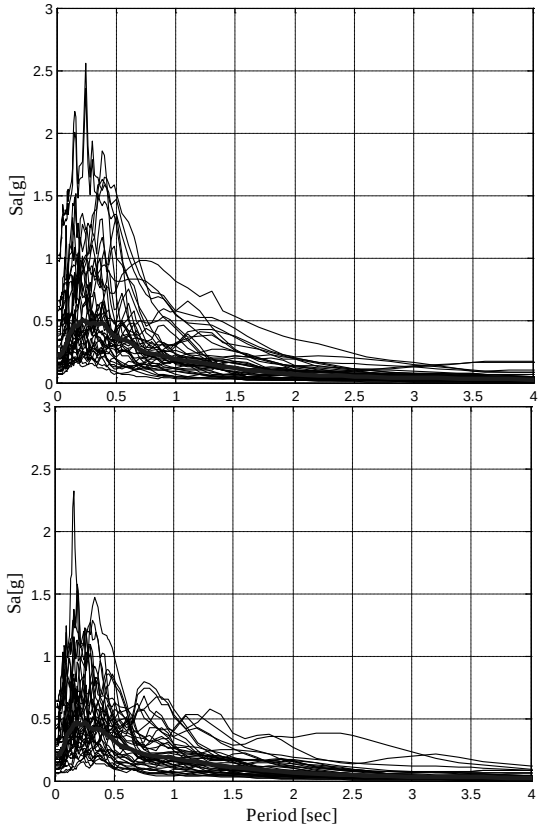


Figure 2 Response spectra of selected ground motions for rock sites. (a) Fault normal comp., (b) fault parallel comp.

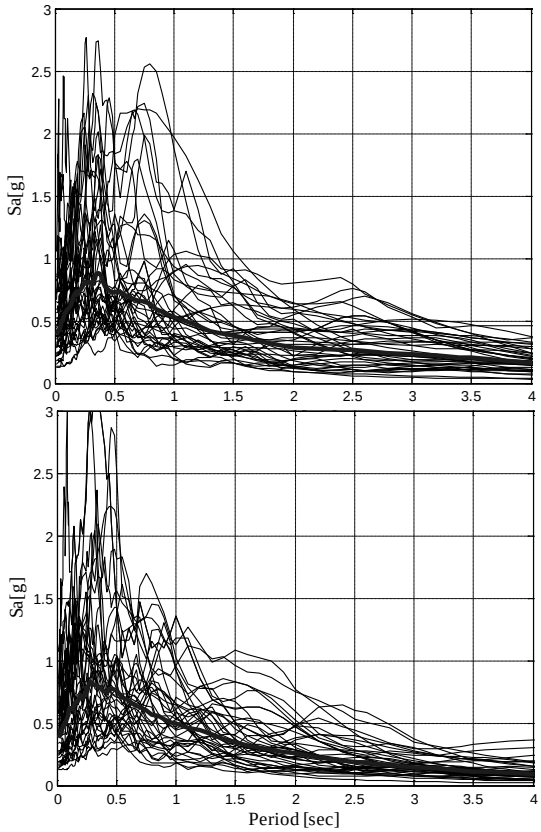


Figure 3 Response spectra of selected pulse type ground motions. (a) Fault normal comp., (b) fault parallel comp.

We investigated the accuracy of ground motion selection and scaling methods to estimate the median bridge response for the M_w = 7 and R = 10km generic scenario. This investigation has two parts. First we obtain the best estimate for the bridge response parameter (e.g., column drift, unseating deformation), denoted as POC (i.e. Point Of Comparison), using a large set of ground motions and a sophisticated mathematical regression form, for the target generic scenario M_w = 7 and R = 10km. Second, we obtain the similar bridge response parameters using smaller sets of ground motions each selected based on a predefined ground motion selection and scaling procedure and compare with POC. Estimation of POC is possible with a large set of ground motions. This large set of ground motions were selected from the PEER-NGA Database available from the Pacific Earthquake Engineering Research Center (PEER 2010). The ground motion set selected for this part of the investigation includes 117 horizontal ground motion pairs selected based on the following detailed criteria. These criteria are similar to those used in the FEMA P695 (ATC-63) project (FEMA 2009). The selected ground motions are from earthquakes with $6.5 \leq M_w \leq 7.5$ recorded on soft rock or stiff soil (Site Classes A-D, with Vs > 180 m/s), all of records come from either strike-slip or reverse (thrust) sources (with only a few records coming from subduction sources) with source-to-site distances from 0-20 km. To ensure that the ground motion recording and processing maintained the important range of frequency contents, only ground motions with useable frequencies

down to at least 0.25 Hz are included in the ground motion record set. Figure 4 provide the spectra of the ground motions included in the set (for each individual ground motion component), and the median spectrum.

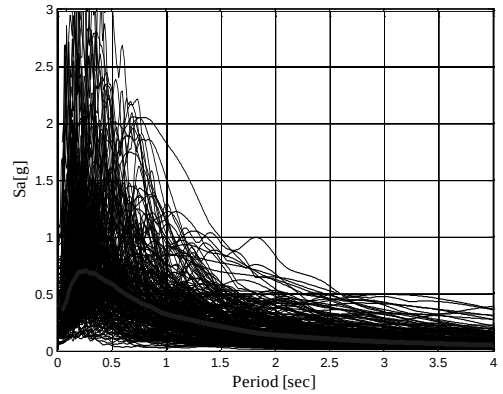


Figure 4 Spectra of ground motions included in the $M_w = 7$ $R = 10$km ground motion set for estimation of POC.

The development of the POC prediction involved: (a) selecting a large bin of records consistent with the target scenario as described in the previous paragraph, (b) completing bridge response analyses using the set of records scaled by arbitrary factors of 1.0, 2.0, 4.0, and 8.0, (c) completing regression analysis (which is designed to remove the effect of scaling bias) to relate bridge response parameters to the important ground motion parameters, and then (d) integrating the regression equation over the proper distributions of the ground motion parameters used in the regression model. Details of calculation of POC can be found in PEER GMSM (2009).

Two ground motion selection and scaling methods are investigated in this study. One is based on fist mode spectral acceleration, denoted as $Sa(T_1)$, and the other is based on the Conditional Mean Spectrum, denoted as CMS. In the $Sa(T_1)$ method, ground motions are selected and scaled from a representative bin for the target scenario, and amplitude scaled to ensure the spectral acceleration at the first mode period in the longitudinal direction matches the target spectral acceleration at the same period. Previous research has shown that spectral shape is an important factor in selection and scaling ground motions. The expected spectra tend to have a "peak" with richer frequency content near the period used to define the ground motion intensity (typically the fundamental period of the structure). Baker and Cornell (2006) showed that proper spectral shape for a given ground motion scenario and associated ε value; this spectrum has been termed a Conditional Mean Spectrum (CMS), as it is the mean response spectrum at all periods, conditional on knowledge of $Sa(T_1)$.

4. ANALYTICAL MODEL

For the purpose of this paper, we have selected a two-Span on single-column bridge (viz., Jack Tone Road Overcrossing). The Jack Tone Road On-Ramp Overcrossing is located in City of Ripon in California, is a two-span bridge with 67.2 m total length, and spans of 33.105 m and 34.095 m. The superstructure is a three-cell continuous reinforced concrete box-girder. The bent cap is integral with the deck and a single concrete column. The column of the bent is 1.68 m in diameter supported on steel piles. The longitudinal reinforcing steel ratio of the column is approximately 2%. The bridge has non-skewed, seat-type abutments with four elastomeric bearing pads per each. The case study bridge is part of a matrix of bridges with geometric characteristics representative of common bridges in California have been studied. These bridges are recently designed (built after 2000) and are located in Southern California, which is a region with high seismicity.

The analytical model of the case study bridge is shown in Figure 5. The bridge structure is modeled through the OpenSees (McKenna et al. 2000) Finite Element Analysis software. The present modeling assumptions generally follow the guidelines proposed by Aviram et al. (2008) and Kaviani et al. (2010) as well as SDC (2006). The three-dimensional spine-model of the bridge structure with line elements located at the centroid of the cross sections following the alignment of the bridge is used. To capture the response of the entire bridge system and individual components under specific seismic demand characteristics, three-dimensional modeling is implemented. The models developed for skewed bridges *do* incorporate nonlinear behavior of individual components. These components include column plastic hinges, abutment transverse and longitudinal springs, and abutment gap components. For simplicity, the superstructure, the cap beam, and the foundation springs are considered as linear elastic components.

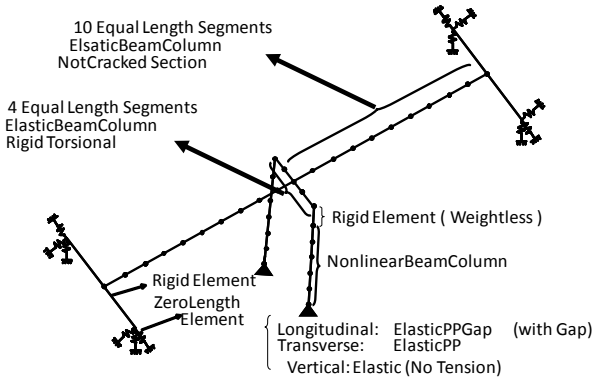


Figure 5 Conceptual depiction of the analytical model for skewed bridges in OpenSees

4.1 Columns

The concrete considered for modeling the columns is based on an enhanced version of the concrete model proposed by Chang and Mander (1994), available in OpenSees under the name *Concrete07* (J. Waugh et al. 2008). The core concrete is confined by circular hoops or spirals,

while the cover concrete is unconfined. The maximum strain in compression for the confined concrete is governed by the first hoop fracture, and it is set equal to 0.025. The compressive strength of the unconfined concrete is equal to 35MPa and its initial Young's modulus is equal to 28GPa, according to SDC (2006), Section 3.2. The characteristics of the confined concrete depend on the level of transverse confinement, which is determined by the circular hoops or spirals of the columns. Figure 6 shows the backbone curves for confined and unconfined concrete used in the column of Bridge 1.

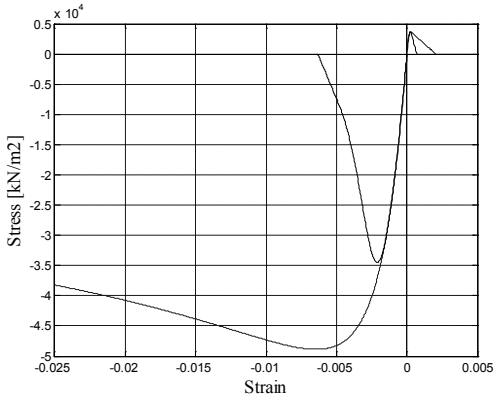


Figure 6 Backbone curves for concrete and steel (negative values refer to compression)

The reinforcing steel is assumed to have an elastic-perfectly plastic behavior. The type of material available in the library of materials of OpenSees that is used is *Steel01*. It is a simple model with no ultimate strain and no hardening after yielding. This material model is selected for its simplicity and the fact that it better represents the behavior of the bridges used in this study compared to other available steel material models. The yielding strength of the steel is equal to 475MPa, and the Young's Modulus, equal to 200GPa, according to SDC (2006), Section 3.2. The maximum strain in tension depends on the type of the steel and the size of the reinforcing bars, and it is equal to 0.09.

4.2 Abutment

The model of the abutments is based on the simplified model developed by Aviram et al. (2008) as part of the project they conducted to establish general guidelines for nonlinear analysis of bridges in California. Each abutment is modeled with a rigid element of length equal to the superstructure width, connected through a rigid joint to the superstructure centerline, and with a zero-length element at each.

In the longitudinal direction, the response is governed by a gap material. The material does not work in tension. In compression, it behaves as an elastic – perfectly plastic material when it reaches the gap length. The gap is defined by the plans, and the stiffness and the ultimate strength are defined according to Caltrans SDC (2006), Section 7.8. The rotation about the longitudinal direction is not allowed.

In the transverse direction; the response is governed by an elastic material that only works in compression. The abutment stiffness and the back wall strength for the longitudinal direction are modified by factors corresponding to wall effectiveness (C_L) of 2/3 and participation coefficients (C_w) of 4/3. The wing wall is assumed to be 1/3 of the back wall length.

In the vertical direction; the response is governed by an elastic material with zero tensile strength. After reaching a vertical deformation in compression equal to the maximum allowed by the bearing pads, the stiffness changes and tends to infinity.

5. SUMMARY OF FINDINGS

The sensitivity of seismic response of case study skewed bridge to variations of structural and ground motion properties was investigated. We focus our study on two major bridge response parameters that affect the bridge performance: deck rotation and column drift ratio. Figure 7 shows the effect of the deck rotation during the M_w = 8.0 Offshore Maule earthquake in Chile, signifying the importance of this parameter in investigating performance of skewed bridges.



Figure 7 Bridge deck rotation during M_w = 8.0 Offshore Maule earthquake in Chile. [*Image Source: Carlos Cabrera*]

Our investigation shows that deck rotation is highly sensitive to bridge structural properties and ground motion characteristics. Figure 8 shows the variation of deck rotation as function of abutment skew angle for the case study bridge for three different types of ground motions. The solid lines show the estimated median, and the individual data points are depicted with solid dots on the plot. Figure 9 shows a similar plot, however, the two spans are not equal in length (i.e., Asymmetrical span).

Investigation of Figure 8 and 9 shows that by increasing abutment skew angle from 0 to 30 degrees, median estimate of deck rotation increases regardless of applied type ground motion or span configuration. However, for higher abutment skew angles, ranging from 30 to 60 degrees deck rotation decreases for the symmetrical span bridge whereas an increasing trend continues for asymmetrical span one. This behavior is particularly pronounced in for pulse-like ground motion.

We conclude that this type of behavior for deck rotation in large abutment skew angles is due to the effect of the abutment gap size orientation. The gap element is always perpendicular to the abutment alignment (Figure 10). In other words, for a skewed abutment, the gap element will skew with the same rate to stay perpendicular to the abutment. Therefore, the distance in global longitudinal direction (X direction) increases by skew angle. Consequently, the springs which connect to the gap element and simulate the backwall engagement in response, contribute less efficiently to seismic response when smaller skew angles of abutment are present. Therefore, the larger the gap size the smaller the deck rotation.

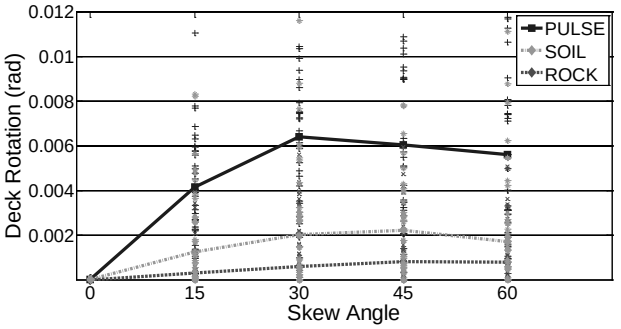


Figure 8 Variation of deck rotation due to ground motion characteristics and abutment skew angle for sym. deck.

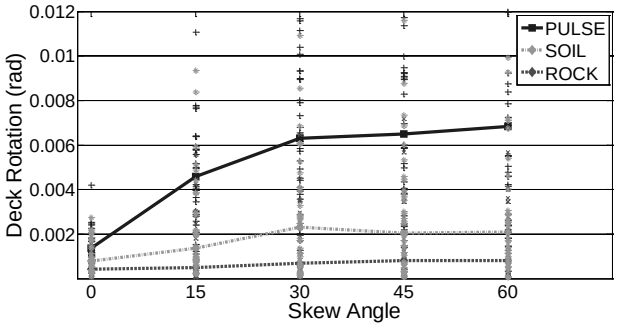


Figure 9 Variation of deck rotation due to ground motion characteristics and abutment skew angle for Asym. deck.

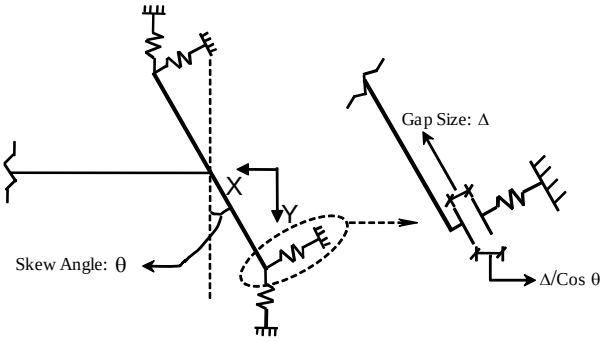


Figure 10 Effect of abutment skew angle on effective gap size.

Column drift ratio for the two-span single column case study is not sensitive to abutment skew angle, see Figures 11 and 12. This behavior is due to the nature of vibration for the single column bridge in which the rotation of the deck increases as the skew angle increases but the column usually remains near the center of rotation.

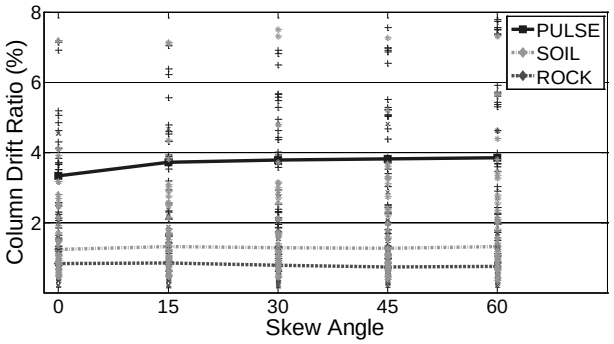


Figure 11 Variation of col. drift ratio due to ground motion characteristics and abutment skew angle for sym. deck.

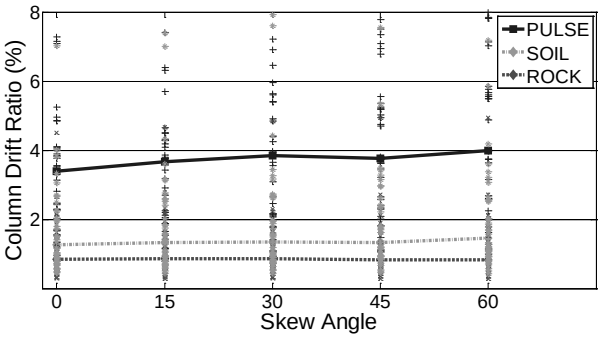


Figure 12 Variation of col. drift ratio due to ground motion characteristics and abutment skew angle for Asym. deck.

Our investigation shows that the ground motion selection scaling methods that use spectral acceleration at the first mode period can well predict the response of the case study bridge and these estimates of the median response is comparable with the estimated median obtained using ground motions selected and scaled using the conditional mean spectrum and the POC. Figure 13 shows the variation of estimated column drift ratio for the case study bridge as function of ground motion selection and scaling methods. The blue dots show the analysis results for each individual ground motion in the selected set and the median estimate of each set is marked with a solid short line. The red line represents the estimated median using the detailed and sophisticated analysis denoted as POC. This The set denoted with $Sa(T_1)$, is set of 84 records all selected based on the bridge fundamental period in the longitudinal direction. Each of CMS1, CMS2, CMS 3, and CMS 4 comprise seven ground motion selected and scaled according to conditional mean spectrum. CMS 5 is similar to other CMS sets; however, it includes 40 ground motions. All ground motions were applied in the longitudinal direction. The similarity between estimated median from using $Sa(T_1)$ and CMS, and with POC is due to small nonlinear behavior of the bridge in

applied ground motions. We postulate using bidirectional ground motions could potentially change the conclusion drawn here. Investigation about this hypothesis is underway.

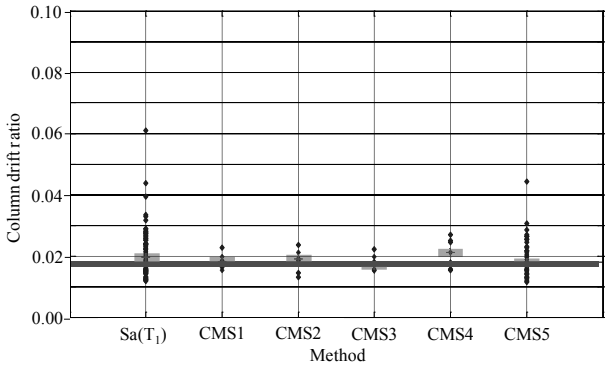


Figure 13 Comparison between estimated column drift ratio from various sets of ground motions and the POC.

Acknowledgements:

This study is based on work supported by the by the PEER Transportation Research Program under Grant No. UCLA-45782 and PEER Lifeline Program under Grant No. UCB-PEER 00006938. This financial support is gratefully acknowledged. Any opinions, findings, and conclusions or recommendations expressed in this paper are those of the authors and do not necessarily reflect the views of sponsors.

References:

Aviram, A., Mackie, K.R. and Stojadinović, B. (2008), "Guidelines for Nonlinear Analysis of Bridge Structures in California," *PEER Report 2008/3*, Pacific Earthquake Engineering Research Center.

Baker, J.W., and Cornell, C.A., (2006). "Spectral Shape, Epsilon and Record Selection," *Earthquake Engineering and Structural Dynamics*, **35**, 1077-1095.

Cornell, C.A., and Krawinkler, H. (2000), "Progress and Challenges in Seismic Performance Assessment," *PEER News*, April 2000.

Caltrans SDC. (2006), "Caltrans Seismic Design Criteria Version 1.4," California Department of Transportation, Sacramento.

Goel, R. K., Chopra A. K. (1997), "Evaluation of Bridge Abutment Capacity and Stiffness During Earthquakes," *Earthquake Spectra*, **13**(1), 1-24.

Ghobarah, A.A., and Tso, W.K., (1974). "Seismic Analysis of Skewed Highway Bridges with Intermediate Supports," *Earthquake Engineering and Structural Dynamics*, **2**(3), 235-248.

Federal Emergency Management Agency (FEMA), (2009). "Recommended Methodology for Quantification of Building System Performance and Response Parameters." FEMA P695 (ATC-63 Project), Prepared for the Federal Emergency Management Agency, Prepared by the Applied Technology Council, Redwood City, CA.

Jayaram, N., Shahi, S. and Baker, J. (2010), "Ground Motion for PEER Transportation Research Program," http://peer.berekeley.edu/transportation/gm_peer_transportation.html.

Jennings, P.C., and Wood, J.H. (1971), "Engineering Feature of the San Fernando Earthquake," *EERL 71-02*, Pasadena, California, 1971.

Johnson, N., Saiidi, M.S., and Sanders, D. (2009), "Nonlinear Earthquake Response Modeling of a Large-Scale Two-Span Concrete Bridge," *ASCE Journal of Bridge Engineering*, **14**(6), 460-471.

Kaviani, P., Zareian, F. and Sarraf, M. (2010). "Comparison of Seismic Response of skewed Bridges to Near vs. Far Field Motions," 7th International Conference on Urban Earthquake Engineering & 5th International Conference on Earthquake Engineering. 1: 1805-1810.

Kotsoglou, A., and Pantazopoulou, S. (2010), "Response Simulation and Seismic Assessment of Highway Overcrossings," *Earthquake Engineering and Structural Dynamics*, **39**(9), 991-1013.

Krawinkler, H., and Miranda, E. (2004), "Performance-based Earthquake Engineering," Earthquake Engineering: from engineering seismology to performance-based engineering, Chapter 9, Bozorgnia Y, Bertero VV (eds); CRC Press: Boca Raton; 9-1 to 9-59

Mander, J.B., Priestley, M.J.N., Park R. (1988). "Theoretical Stress – Strain Model for Confined Concrete," *ASCE Journal of Structural Engineering*, **114**(8), 1804-1826.

McKenna, F., Fenves, G.L. and Scott, M.H. (2000), "Open System for Earthquake Engineering Simulation," University of California Berkeley, California, http://opensees.berkeley.edu

Meng, J.Y., and Lui, E.M. (2000), "Seismic Analysis and Assessment of a Skew Highway Bridge," *Engineering Structures*, **22**, 1433-1452.

Mackie, K. R., and Stojadinovic, B. (2007), "Performance-Based Seismic Bridge Design for Damage and Loss Limit States," *Earthquake Engineering and Structural Dynamics*, **36**(13), 1953-1971.

Paraskeva, T. S., Kappos, A. J., and Sextos, A. G. (2006), "Extension of Modal Pushover Analysis to Seismic Assessment of Bridges," *Earthquake Engineering and Structural Dynamics,* **35**(10), 1269-1293.

PEER GMSM, Haselton, C.B., Editor (2009), "Evaluation of Ground Motion Selection and Modification Methods: Predicting Median Interstory Drift Response of Buildings," *PEER Report 2009/01*, Pacific Engineering Research Center, University of California, Berkeley, California.

PEER. (2010), "Pacific Earthquake Engineering Research Center: PEER NGA Database," University of California, Berkeley, http://peer.berkeley.edu/nga

Shamsabadi, A., Rollins, K. M., and Kapuskar, M. (2007), "Nonlinear Soil–Abutment–Bridge Structure Interaction for Seismic Performance-Based Design," *ASCE Journal of Geotechnical and Geoenvironmental Engineering,* **133**(6), 707-720.

Wakefield, R. R., Nazmy, A. S., and Billington, D.P. (1991), "Analysis of Seismic Failure in Skew RC Bridge," *ASCE Journal of Structural Engineering*, **117**(3), 972-986.

Waugh, J., Aaleti, S., Sritharan, S., Zhao, J. (2008), "Nonlinear Analysis of Rectangular and T-Shaped Concrete Walls," ISU–ERI – Ames Report ERI – 09327. Department of Civil, Construction and Environmental Engineering, Iowa State University.

8CUEE CONFERENCE PROCEEDINGS
8th International Conference on Urban Earthquake Engineering
March 7-8, 2010, Tokyo Institute of Technology, Tokyo, Japan

SHEAR BEHAVIOR OF SEGMENTAL CONCRETE BEAMS WITH DRAPED EXTERNAL TENDONS

Dinh Hung Nguyen[1)], Koji Matsumoto[2)], Tsuyoshi Hasegawa[3)], and Junichiro Niwa[4)]

1) PhD. Candidate, Graduate School of Civil Engineering, Tokyo Institute of Technology, Japan
2) Assistant Professor, Department of Civil Engineering, Tokyo Institute of Technology, Japan
3) Research Engineer, Research and Development Center, DPS Bridge Works Co., Ltd, Japan
4) Professor, Department of Civil Engineering, Tokyo Institute of Technology, Japan
nguyen@cv.titech.ac.jp, matsumoto.k.ar@m.titech.ac.jp, t_hasegawa@dps.co.jp, jniwa@cv.titech.ac.jp

Abstract: This paper presents an experimental result of the structural behavior of segmental concrete beams prestressed with external draped tendons under the shear behavior. The inclined angle of draped tendons and the location of deviators on a shear span are main parameters. The effects of the inclined angle of draped tendons and location of deviators on a deviator force that affects the shear mechanism, such as propagation of cracks, joint opening and shear carrying capacity of segmental concrete beams are investigated. The experimental result shows that shear capacity of segmental beams with draped tendons was higher than that of segmental beams with straight external tendons.

1. INTRODUCTION

Prestressed concrete structures can absorb considerable energy before failure due to impact and thus show improved performance under seismic condition. Precast segmental construction is widely used in bridge structures, because of substantial cost and time saving in construction. In the beginning, internal tendon technology has been used for segmental technology where tendons are located inside the concrete cross section. However, problems such as leakage at epoxy joints or corrosion in tendons may cause damage in segmental bridges. So, the application of external prestressing to precast segmental structures has been used as an innovative method in segmental concrete technology.

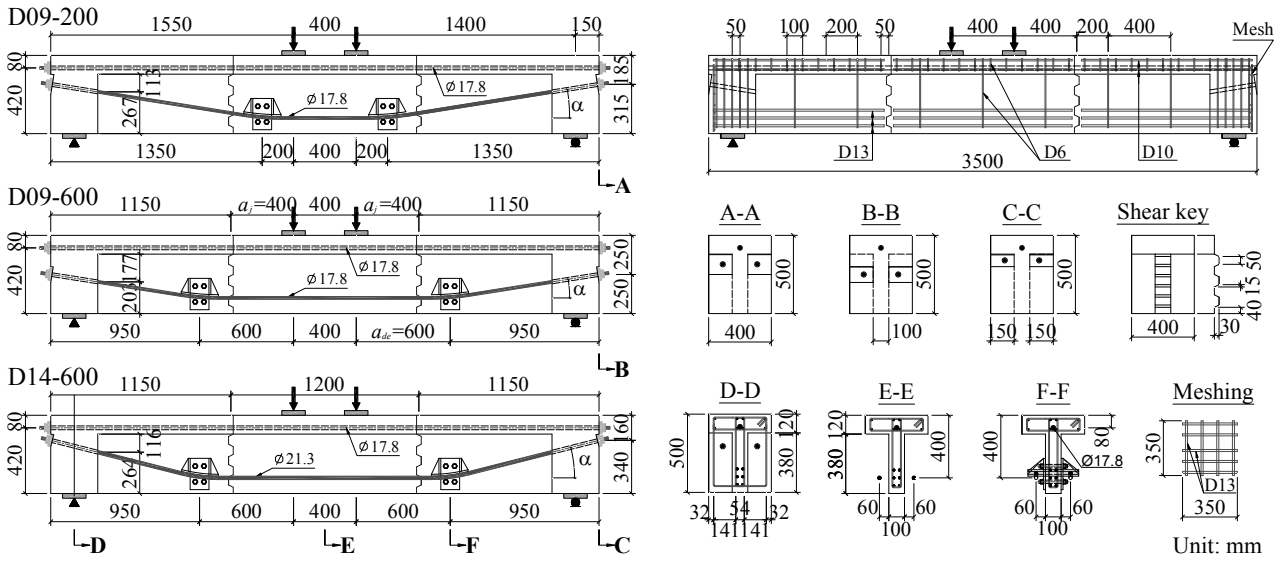
Both straight tendon profile and draped tendon profile have been applied in a segmental concrete beam with external tendons. The difference comparing to the internal tendons is that the prestressing force from external tendons only acts on the structure at the deviators and the ends of a beam through anchorages. The draped profile has been used to alleviate congestion in anchorage zones, to reduce concrete stresses at transfer and to provide a vertical component for shear in the high shear and low moment zone in a simply supported beam. A straight external tendon profile was conducted in the author's previous study (Nguyen et al. 2010). It was concluded that the effect of deviator force in a shear span on the shear capacity is insignificant. However, test data to investigate the effect of draped external tendons on the shear behavior of segmental concrete beams are very limited. Several researchers reported the experimental results focusing on the shear behavior of monolithic concrete beams with draped internal tendons (MacGregor et al. 1960 and Rezai-Joeabi et al. 1986). Some studies focused on flexural behavior of monolithic concrete beams with draped external tendons (Tan and Ng 1997). In addition, in almost current codes, e.g. JSCE Standards 2002, the contribution of draped tendons on the shear capacity has been considered via the vertical component of prestressing force without considering the effect of location of deviators. Therefore, the effect of deviator force such as location of deviators and inclined angle of tendons on the behavior of segmental joint and shear behavior of segmental beams is necessary to be evaluated.

This paper presents experimental and nonlinear finite element analysis results of the structural behavior of segmental concrete beams prestressed with draped external tendons. The paper focuses on the response of the segmental concrete beams under the shear behavior considering the effect of draped external tendons. The inclined angle of draped tendons and the location of deviators on a shear span are main parameters. The effects of the inclined angle of draped tendons and location of deviators on a deviator force that affects the shear mechanism, such as propagation of cracks, joint opening and shear carrying capacity of segmental concrete beams are investigated.

2. TEST PROGRAM

2.1 Detail of testing beams

Figure 1 shows the detail of specimens in this study. Three simply supported concrete beams designed to fail in



(a) General view (b) Reinforcement and cross section

Fig. 1 Detail of specimens

Table 1 Detail of test beams

Beams	a/d	α (deg.)	a_{de} (mm)	a_j/d	Upper fiber stress, σ_u (N/mm^2)	Lower fiber stress, σ_l (N/mm^2)	Compressive strength, f'_c (N/mm^2)		Tensile strength, f_t (N/mm^2)	
							Batch A	Batch B	Batch A	Batch B
D09-200	3.5	9	200	1.0	-1.10	19.56	69.3	65.1	4.5	4.5
D09-600		9	600		-0.89	19.59				
D14-600		14.2	600		-2.00	19.21				

Note: Batches A and B are for ending segments and middle segments, respectively.

Table 2 Mechanical property of reinforcements

Bar	Yield strength (N/mm^2)	Tensile strength (N/mm^2)	Elastic modulus (kN/mm^2)	Area (mm^2)
D6	337	523	200	31.7
D10	370	524	200	71.3
D13	366	515	200	126.7

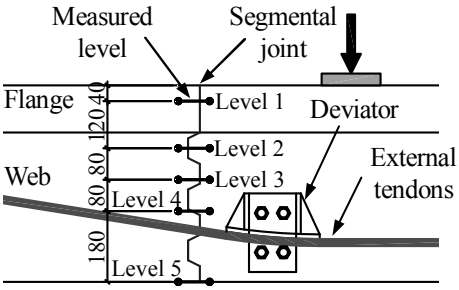
Table 3 Mechanical property of tendons

Beams	Dia. (mm)	Yield strength (N/mm^2)	Tensile strength (N/mm^2)	Elastic modulus (kN/mm^2)	Area (mm^2)
D09-200	17.8	1694	1924	191.6	208.4
D09-600	17.8	1689	1919	192.0	208.4
D14-600	17.8	1689	1919	192.0	208.4
	21.3	1649	1879	188.7	312.5

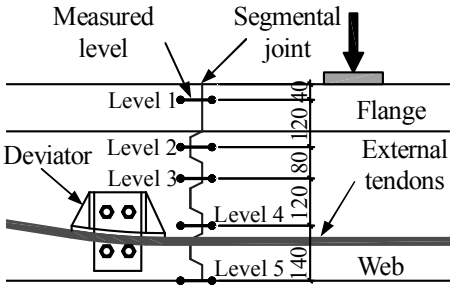
shear with a/d ratio of 3.5 were used. The distance, a_j from the loading point to the joint position in a shear span used in these beams was 1.0d, where d was the effective depth of the beam at deviators. Test specimens were T-shaped section concrete beams with the span length of 3.2 m. The concrete stress at the upper fiber of the segmental beams was about 0 N/mm^2. The concrete stress was about 19 N/mm^2 (positive means compression) at the lower fiber. The inclined angle α of tendons was 9 and 14.2 deg. The location of the deviator from the loading point, a_{de} was 0.5d (200 mm) and 1.5d (600 mm). So the name of beams is D09-200, D09-600 and D14-600. Thus, D09-200 means that the inclined angle α was 9 deg. and a_{de} was 200 mm. Table 1 tabulates the tested segmental beams and the other parameters.

2.2 Materials

The match-cast method was used for casting the segmental beams. In this method, the ending segments of each beam were cast first with a wood shear key as an end formwork. Two days later the formwork was removed and the ending segments themselves were used as the ending formworks for the middle segment in order to provide a perfect matching between the two segments. The design compressive strength of concrete, f'_c was specified as 65.0 N/mm^2 at 28 days. The actual compressive and tensile strengths of concrete are tabulated in Table 1. Epoxy resin was used to connect concrete segments. The tensile and bending strengths of the epoxy resin were about 25 N/mm^2 and 40 N/mm^2, respectively.



(a) Measuring joint opening in D09-200



(b) Measuring joint opening in D09-600 and D14-600

Fig. 2 Measuring at 5 levels of each segmental joint

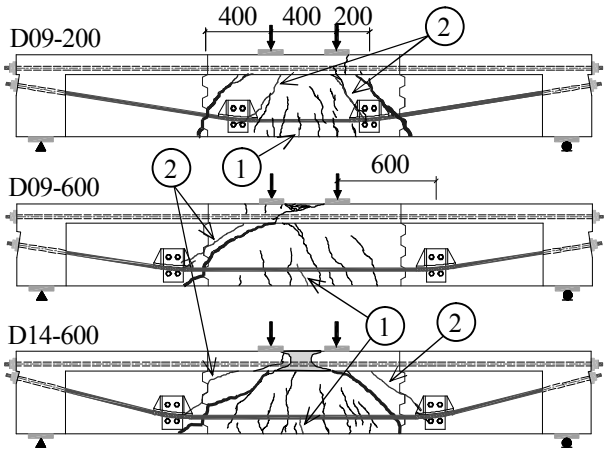
The arrangement of reinforcement in the beam is shown in Fig. 1(b). The non-prestressed steel bars were deformed bars. In all beams, six deformed bars with a nominal diameter of 13 mm (D13), and eight deformed bars with a nominal diameter of 10 mm (D10) were provided as internal longitudinal reinforcement at the bottom and the top flange, respectively. Deformed bars with a nominal diameter of 6 mm (D6) were used for stirrups having at an interval of 400 mm. Stirrups were also provided at the top flange with an interval of 100 mm. Meshing with D13 was utilized at the end of each beam to resist local stress due to prestressing force. The average mechanical properties of the steel bars are given in Table 2.

One unbonded internal tendon of type SWPR19L with a nominal diameter of 17.8 mm was provided in the top flange of the beams. The draped external tendons used for D09-200 and D09-600 were 19-wire type SWPR19L with a nominal diameter of 17.8 mm. The draped external tendons used for D14-600 was 19-wire type SWPR19L with a nominal diameter of 21.3 mm. The mechanical properties of the tendons are given in Table 3. The external tendons were arranged as shown in Fig. 1(a) and were stretched for four days before testing. Steel deviators were connected on the web of the beams by M22 bolts prefabricated in the web of the beams.

2.3 Loading method and measurements

The beams were subjected to a two-point loading test with a distance of 400 mm between two loading points as shown in Fig. 1(a). The applied load was increased monotonically by means of displacement control method.

Various measuring devices were utilized in order to measure the displacement of the beam, as well as joint opening and stress increment in the external tendons. Strain in the tendons was measured by electrical strain gauges at the middles between anchorage and deviators and at the middle of external tendons. Meanwhile, displacement transducers were mounted at the midspan, deviators and the supports of the beams to monitor the vertical deflection. At the same time, joint opening was measured at five levels on the both segmental joints of each beam as shown in Fig. 2. Levels 1 and 2 were measured by pie-gauges while levels 3, 4 and 5 were measured by transducers.



① The fist flexural crack; ② The diagonal crack from the deviator; Bold line is the dominant diagonal crack

Fig. 3 Crack patterns

3. RESULTS AND DISCUSSION

3.1 Generals about Testing Beams

D09-600 was first tested. For the safety, applied load was stopped when the stress in the draped lower tendons became about 1434 N/mm^2 (79 percent of the yield strength of tendons). D09-600, therefore, did not reach totally failure. D14-600 was secondly tested. The applied load was provided until the beam was totally failed. D09-200 was last tested. Until the stress in the draped lower tendon reached the yield strength the applied load was stopped. At the stopped load stage D09-200 had not been totally failed.

3.2 Crack patterns

Figure 3 presents the crack pattern of the tested beams. Some flexural cracks first formed in the maximum moment zone between the loading points. Then flexural shear cracks occurred. Despite the difference in location of deviators and the inclined angle of draped tendons, one diagonal crack was observed to be formed from a deviator to the loading point. After the occurrence of diagonal cracks from deviators the dominant diagonal crack occurred at the lower corner the ending segment toward the loading point. In D14-600 at the ultimate stage dominant diagonal crack penetrated into the

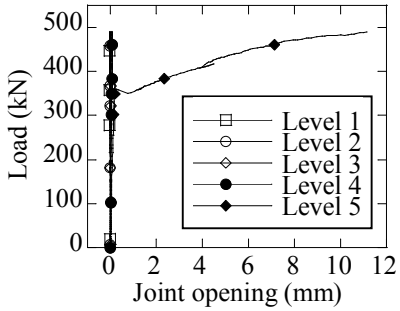


Fig. 4 Joint opening of D09-200

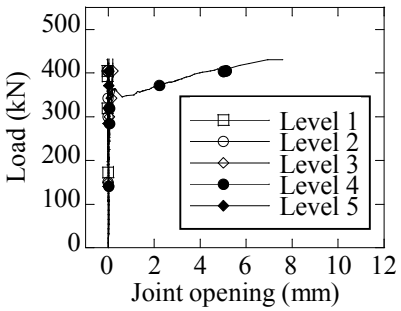


Fig. 5 Joint opening of D09-600

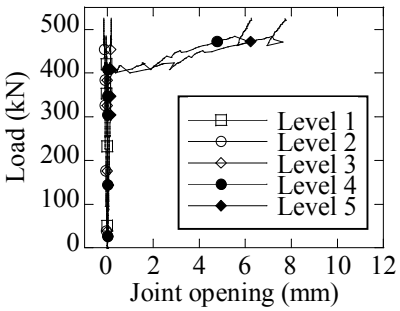
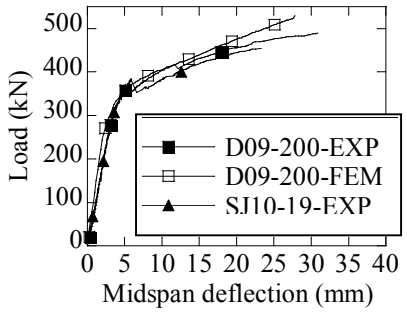
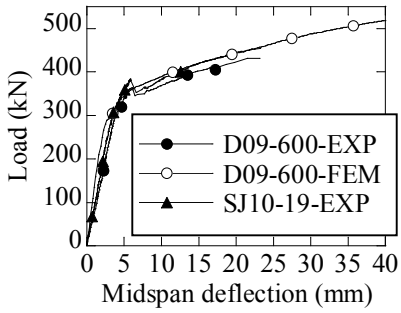


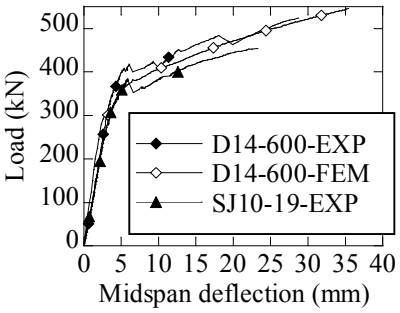
Fig. 6 Joint opening of D14-600



(a) D09-200



(b) D09-600



(c) D14-600

Fig. 7 Load – deflection curves

Table 4 Test results

Beams	α (deg.)	P_{cr} kN	P_{dcr} kN	P_{sh} kN	P_u kN
D09-200	9.0	280	338.4	360.2	489.2
D09-600	9.0	287.3	327.3	364.1	431.6
D14-600	14.2	285.6	408.1	417.5	523.4
SJ10-19	0	290.5	-	381.7	453.9

Note:
P_{cr} is load at the first flexural crack,
P_{dcr} is load at the diagonal crack formed from deviator,
P_{sh} is load at the dominant diagonal crack,
P_u is the peak load.

top flange near the loading point. After the peak load, the crushing occurred near the loading point. In D09-200 and D09-600, before the applied load was stopped the dominant diagonal cracks were observed to penetrate into the top flange. Some cracks were seen on the top flange of a beam near the loading points. It means that these two beams, D09-200 and D09-600, were close to the ultimate state when the applied load was stopped.

3.3 Joint opening

Joint opening was measured at 5 levels in both segmental joints of each beam as shown in Fig. 2. Figure 4 shows the joint opening observed in segmental joint on the right of D09-200 that was the critical segmental joint. Because cracks were observed in the top flange near the loading point and the joint opening was larger. The segmental joint expressed closing the levels 1 and 2. Joint opening in the levels 3 and 4 was very small, 0.04 and 0.09 mm, respectively. Joint opening observed in level 5 where dominant diagonal crack propagated was 11.13 mm.

Figures 5 and 6 show the joint opening observed in segmental joint on the left of D09-600 and the right of D14-600 that were the critical segmental joint. The segmental joint expressed closing in levels 1 and 2 of D09-600 and D14-600. The diagonal crack from deviator was formed and passed, therefore, the level 3 joint opening of D09-600 and D14-600 was 0.28 and 0.17 mm, respectively. In the stopping load of D09-600, joint opening at level 4 was 7.57 mm. Joint opening at level 5 could not be recorded, because the failure in the lower shear key in the ending segment was occurred when the dominant diagonal crack was formed as shown in Fig. 3. At the ultimate stage of D14-600, joint opening of levels 4 and 5 was 6.25 and 7.75 mm, respectively. It noted that the joint opening of SJ10-19 in the previous test was 10.5 mm at the peak load (Nguyen et al. 2010).

The smaller inclined angle of tendon was, the larger joint opening was. Joint opening in D09-200 was larger than that in D09-600 and D14-600. In both D09-600 and D14-600 the joint opening did not connect between the diagonal crack from deviator and the dominant diagonal crack as shown in Fig. 3. It means that the height of opening joint was not affected by the diagonal crack from the deviator.

3.4 Load-Deflection Curves

Figure 7 presents the load-deflection curves of the testing beams and referred beam, e.g. SJ10-19 (Nguyen et al.

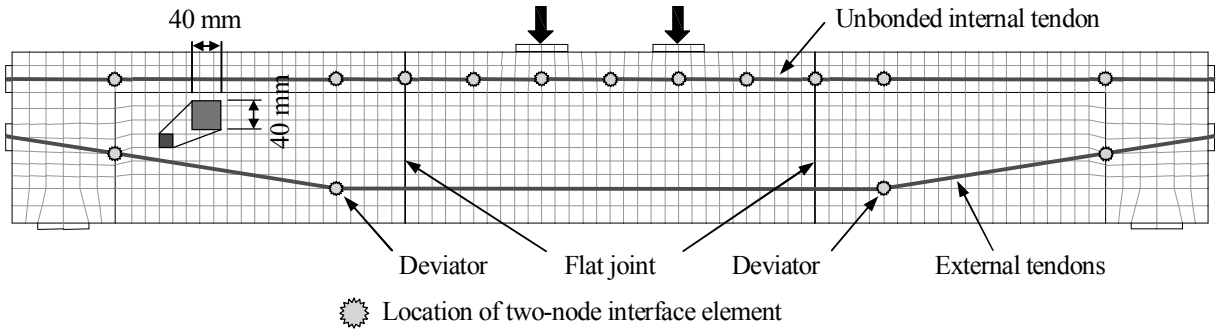


Fig. 8 Mesh for finite element discretization

2010) where incline angle α was of 0 deg. Even though there was a difference of location of deviators and the inclined angle of external tendons, all the segmental beams exhibited the similar linear elastic behavior in the beginning. Linear behavior was prolonged until the first flexural crack occurred with the load, P_{cr} as tabulated in Table 4. The load of first flexural crack was affected insignificantly by the location of deviator and the inclined angle of external tendons. The load at the first flexural crack of segmental beams with draped external tendons was very close to that of the segmental beams with straight external tendons (Nguyen et al. 2010). The load at the diagonal crack from deviator was not affected by the location of deviator, D09-200 and D09-600. In D14-600, higher inclined angle and area of draped external tendons, the load at the diagonal crack from deviator was higher than that of D09-200 and D09-600. The load at the dominant diagonal crack was not affected by the location of deviator. The load at dominant crack of D14-600, higher inclined angle and area of draped external tendons, was higher than that of D09-600 and 09-200 about 13 percent. Because of stopping before failure, the maximum load of D09-600 was smaller that the ultimate load of the segmental beams with straight external tendons. However, the maximum load of D09-200 and the ultimate load of D14-600 were higher than the ultimate load of the beam with straight external tendons, SJ10-19 [5] about 8 and 15 percent, respectively.

3.5 Failure mechanism

The linear elastic behavior of segmental beams was not affected by the location of deviator, inclined angle of draped tendons and area of external tendons. It was expressed by the load at the first flexural crack to be similar. Compared with the same area of external tendons, the load at the dominant diagonal crack of segmental beams with inclined angle of 9 deg., D09-200 and D09-600, was smaller than that of the segmental beam with straight tendons, SJ10-19. It was because that the segmental beams with draped tendons exhibited reduced stiffness (Tan and Ng 1997) higher than beams with straight tendons. However, in D14-600 with inclined angle of 14.2 deg. and higher in tendon area the loads at the diagonal crack from a deviator and the dominant diagonal crack were higher than that of D09-200 and D09-600, inclined angle of 9 deg., and straight tendon SJ10-19 as well. It means that the stiffness of external tendons also affected the stiffness of segmental beams with draped tendons.

The crack from deviator was not formed in segmental beams with straight tendons (Nguyen et al. 2010 and Sivaleepunth et al. 2009). In segmental beams with draped tendons the diagonal cracks from deviators, however, was formed before the occurrence of the dominant diagonal crack from segmental joint to the loading point. It means that deviator force was arisen and it affected the shear transfer mechanism in the segmental beams with draped tendon. The formation of the dominant diagonal crack from segmental joint to the loading point demonstrated that the local behavior of segmental joint (MacGregor et al. 1989) affected significantly the behavior of segmental beams. Although there was a difference in location of deviator and inclined angle of draped tendons, the shear failure mode was designated in the tested beams as the shear compression failure mode. First, the dominant diagonal crack was formed toward the loading point. Finally, the failure took place with the crushing of concrete near the loading point in the shear span. The results of this experiment show that the shear carrying capacity of segmental concrete beams with draped external tendons was higher than that of segmental beams with straight external tendons.

4. FEM ANALYSYS

4.1 Description of models

The nonlinear finite element method (FEM) using DIANA computer program has been conducted to examine the shear mechanism with the effect of draped external tendons. The concrete beams were modeled by means of four-node quadrilateral isoparametric plane stress element as shown in Fig. 8. The behavior of concrete in compression and tension was modeled according to the model proposed by Thorenfeldt et al. 1987 and Hordijk's model (Hordijk 1991), respectively. Longitudinal reinforcements were modeled by means of the embedded reinforcement element. Tendons were modeled by a two-node truss element. A bilinear elasto-plastic constitutive model appropriately represents the stress–strain relationship of reinforcing bars and tendons. The properties of concrete, reinforcing bars and external tendons are shown in Tables 1, 2 and 3.

To represent the interfacial behavior between external

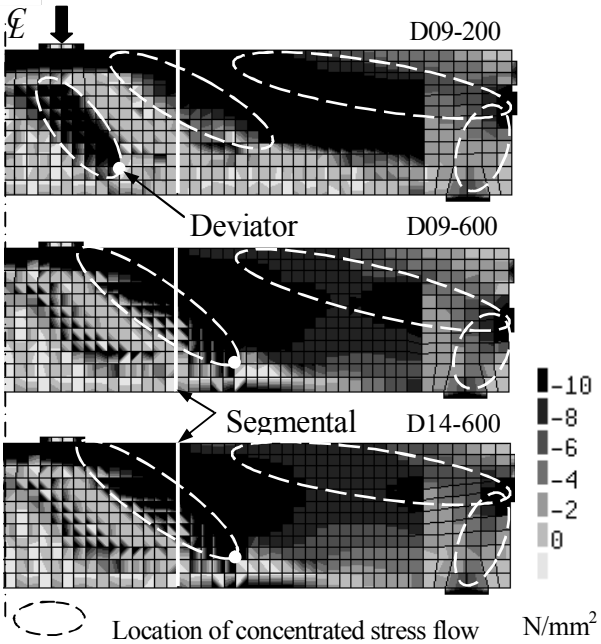


Fig. 9 Principal compressive stress at peak load

tendons and deviators or a concrete beam, the two-node interface element in DIANA system was applied. The stiffness of this interface element was adopted from Sivaleepunth et al. 2009 in order to neglect the friction between tendons and deviators or concrete at beam ends. Two-node interface element was also provided in some positions to model unbonded internal tendon in the top flange as shown in Fig. 8.

Figure 8 also shows that the flat joint model (Turmo et al. 2006) has been applied to reproduce the real geometry of joint by using the two-line interface element in DIANA system. Flat joints have fewer degree of freedom which means less computer calculation time. This can be beneficial especially for complex geometries such as shear keys. The discrete crack model is selected for the interface elements of segmental joints. The normal stiffness, k_n, and tangential stiffness, k_t, in the elastic stage for flat joint model was 10^5 N/mm^3 for segmental beams with draped tendons. The tensile strength of the epoxy is higher than that of concrete. Therefore, the tensile strength of concrete, f_t was selected to model the segmental joint in the nonlinear FEM analysis.

4.2 FEM Results

In order to validate the FEM model, the results obtained from the numerical analysis were compared with the experimental results. Figure 7 also shows a good agreement of the load and deflection curves between the experimental results and FEM analysis. Figure 9 shows the principal compressive stress of all beams at the peak load. It can be seen that one concentrated stress flow formed from the deviator to the loading point. This concentrated stress flow explained the formation to the diagonal crack from the deviator to the loading point. From the anchorage there are two concentrated stress flows. One is formed from the anchorage to support. Other is tended toward the loading point. It means that not only deviator force but also the transfer behavior of prestressing force from anchorage affected the shear transfer mechanism and also the shear failure mechanism in segmental concrete beams with draped external tendons.

5. CONCLUSIONS

The shear failure mechanism and the shear carrying capacity of segmental concrete beams with draped external tendon were discussed in this paper. The shear behavior of segmental concrete beams with draped external tendons was similar to that of segmental concrete beams with straight external tendons in the linear stage. After the linear stage the stiffness of segmental beams with draped tendons exhibited reduced stiffness to compare with segmental beams with straight tendons and was affected by the area of draped tendons. The deviator force, affected by the location of deviator and the inclined angle of draped tendons, and the transfer behavior of prestressing force from anchorage affected significantly on the shear transfer mechanism of segmental concrete beams with draped external tendons. The shear compression failure mode was observed for the segmental concrete beams with draped external tendons. Shear capacity of segmental concrete beams with draped external tendons was higher than that of segmental beams with straight external tendons.

References:

Hordijk, D. A.: Local Approach to Fatigue of Concrete, Ph.D thesis, Delft University of Technology, 1991.

Japan Society of Civil Engineers (JSCE) (2002), "Standard Specification for Concrete Structures," Structure Performance Verification.

MacGregor, J. G, Sozen, M. A. and Siess, C. P.: Effect of Draped Reinforcement of Behavior of Prestressed Concrete Beams, ACI Journal, Vol. 32, No. 6, pp. 649-677, 1960.

Nguyen, D. H., Watanabe, K., Niwa, J. and Hasegawa, T.: Modified Model for Shear Carrying Capacity of Segmental Concrete Beams with External Tendons, Journal of Materials, Concrete Structures and Pavements, JSCE, Vol. 66, No. 1, pp.53-67, 2010.

Rezai-Jorabi, H. and Regan, P. E.: Shear Resistance of Prestressed Concrete Beams with Inclined Tendons, The Structural Engineer, Vol. 64, No. 3, pp. 63-75, 1986.

Sevaleepunth, C., Niwa, J., Nguyen, D. H., Hasegawa, T. and Hamada, Y.: Shear Carrying Capacity of Segmental Prestressed Concrete Beams, Journal of Materials, Concrete Structures and Pavements, JSCE, Vol. 65, No. 1, pp. 63-75, 2009.

Tan, K. H. and Ng, C. K.: Effect of Deviators and Tendon Configuration on Behavior of Externally Prestressed Beams, ACI Journal, Vol. 94, No. 1, pp. 13-21, 1997.

Thorenfeldt, E., Tomaszewicz, A. and Jensen, J. J.: Mechanical Properties of High-Strength Concrete and Application in Design, Symposium Procceding of Utilization of High-Strength Concrete, Norway, 1987.

Turmo, J., Ramos, G. and Aparicio, A. C.: FEM Modelling of Unbonded Post-Tensioned Segmental Beams with Dry Joints, Engineering Structural Journal, Vol. 28, pp. 1852-1863, 2006.

8CUEE CONFERENCE PROCEEDINGS
8th International Conference on Urban Earthquake Engineering
March 7-8, 2011, Tokyo Institute of Technology, Tokyo, Japan

SEISMIC PERFORMANCE OF A FULL-SIZE POLYPROPYLENE FIBER REINFORCED CEMENT COMPOSITE BRIDGE COLUMN BASED ON E-DEFENSE SHAKE TABLE EXCITATIONS

Kazuhiko Kawashima[1], Richelle Zafra[2], Tomohiro Sasaki[3], Koichi Kajiwara[4], and Manabu Nakayama[5]

1) Professor, Department of Civil Engineering, Tokyo Institute of Technology, Japan
2) Graduate Student, Department of Civil Engineering, Tokyo Institute of Technology, Japan
3) Post-Doctoral Fellow, Department of Civil Engineering, Tokyo Institute of Technology, Japan
4) Senior Researcher, Hyogo Earthquake Engineering Research Center, National Research Institute for Earth Science and Disaster Prevention, Miki, Hyogo, Japan
5) Research Fellow, Hyogo Earthquake Engineering Research Center, National Research Institute for Earth Science and Disaster Prevention, Miki, Hyogo, Japan
kawashima.k.ae@m.titech.ac.jp, zafra.r.aa@m.titech.ac.jp, sasaki.t.aa@m.titech.ac.jp, kaji@bosai.go.jp, m-nakayama@bosai.go.jp

Abstract: E-Defense shake table experiments on a full-size bridge column using polypropylene fiber reinforced cement composites (PFRC) at the potential plastic hinge and part of the footing is presented. The column is 7.5 m tall with 1.8 m by 1.8 m square section designed based on the 2002 Japan design code. The column was excited using a ground motion with 80% of the original intensity of the near-field ground motion recorded at the JR Takatori station during the 1995 Kobe, Japan earthquake. Excitations were repeated under increased mass and increased intensity of ground motion. The use of PFRC mitigated cover and core damage, local buckling of longitudinal bars and deformation of tie bars even after six times of excitation. The damage sustained was much less than the normal damage of regular reinforced concrete columns.

1. INTRODUCTION

A large scale bridge experimental program was conducted in 2007-2010 by the National Research Institute for Earth Science and Disaster Prevention (NIED), Japan (Nakashima et al. 2008). In the program, shake table experiments were conducted for two typical reinforced concrete columns which failed during the 1995 Kobe, Japan earthquake (C1-1 and C1-2 experiments), a typical reinforced concrete column designed in accordance with the 2002 Japan design code (JRA, 2002) (C1-5 experiment) and a new generation column using polypropylene fiber reinforced cement composites (PFRC) for enhancing the damage control and ductility (C1-6 experiment). The experiments were conducted using the E-Defense shake table where the table is 20 m by 15 m and has a payload of 1200 tf (12 MN). The maximum stroke of the table is 1 m and 0.5 m in the lateral and vertical directions, respectively. It was designed so that the ground motions during the 1995 Kobe earthquake can be generated.

C1-5 experiment was conducted using the E-Defense shake table with a ground motion 80% of the original intensity of the near-field ground motion recorded at the JR Takatori station during the 1995 Kobe earthquake. This is referred herein as the E-Takatori ground motion. The column performed satisfactorily under this ground motion. However, when the excitations were repeated under much stronger intensity and longer duration near-field ground motion, the column suffered extensive damage with blocks of crushed core concrete spilling out like explosion from the steel cage (Kawashima et al. 2010). Such failure was never seen in past quasi-static cyclic or hybrid loading experiments. Therefore, it is expected to develop columns which contribute to construct damage free bridges using materials that mitigate such damage under severe seismic loading.

Prior to the C1-6 experiment, a series of cyclic loading experiments were conducted on 1.68 m high, 0.4 m by 0.4 m square cantilever regular high strength concrete column and a column each using steel fiber reinforced concrete and polypropylene fiber reinforced cement composite at the plastic hinge region and the footing for deciding the material of C1-6 column (Kawashima et al. 2011). The polypropylene fiber reinforced cement composite column had superior performance in mitigating cover and core concrete damage, longitudinal bar buckling and deformation of tie bars at the plastic hinge region resulting from the crack control capability of polypropylene fiber reinforced cement composite. As a result, C1-6 column was built using

polypropylene fiber reinforced cement composite at the plastic hinge region and a part of the footing.

High performance fiber reinforced cement composites (HPFRCC) are materials that exhibit multiple fine cracks upon loading in tension which leads to improvement in toughness, fatigue resistance and deformation capacity (Matsumoto and Mihashi 2002). Engineered cementitious composite (ECC) is an HPRCC that has tensile strain capacity of about 0.03 to 0.05 resulting from the formation of closely spaced micro cracks due to the bridging action of fibers (Li and Leung, 1992). It has low elastic stiffness compared to concrete, and larger strain at peak compressive strength, due to the absence of course aggregates (Li et al. 1995). Polypropylene fiber reinforced cement composite, referred herein as PFRC, belongs to the class of ECC.

Previous investigations have shown the positive effects of using HPFRCC for structural members subjected to seismic loads. Kosa et al (2007) examined the use of this material with polyvynil alcohol (PVA) fibers for the seismic strengthening of scaled bridge piers similar to concrete jacketing. They found that a pier using HPFRCC on the cover concrete can provide confinement effect as much as the pier whose entire cross section was constructed of this material. Furthermore, the deformation capacity and the energy absorption capacity were also significantly improved compared with a pier constructed of ordinary concrete.

Saiidi et al. (2009) investigated the effect of incorporating ECC with polyvynil alcohol (PVA) fibers and shape-memory alloys (SMA) on model columns subjected to cyclic loading. Use of PVA-ECC substantially reduced damage in the plastic hinge. Furthermore, the combination of PVA-ECC and SMA led to larger drift capacity compared to the conventional steel reinforced concrete column.

This study aims to investigate the effect of PFRC for enhancing the damage control and ductility capacity of a full-size bridge column subjected to a strong near-field ground motion using the E-Defense shake table. This column is called herein as C1-6 column. The information obtained from the shake table experiments can provide reliable data for verification of structure performance and can provide an insight on the response of such structures subjected to real earthquake conditions.

2. E-DEFENSE SHAKE-TABLE EXCITATIONS

2.1 Column Configuration and Properties

C1-6 column is a 7.5 m tall, 1.8 m by 1.8 m square, cantilever column shown in Figure 1. It was designed based on the 2002 Japan design code assuming moderate soil condition under the Type II design ground motion (near-field ground motion). PFRC was used at a part of the footing with a depth of 0.60 m below the column base and a depth of 2.7 m above the column base to minimize the cost. The 2.7 m depth of PFRC is three times the code specified plastic hinge length of one-half the column width (0.90 m). This height was set to avoid failure at the PFRC-concrete interface. The 0.60 m depth of PFRC at the footing was provided to minimize damage. Regular concrete with design compressive strength of 30 MPa was used in the other parts of the column. The actual 28-day cylinder compressive strength of concrete was 41 MPa.

The design compressive strength of PFRC was 40 MPa. PFRC was made by combining cement mortar, fine aggregates with maximum grain size of 0.30 mm, water and 3% volume of polypropylene fibers. Monofilament polypropylene fibers with diameter of 42.6 μ m, length of 12 mm, tensile strength of 482 MPa, Young's modulus of 5 GPa and density of 0.91 kg/m^3 were used (Hirata et al. 2009). Superplasticizers were added to improve the workability of the mix. The actual 28-day cylinder compressive strength of PFRC was 36 MPa with a strain at peak of 0.47%.

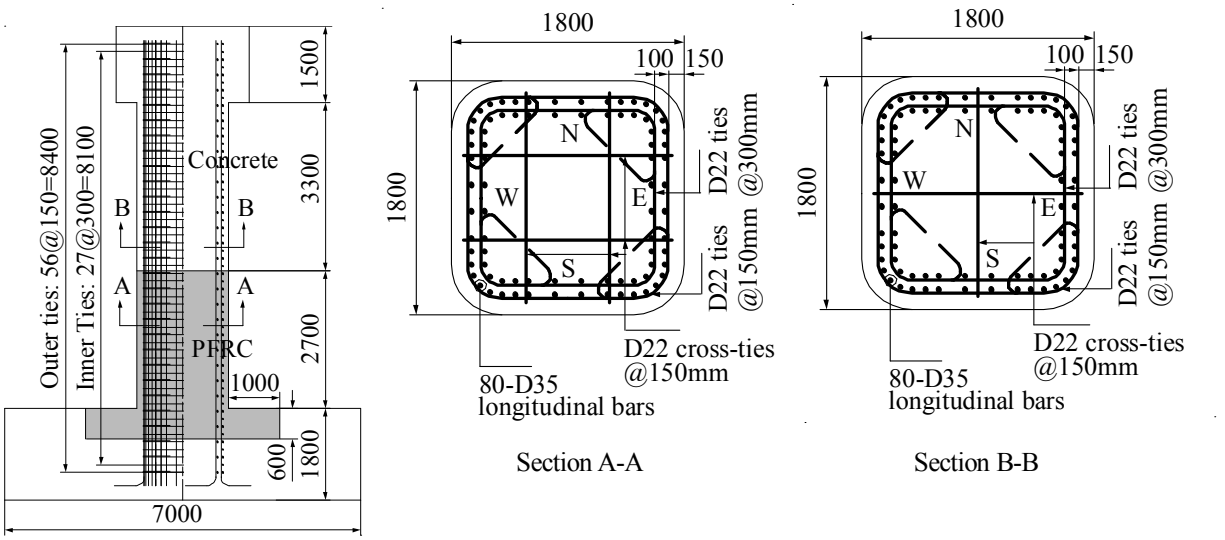


Figure 1 C1-6 column configuration and dimensions (mm)

Eighty-35 mm diameter deformed longitudinal bars were provided in two layers. The corresponding reinforcement ratio ρ_l was 2.47%. The nominal yield strength of longitudinal bars was 345 MPa (SD345) and the actual yield strength was 386 MPa at 0.2% strain. Deformed 22 mm diameter ties with 135 degree bent hooks lap-spliced with 40 times the bar diameter were provided. The outer ties were spaced at 150 mm and the inner ties were spaced at 300 mm throughout the column height. Cross-ties with 180 degree hooks at 150 mm spacing were provided as shown in Figure 1 to increase confinement of the square ties. Volumetric tie reinforcement ratio ρ_s within a height of 2.7 m from the column base was 1.72%. The nominal yield strength of ties was 345 MPa (SD345) and the actual yield strength was 396 MPa at 0.2% strain. Concrete cover of 150 mm was provided.

2.2 Experiment Set-up and Shake-Table Excitations

Photo 1 shows the experiment set-up using the E-Defense shake table. Four mass blocks were set on the column through two simply supported decks. Note that the decks were not designed to idealize the stiffness and strength of real decks. Each deck was supported by the column on one side and by the steel end support on the other side. Tributary mass to the column by two decks including four weights was 307 tf (3011 kN) and 215 tf (2109 kN) in the longitudinal and transverse directions, respectively. The column was excited using the E-Takatori ground motion with the EW, NS and UD components, shown in Figure 2, applied in the longitudinal, transverse and vertical directions of the column, respectively. This ground motion is referred herein as the 100% E-Takatori ground motion.

Shake table excitations were conducted six times. Excitations were repeated to clarify column performance when subjected to much stronger and longer duration near-field ground motion. The column was excited twice with 100% E-Takatori ground motion (1-100%(1) and 1-100%(2) excitations). After the mass in the longitudinal direction was increased by 21% from 307 tf to 372 tf, excitations were conducted with 100% E-Takatori ground motion once (2-100% excitation) and 125% E-Takatori ground motion three times (2-125%(1), 2-125%(2) and 2-125%(3) excitations).



Photo 1 Experiment set-up using E-Defense shake table

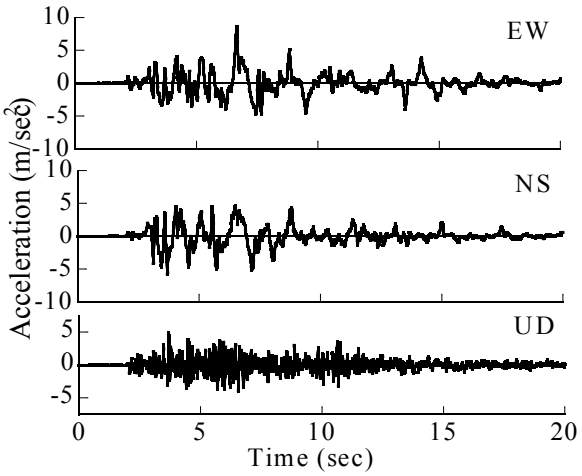


Figure 2 E-Takatori ground motion

3. EFFECT OF POLYPROPYLENE FIBER REINFORCED CEMENT COMPOSITE ON COLUMN SEISMIC PERFORMANCE

3.1 Progress of Failure

Photos 2 to 4 show the damage progress within 1.2 m from the column base at the SW and NE corner during 1-100%(1), 2-100% and 2-125%(3) excitations at the instance of peak response displacement where the SW corner was subjected to compression while the NE corner was subjected to tension. As shown in Photo 2, during 1-100%(1) excitation, only micro cracks were observed around the column. During 1-100%(2) excitation, very thin flexural cracks as wide as 0.1 - 0.2 mm occurred within 1.6 m from the base all around the column.

During 2-100% excitation, with the mass increased by 21%, damage progressed as shown in Photo 3. Flexural cracks propagated and a crack 0.6 m from the column base at the NE corner opened about 8 mm at the peak response displacement. After the excitation, the maximum residual crack at the above location was 1 - 2 mm wide. Although only flexural cracks occurred all around the column with the cover concrete remaining as a whole shell due to the bridging action of fibers, vertical hairline cracks started to occur at the NE and SW corners within 0.6 m from the column base due to the large strut action of cover concrete shell resulting from the footing reaction when the column was laterally displaced.

During 2-125%(1) excitation, in which the seismic excitation intensity was increased by 25%, at the peak response displacement, the crack 0.6 m from the base opened to 14 mm at the NE corner which was subjected to tension while a vertical crack opened to 9 mm at the opposite SW corner subjected to compression. As the loading progressed, at the SW corner subjected to tension, a crack 1.2 m from the base opened to 9 mm and vertical cracks started to widen at the opposite NE corner.

Succeeding excitations resulted to further propagation of flexural cracks within 2 m from the base around the column and the widening of the vertical crack at the SW

corner. As shown in Photo 4, the damage progressed during 2-125%(3) excitation wherein at the peak response displacement, the crack 0.6 m from the base at the NE corner opened to 20 mm and the vertical crack at the SW corner opened to 15 mm. Note that at the NW corner, cover concrete spalled within 200 mm from the column base when it was subjected to compression while flexural cracks opened to 13 mm at the opposite SE corner subjected to tension. After the excitation, the cracks which opened to over 10 mm during the excitation almost closed with widths of only 5 - 8 mm in flexural cracks and 7 - 12 mm in vertical cracks. Moreover, majority of other small cracks closed to hairline cracks after the excitations due to the fiber bridging action of fibers. Cover concrete spalling was much restricted and there were no exposed longitudinal bars and ties in C1-6 column after 2-125%(3) excitation.

To investigate how the damage progressed in the core and in the longitudinal bars at the NE corner after 2-125%(3) excitation, the column was opened at the area shown in Photo 5. Note that removal of cover concrete in the fiber mixed concrete was very difficult because of its solid nature compared to that of regular reinforced concrete.



(a) (b)

Photo 2 Column damage during 1-100%(1) excitation: (a) SW corner and (b) NE corner



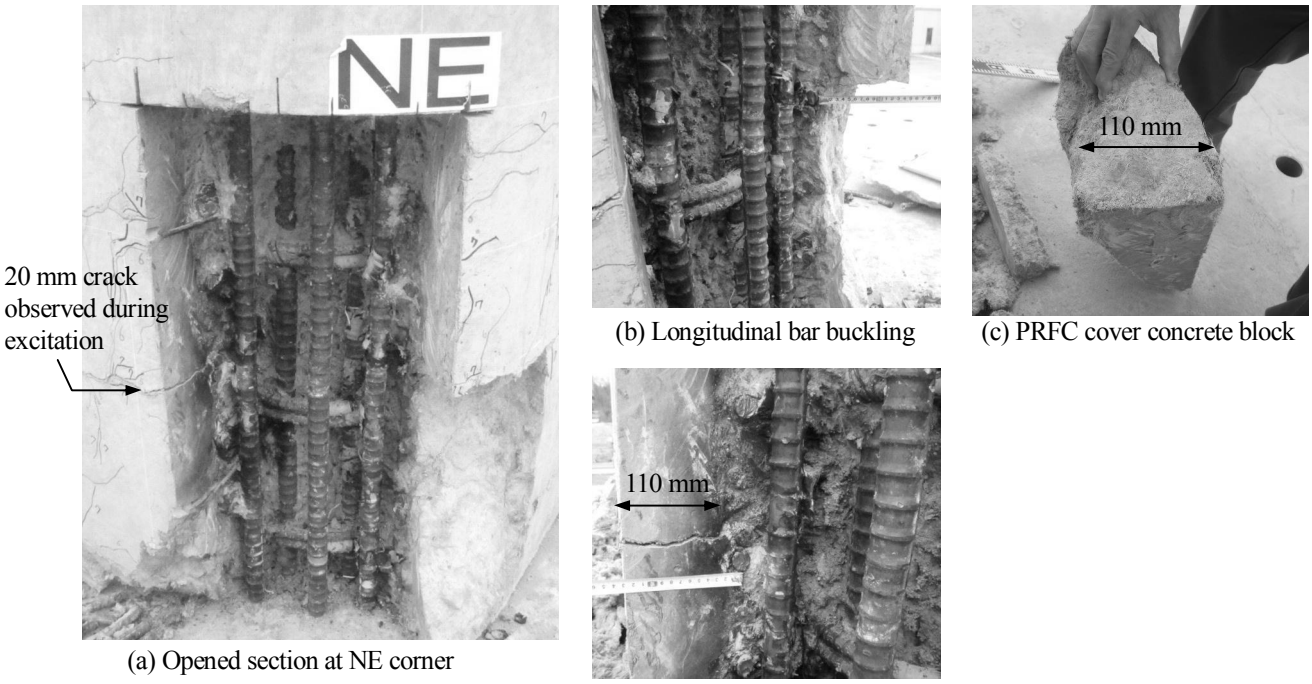
(a) (b)

Photo 3 Column damage during 2-100% excitation: (a) SW corner and (b) NE corner



(a) (b)

Photo 4 Column damage during 2-125%(3) excitation: (a) SW corner and (b) NE corner



(a) Opened section at NE corner

(b) Longitudinal bar buckling

(c) PRFC cover concrete block

(d) Crack on PFRC cover concrete

Photo 5 Damage of PFRC cover concrete and longitudinal bars at the NE corner after 2-125%(3) excitation

In Photo 5, only the outer and inner longitudinal bars and inner ties can be seen because outer ties and a part of the PFRC cover concrete were removed. Maximum lateral offset among three outer longitudinal bars from their original vertical axis was 8 mm. On the other hand, the inner longitudinal bars did not buckle because they were constrained by the undamaged concrete between the outer and inner longitudinal bars. At the SW corner which was subjected to the largest compression during the peak response displacement, the maximum lateral offset of the outer longitudinal bars due to local buckling was 5 mm which was much less than the buckling of bars at the NE corner. In general, local bar buckling was limited.

At the location where crack opening of 20 mm was observed, it was found that the crack occurred only in the PFRC cover concrete with a depth of 110 mm and did not propagate into the core concrete. Also shown is the block of cover concrete that was removed at the bottom right portion where the presence of fibers held the cover concrete together preventing the disintegration of cover concrete. Hence, it is worthy to note that even after six times of excitation, the damage sustained by C1-6 column was much less than the damage of regular reinforced concrete columns.

3.2 Response Acceleration and Displacement

The principal response angle θ_P is defined to identify the principal response direction when the maximum column response displacement occurs . It is given by

$$\theta_P = \tan^{-1}\left(\frac{u_{TR}}{u_{LG}}\right) \qquad (1)$$

where u_{LG} and u_{TR} are the response displacements in the longitudinal and transverse directions, respectively.

Figure 3 shows the acceleration and displacement at the top of column in the principal response direction and Table 1 summarizes the peak acceleration, displacement, residual displacement and moment at each excitation. The principal response angle θ_P varied from 194 to 205 degrees during the six excitations which was almost at the NE-SW direction. The measured peak response acceleration during the series of excitations varied from 13-20 m/s^2.

Due to the high acceleration pulse in the input ground motion, the column experienced high amplitude displacement during each excitation. The peak response displacement was equal to 0.078 m (1% drift) during 1-100%(1) excitation and progressed to 0.45 m (6% drift) during 2-125%(3) excitation. As the excitation progressed with increasing intensity of ground motion, the response displacements increased due to column stiffness deterioration resulting from the damage. The residual displacement was only -0.004 m (0.05% drift) after 2-100% excitation, increased to -0.037 m (0.49% drift) after 2-125%(2) excitation then decreased to -0.013 m (0.13% drift) after the last excitation. Since the allowable residual drift for a cantilever column based on the 2002 JRA code is 1%, the residual drift of the column was still smaller than the allowable limit. It is important to note that residual displacement not only increases but also decreases during seismic excitations because it is more affected by the ratio of post elastic stiffness to elastic stiffness as well as the instantaneous structure period [MacRae and Kawashima, 1997].

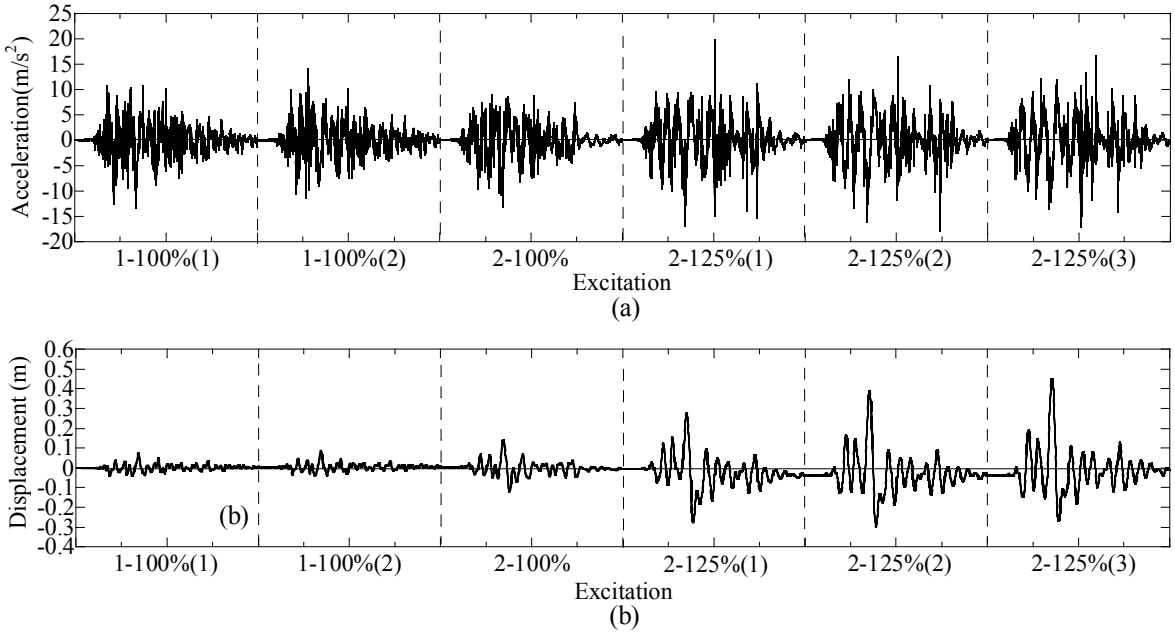


Figure 3 Column response in the principal direction: (a) acceleration and (b) displacement

3.3 Moment and Ductility Capacity

The bending moment at the column base was evaluated as

$$M_k = M_{Bk} + M_{Ck} \tag{2}$$

where M_{Bk} and M_{Ck} represent the moment based on measured load cell forces and based on pier and column mass accelerations, respectively, and are given by

$$M_{Bk} = \sum_{i=1}^{N} \left\{ F_{Lki} h_{Li} - V_{Li} \left(x_{ki} + u_k \right) \right\} \tag{3}$$

$$M_{Ck} = \int_0^{h_B} m_C \ddot{u}_{Ck} dz + \int_{h_B}^{h} m_B \ddot{u}_{Bk} dz \tag{4}$$

where F_{Lki} is the inertia force measured by the i-th load cell in the k direction (k = LG and TR corresponding to the longitudinal and transverse directions, respectively); V_{Li} is the vertical force measured by the i-th load cell in the k direction; h_{Li} is the height from the base to the i-th load cell; x_{ki} is the load cell coordinate in the k direction from the column center; u_k is the response displacement at top of column in the k direction; N is the load cell number ($N = 32$); z is the coordinate of the column from the base upward; m_C and m_B are the mass per unit length of the column and pier cap, respectively; $\ddot{u}_{Ck}$ is the column acceleration response; $\ddot{u}_{Bk}$ is the pier cap acceleration response; h_B is the height from base to the bottom of the pier cap and h is the height from base to the top of pier cap.

Figure 4 shows the hysteresis of moment at the base vs. displacement at the top of the column in the principal response direction. The hysteresis during the entire six times of excitation is stable with sufficient energy dissipation. As summarized in Table 1, the peak moment gradually increased as the excitation progressed. A maximum capacity of 25.3 MNm at 5.2% drift was developed during 2-125%(2) excitation. During this excitation, flexural cracks further propagated all around the column and the vertical cracks at the SW corner widened as described in 3.1. During the subsequent 2-125%(3) excitation, the peak drift increased to 6% while the peak moment slightly deteriorated by 2%. It should be noted that even during the 2-125%(3) excitation, the moment vs. lateral displacement hysteresis was still very stable.

3.4 Strains of Longitudinal and Tie Bars

Figure 5 shows strains of longitudinal and tie bars of C1-6 column at the plastic hinge zone (300-400 mm from the base) at the SW corner where the most extensive damage occurred. Only strains during 1-100%(1), 2-100%, 2-125%(1) and 2-125%(3) excitations are shown due to space limitation. Because longitudinal bars were set in two layers, strains of both the outer and inner longitudinal bars and tie bars are shown here. Noting that the yield strain of both longitudinal and tie bars was nearly 2,000 μ, the longitudinal bars started to yield in tension during 1-100%(1) while tie bars started to yield in tension during 2-125%(1) excitation. The outer and inner longitudinal bars and tie bars exhibited similar response however the amplitude of strains were generally larger in the outer longitudinal and tie bars than the respective inner longitudinal and tie bars.The difference of strain amplitude between outer and inner tie bars is particularly large during and after 2-125%(1) excitation resulting from local buckling of longitudinal bars, which will be described later.

An interesting point in Figure 5 is that the compression strains of the outer and inner longitudinal bars became larger than tension strains during and after 2-125%(1) excitation. For example, compression strain of the outer longitudinal bar reached 19,000 μ while tension strain reached 18,000 μ during 2-125%(1) excitation. This obviously

Table 1 Column response in the principal response direction

Excitation	θ_P (Degrees)	$\ddot{u}_P$ (m/s^2)	u_P (m)	u_P Drift (%)	Residual displacement (m)	M_P (MNm)
1-100%(1)	201.9	-13.4	0.078	1.0	0.005	20.5
1-100%(2)	193.5	14.2	0.089	1.2	0.007	21.8
2-100%	196.0	-13.0	0.144	1.9	-0.004	24.0
2-125%(1)	201.1	19.9	0.280	3.7	-0.035	24.3
2-125%(2)	204.8	-17.9	0.392	5.2	-0.037	25.3
2-125%(3)	204.6	-17.1	0.450	6.0	-0.013	24.9

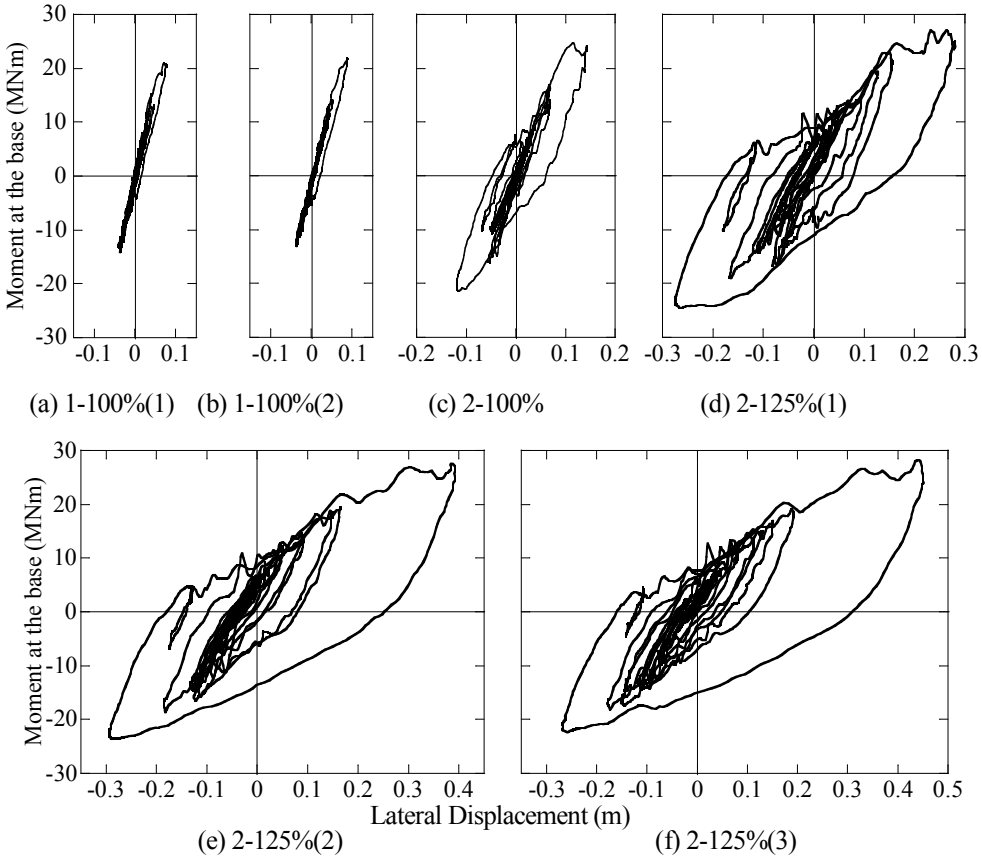


Figure 4 Hysteresis of moment at the base vs. displacement at the top of column in the principal direction

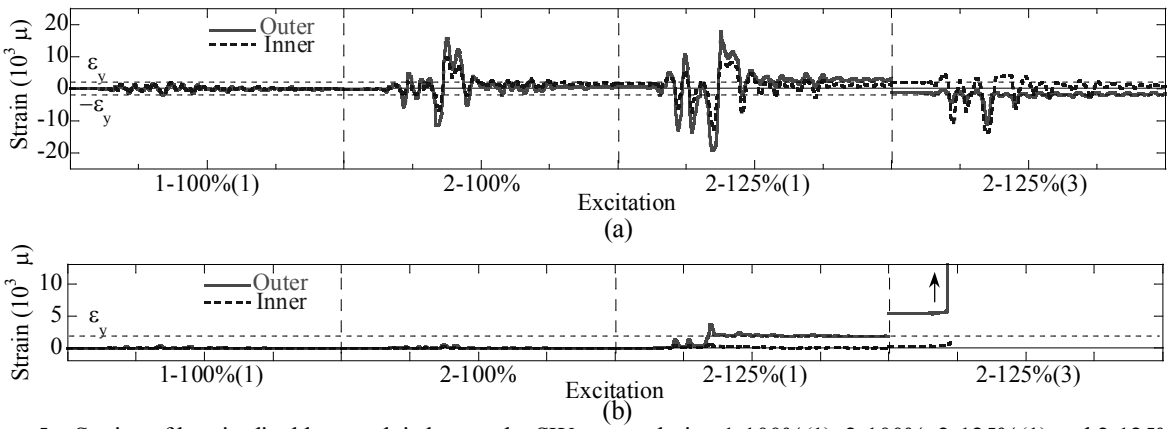


Figure 5 Strains of longitudinal bars and tie bars at the SW corner during 1-100%(1), 2-100%, 2-125%(1) and 2-125%(3) excitations: (a) Longitudinal bars at 300 mm from the base and (b) tie bars at 400 mm from the base

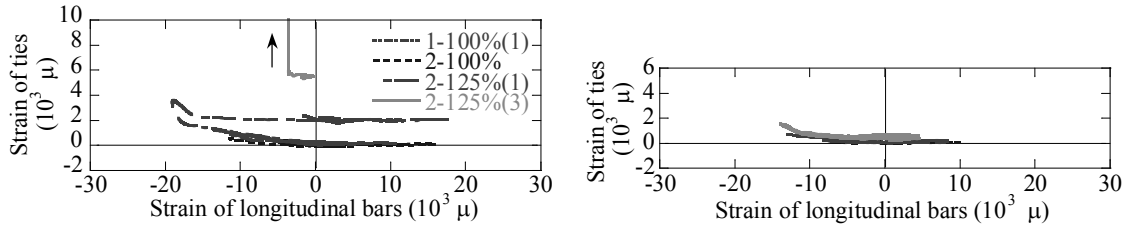


Figure 6 Strain of a tie at 400 mm from the base vs. strain of a longitudinal bar at 300 mm from the base at the SW corner of C1-6 column: (a) Outer bars and (b) inner bars

resulted from the low elastic modulus of PFRC. The large compression strain must have caused the longitudinal bar to buckle. However, in spite of the bar buckling, as described in 3.1, spalling of cover concrete did not occur indicating that the presence of fibers made the cover concrete remain as a whole shell.

On the other hand, the tie bar was still elastic during 1-100%(1) until 2-100% excitations. At the instance when compression strain of the outer longitudinal bar sharply increased during 2-125%(1) excitation, the outer tie strain started to increase to 3,700 μ , indicating that the tie resisted the longitudinal bar buckling. Compression strain of the inner longitudinal bar also sharply increased at the same time, however, the inner tie strain did not increase indicating that the inner longitudinal bar did not buckle. This was because confinement for bar buckling was larger at the inner longitudinal bar than the outer longitudinal bar due to the resistance of core concrete between outer and inner ties which was still intact as shown in Photo 5.

Figure 6 further shows the interaction of a longitudinal bar with a tie bar for outer and inner bars. The tie strains during 2-125%(3) excitation were larger than 5,000 μ and only reliable data are shown here. A sharp increase of the outer tie strain resulting from restraining local buckling of the outer longitudinal bar under high compression strain is clearly seen during and after 2-125%(1) excitation while the inner tie strain remained below 2,000 μ because inner longitudinal bars did not yet buckle.

4. CONCLUSIONS

A series of shake table experiments of a full-size bridge column using polypropylene fiber reinforced cement composites (PFRC) at the potential plastic hinge and part of the footing, referred herein as C1-6 column, were conducted. Based on the results presented, the following conclusions were deduced:

a) PFRC did not have the brittle compression failure of regular reinforced concrete under repeated large inelastic deformation due to the bridging mechanism of fibers. This prevented the brittle crushing of cover and core concrete.

b) As a consequence of a), the use of PFRC reduced buckling of longitudinal bars and deformation of tie bars thus mitigating the damage of C1-6 column even after six times of strong excitations.

c) As a result of the damage mitigation properties of PFRC, the column had a stable flexural capacity and enhanced ductility reaching until 6% drift.

References:

Japan Road Association (2002), "Specifications for Highway Bridges," Maruzen, Tokyo.

Hirata, T., Kawanishi, T., Okano, M. and Watanabe, S. (2009), "Study on Material Properties and Structural Performance of High-Performance Cement Composites using Polypropylene Fiber," *Proc. Japan Concrete Institute*, **31**(1), 295-300.

Kawashima, K., Sasaki, T., Ukon, H., Kajiwara, K., Unjoh, S., Sakai, J., Kosa, K., Takahashi, Y., and Yabe, M. and Matsuzaki, H. (2010), "Evaluation of Seismic Performance of a Circular Reinforced Concrete Bridge Column Designed in Accordance with the Current Design Code based on E-Defense Excitation," *Journal of Japan Society of Civil Engineers*, **65**(2), 324-343.

Kawashima, K., Zafra, R., Sasaki, T., Kajiwara, K. and Nakayama, M. (2011), "Effect of polypropylene fiber reinforced cement composite and steel fiber reinforced concrete for enhancing the seismic performance of bridge columns," *Journal of Earthquake Engineering* (submitted for publication).

Kosa, K., Wakita, K., Goda, H. and Ogawa, A. (2007), "Seismic Strengthening of Piers with Partial Use of High Ductility Cement," *Advances in Construction Materials*, Grosse, C. U. Ed., Springer: Berlin Heidelberg, 269-277.

Li, V. and Leung, C. (1992) "Steady-State and Multiple Cracking of Short Random Fiber Composites," *Journal of Engineering Mechanics*, *ASCE*, **118**(11), 2246-2264.

Li, V., Mishra, D. and Wu, H. (1995) "Matrix Design for Pseudo-strain-hardening Fibre Reinforced Cementitious Composites," *Materials and Structures*, **28**, 586-595.

MacRae, G. and Kawashima, K. (1997) "Post-earthquake Residual Displacements of Bilinear Oscillators," *Earthquake Engineering and Structural Dynamics*, **26**, 701-716.

Matsumoto, T. and Mihashi, H. (2002) "JCI-DFRCC Summary Report on DFRCC Terminologies and Application Concepts," *JCI International Workshop on Ductile Fiber Reinforced Cementitious Composites – Application and Evaluation*, Takayama, Japan. 1-8

Nakashima, M., Kawashima, K., Ukon, H. and Kajiwara, K., (2008) "Shake Table Experimental Project on the Seismic Performance of Bridges using E-Defense," *14th World Conference on Earthquake Engineering*, Beijing, China, Paper S17-02-010 (CD-ROM).

Saiidi, M., O'Brien, M. and Sadrossadat-Zadeh, M. (2009) "Cyclic Response of Concrete Bridge Columns Using Superelastic Nitinol and Bendable Concrete," *ACI Structural Journal*, **106**(1), 69-77.

8CUEE CONFERENCE PROCEEDINGS
8th International Conference on Urban Earthquake Engineering
March 7-8, 2011, Tokyo Institute of Technology, Tokyo, Japan

ADVANCED PRECAST CONCRETE DUAL-SHELL STEEL COLUMNS

Gabriele Guerrini[1] and José I. Restrepo[2]

1) Graduate Student Researcher, Dept. of Structural Engineering, University of California-San Diego, La Jolla, California, USA
2) Professor, Dept. of Structural Engineering, University of California-San Diego, La Jolla, California, USA
gguerrin@ucsd.edu, jrestrepo@ucsd.edu

Abstract: An innovative bridge column technology for application in seismic regions is being developed, designed, and tested at UC San Diego Structural Engineering Department. This element combines a precast concrete hollow-core column with pre-tensioning or on-site post-tensioning and added energy dissipation.
The column consists of two steel shells that run for the full-height of the column, with concrete sandwiched in between. The outer shell acts as permanent formwork, and provides longitudinal and transverse reinforcement. The inner shell also behaves as permanent formwork, and prevents concrete implosion under large compressive strains. Constructability is enhanced by the use of a precast element of reduced weight (hollow-core section) without a reinforcing cage.
Large plastic rotations can be attained with minimal structural damage: column-cap and column-foundation joints are allowed to open in tension under severe earthquake excitation, and to close subsequently upon load reversal. Re-centering behavior is ensured by pre- or post-tensioned tendons, designed to respond elastically. A special connection between column, bent-cap, foundation, and tendon allows for eventual tendon replacement in the post-tensioned layout. Energy dissipation is provided by external devices yielding in flexure, which can be easily replaced if damaged.
Analytical and experimental work is currently in progress.

1. INTRODUCTION

During the last three decades of the 20th century, failure of bridges in densely populated areas of California and Japan under strong earthquakes resulted in a significant evolution of the seismic design approach for these infrastructures. Concepts such as ductility and capacity design were gradually understood and incorporated into practice standards, leading to the current design codes such as the California Department of Transportation's (Caltrans) *Seismic Design Criteria* (Caltrans, 2006).

While the notion of structural damage is accepted in design, resilient communities expect bridges to survive a moderately strong earthquake with little or no disturbance to traffic. This implies that partial or total bridge closures are tolerated with uneasiness, particularly in heavily congested urban areas. As a consequence, research efforts have been prompted into advanced technologies that reduce residual damage to the main structural elements, and encompass self-centering properties which allow the structural system to return to its original position after an earthquake. Moreover, these innovative solutions need to be economically viable when compared to existing technologies.

Replacement of existing infrastructure or construction of new facilities in congested and economically or environmentally sensitive areas is an issue faced by many communities worldwide. For this reason Caltrans, through a Federal Highway Administration's (FHWA) initiative, is moving forward towards the development of Accelerated Bridge Construction (ABC) technologies. Among the several goals of this initiative, reduction of on-site construction time, traffic impact, environmental disruption, and life-cycle costs, require technologies characterized by enhanced constructability.

As an example the State of California, as well as many other countries, is currently planning a new high-speed railway infrastructure, which will connect the largest urban and industrial areas of the State. The size of the required investment, and the social and economic impact caused by an eventual service interruption, make accelerated construction and seismic resilience one of the main concerns for the design of bridges along this transportation facility.

In response to the mentioned needs, researchers at UC San Diego are developing *Advanced Precast Concrete Dual-shell Steel Column* systems. Employment of precast technologies, replacement of traditional time-consuming reinforcing cages with steel pipes, and use of hollow cross-sections resulting in weight reduction by elimination of unnecessary concrete, are aimed to improve constructability and in particular to reduce on-site burdens. In parallel, the combination of pre- or post-tensioned joint connections and added energy dissipators ensure seismic resilience, in the form of self-centering capability, facilitation of structural fuse repair, and minimization of residual structural damage.

The proposed columns are an extension of the steel jacket concept used by Caltrans for retrofitting deficient columns, of the research work on Cast-In-Steel-Shell piles funded by Caltrans (Gebman, Ashford, and Restrepo, 2006), of the studies on self-centering precast walls performed at UC Berkeley (Sakai and Mahin, 2004) and in New Zealand (Rahman and Restrepo, 2000), and of the precast post-tensioned rocking systems developed within the PRESSS program (Priestley and Tao, 1993).

2. DIFFERENT LAYOUTS FOR PRECAST CONCRETE DUAL-SHELL STEEL COLUMNS

2.1 Background

A few years ago, researchers at UC San Diego (Tobolski, 2010) investigated the lateral response of a precast column unit featuring the dual-shell and re-centering characteristics under discussion. The test prototype is depicted in Figure 1. The column consists of two steel shells that run for the full-height of the column with high-performance concrete sandwiched in between the shells. Both shells act as permanent formwork during concrete casting. The outer one substitutes longitudinal and transverse reinforcement, with stresses being transferred between steel and concrete through weld beads on the internal surface of the shell. The inner shell prevents concrete implosion under large compressive strains.

This type of bent assembly is designed to attain large nonlinear drift rotations with minimum structural damage, which differs from the accepted performance criteria for columns being incorporated into bridge construction nowadays. Column-cap and column-foundation joints are allowed to open in tension during a strong and rare earthquake, and to close subsequently upon load reversal as shown in Figure 2(a).

In this particular configuration, re-centering behavior is ensured by unbonded tendons, designed to remain elastic even during a strong shake. Energy dissipation is provided by mild steel bars yielding axially across the joints; these bars are left partially unbonded to concentrate yielding at the

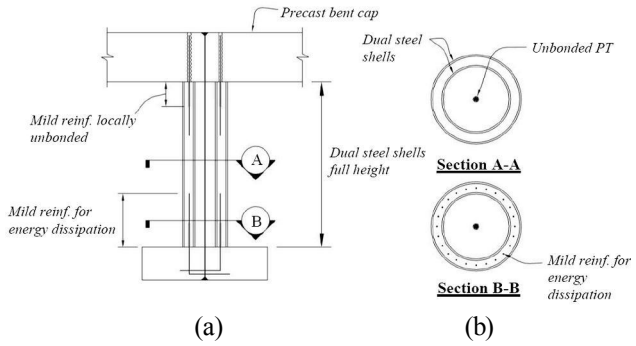


Figure 1 – Advanced Precast Concrete Dual-shell Steel Column, post-tensioned connections with internal energy dissipators: (a) global layout, and (b) cross-sections.

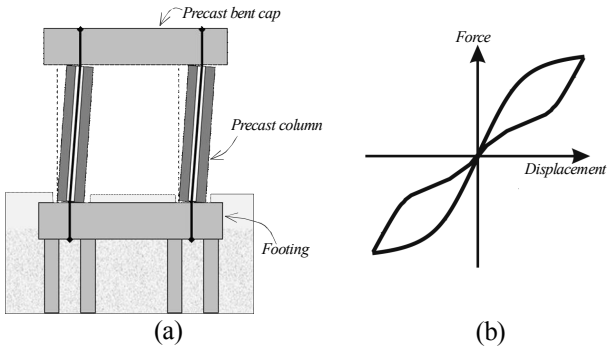


Figure 2 – Hybrid system: (a) swaying bent with opening joints, and (b) flag-shaped force-displacement response.

desired locations (Figure 1). The combination of self-centering capability and added energy dissipation makes the proposed technology to be part of the *hybrid systems* family. A typical flag-shaped hysteretic force-displacement response is sketched in Figure 2(b).

During testing, under large joint opening, the mortar sealing the column-cap interface crushed due to high compressive strains, leading to some post-tensioning force losses. To overcome this inconvenience, polymer-modified mortar is being employed in future specimens.

2.2 Internal and External Energy Dissipators

As mentioned before, energy dissipation in the form of yielding is concentrated within specific components, preventing the remaining members to suffer significant damage. After a strong-intensity shake, only these dissipators are expected to undergo multiple cycles within the inelastic range of response, with possible need of replacement.

The use of mild steel longitudinal bars, crossing the column-cap and column-footing interface, has been proven to be effective in terms of dissipative behavior (Tobolski, 2010) and offers the advantage of avoiding aesthetic interference. As shown in Figure 3, these devices are embedded in the column concrete and protrude within the footing or bent-cap without any visible impact.

However, this layout presents some drawbacks. During plant operations, the presence of mild steel bars would interfere with concrete casting, given the narrow space left in between the two shells. Moreover, the eventual replacement of damaged dissipators would require cutting and repairing the outer steel shell, which may have a thickness of several centimeters, to reach the embedded bars. These inconveniences would make construction and repair more time-consuming and expensive, compared to other solutions.

For this reason, the use of external devices instead of mild steel bars could be advantageous. Tests on hybrid masonry shear-walls have been conducted in New Zealand employing external energy dissipators (Toranzo, 2002). An example of such devices and their possible location around



Figure 3 – Column end at the column-cap interface. Mild steel bars protruding out of the column, subsequently embedded in the bent-cap concrete, work as energy disispators.

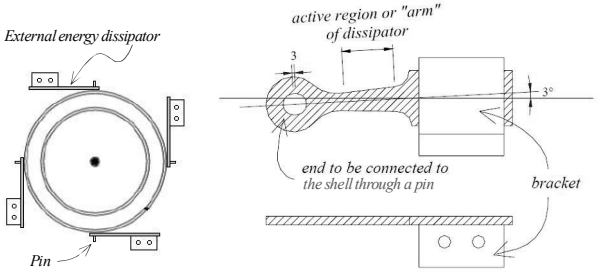


Figure 4 – External energy dissipators: (a) location around the column perimeter, and (b) sketch of device features.

the column perimeter at the column-cap or column-footing interface, are shown in Figure 4.

The proposed external dissipator consists of a stainless steel lever, connected to the outer shell through a pin, and fixed to the footing or the bent-cap through a steel bracket. The lever acts as a cantilever with a transverse force applied to its free end. It is tapered, such that flexural yield may spread throughout its length instead of being concentrated in a narrow portion. The lever longitudinal axis is slightly sloped downward to the free end, to minimize the interaction between axial and flexural stiffness during joint rotation. The slenderness of the arm is limited in order to prevent local or global buckling, allowing for full plasticity development on both tensile and compressive sides.

The pin connecting the lever to the column must transfer only a force transverse to the arm, to prevent weak-axis bending or twisting of the lever. A spherical pin can satisfy this requirement. The fixed end of the lever is welded to a bracket, which is bolted into the footing or the cap. To protect this joint from premature failure, capacity-design principle are applied: in particular, the lever width is increased close to the connection to prevent plasticity from spreading into this region, and welds and bolts are proportioned for the moment transferred by the enlarged cross-section.

Figure 5 depicts an external dissipator during testing in New Zealand: it is shown in its undeflected (a) and deflected (b) configurations, together with its hysteretic response (c).

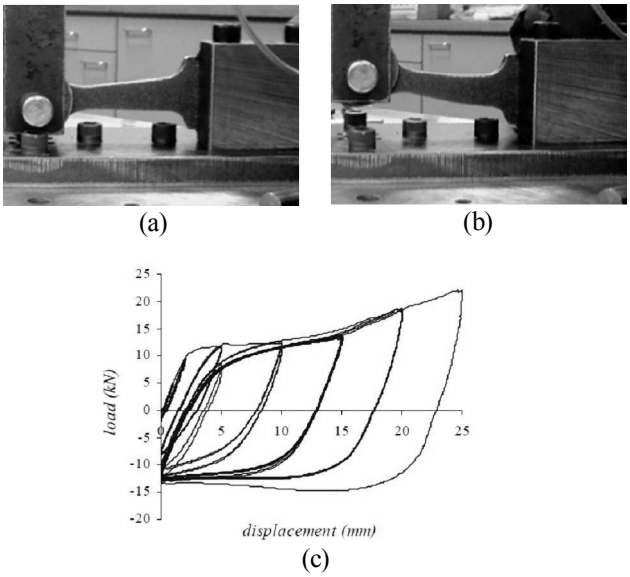


Figure 5 – Testing of external energy dissipators in New Zealand: (a) undeflected configuration, (b) deflected configuration, and (c) hysteretic behavior.

2.3 Post-tensioned and Pre-tensioned Connection

For the specimens of hybrid columns tested at UC San Diego, post-tensioning was employed to confer self-centering capability to the structural system. This technology has proven to be effective and reliable for the scope under investigation, even though post-tensioning losses were recorded due to mortar crushing at the interface in one of these tests. The use of special mortars, such as polymer-modified or fiber-reinforced ones, should provide a valid solution to this problem.

A more insidious issue is represented by eventual corrosion of the post-tensioning tendon, exposed to air and moisture inside the hollow core. This phenomenon may cause serious damage to the tendon, up to the need of replacing it. A special footing-column-cap connection is needed to make the replacement operations easier: different possible solutions are being compared in terms of feasibility and cost. The common idea is to allow for pulling the tendon out from the bent-cap top, leaving the column in place. Minimizing bridge operation disruption is a fundamental objective to be fulfilled with this system.

An alternative is represented by a pre-tensioned connection, with tendons running through the concrete between the shells (Figure 6). This layout allow for better protection of the tendons, reducing the risk of corrosion and the need of replacement.

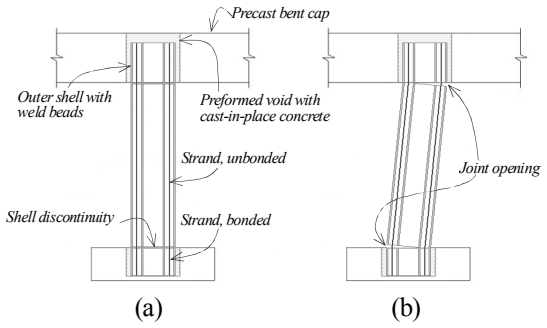


Figure 6 – Pre-tensioned connection: (a) global layout, and (b) deflected configuration.

The precast column unit extends and develops within preformed cavities in the footing and bent-cap, filled with concrete after assemblage. Internal force transfer between the outer shell and the surrounding concrete is enhanced by weld beads on the exterior surface of the shell. The steel shells are discontinuous at locations where joints will open, allowing relative rotation between three segments of the element. Re-centering behavior is ensured by pre-tensioned strands running between the shells for the entire length of the precast unit. These strands are bonded to the concrete within the end segments, anchored in the cap and footing, while they are debonded through greased PVC sheathing along the central segment. Energy dissipation is achieved in the system through the use of stainless steel levers anchored between the end segments and the central segment (not sketched in Figure 6 to avoid graphic congestion).

3. EXPERIMENTAL PROGRAM

Two specimens are being tested at the UC San Diego Powell Laboratories. They represent the column-cap joint of a prototype bent assembly, as illustrated in Figure 7, and they have similar dimensions and testing setup as previous experiments conducted by UC san Diego researchers (Tobolski, 2010). Design is conform to AASHTO *Seismic Guide Specifications* (AASHTO 2009). One specimen combines post-tensioned connection with external energy dissipators, while the other one includes pre-tensioned connection and external dissipators.

In both cases, the column has an outer diameter of 20 in. (0.5 m) and a nominal length of 57.5 in. (1.46 m), thus an aspect ratio of 2.9. The cap beam is simply supported at the inflection points; it has a pin-to-pin length of 10 ft (3.05 m) and a square cross section with 25-in. (0.64-m) sides. The column external shell is made of ASTM A572 GR 50 steel; it has an outer diameter of 20 in. (0.5 m) and a thickness of 0.25 in. (6.35 mm), resulting in a longitudinal reinforcement ratio 0f 5.19%. The inner shell is a corrugated steel pipe with a nominal diameter of 1 ft (0.30 m). Concrete strength at 28 days is specified as 7 ksi (48.3 MPa).

The post-tensioned specimen has a concentric tendon made of high-strength, low-relaxation steel with a specified ultimate strength of 270 ksi (1860 MPa) and yield strength of 245 ksi (1690 MPa). Five 0.6-in. (15.24-mm) strands, stressed at 75% GUTS, run inside a PVC pipe in the hollow core of the column, to reduce the risk of corrosion. These strands are anchored to the cap-beam through a wedge plate. The same prestressing force is applied to the pre-tensioned specimen. In this case, five 0.6-in. (15.24-mm) or seven 0.5-in. (12.7-mm) strands are distributed within the concrete between the steel shells. Here the strands develop along the end segment of the precast column, embedded in the bent-cap (see Figure 6).

External energy dissipators are being designed to induce the same forces on the specimen as the mild steel bars previously used. Four to six devices are disposed around the perimeter as shown in Figure 4. Details are currently under review.

The loading protocol consists of displacement time-histories applied to the free end of the column, subjected to a constant axial force. These time-histories are derived from the response of the prototype structure to selected ground motions, and are applied to induce the correct strain rates on the specimens.

4. CONCLUSIONS

The proposed system is expected to yield a superior performance compared to traditionally cast-in-place bridge bents. Previous tests have proven the ability of hybrid systems, similar to the one under development, in terms of re-centering behavior and energy dissipation. Some drawbacks observed during those tests are being addressed, such as: compressive strength of the mortar at column-cap and column-footing interface; tendon corrosion and eventual replacement; and accessibility of energy dissipators.

Testing of the first unit, which incorporates a post-tensioned tendon, will take place at the University of California, San Diego, Powell Structural Engineering Laboratories during Winter and Spring 2011.

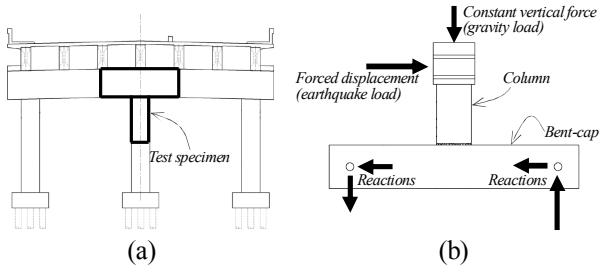


Figure 7 – Testing setup: (a) prototype bent assembly, and (b) test specimen.

Acknowledgements:

The authors acknowledge the support from the Pacific Earthquake Engineering Research Center (PEER).

References:

AASHTO (2009), "Guide Specification for LRFD Seismic Bridge Design", 1st edition, American Association of State Highway and Transportation officials, Washington, DC, USA.

Caltrans (2006), "Seismic Design Criteria", California Department of Transportation, Sacramento, California, USA.

Gebman, M., Ashford, S. and Restrepo, J.I. (2006), "Mechanical Axial Force Transfer within Cast-In-Steel-Shell Piles – Verification through Full-Scale Experimentation and Finite Element Analysis," *Proceedings of the Fifth National Seismic Conference on Bridges and Highways*, San Francisco, California, USA.

Priestley, M.J.N. and Tao, J.R.T. (1993), "Seismic Response of Precast Prestressed Concrete Frames with Partially Debonded Tendons", *PCI Journal*, **38**(1), 58-69.

Rahman, A. and Restrepo, J.I. (2000), "Earthquake Resistant Precast Concrete Buildings: Seismic Performance of Cantilever Walls Prestressed using Unbonded Tendons", *Research Report 2000-5*, Department of Civil Engineering, University of Canterbury, Christchurch, New Zealand.

Sakai, J. and Mahin, S. (2004), "Mitigation of residual displacements of reinforced concrete bridge columns", *Proceedings of the 20th US-Japan Bridge Engineering Workshop*, Tsukuba, Japan.

Tobolski, M.J.(2010), "Improving the Design and Performance of Concrete Bridges in Seismic Regions", *Ph.D. thesis* , Department of Structural Engineering, University of California - San Diego, La Jolla, California, USA.

Toranzo-Dianderas, L.A. (2002), "The Use of Rocking Walls in Confined Masonry Structures: a Performance-Based Approach", *Ph.D. thesis*, Department of Civil Engineering, University of Canterbury, Christchurch, New Zealand.

8CUEE CONFERENCE PROCEEDINGS
8th International Conference on Urban Earthquake Engineering
March 7-8, 2011, Tokyo Institute of Technology, Tokyo, Japan

COMBINED ACTIONS ON REINFORCED CONCRETE BRIDGE PIERS

Thomas M. Frankie[1] and Daniel A. Kuchma[2]

1) Department of Civil Engineering, University of Illinois at Urbana-Champaign, Urbana, IL, USA
2) Professor, Department of Civil Engineering, University of Illinois at Urbana-Champaign, Urbana, IL, USA
frankie2@illinois.edu, kuchma@illinois.edu

Abstract: A series of analyses and small scale experimental tests are performed for circular reinforced concrete bridge piers. These studies are in preparation for a large-scale hybrid simulation of a curved three-pier bridge structure subjected to multi-directional earthquake loading. The small scale tests serve as a proof of concept for six degree of freedom control of the experimental piers. The effects of combined actions resulting from geometrical asymmetry and multi-directional earthquake loading are studied. Specific effort is focused on the interaction effects of applying torsional and lateral loads to the piers.

Small scale specimens are carefully fabricated considering similitude relationships and scaling effects. A series of small scale tests are performed to assess the interaction effects of shear and torsion. In addition, the capacity envelope under individual actions is determined experimentally for scaled down specimens from the curved three-pier bridge. Analysis is performed in OpenSees, and a parametric study is conducted to determine the effects of geometry on torsional and lateral loads sustained by the piers. These results are used in preparation for a small-scale hybrid proof-of-concept to be followed by large-scale testing.

1. INTRODUCTION

Bridge columns can be subjected to various combined loading conditions resulting from complex earthquake ground motions coupled with irregular geometry and asymmetry of the bridge structure itself. The objective of the Network for Earthquake Engineering Simulation (NEES) Combined Actions on Bridge Earthquake Response (CABER) project is to develop a fundamental understanding of the effects of these combined actions on the performance of reinforced concrete (RC) columns and the resulting system response. The investigations are motivated by the inadequacy of existing analytical solutions and lack of experimental data for use in improving model behavior.

Experimental tests have been performed under different combinations of multi-directional bending, shear, axial load, and torsion. Columns have been tested quasi-statically at the Missouri University of Science and Technology (MST), pseudo-dynamically at the University of Illinois at Urbana-Champaign (UIUC), and dynamically at the University of Nevada, Reno (UNR). The remaining task of the CABER project is the hybrid testing of a curved three-pier bridge under multidirectional earthquake loading. The experiment will be performed leveraging the unique capabilities of the NEES Multi-Axial Full-Scale Sub-Structures Testing and Simulation (MUST-SIM) Facility at the University of Illinois, Urbana-Champaign.

A series of small-scale experimental tests were performed on circular reinforced concrete bridge piers to demonstrate structural principles. Five 1/16-scale specimens were tested cyclically under a combination of shear and torsion loads. Small-scale fabrication and microconcrete mix design were modeled based on previous studies on similitude requirements (Holub, 2005). Tests included shear-only, torsion-only, and shear-torsion interaction tests with ratios of 1:3, 1:1, and 3:1 as defined by elastic properties of the specimens observed in the first two tests void of interaction effects.

A single small-scale load and boundary condition box (LBCB) shown in Figure 1 was used to apply displacement input motions. The LBCBs are able to simulate complex loading representative of seismic motion in all six degrees of freedom, with the goal of understanding the response of complex structural systems under realistic loading. Forces and displacements were read from internal load cells and linear variable differential transformer (LVDT) readings of the LBCB. Four external linear potentiometers were used to confirm the LVDT displacement readings. Critical structural values are reported, and these experimental results are compared to the predicted results obtained through analysis methods and code calculations. Combined shear and torsion loading states were used to develop an interaction diagram and illustrate the combined effects of the two types of structural demand.



Figure 1 Small scale set-up with LBCB

A second set of small-scale specimens were tested to develop capacity envelopes under individual actions for scaled properties of the curved three-pier bridge. Analysis of the piers from the curved bridge is performed in OpenSees, and a parametric study is conducted to determine the effects of geometry on torsional and lateral loads sustained by the piers. These results are used in preparation for a small-scale hybrid proof-of-concept to be followed by large-scale testing.

2. HYBRID METHODOLOGY

The Hybrid simulation is enabled by the 6DOF loading equipment and simulation-coordinator software available at the Illinois MUST-SIM testing facility. These features of the UIUC equipment site enable the following hybrid simulation:

- Two 1/3-scale piers will be tested in the large-scale MUST-SIM facility using 6DOF Load and Boundary Condition Boxes (LBCBs).
- One 1/20-scale pier will be tested in the portable LBCB reaction frame of the small-scale MUST-SIM facility.
- Superstructure and abutments are modeled analytically using OpenSees.

Hybrid analysis using experimental and analytical components is enabled through the use of the University of Illinois simulation coordinator (UI-SimCor). The acceleration time history step will be passed into UI-SimCor, which performs numerical time integration and passes displacement targets to the experimental and analytical components of the hybrid simulation. Forces are measured and calculated from the two components and read back into UI-SimCor to command displacements to balance the equations of equilibrium before taking the next step in the earthquake time history.

3. GEOMETRY

Overall geometry of the prototype bridge is based on a seismic design example from the Federal Highway Administration (FHWA). The curved geometry and spacing of the piers is critical to the level of combined response generated in the structure. The skewed geometry shown in the OpenSees wire-frame model (Figure 2) develops torsional, flexural, shear, and axial stresses in the supporting members.

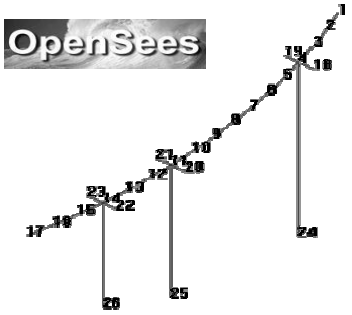


Figure 2 OpenSees model of skewed geometry with optimal pier locations

A parametric study was performed using this OpenSees model to determine the most reasonable column locations that generate maximum torsional moments in the piers. This objective is selected because the torsional component of interaction is specifically of interest in this study. Special effort was made to ensure that the distribution of piers represents a realistic and viable structural design option. The torsional and flexural moment time-history plots resulting from the selected case are shown in Figures 3 and 4, respectively.

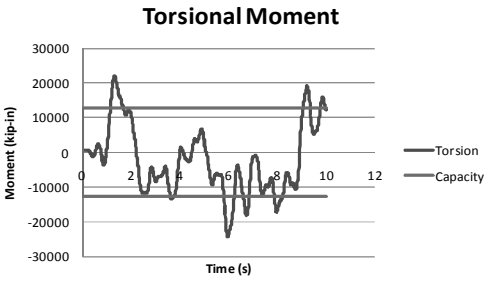


Figure 3 Torsional moment time history

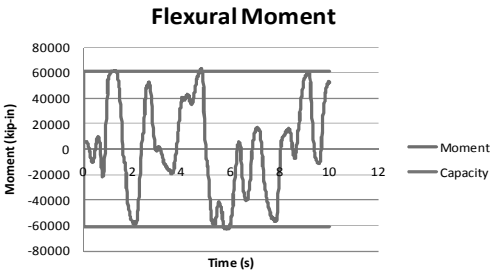


Figure 4 Flexural moment time history

4. SEISMIC DEMAND

The applied earthquake record is a synthetically generated accelerogram from Washington State. SPECTRA was used to generate the response spectrum, and SIMQKE was used to generate time history records.

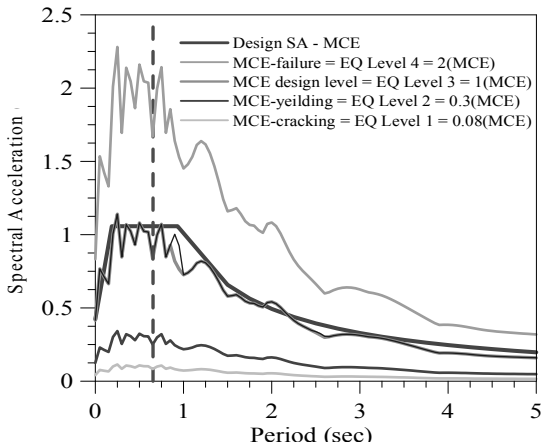


Figure 5 Response spectra of seismic demands

The record will be applied as a sequence of imposed records scaled to four levels corresponding to estimates of the states of structural response listed below. The four levels of scaling are represented as ratios of the Maximum Credible Earthquake (MCE), with definition and response spectra for each level plotted in Figure 5.

5. MATERIALS AND SIMILITUDE

Similitude relationships for the small scale test specimens are based on extensive studies by Holub (2005) where a methodology for consistent and accurate small scale fabrication of reinforced concrete piers was developed. A micro-concrete mix is prepared using appropriately scaled and graded aggregate, along with Type III cement to achieve the desired characteristics, including an early compressive strength of approximately 4 ksi.

The initial set of specimens were produced for this project with the intent of performing five small-scale tests. All specimens consisted of a column with a height of 9.5 in. and a diameter of 2.4 in. The end caps on each column had a height of 1.5 in. and a diameter of 5.0 in. Twenty 4-40 threaded rods were used to provide the longitudinal reinforcement. The rods were annealed for one hour at 1000°F. The spiral reinforcement is provided by smooth annealed wire with a diameter of 0.0348 in. The spiral reinforcement coils were spaced at approximately 3/8 inches.

The scaled down versions of the 3-peir simulation have longitudinal reinforcement provided using 3-48 threaded rods to achieve symmetry in the flexural steel at the desired reinforcement ratio. These rods are heat treated in order to achieve the desired stress-strain response. Transverse reinforcement is smooth black annealed wire of 0.0348 inch diameter. The reinforcement cage prior to enclosure of formwork is shown in Figure 6. Piers are cast using PVC and wood forms. Micro-concrete is poured and consolidated using a vibrating table, specimens are cured for 7 days prior to form removal, and are painted and capped with Hydrocal before finally being ready for testing any time after reaching 21 day strength.

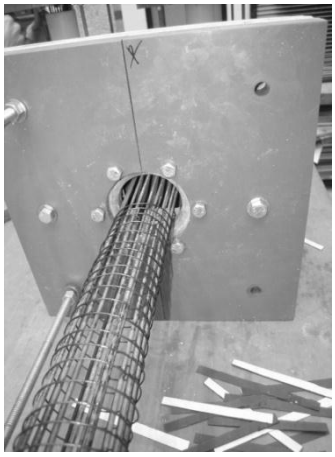


Figure 6 Small scale fabrication of reinforcement

6. SMALL SCALE TESTING PROGRAM

Lateral and rotational actions were applied cyclically with increased amplitude to two sets of small-scale test specimens. The first set of 5 specimens consist of cyclic loading patterns were used for the tests to more closely simulate dynamic loading conditions. The LBCB was given cyclic displacement and/or rotation commands. For each test, the loading protocol was provided via an input file uploaded to the LBCB Plugin. Displacements and rotations were applied in one direction, returned to zero, and then applied in the opposite direction. This pattern was repeated with increasing displacements and rotations after each successive cycle until the specimen lost significant torsional and shear capacity.

The second set of specimens have geometry and material properties identical to the pier that will be included in the final hybrid simulation. The purpose of these simple tests were to confirm the anticipated maximum lateral and rotational capacities of the piers, as well as to test a newly designed reaction frame and updated control systems and software of the small scale facility.

7. RESULTS

The results of the five tests performed are discussed below. Key performance points of yield, peak, loss of

strength, and ultimate limit states are defined according to hysteretic response curves for force-displacement and moment-rotation relationships. Yield is defined as the loss of stiffness, where the specimen enters the inelastic response region. The peak limit state is the maximum strength value achieved by the specimen in units of either force or moment. The first significant drop in load resistance was selected as the loss of strength point, and is often coincidental with large cracks developing. Finally, the ultimate limit state is selected to give an indication of the ductility that can be achieved while still resisting a nominal load on the specimen. An example of one response curve and the four performance states are provided in Figure 7 and Table 1, respectively. Photos of each specimen are provided in Figure 8 at the four corresponding points during the experimental testing.

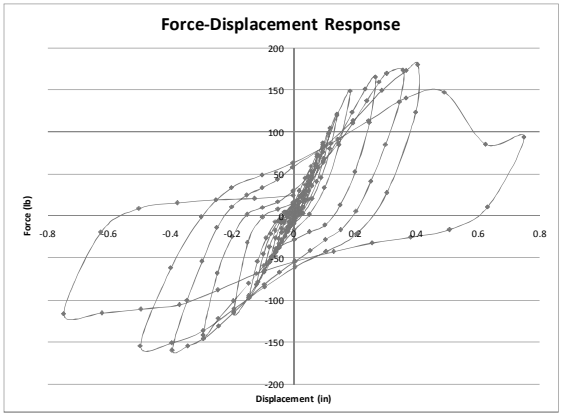
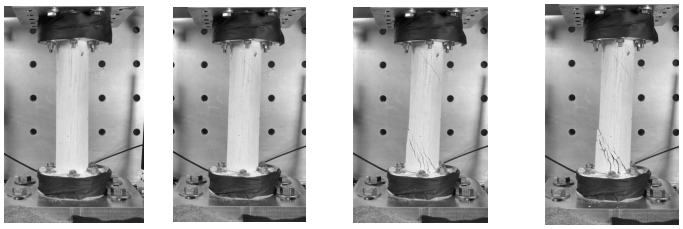


Figure 7 Cyclic force-displacement response curve for 3:1 shear to torsion loading.

Table 1 Performance limit states under 3:1 loading

3:1 Shear to Torsion Ratio				
Shear Test Curves	Force (lb)	Displacement (in)	Moment (in-lb)	Rotation (degrees)
Yield	121.2	0.14	92.4	0.09
Peak	180.3	0.40	139.2	0.17
Strength Loss	147.3	0.49	127.6	0.26
Ultimate	94.1	0.75	36.6	0.61



(a) Yield (b) Peak (c)Strength Loss (d) Ultimate

Figure 8 Photos corresponding to lateral performance limit states for 3:1 shear to torsion loading.

Backbone curves of each specimen are created from the four limit state points defined from the hysteretic responses like those shown in Figure 7 and Table 1. These points are used to provide rough estimates of the peak response of the piers, allowing for more natural comparison of the effects of each loading profile on the specimens. This provides the best visual representation for examining the effects of shear and torsion interaction on the behavior of the bridge piers.

The yield points show that lateral yield force decreases as torsion is added to the loading profile as expected. This yielding will occur earlier as torsion is additive on one face of the pier, causing an increase in shear stress. In addition to lower force capacity, lateral yielding also occurs at a smaller displacement, indicating that deformation capacity is reduced. The inverse is also true as shown by the rotational yield moment, with the exception that the relationship between the loading case with equal application of shear and torsion exhibits a higher yield moment than anticipated when compared to the load application of shear and torsion that is biased toward torsion. Apart from this case, the application of shear reduces the moment and rotational values at which torsional yielding occurs. Hence, it is clear that interaction effects result in inelastic behavior occurring at lower force and moment values than the cases where either of the single components of loading is applied.

It should be noted that minimal amounts of torsion relative to the shear force present do not seem to have a drastic effect on lateral capacities. However, even a very small shear force introduced into a system undergoing rotational input severely reduces the moment and rotation capacity of the structure. Regardless, it is evident that there is a threshold for each limit state where the combined shear and torsion interaction results in specimens more vulnerable to shear or torsional failure than if the other loading component was not present, as can be seen in Figure 9.

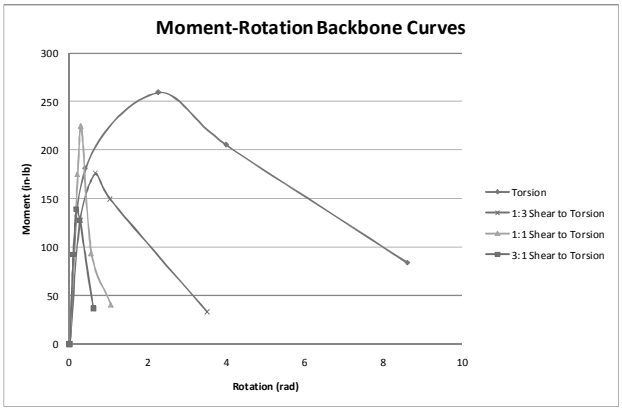


Figure 9 Comparison of backbone curves derived from rotational performance limits

The results of the two additional small scale tests reveal that the small scale fabrication has achieved the desired capacity to achieve reasonable similitude in future hybrid tests. Analysis of the small-scale sections were performed

using Response-2000, and the lateral capacity was estimated at approximately 700 pounds (corresponding to an ultimate moment of 7.1 in-kips) which is 10% above the capacity shown in the results displayed in Figure 10.

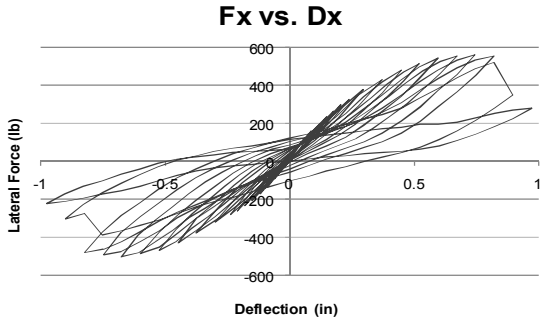


Figure 10 Lateral force-deflection hysteresis

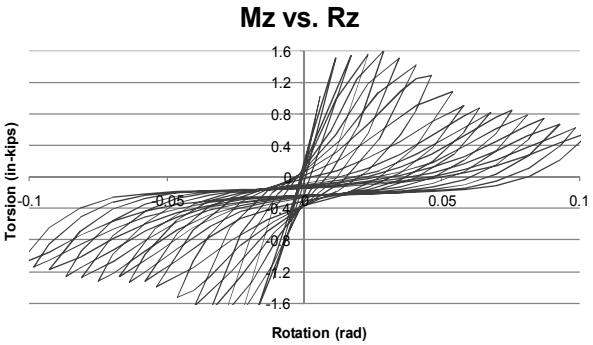


Figure 11 Torsional moment-rotation hysteresis

Torsional capacity was predicted using ACI 318-08 Eq. 11-21 and is conservatively estimated to be 1.3 in-kips. The experimental results (Figure 11) show torsional moments achieving approximately 25% above the code prediction due to conservative safety factors. At full scale, this torsional moment is equivalent to nearly 13,000 in-kips. This is the value that was used for torsional capacity in the parametric study for determining the final configuration of the 3 Pier Hybrid Simulation. It has been shown that rigorous replication of the small scale fabrication techniques developed for this concept test will result in small scale piers with consistent behavior, which is desired in order to apply realistic combined actions to the large-scale specimens.

8. CONCLUSIONS AND FUTURE WORK

A series of small-scale experimental tests were successfully performed on circular reinforced concrete bridge piers to demonstrate structural principles such as shear-torsion interaction. The five 1/16-scale specimens were tested cyclically under shear-only, torsion-only, and shear-torsion interaction tests with ratios of 1:3, 1:1, and 3:1 as determined by elastic properties of the specimens loaded in only one method. A comprehensive program for data acquisition using the facilities of the MUST-SIM NEES facility was employed, with the use of internal and external sensors, LBCB load cells, and external cameras. Forces and displacements are reported, along with moments and rotations, and the resulting behaviors of the specimens are discussed. Critical structural values are reported for each test, and these experimental results are compared to the predicted results obtained through analysis methods and code calculations. Combined shear and torsion loading states are used to develop an interaction diagram and illustrate the combined effects of different loading scenarios. An educational outreach video was also produced to illustrate structural concepts using the results from this experimental program.

Based on analytical analyses and two additional small scale proof tests, it has been determined that the small scale fabrication techniques, 6DOF loading and boundary condition boxes, and simulation coordinating software will provide an adequate means of testing the complete hybrid framework in the small scale facility. The parametric study on interaction effects resulting from various bridge geometry has provided an arrangement of piers that will be used in this test. Earthquake demand has been determined based off of applied ratios to the MCE record. The experimental tests have shown that the facility is capable of accurately capturing the effects of these combined actions. The results from these proof of concept tests will help to determine instrumentation plans and other data acquisition details for the final full scale hybrid simulation. Further studies will be performed to ensure that the magnitude and characteristics of the applied seismic motion will result in levels of actions that demonstrate the combined response of the structure in three dimensions.

Acknowledgements:

The authors acknowledge support from the National Science Foundation (NSF) through the Network for Earthquake Engineering Simulation (NEES). Many thanks also go to the site staff and students of the University of Illinois MUST-SIM facility

References:

ACI 318-08 (2008). *Building Code Requirements for Reinforced Concrete,* American Concrete Institute.

Holub, C. J. (2005). "Similitude considerations for small scale distributed hybrid testing of reinforced concrete bridges." Master's thesis, University of Illinois at Urbana-Champaign.

Holub, C. (2009). *Interaction of Variable Axial Load and Shear Effects in RC Bridges.*

Wight, J. K., & MacGregor, J. G. (2009). *Reinforced Concrete Mechanics and Design.* Upper Saddle River, New Jersey: Pearson Prentice Hall.

8CUEE CONFERENCE PROCEEDINGS
8th International Conference on Urban Earthquake Engineering
March 7-8, 2011, Tokyo Institute of Technology, Tokyo, Japan

BONDING BEHAVIOR OF CFRP SHEET-STEEL CONNECTIONS USING FOR SEISMIC RETROFIT OF HIGHWAY BRIDGE COLUMNS

Guangfeng Zhang[1)], Jun-ichi Hoshikuma[2)], and Junichi Sakai[3)]

1) Researcher, Bridge and Structural Technology Research Group, Public Works Research Institute, Japan
2) Chief Researcher, Bridge and Structural Technology Research Group, Public Works Research Institute, Japan
3) Senior Researcher, Bridge and Structural Technology Research Group, Public Works Research Institute, Japan
tyou44@pwri.go.jp, hosikuma@pwri.go.jp, sakai55@pwri.go.jp

Abstract: This research was conducted with the purpose to obtain basic knowledges for establishing a method for designing carbon fiber reinforced polymer (CFRP) sheet-steel plate connection that can be employed in seismic retrofit of reinforced concrete (RC) bridge columns. Bonding behavior between CFRP sheet and steel plate including effective bond length and relationships between interfacial bond stress and relative displacement were investigated based on double-lap bond tests. Effective bond lengths were determined for the cases with different thickness of CFRP sheet. A bond stress-slip model that can be used for estimating bonding capacity of the connection was proposed based on the test results. Furthermore, the validity of the proposed bond stress-slip model was estimated by three dimensional FEM analyses.

1. INTRODUCTION

Carbon fiber reinforced polymer (CFRP) sheet is often used for seismic retrofit of reinforced concrete (RC) highway bridge columns attributing to the light-weight, high strength and outstanding workability. A typical application of CFRP sheet in seismic retrofit of RC bridge columns in Japan is used for enhancing flexural and/or shear strength of the sections at which the longitudinal reinforcements were cut off prematurely with insufficient development length. In some other cases, CFRP sheet is also used for enhancing ductility of RC bridge columns by jacketing around the plastic hinge in the circumferential direction.

However, due to the reason that the elongation of CFRP sheet is rather lower before fracture, it is not easy to apply CFRP sheet for enhancing the flexural strength around the bottom of RC bridge columns where plastic deformation is expected to occur during the large earthquakes. On the other hand, seismic retrofit method using CFRP sheet will be efficient for the bridges under severe construction work conditions for the reasons such as that it can reduce the construction period, increasing of the death weight after retrofit is little, and so on. With the purpose to develop a retrofit method using CFRP sheet for seismic retrofit of RC bridge columns including the flexural strength of the base, a method by means of using combination of CFRP sheet and steel jacketing as shown in Figure 1 is being studied by the authors. This method takes advantage of both steel plate and CFRP sheet. Steel jacketing is adopted for strengthening the flexural capacity of column base and CFRP sheet jacketing is adopted for strengthening the other sections of the column.

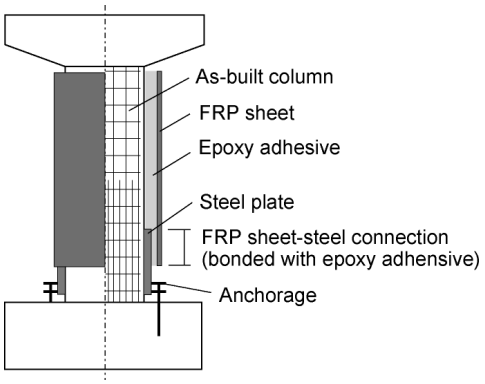
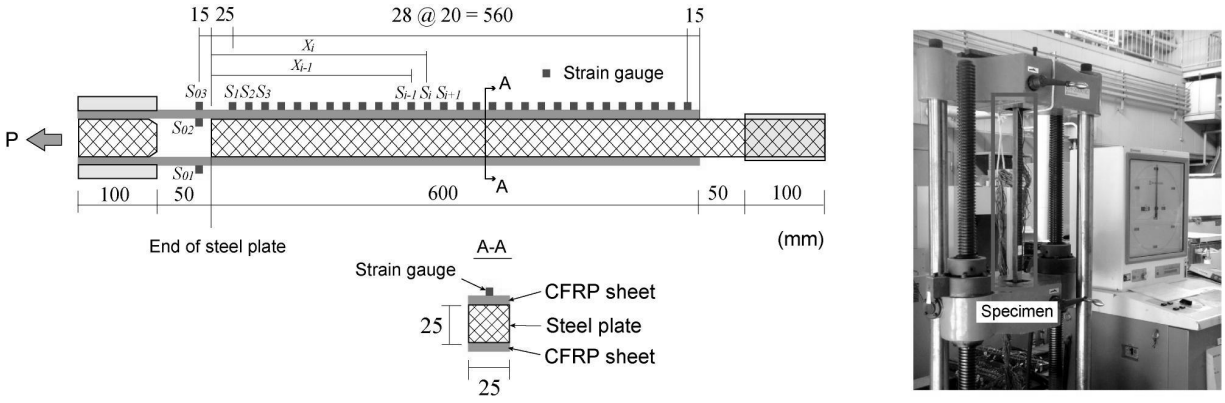


Figure 1 Schematic of seismic retrofit method using combination of FRP sheet and steel jacketing

In this method, CFRP sheet is bonded to the steel plate with epoxy adhesive. It can be noted that bonding capacity of the connection between CFRP sheet and steel plate is a key issue for this method because the longitudinal force induced by the additional anchor bolts that are used for enhancing the flexural strength of the columns must be transferred to the CFRP sheet. In order to design a CFRP sheet-steel plate connection, bonding force that can be transferred by the connection and a minimum bond length that is needed to ensure the bonding force are required to be understood. According to the previous researches (Nozaka et al. 2005, Teng et al. 2006), there is an effective bond length for the CFRP sheet-steel plate connection that is the minimum bond length to ensure the bonding force. Bonding force does not increase even applying a bond length longer than the effective bond length. It is also known that bonding



(a) Details of specimen (b) Setup of tests

Figure 2 Details of specimens and setup of tests

force is mainly affected by the thickness of CFRP sheet and it can be evaluated by using a bond stress-slip model that represents the bonding capacity of the CFRP sheet-steel plate interface (Teng et al. 2006). Consequently, effective bond length and bond stress-slip model are required to be determined for designing a CFRP sheet-steel plate connection.

With the above point of view, in this study, bonding behavior between CFRP sheet and steel plate including effective bond length and bond stress-slip model were investigated through double-lap bond tests with the purpose to obtain basic knowledges for establishing a design method for the CFRP sheet-steel plate connection. Three dimensional FEM analyses were also carried out for estimating the validity of the proposed bond stress-slip model. This paper provides descriptions of the details of tests, FEM analysis methods and results obtained from the experimental and analytical studies.

2. TEST SPECIMENS AND PRECEDURE

Four series of double-lap shear bond tests as shown in Table 1 were designed in this study. Figure 2(a) shows the details of the double-lap shear specimens. Three specimens with same condition were tested for each series. Parameters of the specimens including the thickness of CFRP sheet, the thickness of steel plate and bond length were designed based on the following considerations. The thicknesses of CFRP sheet were varied from 0.333 to 1.332 mm to investigate the influence of the thickness of CFRP sheet on bonding behavior. Here, the thicknesses are the design thickness and correspond to 1 to 4 layers of CFRP sheet with a fiber mass per unit area of 600g/m^2. SS400 steel plates with a thickness of 25mm were used for each of the specimens. The thickness of the steel plate was designed as 25mm in order to ensure that the steel plate does not yield during the tests. CFRP sheet with a length of 50mm at the end of the steel plate that was not being bonded with steel plate was employed to determine the initiation of debonding between CFRP sheet and steel plate. Bond length of 600mm was applied for each of the specimens. This bond length is several times longer than the effective bond length that can be estimated based on the previous researches (Nozaka et al. 2005, Teng et al. 2006). The purpose of using a longer bond length is to investigate the varying of the distribution of strain in CFRP sheet with the progress of debonding between CFRP sheet and steel plate.

Table 1 List of specimens

Series	Thickness of CFRP sheet	Numbers of specimens for each series
Case-1	1 layer, t_f = 0.333mm	3 (No.1, No.2, No.3)
Case-2	2 layer, t_f = 0.666mm	3 (No.1, No.2, No.3)
Case-3	3 layer, t_f = 0.999mm	3 (No.1, No.2, No.3)
Case-4	4 layer, t_f = 1.332mm	3 (No.1, No.2, No.3)

Table 2 Material properties

Materials	Items	Values
CFRP sheet	Fiber mass per unit area (g/m^2)	600
	Design thickness (mm)	0.333
	Young's modulus (N/mm^2)	2.65×10^5
	Tensile strength (N/mm^2)	3,400
Epoxy adhesive	Young's modulus (N/mm^2)	2.202×10^3
	Compressive strength (N/mm^2)	71.8
	Tensile strength (N/mm^2)	47.0
	Tensile shear strength (N/mm^2)	17.6

Surface of steel plate to be bonded with CFRP sheet was grinded with a disc sander. All the specimens were cured for 7 days at ambient temperature after the epoxy adhesive was applied. Strain gauges were placed on CFRP sheet at intervals of 20 mm to measure the strain induced in CFRP sheet in details.

Table 2 shows the material properties of CFRP sheet and epoxy adhesive. The values of Young's modulus and strengths were obtained from tests.

All the tests were performed under unidirectional tensile force with a loading speed of 0.5-1.0 mm per minute. Figure 2(b) shows the setup of the tests.

3. TEST RESULTS

The effective bond length and relationships between

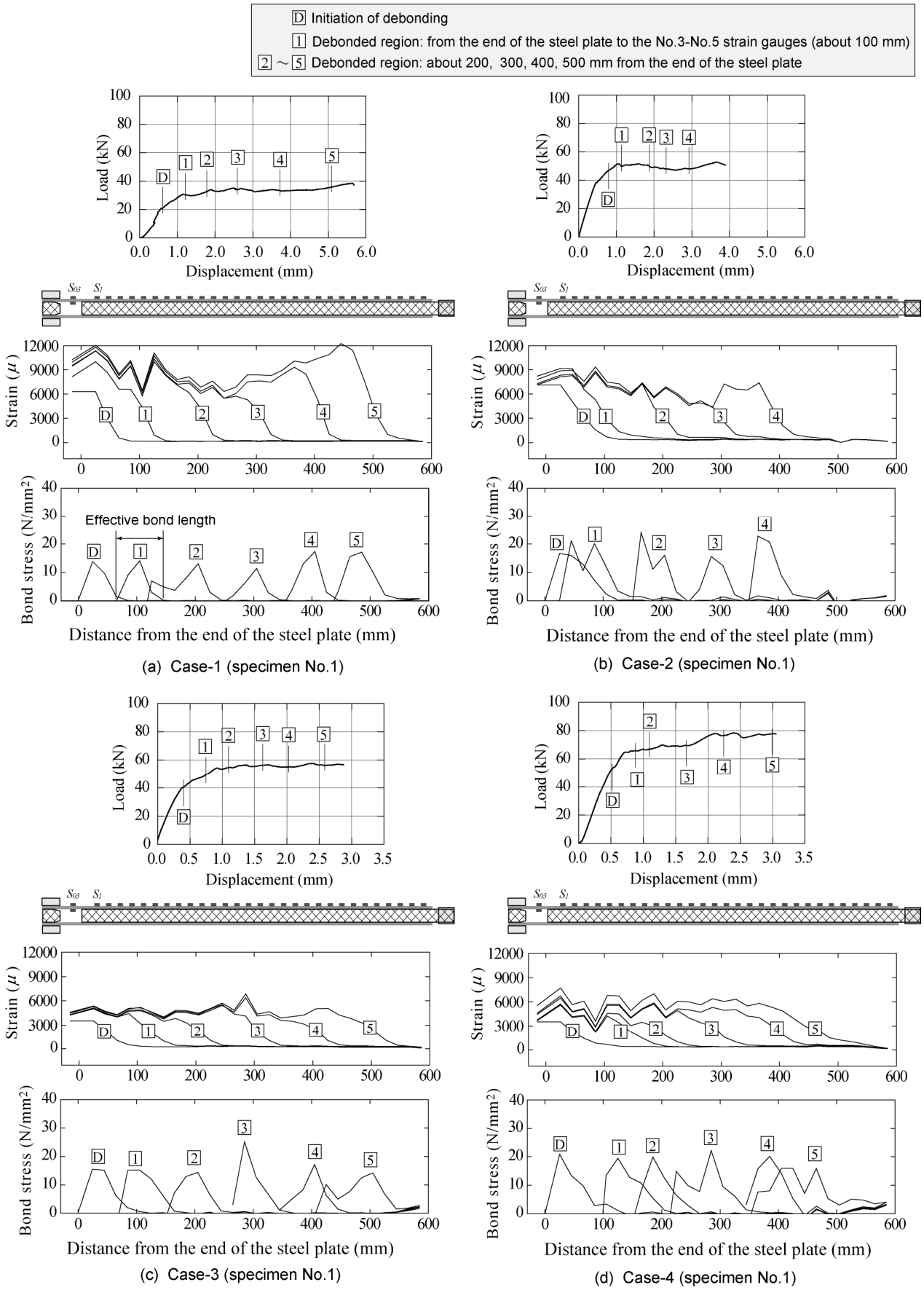


Figure 3 Test results of load-displacement curves, strain distributions in CFRP sheet and interfacial bond stress

Table 3 Debonding strains and effective bond lengths

Series	Debonding strains (μ)		Effective bond length
	No.1, No.2, No.3	Average	
Case-1	6311, 8263, 5728	6763	80-100 mm
Case-2	7127, 6640	6884	100-160 mm
Case-3	3513, 4604, 4937	4351	120-180 mm
Case-4	3555, 5450, 4285	4430	140-200 mm

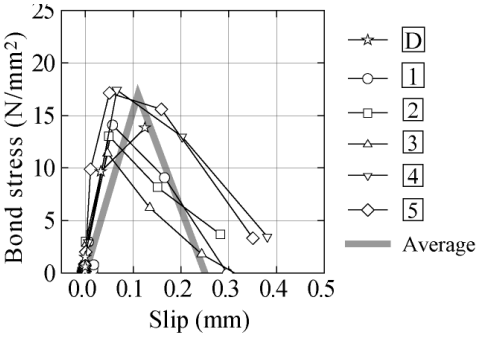


Figure 4 Bond stress-slip curves (case-1)

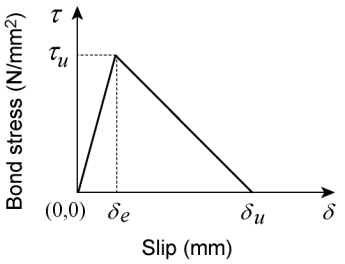


Figure 5 Bond stress-slip model

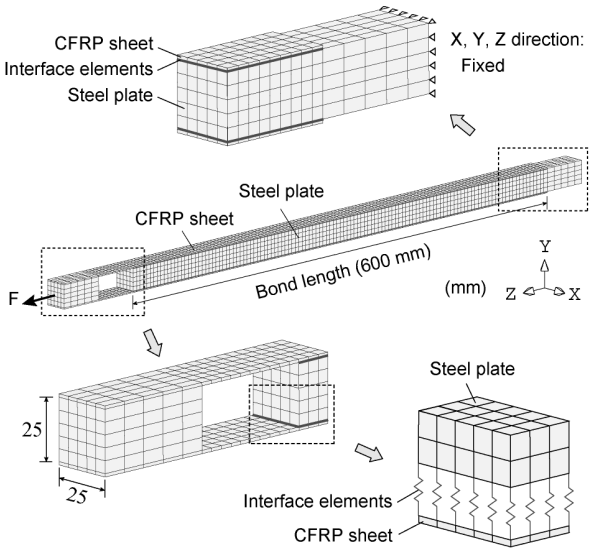


Figure 6 FEM model

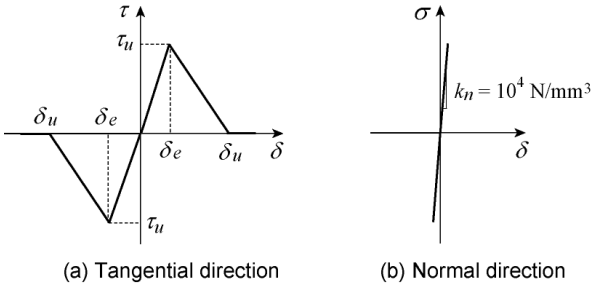


Figure 7 Stress-relative displacement models

interfacial bond stress and relative displacement (slip) were investigated based on the discussions on the following items: relationships between load and displacement of CFRP sheet at the end of steel plate, distributions of strain in CFRP sheet and distributions of interfacial bond stress along the bond length. Figure 3 shows the test results of specimens No.1 for each of the four series. Here, interfacial bond stress τ was calculated from the strain in CFRP sheet using the equation $\tau = d\varepsilon(x)/dx \cdot E_f \cdot t_f$, where E_f and t_f are the Young's modulus and thickness of CFRP sheet respectively. Effective bond length was considered as the distance of the two points at which bond stress is zero as shown in Figure 3(a). Results of specimen No.3 of case-2 were not included in the following discussion because debonding of the CFRP sheet occurred prematurely due to the defects in the bonding condition.

Table 3 shows the results of debonding strains and effective bond lengths obtained based on the distributions of strain in CFRP sheet and distributions of bond stress. Here, debonding strain is defined as the strain occurred in CFRP sheet at the end of the steel plate when debonding initiated. The debonding strain can be employed to evaluate the bonding capacity of the connection. In this research, the debonding strains were determined with the average of strain gauges S_{02} and S_{03} at the point of the debonding initiated (Zhang et al. 2010). It can be noted that the debonding strain decreases with the increasing of the thickness of CFRP sheet. The lowest value was about 3,500 microstrains for the specimens No.1 of both case-3 and case-4. Furthermore, it was determined that the effective bond lengths were about 80-100, 100-160, 120-180 and 140-200 mm for case-1 to case-4 respectively. As the thickness of CFRP sheet increases, the length of the effective bond length increases.

Figure 4 shows bond stress-slip curves for specimen No.1 of case-1. It can be seen that the shape of the bond stress-slip curves show approximately a triangle shape. The same trend was also confirmed from the other tests. Based on this observation, the relationship between bond stress and slip was assumed as a bilinear model as shown in Figure 5. Three parameters of this model including maximum bond stress τ_u, relative displacements δ_e and δ_u were determined as the average values of the results of point 1 for all of the specimens. Only the results of point 1 were used for determining the parameters because of the following two reasons. One is that the relative displacements δ_u cannot be calculated yet at point D when the debonding initiated and the other is that the variations of the stain values become notable after point 2 when the debonded region becomes longer. The values of τ_u, δ_e and δ_u obtained from the test results were 17.0 N/mm^2, 0.11 mm and 0.25 mm, respectively. Consequently, the fracture energy G_f of the CFRP sheet-steel plate interface that was considered as the area of the triangle was evaluated as 2.13 N/mm.

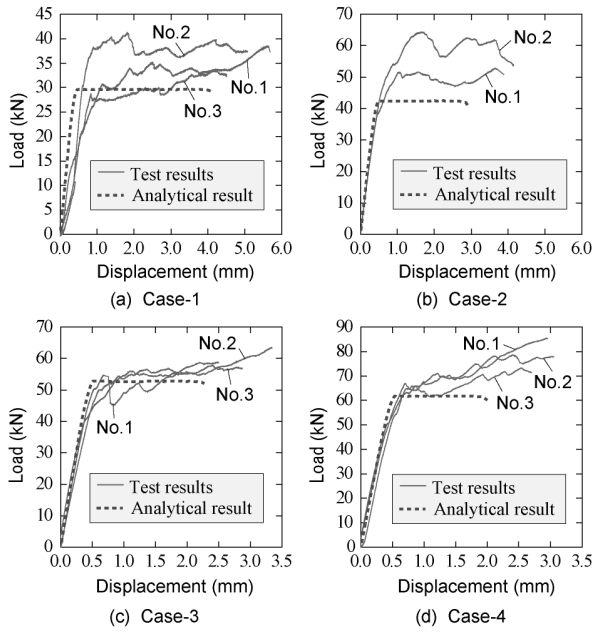


Figure 8 Comparisons of load-displacement curves

4. EVALUATION OF THE BOND STRESS-SLIP MODEL BASED ON FEM ANALYSES

Three-dimensional FEM analyses were carried out for all of the specimens listed in Table 1 in order to estimate the validity of the bond stress-slip model proposed in this research. Figure 6 shows the FEM model adopted in the analyses. The steel plate and CFRP sheet were modeled with 8-node solid element. Interface elements were applied between the steel plate and CFRP sheet to model the stress and relative displacement of the interface. Interface element is a type of element that can be used to model the discontinuous behavior between two surfaces by means of applying a rational stress-relative displacement model (DIANA 9.3, 2008). Figure 7 shows the stress-relative displacement models adopted for the two directions of the interface. The behavior of the interface in the tangential direction was defined by the bond stress-slip model proposed in the previous section. The behavior in the normal direction was defined as linear with a stiffness k_n of 10^4 N/mm^3. Here, the value of k_n was decided considering the stability of the analyses (DIANA 9.3, 2008). Both the steel plate and CFRP sheet were modeled as elastic materials because the steel plate did not yield and the CFRP sheet did not fracture during the tests.

Figure 8 shows the comparisons of load-displacement curves. The analytical results show that load increases sharply in the early stage of loading and then keep a constant value. It was confirmed from the stress and strain condition in the interface elements that once the relative displacement of the interface element at the end of the steel plate exceeds δ_u as shown in Figure 5, the load will not increase and the curve become flat. This means that the load will not increase after the debonding occurred. Figure 9 shows the comparisons of the strain distributions in CFRP sheet and

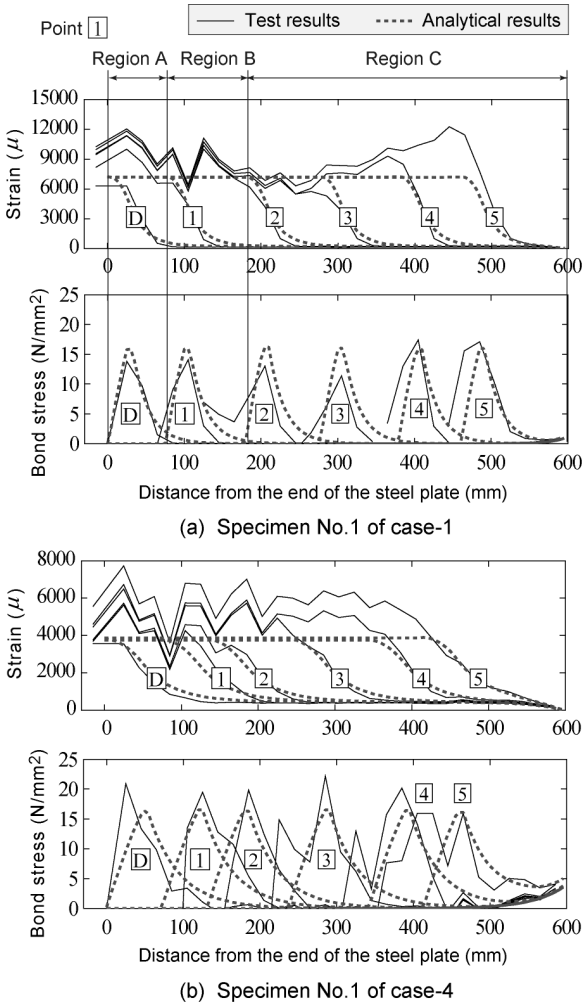


Figure 9 Comparisons of distributions of strain in CFRP sheet and distributions of bond stress

bond stress for specimens No.1 of case-1 and case-4 as examples. Here, strain distribution of CFRP sheet can be divided into three regions as shown in Figure 9 (a). Region A is the region in which debonding occurred entirely. Region B in the region in which interfacial bond stress occurred. Region C is region in which interfacial bond stress do not occur yet. Region B is the region that contributes to the bond force of the connection. It should be noticed that CFRP sheet in region A is debonded entirely from the steel plate and the strain is not affected by the bond stress-slip model. Strain distribution of CFRP sheet in region A may be affected by the length of the region A and progress condition of the debonding of the CFRP sheets bonded on the two side of the steel plate. Based on the same consideration, the load after the debonding occurred is not only affected by the bonding capacity, but also affected by other factors such as the debonding condition of the CFRP sheets. Therefore, comparisons of the load-displacement curves after debonding occurred and the strain distribution of CFRP sheet in the region A were not considered in this paper taking into account of the purpose of the analytical study.

Figures 8 and 9 show that analytical results including load-displacement curves before debonding occurred, strain

distribution of CFRP sheet and bond stress in the region B agree approximately with the test results. This indicates that FEM analysis adopting the bond stress-slip model proposed in the pervious section can provide a good simulation of the bonding behavior of the CFRP sheet-steel plate connection. It can also be considered that the validity of the proposed bond stress-slip model was confirmed by the comparisons.

5. CONCLUSIONS

In this study, bonding behavior between CFRP sheet and steel plate were studied experimentally and analytically with the purpose to obtain basic knowledges for establishing a design method for CFRP sheet-steel plate connection. Effective bond lengths for CFRP sheet-steel plate connection with different thickness of CFRP sheet were investigated. It was confirmed that the effective bond lengths were about 80-100, 100-160, 120-180 and 140-200 mm for the cases bonded with CFRP sheet with thickness of 0.333, 0.666, 0.999 and 1.32 mm respectively. Relationship between bond stress and slip of the interface between CFRP sheet and steel plate was assumed as a bilinear model and the parameters of the model were studied. The values of maximum shear stress τ_u , relative displacement δ_e and δ_u were determined as 17.0 N/mm^2, 0.11 mm and 0.25 mm, respectively. The fracture energy of the CFRP sheet-steel plate interface was evaluated as 2.13 N/mm. Furthermore, the validity of the proposed bond stress-slip model was confirmed by comparing the results obtained from three dimensional FEM analyses with the test results.

References:

Nozaka, K., Shield, C.K. and Hajjar, J.F.: "Effective Bond Length of Carbon-Fiber-Reinforced Polymer Strips Bonded to Fatigued Steel Bridge I-Girders", *Journal of Bridge Engineering*, Vol. 10, No. 2, pp.195-205, 2005.3.

Teng, J.G., Yuan, H. and Chen, J.F.: "FRP-to-Concrete Interfaces between Two Adjacent Cracks: Theoretical Model for Debonding Failure", *International Journal of Solids and Structures*, Vol.43, pp.5750-5778, 2006.

Zhang, G.F., Hoshikuma, J. and Sakai, J.: "Bonding Behavior of FRP-Steel Bonded Connections Using for Seismic Retrofit of Reinforced Concrete Bridge Pier", *Journal of Structural Engineering*, Vol.56A, pp.432-439 , 2010.3.

DIANA User's Manual, Analysis Procedures, release 9.3, TNO DIANA BV, 2008.

8CUEE CONFERENCE PROCEEDINGS
8th International Conference on Urban Earthquake Engineering
March 7-8, 2011, Tokyo Institute of Technology, Tokyo, Japan

MODELING OF PITTING CORROSION IN REINFORCED CONCRETE BRIDGE COLUMNS FOR TIME-VARYING SEISMIC RISK ASSESSMENT

Anirudh S. Rao[1], Michael D. Lepech[2], and Anne S. Kiremidjian[3]

1) Graduate Student, Department of Civil and Environmental Engineering, Stanford University, Stanford, CA, USA
2) Assistant Professor, Department of Civil and Environmental Engineering, Stanford University, Stanford, CA, USA
3) Professor, Department of Civil and Environmental Engineering, Stanford University, Stanford, CA, USA
asrao@stanford.edu, mlepech@stanford.edu, ask@stanford.edu

Abstract: Pitting corrosion of reinforcing steel can lead to a considerable decrease in reliability over time in reinforced concrete members and structural systems. Older structures that have undergone long-term structural deterioration are likely to be at higher risk during extreme events like earthquakes than similar structures that have recently been built. This paper presents a simplified approach for analytically modeling pitting corrosion deterioration in reinforced concrete bridge columns that can be used in a time-dependent risk assessment framework. The model is validated by comparison with experimental tests.

1. INTRODUCTION

1.1 Corrosion and Time Varying Seismic Risk

Corrosion of reinforcing steel combined with poor concrete durability is a major source of structural deterioration in reinforced concrete infrastructure worldwide including bridges, piers, seawalls, dams, and other structures (Vu and Stewart 2000). Several researchers have investigated the effect of reinforcement corrosion on the time-dependent reliability of reinforced concrete structures subjected largely to dead and live gravity loads (Frangopol et al. 1997; Stewart and Rosowsky 1998; Val et al. 1998; Vu and Stewart 2000). These studies have established that the corrosion of reinforcing steel can lead to significant reductions in the reliability of reinforced concrete members and structural systems over time.

Deterioration due to corrosion has been commonly modeled using phenomenological processes proposed by Tuutti (1982) which segments steel corrosion in reinforced concrete into a series of distinct stages. The first stage involves the initial transport of chlorides through the concrete cover leading to depassivation of the reinforcing steel. This is followed by the formation of oxidation products that cause radial cracking around the steel rebar. Eventually, the oxidation process is accelerated ultimately leading to spalling of the concrete cover. The stages of this phenomenon have been quantified, modeled, and reviewed in part or whole by others (Bentz et al. 1996; Liu and Weyers 1998; Middleton and Hogg 1998; Neville 1995). In the majority of these approaches, the corrosion initiation stages involving transport of the chlorides and corrosives through the cover and initial depassivation have been modeled using Fick's Second Law of Diffusion (Eqn 1).

$$T_{int} = \frac{x^2}{4D_c}\left[\text{erf}^{-1}\left(\frac{C_0 - C_{cr}}{C_0}\right)\right]^{-2} \quad (1)$$

where T_{int} = time to corrosion in years; x = concrete cover depth in mm; D_c = diffusion coefficient in mm^2/yr; C_0 = surface chloride concentration in mg/g; and C_{cr} = threshold chloride concentration for steel depassivation in mg/g.

This is followed by uniform rates of steel corrosion that result in expansive hoop stresses on the concrete cover, exceedence of the tensile strength of the cover, and crack formation and spalling of the cover resulting in unchecked steel corrosion. One such model for uniform corrosion is shown as Equation 2 (Enright and Frangopol 1998).

$$D(t) = D_0 - 0.0203 i_{corr}\,(t - T_{int}) \quad (2)$$

where $D(t)$ = rebar diameter as a function of time in mm; D_o = initial rebar diameter in mm; and i_{corr} = corrosion rate measured as a current density in μA/cm^2.

In recent years, researchers have begun recognizing that the time-dependent decrease in structural reliability due to reinforced concrete corrosion can have a profound effect on the probability of failure of aging reinforced concrete structures exposed to seismic hazards (Choe et al. 2009; Padgett and Ghosh 2009; Kumar et al. 2009). Thus there is demonstrably a dire need for time-varying risk assessment models that can characterize risk due to multi-hazard environments, in this case extreme seismic events and long-term structural deterioration that vary over time.

1.2 Research Motivation

While previous researchers have shown that time-dependent corrosion can have a considerable impact on the probability of failure of structures under seismic loads, the simple method in which corrosion initiation and propagation has been modeled reduces the usefulness of these results for either structural reliability prediction or life cycle cost or impact estimation. Furthermore, neglecting to include the effects of pitting corrosion can lead to a significant underestimation of the actual extent of deterioration and an over-prediction of the residual strength of the structure. This study improves upon previous research by explicitly incorporating the effect of concrete cover cracking in the corrosion phenomenon. The appearance of concrete cracks causes a shift from uniform corrosion along the length of the reinforcement to more severe pitting corrosion at the crack location. Consideration of pitting corrosion represents a significant improvement over the existing models in that the corrosion deterioration process is represented more realistically, thus bringing the time-dependent multi-hazard model closer to actual field conditions over time.

2. CORROSION MODELING

2.1 Model for Multi-Stage Reinforcement Corrosion

Transport of chlorides through the uncracked cover is modeled as a Fickian diffusion process up until time T_{int}, as given by Equation 1 and shown in Figure 1. Time to cracking following depassivation, T_{cr}, is modeled as uniform corrosion using the mechanics-based model of Liu and Weyers (Eqn 3).

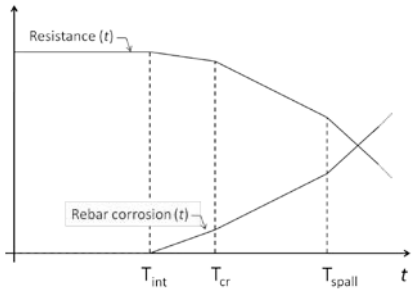


Figure 1 Conceptual multi-stage deterioration process

Time to cracking following depassivation, T_{cr}, is modeled as uniform corrosion using the mechanics-based model of Liu and Weyers (Eqn 3).

$$T_{cr} = \frac{\left[\rho_{rust}\left(\pi\left[\frac{xf_t}{E_{ef}}\left(\frac{a^2+b^2}{b^2-a^2}+\nu_c\right)+d_0\right]D_0+\frac{W_{st}}{\rho_{st}}\right)\right]^2}{\frac{0.208\pi D_0 i_{corr}}{\alpha}} \quad (3)$$

where T_{cr} = time to cover cracking after depassivation in years; ρ_{rust} = density of corrosion products; x = concrete cover depth in mm; f'_t = tensile strength of concrete in MPa; $E_{ef} = E_C/(1+\varphi_C)$; E_C = elastic modulus of concrete in MPa; φ_C = concrete creep coefficient; $a = 0.5(D + 2d_0)$; $b = x + a$; ν_c = Poisson's ratio for concrete; d_0 = thickness of porous band at steel/concrete interface in mm; D_0 = initial diameter of steel reinforcement in mm; W_{st} = mass of corroded steel in mg/mm; ρ_{st} = density of steel; α = molecular weight of steel divided by molecular weight of corrosion products; and i_{corr} = corrosion rate measured as current density in μA/cm^2.

After cracking has occurred, more often than not, instead of a uniform reduction of cross-sectional area, chloride-induced corrosion will lead to localized reductions of rebar cross-sectional area through the formation of pits. Pitting is considered to be more dangerous than uniform corrosion damage. A small, narrow pit with minimal overall metal loss can lead to the failure of an entire reinforced concrete member. Since pitting corrosion is a highly localized phenomenon, it can result in reductions of cross sectional area that are 5 to 10 times greater than that of uniform corrosion given the same corrosion rate (Stewart 2004).

The extent of pitting corrosion has been quantified by others using a pitting factor (Cairns *et al*. 2005; Gonzalez *et al*. 1995; Rodriguez *et al*. 1997; Torres-Acosta and Martínez-Madrid 2003) given as:

$$R = p/P_{av} \quad (4)$$

$$P_{av} = 0.0116 i_{corr}\, t \quad (5)$$

where R = pitting factor; p = maximum pit depth in mm; P_{av} = penetration based on uniform corrosion; i_{corr} = corrosion rate as current density in μA/cm^2.

From Equations 4 and 5 the maximum pit depth along a reinforcing bar is then calculated as

$$p(t) = 0.0116 i_{corr}\, Rt \quad (6)$$

2.2 Reduction of reinforcing steel diameter over time

Given the pit depth as a function of time, Val et al. (1998) suggested that the geometry of the pit can be expressed as a quadrilateral (Figure 2).

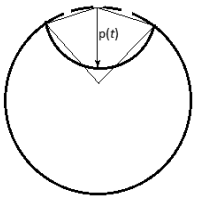


Figure 2 Quadrilateral pit configuration

Therefore, the cross sectional area of steel remaining in an RC component as a function of time is (Stewart and Al-Harthy 2008)

$$A(t) = A_0 - A_{pit}(t) \quad (7)$$

where A = cross sectional area of remaining rebar in mm^2; A_0 = initial cross sectional are of rebar in mm^2; and A_{pit} = cross

sectional area of pit in mm^2 which can be calculated using the equations developed by Val and Melchers (1997).

To facilitate the incorporation of the effects of pitting corrosion in the analytical modeling of the column, a number of simplifications were made on the Val and Melchers model. The mechanical effect of pitting is assumed equivalent to a gross reduction in rebar diameter (Figure 3).

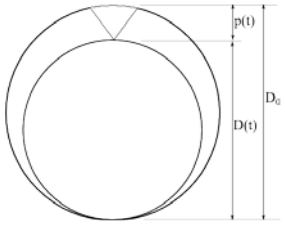


Figure 3 Simplified effect of pitting corrosion on rebar geometry

Combining this with equations 2 and 6, the multi-stage uniform-pitting corrosion model is obtained as

$$D(t) = \begin{cases} D_0, & t \le T_{int} \\ D_0 - 0.0203 i_{corr}\,(t - T_{int}), & T_{int} < t \le T_{int} + T_{cr} \\ D_0 - 0.0116 R i_{corr}\,(t - T_{cr} - T_{int}) & \\ \quad -0.0203 i_{corr}\,(t - T_{int}), & t > T_{int} + T_{cr} \end{cases} \quad (8)$$

where D(t) = diameter of rebar at time t, as shown in Figure 3.

3. STRUCTURAL MODELING

In order to validate the assumptions made in the corrosion model described above, analytical and experimental test results of several reinforced concrete columns were compared. The time-varying nature of the seismic behavior of the columns was accounted for by combining the corrosion model with the finite element structural model in OpenSees. Physical test columns having the same specifications were subjected to different axial loads and varying degrees of accelerated corrosion in an experiment at the State Key Laboratory of Coastal and Offshore Engineering at Dalian University of Technology in China (Li and Gong 2008).

3.1 Tests Used for Validation

The experimental reinforced concrete column test specimens were 1 m tall and had a diameter of 0.26 m. The longitudinal reinforcement consisted of 6x16 mm bars; the distribution of longitudinal bars is shown in the column cross section in Figure 4. The transverse reinforcement consisted of 8 mm stirrups at a spacing of 0.1 m. The concrete cover was 0.03 m. The geometric and structural properties of the test specimens are summarized in Table 1. Table 2 shows the different axial load ratios and corrosion mass loss ratios for the series of tested column specimens.

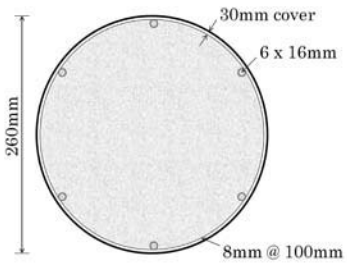


Figure 4 Cross section of the test column specimens (after Li and Gong 2008)

Table 1 Properties of the test column specimens

Height, H	1 m
Diameter, D	0.26 m
Longitudinal Reinforcement Ratio, ρ	2.3%
Longitudinal Rebar Diameter, d_0	16 mm
Transverse Rebar Diameter, d_s	8 mm
Nominal Yield Strength of Steel, f_y	373.2 MPa
Nominal Strength of Concrete, $f_c^{'}$	32.4 MPa

Table 2 Axial load ratios and mass loss ratios for the test specimens (after Li and Gong 2008)

Specimen	A		B		
	A_0	A_{12}	B_0	B_{21}	B_{22}
Mass loss due to corrosion (%)	0.0%	9.4%	0.0%	5.1%	9.4%
Axial Load Ratio	0.15		0.25		

The test columns were subjected to reversed cyclic loading using the triangular waveform shown in Figure 5 and hysteretic and skeleton curves for the columns were obtained. The initial displacement of 2 mm was followed by three full cycles at each subsequent displacement level. Each displacement level was higher than the previous level by 4 mm.

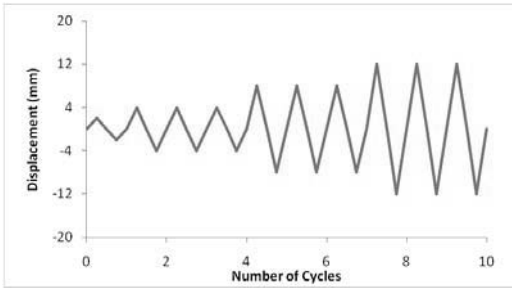


Figure 5 Lateral displacement history (after Li and Gong 2008)

3.2 Analytical Modeling of Test Column

The analytical modeling of the test column was conducted using the Open System for Earthquake Engineering Simulation (OpenSees) software (Mazzoni *et al*. 2009), a finite element method based object oriented software framework for simulating the seismic response of structural systems. The column was modeled as a nonlinear beam-column element, which is a force-based element that considers the spread of plasticity along its length.

The column cross-section was discretized into a number of inelastic fiber segments as shown in Figure 6. The number of elements the cross-section was discretized into was progressively increased starting from a minimal number of elements until a further increase in the number of elements yielded no significant change in the results. This particular discretization was then used for all further analyses.

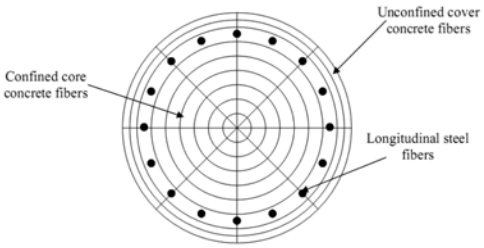


Figure 6 Discretization of cross-section into inelastic fibers

The confined core concrete fibers were modeled using the uniaxial 'Concrete04' material in OpenSees, which uses the Karsan-Jirsa model for unloading and reloading in compression and also provides tensile strength with exponential decay. The unconfined core concrete fibers were modeled using the uniaxial 'Concrete01' material which has no tensile strength. The reinforcement steel was modeled using the uniaxial Giuffre-Menegotto-Pinto 'Steel02' material, which provides isotropic strain hardening.

A zero-length section was introduced at the base of the column to account for the component of the deformation due to bond-slip. The tensile stress-strain model used for the reinforcement was adapted from the modified two-component bond-stress model recommended by Berry and Eberhard (2003).

According to the multi-phase corrosion model described in Equation 8, the diameter of the longitudinal steel bars was reduced as a function of time. While modeling the deterioration due to uniform corrosion, it was assumed that the effects of corrosion are uniform about the perimeter of the column and that all rebars undergo the same reduction in diameter at any given point of time during the service life of the bridge.

For modeling purposes, the reduction in rebar diameter was assumed to be uniform along the height of the column since the formation of cracks due to chloride-induced uniform corrosion is expected to be uniform along the height. Aspects that have not been considered in this study include spalling of the concrete cover, changes in the material properties of steel and concrete due to corrosion and the effect of corrosion on the bond between the rebar steel and concrete. However, as noted by Fang et al. (2004) and Wang and Liu (2004), the effects of corrosion on bonding in well confined concrete are negligible.

3.3 Comparison of analytical and experimental results

The hysteresis curves obtained from the test and the corresponding OpenSees analyses for specimens A_0 and A_{12} are plotted in Figure 7. Similar hysteresis curves were also obtained from the test and the corresponding OpenSees analyses for specimens B_0 and B_{21} and B_{22}, but are not plotted in the figure. Envelope curves are obtained for each of these hysteresis curves by plotting the mean of the absolute values of the three peak forces on either side for each displacement during the revered cyclic load test. The envelope curves obtained from the hysteresis plots are shown in Figure 8.

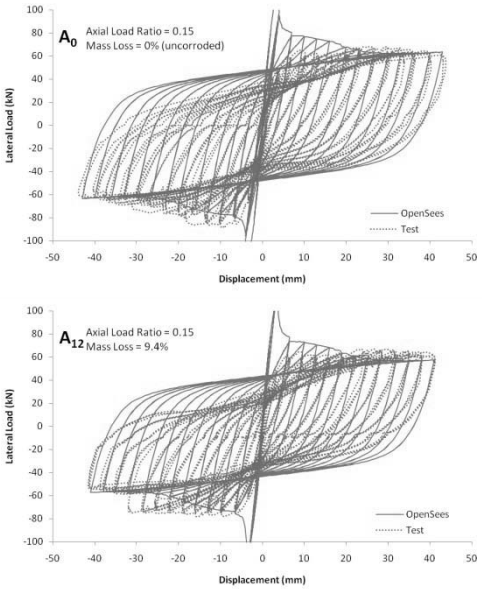


Figure 7 Hysteresis curves from the test (dotted lines) and the OpenSees analysis (solid lines) compared for specimens A_0 (top) and A_{12} (bottom)

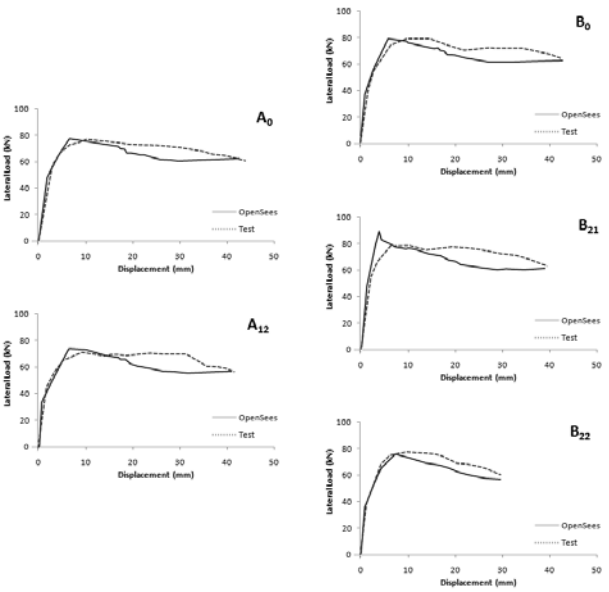


Figure 8 Envelope curves from the test (dashed lines) and the OpenSees analysis (solid lines) compared for the five column specimens

4. DISCUSSION OF RESULTS

Comparing the envelope curves obtained from the test and the analytical model for the uncorroded specimens A_0 and B_0, it can be seen that the nonlinear OpenSees analytical model predicts the envelope or 'backbone' load-displacement response well. Also, the predicted envelope curves for the corroded specimens A_{12}, B_{21} and B_{22} agree well with the test results, indicating that the reinforcing steel deterioration model implemented in OpenSees is able to capture the degradation in the performance of the column due to corrosion sufficiently well at the axial load ratios tested.

Since the objective of the study was to verify that the analytical model can predict the envelope load-displacement response of deteriorating columns, a pinching model was not used to capture the pinching behavior exhibited by reinforced concrete under cyclic loading. This is reflected in the comparison of the hysteresis curves for the test and analytical model. The analytical model under-predicts the energy dissipation during the reversed cyclic loading for all of the specimens. If energy dissipation needs to be predicted, a pinching model such as the 'Pinching4' material in OpenSees could be used.

5. CONCLUSIONS

An improved model for the chloride-induced deterioration of reinforcing steel is presented in this paper that can be used for time-dependent risk assessment of deteriorating structures. The model accounts for the effects of uncracked and cracked concrete covers through the inclusion of pitting corrosion in cracked reinforced concrete. The simplified model used for capturing the deterioration of reinforcement is capable of predicting the envelope load-displacement response of corroded reinforced concrete columns for moderate levels of corrosion, corresponding to less than 10% reinforcement steel mass loss due to corrosion. The improved reinforcing steel deterioration model can thus be used in conjunction with this simplified analytical model to assess the seismic risk of a bridge at various points during its lifetime.

Acknowledgements:

The authors would like to thank the financial support of the John A. Blume Earthquake Engineering Research Center, the Leavell Fellowship, and the Terman Faculty Fellowship at Stanford University.

References:

Bentz, D. P., Clifton, J. R., and Snyder, K. A. (1996). "Predicting service life of chloride-exposed steel-reinforced concrete." *Concrete International*, 18(12), 42–47.

Berry, M., and Eberhard, M. O. (2003). *Performance models for flexural damage in reinforced concrete columns*. Berkeley, CA.

Cairns, J., Plizzari, G. A., Du, Y., Law, D. W., and Franzoni, C. (2005). "Mechanical properties of corrosion-damaged reinforcement." *ACI Materials Journal*, 102(4).

Choe, D.-E., Gardoni, P., Rosowsky, D. V., and Haukaas, T. (2008). "Probabilistic capacity models and seismic fragility estimates for RC columns subject to corrosion." *Reliability Engineering & System Safety*, 93(3), 383-393.

Choe, D.-E., Gardoni, P., Rosowsky, D. V., and Haukaas, T. (2009). "Seismic fragility estimates for reinforced concrete bridges subject to corrosion." *Structural Safety*, 31(4), 275-283.

Enright, M. P., and Frangopol, D. M. (1998). "Probabilistic analysis of resistance degradation of reinforced concrete bridge beams under corrosion." *Engineering Structures*, 20(11), 960–971.

Fang, C., Lundgrenb, K., Chena, L., and Zhu, C. (2004). "Corrosion influence on bond in reinforced concrete." *Cement and Concrete Research*, 34(11), 2159-2167.

Frangopol, D. M., Lin, K.-Y., and Estes, A. C. (1997). "Reliability of reinforced concrete girders under corrosion attack." *Journal of Structural Engineering*, 123(3), 286-297.

Gonzalez, J. A., Andrade, C., Alonso, C., and Feliu, S. (1995). "Comparison of rates of general corrosion and maximum pitting penetration on concrete embedded steel reinforcement." *Cement and Concrete Research*, 25(2), 257–264.

Kumar, R., Gardoni, P., and Sanchez-Silva, M. (2009). "Effect of cumulative seismic damage and corrosion on the life-cycle cost of reinforced concrete bridges." *Earthquake Engineering & Structural Dynamics*, 38(7), 887-905.

Li, J., and Gong, J. (2008). "Influences of Rebar Corrosion on Seismic Behavior of Circular RC Columns." *China Journal of Highway and Transport*, 21(4), 55-60.

Liu, Y., and Weyers, R. E. (1998). "Modeling the time-to-corrosion cracking in chloride contaminated reinforced concrete structures." *ACI Materials Journal*, 95(6), 675-681.

Mazzoni, S., McKenna, F., Scott, M. H., and Fenves, G. L. (2009). "Open System for Earthquake Engineering Simulation User Command-Language Manual." Pacific Earthquake Engineering Research Center, Berkeley, CA.

Middleton, C. R., and Hogg, V. (1998). *Review of deterioration models used to predict corrosion in reinforced concrete structures*. Cambridge University Department of Engineering, Cambridge, UK.

Neville, A. (1995). "Chloride attack of reinforced concrete: an overview." *Materials and Structures*, 28(2), 63-70.

Padgett, J. E., and Ghosh, J. (2009). "Multi-Hazard Consideration of Seismic and Aging Threats to Bridges." *Proceedings of the 2009 Structures Congress*, ASCE, 547-556.

Rodriguez, J., Ortega, L. M., and Casal, J. (1997). "Load carrying capacity of concrete structures with corroded reinforcement." *Construction and Building Materials*, 11(4), 239–248.

Stewart, M. G. (2004). "Spatial variability of pitting corrosion and its influence on structural fragility and reliability of RC beams in flexure." *Structural safety*, 26(4), 453–470.

Stewart, M. G., and Al-Harthy, A. (2008). "Pitting corrosion and structural reliability of corroding RC structures: Experimental data and probabilistic analysis." *Reliability Engineering & System Safety*, 93(3), 373-382.

Stewart, M. G., and Rosowsky, D. V. (1998). "Time-dependent reliability of deteriorating reinforced concrete bridge decks."

Structural Safety, 20(1), 91-109.
Torres-Acosta, A. A., and Martínez-Madrid, M. (2003). "Residual life of corroding reinforced concrete structures in marine environment." *Journal of Materials in Civil Engineering*, 15(4), 344.
Tuutti, K. (1982). "Corrosion of steel in concrete." *Swedish Cement and Concrete Research Institute, Stockholm*, 469.
Val, D. V., and Melchers, R. E. (1997). "Reliability of deteriorating RC slab bridges." *Journal of structural engineering*, 123, 1638.
Val, D. V., Stewart, M. G., and Melchers, R. E. (1998). "Effect of reinforcement corrosion on reliability of highway bridges." *Engineering Structures*, 20(11), 1010-1019.
Vu, K. A. T., and Stewart, M. G. (2000). "Structural reliability of concrete bridges including improved chloride-induced corrosion models." *Structural Safety*, 22(4), 313-333.
Wang, X., and Liu, X. (2004). "Modeling bond strength of corroded reinforcement without stirrups." *Cement and Concrete Research*, 34(8), 1331–1339.

8CUEE CONFERENCE PROCEEDINGS
8th International Conference on Urban Earthquake Engineering
March 7-8, 2011, Tokyo Institute of Technology, Tokyo, Japan

SEISMIC PROPERTIES OF JAPANESE TRADITIONAL WOODEN PAGODAS - STATIC LOADING TEST AND FREE VIBRATION TEST OF A SMALL SCALE MODEL -

Eisuke Nishikawa[1] and Hidekazu Nishizawa[2]

1) Researcher, CUEE, Tokyo Institute of Technology, Japan
2) Professor, Dept. of Architecture, Kansai University, Japan
nishikawa@cuee.titech.ac.jp, sc8h-nszw@asahi-net.or.jp

Abstract: This paper refers to studies on the seismic properties of Japanese traditional wooden pagodas. Because there are few records of collapses of wooden pagodas due to earthquakes available, many researchers have studied this theme, but have done so under the conditions that all pagodas are relatively similar. In reality, pagodas have various scales. In this study, we performed static horizontal loading tests and free vibration tests with a 1/10 model of a three-story pagoda. By changing the weight of the model, we simulated the behavior of pagodas with heights of 18m, 5.4m 1.8m, and examined the effect of the size of the pagoda on its seismic property. The following results have been obtained from these tests. Large pagoda (height: 18m), restoring force is greater and more dissipative than those of small pagodas, and the pagoda bent like a bow, and by an increase in amplitude, the natural frequency tends to be lower, because of the decrease in stiffness. Small pagodas (height: 5.4m, 1.8m), restoring force is smaller than that of the larger one, and these pagodas tilted like a rigid body, and by an increase in amplitude, the natural frequency and damping ratio become small, because of the rocking of the pagoda.

1. INTRODUCTION

1.1 Introduction of Previous Research

This paper refers to studies on the seismic properties of Japanese traditional wooden pagodas. In Japan, many three-story and five-story pagodas have been built, and a great number of these pagodas were built hundreds of years ago. Though in almost all areas of Japan, a big earthquake occurs every hundreds years, there exist few recorded collapses of wooden pagodas due to earthquakes. Therefore, pagodas are believed to have a high seismic performance.

Many researchers have studied this theme, and have often pointed out that the long natural period and high capacity of damping are the keys to the seismic performance of the pagoda.

Microtremor measurements and vibration tests of many pagodas have been performed in the field. According to these tests, the natural frequencies have been observed to range from 0.5～2Hz, the damping factors range from 1～5%, and the natural frequencies are related to the height of the pagoda. But these characteristics relate only to microtremors.

According to tests on a small scaled model, by an increase in amplitude, the natural frequency of vibration and damping ratio become smaller, but the similarity rule between the small model and the full size pagoda is not yet studied. Therefore investigations of the structural characteristics of big amplitude vibrations should be undertaken with consideration of the similarity rule.

1.2 Scope of Model Tests

Pagodas have been built to various scales as shown in Fig.1.1. Depending on the period in which the pagoda was built, the structure varies slightly, but the proportion and the ratio of members are almost the same despite a difference in size. So, from a structural point of view, we can assume that pagodas behave as different-size models with a similar-structure.

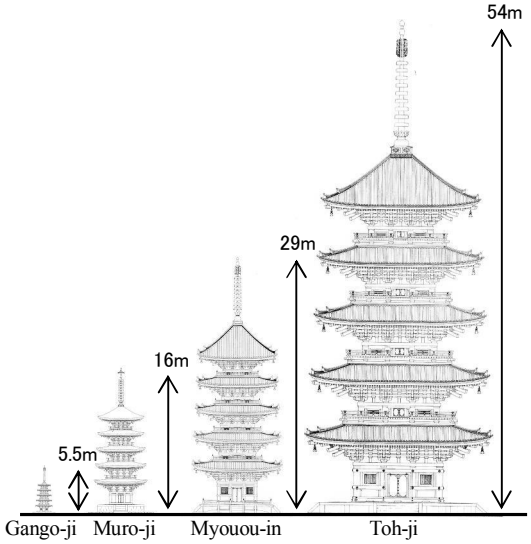


FIGURE 1.1 VARIOUS SCALE PAGODAS

Based on the above, in this study, we performed static horizontal loading tests and free vibration tests with a 1/10 model of a traditional wooden three-story pagoda in order to clarify seismic properties. By changing the weight of the model, we simulated the behavior of three different pagodas with the heights of 18m, 5.4m 1.8m, and we examined the effect of the size of the pagoda on its seismic property.

2. STUDY OF SIMILARITY RULE

2.1 Frame Models of Japanese Traditional Wooden Architectures

As a basic frame of Japanese traditional wooden architectures including the pagoda, we studied the frame models shown in Fig.2.1-① ～ ⑤. Because Japanese traditional wooden buildings are not fixed to their foundation, when they are forced horizontally to some extent, they rock by lifting up the bottom of the frame (Fig.2.1-①) or they slip (Fig.2.1-②). The deformation mechanisms of these frames are as follows:

Frame①: The frame rocks by lifting up its bottom.
Frame②: The frame slips from the foundation.
Frame③: The frame's columns are bent; the joints of the horizontal beam and the columns are rigid.
Frame④: The frame's wooden wall compresses inclined to the column's grain; the joint of the horizontal beam and the columns are pin joints.
Frame⑤: The frame's horizontal beams, which penetrate the columns, compress inclined to the grain of the column's openings.

With the assumption that each of these stress and strain relationships is linear, we studied load deformation relationships of full and small size frames.

2.2 Similarity Ratios of Dimension and Weight

The similarity ratios of dimension and weight of the full and small size frames mentioned above were studied. In this paper, the similarity ratio of dimension is defined by α, that of weight is by β. In Fig.2.1, forces and deformations of the full size frames are expressed by capital letters, and that of the small size frames are expressed by small letters.

2.3 Load Deformation Relationships of Full Size Frames

The load of the full-size frames when the deformation equals X is obtained by Eqs.2.1～2.5. Notations used in the formulas are following.

γ : coefficient of friction
E: Young's modulus of bending deflection
K_s: Young's modulus inclined to the grain

Frame①

$$P_r = \frac{Wg \cdot B_G}{H} \quad \cdots \text{Eq.2.1}$$

Frame②

$$P_s = Wg \cdot \gamma \quad \cdots \text{Eq.2.2}$$

Frame③

$$P_c = \frac{24 \cdot E \cdot I \cdot \delta_c}{H^3}, \quad I = \frac{B^4}{12},$$

$$\therefore P_c = \frac{2 \cdot B^4}{H^3} \cdot E \cdot X_c \quad \cdots \text{Eq.2.3}$$

Frame④

$$P_w = \frac{Z \cdot \varepsilon \cdot K_s}{H}, Z = \frac{T \cdot H^2}{6}, \varepsilon = \frac{X_w}{2 \cdot B},$$

$$\therefore P_c = \frac{T \cdot H}{12 \cdot B} \cdot K_s \cdot X_w \quad \cdots \text{Eq.2.4}$$

Frame⑤

$$P_n = \frac{2 \cdot M_n}{h}, \quad M_n = \varepsilon \cdot K_s \cdot Z,$$

$$\varepsilon = \frac{X_n \cdot b}{2 \cdot h \cdot c}, \quad Z = \frac{d \cdot b^2}{6}$$

$$\therefore P_n = \frac{B^3 \cdot D}{6 \cdot C \cdot H^2} \cdot K_s \cdot X_n \quad \cdots \text{Eq.2.5}$$

2.4 Load Deformation Relationships of Small Size Frames

The load of the small-size frames when the deformation equals x is obtained by Eqs.2. 6～2.10.

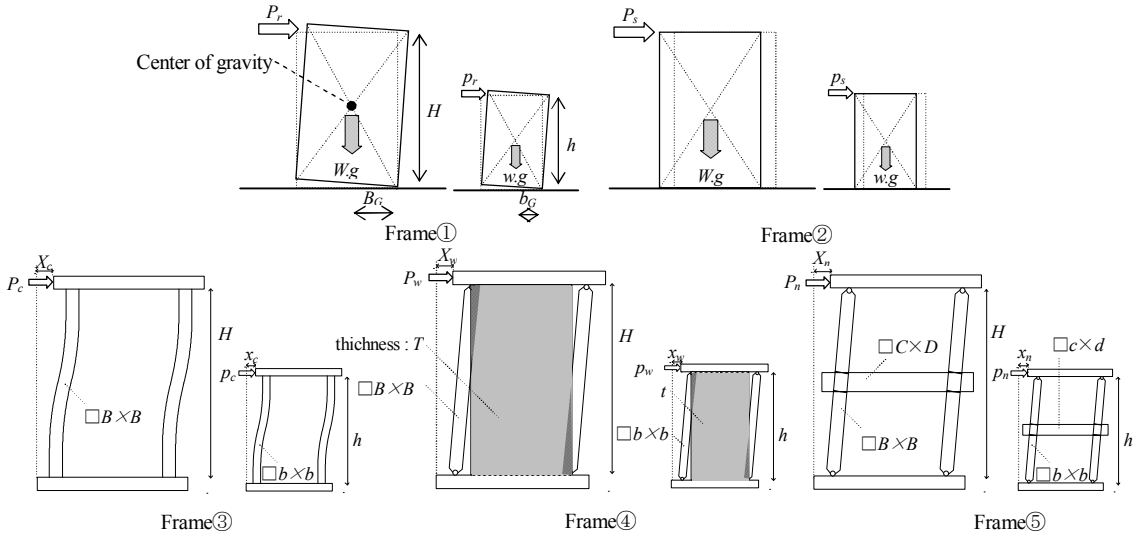


FIGURE 2.1 FRAME MODELS

Frame①

$$p_r = \frac{wg \cdot b_G}{h} = \frac{(\beta \cdot W)g \cdot (\alpha \cdot B_G)}{(\alpha \cdot H)} = \beta \cdot P_r \quad \cdots \text{Eq.2.6}$$

Frame②

$$p_s = wg \cdot \gamma = (\beta \cdot W)g \cdot \gamma = \beta \cdot P_s \quad \cdots \text{Eq.2.7}$$

Frame③

$$p_c = \frac{2 \cdot b^4}{h^3} \cdot E \cdot x_c = \frac{2 \cdot (\alpha \cdot B)^4}{(\alpha \cdot H)^3} \cdot E \cdot (\alpha \cdot X_c) = \alpha^2 \cdot P_c \quad \cdots \text{Eq.2.8}$$

Frame④

$$p_w = \frac{t \cdot h}{12 \cdot b} \cdot K_s \cdot x_w = \frac{(\alpha \cdot T) \cdot (\alpha \cdot H)}{12 \cdot (\alpha \cdot B)} \cdot K_s \cdot (\alpha \cdot X_w) = \alpha^2 \cdot P_w \cdots \text{Eq.2.9}$$

Frame⑤

$$p_n = \frac{b^3 \cdot d}{6 \cdot c \cdot h^2} \cdot K_s \cdot X_n = \frac{(\alpha \cdot B)^3 \cdot (\alpha \cdot D)}{6 \cdot (\alpha \cdot C) \cdot (\alpha \cdot H)^2} \cdot K_s \cdot (\alpha \cdot X_n) = \alpha^2 \cdot P_n$$

$\cdots$Eq.2.10

2.5 Relationship between Similarity Ratios of Dimension and Similarity Ratios of Weight

In order to simulate the structural characteristics of a full-size building composed of the above basic frames, the similarity ratios of load of several frames have to be made the same. According to the above, β has to be made equal to α^2. Table 2.1 shows the similarity ratios of various conditions of a small model in which β is equal to α^2.

TABLE 2.1 SIMILARITY RATIOS OF VARIOUS CONDITIONS

		Full Size	Small Model
Size	m	1	α
Weight	kg	1	α^2
Rotational Inertia	kg.m^2	1	α^4
Load	N	1	α^2
Moment	N.m	1	α^3
Shear Rigidity	N/m	1	α
Rotational Rigidity	N.m/rad	1	α^3
Natural Frequency	Hz	1	$1/\sqrt{\alpha}$
Time	sec.	1	$\sqrt{\alpha}$
Displace	m	1	α
Velocity	m/s	1	$\sqrt{\alpha}$
Accerelation	m/s^2	1	1

2.6 Effect of Similarity Ratio of Weight on Deformation of Small Model of a Pagoda.

Fig.2.2 shows the deformations of the full size pagoda, the small size model in which β is equal to α^2, and the small size model in which β is equal to α^3.

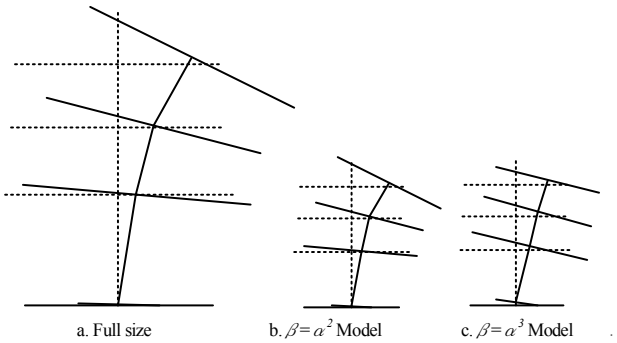


FIGURE 2.2 DEFORMATIONS OF MODELS WITH DIFFERENT WEIGHT

As shown in Fig.2.2, when β is equal to α^2, the deformation of the small size model is similar to that of the full size pagoda. On the other hand, when β is equal to α^3, the small size model rocks by lifting up its bottom more than the full size pagoda.

3. MODEL

3.1 Structure of Model

Fig.3.1 show the 1/10 scale model of the three-story pagoda which was built in Aichi prefecture recently. The model was made like the full size pagoda not only in the proportion but also in detail and was made of Japanese cypress, with height 1.8m. The characteristics of the structure of this model are as follows:

1. The central wooden column (Fig.3.1-A), which is named "shin-bashira", stands on a girder above the first floor, and is independent from surrounding structural frames.
2. The prolonged part of the *shin-bashira* above the roof is covered in bronze ornaments (Fig.3.1-B), which are named "sorin".
3. The frames of each floor are stacked up; the columns (Fig.3.1-C) of the upper floors are erected on the horizontal beams (Fig.3.1-D) which sit on the rafters of the floor below.
4. The columns of the first floor (Fig.3.1-E) are put on base stones (Fig.3.1-F).

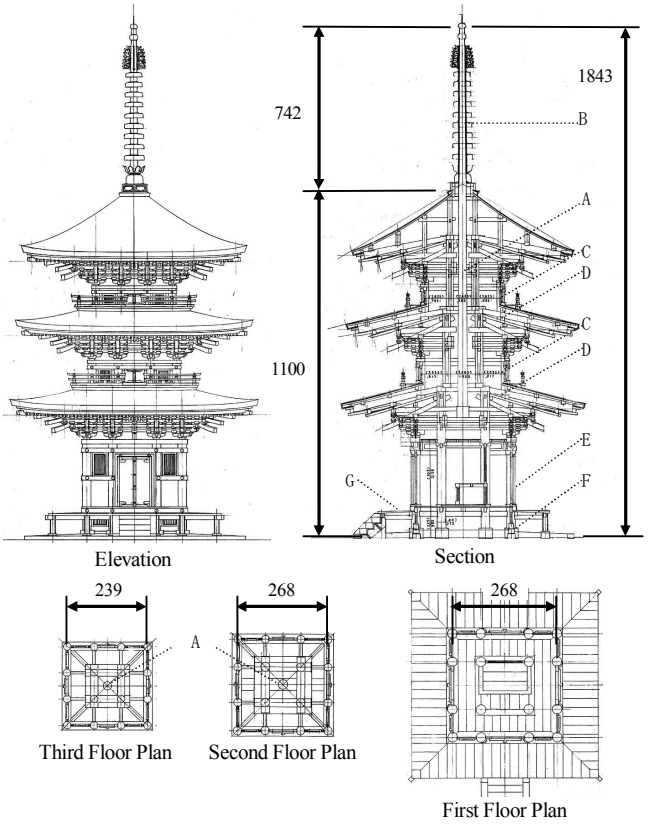


FIGURE 3.1 MODEL OF THREE-STORY PAGODA (unit: mm)

5. The weight of the building and roof covered by thin copper plate of the full size pagoda are 32t and 1.6t respectively. The weight of the roof is 5% of that of the building. So, the former is much smaller than the latter.

3.2 Weight of Model

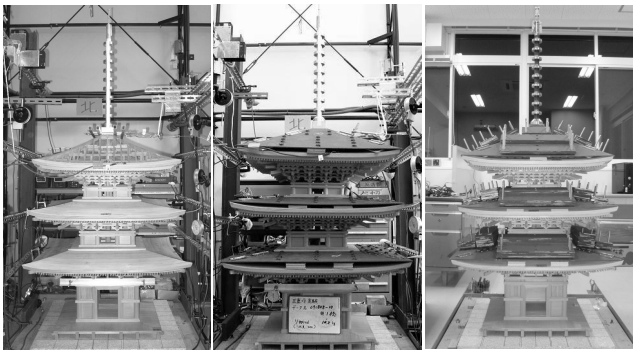
As shown in Photo.3.1, we performed experiments with the model by adjusting its weight by putting steel plates on the roof of each floor. The patterns of the weight are shown in Tab.3.1, [A]: 30kg, [B]: 83kg, [C]: 319kg.

In order to simulate the weight of the *sorin*, as shown in Fig.3.2, 2 types ([X], [Y]) of *sorin* are modeled on the *sorin* of the full size pagoda, which is composed twelve parts put together. These models are made of aluminum ([X]) and steel ([Y]), their weights being 0.35kg ([X]) and 3.15kg ([Y]). The above Model [A], Model [B] are equipped with [X], Model [C] is equipped with [Y].

3.3 Pagoda Simulation

As mentioned in Chapter 2, β (the similarity ratio of weight) is made to equal α^2 (the similarity size ratio). When α of the 18m high pagoda is 1/10, then β is $1/10^2$. Because the weight of the full size pagoda at 18m is 32t, the weight of the model is equivalent to 320kg. [C] corresponds to the simulation of the 18m pagoda. When α of the 5m pagoda is 1/2.7, the weight of the 5m pagoda is 640kg, so β is $1/2.7^2$, the weight of the model is equivalent to 88kg. [B] corresponds to the simulation of the 5m pagoda approximately. Based on the same way of similitude, [A] corresponds to the simulation of the 1.8m pagoda. The similarity ratios of time γ is $\sqrt{\alpha}$, so γ of each of the patterns are $1/\sqrt{10}$ ([A]), $1/\sqrt{2.7}$ ([B]), 1 ([C]).

Based on the above law of similitude, we can simulate the behavior of pagodas of various sizes by changing the weight of the model in keeping with the similarity rule.



MODEL [A] MODEL [B] MODEL [C]

PHOTO. 3.1 MODELS

TABLE 3.1 WEIGHTS AND SCALES OF MODELS

unit of weight : kg

	Model [A]	Model [B]	Model [C]
Third Floor	8.67	29.07	92.07
Second Floor	9.30	24.90	98.50
First Floor	12.01	28.81	125.41
Sorin	0.35	0.35	3.15
Total	30.33	83.13	319.13
Scale	1/1	1/2.7	1/10

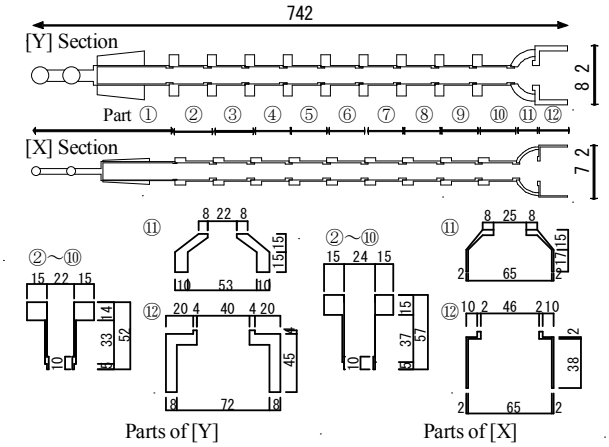


FIGURE 3.2 MODEL OF *SORIN* (unit: mm)

4. HORIZONTAL LOAD TEST

4.1 Test System

Fig.4.1 shows the system of the horizontal loading test. The wires (Fig. 4.1-A) are attached to the base of the *sorin*. The pagoda models were loaded by pulling the wires horizontally with electronic actuators (Fig. 4.1-B) in opposite directions by turns. The targets of the drift angle at the base of the *sorin* are 1/240rad, 1/120rad, 1/90rad, 1/60rad, 1/40rad and, 1/30rad. The loads were measured with load cells (Fig. 4.1-C). The deformations were measured with laser displacement meters (▲) and dial gauges (△).

The horizontal deformations of each floor's eave are noted X1～X4, and the angles of rotation of each floor's eave are obtained by the Eq.4.1.

$$\theta_i = \frac{Y_{i-A} - Y_{i-B}}{l_i} \quad \cdots \text{Eq.4.1}$$

4.2 Comparison of Load Deformation Relationships of Each Model

Fig.4.2 shows the load deformation relationships of each model, and Fig.4.3 shows the +1/30 loops of each model.

The load of Model [A] does not increase when the drift angle is greater than 1/120rad. Similarly, the load of

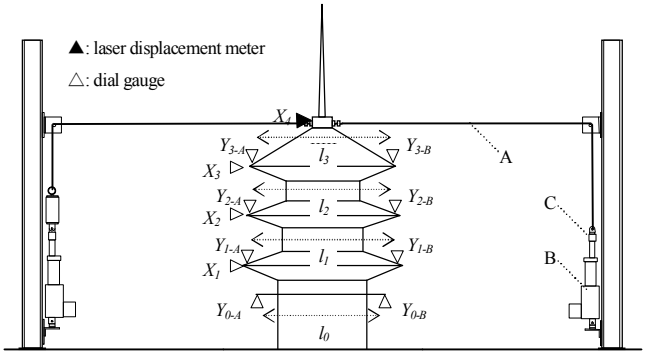


FIGURE 4.1 SYSTEM OF HORIZONTAL LOAD TSET

Model [B] does not increase when the drift angle is bigger than 1/60rad. On the other hand, the load of Model [C] continues to increase until the drift angle equals 1/30rad. The dotted lines in Fig.4.3 are the load deformation of three rigid bodies for comparison. Each body has proportions similar to one of the models. The load deformation of each rigid body is obtained by Eq.4.2.

$$P = W \cdot g \cdot \left(\frac{b}{h_g} - \frac{X_4}{h} \right) \quad \cdots \text{Eq.4.2}$$

P:Load W:Weight

X_4:Displace b:Width of Building(303mm)

h_g:Height of Gravity ([A]:684mm [B]:708mm [C]:684mm)

h:Height of Load Point (1100mm)

In Eq.4.2, the width of the building does not include the width of the first floor veranda, which is called "en" (Fig.3.1-G). The load deformation relationships of Model [A] and [B] are close to that of each rigid body when the deformations are greater than the deformations mentioned above, but the loads of the models exceed slightly those of the rigid bodies. It is thought that the reason for this is that the *en* of each model resists as an outrigger. It is assumed that the load deformation relationships of Model [C] would be close to that of each rigid body when the deformations are bigger than 1/30rad because of rocking by lifting up its bottom.

Table 4.2 shows the restoring force, secant rigidity, absorbed energy, and equivalent damping factor of ±1/30 loop of each model. The highest equivalent damping factor is that of Model [C], the second is that of Model [A] and, the lowest is that of Model [B].

Fig.4.4 shows the relationships between deformation and absorbed energy of each model. The absorbed energy of Model [A] and [B] are smaller than that of Model [C], and slightly increase especially when the deformations are larger than 1/60rad. The absorbed energy of Model [C] largely increases especially when the deformations are larger than 1/240rad.

4.3 Comparison of Deformation of Each Model

Fig.4.5 shows the deformation of each model. In order to clarify the characteristics of deformation, deformations in Fig.4.5 are made 10 times larger than the observed one.

As shown in Fig. 4.5, Models [A] and [B] rock by lifting up their bottom (Photo. 4.1), on the other hand, Model [C] is bent without lifting up its bottom, but the roof of the third floor is lifted up (Photo. 4.2).

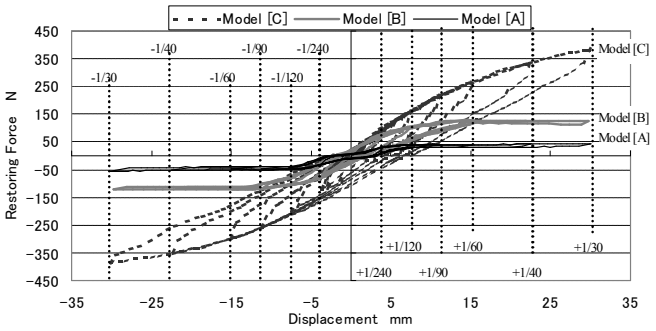


FIGURE 4.2 LOAD DEFORMATION RELATIONSHIPS OF MODELS

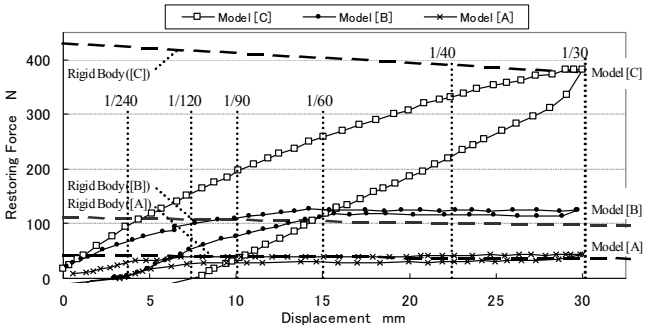


FIGURE 4.3 COMPARISONS OF LOAD DEFORMATION RELATIONSHIPS OF MODEL AND RIGID BODY

TABLE 4.2 LOADS, RIGIDITY, ABSORBED ENERGY AND DAMPING FACTOR OF MODELS (±1/30 LOOP)

		Model [A]	Model [B]	Model [C]
Restoring Force	N	45	126	382
Secant Rigidity	N/mm	1.5	4.2	12.7
Absorbed Energy	J	0.72	1.30	6.93
Damping Factor	%	8.5	5.5	9.6

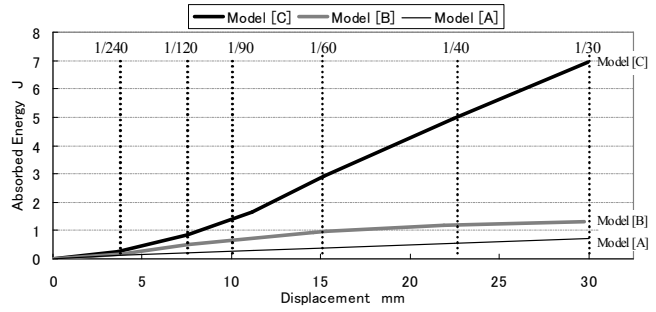


FIGURE 4.4 RELATIONSHIPS BETWEEN DEFORMATIONS AND ABSORBED ENERGY OF MODELS

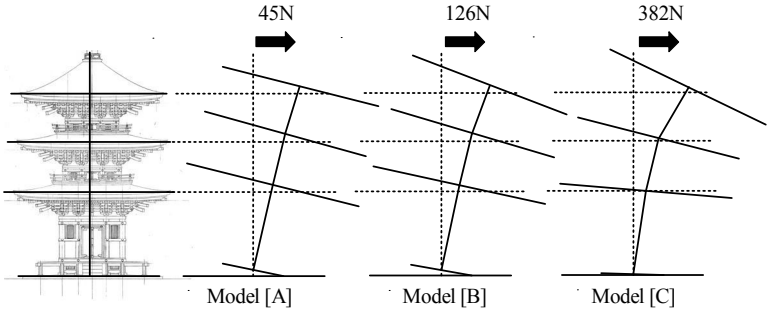


FIGURE 4.5 DEFORMATIONS OF MODELS (+1/30)

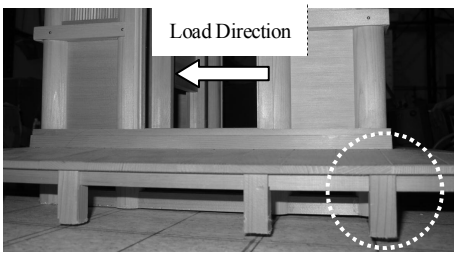
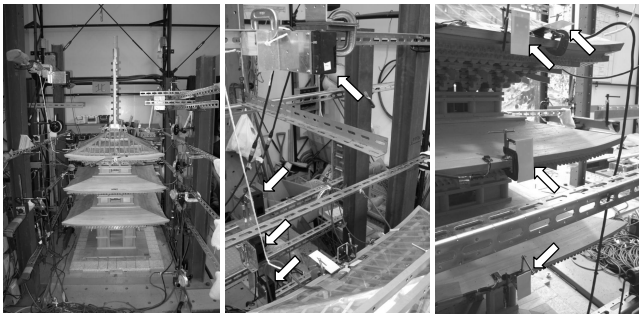


PHOTO 4.1 BOTTOM LIFTED UP (MODEL [B] +1/30)

5. FREE VIBRATION TEST

5.1 Test System

Fig.5.1 and Photo.5.1 show the system of the free vibration test. The model was loaded by pulling a wire attached to it. The targets of the drift angle at the base of the *sorin* are the same as the horizontal load test. After cutting the wire, free vibration of the model was observed. The vibrations of displacement were measured with 6 laser displacement meters as shown in Fig.5.1 and Photo.5.1-B, C. The frequency of sampling is 200Hz, and the duration of the measurement is 8sec. from an instant before cutting the wire.



A: WHOLE SYSTEM B: LASER DISPLACEMENT C: LASER RECEPTOR

PHOTO. 5.1 SYSTEM OF FREE VIBRATION TEST

5.2 Wave Form

Figs.5.2, 5.3, 5.4, show the observed free vibrations of each drift angle of each model. These figures show the frequencies and damping factors from first to third waves of the third floor and the top of the *sorin* with dotted lines, which are obtained from the peaks of each wave. The waves of the third floor and the top of the *sorin* are assumed to represent the waves of the building and the *shin-bashira*.

Model [C]

As shown in Fig.5.2, the frequencies and phases of the waves of building are different from that of the *shin-bashira*. These differences become smaller with an increase of amplitude, and when the amplitude is small the phases of the *shin-bashira* tend to be later than those of the building.

The damping factors of the first wave of the building in the range of 10～20% are high. But, as shown in Fig. 5.2-A, B, the third wave of the building increases compared to the second one, while, the wave of the *shin-bashira* decreases considerably. In terms of the relationship between the phases of the building and the *shin-bashira*, it is thought that the vibration energy of the *shin-bashira* is transferred to the building by collision after the second wave.

Model [B]

As shown in Fig.5.3, as well as Model [C], when the amplitude is small the phases of the *shin-bashira* tend to be later than that of the building. The damping factors of the first wave of the building which is about 10%, is lower than Model [C]. The wave forms of the *shin-bashira*, in comparison with Model [C], are more similar to a triangle than a sine curve, and these waves are damped considerably

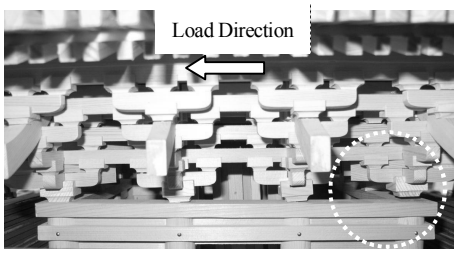


PHOTO 4.2 ROOF OF THIRD FLOOR LIFTED UP (MODEL [C] +1/30)

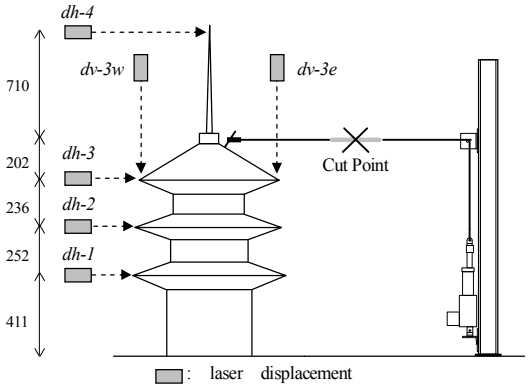
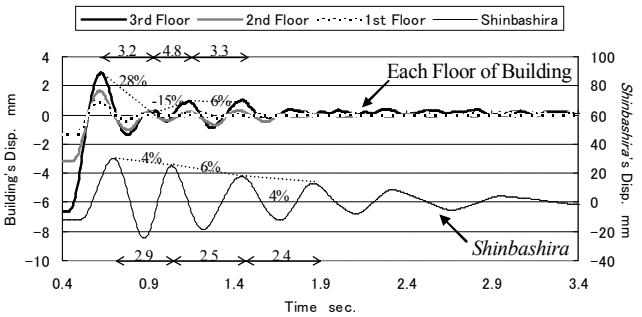
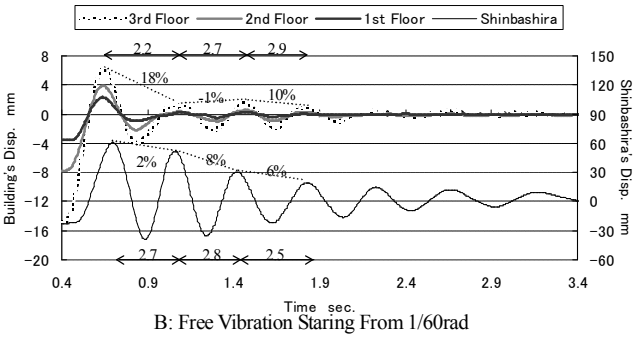


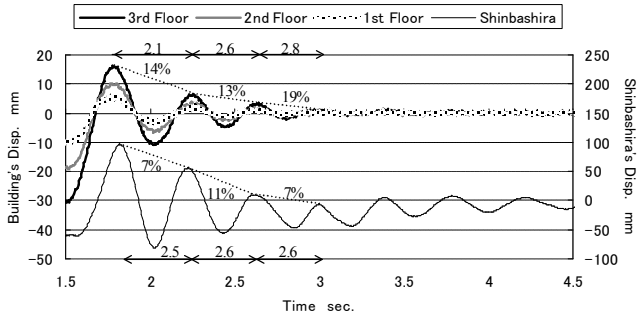
FIGURE 5.1 SYSTEM OF FREE VIBRATION TEST unit: mm



A: Free Vibration Staring From 1/120rad



B: Free Vibration Staring From 1/60rad

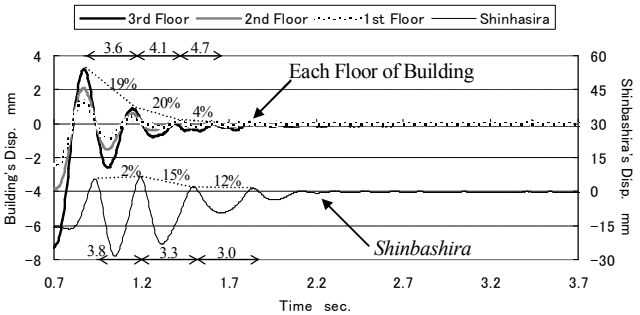


C: Free Vibration Staring From 1/30rad

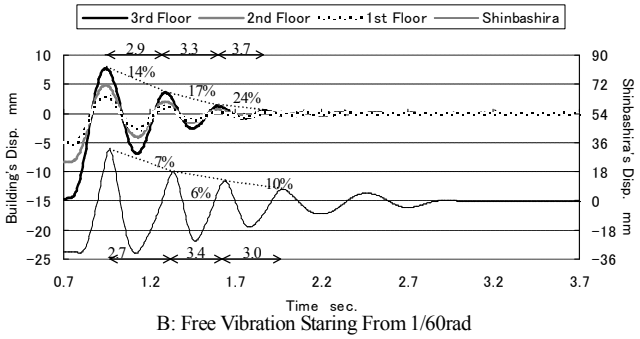
FIGURE 5.2 FREE VIBRATION (MODEL [C])

when the wave's amplitude is smaller than 20mm.

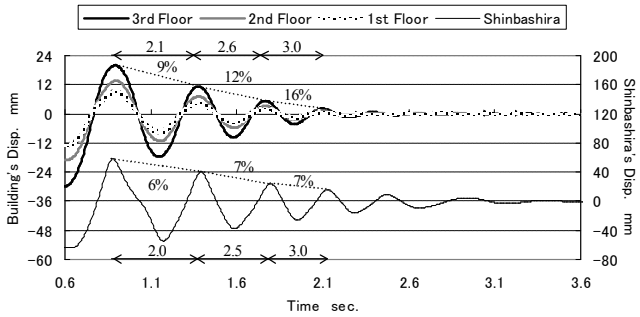
This characteristic of wave form is thought to mean that the restoring force of the joint of the building and *shin-bashira* in the upper portion of the third roof increases considerably after a certain point.



A: Free Vibration Staring From 1/120rad



B: Free Vibration Staring From 1/60rad

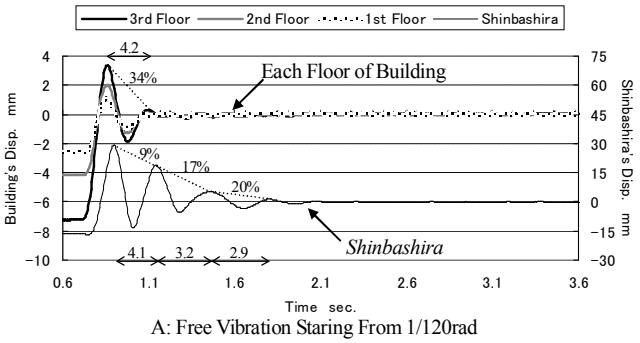


C: Free Vibration Staring From 1/30rad

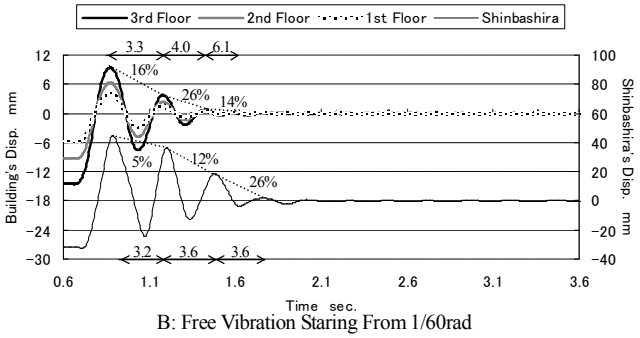
FIGURE 5.3 FREE VIBRATION (MODEL [B])

Model [A]

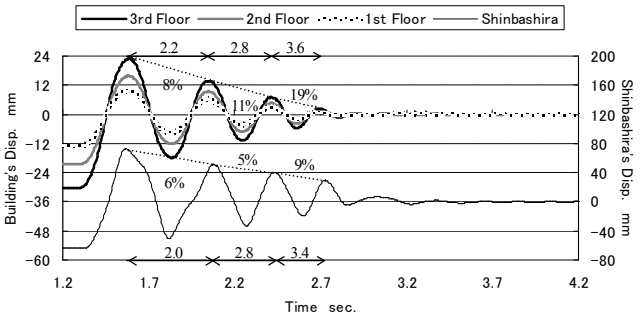
As shown in Fig.5.4, the characteristics of the wave form of Model [A] are similar to those of Model [B].



A: Free Vibration Staring From 1/120rad



B: Free Vibration Staring From 1/60rad



C: Free Vibration Staring From 1/30rad

FIGURE 5.4 FREE VIBRATION (MODEL [A])

5.3 Relationship between Frequency and Amplitude

Figs.5.5 ～ 5.7 show the relationships between frequency and amplitude of each model obtained from all the experiments.

The frequencies of each of the models are around 2Hz, almost the same when the amplitudes of each model are around 20mm (denoted hereafter as "Big Amp.").

The frequencies of all the models become higher with a decrease in amplitude. The frequencies of each of the models are Model [C]: 2.5Hz, Model [B]: 4Hz, Model [A]: 4.7Hz when the amplitudes of each model are around 3mm (denoted hereafter as "Medium Amp."). The frequencies of all the models become considerably higher with a decrease in amplitude when the amplitude is smaller than the Medium Amplitude. The frequencies of each of the models are Model [C]: 3.8Hz, Model [B]: 5Hz, Model [A]: 7Hz when the amplitudes of each model are around 0.5mm (denoted hereafter as "Small Amp.").

The ratios between the frequencies of the Big Amp. and Small Amp. of each of the models are Model [C]: 1.9, Model [B]: 2.5, Model [A]: 3.5.

The approximate two lines of the relationship between frequency and amplitude of each model, which range from the Small Amp. to the Medium Amp. and from the Medium Amp. to the Big Amp., are noted in Fig.5.5～5.7. As shown in these figures, the increase in ratios of frequency of the range from the Small Amp. to the Medium Amp. of all the models are larger than that of the range from the Medium Amp. to the Big Amp..

The main reason for an increase of frequency by a decrease in amplitude is thought to be a decrease of rigidity of each part of the building in Model [C], and an increase of the rocking angle at the bottom of the building in Models [B] and [A].

5.4 Comparison with Frequency of Small Models and Full Size Buildings

Fig.5.8 shows the relationship between the first natural period and the height of the building obtained by micro tremor measurements from previous research. The 23 pagodas with roofs covered by roof tiles are heavy and are denoted by △, the 12 pagodas with roofs covered by another material and therefore with lighter weight are denoted by ◇. All 35 pagodas are noted in Fig.5.8. The approximate line of the relationship between the first natural period and height, which is noted in Fig.5.8 with the dotted line, is represented in Eq.5.1.

$$T = 0.040H \quad \cdots \text{Eq.5.1}$$

T : 1st Natural Period (sec.)

H : Height (m)

The relationships between the first natural period and height of the 18m pagoda, 5.4m pagoda, and 1.8m pagoda, are obtained from the frequency of Models [A], [B], [C] in the Small Amp. with consideration of the similarity rule, and are denoted in Fig.5.8 by ●. As shown in Fig.5.8, the relationships obtained from the model test are similar to that of the full size buildings.

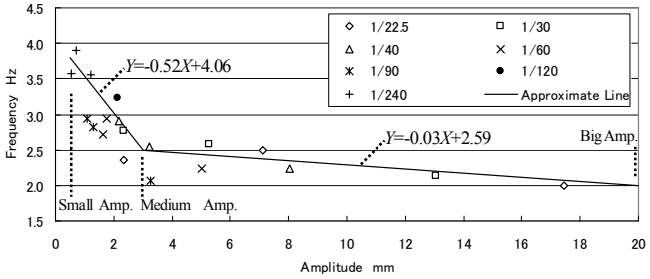


FIGURE 5.5 RELATIONSHIPS BETWEEN FREQUENCY AND AMPLITUDE (MODEL [C])

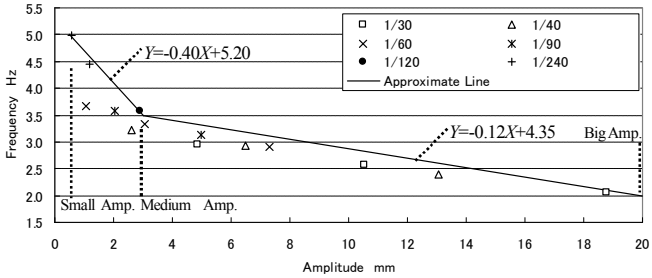


FIGURE 5.6 RELATIONSHIPS BETWEEN FREQUENCY AND AMPLITUDE (MODEL [B])

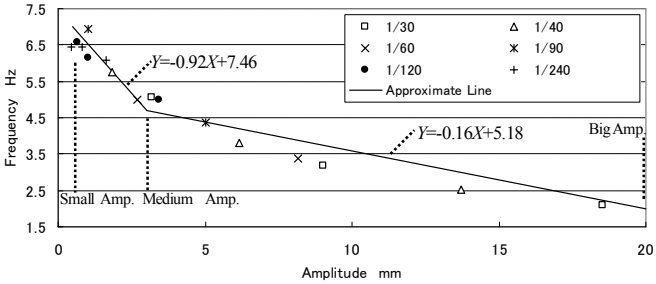


FIGURE 5.7 RELATIONSHIPS BETWEEN FREQUENCY AND AMPLITUDE (MODEL [A])

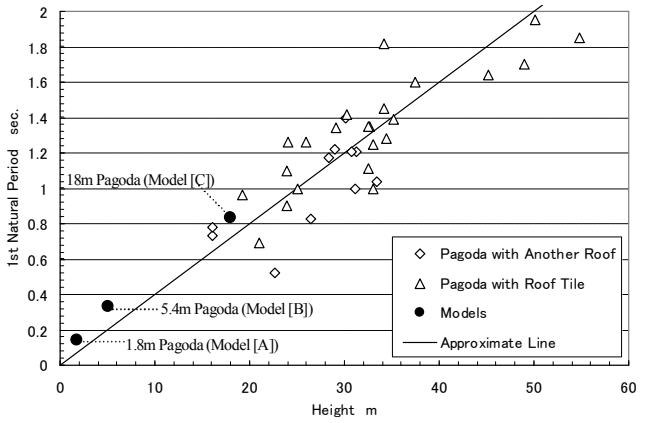


FIGURE 5.8 RELATIONSHIPS BETWEEN 1ST NATURAL PERIOD AND HEIGHT

6. Conclusion

In this study, we performed horizontal load tests and free vibration tests with a 1/10 model of a traditional wooden three-story pagoda. By changing the weight of the model, we simulated the behavior of three different pagodas with heights of 18m, 5.4m and 1.8m. The following results were obtained from these tests:

- When the height of the pagoda is relatively large, the restoring force is greater and more dissipative than that of the smaller one, and the building bends like a bow.
- When the height is small, the restoring force is smaller than that of the above, and the building tilts like a rigid body.
- When the height of the pagoda is relatively large, with an increase of amplitude, frequency of free vibration tends to become smaller, because of a decrease of rigidity.
- When the height is small, with an increase of amplitude, the frequency and damping ratio of free vibration becomes smaller, because of rocking of the building.

Acknowledgements:

The authors acknowledge the support from the Center for Urban Earthquake Engineering (CUEE), Tokyo Institute of Technology. This support made possible successful implementation of the above experimental studies.

References:

Shintaro, O. and Akihiro, K. (2002), "Dynamic Characteristics of Multi-Story Wooden Pagodas", J. Struct. Constr. Eng., AIJ, No.559, pp.47-54.

Kazuki, T., Kaori, F., and the other (2007), "Fundamental Vibration Characteristics of Traditional Timber Five Storied Pagoda by Shaking Table Tests", J. Struct. Constr. Eng., AIJ, No.614, pp.69-75.

Eisuke, N. and Hidekazu, N. (2010), "A Study on the Structural Characteristic of a Traditional Wooden Three Storied Pagoda - Static Loading Test of a Small Scale Model -", J. Archit. Plann. , AIJ, No.652, pp.1631-1638.

Eisuke, N. and Hidekazu, N. (2011), "A Study on the Structural Characteristic of a Traditional Wooden Three Storied Pagoda - Free Vibration Test of a Small Scale Model -", J. Archit. Plann. , AIJ, No.660.

8CUEE CONFERENCE PROCEEDINGS
8th International Conference on Urban Earthquake Engineering
March 7-8, 2011, Tokyo Institute of Technology, Tokyo, Japan

STRUCTURAL COLLAPSE ANALYSIS OF LIGHT-FRAME WOOD SHEAR WALLS UNDER EARTHQUAKE MOTIONS

Weichiang Pang [1], Seyed Masood Hassanzadeh Shirazi [2], John van de Lindt [3], and Shiling Pei [4]

1) Assistant Professor, Department of Civil Engineering, Clemson University, Clemson, SC, USA.
2) Ph.D. Student, Department of Civil Engineering, Clemson University, Clemson, SC, USA.
3) Professor and Garry Neil Drummond Endowed Chair in Civil Engineering, Department of Civil, Construction, and Environmental Engineering, University of Alabama, Tuscaloosa, AL, USA.
4) Assistant Professor, Department of Civil and Environmental Engineering, South Dakota State University, Brookings, SD, USA.
wpang@clemson.edu, shassan@clemson.edu, jwvandelindt@eng.ua.edu, shiling.pei@sdstate.edu

Abstract: Light-frame wood construction makes up the majority of the residential building stock in the North America. Wood-frame buildings have performed relatively well under gravity loadings. However, some of the older wood-frame buildings have suffered costly damage and even structural collapse under moderate earthquake events (e.g. 1994 Northridge Earthquake). In light-frame wood buildings, shear walls act as the main lateral load resisting system. This paper presents the key aspects of modeling collapse of wood-frame shear walls under earthquake motions using nonlinear dynamic analysis. In order to predict the wall behavior from small displacement all the wall to the collapse point, a co-rotational formulation and a large displacement theory are utilized in the formulation of the numerical model. The numerical model specifically accounts for (1) bending and axial elongation of the framing members, (2) separation and bearing contact between the framing members, (3) uplift and anchorage effect of the hold-down devices, (4) shear deformation of the sheathing panels, (5) non-linear shear slip response of the sheathing nails, and (6) second order effect due to gravity loads (P-delta). This numerical model has been coded into computer program. Verification of the numerical model was performed using the results of a shake table collapse test on a light-frame wood garage wall. It has been shown that the model can accurately estimate the displacement time history response and the collapse mechanism of the test wall.

1. INTRODUCTION

Light-frame wood construction is the most common form of construction for residential buildings in the North America. The newer light-frame wood buildings, constructed after the implementation of the 1973 *Uniform Building Code*, have performed fairly well under moderate earthquakes. However, past earthquake events, for example, the 1994 Northridge earthquake, have shown that older light-frame wood buildings are prone to costly damage and even structural collapse. The magnitude 6.7 Northridge earthquake, considered to be a moderate intensity event, resulted in more than $20 billion in property damage making it the costliest earthquake disaster in the United States (US) history (USGS 1996). A recent study estimated that one quarter of the existing wood buildings in the San Francisco Bay Area in the Western US would collapse under a magnitude 7.2 earthquake (ATC 2008). However, the exact collapse mechanism of these at-risk wood buildings is not fully understood at this point. This paper presents a state-of-the-art numerical model that is capable of predicting seismic response and collapse mechanism of the main lateral force resisting system in wood buildings, namely the wood shear walls.

2. SHEAR WALL MODEL FORMULATION

A typical engineered wood shear wall consists of four main components: 1) framing members (studs) 2) sheathing panels, 3) fasteners or nails, and 4) anchorage devices (hold-downs or straps). Older wood buildings are commonly built with non-engineered shear walls, i.e. without hold-down devices and thus are prone to structural collapse during earthquakes. Accurate prediction of the deformation responses of wood shear walls requires accurate modeling of the (1) bending and axial elongation of the framing members, (2) separation and bearing contact between the framing members, (3) uplift and anchorage effect of the hold-down devices, (4) shear deformation of the sheathing panels, (5) non-linear shear slip response of the sheathing nails, and (6) second order effect due to gravity loads (P-delta).

A computer program with graphical user interface, M-CASHEW2 (Matlab - Cyclic Analysis of Wood Shear Walls version 2), was developed for collapse analysis of wood shear walls. The M-CASHEW2 program was developed from its predecessor, a Fortran version of the CASHEW program (Folz and Filiatrault 2001). In the

original CASHEW program, the framing members are modeled as pin-ended rigid elements which do not contribute any lateral stiffness and the in-plane wall stiffness is assumed to be provided solely by the panel-to-frame connections (i.e. sheathing nails). In other words, the CASHEW program is based on small deformation theory and only the pure shear deformation is considered. Past shear wall tests (e.g. Johnston et al. 2006) have shown that the end-post uplift and the anchorage condition have a significant influence on the behavior of shear walls. In order to accurately predict the behavior of wood shear walls all the way to the point of collapse, a co-rotational formulation and large deformation theory are utilized in the formulation of M-CASHEW2 program.

2.1 Frame Element

The wood framing members (studs, sill plates and etc.) are modeled with a two-node co-rotational beam element (herein referred as the *frame element*). Each node of the frame element consists of three degrees of freedom (DOFs): two translations and one rotation (Figure 1).

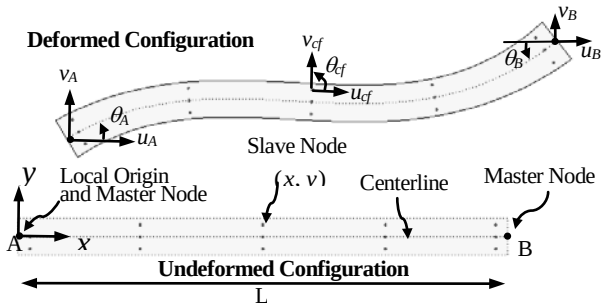


Figure 1: Deformation of a frame element.

The equilibrium of the frame element is given by $\{F_f\}=[K_f]\{D_f\}$ where $\{D_f\}$ is the local element deformation vector and $\{F_f\}$ is the nodal force vector:

$$\{D_f\} = \lfloor u_A \quad v_A \quad \theta_A \quad u_B \quad v_B \quad \theta_B \rfloor^T \tag{1}$$

$$\{F_f\} = \lfloor F_{xA} \quad F_{yA} \quad M_A \quad F_{xB} \quad F_{yB} \quad M_B \rfloor^T \tag{2}$$

The stiffness matrix of the co-rotational beam element, K_f, can be expressed in terms of the summation of the material stiffness matrix, K_e, geometric stiffness matrix, K_g, and initial displacement stiffness matrix, K_d:

$$[K_f] = [K_e] + [K_g] + [K_d] \tag{3}$$

K_e is the well-known elastic stiffness matrix formulated based on the undeformed configuration:

$$K_e = \frac{EI}{L^3}\begin{bmatrix} \frac{AL^2}{I} & 0 & 0 & -\frac{AL^2}{I} & 0 & 0 \\ 0 & 12 & 6L & 0 & -12 & 6L \\ 0 & 6L & 4L^2 & 0 & -6L & 2L^2 \\ -\frac{AL^2}{I} & 0 & 0 & \frac{AL^2}{I} & 0 & 0 \\ 0 & -12 & -6L & 0 & 12 & -6L \\ 0 & 6L & 2L^2 & 0 & -6L & 4L^2 \end{bmatrix} \tag{4}$$

where E, A and I are the elastic modulus, cross-sectional area and moment of inertia, respectively. K_g is the geometric stiffness matrix which accounts for the geometric nonlinearity in the deformed configuration:

$$K_g = \begin{bmatrix} \frac{F_{xB}}{L} & -a_1 & -\frac{M_A}{L} & -\frac{F_{xB}}{L} & a_1 & -\frac{M_B}{L} \\ -a_1 & 2a_2 & a_2 & a_1 & -2a_2 & a_2 \\ -\frac{M_A}{L} & a_2 & a_3 & \frac{M_A}{L} & -a_2 & a_4 \\ -\frac{F_{xB}}{L} & a_1 & -\frac{M_A}{L} & \frac{F_{xB}}{L} & -a_1 & \frac{M_B}{L} \\ a_1 & -2a_2 & -a_2 & -a_1 & 2a_2 & -a_2 \\ -\frac{M_B}{L} & a_2 & a_4 & \frac{M_B}{L} & -a_2 & a_3 \end{bmatrix}$$

$$a_1 = \frac{M_A + M_B}{L^2} \quad , \quad a_2 = \frac{F_{xB}}{10} + \frac{6F_{xB}I}{AL^2} \tag{5}$$

$$a_4 = -\frac{F_{xB}}{30} + \frac{2F_{xB}I}{AL} \quad , \quad a_3 = \frac{2F_{xB}}{15} + \frac{4F_{xB}I}{AL}$$

It should be noted that although the geometric stiffness K_g is formulated based on the deformed configuration, it does not account for the deformed curvature caused by rotations at nodes A and B. Past research have showed that ignoring the deformed curvatures will significantly reduce the accuracy of the analysis when the deformations are large (Zhang and Tong 2008). In this study, the initial displacement matrix, K_d, derived by Zhang and Tong (2008) is employed to account for the effects of the deformed curvature:

$$K_d = \frac{2EI}{L^3}\begin{bmatrix} 0 & 3a_{11} & La_{21} & 0 & -3a_{11} & La_{12} \\ 3a_{11} & 0 & 0 & -3a_{11} & 0 & 0 \\ La_{21} & 0 & 0 & -La_{21} & 0 & 0 \\ 0 & -3a_{11} & -La_{21} & 0 & 3a_{11} & -La_{21} \\ -3a_{11} & 0 & 0 & 3a_{11} & 0 & 0 \\ La_{21} & 0 & 0 & -La_{21} & 0 & 0 \end{bmatrix} + \cdots$$

$$-\frac{EA}{30L}\begin{bmatrix} 0 & 3a_{11} & La_{41} & 0 & -3a_{11} & La_{14} \\ 3a_{11} & 0 & 0 & -3a_{11} & 0 & 0 \\ La_{41} & 0 & 0 & -La_{41} & 0 & 0 \\ 0 & -3a_{11} & -La_{41} & 0 & 3a_{11} & -La_{14} \\ -3a_{11} & 0 & 0 & 3a_{11} & 0 & 0 \\ La_{14} & 0 & 0 & -La_{14} & 0 & 0 \end{bmatrix} \tag{6}$$

$$a_{11} = \theta_A + \theta_B \quad , a_{21} = 2\theta_A + \theta_B \quad , a_{12} = \theta_A + 2\theta_B$$
$$a_{41} = 4\theta_A - \theta_B \quad , a_{14} = 4\theta_B - \theta_A$$

The presented frame element model with co-rotational formulation is suited for nonlinear collapse analysis of shear walls under large deformations.

2.2 Frame Element Shape Functions

The wood shear wall models developed in previous

research (e.g., Folz and Filiatrault 2001, Pei and van de Lindt 2008) utilize centerline modeling approach which ignores the width of the framing members. While the centerline modeling approach is reasonable for most applications, it may not provide accurate estimates of shear wall behavior under large deformations. In M-CASHEW2, a novel geometric model which explicitly considers the actual dimensions of the framing members is employed (Figure 2). Unlike the centerline modeling approach, the geometric model does not allow two frame members to occupy the same space. This modeling capability allows the use of contact element to explicitly model the bearing contact and separation of the framing members as observed in the actual shear wall tests. The contact model will be discussed in a later section.

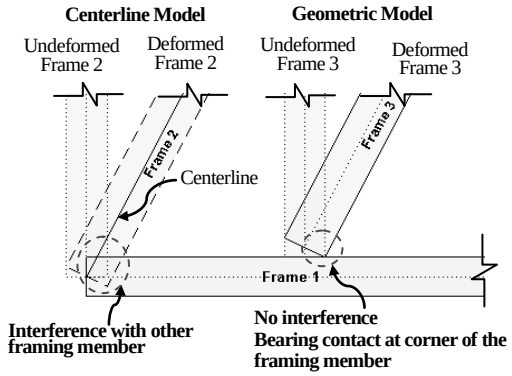


Figure 2: Illustration of centerline and geometric models.

The geometric model is derived using a set of shape functions. Consider the local deformations of a generic point, *slave node*, on a frame with initial local frame coordinates (*x*,*y*) as shown in *Figure 1*. The deformations of the slave node can be expressed in terms of the deformations of the *master nodes* A and B:

$$\{D_{cf}\} = \lfloor N_f \rfloor \{D_f\} \tag{7}$$

where, $D_{cf} = \lfloor u_{cf},\ v_{cf},\ \theta_{cf} \rfloor^T$ is the displacement vector of the slave node on the frame and N_f is the interpolation matrix (i.e. shape functions expressed in a matrix format). Using consistent deformation method, the interpolation matrix considering the width effect is derived and is given in equation (8):

$$N_f = \begin{bmatrix} N_{11}(x) & -N_{32}(x)y & -N_{33}(x)y & N_{14}(x) & -N_{35}(x)y & -N_{36}(x)y \\ 0 & N_{22}(x) & N_{23}(x) & 0 & N_{25}(x) & N_{26}(x) \\ 0 & N_{32}(x) & N_{33}(x) & 0 & N_{35}(x) & N_{36}(x) \end{bmatrix} \tag{8}$$

$$N_{11}(x) = 1 - r \qquad N_{14}(x) = r$$
$$N_{22}(x) = 2r^3 - 3r^2 + 1 \qquad N_{25}(x) = 3r^2 - 2r^3$$
$$N_{23}(x) = (r^2 - 2r + 1)x \qquad N_{26}(x) = (r^2 - r)x$$
$$N_{32}(x) = (r^2 - r)\,6/L \qquad N_{35}(x) = (r - r^2)\,6/L$$
$$N_{33}(x) = 3r^2 - 4r + 1 \qquad N_{36}(x) = 3r^2 - 2r$$

where, $r = x/L$. The use of interpolation matrix allows one to condense the nail DOFs (slave nodes) into just six DOFs (master nodes) regardless of the nail spacing or the total number of nails on a frame thus achieving high computation efficiency.

2.2 Panel Element

The sheathing of shear walls is modeled with a five degrees-of-freedom (DOFs) co-rotational rectangular *panel element*: one rigid body rotation, θ_p, two rigid body translations, u_p and v_p, and two in-plane shear deformations, μ_p and γ_p (*Figure 3*).

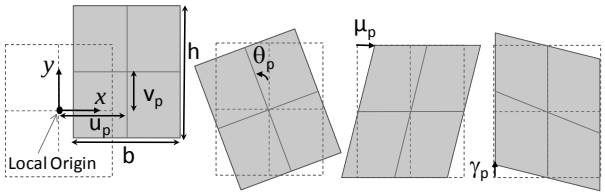


Figure 3: Five DOFs panel elements.

The equilibrium of the panel element is given by $\{F_p\}=[K_p]\{D_p\}$, where$\{D_p\}$ is the local panel deformation vector, $\{F_p\}$ is the local force vector, and K_p, is the stiffness matrix of the panel element:

$$\{D_p\} = \lfloor u_p \quad v_p \quad \mu_p \quad \gamma_p \quad \theta_p \rfloor^T \tag{9}$$

$$\{F_p\} = \lfloor F_{xp} \quad F_{yp} \quad V_{xp} \quad V_{yp} \quad M_p \rfloor^T \tag{10}$$

$$K_p = \begin{bmatrix} 0 & 0 & 0 & 0 & 0 \\ 0 & 0 & 0 & 0 & 0 \\ 0 & 0 & \dfrac{2Gbt}{h} & 0 & 0 \\ 0 & 0 & 0 & \dfrac{2Ght}{b} & 0 \\ 0 & 0 & 0 & 0 & 0 \end{bmatrix} \tag{11}$$

G, *b* and *h* are the shear modulus, width and height of the sheathing panel, respectively.

2.3 Panel Element Shape Functions

Similarly, the deformations of a generic connection point (slave node) on the panel can be determined using an interpolation matrix:

$$\{D_{cp}\} = \lfloor N_p \rfloor \{D_p\} \tag{12}$$

where, $D_{cp} = \lfloor u_{cp},\ v_{cp},\ \theta_{cp} \rfloor^T$ is the deformation vector of the connection point on the panel and $\lfloor N_p \rfloor$ is the interpolation matrix (a set of shape functions):

$$N_p = \begin{bmatrix} 1 & 0 & \dfrac{2y}{h} & 0 & -y \\ 0 & 1 & 0 & \dfrac{-2x}{b} & x \\ 0 & 0 & 0 & 0 & 1 \end{bmatrix} \tag{13}$$

2.4 Connection Elements

Three types of connection elements are employed to model the partial composite action between the shear wall components (i.e. framing members and sheathing panels): panel-to-frame (P2F), frame-to-frame (F2F), and panel-to-panel (P2P) connections (*Figure 4*). The P2F connectors are used for modeling the behavior of the

sheathing nails while the F2F connectors are utilized for modeling the behavior of the framing nails, anchor bolts, hold-down devices, and bearing contact between the framing members. The P2P connectors serve three purposes: (1) to model the bearing contact between the panels, (2) to model the contact between the panel and ground, and (3) to model non-rectangular sheathing panels by connecting multiple rectangular panels together using rigid P2P connections.

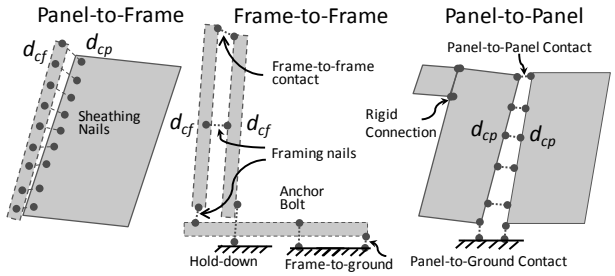


Figure 4: Connection elements.

Each P2F, F2F or P2P connection element is represented by a two-node zero-length element with three uncoupled springs: one rotational and two translational springs (*Figure 5*). Each spring can be assigned with the properties of one of the seven spring models currently available in the M-CASHEW2 program: 1) linear spring, 2) bilinear hysteretic spring, 3) modified Stewart (MSTEW) hysteretic spring (Folz and Filiatrault 2001), 4) evolutionary parameter hysteretic (EPHM) spring (Pang et al. 2007), 5) bearing contact spring, 6) nonlinear hold-down spring (HD1), and 7) nail withdrawal spring (HD2).

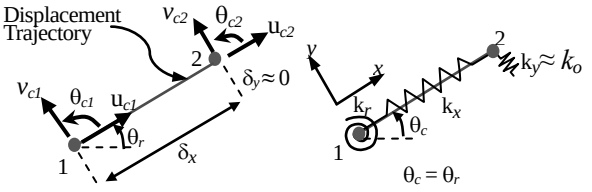


Figure 6: Oriented connection model.

The stiffness matrix of the connector in local coordinate system is:

$$k_c = \begin{bmatrix} k_x & 0 & 0 \\ 0 & k_y & 0 \\ 0 & 0 & k_r \end{bmatrix} \tag{14}$$

where, k_x and k_y are the stiffness of the translational springs, and k_r is the stiffness of the rotational spring.

2.5 Oriented Sheathing Nail Model

The two-node panel-to-frame (P2F) connection is used to model the sheathing nails of wood shear walls. In *Figure 5*, node 1 represents the location of the nail head in the panel and node 2 represents the location of the nail shank in the frame. The rotational spring of a P2F connection is assigned with zero stiffness and the translational springs are assigned with either the MSTEW or EPHM spring. Previous research have shown that the non-oriented P2F spring model tends to overestimate the stiffness and strength of shear walls under reversed cyclic loading (Judd, and Fonseca 2005). Therefore, in M-CASHEW2, an oriented connection model is utilized to model the sheathing nails. The stiffness matrix of the oriented P2F connector in global coordinate system, K_c, is:

$$[K_c] = [R][k_c][R]^T \tag{15}$$

where, R is the transformation (rotation) matrix:

$$R = \begin{bmatrix} \cos\theta_c & -\sin\theta_c & 0 \\ \sin\theta_c & \cos\theta_c & 0 \\ 0 & 0 & 1 \end{bmatrix} \tag{16}$$

$\theta_c = \text{atan}(\delta_y/\delta_x)$ is the angle measured from the global x-axis to the displacement trajectory (*Figure 5*). Since the orientation of the connection element, θ_c, is updated after each time step (or increment), the y-spring of the connection does not contribute to the wall stiffness. The y-spring is only for maintaining stability in the transverse direction of the displacement trajectory.

2.6 Contact Spring Model

For modeling the contact (bearing) and separation (gap) phenomena between the shear wall components, a nonlinear hysteretic contact spring element is introduced. This contact element is used to model the interface (1) between the frames, (2) between the sheathing panels, (3) between the frames and foundation, and (4) between the panels and foundation. Figure 6 depicts the force-displacement response of a contact element and its mathematical representation is given in equation(17).

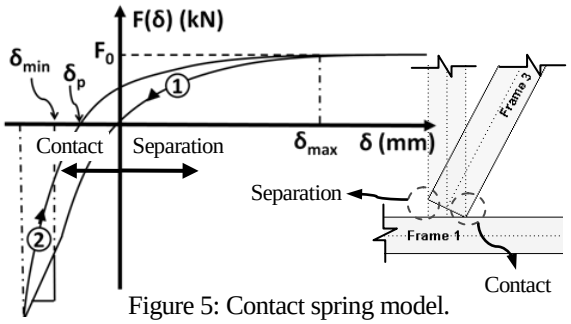


Figure 5: Contact spring model.

$$F(\delta) = \begin{cases} F_o(1-e^{-\frac{\delta_{min}}{\delta_u}}) + k_o e^{-\frac{\delta_{min}}{\delta_u}}(\delta - \delta_p - \delta_{min}) & \delta - \delta_p \le \delta_{min} \\ F_o(1-e^{-\frac{\delta+\delta_p}{\delta_u}}) & \delta_{min} < \delta - \delta_p < \delta_{max} \\ F_o(1-e^{-\frac{\delta_{max}}{\delta_u}}) + k_o e^{-\frac{\delta_{max}}{\delta_u}}(\delta - \delta_p - \delta_{max}) & \delta - \delta_p \ge \delta_{max} \end{cases} \tag{17}$$

The modeling parameters are:

F_o = asymptotic separation force
δ_u = tolerance for contact displacement
δ_{min} = minimum compression displacement
δ_{max} = maximum separation displacement
r_c = permanent bearing deformation ratio

where, $K_o = F_o/\delta_u$ is the initial stiffness and $\delta_p = \min(r_c\delta)$ is a

hysteretic parameter which tracks the permanent bearing deformation (Figure 6). The contact element is formulated such that when gap or separation occurs, the force and stiffness of the element is small enough to be considered zero. In contrary, when contact occurs, the element will respond with a high tangent stiffness to simulate the high reaction force of bearing contact.

2.7 Hold-down Model

A specialized nonlinear hysteretic hold-down spring was developed to model the anchorage effects of hold-down devices (Figure 7). The hold-down spring simulates the uplift force in the hold-down device and uplift deformation of the end studs. This hysteretic model consists of ten parameters:

K_o= initial stiffness,
F_o=asymptotic ultimate tensile force,
F_i = maximum compression force,
δ_u = uplift at maximum tensile force,
r_1 = asymptotic ascending backbone stiffness ratio,
r_d= descending backbone stiffness ratio,
r_u = unloading stiffness ratio,
r_ℓ= reloading stiffness ratio,
r_r = reloading uplift ratio,
r_i= stiffness ratio of line with F_i intercept, $r_i k_o \delta + F_i$

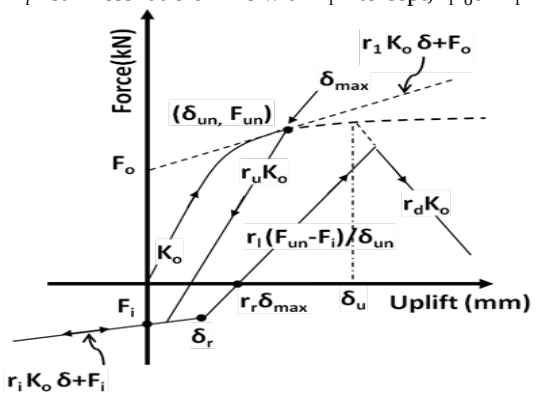


Figure 7: Nonlinear hold-down spring model.

2.8 Nail Withdrawal Model

End nails are commonly used for fastening two framing members together at a 90 degree angle. The end nail connection is an inherently weak connection in withdrawal because the load is applied parallel to the length of the nail. However, it has a good shear resistance under transverse loads. *Figure 8* shows a schematic sketch of an end nail connection modeled using a pair of orthogonal and an translational springs. The withdrawal spring with stiffness k_x in local coordinate is oriented parallel to the length direction of the framing nail (x-spring) and the nonlinear MSTEW or EPHM spring is used to model the shear behavior of the end nail (y-spring). The contact springs are shown at the corners of the stud and are used for modeling the separation and contact between the framing members.

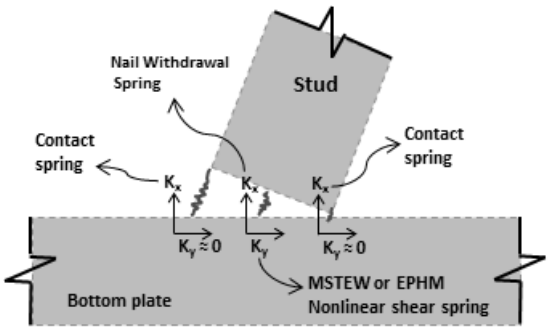


Figure 8: End nail connection model.

3. SHAKE TABLE WALL TEST

The test specimen used to verify the numerical model was a light-frame wood garage wall with a length of 4.52 m, a height of 2.43 m, and an opening width of 3.3 m. Figure 9 shows a sketch of the garage wall. All studs were 2x6 Hem-Fir and sheathing was 12 mm (15/32 inch) thick Oriented Strand Board (OSB). The framing members were assembled using 16d common nails and sheathing nails were 8d common gun-driven nails spaced at 152 mm (6 in.) on the sheathing panel edges and 304 mm (12 in.) on the interior. Two nominally identical specimens were tested simultaneously. The two walls were spaced approximately 2.2 m apart to provide stability and limit accidental torsion since the shake table was uni-axial. Each wall had a tributary seismic weight of 18.2 KN (4.1 kips) at top of the wall. Figure 10 shows the test setup and seismic weight at top of the walls. For safety purpose, the seismic weight was connected to the test setup frames by a set of straps.

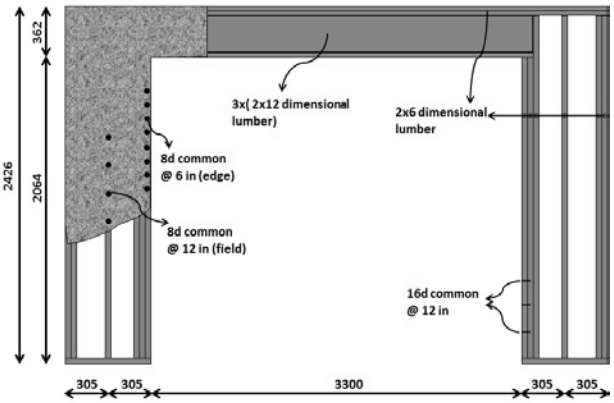


Figure 9: Tested garage shear wall.



Figure 8: Test setup and seismic weight at top

Two historical ground motions that known to collapse wood structures when they occurred were chosen and used during shake table testing of the garage walls. The first ground motion was 100% 1995 Kobe earthquake measured at Akashi station (Test 1), and the second was 85% of the Rinaldi record from the 1994 Northridge earthquake (Test 2). The slight reduction in the seismic intensity to 85% for the Rinaldi record was necessary due to the shake table stroke length limit of 0.5 m. The test started with the Kobe-Akashi ground motion record and this record shook the garage walls to near collapse. At the end of the Kobe-Akashi test, significant damage was observed at the top corners of the garage walls (Figure 11) and sheathing nails were beginning to pull out. With a residual of 0.7%, the walls were still able to support the gravity load. However, they were severely damage and at the verge of incipient collapse.

After the Kobe-Akashi test, the walls were subjected to 85% of Northridge-Rinaldi record. Since the walls were already severely damaged after the first test, collapse occurred almost immediately following the first significant displacement pulse. The failure mechanisms of the specimen were a combined effect of sheathing nail withdrawal, framing nail withdrawal, and damage to sheathing panel near the opening corners.



Figure 11: Damage at the top corner of the garage wall.

4. MODEL VERIFICATION

The M-CASHEW2 was used to model the test wall. Since the test consisted of two nominally identical garage walls, only one wall was modeled numerically. The model consisted of eighteen 6-DOF frame elements and five 5-DOF shear panel elements, resulted in a total of 133 DOFs.

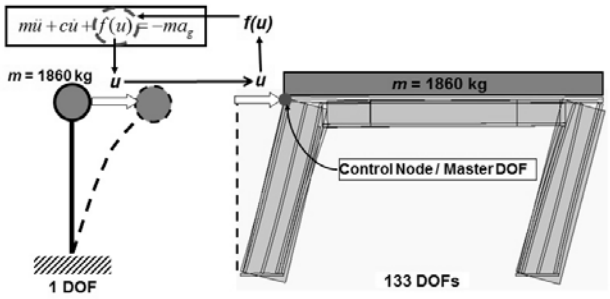


Figure 12: Sub-structuring approach for nonlinear dynamic time history analysis.

A sub-structuring approach was employed in nonlinear dynamic time history analysis to condense the 133 DOFs of the detailed wall model into one master DOF, horizontal displacement at the top of the wall, which can be used to adequately describe the global behavior of the shear wall (Figure 12). Equilibrium in the equation of motion is maintained only for the master DOF. The recorded table accelerations were used as the input ground motion for the dynamic time history analysis.

The 8d common sheathing nails were modeled using the Evolutionary Parameter Hysteretic Model (EPHM) (Pang et al. 2009) (Figure 13) while the Modified Stewart Hysteretic Model (MSTEW) (Folz and Filiatrault 2001) was utilized to describe the shear slip response of the 16d common framing nails. (Figure 14)

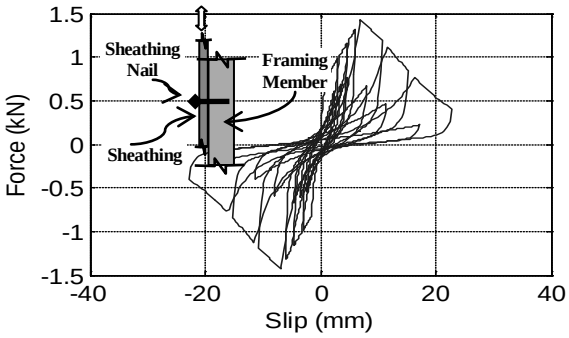


Figure 9: 8d common nails sheathing to framing

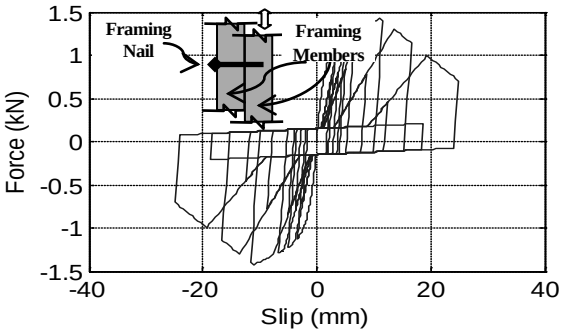


Figure 10: 10d common nails framing to framing.

Two hysteretic elements, a nonlinear hold-down spring (designated as HD1) and a contact element, were utilized to characterize the behavior of each hold-down connection. The HD1 spring was used for describing the uplift response of the hold-down and the contact element was used for modeling the bearing deformation between the end post and the sill plate (Figure 15).

Similarly, the same modeling technique was also employed to model the bearing contact and withdrawal responses of the end nail connections (Figure 16).

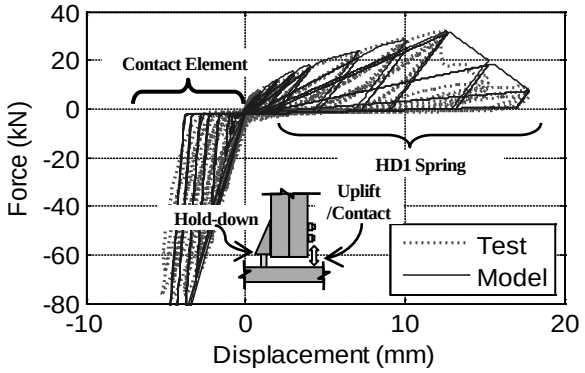


Figure 17: Hysteretic model for hold-down uplift.

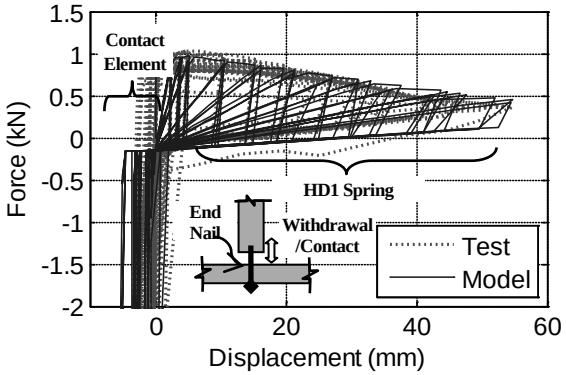


Figure 16: Hysteretic model withdrawal nail.

Bilinear spring elements are utilized to connect two pieces of rectangular panels together (Figure 17). This modeling feature allows the numerical model to capture the moment failure observed at the corner of the sheathing panels of the test walls (Figure 11). Figure 17 shows the model predicted deformed shape at the corner of the garage wall at the end of the dynamic time history analysis. As can be seen, the model was able to reproduce the failure mechanisms observed in the shake table test (i.e. moment failure of the sheathing panels and separation of the framing members).

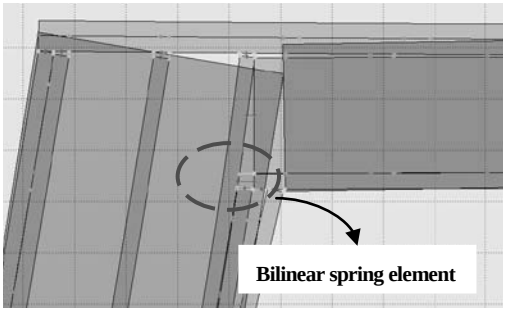


Figure 14: Corner of garage wall (Deformed shape).

5. COMPARISON OF TEST AND MODEL RESULTS

5.2 Hysteresis loops

Figure 18 presents the shake table test and M-CASHEW2 hysteresis loops. The displacements and restoring forces of the model were obtained directly from the M-CASHEW2 program. The forces of the test hysteresis were computed by multiplying the roof accelerations by the tributary seismic weight for one wall. Note that these forces include the restoring forces due to wall deformation in addition to the inherent damping forces. As can be seen, the model is able to reproduce the overall response of the test hysteresis. Clearly it does not reproduce the exact hysteresis, but the overall hysteretic envelopes appear to be well overlaid.

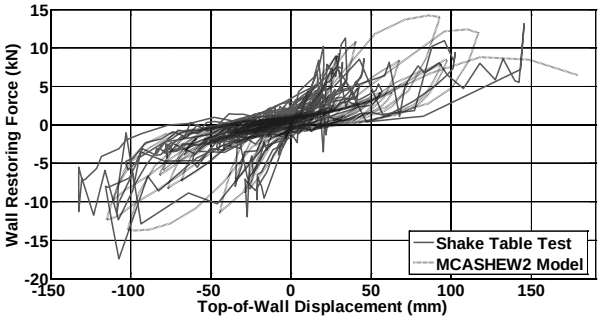


Figure 15: Test and M-CASHEW2 hysteresis loops.

5.1 Displacement Time Histories

Figure 19 shows the inter-story displacement response of the first test with the Kobe-Akashi ground motion. The test displacement time history (Figure 14) shows a residual deformation of about 17 mm (0.7 inches) at the end of the first test. The model predicted peak displacement was 117 mm (4.6 inches), which is close to the test peak displacement 132 mm (5.2 inches) corresponds to 5.5% inter-story drift.

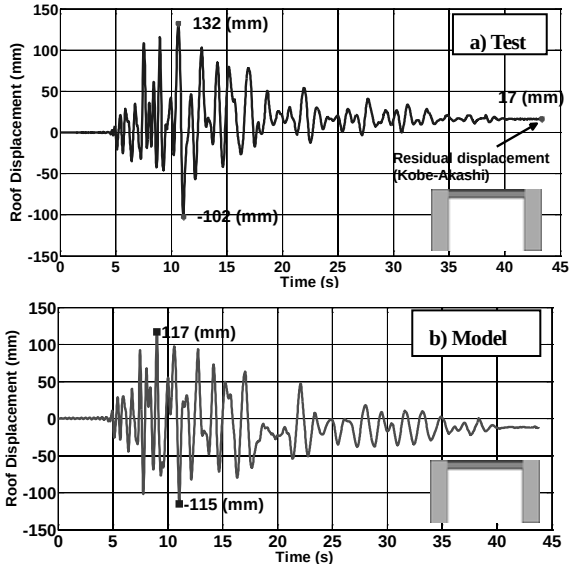


Figure 13: Displacement time histories for test 1 (100% Kobe Akashi) and Model (M-CASHEW2).

5.3 End Post Uplift Time Series

Although hold-downs were installed in the garage walls, significant rocking of wall piers was observed during

the test. Figures 20-23 show the time series of the test and model predicted end post uplifts. The peak test and model uplift responses are identified by square and diamond markers, respectively.

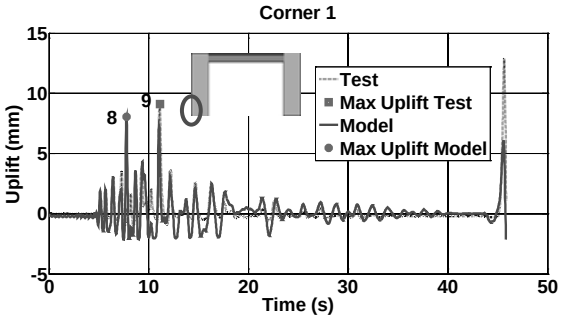


Figure 18: Comparison of test and model uplift

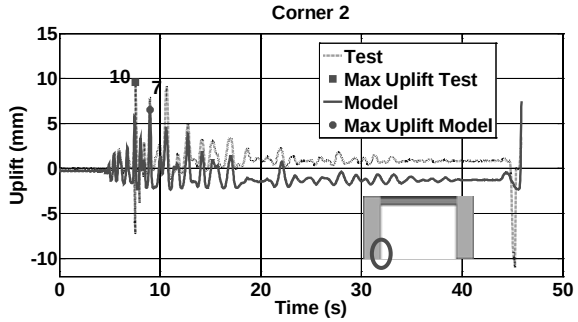


Figure 21: Comparison of test and model uplift

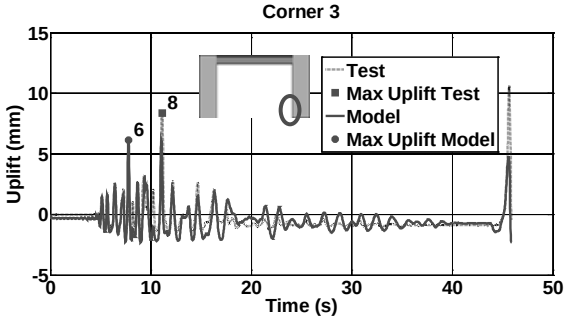


Figure 22: Comparison of test and model uplift

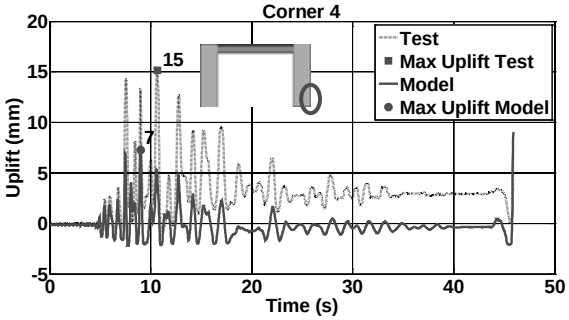


Figure 23 Comparison of test and model uplift

In general, the model was able to reproduce the overall uplift responses of the end posts, especially at corners 1 and 3 with approximately 10 to 20% errors. However, at corner 4, noticeable difference between the test and model predicted uplifts can be seen. The model under predicted the peak uplift at corner 4 by about 50%. This could be attributed to the inherent variability in the uplift resistance or stiffness of the hold-down devices. The model assumed all four hold-downs were identical with the same stiffness and strength. However, examining the uplift time series responses seems to suggest that hold-down at corner 4 was weaker than the other three hold-downs. The test recorded uplift response indicates that there was a gap or slack in hold-down number 4.

6. CONCLUSIONS

The formulation of a detailed mechanistic wood shear wall model which accounts for the non-linear shear slip response of the sheathing nails, bending and axial elongation of the framing members, separation and bearing contact between the framing members, uplift and anchorage effect of the hold-down devices, shear deformation of the sheathing panels, and second order effect due to gravity loads (P-delta) has been developed and coded into a computer program (M-CASHEW2). To verify the numerical model, the M-CASHEW2 program was used to analyze the results of a shake table collapse test of a light-frame wood garage wall. The model predicted peak displacements for Test 1 are within ±15% of the measured values; underpredicting the positive displacement by 11% and overpredicting the negative displacement by 13% and the peak end post uplifts to within +/- 15% (expect for one hold-down). Additionally, it has been shown that the detailed wall model created using M-CASHEW2 is able to predict the failure sequence and mechanism of the wall components all the way to the point of collapse.

According to the analytical and experimental results, the collapse inter-story drift limit for this type of garage walls is more than 6%. The failure mechanisms of the test walls were a combined effect of sheathing nail withdrawal, framing nail withdrawal, and damage to sheathing panel near the opening corners. These governing failure mechanisms observed during the shake table test were also captured by the computer program. Finally, it was observed that variability in the hold-down stiffness has a significant influence on the prediction of the end post uplifts. In order to accurately capture the variability of the shear wall responses, the inherent variability of wood shear wall framing components (frames, panels, nails and etc) should be included in the numerical model. This will be investigated in future studies.

References

Applied Technology Council (ATC) (2008). "Here Today – Here Tomorrow, Earthquake Safety for Soft-Story Buildings." San Francisco Department of Building Inspection, San Francisco, CA.

Dolan, J. D., and Foschi, R. O. (1991), "Structural analysis model for static loads on timber shear walls." *Journal of Structural Engineering*, American Society of Civil Engineers,, **117**(3):851–861.

Folz, B., and Filiatrault, A. (2001), "Cyclic analysis of wood shear

walls.", *Journal of Structural Engineering*, American Society of Civil Engineers, **127**(4):433–441, 2001.

Johnston A.R., Dean P.K., Shenton H.W. (2006), "Effects of Vertical Load and Hold-Down Anchors on the Cyclic Response of Wood Framed Shear Walls." *Journal of Structural Engineering*, American Society of Civil Engineers, **132**(9): 1426-1434.

Judd, J.P. and Fonseca, F.S. (2005), "Analytical Model for Sheathing-to-Framing Connections in Wood Shear Walls and Diaphragms." *Journal of Structural Engineering*, American Society of Civil Engineers, **131**(2):345-352, 2005.

Pang, W.C., Rosowsky, D.V., Pei, S. and van de Lindt, J.W. (2007), "Evolutionary Parameter Hysteretic Model for Wood Shear Walls," *Journal of Structural Engineering*, American Society of Civil Engineers, **133**(8):1118-1129.

Pei S. and van de Lindt J. W. (2008), "Development of seismic analysis package for woodframe structures (SAPWood)" NEESWood Report NW-04, Colorado State University.

USGS (1996), *USGA Responses to an Urban Earthquake*, Northridge 1994, Open File Report 96-263.

White, M. W., and Dolan, J. D.: (1995), "Nonlinear shear-wall analysis." *Journal of Structural Engineering*, American Society of Civil Engineers,, **121**(11): 1629–1635.

Zhang, N. and Tong,. G,: A (2008), "Co-rotational updated Lagrangian formulation for a 2D beam element with consideration of the deformed curvature.," *Journal of Zhejiang University*, SCIENCE A, **9**(11):1480-1489.

8CUEE CONFERENCE PROCEEDINGS
8th International Conference on Urban Earthquake Engineering
March 7-8, 2011, Tokyo Institute of Technology, Tokyo, Japan

EARTHQUAKE RESPONSE ANALYSIS OF TIMBER STRUCTURE WITH PASSIVE CONTROL SCHEME BY DETAILED FRAME MODEL

Kazuhiro Matsuda[1], Kazuhiko Kasai [2], and Hiroyasu Sakata[3]

1) Assistant Professor, Structural Engineering Research Center, Tokyo Institute of Technology, Japan
2) Professor, Structural Engineering Research Center, Tokyo Institute of Technology, Japan
3) Associate Professor, Structural Engineering Research Center, Tokyo Institute of Technology, Japan
matsuda@serc.titech.ac.jp, kasai@serc.titech.ac.jp, hsakata@serc.titech.ac.jp

Abstract: This paper proposes an accurate, member-by-member analytical model for timber structures having energy dissipation walls and/or plywood shear walls. Various member joints are modeled by using nonlinear spring elements whose properties derived from numerous test results, and model's schemes are described in detail. The analyses were found to reproduce both local and global responses obtained from cyclic loading tests and shaking table tests of a variety of one-story mult-span timber frames. Moreover, difference between single wall and linked walls, difference of seismic response by variation of damper and nail volume are discussed.

1. INTRODUCTION

It is said that approximately 10 million wooden houses are insufficient for earthquake resistant in Japan, and those houses need to be reinforced immediately. Moreover, to design new wooden houses to be resistant to earthquakes, it is important to investigate rational methods applying the passive control scheme to wooden houses. In order to mitigate the earthquake response and damage of wooden houses, an energy dissipation wall was developed (Kasai and Sakata et al. 2005, Appendix 1) and a lot of experimental studies using the wall were carried out, such as dynamic cyclic loading tests of the energy dissipation walls (Matsuda et al. 2008), shaking table tests of 1-story and 2-story wooden frames (Sakata et al. 2007 and Matsuda et al. 2007), and so on.

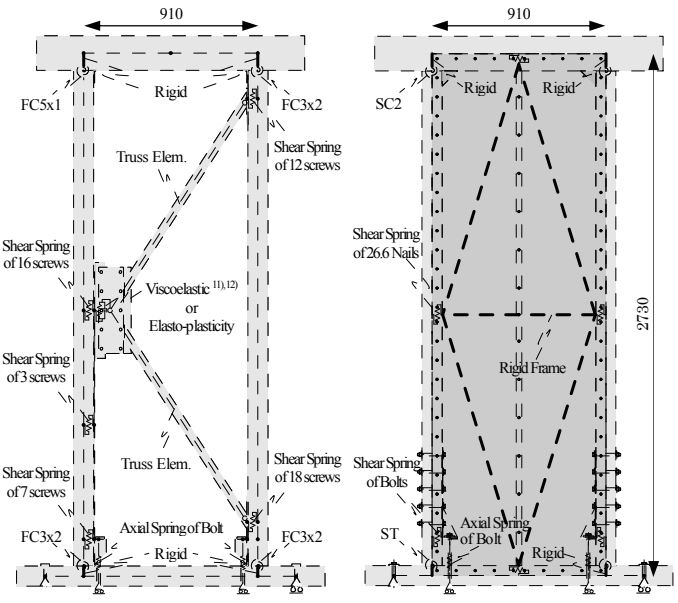
However, analytical studies need to be carried out to develop more effective energy dissipation wall and to propose the design method. In particular, a framed analysis is effective to study their local behavior. Therefore the objective of this study is to propose an accurate, member-by-member analytical model for timber structures having energy dissipation walls and/or plywood shear walls.

To make the model, modeling the joint is important extremely. In this study, various member joints are modeled by using nonlinear spring elements whose properties derived from numerous test results, and model's schemes are described in detail. Also the accuracy of the framed analytical model is confirmed by the comparison between the analytical results and many test results. In addition, the difference of seismic response by variation of damper and nail volume are discussed.

2. ANALYTICAL FRAME MODEL

2.1 Outline of Analytical Frame Model

Fig. 1(a) illustrates frame model of the energy dissipation wall and the plywood shear wall. Basically linear beam elements which have same condition to the test members, are arranged in the center of the members. The column and horizontal member are connected by the joint elements which consist of three springs: axial spring, shear



(a) Energy Dissipation Wall (b) Plywood Shear Wall

Fig. 1 Detail of Frame Model

spring and rotational spring (see Fig. 2). The area between the beam edge and the column edge is assumed rigid and the steel pipe brace is set for truss elements. There are reaction springs under the sill (see Fig. 3). Viscoelastic element which was proposed by Kasai et al. (2001, 2002), or elasto-plasticity element are arranged at the point between the intersection of the braces and the steel plate. Basically following equations are used in viscoelastic element.

$$\tau(t) + aD^{\alpha}\tau(t) = G\,[\gamma(t) + bD^{\alpha}\gamma(t)] \qquad (1)$$

$$a = a_{ref}\lambda^{\alpha} \quad , \quad b = b_{ref}\lambda^{\alpha} \qquad (2a,b)$$

$$\lambda = \exp[-p_1(\theta - \theta_{ref})/(p_2 + \theta - \theta_{ref})] \qquad (3)$$

Where D^{α} is operator of fractional derivative, α is order of fractional derivative. a, b and G are parameter to depend on frequency, a_{ref} and b_{ref} are parameter to depend on temperature.

There are two types of joint element: FC3x2, FC5x1 (see Table 1). The L-type metal includes "FC5" and "FC3" which indicate the number of screws on the column. "x1" and "x2" indicate the number of the metals. Detail of setting the each spring will be described in section 3.2. The shear springs between the two nodes are set depending on shear performance of per screw which is set from the test of the joint, because the steel plate is screwed on column by a number of screws. Also the axial springs of bolt are set from the test of joint.

Fig. 1(b) illustrates frame model of the plywood shear wall. Basically constructing method of the exterior frame is same as energy dissipation wall. Therefore linear beam elements which have same condition to the test members, are arranged in the center of the members. Each beam elements are connected by the joint elements which consist of three springs. There are two types of joint element: ST and SC2 (see Table 1). There are shear springs and axial springs of the bolts. The effect of the nails is concentrated to four shear springs using the shear property of a nail and the sheeted wall theory (Murakami et al. 1999).

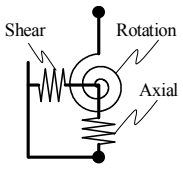
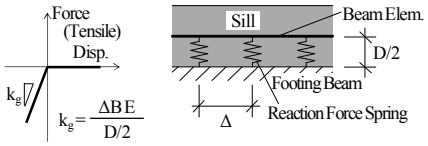


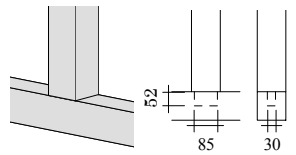
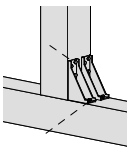
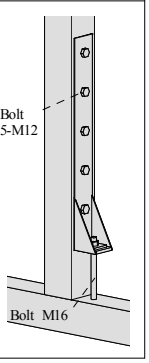
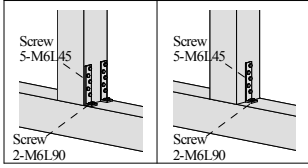
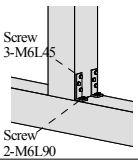
Fig. 2 Joint Elem.



B : Width of Sill
E : Young's Modulus of Orthogonal Direction
Δ : Interval of Springs (= 91mm)

Fig. 3 Reaction Force Spring of Sill

Tab. 1 Joint Types

ST (common specification)		SC2	HD
			
FC5x2	FC5x1	FC3x2	
			

2.2 Method of Concentrating Nail Spring

Murakami and Inayama have proposed a method to calculate the shear performance of plywood shear wall from relationship between shear force of nail and displacement of nail (Murakami et al. 1999). The method assumes the nail behavior to be able to separate to mode X and mode Y (see Fig. 4). The concentrating method which will be proposed here is based on the same idea.

Considering that the center of Fig.4 (mode X) is separated up and down, the effect of nails of upper side is concentrated to point U in Fig. 5. Similarly the effect of lower side is concentrated to point D. The scale factors of up and down are obtained from equation (4).

$$m_U = \sum y(i_u)^2 / H_U^{\,2} \;,\; m_D = \sum y(i_D)^2 / H_D^{\,2} \qquad (4)$$

Where H_U and H_D are distance of each point to neutral axis, i_U and i_D are number of nail, y is distance of each nail to neutral axis. Similarly considering the mode Y, the scale factors of right and left are obtained from equation (5).

$$m_L = \sum x(i_L)^2 / L_L^{\,2} \;,\; m_R = \sum x(i_R)^2 / L_R^{\,2} \qquad (5)$$

The four scale factors are multiplied by the relationship between shear force of nail and displacement of nail (see Fig.

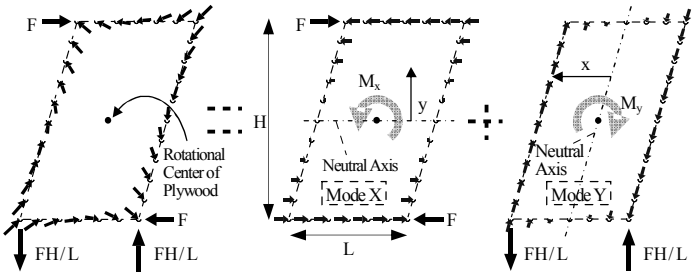


Fig 4 Force Acting on Frame (Elastic)

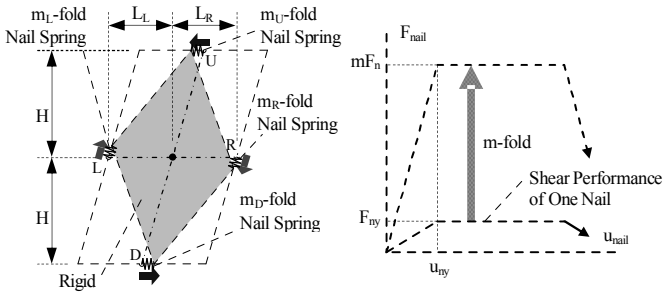


Fig 5 Outline of Concentrating Nail Spring

5), the four springs are connected by the rigid member. It was confirmed that the concentrated model behaves similarly to detailed model and also real structure (Matsuda et al. 2010).

3. CONFIGURATION OF SPRING

3.1 Hysteresis Rule

Fig. 6 illustrates hysteresis rule of Joint. After arriving at the elastic limit, the force increases gradually, and the envelope curve is calculated by Equation (6).

$$P = \frac{(k_0 - k_p)(u - u_a)}{\left(1 + \left|k_0(u - u_a)/P_0\right|^n\right)^{1/n}} + k_p(u - u_a) + P_a \quad (u > u_a) \quad (6)$$

Where P_0 is constant number which is obtained by substituting P_b and u_b into P and u. n is coefficient to decide the shape of the curve.

To duplicate the pinched hysteresis having slippage specific to wooden structure, the hysteresis rule is able to change the slip stiffness depending on maximum displacement (see Fig. 6). This hysteretic rule is applied to the six springs: axial, rotational and shear springs of the joint, and shear springs of the screw, bolt and nail.

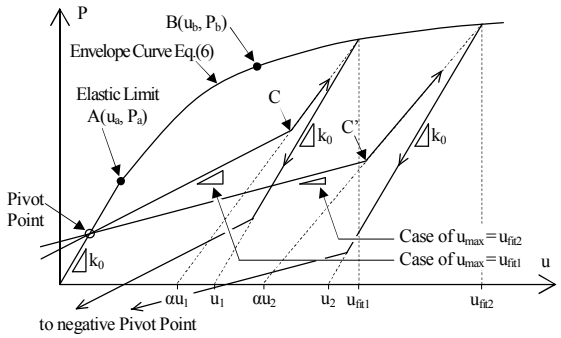


Fig. 6 Hysteresis Rule of Joint

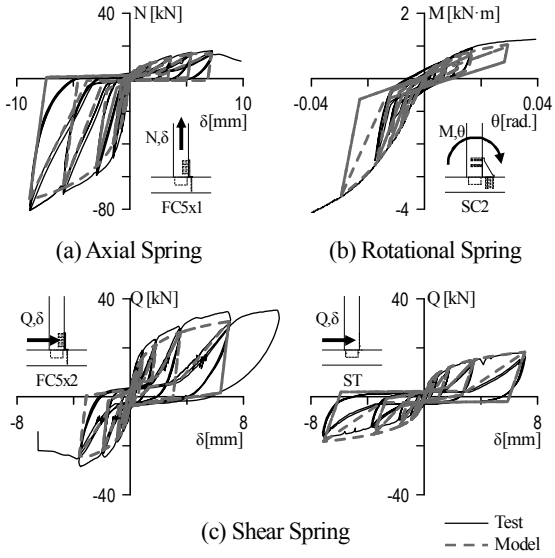
3.2 Joint Spring between Column and Horizontal Member

In order to model the property of the joint spring, a lot of joint test were carried out (Sakata et al. 2009). Fig.7-10 show the modelization of the many kinds of joint. The envelop curves of model are fitted to the average of more than three test results. The models correspond to test results including their cyclic behavior.

4. COMPARISON BETWEEN TEST AND ANARYSIS

4.1 Cyclic Loading Test

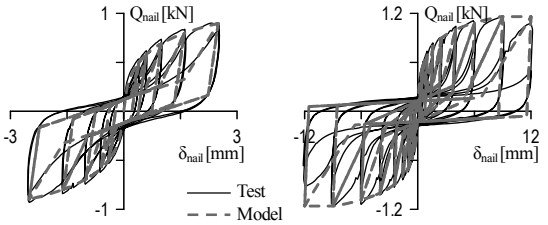
As for cyclic loading test of energy dissipation wall and plywood shear wall, Fig. 11 illustrates the comparison of test results (Matsuda et al. 2008) and analytical results. In the case of plywood shear wall, the analysis result duplicates not only strength but also slip behavior. In the case of energy dissipation wall, in both viscoelastic damper and elasto-plasticity damper, system hysteresis and damper



(a) Axial Spring (b) Rotational Spring

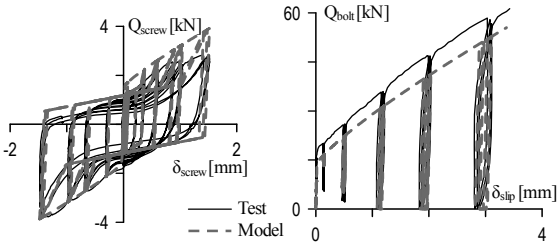
(c) Shear Spring

Fig. 7 Modelization Example of Joint between Column and Horizontal Member



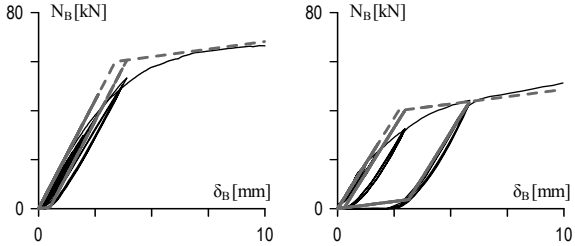
(a) Small Deformation (b) Large Deformation

Fig. 8 Modelization of Shear Spring of Nail



(a) Shear Spring of Screw (b) Shear Spring of Bolt

Fig. 9 Modelization of Shear Spring of Screw and Bolt



(a) Energy Dissipation Wall (b) Plywood Shear Wall

Fig. 10 Modelization of Axial Spring of Bolt

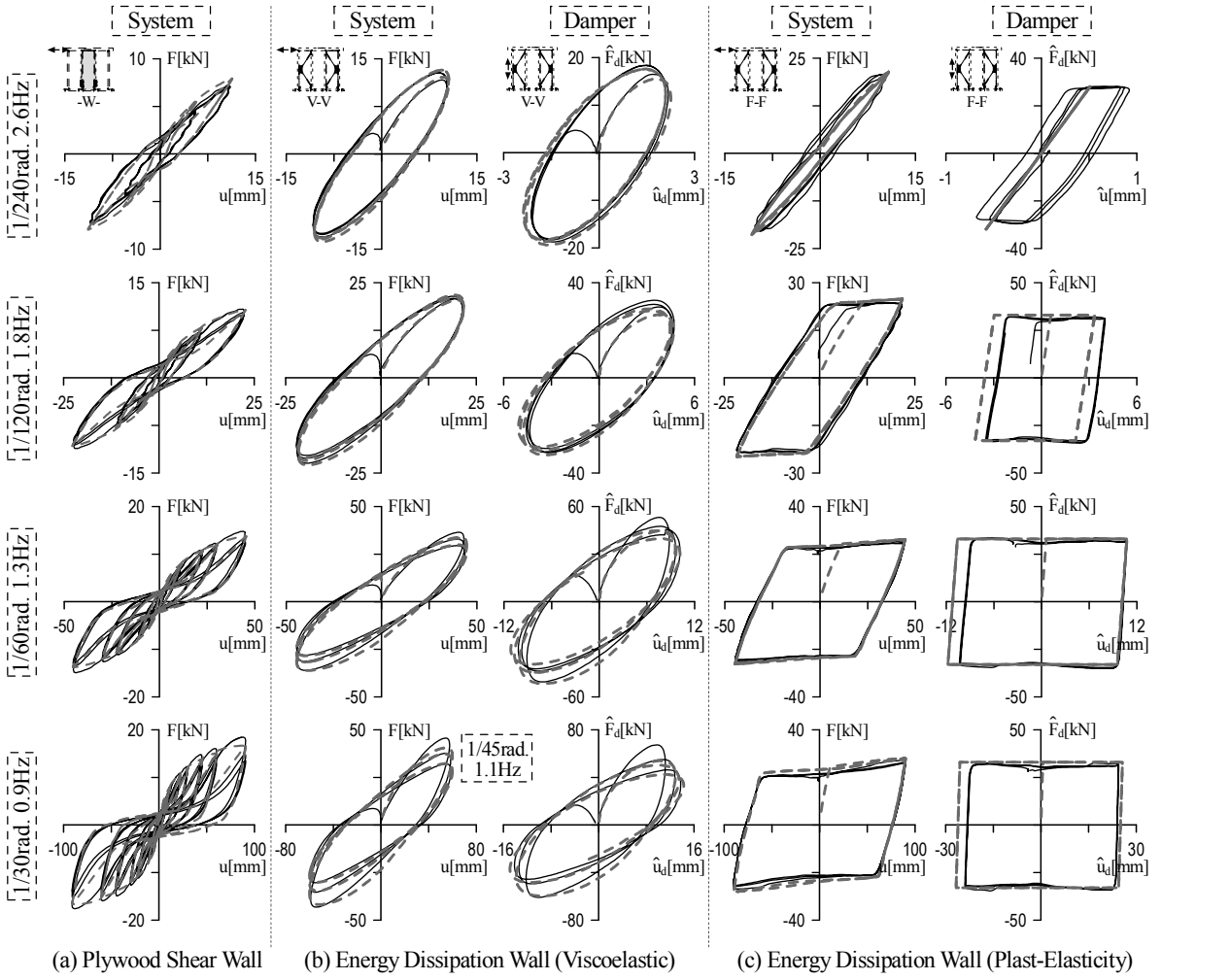


Fig. 11 Comparison of Test and Analysis of Cyclic Loading

hysteresis, analytical results correspond to test results with high accuracy.

4.2 Shaking Table Test

In order to confirm the accuracy of seismic response, the comparison of shake table test and seismic response analysis will be discussed. Fig. 12 indicates the test specimen. Only center plane of the specimen is substituted to frame model since four-cornered columns hardly have horizontal force. Total seismic mass which the frame model has is 3.64 ton including the weight of specimen. Acceleration record which is measured at the specimen's sill is used.

Fig. 13 and 14 show the comparison of test result and analytical result in both global behavior and local behavior. The specimen's character W means plywood shear wall, V or F mean energy dissipation wall which has viscoelastic damper or friction (elasto-plasticity) damper.

The analytical result is similar to test result in both system and damper hysteresis, and the error in the maximum displacement is within 15%. The rotational angle of local behavior shown in upper stage of Fig. 14 is duplicated with high accuracy. In case of axial displacement shown in center stage of Fig. 14, the analytical displacement of capital part is smaller than the test result. Since the analysis is not able to duplicate axial displacement which the rotation provokes (see Fig. 15). In case of also axial force of bolt shown in lower stage of Fig. 14, the analytical result duplicates the test result nearly. As observed above, the frame model is able to duplicate not only global behavior but also local behavior with a high degree of accuracy.

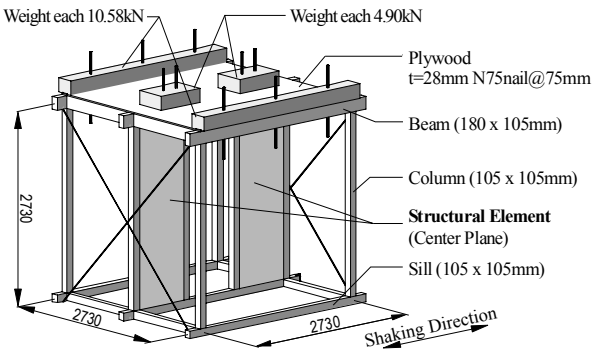


Fig. 12 Shake Table Test of Wood Frame with Damper

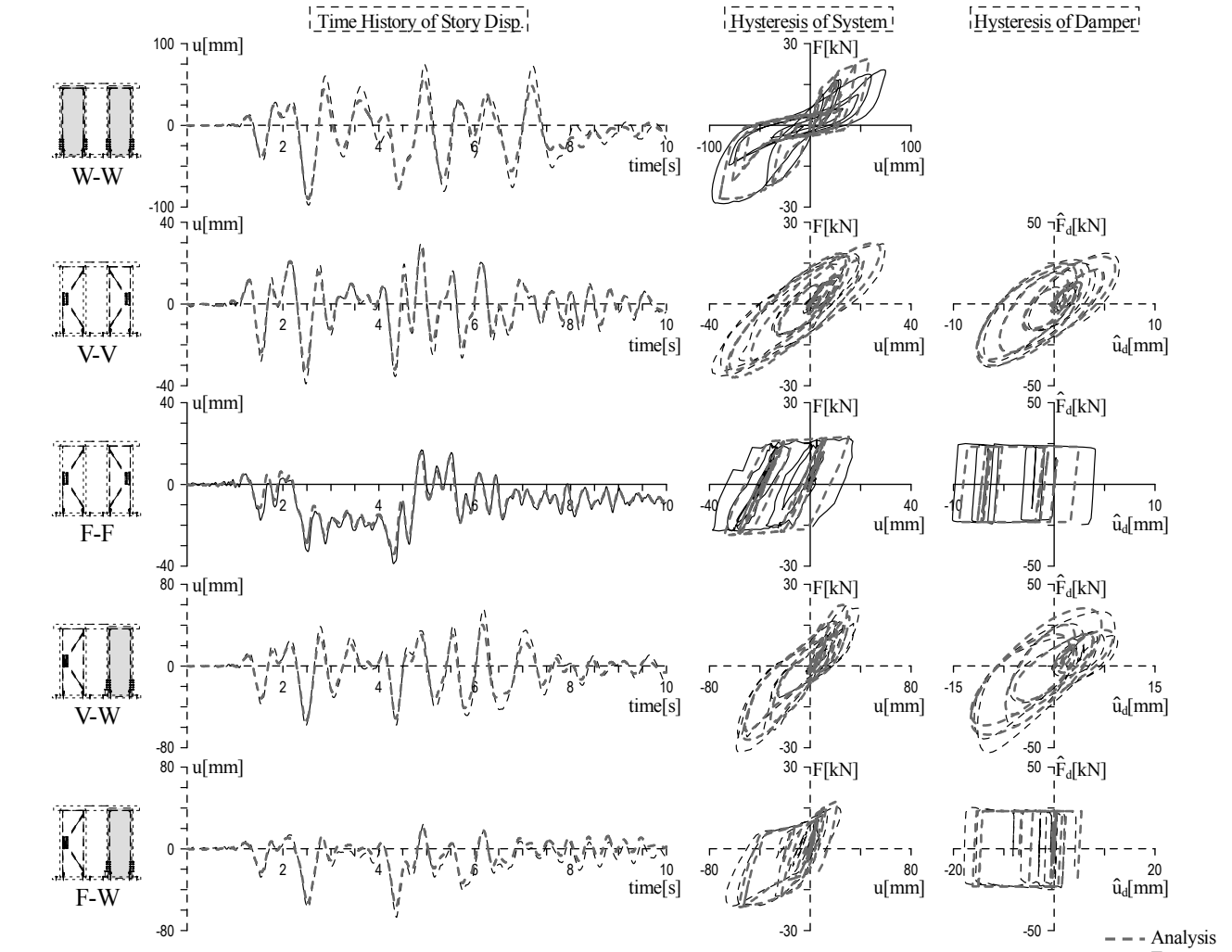
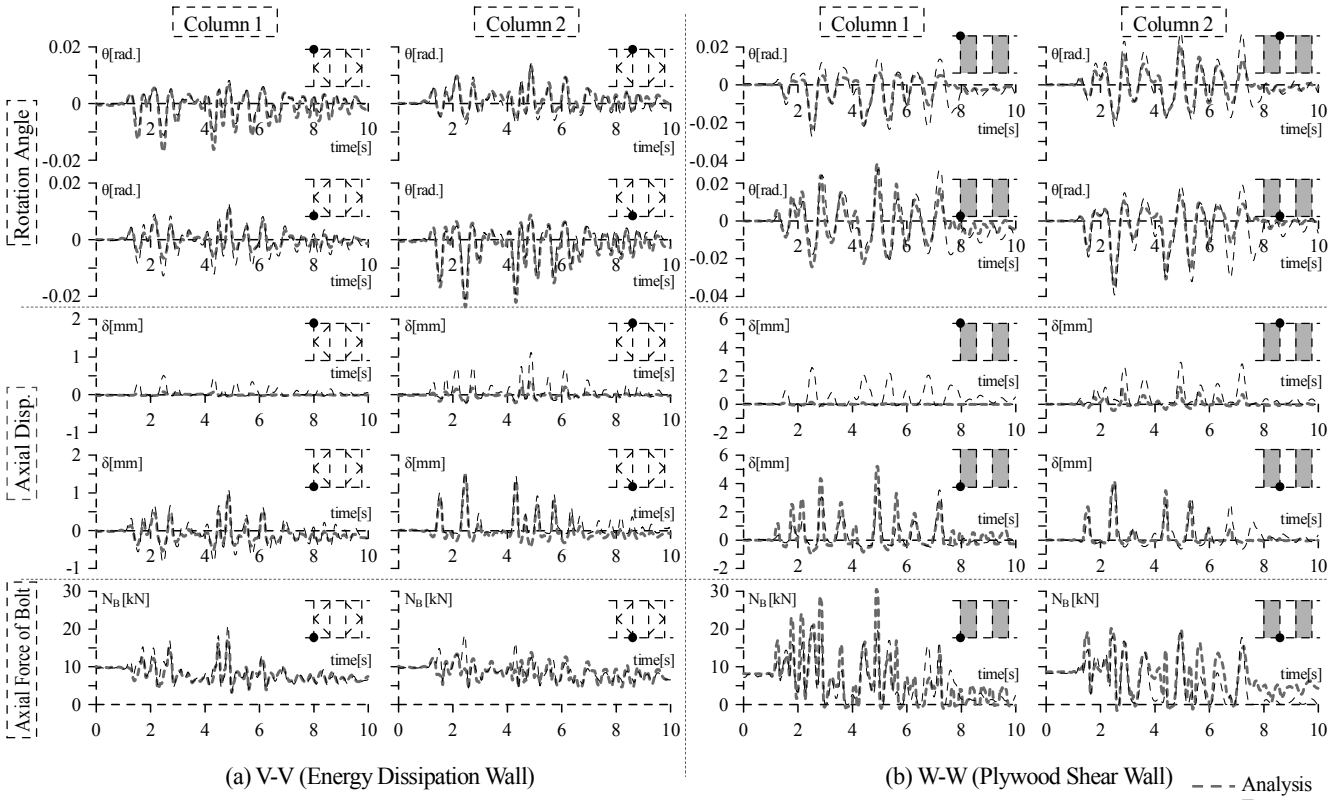


Fig. 13 Comparison of Test and Analysis of Global Behavior (JMAKobe0.6g)



(a) V-V (Energy Dissipation Wall) (b) W-W (Plywood Shear Wall)

Fig. 14 Comparison of Test and Analysis of Local Behavior (JMAKobe0.6g)

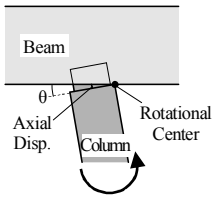


Fig. 15 Axial Disp. by Rotation (Capital)

5. PARAMETORIC STUDY

Using the frame model V, F and W, parametric analysis that the damper quantity and nail quantity are changed will be discussed. Note that each frame models' strengths in case that the model deforms 1/120rad. are from 8.5kN to 8.8kN and they are almost equal. Response spectra of input earthquake waves are showed in Fig. 16. The 6 waves are scaled to target Spa value 1,375cm/s^2 in the case of damping ratio is 2% in the constant area of acceleration.

Fig. 17 shows relationship between story drift and damper quantity. The maximum displacement of model which have viscoelastic damper, V-V, V-W and V-F don't vary among the waves, and it would appear that it is effective for estimating the response. Although the residual displacement of F-F is large, but the residual displacements of F-W and V-F are small. Therefore, adding structural element to friction damper is effective to reduce the residual displacement. The average of displacement of V-F is the smallest, hence combining viscoelastic and friction damper is effective to reduce the maximum displacement.

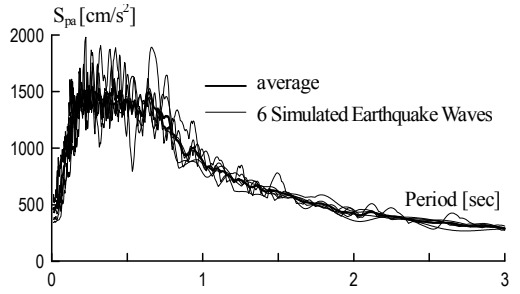


Fig 16 Pseudo-Acceleration Response Spectra of Simulated Earthquake Waves

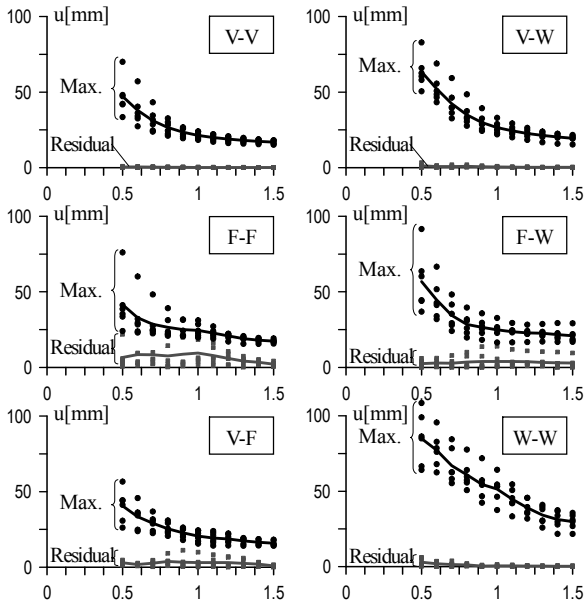


Fig 17 Relationship between Story Drift and Damper Quantity
(Horizontal axis means damper quantity as amount of specimen is 1, and solid line indicates average)

6. CONCLUSION

Accurate, framed analytical models for the wooden energy dissipation wall with damper and plywood shear wall were proposed. In addition, parametric study was carried out using the frame model. Major finding are

- Framed analytical models of energy dissipation wall and/or plywood shear wall were constructed by using many kinds of nonlinear springs whose properties are derived from the test results of the joint. The joint spring between column and horizontal member consists of three types of spring, axial, rotational and shear spring.
- The frame models were able to duplicate not only global behavior but also local behavior with a high degree of accuracy in many kinds of test.
- In the case of the frame which has energy dissipation wall of viscoelastic damper, the maximum displacement doesn't vary among the waves whose response spectra are calibrated equally.
- In the case of the frame which has energy dissipation wall of friction damper, the residual displacement becomes large. But the phenomenon is able to be reduced by combining the friction damper elements with the other structural elements.

References:

Kasai, K., Sakata, H., Wada, A. and Miyashita, T. (2005): "Dynamic behavior of a wood frame with shear link passive control mechanism involving k-brace", Journal of Structural and Construction Engineering, No.598, pp.51-60 (In Japanese)

Matsuda, K., Sakata, H., Kasai, K. and Ooki, Y. (2008): "Experimental study on dynamic response of wooden frames with passive control", Journal of Structural Engineering, Vol.54B, pp.149-156 (In Japanese)

Sakata, H., Kasai, K., Wada, A., Midorikawa, M., Ooki, Y., Nakagawa, T. and Matsuda, K. (2007): "Shaking table tests of wood frames with velocity-dependent dampers", Journal of Structural and Construction Engineering, No.615, pp.161-168 (In Japanese)

Matsuda, K. and Kasai, K. and Sakata, H. and Ooki, Y. and Wada, A. (2007): "Shaking table tests of two-story frames with passive control system", Proceedings of 4th International Conference on Urban Earthquake Engineering, Center on Urban Earthquake Engineering, pp.369-374, Yokohama, JAPAN

Kasai, K., Teramoto, M., Okuma, K and Tokoro, K. (2001): "Constitutive rule for viscoelastic materials considering temperature frequency, and strain sensitivities, part 1 Linear model with temperature and frequency sensitivities", Journal of Structural and Construction Engineering, No.543, pp.77-86 (In Japanese)

Kasai, K. and Tokoro, K. (2002): "Constitutive rule for viscoelastic materials considering temperature frequency, and strain sensitivities, part 2 Nonlinear model based on temperature-rise, strain and strain-rate", Journal of Structural and Construction

Engineering, No.561, pp.55-63 (In Japanese)
Murakami, M. and Inayama, M. (1999): "Formulae to predict the elastic and plastic behavior of sheathed walls with any nailing arrangement pattern", Journal of Structural and Construction Engineering, No.519, pp.87-93 (In Japanese)
Matsuda, K., Kasai, K. and Sakata, H. (2010): "Development of Passively-Controlled Houses with Superior Property-Retention Capability, Part 30: Simple Frame-Modeling Method for Sheathed Shear Wall", Summaries of Technical Papers of AIJ Annual Meeting, C-1, pp.397-398 (In Japanese)
Sakata, H., Suyama, T. and Matsuda, K. (2009): "Study on Hysteresis Model of Joints Using Screws and Holddown Bolts for Conventional Post-and-Beam Wooden House", Journal of Structural and Construction Engineering, No.645, pp.2061-2067 (In Japanese)

Appendix 1: Outline of Energy Dissipation Wall

The feature of K-brace passive control wall is shown below (Fig. A1). When the wall deforms by horizontal force, there is vertical deformation between the brace and the steel plate and the damper is inserted in the place. The wall is classified in to a series of so-called shear link type. In order to reduce the effect of the column's bending, the edge of the brace is fixed near the joint of the column and horizontal member. There are many advantages because the contents of the wall are able to fit in inside of frames. For example it is possible to fix without an attachment of other walls. K-brace is screwed on wooden frames by a lot of screws because of high safety factor.

A stub tenon, L-type metal and bolt (hold-down metal) are allocated in the joint of the column and horizontal member. The square steel pipe is fillet-welded to steel plate B and C (Fig. A1(c)). Energy absorption capacity is increased as much as possible by allocating the bolt closer to the column, and integrating the steel plate C into the hold-down metal.

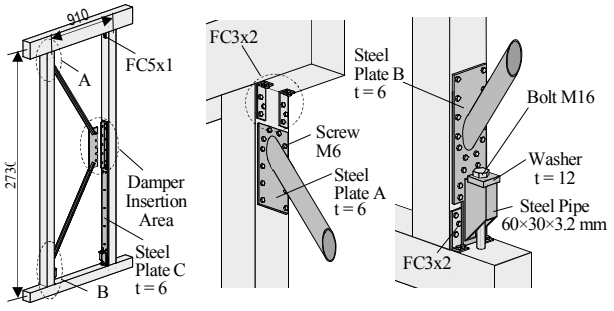


Fig. A1 Detail of Energy Dissipation Wall

8CUEE CONFERENCE PROCEEDINGS
8th International Conference on Urban Earthquake Engineering
March 7-8, 2011, Tokyo Institute of Technology, Tokyo, Japan

A BASIC STUDY ON DYNAMIC PROPERTY AND SEISMIC RESPONSE OF TIMBER STRUCTURE WITH FLEXIBLE FLOOR AND UNI-AXIAL STIFFNESS ECCENTRICITY

Yoshihiro Yamazaki[1)], Kazuhiko Kasai[2)], and Hiroyasu Sakata[3)]

1) JSPS Research Fellow, Structural Engineering Research Center, Tokyo Institute of Technology, Japan
2) Professor, Structural Engineering Research Center, Tokyo Institute of Technology, Japan
3) Associate Professor, Structural Engineering Research Center, Tokyo Institute of Technology, Japan
yamazaki.y.ai@m.titech.ac.jp, kasai@serc.titech.ac.jp, hsakata@serc.titech.ac.jp

Abstract: Dynamic properties and seismic responses of timber structure are discussed, with focus on uni-axial stiffness eccentricity of structural walls and horizontal flexibility of floor diaphragm. The stiffness eccentricity factor R_e defined in Japanese building standard law assumes rigid horizontal diaphragm, which can result in considerable error in estimations for torsional properties/responses of timber structures. Simplified formulations for the dynamic properties considering the diaphragm flexibility are given, and are applied to discuss seismic responses of example structures. The stiffness of horizontal diaphragm appears to affect not only the torsional response but also the translational response of the structure.

1. INTRODUCTION

Most wooden houses have stiffness eccentricity because of their eccentric arrangement of shear walls. Since it should be avoided from the point of view of seismic resistance, eccentric ratio R_e is defined in Japanese Building Standard Law. However, R_e assumes rigid horizontal diaphragm, which can result in considerable error in estimations for torsional properties/responses of timber structure. If horizontal diaphragm such as a floor or a roof is flexible, the building becomes vulnerable to torsion because transverse frames are unlikely to resist torsion. In particular, Japanese traditional wooden houses as well as existing old houses are thought to have flexible floor and large stiffness eccentricity.

In allowable stress design for Japanese timber houses, horizontal diaphragm must have enough *floor strength factors* in order to prevent it from breaking out prior to shear walls. As mentioned above, horizontal diaphragm needs to have not only enough strength but also much stiffness. Agawa showed the effect of floor's flexibility of timber structure by shaking table tests and reported that some changes of natural period and deformation mode are observed when stiffness of horizontal diaphragm is lacked.

Although much verification of seismic performance of timber house designed on the basis of current seismic standard is carried out in recent days, relationship between stiffness of horizontal diaphragm and dynamic torsional behavior does not appear to be clarified. In this paper, simplified formulations for the dynamic properties considering the diaphragm flexibility are given, and are applied to discuss seismic responses of example structures. We assume that horizontal diaphragm maintains parallelogram after it is deformed in order that degrees of freedom are minimized. As a result, behavior of considering model is simplified compared to that of actual building. However, such a basic study is indispensable in order to clarify its complicated behavior theoretically. In addition, characteristics of shear walls and horizontal diaphragm are assumed to be linear.

2. PRIOR CONDITION

2.1 Single Span Structure Considered in This Paper

As shown in figure 1, single story and single span shear wall structure is considered. Stiffness of *x*- directional shear walls are unbalanced, and center of stiffness is located away in *y*- direction from center of mass. Horizontal diaphragm which means floor of 2nd. story is assumed to behave like a shear panel. Both dead load and live load are thought to be distributed uniformly in the plan.

As shown on the right side of figure 1, when structure is subjected to earthquake in *x*- direction, distribution of inertial force becomes triangular or trapezoidal due to rotation and shear deformation of floor. Figure 2 shows equilibrium between inertial forces and resisting forces of shear walls in three cases ; (a) rigid floor without eccentricity, (b) rigid floor with eccentricity and (c) flexible floor with eccentricity. In this study, we consider the response such as figure 2 (c), and assume that horizontal diaphragm maintains

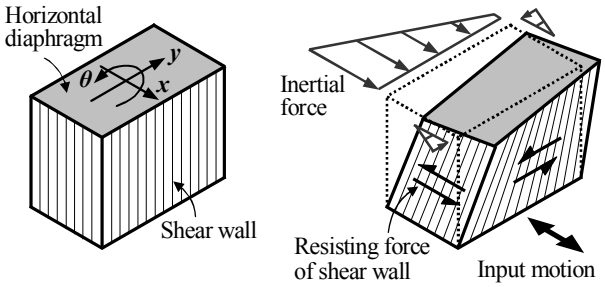
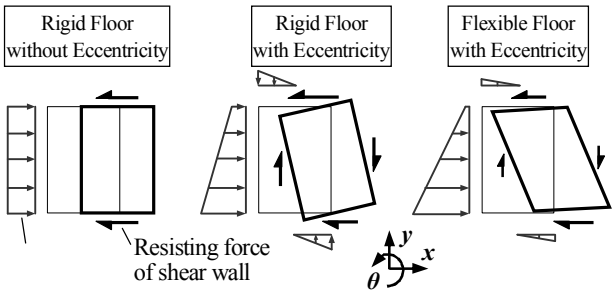


Figure 1 Single Story and Single Span Shear Wall Structure Considered in This Study



(a) Translation (b) (a) and Rotation (c) (b) and Shear deformation

Figure 2 Forces Applied to Horizontal Diaphragm and Deformation of Floor

parallelogram.

3. EQUATION OF MOTION

3.1 In A Case of Rigid Floor

Figure 3 shows structural model considered in this study, and figure 4 shows displacement mode of the structure. In this section, formulation for rigid floor structure is presented. Therefore, displacement mode becomes like a dash line in figure 4, which means horizontal diaphragm maintains rectangle.

k_{xi} and c_{xi} are stiffness and viscosity of i-th structural element in x- direction, respectively. Their distances from center of mass are y_i and y_i'. Similarly, k_{yi} and c_{yi} are stiffness and viscosity of i-th structural element in y-direction. Their distances from center of mass are x_i and x_i'. The origin is set in center of mass. Using above definition, following parameters are obtained.

$$K_x = \sum_i k_{xi}\,, \qquad K_\theta = \sum_i (k_{xi} y_i^{\,2} + k_{yi} x_i^{\,2}) \tag{1a,b}$$

$$C_x = \sum_i c_{xi}\,, \qquad C_\theta = \sum_i (c_{xi} y_i'^{\,2} + c_{yi} x_i'^{\,2}) \tag{2a,b}$$

$$e_y = \sum_i k_{xi} y_i / K_x\,, \qquad e_y' = \sum_i c_{xi} y_i' / C_x \tag{3a,b}$$

Where, K_x and K_θ are total stiffness in x- direction and rotational stiffness around center of mass, respectively. e_y is the distance from center of mass to center of stiffness. Similarly, C_x and C_θ are total viscosity in x- direction and rotational viscosity around center of mass, respectively. e_y' is the distance from center of mass to center of viscosity.

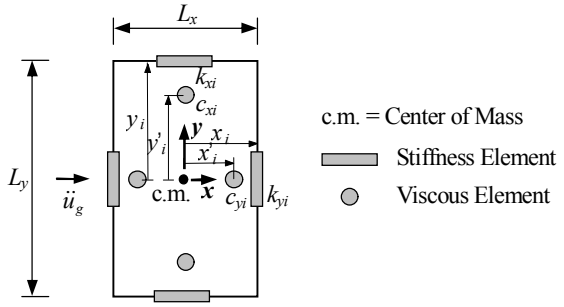


Figure 3 Arrangement of Stiffness and Viscous Element of the Structure

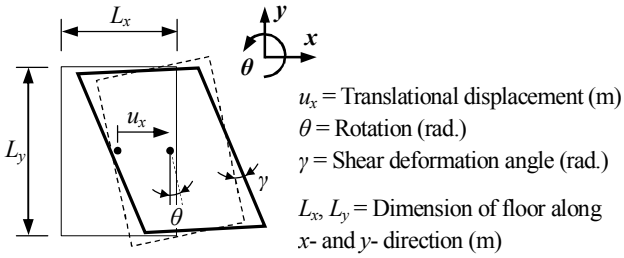


Figure 4 Displacement Mode of the Structure

Using equilibrium of x- directional forces and moment around center of mass, we can obtain the following equation of motion.

$$\begin{bmatrix} m & 0 \\ 0 & I \end{bmatrix} \begin{Bmatrix} \ddot{u}_x \\ \ddot{\theta} \end{Bmatrix} + \begin{bmatrix} C_x & -C_x e_y' \\ -C_x e_y' & C_\theta \end{bmatrix} \begin{Bmatrix} \dot{u}_x \\ \dot{\theta} \end{Bmatrix} + \begin{bmatrix} K_x & -K_x e_y \\ -K_x e_y & K_\theta \end{bmatrix} \begin{Bmatrix} u_x \\ \theta \end{Bmatrix} = -\begin{bmatrix} m & 0 \\ 0 & I \end{bmatrix} \begin{Bmatrix} 1 \\ 0 \end{Bmatrix} \ddot{u}_g \tag{4}$$

Where, m = total mass, I = moment of inertia, $\ddot{u}_g$ = input motion. First entry of displacement vector u_x is translational displacement of center of mass and second entry θ is rotation (rad.) around center of mass, as illustrated in figure 4.

The following parameters are also obtained.

$$\omega_x = \sqrt{K_x / m}\,, \qquad h_x = C_x / (2m\omega_x) \tag{5a,b}$$

$$\omega_\theta = \sqrt{K_\theta / I}\,, \qquad h_\theta = C_\theta / (2I\omega_\theta)\,, \tag{6a,b}$$

$$\bar{e}_y = e_y / r_m\,, \qquad \bar{e}_y' = e_y' / r_m \tag{7a,b}$$

ω_x, h_x are natural circular frequency and damping ratio of the system whose rotation is unfree, and ω_θ, h_θ are those of the system whose translation is unfree, respectively. r_m is radius of gyration. Using r_m, the following transformation is conducted.

$$\Delta u_x = r_m \theta\,, \qquad r_m = \sqrt{I / m} \tag{8a,b}$$

Δu_x is relative displacement from center of mass in the point r_m away in y- direction, which is caused by rotation θ.

Equation (4) can be rewritten using above new parameters as follows.

$$\mathbf{m}\,\ddot{\mathbf{u}} + \mathbf{c}\,\dot{\mathbf{u}} + \mathbf{k}\,\mathbf{u} = -\mathbf{m}\,\{\mathbf{1}\}\,\ddot{u}_g \tag{9}$$

$$\mathbf{m} = \begin{bmatrix} 1 & 0 \\ 0 & 1 \end{bmatrix}, \quad \mathbf{u} = \begin{Bmatrix} u_x \\ \Delta u_x \end{Bmatrix}, \quad \{\mathbf{1}\} = \begin{Bmatrix} 1 \\ 0 \end{Bmatrix}$$
$$\mathbf{c} = 2h_x\omega_x \begin{bmatrix} 1 & -\bar{e}_y' \\ -\bar{e}_y' & \dfrac{h_\theta}{h_x}\dfrac{\omega_\theta}{\omega_x} \end{bmatrix}, \quad \mathbf{k} = \omega_x^2 \begin{bmatrix} 1 & -\bar{e}_y \\ -\bar{e}_y & \dfrac{\omega_\theta^2}{\omega_x^2} \end{bmatrix} \tag{10a-e}$$

Equation (9) is the equation of motion normalized by mass matrix **m**. We can see that the shapes of stiffness matrix **k** and damping matrix **c** are determined by four parameters ; ω_θ / ω_x , $\bar{e}_y$, h_θ / h_x and $\bar{e}_y'$. They are defined as '*torsional properties*' for rigid floor structure.

3.2 In A Case of Flexible Floor

When horizontal diaphragm is flexible, additional degree of freedom, which is shear deformation of floor γ , must be considered as shown in figure 4. It is notable that γ means shear deformation as strain tensor. Therefore, γ is a half of shear deformation angle of horizontal diaphragm.

As shown in figure 5, *x*- and *y*- directional forces produce moment and are balanced through horizontal diaphragm. The moment is replaced with concentric forces Q_x and Q_y applied to floor edge.

$$Q_x L_y = -M^{(x)} - I^{(x)}\left(\ddot{\theta} + \ddot{\gamma}\right), \quad Q_y L_x = M^{(y)} + I^{(y)}\left(\ddot{\theta} - \ddot{\gamma}\right) \tag{11a,b}$$

Equilibrium of moment around center of mass is expressed as follows.

$$Q_x L_y = Q_y L_x \tag{12}$$

$$M^{(x)} + M^{(y)} + I\ddot{\theta} + \left(I^{(x)} - I^{(y)}\right)\ddot{\gamma} = 0 \tag{13}$$

Where, $M^{(x)}$ and $M^{(y)}$ are resisting moment of *x*- and *y*- directional shear walls. $I\ddot{\theta}$ and $\left(I^{(x)} - I^{(y)}\right)\ddot{\gamma}$ are torque when floor rotates θ radian and deforms γ radian, respectively. Their proportional constant I, $I^{(x)}$ and $I^{(y)}$ are calculated by integrating moment by inertial force applied to small body as shown in figure 6.

$$I = \sum_j m_j\left(x_{mj}^2 + y_{mj}^2\right) = I^{(y)} + I^{(x)}\left(= \frac{m}{12}\left(L_x^2 + L_y^2\right)\right), \quad m = \sum_j m_j$$

$$I^{(x)} = \sum_j m_j\, y_{mj}^2\left(= \frac{mL_y^2}{12}\right), \quad I^{(y)} = \sum_j m_j x_{mj}^2\left(= \frac{mL_x^2}{12}\right) \tag{14a-d}$$

Where, m_j is mass of small body, and x_{mj} and y_{mj} are the distances from center of mass in *x*- and *y*- direction, respectively. The last members of equation (14a), (14c) and (14d), which are parenthetic, are realized in the case of uniformly distributed mass.

Moreover, horizontal diaphragm is assumed to be a shear panel whose shear modulus is *G*. Its plan dimension is L_x in *x*- direction and L_y in *y*- direction, and thickness is *t*, respectively. Thus, constitutive laws of floor are expressed as follows.

$$Q_x / \left(tL_x\right) = 2G\gamma\,, \qquad Q_y / \left(tL_y\right) = 2G\gamma \tag{15a,b}$$

In addition, by expressing left members of equation (15) using moment applied to floor (figure 5) instead of shear stress,

$$Q_x L_y = 2GV\gamma\,, \qquad Q_y L_x = 2GV\gamma$$
$$V = tL_xL_y \tag{16a-c}$$

V means volume of the floor. By adding equation (16a) to equation (16b) in both members and substituting equation (11), the following equation of equilibrium is obtained.

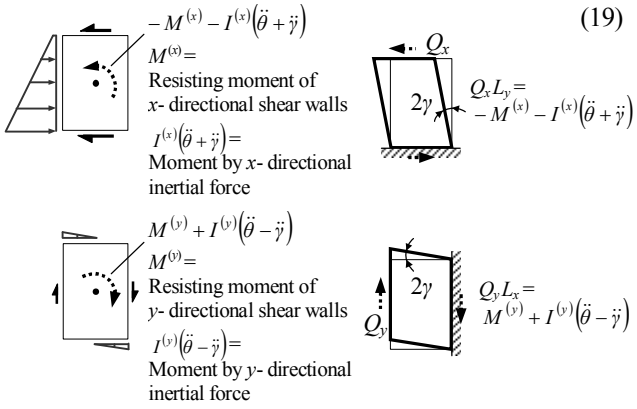
$$M^{(x)} - M^{(y)} + \left(I^{(x)} - I^{(y)}\right)\ddot{\theta} + I\,\ddot{\gamma} + 4GV\gamma = 0 \tag{17}$$

Where, $M^{(x)}$ and $M^{(y)}$ are expressed as follows.

$$M^{(x)} = -C_x e_y' \dot{u}_x + C_\theta^{(x)}\left(\dot{\theta} + \dot{\gamma}\right) + -K_x e_y u_x + K_\theta^{(x)}\left(\theta + \gamma\right)$$
$$M^{(y)} = C_\theta^{(y)}\left(\dot{\theta} - \dot{\gamma}\right) + K_\theta^{(y)}\left(\theta - \gamma\right) \tag{18a,b}$$

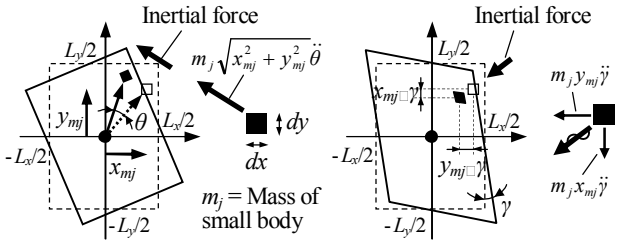
Thus, equation of motion considering flexibility of floor are obtained as follows.

$$\begin{bmatrix} m & 0 & 0 \\ 0 & I & I^{(x)} - I^{(y)} \\ 0 & I^{(x)} - I^{(y)} & I \end{bmatrix}\begin{Bmatrix} \ddot{u}_x \\ \ddot{\theta} \\ \ddot{\gamma} \end{Bmatrix} + \begin{bmatrix} C_x & -C_x e_y' & -C_x e_y' \\ -C_x e_y' & C_\theta & C_\theta^{(x)} - C_\theta^{(y)} \\ -C_x e_y' & C_\theta^{(x)} - C_\theta^{(y)} & C_\theta \end{bmatrix}\begin{Bmatrix} \dot{u}_x \\ \dot{\theta} \\ \dot{\gamma} \end{Bmatrix}$$
$$+ \begin{bmatrix} K_x & -K_x e_y & -K_x e_y \\ -K_x e_y & K_\theta & K_\theta^{(x)} - K_\theta^{(y)} \\ -K_x e_y & K_\theta^{(x)} - K_\theta^{(y)} & K_\theta + 4GV \end{bmatrix}\begin{Bmatrix} u_x \\ \theta \\ \gamma \end{Bmatrix} = -\begin{bmatrix} m & 0 & 0 \\ 0 & I & I^{(x)} - I^{(y)} \\ 0 & I^{(x)} - I^{(y)} & I \end{bmatrix}\begin{Bmatrix} 1 \\ 0 \\ 0 \end{Bmatrix}\ddot{u}_g \tag{19}$$



(a) Moment Attributed to *x*- and *y*- Directional Forces (b) Equivalent Shear Forces

Figure 5 Forces Applied to Horizontal Diaphragm



(a) Only Rotation (b) Only Shear Deformation

Figure 6 Calculation of Moment of Inertia

Where,

$$K_\theta^{(x)} = \sum_i k_{xi} y_i^{\,2}, \qquad C_\theta^{(x)} = \sum_i c_{xi} y_i'^{\,2} \tag{20a,b}$$

$$K_\theta^{(y)} = \sum_i k_{yi} x_i^{\,2}, \qquad C_\theta^{(y)} = \sum_i c_{yi} x_i'^{\,2} \tag{21a,b}$$

$$K_\theta = K_\theta^{(x)} + K_\theta^{(y)}, \qquad C_\theta = C_\theta^{(x)} + C_\theta^{(y)} \tag{22a,b}$$

$K_\theta^{(x)}$ and $K_\theta^{(y)}$ are contributions of *x*- and *y*- directional shear walls to rotational stiffness K_θ, respectively. Similarly, $C_\theta^{(x)}$ and $C_\theta^{(y)}$ are those of *x*- and *y*- directional shear walls to rotational vicosity C_θ, respectively. The following nondimensional parameters are also defined due to simplified expression.

$$\cos^2\psi_x = K_\theta^{(x)} / K_\theta, \qquad \sin^2\psi_x = K_\theta^{(y)} / K_\theta \tag{23a,b}$$

$$\cos^2\psi_x' = C_\theta^{(x)} / C_\theta, \qquad \sin^2\psi_x' = C_\theta^{(y)} / C_\theta \tag{24a,b}$$

$$\alpha = \left(I^{(x)} - I^{(y)}\right) / I, \qquad \beta = \sqrt{4GV/I} \tag{25a,b}$$

The following transformation is conducted alike equation (8a).

$$\Delta u_x' = r_m \gamma \tag{26}$$

$\Delta u_x'$ is relative displacement from center of mass in the point r_m away in *y*- direction, which is caused by shear deformation angle γ. The difference between Δu_x and $\Delta u_x'$ are shown in figure 7.

Accordingly, **m**, **c** and **k** considering flexibility of floor are expressed as follows.

$$\mathbf{m} = \begin{bmatrix} 1 & 0 & 0 \\ 0 & 1 & \alpha \\ 0 & \alpha & 1 \end{bmatrix}, \quad \mathbf{u} = \begin{Bmatrix} u_x \\ \Delta u_x \\ \Delta u_x' \end{Bmatrix}, \quad \{\mathbf{1}\} = \begin{Bmatrix} 1 \\ 0 \\ 0 \end{Bmatrix}$$

$$\mathbf{c} = 2h_x\omega_x \begin{bmatrix} 1 & -\bar{e}_y' & -\bar{e}_y' \\ -\bar{e}_y' & \dfrac{h_\theta}{h_x}\dfrac{\omega_\theta}{\omega_x} & \dfrac{h_\theta}{h_x}\dfrac{\omega_\theta}{\omega_x}\cos 2\psi_x' \\ -\bar{e}_y' & \dfrac{h_\theta}{h_x}\dfrac{\omega_\theta}{\omega_x}\cos 2\psi' & \dfrac{h_\theta}{h_x}\dfrac{\omega_\theta}{\omega_x} \end{bmatrix} \tag{27a-e}$$

$$\mathbf{k} = \omega_x^{\,2} \begin{bmatrix} 1 & -\bar{e}_y & -\bar{e}_y \\ -\bar{e}_y & \dfrac{\omega_\theta^2}{\omega_x^2} & \dfrac{\omega_\theta^2}{\omega_x^2}\cos 2\psi_x \\ -\bar{e}_y & \dfrac{\omega_\theta^2}{\omega_x^2}\cos 2\psi_x & \dfrac{\omega_\theta^2}{\omega_x^2}\left(1+\dfrac{\beta^2}{\omega_\theta^2}\right) \end{bmatrix}$$

We can see that there are eight '*torsional properties*' for flexible floor structure ; α, $\cos 2\psi_x$, $\cos 2\psi_x'$ and β/ω_θ added to those for rigid floor structure. α, $\cos 2\psi_x$ and $\cos 2\psi_x'$ represent influence of arrangement of mass, stiffness and viscosity upon floor deformation, respectively. β/ω_θ means the ratio of floor shear stiffness to rotational natural circular frequency, which is explained for details in the next chapter.

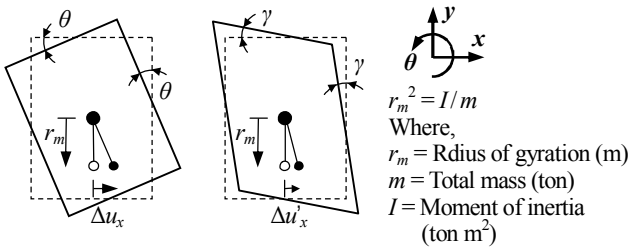


Figure 7 Definition of Δu_x and $\Delta u'_x$

4. DYNAMIC PROPERTIES

4.1 Supposed Range of Torsional Properties

In this section, some example structures are shown and their torsional properties are examined. Figure 8 shows structure model considered. The length of black rectangle expresses stiffness of each shear walls. Viscous elements are neglected. Constant proportional *a*, *b* and *c* are used ; *a* = the ratio of stiffness of two *x*- directional shear walls, *b* = the ratio of total stiffness of *y*- directional shear walls to that of *x*- direction and *c* = aspect ratio of floor.

Torsional properties calculated using above *a*, *b* and *c* are shown in table 1. *a* is changed from 0.5 to 0. *x*-directional eccentric ratio R_{ex} is also shown in the table. In the current Japanese design code for timber houses, R_{ex} must not exceed 0.3. Note that $\bar{e}_y = \bar{e}_y'$, $\omega_\theta/\omega_x = h_\theta/h_x$ and $\cos 2\psi_x = \cos 2\psi_x'$ are assumed because damping matrix **c** is typically considered to be proportional to stiffness matrix **k**.

Furthermore, physical meaning of β/ω_θ is explained here. By replacing β/ω_θ with equations (6a) and (25b),

$$\left(\beta/\omega_\theta\right)^2 = 4GV/K_\theta \tag{28}$$

It is found that β/ω_θ represents the ratio of floor shear stiffness to rotational stiffness of structure.

In Japan, floor strength factor is defined for each floor specification, which are based on experimental results. It is convenient to think that floor strength factor are decided by its strength in 1/150 rad. and means the shear stiffness of floor. Let α_f be floor strength factor, and GV is expressed as follows.

$$GV = 1.96\times 150\,\alpha_f L_x L_y \tag{29}$$

1.96 (kN/m) means standard strength value corresponding to α_f = 1. Similarly, let α_x (m/m^2) be wall length, which means summation of product of bracing unit multipliers and length of shear walls per unit area. Bracing unit multipliers is the strength of shear walls per unit length, and appears to means its stiffness. As a result, K_θ is expressed as follows.

$$K_\theta = \frac{1.96\times 150\,\alpha_x L_x L_y\left(b+c^2\right)}{h}\left(\frac{L_x}{2}\right)^2 \tag{30}$$

Where, *h* is floor height. By substituting equation (29) and (30) into equation (28),

$$(\beta/\omega_\theta)^2 = \frac{16\alpha_f h}{\alpha_x L_y^2\left(1+b/c^2\right)} \tag{31}$$

It is found that β/ω_θ has the following characteristics. β/ω_θ is proportional to α_f and inversely proportional to α_x, which means stiff floor is needed on the basis of the amount of shear walls. β/ω_θ is affected by other parameters ; b/c^2 and h/L_y^2. b/c^2 means the contribution of transverse walls to rotational stiffness. h/L_y^2 does three-dimensional shape of building.

Table 2 shows corresponding values of floor strength factor when the other parameters are given. $L_x = L_y =$ 5.46m (c = 1), α_x = 0.15, 0.3, 0.45m/m^2, b = 0.5, 1, 2 and β/ω_θ = 0.5, 1, 1.5, 2, 3 are considered in this table (Appendix A). $\beta/\omega_\theta = 0$ and infinity (Rigid floor) are also examined in a later chapter.

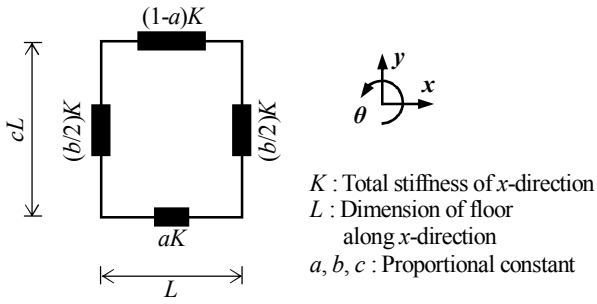


Figure 8 Structural Model Considered
(Except for Viscous Element)

Table 1 Relationship between Torsional Properties and Structural Parameters

b	c	$\bar{e}_y$ (*)	ω_θ/ω_x	$\cos 2\Psi_x$	α	R_{ex}
0.5	0.5	0 ~ 0.78	1.34	-0.33	-0.6	0 ~ 0.71
1			1.73	-0.6		0 ~ 0.5
2			2.32	-0.78		0 ~ 0.35
0.5	1	0 ~ 1.23	1.5	0.33	0	0 ~ 1.41
1			1.73	0		0 ~ 1
2			2.12	-0.33		0 ~ 0.71
0.5	2	0 ~ 1.55	1.64	0.78	0.6	0 ~ 2.82
1			1.73	0.6		0 ~ 2
2			1.9	0.33		0 ~ 1.41

(*) When a is changed from 0.5 to 0
(**) $\bar{e}_y' = \bar{e}_y$, $h_{\theta\square}/h_x = \omega_\theta/\omega_x$, $\cos 2\Psi'_x = \cos 2\Psi_x$

Table 2 Equivalent Values of Floor Strength Factors

Wall length	b	β/ω_θ 0.5	1	1.5	2	3
0.15	0.5	0.05	0.21	0.48	0.85	1.92
	1	0.07	0.28	0.64	1.14	2.56
	2	0.11	0.43	0.96	1.71	3.84
0.3	0.5	0.11	0.43	0.96	1.71	3.84
	1	0.14	0.57	1.28	2.28	5.12
	2	0.21	0.85	1.92	3.41	7.68
0.45	0.5	0.16	0.64	1.44	2.56	5.76
	1	0.21	0.85	1.92	3.41	7.68
	2	0.32	1.28	2.88	5.12	11.52

(***) Floor strength factors in the case of $L_x = L_y =$ 5.46m

4.2 Dynamic Properties of the Structure

Natural circular frequency ω_i and eigen vector $\boldsymbol{\varphi_i}$ with respect to i-th mode are obtained by solving the following real eigen equation.

$$(-\omega_i^2 \mathbf{m} + \mathbf{k})\,\boldsymbol{\varphi_i} = \mathbf{0} \tag{32}$$

Higher mode response can be neglected because timber houses are likely to have short natural period. Therefore, characteristics of natural circular frequency ω_1 and eigen vector $\boldsymbol{\varphi_1} = \{\varphi_{11}, \varphi_{21}, \varphi_{31}\}^{\mathbf{T}}$ are discussed in this section. As shown in figure 9, φ_{j1} represents j-th degree of freedom based on 1st. mode ; j = 1(translation), = 2 (rotation) and =3 (shear deformation). Figure 10 shows ω_1/ω_x, $(\varphi_{21} + \varphi_{31})/\varphi_{11}$ and $\varphi_{31}/\varphi_{11}$.

In the case of a = 0.5 (without eccentricity), ω_1/ω_x becomes 1 regardless of either b or β/ω_θ. Reduced a leads to decreasing of ω_1/ω_x, which is more remarkable in the case of smaller β/ω_θ. In addition, β/ω_θ more affects the reduction of ω_1/ω_x when b is larger.

$(\varphi_{21} + \varphi_{31})/\varphi_{11}$, which means torsion between two x-directional walls, becomes large when β/ω_θ is small. If b is larger, β/ω_θ more affects the increase of $(\varphi_{21} + \varphi_{31})/\varphi_{11}$.

A few previous researches led to the fact that $\varphi_{31}/\varphi_{11}$ is not changed when a is constant. However, we can find that $\varphi_{31}/\varphi_{11}$ has some relation to a, as shown on the right side of figure 10. It is because the former researches considered static concentric forces applied to center of mass.

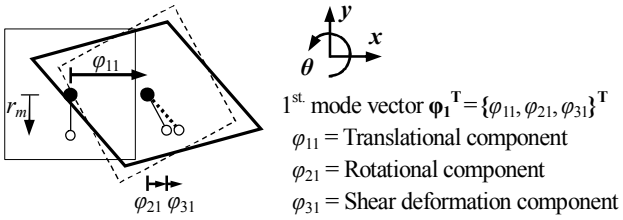


Figure 9 1st. Mode Shape of the Structure

4.3 Equivalent Eccentric Ratio Considering Floor Flexibility

Deformation of floor leads to reduced deformation of transverse walls as shown on the left side of figure 11. It can be replaced with reduced stiffness of transverse walls of rigid floor model as shown on the right side of figure 11. The two models are described as '*Flexible floor model*' and '*Equivalent rigid floor model*', respectively. In this section, influence of flexible floor is quantitatively presented using these two models.

The reduction ratio of transverse walls' stiffness of equivalent rigid floor model is defined as '*Effective transverse walls' stiffness coefficient k*'. This reduction results in decreasing of ω_θ/ω_x. Let $\overline{\omega}_\theta/\omega_x$ be that of equivalent rigid floor model. Its natural circular frequency of 1st. mode $\overline{\omega}_1$ is obtained by solving equation (10) and (32).

$$\overline{\omega}_1^2 = \frac{\omega_x^2}{2}\left[1 + \frac{\overline{\omega}_\theta^2}{\omega_x^2} - \sqrt{\left(1+\frac{\overline{\omega}_\theta^2}{\omega_x^2}\right)^2 - 4\left(\frac{\overline{\omega}_\theta^2}{\omega_x^2} - \bar{e}_y^2\right)}\right] \tag{33}$$

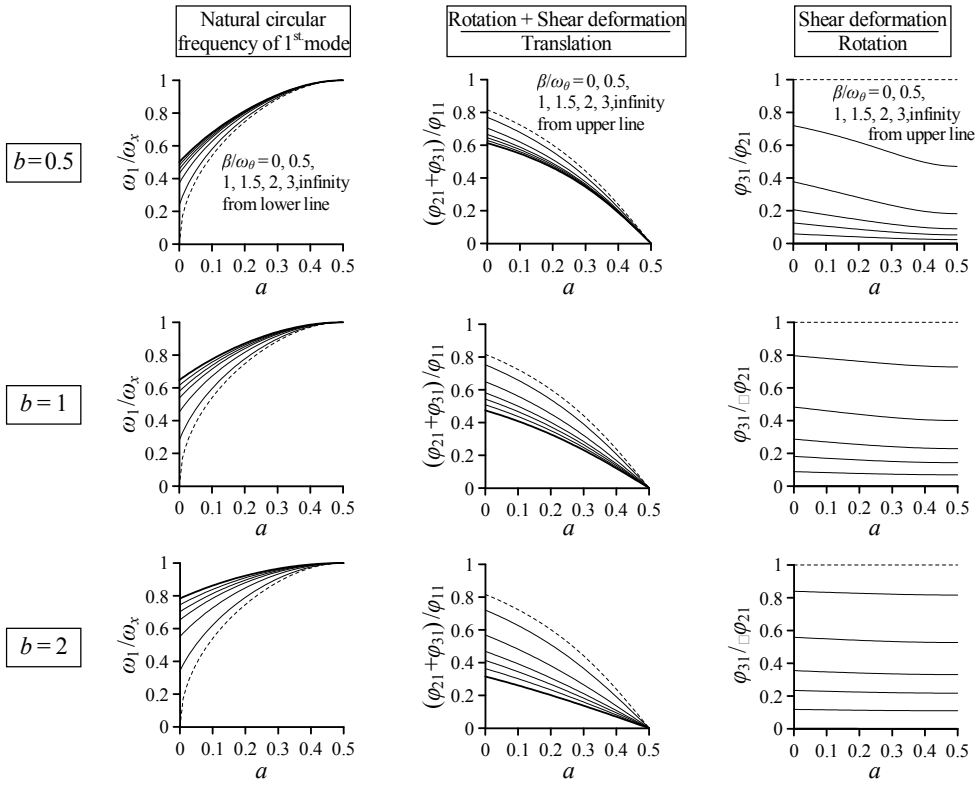


Figure 10 Relationship between β/ω_θ and Dynamic Properties of the System ($\beta/\omega_\theta = 0$ (Dash lines), 0.5, 1, 1.5, 2, 3 and infinity (Bold lines), $c = 1$)

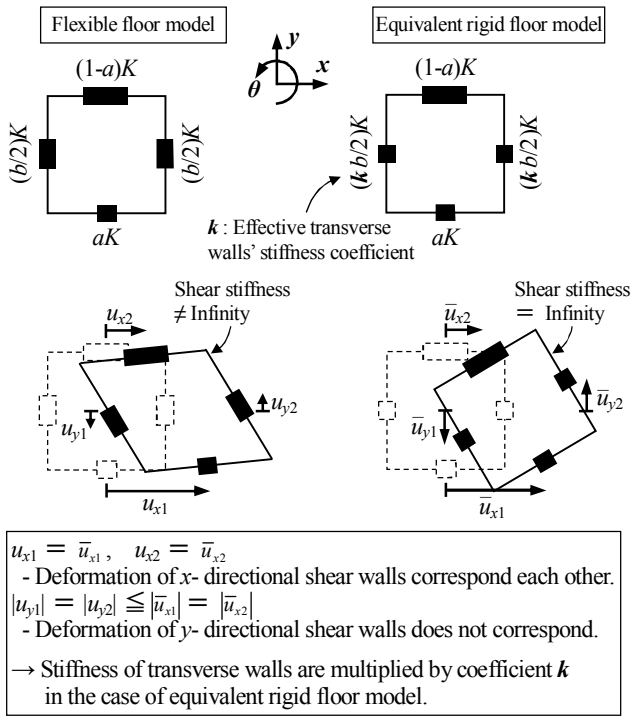


Figure 11 Flexible Floor Model and Equivalent Rigid Floor Model

By solving equation (33) for $\overline{\omega}_\theta / \omega_x$,

$$\frac{\overline{\omega}_\theta}{\omega_x} = \sqrt{\frac{\overline{\omega}_1^2}{\omega_x^2} + \frac{\overline{e}_y^2}{1 - \overline{\omega}_1^2 / \omega_x^2}} \tag{34}$$

By substituting ω_1, which is natural circular frequency of flexible floor model, into $\overline{\omega}_1$, we can obtain k as well as $\overline{\omega}_\theta / \omega_x$. As a result, natural circular frequencies and displacement modes of x- directional walls of both models agree exactly with respect to one another (Appendix B). Moreover, eccentric ratio of equivalent rigid floor model is calculated using above k. This is defined as '*Equivalent eccentric ratio considering floor flexibility* R'_{ex}'.

Figure 12 shows k and R'_{ex}. Other parameters are the same as those of figure 10. Reduced a leads to decreasing of k, which is more remarkable in the case of smaller β/ω_θ. In addition, the larger b is, the smaller k becomes if a and β/ω_θ are fixed. Right side of figure 12 shows relationship between R_{ex} and R'_{ex}. R_{ex} corresponds to R'_{ex} exactly when β/ω_θ is infinity. R'_{ex} nearly equals to R_{ex} in the case of b = 0.5. However, R'_{ex} obviously becomes larger than R_{ex} in the case of b = 1 or 2.

According to above discussion, flexible floor apparently leads to decreasing of stiffness of transverse walls or increasing of eccentric ratio. The influence is demonstrated theoretically.

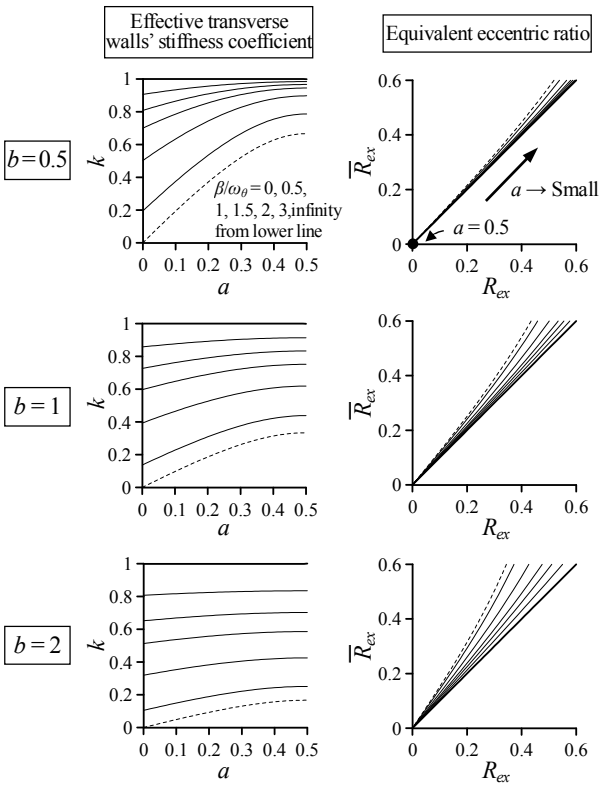


Figure 12 Effective Transverse Walls' Stiffness Coefficient k and Equivalent Eccentric Ratio $\overline{R}_{ex}$ (β/ω_θ = 0 (Dash lines), 0.5, 1, 1.5, 2, 3 and infinity (Bold lines), c = 1)

5. SEISMIC RESPONSE ANALISIS

5.1 Maximum Displacement of the System Subjected to Earthquake Characterized by Constant Acceleration Spectrum

In this chapter, basic characteristics of earthquake response of flexible floor structure are examined. For simplified discussion, input motion is characterized by its pseudo acceleration spectrum. In addition, the response derived from only 1st. mode is considered.

Modal participation factor β_1 is obtained as follows.

$$\beta_1 = \boldsymbol{\varphi}_1^{\mathrm{T}}\mathbf{m}\{\mathbf{1}\}/\boldsymbol{\varphi}_1^{\mathrm{T}}\mathbf{m}\boldsymbol{\varphi}_1 \tag{35}$$

Let $S_{pa}(h_0=0.05)$ be constant pseudo acceleration spectrum for damping ratio $h_0 = 0.05$. $S_{pa}(h_0 = 0.05)$ = 196cm/s^2 is used, which shows that base shear coefficient C_0 = 0.2 is assumed. Note that natural period of 1st. mode T_1 (= $2\pi/\omega_1$) is located in the spectrum constant area.

Maximum displacement vector $\mathbf{u_{max}}$ is calculated as follows.

$$\mathbf{u_{max}} = \beta_1 \boldsymbol{\varphi}_1 S_{pa}(h_0 = 0.05)/\omega_1^2 \tag{36}$$

Damping ratio of 1st. mode is assumed to be 0.05 in all cases, so that response reduction by damping is not considered.

5.2 Distribution of Maximum Displacement

Maximum displacement in three points are compared ; center of mass (c.m.), flexible side wall and stiff side wall in x- direction. a = 0.15, 0.2, 0.25, 0.33, 0.4 and β/ω_θ = 0, 0.5, 1, 1.5, 2, 3, infinity are examined. T_x (= $2\pi/\omega_x$) = 0.4 second is assumed.

At first, c = 1 is assumed, and three cases of b (= 0.5, 1 and 2) are shown in figure 13(a). In the case of small a, structure becomes more vulnerable to torsion according as β/ω_θ is reduced. In other words, the smaller β/ω_θ becomes, the larger maximum displacement in flexible side wall becomes. In addition, It is particularly notable that translational displacement in c.m. is also increased when β/ω_θ is small, compared to β/ω_θ = infinity especially in the case of small a. This certainly results from reduced ω_1 attributed to small β/ω_θ. Since timber houses have short natural period T_1 as mentioned above, maximum displacement is likely to be proportional to square of T_1.

In figure 13(b), b = 1 is assumed, and two cases of c (= 0.5 and 2) are shown. In the case of c = 2, the response is unlikely to be greatly affected by reduced β/ω_θ because transverse walls are not effective to resist torsion due to its plan shape. In other words, reduced floor stiffness especially affects the maximum responses of stiffness eccentric buildings which rely on transverse walls for their rotational stiffness.

Finally, we try to set the condition that horizontal diaphragm can be assumed to be rigid. Judging from figure 10 and 13, β/ω_θ > 1.5 can be the criteria of rigid floor apparently. In other words, dynamic properties/responses when β/ω_θ is larger than 1.5 are about the same as those of structure with rigid floor. Thus, we can solve equation (31) for α_f using β/ω_θ = 1.5 and h = 2.73m.

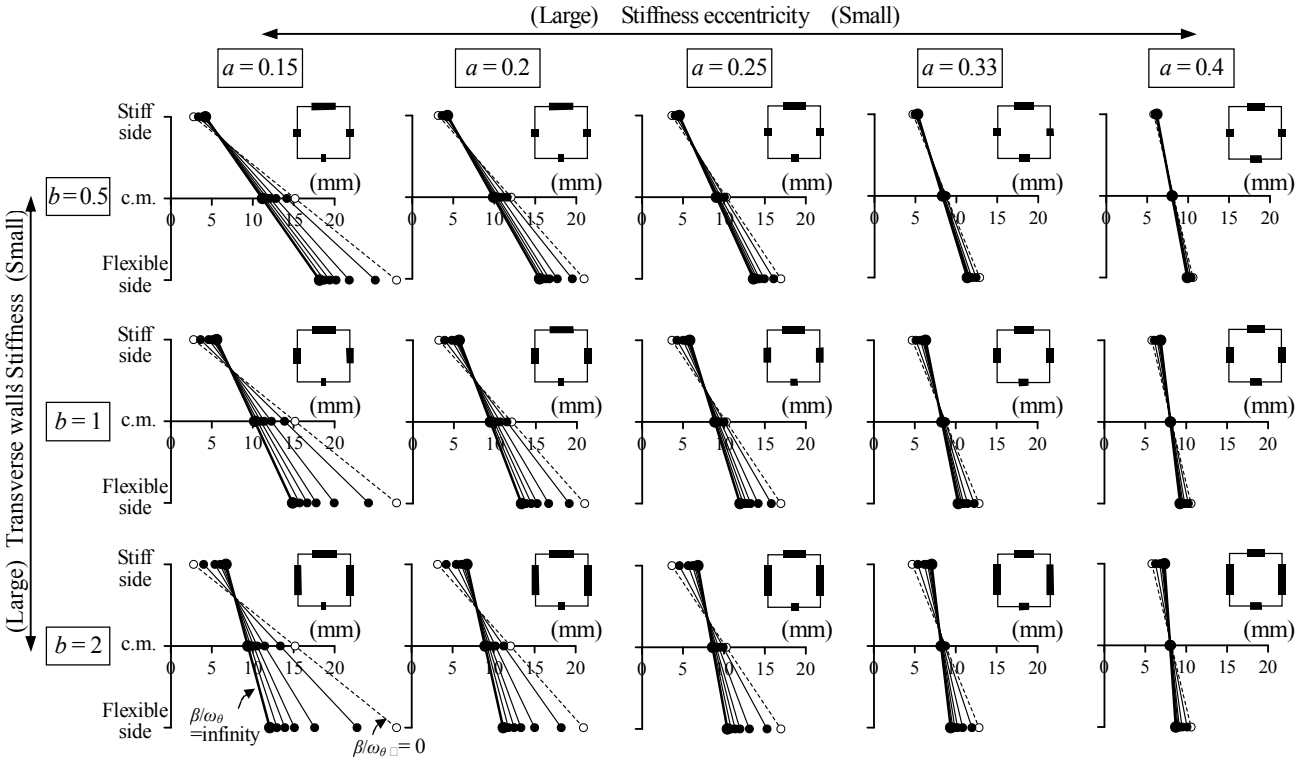
$$\alpha_f = 0.052\left(1+b/c^2\right)\alpha_x L_y^2 \approx \frac{L_y\left(1+b/c^2\right)}{9.7}\frac{\alpha_x}{2}L_y \tag{37}$$

Equation (37) means minimum floor strength factor for rigid floor assumption derived from structural dynamics. However, more close investigation should be required regarding the criteria of β/ω_θ.

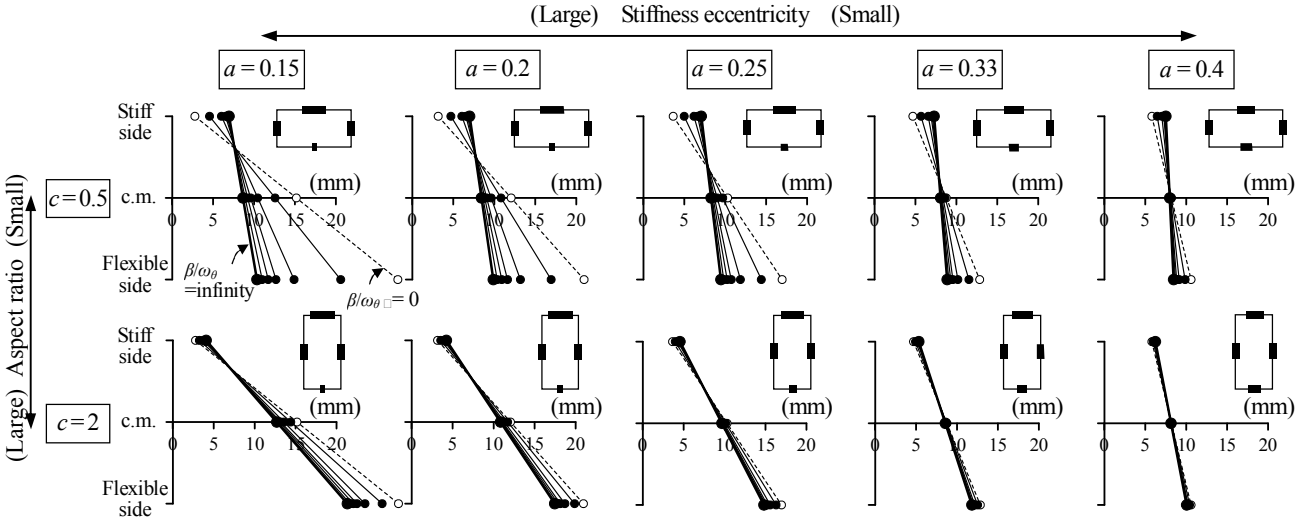
6. CONCLUSIONS

In this paper, evaluation method for dynamic properties of timber structure with flexible floor and uni-axial eccentricity is proposed. Based on the method, estimation of earthquake response is also demonstrated. The following are findings obtained.

1) Flexibility of horizontal diaphragm is represented by β/ω_θ derived from equation of motion for simplified model. β/ω_θ has two interpretations ; one is the ratio of floor shear stiffness to rotational stiffness of the structure (equation (28)), and another is the value determined by wall length, stiffness balance of x- and y-directional walls and the dimension of the building as well as floor strength factor (equation (31)).



(a) Influence of Stiffness Eccentricity a and Transverse walls' Stiffness b (c = 1 = Constant)



(b) Influence of Stiffness Eccentricity a and Aspect Ratio c (b = 1 = Constant)

Figure 13 Maximum Displacement of the System Subjected to Earthquake Characterized by Constant Acceleration Spectrum (β/ω_θ = 0 (Dash lines), 0.5, 1, 1.5, 2, 3 and infinity (Bold lines))

2) Relationship between floor flexibility and dynamic properties is obtained by solving eigen equation (equation (32)) as shown in figure 10.
3) Shear Deformation of floor leads to reduced deformation of transverse walls. It is replaced with reduced stiffness of transverse walls, and equivalent eccentric ratio considering floor stiffness is evaluated (figure 12).
4) Reduced stiffness of floor results in not only increasing of torsion but also increasing of translational displacement in center of mass.
5) Dynamic properties/responses are about the same as those of structure with rigid floor when β/ω_θ is larger than 1.5. Therefore, minimum floor strength factor for rigid floor assumption is expressed by equation (37).
6) Reduced floor stiffness remarkably affects the maximum responses of stiffness eccentric buildings which rely on transverse walls for their rotational stiffness.

References:

Architectural Institute of Japan et al. : Report on the Hanshin-Awaji Earthquake Disaster, Building Series Volume4, Editorial

Committee for the Report on the Hanshin-Awaji Earthquake Disaster, pp.228-231, 1998.3

Yamazaki, Y., Kasai, K., Sakata, H. and Ooki, Y. : Torsional Seismic Response Control by Viscoelastic Damper for Three-dimensional Wood-frame Structure with Stiffness Eccentricity, *Journal of structural and construction engineering. Transactions of AIJ*, Architectural Institute of Japan, **655**, 1691-1700, 2010.9

Shimizu, H. et al. : Study on Seismic Performance of Traditional Wooden Structure by Full Scale Shaking Table Tests: Result of Suburban Typical House with Large Wooden Section, *Journal of structural and construction engineering. Transactions of AIJ*, Architectural Institute of Japan, **657**, 2001-2008, 2010.11

Japan Housing and Wood Technology Center : Mokuzoujikugumikohojutakuno Kyoyoouryokudosekkei (In Japanese), pp.75-76, 2009.6

Agawa, M. et al. : Experimental Study on Dynamic Properties of Timber Shear Wall Structures with Eccentricity, *Journal of structural and construction engineering. Transactions of AIJ*, Architectural Institute of Japan, **558**, 157-164, 2002.8

Kawai, N. et al. : Design Method and Shaking Table Test on 3-story Wood Houses by Post and Beam Construction, *Summaries of technical papers of Annual Meeting Architectural Institute of Japan*, Architectural Institute of Japan, C-1:229-230, 2010.9

Odani, R. et al. : Calculation Method for Eccentricity and Correction Coefficient of Torsional on Consideration with Flexible Horizontal Diaphragm: in Case of Single Span Model, *Journal of structural and construction engineering. Transactions of AIJ*, Architectural Institute of Japan, **654**, 1483-1490, 2010.8

The Japan Building Disaster Prevention Association : Mokuzoujutakuno Taishinshindanto Hokyouhoho (In Japanese), pp.74-75, 2006.6

Kasai, K., Yamashita, T., Yamazaki, Y. and Igusa, T. : Spectrum-Based Response Prediction of Asymmetric Structure with Supplemental Viscous Dsmping, *Journal of structural and construction engineering. Transactions of AIJ*, Architectural Institute of Japan, **636**, 225-234, 2009.2

Miyazawa, K. et al. : A Study on Static and Dynamic Behavior of Wooden Houses with Three Dimensional Eccentricity of Shear-Walls Part6 Seismic Behavior of Three Dimensional Eccentric Structure and Guideline for Earthquake-Proof Design, *Summaries of technical papers of Annual Meeting Architectural Institute of Japan*, Architectural Institute of Japan, C-1:277-278, 2010.9

Kajikawa, H. et al. : The Scope of Rigid Floor Assumption for Single-Story Box Type Building : A Study on Horizontal Twist Behavior Considering Floor Stiffness by Wooden Construction (Part 1), *Journal of structural and construction engineering. Transactions of AIJ*, Architectural Institute of Japan, **595**, 79-85, 2005.9

Appendix:

A. Wall Length Considered in This Paper

In wall length method which is the most popular design method for timber houses provided by Japanese building standard law, timber houses are categorized into heavy buildings or light buildings. Demand length of wall depends on such a building type and the number of story etc.. In this study, wall length α_x = 0.15, 0.3 and 0.45m/m^2 are demonstrated, and it is determined by referring to the amount provided by the law.

B. Relationship between Flexible Floor Model and Equivalent Rigid Floor Model

In section 4.3, we made a condition that natural circular frequencies of two models, flexible floor model and equivalent rigid floor model, agree with respect to one another. Eigen vector and participation factor of two models are also presented here.

Eigen equation of 1$^{st.}$ mode is expressed as follows.

$$(-\omega_1^2\,\mathbf{m}+\mathbf{k})\,\boldsymbol{\varphi}_1 = 0 \tag{B1}$$

By expanding above matrix and vector into three equations, we can obtain the following relation from the fist row.

$$\frac{\varphi_{21}+\varphi_{31}}{\varphi_{11}} = \frac{1-\omega_1^2/\omega_x^2}{\bar{e}_y}, \qquad \beta_1 = \frac{\varphi_{11}}{\varphi_{11}^2+\varphi_{21}^2+\varphi_{31}^2+2\alpha\varphi_{21}\varphi_{31}} \tag{B2a,b}$$

Let $\bar{\boldsymbol{\varphi}}_1 = \{\,\bar{\varphi}_{11}, \bar{\varphi}_{21}\,\}^{\mathrm{T}}$ and $\bar{\beta}_1$ be eigen vector and participation factor of equivalent rigid floor model, respectively. They are obtained as follows.

$$\frac{\bar{\varphi}_{21}}{\bar{\varphi}_{11}} = \frac{1-\omega_1^2/\omega_x^2}{\bar{e}_y}, \qquad \bar{\beta}_1 = \frac{\varphi_{11}}{\varphi_{11}^2+\varphi_{21}^2} \tag{B3a,b}$$

We can see that $\bar{\varphi}_{21}/\bar{\varphi}_{11}$ agrees to $(\varphi_{21}+\varphi_{31})/\varphi_{11}$ exactly, which means displacement modes of *x*- directional walls of two models are similar. In addition, participation factors also agree in the case of $\alpha = 1$.

8CUEE CONFERENCE PROCEEDINGS
8th International Conference on Urban Earthquake Engineering
March 7-8, 2011, Tokyo Institute of Technology, Tokyo, Japan

PROBABILISTIC EVALUATION OF COLLAPSE POTENTIAL OF STRUCTURES WITH MAGNETO-RHEOLOGICAL (MR) DAMPERS

Yunbyeong Chae[1], James M. Ricles[2], and Richard Sause[2]

1) Graduate Research Assistant, Dept. of Civil and Environmental Engineering, Lehigh University, PA, USA
2) Professor, Dept. of Civil and Environmental Engineering, Lehigh University, PA, USA
yuc206@lehigh.edu, jmr5@lehigh.edu, rs0c@lehigh.edu

Abstract: The seismic collapse potential of a multi-story building with Magneto-Rheological (MR) dampers is investigated by performing incremental dynamic analyses (IDAs) to develop fragility curves for collapse. The building is designed with MR dampers to achieve a performance objective of 1.5% story drift and 3.0% story drift under the design basis earthquake (DBE) and maximum consider earthquake (MCE), respectively. Nonlinear time history analyses are conducted using OpenSees as a tool for the IDAs. A set of 22 recorded far-field ground motion pairs provided in the Applied Technology Council (ATC) Project 63 are used for the IDAs. A phenomenological based deterioration model for beam-to-column connections calibrated from experimental data is incorporated into OpenSees to enable strength degradation in the lateral load resisting system to be modeled, along with the Maxwell Nonlinear Slider (MNS) MR damper model. The MR dampers are controlled either in passive or semi-active mode, where five different semi-active control strategies are considered for the MR dampers. The collapse fragility curves for the various control strategies are obtained along with the case where the building is designed as a conventional MRF without MR dampers. Collapse fragilities and the collapse margin ratio are compared for each case in order to assess the effectiveness of semi-active and passive dampers in reducing seismic collapse.

1. INTRODUCTION

In earthquake engineering, collapse implies that a structural system, or a part of it, is incapable of maintaining gravity load carrying capacity in the presence of seismic effects (Ibarra and Krawinkler 2005). When a building is subjected to large story drifts, it is vulnerable to dynamic instability due to P-Δ effects and deterioration in strength and stiffness of its structural components, subsequently, resulting in collapse of the system. Protection against collapse has always been a major concern in the design of structures. The recently developed FEMA P695 (ATC 2009) document provides a methodology for seismic collapse assessment of structures.

While several studies have been conducted to assess the performance of supplemental damping systems and their effectiveness in mitigating the seismic hazard of structures under the design basis earthquake (DBE) and maximum considered earthquake (MCE), the collapse resistance of buildings with Magneto-Rheological (MR) dampers has not been investigated. The seismic collapse potential of structures with passive supplemental damping systems has been investigated by a few researchers using the incremental dynamic analysis (IDA) method (Solberg et al. 2007; Marshall and Charney 2010; Miyamoto et al. 2010). In this paper, the collapse resistance capacity of a 3-story building with MRFs and braced frames with MR dampers designed for seismic performance under the DBE and MCE is assessed for seismic collapse using the procedure given in FEMA P695. The nonlinear time history analyses used in the IDA method are conducted using OpenSees (2009). A phenomenological-based model developed by Ibarra and Krawinkler (2005) and modified by Lignos (2008) for modeling deterioration in beam plastic hinge regions in MRFs is incorporated into OpenSees. The IDA are performed on the building using five different controllers (Chae 2011), including: i) passive control; ii) linear quadratic regulator (LQR); iii) sliding mode control (SMC); iv) decentralized bang-bang control (DBB); and v) phase angle control (PAC). Collapse fragility curves are obtained using the ensemble of 22 recorded far-field ground motion pairs (i.e., 44 far-field ground motions) provided in FEMA P695. The collapse fragility curves for the various control strategies are compared in order to assess the performance of the MR damper control strategies in mitigating structural collapse under extreme earthquake ground motions.

2. BEAM PLASTIC HINGE DETERIORATION MODEL

The P-Δ effect and the strength and stiffness deterioration of structural components are considered to be

the major contributors to the collapse of a structural system under seismic loading. The P-Δ effect is well-understood and mathematical models have been formulated for use in linear and nonlinear structural analysis, while the modeling of strength and stiffness deterioration under seismic loading is an on-going research topic. For the accurate evaluation of the collapse of a structure, it is necessary to construct a model that is capable of capturing the strength and stiffness deterioration of structural components under seismic loading. In this section, recently developed deterioration models are introduced. The models are used for the IDA presented later in this paper.

Ibarra and Krawinkler (2005) developed a hysteretic inelastic deterioration model to describe the moment-rotation behavior in the plastic hinge region of a steel or concrete beam. The model is based on a backbone curve that defines a reference skeleton behavior of a non-deteriorated system. A set of rules are used to define the basic characteristics of the hysteretic behavior between the bounds defined by the backbone curve as well as deterioration in strength and stiffness with respect to the backbone curve.

Lignos (2008) modified the Ibarra-Krawinkler model based on observations from data from several hundred tests that had been conducted on steel and reinforced concrete beams. Lignos modified the backbone curve and the cyclic deterioration modeling in the original Ibarra-Krawinkler model, where the new backbone curve proposed by Lignos is shown in Figure 1. In Figure 1, δ_c is the cap deformation (deformation associated with capacity F_c for monotonic loading); F_y is the effective yield strength; δ_y is the effective yield deformation (=F_y/K_e); K_e is the effective elastic stiffness; F_r is the residual strength capacity; δ_r is the deformation at residual strength; δ_u is the ultimate deformation capacity; δ_p is the plastic deformation capacity associated with monotonic loading; δ_{pc} is the post-capping deformation capacity associated with monotonic loading; F_{yp} is the predicted effective yield strength; F_{yn} is the nominal effective yield strength; and κ is the residual strength ratio (=F_r/F_y). The capacity F_c mentioned above is the strength cap associated with the maximum strength incorporating average strain hardening. The strain hardening ratio α_s and the post-capping stiffness ratio α_c are defined as $\alpha_s = K_s/K_e = [(F_c/F_y)/\delta_p]/K_e$ and $\alpha_c = K_{pc}/K_e = (F_c/\delta_{pc})/K_e$, respectively. The reference energy dissipation capacity E_t, which is used to describe the cyclic deterioration, is defined by using the parameter δ_p in the normalization of the reference energy dissipation capacity, i.e., $E_t = \Lambda\delta_p$, where Λ denotes the reference cumulative deformation capacity.

3. MODELING OF 3-STORY BUILDING

The 3-story building shown in plan and elevation in Figures 2 and 3, respectively, was used for the study. The building has two perimeter MRFs along each of its sides and braced internal bays with MR dampers (called *damped brace frames* (DBFs)) at the 2nd and 3rd floors. The structure was designed using the simplified design procedure developed by Chae et al. (2011) to achieve a performance objective of 1.5% story drift and 3.0% story drift under the DBE and MCE, respectively. The 3-story building was scaled down using a scale factor of 0.6 for the study since a reduced scale model of the building will be constructed and tested in the laboratory in future research. The members of the MRF are proportioned using a weak beam-strong column design. Yielding is expected to occur predominately at the ends of the MRF beams and at the base of the columns in the first story of the MRF and DBF. The beams and diagonal bracing members in the DBF have pin-ended connections. The beams are axially restrained in the DBF by the floor diaphragm (which is assumed to be rigid in-plane) at each floor level and expected to remain elastic. The diagonal bracing is expected to remain elastic up to 135% story drift (Chae 2011). Tables 1 and 2 summarize the member sizes for the 0.6-scale building. The OpenSees model for the scaled building is shown in Figure 4. Symmetry in the floor plan and ground motions along only one principal axis of the building were considered in the analysis. Hence, only one-quarter of the building was modeled consisting of one MRF, one DBF, and the gravity frames that are within the tributary area of the MRF and DBF.

Each beam of the MRF in the model consists of three elements: two inelastic deterioration elements with zero length at the column faces based on the modified Ibarra-Krawinkler model; and one linear elastic element between the deterioration elements. The parameters for the deterioration element are summarized in Table 3, where M_y, θ_p and θ_{pc} denote the yield moment, plastic rotation capacity and the post-capping rotation capacity, respectively. The values of these parameters are based on Lignos and Krawinkler (2009) for the beam sections used in the MRF.

The columns of the MRF and DBF are modeled using a nonlinear distributed plasticity force-based beam-column element. Each fiber is modeled with a bilinear stress-strain relationship with a post-yielding stiffness that is 0.01 times the elastic stiffness. The columns extend below the ground level in the model to the base, where they are pinned. The beam-to-column joints in the MRF are modeled using a nonlinear panel zone element, where shear and symmetric column bending deformation modes are considered (Seo et al. 2009). Doubler plates in the panel zones of the MRF are included in the model. The beams and braces of the DBF are modeled using linear elastic truss elements. The gravity frames are idealized using the concept of a lean-on column, where an elastic beam-column element with geometric stiffness is used to model the lean-on column. The section properties of the lean-on column are obtained by taking the sum of the section properties of each column of the gravity frames within the tributary area (i.e., one quarter of the floor plan) of the MRF and the DBF.

The structural model in Figure 4 has two major structural components that can lead to dynamic instability under extreme earthquake ground motions: (1) negative stiffness induced by the gravity loads acting on the lean-on

column (the P-Δ effect); and (2) strength deterioration in the inelastic deterioration elements in the beams of the MRF. The columns of the MRF and DBF are assumed to have sufficient strength and compactness of their cross-sections such that no deterioration in strength or stiffness of the columns is expected to occur.

To model a rigid floor diaphragm at each floor level the top node of each panel zone element in the MRF and the beam-column joint in the DBF are horizontally constrained together with the node of the lean-on column, while the vertical and rotational DOFs are released. The MR damper is assumed to be located between the top of the diagonal bracing and beam-to-column joint of the DBF. The variable current MNS model developed by (Chae 2011) is used to model the MR dampers for the nonlinear time history analysis.

Large-scale MR dampers were used for the study which can generate a 200kN damper force at a velocity of 0.1m/sec. (Chae et al. 2010). The damper has a stroke limit of ±279mm. The story height of the 3-story building is 2.286m, implying that the dampers will reach their stroke limit at 12.2% story drift. Since large story drifts can be expected in a collapse simulation, the MR damper may bottom out with respect to their stroke limit under extreme earthquake ground motions. In this case, a gap or the hook element should be included in the model to account for the dynamic behavior associated with reaching the stroke limit, as suggested by Miyamoto et al. (2010). The MR dampers in this study are assumed to have sufficient stroke limit to accommodate the large story drifts during a collapse simulation since no experimental data exists that can be used to model the effect of bottoming out of the dampers.

4. GROUND MOTIONS

As noted previously, the far-field ground motion record set provided in FEMA P695 (ATC 2009) was selected as ground motions for the IDA. These ground motions were selected from the PEER-NGA data base to permit evaluation of the record-to-record (RTR) variability of the structural response and calculation of the median of the intensity of spectral acceleration at which collapse occurs. Among the 22 earthquakes, 14 occurred in the United States and 7 in other countries. Event magnitudes range from M6.5 to M7.6, with an average magnitude of M7.0. Each earthquake has two horizontal components so that a total of 44 ground motions are used for the IDA.

FEMA P695 recommends the use of spectral acceleration at the fundamental period of a structure, S_{aT_1}, as the intensity measure (IM). The ground motions are scaled up (or down) based on the spectral acceleration at the fundamental period of the structure. The MR damper stiffness depends on its displacement amplitude (Chae 2011). Hence, the effective fundamental period of the structure is dependent on the amplitude of the damper displacements, which is a function of the intensity of ground motion. In this paper, the fundamental period of the structure without MR dampers is used to determine the spectral acceleration corresponding to the IM, rather than using the effective fundamental period of the structure with the dampers. The fundamental period without the MR dampers is 0.94 sec. (Chae 2011), and the scaling of ground motions is performed based on the spectral acceleration at this period.

5. CONTROLLERS

As noted previously, five different control strategies for MR dampers are used in this study, namely: i) passive control; ii) linear quadratic regulator (LQR); iii) sliding mode control (SMC); iv) decentralized bang-bang control (DBB); and v) phase angle control (PAC). More details on these controllers can be found in Chae (2011). A constant current with I=2.5A is supplied to the MR dampers for passive control, while either I=0.0A or 2.5A is used for the semi-active controllers.

6. INCREMENTAL DYNAMIC ANALYSES

The incremental dynamic analysis (IDA) curves are a set of plots that correlate a damage measure (DM) with the IM that characterizes the applied scaled accelerograms (Vamvatsikos and Cornell 2002). The roof drift ratio of the building structure, θ_{roof}, is selected as the DM for this study. A ground motion is scaled up until dynamic instability occurs, where an IDA curve becomes a flat line, i.e., at collapse. Each selected ground motion is gradually scaled up until θ_{roof} reaches 17% or collapse occurs. For the 44 ground motions in the ensemble, the IDA curves all became flat indicating collapse before θ_{roof} reached 17%. The median roof drift when the IDA curves become flat was approximately 14%.

Figures 5 through 10 show the IDA curves for the structure with various control strategies. These results are for the 44 ground motions. The collapse margin ratio (CMR) was determined for each case, where the CMR is defined by FEMA P695 (ATC 2009) as the ratio of the median value for the collapse spectral acceleration, $\hat{S}_{CT}$, to the spectral acceleration of the MCE, S_{MT}, at the fundamental period of the structural system:

$$\text{CMR} = \frac{\hat{S}_{CT}}{S_{MT}} \tag{1}$$

$\hat{S}_{CT}$ for each control case is calculated from the IDA curves and marked in Figures 5 through 10 along with the S_{MT}. Table 4 shows the CMR values for each control strategy. Since the purpose is to evaluate the collapse capacity of a structure with MR dampers with various control strategies, the further adjustment of the CMR values based on the spectral shape factor (SSF) (ATC 2009) is not considered in this study. The results in Table 4 show that when passive control is used that the CMR value increases by about 26% compared to the no damper case, demonstrating the benefit of using MR dampers. The overall performance of each semi-active controller is similar to that of the passive control case, except for the LQR controller.

The LQR controller shows the highest CMR value, but the improvement over passive control is about 7%.

7. COLLAPSE FRAGILITY CURVES

A collapse fragility curve is the cumulative distribution function (CDF) which relates the intensity of ground motion to the probability of collapse, and is constructed utilizing the results of the IDAs (ATC 2009). For a prescribed level of spectral acceleration S_{aT_1} the number of cases, N_{SaT1}, where collapse occurs for a spectral acceleration equal to or less than this value of S_{aT_1} among the IDA curves for the various ground motions is counted. The probability of collapse associated with this value of S_{aT_1} is N_{SaT1}/N_{tot}, where N_{tot} is the total number of IDA curves (i.e., ground motions). The probability of collapse typically follows a lognormal distribution. A set of collapse data points can then be fitted using the lognormal distribution to construct the collapse fragility curve. The fitted lognormal distribution is defined by two parameters, namely, the median collapse spectral acceleration ($\hat{S}_{CT}$), and the standard deviation of the natural logarithm of the collapse spectral accelerations (ζ). The CDF with a lognormal distribution, $F(x)$, is mathematically expressed as

$$F(x) = \int_0^x \frac{1}{s\zeta\sqrt{2\pi}} \exp\left[-\frac{(\ln s-\lambda)^2}{2\zeta^2}\right] ds = \Phi\left(\frac{\ln x-\lambda}{\zeta}\right) \quad (2)$$

where, Φ is the cumulative distribution function of the standard normal distribution and $\lambda = \ln \hat{S}_{CT}$. Figure 11 compares the collapse fragility curves for passive control with the no damper case. The fragility curve for passive control is located to the right of the fragility curve for the no damper case, which means the collapse potential of the structure with passive control is lower than that for the structure with no dampers. This result is also illustrated in Table 4 by a comparison of the CMR values, where passive control has a higher CMR value. The collapse fragility curve for various semi-active control strategies are compared to the collapse fragility curve for passive control in Figures 12 through 15. The collapse fragility curves for the semi-active control strategies are shown to be similar to passive control, except for the LQR controller. The collapse fragility curve for the building with the LQR controller is more notably to the right of that for the passive control case (Figure 12) than for the other comparisons, indicating a lower probability of collapse compared to passive control, and consistent with having a higher CMR value in Table 4.

8. COLLAPSE MODE

The collapse mode of the building structure studied is characterized by the formation of plastic hinges in the beams and columns leading to a collapse mechanism. A soft story mechanism, where both ends of all columns at a particular story level develop plastic hinges, did not occur in any of the cases. The design methodology based on a strong column-weak beam design appears to have helped avoid a soft story collapse mechanism.

Figure 16 shows the deformed shape of the building with passively controlled MR dampers at the time of maximum drift under the 1994 Northridge earthquake (Canyon country, 000 component), where the ground motion was scaled to a spectral acceleration of S_{aT_1} =2.25g. Collapse for this ground motion occurs when S_{aT_1}=2.27g. Both ends of each beam in the 1st through 3rd floors in the MRF and the ground level of the 1st story columns for both the MRF and DBF form plastic hinges during the earthquake.

9. CONCLUSIONS

In this paper, the collapse potential of a 3-story steel frame building with MR dampers controlled by various control strategies was investigated. A model of the structure was developed using OpenSees that included strength and stiffness deterioration along with the P-Δ effect. Incremental dynamic analyses based on nonlinear time history earthquake simulations were performed to obtain the statistical response and collapse margin ratios (CMRs) for the structure. Five different control strategies for the MR dampers were used, and the collapse potential for each case was compared. The passive control of MR dampers with a 2.5A constant current input improved the CMR value by about 26% compared to the structure without MR dampers. The collapse fragility curves for sliding mode control, decentralized bang-bang control, and phase angle control resulted in almost the same collapse potential as passive control, while the LQR controller provided a reduction in the collapse potential. The CMR is about 7% greater for the structure with an LQR controller compared to passive control.

The LQR and SMC controllers require control gains to be specified. To reach more general conclusions about the seismic collapse potential of buildings with semi-active controlled MR dampers it is recommended that the effect of the control gains on the collapse potential be further investigated. In addition, other semi-active controllers and various structural geometries (e.g. the height of the building) should be included. The effect of a damper bottoming out on the collapse potential of structures with MR dampers also needs to be investigated.

Acknowledgements:

This paper is based upon work supported by grants from the Pennsylvania Department of Community and Economic Development through the Pennsylvania Infrastructure Technology Alliance, and by the National Science Foundation under Award No. CMMI-1011534, within the George E. Brown, Jr. Network for Earthquake Engineering Simulation Research (NEESR) program, Award No. CMS-0612661, and Award No. CMS-0402490 NEES Consortium Operation.

References:

Applied Technology Council (2009), *Quantification of Building Seismic Performance Factors*, ATC-63 Project Report (FEMA P695), Redwood City, CA.

Chae, Y. (2011), "Seismic Hazard Mitigation of Building Structures Using Magneto-Rheological Dampers," *Ph.D. Dissertation*, Lehigh University, PA.
Chae, Y., Dong, B., Ricles, J.M., and Sause, R. (2011), "Development of Simplified Design Procedure for Structures with Magneto-Rheological (MR) Dampers," *8th International Conference on Urban Earthquake Engineering*, Tokyo, Japan.
Chae, Y., Ricles, J.M., and Sause, R. (2010), "Development of a Large-Scale MR Damper Model for Seismic Hazard Mitigation Assessment of Structures," *9th US National and 10th Canadian Conference on Earthquake Engineering*, Toronto, Canada.
Ibarra, L.F. and Krawinkler, H. (2005), "Global Collapse of Frame Structures under Seismic Excitations," *John A. Blume Earthquake Engineering Center, Report No. 152*.
Lignos, D. (2008), "Sidesway Collapse of Deteriorating Structural Systems under Seismic Excitations" *Ph.D. Dissertation*, Stanford University, Stanford, CA.
Lignos, D., and Krawinkler, H. (2009), "Sidesway Collapse of Deteriorating Structural Systems under 17 Seismic Excitations," *John A. Blume Earthquake Engineering Center Report No. TR 172*, Department of Civil Engineering, Stanford University.
Marshall, J.D. and Charney, F.A. (2010), "A Hybrid Passive Control Device for Steel Structures, I: Development and Analysis," *Journal of Constructional Steel Research*, **66**, 1278-1286.
Miyamoto, H.K., Gilani, A.S.J., Ariyaratana, Ch., and Wada, A. (2010), "Probabilistic Evaluation of Seismic Performance of Steel Moment Framed Buildings Incorporating Damper Limit States" *ASCE Structures Congress*, Orlando, FL.
OpenSees (2009), *Open System for Earthquake Engineering Simulation*, Pacific Earthquake Engineering Research Center, University of California, Berkeley.
Seo, C.Y., Lin, Y.C., Sause, R, and Ricles, J.M. (2009), "Development of Analytical Models for 0.6 Scale Self-Centering MRF with Beam Web Friction Devices," *6th International Conference for Steel Structures in Seismic Area (STESSA)*, Philadelphia.
Solberg, K., Bradley, B., Rodgers, G., Mander, J., Dhakal, R., and Chase, J. (2007), "Multi-Level Seismic Performance Assessment of a Damage-Protected Beam-Column Joint with Internal Lead Dampers," *New Zealand Society for Earthquake Engineering Annual Conference (NZSEE 07)*, Palmerston North, New Zealand.
Vamvatsikos, D. and Cornell, C.A. (2002), "Incremental dynamic analysis" *Earthquake Engineering and Structural Dynamics*, **31**, 491-514.

Table 1 Member sizes for MRFs and gravity frames

Story (or Floor Level)	MRFs		Gravity Frames	
	Column	Beam	Column	Beam
1	W8X67	W18X46	W8X48	W10X30
2	W8X67	W14X38	W8X48	W10X30
3	W8X67	W10X17	W8X48	W10X30

Table 2 Member sizes for DBFs

Story (or Floor level)	Column	Beam	Diagonal bracing
1	W10X33	W10X30	-
2	W10X33	W10X30	W6X20
3	W10X33	W10X30	W6X20

Table 3 Parameters for inelastic deterioration element for MRF beams

Parameters	Beam size		
	W10X17	W14X38	W18X46
K_e (kN-m/m)	103531	462520	855748
M_y (kN-m)	116	383	564
α_s	0.002	0.002	0.002
θ_p (rad)	0.062	0.043	0.033
θ_{pc} (rad)	0.207	0.171	0.186
Λ	1.244	1.084	1.104
κ	0.01	0.01	0.01

Table 4 Collapse margin ratio (CMR) for 3-story building with various control strategies

	No damper	Passive	LQR	SMC	DBB	PAC
CMR	2.39	3.02	3.23	3.03	3.02	3.05

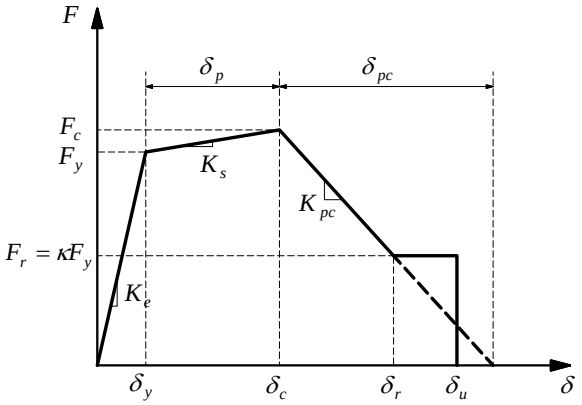


Figure 1 Modified backbone curve of Ibarra-Krawinkler model (after Lignos 2008)

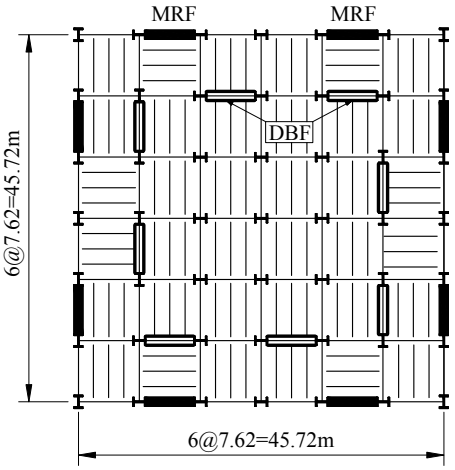


Figure 2 Floor plan of prototype building

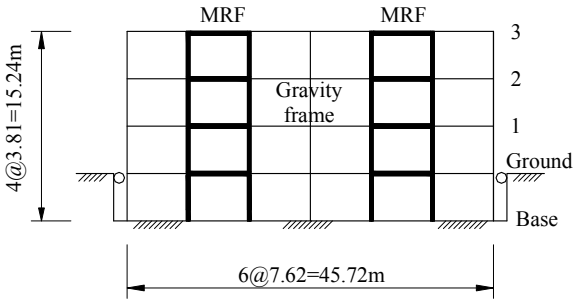


Figure 3 Exterior elevation of prototype building

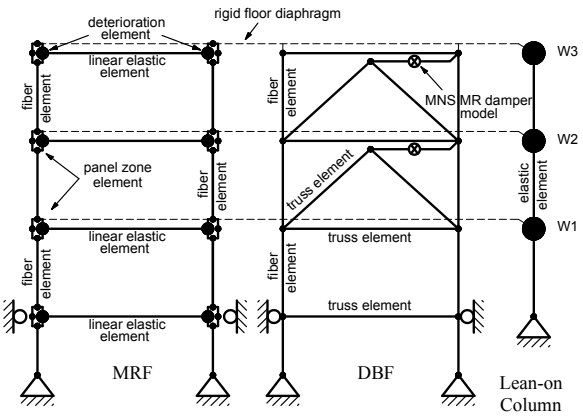


Figure 4 OpenSees model of the 3-story structure for the incremental dynamic analysis

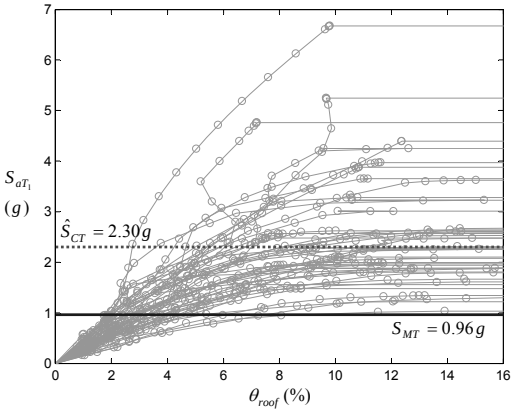


Figure 5 IDA curves: no damper case

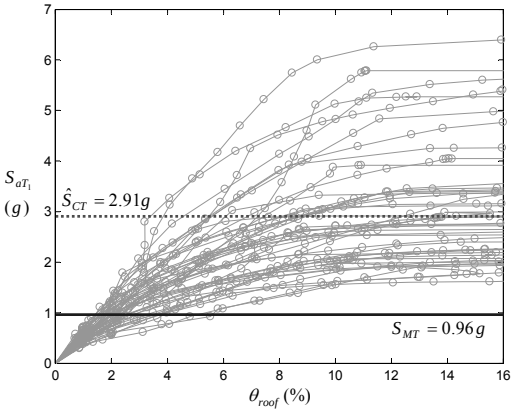


Figure 6 IDA curves: passive control

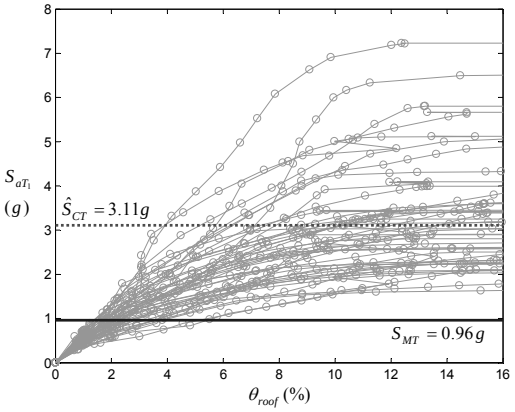


Figure 7 IDA curves: LQR control

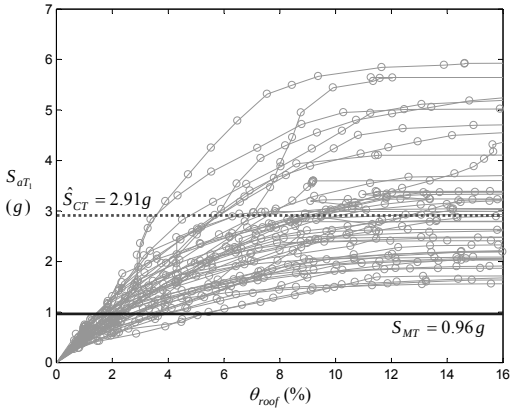


Figure 8 IDA curves: SMC

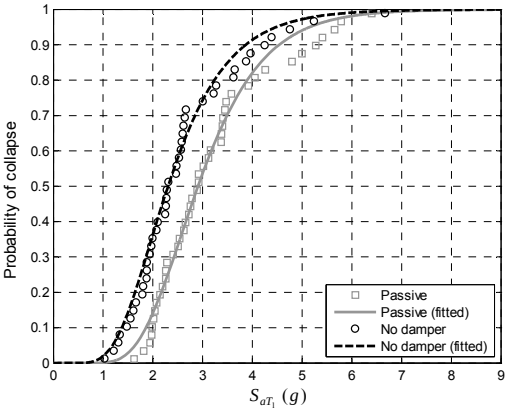


Figure 11 Collapse fragility curves where the no damper case is compared with passive control

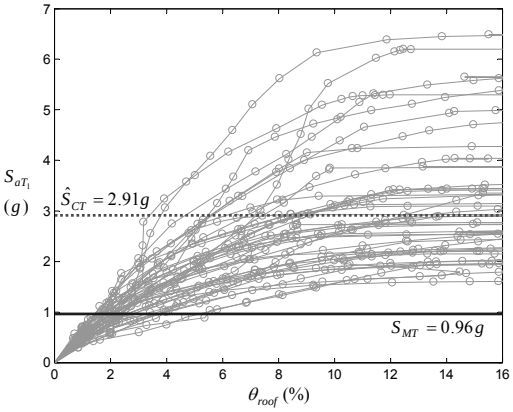


Figure 9 IDA curves: DBB control

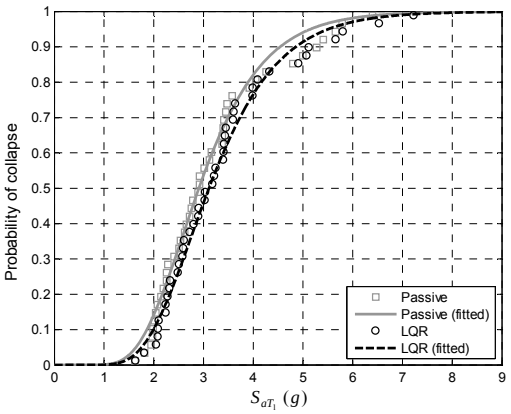


Figure 12 Collapse fragility curves where the LQR controller is compared with passive control

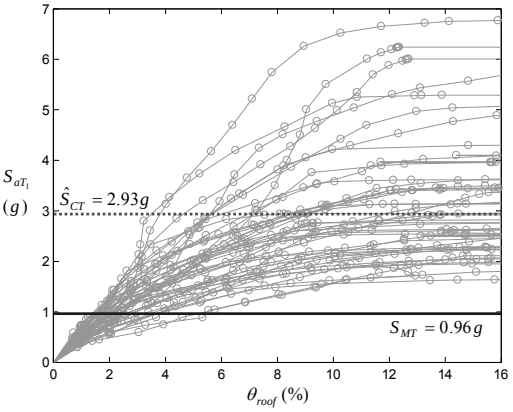


Figure 10 IDA curves: PAC

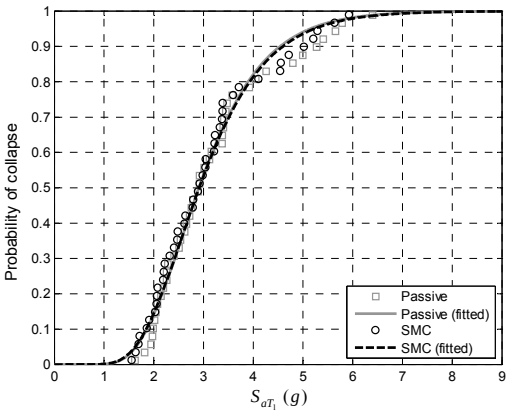


Figure 13 Collapse fragility curves where the SMC controller is compared with passive control

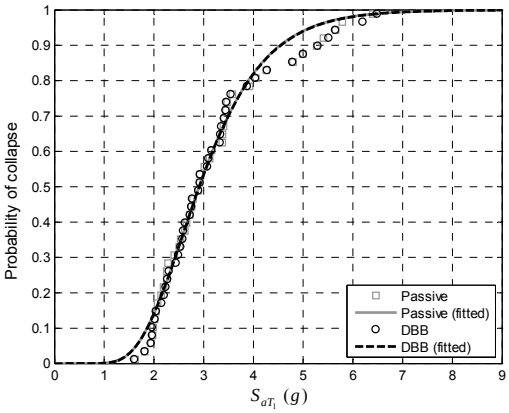


Figure 14 Collapse fragility curves where the DBB controller is compared with passive control

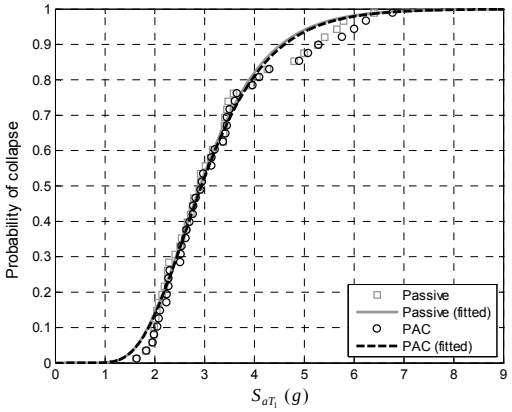


Figure 15 Collapse fragility curves where the PAC controller is compared with passive control

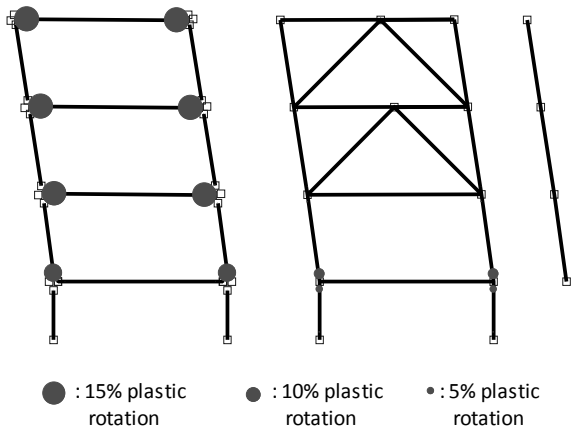


Figure 16 Deformed shape of the building structure at incipient collapse, where the solid circles represent the location of plastic hinges and their size denotes the magnitude of plastic rotation

8CUEE CONFERENCE PROCEEDINGS
8th International Conference on Urban Earthquake Engineering
March 7-8, 2011, Tokyo Institute of Technology, Tokyo, Japan

USE OF RESPONSE MODIFICATION AND MODULAR CONSTRUCTION TECHNOLOGIES FOR NEXT-GENERATION NUCLEAR POWER PLANTS

Bozidar Stojadinovic[1], Eric Keldrauk[2], and Michael Mieler[3]

1) Professor, Department of Civil and Environmental Engineering, University of California Berkeley, Berkeley, USA
2) Doctoral Candidate, Department of Civil and Environmental Engineering, University of California Berkeley, Berkeley, USA
3) Doctoral Candidate, Department of Civil and Environmental Engineering, University of California Berkeley, Berkeley, USA
boza@ce.berkeley.edu, keldrauk@berkeley.edu, mieler17@berkeley.edu

Abstract: Building of new Generation III+ passively safe nuclear power plants (NPPs) and commercial development of Generation IV advanced reactor concepts has started. There are strong indications that NPP vendors are considering seismic response modification through base isolation and modular construction to achieve greater economy while maintaining or improving safety of the new plant designs. Seismic isolation has been used for conventional buildings and non-building structures for more than forty years. Advances in this technology (new materials, development of new motion isolation and damping devices, advances in combating aging, and improved analysis methods) support deployment of base isolation systems for nuclear facility structures. Modular construction using sandwich steel/concrete (S/C) composite walls, featuring steel plates that function as a stay-in-place form for concrete and reinforce it, has shown great promise for factory pre-fabrication, shipping and installation of large NPP modules simultaneously reducing construction time and increasing quality. Aspects of the risk-informed performance-based design codes and regulatory frameworks needed to successfully design and license NPPs featuring seismic isolation and S/C composite walls are discussed.

1. INTRODUCTION

Advanced technologies for structural design and construction have the potential for major impact not only on nuclear power plant construction time and cost, but also on the design process and on the safety, security and reliability of next generation of nuclear power plants. In future next-generation reactors structural and seismic design should be much more closely integrated with the design of nuclear and industrial safety systems, physical security systems, and international safeguards systems. Overall reliability will be increased through the use of replaceable and modular equipment, and through design to facilitate on-line monitoring, in-service inspection, maintenance, replacement, and decommissioning. Economics will also receive high design priority, through integrated engineering efforts to optimize building arrangements to minimize building heights and footprints. Finally, the licensing approach will be transformed by becoming increasingly performance based and technology neutral, using best-estimate simulation methods with uncertainty and margin quantification.

In this context, two structural engineering technologies, seismic base isolation and modular steel-plate/concrete (S/C) composite structural wall, are discussed. These technologies have major potential to 1) enable standardized reactor designs to be deployed across a wider range of sites; 2) reduce the impact of uncertainties related to site-specific seismic conditions; and 3) alleviate reactor equipment qualification requirements. Two principal hazards, the seismic hazard and the hazard of deliberate aircraft impact, must be considered. Aspects of the risk-informed performance-based design codes and regulatory frameworks needed to successfully design and license NPPs featuring seismic isolation and S/C composite walls are discussed.

2. SEISMIC ISOLATION

Seismic isolation is a civil/structural technology that enables engineered modification of the seismic response of a seismically isolated structure. Such response modification is accomplished by placing a seismic isolation system between the superstructure and its substructure. A seismic isolation system typically comprises seismic isolator units, structural elements that transfer forces to and from the isolator units, and their connections. Seismic isolator units are horizontally flexible structural elements designed to enable large lateral deformations of the isolation system under seismic loads. They may also be used as a part of the vertical load supporting system of the structure. Seismic isolation system may also include a wind load resisting system, a system of energy dissipation devices, and/or a displacement restraint system. Because the seismic isolator units are usually (but not necessarily) installed at the base of a structure, seismic isolation is often referred to as base isolation.

Seismic isolation changes the dynamics of the structure such that the dynamic response of the isolated

superstructures to seismic excitation is decoupled from that of its substructure (Naeim and Kelly, 1999). The decoupling is accomplished using one or a combination of the following two horizontal deformation mechanisms: shear deformation of a flexible device; and sliding on friction-controlled surfaces (Kelly, 1993). The flexible device mechanism works by introducing an additional natural vibration mode shape of the isolated structural system: this mode shape is orthogonal to the vibration mode shapes of the superstructure and thus works as a filter that minimizes the vibration of the isolated superstructure. The sliding mechanism limits the force to the level of friction generated between the sliding surfaces: it allows the isolated structure to move when inertia of the isolated superstructure exceeds the friction.

While the initiation of motion is different, both horizontal deformation mechanisms perform in a similar manner once the isolated superstructure is moving. They modify the dynamic response of the structure by making the fundamental horizontal-direction vibration period of the isolated structural system significantly longer than that of the original fixed-base (non-isolated) structure. This leads to significant reductions in the horizontal accelerations and inertial forces transmitted to the isolated superstructure during an earthquake compared to the traditional fixed-base structure. Making use of a typical seismic design spectrum and the fact that horizontal acceleration are roughly inversely proportional to the fundamental vibration period of the structure in the range of interest, it is evident that elongation of the fundamental vibration period achieved by seismic isolation is a very effective method of reducing inertial forces experienced by the isolated superstructure. Reduction of seismic loads in the superstructure offers another benefit: the superstructure can easily be engineered to be sufficiently strong and stiff to control its deformation and acceleration to acceptably small levels and thus protect its integrity and the integrity of the systems and components it contains. At the same time, the seismic isolation devices undergo large horizontal deformations: they are engineered to safely sustain such motions and thus protect the isolated superstructure.

2.1 Benefits of Seismic Isolation

A properly engineered seismically isolated superstructure will, with high confidence, be decoupled from the earthquake-induced motion of its foundation and experience significantly smaller inertial forces than if that same structure was fixed to its base in the same earthquake shaking event. The reduced forces make it easier to design the superstructure to remain essentially elastic: this, in turn, ensures that the deformations of the structure will remain small and in the acceptable range, improving its seismic performance and protecting the internal systems and components. The mechanical properties of seismic isolator units vary among different units produced in a series and change with time, but to a significantly lesser extent than the mechanical properties of other structural elements. Taken together, reduction in inertial forces and deformations experienced by the superstructure achieved by the seismic isolation system, and the repeatable performance of seismic isolator units, can substantially reduce the contribution of seismic hazard to the total probability of large radiation does release. This directly increases the safety margins of seismically isolated nuclear facilities. Seismic isolation can be custom-engineered to specific nuclear facility site characteristics, both with respect to site seismic hazard exposure and to local soil conditions and configurations. Engineering the substructure and the seismic isolation system provides an opportunity to engineer the isolated superstructure for essentially the same level of seismic demand regardless of the site characteristics. This, in turn, facilitates standardization of nuclear facility design and makes the seismic behavior of the isolated superstructure more predictable, leading to increased reliability of isolated nuclear facilities. Equally important, standardization facilitates regulatory review and design certification of seismically isolated nuclear facilities.

While seismic isolation adds a structural system between the substructure and superstructure, the added cost and complexity is very likely to be compensated for by the savings realized through the increase of safety margins despite the smaller strength, size and complexity of the superstructure. However, a significantly larger economy can be derived from simplified, standardized designs made to suite modular construction methodology. Today, modular construction is being implemented at the level of components and systems: use of seismic isolation enables expansion of the modular concept to the entire isolated superstructure and provides the all-important cost driver for use of seismic isolation in new nuclear power plants.

2.2 Challenges of Seismic Isolation

Use of seismic isolation systems brings about a number of challenges. Seismic hazard analysis for seismically isolated structures must consider the long fundamental vibration period of such structures, typically 2 seconds or longer. Thus, ground motion records must be filtered differently to provide reliable data in this long-period (low-frequency) range, ground motion attenuation relations must be developed accordingly, and design spectra and ground motion selection procedures must be modified. Maximum horizontal deformation of the isolator units occurs under combined effects of the horizontal components of ground motion and the relative eccentricity of the isolated superstructure with respect to the isolation system. Effect of the vertical motion of the isolated superstructure on the isolator units must be accounted for, regardless of the cause: overturning moment in the superstructure, ground motion in the vertical direction, or the rotational (rolling) components of the ground motions. Therefore, ground motion selection and scaling must account for all components of ground motion. Modeling of the response of seismically isolated structures must directly account for the three-dimensional non-linear behavior of seismic isolators under both design-basis and beyond-design-basis earthquake ground motions. This is particularly challenging for the traditional

frequency-domain methods used to evaluate the effects of soil-structure interaction on the structural demands and floor spectra. To overcome this challenge, it is imperative to develop effective time-domain non-linear modeling and analysis methods to account for soil-structure interaction between the foundation, the seismic isolation system, and the isolated superstructure, and to develop validated and verified models of the isolator units.

Non-redundancy of the seismic isolation system is a profound challenge. The seismic isolation system comprises a large number of essentially identical seismic isolation units that act in parallel. The performance of the seismic isolation system will not be significantly affected by failure of a one or even a few seismic isolation units or components. However, the seismic isolation layer connects the isolated superstructure to the substructure forming a series system. As such, the seismic isolation layer is not redundant. Therefore, engineering measures must be taken to prevent simultaneous or cascading failure of many seismic isolation units due to exceeding their deformation or force capacities. Such engineering measures include fail-safe system such as deformation limiters achieved by physical (bumpers, stoppers, walls) or mechanical (increasing isolator unit stiffness, slider breaks) means, and additional passive or semi-active dampers. These measures, when engaged, may result in impact and/or gradual increase in forces transmitted to the isolated superstructure. The engineering objective is to provide sufficient space for the isolation system to move without obstacles and for graceful degradation of the seismic isolation layer in extreme situations: a cliff-edge sudden seizure of its isolation function must be avoided.

This engineering objective is particularly challenging when another important beyond-design basis load is considered: aircraft impact. The U.S. Nuclear Regulatory Commission issued a final rule that requires new reactor applicants to assess the ability of their reactor designs to avoid or mitigate the effects of a large commercial aircraft impact (USNRC, 2009). The specific aircraft attributes the USNRC requires applicants to consider are considered to be "safeguarded" information and are restricted from public disclosure. To adequately represent the full range of possible impacts now and over a typical 60 to 100 year lifetime of a nuclear power plant, two airplanes are considered: the Boeing 747-400 and the Boeing 737-900. The Boeing 747 is one of the heaviest and fastest commercial airliners currently in use. While significant further evolution of aviation technology will occur over the typical 60 to 80 year lifetime of new nuclear power plants, the 747 provides a reasonable example for a very severe aircraft crash. Conversely, the 737 is one of the lighter commercial airliners in use, providing a reasonable lower bound for commercial aircraft collision loading. The loading functions for these two aircraft, developed using a method developed by Riera (1968) using the available data on the length, weight and possible impact velocity of the aircraft, are shown in Figure 1.

The deformation of the base isolation system when an aircraft impacts a seismically isolated nuclear facility structures depends on the ratio of the masses of the aircraft and the balance of the facility above the isolation layer. This is because the duration of the impact (about 0.3 sec) and the time when the structure attains peak acceleration is significantly shorter than the isolated period of the structure (about 2.0 sec), making the impulse momentum balance the primary determinant of peak post-impact isolation system displacement. Therefore, given that the mass of the model aircraft is constant, the displacement of the isolation system will be inversely proportional to the weight of the balance of the plant above isolation layer. In contrast, deformation of the isolation system under seismic loading depends on the fundamental period of the isolated system, making it, in general, directly proportional to the weight of the balance of the plant above the isolation layer. Therefore, deformation of the seismic isolation layer of a relatively light plant may be controlled by aircraft impact, while that of a relatively heavy plant is likely to be controlled by seismic demands. This situation is further complicated by the different seismicity in the West and the Central and Eastern US, and different estimates of the magnitude of beyond-design basis seismic demand.

3. STEEL/CONCRETE MODULAR WALLS

Conventional, fixed-base, nuclear power plant structures are constructed using the reinforced concrete structural shear wall elements to form the primary gravity and lateral load structural systems. In addition to their load-carrying ability, such walls offer good radiation protection, provide a satisfactory pressure barrier, and offer good fire resistance. The isolated superstructure and the foundations of seismically isolated nuclear power plants may also be constructed using this conventional technology.

The structural reinforced concrete shear walls are erected using the cast-in-place construction method. The forms for such walls are erected first. The reinforcement is placed into the forms, usually using pre-assembled reinforcement cages. Finally, the concrete is poured into the forms, vibrated into place, and left to cure to a strength that allows for removal of forms. While there is ample experience with such construction method in the industry, three obstacles still remain. One is the design of the forms to sustain the weight of the flowing concrete: this limits the height of the pouring lifts, thus constraining the speed of construction. Second is the time needed for concrete to cure to the level where forms can be removed to advance construction. Use of slip-forming for cylindrical walls can accelerate construction. And third is the need to completely remove the forms such that, over time, wood debris left behind does not cause unwanted corrosion. Liner corrosion problems have been observed at existing U.S. nuclear plants due to wood debris left during construction.

The solution for these construction problems is to use so called "stay-in-place" forms. Such forms are, by themselves, structural elements that are capable of sustaining the load of flowing concrete and additional formwork above the pour level. In addition, they can be composited with the poured

concrete to become part of the larger structural element. Stay-in-place forms can, furthermore, be pre-fabricated and pre-assembled into large modules, enabling significant speedup in construction.

Stay-in-place forms have been made using a variety of materials. It is not uncommon to use thin reinforced concrete plate elements, or plates made of fiber-reinforced mortars or polymer composites to form structural walls and leave them in place. However, the most common material used for stay-in-place forms is steel plate. Steel plates forms can be pre-fabricated as modules of significant size, lifted and assembled into place, and welded at the contacting seams before additional reinforcement is placed into them (if needed). The concrete pour is then the same as in conventionally-formed walls.

3.1 Benefits of S/C Modular Construction

The principal advantage of steel stay-in-place forms is that the form steel can be composited with the interior concrete to form a composite steel-concrete structural element. Steel studs, steel through-bars and/or light steel frames can be used to achieve the composite action between steel and concrete. In addition, stiffeners are used to stiffen the steel plates such that they can sustain the hydrostatic pressure of flowing concrete and maintain their form. Steel-concrete composite construction is regulated by structural design code documents: ASCE 7-05 for design of composite structural systems, and ANSI/AISC 360-05 and ANSI/AISC 341-05 for design of composite structural elements for non-seismic and seismic applications, respectively. However, the existing US design provisions do not cover composite steel plate shear walls where structural concrete is encased by steel plates and the bond between steel and concrete is maintained to ensure composite load carrying action. Research to support the provisions proposed for the next edition of the AISC code is ongoing.

Additional advantage of stay-in-place steel forms is the ability to pre-fabricate large and complex modules. Using ship-building techniques, modules comprising a variety of structural openings, corners and attachments can be pre-fabricated in a controlled factory environment and shipped to the construction site. The only limit is the shipping and lift-and-place capability. Such modules can pre inspected at the construction yard and match-assembled to ensure easy installation and welding on site (a technique long-used in long-span bridge construction).

The final advantage of S/C modular walls is their ability to resist penetration of missiles and parts of aircraft engine better than conventionally reinforced walls.

3.2 Challenges of S/C Modular Construction

Steel-plate/concrete construction has been identified as a very promising technology for construction of new nuclear power plants (Schlaseman, 2004). However, while earlier experience exists with BWRs, this technology still entails significant challenges.

The first group of challenges concerns the design and modeling of steel-plate/concrete walls. The experimental data available for such walls has been obtained by testing scaled-down specimens, with overall thickness between 100mm and 300mm and steel plate thickness between 2mm and 6mm. The prototype wall thicknesses are larger than 1,000mm while the plate thicknesses remain between 6mm and 12mm. Recognizing that full-scale test may not be possible using the existing structural laboratories, more tests on correctly scaled specimens are needed to establish the benchmarks for calibrating computer models for thick steel-plate/concrete walls. That said, the existing computer models for composite steel concrete structures need to be validated for situations where structural shapes are used to tie the two plates together, to carry the bi-axial shears, and where studs are provided to prevent the thin liner plates from debonding during pouring or unexpected internal out-gassing pressures. For limitation of buckling the studs also play a useful role because only a small amount of support is needed to prevent buckling from occuring.

The second group of challenges concerns construction of steel/plate composite walls. While construction of the wall itself is made much easier, implementation of the wall-to-floor connections is challenging. Design and construction of structural connections between steel-plate/concrete and conventional reinforced concrete elements has not been extensively studied. Finally, implementation and anchoring of piping and equipment attachments to the steel skin of steel-plate/concrete walls remains an important design issue.

The third group of challenges concerns inspection and service of steel/plate composite walls over the life of the nuclear power plant. It is universally recognized that the composite walls offer superior resistance to extreme loading conditions, such as aircraft impact and earthquake loading. Under impact, the steel skin increases the resistance of the wall to local perforation, scabbing and penetration (shear cone punching) compared to conventional reinforced concrete walls. Under earthquake loading, properly designed steel-plate/concrete walls (with details to delay elephant-foot buckling and formation of buckled compression diagonals) should be significantly more ductile than the correspondingly reinforced conventional reinforced concrete walls. However, long-term degradation of steel-plate/concrete walls is not fully understood, although experience exists with steel liners commonly used on the internal surfaces of reactor containments. The exposed steel plates may need to be protected against corrosion. Inspection methods to establish the conditions of inaccessible portions of the walls have not been evaluated, particularly concerning the state of bond between steel plates and concrete. Behavior of such walls under elevated temperatures during accidents and fires has not been studied at the size and scale used in nuclear power plants.

Finally, the forth group of challenges concerns decommissioning of nuclear power plants after the end of their service life. Methods for effective deconstruction of the steel-plate/concrete walls have not been investigated. In particular, it is not clear how to deal with portions of such walls that may be irradiated or otherwise contaminated

during the regular service life of a nuclear power plant.

4. PERFORMANCE-BASED DESIGN AND EVALUATION FRAMEWORK

A framework, a consistent set of requirements and guidelines for design and regulatory approval, is needed to successfully design seismically isolated nuclear power plant structures. The framework proposed in this paper builds on the design framework for conventional seismically isolated structures defined in Chapter 17 of ASCE 7-10 (ASCE 2010), on the design objectives for nuclear facility structures contained in ASCE 43-05 (ASCE, 2006), and on design provisions proposed for the upcoming ASCE 4-11 (ASCE 2011) standard.

The proposed framework is performance-based, and applies to both seismic isolation and composite steel/concrete wall construction. It comprises the following phases: 1) setting the performance objectives; 2) preliminary design for seismic and aircraft impact loads; 3) design, manufacturing and prototype testing consistent with the requirements for prototype testing for conventional facilities; 4) detailed modeling of the NPP structure; 5) evaluation of the design-basis and beyond-design-basis performance of the structure under seismic and aircraft impact loads; 6) specification of quality acceptance and quality control for manufacturing and installation; and 7) specification of in-service monitoring procedures and alert levels.

4.1 Performance Objectives

ASCE 43-05 defines five Seismic Design Categories (SDC). Categories 3, 4 and 5 are associated with nuclear facility structures, systems and components through ANSI/ANS 2.26. ASCE 43-05 defines four Limit States based on structural deformations to describe levels of acceptable structural damage. These damage states range from significant damage with a structure close to collapse (state A) to no significant damage with a structure in operational condition (state D). The performance objective for a seismically isolated nuclear power plant structure is SDC5-D. ASCE 43-05 also defines the Design Basis Earthquake (DBE) using a Probabilistic Seismic Hazard Assessment (PSHA) to derive a Uniform (or Equal) Hazard Response Spectrum (UHRS) for the site and modifies it further using a Design Factor. The Design Factor is calibrated to achieve a mean annual seismic core damage frequency of 10-6 considering the failure probabilities inherent to current design codes and the design goal proposed in ASCE 43-05 (Kennedy, 2007). The design goal for structural components not explicitly covered in ASCE 43-05 is to *reasonably* achieve both of the following design objectives (Section 2.0 of ASCE 43-05):

1. Less than 1% probability of unacceptable performance for the DBE ground motion (defined in).
2. Less than 10% probability of unacceptable performance for 150% of the DBE ground motion (defined in Section 2.0 of ASCE 43-05).

Acceptable performance for structural framing such as concrete shear walls and moment frames typically found in nuclear power plant structures is described as "essentially elastic behavior." This performance objective can be extended to S/C modular walls. In addition, the response of the S/C walls in beyond-design-base load cases should not exhibit a cliff-edge effect, i.e. the response should be ductile and degrade gracefully without sudden local fractures or instabilities that induce significant redistributions of the applied load among the S/C wall resistance mechanisms. A principal method for achieving such behavior is the provision of sufficient connectivity between the steel skin plates. Ongoing research is addressing this issue starting from the minimum transverse reinforcement requirements for conventional reinforced concrete walls.

Acceptable performance of the seismically isolated structure is defined through acceptable behavior of its components. The foundation and the seismically isolated superstructure are expected to remain in ASCE 43-05 state D, i.e. "essentially elastic". The structures, systems and components are expected to remain operational in case of impact generated by failure of the seismic isolation system. The seismic isolation system is expected to also develop no significant damage and remain in operational condition (state D). This means that the structural elements framing the seismic isolation system (the foundation and the isolation diaphragms) must remain "essentially elastic" and capable of distributing and transferring the gravity and ordinary lateral loads even if some of the seismic isolator units fail. Unacceptable performance of the seismic isolator units under seismic and aircraft impact loads is defined as:

1. Permanent damage to the seismic isolator unit, such as tearing, buckling or disassembly, that prevents it from functioning as intended;
2. Excedance of the design displacement limit of the seismic isolator unit.

It is important to note that ASCE 43-05 is calibrated to the mean annual frequency. US NRC requires a design to achieve high confidence of low probability of failure (HCLPF).

4.2 Preliminary Design

A preliminary assessment of seismically isolated nuclear structures for design basis and beyond-design basis ground motions at three different sites has recently been conducted by Huang, Whittaker, Kennedy and Mayes (Huang et.al, 2009). The main outcome of this study is a triplet of performance statements aimed at achieving the two ASCE 43-05 probability-based design goals. Namely:

1. Individual isolators shall suffer no damage in DBE shaking.
2. The probability of the isolated nuclear structure impacting the surrounding structure (moat) for 100% (150%) DBE shaking is 1% (10%) or less.
3. Individual isolators shall sustain gravity and earthquake-induced axial loads at 90th percentile lateral displacements consistent with 150% DBE shaking.

These performance statements, derived for seismic loading, are extended to aircraft impact loading by

considering it as beyond-design basis event in the same category as the 150% DBE event. Preliminary design of the seismic isolator units can be conducted using the following procedure. A target isolation system horizontal fundamental vibration period can be at least 4 times longer than the fundamental vibration period of the isolated superstructure, and outside any regions where UHRS has an unusual amplification. Typical values are between 2 and 4 seconds. A target characteristic horizontal strength of the isolation system may be between 3% and 9% of the weight of the isolated superstructure. These values are based on the ranges of parameters considered in (Huang et.al, 2009). A target effective damping may be between 15% and 20% of critical damping (Naeim and Kelly, 1999).

Performance statements 1 and 2 can be utilized for preliminary assessment of the design displacement of the seismic isolator unit. To do this, a stick model representing the principal mass and stiffness characteristics of the isolated superstructure should be combined with a model of the seismic isolator unit capable of representing the force-deformation response of the unit in two horizontal directions. Best-estimate values for mechanical properties of the units should be used at this stage. Huang et.al (2009) find that the seismic displacement with a 10% exceedance probability in 150% DBE shaking governs the design. Using their Approach I, select or generate 11 seed three-component ground motions to appropriately represent the site conditions and the controlling hazard, spectrally match these motions to the DBE spectra, perform 11 non-linear response history analyses, compute the vector-sum maximum displacement of the seismic isolator units in each analysis and then find the median value of these maxima. Multiply this median value by 3 to determine the seismic design displacement of the isolator unit. The aircraft impact displacement can be computed using the same computer model of the facility used for preliminary seismic analysis and the aircraft impact load models including the USNRC aircraft impact model. The obtained aircraft impact displacements are expected to represent the mean and HCLPF displacements, respectively. The mean aircraft impact and the mean seismic displacements of the isolation system should be compared to determine the governing displacement for the next design phase. A procedure suggested in (Naeim and Kelly, 1999) or in (Buckle, 2006) can be used to compute the remaining properties of the seismic isolator unit and to design the unit. Using a procedure suggested in (Naeim and Kelly, 1999), a manufacturer should be selected and a proof-test isolator unit should be manufactured. The proof-test should be conducted using a test procedure suggested in (Buckle, 2006).

Preliminary design of S/C modular walls should be conducted using the minimum design provisions for conventional reinforced concrete structures and the current design provisions for composite steel/concrete structures. These provisions will provide the designer with the fundamental estimates of the thickness of the steel plates and the amount of steel needed to connect the steel plates and resist the seismic and aircraft impact shear. The thickness of the S/C wall will be governed by aircraft impact demands and by the demands to transfer the forces at the connections between the S/C and conventional R/C walls and/or foundations. US code provisions for verification of such designs are under development.

4.3 Modeling and Evaluation

Design of the seismic isolation system may also include design of supplemental dampers intended to further reduce design displacements, vertical restraint or isolation devices, and fail-safe devices intended to reduce or eliminate adverse consequence of superstructure impact on the surrounding soil or structure. A detailed model of the seismically isolated nuclear power plant can then be made. This model should be used to evaluate the response of the nuclear power plant structure under design and beyond-design basis earthquake shaking and aircraft impact. The limit states associated with the seismic isolation system include (but are not limited to): 1) failure of isolator units due to exceedance of design displacement; 2) failure due to tearing or instability such as buckling, rollout or disassembly; 3) impact of the isolated superstructure against the isolation mote; 4) vertical motion and uplift due to ground motion, and overturning or rocking due to aircraft impact; 5) local failure of the S/C walls due to in-plane bending or out-of-plane shear forces; 6) failure of connections between S/C walls and other conventional structural elements; 7) local penetration failure of the S/C wall; and 8) global or partial collapse of the S/C wall due to aircraft impact.

The challenge posed by seismic isolation response modification technology is that the seismic isolator units are expected, and relied upon in design, to behave in a non-linear manner during design-basis and beyond-design-basis earthquake shaking. Even though the isolated superstructure is expected to remain essentially elastic (and can be modeled assuming it remains within its elastic response range), and the soil and the foundation may behave in a manner such that they can be modeled using equivalent elastic properties, the seismic isolator units must be modeled as non-linear using a model capable of accurately computing the isolator force-deformation response under bi-directional horizontal excitation. Even such relatively simple non-linear models cannot be linearized with sufficient accuracy to represent the response of the seismically isolated structure over the range of excitations of interest. Yet, it is likely that more sophisticated models of seismic isolators and other devices, such as dampers and displacement restrainers if used in design, will be needed to demonstrate satisfactory performance of the seismically isolated structure with the high confidence required by licensing regulators.

Development of verified and validated tools for time-domain non-linear analysis of seismically isolated S/C modular structures and soil is on the critical path for successful design and licensing of new seismically isolated nuclear power plants. Such tools should include sophisticated 3-directional interaction models of seismic isolators, models of contact, uplift and impact, non-linear models of S/C walls, and non-linear models of soil. Ideally,

such models should enable propagation of seismic wave excitation from the source (or rock layer), eliminating the need for additional software. Finally, these tools should enable non-linear modeling of the response of the isolated superstructure capable of capturing its response in higher vibration modes, propagation of horizontal and vertical excitation through the isolation system and into the structure, and the corresponding floor response spectra to enable coupling to equipment fragility evaluation. The time scales of the response quantities of interest span approximately three orders of magnitude (0.1Hz to 10 Hz). The dimensions of the model elements also span roughly four orders of magnitude (0.1m to 100m). Even without non-linear behavior, the time and length scales present a significant challenge for development and implementation of efficient and accurate solution algorithms. Nevertheless, some of solid finite element software package used by industry today can handle such complex problems. But, then need to be verified and validate for use for seismically isolated structures, and sped-up, simplified and hardened for use in design practice.

5. CONCLUSIONS

Seismic isolation response modification and compsite steel/concrete modular structural wall technologies are mature and ready for application in safety critical nuclear power plants. The benefits of using these technologies (improved safety, reliability and economy) clearly outweigh the challenges. Three major issues are on the critical path for adoption of these new technologies in nuclear engineering practice and regulation. The first is the development of the regulatory guidelines to define the way seismically isolated and S/C modular nuclear power plant license applications are going to be evaluated. Work in this direction is ongoing. The second is the development of practical non-linear seismic and aircraft impact soil-structure interaction response analysis of the seismically isolated S/C modular nuclear power plants. Research in this direction is starting. Third is the work by vendors to develop seismically isolated S/C modular nuclear power plant designs and the willingness of the utilities to support the licensing process of the first such license application. The risk for such first movers is significant, but taking this risk on is essential.

Acknowledgements:

The authors acknowledge support from the US Department of Energy and the Nuclear Regularity Commission. The opinions presented in this paper are those of the authors and are not necessarily shared by the sponsors.

References:

American Society of Civil Engineers (ASCE). (2010a). "Minimum design loads for buildings and other structures." *ASCE/SEI 7-10*, ASCE, Reston, VA.

American Society of Civil Engineers (ASCE). (2010b). "Seismic analysis of safety-related nuclear structures and commentary." *ASCE 4-11*, ASCE, Reston, VA.

Blandford, E., Keldrauk, E., Laufer, M., Mieler, M., Wei, J., Stojadinovic, B. and Peterson, P. F, "Advanced Seismic Base Isolation Methods For Modular Reactors", Technical report UCBTH-09-004, Dept. of Civil and Env. Engineering and Dept. of Nuclear Engineering, University of California Berkeley, Berkeley, CA, USA.

Buckle, I., Constantinou, M., Dicleli, M. and Ghasemi, H. (2006), "Seismic Isolation of Highway Bridges", Technical Report MCEER-06-SP07, University at Buffalo, The State University of New York.

Japan Electric Association (JEAG). (2000). "Technical Guidelines on Seismic Base Isolation Systems for Structural Safety and Design of Nuclear Power Plants", JEAG-4614, Special Subcommittee on Nuclear Power.

Japan Nuclear Energy Safety Organization (JNES). (2010). "Regulatory Guidelines for Reviewing Seismic Isolation Structures", JNES-SS-1001, Seismic Safety Division.

Huang, Y.-N., Whittaker, A. S., Kennedy, R. P. and Mayes, R. L. (2009). "Assessment of base-isolated nuclear structures for design- and beyond-design basis earthquake shaking." *MCEER-09-0008*, Multidisciplinary Center for Earthquake Engineering Research, State University of New York, Buffalo, NY.

Kato, A., Moro, S., Morishita, M., Fujita, T., and Midorikawa S. (2003) "A Development program of Three-Dimensional Seismic Isolation for Advanced Reactor Systems in Japan", Transitions of 17th International Conference on Structural Mechanics in Reactor Technology (SMiRT 17), K09-1.

Kelly, J. M. (1993). *Earthquake-Resistant Design with Rubber*, Springer-Verlag, London.

Kennedy, R., (2007). "Performance-Goal Based (Risk Informed) Approach for Establishing the SSE Site Specific Response Spectrum for Future Nuclear Power Plants', Transitions of 19th International Conference on Structural Mechanics in Reactor Technology (SMiRT 19), Jaeger lecture.

Malushte, S. and Whittaker A. (2005). "Survey of Past Base Isolation Applications in Nuclear Power Plants and Challenges to Industry/Regulatory Acceptance." Transitions of 18th International Conference on Structural Mechanics in Reactor Technology (SMiRT 18), K-10-7.

Naeim, F., and Kelly, J. M. (1999). *Design of seismic isolated structures: from theory to practice*, John Wiley, NY.

Riera, Jorge D. "On the Stress Analysis of Structures Subjected to Aircraft Impact Forces." Nuclear Engineering and Design (1968): 415 – 426.

Renault, J., Jolivet, F., Plichon, C., & Bordet, R. (1976) Patent 05/697632, "*Device for protecting a structure against the effects of high horizontal dynamic stresses"*

Schlaseman, C. "Application of Advanced Construction Technologies to Nuclear Power Plants," Technical Report, MPR-2610, Revision 2, P. 132, US Department of Energy, Sept. 24, 2009.

U.S. Nuclear Regulatory Commission, "NRC Issues Final Rule on New Reactor Aircraft Impact Assessments," NRC News, 09-030, Feb. 17, 2009.

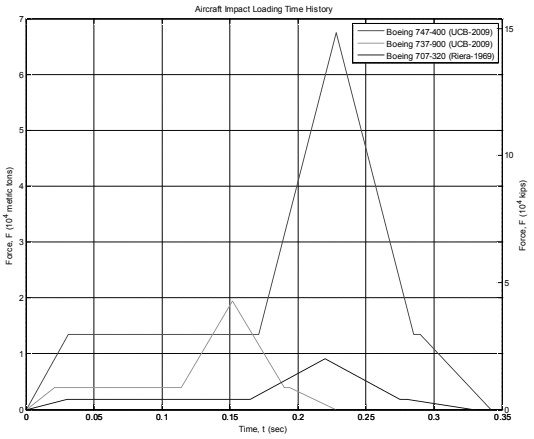


Figure 1. Aircraft impact load functions.

8CUEE CONFERENCE PROCEEDINGS
8th International Conference on Urban Earthquake Engineering
March 7-8, 2011, Tokyo Institute of Technology, Tokyo, Japan

THE SEISMIC RESPONSES OF 14-STORY RC STRUCTURES INSTALLED WITH THREE-PIN STEEL DAMPER

Huei-Tsyr Chen[1], Yung-Feng Su[2], and Hsun-Hua Tang[3]

1) Professor, Dept. Civil Engineering, National Central University, Taiwan
2) Adjunct Associate Professor, Dept. Civil Engineering, National Central University, Taiwan
3) Former Graduate Student, Dept. Civil Engineering, National Central University, Taiwan
Chenht@cc.ncu.edu.tw

Abstract: In this study a damper called three-pin steel damper was developed. The experimental results showed that the energy dissipation mechanism was stable with a large area of hysteresis loops while it can eliminate the defects of the X type and the triangular type steel damper called ADAS. A 14-story RC building structure was designed and installed with the damper. The nonlinear dynamic responses of the designed RC structures were conducted to investigate the effectiveness of the developed damper using the earthquake records of Taipei Basin and SAP 2000. The results demonstrated that the use of developed dampers is effective in reducing the seismic responses. From the results obtained for all the cases investigated, the maximum reduction in story ductility ratio is 70% and that in story drift ratio is 54%.

1. INTRODUCTION

Different measures have been proposed over the last years to reduce the responses of the structures subjected to earthquakes and one of them is to use energy dissipation device called damper which is developed by exploiting the stable hysteretic behavior of the selected material. The main philosophy of using dampers is to dissipate the input energy by dampers not by the inelastic behavior of the primary structural members.

Among many types of energy dissipation device proposed is the type called steel plate damper which uses the steel's stable hysteretic behavior to dissipate the input energy. Added Damping and Stiffness device (ADAS) is a mechanical device made of steel plates with X or triangular shape and assembled with bolts and/or welds to end blocks, the top of which is connected to girder while the end block is attached to the brace members. Investigations (Su, 1992; Chen, 1994; Juang et al., 2001) have demonstrated that ADAS can provide initial stiffness and stable and large hysteretic energy dissipation capability, leading to the effective reduction in structural responses. Other types of steel damper such as shear-panel damper (Masayoshi and Satoshi, 1994; Masatoshi et al., 1995) and damper with honeycomb-shapes opening (Naoki, et al., 1989) also showed the effectiveness of steel plate dampers.

For the previous steel dampers, they must be installed on bracing members within a panel. In this paper a new device called three-pin steel damper is developed which can be installed on a separated wall within a panel/.

2. THREE-PIN STEEL DAMPER

2.1 Geometrical Shape

Figure 1 shows the sketch of the developed three-pin steel damper. When the three-pin steel dampers are used, they are always in pairs and connected using pins at locations A, B and C. As compared with the previous steel dampers, such hinge-type connections lead to easy manufacture and avoidance of effect of welding quality. In the figure, b is the width of any cross section between the cross sections AA and BB and h is the distance of this cross section to the pin at the end pin on the same side. The width b varies with the distance h such that $bh^{-0.5}$ remains constant. Two types of three-pin steel damper were initially developed on the basis of predicted location of breakage. Type A damper is designed to ensure that the steel damper remains elastic behavior at the location of pin connections and the breakage occurs at some distance from the center pin as shown in Figure 2. Type B damper, on the other hand, is designed to let the plastic zone be developed near the center pin and the breakage extends from the edge of the steel damper to the center pin as shown in Figure 3.

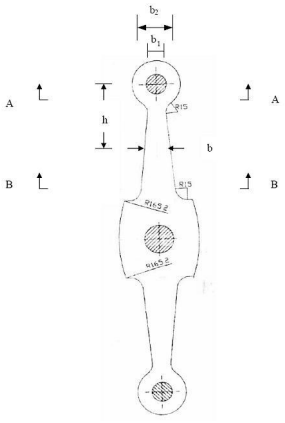


Figure 1 Sketch of three-pin steel damper



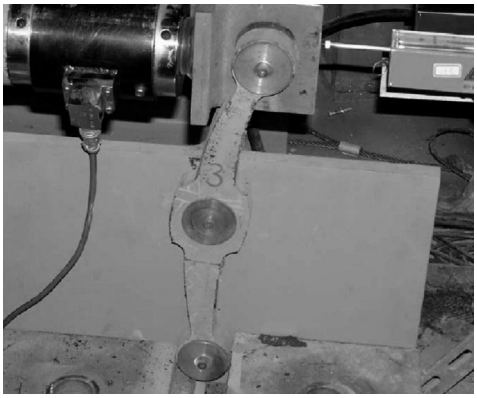
Figure 2 Failure of Type A damper



Figure 3 Failure of Type B damper

2.2 Experimental Results and Numerical Simulations

For type A damper, the experiments were conducted for a pair only as shown in Figure 4. The displacement-control cyclic tests were performed for displacements of 20mm, 30mm, 40mm, 50mm and 60mm, respectively. Figure 5 shows the number of cycles before failure. It can be seen that the number of cycles leading to failure decreases with increasing displacement. Since the code requires that the number of cycles before the failure must be greater than 5, we took the 50mm as the ultimate displacement for the developed steel damper.



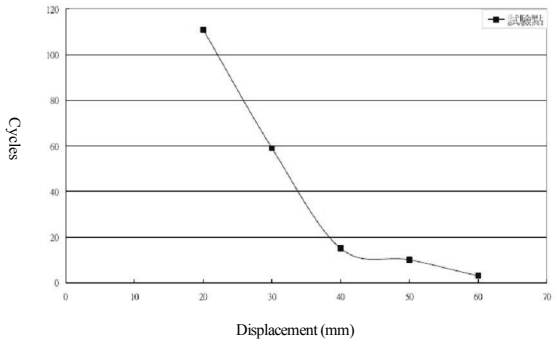


Figure 5 Cycles of loading before failure

For type B damper the experiments were conducted for 10 dampers (5 pairs) as shown in Figure 6. The displacement-control cyclic tests were performed for displacements of 12.5mm, 25m, 37.5mm and 50mm respectively. The results shown in Figure 7 show the stable hysteretic loop and no signs of decrease in strength.

Since the effectiveness of the three-pin steel damper on the reduction of seismic responses of structures will be investigated using SAP2000, a constitutive relation for numerical analysis must be developed for the three-pin steel damper. In this study the three-pin steel damper is modeled as a link member with bilinear constitutive relation and to fully describe the hysteretic behavior, the parameters required are initial stiffness (K), yield strength (P_y), post yield ratio (R) and yielding exponent (E) which is the curvature at the junction of bilinear model. The SAP2000

was used to determine these parameters. For type B damper, the parametric values obtained are P_y=490.5 kN, K=882.9kN/mm, R=0.005 and E=2. Figure 8 compares the experimental results and numerical simulations (smooth curves) for the type B damper. Since the arrangement of the dampers are in parallel, the parametric values for each pair of damper are P_y=98.1kN, K=176.58kN/mm, R=0.005 and E=2. These values were used for the study on the effectiveness of the three-pin steel damper on the reduction of seismic responses of structures.

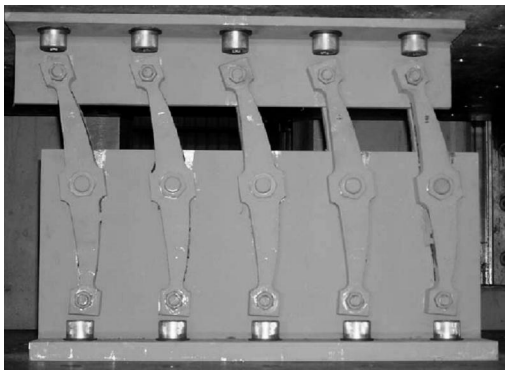


Figure 6 Type B steel damper under test

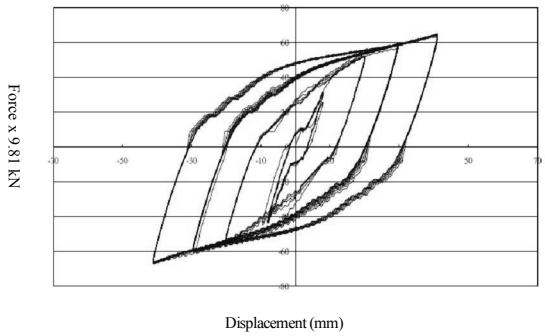


Figure 7 Hysteresis loop for Type B damper

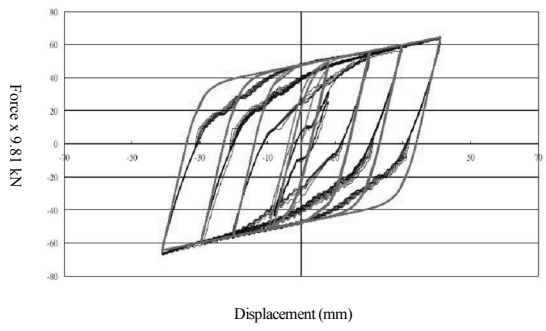


Figure 8 Numerical simulation of hysteresis loop for Type B damper

3. DISCUSSIONS OF ANALYSIS RESULTS

To investigate the effectiveness of three-pin steel damper, a 14-story reinforced concrete building was designed according to the design code of Taiwan and the design spectrum of Zone III of Taipei basin. The building has three bays in each direction and each bay has a length of 8m. The height of first story is 5.4m and all the other floors have the same height of 3.4m with a total building height of 49.l6m. Detailed information about this building can be found in (Tang, 2010). To install the three-pin steel dampers, within a panel a wall-type column is constructed between the beams at the top and the bottom and cut into two parts with a distance of 500mm apart vertically which is used for the installation. The thickness of the wall is 300mm the horizontal length is 1300mm in this study. In this study the three-pin steel damper consists of 7 pairs at each location and is installed up to 11th floor.

The analyses were conducted by simplifying the building as a stick model where each story is modeled as a link member as shown in Figure 9. The pushover analysis was performed to obtain the relation between the story shear and the story displacement. With this relation and the selection of Takeda model, the hysteresis relation was set up by the SAP 2000 which was then used for the seismic analyses of reinforced concrete building. For three-pin steel damper, it was models as a link with P_y=2774kN, K=4944.24kN/mm, R=0.005 and E=2.

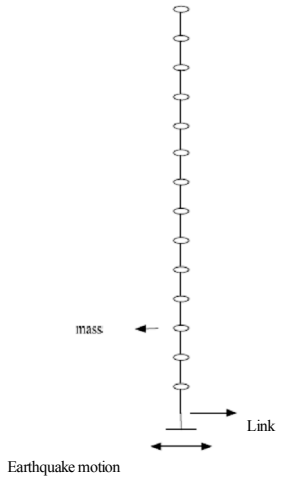


Figure 9 Building model for analysis

The ChiChi earthquake recorded in Taipei basin denoted as TAP013, TAP014, TAP090 and TAP100 were adopted for the analyses. Both the peak ground velocity (PGV) of the NS and EW components of the selected records were normalized to have PGV= 250mm/sec (PGV25), 500mm/sec (PGV50) and 750mm/sec (PGV75). However, in the following discussions only the results using TAP090, located in zone III of Taipei basin, as input will be presented.

Figures 10 and 11 show the story ductility ratios for each component of earthquake motion, respectively. Shown in Figures 12 and 13 are the story drift ratios for each component of earthquake motion, respectively. It can be seen that the use of three-pin steel damper can lead to the reduction in both story ductility ratios and the story drift ratios. The amount of reduction increases with increasing PGV with maximum of reduction of 63% for story ductility ratio and of 53.1% for story drift ratio.

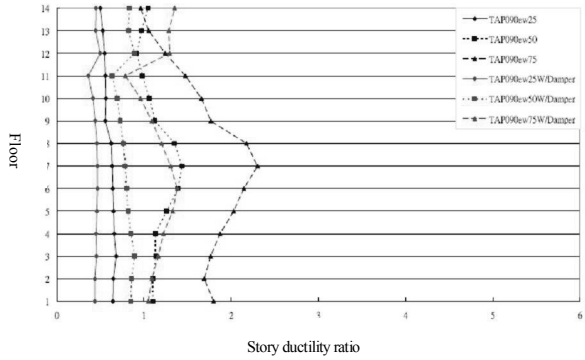


Figure 10 Story ductility ratios for EW component

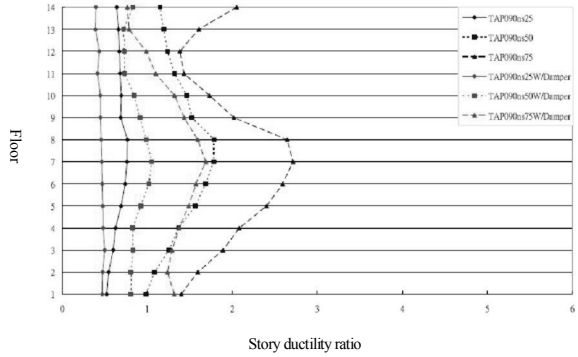


Figure 11 Story ductility ratios for NS component

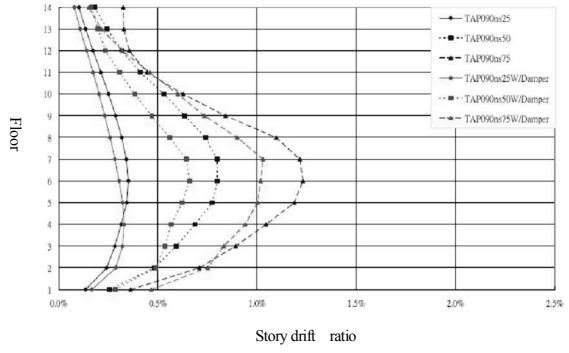


Figure 12 Story drift ratios for EW component

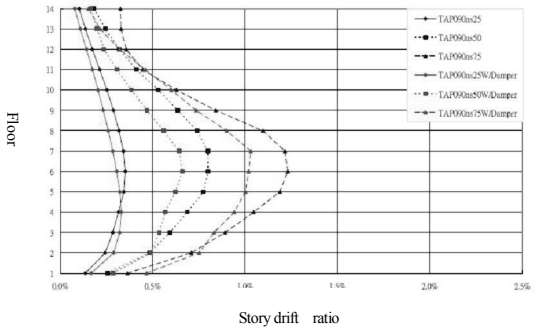


Figure 13 Story drift ratios for NS component

4. CONCLUSIONS

In this study a damper called three-pin steel damper was developed. The experimental results showed that the energy dissipation mechanism was stable with a large area of hysteresis loops while it can eliminate the defects of the X type and the triangular type steel damper called ADAS. 14-story RC building structures were designed with or without installing the damper. The nonlinear dynamic responses of the designed RC structures were conducted to investigate the effectiveness of the developed damper using the earthquake records of Taipei Basin and SAP 2000. The results demonstrated that the use of developed dampers is effective in reducing the seismic responses. From the results obtained for all the cases investigated, the maximum reduction in story ductility ratio is 70% and that in story drift ratio is 54%.

References:

Su, Y.F. (1992), "Pseudo-dynamic Testing of a Two-Story Steel Frame with Added Stiffness and Damping Elements," SFRDEST, R-93-ST-01-2, Sinotech Foundation for Research and Development of Engineering Science and Technology, Taiwan. (in Chinese)

Chen, F.S. (1994), "Design and Analysis for Steel Building with Added Stiffness and Damping Device," Master Thesis, Department of Civil Engineering, Jhongli, Taiwan. (in Chinese)

Juang, D.S., Chong, N.S., Chen, H.T. and Su, Y.F. (2001), "Seismic Resistant Design with Added Stiffness and Damping Device," Journal of Structural Engineering, Chinese Society of Structural Engineering, **16**(2), pp.77-96. (in Chinese)

Massayoshi, N. and Satoshi, I. (1994), "Energy Dissipation Behavior of Shear Panels Made of Low Yield Steel," Earthquake Engineering and Structural Dynamics, **23**, pp.1299-1313.

Massayoshi, N., Takashi, A. and Bunzo, T. (1995), "Strain-Hardening Behavior of Shear Panels Made of Low Yield Steel," Journal of Structural Engineering, American Society of Civil Engineers, **121**(12).

Noaki, T., Takuji, K. Toshikazu, Y. and Toshiyuki, F. (1989), "A Study on Steel Plate Damper with Honeycomb-Shaped Openings Subjected to Low Cycle Fatigue," Journal of Structural Engineering, 37, pp.1-23.

Tang, H.H. (2010), "Design and Analysis of Reinforced Concrete Buildings with Three-Pin Steel Damper," Master Thesis, Department of Civil Engineering, National Central University, Jhongli, Taiwan. (in Chniese)

8CUEE CONFERENCE PROCEEDINGS
8th International Conference on Urban Earthquake Engineering
March 7-8, 2011, Tokyo Institute of Technology, Tokyo, Japan

RETROFIT OF SOFT STORY STRUCTURE USING SEISMIC ISOLATION TECHNOLOGY

Lieping Ye[1)2)], Peng Pan[1)2)], Yujun Qi[1)2)], Zhenhua Pan[1)], Haiyun Cao[1)], and Shichun Zhao[3)]

1) Department of Civil Engineering, Tsinghua University, Beijing, 100084, China
2) Key Laboratory of Structural Engineering and Vibration of China Education Ministry, Tsinghua University, Beijing, 100084, China
3) Department of Civil Engineering, Xinan Jiaotong University, Chengdu, 610031, China
ylp@tsinghua.edu.cn, panpeng@tsinghua.edu.cn, jyj02@mails.tsinghua.edu.cn

Abstract: During the 2008 Wenchuan earthquake China, a 6-story RC frame structure located in Dujiangyan city sustained serious damage at the bottom story, which served as a parking area, whereas the upper stories were almost undamaged. To retrofit the structure, the seismic isolation technology was applied. The bottom columns were restored and strengthened, and lead rubber bearings were installed at the top of these columns. The soft story of the structure was replaced to an isolation story, and the function of the bottom story was recovered. This paper reviews the state-of-the-practice of Chinese design of seismic isolation and presents the retrofit of the 6-story structure as an example. Major conclusions obtained in this study are as follows: (1) Chinese design of seismic isolation is getting mature; (2) seismic isolation technology is effective in the retrofit of the soft story structures damaged in the earthquakes.

1. INTRODUCTION

A strong earthquake with a magnitude of 8.0 hit Wenchuan of Sichuan province, China in 2008. A huge number of buildings were damaged in the earthquake, leading heavy casualties and property losses. Post-earthquake investigation showed that serious damages at the bottom story were quite common for reinforced concrete frames as shown in Fig. 1 (Lin et al. 2009). This is mainly because that the bottom story, commonly used as a sales area or parking, has less infill wall, leading the story essentially a weak story. Thanks to the damage of the bottom story, which played a role as an isolated story, the upper stories were "protected".



Figure 1 Serious Damage at Bottom Soft Story

To retrofit the structures, the stiffness and strength of the bottom story will be significantly increased if using conventional methods, such as adding shear walls or enlarger the columns, commonly cost much, and also affect the functionality of the original structure. On the other hand, a large number of regions affected in the Wenchuan earthquake increase their earthquake fortification intensity, meaning that the seismic forces considered in these regions are enlarged after the earthquake. The damaged structure should be retrofitted according to the new earthquake fortification intensity, and the "protected" upper stories should also be strengthened if using the conventional retrofit methods. Strengthening these upper stories costs even more.

Seismic isolation technology was considered for the retrofit of the structures. Specifically, the bottom story columns were restored and strengthened, seismic isolators were installed on the tops of the columns, and the bottom story was changed to a seismic isolation story. Compared to the conventional retrofit methods, the retrofit method using seismic isolation has significant advantages: (1) it enhances the earthquake resistant capability of the entire structures without strengthening the upper stories; (2) it maintains the functionality of the bottom story as parking or sales areas; (3) it provides better protection to the contents of the structures in addition to the structures themselves; (4) it cost much less than the conventional retrofit methods. (National Standard of China, 2001)

The seismic isolation has been applied to the retrofit of building structure for many years in some oversea countries. The earliest case is the Salt Lake Mansion in USA, which was built in 1894, suffered partial failure in an earthquake in 1934, and was retrofitted in 1989 (Xu et al. 2001). However, retrofit using seismic isolation is still rather rare in China. This paper mainly briefs Chinese design practise of seismic isolation buildings and explains a specific design of a building that sustains soft story damage in the Wenchuan earthquake as an example.

2. CHINESE DESIGN PRACTICE FOR SEISMIC ISOLATED BUILDING

2.1 Performance targets

Three levels of earthquakes are considered in Chinese structure design practice, i.e. frequent earthquake, local fortification intensity earthquake, and rare earthquake. The three levels of earthquakes have return periods of about 50, 475, and 2000 years, respectively, corresponding to the three levels of earthquakes, the seismic fortification targets of buildings are as follows: (1) When subjected to frequent earthquakes, the buildings should sustain no damage or only slight damage, and be serviceable without repair. (2) When subjected to local fortification intensity earthquakes, the buildings are allowed for some damage but should be serviceable after ordinary repair or without repair. (3) When subjected to rare earthquake, the buildings shall neither collapse nor suffer severe damage that can endanger human lives.

To achieve the design targets, two stages of design are conducted: (1) First stage design is to ensure the seismic performance of buildings under frequent earthquakes. Essentially a Load and Resistance Factor Design method is applied in this stage. Structure members are designed, and story drifts are checked. (2) Second stage design is to ensure the seismic performance of buildings under rare earthquakes. Detailing design and story drift control under rare earthquakes are considered in this stage.

According to Chinese seismic design code issued in 2001, the seismic isolation structures under the frequent, fortification and rare earthquakes shall meet the requirements higher than conventional structures. Such provisions imply enhanced performance requirements for base-isolation compared to the general design of structures in China. In the release of 2008 Chinese seismic design code, the provision is removed, meaning that the seismic isolation structures do not have to use higher performance standard. This is particularly to promote the application of seismic isolation after the Wenchuan earthquake.

2.2 Ground Motions

In Chinese design practise, nonlinear time history analyses are recommended for seismic isolation structures. According to the seismic design code, at least 2 sets of real ground motions and 1 set of synthetic ground motion shall be selected based on the design spectra. Their average seismic response spectra shall be in conformity with the seismic spectra given in the code. The peak ground accelerations (PGAs) for the ground motions are adjusted according to the values given in Table 1. The linear elastic time-history analyses should be applied to justify the selection of the ground motion before the nonlinear analyses. The structure base shear obtained from each ground motion shall not be less than 65% of that from the response spectrum method, and the average value from the three ground motions shall not be less than 80% of that from the response spectrum method.

Table 1 Peak ground accelerations (PGAs) for time-history analysis (cm/s^2)

Seismic Fortification Intensity	6	7	7.5	8	8.5	9
Frequently earthquake	18	35	55	70	110	140
Rare earthquake	-	220	310	400	510	620

2.3 Common Design Procedure

As shown in Fig. 2, the design of seismic isolation structure mainly commonly adopts the following four steps, i.e. design of super-structure, design of base-isolation layer, validation of superstructure design, and design of base structure and foundation, with step 1 to 3 conducted in an iterative manner.

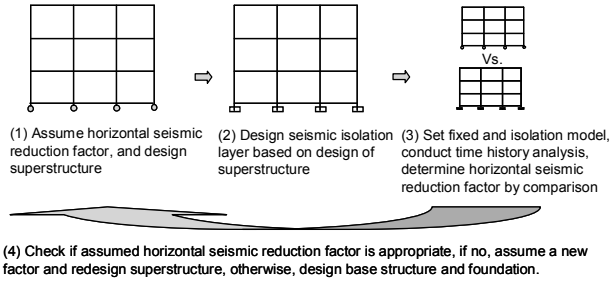


Figure 2 Flow chart for design of seismic isolation buildings

(1) The superstructure is first to be designed. In Chinese design practise, the seismic forces of the superstructure adopt the multiplication of the seismic force for the non seismic isolation structure and the seismic reduction factor. The seismic reduction factor is assumed to be a specific value, e.g. 0.5, in the beginning. Once the seismic forces are determined, the superstructure can be designed by following the design method for conventional structures.

(2) The base-isolation layer is then designed. For the design of seismic isolation layer, the following major issues are considered: the ratio of the fixed-base period to the base-isolated period of the structure is recommended to be greater than three to achieve an effective reduction of the earthquake demands. The isolator configuration is determined by the gravitational loads. The vertical average stress of the isolators is set to be about 10 to 15N/mm2. The number of dampers is assessed in order to obtain an equivalent damping for rare earthquake of about 15% to 20% to control the maximum lateral deformation of seismic isolation layer. Hysteretic dampers, if used, are designed to resist the frequent lateral loads in the elastic domain. The common yield threshold of the hysteretic dampers is commonly in the range of 3% to 5% of the weight of the structure. The maximum displacement of the isolation layer for rare earthquake should not exceed the limit, which is specified as the maximum of 0.55 times diameter and 3.0 times total rubber thickness of the rubber bearings.

(3) The seismic reduction factor assumed in Step (1) need to be validated after the superstructure and base-isolation layer are determined. Two models, i.e. seismic isolation and non seismic isolation models are established, and time history analyses are conducted. The seismic reduced factor is determined according to Table 2 and depends upon the maximum ratio of isolated story shear forces to non-isolated story shears forces, in of all stories. The horizontal seismic reduction factor shall not be smaller than 0.25. The difference between horizontal seismic reduction factor and maximum ratio of story shear forces is considered as the safety margin. If the seismic reduction factor obtained in this step is larger or too much smaller than that assumed in Step (1), the superstructure and the base-isolation layer need to be redesigned.

(4) The design of base structure and foundation is preceded after the design of the superstructure and seismic isolation layer is completed. The design is similar to conventional structures, but the vertical force, horizontal force and moment of force at the bottom of the isolators under rare earthquake, which are transferred from the superstructure, should be considered.

Table 2 Relation of the maximum ratio of story shear force and the horizontal seismic reduced factor

Maximum ratio of story shear force	0.53	0.35	0.26	0. 18
Horizontal seismic-reduced factor	0.75	0.50	0.38	0.25

3. APPLICATION EXAMPLE

3.1 Structure Brief

As shown in Fig. 3, the example building is a 6-story RC-frame structure located in Dujiangyan City, with a height of 21.22m and a floor area of 5400m2. The first floor is used as a parking place thus having no infill walls and its upper stories are apartments with both horizontal and vertical infill walls. Concrete C30 is used in this frame, and HRB335 is used in longitudinal reinforcement. Cross-sections of the column are ranged from 650mm × 450mm to 400mm × 400mm along the height; and those of the beams are 720mm × 250mm in short direction, and 620mm × 200mm in long direction. The thickness of slab is 120mm, and 240mm of wall.

During the Wenchuan earthquake, the bottom story was seriously damaged (refer to Fig. 4). The plastic hinges occurred at the ends of columns, and the maximum residual displacement was over 200mm corresponding to a story drift angle of 1/15. However, the upper stories were almost untouched. In addition, the earthquake intensity of Dujiangyan City was increased from intensity 7 to 8. Accordingly, the design spectra of the city got doubled. The maximum value of the design spectra was changed from 0.04g to 0.08g for frequent earthquake, and from 0.08g to 0.16g for rare earthquake. The seismic design group of the city, which represents the distance from the epicenter of possible earthquake, is changed from Group 1 to Group 2. The site class for the building, which is determined according to the equivalent shear-wave velocity and the overlaying depth of soil profile, is Site Class 2. The design characteristic period of the ground motions for this building is 0.4s.

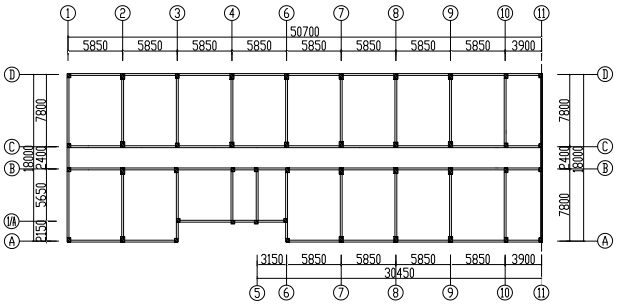


Figure 3 Structure plane



Figure 4 Damages of bottom columns

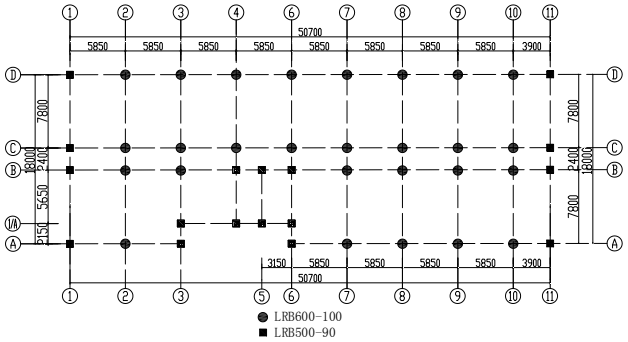


Figure 5 Arrangement of seismic isolator

3.2 Retrofit Using Seismic Isolation

Seismic-isolation technology is applied to the retrofit of this building. The retrofit procedure is considered as follows: (1) enlarge the columns of the bottom story; (2) jack the superstructure above the second floor, and cut the columns of bottom story at the top; (3) install slide bearings, and restore the structure to the original position; (4) replace the slide bearings with rubber bearings. As shown in Fig. 5, two types of lead rubber bearings are adopted in this project, i.e. LRB500-90 and LRB600-100. The rubber bearings are carefully arranged so that the stiffness and the mass centres match well.

The equivalent damping ratios at 100% horizontal deformation are 23.9% and 21.9%, respectively. The second shape factors are 5.00 for both two types of rubber bearings. The rubber bearings are set at the top of columns at the first story. The compressive stresses when subjected to 1.0 times

Dead Load plus 1.0 times Live Load are less than 12MPa, the limit for allowable long term compressive forces.

3.3 Computational Model

In this project, a structure analysis program called SAP2000 is used for the time history analyses. As shown in Fig. 6, two models are built: one is for the original structure. It uses a mass-spring model, in which each story is represented by a mass and a spring. The other is for the building after seismic isolation. In this model, a nonlinear LINK element, provided by SAP2000, is used to represent the rubber bearings. The isolation layer is modelled in detail, and the eccentricities of the superstructure are also carefully modelled, so that the torsion effect on the displacement of the seismic isolation layer can be taken into account.

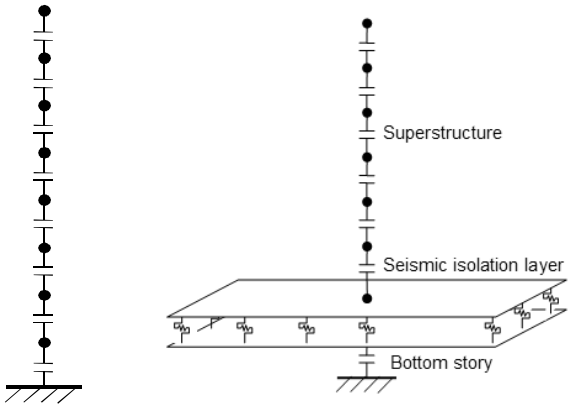


Figure 6 Computational models of structure (a) Model 1 Original structure, (b) Model 2 Seismic isolation structure

3.4 Ground Motions

According to the Chinese seismic design code, 2 sets of real ground motions (El Centro(NS) and Taft(NS)) and 1 set of synthetic ground motion were selected based on the site class. The acceleration histories and the associated spectra are given in Fig. 7. The maximum accelerations of ground motions are adjusted to 70gal for frequent earthquake, 200gal for local fortification intensity earthquake, and 400gal for rare earthquake.

3.5. Modal Analysis

Modal analyses are conducted and the results are given in Table 3. According to the modal analysis results of the original structure and seismic isolation structure models, it is found that after seismic isolation the period of the first mode extends from 0.609s to 2.281s in X direction, and from 0.569s to 2.267s in Y direction. Note that the modal analysis for the seismic isolation structure uses the stiffness of rubber bearing corresponding to 100% shear strain. The first vibration mode is characterized by the translation in X direction, the second vibration mode is characterized by the translation in Y direction, and the third vibration mode is a torsion mode around Z direction.

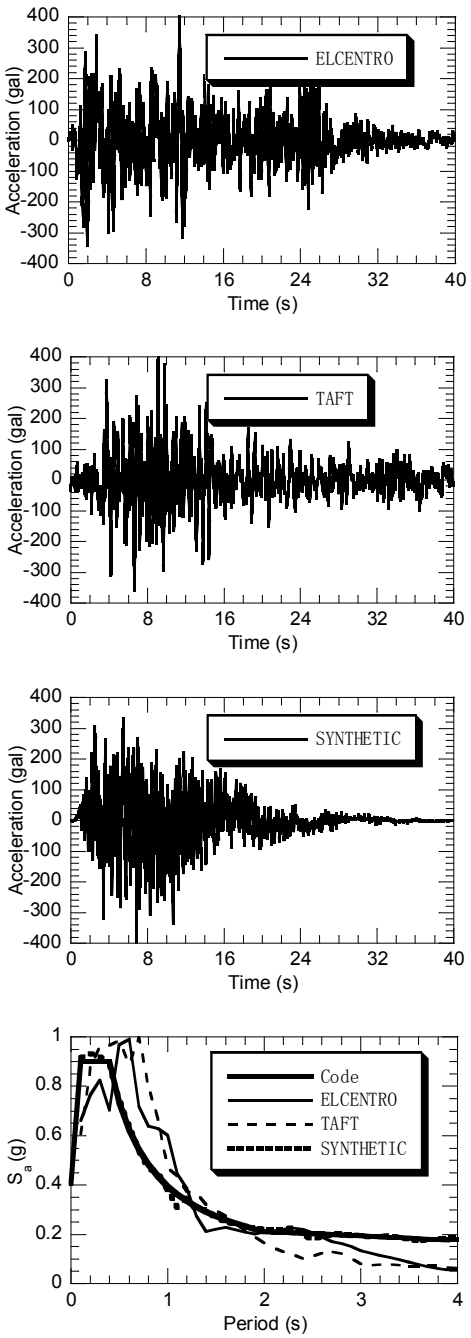


Figure 7 Time history and spectra for rare earthquake

Table 3 Natural period of the first three modes and quality participation coefficient

Mode	Time/s	UX	UY	RZ
1	2.281	0.938	0.003	0.115
2	2.267	0.003	0.975	0.668
3	2.075	0.037	0.000	0.200

3.6 Maximum Story Shear of Superstructure

Time history analyses are conducted, and average of the maximum story shears of the superstructure when subjected to three ground motions for intensities 7 and 8 are obtained

(refer to Fig. 8). Analysis results show that after seismic isolation the story shear is decreased to no more than 40% of the original non seismic isolated structure, and the story shears of the seismic isolation model for Intensity 8 are smaller than those of the original structure model for Intensity 7, suggesting that the after seismic isolation the superstructure satisfies the requirement of new intensity without strengthening.

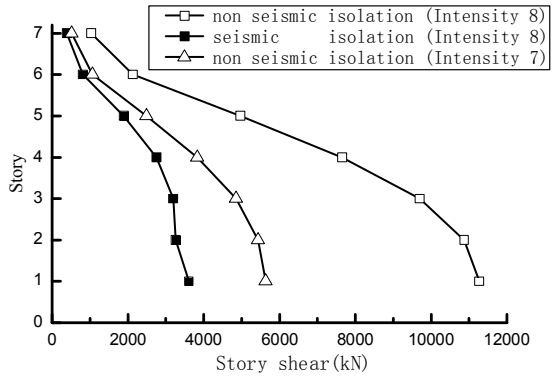


Figure 8 Story shear of superstructure

3.7 Maximum Displacement of Isolation Layer for Rare Earthquake

As shown in Table 4, the maximum displacement of the isolation layer under rare earthquake is investigated. In the table, the data for the cases including and not including torsion effects are given separately. It can be observed that the maximum displacements are all smaller than the limit values, which are specified as the maximum of 0.55 times diameter and 3.0 times total rubber thickness of the rubber bearings. The results also suggest that no significant torsion effects can be observed in the isolation layer. This is mainly thanks to the well arrangement of the LRBs so that the mass and the stiffness centres match.

Table 4 The maximum horizontal displacement of the isolation layer under rare earthquake (mm)

Without/with consideration of torsion effect				
Direction of the seismic wave	ELNS	TAFT	SYNTHETIC	AVERAGE
X direction	118/119	122/123	158/161	132.7/133.7
Y direction	117/117	123/123	157/158	132.3/132.7

3.8. Design of Bottom Column and Foundation

The design of the bottom columns and foundation is similar to the design of conventional structures. However, the following issues were considered: (1) the shear forces, axial forces, and moments transferred from the superstructure under the rare earthquakes are exerted as external load at the top of the columns. (2) The performance of the bottom columns is set to be elastic under rare earthquake (Xu et al. 2001).

4. CONCLUSIONS

This paper mainly presents the design methodology and engineering application of seismic isolation. The seismic isolation design of a building damaged in the Wenchuan earthquake in soft bottom story mode and retrofitted after the earthquake is outlined. Major conclusions obtained in this study are as follows:

(1) Chinese design of seismic isolation is getting mature.

(2) The retrofit solutions using the mid-story isolation technology effectively improve the seismic performance of the structure.

References:

Lin X. Ch. , Pan P. , Ye L.P. , Lu X. Zh. , and Zhao Sh.Ch. (2009) , "Analysis on damage mechanism of a typical RC frame in Wenchuan Earthquake", *China Civil Engineering Journal*, 42(5), 13-20.

National Standard of China (2001), Code for seismic design of building, GB50011-2001. Beijing: *China Architecture and Building Press*, 2001:116.

Xu Zh. G, Xie J. L., Zhou F. L(2001)., "Isolation retrofitting design of a multi-story building", *Earthquake Engineering and Engineering Vibration*, 21(3), 132-139.

Xu Zh. G , Zhou F. L, Kong L.(1999), "A Survey of Retrofitting Buildings with Isolation Technique at Home and Abroad", *Journal of South China Construction University*, 7(2),14-20,.

8CUEE CONFERENCE PROCEEDINGS
8th International Conference on Urban Earthquake Engineering
March 7-8, 2011, Tokyo Institute of Technology, Tokyo, Japan

FUNDAMENTAL STUDY ON PROBABILISTIC EVALUATION OF THE ULTIMATE STATE OF BASE ISOLATED STRUCTURES

Toshiyuki Nakazawa[1], Zhe Qu[2], Arata Miyoshi[3], Shoichi Kishiki[4], and Akira Wada[5]

1) Tokyo-Kenchiku Structural Engineers, Japan
2) Postdoctoral research fellow, Center for Urban Earthquake Engineering, Tokyo Institute of Technology, Japan
3) Graduate student, Tokyo Institute of Technology, Japan
4) Assistant professor, Structural Engineering Research Center, Tokyo Institute of Technology, Japan
5) Professor, Structural Engineering Research Center, Tokyo Institute of Technology, Japan
nakazawa-t@tkse2000.co.jp, m.quzhe@gmail.com, miyoshi.a.aa@m.titech.ac.jp, kishiki@serc.titech.ac.jp, wada@serc.titech.ac.jp

Abstract: Seismic base isolation is effective to control the seismic responses of building structures. However, compared with conventional seismic systems, the robustness of the base-isolated buildings is generally considered lower and thus the selection of input ground motions becomes a more crucial issue in assessing the seismic safety of base-isolated buildings. Extensive incremental dynamic analysis (IDA) is carried out to evaluate the ultimate state of base isolated buildings in terms of the fragility curves. The ground motion record set in FEMA P695 is adopted for analysis. The influences of the stiffness of isolation layer, the height of rubber bearings, clearance and hysteretic behavior of the retaining walls as well as the strength of the superstructures are examined. Based on the analysis results, the following can be concluded:(1) increasing the clearance of retaining walls is the most effective manner to enhance the seismic safety of base isolated buildings; (2) the seismic safety margin of base-isolated buildings might be significantly increased with stronger superstructures only if the retaining wall is appropriately proportioned so that the yielding of retaining wall is prior to that of the superstructure.

1. INTRODUCTION

The deformation pattern of base-isolated structures is clearly defined by employing a soft isolation layer at the bottom of the building, which is usually composed of both isolators and energy dissipating devices. Under earthquakes, most deformations and energy dissipations are expected to concentrate in the isolation layer so that the superstructure suffers only slight damage. But on the other hand, the robustness of isolated structures subjected to unexpected violent earthquakes remains questionable (Kikuchi *et al*, 1995). Shaking table test reveals that reinforced concrete walls in the superstructure of isolated structures are likely to suffer severe damage if hardening of the rubber bearing in the isolation layer occurs (Kitamura *et al*, 2009).

In order to assess the seismic safety of base-isolated structures under unexpected earthquakes, the incremental dynamic analysis proposed by Vamvatsikos *et al* (2002) is employed and the collapse margin ratios (CMR) of base-isolated structures with various parameters are evaluated in accordance with the framework in FEAM P695 (2009). The following ultimate states are considered in this study: (1) hardening and fracture of rubber bearing; (2) collision of the superstructure with surrounding retaining walls; (3) excessive damage in the superstructures. The failure of dampers is not considered.

2. ANALYSIS MODEL

The base-isolated structure is modeled by a 2-DOF system as shown in Figure 1. The weight of superstructure and isolation layer is 150,000kN and 40,000kN, respectively. Hysteretic behavior of each component is introduced below.

2.1 Superstructure

The superstructure is modeled by a SDOF system with tri-linear degrading hysteresis (Takeda *et al*, 1970) as shown in Figure 1(a). Yield strength Q_y is set to be base shear coefficient C_0 times the superstructure weight W_S (150,000kN). Cracking strength is $0.3Q_y$ and the secant stiffness at yielding point is 0.3 times the initial stiffness. Post-yielding tangent stiffness is 0.001 times the initial stiffness. Unloading stiffness ratio β=0.4. Damping of the superstructure is assumed proportional to the tangent stiffness with a 2% damping ratio at the fixed-base period. For non-isolated structure, 3% damping ratio is assumed to consider the damping induced by soil-structure interaction.

In this study, C_0 varies from 0.15 to 0.40 with an increment of 0.05. The initial stiffness is assumed to be proportional with C_0 value. In the case of C_0=0.3, which is a common practice in Japan, the fundamental period of fixed-base structure is assumed to be 0.3s, and the

corresponding initial stiffness is 6,709❹$10^3$kN/m.

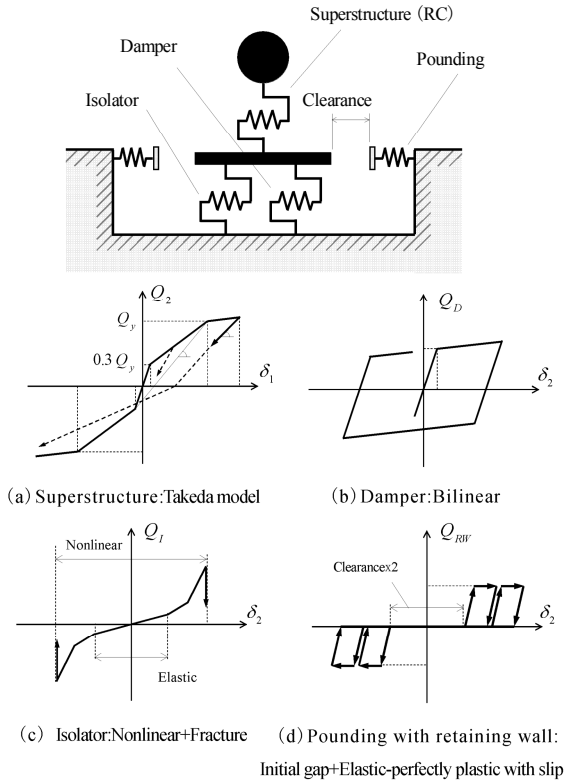


Figure 1 Analysis model and the hysteretic behavior

2.2 Damper

It is assumed that the damper have adequate deformation capacity up to the collapse of the structure. Bilinear hysteretic behavior with an initial stiffness of 240.0❹$10^3$kN/m and a post-yielding stiffness ratio of 1/60 is assumed for the damper (Figure 1b). The damper yield strength is 7,600kN, which is 0.04 times the total weight of the whole structure.

2.3 Isolator

It is assumed that natural rubber bearing is used as seismic isolator. Nonlinear elastic behavior with deformation limit as shown in Figure 1(c) is assumed. The initial stiffness k_{i1} is determined by tuning the isolation period T_f (Equation 1) to 4.0s, 5.0s and 6.0s. The corresponding k_{i1} is 47800, 30600 and 21300kN/m, respectively.

$$T_f = 2\pi\sqrt{M/k_{i1}} \quad (1)$$

where M is the total weight of the structure.

It is assumed that the tangent stiffness of the isolator increases to $k_{i2}=2k_{i1}$ in the shear strain range of 250%~350%, and $k_{i3}=7.0k_{i1}$ in the range of 350%~450%. Shear strain of 450% defines the ultimate deformation of the isolator. These assumptions are made based on the test results reported in previous studies (Takayama, 1995; Yabana *et al*, 1996; Uryu *et al*, 1996; JSI, 1995). The isolator fracture deformation can be adjusted by varying the total rubber thickness nt_R. In this study, nt_R varies from 160mm, 200mm to 240mm. The corresponding fracture deformations of the isolator are 720mm, 900mm to 1080mm, respectively.

Beyond 450% shear strain, the isolator fractures and the restoring force is replaced by the friction between the isolation layer and its foundation. This is modeled by an elastic-perfectly plastic behavior with an elastic stiffness of 1600~3600 times the isolator stiffness and a strength of 0.4 times the total weight of the structure. The fall down of the isolation layer due to isolator fracture is not considered.

2.4 Pounding with retaining wall

An elastic-perfectly plastic spring with slip and initial gap is used to model the retaining wall and the clearance to the superstructure (Figure 1d). The same retaining wall as used by Kashiwa *et al* (2005) is assumed. Elastic stiffness is 57.5❹$10^3$kN/m and the yield strength is 34,500kN. The clearance varies from 500mm, 800mm to infinity (no pounding).

3. GROUND MOTIONS

A set of strong ground motions representing an earthquake scenario is required when evaluating the seismic performance using the incremental dynamic analysis. In this study, the selection of ground motion records is based on the Far-Field set in FEMA P695 (2009). Among the 22 records in the Far-Filed set, 8 components from 6 records are considered not appropriate for evaluating the seismic performance of seismic isolated buildings in this study since their lowest usable frequencies are no less than 0.167Hz, which indicates the long period contents with period longer than 6.0s are not reliable. For this reason, these 6 records are removed from the record set and only the remaining 16 records are used in this study.

3.1 Normalization of ground motion records

In order to remove the unwarranted variability in the ground motions, the selected records should be appropriately normalized. In FEMA P695, the records are normalized by the geometric mean of the peak ground velocities (PGV) of the two horizontal components. This method is dependent on the direction of observation.

In this study, each record is first rotated to the direction where the maximum PGV occurs. The ground acceleration in this direction is denoted as GA_{MV}, where the subscript MV stands for "Maximum Velocity". The normalization factor is then calculated by Equation 2.

$$NM_i = \text{median}\left(PGV_{MV,i}\right)/PGV_{MV,i} \quad (2)$$

where PGV_{MV} is the PGV of GA_{MV}, the subscript i denotes the record number.

3.2 Scaling of record set

In an incremental dynamic analysis, the intensity of the scenario earthquake represented by the ground motion record set needs to be scaled incrementally until the ultimate

failure of the structure is achieved. Before doing so, some intensity measure (IM) needs to be defined. In FEMA P695, the median of the 5% damping spectral accelerations at the fundamental period $S_a(T_1, 5\%)$ of the record set is used as the IM. However, as recommended by Akiyama (1980), the equivalent velocity at the isolation period $V_E(T_f)$ can better represent the seismic response of base-isolated structures, which usually have long natural periods of vibration. T_f is given in Equation 1. The equivalent velocity V_E is a representation of the earthquake input energy with the unit of velocity. It is calculated by Equation 3.

$$V_E(T) = \sqrt{2E_I(T,10\%)/M} \quad (3)$$

where T is the natural period, $E_I(T, 10\%)$ is the input energy for a SDOF system with a period of T and 10% damping. M is the total mass of the system.

In this study, the median $V_E(T_f)$ of the normalized records is chosen to be the IM in the incremental dynamic analysis for base-isolated structure. For conventional non-isolated structures, the median $S_a(T_1)$ of the normalized records is used as the IM following FEMA P695. Note that the method of normalizing the records for both isolated and non-isolated structures is the same.

Since the IM for based-isolated and non-isolated structures are different, the intensity ratio (IR) defined as the ratio of the currently-used IM and design level IM is used to interpret the incremental dynamic analysis results (Equation 4).

$$\mathrm{IR} = \mathrm{IM}/\mathrm{IM}_D \quad (4)$$

IM_D is the design equivalent velocity $V_S(T_f)$ for base-isolated structures, and the design spectral acceleration $S_a(T_1)$ for non-isolated structures. $V_S(T_f)$ and $S_a(T_1)$ at the engineering bedrock recommended by BCJ (2005) are adopted. They can be easily transformed to those at other site conditions by multiplying the surface geology factor $G_s(T)$ recommended by BCJ (2005).

Figure 2 shows the equivalent velocity of the 16 ground motion records after being normalized and scaled to IR=1.0 for isolated structures with a period of 4.0s. Details of the selected ground motions are given in the appendix.

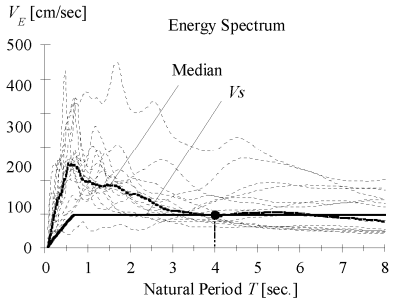


Figure 2 Equivalent velocity spectrum of normalized records when IR=1.0

4. INCREMENTAL DYNAMIC ANALYSIS

The IDA curves of the based-isolated structures with T_f=4.0s and C_0=0.3 as well as the corresponding non-isolated conventional structure are compared in Figure 3. In the IDA curves, the ductility of the superstructure defined as the ratio of the maximum and the yield deformation is chosen as the damage measure (DM).

For the based-isolated structure, 3 models denoted as Model A, B and C are used to examine the effect on the seismic performance of isolator fracture and pounding against the retaining wall. The 3 models are:

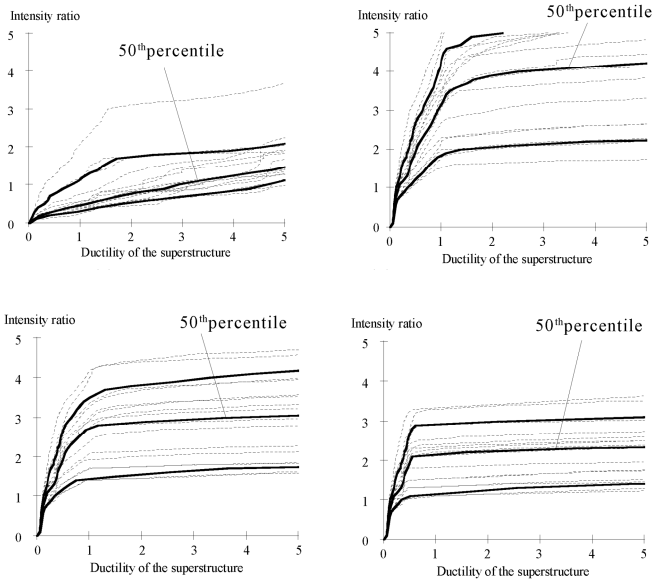
Model A. Ideal isolation. The isolator is assumed linearly elastic and no retaining wall is modeled (or the clearance is infinite).

Model B. The total rubber thickness of the isolator nt_R is 200mm and the hardening and fracture of the isolator as described above is considered. Still, no retaining wall is modeled.

Model C. Linearly elastic retaining wall with a 500mm clearance to the structure is modeled. All the other parameters are the same as in Model B.

Figure 3 gives the IDA curves for the non-isolated and the 3 models of the isolated structure. Dotted lines are the IDA curves for individual ground motions and bold solid lines mark the 16th, 50th (median) and 84th percentile of the IDA curves.

In terms of the median IDA curve, damages to the non-isolated structure increases gradually with the increase of intensity ratio (Figure 3a). No obvious softening of the median IDA curve can be observed since neither strength deterioration nor P-Δ effect are considered in the modeling, i.e. the structure does not exhibit negative stiffness.



(c) Model B: Isolator fracture (d) Model C: Pounding

Figure 3 IDA curves of non-isolated and based-isolated structure

In contrast, the damage of the superstructure in the isolated building is limited to a very low level (say the ductility is below 1.0) prior to a certain limit of earthquake intensity. Beyond the limit, significant softening occurs even if the *P-Δ* effect is not considered. The superstructure ductility grows rapidly with slight increase of earthquake intensity.

From Figure 3(b)-(d), it is evident that the nonlinearity of the isolator and the pounding with the retaining wall significantly deteriorates the seismic performance of base-isolated structure. The value of IR when median IDA curve softens is about 4 for ideally isolated structure (Model A, Figure 3b). It is reduced to about 3 when nonlinearity of the isolator is considered (Model B, Figure 3c) and is further reduced to only about 2 if pounding occurs (Model C, Figure 3d).

It is also worth noting that the dispersions of IDA curves of isolated structures that can be visually identified by the range between 16th and 84th percentile in Figure 3(b)-(d) are also significantly reduced if the isolator's nonlinearity and the pounding are considered.

5. COLLAPSE MARGIN RATIOS

It is assumed herein that the structure or the superstructure in an isolated building collapses at the ductility of 4.0. The corresponding intensity ratios (IR) under individual ground motion input are collected from the IDA curves. By assuming a lognormal distribution, fragility curves as demonstrated in Figure 4 can be produced, where the vertical axis is the probability of collapse, i.e. the ductility equals or exceeds 4.0, and the horizontal axis is the intensity ratio (IR). Figure 4 gives an example of fragility curves of the above mentioned Model A, B and C for isolated structures. The IR corresponding to the 50% probability of collapse is taken as the collapse margin ratio (CMR). It is obvious from Figure 4 that CMR decreases significantly from Model A (ideal isolation) to B and C.

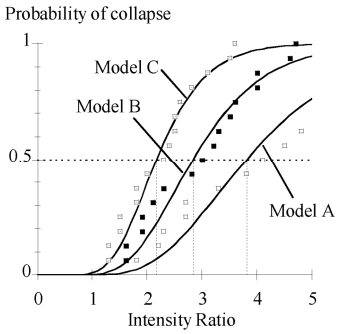


Figure 4 An example of fragility curves of isolated structure

The influences of various parameters on the CMRs of base-isolated structures are discussed. In order to help identifying the sequence of isolator fracture and retaining wall pounding, characteristic deformations (i.e. hardening limit and fracture limit) of the isolator with various total rubber thicknesses nt_R are compared with the size of clearance in Figure 5. For example, if the total rubber thick is 160mm and the clearance is 800mm, the isolator will fracture prior to the pounding. In other words, pounding is not likely to occur in this case.

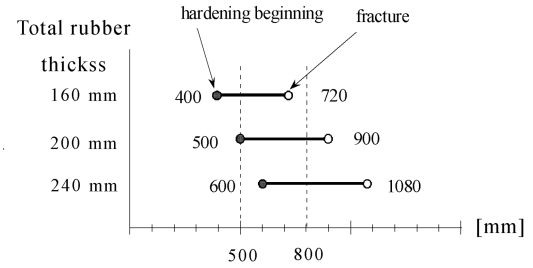


Figure 5 Characteristic deformations of the isolator compared with the size of clearance

Figure 6 summaries the CMRs of the base-isolated structures with various superstructure strengths, total rubber thicknesses, isolation periods, retaining wall properties and sizes of clearance.

For 500mm clearance, as indicated by Figure 5, pounding with the retaining wall occurs prior to the fracture of the isolator and hence dominates the ultimate behavior of the isolated structure no matter the total rubber thickness is 160mm, 200mm or 240mm. In this case, the superstructure strength has only marginal effect on the CMRs, regardless of the total rubber thickness and the isolation period (Figure 6a).

If the retaining wall behaves in an elastic-plastic manner, as shown in Figure 6(b), CMR can be increased considerably with larger superstructure strength, especially when superstructure strength is large enough to resist the shear force in the isolation layer when the retaining wall yields. Meanwhile, larger fracture deformation of the isolator (i.e. larger total rubber thickness) can increase the CMR. Table 1 lists the shear coefficient of the isolation layer when the retaining wall yields in various cases.

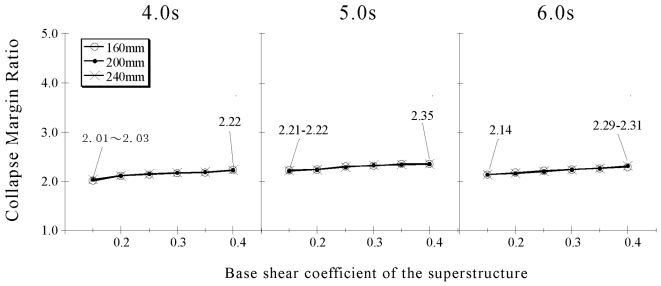
Table 1 Shear coefficient of isolation layer when retaining wall yields

Clearance (mm)	Isolation period T_I (s)	Total rubber thickness (mm)		
		160	200	240
500	4.0	0.41	0.39	0.37
	5.0	0.35	0.33	0.32
	6.0	0.31	0.30	0.29
800	4.0	No pounding	0.75	0.52
	5.0		0.56	0.42
	6.0		0.46	0.36

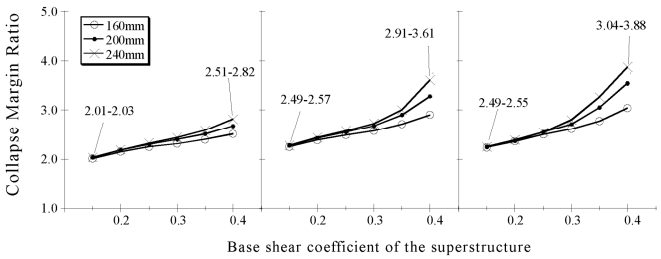
On the other hand, if the clearance of the retaining wall is increased to 800mm, the pounding is not likely to occur since the isolator fractures prematurely if the rubber thickness is only 160mm (See Figure 5). In this case, it makes no difference whether the retaining wall is elastic or elastic-plastic (see Figure 6c and 6d). Otherwise, when the total rubber thickness is 200mm or 240mm, pounding occurs

during the hardening range of the isolator. In these cases, yielding of the retaining wall will permit the isolator to develop larger deformation up to its fracture. As a result, CMR is increased with larger fracture deformation of the isolator (Figure 6d).

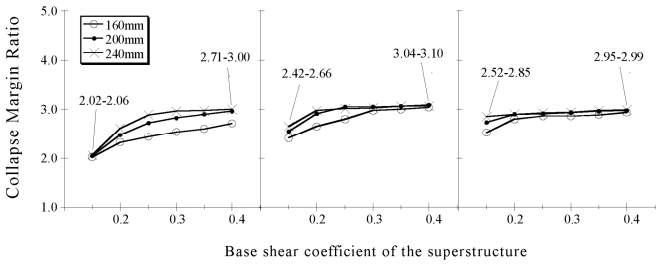
It's also worth noting that the CMRs with 800mm clearance are generally larger than those with 500mm clearance.



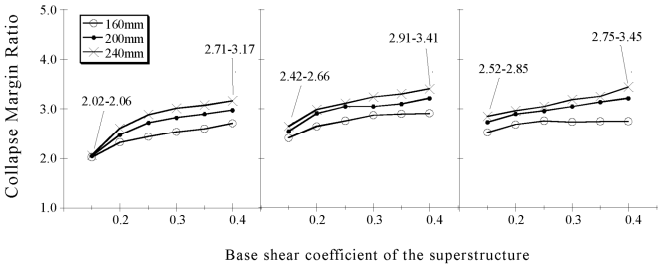
(a) Elastic retaining wall with 500mm clearance



(b) Elastic-plastic retaining wall with 500mm clearance



(c) Elastic retaining wall with 800mm clearance



(d) Elastic-plastic retaining wall with 800mm clearance

Figure 6 Influence of various parameters on CMR of base-isolated structures

Figure 7 shows the variations of CMRs of the isolated structure with 5.0s isolation period and 200mm total rubber thickness. If the structure is ideally isolated (i.e. neither pounding nor isolator's nonlinearity is considered), CMR is large and increases dramatically with higher superstructure strength. But this is not realistic. If the clearance is not adequate (say 500mm) and the retaining wall is very strong, CMRs become much smaller and keeps almost constant regardless of the superstructure strength. Yielding of the retaining wall in this case will increase the CMR with the assistance of stronger superstructure. On the other hand, the CMR can be significantly increased if the clearance is enlarged from 500mm to 800mm.

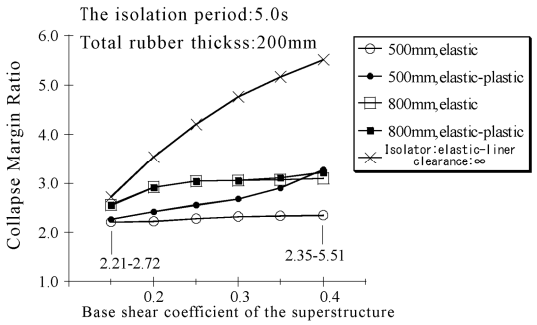


Figure 7 Influence of retaining wall behavior, superstructure strength and clearance size

6. CONCLUSIONS

As a fundamental study on the ultimate state of seismic isolated structure subjected to unexpected strong earthquakes, the seismic performance of base-isolated structures is assessed by incremental dynamic analysis of a 2DOF model with one directional ground motion input. Collapse margin ratios of the models with various influencing parameters are evaluated. From the above discussions, the following conclusions can be drawn:

(1) The seismic safety margin of the base-isolated structures can be significantly increased by increasing the clearance to the retaining walls.

(2) Increasing the strength of superstructure has marginal effect on the overall seismic safety of the base-isolated structure if pounding with the retaining wall occurs and the retaining wall would not yield.

(3) If the retaining wall is appropriately proportioned so that the yielding of retaining wall is prior to that of the superstructure, the seismic safety of base-isolated buildings can be considerable enhanced.

Note that these conclusions are based on the many assumptions made in this study. They should be carefully interpreted in cases where, for example, the higher modes of the superstructure, the vertical failure of the isolator, or the bi-directional ground motion input needs to be considers. These outline the scope of the future study.

References:

Kikuchi, M., Tamura, K. and Wada, A. (1995), "Safety evaluation of base-isolated structures," *J. Struct. Constr. Eng., AIJ*, 470, 65-73.

Kitamura, S., Morishita, M., Yabana, S. and Hirata, K. (2009), "Ultimate behavior tests of seismic isolation system for FBR with A large shaking table (Part1～6)." *Summaries of Technical Papers of Annual Meeting*, *AIJ*, B-2, 1063-1074.

Vamvatsikos, D. and Cornell, C.A. (2002), "Incremental dynamic

analysis." *Earthquake Engineering and Structural Dynamics*, **31**(3), 491- 514.

FEMA P695 (2009), "Quantification of building seismic performance factors." Federal Emergency Management Agency, Washington, D.C.

Takeda, T., Sozen, M.A. and Nielsen, N.N. (1970), "Reinforced concrete response to Simulated Earthquakes." *Journal Structural Division, ASCE*, **96**(ST12)，2257-2573.

Takayama, M. (1995), "Ultimate capacity of natural rubber bearings used in seismic isolation system." *Journal of Technical Des*., *AIJ*, 1, 160-165.

Yabana, S., Ohtori, Y., Hirata, K., Yasui, K. and Mazda, T. (1996), "Study on linear limits of rubber bearings (Part1 and Part2)," *Summaries of Technical Papers of Annual Meeting*, *AIJ*, B-2, 691-694.

Uryu, M., Nakayama, K. and Takayama, M. (1996), "Experimental study on natural rubber bearings under high vertical load for base isolation system (Part5)." *Summaries of Technical Papers of Annual Meeting*,*AIJ*, B-2, 705-706.

JSSI (1995), "Introduction to base-isolated structures." The Japan Society of Seismic Isolation, Ohmusha, 69-71.

Kashiwa, H., Nakayasu, N. and Nakashima, M., (2005). "Response and damage of base-isolated buildings subjected to very varge earthquakes." *Journal of Structural Engineering*, *AIJ*, 51B, 237-246.

Akiyama, H. (1980). "Earthquake-resistant limit-state design for buildings", The University of Tokyo.

BCJ (2005). "Commentary and design examples for the earthquake-resistant design based on energy balance." The Building Center of Japan.

Appendix: Ground motion record set used in the study

Table A1 lists the details of all the 16 ground motion records that are used in this study. These ground motion data are obtain from the PEER/NGA database and the data in Table A1 are also from the database with the exception of the last 3 columns. In these columns, the PGV_{MV} defined in this study and the rotating angles where the PGV_{MV} occurs are listed. These angles are with respect to the 1st component of the original record. In the last column, the normalization factors in accordance with the normalization method in this study are given.

Table A1 Details of the input ground motion records

ID No. (FEMA)	Recording Data					Original Data					Rotated Data		
	Date	Name (Country)	Recording Staion	Epicentral [km]	Magnitude	Component	Lowest Usable Freq [Hz]	PGA [cm/s^2]	PGV [cm/s]	Duration [sec]	PGV_{MV} [cm/s]	θ	*NMi*
2	1994/01/17	Northridge (USA)	Canyon Country-WLC	26.5	6.7	LOS000	0.06	402.11	42.98	20.48	56.88	127°	0.85
						LOS270	0.13	472.68	45.37				
3	1999/11/12	Duzce (Turkey)	Bolu	41.3	7.1	BOL000	0.06	713.50	56.44	81.92	63.69	73°	0.76
						BOL090	0.06	806.50	62.07				
4	1999/10/16	Hector Mine (USA)	Hector	26.5	7.1	HEC000	0.03	260.44	28.56	81.92	44.16	109°	1.09
						HEC090	0.04	330.25	41.72				
5	1979/10/15	Imperial Valley (USA)	Delta	33.7	6.5	H-DLT262	0.06	233.16	25.98	163.84	33.76	103°	1.43
						H-DLT352	0.06	344.32	32.99				
7	1995/01/16	Kobe (Japan)	Nishi-Akashi	8.7	6.9	NIS000	0.13	499.48	37.27	40.96	38.52	109°	1.25
						NIS090	0.13	493.02	36.65				
8	1995/01/16	Kobe (Japan)	Shin-Osaka	46.0	6.9	SHI000	0.13	238.53	37.84	40.96	44.20	31°	1.09
						SHI090	0.10	207.82	27.92				
10	1999/08/17	Kocaeli (Turkey)	Arcelik	53.7	7.5	ARC000	0.09	214.60	17.68	40.96	42.70	66°	1.13
						ARC090	0.05	147.00	39.53				
11	1992/06/28	Landers (USA)	Yermo Fire Station	86.0	7.3	YER270	0.07	344.53	51.40	81.92	56.47	156°	0.86
						YER360	0.07	240.07	29.69				
12	1992/06/28	Landers (USA)	Coolwater	82.1	7.3	CLW-LN	0.13	277.35	25.62	40.96	42.50	84°	1.14
						CLW-TR	0.13	408.82	42.30				
14	1989/10/18	Loma Prieta (USA)	Gilroy Array #3	31.4	6.9	G03000	0.13	544.28	35.67	40.96	49.71	45°	0.97
						G03090	0.13	360.25	44.63				
15	1990/06/20	Manjil (Iran)	Abbar	40.4	7.4	ABBAR-L	0.13	504.61	43.21	81.92	54.92	129°	0.88
						ABBAR-T	0.13	486.75	54.06				
16	1987/11/24	Superstition Hills (USA)	El Centro Imp. Co.	35.8	6.5	B-ICC000	0.13	350.93	46.31	40.96	52.42	28°	0.92
						B-ICC090	0.13	253.33	40.83				
18	1992/04/25	Cape Mendocino (USA)	Rio Dell Overpass	22.7	7.0	RIO270	0.07	377.96	43.78	40.96	51.57	37°	0.94
						RIO360	0.07	538.31	42.04				
19	1999/09/20	Chi-Chi (Taiwan)	CHY101	32.0	7.6	CHY101-E	0.04	346.06	70.59	81.92	115.01	89°	0.42
						CHY101-N	0.05	431.59	114.92				
20			TCU045	77.5	7.6	TCU045-E	0.03	465.17	36.67	81.92	46.96	124°	1.03
						TCY045-N	0.05	502.11	39.07				
22	1976/05/6	Friuli (Italy)	Tolmezzo	20.2	6.6	A-TMZ000	0.13	344.53	22.02	40.96	31.02	82°	1.56
						A-TMZ270	0.13	308.72	30.78				

8CUEE CONFERENCE PROCEEDINGS
8th International Conference on Urban Earthquake Engineering
March 7-8, 2011, Tokyo Institute of Technology, Tokyo, Japan

SEISMIC DESIGN FOR A RESILIENT AND SUSTAINABLE SOCIETY

Victor Zayas

President, Earthquake Protection Systems, California, USA
Victor@EarthquakeProtection.com

Abstract: A seismic resistant construction method is presented that reduces initial construction costs, and reliably avoids seismic damage to structures, non-structural components, and building contents. Avoiding seismic damage to structures, non-structural components and contents of a building is necessary if we are to avoid the devastating economic losses and disruption that major earthquakes cause urban regions. New buildings are typically designed to comply with only the minimum seismic safety requirements of the building codes. Building codes do not require avoiding damage to structures, non-structural components, or building contents during severe earthquakes. Sustainable construction does however require structures that are not damaged. Moreover, resilient construction requires that contents and non-structural components maintain their ability to function after a severe earthquake. Example applications are presented for major buildings, bridges, and industrial facilities, that avoid seismic damage and have lower initial construction costs as compared to ductility based design methods. A design method for Triple Pendulum seismic isolation is presented that achieves 98% reliably of maintaining function of the non-structural components, contents, and structure, for an earthquake having only a 2% chance of being exceeded in 50 years. The Triple Pendulum is a multi-stage seismic isolation bearing. Each bearing has three independent isolation mechanisms that can be optimized to protect contents, non-structural components and structures from damage. With their compact size and lower bearing costs, Triple Pendulum bearings can actually lower construction costs as compared to traditional ductility design methods.

SEISMIC DESIGN BACKGROUND

Modern building codes have saved the lives of hundreds of thousands of people. Building engineers worldwide have achieved seismic safety and construction cost savings by designing structures to comply with modern codes at the lowest construction cost. Yet every year, major earthquakes cause devastating economic losses and disruption to the urban areas they affect. Facility owners and occupants are always very surprised when code compliant facilities suffer extensive damage, loss of use, and disruption as a result of earthquakes. Government-reported loss data from the Kobe and Northridge earthquakes shows that total economic losses including loss of use and disruption were ten times greater than the direct costs for repairing damaged structures. In modern code compliant buildings, the loss of use and costs of damage to nonstructural elements and contents can be substantial even for moderate seismic events. Today, the public expects engineers to protect them from the economic losses and disruption caused by earthquakes.

Although it is possible to design buildings strong enough to remain elastic during earthquakes, these structures are expensive, and the increase in structure strength causes higher in-structure accelerations, and results in greater damage to nonstructural components and contents.

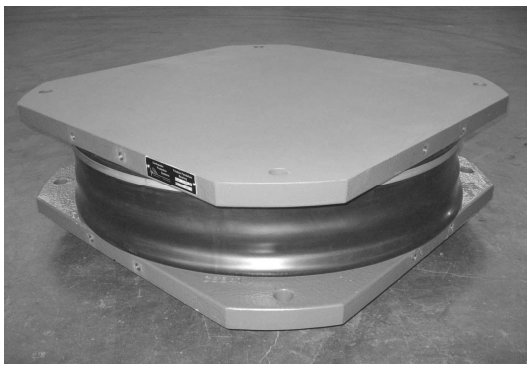


Figure 1: Triple Pendulum Bearing

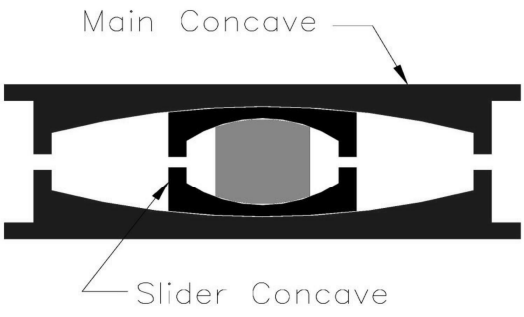


Figure 2: Three Internal Sliders in Triple Pendulum

Figures 3 to 7 show newer code compliant buildings that could not function after moderate earthquake shaking because of non-structural and content damage. Figures 7 to 14 show the severe non-structural and content damage observed in code compliant buildings that had no structural damage. California's Olive View Hospital experienced only modest ground shaking during the 1994 Northridge Earthquake (Fig. 6), but had to be evacuated because of the extensive damage to nonstructural components. Consequently, this hospital was not available at the time when it was needed the most.

The intent of modern seismic codes has been to achieve life-safe buildings at the minimum construction cost. Triple Pendulum seismic isolation (Figs. 1 and 2) can avoid seismic damage to structures, non-structural components, and contents, and in many cases at a lower initial construction costs as compared to ductility designs. To achieve a resilient and sustainable society, avoiding seismic damage should become the performance objective of building codes.

Examples of Friction Pendulum Seismic Isolation

Friction Pendulum technology (Ref. 1 to 4) has been used to avoid seismic damage and reduce construction costs for over 20 years. Over US $ 40 Billion in constructed value of important facilities in over 20 countries rely on Friction Pendulum bearings for seismic protection. In 1991, the retrofit of the US Federal Court building in San Francisco was designed to avoid seismic damage, with Friction Pendulum bearings saving 25% of the construction costs as compared to using rubber bearings (Fig. 15). Four major hospitals in California have been designed using Triple Pendulum bearings for continued functionality following a major earthquake (Fig. 16). The Cathedral of Christ in Oakland California is an example of elegant architecture, designed for no seismic damage, and constructed at a 50% reduction in cost as compared to the alternative strength and ductility design (Figs. 17 and 18). Triple Pendulum bearings (Refs. 3 and 4) have made significant advances in both reducing construction costs, and protecting structures, non-structural components, and contents from seismic damage. The three pendulum stages are three independent degrees of freedom that can be optimized for the different performance requirements needed to protect contents, non-structural components and structures. The 200,000 square meter Sabiha Gokcen Airport building in Turkey was built using Triple Pendulum bearings to avoid seismic damage, and was constructed at approximately the same cost as a minimum code design (Figs. 19 and 20). The San Francisco Airport International Terminal was designed to avoid damage to the architectural glass façade, with Friction Pendulum bearings saving 3% of the construction costs as compared to using rubber bearings (Fig. 21). Many government buildings in California have been seismically isolated to maintain function after a seismic event (Figs. 22 and 23).



Figure 3: New Rail Control Building, Chile 2010



Figure 4: New Commercial Building, Chile 2010



Figure 5: Court Building, Chile 2010



Figure 6: Olive View Hospital, California 1994



Figure 7: Damage to Commercial Building, Chile



Figure 8: Contents and Non-Structural, Chile 2010



Figure 9: Content Damage, Commercial, Chile 2010



Figure 10: Content Damage, Court, Chile 2010



Figure 11: Damage, Rail Control Bldg, Chile 2010



Figure 12: Damage, Santiago Airport, Chile 2010



Figure 13: Damage, Seattle Airport Control Tower



Figure 14: Non-Structural Damage, 1994 Northridge



Figure 15: U.S. Federal Court, San Francisco, California



Figure 16: Mills-Peninsula Hospital, California



Figure 17: Cathedral of Christ the Light, California



Figure 18: Interior of Cathedral, California



Figure 19: Sabiha Gokcen Airport, Turkey



Figure 20: Installed Bearings, Sabiha Gokcen Airport



Figure 21: San Francisco Airport, California



Figure 22: Hayward City Hall, California

Three major Offshore Oil Platforms have been designed using Friction Pendulum bearings to minimize the disruption and lost production that would result from damage to the equipment and facilities on the platform deck (Fig 24).

Eight large LNG Tanks, containing over 1.2 billion liters of liquid natural gas, have used Friction Pendulum bearings to avoid seismic damage to the concrete tanks. Two LNG Tanks at Quintero Chile, using 520 Triple Pendulum bearings, had no disruption to operations after the 2010 Magnitude 8.8 earthquake (Fig 25). Over 30 bridges have used Friction Pendulum bearings to avoid seismic damage, and were constructed at an average 15% lower construction cost as compared to typical minimum code ductility designs (Figs. 26 to 30).

Design Methodology for 98% Reliability of Avoiding Seismic Damage for a 50 Year Design Life

Using Triple Pendulum seismic isolation, 98 % reliability in 50 years is achievable, quantifiable, and surprisingly cost-effective for a wide range of structures. Triple Pendulum Bearings provide the opportunity to tune the different stages of the seismic isolation system to accommodate the multiple performance objectives for the structure, architectural components, and contents. Achieving 98 % reliability in 50 years requires the facility design to be such that the structure, non-structural components, and contents can withstand an earthquake with a 2500-year return period without damage. Although this level of seismic hazard is higher than required for minimum code compliance, it is consistent with society's expectations that new structures should not have seismic damage. By designing to protect against damage, instead of just minimum code requirements, the structural engineer can help achieve a sustainable and resilient society that can avoid the widespread damage and disruption that is seen every time a major earthquake occurs in a metropolitan area.

Design Method for 98% Reliability of Avoiding Damage to Building Structures, Non-Structural Components, and Contents Damage for a 50 Year Design Life

1) Design for an earthquake strength that has less than a 2% chance of being exceeded in 50 years (2500 year return period). Design the structure and isolation system to reliably avoid structure damage, non-structural damage, and content damage for the 2500 year earthquake hazard.
2) Design the structure to be reliably elastic during seismic events. Use a seismic reduction factor Rw = 1.0, and standard member capacity factors, and a seismic load factor = 1.0. This avoids damage caused by typical structure irregularities, asymmetries, construction imperfections, structure modeling limitations, and design errors.
3) Limit story drifts to 0.5% maximum. This avoids

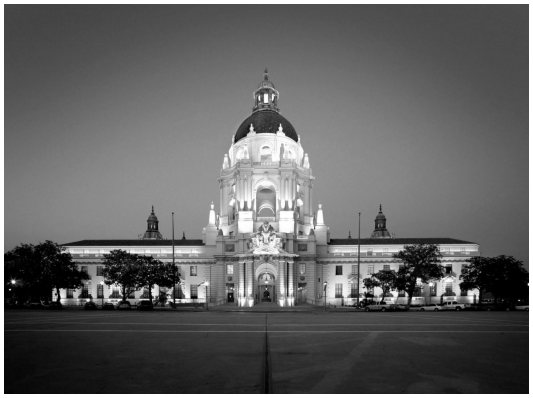


Figure 23: Pasadena City Hall, California



Figure 24:Shell Offshore Platform, Russia



Figure 25: Chile LNG Tank after 8.8 mag. EQ

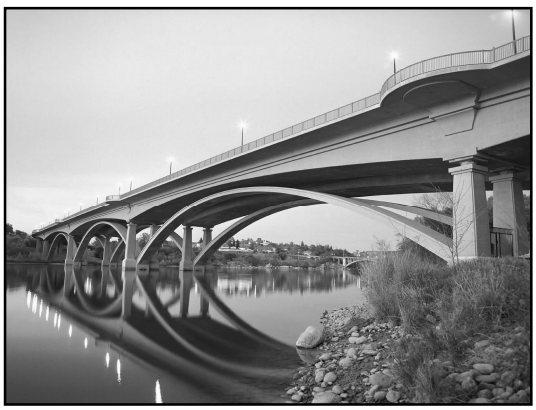


Figure 26: America River Bridge, California

significant damage to most nonstructural components and contents that are drift sensitive.

4) Limit the in-structure floor accelerations to less than 0.4g, and in-structure velocities to less than 180 cm/sec. This avoids serious damage to most ordinary contents and non-structural components.

A design example for avoiding seismic damage is provided for an ordinary concentric braced frame (Fig. 31), at a site having the 2% in 50 year spectra as shown in Figure 32. Triple Pendulum bearings are used having the multi-stage force-displacement properties shown in Figure 34. Also evaluated are the responses of an isolated ordinary moment frame, and code compliant conventional fixed base structures including a special ductile moment frame, and a special ductile concentric braced frame. The building responses for the 2% in 50 year earthquake are provided in Figure 33, together with estimated structural frame construction costs (including isolation bearings), and expected seismic losses as a percentage of the total value of the building, content, and use, and expected loss of use days for the facility.

The fixed base ductile moment frame has in-structure velocities of 274 cm/second, and a structure drift of 3.5%, which is a near collapse condition, and results in an estimated 100% economic loss for the building, contents, and function.

The fixed base ductile braced frame has a structure drift of 1.5%, which would cause major damage to the structure, and moderate damage to non-structural components; and in-structure accelerations of 1.7g, and in-structure velocities of 400 cm/second, which would cause major damage for contents and non-structural components; and which results in an estimated 70% economic loss of the total value of the building, contents, and function.

The isolated moment frame has a calculated structure drift of 1.1%, 0.2g in-structure accelerations, and in-structure velocities of 137 cm/second. Using special details for the interior partitions and non-structural components for a 1% drift would result in modest damage to non-structural components, with an estimated 3% economic loss for nonstructural components and function.

The Triple Pendulum isolated braced frame has a calculated structure drift of 0.3%, 0.3g in-structure accelerations, and in-structure velocities of 130 cm/second, and with no special details for the interior partitions would result in an estimated 0.1% economic loss due to minor disruption to non-structural components and function. The analysis results show that Triple Pendulum bearings with an ordinary concentric braced frame, provides the lowest estimated seismic damage and loss of use days.

Triple Pendulum bearings with a concentric braced frame also had the lowest structure cost of $422/square meter. The fixed base moment and braced frames had structures costs of $600 and $516/square meter, and the isolated moment frame had a cost of $613/square meter.



Figure 27: Trans-European Motorway, Turkey



Figure 28: Installed Bearing, TEM Turkey



Figure 29: Benicia-Martinez Bridge, California



Figure 30: Dumbarton Bridge, California

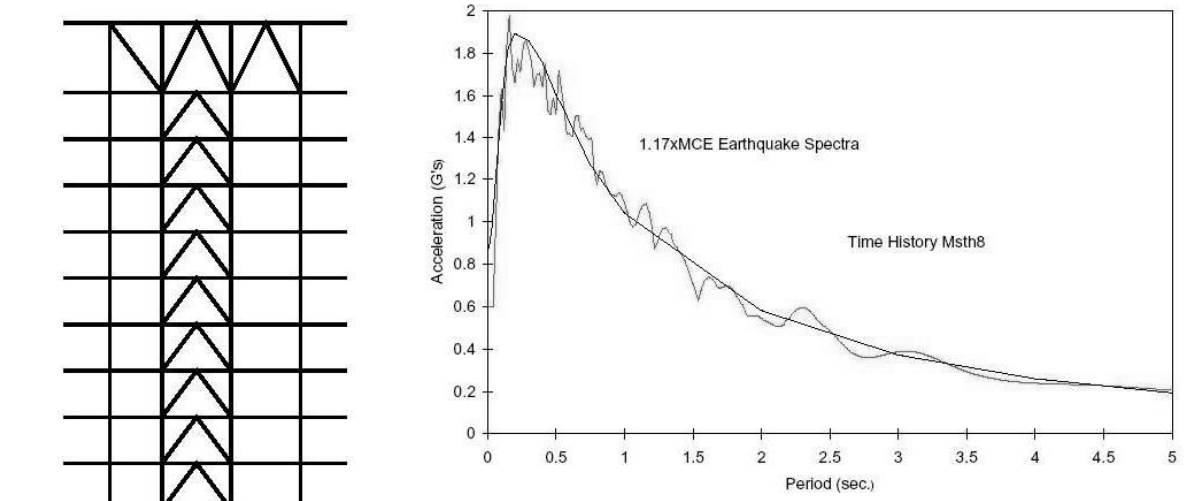


Fig. 32. 2% in 50 Year Earthquake Spectra

Fig. 31. Continued Fuctionality Design Isolated Braced Frame

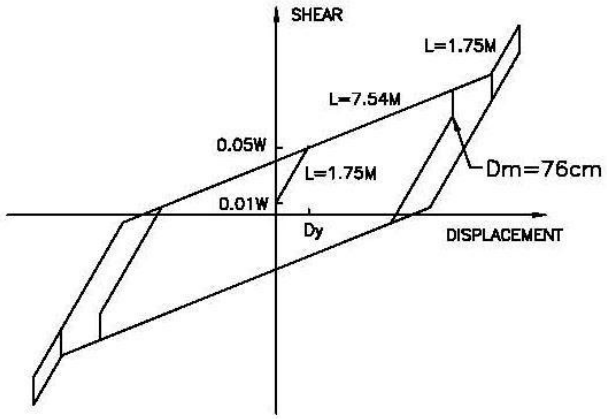


Fig. 34. Triple Pendulum Force Displacement Loop for Brace Frame

Structure Type	Story Drift (%)	Floor Accel. (G's)	Floor Velocity (cm/s)	Base Shear (W)	Design Shear (W)	Steel Structure Cost/m^2 ($U.S.)	Expected Sesmic Losses for Building, Contents and Function	Expected Loss of Use (Days)
Code Compliant Moment Frame	3.5%	0.4	274	0.14	0.05	$600	100%	1400
Code Compliant Braced Frame	1.5%	1.7	400	0.57	0.05	$516	70%	700
Triple Pendulum Moment Frame	1.1%	0.2	137	0.10	0.10	$613	3%	10
Triple Pendulum Braced Frame	0.3%	0.3	130	0.14	0.14	$422	0.1%	5

Fig. 33. Structure Response, Structure Costs, Expected Losses, and Expected Loss of Use for the 2% in 50 Year Earthquake

The ordinary concentric braced frame had the lowest structural frame costs because of the savings from avoiding ductility detailing for the concentric braced frame, and the relatively low cost of the Triple Pendulum bearings. The structure with the best seismic performance and most reliable fully elastic behavior also has the lowest initial construction cost. Thus, the Triple Pendulum has improved the seismic performance, increased the design reliability, and reduced the cost of construction to design for avoiding seismic damage.

The first application of Triple Pendulum bearings in Japan was for the Todaiji Temple Exhibit Museum (Figs. 35 to 38). Ancient Japanese cultural artifacts are displayed on a concrete exhibit floor that is seismically isolated with Triple Pendulum bearings. During the museum design phase, shake table tests of the Todaiji bearings were performed by Obayashi Corporation to demonstrate the effectiveness of the Triple Pendulum bearings to protect these historic cultural artifacts. Triple Pendulum bearings designed to avoid non-structural and content damage will again be tested at Japan's E-Defense Laboratory in August of 2011. A five story full scale building outfitted with non-structural components and building contents will be tested subject to the most extreme earthquake shaking motions considered possible to occur in Japan. An opening ceremony for the Todaiji Exhibit Museum will be held during September 2011.

The sliding mechanisms of Triple Pendulum bearings are compared to single stage Friction Pendulum bearings in Fig. 39. Triple Pendulum bearings allow explicit control of the various aspects of a seismic response that affects the structure, non-structural components, and contents. The period, damping, and displacement capacity of each of the three pendulum mechanisms can be selected independently. There are nine bearing design parameters that can be selected to optimize the isolation system for the desired response of the structure, nonstructural components, and contents. The period and damping for the first pendulum stage are selected specifically to limit the in-structure accelerations to 0.4g. The period and damping for the second pendulum mechanism are selected to limit the structure drifts to ½ %. The period and damping for the third pendulum mechanism are selected to keep the structure response reliably elastic, and the isolator displacements within the available seismic gap.

The inside of a Triple Pendulum bearing is shown in Figure 40. The upper and lower slider concaves are seen attached together with an ethylene propylene seal, concealing the inner slider. The three sliders, having three different friction coefficients, achieve three independent single pendulum mechanisms in one bearing. The concept of a single stage sliding pendulum is shown in Figure 41. For all Friction Pendulum bearings the dynamic properties are verified through testing at the bearing's natural period, and the full design loads and displacements (Fig. 42), providing high very reliability for the bearing properties as used in dynamic analyses.

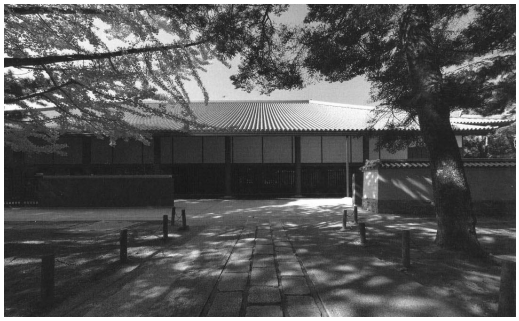


Figure 35: Todaiji Temple, Japan



Figure 36: Statue, Todaiji Temple

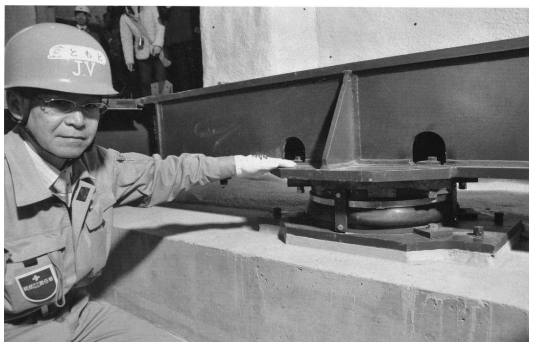


Figure 37: Installed Bearing, Todaiji Temple

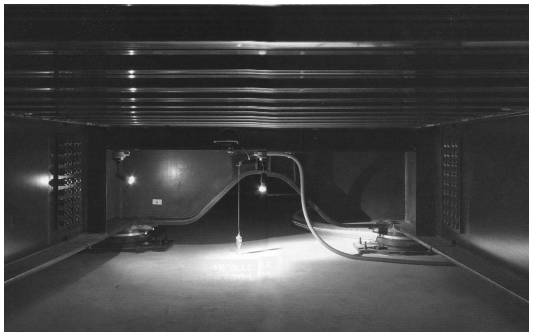


Figure 38: Installed Bearings, Todaiji Temple

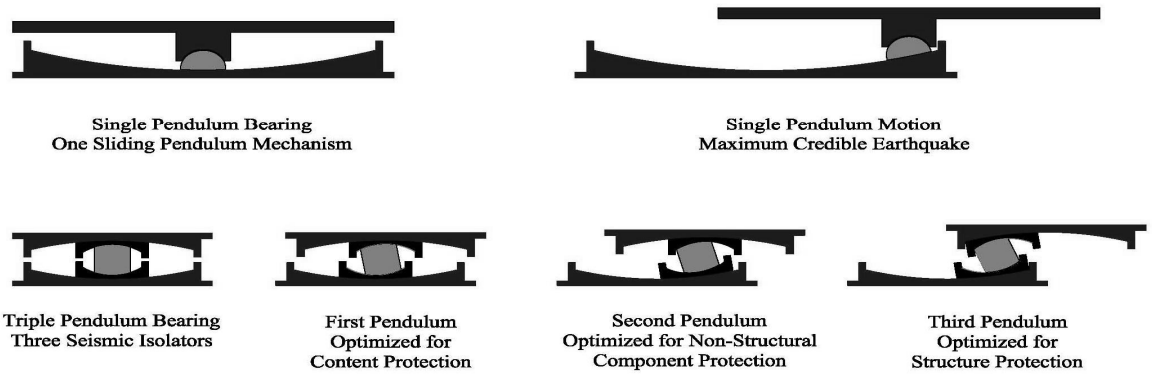


Figure 39: Single and Triple Pendulum Mechanisms
With Comparison of Bearing Sizes

CONCLUSIONS

1) The three stages of Triple Pendulum bearings can be optimized for the seismic protection of structures, non-structural components, and building contents.

2) The initial construction costs of an ordinary concentric braced frame with Triple Pendulum bearings can be less than for traditional moment and braced frames designed for minimum code requirements.

3) Multi-stage Triple Pendulum bearings can significantly reduce structure drifts, in-structure accelerations, and in-structure velocities, sufficient to avoid significant damage to non-structural components and contents.

4) Owners and occupants expect newer code compliant buildings to resist earthquakes with very little or no damage to structures, non-structural components, and contents.

5) Using multi-stage seismic isolation technology, engineers can help achieve a resilient and sustainable society by designing buildings, bridges, and industrial facilities to withstand earthquakes without damage.

References:

1) Zayas, Victor A., 1985, "Earthquake Protective Column Support", United States Patent No. 4,664,714, United States Patent Office, Washington D.C., USA
2) Zayas; Low; Mahin: 1987, "The FPS Earthquake Resisting System", Report UCB/EERC-87/01, Earthquake Engineering Research Center, College of Engineering, University of California, Berkeley.
3) Zayas, Victor A.; Low, Stanley S., 2006: "Sliding Pendulum Seismic Isolation System", United States Patent Publication No. US 2006/0174555 A1, United States Patent Office, Washington D.C., USA
4) Fenz, Daniel M.; Constantinou, Michael C., 2007; "Spherical Sliding Isolation Bearings with Adaptive Behavior: Experimental Verification", Earthquake Engineering and Structural Dynamics, Wiley InterScience, 10.1002/eqe.750



Figure 40: Bearing Concaves and Triple Slider Assembly

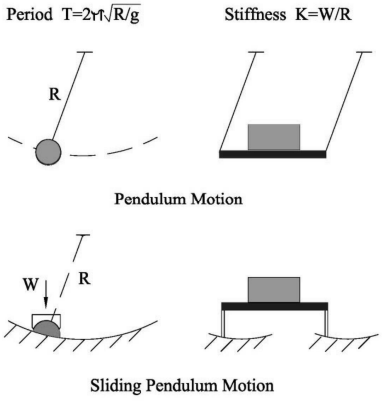


Figure 41: Sliding Pendulum Concept



Figure 42: 100% Real-Time Quality Control Testing

8CUEE CONFERENCE PROCEEDINGS
8th International Conference on Urban Earthquake Engineering
March 7-8, 2011, Tokyo Institute of Technology, Tokyo, Japan

CHINA-JAPAN (NSFC-JST) RESEARCH ON USE OF DAMPERS FOR REPAIR OF RC BUILDING DAMAGED DURING 2008 WENCHUAN EARTHQUAKE PART 1: ANALYTICAL SIMULATION BASED ON FULL-SCALE DAMPER TESTS

Xilin Lu[1], Kazuhiko Kasai[2], Dagen Weng[3], Wuchuan Pu[4], Ying Zhou[5], and Akira Wada[2]

1) Professor, Tongji University, State Key Laboratory of Disaster Reduction in Civil Engineering, Tongji University, Shanghai, China
2) Professor, Structural Engineering Research Center, Tokyo Institute of Technology, Japan
3) Professor, College of Civil Engineering, Tongji University, Shanghai, China
4) Postdoctoral Research Fellow of COE, Center for Urban Earthquake Engineering, Tokyo Institute of Technology, Japan
5) Associate Professor, State Key Laboratory of Disaster Reduction in Civil Engineering, Tongji University, Shanghai, China
lxlst@tongji.edu.cn, kasai@serc.titech.ac.jp, wdg@tongji.edu.cn, pu.w.aa@m.titech.ac.jp,
yingzhou@tongji.edu.cn, wadai@serc.titech.ac.jp

Abstract: Key issues related to repair of RC buildings using dampers are discussed, based on actual repair work performed in China and extensive full-scale experiments for dampers conducted in Japan. This Part 1 paper describes the 7-story RC building damaged due to the 2008 Wenchuan Earthquake, actual repair work performed, detailed full-scale damper tests, and hypothetical repair and analysis using the damper test results.

1. INTRODUCTION

1.1 General

As a apart of Strategic China-Japan Cooperative Program on Science and Technology organized by the National Natural Science Foundation of China (NSFC) and Japan Science and Technology Agency (JST), the joint research on the seismic evaluation and mitigation technologies is being conducted by the researchers in Tongji University, China and in Tokyo Institute of Technology (Tokyo Tech.) and Hokkaido University, Japan.

The first stage of the research focuses on the use of seismic energy dissipaters, hereby called as "dampers", for seismic repair or upgrade of the existing reinforced concrete (RC) buildings. The dampers have been extensively utilized to steel buildings, since connecting the dampers to the steel frames is convenient and simple. However, there exist many RC buildings with a variety of serious problems in terms of seismic vulnerability, and extended use of the dampers to such buildings is of strong interest not only to China and Japan, but also to many other countries of high seismic activity.

1.2 Scope and Objectives

Accordingly, the present paper and the companion paper (Kasai et al. 2011) discuss key issues related to repair and retrofit of RC buildings using dampers, based on actual repair work performed in China and extensive full-scale experiments for dampers conducted in Japan. The present paper, designated as Part 1, describes the 7-story RC building damaged due to the 2008 Wenchuan Earthquake, actual repair work performed, detailed full-scale damper tests, and hypothetical repair and analysis using the damper test results.

2. 7-STORY RC-BUILDING DAMGED DURING THE 2008 WENCHUAN EARTHQUAKE

The 7-story RC building is an office building of a Power Gas Company in Dujiangyan, Sichuan Province. It is a reinforced concrete (RC) frame structure. The structure was originally designed based on a seismic intensity of 7 in 1997, the plan layout and elevation are shown in Figure 1 and Figure 2. The structure has a plan dimension of 50.4m by 17.4m. There are seven stories with a story height of 4.6m, 4.2m, 3×3.6m, 4.2m and 3.6m from Story 1 to 7, respectively. The total height of the structure is 27.4m. RC frame structural system is applied to undertake the gravity loads and lateral forces. The cross sections of frame beams are 350 mm by 600 mm and those of columns changed along the structural height from 800 mm by 800 mm to 500 mm by 500 mm. The thickness of the slab is 100 mm. All concrete design grades are C30

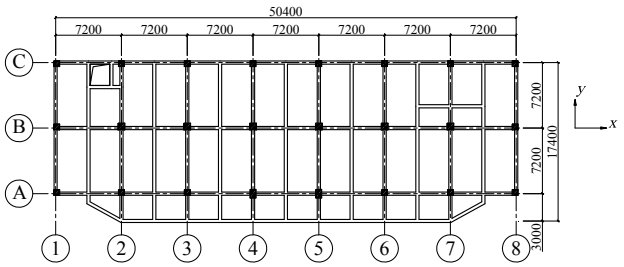
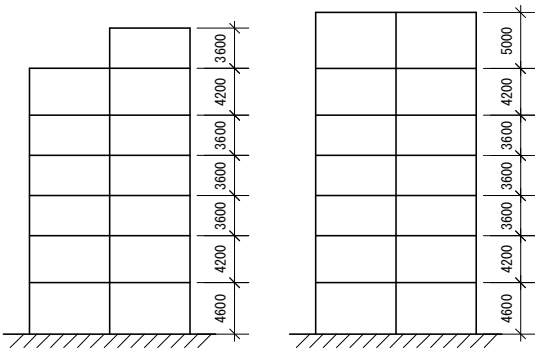


Figure 1 Plan layout of the building



(a) Before retrofit (b) After retrofit

Figure 2 Elevation of the building



Figure 4 Damage at beam and column ends



Figure 3 Horizontal cracks of infilled walls

that has a compressive strength of 14.3 MPa. The infilled wall is made by hole brick with a thickness of 200mm. The total mass of the building is about 6456 t.

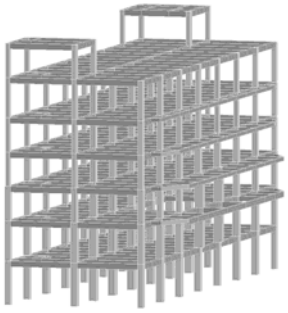


Figure 5 Building analytical model (before retrofit)

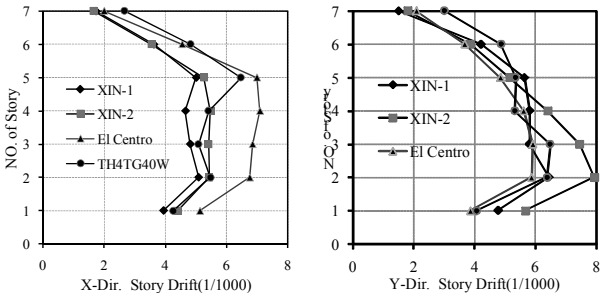


Figure 6 Inter-story drift in *X* and *Y* direction

During the time when the building was designed and constructed, the seismic protection intensity in that area is 7 with a basic peak ground acceleration (PGA) of 0.1g, and the design code was the version of 1989 in which lower requirements and structural detailing were suggested compared to the current one.

The building was damaged during the 2008 Wenchuan Earthquake. Most visible damages are the horizontal infilled wall cracks in the longitudinal direction (Figure 3). Cracks with a width of 0.1 mm to 3 mm were observed at the structural beam ends in longitudinal direction. In Story 3 and 4, minor cracks (0.1 mm~0.5 mm) were also observed at the ends of the columns (Figure 4). Because of the limited structural elements damage found, the structure was evaluated as "minor damage" grade by the seismic evaluation team although the earthquake intensity in that area was evaluated by China Earthquake Administration as 9 that is substantially larger than expected. Therefore soon after the Wenchuan earthquake, the seismic design intensity in Dujiangyan city is increased to 8 with a basic PGA of 0.2g.

An analytical structural model is built up by PKPM2008 to investigate the seismic response, as shown in Figure 5. Four sets of time histories, including two strong earthquake records and two artificial accelerograms, are applied to obtain the dynamic responses of the structure. The peak ground acceleration in the time-history analysis is taken as 0.3g to accommodate the seismic intensity 8 in Dujiangyan area. The maximum inter-story drifts under four ground motions are shown in Figure 6.

One can easily find that the structural inter-story drifts in both directions are just beyond the code limitation of 1/200 under basic earthquake of intensity 8.5. The minor damage characteristic is in accordance with the results of analysis. Therefore strengthening of this building is required by Building Regulations and Codes to control the structural responses and to meet the code provisions because the building is lifeline structure.

3. REPAIR PERFORMED TO THE BUILING

The common practice to strengthen earthquake damaged buildings in China is to strengthen damaged members and joints with concrete or steel jacketing and to increase the size of most structural members so as to meet the new design requirements. This practice is suitable for most of the strengthening applications. However, it needs to demolish all the decorations of undamaged members, which is a time-consuming process, and the site construction may pollute the environment. Considering the above disadvantages and the importance of the building, a comprehensive strengthening scheme with less labor work was selected as follows. First, to strengthen the damaged joints with steel jacketing and to inject epoxy resin into the cracks. And then to use viscous damper and steel bracing to increase the overall stiffness of the structure while to reduce the seismic force to the structure. Detailed and optimal analysis was done to select steel jacketing, dampers and their locations. Figures 7 and 8 show the photos of steel jacketing for the damaged joint and damper and steel bracing in construction site.

On the selection of dampers in preliminary design phase, the added stiffness to the frame provided by viscous dampers and braces is approximately neglected, so as to easily estimate the required supplementary damping ratio of the structure, and therefore viscous dampers can be designed according to the required equivalent damping ratio. Typically, for RC frames which are mainly of shearing deformation, its required damping ratio can be estimated based on Chinese Code Response Spectrum (GB 50011-2010), as given in Eq. (1):

$$\Delta_{\max} / \Delta_T = \alpha_{0.05} / \alpha_{(\zeta_r + 0.05)} \tag{1}$$

Where $\Delta_{\max}$ is the maximum value of story drift in the structure (obtained under moderate earthquake), Δ_T is the corresponding target value of story drift, ζ_r is the required equivalent damping ratio, $\alpha_{0.05}$ is seismic influence coefficient for the damping ratio of 5%, while $\alpha_{(\zeta_r+0.05)}$ is for the damping ratio of $(\zeta_r+0.05)$ (based on GB 50011-2010).

Moreover, the Code requires that the final damping ratio shall not exceed 25% in general, whereas it should be counted to 25% once exceeds, which also means that the primary frame shall be further strengthened in this case.



Figure 7 Photo of steel jacketing

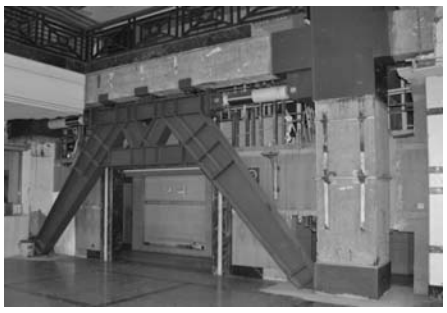


Figure 8 Photo of damper and bracing

According to the calculated required damping ratio, the expected designed damping force can be obtained by the following equations (2) ~ (6):

$$F_{di} = \zeta_r \cdot \beta \cdot Q_i \tag{2}$$

$$\beta = \left[\pi \sum_{j=1}^{N} \Delta_j Q_j \right] \Big/ \left[2 \sum_{i=j_1}^{N_1} \Delta_i Q_i (1 - \mu_i) \right] \tag{3}$$

$$\mu_i = \Delta_{di} / \Delta_i \tag{4}$$

Where F_{di} is the expected damping force on the i-th floor, β is the design coefficient related to story damping force and shear force, Q_i is the story shear force on the i-th floor under moderate earthquake, N is the total number of floors for calculation, N_1 is the total number of floors equipped with viscous dampers, j_1 is the initial number of floor equipped with viscous dampers, μ_i is the ratio of yield displacement of viscous damper and peak value of story drift on the i-th floor, Δ_{di} is the yield displacement of viscous damper on the ith floor.

Specially, to achieve the best damping effect of supplementary viscous dampers, an optimizing coefficient is introduced to modify the designed damping forces given by Eq. (2), which conducted as follows:

$$F_{(di)m} = \Omega_i \cdot F_{di} \tag{5}$$

$$\Omega_i = \Delta_i \Big/ \left(\sum_{j=1}^{N} \Delta_j / N \right) \tag{6}$$

Where: $F_{(di)m}$ is the modified designed damping force on the ith floor, Ω_i is the optimizing coefficient on the ith floor. However, it is noteworthy that the optimizing process of designed damping forces here is advisory but not compulsory step, and therefore the final designed damping forces are usually interpolated in the value range between the designed damping forces given by Eq. (2) and the modified damping forces given by Eq. (5) with the combination of the allowable story drift rotation for buildings in China's seismic design code (i.e. GB 50011-2010).

Based on above steps of design and distribution of expected damping force on certain floor, it is concluded that the expected supplementary damping forces of the existing frame are designed on the basis of story shear forces, and optimized in the light of story drifts. Nonlinear viscous dampers manufactured in China were installed, and they will be named as Type 1 nonlinear viscous damper from now on. Properties of the Type 1 damper will be given in Sec. 6.

4. FULL-SCALE TEST OF VISCOUS DAMPERS

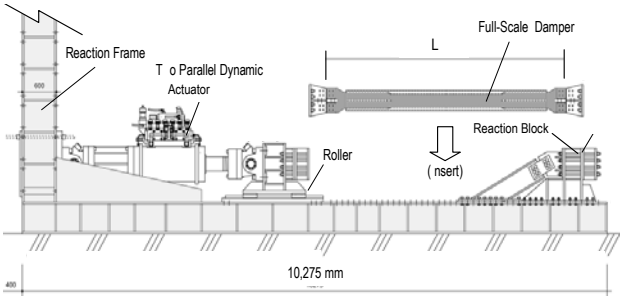
4.1 Damper Test Scheme

In addition to the Type 1 damper used in the actual repair project explained above, the present study will also consider Type 2 damper. Twelve full-scale nonlinear viscous dampers of Type 2 are tested at Tokyo Tech. They were the dampers in the full-scale 5-story building tested using the world's largest shake-table, "E-Defense" (Kasai et al. 2007, 2009, 2010), and were produced by a manufacturer in the United States. Steel, oil, and visco-elastic dampers produced by Japanese manufacturers were also tested at E-Defense and Tokyo Tech., but they are not included in the present study.

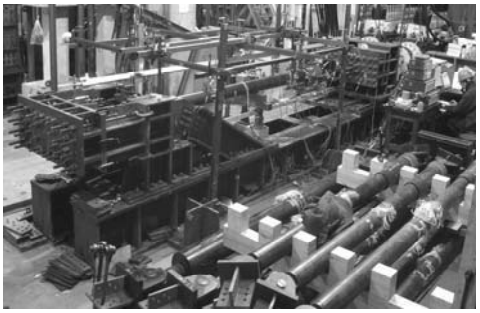
The purpose of the Tokyo Tech. test is to confirm accuracy of load monitoring gages that were attached on the damper and used during the E-Defense tests, and to compare effects of boundary conditions for the two tests. Note that Tokyo Tech. tests consider the typical boundary conditions used for proof tests of manufactured dampers, and the comparison will be important for evaluating on-going practical test method.

As shown by Figure 9, the test set-up utilizes two parallel dynamic actuators whose maximum possible stroke, velocity, and load are 400 mm, 500 mm/s, and 2000kN, respectively. Deformations of various components of the damper-brace assembly are measured (Figure 10a), and Figure 10b are used to estimate properties of the analysis models.

The material used in the damper is polymer liquid, and its resistance against flow produces the damper force (JSSI Manual 2005, 2007, Chinese Translation 2008). Damper-brace assemblies are categorized into three types according to load capacity of 1700, 850, and 425 kN, respectively. The load capacities are defined as the damper force at stroke speed of 300 mm/s. Table 1

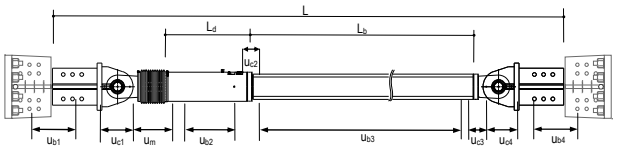


(a) Elevation



(b) Photo

Figure 9 Experimental Set-up for Full-Scale Viscous Dampers

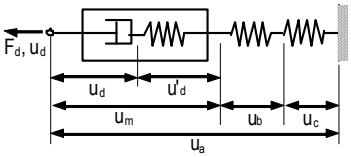


(a) Dimensions and deformation measurement

$u_m = u_d + u'_d$

$u_b = u_{b1} + u_{b2} + u_{b3} + u_{b4}$

$u_c = u_{c1} + u_{c2} + u_{c3} + u_{c4}$



(b) Model for Deformation Components

Figure 10 Deformation Measurement Scheme for Viscous Dampers

indicates dimensions of the three types, where the diameters of the cylinders vary from 286 to 152 mm, and those of the braces 236 to 140 mm. The damper-brace assemblies of the same type had difference only in the length of the extenders, and average value of the total length L is specified in Table 1. In the order of types 1 to 3, the number of assemblies tested is two, six, and four, and variations of test results within each type are found insignificant.

Sinusoidal deformation tests are performed. As indicated in Table 2, one damper from each type is selected for detailed tests using seven different peak

Table 1. Dimensions and dynamic properties determined for three damper-brace assembly types tested at E-Defense and Tokyo Tech.

Type	F_d [1] (kN)	L [2] (mm)	Brace Dimension			Damper Dimension			Damper Properties [3]		
			L_b (mm)	A_b (mm^2)	D_b (mm)	L_d (mm)	A_d (mm^2)	D_d (mm)	C_d (kN/(mm/ses)$^\alpha$)	K_d (kN/mm)	α
1 (2 dampers)	1700	4238.8	1932	15323	236	689	28124	285.8	181 (196)	547 (∞)	0.39 (0.38)
2 (6 dampers)	850	4199.8	2357	8380	159	606	12880	184.2	85 (98)	218 (∞)	0.38 (0.38)
3 (4 dampers)	425	4024.5	2429	9121	140	535	8034	152.4	48 (49)	146 (∞)	0.34 (0.38)

Notes: 1) F_d = Nominal damper force at stroke velocity of 300 mm/s.
2) L = Average length of the same type damper-brace assembly.
3) Parenthesis indicates the catalogue value provided by the manufacturer.

Table 2. Damper stroke velocities (mm/s) under different frequency and stroke

Maximum Displacement	Excitation Frequency							
	0.1 Hz	0.5 Hz	1.0 Hz	2.0 Hz	3.0 Hz	6.0 Hz	10 Hz	15 Hz
0.5 mm	0.3	1.6	3.1	6.3	9.4	(18.9)	(31.4)	(47.1)
1.0 mm	0.6	3.1	6.3	12.6	18.9	(37.7)	(62.8)	(94.3)
3.0 mm	1.9	9.4	18.9	37.7	56.6	(113.1)	(188.5)	(282.7)
6.0 mm	3.8	18.9	37.7	75.4	113.1	(226.2)	(377.0)	—
12.0 mm	7.5	37.7	75.4	150.8	226.3	(452.4)	—	—
24.0 mm	15.1	75.4	150.8	301.6	452.4	—	—	—
36.0 mm	22.6	113.1	226.2	452.4	—	—	—	—

Note: The velocity in parenthesis was applied to only one damper per type.

displacements (0.5, 1, 3, 6, 12, 24, and 36 mm) and eight frequencies (0.1, 0.5, 1, 2, 3, 6, 10, and 15Hz). By eliminating cases exceeding the stroke velocity limit of 500 mm/s aforementioned (Table 2), total of forty-one cases are tested. All other dampers are tested for the same peak displacements, but for a smaller range of frequency 0.1 to 3 Hz (Table 1).

Random deformation tests are also performed at Tokyo Tech. The input for each damper is its deformation history recorded at the E-Defense test, where the damper was connected to the 5-story building. The building was subjected to varied levels of JR Takatori ground motion, one of the strongest recorded during the 1995 Kobe earthquake. The Tokyo Tech. test utilizes the damper deformation histories at 15, 50, and 100% JR Takatori motions, respectively.

4.2 Deformation Measurements

As shown in Figure 10a, the deformation of the damper-brace assembly u_a is broken down to those of three portions defined as damper, brace, and connection deformations, u_m, u_b, and u_c, respectively, i.e.,

$$u_a = u_m + u_b + u_c \tag{7}$$

where deformation of each portion is subdivided further, as will be explained below (Figure 10a):

First, damper deformation (stroke) u_m is subdivided as:

$$u_m = u_d + u'_d \tag{8}$$

where u_d , u'_d = deformations of nonlinear dashpot and spring representing the elastic flexibility of the viscous fluid (Figure 10b).

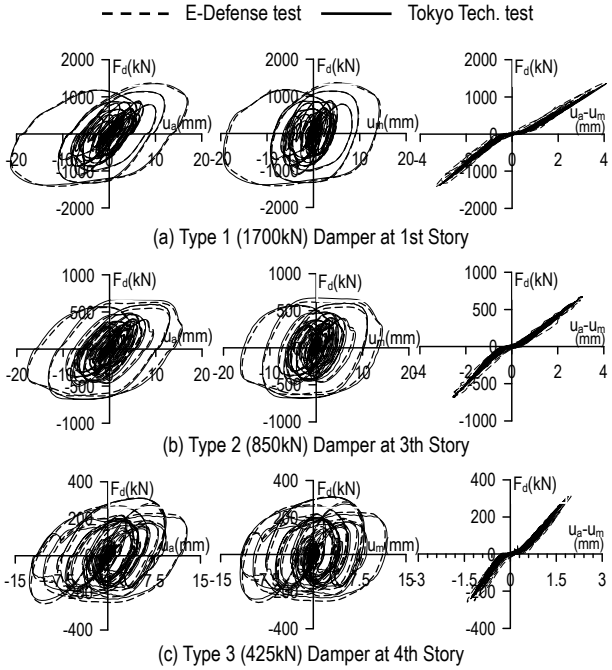


Figure 11. Comparison between E-Defense test results and Tokyo Tech. test results for Type 2 dampers of different size and orientation

Second, brace deformation u_b is expressed as:

$$u_b = u_{b1} + u_{b2} + u_{b3} + u_{b4} \tag{9}$$

where u_{b1} , u_{b2} , u_{b3} , u_{b4} = deformations of left splice, damper cylinder, extender (typical brace), and right splice, respectively (Figure 10a).

Third, connection deformation u_c is expressed as:

$$u_c = u_{c1} + u_{c2} + u_{c3} + u_{c4} \tag{10}$$

where u_{c1} , u_{c2} , u_{c3} , u_{c4} = play of left pin, deformation of screw joint between cylinder and extender, deformation of screw joint between extender and right clevis, and play of right pin, respectively (Figure 10a).

4.3 Tests Results

Figure 11 compares responses of the same viscous damper tested at E-Defense and Tokyo Tech., respectively. In spite of very different boundary conditions of the two tests, the results are almost the same. This suggests appropriateness of the typical damper tests performed under idealized boundary conditions like the Tokyo Tech. test.

Damper force F_d is plotted against damper deformation (stroke) u_m, total deformation of the damper-brace assembly or added component u_a , and race and connection deformations $u_b + u_c$ (= u_a - u_m) , see Eq. (7). Note that $u_b + u_c$ is about 15% of u_a and cannot be neglected. Because of such deformation, the hysteresis becomes inclined, leading to increased elastic stiffness and reduced damping.

Note also from F_d vs. (u_a - u_m) that the stiffness of the brace and connection is smaller when the force is tension, indicating influence of some of the screw joints more flexible in tension. The flat curves at F_d = 0 are due to slackness and play of the pins, and cannot be neglected at small amplitude shaking.

5. ANALYTICAL MODELING FOR DAMPERS

5.1 Determination of Three Parameters

The basic equations for the force and deformation are as follows:

$$F_d = C_d |\dot{u}_d|^{\alpha} \mathrm{sgn}(\dot{u}_d) \quad , \qquad u_m = u_d + F_d / K_d \tag{11a,b}$$

where C_d and K_d are nonlinear viscous coefficient and elastic spring stiffness of the Maxwell model, and α is the fraction to determine the power (Eq. (11a)).

Using Eq. (11) and $u_d = u_m - F_d/K_d$ from Figure 10b, the constants C_d , K_d , and α are determined by the least square method minimizing the following error:

$$R = \sum_i [F_d^{(i)} \mp C_d |\dot{u}_m^{(i)} - \dot{F}_d^{(i)} / K_d|^{\alpha}] \tag{12}$$

where i = step number for data $F_d^{(i)}$ and $u_m^{(i)}$. The negative and positive signs in Eq. (12) are used, when

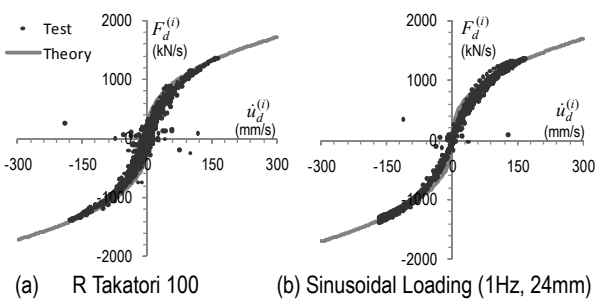


Figure 12. Plots of experimental damper force $F_d^{(i)}$ and estimated dashpot velocity $\dot{u}_d^{(i)}$ (see Sec.5.1) compared with model curve

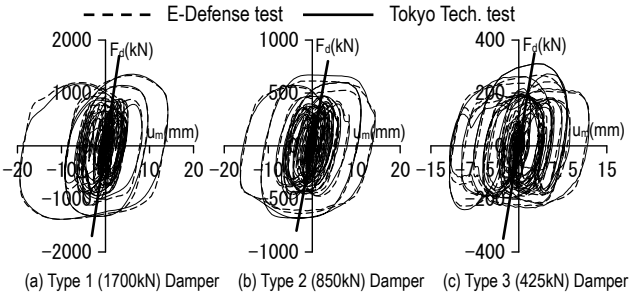


Figure 13. Comparison between test and analysis results (JR Takatori 100%)

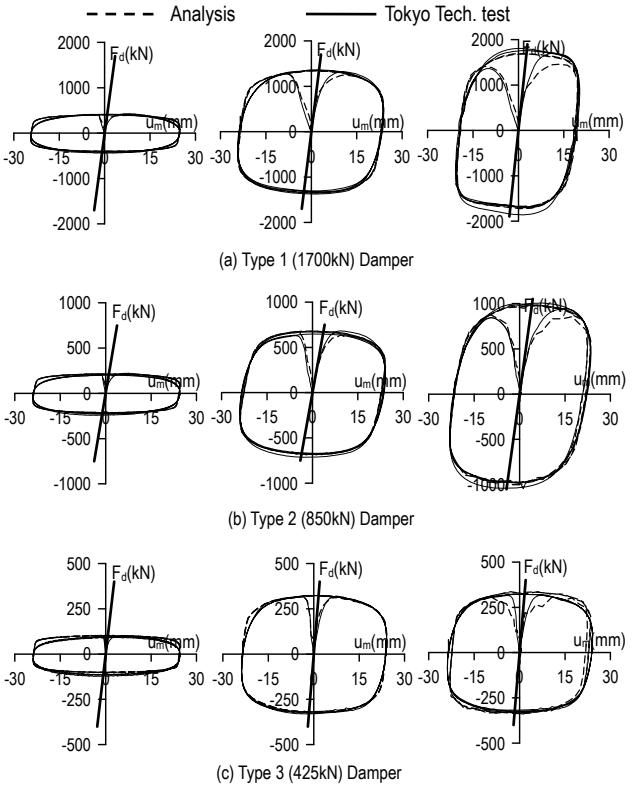


Figure 14. Comparison between test and analysis results (sinusoidal loading, 0.1, 1, and 3 Hz from left)

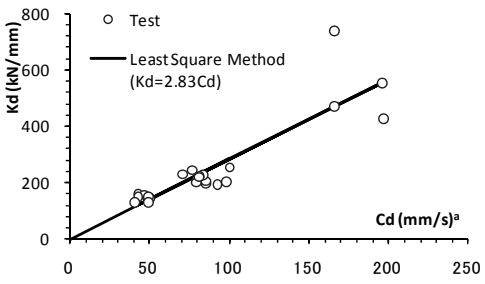


Figure 15. C_d vs. K_d obtained from Type 2 damper test and linear regression

the content in the absolute value bracket is positive and negative, respectively.

In Figure 12, force $F_d^{(i)}$ is plotted against estimated dashpot velocity $\dot{u}_d^{(i)}(=\dot{u}_m^{(i)}-\dot{F}_d^{(i)}/K_d)$, and is compared with the model curve given by Eq. (11a). The curve agrees well with the test data, except for the small velocity range. Because it was difficult to fit the curve in this range, Eq. 12 is applied to $\dot{u}_m^{(i)}$ whose absolute value larger than 50 mm/s.

In the above manner, C_d , K_d , and α values are obtained from each damper and each test applying deformation that corresponds to either 50% or 100% Takatori input. The values are alternatively determined from many other tests applying various sinusoidal deformations to the dampers.

The values of the three parameters thus-determined appear to be very similar for the same damper type, regardless of loading.

5.2 Damper Model and Accuracy

Figure 13 comparers the load-deformation curves obtained from the experiments with those predicted by the analytical model (Figure 10b). The dampers and their loading histories at Tokyo Tech. are the same as those in Figure 11. The analytical model agrees well with the experiment for the random loading.

The straight inclined line shows the value of K_d in the models, and indicates that it determines inclination of the hysteresis, which can be easily proved by Eq. 11. Modeling K_d as infinity was advised by the damper manufacturer (Table 1), but such an idealization is unreasonable for the cases shown in Figure 13.

Figure 14 shows comparison for cases of sinusoidal deformations, and again confirms accuracy of the analytical model for the loading.

The values C_d , K_d , and α values are then averaged over dampers of the same type and the two Takatori input cases, and the results are indicated in Table 1.

Like the Type 1 dampers adopted for the actual retrofit (Sec. 3 and Sec. 6), the Type 2 dampers tested in this study produce hysteresis loops of combined ellipse and rectangle. However, $\alpha = 0.2$ for the Type 1 dampers, and $\alpha = 0.34$ to 0.39 (Table 1) for the Type 2 dampers, making hysteresis curve of the latter more round.

Figure 15 shows values of C_d vs. K_d obtained for the twelve dampers (Table 1) and the two Takatori input cases. Because of strong linear relationship as Kasai et al. indicated for other viscous dampers (Kasai et al. 2007, JSSI Manual 2005, 2007), the following relationship is considered from now on:

$$K_d = \beta C_d \tag{7}$$

where $\beta = 2.83$ mm$^{\alpha-1}$/s$^{\alpha}$, if the length unit of mm is used.

As Figures 13 and 14 indicate, the inclination of damper force-stroke curve produces equivalent stiffness, less phase angle between the force and stroke, and less energy dissipation compared with the case of infinite K_d (Kasai et al. 2007). Likewise, if a flexible brace is attached in series with the damper (Figure 10b), the trends will be more prominent.

6. REDESIGN AND ANALYSIS

For comparative research, the Type 1 damper used in the repair project of actual RC building in China and the Type 2 dampers experimented in the present study are considered. They are now analytically used to achieve the aforementioned retrofitting objective on the premise that the design and distribution of these two dampers are equal expected damping forces under moderate earthquake. Thus, three different structural states (ST0, ST1 and ST2) are denoted in the comparative analysis, here ST0 is the primary frame (after repairing and story-adding transformation), ST1 is the damped frame using Type 1 dampers, and ST2 is the damped frame using Type 2 dampers.

Firstly, the finite element modeling and analysis are performed by PKPM2008 and SAP2000 software, and the corresponding structural properties of ST0 under seismic protection intensity 8 are shown in Table 3. It is noted that the X-direction here is the longitudinal direction (i.e. along West-East direction), and the Y-direction is the transverse direction (i.e. along North-South direction). Moreover, after primary analysis, 2 sets of strong earthquake records and 2 sets of artificial acceleration time-histories are adopted to the later time-history analysis.

Based on the simplified retrofitting design procedure introduced in Sec. 3, design and distribution of expected damping forces of ST1 and ST2 are conducted respectively. Therefore, with the consideration of retrofitting objective and architecture function of the existing frame, 4 buckling-restrained-braces (BRB) are installed on the ground floor, and 48 viscous dampers (with 24 chevron braces) are installed on the 2nd to 7th floor, as listed in Table 4. Here it is noteworthy that the total numbers of BRB and viscous dampers, as well as their locations are the same in ST1 and ST2, while the only difference is the damper categories and their design mechanical properties, as shown in Table 5.

As to Table 5, where α is the velocity exponent, C_d is the damping coefficient, and K_d is the interior stiffness of the viscous damper. Here K_d is obtained by the E-Defense test for Type 2 dampers, and assigned by 70% of C_d for Type 1 dampers. In minor earthquake response analysis, the all K_d are assigned by ∞ for ST1 and ST2. Besides, it is also noted that the damper category *A*, *B*, *C*, *D* of Type 1 dampers are expected to provide the designed damping forces of 600, 360, 240, and 120 kN, respectively, at the expected velocity of 80 mm/s under the moderate earthquake. Likewise, the damper category *A*', *B*', *C*' of Type 2 dampers are expected to provide the design damping forces of 1040, 520, and 260 kN, respectively, in the same condition.

Table 3 Structural properties of ST0 under earthquake intensity 8

Floor	Height (*m*)	Storey mass (*t*)	X-direction			Y-direction		
			Stiffness (*kN/mm*)	Shear force (*kN*)	Drift Angle (*rad*)	Stiffness (*kN/mm*)	Shear force (*kN*)	Drift Angle (*rad*)
7	5	601	99	2841	1/519	139	2788	1/592
6	4.2	923	257	4912	1/636	238	4886	1/477
5	3.6	967	354	6208	1/558	322	6416	1/417
4	3.6	981	400	7183	1/515	358	7038	1/381
3	3.6	1002	431	8130	1/482	396	8021	1/367
2	4.2	907	411	8509	1/488	390	8781	1/380
1	4.6	1075	712	9216	1/828	701	9442	1/660

Note: Story shear forces of the frame structure are obtained under moderate earthquake.

Table 4 Design and distribution of added viscous dampers

Floor	Type 1 damper		Type 2 damper	
	X-direction Dampers (N×category)	Y-direction Dampers (N×category)	X-direction Dampers (N×category)	Y-direction Dampers (N×category)
7	4×*C*	4×*C*	4×*C*’	4×*C*’
6	4×*C*	2×*B*+2×*D*	4×*C*’	4×*C*’
5	4×*B*	2×*A*+2×*D*	2×*B*’+2×*C*’	2×*B*’+2×*C*’
4	4×*B*	2×*A*+2×*D*	2×*B*’+2×*C*’	2×*B*’+2×*C*’
3	4×*A*	4×*A*	2×*A*’+2×*C*’	2×*A*’+2×*C*’
2	4×*A*	4×*A*	2×*A*’+2×*C*’	2×*A*’+2×*C*’
1	2×BRB	2×BRB	2×BRB	2×BRB

Note: Categories (*A*, *B*, *C*, *D*) and (*A′*, *B′*, *C′*) denote the Type 1dampers and Type 2 dampers, respectively.

Table 5 Mechanical properties of different categories of Type 1 and Type 2 dampers

Properties	Type 1 damper				Type 2 damper		
	A	***B***	***C***	***D***	***A’***	***B’***	***C’***
$\bar{C}_d$	250	150	100	50	196	98	49
α	0.2	0.2	0.2	0.2	0.38	0.38	0.38
K_d	175	105	70	35	526	220	146

Note: Unit of C_d is kN/(mm/s)$^{\alpha}$, and unit of K_d is kN/mm.

Accordingly, comparative analysis of ST1, ST2 and ST0 are conducted through time-history analysis method with the aforementioned ground accelerations, which refer to the comparison of the envelops of the inter-story drifts and story shear forces under minor earthquake, moderate earthquake and major earthquake respectively, as shown in Figures 16 and 17.

Here it is noted that the story shear forces are obtained from section forces of frame columns (without damper-braces). Moreover, for analysis cases under minor earthquake, the installation errors may have heavy influence on damping effect of the viscous damper due to its relatively small stroke, thus the interior stiffness of viscous damper is artificially modified to a larger value; while for analysis case under strong earthquake, the elastic modulus of concrete decrease with the structure going into plastic state, therefore the lateral stiffness of story is approximately reduced by a discount factor of $1/\mu$ (where μ is the displacement ductility coefficient, here in this frame it is assigned to 2) for simplified calculation.

In addition, from above figures, it is easily seen that both ST1 and ST2 have excellent structural performances and remarkable control effect compared to ST0, which means that both Type 1 and Type 2 dampers can be appropriately designed to control seismic behavior of non-ductile structures. With the equal expected damping forces provided by supplemental viscous damper (and BRB) under moderate earthquake, performances of ST1 are apparently superior to that of ST2 under minor earthquake, as shown in the left columns of Figures 16 and 17. However, these two damping scheme acquire similar control effect of story drifts and story shear forces, as shown in the middle columns of Figures 16 and 17. Whereas, performances of ST2 are relatively better than that of ST1 under strong earthquake, as shown in the right columns of Figures 16 and 17, which may partly derive from a larger velocity exponent of the Type 2 dampers, as compared to the Type 1 dampers.

7. CONCLUSIONS

This paper has described a 7-story RC building damaged due to the 2008 Wenchuan Earthquake, actual repair work performed, detailed full-scale damper tests, comparison of using two distinct types of nonlinear viscous dampers, herein called as Type 1 and 2 dampers, in the analysis of retrofit design.

Compared with Type 1 damper, Type 2 damper has higher velocity exponent and interior stiffness. Regardless of their differences in mechanical properties, it is concluded that when designed and distributed according to the simplified procedure proposed in this paper, both types have excellent damping effect and evidently can be used to achieve the structural retrofitting objective to increase one grade of seismic protection intensity without heavy strengthening work.

As to the application in seismic retrofit of the damaged frame, when Type 1 and Type 2 dampers are designed with the equal expected damping forces under moderate earthquake, it is apparent that Type 2 can provide relatively larger damping forces at a higher velocity, and consequently it has better control effects of story drifts and story shear forces under strong earthquake. Likewise, Type 1 can provide relatively large damping forces at a lower velocity due to its smaller velocity exponent. It is thus proved to have better damping effect under minor earthquake.

ACKNOWLEDGEMENTS

This study is a part of the Strategic Chinese-Japanese Cooperative Program on “Science and Technology (S&T)

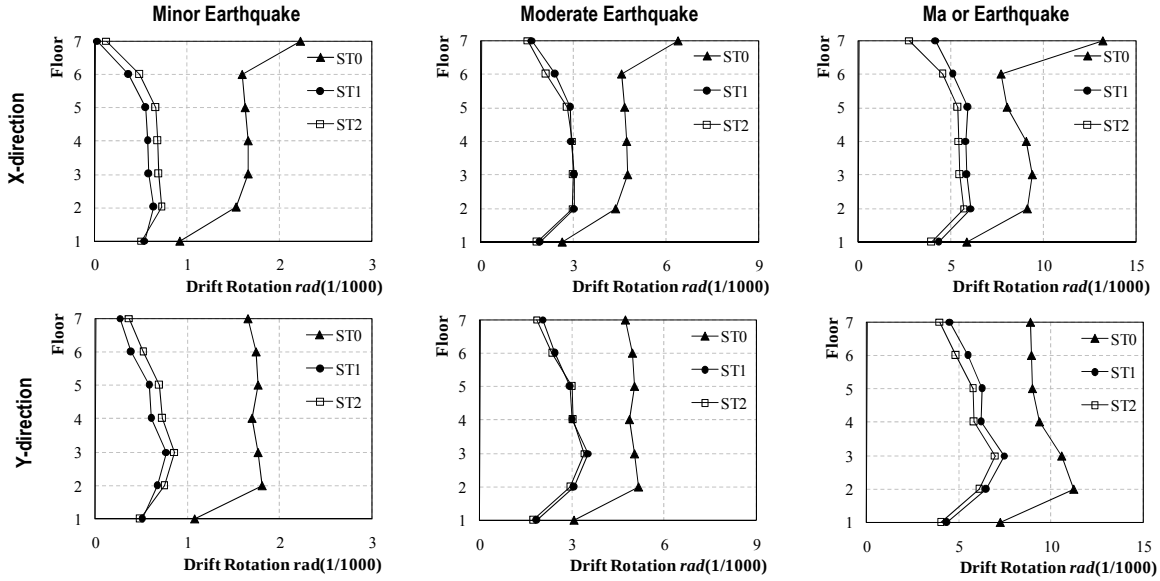


Figure 16 Story drift angles of the building with no dampers, with Type 1 dampers, and with Type2 dampers

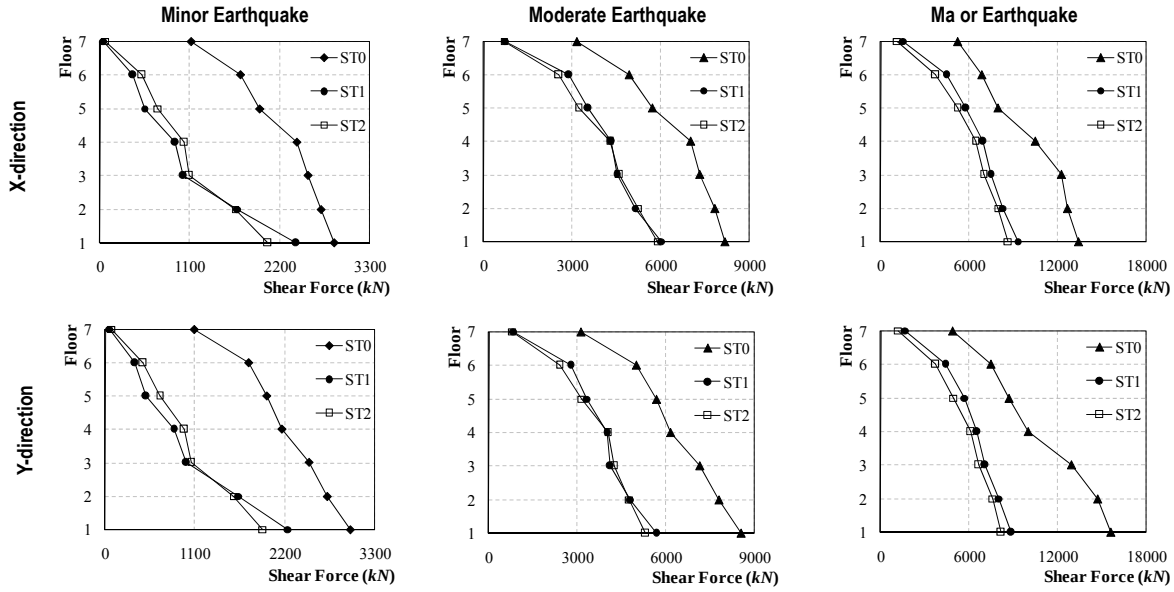


Figure 17. Story shear forces of the building with no dampers, with Type 1 dampers, and with Type2 dampers

for Environmental Conservation and Construction of a Society with Less Environmental Burden". The research field of the program is "Evaluation and mitigation of environment impacts of earthquake and typhoon disaster on urban area and infrastructures".

The principal investigators of the China and Japan teams, respectively, are Xilin Lu, Tongji University, and Kazuhiko Kasai, Tokyo Institute of Technology. The writers acknowledge financial support provided by the National Natural Science Foundation of China (NSFC) and Japan Science and Technology Agency (JST). Special thanks are given to the working group members, Linhai Peng, Chao Zhang, Ruifu Zhang, Shiming Zhang, for their analysis and design.

REFERENCES

Chang, K., Lin, Y. and Chen, C. (2008), "Shaking table study on displacement-based design for seismic retrofit of existing buildings using nonlinear viscous dampers." *Journal of Structural Engineering*, ASCE, **134**(4), 671-681.

Diotallevi, P. P., Landi, L. and Busca, A. (2008), "Seismic assessment of an existing RC hospital building study for the rehabilitation with supplemental fluid viscous dampers." *Proceedings of 14th World Conference on Earthquake Engineering*, Paper No. 11-0151.

Hwang, J., Wang, S., Huang, Y. and Chen, J. (2008), "Seismic retrofit of microelectronics factories using viscous dampers." *Proceedings of 14th World Conference on Earthquake Engineering*, Paper No. 05-01-0079.

JSSI Manual 2nd Edition (2005, 2007), *Design and Construction Manual for Passively Controlled Buildings*, Japan Society of Seismic Isolation (JSSI), Tokyo, JAPAN, 1st Ed., 405 pages, 2003, 2nd Ed., 515 pages, 2005, 2nd Ed. and 2nd Print, 509 pages, 2007 (in Japanese)

JSSI Manual, Chinese Translation (2008), *Design and Construction Manual for Passively Controlled Buildings*, Japan Society of Seismic Isolation (JSSI), China Architecture and Building Press, Beijing, China, 552 pages, (in Chinese)

Kasai, K., Suzuki, A., and Oohara, K. (2003), "Equivalent Linearization of a Passive Control System Having Viscous Dampers Dependent on Fractional Power of Velocity", *Journal of Structural and Construction Engineering*, AIJ, No. 574, 77-84 (in Japanese).

Kasai, K., Oohara, K., and Sekiguchi, Y. (2004), "JSSI Manual for Building Passive Control Technology: Part-11 Time-History Analysis Model for Viscous Dampers", *13th World Conference on earthquake Engineering*, No. 1427, Aug. 1-6, Vancouver, Canada.

Kasai, K., Ogura, T., and Suzuki, A. (2007), "Passive Control Design Method Based on Tuning of Equivalent Stiffness of Nonlinear Viscous Damper", *Journal of Structural and Construction Engineering*, AIJ, No. 618, 97-104 (in Japanese).

Kasai, K., Ooki, Y., Ishii, M., Ozaki, H., Ito H., Motoyui S., Hikino, T., and Sato, E. (2008), "Value-Added 5-Story Steel Frame and Its Components: Part 1 – Full-Scale Damper Tests and Analyses", *14th World Conference on Earthquake Engineering*, S17-01-013, Beijing, China.

Kasai, K., Motoyui, S., Ozaki, H., Ishii, M., Ito, H., Kajiwara, K., and Hikino, T. (2009), "Full-Scale Tests of Passively-Controlled 5-Story Steel Building Using E-Defense Shake Table, Part 1: Test concept, method, and building specimen", *STESSA 2009*, Philadelphia, USA.

Kasai, K., Ito, H., Ooki, Y., Hikino, T., Kajiwara, K., Motoyui, S.,, Ozaki, H., and Ishii, M.(2010), "Full-Scale Shake Table Tests of 5-Story Steel Building with Various Dampers", *Proceedings, 7CUEE and 5ICEE*, Tokyo Institute of Technology, Keynote Paper pp. 11 -22, March

Kasai, K., Lu, X., Pu, W., Weng, D., Zhou, Y., and Wada, A. (2011), "Design Method for RC Building Repair Using Dampers", *Proceedings, 8CUEE*, Tokyo Institute of Technology, March

Lin, Y. Y., Chang, K. C. and Chen, C. Y. (2008), "Direct displacement-based design for seismic retrofit of existing buildings using nonlinear viscous dampers." *Bulletin of Earthquake Engineering*, **6**(3), 535-552.

Martinez-Rodrigo, M. and Romero, M. L. (2003), "An optimum retrofit strategy for moment resisting frames with nonlinear viscous dampers for seismic applications." *Engineering Structures*, **25**(7), 913-925.

Ooki, Y., Kasai, K., Motoyui, S., Kaneko, K., Kajiwara, K., and Hikino, T. (2009) "Full-Scale Tests of Passively-Controlled 5-Story Steel Building Using E-Defense Shake Table, Part 3: Full-Scale Tests for Dampers and Beam-Column Subassemblies", *STESSA 2009*, Philadelphia, USA.

PRC National Standard, (1989), "Code for Seismic Design of Buildings (GBJ 11-89)," issued by the Ministry of Housing and Urban-Rural Construction of the People's Republic of China, China Architecture & Building Press, Beijing, China.

PRC National Standard, (2008), "Standard for Classification of Seismic Protection of Building Construction (GB 50223-2008)," issued by the Ministry of Housing and Urban-Rural Construction of the People's Republic of China, China Architecture & Building Press, Beijing, China.

PRC National Standard, (2010), "Code for Seismic Design of Buildings (GB 50011-2010)," issued by the Ministry of Housing and Urban-Rural Construction of the People's Republic of China, China Architecture & Building Press, Beijing, China.

Sorace, S. and Terenzi, G. (2008), "Seismic Protection of Frame Structures by Fluid Viscous Damped Braces," Journal of Structural Engineering, ASCE, **134**(1): 45-55.

Symans, M. D., and Constantinou, M. C. (1998), "Passive Fluid Viscous Damping Systems for Seismic Energy Dissipation," *Journal of Earthquake Technology*, Special issue on passive control of structures, **35**(4), 185-206.

Uetani, K., Tsuji, M. and Takewaki, I. (2003), "Application of an Optimum Design Method to Practical Building Frames with Viscous Dampers and Hysteretic Dampers," *Journal of Engineering Structure*, **25**, 579-592.

Uriz P. and Whittaker, A. S. (2001), "Retrofit of pre-Northridge steel moment-resisting frames using fluid viscous dampers." *Structural design of tall buildings*, **10**(5), 371-390.

Weng, D. G. and Lu, X. L. (2004), "Study on Design Parameters of Energy Dissipation Structures with Experiment Verification", *Journal of Earthquake Engineering and Engineering Vibration*, **24**(2), 150-157.

Weng, D. G., Zhang, R. F., Zhang, S. M. and Lu, X. L. (2009), "Application of energy dissipation method based on seismic performance and demand for post-earthquake R.C. frame retrofit." *Proceeding of 11th World Conference on Seismic Isolation, Energy Dissipation and Active Vibration Control of Structures*.

Weng, D. G., Zhang, C. and Lu, X. L. (2011), "Application of Energy Dissipation Technology to C-category Frame Structure of School Buildings for Seismic Retrofit of Increasing Precautionary Intensity," *Journal of Advanced Materials Research*, 163-167, 3480-3487.

8CUEE CONFERENCE PROCEEDINGS
8th International Conference on Urban Earthquake Engineering
March 7-8, 2011, Tokyo Institute of Technology, Tokyo, Japan

CHINA-JAPAN (NSFC-JST) RESEARCH ON USE OF DAMPERS FOR REPAIR OF RC BUILDING DAMAGED DURING 2008 WENCHUAN EARTHQUAKE PART 2: DESIGN METHOD FOR RC BUILDING REPAIR USING DAMPERS

Kazuhiko Kasai[1], Xilin Lu[2], Wuchuan Pu[3], Dagen Weng[4], Akira Wada[1], and Ying Zhou[5]

1) Professor, Structural Engineering Research Center, Tokyo Institute of Technology, Japan
2) Professor, Tongji University, State Key Laboratory of Disaster Reduction in Civil Engineering, Tongji University, Shanghai, China
3)Postdoctoral Research Fellow of COE, Center for Urban Earthquake Engineering, Tokyo Institute of Technology, Japan
4) Professor, College of Civil Engineering, Tongji University, Shanghai, China
5) Associate Professor, College of Civil Engineering, Tongji University, Shanghai, China
kasai@serc.titech.ac.jp, lxlst@tongji.edu.cn, pu.w.aa@m.titech.ac.jp,
wdg@tongji.edu.cn, wada@serc.titech.ac.jp, yingzhou@tongji.edu.cn

Abstract: Following the companion paper (Part 1) that described the 7-story RC building damage, actual repair work and analyses, and full-scale damper test, the present paper (Part 2) proposes a design method to determine the required capacity of viscous damper and its story-by-story distribution for RC building structure whose hysteresis is modeled as a stiffness-degrading type. The design method maintains the story drift uniformly at the target value. Its accuracy is verified by example damper design and time history analyses of the 7-story RC building.

1. INTRODUCTION

1.1 RC building repair using dampers

Use of dampers for seismic repair and retrofit of reinforced-concrete (RC) buildings is an attractive option. The cracking and spalling of concrete that can require extensive repair will be reduced significantly, if the dampers are attached to the building in a manner to efficiently absorb seismic energy.

The companion paper (Lu et. al. 2011) has described the 7-story RC building damaged due to the 2008 Wenchuan Earthquake, actual repair work performed by using nonlinear viscous dampers, detailed full-scale damper tests, and hypothetical repair and analysis using the damper test results. In the studies, the viscous dampers have been sized through design iterations utilizing time history analyses.

1.2 Damper distribution rule

RC frame shows complex hysteretic characteristics of degrading stiffness, and nonlinear viscous damper depends on not only velocity but also displacement. Because of these, the aforementioned design iterations based on trial and errors require significant effort.

Thus, it is highly desirable to develop a comprehensive design rule that clearly indicates effects as well as necessary capacities of the dampers for the target performance of nonlinear RC frames. This paper proposes such a rule, by extending the writers' earlier design method for the elastic frame and nonlinear viscous dampers (Kasai et al. 2003b, 2007, JSSI Manual 2005, 2007, Chinese Translation 2008).

Like typical performance-based design, it is considered that the design earthquake level and corresponding limit for the story drift are given. The design rule then determines the distribution of required damper capacities throughout the building height, so as to maintain the story drift uniformly at the target value, thereby avoiding damage concentration to a particular story.

The sample RC building discussed in Part 1 (Lu et al. 2011) is briefly introduced, and the target performance for its repair design is explained in Section 2. Modeling scheme for the original RC building is proposed in Section 3. The damper distribution rule and specific steps are described in Section 4. Accuracy of the rule and design will be demonstrated in Section 5, where the design example will consider Type 2 dampers discussed in Part 1 (Lu et al. 2011).

2. SEISMIC DESIGN CRITERIA FOR REPAIR

2.1 Description of RC Building

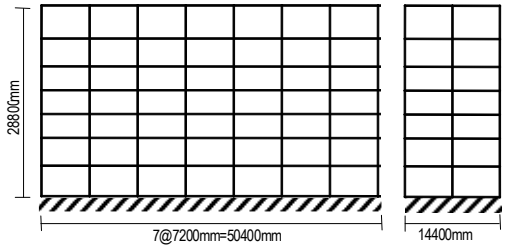
The existing building under investigation was originally a 6-story RC frame (with partial 7-story extruded) constructed in 1997, and it was damaged by the Wenchuan earthquake in 2008. After earthquake, the building was strengthened by adding steel columns, and reconstructed into a 7-story building. All analysis of this study will be based on the existing 7-story building. Figure 1 shows the front view of the building damaged by the earthquake, as well as the elevation of the building frame. The companion paper (Lu et al. 2011) describes more details.

2.2 Design criteria based on Chinese spectrum

The writers consider the same design criteria as used for the actual repair project (Lu et al. 2011). In order to



(a) Building damaged by earthquake



(b) Elevation of 7-sotry building (X and Y- direction)

Figure 1. RC building damaged by the 2008 Wenchuan earthquake and its elevation after repair and strengthening

meet the increased requirement of Chinese code after the quake (GB50011-2010), and to provide redundant load carrying capacity of structure, the target story drift angles of the building are set as 1/800, 1/300 and 1/100, at minor, moderate, and major earthquakes, respectively.

A suit of four ground acceleration histories are used to examine the structural performance, of which two are artificial and two others are recorded ones. According to the China seismic code, the peak ground acceleration (PGA) for seismic intensity 8 should be 70, 200, and 400 cm/s^2 for minor, moderate, and major earthquakes, respectively. However, as described previously (Lu et al. 2011, Weng et al. 2009, 2011), in order to consider the contribution of partition walls to the stiffness of the building, the PGA is amplified by 22%, and 85.4, 244, and 488 cm/s^2 will be used, respectively. Figure 2 shows four acceleration histories thus-amplified to PGA = 488 cm/s^2, and corresponding pseudo-acceleration spectra with 5% damping ratio.

3. RC FRAME NONLINEAR MODEL

3.1 Static push-over analysis of 7-story RC frame

The RC frame was modeled in the actual repair project by using the nonlinear member-to-member model, hereby defined as "frame model". The Chinese computer program PKPM2008 is used to analyze the model.

Figures 3a and b show results of static push-over analyses in X- and Y-directions, respectively. Relationship of story shear Q_i vs. story drift $h_i\theta_i$ at i-th story level is shown, where h_i and θ_i = story height and story drift angle at i-th story level, respectively. The lateral load distribution corresponds to the story shear distribution calculated from Chinese code (GB50011-2010).

The frame tends to show highly non-uniform deformation, with larger story drifts at the 2nd and 3rd story levels.

3.2 Story-by-story idealization of cyclic behavior

For the rule to estimate required damper capacities, hysteretic characteristics of the RC frame must be known beforehand. Instead of time-consuming analysis applying

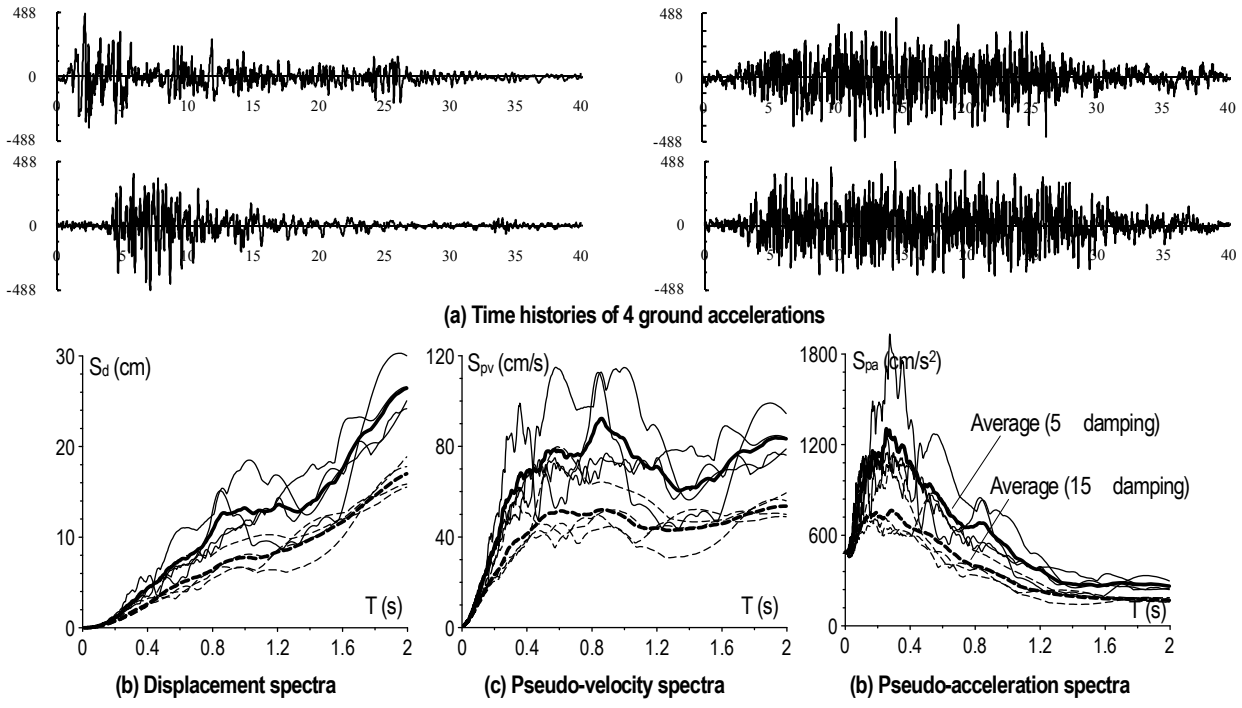
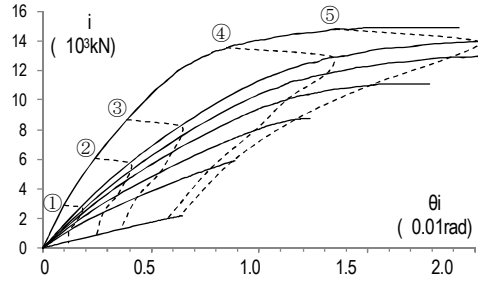


Figure 2. Time histories of 4 ground accelerations and their response spectra with different damping ratios (Solid line =5% damping ratio, broken line = 15% damping ratio)



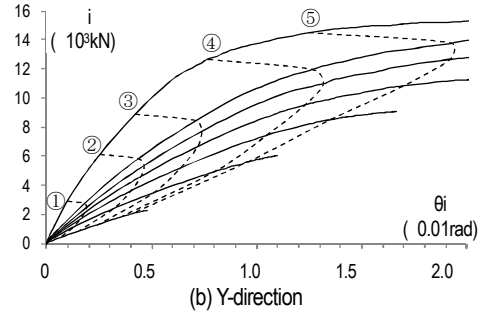


Figure 3. Static pushover analysis results for the frame model (Average drift angle = 1/800, 1/300, 1/200, 1/100, 1/75 in the order of ①~⑤)

cyclic load to the nonlinear member-to-member model (Sec. 3.1), such characteristics will be idealized story-by-story using the stiffness degrading model called "Takeda model" (Takeda et al. 1970) as follows.

In the model, hysteresis depends on experienced maximum story drift angle θ_i, where i = story level. The model is elastic at $\theta_i<\theta_{ci}$, where θ_{ci}= cracking drift angle defined by micro-cracking of the concrete material. Figure 4a shows the model at $\theta_{ci}<\theta_i<\theta_{yi}$, where θ_{yi}= yield drift angle when the steel reinforcing bars yield significantly and plastic hinge formed at the member. Figure 4b shows the model at $\theta_{ci}<\theta_{yi}<\theta_i$.

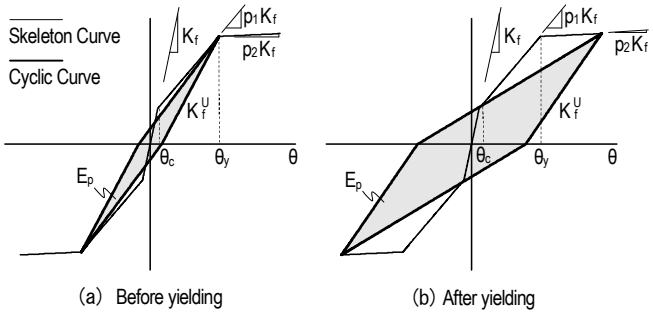


Figure 4 Idealized hysteresis (Takeda) model for RC frame (Note: subscript "i" to denote story level is not indicated)

Accordingly, Takeda model has tri-linear skeleton curve, and the first, second, and third lines represent elastic stiffness K_{fi}, post-crack stiffness $p_{1i}K_{fi}$, and post-yield stiffness $p_{2i}K_{fi}$ against the story drift $h_i\theta_i$, respectively.

The most significant characteristics that differentiate Takeda model with other models are the loading and unloading rules. The stiffness K_{fi}^U when unloading from skeleton curve depends on θ_i experienced, and is given as:

$$\theta_i \le \theta_{ci}: \quad K_{fi}^U = K_{fi} \tag{1a}$$

$$\theta_{ci} < \theta_i \le \theta_{yi}: \quad K_{fi}^U = K_{fi}\frac{2\theta_{ci} + p_{1i}(\theta_i - \theta_{ci})}{\theta_i + \theta_{ci}} \tag{1b}$$

$$\theta_{yi} < \theta_i: \quad K_{fi}^U = K_{fi}\frac{2\theta_{ci} + p_{1i}(\theta_{yi} - \theta_{ci})}{(\theta_{yi} + \theta_{ci})(\theta_i/\theta_{yi})^{0.4}} \tag{1c}$$

After one or more loading cycles have occurred, the loading curve can be constructed by connecting the point at zero load to the point reached in the previous cycle, if that point lies on the skeleton curve or on a line aimed at a point on the skeleton curve. The more details about loading and unloading rules can be found in Takeda et al. (1970).

In order to perform analysis using Takeda hysteretic model, tri-linear skeleton curves are constructed to substitute the continuous nonlinear curves, as depicted by Figure 5. After the initial stiffness K_{fi} is specified from the pushover curve (step 1 in Figure 5), the third segment of skeleton curve crossing the original nonlinear curve at drift angle of

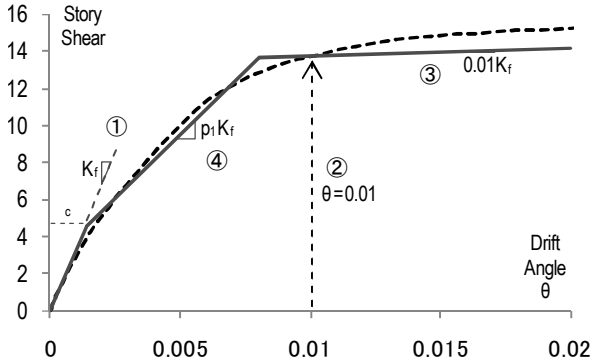


Figure 5. Tri-linear approximation of frame pushover curve

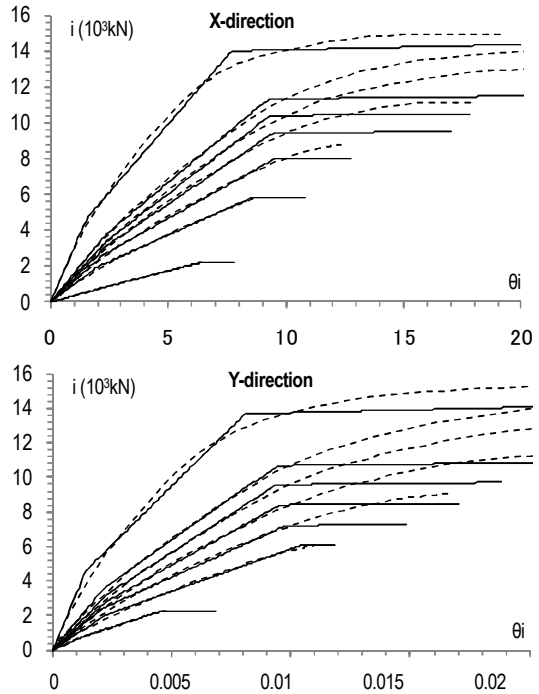


Figure 6. Tri-linear approximation compared with pushover curve at each story

Table 1. Properties of RC building and parameters for idealized stiffness-degrading model

Story No.	W_i (kN)	h_i (mm)	X-direction							Y-dirction						
			K_{fi} (kN/mm)	$p_{1i}K_{fi}$ (kN/mm)	$p_{2i}K_{fi}$ (kN/mm)	θ_{ci} (×0.01)	θ_{yi} (×0.01)	Q_{ci} (kN)	Q_{yi} (kN)	K_{fi} (kN/mm)	$p_{1i}K_{fi}$ (kN/mm)	$p_{2i}K_{fi}$ (kN/mm)	θ_{ci} (×0.01)	θ_{yi} (×0.01)	Q_{ci} (kN)	Q_{yi} (kN)
7	5351	5000	73	68	0.7	0.2	0.63	733	2200	128	90	1.3	0.12	0.45	760	2280
6	10417	4200	238	140	2.4	0.2	0.86	1947	5840	221	117	2.2	0.22	1.04	2020	6060
5	10084	3600	327	203	3.3	0.23	0.95	2667	8000	324	171	3.2	0.21	0.98	2405	7216
4	10221	3600	366	245	3.7	0.24	0.94	3139	9419	348	212	3.5	0.22	0.95	2804	8414
3	10427	3600	395	280	4.0	0.24	0.93	3467	10400	395	249	4.0	0.22	0.94	3194	9584
2	9369	4200	382	259	3.8	0.24	0.92	3776	11328	400	232	4.0	0.21	0.94	3560	10681
1	11152	4600	658	329	6.6	0.16	0.77	4686	14059	726	298	7.3	0.14	0.81	4580	13740

1/100 (step 2) with the post-yield stiffness $p_{2i}K_{fi} = 0.01K_{fi}$ is drawn (step 3). Further, post-crack stiffness $p_{1i}K_{fi}$ is drawn (step 4) on the basis of energy equivalence and condition that the force at cracking is 1/3 of the yield force. (Figure 5)

In this manner, for the *i*-th story level, all parameters K_{fi}, p_{1i}, p_{2i}, θ_{ci}, and θ_{yi} to construct Takeda model are evaluated, and the values are listed in Table 1. Additionally, for the stories where drift angle could not reach 1/100 in pushover analysis, the maximum drift angle can be used instead of 1/100 in step 2 mentioned above. The tri-linear skeleton curve obtained for the 7-story RC building agrees reasonably well with the push-over curve in both X- and Y-directions, see Figure 6.

3.3 Accuracy of story-by-story idealization

In order to check appropriateness of the story-by-story idealization explained above, a stick model having the idealized hysteresis (Figure 4) of the 7-story RC frame is produced. Seismic responses of the stick model and the original frame model (Sec. 3.1) are compared using four different ground acceleration histories and three different levels explained in Sec. 2.2.

Figure 7 shows average of story drifts due to the four acceleration histories at each excitation level. For the minor and moderate excitation levels, the stick model shows excellent match with the frame model. For the major level, the former shows more deformation at the 2nd and 3rd story levels, indicating sensitivity of responses against plastic stiffness of each story. Thus, as a conservative and simplified approach for the stories developing large deformations, the idealized hysteresis will be considered throughout the present paper.

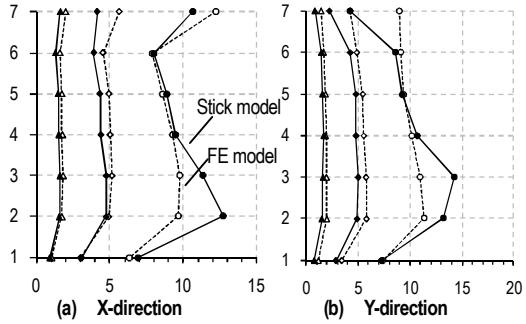


Figure 7. Comparison of analysis results obtained by finite element model and a stick model with idealized hysteresis

The 7-story multi-degree-of-freedom (MDOF) stick model without dampers will be called as the "*MDOF system*", and the system combining it with dampers story-by-story will be called as the "*damped MDOF system*" from now on. Further, for the single-degree-of-freedom system to be discussed, the "*SDOF system*" and the "*damped SDOF system*" are defined.

3.4 Energies produced from idealized frame hysteresis

The present rule aims to produce uniform story drift angle of the target value θ_t. Using idealization depicted by Figure 4, Secs. 3.2 and 3.3, stored and dissipated energies E_{si}, E_{di} at *i*-th story of the MDOF system developing the target drift angle θ_t uniformly are given as:

$$E_{si}=\beta_i K_{fi}(h_i\theta_t)^2/2 \quad , \quad E_{pi}=\zeta_i K_{fi}(h_i\theta_t)^2 \tag{2a,b}$$

where β_i and ζ_i are used to compare energies E_{si}, E_{di} with the stored energy of an elastic MDOF system, and they depend on the magnitude of θ_t, *i.e.*,

$$\theta_t \le \theta_{ci}: \quad \beta_i=1 \quad , \quad \zeta_i=0 \tag{3a,b}$$

$$\theta_{ci}<\theta_t \le \theta_{yi}: \quad \beta_i=p_{1i}+(1-p_{1i})\frac{\theta_{ci}}{\theta_t} \tag{4a}$$

$$\zeta_i=\frac{2(1-p_{1i}(1-\theta_{ci}/\theta_t)\{p_{1i}+(1-p_{1i}\theta_{ci}/\theta_t)\}}{2+p_{1i}(\theta_t/\theta_{ci}-1)} \tag{4b}$$

$$\theta_{yi}<\theta_t: \quad \beta_i=-p_{2i}+(1-p_{1i})\frac{\theta_{ci}}{\theta_t}+(p_{1i}-p_{2i})\frac{\theta_{yi}}{\theta_t} \tag{5a}$$

$$\zeta_i=2\beta_i-\frac{\beta_i^2(1+\theta_{ci})(\theta_t/\theta_{yi})^{0.4}}{2\theta_{ci}+p_{1i}(1-\theta_{ci})} \tag{5b}$$

The above equations will be used in the next sections.

4. SEISMIC CONTROL DESIGN

The present rule finds damper distributions to achieve uniform story drift angle θ_t, even for frames of irregularly distributed structural parameters (Sec. 1.2). Considering the MDOF system with idealized hysteresis (Secs. 3.2 and 3.4), damper design for the given earthquakes and target performance is outlined below:

Step 1: The MDOF system is converted to a SDOF system, such that stored and dissipated energies of both

systems are equal at the target θ_t (Sec. 4.1).

Step 2: For the above SDOF system, required capacity of a viscous damper to be added to satisfy θ_t is found by time history analyses (Sec. 4.2).

Step 3: The required damper capacity found in step 2 for the SDOF system is converted and distributed story-by-story to the MDOF system (Sec. 4.3).

The following sections describe each step:

4.1 Conversion from MDOF system to SDOF system

The first step converts the MDOF system to an equivalent SDOF system. By imposing uniform deformation to the MDOF system and equating its stored and dissipated energies to those of the SDOF system,

$$E_s = \frac{1}{2}\beta K_f (H_{eff}\theta_t)^2 = \sum_{i=1,N} E_{si} \tag{6a}$$

$$E_p = \zeta K_f (H_{eff}\theta_t)^2 = \sum_{i=1,N} E_{pi} \tag{6b}$$

where E_s, E_p = stored and dissipated energies of the SDOF system, β, ζ = factors to determine E_s and E_p, respectively, and H_{eff} = effective height of the RC building estimated by assuming uniform deformation (e.g., Kasai et al. 1998, 2010b, Kasai and Pu 2010a, JSSI Manual 2005, 2007) as follows:

$$H_{eff} = \sum_{i=1,N} m_i H_i^2 / \sum_{i=1,N} m_i H_i \tag{7a,b}$$

Using Eq. 6 and other conditions set for the elastic range, post-crack range, and post-yield range, respectively. parameters defining hysteresis of the SDOF system will be determined as follows:

Elastic stiffness K_f is obtained by substituting $\beta = 1$ into Eq. (6a). Other parameters characterizing the hysteresis loops are named as p_1, p_2, θ_c, and θ_y (Figure 4), like those in the MDOF system. They are obtained in the following two ways:

If $\theta_t < \theta_{yi}$ in all stories of the MDOF system, the SDOF system is considered to be at either elastic or post-crack state, and only p_1 and θ_c are needed to define its hysteresis. After obtaining β_i and ζ_i from Eq. (3) or (4) and estimating the energies of the MDOF system by Eq. (2), the β and ζ of the SDOF system are calculated using Eq. (6). Then, p_1 and θ_c are obtained by solving the following equations:

$$\beta = p_1 + (1-p_1)\frac{\theta_c}{\theta_t} \tag{8a}$$

$$\zeta = \frac{2(1-p_1)(1-\theta_c/\theta_t)\{p_1 + (1-p_1)\theta_c/\theta_t\}}{2 + p_1(\theta_t/\theta_c - 1)} \tag{8b}$$

Note that the same hysteresis type as that of the MDOF system is considered, thus, Eq. (8) is similar to Eq. (4).

If $\theta_t > \theta_{yi}$ in at least one story of the MDOF system, the SDOF system is considered to be at post-yield state. Thus, all parameters p_1, p_2, θ_c, and θ_y must be obtained. Like the post-crack state discussed above, equations similar to Eqs. (5a) and (5b) can be used to solve for the two of the four unknowns. In the present study, p_2 and θ_c are considered less important than p_1 and θ_y, and they are simply estimated as average of the values at all stories of the MDOF system. Thus, p_1 and θ_y are obtained by solving Eqs. (9a,b) below:

$$\beta = -p_2 + (1-p_1)\frac{\theta_c}{\theta_t} + (p_1 - p_2)\frac{\theta_y}{\theta_t} \tag{9a}$$

$$\zeta = 2\beta - \frac{\beta^2 (1+\theta_c)(\theta_t/\theta_y)^{0.4}}{2\theta_c + p_1(1-\theta_c)} \tag{9b}$$

$$p_2 = \sum_{i=1,N} p_{2i}/N \quad , \quad \theta_c = \sum_{i=1,N} \theta_{ci}/N \tag{9c,d}$$

Figure 8 plots an example for hysteresis curves of the MDOF system at drift angle of ± 1/100 rad , from which different extent of plastification and degradation can be recognized story-by-story. Figure 8 also shows the hysteresis curve of the equivalent SDOF system determined by the above method.

Like the actual repair project (Lu et al. 2011), the above conversion was performed for two principle directions of the building, with the target story drift angle θ_t = 1/300 against the moderate earthquake (Sec. 2.2). After designing the dampers, the performance of the damped MDOF will be checked by considering the minor and major earthquakes (Sec. 2.2) and their drift limits 1/800 and 1/100, respectively.

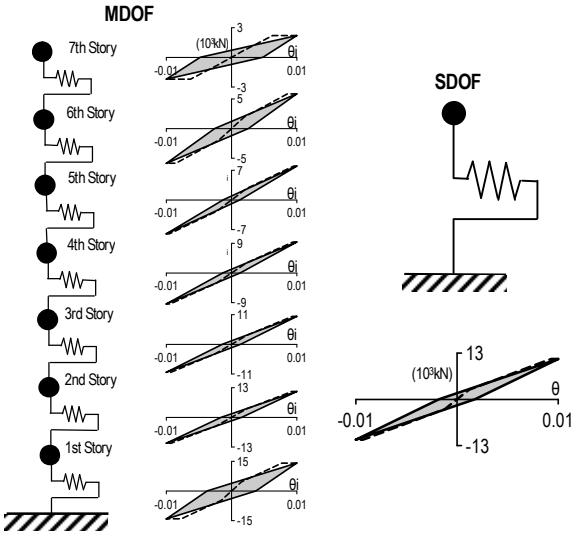


Figure 8 Conversion of MDOF system to SDOF system without damper (X-direction)

4.2 Damper Design for SDOF system

A system combining the SDOF system and a nonlinear viscous damper element with assigned values of C_d, K_d, and α is created, and it will be named as the damped SDOF system. Type 2 damper will be considered (Sec. 1.2).

As shown in Figure 9, an "added component" consists of a series combination of the nonlinear dashpot of with the viscosity coefficient of C_d, the spring simulating damper internal stiffness K_d, and the spring simulating the stiffness of support brace and connections K_b. In the present study, K_d is considered to be much smaller than K_b, thus only the

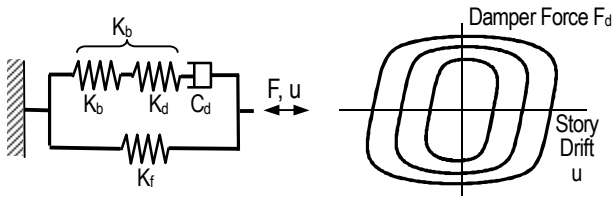


Figure 9. Damper force vs. story drift curve for equivalent damped SDOF system under different target drifts

value of K_d is used to simulate the flexibility of the spring.

The time history responses of the damped SDOF system are obtained for the set of earthquakes (Sec. 2.2.). Note that the method to create the analytical model requires some caution due to nonlinearity of viscous damper, and details are explained in Appendix-I.

Figure 10 shows such analyses using one of the artificial earthquakes. The value of C_d is increased from 0, and analysis repeated only a few times until the maximum displacement of the damped SDOF system is about equal to the target θ_t. Based on full-scale tests (Lu et al. 2011), α = 0.38 and K_d= 2.83C_d are considered, with units kN/mm and kN/(mm/s)$^{0.38}$ for K_d and C_d, respectively.

The example in Figure 10 considers the moderate earthquake (one of the artificial earthquakes) and target θ_t= 1/300, as explained in Sec. 4.1. The undamped SDOF system 1 develops the drift angle 1/232, but the damped SDOF system 2 has reduced it to 1/300 rad. The values are based on the assumption of uniform drift angle, and may be viewed as the indicator of an average drift angles throughout the building. Note also that the curve indicating peak base shear vs. peak deformation of the damped SDOF system follow the profile of the frame skeleton curve, with added force produced by the nonlinear viscous damper (Figure 10).

In the present design, the required C_d value is found such that the average of the drift angles of the SDOF system due to the four moderate earthquakes reaches the target θ_t= 1/300. Using the values of C_d, K_d, and $u_{d,\max}$ thus-obtained, as well as β from either Eq. (8a) or (9a), effective circular

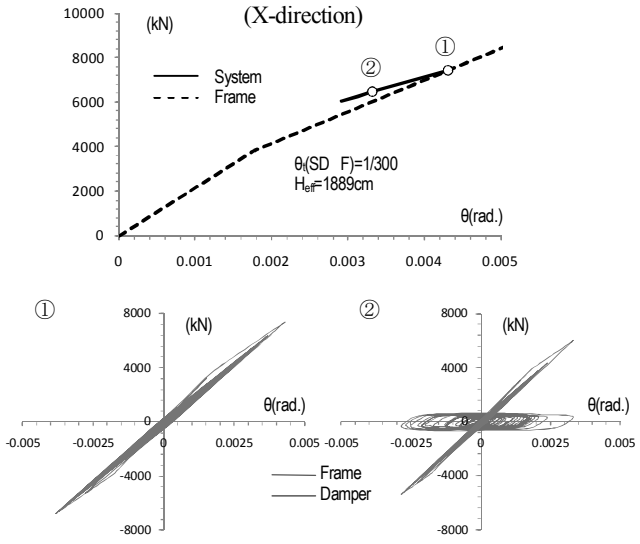


Figure 10 Time history analysis of SDOF system with damper

frequency ω_{eq} is obtained from Eq. (10a) with a few iterations, *i.e.*,

$$\omega_{eq}=\sqrt{\frac{K'_a(\omega_{eq})+\beta K_f}{M_{eff}}} \quad , \quad M_{eff}=\frac{\sum_{i=1,N}(m_i H_i)^2}{\sum_{i=1,N} m_i H_i^2}$$

$$K'_a=\frac{\lambda^{1+\alpha}}{1+\lambda^{1+\alpha}}K_b^* \quad , \quad \lambda=\frac{C_d \omega_{eq}^{\alpha} u_{d,\max}^{\alpha-1}}{K_b^*} \qquad \text{(10a-d)}$$

where M_{eff} = effective modal mass estimated by assuming a straight-line mode shape, $K'_a(\omega_{eq})$ = storage stiffness of the added component, K_b^* = equivalent brace stiffness combining effects of K_b and K_d (Figure 9), approximately equal to K_d in the present study, as mentioned above. Eqs. (10c,d) were derived previously (Kasai et al. 2003b, 2007, JSSI Manual 2005, 2007, Chinese Translation, 2008).

After obtaining ω_{eq} , the supplemental equivalent damping ratio ξ_{eq} is calculated as follows:

$$\xi_{eq}=\frac{E_p+E_v}{2\pi(K'_a(\omega_{eq})+\beta K_f)(H_{eff}\theta_t)^2} \qquad (11)$$

where E_p is already known from Eq. (6a), and E_v is the energy dissipated by the viscous damper. Using the formulas derived earlier (Kasai et al. 2003b, 2007), E_v is expressed as follows:

$$E_v=4\left(\frac{1+\lambda^{1+\alpha}}{e^{0.24}}\right)^{\alpha} C_d \omega_{eq}^{\alpha} u_{d,\max}^{\alpha-1}(H_{eff}\theta_t)^2 \qquad (12)$$

The calculated values for θ_t = 1/300 are as follows: Compared with the x- and y-direction elastic vibration periods 1.41 and 1.43 seconds, the effective periods ($2\pi/\omega_{eq}$) has changed to 1.59 and 1.55 seconds, due to softening of the frame and stiffening by the damper. Supplemental effective damping ratios ξ_{eq}'s are somewhat small and 0.034 and 0.031, respectively, where E_p is about 2 times the E_v .

The values of ω_{eq} and ξ_{eq} of the damped SDOF system will be utilized for design of the damped MDOF system in the next section.

4.3 Damper distribution rule for MDOF system

The required damper capacity for the damped SDOF mentioned above will be distributed story-by-story to the MDOF system, satisfying the constraining conditions below:

(1) The equivalent damping ratios of the damped SDOF system and damped MDOF systems are equal.
(2) Equivalent story stiffness of the damped MDOF system at a uniform target drift angle θ_t is proportional to the design story shear force.

The design story shear force distribution is calculated based on the Chinese seismic code. The writers derived distribution rules for many combinations of the dampers and frames (e.g., Kasai et al. 1998, 2005-2008). Based on the previous work, the distribution rule for the required damper force $F_{di,\max}$ is proposed below:

$$F_{di,\max}=\left(\frac{1+\lambda^{1+\alpha}}{\lambda^2}\right)^{\alpha/2}\left\{\frac{\sum_{i=1,N}(A\beta_i-\zeta_i)K_{fi}h_i^2}{A\sum_{i=1,N}Q_ih_i-2\pi\xi_{eq}}\frac{Q_i}{h_i}-K_{fi}\beta_i\right\}h_i\theta_t$$

$$u_{di,\max}=\frac{h_i\theta_t}{(1+\lambda^{1+\alpha})^{1-0.5\alpha}}\quad,\quad A=\frac{4e^{-0.24\alpha}}{\lambda^{\alpha}(1+\lambda^{1+\alpha})^{1-\alpha}} \qquad (13a\text{-}c)$$

where α = 0.38, Q_i = design story shear force, and $u_{di,\max}$= expected maximum deformation of the dashpot (Figure 9) at i-th story of the damped MDOF system.

Eq. (13) assumes the dampers are oriented horizontally, following the actual project (Lu et al. 2011). A negative value of $F_{di,\max}$ means that the frame at the i-th story is stronger than necessary, and no damper is assigned to such a story. Detailed derivation of Eq. (13) will be given elsewhere.

Note that Eq. (13b) indicates effectiveness of the damper: It clarifies how much damper deforms relative to the maximum story drift $h_i\theta_t$, and depends largely on the "support deformation ratio" λ (Eq. (10d)), a ratio between the maximum deformations of the spring of equivalent brace stiffness K_b^* and the nonlinear dashpot (Figure 9). Larger λ means larger spring deformation, and consequently less damper deformation and energy dissipation.

In the present formulation, λ is assumed constant, thus, approximate proportioning K_b^* to C_d is required at each story. This is automatically satisfied in the present study, since K_b^* is approximately set to K_d which is also proportional to C_d (Sec. 4.2). However, if K_b happens to be small, it should be adjusted to satisfy the above assumption.

Since the nonlinear viscous damper force is proportional to fractional power of velocity, the required viscosity coefficient C_{di} is obtained from:

$$C_{di}=\frac{F_{di,\max}}{(\omega_{eq}u_{di,\max})^{\alpha}} \qquad (14)$$

Table 2. MDOF design results for viscous dampers (α=0.38)

Story No.	X-direction				Y-direction			
	$F_{di,max}$ (kN)	$u_{di,max}$ (mm)	λ_i	C_{di} (kN/(mm/s)$^{\alpha}$)	$F_{di,max}$ (kN)	$u_{di,max}$ (mm)	λ_i	C_{di} (kN/(mm/s)$^{\alpha}$)
7	308	15.9	0.11	60	—	—	—	—
6	—	—	—	—	96	13.3	0.12	20
5	562	11.4	0.14	125	949	11.4	0.13	213
4	1147	11.4	0.14	254	1675	11.4	0.13	376
3	1640	11.4	0.14	364	1848	11.4	0.13	415
2	1458	13.3	0.12	305	1393	13.3	0.12	295
1	—	—	—	—	—	—	—	—

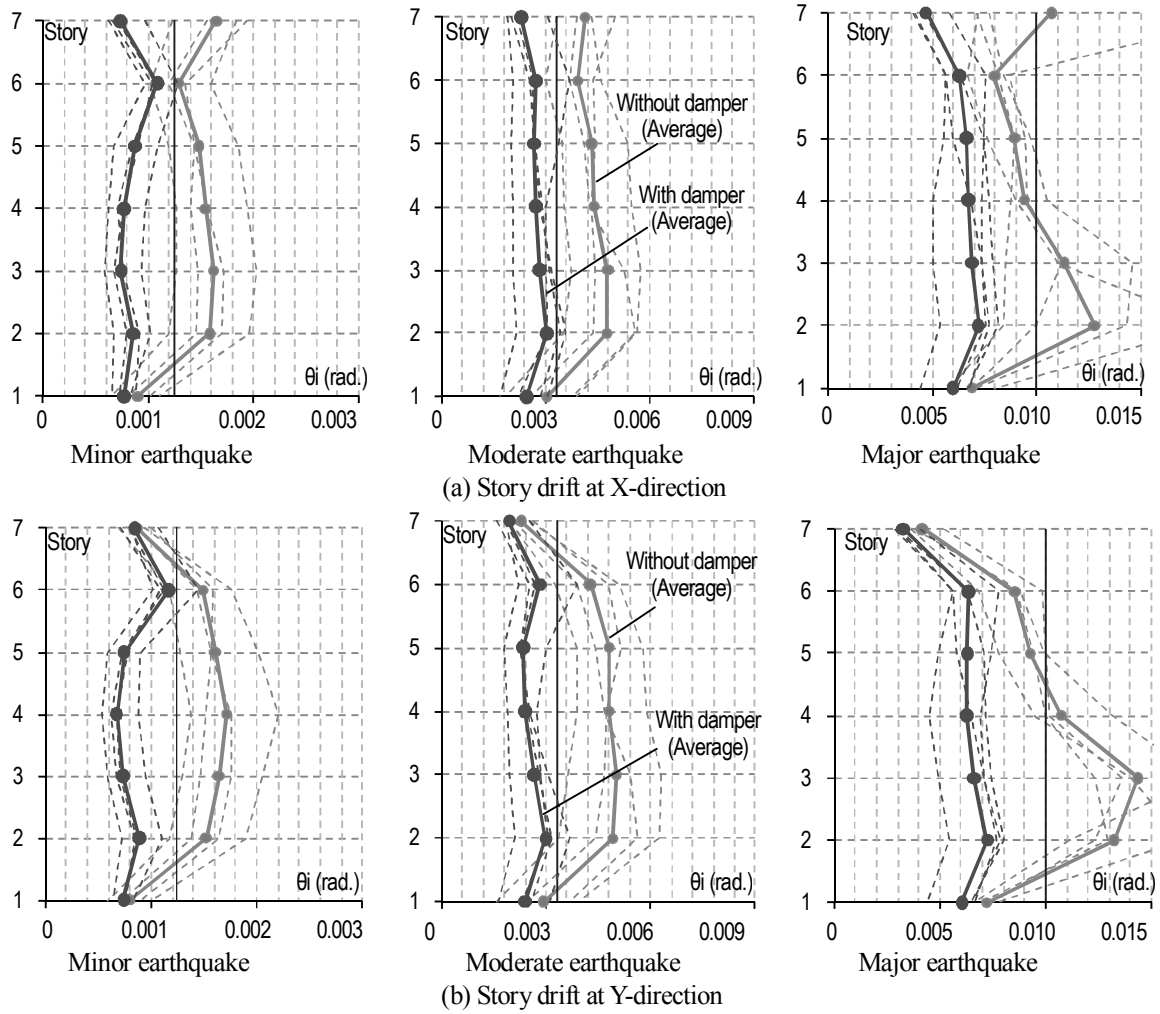


Figure 11. Drift angles of RC building with and without dampers (dampers designed for the moderate earthquake)

and $K_{di} = 2.83 C_{di}$ with the unit kN/mm (Sec. 4.2).

Table 2 lists required damper capacities for the moderate earthquake and target θ_t = 1/300 in X- and Y-directions, respectively. In order to obtain equivalent stiffness distribution proportional to story shear force (Sec. 4.3), the dampers are distributed to relatively weak stories but not all stories based on their stiffness. Namely, the added components compensate the stiffness of frame, while dissipating earthquake energy as required by the rule.

The dynamic analysis on existing undamped frame building (Sec. 3, Figure 7) showed relatively small responses in 1st and 6th stories of X-direction, and 1st and 7th stories of Y-direction. Eq. (13) using the static load captures this dynamic trend, and requires no dampers in these stories for the moderate earthquakes considered.

5. ANALYTICAL VALIDATION AND COMMENTS

5.1 Validation by Dynamic Analyses

As commented earlier, repair design of the 7-story RC building is completed for the moderate earthquakes with the target story drift angle θ_t = 1/300. It is then checked against the minor and major earthquakes and the corresponding drift limits 1/800 and 1/100, respectively.

Broken lines in Figure 11 show drift angles of the (undamped) MDOF system as well as damped MDOF system against the four minor earthquakes, the four design (moderate) earthquakes, and the four major earthquakes, respectively. The thick solid line shows the average of the responses over the four earthquakes, and vertical and thin solid straight line indicates the design limit for each earthquake level.

Story drift angles of the damped MDOF system under the design (moderate) earthquakes match well with the target angle θ_t = 1/300 with some conservatism, indicating appropriateness of the proposed damper distribution rule. Also, those under the minor and major earthquakes are below the design limits, respectively, and the system designed for the moderate earthquake appears to be adequate for the other levels of earthquakes as well.

As an example, responses due to a major earthquake are shown in Figure 12, where hysteretic curves show story shear and story drift angle relationship for every story of the 7-story undamped system (Figure 12 left) and damped system (Figure 12 right), respectively. The former shows considerable deformations and stiffness degradation in the 2nd and 3rd stories, whereas the latter using the dampers mitigates such a problem. Figure 12 right also shows the frame of the latter responds almost elastically, by virtue of the dampers sharing story shear and dissipating energy. The damper distribution rule achieving uniform deformation at the design level (Figure 11) appears to be reasonably effective at the major earthquake level as well. The stories where the rule indicated no need for dampers has performed satisfactorily without dampers (Figure 12 right).

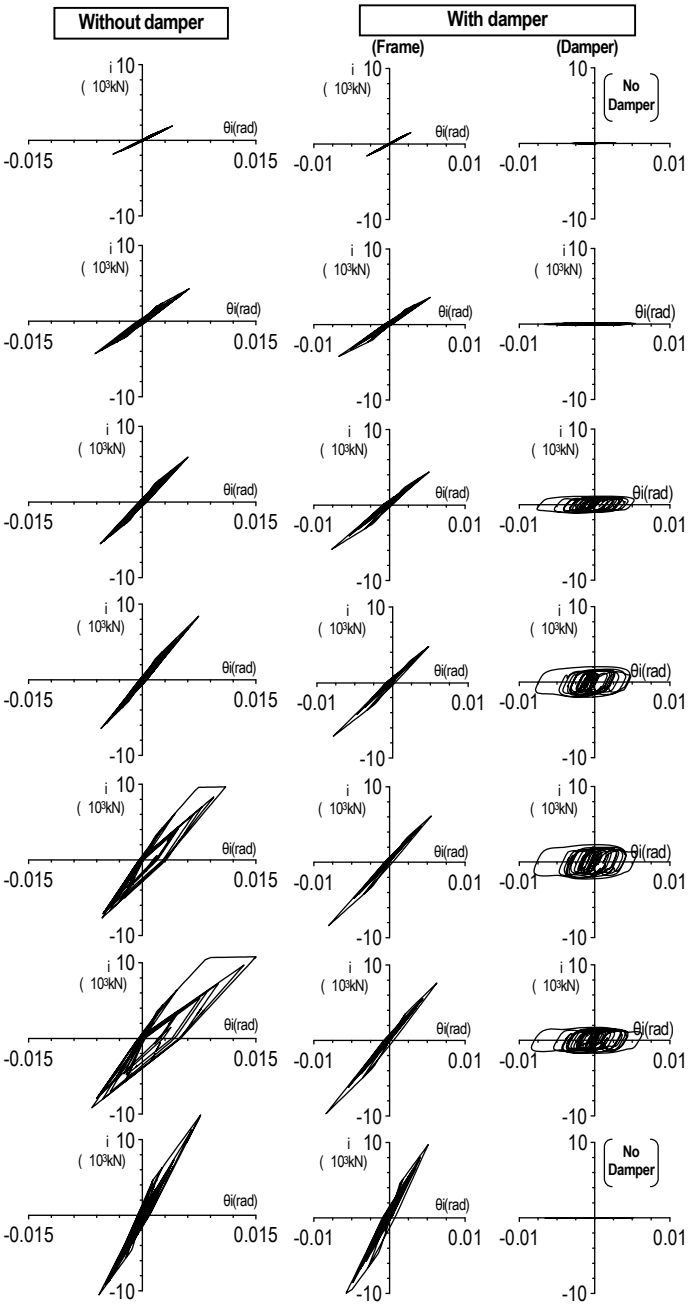


Figure 12. Hysteresis example for design against major earthquake (Y-direction)

5.2 Important Comments

It is interesting to compare the present damper design with the previous design performed on a trial basis assuming the same damper type (Type 2), as discussed in the companion paper. Both designs consider the same moderate earthquakes and target θ_t.

From Tables 4 and 5 of the companion paper (Lu et al. 2011), the sum of required C_{di}'s (i = 1 to 7) of the Type 2 dampers was 1,960 kN/(mm/s)$^{0.38}$ in each of X- and Y-directions. Whereas, from Table 2 of the present paper, the values are 1,108 and 1,319 kN/(mm/s)$^{0.38}$ in X- and Y-directions, respectively. They are 0.57 and 0.67 times that of the previous design, which is significant difference, even considering that the previous design was limited by

commercially available C_{di}-values and thus over-sizing of damper was inevitable.

The main reason for such difference of the two designs is that the present distribution rule can optimize the damper capacity story-by-story, thereby requiring less capacities. As discussed in Sec. 4.3, dampers were not used in 1st and 6th stories for X-direction, and 1st and 7th stories for Y-direction. Further, in contrast to the previous design increasing the damper capacity gradually from upper to lower stories, the present design provides larger amount of damper wherever necessary.

However, it is also noted that, due to nonlinearity of the frame and dampers, optimum damper capacities and distributions vary, depending on the level of the earthquake and target performance. Thus, once design is complete at one level, its adequacy must be confirmed at other stipulated levels. In Sec. 5.1, the design was confirmed in such a manner (Figure 11).

Comparing the earthquake levels and corresponding drift limits, which level governs the design is almost obvious in the present building case. However, if it were not the case, or if preliminary estimate for required damper capacity were necessary, the check using the SDOF system (Sec. 4.2) would be simple and useful. By this check, one can find the earthquake level requiring the most control, hence the largest damper quantity, and corresponding dynamic properties such as effective period and damping ratio. The result of this SDOF check will also be directly utilized to the damper distribution rule for the MDOF system.

Accordingly, the writers are currently developing a simplified tool to perform the same SDOF check. Considering a graphical approach as one of the practical methods to solve nonlinear problem, the writers developed various "performance curves" expressing response reduction in term of the amount of linear or nonlinear dampers and linear or nonlinear frame properties (Kasai et al. 1998, 2005-2009, 2010a and b, JSSI Manual 2005, 2007, Chinese Translation 2008.) The curves are being extended to include nonlinear viscous dampers and stiffness-degrading frames discussed in the present paper.

6. CONCLUSION

This paper has proposed a design method to determine the required capacity of viscous damper and its story-by-story distribution for RC building structure whose hysteresis is of stiffness-degrading type. The design method maintains the story drift uniformly at the target value. Its accuracy is verified by example damper design and time history analyses of an existing 7-story RC building damaged during the 2008 Wenchuan Earthquake and repaired using nonlinear viscous dampers of different type (Lu et al. 2011).

Compared with the trial-based design reported in Part 1, the present design method requires considerably less damper capacities, by optimizing the damper capacity story-by-story. The optimized solution is hardly obtained by trial-based design, and it is significant advantage for the economy of dampers, connections, surrounding frame members, and foundations transmitting the damper forces.

The initial step for the design method using the SDOF system and its time history analyses is unique, and provides many significant information for the passive control design. On the other hand, it will be replaced by a simplified graphic approach in order to simplify the whole design procedure.

ACKNOWLEDGEMENTS

This study is a part of the Strategic Japanese-Chinese Cooperative Program on "Science and Technology (S&T) for Environmental Conservation and Construction of a Society with Less Environmental Burden". The research field of the program is "Evaluation and mitigation of environment impacts of earthquake and typhoon disaster on urban area and infrastructures".

The principal investigators of the Japan and China teams, respectively, are Kazuhiko Kasai, Tokyo Institute of Technology, and Xilin Lu, Tongji University. The writers acknowledge financial support provided by the Japan Science and Technology Agency (JST) and National Natural Science Foundation of China (NSFC). Special thanks are given to the working group members, Kazuhiro Matsuda, Mitsumasa Midorikawa, Linhai Peng, Chao Zhang, Ruifu Zhang, and Shiming Zhang, for their advice and asssitance.

REFERENCES

JSSI Manual 2nd Edition (2005, 2007), *Design and Construction Manual for Passively Controlled Buildings*, Japan Society of Seismic Isolation (JSSI), Tokyo, JAPAN, 1st Ed., 405 pages, 2003, 2nd Ed., 515 pages, 2005, 2nd Ed. and 2nd Print, 509 pages, 2007 (in Japanese)

JSSI Manual, Chinese Translation (2008), *Design and Construction Manual for Passively Controlled Buildings*, Japan Society of Seismic Isolation (JSSI), China Architecture and Building Press, Beijing, China, 552 pages, (in Chinese)

Kasai, K., Fu, Y., and Watanabe, A., (1998) "Two Types of Passive Control Systems for Seismic Damage Mitigation." Journal of Structural Engineering, ASCE 122 [10], 501-512.

Kasai K., Ito H., and Watanabe A., (2003a), "Peak Response Prediction Rule for a SDOF Elasto-Plastic System Based on Equivalent Linearization Technique," *Journal of Structure and Construction Engineering*, No.571, pp.53~62, Sep. (in Japanese).

Kasai, K., Suzuki, A., and Oohara, K. (2003b), "Equivalent Linearization of a Passive Control System Having Viscous Dampers Dependent on Fractional Power of Velocity", *Journal of Structural and Construction Engineering*, AIJ, No. 574, 77-84 (in Japanese).

Kasai, K. and Ito, H., (2005), "Passive Control Design Method Based on Tuning of Equivalent Stiffness of Elasto-Plastic Damper", *J. Structural and Construction Eng., Trans. AIJ,* No.595, 45-55, Sep. (in Japanese)

Kasai K., Minato N., and Kawanabe Y., (2006) "Passive Control Design Method Based on Tuning of Equivalent Stiffness of Visco-Elastic Damper," *Journal of Structure and Construction*, No. 610, pp. 75-83, Dec. (in Japanese).

Kasai, K., Ogura, T., and Suzuki, A., (2007), "Passive Control Design Method Based on Tuning of Equivalent Stiffness of Nonlinear Visous Damper", J. Structural and Construction Eng., Trans.AIJ, No.618, 97-104, Aug. (in Japanese)

Kasai, K. Ito, H., and Ogura, T., (2008), "Passive Control Design Method Based on Tuning of Equivalent Stiffness of Bilinear Oil Damper", J. Structural and Construction Eng., Trans. AIJ, No.630, 1281-1288, Aug. (in Japanese)

Kasai K., Nishihara K., Pu W. et al., (2009) " Peak Response Evaluation Method for Slip-Hysteretic Structure Added with Visco-elastic Damper," *Journal of Structure and Construction Engineering*, No.646, pp.2227~2236, Dec. (in Japanese).

Kasai K. and Pu W., (2010a), " Passive Control Design Method for MDOF Slip-Hysteretic Structure Added with Visco-elastic Damper." *Journal of Structure and Construction Engineering*, No.650, pp.781~790, April (in Japanese).

Kasai K., Ogawa, R., Pu W., and Kiyokawa, T. (2010b), " Passive Control Design Method for Elasto-Plastic Frame Added with Visco-Elastic Damper." *Journal of Structure and Construction Engineering*, No.655, pp.1625~1634, Sep. (in Japanese).

Lu, X.L., Kasai, K., Weng, D.G., Pu, W., Zhou, Y., and Wada, A. (2011), "China-Japan (NSFC-JST) Research on Use of Dampers for Repair of RC Building Damaged During 2008 Wenchuan Earthquake. Part I : Analytical Simulation Based on Full-Scale Damper Tests," *Proceedings of the 8th International Conference on Urban Earthquake Engineering, March 7-8, 2011, Tokyo, Japan*.

Newmark, N.M. and Rosenblueth, E. , (1971) "Fundamentals of Earthquake Engineering." Prentice-Hall Inc..

PRC National Standard, (2010), "Code for Seismic Design of Buildings (GB 50011-2010)," issued by the Ministry of Housing and Urban-Rural Construction of the People's Republic of China, China Architecture & Building Press, Beijing, China.

Takeda T., Sozen M.A. and Nielsen N.N., (1970), "Reinforced concrete response to simulated earthquakes", Journal of Strucutral Division, ASCE, Vol.96, ST12, 2557 2573, Dec.

Weng, D. G. and Lu, X. L. (2004), "Study on Design Parameters of Energy Dissipation Structures with Experiment Verification", *Journal of Earthquake Engineering and Engineering Vibration*, **24**(2), 150-157.

Weng, D. G., Zhang, R. F., Zhang, S. M. and Lu, X. L. (2009), "Application of energy dissipation method based on seismic performance and demand for post-earthquake R.C. frame retrofit." *Proceeding of 11th World Conference on Seismic Isolation, Energy Dissipation and Active Vibration Control of Structures*.

Weng, D. G., Zhang, C. and Lu, X. L. (2011), "Application of Energy Dissipation Technology to C-category Frame Structure of School Buildings for Seismic Retrofit of Increasing Precautionary Intensity," *Journal of Advanced Materials Research*, 163-167, 3480-3487.

APPENDIX-I

The undamped MDOF system is firstly converted to an equivalent SDOF with equivalent height estimated by Eq. (7a). Time history analysis on SDOF system with increased damper is repeated until the target drift angle is achieved. Figure A1 shows two analysis models used for the SDOF system. In model A, the damper is added at the equivalent height H_{eff}=1889cm together with the spring denoting the stiffness of frame K_f. Obviously, the damper in SDOF system will experience deformation much larger than the actual deformation of dampers in MDOF system.

Due to the nonlinear viscosity, the damper obtained in such a way may not reflect the correct relationship between damper and frame. Therefore, a substituted Model B is used, where the frame stiffness and damper are added to a typical story height H_0 (360cm used in this study) of the original MDOF system, so that damper in the SDOF system experiences approximately the same deformation and velocity as those in the MDOF system at target drift angle θ_t (Figure A1).

It is noted that the displacement of spring of frame in Model B is reduced to be H_0/H_{eff} times, the force of SDOF frame is accordingly scaled up by multiplying it by H_{eff}/H_0. Namely, the stiffness of frame in Model B is set as Eq. (A1), while the equivalent periods of two systems without dampers remain equal.

$$K'_f = K_f (H_{eff}/H_0)^2 = M_{eff}\omega_{eq}^2 (H_{eff}/H_0)^2 \qquad \text{(A1)}$$

After the required values of C'_d, K'_d in Model B are determined by repeated time history analyses, the values of the equivalent C_d, K_d in Model A are estimated by Eq.(A2a) and (A2b), while $u_{d,max}$ keeps unchanged (Eq. (A2c)).

$$C_d = C'_d (H_{eff}/H_0)^2 \ , \ K_d = K'_d (H_{eff}/H_0)^2 \ ,$$

$$u_{d,\max} = u'_{d,\max} \qquad \text{(A2a-b)}$$

The obtained values of C_d, K_d, $u_{d,max}$ will be used in Eqs. (10) and (11). In the time history analysis, tangent stiffness proportional damping is used for the spring to simulate the frame, with damping ratio set to 5% at elastic state. Vibration period is 1.4 sec. These are consistent with the analysis of the MDOF system.

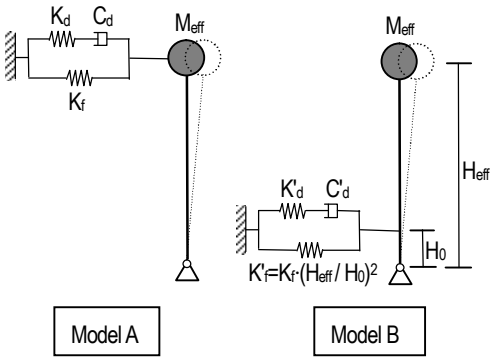


Figure A1. E uivalent SD F models used in time history analysis

8CUEE CONFERENCE PROCEEDINGS
8th International Conference on Urban Earthquake Engineering
March 7-8, 2011, Tokyo Institute of Technology, Tokyo, Japan

TORSIONAL VIBRATION CONTROL OF HIGH-RISING STRUCTURE WITH LARGE LOCAL SPACE BY USING BIDIRECTIONAL TMD

Bin Zhao[1], Hui Gao[2], and Xilin Lu[3]

1) Professor, State Key Laboratory of Disaster Reduction in Civil Engineering, Tongji University, Shanghai, P. R. China
2) Engineer, Central-south Architectural Design Institute Co. Ltd, Wuhan, P. R. China
3) Professor, State Key Laboratory of Disaster Reduction in Civil Engineering, Tongji University, Shanghai, P. R. China
binzh@tongji.edu.cn, gaohui831019 @163.com, lxlst@ tongji.edu.cn

Abstract: According to the shake table test results of a complex high-rising building with large local space, the dynamic characteristics of such structure are complex and the torsional mode becomes the first mode, while the torsional responses under earthquake excitation, especially of the floor just above the large local space, are very remarkable. Special measures are required for such structural system for maintaining its seismic safety. The bidirectional Tuned Mass Damper (TMD) is employed for reducing the torsional vibration of the high-rising building with large local space. The optimization of the TMD parameters, such as natural frequency, damping ratios and mass ratio, is performed. The time history analysis results indicate that the proposed bidirectional TMD is very effective in torsional vibration control.

1. INTRODUCTION

For some high-rising buildings, large local space is very useful for the special function needs, such as conference hall and hotel lobby. The high-rising structures with large local space obviously belong to complex irregular structural system which may suffer serious damages induced by the torsional vibration under earthquake condition. A shake table test on such structural system has been performed by Zhao et al. (2007) that indicate the dynamic characteristics are complex and the torsional mode has become the first mode of the structure. The torsional responses under earthquake excitation, especially of the floor just above the large local space, are quite remarkable and special measures are required for such structural system for maintaining its seismic safety.

During the past 30 years, several innovative passive and active control devices have been developed and constructed for reducing vibrations in structures caused by wind loads and earthquakes (Housner et al. 1997, Lu and Zhao 2003). Tuned Mass Damper (TMD) is an example of such devices, and their design has been a subject of much interest to researchers all over the world, with a wealth of theoretical and experimental work in the literature (Ankireddi and Yang 2000). A simple unidirectional TMD consists of a single mass m, connected to the structure by a viscous dashpot c and a linear spring k. The mass is constrained to move in one direction alone, and is usually most effective when the response of the structure is predominantly in the direction in which the damper can move. However, if the structural response is such that there is a very small component of its motion along the path of the damper, or a quite large component perpendicular to the path of the damper, or the structure is suffered large torsional responses, then the unidirectional TMD may not be very effective. For reducing the seismic responses of the complex building structures, such as the high-rising building structure with large local space, a bidirectional TMD system which is shown as Figure 1 may be applied.

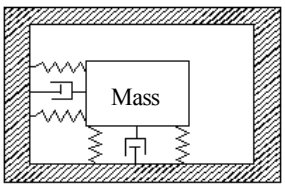


Figure1 Schematic diagram of the bidirectional TMD

In this paper, the seismic behavior and the torsional responses of a complex high-rising building with large local space are studied. A simple multi-floor building model is established and the bidirectional TMD system is employed to reduce the torsional responses of the structure under seismic condition. The numerical results indicate that the well-designed bidirectional TMD system is effective in reducing the torsional responses of the whole structure as well as the top of the large local space.

2. FORMULATION OF BUILDING WITH TMD

2.1 Mechanical Model of the Building

A sample multi-floor model of a building, shown as

Figure 2, is considered in this research. The mass of the structure is concentrated at the floors, which are linked by massless springs to represent horizontal and rotation stiffness of the walls and columns. Each floor has a mass center and a stiffness center, and the story has three degrees of freedom - the horizontal orthogonal translations along the x- and y-directions and the rotation.

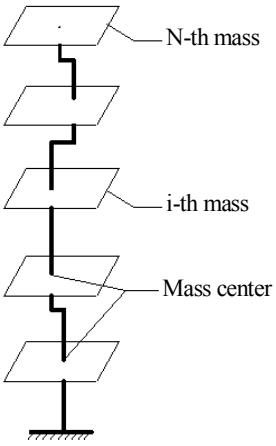


Figure 2 Schematic diagram of the building model

2.2 Equations of Motion of the Building with TMD

The equations of motion of the building in the presence of seismic forces is

$$[M]\{\ddot{D}\}+[C]\{\dot{D}\}+[K]\{D\}=-[M]\{\ddot{D}_g(t)\}+[H]\{U(t)\} \quad (1)$$

and the equation of motion of the TMD system is

$$[M_0]\{\ddot{D}_0\}+[C_0]\{\dot{\gamma}\}+[K_0]\{\gamma\}=-[M_0]\{\ddot{D}_g(t)\} \quad (2)$$

while the control forces can be expressed as

$$\begin{aligned}\{U(t)\} &= -[M_0](\{\ddot{D}_0\}+\{\ddot{D}_g(t)\}) \\ &= [K_0](\{D_0\}-\{D_i\})+[C_0](\{\dot{D}_0\}-\{\dot{D}_i\})\end{aligned} \quad (3)$$

where,

$$\{\gamma\}=\{D_0\}-\{D_i\},\{\dot{\gamma}\}=\{\dot{D}_0\}-\{\dot{D}_i\}$$

$$[K]=\begin{bmatrix}[K_{xx}] & [0] & [K_{x\varphi}]\\ [0] & [K_{yy}] & [K_{y\varphi}]\\ [K_{\varphi x}] & [K_{\varphi y}] & [K_{\varphi\varphi}]\end{bmatrix}_{3n\times 3n}$$

$$[C]=\begin{bmatrix}[C_{xx}] & [0] & [C_{x\varphi}]\\ [0] & [C_{yy}] & [C_{y\varphi}]\\ [C_{\varphi x}] & [C_{\varphi y}] & [C_{\varphi\varphi}]\end{bmatrix}_{3n\times 3n}$$

$$[M]=diag[[m]\ \ [m]\ \ [J]]$$

$$[C]=a[M]+b[K]$$

$$[C_0]=\begin{bmatrix}c_{dx} & \\ & c_{dy}\end{bmatrix},[K_0]=\begin{bmatrix}k_{dx} & \\ & k_{dy}\end{bmatrix},$$

$$c_{dx}=2m_0w_{dx}\xi_d,k_{dx}=m_0w_{dx}^2,$$

$$c_{dy}=2m_0w_{dy}\xi_d,k_{dy}=m_0w_{dy}^2$$

$[H]$ is the matrix defining the location of TMD, when TMD is setup on the i-th floor,

$$[H]=\begin{bmatrix}0 & \cdots 1 & \cdots\cdots 0 & \cdots l_y\cdots & 0\\ 0 & \cdots 0 & \cdots\cdots 1 & \cdots -l_x\cdots & 0\end{bmatrix}^T_{2\times 3n}$$

$$\begin{matrix}\vdots & \vdots & \vdots\\ i & n+i & 2n+i\end{matrix}$$

$[D_0]$ is displacement vector of the TMD,

$$[D_0]=\{x_0,y_0\}^T$$

$[D_i]$ is the displacements of i-th floor,

$$[D_i]=\{x_i+l_y\cdot\varphi_i,y_i-l_x\cdot\varphi_i\}^T$$

where, l_x and l_y indicate the distances between the floor mass center and the TMD in x and y directions.

Then, the general equations of motion of the building with TMD can be expressed as

$$[M^*]\{\ddot{D}^*\}+[C^*]\{\dot{D}^*\}+[K^*]\{D^*\}=-[M^*]\{\ddot{D}_g^*(t)\} \quad (4)$$

where, $[M^*]$, $[K^*]$ and $[C^*]$ are the combined mass, stiffness and damping matrixes, and $[D^*]$ is the combined displacement vector.

$$[M^*]=diag[[m]\ \ [m]\ \ [J]\ \ \ [M_0]]$$

$$[K^*]=\begin{bmatrix}[K^*_{xx}] & [0] & [K^*_{x\varphi}] & \\ [0] & [K^*_{yy}] & [K^*_{y\varphi}] & [K_{c\infty}]\\ [K^*_{\varphi x}] & [K^*_{\varphi y}] & [K^*_{\varphi\varphi}] & \\ & [K_{c\infty}]^T & & [K_0]\end{bmatrix}_{(3n+2)\times(3n+2)}$$

$$[K_{c\infty}]=-[H][K_0]$$

In which $[K^*_{xx}]$ and $[K^*_{yy}]$ are turn out from $[K_{xx}]$ and $[K_{yy}]$ by adding k_{dx} and k_{dy} to their i-th diagonal element, respectively. $[K^*_{\varphi\varphi}]$ is turn out from $[K_{\varphi\varphi}]$ by adding $(l_y^2k_{dx}+l_x^2k_{dy})$ to its i-th diagonal element. $[K^*_{x\varphi}]$ and $[K^*_{y\varphi}]$ are turn out from $[K_{x\varphi}]$ and $[K_{y\varphi}]$ by adding $l_y\cdot k_{dx}$ and $-l_x\cdot k_{dy}$ to their i-th diagonal element, respectively. Take $[K^*_{\varphi\varphi}]$ as an example, its formation procedure is shown as

$$\left[K^*_{\varphi\varphi}\right]=\begin{bmatrix} k_{\varphi 11} & -k_{\varphi 12} & & & & & \\ -k_{\varphi 21} & k_{\varphi 22} & -k_{\varphi 23} & & & & \\ & \ddots & \ddots & & & & \\ & & -k_{\varphi i(i-1)} & k_{\varphi ii}+(l_y^2k_{dx}+l_x^2k_{dy}) & -k_{\varphi i(i+1)} & & \\ & & \ddots & \ddots & \ddots & & \\ & & & -k_{\varphi(n-1)(n-2)} & k_{\varphi(n-1)(n-1)} & -k_{\varphi(n-1)n} & \\ & & & & -k_{\varphi n(n-1)} & k_{\varphi nn} & \end{bmatrix}$$

The combined damping matrix $[C^*]$ follows the same formation of the matrix $[K^*]$.

In the state space, Eq. 4 becomes

$$\dot{Z}(t)=AZ(t)+B\ddot{D}^*_g(t) \tag{5}$$

where

$$Z(t)=\begin{bmatrix} D^*(t) \\ \dot{D}^*(t)\end{bmatrix}_{1\times 2(3n+r)}$$

$$A=\begin{bmatrix} 0 & I_{3n+r} \\ -\left[M^*\right]^{-1}\left[K^*\right] & -\left[M^*\right]^{-1}\left[C^*\right]\end{bmatrix}_{2(3n+r)\times 2(3n+r)}$$

$$B=\begin{bmatrix} 0 \\ -E\end{bmatrix}_{2(3n+r)\times(3n+r)}$$

$$E=\begin{bmatrix} I_{n\times 1} & 0 & 0_{n\times 1} & 1 & 0 \\ 0 & I_{n\times 1} & 0_{n\times 1} & 0 & 1\end{bmatrix}^T$$

$$\ddot{D}^*_g=\begin{bmatrix}\ddot{d}_{gx} \\ \ddot{d}_{gy}\end{bmatrix}$$

3. MODELING OF A HIGH-RISING STRUCTURE WITH LARGE LOCAL SPACE

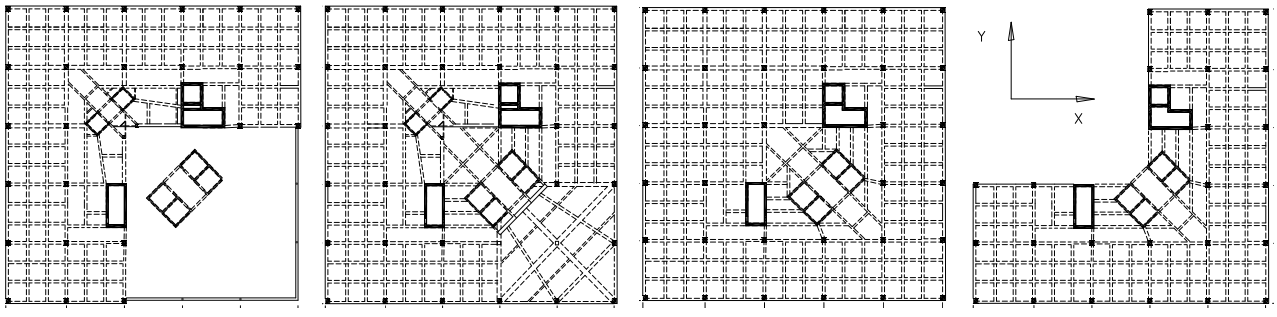
A typical high-rising building with large local space (Zhao et al. 2007) is used for verification of the strategy of using bidirectional TMD system to reduce the torsional responses of the structure under seismic excitation. The prototype is a 18-story building with totally height of 98 m, while the height of the first, fourth, ninth and tenth story reach 8.4 m, the height of the top story is 5.8 m and the other story with height of 4.2 m. The plan size of the structure is 44 m × 44 m, through deleting some columns of the lowest 4 stories, a 26.3 m × 26.3 m large hall is turn out at a corner of the building. Above the tenth floor, some opposite columns are also deleted which forms a series of L- type floors. The general plan layout of the structure is given in Figure 3. Obviously, the mass and stiffness center of lower and higher part of the structure are far away from the vertical axis.

The multi-floor model of the building can be achieved through a response spectrum analysis on its 3-D structural model (He 2008). All the parameters of the established multi-floor model are listed in Table 1 (Gao 2010).

The mode analysis is carried out and the period, direction factor and mass participation factor of the first 6 modes are listed in Table 2. The pattern of the first mode is rotation which is exactly in accordance with the test result (Zhao et al. 2007). One can also find that the rotation component is very remarkable and the rotation factors of mode number 3, 4, 5 and 6 are equal to or greater than 30%. Under earthquake condition, the structure will suffer large torsional displacements.

4. DESIGN OF THE BIDIRECTIONAL TMD

According to the plan layout of the building, there are three options to setup the bidirectional TMD system: (1) To hang the TMD at the top of the large local hall - fourth floor; (2) To put the TMD at the vertical layout changing location – ninth floor; or (3) to put the TMD on the top floor of the structure – eighteenth floor. Physically, it is more convenience to choose option (2) and (3), both the tenth floor and eighteenth floor can provide ideal space holding the TMD. From the original objective of reducing the torsion responses of the structure, mainly the torsion responses at the top of the large local hall, option (2) has been chosen and the TMD is set up on the ninth floor.



(a) Floor 1 to 4 (b) Floor 5 (c) Floor 6 to 9 (d) Floor 10 to 18

Figure 3 Plan layout of the structure

Table 1 Parameters of the building model

Floor	Mass (kg)	Moment of inertia(kg× m× m)	Coordinate of the mass center (m)		Horizontal stiffness (N/m)		Rotational stiffness (N× m/rad)
			X	Y	X	Y	
1	1.95E+06	7.48E+08	18.171	26.303	2.92E+09	2.214E+09	1.03E+12
2	1.75E+06	6.79E+08	17.676	26.546	4.12E+09	3.976E+09	1.33E+12
3	2.53E+06	9.19E+08	17.910	26.280	3.54E+09	3.572E+09	1.21E+12
4	4.50E+06	1.92E+09	23.551	20.353	1.60E+09	1.565E+09	5.03E+11
5	2.60E+06	1.07E+09	22.043	22.099	2.69E+09	2.988E+09	8.89E+11
6	2.50E+06	1.03E+09	22.290	21.898	2.28E+09	2.450E+09	7.40E+11
7	2.41E+06	8.71E+08	24.696	19.439	2.03E+09	2.108E+09	6.66E+11
8	2.57E+06	1.32E+09	22.380	21.642	1.89E+09	1.891E+09	7.60E+11
9	3.01E+06	1.53E+09	23.108	21.044	1.18E+09	8.278E+08	3.33E+11
10	2.23E+06	8.26E+08	26.452	17.831	1.02E+09	7.628E+08	3.35E+11
11	1.71E+06	6.08E+08	26.604	17.727	1.56E+09	1.476E+09	6.24E+11
12	1.67E+06	5.93E+08	26.749	17.878	1.55E+09	1.411E+09	7.34E+11
13	1.64E+06	6.50E+08	26.575	17.654	1.56E+09	1.345E+09	6.18E+11
14	1.64E+06	6.50E+08	26.575	17.654	1.52E+09	1.270E+09	7.20E+11
15	1.64E+06	6.50E+08	26.575	17.654	1.45E+09	1.163E+09	6.52E+11
16	1.67E+06	6.53E+08	26.551	17.700	1.30E+09	1.012E+09	6.55E+11
17	1.94E+06	7.27E+08	26.511	17.802	1.05E+09	7.942E+08	7.07E+11
18	1.85E+06	7.02E+08	26.633	17.643	4.44E+08	3.234E+08	3.16E+11

Table 2 Mode analysis result of the established model

Mode No.	Period (s)	Direction factor			Mass participation factor		
		X	Y	Rotation	X	Y	Rotation
1	2.71	25.5%	23.9%	50.6%	17.9%	15.9%	39.0%
2	2.38	27.4%	68.8%	3.8%	20.1%	50.8%	3.0%
3	2.10	47.4%	7.8%	44.8%	36.8%	6.4%	32.9%
4	0.98	11.7%	58.3%	30.0%	1.3%	9.2%	6.8%
5	0.96	25.9%	41.2%	33.0%	3.3%	7.8%	4.6%
6	0.87	62.7%	0.9%	36.4%	10.1%	0.2%	4.0%

Generally, the frequency of the TMD system should be set to the main frequency of the controlled structure (Zhang 2007). For such complex structure, according to the mode analysis result which is listed in Table 2 and the objective of torsion response control, the frequency in x-direction of the TMD system is defined as 0.48 Hz (the frequency of Mode No. 3) while the frequency in y-direction is defined as 0.37 Hz (the frequency of Mode No. 1).

5. NUMERICAL ANALYSIS

Based on the equation of motion of the building with TMD of the Eq. 5, a program is developed to assess the effect of the bidirectional TMD system on torsion responses reduction of the seismically excited structure.

5.1 Assessment Index

In order to consider the overall effect of the torsion response reduction under different earthquake waves, a common control ratio is defined as

$$\eta = \sum_{i=1}^{i=n} \eta_i / n \,, \quad \eta_i = (U_i^o - U_i^c)/U_i^o$$

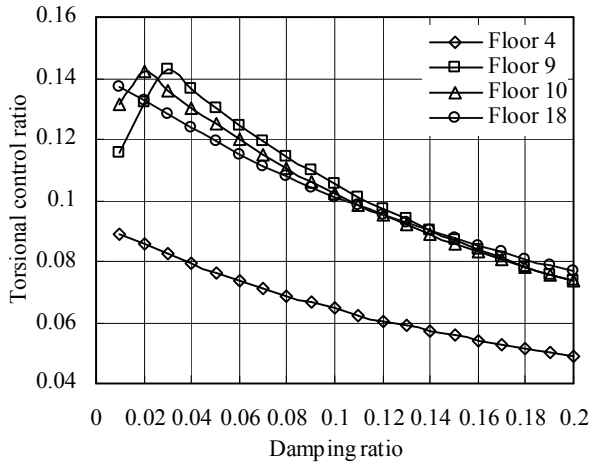
where, U_i^o is the maximum response of the un-controlled structure under i-th earthquake wave and U_i^c is the maximum response of the structure with TMD system.

5.2 Numerical Result

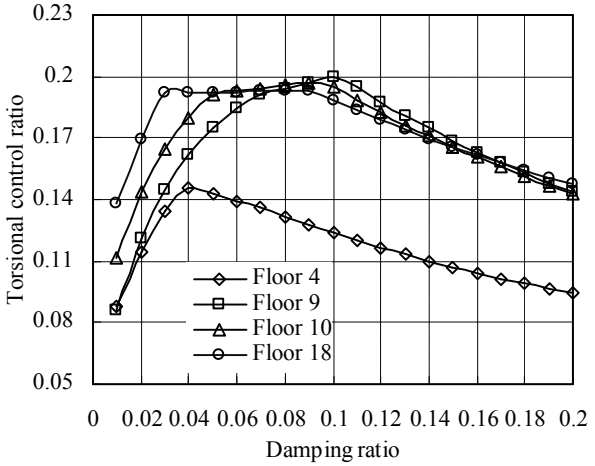
The widely used El Centrol and Talf earthquake records and an artificial earthquake wave are chosen as the input ground accelerations for the numerical analyses. The peak accelerations of the waves are adjusted to 0.2 g. The relationship of the rotation control ratios and the TMD damping ratios with different TMD mass ratio of 0.005, 0.01, 0.015, 0.02, 0.025 and 0.03 are given as Figure 4. From these diagrams, it is easy to find that the rotation control ratios increase as the TMD mass ratio increase from 0.005 to 0.03. But when the mass ratio is greater than 0.01, the rotation control ratio increase is only about 4% as mass ratio increase of each 0.005. The optimal damping ratio increase as the mass ratio becomes large, and the control effect

changes gently when the damping ratio greater than the optimal damping ratio.

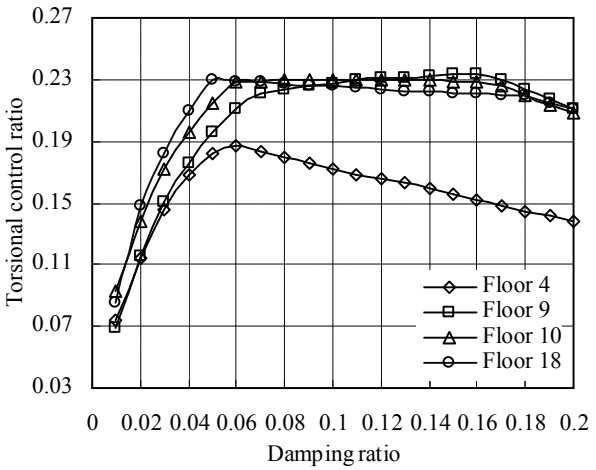
As mentioned before, the sample way for determining the TMD parameters is to set its frequencies in both x- and y-direction equaling the first frequency of the structure. The relationship of the rotation control ratios and the TMD damping ratios with different TMD mass ratio of 0.01 and 0.02 are given as Figure 5. Comparing Figure 5 with Figure 4 (b) and (d), one can find the above two modes control strategy is more effective than this first mode strategy.



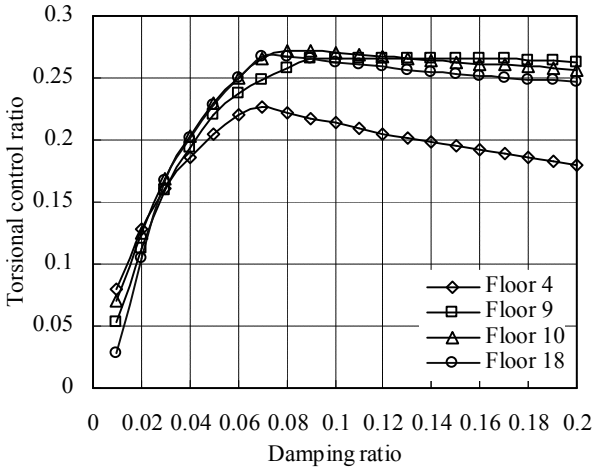
(a) TMD mass ratio=0.005



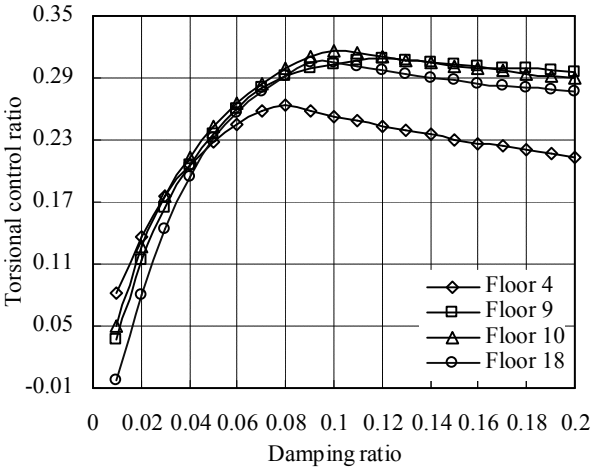
(b) TMD mass ratio=0.01



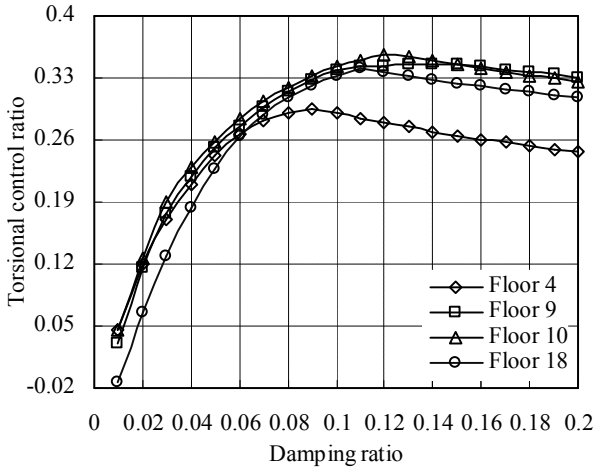
(c) TMD mass ratio=0.015



(d) TMD mass ratio=0.02

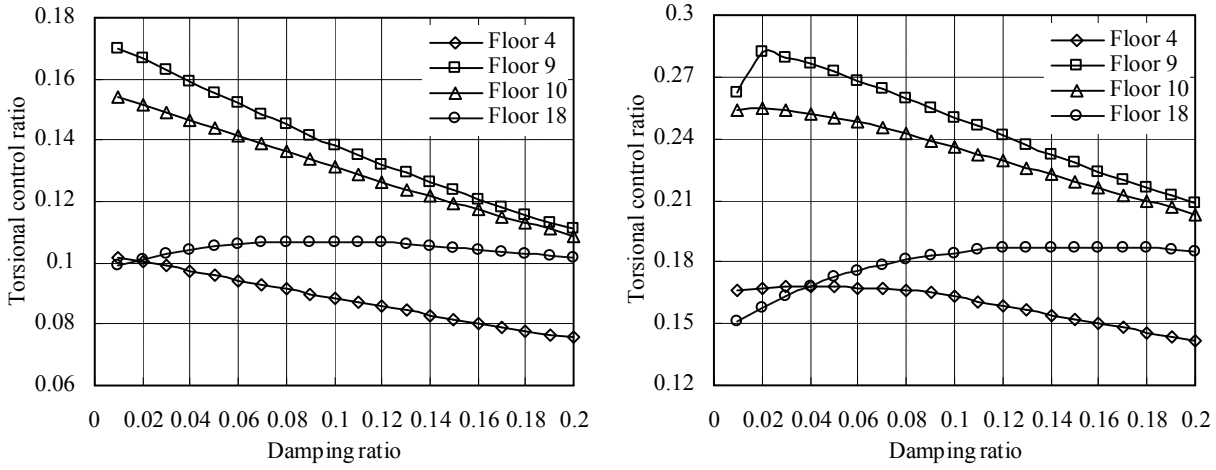


(e) TMD mass ratio=0.025



(f) TMD mass ratio=0.03

Figure 4 Relationship between torsional control ratio and damping ratio



(a) TMD mass ratio=0.01

(b) TMD mass ratio=0.02

Figure 5 Relationship between torsional control ratio and damping ratio

6. CONCLUSIONS

In this research, the seismic behavior, mainly the torsional responses and its control strategy, of a complex high-rising building with large local space are studied. The simple multi-floor building model is established and the bidirectional TMD system is applied to reduce the torsional responses of the structure under seismic condition. The numeric analyses indicate that:

(1) A well-designed bidirectional TMD system is very effective in reducing the torsional responses of the whole structure as well as the tope of the large local space.

(2) As the complex of the dynamic property of the highly irregular structure like high-rising building with large local space, different dynamic mode should be considered in the TMD parameter design, and an optimal combination of structural modes is more effective than the first mode control strategy.

Acknowledgements:

This research is sponsored by the National Natural Science Foundation of P. R. China under Grant No. 50678126.

References:

Ankireddi, S., Yang, H. T. Y. (2000), "Directional Mass Dampers for Buildings under Wind or Seismic Loads". *Journal of Wind Engineering and Industrial Aerodynamics*, 85, 119-144.

Gao, H. (2010), "The Research of Torsional Response Control of Tall Building with Large Local Space", *A Dissertation Submitted to Tongji University for the Master's Degree.*

He, S. (2008), "Seismic Vulnerability of Complex High-rise Building with Large Local Space", *A Dissertation Submitted to Tongji University for the Master's Degree.*

Housner, G. W., Bergman, L. A., Caughey, T. K., et al (1997), "Structural Control: Past Present, and Future", *ASCE Journal of Engineering Mechanics, 123(9), 897-971.*

Lu X., and Zhao, B. (2003), "Recent Advance in Structural Control Research and Application in China Mainland", *Earthquake Engineering and Engineering Vibration*, 2(1), 117-132.

Zhang, M. (2007), "Seismic Analysis and Vibration Reduction Control", *Xinan Jiaotong University Press*.

Zhao, B., Lu X., Lu, W. and Zhang, Y. (2007), "Shake Table Experimental Study of Complex High-rising Building with Large Local Space". *Journal of Building Structures*, 27(Sup), 1-7

8CUEE CONFERENCE PROCEEDINGS
8th International Conference on Urban Earthquake Engineering
March 7-8, 2011, Tokyo Institute of Technology, Tokyo, Japan

ACHIEVING ENHANCED SEISMIC PERFORMANCE OF TALL BUILDINGS THROUGH BASE ISOLATION

Troy A. Morgan[1] and Kazuhiko Kasai[2]

1) Assistant Professor, Center for Urban Earthquake Engineering, Tokyo Institute of Technology, Japan
2) Professor, Structural Engineering Research Center, Tokyo Institute of Technology, Japan
morgan@cuee.titech.ac.jp, kasai@serc.titech.ac.jp

Abstract: The design of tall buildings in Japan have recently incorporated seismic isolation systems as a means of providing enhances seismic protection. Whereas seismic isolation has traditionally been applied to short, stiff structures, several successful projects have demonstrated the viability of seismic isolation for tall buildings. However, a general methodology describing an approach for selecting appropriate isolation system parameters given a range of superstructural characteristics has yet to be developed. In this paper, a procedure for generating an equivalent viscoelastic system to describe a tall isolated building is described. In this procedure, the problem of a significant non-proportionally damped multi-DOF structure is overcome by introducing an assumption of steady-state vibration combined with a correction to account for the difference in peak velocity compared to peak pseudo-velocity. Analysis of a wide range of isolated building models indicates excellent agreement between response prediction from response history analysis of the non-proportionally damped model and the proposed spectrum-based equivalent viscoelastic analysis. A methodology is proposed to select optimal isolation system period and damping given a superstructure height, seismic intensity, and acceptance criteria for drift and isolator displacement.

1. INTRODUCTION

Recent trends in urban planning have led to the development of high-density residential and commercial areas. Due to limitations in available space, tall buildings must be constructed to accommodate such high-density areas. Given the large number of occupants in these tall buildings, combined with the financial significance of organizations which inhabit them, the consequences of damage due to a seismic event must be carefully assessed. In the past 25 years, seismic isolation has been applied worldwide to achieve enhanced seismic performance in structures subjected to earthquakes. There have been recent applications of seismic isolation technology to tall, flexible building in Japan [Ariga, et al. 2006, Kani 2009, Miyazaki 2009]. Given this trend, there has been recent research dedicated to examining the behavior of tall buildings with seismic isolation systems [Takewaki 2007, Takewaki and Fujita 2009.]

Traditionally, base isolation has been seen as applicable only to short, stiff structures. For tall, flexible structures, the period is already longer than the predominant period of most ground motions. Therefore, it is assumed that the addition of an isolation system is ineffective for the enhancement of seismic performance. However, the addition of an isolation layer can alter the mode shape such that a significant portion of the deformation response is concentrated in the isolations system rather than the supported structure. Since there is very little information about the behavior of tall or flexible structures on isolation systems, it is necessary to develop robust design methodologies to target desired levels of performance.

2. DEFINITION OF PARAMETERS

To develop equations of motion for generic 2-DOF isolated structures, a coordinate system must be chosen. Since relative deformations of the superstructure and isolation system are of primary interest, equations of motion are expressed using relative deformations. Relative to some fixed reference frame, let the ground displacement, isolation level displacement, and structural displacement be u_g, x_b, and x_s, respectively. Here we define the isolator displacement as $u_b = x_b - u_g$ and the structural displacement as $u_s = x_s - x_b$. We also define the mass at the isolator and structure level as m_b and m_s, respectively. Between the ground and base mass, the isolation system is represented as a Kelvin element having spring stiffness k_b and linear viscous damping coefficient c_b. Between the base mass and superstructure mass, a second Kelvin element with spring stiffness k_s and linear viscous damping coefficient c_s is defined to represent the superstructure. The 2-DOF structure with the above parameters is depicted in Figure 1.

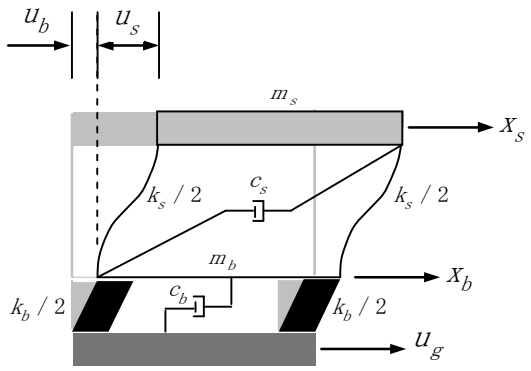


Figure 1: Definition of parameters for 2-DOF isolated structure

With these definitions, it is possible to develop the equations of motion for this system subjected to some ground acceleration $\ddot{u}_g$. First, it is convenient to define a mass ratio $\gamma = m_s / (m_s + m_b)$, which tends to unity at the superstructure mass becomes very large compared to the base mass. Additionally, it is useful to define the natural frequencies of the isolation system and the superstructure. The squares of the natural frequencies of the isolation system and superstructure, ω_b^2 and ω_s^2 are defined as

$$\omega_b^2 = \frac{k_b}{m_s + m_b}, \quad \omega_s^2 = \frac{k_s}{m_s} \tag{1}$$

Notice that ω_b is the natural frequency of the isolated structure assuming the superstructure is infinitely rigid. This definition follows that of modern building codes (e.g. ASCE-7, 2005.) Similarly, we can define critical viscous damping ratios for the isolation system and superstructure as

$$\zeta_b = \frac{c_b}{2(m_s + m_b)\omega_b}, \quad \zeta_s = \frac{c_s}{2m_s\omega_s} \tag{2}$$

3. VISCOELASTIC REPRESENTATION

In order to develop an equivalent SDOF system which may be used to estimate the response of the previously-described 2DOF structure, a steady-state response approach is taken. For tall isolated buildings, the superstructure mass will be much larger than the base mass, which implies that γ approaches unity. If the superstructure mass m_s is assumed to be much larger than the base mass m_b (i.e. $\gamma \to 1$), the isolated structure may be represented by a viscoelastic (VE) system subjected to some forcing function f, as shown in Figure 2. All other definitions remain as defined above, except the damping ratio of the superstructure, ζ_s, is assumed negligible compared to that of the isolation system, and is therefore assumed to be zero.

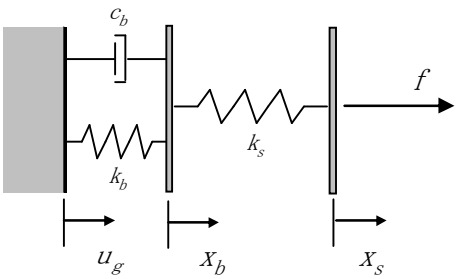


Figure 2: Viscoelastic representation of isolated 2DOF structure

We define the displacement of the equivalent system as $u = x_s - u_g$, which could be expressed equivalently as $u = u_b + u_s$. Suppose that the response of the equivalent system is described by

$$u = u_0 \sin \omega_{eq} t \tag{3}$$

Where u_0 is the maximum displacement response and ω_{eq} is some frequency of excitation of the equivalent VE system. With no loss of generality, we assume the mass of the equivalent VE system is equal to unity. As a result, the total mass-normalized force f acting on the system can be described by either the isolation system force f_b as

$$f = f_b = \omega_b^2 u_b + 2\zeta_b \omega_b \dot{u}_b \tag{4}$$

or the superstructure force f_s as

$$f = f_s = \omega_s^2 u_s \tag{5}$$

The individual component deformations may be expressed as

$$u_b = \frac{f - 2\zeta_b \omega_b \dot{u}_b}{\omega_b^2}, \quad u_s = \frac{f}{\omega_s^2} \tag{6}$$

Applying the relations $u = u_b + u_s$ and $\dot{u} = \dot{u}_b + \dot{u}_s$, the deformation u is given by

$$u = \frac{f - 2\zeta_b \omega_b (\dot{u} - \dot{u}_s)}{\omega_b^2} + \frac{f}{\omega_s^2} \tag{7}$$

Substituting $u = u_0 \sin \bar{\omega} t$, $\dot{f} = \omega_s^2 \dot{u}_s$, and applying algebraic manipulation leads to the following first-order differential equation

$$f\left(\frac{\omega_b^2 + \omega_s^2}{\omega_b^2 \omega_s^2}\right) + \dot{f}\left(\frac{2\zeta_b}{\omega_b \omega_s^2}\right) = u_0 \sin \omega_{eq} t + u_0 \omega_{eq} \left(\frac{2\zeta_b}{\omega_b}\right) \cos \omega_{eq} t \tag{8}$$

It can be shown that the solution to this differential equation is given by

$$f = \left(\frac{\omega_s^2 \omega_b^2}{\omega_b^2 + \frac{\omega_s^2}{\Gamma}} \right) u_0 \sin \omega_{eq} t + \left\{ \frac{\omega_s^2 \omega_b^2 \eta_b}{\left(\omega_b^2 + \frac{\omega_s^2}{\Gamma} \right) \left[1 + \frac{\omega_b^2}{\omega_s^2} \left(1 + \eta_b \right)^2 \right]} \right\} u_0 \cos \omega_{eq} t \tag{9}$$

Where the loss factor $\eta_b = 2\zeta_b$ and the non-dimensional parameter Γ is defined as

$$\Gamma = 1 + \frac{\omega_s^2 \eta_b^2}{\omega_s^2 + \omega_b^2} \tag{10}$$

In general, the total force in the equivalent VE system undergoing stead-state vibration can be described as

$$f = k'_{eq} u_0 \left(\sin \omega_{eq} t + \eta_{eq} \cos \omega_{eq} t \right) \tag{11}$$

where k'_{eq} is the storage stiffness and η_{eq} is the loss factor. Here, we introduce a term to account for the inexact assumption of steady state response for a system subjected to earthquake excitation. Under steady-state response, the peak velocity of the system can be computed through differentiation as

$$\dot{u}_0 = \max \left[\dot{u}(t) \right] = \omega_{eq} u_0 \tag{12}$$

This definition follows that of the peak pseudo-velocity (Chopra, 2007) where u_0 is the peak earthquake displacement response of an SDOF oscillator having natural frequency ω_{eq}. However, the damping force is related to the actual velocity, whose peak is generally not equal to the peak pseudo-velocity. For some ground motion excitation, we define a correction term

$$\alpha_v = \frac{\dot{u}_0}{\omega_{eq} u_0} \tag{13}$$

where u_0 and $\dot{u}_0$ are the peak displacement and velocity at frequency ω_{eq}, respectively. The correction term α_v is generally a function of frequency and damping, and varies depending on the ground motion under consideration. Using the relationship $\dot{u}_0 = \alpha_v \omega_{eq} u_0$, the corrected force in the VE system is described by

$$f = k'_{eq} u_0 \left(\sin \omega_{eq} t + \eta_{eq} \alpha_v \cos \omega_{eq} t \right) \tag{14}$$

An important observation is that the maximum force in the VE system can be expressed as

$$f_{\max} = k'_{eq} u_0 \sqrt{1 + \eta_{eq}^2 \alpha_v^2} \tag{15}$$

The derived force from Eq. (9) can be expressed in the same form as Eq. (15) where

$$k'_{eq} = \frac{\omega_s^2 \omega_b^2}{\omega_b^2 + \frac{\omega_s^2}{\Gamma}}, \quad \eta_{eq} = \frac{\eta_b}{\left[1 + \frac{\omega_b^2}{\omega_s^2} \left(1 + \eta_b \right)^2 \right]} \tag{16}$$

Therefore, the equivalent VE representation of the 2DOF isolated structure undergoing steady-state vibration is described by the parameters k'_{eq} and η_{eq}. From this we can conclude that the natural frequency of the equivalent system is given by $\omega_{eq} = \sqrt{k'_{eq}}$, or

$$\omega_{eq} = \sqrt{\frac{\omega_b^2 \omega_s^2}{\omega_b^2 + \frac{\omega_s^2}{\Gamma}}} \tag{17}$$

Similarly, the viscous damping ratio of the equivalent system can be computed by recognizing that the critical damping $\zeta_{eq} = \eta_{eq} / 2$, or

$$\zeta_{eq} = \frac{\zeta_b}{1 + \left[\frac{\omega_b}{\omega_s} \left(1 + 2\zeta_b \right) \right]^2} \tag{18}$$

The relationship of the equivalent period $T_{eq} = 2\pi / \omega_{eq}$ and the equivalent damping ζ_{eq} to the isolation period T_b for various fixed-base periods T_s and isolation damping ζ_b is shown below in Figure 3.

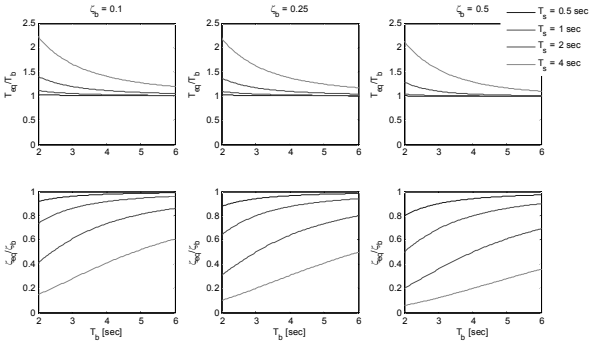


Figure 3: Equivalent period T_{eq} and equivalent damping ζ_{eq} as a function of isolation period T_b

With these definitions, it is possible to analyze an equivalent SDOF system subject to earthquake ground motion, and obtain an estimate for the maximum displacement response u_0. However, it is important that the individual displacements of the isolation system and superstructure are captured from this equivalent analysis. Therefore, a procedure is needed to extract u_{b0} and u_{s0} from the computed u_0. Suppose the steady-state isolator displacement is described by $u_b = u_{b0} \sin \omega_{eq} t$. Substituting u_b and its derivative into Eq. (4), the maximum force developed in the isolation system is

$$f_{b\max} = u_{b0} \sqrt{\omega_b^4 + 4\alpha_v^2 \zeta_b^2 \omega_b^2 \omega_{eq}^2} \tag{19}$$

Noting $f_{b\max} = f_{\max}$ and solving for u_{b0} gives

$$u_{b0} = u_0 \frac{\omega_{eq}^2}{\omega_b^2} \sqrt{\frac{1+4\alpha_v^2\zeta_{eq}^2}{1+4\alpha_v^2\zeta_b^2\left(\frac{\omega_{eq}^2}{\omega_b^2}\right)}} \tag{20}$$

Similarly, we let $u_s = u_{s0}\sin\omega_{eq}t$ and substitute $f_{s\max} = f_{\max}$ from Eq. (15) into Eq. (19) to obtain

$$u_{s0} = u_0 \frac{\omega_{eq}^2}{\omega_s^2}\sqrt{1+4\alpha_v^2\zeta_{eq}^2} \tag{21}$$

With these definitions, it is straight-forward to estimate the peak deformation in both the isolator and superstructure based on a ground motion displacement spectrum developed for a damping level of ζ_{eq}.

4. TRANSFORMATION OF NDOF TO 2DOF

To conduct realistic analytical simulations, a procedure is needed to convert a generic *N*-story building to an idealized 2DOF structure. The necessary properties for the 2DOF system are: number of stories *N*, superstructure period T_s, superstructure damping ratio ζ_s, isolation period T_b, isolation damping ratio ζ_b, and mass ratio γ. It is necessary to make some assumption regarding T_s based on *N*, so the well-known approximation $T_s = 0.1N$ is made here. Therefore, assuming equal floor weights, the mass ratio γ can be expressed as $\gamma = (N-1)/N$. This idealization is described below in Figure 4.

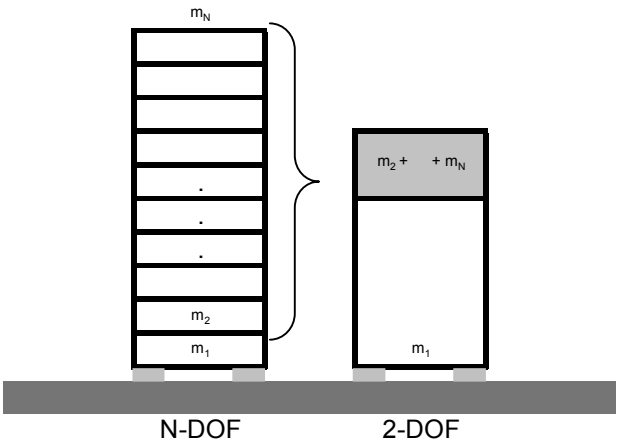


Figure 4: Description of the idealization of N-story building to a 2DOF structure

Given the assumptions of T_s, ζ_s, T_b, and ζ_b, we can define the properties of the 2DOF system, shown in detail in Figure 1, as follows. For the superstructure, the spring stiffness k_s and damping coefficient c_s are computed as

$$k_s = \left(\frac{2\pi}{T_s}\right)^2 \sum_{i=2}^{N} m_i, \quad c_s = 2\zeta_s\left(\frac{2\pi}{T_s}\right)\sum_{i=2}^{N} m_i \tag{22}$$

Similarly, for the isolation level, the spring stiffness k_b and damping coefficient c_b are computed as

$$k_b = \left(\frac{2\pi}{T_b}\right)^2 \sum_{i=1}^{N} m_i, \quad c_b = 2\zeta_b\left(\frac{2\pi}{T_b}\right)\sum_{i=1}^{N} m_i \tag{23}$$

These parameters are sufficient to characterize the 2DOF system for response history analysis.

5. GROUND MOTIONS

To both facilitate the development of statistical descriptions of demand and to consider a variety of seismic characteristics, an ensemble of ground motions is selected to represent possible realizations of ground motion at a site. As part of the SAC Steel Project, several ensembles of ground motions were developed for the Los Angeles basin. Since the objectives of these studies is to identify demand parameter sensitivities to inputs having multiple frequencies of occurrence, three ground motions ensembles were selected. Each of the three ensembles contains 20 acceleration records, and were developed for return periods of 72-years, 475-years, and 2475-years. For further details of the development of the SAC ground motions, see Somerville et al. [1997.]

Figure 5 through Figure 7: Elastic response spectra for 2475-yr records (median shown bold) show the elastic response spectra for each ground motion for the 72-yr, 475-yr, and 2475-yr ensembles, respectively. Figure 8 shows a comparison of the median spectra for all three return periods, including an overlay of the USGS prescriptive spectra with best fit parameters. Best-fit parameters are determined by selecting S_{DS} and S_{D1} such that the error between the median spectrum and the USGS spectrum is minimized for both constant acceleration and constant velocity regions, for all three return periods.

A key ingredient of the VE analysis procedure described previously is a relationship that describes the ratio between peak velocity and peak pseudo-velocity, defines as α_v. While estimates of this ratio are available in the literature for the period range $0.1\,\text{sec} \le T \le 3\,\text{sec}$ (Kasai et al., 2009,) there is little information regarding its characteristics at long-periods of vibration, which are important for isolated tall buildings. For the purpose of estimating this parameter, linear least-squares regression analysis was performed using the SAC suite of ground motions and the following 6-parameter linear model for α_v:

$$\begin{aligned}\alpha_v(T,\zeta) &= \frac{\dot{u}_0}{\omega_{eq}u_0} \\ &= \beta_0 + \beta_1 T + \beta_2 T^2 + \beta_3\zeta + \beta_4\zeta^2 + \beta_5 T\zeta\end{aligned} \tag{24}$$

Where the input factors T and ζ are the period and damping of an SDOF oscillator. From this analysis, the following least-squares estimates were determined for each regression coefficient:

$$\begin{aligned}&\hat{\beta}_0 = 0.7062,\ \hat{\beta}_1 = 0.1186,\ \hat{\beta}_2 = 0.0265, \\ &\hat{\beta}_3 = 1.5101,\ \hat{\beta}_4 = -1.1248,\ \hat{\beta}_5 = 0.0334\end{aligned} \tag{25}$$

This equation defines the assumed relationship for $\alpha_y(T,\zeta)$ used in subsequent analyses, and is valid for the period range $2\,\text{sec} \le T \le 10\,\text{sec}$ and a damping range $0.02 \le \zeta \le 0.40$.

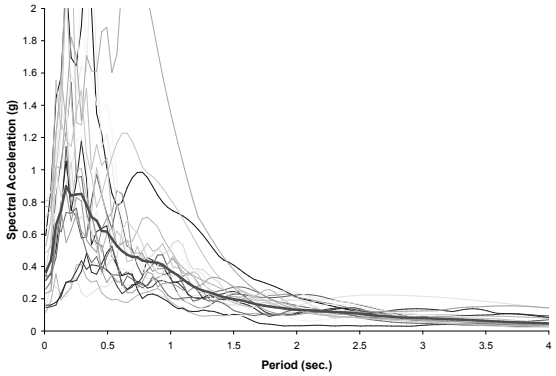


Figure 5: Elastic response spectra for 72-yr records (median shown bold)

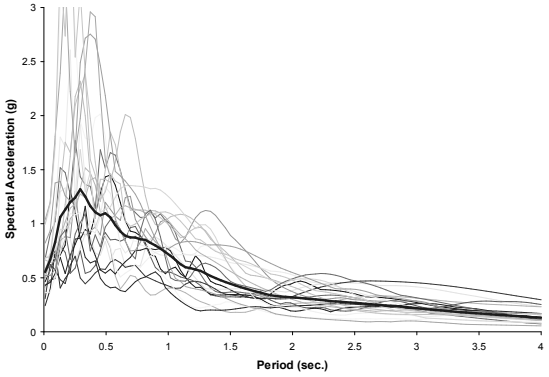


Figure 6: Elastic response spectra for 475-yr records (median shown bold)

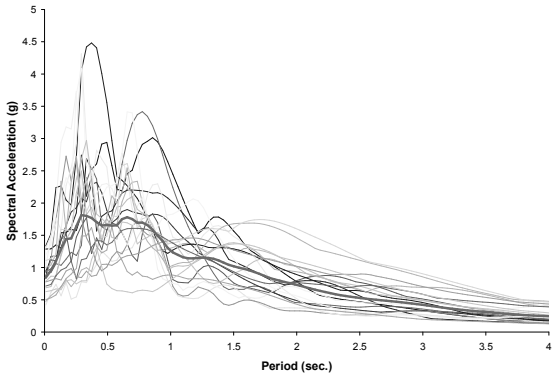


Figure 7: Elastic response spectra for 2475-yr records (median shown bold)

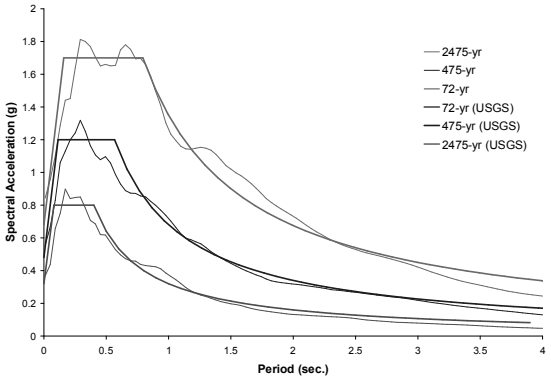


Figure 8: Median elastic response spectra for all three ground motion ensembles, including overlay of best-fit USGS prescriptive spectra

6. LINEAR 2DOF STUDIES

To study the accuracy of the equivalent VE analysis method presented previously, a comparison of displacement demands based on response spectrum and explicit response history analysis (RHA) is made. In the case of response history analysis, the 2DOF system with non-classical damping behavior is analyzed exactly through numerical integration using input earthquake acceleration records. The peak isolator displacement $\max\left[u_b(t)\right]$ and peak structural displacement $\max\left[u_s(t)\right]$ is computed for each of the 60 ground motions described. These peak deformations of the isolation system and superstructure are compared to those estimated by Eq. (20) and (21) based on the VE approximation and individual ground motion response spectra.

Figure 9 describes the response of a 2DOF structure having $T_b = 4$ sec, $T_s = 1$ sec (i.e. $N = 10$ stories.) It appears that, for both levels of isolation system damping ζ_b considered (10% and 25%) there is very close agreement between the 2DOF RHA and the equivalent SDOF analysis, with very little observable bias and dispersion.

Figure 10 through Figure 12 present similar response comparison data for 2DOF and SDOF analyses, but for superstructure periods $T_s = 2$, 3, and 4 sec ($N = 20$, 30, and 40 stories) respectively. It is clear that, as the superstructure period becomes longer, there is similar variation in the estimate of isolator displacement u_b and structural displacement u_s, with negligible bias and dispersion. The results presented here demonstrate that an accurate, response spectrum-based method of estimating isolator displacements and superstructural drift is feasible for tall, isolated buildings with a range of period and damping characteristics.

To investigate the accuracy of the proposed method for *all* SDOF systems studied, the statistical relationship between the exact and the estimated displacement response is described. Here we assume some linear relationship $u_{RHA} = \lambda u_{VE}$ where u_{RHA} is the exact displacement response computed from response history analysis and u_{VE}

is the same displacement response estimated from the proposed equivalent viscoelastic method. The slope parameter λ may be estimated using least-squares regression from the computed data for all 60 ground motion records. If we define $\hat{\lambda}$ as the least-squares estimate of the true slope $\lambda = u_{RHA} / u_{VE}$, then $\hat{\lambda} > 1$ indicates unconservative bias, $\hat{\lambda} < 1$ indicates conservative bias, and $\hat{\lambda} = 1$ indicates a lack of bias. The estimated slope parameters for both isolator and structural displacement are summarized for ζ_b = 10% and 25% in Table 1 and Table 2, respectively. This data demonstrates that the proposed method gives reliable estimates of both isolator displacement and superstructure drift for buildings having natural periods between 1 and 4 seconds (number of stories between 10 and 40) and isolation systems between 2 and 4 seconds for both levels of isolation system damping considered (ζ_b = 10% and 25%.) The estimates for isolator displacement show negligible unconservative bias ($\hat{\lambda} < 1.014$) and those for structural drift show low unconservative bias ($\hat{\lambda} < 1.070$.)

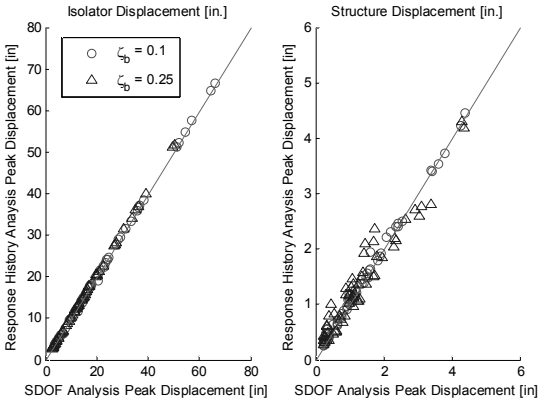


Figure 9: Response of moderately-damped 2DOF structures having $T_b = 4$ sec, $T_s = 1$

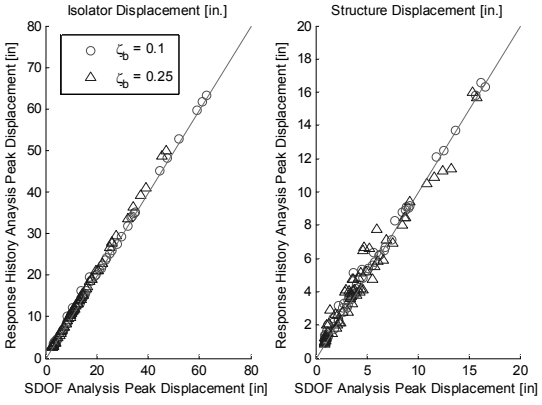


Figure 10: Response of moderately-damped 2DOF structures having $T_b = 4$ sec, $T_s = 2$

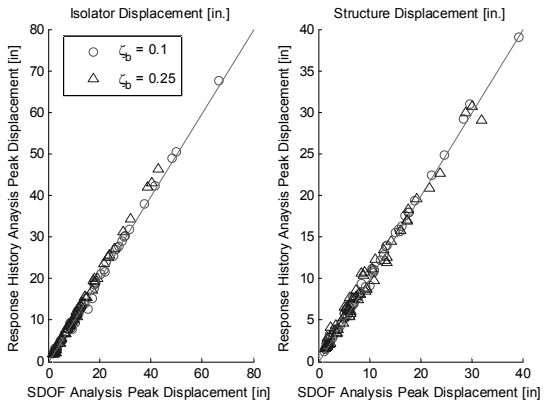


Figure 11: Response of moderately-damped 2DOF structures having $T_b = 4$ sec, $T_s = 3$

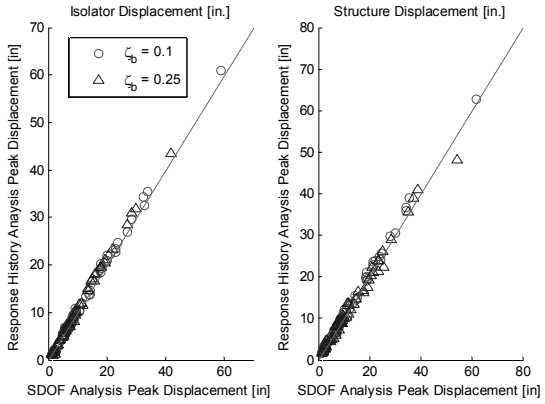


Figure 12: Response of moderately-damped 2DOF structures having $T_b = 4$ sec, $T_s = 4$

Table 1: Estimated slope parameter $\hat{\lambda}$ of isolator displacement and structural displacement regression lines between response history result and equivalent viscoelastic result for ζ_b = 10% (slope = 1.0 indicates lack of bias)

	Isolator Displacement			Structural Drift		
	$T_b = 2$ s	$T_b = 3$ s	$T_b = 4$ s	$T_b = 2$ s	$T_b = 3$ s	$T_b = 4$ s
$T_s = 1$ s	1.0043	1.0059	1.002	1.0329	1.0429	1.031
$T_s = 2$ s	0.9983	1.004	1.0037	1.0258	1.0346	1.0357
$T_s = 3$ s	0.9887	1.0009	0.9937	1.0227	1.0318	1.0314
$T_s = 4$ s	0.9456	0.9908	1.0129	0.9771	1.0211	1.0519

Table 2: Estimated slope parameter $\hat{\lambda}$ of isolator displacement and structural displacement regression lines between response history result and equivalent viscoelastic result for $\zeta_b = 25\%$ (slope = 1.0 indicates lack of bias)

	Isolator Displacement			Structural Drift		
	$T_b = 2$ s	$T_b = 3$ s	$T_b = 4$ s	$T_b = 2$ s	$T_b = 3$ s	$T_b = 4$ s
$T_s = 1$ s	0.9889	1.002	1.0127	1.0314	1.0568	1.0696
$T_s = 2$ s	0.9459	0.9927	1.0135	0.9819	1.0294	1.0665
$T_s = 3$ s	0.9297	0.9636	0.9858	0.9621	0.9875	1.0443
$T_s = 4$ s	0.9942	0.9558	0.9655	1.026	0.9948	1.0165

6. DESIGN METHODOLOGY

The preceding development of a simplified approach to estimating seismic demands on tall base isolated buildings can be extended to form a robust design methodology. Consider the task of selecting an isolation system for a tall building, subject to some limitations on seismic demand for one or several levels of ground shaking intensity. For a given level of seismic intensity, defined simply by the displacement spectrum, we can estimate the roof displacement of the fixed-base tall building. Additionally, from the same displacement spectrum adjusted to account for the effective damping computed by Equation (18), we can estimate both the displacement of the isolation layer and the roof displacement of the building relative to the isolation layer (the drift in the superstructure), from Equations (20) and (21), respectively. This is indicated graphically below in Figure 13. This corresponds to a 40 story building with an isolation system having a 4 second natural period, and 40% equivalent viscous damping. From this figure, it is clear how the introduction of an isolation layer, even where very little period shift is attained, leads to a significant reduction of story drift demand in the supported tall structure.

With these derived closed-form expressions for both peak interstory drift and peak isolator displacement, it is possible to map contours of each demand parameter as a function of two basic isolation system parameters: natural period T_b and viscous damping ratio ζ_b. Figure 14 shows how these contour plots may be constructed such that a permissible region of isolation system period and damping, (T_b, ζ_b), is defined for a given building height and particular earthquake return period. Such a tool is useful for preliminary design, with the performance of the final combination of structure and isolation system verified through nonlinear response history analysis.

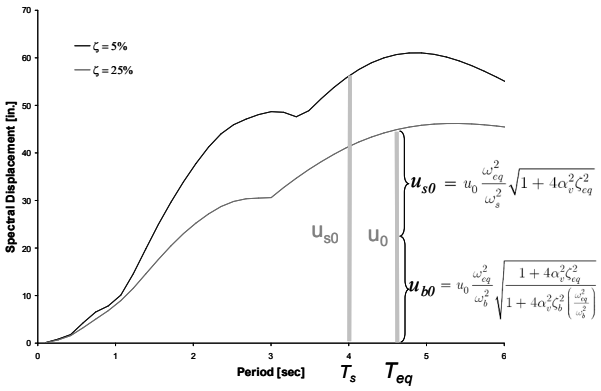


Figure 13: Response of moderately-damped 2DOF structures having $T_b = 4$ sec, $T_s = 4$

3. CONCLUSIONS AND FUTURE STUDIES

This study focuses on the response of isolated tall buildings subjected to seismic excitation. A methodology is described to convert a generic *N*-story isolated structure to an idealized 2DOF system using basic natural parameters such as isolation system period and damping, and superstructure period and damping. An equivalent viscoelastic SDOF system is derived in such a away to allow closed-form expressions for isolator and structure displacements given some earthquake response spectrum. This development is made tractable by letting the

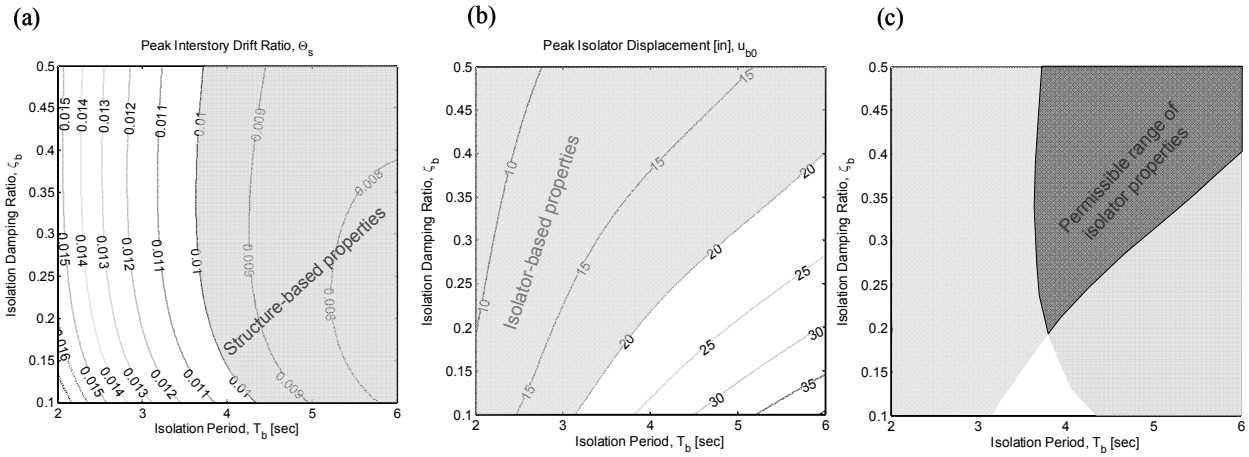


Figure 14: For a 40-story building subjected to DBE, permissible range of isolator properties based on (a) peak interstory drift ratio $\Theta_s \leq 0.01$, (b) peak isolator displacement $\underline{u_{bo}} \leq 20$ in. and (c) combination of drift criteria in (a) and isolator displacement criteria in (b)

superstructure mass become large relative to the base mass, which is a reasonable assumption for tall isolated buildings. The described approach leads to accurate estimates of peak isolator displacement and peak structural drift through the simple use of a response spectrum. The proposed method gives accurate results even in cases of long isolation period and high isolation system damping, both of which give are characterized by highly non-proportional damping.

Future work includes:

1. Development of spectrum-based design procedures that give estimates of displacement *and* acceleration demand
2. Investigation of the relationship between linear and nonlinear response for isolated tall buildings considering MDOF representations
3. Quantification of the relative reliability of isolated tall buildings compared to conventional tall buildings in terms of probabilistic hazard analysis.

ACKNOWLEDGEMENTS:

The first author is grateful for research funding provided under the Global Center of Excellence (GCOE) Program at the Tokyo Institute of Technology.

REFERENCES:

Ariga T, Kanno Y, Takewaki I. [2006] "Resonant behavior of base-isolated high-rise buildings under long-period ground motions," *Struct. Design Tall and Special Bldgs*; **15**(3): 325–338.

Fu, Y. and Kasai, K. [1998] "Comparative Study of Frames Using Viscoelastic and Viscous Dampers," *J. Struct. Eng.*, ASCE, **124**(5): 513–522

Kani N. [2009] "Current State of Seismic Isolation Design," *J. Disaster Res.*; **4**(3): 175-181

Kasai, K., Yamashita, T., Yamazaki, Y., and Igusa, T. [2009] "Spectrum-Based Response Prediction of Asymmetric Structure with Supplemental Viscous Damper," *J. Struct. Constr. Eng.*, AIJ, **74**(636): pp. 225-234 (in Japanese)

Miyazaki M. [2009] "The Next Generation of Seismic Isolation: Going Beyond Seismic Design Dominated by Earthquakes," *J. Disaster Res.*; **3**(6): 479-502

Somerville, P., Anderson, D., Sun, J., Punyamurthula, S., and Smith, N. [1998] "Generation of Ground Motion Time histories for Performance-Based Seismic Engineering," *Proceedings*, 6th National Earthquake Engineering Conference, Seattle, WA

Takewaki I, Fujita K [2009] "Earthquake input energy to tall and base-isolated buildings in time and frequency dual domains," *Struct. Design Tall and Special Bldgs*; Online: 589-606

Takewaki I. [2007] "Robustness of base-isolated high-rise buildings under code-specified ground motions," The Structural Design of Tall and Special Buildings; **17**(2): 257–271

8CUEE CONFERENCE PROCEEDINGS
8th International Conference on Urban Earthquake Engineering
March 7-8, 2011, Tokyo Institute of Technology, Tokyo, Japan

CONCEPTS FOR THE DESIGN OF MASS ISOLATED STEEL BUILDINGS

Luis E. Peternell-Altamira[1], and Gary T. Fry[2]

1) Graduate Assistant Researcher, Zachry Department of Civil Engineering, Texas A&M University, College Station, TX, USA
2) Associate Professor, Zachry Department of Civil Engineering, Texas A&M University, College Station, TX, USA
lepa@tamu.edu, garyfry@tamu.edu

Abstract: Different seismic control and isolation techniques with inherent advantages and disadvantages have been developed to manage the amount of seismic energy that is input into a building as well as its dissipation. Their ultimate purpose is to reduce the demands on the primary structural elements and, thus, improve the global performance of the structure. The authors have combined the positive aspects of some of these techniques while eliminating their negative side-effects to create a novel seismic isolation/control system that has the potential to outperform technically and economically the currently available control and isolation strategies. This paper introduces the ideated system and presents the initial analytical steps that will be taken for its complete development.

1. INTRODUCTION

Earthquakes have caused the death of millions of people as well as wide-spread infrastructure destruction (USGS 2009). Although earthquake engineering has advanced quickly, major seismic events continue to show us that we are still vulnerable to them. Many of the advancements are in the area of seismic control whose strategies use a variety of damper and shock-absorbing technologies. These strategies have been proven to reduce the structural demands, improve the structural performance and, in cases, make up for the additional cost of installing them by allowing lighter structural designs. In general, however, the control techniques are expensive, need regular inspection, maintenance and component replacement after major earthquakes. They also have limited applicability, interfere with architectural features, require special mountings and reinforcements in the places where dampers/actuators are installed, etc. Base Isolation, on the other side, is effective in reducing interstory drifts and floor accelerations; however, its use has been limited by the isolating technologies as well as by the prevention of the mechanisms that would jeopardize the safety of the base-isolated structure.

This project attempts to use the virtues of some seismic control/isolation tools and combine them into a new, but simple earthquake resistant product that has the potential to outperform through the isolation of the floor masses from the seismic accelerations, the currently available seismic control and isolation strategies. Since the ideated system is simple and most of its components have already been approved for their application, the implementation of the concept should follow directly after a small amount of studies have been carried out. The proposers also believe that their concept of mass isolation is easy to implement in new buildings and with retrofitting purposes.

2. BACKGROUND

Recent structural design philosophies require the provision of sufficiently ductile structural elements in buildings to cope with and limit the seismic input energy of an earthquake. By providing ductility, structural materials will dissipate energy by incursions in their nonlinear range; however, inelastic deformations cause structural and non-structural damage which has to be kept within acceptable limits.

Alternatively, innovative concepts for the seismic protection of structures that consist in the incorporation of energy dissipating devices and/or the modification of dynamic characteristics of the structures have been

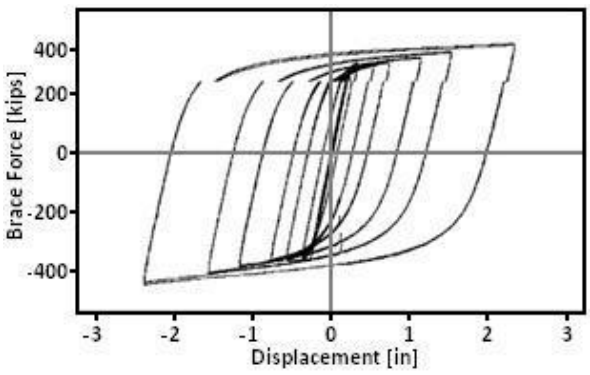


Figure 1 Force displacement plot of buckling-restrained braces (Sabelli, Mahin et al. 2003)

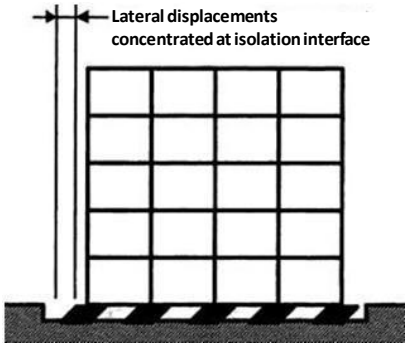


Figure 2 Base Isolation (ASCE 2004)

engineered with the objective of reducing the energy dissipation demand (and damage) in the primary structural members. The intention of including energy dissipating devices in buildings is that they perform most of the task of energy dissipation instead of the building's structural elements, one example of such devices are buckling-restrained braces (Figure 1). Since now damage is concentrated in these elements, they have to be inspected and/or replaced after a number of earthquakes or immediately after major ones to guarantee the safety of the building, which can be expensive and time consuming (PDL 2009).

Another technique of earthquake protection that has proven to be very effective and surprisingly simple (Naeim and Kelly 1999) is Base Isolation; it consists in providing a relatively flexible (isolating) layer between the structure and its foundation. This layer "detaches" the building from the ground, making the former less susceptible to the accelerations of the latter (Figure 2). Implementation of Base Isolation modifies the inherent dynamic properties of a structure in a way that promotes the predominance of the first mode of vibration in its seismic response. Also, like yielding or friction energy dissipaters do, Base Isolation lengthens the fundamental period of the building, thus, reducing the input of seismic energy. However, the flexibility and dependence of the good functioning of the system on the single-mode behavior of the system makes it vulnerable and susceptible to problems derived from these conditions. These include the possibility of resonance and excessive lateral displacements (Komodromos, Polycarpou et al. 2007); therefore, special considerations are necessary to accommodate this side-effects. These include, among others, the provision of a seismic moat and the inconvenient installation of additional springs and/or energy dissipaters at the base-level of the building (Kelly 1999; ASCE 2004).

The existence of a moat makes pounding a possibility. Pounding is a very serious problem in Base Isolation because it causes a sudden and important excitation of higher response modes which, first of all, eliminates the advantages that are inherent to the "first-mode" structural behavior. But more important is that pounding can result in an unexpected structural behavior for which the building might not have been designed. Therefore, pounding can raise the structural response parameters to critical levels (Komodromos, Polycarpou et al. 2007) which translates into severe structural and non-structural damage. Since the issue of large lateral displacements at the base and the associated danger of pounding constitute major concerns, design codes need to specify conservative general provisions that minimize their occurrence and/or their effects, but that reduce the effectiveness and benefits of Base Isolation (Pan and Cui 1998; Kelly 1999).

Different approaches have been proposed to alleviate the problem of pounding and, in general, the one of large displacements of base-isolated structures. One of them consists in the installation of additional springs and/or energy dissipaters at the base level; however, as Kelly (1999) demonstrated, this is detrimental to the performance of the Base Isolation technique, since it reduces the level of isolation and allows the participation of higher modes of vibration. In a more radical way, Pan and other researchers (Pan, Ling et al. 1995; Pan and Cui 1998; Earl and Ryan 2006; Komodromos, Polycarpou et al. 2007) have attempted to solve the problem by studying variations to the concept of Base Isolation. Pan et al. (1995; 1998) have proposed to insert isolation layers at various levels of a building (including the base) to reduce the magnitude of the lateral displacements throughout the height of the building, but mainly at the base (Figure 3). Their analyses show that with their idea, significant reductions of the base displacements can be achieved while the characteristic outstanding interstory and acceleration performance of Base Isolation is kept.

Another shortcoming of Base Isolation arises from the limited vertical-load resistance of the isolating devices (isolators). Apart from the issue with the displacements, this has also limited the use of Base Isolation to low-rise structures. The elevated forces necessary to test at full-scale and develop current and new isolating technologies for heavier (taller) structures cannot be achieved in laboratories (ASCE 2004). This adds to the difficulties of developing and, hence, accepting new isolating technologies and code provisions related to their implementation.

Finally, the interaction of the large displacements of the isolators with the large vertical forces imposed on them by the building generates stability problems due to the p-delta effect that is induced (Figure 4). This issue has already been the subject of several research studies (Haringx 1948;

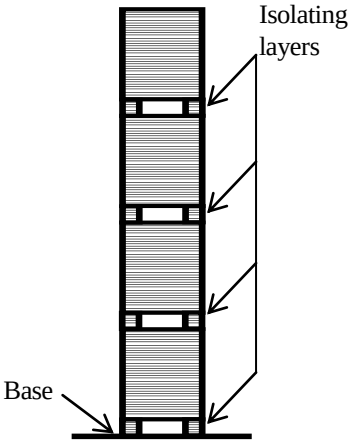


Figure 3 Segmental building concept (Pan and Cui 1998)

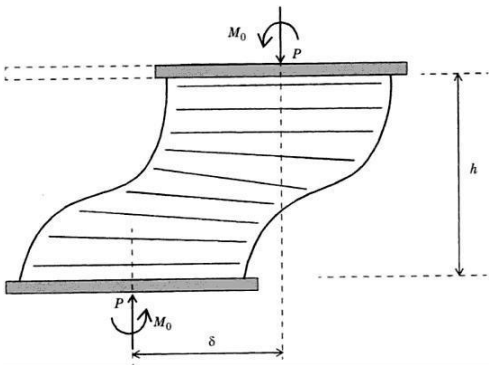


Figure 4 P-delta in rubber isolator (Naeim and Kelly 1999)

Gent and Lindley 1959; Gent 1964; Kircher, Delfosse et al. 1979); however, it is still and will inevitably always be a concern in the development of isolators and the design of base isolated systems.

From the economical point of view, although the isolation of the base of a new building is technically simple, it becomes expensive and complicated in retrofit applications, since it requires excavations, temporary load transfer and sometimes the removal from service of the structure during certain stages of the isolation process (Earl and Ryan 2006).

3. MASS ISOLATION

3.1 Principles

Conventional buildings have their bases attached to the ground through their foundations and, in practical terms, fully experience the accelerations imposed by earthquakes when they take place. The concept of structural isolation attempts to detach the structure from the source of the excitation so that the induction of forces is reduced. An example of this is the case of Base Isolation explained before where a whole building is "separated" from the ground through the use of low-stiffness isolators. It is not necessary to separate the whole bulky and heavy structure from its foundation to achieve its isolation, the isolation of only the individual mass concentrations produces in theory the same effect.

Buildings are designed and built to resist gravity and lateral loads; this requires two different structural sub-systems, one that provides resistance to the vertical loads and another one that resists forces in the horizontal planes. In practice, both sub-systems are built into a single system in which they work in a coupled manner.

The masses in buildings are considered lumped at the floor slabs, which are part of the gravity system and are linked to the ground by the lateral resisting sub-system. The general concept of mass isolation is based on introducing a discontinuity between the floor masses (gravity sub-system) and the lateral sub-system to reduce or, ideally, eliminate the interaction between the two. By placing an isolating gap between the two systems, the masses are automatically "detached" from the ground and, consequently, their participation and ease of excitation by earthquake accelerations decreases (Figure 5). Lower excitations of the masses translate into reduced demands on the lateral sub-system, which ultimately results in better structural performance and the need for lighter (more economical) designs.

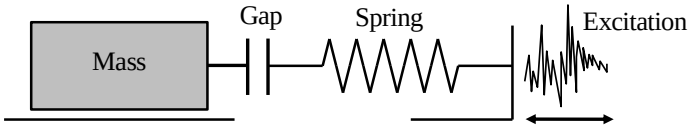


Figure 5 Mass isolation (Ziyaeifar 2002)

The "elimination" of the physical links between the masses and the lateral springs leaves a loose gravity system that undergoes large velocities and displacements relative to the stiffness system when it is subjected to earthquake excitations. While they may look as an inconvenient at first, the increased relative velocities and displacements can actually be used to dissipate the input seismic energy through velocity-dependent or displacement-dependent energy dissipaters to further improve the performance of the already less demanded mass-isolated system.

3.2 Current state of knowledge

A certain number of researchers have already worked with ideas that are in some form associated to the concept of mass isolation. In Japan, for example, Niiya et al. (1992) and Sakamoto et al. (2000) describe structural systems in which auxiliary masses or the actual masses of the floors are used as vibration absorbers to reduce the seismic response of buildings (Figure 6). An example of this is the case of the Active-Passive Composite Tuned-Mass Damper presented in (Sakamoto, Koshika et al. 2000).

Other approaches to seismic isolation that are more similar to what has been described as mass isolation have been proposed by Pan et al. (1995; 1998), Ziyaeifar and Noguchi (1998), Villaverde (1998), Villaverde and Mosqueda (1999), Ziyaeifar (2000; 2002), Villaverde et al. (2005), Pourmohammad et al. (2006), Earl and Ryan (2006), and Phocas and Pamboris (2009). As described earlier, Pan and his co-researchers proposed an extension of the concept of Base Isolation to other levels of the building, which consists in introducing isolation layers between various segments of a building (Figure 3). They showed that reduced displacements, especially at the base, can be achieved with

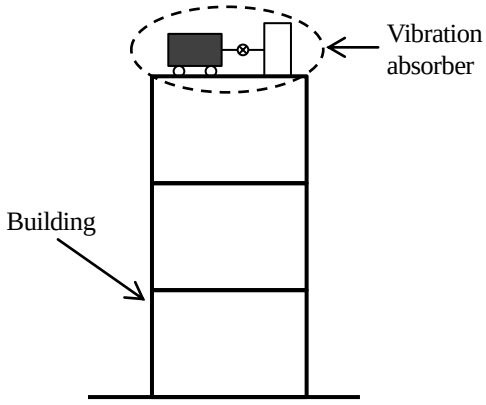


Figure 6 Building with active vibration absorber (Sakamoto, Koshika et al. 2000)

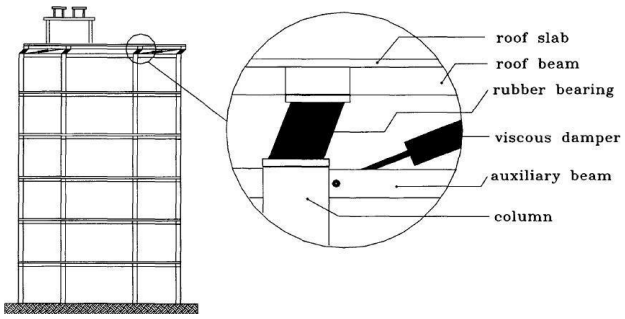


Figure 7 Typical building with roof isolation (Villaverde 1998)

their system. On the other hand, Villaverde and his co-researchers have focused on isolating only the mass of the building roof in a way similar to the method of Base Isolation, but rather approached their idea as that of turning the roof into a vibration absorber (Figure 7). Villaverde recognized that a very large roof mass is needed for an effective implementation of his idea and, also, that the very large displacements of the roof that result require special care. However, his studies, both analytical and experimental, demonstrated that the appropriate isolation of part of the total mass of a structure leads to significant reductions in the seismic demands of the lateral-force resisting system. For retrofitting works, he pointed out that the isolation of the roof should be less disruptive for the service of the building than the implementation of Base Isolation.

Ziyaeifar (1998; 2000; 2002) carefully explained the concept of mass isolation and proposed mass-isolated structural systems that agree with the definition of the mass isolation concept in this document. His systems isolate the mass subsystem from the ground by diverse methods (Figure 8). He supported his ideas with limited analytical testing whose outcomes clearly show technical benefits of isolating the main mass concentrations in buildings from the lateral system and, thus, the ground. Pourmohammad and his colleagues (2006) proposed to isolate each floor of a building in the way Villaverde proposed to isolate the roof; that is, by introducing (rubber) isolators between the floor slabs and the beams that support them (Figure 8a).

Earl and Ryan (2006) deepened the concept of segmental isolation that was initially developed by Pan et al. (1995) and compared the effectiveness of placing various isolating layers at different levels of a building. They point out the technical benefits of placing the isolation layer(s) above the ground instead of placing it at the base level like in Base Isolation. These include the achievement of a level of reductions of the dynamic response of the structure of the same order as those achieved when Base Isolation is used, but eliminating the risk of pounding and the necessity for provisions for the accommodation of large displacements at the base.

Mass isolation is an appealing and simple concept with proved potential; however, to date only limited research related to its development has been done. The technical, architectural and economic benefits (or disadvantages) that could be drawn from this system are far from having been

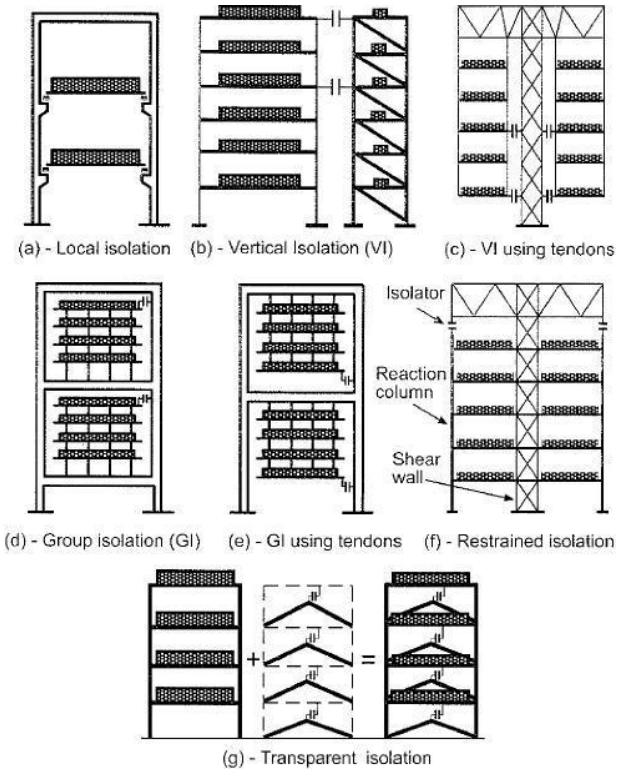


Figure 8 Some methods of mass isolation (Ziyaeifar 2002)

accurately addressed; in fact, the studies on the concept that have been carried out, have many times served to only introduce the concept.

4. STABILITY-DEPENDENT MASS-ISOLATION

4.1 System description

The system proposed for the application of mass isolation in buildings, depicted in Figures 9 and 10, has the following characteristics:

- The concept is intended to be applied to steel buildings where hinged end-conditions of the structural elements can be produced more naturally. The building does not show major physical differences compared to a typical "fixed-base" building, only that the mass sub-system is built detached from the lateral system; that is, there are no primary structural links between the two structural sub-systems.
- All connections in the mass system are pinned, including possibly those at both ends of the columns joining adjacent floor levels, so that free relative motion of a floor slab with respect to the adjacent ones is intentionally allowed.
- The lateral-load-resisting system can consist of any system currently used in practice, namely, shear walls, moment frames, concentrically and eccentrically braced frames, or variations thereof.
- Since the mass sub-system is detached from the lateral system it is inherently unstable. In order to provide it with stability, linear (nodal) springs are placed at each floor level between the slabs and the lateral system.

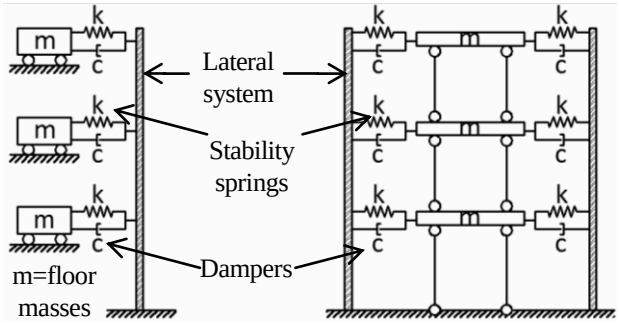


Figure 9 Equivalent sketches of proposed method of SDMI

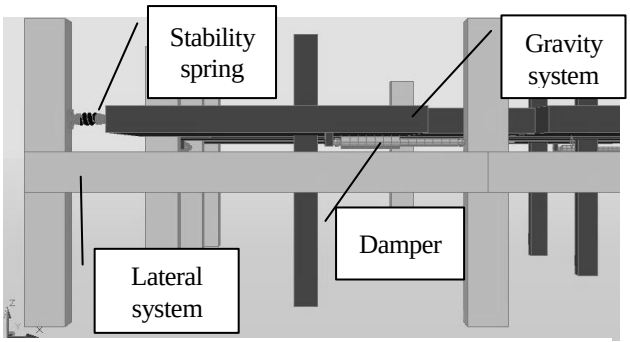


Figure 10 Scheme of proposed SDMI

These springs are referred to as stability springs. Their provision will couple the mass and lateral systems to some extent; that is why, to minimize the coupling of the two systems and, thus, maximize the level of isolation, the stiffness of the stability springs has to be the minimum that guarantees the safety and full restoration of the mass sub-system after the action of an earthquake.

- Since the stiffness of the stability spring springs is relatively low, they act as low-stiffness isolators. The flexibility of these links joining the two sub-systems allow large velocities of the floor masses during seismic excitations which are used for energy dissipation through the use of velocity-dependent energy dissipaters.

Since the level of isolation of the floor masses of the building is limited by the stability requirements of the mass sub-system, the concept is named Stability-Dependent Mass Isolation (SDMI). Some of its advantages compared to typical fixed-base, base-isolated buildings and the other isolation systems mentioned before are:

- As an isolated structure it possesses the associated advantages of reduced floor accelerations and interstory drifts.
- It incorporates the concept of segmental and/or interstory isolation which eliminates the disadvantages and d angers of Base-Isolation (high displacements and associated risk of pounding); in fact, in the case of SDMI there will be no lateral displacements at the base at all.
- The length of the stability springs can be designed to accommodate the maximum relative displacements between the mass and lateral (stiffness) sub-systems. Since adjacent floor levels are not linked with each other in the horizontal direction, the displacements throughout the height of the building are not cumulative.
- Since there are no interstory springs in the mass system, the excitation of higher modes of response and the associated increase in floor accelerations and interstory drifts is kept within certain limits.
- The incorporation of viscous dampers at various levels of the building allows greater energy dissipation than in the case of Base Isolation, Segmental Isolation, Roof Isolation, etc., or than by system damping only and ductile deformations.
- Since it does not use rubber isolators the concept can be applied to high rise structures.
- Since there are actually no complex elements or mechanisms in this system, its cost should be low compared to that of other isolation or control systems. Even in the case of retrofit problems, the implementation of this concept should cause minimal or no disruptions to the service of a building.
- Any additional cost derived from the installation of the energy dissipaters should be compensated with the reduced cost of a lighter lateral system. Moreover, once built, the structural performance of the building during earthquakes will be significantly improved and the damage to primary structural members will be reduced considerably. This will also result in a lower life-cycle cost of the building and a greater probability that the structure will be available for service even after major seismic events.
- The way SDMI is outlined allows the resistance to wind excitations in practically the same way it is achieved in typical fixed-base buildings; i.e., the wind forces will hit the surface of the building which is directly supported by the lateral system.

4.2 Description of requirements for stability springs and dampers

The provision of stability to the mass sub-system is a fundamental requirement. However, for the SDMI system to function as intended, there are issues that have to be considered in the selection/design of the stability springs in order to comply with the stability requirements without compromising the effectiveness of the isolation of the mass sub-system.

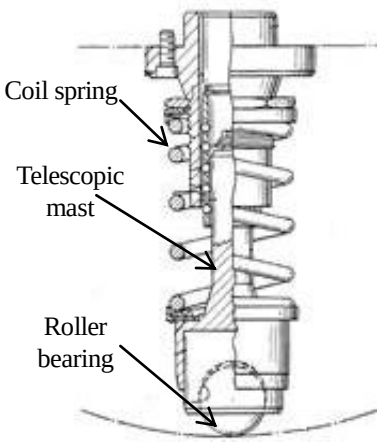


Figure 11 Earthquake isolating support (Yaghoubian 1988)

The fact that the motion of the floor slabs in the building is a three-dimensional phenomenon, it is important that the stability springs do not couple the displacement of the floors with that of the lateral system in any direction, since this would preclude the proper isolation of the floor masses. Yet, at the same time, restoration forces have to be provided in all directions of movement. To achieve this dual purpose, it is necessary to use supports of the form of the U.S. patented seismic isolation support by Yaghoubian (1988) (Figure 11). This support consists of a coil spring mounted around a telescopic mast with a roller bearing, thus, it resists axial forces while allowing lateral motions. These springs would be placed at all floor levels and bearing against all the sides of the slabs. It is also necessary that these springs remain always elastic so that the original positions of the floors can be fully restored.

In the same way, the selection of the type of the energy dissipaters that should be used in conjunction with the stability springs has to be made considering the need for a full restoration of the undisturbed (original) position of the building. Of the many commercially available energy dissipaters, fluid viscous dampers are likely best suited to perform this job. Yielding dampers, for example, would not let the stability springs bring the floor masses to their original position after an earthquake since, once they yield, they adopt a new equilibrium position. Practically the same happens with friction dampers, which would require the stability springs to provide restoring forces greater than the friction forces of the dampers to return the slabs to their initial positions. Viscous dampers allow the stability springs perform the restoration of the system until it is completed. Moreover, the fluid viscous damper technology is already sufficiently developed and tested to provide with the energy dissipation needs for this project (TDI 2009).

5. OBJECTIVES

An analytical study has been designed with the following objectives:

- The construction of computer models using available powerful computational tools for the nonlinear dynamic analysis of SDMI buildings,
- The determination of the appropriate configuration of the stability springs and dampers,
- The establishment of the dynamic properties of the SDMI buildings,
- The analysis of the computer models using standardized methodologies, tools and criteria to identify and assess key design parameters influencing the response of SDMI buildings,
- The generation of optimized designs of SDMI buildings,
- The assessment of dynamic response quantities of interest such as accelerations and interstory drifts, among others, to determine the technical advantages and disadvantages of the SDMI system,
- The proposal of design guidelines for SDMI buildings, and
- The eventual design of experimental models to calibrate and corroborate the analytical results and design guidelines.

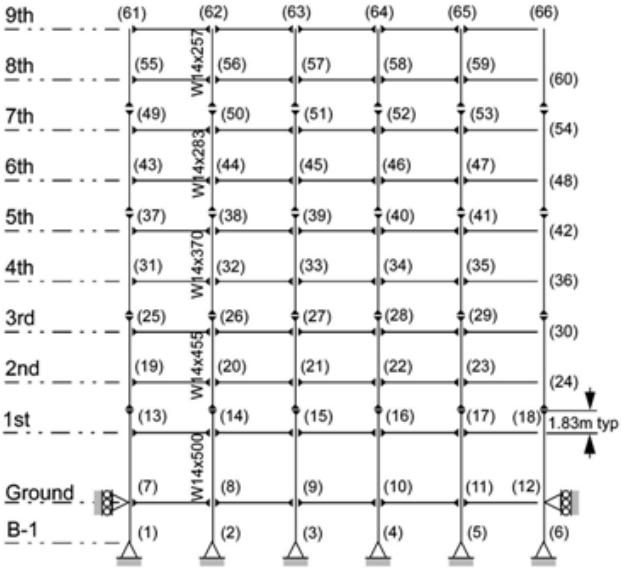


Figure 12 9-Story benchmark building (Ohtori, Spencer Jr et al. 2004)

6. PRELIMINARY STUDIES

6.1 Seismic response of a SDMI building compared to that of a fixed-base building

Preliminary nonlinear dynamic analyses of a 9-story SDMI frame were carried out to determine very roughly the potential reductions in the structural response that can be achieved when a possible form of a SDMI is implemented. For this purpose, the 9-story benchmark building (Figure 12) (Ohtori, Spencer Jr et al. 2004) designed for the SAC Steel Project was selected and the SDMI concept was applied to it. The modeling and analysis of the frame were carried out with the commercial computer program SAP2000 (CSI 2007). It is important mentioning that, in these preliminary studies, none of the design parameters like damper

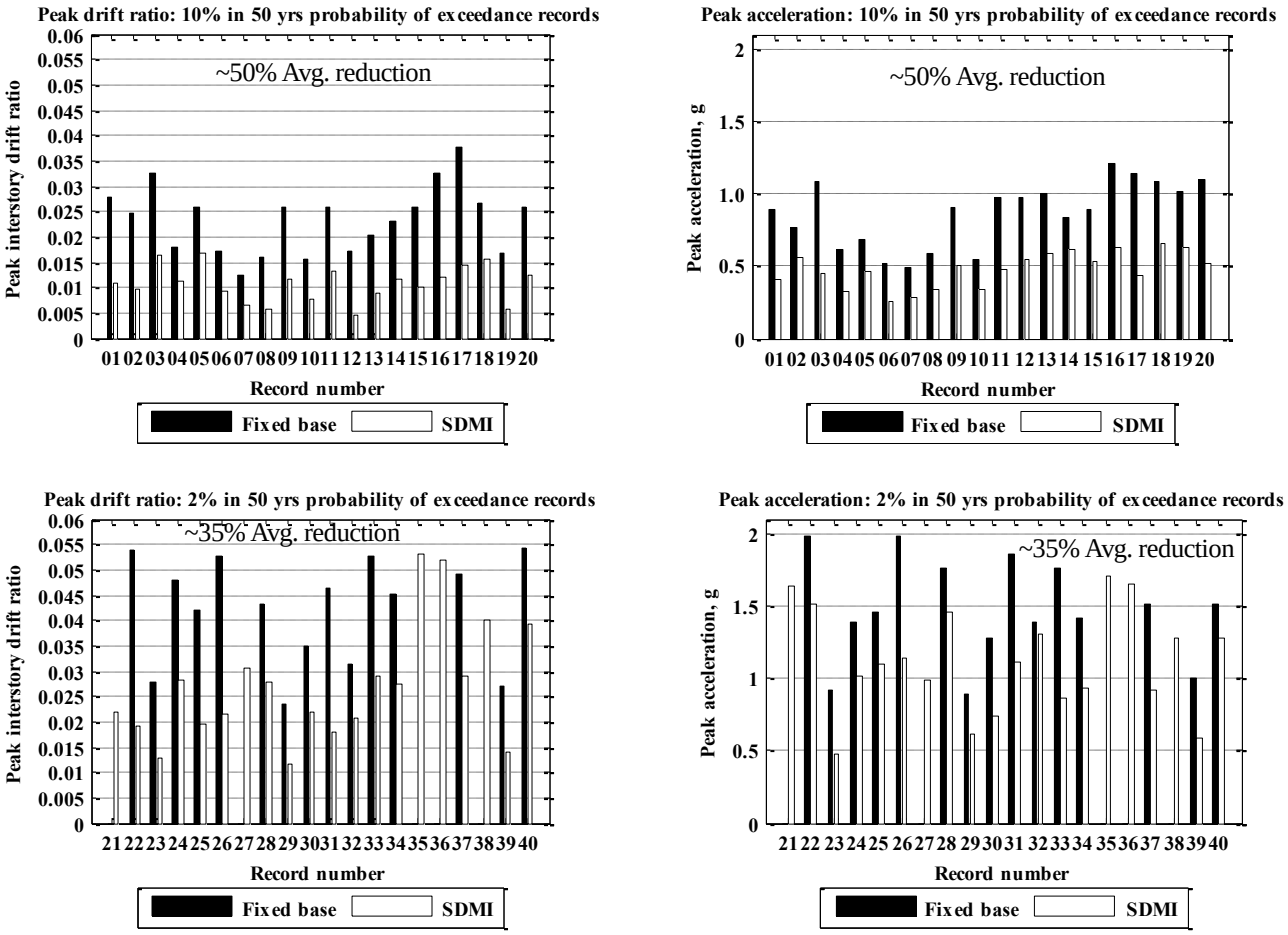


Figure 13 Comparative peak dynamic response of SDMI building vs. fixed-base building

configuration, damper properties, spring properties, etc. in the SDMI building model was optimized to yield the minimum response, which means that the performance of the structure can be further improved if optimal values for these parameters are specified.

The fixed-base and SDMI models were subjected to 40 earthquake records consistent with the location of the building (Los Angeles, CA), 20 having a probability of exceedance of 10% in 50 years (records 01-20) and 20 having a probability of exceedance of 2% in 50 years (records 21-40). The ground acceleration histories that were used are the ones developed by Somerville (1997) for the SAC Steel Project (FEMA 1994). The results provided in Figure 13 show the impressive performance of the SDMI building compared to the original fixed-base building even without optimization. It is also worth mentioning that the fixed-base structure collapsed under records 21, 27, 35, 36 and 38 (no bars are shown on charts for these cases), but the SDMI building was able to resist them.

6.2 Determination of damper configuration

For the generation of the optimized designs of the SDMI buildings, extensive use will be made of genetic algorithms (Haupt 2004). The design optimization process begins with the determination of the most convenient configuration for the dampers based on the configuration

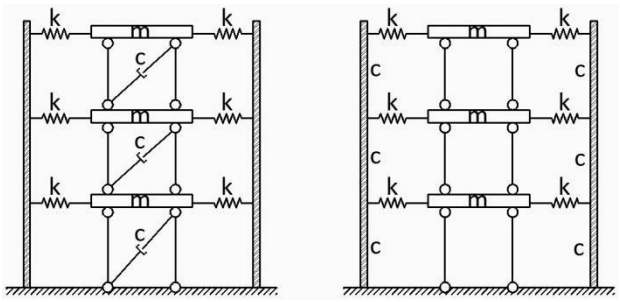


Figure 14 a) SDMI with dampers within gravity sub-system, b) SDMI with dampers within the lateral sub-system

that will minimize particular structural response parameters. For this and for now, the objective function is preliminarily selected to be the interstory drift ratio in the lateral sub-system. Three main damper configurations are considered:

1. Dampers are joining the lateral sub-system with the gravity sub-system as depicted in Figure 9,
2. Dampers are within the gravity sub-system joining adjacent floor levels (Figure 14a), and
3. Dampers are within the lateral sub-system joining adjacent floor levels (Figure 14b).

In order to find which of the three options is technically most convenient, a genetic algorithm based on the blend crossover method (Haupt 2004) is applied to all damper

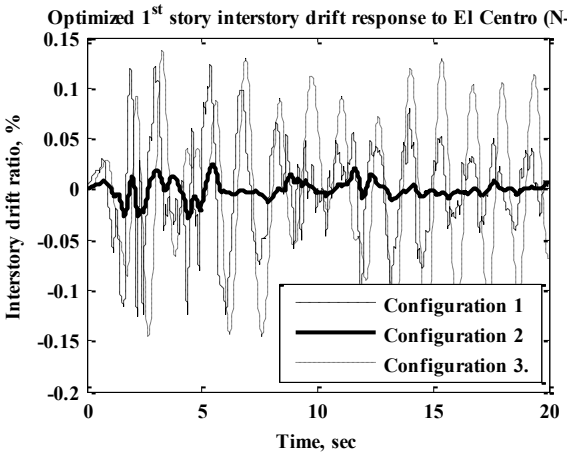


Figure 15 Interstory drift ratio time histories for the different configurations considered subjected to El Centro (N-S)

configurations to find optimal values for the stiffness of the stability springs and damping coefficients for the dampers. The 3-story benchmark building (Ohtori, Spencer Jr et al. 2004) is modeled using Matlab (TheMathWorks 2008), where the gravity sub-system is modeled as a triple pendulum attached through the stability springs to the lateral subsystem. The model is subjected to the north-south component of *El Centro* as part of the optimization process. The genetic algorithm that is used already includes a subroutine that will check that the values found for the stiffness of the springs are sufficient to provide static stability to the gravity system; compliance with dynamic stability requirements is implicit in the process of minimizing the structural response.

Results of the genetic algorithm show that the best way to place the dampers is within the gravity sub-system joining adjacent floor levels (Figure 14a) and not in the configuration used in Figure 9 and in the preliminary analyses of the SDMI system (Figure 15). This outcome makes sense, since placing the dampers joining the two structural sub-systems enables additional coupling of the two, thus, the isolation of the floor masses is lowered and, therefore, the benefits of SDMI are also reduced.

7. CONCLUSIONS

The development of the proposed concept of seismic mass isolation will constitute an important advancement in the field of seismic isolation of buildings which, at present, has practically been limited to the case of Base Isolation. Although attempts have already been made to diversify the strategy and generalize the concept of isolation, until now, these have been discrete and have fallen short in the scope that is necessary for a newly developed system to be considered for practical applications.

The proposed study intends to address every analytical aspect necessary to take SDMI to a level that permits its practical implementation. With the already available and encouraging results provided by Base Isolation and the preliminary analyses carried out on the SDMI concept, the authors believe that SDMI promises technical and economic advantages and, therefore, has the potential to become a wide-spread strategy for improving the seismic performance of buildings in the future. At the same time, it should open an important amount of new possibilities for earthquake protection.

References:

ASCE. (2004). Primer on seismic isolation, American Society of Civil Engineers, Reston, VA.

CSI. (2007). "SAP2000 Advanced." Computer and Structures Inc, Berkeley, CA.

Earl, C. L., and Ryan, K. L. (2006). "Effectiveness and feasibility of inter-story isolation systems." Proc. 8th U.S. National Conference on Earthquake Engineering, San Francisco, CA.

FEMA. (1994). "SAC Steel Project." Richmond, CA.

Gent, A. N. (1964). "Elastic stability of rubber compression springs." Journal of Mechanical Engineering, 6(4), 318–326.

Gent, A. N., and Lindley, P. B. (1959). "Internal rupture of bonded rubber cylinders in tension." Proc. of the Royal Society of London. Series A., 195-205.

Haringx, J. A. (1948). "On Highly Compressive Helical Springs and Rubber Rods and their Applications to Free Mountings - Part III." Philips Research Reports, 4, 206-220.

Haupt, R. L. a. H., S. E. (2004). Practical genetic algorithms, Wiley Interscience, New Jersey.

Kelly, J. M. (1999). "The role of damping in seismic isolation." Earthquake Engineering & Structural Dynamics, 28(1), 3-20.

Kircher, C. A., Delfosse, G. C., Schoof, C. C., Khemici, O., and Shah, H. C. (1979). "Performance of a 230 KV ATB 7 power circuit breaker mounted on GAPEC seismic isolators." Rep. No. 40, The John A. Blume Earthquake Engineering Center, Stanford University, Stanford, CA.

Komodromos, P., Polycarpou, P. C., Papaloizou, L., and Phocas, M. C. (2007). "Response of seismically isolated buildings considering poundings." Earthquake Engineering & Structural Dynamics, 36(12), 1605-1622.

Naeim, F., and Kelly, J. M. (1999). Design of seismic isolated structures - From theory to practice, John Wiley and Sons, New York.

Niiya, T., Ishimaru, S., Yamaguchi, N., and Hayashida, T. (1992). "Seismic response control by 'mode(s)-isolation' method - Part II: Control of a tall building by tuned multi-masses damper system." Proc. 10th World Conference on Earthquake Engineering, Balkema, Rotterdam, 2337-2337.

Ohtori, Y., Spencer Jr, B. F., and Dyke, S. J. (2004). "Benchmark control problems for seismically excited nonlinear buildings." Journal of Engineering Mechanics, 130(4), 366-385.

Pan, T. C., and Cui, W. (1998). "Response of segmental buildings to random seismic motions." ISET Journal of Engineering Technology, 35(4), 105-112.

Pan, T. C., Ling, S. F., and Cui, W. (1995). "Seismic response of segmental buildings." Earthquake Engineering & Structural Dynamics, 24(7), 1039-1048.

PDL. (2009). "Pall Dynamics Ltd." Montreal, Canada.

Phocas, M. C., and Pamboris, G. (2009). "Multi-storey structures with compound seismic isolation." Proc. 7th World Conference on Earthquake Resistant Engineering Structures, Nicosia, Cyprus, 207-216.

Pourmohammad, H., Ashtiany, M. G., and Ziyaeifar, M. (2006). "Buildings with local isolation system: Performance and simplified method of dynamic analysis." Asian Journal of Civil Engineering (Building and Housing), 7(5), 501-516.

Sabelli, R., Mahin, S., and Chang, C. (2003). "Seismic demands on steel braced frame buildings with buckling-restrained braces." Engineering Structures, 25(5), 655-666.

Sakamoto, M., Koshika, N., and Kobori, T. (2000). "Development and applications of structural control systems - Active-passive

composite tuned mass damper." Der Stahlbau, 69(6), 455-463.
Somerville, P. G. (1997). "Development of ground motion time-histories for phase 2 of the FEMA/SAC steel project." Rep. No. SAC/BD-97/04, SAC Joint Venture, Sacramento, CA.
TDI. (2009). "Taylor Devices Inc.", North Tonawanda, NY.
TheMathWorks. (2008). "MATLAB." TheMathWorks, Natick, MA.
USGS. (2009). "U.S. Geological Survey Earthquake Hazards Program." Reston, VA.
Villaverde, R. (1998). "Roof isolation system to reduce the seismic response of buildings: A preliminary assessment." Earthquake spectra, 14(3), 521-532.
Villaverde, R., Aguirre, M., and Hamilton, C. (2005). "Aseismic roof isolation system built with steel oval elements: exploratory study." Earthquake Spectra, 21(1), 225-241.
Villaverde, R., and Mosqueda, G. (1999). "Aseismic roof isolation system: Analytic and shake table studies." Earthquake Engineering & Structural Dynamics, 28(3), 217-234.
Yaghoubian, N. F. (1988). "Earthquake isolating support." U.S. Patent 4,726,161, February 23, 1988.
Ziyaeifar, M. (2000). "Method of mass isolation in seismic design of structures." Proc. 12th World Conference on Earthquake Engineering, Pergamon, Auckland, New Zealand, 1411-1411.
Ziyaeifar, M. (2002). "Mass isolation, concept and techniques." European Earthquake Engineering, 16(2), 43-55.
Ziyaeifar, M., and Noguchi, H. (1998). "Partial mass isolation in tall buildings." Earthquake Engineering & Structural Dynamics, 27(1), 49-65.

8CUEE CONFERENCE PROCEEDINGS
8th International Conference on Urban Earthquake Engineering
March 7-8, 2011, Tokyo Institute of Technology, Tokyo, Japan

RESPONSE BEHAVIOUR OF ISOLATED BUILDINGS TO EARTHQUAKE EXCITATIONS CONSIDERING SOIL FLEXIBILITY

Sayed Mahmoud[1], and Per-Erik Austrell[2]

1) Postdoctoral Research Fellow, Division of Structural Mechanics, Lund University, Lund, Sweden
2) Assistant Professor, Division of Structural Mechanics, Lund University, Lund, Sweden
elseedy@hotmail.com, per_erik.austrell@construction.lth.se

Abstract: Seismic response time history analysis of isolated-base buildings considering and ignoring supporting soil flexibility is investigated. In the analysis, a large number of parametric studies in which different earthquake excitations, and building natural periods has been performed. Moreover, several values of shear wave velocities have been considered. The action of the underlying soil has been modelled through a lumped parameter model with swaying and rocking spring-dashpot system. Compared are certain aspects of the response with and without soil-structure interaction (SSI) effect leading to the following conclusions. (1) Soil flexibility significantly affects the rigid superstructure response and slightly influences the response of the flexible base bearing. (2) The peak response of the SSI system with a nonlinear bearing is shown to be larger than those obtained with the SSI system having a linear base particularly for moderate and high earthquake actions. (3) Although the peak response is highly affected by the inclusion of soil flexibility; it appears insensitive to the variation of soil velocity. (4) As the building natural periods become larger, a decrease trend in the effect of SSI on the obtained response has been observed for all the considered ground motions, base isolations, and shear waves.

1. INTRODUCTION

Seismic isolation is a strategy to reduce the response and the seismic forces to or near the structure elastic capacity. Isolation systems applied in base-isolated buildings are generally effective due to their flexibility and energy dissipation characteristics. Flexibility in the horizontal direction will lower the fundamental frequency of the building below the range of frequencies which dominate general earthquake input. Providing means of energy dissipation reduce the seismic energy transmitted to the system during earthquakes so that the structural response will be reduced.

A number of base isolation systems has been proposed and their effects on the dynamic behaviour of structures have been accurately reviewed by many authors (Buckle and Mayes 1990, Jangid and Datta 1995, Chopra 1995, Kelly 1997, Kelly 1998, Kelly 1999). Two of the most commonly used isolation systems consist of laminated rubber bearings (LRBs) and high damping rubber bearings (HDRBs). LRBs are often used with passive dampers for the purpose of controlling the excessive base displacements. On the other hand, the application of HDRBs is considered as one of the most promising among several methods of seismic isolation. However, most of the research works investigating the performance of seismically isolated buildings have been focused on the dynamic behaviour of sliding structures based on the PF system subjected to harmonic support motion (Mostaghel et al. 1983, Westermo and Udwadia 1983, Jangid 1997, Calio et al. 1998), to earthquake excitations (Toki et al. 1981, Constantinou and Kneifati 1987, Liaw et al. 1997, Ryan 2004) and to randomly moving foundation (Constantiou and Tadjbakhsh 1983, Constantiou and Tadjbakhsh 1984). A review of the above cited papers indicates that the conducted analyses ignore the influence of soil-structure interaction (SSI) on the dynamic response of a structure. Moreover, the isolated bases of the analysed structures were usually modelled as PF base isolation systems.

Ignoring the SSI effects may lead to incorrect structural response assessment since it has been recognized that it may have a significant impact on the dynamic system response. Two general methods are available for rationally incorporating SSI effects into structural analysis (Wolf 1994). The first one is a direct method in which the structure and a portion of the base soil are both incorporated into a finite element mesh. In the second method, known as a substructure method, the structure and the soil are analyzed separately. A simplified model, which is typically composed of one or more springs or spring-damper combinations to approximate the behaviour of the soil, is coupled with the structural model at its base. The most common analytical model is the one in which the soil domain is considered to be a homogeneous elastic half-space. For the dynamic SSI problems, several studies proposed lumped-parameter models (Wolf and Somaini 1986, De Barros and Luco 1990,

Wolf 1994, Wolf 1997, Wu and Chen 2001, Wu and Lee 2002, Wu and Lee 2004) to simulate unbounded soil so that these models can be used directly in the time domain analysis.

Quite extensive research works have been conducted in order to investigate the impact of considering SSI effects on the response of isolated bridge structures (Zheng and Takeda 1995, Vlassis and Spyrakos 2001, Tonganokar and Jangid 2003, Jangid 2004, Kunde and Jangid 2006). However, very limited research works have been carried out for the response of seismically isolated buildings with SSI effects (Spyrakos et al. 2009a, Spyrakos et al. 2009b).

The aim of this paper is to evaluate the effect of SSI on the seismic response behaviour of isolated buildings. A large number of simulations using isolated building model with different natural periods subjected to three different ground motion records has been performed. The response and peak responses in the mean of accelerations, velocities and displacements with and without SSI effects have been analyzed. Also, the sensitivity of the response has been investigated for a variety of shear wave velocities.

2. MODELLING AND IDEALIZATION

2.1 Isolated Building Model

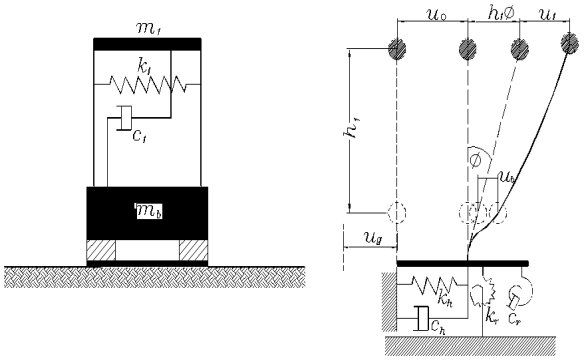


Figure 1 Idealized SDOF Mathematical Model

Figure 1 shows the idealized SDOF mathematical model for the isolated one-storey building of height h_1. A rigid deck of mass m_1 is connected to a rigid mat of mass m_b through massless columns of stiffness k_1 and damping coefficient c_1. The values of structural stiffness and damping coefficients can be calculated from the formulas (Harris and Piersol 2002):

$$k_1 = \frac{4\pi^2 m_1}{T_1^2}; \qquad c_1 = 2\xi_1\sqrt{k_1 m_1} \tag{1}$$

where T_1 and ξ_1 denote the natural structural vibration period and structural damping, respectively.

2.2. Isolation Base Model

Laminated rubber bearing (LRB) is one type of elastomeric bearings. It exhibits the parallel action of linear spring and damper. The restoring force developed in the LRB can be written as:

$$F_b = k_b u_b + c_b \dot{u}_b \tag{2}$$

where k_b, c_b, u_b and $\dot{u}_b$ are the stiffness, damping coefficient, displacement and velocity of the LRB system, respectively.

The isolation time-period T_b in terms of the stiffness, damping coefficient and the total mass M_t of the base-isolated building (including the base mass) can be written as:

$$T_b = 2\pi\sqrt{\frac{M_t}{k_b}} \tag{3}$$

On the other hand, the damping ratio ξ_b can be related to the damping coefficient, total mass and the isolation base frequency ω_b by the formula:

$$\xi_b = \frac{c_b}{2M_t\omega_b} \tag{4}$$

2.3. Soil Modelling

The considered building model rests on a half-space elastic flexible soil with no slippage between the base and the soil. The soil flexibility allows for horizontal translation and rocking at the structure's base making a system with four degree-of-freedom for the one-storey building and six degree-of-freedom for the three-storey building models. For a foundation of length L and width B, the spring stiffness and damping coefficients of swaying and rocking effects, which represent the SSI, are computed using the following expressions (Whitman and Richart 1967):

$$\begin{aligned} k_h &= 2(1-\nu)G\beta_x\sqrt{BL}, \\ c_h &= 0.576k_h r_h\sqrt{\frac{\gamma}{gG}} \\ k_r &= \frac{G}{1-\nu}\beta_\phi BL^2 \\ c_r &= \frac{0.3}{1+\beta_\phi}k_r r_r\sqrt{\frac{\gamma}{gG}} \end{aligned} \tag{5}$$

where k_h, and c_h are stiffness and damping coefficients of swaying spring, k_r and c_r are stiffness and damping coefficients of rocking spring, ν is the Poisson's ratio of soil, β_x and β_ϕ are the constants of swaying and rocking springs (depending on the ratio L/B), r_h and r_r denotes the equivalent radii of isolated foundation for swaying and rocking springs, respectively; γ is the density of soil, g refers to the acceleration of gravity and G is the shear modulus which depends on of the shear wave velocity, V_s, and can be calculated as (Whitman and Richart 1967):

$$G = \frac{\gamma(V_s)^2}{g} \tag{6}$$

2.4. Earthquake Modelling

The effects of SSI on the response time history of the considered building models have been studied under three different ground motions. The analysis has been carried out under the El Centro earthquake (18.05.1940, PGA=0.34*g*), the N. Palm Springs earthquake (08.07.1986, PGA=0.59*g*) and the The Chi-Chi (Taiwan) earthquake (20.09.1999, PGA=1.13*g*). .

3. EQUATION OF MOTION

The equation of motion for the superstructure and base of the isolated system incorporating the horizontal and rotation motions of the soil at the structure's base can be written as:

$$\mathbf{M}\ddot{\mathbf{U}} + \mathbf{C}\dot{\mathbf{U}} + \mathbf{K}\mathbf{U} + \mathbf{F_b} = -\mathbf{M}\mathbf{R}\ddot{\mathbf{U}}_\mathbf{g} \qquad (7)$$

where $\mathbf{M}$, $\mathbf{C}$, and $\mathbf{K}$ is the mass, damping and stiffness matrix, respectively; $\mathbf{R}$ is an influence matrix; $\ddot{\mathbf{U}}$, $\dot{\mathbf{U}}$, and $\mathbf{U}$ represent the acceleration, velocity and displacement vectors, respectively; $\ddot{\mathbf{U}}_\mathbf{g}$ is the ground acceleration vector and $\mathbf{F_b}$ denotes vector containing the forces mobilized in the isolation bearing. Details of the matrices and vectors can be defined as

$$\mathbf{M} = \begin{pmatrix} m_1 & 0 & m_1 & m_1 h_1 \\ 0 & m_b & m_b & 0 \\ m_1 & m_b & m_1 + m_b & m_1 h_1 \\ m_1 h_1 & 0 & m_1 h_1 & m_1 h_1^2 \end{pmatrix}, \quad \mathbf{C} = \begin{pmatrix} c_1 & -c_1 & 0 & 0 \\ -c_1 & c_1 & 0 & 0 \\ 0 & 0 & c_h & 0 \\ 0 & 0 & 0 & c_r \end{pmatrix}, \quad \mathbf{K} = \begin{pmatrix} k_1 & -k_1 & 0 & 0 \\ -k_1 & k_1 & 0 & 0 \\ 0 & 0 & k_h & 0 \\ 0 & 0 & 0 & k_r \end{pmatrix}$$

$$\mathbf{R} = \begin{pmatrix} 1 & 0 & 0 & 0 \\ 0 & 1 & 0 & 0 \\ 0 & 0 & 1 & 0 \\ 0 & 0 & 0 & 1/h_1 \end{pmatrix}, \ddot{\mathbf{U}} = \begin{pmatrix} \ddot{u}_1 \\ \ddot{u}_b \\ \ddot{u}_0 \\ \ddot{\phi} \end{pmatrix}, \quad \dot{\mathbf{U}} = \begin{pmatrix} \dot{u}_1 \\ \dot{u}_2 \\ \dot{u}_0 \\ \dot{\phi} \end{pmatrix}, \quad \mathbf{U} = \begin{pmatrix} u_1 \\ u_b \\ u_0 \\ \phi \end{pmatrix}, \quad \mathbf{F_b} = \begin{pmatrix} 0 \\ f_b \\ 0 \\ 0 \end{pmatrix}$$

where u_1 and u_b is the displacement of the superstructure and the isolation bearing, respectively; u_0 and ϕ describe the soil horizontal translation and rocking movements. The corresponding velocities and accelerations are represented with dots (derivatives with respect to time).

4. RESPONSE ANALYSIS

Extensive numerical simulations have been conducted to investigate the effects of soil flexibility on the response of single and multi-storey base-isolated buildings having different natural periods. In the analysis, different sandy soil types (Wei et al. 1996) and earthquake motions have been used. Due to the paper length limitation, representative results for one sandy soil type with different shear wave velocities at depth of 15 m are presented. The soil properties characterized by the shear wave velocities and densities are shown in Table 1. The isolated buildings have been excited by a suit of ground motion records. The records are intended to encompass low, moderate and high PGA levels to better understand the effect of SSI under different earthquake excitations. Numerical study has been carried out using lumped mass models of the base-isolated building under consideration for calculation of response quantities of interest in terms of displacements, velocities and accelerations.

Table 1 Sandy Soil type with Different Densities and Shear Wave Velocities at Depth of 15 m.

Soil density γ (kg/m^3)	Shear wave velocity V_s (m/sec)
1.89×10^3	196
1.94×10^3	220
2.00×10^3	255
2.07×10^3	275

The building superstructure fundamental period, damping ratio and mass are: $T_n = 1$ s, $\xi = 0.05$ and $m_1 = 30\times10^3$ kg. The storey height is $h = 3.5$ m. For the isolation system, the natural period and the viscous damping ratio of LRBs system are $T_b = 2$ s and $\xi_b = 0.1$. The base mass is $m_b = 90\times10^3$ kg. The stiffness of swaying and rocking springs and the damping coefficients of dashpots have been evaluated using the formula given by Eq. (1). The soil mass density and Poisson's ratio are: $\gamma = 1.89\times10^3$ kg/m^3 and $\nu = 0.3$. The shear wave velocity is given by $V_s = 196$ m/sec. The radii of equivalent circular foundation for swaying and rocking have been estimated and found to be of equal values $r_h = r_r = 4$ m (Takewaki 2005).

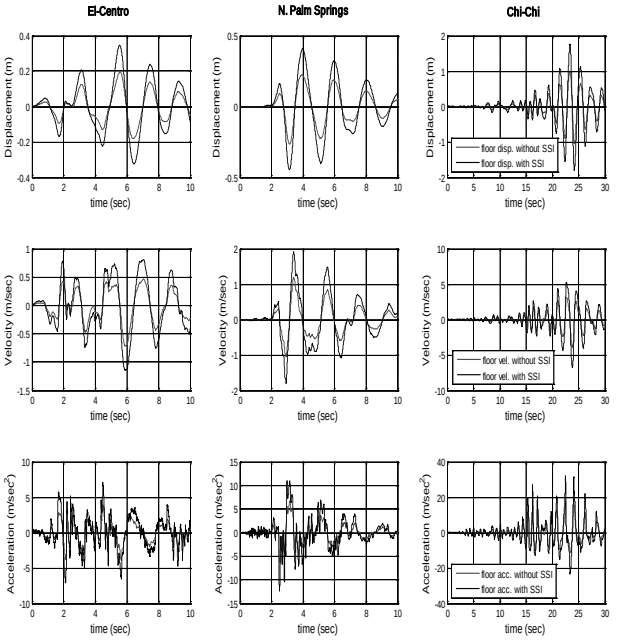


Figure 2 Displacement, Velocity and Acceleration Time Histories with and without SSI under The El Centro, N. Palm Springs and Chi-Chi Earthquakes

Figure 2 shows the storey displacement, velocity and acceleration time histories of one-storey building isolated by the LRB system with and without SSI under the El Centro earthquake, N. Palm Springs earthquake and Chi-Chi (Taiwan) earthquake. The plot indicates that the displacement, velocity and acceleration are higher when SSI is considered. The peak values of storey acceleration of 4.835, 8.684 and 20.156 m/sec^2 without SSI is increased upto 7.045, 12.404 and 32.119 m/sec^2 under the El Centro earthquake, N. Palm Springs and Chi-Chi (Taiwan) earthquake, respectively. However, the capacity demand for the superstructure increases due to increased superstructure accelerations with soil flexibility consideration.

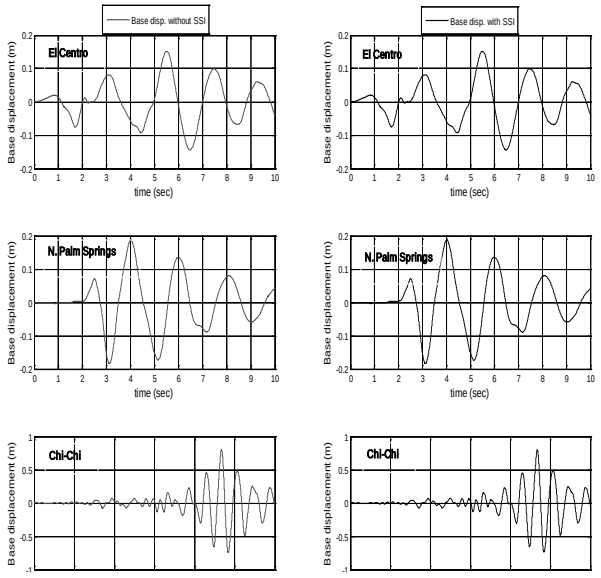


Figure 3 Displacement Ttime Histories at The Base of The Seismically Isolated Building under Different Earthquakes with Three PGA Llevels for The Case without and with SSI

Displacement time histories at the base of the seismically isolated building under different earthquakes with three PGA levels considered in the study are shown in Figure 3 for the case without and with SSI. It can be observed that the differences between the two plots are very difficult to be identified. Only a slight increase in the peak values due to incorporation of soil flexibility is detected. This implies that considering the flexibility of soil does not affect the response of the flexible base-isolation system. It has also been found that the peak base displacements obtained by ignoring the effect of underlying soil are of 0.1519, 0.1882 and 0.8033 m while for the case of considering the SSI effect the corresponding values have been recorded to be of 0.1524, 0.1883 and 0.8040 m for the El Centro, N. Palm Springs and Chi-Chi earthquake, respectively. This confirms the fact that the flexibility of soil significantly affects the rigid superstructure response and unables to influence the behaviour of the flexible base-isolation system. Similarly, velocity and acceleration time histories at the base of the seismically isolated building under different earthquakes with three PGA levels considered in the study confirm the previous results for displacement time histories with and without SSI.

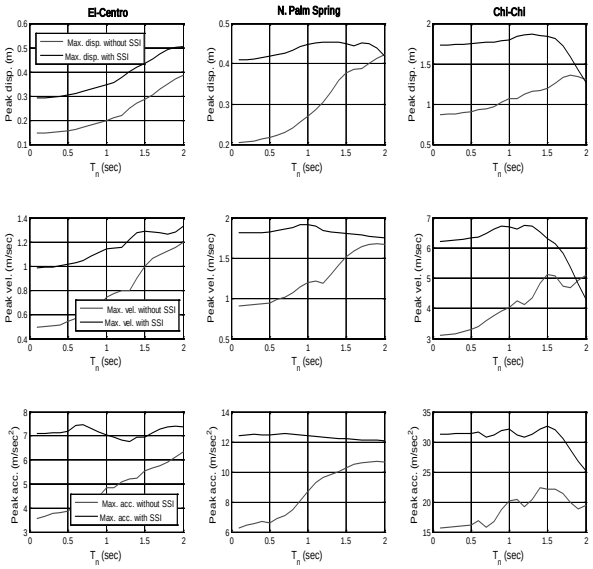


Figure 4 Peak displacement, velocity and acceleration responses for the SDOF system with different natural periods and LRBs as an isolation system with and without SSI effects under different earthquakes

Figure 4 shows the peak displacement, velocity and acceleration responses for of the linear isolation system with LRBs for different natural structural periods with and without SSI effects under different earthquakes. It can be observed from the figure that as the building period increases, the peak response of the isolated building, ignoring SSI effects, increases as well. Similar trends can be observed for the system with the incorporation of soil flexibility. For the earthquakes with higher PGA with the increase in the building natural period a slight increase trend can be observed for the peak response curves with SSI effects and with further increase in the natural period a sharp decrease trend occurs.

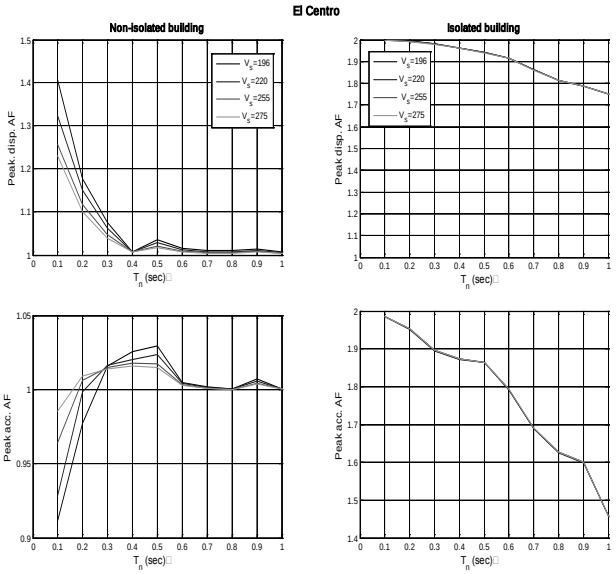


Figure 5 Peak Displacement and Acceleration Amplification Factors for the Non-isolated and Isolated Buildings with Respect to the Structural Natural Period under the El Centro Earthquake for Different Shear Wave Velocities

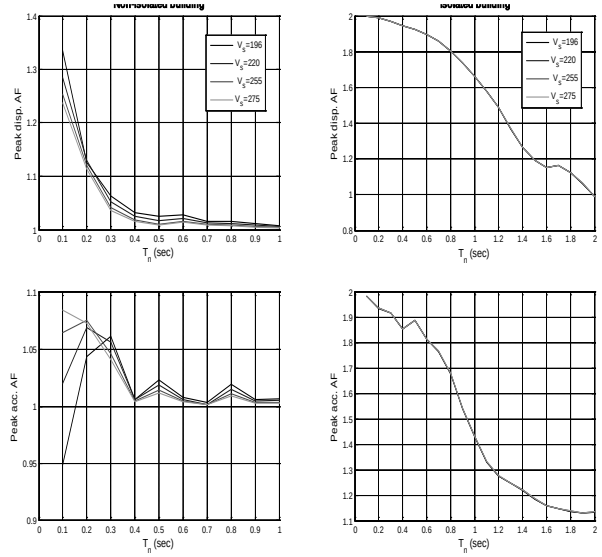


Figure 6 Peak Displacement and Acceleration Amplification Factors for the Non-isolated and Isolated Buildings with Respect to the Structural Natural Period under the N. Palm Springs earthquake for different Shear Wave Velocities

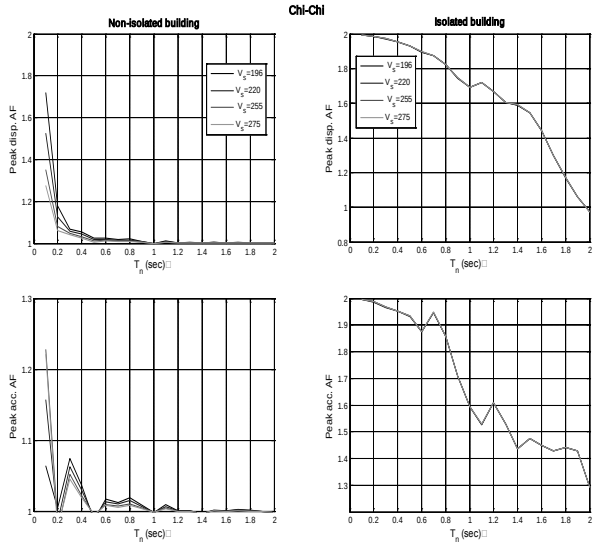


Figure 7 Peak Displacement and Acceleration Amplification Factors for the Non-isolated and Isolated Buildings with Respect to the Structural Natural Period under the Chi-Chi Earthquake for Different Shear Wave velocities

Figures 5-7 show the peak displacement and acceleration amplification factors (AF) for the non-isolated and isolated buildings with respect to the structural natural period under the El Centro, N. Palm Springs and Chi-Chi earthquakes with different shear wave velocities in the soil specified in Table 1. It can be seen from the figures that, for the non-isolated building, variations in shear wave velocities significantly change the values obtained for the peak response AF, especially for low structural natural periods. Moreover, as the soil condition becomes soft, i.e. shear wave velocity decreases, the corresponding peak displacement AF increases, while the peak AF for the acceleration decreases. It is also worth noting that the PGA levels have been found to be important in affecting the peak acceleration. Figure 5 shows that, for the El Centro earthquake with PGA=0.34*g*, the peak acceleration AF appears to be below the unity for lower shear wave velocities and slightly above the unity for higher velocity values. For the N. Palm Springs earthquake (see Figure 6), which has PGA level greater than the PGA level of the El Centro earthquake, the values for the peak acceleration AF exceed the unity, except for the lowest shear wave velocity. On the other hand, for high PGA levels represented by Chi-Chi earthquake (see Figure 7) the peak acceleration AF is higher than the unity for all considered shear wave velocities in the soil.

Figures 5-7 also show that the response of the base-isolated building is not altered by the shear wave velocity variations, although it is highly affected by the soil flexibility. The simulation results indicate that as the natural period of the building decreases the peak displacement and acceleration AF significantly increase. For all the considered shear wave velocities in the soil, the peak response of the isolated building is uniformly amplified. Similar trends have been observed for all the earthquakes considered.

5. CONCLUSIONS

The present paper has been focused on the seismic response behaviour of single-storey buildings isolated by LRB system with and without SSI effects under different earthquakes. In the analysis, the records of the 1940 El Centro, 1986 N. Palm Springs and 1999 Chi-Chi earthquakes have been used, as examples of ground motions with different PGA. The seismically isolated building has been considered to have different natural periods as well as resting on soils with different densities and shear wave velocities. From the results of present study, the following conclusions can be drawn:

Numerical simulations demonstrate that soil flexibility has a significant influence on the earthquake-induced response of base-isolated buildings.

Considering the flexibility of soil significantly affect the rigid superstructure response and unable to influence the behaviour of the flexible base-isolation system.

The influence of the SSI effects on the response of base-isolated buildings is more significant for structures with longer natural period, particularly in the case of earthquakes with high PGA.

The response of non-isolated buildings has been found to be sensitive to the variations in shear wave velocity in the soil, especially for low structural natural periods. On the other hand, the response of isolated buildings seems to be insensitive to the shear wave velocity variations.

References

Buckle, I.G., and Mayes, R.L. (1990), "Seismic isolation: history, application and performance. A world overview," *Earthquake Spectra*, **6** (2), 161–202.

Jangid, R.S., and Datta, T.K. (1995), "Seismic behaviour of base isolated buildings: a-state-of-the-art-review," *Proceedings of the ICE - Structures and Buildings* **110**, 186–203.

Chopra, A.K. (1995), "Dynamics of Structures: Theory and Applications to Earthquake Engineering," Englewood Cliffs (NJ): Prentice-Hall.

Kelly, J.M. (1997), "Earthquake-resistant Design with Rubber (2nd edn)," Springer: New York.

Kelly, J.M. (1998), "Seismic isolation as an innovative approach for the protection of engineering structures," Proceedings *of the Eleventh European Conference on Earthquake Engineering*, Rotterdam: A.A. Balkema.

Kelly, J.M. (1999), "Progress of applications and development in base isolation for civil and industrial structures in the United States," *Proceedings of the International Post-SMiRT Conference Seminar*, Cheju, Korea (I), 71–84.

Mostaghel, N., Hejazi, M., and Tanbakuchi, J. (1983), "Response of sliding structure to harmonic support motion," *Earthquake Engineering and Structural Dynamics*, **11** (3), 355–66.

Westermo, B., and Udwadia, F. (1983), "Periodic response of a sliding oscillator system to harmonic excitation," *Earthquake Engineering and Structural Dynamics*, **11** (1), 135–46.

Jangid, R.S. (1997), "Response of pure friction sliding structures to bi-directional harmonic ground motion," *Engineering Structures*, **19** (2), 97–104.

Calio, I., Greco, A., and Santini, A. (1998), "A parametric study of sliding multistorey buildings under harmonic excitations," *Proceedings of the Eleventh European Conference on Earthquake Engineering*, Rotterdam: A.A. Balkema.

Toki, K., Sato, T., and Miura, F. (1981), "Separation and sliding between soil and structure during strong ground motion," *Earthquake Engineering and Structural Dynamics*, **9** (3), 263–77.

Constantinou, M.C., and Kneifati, M.C. (1987), "Dynamics of soil-base isolated structure systems," *Journal of Structural Engineering*", *American* Society of Civil Engineers, **114** (1), 211–221.

Liaw, T.C., Tian, Q.L., and Cheung, Y.K. (1988), "Structures on sliding base subjected to horizontal and vertical motion," *Journal of Structural Engineering*, *American* Society of Civil Engineers, **114** (9), 2119–2129.

Constantinou, M.C., and Tadjbakhsh, I.G. (1983), "Probabilistic optimum base isolation of structures," *Journal of Structural Engineering*, *American* Society of Civil Engineers, **109** (3), 676–89.

Ryan, K.L. (2004), "Estimating the seismic response of base-isolated buildings including torsion, rocking and axial-load effects," Ph.D dissertation, University of California, Berkeley, 248 pages.

Constantinou, M.C., and Tadjbakhsh, I.G. (1984), "The optimum design of a base isolation system with frictional elements," *Earthquake Engineering and Structural Dynamics*, **12** (2), 203–14.

Wolf, J.P. (1994), "Foundation vibration analysis using simple physical models," Englewood Cliffs: Prentice-Hall.

Wolf, J.P., and Somaini, D.R. (1986), "Approximate dynamic model of embedded foundation in time domain," *Earthquake Engineering and Structural Dynamics*, **14** (5), 683–703.

De Barros, F.C.P., and Luco, J.E. (1990), "Discrete models for vertical vibrations of surface and embedded foundations," *Earthquake Engineering and Structural Dynamics*, **19** (2), 289–303.

Wolf, J.P. (1997), "Spring-dashpot-mass models for foundation vibrations," *Earthquake Engineering and Structural Dynamics*, **26** (9), 931–949.

Wu, W.H., and Chen, C.Y. (2001), "Simple lumped-parameter models of foundation using mass-spring-dashpot oscillators," *Journal of the Chinese Institute of Engineering*, **24**, 681–697.

Wu, W.H., and Lee, W.H. (2002), "Systematic lumped-parameter models for foundations based on polynomial-fraction approximation," *Earthquake Engineering and Structural Dynamics*, **31** (7), 1383–1412.

Wu, W.H., and Lee, W.H. (2004), "Nested lumped-parameter models for foundation vibrations," *Earthquake Engineering and Structural Dynamics*, **33** (9), 1051–1058.

Zheng, J., and Takeda, T. (1995), "Effects of soil-structure interaction on seismic response of PC cable-stayed bridge," *Soil Dynamics and Earthquake Engineering*, **14** (6), 427–437.

Vlassis, A.G., and Spyrakos, C.C. (2001), "Seismically isolated bridge piers on shallow soil stratum with soil-structure interaction," *Computers and Structures*, **79** (32), 2847–2861.

Tongaonkar, N.P., and Jangid, R.S. (2003), "Seismic response of isolated bridges with soil-structure interaction," *Soil Dynamics and Earthquake Engineering*, **23** (4), 287–302.

Jangid, R.S. (2004), "Seismic response of isolated bridges," *J ournal of Bridge Engineering*, *American* Society of Civil Engineers, **9** (2), 156–166.

Kunde, M.C., and Jangid, R.S. (2006), "Effects of pier and deck flexibility on the seismic response of isolated bridges," *J ournal of Bridge Engineering*, *American* Society of Civil Engineers, **11** (1), 109–121.

Spyrakos, C.C., Koutromanos, I.A., and Maniatakis, C.A. (2009a), "Seismic response of base-isolated buildings including soil-structure interaction," *Soil Dynamics and Earthquake Engineering*, **29** (4), 658–668.

Spyrakos, C.C., Maniatakis, C.A., and Koutromanos, I.A. (2009b), "Soil-structure interaction effects on base-isolated buildings founded on soil stratum," *Engineering Structures* **31** (3), 729–737.

Harris, C.M., and Piersol, A.G. (2002), "Harris' Shock and Vibration Handbook," McGraw-Hill; New York.

Whitman, R.V., and Richart, F.E. (1967), "Design procedures for dynamically loaded foundations," *Journal of Soil Mechanics and Foundations* Division , *American* Society of Civil Engineers, **93** (SM6).

Takewaki, I. (2005), "Bound of earthquake input energy to soil-structure interaction systems," *Soil Dynamics and Earthquake Engineering*, **25** (7-10), 741-752.

Wei, B.Z., Pezeshk, S., Chang, T.S., Hall, K.H., and Liu, H.P. (1996), "An empirical method to estimate shear wave velocity of soils in the New Madrid seismic zone," *Soil Dynamics and Earthquake Engineering*, **15** (6), 399-408.

8CUEE CONFERENCE PROCEEDINGS
8th International Conference on Urban Earthquake Engineering
March 7-8, 2011, Tokyo Institute of Technology, Tokyo, Japan

NONLINEAR SEISMIC RESPONSE OF BASE-ISOLATED BUILDINGS CONSIDERING POUNDING

Deepak Raj Pant[1)] and Anil C. Wijeyewickrema[2)]

1) Graduate Student, Department of Civil and Environmental Engineering, Tokyo Institute of Technology, Japan
2) Associate Professor, Department of Civil and Environmental Engineering, Tokyo Institute of Technology, Japan
pant.d.aa@m.titech.ac.jp, wijeyewickrema.a.aa@m.titech.ac.jp

Abstract: Previous studies have shown that pounding of seismically isolated buildings during earthquakes could significantly affect the performance of these buildings. In this paper analysis of seismic pounding of a typical 4-story base-isolated reinforced concrete (RC) building with retaining walls at the isolation level is presented. A modified Kelvin-Voigt impact force model, which does not have the limitations of the conventional model, is used to simulate impact. Geometric and material nonlinearities are considered in the analysis. The effect of seismic pounding on the performance of the building is evaluated based on drift demands and damage indices. The findings of the study are expected to assist design and evaluation of typical mid-rise base-isolated RC buildings.

1. INTRODUCTION

Seismic pounding refers to collision between adjacent structures during earthquakes. It occurs when structures with different dynamic characteristics, having insufficient separation between them vibrate out of phase. Earthquake reconnaissance surveys have reported that seismic pounding of *fixed-base buildings* may lead to severe damage and even result in complete collapse (Rosenblueth and Meli 1986, Kasai and Maison 1997). At least one case of seismic pounding of *base-isolated buildings* has been reported viz. the Fire Command and Control (FCC) building in Los Angeles experienced one-sided pounding with the entry bridge during the 1994 Northridge earthquake. Increased story shear, drift and acceleration demands on the steel structure were evident due to pounding (Nagarajaiah and Sun 2001). Although seismic pounding of fixed-base buildings has been studied extensively (Maison and Kasai 1992, Pant et al. 2010) for two decades, it is only recently that the seismic pounding of base-isolated buildings has drawn the attention of researchers (see for example Matsagar and Jangid 2003, Polycarpou and Komodromos 2010). All previous studies related to seismic pounding of base-isolated buildings have been carried out where the buildings were modeled as elastic or elastoplastic shear beams or elastic multi-degree-of-freedom lumped mass systems. However, these simplified models cannot incorporate characteristics of the realistic building materials such as reinforced concrete (RC). Therefore, the response of a base-isolated RC building considering seismic pounding is not well understood. Owing to the increasing use of base isolation technology for seismic protection of mid-rise RC buildings around the world, it is important to study the seismic pounding response of such buildings.

In this study, seismic pounding of a typical mid-rise base-isolated RC building with retaining walls at the base is studied. The effect of seismic pounding on the performance of the building is assessed using three-dimensional nonlinear finite element (FE) analysis.

2. IMPACT SIMULATION

The contact element approach is widely used for the simulation of impact between structures, due to its clear physical meaning and simple algorithm. The appropriate force-deformation relationship of the contact element is one of the important issues in pounding simulations. Hence, there have been numerous efforts to develop various impact force models for these contact elements. Although nonlinear impact force models are also available, the linear impact force models provide a good balance between simplicity and accuracy. The Kelvin-Voigt (KV) model, which can be represented by the combination of a spring and a dashpot in parallel, is the most widely used impact force model. In this model, the impact force F between the impacting bodies is,

$$F = \begin{cases} k_l \delta + c\dot{\delta} & \delta > 0, \\ 0 & \delta \le 0, \end{cases} \tag{1}$$

where k_l is stiffness of spring element, c is damping coefficient and indentation δ and relative velocity of impact $\dot{\delta}$ are given by,

$$\delta = u_i - u_j - d_g, \qquad \dot{\delta} = \dot{u}_i - \dot{u}_j, \tag{2}$$

where u_i and u_j are displacements and $\dot{u}_i$ and $\dot{u}_j$ are velocities of impacting nodes *i* and *j*, respectively and d_g is at-rest gap distance between the impacting nodes. The damping coefficient c in Eq. (1) can be expressed in terms of the coefficient of restitution r, which is defined as the ratio of the relative velocity after impact to the relative velocity before impact. The expression for the damping coefficient in the KV model is (Anagnostopoulos 2004),

$$c = 2\xi\sqrt{\left(k_l m_{eff}\right)}, \tag{3}$$

where the stiffness k_l in the absence of experimental studies is determined based on the axial stiffness of colliding bodies and the effective mass m_{eff} and damping ratio ξ are given by,

$$m_{eff} = \frac{m_1 m_2}{m_1 + m_2}, \quad \xi = -\frac{\ln(r)}{\sqrt{\pi^2 + (\ln(r))^2}}, \tag{4}$$

where m_1 and m_2 are masses of the colliding bodies. Although the model is attractive due to its simplicity, the limitations are:

(i) Due to a constant damping coefficient, it shows a sudden jump in the impact force at the beginning of impact, which is not reasonable for concrete-to-concrete impact (Fig. 1(a)). This sudden jump in the force induces unrealistic high accelerations in the impacting bodies.

(ii) Due to the dashpot being activated even in the restitution phase, the colliding bodies exert tension on each other just before the separation (Fig. 1(a)), which has no physical meaning.

Hence, a modification to the KV model referred to as the Modified Kelvin-Voigt (MKV) model was proposed by Pant et al. 2010. The MKV model is based on the assumption that most of the energy during impact is dissipated in the compression phase. Hence, the energy dissipated in the restitution phase can be neglected. This assumption allows for the removal of the dashpot from the spring-dashpot assembly in the restitution phase. The impact force F between the impacting bodies can be expressed as,

$$F = \begin{cases} k_l\delta + c\dot{\delta} & \delta > 0 \text{ and } \dot{\delta} > 0, \\ k_l\delta & \delta > 0 \text{ and } \dot{\delta} \le 0, \\ 0 & \delta \le 0. \end{cases} \tag{5}$$

In order to avoid a sudden jump in the impact force at the beginning of impact, the damping coefficient c is taken to be directly proportional to the indentation δ as,

$$c = \xi\delta. \tag{6}$$

This leads to a new relationship between ξ and r as,

$$\xi = \frac{3k_l\left(1 - r^2\right)}{2r^2\dot{\delta}_0}, \tag{7}$$

where $\dot{\delta}_0$ is relative velocity before impact. The relationship between impact force and indentation for the MKV model is shown schematically in Fig. 1(b). It is clear from Fig. 1(b) that the sudden jump in impact force at the beginning of impact and the tensile impact force just before the separation of the KV model are no longer present. Thus, all the major limitations of the KV model are eliminated in the MKV model, while maintaining the simplicity and clear physical meaning of the KV model. Furthermore, the model is implemented in FE program OpenSees 2010 in the form of a uniaxial material and is used to simulate seismic pounding of a base-isolated building in subsequent sections.

It is noted that other researchers have also proposed different modifications to the KV model. However, a comparison of these models with the MKV model has shown that the MKV model is more rational for seismic pounding simulation of multi-story buildings (Pant 2010).

To verify the correctness of the derived formula (Eq. (7)) and its proper implementation in OpenSees, numerical verification is conducted by simulating the first instance of impact between a spherical ball and a stationary rigid surface. A ball of mass $m = 1.0\ kg$ is dropped freely from a height $h = 0.5\ m$ on a stationary rigid surface (Fig. 2(a)). Different values of coefficient of restitution r_{pre} are specified, pounding simulations are performed and the coefficient of restitution from the simulation r_{post} are obtained and compared with the pre-specified values. In OpenSees, the simulation is conducted using two-dimensional FE method. The FE model of the problem is shown in Fig. 2(b). The stationary rigid surface and the spherical ball are modeled as node 1 and node 2, respectively. Node 1 is fixed and node 2 is free to move

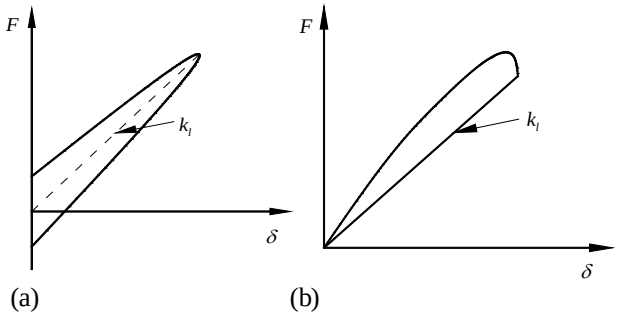
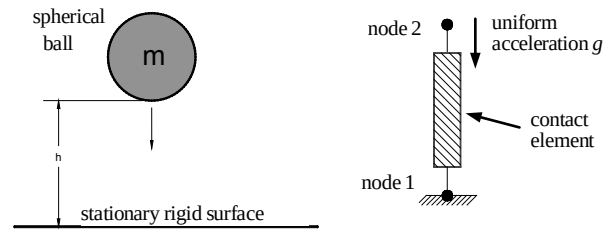


Fig. 1. Schematic force-indentation curve for one instance of impact for: (a) KV model; (b) MKV model.



(a) (b)

Fig. 2. Drop weight impact simulation: (a) schematic diagram; (b) finite element idealization.

Table 1. Comparison of pre-defined and simulated values of coefficient of restitution using MKV model.

r_{pre}	r_{post}	**Relative error (%)**
0.10	0.113	13.4
0.20	0.223	11.5
0.30	0.328	9.2
0.40	0.428	7.0
0.50	0.525	5.0
0.60	0.620	3.3
0.70	0.713	1.9
0.80	0.807	0.9
0.90	0.902	0.2
1.00	1.000	0.0

only in the vertical direction. A contact element needs to be placed between the nodes to simulate the pounding phenomenon. Here, a so called zero-length element available in OpenSees is chosen. With the zero-length element, end nodes of the element can have same coordinates. Particular choice of zero-length element as contact element becomes very advantageous while performing a large number of numerical simulations of seismic pounding between structures with various at-rest gap distances. The nodal coordinates of the adjacent structures need not to be revised for each gap case; rather the gap parameter in the associated uniaxial material only needs to be changed. For the present simulation, the MKV model is assigned to the aforementioned contact element. The stiffness of spring element k_1 is set to 2.0×10^7 N/m. In the free fall condition, node 2 has a constant acceleration of g in downward direction. Hence, a uniform acceleration loading is applied at node 2. To be consistent with the seismic pounding simulations going to be discussed in forthcoming sections, the applied acceleration is treated from the viewpoint of *uniform ground acceleration.* The resulting system of nonlinear equations is solved using Newmark's method of constant acceleration ($\beta = 0.25$, γ=0.5), where Modified Newton-Raphson method is used for iterative solution. The analyses are performed for 0.35 sec with a time step of 1×10^{-7} sec. The values of r_{post} obtained from pounding simulation are compared with r_{pre} and relative error is computed as $\left|r_{pre}-r_{post}\right|/r_{pre}$. The comparison is shown in Table 1. The relative error reduces with increasing r. The coefficient of restitution used to simulate structural pounding ranges from 0.5 to 0.75 (Jankowski 2005). It is clear from Table 1 that the relative error is small for the values of coefficient of restitution in this range. This shows that the relationship between ξ and r given by Eq. (7) is correct and hence can be used for rational simulation of structural pounding.

3. SEISMIC POUNDING CASES

A 4-story, 2-bay by 2-bay base-isolated RC building is considered to investigate the effect of pounding on the response of a typical mid-rise structure. The bay widths and story heights are 6 m and 3.6 m, respectively. The building is supposed to be used as an elementary school such that substantial hazard to human life is expected in case of failure. The building is assumed to be located at a stiff soil site. Two cases of seismic pounding of this building are examined:

(i) Pounding with the retaining wall on one side (Fig. 3(a)),
(ii) Pounding with the retaining walls on both sides (Fig. 3(b)).

The retaining wall extends from ground level up to the isolation level (Fig. 3). The building was designed following the 2009 International Building Code (ICC 2009). According to the code, an equivalent lateral force procedure was used for the design of this building. ACI 318-08 (ACI 2008) was followed for the design of the structural concrete. Compressive strength, unit weight and modulus of elasticity of concrete are taken as 28 MPa, 22.76 kN/m^3 and 2.5×10^4 MPa, respectively. The yield strength of main steel reinforcement bars and ties are taken as 420 MPa and 300 MPa, respectively. The unit weight and modulus of elasticity of steel are assumed to be

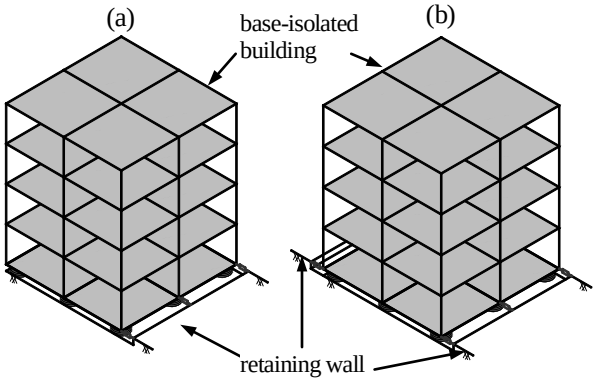


Fig. 3. The base isolated building with: (a) retaining wall on one side; (b) retaining walls on both sides.

76.97 kN/m^3 and 1.99×10^5 MPa, respectively. Live loads on floors and roofs are assumed to be 4.79 kN/m^2 and 0.96 kN/m^2, respectively. Total wall thickness is taken as 113 mm with a unit weight of approximately 15.0 kN/m^3. The slab thickness is 200 mm. For the floor finish, a 10 mm thick porcelain tile with a unit weight of 23.57 kN/m^3 is taken. Seismic force-resisting system of the building is chosen as special moment-resisting frame (SMRF). The lead rubber bearing (LRB) isolation system is selected for the building. Bearings are designed for gravity and earthquake loads using SAP2000 (2009) and Microsoft Excel spreadsheets. Identical circular bearings of 750 mm diameter and 572 mm height are provided under each of the 9 column bases. A total of 30 layers of rubber with a layer thickness of 15 mm are used. Steel shim thickness is taken as 2 mm. The design displacement D_D and total maximum displacement D_{TM} of the isolation system are 225 mm and 462 mm, respectively. Figure 4 shows the cross-section of the bearing.

In order to investigate the influence of separation, the structures are assumed to be separated by different at-rest gap distances d_g in both of the pounding cases. It is considered that the gap between buildings can be as small as half of the design displacement D_D. Therefore, ratio of at-rest gap distance to the design displacement is taken as 1.0, 0.9, 0.8, 0.7, 0.6 and 0.5.

For performance evaluation, four earthquake ground motions are selected from 1968 Hachinohe, 1940 El Centro, 1995 Kobe and 1994 Northridge earthquakes (see Table 2 for details of ground motions). The earthquake ground motions are matched to the design response spectrum at 5% damping using wavelet adjustments. The program RspMatch2005 (Hancock et al. 2006) is used to match the ground motions simultaneously to the design acceleration response spectrum (Fig. 5) and the design displacement response spectrum for natural periods up to 6 sec.

4. NUMERICAL MODELING AND ANALYSIS

A macromodel-based approach is adopted for three-dimensional modeling of seismic pounding of the base-isolated building in OpenSees. There are three

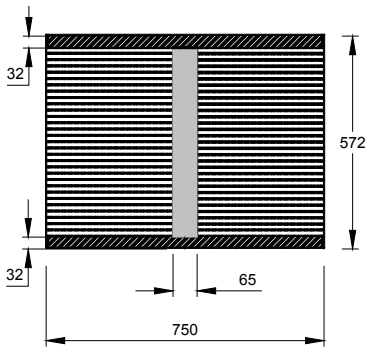


Fig. 4. Cross-section of the bearing (all dimensions are in mm)

Table 2. Details of earthquake ground motions.

Earthquake	Date	Station	PGA (g)
Hachinohe	1968/05/16	Hachinohe city	0.239
El Centro	1940/05/19	El Centro Array #9	0.313
Kobe	1995/01/17	JMA Kobe	0.821
Northridge	1994/01/17	Rinaldi Receiving Station	0.825

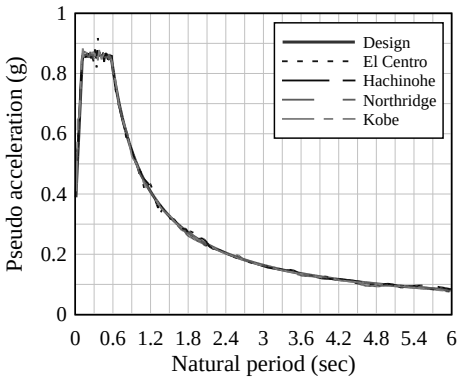


Fig. 5. Comparison of elastic pseudo acceleration response spectra of matched ground motions with design acceleration response spectrum.

modeling issues to be addressed viz. modeling of structural members which are beams, columns, lead rubber bearings and slabs, modeling of retaining walls and modeling of impact. Reinforced concrete beams and columns are modeled using force-based, fiber beam-column elements, which are considered as most accurate and robust distributed plasticity elements. In fiber beam-column elements, the element response is evaluated at certain number of integration points i.e. sections along the length of the element and each section is discretized into unconfined concrete, confined concrete and steel fibers (Fig. 6, 7). Uniaxial materials with nonlinear constitutive relationship are assigned to these fibers. Section constitutive relationship is derived from the integration of constitutive relationship of fibers. There are several material models to describe nonlinear constitutive relationship of concrete and steel under monotonic as well as cyclic loading. In this study the modified Kent and Park model (Park et al. 1982) is used for the response of concrete in compression. In tension, a linear elastic branch is followed by a linear softening branch up to zero stress (Fig. 8(a)). For reinforcing steel, the constitutive model of Menegotto and Pinto (Menegotto and Pinto 1973) is used (Fig. 8(b)). Lead rubber bearings are modeled using elastomeric bearing elements. A bilinear hysteretic model (Fig. 8(c)) is used to describe shear force-deformation relationship of these elements. Floor and roof slabs are not modeled explicitly; rather their restraining effect is accounted for by assuming an in-plane rigid diaphragm response. Retaining walls are modeled as rigid objects. Backfill soil-structure

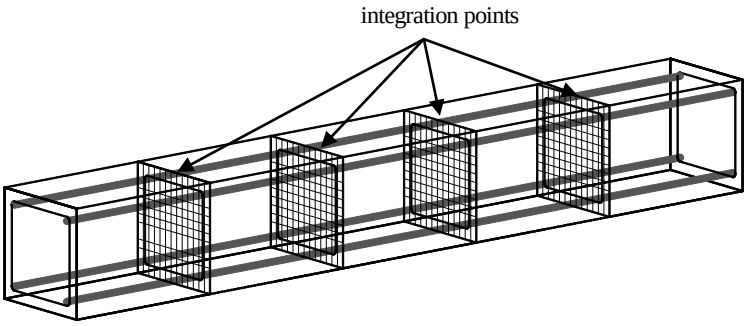


Fig. 6. A fiber beam-column element.

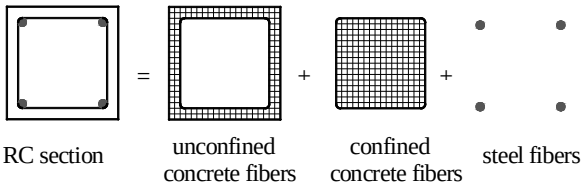


Fig. 7. Discretization of RC section into unconfined concrete, confined concrete and steel fibers.

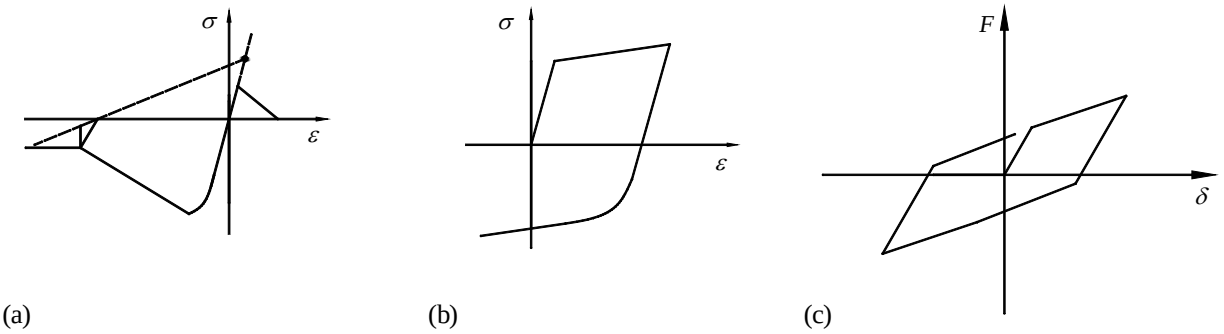


Fig. 8. (a) Stress-strain relationship of concrete; (b) stress-strain relationship of reinforcing steel; (c) bilinear hysteretic model of elastomeric bearing elements.

interaction is considered outside the scope of this study. Impact is modeled using zero length elements, which are used as contact elements between structures at floor levels (Fig. 3). The material property of the contact elements is based on the MKV model. The coefficient of restitution r is taken as 0.65 and stiffness of spring element k_i is assessed based on the axial stiffness of a slab.

Nonlinear time-history analyses are performed. Time integration of equations of motion is accomplished using Newmark's method of constant acceleration. A time step of 0.005 sec is used for all the cases. The nonlinearity of the problem demands an iterative solution procedure. At the beginning of each time step modified Newton-Raphson method is employed for the iterative solution and the method is changed if the convergence is not achieved in the time step. There are many alternatives to modified Newton-Raphson method in OpenSees such as Newton with line search or Broyden method. The convergence of the solution is based on energy increment. For damping in the building, stiffness proportional damping is applied to the superstructure only. A damping ratio of 5% is used for the first mode of the isolated structure.

The accuracies of impact force model and FE modeling have been validated using an available impact experiment and a shake table test of a base-isolated RC building, respectively. Details of the validation are shown elsewhere (Pant 2010).

5. RESULTS AND DISCUSSION

Inter-story drift ratio and overall damage index (ODI) based on Park and Ang damage index (Park et al. 1985) are presented to illustrate the influence of pounding on the structural performance of the base-isolated building.

Table 3. Values of inter-story drift ratios and overall damage indices for performance evaluation of RC buildings.

Degree of damage	Physical appearance	Inter-story drift ratio (%)	ODI
No damage	Minor localized cracking	drift ratio $<$ 0.5	ODI $<$ 0.1
Minor to moderate damage	Light cracking throghout to extensive cracking and localized spalling of concrete	0.5 $\leq$ drift ratio $<$ 1.5	0.1 $\leq$ ODI $<$ 0.4
Severe damage	Extensive crushing of concrete and exposure of buckled reinforcement	1.5 $\leq$ drift ratio $<$ 3.0	0.4 $\leq$ ODI $<$ 1.0
Total collapse	Complete loss of load carrying capacity	drift ratio $\geq$ 3.0	ODI $\geq$ 1.0

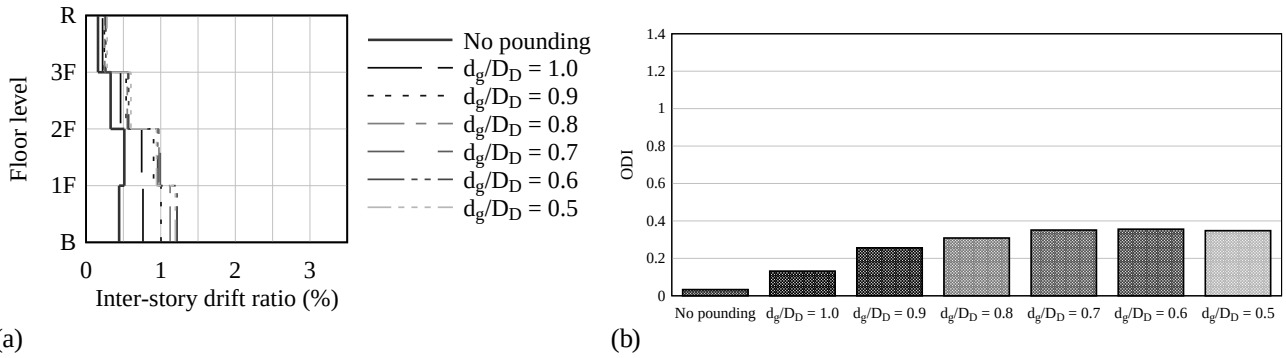


Fig. 9. Response of the base-isolated building considering pounding with the retaining wall on one side: (a) peak inter-story drifts; (b) overall damage indices.

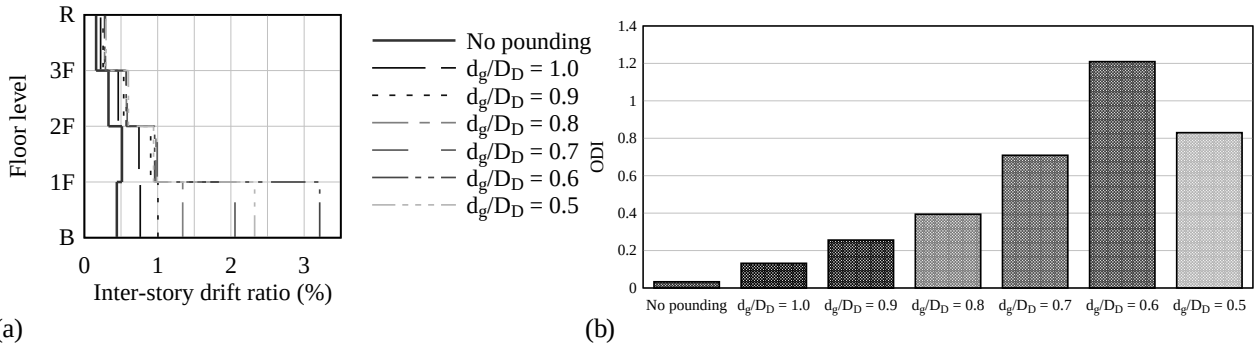


Fig. 10. Response of the base-isolated building considering pounding with retaining walls on both sides: (a) peak inter-story drifts; (b) overall damage indices.

The damage can be classified as no damage, minor to moderate damage, severe damage and total collapse based on inter-story drift ratio and ODI as shown in Table 3. Note that to highlight the trends in the response, the results presented represent maximum responses generated due to all four earthquake excitations.

When the pounding of the base-isolated building is considered with the retaining wall on one side, the peak inter-story drift ratio, which is less than 0.5% at the first story when there is no pounding, becomes more than 1.2% due to pounding (Fig. 9(a)). This implies that the base-isolated building experiencing no damage without any interaction with adjacent structures undergoes minor to moderate damage due to pounding. In general, the inter-story drift demand increases with reduction in the gap. In addition, the maximum inter-story drift occurs at the first story and gradually reduces at upper stories. The minor to moderate damage to the building is also evident from Fig. 9(b), where ODI remains less than 0.4. A clear pattern of overall damage is also observed from Fig. 9(b). Overall damage index increases rapidly for the gaps up to 70% of the design displacement and becomes nearly constant for further reduction in the gap.

Significant increase in the demands is observed in case

of pounding with the retaining walls on both sides compared to one-sided pounding (Fig. 10(a)). The peak inter-story drift demand at the first story clearly exceeds 1.5% for the gaps smaller than 80% of design displacement, denoting severe damage to the story. Imminent collapse of the story is evident at a gap equal to 60% of the design displacement. The influence of pounding is less severe at upper stories. Fig. 10(b) shows clear trend in the overall damage to the building for various gaps. With decreasing gap, the ODI first increases and then reduces with further reduction of the gap. This implies that there exists a critical at-rest gap distance causing maximum damage to the base-isolated building.

6. CONCLUDING REMARKS

This study investigates the performance of a typical mid-rise base-isolated RC building considering seismic pounding. It is found through series of numerical analyses that the seismic pounding has detrimental effects on the response of a base-isolated RC building. While one-sided pounding with a retaining wall at the base causes minor to moderate damage to the base-isolated building, two-sided pounding with retaining walls at the base could even lead to its collapse, depending upon the clear space maintained around the building.

The present study only focuses on the evaluation structural damage to the building due to pounding. Evaluation of the non-structural damage, which requires accurate estimation of floor accelerations in the building, could be studied in the future. Furthermore, the present study is only focused on the seismic performance evaluation of base-isolated buildings. The mitigating measures against pounding should also be studied in the future.

Acknowledgements:

The first author is pleased to acknowledge a Monbukagakusho (Ministry of Education, Culture, Sports, Science and Technology, Japan) scholarship for graduate students. Financial support from the Center for Urban Earthquake Engineering (CUEE) through the GCOE Program "International Urban Earthquake Engineering Center for Mitigating Seismic Mega Risk," is gratefully acknowledged.

References:

ACI (2008), "Building Code Requirements for Structural Concrete (ACI 318-08) and Commentary (ACI 318R-08)", ACI Committee 318, American Concrete Institute, Farmington Hills, MI.

Anagnostopoulos S.A. (2004), "Equivalent viscous damping for modeling inelastic impacts in earthquake pounding problems", *Earthquake Engineering and Structural Dynamics*, **33**, 897-902.

Hancock, J., Watson-Lamprey, J., Abrahamson, N.A., Bommer, J.J., Markatis, A., Mccoy, E. and Mendis, R. (2006), "An improved method of matching response spectra of recorded earthquake ground motion using wavelets", *Journal of Earthquake Engineering*, **10** (Sp. 1), 67-89.

International Code Council (ICC) (2009), "International Building Code", IBC 2009, Country Club Hills, Illinois.

Jankowski, R. (2005), "Non-linear viscoelastic modelling of earthquake-induced structural pounding", *Earthquake Engineering and Structural Dynamics*, **34**, 595-611.

Kasai, K. and Maison, B. (1997), "Building pounding damage during the 1989 Loma Prieta earthquake", *Engineering Structures* , **19**, 195-207.

Maison, B.F. and Kasai, K. (1992), "Dynamics of pounding when two buildings collide", *Earthquake Engineering and Structural Dynamics*, **21**, 771-786.

Matsagar, V.A. and Jangid, R.S. (2003), "Seismic response of base-isolated structures during impact with adjacent structures", *Engineering Structures*, **25**, 1311-1323.

Menegotto, M. and Pinto, P. (1973), "Methods of analysis for cyclically loaded R/C frames", *Proceedings of the Symposium of Resistance and Ultimate Deformability of Structure Acted by Well Defined Repeated Load*, IABSE, Lisbon, Portugal.

Nagarajaiah, S. and Sun, X. (2001), "Base-isolated FCC building: impact response in Northridge earthquake", *Journal of Structural Engineering*, ASCE, **127**(9), 1063-1075.

OpenSees (2010), Open system for earthquake engineering simulation. <http://opensees.berkeley.edu>

Pant, D.R. (2010), "Seismic Pounding of a Base-Isolated Building with Adjacent Structures", *M. Eng. Thesis*, Tokyo Institute of Technology.

Pant, D.R., Wijeyewickrema, A.C. and Ohmachi, T. (2010), "Three dimensional nonlinear analysis of seismic pounding between multi-story reinforced concrete buildings", *Proceedings of the Seventh International Conference on Urban Earthquake Engineering (7CUEE) and Fifth International Conference on Earthquake Engineering (5ICEE)*, March 3-5, Tokyo, Japan, 1829-1840.

Park, R., Priestley, M.J.N. and Gill, W.D. (1982), "Ductility of square-confined concrete columns", *Journal of Structural Engineering*, ASCE, **108**, 929-950.

Park, Y., Ang, A.H. and Wen, Y.K. (1985), "Seismic damage analysis of reinforced concrete buildings", *Journal of Structural Engineering*, ASCE, **111**(4), 740-757.

Polycarpou, P.C. and Komodromos, P. (2010), "Earthquake-induced poundings of a seismically isolated building with adjacent structures", *Engineering Structures*, **32**, 1937-1951.

Rosenblueth, E. and Meli, R. (1986), "The 1985 earthquake: causes and effects in Mexico City", *Concrete International* (ACI), **8**, 23-36.

SAP2000 (2009), Integrated finite element analysis and design of structures, Computers and Structures, Inc., Berkeley, CA.

8CUEE CONFERENCE PROCEEDINGS
8th International Conference on Urban Earthquake Engineering
March 7-8, 2011, Tokyo Institute of Technology, Tokyo, Japan

POUNDING OF BASE ISOLATED STRUCTURES CONSIDERING INELASTIC BEHAVIOR OF SUPERSTRUCTURE

Parisara Thiravechyan[1)], Troy A. Morgan[2)], and Kazuhiko Kasai[3)]

1) Graduate student, Dept. of Built Environment, Tokyo Institute of Technology, Japan
2) Assistant Professor, Center of Urban Earthquake Engineering, Tokyo Institute of Technology, Japan
3) Professor, Structural Engineering Research Center, Tokyo Institute of Technology, Japan
thiravechyan.p.aa@m.titech.ac.jp, morgan@cuee.titech.ac.jp, kasai@serc.titech.ac.jp

Abstract: Designed according to modern seismic provisions, base isolated structures are required to develop sufficient strength such that they remain essentially elastic in the expected Design Basis Earthquake (DBE). Additionally, a sufficient seismic separation distance (or moat) must be provided to accommodate expected displacement in a Maximum Considered Earthquake (MCE). However, little consideration is given to the effect of inelastic superstructural behavior on the seismic performance given the occurrence of an event greater than the DBE. This study investigates parametrically the effect of superstructure yield strength and seismic separation on the ultimate behavior of base isolated structures. Nonlinear response history analysis including pounding is then utilized to examine the tradeoffs between providing a weaker superstructure and a smaller seismic gap. Results indicate that a decrease in superstructural strength significantly increases ductility demand but the likelihood of pounding reduces. In contrast, an increase in gap size does not assure a decrease in ductility.

1. INTRODUCTION

Base isolation is an approach to mitigate earthquake damage that has been used over the past 25 years. The concept is to reduce seismic demand by adding horizontally flexible elements called isolators between the structure above and its base, thereby isolating the building from the horizontal components of ground motion. However, large deformation is expected at the isolation interface, and as a result, sufficient separation between the structure and surrounding moat walls must be provided to prevent pounding.

Following modern US building code provisions, a separation gap between the isolation level and surrounding walls is required to accomodate the displacement in a Maximum Considered Earthquake (MCE), an event having a 2475-year return period. Moreover, the superstructure is expected to remain elastic for the expected Design Basis Earthquake (DBE), an event whose response spectrum is 2/3 of the MCE. Figure 1(a) schematically shows the behavior of the isolated structure implied by the code, whereby pounding is avoided and yielding in the superstructure is prevented. Previous studies on base isolated structures have primarily focused on this case.

On the other hand, for an earthquake greater than DBE level, yielding is expected to occur, as shown in Figure 1(b). Also, insufficient seismic gap may cause pounding, as shown in Figure 1(c), which can significantly increase the building acceleration and force (Kasai et al. 1990), and may cause much damage to the structure. Additionally, a combination of pounding and yielding may occur, as indicated in Figure 1(d). Although yielding causes structural damage, it impedes the base from moving further and reduces the possibility of pounding. Therefore, selecting an appropriate combination of superstrucutural strength and separation distance is a potentially useful approach to

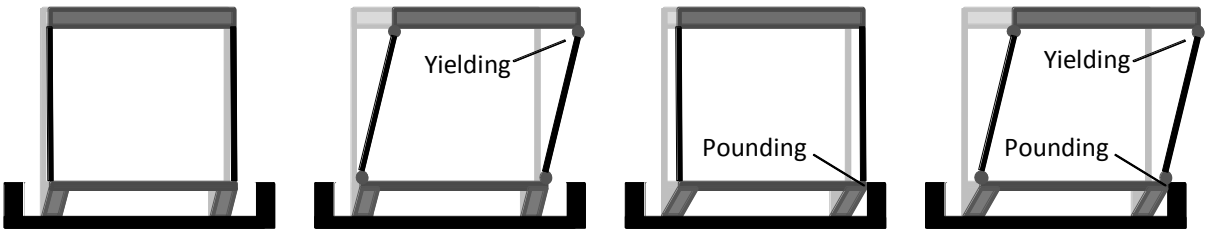


Figure 1 Possible modes of behavior for base isolated buildings

achieve the desired performance of the structure. This study investigates parametrically the combined effects of superstructure yield strength and seismic separation.

2. MODELING ASSUMPTIONS

As depicted in Figure 2, the base isolated structure is modelled as a 2 degree-of-freedom (2DOF) system. Assuming equal floor masses, the superstructure mass to total mass ratio can be calculated as $\gamma = (N-1)/N$ where N represents number of stories of the structure. Letting $m_s + m_b = 1$, we can compute $m_s = \gamma$, and $m_b = 1-\gamma$. During earthquake excitation, the isolation system is assumed to behave linearly with stiffness k_b and damping coefficient c_b, while the superstructure behaves elasto-perfectly-plastically with superstructural stiffness k_s, damping coefficient c_s, and ratio of superstructure yield strength f_{ys} to superstructural weight $m_s g$, namely $\overline{f}_{ys}$ ($=f_{ys}/m_s g$). Pounding is assumed to occur at the isolation level, the most common case of impact for base isolated buildings. Contact elements are simulated using a linear elastic spring with stiffness k_w arbitrarily taken as 10 times the superstructure stiffness k_s, following the general assumption of previous researchers (Tsai 1997, Komodromos 2008). This contact element is located a separation distance, s, away from both sides of the base structure. Energy dissipation due to pounding is not considered based on previous studies (Tsai 1997).

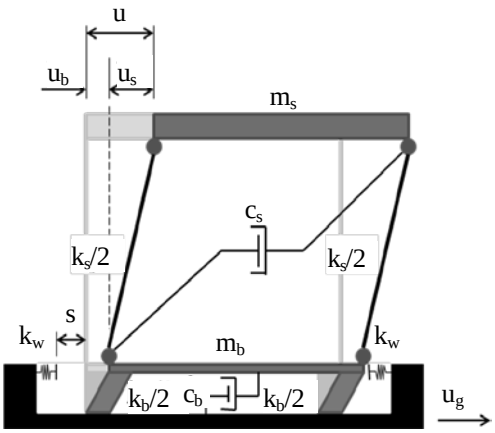


Figure 2 Analysis model

3. GROUND MOTIONS

The SAC suite of ground motions with 2% possibility of exceedance in 50 years for the Los Angeles area, LA21-LA40, are used in this study (Somerville et al. 1998). These ground motions were developed to represent the MCE for downtown Los Angeles. Figure 3 shows response spectra of these 20 ground motions, including a comparison of the median acceleration spectrum with the code-prescribed DBE and MCE for the site. Previous researchers have indicated that ground motion parameters are lognormally distributed (Mcguire 2004), and as a result, the geometric mean provides a good measure of central tendency of a sample and is used here to estimate the median.

4. PARAMETRIC STUDIES

The superstructure vibration period is defined as $T_s = 0.1N$. Base and superstructural masses and stiffnesses are selected to obtain the desired isolation system and superstructural periods and damping ratios from the following equations:

$$T_s = 2\pi\sqrt{\frac{m_s}{k_s}}, \quad T_b = 2\pi\sqrt{\frac{m_s + m_b}{k_b}} \qquad \text{(1a,b)}$$

$$\zeta_s = \frac{c_s T_s}{4\pi m_s}, \quad \zeta_b = \frac{c_b T_b}{4\pi(m_s + m_b)} \qquad \text{(2a,b)}$$

From the parameters above, "Elastic No-Pounding (ENP) Response" for a particular ground motion with given T_s, ζ_s, T_b and ζ_b can be obtained. For the selected strength reduction factor R and separation ratio β, superstructure

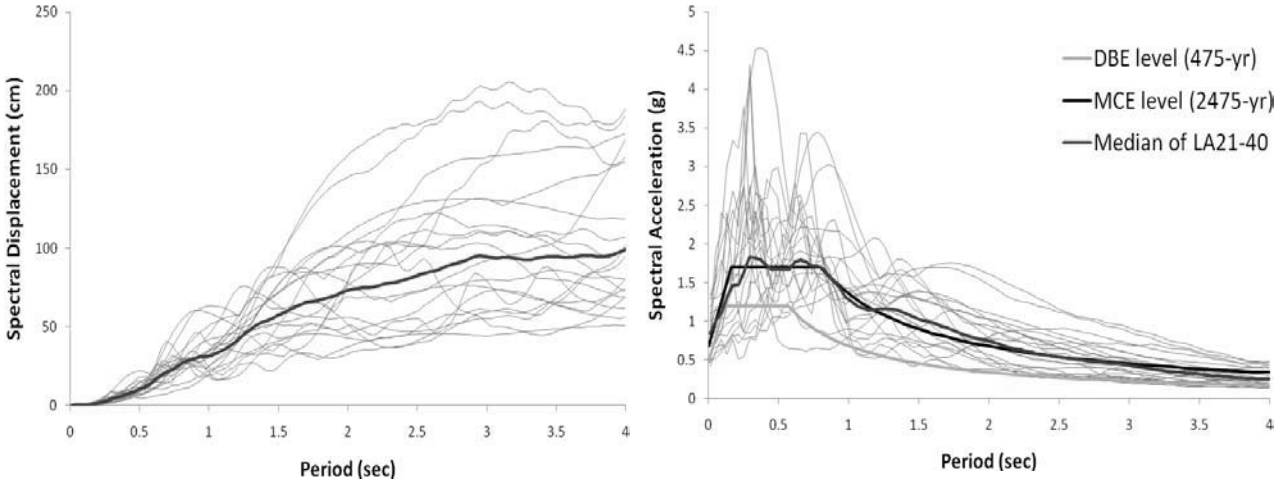


Figure 3 Response spectra of SAC LA21-40 ground motions and comparison with code spectra

yield strength f_{ys} and separation distance s for the simulation can be computed based on the definitions as follows:

$$R = f_{s0}^{ENP} / f_{ys}, \quad \beta = s / u_{b0}^{ENP} \qquad (3a,b)$$

where f_{s0}^{ENP} is the maximum superstructural force for the ENP case and u_{b0}^{ENP} is the maximum displacement of the isolator relative to the ground for the ENP case.

This study focuses on the case of a 5-story building, so T_s = 0.5 sec. is assumed and superstructure damping is taken as ζ_s = 0.02. Six isolation systems are considered, with period T_b = 2, 3, and 4 sec., and damping ζ_b = 0.10 and 0.30. R is varied from 0.1 to 1.0 with increments of 0.1 and from 1.5 to 4.0 with increments of 0.5. β is varied from 0.0 to 1.0 with increments of 0.2. The result for each combination of system parameters are discussed using median response from the suite of 20 ground motions.

5. EXAMPLE RESPONSE HISTORIES

5.1 Four cases of pounding / no-pounding histories

As an example, four cases of dynamic response of a structure with T_s = 0.5 sec., ζ_s = 0.02, T_b = 2 sec., and ζ_b = 0.10 subjected to the LA29 excitation is discussed. Peak ground acceleration of the LA29 record is 0.81g. The maximum superstructural force normalized by superstructural weight, $\overline{f}_{s0}^{ENP}$, for this ground motion is 0.32. Case 1, presented as thick solid lines in Figure 4 for which R = 1.0 and β = 1.0, corresponds to the ENP case (as shown in Figure 1(a)). Case 2, presented as thick dotted lines, describes the response when R is increased to 1.5 which represents yielding with no-pounding case (Figure 1(b)). Case 3, shown as thin solid lines, corresponds to Figure 1(c) which is pounding with elastic response of the superstructure. The separation ratio is reduced to 0.4 while R is reduced to 0.3. Case 4, shown as thin dotted lines, has the same separation distance of 0.4, but R is increased to 1.5, resulting in a combination of yielding and pounding as in Figure 1(d).

5.2 Observations

Figure 4(a) shows the superstructure displacement relative to the base, u_s (as shown in Figure 2). The first case, which represents the ENP response, shows elastic behavior with the maximum superstructure displacement u_{s0}^{ENP} = 2 cm. When R is increased for Case 2, a single yield excursion occurs at around 12.3 sec., resulting in the largest residual structural displacement among the four cases shown. In Cases 3 and 4 where the gap size is reduced, pounding first occurs at approximately 11.4 seconds and results in a sudden displacement increase in the superstructure. However, the responses are different due to the difference in superstructural strength.

Figure 4(b) represents superstructure ductility demand $\mu_s = u_s / u_{ys}$ where u_{ys} is the superstructure yield displacement computed from $u_{ys} = f_{ys} / k_s$ and f_{ys} is the superstructure yield strength obtained from Eq. (3a). Ductility demand of the ENP case is in the range of -1.0 to 1.0, meaning yielding does not occur. Case 2 shows significant yielding when R is increased as described above, resulting in the largest ductility demand (μ_s = 8.54) among all cases. Due to the increased strength, large displacements caused by pounding in Case 3 do not exceed the yield displacement and therefore the superstructure responds elastically. This can be seen by observing that μ_s is in the range between -1.0 to 1.0. Considering Case 4, which has the same strength as Case 1 but with the gap size reduced to 0.4, the response due to pounding causes yielding of the superstructure, and the ductility demand is increased to 5 relative to Case 1 in which no pounding occurs. The occurrence of both pounding and yielding in Case 4 results in a residual displacement smaller than that obtained from Case 2, but this may not be a general trend for all ground motions.

Base displacement u_b normalized by the maximum base displacement of the ENP case u_{b0}^{ENP} is shown in Figure 4(c). For this example, u_{b0}^{ENP} is 29 cm. Using this number as the normalizing value, u_b / u_{b0}^{ENP} of Case 1 reaches the maximum of -1.0 at 12.5 sec. In Case 2, yielding of the superstructure reduces the base displacement, implying that a weaker structure decreases the possibility of pounding. In Cases 3 and 4, pounding limits the base displacement so that the peaks and troughs of both cases are flattened at 0.4 which correspond to the separation ratio (Eq.(3b)) provided. Differences in superstructural strength causes yielding that affect response at the base. Pounding occurs five times between 11 to 14 seconds in Case 3 while occuring only three times in Case 4 and another two times between 16-17 seconds.

Figure 4(d) describes the total superstructure acceleration $\ddot{u}_{s,tot} = \ddot{u}_s + \ddot{u}_b + \ddot{u}_g$. In Cases 1, 2 and 4 where superstructural strengths are limited, the effect of pounding to superstructural acceleration is not significant because yielding prevents the impact force from propagating to the above structure (Tsai 1997). But when R=0.3 in Case 3, the superstructure behave elastically and pounding causes high acceleration that even larger than the peak ground acceleration of the excitation. This agrees with previous studies (Tsai 1997, Komodromos 2008).

Base acceleration $\ddot{u}_{b,tot} = \ddot{u}_b + \ddot{u}_g$ is presented in Figure 4(e). For the first 2 cases without pounding, the response is very smooth. However, the occurrence of pounding excites large acceleration spikes at the isolation system level. This agrees with previous research findings (Kasai et al. 1990, Ye et al. 2009).

Because acceleration response is highly sensitive to the characteristic of the wall, effect of superstructure strength and separation distance on the acceleration response should be a subject of further study. However, the subsequent chapter focuses only on ductility demand, μ_s.

6. RESULTS OF PARAMETRIC STUDIES

6.1 Superstructural yield strength f_{ys}

The strength reduction factor R is varied from 0.1 to 4.0 to study the ductility demand resulting from a specified

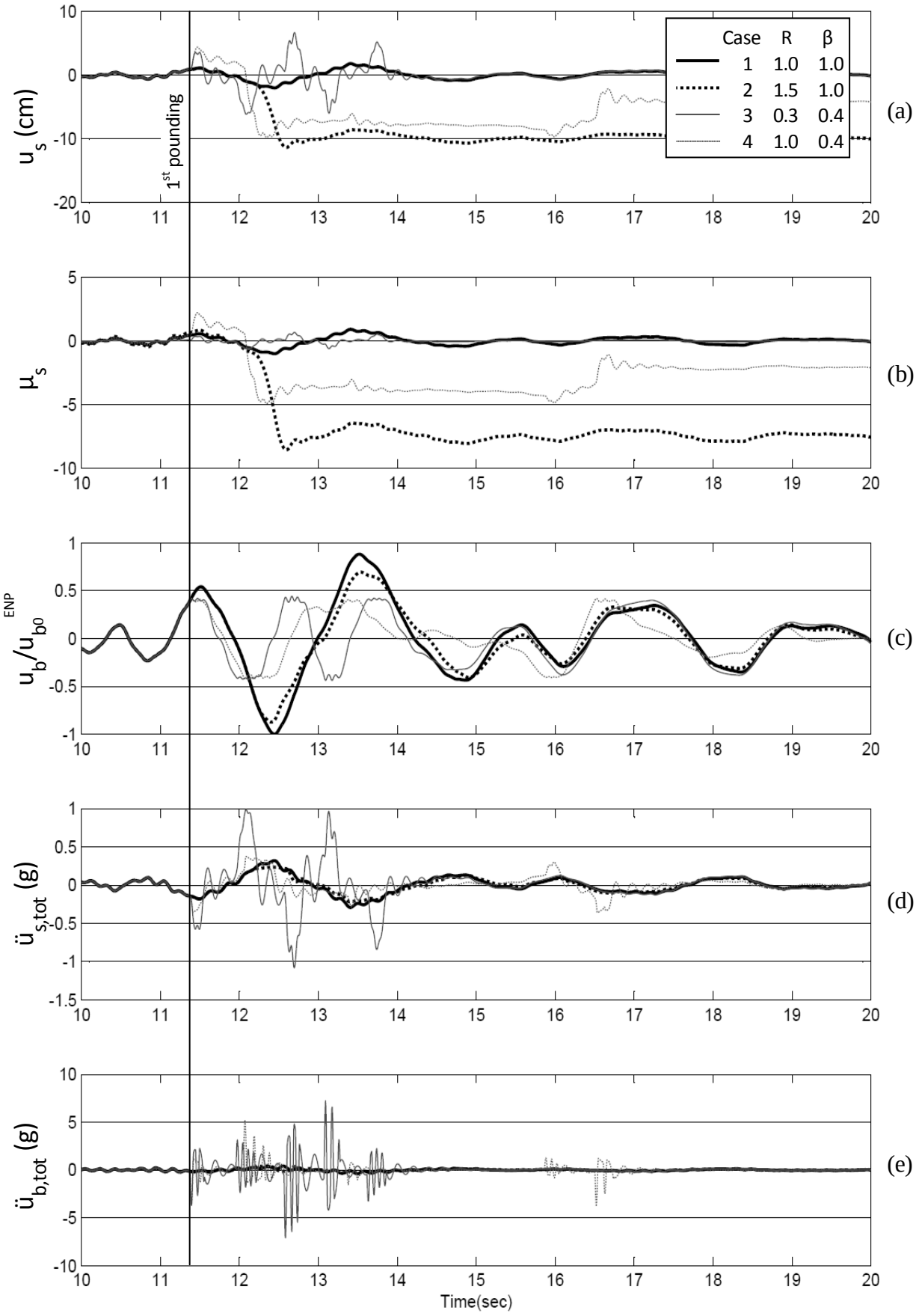
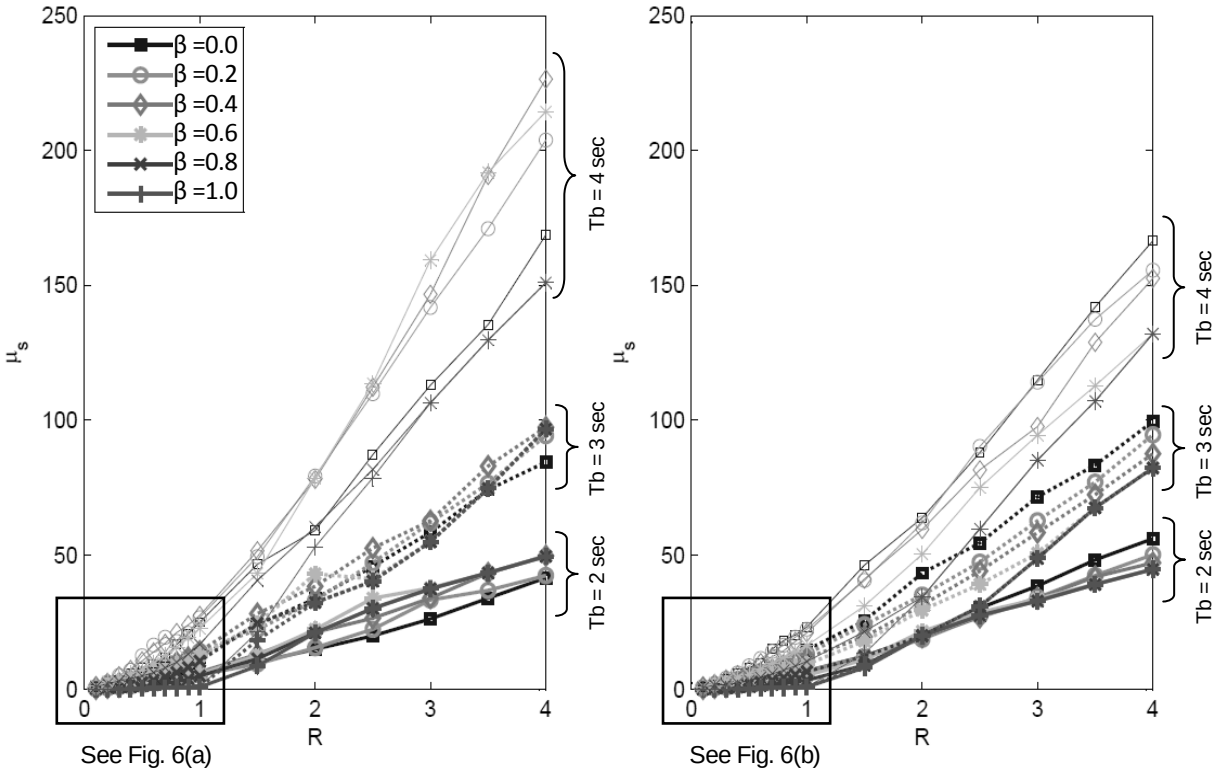
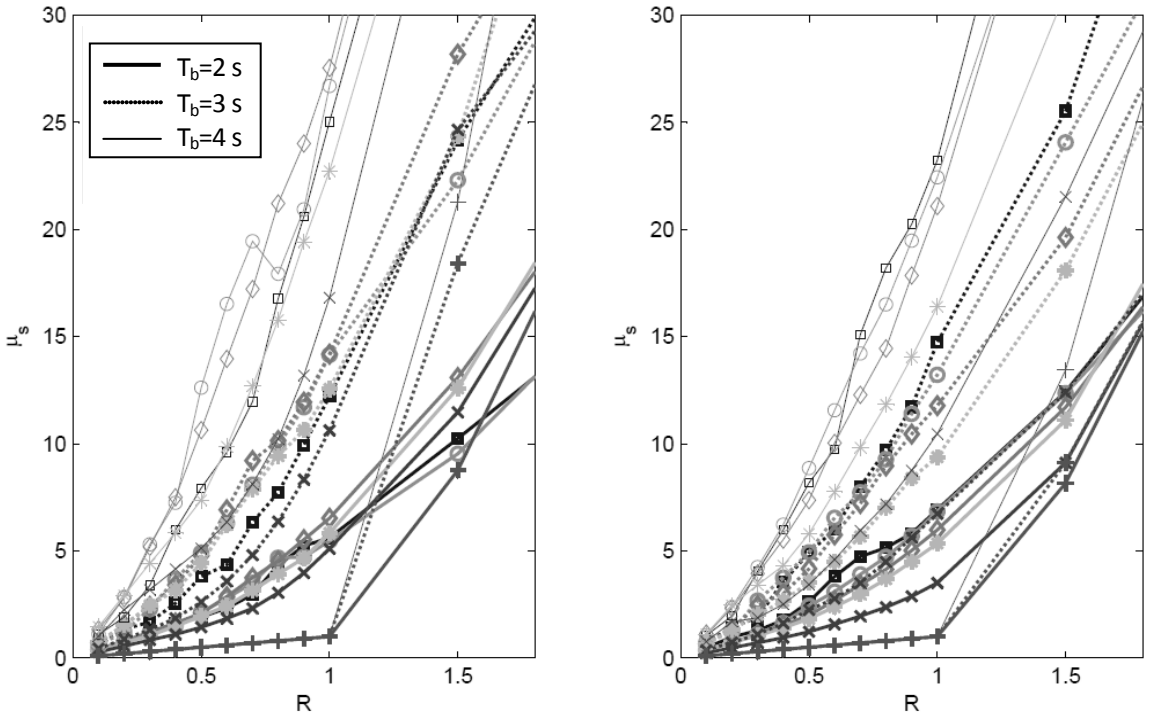


Figure 4 Response history results of a T_b = 2 sec., ζ_b = 0.1 structure subjected to LA29 excitation



(b) $\zeta_b = 0.1$ (b) $\zeta_b = 0.3$

Figure 5 Effect of superstructural yield strength on median ductility demand for given separation distance



(a) $\zeta_b = 0.1$ (b) $\zeta_b = 0.3$

Figure 6 Effect of superstructural strength on ductility demand when the strength reduction factor $R \leq 1$

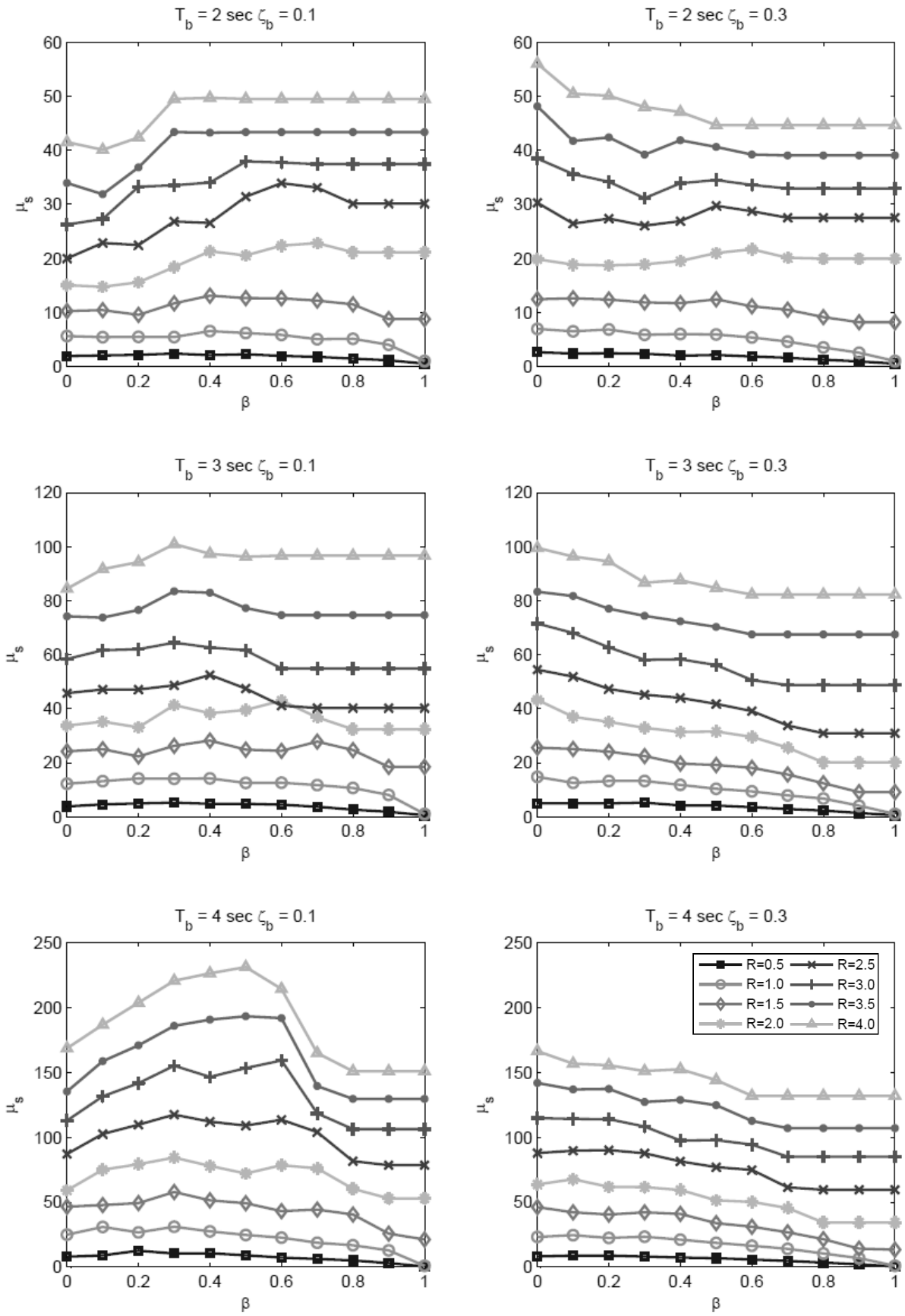


Figure 7 Effect of separation distance on median ductility demand for given superstructural yield strengths

superstructural strength for base isolated structures. Results indicate that yield strength has a significant effect on resulting ductility demand in the superstructure. Each graph in Figure 5 describes the median ductility demand as a function of strength reduction factor R, from the suite of ground motions for each isolation system damping ratio ζ_b considered. Each line in the graph corresponds to a distinct isolation system period T_b and separation distance s. The square data points shows the case that β is equal to 0 (similar to a fixed base building) while the '+' data points represent β = 1.0 (no pounding). Figure 6 is enlarged from Figure 5 to present the response when R less than 1. From this figure, when β = 1.0, the ductility damand is equal to strength reduction factor R. Moreover, ductility demand is exactly 1.0 when β = 1.0 and R = 1.0 for every isolation period and damping ratio. These indicate the ENP cases for which no yielding or pounding occurs. Note that the same R gives different values of superstructure yield strength for different combinations of T_s, ζ_s, T_b, ζ_b and earthquake ground motion, depending on the ENP response. For larger R and other value of β, as the superstructural strength decreases, ductility demand of the superstructure increases dramatically for all gap sizes.

6.2 Separation ratio β

The separation ratio β is varied from 0.0 to 1.0 to study the effect of separation distance on ductility demand.

In Figure 7, the median ductility demand is presented as a function of separation ratio β. Each graph in the figure corresponds to a distinct isolation period T_b and damping ratio ζ_b. For $R \leq 1.0$, the ductility demand is equal to R when β = 1.0, and increases as β decreases due to yielding of superstructure that caused by the high impact forces resulted from pounding.

When $R > 1.0$, the lines become flat as β is increased to 1.0, meaning that the resulting ductility demand eventually becomes insensitive to the seismic separation after some threshold gap size. This can be seen also in Figure 5, since for large cases of β the results are converging to a single line. The ductility demands observed when β is small result from yielding that results from pounding. However, when the gap size is sufficiently large such that the superstructure yields before pounding occurs, the base ceases to move further and an increased gap size no longer provides any benefit. The resulting ductility demand is due to yielding alone, not pounding. Therefore, a decrease in gap size does not significantly affect the ductility demand so long as the gap size provided is large enough to accommodate the isolation level displacement which results in a shear causing yielding of the superstructure.

6.3 Isolation period T_b and damping ratio ζ_b

Base isolated structures with isolation system period T_b = 2, 3, and 4 sec. and isolation system damping ratio ζ_b = 0.10 and 0.30 have been considered in this study. Figure 5 clearly indicates that, for a given R, median ductility demand increases with isolation system period. An increase in isolation damping results in minor reductions in ductility demand, particularly for the long period cases. From Figure 7, for high damping isolation systems, the ductility demand decreases more significantly as the gap size increase. However, for the low damping cases, an increase in gap size does not necessarily lead to a decrease in ductility demand.

7. CONCLUSIONS

Parametric studies of the response of base isolated structures considering yielding of the superstructure and pounding of the isolation level against the surrounding moat wall have been described. Results indicate that a decrease in superstructural strength significantly increases ductility demand but the likelihood of pounding reduces. Separation gap size does not significantly affect the ductility demand compared with superstructure strength, and an increase in gap size does not assure a decrease in ductility demand. For a particular yield strength, a specific gap size exists beyond which further increase has no effect on structural behaviour. Moreover, for a given superstructure strength, an increase in isolation period leads to an increase in ductility demand.

In future studies, various parameters such as number of stories, and multiple classes of contact elements will be considered. In addition to ductility demand of superstructure, acceleration response will be investigated.

Acknowledgements:

The first author acknowledges the scholarship from the Japan Ministry of Education, Culture, Sport, Science, and Technology (MEXT). Supports from the Center for Urban Earthquake Engineering (CUEE) in Tokyo Institute of Technology are greatly appriciated.

References:

KASAI K., JENG V., MAISON B.F., "The Significant Effects of Pounding Induced Accelerations on Building Appurtenances", *Proc. of Seismic Design and Performance of Equipment and Nonstructural Components in Buildings and Industrial Structures, Applied Technology Council Seminar ATC-29*, Irvine, CA, 1990.

TSAI H.C., "Dynamic Analysis of Base-Isolated Shear Beams Bumping Against Stops", *Earthquake Engineering and Structural Dynamics*, Vol. 26, 1997, p. 515-528.

KOMODROMOS P., "Simulation of the Earthquake-Induced Pounding of Seismically Isolated Building", *Computers and Structures*, Vol. 86, 2008, p. 618-626.

SOMERVILLE P., ANDERSON D., SUN J., PUNYAMURTHULA S., and SMITH N., "Generation of Ground Motion Time histories for Performance-Based Seismic Engineering," Proceedings, *6th National Earthquake Engineering Conference*, Seattle, WA, 1998.

McGUIRE R.K., "Seismic Hazard and Risk Analysis", *EERI Monograph*, Earthquake Engineering Research Institute, Oakland, CA, 2004.

YE K, LI L, ZHU H.P.,"A modified Kelvin impact model for pounding simulation of base-isolated building with adjacent structures", *Earthquake Engineering and Engineering Vibration*, Vol. 8 No. 3, 2009, p. 433-446.

8CUEE CONFERENCE PROCEEDINGS
8th International Conference on Urban Earthquake Engineering
March 7-8, 2011, Tokyo Institute of Technology, Tokyo, Japan

MODELLING HYBRID BASE ISOLATION SYSTEMS FOR FREE VIBRATION SIMULATIONS

Anastasia Athanasiou[1] and Giuseppe Oliveto[2]

1) Postgraduate Student, Structural Division, Department of Civil and Environmental Engineering, University of Catania, Italy
2) Professor, Structural Division, Department of Civil and Environmental Engineering, University of Catania, Italy
athanasiou@dica.unict.it, goliveto@dica.unict.it

Abstract: An analytical model is derived for the simulation of the free vibration motion of hybrid base-isolation systems. The high damping rubber bearing component of the isolation system is modeled by a bi-linear spring while the low friction sliding bearing component is modeled by a linear Coulomb friction damper. After the formulation of the equation of motion of the combined system, an analytical solution is provided. A numerical application is then presented where the behavior of each component of the model is analyzed. The solution of the inverse problem is then considered whereby the system parameters must be evaluated given the acceleration response of the system being released after an initially imposed displacement. An evolution strategy has been used to solve a mathematically formulated inverse problem by using an imperfect model and a perfect one, demonstrating the importance of appropriate models in dynamic structural identification. Finally the model has been used for the identification of a hybrid base-isolation system in a real building, from acceleration records obtained in full scale free vibration tests on the building. The paper ends with a comparison of the results obtained by two different Coulomb friction models (constant and linear) and by quantifying the amount of energy dissipation in the various components of the system.

1. INTRODUCTION

At the beginning of the last decade two reinforced concrete buildings, originally not designed to withstand earthquake action, were seismically retrofitted by Hybrid Base Isolation Systems (HBIS) in Solarino, a small town in eastern Sicily. Some details of the buildings considered and of the base-isolation systems adopted are provided in the papers by Oliveto et al. (2004) and by Oliveto and Marletta (2005). The retrofitting works were completed in the summer of 2004 and in July of the same year several free vibration tests were performed on one of the retrofitted buildings upon static application and sudden release of a displacement of the same order of magnitude as the design one. A description of the testing apparatus and some of the results obtained were presented by Oliveto et al. at the 10th Anniversary Symposium of the JSSI held at Yokohama (2004).

Much of the work by the senior author and his research associates in the following years was devoted to the interpretation of the experimental results with the goal of extracting from them as much information as possible. Earlier work, based on elementary dynamics, provided basic results presented by Oliveto and Scalia at the 8NCEE-EERI (2006). Among the results derived in the work above are the dependence of the vibration period on the displacement amplitude and the separation of the equivalent damping in a fraction due to friction in the Low Friction Sliding Bearings (LFSB) and the complementary fraction concerning the High Damping Rubber Bearings (HDRB). These results are shown graphically and analytically by the same couple of authors in a following paper presented at the ANIDIS conference (2007).

The following studies were devoted to dynamic identification of the Solarino base isolation system. As was shown by N. D. Oliveto et al. (2008), identification in the frequency domain is not well suited for base isolation systems and the results were not encouraging. However those studies provided the setting for further identification work in the time domain, N. D. Oliveto et al. (2010). The hybrid base isolation system typical of the Solarino buildings was described by two models working in parallel; one describing the HDRB system and the other the LFSB one. The model describing the HDRB system is composed by a bilinear (elastic-plastic) spring in parallel with a viscous damper while the one describing the LFSB system consists of a Coulomb friction system. The matching between the experimentally measured acceleration and the simulated one was much better in the present case than in the previous identification studies performed in the frequency domain.

Most relevant in the dynamic identification work is that all the system parameters are identified and that these can be compared with the corresponding ones obtained by performing mechanical tests on individual components. In fact the field experimental tests combined with the system identification can serve as an assessment of the design and construction work. The results of the identification process can be used for building certification purposes.

In the case of the Solarino building an identification procedure based on the least squares method was formulated ad hoc and used. The procedure was preliminarily tested against a mathematically generated solution and it was shown that the given solution could be approximated to any required degree of accuracy. However, when the procedure was applied to experimental data, the degree of accuracy, although acceptable for engineering purposes, was not comparable with the one obtained for the test problem. The diminished accuracy with the experimental data may be due as usual to measurement noise and/or to model consistency. Two different models were used in the already quoted study by N. D. Oliveto et al. (2010) differing by whether or not a viscous damper was used in parallel with a bilinear spring to model the HDRB isolators. Recent work to be published elsewhere shows that the model including the viscous damper provides a better fitting between experimental and simulated results and the identified physical parameters from several tests performed show a smaller dispersion than with the other model.

2. THE PHYSICAL MODEL

The physical model is composed of two independent systems acting in parallel as shown in Fig. 1. The first one models the HDRB isolators and is composed by a bilinear spring acting in parallel with a linear viscous dashpot; the second one models the LFSB isolators and is represented in the figure by a friction slider. Both systems are connected to the same mass. The resulting model is a single degree of freedom system and its suitability for the simulation of the dynamic behavior of base isolation systems has been explained in the literature, see for instance Furukawa et al. (2005) and N. D. Oliveto et al. (2010).

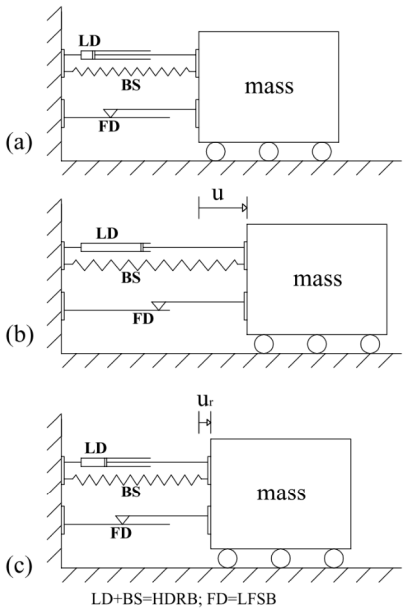


Figure 1 The physical model: (a) Initial configuration, (b) Deformed configuration during the dynamic test, and (c) Rest configuration after the dynamic test

As shown in Fig. 2, the constitutive behavior of the bilinear spring is described by only three parameters which, for coherence with previous work, are chosen to be the elastic stiffness k_0, the post-yielding stiffness k_1 and the first yielding displacement u_y.

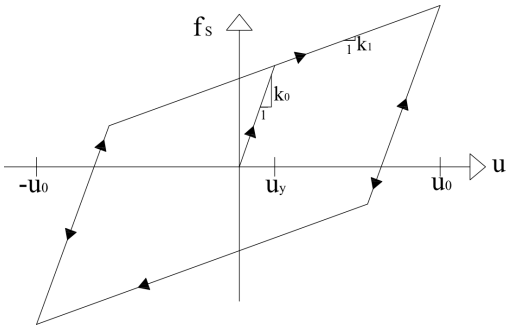


Figure 2 Bi-linear spring constitutive behavior

The present work departs from the previous one for the constitutive behavior of the friction damper which is shown in Fig. 3.

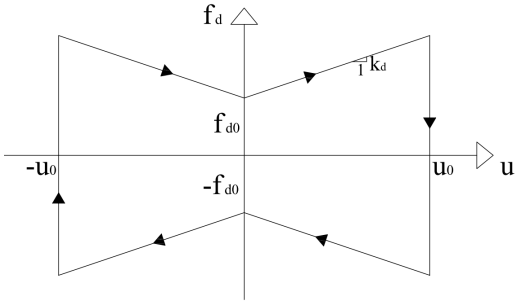


Figure 3 Friction force-displacement relationship

In a standard Coulomb model the friction force is independent of the amplitude of motion and opposes the velocity. The model itself is characterized by a single parameter which is the amplitude of the friction force or equivalently the friction coefficient. The present model differs from a standard Coulomb model because the friction force (or friction coefficient) is no longer constant but a linear function of the displacement amplitude. The constitutive equation for this model is described by only two parameters that are chosen as the friction force at zero displacement f_{d0} and the slope k_d of the force-displacement linear relationship.

3. EQUATION OF MOTION

The equation of motion for the model considered may be written in the following form:

$$m\ddot{u} + c\dot{u} + f_s(u,\dot{u}) + f_d(u,\dot{u}) = 0 \qquad (1)$$

It is easy to recognize that the inertia forces in the

equation above are balanced by the resisting force in the viscous damper (dashpot), the restoring force in the bilinear spring and by the friction force in the slider. The restoring force in the bilinear spring takes different forms according to whether the system experiences an elastic phase of motion or a plastic or yielding one. When the system, after yielding, enters an elastic phase with displacement u_i, the restoring force in the bilinear spring takes the following expression:

$$f_s(u,\dot{u}) = k_0[u - u_i - u_y sign(\dot{u})] + \\ +k_1[u_i + u_y sign(\dot{u})] \tag{2}$$

During a yielding phase the restoring force in the bilinear spring may be written as:

$$f_s(u,\dot{u}) = k_0 u_y sign(\dot{u}) + k_1[u - u_y sign(\dot{u})] \tag{3}$$

Independently of the phase of motion, the resisting force in the slider always takes the expression:

$$f_d(u,\dot{u}) = (f_{d0} + k_d \mid u \mid) sign(\dot{u}) \tag{4}$$

It may be worthwhile to notice at this point that the model considered can reach a position of static equilibrium different from the original unstrained one, satisfying the following equation:

$$f_s(u_r,0) + \tilde{f}_d(u_r,0) = 0 \tag{5}$$

where u_r is the residual displacement, Fig. 1(c), and

$$-\left|f_d(u_r,0)\right| \le \tilde{f}_d(u_r,0) \le \left|f_d(u_r,0)\right| \tag{6}$$

4. ANALYTICAL SOLUTION

In the following an analytical solution is provided for the equation of motion (1) under the initial conditions:

$$u(0) = u_0;\ \dot{u}(0) = 0 \tag{7}$$

Three different phases of motion need to be considered which are: 1) elastic behavior after yielding, 2) yielding behavior and 3) purely elastic behavior. A phase of pure elastic behavior is one which is not followed by a yielding phase, but instead is followed by static equilibrium, that is rest. A phase of pure elastic equilibrium ends with the system satisfying equation (5). In the following an analytical solution will be provided for each of the phases listed.

4.1 Elastic Behavior after Yielding

After using equations (2) and (4), performing some algebraic manipulations and making appropriate settings, the equation of motion (1) takes the following form:

$$\ddot{u} + 2\zeta_0\omega_0\,\dot{u} + \tilde{\omega}_0^2 u = \tilde{\omega}_0^2 u_p \tag{8}$$

where

$$\omega_0 = \sqrt{\frac{k_0}{m}};\ \zeta_0 = \frac{c}{2m\omega_0};\ \omega_{0D} = \omega_0\sqrt{1-\zeta_0^2} \tag{9}$$

$$r_{d0} = \frac{k_d}{k_0};\ \rho_0 = \sqrt{1 + r_{d0} sign(u) sign(\dot{u})} \tag{10}$$

$$\tilde{\omega}_0 = \rho_0\omega_0;\ \tilde{\omega}_{0D} = \omega_0\sqrt{\rho_0^2 - \zeta_0^2} \tag{11}$$

$$u_p = \frac{-u_{d0} sign(\dot{u}) + \left(1 - \dfrac{\omega_1^2}{\omega_0^2}\right)\left[u_i + u_y sign(\dot{u})\right]}{\rho_0^2} \tag{12}$$

The analytical expressions obtained for displacement, velocity and acceleration are given by equations (13)-(15).

$$u(t) - u_p = u_a e^{-\zeta_0\omega_0(t-t_i)}\cos[\tilde{\omega}_{0D}(t-t_i) - \theta_0] \tag{13}$$

$$\dot{u}(t) = -\dot{u}_a e^{-\zeta_0\omega_0(t-t_i)}\sin\tilde{\omega}_{0D}(t-t_i) \tag{14}$$

$$\ddot{u}(t) = -\ddot{u}_a e^{-\zeta_0\omega_0(t-t_i)}\cos[\tilde{\omega}_{0D}(t-t_i) + \theta_0] \tag{15}$$

where t_i is the starting time for the present phase, $t \ge t_i$ and

$$\sin\theta_0 = \frac{\zeta_0}{\rho_0};\ \cos\theta_0 = \frac{\sqrt{\rho_0^2 - \zeta_0^2}}{\rho_0} \tag{16}$$

$$u_a = (u_i - u_p)\frac{\rho_0}{\sqrt{\rho_0^2 - \zeta_0^2}} \tag{17}$$

$$\dot{u}_a = \tilde{\omega}_0 u_a;\ \ddot{u}_a = \tilde{\omega}_0\dot{u}_a = \tilde{\omega}_0^2 u_a \tag{18}$$

4.2 Yielding Behavior

After yielding occurs, the equation of motion (1) takes the following form:

$$\ddot{u} + 2\zeta_1\omega_1\,\dot{u} + \tilde{\omega}_1^2 u = \tilde{\omega}_1^2 u_p \tag{19}$$

where:

$$\omega_1 = \sqrt{\frac{k_1}{m}};\ \zeta_1 = \frac{c}{2m\omega_1};\ \omega_{1D} = \omega_1\sqrt{1-\zeta_1^2} \quad (20)$$

$$r_{d1} = \frac{k_d}{k_1};\ \rho_1 = \sqrt{1 + r_{d1} sign(u) sign(\dot{u})} \quad (21)$$

$$\tilde{\omega}_1 = \rho_1\omega_1;\ \tilde{\omega}_{1D} = \omega_1\sqrt{\rho_1^2 - \zeta_1^2} \quad (22)$$

$$u_p = -\frac{\left[\frac{\omega_0^2}{\omega_1^2}u_{d0} + \left(\frac{\omega_0^2}{\omega_1^2} - 1\right)u_y\right] sign(\dot{u})}{\rho_1^2} \quad (23)$$

The analytical solution is given by equations (24)-(26).

$$u(t) - u_p = u_a e^{-\zeta_1\omega_1(t-t_j)}\cos[\tilde{\omega}_{1D}(t-t_j) - \theta_1] \quad (24)$$

$$\dot{u}(t) = -\dot{u}_a e^{-\zeta_1\omega_1(t-t_j)}\sin[\tilde{\omega}_{1D}(t-t_j) - \theta_1 + \theta_2] \quad (25)$$

$$\ddot{u}(t) = -\ddot{u}_a e^{-\zeta_1\omega_1(t-t_j)}\cos[\tilde{\omega}_{1D}(t-t_j) - \theta_1 + 2\theta_2] \quad (26)$$

where t_j is the starting time for this phase, $t \geq t_j$ and

$$u_a = \sqrt{(u_j - u_p)^2 + \left[\frac{\dot{u}_j + \zeta_1\omega_1(u_j - u_p)}{\tilde{\omega}_{1D}}\right]^2} \quad (27)$$

$$\dot{u}_a = \tilde{\omega}_1 u_a;\ \ddot{u}_a = \tilde{\omega}_1\dot{u}_a = \tilde{\omega}_1^2 u_a \quad (28)$$

$$\sin\theta_1 = \frac{\dot{u}_j + \zeta_1\omega_1(u_j - u_p)}{u_a\tilde{\omega}_{1D}};\ \cos\theta_1 = \frac{u_j - u_p}{u_a} \quad (29)$$

$$\sin\theta_2 = \frac{\zeta_1}{\rho_1};\cos\theta_2 = \frac{\sqrt{\rho_1^2 - \zeta_1^2}}{\rho_1} \quad (30)$$

4.3 Purely Elastic Behavior

The same equations hold as in the elastic phase, with

$$u_p = \frac{-u_{d0} sign(\dot{u}) + \left(1 - \frac{\omega_1^2}{\omega_0^2}\right)\left[u_i + u_y sign(\dot{u}_i)\right]}{\rho_0^2} \quad (31)$$

Here u_i is the displacement at the end of the last yielding phase, $sign(\dot{u}_i)$ is the velocity sign in the following phase of elastic recovery and $sign(\dot{u})$ is the velocity sign in the considered phase.

4.4 Rest Conditions

In a free vibration test or in a phase of free vibration following a forced vibration motion, equation (5) is satisfied when the system finally comes to rest. However, for the system to come to rest and equation (5) to be satisfied the following relationships must hold

$$|\ddot{u}| \leq 2\frac{|f_d(u_r, 0)|}{m} \quad (32)$$

$$sign(\ddot{u}_) = -sign(\dot{u}_) \quad (33)$$

The suffix _ in equation (33) indicates that the condition must be satisfied just before the system comes to rest.

5. NUMERICAL APPLICATION

A numerical application will be presented in the following in order to show in graphical form the dynamic response of the system considered following its release after a statically imposed initial displacement. The parameters that characterize the system are collected in a vector S_0 that for later reference shall be called system parameter vector, Oliveto et. al. (2010). For convenience the imposed initial displacement u_0 shall be enclosed as the first component of this vector, Tab.1. The remaining components have all been defined in the previous section 2 and are listed in the following order: the yield displacement u_y, the friction displacement u_{d0}, the elastic frequency ω_0, the yielding frequency ω_1, the stiffness ratio r_{d0} and the damping ratio ζ_0. The values given to the considered parameters were chosen in order to produce results similar to the recorded experimental ones and to those used earlier in the literature, Oliveto et. al. (2010).

Table 1 System parameter vector S_0

u_0 (m)	u_y (m)	u_{d0} (m)	$\omega_0/2\pi$ (s^{-1})	$\omega_1/2\pi$ (s^{-1})	r_{d0}	ζ_0
0.12	0.02	0.003	0.50	0.40	0.10	0.01

The graph of the evaluated displacement function is shown in Fig. 4. It can be seen that the motion stops after 5.539 s and the residual displacement is -1.22 mm. Due to the presence of the friction damper and of the bi-linear spring the system completes only two full cycles of motion and stops during the third one.

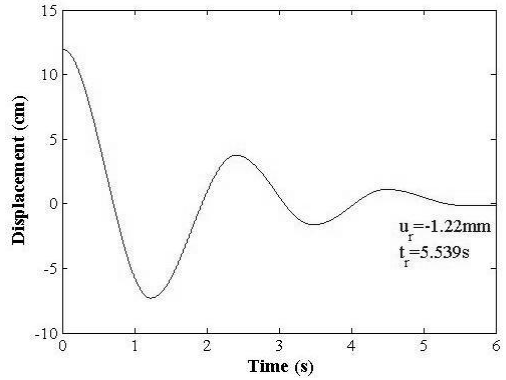


Figure 4 Displacement time history corresponding to the set of system parameters S_0 specified in Table 1

The graph of the velocity function is shown in Fig. 5. It is easy to see when the motion stops because the velocity remains equal to zero ever after. Another point that can be noticed in the velocity graph is the presence of a discrete number of slope discontinuities which correspond to velocity sign changes and jump discontinuities in the friction force.

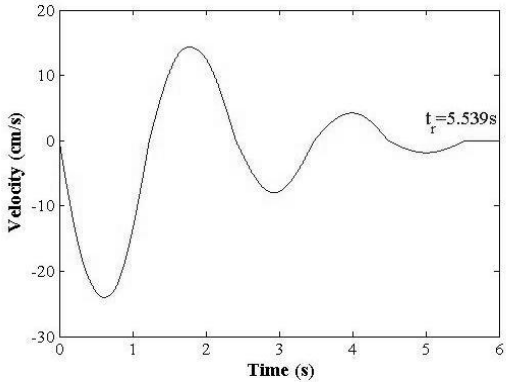


Figure 5 Velocity time history corresponding to S_0

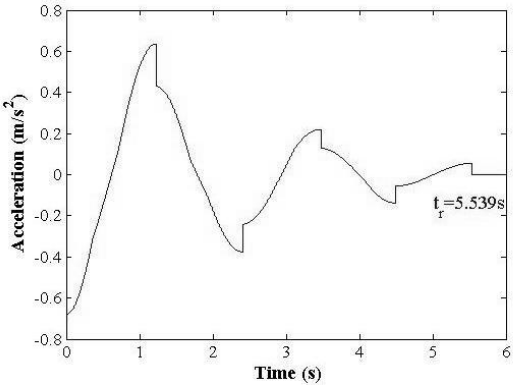


Figure 6 Acceleration time history corresponding to S_0

The acceleration graph is shown in Fig. 6. A number of function discontinuities corresponding to changes of sign in the velocity and the friction force are clearly visible. Due to the particular friction model being used the jumps are larger in the early stages of the motion, when the displacement is larger, and become smaller as the amplitude of the displacement decays. The significant decay in the amplitude of the acceleration jumps is due to the relatively large value of the stifness ratio r_{d0}. Should this have been smaller the decay would have been barely visible.

In order to complete the picture of the behavior of the system considered it is useful to present the force-displacement relationship for the restoring force in the bi-linear spring and of the resisting force in the friction damper. To evaluate these forces in dimensional form another system parameter is required. By assuming this to be the mass m and setting its value to 1200 kNs^2/m, the graph of force-displacement relationship in the bi-linear spring is shown in Fig.7. It may be useful to realize that the initial value of the restoring force is 994.85 kN while the value when the motion stops, with a residual displacement u_r=-1.22 mm, is -30.40 kN.

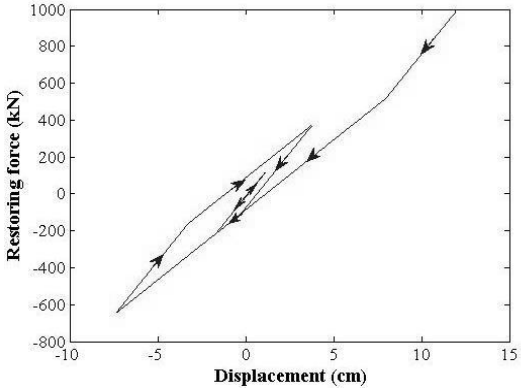


Figure 7 Restoring force-displacement relationship corresponding to the system parameter vector S_0

The force-displacement relationship for the friction damper is shown in Fig. 8. It may be worth noticing that the initial value of the friction force is -177.65 kN while the value at rest is -30.40 kN, exactly balancing the force in the bi-linear spring.

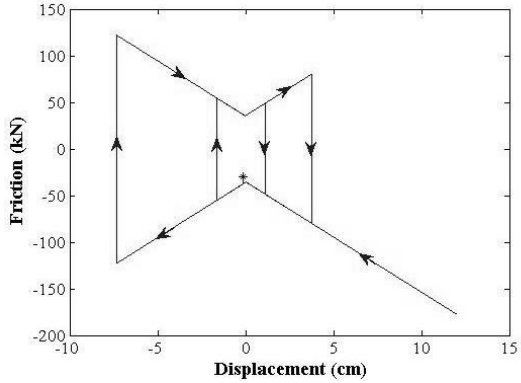


Figure 8 Friction force-displacement relationship corresponding to the system parameter vector S_0

6. INVERSE PROBLEM

The problem that we are going to address now is that of

finding the system parameters as given in the system parameter vector S_0, for example the values shown in Tab.1, once the acceleration record shown in Fig. 6 is known in sampled form. The sample is given by N acceleration values calculated at N discrete times $t_n=n\cdot\Delta t$ with $n=1,....N$. The sampling frequency shall be given by $f_s=\Delta t^{-1}$. At the present the sample is generated mathematically by using the equations developed in section 4. In real applications the data sample could be generated by dynamic testing. In doing this we are following the lead in Oliveto et al. (2010). However we want to gain some additional insight in the solution of inverse problems by using a different model from that which was used to generate the data sample. In real life applications we may collect accurate data, but we may not have a sufficiently accurate model as to match the experimental data exactly. Just to show what happens in such a case we shall use an inaccurate model to solve the inverse problem, namely the classical Coulomb friction model which in our case amounts to set r_{d0} in all our equations. In a geometrical description the stiffness k_d in the graph of Fig.3 shall be set equal to zero.

6.1 Solution Strategies

In previous work by the senior author and his research associates, Oliveto et al. (2010), the least squares method was used in the solution of the inverse problem. A suitable error function was defined in order to measure the distance between any trial solution and the given data set. In the present work we generate the error function in exactly the same way, taking care of the matching of both acceleration and corresponding time. More details about the error function used can be obtained from the reference quoted above.

An ongoing research cooperation with researchers from the School of Computing Science of the University of Birmingham (UK), has shifted our interest from the use of in house developed optimization methods based on least squares to evolution strategies, Hansen and Ostermeier (2001). Details on the performance of evolution strategies in the solution of inverse problems deriving from dynamic structural identification shall be reported elsewhere in the specialized literature. Here the focus shall be on the model rather than on the identification method.

6.2 Constant Coulomb Friction Model

We cannot expect to obtain an exact solution of the inverse problem because the model we are using is not consistent with the model that was used to generate the data. In real life applications this is equivalent to not having a sufficiently accurate model to describe the problem considered. One problem with evolution strategies is that at each run the algorithm considered may provide a different solution. Having fixed the number of fitness (error) evaluations for each run of the algorithm and the number algorithm runs, one usually chooses the solution with maximum fitness (minimum error). The best solution found in the present case is shown in Tab.2 where the estimated system parameters are compared to the real ones. Of course the parameter r_{d0} is equal to zero in the classical Coulomb friction model and so it was not identifiable. The matching between the data function and the identified one is shown in Fig. 9. The main discrepancy between the given function and the identified one appears to be in the size of the acceleration jumps. As it should have been expected the system parameter with the largest error (63%) is u_d because it is affected by the fact that the model used does not allow for the friction force to be dependent on the displacement amplitude. Viscous damping is the other parameter that shows a considerable error while all the others show an error smaller than 10%. The most important aspect of the present application is that the errors measured are all model errors and not identification errors as it will be shown in the next paragraph.

Table 2 Identified system parameter vector using the Constant Coulomb Friction Model (CCFM)

u_0 (m)	u_y (m)	u_{d0} (m)	$\omega_0/2\pi$ (s^{-1})	$\omega_1/2\pi$ (s^{-1})	r_{d0}	ζ_0
Real system parameter vector						
0.1200	0.0200	0.0030	0.5000	0.4000	0.10	0.0100
Identified system parameter vector						
0.1095	0.0200	0.0049	0.4911	0.3921	0.00	0.0076
Error regarding the system parameters (%)						
9	0	63	2	2	-	24
Overall error: $e^2 = 8.5222\cdot10^{-3}$						

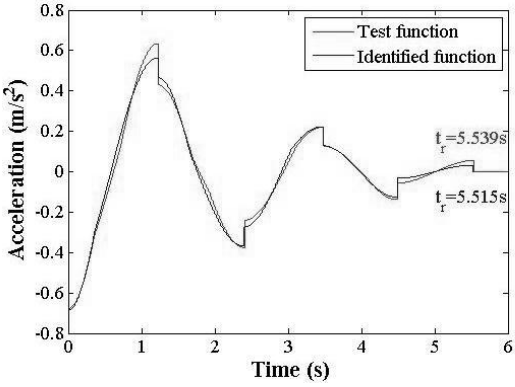


Figure 9 Test and identified function using the CCFM

6.3 Linear Coulomb Friction Model

The data function used for the system identification was generated by the linear Coulomb friction model. Therefore it is expected that the system parameters should be evaluated very accurately. In the present application the tolerated error or optimal fitness was set equal to 10^{-10} and the algorithm used successfully completed the search in just one run. All the system parameters were identified to all significant digits. This confirms what anticipated in the previous paragraph when asserting that the measured errors were all model errors rather than identification errors.

7. APPLICATION TO REAL SYSTEMS

The present model will now be applied to data obtained from free vibration tests performed on a real base-isolated building and the model parameters will be identified. Of course the parameters obtained shall be only as good as the model is. This is the reason why the application in section 6.2 was performed. We should recognize that the parameters obtained shall be the best ones to fit our model into the experimental data, but it does not mean that the present model is the best that could be conceived. The results shall be compared to those obtained by using the constant Coulomb friction model to see if any improvement is achieved, and then some conclusions shall be drawn.

7.1 Results from Test 3

The identification procedure described in section 6 for a mathematically generated data set is applied to the acceleration record obtained from test 3 performed on the Solarino building, Oliveto et al. (2004). The matching shown in Fig. 10 is obtained using the constant Coulomb friction model (CCFM) while that shown in Fig. 11 is obtained using the linear Coulomb friction model (LCFM). The two models produce two very close acceleration functions and, in fact, differences are barely visible at first sight, as may be seen from the superimposed graphs of Fig. 12. The identified system parameters are shown in Tab.3 along with the resulting error, or solution fitness in computer science jargon. Although the error appears to be roughly the same for both models, careful comparison shows an improvement in the solution fitness of more than 5%.

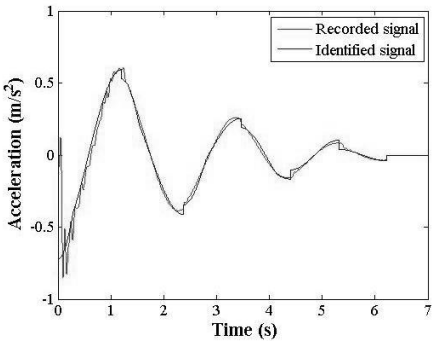


Figure 10 Recorded and identified signal for the CCFM

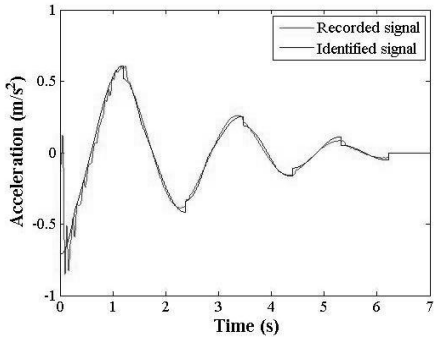


Figure 11 Recorded and identified signal for the LCFM

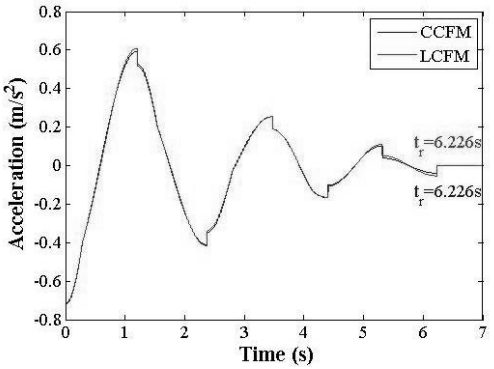


Figure 12 Comparison of the identified signals using the two friction models

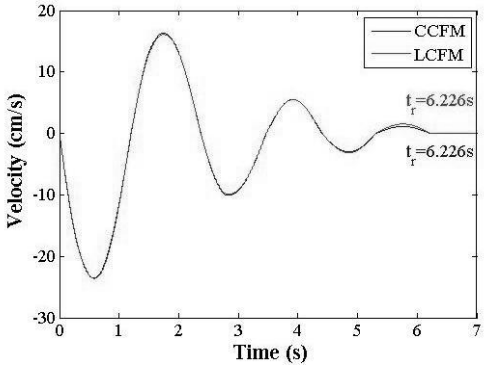


Figure 13 Velocity time histories for the two friction models

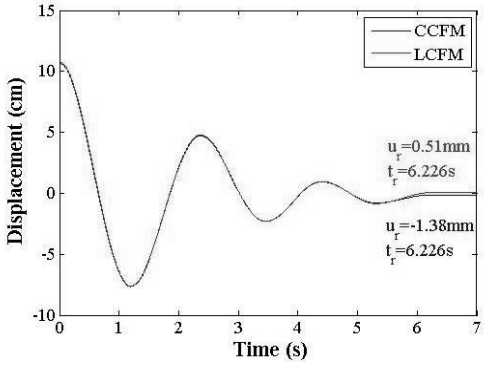


Figure 14 Displacement time histories for the two friction models

Table 3 Identified system parameter vector using the Constant Coulomb Friction Model (CCFM) and the Linear Friction Model (LCFM)

u_0 (m)	u_y (m)	u_{d0} (m)	$\omega_0/2\pi$ (s^{-1})	$\omega_1/2\pi$ (s^{-1})	r_{d0}	ζ_0
CCFM [Overall error: e^2= 1.4730·10^{-2}]						
0.1068	0.0136	0.0027	0.5490	0.4008	0.000	10^{-10}
LCFM [Overall error: e^2=1.3948·10^{-2}]						
0.1079	0.0132	0.0022	0.5528	0.4035	0.0211	10^{-10}

Another interesting aspect is that viscous damping is predicted as vanishingly small by both models so that energy dissipation is accounted almost entirely by the bi-linear spring and by the friction damper. The constant friction force in the CCFM can be compared to the minimum friction force in the LCFM and obviously the former turns out to be larger, see third column in Tab.3. The bi-linear spring yield displacement is slightly larger for the CCFM while the initial imposed displacement is predicted a little larger by the LCFM. As shown in the literature, Oliveto et al. (2004) and Oliveto et al. (2010), the nominal initial displacement is 11.48 cm; however, due to preliminary tests performed prior to the considered one (at least 2) and not having recorded the history of the residual displacement after each test, the precise value of the imposed displacement is unknown and the actual value is a part of the identification process. The predicted values are 10.68 cm according to the CCFM, 10.79 cm according to the LCFM, see first column of Tab.3, and 11.08 cm according to the identification performed by Oliveto et al. (2010) using the CCFM and a least squares based identification procedure. It may be interesting to notice that the residual displacement predicted by the present identifications from test 3 is rather small: 0.51mm using the LCFM and -1.38 mm using the CCFM.

7.2 Mass Identification

For the identification of the physical parameters of the models considered, a preliminary estimate of the system mass is required. This can be done via a formula derived by Oliveto et al. (2010) based on the results of the static test preceding the dynamic one:

$$m = \frac{f_0 - f_{ds}}{\omega_0^2 u_y + \omega_1^2 (u_0 - u_y)} \tag{34}$$

All the terms in the denominator of equation (34) are obtained as a result of the dynamic identification procedure and can be read from Tab. 3. The two forces on the nominator are the externally applied force needed to impose the initial displacement and the static force in the friction damper f_{ds} which balances the external force f_0 before the system starts to move. By using the minimum estimate for the static friction force f_{ds}=100 kN and the measured value of the external force f_0=1027.04 kN, Oliveto et al. (2004) and Oliveto et al. (2010), the estimates for the system mass and for the other physical parameters of the model considered are shown in Tab. 4.

Table 4 Identified physical parameters

Model	m (kNs^2/m)	k_0 (kN/m)	k_1 (kN/m)	k_d (kN/m)	f_{sy} (kN)	f_{d0} (kN)
CCFM	1231	14651	7807	0	199	39
LCFM	1207	14561	7758	307	193	32

7.3 Force-Displacement Relationships

The knowledge of the values of the physical parameters of the system from Tab. 4 enables the construction of the force-displacement relationships using the expressions given by equations (2), (3) and (4). The force-displacement relationship for the bi-linear spring is shown in Fig. 15 for the CCFM and in Fig.16 for the LCFM. For the friction damper the corresponding relationships are given in Fig. 17 and in Fig.18.

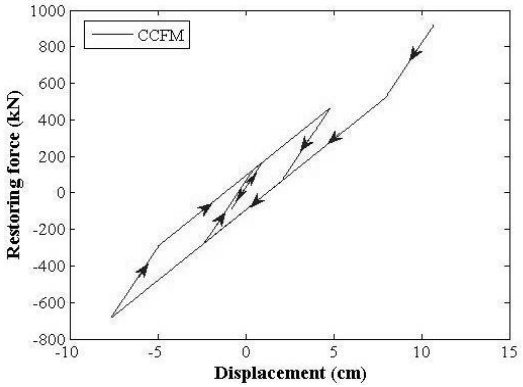


Figure 15 Restoring force-displacement relationship for the CCFM

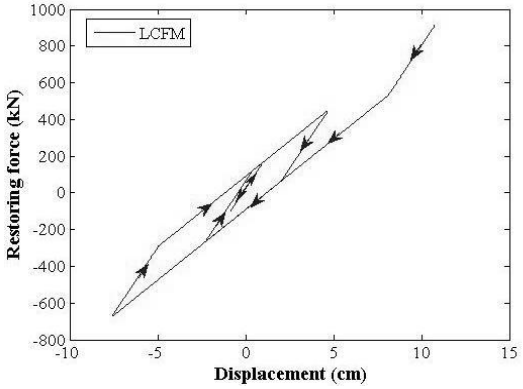


Figure 16 Restoring force-displacement relationship for the LCFM

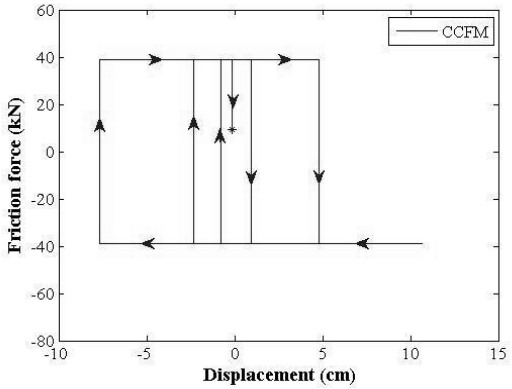


Figure 17 Friction force-displacement relationship for the CCFM

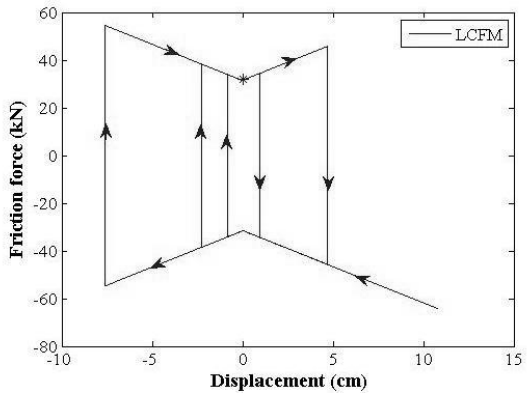


Figure 18 Friction force-displacement relationship for the LCFM

7.4 Energy Balance

The energy balance for the system considered can be formulated in terms of the following equation:

$$E_K(t) + W_{VD}(t) + W_{BS}(t) + W_{FD}(t) = 0 \tag{35}$$

where the first term is the kinetic energy of the system and the remaining terms represent the work performed by the forces in the viscous damper, in the friction damper and in the bi-linear spring over the time interval *(0,t)*. Equation (35) can be rearranged in a more expressive form as follows:

$$\begin{aligned} &E_K(t) + E_S(t) + \\ &+E_{VD}(t) + E_{BSD}(t) + E_{FD}(t) = E_S(0) \end{aligned} \tag{36}$$

where the energy terms referring to the viscous damper and to the friction damper coincide with the corresponding work terms in equation (35) while the energy dissipated in the bilinear spring may be calculated by using the following expression:

$$E_{BSD}(t) = W_{BS}(t) + E_S(0) - E_S(t) \tag{37}$$

For completeness the expressions used for the calculation of each term in the balance equations (35) and (36) are given below.

$$E_K(t) = \frac{1}{2} m \cdot \dot{u}^2(t) \tag{38}$$

$$W_{VD}(t) = \int_0^t c \cdot \dot{u}^2(\tau) \cdot d\tau \tag{39}$$

$$W_{BS}(t) = \int_0^t f_s(u,\dot{u}) \cdot \dot{u}(\tau) d\tau \tag{40}$$

$$W_{FD}(t) = \int_0^t f_d(u,\dot{u}) \cdot \dot{u}(\tau) d\tau \tag{41}$$

The calculation of the strain energy $E_s(t)$ which concurs in the definition of the energy dissipated in the bi-linear spring $E_{BSD}(t)$ can be carried out by means of the following formula, Sivaselvan et al. (2009):

$$E_S(t) = \frac{1}{2} \frac{f_s^2(u,\dot{u},t)}{k_e} + \frac{1}{2} \frac{f_h^2(u,\dot{u},t)}{k_h} \tag{42}$$

where the meaning of the newly introduced symbols is given below:

$$k_e = k_0;\ k_h = \frac{k_0 \cdot k_1}{k_0 - k_1};\ f_{sy} = k_0 \cdot u_y \tag{43}$$

$$f_h(u,\dot{u},t) = f_s(u,\dot{u},t) - f_{sy} \cdot sign(\dot{u}) \tag{44}$$

in the yielding phases, and

$$f_h(u,\dot{u},t) = f_h(u_i,\dot{u}_i,t_i) \tag{45}$$

in the elastic phases, with the suffix "*i*" indicating the value of the variables at the end of the previous yielding phase.

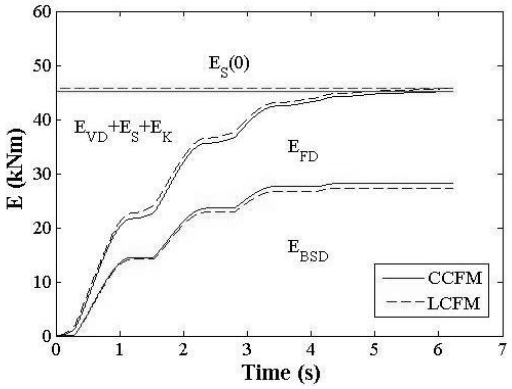


Figure 19 Energy dissipation by friction damper and bilinear spring

The contribution to energy dissipation by the viscous damper turns out to be negligible in both models (CCFM and LCFM). As it should have been expected the contribution of the bi-linear spring to energy dissipation is larger than that of the friction damper with the former accounting for about 60% of the total energy dissipated and the latter for about 40%, Fig. 19. However the LCFM results in a larger energy dissipation in the friction damper compared to the CCFM. By assuming that the former model is more accurate than the latter, this means that the CCFM underestimates the energy dissipation by the LFSB. This underestimation, approximately 8% of the final value, is not excessive but also not negligible.

8. CONCLUSIONS

An improved model for the dynamic identification of hybrid base isolation systems has been presented. The model is the evolution of a previous one already available in the literature, Oliveto et al. (2010). In the previous model a bi-linear spring was used to characterize the HDRB component of the system, while a constant Coulomb friction damper was used to describe the LFSB component. The present model differs from the previous one in that it replaces the constant Coulomb friction model with a linear one characterized by two parameters instead of just one. The response of the system to the sudden release of a statically imposed displacement is provided in closed form. The response provided by the system has been shown graphically in terms of displacement, velocity, acceleration and resisting forces in the bi-linear spring and in the friction damper.

The analytical solution provided has then been used to solve an inverse problem whereby the acceleration response is assumed to be known while the system parameters and the initial displacement are assumed to be unknown. An evolution strategy is used to provide a solution to the inverse problem but this will be discussed elsewhere. Here the importance of the suitability of the model for structural dynamical identification is addressed instead. An acceleration response produced using a LCFM is used as experimental data. When the CCFM is used for the system identification, the error of the optimal solution is of the order of 10^{-2} which, in computer jargon, says that the solution fitness is rather poor. This is demonstrated also by the errors in the individual system parameters which in some cases appear to be exceedingly large. On the other hand, when the LCFM is used for the identification, given enough time, the error can be made as little as desired, meaning that the real solution can be found.

The next step has been that of applying the newly developed model solution to the identification of a real hybrid isolation system, that existing in a base-isolated building in the little Sicilian town of Solarino. An improvement of the order of 5% in the fitness of the solution obtained was observed as compared to previous results obtained by using the CCFM. Interestingly enough both models showed that viscous damping did not play a role in the identification suggesting that the viscous damper could be removed from the physical model without affecting the final results.

An interesting feature of the identification procedure presented is the possibility of identifying the initial and residual displacements besides the system parameters. While the identified initial displacements differ by only about a unit per cent from one model to the other, the residual displacements differ by a large amount. It is therefore evident that the reliability of the model shall be relevant if one wants to predict the residual displacement accurately.

An additional feature of the present work which had not yet been expounded in the existing literature is the evolution of the energy balance during the test. The initial input provided in the form of stored elastic strain energy is split in various components and their evolution with time is depicted. Confirming what had already emerged, the contribution of the viscous damper to energy dissipation is negligible. The contribution of the bilinear spring to energy dissipation is discontinuous and limited to the yielding phases which are interrupted by elastic recovery phases that become permanent sometime before the motion stops. On the contrary the contribution of the friction damper to energy dissipation is continuous. The LCFM leads to a larger energy dissipation than the CCFM. The difference is of about 8%, which is not excessive but negligible either.

Finally it is interesting to observe how in a hybrid base isolation system, like the one in the Solarino building, the LFSB component only accounts for about 4% of the base shear force while contributing to nearly 1/3 of the overall energy dissipation, the remaining 2/3 being dissipated by the HDRB component.

References:

Oliveto, G., Caliò, I. and Marletta, M. (2004). "Retrofitting of Reinforced Concrete Buildings not Designed to withstand Seismic Action: A Case Study using Base Isolation," *Paper No. 954, 13th WCEE, Vancouver.*

Oliveto, G. and Marletta, M. (2005). "Preliminary results from full-scale free vibration tests on a four story reinforced concrete building after seismic rehabilitation by base isolation," *JSSI 10th Anniversary Symposium on Performance of Response Controlled Buildings*, *Yokohama, Japan.*

Oliveto, G. Granata, M., Buda, G. and Sciacca, P. (2004). "Preliminary results from full-scale free vibration tests on a four story reinforced concrete building after seismic rehabilitation by base isolation," *JSSI 10th Anniversary Symposium on Performance of Response Controlled Buildings, Yokohama, Japan.*

Oliveto, G. and Scalia, G., (2006). "Free-Vibration Tests following Seismic Retrofitting by Base Isolation on the Solarino Buildings," *Paper No. 1254, Proceedings of the 8th U.S. NCEE, San Francisco.*

Oliveto, G. and Scalia, G., (2007). "Wavelet Identification of Base Isolated Buildings Buildings: Application to the Solarino Buildings," *ANIDIS 2007, Pisa, Italy.*

Oliveto, N.D., Scalia, G. and Oliveto., G. (2008). "Dynamic Identification of Structural Systems with Viscous and Friction Damping," *Journal of Sound and Vibration, 318(2008), 911-926.*

Oliveto, N.D., Scalia, G. and Oliveto., G. (2010). "Time domain identification of hybrid base isolation systems using free vibration tests," *Earthquake engineering and structural dynamics, 39(9):1015–1038.*

Fukurawa, T., Ito, M., Izawa, K. and Noori, M. N., (2005). "System Identification of Base-Isolated Building using Seismic Response Data," *Journal of Engineering Mechanics, Vol.131, No.3.*

Hansen, N. and Ostermeier, A. (2001). "Completely Derandomized Self-Adaptation in Evolution Strategies," *Evolutionary Computation, 9(2), pp. 159-195.*

Sivaselvan, M.V., Lavan, O., Dargoush, G.F., Kurino, H., Hyodo, Y., Fukuda, R., Sato, K., Apostolakis, G. and Reinhorn, A.M. (2009). "Numerical collapse simulation of large-scale structural systems using an optimization-based algorithm," *Earthquake Engineering & Structural Dynamics, 38:655-677.*

8CUEE CONFERENCE PROCEEDINGS
8th International Conference on Urban Earthquake Engineering
March 7-8, 2011, Tokyo Institute of Technology, Tokyo, Japan

SEISMIC ISOLATION OF TALL CANTILEVER WALL BUILDINGS USING ONE OR MORE ISOLATION PLANES

Vladimir Calugaru[1)] and Marios Panagiotou[2)]

1) Graduate Student Researcher, Department of Civil and Environmental Engineering, University of California, Berkeley, USA
2) Assistant Professor, Department of Civil and Environmental Engineering, University of California, Berkeley, USA
calugaru@berkeley.edu, panagiotou@berkeley.edu

Abstract: This paper investigates numerically the effect of seismic isolation on the response of tall reinforced concrete cantilever wall buildings subjected to strong pulse-type near-fault ground motions. Five 20-story reinforced concrete cantilever wall buildings are considered. Two building designs are fixed-base and three use seismic isolation. The first fixed-base design allows the formation of a plastic hinge only at the base of the wall, with the wall above the plastic hinge region detailed to remain elastic. In the second fixed-base design plasticity is allowed to spread anywhere along the height of the wall. The three designs using seismic isolation vary in the location and number of isolation planes. The isolation plane consists of low-damping laminated rubber bearings, and is either only at the base, only at mid-height, or at both base and mid-height. The buildings are subjected to seven strong near-fault ground motions. The nonlinear dynamic time history analysis of the buildings shows a significant reduction in the engineering response parameters of the base isolated building in comparison with those of the fixed-base buildings. Using two seismic isolation planes further reduces, in comparison with the base isolation building, bending moments, inelastic section curvatures, and inter-story drifts. The building with a single isolation plane at its mid-height is not effective in reducing response parameters.

1. INTRODUCTION

Construction of tall buildings worldwide is increasing at an exponential pace due to the rapid growth of cities and their dense inner cores in the U.S. and around the world. Not only are super tall buildings—100 or more stories—continuing at a rapid pace, but construction of 20- to 80-story tall buildings has also increased significantly (CTBUH 2011). This trend has been slower in regions of high seismicity, but numerous tall buildings are being planned or designed in regions vulnerable to earthquakes. Currently, two hundred buildings taller than 120 m (394 ft) are proposed or under construction in U.S. with 21 of them in highly seismic regions: 7 in Los Angeles, 8 in San Francisco, and 6 in Seattle (CTBUH 2011).

Many tall buildings in highly seismic regions are now designed with reinforced concrete core walls as the main lateral force resisting system. Currently, RC core-wall buildings are designed to develop nonlinear deformations in regions defined as plastic hinges located at the base of the walls (LA 2005, SEAONC 2007, TBI 2010). Numerical studies have shown, however, that tall cantilever wall buildings undergoing strong ground shaking experience high acceleration and force demands along their entire height with significant contribution from the higher modes of response (Moehle 2007, Panagiotou and Restrepo 2009, Panagiotou et al. 2009). For walls designed to develop significant inelastic response at a single plastic hinge at their base, studies have shown that large bending moment demands develop around their mid-height (Panagiotou and Restrepo 2009, Panagiotou et al. 2009). If these regions have to remain elastic, a large amount of longitudinal reinforcement is required. On the other had if plasticity is allowed to develop anywhere along the height of the wall then special detailing is required over the entire wall height in order for these regions to be able to accommodate inelastic deformations. In this study the effect of seismic isolation is investigated to reduce the acceleration, force, and inelastic deformation demands along the height of the walls of such buildings, to reduce their post-earthquake damage and thus to enhance their seismic performance.

Seismic isolation is a well-established approach for improving the seismic performance of structures (Kelly 1999). Hundreds of applications of seismic isolation have been made around the world over the last 40 years. Traditionally seismic isolation has been considered effective for relatively short and stiff structures by elongating their fundamental period, and thus reducing the accelerations and forces they develop. In tall buildings the main goal of seismic isolation is not to increase the already long fundamental period, but to reduce forces and accelerations by controlling the response of a few robust regions while the rest of the building is designed to remain elastic, reducing post-earthquake structural damage. Several applications of base isolation to tall buildings have been made, primarily in Japan (Komuro 2005, Kani 2009). Most of these buildings have a single seismic isolation plane at their base, while cases where this plane is located on the upper part of the building have been reported. (Sueoka 2004, Tsuneki et al. 2009). One third of all recorded isolated buildings in Japan

are over 40-m tall, with the tallest being 50 stories (Kani 2009).

This study investigates the effect of seismic isolation on the performance of tall reinforced concrete core-wall buildings and compares their performance with that of buildings designed according to current building codes. The effectiveness of three seismic isolation designs which differ in the number (one or two) of the seismic isolation planes and the location (base and/or mid-height) of these planes is also investigated.

2. BUILDING AND ISOLATION PLANE DESIGN

2.1 Building Design

Five buildings are considered, two of them fixed-base, and three – seismically isolated. Figure 1 shows the common floor plan view of the buildings considered. A reinforced concrete core-wall provides all the lateral force resistance in the fixed-base buildings. Table 1 lists the main characteristics of the buildings, including the main building and core-wall geometrical properties, floor height h, the seismic weight per floor w, the axial load per floor ΔP, acting on the wall, and the axial stress ratio at the wall base. The axial load ratios are based on a specified concrete compressive strength of $f_c^{'}$ = 50 MPa (8 ksi).

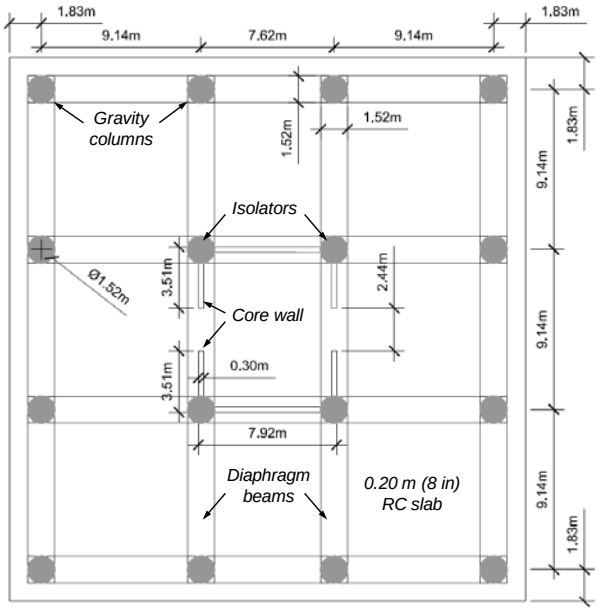


Figure 1. Floor plan view of the studied 20-story RC core-wall buildings showing the isolation plane.

The fixed-base buildings are designed according to ASCE 7-05 (2006) seismic provisions. The mean of seven ground motions, described in section 3.2 below, and a response modification factor R = 5 were used for design with the modal response spectrum analysis (MRSA) method. For the fixed-base buildings, described below, the bending moment, shear force, and axial force capacity along the height of the walls exceeds the design demands.

The first considered fixed-base design is referred to as single plastic hinge (SPH) and is designed to form a single flexural plastic hinge extending over the bottom two stories [see Figure 2]. The reinforcing steel ratio in the plastic hinge region is equal to ρ_b = 0.7%. Above the plastic hinge region the wall is modeled with a high longitudinal steel ratio ρ_E = 3.0%, sufficient to ensure nearly elastic response of this part of the wall. The SPH design follows the methodologies of the EC8 code (2004), which advocates that all plasticity be restrained to a single plastic hinge region at the base of the wall with all other regions designed to remain elastic. The expected flexural strength at the base of the wall, $M_{y,b}$, is computed with moment -curvature analysis using the provided reinforcement and axial loads, and is 1.13 times the moment at which the outer steel yields. The expected flexural strength, $M_{y,b}$, and the corresponding curvature, $\varphi_{y,b}$, are presented in Table 1.

Table 1. Main characteristics of studied buildings.

Floor height h, m (ft)	3.35 (11)
Building height H, m (ft)	67.1 (220)
Floor plan view dimension L_o, m (ft)	31.1 (102)
Base axial load ratio $P / (f'_c A_g)$	0.15
Seismic weight / floor w, kN (kip)	5502 (1237)
Length of core L_w, m (ft)	7.9 (26)
Core thickness t_w, m (ft)	0.3 (1.0)
Expected base flexural strength $M_{y,b}$, kN·m (kip·ft)	504100 (371840)
Curvature at expected base flexural strength $\varphi_{y,b}$, rad/m (rad/in)	$5.5 \cdot 10^{-4}$ ($1.4 \cdot 10^{-5}$)

In the second fixed-base building, referred to as extended plasticity (EP), plasticity is allowed to develop in any region along the height of the wall. Steel reinforcement is curtailed at thirds of the height of the wall with longitudinal steel ratios ρ_l = 0.7%, 0.6%, 0.5% at the base, middle, and top third of the wall height, respectively.

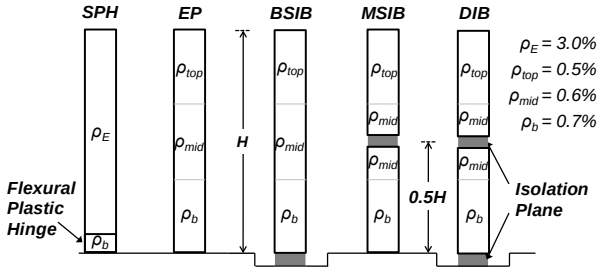


Figure 2. Schematic view of the five building designs including location of isolation planes and longitudinal reinforcement ratio along the height of the walls.

The core walls of the three seismically isolated buildings have the same details as the wall of the EP building. These buildings are seismically isolated using one

or two isolation planes at the base, mid-height, or at both base and mid-height. Building height, *H*, is defined as the height above the ground surface. For the isolated buildings with an isolation plane at their base, base is defined the base of the levels below ground. The system with a single plane of isolation at the base is referred to as BSIB, while that with the isolation plane at mid-height as MSIB. The system with two isolation planes, at base and at mid-height is termed DIB.

Diaphragm beams are utilized at the mid-height isolation plane to distribute the isolators over the entire floor plan and minimize tension demand in the bearings. These beams are installed at the top of the story below the isolators to allow full use of that story, and above the isolators, below the floor slab of the above story.

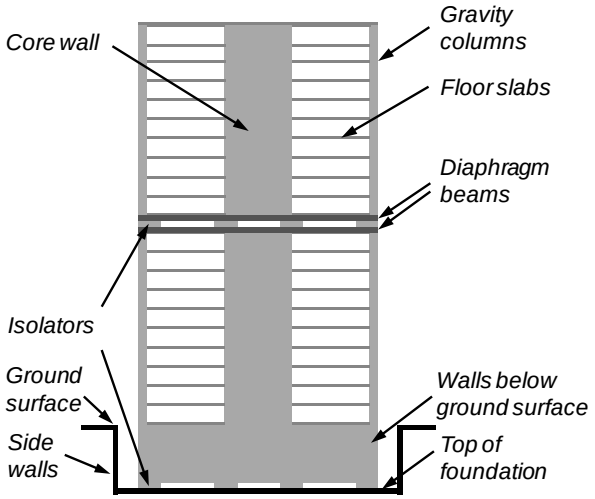


Figure 3. Elevation showing the location of isolation levels at building base and mid-height.

2.2 Seismic Isolator Design

Low-damping laminated rubber bearings were used for all isolated buildings. The main objective of the isolated buildings was to reduce acceleration and force demands and achieve a nearly elastic response of the walls. This could be accomplished by controlling the force that is transferred through the isolation plane at a target displacement of the isolation plane. For this target peak displacement the stability of the bearings under the combined axial and shear force has to be ensured (Kelly and Takhirov 2006). The target peak shear strain was 200% while the maximum tensile strain was 1%. The peak allowable ratio of peak vertical load to critical buckling load, P/P_{cr}, was considered equal to 0.3 (Kelly 1999). For the BSIB the target peak shear force was 0.15W at 0.75 m (30 in) target isolator displacement. Iterations, including preliminary numerical time history analyses, were performed to arrive at the design described in this study.

The base isolation plane of the BSIB, and DIB buildings were identical as they were the mid-height isolation planes of the DIB, and MSIB buildings, respectively. The ratio of the mid-height to the base isolation plane stiffness determines the difference in the response of the DIB in comparison with the BSIB. In order for this system to be effective, the stiffness of the mid-height isolation plane should be selected to reduce the force transmitted through it without the isolators exceeding a specific level of deformation. By preliminary analysis, a ratio of base to mid-height isolation plane stiffness of 0.7 was selected. Table 2 summarizes the main characteristics of the isolators. Sixteen isolators were used at both the base and the mid-height isolation planes. The diameters of the isolators used at the base and mid-height isolation planes were 1524 mm (60 in) and 1270 mm (50 in), respectively. All other design parameters for the isolators were identical.

Table 2. Main characteristics of seismic isolators.

Isolation Level	Base	Mid-height
Number of bearings	16	16
Outer diameter, mm (in)	1524 (60)	1270 (50)
Total rubber thickness t_r, mm (in)	635 (25)	635 (25)
Individual plane rubber thickness t, mm (in)	12.7 (0.5)	12.7 (0.5)
Steel plate thickness t_s, mm (in)	3.18 (0.125)	3.18 (0.125)
Individual bearing lateral stiffness K_h, kN/m (kip/in)	1386 (7.92)	963 (5.50)
Individual bearing vertical stiffness in compression, $K_{v,c}$, kN/m (kip/in)	3741000 (21375)	1804000 (10308)

2.3 Numerical Modeling of the Buildings

The Open System for Earthquake Engineering Simulation (OpenSees) software was used in this numerical study. Nonlinear beam-column elements with fiber sections were utilized to model the RC walls. An initial concrete modulus E_c = 33.8 GPa (4900 ksi) was used. Linear vertical, horizontal, and rotational zero-length springs were used to model the force-displacement behavior of each isolator at the corresponding direction. The vertical force, shear force, and bending moment interaction (Kelly and Takhirov 2004, Ryan et al. 2005) was not modeled. The vertical stiffness of the isolators in tension was modeled five times smaller than the compressive one (Fujita 1991, Kato 2003), however the isolators did not undergo tension in this numerical study. Rubber with shear modulus G = 483 KPa (70 psi) was assumed for the isolators. At each isolation plane "rigid" beam-column elements were used to model the diaphragm beams [see Figure 4]. The axial effect of the gravity columns was ignored. Vertical mass equal to half the lateral mass was modeled. Rayleigh damping with 2% damping in the first and the sixth mode was used.

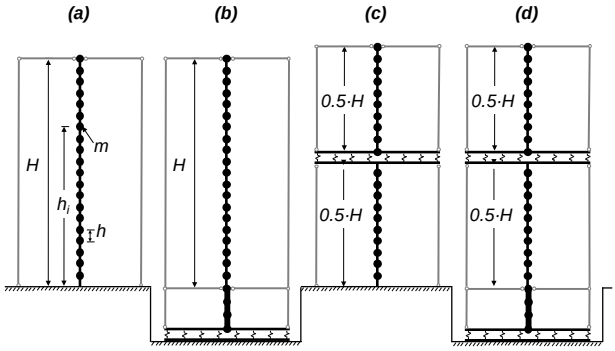


Figure 4. Elevation of numerical models showing lumped masses, diaphragm beams, and isolator springs.

3. NUMERICAL ANALYSIS RESULTS

3.1 Modal Analysis

The modal periods of the five buildings are presented in Table 3. The periods of the modes of lateral vibration elongate at least 120% for the isolated buildings. Compared with EP, the fundamental vertical periods of BSIB, MSIB, and DIB are 8%, 11%, and 18% longer, respectively.

Table 3. First three lateral ($T_{L,i}$) and first vertical ($T_{V,1}$) modal periods of the studied buildings.

Period (sec)	SPH	EP	BSIB	MSIB	DIB
$T_{L,1}$	1.91	1.99	5.17	4.42	6.13
$T_{L,2}$	0.30	0.31	1.35	0.67	2.62
$T_{L,3}$	0.11	0.11	0.26	0.30	0.66
$T_{V,1}$	0.13	0.14	0.15	0.16	0.17

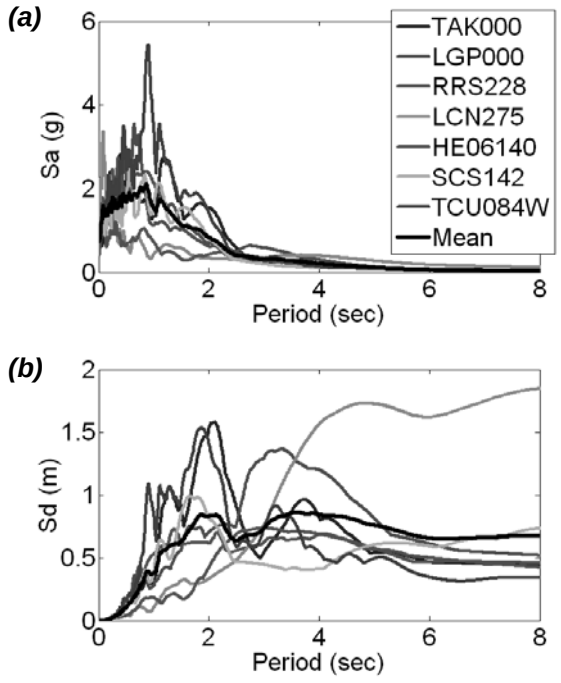


Figure 5. Total acceleration and relative displacement spectra of the 7 considered ground motions, 2% damping.

3.2 Ground Motions

Seven strong pulse-type near-fault ground motions from the Imperial Valley (1979), Loma Prieta (1989), Landers (1992), Northridge (1994), Kobe (1995), and Chi-Chi (1999) earthquakes were used in this study. Their spectral total acceleration and relative displacement spectra for 2% damping are presented in Figure 5. The ground motions were selected to have different predominant frequency content.

3.3 Comparison of Mean Results

Mean computed response envelopes, for the seven strong ground motions are shown in Figure 6 for six response quantities. The following six response quantities are considered: bending moment M normalized by the expected flexural strength at the base of the wall $M_{y,b}$, curvature ductility μ_φ defined as the measured curvature divided by $\varphi_{y,b}$, shear force V normalized by the total corresponding building weight W_t, total acceleration A normalized by the mean peak ground acceleration PGA, relative displacement D, and interstory drift ID.

BSIB, in comparison with the fixed base buildings reduces significantly accelerations, forces, interstory drifts and inelastic curvatures. In comparison with the EP building, BSIB reduces mid-height bending moment, base shear force, average floor acceleration along the building's height, and average interstory drift along the building's height by 28%, 74%, 65%, and 34%, respectively. In comparison with the SPH building, which has the largest mid-height bending moment, due to the "elastic" design of this building above the bottom plastic hinge and the significant contribution of the second mode to the response, the BSIB reduces mid-height bending moment by 56%.

The mean base curvature ductility demand μ_φ for the BSIB is equal to 4.1, which is 60% and 64% smaller than the corresponding values of the SPH and EP buildings. The mean curvature ductility at the base for BSIB is heavily influenced by the high value of μ_φ =15.3 recorded for LCN275 ground motion, which was the motion with the highest Sd for periods larger than 3.6 sec. The mean curvature ductility at the base for BSIB for the remaining six ground motions, omitting LCN275, is μ_φ = 2.2. Above the bottom three stories the BSIB remains elastic in comparison with the EP building which reaches a mean μ_φ = 3.2 at 45% of the height.

In comparison with the BSIB, the DIB reduces base bending moment and average interstory drifts along the height by 19% and 36%, respectively. The DIB building remains nearly elastic with a mean curvature ductility μ_φ = 1.9.

Similar mean roof displacements were computed for all buildings [see Figure 6(e)] since for most of the ground motions the spectral displacement for periods larger than 2.5 sec do not vary significantly, see Figure 5.

The MSIB develops forces and acceleration closer to those of the fixed-base buildings while it develops highly

inelastic response at its base, higher than the corresponding response of the fixed-base buildings. This occurs because the isolation plane at the mid-height of the structure controls the force that can be transferred through it while the forces that develop below this plane are bounded only by inelastic response of the wall in flexure. The bending moment and shear force envelopes of the MSIB are similar to those of the EP building. The above observations indicate the inefficiency of the MSIB design with the specific characteristics described in this paper.

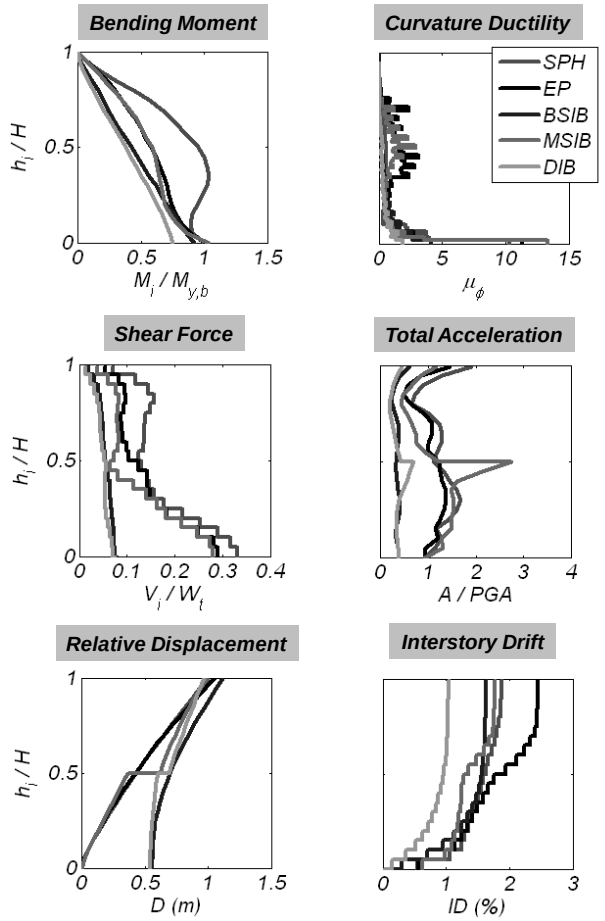


Figure 6. Mean response envelopes based on numerical analysis with seven strong near-fault records.

Response quantities of the bearings are summarized in Tables 4 and 5. The mean displacements of the bearings did not exceed 50% of their diameter *D*, while the peak was equal to 0.63*D* at the base for BSIB and 0.57*D* at mid-height for DIB. These peak displacements correspond to a shear strain of 147% and 111%, respectively. The peak compressive stress of 7.0 MPa (1.12 ksi) and 9.6 MPa (1.53 ksi) was reached for the isolators in the base plane of BSIB and in the mid-height plane of the DIB, respectively, corresponding to peak axial load ratio P / Pcr = 0.27 and 0.23.

Table 4. Mean of 7 near-fault ground motions, and peak (in parenthesis) displacements of the bearings (meters).

Isolation Plane	Base	Mid-height
BSIB	0.56 (0.95)	-
MSIB	-	0.54 (0.66)
DIB	0.54 (0.73)	0.51 (0.72)

Table 5. Mean of 7 near-fault ground motions, and peak (in parenthesis) isolator compressive strains (percent).

Isolation Plane	Base	Mid-height
BSIB	0.30 (0.33)	-
MSIB	-	0.30 (0.32)
DIB	0.26 (0.32)	0.25 (0.30)

3.4 Response to Individual Ground Motions

The response envelopes to each of the seven ground motions are presented in Figure 7. Less variability in the shear force and bending moment envelopes is observed for the BSIB compared with the fixed-base buildings. The bending moment envelopes of BSIB have a nearly linear profile along the building height.

For the LCN275 record, which has the largest spectral displacement demands for periods larger than 3.6 sec, the response of BSIB and DIB was highly inelastic at their base. To accommodate these high demands, the longitudinal reinforcement has to be increased along the height of the wall to remain elastic. For the isolated buildings the relative displacements for the LCN275 record are much higher in comparison to the other records. This record had significantly larger spectral displacements for T larger than 4.5 sec which was the fundamental period range of the isolated buildings.

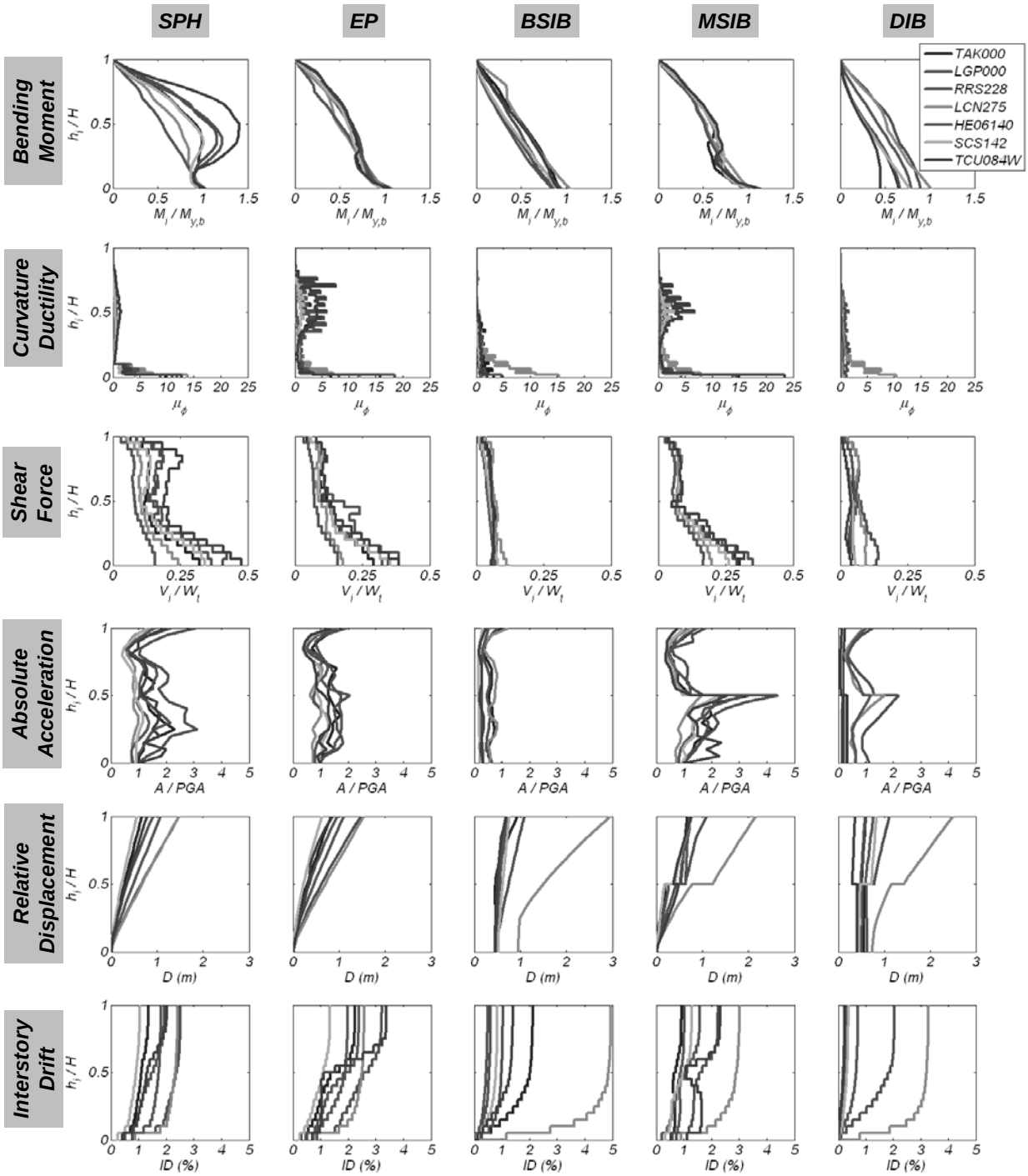


Figure 7. Response envelopes to individual ground motions of the five studied buildings.

4. CONCLUSIONS

This study investigated numerically the effect of seismic isolation on the response of 20-story tall reinforced-concrete core-wall buildings. The response of three seismic-isolated buildings was compared with this of two fixed-base buildings. The seismic isolation designs, differed in terms of number and location of the isolation planes. The buildings were subjected to seven strong pulse-type near-fault ground motions. The following conclusions are drawn:

- Base isolation reduced mid-height bending moment, base curvature ductility, base shear force, average along the height floor acceleration, and average along the height interstory drift demands in the fixed-base building by 28%, 64%, 74%, 65%, and 34%, respectively.
- Using and isolation plane at mid-height of the building in addition to the base, in comparison with using the isolation plane only at the base, resulted in a decrease of base bending moment, and average interstory drift along the wall height equal to 19% and 36%, respectively.
- The building with an isolation plane only at its mid-height was ineffective, and resulted in acceleration

and force demands closer to those of the fixed-base buildings, while its response was highly inelastic at the base.

- Base isolation, in comparison with the fixed base buildings, resulted in smaller sensitivity of the computed shear force and bending moment envelopes to the ground motion characteristics.

Acknowledgements:

The authors would like to thank UC MEXUS, which partially supported the first author.

References:

ACI 318-08. *Building Code Requirements for Structural Concrete (ACI 318-08) and Commentary*. ACI Committee 318, Farmington Hills, 2008.

ASCE 7-05. *Minimum Design Loads for Buildings and Other Structures*. American Society of Civil Engineers, 2006.

CEN EC8: *Design of Structures for Earthquake Resistance*. European Committee for Standardisation: Brussels, Belgium, 2004.

Council on Tall Buildings and the Urban Habitat (2011). "CTBUH Tall Building Database," http://www.ctbuh.org/Resources/WorldsTallest/tabid/123/Default.aspx

Fujita T. Seismic isolation rubber bearings for nuclear facilities. *Nuclear Engineering and Design* 1991; **127**: 379-391.

Kani N. Current state of seismic-isolation design. *Journal of Disaster Research* 2009; **4**(3): 175-181.

Kato R. The tensile tests of natural rubber bearings focused on the effect of the steel flange plates. *Proceedings, ASME Pressure Vessels and Piping Conference*, Cleveland, OH, USA 2003.

Kelly JM, Naeim F. *Design of Seismic Isolated Structures: from Theory to Practice*. John Wiley & Sons Ltd, 1999.

Kelly JM, Takhirov SM. Analytical and numerical study on buckling of elastomeric bearings with various shape factors. *Earthquake Engineering Research Center Report* December 2004.

Komuro T, Nishikawa Y, Kimura Y, Isshiki Y. Development and realization of base isolation system for high-rise buildings. *Journal of Advanced Concrete Technology* 2005; **3**(2):233-239.

Los Angeles Tall Buildings Structural Design Council. *An Alternative Procedure for Seismic Analysis and Design of Tall Buildings Located in the Los Angeles Region*. Los Angeles, CA, 2005.

Moehle J, Bozorgnia Y, Yang TY. The Tall Buildings Initiative. *Proceedings SEAOC Convention*. 2007; 315-324.

Pacific Earthquake Engineering Research Center (PEER) as part of the Tall Building Initiative (TBI). *Guidelines for Performance-Based Seismic Design of Tall Buildings*. PEER Report No. 2010/05.

Panagiotou M, Calugaru V, Visnjic T. Higher mode effects on the seismic response of tall cantilever wall buildings subjected to near fault ground motions. *Proceedings, Structural Engineers Association of California Convention*, San Diego, CA 2009; 345–357.

Panagiotou M, Restrepo JI. Dual-plastic hinge design concept for reducing higher-mode effects on high-rise cantilever wall buildings. Published online, *Earthquake Engineering and Structural Dynamics*, Feb. 2009.

Ryan KL, Kelly JM, Chopra AK. Nonlinear model for lead–rubber bearings including axial-load effects. *Journal of Engineering Mechanics* December 2005; 1270-1278.

Sueoka T, Torii S, Tsuneki Y. The application of response control design using middle-story isolation system to high-rise building. *Proceedings, 13th World Conference on Earthquake Engineering*, Vancouver, B.C., Canada 2004, Paper No. 3457.

Structural Engineers Association of Northern California (SEAONC). *Seismic Design & Review of Tall Buildings Using Non-Prescriptive Procedures*. Recommended Administrative Bulletin, San Francisco, April 23, 2007.

Tsuneki Y, Torii S, Murakami K, Sueoka T. Middle-story isolated structural system of high-rise building. *Journal of Disaster Research* 2009; **4**(3): 229-238.

8CUEE CONFERENCE PROCEEDINGS
8th International Conference on Urban Earthquake Engineering
March 7-8, 2011, Tokyo Institute of Technology, Tokyo, Japan

SHAKING TABLE TEST STUDY OF SYMPATHETIC VIBRATION IN BASE ISOLATION STRUCTURE

Yuxiang Xu[1)], Yuhua Zhu[2)], Wensheng Lu [3)]

1) Master, College of Civil Engineering, Tongji University, China
2) Professor, College of Civil Engineering, Tongji University, China
3) Professor, State Key Laboratory of Disaster Reduction in Civil Engineering, Tongji University, Tongji University, China
shujunxyx@126.com, zyhua@tongji.edu.cn, wenshenglu@vip.163.com

Abstract: Natural periods of isolation buildings in stiff construction sites were usually much larger than sites' characteristic period. But the two kinds of periods may be close to each other for isolation buildings and soft sites, this may cause resonance easily. In the paper, the resonance of a base isolation model under long-period seismic wave was studied by means of shaking table test, and the variations of acceleration, displacements and bearings' hysteretic curve were analyzed. The results showed that the resonant base isolation structure had distinctive feature which was different from non-resonant structure. The acceleration amplification factors, relative displacements and interstory drift of the super-structure in resonant isolation buildings were large, and deformations of bearings, with their hysteretic curves being pinched and hardened obviously, were super-large. As the seismic energy was accumulated, displacement of isolation storey would increase continuously, and it was very easy to cause damage or instability of the isolators even the isolation storey.

1. INTRODUCTION

The main objective of seismic isolation is to introduce horizontally flexible but vertically stiff isolation storey at the base of a building to substantially uncouple the superstructure from earthquake motion. By means of large deformation, the isolation storey can absorb most of the seismic energy transmitting to the building, and finally bring down seismic reactions of the structure. Fixed-based structures usually have large interstory drift and strong acceleration response under earthquake ground motion which tend to cause damage for structural members and non-structural components. However, the superstructure which has very small acceleration and interstory drift is almost rigid body motion and basically intact with deformations and hysteretic energy mainly occurring in the isolation storey.

The primary reason why isolation buildings could mitigate seismic reaction is that the stiffness of isolation story is very small which can lengthen the natural vibration period greatly. The period of isolation building is usually far from predominant period of construction site and is in the descending stage of seismic reaction. Furthermore, isolation bearings have excellent characteristics of large deformation, big damping ratio and good energy dissipation, and they can absorb most seismic energy which would be transmitted to the super-structure in fixed based building.

The relation between isolation structure's natural period and site's predominant period has great influence on efficacy of absorption of energy. Only if building's natural period is much greater than site's period, could the structure get good isolation efficacy. But when the natural period is close to the predominant period, the building may cause violent resonant reaction.

In the test, the model of a isolation building with small height-width ratio in soft site (e.g. 4 class or softer) is excited by high frequency and long period ground motions respectively, and the model gives rise to two kinds of responses, namely non-resonant and resonant reactions. After comparative study of these two kinds of phenomena, the resonant characteristics of base isolation building is known clearly.

2. MODEL TEST

2.1 General Situation of Model

The real structure is a large 6-story isolation building with small height-width ratio, and the plane dimension of the building is 105m×105m. There is a 4-story high, 40m × 40m sized atrium in the middle of the building, and the atrium's roof is 40m length long span trusses. The six storey test model is made in accordance with 1/30 similar ratio, and the plane size is 3.5m×3.5m. Total height of the super-structure, isolation storey and sensors under the bearings is 1.86m, and the super-structure is 1.178m high. The atrium's top roof truss is installed on the 4th floor column cap, and two storeys are suspended under the truss. The shaking table test model is shown in Figure 1.

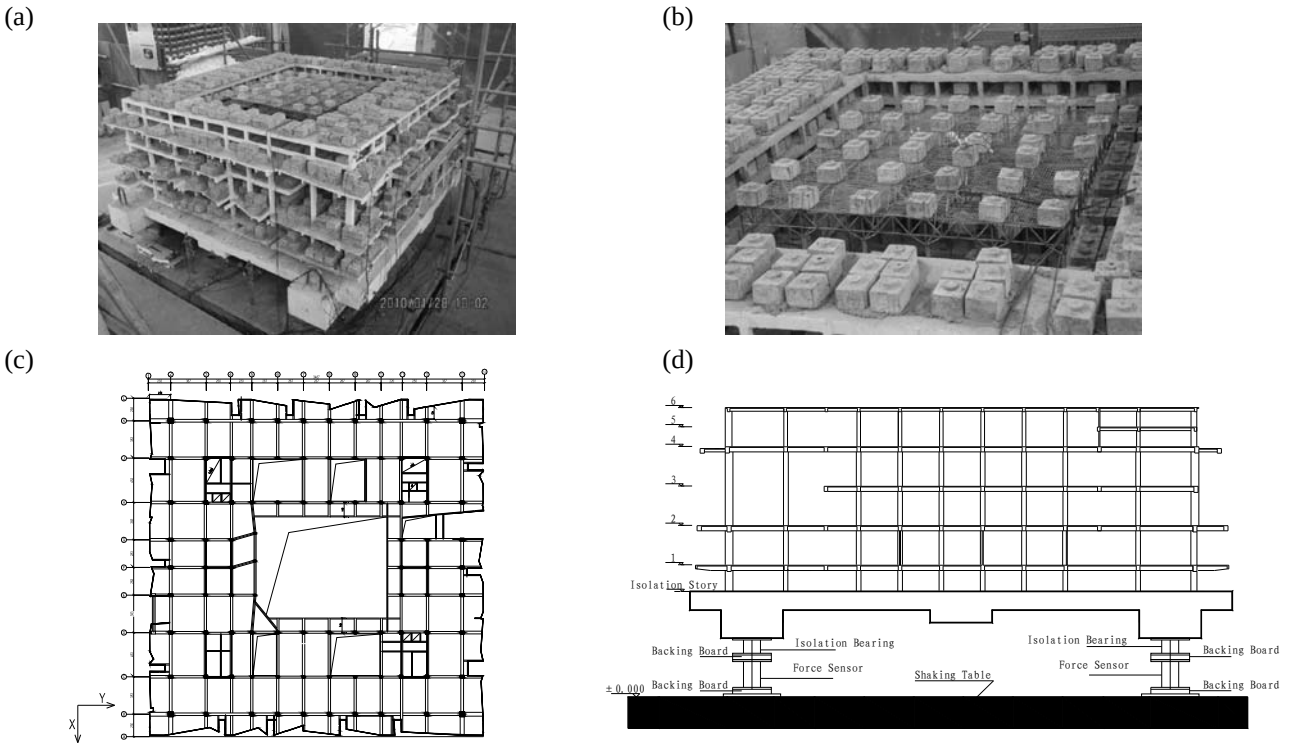


Figure 1 Shaking Table Test Model: (a) Shaking Table Test Model, (b) Truss on The Top Floor,(c) Plan Layout of Typical Storey, and (d) Typical Elevation of The Test Model

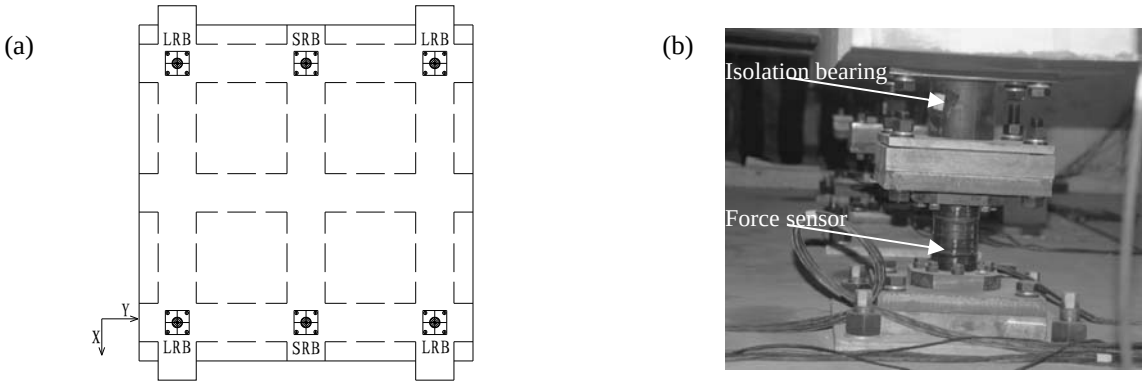


Figure 2 Isolated Bearings:(a)Locations of Isolation Bearings, and (b) Arrangement and detail of Isolation Bearing

The isolators' locations and arrangement detail of a typical LRB are shown in Fig 2, and there are 6 isolators in the isolation storey. 4 of them are lead rubber bearings (LRB) which located in the corners, the others are polysaccharide sliding rubber bearing（SRB）which located in the mid of two sides. According to similarity theory, the acceleration similar ratio is 1.888, and time similar ratio is 0.2.

2.2 Earthquake Records And Features

In the previous test, the isolation test model is not resonant under earthquake wave records of stiff sites such as El-Centro waves, Tanjin waves, Taft waves and LWD waves, and it has excellent ability of seismic reduction. The acceleration record of North-South direction of El-Centro waves (e.g. El-NS) is shown in Fig 3, and response spectrums of 3 direction acceleration of El-Centro records are shown in Fig 4. It shows that predominant periods of El-Centro wave records are less than 0.6s, while isolation buildings' natural periods are usually larger than 2s which is much greater than the predominant period of the wave records. Accordingly, El-Centro waves which can reduce reactions in the isolation structure can be representative of typical non-resonant earthquake waves in stiff sites..

Wenchuan earthquake (which happened in Sichuan province, China) wave records were recorded by State Key Laboratory of Disaster Reduction in Civil Engineering, Tongji University, in may 12, 2008. The duration of the wave records was 200s long, and the velocity was 3.2km/s. The acceleration peak values of south-north direction record (WC-SN), east-west direction record (WC-EW), and vertical direction record (WC-VER) are 2.32cm/ s^2, 1.96cm/s^2 and 1.17cm/s^2

respectively, and East-west direction record (WC-EW) is selected as the long-period resonant wave in the test. The acceleration record is shown in Fig5, and Fig 6 shows acceleration spectrums of the 3 records.

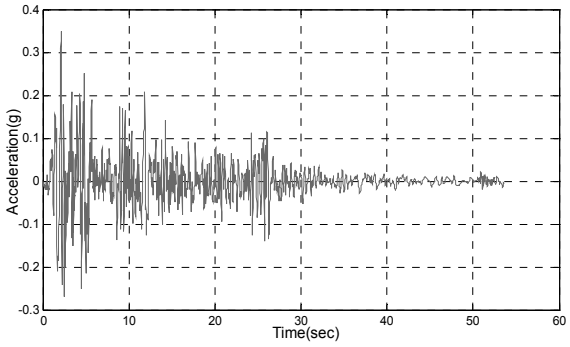


Figure 3 El-Centro(NS) earthquake wave record

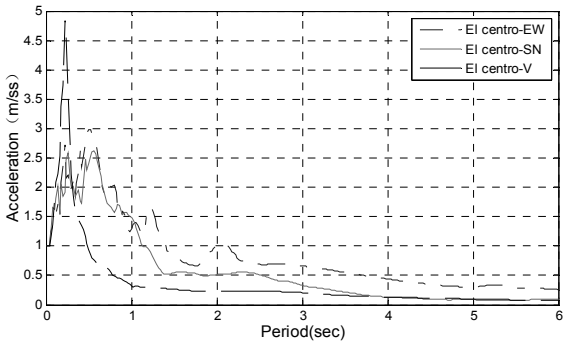


Figure 4 Acceleration response spectrum of El-Centro wave records

Fig 6 shows that predominant periods of WC-EW, WC-SN and WC-VER wave records are 2.4s, 2.6s and 2.3s respectively. Wenchuan waves' predominant periods are close to the natural period of high-rise, isolated and other long-period buildings, and these buildings would have violent reactions under long-period ground motions.

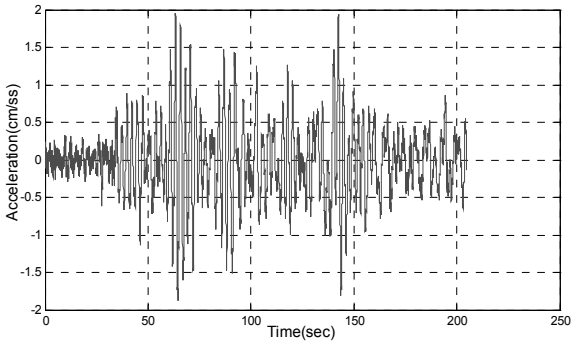


Figure 5 WC-EW Wave Record of Wenchuan Earthquake

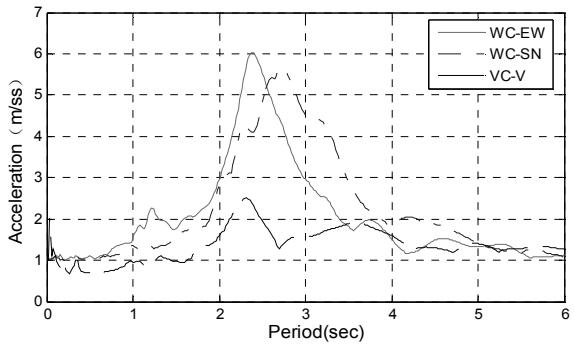


Figure 6 Acceleration Response Spectrum of WC Wave Records

2.3 Test Conditions

The test consists of two stages: base isolation structure's typical non-resonant reactions are verified in the first stage, and base isolation structure's resonant reactions are did in the second stage. In order to get dynamic properties, white noise is inputted before and after each stage, and base isolation model's shaking table test conditions is shown in table 1. Note that, the peak values of white noises in condition 1 and 4 are 0.1g, and the peak value in condition 7 after test of stage 2 is 0.05g so as to avoid further damage in superstructure especially in isolation layer,

Table 1 Test Conditions of Base Isolation Model

NO.	Earthquake Records	X	Y	Z	Notes	
1	White noise	0.100g	0.100g	0.100g	Sweep	Test of the first stage
2	El(NS)-x	0.100g	--	--	Frequent	
3	El(NS+EW+V)-xyz	0.200g	0.123g	0.121g	Design	
4	El(NS+EW+V)-xyz	0.400g	0.246g	0.242g	Rare	
5	White noise	0.100g	0.100g	0.100g	Sweep	Test of the Second stage
6	WC-EW	0.400g	--	--	Rare	
7	White noise	0.050g	0.050g	0.050g	Sweep	

In the test, the peak value of really inputing X direction acceleration of El-Centro wave is 0.393g in condition 4, and real peak value of X direction WC-EW wave is 0.317g in condition 6. These two peak values are similar, so they can be compared effectively.

3. EXPERIMENTAL PHENOMENA AND DYNAMIC CHARACTERISTICS

3.1 Experimental Phenomena

After white noise was inputted, the isolation storey has obvious vibration, but no overlarge displacement.

In the tests of first stage, the isolation storey has obvious displacement respectively under degree frequent wave, design wave and rare earthquake wave. The super-structure is nearly rigid body motion, and it almost has no torsion reaction and no obvious deformation. There are no new cracks in beams and columns, and at the same time, roof truss, suspended members and other components are well with the prism brick on isolation storey vibrating small. The test shows that normal base isolation buildings can reduce the earthquake reactions.

(a)





(b)





Figure 7 Bearing Deformation:(a)Small Deformation, and(b) Large Deformation

(a)



(b)



Figure 8 Typical Cracks on Super-structure's Beam and Column

7 degree rare WC-EW earthquake wave is inputted in the second stage. Because the acceleration amplitude is small in the first 15s, the isolation storey has no large deformation. As the wave is inputted, isolation story's deformation becomes obvious, larger and larger, and finally, the deformation is much larger than the deformation limit. Fig 6 shows the change of bearing deformation, (a) is bearing's small deformation, and (b) is bearing's super large deformation. At the moment of super large deformation, lead rubber bearings' appearance is well, but the inner lead may be destroyed and one slider has slide out from the Teflon slide type rubber bearing. The responses of super-structure are violent: the interstory drift is large with more and more concrete members cracking and many of cracks becoming wider, the diagonal bracings and the suspended members' bending deformation becomes aggravated, and the prism on isolation storey is overturned. Fig 8 shows the typical cracks on column and beam. The second stage test implies that the model has 'resonant' phenomena which are completely different from the first stage, and resonance has great influence on isolation storey and super-structure. After the super-large displacement, to avoid serious damage in bearings and the model, the test is stopped.

3.2 Dynamic Properties of Model

Table 2 shows variation of model's dynamic characteristics. Natural frequencies of model's Y direction and X direction were 1.712Hz and 1.953Hz respectively before tests. During tests of the first stage, model's natural frequency and vibration mode did not change, implying that the earquake waves had no influence on non-resonant isolation structure, and the model is basically intact. Model's X direction natural period was 0.512s before the second stage tests, while predominant period of the wave inputted in second stage was 0.48s which is 7 percent lesser than structural. According to structural dynamics, the predominant period was in structural resonance zone, and the model was liable to be resonant for the WC-EW wave record.

In table 2, it is known that model's X direction nominal natural frequency has no change under 0.05g white noise after stage 2. In fact, model's X direction frequency should be less than 1.953HZ under 0.1g white noise and has decreased, and the damping ratio is greater than the before. Furthermore, Y direction is model's first vibration mode before stage 2, but X direction becomes model's first vibration mode after stage 2, so it shows that isolation bearings are destroyed in large deformation, and this affects model's Vibration Characteristics.

4. ANALYSIS OF TEST RESULTS

4.1 Acceleration Reaction of Model

Fig 9 shows comparisons of X direction acceleration time history between isolation storey, 6th floor and shaking table under El-Centro 3 direction wave records. When the peak value of shaking table acceleration time history is 0.394g, peak value of 6th floor in super-structure is only 0.18g and isolation story's peak value is only 0.134g, so isolation model could reduce acceleration response effectively under El-Centro wave records. The tests also shows that the acceleration is larger, the isolation system mitigate the acceleration

reaction better.

Table 2 Model's Dynamic Characteristics

Sweep	Frequency(HZ)	Period(sec)	Damping Ratio	Vibration Mode
Before First Stage(0.1g)	1.712	0.584	0.372	Y direction motion
	1.953	0.512	0.374	X direction motion
Before Second Stage(0.1g)	1.709	0.585	0.374	Y direction motion
	1.953	0.512	0.375	X direction motion
After Second Stage(0.05g)	1.953	0.512	0.427	X direction motion
	2.197	0.455	0.283	Y direction motion

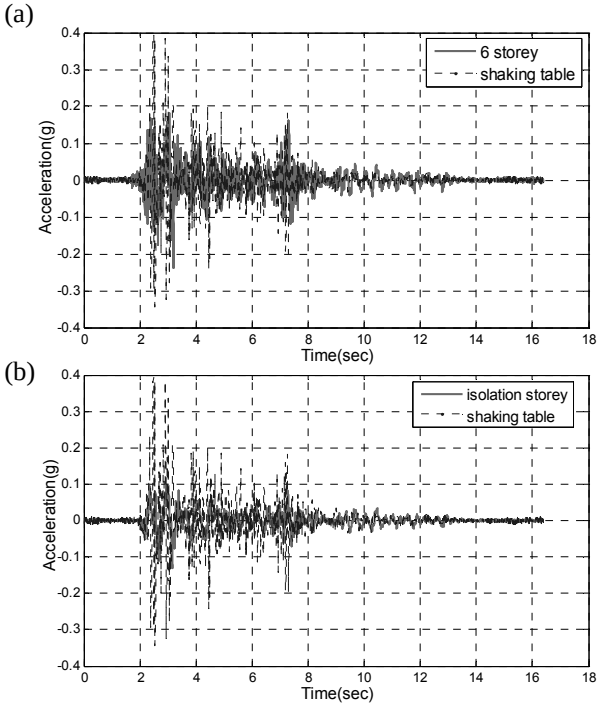


Figure 9 Comparison of Model's X Direction Acceleration Time History of El-Centro Wave: (a) 6th Floor and Shaking Table, and (b) Isolation Storey and

Fig 10 shows comparisons of X direction acceleration time history between isolation storey, 6th floor and table under WC-EW wave. The model amplifies acceleration response greatly under WC-EW wave: when the peak value of acceleration of table is 0.32g, the 6th floor's peak value of time history is as large as 0.76g, and isolation story's peak value is 0.69g. As the energy is accumulated, the model amplifies the acceleration reaction much greater. For example, at 27th second, the peak value of inputting acceleration is 0.21g, but the maximum acceleration is 0.76g in 6 floor and 0.69g in isolation storey. The result indicates that base isolation building can not mitigate acceleration when resonant.

Maximum accelerations of each floor under El-Centro and WC-EW waves are shown in Fig 11, and Fig 12 shows acceleration amplification factors of each floor. When El-Centro wave is inputted, maximum acceleration of each floor is much smaller than the table value: when maximum acceleration of table is 0.393g, peak values of the isolation storey and super-structure are between 0.132g and 0.238g respectively, and the acceleration amplification factors are between 0.34 and 0.61, so base isolation structure could mitigate each floor's acceleration obviously. However, when WC-EW wave is inputted, each story's acceleration is much larger than the table value: when the inputted acceleration is 0.318g, while the maximum accelerations of super-structure vary from 0.635g to 0.916g, and the acceleration amplification factors are between 2.06 and 2.88. Base isolation structure amplifies acceleration reaction of each floor obviously when resonant.

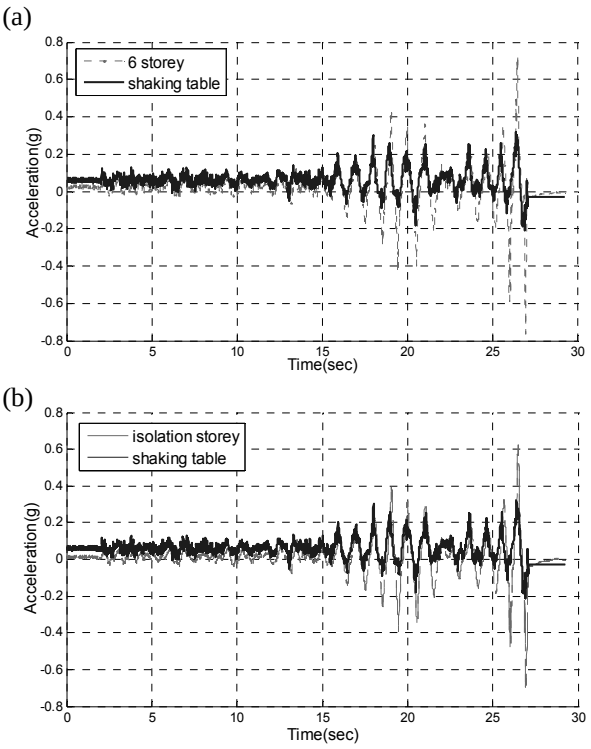


Figure 10 Model's X Direction Acceleration Time History of WC-EW Wave: (a) 6th Floor and Shaking Table, and (b) Isolation Storey and Shaking Table

As the numbers of storey increase, each floor's maximum acceleration is similar and change gently in non-resonant base isolation building rough the horizontal stiffness changed greatly. However, story's maximum

acceleration became larger as the numbers of storey increase in resonant condition, and the floor acceleration changed greatly when the horizontal stiffness varied. The accelerations are sensitive to the storey horizontal stiffness, for example, 3rd floor acceleration changed greatly along with the change of the horizontal stiffness. In brief, non-resonant base isolation building reduces the acceleration reaction greatly, but resonant isolation building amplifies the acceleration seriously and the acceleration is more sensitive to the variation of horizontal stiffness.

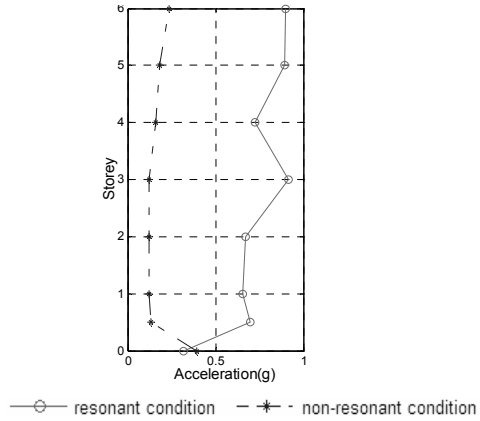


Figure 11 Maximum Acceleration For Different Storey

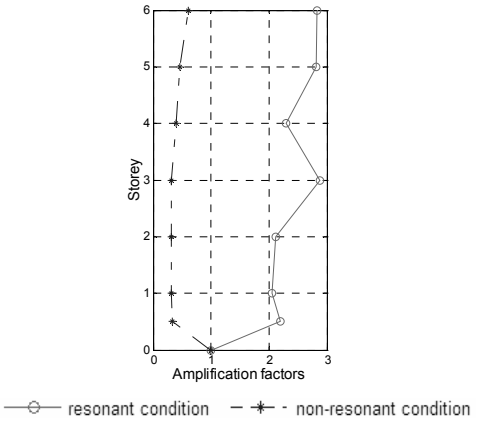


Figure 12 Maximum Acceleration Amplification Factors for Different Storey

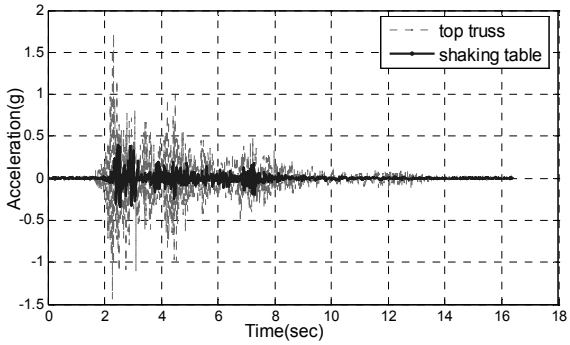


Figure 13 Acceleration Time-history of Truss and Shaking Table Under El-Centro Wave

Acceleration time histories of roof truss under El-Centro wave and WC-EW wave are shown in Fig13 and Fig 14 respectively. The truss acceleration is large under both two waves, and the acceleration amplification factors are larger than 4 which are much greater than the main structure's. Therefore resonance has little influence on the truss, but truss' response is still serious.

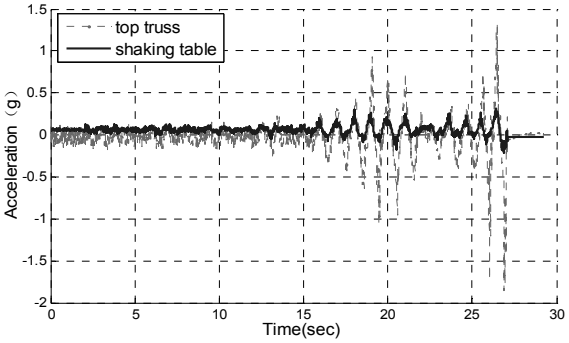


Figure 14 Acceleration Time-history of Truss and Shaking Table Under WC-EW Wave

4.2 Displacement Reaction of Model

The comparison of displacement time history of shaking table and isolation storey under El-Centro earthquake waves is shown in Fig 15. The isolation storey displacement is a little larger than the table, and displacement of isolation storey do not increase obviously as the earthquake wave inputted continuously. Fig 16 shows the comparison of displacement time histories of shaking table and isolation storey under WC-EW ground motion. Displacement of the isolation storey is larger than the table, and the displacement of isolation storey amplifies greatly as the earthquake wave is inputted continuously.

The relative displacement of isolation storey under El-Centro wave is shown in Fig 17, and the peak displacement is 5.34mm (LRB shear deformation 37.4%), implying that the isolation storey has "small" displacement. Fig 18 shows the relative displacement of isolation storey under WC-EW wave. As the wave is inputted and energy is accumulated, the isolation storey displacement increases continuously (this also can be seen from Fig 16). The largest relative displacement of isolation storey reached 59.9mm (LRB shear deformation 419%), and bearings' stability is very bad and may be destroyed easily.

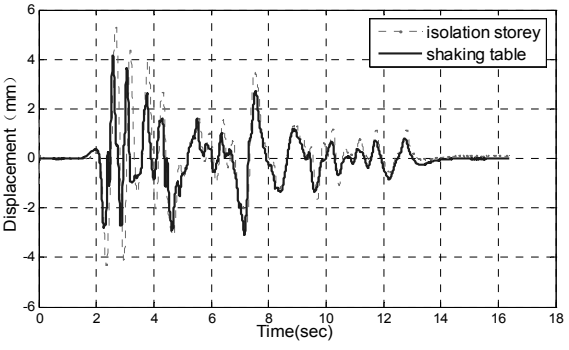


Figure 15 Displacement Time History of El-Centro wave

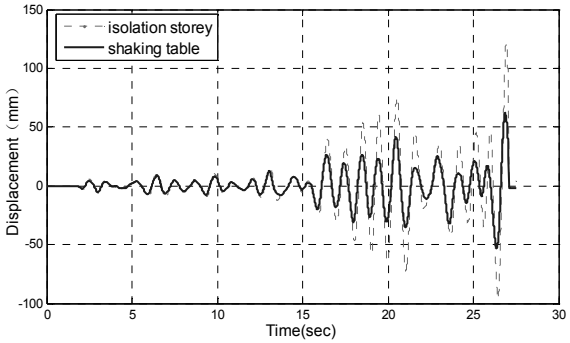


Figure 16 Displacement Time History of WC-EW Wave

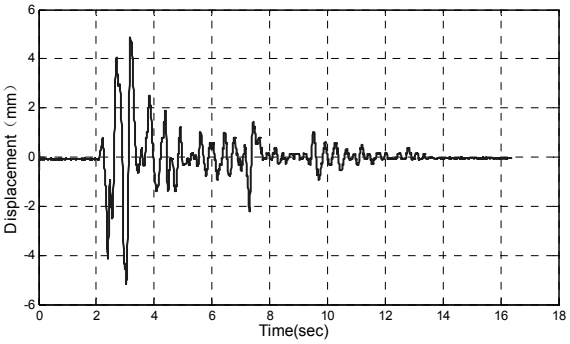


Figure 17 Relative Displacement Time History of Isolation Storey Under El-Centro Wave

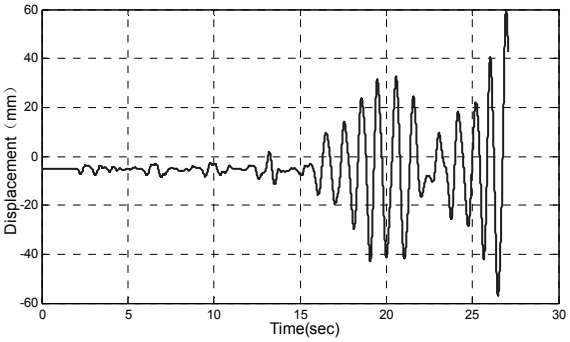


Figure 18 Relative Displacement Time History of Isolation Storey Under WC-EW Wave

Fig 19 shows peak displacements of isolation storey and super-structure under El-Centro and WC-EW waves. Under El-Centro wave, displacement of isolation storey is very small (5.34mm), and super-structure displacement is nearly "rigid body motion", namely displacement of each floor in super-structure is almost the same. But when WC-EW wave is inputted, both isolation storey deformation and floor relative displacements in super-structure are very large, and the model is not "rigid body motion" any more.

Displacement reaction of each floor in super-structure is shown in Fig 20. The peak value of interstory drift is only 0.22mm under El-Centro wave, and the largest drift angle is 1/1151. But in resonant condition, the relative displacement between 6th floor and isolation storey is 13.98mm. Interstory drift between 1st and 2nd floor is 4.5mm with drift angle 1/58, and storey drift between 4th and 6th floor is 6.8 mm with the drift angle 1/38. The storey relative displacement, interstory drift and drift angle in superstructure exceed the non-resonant condition greatly.

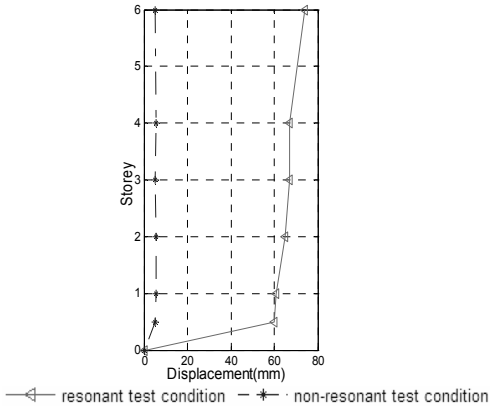


Figure 19 Model Absolute Displacement

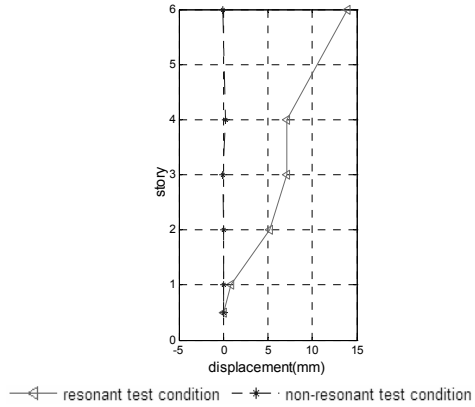


Figure 20 Superstructure Relative Displacement

According to "Technical Specification For Seismic-isolation With Laminated Rubber Bearing Isolators(CECS126:2001, Chinese)", isolation bearing's largest displacement should satisfy the following expressions :

$$u_{\max} \le 0.55d \quad (1)$$

$$u_{\max} \le 3t_r \quad (2)$$

Where,

$u_{\max}$ is bearing's largest horizontal displacement, and 59.9mm in the test.

d is diameter of the isolation bearing, and 100mm in the test.

t_r is total thickness of bearing's rubber layers, and 14.3mm in the test.

However, in the test,

$$u_{\max} = 59.9mm = 0.6d > 0.55d = 55mm$$

&

$$u_{\max} = 59.9mm = 4.2t_r > 3t_r = 42.9mm$$

the relative displacement of isolation storey is super large, and it would cause instability and damage in isolation bearings.

According to "Code For Seismic Design of Building

(GB50011-2010, china)", the allowable value of storey drift angle of earthquake resistant structure should be less than 1/50, and the storey drift angle limit in "CECS126" is 1/100, so interstory drift and storey drift angle of the superstructure exceed the limits of codes seriously.

4.3 Hysteretic Characteristics of Isolation Bearings

Hysteretic curve of typical lead rubber bearing under El-Centro wave is shown in Fig 21. The hysteretic curve is plump, elliptical and spindle shape with good energy dissipation, and its biggest horizontal force and displacement are 4.2Kn and 5.2mm respectively.

Fig 22 shows hysteretic curve of the same bearing under WC-EW wave. The curve has very large horizontal force (30kn) and displacement (59.9mm),which are 7.14 times and 11.54 times of non-resonant structure respectively, therefore the resonant hysteretic curve is much larger than the non-resonant curve.

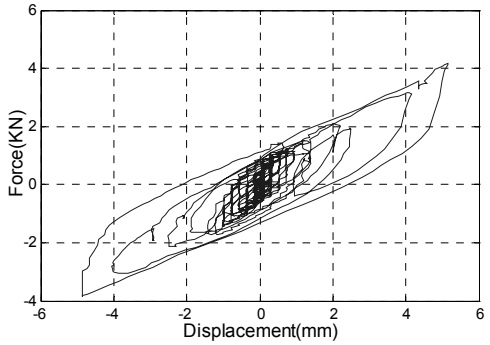


Figure 21 LRB Hysteretic Loop of El-Centro Wave

For resonant condition, when the bearing's displacement is small, such as 28mm (about 200% shear deformation), the hysteretic curve is plump, elliptical and spindle, and the bearing has good capacity of energy dissipation. As the displacement increases, the hysteretic loop becomes larger with more energy is absorbed, but the hysteretic loop began to be pinched. When bearings displacement is less than 40mm (about 300% shear deformation), it still is stable and possesses good capability of energy consumption rough the curve begins to be pinched. When the displacement is larger than 40mm, the hysteretic loop becomes larger while the displacement increases sharply. For large deformation, The lead rubber bearings are pinched seriously, and bearing's horizontal stiffness is hardened obviously. Bearing's characteristics have changed greatly, and it is not stable. So the largest shear deformation of bearing must be less than 300%, the limit is same to formula (2), and the suggesting peak value should not be larger than 200% for base isolation building in soft site.

Hysteretic curve of typical sliding rubber bearing under El-Centro wave is shown in Fig 23. The hysteretic curve is plump and the capability of energy consumption is stable and good.

Fig 24 shows the bearing's hysteretic curve under WC-EW wave. When the displacement is larger than 40mm, the hysteretic curve increase greatly and is pinched, not stable.

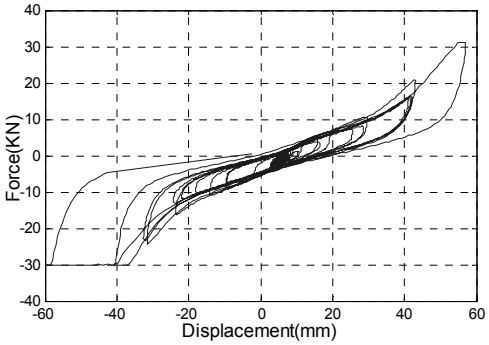


Figure 22 LRB Hysteretic Loop of WC-EW Wave

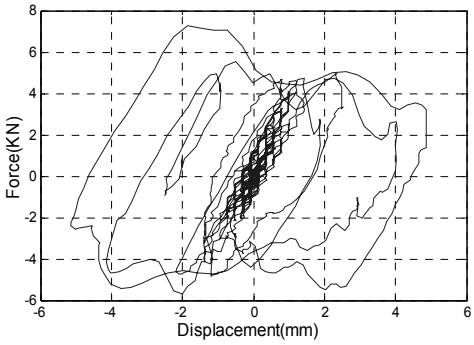


Figure 23 Sliding Bearing Hysteretic Loop of El-Centro Wave

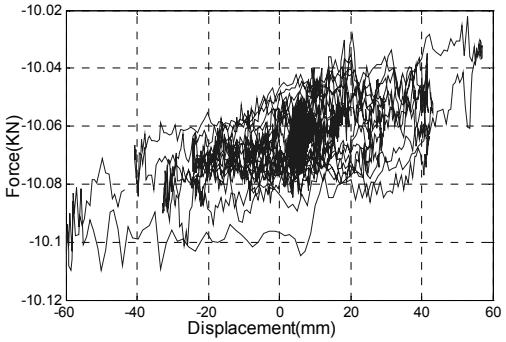


Figure 24 Sliding Bearing Hysteretic Loop of WC-EW Wave

5 CONCLUSIONS

According to resonance in shaking table test, the isolation buildings in soft sites are liable to be resonant if the natural period is close to site's predominant period. And the following main conclusions could be drawn.

(a) Horizontal relative displacement of isolation storey increase continuously in resonant base isolation buildings. The peak value can reach 59.9mm(4tr, 400% shear deformation, and this would lead to damage of bearings in isolation layer.

(b) When deformation of LRB is less than $2.0t_r$, the hysteretic curve with good energy consumption is plump and spindle. when deformation is larger than $2.0t_r$, the curve begins to be pinched and the lead core begins to be hardened. When the deformation is larger than $3.0t_r$, the hysteretic curve increases sharply and is pinched

seriously. The lead core is hardened obviously in large deformation and the bearings are not stable. To ensure some Safety Margin, the largest deformation of LRB in soft site should be less than 2.5 t_r, and must be smaller than 3.0t_r.

(c) The acceleration amplification factor of each floor in resonant isolation building is larger than 2, and both isolation storey and superstructure amplify shaking table's (also ground's) acceleration greatly. With storey numbers increasing, floor amplification factor becomes larger.

(d) Super-structure in resonant base-isolation building is not "rigid body motion" any more. The peak interstory drift angle is 1/37 in test, and it is much larger than the allowable limit. Many concrete members crack, and some steel members are bended and largely deformed. When the storey horizontal stiffness changed, the acceleration and displacement varied greatly, and seismic reactions of resonant building are more sensitive to the variation of horizontal stiffness.

(e) When a base-isolation building is resonant, not only it can't mitigate the seismic reaction, but also its isolation storey and super-structure are liable to be destroyed. Accordingly, if a base isolation building is built in soft site, structure's resonance should be avoided, and the limit of bearing's largest deformation should be more strict.

Acknowledgements:

The financial and technical supports from SLDRCE08-B-02 and prof. Wenguang Liu of Shanghai University are gratefully acknowledged.

References:

Liu, J.J. and Wang, J.Q.(2005), "The Discussion of Predominant Period of Site And Resonance Phenomenon of The site Building," *Journal of Guangxi Institute of Technology,***16**(3),47-50.

Yang, W.L., Zhu, S.C. And Hong, HC.,etc.(2009), "Characteristics of Far-field Ground Motion of Wenchuan Earthquake and The Effect on Long-Periodic Structures," *journal of disaster prevention and mitigation engineering*, **29**(4), 473-478

Xie, L.L., Zhou, Y.N. and Hu, C.X. (1990), "Characteristics of Response Spectra of Long Period Earthquake Ground Motion," *Earthquake Engineering And Engineering Vibration*, 10(1),1-20.

Li, J. and Li, G.Q.(1992), "Introduction to Earthquake Engineering," Seismological Press.

Architectural Institute of Japan (2005), "Design of Isolation Building," Trans Liu, W.G., Seismological Press.

R.S. Jangid and J.M.Kelly. (2001), "Base Isolation For Near-fault Motions," *Earthquake Engineering And Structural Dynamics*,30:691-707

M.R. Shekari, N.Khaji and M.T. Ahmadi(2010), "On The Seismic Behavior of Cylindrical Base-isolated Liquid Storage Tanks excited by Long-period Ground Motions," *Soil Dynamics and Earthquake Engineering*,30:968-980

8CUEE CONFERENCE PROCEEDINGS
8th International Conference on Urban Earthquake Engineering
March 7-8, 2011, Tokyo Institute of Technology, Tokyo, Japan

A DESIGN APPROACH FOR SEISMIC VIBRATION CONTROL OF RC BUILDING STRUCTURES USING VISCO-ELASTIC DAMPER

Wuchuan Pu[1] and Kazuhiko Kasai[2]

1) Post-doctoral Researcher, Center for Urban Earthquake Engineering, Tokyo Institute of Technology, Japan
2) Professor, Structural Engineering Research Center, Tokyo Institute of Technology, Japan
pu.w.aa@m.titech.ac.jp, kasai@serc.titech.ac.jp

Abstract: This paper proposed a passive control design method for reinforced concrete (RC) structures with visco-elastic dampers. The dynamic properties of the passive system are described, and the variation of equivalent parameters of system is discussed. The performance curves for reinforced concrete structures, which describe the interaction between dampers, structural component, and seismic input intuitively, are developed, and a damper distribution method for MDOF RC building structure is proposed. The time history analysis over a wide range of system parameters and input earthquakes shows good accuracy of the proposed method.

1. INTRODUCTION

Energy dissipation technology for seismic protection of building structures has got significant advance and active practice in recent years. As one of the major types of energy dissipation device, visco-elastic (VE) damper is being widely used both in new construction and in retrofitting of various types of strucutres, including reinforced concreted (RC) building structures. Compared with other velocity-dependent dampers, VE damper has the spring element in addition to the damping element, which functions to restore the objective structure to the original position after deformation. On the other hand, VE dampers have some characteristics such as the frequency dependency, temperature dependency, which lead to the necessity of careful consideration of environment where the VE damper is installed during the design.

Due to the complex mechanical behavior of RC materials and VE dampers, it is highly desirable to develop a comprehensive design rule that clearly indicates effects as well as necessary capacities of the dampers for the target performance of RC buildings. The writers have extended earlier design method (JSSI 2005, 2007) for the elastic frame and VE dampers to nonlinear behavior frames including steel frame and timber frame (Kasai and Pu 2010, Kasai et al. 2010). This study will propose a design method for RC building structure by extending the previous method.

The aim of the present design method is to provide an optimum distribution of VE damper for multi-story RC building so that each story develops same story drift prescribed beforehand. That will be realized by tuning the equivalent stiffness of the system, as will be described in the next sections.

2. DYNAMIC PROPERTIES OF SYSTEM

2.1 Degrading stiffness model for RC frame

The degrading Takeda model is used for the hysteresis rule of RC building. In the model, hysteresis depends on experienced maximum deformation $u_{\max}$. The model is elastic at $u_{\max}<u_c$, where u_c= cracking deformation defined by micro-cracking of the concrete material. Figure 1a shows the model at $u_c<u_{\max}<u_y$, where u_y= yield deformation when the steel reinforcing bars yield significantly and plastic hinge formed at the member. Figure 1b shows the hysteresis at $u_c<u_y<u_{\max}$.

Accordingly, Takeda model has tri-linear skeleton curve, and the first, second, and third lines represent elastic stiffness K_f, post-crack stiffness $\alpha_1 K_f$, and post-yield stiffness $\alpha_2 K_f$ against the displacement $u_{\max}$, respectively. From now on, ductility ratio μ and normalized cracking displacement μ_c will be used, where

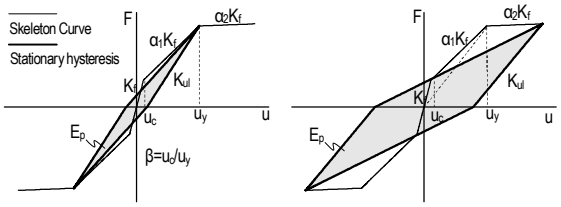
$$\mu = u_{\max}/u_y , \quad \mu_c = u_c/u_y \tag{1a,b}$$

The most significant characteristics that differentiate Takeda model with other models are the loading and unloading rules. The stiffness K_f^U when unloading from skeleton curve depends on μ experienced, and is given as:

$$\mu_c<\mu\le 1: \quad K_f^U = K_f \frac{2\mu_c+\alpha_1(\mu-\mu_c)}{\mu+\mu_c} \tag{2a}$$

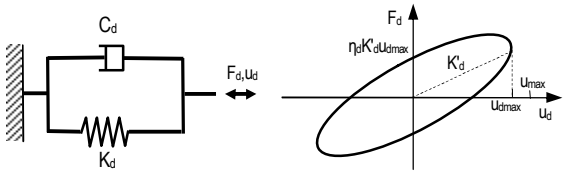
$$1<\mu: \quad K_f^U = K_f \frac{2\mu_c+\alpha_1(1-\mu_c)}{(1+\mu_c)\mu^{0.4}} \tag{2b}$$

After one or more loading cycles have occurred, the loading curve can be constructed by connecting the point at zero load to the point reached in the previous cycle, if that point lies on the skeleton curve or on a line aimed at a point



(a) Hysteresis before yielding (b) Hysteresis after yielding

Figure 1. Hysteresis loop of stiffness degrading model



(a) Kelvin Model for VE damper (b) Typical hysteresis loop of VE Damper

Figure 2. Typical hysteresis loop of VE Damper

on the skeleton curve. The more details about loading and unloading rules can be found in Takeda et al. (1970).

The equivalent stiffness at maximum displacement is given by Eq. (3),

$$K_{f,eq}=K_f p \tag{3}$$

where p is ratio of equivalent stiffness to initial stiffness of frame and given as Eq. (4).

$$\mu_c<\mu\le 1: \quad p=[\mu_c+\alpha_1(\mu-\mu_c)]/\mu \tag{4a}$$

$$1<\mu: \quad p=[\mu_c+\alpha_1(1-\mu_c)+\alpha_2(\mu-1)]/\mu \tag{4b}$$

2.2 Model for VE damper

Figure 2 shows the typical stationary-state hysteresis for visco-elastic damper. The VE damper produces the elastic force and viscous force proportional to the deformation and velocity, respectively, so VE damper develops hysteresis loop of an inclined ellipse. The secant stiffness at maximum deformation is defined as storage stiffness K'_d, and loss stiffness K''_d is defined as the force at deformation u=0 divided by maximum deformation u_{dmax}. Loss factor $\eta_d = K''_d/K'_d$ is used to denote the ratio of loss stiffness to storage stiffness (Fu and Kasai 1998).

2.2 Dynamic properties of system

Figure 3 shows the constitution of RC frame and VE damper system. The damper is connected to elastic brace in series, and the damper-brace assembly is called as "added component". The added component is connected to main frame in parallel to form the passive control system. Obviously, damper and brace experience the same force, added component and frame experience the same deformation.

Given the stiffness of brace K_b, storage stiffness of damper K'_d, and loss factor of damper η_d, the storage stiffness K'_a and loss factor η_a for added component can be easily obtained as following.

$$K'_a=\frac{K'_d}{1/\Gamma_d+K'_d/K_b}, \quad \Gamma_d=1+\frac{\eta_d^2}{1+K_b/K'_d} \tag{5a-c}$$

$$\eta_a=\frac{\eta_d}{1+(1+\eta_d^2)K'_d/K_b}$$

Similarly, storage stiffness of system K' and loss factor η are expressed by

$$K'=K_f+K'_a, \quad \eta=\eta_a\frac{K'_a}{K_f+K'_a} \tag{6a,b}$$

Let T_f, h_f denote the initial period and damping ratio of frame, the natural period T_0, damping ratio h_0 of the elastic system with added component can be easily obtained.

$$T_0=T_f\sqrt{K_f/(K_f+K'_a)}, \quad h_0=h_f+0.9\frac{\eta}{2} \tag{7a,b}$$

where the factor 0.9 in Eq. (3b) serves to modify the damping effect of system in random response when damping factor estimated from stationary response is used (Kasai & Okuma 2004).

For elasto-plastic system, using the equivalent stiffness of frame defined by Eq. (3), the equivalent period of system at maximum displacement can be calculated by Eq. (8).

$$T_{eq}=T_f\sqrt{1/(p+K'_a/K_f)} \tag{8}$$

Based on the previous definitions for frame and damper, the dissipated energies of damper and frame at maximum deformation u_{max} are given as Eq. (9).

$$E_v=\pi\eta_a K'_a u_{\max}^2, \quad E_p=qK_f u_{\max}^2 \tag{9a,b}$$

where q in Eq. (9b) is given as,

$$\mu\le\mu: \quad q=0$$

$$\mu_c<\mu\le 1: \quad q=2\beta(1-\beta)/\{1+(1-\beta)\mu/\mu_c\} \tag{10a-d}$$

$$\beta=(1-\alpha_1)\{1-(\mu_c/\mu)\}$$

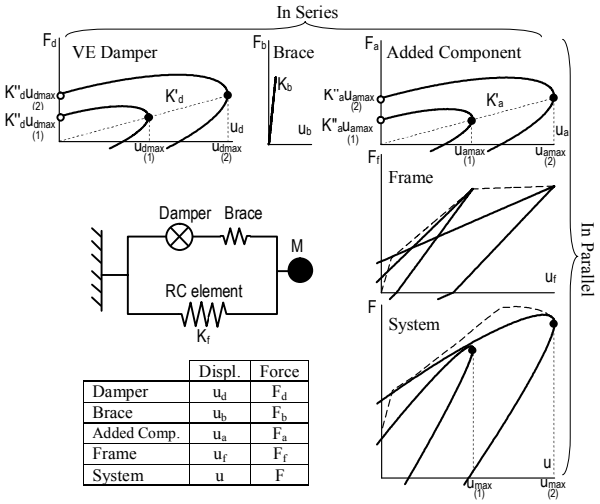


Figure 3. Force and displacement relationship of structural components of SDOF system.

$1<\mu$: $q=2p[1-p\mu^{0.4}(1+\mu_c)/\{2\mu_c+\alpha_1(1-\mu_c)\}]$

The stored energy of system can be easily estimated by

$$E_s=(pK_f+K'_a)\cdot u_{\max}^2/2 \tag{11}$$

The damping ratio of system is estimated by Eq. (12).

$$h_{eq}=h_{eq,v}+h_{eq,p}=\frac{E_p+E_v}{4\pi E_s} \tag{12}$$

$$h_{eq,v}=\frac{E_v}{4\pi E_s},\quad h_{eq,p}=\frac{E_p}{4\pi E_s} \tag{13a,b}$$

When building frame subjected to random excitation, it develops different hysteresis loops because loading stiffness depends on the maximum deformation experienced by frame. The ductility ratio of frame varies from 0 to maximum randomly. In order to include this effect in the analysis, the average damping method proposed by Newmark & Rosenbluth (1971) is used in this study. The average damping ratio of system was estimated by Eq. (14).

$$h_{eq,ave}=\frac{1}{\mu}\int_0^{\mu}h_{eq}(\mu')d\mu' \tag{14}$$

3 DAMPER DESIGN BASED ON PERFORMANCE CURVE

3.1 Response reduction of VE system

The evaluation method of response reduction of passive control building has been proposed based on the elastic response spectrum previously. In this section, the design method for RC structure added with VE damper is constructed by extending the previous method. The displacement spectrum, pseudo-velocity spectrum, pseudo-acceleration spectrum are defined as S_d, S_{pv} and S_{pa}, respectively. From any one of the three spectra, the other two spectra can be calculated in terms of Eq. (15).

$$S_d(T_f,h_f)=\frac{T_f}{2\pi}S_{pv}(T_f,h_f)=\left(\frac{T_f}{2\pi}\right)^2 S_{pa}(T_f,h_f) \tag{15}$$

The response reduction is the combination effect of decreased vibration period and increased damping effect by adding VE damper into structure. We define the ratios of the displacement u, force F of passive system to the displacement and force of original elastic frame u_{el}, F_{el} as displacement reduction ratio R_d, pseudo-acceleration reduction ratio R_{pa}, respectively.

$$R_d=\frac{S_d(T_{eq},h_{eq})}{S_d(T_f,h_f)}=D_h\frac{T_{eq}}{T_f}\frac{\bar{S}_{pv}(T_{eq},h_f)}{S_{pv}(T_f,h_f)} \tag{16a}$$

$$R_{pa}=\frac{S_{pa}(T_{eq},h_{eq})}{S_{pa}(T_f,h_f)}=D_h\frac{T_f}{T_{eq}}\frac{\bar{S}_{pv}(T_{eq},h_f)}{S_{pv}(T_f,h_f)} \tag{16b}$$

where $\bar{S}_{pv(T_{eq},h_f)}$ is the average pseudo-velocity spectrum over period range from T_0 to T_{eq} (Kasai et al. 2005, 2009). The reason to use averaged pseudo-velocity spectrum is in that the spectrum is smoothed and the possible difference between the spectrum value at T_f and T_{eq} can be reduced in such a way.

Assume the pseudo-acceleration spectrum in short-period and pseudo-velocity spectrum in medium- to long-period are identical, respectively, the response reductions of structure can be rewritten as

$$R_d=D_h\frac{T_{eq}(T_{eq}+T_0)}{2T_f^2},\ R_{pa}=R_d\left(\frac{T_f}{T_{eq}}\right)^2\quad(S_{pa}=\text{Const.}) \tag{17a,b}$$

$$R_d=D_h\frac{T_{eq}}{T_f},\qquad R_{pa}=R_d\left(\frac{T_f}{T_{eq}}\right)^2\quad(S_{pv}=\text{Const.}) \tag{18a,b}$$

where D_h is called as damping effect factor, it describes the response reduction ratio due to increase of damping of system. Equation (19) is used for calculating D_h, where a=25 in case of real earthquake motions, and other different values will be used if artificial earthquake motions are used. (Kasai et al. 2003).

$$D_h=\sqrt{(1+\alpha h_f)/(1+\alpha h_{eq})} \tag{19}$$

Given the loss factor η_d and storage stiffness ratio K''_d/K_f, calculate T_0/T_f, T_{eq}/T_f, and h_{eq}, and then obtain R_d and R_{pa} by using Eqs. (17) and (18). The plot for R_d-R_{pa} estimated for varied parameters is defined as "performance curve".

Assume K_b/K_f =3, μ_c = 0.1, α_1 = 0.22, α_2 = 0.01 and h_f = 0.02, the performance curves for μ = 0.75 and μ=1.5 are plotted in Fig. 4 and Fig. 5, respectively. Fig. 4(a) and Fig. 5(a) are based on constant pseudo-acceleration spectrum S_{pa}, Fig. (4b) and Fig. (5b) are based constant pseudo-acceleration spectrum S_{pa}. For comparison, the performance curves for elastic system with μ=1 are plotted in broken line in each figure.

The performance curves as plotted in Figs. 4 and 5 show the ratios of the displacement and acceleration responses of VE system to those of initial elastic frame. Using the performance curves, the responses of elasto-plastic VE system can be easily obtained after the elastic response of initial system is calculated. The necessary damper quantity for achieving a target response level can also be easily determined bases on such performance curves.

3.2 Passive control design based on performance curve

The already-known include the initial period T_f, initial damping factor h_f, all structural parameters for RC frame, brace stiffness ratio K_b/K_f, target ductility ratio μ. Based on the performance curve, the passive control design to determine the quantity of damper can be performed as following.

(1). Make performance curves for target ductility ratio μ.
(2). Calculate responses of elastic frame u_{el}, F_{el}.
(3). Calculate the response reductions R_d, R_{pa}.
(4). Determine the storage stiffness ratio K''_d/K_f, with an assumed loss factor η_d.
(5). Get the pseudo-acceleration reduction R_{pa}, and subsequently get maximum shear force of system.

If both the target maximum force and maximum displacement are satisfied, the design is finished.

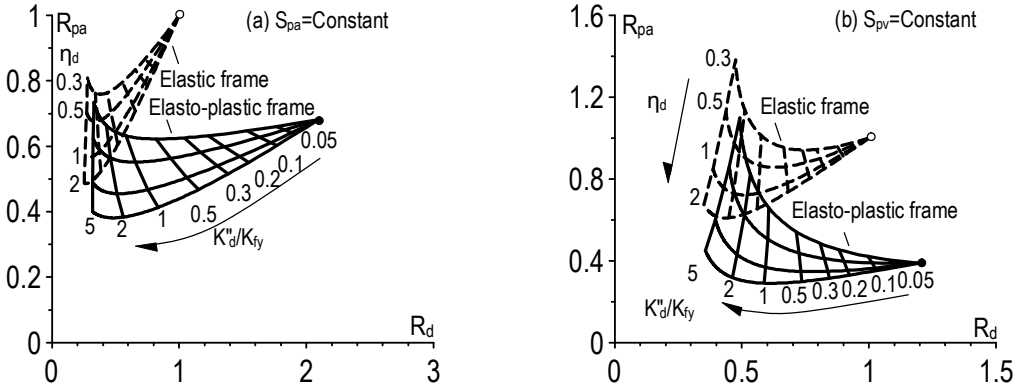


Figure 4 Performance curve (μ=0.75, K_b/K_f=3, μ_c=0.1, α_1 = 0.22, α_2 = 0.01)

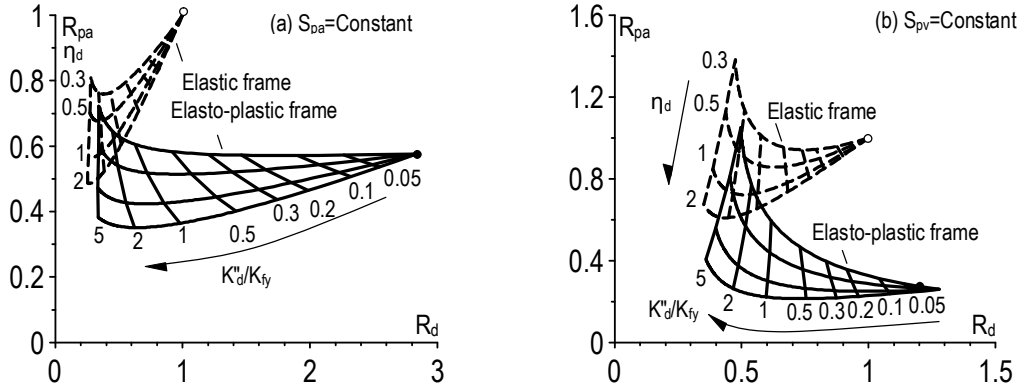


Figure 5. Performance curve (μ=1.5, K_b/K_f=3, μ_c=0.1, α_1 = 0.22, α_2 = 0.01)

4. DAMPER DISTRIBUTION RULE FOR MDOF SYSTEM

4.1 Design procedure

As outlined in Sec. 1, the present design method contains a rule to optimize damper distributions so as to produce uniform story drift angle that matches with the target value even for frames of irregularly distributed structural parameters.

The writers developed a series of design methods for elastic and elasto-plastic frames with various types of dampers, and validated them by extensive numerical tests considering arbitrary parametric distributions. The present study for the first time extends the previous methods to RC building typically having complex hysteretic properties.

The general design procedure is shown as follows.

Step 1. Establish the required basic design data, including mass m_i and story height h_i of each story of building, and specify the target drift angle, design spectrum and earthquake motions for dynamic analysis.

Step 2. Establish the constitutive model for each story based on the pushover analysis, and construct a MDOF shear beam model for building.

Step 3. Reduce the degree of freedoms to get an equivalent SDOF model at target displacement level.

Step 4. Determine the necessary damper quantity for SDOF system through performance curves.

Step 5. Distribute damper into each story of MDOF system (Section 4.3).

Step 6. Examine the performance of passive control building by time history analysis.

4.2 Conversion of MDOF frame to SDOF frame

The conversion of MDOF structural frame into an equivalent SDOF frame is divided into three cases according to the target drift angle θ_t. Firstly, the elastic stiffness of the equivalent SDOF system is estimated by,

$$K_f=\sum_{i=1}^{N}K_{fi}h_i^2/H_{eff}^2\,,\quad H_{eff}=\sum_{i=1}^{N}m_iH_i^2/\sum_{i=1}^{N}m_iH_i \qquad (20a,b)$$

where H_{eff} is the effective height of the RC building, and straight-line mode giving uniform story drift angle is assumed, as often considered by the writers (Kasai et al. 2006, 2010).

The storage and dissipated energies are respectively assumed equal between equivalent SDOF system and MDOF system, namely,

$$\frac{1}{2}pK_f(H_{eff}\theta_t)^2=\sum_{i=1}^{N}E_{si}\,,\quad qK_f(H_{eff}\theta_t)^2=\sum_{i=1}^{N}E_{pi} \qquad (21a,b)$$

In case of μ_i>1, namely, yielding happens in one or more stories at target drift angle θ, it is assumed similarly that μ>1 holds true for SDOF system. In addition to the previous two constraint conditions, μ_c and α_2 of SDOF system are assumed to be the average value of μ_{ci} , α_{2i} of each story level of MDOF frame (Eq. (22)). v

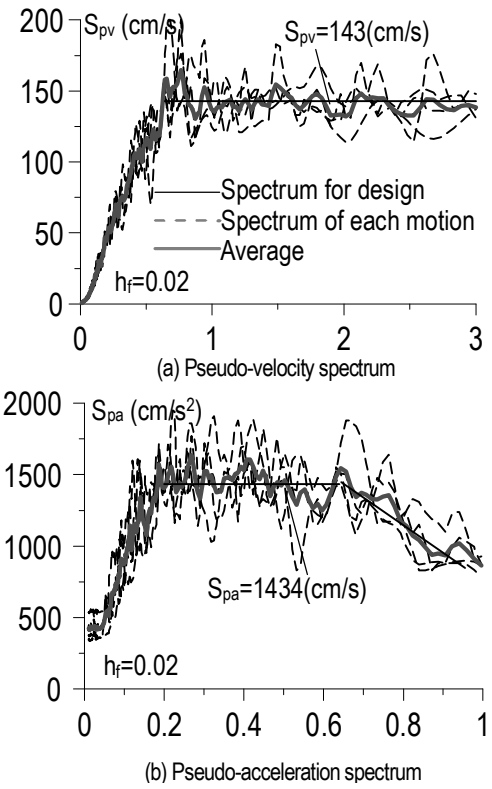


Figure 6 Response spectra of ground accelerations

$$\alpha_2=\frac{1}{N}\sum_{i=1}^{N}\alpha_{2i}\ ,\quad \mu_c=\frac{1}{N}\sum_{i=1}^{N}\mu_{ci} \tag{22a,b}$$

In this way, an equivalent SDOF system is determined. It is noted that the equivalent SDOF system depends on the target displacement level, because the equivalent SDOF is made based on the equivalence of damping and period SDOF and MDOF systems at specified performance level.

4.3 Damper distribution rule for MDOF system

The damper quantity obtained for equivalent SDOF system is distributed to each story of MDOF system by using the following two constraint conditions.

(a) The equivalent damping factors of SDOF and MDOF passive control systems are equal.

(b) The equivalent stiffness of passive control MDOF system at target drift angle is proportional to the story shear force Q_i acting on each story.

Equations (23) and (24) are constructed based on the above conditions.

$$\frac{E_v+E_p}{2\pi(K'_a+K_{eq,f})(H_{eff}\theta)^2}=\frac{\pi\sum_{i=1}^{N}\eta_{ai}K'_{ai}(h_i\theta_t)^2+\sum_{i=1}^{N}E_{pi}}{2\pi\sum_{i=1}^{N}\{(K'_{ai}+K_{eq,fi})(h_i\theta)^2\}} \tag{23}$$

$$\frac{Q_i}{\{K_{fi}p_i+K'_{ai}\}h_i}=\frac{\sum Q_i}{\sum\{K_{fi}p_i+K'_{ai}\}h_i} \tag{24}$$

The storage stiffness of viscous damper distributed to i-th story K''_{di} is obtained as Eq. (25).

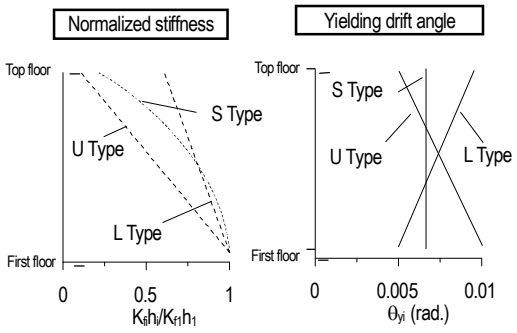


Figure 7. Stiffness and yielding drift distributions

$$K'_{di}=\left[\frac{\sum E_{pi}/\pi\theta^2-\eta_a\sum K_{fi}p_ih_i^2}{(2h^m-\eta_a)\sum Q_ih_i}\cdot\frac{Q_i}{h_i}-K_{fi}p_i\right]\cdot\left(\frac{K'_d}{K_b}+\frac{1}{\Gamma_d}\right) \tag{25}$$

5. ACCURACY VERIFICATION

Time history analysis is performed to verify the accuracy of present design method. A suit of 6 artificial earthquake motions are used. The motions are scaled so that the averaged S_{pa} between 0.16s and 0.64s equal to 1434cm/s^2, and averaged S_{pv} over 0.64s equal to 143cm/s. Figure 6 shows the pseudo-velocity and pseudo-acceleration spectrum for each earthquake motion and their average.

10-story RC building structures are considered. The building has height of 42m and elastic period of 1.26s. Three distribution patterns of initial stiffness are considered, which include S-type where stiffness is proportional to the shear force Q_i, and L-type and U-type where the lower stories and upper stories, respectively, are relatively weak compared to S pattern. Three yield drift angle distribution patterns are considered. S-type has identical yielding drift angle of 1/150 in each story. L-type, U-type have linear distribution of θ_{yi} between 1/200 and 1/100 over the height (Fig.7). The target drift angle is set to be 1/150 and 1/100, respectively. Accordingly, 9 frames designed to 2 types of target drift angle and 6 earthquake motions, a total of 108 cases are investigated.

Figure 8 shows the accuracy of the present damper design methods per frame stiffness distribution type. The broken line denotes the averaged story drift of frame of 3 types of yielding drift angle distribution pattern, for each earthquake motion. The solid line shows the averaged story drift of passively controlled system designed by the present method, the story drift is averaged over three types of yielding drift distribution pattern and 6 earthquake motions. One can see that the present method shows good accuracy.

6. CONCLUSIONS

This paper proposed a passive control design method for RC structure added with elasto-plastic damper. The dynamic properties of the system constituted by the main frame and the added component in parallel are discussed, the variation of equivalent period and damping with respect to system's parameters were described.

The dampers are designed by tuning the equivalent stiffness of the system so that an optimum equivalent

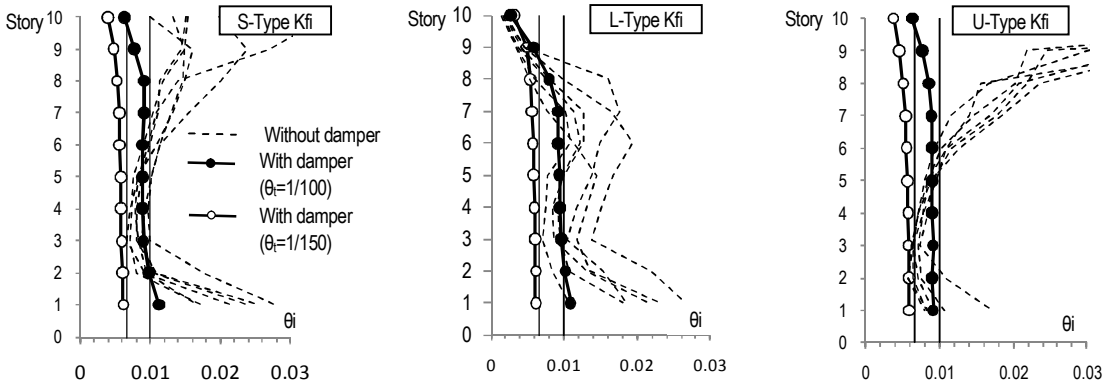


Figure 8. Comparison of story drift between structures with and without damper

stiffness distribution can be achieved at target drift by adding VE dampers, while the earthquake energies are dissipated by VE dampers as well. The time history analysis on structures with irregular distribution of structural parameters was performed, the good accuracy of the proposed method was verified.

REFERENCE

JSSI Manual 2nd Edition (2005, 2007), *Design and Construction Manual for Passively Controlled Buildings*, Japan Society of Seismic Isolation (JSSI), Tokyo, JAPAN, 1st Ed., 405 pages, 2003, 2nd Ed., 515 pages, 2005, 2nd Ed. and 2nd Print, 509 pages, 2007 (in Japanese)

Kasai K., Ito H., and Watanabe A., "Peak Response Prediction Rule for a SDOF Elasto-Plastic System Based on Equivalent Linearization Technique," *Journal of Structure and Construction Engineering*, No.571, pp.53~62, 2003.9.

Kasai K., Minato N., and Kawanabe Y., "Passive Control Design Method Based on Tuning of Equivalent Stiffness of Visco-Elastic Damper," *Journal of Structure and Construction*, No. 610, pp. 75-83, 2006.12.

Fu Yaomin and Kasai Kazuhiko, "Comparative Study of Frames Using Viscoelastic and Viscous Dampers," *Journal of Structural Engineering*, Vol. 124, No. 5, pp. 513-522, 1998.5.

Kasai Kazuhiko and Okuma Kiyoshi, "Evaluation Rule and Its Accuracy for Equivalent Period and Damping of Frequency-Dependent Passive Control Systems: Global damping model of one-mass system having elastic frame and either viscoelastic or oil damper," *Journal of Structure and Construction Engineering*, No. 580, pp. 51~59, 2004.6.

Kasai K., Nishihara K., Pu W. et al." Peak Response Evaluation Method for Slip-Hysteretic Structure Added with Visco-elastic Damper," *Journal of Structure and Construction Engineering*, No.646, pp.2227~2236, 2009.12.

Newmark, N.M. and Rosenblueth, E. "Fundamentals of Earthquake Engineering." Prentice-Hall Inc., 1971.

Kasai K., Kawanabe Y., "Equivalent Linearization to Predict Dynamic Properties and Seismic Peak Responses of a Structural System with High Viscous Damping and Hysteretic Damping," *Journal of Structure and Construction Engineering*, No. 591, pp.43~51, 2005.5.

Takeda T., Sozen M.A. and Nielsen N.N. "Reinforce Concrete Response to Simulated Earthquakes", *Journal of the Structural Division*, ASCE, Vol. 96, No.ST12, 1970.12.

Kasai K., Ogawa R., Pu W. et al. "Passive control design method for elasto-plastic frame added with visco-elastic Dampers" , *Journal of Structure and Construction Engineering*, No.655, pp.1625~1634, 2010.9.

Kasai K., Pu W. "Passive control design method for MDOF slip-hysteretic structure added with visco-elastic damper", *Journal of Structure and Construction Engineering*, No.650, pp.781~790, 20010.4.

8CUEE CONFERENCE PROCEEDINGS
8th International Conference on Urban Earthquake Engineering
March 7-8, 2011, Tokyo Institute of Technology, Tokyo, Japan

SEISMIC RESPONSE ANALYSIS OF STEEL MOMENT FRAMES WITH VISCOELASTIC DAMPERS BASED ON QUASI-LINEAR MOTION MECHANISM

Jaedo Kang[1] and Hiroshi Tagawa[2]

1) Graduate Student, Nagoya University, Japan
2) Assoc. Professor, Nagoya University, Japan
kang.jaedo@j.mbox.nagoya-u.ac.jp, h.tagawa@nagoya-u.jp

Abstract: This paper presents a new vibration control system using the viscoelastic dampers. In the proposed devices, the vibration energy is absorbed through shear deformation of viscoelastic material. The system is based on a quasi-linear motion mechanism. Consequently, bracing members are subjected only to tensile force. This can eliminate the brace-buckling problem and the rod members can be employed as bracing. The seismic response analysis is conducted for steel moment frames with the proposed vibration control system. Energy dissipation characteristics are examined using time-history response results of energy. Maximum story drift angle distributions and time-history response results of displacement show that the proposed device can reduce the seismic response of the frames effectively.

1. INTRODUCTION

Recent research has developed various devices for vibration control systems to reduce earthquake damage to structures. Passive dampers, one type of vibration control device, absorb seismic energy and enhance the seismic performance of structures by reducing drift, velocity, and acceleration demands of structures.

Viscoelastic dampers have been investigated extensively as passive dampers. The damper comprises some layers of viscoelastic material bonded with steel plates. The energy input to structures is absorbed through shear deformation of the viscoelastic material. For velocity-dependent dampers such as viscoelastic dampers, numerous mechanical models and damper devices have been developed (Ibrahim et al. 2007). Ooki et al. (2009) proposed application of viscoelastic dampers to light-gage steel frames having tension braces. Kasaki et al. (2005) investigated the dynamic behavior of a wood frame with a shear link passive control mechanism involving a K-brace. Natsubori et al. (2005) proposed a wall-type viscoelastic damper using styrene-olefin material.

Steel dampers have also been developed. They dissipate seismic energy through the yield deformation of steel dampers, which are inexpensive and which require minimal maintenance. Therefore they have been widely adopted to reduce the seismic response of structures. Steel dampers are classifiable into three types by their yield deformation: axial-yield type such as buckling-restrained braces (Sabelli et al. 2003); shear-yield type such as shear panels (Chan et al. 2009); and bending-yield type such as U-shaped steel dampers (Gao and Tagawa 2009).

This study investigates passive energy dissipation devices using viscoelastic dampers based on a quasi-linear motion mechanism. In the proposed device, only tension force is generated in bracing members and brace buckling need not be considered. In this paper, seismic response analysis is conducted for steel moment frames considering the proposed vibration control system. Energy dissipation characteristics are examined using time-history response results of energy. Maximum story drift angle distributions and time-history response results of displacement show that the proposed device can reduce the seismic response of the frames effectively.

2. OUTLINE OF ENERGY DISSIPATION DEVICE

2.1 Quasi-Linear Motion Mechanism

Figure 1 portrays the Chebyshev linkage, which realizes a quasi-linear motion mechanism. While hinges C and D move rightward and leftward, middle point E moves on the approximate straight line g. Figure 2 portrays the proposed energy dissipation system. Figure 3 portrays the proposed energy dissipation scheme. As presented in Figure 3(a), a connection member is pin-supported and viscoelastic dampers are installed under the connection member. Two rods intersect from the edge of the connection member. As presented in Figure 3(b), when the frame deforms under a lateral load, the viscoelastic materials in the damper exhibit shear deformation. Tensile axial force is generated in the rods, but compression axial force is not generated. When the direction of the lateral load reverses, tensile axial force is generated immediately in an opposite rod. This behavior is based on characteristics of the quasi-linear motion mechanism.

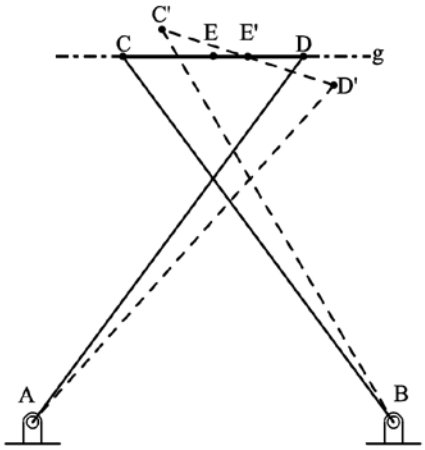


Figure 1 Quasi-Linear Motion Mechanism

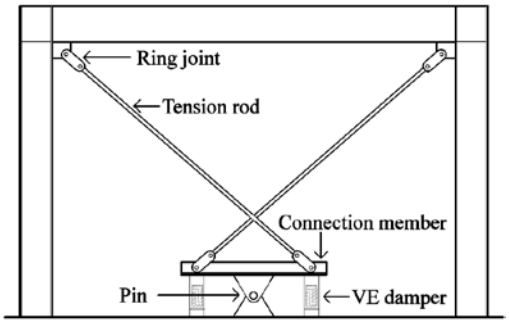
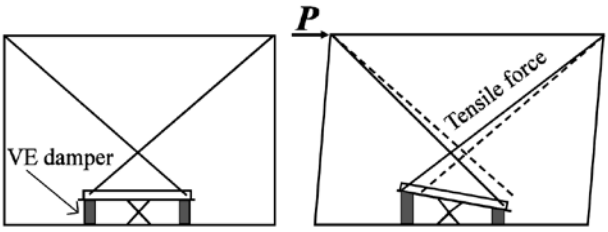


Figure 2 Proposed Energy Dissipation System



(a) Before Deformation (b) After Deformation

Figure 3 Energy Dissipation Scheme

2.2 Viscoelastic Damper

Viscoelastic (VE) materials usually consist of polymers or glassy substances and have the property of dissipating energy in the form of heat when subjected to deformation (Ou et al. 2007). The VE materials in dampers show a complicated behavior that is dependent on the vibration frequency, velocity and temperature. Reportedly, the VE material of styrene-olefin can reduce the influence of temperature variation(Natsubori et al. 2005).

The overall behavior of typical VE dampers can be represented using a spring and a dashpot in parallel such as a Kelvin model. Styrene-olefin material can be represented using a four-element model, as shown in Figure 4, where dynamic characteristics K_1, C_1, and C_2 depend on shear strain. K_2 is the elasto-plastic spring. The VE materials damping modulus and stiffness decrease when the shear strain of the VE material increases.

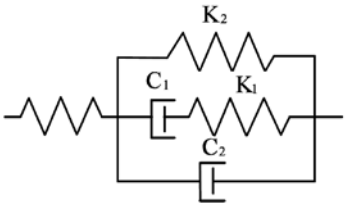


Figure 4 Four-Element Model

3. DESIGN OF ANALYSIS STRUCTURES

3.1 Design of the Moment Frame

Figure 5 shows the steel moment frame without dampers that consist of three bays of 6.0 m and the story heights of 4.0 m. The steel sections of H-350×350×12×19 for columns and H-450×200×9×14 for beams are used in the Model frame, and the yield strength of the steel material are assumed to be 259 N/mm^2. The mass of each story is set as 87 tons. The story shear coefficient in the first story at the final stage of the nonlinear static pushover analysis was obtained as C_B=0.432. The eigenvalue analysis provided the fundamental natural period as 0.845 s. Stiffness-proportional damping is considered with a 2% damping ratio for the first mode throughout this paper.

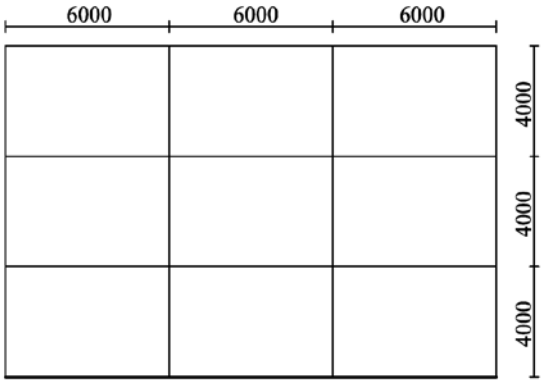


Figure 5 Steel Moment Frame (Model-A)

3.2 Design of the Damping Device

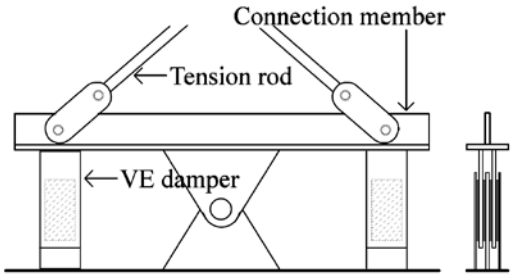
Figure 6(a) portrays the damping device detail that composes of VE dampers, tension rods, and pin-supported connection member. Figure 6(b) shows the analysis model in which some rigid truss member form both the connection member and the pin-support. The bracing members were 52 mm diameter tension rods. Table 1 presents values of VE damper parameters.

3.3 Description of Analysis Structures

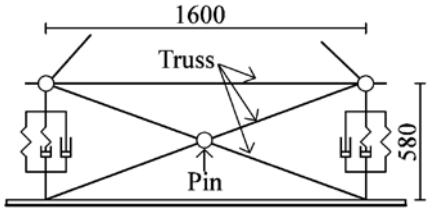
Figure 7 shows analysis models. Model A is the moment frame without dampers described in Section 3.1. Models B, C, and D have the proposed dampers. For Models B and C, one damping device is located on the ground level. For Model B, tension rods are connected to the top story at the center bay. For Model C, tension rods are connected to the top story at the outside bay. For Model D, damping devices are located at all stories.

Table 1 VE Damper Parameters

Height (mm)	Width (mm)	Thickness (mm)	Number of Layers	VE Area (mm^2)	Temperature (C°)
300	200	15	4	240,000	20

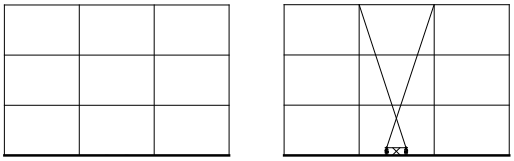


(a) Details of the Damping Device

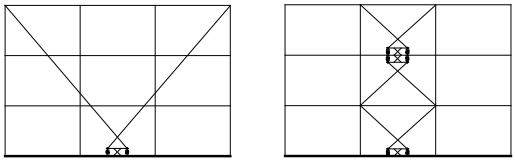


(b) Analysis Model

Figure 6 Modeling of Damping Devices



(a) Model A (b) Model B



(c) Model C (d) Model D

Figure 7 Analysis Models

4. SEISMIC RESPONSE ANALYSIS

This section presents results of nonlinear dynamic analysis for moment frames with and without proposed devices. The characteristics and advantages of the proposed device are examined through comparison of analysis results.

4.1 Analysis Models and Conditions

The nonlinear dynamic analysis program SNAP ver. 5 was adopted for this study. The beams and columns were modeled using beams and columns elements. The rods were molded using the elastic spring element "EL1". The VE material was modeled using the VE damper element "VET".

Figure 8 shows hysteresis loops of member ends in beams and columns. The following values are assumed: f_y=644.9 kN·m, α=0.99, β=0.001, and ξ=0.7 for columns, and f_y =426.53kN·m, α=0.99, β=0.001, and ξ=0.7 for beams. Tension rods were assumed to be elastic and modeled using spring elements.

The 1940 El Centro earthquake record, the 1952 Taft earthquake record, the 1968 Hachinohe earthquake record, and the 1995 Japan Meteorological Agency (JMA) Kobe record were used for input ground motions. The seismic duration of 30 s was considered for all motions. Acceleration records used in the analysis were scaled so that the maximum velocity was equal to 25 and 50 cm/s. Table 2 shows the maximum velocity (Max. *V*) and maximum acceleration (Max. Acc.) of the scaled motions. The scaled ground motions of Max. *V*=50 cm/s represent severe earthquakes considering the fact that the dynamic design practices of high-rise buildings in Japan often use the scaled motions of Max. *V*=50 cm/s as severe earthquakes.

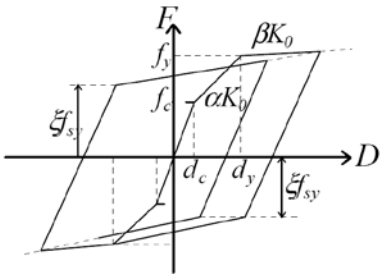
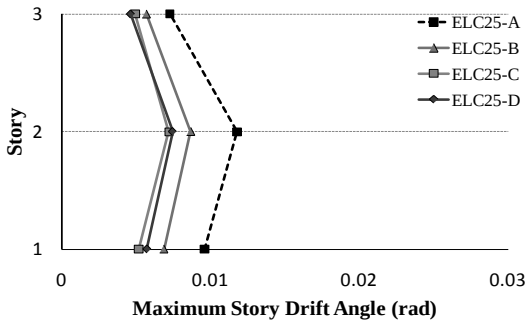


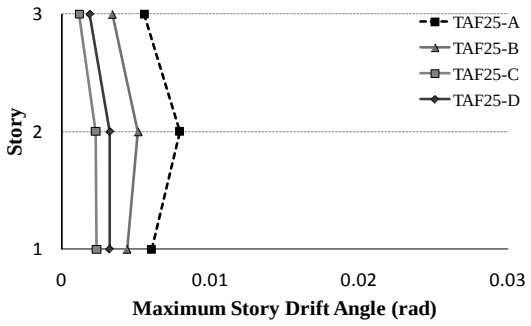
Figure 8 Hysteresis Loops

Table 2 Seismic Ground Motions Used for Analysis

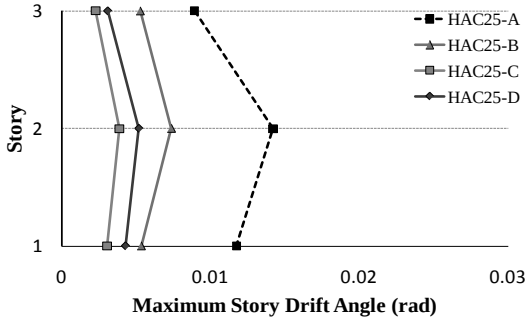
Input motion	Max *V*	Max. Acc.	Duration
El Centro	25 cm/s	255.4 cm/s^2	30 s
	50 cm/s	510.8 cm/s^2	30 s
Taft	25 cm/s	248.4 cm/s^2	30 s
	50 cm/s	496.9 cm/s^2	30 s
Hachinohe	25 cm/s	165.0 cm/s^2	30 s
	50 cm/s	329.9 cm/s^2	30 s
Kobe	25 cm/s	225.0 cm/s^2	30 s
	50 cm/s	499.9 cm/s^2	30 s



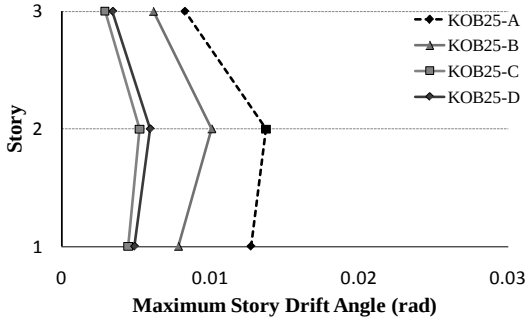
(a) El Centro 1940 NS



(b) Taft 1952 EW

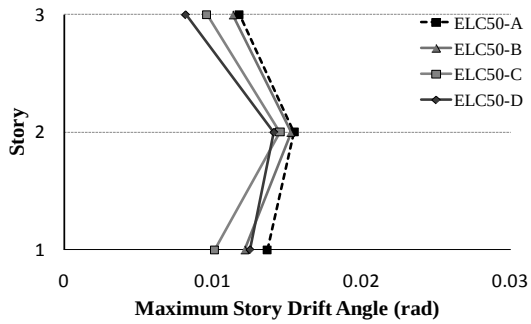


(c) Hachinohe 1968 NS

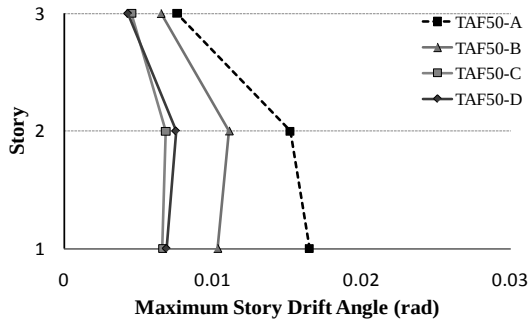


(d) Kobe 1995 NS

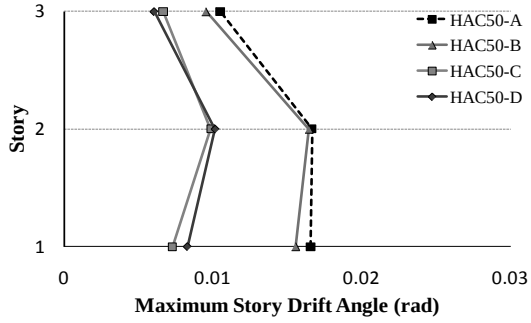
Figure 9 Max. V=25 cm/s



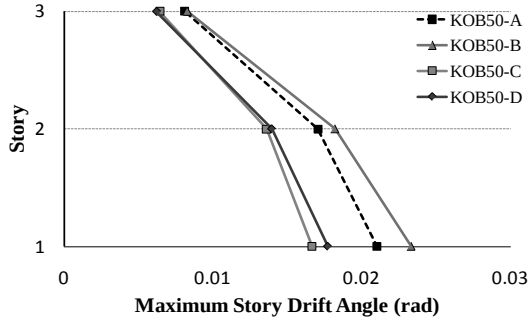
(a) El Centro 1940 NS



(b) Taft 1952 EW



(c) Hachinohe 1968 NS



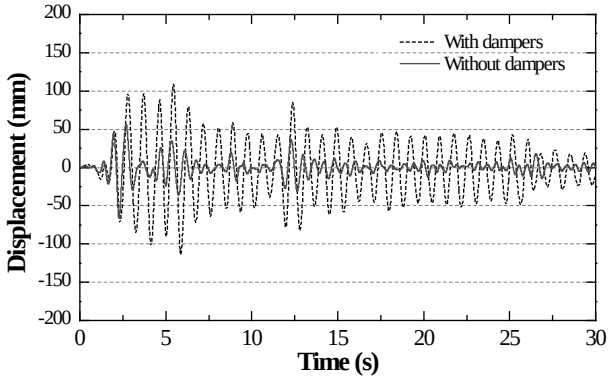
(d) Kobe 1995 NS

Figure 10 Max. V=50 cm/s

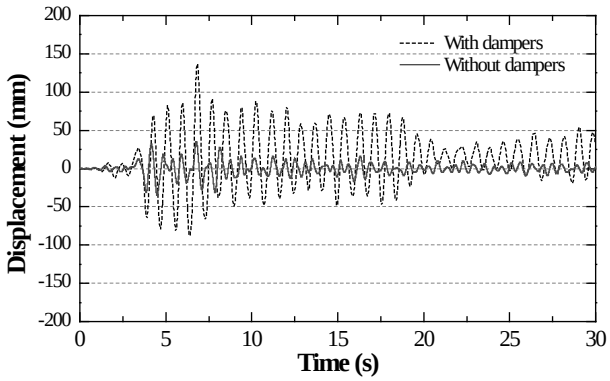
4.2 Analysis Results

Figures 9 and 10 depict the maximum story drift angle distributions for the cases of Max. V=25 cm/s and 50 cm/s, respectively. For Max. V=25 cm/s, the maximum story drift angle in the models with dampers is smaller than 0.01 rad. Model C exhibits the lowest story drift.

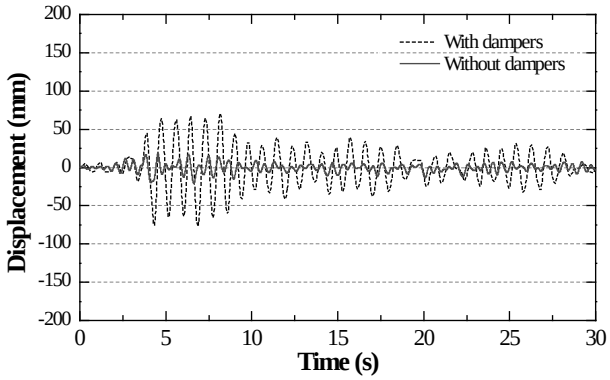
For Max. V=50 cm/s, in all cases except for Kobe 50 of Model B, the maximum story drift angle distributions were reduced by locating the proposed damping device. Models C and D show similar amounts of story drift angle reduction. It can be described that Model C is more effective because only one damping device is used.



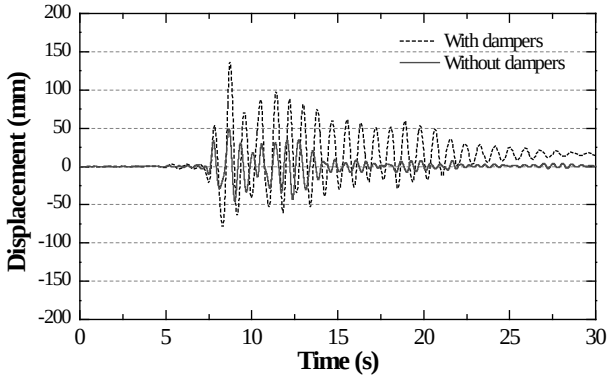
(a) El Centro 1940 NS



(b) Taft 1952 EW

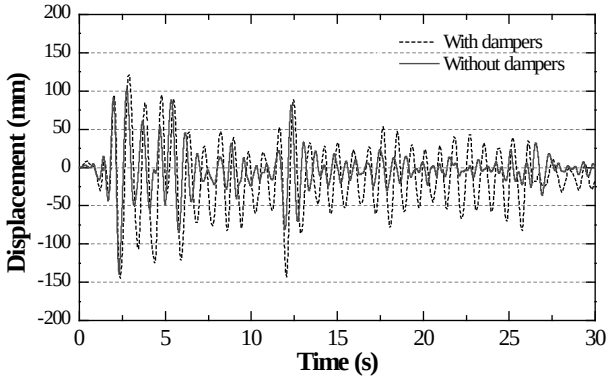


(c) Hachinohe 1968 NS

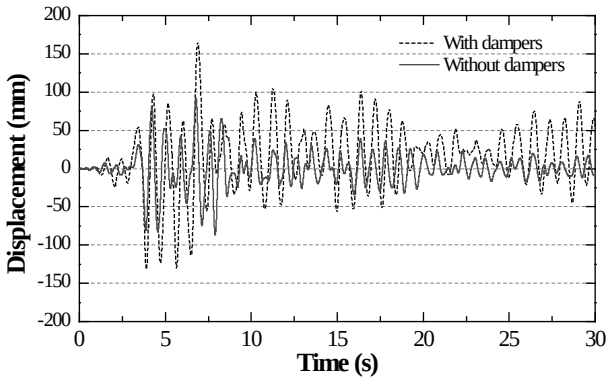


(d) Kobe 1995 NS

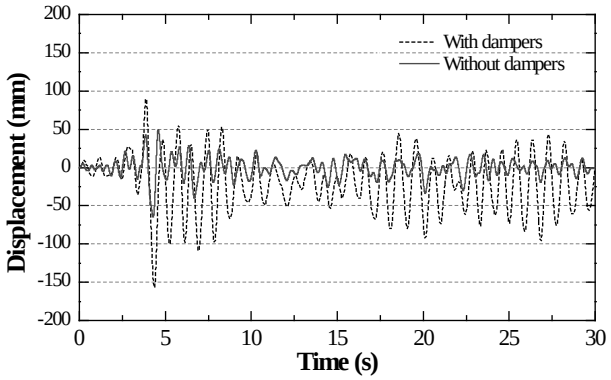
Figure 11 Time-History Response of Displacement at the Top Floor of Model C for the Case of Max. V=25 cm/s



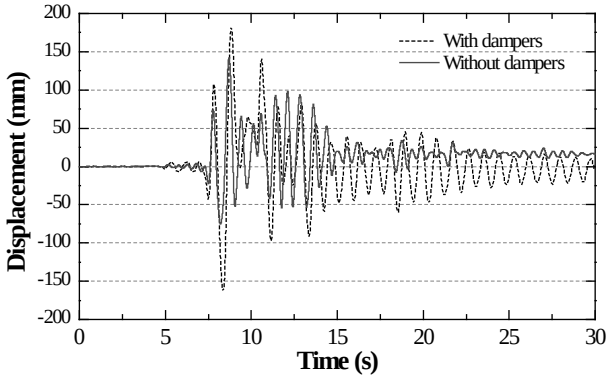
(a) El Centro 1940 NS



(b) Taft 1952 EW



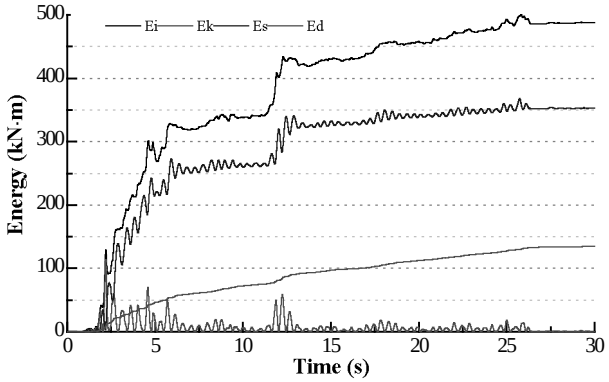
(c) Hachinohe 1968 NS



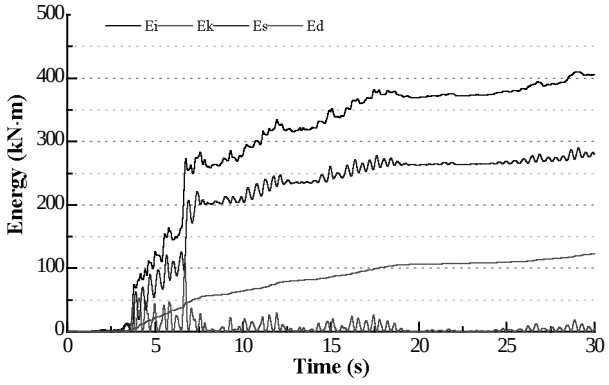
(d) Kobe 1995 NS

Figure 12 Time-History Response of Displacement at the Top Floor of Model C for the Case of Max. V=50 cm/s

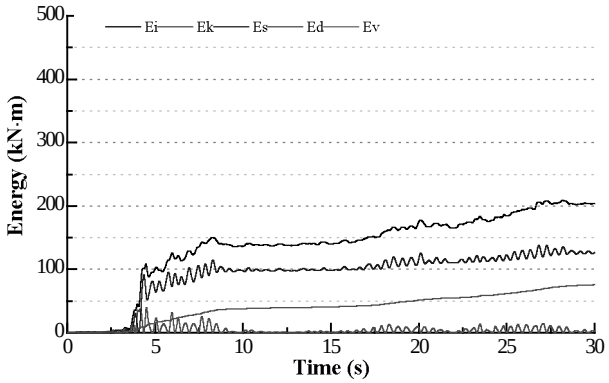
Ei, total input energy; Ek, kinetic energy; Es, strain energy; Ed, damping energy; Ev, viscoelastic energy



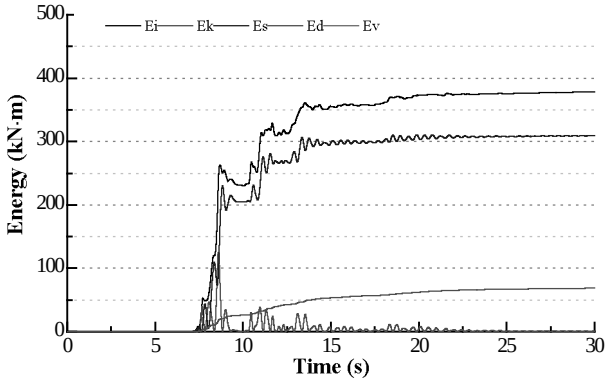
(a) El Centro 1940 NS



(b) Taft 1952 EW

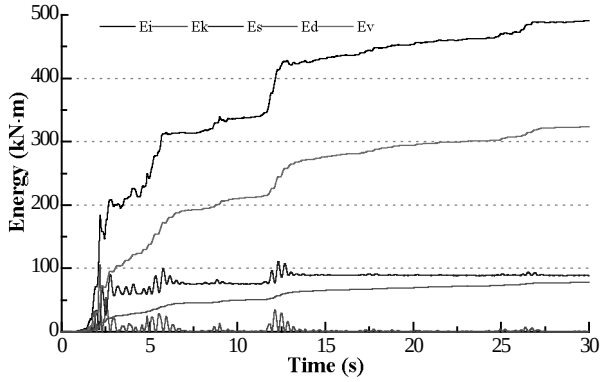


(c) Hachinohe 1968 NS

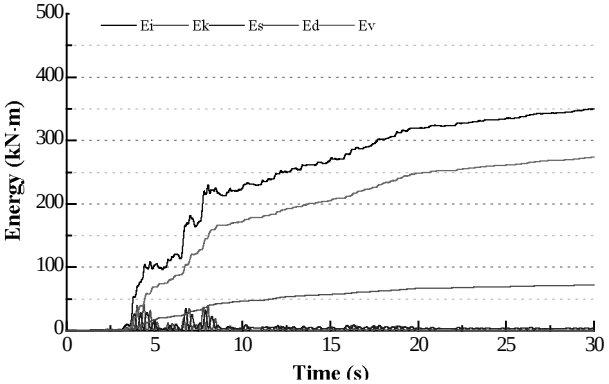


(d) Kobe 1995 NS

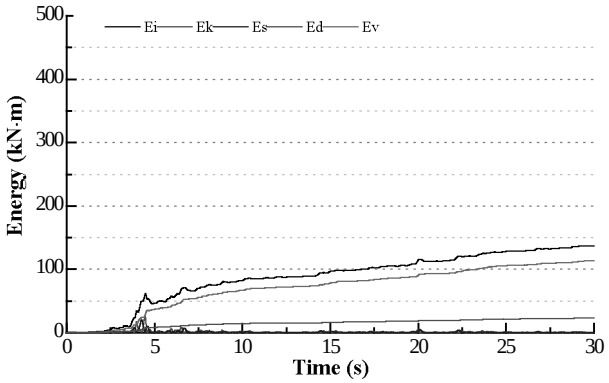
Figure 13 Time-History Response of Energy in the Model A for the Case of Max. V=50 cm/s



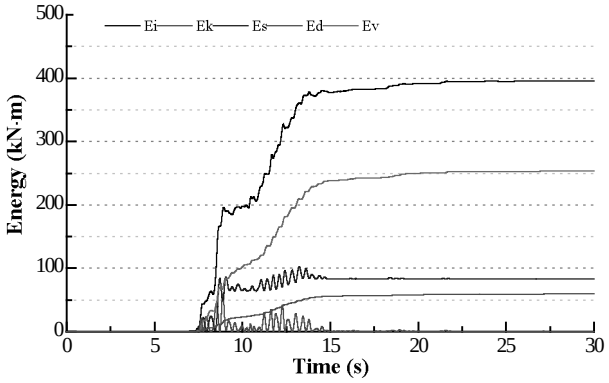
(a) El Centro 1940 NS



(b) Taft 1952 EW

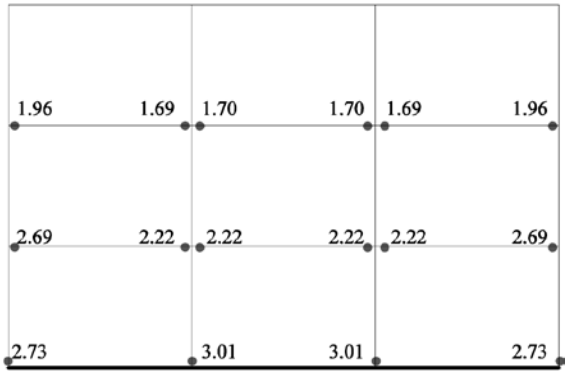


(c) Hachinohe 1968 NS

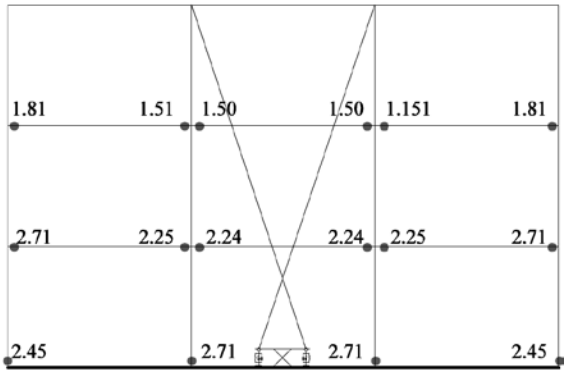


(d) Kobe 1995 NS

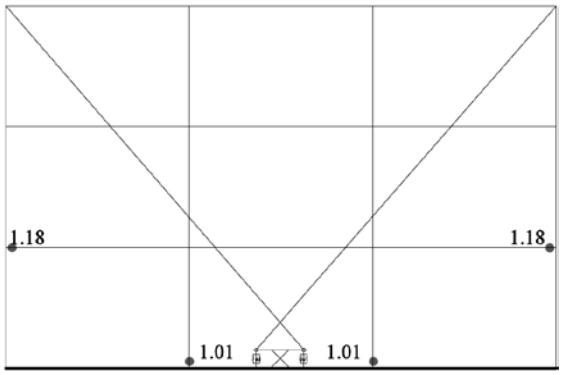
Figure 14 Time-History Response of Energy in the Model C for the Case of Max. V=50 cm/



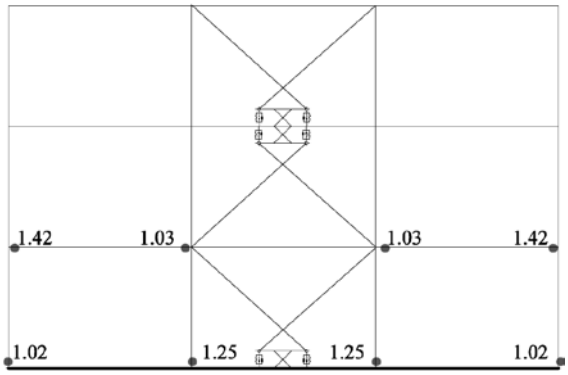
(a) Model A



(b) Model B



(c) Model C



(d) Model D

Figure 15 Plastic Hinge Formation for the Taft Earthquake [Max. V=50 cm/s]

Figures 11 and 12 show time-history responses of displacement for Max. V=25 cm/s and 50 cm/s. From these figures, the performance of the proposed device can be examined by comparing cases with and without the proposed devices. Displacement is reduced by implementing the proposed device. Table 3 presents maximum displacement and the rate of the value with the device to that without the device. The rate for the cases of Max. V=25 cm/s is lower than that of Max. V=50 cm/s for each input ground motion.

Table 3 Maximum Displacement (mm)

Input motion		Without Device	With Device	Rate
El Centro	25 cm/s	113.84	66.745	0.59
	50 cm/s	145.49	136.49	0.94
Taft	25 cm/s	136.72	35.67	0.26
	50 cm/s	165.22	92.332	0.56
Hachinohe	25 cm/s	76.484	21.052	0.28
	50 cm/s	156.49	64.519	0.41
Kobe	25 cm/s	136.77	49.022	0.36
	50 cm/s	181.58	142.17	0.78

Figures 13 and 14 depict the time-history response of energy for Max. V=50 cm/s in Models A and C, respectively. The performance of the proposed device can be examined by comparing the results for Model A and Model C. In the figures, Ei, Ek, Es, Ed, and Ev represent the total input energy, kinetic energy, strain energy, damping energy, and viscoelastic energy. As Figure 14 shows, the strain energy is reduced dramatically, but the viscoelastic energy increases, which indicates that a large amount of input energy is dissipated in the proposed damping device.

Figure 15 portrays the location of plastic hinges and indicates their yield ratio at the final stage of seismic response analysis for Taft earthquake of Max. V=50 cm/s. In Model A, the plastic hinges form at all beam-ends, except for the top beams and at the column-base in the first story. For Model B, the number of forming plastic hinges did not decrease, although the yield ratios decreased. For Models C and D, both the number of plastic hinges and their yield ratios decreased. Especially for Model C, the deformations were reduced dramatically, implying that the location method of the proposed damping device for Model C is best if the bracing members are permitted to connect the ground level damping device directly to the top story beams in the other bay.

5. Conclusions

This paper presented the seismic response analysis of the steel building frames to investigate the effectiveness of

the proposed vibration control system with VE dampers. The system is based on the quasi-linear motion mechanism. Consequently, the brace buckling problem is eliminated. For that reason, the steel rod members are applicable as the bracing member.

To confirm the applicability of the proposed device, seismic response analyses were conducted for three-story frame models with and without the proposed device. The maximum story rotation angle distributions, the time-history responses of top displacement and energy and plastic hinge formations were examined. The results of analyses demonstrated that the proposed device can reduce the seismic response of the frames. The location method of the damping device influenced the damping effect. The analysis model in which the bracing members connect the damping device at the ground level directly to the top story beams in the other bay exhibited the greatest reduction of deformation.

References:

Ibrahim, Y.E., Marshall, J. and Charney, F.A. (2007), "A Visco-Plastic Device for Seismic Protection of Structures," *Journal of Construction Steel Research*, **63**, 1515-1528.

Ooki, Y., Kasai, K., Yokoyama, S., Wada, A. and Midorihawa, M. (2009), "A Study on Application of Viscoelastic Dampers to Light-Gage Steel Frames Having Tension Braces [in Japanese]," *Journal of structural and construction engineering. Transactions of AIJ*, **645**, 2011-2020,

Kasai, K., Sakata, H., Wada, A. and Miyashita, T. (2005), "Dynamic Behavior of a Wood Frame with Shear Link Passive Control Mechanism Involving K-Brace [in Japanese]," J*ournal of structural and construction engineering. Transactions of AIJ* ,**598**, 51-59,

Natsubori, I., Hanazawa, T., Senda, S., Nnishimura, T., Terada, T. and Nakamura, Y. (2005), "Development of Wall-Type Viscoelastic Damper Using Styrene-Olefin Material : (Part 1) Basic Properties, Mechanical Model and Simulation of Viscoelastic Material [in Japanese]," *Summaries of technical papers of Annual Meeting Architectural Institute of Japan*. **B-2**, Structures II, 919-920,

Sabelli, R., Mahin, S. and Chang, C. (2003), "Seismic Demands on Steel Braced Frame Buildings with Buckling-Restrained Braces," *Engineering Structures*, 25, 655-666.

Chan, R.W.K., Albermani, F. and Williams, M.S. (2009), "Evaluation of Yielding Shear Panel Device for Passive Energy Dissipation," *Journal of Construction Steel Research*, **65**, 260-268.

Gao, J. and Tagawa, H. (2010), "Passive Energy Dissipation Device using U-Shaped Steel Dampers Based on Quasi-Linear Motion Mechanism," *Proceedings 7CUEE & 5ICEE*, 1231-1236, Tokyo Institute of Technology, Tokyo, Japan

Ou, J.P., Long, X. and Li, Q.S. (2007), "Seismic Response Analysis of Structures with Velocity-Dependent Dampers," *Journal of Constructional Steel Research*, **63**, 628-638.

SNAP Technical manual, ver.5, **2009**, Kozo System, Inc.

8CUEE CONFERENCE PROCEEDINGS
8th International Conference on Urban Earthquake Engineering
March 7-8, 2011, Tokyo Institute of Technology, Tokyo, Japan

A SIMPLIFIED DESIGN METHOD FOR ENERGY-DISSIPATED STRUCTURE WITH VISCOUS DAMPERS

Chao Zhang[1], Da G. Weng[2], and Xi L. Lu[3]

1) PhD. Candidate, State Key Laboratory for Disaster Reduction in Civil Engineering, Tongji University, Shanghai, China
2) Professor, State Key Laboratory for Disaster Reduction in Civil Engineering, Tongji University, Shanghai, China
3) Professor, State Key Laboratory for Disaster Reduction in Civil Engineering, Tongji University, Shanghai, China
2009_zhangchao@tongji.edu.cn, wdg@tongji.edu.cn, lxlst@tongji.edu.cn

Abstract: Passive energy dissipation technology has been proven to be thoroughly reliable and robust through numbers of practical applications, hence various supplemental dampers have been applied to the building structure for acquiring better performance when it is subjected to earthquakes, severe windstorm, bomb blast and other transient disturbances. The focus of this paper is on a simplified design method for energy-dissipated building structure with viscous dampers. The analytical model of viscous damping structure is researched, and the specific process scheme and content frame are proposed, with the thought of designing the main structure and energy-dissipating components respectively. Besides, the related calculating equations about performance parameter design of energy-dissipating components are also listed. In the end, with the combination of a practical milt-story reinforced concrete frame which is retrofitted by energy dissipation devices, the corresponding analysis and demonstration are conducted. It is concluded that this simplified design method is feasible and effective, and can be well applied to energy-dissipated structure with viscous dampers, so as to satisfy various demands of structural performance objectives under different earthquake risk levels.

1. INTRODUCTION

In the past several decades, a variety of energy dissipation devices have been developed, such as oil dampers, viscous dampers, visco-elastic dampers, metallic dampers, friction dampers, etc. However, for the control target of simultaneous stress and deflection reduction in the structure subjected to a transient, maybe viscous damper is a better option among above dampers, due to its pure viscous behavior of having an out-of-phase relationship between the column restoring force and damper force (Symans and Constantinou, 1998). Fluid viscous dampers, which are initially used in the military and aerospace industry, typically consist of a piston head with orifices contained in a cylinder filled with a highly viscous fluid, and dissipate the external energy by transferring it into heat (Housner et al., 1997; Hanson and Soong, 2001). Since viscous dampers have such characteristic, they are regarded as a more effective approach for structural vibration control and consequently applied to seismic protective design of many new constructions or retrofitting buildings after the cold war in 1990. The projects of new constructions using viscous dampers mainly refer to Dubai Racetrack Stadium (Dubai/United Arab Emirates, 2009), Hydra Waves (Mazatlan/Mexico, 2009), T.F.Green Airport Parking Garage (Providence/USA, 2009), Meguro Gajoen Extension Project (Tokyo/Japan, 2010), etc. And the projects of retrofitting buildings equipped with viscous dampers contain 865 Market Street – San Francisco Centre (San Francisco/USA, 2009), Nagoya-Port Government Office Main Building (Nagoya/Japan, 2009), ASE I – Mihai Eminescu Project (Bucharest/Romania, 2009), Gas Company Building (Sichuan/China, 2009), Dujiangyan Middle School Buildings (Sichuan/China, 2010), etc.

With the extensive application of passive energy dissipation technologies in the industry and the civil construction field, researches on practicable and feasible design methods, as well as rational analytical model, become hot topic and key issues recently (Martinez-Rodrigo and Remero, 2003; Uetani et al., 2003; Kasai and Kibayashi, 2004; Sorace and Terenzi, 2008). As to energy-dissipated structures with viscous dampers, the corresponding design process and analysis methods are given by various standards from different countries, such as ATC-33 (Applied Technology Council, 1997), FEMA-273/274 (Federal Emergency Management Agency, 1997), NEHRP 2000 Provision (National Earthquake Hazards Reduction Program, 2000), FEMA-368, NEHRP 2003: Chapter 15 – Structures with Damping Systems, EC 8: Design of Structures for Earthquake Resistance – Part 1 (Eurocode 8, 2003), ASCE 7-05: Seismic Provisions (American Society of Civil Engineering, 2005), JSSI Manual: Design and Construction Manual for Passively Controlled Buildings (Japan Society of Seismic Isolation, 2003/2005/2007), Technical Specification for Building with Energy Dissipation Devices (People's Republic of China Profession standard, 2011), etc.

Although the proposed design procedures for viscous damping structures vary with different standards, their philosophies are essentially based on the response spectrum

modal analysis method. And besides, it is probably no exaggeration to say that, among above standards, only JSSI Manual provides instructions and specific steps for design of viscous dampers in passive control system at present. Pursuant to this Manual, the main design process of passive control system with viscous dampers can be depicted as follows (Kasai and Kibayashi, 2004): Firstly, given an earthquake input of a smooth response spectrum, the peak displacement and base shear of the frame prior to damper installment can be predicted easily from the response spectrum. Then, the target reduction ratios of displacement and base shear can be estimated based on the required performance. Finally, considering the target reduction ratios and the performance curve, the necessary stiffness of viscous dampers and braces can be determined, while optimum design solution to control both displacement and force can also be found from the performance curve. Moreover, it is noteworthy that the performance curves model buildings as an equivalent SDOF system, and therefore design of viscous dampers in the multistory case can be conducted by modeling the MDOF frame to an equivalent SDOF system.

In this case, for optimum design of energy-dissipated structure with viscous dampers in Japan, adopting the design method in JSSI Manual and performing time-history analysis (using appropriately selected ground motions) to confirm or make modification in design may be a good option. However, as to the building constructions using passive control technology in China, it is difficult to directly apply the JSSI Manual method to practical design, because of the limitations in performance curves caused by different response spectrum. Furthermore, several controversial points in JSSI Manual method are still needed to be think over: (a) the validity of SDOF system correspond to MDOF system; (b) determination of the target DRR (displacement reduction ratio), especially for the design of existing MDOF system with different DRR on each storey; (c) distribution of total viscous dampers is conducted based on their loss stiffness (which is defined as the force at zero displacement divided by the peak deformation in steady-state responses of the viscous damper, JSSI Manual) proportioning to storey stiffness of MDOF system, while the influences of weak floors are not taken into account. Pursuant to this, improving the JSSI Manual method to suit China's current seismic design codes, or exploring a new simplified design procedure for energy-dissipated structures with viscous dampers will definitely be helpful for the application of viscous dampers to seismic design in China, and which is also the focus and purpose of this paper.

2. VISCOUS DAMPING PRINCIPLE

Regardless of new constructions or existing buildings need to be damped, the added viscous dampers (usually with required braces or support members) are deemed as supplemental system to main structure, hence the design of viscous dampers-braces and design of frame can be conducted respectively (it is particularly easy to understand for seismic retrofit of existing buildings). Based on this idea, the analytical model of viscous damping frame structures can be divided into the model of main frame and the model of viscous dampers-braces (VDB), as shown in Figure 1.

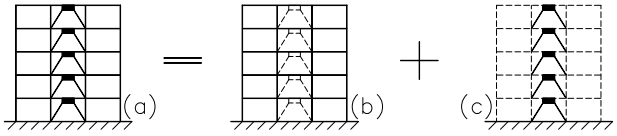


Figure 1 Analytical Model of Viscous Damping Structure: (a)damping model, (b)model of frame, and (c)model of VDB

Based on Dynamics of Structure, it is assumed that the actual damping in structures can be idealized satisfactorily by a linear viscous damper or dashpot with a equivalent viscous damping, hence for the frame structure without dampers, the equation of motion is:

$$[M]\{\ddot{u}(t)\}+[C]\{\dot{u}(t)\}+[K]\{u(t)\}=-[M]\{\ddot{u}_g(t)\} \quad (1)$$

Where [*M*], [*C*], [*K*] are the mass matrix, the damping matrix, the stiffness matrix of the frame structure respectively; $u(t)$, $\dot{u}(t)$, $\ddot{u}(t)$ are its displacement vector, velocity vector, acceleration vector respectively; and $\ddot{u}_g(t)$ is the ground acceleration vector.

For viscous damping structures, the effect from added viscous dampers and required braces should be taken into account and represented by the Γ operator. Generally speaking, the Γ operator has the comprehensive force provided by added mass, added damping and added stiffness, the equation of motion for such system becomes:

$$[M]\{\ddot{u}(t)\}+[C]\{\dot{u}(t)\}+[K]\{u(t)\}+\Gamma = -([M]+[M_a])\{\ddot{u}_g(t)\} \quad (2)$$

$$\Gamma=[M_a]\{\ddot{u}(t)\}+[C_a]\{\dot{u}(t)\}+[K_a]\{u(t)\} \quad (3)$$

Where [M_a], [C_a], [K_a] are the added mass matrix, the added damping matrix, the added stiffness matrix provided by viscous dampers and required braces respectively.

However, for practical design and analysis, the added mass of viscous dampers and required braces is far less than the whole structural mass, and the added stiffness of required braces closely depend on braces stiffness, damping constant and load frequency (Fu and Kasai, 1998). Thus, to simplify calculations in preliminary design phase, usually assuming [M_a] = 0, and approximately neglecting the added stiffness (i.e. [K_a] = 0, only for handily estimate the required added damping in preliminary design), thus, the Γ operator can be consequently expressed by the pure viscous damping force:

$$\Gamma=\{F_d(\dot{u}(t))\}=\left\{C_d\cdot Sgn(\dot{u}(t))\cdot|\dot{u}(t)|^{\alpha}\right\} \quad (4)$$

Where $F_d(\dot{u}(t))$ is the viscous damping force, which directly depends on the relative velocity across the damper; *Sgn* denotes the symbolic function, C_d is the damping

coefficient, α is the velocity exponent ($0 \le \alpha \le 1$). Apparently, equation (4) signify linear viscous damper when α=1, and friction damper when α=0.

Besides, it is noted that whether the viscous dampers are linear or nonlinear, the damping force can be approximately converted into an equivalent linear expression under the equal dissipated energy, hence we get:

$$\Gamma = \left\{ F_d \left(\dot{u}(t) \right) \right\} = [C_0] \left\{ \dot{u}(t) \right\} \tag{5}$$

Where $[C_0]$ is the matrix of added equivalent linear damping (while α=1 in this case).

Substituting equations (3), (4) and (5) in Eq. (2) gives:

$$[M] \left\{ \ddot{u}(t) \right\} + ([C] + [C_0]) \left\{ \dot{u}(t) \right\} + [K] \left\{ u(t) \right\} = -[M] \left\{ \ddot{u}_g(t) \right\} \tag{6}$$

Equation (6) can be solved by the Implicit Newmark Iterative method or the Discrete Fourier Transform method (Soong and Dargush, 1997), it is noteworthy that the added viscous dampers can be preliminarily designed according to the added equivalent damping ratio to the main frame structure (here the impact of added stiffness provided by viscous dampers and braces doesn't take into account, but it actually has on the structure).

3. SIMPLIFIED DESIGN PROCESS

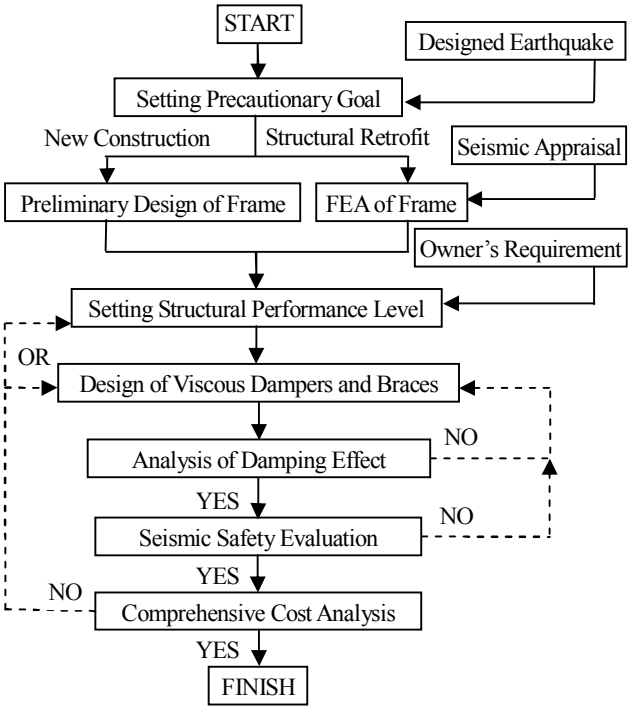


Figure 2 Process of Simplified Design Method for Viscous Damping Structures

Based on above viscous damping principle and design philosophy, a simplified design method for energy dissipated frame structure using viscous dampers (and required braces) is presented in this paper, and its design process and contents are briefly introduced, as shown in Figure 2, It is seen that the simplified design process has the following steps:

Step (1): Setting precautionary goal. According to certain seismic precautionary grade and seismic protection classification of the structure, given by Code for seismic design of buildings (GB 50011-2010) and Standard for classification of seismic protection of building constructions (GB 50023-2008), the seismic precautionary goal shall be determined under designed earthquake.

Step (2): Design and analysis of the frame structure. Design of viscous dampers used in new constructions is surely different with that used in retrofitting buildings, thus work in this step has the following two cases: (a) for seismic retrofit of existing buildings, three-dimensional finite element model of the primary structure shall be established to estimate its present seismic performances, with the combination of seismic appraisal results (while sometimes a simplified model under the hypothesis of lumped mass is used for fast design). However, (b) for damping design of new constructions, the preliminary design of the frame shall be conducted based on the requirements which are half grade or one grade lower than those of the precautionary goal preset in step (1), and then the design of supplemental system shall be conducted in the light of designed performances of the frame.

Step (3): Setting structural performance level. For energy dissipated structure, its performance level shall be set in conformity with the owner's requirements and the seismic precautionary goal determined in Step (1). To be specific, the seismic precautionary goal of structure closely associates with Code's requirements, hence the limit values of storey drift rotation of structures, which can be taken as the representative of structural performance level, vary with different Codes in different countries (e.g.: the three-level design objective of China's current codes, the classified performance levels from SEAOC, etc.).

Step (4): Design of viscous dampers and braces. As presented by Weng (Weng et al., 2011), the damping forces given by viscous dampers can be calculated according to the required added damping ratio (obtained by structural performances set in Step (3)) for certain design objective. Thus, as to the calculated damping forces, location of added viscous dampers and pattern of required braces (e.g.: diagonal brace and chevron brace) shall be firstly determined in the light of architecture function and structural arrangement, and then distribution of added viscous dampers corresponding to different storey shall be conducted, as well as the design of component parameters, such as damping coefficient and velocity exponent of viscous dampers, stiffness of required braces, etc.

Step (5): Analysis of damping effect. Since viscous dampers are of nonlinear characteristic, time-history method shall be adopted to analyze the viscous damping structure in practical design. Combining the philosophy of performance-based design under moderate earthquake and the reference to load-based design under minor earthquake (in China's seismic design code), the damping effect

provided by added viscous dampers (and required braces) is verified based on the control of structural dynamic behavior under minor earthquake and moderate earthquake. Specially, the main contents in this step include the calculation of added equivalent damping ratio, the comparison of storey shear forces, storey drifts (or storey drift rotation) between primary frame and damped frame, the check of damped frame's performances, etc (Weng et al., 2011). Whereas, if the damping effect to the frame structure is unsatisfactory, then the design process must return to Step (4) and design of viscous dampers and braces must be readjusted until acquiring desirable damping effect.

Step (6): Seismic safety evaluation. After acquiring satisfactory damping effect in Step (5), seismic safety evaluation to the whole structure shall be conducted subsequently, it is mainly comprised of the elastoplastic deformation check, the safety assessment of added system and the verification of seismic design details. Likewise, if the results of seismic safety evaluation in this step are unsatisfactory, the design process shall also return to Step (4) for a new circular iterative calculation.

Step (7): Comprehensive cost analysis. As to adopting a new strategy (e.g.: using viscous dampers), an estimate of its total cost shall be required in contrast to traditional strategies. It is noteworthy that this cost analysis shall be conducted with taking various factors into account, such as the construction cost of supplemental system, its maintenance charge for operation, the reduced losses of damped frame under new seismic hazard (and the inherent value of primary building only for structural retrofit), etc. A key task for designers is to seek the optimal safety-cost ratio for seismic design of the structure, which means to give reasonable seismic safety at significantly lower cost. Thus, if the owner dissent from the cost of current damping scheme, the design process shall be back to Step (4) or Step (3) for a redesign.

4. DAMPER PARAMETER DESIGN

For viscous damping structures, viscous damper is an indispensable part of supplemental system to dissipate seismic energy, however sometimes the brace or support member (for diagonal brace-damper) and also the lead rubber bearing (LRB, for chevron brace-damper) are required, as shown in Figures 3~4.

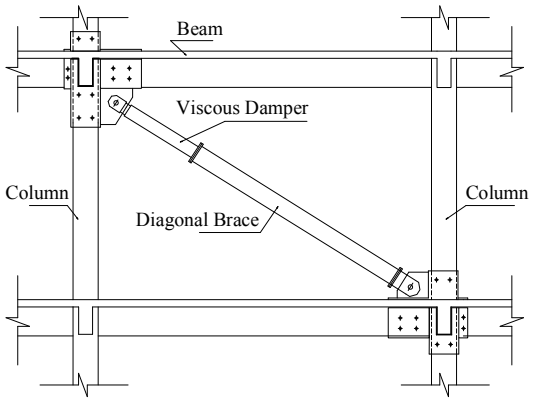


Figure 3 Diagonal Brace-Dampers

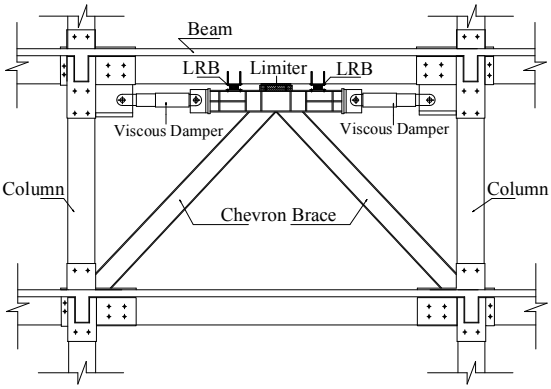


Figure 4 Chevron Brace-Dampers

4.1 Estimate of Required Equivalent Damping Ratio

Based on the viscous damping principle mentioned above, for simplified analysis in preliminary design phase, the added stiffness to the frame provided by viscous dampers and braces is approximately neglected, so as to handily estimate the required added damping ratio of the structure, and therefore viscous dampers can be designed according to the required equivalent damping ratio.

Under this circumstance, rational estimate of the required damping ratio seems to be crucial for the whole design process. And usually, for RC frames which are mainly of shearing deformation, its required damping ratio can be estimated based on energy concept (Uang and Bertero, 1988), or Code Response Spectrum (e.g.: GB 50011-2010):

$$\Delta_{\max} / \Delta_T = \alpha_{0.05} / \alpha_{(\zeta_r+0.05)} \tag{7}$$

Where Δ_{max} is the maximum value of storey drift in the structure (obtained under moderate earthquake), Δ_T is the corresponding target value of storey drift, ζ_r is the required equivalent damping ratio, $\alpha_{0.05}$ is seismic influence coefficient for the damping ratio of 5%, while $\alpha_{(\zeta_r+0.05)}$ is for the damping ratio of $(\zeta_r+0.05)$ (based on GB 50011-2010).

Moreover, it is noteworthy that the final required damping ratio shall not exceed 25% in general, whereas it should be counted according to 25% once exceeds, and which also means that the primary frame shall be further strengthened in this case.

4.2 Calculation of Expected Damping Force

According to the calculated required damping ratio, the expected designed damping force can be obtained by the following equations (14) ~ (18):

$$F_{di} = \zeta_r \cdot \beta \cdot Q_i \tag{8}$$

$$\beta = \left[\pi \sum_{j=1}^{N} \Delta_j Q_j \right] \Big/ \left[2 \sum_{i=j_1}^{N_1} \Delta_i Q_i (1 - \mu_i) \right] \tag{9}$$

$$\mu_i = \Delta_{di} / \Delta_i \tag{10}$$

Where F_{di} is the expected damping force on the i^{th} floor, β is the design coefficient related to storey damping force and shear force, Q_i is the storey shear force on the i^{th} floor under moderate earthquake, N is the total number of floors for calculation, N_1 is the total number of floors equipped with viscous dampers, j_1 is the initial number of floor equipped with viscous dampers, μ_i is the ratio of yield displacement of viscous damper and peak value of storey drift on the i^{th} floor, Δ_{di} is the yield displacement of viscous damper on the i^{th} floor.

Specially, to achieve the best damping effect of added viscous dampers, an optimizing coefficient is introduced to modify the designed damping forces given by Eq. (8), which conducted as follows:

$$F_{(di)m} = \Omega_i \cdot F_{di} \tag{11}$$

$$\Omega_i = \Delta_i \Big/ \left(\sum_{j=1}^{N} \Delta_j / N \right) \tag{12}$$

Where: $F_{(di)m}$ is the modified designed damping force on the i^{th} floor, Ω_i is the optimizing coefficient on the i^{th} floor. However, it is noteworthy that the optimizing process of designed damping forces here is advisory but not compulsory step, and therefore the final designed damping forces are usually interpolated in the value range between the designed damping forces given by Eq. (8) and the modified damping forces given by Eq. (11) with the combination of the allowable storey drift rotation for buildings in China's seismic design code (i.e. GB 50011-2010).

Based on above equations in this section, it is concluded that the expected added damping forces in the frame are designed based on storey shear forces, and optimized in the light of storey drifts.

4.3 Design of Brace Stiffness and LRB

As to the system of viscous dampers and required braces, the brace stiffness definitely affects the energy-dissipated capability of viscous dampers (Weng and Lu, 2004), and therefore the brace stiffness related to viscous dampers is recommended as:

$$K_b \geq \left(6\pi / T_1\right) \cdot C_v \qquad \text{(Linear VD)} \tag{13}$$

$$K_b \geq 3K_c = F_{d,\max} / u_{d,\max} \qquad \text{(Nonlinear VD)} \tag{14}$$

Where K_b is the stiffness of the brace used to support the viscous damper in the frame structure; T_1 is the fundamental vibration period of the damped frame structure; C_v is the linear damping factor of the linear viscous damper (VD), which corresponds to T_1 and is usually determined by testing; K_c is the loss stiffness of the nonlinear VD (while in practical design it may be approximately replaced by elastic stiffness for simplicity); $F_{d,\max}$, $u_{d,\max}$ are the maximum designed damping force and the maximum relative displacement of the nonlinear VD under moderate earthquake respectively.

Besides, when the chevron brace is used to install the viscous dampers, a lead rubber bearing (LRB) corresponds to a viscous damper is used to prevent the out-of-plane instability of supplemental system, and also to improve the seismic performance of damped frame, especially for the structure with inadequate lateral stiffness. In practical design, analysis of LRB is typically conducted by using Bouc-Wen plastic model or bilinear model.

4.4 Examination of Equivalent Damping Ratio

Since the added viscous dampers are designed based on the estimate of required damping ratio (in section 4.1), thus the real equivalent damping ratio provided by designed viscous dampers shall be examined in contrast to the predicted required damping ratio. As to the damped frame structure (mainly exhibit shearing deformation), when the torsion effect is not taken into consideration, its total strain energy and energy dissipated by viscous dampers can be estimated by the following equations (15) ~ (18):

$$\zeta_a = W_c / (4\pi \cdot W_s) \tag{15}$$

$$W_c = \sum_{i=1}^{m} W_{ci} \tag{16}$$

$$W_{ci} = \sum_{j=1}^{d_i} E_{d(ij),\max} = 4 \sum_{j=1}^{d_i} \gamma \cdot \left| F_{d(ij)}(t) \cdot \Delta_{d(ij)}(t) \right|_{\max} \tag{17}$$

$$W_s = \frac{1}{2} \sum (F_i \cdot u_i) = \frac{1}{2} \sum_{j=1}^{n} (M_j \cdot \left| \ddot{u}_j(t) \cdot u_j(t) \right|_{\max}) \tag{18}$$

Where ζ_a is the equivalent damping ratio added by the viscous dampers; W_c is the energy dissipated by all added viscous dampers in one cycle under expected displacement of the structure; W_s is the total strain energy of the damped structure under expected displacement; W_{ci} is the energy dissipated by viscous dampers on the i^{th} floor in one cycle under expected displacement of the structure; $E_{d(ij),\max}$ is the peak energy in one cycle dissipated by the j^{th} damper on the i^{th} floor; γ is the discount coefficient of hysteresis hoop area of dampers; $E_{d(ij)}(t)$ is the damping force of the j^{th} damper on the i^{th} floor at the fixed time t; $\Delta_{d(ij)}(t)$ is the stroke of the j^{th} damper on the i^{th} floor at the fixed time t; F_i is the horizontal seismic action characteristic value of the i^{th} mass, and u_i is the displacement of the i^{th} mass correspond to aforementioned F_i; M_j is the lumped mass of the j^{th} floor; $u_j(t)$ is the peak displacement of the center of mass on the j^{th} floor at the fixed time t, $\ddot{u}_j(t)$ is the peak acceleration of the center of mass on the j^{th} floor at the fixed time t.

5. CASE STUDY

The engineering case used for this paper is an existing RC frame in Sichuan, China, which was constructed in 2007 and performed well in 2008 Wenchuan earthquake. The

frame was originally designed based on seismic precautionary intensity 7, measure grade 3-rd, design earthquake group 1-st and the response spectra characteristic period 0.35 *s* (design parameters in China's code). However, after Wenchuan earthquake, the precautionary grade of the frame is increased to seismic precautionary intensity 8, and therefore the corresponding design parameters are upgraded to measure grade 2-nd, design earthquake group 2-nd and the response spectra characteristic period 0.4 *s*.

Since the present seismic capability of the frame under original design is obviously insufficient to resist the new precautionary earthquake, as seen in Table 1, the frame was retrofitted by using viscous dampers (with braces and/or LRB in necessary) after earthquake, and therefore it can be used to demonstrate the feasibility and reliability of the simplified design method proposed in this paper for energy-dissipated frame structure with viscous dampers.

Table 1 Structural Information under Intensity 8

Floor	Height (*m*)	Storey mass (*t*)	X-direction			Y-direction		
			Stiffness (*kN/mm*)	Shear force (*kN*)	Rotation (*rad*)	Stiffness (*kN/mm*)	Shear force (*kN*)	Rotation (*rad*)
5	3.6	1122	776	4844	1/1560	472	4894	1/966
4	3.6	1294	1066	9474	1/1213	718	9284	1/809
3	3.6	1232	1088	12690	1/896	758	11852	1/629
2	3.6	1232	1062	15224	1/716	760	13186	1/520
1	4.4	1270	654	16864	1/476	564	14826	1/422

Noted: here the storey shear forces of the frame structure are obtained under moderate earthquake.

For comparative research, two approaches are used to distribute viscous dampers to the multistory frame, one is the simplified method (i.e. Designed based on storey shear forces and optimized by storey drifts), and the other is the JSSI Manual method (i.e. Distributed by dampers' loss stiffness in proportion to storey stiffness). It is also noted that the total designed horizontal forces provided by added viscous dampers under moderate earthquake (i.e. total viscous coefficient in horizontal direction) in these two approaches are expected to be equal and obtained by the simplified method. Pursuant to this, three different structural states (ST0, ST1 and ST2) are denoted in the comparative analysis, and here ST0 is the primary frame, ST1 is the damped frame using the JSSI Manual method, ST2 is the damped frame using the simplified method.

Table 2 Designed Damping Force of ST2 (*kN*)

Floor	X-direction		Y-direction	
	Design value (Optimal value)	Actual value	Design value (Optimal value)	Actual value
4	3846 (2086)	3600	3816 (2314)	2800
3	5151 (3783)	3600	4872 (3799)	4000
2	6180 (5679)	6400	5420 (5113)	6000
1	6845 (9463)	7200	6094 (7084)	6400
Total horizontal damping forces			X: 20800 *kN*, Y: 19200 *kN*	

Table 2 shows the design of expected damping forces provided by added viscous dampers of ST2, as explained in Section 4.2, the final designed damping forces are usually interpolated in the value range between the originally designed damping forces (i.e. based on storey shear forces) and the optimal damping forces (i.e. based on storey drifts), and it is also noted that the actual damping forces may be partly different with the aforementioned final designed damping forces, due to the limitation of damper categories.

According to the actual damping forces in Table 2, distribution of added viscous dampers (with required braces) in ST1 and ST2 can be conducted, as listed in Table 3, here the DB signifies Diagonal Brace to the damper, while the other dampers default to the brace pattern of Chevron Brace. Moreover, for cost saving, viscous dampers of a Chinese product are used in this engineering case, and the corresponding design mechanics properties of which are assigned to: α=0.18, and C_v=150, 200, 300, 450 $kN/(mm/s)^{\alpha}$ for the categories of ***A***, ***B***, ***C*** and ***D*** respectively (as listed in Table 3), where α is the velocity exponent, C_v is the damping coefficient. Besides, damper category ***A***, ***B***, ***C***, ***D*** are expected to provide the designed damping forces of 300 *kN*, 400 *kN*, 600 *kN*, 900 *kN* respectively at the expected velocity of 150 *mm/s*, here it is also noted that the peak damping force of the viscous damper shall be no less than 120% of the designed damping force.

Table 3 Distribution of Added Viscous Dampers

Floor	ST1		ST2	
	X-direction Dampers (N×category)	Y-direction Dampers (N×category)	X-direction Dampers (N×category)	Y-direction Dampers (N×category)
4	8×***D*** (DB)	8×***C***	8×***C*** (DB)	4×***B*** +4×***A***
3	8×***D*** (DB)	8×***C***	8×***C*** (DB)	4×***C***+4×***B***
2	16×***A***	8×***C***	16×***B***	4×***D*** +4×***C***
1	16×***A***	8×***C***	8×***C*** +8×***A***	8×***C*** +4×***B***
total damping forces	20400 *kN*	19200 *kN*	20800 *kN*	19200 *kN*

Noted: the horizontal damping force of the viscous damper with DB pattern shall be reduced by a discount coefficient of 0.75, and here the minor deviation of total horizontal damping forces along X direction between ST1 and ST2 is neglected.

The installed location of viscous dampers and braces in this engineering case are shown in Figures 5~6, which are installed on the 1st to 4th Floor. Here it is also noted that VD: DB signifies viscous damper with diagonal brace, and VD: CB signifies viscous damper with chevron brace.

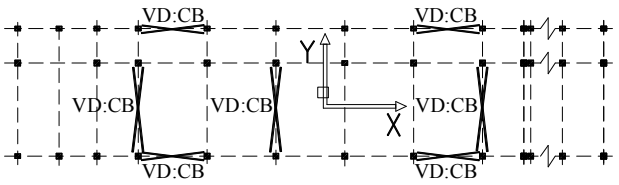


Figure 5 Schematic Diagrams of Installed Location for Viscous Dampers and Braces on the 1st ~2nd Floor

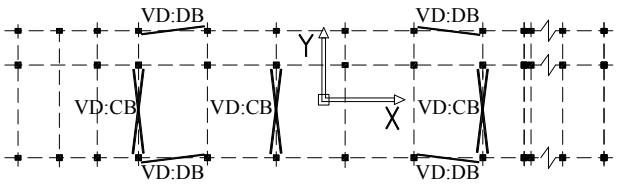


Figure 6 Schematic Diagrams of Installed Location for Viscous Dampers and Braces on the 3rd ~4th Floor

Comparative analysis of these three structural states under minor earthquake (Mi-E), moderate earthquake (Mo-E) are conducted through time-history analysis method, the corresponding analytical results are shown in Figures 7~14, and the elasto-plastic analysis results of ST0 and ST1 are obtained through static elasto-plastic analysis (pushover) method, as listed in Table 4.

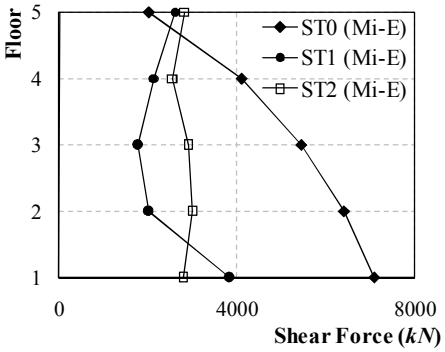


Figure 7 Comparison of Storey Shear Forces along X direction under Minor Earthquake

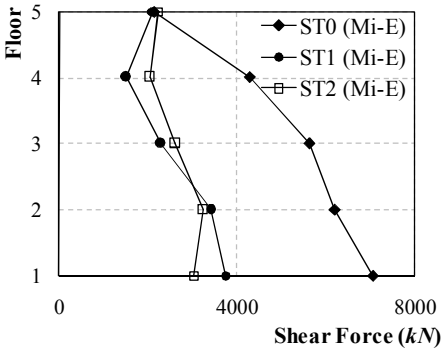


Figure 8 Comparison of Storey Shear Forces along Y direction under Minor Earthquake

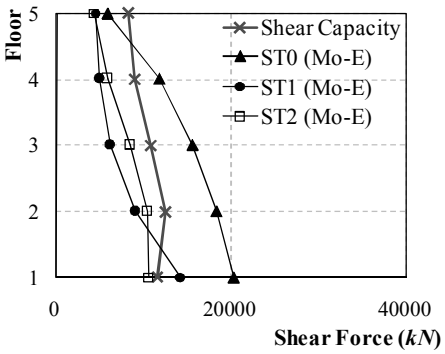


Figure 9 Comparison of Storey Shear Forces along X direction under Moderate Earthquake

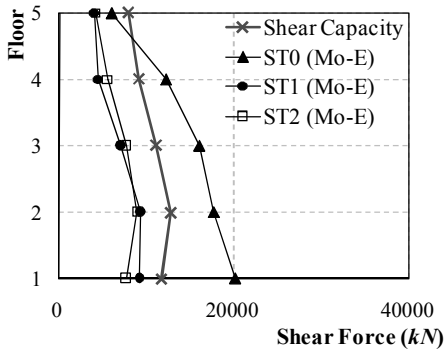


Figure 10 Comparison of Storey Shear Forces along Y direction under Moderate Earthquake

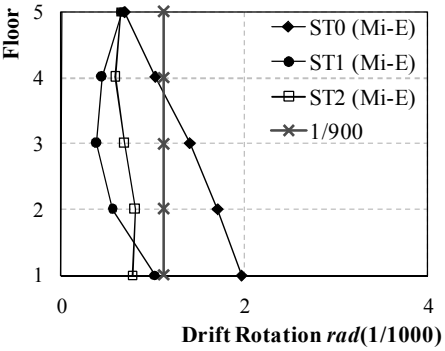


Figure 11 Comparison of Storey Drift Rotation along X direction under Minor Earthquake

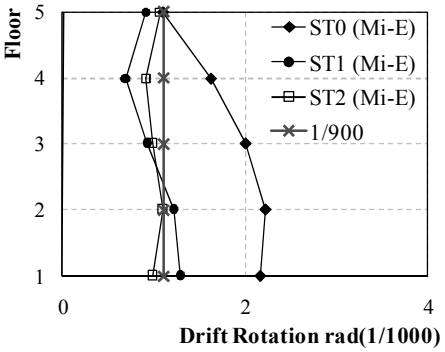


Figure 12 Comparison of Storey Drift Rotation along Y direction under Minor Earthquake

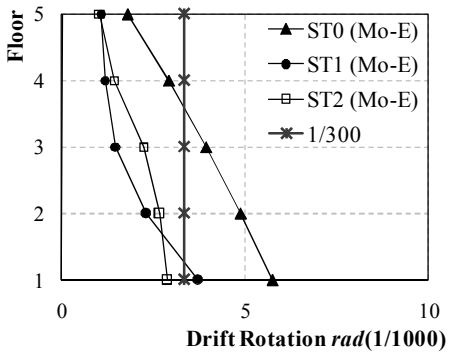


Figure 13 Comparison of Storey Drift Rotation along X direction under Moderate Earthquake

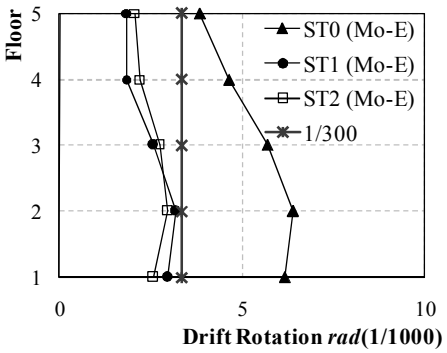


Figure 14 Comparison of Storey Drift Rotation along Y direction under Moderate Earthquake

Table 4 Comparison of Elasto-Plastic Analysis of ST0 and ST2

Seismic action direction	ST0		ST2		Comparison	
	Base shear $Q1(kN)$	Drift rotation $R1(rad)$	Base shear $Q2(kN)$	Drift rotation $R2(rad)$	$\frac{Q2-Q1}{Q1}$	$\frac{R2-R1}{R1}$
X-dir.	16616	1/108	13762	1/143	-17.2%	-24.5%
Y-dir.	14574	1/94	12260	1/123	-15.9%	-23.6%

Noted: here the pushover analysis is conducted based on Chinese design response spectrum (GB 50011-2010).

As to Figures 7~10, it is noted that the Shear Forces on each storey here are obtained from section cut forces of frame columns (without damper-braces), and Shear Capacity is represented by the calculated bearing shear force of floors in primary frame (i.e. according to the original design under seismic precautionary intensity 7), which can be obtained through PKPM2008 software and be surely below the actual bearing shear force of Floors in the light of real reinforcing bars. Thus, it is concluded that demonstration and comparison of storey shear forces conducted here is still conservative and safe to some degree.

In addition, from above Figures, it is easily seen that both ST1 and ST2 have excellent structural performances and remarkable control effect compared to ST0, which means the viscous dampers can be appropriately designed to control seismic behavior of non-ductile structures. Performance of ST2 is deemed to be more rational and well-distributed than that of ST1, which indicates that the principle of distributing viscous dampers by their loss stiffness in proportion to storey stiffness of the frame in JSSI Manual method sometimes may be inappropriate, especially for multistory frame structures with weak floors, seismic behavior of some weak floors may not be effectively controlled in such method. Whereas, as addressed in the simplified design method in this paper, viscous damping forces to multistory frame structure are firstly designed by storey shear forces and consequently optimized by storey drifts, which is demonstrated to have good control effect of the whole structure compared to the distribute principle of only in proportion to storey stiffness in the JSSI Manual method.

Table 4 shows the comparative elasto-plastic analysis results of ST0 and ST2, it can be seen that the storey drift of ST2 is reduced by about 24% than that of ST0, and the base shear force is reduced by about 15%, which also indicates that the simplified design method proposed in this paper can be used to control and improve the structural seismic behavior under strong earthquake.

6. CONCLUSIONS

For any simplified design methods proposed for energy-dissipated structures, the demonstration of its validity and reliability shall be absolutely required, and always conducted with comprehensive considerations, such as the damping effect analysis and seismic safety evaluation of the damped structure (designed in this simplified method), the cost analysis and comparison of the selected damping strategy with other control strategies (to seek the optimal safety-cost ratio for seismic design).

In preliminary design phase, the required added damping ratio, which can be given based on Code Response Spectrum or energy concept, is usually estimated under the assumption of neglecting the added stiffness provided by viscous dampers and braces (but it actually has on the structure), and therefore obtain the expected damping forces.

In JSSI Manual method, the viscous dampers to multistory structure are distributed based on their loss stiffness being in proportion to storey stiffness, which sometimes may be inappropriate in practical design, especially for multistory structures with weak floors, the control effect of the whole structure is always unsatisfactory. Whereas, in the simplified method proposed in this paper, viscous damping forces are firstly designed by storey shear forces and consequently optimized by storey drifts, which is proved to have better control effect and well-distributed performance of the whole structure.

With the combination of case study, it is concluded that the simplified design method proposed in this paper can evidently decrease complex iterative steps of computational analysis, but still be accurate enough for practical design; furthermore, since the required damping ratio for structural seismic design can be flexibly adjusted, this simplified design method can well conform with China's current design codes, and also can be well applied to engineering design for satisfying various demands proposed by owners or achieving structural performance objectives under different earthquake risk levels.

Acknowledgements:

The authors wish to gratefully acknowledge the generous support of this work partially by the National Key Technology R&D Program of China under Grant No. 2009BAJ28B02 and the Key Consulting & Research Project of Chinese of Academy Engineering under Grant No. 2010-ZD-4.

References:

Symans, M. D., and Constantinou, M. C. (1998), "Passive Fluid Viscous Damping Systems for Seismic Energy Dissipation," *Journal of Earthquake Technology*, Special issue on passive

control of structures, **35**(4), 185-206.
Housner, G.W., Bergman, L.A., Caughey, T.K., Chassiakos A.G., Claus R.O., Masri, S.F., Skelton R.E., Soong T.T., Spencer B.F., Jr., and Yao, J.T.P. (1997), "Structural Control: Past, Present and Future." *Journal of Engineering Mechanics*, American Society of Civil Engineers, **123**(9), 897-971.
Hanson, R. D. and Soong, T. T. (2001), "Seismic design with supplemental energy dissipation devices (MNO-8)," Earthquake Engineering Research Institute, Oakland, CA.
Martinez-Rodrigo, M. and Remero, M. L. (2003), "An Optimum Retrofit Strategy for Moment Resisting Frames with Nonlinear Viscous Dampers for Seismic Applications," *Journal of Engineering Structure*, **25**, 913-925.
Uetani, K., Tsuji, M. and Takewaki, I. (2003), "Application of an Optimum Design Method to Practical Building Frames with Viscous Dampers and Hysteretic Dampers," *Journal of Engineering Structure*, **25**, 579-592.
Kasai, K. and Kibayashi, M. (2004), "JSSI Manual for Building Passive Control Technology Part-1 Manual Contents and Design/Analysis Methods," *Proceedings of the 13th World Conference on Earthquake Engineering*, Paper No. 2989.
Sorace, S. and Terenzi, G. (2008), "Seismic Protection of Frame Structures by Fluid Viscous Damped Braces," Journal of Structural Engineering, ASCE, **134**(1): 45-55.
ATC-33.03. (1997), "BSSC Guidelines for the Seismic Rehabilitation of Buildings: Seismic Isolation and Energy Dissipation," prepared by Applied Technology Council for the Building Seismic Safety Council and the Federal Emergency Management Agency, Redwood City, California
FEMA 273. (1997), "NEHRP Guidelines for the Rehabilitation of Buildings," prepared by the Building Seismic Safety Council for the Federal Emergency Management Agency, Washington, D. C.
FEMA 274. (1997), "NEHRP Commentary on the Guidelines for the Rehabilitation of Buildings," prepared by the Building Seismic Safety Council for the Federal Emergency management Agency, Washington, D. C.
NEHRP 2000 Proposal 12-7 and Chapter 15, (2000), "Structures with Damping Systems," prepared by the National Earthquake Hazards Reduction Program, Washington, D. C.
EC8. (2003), "Euro code 8: Design of Structures for Earthquake Resistance. General rules, Seismic Actions and Rules for Buildings," EN1998-1: 2003, British Standards Institution, London.
ASCE 7-05 Seismic Provisions, (2005), "Section 18: Seismic Design Requirements for Structures with Damping Systems," prepared by the American Society of Civil Engineers for the Federal Emergency Management Agency, Washington, D. C.
JSSI Manual, (2003, 2005, 2007), "Design and Construction Manual for Passively Controlled Buildings, Japan Society of Seismic Isolation," Tokyo, Japan, 1st Ed. 405pages, 2nd Ed. 515 pages, 2nd Ed & 2nd Print 509 pages.
People's Republic of China Profession Standard, (2011), "Technical Specification for Building with Energy Dissipation Devices (Questionnaire Opinion Manuscript)," issued by the Ministry of Housing and Urban-Rural Construction of the People's Republic of China, Beijing.
Fu, Y. and Kasai, K. (1998), "Comparative Study of Frames Using Viscoelastic and Viscous Dampers," *Journal of Structural Engineering*, American Society of Civil Engineers, **124**(5), 513-522.
Soong, T. T. and Dargush, G. F. (1997), "Passive Energy Dissipation Systems in Structural Engineering," John Wiley and Sons, Ltd., New York
PRC National Standard, (2010), "Code for Seismic Design of Buildings (GB 50011-2010)," issued by the Ministry of Housing and Urban-Rural Construction of the People's Republic of China, China Architecture & Building Press, Beijing, China.
PRC National Standard, (2008), "Standard for Classification of Seismic Protection of Building Construction (GB 50223-2008)," issued by the Ministry of Housing and Urban-Rural Construction of the People's Republic of China, China Architecture & Building Press, Beijing, China.
Uang, C. M. and Bertero, V. V. (1988), "Use of Energy as a Design Criterion in Earthquake-Resistant Design," Report No. UCB/EERC-88/18, University of California, Berkeley
Weng, D. G. and Lu, X. L. (2004), "Study on Design Parameters of Energy Dissipation Structures with Experiment Verification", *Journal of Earthquake Engineering and Engineering Vibration*, **24**(2), 150-157.
Weng, D. G., Zhang, C. and Lu, X. L. (2011), "Application of Energy Dissipation Technology to C-category Frame Structure of School Buildings for Seismic Retrofit of Increasing Precautionary Intensity," *Journal of Advanced Materials Research*, **163-167**, 3480-3487

8CUEE CONFERENCE PROCEEDINGS
8th International Conference on Urban Earthquake Engineering
March 7-8, 2011, Tokyo Institute of Technology, Tokyo, Japan

SEISMIC PERFORMANCE OF A STEEL SELF-CENTERING MOMENT RESISTING FRAME: MCE-LEVEL HYBRID SIMULATIONS AND QUASI-STATIC PUSHOVER EXPERIMENTS

Ying-Cheng Lin[1)], James M. Ricles[2)], and Richard Sause[3)]

1) PhD Candidate, Dept. of Civil and Environmental Engineering, Lehigh University, USA
2) Professor, Dept. of Civil and Environmental Engineering, Lehigh University, USA
3) Professor, Dept. of Civil and Environmental Engineering, Lehigh University, USA
ycl206@lehigh.edu, jmr5@lehigh.edu, rsause@lehigh.edu

Abstract: The behavior of a self-centering moment resisting frame (SC-MRF) is characterized by connection gap opening and closing at beam-to-column interfaces under earthquake loading. An SC-MRF uses high strength post-tensioning (PT) strands to precompress the beams to the columns and to close the gaps that develop under earthquake loading, returning the frame to its initial position (i.e. the frame is "self-centering"). In this study, a beam web friction device (WFD) is included in each beam-to-column connection to dissipate energy under seismic loading. Unlike a special steel moment-resisting frame with welded connections (W-SMRF), an SC-MRF can be designed to survive the design basis earthquake (DBE) without structural damage, providing the potential for immediate occupancy (IO) performance, and to suffer only modest damage under the maximum considered earthquake (MCE), providing collapse prevention (CP) performance. A 7-bay, 4-story SC-MRF prototype building located in the Los Angeles area was designed using a performance-based design procedure. A 0.6-scale model of two bays of the SC-MRF building was developed and subjected to simulated earthquakes using the hybrid simulation method. This paper focuses on the MCE-level performance of the SC-MRF. Results from MCE hybrid simulations and quasi-static pushover tests are presented. A special PT strand fuse was developed and installed in the SC-MRF. The behavior of the SC-MRF with the fuses in a quasi-static pushover test is also presented.

1. INTRODUCTION

Conventional steel moment resisting frames (MRFs) are often used in building systems to resist earthquake loading. Under the maximum considered earthquake (MCE), conventional MRFs are designed to develop plastic deformation and significant damage in main structure members, resulting in buildings with large residual drift and the potential for being near collapse. To avoid large residual drift, post-tensioned (PT) beam-to-column connections for self-centering MRFs (SC-MRFs) were developed by Ricles et al. (2001). These connections are designed to develop gap opening at the beam-to-column interface rather than permanent plastic deformation in the beams. PT forces close the gap and enable the connections to self-center upon unloading. Energy is dissipated by special devices located in the connection regions.

This paper presents the seismic response of a 0.6-scale 2-bay 4-story SC-MRF test frame. This SC-MRF uses beam web friction devices (WFDs) at beam-to-column connections to dissipate energy. WFDs are attached to the columns and located on the beam webs to avoid interference with the floor slab. PT strands are used to provide self-centering forces. The floor diaphragm is attached to only one bay of the SC-MRF to avoid restraining the gap opening behavior at the connections. The SC-MRF is designed using a performance based design (PBD) approach and associated design criteria to achieve immediate occupancy (IO) performance under the design basis earthquake (DBE) and collapse prevention (CP) performance under the MCE. The details of the SC-MRF prototype frame, the test frame, the simulated floor diaphragm in the experiments, DBE simulation results, and the IO performance evaluation are given by Lin et al. (2009) and Ricles et al. (2010). This paper focuses on the MCE performance. MCE-level design criteria, results from MCE simulations and quasi-static tests, and a CP performance evaluation are presented and discussed in this paper. A fuse that helps to control the force in the PT strands under the MCE is also presented in this paper.

2. SC-WFD CONNECTION

2.1 Connection Details

Figure 1(a) schematically shows an SC-MRF with self-centering WFD (SC-WFD) beam-to-column connections. The PT strands run parallel to the beams across multiple bays. The WFD (Figure 1(b)) includes two channel sections (denoted friction channels) welded to the column flange. Brass plates are sandwiched between the webs of the friction channels and the beam web to enable reliable

friction at the interface. The channels are clamped to the beam web by friction bolts shown in Figure 1(b) which produce normal force on the friction surface. The friction channels are welded to the column flange after the friction bolts are tightened. The shape of the friction channels reduces the tendency for weld shrinkage to pry the friction channels away from the friction surface. Slotted holes in the beam web shown in Figure 1(c) accommodate the travel of the friction bolts during connection gap opening and closing. Shim plates shown in Figure 1(b) are welded to the column flange to provide good contact surfaces for the beam flanges. Reinforcing plates are welded to the outside surfaces of the beam flanges to avoid excessive yielding in the beam flanges. Reinforcing plates are also welded to the inside surfaces of the column flanges to avoid excessive yielding around the holes for the PT strands.

2.2 Moment-Rotation Behavior

The moment M in the SC-WFD connection is controlled by the axial force in the beam (P) and friction force resultant in the WFD (F_f) as follows:

$$M = Pd_2 + F_f r \quad (1)$$

Where d_2 = distance from the beam section centroid to the center of rotation (COR) and r = distance from the WFD friction force resultant to the COR. The COR is at the point of contact of the beam compression flange with the column. The product $F_f r$ is the friction moment denoted M_{Ff}. F_f is calculated as:

$$F_f = 2\mu N_b n_b \quad (2)$$

where μ = friction coefficient, N_b = normal force produced by one friction bolt, n_b = total number of friction bolts in a WFD, and the factor 2 accounts for the two friction surfaces in the WFD, one for each friction channel. μ=0.4 is used for design. P includes the PT force, T, and an axial force from inertial force transferred by the floor diaphragm P_{fd} as follows:

$$P = P_{fd} + T \quad (3)$$

where T can be estimated as follows:

$$T = T_o + \bar{\theta}_r [2 d_2 k_b k_s / (k_b + k_s)] \quad (4)$$

where T_o = initial PT force; k_b and k_s = axial stiffness of the beam and axial stiffness of the PT strands within one bay, respectively; and $\bar{\theta}_r$ = average relative rotation of the connections over one floor level.

The imminent gap opening moment (M_{IGO}) is calculated from Eq. (1) using $P=T_o$. The effective energy dissipation ratio β_E for a connection can be estimated as follows:

$$\beta_E = M_{Ff}/M_{IGO} \quad (5)$$

Studies by Seo and Sause (2005) show that as β_E is increased, the lateral drift demand for an SC system is reduced. The theoretical maximum value of β_E for an SC system is 50%. Based on results from Seo and Sause (2005), 25% is selected as the lower bound design value for β_E.

3 PERFORMANCE-BASED DESIGN

3.2 Design Objectives

Performance-based design (PBD) objectives for SC-MRFs (Figure 2) were modified from previous work by Garlock et al. (2007). The DBE and MCE are the two seismic input levels considered. The MCE is a ground motion intensity with a 2% probability of exceedance in 50 years (BSSC 2003). The DBE is a ground motion intensity that is two-thirds that of the MCE (BSSC 2003), with an approximate return period of several hundred years. Immediate occupancy (IO) and collapse prevention (CP) are the target performance at the DBE and MCE level, respectively. IO performance requires essentially no structural damage, and as shown later, does not require the SC-MRF to be unusually strong. Gap opening and minimal yielding (e.g., column base yielding and beam flange yielding with the strain less than twice the yield strain ($2\varepsilon_y$)) are permitted for IO performance. Panel zone yielding, beam web yielding, and beam flange yielding with the strain greater than $2\varepsilon_y$ are permitted for CP performance. PT strand yielding, which can lead to strand fracture, and beam web buckling, which can lead to loss of beam axial and flexural resistance, are not permitted for CP performance.

3.2 MCE Design Criteria

This paper focuses on MCE-level performance. To avoid beam web buckling and PT strand yielding under the MCE. The following design criteria are used:

(i) Beam web compactness criterion: SC-MRF beams should satisfy the compactness criterion of the AISC Seismic Provision (2005):

$$(h/t_w) / \lambda_{ps,MCE} \leq 1.0 \quad (6)$$

where h/t_w = beam web width-thickness ratio, and $\lambda_{PS,MCE}$ = limiting width-thickness ratio calculated as follows:

$$\lambda_{PS,MCE} = \max\{1.12(2.33 - C_a)\sqrt{E/\sigma_y}, 1.49\sqrt{E/\sigma_y}\} \quad (7)$$

where E = Young's modulus, σ_y = nominal yield stress, and $C_a = P_{MCE}/0.9P_y$. P_{MCE} = beam axial force demand under the MCE P_{MCE}. P_y = nominal beam axial yield strength.

(ii) Strand yield criterion: the total PT strand force under the MCE (T_{MCE}) should not exceed 90% of the total PT strand design yield force ($0.9T_{y,des}$) as follows:

$$T_{MCE} / 0.9T_{y,des} \leq 1.0 \quad (8)$$

where $T_{y,des}=0.9T_{u,n}$ and $T_{u,n}$ = total PT strand nominal

ultimate force capacity.

4 EXPERIMENTAL PROGRAM

4.1 Experimental Setup

A 7x7-bay prototype office building shown in Figure 3(a) was designed using the above PBD objectives. The building has four stories above ground level and one basement story. The building is assumed to be located on a stiff soil site in Van Nuys, California in the Los Angeles area. Each perimeter frame has two 2-bay steel SC-MRFs with SC-WFD connections. The SC-MRF design demands (Lin et al. 2009; Ricles at el. 2010) are summarized in Table 1. $\theta_{rf,DBE}$ and $\theta_{rf,MCE}$ are the roof drift demands, $\theta_{s,DBE}$ and $\theta_{s,MCE}$ are the story drift demands, $\overline{\theta}_{r,DBE}$ and $\overline{\theta}_{r,MCE}$ are the demands for the average relative rotation demands under the DBE and the MCE, respectively. The MCE demand-capacity ratios from Eq. (6) and (8) are listed in Table 2. In each SC-MRF, the floor diaphragm (FD) is attached to the beam in one bay (labeled "FD bay" in Figure 3). The beam in the other bay (labeled "sliding bay" in Figure 3) and the columns are free to move horizontally relative to the floor diaphragm to avoid restraining gap opening of the SC-WFD connections.

Considering the symmetry of the building plan, the earthquake response of one quarter of the building was simulated at the NEES Real-Time Multi-Directional (RTMD) earthquake simulation facility at Lehigh University. The hybrid simulation method was used. One 2-bay SC-MRF acting in one direction of the building was simulated by the SC-MRF test frame (Figure 3(b)) as an experimental substructure, and the remainder of one quarter of the building was simulated as an analytical substructure. The SC-MRF test frame is a 0.6-scale model of one 2-bay SC-MRF in the prototype building (Lin 2011). The gravity load bearing system, associated gravity loads, and seismic mass tributary to one SC-MRF, as well as the damping were included in the analytical substructure. Rayleigh damping was used with 2% and 5% damping in the 1st and 3rd modes. The equations of motion were solved using the CR integration algorithm (Chen and Ricles, 2009).

4.2 Floor Diaphragm

During the experiments, the lateral force (i.e., the simulated diaphragm force acting on the SC-MRF test frame) at each level is applied by a hydraulic actuator through a simulated floor diaphragm (Lin 2011). The floor diaphragm is connected to the test frame with steel diaphragm plates, which are fillet welded to the middle of the north-bay beam to simulate the FD bay in the prototype structure.

As shown in Figure 4, when the SC-MRF test frame is subjected to a lateral force at the x^{th} floor (F_x) toward the north (Figure 4(b)), the maximum beam axial force is at the north end of the north-bay beam (denoted NN) and can be estimated as follows:

$$P_{N,x}^{NN} = T_x + (1/4)F_x \quad (9)$$

When F_x is toward the south (Figure 4(c)), the maximum beam axial force is at the south end of the north-bay beam (denoted NS) and can be estimated as follows:

$$P_{S,x}^{NS} = T_x + (3/4)F_x \quad (10)$$

Therefore, the maximum strain in beam flange will occur in the bottom flanges at the NN and NS connections.

4.3 Matrix of Experiments

This paper focuses on the MCE-level performance. The MCE-level experiments (Table 3) included two earthquake hybrid simulations (MCE-1 and MCE-2) and three quasi-static tests (PH, TU, and FU). The spectral acceleration S_a of the ground motion records for the MCE-1 and MCE-2 simulations (Figure 5) are compared with the USGS uniform hazard spectrum (denoted USGS-UHS) for ground motions with a 2% probability of exceedance in 50 years and the ASCE7 (2005) (denoted ASCE7-05) MCE design spectrum. The scaling of the ground motion records is similar to that given in Lin et al. (2009) and Ricles et al. (2010) for DBE ground motions. The S_a values at the test frame fundamental period (T_1=1.26 sec), denoted $S_a(T_1)$, are 0.55g for the USGS-UHS and the ASCE7-05 MCE spectra. For MCE-1 $S_a(T_1)$=0.67g, and for MCE-2 $S_a(T_1)$=0.65g.

The floor displacement profiles used for the quasi-static pushover tests are shown in Figure 6, where a positive floor displacement indicates a displacement to the north. The PH and TU tests were conducted to evaluate the beam buckling and PT strand yield strengths, respectively. The FU test was conducted to evaluate the behavior of the SC-MRF test frame when PT strand fuses were installed at the 3rd floor.

5. EXPERIMENTAL RESPONSES

5.1 MCE-1 and MCE-2 Simulation Results

The floor displacement time histories from the MCE-1 and MCE-2 simulations are shown in Figure 7. The residual story drifts (obtained by dividing the difference in residual displacements of adjacent floors by the story height) are listed in Table 4. The largest residual drift is 0.18% rad from the MCE-2 simulation in the 1st story. These results demonstrate the self-centering behavior of the SC-MRF under the MCE. Table 4 also gives the maximum roof drift $\theta_{rf,max}$, the maximum story drift $\theta_{s,max}$, the maximum of average relative rotation $\overline{\theta}_{r,max}$, the maximum total PT force T_{max}, the loss of PT force after the simulation ΔT normalized by $T_{u,n}$, and the estimated β_E. The average relative rotation $\overline{\theta}_r$ for each floor is taken over four connections, and a positive value corresponds to a north floor displacement. ΔT is the difference in the PT force before the simulation (T_i) and after the simulation (T_{end}). The estimated β_E is based on Eq. (5). $\theta_{rf,max}$=3.2% and 4.6%

rad respectively for MCE-1 and MCE-2, which are smaller and larger values than the design demand $\theta_{rf,MCE}$ =3.9% rad (Table 1). The largest $\theta_{s,max}$=5.8% and 7.2% rad respectively in the 4th story for MCE-1 and MCE-2, which are smaller and larger values than the design demand $\theta_{s,MCE}$=5.9% rad (Table 1). The largest $\overline{\theta}_{r,max}$=5.4% and 6.7% rad for MCE-1 and MCE-2, respectively, which are both larger than the design demand $\overline{\theta}_{r,MCE}$=4.7% rad (Table 1).

The largest $T_{max}=0.81T_{u,n}$ at the 3rd floor from MCE-2, which equals $0.9T_{y,des}$ in Eq. (8). However, yielding did not occur in the PT strands. The measured total PT force T_{exp} (normalized by $T_{u,n}$) vs. measured $\overline{\theta}_{r}$ from MCE-2 simulation is shown in Figure 8, where T_{exp} is compared with the theoretically predicted total PT force T_{th} (calculated from Eq. (4) using the measured T_o, $\overline{\theta}_{r}$, and d_2, as well as the nominal k_s and k_b). The measured $\overline{\theta}_{r}$ is the average of the measured θ_r for the four connections in one floor. θ_r varies for connections at the same floor, and $\overline{\theta}_{r}$ in Eq. (4) accounts for the variation. T_{th} and T_{exp} have good correlation. The difference is within 3% of $T_{u,n}$. T_{exp} decreased during the simulation due to seating of the PT anchorages, and the largest ΔT was 2.5% of $T_{u,n}$ at the 3rd floor during MCE-2 (Table 4).

The typical measured connection moment M_{exp} (normalized by the nominal plastic moment $M_{p,n}$) vs. the measured relative rotation θ_r for each connection in the south bay from the MCE-2 simulation are shown in Figure 9. The positive moment and positive θ_r are when the beam top flange is in compression. θ_r returns to zero upon unloading, which demonstrates self-centering behavior. M_{exp} is compared to theoretical connection moment M_{th} in Figure 9. M_{th} is calculated from Eq. (1) using the measured P, d_2, r, and estimated F_f (using Eq. (2) with N_b=12 kip, which is the design normal force). Good agreement between M_{exp} and M_{th} is shown in Figure 9. M_{exp} is larger than M_{th} while θ_r is larger due to the friction bolt bearing against the longitudinal edge of the beam web slots. Each connection has different post gap opening M-θ_r stiffness for positive and negative θ_r. The stiffness is higher when the inertial force from the floor diaphragm generates a compression force in the beam (Figure 4(c)). The compression force increases the beam axial force P in Eq. (1) and therefore increases the moment M. The estimated β_E from the MCE simulations (Table 4) ranges from 27% to 38%, which is larger than the target β_E as shown in Figure 3(b) due to the friction bolt bearing.

During the MCE simulations, beam flanges yielded at the end of the reinforcing plates. The maximum beam flange strain at the end of reinforcing plates $\varepsilon_{rp,max}=8.65\varepsilon_y$ (MCE-1) and $9.02\varepsilon_y$ (MCE-2) in the bottom flange of the south end of the north-bay beam in the 4th floor (denoted 4FNS). Figure 10 shows the beam yielding and flange distortion from the MCE-2 simulation, but beam web buckling did not occur.

Beam flange strain larger than $2\varepsilon_y$ is expected under the MCE. No the PT strand yielding and no beam web buckling occurred during the MCE simulations, which demonstrated the SC-MRF achieved the CP performance under the MCE.

5.2 PH and TU Quasi-Static Pushover Results

As described earlier, the PH and TU quasi-static pushover tests were conducted to evaluate the beam buckling and PT strand yield strength, respectively. The largest $\theta_{s,max}$=8.4% and 11.1% rad in the 4th story for the PH and TU tests, respectively, which are larger than the design demand $\theta_{s,MCE}$=5.9% rad (Table 1). The largest $\overline{\theta}_{r,max}$=6.8% and 7.9% rad for the PH and TU tests, which are larger than the design demand $\overline{\theta}_{r,MCE}$ =4.7% rad (Table 1).

During the PH test, the largest $\overline{\theta}_{r,max}$=6.8% rad is at the 4th floor, but the largest $T_{max}=0.81T_{u,n}$ is at the 3rd floor, because the nominal value of $d_2k_bk_s/(k_b+k_s)$ in Eq. (4) at the 3rd floor is larger than that at the 4th floor. During the TU test, the largest $T_{max}=0.82T_{u,n}$ at the 4th floor. Although the largest T_{max} from PH and TU tests respectively equals and exceeds 90% the PT strand design yield strength, $0.81T_{u,n}$, yielding did not occur in the PT strands.

The beam bottom flange and web buckled at the south end of the north-bay beam (NS) at the 4th floor during the PH test (Figure 11(a)) and at north end of the north-bay beam (NN) during the TU test (Figure 11(b)). The beam buckled as $\overline{\theta}_{r,max}$=6.8% and 7.9% rad (Table 5) during the PH and TU tests, respectively, which are larger than the design demand $\overline{\theta}_{r,MCE}$=4.7% rad (Table 1). The beam buckling at NS in the PH test occurred at a smaller $\overline{\theta}_{r,max}$ than at NN in the TU test due to the larger beam axial force (compare Eq. (9) and (10)). The largest $\Delta T=0.014T_{u,n}$ and $\Delta T=0.058T_{u,n}$ from the TU and PH tests (Table 5) due to the beam buckling and seating of the PT anchorages.

Figure 12 shows the total PT force (normalized by $T_{u,n}$) vs. $\overline{\theta}_{r}$ at the 4th floor from the TU test. From Points A to B, the beam buckling shortened the beam and caused a loss of the PT force, $\Delta T_{AB}=0.04T_{u,n}$. From Points B to C, the total PT force increased due to the increase of $\overline{\theta}_{r}$. At point C, the PT force decreased due to unloading of $\overline{\theta}_{r}$.

6. PT Strand Fuses

Based on the PBD objectives as shown in Figure 2, under the MCE, the SC-MRF should achieve CP performance by avoiding beam web buckling and PT strand yielding. To prevent beam web buckling under the MCE, beam sizes can be selected to satisfy the beam web compactness criterion (Eq. (6)). Alternatively, beam web longitudinal stiffeners (Kim and Christopoulos, 2008) can be used to avoid beam web buckling. To prevent PT strand yielding, one approach is to increase the number of PT strands, so the stress in each strand remains low under the MCE. However, additional PT strands require larger holes or more holes in the column flanges, which can lead to low cycle fatigue from net section yielding in the flanges. Another approach is to use better anchorages and wedges so PT strands have ductile behavior before fracture (Walsh and

Kurama, 2010). The approach proposed in this paper is using a PT strand "*fuse*", which yields at a specific load to limit the force developed in the PT strands. The developed PT fuse is shown in Figure 13. In the SC-MRF test frame, the fuses were installed at the 3rd floor (Figure 13(a)). Each fuse is aligned with the PT strand, and the PT strand passes through the center of the fuse. Each fuse is supported by the column flange at one end and supports the PT anchorage at the other end. Therefore, each fuse carries the same force as developed in the PT strand.

The typical fuse (Figure 13) is composed of an annealed A513 steel tube and wood (poplar) discs as shown in Figure 13(c) and (d). The typical steel tube has a length of 4 in. and four 3/16 in. diameter holes drilled around the wall at quarter length locations. The purpose of the wood and the holes is to provide controllable inelastic buckling of the tube. The typical normalized force-deformation response of the fuse from a uniaxial test is shown in Figure 14(a), where p_{fs} is the compression force in the fuse, $t_{u,n}$ is the nominal force capacity of a single PT strand used at the 3rd floor of the SC-MRF test frame, $L_{o,fs}$ is the length of the steel tube (i.e. 4 in.), and Δ_{fs} is the fuse axial deformation. The fuse buckled sequently at Points 1 and 2 with $p_{fs}/t_{u,n}$=0.7 and 0.76, respectively, which are less than the value of $0.9T_{y,des}/T_{u,n}$=0.81 given in Eq. (8). The typical deformed fuse from a uniaxial test is shown in Figure 14(b), where the buckling forms uniformly around the circumference of the steel tube wall. The buckling formed at the ends is corresponding Point 1 bucking, and the buckling formed at the mid length is corresponding to Point 2 buckling.

The fuses were installed for each PT strand at the 3rd floor of the SC-MRF test frame, and the FU quasi-static pushover test was conducted to evaluate the response of the SC-MRF test frame with the fuses. Table 5 shows that at the 3rd floor in, T_{max}=0.64$T_{u,n}$ from the FU test is smaller than T_{max}=0.81$T_{u,n}$ from the PH test while $\overline{\theta}_{r,max}$=6.7% rad from FU test is larger than $\overline{\theta}_{r,max}$=6.3% rad from PH test. This result demonstrates that the fuses controlled the force developed in the PT strands, preventing PT strands from yielding. The total PT force (normalized by $T_{u,n}$) vs. $\overline{\theta}_r$ at the 3rd floor from FU test is shown in Figure 15. All fuses started buckle at Point a, which caused a decrease in the total PT force. Then, the total PT force remained constant until unloading at Point b. The response from Point a to Point b shows the ductile behavior of the PT strands with the fuses. The deformed fuses after the FU test are shown in Figure 16. The largest $T/T_{u,n}$=0.64 at Point a, which is less than $p_{fs}/t_{u,n}$=0.7 at Point 1 in Figure 14(a) because the buckling of the fuses did not form uniformly around the steel tube circumferences as observed in the uniaxial test. The permanent buckling of the fuses caused ΔT=0.2$T_{u,n}$ at the end of the FU test. As a result, the fuses need to be replaced after they deform permanently during a severe ground motion.

6. SUMMARY AND CONCLUSIONS

This paper focuses on MCE performance evaluation of an SC-MRF. Performance-based design (PBD) objectives were described, and MCE design criteria used for a SC-MRF to achieve CP performance were given. A 0.6-scale 2-bay 4-story SC-MRF test frame was developed and tested. Two MCE-level ground motions were imposed to the test frame using the hybrid simulation method. Three quasi-static pushover tests were conducted to investigate beam buckling, PT strand yielding strengths, and behavior of PT strands with special fuses, respectively.

The MCE hybrid simulations produced essentially no residual drift, which demonstrates the self-centering behavior of the SC-MRF. The SC-WFD connections provided reasonable energy dissipation for the SC-MRF. β_E was found to be larger than the design due to the friction bolt bearing against the longitudinal edges of the beam web slots. During the MCE hybrid simulations, beam flanges yielded with the largest strain larger than $2\varepsilon_y$ as expected in the PBD approach. Beam web buckling did not occur in the SC-MRF test frame. The largest total PT force reached 90% of the strand design yield strength $0.9T_{y,des}=0.81T_{u,n}$, but yielding did not occur in the PT strands. Therefore, beam web buckling and PT strand yielding in the SC-MRF did not occur during the MCE hybrid simulations, showing that the SC-MRF satisfied the PBD objectives under the MCE and achieved CP performance.

Test results from the PH and TU quasi-static pushover tests showed that the north-bay beam at the 4th floor buckled in the webs and bottom flanges when the largest $\overline{\theta}_{r,max}$ exceeded the design demand for $\overline{\theta}_{r,,MCE.}$ Therefore, the beam web compactness criterion gave the SC-MRF beams sufficient web buckling strength under the MCE. The beam always buckled in the bottom flange, so full plastic hinges do not form in the beam as in a conventional MRF. The largest total PT force exceeded $0.9T_{y,des}=0.81T_{u,n}$ by $0.01T_{u,n}$, but strand yielding did not occur. The strand yield criterion helped prevent PT strands from yielding under the MCE.

To avoid PT strands from yielding under the MCE, a special fuse was developed for the PT strands. The fuses were installed at the 3rd floor of the SC-MRF test frame. The FU quasi-static pushover test was conducted to study the behavior of the PT strands with the fuses. Test results showed that the fuses limited the force developed in the PT strands successfully and helped prevent PT strand yielding. The PT strands with the fuses had ductile behavior. Therefore, using the fuses to protect PT strands from yielding is an option for a SC-MRF to achieve CP performance.

Acknowledgements:

This paper is based upon work supported by the National Science Foundation under Grant No. CMS-0420974, within the George E. Brown, Jr. Network for Earthquake Engineering Simulation Research (NEESR) program. Support for the experiments was also provided through NSF Award No. CMS-0402490 NEES Consortium Operation. The work was also supported by the Pennsylvania Infrastructure Technology Alliance (PITA). The work was conducted at the NEES Real-Time

Multi-Directional (RTMD) earthquake simulation facility located in the ATLSS Center at Lehigh University.

References:

AISC (2005), Seismic Provision for Structural Steel Buildings, American Institute of Steel Construction, Chicago, IL

ASCE 7 (2005), Minimum Design Loads for Buildings and Other Structures, American Society of Civil Engineers, Reston, VA

BSSC (2003). NEHRP Recommended Provisions for Seismic Regulations for New Buildings and Other Structures. FEMA 450. Building Seismic Safety Council, National Institute of Building Sciences, Washington, D.C.

Chen, C., Ricles J.M. (2009), "Real-Time Hybrid Testing Using the Unconditionally Stable Explicit CR Integration Algorithm," Earthquake Engineering and Structural Dynamics; 38, 23-44.

Garlock M., Sause R., Ricles J.M. (2007), "Behavior and Design of Post-tensioned Steel Frame Systems," Journal of Structural Engineering, ASCE; 133:3, 389-399.

Kim, H.J., Chirstopoulos, C. (2008), "Friction Damped Posttensioned Self-Centering Steel Moment-Resisting Frames," Journal of Structural Engineering, ASCE; 134:11, 1768-1779.

Lin, Y.C. (2011), "Seismic Performance of a Self-Centering Steel Moment Resisting Frame System with Beam Web Friction Devices," Ph.D. Dissertation, Department of Civil and Environmental Engineering, Lehigh University, Bethlehem, PA, USA.

Lin, Y.C., Ricles, J.M., and Sause, R. (2009), "Experimental Assessment of the Seismic Performance of a Steel Self-Centering MRF System with Beam Web Friction Devices," Proceddings of the 6th International Conference on Behavior of Steel Structures in Seiemic Areas, PA, USA.

Ricles, J.M., Sause, R., Lin, Y.C., Seo, C-Y. (2010) "Self-Centering Moment Connections for Damage-Free Seismic Response of Steel MRFs," ASCE 2010 Structures Congress, FL, USA.

Ricles, J.M., Sause, R., Garlock, M., Zhao C. (2001), "Post-Tensioned Seismic-Resistant Connections for Steel Frames," Journal of Structural Engineering, ASCE; 127:2, 113-121.

Seo, C-Y., Sause R. (2005), "Ductility Demands on Self-Centering Systems under Earthquake Loading," ACI Structural Journal; 102:2, 275-285.

Walsh, K.Q. and Kurama, Y.C. (2010), "Behavior of Unbonded Post-Tensioning Monostrand Anchorage Systems under Monotonic Tensile Loading," PCI Journal, Winter 2010; 97-11.

Table 1 Design demands (% rad).

$\theta_{rf,DBE}$	$\theta_{s,DBE}$	$\overline{\theta}_{r,DBE}$	$\theta_{rf,MCE}$	$\theta_{s,MCE}$	$\overline{\theta}_{r,MCE}$
2.6	3.9	3.1	3.9	5.9	4.7

Table 2 MCE demand-capacity ratios.

Floor	$(h/t_w) / \lambda_{ps,MCE}$ from Eq. (6)	$T_{MCE} / 0.9T_{y,des}$ from Eq. (8)
4	0.87	0.91
3	0.92	0.96
2	0.89	0.98
1	0.89	1.00

Table 3 Test matrix for MCE performance evaluations.

Test	Description	GM Record	Scale Factor	Method
MCE-1	1979 Imperial Valley	5082-235	0.94	Hybrid simulation
MCE-2	1989 Loma Prieta	STM090	-2.23	
PH	Beam flange buckling evaluation	--	--	Quasi-Static Pushover
TU	PT strand strength evaluation	--	--	
FU	PT strand fuse evaluation	--	--	

Table 4 Test results from MCE hybrid simulations.

	Floor	Residual story drift (%rad)	$\theta_{rf,max}$ (%rad)	$\theta_{s,max}$ (%rad)	$\overline{\theta}_{r,max}$ (%rad)	$T_{max}/T_{u,n}$ (%)	$\Delta T/T_{u,n}$ (%)	β_E (%)
MCE-1	4	-0.094	-3.2	-5.8	-5.4	69	-1.0	38
	3	-0.056	--	-4.2	-4.7	72	-0.8	33
	2	-0.031	--	-3.2	-3.3	64	-0.5	28
	1	-0.031	--	-1.8	-2.2	62	0.0	28
MCE-2	4	-0.059	-4.6	-7.2	-6.7	76	-1.3	37
	3	-0.086	--	-6.2	-6.2	81	-2.5	33
	2	-0.110	--	-4.6	-5.2	77	-1.9	27
	1	-0.180	--	-2.6	-3.6	71	-1.3	28

Table 5 Test results from quasi-static pushover tests.

	Floor	$\theta_{s,max}$ (%rad)	$\overline{\theta}_{r,max}$ (%rad)	$T_{max}/T_{u,n}$ (%)	$\Delta T/T_{u,n}$ (%)
PH	4	-8.4	-6.8	74	-1.4
	3	-5.1	-6.3	81	-0.0
	2	-2.2	-2.7	59	-0.1
	1	-2.0	-1.9	55	-0.6
TU	4	11.1	7.9	82	-5.8
FU	4	7.9	7.4	81	-1.8
	3	6.7	6.7	64	-20.5
	2	4.7	4.8	71	-0.4
	1	2.3	2.9	61	-0.5

Table 6 Normalized maximum beam flange strains at the end of beam reinforcing plates $\varepsilon_{rp,max} / \varepsilon_y$.

Floor	MCE-1	MCE-2
4	-8.65	-9.02
3	-1.14	-1.33
2	-0.89	-1.16
1	-0.87	-1.15

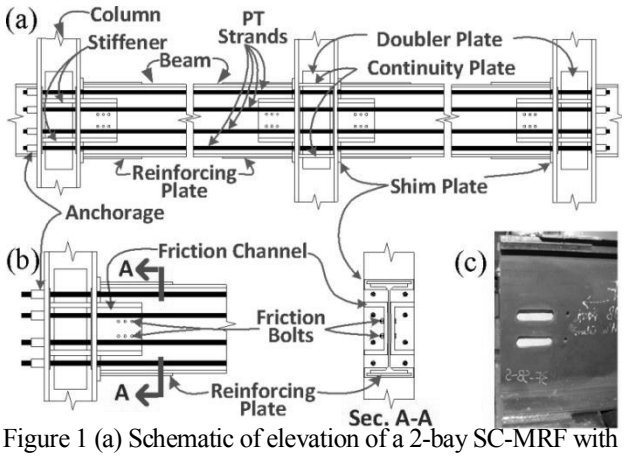


Figure 1 (a) Schematic of elevation of a 2-bay SC-MRF with PT strands and WFDs, (b) connection details, and (c) slotted holes in the beam web.

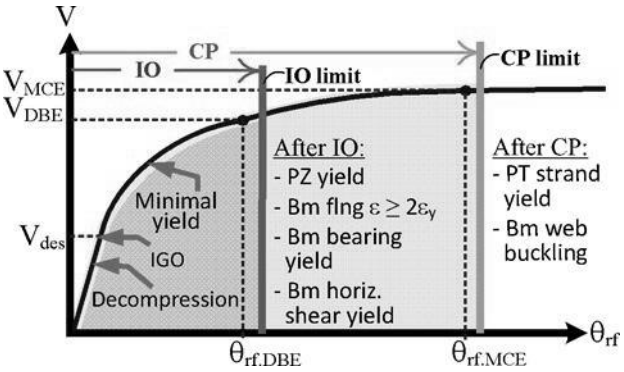


Figure 2 Performance based design objectives.

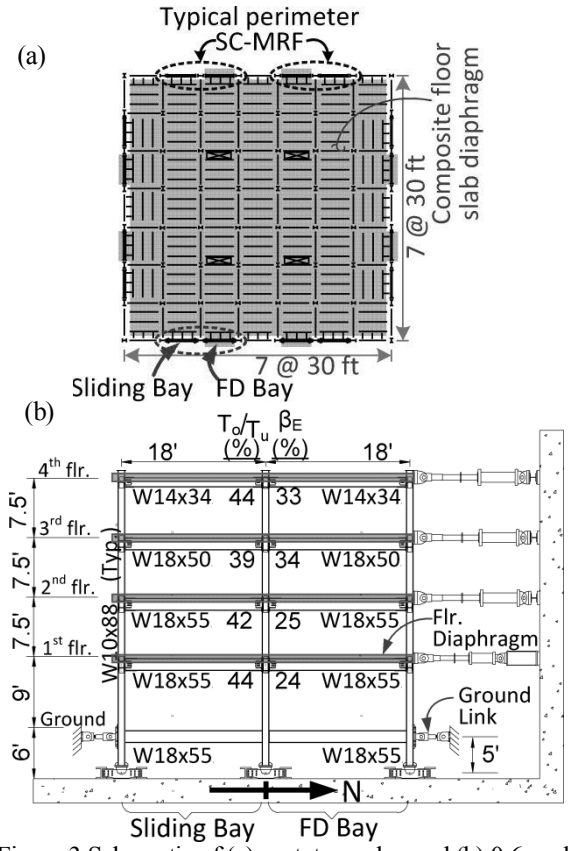


Figure 3 Schematic of (a) prototype plan and (b) 0.6-scale perimeter SC-MRF test frame elevation.

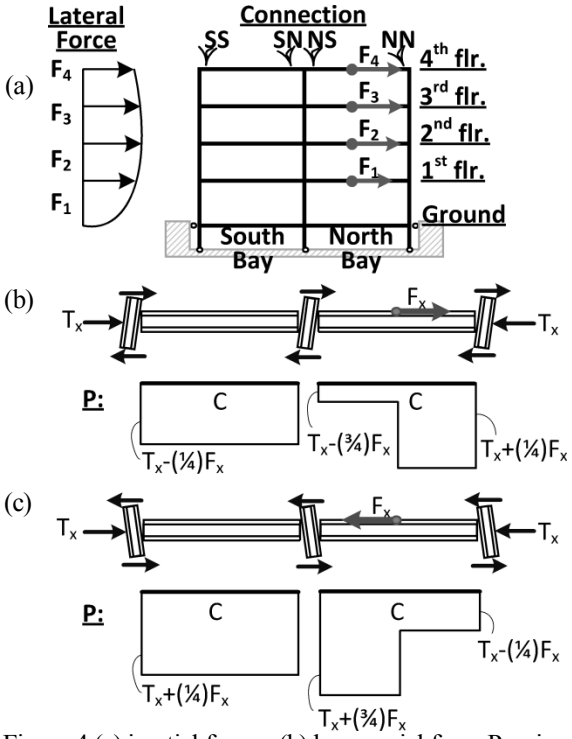


Figure 4 (a) inertial forces, (b) beam axial force P as inertial force acting to north, and (c)) beam axial force P as inertial force acting to south.

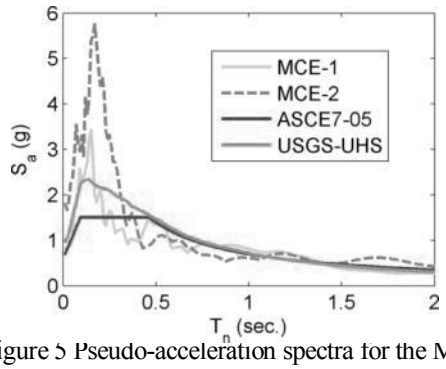


Figure 5 Pseudo-acceleration spectra for the MCE.

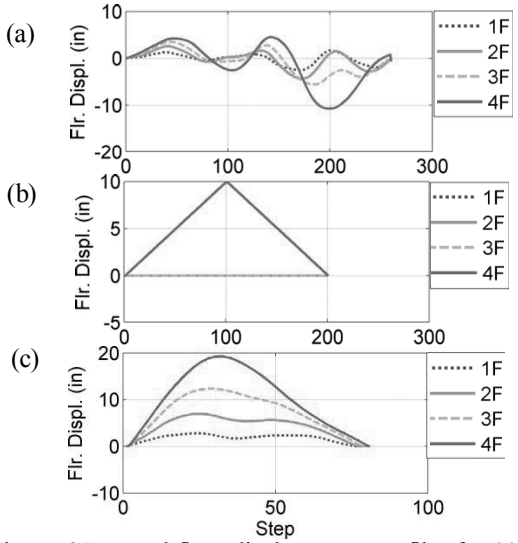


Figure 6 Imposed floor displacement profiles for (a) PH, (b) TU and (c) FU tests.

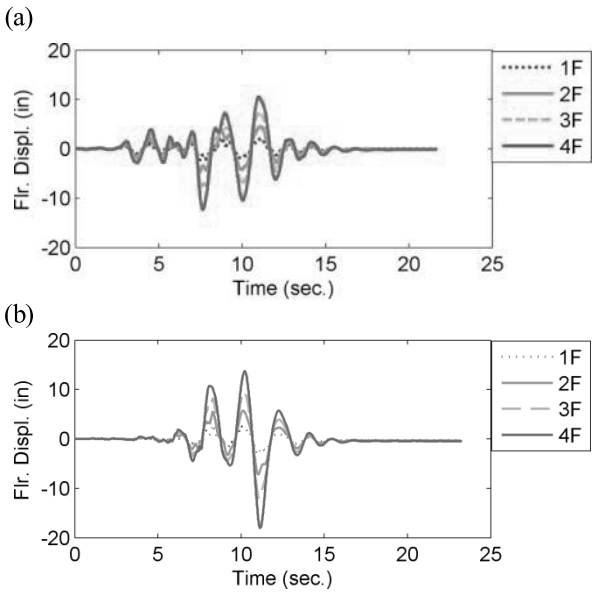


Figure 7 Floor displacements time histories from (a) MCE-1 and (b) MCE-2.

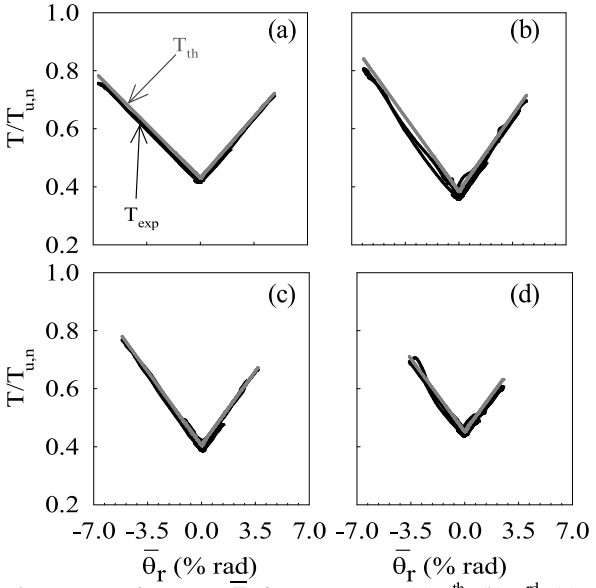


Figure 8 PT force vs. $\bar{\theta}_r$ from MCE-2: (a) 4th, (b) 3rd, (c) 2nd, and (d) 1st floors.

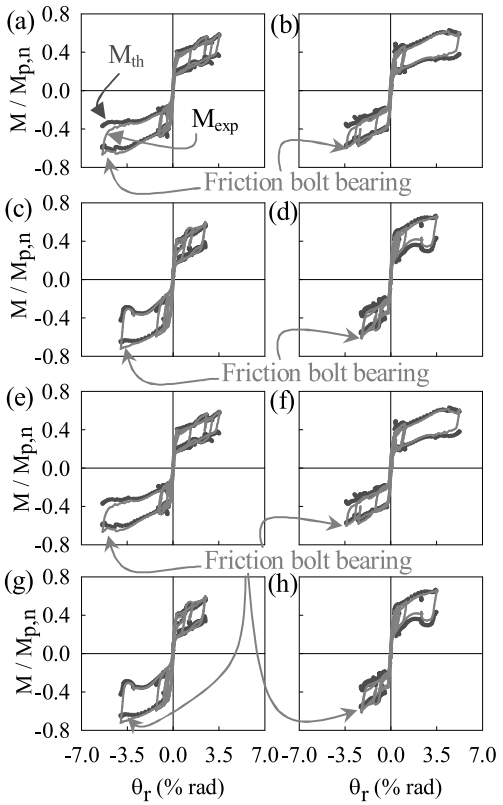


Figure 9 Connection M-θ_r responses from MCE-2 at (a) 4FSS, (b) 4FSN, (c)3FSS, (d)3FSN, (d) 2FSS, (e)2FSN, (f) 1FSS, and (g) 1FSN.



Figure 10 Beam yielding at 4FNS connection from MCE-2.

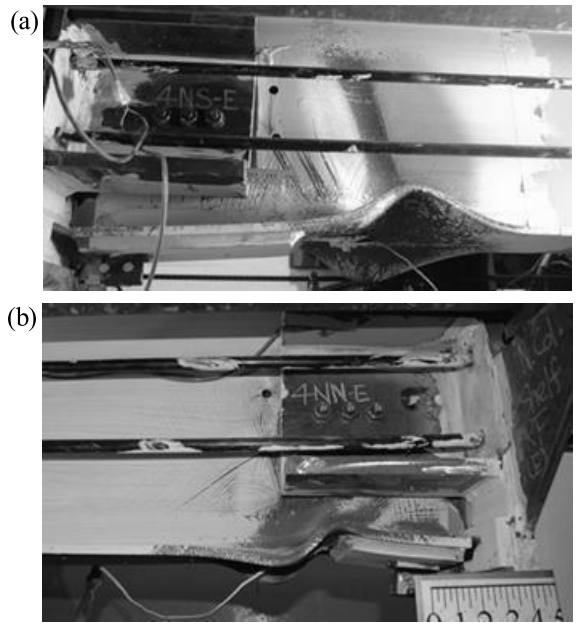


Figure 11 Damage of bottom flanges of (a) 4FNS connection from the PH test and (b) 4FNN connection from the TU test.

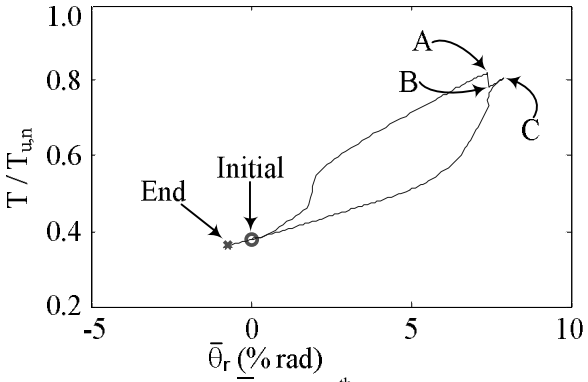


Figure 12 PT force vs. $\bar{\theta}_r$ at the 4th floor from the TU test.

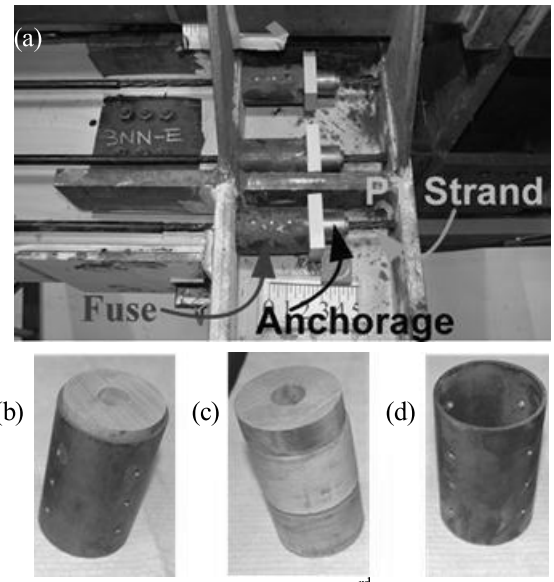


Figure 13 (a) Fuses installed at the 3rd floor of the SC-MRF test frame; (b) fuse, (c) wood discs, and (d) annealed steel tube.

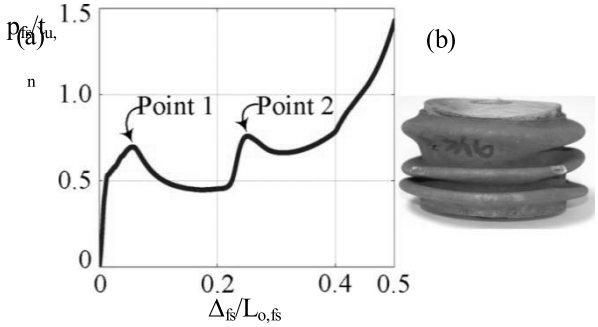


Figure 14 (a) Typical fuse normalized strength-deformation behavior; (b) deformed fuse.

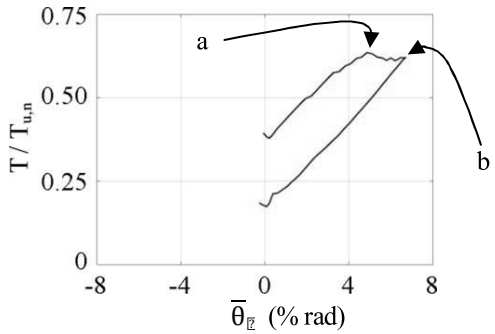


Figure 15 PT force vs. $\bar{\theta}_r$ at the 3rd floor from the FU test.

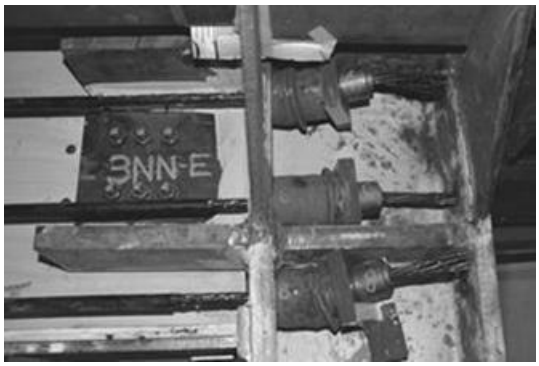


Figure 16 Fuse buckling from the FU test.

8CUEE CONFERENCE PROCEEDINGS
8th International Conference on Urban Earthquake Engineering
March 7-8, 2011, Tokyo Institute of Technology, Tokyo, Japan

BIO-INSPIRED PASSIVE ACTUATOR FOR STRUCTURAL CONTROL

Chun-Hung Lin[1], Paul K. Hansma[2], and Henry T.Y. Yang[3]

1) Research Assistant, Department of Mechanical Engineering, University of California, Santa Barbara, CA 93106, USA
2) Professor, Department of Physics, University of California, Santa Barbara, CA 93106, USA
3) Professor, Department of Mechanical Engineering, University of California, Santa Barbara, CA 93106, USA
lin@engineering.ucsb.edu

Abstract: An energy dispersion mechanism called "Sacrificial Bonds and Hidden Length" found in some biological systems, such as abalone shells and bones, is the inspiration for new mechanisms for structural control. Sacrificial bonds and hidden length can substantially increase the stiffness and enhance energy dissipation in the constituent molecules of abalone shells and bone. This paper presents a fundamental method for designing and optimizing bio-inspired passive actuators for structural control. A simple optimization method utilizing the Force-Displacement-Velocity (FDV) plots and a statistic approach of linear regression are adopted in this research to find the initial values of the desired parameters for the bio-inspired passive actuator. The illustrative examples, conducted by numerical simulation with experimental validation, suggest that the bio-inspired passive actuator based on sacrificial bonds and hidden length may be comparable in performance to state-of-the-art semi-active actuators, and can also be adaptive to different earthquakes.

1. INTRODUCTION

Abalone shell is 3,000 times more fracture resistant than crystalline calcium carbonate even though it is composed of 97% crystalline calcium carbonate (Jackson, Vincent et al. 1988). Part of the secret is the amazing mechanical performance of the other 3%, which is organic, primarily proteins (Smith, Schaffer et al. 1999), working together with the structural geometry (Fritz, Belcher et al. 1994; Zaremba, Belcher et al. 1996; Schaffer, IonescuZanetti et al. 1997; Evans, Suo et al. 2001). In bone as well, a small percentage by weight of non-collagenous proteins, such as osteopontin, contributes significantly to the fracture resistance (Thompson, Kindt et al. 2001; Hansma, Fantner et al. 2005; Fantner, Rabinovych et al. 2006; Fantner, Adams et al. 2007).

The key points in both abalone shells and bones are: 1) the work that must be done against entropy to stretch the hidden length is of order 30 times greater than the work to break strong bonds, and 2) sacrificial bonds can reform and the work done against entropy is non-destructive (Thurner, Erickson et al. 2006; Thurner, Erickson et al. 2007). This is the goal of this research: to find new ways to dissipate energy from threats such as earthquakes, winds, impacts, or even blasts to civil and mechanical infrastructures, flutter of aircraft wings, bridges, cooling towers, and more.

What can be learned from abalone shell and bone that could help move the field of structural control forward? One lesson that can be learned is how to develop bio-inspired autonomous passive actuators. Both abalone shells and bones have distributed passive actuators that use the mechanism of sacrificial bonds and hidden length. Figure 1 shows a Scanning Electron Microscope image of bone being fractured: the molecules with sacrificial bonds and hidden length can be seen resisting the start of the fracture (Smith, Schaffer et al. 1999; Fantner, Hassenkam et al. 2005; Fantner, Oroudjev et al. 2006). The biological system with sacrificial bonds and hidden length mechanism can dissipate energy from threats. A schematic drawing of the basic principle of the sacrificial bond and hidden length mechanism is shown in figure 2. Before the sacrificial bond is broken, only the solid length of the molecule contributes to the entropic spring and therefore to the force with which the molecule resists the stretching. The dotted length of the molecule is hidden from the applied force by the sacrificial bond. When the bond breaking force is reached, only a small amount of energy is required to break the sacrificial bond. After that, the whole length (solid plus dotted) contributes to the entropy of the molecule. This mechanism is very different from the mechanisms of dashpots and springs used in conventional engineered actuators.

Various state-of–the-art semi-active devices have been proposed and developed for civil infrastructural applications. For example, Dyke et al (1996) and Spencer et al (1997) have proposed the magnetorheological (MR) dampers for seismic response reduction. Scruggs and Iwan (2003) have proposed another semi-active electrical machine for civil structural control. Chen and Chen (2004) have designed and tested the semi-active piezoelectric friction dampers on a quarter-scale building model.

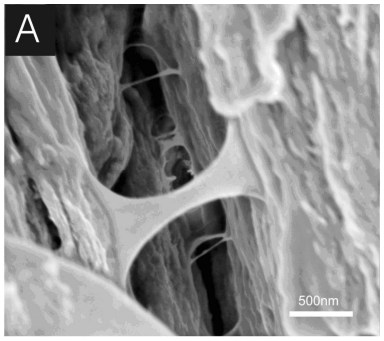


Figure 1 The molecules with sacrificial bonds and hidden length in the Scanning Electron Microscope Image of bone being fractured (Smith, Schaffer et al. 1999; Fantner, Hassenkam et al. 2005; Fantner, Oroudjev et al. 2006).

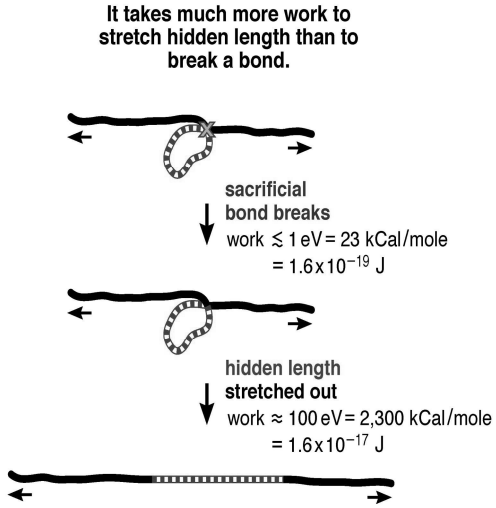


Figure 2 Schematic drawing of the sacrificial bond – hidden length mechanism (Fantner, Oroudjev et al. 2006).

In order to illustrate and prove the concept of using the inspiration from sacrificial bonds and hidden length to design bio-inspired and bio-autonomous actuators for structural control applications, a building structural model is chosen as an example with earthquake as the threatening force. The primary reason for using building response to earthquake excitation as the present model is because of the high level of work done in the field: it will be possible to compare the present results to the state-of-the-art examples which have already been developed. Additionally, structural models similar to those already constructed (Spencer Jr, Dyke et al. 1998) can be tailor built to experimentally test the usefulness and effectiveness of the bio-inspired passive actuators invented in this study.

In this research, the authors test the biologically inspired passive actuators on a three-story model building similar to that proposed by Dyke et al (1996). This research is done by numerical simulation with experimental validation. The control performance of the proposed bio-inspired passive actuator is compared with the well developed semi-active actuators using the same structural control example. Within the illustrative examples shown here, it is found that the current bio-inspired passive control devices can achieve comparable performance to the state-of-the-art semi-active devices.

2. OPTIMAL PASSIVE ACTUATOR

The force vs. displacement and velocity for the sacrificial bond–hidden length mechanism is very different from that of conventional passive actuators. A new type of plot, the Force-Displacement-Velocity plot (FDV plot), is presented in this study to facilitate the optimization of passive actuator systems to each structural system.

Considering a seismically excited structure with actuators on given floors, the equation of motion can be written as

$$\mathbf{M}_s\ddot{x} + \mathbf{C}_s\dot{x} + \mathbf{K}_s x = \Gamma f - \mathbf{M}_s \Lambda \ddot{x}_g \tag{1}$$

where x is a vector of the displacements of each floor, $\ddot{x}_g$ is, for simplicity, a one-dimensional ground acceleration, f is the control force applied by the actuator installed on the structure, $\mathbf{\Gamma}$ and $\mathbf{\Lambda}$ are the location matrices, and Ms, Cs and Ks are the mass, damping and stiffness matrices of the linear system, respectively. Equation (1) can be written in state-space representation as

$$\dot{z} = \mathbf{A}z + \mathbf{B}f + \mathbf{E}\ddot{x}_g \tag{2}$$

where z is the state vector. The measurement equation is given by

$$y = \mathbf{C}z + \mathbf{D}f + v \tag{3}$$

where y is the vector of measured outputs, v is the noise vector in measurement, and A, B, C, D and E are the state-space matrices, which are the same as those defined in (Dyke, Spencer Jr et al. 1996) and given by

$$\mathbf{A} = \begin{bmatrix} \mathbf{0} & \mathbf{I} \\ -\mathbf{M_s}^{-1}\mathbf{K_s} & -\mathbf{M_s}^{-1}\mathbf{C_s} \end{bmatrix} \quad \mathbf{B} = \begin{bmatrix} \mathbf{0} \\ \mathbf{M_s}^{-1}\mathbf{\Gamma} \end{bmatrix} \quad \mathbf{E} = -\begin{bmatrix} \mathbf{0} \\ \mathbf{\Lambda} \end{bmatrix} \tag{4}$$

and

$$\mathbf{C} = \begin{bmatrix} -\mathbf{M_s}^{-1}\mathbf{K_s} & -\mathbf{M_s}^{-1}\mathbf{C_s} \\ 1\ 0\ 0 & 0\ 0\ 0 \end{bmatrix} \quad \mathbf{D} = \begin{bmatrix} \mathbf{M_s}^{-1}\mathbf{\Gamma} \\ \mathbf{0} \end{bmatrix} \tag{5}$$

The FDV plot presented here is a contour plot of the control force applied on a structure as a function of the displacement and velocity under a specific excitation. Figure 3 shows two kinds of typical passive control forces at the first floor of the three-story structural model considered by Dyke et al (1996) for 1,250 sets of values of displacement (x_1) and velocity (v_1) over the first 5 seconds, with Δt=0.004 seconds, while excited by the N-S acceleration components of the scaled 1940 El Centro Earthquake.

With the aid of FDV plots, the bio-inspired passive actuators in model structures can be optimized. First, for example, the linear-quadratic regulator (LQR) optimization (Kwakernaak and Sivan 1972) is used to find the ideal FDV plot (shown in figure 4) of an active actuator during a simulated earthquake. The objective of using a LQR optimization is to minimize a cost function of

$$J = \lim_{t\to\infty} \int_{-\infty}^{t} \left(y^T \mathbf{Q} y + f^T \mathbf{R} f \right) dt \qquad (6)$$

where Q and R are the weighting matrices and can be defined according to the mechanical dynamics of the system under consideration.

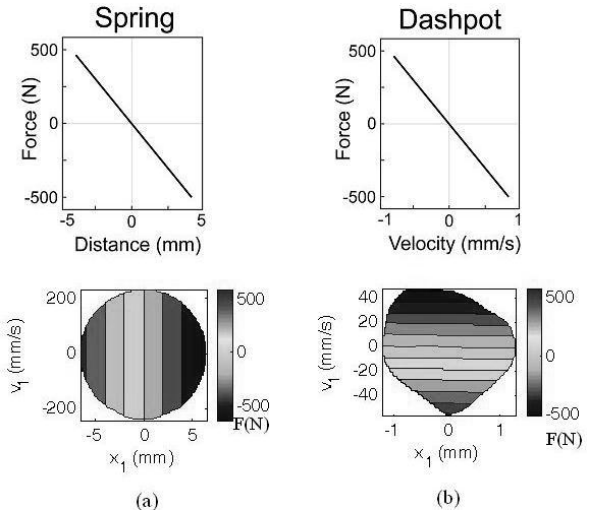


Figure 3 FDV plots of two kinds of passive control forces at the first floor of the model considered by Dyke et al (1996) for 1,250 sets of values of displacement x_1 and velocity v_1 over the first 5 seconds, with Δt=0.004 seconds, of N-S acceleration components of the scaled 1940 El Centro Earthquake: (a) spring constant = 1,000 (N/cm); (b) damping coefficient = 110 (N s/cm).

Efforts are then made to try to replicate this Force-Displacement-Velocity plot of an active actuator with a combination of components from the current bio-inspired pallet of passive actuators. By choosing the appropriate parameters of the bio-inspired passive actuator, it is possible to construct the optimal passive actuator to control the structure during a specific earthquake.

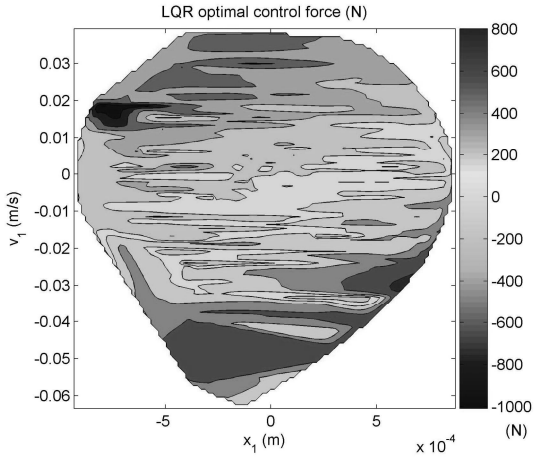


Figure 4 FDV plot calculated on the model considered by Dyke et al (1996) over the N-S acceleration components of the scaled 1940 El Centro Earthquake with LQR optimal control force. The LQR is based on the minimization of cost function:

$$J = \lim_{t\to\infty} \int_{-\infty}^{t} \left(1.83\times10^{6}\, \ddot{x}_3^2 + 7.2\times10^{12}\, x_1^2 + 1.0 f_1^2 \right) dt \,.$$

3. DESIGN OF BIO-INSPIRED ACTUATOR

For the three-story model structure considered by Dyke et al (1996), the Force-Displacement-Velocity plot cannot be simulated using a linear combination of conventional dampers and springs. In fact what is needed is the addition of a component to tilt the Force-Displacement-Velocity plot of a damper the opposite way from adding a conventional spring. From biology, the authors are inspired to evolve a device that will optimize Force-Displacement-Velocity plot and hence optimize the control of structural vibrations. The simple mechanical model of the bio-inspired system is shown in Figure 6, which formed the basis for the numerical simulation model and for the construction of the passive actuators used in this research. The applied force f predicted by the model is given by

$$f = \mathrm{BIO}(x, \dot{x}) + C_0 \dot{x} \qquad (7)$$

where $\mathrm{BIO}(x, \dot{x})$ is the force generated by the bio-inspired mechanism, and C_0 is the damping coefficient.

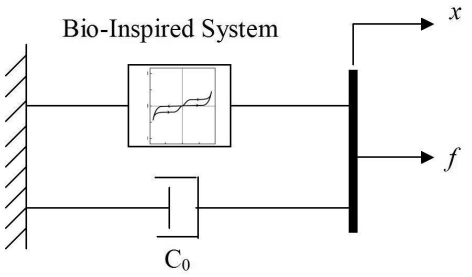


Figure 5 Simple mechanical model of the bio-inspired system as the basis for the numerical simulation and the construction of passive actuators.

In this study, the function $\mathrm{BIO}(x,\dot{x})$ is defined by

$$\mathrm{BIO}(x,\dot{x}) = \begin{cases} f_{\max} & if \quad x \geq 0 \ \ and \ \dot{x} \leq 0 \\ -f_{\max} & if \quad x \leq 0 \ \ and \ \dot{x} \geq 0 \\ 0 & if \quad x \cdot \dot{x} > 0 \end{cases} \tag{8}$$

where f_{max} is the maximum force assumed in the sacrificial bond-hidden length mechanism.

A statistic approach is utilized in this study to determine the parameters of the optimal passive actuator. Since the FDV plot of LQR control over a specific earthquake (Figure 4) is desired, the linear regression is used to fit every point on the FDV plot:

$$F = \beta_{spring} \times x_1 + \beta_{damping} \times v_1 + \beta_{bio} \times BIO \tag{9}$$

where F is the desired control force from LQR control, and x_1 and v_1 are the displacement and velocity of the controlled floor, respectively. BIO is the force generated by the bio-inspired mechanism based on the negative sacrificial bonds and hidden length with f_{max} = 1 N. The coefficients on the independent variables, x_1, v_1, and BIO, are β_{spring}, $\beta_{damping}$, and β_{bio}, respectively. The values of β_{spring} and $\beta_{damping}$ are equivalent to the stiffness coefficient, K_0, and the damping coefficient, C_0, respectively. The value of β_{bio} is equivalent to f_{max} in the $\mathrm{BIO}(x,\dot{x})$ function.

The spring coefficient in (9) is used to show the idea of negative spring, which is similar to the negative sacrificial-bond/hidden-length mechanism and is not included in Figure 5. The optimal control parameters of the bio-inspired passive controller defined in (9) can be obtained by linearly regressing (9) to the ideal FDV plot (Figure 4). These values can be used as the initial values when optimizing the parameters of the control device.

4. EXAMPLES

4.1 Numerical Example

In order to prove the concept and to demonstrate the applicability and performance of the proposed bio-inspired passive actuator, a three-story numerical structure model is considered in this study. The equation of motion of the structure is given in Equation (1), where $x = [x_1\ x_2\ x_3]^T$ is the vector of displacements of the three floors. Since the bio-inspired actuator is installed on the first floor, the variable x in (7) and (8) is equal to x_1. The system matrices are the same as those documented in (Dyke, Spencer Jr et al. 1996) and given by

$$\mathbf{M_s} = \begin{bmatrix} 98.3 & 0 & 0 \\ 0 & 98.3 & 0 \\ 0 & 0 & 98.3 \end{bmatrix} \text{kg}$$

$$\mathbf{C_s} = \begin{bmatrix} 175 & -50 & 0 \\ -50 & 100 & -50 \\ 0 & -50 & 50 \end{bmatrix} \frac{\text{N s}}{\text{m}}$$

$$\mathbf{K_s} = 10^5 \begin{bmatrix} 12.0 & -6.84 & 0 \\ -6.84 & 13.7 & -6.84 \\ 0 & -6.84 & 6.84 \end{bmatrix} \frac{\text{N}}{\text{m}}$$

$$\mathbf{\Gamma} = \begin{bmatrix} 1 \\ 0 \\ 0 \end{bmatrix} \qquad \mathbf{\Lambda} = \begin{bmatrix} 1 \\ 1 \\ 1 \end{bmatrix}.$$

To account for the model scale and to compare with the simulating results by Dyke et al. (1996), the N-S acceleration components of the 1940 El Centro Earthquake is time-scaled by a factor of 5 and used as the excitation to the structure model in the proposed simulation. Due to the passive nature of the proposed bio-inspired actuator, there is no need to design a control strategy such as those usually used by active or semi-active control devices. In this example, the cost function of the LQR control is chosen in a way to minimize the third floor acceleration, the first floor displacement, and the applied control force. The cost function then is defined by

$$\begin{aligned} J &= \lim_{t\to\infty} \int_0^t \left(y^T \mathbf{Q} y + f^T \mathbf{R} f \right) dt \\ &= \lim_{t\to\infty} \int_0^t \left(Q(3,3)\ddot{x}_3^2 + Q(4,4)x_1^2 + R(1,1)f_1^2 \right) dt \end{aligned} \tag{10}$$

where $\ddot{x}_3$ is the acceleration measured on the third floor of the structure model, x1 and f1 are the displacement and control force on the first floor, respectively. In this research, Q(3,3), Q(4,4), and R(1,1) are chosen to be 1.83×10^6, 7.20×10^{12}, and 1.0, respectively, to minimize the largest floor-to-floor drift, while the maximum control force is set to be 941 N to be the same as in the work done by Dyke et al. (1996). This choice is different from those chosen by Scruggs and Iwan (2003), which can also successfully reduce the structural response. However, the results of control performance are close to each other. The LQR optimal control force based on (10) is used to derive the parameters of the bio-inspired passive controller defined in (9).

For example, if only the combination of damping and negative sacrificial-bond/hidden-length mechanism are considered, the result of the regression shows the damping coefficient to be 104.5 N s/cm and the f_{max} of negative sacrificial bond – hidden length to be 133.8 N with an R-squared value of 0.81. These two coefficients are both significant at 95% confidence level.

If only the stiffness and damping coefficients are considered, the regression suggests a negative spring constant of -2,139 N/cm and a damping coefficient of 126.1 N s/cm. The negative spring constant means the structure is too stiff and can be softened to reduce the structural response. The R-squared value of the regression is 0.83, and both coefficients are significant at 95% confidence level.

If all three variables are considered, the regression suggests a negative spring constant of -1,795.5 N/cm, a damping coefficient of 120.6 N s/cm, and f_{max} of 34.8 N. The R-squared value of the regression is 0.83. All

coefficients are significant at 95% confidence level.

The statistic approach based on linear regression can provide a good estimation of the parameters of the passive actuator. A better control performance can be achieved by tuning the parameters starting from the estimated values.

In this study, the value of C_0 and f_{max} are chosen to be 70 (N s/cm) and 350 (N), respectively, to improve the performance. The simulation comparison of the bio-inspired passive actuator to the MR damper proposed by Dyke et al (1996) due to a 2.5 Hz sinusoid excitation with an amplitude of 1.5 cm is shown in Figure 6. The Force-Displacement-Velocity plot of this passive actuator is then calculated and shown in Figure 7. It is noticed that the FDV plot here is tilted in the same way as the FDV plot based on LQR optimal control force (Figure 4).

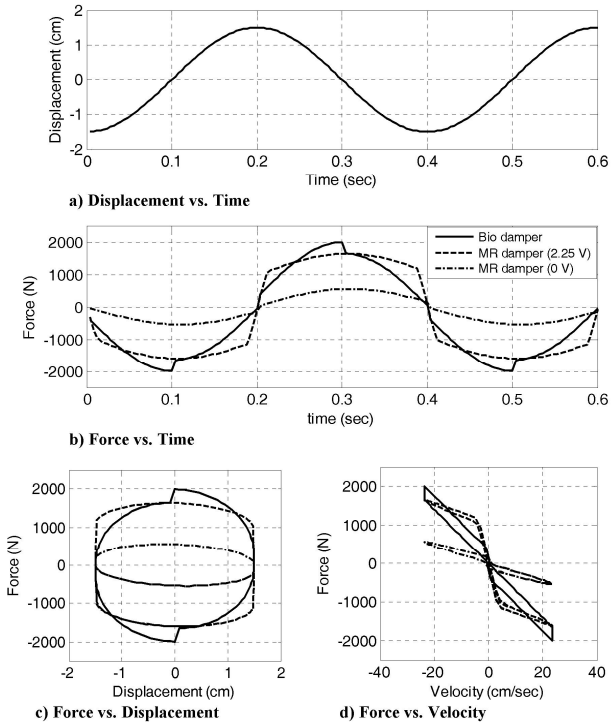


Figure 6 Simulation results of the bio-inspired passive actuator and MR damper for 2.5 Hz sinusoidal excitation with an amplitude of 1.5 cm.

The structural response of the example are compared to those using the semi-active MR damper (Dyke, Spencer Jr et al. 1996; Spencer Jr, Dyke et al. 1997) and both shown in Figure 8. The proposed bio-inspired passive actuator can achieve a similar level of performance in floor displacements and acceleration response as the semi-active MR damper.

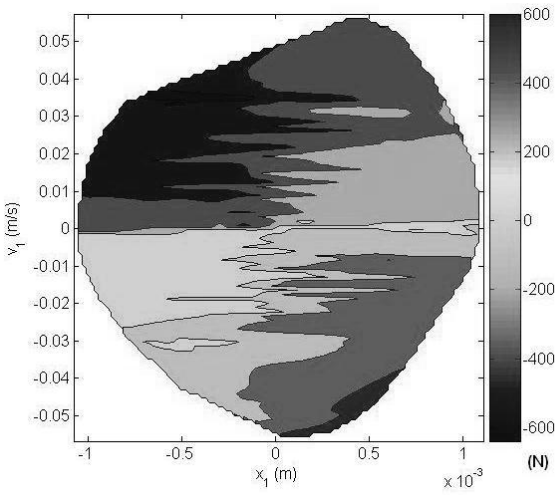


Figure 7 Force-Displacement-Velocity plots calculated on the model considered by Dyke et al. (1996) over the N-S acceleration components of the scaled 1940 El Centro Earthquake with bio-inspired passive actuator (C_0 = 70 N s/cm and f_{max} =350 N).

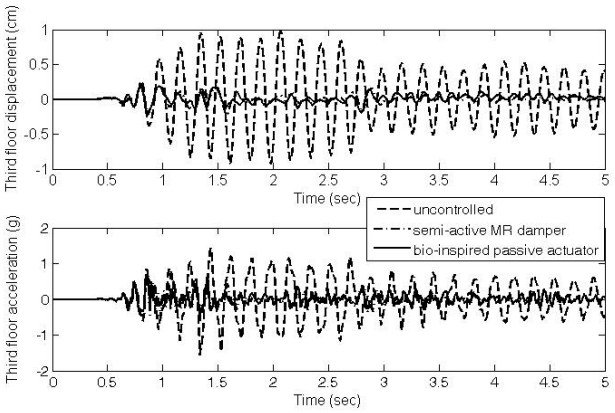


Figure 8 Uncontrolled structural responses as compared to these controlled by semi-active MR damper and bio-inspired passive actuator (C_0 = 70 N s/cm and f_{max} = 350 N), respectively, due to the N-S acceleration component of the scaled 1940 El Centro Earthquake.

In the illustrative example, it seems that bio-inspired passive actuator systems based on sacrificial bonds and hidden length coupled with dampers could yield results comparable in performance to the state-of-the-art semi-active actuators developed by widely referenced publications in the field (Dyke, Spencer Jr et al. 1996; Spencer Jr, Dyke et al. 1997; Scruggs and Iwan 2003).

To account for the model scale and to compare with the simulating results by Dyke et al. (1996), the considered earthquakes are time-scaled by a factor of 5 and used as the excitation to the structure model in the proposed simulation. The simulation results using the proposed methods, the previous bio-inspired actuators (Yang et al., 2010), and a simulation model of a conventional Magnetorheological

(MR) damper built by the authors that follows the computational model proposed by Spencer Jr et al. (1997), subjected to the three different earthquakes, are shown in the Tables 1-3. It is shown that the proposed methods may be adaptive to different earthquakes.

Table 1 Comparisons of peak responses of displacements, drifts, and accelerations over the scaled 1940 El Centro earthquake using:
(a) Active LQR control;
(b) Bio-inspired passive actuator;
(c) Conventional Semi-Active MR damper.

		Uncontrolled	**Active** LQR optimal control (a)	Bio-inspired **passive** actuator (Sacrificial Bond and Hidden Length) (b)			**Semi-active** MR damper (c)
K_0 (N s/cm)				0	0	-1689	
C_0 (N s/cm)				100	70	85	
f_{max} (N)				260	350	260	
Displacement (cm)	x_1	0.549	0.093	0.106	0.112	0.108	0.114
	x_2	0.837	0.139	0.173	0.169	0.149	0.185
	x_3	0.973	0.191	0.246	0.230	0.202	0.212
Drift (cm)	d_1	0.549	0.093	0.106	0.112	0.108	0.114
	d_2	0.318	0.093	0.103	0.092	0.090	0.090
	d_3	0.203	0.065	0.080	0.071	0.068	0.101
Acceleration (cm/s^2)	a_1	882	603	348	424	347	696
	a_2	1066	290	368	398	303	739
	a_3	1413	450	556	494	473	703
Max force (N)	f	0	941	780	754	763	941

Table 2 Comparisons of peak responses of displacements, drifts, and accelerations over the scaled 1989 San Francisco earthquake using:
(a) Active LQR control;
(b) Bio-inspired passive actuator;
(c) Semi-Active MR damper.

		Uncontrolled	**Active** LQR optimal control (a)	Bio-inspired **passive** actuator (Sacrificial Bond and Hidden Length) (b)			**Semi-active** MR damper (c)
K_0 (N s/cm)				0	0	-1689	
C_0 (N s/cm)				100	70	85	
f_{max} (N)				260	350	260	
Displacement (cm)	x_1	0.438	0.107	0.111	0.113	0.116	0.155
	x_2	0.664	0.167	0.204	0.196	0.175	0.246
	x_3	0.821	0.224	0.264	0.246	0.220	0.267
Drift (cm)	d_1	0.438	0.107	0.111	0.113	0.116	0.155
	d_2	0.267	0.095	0.105	0.094	0.088	0.095
	d_3	0.173	0.063	0.060	0.053	0.048	0.067
Acceleration (cm/s^2)	a_1	773	224	312	345	334	837
	a_2	866	276	335	343	290	504
	a_3	1202	439	418	369	334	466
Max force (N)	f	0	766	673	639	677	744

Table 3 Comparisons of peak responses of displacements, drifts, and accelerations over the scaled 1995 Kobe earthquake using:
(a) Active LQR control;
(b) Bio-inspired passive actuator;
(c) Semi-Active MR damper.

		Uncontrolled	**Active** LQR optimal control (a)	Bio-inspired **passive** actuator (Sacrificial Bond and Hidden Length) (b)			**Semi-active** MR damper (c)
K_0 (N s/cm)				0	0	-1689	
C_0 (N s/cm)				100	70	85	
f_{max} (N)				260	350	260	
Displacement (cm)	x_1	1.496	0.370	0.480	0.560	0.520	0.699
	x_2	2.373	0.549	0.811	0.917	0.752	1.180
	x_3	2.877	0.691	1.023	1.134	0.908	1.445
Drift (cm)	d_1	1.496	0.370	0.480	0.560	0.520	0.699
	d_2	0.888	0.283	0.381	0.386	0.307	0.488
	d_3	0.529	0.177	0.212	0.217	0.169	0.327
Acceleration (cm/s^2)	a_1	2354	578	723	797	623	1873
	a_2	2825	873	1250	1321	1007	1934
	a_3	3679	1231	1477	1508	1173	2274
Max force (N)	f	0	2245	1729	1603	1824	1298.4

4.2 Experimental Validation

During this research, a specific three story model is built out of aluminum, as shown in Figure 9. The first three natural frequencies calculated from the finite element model are 2.15 Hz, 6.79 Hz, and 10.59 Hz, respectively. The experimentally measured frequencies are 2.00 Hz, 6.37 Hz, and 10.16 Hz, respectively.

Two types of passive actuators to be installed on the first floor of this model are designed, built, and tested using the N-S acceleration component of the 1940 El Centro Earthquake as the excitation. The first device is a simple friction block that slides on the platform of the present test model building (friction force = 0.2 N). The second one is a "negative spring" (spring constant = -4.3 N/cm) plus a damper (damping coefficient = 0.117 N s/cm) mounted on the test model building. The negative spring with damping prototype device uses a commercial airpot damper (the black cylinder) together with a novel element that uses three magnets. Two magnets on a linear slide are attracted to a stationary magnet that is held in the arched structure mounted on the base. Figure 10 shows a comparison between theoretically predictions and experimentally measurements using FDV plots for the two sets of prototype devices – friction damper and negative spring damper. The friction damper is employed here because it is a simple and common device. The negative spring damper has the desired property indicated in Figure 4, and the proposed bio-inspired passive actuator is inspired by this kind of damper. Furthermore, the structural response of third floor displacement corresponding to the comparison in Figure 10 is shown in Figure 11. The agreements in the two sets of the time-history displacement data for the first 10 seconds are convincing. Such comparison may indicate that reliable results can be obtained in the subsequent numerical

simulations and validations of the presently suggested concept of bio-inspired passive actuator.

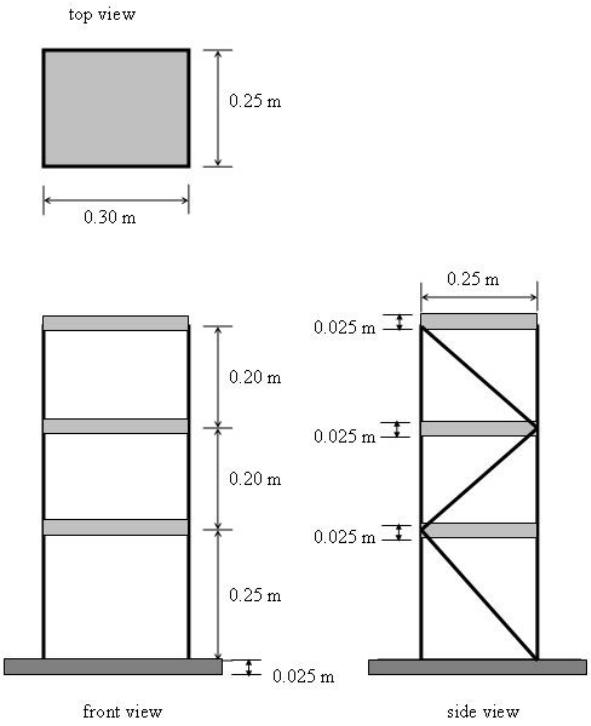


Figure 9 Three-story aluminum test model structure.

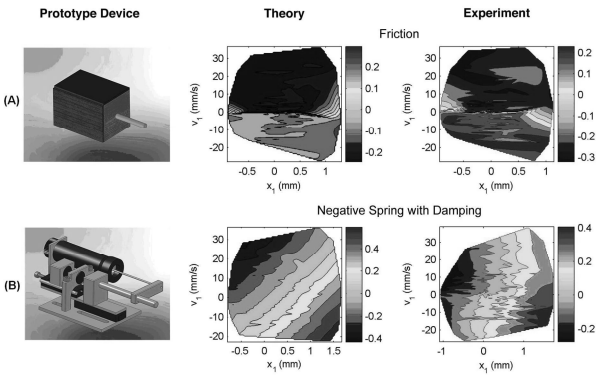


Figure 10 Passive actuators developed in this study and its FDV plots: (A) friction damper; (B) negative spring with damping prototype device uses a commercial airpot damper.

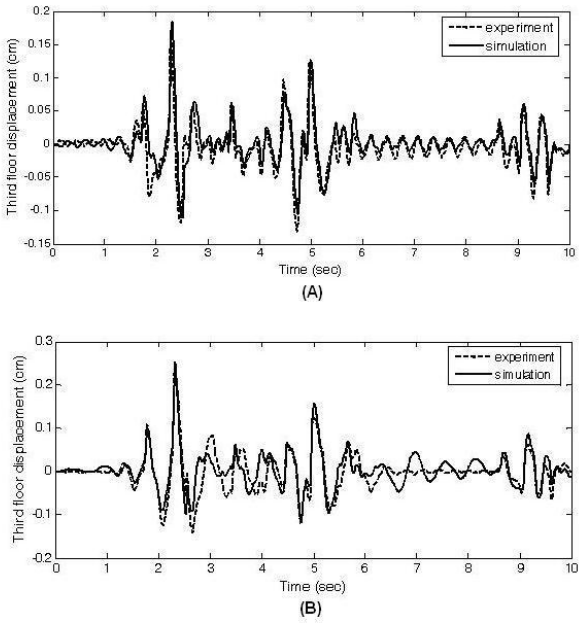


Figure 11 Third floor displacement of the present three-story aluminum test model building with the passive actuators: (A) friction damper; (B) negative spring with damping prototype device uses a commercial airpot damper.

5. CONCLUSIONS

Inspired and challenged by the simplicity and enormous capability of actuators present in bio-organisms, the authors have successfully built passive actuators which compare favorably with state-of-the-art semi-active actuators, and with potential in the direction of bio-inspired research in the future. This paper presents a fundamental method of designing and optimizing bio-inspired passive actuators for structural control. The Force-Displacement-Velocity plots based on LQR control and the statistic approach based on linear regression are adopted in this research.

Illustrative examples of two prototype passive dampers tested both theoretically and experimentally validate the development and also demonstrate the applications. The proposed bio-inspired actuators, although passive, are comparable in performance to the state-of-the-art semi-active actuators in numerical simulations. It is noted that once the peak ground acceleration is changed, the situation will likely change. The accuracy of the control parameters used in numerical simulations, such as damping coefficient, spring constant, and f_{max} are important in order to predict the structural response more realistically. Besides, due to the simplicity of the bio-inspired actuator, the control devices are easy to design, and there is no need of any active control strategy. Furthermore, the control device is independent of inadvertent condition such as power outage.

The illustrative examples of a three story building model under three different earthquakes are used in this research to demonstrate the effectiveness of the proposed methods. The proposed bio-inspired actuators, although

passive, are comparable in performance to the state-of-the-art semi-active actuators in numerical simulations. The proposed bio-inspired actuator is also shown to be more adaptive to different earthquakes. It is noted that once the peak ground acceleration is changed, i.e. under different earthquakes, the control performance will also change.

Acknowledgements:

This study is sponsored by the National Science Foundation grants CMMI 0511046 and CMMI 1014958.

References:

Chen, C. and Chen, G. (2004), "Shake Table Tests of a Quarter-Scale Three-Storey Building Model with Piezoelectric Friction Dampers." *Structural Control and Health Monitoring* **11**(4), 239-257.

Dyke, S. J., Spencer Jr, B. F., et al. (1996), "Modeling and Control of Magnetorheological Dampers for Seismic Response Reduction." *SMART MATERIALS AND STRUCTURES* **5**, 565-575.

Evans, A. G., Suo, Z., et al. (2001), "Model for the Robust Mechanical Behavior of Nacre." *Journal of Materials Research* **16**(9), 2475-2484.

Fantner, G. E., Adams, J., et al. (2007), "Nanoscale Ion Mediated Networks in Bone: Osteopontin Can Repeatedly Dissipate Large Amounts of Energy." *Nano Letters* **7**(8), 2491-2498.

Fantner, G. E., Hassenkam, T., et al. (2005), "Sacrificial Bonds and Hidden Length Dissipate Energy as Mineralized Fibrils Separate During Bone Fracture." *Nature Materials* **4**(8), 612-616.

Fantner, G. E., Oroudjev, E., et al. (2006), "Sacrificial Bonds and Hidden Length: Unraveling Molecular Mesostructures in Tough Materials." *Biophysical Journal* **90**(4), 1411-1418.

Fantner, G. E., Rabinovych, O., et al. (2006), "Hierarchical Interconnections in the Nano-Composite Material Bone: Fibrillar Cross-Links Resist Fracture on Several Length Scales." *Composites Science and Technology* **66**(9), 1205-1211.

Fritz, M., Belcher, A. M., et al. (1994), "Flat Pearls from Biofabrication of Organized Composites on Inorganic Substrates." *Nature* **371**(6492), 49-51.

Hansma, P. K., Fantner, G. E., et al. (2005), "Sacrificial Bonds in the Interfibrillar Matrix of Bone." *J Musculoskelet Neuronal Interact* **5**(4), 313-315.

Jackson, A. P., Vincent, J. F. V., et al. (1988), "The Mechanical Design of Nacre." *Proceedings of the Royal Society of London Series B-Biological Sciences* **234**(1277), 415-&.

Kwakernaak, H. and Sivan, R. (1972). Linear Optimal Control Systems, Wiley-Interscience New York.

Schaffer, T. E., IonescuZanetti, C., et al. (1997), "Does Abalone Nacre Form by Heteroepitaxial Nucleation or by Growth through Mineral Bridges?" *Chemistry of Materials* **9**(8), 1731-1740.

Scruggs, J. T. and Iwan, W. D. (2003), "Control of a Civil Structure Using an Electric Machine with Semiactive Capability." *Journal of Structural Engineering* **129**(7), 951-959.

Smith, B. L., Schaffer, T. E., et al. (1999), "Molecular Mechanistic Origin of the Toughness of Natural Adhesives, Fibres and Composites." *Nature* **399**(6738), 761-763.

Spencer Jr, B. F., Dyke, S. J., et al. (1998), "Benchmark Problems in Structural Control: Part 1-Active Mass Driver System." *Earthquake Engrn. Struct. Dyn.* **27**(11), 1127-1139.

Spencer Jr, B. F., Dyke, S. J., et al. (1997), "Phenomenological Model for Magnetorheological Dampers." *Journal of Engineering Mechanics* **123**(3), 230-238.

Thompson, J. B., Kindt, J. H., et al. (2001), "Bone Indentation Recovery Time Correlates with Bond Reforming Time." *Nature* **414**(6865), 773-776.

Thurner, P. J., Erickson, B., et al. (2007), "High-Speed Photography of Compressed Human Trabecular Bone Correlates Whitening to Microscopic Damage." *Engineering Fracture Mechanics* **74**(12), 1928-1941.

Thurner, P. J., Erickson, B., et al. (2006), "High-Speed Photography of the Development of Microdamage in Trabecular Bone During Compression." *Journal of Materials Research* **21**(5), 1093-1100.

Zaremba, C. M., Belcher, A. M., et al. (1996), "Critical Transitions in the Biofabrication of Abalone Shells and Flat Pearls." *Chemistry of Materials* **8**(3), 679-690.

8CUEE CONFERENCE PROCEEDINGS
8th International Conference on Urban Earthquake Engineering
March 7-8, 2011, Tokyo Institute of Technology, Tokyo, Japan

DEVELOPMENT OF SIMPLIFIED DESIGN PROCEDURE FOR STRUCTURES WITH MAGNETO-RHEOLOGICAL (MR) DAMPERS

Yunbyeong Chae[1], Baiping Dong[1], James M. Ricles[2], and Richard Sause[2]

1) Graduate Research Assistant, Dept. of Civil and Environmental Engineering, Lehigh University, PA, USA
2) Professor, Dept. of Civil and Environmental Engineering, Lehigh University, PA, USA
yuc206@lehigh.edu, bad209@lehigh.edu, jmr5@lehigh.edu, rs0c@lehigh.edu

Abstract: Magneto-rheological (MR) dampers are a type of smart damper whose characteristics can be varied under dynamic loading by semi-active controllers. Currently, the application of MR dampers in seismic design is limited due to the non-existence of a performance-based design procedure. In this paper, a simplified design procedure (SDP) is presented for the performance-based design of structures with MR dampers. The SDP utilizes the characteristics of an equivalent linear structural system, where the loss factor and equivalent stiffness of the MR dampers are calculated from quasi-static MR damper models such as the simple frictional model or the Hershel-Bulkley visco-plastic model. The simple frictional MR damper model enables the required MR damper capacity to be approximated that has the structure satisfy performance objectives. Once the required MR damper capacity and properties are determined, the Hershel-Bulkley quasi-static MR damper model is used to more accurately predict the design demand for the structure and the design revised accordingly. The SDP is used to design a 3-story building, where steel moment resisting frames (MRFs) combined with the damped braced frames (DBFs) are selected as the lateral force resisting system for the building. The MRF is designed to satisfy the code strength requirement, and the story drift is controlled by the damped braced frames (DBFs) in which the MR dampers are installed. Statistical response of the nonlinear time history analysis of the structure using OpenSees and a suite of ground motions shows the performance objectives for the 3-story building are satisfied, demonstrating the robustness of the simplified design procedure for structures with MR dampers.

1. INTRODUCTION

It is well-known that supplemental damping devices increase the energy dissipation capacity of structures, reducing the seismic demand on the primary structure (Constantinou et al. 1998; Soong and Dargush 1997). A structural system with supplemental dampers is often represented by an equivalent linear system. Kwan and Billington (2003) derived optimal equations for the equivalent period and damping ratio of SDOF systems with various nonlinear hysteresis loops based on time history analysis and regression analysis. Symans and Constantinou (1998) studied the dynamic behavior of SDOF systems with linear or nonlinear viscous fluid dampers and derived an equation for the equivalent damping ratio of the nonlinear viscous fluid damper. Ramirez et al (2002) proposed a simplified method to estimate displacement, velocity and acceleration for yielding structures with linear or nonlinear viscous dampers. Lin and Chopra (2003) investigated the behavior of SDOF systems with a diagonal brace in series with a nonlinear viscous damper by transforming the system to an equivalent linear Kelvin model.

Fan (1998) investigated the behavior of non-ductile reinforced concrete frame buildings with viscoelastic dampers. He derived an equivalent elastic-viscous model based on the complex stiffness and energy dissipation of the viscoelastic system, and proposed a simplified design procedure for a structure with viscoelastic dampers. Lee et al. (2005 and 2009) applied this method to structures with elastomeric dampers and validated the simplified design procedure by comparing the design demand with the results from nonlinear time history analysis..

In this paper, a systematic procedure for the design of structures with MR dampers, referred to as the *Simplified Design Procedure* (SDP), is developed. The procedure is similar to that developed by Lee et al. (2005 and 2009), but with modifications to account for the characteristics of the MR dampers. A quasi-static MR damper model for determining the loss factor and the effective stiffness of an MR damper is introduced and incorporated into the procedure to calculate the design demand for the structure with MR dampers. The procedure is evaluated by comparing the predicted design demand to the seismic response determined from nonlinear time history analysis.

2. SIMPLIFIED DESIGN PROCEDURE (SDP)

In the SDP developed by Lee et al. (2005 and 2009), the supplemental damper properties are represented by β, which is the ratio of the damper stiffness per story in the

global direction to the lateral load resisting frame story stiffness, k_0, without dampers and braces of the structural system. The structural system with dampers is converted into a linear elastic system characterized by the initial stiffness of the structure, α (the ratio of brace stiffness per story in the global direction to the lateral load resisting frame story stiffness k_0), β, and η. α, β, and η may vary among the stories of the structure. By conducting an elastic-static analysis with the RSA method the design demand for the structure is determined.

Since the loss factor of an MR damper depends on the displacement of the structure, as can be shown below in Equation (8), the SDP for an elastomeric damper developed by Lee et al. (2005, 2009) needs to be modified for structures with MR dampers. The loss factor η is associated with the energy dissipation of the damper over a cycle. For the purpose of determining the energy dissipation over a cycle of displacement the properties of the MR damper are assumed to remain constant. The linearization and energy dissipation of an MR damper are discussed later.

Figure 1 summarizes the SDP for structures with MR dampers. In Step 1, the seismic performance objectives and associated design criteria are established for the design of the structure. In Step 2, the structure is designed without MR dampers in accordance with the design code selected in Step 1 to satisfy the strength requirement for the members in the structure. In Step 3, the MR dampers are incorporated into the design of the structure to satisfy the specified performance objectives. The design demand for the structure is estimated for a range of selected values for α, β, and a constant loss factor $\eta = 4/\pi$ using a *simplified analysis procedure*, discussed later. In the simplified analysis procedure the MR damper behavior is based on the simple frictional MR damper model (Chae 2010). The required MR damper sizes are then selected in Step 4 based on the smallest β value that meets the design criteria and performance objectives in Step 1. Since the simple frictional damper model does not account for the velocity dependent behavior of an MR damper, a more accurate determination of the design demand are determined in Step 5 using a more sophisticated MR damper model (i.e., Hershel-Bulkley model) in the simplified analysis procedure. The design is then revised with final member sizes and the MR damper sizes are selected (location, number, force capacity, etc.). If the performance objectives cannot be met in an economical manner, then the performance objectives and/or structural system design need to be revised as indicated in Figure 1.

3. EQUIVALENT LINEAR SYSTEM FOR AN MR DAMPER

The SDP requires that the structure with the nonlinear MR dampers be linearized. In order to linearize the system for estimating the response of structures with MR dampers, the Hershel-Bulkley quasi-static MR damper model is used. Figure 2 shows the force-velocity and force-displacement relationships for the model where the damper force f is given as

$$f = \text{sign}(\dot{u})\{f_0 + C|\dot{u}|^n\} \tag{1}$$

In Equation (1) u is the damper displacement relative to the initial position of the damper and $\dot{u}$ is the damper velocity. f_0 is the frictional force. C and n are the coefficients of the nonlinear dashpot. Suppose that the MR damper is subjected to a harmonic displacement motion

$$u(t) = u_0 \sin(\omega t) \tag{2}$$

where, u_0 is the amplitude of displacement and ω is the excitation frequency of the damper. The energy dissipated by the damper over one cycle of the harmonic motion is equal to

$$\begin{aligned} E_{MRD} &= \int_0^{\frac{2\pi}{\omega}} f(t)\dot{u}(t)dt \\ &= 4f_0u_0 + 2^{n+2}C\gamma(n)u_0^{1+n}\omega^n \end{aligned} \tag{3}$$

where

$$\gamma(n) = \frac{\Gamma^2\left(1+\frac{n}{2}\right)}{\Gamma(2+n)} \tag{4}$$

In Equation (4), $\Gamma()$ is the gamma function (Soong and Constantinou 1997). In general, diagonal bracing is installed in the building in series with the dampers. Therefore, the energy dissipation of an MR damper needs to be studied considering the stiffness of the diagonal bracing. Figure 3 shows an SDOF system with an MR damper and diagonal bracing. Under the harmonic motion $x = x_0 \sin(\omega t)$ the maximum damper displacement, u_{d0}, and velocity, $\dot{u}_{d0}$, of the MR damper occurs when the displacement x and velocity $\dot{x}$ are a maximum, respectively, where u_{d0} and $\dot{u}_{d0}$ can be calculated as (Chae 2011)

$$u_{d0} = x_0 - f_0/k_{br} \tag{5a}$$
$$\dot{u}_{d0} = \dot{x}_0 = x_0\omega \tag{5b}$$

In Equation (5) k_{br} is the stiffness of the diagonal bracing. Substitution of Equation (5a) into Equation (3) results in the expression for the energy dissipation of the MR damper for a SDOF system

$$E_{MRD} = 4f_0u_{d0} + 2^{n+2}C\gamma(n)u_{d0}^{n+1}\omega^n \tag{6}$$

The strain energy of the MR damper, E_S, is calculated from the equivalent stiffness of the damper and the maximum damper displacement:

$$E_S = \frac{1}{2}k_{eq}u_{d0}^2 \tag{7}$$

where k_{eq} is the equivalent stiffness of the MR damper, defined as $k_{eq} = f_0/u_{d0}$ and based on the secant stiffness from the force-displacement relationship of the Hershel-Bulkley model. The loss factor η of the MR damper by definition is

$$\eta = \frac{1}{2\pi}\frac{E_{MRD}}{E_S} = \frac{4\{f_0 + C\gamma(n)(2u_{d0}\omega)^n\}}{\pi k_{eq} u_{d0}} \quad (8)$$

4. SIMPLIFIED ANALYSIS PROCEDURE

The simplified analysis procedure provides an elastic-static method for calculation of the design demand of an MDOF system with MR dampers. The simplified analysis procedure utilizing the response spectrum analysis (RSA) method is summarized in Figures 4 and 5.

In the simplified analysis procedure, the maximum structural displacements are determined by the well-known equal displacement rule. In the equal displacement rule the maximum displacement of the nonlinear structure, whose lateral stiffness is based on its initial tangent stiffness, is assumed to be equal to that of a linear structure. The equal displacement rule is only applicable to structures that lie in the low-frequency and medium frequency spectral regions (Newmark and Hall 1973).

In order to obtain the equivalent period for an MDOF structure with MR dampers, the combined stiffness of the MR dampers and diagonal bracing needs to be added to the stiffness of the structure. Thus, the global effective stiffness of the MDOF system is given as

$$\mathbf{K_{eff}} = \mathbf{K_0} + \mathbf{K_{brsystem}} \quad (9)$$

where $\mathbf{K_0}$ is the stiffness of the structure without diagonal braces and MR dampers, and $\mathbf{K_{brsystem}}$ is the stiffness associated with the braces and MR dampers. The structure is assumed to have N DOF, thus the dimension of $\mathbf{K_{eff}}$ is $N \times N$. The combined stiffness $\mathrm{K}^i_{\mathrm{brsystem}}$ of the diagonal bracing and MR damper at the *i*-th MR damper location is

$$\mathrm{K}^i_{\mathrm{brsystem}} = \frac{k^i_{br} k^i_{eq}}{k^i_{br} + k^i_{eq}} \quad (10)$$

where k^i_{br} and k^i_{eq} are the horizontal stiffness of the diagonal bracing and the MR damper associated with the i^{th} MR damper, respectively. k^i_{eq} can be calculated utilizing the secant stiffness method as noted above. The individual combined stiffnesses based on Equation (10) are appropriately assembled to form $\mathbf{K_{brsystem}}$. The effective periods and mode shapes of the structure are then obtained by performing an eigenvalue analysis of the structure, considering the seismic mass of the structure.

The equivalent damping ratio ξ_{eq} of an MDOF system is determined using the lateral force energy method proposed by Sause et al. (1994), where

$$\xi_{eq} = \frac{1}{2}\frac{\sum_{i=1}^{L} \eta_i F^i_d u^i_d}{\mathbf{F}^{\mathrm{T}}\mathbf{x_0}} + \xi_{in} \quad (11)$$

In Equation (11) η_i and u^i_d are the loss factor and maximum damper displacement of the i^{th} MR damper, respectively, and L is the number of MR dampers. Since the damper displacement is unique for each MR damper, the loss factor of each MR damper, which is a function of damper displacement, is also unique for each damper. For each damper η_i is obtained from Equation (8). ξ_{in} in Equation (11) is the inherent damping ratio and $\mathbf{x_0}$ is the vector of the displacements of the structure that develop under the lateral force $\mathbf{F}$. The individual damper force F^i_d and the lateral force vector $\mathbf{F}$ are defined as

$$F^i_d = k^i_{eq} u^i_d, \ \mathbf{F} = \mathbf{K_{eff}}\mathbf{x_0} \quad (12)$$

In the simplified analysis procedure using the RSA, the relationships in Equation (12) are substituted into Equation (11), and the inherent damping ξ_{in} and $\mathbf{x_0}$ from each mode are considered, as indicated in Substep 3 in Figure 5.

5. PERFORMANCE-BASED DESIGN OF A 3-STORY BUILDING WITH MR DAMPERS

5.1 Prototype Building Structure

Based on the proposed SDP, a 3-story building with MR dampers is designed. The floor plan and elevation of the prototype structure is shown in Figures 6 and 7, respectively. It consists of a 3-story, 6-bay building and represents a typical office building located in Southern California. Lateral loads are resisted by a four perimeter moment resisting frames (MRFs) and four damped braced frames (DBFs) in the two orthogonal principle directions of the building's floor plan. MR dampers are installed in the DBFs to control the drift of the building, adding supplemental damping to the structure. The DBFs have continuous columns, with pin connections at the beam-to-column connections and at the ends of the diagonal bracing. A rigid diaphragm system is assumed to exist at each floor level and the roof of the building to transfer the floor inertia loads to the MRFs and DBFs. The building has a basement where a point of inflection is assigned at 1/3rd of the height of the column from the column base in the analysis model.

5.2 Performance Objectives

In this design, three different performance objectives for the building are considered:

1) Limit the story drift to 1.5% under the DBE ground motion;
2) Limit the story drift to 3.0% under the MCE ground motion;
3) Design strength of members in the DBF shall not be exceeded by the demand imposed by the DBE ground motion.

The MCE ground motion is represented by a response spectra that has a 2% probability of exceedance in 50 years, and the DBE ground motion is 2/3rd the intensity of the MCE ground motion. (FEMA 2000a). The performance objectives of 1.5% story drift satisfies the life safety performance level under the DBE and the 3% story drift satisfies the collapse prevention level under the MCE. The performance levels are defined in FEMA-356 (2000b). To minimize the damage and repair cost to the DBF structure,

the third performance objective is adopted to have the DBF structure remain elastic under the DBE.

5.3 Performance-Based Design

The prototype building structure is intended to provide the basis for an MRF and DBF with MR dampers which can be constructed in the laboratory for future tests. Due to laboratory constraints, the prototype building structure and resulting MRF and DBF were designed at 0.6-scale. The MRFs are designed to satisfy the strength requirement of the current building seismic code of ICC (2006); the member design criteria is based on the AISC steel design provisions (2005b). The design response spectrum is based on a site in Southern California where the spectral acceleration for the short period, S_S, and for a 1 second period, S_1, are equal to 1.5 and 0.6, respectively. The strength contribution from the DBFs and MR dampers is not considered when the MRFs are designed since, as noted above,+ the DBFs and MR dampers are intended only to control the story drift of the building system. More detailed information on the design of the MRFs and gravity frames can be found in Chae (2011).

Once the MRFs and gravity frames are designed for strength, the required capacity of the MR dampers to control the drift is determined. The DBF members are then designed by imposing the displacement and damper force demands on the DBF, which are obtained from the simplified analysis procedure and the required MR damper capacity. The maximum displacements and the maximum MR damper forces are assumed to occur concurrently in the SDP. The design of the 3-story building is revised until the performance objectives and strength requirements are satisfied.

Large-scale MR dampers were used for the study which can generate a 200kN damper force at a velocity of 0.1m/sec. (Chae et al. 2010). ,The parameters for the Hershel-Bulkley model associated with the large-scale MR damper are: $f_0 = 138.5$kN, $C = 161.8$kNsec/m, and $n = 0.46$.

The optimal damper location which satisfies the performance objectives is determined by using the simplified analysis procedure, resulting in one large-scale MR damper in the 2nd and 3rd stories, respectively, with $\alpha = 10$ and $\beta = 0.3$ (Chae 2011). Tables 1 and 2 summarize the member sizes for the MRFs, gravity frames, and DBFs. Table 3 summarizes the calculated design demand associated with maximum story drift and maximum damper forces. As can be observed, the design demand for the story drift under the DBE and MCE are less than 1.5% and 3.0%, respectively, in order to satisfy the performance objectives. Table 4 shows the DBE demand-to-capacity ratios for the DBF members. The demand-to-capacity ratio for each member is less than 1.0, which means the members are designed to remain elastic under the DBE. The design of the braces was controlled by stiffness, $\alpha = 10$, and not strength, hence, the demand-to-capacity ratios for the braces are small in Table 4.

6. ASSESSMENT OF SIMPLIFIED DESIGN PROCEDURE

The SDP is assessed by comparing the design demand from the SDP with results from a series of nonlinear time history analyses (NTHA) of the 3-story building using the nonlinear finite element program OpenSees (2009).

6.1 OpenSees Model

Symmetry in the floor plan and ground motions along only one principal axis of the building were considered in the analysis. Hence, only one-quarter of the building was modeled consisting of one MRF, one DBF, and the gravity frames that are within the tributary area of the MRF and DBF. The OpenSees model is shown in Figure 8. The beams and columns of the MRF structure are modeled with a nonlinear distributed plasticity force-based beam-column element with five fiber sections along the element length. The cross section of the element is discretized into 18 fibers, including 12 fibers for the web and 3 fibers each for the top and bottom flanges. Each fiber is modeled with a bilinear stress-strain relationship with a post-yielding stiffness that is 0.01 times the elastic stiffness. The beam-column joints in the MRF are modeled using a panel zone element, where shear and symmetric column bending deformations are considered (Seo et al. 2009). The doubler plates in the panel zones of the MRF are included in the model. The nonlinear force-based fiber element is also used to model the columns of the DBF. The beams and braces of the DBF are modeled using linear elastic truss elements. The gravity frames are idealized using the concept of a lean-on column, where an elastic beam-column element with geometric stiffness is used to model the lean-on column. The section properties of the lean-on column are obtained by taking the sum of the section properties of each gravity column within the tributary area (i.e., one quarter of the floor plan) of the MRF and the DBF. The MR dampers are modeled using the MNS MR damper model implemented into OpenSees by Chae et al. (2010). The MR damper is assumed to be located between the top of the brace and the adjacent beam-column joint, as shown in Figure 8. The results reported in this paper are for MR dampers that are passive controlled with a constant current input of 2.5A. Studies with the MR dampers in semi-active control mode are presented in Chae (2011).

The gravity loads from the tributary gravity frames are applied to the lean-on column to account for the P-Δ effect of the building. To model the effect of the rigid floor diaphragm the top node of the panel zone element in the MRF and the beam-column joint in the DBF are horizontally constrained to the node of the lean-on column at each floor level, while the vertical and rotational degrees of freedom of these nodes are unconstrained.

Rayleigh damping is used to model the inherent damping of the building with a 5% damping ratio for the 1st and 2nd modes.

6.2 Comparison of Response

An ensemble of 44 ground motions listed in FEMA P695 (ATC 2009) is scaled to the DBE and MCE levels using the procedure by Somerville et al. (1997) for the NTHA.

A summary of the median and standard deviation of maximum story drift and residual story drift from the NTHA is given in Table 5. Figures 9 and 10 compare the calculated design demand for drift from the SDP with the median values for maximum story drift from the NTHA under the DBE and MCE ground motions. The story drift design demand calculated by the SDP shows good agreement in Figure 9 with the median maximum story drifts from the NTHA. The calculated design demand for story drift from the SDP also shows good agreement with the median values from the NTHA under the MCE, see Figure 10. Figures 9 and 10 show that the median values of the maximum story drift from the NTHA satisfies the performance objectives of 1.5% and 3.0% under the DBE and MCE levels, respectively. The residual story drift of the building after the DBE has a maximum median value and standard deviation of 0.22% and 0.27%, respectively, which occurred in the 3rd story as summarized in Table 5. The residual drift is small.

Table 6 compares the design demand for maximum MR damper forces calculated by the SDP with the median maximum MR damper forces from the NTHA. The MR damper force design demands from the SDP are slightly smaller than the median NTHA results for the DBE. However, the differences between the SDP and the NTHA are only 3.9% and 3.3% for the MR dampers in the 2nd and 3rd stories, respectively. For the MCE, the differences between the median NTHA results and the SDP for the MR damper forces in the 2nd and 3rd stories are 1.6% and 0.5% respectively. The design demand calculated by the SDP shows reasonably good agreement with the median results from the NTHA for the maximum MR damper forces.

The linear elastic behavior of the DBF columns under the DBE is confirmed by checking the plastic rotation developed in the columns. Summarized in Table 7 are the median and standard deviation of the DBF maximum magnitude of column plastic rotation from the NTHA for the DBE ground motions. In the first story, some plastic rotation developed at the base of the column under the DBE. However, the median is zero and the standard deviation is 0.0005 radians for the maximum plastic rotation. The median and standard deviation of the maximum plastic rotation in the 2nd and 3rd stories columns are zero under the DBE ground motion, as given in Table 7, which indicates linear elastic behavior of the columns at these stories. The median of the residual plastic rotation at the base of the column is zero and the standard deviation for the residual plastic rotation is 0.0004 radians.

The building's response under the DBE and MCE determined by the NTHA appears to have met the performance objectives for the structure. Moreover, the performance under the DBE meets the immediate occupancy level (FEMA 2000b), where the maximum residual drift is practically equal to the allowable construction tolerance of 0.2% for steel structures (AISC 2005a), with minimal damage occurring in the building (the median of the maximum plastic rotations in the beams and columns of the MRF are 0.37% and 0.07% radians, respectively, with the MRF having the same residual drift statistics as the DBF due to the rigid diaphragm (Chae 2011)).

7. CONCLUSIONS

A simplified design procedure was developed to enable the performance-based design of structures with MR dampers. The design procedure utilizes a systematic approach to calculate the design demand of structures with MR dampers. The simplified analysis procedure enables the design demand to be determined without performing a nonlinear time history analysis by linearizing the structure and utilizing the response spectrum analysis method.

To linear the nonlinear MR dampers, the simplified analysis procedure is based on an equivalent linear MR damper model using the Hershel-Bulkley quasi-static MR damper model. The energy dissipated by the MR damper over one cycle of a harmonic motion is calculated and the equivalent stiffness determined based on the secant stiffness method from the damper force-displacement relationship. The loss factor of the MR damper is obtained from the energy dissipated by the damper and the strain energy calculated from the equivalent stiffness of the damper. Both the equivalent stiffness and loss factor of the MR damper are dependent on the maximum displacement of the damper. A 3-story building was designed using the SDP, where three performance objectives associated with two seismic hazard levels were selected. The SDP was assessed by comparing the design demand calculated by the SDP with the response determined from nonlinear time history analyses. The MNS MR damper model was implemented into the OpenSees computer program and statistics for the response to DBE and MCE ground motions were obtained from a series of nonlinear time history analyses using 44 different ground motions. The performance of the building from the nonlinear time history analysis indicated that building design satisfies the three performance objectives. The design demand associated with story drift and maximum MR damper forces from the SDP showed good agreement with the median values from the nonlinear time history analyses, confirming the robustness of the SDP.

Acknowledgements:

This paper is based upon work supported by grants from the Pennsylvania Department of Community and Economic Development through the Pennsylvania Infrastructure Technology Alliance, and by the National Science Foundation under Award No. CMMI-1011534, within the George E. Brown, Jr. Network for Earthquake Engineering Simulation Research (NEESR) program, Award No. CMS-0612661, and Award No. CMS-0402490 NEES Consortium Operation.

References:

AISC (2005a), *Code of Standard Practice for Steel Buildings and Bridges*, American Institute of Steel Construction,.

AISC (2005b), *Seismic Provisions for Structural Steel Buildings*, American Institute of Steel Construction, Chicago, IL.

Applied Technology Council (2009), *Quantification of Building Seismic Performance Factors*, ATC-63 Project Report (FEMA P695), Redwood City, CA.

Chae, Y. (2011), "Seismic Hazard Mitigation of Building Structures Using Magneto-Rheological Dampers," *Ph.D. Dissertation*, Lehigh University, PA.
Chae, Y., Ricles, J.M., and Sause, R. (2010), "Development of a Large-Scale MR Damper Model for Seismic Hazard Mitigation Assessment of Structures," *9th US National and 10th Canadian Conference on Earthquake Engineering*, Toronto, Canada.
Constantinou, M. C., Soong, T. T., and Dargush, G. F., (1998) *Passive Energy Dissipation Systems for Structural Design and Retrofit*, Monograph Series, MCEER, State Univ. of New York at Buffalo, Buffalo, N.Y.
Fan, C. P. (1998), "Seismic Analysis, Behavior, and Retrofit of Non-ductile Reinforced Concrete Frame Buildings with Viscoelastic Dampers," *Ph.D. Dissertation*, Lehigh University, Bethlehem, PA.
Federal Emergency Management Agency (2000a), *Recommended Seismic Design Criteria for New Steel Moment-Frame Buildings*, Report No. FEMA-350, Washington, DC.
Federal Emergency Management Agency (2000b), *Prestandard and Commentary for the Seismic Rehabilitation of Buildings*, Report No. FEMA-356, Washington, DC.
International Code Council (2006),. *International Building Code*, Falls Church, VA
Kwan, W. P. and Billington, S. L. (2003), "Influence of Hysteretic Behavior on Equivalent Period and Damping of Structural Systems," *ASCE Jrnl of Structural Eng.*, **129**(5), 576-585.
Lee, K.-S., Fan, C.-P., Sause, R., and Ricles, J. (2005), "Simplified Design Procedure for Frame Buildings with Viscoelastic and Elastomeric Structural Dampers," *Earthquake Eng. Struct. Dyn.*, **34**, 1271–1284.
Lee, K.-S., Ricles, J., and Sause, R. (2009), "Performance-Based Seismic Design of Steel MRFs with Elastomeric Dampers," *Journal of Structural Engineering*, **135**(5), 489-498.
Lin, W.H. and Chopra, A.K. (2003), "Earthquake Response of Elastic Single-Degree-of-Freedom Systems with Nonlinear Viscoelastic Dampers," *ASCE Journal of Engineering Mechanics*, **129**(6), 597-606.
Newmark, N.M. and Hall, W.J. (1973), "Seismic Design Criteria for Nuclear Reactor Facilities," *Report No. 46, Building Practices for Disaster Mitigation, National Bureau of Standards, U.S. Department of Commerce*, 209-236.
OpenSees (2009), *Open System for Earthquake Engineering Simulation*, Pacific Earthquake Engineering Research Center, University of California, Berkeley.
Ramirez, O.M., Constantinou, M.C., Gomez, J.D., and Whittaker, A.S. (2002), "Evaluation of Simplified Methods of Analysis of Yielding Structures with Damping Systems," *Earthquake Spectra*, **18**(3), 501-530.
Seo, C.Y., Lin, Y.C., Sause, R, and Ricles, J.M. (2009), "Development of Analytical Models for 0.6 Scale Self-Centering MRF with Beam Web Friction Devices," *6th International Conference for Steel Structures in Seismic Area (STESSA)*, Philadelphia.
Somerville P, Smith N, Punyamurthula S, and Sun J. (1997), "Development of Ground Motion Time Histories for Phase 2 of the FEMA/SAC Steel Project," *Report No. SAC/BD-97/04, SAC Joint Venture*, Sacramento, CA.
Soong, T.T. and Dargush, G.F. (1997), *Passive Energy Dissipation Systems in Structural Engineering*, Wiley, West Sussex.
Symans, M.D. and Constantinou, M.C. (1998), "Passive and Fluid Viscous Damping Systems for Seismic Energy Dissipation," *ISET Journal of Earthquake Technology*, **35**(4), 185-206.

Table 1 Member sizes for MRFs and gravity frames

Story (or Floor Level)	MRFs		Gravity Frames	
	Column	Beam	Column	Beam
1	W8X67	W18X46	W8X48	W10X30
2	W8X67	W14X38	W8X48	W10X30
3	W8X67	W10X17	W8X48	W10X30

Table 2 Member sizes for DBFs

Story (or Floor level)	Column	Beam	Diagonal bracing
1	W10X33	W10X30	-
2	W10X33	W10X30	W6X20
3	W10X33	W10X30	W6X20

Table 3 Calculated design demand associated with maximum story drift and maximum damper force from SDP

Story	Maximum story drift (%)		Maximum damper force (kN)	
	DBE	MCE	DBE	MCE
1	1.18	1.91	-	-
2	1.35	2.32	222.9	244.4
3	1.41	2.57	233.6	261.6

Table 4 Demand-to-capacity ratio for DBF frames, DBE

Story (or Floor level)	Column (W10X33)	Beam (W10X30)	Brace (W6X20)
1	0.955	0.521	-
2	0.303	0.576	0.270
3	0.079	0.354	0.283

Table 5 Median and standard deviation of maximum and residual story drift from nonlinear time history analysis

Story	DBE level		MCE level	
	Max story drift (%)	Residual drift (%)	Max story drift (%)	Residual drift (%)
1	1.18 (0.35)*	0.11 (0.21)	1.86 (0.85)	0.42 (0.62)
2	1.35 (0.36)	0.17 (0.26)	2.10 (0.85)	0.57 (0.66)
3	1.46 (0.33)	0.22 (0.27)	2.32 (0.84)	0.63 (0.69)

* Value in () indicates standard deviation response

Table 6 Comparison of maximum damper forces

Story	DBE level		MCE level	
	SDP	NTHA	SDP	NTHA
1	-	-	-	-
2	222.9	231.9 (6.4)*	244.4	248.4 (7.3)
3	233.6	241.5 (8.3)	261.6	260.2 (9.4)

* Value in () indicates standard deviation response

Table 7 Median and standard deviation of DBF maximum magnitude of column plastic rotation from nonlinear time history analysis, DBE ground motions

Story	Location along column	Max plastic rotation (rad %)	Residual plastic rotation (rad %)
1	bottom	0.00 (0.05)*	0.00 (0.04)
	top	0.00 (0.00)	0.00 (0.00)
2	bottom	0.00 (0.00)	0.00 (0.00)
	top	0.00 (0.00)	0.00 (0.00)
3	bottom	0.00 (0.00)	0.00 (0.00)
	top	0.00 (0.00)	0.00 (0.00)

* Value in () indicates standard deviation response

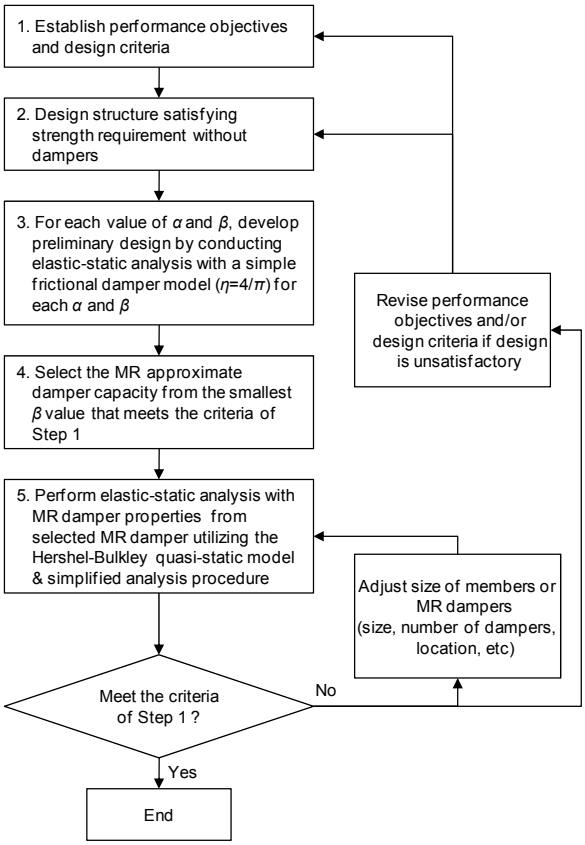


Figure 1 Generalized simplified design procedure (SDP) for structures with MR dampers

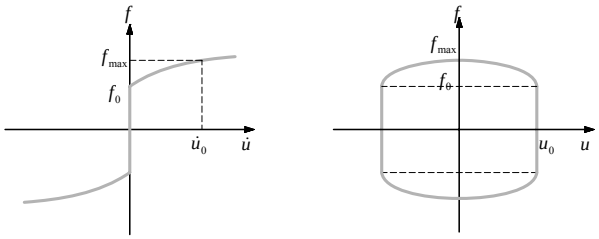
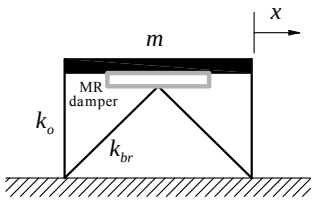
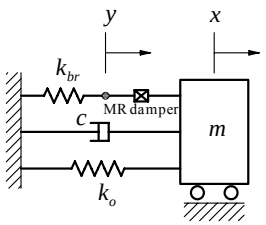


Figure 2 Hershel-Bulkley visco-plasticity MR damper model: (a) force-velocity relationship; (b) force-displacement relationship



(a)



(b)

Figure 3 SDOF system: (a) schematic of equivalent SDOF system with MR damper and brace; (b) mechanical model

Given:

- MR damper properties: $f_0^i,\ C_i,\ n_i$ (i: index for MR damper location)
- Structural properties: $\mathbf{M},\ \mathbf{K_0},\ k_{br}^i,\ \xi_{in}^j$ (inherent damping ratio of the j-th mode)

Step 1. Assume $\mathbf{x_0}$ and set $\omega_{eff}^1 = \omega_n^1$ (fundamental frequency of structure without MR dampers)

Step 2. Determine maximum damper displacements

$$u_{d0}^i = u_0^i - f_0^i/k_{br}^i$$

u_0^i: maximum deformation of damper and bracing of the i^{th} MR damper

Step 3. Calculate equivalent stiffness of each MR damper

$$k_{eq}^i = f_0^i/u_{d0}^i$$

Step 4. Determine $\mathrm{K}_{\mathrm{brsystem}}^i = \frac{k_{br}^i k_{eq}^i}{k_{br}^i + k_{eq}^i}$ for each MR damper and update $\mathbf{K_{eff}}$

Step 5. Update modal frequency ω_{eff}^j and modal vector $\boldsymbol{\phi}_j$ $(j = 1, \dots, N)$

ω_{eff}^j, $\boldsymbol{\phi}_j$ ← eig($\mathbf{K_{eff}}, \mathbf{M}$)

where $\mathbf{M}$ is the mass matrix of the structure

Step 6. Calculate loss factor of each MR damper

$$\eta_i = \frac{4\left\{f_0^i + C_i\gamma(n_i)\left(2u_{d0}^i\omega_{eff}^1\right)^{n_i}\right\}}{\pi k_{eq}^i u_{d0}^i}$$

where ω_{eff}^1 is the fundamental modal frequency

Step 7. Perform modal analysis described in Figure 5

Step 8. Apply the modal combination rule (e.g., SRSS or CQC) to get the final displacement $\mathbf{x_0}$ and velocity of each MR damper $\dot{u}_{d0}^i$

$\mathbf{x_0}$ = function of ($\mathbf{x_0^1}, \dots, \mathbf{x_0^N}$),

$\dot{u}_{d0}^i$ = function of ($\dot{u}_{d0}^{i1}, \dots, \dot{u}_{d0}^{iN}$)

Step 9. Repeat **Step 2** ~ **Step 8** until $\mathbf{x_0}$ convergence is achieved.

Step 10. Calculate maximum damper force for each MR damper

$$f_{max}^i = f_0 + C\left(\dot{u}_{d0}^i\right)^n$$

Figure 4 Simplified analysis procedure used to design MDOF structures with passive MR dampers utilizing response spectrum analysis (RSA) method

Step 7. For j=1 to N^{th} mode

Substep 1. Assume modal displacement vector $\mathbf{x_0^j}$

Substep 2. Determine maximum displacement for each damper u_{d0}^{ij}

$u_{d0}^{ij} = u_0^{ij} - f_0^i/k_{br}^i$

u_0^{ij}: maximum deformation of damper and bracing at the i^{th} MR damper in mode j

Substep 3. Calculate equivalent modal damping ratio

$$\xi_{eq}^j = \frac{1}{2}\frac{\sum_{i=1}^{L}\eta_i k_{eq}^i (u_{d0}^{ij})^2}{\mathbf{x_0^{jT}K_{eff}x_0^j}} + \xi_{in}^j$$

Substep 4. Find maximum modal displacement (y_0^j) from response spectrum

$y_0^j = S_d(T_{eff}^j, \xi_{eq}^j)$ where $T_{eff}^j = 2\pi/\omega_{eff}^j$

Substep 5. Update modal displacement vector $\mathbf{x_0^j}$

$\mathbf{x_0^j} = \Gamma_j \boldsymbol{\phi}_j y_0^j$

$\boldsymbol{\phi}_j$: mode vector; $\Gamma_j = \boldsymbol{\phi}_j^T\mathbf{M1}/\mathrm{M_j}$; $\mathbf{1}$: unit vector; $\mathrm{M_j}$: modal mass ($=\boldsymbol{\phi}_j^T\mathbf{M}\boldsymbol{\phi}_j$)

Substep 6. Repeat Substep 2 ~ 5 until convergence in $\mathbf{x}_0^j$ is achieved

Substep 7. Calculate maximum velocity $\dot{\mathrm{u}}_{\mathrm{d0}}^{\mathrm{ij}}$ for each MR damper, where for the i^{th} MR damper

$\dot{u}_{d0}^{ij} = u_0^{ij}\omega_{eff}^j$

Figure 5 Modal analysis method for the simplified analysis procedure utilizing response spectrum analysis (RSA) method

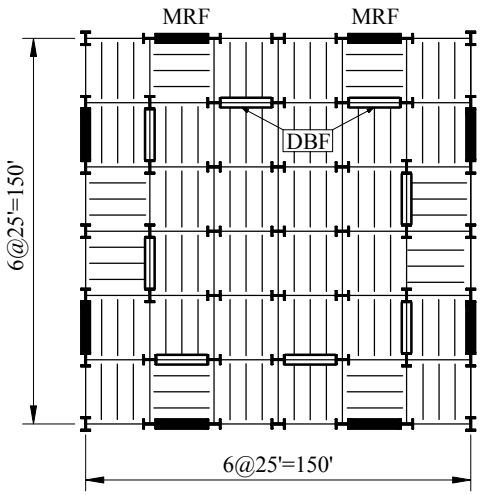


Figure 6 Floor plan of prototype building

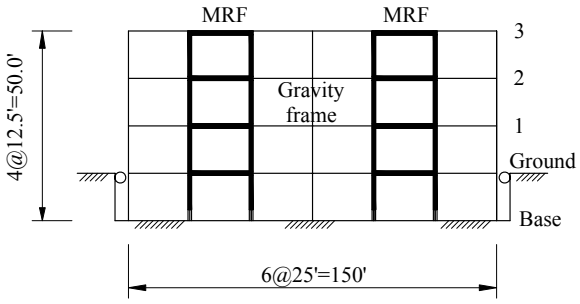


Figure 7 Elevation of prototype building

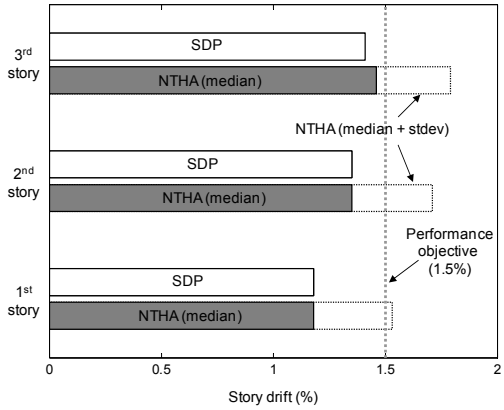


Figure 9 Comparison of story drift between SDP and NTHA, DBE ground motions

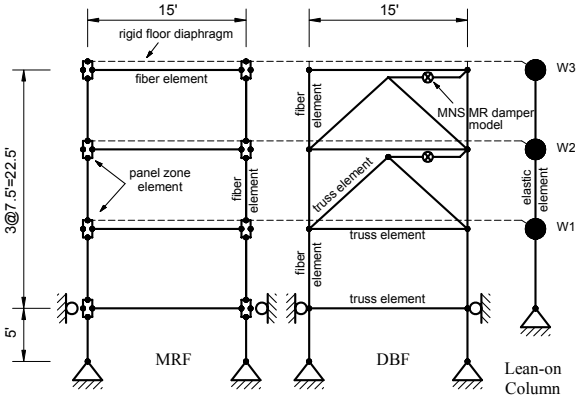


Figure 8 OpenSees model for 0.6-scale building

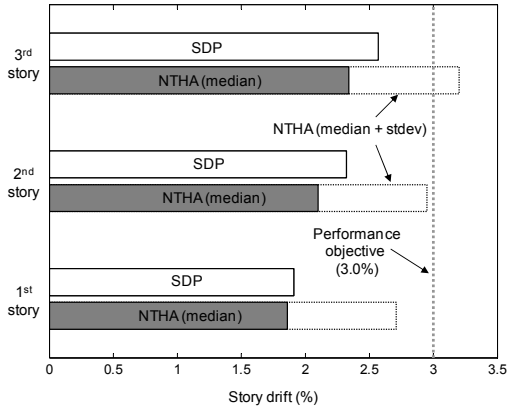


Figure 10 Comparison of story drift between SDP and NTHA, MCE ground motions

8CUEE CONFERENCE PROCEEDINGS
8th International Conference on Urban Earthquake Engineering
March 7-8, 2011, Tokyo Institute of Technology, Tokyo, Japan

SEISMIC INSTRUMENTATION OF BUILDINGS BY THE CALIFORNIA STRONG MOTION INSTRUMENTATION PROGRAM

Moh-jiann Huang and Anthony F. Shakal

California Geological Survey, Department of Conservation, Sacramento, California, U.S.A.
moh.huang@conservation.ca.gov, tony.shakal@conservation.ca.gov

Abstract: During the last 35 years the California Strong Motion Instrumentation Program (CSMIP) in the California Geological Survey has instrumented over 220 buildings, typically installing 12 to 32 sensors in each building. The primary objectives of the CSMIP building instrumentation are to obtain strong earthquake shaking data for improving seismic design codes and engineering design practices, and for post-earthquake evaluations of existing buildings. The instrumented buildings include steel, concrete, masonry and wood structures. Building heights range from one to 58 stories. Buildings with base isolators or other energy dissipation devices have also been instrumented.

CSMIP has obtained strong-motion earthquake records with building base motions larger than 0.1g from more than 80 instrumented buildings. Several of these buildings were damaged during earthquakes. These building records are available at the Center for Engineering Strong Motion Data (http://www.strongmotioncenter.org) for analyses of building response by researchers. Building records from new earthquakes are routinely processed and added to the Center. This paper presents several aspects of building instrumentation including strategies and criteria for the selection of buildings, development of sensor locations and instrumentation schemes, instrumentation installation and maintenance, data dissemination and utilization, and other factors considered by CSMIP in building instrumentation in California.

1. INTRODUCTION

The California Strong Motion Instrumentation Program (CSMIP) was established following the destructive 1971 San Fernando earthquake to increase data on strong earthquake shaking. The program installs and maintains strong-motion instruments in representative structures and geological environments throughout California. Strong-motion data recovered from the instruments are processed by CSMIP and made available to engineers and seismologists involved in designing for earthquake shaking and assessing seismic hazards. In addition, CSMIP funds data interpretation projects to facilitate utilization of strong-motion data in improving post-earthquake response and seismic design codes and practices.

Since the inception of the program over 1150 stations of various types have been instrumented, including 810 ground-response stations, 220 buildings, and 120 lifeline structures (bridges, dams and other structures). Locations of CSMIP stations are shown in Figure 1. Ground-response sites and structures are selected for instrumentation on the basis of recommendations of the Strong Motion Instrumentation Advisory Committee (SMIAC), an advisory committee that is part of the California Seismic Safety Commission. The Committee is made up of leading engineers and seismologists from universities, government, and private industry. The program funding is primarily provided through an assessment on construction costs for building permits issued by cities and counties in California (Shakal and Huang, 1989).

In 1989, the California Office of Statewide Health Planning and Development (OSHPD), which has responsibility for approving hospital design in California since the 1971 San Fernando earthquake, initiated a program providing funding for instrumentation of hospitals by CSMIP. In addition, base-isolated hospital buildings are required by OSHPD to be instrumented by the owner and maintained by CSMIP. The Instrumentation Committee of the Hospital Building Safety Board recommends the hospital buildings for instrumentation. A total of 48 hospital buildings have been instrumented and are now part of the CSMIP network.

Significant earthquakes, including the 1979 Imperial Valley, 1984 Morgan Hill, 1989 Loma Prieta, 1992 Landers, 1994 Northridge and 1999 Hector Mines earthquakes, have been recorded. Stations installed in the last few years include modern digital instruments and utilize a communication system that can transmit the recorded data to a central facility in Sacramento within a few minutes after the shaking occurs where the data are automatically processed (Shakal et al., 1995). The results are then disseminated rapidly to the users via the Internet at the Center for Engineering Strong Motion Data (Haddadi, et al., 2008).

CSMIP funds data interpretation projects to facilitate utilization of strong-motion data in improving

post-earthquake response, seismic design codes and practices. Twenty seminars have been held to disseminate research results to earthquake engineers and seismologists.

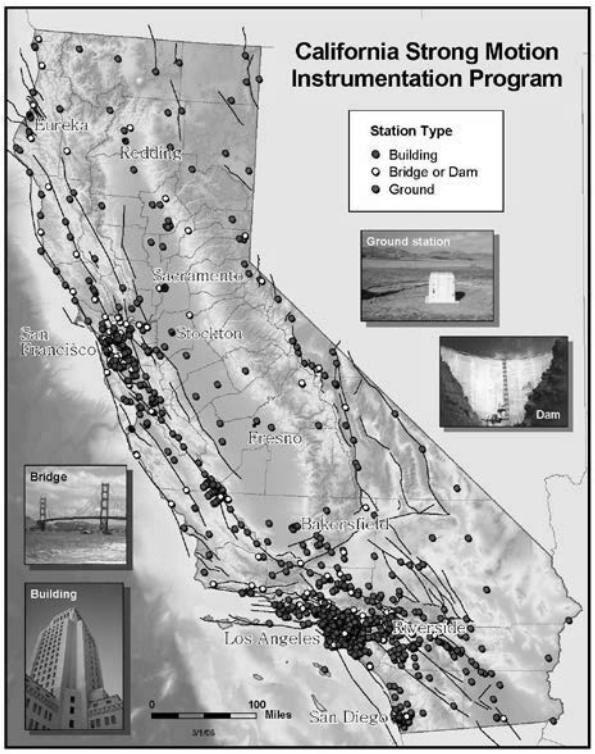


Figure 1. Locations of the California Strong Motion Instrumentation Program (CSMIP) stations in California.

2. CSMIP BUILDING INSTRUMENTATION

2.1 Building Selection Criteria

In 1985, the Buildings Subcommittee of the Strong Motion Instrumentation Advisory Committee (SMIAC) developed a long-term plan and established selection criteria for CSMIP building instrumentation (Shakal, et al., 2001). More than 200 buildings in California have been instrumented by CSMIP and these buildings have been selected for instrumentation based on these criteria. The primary goals of CSMIP building instrumentation are to obtain data to improve engineering design practices and to assess and mitigate the hazards posed by existing buildings. The ultimate goal is to save lives and property through the design of safer structures and the mitigation of seismic hazards posed by existing buildings. As shown in Figure 1, most of CSMIP-instrumented buildings are located in areas where significant ground shaking is likely to occur, one of the criteria for selection.

There are many thousands of buildings in California, and it is impossible to instrument all the buildings. In the building selection criteria, buildings in California were categorized into 30 representative groups by the construction materials (steel, concrete, masonry and wood) and the primary lateral force resisting systems (frames, shear walls and base isolation). These 30 groups are shown in Table 1. Each group is divided into several representative types according to distribution of the lateral force resisting elements and the vulnerability of each structural system. There are a total of 133 representative building types in the 30 groups. Representative buildings of all types are to be instrumented. It is planned that a total of 400 buildings will eventually be instrumented by CSMIP.

The long-term objective of CSMIP building instrumentation is to record significant structural response data in each of the representative building types. Strong-motion records from a specific building will be analyzed not only to learn about that specific building, but most importantly to study the behavior of the class of buildings of which the specific building has been selected as a typical member. It is expected that through study of the behavior of specific buildings of a class, representative lessons learned can be applied to all buildings of that class.

Table 1. Building Groups for CSMIP Instrumentation

Group No.	Building Type - Structural System [Height]	Total No. Needed	Instrumented as of Dec 2010
1	Unreinforced Masonry Bearing Wall [M]	6	0
2	Unreinforced Masonry Bearing Wall [L]	9	2
3	Unreinforced Masonry with Load Bearing Frame [M]	6	2
4	Unreinforced Masonry with Load Bearing Frame [L]	9	1
5	Unreinforced Masonry Bearing Wall [H]	6	0
6	Unreinforced Masonry with Load Bearing Frame [H]	6	2
7	Non-ductile Concrete Moment Frame [L]	9	1
8	Concrete Tilt-up [L]	12	7
9	Reinforced Masonry Wall w/o Moment Frame [M]	9	2
10	Concrete Shear Wall w/o Moment Frame [M]	12	6
11	Reinforced Masonry Shear Wall w/o Moment Frame[L]	15	8
12	Concrete Shear Wall w/o Moment Frame [L]	12	6
13	Non-ductile Concrete Moment Frame [M]	3	1
14	Concrete Shear Wall & Moment Frame [H]	24	8
15	Steel Braced Frame [M]	12	7
16	Precast Concrete (Not Tilt-up) [H]	6	3
17	Precast Concrete (Not Tilt-up) [M]	6	2
18	Concrete Shear Wall w/o Moment Frame [H]	3	1
19	Non-ductile Concrete Moment Frame [H]	3	2
20	Reinforced Masonry Shear Wall w/o Moment Frame[H]	6	3
21	Precast RC (Not Tilt-up) [L]	6	0
22	Braced Steel Frame [H]	21	11
23	RM Shear Wall & Moment Frame [H]	3	0
24	Ductile Concrete Moment Frame [H]	3	1
25	Moment Resisting Perimeter Steel Frame [H]	9	9
26	Wood Frame [L]	6	7
27	Base Isolated [L,M,H]	9	11
28	OSHPD Hospitals		48
29	Retrofitted		20
30	All Other Building Types	169	49
	Total:	400	220

[L] = Low Rise (1 to 3 stories); [M] = Medium Rise (4 to 7 stories); [H] = High Rise (8 or more stories)

2.2 Building Instrumentation Objectives

Instrumentation of a building involves the installation of small sensors (accelerometers in most cases), distributed throughout the structure, all connected to one or several central recorders, generally by low-voltage electrical cabling. Optimal locations for installing sensors in a building are developed by CSMIP engineering staff by studying lateral force resisting systems from the building design plans. Sensors are installed at key structural members so the important modes of vibration will be recorded and specific measurement objectives can be achieved. The sensor locations are reviewed by members of the SMIAC Buildings Subcommittee before the sensors are installed by CSMIP

technical staff. Procedures are implemented and followed to ensure the quality control in field installations of the instrumentation system in the building (Shakal and Petersen, 2001).

CSMIP instrumentation of buildings always includes installation of sensors at the base and the roof of the building. The instrumentation plan includes as many intermediate levels as appropriate for a particular building and a reference free-field site if possible. A typical instrumentation scheme is illustrated in Figure 2, and includes 10 to 30 sensors distributed on 3 or more levels of the building (Huang and Shakal, 2001 & 2002).

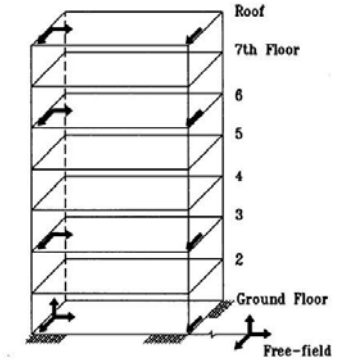


Figure 2. Sensor locations in a typical building instrumented by CSMIP.

The number of intermediate levels instrumented depends on the building height and configuration:

(a) For buildings up to three stories in height, each level is usually instrumented in order to calculate inter-story drift at each story from the records. An example, shown in Figure 3, is a 3-story steel building instrumented with 15 sensors in the building and 3 sensors at a reference free-field site in the parking lot.

(b) For mid-rise buildings, from four to seven stories, two intermediate levels are usually instrumented;

(c) For high-rise buildings, eight stories or more, at least two or three intermediate levels are instrumented, and additional instrument may be added at levels where there is a discontinuity in stiffness. An example of a 52-story building is shown in Figure 4.

As shown in Figure 2, torsional motion of the building base is measured and the instrumentation scheme provides information on soil-structure-interaction. However, a free-field station is not always possible in a metropolitan area where a lot of buildings surround the instrumented building. For concrete shear wall or steel braced frame buildings, vertical sensors can be added to measure rocking motion of the shear wall or braced frame. For a building with flexible diaphragms, such as tilt-up buildings, a sensor is added at the middle of a selected floor to measure diaphragm motion.

In general, the number of sensors installed in a building depends on the budget, instrumentation objectives and complexity of the structural system. Building instrumentation objectives generally include measurements of

(1) input ground motion,
(2) building base motion,
(3) lateral floor motion,
(4) torsional floor motion,
(5) floor or wall diaphragm motion,
(6) shear wall/braced frame rocking motion, and
(7) relative displacement/deformation of special structural members such as isolators, dampers or unbonded braces.

Other information such as building periods, damping ratios, base shears and inter-story drifts can generally be computed or derived from these measurements.

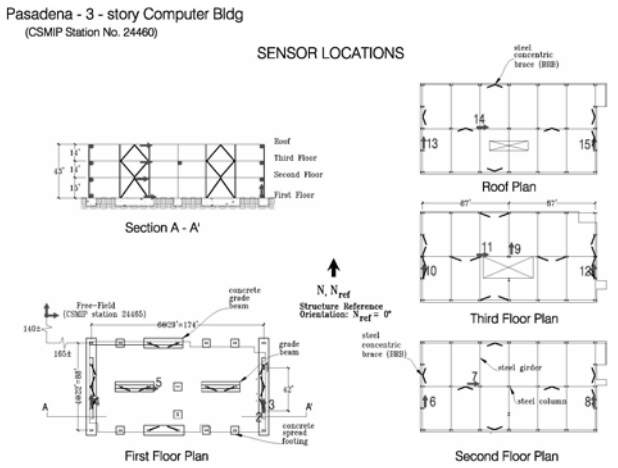


Figure 3. Locations of 15 sensors in a 3-story building in Pasadena and 3 sensors at a reference free-field site in the parking lot.

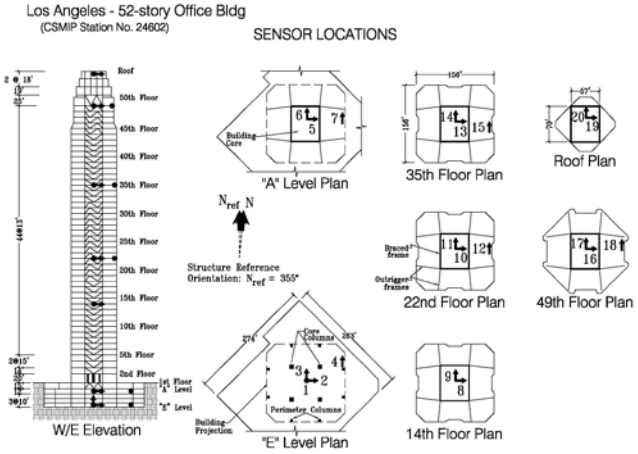


Figure 4. Locations of 20 sensors installed in a 52-story office building in downtown Los Angeles.

2.3 Building Record Processing

Strong motion records from a building include accelerations measured by individual accelerometers installed at various locations in the building. The data can be recorded by one or several recorders. The acceleration record from each sensor will have different amplitudes and frequencies. The record from each sensor may have a unique character or problem, and a different noise spectrum.

CSMIP routinely processes building records to compute velocities, displacements and response spectra by using the same procedure used for processing ground motion records (Shakal, et al., 2004). The records are processed uniformly for all channels despite the fact that each record has different a signal-to-noise ratio at long periods (Huang, 2004). If the record from a particular sensor has a unique problem, it is examined separately and a special procedure may be used to process the record.

CSMIP has processed building records using the following practices:

(1) Records from all the sensors in the building are processed with the same usable data bandwidth, i.e., same filter corners.

(2) The free-field record is processed using the same usable data bandwidth as the building records. The free-field data are distributed with the building data. However, it may be processed with a wider bandwidth for ground motion study purposes.

(3) The filter corners are chosen based on the horizontal sensor records rather than the vertical. Vertical records have a lower signal-to-noise ratio at long periods. Also, most CSMIP buildings have only one vertical sensor at the base of the building.

The fundamental period of a building depends on the lateral force resisting system and distribution of the resisting structural elements. It can be derived from previous earthquake records and ambient vibration data, or estimated from a rule-of-thumb formula, T=0.1N, where N is the number of stories. In general, a moment frame building would have a longer period, and a shear wall or braced-frame building would have a shorter period. In processing a building record, one has to avoid filtering out the motion of the building fundamental period. For example, the 52-story building in Los Angeles of Figure 4 has a fundamental period of about 6 seconds in each direction. The records from the 1994 Northridge earthquake, shown in Figure 5, were filtered at about 10 seconds. As shown in the acceleration response spectra in Figure 6, the fundamental mode was less prominent than the second and third modes in the building response to the Northridge earthquake.

The response of a building depends on the flexibility of the building, size of the earthquake, and the distance from the earthquake. For flexible building, the long-period filter corner has to be larger than the building fundamental period to avoid filtering out fundamental mode motions. On the other hand, it is better to filter out more long-period motions for stiff buildings, for record analysis purposes. If the building structural element had undergone permanent deformations during an earthquake, these permanent deformations cannot be obtained from acceleration records by the routine record processing using filters. At locations at which permanent displacements are expected to occur, such as base-isolators or buckling-restrained steel braces, relative displacement sensors can be installed, in addition to accelerometers, to provide direct measurement of the movement.

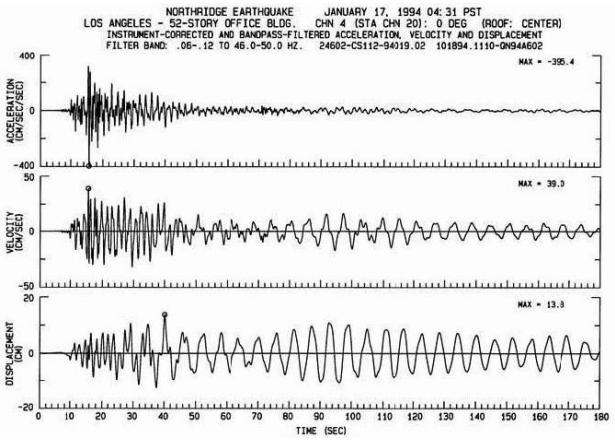


Figure 5. Acceleration, velocity and displacement records from sensor 20 on the roof of a 52-story building in Los Angeles during the 1994 Northridge earthquake.

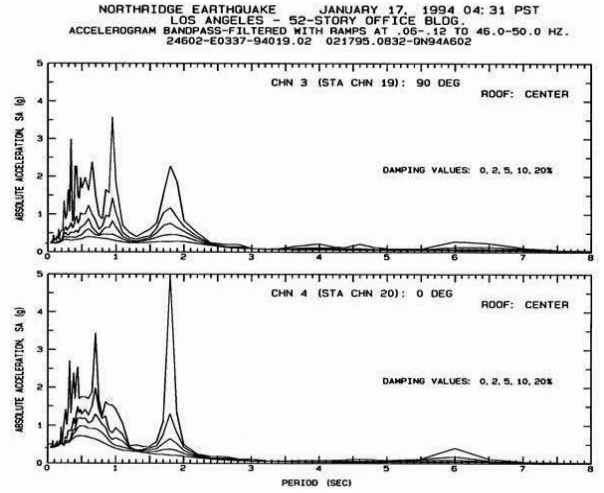


Figure 6. Response spectra of the roof records of a 52-story building in Los Angeles during the 1994 Northridge earthquake.

3. DATA DISSEMINATION VIA INTERNET

CSMIP has obtained strong-motion records with building base motions larger than 0.1g from more than 80 instrumented buildings. Several of these buildings were damaged during earthquakes (Huang, et al., 1996). These records are available at the Center for Engineering Strong Motion Data (CESMD) for analyses of building response by researchers. Figure 7 shows the home page of the CESMD (http://www.strongmotioncenter.org). The Center is a cooperative center established by the US Geological Survey (USGS) and the California Geological Survey (CGS) to integrate earthquake strong-motion data from the CGS California Strong Motion Instrumentation Program, the USGS National Strong Motion Project, and the Advanced National Seismic System (Haddadi, et al., 2008).

Buildings records from new earthquakes are routinely processed and the usable data bandwidth is always included in the text headers of the processed data. The processed data as well as raw data from new earthquakes are added to

the Center and available for earthquake engineering applications.

In addition to the strong-motion data, the Center also contains the metadata for the instrumented buildings. Users can find descriptions of the building structural system, design dates, and the sensor location diagram for a specific building, such as the 52-story building in Figure 8. At the Center, the users can also search for all the earthquakes which were recorded at a specific building, as shown in Figure 9. The records can be viewed and downloaded for analyses. The CESMD Center provides an interface with Google maps to show the building locations on street, terrain, or satellite maps. New features are periodically added to the CESMD Center to facilitate access by users to the data and information on buildings and earthquakes (Haddadi, et al., 2009).

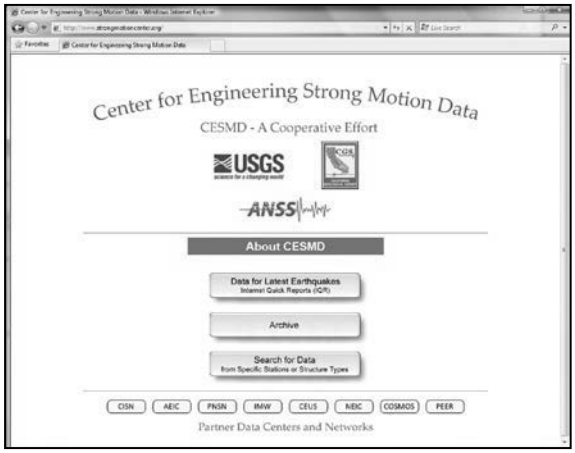


Figure 7. Home page of the Center of Engineering Strong Motion Data (http://www.strongmotioncenter.org).

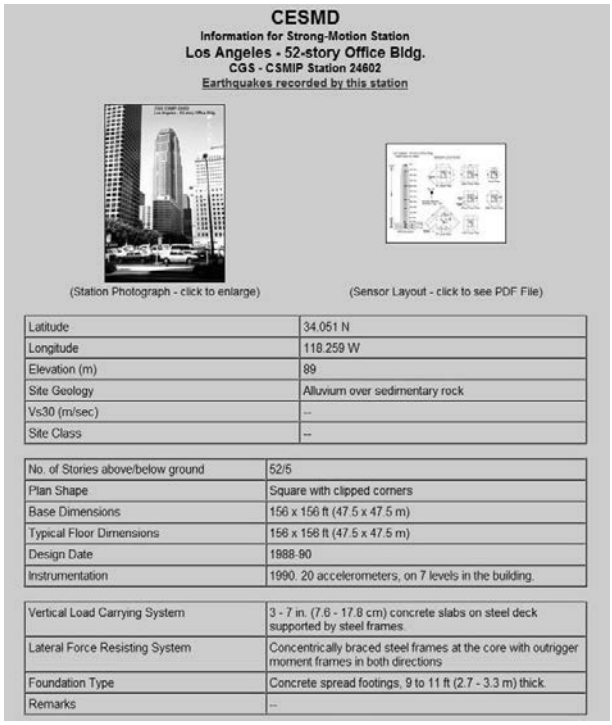


Figure 8. Description of the 52-story building and the sensor location diagram are available at CESMD.

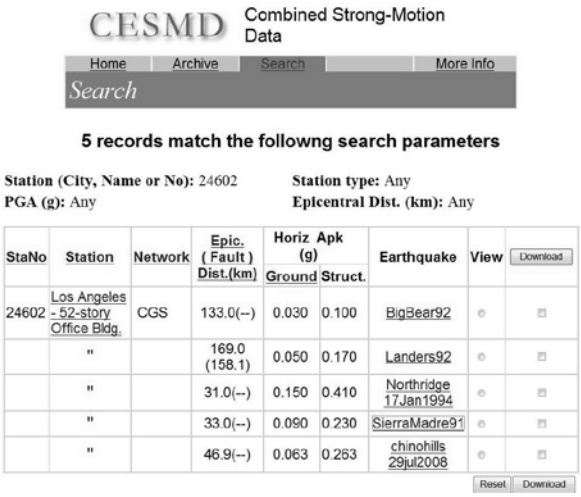


Figure 9. Result of search at CESMD for earthquakes that were recorded at the 52-story building.

4. ANALYSES OF BUILDING RECORDS

CSMIP established a Data Interpretation Project in 1989 to fund data interpretation projects for the analysis and utilization of strong-motion data. The primary objectives of the Data Interpretation Project are to further the understanding of strong ground shaking and the response of structures, and to increase the utilization of strong-motion data in improving post-earthquake response, seismic code provisions and design practices. Building records obtained during the 1989 Loma Prieta and the 1994 Northridge earthquakes have been the most significant data sets analyzed in the Project.

As part of the Data Interpretation Project, CSMIP holds annual seminars to transfer recent research findings on strong-motion data to practicing seismic design professionals, earth scientists and post-earthquake response personnel. The seminars include presentations by the investigators on the CSMIP-funded projects and invited speakers on topics related to strong-motion data. Twenty seminars have been held since 1989. The purpose of these seminars is to provide information that will be useful immediately in seismic design practice and post-earthquake response, and in the longer term, useful in the improvement of seismic design codes and practices. Proceedings and individual papers for each of the seminars are available at http://www.consrv.ca.gov/cgs/smip/pages/proceedings.aspx

Building records are traditionally analyzed to verify and improve analytical procedures for seismic response of a building, and to improve seismic design provisions in the building codes (e.g., Chopra, et al., 1998). Key response parameters are derived from the records and then compared with the results from a computer model based on the design plans. Frequently, a dynamic analysis using the recorded input motion is performed. The predicted response is compared with the recorded response to verify or improve the analysis procedure (e.g., Nagarajaiah, et al.; 1995, Naeim, et al., 1998 & 1999). Recently, the records have been utilized for post-earthquake damage assessment and safety

evaluation of buildings by rapid interpretation of the data (e.g., Rojahn, et al., 2003; Naeim, et al., 2005).

The dynamic characteristics of a building that can be obtained from strong-motion records include periods, damping, and participation factors of the first few modes. The mode shapes can also be estimated from the records if a sufficient number of floors are instrumented. The most important parameters that are related to the building performance during the earthquake are probably base shear force and inter-story drift, which can be derived directly or indirectly from the records (e.g., Jennings, 1997; Naeim, et al., 2005). The records can also be analyzed to study the nonlinear response of the building (e.g., Goel and Nishimoto, 2009), and the performance of non-structural components in the building.

In 2005, a CSMIP 3-D visualization software system was developed to visualize the response of instrumented buildings during earthquakes based on the recorded building response data (Naeim, et al., 2004). The system also allows users to analyze the building response data and learn about the performance of buildings during earthquakes. It has been a useful educational tool for understanding the seismic response of buildings.

5. CONCLUSIONS

The California Strong Motion Instrumentation Program (CSMIP) continues to instrument buildings to measure the ground motions and the building responses to these motions during earthquakes. The CSMIP building selection process and building instrumentation objectives and models continue to follow the long-term plan and criteria developed with the Strong Motion Instrumentation Advisory Committee. Strong-motion data recorded at these buildings have provided valuable information for understanding the seismic response of buildings and for improving seismic design and analysis procedures. In addition, the near-real-time recovery and processing of the recorded data is useful for post-earthquake evaluation of buildings. CSMIP continues to fund and facilitate efforts towards utilizing the near-real-time data for post-earthquake response and structural integrity assessments of buildings.

References:

Chopra, A., Goel, R. and De la Llera, J. (1998), "Seismic Code Improvements Based on Recorded Motions of Buildings During Earthquakes," *Proceedings of SMIP98 Seminar on Utilization of Strong-Motion Data*, p. 135 - 154.

Goel, R. and Nishimoto, K. (2009), "Seismic Analysis of Buildings to Recorded Motions: Modeling and Software Challenges," *Proceedings of SMIP09 Seminar on Utilization of Strong-Motion Data*, p. 39 - 60.

Haddadi, H., Shakal, A., Stephen, C., Savage, W., Huang, M., Leith W., Parrish, J. and Borcherdt, R. (2008), "Center for Engineering Strong-Motion Data (CESMD)," *Proceedings of the 14th World Conference on Earthquake Engineering*, Paper 02-0168.

Haddadi, H., Stephen, C., Shakal, A., Huang, M., Oppenheimer, D., Savage, W., Leith W. and Parrish, J. (2009), "Update and New Features of the Center for Engineering Strong Motion Data (CESMD)," *Proceedings of SMIP09 Seminar on Utilization of Strong-Motion Data*, p. 89 - 106.

Huang, M., Malhotra P. and Shakal, A. (1996), "Strong-Motion Records from Buildings Damaged in Earthquakes," *Proceedings of SMIP96 Seminar on Seismological and Engineering Implications of Recent Strong-Motion Data*, p. 99 - 116.

Huang, M. and Shakal, A. (2001), "CSMIP Building Instrumentation Measurement Objectives and Models," *Proceedings of COSMOS Invited Workshop on Strong-Motion Instrumentation of Buildings*, p. 15 - 19.

Huang, M. and Shakal, A. (2002), "Building Instrumentation Objectives and Models," *Proceedings of the 7th U.S. National Conference on Earthquake Engineering*, Paper ST-1d.

Huang, M. (2004), "Recording Processing Consideration for Analysis of Building," *Proceedings of COSMOS Invited Workshop on Strong-Motion Record Processing*, p. 155 - 169.

Jennings, P. (1997), "Use of Strong-Motion Data in Earthquake Resistant Design," *Proceedings of SMIP97 Seminar on Utilization of Strong-Motion Data*, p. 1 - 8.

Naeim, F., Lobo, R., Li, J., Sabol, T. and Li, R. (1998), "Response Evaluation of Three Concrete Frame Buildings to the January 17, 1994 Northridge Earthquake," *Proceedings of SMIP98 Seminar on Utilization of Strong-Motion Data*, p. 91 - 118.

Naeim, F., Lobo, R., Skiliros, K., and Sgambelluri, M. (1999), "Seismic Performance of Four Instrumented Steel Moment Resisting Frame Buildings during the January 17, 1994 Northridge Earthquake," *Proceedings of SMIP99 Seminar on Utilization of Strong-Motion Data*, p. 51 - 82.

Naeim, F., Lee, H., Bhatia, H., Hagie, S. and Skiliros, K. (2004), "CSMIP Instrumented Building Response Analysis and 3-D Visualization System (CSMIP-3DV)," *Proceedings of SMIP04 Seminar on Utilization of Strong-Motion Data*, p. 83 - 102.

Naeim, F., Hagie, S. and Alimoradi, A. (2005), "Automated Post-Earthquake Damage Assessment and Safety Evaluation of Instrumented Buildings, "*Proceedings of SMIP05 Seminar on Utilization of Strong-Motion Data*," p. 71 - 88.

Nagarajaiah, S. and Sun X. (1995), "Response of Base-Isolated Buildings during the 1994 Northridge Earthquake," *Proceedings of SMIP95 Seminar on Seismological and Engineering Implications of Recent Strong-Motion Data*, p. 41 - 56.

Rojahn, C., Comartin, C. and King, S. (2003), "Guidelines for Utilizing Strong-Motion and ShakeMap Data in Post-Earthquake Response (ATC-54)," *Proceedings of SMIP03 Seminar on Utilization of Strong-Motion Data*, p. 47 - 58.

Shakal, A. and Huang, M. (1989), "Overview of the Strong Motion Instrumentation Program - May 1989," *Proceedings of SMIP89 Seminar on Seismological and Engineering Implications of Recent Strong-Motion Data*, p. 1-1 - 1-10.

Shakal, A., Petersen, C., Cramlet, A. and Darragh, R. (1995), "CSMIP Near-Real-Time Strong Motion Monitoring System: Rapid Data recovery and Processing for Event Response", *Proceedings of SMIP95 Seminar on Seismological and Engineering Implications of Recent Strong-Motion Data*, p.1-10.

Shakal, A. and Petersen, C. (2001), "Quality Control in Structural Instrumentation," *Proceeding of COSMOS Invited Workshop on Strong-Motion Instrumentation of Buildings*, p. 95 - 97.

Shakal, A., Huang, M. Rojahn, C. and Poland, C. (2001), "Strategies and Criteria for the Selection of Buildings for Instrumentation," *Proceeding of COSMOS Invited Workshop on Strong-Motion Instrumentation of Buildings*, p. 5 - 14.

Shakal, A., Huang, M. and Graizer, V. (2004), "California Strong-Motion Instrumentation Program Processing Methods and Procedures," *Proceeding of COSMOS Invited Workshop on Strong-Motion Record Processing*, p. 111 - 122.

8CUEE CONFERENCE PROCEEDINGS
8th International Conference on Urban Earthquake Engineering
March 7-8, 2011, Tokyo Institute of Technology, Tokyo, Japan

STRONG MOTION OBSERVATION FOR BUILDINGS BY BUILDING RESEARCH INSTITUTE

Toshihide Kashima[1] and Shin Koyama[2]

1) Senior Research Engineer, Building Research Institute, Japan
2) Chief Research Engineer, Building Research Institute, Japan
kashima@kenken.go.jp, skoyama@kenken.go.jp

Abstract: Strong motion observation in Japan has a history for more than 50 years. Building structures have been the main target of instrumentation at the dawn of the strong motion observation. Currently, many buildings are equipped with strong motion instruments by various bodies, such as national institutes, universities or private companies.
The Building Research Institute (BRI) of Japan is a national research institute specialising in the fields of architecture, building engineering and urban planning. BRI is operating the nationwide strong motion network as part of its research activities. The network has more than seventy strong motion stations located in major cities throughout Japan. The most important objective of strong motion observation is to contribute to an improvement in seismic safety of houses and buildings. The related researches are being conducted to elucidate dynamic properties and seismic performance of buildings, evaluate the effects of input seismic motions on buildings, and verify new earthquake-resistant technologies.
First this paper describes a state of the strong motion observation for buildings in Japan. Second, the outline of the BRI strong motion network and some outcomes are introduced.

1. INTRODUCTION

Strong motion observation in Japan has been started in 1950's under a cooperative project between universities and national institutions. Building Research Institute (BRI) is one of the members participating in the project from its launching. Expansion of the strong motion network and improvement of strong motion instruments have been continued for more than 50 years (Kashima 2010b).

With the 1995 Kobe Earthquake as a start, the strong motion network for monitoring earthquake ground motions has made great strides. Nearly 5,000 stations have been newly deployed all across Japan. The strong motion network for buildings is essential to preserve seismic safety of buildings; however, it has made very slow progress. BRI is making best efforts to accelerate the progress of the strong motion observation of building structures. The paper introduces the BRI strong motion network targeted at building structures and some of research activities using strong motion records of recent earthquakes.

2. STATE OF STRONG MOTION OBSERVATION FOR BUILDINGS IN JAPAN

In Japan, many bodies are conducting strong motion observation aimed at seismic response of buildings for their specific purposes. The chapter intends to take a general view of the situation of building instrumentation in Japan.

For instance, BRI is operating the nation-wide strong motion network of buildings as a part of research activities. The purpose of the observation is to contribute to the improvement in seismic safety of buildings as a national research institute. The chapter 3 described the BRI network in detail.

Urban Renaissance Agency (UR) is in charge of the urban development and the provision of residential and office buildings. UR has instrumented around 20 residential buildings to verify and preserve their seismic safety. Nippon Telegraph and Telephone Corporation (NTT) is the largest company providing communication service in Japan. NTT has a strong motion network with more than 50 stations. The target of instrumentation is office buildings of NTT and its group companies.

Many general contractors are maintaining their own strong motion networks. It is guessed that a large number of buildings and civil structures are instrumented. Generally, the observation is planned for development and investigation of new technology. The instrumented structures were constructed by them and owned by others. Therefore, it is difficult to bring the whole condition to light.

On the other hand, several universities are conducting strong motion monitoring in buildings for the purpose of research and education. The targets of instrumentation are usually their school buildings. Although the number of buildings is limited, creative plans specialised in research subjects can be found.

BRI investigated the actual conditions of the strong motion observation of buildings conducted by private bodies by means of questionnaires in 2003. Koyama et al. (2004) reported that 160 buildings were instrumented by 38 bodies in total. One fourth of the buildings were located in Tokyo, and a half of the buildings were equipped with base-isolation

devices or seismic control systems.

Okawa et al. (2003) reported the status of the strong motion recordings for buildings in Japan based on the literature survey by the study group of Tsukuba Building Research Institute Consortium. They surveyed technical papers of the AIJ annual meeting from 1990 to 2001 and summarised 128 cases. In addition, Kataoka et al. (2010) surveyed technical papers of the AIJ annual meeting from 2002 to 2008 and detected 119 instrumented buildings. They concluded that the total number of instrumented buildings would be estimated at approximately 300.

3. BRI STRONG MOTION NETWORK

3.1 Outline

To enhance the seismic safety of building structures, it is necessary to understand the characteristics of earthquake ground motions and the behaviours of buildings during an earthquake. BRI is performing strong motion observation to reveal the actual dynamic behaviours of buildings and is conducting research projects to clarify these motions.

BRI has installed strong motion instruments in major cities throughout Japan. Seventy-five observation stations are now in operation as shown in Fig. 1. One third of these stations are located in Tokyo and its outskirts. All of the stations are equipped with up-to-date digital instruments and most of them are connected to BRI via public telephone lines so that these instruments may be appropriately maintained and strong motion data may be collected immediately after an earthquake.

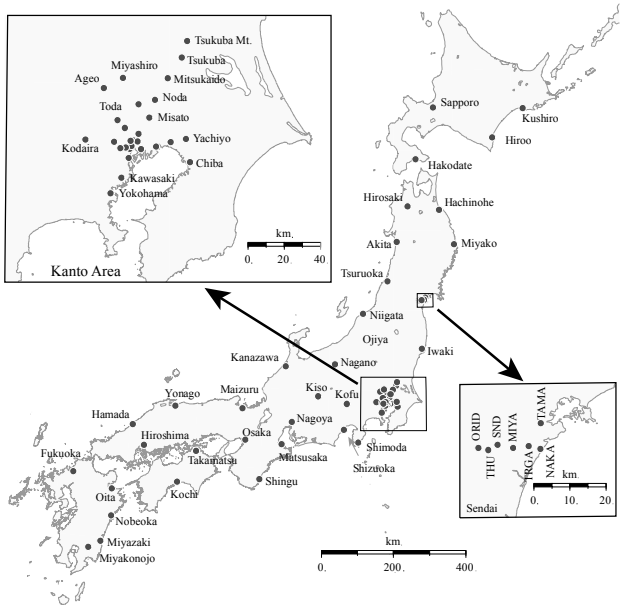


Figure 1 Locations of observation stations of BRI strong motion network

3.2 Installation Pattern

The stations of the BRI strong motion network can be classified according to installation patterns as shown in Fig. 2. Strong motion instruments are set up on the ground (and/or in the ground in some cases) at nine stations. A sensor is set up only on the first floor of a low-rise building at each of other eight stations. A quarter of the stations, therefore, are being operated for getting deep insight into characteristics of earthquake motions.

A half of the stations have two or more sensors placed on both the basement and top of their buildings. In some cases, additional sensors have been installed depending on building features. For example, sensors have been added at intermediate floors of high-rise buildings. In case of a base-isolated building, at least two sensors are necessary just above and below the floor on which base-isolation devices are installed. The dynamic soil-structure interaction is an important factor in estimating seismic responses of buildings; therefore, a sensor is preferably installed on the ground.

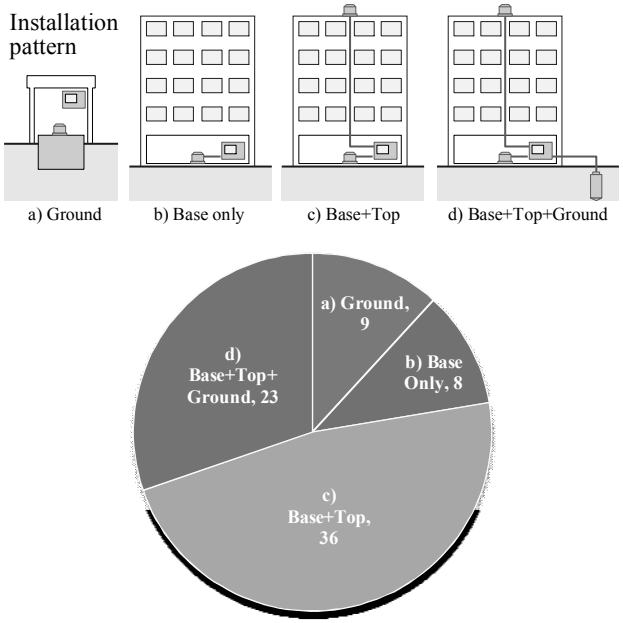


Figure 2 Classification of stations according to installation patterns

3.3 Building Types

Thus, 67 buildings are equipped with strong motion instruments. Most of the buildings are used as offices of the national or local governments. Figure 3 indicates the number of storeys and structural types of these buildings. Eighty percent of the buildings are of low- and middle-rise types which have ten or less storeys. There are five high-rise buildings with storeys more than 20, among which the highest one is a 37-storey residential building with the height of 119 meters. Low-rise buildings are usually built using reinforced concrete (RC) structures in Japan; therefore, a half of the buildings have the RC structure. The steel-framed reinforced concrete (SRC) structure is often used in middle-rise buildings with five or more storeys. Most of high-rise buildings are constructed using steel structures. There are seven steel high-rise buildings with 15 or more storeys in the BRI strong motion network.

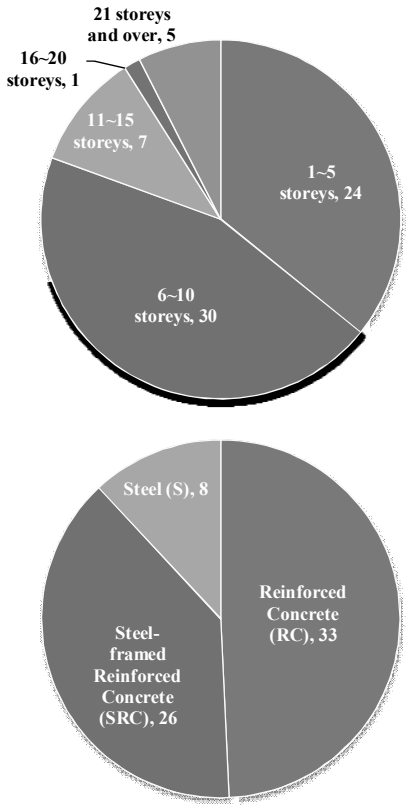


Figure 3 Classification of target buildings according to the number of storeys (upper) and structural type (lower)

4. RECENT TOPICS

4.1 Input Seismic Motions on Building

To evaluate the seismic safety of buildings, we need to understand the effects of input seismic motions on buildings correctly. Currently, we have about 5,000 strong motion stations on the ground throughout Japan. A huge number of ground motion records of every big earthquake have been accumulated. It is known, however, that the earthquake motions on the ground surface differ from the input seismic motions of buildings.

The mechanism of input seismic motions of buildings is extremely complicated, and no practical method for evaluating the input motions has been established. To address this problem, it is necessary to enhance simultaneous recording of strong motions both on the ground and of the buildings. The BRI strong motion network is tackling this problem proactively.

An example of observation results is introduced here. The annex building of the Hachinohe City Office is a ten-storey SRC building with the base isolation system. Hachinohe City, known as one of the most earthquake-prone areas, lies on the coast of the Pacific Ocean in the northernmost part of Honshu of Japan. Considering such a situation, BRI installed strong motion instrumentation in the annex building in 1999 (Kashima 2010a). The instrument has three sensors in the building and three sensors on/in the ground. One of the sensors is set up on the building basement (B1F) and other one is placed on the ground (GL) at a distance of about 50 meters from the building as shown in Fig. 4. The characteristics of input seismic motions of the building can be evaluated by comparing two strong motion records observed on both the ground and the building basement.

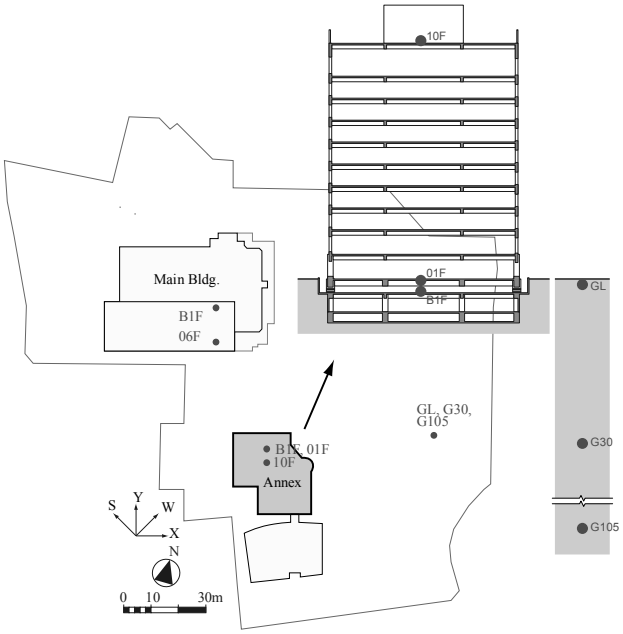


Figure 4 Sensor configuration at Hachinohe City Hall

Ninety-five strong motion records have been accumulated for the last ten years at this station. Figure 5 shows the correlations of peak accelerations between the ground (GL) and basement (B1F) levels. Red diamonds and blue squares correspond to X- and Y-directions, respectively (cf. Fig. 4). The peak acceleration on the basement is always smaller than that on the ground surface. The average of the ratio of the peak acceleration on the basement to that on the ground surface is less than 0.4.

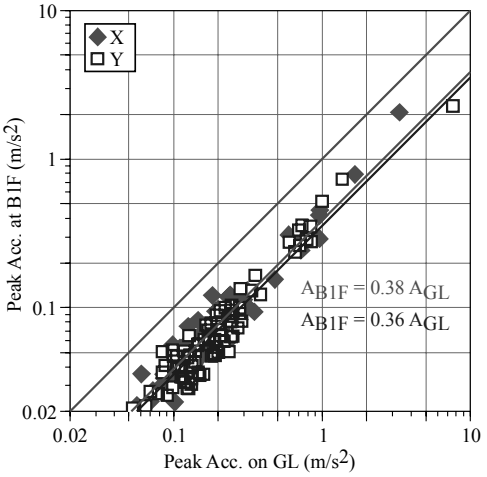


Figure 5 Correlations of peak accelerations and peak velocities between the ground and basement levels

As an example, the strong motion record of the Northern Coast of Iwate Prefecture Earthquake of 24 July,

2008, is shown in Fig. 6. The upper three waveforms and lower three waveforms show accelerations on the ground (GL) and on the basement (B1F), respectively. A difference in Y-direction acceleration is especially large, the peak acceleration on the basement attenuating down to 30 percent of that on the ground.

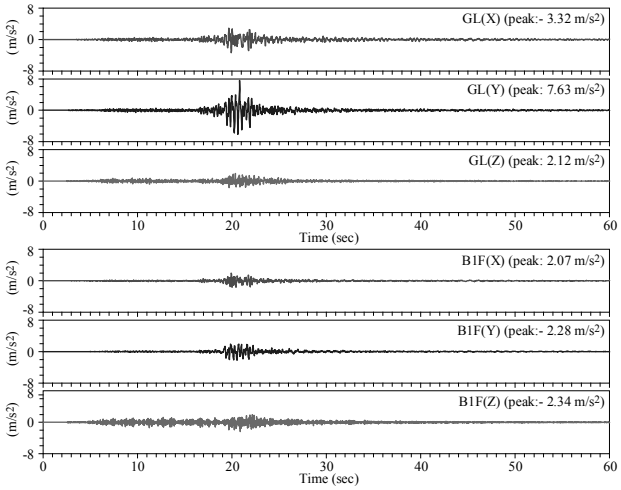


Figure 6 Acceleration records of the Northern Coast of Iwate Prefecture Earthquake of 24 July, 2008

The averaged Fourier spectrum ratios of the motions between the basement and ground levels (B1F/GL) for the 95 strong motion data are plotted in Fig. 7. Red and blue solid lines represent the average spectra in the X- and Y-directions, respectively. Dashed lines indicate positive-or-negative standard deviations. The Fourier spectra are smoothed using the Parzen window (Parzen, 1962) with a width of 0.1 Hz. The spectral ratios, which indicate about 1 in the low frequency of 1 Hz or less, drop significantly in the frequency range higher than 1.4 Hz. Consequently, it is suggested that the reduced acceleration on the building basement compared with that on the ground surface is caused by the loss of high frequency components of the earthquake motion.

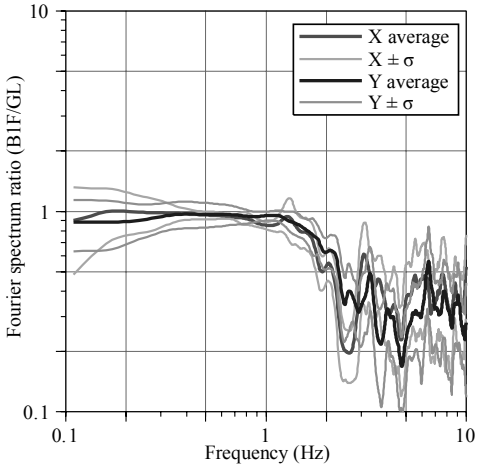


Figure 7 Fourier spectrum ratios between B1F and GL

4.2 Long-Period Earthquake Motions and Building Responses

In the urban areas in Japan, e.g. Tokyo, Osaka and Nagoya, the importance of the study on long-period earthquake motions has grown with an increase of high-rise buildings and base-isolated structures. This chapter discusses the characteristics of ground motions in Tokyo and seismic responses of a high-rise building using the strong motion data recorded in the BRI strong motion network.

The target building is a 37-storey apartment building made of reinforced concrete (RC) located in the waterfront of Tokyo. The instrumentation installed in this building has three sensors, each on the first, 18th and 37th floors.

Three major strong motion data recently recorded are taken up for discussion. Table 1 lists peak accelerations and peak velocities recorded on the first floor of the building with the earthquake parameters. The peak accelerations of EQ1 are lower than others, but the peak velocities are higher. The locations of the building and the epicentres are plotted in Fig. 8. The seismic waves of three earthquakes come from quite different directions.

Table 1 List of earthquakes and peak accelerations on the first floor

#	Date	h (km)	M_{JMA}	Δ (km)	Peak acc. (m/s^2)		
					N-S	E-W	U-D
EQ1	2007/07/16	17	6.8	235	0.050	0.058	0.025
EQ2	2008/05/08	51	7.0	175	0.123	0.095	0.051
EQ3	2009/08/11	23	6.5	153	0.141	0.132	0.046

h: focal depth, M_{JMA}: Magnitude by Japan Meteorological Agency (JMA), Δ: epicentral distance

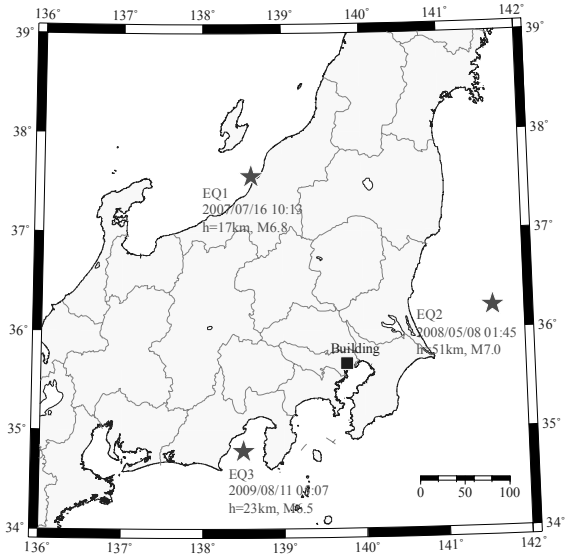


Figure 8 Locations of the instrumented building and the epicentres

Figure 9 shows acceleration waveforms of the strong motion data listed in Table 1. The upper, middle, and lower pairs of waveforms indicate accelerations in the North-South direction of EQ1, EQ2, and EQ3, respectively. The upper waveform of each pair is recorded on the 37th floor (37F) and the lower one is on the first floor (01F). Later phases of

long-period components can be clearly recognised on the waveform on the first floor of EQ1 recorded 60 seconds after the earthquake. In the cases of EQ1 and EQ2, the acceleration on the 37th floor is remarkably high and continues for long time of 4 minutes or more.

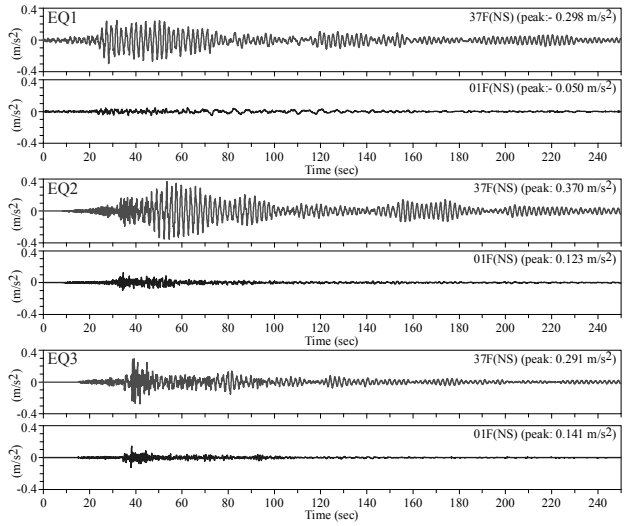


Figure 9 Acceleration records on the first and 37th floors in N-S direction

Pseudo velocity response spectra with the damping ratio of 5% of the acceleration records on the first floor are plotted in Fig. 10. The curve of the EQ1 response spectrum quite differs from others. The response spectrum has the highest peak at the period of around 7 seconds after the earthquake and attenuates gradually. The EQ3 response spectrum in the period longer than 2 seconds is extremely low in contrast to that of EQ1. The EQ2 response spectrum has high peaks in the period ranging from 2 to 3 seconds after the earthquake and attenuates to half or less in the period longer than 4 seconds.

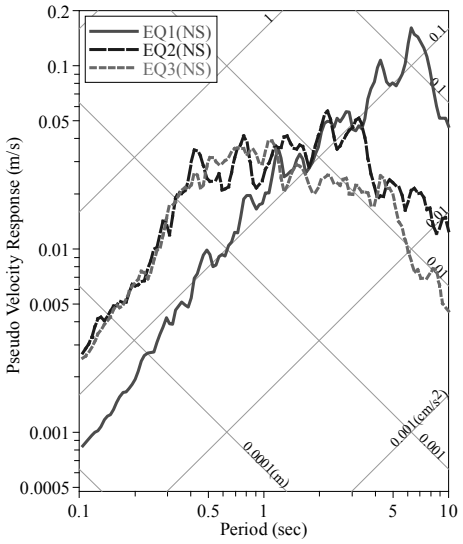


Figure 10 Pseudo velocity response spectra of N-S components of accelerations on the first floor

4.3 Strong Motion Database

BRI opened a website of the strong motion network at the address of http://smo.kenken.go.jp/ in 2009. The web site has a database which stores more than 5,000 strong motion data sets recorded on/in the ground or on the building basement levels. The search page of the website of the BRI strong motion network is shown in Fig. 11.

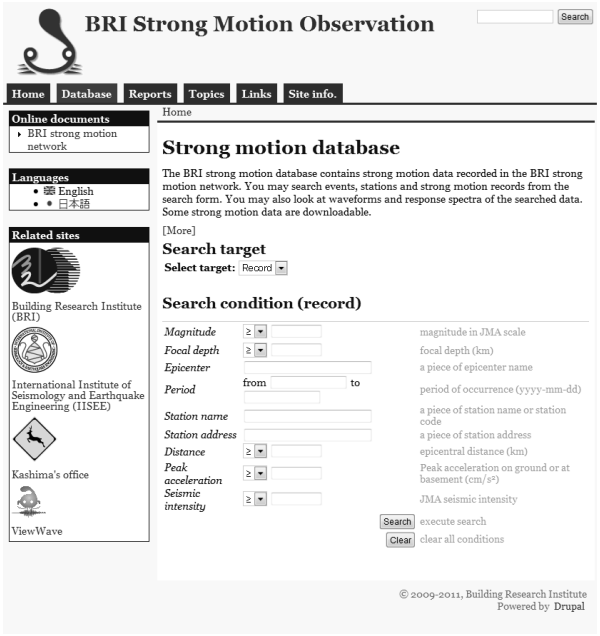


Figure 11 Search interface in the website of the BRI strong motion network (http://smo.kenken.go.jp/)

5. CONCLUSIONS

The paper summarised the current state of the strong motion observation for buildings in Japan. Approximately 300 buildings are instrumented by various institutions for various purposes.

The strong motion network operated by Building Research Institute (BRI) and some of the outcomes were also introduced. BRI is operating 76 strong motion stations aiming at capturing data on seismic responses of building structures. Importance of sensor installation both on the ground and in the building was suggested through the strong motion data analysis. This is essential for the estimation of motions input to buildings accurately. The characteristics of the earthquake motions in the Tokyo waterfront and seismic response of the high-rise building were also discussed. High-rise buildings may show strong and long responses even to moderate intensities of earthquake motions.

Acknowledgements:

The strong motion observation project of BRI is being executed with large cooperation of the owners and administrators of the target buildings. We express my gratitude to them for the assistance they gave.

References:

Akagi, H, et al. (2004), "String-Motion Earthquake Observation of NTT Telecommunication Buildings," *Proceedings of the*

Symposium The 50th Anniversary of Strong-Motion Earthquake Observation in Japan – History and Perspective -, Technical Note of National Institute for Earth Science and Disaster Prevention, No. 264, 73-76 (Japanese)

Kashima T. (2010a), "Dynamic Behavior of Hachinohe City Hall Buildings Examined based on Strong-Motion Data," *Proceedings of 9th US National and 10th Canadian Conference on Earthquake Engineering*, Paper No. 1187

Kashima T. (2010b), "Strong motion network for buildings operated by Building Research Institute of Japan," *Proceedings of the 14th European Conference on Earthquake Engineering*, Paper No. 1714

Kataoka, S., et al. (2010), "Survey for present state of Earthquake Motion Observation in Buildings," *AIJ Journal of Technology and Design*, Architectural Institute of Japan, **Vol. 16, No. 32**, 87-90 (Japanese)

Koyama, S., et al. (2004), "Investigation of the present strong motion observation on building," *Summary of Technical Papers of Annual Meeting*, Architectural Institute of Japan, **B-2**, 877-878 (Japanese)

Okawa, I., et al. (2003), "Status Report on Strong Motion Recording for Buildings in Japan," *Proceedings of the 35th Joint Panel Meeting on Wind and Seismic Effects*, Public Works Research Institute

Parzen E. (1962). "On estimation of a probability density function and mode," *Annals of Mathematical Statistics*. **33:3**, 1065–1076.

8CUEE CONFERENCE PROCEEDINGS
8th International Conference on Urban Earthquake Engineering
March 7-8, 2011, Tokyo Institute of Technology, Tokyo, Japan

BUILDING HEALTH MONITORING AND DIAGNOSIS FROM EARTHQUAKE RESPONSE RECORDS

Chi-Chang Lin[1], Jer-Fu Wang[2], and Ging-Long Lin[3]

1) Distinguished Professor, Department of Civil Engineering, National Chung Hsing University, Taichung, Taiwan, ROC.
2) Assistant Research Fellow, 921 Earthquake Museum of Taiwan, National Museum of Natural Science,Taichung, Taiwan, ROC.
3) Post-Doctoral Research Fellow, Department of Civil Engineering, National Chung Hsing University, Taichung, Taiwan, ROC.
cclin3@dragon.nchu.edu.tw, jfwang@nmns.edu.tw, gllin@dragon.nchu.edu.tw

Abstract: To better understand the seismic behavior of structures, the Central Weather Bureau in Taiwan initiated a strong-motion instrumentation program in 1993. Nowadays, 50 buildings and 17 bridges have been instrumented with accelerometers. The structural dynamic motions are continuously monitored and recorded when accelerations at certain accelerometers exceed a specific value. The 50 instrumented buildings are classified into low-rise (flat), mid-rise (ordinary), and high-rise (slender) buildings, and are located at soft, medium, and firm sites, respectively. The measured earthquake response records provide a great opportunity to make health monitoring and damage assessment of such buildings. In this paper, a story damage index was developed to evaluate the damage degree of a torsionally-coupled building based on its dominant modal frequencies and mode shapes. This index is expressed in an analytical formula and ranges from 0 (intact undamaged) to 1.0 (collapsed). It can be easily calculated once the modal parameters are obtained through system identification techniques from the acceleration measurements of an instrumented building. The damaged region in a specific floor can also be identified through tracking the change of floor eccentricity. This index was applied to the damage assessment of a four-story reinforced concrete building in Taitung, Taiwan, which experienced severe damage during the 2006 Taitung Beinan Earthquake (M=6.2). The results agree well with the visual inspection to show the applicability of the proposed damage assessment technique.

1. INTRODUCTION

Earthquake resistant design of buildings usually allows for a building to experience repairable damage during moderate and large earthquakes. It is important to acquire damage information of buildings to take appropriate actions after a strong earthquake event. Damaged buildings without immediate repair will probably encounter further damage and have the potential to collapse in the next extreme event. Therefore, the development of damage assessment techniques which can detect, locate, and quantify the damage of a structure, receives considerable attention and becomes a crucial topic in earthquake engineering research and practice. Damage assessment techniques are classified into global and local assessment techniques. The former is usually referred to as structural health monitoring (SHM), whereas the latter is called as non-destructive testing (NDT) which requires that the vicinity of the damage is known in advance. A well-established SHM system needs the installation of hardware incorporation with damage assessment algorithms. Nowadays, hardware technologies for SHM, such as sensors and data acquisition systems, are extensively developed, whereas a robust damage assessment technique remains unrecognized.

Damage assessment techniques based on vibration responses of structures are considered to be practical for SHM. This is due to the fact that damage in a structure will alter its dynamic characteristics, and then affect its vibration behavior (Elenas and Meskouris 2001, Park and Ang 1985). To employ these techniques, measurements of structural responses, such as acceleration and/or velocity are required. Then, damage-related features, calculated either from the measurements directly or on the basis of dynamic parameters extracted from the measurements, are obtained. With the pre-damaged and post-damaged features, damage information can be evaluated using developed algorithms. In the studies by Farrar et al. (2001) and by Yan et al. (2007), various vibration-based damage assessment techniques were summarized and reviewed.

Damage detection of a structure based on change of modal frequencies is intuitive because structural damage always leads to reduction of stiffness that is related to vibration frequency. Damage in different locations and components will cause different frequency changes in each vibration mode. Nevertheless, it remains difficult to determine the damage location just by observing the changes of modal frequencies. Among the modal parameters, mode shape is obviously the only location-related parameter. In previous studies, mode shape-based indices with simple expression, such as MAC (modal assurance criterion) (Allemang and Brown 1982), COMAC (coordinate modal assurance criterion) (Lieven and Ewins 1988), and modal

curvature index (Pandey et al. 1991, Farrar and Jauregui 1998), were applied to detect and locate structural damages. However, it was shown that these indices are insensitive to damages in some cases (Ndambi et al. 2002, Brasiliano et al. 2004). Considering both modal frequencies and mode shapes to detect the occurrence, degree, and location of a damage is a better way than relying on either one of them such as modal flexibility damage index (MFDI) (Pandey and Biswas 1994).The principle of this approach is based on flexibility matrices obtained from two sets of normalized modal parameters. Furthermore, some researchers developed more accurate damage indices but complicated expressions for various types of structures (Kim and Chun 2004, Kim et al. 2003, Di and Law 2007, Jiang and Mahadevan 2008, Gomes and Silva 2008). In recent, the authors (2007) developed a new story damage index (SDI) with analytical expression to accurately identify the damaged degree and location in elevation for buildings.

For the damage detection of a building, most of the previous researches regarded the building as a planar structure. However, it is generally recognized that the floor asymmetry resulting from the non-coincidence of its center of rigidity (C.R.) and center of mass (C.M.) always exists in a building. This results in the coupling of translational and torsional motions when the building is subjected to translational ground excitations. Relevant studies (Ueng et al. 2000, Lin et al. 2005a) reveal that this torsion-coupling (TC) effect will alter the dynamic characteristics as well as the vibration behavior of a building. To consider the TC effect, this study developed an innovative story damage index for TC buildings, called SDITC, based on the reduction of lateral story stiffness. A multi-story TC building model with two-way eccentricities is established for the derivation of SDITC which is expressed in terms of floor masses and only one modal frequency and mode shape. From the floor and excitation acceleration measurements, the dominant modal parameters of a TC building can be identified by employing the SRIM system identification technique (Juang 1997, Lin et al. 2005b, Lin et al. 2008) and then the change of floor eccentricity is used to detect the damaged region at each floor. To verify the applicability of SDITC, numerical analyses of a TC building model were performed using ETABS software with a series of damage scenarios. A planar building-based damage index (SDI) was also applied for comparison. It was proved that the SDITC can accurately identify the damaged degree and location in plan and in elevation of a building. The SDI will overestimate the damage degree. In this study, the SDI and SDITC were applied to evaluate two instrumented RC buildings in Taiwan which experienced moderate and severe damages during the 1999 Chi-Chi earthquake (M=7.3) and 2006 Taitung Beinan earthquake (M=6.2), respectively, based on their earthquake records before and after the damaged earthquake event. The agreement with the field visual inspection shows the accuracy and applicability of the proposed damage assessment technique.

2. PRATICAL CONSIDERATIONS OF MEASUREMENTS

In general, the soil surrounding the foundation of a building is not rigid resulting in complex 3-D soil-structure interaction (SSI) motions. The SSI effect affects building responses significantly and must be taken into account in the parametric identification of building systems. According to recent studies by the authors (Wu et al. 2001, Lin et al. 2008), the foundation of an irregular building-soil system behaves not only in lateral but also in torsional and rocking motions under translational seismic excitations, as shown in Figure 1. To catch these 3-D dynamic motions, measurements at free-field, base, ground floor, and the superstructure in horizontal and vertical directions are required to investigate the effects of SSI and embedment, and the vibration amplification of buildings. Because of limited number of sensors, it is not possible to measure all floor responses. Therefore, the measurements at intermediate floors with large change of story stiffness should be considered to evaluate the non-instrumented floor responses. The minimum number of sensors and their locations for different engineering purposes are illustrated in Table 1. In summary, at least total of 24 sensors are required for a general TC shear building as shown in Figure 2.

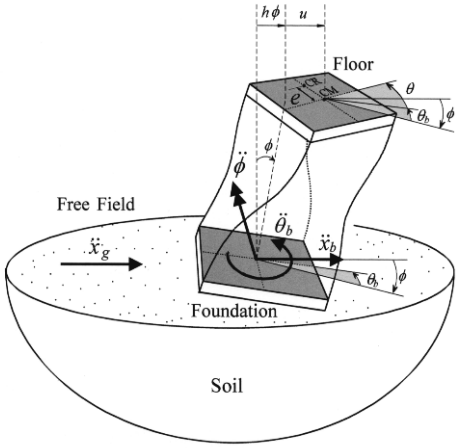


Figure 1. Irregular building-soil interaction system

Table 1. Number of sensors and locations for different engineering purposes

Consideration	Sensor location	Number of sensor	Engineering purpose
Soil-structure interaction	Free-field	3	Building input motions (translation, torsion and rocking)
	Ground level	6	
Embedment	Ground level	6	Underground structures
	Base	6	
Floor amplification building rocking	Roof	6	Nonstructural components
	Intermediate floors	3	
Vibration mode shape	Intermediate floors with discontinuous stiffness or mass	3	Non-instrumented floor responses

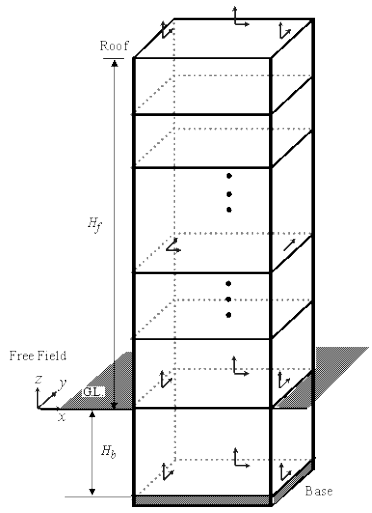
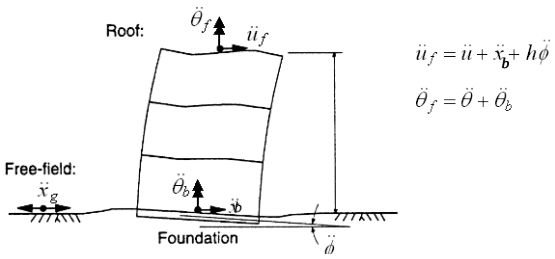


Figure 2. Sensor locations for practical considerations

For the identification of physical parameters (such as story stiffness) in the superstructure of an irregular building with consideration of SSI effect, the selected input motions should include horizontal, torsional as well as rocking motions of the foundation. Different input/output selections represent different structural systems as shown in Figure 3 (Stewart and Fenves 1998, Lin et al. 2008)



	Input	Output	System Model	ID Parameters
w/o SSI	$\ddot{x}_g$ (or $\ddot{x}_b$)	$\ddot{u}_f$, $\ddot{\theta}_f$	Fixed base	Structure
SSI	$\ddot{x}_g$	$\ddot{u}_f$, $\ddot{\theta}_f$	Flexible base	Soil + Structure
	$\ddot{x}_b$	$\ddot{u}_f$, $\ddot{\theta}_f$	Pseudo flexible-base (Stewart and Fenves 1998)	Pseudo Structure
	$\ddot{x}_b$, $\ddot{\phi}$, $\ddot{\theta}_b$	$\ddot{u}_f$, $\ddot{\theta}_f$	Fixed base (Lin et al. 2008)	Structure

Figure 3. Input/output selection in building identification

3. BUILDING INSTRUMENTATION IN TAIWAN

To better understand the seismic behavior of structures, the Taiwan Central Weather Bureau (CWB) initiated a strong-motion instrumentation program in 1993. Nowadays, 50 buildings and 17 bridges have been installed with accelerometers, as shown in Figure 4. The 50 instrumented buildings are classified into low-rise (flat), mid-rise (ordinary), and high-rise (slender) buildings, and are located at soft, medium, and firm sites, respectively. The variety of slenderness and site condition is useful for the study of both SSI and embedment effects and seismic response analysis of building systems.

For a typical building, about 30 sensors are distributed at the base, the ground floor, middle floors, and the roof. Most instrumented building systems are also equipped with a triaxial accelerometer in the free-field. The building motions are continuously monitored and the recording is triggered when accelerations of certain accelerometers exceed a specific value. All earthquake records are stored in an on-site computer and collected periodically to save at CWB. Since 2003, most measured stations have been updated with new data acquisition systems so that measurements can be on-line transmitted to CWB through ADSL (Asymmetric Digital Subscriber Line).

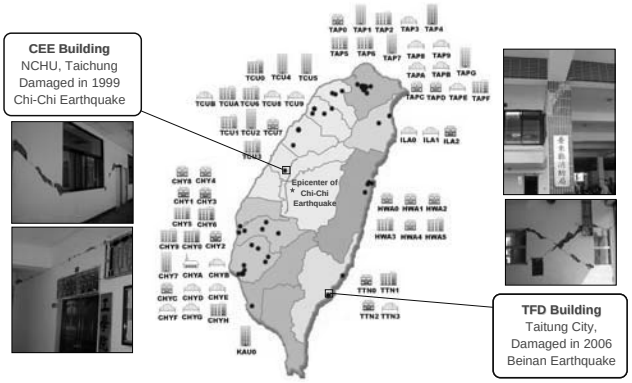


Figure 4 Map of instrumented buildings and bridges in Taiwan (http://www.cwb.gov.tw)

Among the 50 instrumented buildings, the Civil and Environmental Engineering (CEE) department building at National Chung Hsing University (NCHU) in central Taiwan experienced moderate damages during the 1999 Chi-Chi earthquake (M=7.3). Later on, the Taitung Fire Department (TFD) building was severely damaged by the 2006 Taitung Beinan earthquake (M=6.2). The measured earthquake records before and after the damaged earthquake event (such as aftershocks) are very useful for the health monitoring and damage assessment of such buildings.

4. STORY DAMAGE INDEX

4.1 Story Damage Index for TC Buildings

Define story damage of a building as the reduction ratio of lateral story stiffness after damage to that before damage. For an *N*-story TC building system, the damage index of the *l*th story in *x* direction, termed SDITC_{x_l}, can be expressed as

$$\mathrm{SDITC}_{x_l} = 1 - \frac{k^*_{x_l}}{k_{x_l}} = 1 - \frac{\omega^{*2}_j}{\omega^2_j} \frac{\sum_{i=l}^{N} \frac{m_i \phi^*_{x_i j}}{\Delta\phi^{CR*}_{x_l j}}}{\sum_{i=l}^{N} \frac{m_i \phi_{x_i j}}{\Delta\phi^{CR}_{x_l j}}} \qquad (1)$$

where k_{x_l} = story stiffness at the *l*th floor in *x* direction and m_l = the *l*th floor mass. The superscript asterisk (*) marks the

damage-state modal parameters. Superscript *CR* denotes the center of rigidity. ω_j represents the *j*th modal frequency while $\phi_{x_i j}$ represents the *j*th mode-shape values at the *i*th floor in *x* direction. *j* can be 1, 2, … or 3*N*, and

$$\Delta\phi_{x_l j}^{CR} = \begin{cases} \phi_{x_l j}^{CR} - \phi_{x_{l-1} j}^{CR} & \text{for } l = 2, 3, \ldots, N \\ \phi_{x_l j}^{CR} & \text{for } l = 1 \end{cases}$$

In the above equation,

$$\phi_{x_{l-1} j}^{CR} = \phi_{x_{l-1} j} - e_{y_{l-1,l}} \phi_{\theta_{l-1} j}, \quad \phi_{x_l j}^{CR} = \phi_{x_l j} - e_{y_{l,l}} \phi_{\theta_l j}$$

where $e_{x_{r,s}}$ (*r*, *s* =*l*-1, *l*, or *l*+1) represents the eccentricity of the center of rigidity (C.R.) from the center of mass (C.M.) of the *r*th floor due to the elements in *s*th story in *x* direction.

Similarly, damage index in *y* direction, SDITC_{y_l} can be obtained by replacing *x* by *y* in Equation (1). The value of SDITC, ranging from 0 (intact) to 1.0 (collapsed), provides a convenient index to indicate the location and degree of story damage.

As seen in Equation (1), the value of SDITC in both *x* and *y* directions can be easily obtained based on only the first dominant modal frequencies and mode shapes. This is highly beneficial in practice because the fundamental modal parameters can be identified accurately through system identification technique even with noise-contaminated measurements.

Moreover, the floor eccentricities can also be obtained based on the first three sets of modal frequencies and mode shapes and take the form as

$$\begin{Bmatrix} e_{x_{l,l}} \\ e_{x_{l-1,l}} \end{Bmatrix} = \frac{1}{(A_{x_{11}} A_{x_{22}} - A_{x_{21}} A_{x_{12}})} \begin{Bmatrix} A_{x_{22}} A_{x_{13}} - A_{x_{12}} A_{x_{23}} \\ -A_{x_{21}} A_{x_{13}} + A_{x_{11}} A_{x_{23}} \end{Bmatrix} \quad (2)$$

where

$$A_{x_{11}} = \phi_{\theta_l p_1} F_{y_l p_2} - \phi_{\theta_l p_2} F_{y_l p_1} \quad A_{x_{12}} = \phi_{\theta_{l-1} p_2} F_{y_l p_1} - \phi_{\theta_{l-1} p_1} F_{y_l p_2}$$

$$A_{x_{13}} = (\phi_{y_l p_2} - \phi_{y_{l-1} p_2}) F_{y_l p_1} - (\phi_{y_l p_1} - \phi_{y_{l-1} p_1}) F_{y_l p_2}$$

$$A_{x_{21}} = \phi_{\theta_l q_1} F_{y_l q_2} - \phi_{\theta_l q_2} F_{y_l q_1} \quad A_{x_{22}} = \phi_{\theta_{l-1} q_2} F_{y_l q_1} - \phi_{\theta_{l-1} q_1} F_{y_l q_2}$$

$$A_{x_{23}} = (\phi_{y_l q_2} - \phi_{y_{l-1} q_2}) F_{y_l q_1} - (\phi_{y_l q_1} - \phi_{y_{l-1} k_1}) F_{y_l q_2}$$

in which $\phi_{\theta_l j}$ and $\phi_{y_l j}$ denote the *j*th mode-shape values at θ and *y* directions in the *l*th floor, and

$$F_{y_l m} = \sum_{i=l}^{N} \omega_m^2 m_i \phi_{y_i m}, \quad F_{y_l n} = \sum_{i=l}^{N} \omega_n^2 m_i \phi_{x_i n} \quad (3)$$

In Equation (3), $m=p_1$ or p_2 and $n=q_1$ or q_2 which indicate specific structural modes. To make Equation (2) solvable, p_1 and p_2 have to be different, so are q_1 and q_2.

To interpret the story stiffness in Equation (1) from a physical point of view, one can imagine a building vibrating in *x* direction and in its *j*th mode. In this situation, the vibration frequency of the building is the *j*th modal frequency, ω_j, and mode shape value, $\phi_{x_l j}$ can be regarded as the displacement of the *l*th floor in *x* direction. Therefore, the *l*th floor acceleration in *x* direction equals to $\omega_j^2 \phi_{x_l j}$. Also, the inertial force of the *l*th floor in *x* direction is the mass multiplied by the acceleration, expressed as $m_l \omega_j^2 \phi_{x_l j}$. The resultant force (story shear force) applying to the *l*th story is the summation of the inertial forces above the story, $\sum_{i=l}^{N} m_i \omega_j^2 \phi_{x_i j}$. In addition, the lateral resisting force at the *l*th story is equal to the relative displacement at CRs of the *l*th and the (*l*-1)th floors, $\Delta\phi_{x_l j}^{CR}$, times the story stiffness k_x. Equating the resultant force and the resisting force, the formula of k_x is obtained and expressed as

$$k_{x_l} = \omega_j^2 \sum_{i=l}^{N} \frac{m_i \phi_{x_i j}}{\Delta\phi_{x_l j}^{CR}} \quad (4)$$

4.2 Story Damage Index for Planar Buildings

For a symmetric building, Wang et al. (2007) derived an approximate story damage index (ASDI) equation, which can be reduced from Equation (1) with same floor masses, to evaluate the damage degree of the *l*th story. The formula of ASDI takes the form as

$$\mathrm{ASDI}_l = 1 - \frac{\omega_j^{*2} \sum_{i=l}^{N} \frac{\phi_{ij}^*}{\Delta\phi_{lj}^*}}{\omega_j^2 \sum_{i=l}^{N} \frac{\phi_{ij}}{\Delta\phi_{lj}}} \quad (5)$$

This index has been proved superior to other indices (i.e. COMAC, MAC, and MFDI) for the damage assessment of a planar building (Wang et al, 2007). In this study, ASDI was also implemented to assess the damage of CEE and TFD buildings with neglect of TC effect. The results from ASDI overestimate the degree of story damage as compared with those of SDITC, as expected.

5. DAMAGE ASSESSMENT OF REAL BUILDINGS

5.1 CEE Building at NCHU

The Civil and Environmental Engineering Department building is located in the campus of National Chung Hsing University in central Taiwan. It is a seven-story reinforced concrete building with one-story basement, as shown in Figure 5. It is closely contacted with another three-story building at the right-hand side.

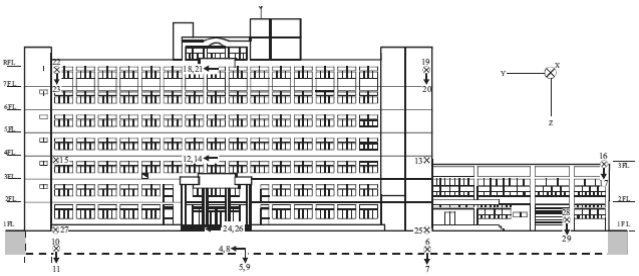


Figure 5. Elevation-view of CEE Building

A triaxial accelerograph is installed in the free-field near the CEE building and 26 unidirectional accelerometers are installed on the base, the ground floor (1FL), the fourth floor (4FL) and the roof. The location and measuring direction (indicated by arrows) of each accelerometer are shown in Figure 6. Building acceleration responses induced by the main shock and several aftershocks of the 1999 Chi-Chi earthquake were completely recorded. Cracks in the partition walls and at the junction of beams and walls of lower stories (1-4 FL) were visible after the main shock.

Table 2 presents the identified first modal parameters of the CEE building before and after the Ch-Chi earthquake using SRIM system identification technique. The values of ASDI in both horizontal directions were also calculated and shown in Table 2. It is seen that $(ASDI)_{EW} > (ASDI)_{NS}$ and $(ASDI)_{(1F-4F)} > (ASDI)_{(4F-RF)}$. Indicating that the damages at lower story and in EW direction are more serious than those at upper stories in NS direction. Moreover, the calculated ASDI values agree well with the results by visual inspection and by NDT.

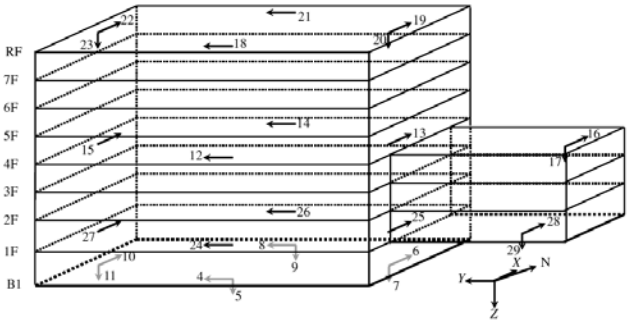


Figure 6. Sensor location and direction in the NCHU CEE building

Table 2. ASDI of CEE building under the 1999 Chi-Chi earthquake

Direction		X (NS)		Y (EW)	
Earthquake date		1999/7/7	1999/10/19	1999/7/7	1999/10/19
ω_1 or ω_1^* (Hz)		3.077	2.524	3.096	2.272
$1-\omega_1/\omega_1^*$		0.33		0.46	
ϕ_1 or ϕ_1^*	RF	1.000	1.000	1.000	1.000
	4F	0.460	0.506	0.459	0.486
ASDI	4F-RF	0.27		0.43	
	1F-4F	0.37		0.48	

5.2 TFD Building at Taitung

The Taitung Fire Department (TFD) building, located in Taitung City, was severely damaged by the 2006 Taitung Beinan earthquake. Acceleration measurements before, during, and after the earthquake were obtained and used for the verification of damage index SDITC.

The TFD building is a plan-irregular, four-story reinforced concrete building with one-story, half-excavated basement. The story height above the second floor is identical with 3.5 meters. However, the first story is 5 meter high with fewer walls than other stories to park fire fighting trucks and store essential equipments, as shown in Figure 7. Therefore, the outer and inner partition walls provide very large stiffness above the second floor resulting in soft first-story. Consequently, it is expected that the damage of this building will concentrate at the first story.



Figure 7. Photo of TFD Building

Twenty-two accelerometers were installed in the free field, ground level (GF), second floor (2F), and the roof (RF), respectively, as shown in Figure 8. The architectural drawings shown in Figure 9 indicate that the TFD building is irregular in plan which leads to translation-torsion coupling. Because each instrumented floor has four sensors, the translation along x and y directions and the torsion about the z- axis at center of mass of each floor can be calculated.

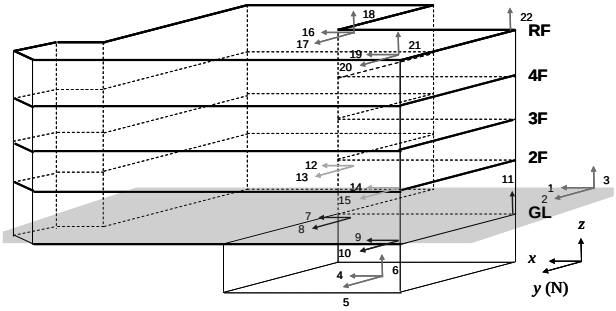


Figure 8. Sensor location and direction in the TFD building

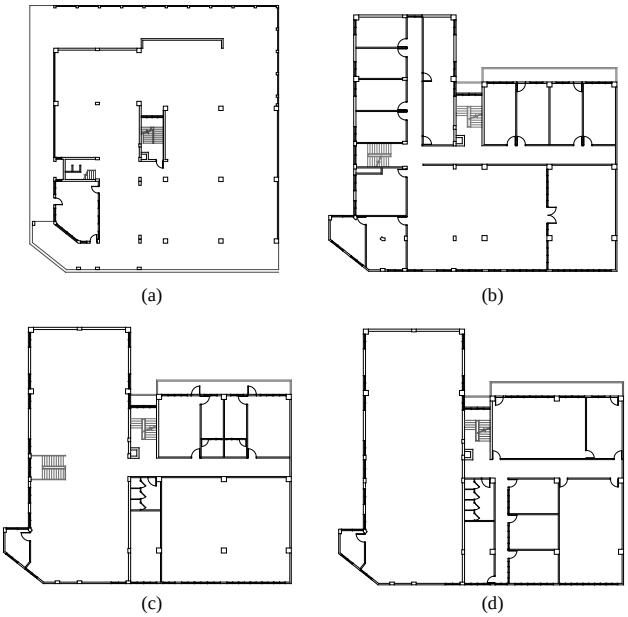


Figure 9. Plan view of TFD building: (a) GL; (b) 2F; (c) 3F; (d) 4F

During the 2006 Taitung Beinan earthquake, many columns and walls in the first story were severely damaged. It is seen from Figure 10 that most damages occurred at the north-side columns and east-side walls. For the damaged columns, moment failure near beam-column joint and shear failure due to short-column effect were observed. As to the walls, typical X-shape shear cracks happened. For the stories above second floor, no significant damage was found.

To evaluate the TFD building, the earthquake records of December 28, 2005, and aftershocks of the Taitung Beinan earthquake were used. Because this building has a soft bottom story, the SDITC was calculated only for the first story. Table 3 presents the identified first three modal parameters of the TFD building before and after the main earthquake event using SRIM system identification technique. The large reduction of fundamental modal frequencies (55% in the first mode and 42% in the second mode) reflects the occurrence of serious damage of the building. The changes of eccentricities (calculated by Equation (2)) in *x*- and *y*-directions and then the $SDITC_1$ are calculated and shown in Table 4. It is seen that the C.R. moved toward southwestern direction indicating that the damage is located at the northeastern region of the building. It agrees well with the results of visual inspections as shown in Figure 10. Moreover, the $(SDITC_1)_{EW}$ is larger than $(SDITC_1)_{NS}$, representing that the damage in EW direction is more severe than that in NS direction. The results can be reasonably expected because a wall contributes large lateral stiffness and more wall damages encountered along the EW-direction. For comparison, the $ASDI_1$ is also presented in Table 4. The results indicate that 81% of the EW-direction stiffness was reduced, which is overestimated due to large torsion coupling effect.

Table 3. Identified fundamental modal parameters of TFD building before and after the 2006 Taitung Benan earthquake

Earthquake Date		12/28/2005	4/1/2006
Peak Base Acceleration (gal)		x: 0.40 y: 0.53	x: 8.90 y: 12.7
Modal Frequency (Hz)		$\begin{Bmatrix}3.3350\\4.6480\\6.7563\end{Bmatrix}$	$\begin{Bmatrix}1.5129\\2.6968\\5.5340\end{Bmatrix}$
Mode Shape	2F-*x* 2F-*y* 2F-θ RF-*x* RF-*y* RF-θ	$\begin{Bmatrix}-0.7312 & -0.1948 & -0.2196\\0.3033 & -0.5379 & 0.1327\\0.0002 & -0.0002 & -0.0004\\-1.0000 & -0.4216 & -0.4516\\0.2670 & -1.0000 & 1.0000\\0.0002 & -0.0003 & -0.0008\end{Bmatrix}$	$\begin{Bmatrix}-0.8375 & -0.7817 & -0.1032\\0.6582 & -0.5436 & 0.1370\\0.0004 & -0.0003 & -0.0004\\-1.0000 & -1.0000 & -0.2678\\0.6170 & -0.7443 & 1.0000\\0.0004 & -0.0003 & -0.0008\end{Bmatrix}$

Table 4. Damage indices of TFD building under the 2006 Taitung Beinan earthquake

Damage Index	EW-direction	NS-direction
Changes of Eccentricities	-369 cm	-433 cm
$SDITC_1$	0.66	0.49
$ASDI_1$	0.81	0.70

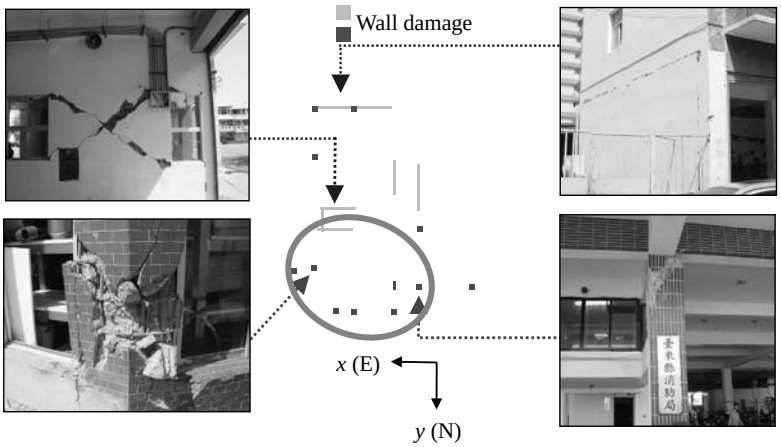


Figure 10. Wall and column failures in the first story of TFD building

6. CONCLUSIONS

Damage assessment of a building after a strong earthquake is very essential for post-earthquake recovery and has received great research interest from researchers and engineers in recent decade. This study applied a story damage index for TC buildings, named SDITC, expressed with closed form in terms of the first three modal frequencies and mode shapes of the building. For the damage assessment of the Taitung Fire Department building based on its real earthquake records, SDITC proves its accuracy and applicability to detect the damage degree and to identify the damage region in plan of a particular story. It is also shown that the assessed damage degrees in two directions agree with the visual inspection of the damaged buildings. Meanwhile, the damage degree indicated by SDITC is more reasonable than that by the planar damage index, ASDI.

Acknowledgements

This work was supported by the National Science Council of the Republic of China under Grant NSC 97-2625-M-005-004 and by the Central Weather Bureau under Grant MOTC-CWB-97-E-10. These supports are greatly appreciated.

References

Allemang R.J. and Brown D.L. (1982), "A correlation coefficient for modal vector analysis," *Proceedings of the International Modal Analysis Conference & Exhibit* , 110-116.

Brasiliano A., Doz G.N. and Brito J.L.V. (2004), "Damage identification in continuous beams and frame structures using the Residual Error Method in the Movement Equation," *Nuclear Engineering and Design*, **227**(1): 1-17.

Di W. and Law S.S. (2007), "Eigen-parameter decomposition of element matrices for structural damage detection," *Engineering Structures*, **29**(4), 519-528.

Elenas A. and Meskouris K. (2001), "Correlation study between seismic acceleration parameters and damage indices of structures," *Engineering Structures*, **23**(6), 698-704.

Farrar C.R. and Jauregui D.A. (1998), "Comparative study of damage identification algorithms applied to a bridge," *Smart Materials and Structures*, **7**(5), 704-731.

Farrar C.R., Doebling S.W. and Nix D.A. (2001), "Vibration-based structural damage identification," Philosophical *Transactions of the Royal Society*, **359**, 131-149.

Gomes H.M. and Silva N.R.S. (2008), "Some comparisons for damage detection on structures using genetic algorithms and modal sensitivity method," *Applied Mathematical Modeling* , **32**(11), 2216-2232.

Jiang X. and Mahadevan S. (2008), "Bayesian wavelet methodology for structural damage detection," Structural Control and Health Monitoring, **15**(7), 974-991.

Juang J.N. (1997) System realization using information matrix. *Journal of Guidance*, Control, *and Dynamics*, **21**(3): 492-500.

Kim H.S. and Chun Y.S. (2004), "Structural damage assessment of building structures using dynamic experimental data," *Structural Design of Tall and Special Buildings*, **13**(1): 1-8.

Kim J.T., Ryu Y.S., Cho H.M. and Stubbs N. (2003), "Damage identification in beam-type structures: frequency-based method vs mode-shape-based method," *Engineering Structures*, **25**(1), 57-67.

Lieven N.A.J. and Ewins D.J. (1988), "Spatial correlation of mode shapes, the coordinate modal assurance criterion (COMAC)," *Proceedings of the Sixth International Modal Analysis Conference*, 690-695.

Lin C.C., Hong L.L., Ueng J.M., Wu K.C., Wang C.E. (2005a), "Parametric identification of asymmetric buildings from earthquake response records," *Smart Materials and Structures* 2005, **14**(4), 850-861.

Lin C.C., Wang C.E., Wu H.W., Wang J.F. (2005b), "On-line

building damage assessment based on earthquake records," *Smart Materials and Structures*, **14**(3), S137-S153.

Lin C.C., Wang J.F. and Tsai C.H. (2008), "Dynamic parameter identifications for irregular buildings considering soil-structure interaction effects," *Earthquake Spectra*, **24**(3), 641-666.

Ndambi J.M., Vantomme J. and Harri K. (2002), "Damage assessment in reinforced concrete beams using eigenfrequencies and mode shapes derivatives," *Engineering Structures*, **24**(4): 501-515.

Pandey A.K., Biswas M. and Samman M.M. (1991) "Damage detection from changes in curvature mode shapes," *Journal of Sound and Vibration*, **145**(2), 321-332.

Pandey A.K. and Biswas M. (1994), "Damage detection in structures using changes in flexibility," *Journal of Sound and Vibration*, **169**(1), 3-17.

Park Y.J. and Ang A.H.S. (1985), "Mechanistic seismic damage model for reinforced concrete," *Journal of Structural Engineering (ASCE)*, **111**(4), 722-739.

Stewart, J.P. and Fenves, G.L. (1998), "System identification for evaluating soil-structure interaction effects in buildings from strong motion recordings," *Earthquake Engineering and Structural Dynamics*, **27**(8): 869-885.

Ueng J.M., Lin C.C., Lin P.L. (2000), "System identification of torsionally-coupled buildings," *Computers and Structures*, **74**(6), 667-686.

Wang J.F., Lin C.C. and Yen S.M. (2007), "A story damage index of seismically-excited buildings based on modal frequency and mode shape," *Engineering Structures*, **29**(9), 2143-2157.

Wu, W.H., Wang, J.F., and Lin, C.C. (2001), "Systematic assessment of irregular building-soil interaction using efficient modal analysis," *Earthquake Engineering and Structure Dynamic*, **30**, 573–594.

Yan Y.J., Cheng L., Wu Z.Y. and Yam L.H. (2007), "Development in vibration-based structural damage detection technique," *Mechanical Systems and Signal Processing*, **21**(5), 2198-2211.

8CUEE CONFERENCE PROCEEDINGS
8th International Conference on Urban Earthquake Engineering
March 7-8, 2011, Tokyo Institute of Technology, Tokyo, Japan

OBSERVATION OF STRONG EARTHQUAKE MOTION AT PUBLIC WORKS BY NILIM

Shojiro Kataoka

Senior Researcher, National Institute for Land and Infrastructure Management, Japan
kataoka-s92rc@nilim.go.jp

Abstract: National Institute for Land and Infrastructure Management (NILIM) administers the observation of strong earthquake motion at public works throughout Japan. This paper describes current status of the observation at road and river facilities by NILIM and examples of utilization of observed records.

1. INTRODUCTION

The observation of strong earthquake motion at public works was initiated in 1957, when a SMAC-type strong motion accelerometer was installed at Sarutani Dam. Strong motion accelerograms recorded during the 1964 Niigata earthquake greatly contributed to study of damage caused by the earthquake, especially liquefaction of sandy soil, demonstrating necessity of the strong earthquake motion observation.

Therefore, a nationwide instrumentation plan of SMAC-type accelerometers was drawn up and has been steadily implemented by the Ministry of Land, Infrastructure, Transport and Tourism (MLIT) and other organizations. National Institute for Land and Infrastructure Management (NILIM) has been in charge of collection, processing, and analysis of the strong motion records and conducts research on seismic design and earthquake disaster mitigation using the accumulated records.

Currently, NILIM administers two types of strong earthquake motion observation, in addition to supervising the MLIT Seismograph Network. Table 1 shows outlines and objectives of these strong motion observation systems. Locations of the observation stations at river and road facilities and those for dense instrument array observation are shown in Figure 1. Strong earthquake motion observations at national dams and ports are mainly conducted by dam work offices and Port and Airport Research Institute, respectively.

2. OBSERVATION AT RIVER FACILITIES

65 observation stations were installed at river facilities: 56 stations are at levees, 8 at weirs, and one at a sluice gate. A typical configuration of instruments at levee sites is shown in Figure 2. Accelerometers are located at the crown of the levee, on the ground surface nearby, and in the bedrock layer, while piezometers are set in the sandy soil layer.

Some stations have specific purposes such as observing influence of microtopography and examination of soil improvement. Figure 3 shows locations of accelerometers and piezometers at Nakashimo station, right-bank of Naruse River, Miyagi prefecture. The sensor arrays were installed at the berm, where liquefaction strength had been improved by the sand compaction pile (SCP) method, and near the crown, where no liquefaction remediation had been conducted.

Table 1 Outline of strong-motion observation administered by NILIM

Type of observation	Description of observation	Number of stations
Strong motion observation at public works	1) River facilities (levees, weirs, sluice gate) 2) Road facilities (bridges, embankments, slopes, retaining wall, common ducts) 3) Ground surface	123 stations (65 river facilities, 30 road facilities, 28 ground surface)
Dense instrument array observation of strong motion	Observation of amplification or attenuation characteristics caused by variations of local topography and geological conditions	92 stations in 9 areas
MLIT Seismograph Network	The stations are installed on ground surface with intervals of 20 to 40 km along rivers and national highways administered by MLIT. The observed data are sent to responsible sectors by telecommunication network for estimating seismic intensity distribution.	718 stations (http://www.nilim.go.jp/japanese/database/nwdb/index.htm)

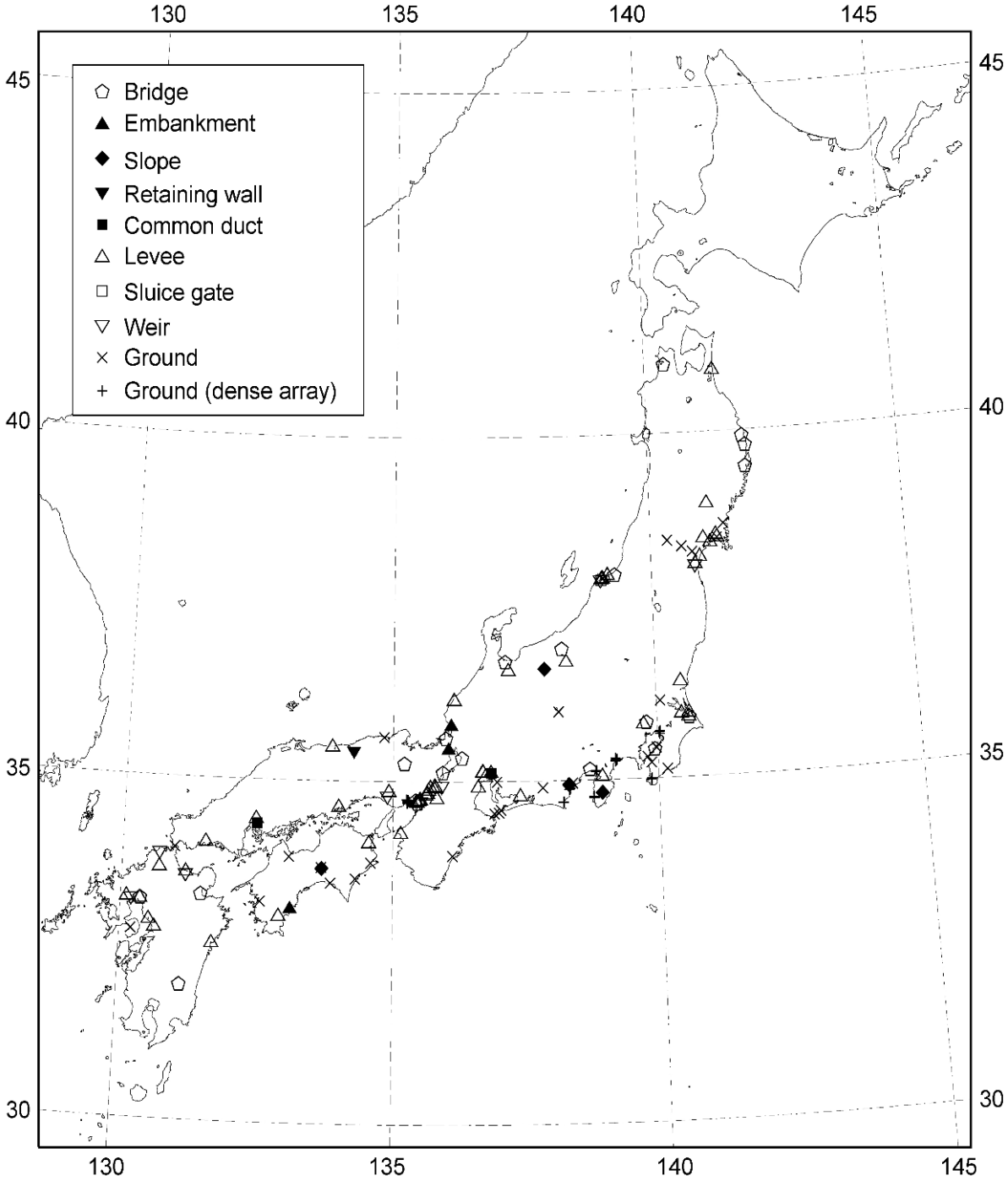


Figure 1 Strong motion observation stations at road and river facilities and those for dense instrument array observation.

Time history records of ground acceleration and pore water pressure were obtained at the station during northern Miyagi earthquakes on July 26, 2003. Figure 4 shows those recorded during the main shock (M6.4). Though the pore water pressure at 9m below the crown exceeded the maximum measurable value, 101.3[kPa]=1[atm], remarkable difference can be seen between the pore water pressure in the improved and non-improved soils. Liquefaction strengths of the improved and non-improved sandy soils were estimated using these observed records based on the accumulated damage analysis (Kataoka *et al.*, 2010). Cyclic triaxial strength ratios (R_L) of soils where the piezometers are located were estimated 0.34 and 0.40 for SCP-improved soil and 0.26 for non-improved soil.

These values are larger than R_L calculated from the equations in Specifications for highway bridges (Japan Road Association, 2002). Since the equations are used for liquefaction judgment in the seismic performance evaluation of river facilities (River Improvement and Management Division, 2007), this result can be used to reduce the cost for liquefaction remediation.

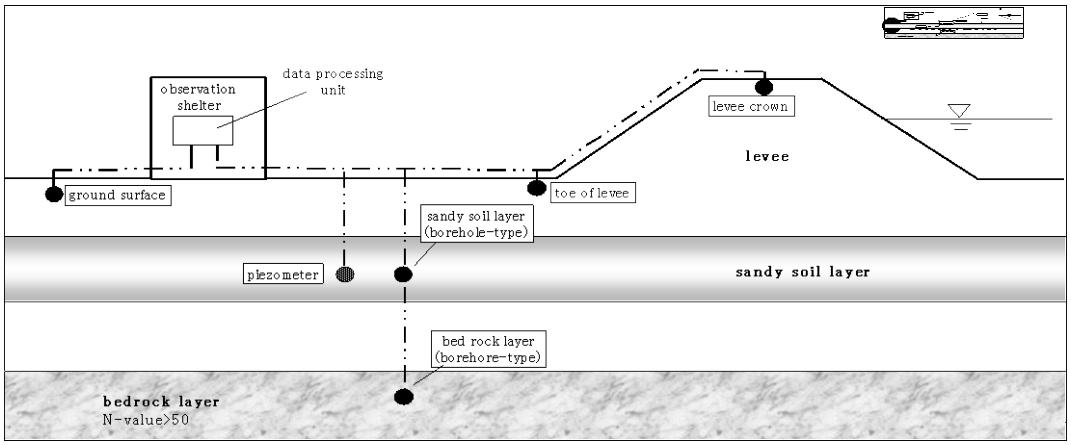


Figure 2 Typical configuration of instruments at a levee site.

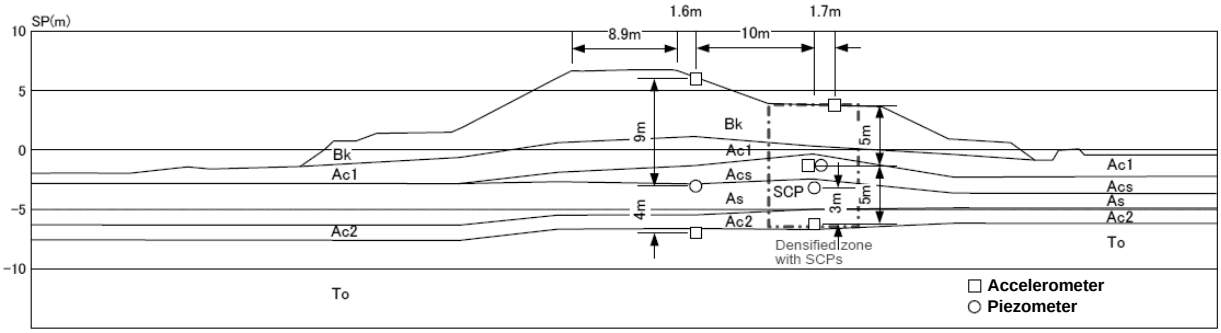
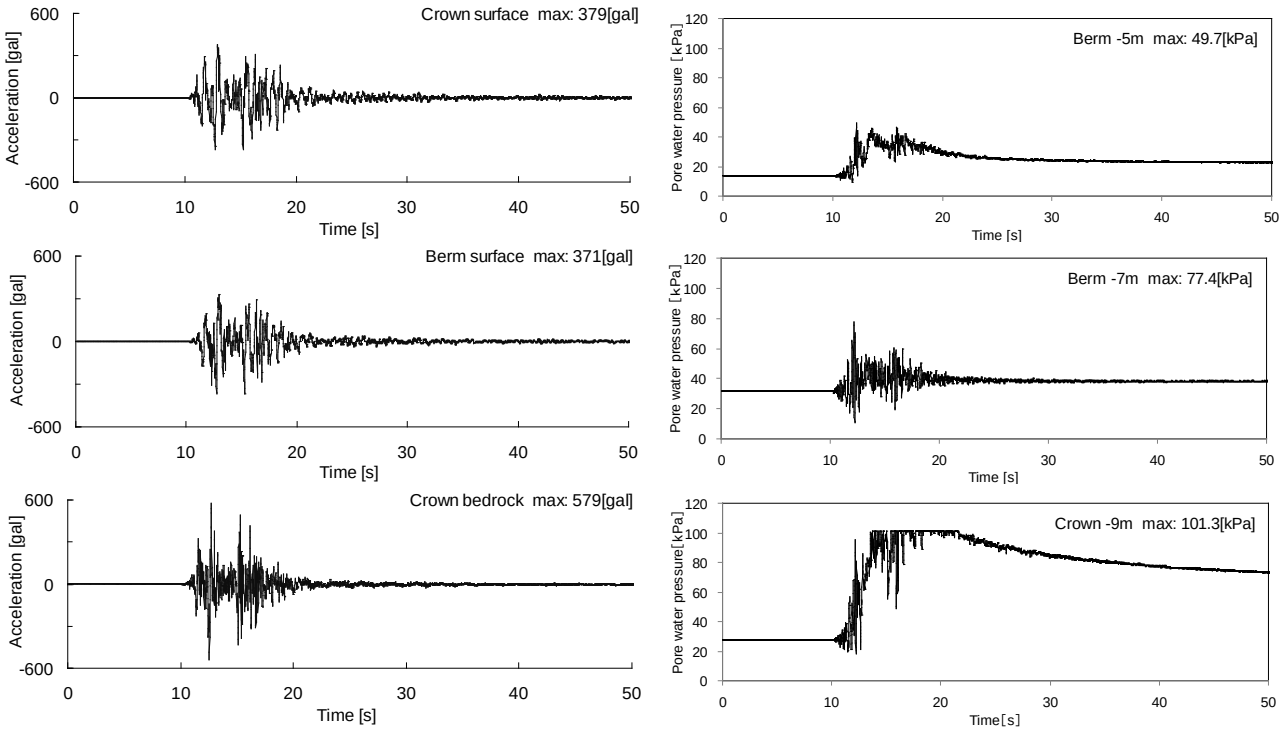


Figure 3 Locations of accelerometers and piezometers at Nakashimo station.



(a) Acceleration (b) Pore water pressure

Figure 4 Time history records observed at Nakashimo station during the main shock (M6.4) of the northern Miyagi earthquakes on July 26, 2003.

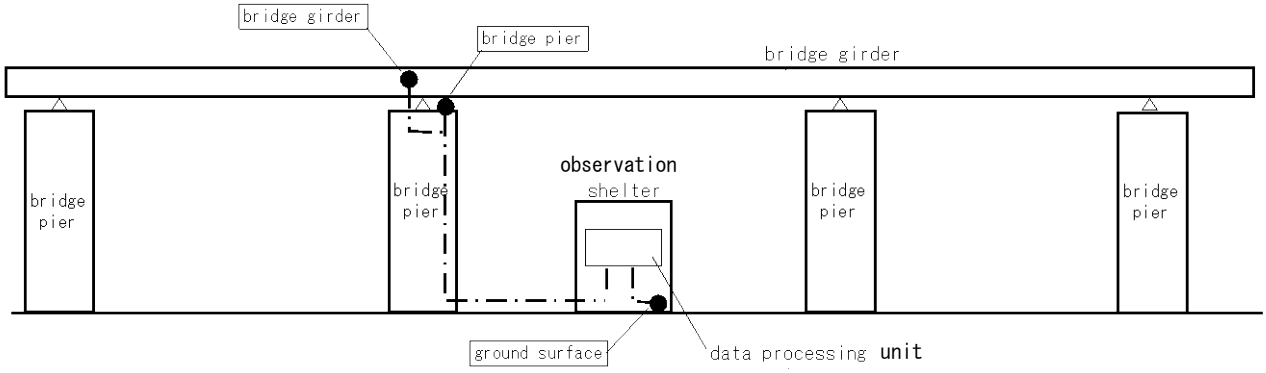
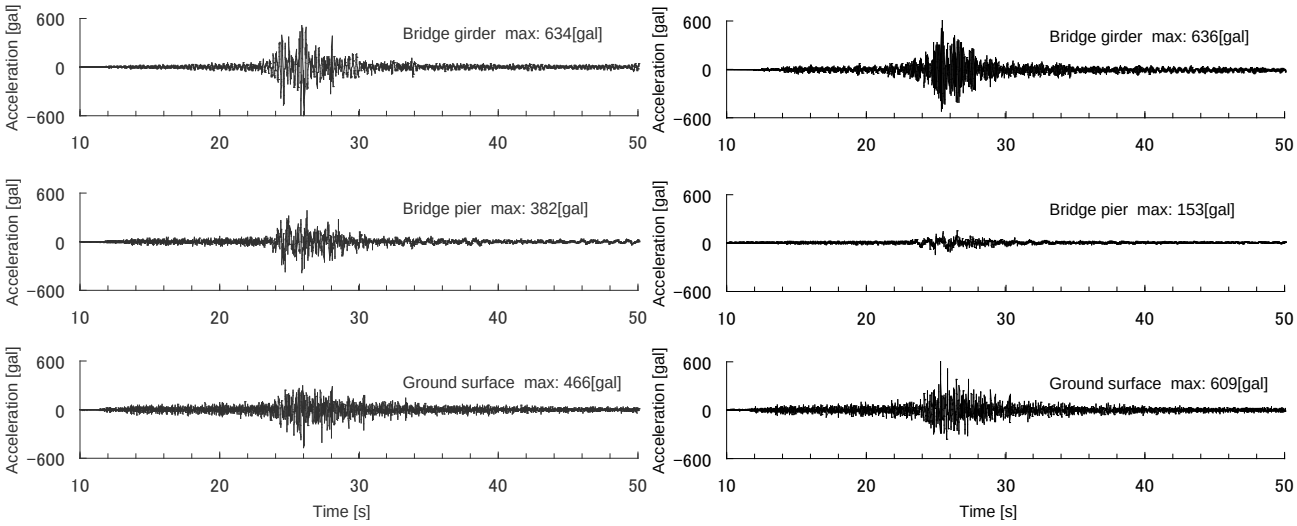


Figure 5 Typical configuration of instruments at a bridge site.



(a) Longitudinal direction (b) Transverse direction

Figure 6 Accelerograms recorded at Yamada viaduct during the northern Iwate coast earthquake (M6.8) on July 24, 2008.

3. OBSERVATION AT ROAD FACILITIES

30 observation stations were installed at road facilities: 20 stations are at bridges, 4 at slopes, 3 at embankments, 2 at common ducts, and one at a retaining wall. A typical configuration of instruments at bridge sites is shown in Figure 5. Accelerometers are located at the girder, pier, and on the ground surface nearby.

Figure 6 shows accelerograms recorded at Yamada viaduct during the northern Iwate coast earthquake (M6.8) on July 24, 2008. Horizontal force distribution structure was adopted for the viaduct, 470.7m long with two 4-span continuous steel box girders, using multi-layered rubber bearings. We conducted dynamic response analysis of the viaduct using the observed records and found the earthquake response of the viaduct cannot be reproduced well by a simple model (Matsuhashi *et al*., 2010). We have been investigating the reason that causes the difference between observed and analytical responses.

4. CONCLUDING REMARKS

NILIM has been intent on maintenance of the strong earthquake motion observation systems and utilizing the observed records for improving seismic design and earthquake disaster mitigation. We will be working on further development of the observation systems and improvement of the data utilization.

References:

Japan Road Association (2002), "Seismic design", Specifications for highway bridges, Part V.

Kataoka, S., Tanimoto, S., Nakajima, S., Matsuhashi, M. and Takamiya, S. (2010), "Study on effectiveness of soil improvement of levee using observed records", *Proceedings of the 13th Japan Earthquake Engineering Symposium*, pp. 3372-3378.

Matsuhashi, M., Kataoka, S. and Takamiya, S. (2010), "Earthquake response analysis based on earthquake record for the bridge with horizontal force distributed structure", *Proceedings of the 13th Japan Earthquake Engineering Symposium*, pp. 3268-3275.

River Improvement and Management Division (2007), "Guideline for the seismic performance evaluation of river structures against large earthquake (draft)", http://www.mlit.go.jp/river/shishin_guideline/bousai/wf_environment/structure/index.html

Uehara, H. and Kusakabe, T. (2004), "Observation of strong earthquake motion by National Institute for Land and Infrastructure Management", *Journal of Japan Association for Earthquake Engineering*, Vol.4, No.3 (Special Issue), pp.90-96.

8CUEE CONFERENCE PROCEEDINGS
8th International Conference on Urban Earthquake Engineering
March 7-8, 2011, Tokyo Institute of Technology, Tokyo, Japan

A NEW APPROACH FOR STRONG-MOTION OBSERVATION USING LOW-COST SENSORS IN COLLABORATION WITH NONPROFESSIONAL PARTNERS

Jun Tobita[1] and Nobuo Fukuwa[2]

1) Associate Professor, Graduate School of Environmental Studies, Nagoya University, Japan
2) Professor, Graduate School of Environmental Studies, Nagoya University, Japan
tobita@sharaku.nuac.nagoya-u.ac.jp, fukuwa@sharaku.nuac.nagoya-u.ac.jp

Abstract: A new strong-motion observation system, P-NET, is introduced and discussed for application of building response observation in collaboration with non-professional persons. The first aspect of the system is utilizing low cost seismometers including old and reused instruments of other observation systems such as seismic intensity networks for local governments. Daily maintenance, inspection and preservation of observed earthquake data are performed by non-professional users who are interested in earth and building science, aseismic building and disaster mitigation. To encourage such partners in continuous collaboration on earthquake observation, various vibration analysis and utility software, Web GIS contents and study programs are offered. The observation has already tested and performed in some high schools and houses by science teachers, engineers and university students. Observed data will be analyzed to show the effectiveness of the proposed system for long term observation in many buildings spread over a wide area. Furthermore the most important effect of the P-NET is that the partner will be interested in the field of earth science, earthquake engineering and disaster mitigation.

1. INTRODUCTION

An earthquake observation system that can be used to monitor various sites of ground and buildings over a wide area can contribute greatly to the disaster-mitigation measures for future earthquakes, and can be effective for the immediate reactions for an earthquake disaster.

There has been remarkable progress in Japan's strong-motion observation since the 1995 South Hyogo Prefecture Earthquake (NIED, 2004). Consequently, nationwide observation networks have been established by the central government and local authorities. Seismometers have been placed at a few thousand stations across the country by the Japan Meteorological Agency and local governments. The seismic intensity data provided by these stations are readily available for disaster response. An earthquake early-warning system based on real-time observation and data collection is also in use. However, seismic waveform records from these observation networks are not often collected, disseminated, and used. The Metropolitan Strong-Motion Observation Networks have been developed in 2000 for the major six urban areas in Japan and has created a database of waveform records such as the intensity networks measured by local governments (Tobita, *et al.*, 2001). However the networks have been continuously operated only in the districts of Tokai and Kanto until now.

NIED's K-NET and KIK-net uniformly cover all parts of the country, accumulate high-quality waveform data, and release them on the Internet. Then, these data are widely used for seismic engineering and disaster prevention (Okada, *et al*., 2004). However, the seismometers spaced within several tens of kilometers of each other in these networks do not provide sufficient data for the evaluation of strong motion with respect to the local ground conditions.

While a large number of observations have been carried out to analyze the earthquake response of the ground, there are very few observations of the earthquake response of buildings. Earthquake responses of buildings were observed at around 2000 sites in 1990 (NIED, 2004). However, only a few such records were released and used because many of the observed buildings are special ones such as high-rise buildings, base-isolated buildings and some large buildings for public use. The observed records are used only to confirm the basic response characteristics of the buildings because the good results are enough for engineers, and because the costs and labor required for long-term observation were relatively expensive. In addition, most of the buildings are private assets and thus the owners and users of the building are usually nervous to open the data to the public on the behavior of their buildings against earthquake. Such engineers' overconfidence in the existing technologies and the public's indifference to the observations are believed to contribute to the limited use of the observed data.

In light of the above, it is essential to ensure that there are as many observation targets and waveform observation records as possible and to establish a framework for the wide use of these records. We therefore propose a new strong-motion observation system, P-NET, which encourages collaboration with nonprofessional partners. P refers to the initials of People, Person, and Partner, etc. The two main objectives for the development of this system are as follows:

(1) To form a simplified observation system using low-cost and reused seismometers and to request local nonprofessional partners to maintain them and collect strong-motion records.

(2) To provide the partners software and web environments so that they understand the advantages of strong-motion observations, as well as educational programs related to the observations, in exchange for their contribution.

The system aims to reuse observation equipment and materials that have been discarded by local governments to provide stations at the lowest cost, and to increase the partners' awareness of and interest in strong-motion observations. This will lead to better seismic strengthening of buildings and improvement in the quality of education on earthquake disaster prevention. In this paper we summarize the development of equipment and materials, including recycled sensors and the Web GIS-based environment, as well as the installation of the seismometers and the observation results. We also describe the future development plans for this system in the later section.

2. BASIC SYSTEM FOR SEISMIC OBSERVATION

The basic system focuses on offline standalone observations on the assumption of the reuse of discarded seismometers and other low-cost sensors. Local partners are requested to collect observation records, transfer them to the servers, and maintain the equipment and materials. We provide a software package that can be individually used for strong-motion observations (Tobita, *et al*., 2009).

We tested the system in a school building; high-school science teachers were asked to help. The basic observation system is shown in Fig. 1. Sensors are individually placed on the first and top floors of the building. GPS-based time calibration and UPS-based power backup are performed to the extent possible. When an earthquake occurs, the school's PC and its special software are used to collect observation records. The records are attached to an email and sent to the University's server. The server creates a database for the records. The results are then made available on the Web GIS. The high-school staff can analyze the records collected offline and refer to area-wide observation records on the Web as well. The records can be used for education in science, social studies, disaster mitigation, and other subjects, in combination with other relevant information on the area. An example of such a learning tool is shown in Fig. 2. The left side of the figure shows the PC tool that is provided to users. This tool displays the maximum values, seismic intensities, waveforms, and response spectra calculated on the basis of the records collected from the sensors. It also displays one-degree-of-freedom response animations (Hirono, *et al*., 2008). The software is also effective for educational experiment using sensors. The right side of the figure shows an example where the Web GIS is used to display the status of strong-motion observation at the school and other sites in the area.

Because the responsibility of data observation and record collection should be entrusted to nonprofessional partners, we must set reasonable expectations for the precision, reliability, and immediacy of the records. This reduces the cost of the equipment and the installation and maintenance costs. It also reduces the effort involved, thereby enabling the development of the easy and rapid observation. Even if a large-scale disaster damages the network and electric power infrastructure, some data can be collected by this type of simple observation, and a database containing observation records for more buildings may be constructed than highly developed observation systems.

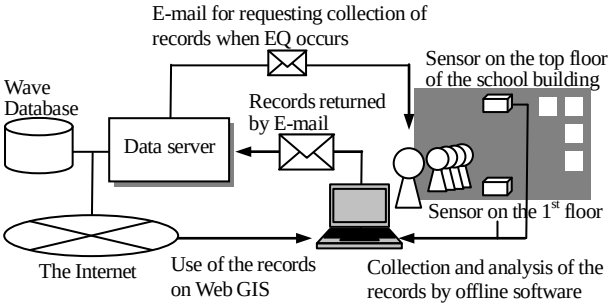


Figure 1 Strong-Motion Observation System

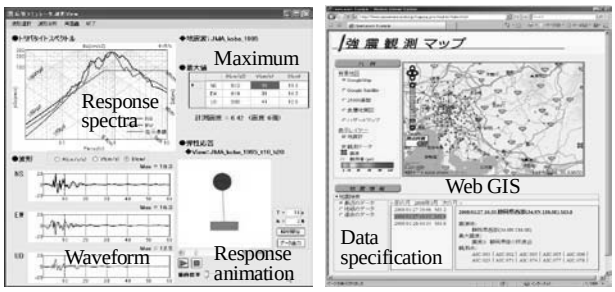


Figure 2 Example of Learning Tool

3. OBSERVATION EQUIPMENTS

The sensors used in this paper are mainly K-NET95 seismometers that were installed during 1995 and 1996, and removed for renewal during 2003 and 2004. An operational test on 133 sensors was conducted in Nagoya University in 2008. Out of the 133 sensors, 13 sensors could not be used for normal observations, while 11 others had some problems during use.

Before using the sensor, the battery box was removed and modified for direct connection to the AC power supply. When the battery is crucial to ensure uninterrupted power supply, a low-cost external UPS is connected to the seismometer to eliminate the need for inspection and

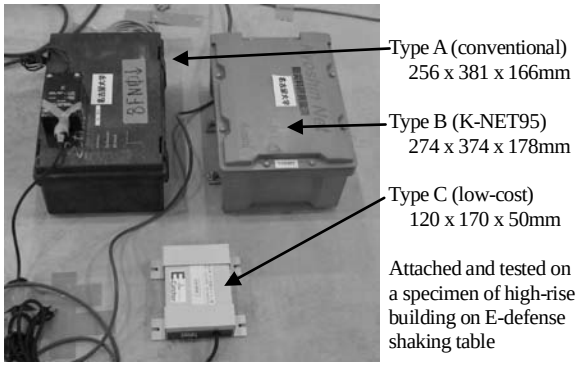


Figure 3 Observation Test on Shaking Table Experiment

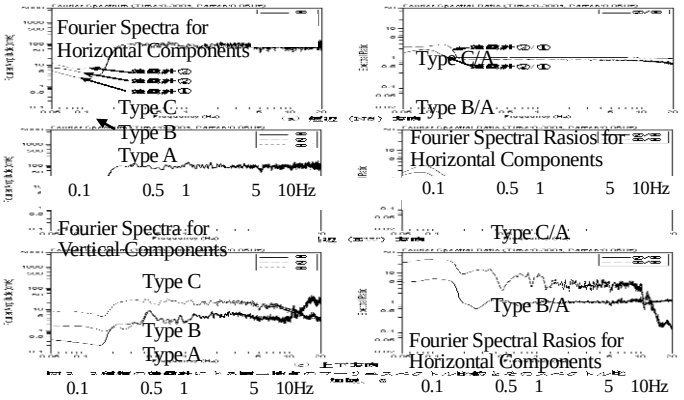


Figure 4 Spectral Characteristics under White-Noise Excitation

Table 1 Strong-Motion Sensors

	Type A (conventional)	Type B (K-NET95, reused)	Type C (low-cost, compact)
Sensor	servo (force balance)	servo	semiconductor
Range	2 G (0.25—4G available)	2 G	2 G (horizontal), 1 G (vertical)
Frequency response	DC—80 Hz (200 Hz sps)	DC—30Hz	DC—20 Hz (h), DC—4Hz (v)
Resolution	18 bits	24 bits	16 bits
Dynamic range	108 dB	114 dB	(noise level 2 gal)
Sampling	100 & 200 Hz	100 Hz	100 Hz
Time calibration	GPS	GPS	NTP
Storage	PCMCIA, 512 MB*2	Flash memory 8 MB	Internal Memory (100s x 56 data)
Communications	serial (RS-232C)	serial (RS-232C)	serial (RS-232C), Ethernet (10M)
Power supply	AC + built-in buttery	AC, battery can be added	AC, dry cell battery
Size and weight	256 x 381 x 178 mm, 9 Kg	274 x 374 x 178 mm, 7Kg	120 x 170 x 50 mm

replacement of the built-in battery of conventional all-in-one type seismometers. Because its small capacity memory (8 MB) is not expandable, the seismometer requires frequent maintenance in the case of continuous noises and aftershocks. With GPS-based time calibration, the sensor can easily receive time data if an antenna is placed at the window with an unobstructed view of the sky. The seismometer has a serial interface that maintains the transfer rate at a value of up to 38,400 bps.

We performed a strong-motion observation test in the E-Defense using a conventional all-in-one type seismometer, the K-NET95 seismometer and a low-cost compact sensor (Tobita, *et al*., 2010). Outline of sensors and setup are shown in Fig. 3, and the specifications of the three sensors are given in Table 1. We compared the spectral characteristics of the sensors under white-noise excitation; see Fig. 4. The results revealed that the K-NET95 showed satisfactory performance for our applications. For reference, we used a low-cost compact semi-conductor type acceleration sensor that had problems in frequency content of upper/lower component and in its low resolutions but showed satisfactory characteristics in the horizontal components for amplitude level of large earthquake response.

We considered new approaches for the collection of the data recorded by the sensors, as the existing sensors have certain limitations. If the sensor is connected to a network such as ADSL or Cable TV, it can automatically transfer observation records to the server via email. Figures 5 and 6 show a network interface with a compact Linux Box and its application for observation. The interface gains access to the sensor on a regular basis, reads any new records, clears existing records when the available memory is low, and adjusts the time via NTP (Network Time Protocol). The interface automatically transmits collected records and its status via email. This significantly alleviates the memory restriction of the seismometer and the effect of GPS reception. Because of the non-direct external connection to the Internet, this method is suitable for ordinary households, where a global address cannot be used, and/or in cases where the rigid network security constraints were applied in the observation building, such as local governments' buildings.



Figure 5 Network Interface with Compact Linux Box

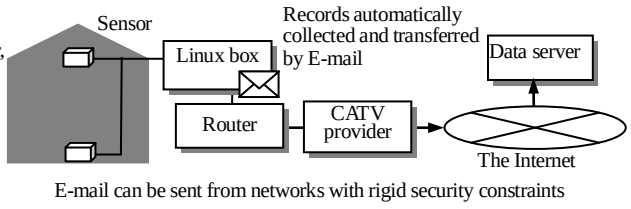


Figure 6 Observation System Using Linux Box

Thus, we can deal with constraints such as network connection, interface speed, time synchronization, and memory capacity and use any old or low-cost equipment. The seismometers installed by local governments have been upgraded nationwide since 2009. Our approach allows the reuse of large quantities of discarded equipment without any associated costs or labor.

4. EXAMPLE OF HIGH-SCHOOL OBSERVATION

We have used the introduced system to observe strong motions at high school buildings in Aichi Prefecture in cooperation with science teachers. Figure 7 shows the sensors placed on the first and fourth floors of a reinforced concrete four-story school building, and Fig. 8 shows an example of the observation records. In 2009, records for six earthquakes were obtained from this school in Okazaki City, Aichi Prefecture. The maximum seismic intensity (3 on the first floor) and response (approximately 50 cm/s^2 on the fourth floor of the building) were observed during the Suruga Bay Earthquake that occurred on August 11, 2009. A trigger interlock between the two sensors was not made, and it can also be seen that the GPS on the first floor did not receive data. However, the time could be adjusted with sufficient precision by using cross correlation of vertical components of observed data in the range of 0.5 to 3 Hz. Consequently, the transfer functions on the fourth/first floors were stably determined, as shown in Figs. 8(d) and 8(e). The

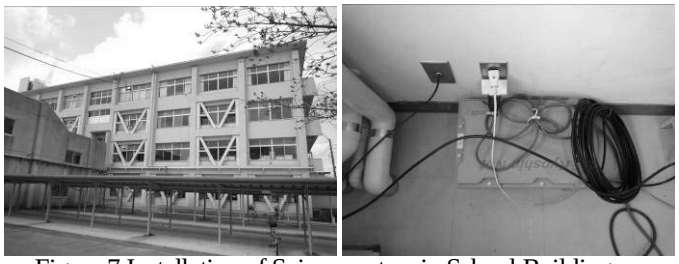


Figure 7 Installation of Seismometers in School Building
(Left: Appearance, Right: 4th floor)

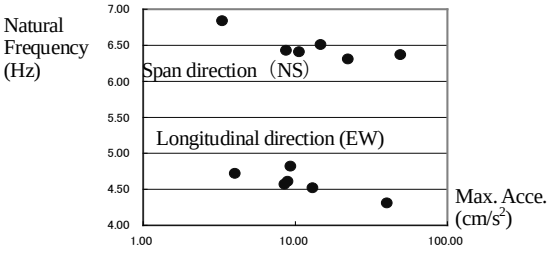
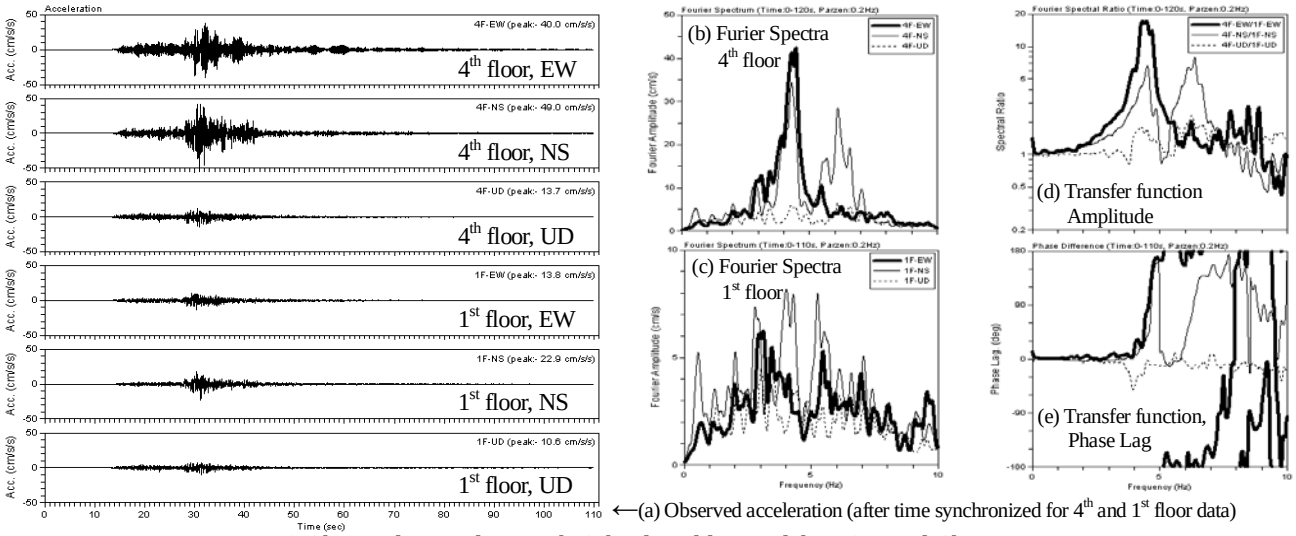
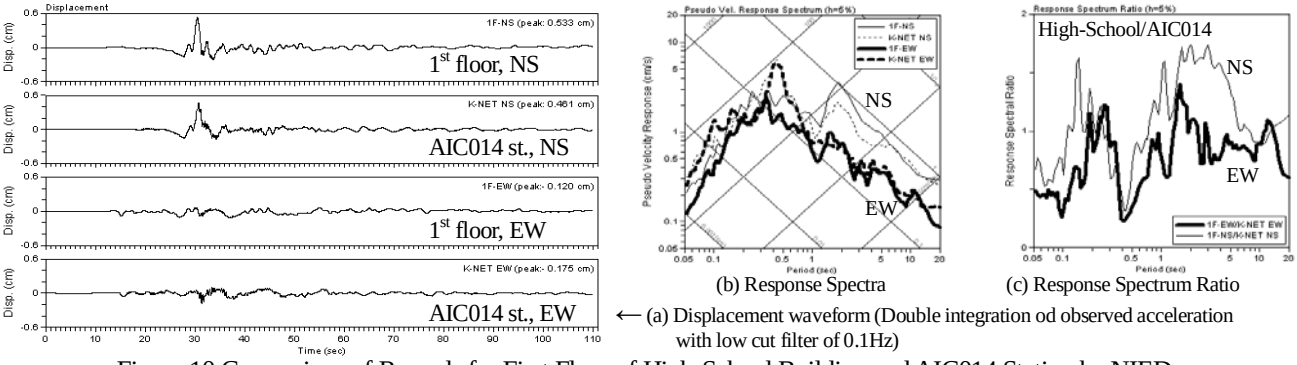


Figure 9 Amplitude Dependency of Natural Frequencies Estimated from Observed Data for Earthquakes



←(a) Observed acceleration (after time synchronized for 4th and 1st floor data)

Figure 8 Observed Records at High-School Building and their Spectral Characteristics
(Suruga Bay Earthquake on August 11, 2009)



(b) Response Spectra (c) Response Spectrum Ratio

← (a) Displacement waveform (Double integration od observed acceleration with low cut filter of 0.1Hz)

Figure 10 Comparison of Records for First Floor of High-School Building and AIC014 Station by NIED
(Suruga Bay Earthquake on August 11, 2009)

natural frequencies identified for the different earthquakes are shown in Fig. 9. The structure is modeled as a linear, time-invariant system with classical normal modes. Two orthogonal horizontal acceleration records at the basement of the structure are used as system input to explain two-dimensional behavior of the structure (Tobita, 1996). Natural frequencies, damping ratios and participation vectors are estimated in the frequency domain. By using the system identification procedure, nonlinear inelastic behavior of the structure is evaluated by the equivalent linear system. Responses ranging from 4 to 50 cm/s^2 are recorded in the span and longitudinal directions, and the amplitude dependence of the natural frequencies can be clearly seen.

Figure 10 shows a comparison of the records from the K-NET station (AIC014) closest to the school building and on the first floor. Although the station and the building are separated by a distance of about 10 km, the characteristics of the long-period components in the displacement waveforms at the school are in good agreement with those at the station. From a performance test on a shaking table, it was confirmed that the displacements were stably determined by double integration of the acceleration by a low-cut filter of approximately 0.1 Hz. In the case of a large-amplitude response, the damage to the building can be assessed on the basis of story deformation (Tobita, *et al*., 2010).

5. FUTURE DEVELOPMENT

Good and reliable observation data are collected by the sensors installed in the school buildings, as described in the previous section, but only keen science teachers and some particularly active students associate the observations with disaster mitigation education. Our next challenge is to make more high-school students as well as elementary-school and junior-high-school students aware of the school observations. High-school teachers often desire practical course materials for disaster prevention and physics (vibration) education as well as for geoscience (earthquake) and geography (society and disaster) classes, as these subjects might capture the attention of the students. Disaster-prevention education has been introduced in elementary-, junior-high-, and high-school curriculums. We believe that it is necessary to revitalize the education in existing subjects with strong focus on disaster mitigation.

Recent attempts to link observations and education include the earthquake observations at elementary schools in the Metropolitan area carried out by ERI, the University of Tokyo (Kasahara, *et al*., 2009), and educational application of observations with high-precision seismometer network "Manten project" by Prof. K. Yamori, DPRI, Kyoto University. In another project, many network-connected vibration observation instruments are provided to applicants and real-time motion information is released nationwide on a website ("Yure-project" by Weather News Inc., http://weathernews.jp/yure/, accessed on January 2nd, 2011). Recently, an attempt has been made with using high-performance smart phones, which have acceleration sensors and GPS-based location information. Observed vibration data is displayed on Web-GIS based map ("*i*Jishin" project with free software by Hakusan corporation, http://i-jishin.appspot.com/, and its introduction in English: http://www.hakusan.co.jp/LABO/i-jishin/iJishin_en.shtml, accessed on January 2nd, 2011). With this attempt, it has been possible to receive the attention of a large number of people.

However, our observation approach is clearly different from the above mentioned projects and attempts. The main purpose of our system is to observe wave data of earthquake response of as many buildings as possible. The observation partners will include high-school teachers, building engineers and researchers who are not specialized in strong-motion observation, engineers and researchers from other fields, administration and mass-media personnel, and interested individuals and building managers. Collaborations with these partners would enable various kinds of new functions by observation.

For example, seismic diagnosis of buildings could be performed not only based on the building information but also using observed building response. Damage prediction for coming large earthquake disaster could be performed clearly on the basis of the Web GIS-based ground conditions and predicted earthquake ground motions at the site of the building. Structural health monitoring and damage assessment of the building are also required by using the appropriate predictions and observations. Based on continuous observation, a building engineer can confirm whether a building under construction will show the desired performance or not and conduct long-term deterioration monitoring. The accumulation of small- and medium-level earthquake records clearly shows the actual response characteristics of the building and their changes, thereby enabling deterioration and damage assessments.

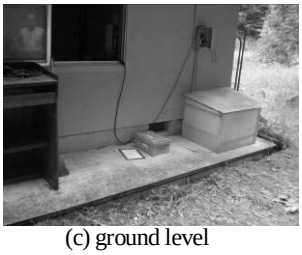
Another important aspect is that the observation is performed by the users and owners of the building, who are most influential with its safety. Figure 11 shows seismometers installed on wooden houses. Earthquake response data on their own house will lead their interest and positive preparedness on future earthquake disasters, e.g. seismic reinforcement of their houses.



(a) 2nd floor



(b) 1st floor



(c) ground level

Seismometers were fixed using double-sided adhesive sheets and were covered with plain covers. These are examples without using Linux Boxes.

Figure 11 Installed Seismometers in Private Houses

6. CONCLUSION

Nonprofessional partner involvement in strong-motion observation through P-NET is expected to reduce operational loads and costs, promote data distribution, and broaden the base of strong-motion observation. In addition, a collaborative relationship with partners with various positions, interests, knowledge, and techniques could allow us to improve the use of strong-motion observation records for disaster prevention.

Acknowledgements:

High-school science teachers have contributed to our continuous observations; FALCON and HAKUSAN Corporation helped us in developing the software and other tools; and NIED permitted us to use the K-NET records. We are grateful for their cooperation. The part of this study was supported by Grant-in-Aid for Scientific Research (KAKENHI (B) No.20360250).

References:

Hirono, E., Makihara, S., Fukuwa, N., Tobita, J., Mori, M. and Kojima, H. (2008), "Development of Animated Application for Effective Analysis of Multi-point Multi-channel Vibration Data," *AIJ Journal of Technology and Design*, **14**(28), 423-428. (in Japanese)

Kasahara, K., Sakai, S., Morita, Y., Hirata, N., Tsuruoka, H., Nakagawa, S., Nanjo, K. and Obara, K. (2009), "Development of the Metropolitan Seismic Observation network (MeSO-net) for Detection of Mega-thrust beneath Tokyo Metropolitan Area," Bulletin of Earthquake Research Institute, the University of Tokyo," 84, 71-88. (in Japanese)

NIED (2004), "Symposium on The 50th Anniversary of Strong-Motion Earthquake Observation in Japan ―History and Perspective―," (in Japanese)

Okada, Y., Kasahara, K., Hori, S., Obara, K., Sekighchi, S., Fujiwara, H. and Yamamoto, A. (2004), "Recent Progress of Seismic Observation Networks in Japan ―Hi-net, G-net, K-NET and KiK-net―," *Earth Planets Space*, 56, xv-xxviii.

Tobita, J. (1996), "Evaluation of Nonstationary Damping Characteristics of Structures under Earthquake Excitations," *Journal of Wind Engineering and Industrial Aerodynamics*, **59**(2,3), 283-298.

Tobita, J., Fukuwa, N., Nakano, M. and Yamaoka, K. (2001), "Development of On-line Data Acquisition System for Strong Motion Seismic Records and its Application to Existent observation Systems," *AIJ Journal of Technology and Design*, 13, 49-52. (in Japanese)

Tobita, J., Fukuwa, N. and Kurata, K. (2009), "Integrated Observation and Database System for Seismic Records using Web GIS and Data Interoperation," *Journal of Japan Association for Earthquake Engineering*, **9**(2), 51-60. (in Japanese)

Tobita, J., Fukuwa, N., Hirata, Y. and Nagae, T. (2010), "Monitoring of Earthquake Response and Damage of High-rise Buildings by Ordinary Strong Motion Sensors," *Journal of Structural Engineering*, 56B, 229-236. (in Japanese)

8CUEE CONFERENCE PROCEEDINGS
8th International Conference on Urban Earthquake Engineering
March 7-8, 2011, Tokyo Institute of Technology, Tokyo, Japan

DEVELOPMENT OF SHAKE TABLE MOTIONS FOR SIMULATION OF THE SEISMIC RESPONSE OF NONSTRUCTURAL SYSTEMS

Manos Maragakis[1], Arash E. Zaghi[2], Siavash Soroushian[3], Ahmad Itani[4], and Gokhan Pekcan[5]

1) Dean, College of Engineering, University of Nevada, Reno, USA
2) Research Scientist, Dept. of Civil and Environmental Engineering, University of Nevada, Reno, USA
3) Graduate Student, Dept. of Civil and Environmental Engineering, University of Nevada, Reno, USA
4) Professor, Dept. of Civil and Environmental Engineering, University of Nevada, Reno, USA
5) Associate Professor, Dept. of Civil and Environmental Engineering, University of Nevada, Reno, USA
maragaki@unr.edu, esmailiz@unr.edu, siyavashs@yahoo.com, Itani@unr.edu, Peckan@unr.edu

Abstract: As part of the project entitled "NEESR-GC: Simulation of the Seismic Performance of Nonstructural System," a series of system-level full-scale experiments of ceilings-piping-partition systems will be conducted at the University of Nevada, Reno NEES Site. This project is aimed at understanding the seismic response of these systems and their interaction with each other and the parent structure. A two-story, two-bay steel braced frame spanning across three biaxial shake tables was designed as a Test-Bed structure to simulate a variety of dynamic environments. After introducing the design considerations of the Test-Bed structure within this paper, the method proposed to develop the shake table drive motions is explained. To obtain the drive motion of the linear Test-Bed, a transfer function (TF) was formulated for a multi-support dynamic system under differential support excitation and combined with a TF previously developed for target floor acceleration of a generic structure. For the nonlinear Test-Bed structure, the drive motion was developed using the concept of drift TF. In the later case, the nonlinearities were accounted for in the formulations by using equivalent damping and effective frequency for the first mode.

1. INTRODUCTION

After an earthquake, the functionality of an essential facility, such as a hospital, relies heavily on the functionality of its nonstructural components, such as piping systems, fire suppression systems, elevators, and other equipment. In recent earthquakes, nonstructural components of hospitals and medical facilities have suffered severe damage, which consequently interrupted the functionality of these facilities (OSHPD, 2010). The 1971 San Fernando Earthquake caused excessive damage to many hospitals and medical facilities, which led to evacuation of four of the eleven damaged medical facilities in the area (Wasilweski, 1998). Due to this unacceptable performance, the State of California passed the Hospital Seismic Safety Act in 1973, requiring medical facilities to remain operational after earthquake events.

The repair and replacement costs of nonresidential buildings after the Northridge earthquake were $6.3 billion, with only $1.1 billion of the total in structural damage (Kircher, 2003). Immediately after this earthquake, 88% of the occupants of the hospital beds in the damaged area (13 hospitals) had to be evacuated as a result of nonstructural damage such as water damage, elevator failure, etc. (Ayres et al., 1998). Hospitals built in accordance with the 1973 Hospital Act, however, were successful in resisting structural damage. Nevertheless, nonstructural damage (plumbing, ceiling systems, etc.) in post 1973 construction was, and still is, extensive after strong seismic activities. This shows an urgent need to better understand the seismic behavior of nonstructural systems.

Extensive systematic experimental data is required as a supplement to previous experience to improve available nonstructural design provisions. Several studies have been conducted on the seismic response of nonstructural subassemblies and their components as early as 1980s on ceiling tiles and piping systems (ANCO, 1983; Hoehler et al., 2009; ATC, 2007); however, the understanding on the system-level response of these subassemblies is significantly limited necessitating the design of large-scale experiments on complete systems (Zaghi, 2010).

As a part of the NEESR Grand Challenge project "Simulation of the Seismic Performance of Nonstructural Systems," a large scale Test-Bed structure is constructed to conduct system-level experiments of full-scale, complex, nonstructural systems. The NEES earthquake simulator (three biaxial shake tables) at the Large Scale Structure Laboratory of University of Nevada, Reno will be used to subject the Test-Bed structure and nested nonstructural systems to desired levels of dynamic excitations.

Nonstructural components can be divided into two categories in terms of seismic performance: 1) acceleration sensitive elements such as ceiling and horizontal pipe runs;

and 2) drift sensitive components, including partition and riser pipes. The Test-Bed structure is designed in a way that it can subject the nested subassemblies to large accelerations as well as large inter-story drifts.

Before describing the methodology used for the development of the shake table input motion, a brief review of the NEESR Grand Challenge is presented, followed by the design philosophy and provisions of the proposed Test-Bed structure.

2. NEESR NONSTRUCTURAL GRAND CHALLENGE PROJECT

The Grand Challenge Project entitled "Simulation of the Seismic Performance of Nonstructural Systems" integrates multidisciplinary system-level studies that develop, for the first time, the simulation capabilities and implementation process for enhancing the seismic performance of ceiling-piping-partition (CPP) nonstructural systems. This project is led by the University of Nevada, Reno in collaboration with the Consortium of Universities for Research in Earthquake Engineering (CUREE), Cornell University, Georgia Institute of Technology, North Carolina Agricultural and Technical State University, North Carolina State University, Rutherford & Chekene, State University of New York at Buffalo, and University of California, San Diego. This paper reports on design considerations and characteristics of UNR Test-Bed structure.

3. TEST-BED STRUCTURE DESIGN PHLOSOPHY

To achieve the objectives of system-level experimental investigation, several key requirements were identified, particularly with respect to the design of the Test-Bed structure. During the experiments, it will be utmost importance to simulate experimentally and to capture the various types of interactions that will take place among the subassemblies and the parent Test-Bed structure. Moreover, the Test-Bed structure should allow investigators to study the effects of structural yielding on the response of the subassemblies. A discussion of the performance design concepts were utilized in the design of the Test-Bed structure with the provisions follows.

A two-story, two-bay (18.6 m-long, 3.66 m-wide, 7.57 m-high) Test-Bed structure was designed. The dimensions are typical of spans and story heights in multi-story buildings and allow for the installation of full height partition walls as well as large ceiling areas. The view of this structure is shown in Fig.1.

To study drift sensitive and acceleration sensitive nonstructural components, two designs were considered for the Test-Bed structure by implementing two sets of bracing systems. Elastic braces restrained against buckling (BRBs), used to achieve large floor accelerations, and buckling resistant braces, used to produce large inter-story drifts.

The test bed is designed for longitudinal excitation. Therefore, the transverse bracing system of the Test-Bed structure was significantly overdesigned to ensure that the longitudinal dynamic modes dominate vibration of the frame.

To understand the effects of the nonstructural subassemblies on the seismic response of structures (specifically stiffness, lateral strength, and added damping) structural dynamic characteristics of the Test-Bed structure should be well known, predictable, and controllable. The Test-Bed structure was designed with 'frictionless' tight-fit hinges in order to avoid any possible deviation of the physical responses from that of numerical models. The column-base and beam-column connections were pinned, minimizing the rotational fixity. The lateral stiffness and strength of the frame is provided by a set of eight brace members that are installed in a chevron configuration. This design methodology allows yielding to take place in predefined members (BRBs).

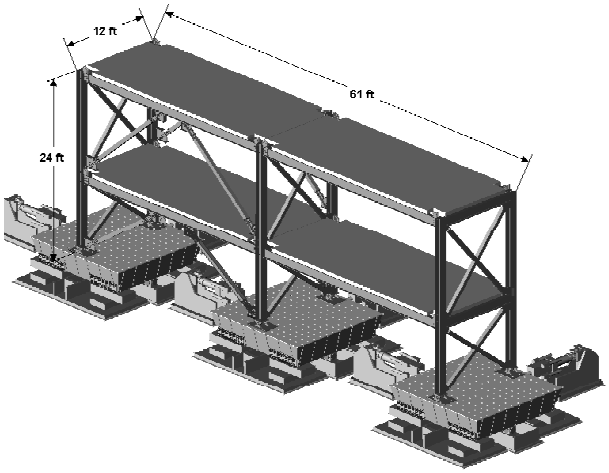


Figure 1 View of the Test-Bed Structure

The Test-Bed structure is planned to be used for multiple experiments, and therefore, should remain linear-elastic during the shake table testing. Utilization of the buckling restrained members as lateral resisting members enables the Test-Bed structure to be used a number of times after replacement of the yielded braces. Furthermore, to allow for a safe assembly and disassembly of the structure, each floor is divided into two prefabricated 5.5-in thick steel deck concrete composite slabs panels that were built off-site and will be shipped to the laboratory. These floor panels as well as other structural members can be stored in a small area before and after the test.

4. TARGET PERFORMANCE OF THE TEST-BED

Although the Test-Bed structure is a two-story frame, it may represent any two adjacent floors of a multi-story building (i.e., the j^{th} and $j+1^{th}$ floors.) Taking the limitations of the shake table into consideration, the Test-Bed was designed to reach a minimum for the inter-story drift and peak floor acceleration without exceeding the hydraulic

system restraints. The target performances of linear and nonlinear Test-Bed structures are separately discussed in this section.

4.1 Nonlinear Test-Bed Structure

This setup was designed to achieve large inter-story drifts similar to that of nonlinear frame structure. This setup was aimed at the evaluation of drift sensitive subassemblies such as in-plane partitions, pipe risers, and riser ducts. Design target of the nonlinear Test-Bed was to achieve an inter-story drift larger than 3% on both stories.

The nonlinear BRBs were designed for this setup and, on each floor, additional mass was provided using low profile lead baskets bolted to the floor to provide required inertial forces. The natural period of the structure was calculated as 0.43sec and the effective period of the structure at 3% drift was found to be 1.21sec.

4.2 Linear Test-Bed Structure

This setup was designed to investigate acceleration sensitive subassemblies including ceilings, sprinkler piping, and out-of-plane partitions. The linear Test-Bed was designed to simulate linear or stiff structures in which large floor acceleration is expected. The target peak floor acceleration (PFA) was larger than 2.0g on both floors.

Because conventional braces required a large cross-section area for local or global buckling requirements, buckling restrained elastic braces were used for the linear structure. This large area increases the elastic stiffness of the structure and as a consequence significantly reduces the effective periods. Although a high frequency Test-Bed experiences large floor accelerations, its period does not fall within the range of practical structures. To avoid yielding of the brace members in the linear structure, strength of the brace members was increased by using higher-grade steel for the brace cores to control the lateral stiffness. An additional mass was provided on the first floors to achieve the target period. The natural period of the structure was found to be 0.19sec.

It should be mentioned that the Test-Bed structure may be modified to achieve other performance limits in accordance with the purpose of the experiment.

5. DEVELOPMENT OF THE SHAKE TABLE INPUT MOTION

It is evident that if a ground acceleration is used as the shake table input motion, the Test-Bed structure will simulate the response of a two-story building supported on the ground. However, the Test-Bed structure is meant to simulate the floor response of any multistory building: a method was developed as part of this project to allow simulation of floor acceleration responses of multistory buildings by using the Test-Bed structure. The theory of a reduced-order earthquake demand assessment that is presented in detail by Taghavi and Miranda (2005) was adopted. The absolute acceleration transfer function (TF) was obtained by superposition of modal TFs. This TF was multiplied by the inverse of a TF for the Test-Bed structure that was formulated with the effect of multi-support excitation in mind. To satisfy the displacement and velocity limitations of the shake-tables, a high-pass filter was added to TF of the system. This method is described in detail in this section.

5.1 Description of Generic Buildings

The dynamic characteristics of multistory buildings are approximated (Taghavi and Miranda, 2005) by using an equivalent continuum model consisting of a flexural cantilever beam and a shear cantilever beam deforming in bending and shear, respectively (Fig. 2). These flexural and shear cantilever beams were assumed to undergo the same lateral deformation. Under a horizontal acceleration at the base, response of this continuum system can be expressed by the following partial differential equation (Taghavi and Miranda, 2005):

$$\rho(x)\frac{\partial^2 u(x,t)}{\partial t^2}+c(x)\frac{\partial u(x,t)}{\partial t^2}+\frac{1}{H^4}\frac{\partial^2}{\partial x^2}\left[EI(x)\frac{\partial^2 u(x,t)}{\partial x^2}\right] -\frac{1}{H^2}\frac{\partial}{\partial x}\left[GA(x)\frac{\partial u(x,t)}{\partial x}\right]=-\rho(x)\frac{\partial^2 u_g(t)}{\partial t^2} \quad (1)$$

where $\rho(x)$ is mass per unit height, $u(x,t)$ is the displacement at normalized height x at time t (x varies between zero, at the base of the building, and one, at the roof level), H is the total height of the building, $c(x)$ is damping coefficient per unit height, $EI(x)$ is flexural rigidity of the flexural beam along the height, $GA(x)$ is shear rigidity of the shear beam and $u_g(t)$is the ground displacement at time t.

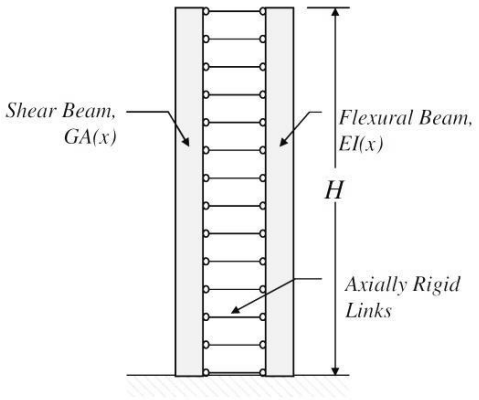


Figure 2 Generic Model to Estimate Dynamic Properties of Multi-Story Buildings (Taghavi and Miranda, 2005)

By solving Eq. (1), the shape of the mode of vibration corresponding to the i^{th} mode, normalized to unity at $x=1$ is found by:

$$\phi_i(x)=\frac{\begin{array}{l}\sin(\gamma_i x)-\gamma_i\left(\gamma_i^2+\alpha_o^2\right)^{-0.5}\sinh\left(x\sqrt{\gamma_i^2+\alpha_o^2}\right)\\+\eta_i\left[\cosh\left(x\sqrt{\gamma_i^2+\alpha_o^2}\right)-\cos(\gamma_i x)\right]\end{array}}{\begin{array}{l}\sin(\gamma_i)-\gamma_i\left(\gamma_i^2+\alpha_o^2\right)^{-0.5}\sinh\left(\sqrt{\gamma_i^2+\alpha_o^2}\right)\\+\eta_i\left[\cosh\left(\sqrt{\gamma_i^2+\alpha_o^2}\right)-\cos(\gamma_i)\right]\end{array}} \quad (2)$$

Where:

$$\eta_i=\frac{\gamma_i^2\sin(\gamma_i)+\gamma_i\sqrt{\gamma_i^2+\alpha_o^2}\sinh\left(\sqrt{\gamma_i^2+\alpha_o^2}\right)}{\gamma_i^2\cos(\gamma_i)+\left(\gamma_i^2+\alpha_o^2\right)\sinh\left(\sqrt{\gamma_i^2+\alpha_o^2}\right)} \quad (3)$$

In Eq. (2), γ_i is obtained from the solution of the characteristic equation shown as Eq. (4):

$$\begin{array}{l}2+\left[2+\dfrac{\alpha_o^4}{\gamma_i^2\left(\gamma_i^2+\alpha_o^2\right)}\right]\cos(\gamma_i)\cosh\left(\sqrt{\gamma_i^2+\alpha_o^2}\right)\\+\left[\dfrac{\alpha_o^2}{\gamma_i\left(\gamma_i^2+\alpha_o^2\right)}\right]\sin(\gamma_i)\sinh\left(\sqrt{\gamma_i^2+\alpha_o^2}\right)=0\end{array} \quad (4)$$

The dimensionless parameter α_o in Eq. (2) controls the degree of participation of overall flexural and overall shear deformations in the generic model of multistory buildings. A value of α_o equal to zero represents a pure flexural and a value larger than 30 corresponds to a shear dominated deformation for a building. In these equations *i* represent the mode number.

For a continuum model with uniformly distributed mass, the modal participation factor of the i^{th} mode of vibration is given by:

$$\Gamma_i=\frac{\int_0^1\phi_i(x)dx}{\int_0^1\phi_i^2(x)dx} \quad (5)$$

Eqs. (2) and (5) were implemented to generate the TF for the absolute acceleration of q^{th} floor of generic building. A method that is discussed in detail in Maddaloni et al. (2010) was utilized to obtain the TF shown in Eq. (6):

$$H_q(\omega)=\sum_{im=1}^{k}\frac{-\left(2i\omega\xi_{im}\omega_{im}+\omega_{im}^2\right)}{\omega_{im}^2-\omega^2+2i\omega\xi_{im}\omega_{im}}\phi_{im,q}\Gamma_{im} \quad (6)$$

Where ω_{im}^2 , Γ_{im} and ξ_{im} are the circular frequency, modal participation factor, and damping ratio of im^{th} mode of generic building, respectively. Only the first *k* significant modes were participated in this derivation. In this equation, $\phi_{im,q}$ corresponds to the value of the im^{th} mode in the q^{th} floor of the building.

5.2 Development Drive Motion of the Linear Test-Bed Structure for the Target Absolute Floor Acceleration

The Test-Bed structure is supported on three shake tables. Each shake table responds slightly different to the drive motion as can be explained by servo-valve control basics. The following formulation for a dynamic system with multiple support excitations was extended to include the support degrees of freedom (DOFs) in the system TF equations. The matrix form of the equation of motion for the Test-Bed Structure with two dynamic DOFs and three support DOFs can be written as (Chopra, 2001):

$$\begin{array}{l}\begin{bmatrix}{}_{2x2}M_{ss} & 0\\ 0 & {}_{3x3}M_{tt}\end{bmatrix}\begin{bmatrix}{}_{2x1}\ddot{u}_s^t\\ {}_{3x1}\ddot{u}_t\end{bmatrix}+\begin{bmatrix}{}_{2x2}C_{ss} & {}_{2x3}C_{st}\\ {}_{3x2}C_{ts} & {}_{3x3}C_{tt}\end{bmatrix}\begin{bmatrix}{}_{2x1}\dot{u}_s^t\\ {}_{3x1}\dot{u}_t\end{bmatrix}+\\ \begin{bmatrix}{}_{2x2}K_{ss} & {}_{2x3}K_{st}\\ {}_{3x2}K_{ts} & {}_{3x3}K_{tt}\end{bmatrix}\begin{bmatrix}{}_{2x1}u_s^t\\ {}_{1x3}u_t\end{bmatrix}=\begin{bmatrix}0\\ {}_{3x1}p_t(t)\end{bmatrix}\end{array} \quad (7)$$

The total displacements include contributions from dynamic and static displacements as:

$$\begin{bmatrix}{}_{2x1}u_s^t\\ {}_{3x1}u_t\end{bmatrix}=\begin{bmatrix}{}_{2x1}u_s^s\\ {}_{3x1}u_t\end{bmatrix}+\begin{bmatrix}{}_{2x1}u_s\\ 0\end{bmatrix} \quad (8)$$

Where [M], [C], [K] are the mass, stiffness, and viscous damping matrices, respectively. The vectors $[\ddot{u}]$, $[\dot{u}]$, $[u]$ are the acceleration, velocity, and displacement, respectively. The superscripts *t* and *s* stand for the total and static responses, accordingly. The subscripts *t* and *s* are related to the shake table's and the structure's responses, respectively. The $P_t(t)$ is the table force vector. Equation (7) can be reduced to Eq. (9) after satisfying static equilibrium.

$$\begin{array}{l}{}_{2x2}M_{ss}\,{}_{2x1}\ddot{u}_s(t)+{}_{2x2}C_{ss}\,{}_{2x1}\dot{u}_s(t)+{}_{2x2}K_{ss}\,{}_{2x1}u_s(t)=\\ -{}_{2x2}M_{ss}\,{}_{2x3}\iota\,{}_{3x1}\ddot{u}_t(t)\end{array} \quad (9)$$

Where ${}_{2x3}\iota=-{}_{2x2}K_{ss}^{-1}\,{}_{2x3}K_{st}$ describes the influence of support displacements (or accelerations) on structure displacement (or acceleration) at dynamic DOFs. Dynamic response of the structure may be decomposed in modal coordinates, $q_i(t)$, that $u(t)=\phi_i q_i(t)$ and ϕ_i is the i^{th} mass-normalized mode shape. Assuming that response is composed of harmonic functions, Eq. (9) can be transformed to Eq. (10) infrequency domain:

$$\begin{array}{l}-\omega^2 q_i(\omega)+2i\omega\xi_i\omega_i q_i(\omega)+\omega_i^2 q_i(\omega)=\\ -{}_{1x2}\Gamma_{i\,2x3}\iota\,{}_{3x1}\ddot{u}_t(\omega)\end{array} \quad (10)$$

Where $(\phi_i^T K_{ss}\phi_i)/M_{ss,i}^*=\omega_i^2$ is the circular frequency and $(C_{ss,i}^*/M_{ss,i}^*)/2\,\omega_i=\xi_i$ is the damping ratio of i^{th} mode of vibration. The absolute acceleration response vector, $\ddot{u}_s^t$, for the Test-Bed structure with two horizontal dynamic DOFs is the summation of the relative acceleration vector and the influence of table acceleration:

$${}_{2x1}\ddot{u}_s^t(\omega)=\sum_{i=1}^{2}-\omega^2\,{}_{2x1}\phi_i q(\omega)_i+{}_{2x3}\iota\,{}_{3x1}\ddot{u}_t(\omega) \quad (11)$$

Equation (11) was pre-multiplied by $({}_{1x2}\phi_i^T\,{}_{2x2}M_{ss})=-{}_{1x2}\Gamma_i$ and combined with Eq. (10) to obtain:

$$ {}_{1x2}\phi_i^T\ {}_{2x2}M_{ss}\ {}_{2x1}\ddot{u}_s^t(\omega) = \frac{-\left(2i\omega\xi_i\omega_i+\omega_i^2\right)}{\omega_i^2-\omega^2+2i\omega\xi_i\omega_i}\ {}_{1x2}\Gamma_{i\ 2x3}\iota_{3x1}\ddot{u}_t(\omega) \quad (12) $$

The mode shape is mass normalized, $\Phi^T M = \Phi^{-1}$, thus Eq. (12) can be manipulated to achieve the absolute acceleration of the j^{th} floor of the Test-Bed structure as:

$$ \ddot{u}_s^t(\omega)_j = \left[\sum_{i=1}^{2}\frac{-\left(2i\omega\xi_i\omega_i+\omega_i^2\right)}{\omega_i^2-\omega^2+2i\omega\xi_i\omega_i}\phi_{i,j\ 1x3}\kappa_i\right]_{3x1}\ddot{u}_t(\omega) \quad (13) $$

The term shown in the bracket is a TF that relates the accelerations of shake tables to the absolute floor acceleration of the Test-Bed. The TF that relates motion of the n^{th} shake table to the acceleration of the j^{th} floor is defined by Eq. (14).

$$ H_{sn,j}(\omega) = \frac{\ddot{u}_s^t(\omega)_j}{\ddot{u}_t(\omega)_n} = \sum_{i=1}^{2}\frac{-\left(2i\omega\xi_i\omega_i+\omega_i^2\right)}{\omega_i^2-\omega^2+2i\omega\xi_i\omega_i}\phi_{i,j}\kappa_{i,n} \quad (14) $$

In this equation, parameter $\kappa_{i,n} = ({}_{1x2}\Gamma_{i\ 2x3}\iota)_n$ is a measure of the participation of n^{th} table on the absolute acceleration of the j^{th} floor in i^{th} mode of vibration. As was mentioned earlier, the achieved table motions may be different from the drive motion (or target motion) due to several factors including the servo valve's dynamic response, the compressibility of the actuator fluid, oil leakage through the actuator seals, and the influence of the mass and stiffness of the test specimen (Maddaloni et al., 2010). The achieved and target shake table motions are assumed to be related through a transfer function H_{tn} for the n^{th} shake table. The TF that relates acceleration of the j^{th} floor to the drive motion can be obtained from the summation of the multiplication of structure TFs, as shown in Eq. (14), with H_{tn}. Figure 3 shows the structure-table dynamic system.

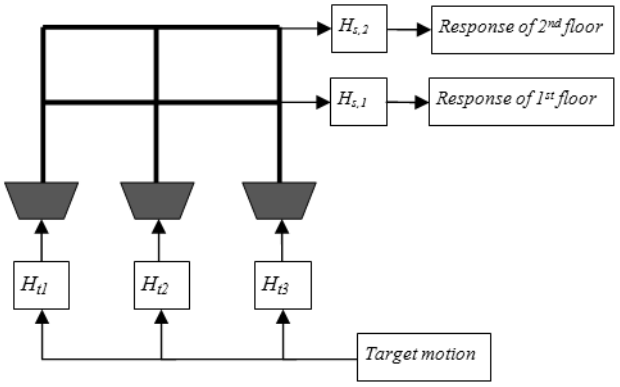


Figure 3 Structure-Table Dynamic System

$$ H_j(\omega) = \sum_{n=1}^{3} H_{tn}(\omega)\cdot H_{sn,j}(\omega) \quad (15) $$

The Test-Bed structure should simulate the specific floor responses of any target building. Floor response of a multistory building subjected to a ground motion, $\ddot{u}_g(\omega)$, can be obtained by using the TF presented as Eq.(6).

The drive motion of the shake tables to achieve the target floor motion can be generated by multiplication of the inverse of the TF of the Test-Bed shake table system shown in Fig. (3) and can express as:

$$ \ddot{u}_{Drive}(\omega) = H_q(\omega).H_j(\omega)^{-1}.\ddot{u}_g(\omega) \quad (16) $$

Expression of $\ddot{u}_{Drive}(\omega)$ in the time domain gives the time history of the drive motion of the shake tables. A suitable high-pass filter may be needed to insure that the demands on the shake tables are within acceptable limits to permit continued use. This method allows for the simulation of floor accelerations of any type of structural system subjected to any set of ground motions.

This work will be continued to develop a similar formulation that can be used for simulation of the inter-story drifts of the generic building. A simplified method will be used to account for the structural nonlinearities.

5.3 Development Drive Motion of the Nonlinear Test-Bed Structure for the Target Inter-Story Drift

Approximate solutions for nonlinear response of yielding structures have gained a wide interest as a simple analysis technique for seismic design procedures. One of the techniques used involves replacing the nonlinear structure with an equivalent linear structure whose maximum displacement response will be, approximately, equal to the original nonlinear structure response. Equivalent linear systems with equivalent damping and effective period were proposed to approximate the steady-state response of a damped nonlinear system after Jacobsen (1939). For a nonlinear system with a hysteretic response shown in Fig. 4, the equivalent hysteretic damping and frequency in a ductility of μ can be found as Eqs. (17) and (18), respectively.

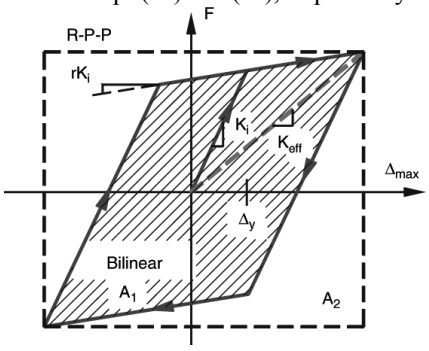


Figure 4 Equivalent Damping for Bilinear and R-P-P Hysteretic Models (Dwairi et. al, 2007).

$$ (\xi_{eq})_{Bilinear} = \xi_{viscus} + \frac{2(\mu-1)(1-r)}{\mu(1+r\mu-r)} \quad (17) $$

$$ \frac{\omega_{eff}}{\omega_i} = \sqrt{\frac{1+r\mu-r}{\mu}} \quad (18) $$

Extensive study was conducted by Dwairi et. al (2007) on four different hysteretic models, namely, (1) Ring-Spring, (2) Large Takeda, (3) Small Takeda, and (4) Elasto-Plastic. These models cover a wide range of structural systems including, concrete and steel frames. Four sets of formula for equivalent damping and effective stiffness have been developed for each hysteresis model.

To account for the nonlinearities of the generic structure, it was assumed that all the inelastic response happens in the first mode of vibrations which has the largest dynamic participation. This was accomplished by using equivalent and effective values for ξ_1 and ω_1, respectively in Eq. 6. For simplicity the shape of the first mode and modal participation factor were assumed to remain unchanged. For all the other dynamic modes, the same values of elastic system were used to develop the TF. In the same way, the damping and frequency of the first mode of vibration of the Test-Bed structure were incorporated in formulation of TF as shown in Eq. (14). Figure 5 shows how the yielding changes the shape of the TF of the test-bed structure. These curves were generated by subjecting the analytical model of the Test-Bed structural to increasing amplitudes of a white noise input motion.

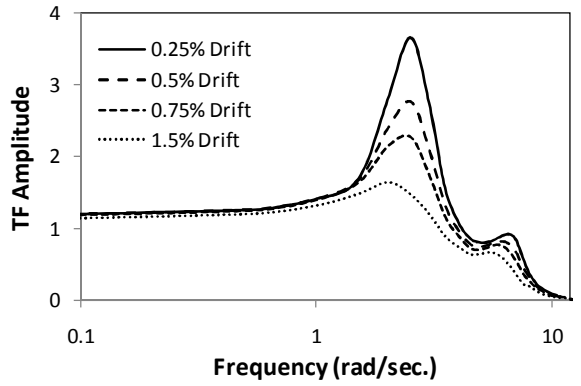


Figure 5 Change of the Shape of the Transfer Function of the Test-Bed Structure due to Yielding

This figure confirms that yielding introduces significant damping into the first mode of vibration. Slight change in value of the frequency of the first mode can also be detected.

The main goal for the nonlinear Test-Best structure is to achieve the drifts equivalent of the ones expected in the generic building with consideration of nonlinearities. Therefore, for the nonlinear Test-Bed, the transfer function for drifts was used, as oppose to the previously developed acceleration TF. This was done by finding the derivative of the TF functions of the displacement with respect to the height (i.e. the differential displacements of the floors divided by the height of the story.) Equation (19) shows how the Eq. (16) can be modified to develop the input motions to achieve any desired drift. This equation leads to a good estimate for the maximum drift response; however, it may not achieve the exact time history response of the drift.

$$\ddot{u}_{Drive}(\omega) = \frac{H_q(\omega) - H_{q-1}(\omega)}{h_q \sum_{im=1}^{k} \left(2i\omega\xi_{im}\omega_{im} + \omega_{im}^2\right)} \cdot \left[\frac{H_j(\omega) - H_{j-1}(\omega)}{h_j \sum_{i=1}^{2} \left(2i\omega\xi_i\omega_i + \omega_i^2\right)}\right]^{-1} \cdot \ddot{u}_g(\omega) \quad (19)$$

In this equation, h_q and h_j are the heights of the stories in the generic building and the Test-Bed Structure, respectively.

6. SUMMARY AND CONCLUSIONS

A reusable Test-Bed structure was developed for shake table investigations of nonstructural systems. The Test-Bed structure simulates two adjacent floors of a multistory building. This two-story, two-bay frame can accommodate full-scale subassemblies and subject them to large drifts and/or accelerations. The design of this frame allows for reusing the Test-Bed.

The drive motion of the shake tables was obtained in order to achieve a target floor motion for the linear Test-Bed and a target drift for nonlinear Test-Bed structure. This target floor motion, or drift, was obtained from analysis of a continuum dynamic system representing a generic multistory building, offering a notable versatility to simulate floor acceleration of any type of structure. Nonlinearities were included in this formulation making use of effective frequency and equivalent damping for the first mode of vibration.

Acknowledgements:

This material is based upon work supported by the National Science Foundation under Grant No. 0721399. Any opinions, findings, conclusions or recommendations expressed in this document are those of the investigators and do not necessarily reflect the views of the NSF. The input provided by the Practice Committee of the NEES Nonstructural Project, composed of W. Holmes (Chair), D. Allen, D. Alvarez, and R. Fleming; by the Advisory Board, composed of R. Bachman (Chair), S. Eder, R. Kirchner, E. Miranda, W. Petak, S. Rose and C. Tokas; and by the other members of the Experimental Group, A, Filiatrault, G. Mosqueda, A. Reinhorn, and J. T. Hutchinson, has been crucial for the completion of this research. The authors are grateful to Dan Andreason of Yajima USA Ltd. for the cooperation during construction of the Test-Bed structure.

References:

ANCO Engineers, Inc. (1983). "Seismic Hazard Assessment of Nonstructural Ceiling Components Phase I," *NSF grant CEE-8114155, ANCO Engineers, Inc.,* Culver City, CA.

ATC.(2007). "FEMA 461-Interim protocols for determining seismic performance characteristics of structural and nonstructural components through laboratory testing," Redwood City, CA.

Ayres, J.M., Phillips, R.J. (1998)."Water Damage in Hospitals Resulting from the Northridge Earthquake," *ASHRAE Trans.*, Vol. 104, Part 1, American Society of Heating, Refrigerating and Air-Conditioning Engineers, Atlanta, Georgia.

Chopra A. K. (2001). "*Dynamics of Structures, Theory and Applications to Earthquake Engineering (2nd edn)*".Prentice-Hall: Upper Saddle River, NJ.

Dwairi, H. M. , Kowalsky, M. J. and Nau, J. M. (2007) "Equivalent Damping in Support of Direct Displacement-Based Design", *Journal of Earthquake Engineering*, **11**(4), 512 – 530.

Jacobsen, L. S. (1930) "Steady forced vibrations as influenced by damping", *ASME Transaction* **52**(1) , 169-181.

Hoehler, M. S., Panagiotou, M., Restrepo, Silva, J. F., Floriani, L., Bourgund, U., and Gassner, H. (2009). "Performance of Suspended Pipes and Their Anchorages During Shake Table Testing of a Seven-Story Building," *Earthquake Spectra* 25, 71.

Kircher, C. A. (2003), "It Makes Dollars and Sense to Improve Nonstructural System Performance." *ATC-29-2 Proceedings of Seminar on Seismic Design, Performance, and Retrofit of Nonstructural Components in Critical Facilities*.

Maddaloni G, Ryu P.K, Reinhorn A.M. (2010). "Simulation of floor response spectra in shake table experiments," *Earthquake Engineering and Structural Dynamics* DOI:10.1002/eqe.1035.

Miranda E, Taghavi S. (2005a). "Approximate floor acceleration demands in multistory buildings. I: Formulation". *Journal of Structural Engineering* **131**(2), 203–211.

OSHPD.(2010). "California Senate Health Committee Hearing on Hospital Seismic Safety," *The Office of Statewide Health Planning and Development*, Sacramento, CA.

Wasilweski, R.J.(1998). "Seismic Restraints for Piping Systems," *ASHRAE Trans*., Vol. 104, Part 1, American Society of Heating, Refrigerating and Air-Conditioning Engineers, Atlanta, Georgia.

Zaghi, A. E., Maragakis, E. M., Itani, A., and Goodwin, E. (2010) (In Press)."Experimental and Analytical Studies of Hospital Piping Subassemblies Subjected to Seismic Loading," *Earthquake Spectra*, EERI

8CUEE CONFERENCE PROCEEDINGS
8th International Conference on Urban Earthquake Engineering
March 7-8, 2011, Tokyo Institute of Technology, Tokyo, Japan

SHAKING TABLE TEST FOR THE EXAMINATION OF THE POUNDING PHENOMENON BETWEEN SPRINKLER HEADS AND CEILINGS

Kunio Mizutani[1] and Shojiro Motoyui[2]

1) Professor, Dept. of Architecture, Faculty of Engineering, Tokyo Polytechnic University, Japan
2) Associate Professor, Dept. of Built Environment, Tokyo Institute of Technology, Japan
mizutani@arch.t-kougei.ac.jp, motoyui.s.aa@m.titech.ac.jp

Abstract: When the big damage does not occur for building structure by an earthquake, the damage occurs to the non-structural element, and there is the case that a building is not available for a long term. And when the disaster prevention facilities such as sprinklers are damaged, what cannot prevent a second fire after the earthquake not only the direct damages such as floods occur is the problem that is very important in disaster prevention.
In this study, we perform the vibration experiment of the ceiling where a sprinkler is installed in and aim at elucidating the mechanism of the damage of the sprinkler head at the time of the earthquake and the collision.

1. INTRODUCTION

Earthquakes not only damage the major structural parts of buildings, causing them to collapse, but they also cause serious damage to non-structural parts, such as ceilings, ducts and pipes. Severe loss may happen in buildings of which structures have no damage during an earthquake, for example, when collapsed or falling ceilings, furniture and facilities cause fatalities, or when buildings become non-functional and unusable because of damaged ducts and pipes. Even when building facilities can be restored in a short period of time, damaged pipes may lead to leaks and serious damage to the interiors of buildings, and expensive equipment and products.

There have been recent cases of damaged facilities or flooded rooms, such as in the damage caused by the Niigata Chuetsu-oki Earthquake on July 16, 2007, and the Iwate-Miyagi Nairiku Earthquake on June 14, 2008, and the Iwate Engan-hokubu Earthquake on July 24, 2008.

In some of these cases, damage to fire protection systems, such as broken sprinkler pipes and malfunctioning sprinkler heads, may cause leakage causing flooding, and prevent secondary fire occurring after an earthquake from being extinguished, which presents a very important issue in terms of fire protection.

Against this background, this study presents recent cases of damaged sprinkler systems. The study also aims to clarify the mechanisms behind sprinkler system damage and collision using vibration experiments with buildings and ceilings with sprinkler systems installed in them to understand the phenomenon of sprinkler heads and ceilings hitting each other during earthquakes. It is hoped this will provide useful data for earthquake-resistant measures for fire protection systems.

2. Examples of sprinklers damaged by earthquakes

Photos 1 to 3 show a sprinkler system and sprinkler heads damaged by the Iwate Engan-hokubu Earthquake on July 24, 2008. Photo 1 (sprinkler heads on the ceiling) and Photo 2 (the sprinkler system above the ceiling) show the resulting damage after sprinkler heads and ceiling tiles hit against each other in an amusement facility. Because sprinkler heads are made of precision components, the sprinkler heads malfunctioned and leaked when the sprinkler heads and the ceiling hit against each other. It is thought that the sprinkler heads and the ceiling hit against each other, because head fasteners were worn out, which changed the distance between the sprinkler heads and the ceiling

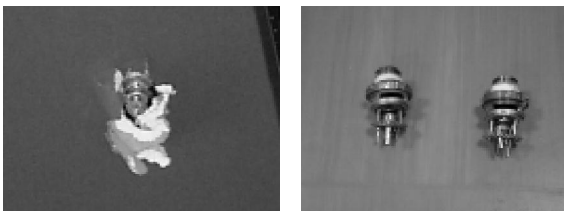


Photo 1 Damaged ceiling and sprinkler heads after hitting against each other



Photo 2 Damaged sprinkler pipes that had been fixed above the ceiling

openings.

Photo 3 shows ruptured sprinkler pipes in the Hachinohe City Auditorium. In this case, sprinkler heads did not hit against the ceiling openings, because the sprinkler pipes near the sprinkler heads were fixed firmly. However, because the sprinkler pipes swayed considerably, it is thought that great force was exerted on the bifurcation of adjoining vertical sprinkler pipes, and the sprinkler pipes ruptured at screwed sections.

These examples of damaged sprinkler systems indicate that a locational deviation between ceiling openings and sprinkler pipes affects sprinkler systems greatly at the time of an earthquake

3. Method of setting sprinklers

Figure 1 shows a typical method of setting sprinkler heads in the ceiling.

Water for sprinklers is drawn from water pipes to sprinkler heads via adjoining vertical sprinkler pipes. The sprinkler heads are fixed to metal carrying channels using main fasteners and auxiliary fasteners. With the ceiling and fasteners stabilized using this method, sprinkler heads are displaced simultaneously even when the ceiling surface is displaced by seismic activity. Therefore, this structure can prevent sprinkler heads and ceiling openings from hitting against each other.

However, as shown in Photos 1 and 2, the ceiling and sprinkler heads actually hit against each other. This damaged the ceiling tiles and sprinkler heads, and impaired the function of water sprinkling. Several instances of ceiling tiles and sprinkler heads being damaged during an earthquake, as in this case, have been confirmed. It is thought that one of the reasons for the damage is the sprinkler heads are fixed with wire and thumbscrews of a simple structure, so the fastening devices for sprinkler heads slide or drop, and the sprinkler heads move differently from the ceiling during an earthquake disturbance.

Because fastening devices for sprinkler heads are fastened to carrying channels, ceiling tile openings and sprinkler heads may jolt out of alignment and hit against each other when a hold-down clip between a main runner and a carrying channel slides, and even when fastening devices for sprinkler heads do not slide or drop.

The fact that hold-down clips between main runners and carrying channels slide during the occurrence of an earthquake has been confirmed by experiments conducted by Motoyui et al., and this causes the hold-down clips to fall and ceilings to collapse. Therefore, in order to prevent ceiling openings and sprinkler heads hitting against each other, attention must be paid to prevent the falling of hold-down clips.

Since vertical sprinkler pipes connected to sprinkler heads are particularly inflexible, stress generated in fastening devices for sprinkler heads becomes greater depending on the difference between the vibration properties of ceilings and water pipes. As a result, it is thought that fastening devices for sprinkler heads and hold-down clips start to slide easily. However, if fastening devices are reinforced to prevent them from sliding, all the stress generated due to the different motions of ceilings and water pipes will be placed on the vertical sprinkler pipes connected to sprinkler heads, and this may cause the pipes to rupture and lead to devastating flooding, as shown in Photo 3.

Because an emphasis has been put recently on the deformability of ceilings, flexible pipes are often used in place of vertical sprinkler pipes connected to sprinkler heads. Even in this case, the movement of hold-down clips between main runners and carrying channels cannot be controlled, so sprinkler heads and ceiling openings may hit against each other when the hold-down clips slide.

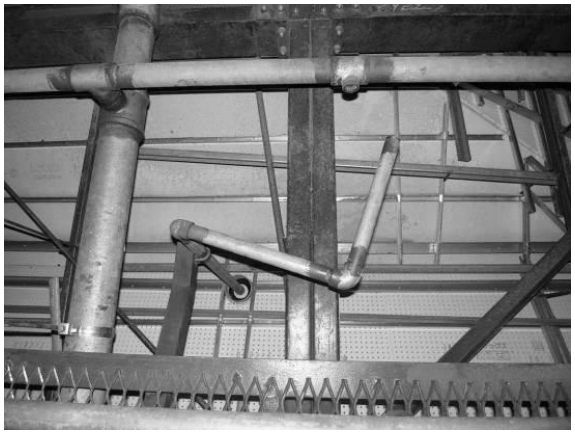
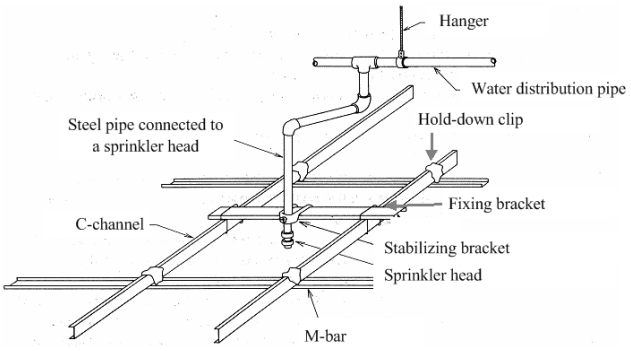
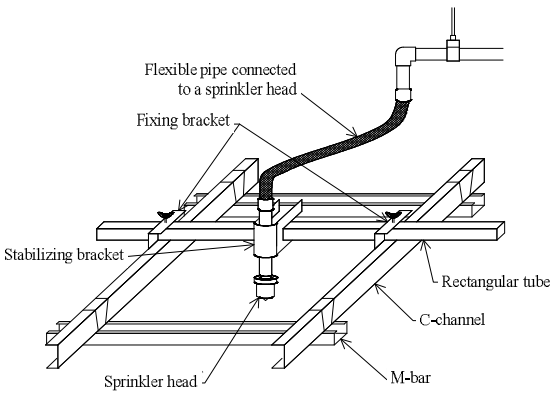


Photo 3 Ruptured sprinkler pipes in the Hachinohe City Auditorium



(1) Steel pipe connection[1)]



(2) Flexible pipe connection

Figure 1 Method of setting sprinklers

4. Preliminary dynamic experiment using an shaker

In order to recreate a situation in which a ceiling and sprinkler heads hit against each other, sprinklers were installed in a device with a ceiling shaker, as shown in Figure 2 and Photo 4, and a sweep vibration test was conducted with the frequency changed at a fixed rate. Photo 5 shows the damage caused after conducting the test. It was confirmed that the main fasteners that fixed the sprinkler heads slid considerably when vibration was added, and that the sprinkler heads hit against the ceiling tiles. It was also confirmed that when vibration was added with the main fasteners fixed firmly auxiliary fasteners sometimes dropped due to deformation of carrying channels, and the sprinkler heads hit against the ceiling tiles.

In addition, when vibration was added with the auxiliary fasteners fixed firmly, hold-down clips that connected the main runners and carrying channels slid and dropped, and this caused the collapse of the ceiling. It is thought that because the connection of the sprinkler heads was reinforced stress concentrated in the area near the fastening devices, and the hold-down clips started sliding quickly, leading to the collapse of the ceiling.

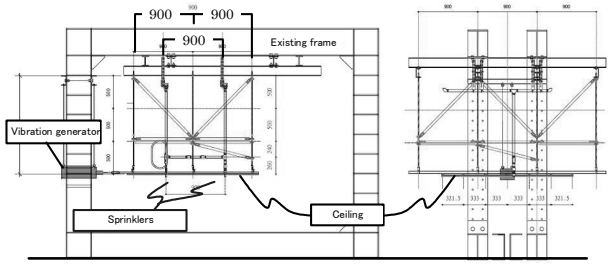


Figure 2 Apparatus of dynamic test with shaker

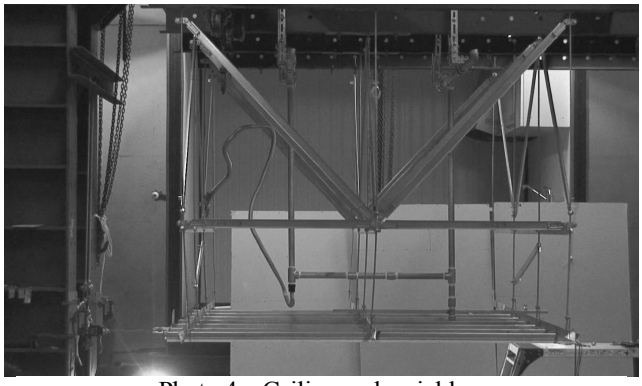
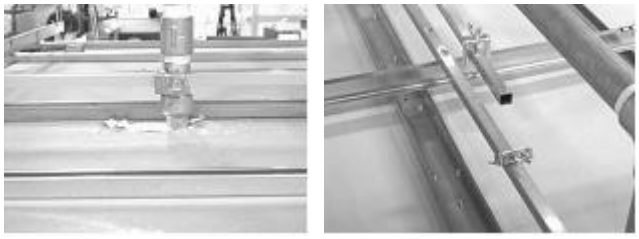


Photo 4 Ceiling and sprinklers



(a)Sprinkler head hitting the ceiling (b) Dropped auxiliary fastener

Photo 5 Damage simulated in the experiment with the use of an shaker

5. Shaking table test

When an earthquake actually occurs, the vibration of floor slabs prompts the vibration of sprinkler pipes and ceilings that are connected with the floor slabs. Therefore, a vibration test was conducted with the use of a shaking table as shown in Photo 6. Two types of pipes were used to connect with sprinkler heads: a conventional steel pipe and a flexible pipe.

Figure 3 shows the chronological change of the ceiling surface and sprinkler heads when 300% of El-Centro waves were added. The difference in displacement (relative displacement) between the ceiling and sprinkler heads was between 10 mm and minus 10 mm, and this indicates that the sprinkler heads repeatedly hit, touched or moved away from the ceiling openings. Photo 6 shows the final stage where 400% of El-Centro waves were added. The entire ceiling collapsed, though the ceiling without sprinkler heads did not collapse entirely. This indicates that increased rigidity and strength of sprinkler heads do not necessarily improve the earthquake-resistance of the ceiling, but they generate a concentration of stress and cause damage to the ceiling, like diagonal bracings. It was judged from the final stage that the fire-extinguishing function of the sprinklers was lost due to the collapse of the ceiling, even though the sprinkler system did not collapse.

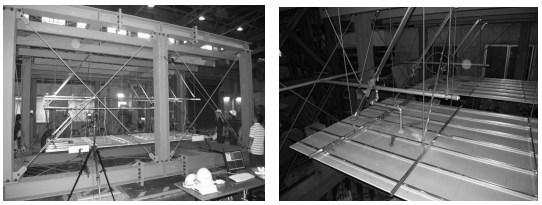


Photo 6 Apparatus of dynamic test with shaking table

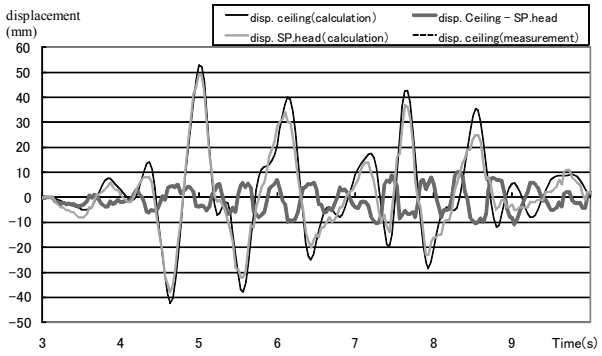
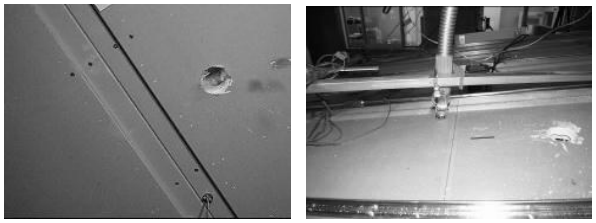


Figure 3 Deformation of the ceiling and sprinkler heads at the time of vibration



(a)5.08 seconds after starting vibration (b)Flexible pipe after vibration

Photo 7 Damage made after 300% of El-Centro waves were added

6. Shaking table test with a full-scale five-story steel-frame building

In order to understand the behavior of a ceiling and a sprinkler system in a full-scale building at the time of an earthquake, we prepared a ceiling and sprinkler system on the fifth floor of a full-scale five-story steel-frame building for vibration testing (Photo 8) with the E-Defense table of the National Research Institute for Earth Science and Disaster Prevention, and conducted a vibration test using a JR Takatori wave in order to confirm the behavior of the ceiling and sprinkler system at the time of an earthquake.

As a result (Photo 9, Figure 4), we confirmed that, when the ceiling swayed significantly, vertical sprinkler pipes that were connected to sprinklers and steel pipes on the other end ruptured at points that were screwed. We also confirmed that, even when flexible pipes were used, sliding hold-down clips caused the ceiling and sprinkler heads to start hitting against each other, and that, after auxiliary fasteners came off, sprinkler heads moved and the sprinkler system was impaired.

7. Conclusion

We conducted various vibration tests for a sprinkler system installed above a conventional ceiling with steel framing, and confirmed the dynamic behaviors of the sprinkler system at the time of an earthquake. We will conduct a detailed study on the interaction of the ceiling and the sprinkler system in the future.



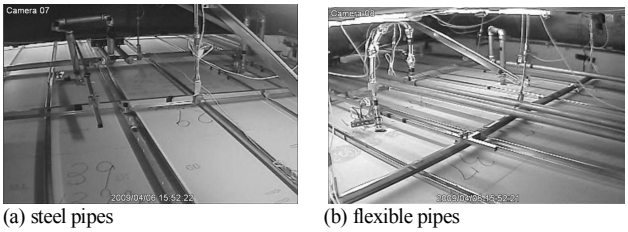
Photo 8 Test conducted with the full-scale five-story steel-frame building for vibration testing

Acknowledgements:

This research was conducted as part of activities for the Ceiling Work Group (Leader: Shojiro Motoyui, Tokyo Institute of Technology) under the Comprehensive Technological Development Project of the Ministry of Land, Infrastructure, Transport and Tourism, "Development of the Performance Assessment of New Structures and Buildings Made of High-Strength Steel and Other Innovative Structural Materials," and also as part of activities for the Vibration Control and Base Isolation Work Group (Leader: Kazuhiko Kasai, Tokyo Institute of Technology) under the Research Group on Steel Structures and Buildings with the Use of E-Defense (Leader: Kazuhiko Kasai, Tokyo Institute of Technology), run by the National Research Institute for Earth Science and Disaster Prevention. We would like to express our gratitude to all the parties concerned.

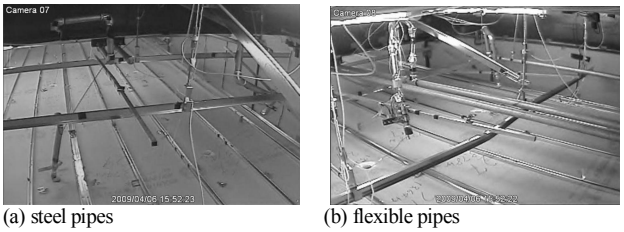
References:

1) "Earthquake-Resistant Design and Construction Methods for Architectural, Mechanical, Electrical and Plumbing Facilities," p.162, The Society of Heating, Air-Conditioning and Sanitary Engineers of Japan (October 1997)
2) "Guidelines for the Design and Construction of Earthquake-Resistant Architectural Facilities 2005," The Building Center of Japan (December 2005)



(a) steel pipes (b) flexible pipes

(1)40% of JR Takatori wave being added



(a) steel pipes (b) flexible pipes

(2)At the time of the ceiling collapse

Photo 9 Behavior of sprinklers connected with steel pipes (a) and flexible pipes(b) above the 5th floor ceiling at the time of vibrating the full-scale five-story steel-frame building for vibration testing

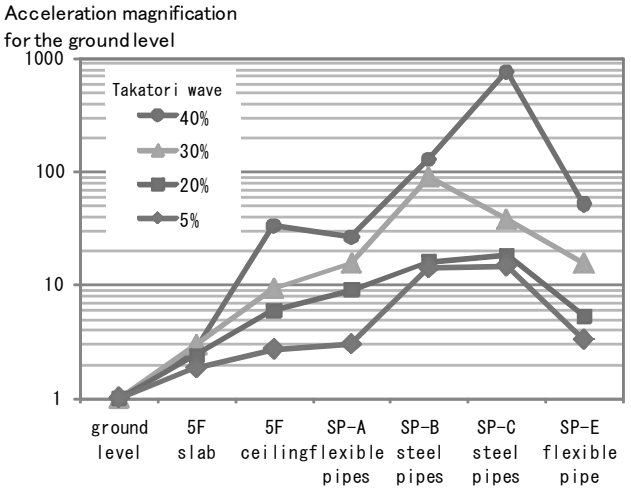


Figure 4 Relations of the biggest ground level input acceleration and the each section's biggest acceleration

8CUEE CONFERENCE PROCEEDINGS
8th International Conference on Urban Earthquake Engineering
March 7-8, 2011, Tokyo Institute of Technology, Tokyo, Japan

MECHANICAL CHARACTERISTICS OF METAL JOINT PARTS IN JAPANESE STYLE OF CEILING

Shojiro Motoyui[1)], Yasuaki Sato[2)], Yuichiro Shimizu[2)], and Tomonari Koshikawa[2)]

1) Associate Professor, Dept. of Built Environment, Tokyo Institute of Technology, Japan
2) Graduate Student, Dept. of Built Environment, Tokyo Institute of Technology, Japan
motoyui@enveng.titech.ac.jp, yasuaki.s.aa@m.titech.ac.jp, shimizu.y.aj@m.titech.ac.jp, koshikawa.t.aa@m.titech.ac.jp

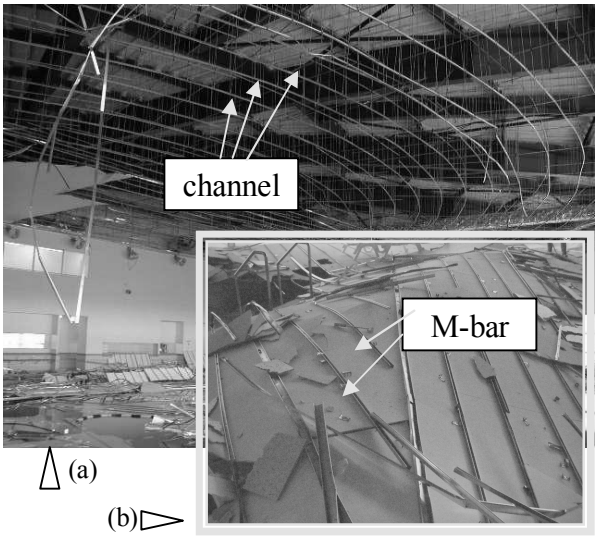
Abstract: The damage of non-structural components like a ceiling in earthquakes brings about the huge economical loss. There have been vague issues with regard to the reason of failure of ceiling while some significant properties have been found through our recent research. The structural characteristics of the ceiling are greatly influenced with metal joint parts used in the connection of steel furring. In this paper, we focus on the metal joint parts and show the mechanical characteristics via experimental results. Finally we suggest the numerical method for the system using metal joint parts.

1. INTRODUCTION

In the recent earthquakes, non-structural components like ceilings, walls and various equipments suffered several damage while structural frames in the buildings did not so. It is no doubt that such damage of non-structural components interrupts daily activity of people or discontinues running of its facility. Then it has been one of the most important issues to overcome immediately.

We have been already researched the characteristics of the Japanese style of ceiling and found out the reason why ceilings fell down during earthquakes. It is obvious that the detachment behavior of clips is the trigger of the falling of ceiling through the observation of the actual falling situation of ceilings after earthquakes. Photographs 1 show (a) the overview of damage situation after an earthquake and (b) gypsum boards fell down. In Photograph (a), it can be seen that a group of steel furring members called "channel" held the original position (height) though the most of gypsum boards fell down. Furthermore, in Photograph (b), another group of steel furring members called "M-bar" which was attached with screws to gypsum boards fell down with gypsum boards. The connection between M-bars and channels is jointed with unique metal parts called "clip". The detachment of clips causes the failure of the ceiling. Furthermore, according to our dynamic test of ceilings, the fatigue of metal joint parts between channels and M-bars is observed.

The main purpose in this paper is to clarify the mechanical characteristics of such metal joint parts and to establish the numerical method and model for accurately simulating the behavior of a ceiling during an earthquake including the strong nonlinear behavior of the connection by the metal joint parts.



Photograph 1 Typical damage of ceiling with earthquake (a)Overview of damage situation and (b) Gypsum board fell down

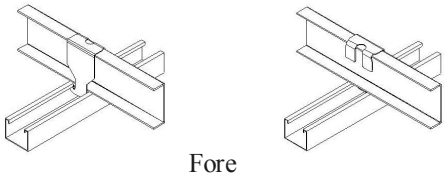


Figure 1 Setting pattern of Clips

2. EXPERIMENT FOR METAL JOINT PARTS

2.1 Clip

Clips are set in two ways. Each setting is called "Front setting" or "Back setting" shown in Figure 1. We have studied the mechanical characteristics of the fore setting type

but have not done ones of the back setting type. Then, we executed a test for the back setting type shown in Figure 2. The parameters are the length (L=250mm and 900mm) of a channel and the velocity (v=0.2cm/sec and 10cm/sec) of loading (see Figure 2).

Figures 4 show the experimental results. The influence of the loading velocity on the behavior of a clip is not considerable because the results in different velocity are the same load-displacement relationship macroscopically. At first, a clip slips with keeping the constant strength, of which value is less than 0.1kN. After unloading and reloading; point B, the clip resists to the horizontal load. At point C, the root of the clip buckles and the strength slightly decreases. The strength rapidly increases at Point D since another part of the clip root contacts with the M-bar. The strength of the connection reaches to the maximum value at Point E. After that, the contact point of the clip root slips and the strength sharply decreases. On the other hand, the influence of the length of a channel is much greater and the relationship between the load and displacement for L=900 is different from the above case; L=250. In particular, it is observed that the plateau and recovery of strength in the resistance phase for Point C and D in Figure 4(a) varnishes and the strength monotonically increases until reaching to the maximum strength.

It should be noted that the clip just slips without resisting to the horizontal load in both results. The behavior is quite different from one during the initial loading at the virgin condition. The reason is why the clip looses owing to the buckling of the clip root. Furthermore, in case of the Back setting, the detachment behavior cannot be observed at this test which extracts a joint part by a clip though such behavior occurred in case of the Fore setting.

2.2 Hanger

The mechanical characteristics of a hanger are examined with the simple test extracting only a hanger. Figure 5 show the apparatus of the test. The two loading patterns are considered. One is the cyclic loading and another is the cyclic in the uni-direction. Figure 6 is the load-displacement curve. The play in the connection is observed at the initial phase or neutral phase of the loading process. After some points on the hanger contact to the surface of the channel, the strength steadily increases. The maximum strength is determined with the yielding of the plate at the bottom of the hanger.

3. NUMERICAL METHOD FOR METAL JOINT PARTS

3.1 Outline of Numerical Method

The various resultant stresses generally act on the metal joint parts subject to the 3-dimensional forces and moments. The elastoplastic condition should be judged accurately to simulate the behavior of such members. The effect of shear stresses caused with shear forces and torsion is often

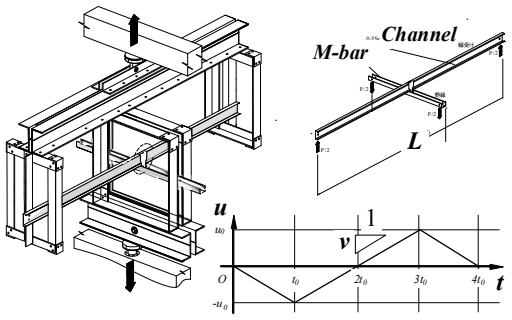


Figure 2 Test for Back setting type of connection with Clip

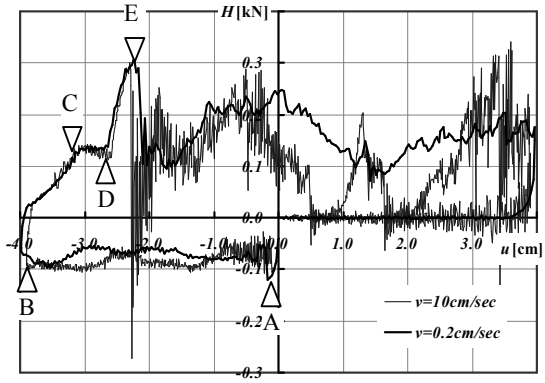


Figure 4(a) Experimental results for L=250

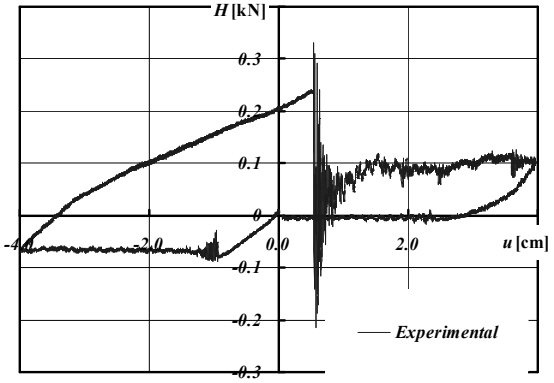


Figure 4(b) Experimental results for L=900

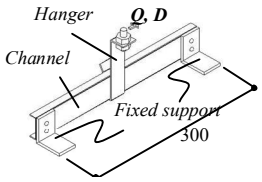


Figure 5 Test for Hanger

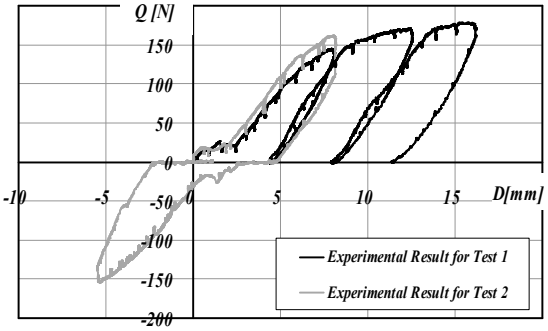


Figure 6 Experimental results for Hanger

neglected in using a co-rotational beam element. Particularly the influence of shear stresses in torsion should be considered when analyzing the 3-dimensional behavior of a hanger because the behavior of the hanger subjected to the lateral horizontal load is affected by the torsion of the bottom plate as mentioned in 2.2. On the other hand, when using the co-rotational beam element, the shear deformation including the pure torsion which is the so-called the Saint Venant's torsion, is generally assumed to keep the elastic condition while the yielding behavior is considered for the axial normal component of stress including the effect of the warping torsion which is the so-called the Wagner's torsion. In this paper, the yielding is considered for both types of torsion behavior. We explain the outline of the present method.

At first, we consider the relationship between the total strain and the displacement at both nodes. As the nodal displacement vector for calculating strains in the co-rotational formulation, one generally uses the vector $\tilde{\boldsymbol{u}}$ that is got with eliminating the effect of a rigid motion and rotation from the total displacement. Now $\boldsymbol{u}$ at an arbitrary point in the beam element is assumed to be expressed as

$$u(r,s,t)=u_0(r)-\gamma(r)s+\beta(r)t+\omega(s,t)\alpha'(r) \qquad (1.a)$$

$$v(r,s,t)=v_0(r)-\alpha(r)t\,,\quad w(r,s,t)=w_0(r)+\alpha(r)s \qquad (1.b,c)$$

where $(u_0,v_0,w_0),(\alpha,\beta,\gamma)$ are the displacement and rotations at the centroid axis of the element. ω,α' are a warping function and the rate of torsional rotation. (*r, s, t*) are co-rotational coordinate shown in Figure 7.Restricting to the thin plate, the strain components to be took account are only two components of ε_{rr}, ε_{rs}. Each component can be expressed by the nodal displacement vector through the definition of strain respectively and the usual finite element formulation.

$$\varepsilon=\boldsymbol{B}\tilde{\boldsymbol{u}}\,,\qquad \varepsilon^T=\langle\varepsilon_{rr}\quad\varepsilon_{rs}\rangle \qquad (2.a,b)$$

$$\tilde{\boldsymbol{u}}^T=\langle\tilde{u}\ \ \tilde{\alpha}_i\ \ \tilde{\beta}_i\ \ \tilde{\gamma}_i\ \ \alpha_i'\ \ \tilde{\alpha}_j\ \ \tilde{\beta}_j\ \ \tilde{\gamma}_j\ \ \alpha_j'\rangle \qquad (2.c)$$

where $\tilde{u},(\tilde{\alpha}_i,\tilde{\beta}_i,\tilde{\gamma}_i)$ are a stretch of beam, rotations around *r,s,t* axis at i-node, and α_i' are the rate of torsion at i-node.

Next, describe the treatment of the present elastoplastic problem. We apply the following yielding function to specify the allowable stress space.

$$f(\sigma,\lambda)=\sqrt{{\sigma_{rr}}^2+3{\sigma_{rs}}^2}-\sigma_y(\lambda) \qquad (3)$$

In this paper, the isotropic hardening is only considered. The associated flow rule for Eq.(3) is assumed to be satisfied and the plastic strain rate can be expressed as

$$d{\varepsilon^p}_{rr}=\frac{\partial f}{\partial\sigma_{rr}}d\lambda=\frac{\sigma_{rr}}{\sigma_y}d\lambda \qquad (4.a)$$

$$d{\varepsilon^p}_{rs}=\frac{\partial f}{\partial\sigma_{rs}}d\lambda=\frac{3\sigma_{rs}}{\sigma_y}d\lambda \qquad (4.b)$$

where $d\lambda\geq 0$ is the plastic consistent parameter. The return mapping algorithm is applied to the numerical

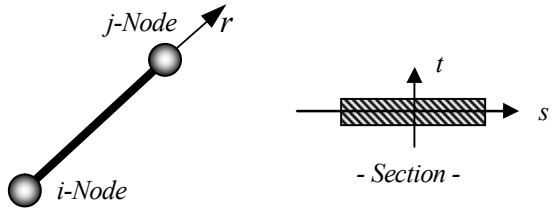


Figure 7 Co-rotational coordinate

calculation of actual stresses.

The tangent coefficient can be derived by using Eqs.(3) and (4) as following.

$$\begin{Bmatrix}d\sigma_{rr}\\ d\sigma_{rs}\end{Bmatrix}=\boldsymbol{D}^{ep}\begin{Bmatrix}d\varepsilon_{rr}\\ d\varepsilon_{rs}\end{Bmatrix},\quad \boldsymbol{D}^{ep}=\boldsymbol{E}-\frac{1}{\boldsymbol{g}\cdot\boldsymbol{E}\boldsymbol{g}}(\boldsymbol{E}\boldsymbol{g})\otimes(\boldsymbol{E}\boldsymbol{g})$$

$$\boldsymbol{E}=\begin{bmatrix}E & \cdot\\ \cdot & G\end{bmatrix},\quad \boldsymbol{g}^T=\begin{Bmatrix}\dfrac{\sigma_{rr}}{\sigma_y} & \dfrac{3\sigma_{rs}}{\sigma_y}\end{Bmatrix} \qquad (5)$$

The numerical method to simulate the slip or contact behavior is based on the 'master-slave model' which was suggested by Crisfield et.al.(2000). We have extended the master-slave model to the contact, slip and detachment problem. And the validation and efficiency of the extended method have already been shown by the authors (Motoyui 2009) through the application to the complicate nonlinear behavior of a Front setting type of a clip. In this paper, we extend it to more general problems like the slip behavior with Coulomb's friction condition.

$$\Phi^{\pm}=|T|+\mu N+c=0 \qquad \text{for } N<0 \qquad (6.a)$$

$$\Phi^{0}=T=0 \qquad \text{for } N\geqq 0 \qquad (6.b)$$

where *N,T* are forces normal or tangent to a slip surface, μ is a coefficient of friction and *c* is a coefficient of cohesion

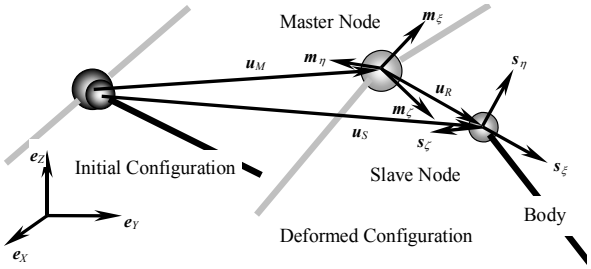


Figure 8 Master-slave model

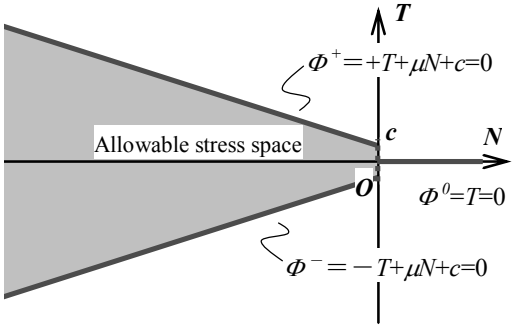


Figure 9 Coulomb's friction criteria

3.2 Validation of the present beam element

To examine the validation of our numerical method, we consider some simple numerical examples as shown in Figure 8. The first one is a thin plate subject to torsion. The second is a single of hanger with the clear boundary condition. In two cases, the width and thickness of plates are 24mm and 2mm. The material properties are also common: Young modulus; 206GPa, Poisson's ratio; 0.3, yield stress; 315MPa, Hardening coefficient; 0.0. The seven numerical integral points are arranged in the both direction of width and thickness.

Figure 9 shows the relationships between torque moment and torsional rotation for the thin plate in the Saint Venant's torsion and the Wagner's torsion. The warping of both ends can be freely developed in the Saint Venant's torsion model while it is constrained and a bi-moment is developed in the Wagner's torsion model. Solid lines are results by shell elements and symbols are ones by the present beam element. The results with the present beam elements both for the Saint Venant's torsion and the Wagner's torsion are close to ones with shell elements. Then, the present element can simulate the effect of the warping and the shear strain in torsion after yielding.

Figure 10 shows the load-displacement curve for the elastic or elastoplastic results of the hanger model with H=98mm. We calculate them using the present beam elements and shell elements. In the beam model, the effect of warping is considered. Each result with the present beam agrees with one with shell elements. These agreement means it is valid for the present beam element to be applied to the elastoplastic torsion problem. Furthermore, the full plastic strength is approximately equal to H times of the full plastic strength of the plate model. Through this equality, we should consider the effect of the warping when simulating the behavior of the hanger subject to the horizontal loading.

4. NUMERICAL ANALYSIS OF METAL JOINT PARTS

4.1 Modeling

For the connection with a clip, the numerical model as shown in Figures 11 and 12. The master nodes are arranged as shown in Figure 11. The master nodes in a channel, a M-bar and a clip are connected by some dummy elements. The dummy elements to represent contact and release, slipping and detaching are arranged and the total number of the dummy elements amounts to six. Show dummy element for contact between a channel and a M-bar as a example in Figure 12. The direction of contact or slipping is defined with the co-rotational unit basis ($\boldsymbol{e}_r$, $\boldsymbol{e}_s$, $\boldsymbol{e}_t$) . The unit basis initially is specified with both slave nodes of the dummy element. After deformation, they rotate with the rotation at the master nodes. Therefore, the slave nodes should be arranged correctly to simulate the contact or slipping behavior.

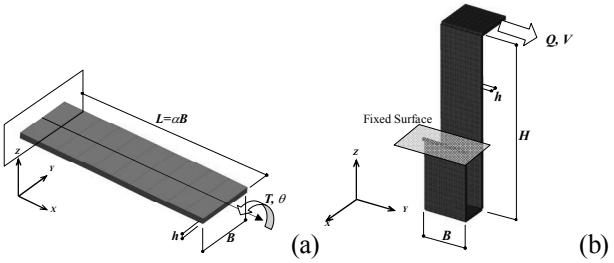


Figure 8 Numerical examples for validation

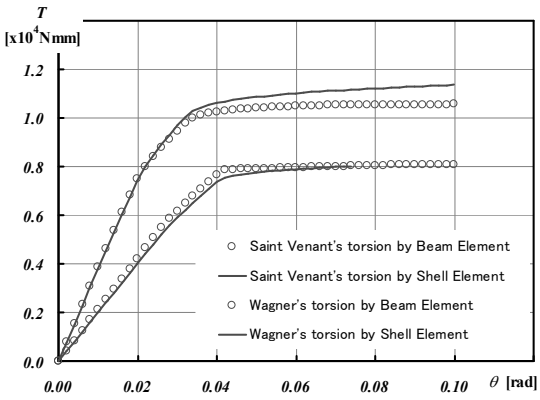


Figure 9 Torque moment-torsional rotation curve

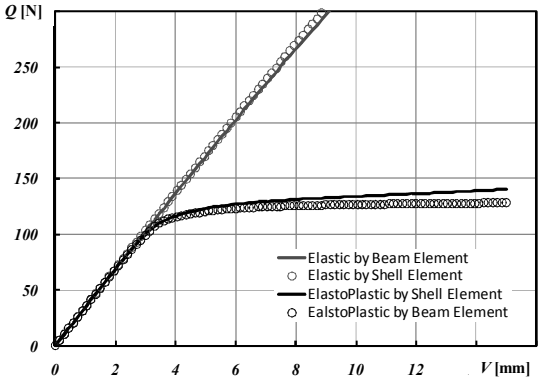


Figure 10 Load-displacement curve

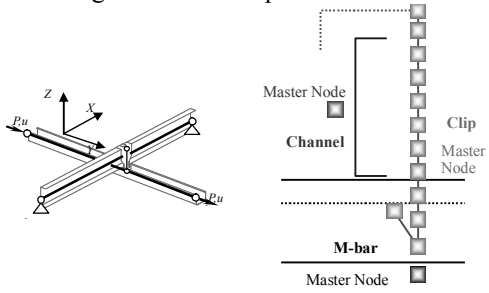


Figure 11 Layout of Master nodes

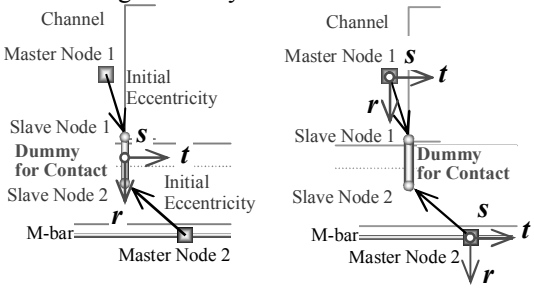
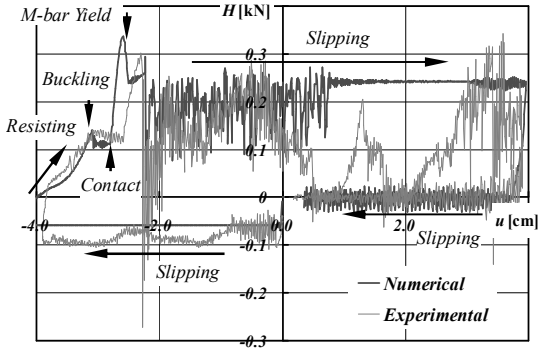
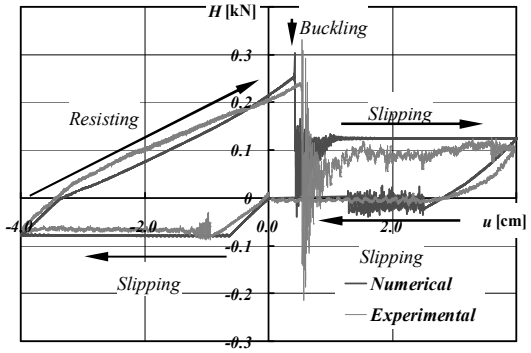


Figure 12 Example of Slave nodes

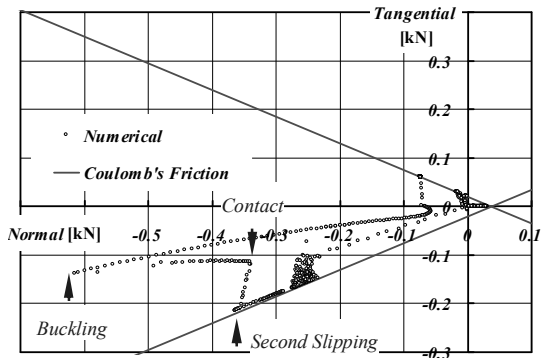


(a) Load-displacement curve L=250

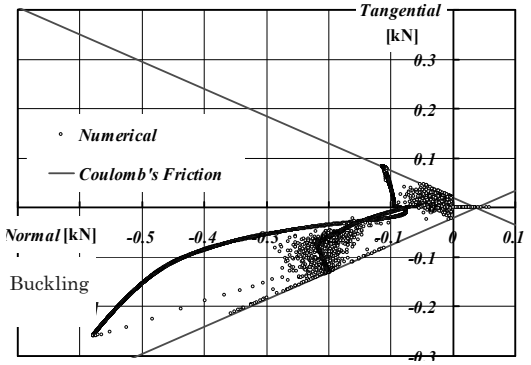


(b) Load-displacement curve L=900

Figure 13 Comparison between Numerical and experimental



(a) L=250



(b) L=900

Figure 14 Interaction of tangential and normal force at slipping surface

4.2 Numerical results

Figures 13 show the load-displacement curves for the connection with clips. We dynamically analyze this problem since the vibration with high frequency occurs. The numerical results for both length of a channel are coincident to the experimental results in all the phase of initial slipping, resisting, second slipping after the maximum strength and slipping with loosening. Figures 14 show the interaction of tangential and normal forces at the slip surface between the clip and the M-bar. The plateau of strength after buckling of the root in the clip vanish in the load-displacement curve for L=900 as I mentioned above. The reason is that the slope of the channel delay the buckling of the root and the rate of the tangential and normal forces is different from one in the model of L=250.

Figure 15 shows the load-displacement curve for the connection with a hanger. The results for two types of loading agree with the experimental results respectively.

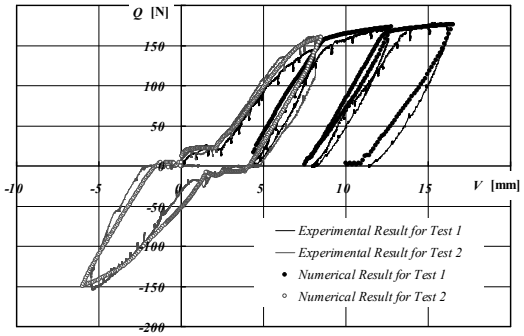


Figure 15 Load-displacement curve of Hanger

5. CONLUSION

In this paper, we examined and clarified the mechanical characteristics of the metal joint parts experimentally and numerically. And we suggested the numerical method and model for the connection by such parts and showed the validity of the present numerical method through some numerical examples and comparison with experimental results.

References:

Crisfield, M.A. (2000), "Non-linear Finite Element Analysis of Solids and Structures Volume 2 Advanced Topics", John Wiley & Sons Inc.

Motoyui, S. et.al.(2009), "DAMAGE IN EARTHQUAKES AND DYNAMIC CHARACTERISTICS OF HANGING CEILING SYSTEM IN JAPAN", 6th International Conference on Urban Earthquake Engineering, 2009, Tokyo, Japan

8CUEE CONFERENCE PROCEEDINGS
8th International Conference on Urban Earthquake Engineering
March 7-8, 2011, Tokyo Institute of Technology, Tokyo, Japan

CEILING DAMAGE IN THE 2010 CANTERBURY EARTHQUAKE

Gregory MacRae[1], James Hair[2] and Rajesh P Dhakal[1]

1) Associate Professor, Dept. of Civil and Natural Resources Engineering, University of Canterbury, New Zealand
2) Structural Engineer, BECA Consultants, Christchurch, New Zealand

Abstract: The Canterbury (Darfield) earthquake of 4th September 2010 caused an intense shaking in New Zealand's second largest city, Christchurch. Fortunately there were no fatalities resulting from the earthquake. However, there was significant loss to structures on liquefiable soil, to URM structures, and due to non-structural damage in buildings subject to the strong shaking. Damage to ceilings contributed significantly to the non-structural damage which caused major business interruption. This paper describes the type of ceiling systems commonly used in NZ and the types of ceiling damage observed in the earthquake.

1. INTRODUCTION

The magnitude 7.1 Darfield (Canterbury) earthquake occurred at 4:35am on 4 September 2010 (NZST) on the previously unknown Greendale fault. The surface rupture was a right strike-slip extending about 30km. The maximum surface ground movement was approximately 4.6m and the rupture zone was 30 to 300 m. The focus was approximately 11km deep and was located about 8km southeast of Darfield and about 37km west of the centre of New Zealand's second largest city, Christchurch. This area is considered to be in a zone of moderate seismicity. In the weeks subsequent to the main shock a number of aftershocks, several with magnitudes greater than 5.0, rocked the Canterbury region and caused strong localized shaking leading to further damage and liquefaction. At the time of writing of this paper (almost 5 months after the earthquake), aftershocks are still very frequent; the most recent big one being the 5.1 magnitude aftershock on 20 January 2011.

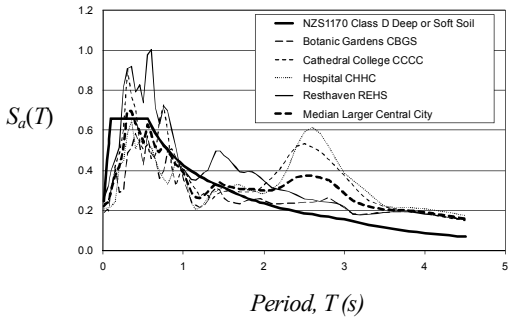


Figure 1. Recorded and NZS1170 Spectra (Cousins and McVerry, 2010)

The acceleration response spectra from the larger horizontal component for 4 sites within the Christchurch central business district (CBD) is compared with the NZS1170.5 elastic design spectra for deep soils, in Figure 1. It may be seen that both for structures with periods between 0.2s and 0.8s and greater than 2.2s that the elastic design level spectra is exceeded.

Possibly one of the most significant effects of the earthquake was the extensive damage to lifelines and residential houses resulting from liquefaction and lateral spreading. This occurred primarily in areas close to major streams, rivers and wetlands throughout Christchurch as well as Kaiapoi, approximately 19km north of Christchurch. Ejection of silt causing a blanket over 200mm thick occurred in many regions. Lateral spreading of up to 3m caused large cracks and damaged houses severely. Houses settled unevenly. Many kilometres of water pipe and wastewater pipe were damaged. Empty sumps floated and roads had up to 0.5m vertical offsets.

Older residential houses suffered collapse of brick chimneys, some of which fell through house roofs. Older houses often had vertical and horizontal cracks around the interior gypsum board. Many houses on good soil, especially those with lighter roofs built on a slab-on-grade foundation suffered no damage at all, but many lost brittle contents such as glasses and china.

A number of older unretrofitted unreinforced masonry (URM) structures in the CBD partially collapsed resulting in total demolition. Many unreinforced brick parapets collapsed onto the footpath below.

Newer multi-storey structures generally seemed to behave well, but information is still becoming available. One structure made from concrete indicated beam plastic hinge rotations with cracks in the hinge zone as big as 5mm. In another, damage was evident in gravity columns which had to follow through the displacements of the rest of the frame. In another, at the ends of simply supported precast beams, 45° cracking at the supports was evident. Most structures showed no distress, and the base-isolated hospital behaved well.

Whereas structural damage was mainly restricted to

old unretrofitted buildings, non-structural and contents damages were observed in all types of building (Dhakal 2010). The non-structural damages involved cracking in internal linings and contents falling to the ground, damage at separation joints and water damage from broken pipes which led to falling wall tiles. It occurred in both older and newer structures. Perhaps the damage which caused the most business interruption in non-URM structures on good soil conditions was that due to ceiling panels falling in many structures. This paper describes the damage to ceiling panels in the Canterbury (Darfield) earthquake. Many of these are taken from a ceiling damage reconnaissance report prepared after the earthquake (MacRae et al. 2010).

2. NZ CEILING SYSTEMS

New Zealand uses suspended ceilings; mainly manufactured and supplied by Rondo™, USG™ and Armstrong™. Many of these have used high mass to limit sound transmissibility. Even buildings constructed in the last 10 years have ceiling panels weighing 16kg/m^2 or more. More recently lighter panels with the same acoustic rating have been used. While concealed ceiling grids with screw fixed plasterboard sheets (such as are used in Japan) are available from companies such as USG, they are not popular. The most popular systems are two-way exposed ceiling grids with drop in panels sitting on the flanges of the inverted 'T' shaped members in the grid. One of these is shown in Figure 2. Here, the ceiling grid is suspended from the floor above using rods or wires. The panels fit loosely in the grid so that they can easily be popped up for access to services. The panels may be punctuated by HVAC or fire sprinkler services. Also, in some cases panels are removed and replaced by fluorescent lighting. Tile/panel tie downs are seldom used.

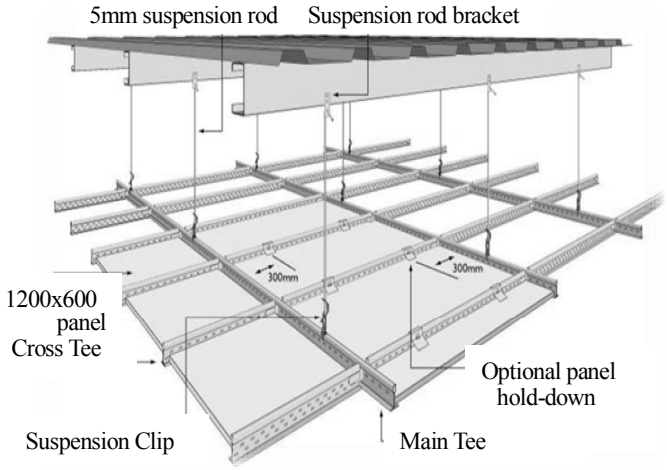


Figure 2: Typical Suspended Ceiling Installation (modified from Rondo DUO, 2008)

There are two common installation methods. *Floating ceilings* are braced to the floor above and a gap is left around the ceiling perimeter so that impact does not occur with the walls during the expected excitations. *Perimeter restrained* ceilings are restrained laterally by the walls around their perimeter. As the building moves laterally, the suspension clips and rods move on an angle to follow the deformations of the ceiling. Since the ceiling panels do not sit tightly in the grid, force is not directly transferred from one panel to another. Instead, forces from panel horizontal accelerations are transferred through the grid. In New Zealand, most of the ceilings are *perimeter restrained*.

Different framing systems have been developed by the major suppliers for use in zones of different seismicity. However, there are a number of issues which make the ceilings vulnerable. They are:

1. Seismic design methods for ceilings were first introduced in the 1970s so the many ceilings in existing structures are not designed for seismic loading.
2. Standards have been written for the design and installation of ceilings (e.g. AS/NZS 2785). The standards tend to be followed by the major installers but they are not enforced by national or local authorities and are not followed by all installers.
3. Ceiling seismic design tends to be inspired by seismic code provisions being used for other components which are designed to resist a level of seismic force less than that expected in a design level earthquake. While other elements of a building system may possess significant ductility, those in NZ ceilings generally do not.
4. Licensing of ceiling installers is not mandatory so it is possible for people without any training, or any appreciation of the important issues, to install ceilings. This may result in a significant range of construction quality.
5. The installation of the ceiling is usually performed by a subcontract to the main contractor. There is an incentive for the major contractor to obtain the cheapest possible ceiling installation in order to win the contract.
6. There are no enforced standardized protocols to ensure different services (e.g. HVAC, fire sprinkler systems, etc) work together to ensure that the final result is likely to meet specified minimum performance.
7. Anecdotal evidence indicates that both the cost and the quality of installation in Christchurch tends to be lower than that in other NZ centres.
8. There is evidence of some cases of very poor practice including such things as vertical partition walls having no out-of-plane resistance. This means that instead of them bracing the ceiling, they actually impart load to it during earthquake shaking.

3. DAMAGE SUSTAINED

The damage sustained by ceilings has been organised by damage type: grid damage; perimeter damage; interaction with services; one-way grid spreading; and combinations of these damage types. The photos given below are courtesy of Hush Interiors Ltd. unless otherwise stated.

Grid damage results from excessive force on the grid members or connections. This then results in buckling of the

grid members or failure of the connections. Figures 3-4 show grid damage sustained.

Perimeter damage results from the main tee or cross-tee losing seating on the perimeter angle around the ceiling. Loss of seating can result due to a lack of a rivet to connect the grid member to the angle or failure of the rivet itself. This results in the grid members and panels dropping from the ceiling. Edge perimeter hanging wires can prevent the member and panels from falling, however, this can result in the panel and members being forced back into the angle causing damage to the panels and members as shown in Figure 5.



Figure 3: Damage resulting from the disconnection of the cross-tee from the main beam resulting in localized grid collapse and panel loss

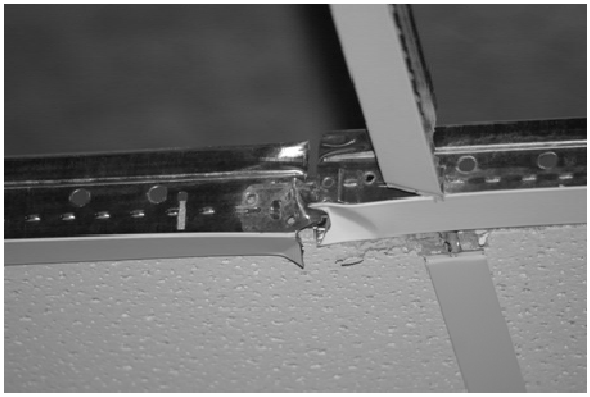


Figure 4: Damage resulting from main beam splice failure



Figure 5: Grid damage leading to panels being forced back into the wall angle causing damage

Damage to suspended ceilings resulted from force being transferred from services above the ceiling into the ceiling itself as shown in Figure 6. In a standard installation of a suspended ceiling the hanger wires are placed @ 1200c/c. However, the presence of services (e.g. HVAC and fire sprinklers) above the ceiling can mean this is not possible. As a result suspended ceiling are sometime partially hung from services within the ceiling (most commonly HVAC ducting and plant). As this plant is rarely secured properly when it moves it imparts force into the ceiling causing damage. Additionally, services above the ceiling moving during an earthquake can hit and impact the hanging wire of the suspended ceiling. Suspended ceilings are not designed to take these additional forces. Grills within the ceiling plane were often observed to have fallen from the ceiling and localized loss of panels often occurred around the location of these grills.



Figure 6: Damage caused by interaction with services above the ceiling

Older one-way grid systems were particularly susceptible to damage. An example is given in Figure 7. These grids consist of main beams hung from the structure above spanning one way. There are typically no transverse runners except where the ceiling may have been retrofitted with these. The drop-in panels limit the possibility of the grids spreading apart during an earthquake. However, if panels do drop out there are no members to stop the grids spreading apart. Further panels then fall from the ceiling. Also, as opposed to the two-way systems discussed above, the panels are not supported on all four edges by the grid system. The panels are instead interlocked, so when one panel falls it leaves the next panel susceptible to falling.

Damage to suspended ceilings can also result from elements connected to the ceiling that should actually be independent. Common examples of this are timber or steel framed bulkheads and partitions. Partitions in particular should not rely on lateral support during an earthquake from the suspended ceiling. This type of construction applies extra

force into the ceiling for which it is neither designed nor installed to carry; thereby causing damage during a seismic event.



Figure 7: Spreading and damage of Older One-Way Grids

Damage to residential ceiling also occurred during the earthquake. These types of ceilings are not suspended like the ceilings discussed above but are rather fixed directly to roof framing using glue and/or nails. Damage to these ceilings results from load being applied to the ceiling from the adjacent walls as the house undergoes lateral displacement. Some damage sustained to a residential structure is shown in Figure 8.



Figure8: Damage to residential ceilings
(courtesy Michael Newcombe)

The forms of damage described above can occur simultaneously during an earthquake causing widespread damage to a single ceiling system. Some examples of this are shown in Figures 9 and 10.

4. DISCUSSION

The widespread damage to ceilings from the earthquake resulted in business interruption as well as direct damage costs. For example, the University of Canterbury was closed for 2 weeks while fallen and not-fallen heavy ceiling panels were replaced with lighter panels in a better way over some lecture theatres.

While the Darfield Earthquake was similar in magnitude to the 2010 Mw 7.0 Haiti earthquake, there was no loss of life and only 2 injuries. One of the major reasons for this is the time of day the earthquake occurred. Nevertheless, it shows that a system of building construction controls, while never perfectly followed, can be very effective in limiting life and other losses.



Figure 9: Widespread Ceiling damage
(courtesy Univ. of Canterbury)



Figure 10: Further Widespread Ceiling Damage

In addition to the damage in the earthquake main shock, more ceiling panel and other damages occurred in the subsequent aftershocks.

In order to reduce damage to ceilings in the future the technical and political issues in the introduction need to be addressed for new ceilings and retrofit or replacement may be required for older ceilings. To have well behaving ceiling systems it is necessary to consider more than the ceiling itself. Appropriate consideration of all of the other design requirements for all elements interacting with the ceilings including services, walls etc. is necessary.

The aim of the NZ earthquake design of building structures criteria is to meet the “loss of life” limit state. While performance of modern buildings in recent earthquakes indicates that the seismically designed structural systems meet this criterion, the ongoing practice of designing and building non-structural components and

storing contents still pose a reasonable risk to life safety. For example; heavy ceiling panels falling from 7-8m high lecture theatres (as observed in the University of Canterbury) could have seriously injured a few students (with a fair probability of fatality) had the earthquake occurred during lecture hours. Similarly, masonry wall blocks and chimney blocks falling from a house (as observed in several buildings in Christchurch) and heavy/fragile contents falling from racks in supermarkets and industrial storages could easily have seriously injured a few people if the earthquake had struck in a normal business hour.

Whereas structural framing systems are designed for lower forces than the expected elastic response level due to their inelastic deformation capacity, such an approach is not appropriate for NZ ceilings. These are constructed of light-weight steel with connections which perform in a relatively brittle manner. Special consideration of this is required and they are likely to need to be designed for significantly higher accelerations than many other parts of the frame in order to protect life. Mandated regulations for the trades are required to ensure good and coordinated construction.

In early 2010, the University of Canterbury was awarded funding from the NZ Foundation for Research in Science and Technology (FRST) through the Natural Hazards Platform (NHP) in order to address the issues with non-structural elements including vertical elements (partitions and cladding) and horizontal elements (ceilings). The widespread damage to non-structural elements observed in this earthquake has emphasized the need of this research. Collaborations also exist between the Tokyo Institute of Technology (the Motoyui laboratory (e.g. Sato et al. 2011)) and the University of Canterbury. This allows not only the whole range of western ceiling systems to be evaluated (e.g. with the use of light weight panels), but also the Japanese approach to ceiling construction. This work, along with other efforts at the University of Canterbury, is aiming to produce cost-effective low damage seismically sustainable buildings. These are expected to have a lot less damage to the frame, slab, non-structural elements or contents during a major earthquake than that experienced in recent earthquakes.

5. CONCLUSIONS

The 2010 Darfield earthquake caused widespread structural and non-structural damage. Suspended ceilings and residential ceilings sustained damage of different forms, such as grid damage, perimeter damage, interaction with services, grid spreading damage. Major improvements in the ongoing practice of ceiling design and installation are required to achieve ceiling systems that do not incur significant damage in design level earthquakes as has been observed in this earthquake.

Acknowledgements:
The authors are grateful to HUSH Interiors for discussions and for making many photos available.

References:

AS/NZS 2785:2000. Suspended Ceiling – Design and Installation. Standards New Zealand, Wellington.

Dhakal R. P. "Damage to Non-Structural Components and Contents in 2010 Darfield Earthquake", Bulletin of the NZ Society of Earthquake Engineering, 43(4): 404-411, Dec 2010.

MacRae G. A. "2010 Darfield (Canterbury) Earthquake Sequence - Initial Report", ICUS newsletter Vol. 10, No.2, 2010.

MacRae, G. A., Dhakal, R. P., Hair J., Paganotti G. and Singh J. "Report on Ceiling Damage during the 2010 Darfield Earthquake", Internal report, Department of Civil and Natural Resources Engineering, University of Canterbury, Christchurch, New Zealand. 27 September 2010.

Sato Y., MacRae G. A., Dhakal R. P. and Motoyui S. "Seismic Fragility of Japanese Ceiling Systems", Proceedings of the 8th International Conference on Urban Earthquake Engineering, March 7-8, 2011, Tokyo Institute of Technology, Tokyo, Japan.

8CUEE CONFERENCE PROCEEDINGS
8th International Conference on Urban Earthquake Engineering
March 7-8, 2011, Tokyo Institute of Technology, Tokyo, Japan

ROLE OF STANDARDS AND REGULATIONS FOR BUILDINGS

Jun Kanda

Professor, Graduate School of Frontier Sciences, University of Tokyo, Japan
kandaj@k.u-tokyo.ac.jp

Abstract: In Japan, building regulations are provided by Ministry in terms of laws and enforcement orders. The standard should provide a basic framework for engineers to follow. When Building Standard Law was first established in 1950, the structural requirements in the regulation were simple. Only simple rules for the design load and allowable stresses for structural materials were specified. After several occasions of revision, now enforcement orders are extensive and complex. Then some discussions for a new Building Basic Law are introduced. A scheme for conference by stakeholders in order to make decisions for appropriate safety for the society can be proposed. New role of standards and regulations are discussed for sustainable society.

1. INTRODUCTION

Building regulations are provided by the government in terms of laws and enforcement orders. In Japan, the fundamental law for buildings is called Building Standard Law which clearly states that the minimum requirements of performances including the safety are specified. Nevertheless most people understand that if buildings are designed to be consistent to the regulations, they are sufficiently safe.

When Building Standard Law was first established in 1950, the structural requirements were simple. Only simple specifications for the load and allowable stresses for structural materials were described. Now enforcement orders are extensive and complex, after revisions for taking engineering advances into account. Calculation procedures are also specified.

The building approval system in Japan is called as a conformity system and building officials are believed to have no choice for their own decision but only to check if building documents are consistent to the regulations. This is one of reasons to introduce conformity check offices of private sector in 1999.

However in reality it is not possible to write every condition and situation in regulations. Then the structural design becomes restricted and only possible when evaluation procedures are specified in the regulations. The uniform specifications for minimum requirements do not mean the uniform degree for the safety for different locations or different types of structures.

Regulations with detailed uniform specifications may be convenient for efficient designs and constructions in an economically growing society, but when the quality of buildings is preferred for a longer life and safer and sustainable society, building approval system should be based on the consensus of stakeholders in the society. Then the role of regulations has to be also reconsidered.

2. CURRENT REGULATIONS IN JAPAN

The Building Standard Law of Japan was enacted in 1950 together with the architectural engineer law at the same time. The structural requirements are specified in enforcement orders which mostly followed the structural rules specified in the Law of Buildings in Urban Area established at the time of the Kanto earthquake (1923). The seismic safety checking is quite simple as the allowable stress design procedure is only one available structural calculation procedure and the allowable stresses of structural materials are given together with the base shear coefficient of 0.2 for the seismic safety. Qualified architectural engineers can make structural calculations by hands before the introduction of capacity design for the seismic safety in 1981.

For the improvement of seismic safety a new structural performance parameter called Ds factor was introduced to take the deformation capability into account. The corresponding base shear coefficient is 1.0 which is 5 times of the allowable stress design criteria. The Ds factor varies from 0.25 to 0.6 according to the deformation capability after the elastic limit of strength and is multiplied to the base shear coefficient as a reduction factor. This reduction is rather conservative in comparison with a similar factor in other countries such as U.S. and New Zealand.

Many computer programs have been developed not only for the structural analysis but also for the design of sections of components. Since the local authority cannot have sufficient engineering staff for checking the conformity as the regulation becomes rather complicated. Some of computer programs for structural calculations are approved

by the Ministry for the purpose of reduction of checking time by the authority.

After the Hyogoken Nambu Earthquake in 1995, the performance-based design was discussed to be implemented in the regulations, as discussed in California after Northridge earthquake in 1994. Then in 1998 another revision was made for the Building Standard Law by the Ministry of Construction (Now it is reformed as Ministry of Land, Infrastructure, Transport and Tourism (MLIT)). In the approval system, private organizations were newly introduced for conformity checking of applied design documents including structural calculations. Another great change of the law for the structural design is that the structural calculations are specified in the enforcement order. In other words, the only calculation procedures specified by MLIT are accepted for building conformity applications.

A rather serious offence in building approval system occurred. It was reported that Mr. Aneha (formerly qualified architectural engineer) intentionally falsified structural calculation documents by reducing the input seismic load into a half of required value or in a similar order in order to reduce the structural cost. Local authorities as well as private organizations could not find the inconsistency during their checking procedures. Number of buildings with insufficient strengths was reported as 60 to 80 for 8 years. The MLIT took this incident seriously and proposed a revision of the Law in order to make the conformity checking process very strict by introducing new organizations for structural calculation conformity checking at the same time additional structural requirements were also introduced for calculation procedures.

Engineers are forced to produce much thicker calculation documents than before and only officially approved calculation procedures are accepted. When this restricted system was first introduced, the new approval system was very inefficient and building construction market was seriously influenced. The reduction of GDP in 2006 due to this revision was reported to be 0.8%. The efficiency of conformity checking system can be improved once people are accustomed to the system, but the influence of restricted regulations on the structural design or the quality of structure is more serious as the creative efforts by engineers are discouraged and people tend to concern about only the conformity to the regulation but do not consider the quality of real safety. Although the Building Standard Law clearly states that the minimum requirements are specified, MLIT claimed that strict rules of regulations are necessary to keep the consistency of the safety. Then people tend to consider that the buildings are safe once the conformity checking was made.

3. PROPOSAL OF BUILDING BASIC LAW

A movement for the building basic law was formed in August 2003 by a group of building professionals including the author. The purpose of the movement is to reform whole social system for buildings in Japan. The main idea for the new system is to establish basic understandings for good quality buildings. As in most countries the regulation specifies the minimum requirements. But the minimum safety is not sufficient or even appropriate. It worked well when we needed to build houses efficiently but now we have more houses than the necessary demand in Japan. The average lifetime of houses in Japan is about only 30 years which is very short in comparison with European or American statistics. We need to design a good quality houses for a longer life.

The constitutional reasoning for the current building standard law is to assure the private property right for land. It may apply to an isolated private house in a wide land, but now houses in a city have some interactions with neighboring houses. Some condominiums are sometimes huge residential complexes. Some tall office buildings have spaces for more than 10,000 people. In these cases the building owner should obtain sufficient consent from neighbors. Buildings in general are regarded as social properties and performances and qualities of buildings should be approved by the local community. Only the fulfillments of specifications of minimum requirements may not be sufficient.

Engineering developments are so rapid and the social acceptance criteria differ based on the cultural and historical background. Therefore the law should only provides basic rules and local communities should prepare specific rules if necessary. The quality and performance of building has to be good enough and the owner is responsible for them. The safety, health and environment are basic demands for buildings and professionals have to provide sufficient information regarding design performances to the client, users and even to the neighbors. The accountability and the transparency are commonly essentially required.

When detailed specifications are provided by regulations, the consistency to the regulation tends to mean the quality of building is approved by the society. However since the regulation does not necessarily provide appropriate qualities in various aspects for the society, such appropriateness can only be achieved by the decision of building owners consulted by architects and engineers.

One of important purposes of Building Basic Law is to make responsibilities of stakeholders clear, in particular the building owner must make appropriate decisions on the quality of building for the society. We should recognize that the appropriateness of structural safety is not the same for different stakeholders. Therefore the social consensus is important

It is expected that proper considerations for the quality of buildings are made when deregulations are introduced. Regulations should be simplified to be understood by every stakeholder, but the accountability has to be recognized in a more transparent manner and the local society should be able to observe the safety quality of buildings.

MLIT in Japan was rather reluctant to discuss the Building Basic Law, as the Building Standard Law is a basic law for many related legislations. And the power of controlling the safety requirements based on the Building Standard Law is centralized in MLIT. However, since laws

for scenery of buildings were established in 2004, more discussions in local community have been encouraged, and decisions for the approval are made by local governments.

In September 2008, MLIT organized a committee for governmental actions for buildings with a higher quality including discussions of Building Basic Law. Although MLIT did not consider the whole reformation of legislation system for buildings then, a new government formed in September 2009 has been keen to establish the Building Basic Law in order to reform the current legislation system as well as the qualification system.

Discussions on the new building legislation system among professionals and industries are now quite frequent. They may influence the political direction of building regulations. We should make efforts to establish a new system which maximizes the potentials of architects and engineers for a sustainable society.

4. SOCIAL CONSENSUS SYTEM

Since buildings occupy the space of land for a long period of time, the owner is responsible for the consequences due to the existence of building. If a natural or man-made disaster occurs, the society will be affected by its consequences. Therefore buildings are sufficiently safe against such expected events.

However future natural or man-made hazard is not easily expected and the failure probability of a building is controlled based on the safety performance of structure. Engineers should provide sufficient information on the safety with possible consequences to the client and the final decision should be made by the consensus in the society.

In the past, the safety requirements were believed to be determined by experts based on scientific findings. Then people can simply follow the decision by experts. But the safety quality is quantitative as expressed in terms of probability and cost dependent. Then demands for the safety can be different among different stakeholders. Investors may require less safety than the neighbors to the building.

As discussed in Risk and Culture by Douglas and Wildavsky(1982), hierarchists and individualists both have disadvantages for risk managements of environments in particular when large uncertainties exist. Sectarians instead have better opportunities for good risk managements. Transparent discussions among stakeholders will provide consensus base decision making for the society. Local community should participate for decision making for the safety of their public facilities, including power plants, schools, city halls and even condominiums.

Failure of structures by an earthquake influences the activity of local community seriously. The consequences of failure may be different from buildings to buildings. Then the local community has rather a power to contProl the safety rather than the central government. Optimal safety of structure has been discussed since 1970's and more individual decisions should be made for an individual building. A basic equation for the optimal safety can be written as minimizing the total expected costs as,

$$C_T = C_I + C_M + \sum \Delta P_{Fi} C_{Fi} \qquad (1)$$

where C_T is the total cost, C_I is the initial construction cost, C_M is the maintenance cost, ΔP_{Fi} is the increment of probability of failure for the i-th damage, C_{Fi} is the failure cost for the i-th damage.

It is the time to use the cost-benefit discussions more seriously for the decision making by individuals. (Kanda, 2009) The cost in ordinary terms in equation (1) is the initial cost and the benefit is the reduction of failure probability or the expected failure cost.

Then engineers are expected to provide more information contributing to the target structural safety. Among many factors for considering the target safety, consequences of failure are important factors formulated in cost-benefit consideration. Engineers should pay sufficient attentions to possible consequences. (Kanda and Shah, 1997) It may be difficult for ordinary people to understand the meaning of probability especially when it is very small, but it may be rather imaginable for anybody to make a scenario for failure consequences with cost estimations. The optimal safety obtained as minimization of equation (1) can transfer the discussion of safety degree or probability of failure to that of failure cost.

As an example of the conference for consensus of the structural safety by stakeholders, the target seismic safety of a school gymnasium may be discussed as one of familiar examples for social decision making in a local community. Should parents provide a safer building for young children? When the school gymnasium is to be used a shelter for refugee at the occasion of earthquake disaster, it must be significantly safer. If the school gymnasium collapsed or even severely damaged after the earthquake, the failure cost is much greater than its construction cost. The quantitative decision may not be easily achieved as the minimization of equation (1) may not be fully understood by ordinary people. Nevertheless discussions with many materials related to the seismic safety of building, such as the soil condition, the seismic hazard including active fault information, current safety degree of buildings with statistical information of past earthquake disaster such as the Hyogoken-Nambu earthquake and the estimated cost due to failure are extremely helpful for making their own community protective to the natural disaster.

Catastrophic risk exists in the modern society with buildings of huge scale and sophisticated technologies. One way control by regulations and conformity checking cannot optimize the minimization of failure consequences. Since the local community has direct consequences from failures, it should have the role to make decision and controlling power in constructions. Contributions from citizens with fully support of professional experts are essential for such decision making procedures.

5. INTERNATIONAL STANSARDS

Many International standards are published in structural engineering area as documents of ISO. International standards for construction materials are beneficial for fair trades, but international standards for structural safety have been also developed for fair engineering services of overseas activities.

ISO 2394: General Principles on Reliability of Structures is the basic documents for the structural engineering. In many countries the structural engineering practices have shifted from the allowable stress design to the limit state design which is developed based on the reliability theory. Therefore if principles provided in ISO 2394 are adopted for the developments of national codes, the structural safety concept can be commonly understood or harmonized in different countries.

ISO documents are also published for actions and loads for the structural design. The uncertainties in actions on structures are significant and common probabilistic models are described according to ISO 2394. When transparency and accountability are essential to achieve the appropriate degree of safety for structures as discussed above, ISO documents have an important role to provide rational procedures for determining the design loads for structures.

In general ISO documents for basis of structural design are developed for code writers. Therefore it is expected for national standard bodies or governments to make their standards and regulations consistent to ISO. But the incentive is not generally so strong in comparison with industries' attitudes to adopt ISO for their products. However the common understanding of structural design against natural hazard among professionals representing their national bodies can be expected in Working Groups for drafting documents. Discussions in technical committees and sub-committees under TC also contribute to the international harmonization of codes.

Unfortunately Japanese structural regulations provided in enforcement orders of the Building Standard Law are not consistent to ISO 2394. The wind load and the snow load is given in terms of the return period such as 50 years for the damage limit and 500 years for the safety limit, but the earthquake loads are considerably inconsistent to the hazard map as the same regional factor from 0.8 to 1.0 has been still used since 1981.

6. ATTITUDE AGAINST CATASTROPHES

Buildings are vulnerable against extreme actions such as terrorist attacks, typhoons and earthquakes. Although regulations require the safety performance of buildings, the minimum requirements cannot cover these rare events except for very important structures such as nuclear power plants or major hospitals.

As discussed in previous chapters, technologies are available to avoid the catastrophic losses by proper design with a higher target safety when the economy allows. And many experiences have been studies for the nature of environmental extremes and extraordinary consequences of disasters in densely populated area.

We have to consider rational attitude against global catastrophes. (Smil, 2008) In general we cannot be free from global catastrophes, then our actions should be minimizing risks. And such decisions should only be possible by decisions of society. According to Smil,

We can do much to be better prepared for a number of anticipated catastrophes, and we can take many steps to moderate negative impacts of some of the most worrisome trends. The precautionary principle should be involved precisely when facing those high risks whose understanding is characterized by uncertainty or outright ignorance. Preventive, preparatory, or mitigating actions are called for in order to avoid extreme consequences of unmanaged outcomes, whether a viral pandemic, global warning, or the use of weapons of mass destruction by terrorists. In such situations imperfect scientific understanding or substantial uncertainties regarding the most likely mode and intensity of the next catastrophic event should not be used as an excuse for inaction or for postponing known effective measures.
(Smil, 2008, p.238)

Regulations cannot deal with such catastrophe preventions. Local communities with a help from the central government by providing sufficient information and supported by professional experts have to make decisions of safety of environments including buildings and houses. Communications between professionals and citizens are essential tools for the decision makings of society.

7. ROLE OF REGULATIONS AND ROLE OF ENGINEERS

The role of national government and that of local government should be identified. The major role of government is to help the local government by providing technical information for building approval system. The local government should have a leading role for regional planning of cities and towns. More active contributions from structural engineers to mitigate natural disaster by considering the hazard potential are expected for regional planning.

Professionals should contribute more to the society in a wide aspect. A new system for the approval of buildings is expected for a sustainable society. Professionals can lead a consensus based discussions for the appropriate safety of a building in their local communities.

The current Building Standard Law only deals each building in a site and a group of buildings in an area is not an object of the law. When scenery of a group of buildings is discussed or when the seismic robustness of a city is considered, the local culture and life style are important factors as well as natural conditions such as soil conditions or climates. Then the collaboration between the local government and architects and engineers becomes extremely

important for sustainable development of the area.

Academic associations of professional are also expected to play an important role by publishing good technical standards and codes for engineering practices. It is common to make excuse that the association does not take responsibility for the results caused by the standards and codes. The engineer should take his/her responsible decision on the application of standards in practices.

When regulations do not cover detailed rules for the structural evaluation, engineers have to choose and use a most appropriate technical code which they can understand well and rely on. This situation is much better than the current system of detailed regulations under Building Standard Law for the safety quality of buildings.

8. CONCLUSIONS

Current Japanese building system under the Building Standard Law is critically reviewed as it is rather old-fashion. Role of standard and regulations in the sustainable society is discussed. Performance-based design is almost global standard as clearly described by ISO documents. In order to mitigate disasters the local community should take actions with supports by professional engineers. The social consensus of local community is a key issue for the structural safety. The regulations should be minimized for encouraging such actions. Engineers should fully utilize available standards to provide sufficient information to the society.

References:

Douglas, M. and Wildavsky, A. (1982), *Risk and Culture*, University of California Press.

I.S.O.(1998), "ISO2394: General principles on reliability for structures," International Organization for Standards.

Kanda, J. (2009), "Optimal design safety as a risk communication tool," *Australian Journal of Structural Engineering*, Vol.9 No.1 .

Kanda, J. and Shah, (1997), "Engineering role in failure cost evaluation for buildings," *Structural Safety*, Vol.19 No.1 pp.79-90

Smil, V. (2008), *Global Catastrophes and Trends*, MIT Press.

8CUEE CONFERENCE PROCEEDINGS
8th International Conference on Urban Earthquake Engineering
March 7-8, 2011, Tokyo Institute of Technology, Tokyo, Japan

GUIDELINES FOR PERFORMANCE-BASED SEISMIC DESIGN OF TALL BUILDINGS

J. P. Moehle[1], Y. Bozorgnia[2], and R. O. Hamburger[3]

1) Professor, Department of Civil & Environmental Engineering, University of California, Berkeley, California, USA
2) Executive Director, PEER, University of California, Berkeley, California, USA
3) Senior Principal, Simpson Gumpertz & Heger Inc., San Francisco, California, USA
moehle@berkeley.edu, yousef@berkeley.edu, rohamburger@sgh.com

Abstract: This paper presents an overview of a recently released document *Guidelines for Performance-Based Seismic Design of Tall buildings*. The Guidelines were developed as part of a larger program, the Tall Buildings Initiative (TBI). The TBI was coordinated by the Pacific Earthquake Engineering Research Center (PEER), with close collaboration with practicing structural and geotechnical engineers in the tall building design community. The Guidelines represent the latest practical implementation of performance-based seismic design (PBD), and improve upon the PBD procedures developed during the past 10 years. A brief review of the evolution of the PBD in the United States is presented in this paper, followed by an overview of the TBI and development of the Guidelines. Few specific critical items proposed in the Guidelines are also elaborated in this paper.

1. INTRODUCTION

Performance-based seismic design methods in the United States originated as a practical and effective means to mitigate the seismic risks posed by existing buildings and were later extended to permit development of new buildings capable of superior seismic performance. These methods were quickly adapted to justify design of new buildings that do not conform to building code requirements, and which are intended only to provide equivalent performance to buildings conforming to code criteria. This practice has become particularly prevalent in the design of very tall buildings in the Western United States.

Initial development of performance-based seismic design procedures in the United States occurred in response to societal reactions to the nearly annual occurrence of damaging earthquakes in the Western United States during the period 1979-1994. These earthquakes provided many illustrations of both the strengths and weaknesses of seismic provisions in U.S. building codes and spurred substantial evolution and improvement of these provisions. Most buildings designed to the code provisions achieved the life-safety intent of the building code, but several experienced extensive damage resulting in large economic loss. These earthquakes also provided frequent reminders that the inventory of existing buildings included many older structures that were susceptible to life-threatening damage and which posed unacceptable seismic risks.

Some corporations and institutions became interested in voluntary seismic upgrades. Engineers working on their behalf quickly found that decision-makers in these organizations wanted to know how their buildings would perform, in terms meaningful to them, before they would commit to retrofit. Often these decision-makers wanted to tailor retrofit programs to optimize their costs and benefits. These same decision-makers quickly became interested in seismic performance issues in the design of new buildings as well, to assure that their important facilities would adequately protect their business and operational needs and that they did not encumber unacceptable future economic losses.

Many owners of hazardous buildings were not interested in seismic upgrades, prompting governments to adopt mandatory upgrade programs. To justify adopting such programs, it was necessary to contrast the likely performance of hazardous buildings and the consequences if no action were taken. Performance-based seismic engineering was developed to enable engineers to respond to the need to reliably assess the probable performance of new and existing buildings under a variety of design scenarios

The Federal Emergency Management Agency (FEMA) provided the primary financial support for development of performance-based seismic engineering procedures. FEMA funded the Applied Technology Council's (ATC) development of a series of performance-based engineering criteria and guidelines including FEMA-273/274(ATC, 1997a, b) that form the basis for present generation performance-based seismic engineering practice. The American Society of Civil Engineers subsequently converted these documents into the ASCE-31(ASCE, 2002) and ASCE-41(ASCE, 2006) standards that could be adopted by building codes.

These first-generation procedures experienced widespread acceptance and application, both in their intended use, evaluation and upgrade of existing buildings; and also for application to the new building design.

However, for new building design, the primary application of these procedures is to demonstrate that nonconforming designs have equivalent performance capability as that intended by the building code, allowing development of buildings at lower cost or with other attributes attractive to developers. This practice became particularly popular in design of very tall buildings, contributing to the development of many of these structures in the period 2003-2008 in Los Angeles, Seattle, San Francisco and other western cities with significant seismic hazards.

Many of these structures are tall residential buildings, having post-tensioned concrete flat slabs supported by a ring of perimeter reinforced concrete columns and tubular bearing walls surrounding the central core. Prescriptive U.S. code provisions prohibit such construction in excess of 50 meters tall, without provision of a dual special moment-resisting frame capable of resisting at least 25% of specified seismic design forces. By using performance-based procedures, engineers were able to eliminate the moment-resisting frame, saving cost, and more importantly permitting exterior designs that accommodated floor to ceiling windows and reduced story heights in buildings extending to 200 meters tall.

2. BUILDING CODE COMPLIANCE

In 2003, Western U.S. cities generally adopt and rigorously enforce building regulations based on the *International Building Code* (ICC, 2006). These codes adopt prescriptive seismic design provisions through reference to the *ASCE 7*(ASCE, 2005) standard, which is based on the *NEHRP Recommended Provisions for Buildings and Other Structures* [BSSC, 2003]. The *International Building Code* also includes permissive language that enables the use of alternative procedures demonstrated to provide performance equivalent to the prescriptive requirements. The design professional must demonstrate equivalence to the satisfaction of the building official. Many, but not all building officials have proven amenable to the use of these procedures.

The code does not limit the procedures that can be used to demonstrate equivalence, nor does the code state, in other than generic and qualitative terms, what performance is acceptable. Most engineers and building officials adopt target performance based on the commentary to the *NEHRP Recommended Provisions*. This commentary states that for ordinary structures the objective is to provide a low conditional probability of collapse, given the occurrence of Maximum Considered Earthquake shaking, and to preclude, to the extent practicable, economic losses associated with more frequent and moderate events. The recently published *FEMA P695* [ATC, 2009a] and *FEMA P750* [BSSC, 2009] reports clarify that the acceptable conditional collapse probability is 10% and specify rigorous analytical and statistical methods for collapse probability quantification. However, these methods are complex and have not yet been adopted into general practice. Instead, engineers have adapted procedures based on ASCE-41.

Engineers have typically performed preliminary design in general conformance with the prescriptive code requirements, but taking a limited number of well-defined exceptions. The resulting near conformance to the code requirements provides both building officials and engineers a foundation level of comfort with the designs. Nonlinear response history analysis is used to demonstrate adequate collapse resistance. Performance is evaluated on an element by element basis using acceptance criteria contained in the ASCE-41 standard, sometimes supplemented with project-specific criteria derived from available laboratory testing to demonstrate acceptable behavior. Since analysis tools used in most design offices are incapable of reliably predicting response of structures nearing collapse, acceptance criteria are often conservatively selected to assure response within the range of analysis reliability.

Many building officials lack the technical expertise to review complex analyses or interpret laboratory test reports and have required independent third party review as a condition of acceptance of performance-based designs. Though procedures vary, third party reviews are typically performed by teams including a practicing engineer with expertise in tall building design and seismic technology, a researcher with particular knowledge of the types of structural systems to be employed (e.g., reinforced concrete walls, steel frames, etc.) and a geotechnical engineer. Reviews can be rigorous and include consideration of the design criteria, ground motion selection and scaling, analytical modeling and results, and structural detailing. The review process can be lengthy and can have significant effect on the design.

3. FIRST-GENERATION PERFORMANCE-BASED PROCEDURES

Initially engineers adopted ad hoc procedures for performance-based design of tall buildings. Later, documents produced by engineers in Northern California (SEAOC, 2007) and Southern California (LATBC, 2006) formalized these procedures. Generally, designs conform to the prescriptive code provisions with limited exceptions. These exceptions may include exceedance of code-specified height limits, violation of code requirements with regard to redundancy, and occasional use of materials, e.g., high strength steel and detailing procedures not specifically recognized by the code. Given the general similarity of these buildings to code-prescriptive designs, the procedures that developed typically included: development and approval of a formal criteria document, preliminary design, code-level analysis; and verification of adequacy for Maximum Considered Earthquake shaking.

Design criteria development and approval is an important first step. The formal criteria document includes a description of the overall structure and its intended load-resisting mechanisms; identification of any exceptions to the building code requirements and the justification for these exceptions; and identification of analytical procedures, load combinations, design ground motions, material properties, and detailing. The intent is to identify all substantive issues before the designer has expended large

effort in actually performing the design. In theory, if all procedures and assumptions are agreed to at project inception, approval of the finished design should be straightforward and attainable without controversy. In practice, however, it is rarely possible to foresee all issues that will arise during the design development, and many substantive criteria issues are resolved through cooperative efforts of the designers and reviewers throughout the project.

The preliminary design provides the basis for succeeding steps. Capacity-based design procedures, wherein a preferred yield mechanism is identified and other elements of the structure are proportioned to remain elastic, or essentially so, are typically used. Initial sizing of elements is often controlled by considerations of dead, live, and wind loads. In many structures, lateral design for wind forces controls even the final sizing of many elements.

The-code level design is used to confirm the adequacy of preliminary sizing and also to provide building officials with confidence, at a primary level, that the structure is comparable to one designed to conform to the code in all respects. In this step, the engineer typically performs the code-prescribed analyses, and evaluates all relevant code-prescribed strength, deformation, and detailing requirements, except those which were specifically exempted in the formal design criteria. Since the building systems used in these structures are not strictly code-compliant, *R*-coefficients and other factors required in the code procedures are typically selected jointly by the designers and reviewers based on judgment.

Verification of behavior in MCE-level shaking is performed using three-dimensional nonlinear response history analyses. Typically, suites of seven horizontal ground motion pairs are used. Ductile behaviors including wall, slab, and beam flexure are evaluated using the mean of the maxima for relevant demand parameters (flexural strain, plastic rotation, etc.). Brittle behaviors, and those with a potential to result in catastrophic failure, including wall shear, column axial force, slab punching shear, etc. are typically evaluated using either maximum demands obtained from the suites of analyses or mean demands that have been amplified by an estimated value of the standard deviation with the intent to provide a low probability of failure. Following procedures contained in *ASCE-41,* models and acceptance criteria for ductile behaviors are typically constructed using expected (mean) values of material properties, considering potential variability and strain hardening effects. Acceptance criteria for brittle and catastrophic behaviors are typically developed using lower bound material properties and sometimes using resistance factors to account for potential dimensional variability and construction quality issues.

4. THE TALL BUILDINGS INITIATIVE

The PEER Tall Buildings Initiative is a cooperative program of research and development undertaken by researchers at the Pacific Earthquake Engineering Research Center (PEER) and practicing structural and geotechnical engineers experienced in tall building design. Spurred by the rapid growth in the use of performance-based seismic design methodologies for the design of tall buildings, the goal of this initiative is to provide a sound and reliable basis for these procedures and to help assure appropriate seismic performance of the resulting new generation of tall buildings.

The program, initiated in 2006, encompasses a range of tasks intended to investigate: the dynamic characteristics of tall buildings; the performance capability of buildings designed using alternative procedures; societal preferences for tall building performance; alternative means of developing ground motions for design; soil-foundation-structure interaction effects, modeling, and analysis procedures; and development of design guidelines. An important companion report on modeling, analysis, and acceptance criteria for tall buildings [ATC, 2009b] is available from the Applied Technology Council. Reports on other task activities can be obtained at http://peer.berkeley.edu/tbi/index.html.

5. SEISMIC DESIGN GUIDELINES

The TBI Guidelines for Performance-Based Seismic Design of Tall Buildings (TBI Guidelines] represents an evolutionary step in the practice of performance-based seismic design of tall buildings. The guidelines embrace the same analytical technologies adopted by engineers following the San Francisco AB-083 and Los Angeles Tall Buildings Council criteria but provide more guidance on structural modeling, acceptance criteria, and ground motion selection and scaling. There are two important departures from prior practice. First, the guidelines do not require a code-level analysis in that it is anticipated that the procedures may be applied to structural systems for which the code response modification coefficients will not be defined, leaving the code analysis with questionable value. Second, the guidelines use more advanced procedures for evaluating structural performance, anticipating the availability of software that can reliably assess the response of structures in a near-collapse state.

The guidelines focus evaluation procedures on verification that the design performance objectives can be achieved, rather than verification that the building mostly complies with prescriptive criteria. The design performance objectives are those most commonly adopted by leading earthquake professionals today as the intent of the building code, that is, serviceability with minimal repair for frequent earthquake shaking levels and safety for rare earthquake shaking levels. With the exception of exterior cladding systems, the failure of which could cause numerous casualties in a crowded city, the guidelines address structural performance only. The procedures presume that nonstructural components and systems will be designed to conform to the prescriptive code criteria, but do caution that if a building's response characteristics are substantially different from that of typical code-conforming buildings, additional precautions may be required. The guidelines are written in a "recommendation" and commentary format. Recommendations are written in mandatory language, while commentary explains the basis for the recommendations

and warns of significant design issues that may not be adequately covered by the recommendations.

As with the AB-083 and Los Angeles Tall Buildings Council criteria, designers must prepare a formal, project-specific design criteria document. The guidelines recommend independent third party review of the criteria, the analyses, and the design. The guidelines employ two levels of analysis: a Service level and a Maximum Considered level.

5.1 Service-Level Evaluation

The purpose of the Service-level check is to assure that the buildings will not experience significant damage from frequent earthquakes. Much controversy surrounded the selection of a Service-level shaking intensity. The 2008 edition of the Los Angeles Tall Buildings Council guidelines[LATBC, 2008] specified service-level shaking with a 50% exceedance probability in 30 years (43-year mean recurrence interval), but permitted Service-level analyses to use 5% viscous damping. Studies conducted by the Applied Technology Council as part of the TBI effort, and summarized in the ATC-72 (ATC, 2009b) report, suggest that 5% viscous damping is excessive for tall buildings. Instead, 2.5% equivalent viscous damping is more justifiable and, in keeping with this, some participants argued for use of a Service-level event with a 25-year mean recurrence, arguing that the response spectrum for such an event, when used with 2.5% damping, would be comparable to the 5%-damped 50%-30 year spectrum. Other participants believed that a 25-year recurrence for onset of damage to these buildings was not an appropriate design objective. Eventually consensus support was achieved for the use of a 2.5% damped, 50%-30 year spectrum as the Service-level loading.

The stated performance goal for the Service-level loading is to avoid onset of damage that would reduce the building's ability to withstand Maximum Considered-level shaking or which would require repair that would necessitate removing the building from service. It is expected that some repair of structural elements may be necessary to restore cosmetic appearance, and fire and weather resistance. Nonstructural damage is anticipated to be minor, but is not specifically evaluated.

The guidelines recommend an elastic, three-dimensional response spectrum analysis for the Service-level because the desired behavior is intended to be essentially elastic and also because it is desired to assure that an elastic analysis is available to benchmark and evaluate nonlinear models used in the Maximum Considered-level evaluation. Carrying out a nonlinear response history analysis, to distribute the loads on very limited number of overstressed elements, is optional. Analytical models must extend to the structure's true base, which for most tall buildings is located several levels below grade. Soil-foundation-structure interaction effects need not be explicitly modeled, though it is permitted to do so. Based on analytical studies of typical buildings conducted under the Tall Buildings Initiative, when soil-foundation-structure interaction effects are not modeled explicitly, mass of subgrade levels is permitted to be neglected.

Acceptance criteria include both strength and deformation. Strength is evaluated by comparing computed strength demands against design strength. Design strength is computed using the strength formula contained in the design specifications referenced by the building code using specified material properties multiplied by strength reduction factors. Recognizing that expected strength will exceed this design strength by a considerable margin, and that some overload is acceptable in a ductile structure, computed demand to capacity ratios may be as large as 1.5. Story drift at any level is not permitted to exceed 0.5% of the story height.

If some computed demand to capacity ratios exceed a value of 1.5, designers are permitted to use three-dimensional nonlinear response history analysis to demonstrate acceptable Service-level performance. When such analyses are performed, a suite of not less than three horizontal ground motion pairs must be selected and modified to be compatible with the Service-level spectrum previously discussed. Either amplitude scaling or spectral matching may be used to achieve spectrum compatibility following procedures presented in the guidelines. Acceptance criteria must be developed based on suitable laboratory test data. Mean values of response parameters obtained from the suite of analyses cannot exceed demand levels at which the test data suggest the onset of strength degradation or damage, the appearance or repair of which would result in occupancy loss.

The Service-level event in effect serves to define the minimum required base shear strength of the building. In some highly active seismic regions such as Los Angeles and San Francisco the 2.5% damped 50%-30 year spectrum will result in strength demand comparable to that obtained following the prescriptive code criteria. In regions of lower seismicity such as Portland, Oregon, and Salt Lake City, Utah, the Service-level spectrum will result in substantially less strength than would be required for a code-conforming building. Commentary warns designers in these regions that additional strength may be required to provide adequate margin against collapse at the Maximum Considered level.

5.2 Maximum Considered-Level Evaluation

MCE-level evaluations are performed for the same level of shaking specified by the building code for this hazard level. The intent of the MCE evaluation is to demonstrate that the structure is capable of surviving this level of shaking with low probability of collapse. However, since the procedure does not include either explicit collapse or statistical analyses as does the *FEMA P-695* procedure, building adequacy is implied through limiting nonlinear response to levels at which significant margin would seem to remain. MCE evaluations are performed using nonlinear response history analysis and at least seven pairs of motions that are modified, either amplitude scaled or spectrally matched, to be compatible with the MCE spectrum.

The guidelines provide extensive discussion of structural modeling techniques and assumptions. The subject

of strength degradation, in particular, receives extensive discussion. Where strength degradation is explicitly modeled in a manner that reasonably predicts the hysteretic behavior obtained from testing using varied loading protocols, permissible levels of nonlinear response are relaxed relative to analyses conducted with models that have less explicit incorporation of cyclic strength degradation. Specifically, there are no limitations on the acceptability of nonlinear deformation demand for ductile elements, so long as element response remains within levels at which the hysteretic models employed are valid and loss of gravity load carrying capacity does not occur. The guidelines suggest limitations on deformation demand when analytical models are used that do not properly account for element strength and stiffness degradation effects.

As with Service-level evaluations, models must extend to the structure's true base level. Modeling of soil-foundation-structure interaction is not required but can be performed. Models are based on mean material properties. Acceptance criteria include both strength and deformation considerations.

Actions that are not ductile are evaluated using demand obtained from the equation:

$$Q = D + L_{\text{exp}} + F_E \tag{3}$$

where D is the dead load and L_{exp} is the expected live load, taken as 25% of the code-specified load. The earthquake effect, F_E is taken either as 150% of the mean earthquake demand $\overline{E}$ computed for the suite of analyses or, for actions with strength demand limited by yielding of other elements, FE may be taken as $\overline{E} + 1.3\sigma \geq 1.2\overline{E}$, where σ is the standard deviation of the response parameter as obtained from the suite of analyses. It is widely recognized that the true dispersion of responses cannot be adequately gauged using only seven earthquake ground motion pairs. The factor 1.5 applied to the mean response is intended to produce a low probability (around 10%) of exceeding the reliable strength in any one earthquake ground motion at the MCE level. It would be applicable, for example, to wall shear strength. The alternative equation is applicable, for example, to shear in an outrigger beam designed by capacity design methods to be limited by flexural strength. Strength capacities are computed using expected material properties and a resistance factor. The resistance factor may be taken as unity where failure of the element would not result in catastrophic failure and must be taken in accordance with the building code otherwise.

The mean story drift from the suite of response history analyses in any story is not permitted to exceed 3% and the story drift for any single analysis run is not permitted to exceed 4.5%. These limits were selected somewhat arbitrarily based on the guideline writers' comfort with the ability of present analytical methods to predict response at very large deformation. In addition to limits on maximum transient story drift, the guidelines also limit maximum residual (permanent) drift. The mean value of residual drift from the suite of analyses cannot exceed 1% of story height in any story and the maximum residual drift in any story from any analysis cannot exceed 1.5% of story height.

6. CONCLUSIONS

The PEER Tall Buildings Initiative has been a successful collaboration of earthquake engineering researchers, practicing structural and geotechnical engineers, and building code officials to address the need for appropriate consensus criteria for performance-based design of tall buildings in the Western U.S. Though evolutionary rather than revolutionary in nature, the PEER Tall Building Design Guidelines introduce significant improvements to practice in the design of these buildings. Of particular note is the provision of modeling guidelines that more realistically account for the nonlinear behavior of buildings than approaches previously used by the profession, together with incorporation of more rational acceptance criteria. The authors believe that the new guidelines will permit the development of tall buildings that are more likely to meet the intended performance objectives embedded in the building code, either than buildings designed to the prescriptive code provisions, or buildings that have been recently designed using performance-based approaches. Future development in this area should include further guidance on selection and scaling of ground motions, direct consideration of nonstructural behaviors, and incorporation of explicit collapse margin investigations.

Acknowledgements:

The TBI was funded by the US National Science Foundation, Federal Emergency Management Agency, California Geologic Survey, California Seismic Safety Commission, and the City of Los Angeles. Charles Pankow Foundation provided funding for the development of the seismic design Guidelines. Members of the design Guidelines development committee are (alphabetically): Yousef Bozorgnia (PEER, UC Berkeley), CB Crouse (URS Corp), Ronald Hamburger (SGH, Inc.), Ron Klemencic (Magnusson-Klemencic Associates), Helmut Krawinkler (Stanford), James Malley (Degenkolb Engineers), Jack Moehle (PEER, UC Berkeley), Farzad Naeim (John A. Martin & Associates), and Jonathan Stewart (UCLA).

References:

American Society of Civil Engineers (ASCE), 2002, *Seismic Evaluation of Existing Buildings, ASCE-31*, American Society of Civil Engineers, Reston, Va, USA.

American Society of Civil Engineers (ASCE), 2005, *Minimum Design Loads for Buildings and Other Structures, ASCE-7*, American Society of Civil Engineers, Reston, Va, USA.

American Society of Civil Engineers (ASCE), 2006, *Seismic Rehabilitation of Existing Buildings, ASCE-41*, American Society of Civil Engineers, Reston, Va, USA.

Applied Technology Council (ATC), 1996, *Seismic Evaluation and Retrofit of Buildings, Report No. ATC-40*, Applied Technology Council, Redwood City, CA, USA.

Applied Technology Council (ATC), 1997, *NEHRP Guidelines for the Seismic Rehabilitation of Buildings, FEMA-273*, Federal Emergency Management Agency, Washington, D.C., USA.

Applied Technology Council (ATC), 1997, *Commentary on the Guidelines for Seismic Rehabilitation of Buildings, FEMA-274*, Federal Emergency Management Agency, Washington, D.C., USA.

Applied Technology Council (ATC), 2009, *Qualification of Building Seismic Performance Factors, FEMA P695*, Federal Emergency Management Agency, Washington, D.C., USA.

Applied Technology Council (ATC), 2009, *Interim Guidelines on Modeling and Acceptance Criteria for Seismic Design and analysis of Tall Buildings,* Applied Technology Council, Redwood City, CA.

Building Seismic Safety Council (BSSC), 2003, *NEHRP Recommended Provisions for Seismic Regulation of Buildings and Other Structure, FEMA 450*, Federal Emergency Management Agency, Washington, D.C., USA.

Building Seismic Safety Council (BSSC), 2009, *NEHRP Recommended Provisions for Seismic Regulation of Buildings and Other Structure, FEMA P750*, Federal Emergency Management Agency, Washington, D.C., USA.

International Code Council (IBC), 2006, *International Building Code*, International Code Council, Whittier, CA, USA.

Los Angeles Tall Buildings Council (LATBC), 2006, *An Alternative Procedure for Seismic Analysis and Design of tall Buildings Located in the Los Angeles Region*, Los Angeles Tall Buildings Council, Los Angeles, Ca, USA.

Los Angeles Tall Buildings Council (LATBC), 2008, *An Alternative Procedure for Seismic Analysis and Design of tall Buildings Located in the Los Angeles Region*, Los Angeles Tall Buildings Council, Los Angeles, Ca, USA.

Structural Engineers Association of Northern California (SEAONC), 2007, *Administrative Bulletin – Requirements and Guidelines for the Seismic Design of New Tall Buildings using Non-Prescriptive Seismic-Design Provisions AB-083*., City of San Francisco, San Francisco, CA, USA.

TBI Guidelines for Performance-Based Seismic Design of Tall Buildings, *PEER Report 2010/05*, Pacific Earthquake Engineering Research Center, University of California, Berkeley, November 2010.

8CUEE CONFERENCE PROCEEDINGS
8th International Conference on Urban Earthquake Engineering
March 7-8, 2011, Tokyo Institute of Technology, Tokyo, Japan

NEAR FAULT EARTHQUAKES OF MEDIUM MAGNITUDE: THE CASE OF THE ATHENS 1999 EVENT

C. Spyrakos[1], E. Skiada[2], and I. Taflampas[3]

1) School of Civil engineering, National Technical University of Athens, Polytechnic campus, Zografos, Athens
2) School of Civil engineering, National Technical University of Athens, Polytechnic campus, Zografos, Athens
3) School of Civil engineering, National Technical University of Athens, Polytechnic campus, Zografos, Athens
cspyrakos@central.ntua.gr, evmaly@hotmail.com, taflan@central.ntua.gr

Abstract: In this paper the moderate earthquake event of 1999, which affected the large urban area of Athens, is presented as a case study for the evaluation of the effects of strong directivity in the near field region for small to moderate events. Ground motion records at a distance from the causative fault are analyzed in order to estimate crucial characteristics associated with the event, as possible directivity pulses and their predominant period. Ground motions recorded at rock sites are scaled up to new generation attenuation models of characteristic spectra, accounting for either mean, near field, acceleration amplification or possible directivity related velocity pulses. These ground motions are used as input at the bedrock of typical soil deposits in order to obtain surface ground motions accounting for different soil profiles at various distances from the causative fault in the near field region. Inelastic spectra are generated and the difference between mean and strong, directivity affected, ground motion is established. For ground motions affected by forward directivity it is concluded that even for medium events seismic coefficients, provided by aseismic codes are inadequate for safe structural design. Seismic zonation coefficients must be re-examined and most likely upgraded in order to account for near field directivity, even in the case of moderate earthquake events.

1. INTRODUCTION

During the last decade a serious effort has been made in order to estimate the expected ground motion and spectral values in the near field region. New generation attenuation relationships have been developed in order to account for different parameters affecting the response of ground motion. Such parameters are associated with characteristics as moment magnitude, distance from the fault, type of fault, soil conditions, etc. These new generation attenuation relationships estimate ground motion values associated with a geometric mean of the horizontal spectral demand, lower than the maximum demand in the near field region affected by forward directivity. As a result, further investigation has been conducted in order to associate the predicted spectral values with this maximum spectral demand (Huang et al, 2008). Up to now this investigation has been undertaken for events with moment magnitude greater than 6.5. In the present paper such an investigation is conducted for events with a moment magnitude in the range of 6.0 presenting a larger frequency of occurrence and consequently more probable events at the vicinity of great urban centers.

As a case study, the Athens earthquake of 1999 is presented and an effort is made to develop the elastic and inelastic spectra associated with such an event of M_w = 5.9, for different soil conditions, at a distance of 2 and 5 kilometers from the causative fault. Two cases of spectral values are considered, associated, on the one hand with new generation relationships, predicting mean values at the near field zone, and, on the other, with the maximum spectral demand in the region, associated with directivity effects. In the case of the Athens earthquake the existing data for the earthquake ground motion are records taken at a distance from the most affected region. These records are at soft rock sites mostly, next to subway stations, near the center of the metropolitan area of Athens.

The analysis of these records presents a pulse with a period of around 1.5 to 2.0 seconds on the time history of ground velocity, which appears to be associated with the directivity pulses expected for events of such magnitude, according to existing relationships. Pulses of that period affect the frequency content lower than 1 Hz, an observation conforming with the prediction of Somerville (1998), separating the frequency content in a region higher than 1 Hz that remains unaffected from directivity amplification, and a region lower than 1 Hz, affected by the directivity phenomenon and presenting amplification dependent on the azimuth of the recording site. This directivity amplification is expected to strongly influence the ratio between the maximum spectral demand and the geometric mean spectral values at the near field region.

Up to now, comparison between the maximum and the

mean spectral values has been conducted for earthquakes larger than 6.5 and distances from the fault plane less than 15 kilometers. The ratios between maximum and mean spectral demands have been evaluated for different period ranges. According to Huang et al (2008), for most periods the strike normal component of the forward directivity records can be considered to represent the maximum spectral demand. Furthermore, for strong forward directivity and for periods 1.0 and 3.0 seconds, spectral ratios of 1.5 to 2.0 have been estimated.

These results present average values for magnitudes larger than 6.5 and do not account for the effect of magnitude variation on the estimated ratios. As well known from many studies (Alavi and Krawinkler (2000), Rodriguez-Marek (2000), Somerville (2003)), the predominant period of the directivity pulses depends on the moment magnitude of the event and varies exponentially with magnitude. Consequently, the spectral amplification associated with these pulses is magnitude and period dependent. In order to estimate appropriate ratios between maximum and mean spectral demands for moderate events, the case of the Athens earthquake is presented in this study.

2. THE ATHENS 1999 EARTHQUAKE

On September 7 1999, an earthquake event with moment magnitude 5.9 rocked the city of Athens (Psycharis et al, 1999). The strongly affected area was within a radius of 12 km from the epicenter. A number of modern buildings collapsed causing the death of 140 persons. About a hundred thousand people became homeless.

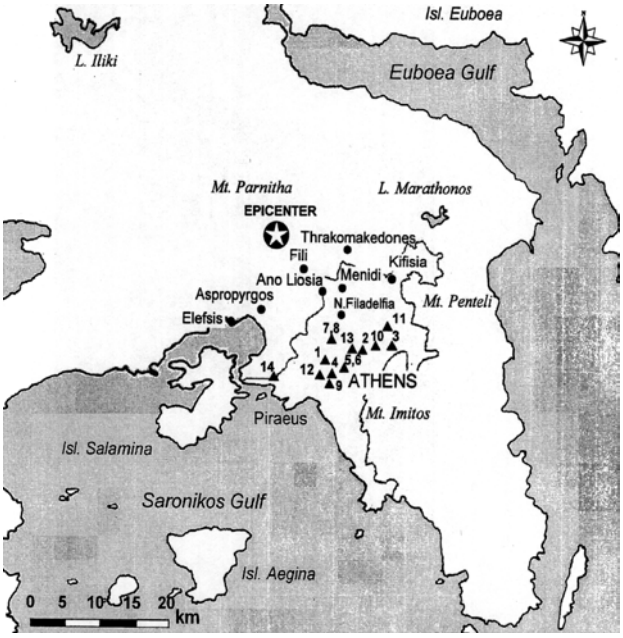


Fig.1. The urban area of Athens affected by the 1999 earthquake. Circles show the mostly affected sites and triangles the sites of recording stations (Psycharis et al, 1999) (see Table 1).

A number of strong ground motion time histories were recorded on soft rock sites at distances of 15 to 20 km from the epicenter (see Fig.1 and Table 1).

Table 1. Characteristics of main records of the Athens 1999 event (Psycharis et al, 1999).

No.	CODE	SITE	GEOLOGY	PLACE	EPICEN. DIST. Km	Max ACCELER., g		
						L	V	T
1	MNSA1	Monastiraki	Schist of bad quality, black soft phylite, archaeological deposits, underground caves	Free field	17	0.223	0.223	0.534
2	ATHA1	Neo Psychiko	Tertiary deposits	Basement, 3-story bldg	18	0.083	0.121	0.104
3	DMK1	Ag. Paraskevi	Limestone	Free field	19	0.052	0.042	0.073
4	FIX1	Syngrou-FIX	Limestone / Sandstone of good quality	Metro station, level –1	19	0.086	0.046	0.122
5	SMGA1	Syntagma	Limestone / schist	Metro station, level –1	18	0.146	0.051	0.239
6	SMGB1	Syntagma	Limestone / schist	Metro station, level –3	18	0.115	0.088	0.092
7	SPLA1	Sepolia	Deposits of Kifissos river	Metro station, level –1	15	0.248	0.093	0.226
8	SPLB1	Sepolia	Deposits of Kifissos river	Basement, 2-story steel bldg	15	0.356	0.204	0.326
9	DFN1	Dafni	Schist	Metro station, level –2	21	0.038	0.041	0.112
10	PNT1	Papagos	Tertiary deposits	Metro station, level –2	19	0.090	0.057	0.080
11	ATHO2	Chalandri	Alluvial deposits	Basement, 2-story bldg	17	0.130	0.190	0.110
12	ATH03	Piraeus str – KEDE	Alluvial deposits	Ground floor, 1-story bldg	16	0.290	0.350	0.190
13	ATH04	Kypseli	Schist	Basement, 4-story bldg	16	0.140	0.120	0.060
14	KERA	Keratsini	Soft rock	Basement, Administr. bldg	15	0.186	0.220	0.157

3. PRESENTATION OF THE ANALYSIS PROCEDURE

The existing records have been used in order to determine the referred ratios between maximum and mean spectral demands according to the following procedure:

- The original accelerograms FIX1 and DFN1 are filtered in order to obtain two frequency components, a component of high frequency, i.e., higher than 1 Hz, and a component with frequencies lower than 1 Hz.
- The two components are scaled in order to represent mean near field ground motion at rock sites, at a distance of 2 and 5 kilometers from the fault plane. Consequently, the high and low frequency components are scaled up to the values given by a representative attenuation relationship for the near field ground motion acceleration spectra, given by Ambraseys and Douglas (2003). The target spectral values are related to the 50% and 84% probability of non-exceedence and the frequency components are combined after scaling. The resulting time histories are considered to represent the mean near field records at rock sites at the referred distances from the fault and probabilities.
- The two components of the original accelerograms are scaled in order to represent maximum near field records, affected by forward directivity, at rock sites located at distances of 2 and 5 kilometers from the fault plane. The high frequency component is scaled, as before, up to the values given by Ambraseys and Douglas (2003). This scaling conforms to the observation presented by Somerville (1998) that the high frequency component of the ground motion remains unaffected from near field directivity. The low frequency component is scaled in order to attain a

maximum velocity, comparable to that predicted by the attenuation relationship proposed by Rodriguez-Marek (2000), for near field ground motions affected by forward directivity. The scaling is performed for 5.9 moment magnitude, rock sites at 2 and 5 km distance from the fault and 50% as well as 84% probabilities of non-exceedance.

- The artificial accelerograms generated by this procedure are used as rock outcrop ground motions in order to estimate the response and the subsequent ground motions at the top of soil deposits corresponding to A, B and C categories of the EC8 regulations. As a result of this procedure, a large sample of artificial time histories, approximating cases of near field ground motions, were generated. These time histories represent ground motion either affected or not by forward directivity, for a moment magnitude 5.9, distance from the fault plane of 2 and 5 kilometers, three different soil conditions and two levels of non-exceedance probability.
- The spectra of these artificial ground motions are used in order to determine the ratios between maximum and mean near field spectral demands.
- The artificial ground motions are used in order to estimate inelastic spectra and especially the design spectral acceleration values in order to attain a ductility level of 2 for representative SDOF systems.
- Finally, the obtained elastic and inelastic spectra are compared with spectra obtained during the San Salvador 1986 earthquake, an event considered to represent the case of near field directivity effects for small to moderate earthquakes (Bommer et al, 2001).

4. SPECTRAL ACCELERATIONS GIVEN BY AMBRASEYS AND DOUGLAS

Ambraseys and Douglas (2003) have studied the horizontal and vertical ground motions for near field and developed attenuation relationships for spectral accelerations. These relationships depend on the surface-wave magnitude, the distance from the horizontal projection of the fault plane and the soil conditions. Forward directivity is not taken into account. Consequently, the corresponding spectra are associated with the mean near field ground motions. The general form of the relationship given by Ambraseys and Douglas is:

$$logy = b_1 + b_2 M_s + b_3 d + b_4 S_A + b_s S_S \qquad (1)$$

with M_S denoting the surface wave magnitude, d is the distance from the horizontal projection of the fault plane, S_A and S_S take the value of 1 for stiff and for soft soil respectively. For rock S_A and S_S are zero. The relationships have been developed with the aid of a worldwide set of 186 strong ground motion records recorded within 15 kilometers from the surface projection of the fault rupture and for event surface magnitudes of 5.8 up to 7.8. Figures 2 and 3 present the target near field spectral accelerations, used for scaling the original records.

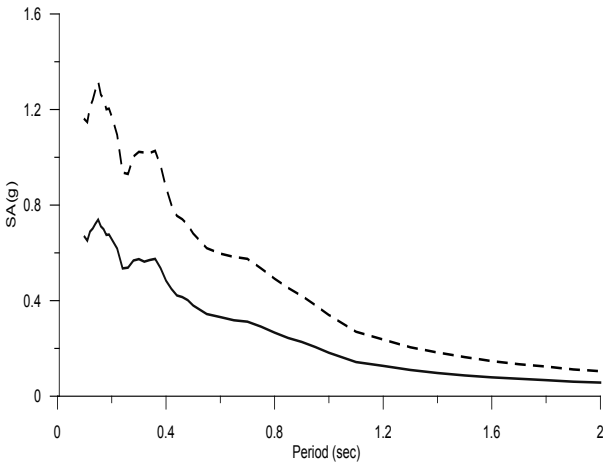


Fig.2 Target acceleration spectra as developed by Ambraseys and Douglas (2003) for surface magnitude 5.9, rock sites at 2 km from the fault and 50%, 84% probabilities in non exceedance.

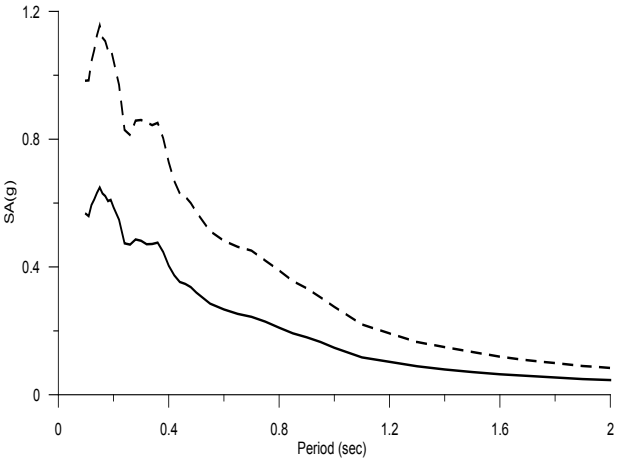


Fig.3 Target acceleration spectra as developed by Ambraseys and Douglas (2003) for surface magnitude 5.9, rock sites at 5 km from the fault and 50%, 84% probabilities in non exceedance.

5. RELATIONSHIPS PROPOSED BY RODRIGUEZ-MAREK TO ESTIMATE DIRECTIVITY PULSE PERIOD AND MAXIMUM GROUND VELOCITY

Rodriguez-Marek in his dissertation (2000) presented relationships to estimate the pulse periods associated with forward directivity, as well as attenuation relationships for the maximum ground velocity associated with directivity velocity pulses. The former relationship is presented in Fig. 4 in order to demonstrate that the pulse period estimated for the Athens records is close to those estimated for 5.9 moment magnitude. The velocity attenuation relationship presented in Fig. 5 was used to scale the low frequency component of the original records in order to simulate near field time histories affected by near field forward directivity.

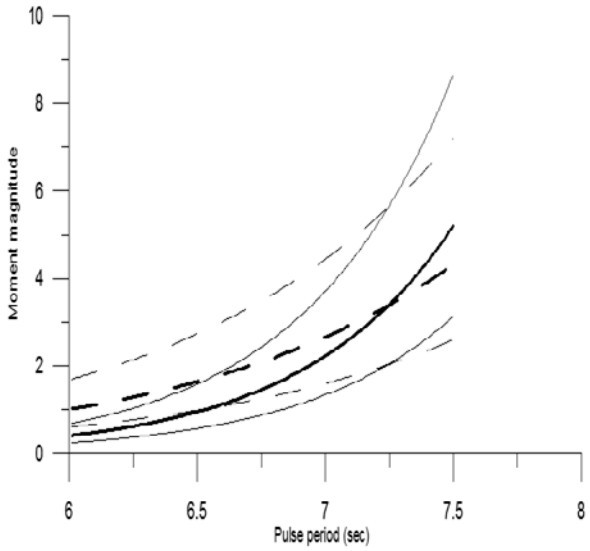


Fig 4. Relationships estimating directivity pulse period for rock sites (continuous line, mean-σ,mean,mean+σ) and soil sites (dashed, mean-σ,mean,mean+σ) (Rodriguez-Marek 2000)

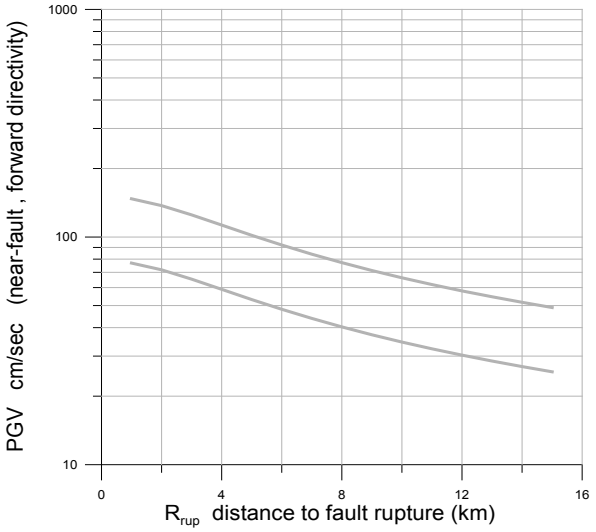


Fig 5. Relationships estimating max ground velocity for 6.1 and 7.4 moment magnitude. (Rodriguez-Marek 2000)

6. ANALYSIS RESULTS

In fig.6 spectra produced from the scaling of the original FIX1 accelerogram are presented. The maximum ground accelerations range from 0.30g for mean near field ground motion and B soil category at a distance of 5 km from the fault plane for a 50% percentile of non exceedance to 0.70g for strong forward directivity and B soil category at a distance of 2 km from the fault plane for a 84% percentile of non exceedance. At the 1 sec period the estimated spectral values are the following, for B soil category:

- At a distance of 5 km from the fault plane, for mean near field ground motion and a 50% probability of non exceedance 0.35g.
- At a distance of 5 km from the fault plane, for mean near field ground motion and a 84% probability of non exceedance 0.6g.
- At a distance of 2 km from the fault plane, for mean near field ground motion and a 50% probability of non exceedance 0.4g.
- At a distance of 2 km from the fault plane, for mean near field ground motion and a 84% probability of non exceedance 0.7g.
- At a distance of 5 km from the fault plane, for near field strong forward directivity and a 50% probability of non exceedance 0.7g.
- At a distance of 5 km from the fault plane, for near field strong forward directivity and a 84% probability of non exceedance 1.2g.
- At a distance of 2 km from the fault plane, for near field strong forward directivity and a 50% probability of non exceedance 0.9g.
- At a distance of 2 km from the fault plane, for near field strong forward directivity and a 84% probability of non exceedance 1.4g.

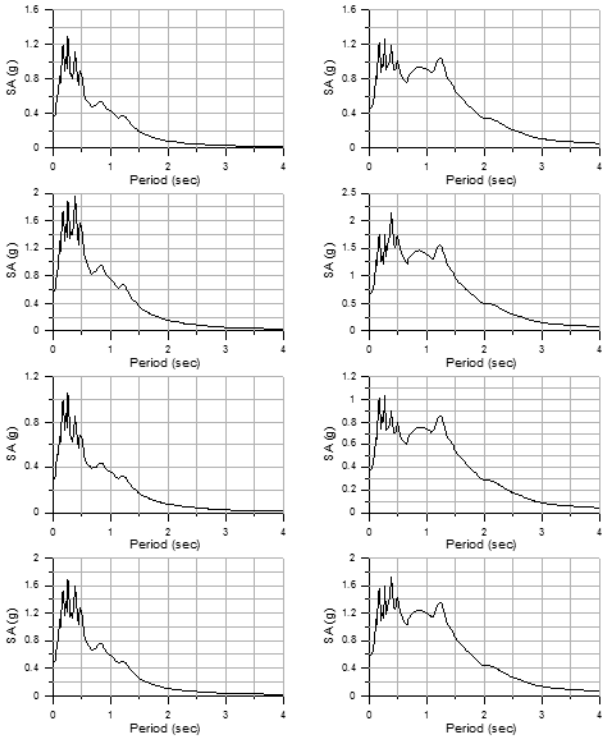


Fig.6 Spectra of artificial accelerograms produced from the FIX1 record. First column presents scaling to the Ambraseys-Douglas spectral values a) mean at 2 km b) mean+σ at 2 km c) mean at 5 km d) mean+σ at 5 km and the second column the same cases but with the low frequency range scaled up to the appropriate max ground velocity as given by Rodriguez-Marek.

In Fig.7 spectra produced from the scaling of the original DFN1 accelerogram are presented. The maximum ground accelerations range from 0.35g for mean near field ground motion and B soil category, at a distance of 5 km

from the fault plane for a 50% percentile of non exceedance to 0.60g for strong forward directivity and B soil category at a distance of 2 km from the fault plane for a 50% percentile of non exceedance. At the 1 sec period the estimated spectral values are the following, for B soil category:

- At a distance of 5 km from the fault plane, for mean near field ground motion and a 50% probability of non exceedance 0.25g.
- At a distance of 2 km from the fault plane, for mean near field ground motion and a 50% probability of non exceedance 0.30g.
- At a distance of 5 km from the fault plane, for near field strong forward directivity and a 50% probability of non exceedance 0.6g.
- At a distance of 2 km from the fault plane, for near field strong forward directivity and a 50% probability of non exceedance 0.8g.

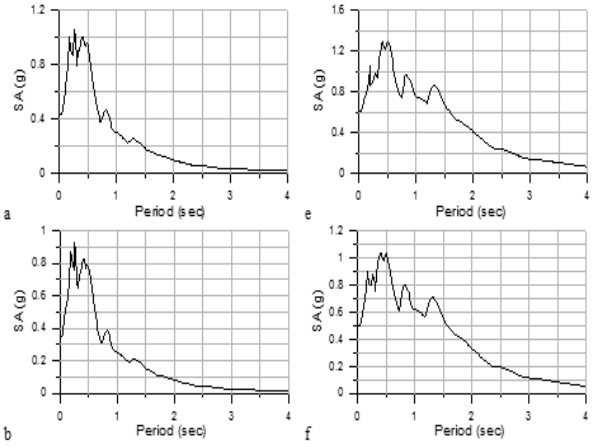


Fig.7 Spectra of artificial accelerograms produced from the DFN1 record. First column presents a) scaling to the Ambraseys-Douglas spectral values mean at 2 km b) at 5km.The second column presents the same with the low frequency range scaled up to the appropriate max ground velocity as given by Rodriguez-Marek.

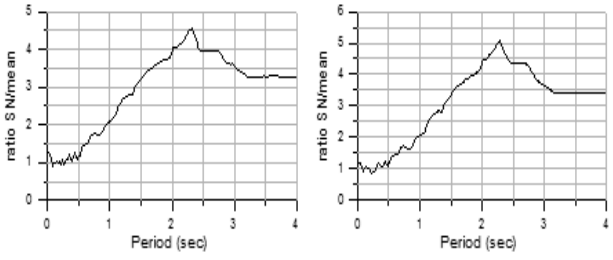


Fig. 8 Ratios between strike-normal (maximum) and mean spectral demand for different artificial accelerograms produced from the FIX1 record.

The values for the latter cases are slightly lower than those for the FIX1 record. For both records, as shown in Figs 6 and 7, a strong amplification in the range of 1 to 2 seconds characterizes the forward directivity records. This amplification is associated with the velocity pulse presenting a period around 1.5 sec.

In what regards the amplification factors between the mean near field and the maximum forward directivity spectra for the artificial accelerograms, these, for all cases, fluctuate between the values of 2 and 4 with a mean value about 3. These amplification values refer to the period range between 1 and 2 sec, where quite a lot of existing structures have their larger natural period. The amplification values given by Huang et al (2008) to estimate forward directivity spectra through new generation attenuation relationships range from 1.5 to 2. This discrepancy could be attributed to the fact that amplification factors for those studies are computed from earthquakes with moment magnitudes larger than 6.5. For such earthquakes the pulse period is expected to be larger than 2 seconds. Consequently, the amplification in the range from 1 to 2 seconds is not associated with the velocity pulses of the directivity effects. In the case presented in our study, earthquake events with magnitude around 6.0 present, as already seen, periods in the referred range of 1 to 2 seconds.

In order to assess the obtained results, a real record obtained at San Salvador in 1986 for a 5.6 earthquake, near the fault plane, at an epicentral distance of 4 km, is compared with the spectra obtained through the presented procedure from the Athens strong motion records. Bommer et al (2001) presented such records as a justification of the assumption that there exist forward directivity effects even for small to moderate earthquake events. Figure 9 shows the acceleration response spectrum of the San Salvador record and the spectrum corresponding to the artifical FIX1 record for a B soil deposit at a distance of 5 klm from the fault plane. The artificial record spectral values correlate very well to those of the real record for the forward directivity effects, which permits the assumption that the Rodriguez-Marek relationships are a good estimator for the maximum ground velocity caused by directivity effects.

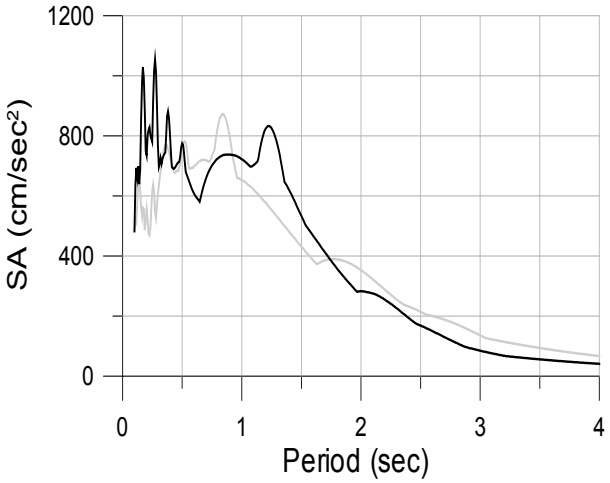


Fig.9 Comparison of spectral acceleration for the artificial ground motion (strong forward directivity, B soil category, at 5 km distance from fault plane, with 50% probability of non-exceedance),(black line), produced from the FIX1 record, with the CIG (San Salvador, 1986),(gray line) record.

Accordingly, these relationships appear to be an appropriate tool to scale accelerograms in the low frequency range, in order to simulate ground motions affected by forward directivity.

Further evaluation of the effects of strong forward directivity on structures with natural periods in the range of 1 to 2 seconds is presented by a series of inelastic spectra, for the artificial FIX1 record, as well as, for the CIG San Salvador record. From the inelastic analyses of SDOF systems the design spectral acceleration for a ductility 2 has been determined.

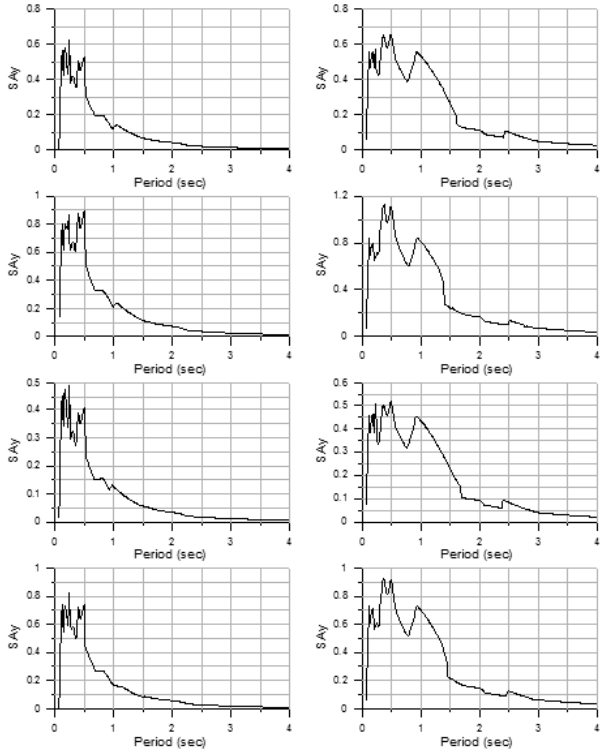


Fig.10 Design spectral acceleration for μ=2 for artificial ground motions produced from the FIX1 record, (first column) scaled to Ambraseys-Douglas for mean and mean+σ at 2 and 5 km and (second column) low frequencies scaled to max ground velocity given by Rodriquez-Marek for the same cases.

As can be seen from Fig.10, at the 1 sec period the estimated design spectral values, for a ductility of 2 and soil category B, are the following:

- At a distance of 5 km from the fault plane, for near field strong forward directivity and a 50% probability of non exceedance, 0.45g.
- At a distance of 5 km from the fault plane, for near field strong forward directivity and a 84% probability of non exceedance, 0.7g.
- At a distance of 2 km from the fault plane, for near field strong forward directivity and a 50% probability of non exceedance, 0.55g.
- At a distance of 2 km from the fault plane, for near field strong forward directivity and a 84% probability of non exceedance, 0.8g.

In Fig. 11 a comparison is made with the design spectral values for ductility 2 for the CIG record. The values are close to those of the FIX1 artificial record at a distance of 5 km from the fault plane, for near field strong forward directivity and a 50% probability of non exceedance.

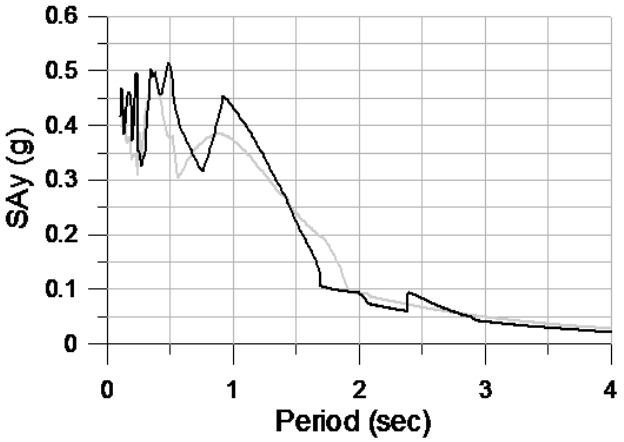


Fig.11 Comparison of design spectral values (μ=2) for the artificial ground motion (strong forward directivity, B soil category, at 5 km distance from fault plane, with 50% probability of non-exceedance),(black line), produced from the FIX1 record, with the CIG (San Salvador, 1986),(gray line) record.

7. CONCLUSIONS

This paper presents a procedure to determine spectral acceleration accounting for strong forward directivity effects of moderate earthquakes, in the period range of 1 to 2 sec. Ground motions recorded at rock sites during the Athens 1999 earthquake are scaled up using new generation attenuation models of characteristic spectra, that account for either mean, near field, acceleration amplification or possible directivity related velocity pulses. Consequently, the ground motions are used as input at the bedrock of typical soil deposits. Surface ground motions, accounting for different soil profiles at various distances from the causative fault, are produced. Elastic and inelastic spectra have been generated and the difference between mean and strong forward directivity ground motion is established. Recent studies estimate the ratio between maximum and mean near field spectral values at about 1.5 to 2. This study, taking explicitly into account the amplification attributed to directivity velocity pulses for moderate events, demonstrates that the ratios may present values of 2 to 4, almost doubling the expected effects. As a result, the spectral values at a period of 1 sec, caused by this strong amplification, may range from 0.7 to 1.4g, according to the distance from the fault plane and the estimated probability of non exceedance. The produced spectral values are compared with those of a characteristic near field record for moderate events. The real spectrum appears to correlate very well to the spectral values of artificial ground motion at a similar distance from the causal fault. Consequently, even for moderate events in the

period range of 1 to 2 sec, a larger amplification of spectral values, even for moderate events, in the period range of 1 to 2 sec, appears to be induced by near field directivity effects.

References:

Huang, Y. N., Whittaker A. S. and Luco, N. (2008), "Maximum Spectral Demands in the Near Fault Region," *Earthquake Spectra*, 20, 347-376.

Somerville, P.G. (1998), "Development of an Improved Representation of Near Fault Ground Motions," *Proceedings SMIP98 Seminar on Utilization of Strong Motion Data, California Strong Motion Instrumentation Program*, Sacramento, California, 1-20.

Alavi, B. and Krawinkler, H. (2000), "Consideration of near-fault ground motion effects in seismic design," *Proceedings 12th World Conference on Earthquake Engineering*, New Zealand.

Somerville, P.G. (2003), "Magnitude Scaling of the Near Fault Rupture Directivity Pulse," *Physics of the Earth and Planetary Interiors*, 137, 201-212.

Rodriguez-Marek, A. (2000), "Near-Fault Seismic Site Response," Ph.D. Dissertation, Department of Civil Engineering, University of California, Berkeley.

Psycharis, I., Papastamatiou, D., Taflampas, I. And Carydis, P. (1999), "The Athens, Greece earthquake of Septemper 7, 1999," EERI, Special Earthquake Report.

Ambraseys, N.N. and Douglas, J. (2003),"Near field horizontal and vertical earthquake ground motions," Soil Dynamics and Earthquake Engineering, 23, 1-18.

Bommer, J.J., Georgallides, G. and Tromans, I. J. (2001), "Is there a Near field for small-to-moderate magnitude earthquakes ? ," *Journal of Earthquake Engineering*, 5(3), 395-423.

8CUEE CONFERENCE PROCEEDINGS
8th International Conference on Urban Earthquake Engineering
March 7-8, 2011, Tokyo Institute of Technology, Tokyo, Japan

RECENT REVISION OF CHINA CODE FOR SEISMIC DESIGN OF BUILDING STRUCTURES

Yingmin Li[1)2)], Qian Tan[3)], Akira Wada[4)], Pu Yang[5)], Hongliu Xia[5)], Liping Liu[5)], Yuntian Wu[5)], Shuyan Ji[5)], Zhe Qu[6)], Nina Zheng[7)], and Jun Han[7)]

1) Professor, College of Civil Engineering, Chongqing University, Chongqing, China
2) Key Laboratory of New Technology for Construction of Cities in Mountain Area (Chongqing Univ.), Ministry of Education, China
3) PhD Candidate, College of Civil Engineering, Chongqing University, Chongqing, China
4) Professor, Structural Engineering Research Center, Tokyo Institute of Technology, Japan
5) Associate Professor, College of Civil Engineering, Chongqing University, Chongqing, China
6) Postdoctoral Fellow, Structural Engineering Research Center, Tokyo Institute of Technology, Japan
7) Lecturer, College of Civil Engineering, Chongqing University, Chongqing, China
liyingmin@cqu.edu.cn, wada@serc.titech.ac.jp

Abstract: Structural damages induced during the Wenchuan Earthquake have revealed the inadequacy of the previous version China Code for Seismic Design of Building Structures in many aspects and the room for potential improvement. Recently a new round of code revision has been completed. In this paper, the major revision, supplement and refinement made to the previous version code is introduced in terms of seismic fortification intensity, performance-based design method, structural analysis requirement, selection of structural system, failure pattern control and miscellaneous structural seismic measures. The impact and change on future seismic design due to the code revision is briefly discussed. In addition, the difference between the seismic design methods of China and Japan is compared and analyzed.

1. INTRODUCTION

Building structures and engineering facilities were destroyed in large numbers during the Wenchuan Earthquake of May 12, 2008. Ever since then progress has been made in terms of the understanding on failure mechanisms of structures, owing to the in-depth investigation work on the observed structural damages caused by the Wenchuan earthquake and the study on the collected information. In order to comply with the national laws and regulations regarding the earthquake hazard prevention policies and to fulfill the needs for the reconstruction of Wenchuan, the Ministry of Housing and Urban-rural Development of China set up boards and committees consisting of experts in related fields shortly after the earthquake to revise the standard code for seismic design of buildings based on the lessons learnt from the Wenchuan earthquake. As a result, the partial revisions of the Standard for Classification of Seismic Protection of Building Constructions (GB50223-2008) and the Code for Seismic Design of Buildings (2008 version of GB50011-2001, or the 2001 code later on) were completed very soon. The Code for Seismic Design of Buildings (GB50011-2010, or the 2010 code later on) was then issued on May 31, 2010, considering the economic conditions and the characteristics of engineering practice in China and adopting the most recent research results in earthquake engineering. In this paper, the major revisions that were incorporated into the new version Code for Seismic Design of Buildings are introduced. The codes for seismic design of buildings used in China and Japan are also compared so as to identify their common points as well as their differences, which will be of great significance for the reconstruction after the Wencuan earthquake and the improvement of the seismic performance of newly built structures.

2. OVERVIEW OF REVISIONS IN CODE 2010

Compared with the Code 2001, the following revisions were incorporated into the Code 2010:

In terms of the seismic parameters of ground motion, the seismic fortification intensities of seismic regions were partially adjusted, i.e. provisions were added regarding the seismic fortification measures in seismic regions with 0.15g and 0.30g PGA. The classification of design earthquakes was adjusted according to the Seismic Ground Motion Parameter Zonation Map of China. In terms of the site soil liquefaction, the liquefaction discrimination equation was improved; in terms of the calculation of design earthquake action, the damping adjusting coefficient of the design response spectrum, damping ratio and seismic adjusting factor for bearing capacity of members of steel structures, the horizontal seismic-reduced factor for seismic-isolated structures were adjusted and the calculation method for the horizontal and vertical earthquake actions of long-span roof

structures was added; for reinforced concrete structures, the seismic fortification criteria for frame buildings and masonry buildings with bottom-frame; for masonry structures, seismic fortification measures for multi-story masonry buildings, concrete seismic-wall structures and reinforced masonry structures were improved; for steel structures, anti-seismic grade of steel buildings was introduced and the design requirements for seismic fortification measures were adjusted accordingly; for seismic-isolated and seismic-energy-dissipating buildings, the range of their applicability was expanded. In addition, the following contents were adjusted: the performance-based design method was added; seismic design provisions for large-span roof structures, underground structures, portal frame factory structures, reinforced concrete frames with steel brace and the steel frame-reinforced concrete core structures were added; the contents regarding the brick buildings with inner-frame were deleted.

3. MAIN REVISED CONTENTS OF CODE 2010

3.1 Seismic Fortification and Basic Principle of Design

The main revised contents include:

(1) Adjustment of parameters of design earthquake

According to the distribution characteristics of earthquake hazard in Wenchuan Earthquake, 2008, the parameters of design earthquake (fortification intensity or design earthquake groups) in some influenced-places are adjusted. It is shown in Table 1.

Table 1 Adjustment on Fortification Intensity and PGA of Some Places

Location	Code 2001	Code 2010
Wenchuan	7(0.10g)	8(0.20g)
Beichuan*	7(0.10g)	8(0.20g)
Qingchuan	7(0.10g)	7(0.15g)
Pingwu	7(0.15g)	8(0.20g)
Dujiangyan	7(0.10g)	8(0.20g)
Pengzhou	7(0.10g)	7(0.15g)
Shifang	7(0.10g)	7(0.15g)
Mianzhu*	7(0.10g)	7(0.15g)
Anxian*	7(0.10g)	7(0.15g)
Jiangyou	7(0.10g)	7(0.15g)
Chengdu*	7(0.10g)	7(0.10g)
Deyang*	6	7(0.10g)
Mianyang	6	7(0.10g)

Notes: *The design characteristic period, T_g, of response spectra are increased by 0.05 second than Code 2001.

(2) Adjustment on classification of seismic fortification

According to the Standard for classification of seismic protection of building constructions (GBJ50223-2008), the classification of seismic fortification of some important buildings such as hospital buildings and school buildings is changed from "standard fortification" to "important fortification". That means the seismic measurement of theses buildings should be taken according to higher intensity than the fortification intensity.

(3) Adjustment on internal forces of irregular structure

According to the damage phenomenon of irregular structure under earthquake and design experience, the Code 2010 provides the ways to adjust the internal forces based on the different irregularities respectively. For plan irregular and vertical regular structure, the limit value of rotation displacement ratio is loosened in Code 2010. For plan regular and vertical irregular structure, the adjustment focuses on the cases of vertical lateral-force-resisting member with discontinuity. In theses cases, the adjustment factors of seismic internal force for the horizontal transmission members were changed from 1.25~1.5 to 1.25~2.0, which shall be determined by fortification intensity, types of horizontal transmission members, stress type and dimension of cross-section of the members.

(4) Performance based design method

In Code 2010, the newly involved performance based design method provides four performance levels, as shown in Table 2. For the seismic design method of structure members, the demonstration on referenced index of load capacity, story drift, etc. is shown in Table 3, Table 4 and Table 5 respectively.

Table 2 Expected Four Performance Levels Specified in Code 2010

Standard of Earthquake Influence	Level 1	Level 2	Level 3	Level 4
Frequent earthquake	No damage	No damage	No damage	No damage
Fortification earthquake	No damage, can be used without repair	Basically inact, can be continuously used after checking	Slightly damage, can be use after simple repair	Slightly to moderate damage, displacement<3[⊿ue]
Rare earthquake	Basically inact, can be continuously used after checking	Slightly to moderate damage, can be continuously used after repair	Can be used after reinforcing the damage place	Near to serious damage, Can be used after thorough repair

Table 3 Demonstration on Referenced Index of Load Capacity for Structural Members

Requirement of performance	Frequent earthquake	Fortification earthquake	Rare earthquake
Level 1	No damage, can be designed as usual	No damage, load capacity should be checked while design value is employed	Seldom damage, load capacity should be checked while design value is employed and

		and the seismic effects shall be adjusted considering earthquake measure grade	the seismic effects shall not be adjusted considering earthquake measure grade
Level 2	No damage, can be designed as usual	Basically inact, load capacity should be checked while design value is employed and the seismic effects shall not be adjusted considering earthquake measure grade	Slightly to moderate damage, load capacity should be checked while ultimate value is employed
Level 3	No damage, can be designed as usual	Slightly damage, load capacity should be checked while standard value is employed	moderate damage, load capacity shall be maintained in a steady status as the ultimate value is achieved, even has some decrease, the decrease ratio is lower than 5%
Level 4	No damage, can be designed as usual	Slightly to moderate damage, load capacity should be checked while ultimate value is employed	Unserious damage, load capacity shall be maintained in a almost steady status as the ultimate value is achieved, even has some decrease, the decrease ratio is lower than 10%

Table 4 Demonstration on Referenced Index of Story Drift for Structural Members

Requirement of performance	Frequent earthquake	Fortification earthquake	Rare earthquake
Level 1	No damage, drift is far less than the limit value of elastic story drift	No damage, drift is less than the limit value of elastic story drift	Basically inact, drift is slightly great than the limit value of elastic story drift
Level 2	No damage, drift is far less than the limit value of elastic story drift	Basically inact, drift is slightly great than the limit value of elastic story drift	Slightly plastic drift occurred, drift is less than the 2 times limit value of elastic story drift
Level 3	No damage, drift is obviously less than the limit value of elastic story drift	Slightly damage, drift is less than the 2 times limit value of elastic story drift	Obvious plastic drift occurred, drift is about to the 4 times limit value of elastic story drift
Level 4	No damage, drift is less than the limit value of elastic story drift	Slightly to moderate damage, load capacity should be checked while ultimate value is employed	Unserious damage, drift is less than the 0.9 times limit value of plastic story drift

Table 5 Demonstration on Grade for Seismic Details for Structural Members

Requirement of performance	Earthquake measure grade of seismic details
Level 1	Basic seismic details
Level 2	Low-ductility requirement seismic details
Level 3	Moderate-ductility requirement seismic details
Level 4	High-ductility requirement seismic details

3.2 Site, Soil and Foundation

(1) Adjustment on plat category

Based on the three categories of site, favorable plat, unfavorable plat and hazard plat specified in Code 2001, a new plat category, general plat, is assigned to describe the common plat between the favorable plat and the unfavorable plat.

Considering the phenomenon of historical earthquake hazard, the minimum distance of avoidance for seismogenic fault is decreased, as shown in Table 6.

Table 6 Adjustment on the Minimum Distance of Avoidance for Seismogenic Fault(uints:m)

Fortification intensity	Fortification category of buildings	
	Important Fortification	Standard Fortification
8	200(300)	100(200)
9	400(500)	200(300)

Note: The values in brackets are given by Code 2001

(2) Adjustment on the criterion of site category

The construction sites can be classified as four categories depending on the equivalent shear-wave velocity and the overlay depth of soil profile. Category I is divided into two sub-categories, Category I_0 and Category I_1, as shown in Table 7.

Table 7 Two Sub-categories of Site Category I

Code 2010		Code 2001
I_0	I_1	I
V_s>800, D_o=0		V_s>500, D_o=0
	800>V_s>500, D_o=0	

Note: Vs is the equivalent shear-wave velocity, D_o is the overlay depth of soil profile.

(3) Adjustment on the criteria for liquefaction discrimination

The adjustments on the criteria for liquefaction discrimination include two aspects. First, the required depth of soil on liquefaction discrimination is enlarged from 15m (Code 2001) to 20m (Code 2010). Second, the calculate equation of critical value of standard penetration resistance for liquefaction discrimination is changed as a logarithm one, which is deduced based on method of probability theory.

3.3 Seismic Action and Seismic Checking for Structures

(1) Adjustment on the characteristic parameters of standard design response spectrum

There was a mistake that the response spectra would cross each other when the period is larger than 5.0sec in Code 2001. The characteristic parameters of standard design response spectra have been changed to correct the mistake. Figure 1 shows an example of the revised response spectra.

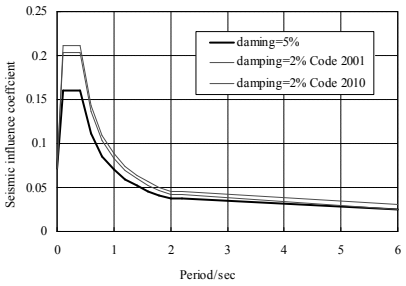


Figure 1 An Example of Design Spectra

(2) Adjustment on the minimum value of story seismic shear force

The minimum values of factor for story seismic shear force are revised. For Intensity 6, it may be 0.006 or 0.008; for long period structures in Intensity 9, it is increased from 0.040 to 0.048.

3.4 RC Buildings

(1) Applicable maximum height for RC buildings

The applicable maximum height for RC buildings in intensity 8 (0.30g) is added in Code 2010. And the one for Slab-Column-Wall structure is also increase from 40m, 35m and 30m to 80m, 70m and 40m respectively corresponding to Intensity 6, 7 and 8. The aspect ratio of the diaphragm between two adjacent seismic walls of slab-column-wall structure is also required in Code 2010.

(2) Grade of RC structures

For RC Frame-seismic Wall structure and Seismic-wall structure, different measure grade shall be adopted according to the intensity, the buildings height and Fortification Category. In Code 2010, the height boundary of 24m is used to classify the structural grade more accurately. And the frame with only one bay is not permitted for the building whose Fortification Category is A, B or its height is over 24m.

(3) The minimum clear width of the isolated joint

In Code 2010, the minimum clear width of the isolated joint has been increased. Taken a frame in intensity 7 as an example, the minimum clear width of the isolated joint would be increased from 110mm to 140mm when the lower building height is 23m.

(4) Requirement for stairs

Because much severe damage had been happened for RC stairs, the effect of component of stairs should be considered in structural analysis.

(5) Factors of the combinatory force design value

Because failure mechanism of strong column-weak beam was rarely developed during Wenchuan earthquake occurred in China on May 12th 2008, the factors of the combinatory force design value have been adjusted in Code 2010 as Table 8.

Table 8 Amplifying Factors of Combined Force Design Values

Grade of RC structures	Amplifying factors			
	Moment of columns	Moment of columns' foot	Shear of columns	Shear of joints
Grade 1	1.7(1.4)	1.7(1.5)	1.5(1.4)	1.50(1.35)
Grade 2	1.5(1.2)	1.5(1.2)	1.3(1.2)	1.35(1.20)
Grade 3	1.3(1.1)	1.3(1.1)	1.2(1.1)	1.20(1.00)
Grade 4	1.2(1.0)	1.1(1.0)	1.1(1.0)	1.0

Note: The factors in brackets are given by Code 2001.

(6) The compression ratio of columns

The compression ratio of columns for frame, frame-seismic-wall, slab-column-wall, frame-core-tube and tube-in- tube structures is strictly limited in Code 2010 shown in Table 9.

Table 9 Comparison of Compression Ratio of Columns

Type of structures	Grade of RC structures			
	Grade 1	Grade 2	Grade 3	Grade 4
Frame	0.65 (0.70)	0.75 (0.80)	0.85 (0.90)	0.90 (-)
Frame-Seismic-Wall Slab-Column-Wall Frame-Core-Tube Tube-In- Tube	0.75 (0.75)	0.85 (0.85)	0.90 (0.95)	0.95 (-)

(7) Requirement of longitudinal bars

The requirement of longitudinal bars for columns, seismic walls and ordinary boundary elements of seismic walls are increased in Code 2010.

(8) Seismic checking for joints

Seismic check for joints in frame of Grade 3 and Slab-Column-Wall has been required in Code 2010 but not in Code 2001.

(9) The minimum seismic shear forces for Frame-Core-Tube structures

For Frame-Core-Tube structures, the seismic story shear force distributed to columns of frame is supplemented in Code 2010, i.e. the seismic story shear force of column shall be not less than 10% of total base shear force of structures.

3.5 Masonry Buildings and Brick Buildings with Bottom-Frame

(1) Limit values of total height and number of stories

The limit values of total height and number of stories are supplemented for structures in intensity 7 (0.15g) and intensity 8 (0.30g) in Code 2010 and the one for other structures is adjusted. The maximum spacing of adjacent transverse seismic-walls is also adjusted in Code 2010 shown in Table 10.

Table 10 Maximum Spacing of Adjacent Transverse Seismic-walls (units: m)

Type of buildings	Type of floor or roof	Intensity			
		6	7	8	9
Multi-Story Masonry	Cast-in-place RC	15 (18)	15 (18)	11 (15)	7 (11)
	Assembled RC	11 (15)	11 (15)	9 (11)	4 (7)
	Timber	9 (11)	9 (11)	4 (7)	- (4)
Multi-Story Masonry with Bottom-Frame	Frame stories	18 (21)	15 (18)	11 (15)	-

(2) Requirement for Multi-Story Masonry with Bottom-Frame

The effect of tie-columns shall be considered to

calculate the stiffness of upper masonry wall. The details for the transition story between the Bottom-Frame and upper masonry wall are required in Code 2010. And seismic shear bearing capacity for Multi-Story Masonry with Bottom-Frame structures with small concrete blocks in intensity 6 should be checked. The details for stairs are required more strictly and use of fabricated stairs is limited.

3.6 Steel Buildings

(1) Applicable maximum height for RC buildings

The applicable maximum height for steel buildings in intensity 7 (0.15g) and intensity 8 (0.30g) is added in Code 2010. And the former frame-braced structure was divided into two types, frame-central braced and frame- eccentric braced structure. Their applicable maximum heights are also established. Meanwhile, the single-bay frame is banned if its fortification category is A or B.

(2) The amplifying factors of design moment force for columns

The measures are given to classify the Grade of steel structures and the amplifying factors of design moment force for columns are adjusted according to their Grade shown in Table 11.

Table 11 Amplifying Factors of Design Moment Force for Columns

Grade of steel structures			
Grade 1	Grade 2	Grade 3	Grade 4
1.15(1.15)	1.10(1.05)	1.05(1.00)	-(-)

3) The damping ratio of the steel structure

The damping ratio of the steel structure is adjusted as Table 12.

Table 12 Damping Ratio of Steel Structures

Earthquake level	Code 2001	Code 2010
Frequently Earthquake	0.035, <=12 stories 0.020, >12 stories	0.04, H<50m 0.03, H=50~120m 0.02, H>120m
Rarely Earthquake	0.05	

Note: H is total height of the structure.

3.7 Single-story Factory Buildings

(1) Single-story factory buildings with reinforced concrete columns

The construction requirement of the dense stirrup region for the lateral restraint bent column which the shear-span ratio is less than 2 is added. The section and reinforcement requirements of column for large-span factory are also added.

(2) Single-story steel factory buildings

Supplementary provisions are proposed as follows. The column braces should be used for factory in intensity 8 or 9 zone and the slenderness ratio limit values of frame columns are determined by different axial-force-ratio. The damping ratios of single-story steel factory buildings could be selected as 0.045~0.05 according to the type of the roof and the enclosure wall. The width thickness ratios of the plates are determined according to whether the contribution of the seismic load is dominated. The stiffness value chosen methods for different type of enclosure wall are also added for the calculation of earthquake action.

(3) Single-story factory buildings with brick columns

The provisions, single-story factory buildings with brick columns used in intensity 9, are deleted.

3.8 Single-story Spacious Buildings and Structures with Large-span Roof

The single-story spacious buildings are consisted of different types of structures，including spacious single-story hall and multilayer annex buildings. In the new code，the structural styles and details of seismic design of the single-story spacious buildings are revised，mainly includes：

(1)The single-story space building with brick column is only applicable to low intensity zone, the span of the brick column and the height of the column are proposed a stricter request than the 2001 Code.

(2)The seismic grade of reinforced column and cross wall of the single-story hall is upgraded. It is cleared that the brick wall on the girder in front of the stage should be light partition wall in intensity 9 zone.

In recent years, the large-span roof buildings are widely used. The content of seismic design of the large-span roof buildings is added in this revision, mainly includes：

(1)The types of the steel roof are classified to the following 7 basic types and their combination，including：arch, plane truss, space truss, grids, network shell，beam string structure and suspending system.

(2)The calculation method of the earthquake reaction，seismic analysis model, combination method of the earthquake reaction and the adjustment method of designed internal forces value of earthquake combination are proposed.

(3)The damping ratio of the steel roof and the concrete supporting structure is different，The damping ratio of the entire structure is ruled in the new Code.

(4)The slenderness ratio of the steel member of the roof is proposed, the details of seismic design of the joint and the support are specified.

3.9 Seismic-isolation and Seismic Energy-dissipating Design

Seismic-isolation and seismic energy-dissipating are effective technology for mitigation of earthquake hazards of the building structure. The new code modifies the design range of the seismic-isolation and seismic energy-dissipating.

New location for the isolation story is added. The isolation story can not only be installed on the base of the structure but also can be installed on the top of the column in ground floor or the chassis of multi-tower-building.

The limitation applied seismic-isolation technology only for multi-story masonry and reinforced concrete frame building is deleted.

Seismic-isolation technology is more appropriate for low-rise and multi-storey buildings. But the correlated studies both at home and abroad show that the technology is still effective for the structure which the fundamental period is more than 1.0s when it non-isolated. So the limitation

applied seismic-isolation technology only for the structure which the fundamental period is less than 1.0s is canceled.

Since the rubber isolation units have low tensile resistance, the horizontal load of non-earthquake action should be limited. So the limitation of height-width ratio of the buildings, which general should be less than 4, is added in the new code.

The concept of horizontal seismic-reduced factor is adjusted. It defined as the ratio of maximal horizontal shear force between the seismic-isolation structures and non-seismic-isolation structures.

The provisions for the total thickness, ultimate displacement and limited velocity of the viscoelastic material are added.

Energy-dissipation device and joint unit for main structure should work in the elastic range.

When the seismic influence coefficient of energy dissipation designed structure is less than 50% of that the non-energy dissipation designed structure, the seismic details requirements of the main structure could be taken as that for intensity of one grade lowers than local fortification intensity.

3.10 Nonstructural Components

During the Wenchuan earthquake, nonstructural components were severely damaged. As a consequence, the new code enhanced the design requirements and seismic measures for the nonstructural components. The major revisions included:

(1) Masonry parapet

Different anchorage methods at different locations of a parapet and the limiting parapet heights corresponding to different seismic fortification intensity were specified. The clear width of the isolation joints should be sufficient, and the free ends of the parapet at the two sides of the joints should be intensified.

(2) Infill wall

Strength indices for different unit types for masonry infill walls in RC structures were introduced. The development lengths for the splice bars between infill walls and columns were increased. Intensifying measures for stairwells and flow channels were added.

In terms of the envelop structures and partition walls of single story RC factory buildings, layout requirements for the perimeter beams of the masonry envelop walls were increased

3.11 Underground Structures

Seismic design for underground structures has attracted more and more attention. This round of code revision introduced the seismic design method for single building type underground structures such as underground parking structures.

(1)Seismic fortification objectives and general requirements

Seismic fortification criteria for underground structures are basically the same as or even higher than those for superstructures. Due to the uniqueness of the underground structures, the structural system should be as simple, uniform and regular as possible to ensure the seismic performance. The anti-seismic grade of RC underground structures is higher than that of basement of high rise buildings,

(2) Computing model and method for seismic design of underground structures

The computing model of underground structures should be able to simulate the influence of surrounding soils. Generally it is preferred to use spatial structural model for the analysis.

Simplified methods such as response displacement method, equivalent horizontal earthquake acceleration method and equivalent lateral force method are only applicable to seismic response analysis of plane strain problems. In most cases the time history method should be used for calculation.

(3) Main design parameters of seismic calculation for underground structures

In terms of the earthquake actions on underground structures, the design fundamental earthquake acceleration can be reduced according to the location. Rock foundation can be taken as one half of the ground surface and others can be reduced in proportion.

Characteristic values of gravity loads should account for water and soil pressure.

(4) Seismic design of underground structures

In general the load carrying capacity and deformation under frequent earthquakes should be checked. Considering the difficulty in repairing, elasto-plastic interstory drift angle of RC underground structures under rare earthquakes should be limited by1/250.

(5) seismic details for underground structures

Construction method of components, connections between components, minimum dimensions, steel ratio and the anti-liquefaction measures for top slab, bottom slab and floor slab are introduced.

4. COMPARISON OF SEISMIC FORTIFICATION OBJECTIVES AND DESIGN METHOD FOR RC BUILDINGS IN CHINA AND JAPAN

In recent years, the comparative studies on seismic fortification objectives and design methods among codes of different countries have attracted attention. Table 13 and Table 14 demonstrate the differences in the seismic fortification objectives and design methods for RC buildings in China and Japan.

Table13 Comparison of the First Stage Design

	China Code	Japan Code
Earthquake level	exceeding probability of 63.2% in 50 years; 50 years of return period	exceeding probability of 50% in 50 years; 43 years of return period
Performance level	The buildings will no damage or slightly damage with continue serviceable without repair subjected to frequently earthquake.	Main structural components remain elastic and no significant damage to nonstructural components
Analysis method	Linear elastic method (without reduction in stiffness)	Linear elastic analysis(with reduction in stiffness）
Member design	Limit state design	Allowable stress design
Deformation control	Inter-story drift angle less than: 1/550 for frame structure; 1/1000 for shear wall structures; 1/800 for frame-shear wall structures	1/200

Note: design at stage one in China code includes the performance level of reparable under moderate earthquake by conceptual design and seismic measures corresponding to the earthquake level with 10% of exceeding probability in 50 years.

Table14 Comparison of the Second Stage Design

	China code	Japan code
Earthquake level	exceeding probability of 2%-3% in 50 years; 2000 years of return period	exceeding probability of 10% in 50 years; 475 years of return period 5
Performance level	The buildings will no damage or slightly damage with continue serviceable without repair subjected to rarely earthquake.	Design limit state(reparable limit state）：sufficient load carrying capacity sustained at deformation corresponding to limit state(ensured by expected load carrying capacity of plastic hinge) and reusable by simple retrofit after earthquake； Safety limit state: ensured by the load carrying capacity of non plastic hinge regions and the ultimate deformation capacity of system
Analysis method	simplified method, static elasto-plastic analysis or dynamic elasto-plastic analysis	Yield mechanism design: Mechanism analysis method, pushover analysis method or linear elastic method (stiffness reduction and internal forces redistribution) to ensure the yield mechanism Mechanism analysis method or pushover analysis method(reliable material strength)
Deformation control	Inter-story drift angle less than: 1/50 for frame structure; 1/1000 for shear wall structures; 1/100 for frame-shear wall structures	Design limit state: 1/100 Safety limit state: 1/67

It can be seen that codes of China and Japan are different in earthquake action calculation, internal force calculation, control of structural performance level, etc. Both countries can learn from each other by conducting comparative studies in terms of specific topics.

5. SUMMARY

This paper summarizes the major revisions that were incorporated into the recently issued new version of China Code for Seismic Design of Buildings (GB50011-2010). The main differences between the old and new versions of code are briefly introduced. The seismic fortification criteria and design method of RC structures specified in the Chinese and Japanese codes are compared and studied, aiming to provide reference for better understanding the new code.

Acknowledgements

This research is supported by the National Key Technology R&D Program of China(2009BAJ28B01-2). The authors would like to appreciate the supports from various sponsoring agencies. The authors also would like to express sincere thanks to Professor Akira Wada for his invaluable contribution to this paper.

References

GB50011-2001 (2008), "Code for seismic design of buildings(2008 version)". Beijing: China Architecture & Building Press

GB50011-2010 (2010), "Code for seismic design of buildings". Beijing: China Architecture & Building Press

Wang Yayong, Dai Guoying (2010), "Evolution and p resent updation of 'Code for seismic design of buildings'," *Journal of Building Structures*, **42**(5):7-16.

Wang Yayong (2009), "An overview of recent revision of seismic design codes after the 5.12 Wenchuan Earthquake," *China Civil Engineering Journal*, **42**(5): 1-12

Wang Ruimin, Luo Qifeng (1998), "Analysis on the damage to underground structure and tunnel in Kobe are caused by Hanshin earthquake," *Journal of Catastrophology*, 13(2):63-66

Ye Lieping, Sun Yuping, Zhu Shan, Zhao Shichun (2010), "Introduction of design method for RC structures under severe earthquake in Japan," *building structure*, **40**(6): 114-118

Ye Lieping, Sun Yuping, Zhu Shan, Zhao Shichun (2010), "Introduction of evaluation method of the seismic capacity of existing multistory RC buildings in Japan", *building structure*, **40**(8): 110-117

Li Yingmin, Liu Liping(2008), "Overview and Inspiration on Building Seismic Disaster in Wenchuan Earthquake", Chongqing University Press. ISBN:978-7-5624-4645-3.

8CUEE CONFERENCE PROCEEDINGS
8th International Conference on Urban Earthquake Engineering
March 7-8, 2011, Tokyo Institute of Technology, Tokyo, Japan

HISTORICAL REVIEW OF THE ITALIAN SEISMIC CODE FROM THE PERSPECTIVE OF THE 2009 L'AQUILA EARTHQUAKE

Giuseppe Oliveto[1] and Luis D Decanini[2]

1) Professor, Structural Division, Department of Civil and Environmental Engineering, University of Catania, Italy
2) Professor, Department of Structural and Geotechnical Engineering, University of Rome "La Sapienza", Italy
goliveto@dica.unict.it, luis.decanini@uniroma1.it

Abstract: The evolution of the Italian seismic code is traced for about a century, starting from the document issued after the 1908 Messina and Reggio Calabria earthquake and ending with the current NTC-08 code. The aspects that have been mainly investigated are the provisions for seismic inputs and for ductility requirements. The NTC-08 design spectrum parameters for the L'Aquila area are compared to measured ground motion characteristics showing that the earthquake had spectral peculiarities not covered by the present code. Finally the behavior of reinforced concrete buildings is considered with the goal of identifying the sources of vulnerability which determined catastrophic collapses and loss of human lives.

1. INTRODUCTION

The 6.3 Mw earthquake that struck L'Aquila on April 6th 2009 was ranked 14th in a list of the most severe historical Italian earthquakes which include, among others, the 1693 Sicily (M=7.5), the 1908 Messina and Reggio Calabria (M=7.2), the 1703 L'Aquila (M=6.9) and the 1915 Avezzano (or Marsica) (M=6.8) earthquakes.

The latter two are of some relevance because the first one, locally known as *the great earthquake*, occurred in the same area as the 2009 one, while the *Marsica* event invested a neighboring area, south west of L'Aquila. Most relevant is the fact that, following the 1915 Avezzano (Marsica) earthquake, a new law was passed which classified L'Aquila and several municipalities in its proximity as seismic zones.

The 2009 earthquake has several characteristics which make it quite unique and worth studying. The city of L'Aquila is in a near fault, hanging wall position about 6 km northeast of the epicenter. With the hypocenter of the main shock located by INGV at a depth of 8.8 km, the earthquake is a shallow one.

These aspects were reflected in the characteristics of the ground motion which determined the collapse of a number of buildings causing 305 casualties, thousands of injuries, tenths of thousands of homeless, and significant damage to a vast majority of masonry historical buildings, to a number of essential and modern facilities, to several commercial and industrial buildings, to transportation facilities, electrical substations, lifelines and utilities.

The second author has had a role as a forensic engineer, advising the local court of justice on the collapse of a number of reinforced concrete buildings, 11 of which caused casualties. Seismic codes in Italy have evolved continuously, with more or less significant improvements after every moderate or catastrophic earthquake. Reinforced concrete buildings have been constructed starting from the early thirties and have evolved according to technological enhancements and, to some extent, according to the technical regulations that have interpreted such changes and absorbed the improvements in the state of the art of structural and earthquake engineering.

The purpose of the present work is twofold; on one side the characteristics of the recorded ground motion, which are typical of near fault conditions, shall be examined and on the other the collapse of some reinforced concrete buildings shall be analyzed in the light of the statutory seismic regulations at the time of construction. Some conclusions shall be drawn on the causes of the collapses and whether these could have been avoided if all the pro-tempore statutory recommendations for anti-seismic design and construction had been applied.

Since the scope of the present work is limited, the reader interested in the general aspects of the 2009 L'Aquila earthquake is referred to several reports published by private and public institutions such as Global Risk - Miyamoto (2009), EERI (2009), INGV (2009), AON Benfield UCL HRC (2010), Mori (2010), Celebi (2010), Decanini et al. (2009, 2010a, 2010b, 2011).

2. SEISMOLOGICAL ASPECTS

The earthquake occurred in a region characterized by a normal faulting system striking at 147 and dipping at 43 degrees approximately. Interestingly the striking angle is approximately coincident with the NW-SE orientation of the Italian peninsula. Interferometric Synthetic Aperture Radar

(InSAR), body wave seismology and GPS data identified with the Paganica fault the causative normal fault dipping 50° SW and estimated the maximum slip at 0.6-0.9 m. For more details and specific references AON Benfield UCL HRC (2010) may be consulted. Evidence of the surface traces of this fault rupture is provided by the INGV (2010) EMERGEO Working Group. The InSAR analysis allowed for the identification of the overall surface area where permanent vertical displacements were measurable distinguishing between the uplifted part NE of the fault line and the subsided one to the SW, with the separation line clearly identifying the trace of the rupture plane on the ground surface. The fringe lines that identify the subsided area are ellipsoids with the main axis oriented from NW to SE.

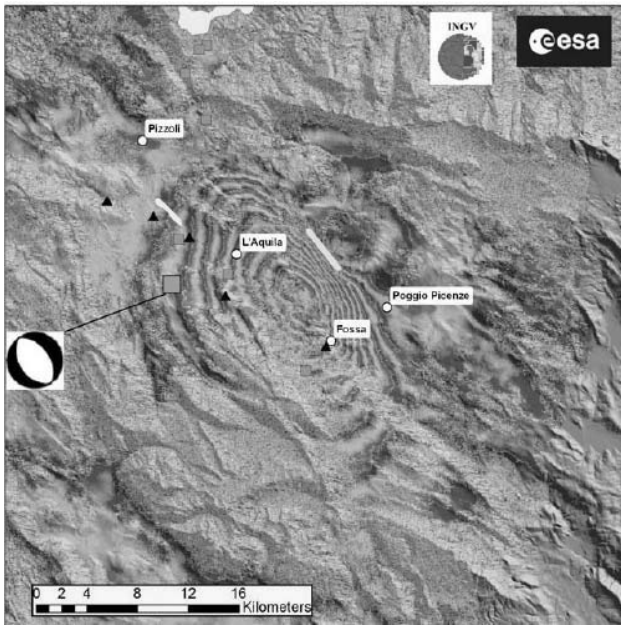


Figure 1 ENVISAT interferogram, focal mechanism and fault line (yellow).

As it may be seen from Fig. 1, the city of L'Aquila lies in the middle of the subsided area, midway between the fault line and the epicenter of the main shock, somewhat along the main axis of the ellipsoid towards NW. Two aftershocks of magnitude larger than 5 followed the main shock. The first one of magnitude M_w=5.6 occurred on April 7th , 40 hours after the main shock, along the principal axis of the fringes of the top event, towards SE. The second aftershock of magnitude M_w=5.4 occurred on April 9th near Campotosto, about 16 km north of L'Aquila. This shows that the rupture process initially progressed towards SE and later migrated to the north and NW. As it may be seen from Fig.1 of INGV EMERGEO Working Group (2009), the city of L'Aquila is roughly located at the centroid of a triangle with vertices at the epicenters of the three main shocks of the seismic sequence of April 2009. Finally it is worth noticing that the subsided area identified by the InSAR fringes lies on the hanging wall of the normal fault, while the uplifted area belongs to its foot wall.

3. GROUND MOTION CHARACTERISTICS

A study of the ground motion characteristics of the earthquake considered has been presented by Akinci et al. (2010). The main conclusions of this study are the presence of long pulses in the near fault records, the presence of some local amplification effects, the dependence of those effects on the magnitude of the shock, with smaller amplifications for larger magnitudes indicating nonlinear material behavior, elastic spectral responses much larger than present code requirements in the short period range.

The ground motion has been recorded by 58 stations of the Italian Strong Ground Motion Network (RAN) managed by the Italian Department of Civil Defense. These concur with the findings of the present study in the assessment of the relative severity of the earthquake and of its short effective duration 3-10 s.

In the present study only the near fault records shall be considered, that is those collected at stations within 6 km from the epicenter.



Figure 2 Strong ground motion recording stations in and around the city of L'Aquila

The recording stations considered are all located within the great metropolitan area of L'Aquila, Fig. 2. Two of the stations are situated downtown with AQU near the castle and AQK near the main bus station; three are located in the Aterno river valley with AQG on the southern bank, AQA and AQV on the northern bank, and finally AQF and AQP are somewhat NE of the latter three. However, stations AQF and AQP did not record due to failure of power supply, while station AQM was found faulty due to maintenance problems; therefore only the records from the remaining five stations are considered. The typical ground motion parameters PGA, PGV and PGD are shown in Tab.1 together with the Effective Peak Acceleration (EPA), evaluated in the 01-05 s period range, and the maximum spectral displacement $S_{D,max}$.

New Technical Rules for Constructions in the Italian Republic were enforced by Inter-Ministry Decree on January 14th 2008 (NTC-08).

Table 1 Ground motion parameters; recorded PGA and calculated PGV, PGD, EPA, $S_{D,max}$

Considered Record	PGA (g)	PGV (cm/s)	PGD (cm)	EPA (g)	$S_{D,max}$ (cm)
AQV-EW	0.626	36.7	8.4	0.471	12.2
AQV-NS	0.598	40.5	4.2	0.502	8.0
AQG-EW	0.416	33.6	8.0	0.316	13.1
AQG-NS	0.434	35.9	3.9	0.309	12.0
AQA-EW	0.394	30.5	6.4	0.254	10.1
AQA-NS	0.451	24.5	4.0	0.384	7.2
AQK-EW	0.342	30.3	8.0	0.220	24.2
AQK-NS	0.340	38.6	11.0	0.245	22.6
AQU-EW	0.263	20.6	3.6	0.209	9.5
AQU-NS	0.316	30.7	5.8	0.157	12.4
Mean	0.418	32.2	6.3	0.307	13.1

These rules superseded previous ones and in fact replaced the four seismic zones in which the Italian territory was divided by a continuous medium where spectral parameters are provided on the basis of the site coordinates in terms of latitude and longitude. For instance the recording stations quoted above are identified by the coordinates shown in Tab.2.

Table 2 Geographical coordinates of recording stations

Station	Latitude	Longitude	Soil Class
AQA	42.375530	13.339298	B
AQG	42.373474	13.337026	B
AQK	42.344967	13.400949	B
AQU	42.353880	13.401930	B
AQV	42.377222	13.343888	B

The soil class profile according to the Eurocode 8 is also provided for the station site because the spectral parameters are affected by the soil properties.

Table 3 Life safety design spectrum parameters

Station	a_g (g)	F_0	T_C^* (s)
AQA	0.260	2.360	0.347
AQG	0.260	2.360	0.347
AQK	0.261	2.360	0.349
AQU	0.261	2.360	0.350
AQV	0.261	2.360	0.350

According to NTC-08 two performance classes are considered; the life safety limit state and the collapse prevention one. For each limit state the code provides a set of parameters for the definition of the elastic design spectrum of the site. The parameters associated with the life safety limit state are given in Tab. 3 for each of the recording stations identified in Tab. 2.

These parameters are almost identical because the stations are not too far apart and the soil class is the same for all of them. Of the four parameters shown in Tab. 4, a_g (g) is the anchorage acceleration of the spectrum to be compared with either the PGA or with EPA, v_g is the peak ground velocity and derives from the spectrum formulation, d_g is the peak ground displacement associated to the given design spectrum, and d_{max} is the maximum predicted displacement.

Table 4 Life safety design ground motion parameters and maximum spectral displacement

Station	a_g (g)	v_g (cm/s)	d_g (cm)	d_{max} (cm)
AQA	0.260	27.4	12.6	21.6
AQG	0.260	27.4	12.6	21.6
AQK	0.261	27.5	12.6	21.8
AQU	0.261	27.5	12.6	21.9
AQV	0.261	27.5	12.6	21.9

Comparison between the first column of Tab. 1 and the first column of Tab. 4 shows that the recorded PGA is generally much larger than the anchorage acceleration for the spectrum, nearly 2.4 times larger for AQV-EW and on average 1.6 times larger. On the other hand, if EPA is considered, which is the average spectral acceleration in the period range 0.1-0.5 s divided by 2.5, the average ratio is about 1.18. In fact the code PGA cannot be compared to the instrumental PGA; the significant comparison is between code PGA and EPA. The most reliable seismic codes in the world make reference to EPA, not to instrumental PGA.

When the PGV is considered, the largest measurement of 40.5 cm/s is provided by AQV-NS; this exceeds the corresponding spectrum value by 1.47 while on average the ratio is about 1.17. It is evident that the code Design Spectrum underestimates both the acceleration and velocity ground motion parameters of the earthquake considered by about 20 % on average. This poses doubts on the reliability of the present specification of the Life Safety Design Spectrum for the area considered, especially when it is realized that the 2009 earthquake has a shorter return period (325 years) than the Life Safety Design event (475 years), Decanini (2010).

However it should be recognized that the two stations closer to the damaged buildings were AQU and AQK. The pseudo-acceleration spectra of these stations are large for periods shorter than 0.5s, but for longer periods their decay is rather steep, Fig. 3. Therefore, the demands for reinforced concrete buildings, especially the inelastic ones, have not been extraordinarily large. This points to intrinsic vulnerability of the affected buildings rather than to exceptional demands.

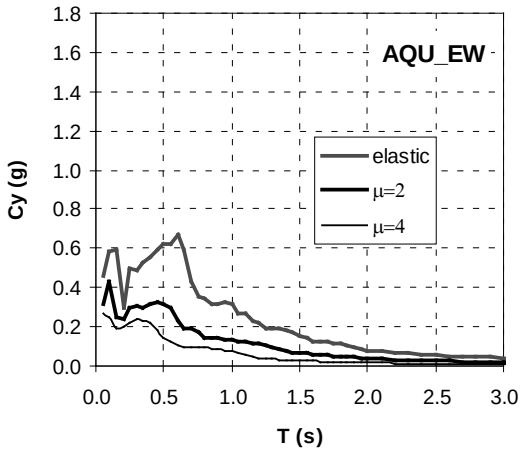


Figure 3 Inelastic acceleration spectra for ductility ratios $\mu=1$, $\mu=2$ and $\mu=4$.

Contrary to acceleration and velocity, the code specification largely overestimates the peak displacements, both for the ground motion and for the structure, as can be seen by comparison between the PGD column of Tab. 1 and the d_g column of Tab. 4, for ground displacements, and between the $S_{D,max}$ column of Tab. 1 and the d_{max} column of Tab. 4 for structural displacements. Only with reference to station AQK the peak structural displacement predicted by the code (21.8 cm) slightly underestimates the corresponding one from the ground motion record (24.2 cm).

A word of caution should be spent with regard to the records of station AQK where the peak ground displacement and the peak structural deformation appear to be much larger than in any other station. This might be due to the positioning of the recording station on a secondary structure, and therefore the recorded motion may not refer to the ground but to the supporting structure.

In concluding this section it appears that the present code specification underestimates by a considerable margin the seismic demands in the acceleration and velocity sensitive parts of the spectrum while it overestimates them in the displacement sensitive portion. On one hand, this may be due to the particular characteristics of the present earthquake, that is near fault and hanging wall position for L'Aquila city. On the other hand, the fact that the earthquake considered appears to be more frequent than the one considered by the code, see previous observation on return period, seems to suggest that stronger events can be expected. Overall it appears that it would be advisable to include the L'Aquila area within the 1st category seismic zones.

4. SEISMIC CODE EVOLUTION FOR L'AQUILA

In what follows a synthesis of the evolution of the Italian seismic code is presented with specific reference to its application to the Abruzzo region of which L'Aquila is the capital city. The topic is covered from the aspect of specification of the ground motion and from the perspective of applying the seismic action to a structural model.

4.1 Specification of the Ground Motion

A synthetic history of the evolution of the seismic code with reference to the L'Aquila area under the aspect considered is provided by Meletti and Stucchi (2009). A brief summary is provided herein in order to clarify some concepts introduced in the previous section and for setting the stage for the following analyses.

The municipality of L'Aquila was classified as seismic after the Avezzano earthquake of 1915, RDL 29 April 1915, No 573. In 1927 seismic classes (later called seismic zones) were introduced and L'Aquila was assigned to class 2, RDL 13 March 1927, No 431. Following the 1980 Campania and Basilicata earthquake, all the Italian territory was reclassified according to homogenous criteria and for the L'Aquila area the earlier classification was maintained, DM 13 September 1982. The municipalities struck by the 1915 (Marsica) and 1933 (Maiella) earthquakes were assigned to class 1 (zone 1 with the highest level of seismic shaking) while L'Aquila city and the remaining areas were assigned to class 2 (zone 2 with medium level of ground shaking).

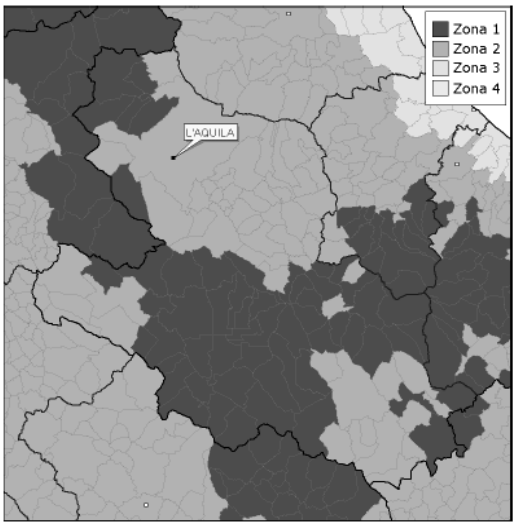


Figure 3 Seismic zones of the Abruzzo region according to OPCM 3274/2003

After the 2002 San Giuliano di Puglia earthquake, with the so called OPCM 3274/2003, the classification of the Italian territory in seismic zones was updated with the introduction of zone 4 in addition to the previously existing zones 1, 2 and 3. At this stage the situation for the Abruzzo region appeared as shown by the map of Fig. 3. Each zone was characterized by a zero period spectral acceleration respectively equal to 0.35g, 0.25g, 0.15g and 0.05g with a probability of being exceeded of 10% in 50 years.

However, with the publication and enforcement of the "Norme tecniche per le costruzioni" (Technical rules for constructions), D.M. 14 January 2008, the seismic zones no longer exist because the whole Italian territory is one large seismic zone with shaking intensity varying smoothly from point to point defined in terms of geographical coordinates.

4.2 Structural Aspects

After the 1908 Messina and Reggio Calabria earthquake, Compulsory Building Rules were issued by the Italian government for the municipalities struck by that earthquake and by previous ones, Committee Report (1909) and Oliveto (2004). The report clearly specified the actions to be considered in the resistance and stability calculations as follows at article 24:

1) static actions representing self weight, dead and live loads increased by a percentage to represent the effects of up and down vibratory motion;
2) Dynamic actions due to lateral ground motion, represented as accelerations applied to the masses of the building in the two directions (longitudinal and transverse) and acting in both senses for each direction.

At the time buildings had mostly two storeys and the horizontal forces were specified as 1/12 of the story weight at the first story and 1/8 of the story weight on the second story. It is apparent that the Committee was aware of the increase of the seismic acceleration along the height of the building and that all the three components of the ground motion needed to be considered. Most important were the examples of calculations that were provided as Annexes to the rules.

The first complete evolution of this set of rules appeared with the RDL 13 March 1927 No 431. The territories struck by earthquakes are divided into two categories according to the severity of the expected shaking and to the local geology, article 2 of the law. The rules for the stability and resistance calculations of buildings with frame structure are provided separately for each seismic zone by article 28 of the law. Notably, the three components of the ground motion are accounted for by three sets of forces. To account for the vertical component of the ground motion, the dead weight of each construction part and the corresponding maximum live load are increased by 50%. Horizontal forces are applied to the various masses of the building according to the experienced horizontal acceleration. Such forces should be applied in both senses in the longitudinal direction of the building as well as in the transverse one. In 1st category zones such forces shall be equal to 1/8 of the weight of the corresponding masses on the ground storey and to 1/6 of the weight of the higher storeys for buildings of height less than 12m (two or three story buildings). For all other buildings such ratio shall be 1/6 at all storeys. In 2nd category zones the effect of the vertical ground motion shall be accounted for by increasing the weight of each structural mass and the corresponding maximum live load by one third. For buildings of height less than 15 m the ratio of the horizontal force to the storey weight shall be 1/10 while for buildings of height equal or greater than 15 m such ratio shall be 1/8. At this point it is apparent that buildings designed and constructed in the following years were calculated as if they were subjected to a constant (spatially independent) acceleration. Also, the horizontal forces were increased considerably with respect to the 1909 regulations.

Ten years later a further evolution occurs with the RDL 22 November 1937, No 2105. Again the forces are specified separately for each category or seismic zone. For the first category the vertical component of the ground motion is accounted for by considering the dead weight and one third of the maximum live load increased by 40%, provided that the resulting load is not smaller than the sum of the dead and the live load. This can be expressed mathematically by the following inequality:

$$\left(D+\frac{L}{3}\right)\left(1+\frac{4}{10}\right)\geq D+L \qquad (1)$$

where D is the dead load and L is the live and/or accidental load. Horizontal forces to account for the horizontal components of the ground motion are taken equal to 1/10 of the weight of the masses on which they are acting, independently of the number of storeys of the building considered. As a contribution to the mass of the building the live load should be accounted only for one third of its maximum value. For the second category zones the forces considered above change as follows. The forces to be considered to account for the vertical component of the ground motion are given by the following expression:

$$\left(D+\frac{L}{3}\right)\left(1+\frac{1}{4}\right)\geq D+L \qquad (2)$$

Horizontal forces are evaluated as before and taken equal to 5% of the weight of the masses producing them.

This new version of the code presents significant changes, as compared to the previous one which represented the completion of the process started after the 1908 earthquake. Probabilistic concepts appear in the evaluation of the masses to be considered for establishing the vertical and the horizontal seismic forces. The seismic acceleration, albeit considered again spatially constant, is considerably abated. From g/6 is reduced to g/10 for 1st category seismic zones and from g/8 is reduced to g/20 for 2nd category zones. This amounts to a substantial reduction, especially for 2nd category zones. The reduction is even more significant when considered in the light of the reduced amount of live load in the evaluation of the seismic weights.

The next significant overhaul of the seismic code occurs in 1962 with Law 25 November 1962, No 1684. The specific reference to the effects of the vertical ground motion is lost in this version of the code, apart from the general prescription that the accidental and/or live load should be applied in such a way as to produce in each structural element the most unfavorable loading condition, prescription already existing in the previous code. The horizontal seismic acceleration is confirmed to be g/10 for 1st category seismic zones and increased to 0.07g, which is slightly larger than

g/15, for 2nd category seismic zones.

The Law 2 February 1974 represents a milestone in the historic development of the Italian seismic code, although it becomes fully operational only with the approval of DM 24 January 1986 dictating " Technical Rules for Anti-Seismic Constructions ". Terms like *"Fundamental Period"* of a structure, *"Response Coefficient"* (alias *Response Spectrum*), *"Dynamic Analysis"* become parts of the knowledge patrimony of the Italian community of practicing Structural Engineers. Also three levels of seismic protection are introduced through the *Importance Coefficient I* which is given the values 1, 1.2 and 1.4. Static Analysis is permitted for buildings with fundamental period less than 1.4 s but dynamic analysis is compulsory for structures with longer periods. Most relevant is also the introduction of the spatial distribution of the seismic forces according to the first mode of vibration when the static analysis is used, albeit through a linear mode shape for buildings with framed structure. Three levels of seismic acceleration are assigned to each of the three seismic zones that are established in the Italian territory. In the zones of *high seismicity*, corresponding to the previous 1st category, the value g/10 is maintained. The previous 2nd category zones are now labeled as zones of *medium seismicity* and the 0.07g seismic acceleration is also preserved. To the newly introduced third category, including *low seismicity* zones, a seismic acceleration level of g/25 is assigned. Little attention is paid to the vertical component of the ground motion for ordinary buildings, while for long span structures or for important structures a theoretical or experimental dynamic analysis is required. For the evaluation of the seismic weight, the contribution of the live or accidental load is evaluated on a statistical base. For residential and commercial buildings 1/3 of the maximum value is considered, for public buildings such as shops, restaurants, coffee houses, schools, military barracks, hospitals etc. 1/2 of the maximum is considered, while the maximum value is considered for theatres, churches, libraries, archives etc. Perhaps it may be useful to observe that these changes in the seismic code matured after the Campania and Basilicata (Southern Italy) earthquake of November 23 1980, M_w=6.5.

Some further evolution in the code occurred a decade later with the DM 16 January 1996. The epochal change was in the safety checks that for the first time were allowed in terms of stress resultants with reference to specified ultimate resistance limit states, instead of the method of allowable stresses that had been used ever before. Notable is also the specific reference to structural regularity with static analysis allowed only for regular structures. Finally the attention returned to the vertical component of the ground motion with the specification of vertical seismic forces proportional to the existing masses evaluated through a constant seismic acceleration. However, when buildings with framed skeleton are addressed, it is suggested that vertical action not be considered with the exception of large spans or overhanging elements.

The next steps of the code evolution have occurred in the third millennium with the issue of OPCM No 3274 on 20 March 2002 and of OPCM No 3431 on 3 May 2005. These led to the introduction of 4 seismic zones as described in section 4.1 Although the two documents were short lived, they are important because they set the ground for the present code NTC-2008 (D.M. 14 January 2008). This is a performance based code that aims at controlling damage from earthquakes occurring at the construction site during the life of the structure. Two service and two ultimate limit states are considered. The service limit states are the Operational Limit State (OLS) and the Damage Limit State (DLS) while the ultimate limit states are the Life Safety Limit State (LSLS) and Collapse Prevention Limit State (CPLS). A reference time span V_R is defined as a function of the nominal life of the construction V_N and of its utilization class C_U with $V_R = C_U \times V_N$. To each considered Limit State corresponds a given probability that the corresponding seismic action is exceeded in the V_R time span. These probabilities are assigned as follows OLS (0.81), DLS (0.63), LSLS (0.10), CPLS (0.05). The return period of the earthquake is calculated through the formula:

$$T_R = -\frac{V_R}{\ln(1-P_{V_R})} \tag{3}$$

A database is provided for the ground motion spectral parameters corresponding to return periods of 30, 50, 72, 101, 140, 201, 475, 975, 2475 years. When the calculated return period does not correspond to any of the above ones, an interpolation formula is provided as a function of the two adjacent return periods. Elastic response spectra are provided for both vertical and horizontal components of the ground motion. For the service limit states the design spectrum shall be the elastic spectrum associated to the probability of being exceeded evaluated as previously outlined. Ultimate limit states should be checked through step by step non linear dynamic analyses using three components of ground motion which can derive from recorded ground motions, artificial and/or simulated ground motions. The ground motions used, whether natural, artificial or simulated should be consistent with the specified elastic design spectrum. Response spectrum analysis and design is also allowed through a reduction of the elastic forces which accounts, in a simplified way, for the inelastic dissipation capacity of the structure, its over-strength and the lengthening of its period of vibration following plastic deformation as described above.

5. EVOLUTION OF DESIGN PGA

At this point it may be interesting to compare the seismic accelerations used by the Italian codes of various epochs. This comparison will be made exclusively for 1st and 2nd category seismic zones, the first being important for obvious reasons and the second referring specifically to the L'Aquila territory. From the previous analysis it may be gathered that from 1909 until 1996 the method of allowable stresses has been used for safety checks. This method is

characterized by an implicit safety factor s_A which is the product of the load safety factor s_L and of the material safety factor s_M. Therefore the elastic spectral acceleration S_E which may be attributed to the old codes can be expressed by the following equality:

$$S_E = s_A \cdot q \cdot S_A = s_L \cdot s_M \cdot q \cdot S_A \qquad (4)$$

where q is a factor accounting for the plastic dissipation capacity of the structure and S_A is the spectral acceleration used to evaluate the seismic loads when using the allowable stress method. It is obvious that any comparison depends on reliable values for s_L, s_M and q. While the values for s_L and s_M can be reasonably set to 1.5, the energy dissipation capacity factor q is affected by many variables and may be different from case to case. For this reason three different values of q will be used here, namely 1, 2 and 4. The actual value will in fact remain unknown, but the behavior of buildings during earthquakes occurred in various epochs could give a fair idea of the most appropriate value of q for each epoch. By assuming a dynamic amplification factor F_0=2.5, the results can be compared directly in terms of effective peak ground acceleration. For each of the time periods between significant code changes, the results obtained are shown in Tab. 5. The analysis of the results provides an interesting perspective in the EPA used for about a century of Italian seismic history in the design of buildings and other structures. After the 1908 Messina and Reggio Calabria earthquake the EPA or design PGA could vary from a minimum of *0.09g*, for buildings without any energy dissipation capacity, to *0.36g* for buildings with a dissipation capacity corresponding to *q=4*. It is unlikely that a dissipation capacity factor q=4 could be provided at the time; a factor *q=2* would seem more appropriate, leading to an *EPA=0.18g*. This however appears too small for a first category zone. This may be the reason why, with the 1927 code, seismic acceleration was increased by *2/3* leading to EPA values in the range 0.*15g* to *0.60g* with a *0.30g* value corresponding to *q=2* .

Table 5 Historic Effective Peak Ground Acceleration (g)

Time Period	First Category			Second Category		
	q=1	q=2	q=4	q=1	q=2	q=4
1909-1927	0.09	0.18	0.36			
1928-1937	0.15	0.30	0.60	0.11	0.23	0.45
1938-1962	0.09	0.18	0.36	0.045	0.09	0.18
1963-1986	0.09	0.18	0.36	0.06	0.12	0.255
1987-2002	0.09	0.18	0.36	0.06	0.12	0.255
2003-2008	0.35			0.25		

That same code introduced second category zones and attributed to them an EPA equal to ¾ of that assigned to the first category zones, that is in the range 0.11-0.45g. By 1937 it must have been realized that the applied seismic forces were too large and therefore they were taken back to the initial value of 0.09-0.36g for 1st category zones, while the corresponding value for 2nd category zone was set to ½ of the value for 1st category, that is 0.045-0.18g. Apparently the EPA value for the 2nd category zones appeared to be too low and so it was increased to 70% of the value for the 1st category zones in 1962.

It may be interesting to notice that, with the exception of the decade 1928-1937, the results shown in Tab. 5 seem to suggest that the Italian code has always assumed an EPA of about 0.35-0.36g for first category zones and of 0.25g for second category zones with an implied seismic dissipation capacity factor *q=4*. With an insider's view it can be said that the situation improved considerably starting from the mid eighties because in the seventies the Italian universities started to offer courses on Structural Dynamics to Civil Engineering students. The 1986 changes in the code were made possible because of the newly acquired background by the structural engineering community. The changes that occurred in the early years of the last decade led to the inclusion of Performance Based Earthquake Engineering concepts and methods.

As a general comment on the seismic regulations of the XX century in Italy, the design effective peak ground acceleration (EPA) has always had the present values if not larger ones for an implied energy dissipation factor *q=4*. When this capacity was not assured by adequate structural detailing, the result was an extremely unsatisfactory behaviour during actual earthquakes, as the three most severe events of the past 50 years have clearly shown.

6. REINFORCED CONCRETE BUILDINGS

According to the Italian Institute of Statistics (ISTAT) the building stock in the L'Aquila region is composed by 24% of reinforced concrete buildings, by 68% of unreinforced masonry buildings and the remaining 8% is qualified as others. Furthermore about 55% of all buildings was erected after 1945. Concerning the height it is found that 20% of the stock has just one storey, 53% has two storeys, 23% has three storeys and only 5% has more than three storeys.

Reinforced concrete buildings were mostly built after the second world war and are mostly low rise (2-4 storeys) and mid rise (5-8 storeys) residential buildings. The most recent ones sometimes present commercial activities on the ground floor. The structural framework is predominantly composed of plane frames along only one direction with slabs of the mixed reinforced concrete - hollow brick system. Shear walls are rare and only present at times as staircase and lift elements.

Out of 4113 reinforced concrete buildings, according to the 2001 census, about 20 overall collapses were reported and about 130 buildings suffered serious damage. Therefore the buildings collapsed were in number slightly less than five in a thousand and the seriously damaged ones only little more than three in a hundred. The unfortunate circumstance that 134 lives were lost in a dozen of collapsed reinforced concrete buildings attracted a lot of attention from the media.

6.1 Age of Collapsed Reinforced Concrete Buildings

Out of the 12 reinforced concrete buildings where loss of life occurred, 9 were built between 1961 and 1965, 2 were built between 1950 and 1955 and another between 1959 and 1960. Also a hospital building complex, built between 1972 and 1992, experienced overall collapses in some of its units. No information is currently available to the authors about the age of the remaining collapsed buildings. Most of the collapsed buildings for which the epoch of construction is known were built in the postwar period of economic expansion when the 1937 code was still statutory and quality control was probably lax. It may be easily observed, Tab.5, that in that construction period the seismic action for 2nd category zones, where the L'Aquila area belonged, was assigned the lowest value ever.

6.2 Probable Causes of Collapse

One of the causes that may have contributed to the collapse of the buildings considered is the pro tempore design seismic action which in some cases may have been insufficient for the event considered. Comparison between data in Tab.1 and Tab.5, with reference to the time of construction, seems to suggest this as a possibility at least. However, this cause has been compounded with several other sources of vulnerability present in the collapsed buildings and discovered by inspection and study of available documents after the event. The design and construction deficiencies that led to structural vulnerability are listed as follows.

a) Resisting frameworks present only along one direction in the horizontal plane, but lacking in the perpendicular direction or in any other direction.
b) Soft storey configurations.
c) Inadequate detailing to assure implied ductility.
d) Poor concrete quality.
e) Strong beam – weak column frameworks.
f) Presence of short columns.
g) Structural irregularity.

Some comments will be provided below for each of the causes of collapse.



Figure 4 Unidirectional resistant system

6.3 Unidirectional Structural Skeleton

With reference to the cause considered at point a), this is the standard arrangement used in Italy for structures designed to resist vertical loads only, Fig. 4. The resistance in the direction perpendicular to the main frames is assured by the frame action provided by the mixed slabs composed of parallel thin concrete beams and hollow bricks. Sometimes slab–thick concrete beams are present along the columns alignments. In both cases the provided resistance is considerably smaller than the one in the perpendicular direction and of the required one. This structural arrangement determines a weaker direction for the building structures along which the collapse can develop.

6.4 Soft Storey

Soft storey configurations may derive from several factors among which the most important can be the need to provide large open spaces for commercial uses, often on the first storey, special architectural space distributions, and finally the search for an overall architectural form totally disjointed from the requirements of structural soundness and efficiency. These situations may have been favored at a time when seismic resistance was still little understood, mainly due to the insufficient background of the field structural engineers and architects.

6.5 Ductility Provisions

For a long time Italian seismic and structural codes have paid little attention to member and joint detailing as essential to ensure an adequate ductility level to structural members and to the overall structure. Until 1939 the only prescription about reinforcement concerned only the longitudinal one; it was only with RDL 25 March 1939, No 640, that transverse reinforcement was explicitly mentioned by requiring stirrups at a distance not larger than half the minimum size of the cross-section nor than ten times the diameter of the longitudinal reinforcement. Again in the seventies a specification required longitudinal reinforcement of diameter not smaller than 12mm and stirrups at a distance not larger than 15 times the minimum diameter of the longitudinal reinforcement with a maximum of 25cm. The diameter of the stirrups could not be smaller than 6mm. All these requirements appear insufficient to ensure a ductile seismic behavior. Finally in 1997 some instructions issued by the Ministry of Public Works with CMLLPP 10 April 1997, No 65, provided considerable improvement towards the objective of achieving a design that ensured ductile seismic behavior. Minimum and maximum bounds (1% and 4%) are provided for the longitudinal reinforcement while the transverse reinforcement must satisfy strict requirements. The distance shall be shorter at the two ends (never larger than 15cm) for a length not shorter than 45cm, and can be longer in the central part but not longer than 25cm. Of course most times the limits turn out to be more strict than the bounds provided here only to convey the idea. At any rate the transverse reinforcement must pass the check for shear resistance. For the first time in an Italian technical regulation, provisions are given for providing confining

transverse reinforcement to columns within the body of beam-column joints. It is prescribed that this reinforcement should not be less than the maximum between that provided at the column end below the joint and that provided at the end above the joint. Because this provision came so late it is not surprising that most of the Italian reinforced concrete buildings built in the XX century present brittle joints and most of the collapses are initiated by joint failure, Fig.5.



Figure 5 Joint failures showing careless detailing

6.6 Structural Irregularities

Several types of irregularities in the collapsed buildings have already been described at previous points. Other irregularities such as the presence of short columns and/or strong beam-weak column frame design have long been recognized as sources of seismic vulnerability. However, weird cases of spatial irregularities have been discovered



Figure 6 Irregular building before earthquake

among the collapsed buildings. In a single case plan irregularities, height irregularities, soft-weak storey conditions and more can be discovered. As mentioned at section 6.3, a cause of seismic vulnerability is the existence of plane frameworks in one direction, but not in the perpendicular one, providing some seismic resistance along one direction but a much smaller one along the orthogonal one. Due to the continuously varying direction of the seismic motion, this results in an extremely vulnerable construction even if it had sufficient resistance in the direction of the plane frames.

But in some cases reality can exceed even imagination in conceiving special types of irregularities. In one of the collapsed buildings the first four storeys showed the main beams aligned along one direction and the next three exhibited main beams aligned along the perpendicular direction. Given sufficient resistance and ductility to structural members and joints and provided that the seismic input can be described with sufficient accuracy such situations should not result in structural vulnerability. However, considered that structural detailing ensures little or no ductility, that structural models are even today inadequate to describe such situations, that the seismic input prescribed by the pro-tempore regulations was largely under-estimated, the result could be nothing else but catastrophic collapse.



Figure 7 Irregular building after earthquake; collapsed left wing

Torsion effects derive also from structural irregularities, Fig 6 and Fig.7. Such effects must have been present in most of the occurred collapses. However, the technical regulations of the time never considered explicitly torsion effects. It was only with the Law 25 November 1962, No 1684 that these effects were fully recognized in the form of mass, stiffness and accidental eccentricities.

6.7 Steel and Concrete Quality

Smooth steel bars were used as reinforcement according to the standards at the time of construction. The mechanical properties of the steel used were in agreement with the statutory code requirements. Concrete strength was generally below the pro tempore code requirements and sometimes below by a large amount. Moreover concrete strength showed a great spatial variability within the same building, perhaps due to the fact that the material was manually mixed at the construction site. Local defects like aggregate segregation and cold joints were also observed.

7. CONCLUSIONS

The earthquake that struck the city of L'Aquila on April 6 2009 had several aspects that made it interesting for their implications in the enhancement of Earthquake Engineering. The earthquake was caused by a normal fault mechanism with the metropolitan area of L'Aquila on the hanging wall. The fault line and fault rupture surface were identified with great accuracy by a combination of scientific means.

Several strong motion recording stations were within the near fault area and five produced useful records. Some ground motion parameters were compared indirectly with the spectral parameters provided for the area by NTC-08, showing disagreement in the short, medium and long period range, underestimating the response in the short-medium range and overestimating it in the long period one.

Since the earthquake was less severe in terms of magnitude and seismic intensity than the design one, it should be considered whether the assumed design spectral parameters are appropriate for the description of a similar event of the expected magnitude.

The historical analysis of the Italian seismic code has shown that until the turn of the century the provisions were somewhat defective in terms of specification of the intensity of the ground motion and of the provision of ductility, especially in view of the synergy played by strength and energy dissipation capacity in earthquake resistant design .

After the 1908 Messina and Reggio Calabria earthquake perhaps Italy had the most advanced seismic code in the world. This code was subject to a continuous improvement until the 1927 version. A relatively large design spectral acceleration was considered, probably to account for the limited ductility that the building technology of the time was able to provide.

Ominously, in the code version of 1937, the spectral acceleration was nearly halved for first category zones and more than halved for second category ones. The spectral acceleration for second category zones was a little increased with the code issue of 1962, but just enough to put the requirements on the same basis as for first category zones.

However, as it is always the case in those circumstances, the new code was not used for the buildings that had already been designed and were being built at the time. Thus it can be established with reasonable accuracy that most of the collapsed buildings were designed according to the 1937 code. This, together with the other sources of vulnerability considered, can explain the catastrophic collapses of reinforced concrete buildings during the 2009 L'Aquila earthquake.

The near fault on hanging wall position of the city of L'Aquila, the intense damage produced by the 6 April 2009 earthquake, the recognition that a stronger earthquake can be expected in the area with a 10% probability of being exceeded in 50 years, as specified by the current code for the Life Safety Limit State, appear to justify a proposal for the inclusion of the area among the 1st category seismic zones.

Acknowledgements:

The authors acknowledge support from the Japan Ministry of Education, Culture, Sport, Science, and Technology (MEXT) for establishing the Center for Urban Earthquake Engineering (CUEE) in Tokyo Institute of Technology. This support makes possible the forthcoming international conference, as well as international joint research projects and exchange programs with overseas universities.

References:

Global Risk – Miyamoto (2009), "2009 L'Aquila M6.3, Italy, Earthquake Field Investigation Report,", Lafayette, CA 94549, USA.

EERI Special Earthquake Report (2009), "Learning from Earthquakes - The M_w 6.3 Abruzzo, Italy, Earthquake of April 6, 2009," Earthquake Engineering Research Institute, USA.

INGV EMERGEO Working Group (2009), "Evidence for Surface Rupture Associated with the M_w 6.3 L'Aquila Earthquake Sequence of April 2009 (Central Italy)," *Terra Nova*, Vol. **22**, No.1, 43-51,Blackwell Publishing Ltd.

AON Benfield UCL Hazard Research Centre (2010), "The 2009 L'Aquila Earthquake: Findings and Implications, " *Event Science Report 02*, London, UK .

Mori, J. (2010), "The 2009 L'Aquila, Italy, Earthquake (M6.3): Damage and Response to a Moderate Event," *Annuals of Disas. Prev. Res. Inst.*,, Kyoto Univ., No.53 A, Japan.

Akinci, A., Malagnini, L. and Sabetta, F. (2010), "Characteristics of Strong Ground Motions from the 6 April 2009 L'Aquila Earthquake, Italy," *Soil Dynamics and Earthquake Engineering*, **30**, 320-335.

Sorrentino, L., Raglione, E., Liberatore, D. and Decanini, L. D. (2010), "Chiesa di S. Biagio d'Amiternum a L'Aquila – Catalogo Sismico Locale e Meccanismi di Collasso," *L'Università e la Ricerca per l'Abruzzo – Il Come e il Perché dei Danni ai Monumenti*, L'Aquila.

Meletti, C. and Stucchi, M. (2009), "Pericolosità Sismica, Normativa e Zone Sismiche nell'Aquilano," *INGV, on-line report.*

Committee Report (1909), "Norme Edilizie Obbligatorie per I Comuni Colpiti dal Terremoto del 28 Dicembre 1908 e da Altri Anteriori," *Giornale del Genio Civile*, Roma, Italy.

Oliveto, G. (2004), "Review of the Italian Seismic Code Released After the 1908 Messina Earthquake," *Passive Control Symposium 2004*, 1-20, Structural Engineering Research Center, Yokohama, Japan.

Çelebi, M., Bazzurro, P., Chiaraluce, L., Clemente, P., Decanini, L., De Sortis, A., Ellsworth, W., Gorini, A., Kalkan, E., Marcucci, S., Milana, G., Mollaioli, F., Olivieri, M., Paolucci, R., Rinaldis, D., Rovelli, A., Sabetta F. and Stephens, C. (2010). Recorded Motions of the 6 April 2009 Mw 6.3 L'Aquila, Italy, Earthquake and Implications for Building Structural Damage: Overview. Earthquake Spectra, Volume 26, No. 3, pages 651–684, August 2010; © 2010, Earthquake Engineering Research Institute.

Decanini, L.D., Liberatore, L., Mollaioli, F., Monti, G., Al Shawa, O. (2009). Studio preliminare della domanda sismica elastica ed anelastica in termini di energia, spostamento e forze (Rel. 1.0). Report available at http://www.reluis.it

Decanini, L.D., Liberatore, L., Mollaioli, F., Monti, G. (2010a). 2009 L'Aquila earthquake, seismic demand and damage characterization. *14th European Conference on Earthquake Engineering.* Paper 445.

Decanini, L.D., Liberatore, L., Mollaioli, F. (2010b). Damage suffered by RC buildings during the 2009 L'Aquila earthquake, a general overview and a case study. *14th European Conference on Earthquake Engineering.* Paper 443.

Decanini, L.D., Liberatore, L., Mollaioli, F. (2011). Damage Potential Of The 2009 L'Aquila, Italy, Earthquake. Accepted for publication in the *Journal of Earthquake and Tsunami*.

8CUEE CONFERENCE PROCEEDINGS
8th International Conference on Urban Earthquake Engineering
March 7-8, 2011, Tokyo Institute of Technology, Tokyo, Japan

DEVELOPMENT AND IMPLEMENTATION OF MEGA URBAN EARTHQUAKE DAMAGE ASSESSMENT AND RECONSTRUCTION PROGRAM: 2010 HAITI EARTHQUAKE

H. Kit Miyamoto[1] and Amir S. Gilani[2]

1) President, Miyamoto International Inc., Pétion Ville, Haiti
2) Structural Specialist, Miyamoto International Inc., 1450 Halyard Drive, Suite One, West Sacramento, CA 95691
kmiyamoto@miyamotointernational.com, agilani@miyamotointernational.com

Abstract: The 2010 Haiti Earthquake resulted in 300,000 deaths, 1.3 million homeless people, and 200,000 damaged or collapsed structures. An unprecedented earthquake damage assessment and reconstruction program under the authorization of the Haitian Public Works with United Nations Office of Project Services and Pan American Development Foundation was developed and implemented. A massive damage assessment program was undertaken with three strategic goals: (1) rapid damage and safety assessment; (2) reconstruction database development; and (3) development of technical capabilities of Haitian engineers. A modified ATC-20 technical platform, accounting for Haitian construction, was developed. As part of this program, personal digital assistant–based data collection techniques and quality assurance programs were implemented. 600 Haitian engineers were trained and 400,000 buildings have been assessed. This database was used to develop; 1) repair construction strategic plan of damaged structures, and 2) demolition and debris plan of collapsed structures. Based on this database and plans, construction management platform was developed and repair of 100,000 damaged structures are underway. This ambitious program combines rapid damage assessment, reconstruction strategic plan development, and construction management platform development. It is considered state of the art practice. This methodology can be implemented as a platform for damage evaluation and reconstruction in other parts of the world including developed countries.

1. INTRODUCTION

The 2010 Haiti Earthquake affected on the lives of more than 3 million people. This paper describes the work performed by The Haitian Ministry of Public Works, Transport, and Communications (MTPTC) to assess rapidly the safety and reparability of much of the affected building inventory in Port-au-Prince and other affected communities..

In light of the enormity of the damage caused by the earthquake, the MTPTC created the Bureau d'Évaluation Technique des Bâtiments (BETB), charged with the task of assessing damage to all buildings in earthquake-affected areas, developing criteria for repair and reconstruction, and providing QC reconstruction. With funding provided by the World Bank (WB), and U.S. Agency for International Development (USAID), field logistics provided by United Nations Office of Project Services (UNOPS), and Pan American Development Foundation (PADF), and technical expertise provided by the authors, BETB embarked on an ambitious program to organize and train a cadre of approximately 250 Haitian national engineers to perform rapid evaluation of all affected buildings using the internationally accepted ATC-20 (ATC 2005) and FEMA 310 (FEMA 1998) methodology

The authors led a four-day intensive classroom session on the fundamentals of earthquake engineering and assessment for more than 600 applicants. Course work was followed by a written examination, from which approximately 250 candidates were selected as evaluators. Among these, 10 of the most qualified were selected as division leaders. Each division consisted of a division leader, four team leaders, and eight to ten evaluators, all taken from the ranks of the 250 trainees.

2. 2010 HAITI EARTHQUAKE

2.1 Overview

The magnitude 7.0 Haiti Earthquake occurred at 1653 local time on Tuesday, 12 January 2010, with an epicenter approximately 25 km west-southwest of the densely populated capital city of Port-au-Prince. This event caused shaking of Modified Mercalli Intensity (MMI) X in the city; see Figure 1 (USGS 2010). In the two weeks following the main event, at least 52 aftershocks in the magnitude range of 4.2 to 5.9 were recorded.

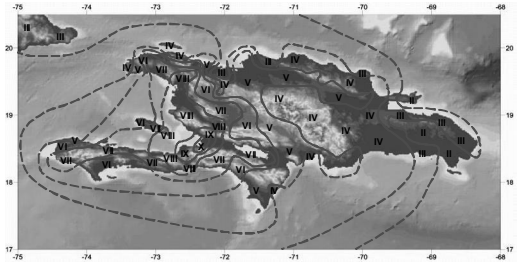


Figure 1. MMI shaking in Haiti (USGS 2010)

The earthquake caused major damage to Port-au-Prince

and other cities in the region. More than 200,000 structures were damaged or collapsed, including many essential buildings, such as the Presidential Palace National Assembly building, Port-au-Prince Cathedral, and main jail. The headquarters of the United Nations Stabilization Mission in Haiti (MINUSTAH) also collapsed, killing many, including the mission's chief.

The Haitian government reported that more than 230,000 people died, 300,000 were injured, and 1.3 million were made homeless. Six months after the earthquake, more than 1.3 million people still lived in temporary camps many of which may offer only minimal services and protection from natural hazards such as hurricanes, floods, and landslides (see Figure 2).

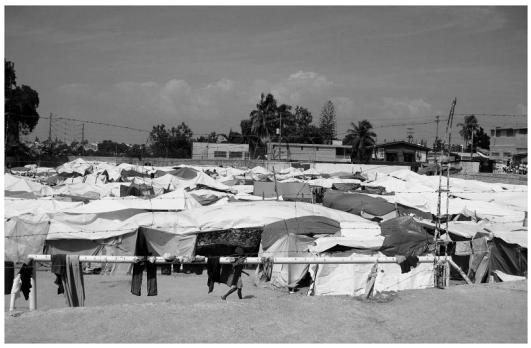


Figure 2. Temporary camps

2.2 Main causes of observed damage

This earthquake caused devastation disproportional to its magnitude. If the international standards of seismic design and construction had been used in Haiti, much of the life and economic loss could have been avoided. The main contributing factors exacerbating this tragedy were the following:

a. In Haiti, design and construction practices had not considered earthquake forces. In addition, many engineers and contractors had neither education nor experience in earthquake-resistant design methodology.
b. Haiti lacked an seismic code.
c. The past decade has seen rapid growth of low-income neighborhoods because of migration into the city from outlying areas. In these neighborhoods, unsafe housing had been built using substandard construction materials and practices.

Many of the structures in Haiti are of a building type that is vulnerable to seismic damage. These buildings use a variation of confined masonry construction comprising weak hollow concrete blocks (HCBs) with lightly reinforced and nonductile beams and columns.

3. DAMAGE ASSESSMENT

3.1 Methodology

The evaluation method chosen for this program was the ATC-20 (ATC 2005) Rapid Assessment, with modifications to adapt to Haitian conditions and to provide more useful information to the MTPTC. This methodology, which was first developed in California in the 1980s, has been used successfully for evaluation after many major earthquakes in the United States. The Rapid Assessment Form allows evaluators to characterize buildings in one of three ways: "Inspected" (also known as "green-tagged"), meaning that the building is structurally undamaged and may be occupied full-time; "Restricted Entry" (or "yellow-tagged"), meaning that the building should not be occupied for extended periods and that parts of the building might be considered off-limits; or "Unsafe" (or "red-tagged"), meaning that the building cannot be safely inhabited. The form was modified to provide evaluators with a checklist of Earthquake Vulnerability Factors per FEMA 310 (FEMA 1998), which has allowed evaluators to list the features of each structure that would make it more prone to earthquake damage.

One important consideration that was stressed to the evaluators is that while the three-color evaluation system provides an understanding of the hazard associated with a building at the time of the evaluation, it does not state whether a building must be demolished. Some buildings given "Unsafe" ratings are considered repairable, but the nature of the damage has rendered them hazardous to occupy until repairs can be completed. In the same way, the "Inspected" rating does not guarantee that a building will not be seriously damaged in the event of future earthquakes. If another major event of equal or greater magnitude were to take place along a section of the fault closer to the city, damage would in all likelihood be much more widespread. In general, the nature of local design and construction in Haiti is such that nearly all buildings can be considered seismically hazardous.

One feature of the process has been the use of Personal digital assistant (PDA)s with Global Positioning System (GPS) capability to assist in performing the evaluations. The PDAs are preloaded with the modified ATC-20 Damage Assessment Form, and evaluators would fill out the forms electronically during the course of each assessment. At the end of the day, all information from the more than 150 PDAs is uploaded to a main server. Because some of the street layout of Port-au-Prince is unmapped and many residences have no addresses, the GPS coordinates of each structure have been used as the primary means of identification. The use of GPS has also proved to be an invaluable tool in developing overall damage maps and a reconstruction strategic plan.

Evaluations have been performed systematically, with each division given the responsibility to evaluate all the structures in a given zone each day. Zones are determined by MTPTC using aerial maps, which are updated daily to show the status (green, yellow, red) of each evaluated structure. As each zone is completed, new ones are assigned.

As the program evolved, and as additional funding became available through USAID and PADF, the 10 teams were expanded to 17. With all 17 teams working at capacity, it was possible to assess more than 3,000 structures daily. The initial target of 100,000 structures evaluated was met on

31 May 2010, and by 15 June 2010, 132,662 buildings had been assessed. By the end of August 2010, more than 250,000 structures had been evaluated. Over 400,000 structures in the earthquake-affected area were assessed by December 2010.

3.2 Typical building properties

Although the buildings observed have displayed a wide variety of sizes and architectural styles, virtually all were constructed using a similar structural system: a cast-in-place concrete gravity frame with unreinforced HCB infill panels acting as incidental infill shear walls.

In such structures, the concrete floor and roof slabs are supported by lightly reinforced concrete columns, sometimes as small as 150 mm on side. Floor and roof framing consists in some cases of a grid of concrete joists framing between the beams; voids between the joists are formed using HCBs as stay-in-place forms. Exterior wall cladding and interior partition walls universally consist of HCBs joined with cement mortar. These infill wall panels effectively serve as the seismic-force-resisting system; however, there has typically been no evidence of any system intentionally designed for that purpose. Buildings typically have lacked a seismic load path; in other words, they do not appear to have a system by which inertial forces generated in one portion of the structure could be transferred to other parts of the structure and then to the ground. In seismic zones, this load path commonly comprises diaphragms, collector elements such as chord and drag reinforcing, special vertical reinforcing at shear wall corners, and doweling between the walls and surrounding elements. None of these have been present in the vast majority of buildings observed.

Concrete gravity frames have displayed numerous design and construction practices that would be considered defective by international standards, particularly in seismic zones. Figure 3 through Figure 5 show some of the common seismic deficiencies.



Figure 3. Beam with exposed reinforcement



Figure 4. Poor concrete consolidation in column



Figure 5. Overhanging upper floor

The design defects include the following:

a. Use of smooth reinforcing bars,
b. Lack of column confinement reinforcing,
c. Inadequate lap splices and rebar development length

The construction defects consist of the following:

a. Segregation, voids, and rock pockets evident in finished concrete, particularly in columns and at construction joints
b. Exposed rebar, poor aggregate shape and grading
c. Poorly located construction joints, and paper and other debris left in joints; formwork embedded in finished concrete
d. Out-of-plumb columns.

Typical masonry construction also has numerous defects, including irregular coursing, missing or inadequate vertical mortar joints, inadequate horizontal joints, poor material quality, and extensive use of broken block. These conditions have been commonly found in nearly all buildings, regardless of age, size, or number of stories. These design and construction practices led to a combination of heavy buildings with little lateral strength and essentially no post-yielding capacity, and were key factors in the vast majority of failures observed.

4. BUILDING DAMAGE SUMMARY

4.1 Overview

By 15 June 2010, 130,000 buildings have been assessed. The damage from this population sample is presented in this paper. Data from the complete population sample of 410,000-surveyed building is currently being analyzed and the results will be presented at a later date.

4.2 Summary data

Table 1summarizes the number and the median (50th percentile) damage estimate for the population sample. As indicated in the table, the median damage estimate for buildings in all assessment categories was in the 1% to 10% damage range. Forty-eight percent is building stock that is undamaged and safe to use. Twenty-eight percent has moderate damage and most likely can be repaired. These numbers are significant, because they indicate that 76% of buildings affected by the earthquake can be immediately occupied or repaired with relative ease.

Table 1. Summary data for damage assessment

Category	Green-tagged	Yellow-tagged	Red-tagged
Number of structures	62,000	36,000	32,000
Percentage	48%	28%	24%
Median damage estimate	0–1%	1–30%	60–100%

The majority of damaged and collapsed buildings are located in the low-lying districts west of the airport, which includes downtown Port-au-Prince, Nazon, Turgeau, Canape Vert, Carrefour, and the lower portion of Delmas. By contrast, more southerly and easterly regions, in particular Juvenat and Pétionville, suffered much lighter damage. The difference in damage levels is mainly a result of soft-soil amplification. Softer soil is found in many of the highly-damage areas.

4.3 Damage classification

By far, the most common damage found among the buildings evaluated has been cracking or collapse of the HCB walls, which is a natural consequence of both the lack of reinforcing and the poor material quality, (see Table 2).. Among the buildings evaluated, moderate or serious wall cracking was cited in nearly 56,000 cases. Wall collapse was noted in slightly more than 40,000 cases. Cracking was observed to be most widespread in the lower levels of multistory buildings, where shear forces were highest. The next most common damage mode was either cracking or crushing failure of concrete columns in about 31,000 cases which was typically a result of flexural forces. Soft-story conditions were observed to be a major contributor to column bending and shear failures.

Table 2. Damage types found in greater Port-au-Prince area

Damage classification	Moderate	Serious
Column cracking or spalling	15,468	15,762
Slab, beam, joist cracking or spalling	12,360	11,715
Ground movement or cracking	12,124	6,204
Exterior, interior wall collapse	20,952	19,536
Exterior, interior wall cracking	30,207	25,711
Parapet, canopy, deck, stair damage	10,479	10,281

4.4 Damage by building occupancy

Overall damage has not varied significantly between building occupancies, but some trends can be seen from the data. The vast majority of buildings evaluated, nearly 95%, were residential structures. These structures varied widely in quality of construction, and ranged from large, engineered mansions to improvised shacks. Table 3 presents the distribution of damage for various building occupancies. Examination of data in this table shows the following:

a. Commercial/industrial, healthcare, and civic buildings, which are often larger engineered structures, had better performance overall, with 52% to 57% of these building types being green-tagged, as opposed to 48% for single-family housing.
b. The performance of essential facilities such as hospitals and public-safety facilities is not adequate. In healthcare, for example, the damage rate corresponds to a loss of healthcare capacity of approximately 44% immediately after the earthquake, a time when this capacity is needed most.
c. The best overall performance (as measured by the largest percentage of green-tagged buildings) was experienced not by essential facilities (such as hospitals and police and fire stations), but by commercial/industrial facilities.
d. One alarming finding was that one of the worst performance among occupancy types was experienced by schools with only 44% of the structures being green tagged.

Table 3. Damage classification for various occupancy types

Building occupancy	Green-tagged	Yellow-tagged	Red-tagged
Single-family residential buildings	48%	27%	25%
Multifamily residential buildings	45%	32%	23%
Schools	44%	34%	22%
Healthcare buildings	56%	25%	19%
Civic/public-safety facilities	52%	30%	18%
Commercial/industrial facilities	57%	24%	19%
Other	51%	32%	17%

4.5 Damage by number of stories

In general, among the structures evaluated, building

performance (as measured by the percentage of red-tagged structures in each group) was progressively worse as building height increased, and tall buildings were much more prone to severe damage. Of the buildings that were four stories or more in height, 44% were red-tagged; versus 24% for one-story buildings (see Table 4). In other words, the potential for catastrophic failure or collapse is almost twice as high for four-story or taller buildings than for one-story buildings.

Table 4. Damage classification for various number of stories

No. of stories	Green-tagged	Yellow-tagged	Red-tagged
One	49%	27%	24%
Two	46%	29%	25%
Three	36%	29%	35%
Four and more	30%	26%	44%

5. REPAIR AND RECONSTRUCTION

5.1 Yellow-tagged buildings

A large number of buildings with HCB and masonry construction have experienced HCB cracking damage. Given the need to use of readily available local material, considering the capabilities of Haiti's masons, and accounting for the economics involved in the repair of such a large number of structures, many of these options are not feasible for the current program in Haiti. For the vast majority of Haitian structures, therefore, the preferred method is placing of horizontal and vertical reinforcement in the HCB walls, and using superior concrete mortar mix and masonry blocks. This is one of the procedures discussed in ASTM (1993). This method was selected as the primary approach for the repairing of failed HCB due to good earthquake performance, economic benefits, and the presence of locally available labor and material for implementation. To demonstrate its efficacy, a sample zone has been selected and is undergoing reconstruction before the effort is extended to wider areas of the country.

The assessment of data shows that approximately 27% are classified as yellow-tagged. These structures must be repaired expediently using safe earthquake engineering techniques to help reduce the number of people living in temporary camps.

Unfortunately, there is ample evidence of reconstruction and repair of these collapsed or damaged structures using pre-earthquake, unsafe methods. Such an approach would place the lives of the citizens of Haiti at risk again in the event of another large earthquake. Therefore, it is imperative to use an improved and safe repair and reconstruction plan that focuses on techniques, quality-control quality assurance (QC-QA), and an approval mechanism to reduce the future life-safety risk. The proposed plan comprises the following components:

a. Develop cost-effective and simple repair methodologies for typical residential buildings. The platform uses the existing research undertaken at leading technical research institutes that focus on these and similar types of construction as described previously.
b. Develop guidelines and programs to communicate and train contractors and communities to repair and reconstruct residential structures. A simple illustrated guideline and training program was developed based on the information listed above. This guideline and training program has been developed for community implementation.
c. Develop a repair assessment method and construction inspection plan. PDA-based repair assessment and QA was developed.
d. Develop community-based reconstruction strategic plans based on the damage assessment database. The damage assessment database and the field knowledge developed during the assessment will be used to create a reconstruction strategic plan for each community. This plan will include possible total reconstruction areas, utilities requirements, and the cost of reconstruction and repair.
e. Develop and implement a project communications program for the repair guidelines. A mass media, strategic public communications campaign will be initiated using the available modes of communication (including radio and community meetings) to inform the public about the reconstruction plan and promote the use of improved repair and reconstruction methods.

5.2 Red-tagged buildings

The non-collapsed structures will be assessed in detail to confirm their red-tagged status and reparability. If the red-tagged structures are evaluated as feasible for repair, the repair assessment program will be conducted on the structure. If the red-tagged status and condition as infeasible for repair are confirmed, then the following data is recorded:

a. Classification of demolition. The demolition will be classified into one of the four groups listed in the following section and information will be recorded to document the reasoning behind the qualification.
b. Means and method of demolition. Given the classification of the demolition, on-site recommendations will be recorded on the means of demolition and the type of equipment and personnel that would be required for a removal.
c. Quality of site access. The quality of access to the site will be determined; for example, what type of construction and demolition equipment can be brought to the site, if any, and whether the site allows for debris-hauling equipment. In addition, it will be determined whether the site would allow access for implementing the demolition requirements listed in the next section.
d. Estimation of debris volume. An estimate of the volume of debris that would be generated after the demotion is completed will be identified.

e. Means and methods of debris removal. Given the volume and type of debris, on-site recommendations will be recorded on the type of debris removal and equipment needed to achieve such a task.
f. Identification of T shelter requirements. Given the size of the site and the number of tenants that the building had, an estimate will be made of the size and number of temporary shelters and housing that would be required until a new replacement structure had been erected.
g. Identification of natural- and geohazard conditions. An estimate of flood hazards and geohazards at the site will also be made. This estimate involves documenting any unusual site conditions, including flooding potential; noting any peculiarities about the site that had amplified the response; and noting other hazards such as slope stability and proximity to faulting. This data will then help engineers in the next phase of the reconstruction effort

5.3 Classification of the demolition

During the detailed red-tagged structure evaluation, the engineers will also assess and document the means by which the building could be demolished. Four categories will be used:

a. None or Minor. These buildings collapsed completely, essentially turning into rubble. No or only minor demolition or structural removal is required. The only task remaining is the debris removal and cleaning of the site.
b. Simple. These buildings are typically one story tall. They still have some small parts standing. However, the remaining portions can be dismantled and removed by hand crews using simple hand tools. No engineering technical support is needed because the remaining structure does not present a life-safety hazard to the crew removing it.
c. Medium. These structures are two to three stories tall and experienced partial collapse at some floors. They require engineering expertise to safely remove the remaining portions of the units.
d. Complex. These groups of buildings are typically tall and experienced collapse of floors at intermediate levels. The buildings are still standing. The removal of these buildings should be undertaken by construction and demolition specialists who have the experience, technical support, and heavy equipment required to remove the buildings safely and incrementally.

5.4 Quality management

Ten engineering divisions (150 national engineers) should be deployed as part of the repair assessment program and another 10 engineering divisions should be deployed for a red-tagged structure assessment program to conduct detailed engineering assessment of 200,000 damaged structures for reconstruction within a reasonable time frame. The repair assessment program was initiated in Delmas 32 in August 2010.

The QC program should support yellow- and red-tagged structure assessment and reconstruction programs. The QC-QA program includes:

a. QC of yellow- and red-tagged structure assessment programs. A construction-quality monitoring platform has been developed and a PDA-based monitoring tool is being implemented for yellow-tagged structure repair and reconstruction. This tool should also be used to provide a construction QA process. A similar tool will be developed for new construction.

These programs are critical activities for reconstruction. The authors have found that many Haitian engineers are more than capable of being trained in and implementing these yellow- and red-tagged structure programs with a proper QA program. This QC-QA program is also an integral part of the capacity development program in Haiti. Trained and experienced engineers from damage assessment, yellow-tagged structure assessment, and red-tagged structure assessment programs should be brought over to the QC-QA programs

6. CONCLUSIONS

The 2010 Haiti Earthquake once again revealed the vulnerability of unreinforced masonry and nonductile concrete construction to earthquake damage. The problem was more severe in Haiti because the country was unprepared for a major earthquake. To address the special circumstances and damage assessment in Haiti, an international and national partnership was formed, and it focused on inspection and reconstruction. This effort showed that:

a. An innovative assessment approach that relies on the expertise of international engineers to train national engineers in using state-of-the-art technology—such as ATC-20 and FEMA 310 protocols, PDAs, and GPS—is effective for rapid assessment and data collection.
b. Such an event provides a unique opportunity to collect field data and to develop fragility functions for various building types, occupancies, and construction.
c. Using a rapid assessment program as a database for reconstruction is an effective methodology. The methodology developed in Haiti can be implemented in other parts of the world as an effective damage assessment and reconstruction method.

Acknowledgements:

The The authors express gratitude to the management of MTPTC, including: Mr Jacques Gabriel (The Minister), Mrs. Viviane St Dic (Chief of Staff), Mr Evelt Eveillard (General Director), Mr Alfred Piard, (Director of Public Work) and, Mr Raymond Hygin (Assistant Director of Public Work). The work

described in this paper would not have been possible without the tireless efforts of the 250 Haitian engineers that participated in this unprecedented task. Similarly, the efforts of the many engineers from the US offices of the Miyamoto International who have spent many months in Haiti participating in this program are recognized. The financial and technical contributions of UNOPS, PADF, and WB OFDA/USAID are acknowledged. Their leadership and understanding of Haiti has been fundamental to the success of this project.

Most important of all, the authors wish to thank and acknowledge the citizens of Haiti. Their resiliency, hospitality, and courage are remarkable. They never quit hoping and smiling in the face of the most severe disaster any human has ever had to endure. They are an incredible people..

References:

Applied Technology Council (ATC), 2005. ATC-20_Set Procedures for Postearthquake Safety Evaluation of Buildings & Addendum, Applied Technology Council, Redwood City, CA.

ASTM, 1993. Masonry: Design and Construction Problems Repair, ASTM International, West Conshohocken, PA.

FEMA 1998, Handbook for the Seismic Evaluation of Buildings, Federal Emergency Management Agency, Washington DC.

United States Geological Survey (USGS), 2010. The Modified Mercalli Intensity Scale webpage, http://earthquake.usgs.gov/learn/topics/mercalli.php.

8CUEE CONFERENCE PROCEEDINGS
8th International Conference on Urban Earthquake Engineering
March 7-8, 2011, Tokyo Institute of Technology, Tokyo, Japan

SEISMIC SEPARATION OF ADJACENT BUILDING

James Anderson[1] and Fabian Rojas[2]

1) Professor, Department of Civil and Environmental Engineering, University of Southern California, USA
2) PhD Student, Department of Civil and Environmental Engineering, University of Southern California, USA
jamesa@usc.edu, rojasbar@usc.edu

Abstract: During the San Fernando earthquake (1971) two of the three triaxial recording instruments placed in an 16 story steel building in Los Angeles recorded the impact with an adjacent reinforced concrete parking structure. This provided an excellent opportunity to evaluate the modeling of such an event using current computer programs (time step, structure damping, impact damping and use of a gapped element), to evaluate the effect of the impact on the strength demands and to evaluate the design implications (necessary separation). Although only the base recorder functioned during the Northridge earthquake, it was possible to evaluate the computer modeling using the San Fernando data and then use the model to evaluate the building behavior under the stronger Northridge earthquake (1994). Results indicate that the extensive cracking indicated in the two transverse frames of the steel building show general agreement with the results of a damage investigation following the Northridge earthquake. Much of this damage in the lower ten floors of the transverse frames was probably due to the impact with the adjacent parking structure at the fifth floor level. Damage in the upper portions is thought to be due to the increased response in the higher modes of vibration caused by the impact and by the horizontal setback at the fifth level.

1. INTRODUCTION

For more than 40 years, the collisions (pounding) of buildings during earthquakes has been of concern to structural engineers. The pounding between buildings during the Tokatioki Earthquake (1968) in Japan has been discussed by Shimazu (T. Shimazu, 2007). During the San Fernando Earthquake (1971) pounding occurred between a 16 story building and an adjacent parking structure (Gates, 1973). At the same time, pounding between the stair towers and the main building of the Olive View Hospital had a significant effect on the damage experienced (Bertero and Collins, 1973). Following. the Mexico City Earthquake (1985), pounding was identified as present in over 40% of the 330 buildings that collapsed (Rosenblueth and Meli, 1986). Bertero (1986), has also documented much of the structural pounding that occurred during this earthquake. During the Northridge earthquake (1994), the 16 story building mentioned above suffered much more severe pounding between the building and an adjacent parking structure. The steel building required substantial repair as did the reinforced concrete parking structure. The behavior of this building during these two earthquakes will be the main topic of this paper.

While data-mining the records obtained during the San Fernando Earthquake for another study, the authors noted that instruments located at the mid-height and roof levels of the 16 story building had recorded the impacts with the five story adjacent structure. This provides an excellent opportunity to evaluate the analytical modeling of this type of event using current, commercial computer programs and to evaluate the effect of these impacts on the overall performance of the building during the San Fernando earthquake.

Unfortunately, the instrumentation at the mid-height and roof did not function properly during the much stronger Northridge earthquake and important records at these locations are not available. However, the base motions were recorded. Therefore, a computer model has been developed and correlated with the recorded San Fernando data. It was then used to predict the response due to the much stronger Northridge earthquake and the effects of multiple impacts on the structure. Calculated response from the computer model is compared with the damage reported by investigators following the two earthquakes.

2. CASE STUDY BUILDING

2.1 Description of Building

The building considered in this study is a 16 story, structural steel office tower, shown in Figure 1. It was designed in 1969 under the building code requirements of the City of Los Angeles. The typical floor plan, shown in Figure 2, is rectangular with three bays in the transverse (N-S) direction and six bays in the longitudinal (E-W) direction. A typical bay width is 8.4 m. The tower rises out of a four story base structure and has a horizontal offset on three sides. On the fourth (longitudinal) side it abuts an adjacent four story parking structure that has a seismic

separation of two inches. Seismic resistance is provided by rigid moment frames on the perimeter of the tower. Due to the location of the building relative to both the San Fernando and Northridge earthquakes, the transverse moment frames experienced the strongest motion. In the case of the Northridge earthquake these frames also experienced the most damage, which required extensive repair. Therefore this study will be focused one of these two identical frames.

A typical elevation of a transverse frame is shown in Figure 3, which is taken from an earlier study following the San Fernando earthquake (Gates, 1973). The beams of the frames consist of 107 cm deep welded plate girders and standard W14, wide flange columns. According to the reference, the deep girders were used to stiffen the frame, thereby reducing the lateral story drift under lateral loading. However, this results in a strong girder/weak column design that will force the higher stresses and possible plastic hinging into the more vulnerable columns rather than the girders. Also shown in Fig. 3 are the locations of the three recording instruments (SMA-1's); one at the base, one on the ninth floor and one on the roof. All three are located near to the center of the floor plan.



Figure 1: 16 Story Building

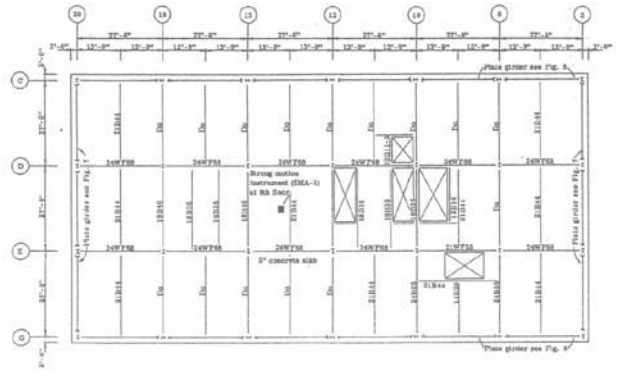


Figure 2: Typical Floor Plan (Gates, 1973)

The adjacent parking structure is constructed with pre-stressed concrete girders resting on column haunches with shear walls providing the lateral resistance. This structure has five levels of parking and is similar to several others that were built in Los Angeles during this time period. An instrumented parking structure of this type is located on the USC campus so that the dynamic properties are well known. There is a two inch seismic separation between the two structures.

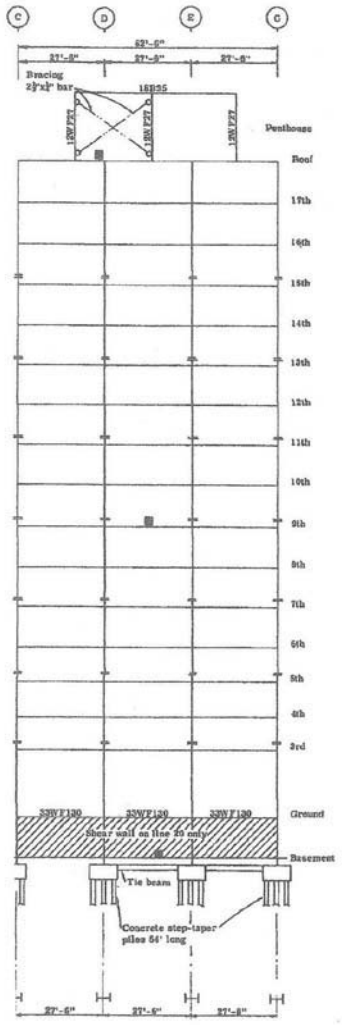


Figure 3: Elevation and Instrument Locations (Gates, 1973)

The computer model of the transverse frame developed for SAP2000 vs.14 (CSI, 2009) is shown in Figure 4. The main tower is modeled using standard beam and column elements with rigid connections. The story weight (mass) is equally divided between the two frames and lumped at the nodal points. The dynamic response of the parking structure is simulated using a lumped mass, chain model having the dynamic properties that approximate those of the actual structure Based on the results reported by Gates (1971) and on the results of preliminary studies by the authors, it was concluded that the response of the structural members to this earthquake was only weakly nonlinear.

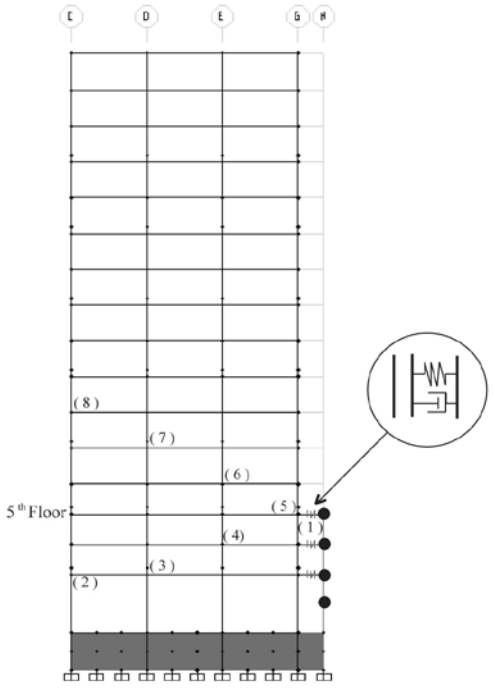


Figure 4: 2D Sap2000 Model

The maximum demand/capacity ratio (DCR) occurred in an interior column of the 15th floor and had a value of 1.6. Therefore it was decided to use the SAP model with linear elastic material properties and with nonlinear geometric properties for the gap elements. The adjacent parking structure is connected to the main building using the gap element available in the SAP program. This element uses a linear spring of stiffness k and a linear dashpot. The stiffness was determined from a three-dimensional analysis of a similar structure on the USC campus. The damping constant c, which is related to the coefficient of restitution, was determined as suggested by Anagnostopoulos (2004). Although the recorded data was digitized with a time step of 0.02 seconds, a time step of 0.005 seconds was used for the analysis in order to more accurately capture the action in the gap. An initial Fourier analysis of the recorded data indicated a damping of 5% of critical in the first mode with lower damping in the next three modes. However, later analysis of the building response indicated that a higher damping was needed to obtain a better agreement with the recorded response. Therefore, the damping in the first mode was increased to 8% and the modified damping function is shown in Figure 5.

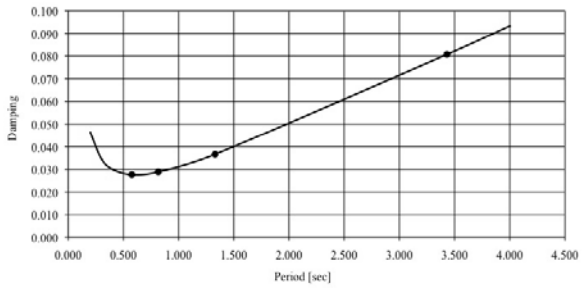


Figure 5: Percent Critical Damping

2.2 San Fernando Earthquake (1971)

Nine excellent records of seismic response were obtained from the three instruments during the San Fernando earthquake, approximately 28.2 Km from the building site. The recorded response in the transverse direction at the roof level is compared with the calculated response in Figure 6. The acceleration responses are compared in Figure 6a. It can be seen that the maximum recorded acceleration is 0.22g, whereas, the maximum calculated acceleration is an acceleration spike that reaches 0.43g at 20.2 seconds. It will be shown that this acceleration spike is due to contact with the parking structure. The maximum displacement, shown in Figure 6b, occurs at the same time and is recorded as 14.5 inches compared with the calculated 48.3 cm. The recorded acceleration response at the ninth level is compared with the calculated response in Fig. 6c. The comparison is quite good with the exception of the two acceleration spikes that occur 12.6 seconds and 19.4 seconds which are due to contact with the parking structure. The displacements, shown in Figure 6d, are in good agreement.

The forces in the link elements which represent impacts with the garage are shown in Figure 6e. Relatively strong impacts can be seen to occur at 12.6 seconds and 19.5 seconds. Recall that these impacts are occurring at the fifth floor level, which is 51 m below the roof. Measuring the time lag in the acceleration spike between the hit at the fifth level and the roof (20.1s – 19.4s) and dividing this into the distance to the roof gives an estimate of the shear wave velocity in the building, which is 72.85 m/sec. An analytical calculation suggested by Tedesco et.al., 1999, expresses the shear wave velocity for a shear building having uniform properties as: $c = 4L/T_n(2n-1)$, where L is the height and T_n is the period of the nth mode. Using L=64 m and T_n = 3.43 seconds this results in a shear wave velocity of 74.83 m/sec.

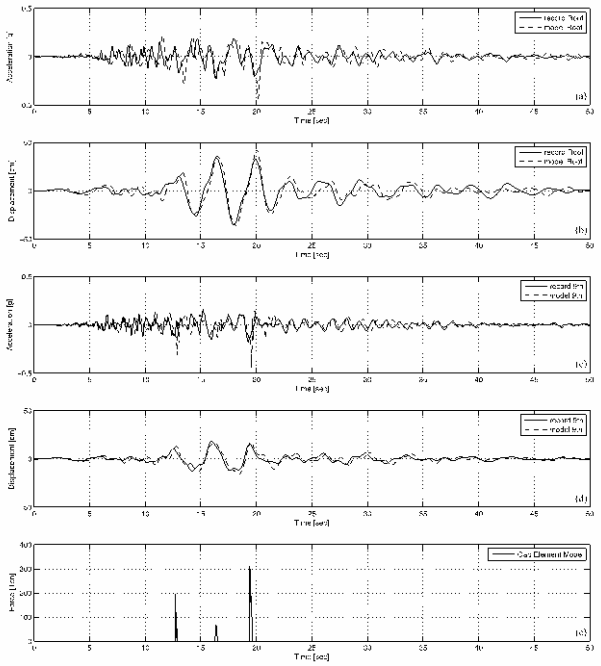


Figure 6: Response Comparisons between Recorded vs Calculated, San Fernando 1971

Demand Capacity Ratios (DCR's) are shown in Figure 7 for the beams and columns of the transverse frames. Two conditions are considered: one with the parking structure in place (P) and the other without the parking structure (N). It can be seen that for the beams, shown in Fig. 7a, the behavior has remained elastic with the exception of the exterior beam at the sixteenth level and the interior beam at the 15th level where the inclusion of the parking structure has increased the DCR's to 1.1 and 1.06 respectively. It can also be seen that in general, the effect of the impact at the fifth level is to increase the DCR's relative to the case where the parking structure is removed as shown by the broken lines. Considering the columns, shown in Fig. 7b, substantial inelastic behavior is indicated in the upper half of the building by several of the DCR 's exceeding unity. A maximum value of 1.5 occurs at the sixteenth floor level, representing a 25% increase due to the impact.. This may indicate the effect of an amplified second mode response due to the impact. In the mid-height region, the opposite is true and the DCR's without the impact are greater than those with the impact and in the lower third of the tower the the DCR's without the parking structure are larger than those with parking although both are less than unity. This may be representative of the restraining effect or the of the adjacent structure. Note that below the 10th floor level, the DCR's are all less than unity indicating elastic behavior.

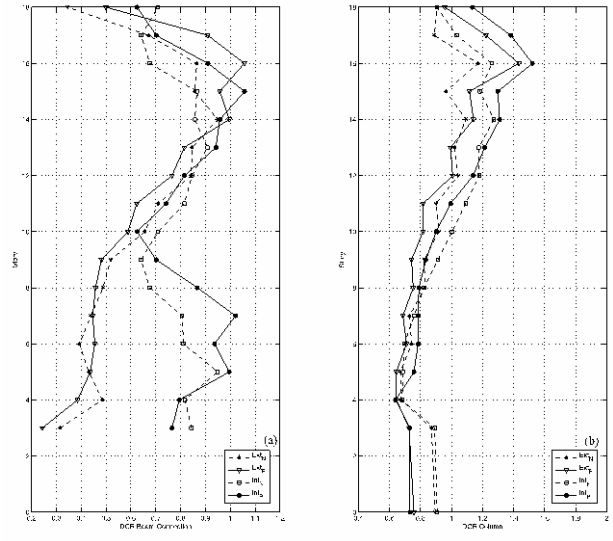


Figure 7: Demand Capacity Ratios, San Fernando 1971

The strong motion portion of the column shear response is shown in Figure 8 for the four locations across the transverse frame shown in Figure 4. The initial impact with the parking structure occurs at 12.6 seconds into the record as shown in Fig. 8 at position 5 which represents the top of the parking structure. This initiates a shear wave that propagates up and down across the structure. The time history of the shear at the first exterior column is shown in Fig. 8(5). Here, the impact effect appears as a short duration blip on the shear response curve of the building without the impact, shown by the dashed line.

The path of the impact wave moving up the structure is tracked across the structure in Figures 8(5), 8(6), 8(7) and 8(8). The second major impact occurs at 19.3 seconds into the record as shown in Fig. 8. Note that the pulse reaches location 8, three stories and three bays from the impact point, at 19.43 seconds into the record for a travel time of 0.13 seconds. As might be expected, the largest effect of the impact on the shear force occurs at position 6 which is the column next to the impact point and results in an increase of 33% over the condition without impact. By the time the pulse reaches position 8, the maximum shear with the impact is just equal to that without impact. The path of the impact wave moving down the structure is tracked across the structure in Figures 8(5), 8(4), 8(3) and 8(2). At these locations, the effect of the impact produces a shear that is either equal to or less than that of the unrestrained structure. However, this was a rather mild impact that did not cause any known damage to either building but left marks indicating that it had occurred. Repair costs were reported to be very minimal.

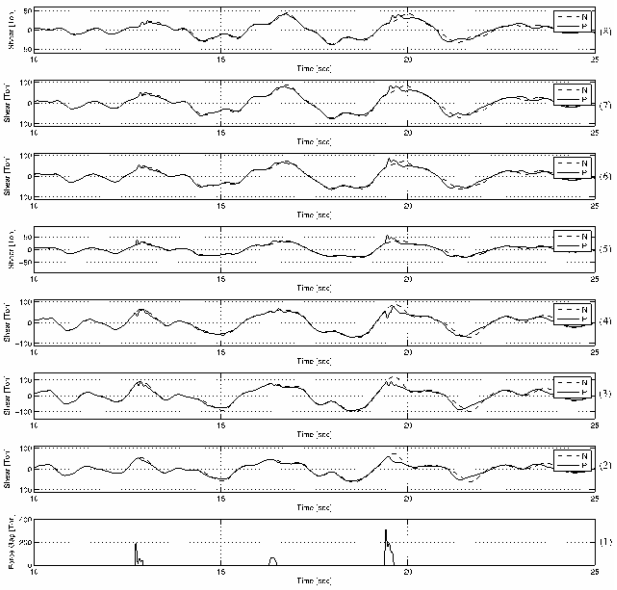


Figure 8: Column Shear Time History, San Fernando 1971

2.2 Northridge Earthquake (1994)

As mentioned previously, at the time of the Northridge earthquake, only the recording instrument at the base of the building was operational. Therefore, comparisons cannot be made with the calculated and recorded response data for this earthquake. The recorded acceleration at the base for the San Fernando earthquake is shown in Figure 9a along with the calculated displacement in Figure 9b. The calculated hits against the parking structure are shown in Figure 9c. Similar data for the Northridge earthquake are presented in Figures 9d, 9e and 9f respectively.

It can be seen immediately that the motion at this site due to the Northridge earthquake was considerably stronger than that due to the San Fernando earthquake. Note that the peak acceleration for San Fernando is approximately 0.12g whereas that for Northridge is almost 0.3g. The increase in displacement is not as large with San Fernando having a

peak displacement of 8.9 cm and Northridge reaching 10.7 cm. This increased response for Northridge has increased both the number and intensity of hits against the adjacent structure. As can be seen in Figure 9f, there are six hits for Northridge versus only three for San Fernando, Figure 9c. These figures also indicate that the intensity of the impact for Northridge is approximately three times that due to the San Fernando ground motion.

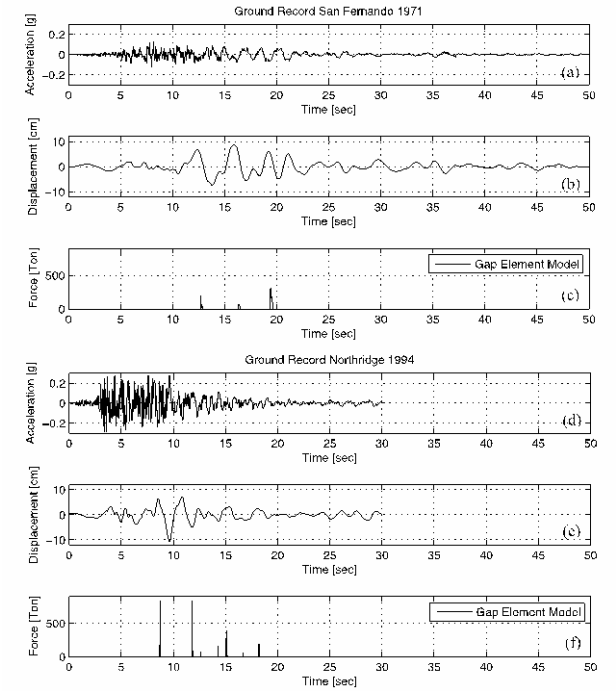


Figure 9: Ground Motion Comparisons

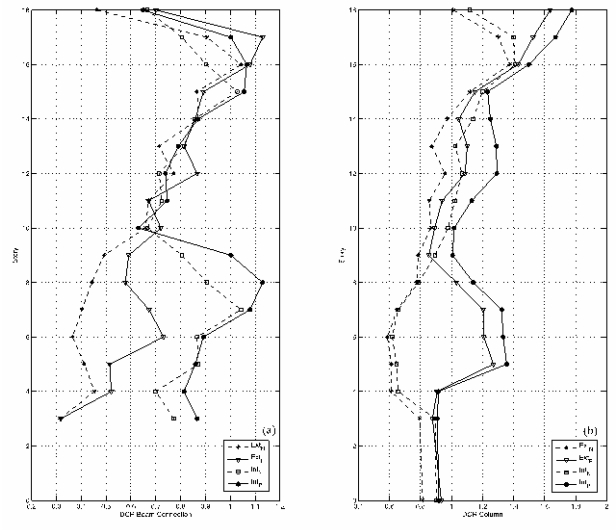


Figure 10: Demand Capacity Ratios, Northridge 1994

The Demand Capacity ratios for the beams and columns of the transverse frames considering both with and without the parking structure are shown in Figure 10. Considering the beams, shown in Figure 10a, there is no significant change in the DCR's over the height of the structure. Most of the increases are in the elastic range and all values are less than 1.2. However, at all beam locations over the height, the impact with the parking structure increases the DCR's. The column DCR's are shown in Figure 10b. Here there is a significant change beginning at the 5th floor level and extending to the 8th floor level. Recall that this is the region shown in Figure 8 that was affected by the impact pulse. The columns in this region have had the DCR's increase from a maximum of just under 0.6 to as much as 1.3, indicating an increase of more than 100% and the initiation of inelastic behavior in levels 5 to 8. The columns in the upper three floors are also increased from values of 1.1 to values of 1.7. This indicates that the amount of inelastic behavior has increased significantly and particularly in the more vulnerable columns.

The strong motion portion of the column shear response is shown in Figure 11 for the four locations across the transverse frame shown in Figure 4. The initial impact with the parking structure occurs at 8.7 seconds into the record as shown in Fig. 11(1). As for the San Fernando record, this initiates a shear wave that propagates up and across the structure. The time history of the shear at the first exterior column is shown in Fig. 11(5). Here, the impact effect appears as a short duration blip on the shear response curve of the building without the impact, shown by the dashed line. The path of the impact wave is tracked across the structure in Figures 11(5), 11(6), 11(7) and 11(8). A second major impact occurs at 11.7 seconds into the record as shown in Fig. 11(1) and this impact results in the largest shear increase of 50% at position 6 shown in Figure 11(6). Note that the pulse reaches location 8, three stories and three bays from the impact point, at 8.82 seconds into the record for a travel time of 0.12 seconds. For this earthquake record, the largest effect of the impact on the shear force occurs at position 6, which is the interior column. By the time the pulse reaches position 8, the effect of the impact on the maximum shear is beginning to decrease and by the time it reaches the other side of the structure at position 4 it is no longer affecting the maximum (design) value.

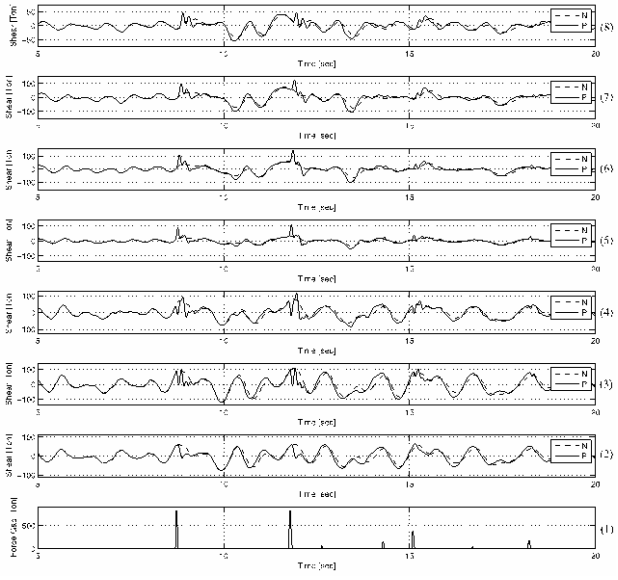
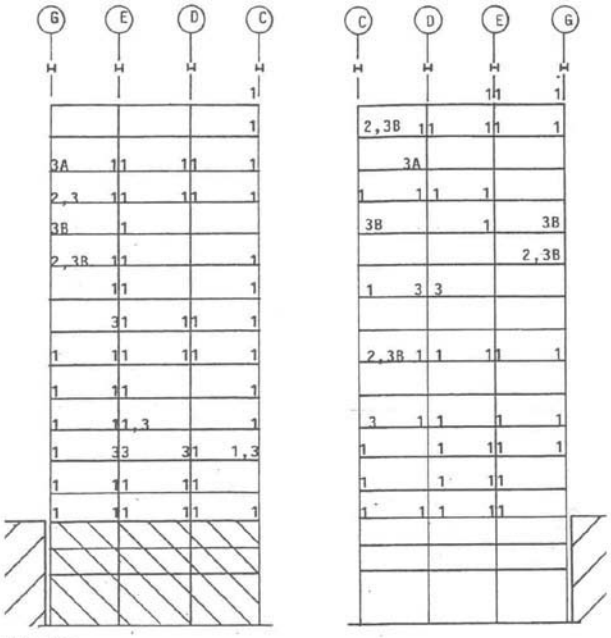


Figure 11: Column Shear Time History, Northridge 1994

Considering the case of no impact (Fig. 10), it can be

seen that below the impact point, the behavior is almost completely elastic with only the columns at the base having DCR's that are just at unity. There are no DCR's greater than unity until reaching the ninth floor level. In the case of the actual building, Fig 10, the impact causes DCR's in all but the far side exterior columns to be in the inelastic range for four story levels, one below the impact level and three above.

Following the Northridge earthquake a comprehensive evaluation and repair program was conducted. The determined damage has been reported (Kariotis, et.al., 1995) as part of the "SAC Program on Steel Moment Frame Structures." This data indicated that the distribution of earthquake damage was primarily confined to the transverse frames. The summary of the damage in the transverse (N-S) frames is reproduced from this reference in Figure 11.This data indicates that there is significant weld cracking at the floor level of the impact (5^{th}) and for two or three levels above the impact level. Data below the impact point were not included in the reference report although the results of this study indicate an increase in the DCR's in the first story below the impact point. In the west elevation there is also cracking in the column flanges two floor levels above the impact point. Increases in the DCR's in the upper half of the structure due to the impact are thought to be a result of the increased response in the second and possibly third mode of vibration.



LEGEND
1. PARTIAL CRACK IN WELD OF BOTTOM FLANGE OF BEAM
2. COMPLETE CRACK THROUGH WELD OF BOTTOM FLANGE OF BEAM
3. PARTIAL CRACK INTO COLUMN FLANGE
3A. COMPLETE CRACK THROUGH COLUMN FLANGE
3B. COMPLETE CRACK THROUGH COLUMN FLANGE PLUS CRACK INTO COLUMN WEB

Figure 11: Damage Report, Northridge 1994 (Kariotis et al., 1995)

3. CONCLUSIONS

The application of an impact load to a steel frame results in a short duration impact load that appears as a blip on the displacement response curve of the frame without the impact. Close to the point of impact, this will cause a significant increase in the calculated DCR. Due to the short duration of the load, it would not appear that there is enough time for a plastic hinge to form. However, the short duration impact may cause cracking in the weld material of welded moment frames. This is particularly true of frames that were constructed prior to 1994 using a weld material with a low fracture-toughness. Since welded plate girders were used for the beams, this may have made the building more susceptible to cracking due to impact load.

The results of this study also illustrate the need for building separation in seismic regions. At the impact point (5^{th} floor level) the displacement due to the San Fernando earthquake was 1.07 cm for the parking structure and 6.81 cm for the main building. For the Northridge earthquake the displacement of the parking structure was calculated to be 2.39 cm and 8.36 cm for the main building. Both of these ground motions required more separation of the buildings than the 5 cm provided in order to prevent pounding. Although there was no apparent danger to life safety, there was undoubtedly a high repair cost for the numerous weld cracks. There was also a substantial repair cost for the concrete parking structure, which came out second best in its encounter with the steel frame and was severely damaged.

It is quite possible that some of these cracks in the steel frame may have been initiated during the San Fernando earthquake. Due to cover by the fire proofing and nonstructural wall boards they remained undetected until the stronger Northridge earthquake required removal of some of this covering material. Hence, the cracking could have been cumulative, particularly in the more critical locations. It is not clear why the post-earthquake investigations did not consider the floors below the impact point.

The results of this study indicate that the effect of the impact on the story shear tends to diminish with distance and after approximately four story levels has no direct effect on the maximum displacement.

A significant increase occurred in the response of the second and possibly the third modes of vibration. Gates (1973) also noted this effect in his earlier study. This may be due to the combination of the horizontal offset at the fifth level and the impact with the parking structure at the fifth level.

The increase in the DCR's above the impact floor level was also noted in an earlier study by Maison and Kasai (1992). This led them to conclude that ignoring these effects may lead to an unconservative evaluation or design.

Many of the results of this study would not have been possible with only a single instrument on the roof. The single instrument most likely would have been to far from the point of impact to even record the resulting change of the acceleration and displacement. Once again the importance of having at least three instruments in tall buildings has been reconfirmed.

References:

Anagnostopoulos, S. A. (2004), "Equivalent Viscous Damping for Modeling Inelastic Impacts in Earthquake Pounding Problems," *Earthquake Engineering & Structural Dynamics*, **33**(8), 897-902.

Bertero, V. V. and Collins, R. G. (1973),"Investigation of the Failures of the Olive View Stair-towers During San Fernando earthquake and their Implications on Seismic Design," *Report no. EERC 73-26*, Earthquake Engineering Research Center, University of California, Berkeley, CA

Bertero, V. V., (1986) "Observations of Structural Pounding," *Proc. Int. Conf., The Mexico Earthquake-1985*, ASCE, New York, NY.

CSI, "SAP 2000 Version 14", *Computers and Structures* , Inc., Berkeley, California.

Gates, W. E. (1973), "KB Valley Center," *San Fernando, California, Earthquake of February 9, 1971*, Vol 1, Effects on Building Structures, Part B, NOAA, Washington, D. C.

Kariotis, J. and Eimani, T. J. (1995), "Analysis of a Sixteen Story Steel Frame Building At Site 5 For The Northridge Earthquake," *Technical Report SAC 95-04*, Part 2.

Kaufmann, E. J., and Fisher, J. W. (1995), "Fracture Analysis of Failed Moment Frame Weld Joints Produced in Full-Scale laboratory Tests and Buildings Damaged in the Northridge Earthquake," *Technical Report, SAC 95-08*.

Maison, B. F. and Kasai, K., (1992), "Dynamics of Pounding When Two Buildings Collide," *Earthquake Engineering and Structural Dynamics*, Vol21, 771-786.

Rosenblueth, E., and Meli, R., (1986), "The 1985 Earthquake: Causes and Effects in Mexico City," Concrete International, 8(5), 23-24.

Shimazu, Takayuki (2007) "Lessons learned from the Earthquake Damages of Reinforced Concrete Building Structures in the Light of the International Point of View," *Concrete Journal*, **45**(8), August.

Tedesco, J. W., McDougal, W. G., and Ross, C. A. (1999), "Structural Dynamics: Theory and Application," *Addison Wesley Longman, Inc*, Chapter 14, 437-494.

8CUEE CONFERENCE PROCEEDINGS
8th International Conference on Urban Earthquake Engineering
March 7-8, 2011, Tokyo Institute of Technology, Tokyo, Japan

EVALUATION OF THE POLICIES FOR SEISMIC RETROFIT OF BUILDINGS

Shoichi Ando

Director of International Institute of Seismology and Earthquake Engineering (IISEE),
The Building Research Institute (BRI), Tsukuba, and Professor of The University of Tokyo,
Department of Urban Engineering, Graduate School of Engineering (Machizukuri-Daigakuin)
ando@kenken.go.jp (IISEE/BRI, Japan), ando@mps.t.u-tokyo.ac.jp (The University of Tokyo)

Abstract: The Japanese government has established a law to promote seismic retrofitting of buildings immediately after the Great Hanshin-Awaji Earthquake in 1995. This paper evaluates the effectiveness, efficiency, administrative feasibility and technological incentives of the policies related to the law. The data shows that the policy target of seismic safety of buildings will be achieved in 2018 if the current trends of improvement will be continued. In the field of school buildings, national government supports the school retrofit works that are carried out by the local governments, using the guideline for school retrofit. However, there are still significant issues to make all houses safe. One of the key challenges is how to persuade the elderly who would not invest their money to improve their old houses. Another challenge is to make housewives understand the importance and have priority in improving the seismic safety of houses. Currently many efforts are taken by the local governments, such as holding seminars for local communities, preparing financial support schemes, providing consultancy for seismic assessment and making earthquake hazard maps. This paper also provides comments on the improvement of the current policies for promoting seismic retrofit based on some international experiences of house and building retrofit.

1. INTRODUCTION

After the Great Hanshin-Awaji Earthquake in 1995, the Japanese government has established around 20 legal systems including the "Act for Promotion of the Earthquake Proof Retrofit of Buildings" (Retrofit Promotion Act) that has been established in 1995 as one of new legal systems. Moreover, many Japanese local governments become to provide various support systems in order to promote seismic retrofit conducted by owners and the private sector. The national government also provides new subsidy systems such as the regional housing grants and the community renovation grants based on the Retrofit Promotion Act. Furthermore a tax reduction system of loans for seismic retrofitting has started from the fiscal year 2006.

Why so many public assistance systems for housing seismic retrofitting exist, though houses are private assets? Originally, this argument arose immediately after the Great Hanshin-Awaji Earthquake. Has the government decided not to appropriate tax revenue (public assistance) for the reconstruction of individual houses, then?

One of the reasons why such a policy change has made, may result from the establishment of the "Act concerning Support for Reconstructing Livelihoods of Disaster Victims" in 1998 and its revision in 2004. This Act is legislation at the instance of house members on the basis of several disasters after the Great Hanshin-Awaji Earthquake. According to this Act, in case of completely or partially destroyed houses, a certain amount of public assistance can be provided to owners of such private assets. For instance, the owner of a completely destroyed house can allow one million yen for purchasing household effects and two million yen for reconstruction of the house, i.e. in total three million yen will be granted.

In addition, collapse of houses often causes streets blockade and this may bring about crucial obstacles to escape, fire fighting and/or relief activities, when an urban fire occurs as the experience at the Great Kanto Earthquake in 1923 and in Nagata ward of Kobe city at the Great Hanshin-Awaji Earthquake. Namely, seismic retrofitting of buildings including house, is indispensable in order to secure entire urban safety. Therefore, public assistance can be provided, even though houses are private assets.

Taking a view of the estimated tolls by the Tokai Earthquake published by the Cabinet Secretary in 2005 as a reference, the maximum number of death toll will reach to approximately 9,200 persons by the assumed ocean-type Tokai Earthquake. And around 85 % of death toll, i.e. approximately 7,900 dead persons will be due to the collapse of buildings and the like. At the same time, the Cabinet Secretary announced a target to reduce those tolls by half in the "Earthquake Disaster Mitigation Strategy" for Tokai Earthquake. For that purpose, a detailed target to improve housing seismic retrofitting ratio was set up from current 75 % to 90 % within 10 years (till 2015). The "Earthquake Disaster Mitigation Strategy" was also created for coming Tohnankai and Nankai (South-east Ocean and South Ocean) Earthquake in 2005 and the main targets consist of housing seismic retrofit and tsunami disaster prevention measures.

These are the backgrounds of movement that many actors established new supporting measures for housing seismic retrofit in all parts of Japan from the establishment of the Strategy in 2005 till now.

2. RETROFIT SYSTEMS IN JAPAN

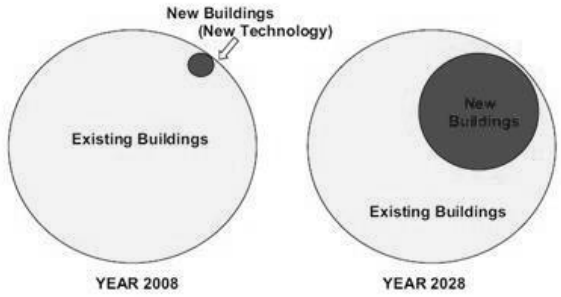
2.1 Technical Background

"The 1995 Great Hanshin-Awaji Earthquake disaster revealed the weakness of reinforced concrete (RC) structures that were designed in accordance with the pre-1981 design code. Failure of RC columns was primarily in the lack of lateral reinforcement. Larger deformation capacity may be attained by enhancing the capacity by (a) jacketing RC columns with steel plates and (b) wrapping RC columns with fiber reinforced plastics (FRP). The use of FRP sheets has merit of easy construction work and of light material weight. Placement of bracing structures (structural walls or steel braces) is effective limiting the response deformation of the structure, thus avoiding the failure of brittle members.

The occupancy of a building during the retrofit work should be considered in selecting retrofit works. For example, the strengthening work of RC columns normally requires the removal of mortar and other finishing materials (tiles) from the concrete surface. The noise, vibration and dust during the retrofit work will not allow occupants to stay in the building.

If advanced technology is affordable, especially in hospitals for post-earthquake medical treatment of the injured, the earthquake induced forces may be reduced by placing isolation devices at the base. The response of a structure may be reduced by installing dampers or energy dissipating devices are available. The failure of foundation piles was reported after the 1995 Kobe earthquake disaster. In some structures, the failure of pile foundation is said to reduce the earthquake ground motion input to the structure and limit the damage in the super-structure. However, the cost of damage investigation of foundation as well as the repair work of damaged foundation is expensive. It is normally desired to provide the foundation structure with higher resistance". (Prof. Shunsuke Otani, 2008)[i]

Fig. 1: Relation of Design Code for New Construction (by Prof. Shunsuke Otani)



2.2 Retrofit Promotion Act and its support systems

The Retrofit Promotion Act was enforced in 1995 immediately after the Great Hanshin-Awaji Earthquake in January 1995, since the lessons learnt from the devastated disaster urged quick response of the government and policy makers to secure the safety of urban built-environment that are mainly consisted of houses and buildings. Key components of the new Act are;

- Obligation of owners to make best efforts to assess and retrofit the buildings that are utilized many people,
- Exemption of retroactive application of building code except for seismic related code to approved retrofit works,
- Guidance, advices and instructions from the responsible governmental agency.

With regard to new obligation for the owners of building that is utilized by many people, such building is defined as, more than 3 stories and more than 1,000 m2 of floor area and its use is in line with designated one such as school, hospital, department store, office, shop, hotel, care facility for the elderly and so on.

When the Retrofit Promotion Act was established, the Japanese Ministry of Land, Infrastructure, Transport and Tourism (MLIT) surveyed the conditions of houses and buildings in terms of applicability to seismic code (in 1981, the current level of seismic safety). The updated result of the survey was indicated in the Table 1. The target of applicable level of seismic code is also shown in the Figure 2.

Table 1:

Number of buildings under (1981) seismic code level

Houses

	Total houses in Japan
Total number of houses	47 million units
Under seismic code level	11.5 million units
(percentage of under level)	around 25 %

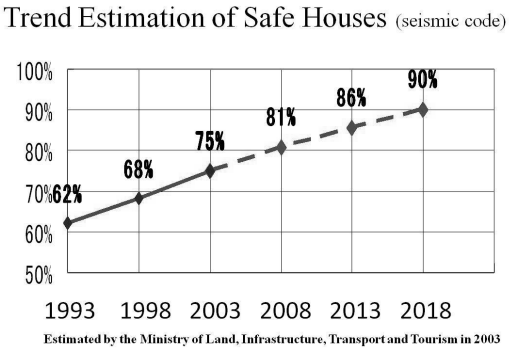
Estimated based on the data in 2003

Non-residential Building

Total number	3.4 million buildings
Under seismic code level	1.2 million buildings
(percentage of under level)	around 35 %

Estimated by the Ministry of Land, Infrastructure, Transport and Tourism in 2002

Figure 2:



The Act was established to introduce retrofit of houses and buildings. Therefore, in addition to regulatory measures some economic measures have been prepared at the same time by the national government. Those economic measures are available only in the local government that established "Plan for Retrofit Promotion". Table 2 shows the number

and ratio of the local governments that have established the Plan for Retrofit Promotion. Table 3 shows the number and percentage of the municipalities that have prepared the subsidy systems for seismic assessment and retrofitting.

Table 2:

Number of Local Governments that have Retrofit Promotion Plans (as of 1 April 2009)

		Have plans	-2009.9	-2010.3	2010.4-
Prefecture		47			
	Total	47			
	(%)	100.0%			
Municipality		1,193	50	185	70
	Total	1,193	1,243	1,428	1,428
	(%)	66.3%	69.1%	79.3%	83.2%

Table 3:

Subsidy System for Seismic Assessment and Retrofit

as of 1 April 2009 (Japan)

Building type	Project type	Applicable Local Govt. for Retrofit subsidy	
		Number of local Govt.	Ratio: Applicable Govt.
Detached house	Assessment	1,227	68.2% (62.7%)
	Retrofitting	857	47.6% (37.2%)
Condominium	Assessment	450	25.0% (19.0%)
	Retrofitting	321	17.8% (12.1%)
Non-residential	Assessment	310	17.2% (13.2%)
	Retrofitting	154	8.6% (5.9%)

Those tables show the fact that even in 2009, one quarter (25%) of municipalities have prepared the subsidy system for condominium to assess/evaluate the vulnerability to earthquake. In case of detached houses, almost 2/3 of municipalities have established subsidy system by 2009 for assessment and almost half of them have prepared financial support for retrofitting of houses. Figures of the Table 4 in the entre- parenthesis indicate the number of percentage of the April 2008. Within only one year, the percentage has been significantly improved because of the following policy measures, while a limit of financial support to the retrofit can be observed especially in the field of condominium and non-residential buildings.

The following policies are described as the MLIT has reported as below;

(1) Formulation of municipal Retrofit Promotion Plans
(2) Establishment of prefectural/municipal subsidy system
(3) Promotion of retrofitting of public buildings
(4) Securing engineers who manage assessment/retrofit
(5) Utilization of tax incentives for business use buildings
(6) Preparation of seismic hazard mapping
(7) Best practices for seismic assessment/retrofit
(8) Model projects on seismic safety houses and buildings

Those measures are comprehensive and are including 1) socio-economic measures, 2) information measures, 3) technical measures, and 4) institutional measures, to promote the policy for seismic assessment and retrofit of buildings.[ii]

2.3 Retrofit of Schools in Japan[iii]

"Because of the Great Hanshin-Awaji Earthquake in 1995, school buildings were also severely damaged by the shake. According to a report provided by the Ministry of Education, Culture, Sports, Science & Technology (MEXT), approximately 4,500 educational facilities were structurally or non- structurally damaged, though there were fortunately no death tolls resulted from damaged schools since the Great Hanshin- Awaji Earthquake occurred in early morning at 5:46 a.m.. After the strike of the Earthquake, 390 schools took the role for evacuation shelter and these schools accommodated approximately 180,000 evacuated people.

Furthermore, at the time of recent major earthquakes such as Niigata-Chuetsu Earthquake in October 2004 and Iwate-Miyagi Nairiku Earthquake in June 2008, while many school buildings were damaged, non-damaged schools accommodated many evacuated people. On the basis of these experiences, it is critical to ensure that school students are safe and school facilities are fit to serve as evacuation shelters for local populations. MEXT's policies on structural and nonstructural retrofitting of school buildings are introduced. Since school buildings have the following crucial roles, it is indispensable to assure the safety of school buildings against earthquakes.

1) Place for educating children: school buildings are the place where many children study and live most part of their days. It is, therefore, vital to keep school buildings in safer and healthier environment.

2) Place for cultural and sporting activities: school is a well-known building to the people who live near the school. School buildings are, therefore, often utilized for the cultural and sporting events for the local population.

3) Place for evacuation: school often becomes an evacuation shelter when a major natural disaster occurs. To this end, it is important that school buildings accommodate necessary functions for evacuation shelter.

The Building Standard Law of Japan was revised in 1981 and new seismic resistant design methods were adopted. According to the revised law, the buildings constructed based on the new design would have no damage in the case of middle class earthquakes (about JMA 5 upper scale). Moreover, there would be no casualties in these buildings and no severe collapse of these buildings even in the case of major earthquakes (about JMA 6 upper).

Table 4:

Difference between New and Old Seismic Resistant Design

Type of Earthquake (JMA Scale)	Medium Scale Earthquake (about 5 Upper)	Larger Scale Earthquake (over 6 Upper)
Old Seismic Resistant Design (until 1981)	No major damage	Not verified
New Seismic Resistant Design (since 1981)	No major damage	Will not collapse

JMA Scale: Scale indicating the strength of seismic motion, which was formed by JMA (Japan Meteorology Agency)

5 Upper: Many people are considerably frightened and find it difficult to move

6 Upper: Impossible to keep standing and to move without crawling

In order to evaluate the seismic capacity of an existing school building, the seismic capacity index of structure (Is) is used in Japan based on the regulation of the Retrofit Promotion Act. The law regulates that a building has low risk of collapsing if the "Is" of the building is more than 0.6. However, in consideration of the importance of school building, MEXT recommends that the "Is" of school building should surpass 0.7 after retrofitting.

Is (Seismic Capacity Index of Structure):
An index to define the seismic capacity of an existing reinforced concrete building

Is = Eo×S×T

Eo : A basic structural seismic capacity index calculated by the elements of Strength index (C), Ductility index (F) and Story Index (St)

Eo= C×F×St

S: A reduction factor to modify Eo index, which is based on the structural balance in both plan and elevation

T: A reduction factor to modify Eo index, which is graded by time-dependent deterioration

Table 5:
Evaluation of Seismic Capacity Index of Structure (Is)

Is < 0.3	There is high risk of collapsing
0.3 < Is <0.6	There is risk of collapsing
0.6 < Is	There is low risk of collapsing

A survey carried out by MEXT in April 2002 showed that public school buildings had not been satisfactorily retrofitted. It emerged from the 2002 survey that seismic assessment/ diagnosis was carried out on only 30% of buildings built based on the pre-1981 Old Seismic Resistant Design, and only about 45% of public primary and junior high school buildings had been retrofitted.

In this connection, a council called "Co-operators' Meeting for the Survey and Study of the Promotion of Earthquake-Resistant School Buildings" was established by MEXT in October 2002. The outcomes of the council's discussions were submitted to MEXT in April 2003 in a report entitled the "Promotion of Earthquake-Resistant School Buildings". Based on this report, the "Guidelines for the Promotion of Earthquake-Resistant School Buildings" was stipulated by MEXT in July 2003.

Chapter 1 of this guideline describes the basic concept of the "earthquake-resistant school building;" and Chapter 2 outlines the methods for devising earthquake-resistant promotion plans, the points to bear in mind, and the suggested methods for determining the urgency of earthquake resistance projects.

The basic principles pointed out in this guideline are:
(1) to prioritize earthquake resistant measures for school buildings at high risk of collapse or severe damage; (2) to implement seismic resistant capacity evaluation promptly; (3) to develop a plan for promoting earthquake resistance promptly; (4) to disclose the results of the seismic resistant capacity evaluation and the plans for promoting earthquake resistance; and (5) to check and take measures for the earthquake resistance of non-structural elements.
(http://www.nier.go.jp/shisetsu/pdf/e-taishinsuishin.pdf)

MEXT has been urging municipal governments, which are responsible for school buildings, to promote school building's retrofitting based on the above-mentioned guideline. In addition, as the following figure shows, MEXT has a subsidy system regarding public school buildings. In line with the Sichuan Earthquake in China in May 2008, MEXT has raised the subsidy rate for vulnerable school buildings (Is<0.3) from a half to two thirds in June 2008.

Table 6: Subsidy Rate for Public School Building

Type of Construction	Subsidy Rate from MEXT
New construction	1/2
Reconstruction	1/3, 1/2 (Is<0.3)
Renovation	1/3
Seismic Rehabilitation	1/3, 1/2 (Is<0.3)

Budget of fiscal 2008: 229 billion JPY

By utilizing the above-mentioned subsidy system, the retrofitting of school buildings has been implemented in Japan. The data shows the status of earthquake resistance on elementary and lower secondary public schools in Japan as of April 1 2008. Approximately 48,000 of school buildings, or 38% of school buildings were found lacking needed earthquake resistance or needed further assessment. Above all, 10,000 of these buildings were estimated to be at high risk of collapse in expected large scale earthquakes. A commitment was made to reinforce all of these buildings at high risk within 5 years. In addition, as mentioned, the subsidy rate for vulnerable school buildings has been raised in June 2008. Moreover, in order to accelerate the 5 years retrofitting program into 4 years, MEXT has added an additional national fund (114 billion JPY) to the regular budget of fiscal 2008 (115 billion JPY, total 229 billion JPY) in the supplementary budget of fiscal 2008 of Japanese government in October 2008.

Even though structural parts of school buildings such as columns, beams and walls are enough retrofitted, if non-structural members such as ceiling materials, various fixtures and furniture are not sufficiently retrofitted, these non-structural members may fall or topple when a major earthquake occurs. Children and evacuated local people can be killed or injured by these vulnerable non-structural members. Therefore, the retrofitting of non-structural members of school building is extremely important.

In order to urge municipalities to implement non-structural seismic retrofitting of school buildings, the National Institute for Educational Policy Research of Japan (NIER) published a reference book on non-structural seismic retrofitting of school building in December 2005.
The following case is an example in this reference book.
(Web: http://www.nier.go.jp/shisetsu/pdf/e-jirei.pdf)"

3. ISSUES OF RETROFIT WORKS

3.1 Technical Issues[iv]

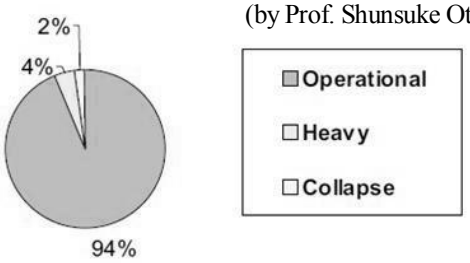
It should be noted that these countermeasures may not be the same from a country to another because the expected performance (minimum required strength and acceptable damage) of buildings varies from a country to another. Each country has different levels of (a) seismic risk, (b) hazard tolerance, (c) economic background, and (d) technical development (construction practices and materials).

Most building codes in the world explicitly or implicitly accept structural damage to occur in a building during strong earthquakes as long as the hazard to life is prevented. Indeed, many earthquakes caused such damage in the past. Then, what percentage of buildings suffered heavy damage in major earthquakes. The Architectural Institute of Japan (AIJ) collected damage statistics in Mexico City and Lazaro Cardenas after the 1985 Mexico Earthquake, Baguio after the 1990 Luzon, Philippines Earthquake, Erzincan after the 1992 Turkey Earthquake, and Kobe after the Hyogo-ken Nambu 1995 (Great Hanshi-Awaji) Earthquake. A heavily damaged area was first identified in each city, and the damage level of all buildings in the identified area was assessed by structural engineers and researchers.

Table 7: Damage Statistics from Major Earthquakes
(by Prof. Shunsuke Otani)

City, year of earthquake	Operational damage	Heavy damage	Collapse	Total
Mexico City, 1985	4,251(93.8%)	194(4.3%)	87(1.9%)	4,532
Lazaro Cardenas, Mexico, 1985	137(83.5%)	25(15.2%)	2(1.2%)	164
Baguio City, Philippines, 1990	138(76.2%)	34(18.8%)	9(5.0%)	181
Erzincan City, Turkey, 1992	328(77.4%)	68(16.8%)	28(6.6%)	424
Kobe (pre-1981 construction), 1995	1,186(79.4%)	149(10.0%)	158(10.6%)	1,493
Kobe (post-1982 construction), 1995	1,733(94.0%)	73(4.0%)	38(2.1%)	1,844

Figure 3: Damage Distribution of Mexico City
(by Prof. Shunsuke Otani)



From damage statistics, the importance of identifying the small percentage of those buildings possibly vulnerable in future earthquakes can be easily realized. Therefore a simple procedure is desirable to examine the vulnerability of all existing buildings in a region, spending a few hours at most for a building, and "screen out" the majority of safe buildings. A more detailed and sophisticated procedure, spending a few weeks, may be utilized to those buildings identified as vulnerable by the simple procedure.

In a screening procedure, for example, dimensions of columns and structural walls per floor areas may be used to roughly estimate lateral load resistance. The lateral load strength is not a single index to represent the safety of a building, but gives some idea if the structure has a sufficient capacity to resist earthquake motions by strength. Those buildings, identified as questionable by the simple procedure, must be analyzed by more sophisticated procedure

The following development and application of technology are needed to mitigate earthquake disaster from construction point of view: i.e.,

(a) Effective earthquake resistant building codes for new construction,
(b) Earthquake vulnerability assessment methods for existing buildings,
(c) Seismic strengthening technology for vulnerable buildings,
(d) Seismic damage evaluation methods for damaged buildings after an earthquake,
(e) Technology to repair damage for immediate occupancy, and
(f) Technology to rehabilitate damaged buildings for permanent use.

3.2 Socio-economic Issues

An examination of allocation of government resources, in terms of financial and human, for pre-disaster and post-disaster disaster programs reveals that more resources are devoted recovery than to disaster prevention. They commit a large amount of financial and human support after a disaster. This is particularly true for the international community. Disaster prevention programs attract little attention. However, because emergency operations take place after a disaster when many lives have already been lost, only few lives can be saved. In contrast, the implementation of disaster preventative measures can potentially save many more lives.

Hence, we must shift our done on seismic resistance and isolation technologies of high rise buildings, but little research is done on conventional houses. But over 80 % of total stock in the world is non-engineered. Because these unsafe buildings are occupied by humans, we cannot reduce disaster losses unless we improve the safety of non-engineered buildings (in case of Japan, wooden houses). However, they attract little attention and research funds. Similarly, when spending habits for new and existing houses are compared, people tend to spend generously for new houses but not as much for the maintenance. However, many more lives can be saved by improving the safety of existing houses.

Another essential aspect is cost reduction. There are several ways to achieve this, for instance, technological development and government subsidies. It is also necessary to train masons and carpenters on available techniques.

The political commitment is also crucial. The reason is that many individual house owners would pay to reinforce their houses if they understand the need; but not all house owners would. Everybody dies eventually. Considering this, the probability of death from an earthquake, which chance of occurrence is 40 percent in every 30 years, might seem negligible. Just like the fact that many smokers wouldn't stop smoking even if they are told to do so, not all individual house owners would

reinforce their houses.[v]

One of the key challenges is how to persuade the elderly who would not invest their money to improve their old houses. Another challenge is to make the housewives understand the importance and have priority in improving the seismic safety of houses.

4. RETROFIT EXAMPLES IN THE WORLD

This section shows four retrofitting examples in the world.

4.1 Example 1 (Houses in Nepal)

Nepal faces a variety of disaster risks owning both to its natural characteristics and human induced factors. Nepal has experienced several major earthquakes: The Bihar Earthquake in 1934 which measured 8.3 on the Richter scale killed 4,300 people, and destroyed 20% of all structures (Earthquake and Megacities Initiatives, 2005). Three earthquakes of similar size occurred in Kathmandu Valley in the 19th century: in 1810, 1833, and 1866. In 1988, there was another earthquake, which caused to loss of 709 lives (The National Society for Earthquake Technology NSET- Nepal).

United Nations Centre for Regional Development (UNCRD) has carried out a training project in Nepal in 2007. The training was organized with technical support from NSET to train practical measures that can be applied at the house level. 20 female members from target communities participated in the training. In the workshop, they learnt the basic science of earthquakes, importance of disaster risk reduction, and how to apply non-structural risk mitigation measures in their homes. For example, they visited several houses to learn practical ways of securing refrigerators and shelves by using brackets and props.

After the initial training, follow-up evaluation meetings were held with the participants. 19 participants reported that they have applied non-structural measurements in their homes within one or two weeks after the training by themselves (13 people) and/or with male members in the family (16 people), while there was one person who hired a handyman. 17 participants reported having talked about the training with relatives and/or friends, and 15 participants had showed their relatives and/or friends what they had done in their homes to secure their furniture.

Furthermore, 14 participants answered that they know relatives/friends who have implemented such non-structural risk reduction measures in their homes after observing their examples. The result showed that there was a strong potential for using women's network and communication to disseminate disaster risk reduction strategy. [vi]

Though the project has not aimed at retrofitting itself, fixture of nonstructural part of a house is recognized as the first step to raise awareness of community people, especially for housewives who must play an important role as decision makers for house maintenance. And this case study shows the communication network among housewives effectively works to disseminate the seismic measures for houses like fixture of furniture.



Fig 4. Household assessment of non-structural part (NSET)



Fig 5. A trainer of NSET secures furniture using anchors in a community participant's home in Kathmandu. (by UNCRD)

4.2 Example 2 (Schools of Indonesia)

Earthquakes in the past have exposed that vulnerability of school buildings is disproportionately high compared to the other infrastructures. For instance, in the 1999 Chi-Chi Earthquake, Taiwan 43 schools in Nantou and Taichung area were completely destroyed and a total of 700 schools nationwide were damaged to different extent. The 2001 Gujarat Earthquake in India caused damages to over 11,600 schools. The 2005 Kashmir earthquake resulted in collapse of 6,700 schools in North-West Frontier Province and 1,300 in Pakistan-administered Kashmir.[vii] Recently in May 2008, Wenchuan Earthquake in China killed about 7,000 students trapped in damaged school buildings. When an earthquake hit Spitak area of Northern Armenia during school hours in 1988, many children lost their lives due to collapse of school buildings. For example, 285 children out of 302 in total died at one school. This resulted in almost 2/3 of total deaths of 25,000 were children and adolescents.

UNCRD and the Center for Disaster Mitigation (CDM) of the Institute of Technology Bandung (ITB) conducted a collaborative project to reduce the vulnerability of existing school buildings in the corridor of the School Earthquake Safety Initiative (SESI) project. Two school buildings, SD Cirateun Kulon II and SD Padasuka II both in

Bandung County, were selected for this project due to the dire needs of improvement and severe deficiencies of earthquake resistant systems. The project included retrofitting and strengthening of school buildings, and other activities to improve school community preparedness regarding earthquake.



Fig 6. Retrofit work of School Building I (ITB)

Prior to conducting any physical work to the structure, the locations and building layouts were checked to ensure that the buildings could be retrofitted. The existing structures were investigated to determine the type and quality of materials used, as well as the existing lateral resisting system. Then, the retrofitting was designed based on the structural deficiencies/weak parts and their accessibilities, weighing in retrofit factors on buildings' life time, earthquake resistance capacity, their function, and appropriate retrofit strategy/ techniques. The design of retrofit strategy also considered factors of continuation of normal function, availability of materials and skilled construction workers, needs of upgrades for non structural components, and total costs.

The retrofitting project was first conducted at the school SD Cirateun Kulon II. The school buildings consisted of two buildings made of RC frames and masonry walls. Each building has four rooms. Based on results from survey and tests, structural analyses were performed on the existing structures using the actual material and structural components. Earthquake risks were introduced to the buildings by applying loads based on potential seismic risks and local soil conditions. The analysis showed that both buildings were considered likely to behave poorly under seismic loadings, thus required retrofitting. The physical works were then conducted to improve the structural quality and reduce the earthquake vulnerability.

Building I which was considered to have lower quality was retrofitted by adding adequate RC frames with mat footings. Anchorage was provided to connect walls with columns and beams. Building II which was in better condition was retrofitted using wire mesh for strengthening wall elements. Double tie beams were added adjacent to the existing one for better foundation system. For both structures, proper detailing was applied to roof truss systems, and repair was carried out for nonstructural elements such as doors/windows and ceilings. Finishing/cosmetic repair and improvement of sanitary facilities were also conducted for both structures.

4.3 Example 3 (Schools of Uzbekistan)

In Tashkent city, there are more than 360 schools. Nearly 20 % of school buildings have had deficiencies of different level at present. Preliminary analysis of seismic risk for Tashkent city showed that more than 25% of school buildings may be completely destroyed and 30% may be heavily damaged in case of design earthquake.

The buildings of schools in Tashkent are represented mainly by two construction systems: bricks and RC frame-panel consisting major portion of school building stock and a few buildings made up of from adobe bricks. Nearly 35 % of school buildings were constructed before Tashkent earthquake of 1966 for design intensity 7 by MSK scale. Since 1966, half of school buildings were constructed using assembled RC frames of IIS-04, which are inherently weak in seismic resistance. The weakness of this construction type was revealed Spitak (1988), Kairakkum earthquakes (1985) and also confirmed by through the engineering analysis of earthquake consequences.

Many school buildings in Tashkent are located in the zone with slumping soils, and as a result many buildings, both brick walled and frame panel type are likely to be damaged. The survey showed that typical structures used for school building in Tashkent basically consist of brick works up to 4 stories in old construction, and reinforced concrete frame-panel for the more recent buildings. Recurrent structure typologies for school buildings are categorized in the following three groups:

1. Mixed type of brickwork and reinforced concrete or wood reinforcing frame - year of construction '40s;
2. Brickwork structures, frequent typology used until '60s;
3. Frame-panel, widely used in the modern construction.

In order to establish an effective and recognizable linkage to the local professional practice in the Central Asian region, and to follow the standard analysis procedure, it is ensured that the characterization is in compliance with the previous study on the Risk Assessment of Tashkent city in the framework of IDNDR RADIUS project in 1990's.[viii]



Fig 7. Retrofit of RC panel school in Tashkent (UNCRD)

4.4 Example 4 (Buildings of China)

Ministry of Housing and Urban-Rural Development of People's Republic of China (MOHURD) has held several investigations on the disaster after the Wenchuan Earthquake. Upon the analysis and research, MOHURD has constituted "Technical Guide for Appraiser and Strengthening of Earthquake Affected Buildings" on July 23rd, 2008, and promptly issued "Seismic Technical Specification for Building Construction in Town and Village" on June 13th, 2008, and implemented on October 1st, 2008.

The Chinese "Standard for Classification of Seismic Protection of Building Constructions" GB50223 -2008 has been enacted on July 30th, 2008. It has been partially amended on the original "Standard for Classification of Seismic Protection of Building Constructions" GB50223 -2004. In addition, "Code for Seismic Design of Buildings" GB50011 -2008 (enacted on July 30th, 2008) has been amended on the original "Code for Seismic Design of Buildings" GB50011 -2001.

Wenchuan earthquake provided abundant experiences for seismic project constructions. In order to improve the capability of disaster area's reconstruction and Chinese project construction disaster-prevention, MOHURD and experts from relevant departments have researched and analyzed earthquake experiences, and have summed up the seismic engineering research results.

On the above amendments, MOHURD has adjusted some seismic standard, especially enhancing the public building seismic standard on secondary & primary schools and hospitals, extending the seismic prevention scope of public seismic buildings including retrofitting works. Besides, MOHURD has also amended the design code and criteria from the aspects of specific technologies.

To learn from Japan's accumulated seismic building technology and further promote the application of seismic technology, to improve the capability of earthquake and hazardous prevention, and to increase the technical level in China, Financing & Foreign Affairs Dept. of MOHURD and Japan International Cooperation Agency (JICA) has reached an agreement on the "China-Japan Seismic Training Program" on May 12th, 2009. This program will last 3 years and be fully supported by Ministry of Land, Infrastructure, Transport and Tourism (MLIT) of Japan.

The International Institute of Seismology and Earthquake Engineering (IISEE) of the Building Research Institute (BRI), Tsukuba, Japan is the implementing agency of the training on assessment, retrofit and design for seismic building since 2009.

5. CONCLUSIONS

The Japanese government has established a law to promote seismic retrofitting of buildings immediately after the Great Hanshin-Awaji Earthquake in 1995. This paper evaluates the policies related to the Retrofit Promotion Act. The data shows that the policy target of seismic safety of buildings (90% of buildings follow the 1981 seismic code) will be achieved in 2015-2018 if the current trends of improvement will be continued. In the field of school buildings, national government supports the school retrofit works that are carried out by the local governments, using the guideline for school retrofit.

However, there are still significant issues to make all houses safe. One of the key challenges is how to persuade the elderly who would not invest their money to improve their old houses. Another challenge is to make the housewives understand the importance and have priority in improving the seismic safety of houses.

Currently many efforts are taken by the Japanese local governments, such as holding seminars for communities, preparing financial support schemes, providing consultancy for seismic assessment and making earthquake hazard maps. This paper also provides comments on the improvement of the current policies for promoting seismic retrofit based on some international experiences of house and building retrofit. Some international cases will help to develop an effective Japanese policy for promoting retrofit, such as the case of Nepal shows the role of females to disseminate the seismic safety of non-structural part of houses.

The Japanese experiences on seismic retrofit will be able to contribute to the disaster risk reduction in the other seismic-prone countries in the world. The lessons from Kobe and lessons from all over the world should be disseminated to find solutions towards challenges to promote policies and actions of seismic assessment and retrofitting.

References:

[i] Shunsuke Otani (2008), "Another Problem, Seismic Protection of Existing buildings": 28 Nov. 2008, International Symposium on Earthquake Safe Housing, Proceedings, National Graduate Institute for Policy Studies (GRIPS), Building Research Institute (BRI) and United Nations Centre for Regional Development (UNCRD)

[ii] The Ministry of Land, Infrastructure, Transport and Tourism (MLIT), Japan (2009), Promotion of assessment and retrofitting, power-point presentation, July 2009, Housing Bureau, MLIT

[iii] Takayuki Nakamura (2009), "From Model Projects to Country -wide Intervention", School Earthquake Safety Initiative (SESI); Reducing Vulnerability of School Children to Earthquake, p.68-79, UNCRD Disaster management Planning Hyogo Office

[iv] Shunsuke Otani (2008), GRIPS, BRI, UNCRD Proceedings of International Symposium 2008, p.40-47

[v] Kenji Okazaki, Professor of National Graduate School for Policy Studies (GRIPS), (2007), "Culture of Disaster Prevention in the Context of housing and urbanization", Proceedings of UNCRD 2007 international symposium, p.45-47

[vi] UNCRD, Disaster Management Planning Hyogo Office, Yoko Saito, Edward Sumoto, et al. (2008), "Gender Perspectives in Community Based Disaster Management (CBDM)"

[vii] UNCRD Disaster Management Planning Hyogo Office, Jishnu Subedi, Ayako Fujieda (2007), "School Earthquake Safety Initiative (SESI); Reducing Vulnerability of School Children to Earthquake"

[viii] UNCRD Disaster Management Planning Hyogo office, Shoichi Ando, Jishnu Subedi, Hayato Nakamura et al. (2009), "Reducing Vulnerability of School Children to Earthquake"

8CUEE CONFERENCE PROCEEDINGS
8th International Conference on Urban Earthquake Engineering
March 7-8, 2011, Tokyo Institute of Technology, Tokyo, Japan

SEISMIC VULNERABILITY INDEX METHOD: ALGERIAN CASE STUDIES

Mahmoud Bensaibi[1], Fouzia Djaalali[2], Fatma I. Belheouane[3], Omar Amellal[4], and Nacim Yousfi[5]

1) Professor, Department of Civil Engineering, University Saad Dahleb, Blida, Algeria
2) Lecturer, Department of Civil Engineering, University M'Hamed Bougara, Boumerdes, Algeria
3) Lecturer, Department of Civil Engineering, University Saad Dahleb, Blida, Algeria
4) Research Student, Department of Civil Engineering, University Saad Dahleb, Blida, Algeria
5) Research Student, Department of Civil Engineering, University Saad Dahleb, Blida, Algeria
bensaibim@yahoo.co.uk, djaalaliben@yahoo.fr, fimenebb@yahoo.fr, omar_tipasien@hotmail.com, nacim_yousfi@hotmail.fr

Abstract: The North of Algeria is an area prone to seismicity. Buildings located in this area, are either made of masonry, reinforced concrete, steel or combined (masonry and steel). The seismic feedback experience showed a great disparity in the behaviour of such structures as a regard to seismic action. Within this paper, an assessment of these structures, using the "Vulnerability Index" method is presented. This method was developed in order to be used by engineers and to allow a good classification and description of the "Seismic Quality" of such structures, by considering numbers of structural and non structural parameters. A technical data sheet and an associated developed calculating computer program named Vulnerability Index Program (VIP) using "Delphi" have been used and validated to get the structural and non structural parameters as well as the vulnerability index to establish their classification. The results show that the established classification confirmed what has been observed in situ.

1. INTRODUCTION

Buildings made from masonry, reinforced concrete and from masonry and steel combined together are the most significant structures found in the Algerian cities, located along the North band, an area prone to seismicity.

Such structures have known consequent damages as a result of the latest earthquakes that stroke many north regions of Algeria such as the 1999 earthquake which hit the city of Ain-Temouchent and 2003 which hit the city of Boumerdes. Thus it is important to quantify the seismic vulnerability of these constructions in order to prevent heavy damages.

There are several tools to estimate the seismic vulnerability functions, it depends mainly of the constituent material of the structure, the purpose of their uses and the typology. To provide these functions several methods do exist.

The two main methods considering vulnerability functions are the global approach method named HAZUS, RISK-UE (2003) or RADIUS (Oyo 1999), and the more specific one named Push-over and Time History Analysis, requesting skilled persons.

However an intermediate method named "Vulnerability Index Method" can be considered to be used by engineers to give a realistic estimation of the seismic quality of structures. This method has been considered in this present work.

One of the first studies carried out on vulnerability index was initiated by the GNDT (Group of National Defense against earthquake) (Corsanego and Petrini 1994), named as the methodology of level II. This method is based upon observations and given data relative to the constructions. The structural and non structural parameters playing a significant role in the seismic response of the structure should belong to one of the four vulnerability classes (A, B, C or D) described by (Benedetti and Petrini 1984) and (Benedetti et al. 1988). This method was used in a study undertaken in the south of Italy. It has allowed a classification of constructions in vulnerability classes with a development of a reinforcement methodology for these constructions (Parisi and Chesi 2006). This method was modified in order to be applied to confined masonry buildings in southern Europe (Franch et al. 2008). Based on the same principles, the group of "vulnerability of existing buildings" of the AFPS (Jacquet and Souloumiac, 1999) has written a guide giving the evaluation of the seismic

vulnerability of buildings. A study on vulnerability of existing buildings was done by Lang (2002) and Yépez et al. (1996). The vulnerability of the city of Catania was investigated by Lagomarsino (Lagomarsino and Giovinazzi 2006).

In Algeria, work relating to the estimate of the constructions vulnerability using vulnerability index was undertaken using the Algerian seismic code (CGS 2003). These studies allowed the classification of buildings in vulnerability class translating its seismic quality (Bensaibi et al. 2003), (Boukri and Bensaibi 2006), (Belheouane 2006), (Boukri and Bensaibi 2007), (Amellal 2008), (Boukri and Bensaibi 2008) (Djaalali and Bensaibi 2009) and (Yousfi 2010).

2. PARAMETERS OF THE DEVELOPED VULNERABILITY INDEX METHOD

This approach considers numbers of structural and non structural parameters. These parameters have an influence on the seismic vulnerability of the structures. These parameters are determined by post-seismic observations and seismic experience feedbacks. The parameters taken into account are chosen for each kind of structure.

2.1 Parameters for Masonry Structure

The considered parameters are as follow:

1) Total shear resistance of walls, 2) Plan regularity, 3) Elevation regularity , 4) Walls connection, 5) Walls type, 6) Floor, 7) Roof, 8) Soil conditions, 9) Pounding effect, 10) Modifications, 11) Details, 12) Maintenance conditions

2.2 Parameters for Reinforced Concrete Structure

For reinforced concrete (RC) structure, the considered parameters are as follow:

1) Frame system, 2) Quality of the Frame system, 3) Seismic capacity, 4) Type of soil, 5) Roof , 6) Plan Regularity, 7) Elevation Regularity, 8) Quality of the nodes, 9) Short column, 10) Details, 11) Maintenance conditions, 12) Modifications, 13) Pounding effect, 14) Ground conditions.

2.3 Parameters for Steel Structure

For steel structure, the considered parameters are set as follow:

1) Ductility, 2) Bearing capacity, 3) Assemblage, 4) Maintenance conditions, 5) Type of soils, 6) Floor, 7) Buckling, 8) Plan regularity, 9) Modifications, 10) Elevation regularity, 11) Pounding effect, 12) Ground conditions, 13) Roof, 14. Details.

2.4 Parameters for Combined Masonry and Steel Structure

For this kind of structure, the considered parameters are:

1) Walls connection, 2) Seismic capacity, 3) Type of soils, 4) Ductility, 5) Assemblage, 6) Floor, 7) Modifications, 8) Plan regularity, 9) Elevation regularity, 10) Maintenance conditions, 11) Ground conditions, 12) Pounding effect , 13) Roof, 14) Details.

3. QUANTIFICATION OF EACH PARAMETER

Weighting factors for each parameter are proposed on table 1, 2, 3 and 4. These factors are determined on a basis of a statistical data containing constructions damaged by different earthquakes (Ain Temouchent (1999) and Boumerdes (2003)). The considered parameter can take only one factor.

For masonry construction, each parameter considered can belong to one of the four defined categories C1, C2, C3 and C4. These categories are declined as follows:

C1 expresses a parameter inducing a good behaviour of the structure during an earthquake,

C4, expresses a parameter inducing a bad behaviour of the structure during an earthquake,

C2 and C3 expresses an intermediate behaviour of the structure during an earthquake.

For the other kind of structure the intermediate behaviour is represented by only one category i.e. (C2).

For each parameter and each category considered, a coefficient (k) is identified expressing its seismic quality.

The “Details” parameter was specified as follows: studwork, dividing walls, balconies, railing, cornices, chimneys, ventilation space, electrical network, gas network, water network and sewage network.

Table 1 Weighting Factors of Vulnerability Index Evaluation for Masonry Structure

N°	Parameter	Categories/k			
		C1	C2	C3	C4
1	Total shear resistance of walls	0	0.05	0.12	0.21
2	Plan regularity	0	0.01	0.04	0.07
3	Elevation regularity	0	0.01	0.04	0.07
4	Walls connection	0	0.03	0.07	0.10
5	Walls type	0	0.01	0.03	0.05
6	Floor	0	0.01	0.03	0.05
7	Roof	0	0.01	0.03	0.05
8	Soil conditions	0	0.02	0.06	0.10
9	Pounding effect	0	0.01	0.04	0.07
10	Modifications	0	0.01	0.04	0.07
11	Details	0	0.00	0.02	0.03
12	Maintenance conditions	0	0.03	0.08	0.13

Table 2 Weighting Factors of Vulnerability Index Evaluation for RC Structure

N°	Parameter	Categories/k		
		C1	C2	C3
1	Frame system	0.25	1.25	2.25
2	Quality of the Frame system	0.25	0.50	0.75
3	Seismic capacity	0.00	0.25	0.50
4	Type of soil	0.25	0.50	0.75
5	Horizontal diaphragm	0.25	0.50	0.75
6	Plan Regularity	0.25	0.50	0.75
7	Elevation Regularity	0.25	0.75	1.75
8	Quality of the nodes	0.25	0.50	0.75
9	Short column	0.25	0.50	0.75
10	Details	0.25	0.50	0.75
11	Maintenance conditions	0.25	0.75	1.25
12	Modifications	0.25	0.50	0.75
13	Pounding effect	0.25	0.50	0.75
14	Ground conditions	0.25	0.50	0.75

Table 3 Weighting Factors of Vulnerability Index Evaluation for Steel Structure

N°	Parameter	Categories/k		
		C1	C2	C3
1	Ductility	0.00	1.5	2.5
2	Bearing capacity	0.25	1.25	2.00
3	Assemblage	0.25	1.5	2.5
4	Maintenance conditions	0.25	1.00	1.5
5	Type of soil	0.50	0.75	1.00
6	Floor	0.50	0.75	1.00
7	Buckling	0.50	1.00	1.5
8	Plan regularity	0.50	0.75	1.00
9	Modifications	0.50	0.75	1.00
10	Elevation regularity	0.50	0.75	1.00
11	Pounding effect	0.50	0.75	1.00
12	Ground conditions	0.50	0.75	1.00
13	Roof	0.50	0.75	1.00
14	Details	0.50	0.75	1.00

Table 4 Weighting Factors of Vulnerability Index Evaluation for Combined Masonry and Steel Structure

N°	Parameter	Categories/k		
		C1	C2	C3
1	Walls connection	0.00	0.12	0.20
2	Seismic capacity	0.00	0.09	0.12
3	Type of soils	0.01	0.08	0.09
4	Ductility	0.01	0.07	0.08
5	Assemblage	0.01	0.04	0.06
6	Floor	0.01	0.04	0.05
7	Modifications	0.01	0.04	0.05
8	Plan regularity	0.01	0.04	0.05
9	Elevation regularity	0.01	0.04	0.05
10	Maintenance conditions	0.01	0.04	0.05
11	Ground conditions	0.01	0.04	0.05
12	Pounding effect	0.01	0.04	0.05
13	Roof	0.01	0.04	0.05
14	Details	0.01	0.04	0.05

Some parameters need calculation and some others are related to the in situ observation.

4. VULNERABILITY INDEX AND CLASSIFICATION

The vulnerability index, VI, of a construction is expressed according to the formula (1):

$$VI = \sum_{i=1}^{n} k_i \qquad (1)$$

According to the value obtained for the vulnerability index, three vulnerability classes Green, Orange and Red are proposed for each category of construction (table 5, 6, 7 and 8).

Table 5 Vulnerability Index Classes for Masonry Structure

Class	Green	Orange	Red
VI	0 - 0.20	0.20 - 0.60	0.60 - 1

Table 6 Vulnerability Index Classes for RC Structure

Class	Green	Orange	Red
VI	3.25 - 6.25	6.25 - 10.25	10.25 - 13.25

Table 7 Vulnerability Index Classes for Steel Structure

Class	Green	Orange	Red
VI	5.75 - 9.5	9.5 - 19	16 - 19

Table 8 Vulnerability Index Classes for Combined Masonry and Steel Structure

Class	Green	Orange	Red
VI	0.12 - 0.44	0.44 - 0.88	0.88 - 1

The first class associated to the green color classifies the construction as resistant with no requirement to any repairs.

The second class associated to the orange color classifies the construction as moderately resistant requiring reinforcement.

The third class associated to the red color classifies the construction to be a construction with low resistance requiring demolition or significant strengthening.

5. ELABORATED CHART

In situ observations on structures are important information required to assess the vulnerability of structures. An investigation chart for a survey was elaborated. The chart contains:

a) General data , b) Geometric characteristics, c) Information on the structural system, d) Information on the ground, e) Details on the non structural elements, f) General maintenance conditions.

6. DEVELOPED PROGRAM

A program called Vulnerability Index Program "VIP" using Delphi was elaborated providing the vulnerability index values for structures. It uses the elaborated chart in order to estimate the coefficient of the different parameters and classify the structures. The front page of the program is given on figure 1.

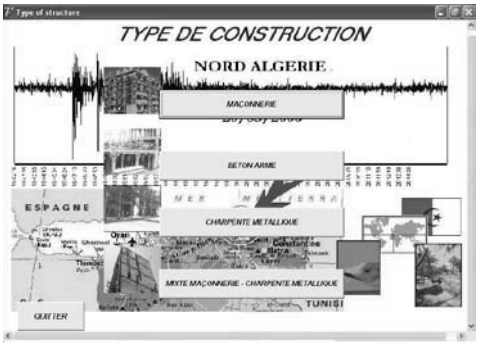


Figure 1 Front Page of the VIP

On the figure 2, a displaying window for masonry structure is shown as a sample.

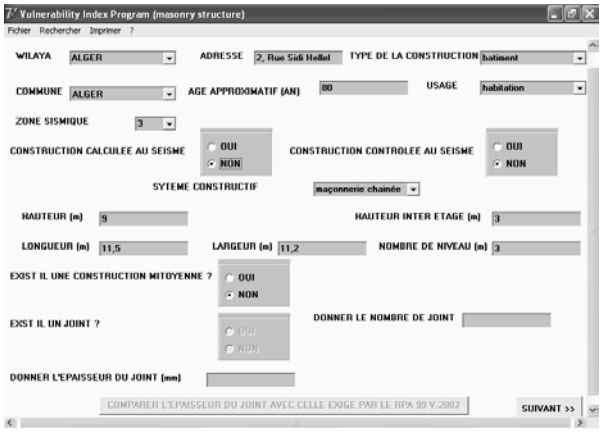


Figure 2 VIP Page for Masonry Structure

7. APPLICATION

Several examples have been treated by the developed program. Here in, are three case studies presented as an example.

7.1 First Case Study

It is a Zinc production manufacture in steel material, built in 1949 and located in the West part of Algeria. The following figures (3, 4 and 5) show the damage undergone by this structure.

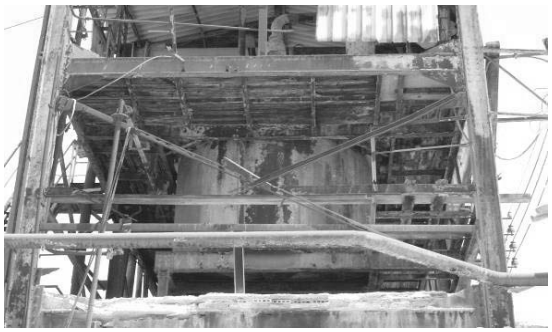


Figure 3 Damage in the Bracing System



Figure 4 Corrosion of Columns



Figure 5 Damage in Beams and Floors

The results given by the program are as follow (table 9):

Table 9 Manufacture Parameters Vulnerability

N°	Parameters	Category	k
1	Ductility	C2	1.5
2	Bearing capacity	C3	2.00
3	Assemblage	C3	2.5
4	Maintenance conditions	C3	1.5
5	Type of soil	C2	0.75
6	Floor	C3	1
7	Buckling	C3	1.5
8	Plan regularity	C3	1
9	Modifications	C1	0.5
10	Elevation regularity	C3	1
11	Pounding effect	C2	0.75
12	Ground conditions	C1	0.5
13	Roof	C2	0.75
14	Details	C3	1

A vulnerability index of 16.25 was found, this indicates that the structure belong to the Red class.

The conclusions provided by the Structural Engineering Control (CTC: official organization in charge of control in Algeria) suggest demolition and the reconstruction according the latest standards.

So, the two conclusions are in adequacy.

7.2 Second Case Study

It is a building in RC located in the city of Blida (a town near Algiers). It has four floors, each one with two dwellings.

An in situ expertise and a data process gave the results presented in table 10.

Table 10 Building in RC Parameters Vulnerability

N°	Parameters	Category	k
1	Walls connection	C1	0.00
2	Seismic capacity	C1	0.00
3	Type of soils	C1	0.01
4	Ductility	C1	0.01
5	Assemblage	C2	0.04
6	Floor	C1	0.01
7	Modifications	C1	0.01
8	Plan regularity	C2	0.04
9	Elevation regularity	C2	0.04
10	Maintenance conditions	C1	0.01
11	Ground conditions	C3	0.05
12	Pounding effect	C1	0.01
13	Roof	C1	0.01
14	Details	C1	0.01

This gives a vulnerability index of 6.50, it means this construction is classified Orange.



Figure 6 Damage in a Node and Short Columns

This result is in adequacy with what have been observed on site (transformation of the balconies into rooms and presence of short columns and node degradation, see figure 6).

7.3 Third Case Study

It is a pavilion in combined materials (masonry and steel) located in Algiers, with a ground floor and two levels. The construction is built on an inclined ground (see figure 7).



Figure 7 Front View of the Pavilion

The VIP gives the following results (table 11):

Table 11 Pavilion Parameters Vulnerability

N°	Parameters	Category	k
1	Frame system	C1	0.25
2	Quality of the Frame system	C1	0.25
3	Seismic capacity	C3	0.50
4	Type of soil	C3	0.75
5	Horizontal diaphragm	C1	0.25
6	Plan Regularity	C1	0.25
7	Elevation Regularity	C1	0.25
8	Quality of the nodes	C2	0.50
9	Short column	C3	0.75
10	Details	C1	0.25
11	Maintenance condition	C2	0.75
12	Modifications	C3	0.75
13	Pounding effect	C3	0.75
14	Soil conditions	C1	0.25

The program gives VI = 0.25, so the structure is classified Green.

This result is in adequacy with the conclusion of an official organism in Algeria witch classify this construction as Green level 1 i.e. a construction with very good resistance.

8. CONCLUSIONS

A vulnerability index method for different type of structures has been developed and presented in this study. Even though the method is an intermediate one, it gives reasonable results regarding the influence of the different parameters on the seismic behaviour of the structure.

A classification has been established according to the damage undergone by the structures. The results from this classification are in accordance with the one done in situ. As a result, this classification can be used by engineers to reduce seismic risk and casualties in case of an earthquake.

Acknowledgements:

The authors acknowledge Mr. B. Kdroussi, director of CTC Tlemcen for his kindly help.

References:

Risk-UE (2003), "An Advanced Approach to Earthquake Risks Scenarios with to Applications Different European Towns, WP4: Vulnerability of Current Buildings," Evk4-ct-2000-00014.

OYO Corp. (1998), "RADIUS (Risk Assessment Tools for Diagnosis of Urban Areas Against Seismic Disaster)," IDNDR – United Nation.

Corsanego, A. and Petrini, V. (1994), "Evaluation Criteria of Seismic Vulnerability of Existing National Building Patrimony on the Territory," *Seismic Engineering*, 1, 16-24.

Benedetti, D. and Petrini, V. (1984), "On the Seismic Vulnerability of Masonry Buildings: Proposal of Year Procedure Evaluation," *The Industry of Construction*, 18, 66-78.

Benedetti, D., Benzoni, G. and Parisi M. A. (1988), "Seismic Vulnerability and Risk Evaluation for Old Urban Nuclei," *Earthquake Engineering and Structural Dynamics*, 16, 183-201.

Parisi, M.A. and Chesi, C. (2006), "Experimenting Seismic Vulnerability Assessment and Strengthening in a Masonry Village," *1st European Conference on Earthquake Engineering and Seismology*, Paper No. 1429, Geneva, Switzerland

Franch, K.A.G., Morbelli, G.M.G., Inostroza M.A.A. and Gori, R.E. (2008), "A Seismic Vulnerability Index for Confined Masonry Shear Wall Buildings and a Relationship with the Damage," *Engineering Structures* , 30, 2605–2612.

Jacquet, G. and Souloumiac, R. (1999), "Evaluation of the Vulnerability of the Existing Buildings," In: *Proceedings of the Fifth National Conference AFPS*, 267-273, Cachan, France.

Lang, K. (2002), "Seismic Vulnerability of Existing Buildings," *Doctorate thesis*, Swiss Federal institute of technology, Zurich, Swiss.

Yépez, F., Barbat, A.H. and Canas, J.A. (1996), "A Method to Perform Computer Simulations of Damage in Buildings for Seismic Risk Evaluation," *Faculty of Civil Engineering*, Technical University of Catalonia, Barcelona, Spain.

Lagomarsino, S. and Giovinazzi, S. (2006), "Macroseismic and Mechanical Models for the Vulnerability and Damage Assessment of Current Buildings," *Bull Earthquake Eng*, 4, 415-443.

CGS (2003), "Réglement Parasismique Algérien Version 2003 (RPA99 version 2003) ," Algeria.

Bensaibi, M., Djaalali, F. and Boukri, M. (2003), "Vulnérabilité Sismique des Bâtiments en Maçonnerie de la Ville d'Alger," *Actes du Colloque International Risque, Vulnérabilité et Fiabilité dans la Construction Vers une Réduction des Désastres*, Algiers, Algeria, 2, 406-415.

Boukri, M. and Bensaibi, M. (2006), "Seismic Vulnerability of Masonry Buildings of Algiers", *1st European Conference on Earthquake Engineering and Seismology (joint event of the 13th ECEE & 30th General Assembly of the ESC)*, Paper No. 507 Geneva, Switzerland.

Belheouane, F.I. (2006), "Détermination de l'Indice de Vulnérabilité des Constructions en Béton Armé," *Master thesis*, University Saad Dahleb, Blida, Algeria.

Boukri, M. and Bensaibi, M. (2007), "Indice de Vulnérabilité des Bâtiments en Maçonnerie de la Ville d'Alger," *Actes du VIIème Colloque National AFPS*, Paper No. 181, Paris, France.

Amellal, O. (2008), "Détermination de l'Indice de Vulnérabilité des Constructions en Charpente Métallique," *Master thesis*, University Saad Dahleb, Blida, Algeria.

Boukri, M. and Bensaibi, M. (2008), "Vulnerability Index of Algiers Masonry Buildings," *14th World Conference on Earthquake Engineering*, Paper No. 0118, Beijing, China.

Djaalali, F. and Bensaibi, M. (2009), "Vulnérabilité Sismiques des Structures de Maçonnerie en Algérie," *9ème Congrès de Méchanique*, 1, pp. 22-24, Marrakech, Morocco.

Yousfi, N. (2010), "Estimation de l'Indice de Vulnérabilité de Structures," *Master thesis*, University Saad Dahleb, Blida, Algeria.

JOINT CONFERENCE PROCEEDINGS
8th International Conference on Urban Earthquake Engineering
March 7-8, 2011, Tokyo Institute of Technology, Tokyo, Japan

REVITALIZATION OF CIRCULAR CONCRETE COLUMNS BY HIGH PERFORMANCE FERROCEMENT

Ivy F.Y. Ho[1] and Eddie S.S. Lam[2]

1) PhD student, Dept. of Civil & Structural Engineering, The Hong Kong Polytechnic University, Hong Kong
2) Associate Professor, Dept. of Civil & Structural Engineering, The Hong Kong Polytechnic University, Hong Kong
ivy.ho@polyu.edu.hk, cesslam@inet.polyu.edu.hk

Abstract: Hong Kong is within the Eurasian Plate with moderate seismic risk. According to the Chinese seismic design code (GB 50011-2001), Hong Kong is an area with seismic intensity 7.5. However, reinforced concrete buildings in Hong Kong are traditionally designed without seismic provision and detailed with low volumetric ratio of transverse reinforcement. These columns fall short of providing sufficient seismic resistance. It is the aim of this study to investigate the use of high performance ferrocement ("HPF") to strengthen reinforced concrete columns detailed with large spacing of transverse reinforcement. Totally 19 full-scale circular reinforced concrete columns were prepared and tested to failure under axial compression. 8 of them were casted in Oct 2009 and tested between Dec 2009 and Jan 2010. The results were reported in the preceding conference of CUEE (Ho and Lam 2010). 11 of them were subsequently casted in July 2010 and tested in Aug 2010 or Jan 2011. In the present study, HPF is applied circumferentially on 8 reinforced concrete columns and 4 plain concrete columns to study the confinement action provided by HPF comprises different mesh density and different rendering materials. It is observed that specimens detailed with volumetric ratios of transverse reinforcement (ρ_s) of 0.230% and strengthened by HPF can achieve a load carrying capacity at 23.3% higher than specimen detailed with ρ_s of 0.918%. In addition, significant increase in peak strength from 29.8-58.7% is observed in plain concrete specimens confined with HPF. These show that HPF is effective to upgrade existing column detailed with low volumetric ratio of transverse reinforcement. Test results also show that compressive strength of confined concrete increases with tensile strength of HPF and better confinement can be provided by HPF using epoxy based rendering material instead of polymer modified cementitious based rendering material or cement-sand screeding. Further study is necessary to fully understand the correlation between overall confinement action provided by HPF and confined compressive strength of concrete in the presence of transverse reinforcement.

1. INTRODUCTION

Although there is no known active fault within the territories of Hong Kong and the risk to have a major tremor is low, Hong Kong is a region with moderate seismic risk with seismic intensity 7.5 ("GB 50011-2001"). Structural condition of our buildings becomes a popular local issue after the collapse of a 55-year-old five storey building and a recently occurred earthquake which can be felt locally with epicenter located in Deep Bay in Shenzhen.

Most buildings in Hong Kong were designed without seismic consideration (Lam et al. 2002) since it is not required by the design code currently in force (i.e. Code of Practice for Structural Use of Concrete 2004 ("CoP2004")). When comparing CoP2004 with its predecessor Code of Practice for Structural Use of Concrete 1987 ("CoP1987"), a few concepts on seismic design have been implemented into CoP2004. For instance, in the provisions on detailing of columns in critical region, CoP2004 takes into account the axial load factor to reduce the maximum allowable spacing of transverse reinforcement. As it is common to find columns with low depth-to-height ratio (i.e. short columns), spacing of transverse reinforcement at critical region is usually applied to the whole column for ease of construction. Thus, columns designed to CoP2004 are usually detailed with high volumetric ratio of transverse reinforcement when compared with those designed to CoP1987. In fact, CoP2004 has reduced the allowable maximum spacing of transverse reinforcement to 1/4 of the preceding requirement specified in CoP1987.

Columns with low volumetric ratio of transverse reinforcement are less sustainable in resisting seismic motion as evidenced for instance in Kobe earthquake 1995, Chi-Chi earthquake in 1999 and Wenchuan earthquake in 2008. Besides, it is well accepted that compressive strength of concrete can be significantly enhanced by proper confinement (Richart et al. 1928, Balmer 1949, Popovics 1973, Sheikh and Uzumeri 1980, Ahmad and Shah 1982, Mander 1983, Mander et al. 1988 and Li 1994). Columns designed to CoP2004 have higher load carrying capacity than columns designed to CoP1987. To strengthen existing columns to meet the current standard, it is necessary to provide additional confinement to existing columns in order to enhance their load carrying capacity. It is the objective of this study to use high performance ferrocement ("HPF") for providing additional confinement to existing columns

detailed to CoP1987.

2. STRENGTHENING USING FERROCEMENT

Many different materials for strengthening of columns were proposed and studied by researchers including, *inter alia*, Ersoy et al. (1993) on the application of steel and concrete jacketing, Wu et al. (2006) on the use of steel/FRP jacketing, and Harries et al (2006) on the use of CFRP jacketing. Study carried out by Han et al. (2006) reveals that it is necessary to provide additional fire protection to steel/FRP jackets in order to avoid rapid reduction in strength at elevated temperature. Similar conclusion is drawn by Tadeu and Branco (2000) on the bonding material used in externally bonded steel plate. In Hong Kong, materials for building works are subjected to stringent requirement on fire rating. Considering the need for strengthening materials to have promising fire resistance, ferrocement and HPF are chosen in this study. HPF has compatible fire resistance as concrete (Williamson and Fisher 1983) and can provide external protection to concrete columns under fire (Kaushik et al. 1996).

Ferrocement can be regarded as a kind of thin reinforced concrete structure. It was extensively used in manufacturing fishing boats in the last century (Abercrombie 1978). Traditionally, it comprises of cementitious based rendering material embedded with multiple layers of closely spaced small-diameter wire mesh. It is recommended to use rendering material with small particle size since large particle may not be able to pass though the closely spaced wire mesh and thus adversely affect the structural integrity and density of ferrocement (ACI 549.1R-93 and Naaman 2000). Besides, workability of rendering material should also be taken into account when designed to be used vertically. Detailed description of ferrocement is referred to publications of Shah et al. (1986), ACI 549.1R-93, Naaman (2000) and CECS 242:2008 (a technical specification in China).

On the subject of strengthening reinforced concrete columns, ferrocement has been used to enhance both ductility and load carrying capacity of columns (卜良桃 2007, Kondraivendhan and Pradhan 2009, Jiang et al. 2009, Kim and Choi 2010). Lim et al. (2000) studied the structural improvement of T-beams strengthened by ferrocement. Cao et al. (2007) studied the use of HPF comprises of high strength steel wire mesh and polymer based rendering material for strengthening beam-column joints. In another paper presented in this conference titled "Reinforced concrete beam-column joint strengthened by HPF jacket with diagonal reinforcements", beam-column joints are strengthened by ferrocement jacket with diagonal reinforcements. All the above have shown that HPF is an effective material for revitalization of existing buildings.

The significant of this study is to quantify the confinement action provided by HPF with two different densities of wire mesh and different rendering materials.

3. THE SPECIMENS

Totally 19 specimens were prepared using Grade C30/20 ready mixed concrete. 8 of them were casted in 2009 ("Group 1") and 11 of them were casted in 2010 ("Group 2"). Group 1 consists of specimens TPC1, TA300C-1, TB75C-1, TB300C, TA300CS3, TA300SD1-1, TA300SD3-1 and TA300ST3-1. They were tested to failure under axial compression in Dec 2009 and Jan 2010. The test results were reported in the preceding conference of CUEE (Ho and Lam 2010). Group 2 consists of specimens TPC2, TA300C-2, TB75C-2, T0SD1, T0SD3, T0ST1, T0ST3, TA300SD1-2, TA300SD3-2, TA300ST1 and TA300ST3-2. They were tested in Aug 2010 or Jan 2011.

5 combinations of HPF consisting of 2 types of mesh density and 3 types of rendering materials are considered. 4 parameters are studied includes (i) angle of hooks, (ii) spacing of transverse reinforcement, (iii) tensile strength of rendering materials and (iv) mesh densities. Rendering materials include cement-sand screeding, polymer modified cementitious based repair mortar and epoxy based repair mortar (denoted as "CS", "PMC" and "EM" respectively in the tables).

All specimens are in full-scale of 350mm diameter and 980mm height with concrete cover of 25mm. Material properties of the specimens are summarized in Table 1. 28-day strength and young modulus of concrete are obtained by carrying out compression test on three 100mm cubes and three 100mm x 150mm cylinders respectively. Material properties of reinforcement are obtained by coupon test on a pair of steel bars.

Table 1 Material properties

Materials	Properties	Group 1	Group 2
Concrete	Density (kg/m^3)	2315	2395
	28-day strength (MPa)	41.7	57.1
	Young modulus (GPa)	25.8	23.1
Main reinforcement	Yield Strength (MPa)	522.9	617.5
	Young modulus (GPa)	218.2	218.6
Transverse reinforcement	Yield Strength (MPa)	523.0	452.2
	Young modulus (GPa)	217.7	213.5

Detailed information of the specimens is listed in Tables 2A and 2B. Specimen TPC1 and TPC2 are control specimens made of plain concrete. Specimens TA300C-1 and TA300C-2 are detailed in accordance with CoP 1987 whereas specimens TB75C-1 and TB75C-2 are detailed to CoP 2004. Specimens strengthened with HPF are designed in the absence of seismic provisions and provided with 8T25 (or 4% main reinforcement ratio) as the main reinforcement. Two volumetric ratios of transverse reinforcement (ρ_s) at 0.230% and 0.918% are considered in accordance with the design provisions of CoP1987 and CoP2004 respectively.

Specimens TA300CS3, TA300SD1-1, TA300SD3-1, TA300ST3-1, TA300ST1, TA300ST3-2, TA300SD1-2 and TA300SD3-2 are detailed to CoP1987 and strengthened with

different types of HPF as per Tables 2A and 2B. Specimen TA300CS3 is detailed to CoP1987, strengthened with traditional ferrocement and served as a control specimen to compare with the result of those strengthened with HPF. These 9 specimens were used to study the confinement action induced by transverse reinforcement together with ferrocement or HPF.

Specimens TA0ST1, TA0ST3, TA0SD1 and TA0SD3 are plain concrete specimens strengthened with different types of HPF as detailed in Table 2. These 4 specimens are used to study the confinement action induced by HPF.

Table 2A Basic properties of specimens – Group 1

Specimen	Transverse reinforcement (hook)	Rendering mortar	Layers of wire mesh
TPC1	Nil	Nil	Nil
TA300C-1	R8@300 (90^0)	Nil	Nil
TB75C-1	R8@75 (90^0)	Nil	Nil
TB300C	R8@300 (135^0)	Nil	Nil
TA300CS3	R8@300 (90^0)	CS	3
TA300SD1-1	R8@300 (90^0)	EM	1
TA300SD3-1	R8@300 (90^0)	EM	3
TA300ST3-1	R8@300 (90^0)	PMC	3

Table 2B Basic properties of specimens – Group 2

Specimen	Transverse reinforcement (hook)	Rendering mortar	Layers of wire mesh
TPC2	Nil	Nil	Nil
TA300C-2	R8@300 (90^0)	Nil	Nil
TB75C-2	R8@75 (90^0)	Nil	Nil
TA300SD1-2	R8@300 (90^0)	EM	1
TA300SD3-2	R8@300 (90^0)	EM	3
TA300ST1	R8@300 (90^0)	PMC	1
TA300ST3-2	R8@300 (90^0)	PMC	3
T0ST1	Nil	PMC	1
T0ST3	Nil	PMC	3
T0SD1	Nil	EM	1
T0SD3	Nil	EM	3

Table 3 Mechanical properties of wire mesh.

	Longitudinal direction	Transverse direction
Diameter (mm)	1.14	1.14
Spacing (mm)	12.7	12.6
Ultimate strength (MPa)	-	548
Corresponding strain	-	0.04874

Table 4 Properties of rendering materials (MPa)

Material	Tensile splitting strength
CS (10-day)	2.70
PMC (30-day)	2.71
EM (30-day)	10.35

Square welded mesh is used as reinforcement in HPF. Measured material properties are listed in Table 3. Table 4 summarizes material properties of rendering materials. Mix proportion of the cement-sand mortar is characterized by water-cement ratio at 0.55 and sand-cement ratio at 3.00. Properties of cement-sand mortar are obtained by carrying out compression tests and tensile splitting tests on a pair of 150mm cubes and 150mm x 300mm cylinders respectively. Properties of the other two types of rendering materials are obtained by carrying out compression tests and tensile splitting tests on three 100mm cubes and three 100mm x 200mm cylinders respectively.

A method statement has been prepared to systematically outline the procedure of strengthening existing reinforced concrete columns using HPF. The method statement is referred to Ho and Lam (2010). Strengthening of all specimens strictly follows the method statement.

Figure 1 shows typical elevations and sections of specimens detailed to CoP1987 and CoP2004. Observed zones of the specimens are at the middle portion and spacing of transverse reinforcement is reduced by half at both ends to prevent failure at the ends due to stress concentration. Strain gauges with 5mm gauge length are installed on all main reinforcement in specimens in Group 1 and on alternative main reinforcement in specimens in Group 2. 5 strain gauges are installed on the transverse reinforcement at mid height of specimens. 2 strain gauges are located next to the hooks and 3 of them are at 90^0 apart. Detailed location and identification of strain gauges installed on the transverse reinforcement are referred to Figure 1. Figure 2 shows the arrangement of LVDTs at 90^0 apart with gauge length of 400mm in the observed zones.

Figure 3 shows the test setup. All specimens were tested by a Computer-Electro-Hydraulic Servo Controlled Multi-Purpose Testing System. The testing system is displacement control with a maximum loading capacity of 10,000kN.

Strain rate varies in different stages and is illustrated in Figure 4. The specimens are subjected to progressive increase in end shortening as follows:-

- At the linear elastic portion of the load-displacement curve, strain rate is applied at 0.5mm/min.
- At the non-linear pre-peak portion, strain rate is reduced to 0.2mm/min.
- When approaching the maximum load, strain rate is further reduced to 0.1mm/min.
- At the post-peak region, the strain rate is 0.05mm/min.

The loading test is terminated when the axial load carrying capacity of a specimen is reduced by more than 15% from the maximum.

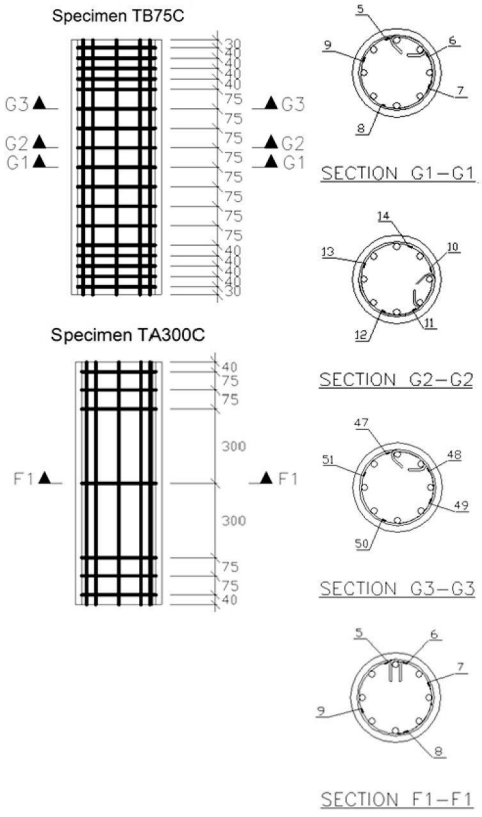
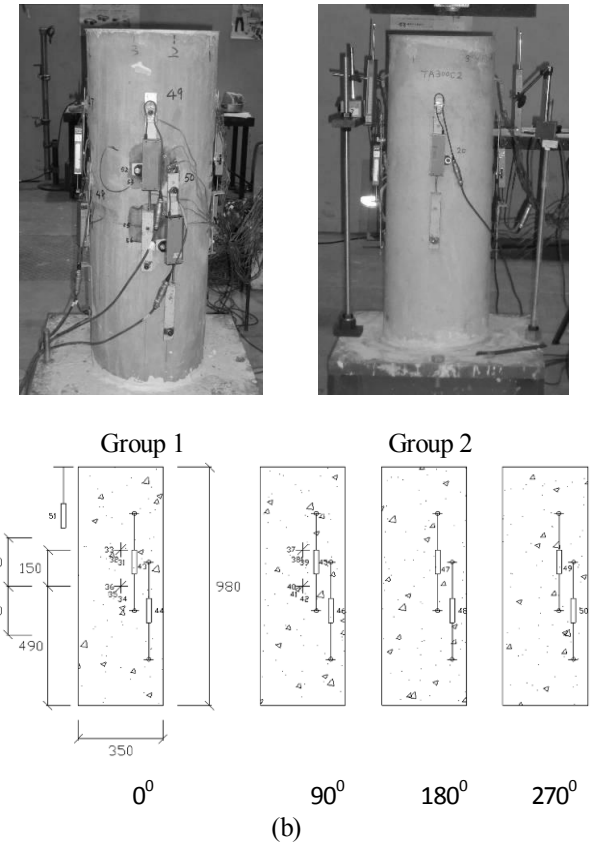


Figure 1 Location of strain gauges.



(b)

Figure 2 Arrangement of LVDTs at four directions.

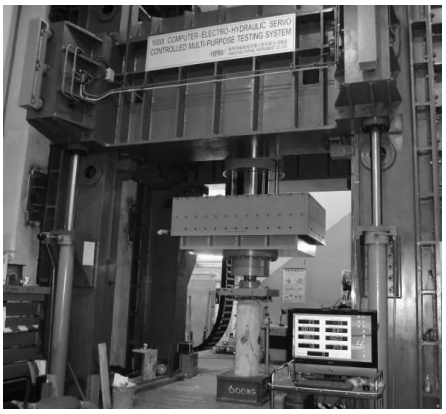


Figure 3 Photo of test setup.

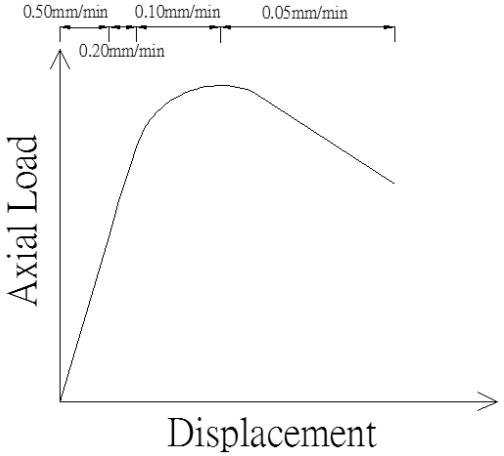


Figure 4 Strain rate.

4. TEST RESULTS

Figures 5(a) and 5(b) show typical modes of failure of specimens provided with 300mm and 75mm spacing of transverse reinforcement and without any HPF confinement.

Figures 5(c) and 5(d) show typical modes of failure of plain concrete specimens strengthened with HPF. Vertical cracks develop on the external HPF layer and steel wires of the wire mesh fractured in transverse direction at peak strength. Core concrete of the specimens fails in a cone shape with fully developed diagonal cracks at approximately 45^0 similar to the modes of failure of plain concrete specimen TPC2.

Figures 5(e) and 5(f) show typical modes of failure of reinforced concrete specimens strengthened with HPF. Crack patterns and condition of steel wires are similar to that observed from the above-mentioned specimens. However, integrity of core concrete is reserved by the HPF without significant damage. Hooks of the transverse reinforcement remain intact throughout the tests. Sign of arching effect can also be observed in the specimens.

In all the tests, concrete covers of non-strengthened specimens spalled off before reaching the peak strength.

Typical load-strain plots of main reinforcement and transverse reinforcement are shown in Figure 6. Strains are

recorded by strain gauges installed on the reinforcement as described in Section 3.

Figure 7 shows the load-strain plots of specimens without strengthening. Strains are based on the overall vertical displacement of the specimens measured by the LVDTs. Figures 8 and 9 show the load-strain plots of the specimens in Group 1 and Group 2 respectively with the strain based on the overall vertical displacement of the specimens obtained from LVDTs.

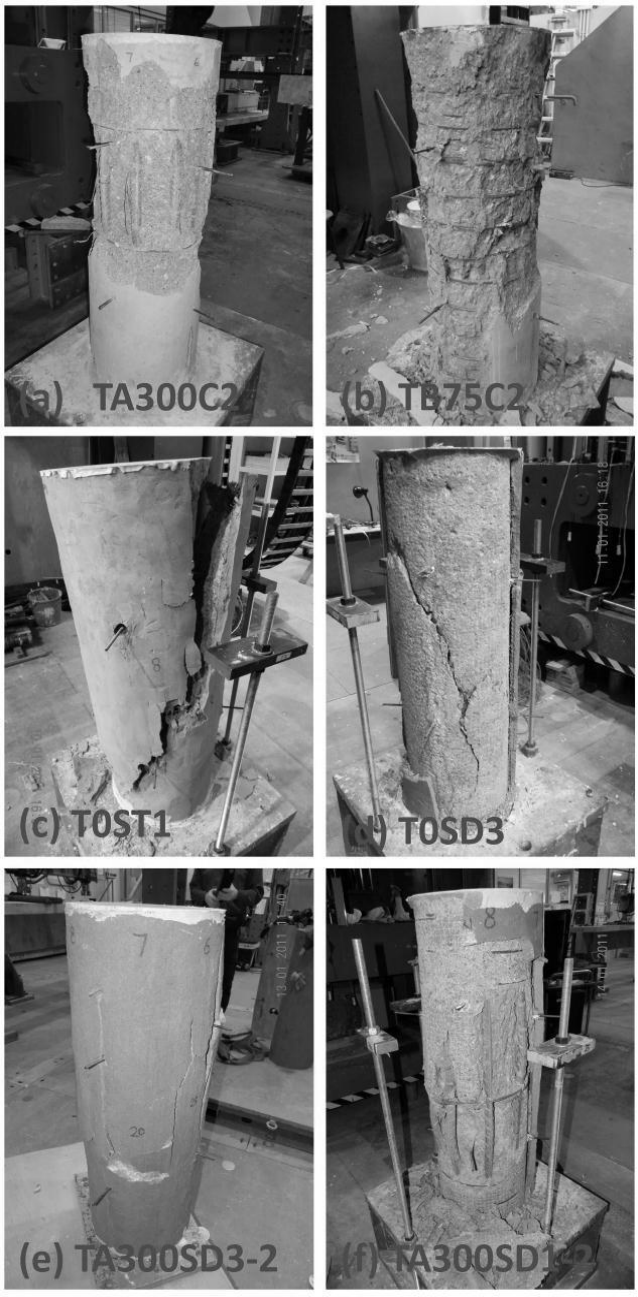


Figure 5 Typical failure modes of specimens.

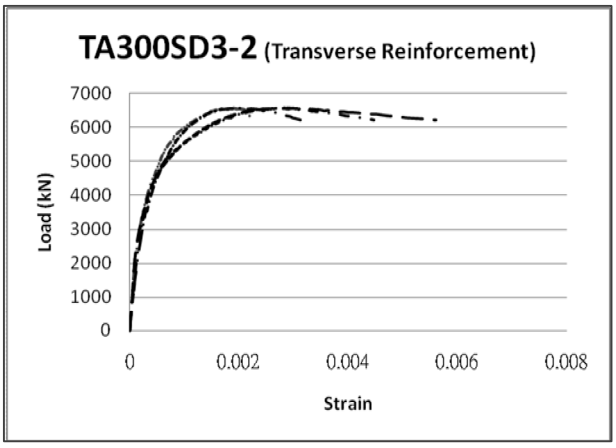


Figure 6(a) Load-strain plots of main reinforcement.

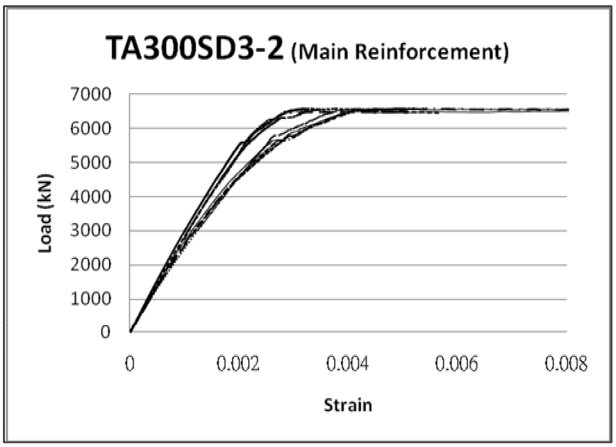


Figure 6(b) Load-strain plots of transverse reinforcement.

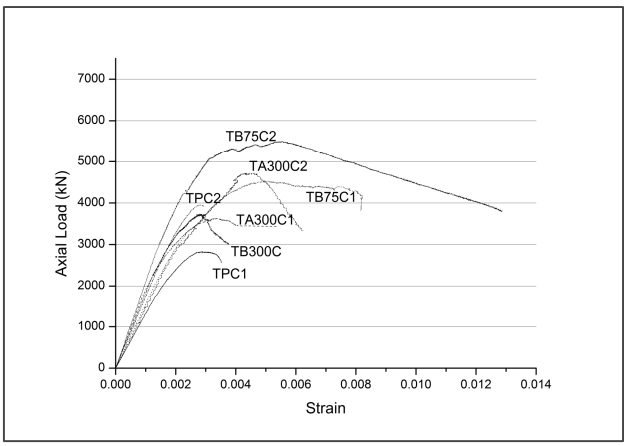


Figure 7 Load-strain plot of non-strengthened specimens.

A non-HPF strengthened reinforced concrete specimen will expand laterally on progressive increase in axial compression. When the lateral expanding stress exceeds the tensile strength of concrete, concrete cover will spall off. As a result, compressive strength of core concrete will increase to compensate for the loss in the load carrying capacity due to reduction on cross sectional area. Compressive force will gradually transfer to and resist by the main reinforcement

and core concrete. When lateral strain of concrete attains a critical level, there will be interaction between core concrete and transverse reinforcement. The transverse reinforcement will provide a confining pressure to confine the core concrete by restraining lateral expansion of concrete. The interaction works in a mechanism similar to the triaxial action of soil and the compressive strength of concrete is enhanced by this interaction (Richart et al. 1928, Balmer 1949, Popovics 1973, Sheikh and Uzumeri 1980, Ahmad and Shah 1982, Mander 1983, Mander et al. 1988 and Li 1994).

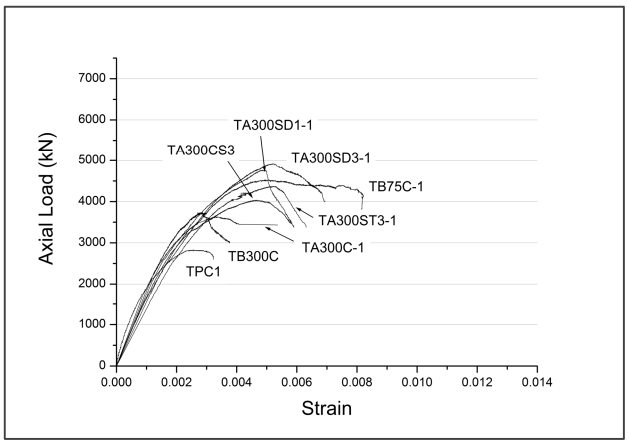


Figure 8 Load-strain plots of specimens in Group 1.

Table 5A Peak strength of specimens – Group 1

Specimen	P_{peak} (kN)	$P_{peak}/P_{peak(TB75C-1)}$
TPC1	2833.4	0.626
TA300C-1	3632.9	0.802
TB75C-1	4529.8	1.000
TB300C	3736.3	0.825
TA300CS3	4036.7	0.891
TA300SD1-1	4765.0	1.052
TA300SD3-1	4918.9	1.086
TA300ST3-1	4368.5	0.964

Table 5B Peak strength of specimens – Group 2

Specimen	P_{peak} (kN)	$P_{peak}/P_{peak(TB75C-2)}$
TPC2	3957.7	0.719
TA300C-2	4717.3	0.857
TB75C-2	5502.5	1.000
TA300SD1-2	6782.2	1.233
TA300SD3-2	6574.1	1.195
TA300ST1	5433.8	0.988
TA300ST3-2	5774.1	1.049
T0ST1	4003.4	0.728
T0ST3	3774.8	0.686
T0SD1	4615.8	0.839
T0SD3	4378.1	0.796

Table 5C Peak strength of plain concrete specimens confined with HPF– Group 2

Specimen	P_{peak} (kN)	$P_{peak}/P_{peak(TPC2)}$
TPC2	2907.7[2]	1.000
T0ST1	4003.4	1.377
T0ST3	3774.8	1.298
T0SD1	4615.8	1.587
T0SD3	4378.1	1.506

Similar interaction between HPF and concrete can be assumed when a HPF strengthened specimen is subjected to uniaxial compression. Increase in peak strength due to confinement action provided by HPF is observed from the test results. However, it is unclear as to the contribution of individual component in situation where confinement action is provided by both transverse reinforcement and HPF. The resulting confinement action may be equal to or less than the sum of the confinement action provided by individual component. Further analysis on the test results is needed.

Tables 5A, 5B and 5C list the peak strengths (P_{peak}) obtained by all 19 specimens. The test results are separated into two groups, namely Group 1 and Group 2, due to different compressive strength of concrete being used in these two groups. In Table 5C, equivalent peak value of specimen TPC2 is estimated based on a diameter of 300 mm instead of 350 mm. For ease of comparison, P_{peak} of specimens in Group 1 are divided by $P_{peak(TB75C-1)}$ (Peak strength of specimen TB75C-1) whereas P_{peak} of specimens in Group 2 are divided by $P_{peak(TB75C-2)}$ (Peak strength of specimen TB75C-2). If the ratio obtained is larger than 1, it means that this particular specimen has a load carrying capacity comparable to column designed to CoP2004. Besides, P_{peak} of plain concrete specimens in Group 2 are divided by $P_{peak(TPC2)}$ (Peak strength of specimen TPC2) to study the improvement in peak strength provided by HPF to plain concrete.

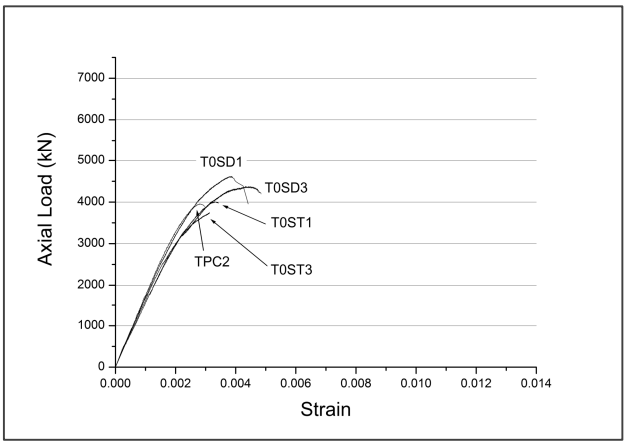


Figure 9(a) Load-strain plots of plain concrete specimens in Group 2.

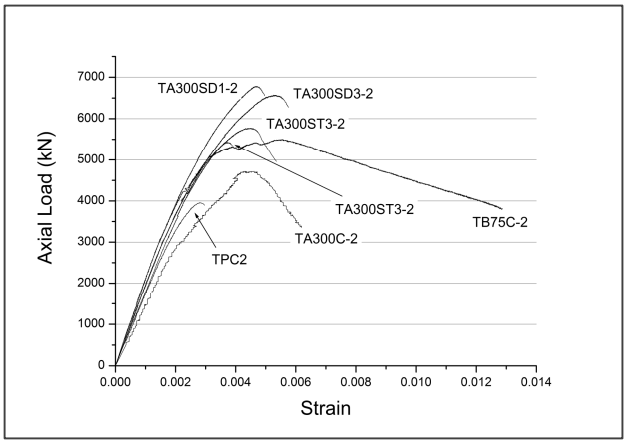


Figure 9(b) Load-strain plots of reinforced concrete specimens in Group 2.

By comparing the peak strengths of specimens TA300C-1 and TB300C, difference in angle of hooks (i.e. 90^0 hooks in specimen TA300C-1 and 135^0 hooks in specimen TB300C) does not have significant influence to load carrying capacity of specimens. This seems to suggest that as far as axial load is considered, the use of 90^0 hooks in lieu of 135^0 hooks causes minor effect to the confinement action.

From Table 5B, it is observed that reinforced concrete specimens (like specimen TA300SD1-2) detailed to CoP1987 and strengthened with HPF can achieved peak strength up to 23.3% higher than reinforced concrete specimens detailed to CoP2004.

Table 5C lists the measured peak strength of plain concrete specimens confined with HPF. Significant increase in peak strength is observed. The improvement in peak strength of specimens T0ST1 and T0ST3 is 29.8-37.7% and of specimens T0SD1 and T0SD3 is 50.6-58.7%. It shows that epoxy based rendering material can provide better confinement to enhance the compressive strength of concrete when compared with polymer modified cementitious based rendering material. HPF strengthening is an effective way to improve the load carrying capacity of columns.

Tables 6A and 6B list the confined compressive strength of concrete ($f_{cc(Meas)}$) estimated based on the following equation

$$f_{cc(Meas)} = (P_{Peak} - A_{st}f_y)/A'_{cc} \quad (1)$$

Where A_{st}, f_y and A'_{cc} are the respective area of main reinforcement, yield strength of main reinforcement and area of confined concrete.

From Table 6A, it is observed that specimens TA300SD1-1, TA300SD3-1 and TA300ST3-1 show substantial increase in confined compressive strength of concrete as compared with specimen TB75C-1. For the other specimens TA300C1, TB300C1 and TA300CS3, core concrete is not effectively confined due to low volumetric ratio of transverse reinforcement. This results in greater reduction of cross sectional area of core concrete. In addition, the result of specimen TA300CS-3 demonstrates that traditional ferrocement may not be able to provide sufficient confinement to core concrete when compared with HPF.

Test results also show that HPF confinement using epoxy based rendering material has better confining capability than using cement-sand screeding or polymer modified cementitious based rendering material. The main difference is that epoxy based rendering material has a tensile strength of 3-4 times higher than polymer modified cementitious based rendering material. It shows that large increase in confined compressive strength of concrete can be achieved by adopting HPF with higher tensile strength.

Similar phenomenon is observed in specimens in Group 2. From Table 6B, it is observed that all specimens except specimens TA300C-2 and TA300ST1 have confined compressive strength of concrete greater than that achieved by specimen TB75C-2. Although specimen TA300ST1 is confined with HPF using polymer modified cementitious based rendering material, confining strength provided by the HPF layer is still insufficient.

Table 6A Confined compressive strength of specimens – Group 1

Specimen	A'_{cc} (mm^2)	$f'_{cc(Meas)}$ (MPa)
TPC1	96211.3	--
TA300C-1	63039.2	25.06
TB75C-1	63039.2	39.28
TB300C	63039.2	26.70
TA300CS3	66540.7	29.81
TA300SD1-1	66540.7	40.75
TA300SD3-1	66540.7	43.06
TA300ST3-1	66540.7	34.79

Table 6B Confined compressive strength of specimens – Group 2

Specimen	A'_{cc} (mm^2)	$f'_{cc(Meas)}$(MPa)
TPC2	96211.3	--
TA300C-2	63039.2	36.36
TB75C-2	63039.2	48.82
TA300SD1-	66540.7	65.48
TA300SD3-	66540.7	62.36
TA300ST1	66540.7	45.22
TA300ST3-2	66540.7	50.33
T0ST1	70685.8	65.30
T0ST3	70685.8	61.94
T0SD1	70685.8	56.64
T0SD3	70685.8	53.40

Tables 7A and 7B list out the predicted compressive strength of confined concrete ($f_{cc(Predicted)}$) of each specimen based on the correlation proposed by Mander et al. (1988), Eq. 2 as follows,

$$f_{cc(Predicted)} = f'_{co}(-1.254 + 2.254\sqrt{1 + \frac{7.94f'_l}{f'_{co}}} - 2\frac{f'_l}{f'_{co}}) \quad (2)$$

Where, f'_{co} is unconfined compressive strength of concrete, and f'_l is overall lateral confining stress on the concrete.

When applying Eq. 2 to the present case, it is assumed

that the overall lateral confining stress (f'_l) induced is the sum of the effective lateral confining stress provided by HPF and transverse reinforcement in the form of,

$$f'_l = f'_{l(Trans)} + f'_{l(HPF)} \quad (3)$$

$f'_{l(Trans)}$ is the effective lateral confining stress on the concrete provided by transverse reinforcement in the form of,

$$f'_{l(Trans)} = 0.5 k_e \rho_s f_{(Trans)} \quad (4a)$$

$$k_e = (1 - 0.5 s'/d_s)^2 / 1 - \rho_{cc} \quad (4b)$$

Where s' is clear distance between consecutive transverse reinforcement, d_s is diameter of core section enclosed by the center lines of the transverse reinforcement, ρ_{cc} is ratio of area of main reinforcement to area of core section, ρ_s is volumetric ratio of transverse reinforcement and $f_{(Trans)}$ is yield strength of transverse reinforcement.

$f'_{l(HPF)}$ is the effective lateral confining stress on the concrete provided by HPF in the form of,

$$f'_{l(HPF)} = 0.5 \rho_{HPF} f_{(HPF)} \quad (4c)$$

$$\rho_{HPF} = 4 t_{HPF} / d_{s(HPF)} \quad (4d)$$

t_{HPF} is the thickness of HPF layer, $d_{s(HPF)}$ is the diameter of core section enclosed by HPF and $f_{(HPF)}$ is the tensile strength of HPF.

Unconfined compressive strength of concrete (f'_{co}) is estimated based on the compressive strength of plain concrete specimens. Considering specimen TCP2 was tested in Aug 2010, the unconfined compressive strength of concrete (f'_{co}) for specimens tested in Jan 2011 is adjusted by correlating the cube strengths measured in Aug 2010 and Jan 2011. The correlation is based on three 100mm cubes tested in Aug 2010 and five 100mm cubes tested in Jan 2011. In general, Eq. 2 provides accurate prediction on the confined compressive strength of concrete for specimens with high volumetric ratio of transverse reinforcement.

In Table 7, percentage different between $f_{cc(Predicted)}$ and $f_{cc(Meas)}$ is denoted by the abbreviation "Diff". "Diff" is defined as $(1- f_{cc(Predicted)}/f_{cc(Meas)})$x100. A positive value means an overestimation of f_{cc} by Eq. 2-4 and a negative value means an underestimation of f_{cc} by Eq. 2-4.

From Table 7B, it is observed that difference between $f_{cc(Predicted)}$ and $f_{cc(Meas)}$ of specimens T0ST1, T0ST3, T0SD1 and T0SD3 is below 10%. The difference between $f_{cc(Predicted)}$ and $f_{cc(Meas)}$ of specimens TA300SD1-1, TA300SD3-1, TA300SD1-2 and TA300SD3-2 are -5.71 to +3.10%. However, the errors of specimens TA300CS3, TA300ST3-1, TA300ST1 and TA300ST3-2 are -28.76 to -10.33%. It shows that Eq. 2 may not be directly applied (i.e. using Eq. 3) to predict the confined compressive strength of concrete in reinforced concrete specimens confined with HPF of low tensile strength.

Further study in this area is necessary to fully understand the correlation between confinement action provided by HPF and confined compressive strength of concrete in the presence of transverse reinforcement.

Table 7A Confined compressive strength of specimens – Group 1

Specimen	$f'_{l(Trans)}$ (MPa)	$f'_{l(HPF)}$ (MPa)	$f_{cc(Predicted)}$ (MPa)	Diff(%)
TPC1	--	--	--	--
TA300C-1	0.1594	--	30.54	-21.90
TB75C-1	1.9987	--	41.42	-5.43
TB300C	0.1594	--	30.54	-14.41
TA300CS3	0.1594	1.276	38.38	-28.76
TA300SD1-1	0.1594	1.942	41.95	-2.95
TA300SD3-1	0.1594	2.377	44.13	-2.48
TA300ST3-1	0.1594	1.278	38.38	-10.33

Table 7B Confined compressive strength of specimens – Group 2

Specimen	$f'_{l(Trans)}$ (MPa)	$f'_{l(HPF)}$ (MPa)	$f_{cc(Predicted)}$ (MPa)	Diff(%)
TPC2	--	--	--	--
TA300C-2	0.1378	--	42.09	-15.73
TB75C-2	1.7282	--	52.03	-6.58
TA300SD1-2	0.1378	1.942	63.46	3.10
TA300SD3-2	0.1378	2.377	65.92	-5.71
TA300ST1	0.1378	0.727	56.08	-24.03
TA300ST3-2	0.1378	1.278	59.52	-18.25
T0SD1	--	1.942	62.66	4.05
T0SD3	--	2.377	65.15	-5.18
T0ST1	--	0.727	55.20	2.54
T0ST3	--	1.278	58.67	-9.87

5. CONCLUSIONS

In this study, 19 full-scale specimens with detailing in accordance with CoP1987 or CoP2004 are subjected to unaxial compression. 12 of the specimens detailed in accordance with CoP1987 are strengthened with different types of HPF. From the results of the compression tests, preliminary conclusions are drawn as follow:-

(i) Variation of angle of hooks does not have significant influence on the load carrying capacity.
(ii) Load carrying capacity increase with volumetric ratio of transverse reinforcement.
(iii) Peak strength of plain concrete specimen can significantly be improved by 29.8-58.7% by HPF strengthening.
(iv) Reinforced concrete specimens detailed to CoP1987 and strengthened with HPF can achieve peak strength up to 23.3% higher than reinforced concrete specimens detailed to CoP2004.
(v) Load carrying capacity of specimens can be enhanced by HPF strengthening.
(vi) Compressive strength of confined concrete increases with tensile strength of HPF.

(vii) Tensile strength of HPF is found to be a crucial factor in providing sufficient confinement.

(viii) Better confinement can be provided by HPF using epoxy based rendering material instead of polymer modified cementitious based rendering material or cement-sand screeding.

All in all, test results have shown that specimens detailed to CoP1987 and strengthened with HPF can achieve axial load carrying capacity comparable to specimens detailed in accordance with CoP2004. The enhancement in axial load carrying capacity is greatly dominated by the tensile strength of HPF.

Further study in this area is necessary to fully understand the correlation between confinement action provided by HPF and confined compressive strength of concrete in the presence of transverse reinforcement.

Acknowledgements:

Financial support from The Hong Kong Polytechnic University and the Research Grants Council of Hong Kong (RGC No: PolyU 5206/08E) is gratefully acknowledged.

The authors would like to thank for the technical assistance provided by the Heavy Structural Laboratory and the Industrial Centre of The Hong Kong Polytechnic University.

References:

Abercrombie S. (1978), "Ferrocement: building with cement, sand, and wire mesh", Robert Hale Ltd, London, 1978.

ACI 549R-97, "Report on Ferrocement", ACI Committee 549, 1997.

ACI 549.1R-93, "Guide for the Design, Construction, and Repair of Ferrocement", reported by ACI Committee 549, reapproved 1999.

Ahmad S.M. and Shah S.P. (1982), "Stress-strain curves of concrete confined by spiral reinforcement", Am. Concr. Inst. J., 79(6), 484-490.

Balmer G. G. (1949), "Shearing strength of concrete under high triaxial stress - computation of Mohr's envelope as a curve", Structural Research Laboratoty Report SP 23, US Bureau of Reclamation, 1949-10-28.

Cao Z., Li A., Wang Y.Y., Zhang W. and Yao Q. (2007), Experimental study on RC space beam-column joints strengthened with high strength steel wire mesh and polymer mortar, J of Southeast University (Natural Science Edition), 37(2), pp 235-239.

CECS 242:2008. Technical specification for strengthening concrete structures with grid rebar and mortar. China Association for Engineering Construction Standardization, 2008. (in Chinese)

CoP1987, "Code of Practice for Structural Use of Concrete 1987", Building Authority Hong Kong.

CoP2004, "Code of Practice for Structural Use of Concrete 2004", Second Edition, The Government of the Hong Kong Special Administrative Region.

Ersoy U., Tankut A.T. and Suleiman R. (1993), Behavior of Jacketed Columns, ACI Structural Journal, 90(3), pp 249-261.

GB 50011-2001, "Code for Seismic Design of Buildings", National Standard of the People's Republic of China.

Han L.H., Zheng Y.Q. and Teng J.G. (2006), Fire resistance of RC and FRP-confined RC columns, Magazine of Concrete Research, 58(8), pp 533-546.

Harries K.A., Ricles J.R., Pessiki S. and Sause R. (2006), Seismic retrofit of lap splices in nonductile square columns using CFR jackets, ACI Structural J, 103(6), pp 874-884.

Ho, I.F.Y. and Lam, S.S.E. (2010), "Strengthening Reinforced Concrete Columns by High Performance Ferrocement", Proc. Joint Conf. of 7th Int. Conf. on Urban Earthquake Engng. & 5th Int. Conf. on Earthquake Engng., March 3-5, 2010, Tokyo Institute of Technology, Tokyo, Japan.

Jiang L., Shang S. and Liu F., "Research on Axially compressed Behavior of RC Strengthening Round Columns Using High Performance Composite Cement Mortar Reinforced with Mesh Reinforcements", Journal of Hunan University of Technology, Vol. 23, No. 1, 2009. (in Chinese)

Kaushik S.K., Singh K.K., Kumar R. and Sharma T.P. (1996), Performance of ferrocement encased concrete under fire exposure, Journal of ferrocement, 26(3), pp 191-196.

Kim S.H. and Choi J.H. (2010), "Repair of Earthquake Damaged RC Columns with Stainless Steel Wire Mesh Composite", Advances in Structural Engineering, Vol. 13, No.2, April 2010, 393-402.

Kondraivendhan B. and Pradhan B. (2009), "Effect of ferrocement confinement on behavior of concrete", Construction and Building Materials, Vol. 23, Issue 3, 2009, 1218-1222.

Lam, S.S.E., Xu, Y.L., Chau, K.T., Wong, Y.L., and Ko, J.M. (2002), "Progress in earthquake resistant design of buildings in Hong Kong", Structural Engineering World Congress, Oct 9-12, 2002, Yokohama, Japan.

Li B. (1994), "Strength and Ductility of Reinforced Concrete Members and Frames Constructed Using High Strength Concrete", Research Report/ Dept. of Civil Engineering, University of Canterbury, Christchurch New Zealand, ISSN 0110-3326.

Lim, C.T.E., Ong, K.C.G. and Paramasivam, P. (2000), "Ferrocement repaired reinforced concrete beams subjected to quasi-static and cyclic loadings", proceedings of fourth international conference on Repair, Rehabilitation, and Maintenance of concrete structures, and innovations in design and construction, Seoul, Korea, pp. 887-907.

Mander (1983), "Seismic Design of Bridge Piers", thesis of PhD at the University of Canterbury, Christchurch New Zealand, 1983.

Mander, J.B., Priestley, M.J.N. and Park, R., (1988a), "Theoretical Stress Strain Model of Confined Concrete," Journal of Structural Engineering, ASCE, Vol. 114, No. 8, pp. 1804-1826.

Mander, J.B., Priestley, M.J.N. and Park, R., (1988b), "Observed Stress Strain Behavior of Confined Concrete," Journal of Structural Engineering, ASCE, Vol. 114, No. 8, pp. 1827-1849.

Naaman A. E. (2000), "Ferrocement and Laminated Cementitious Composites", Techno Press 3000, 2000.

Popovics S. (1973), "A numerical approach to the complete

stress-strain curves for concrete", Cement and Concr. Res., 3(5), 583-599.

Richart F.E., Brandtzaeg A. and Brown R.L. (1928), "A study of failure of concrete under combined compressive stresses", Engineering Experiment Station Bulletin No. 185 (1928) Urbana, IL.

Shah S.P., Lub K.B. and Ronzoni E. (1986), A summary of ferrocement construction and a survey of its durability, RILEM Committee 48-FC, Materials and Structures, 19(4), pp 297-321.

Sheikh S.A. and Uzumeri S.M. (1980), "Strength and ductility of tied concrete columns", J. Struct. Div., A.S.C.E., 106(5), 1079-1102.

Tadeu A.J.B. and Branco F.J.F.G (2000), Shear tests of steel plates epoxy-bonded to concrete under temperature, J of Materials in Civil Engineering, 12(1), pp 74-80.

Williamson R.B. and Fisher F.L. (1983), Fire resistance of a load bearing ferrocement wall, Report no UCB-FRG-83-1, Dept of Civil Eng, U of California, Berkeley, Feb 1983.

Wu Y.F., Liu T. and Oehlers D.J. (2006), Fundamental principles that govern retrofitting of RC columns by steel and FRP jacketing, Advances in Str Eng, 9(4), pp 507-532.

卜良桃 (2007), "高性能复合砂浆钢筋网(HPF)加固混凝土结构新技", 北京:中国建筑工业出版社, 2007. (in Chinese)

8CUEE CONFERENCE PROCEEDINGS
8th International Conference on Urban Earthquake Engineering
March 7-8, 2011, Tokyo Institute of Technology, Tokyo, Japan

IMPROVEMENT OF PARALLEL COMPUTING PERFORMANCE OF INTEGRATED EARTHQUAKE SIMULATION

M. L. L. Wijerathne[1], M. Hori[2], T. Ichimura[3], and T. Kabeyazawa[4]

1) Asst. Professor, GCOE, Dept. of Civil Engineering, the University of Tokyo, Japan
2) Professor, Earthquake Research Institute, the University of Tokyo, Japan
3) Assoc. Professor, Earthquake Research Institute, the University of Tokyo, Japan
4) Researcher, Building Research Institute, Japan
lalith@eri.u-tokyo.ac.jp, hori@eri.u-tokyo.ac.jp, ichimura@eri.u-tokyo.ac.jp, tosikazu@kenken.go.jp

Abstract: This paper presents recent improvements of parallel computing performance of Integrated Earthquake Simulation (IES); parallel computing is applied for IES to carry out seismic structure response of all buildings located in a large urban area. In previous studies, IES has been enhanced with standard parallel computing techniques, but there are bottlenecks which limit the number of buildings analyzed to several tens of thousands with hours of run time. Parallel computing performance is significantly improved by eradicating the bottlenecks; the modules for I/O are replaced with better ones and the link to seismic structure analysis programs is strengthened. In addition, a new program that uses a fiber model is plugged into IES, so that seismic response analysis is applied to mid/high-rise buildings. As test cases, seismic response analysis of all the buildings in a part of central Tokyo has been conducted.

1. INTRODUCTION

Quantitative prediction of infrastructural damages is necessary in preparation for earthquake disasters and both immediate and long term recovery process after a major earthquake. The conventional predictions based on past events would fail to provide a correct picture of damages since drastic changes in the built environment have taken place compared to the time of those past events. Therefore, a numerical tool capable of simulating the existing built environment considering the current conditions of structures, code of practice used for the structure designs, construction materials used, etc. would be indispensable. With the aim of filling the vacancy of such a numerical tool, a system called Integrated Earthquake Simulation (IES) is being developed (Ichimura et al. 2004, Hori et al. 2008). Its long term objective is to simulate earthquakes from source to their aftermaths; namely, strong ground motion from source to site, damages to structures, emergency evacuation and long and short term social and economic recovery. Evidently, most of the IES objectives require seismic response analysis and damage assessment of large number of structures in the target simulation domain within a reasonably short time. Some potential applications of IES are 1) as an aid for accelerating decision making in evacuation, rescue and relief supply right after an earthquake, 2) quantitative estimation of damages due to anticipating large earthquakes with Monte-Carlo simulations, etc... In this paper, we report the strengthening of parallel computation extension of the SRA module making it possible to reach these targets.

The parallel computation extension for the SRA module, developed prior to this work, has several performance bottlenecks. Some of those bottlenecks are due to the use for temporary files to exchange data between IES and independent SRA executable, unbalanced work load assigned to CPUs, large number of unnecessary inter-processor communications and use of large number of temporary files to reorganize the output data. As it will be shown in the next section, these bottlenecks seriously limit the number of building to several tens of thousands and extend the compute time to several hours.

In implementing countermeasures for bottlenecks, priority is given to elimination of temporary files, since extensive use of temporary files in parallel environment can harm computer systems. In this work, the use of temporary files is totally eliminated either with library or system-V shared memory segment and semaphore IPC mechanisms. All-worker model with several orders of magnitude less number of message passing is implemented instead of master-slave model in the current version. We implemented static load balancing based on the previously recorded run time information. Only static load balancing is implemented since changes to the core of IES is required for implementing dynamic load balancing .Since the SRA run time may not differ more than 5%, with different input seismic waves, static load balancing would be a reasonable solution. However, if considerable load imbalance occurs with different input strong ground motion data, a hybrid of static and dynamic load balancing should be added.

The rest of the paper is organized as follows. Section two presents more details of the bottlenecks, countermeasures and details of the implemented countermeasures. The section three presents simulation of

14000 buildings in central Tokyo as a demonstration of IES and discusses scalability of the modified IES. Some concluding remarks are given in the section four. In this paper, the term current IES refers to that with performance bottlenecks and the outcome of this work is referred as the modified IES.

2. PERFORMANCE BOTTLENECKS AND REMEDIES

As mentioned in the previous section, current IES is equipped with standard parallel computing techniques. However, the numbers of structures are limited to several tens of thousands with hours of computing time due to bottlenecks. Figure 1 shows its scalability when simulating 10,000 buildings with a nonlinear Discrete Element Method (DEM) code. Speedup, defined as the ratio of run time with single CPU and many CPUs, is a standard index to measure the scalability of a parallel program. As is seen in Figure 1, it rapidly deviates and from the ideal curve and tends to saturate somewhere around 128 CPUs. Currently, IES uses simplified SRA methods like nonlinear DEM, nonlinear one component model (OCM), etc... Parallel computation is not required to conduct SRA of one building since the run time of these simplified SRA methods is short. It is for simulating a large number of buildings in a reasonably short time, IES needs parallel computation enhancements. In this sense, IES is an embarrassingly parallel program. Obviously, the parallel performance shown in Figure 1 is unacceptably low for an embarrassingly parallel problem and there should be enough room to improve. In this section, details of the parallel performance bottlenecks in current IES and remedies are discussed.

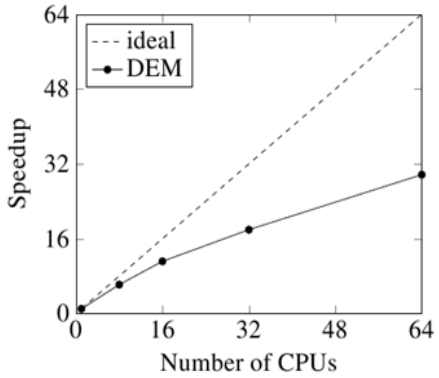


Figure 1 Speedup of the current IES parallel extension.

2.1 Inter-process communication with temporary files

The current IES does not have inbuilt SRA programs. It generates input data for different types of SRA methods and call third party SRA executable with *system*( ) command, using temporary files to exchange data between the two programs. Though this is a common inter process communication (IPC) method in serial computing, it becomes a serious bottleneck in parallel computation. In the current implementation, OCM model requires 10 file I/O operations totaling around 20 million file I/O operations for a city like Tokyo. Further, the file system may stresses heavily when all the CPUs start to simulate two or three storied residential buildings. These small buildings are the most common in any city and the simplified SRA models in IES can simulate these in a very short time.

The standard technique to eliminate the use of temporary files for IPC is calling the external program as a static or dynamic library. We converted some of the SRA programs, with permissions to modify, to libraries. However, converting some of the codes is difficult due to the non-standard compiler options used by their developers. Under such situations, we adopted shared memory and semaphore mechanisms provided by SystemV IPC (commonly abbreviated SysV IPC) (Daniel et al. 2000, Stevens 1999) for inter-process communication and called the SRA programs as independent executable with *system*() command. As the name implies, shared memory mechanism allow multiple processes to share a common segment of memory to exchange a large volume of data. Semaphores can be used to prevent multiple processes simultaneously accessing a shared memory segment. In addition to attaching as libraries, the major SRA programs are attached to IES using these IPC mechanisms. In the future, a propitiatory software code for estimating the life time of damaged concrete structures is to be attached with these two IPC mechanisms.

One disadvantage of using shared memory segments and semaphores is that those persist even after termination of the processes accessing it, unless explicitly cleaned. Under normal operations, IPC classes in IES take care of the cleaning. However, if the main program dies prematurely, allocated IPC resources should be cleaned with the command *ipcrm* <*-s/-m*> <*shmid/semid*>, on each computing node. *shmid* and *semid* of allocated resources can be found with *ipcs* <-s/-m> commands. Otherwise, it become a system wide memory leak and persists until the whole system or all the used nodes are rebooted.

2.2 Large number of file I/O operations in output data handling

When used to simulate a large urban area, IES produces a large volume of output data. The demonstration simulation given in the next section produced 12GB of binary data when seismic responses of 14,000 buildings are saved for 2,400 time steps. Such amount of data may not be needed for some applications. However, the current target is to provide the almost all the available data so that IES can deal with any end user requests. When saving the output data, extremely large amount of file I/O operations are done by the current IES SRA module; two files per time step of each structure are written by all the CPUs using POSIX file I/O functions. Later the master CPUs reads all those back, reorganize, group the buildings in thousands and write to disk formatted for the visualization software. In total, it involves 9.6 million I/O operations per 1000 buildings.

One of the best solutions for this serious file I/O bottleneck is to reorganize data into ready to visualize format (i.e. visualization software can directly read with little or no

preprocessing) and write output into small number of files, large in sizes. However, with POSIX type I/O it's difficult to save data in ready to visualize format. To explain why, it needs to explain how the data is distributed over the CPUs. As will be explained in the section 2.3, buildings from one GIS tile are distributed over many CPUs to attain good load balancing. With POSIX IO, saving data of one GIS tile, scattered over many CPUs, to a single file can be done only with sequential file access; either sending all the data to master CPU to re-organize and save or each CPU opens and saves data to one file sequentially. Utilizing parallel I/O operations, one can attain better performance than either of these options.

We utilized the MPI-IO functionalities comes with the MPI-2 standard to write the SRA output in ready to visualize format, thereby achieving higher parallel performance and reducing the visualization time. Compared to POSIX IO, MPI-IO can deliver much higher IO performance in parallel environment, provided a supporting parallel files system is available. MPI-IO provides four levels of file access; independent or collective access of contiguous or noncontiguous data. We utilized the level 3 access function *MPI_File_write_all*( ) which allow non-contiguous collective access to a file, to write SRA output data to a ready to visualize format.

2.3 Unbalanced work load assigned to CPUs

Though the SRA module of IES is embarrassingly parallel, proper load balancing is important to achieve a good scalability. Current IES SRA module does not assign equal amount of work to each CPU leading to large run time difference among CPUs. The exact run time for each structure cannot be predicted since it depends on location and magnitude of an earthquake, etc... Therefore, some form of dynamic load balancing is necessary to attain a perfect load balance. Possibly, hybrid solution like static load balancing for the first 95% and switching to dynamic load balancing for the remaining would be the best since this involves less number of message passing.

Though hybrid of static and dynamic load balancing is a good choice for this problem, only static load balancing is implemented since dynamic load balancing requires changes to the core of IES. In the simple static load balancer, first all the building shape and previous run time data are shared among all the CPUs by either broadcasting or pipe-lining. The shared shape data contain a group of building shapes from one or more GIS tile and each data set is compressed to reduce to size of the message. CPUs pick a subset of data so that each has equal amount of run time based on the previous run time data. The examples given in the next section provide parallel performance of this static load balancer. The use of static load balancer is an acceptable solution since the run time difference of a given building due different input SGM data would not be greater than 5%.

2.4 More on load balancing

Achieving a perfect load balancing with static or static-cum-dynamic load balancing may not necessarily reduce the total run time. To achieve the best load balance in the modified IES, a building is considered as the smallest computation unit or the grain size in partitioning the computational load. As a result buildings from one GIS tile are scattered over almost all the CPUs. This leads to longer time for collective IO operations since the number of participating CPUs is large and each CPU contribute relatively small amount of data. One potential solution is to form several CPU sub groups and make only the masters of those subgroups to perform the collective IO. However, this method does not perform well when the data size from each CPU is greater than 100kB (Latham et al. 2004), which is the case with IES data.

Another option is to group the buildings from a GIS tile to several sets with approximately equal total run time and use these sets as the smallest computational grain size. When this larger grain sizes have large total run time, buildings from one GIS tile is scattered over less number of CPUs effectively reducing collective IO time. However, larger grain size increases the load imbalance. Therefore, an intermediate grain size should be chosen to get the optimal behavior. The major advantage of this method is possibility to further reduce file saving time with concurrent collective IO of several CPU subgroups. Since buildings are scattered over smaller number of CPUs, it could be possible to finds disjoint sets of CPUs which has data from different GIS tiles. These CPU sub groups can concurrently save corresponding data with collective IO on subgroup communicators. When using over 200 CPUs, this may reduce the total run time.

Though, choosing a moderate computation grain size can reduce the total run time, it may not be the best solution for real-time applications. Having a moderate computation grain size would be good for intended Monte-Carlo simulations or other non-real-time applications. However, what real-time applications needs is not the smaller total run time, but the faster production of outputs even partially. As an example, it would be more useful for relief supply agencies to have results of high priority areas quicker rather than having results of millions of structures at once after longer wait. These high priority areas could be those predicted to suffer severe damage, where most people are depending the time of the earthquake, etc... One method for such early production of results is modifying the core of IES to flush all the data after completing the simulation of one data set and accept new sets of buildings from a different GIS tile. Another method is to implement dynamic processor management of MPI-2 to spawn small groups of CPUs for each GIS tile. Once a spawned processor group dies completing the assigned work, the master CPU spawn new group with those CPUs and assigns the next GIS tile in a queue. The former, modifying core of IES, is preferred to the latter since still processor spawning is complex and not much supported with commodity clusters.

3. ILLUSTRATIVE EXAMPLE WITH FIBER ELEMENT MODEL

The modified parallel extension of IES SRA module involves message passing only at the very beginning and the

very end of a simulation; at the beginning to share some configuration files and building shapes and run time data of each GIS tile and at the end for reorganizing output data and saving with collective IO. The modified parallel module should scale well with the number of CPUs as long as there are large numbers of buildings and SRA data is saved as large group of buildings. To test the scalability of the modified parallel extension, we simulated all the buildings the GIS tile 09ld171 in which 14,000 buildings are located. The objective of this simulation is to demonstrate IES SRA module, check the scalability against number of CPUs, find out the remaining bottlenecks and roughly estimate the necessary computational resources for a given number of buildings, etc...

3.1 Details of the computation model and the computer environment

The most sophisticated SRA method attached to current IES is OCM which is only applicable to low-rise buildings. A modern city is full of medium-rise and high-rise buildings and these tall buildings host most of the economically and administratively important entities. In order to conduct SRA of these important structures, a third party code of fiber element model is attached as a library to IES. Fiber element model is a simple and computationally light, but still allows significant insight to the seismic response of both the structural members and the entire structure. It is said to have the best compromise between the simplicity and the accuracy in non-linear seismic response studies of concrete buildings (Spacone et al. part I- II, 1996). The third party fiber element method code attached to IES uses the modified Kent-Park to model non-linear concrete member response.

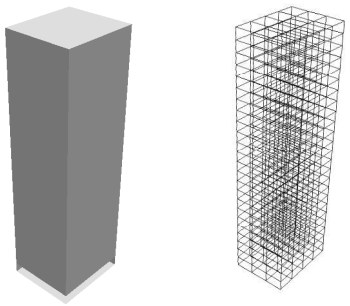


Figure 2 A shape of a building and automatically generated beam column skeleton.

The input beam column structural skeletons for the fiber element model (or other SRA models) are automatically generated from the GIS data since the actual structural details are not available to the authors. Dimensions and the spacing of the beams and columns are decided based on the Japanese code of practice for building design. Figure 2 shows an example of building shape generated from GIS data and its beam column skeleton. IES can simulate different buildings with different SRA program like Fiber, OCM, DEM, MDOF, etc. in a single simulation. However, for this demonstration simulation, all the buildings are simulated with the fiber element model. In addition, all the structures are excited by a strong ground motion data observed during the 1995 Kobe earthquake. Therefore, the current simulation does not reflect the naturally observed complex behavior due to the effects of complicated underground soil and rock structures. IES would be able to capture these complex behaviors either using observed SGM data at the neighborhood of each building or with synthetically generated high resolution SGM data with the multi-scale SGM simulation module of IES, which takes the details of the underground structures in to account.

All the simulations are conducted in a commodity Linux cluster made of connecting 8 workstation nodes with a Gigabit switching hub. Each workstation has a 32GB DDR2 600MHz memory and two Quad-Core AMD Opteron 2379 HE processors. Output data is saved to a raid array, NFS mounted on each node. It is well known that MPI-IO has poor performance on NFS mounted file systems (Latham et al. 2004). Therefore, the current simulation does not reflect the performance advantage of utilizing MPI-IO collective operations.

3.2 Scalability w.r.t the number of CPUs

As shown in Figure 3, the modified parallel module has almost the ideal scalability with respect to the number of CPUs. This is a significant improvement compared to the performance curve shown in Figure 1. When the fiber element model is called as an independent executable with SysV IPC resources for inter-process communication, it only took additional 30 seconds with 64 CPUs. This indicates that there is no serious penalty of calling a third party executable with SysV IPC resources in parallel environment. According to Table 1 the run time for 14,000 structures is around two hours with 64 CPUs. The graphs in Figure 3 and the Table 1 provide run time including and excluding the time for data reorganizing and saving at the last step. According to Table 1, it takes around 200 seconds to cast displacement data from beam-column skeleton actual building shape, reorganize and save 12GB displacement data with MPI collective file operations. As it was mentioned, the cluster used for the simulation had a NFS which is known to have poor support for parallel IO operations. The current file saving time could be reduced by 75% when a file system

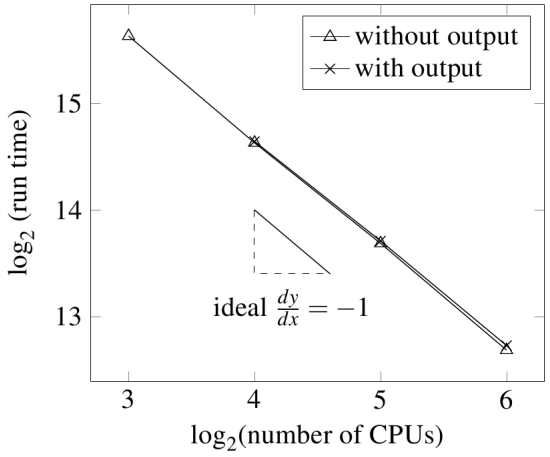


Figure 3 A shape of a building and automatically generated beam column skeleton.

Table 1 Runtimes of 14,000 structures in GIS tile 09ld171

No. of CPUs	Run time /(s)		Time for mapping data to shape and collective file IO
	without output	with output	
8	50631	--	--
16	25606	25820	214
32	13536	13754	218
64	6819	7008	189

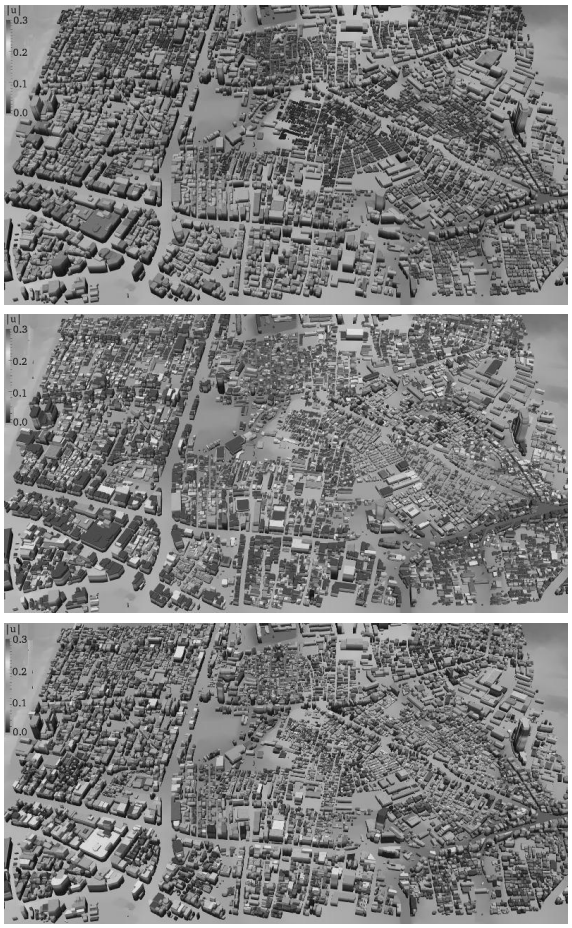


Figure 4 Snapshots of displacement time history of buildings in GIS tile 09ld171, simulated with fiber element model.

with a parallel IO support is used. Figure 4 shows some snapshot of displacement of buildings.

According to the results of this simulation, the shortest run time for an urban area with mid/high rise buildings are to be decided by the time for the fiber model to simulate the most complex mid/high rise building in the selected domain. In the case of this example, the run time for one of the tall building was around 6400 seconds. Therefore, the shortest run time for this GIS tile is around 6600 seconds irrespective of the number of CPUs. In order to further reduce run time, the seismic response programs have to be parallelized either with OpenMP or MPI.

4. CONCLDING REMARKS

We improved the parallel performance of seismic response analysis module of IES by eradicating all the bottlenecks in the former model. The extensive use of temporary files, unreasonably large number of message passing, unbalanced work assignment and poorly designed output data saving are the identified performance bottlenecks. With a relatively small simulation of 14,000 structures, it was demonstrated that the modified parallel module has almost the linear scalability with respect to the number of CPUs. Almost the same linear scalability curve is observed even when saving of a large volume of output data is included. It was observed that using SysV IPC resources for data exchanging between independent executable does not degrade the parallel performance. With SysV IPC, the run time is extended by a relatively small amount compared to the use of libraries. The shortest run time, when simulating a large urban area, could be decided by the runtime for the largest structure in the domain. According to the demonstration problem presented here, 10,000 15,000 CPUs may be needed to simulate whole Tokyo area. In future, increasing the computation grain size used for load balancing and concurrent data saving by multiple groups of CPUs are to be implemented to further improve the parallel performance when using large number of CPUs.

Acknowledgements:

The authors gratefully acknowledge support from the Japan Ministry of Education, Culture, Sport, Science, and Technology (MEXT) for establishing Global Center of Excellence in the University of Tokyo. This work is done under the Global Center of Excellence for Sustainable Urban Regeneration.

References:

Tsuyoshi Ichimura, Muneo Hori, Kenjiro Terada and Takahiro Yamakawa (2004), "On Integrated Earthquake Simulator Prototype: Combination Of Numerical Simulation And Geographical Information System", *Journal of Structural Mechanics and Earthquake Engineering,* **9**-4, 1—12.

Muneo Hori and Tsuyoshi Ichimura (2008), "Current state of integrated earthquake simulation for earthquake hazard and disaster", J. of Seismology, **12**-2, 307-321.

Enrico Spacone, Filip C. Filippou and Fabio F. Taucer (1996), "Fiber beam-column model for non-linear Analysis of R/C frames: Part I. Formulation", *Earthquake Engineering and Structural Dynamics*, **25**, 711-725.

Enrico Spacone, Filip C. Filippou and Fabio F. Taucer (1996), "Fiber beam-column model for non-linear Analysis of R/C frames: Part II. Applications", *Earthquake Engineering and Structural Dynamics*, **25**, 727-742.

Daniel P. Bovet and Marco Cesati (2000), "Understanding the Linux Kernel", O'Reilly, ISBN: 0-596-00002-2.

W. Richard Stevens (1999), "UNIX Network Programming, Volume2: Interprocess Communications", ISBN 0-13-081081-9.

Rob Latham, Rob Ross, and Rajeev Thakur (2004). "The impact of file systems on MPI-IO scalability". *Lecture Notes in Computer Science*, 3241:87-96.

Kwangho Cha, Hyeyoung Cho, and Sungho Kim (2007), "Performance Analysis of the Subgroup Method for Collective I/O", *Int. J. of Electrical and Electronics Engineering*, **1**-8.

8CUEE CONFERENCE PROCEEDINGS
8th International Conference on Urban Earthquake Engineering
March 7-8, 2011, Tokyo Institute of Technology, Tokyo, Japan

AN IMPROVEMENT IN ESTIMATING THE SEISMIC RESPONSES OF ONE-WAY UNSYMMETRIC PLAN TALL BUILDINGS

Mehdi Poursha[1], Faramarz Khoshnoudian[2], and A.S. Moghadam[3]

1) Assistant Professor, Department of Civil Engineering, Sahand University of Technology, Tabriz, Iran
2) Associate Professor, Department of Civil Engineering, Amirkabir University of Technology, Tehran, Iran
3) Assistant Professor, International Earthquake and Seismology Research Centre, Tehran, Iran
Poursha@sut.ac.ir

Abstract: This article presents an extension of the consecutive modal pushover (CMP) procedure for estimating the seismic demands of one-way unsymmetric-plan tall buildings. The procedure employs the multi-stage and classical single-stage pushover analyses and benefits from the elastic modal properties of structure. The seismic demands are obtained by enveloping the peak inelastic responses resulting from the multi-stage and single-stage pushover analyses. To verify and validate the procedure, it is applied to the 10, and 15-storey one-way unsymmetric-plan buildings including torsionally-stiff (TS), torsionally-similarly-stiff (TSS) and torsionally-flexible (TF) systems. The modal pushover analysis (MPA) procedure is implemented for the purpose of comparison as well. The results from the extended pushover procedure and MPA are compared with those obtained by the nonlinear response history analysis (NL-RHA). It is demonstrated that the extended CMP procedure can predict to a reasonable accuracy the peak inelastic responses, such as displacements and storey drifts. The CMP procedure represents an important improvement in estimating the plastic rotations of hinges at the flexible and stiff sides of unsymmetric-plan tall buildings in comparison with the MPA procedure.

1. INTRODUCTION

Several research efforts have been made to extend and apply the pushover analysis to unsymmetric-plan buildings whose inelastic seismic responses are intricate. Kilar and Fajfar [1997; 2001], De Stefano and Rutenberg [1998], Faella and Kilar [1998], Moghadam and Tso [1998; 2000], Ayala et al. [2002], Fujii et al. [2004], Barros and Almeida [2005] investigated on the application of pushover analysis to unsymmetric buildings. Recently, modal pushover analysis (MPA) [Chopra and Goel 2004], the N2 method [Fajfar et al. 2005 and 2008] and a simplified seismic analysis [Lin and Tsai 2007] were extended to the unsymmetric-plan buildings. In the MPA procedure, torsional moments were applied in addition to lateral forces at each floor level. The seismic demands were separately calculated for each of the modal pushover analyses and combined by using CQC modal combination scheme. The MPA procedure is unable to accurately compute the plastic rotation of hinges. In the extended N2 method, the results produced by pushover analysis (based on the N2 method) were combined with the results from elastic spectral analysis by using a correction factor. The correction factor was defined as the ratio between the normalized roof displacements derived from elastic spectral analysis and those resulting from pushover analysis. De-amplification of displacements due to torsion was not taken into consideration. This method is limited to low-rise buildings where higher mode effects are not significant.

The main objective of this paper is to extend the consecutive modal pushover (CMP) procedure to the one-way unsymmetric-plan tall buildings in which torsional and higher mode effects play an important role in estimating the seismic responses.

2. EXTENSION OF THE CONSECUTIVE MODAL PUSHOVER (CMP) PROCEDURE

The consecutive modal pushover (CMP) procedure was proposed to estimate the seismic demands of symmetric tall buildings [Poursha et al. 2009]. Herein, this procedure is extended to the one-way unsymmetric-plan tall buildings. Multi-stage and single-stage pushover

analyses are used in the procedure. In the multi-stage pushover analysis, modal pushover analyses are carried out continuously, so that when one stage (one modal pushover analysis) has been completely performed, the subsequent stage (subsequent modal pushover analysis) starts with an initial structural state (stress and deformation) which is the same as the condition at the end of the previous stage. The lateral forces are incrementally applied in the multi-stage pushover analysis. The number of stages in the multi-stage pushover analysis depends on the period (height) of the structure and type of unsymmetric-plan system. Linearly-elastic modal properties are used to implement the multi-stage pushover analysis. The displacement increment at the roof, in each stage of multi-stage pushover analysis, is determined as the product of a factor, β_i, and the total target displacement, δ_t, at the roof. The factor, β_i, is calculated from the initial modal properties of the structure. Displacement increment, u_{ri}, at the center of mass (CM) at the roof in the *i*th stage of multi-stage pushover analysis, is determined as

$$u_{ri} = \beta_i \delta_t \quad (1)$$

in which

$$\beta_i = \alpha_i \quad \text{for the stages before the last stage} \quad (2)$$

and

$$\beta_i = 1 - \sum_{j=1}^{N_s - 1} \alpha_j \quad \text{for the last stage} \quad (3)$$

where N_s is the number of stages in the multi-stage pushover analysis and α_i is the effective modal mass ratio for the *i*th mode. It is noted that it can be shown that the sum of the effective modal participating mass ratios over all modes is equal to unity [Chopra 2007] .

The two, and three-stage pushover analyses are used for the multi-stage pushover analysis in the torsionally-stiff and torsionally-flexible systems. In the case of torsionally-similarly-stiff systems, a four-stage pushover analysis is utilized in addition to the two, and three-stage pushover analyses. A classical single-stage pushover analysis is separately performed for all of the unsymmetric-plan systems. At the end, the seismic responses are obtained by enveloping the peak responses derived from the multi-stage and single-stage pushover analyses since it is possible to use different pushover analyses and to envelope the results [Fajfar 2000].

Accordingly, the CMP procedure can be expressed as a sequence of following steps:

1. Calculate the natural frequencies, ω_n, and the mode-shapes, Φ_n. The mode-shapes are normalized so that the lateral component of Φ_n, at the roof, equals unity ($\phi_{ryn} = 1$).
2. Compute the incremental lateral forces, $\mathbf{s}_n^* = \mathbf{M}\Phi_n$, over the height of the structure for different stages of multi-stage pushover analysis.
3. Compute the total target displacement, δ_t, at the roof. The target displacement increment for each stage of the multi-stage pushover analysis is obtained by Eqs. (1) to (3).
4. Apply the gravity loads and then perform the single-stage and multi-stage pushover analyses according to the following sub-steps until the control node (CM) at the roof sways to the predetermined total target displacement, δ_t.

    4.1. Perform a single-stage pushover analysis by using an inverted triangular load pattern for medium-rise unsymmetric-plan buildings and a uniform force distribution for high-rise ones until the total target displacement, δ_t, at the roof is reached. For torsionally-flexible buildings, this analysis is carried out by using the force distribution derived from the modal properties of the fundamental effective mode.

    4.2. Perform a two-stage pushover analysis. In the first stage, implement pushover analysis, using the force distribution $\mathbf{s}_1^* = \mathbf{M}\Phi_1$, until the displacement increment at the roof reaches $u_{r1} = \beta_1 \delta_t$ (Eq. (1); $i = 1$) in which $\beta_1 = \alpha_1$ (Eq. (2); $i = 1$). Subsequently, in the second stage, continue the analysis with the incremental lateral forces $\mathbf{s}_2^* = \mathbf{M}\Phi_2$ until the displacement increment at the roof equals $u_{r2} = \beta_2 \delta_t$ (Eq. (1); $i = 2$) where $\beta_2 = 1 - \alpha_1$ (Eq. (3); $i = 2$).

    4.3. The third analysis is a three-stage pushover analysis which can be done in a similar process as defined for the two-stage pushover analysis.

    4.4. Similarly to the previous multi-stage pushover analyses described above, perform a four-stage pushover analysis. This analysis is performed only for torsionally-similarly-stiff systems.
5. Calculate the peak values of the seismic responses for the single- and multi-stage pushover analyses. The peak values for these analyses are denoted by r_i. Index *i* denotes the number of stage(s).
6. Calculate the envelope, r, of the peak responses as follows:

$$r = Max\{r_1, r_2\} \quad \text{for the TS and TF unsymmetric-plan systems with } T < 2.2 \text{ seconds} \quad (4)$$

$$r = Max\{r_1, r_2, r_3\} \quad \text{for the TS and TF unsymmetric-plan systems with } T \geq 2.2 \text{ seconds} \quad (5)$$

$$r = Max\{r_1, r_2, r_3 \; r_4\} \quad \text{for the TSS unsymmetric-plan systems} \quad (6)$$

where *T* is the period of the mode which has the largest effective modal mass ratio for the unsymmetric-plan building in the direction under consideration.

3. DEFENITION OF STRUCTURAL MODELS

Unsymmetric-plan models were created from symmetric-plan model. First, symmetric-plan building and relevant assumptions are described. The original symmetric-plan building considered in this investigation was 10-storey building. The building was 15 m by 15 m in plan and comprised three bays in each direction. All bays were 5 m. The storey heights were equal to 3.2 m.

The lateral load-resisting system of the building was a special steel moment-resisting frame (SMRF) in both directions. P-Δ (second order) effects due to gravity loads were included. The dead and live loads were equal to 650 and 200 kg/m^2 on the floor area. Seismic effects were determined according to the requirements of Iranian code of practice for the seismic resistant design of buildings [Standard No. 2800-05, 2005]. The seismic masses at all floor levels were assumed to be equal and to consist of the dead load plus 20% of the live load. The building was designed according to the allowable stress design method [AISC-ASD 1989]. The structure satisfied the detail requirements of the Iranian seismic code including the deformation limitation and strong column-weak beam criterion.

Unsymmetric-plan buildings were considered as variations of the symmetric-plan building. They were assumed to be mass-eccentric and one-way unsymmetric, i.e. symmetric about x-axis but unsymmetric about y-axis. In order to create the mass-eccentric systems, symmetric-plan building was modified. For this purpose, the stiffness properties of the symmetric-plan building were maintained and the centre of mass (CM) was specified eccentric relative to the centre of stiffness (CS) only along the x-axis [see figure. 1]. The eccentricity between the CM and CS was assumed to be 15% of the plan dimension. Three types of unsymmetric-plan buildings were created corresponding to the symmetric-plan building by modifying the ratio of the floor moment of inertia (I_{oj}) to the floor mass (m_j) [Chopra and Goel 2004]. The created systems, which have different degrees of coupling between the translational and torsional motions, involve torsionally-stiff (TS), torsionally-similarly-stiff (TSS) and torsionally-flexible (TF) systems. The ratios of the floor moment of inertia to the floor mass between the unsymmetric-plan buildings and the symmetric-plan building, the first four periods of linearly-elastic structures, as well as the heights of all buildings are listed in Table 1.

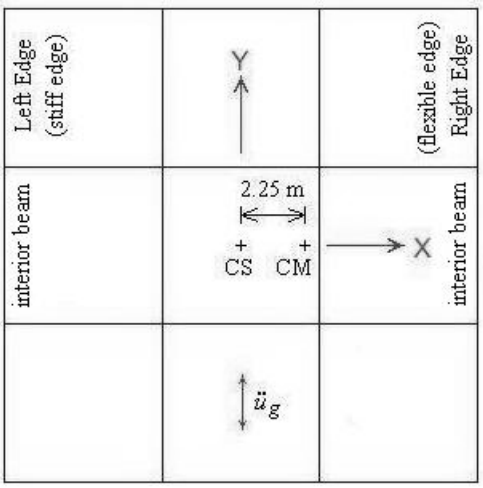


Figure. 1. Plan of the analyzed one-way unsymmetric-plan tall building

Table 1. Details of the analyzed 10-storey building structures

Type of buildings	$\frac{(I_{oj}/m_j)_{unsymmetric}}{(I_{oj}/m_j)_{symmetric}}$	Periods (seconds)			
		T_1	T_2	T_3	T_4
symmetric	-	1.52	0.51	0.29	0.19
TS	.28	1.63h	0.69	0.55	0.31
TSS	1.36	1.84	1.33	0.62	0.45
TF	5.67	3.33	1.50	1.14	0.63

4. DESCREPTION OF ANALYSES

The CMP procedure was performed together with the NL-RHA to investigate the accuracy of the CMP procedure. The MPA procedure was also carried out for the purpose of comparison. The NL-RHA was conducted by using the numerical implicit $Wilson-\theta$ time integration method. Seven ground motion records including the Imperial valley(1979), Victoria(1980), Morgan hill(1984), Hollister(1986), Landers(1992), Northridge(1994) and Duzce(1999) were used in NL-RHA. These selected ground motions were far-field records, and corresponded to locations which were at least 12 km from a rupturing fault. More details of the ground motion records are available in Reference [Poursha et al. 2009]. The records were scaled up to 1g to produce nonlinear responses. The second order ($P-\Delta$) effects were included within all the nonlinear static and dynamic analyses. $P-\Delta$ effects were also taken into consideration for all modes in the MPA and CMP procedures. The responses estimated by the aforementioned approximate pushover procedures were compared with the mean values of maximum seismic responses obtained from seven nonlinear response history analyses (NL-RHAs). In this research, the target displacement at the roof for the CMP procedure was determined as the mean value of the maximum top floor displacements (at the CM in the y-direction) resulting from NL-RHAs. The nonlinear version of computer program SAP2000 was used to perform the nonlinear analyses [Computers and Structures 2004]. It should be noted that point rigid-plastic hinges were used to represent the nonlinear behavior in the static and dynamic analyses. Hinges were defined at the ends of the frame members. The hinge properties and relative modeling parameters were specified according to the FEMA-273 [BSSC 1997]. The hysteretic behavior of the hinges is bilinear with 3% post-yield stiffness. Stiffness degradation was ignored for the NL-RHA.

5. RESULTS AND DISCUSSIONS

Seismic responses including the floor displacements, storey drift ratios and hinge plastic rotations are presented and discussed. The mean value of the maximum responses from NL-RHAs and the mean value plus standard deviation (σ) have been shown. Figure 2 displays displacements for different systems of the 10-storey building at the right (flexible) and left (stiff) edges. The figure demonstrates that the MPA and CMP procedures can estimate the displacements with acceptable accuracy at the flexible and stiff edges of the torsionally-stiff and torsionally-flexible systems. It's of interest to note that the displacements obtained by the MPA and CMP procedures at the flexible edge are more agreeable with the results produced by NL-RHA than those at the stiff edge. At the stiff side of the torsionally-stiff building, the CMP procedure provides relatively better predictions of displacements than the MPA procedure. As seen from figure 2, displacements estimated by the MPA at the flexible edge and by the CMP at the stiff edge may occasionally deteriorate (be underestimated) for the torsionally-similarly-stiff building. Deterioration of the predictions can be due to strong coupling between lateral and rotational motions in each mode of vibration [Chopra and Goel 2004].

A comparison of storey drifts predicted by the CMP and MPA procedures with those obtained by NL-RHA indicates that estimates obtained by these approximate procedures are accurate enough for the torsionally-stiff and torsionally-flexible buildings (see figure 3). The figure illustrates that the estimates of storey drift ratios derived from the CMP procedure are more accurate (sometimes relatively more conservative) than those resulting from the MPA procedure in some cases, especially at the mid and upper storeys. In some other cases, the MPA gives better estimates than the CMP. There is an improvement in estimating the storey drifts through the CMP at the flexible edge of the torsionally-similarly-stiff building (see figure 3(b)), but the predictions from the CMP procedure may occasionally deteriorate at the stiff edge of this building in comparison with the MPA. For example, the storey drift ratios are underestimated by up to 32% by the CMP and overestimated by up to 31% by the MPA at the stiff side of the 10-storey torsionally-similarly-stiff building. Figure 4 shows the height-wise variation of hinge plastic rotations at the interior beam of the frames at the right and left sides of the unsymmetric-plan buildings. The figure obviously demonstrates that the predictions obtained by the CMP procedure are mostly in excellent agreement with results produced by NL-RHA at the flexible and stiff sides of the unsymmetric-plan buildings. The MPA procedure fails to estimate the plastic rotations with acceptable accuracy for all the unsymmetric-plan buildings and it considerably underestimates the plastic rotations. The CMP procedure represents a significant improvement in predicting plastic rotations at the flexible and stiff sides in comparison with the MPA procedure. The improvement is achieved by incrementally applying the lateral forces during the stages in the multi-stage pushover analysis which controls the results at the mid and upper storeys of the unsymmetric-plan tall buildings. By incrementally applying the lateral forces, rotations of the plastic hinges are consecutively accumulated. Then, the plastic hinges, in the CMP procedure, deform into the inelastic range at the mid and upper storeys, whereas in the MPA procedure they remain elastic or deform slightly into the inelastic range at these storeys because the modal pushover analyses are performed independently. It is important to note that cumulative rotations of the plastic hinges due to cyclic hysteretic behavior are not taken

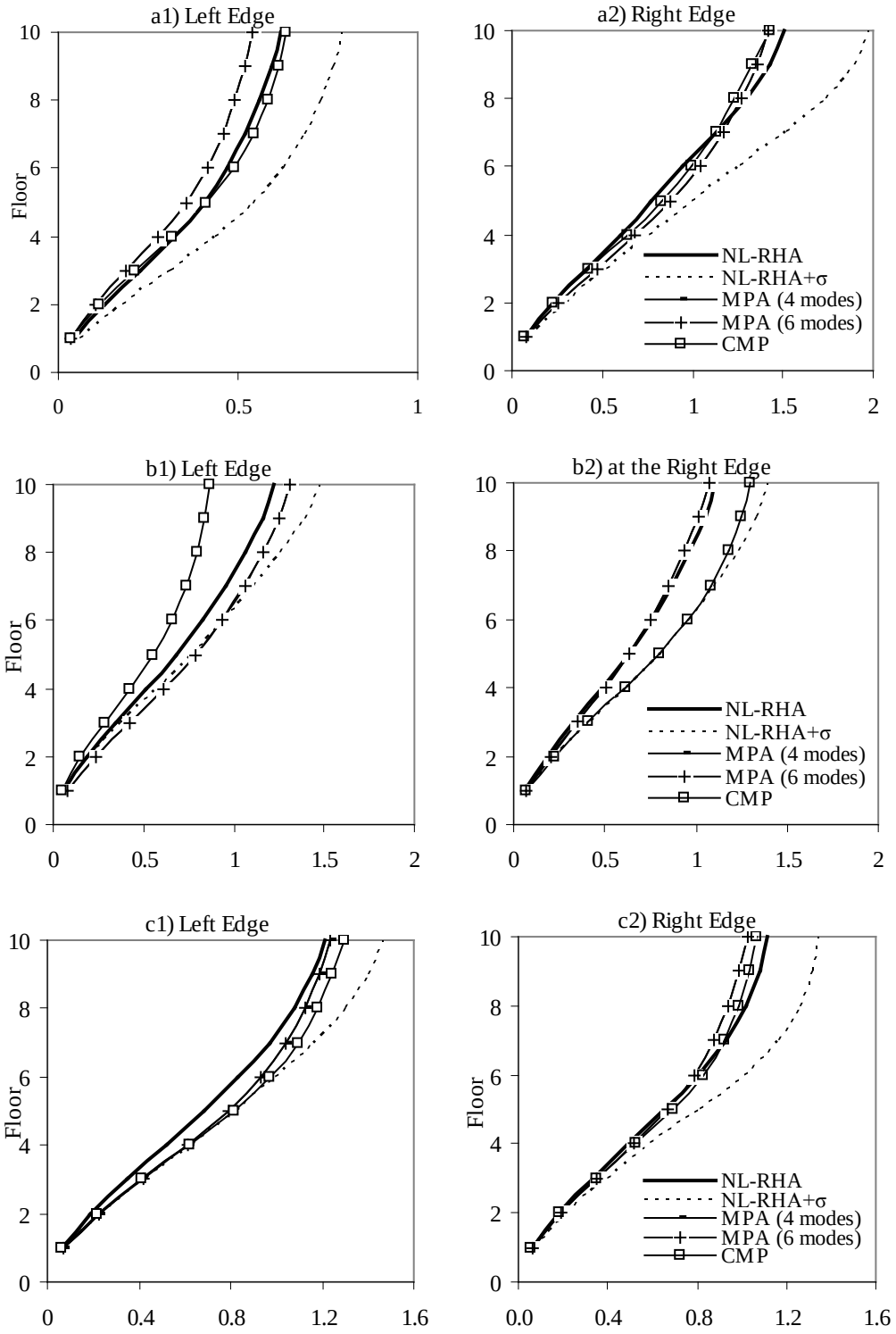


Figure 2. Height-wise variation of the displacements at the left and right edges: a) torsionally-stiff system b) torsionally-similarly-stiff system c) torsionally-flexible system

into consideration in an approximate pushover analysis such as the CMP procedure. As seen from figure 4(c), the improvement through the CMP procedure is also noticeable at the stiff side of torsionally-flexible systems where the prediction on this side was found to be so difficult in the previous investigations [Fajfar et al. 2008].

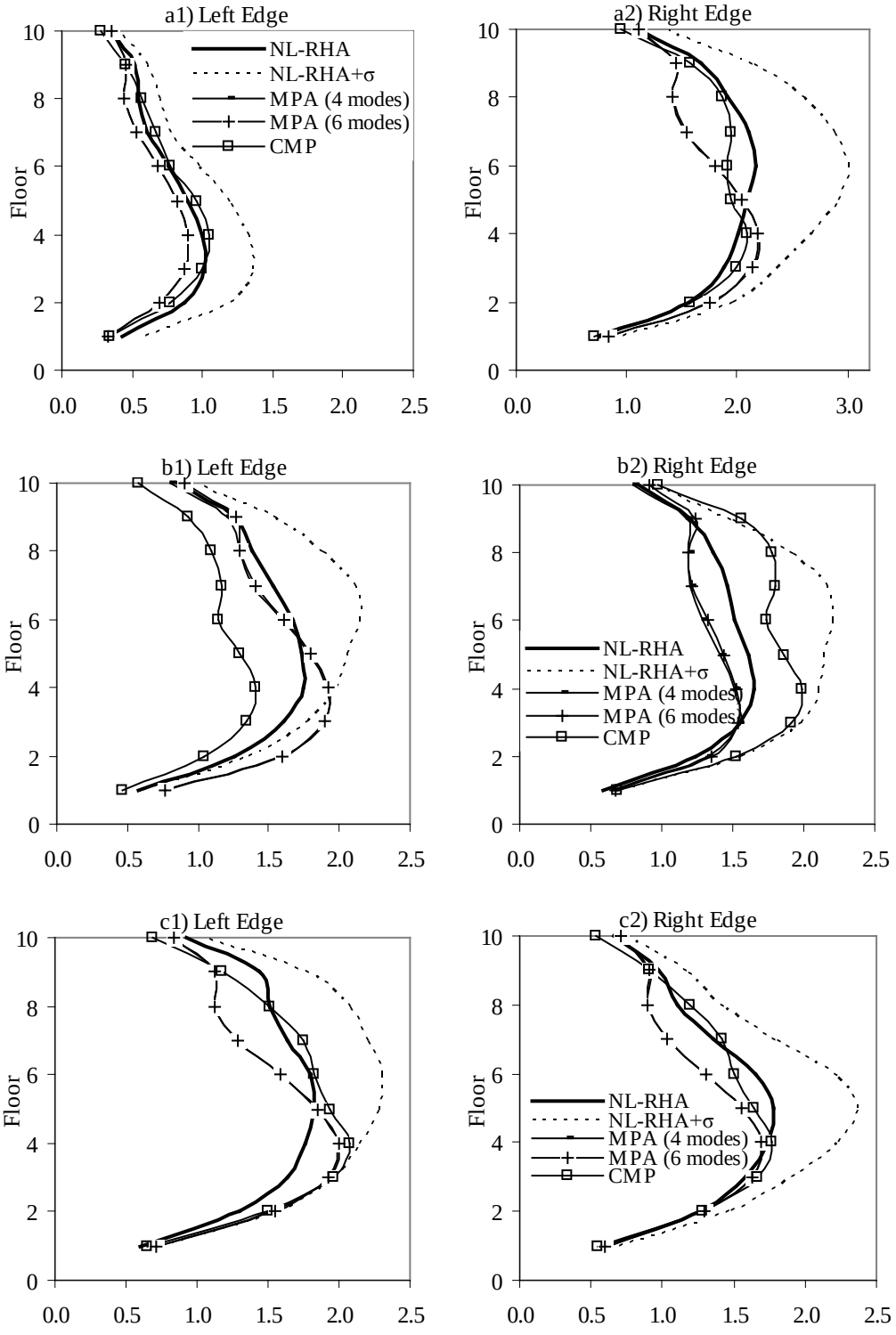


Figure 3. Height-wise variation of the storey drifts at the left and right edges: a) torsionally-stiff system; b) torsionally-similarly-stiff system; c) torsionally-flexible system

6. CONCLUSIONS

This article extends the consecutive modal pushover (CMP) procedure for unsymmetric-plan tall buildings to take torsional and higher mode effects into consideration. By conducting a large amount of analyses for the three types of unsymmetric-plan systems with different heights covering a wide range of periods, several

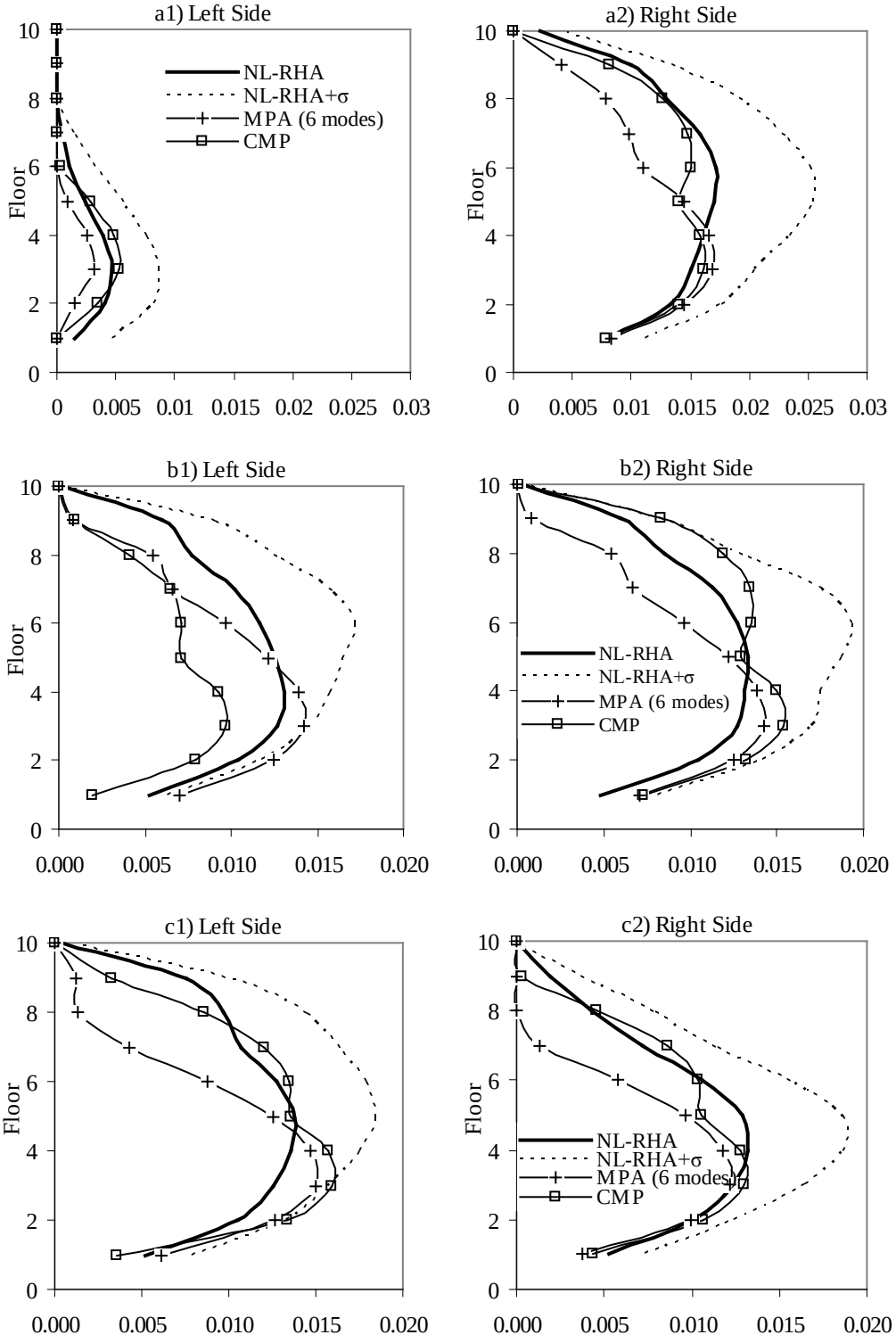


Figure 4. Height-wise variation of the hinge plastic rotations at the left and right edges: a) torsionally-stiff system; b) torsionally-similarly-stiff system; c) torsionally-flexible system

important conclusions are derived. The CMP procedure in general, provides accurate estimates of displacements and storey drifts at both flexible and stiff edges of torsionally-stiff, torsionally-similarly-stiff and torsionally-flexible systems, except at the stiff edge of torsionally-similarly-stiff systems, for which the predictions may occasionally deteriorate to some extent due to strong coupling of the lateral and torsional motions.

- There is, in general, not a large difference between displacements and storey drifts derived from the CMP and MPA procedures. Estimates of the storey drifts from the CMP procedure may be relatively better (sometimes more conservative) than those from the MPA procedure in several cases, especially at the mid and upper storeys. In other cases, the MPA gives better estimates of storey drifts than the CMP. Displacements and storey drifts derived from the CMP are better than those derived from the MPA at the flexible edge of torsionally-similarly-stiff systems, but the MPA procedure gives better estimates than the CMP procedure at the stiff edge of these systems.
- An excellent improvement has been, in general, achieved through the CMP procedure in predicting plastic rotations of the hinges at both flexible and stiff sides of unsymmetric-plan tall buildings in comparison with the MPA procedure. The improvement is achieved by incrementally applying the lateral forces during the stages of the multi-stage pushover analysis. This results in continuous accumulation of the plastic hinge rotations at the mid and upper storeys of unsymmetric-plan tall buildings.

References

AISC-ASD, 1989. Allowable Stress Design and Plastic Design Specification for Structural Steel Buildings, American Institute of Steel Construction: Chicago, IL.

Ayala, A. G. and Tavera, E. A., 2002. A new approach for the evaluation of the seismic performance of asymmetric buildings, *Proc. of the 7th National Conference on Earthquake Engineering*: Boston.

Barros, R.C. and Almeida, R., 2005. Pushover analysis of asymmetric three-dimensional building frames, *Journal of Civil Engineering and Management*, Vol. XI, No. 1, pp. 3-12.

Building Seismic Safety Council (BSSC), 1997. NEHRP Guidelines for the Seismic Rehabilitation of Buildings, FEMA-273, Federal Emergency Management Agency: Washington, D.C.

Chopra, A.K. and Goel, R.K., 2004. A modal Pushover analysis procedure to estimate seismic demand for unsymmetric–plan buildings, *Earthquake Engineering and Structural Dynamics*, 33, pp. 903-927.

Chopra, A.K., 2007. Dynamics of structures. Theory and Applications to Earthquake Engineering, Third Edition, prentice Hall.

Computers & Structures Incorporated (CSI), 2004. SAP 2000 NL: Berkeley, CA, U.S.A.

De Stefano M. and Rutenberg A., 1998. Predicting the dynamic response of asymmetric multi-storey wall-frame structures by pushover analysis: two case studies. *Proceedings of the 11th European Conference on Earthquake Engineering*, Balkema, Rotterdam.

Faella G. and Kilar V., 1998. Asymmetric multi-storey R/C frame structures: push-over versus nonlinear dynamic analysis, *Proceedings of the 11th European Conference on Earthquake Engineering*: Balkema, Rotterdam.

Fajfar, P., 2000. A nonlinear analysis method for performance based seismic design, *Earthquake Spectra*, 16(3), pp. 573-592.

Fajfar, P., Marusic, D. and Perus, I., 2005. Torsional effects in the pushover-based seismic analysis of buildings, *Journal of Earthquake Engineering*, 9(6), pp. 831-854.

Fajfar, P., Marusic, D., Perus and Kereslin, M., 2008. The N2 method for asymmetric buildings, *Workshop of nonlinear static methods for design*/ Assessment of 3D structures: Lisbon, Portugal.

Fujii, K., Nakano, Y. and Sanada, Y., 2004. Simplified nonlinear analysis procedure for asymmetric buildings, *Proc. of the 13th World Conference on Earthquake Engineering*: Vancouver, Canada, Paper No. 149.

Kilar, V. and Fajfar P., 1997. Simple push-over analysis of asymmetric buildings. *Earthquake Engineering and Structural Dynamics*; 26:233–249.

Kilar, V. and Fajfar, P., 2001. On the applicability of pushover analysis to the seismic performance evaluation of asymmetric buildings, *European Earthquake Engineering*, 15, pp. 20–31.

Lin, J.L. and Tsai, K.C. 2007. Simplified seismic analysis of asymmetric building systems, *Earthquake Engineering and Structural Dynamics*, 36, pp. 459-479.

Moghadam, A.S. and Tso W.K. 1998. Pushover analysis for asymmetrical multi-storey buildings. *Proceedings of the 6th U.S. National Conference on Earthquake Engineering*, EERI: Oakland, CA.

Moghadam, A.S. and Tso, W.K. 2000. Pushover analysis for asymmetric and set-back multi-storey buildings, *Proc. of the 12th World Conference on Earthquake Engineering*, Auckland, New Zealand, Paper No. 1093.

Poursha, M., Khoshnoudian, F. and Moghadam, A.S. 2009. A Consecutive modal pushover procedure for estimating the seismic demands of tall buildings, *Engineering Structures*, 31, pp. 591-599.

Standard No. 2800-05, 2005. Iranian code of practice for seismic resistant design of buildings, 3rd edition, Building and Housing Research Centre: Iran.

8CUEE CONFERENCE PROCEEDINGS
8th International Conference on Urban Earthquake Engineering
March 7-8, 2011, Tokyo Institute of Technology, Tokyo, Japan

DEVELOPMENT OF IT TRIAGE SYSTEM (TRACY) TO SHARE REGIONAL DISASTER MEDICAL INFORMATION

Muneyoshi NUMADA[1], Yasunori HADA[2], Miho OHARA[3], and Kimiro MEGURO[4]

1) Research Associate, International Center for Urban Safety Engineering (ICUS), Institute of Industrial Science (IIS), The University of Tokyo, Japan
2) Associate Professor, Department of Education Interdisciplinary Graduate School of Medicine and Engineering, University of Yamanashi, Japan
3) Associate Professor, International Center for Urban Safety Engineering (ICUS), Institute of Industrial Science (IIS), The University of Tokyo, Japan
4) Professor, International Center for Urban Safety Engineering (ICUS), Institute of Industrial Science (IIS), The University of Tokyo, Japan
numa@iis.u-tokyo.ac.jp, yhada@yamanashi.ac.jp, ohara@iis.u-tokyo.ac.jp, meguro@iis.u-tokyo.ac.jp

Abstract: We developed an IT triage system for collecting disaster medical information in real time. FeliCa cards and card readers are used to obtain the number and condition of patients. The system is composed of two elements. First, the number of patients for each triage level and the accepted number of patients in each diagnosis and treatment department are obtained in real time, including response for changing triage level. Second, this information is shared in real time among hospitals, the administration, and residents who are searching for their family. A disaster drill utilizing this system was held at the University of Yamanashi Hospital with 450 participants.

1. INTRODUCTION

Disaster medical care during accidents and disasters both large and small is carried out with less medical resources in normal situations.

Disaster medical care consists of triage, transport and treatment. In the case of a disaster or accident, it is necessary to exert maximum effect with limited medical resources, but to accomplish these hospitals need to estimate the expected number and condition of patients. The advancement of triage, including understanding and ensuring the capacity of beds, tracking the status of patients' visits and transport to other hospitals, managing the assignment of the appropriate medical staff and the distribution of medical materials is necessary. On the other hand, information sharing is important effective acceptance and transportation. These actions are required across the entire region outside the hospital for setting up the disaster headquarters, coordinating all tasks with the government and other hospitals, and supporting the patients' family and media.

To advance the triage, it is necessary to obtain patient information, such as the victim's status and number staying at hospital, discharging from hospital, and being transported to other hospital, in digital form and in real time.

Research using a digital pen with triage results can digitize patient information (Ashida et al. 2008). However, it is difficult to manage patient status when triage level is changed and to understand the number of patient in different triage levels. In addition, the usage of RFID tags and mobile RFID network equipment collection system can collect the patient information using mobile devices in real time (Sonoda et al. 2007, Kusuda et al. 2009), but it is necessary to overwrite data when the triage level is changed so the management is complicated. Furthermore, the flow line of patients cannot be confirmed when patients are moved between departments.

For information sharing across an entire region, an information sharing system has been built to consolidate all kinds of information related to disaster conditions (The Ministry of Health and Welfare Health Policy Bureau 1996). With this system, staffs are necessary for entering the data in this system, but it is difficult to assign staff under the limited conditions during a disaster.

The purpose of this study is to develop a triage system which can collect and share the disaster medical information in real-time among hospitals including emergency medical institution both inside and outside the disaster area, with residents and with the government. In order to examine the feasibility and effectiveness of this system, it was applied to a large-scale disaster drill with 450 participants at the Yamanashi University Hospital.

Using this system, it is possible to estimate the number of patients in different triage levels in real time, to identify the number of patients visiting each department, to manage the triage level changes in real time and to share this information with related institutions across an entire region including

people looking for their family in hospitals.

2. PROBLEM SETTING

Traditional triage problems are summarized from the result of the triage drill held at Yamanashi University Hospital.

2.1 Summary of triage

A triage team normally consists of the triage officer, nurse and support staff. The team conducts the triage in front of the hospital building. Patients taken to the triage are transferred to the treatment zones: the mild zone (green), the moderate zone (yellow), the severe zone (red) and death zone (black), depending on the level of injury. If the hospital cannot treat the patient with heavy injuries or due to lack of resources, the patient is transferred to another other hospital.

2.2 Triage problem

The following problems with the current triage method were obtained from the result of the triage drill at Yamanashi University Hospital.

1. *Real-time information*: It takes a certain amount of time for the disaster headquarters to know the latest patient information such as the number of accepted patients and the number of patients in the different triage levels because the copy of the current triage tag containing patient information such as name, age, etc. and triage level is carried by volunteer staff to the headquarters after a certain amount of information is collected in each zone. Furthermore, it takes time to copy the information to the patient's list handwriting one by one. In addition, patient information is written on a white board in front of the hospital near the triage zone to for people looking for their family in hospitals.

Therefore, it is difficult to grasp the number of patients in real time and assign the proper medical staff to the each zone in this triage method. When there is a change of triage level, the management of its change is very difficult to update in real time. Also, some staff needs to work only for the management of patient's list. It can be wasted work under the limited resources of medical staff in the disaster.

2. *Information sharing with other medical institutions*: It is necessary to determine that; the patient needs to be transferred to other hospitals by such as the doctor helicopter, because of the heavy status of patient or the luck of hospital's resources. However, hospitals which need to transfer the patient cannot make a plan of transference of patient. Because hospitals don't know which other hospitals can accept the patient. On the other hand, the accepting hospital management also doesn't understand the status of coming patients.

The information sharing among related medical institutions is necessary for the effective transport in the entire region.

3. *Information sharing with the family and government*: The people look for the location of hospital in which their family is accepted due to the injury in the disaster. The hospital and the government asked by the people need to answer the location of hospital and the status of the family.

However, immediate response is difficult for the hospital in a situation of a huge number of patients. Because they cannot search the patient whom the family looking for in the paper-based patient's information and it takes a certain time to obtain the latest information.

In the point of the local government, even if the government needs to find the family where they are, the local government has to ask the possible hospitals one by one.
This situation is inefficient for all the relations, the family, the hospital and the government.

3. IT TRIAGE SYSTEM (TRACY)

TRACY has been developed as the triage system to solve the traditional problems observed in the result of triage drill and the things discuss as mentioned above. The structure and framework of this present system has been set after several interview and meetings with doctors and nurses in emergency department. This section describes the overview of this system.

3.1 System framework

We discussed the obtaining patient's information in real time and the sharing it in the whole area as main features. The obtained patient's information including the location, triage level and status of patient need to be updated in real time. It is effective and efficient to share the information for the patient transference to the other hospital. On the other hand, there are some advantages in traditional triage tag. When we need to know the patient's information such as name, age and triage level, the current triage tag can show those by seeing it without special operation. Therefore, both present system and current paper based triage tag are used.

3.2 Management of triage level changing

We discussed when the triage level change the information about triage level also should be changed without special operation of the system in real time. If there is a change of triage level of the patient such as patient moves to the new triage zone. When the patient arrive the entrance of the new zone, we proposed that the change can be recorded by the usual pass-processing used in present system. This method can update the triage level automatically without special and/or additional work. This method also can confirm the movement of the patient correctly.

3.3 Patient's family

To respond quickly to the people who are searching for their family member in the hospital, the staff can search the patient by using the search function of present system in the patient list. In addition, if the list can share in the whole area, it is beneficial for the government and the family living far from disaster area.

3.4 Sharing of patient information for transportation

We discussed that it is important to conduct the effective transporting in the entire region. This could be done

by understanding the condition of accepting patients in other hospital and then to decide whether the transporting is available. Therefore, the present system is required to show the condition of all related hospitals to decide the available transportation in the entire region.

3.5 Discussion of equipment

The following three points in selecting the equipment for this system were considered. 1) Using the equipment on a daily basis, because other than daily-life equipment does not work in a disaster. 2) Using low-cost equipment in order to spread to the lot of hospitals under the current economic condition for sharing information in entire area. 3) Using simple-operating equipment that is not required the special training for operation only for the disaster.

First, we discussed a handheld wireless UHF IC tag reader/writer that can write the patient information to the tag. But when the medical staff try to know the patient's information in the IC tag, the special operation is required. In addition to that, for the sharing information of patient in the entire area, same equipment is necessary to install in all related hospitals. In the consideration of cost, the writing function of the patient information to IC tags/cards is not the low-cost option.

Therefore, the concept of this system is to manage the patient's information in the server side. Then, the three method, IC tag, bar codes and FeliCa, were discussed how to recognize the patient ID. The IC tag is expensive, even for the models without the function of a tag writer. For bar codes, we have to consider the accuracy of reading the bar code, the preparation of bar codes in advance and the problem of cost. As the result of these factors, the bar code is actually difficult to apply to the management of patient for triage. For FeliCa, USB-friendly FeliCa reader can be purchased at lower prices. It is available to use the PC, which is used on the daily treatment in hospitals, for connecting it. In addition, FeliCa cards are used by a lot of people for the train pass, student ID, and electronic money on a daily basis. Recently, there is also mobile phone with a FeliCa function. Therefore, FeliCa can be applied on a daily basis to conduct the triage in the disaster. The operation is simple "waving the card to the reader" and there is potential to be expanded further spread.

From the above discussions, FeliCa is used as the configuration of the equipment in this system.

3.6 Constitution of "TRACY"

Table 1 shows the configuration of the equipment for this system by using FeliCa. There are advantages by applying FeliCa on the daily basis to the triage. For example, the database of the personal information such as name, date of birth and address for the daily service can be applied for the triage to recognize the each patient in the disaster by using FeliCa ID. In this case, the hospital is not required to ask the patient for the personal information and can be understand the patient personal data who cannot speak due to heavy injury. As there are many people who have the FeliCa for daily service, therefore hospitals are not necessary to ready the FeliCa card in advance for all unpredictable large number of patients.

The unique serial number of FeliCa can be considered as the patient ID. Therefore the hospitals and other related institution can easily share and manage the patient transfer by using FeliCa ID for the entire region.

Figure 1 shows an overview of this system. FeliCa reader and PC for pass processing are set at triage zone and each zone such as Black (deceased), Red (immediate), Yellow (delayed) and Green (minor), and the department of medicine and radiation. PC and FeliCa reader at the each point for pass processing can record the patient's zone pass time and location in the database server (Figure 2).

In the case for example, that the symptoms of patient is changed to the worse, the latest triage level can automatically be update in database server without special work or operation by conducting the usual pass processing in this system. This is same case, even if the symptoms improve.

Table 1 Constitution of "TRACY"

Equipment	Content	Setting location
FeliCa card	Managing the FeliCa ID as the patient's ID	Triage tag (bounded at back of triage tag)
FeliCa reader	Connecting to the PC for pass processing to read the FeliCa card	Doorway at each zone
PC for pass-processing	Pass-processing window	
PC for server	Consolidate information	Outside of damaged area

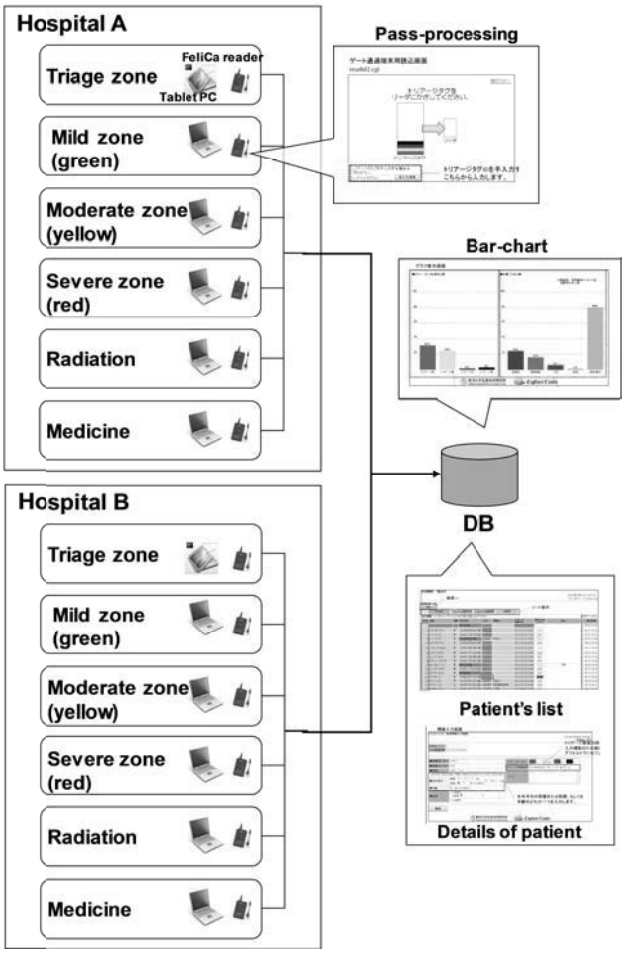


Figure 1 Overview of triage system "TRACY"

3.7 Content of input item

We consider following kinds of information are necessary for triage in TRACY.

From the hospital point of view, patient personal information and medical information are taken in to account as patient detail. But this triage system only covers the personal information (name, gender, date of date, etc.) but not medical information. Because misunderstood medical information may lead to medical errors and troubles.

As the result, input items of personal information such as name, date of birth, age, address, and free entry for the remarks are read with the triage tag. One example of using remarks is to write the patient exterior features such as the color of shirts, jacket, glass etc. to identify an individual who cannot speak due to heavy injured. Figure 3 shows the list of patients.

There is high possibility to stay or transfer to other hospitals for the patient with the level of Red (immediate) and Yellow (delayed). In case of those, the room or building of staying and the hospital name of transferring can be entered in this system.

The interface of the personal information window was made considering easy to be used by hospital staffs (Figure 4).

3.8 Visualization of patient data at the headquarters

It is important for the forward-command-headquarters directing the assignment of medical staff and the emergency-response-headquarters to take a proper action to manage the triage work based on understanding the situation such as the number of current accepted patients in the hospital, the number in the different triage level for each treatment zone in real time.

We discuss how to show those data in present system. As the result, the bar-chart showing the patient number in different triage level and the all patient list are necessary to analyze the condition of hospital for the triage officer at the both headquarters. The chart and the list can be updated automatically every 5 seconds. (Figure 5). When the patient's information is needed to edit, the details window of patient is available from the list of patient.

3.9 Preparation System

When a disaster occurs, the system must quickly starts with a minimum preparation of work as much as possible.

The present system is developed on the CGI (Common Gateway Interface). This system can work by the PC which can use WEB browser, is independent of PC type, and doesn't need any additional installation. The CGI program that runs on the WWW-server is independent of PC type/ OS and it can be work by the access form the browser of PC for pass-processing at the each zone. The result of the working of CGI returns to the browser of each PC at the zone.

As mentioned above, the digitize the patient information by FeliCa in real time can achieve not only the advancement of triage such as tracing of the patient treatment but also the sharing patient's information such as the transfer to the other hospitals, quick response to the person who asking of his/her family's location and coordination with the administration for the entire region.

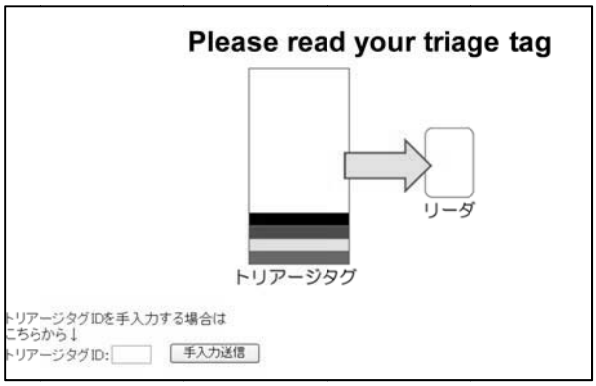


Figure 2 Pass processing window

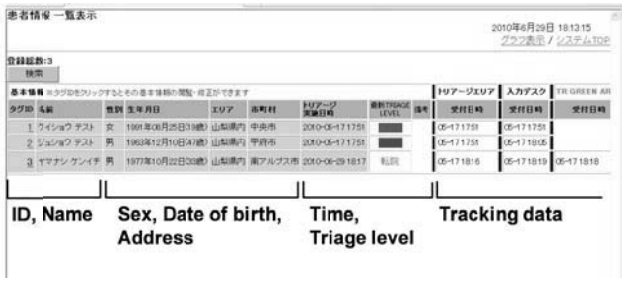


Figure 3 The list of patients



Figure 4 Details window of patient

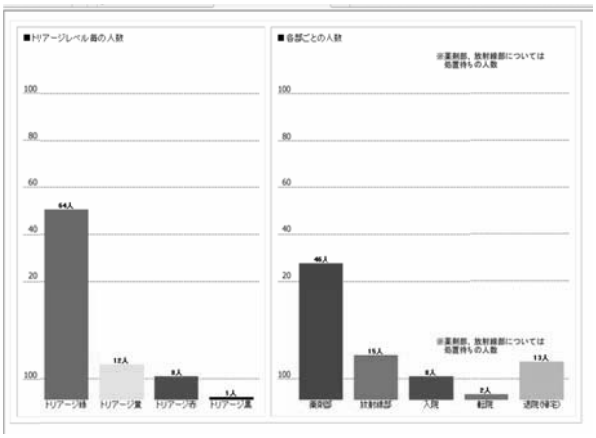


Figure 5 Bar-chart window for the number of patient in triage levels and treatments

4. VERIFICATION OF TRACY BY DEPARTMENT OF YAMANASHI UNIVERSITY HOSPITAL

The Yamanashi University Hospital in Yamanashi prefecture has experienced the triage drill since 2001. This triage drill becomes 10 times in total. The purpose of this drill is that the hospital staff makes accurate safety, accept the patient, implement triage and handle the treatment when the big earthquake occurs in Yamanashi prefecture.

The present triage system, TRACY, was examined its availability and practicality in the real disaster by applying the triage drill on this hospital with enough experience.

4.1 Triage drill of Yamanashi university hospital

In this triage drill, 48 doctors, 21 medical engineers, 48 nurses, 47 office staffs, 145 patients and support staff, totally approximately 450 people were attended. Participants were not only from this hospital, but also from the other hospital, the fire station, the government of Yamanashi Prefecture, the government of Kofu City, the government of Central City and residents.

The drill assumes the disaster level that, there is damage in the hospital building, but the lifeline and other medical equipment work normally. Therefore the triage and treatment are available even for a large number of visiting patients.

At 9:00 am a big earthquake with the epicenter of the west and southern area in Yamanashi prefecture caused a damage of houses, a fire and a traffic accident around the hospital. Then the staff in the hospital checks the status of the building damage and secures the safety of responsible department based on the disaster manuals and according to the instruction of the leaders of each department. All staff prepares to accept the number of patients as soon as possible. The team of triage set the necessary materials in the front of hospital building and to decide the triage level of each patient on the symptoms. After triage, the patient moves to the triage zone or is transferred to other hospital depending on the triage level.

4.2 Outline of installation of system

Table 2 shows the list of equipment of present system used in this triage drill. The PC set at Triage area in the front of hospital building, each triage zone, each treatment department and headquarters. Figure 6 shows the PC and FeliCa reader set at Department of Radiology. FeliCa cards is adhered to the back of triage tag, and managed to integrate triage tag and FeliCa cards together. As the reader of FeliCa card, the FeliCa port/ pasori (RC-S320) which is compatible with USB was used.

In this triage drill, FeliCa card has not been entered personal information such as name and date of birth, and assuming a situation in which these information was enter at the hospital. As for the timing and the person who enter the personal information, the patient information is input at the upstream process of triage to answer the person who asking from patient family as soon as possible. The special person who only input the patient data are assigned beside the doctors, nurses, clerks separately. By this way it can solve the

Table 2 List of equipment and system window

PC location	PC type (number)	FeliCa reader (number)	System window
Triage area	tablet (4)	○(4)	Pass-processing
Input desk	laptop (4)	-	Patient list
Green entrance	tablet (2)	○(2)	Pass-processing
Green zone	laptop (1)	-	Patient list
Green exit	tablet (1)	○(1)	Pass-processing
Yellow entrance	tablet (1)	○(1)	Pass-processing
Yellow exit	laptop (1)	-	Patient list
Red entrance	tablet (1)	○(1)	Pass-processing
Red exit	laptop (1)	-	Patient list
Black zone	laptop (1)	-	Patient list
Pharmacy entrance	tablet (1)	○(1)	Pass-processing
Pharmacy exit	tablet (1)	○(1)	Pass-processing
Inspection entrance	laptop (1)	○(1)	Pass-processing
Radiology entrance	tablet (1)	○(1)	Pass-processing
Radiology exit	tablet (1)	○(1)	Pass-processing
Forward-command-headquarters	laptop (2)	-	Patient list
Emergency-response-headquarters	laptop (2)	-	Patient list
Family answering	laptop (2)	-	Patient list
The government	laptop (2)	-	Patient list
Residents	laptop (2)	-	Patient list



Figure 6 PC and FeliCa reader set at Department of Radiology.

problem that the patient cannot move during the entering their triage result or personal information in present system. In the case of a large number of patients compared with the number of staff for data input, even if all the data entering is not completed, the personal data can be registered on a temporary basis, and then all staff can modify or update the content of the personal data at the each triage zone or headquarter.

All four triage teams consisted of triage officer (doctor), nurse and support staff (clerk) at the triage area.

The triage officer and nurse carry out usual triage work same as traditional triage way. On the other hand, the clerk read the FeliCa card to recognize its ID by Felica reader connected to the mobile PC by USB. Then clerks give the triage tag to triage officer, when just before triage officer

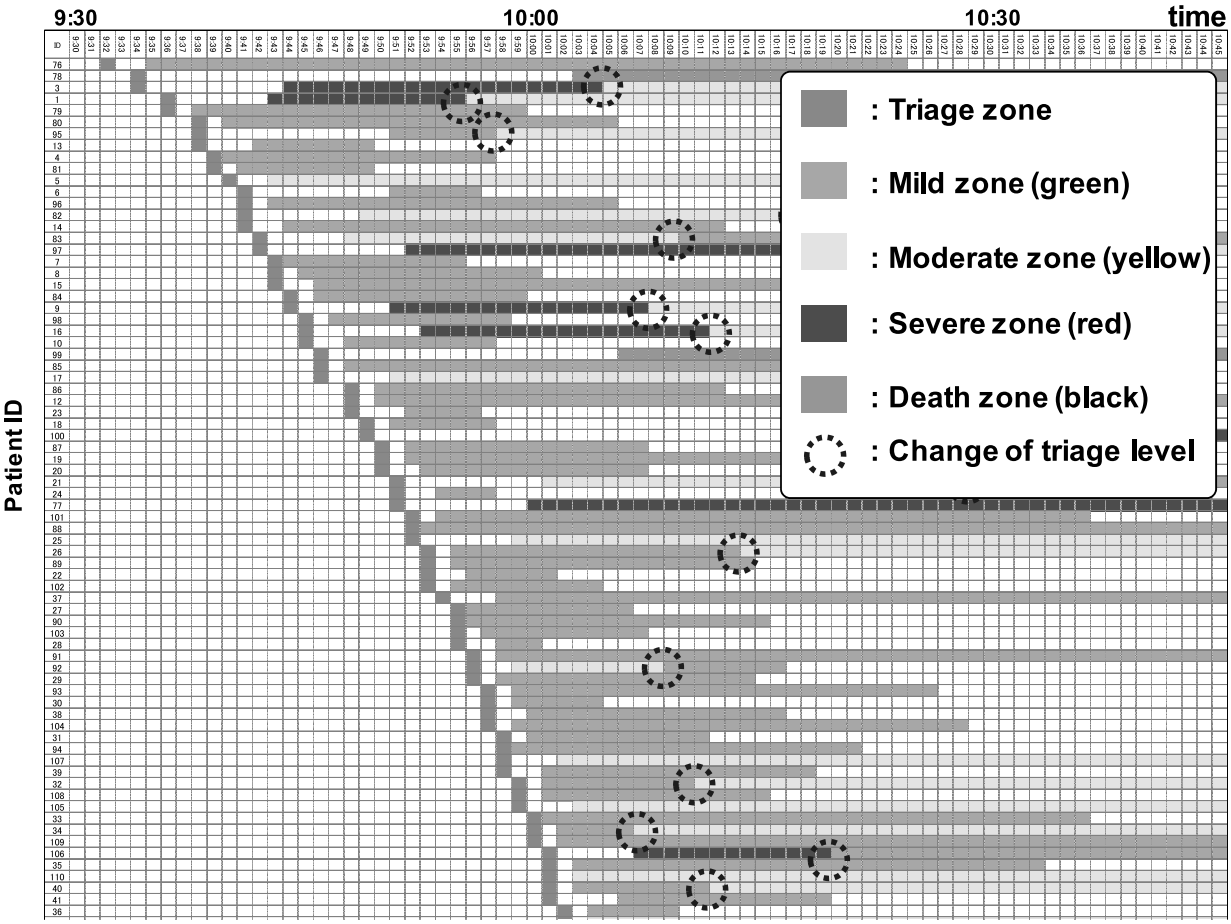


Figure 7 Time history of patient triage level

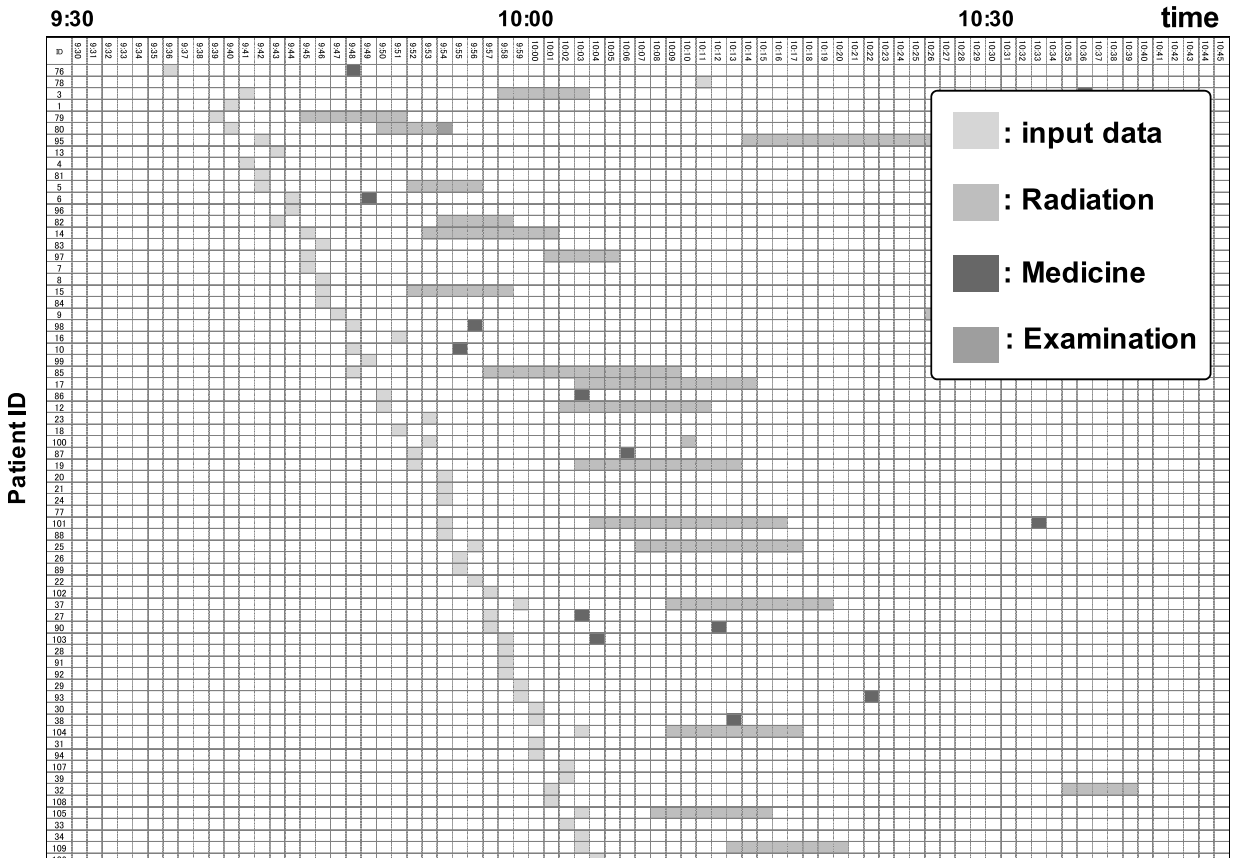


Figure 8 Time history of treatment department

begin to conduct triage. In this time, the only patient ID is input in the database.

After finishing triage, the clerk brings the first piece of triage tag (copy the paper written patient's information by triage officer) to the data-input-desk. Then the staff at the data-input-desk enters the patient's information such as the name, date of birth, age, address, remarks by reading the copy paper in the present system.

On the other hand, the patient who finished the triage moves to the each treatment zone. When the patient arrives at the zone entrance, the FeliCa card is read by the FeliCa reader to record the location and the time automatically as the pass-processing. This is same way for the other zone or department where the PC for the present system is set.

Thus, even if there is a change of triage level, it is possible to conduct the same pass-processing at the new place. The new triage level can be updated in the present system automatically in this way.

4.3 Result

1. *Time history of the patient changes*: Figure 7 shows the time history of each patient's triage level, taking the patient in the vertical axis and time in the horizontal axis. The staff in medical institute and the government can understand the triage level of all patients from the time when the patients are received in hospital to discharge from the hospital by following time history. The change of triage level also can be understood in this figure.

Figure 8 shows the time history of when each patient are taken the treatment in neuroradiology department, pharmaceutical department and inspection department. In the case of neuroradiology department, the time when the patient stay there is shown and maximum time of stay was 14 minutes for this drill.

Figure 9 shows the time history of the number of patients in each triage level. The number of patient in the Green zone has increased just after the triage drill starts, 50 patients stay there at 10:12, then, showing the tendency to decrease until 10:17. After that, the number of patients in green zone reached the maximum at 10:24. The first patient in red zone was accepted at 9:43, 5 patients were received treatment at 9:53. The first patient in black zone was accepted at 10:03, 3 patients were received at 10:21.

Similarly, Figure 10 shows the time history of the number of patients in each treatment zone. Neuroradiology department received the 9 patients at 10:09. Pharmaceutical department received 2 patients at 10:03, and not seeing the any remarkable concentration. Inspection department also did not show the remarkable concentration of patients, receiving 1 patient at 9:54.

2. *Response to the Changes of triage level*: Totally, there is the change of triage level for 20 patients (Figure 11). The change from the green to yellow was 8 patients, 1 patient from green to red, 5 patients from red to yellow, 5 patients from yellow to green, 1 patient from red to green. In this drill, because of over-triage was conscious, the change of triage level was affected by the over-triage.

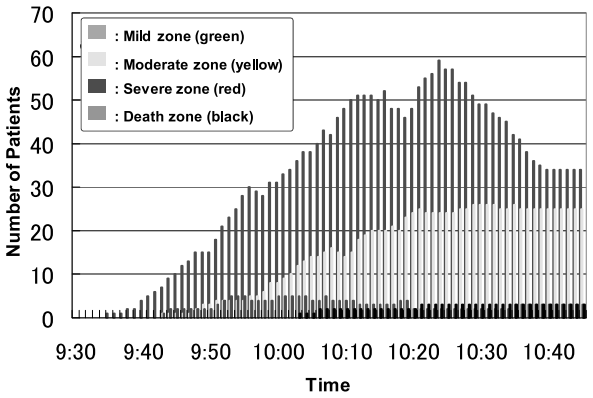


Figure 9 Time history of the number of triage level

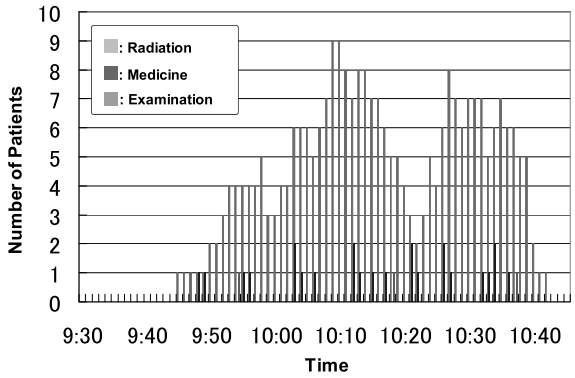


Figure 10 Time history of treatment department

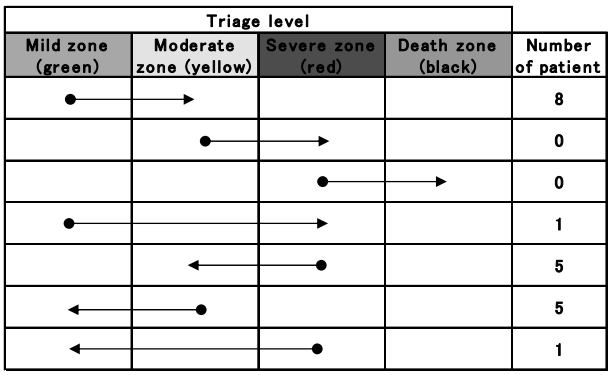


Figure 11 Pattern of triage level change

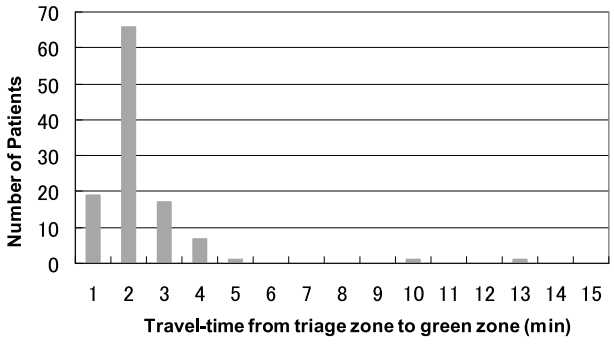


Figure 12 The lead-time from triage zone to green zone

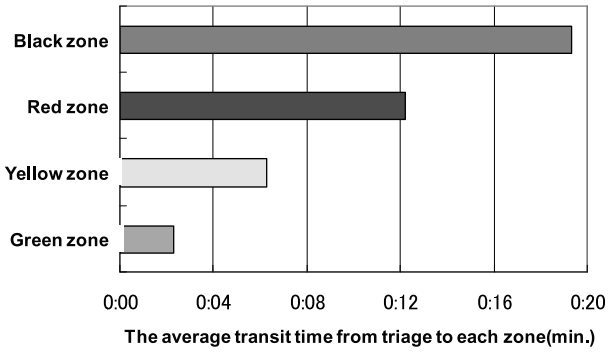


Figure 13 Average lead-time from triage zone to each zone

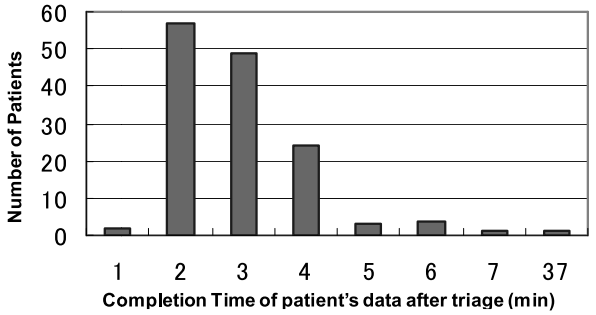


Figure 14 Time until complete the patient data at input desk

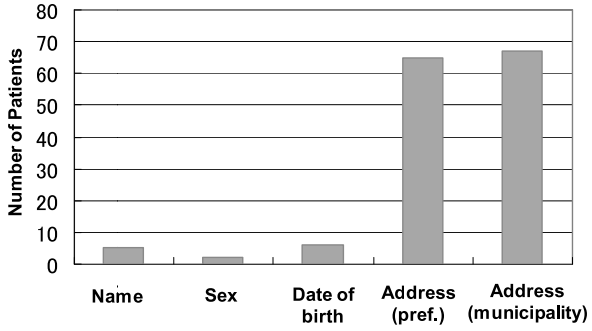
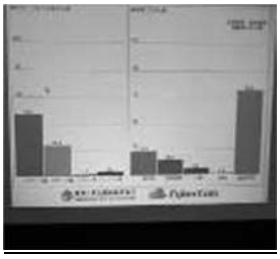


Figure 15 Number of un-entered item of personal information



a) Judge for assignment of medical staff



b) Bar-chart seen at the forward headquarter

Figure 16 The forward headquarter

3. *Transport after triage*: It is possible to start treatment early, if we can reduce the lead-time from the triage zone in the front of hospital building to the each treatment. In particular, it is necessary to transport as soon as possible for the patients to be mild who is the majority to the all patients and not to make dwell time at triage zone in front of hospital building.

Figure 12 shows the lead-time from triage zone to the green zone for the 112 patients who were judged to be mild. 19 patients arrived at the green zone by taking 1 minute after triage, in the same way, 66 patients by 2 minutes, 17 patients by 3 minutes, and the average leading-time was 2 minutes and 18 seconds. This data can be understood that the support member respond quickly to transfer the patients.

Figure 13 shows the average travel time from triage zone to each treatment zone. The green zone shows the shortest time, 2 minutes and 18 seconds as described above. And also, the travel time from triage zone to yellow zone shows the average of 6 minutes and 18 seconds (20 patients), to red zone shows the average 12 minutes and 13 seconds (9 patients) and to the black zone shows the average 19 minutes 20 seconds (3 patients) respectively. The yellow and red zone shows the longer moving time. This is because that these zones locate far from triage zone compared to the green and black zone, and there are many patients transferred by using a stretcher or wheelchair due to the heavily injured.

4. *Input of personal information*: The time take from the triage to the complete of the personal data input such as name, day of birth etc. was average 3 minutes, minimum 1 minute and maximum 37 minutes (Figure 14).

The patient with the longest time of 37 minutes was deceased (black zone), it takes time to identify the individual. There is record that shows the personal features like "blonde hair, blue shirt, confirm of the dead at 9:34" in remarks. And also, from the time history, triage at 9:34, the dead is confirmed 9 minutes after that, transferred to the black zone, and then the personal data is entered.

As for the accuracy of the input item, there are 5 patients is with no input of name, 2 patients with no input of gender, 6 patients without date of birth data, 65 patients without address.(Figure 15). The 3 patients out of 5 patients without input of name are recorded showing with their feature like wearing black clothes as for personally identifiable information in the remarks.

5. *Assignment of medical staff*: The forward-command-headquarters directing the assignment of medical staff could take a proper action to manage the triage work based on understanding the situation such as the number of current accepted patients in the hospital, the number in the different triage level at each treatment zone in real time provided by the present system (Figure 16).

6. *Family support*: The family of patient visits to the hospital, which can be considered as that the family stays to look for patient status and location. However, immediate response is difficult for the hospital in a situation of a huge number of patients. Because they cannot search the patient, for whom the family is looking for in the paper-based patient's information. By using the key-word search function in the

present system in this drill, the all staff in hospital can search immediately the patient they are looking for.

5. CONCLUSION

This research developed an IT triage system for collecting disaster medical information in real time and sharing it among related institution in entire area. Felicia card and card-reader are used to constitute of this system to obtain the number and condition of patients etc. in real time.

A disaster drill was held at the Yamanashi University Hospital with 450 participants. TRACY was examined its availability and practicability by using in this drill. From the result of that, the present system can obtain the number of patients for each triage level and the accepted number of patients in each diagnosis and treatment department in real time, including response for changing triage level and the people looking for their family in hospital. In the point of the information sharing in the entire area, the patient's information can be shared among hospitals, the administration, and residents in real time.

The feedback and opinions were widely obtained from the entire evaluation meeting and the meeting with the mainly triage officer held after the triage drill.

From the results, the present system can solve the traditional problem such as the hospital cannot make a plan to receive the patients, the hospital cannot immediately answer the location and triage level of the patient to their families who are looking for details and it is impossible to take a proper action to manage the staff assignment for the forward-command-headquarters.

In addition, information on the degree of concentration of patients at each hospital can be shared between medical agencies and the governments in real time through the database. Therefore the patient transportation can be conducted by avoiding to the hospital which is busy or over capacity, and effective transportation is able to be achieved in the entire region. Although the patient concentration information is required high real-time data-collection, this system can work even if a large number of patients in the case of large-scale disaster.

Therefore, this system has the availability and practicability to the triage in the disaster.

On the other hand, we also discuss the issues and needs in the future.

(1) How we can consider the patients without reading the FeliCa card in the confusion/busy of hospital and the patient whose arm cannot move due to injury. We discuss the mobile type FeliCa reader is available to those patients.

(2) It is better to show the bar-chart and patient list at each zone or department to understand/share the latest status of entire hospital.

(3) The pass-processing can be additional work for the patients and staff. However, as this system can provide the status of hospital and share the data in entire region, the related people can take a better action.

(4) How we can set up the system as soon as possible after the disaster occurs. The present system can install to the PC which are used in the daily hospital working. This system is developed as the Web application, the client PC is not required installation in advance, and also, the present system can be used in a PC machine-independent. Therefore, the system can work by connecting only FeliCa reader to its PC.

These discussions are implementing to increase more practical level in the next drill. We will expand and examine TRACY according to the result obtained this triage drill.

Acknowledgements:

The authors acknowledge complete cooperation from the Department of Medicine at Yamanashi University hospital. This cooperation makes possible to develop and examine the present system. Especially, the authors got the valuable advice about system function and structures from Professor Kenichi Matsuda and Dr. Shoji Suzuki as a specialist of the emergency medicine. The authors also acknowledge support from the Japan Ministry of Education, Culture, Sport, Science, and Technology (MEXT) for development of present system.

References:

Kusuda, J., Kiyama, N., Utiyama, A., Hiromori, A., Umedu, T., Yamaguchi, H. and Higashino, T. (2009), "Design and Development of Electronic Triage System Using Wireless Sensor Networks," The Institute of Image Information and Television Engineering Technical Report, Vol.33, No.36, 33-38.

Ashida, H., Takeshima, S., Wakisaka, H., Ueki, T., Yamamoto, T., Karasawa, K., Inaba, T., Tsuji, K., and Komura., T. (2008) , "A data input system for triage tag information using a digital pen: a training program for acceptance of a massive number of injured people at the Japan Self Defense Force Central Hospital," *Japanese Journal of Disaster Medicine*, 13(1), 56-60.

Sonoda, A., Inoue, S., Oka, K., and Fujisaki, S. (2007), "Experiment of Large Scale Triage with RFID Tags," *Transactions of Information Processing Society of Japan*, 48(2), 802-810.

The Ministry of Health and Welfare Health Policy Bureau (1996), "Disaster health care system of the 21st century - Ideal way of medical treatment offered to disaster, " Herusu Shuppan, Co. inc., 25-48.

Shimora,H., Matsui, H., Noda, I. (2009), "Cooperation of Disaster Related Systems on Distributed System Architecture, "Journal of JAEE, 9(2), 61-72.

The National Institute of Advanced Industrial Science and Technology (AIST) , "DaRuMa, " http://sourceforge.jp/projects/daruma/

Yamanashi Prefecture HP : Base disaster Hospital , http://www.pref.yamanashi.jp/ft-hokenf/60475114366.html

8CUEE CONFERENCE PROCEEDINGS
8th International Conference on Urban Earthquake Engineering
March 7-8, 2011, Tokyo Institute of Technology, Tokyo, Japan

A PERFORMANCE-BASED FRAMEWORK FOR DESIGN AND EVALUATION OF COMMUNITIES SUBJECT TO HAZARDS

Michael Mieler[1] and Bozidar Stojadinovic[2]

1) Graduate Student, Dept. of Civil and Environmental Engineering, University of California, Berkeley, USA
2) Professor, Dept. of Civil and Environmental Engineering, University of California, Berkeley, USA
mmieler@berkeley.edu, boza@ce.berkeley.edu

Abstract: In recent years, performance-based engineering (PBE) has emerged as a viable alternative to prescriptive code-based procedures for design and analysis of individual buildings. However, growing interest in the prediction of community performance necessitates an updated and expanded design and evaluation framework for communities. This paper explores the many issues that arise when the PBE methodology is extended from individual buildings to entire communities. A conceptual framework for the performance-based design and evaluation of communities is presented and discussed. The proposed framework comprises two main parts: the first part outlines a procedure for establishing a graded set of performance objective for a community; the second part outlines a procedure-neutral methodology for evaluating whether specified performance objectives have been satisfied. An implementation strategy for the proposed framework is also discussed. While the proposed framework is currently in early stages of research and development, it lays foundations for a more consistent and transparent approach to predicting community performance.

1. INTRODUCTION

Currently, the design and evaluation process for individual buildings centers on satisfying various requirements specified in building codes. In the United States, most jurisdictions have adopted the *International Building Code*. These code-based procedures, which are deterministic and prescriptive in nature, provide the minimum criteria considered prudent for the protection of life safety (BSSC 2004, 2009). Structures that satisfy these requirements implicitly achieve certain levels of performance. However, an assessment of actual performance is not required. As a result, a building may perform better or worse than the level implicitly assumed by the building code (ATC 2006).

In recent years, performance-based engineering (PBE) has emerged as a viable alternative to traditional code-based procedures, offering several important improvements to the current design and evaluation process. First, PBE requires establishment of explicit performance objectives for a building. A performance objective typically comprises a reliability target, performance level, and hazard scenario; for example, a 90% probability of being operational immediately following the maximum considered earthquake. And second, PBE requires an evaluation of actual building performance, incorporating uncertainty in both demand and capacity. As a result, PBE provides a more accurate and reliable estimate of the expected performance of individual buildings in different hazard scenarios. Furthermore, building performance can be quantified in terms of repair costs, casualties, and downtime, metrics that are more meaningful to building owners and decision makers than estimates of forces and displacements.

Currently, the PBE methodology addresses the design and evaluation of individual buildings. In general, performance objectives established for individual buildings are not linked to broader performance targets for a community, which can frustrate efforts to reliably predict the performance of communities in different hazard scenarios. This growing interest in community performance necessitates an updated and expanded design and evaluation framework for individual buildings, as well as other important community components (including lifelines and organizations).

This paper explores issues relating to extending the PBE methodology from individual buildings to entire communities. Specifically, a performance-based framework for design and evaluation of communities is proposed and discussed. This conceptual framework enables a more complete understanding of community performance to be obtained.

2. EXTENSION OF PBE METHODOLOGY TO COMMUNITIES

2.1 Definition of Community

A community comprises three primary systems (adapted from Mileti 1999): the natural environment, social infrastructure, and physical infrastructure (see Figure 1). The

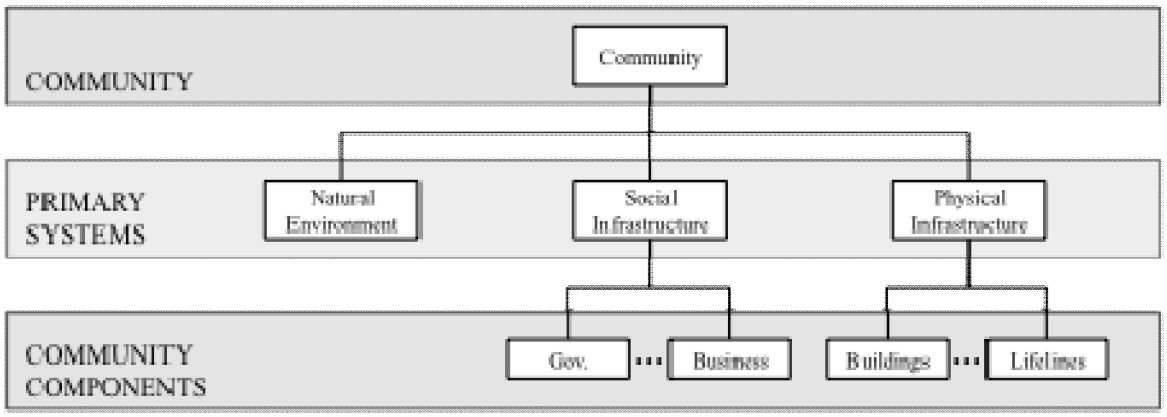


Figure 1 Hierarchal organization of a typical community

natural environment includes the land, water, and air surrounding a community, which give rise to natural hazards (earthquakes, hurricanes, floods, etc.). Social infrastructure refers to the public and private organizations and institutions that provide goods and services to a community. The physical infrastructure includes the human-made structures and systems that support the necessary functions of a community. These three systems are highly interdependent and interrelated. For example, many organizations within the social infrastructure rely on various components within the physical infrastructure to produce and deliver goods and services. These same organizations, however, may also have direct control over how the physical infrastructure is developed and maintained. Therefore, to obtain a more complete understanding of community performance, each system must be adequately addressed.

Each primary system comprises individual community components (see Figure 1). A community component is an element, network, or organization that performs a specific function in a community. Within the social infrastructure are government agencies (police and fire departments, etc.), businesses (banks, grocery stores, etc.), and other organizations. Within the physical infrastructure are buildings and lifelines. Lifelines include communication, electric power, liquid fuel, transportation, water, and waste disposal systems. Again, if a more complete understanding of community performance is to be obtained, all relevant community components need to be addressed in the design and evaluation process.

2.2 Proposed Framework

The proposed framework extends the PBE methodology from individual buildings to entire communities. It comprises two main parts. The first part of the framework (Figure 2) outlines a procedure for establishing performance objectives, first for the community in general and then for specific community components (buildings, lifelines, organizations, etc.). This graded approach ensures that performance objectives for individual community components are consistent with broader objectives established for the community, a step missing from current procedures. It also ensures that performance objectives are specified for all those components necessary to satisfying community-level objectives, including components in the physical and social infrastructure. A clear, well-graded set of performance objectives is crucial to improving the transparency and consistency of the design and evaluation process.

The second part of the framework (Figure 3) describes a methodology for evaluating whether specified performance objectives have been satisfied. The methodology attempts to be procedure-neutral: any analysis procedure can be used to evaluate performance as long as it produces an estimate of component reliability, where reliability is defined as the probability that specified performance levels are satisfied. This neutrality gives the

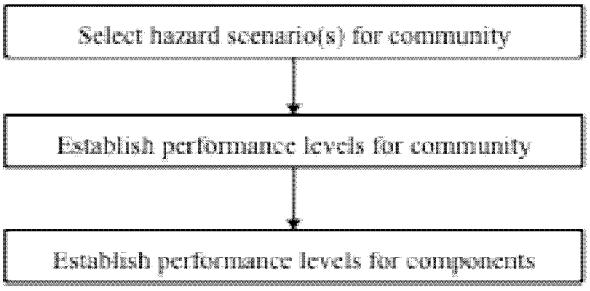


Figure 2 Procedure for establishing a graded set of performance objectives for a community

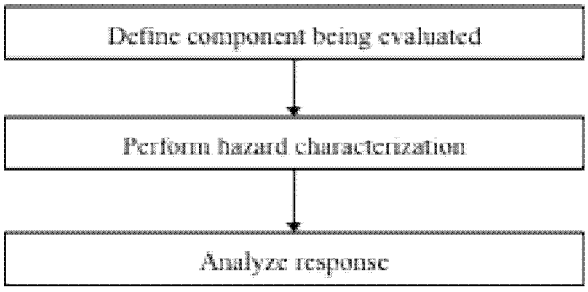


Figure 3 Procedure for evaluating the performance of a specific community component

designer or analyst flexibility in choosing the most appropriate or efficient method for evaluating performance. However, it should be noted that probabilistic procedures that address uncertainty in a consistent and transparent manner are preferable to deterministic ones.

3. DISCUSSION

In extending the PBE methodology from individual buildings to entire communities, many important issues arise. The following subsections discuss several of these issues.

3.1 Functional Correlation

Interaction between community components can significantly affect performance. Therefore, for a complete understanding of community performance to be obtained, these sources of interaction need to be identified and addressed. One source of interaction stems from functional correlation. Functional correlation arises when the functionality of one component depends on the functionality of other components.

To illustrate this concept, consider a hypothetical hospital with the following performance objective: 90% probability of remaining operational immediately after the maximum considered earthquake (MCE). In order to remain operational, the hospital building must suffer only minor structural and nonstructural damage. Furthermore, the hospital must also have uninterrupted access to important utilities (telecommunications, electricity, etc.). Both of these events must occur for the hospital to remain operational. The reliability, P_S, of the hospital can be computed using Eq. (1):

$$P_S = P(E_1 \cup E_2) = P(E_1 | E_2)\, P(E_2) \quad (1)$$

Where: E_1 and E_2 are the events defined in Table 1; the symbol $\cup$ denotes the intersection of two events (both events occur); $P(E_1 \cup E_2)$ is the probability that both E_1 and E_2 occur; $P(E_1 | E_2)$ is the probability that E_1 occurs given that E_2 has occurred; and $P(E_2)$ is the probability that E_2 occurs. So to calculate P_S, both $P(E_1 | E_2)$ and $P(E_2)$ need to be determined. $P(E_2)$ can be calculated directly through an analysis of the lifelines and/or emergency backup equipment that supply required utilities to the hospital. Computation of $P(E_1 | E_2)$ is less straightforward; however, Eq. (2) can be used to establish a lower bound on $P(E_1 | E_2)$:

$$P(E_1 | E_2) \geq P(E_1) \quad (2)$$

Table 1 Description of events that must occur for a hospital to remain operational

Event	Description
E_1	Hospital building suffers only minor structural and nonstructural damage
E_2	Hospital has uninterrupted access to important utilities

Eq. (2) results from the fact that E_1 and E_2 are positively related: if E_2 occurs (the hospital has access to required utilities), then E_1 is more likely to occur (the hospital suffers only minor structural and nonstructural damage). $P(E_1)$ can be calculated directly through an analysis of the hospital building. Using Eq. (2), a lower bound can be established for P_S:

$$P_S \geq P(E_1)\, P(E_2) \quad (3)$$

To make this example more concrete, consider that separate analyses have revealed $P(E_1) = 0.90$ and $P(E_2) = 0.90$. Using Eq. (3), $P_S \geq 0.90^2 = 0.81$. In other words, a lower bound estimate of the reliability of the hospital is 81%. Recall that the specified reliability target is 90%. Therefore, the hospital will likely fail to satisfy its specified performance objective.

This example highlights the significant impact of functional correlation. Under the current design and analysis process, a performance evaluation of the hospital would consider only the response of the building. In this scenario, the reliability of the hospital becomes:

$$P'_S = P(E_1) \quad (4)$$

Using the same quantities as before, $P'_S = P(E_1) = 0.90$. Therefore, the hospital appears to satisfy its specified performance objective. However, due to functional correlation, the actual reliability of the hospital will likely be less than 90% (and probably closer to 81%).

Because of its potentially significant impact on component reliability, functional correlation needs to be included in all applicable performance evaluations.

3.2 Human and Organizational Factors

In expanding the focus of the design and evaluation process to entire communities, the role of the social infrastructure must now be considered explicitly. Performance objectives should be established for important organizations and institutions within a community. The performance of these organizations and institutions should then be evaluated to determine whether specified objectives have been satisfied. These performance evaluations can be quite complex, as the following example illustrates.

Consider a hypothetical fire department with the following performance objective: 90% probability that all fires are suppressed within 24 hours of the MCE. To evaluate whether the department satisfies this objective, it is beneficial to translate it into more traditional engineering parameters of capacity and demand: 90% probability that the capacity of the fire department exceeds the demand induced within 24 hours of the MCE. Both capacity and demand depend on the performance of various components within the physical infrastructure. Capacity depends on the condition of water, electric, transportation, and communication lifelines, while demand depends on the number of damaged buildings and ruptured gas mains throughout the community. Furthermore, the capacity of the

fire department also depends on various human and organizational factors, including (but not limited to) the management structure of the department and the level of training and experience of personnel.

Because of their potentially significant impact on reliability, human and organizational factors need to be included in all applicable performance evaluations.

3.3 Community Boundaries

Unlike buildings, which have well-defined physical boundaries, communities are nebulous, complicated systems of components and interactions. As a result, it may be difficult to establish appropriate boundaries for a community. Geographical boundaries alone may be insufficient. Certain lifelines can span and/or service multiple cities, and may fall under the jurisdiction of various public or private agencies. As a result, individual cities may have varying levels of control over the lifelines within their geographical boundaries.

Furthermore, actions taken (or not taken) by one community may impact adjacent ones. For example, in an effort to improve resilience, a city might require local businesses to retrofit their buildings to decrease downtime and interruption following an earthquake. However, if these businesses rely on goods and services provided by businesses outside the jurisdiction of the city, the retrofit program may not be effective unless nearby cities do the same (because they will likely experience similar earthquake effects).

4. IMPLEMENTATION

The conceptual framework proposed in this paper is currently in early stages of research and development. As a result, many issues identified in the previous section require additional investigation. Despite this, it is beneficial to consider how the proposed framework might eventually be implemented in practice. The following subsections discuss several pertinent issues.

4.1 Community Code

To ensure uniform levels of performance from community to community, a national community code should be developed. This document would serve a similar role for communities as building codes do for buildings. It would specify a graded set of minimum performance objectives for a community. To ensure both consistency and feasibility, this set of minimum performance objectives should be established by a diverse group of community stakeholders, including engineers, government officials, city planners, economists, politicians, residents, and building owners. Minimum performance objectives should be established for all important community components, including buildings, lifelines, and various organizations.

Unlike current building codes, the proposed community code would not contain specific procedures for analysis of individual components. Instead, it would specify confidence factors associated with the use of different types of procedures. For example, more realistic, probabilistic analysis procedures, like those outlined in ATC (2009), would be assigned higher confidence factors than simple, deterministic ones, like those contained in current building codes (ICC 2006). This would allow the designer or analyst flexibility in choosing the most appropriate or efficient method for evaluating performance, while at the same time promoting use of more realistic analysis procedures.

4.2 Rating System

Because a large number of existing buildings, lifelines, and organizations would likely fail to satisfy the minimum performance objectives contained in the community code, a rating system should be developed. This rating system would expand the set of possible outcomes of a performance evaluation; instead of either satisfying or failing to satisfy its performance objective, a component would be given a rating based on its computed reliability.

For example, consider the hypothetical hospital analyzed in the previous section. The performance objective for the hospital specified a 90% probability of remaining operational immediately after the MCE. A performance evaluation revealed the actual reliability to be greater than 81% but less than 90%. Therefore, the hospital fails to satisfy its specified performance objective. However, if the rating system described in Table 2 were employed, the hospital would receive a rating of three stars.

A simple, clearly defined rating system would facilitate communication with the public regarding the expected performance of different components within a community, and may even incentivize retrofits or other performance upgrades.

4.3 Compatibility with Existing Procedures

One important feature of the proposed framework is that it is procedure-neutral: any analysis procedure can be used as long as it produces an estimate of reliability, P_S. As a result, current code-based procedures can be made compatible with the new framework. At the moment, however, these procedures do not require an estimate of P_S to be computed. To address this deficiency, standard values of P_S could be developed for various prototypical buildings with different occupancy categories and lateral force resisting systems. These standard values, which would represent conservative estimates of actual reliability, would automatically be achieved if the requirements of the building code are satisfied. This backwards compatibility is essential if the proposed framework is to be implemented successfully,

Table 2 Description of a simple rating system for community components

Rating	Reliability
Four stars	$P_S \geq 0.90$
Three stars	$0.80 \leq P_S < 0.90$
Two stars	$0.70 \leq P_S < 0.80$
One star	$P_S < 0.70$

as it eases the transition from current code-based procedures to more realistic, probabilistic ones.

5. CONCLUSIONS

The extension of the PBE methodology from individual buildings to entire communities requires consideration of many important issues overlooked by the current design and evaluation process, including functional correlation and human and organizational factors. If an improved understanding of community performance is to be obtained, these issues need to be addressed.

This paper has presented a conceptual framework for the performance-based design and evaluation of communities subject to hazards. The proposed framework comprises two main parts: the first part outlines a procedure for establishing a graded set of performance objective for a community; the second part outlines a procedure-neutral methodology for evaluating whether specified performance objectives have been satisfied. This paper has also discussed a possible implementation strategy for the proposed framework, including development of a community code, rating system, and standard P_S values for current code-based procedures.

While the proposed framework is currently in early stages of research and development, it lays foundations for a more consistent and transparent approach to predicting community performance.

References:

Applied Technology Council (ATC) (2006). *Next-generation performance-based seismic design guidelines: Program plan for new and existing buildings (FEMA 445)*, ATC, Redwood City, CA.

ATC (2009). *Guidelines for seismic performance assessment of buildings (ATC-58 50% Draft)*, ATC, Redwood City, CA.

Building Seismic Safety Council (BSSC) (2004). *NEHRP recommended provisions for seismic regulations for new buildings and other structures (FEMA 450 / 2003 Edition)*, National Institute of Building Sciences, Washington, DC.

BSSC (2009). *NEHRP recommended provisions for seismic regulations for new buildings and other structures (FEMA P-750 / 2009 Edition)*, National Institute of Building Sciences, Washington, DC.

International Code Council (ICC) (2006). *2006 International Building Code*, ICC, Country Club Hills, IL.

Mileti, D.S. (1999). *Disasters by design: A reassessment of natural hazards in the United States*, Joseph Henry Press, Washington, DC.

8CUEE CONFERENCE PROCEEDINGS
8th International Conference on Urban Earthquake Engineering
March 7-8, 2011, Tokyo Institute of Technology, Tokyo, Japan

CEILING FRAGILITY OF JAPANESE CEILING SYSTEMS

Yasuaki Sato[1], Gregory A. MacRae[2], Rajesh P. Dhakal[2] and Shojiro Motoyui[3]

1) Graduated student, Dept. of Built Environment, Tokyo Institute of Technology, Japan
2) Associate Professor, Dept. of Civil and Natural Resources Engineering, University of Canterbury, New Zealand
3) Associate Professor, Dept. of Built Environment, Tokyo Institute of Technology, Japan
yasuaki.s.aa@m.titech.ac.jp, gregory.macrae@canterbury.ac.nz, rajesh.dhakal@canterbury.ac.nz, motoyui.s.aa@m.titech.ac.jp

Abstract: In Japan, the performance of modern seismically designed building structures has been good. However, non-structural damage is still significant and several people were injured by the collapse of ceiling boards in a 2005 earthquake. Ceiling failure can cause significant downtime and economic loss in addition to life safety risk. Previous studies have shown that ceiling collapse generally occurs at the connections behavior. Connection can be simulated by using a detailed numerical model. The ceiling system describes the likelihood of ceiling damage resulting from the connection damage. This paper describes the development of fragility curves for typical Japanese ceilings. Strength of the connection is obtained from previous experimental testing, and the connection shear force demand is calculated by using the elastic and inelastic 2D finite element analysis. The fragility of a typical Japanese ceiling system is then obtained by comparing the member/connection forces obtained from these analyses with the corresponding strengths generated randomly through Monte-Carlo analysis. Thus developed fragility is validated against the response of ceiling system in the shaking table test. The fragility curves can be used to probabilistically interpret ceiling performance as well as to estimate ceiling contribution to the overall building loss in earthquakes.

1. INTRODUCTION

Earthquakes are of concern because they can produce losses. The loss inducing process is simply described in Figure 1. Faulting occurs beneath the ground (1). This results in waves being distributed within the rock and soil which travel to the base of different structures (2). The shaking at the base of the structure, measured by an *Intensity Measure (IM)* such as peak ground acceleration or spectral acceleration, causes the structure to respond. *Engineering Demand Parameters (EDPs)* such as displacements and drifts tend to affect the structural elements and also partitions and cladding elements which are in contact with the different floors. On the other hand, *EDPs* in the form of accelerations at different levels can affect contents and other elements. If the *EDPs* are sufficiently large they can produce different types of damage, quantified by *a Damage Measure (DM)*. This damage results in loss, which can be measured in terms of the 3 D's – damage, death (injuries and life loss) and downtime (or business interruption). All of these can be expressed in terms of dollars, at least by the insurance industry. The probabilistic relationships between the different parameters should consider aleatory and epistemic uncertainty, before being combined through total probability theorem, to enable the uncertainty in the likely loss to be rationally evaluated.

Ceilings are the subject of investigation of this paper.

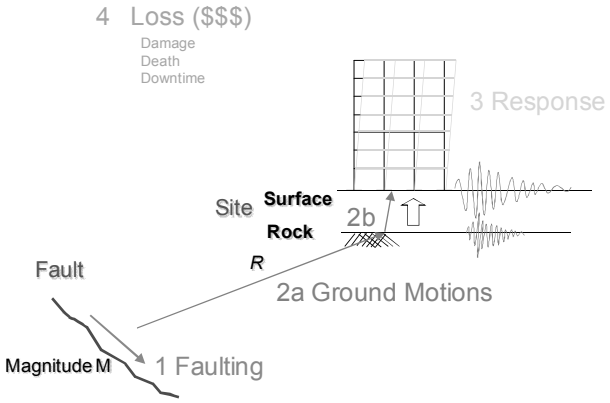


Figure 1. The effects of Earthquake Faulting on a Building



Figure 2. 2005 Miyagi prefecture earthquake damages

These may be attached in different ways to the floor above. Traditionally ceilings have not been designed by structural engineers, but have been considered to be architectural elements. However, as a result of ceiling damage and collapse, which has resulted in injuries and significant loss due to business interruption, it has been realized that a proper ceiling design is necessary.

Significant ceiling damage has been observed in the 2003 Tokachi oki earthquake, the 2005 Miyagi-ken oki earthquake (as shown for a swimming pool in Figure 2), the 2010 Chile earthquake, and the 2010 Canterbury Earthquake (Dhakal.R.P (2010)). In many of these cases the downtime had significant economic consequences. For example, the University of Canterbury was closed for 2 weeks because of heavy tile damage and ceiling collapse in several of the lecture theatres and libraries as a result of the Canterbury earthquake (Dhakal.R.P (2010)).

The aim of this paper is to describe and illustrate a method to answer the following questions:

1. How is a typical Japanese ceiling system constructed?
2. Which component is the most critical and hence important for *a Damage Measure (DM)* of a typical Japanese ceiling system?
3. What models are there to compute the demand force of the clips and the ceiling?
4. What methods are there to determine the capacity of the ceiling? And then, what is the capacity of a specific ceiling configuration, considering the statistical variation in element capacity, for a specified level of shaking?

2. TYPICAL JAPANESE CEILING SYSTEM

The typical Japanese ceiling system considered herein is composed of steel members and plaster board as shown in Figure 3. The M-bar, which is attached directly to the plaster board is connected to the channel with a clip. The clip is a unique metal part. It can be connected either in the front, or back, type of configuration as shown in Figure 4. This system is easily constructed and is widely used in Japan.

3. CEILING SYSTEM BEHAVIOR

The past earthquake damages and the previous studies (Motoyui et al. (2009)) have shown that the clip is the critical element that can cause the ceiling to fail and collapse. For horizontal loading along the axis of the channel, the channel can slide through the clip in both directions. There is no maximum displacement capacity in this direction. The failures that have been observed are due to horizontal loading of the ceiling perpendicular to the direction of the channel in Figure 4. To evaluate this behavior, experiments were performed with the setup shown in Figure 5 (Motoyui et al. (2009)). Here the ceiling is tested vertically, rather than horizontally, for simplicity in the direction perpendicular to the channel.

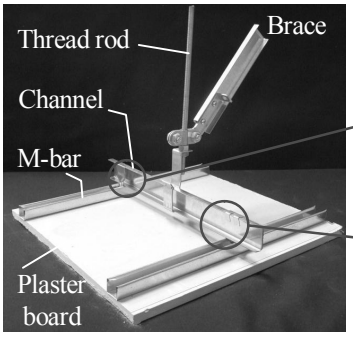


Figure 3. The typical Japanese ceiling

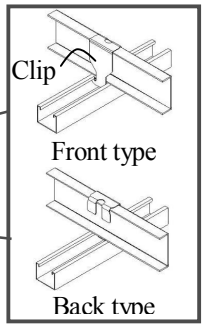


Figure 4. Clip type

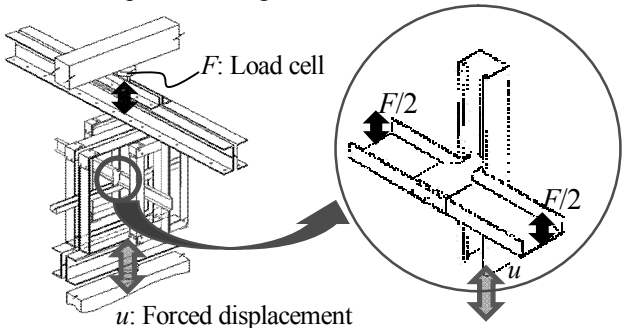
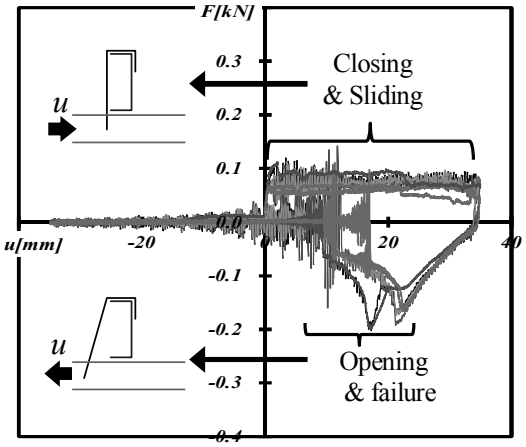
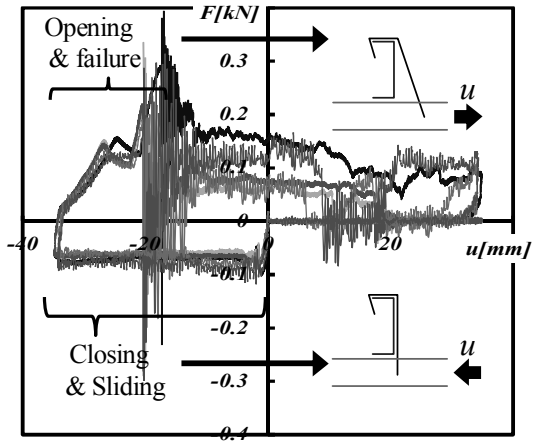


Figure 5. Experiment for Clip connection



a) The front type of clip



b) The back type of clip

Figure 6. The behavior of the clip connection

Figure 6 shows the cyclic push-pull behavior of the clip connection. It may be seen that the connection has two maximum strengths. When the clip moves away from the channel, it opens. As it opens, it undergoes plastic deformation and eventually separates from the channel allowing collapse. When the clip moves toward the channel, it slides on the m-bar when it reaches the sliding strength.

Table 1 describes the maximum strength in each test. The means and the standard deviation are obtained from these strengths. The information is used to create the connection strength in Monte Carlo method. Note that the sliding and failure strengths are different for opening and closing loading. This is because in one case the clip is on the back of the channel, and in the other case it is on the front.

4. THE ANALYSIS MODEL OF CEILING

4.1 THE CONNECTION MODEL

The clip that first reaches its "failure" force, then governs the capacity of the system and determines the horizontal force resisted by the ceiling. The force in each clip can be computed with a structure analysis. The previous studies have developed numerical models to simulate the behavior of clip connections using sophisticated FE models (Motoyui et al. (2010)). This model is complicated and a long time is needed to perform the analysis. A simpler model described in Figure 7 is used in this paper. The model is composed of several beam elements. Element (1) has the sliding behavior by elastoplastic type restoring characteristic. The yield strength is equivalent to the sliding strength. Element (2) releases from or contacts with the channel. The gap between the m-bar and the channel occurs when the clip is opening. The compressive force in this element does not occur until the gap reaches zero. Element (3) has the opening behavior and failure strength, and resists only compressive force. Element (4) is the elastic element for supplying the stiffness when the clip is opening. The node between element (1) and element (2) (and between element (3) and element (4)), is independent of the m-bar element.

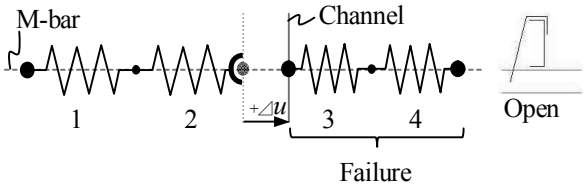
It may be seen in Figure 8 that the numerical model simulate the clip behavior well until the peak opening strength is reached. After this peak, the clip loses the performance of connection in the experiment. A more complex model is required to simulate the performance loss of connection. However, the model shown in Figure 7 can be reasonable to investigate the limit state of the ceiling system which changes from linear to nonlinear.

4.2 THE CEILING MODEL

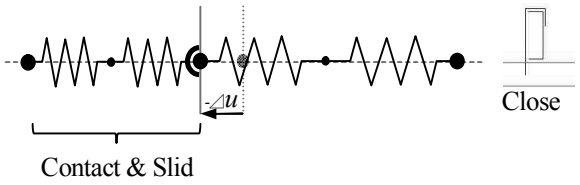
The ceiling configuration selected for this study is one which was set on the roof slab in the 5 story full-scale building test on E-defense in 2009 (Motoyui et al. (2009)). The ceiling has the area of 4.5m x 6.5m and the mass of 585kg. The m-bars are placed 0.303 meters apart. The ground motions used were scaled versions (5%, 20%, 30%, 40%) of the records from the JR Takatori station captured during the

Table 1. Strengths of the clip

Number of test	Front		Back	
	Sliding	Failure	Sliding	Failure
1	0.101	0.203	0.098	0.300
2	0.080	0.193	0.104	0.243
3	0.088	0.175	0.088	0.191
4	0.067	0.167	0.083	0.220
5	0.111	0.200	0.079	0.212
6	0.068	0.160	0.101	0.292
7	–	0.174	–	0.256
8	–	0.185	–	0.202
9	–	0.159	–	0.173
10	–	0.165	–	0.205
Mean	0.086	0.178	0.092	0.222
Std	0.016	0.015	0.009	0.034
Cov	0.188	0.087	0.101	0.156

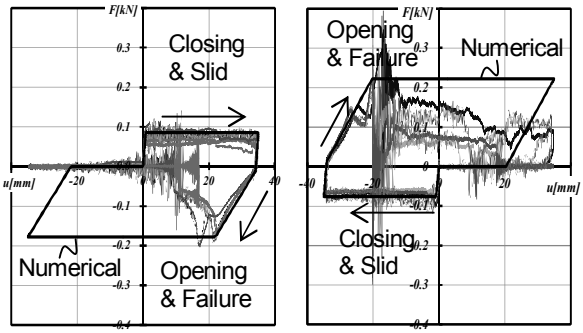


a) Clip is opening and failure



b) Clip is closing and slides

Figure 7. Connection model (overhead view of clip)



a) Front type b) Back type

Figure 8. Comparison analysis and experiment

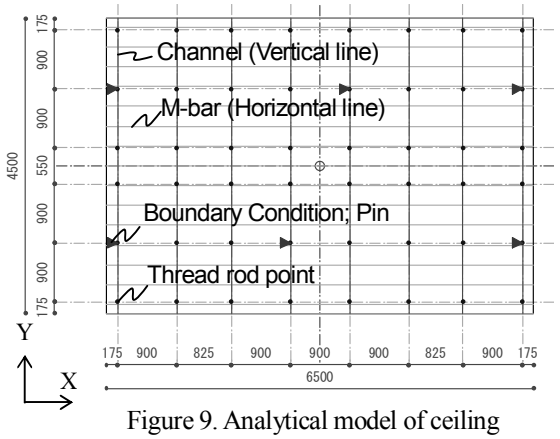


Figure 9. Analytical model of ceiling

M6.9 Kobe earthquake in Japan on 17th January, 1995.

The analysis model for investigating the capacity of the ceiling is described in Figure 9. This model has pin as the boundary condition at the points on Channels which have a brace. The direction of loading is parallel to the mbar, because the clips can be damaged significantly in this way of loading. Several models can be made by considering different combinations of the two types of clip.

Figure 10 shows the experimental measured response acceleration records of the ceiling when the ground motion was scaled to 5% and 20%. The result for the 5% records is scaled up 4 times in Figure 10. When the ground motion level was 20% in the E-defense test, it was observed in Figure 10 that the restoring force characteristic of the ceiling specimen became nonlinear. As a result of this the ceiling was damaged. When the ceiling behavior became nonlinear, the response acceleration of the ceiling was about 0.4g.

5. THE CAPACITY OF CEILING

The performance of a ceiling can be obtained directly from a suite of floor acceleration records. However, this is too complex for most designers. Also, it would be difficult to know if an error had been made in the analysis. For this reason two different methods are described below.

5.1 ELASTIC ANALYSIS

Computation of either the sliding or failure limit state acceleration is easily conducted using the following process.

For sliding and failure, the likely strengths of each connection, F_c, can be generated by the statistical Monte Carlo analysis. An analysis is carried out to determine the demand in each clip, F_d. The analysis model of a ceiling is composed of elastic beam elements and an arbitrary horizontal force, F_H, is applied to the ceiling model. The demand-to-capacity ratio for all clips, R (i.e. $R = F_d/F_c$), is determined for the limit state considered. The clip with the highest ratio is critical. The ceiling horizontal force for the limit state can therefore be computed by scaling the applied horizontal force by R, (i.e. $F_H/R = F_H'$). The acceleration corresponding to this limit state is $F_H'/m = A_{elastic}$. This calculation is then repeated many times with different values of capacity randomly generated from the capacity probability distribution obtained from MC analysis. The resulting accelerations therefore form a distribution which can be described by a cumulative density function or fragility curve.

The ceiling fragility curve from this process is shown in Figure 11. The ceiling can slide with the ceiling acceleration, about 0.2g and occurs of about 0.4g. For a given failure probability, the ceiling acceleration required to cause failure is about twice of that required for sliding. The ceiling fragility is close to the response acceleration of the ceiling obtained from the shaking table test; i.e. about 0.4g. This indicates that this simple approach of generating ceiling fragility curve is reasonably reliable.

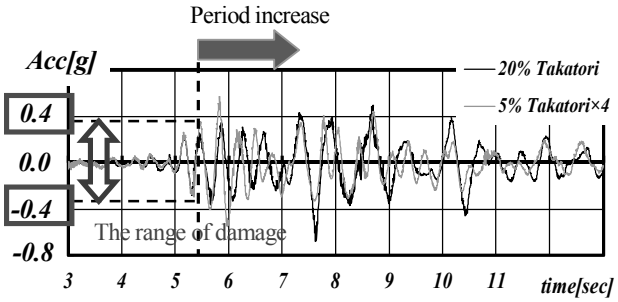


Figure 10. The response acceleration of ceiling

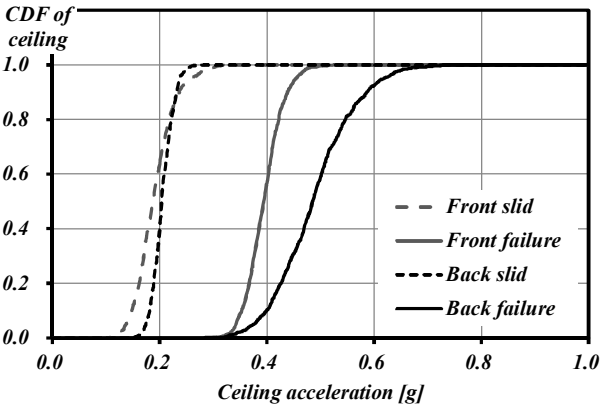
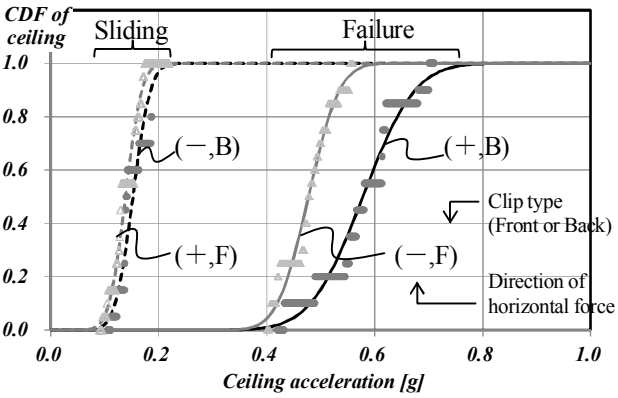
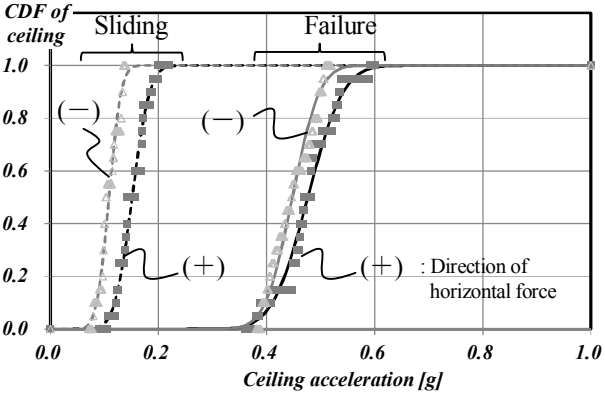


Figure 11. Ceiling fragility by elastic



a) All of clips are either front or back type



b) Front and back type alternately

Figure 12. Ceiling fragility by pushover analysis

5.2 PUSHOVER ANALYSIS

In the pushover method, strengths are generated for all clips based on Monte Carlo approach. A nonlinear static analysis is then conducted on the ceiling. Analysis stops when the force (or displacement) corresponding to the critical limit state is reached. Because of non-linearly, a new analysis must be conducted each time. This analysis is repeated with different sets of randomly generated clip strengths until a distribution of failure force is obtained. The failure force then needs to be converted into a failure acceleration. This may be done in several ways. In this study, the following method was used for simplicity. A conservative estimate of the acceleration may be simply determined as the forces divided by the mass, F_{max}/m.

In this study, three models were made; the first two had either front or back type at all clips while the thirds had both types alternately. The ceiling fragility curves from this method are shown in Figures 12. The connection can slide at a ceiling acceleration of, about 0.15g, and fail at about 0.5g. It is seen in Figure 12(a) that the capacity of ceiling depends on the direction of horizontal force when all clips are either front or back type. This is because the clips engage the sliding or failure strength according to the direction of loading. However, it is seen in Figure 12(b) that the effect of loading direction can be modified if two types of clip are arranged alternately in the ceiling. The ceiling fragility obtained from this approach is also close to the response acceleration of the ceiling measured in the shaking table test.

6. CONCLUSIONS

This paper describes methods of assessing the level of safety of a typical Japanese ceiling system. It was shown that:

1) The typical Japanese ceiling considered herein is composed of steel members and plaster board. The steel members are made of thin plate and have unique shapes. The clips, which connect the m-bar with the channels, can be connected either in the front or back type
2) The damage of clip can cause the ceiling to fail and collapse. The failures are due to horizontal loading of the ceiling perpendicular to the direction of the channel. The clip has two different values of maximum strengths in two directions of loading which correspond to the sliding and failure strength.
3) The behavior of clip can be simulated by using a simple model consisting of an elastoplastic beam element and contact beam element.
4) The capacity of ceiling was computed with 2 different methods which include a 2D static analysis and a statistical Monte Carlo analysis. These methods have different levels of conservatism and accuracy. The ceiling fragility curves by both methods were close to the response acceleration of ceiling when the ceiling was tested on a shaking table. This result describes that these methods to generate ceiling fragility curves are valid.

References:

Dhakal, R.P. (2010), "Damage to Non-Structural Components and Contents in the 2010 Darfiled Earthquake," *Bulletin of the NZ Society for Earthquake Engineering, 43(4), 404-411*

Motoyui, S. and Sato, Y. (2009), "Damage in Earthquakes and Dynamic Characteristics of Hanging Ceiling System in Japan," *6th International Conference on Urban Earthquake Engineering, 705-710*

Motoyui, S., Sato, Y. and Kawanishi, T. (2010), "Dynamic Characteristics of Japanese style of ceiling," *7th International Conference on Urban Earthquake Engineering & 5th International Conference on Earthquake Engineering Joint Conference, 1307-1311*

8CUEE CONFERENCE PROCEEDINGS
8th International Conference on Urban Earthquake Engineering
March 7-8, 2011, Tokyo Institute of Technology, Tokyo, Japan

RESIDUAL HORIZONTAL DISPLACEMENT OF WATER PARTICLES IN THE VICINITY OF TSUNAMI SOURCE

Mikhail A. Nosov

Professor, Faculty of Physics, M.V. Lomonosov Moscow State University, Russia
nosov@phys.msu.ru

Abstract: Along with the tsunami waves, co-seismic bottom deformations result in formation of residual hydrodynamic fields in the ocean such as horizontal displacements of water particles and geostrophic vortex. This study is aimed at developing a method of calculation of the residual hydrodynamic fields. Initially, the problem is considered in the case of ocean of constant depth and cylindrically symmetric analytical solution of the problem is obtained. It is shown that under typical conditions the residual horizontal displacements of water particles can exceed tens or even hundreds of meters. At the same time, velocity and free surface disturbance in the geostrophic vortex exhibits negligibly small values. Considering the assumption of zero disturbance of free surface in the geostrophic vortex a practical method of calculation of the residual horizontal displacements of water particles is suggested. The method takes into account sphericity of the Earth, real bathymetry and co-seismic bottom deformation in a tsunami source. Finally, the method is applied for the estimation of the residual horizontal displacements of water particles in the vicinity of the 2003 Tokachi-oki tsunami source. Perspectives of usage of the static hydrodynamic fields for the sake of tsunami warning are discussed.

1. INTRODUCTION

Strong bottom earthquakes are the most widespread cause of origin of tsunami waves (Historical Tsunami Database for the World Ocean, http://tsun.sscc.ru/nh/tsunami.php). The most effective mechanism of tsunami generation is associated with the so called co-seismic (residual, permanent, static) deformation of ocean bottom resulted from earthquake (e.g. Dotsenko and Soloviev 1995, Levin and Nosov 2008, Nosov and Kolesov 2010). The permanent deformation implies that during the generation process of a tsunami a huge volume of water (up to tens of cubic kilometers) is been displaced from its equilibrium position (Grilli et al. 2007, Nosov and Kolesov 2009, Bolshakova and Nosov 2011). The spreading of this huge volume of water in the vicinity of tsunami source has certainly to result in a horizontal displacement of water particles from their initial positions. At the same time, due to the Earth rotation, a geostrophic vortex should arise in the vicinity of tsunami source (e.g. Dotsenko 1999). In what follows, we shall call the horizontal displacements of water particles and the geostrophic vortex the "residual hydrodynamic fields".

The main purpose of this study is to develop a practical method of calculation of the residual hydrodynamic fields and to reveal which of them could be detectable in reality, e.g. by means of GPS buoys (drifters). In fact, along with DART and JAMSTEC deep-water tsunami measurements (Hirata et al 2002, Meinig et al 2005), the residual hydrodynamic fields represent an additional set of parameters which may be useful in tsunami warning system.

Note that the idea of using of GPS buoys for tsunami detection had been already discussed in some papers (Kato et al. 2000, Falck et al. 2010, Nagai 2010). However, authors of these publications suggested detecting tsunamis by means of measurement of vertical displacement of a GPS buoy while a tsunami is passing. In the long oceanic waves (including tsunamis) the horizontal displacements of water particles turn out to be many times larger as compared with the vertical ones and, in particular, with the displacements of ocean surface. So, as for tsunami detection in the open ocean with use of GPS buoys, measurements of the horizontal displacements are surely more promising.

In this study, first, we suggest a method of calculation of the residual fields. Second, we consider a simplified case of constant ocean depth and analytically derive some general assessments for the horizontal displacements of water particles and for the velocity in geostrophic vortex. Third, we develop practical method of calculation of the horizontal displacements taking into account sphericity of the Earth, real bathymetry and bottom deformation. Finally, we apply the developed method to the 2003 Tokachi-oki tsunami source and discuss perspectives of usage of the residual hydrodynamic field in tsunami warning system.

2. MATHEMATICAL MODEL

2.1 Basic Equations and Assumptions

Consider a layer, infinite in the horizontal directions, of an ideal incompressible homogeneous liquid of variable

depth H in the field of gravity on a rotating Earth. We restrict ourselves to the linear long-wave theory which represents traditional approximation in tsunami simulation technique. Initially we assume the domain under consideration to be small enough to neglect the sphericity of the Earth. So, the set of shallow water equations can be written in the Cartesian reference frame ($0x$-axis is directed eastward, $0y$-axis - northward)

$$\frac{\partial \xi}{\partial t} - \frac{\partial \eta}{\partial t} + \frac{\partial M}{\partial x} + \frac{\partial N}{\partial y} = 0, \quad (1)$$

$$\frac{\partial M}{\partial t} = -gH\frac{\partial \xi}{\partial x} + fN, \quad (2)$$

$$\frac{\partial N}{\partial t} = -gH\frac{\partial \xi}{\partial y} - fM, \quad (3)$$

where ξ is the free-surface displacement from the equilibrium position, $M = UH$, $N = VH$ are components of the total water flux along the $0x$ and $0y$ axes, respectively, U and V are the respective flow velocity components, η is vertical bottom deformation, g is the acceleration of gravity, $f = 2\omega \sin\varphi$ is the Coriolis parameter, ω is the angular velocity of the Earth's rotation, φ is the latitude.

The liquid is at rest until the time moment $t = 0$, i.e. $M = N = \xi = \eta = 0$. The dynamic bottom deformation occurs in accordance with an arbitrary law, $\eta(x,y,t)$. The motion will take place during a time interval τ, upon which the ocean bottom stops. Such a process results in a residual deformation of bottom, $\eta(x,y,\tau)$. Bottom motions give rise to disturbances of water layer including tsunami waves and residual hydrodynamic fields: potential and rotational.

According to Helmholtz's theorem, a vector field can be resolved into the sum of an irrotational (curl-free) vector field and a solenoidal (divergence-free) vector field. Let us express the 2D vector field of water flux (M,N) via the potential φ and the stream function ψ

$$M = \frac{\partial \varphi}{\partial x} + \frac{\partial \psi}{\partial y}, \quad (4)$$

$$N = \frac{\partial \varphi}{\partial y} - \frac{\partial \psi}{\partial x}. \quad (5)$$

Substituting expressions (4) and (5) in the continuity equation (1) we readily eliminate the stream function ψ and arrive at the following equation:

$$\Delta\varphi = \frac{\partial \eta}{\partial t} - \frac{\partial \xi}{\partial t}. \quad (6)$$

Integrating equation (6) with respect to time from 0 to T, we reduce the evolutionary problem to static problem

$$\Delta\Phi = \eta_T - \xi_T, \quad (7)$$

$$\Phi \equiv \int_0^T \varphi \, dt, \quad (8)$$

where T is the time moment upon which tsunami waves leave the area under consideration, $\eta_T \equiv \eta(x,y,T) = \eta(x,y,\tau)$ is the residual deformation of bottom, ξ_T is the residual free surface disturbance associated with geostrophic vortex in tsunami source. In formula (7) we introduce, instead of the velocity potential, a new quantity Φ which can be interpreted as the displacement potential. Potential residual field, i.e. residual displacements of water particles in the horizontal direction, can be expressed via Φ in the following way:

$$X_T = \frac{1}{H}\frac{\partial \Phi}{\partial x}, \quad (9)$$

$$Y_T = \frac{1}{H}\frac{\partial \Phi}{\partial y}. \quad (10)$$

In case of arbitrary bottom topography, determining of the vortex residual field involves certain difficulties. The point is that a static vortex current should be adapted to the bottom topography so that the current is directed along isobath (e.g. Zyryanov 2006). Considering the case of constant depth, one easily avoids the problem of adaptation. So, in the next section, we process further evaluations of the equation (2) and (3) under the following condition: $H = const$.

2.2 Constant Depth Case: Analytical Solution

In what follows, along with the assumption of constant ocean depth, for simplicity, let us also consider the Coriolis parameter to be constant. Note that this assumption is quite reasonable if the domain under consideration is small enough. Taking the x-component partial derivative of (3) and subtracting from it the y-component partial derivative of (2) we eliminate the quantity ξ. Introducing potential and stream function in accordance with formulae (4) and (5), we ultimately obtain

$$\frac{\partial}{\partial t}\Delta\psi = f\Delta\varphi. \quad (11)$$

Integrating equation (11) with respect to time from 0 to T, we arrive at the following formula:

$$\Delta\psi_T = f\Delta\Phi, \quad (12)$$

where ψ_T is the stream function at the time moment T. Velocity components in the residual geostrophic vortex can be expressed via the stream function in the following way:

$$U_T = \frac{1}{H}\frac{\partial \psi_T}{\partial y}, \quad (13)$$

$$V_T = -\frac{1}{H}\frac{\partial \psi_T}{\partial x}. \quad (14)$$

From the time moment $t = T$, all the motions of water exist in the form of a static geostrophic vortex. Setting in equations (2) and (3) $\partial/\partial t = 0$ and taking the x-component partial derivative of (2) and the y-component partial derivative of (3), we summarize the equations. Finally, expressing components of vortex flux via the stream

function, we arrive at the following equation:

$$\Delta\xi_T + \frac{f}{gH}\Delta\psi_T = 0. \qquad (15)$$

Equations (7), (12) and (15) represent a closed system of equations (unknown functions: ξ_T, ψ_T, and Φ) which allows determining all the residual hydrodynamic fields in the vicinity of tsunami source from the known static bottom deformation, η_T.

From equations (7), (12) and (15) one can easily derive the following equation for the static disturbance of water surface, ξ_T:

$$\Delta\xi_T + \frac{f^2}{gH}(\eta_T - \xi_T) = 0. \qquad (16)$$

Note that the equation (16) can be solved separately. This is the first step in solving the whole problem (7), (12) and (15). Knowing the function ξ_T, one can make the next steps, i.e. solve equations (7) and (12).

In practice, ξ_T turns out often to be negligible as compared with η_T. In order to prove it, let us introduce the horizontal scale L which can be interpreted as horizontal extension of tsunami source. Equation (16) gives us ground to link amplitudes of ξ_T and η_T by the following approximate formula:

$$|\xi_T| \sim \frac{\alpha}{1-\alpha}|\eta_T|, \qquad (17)$$

$$\alpha = \frac{f^2 L^2}{gH}.$$

Under typical conditions ($f \sim 10^{-4} s^{-1}$, $H \sim 10^3 m$, $L \sim 10^5 m$, $g \sim 10\, m \cdot s^{-2}$: $\alpha \sim 0.01$) the free surface disturbance in geostrophic vortex turns out to be much smaller than bottom deformations, $|\xi_T| << |\eta_T|$. This makes it possible to essentially simplify equation (7) at the expense of neglecting the unknown term, ξ_T. So, equation (7) is reduced to the following one:

$$\Delta\Phi = \eta_T. \qquad (18)$$

Poisson's equations (18) can be readily solved. At the same time, with account of equation (18), formula (12) reduces to the following form:

$$\Delta\psi_T = f\,\eta_T. \qquad (19)$$

Ultimately, with use of Poisson's equations (18) and (19) the residual hydrodynamic fields can be estimated from known static deformation of bottom, η_T.

Let us next consider the case of cylindrical symmetry. We shall further restrict ourselves to dealing with the residual bottom deformations specified by formula

$$\eta_T(r) = \eta_0[1 - \theta(r - R)], \qquad (20)$$

where θ is the Heaviside step function, R is the radius of tsunami source, η_0 is the amplitude of vertical bottom deformation.

In the cylindrical coordinates, equations (18) and (19) take the following forms:

$$\frac{1}{r}\frac{\partial}{\partial r}\left(r\frac{\partial\Phi}{\partial r}\right) = \eta_T(r), \qquad (21)$$

$$\frac{1}{r}\frac{\partial}{\partial r}\left(r\frac{\partial\psi_T}{\partial r}\right) = f\,\eta_T(r). \qquad (22)$$

Analytical solutions of (21) and (22) allow determining residual displacements of water particles in horizontal direction (along radius)

$$D_T(r) = \frac{1}{rH}\int_0^r \hat{r}\,\eta_T(\hat{r})\,d\hat{r} \qquad (23)$$

and vortex velocity (normal to radius)

$$V_T(r) = -\frac{f}{rH}\int_0^r \hat{r}\,\eta_T(\hat{r})\,d\hat{r}. \qquad (24)$$

The sign in formula (24) means that in the Northern hemisphere bottom uplift ($\eta_T > 0$) result in formation of geostrophic vortex rotating in the negative direction, i.e. clockwise.

Substituting formula (20) in the solutions (23) and (24), one can derive the following simple formulae for the horizontal displacement, D_T and the vortex velocity, V_T:

$$D_T(r) = \frac{\eta_0 R}{2H}\begin{cases} r/R, r \le R \\ R/r, r > R \end{cases}, \qquad (25)$$

$$V_T(r) = -\frac{\eta_0 R f}{2H}\begin{cases} r/R, r \le R \\ R/r, r > R \end{cases}. \qquad (26)$$

Functions (25) and (26) have local maxima at the boundary of the tsunami source, i.e. at $r = R$. Under typical conditions ($\eta_0 = 1\,m$, $R \sim 10^5 m$, $H \sim 10^3 m$, $f \sim 10^{-4} s^{-1}$), the horizontal displacement and the vortex velocity reach the value of $D_{max} = 50\,m$ and $V_{max} = 5 \cdot 10^{-3}\, m \cdot s^{-1}$. In accordance with formula (17), free surface disturbance in geostrophic vortex can be estimated as $|\xi_T| \sim 0.01|\eta_T| = 0.01m$. So, the horizontal displacement is large enough to be detected in-situ whereas the vortex velocity and free surface disturbance in geostrophic vortex are negligible and hardly detectable on practice. However, the maximal values can be significantly increased in the case of large amplitude of bottom deformation and shallow water. For example, taking the following set of parameters: $\eta_0 = 5\,m$, $R \sim 10^5 m$, $H \sim 250\,m$, $f \sim 10^{-4} s^{-1}$, one readily obtains $D_{max} = 1000\,m$ and $V_{max} = 0.1 m \cdot s^{-1}$. Note that in this case, in accordance with formula (17), free surface disturbance in geostrophic vortex still remains much smaller as compared with bottom deformation, $|\xi_T| \sim 0.04|\eta_T| = 0.2\,m$.

2.3 Arbitrary Bathymetry Case: Numerical Solution

The most important outcome of the analytical part of this study is that the residual horizontal displacements of water particles due to co-seismic bottom deformation can

reach tens or even hundreds of meters. Such values can be easily registered in-situ, e.g. by means of GPS drifters. At the same time, velocity in geostrophic vortex due to co-seismic bottom deformation is very slow, i.e. the vortex can not disturb the field of residual horizontal displacements much. Moreover, as it has been shown in previous section, $|\xi_T| << |\eta_T|$. This relation gives us ground to assume the function $\xi_T = 0$ in equation (7).

In this section we suggest a practical method of calculation of the residual horizontal displacements of water particles for real tsunami source and real bathymetry. Here we cancel the restriction of smallness of the domain under consideration. Taking into account the sphericity of the Earth we write the equation of continuity in spherical coordinates

$$\frac{\partial \xi}{\partial t} - \frac{\partial \eta}{\partial t} + \frac{1}{\rho \cos(Lat)} \frac{\partial M}{\partial Lon} + \frac{1}{\rho \cos(Lat)} \frac{\partial (\cos(Lat) N)}{\partial Lat} = 0, \quad (27)$$

where Lon is the longitude, Lat is the latitude, $\rho = 6371\,km$ is the mean radius of the Earth, $M = HV_{Lon}$, $N = HV_{Lat}$ are the water flux components along the parallel (west–east) and along the meridian (north–south), respectively.

In the same way as it has been done in section 2.1, introducing potential φ and stream function ψ in (27) and integrating the equation with respect to time from 0 to T, we arrive at the following expression:

$$\frac{1}{\rho^2 \cos^2(Lat)} \frac{\partial^2 \Phi}{\partial Lon^2} + \frac{1}{\rho^2 \cos(Lat)} \frac{\partial}{\partial Lat} \left(\cos(Lat) \frac{\partial \Phi}{\partial Lat} \right) = \eta_T . \quad (28)$$

While deriving equation (28), we assume $\xi_T = 0$.

Components of the residual displacements of water particles along the parallel, D_{Lon}, and along the meridian, D_{Lat}, are expressed via the potential as follows:

$$D_{Lon} = \frac{1}{H \rho \cos(Lat)} \frac{\partial \Phi}{\partial Lon}, \quad (29)$$

$$D_{Lat} = \frac{1}{H \rho} \frac{\partial \Phi}{\partial Lat}. \quad (30)$$

At the coastline the residual displacements of water particles normal to the coastline vanishes. So, at the coastline one have to require the equality to zero of the derivative normal to the coastline of the potential, Φ:

$$\frac{\partial \Phi}{\partial \vec{n}} = 0. \quad (31)$$

Simple free pass boundary condition is specified on the ocean-crossing outer borders of the computational domain

$$Lon = Lon_{min}, Lon_{max} : \frac{\partial^2 \Phi}{\partial Lon^2} = 0, \quad (32)$$

$$Lat = Lat_{min}, Lat_{max} : \frac{\partial^2 \Phi}{\partial Lat^2} = 0. \quad (33)$$

The conditions (32) and (33) imply that the residual displacements at boundary and at the closest internal points are equal.

Poisson's equation (28), supplemented with the boundary conditions (31) – (33) was solved numerically on a rectangular net with use of implicit finite differences method.

3. RESULTS AND DISCUSSION

In this section, taking the 2003 Tokachi-oki earthquake as an example, we shall describe how the method developed above can be applied in practice. The 2003 Tokachi-oki earthquake of JMA magnitude (MJ) 8.0 occurred off the south-eastern coast of Tokachi district at 04:50:06 JST on September 26, 2003. This earthquake turned out to be the strongest seismic event of the year. In spite of its strength, the 2003 Tokachi-oki earthquake generated rather moderate tsunami with a wave height up to 4.3 m (Ohmachi and Inoue 2010).

The computational domain extends from 139.6^oE to 149.2^oE in longitude and from 39^oN to 45.7^oN in latitude. Bathymetric data extracted from the 1-minute digital atlas GEBCO (General Bathymetric Chart of the Oceans) were employed to build the computational grid. In calculations the following values of space increments were used: $\Delta Lon = \Delta Lat = 1'$. For specification of the boundary condition (31) the isobath of $H = -1\,m$ was chosen.

The residual bottom deformation was calculated by group of Prof. Ohmachi on the base of the fault model proposed by Koketsu et al. (2004). We adopted this data to the computational grid with use of triangulation with linear interpolation gridding method.

Input data, such as the bathymetry and the residual bottom deformation in the 2003 Tokachi-oki tsunami source, and results of numerical computations, i.e. residual horizontal displacements of water particles, are presented in Figure 1. The isobaths are drawn with an interval of 1 km. The residual bottom deformation is shown by white isolines: solid lines stand for uplift, dashed lines – for subsidence. The maximum values of uplift and subsidence reach of 1.4 m and 0.4 m, respectively. Black arrows denote residual horizontal displacements of water particles in terms of "total fluxes", i.e. the length of each vector is proportional to the value of displacement multiplied by ocean depth. Areas within which the amplitude of the residual horizontal displacements exceeds 3 m are shown by different colors in accordance with the color scale depicted in the left bottom corner.

As it is seen from Figure 1, there exist rather wide areas within which the amplitude of the residual horizontal displacements of water particles exceeds 10 meters. In some cases the amplitude reaches tens or even hundreds of meters.

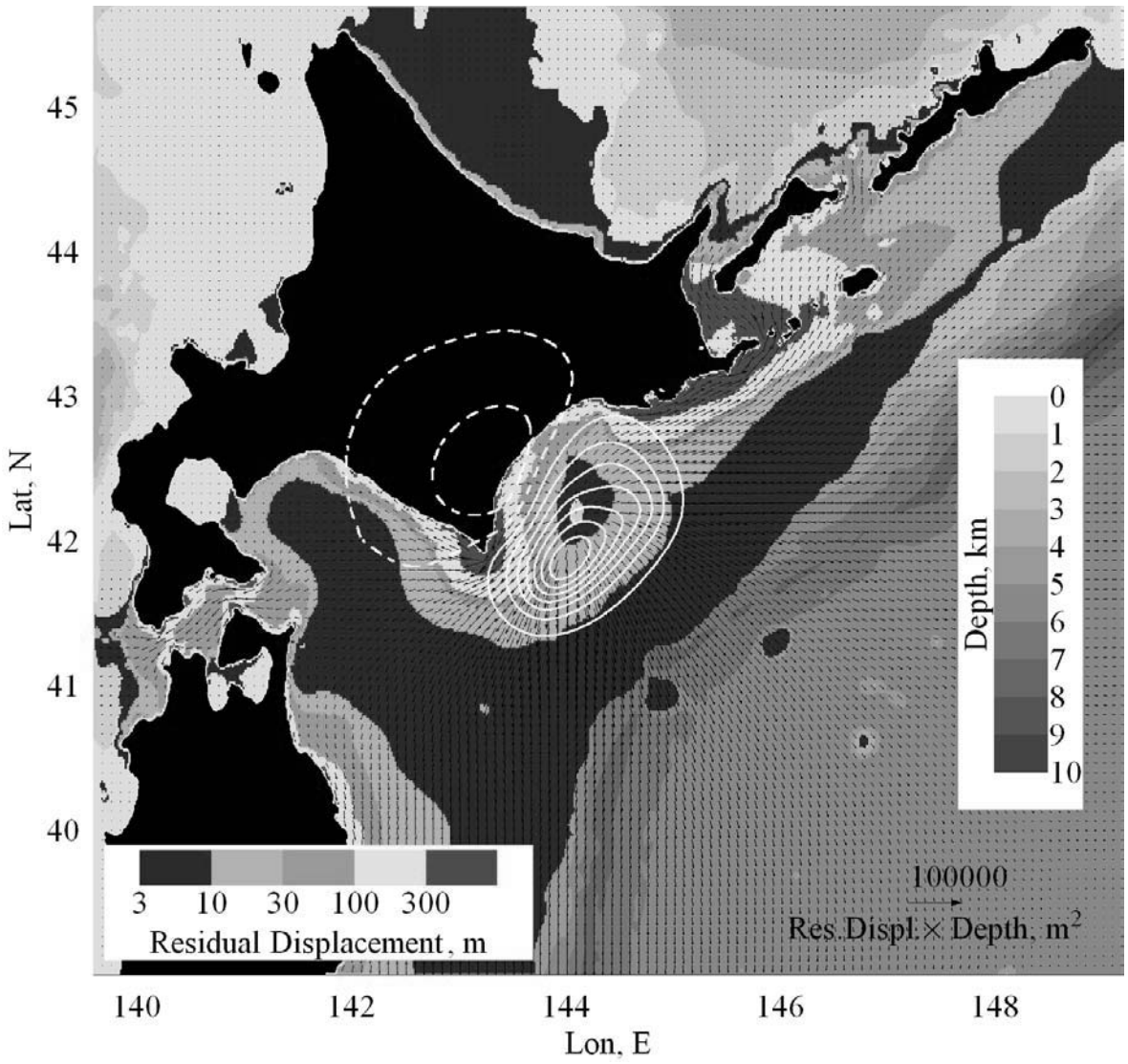


Figure 1 Computational domain. The residual bottom deformation is shown by white isolines: solid lines stand for uplift (up to 1.4 m), dashed lines – for subsidence (up to 0.4 m). Black arrows denote residual horizontal displacements of water particles in terms of "total fluxes", i.e. the length of each vector is proportional to the value of displacement multiplied by ocean depth. Areas within which amplitude of horizontal displacements exceeds 3 m are shown by different colors in accordance with the color scale depicted in the left bottom corner

Amplitude and direction of the residual horizontal displacements is a complex function of residual bottom deformation and bathymetry. Far from shore, direction of displacement of water particles is mostly defined by distribution of bottom deformation in tsunami source. In the vicinity of shoreline, vectors tend to be directed parallel to the shore. The most significant displacements are observed in the vicinity of Cape Erimo and near east coast of Hokkaido (Kushiro – Nemuro – Rausuin).

Among all other factors, amplitude of displacement of water particles strongly depends on water depth. Large displacements are mostly associated with shallow water areas. The amplitude of the residual horizontal displacements of water particles versus ocean depth for all the points in the computational domain is shown in Figure 2. From the figure one can quickly assess that the amplitude of horizontal displacement of 100 m can be achieved only in case of ocean depth $H < 300\ m$, whereas the amplitude of 1000 m – in case of $H < 50\ m$. So, it makes sense to detect the horizontal displacements of water particles in-situ in a shallow water (shelf) area where the amplitude is expected to be large enough. Displacements of large amplitude can be easily detectable by means of GPS drifters. The other option here involves processing of sequential satellite imagery with use of the maximum cross correlation technique (e.g. Crocker et al. 2007).

Vertical profile of horizontal velocity measured by means of bottom ADCP also can be used to derive residual horizontal displacements in-situ. Note that horizontal currents associated with long waves (tsunamis and tides) virtually do not depend on the vertical coordinate. Taking advantage of this feature one can easily select tsunami signal on the background of other currents. As for the tides, these currents can be precalculated. For the sake of tsunami

forecast ADSPs should be deployed at shelf depths of 100 m or so. In deep water areas, due to relatively small velocities, measurements of much higher accuracy are required. Anyway, just after the 2003 Tokachi-oki earthquake, at the depth 2540 m (Cable-end station, electro-magnetic current meter) a bottom velocity disturbance of a few centimeters per second in amplitude was registered (Mikada et al. 2006). Cable-end station is also equipped by ADSP. Unfortunately, because of too long sampling interval (30 min), tsunami signal was not registered by means of ADSP.

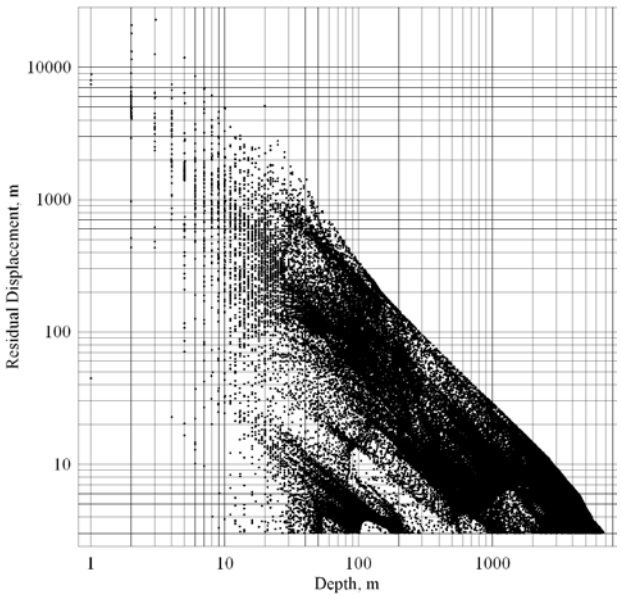


Figure 2 Residual horizontal displacements of water particles versus ocean depth

Inside of the tsunami source a "dead area" exists (approx. $144^o E, 42.2^o N$). Within this area the amplitude of horizontal displacement of water particles nearly vanishes. In case of a single measurement within such dead area a tsunami may be underestimated or even missed. This is why for the sake of tsunami warning, not a single GPS buoy or bottom ADSP but a number of devices should be used. Estimation of minimal number of devices necessary to provide reliable forecast of tsunami as well as the influence of existing oceanic currents on the detection of residual displacements lie beyond of the present study.

Obviously, we do not intend to make a tsunami warning system fully rely on the method of residual hydrodynamic fields. Seismic data and deep water bottom pressure measurements had already proved their efficiency in tsunami warning. However, residual hydrodynamic fields can serve as an alternate set of data to confirm the fact of tsunami generation and estimate its strength.

Acknowledgements:

This work was supported by the Russian Foundation for Basic Research, project 10-05-00562. We are grateful to Professor Tatsuo Ohmachi and his colleagues for providing us with bottom deformation data.

References:

Bolshakova, A.V. and Nosov, M.A. (2011), "Parameters of tsunami source versus earthquake magnitude," *Pure and Applied Geophysics* (in print).

Crocker, R. I., Matthews, D. K., Emery, W. J., and Baldwin D. (2007), "Computing coastal ocean surface currents from infrared and ocean color satellite imagery," *IEEE Transactions on Geoscience and Remote Sensing*, **45**(2), 435-447.

Dotsenko, S. F. and Soloviev, S. L. (1995), "On the role of residual shifts of ocean-bottom in tsunami generation underwater earthquakes," *Okeanologiya*, **35**(1), 25-31.

Dotsenko, S.F. (1999), "Effects of earth rotation during tsunami generation by underwater earthquakes," *Izvestiya Akademii Nauk Fizika Atmosfery i Okeana*, **35**(5), 706-714.

Falck, C., Ramatschi, M., Subarya, C., Bartsch, M., Merx, A., Hoeberechts, J., and Schmidt, G. (2010), "Near real-time GPS applications for tsunami early warning systems," *Natural Hazards and Earth System Sciences*, **10**, 181-189.

Grilli, S.T., Ioualalen, J.M., Kirby, J.T., Watts, P., Asavant, J., and Shi, F. (2007), "Source Constraints and Model Simulation of the December 26, 2004, Indian Ocean Tsunami," *Journal of Ocean Engineering*, **133**(6), 414-428.

Hirata, K., Aoyagi, M., Mikada, H., Kawaguchi, K., Kaiho, Y., Iwase, R., Morita, S., Fujisawa, I., Sugioka, H., Mitsuzawa, K., Suyehiro, K., Kinoshita, H., and Fujiwara, N. (2002), "Real-time geophysical measurements onthe deepseafloor using submarine cable in the southern Kurile subduction zone," *IEEE Journal of Oceanic Engineering*, **27**(2), 170-181.

Kato, T., Terada, Y., Kinoshita, M., Kakimoto, H., Isshiki, H., Matsuishi, M., Yokoyama, A., and Tanno, T. (2000), "Real-time observation of tsunami by RTK-GPS," *LETTER Earth Planets Space*, **52**, 841-845.

Koketsu, K., Hikima K., Miyazaki, S. and Ide, S. (2004), "Joint inversion of strong motion and geodetic data for the source process of the 2003 Tokachi-oki, Hokkaido, earthquake," *Earth Planets Space*, **56**(3), 329-334.

Levin, B.W. and Nosov, M.A. (2008), "Physics of Tsunamis," Springer.

Meinig, C., Stalin, S.E. Nakamura, A.I. and Milburn, H.B. (2005), "Real-Time Deep-Ocean Tsunami Measuring, Monitoring, and Reporting System: The NOAA DART™ II Description and Disclosure" (unpublished, available on-line at http://nctr.pmel.noaa.gov/Dart/Pdf/DART_II_Description_6_4_05.pdf)

Mikada, H., Mitsuzawa, K., Matsumoto, H., Watanabe, T., Morita, S., Otsuka, R., Sugioka, H., Baba, T., Araki, E., and Suyehiro, K. (2006), "New discoveries in dynamics of an M8 earthquake - Phenomena and their implications from the 2003 Tokachi-oki Earthquake using a long term monitoring cabled observatory," *Tectonophysics*, **426**, 95-105.

Nagai, T. (2010), "Introduction of Japanese coastal wave Monitoring network," *JOINT CONFERENCE PROCEEDINGS 7th International Conference on Urban Earthquake Engineering (7CUEE) & 5th International Conference on Earthquake Engineering (5ICEE)*, 1649-1653.

Nosov, M.A. and Kolesov, S. V. (2010), "Optimal Initial Conditions for Simulation of Seismotectonic Tsunamis," *Pure and Applied Geophysics*, DOI 10.1007/s00024-010-0226-6.

Nosov, M.A., and Kolesov, S.V. (2009), Method of Specification of the Initial Conditions for Numerical Tsunami Modeling, *Moscow University Physics Bulletin*, **64**(2), 208-213.

Ohmachi, T. and Inoue, S. (2010), "Dynamic tsunami generation process observed in the 2003 Tokachi-oki, Japan, earthquake," *Advances in Geosciences - Ocean Science*, **18**, 159-168.

Zyryanov, V. N. (2006), "Topographic eddies in a stratified ocean," *Regular and Chaotic Dynamics*, **11**(4), 491-521.

8CUEE CONFERENCE PROCEEDINGS
8th International Conference on Urban Earthquake Engineering
March 7-8, 2011, Tokyo Institute of Technology, Tokyo, Japan

FIELD SURVEY OF THE 2010 TSUNAMI IN CHILE

Shunichi Koshimura[1)], Masashi Matsuoka[2)] , Masafumi Matsuyama[3)], Takumi Yoshii[4)], Erick Mas[5)], Cesar Jimenez[6)] and Fumio Yamazaki[7)]

1) Associate Professor, Disaster Control Research Center, Graduate School of Engineering, Tohoku University, Japan
2) Senior Research Scientist, Geoinformation Center, Geological Survey of Japan, National Institute of Advanced Industrial Science and Technology, Japan
3) Senior Researcher, Civil Engineering Research Laboratory, Central Research Institute of Electric Power Industry, Japan
4) Research Scientist, Environmental Science Research Laboratory, Central Research Institute of Electric Power Industry, Japan
5) Graduate Student, Graduate School of Engineering, Tohoku University, Japan
6) Research Scientist, Direccion de Hidrografia y Navegacion, Peru
7) Professor, Department of Urban Environment Systems, Graduate School of Engineering, Chiba University, Japan
koshimura@tsunami2.civil.tohoku.ac.jp, m.matsuoka@aist.go.jp, matsu@criepi.denken.or.jp, takumi@criepi.denken.or.jp, erick@tsunami2.civil.tohoku.ac.jp, cesarsud86@hotmail.com, fumio.yamazaki@faculty.chiba-u.jp

Abstract: We conducted the field survey of the tsunami generated by the M8.8 great earthquake in Chile triggered on 27 February 2010 (UTC). The survey focused on the measurements of tsunami inundation/run-up height, flow depth, extent of inundation zone, structural damage inspection, and collecting eyewitness accounts. In total, tsunami heights and flow depths at approximately 155 points were measured along the coast of Biobio region, Chile, to understand the tsunami features during this event.

1. INTRODUCTION

On 27 February 2010, a megathrust earthquake of M8.8 (Figure.1) generated a destructive tsunami. It struck not only Chilean coast but propagated all the way to Japan. After the event occurred, the post-tsunami survey team was assembled, funded by JST, to survey the area of severely affected by the tsunami. The main purpose of the survey was to examine the damage, measure the tsunami run-up and inundation height, flow depth and extent of inundation, and interview the eyewitnesses of the tsunami. A joint survey team was consisted of the members from SATREPS and the researchers from Central Research Institute of Electric Power Industry (5 researchers from Japan and two researchers from Peru).

The following report aims to describe the findings and knowledge from the survey.

2. POST TSUNAMI FIELD SURVEY

2.1 Logistics

Because the tsunami hit quite long extent of Chilean coast, the survey area needed to be prioritized. We decided to deploy the most severely affected area in Biobio region. The survey team was deployed along the central coast of Chile from 18 to 25 April 2010. Figure.2 shows the route of the survey team. Setting the base lodging in Concepcion, we started the survey on 18 April from Talcahuano to visit eight coastal communities using a car.

2.2 Methods

Conventionally, the post-tsunami survey measures tsunami inundation and run-up height, flow depth, and extent of inundation zone. The inundation height is measured as the height of watermarks on structures or debris on trees above sea level (after tide correction), and the run-up height as the altitude of the inland limit of tsunami penetration. Flow depth is the thickness of tsunami inundation flow measured as the height of the watermark from the local ground level. Measurements were conducted using the laser range finder (Laser Technology Inc.) with survey rods and digital cameras with GPS and compass. During the survey, we inter-viewed witnesses to collect the information of tsunami features (time of the tsunami arrival, polarity of the first wave, timing of maximum wave). In total, we obtained 155 points along the coast as the measurement of tsunami inundation and run-up heights, and flow depths. Figures. 3 and 4 show the longshore distribution of the measured tsunami heights and depths. We made the tide correction for all the data by using tide table at Talcahuano.

Along with the field measurements, we used high-resolution optical satellite images to inspect the impact of tsunami disaster. Table 1 is the list of high-resolution satellite images used in the inspection of tsunami-affected area.

3. RESULTS

3.1 Talcahuano

Talcahuano is the port city in Biobio Region, which contains the naval base, and has approximately 250,000 inhabitants as a population (2002 census). According to the tide gauge record (NOAA, 2010), the first wave of tsunami reached Talcahuano at 3:30 (Local time) with receded wave. After the arrival of first wave, the tide gauge at Talcahuano did not successfully record the tsunami and stopped transmitting data. CATOE (Centro de Alertamiento Temprano y Oficina de Emergencia) reported that the tsunami attacked the coast at least four times with its period of 45 to 60 minutes, and the fourth wave was the largest.
Figure. 5 represents the result of tsunami inundation height measurement in Talcahuano. The tsunami penetrated approximately 300 m inland in the port-town area and more than 1 km in the southern coastal marsh. Tsunami inundation reached to 6-8 m in port-town area and 10 m in the coastal marsh. This figure also shows the comparison of pre and post event satellite images in Talcahuano port (Figures. 5(b), (c)). Significant amount of containers and fishing boats were left as tsunami debris, which caused long duration of failure of port and harbor facilities. While the tsunami left considerable damage to the town of Talcahuano (eastern bottom of the bay), no damage was found in the western port area (San Vicente). The measured tsunami run-up height in San Vicente was 3.4 m (Figure. 5(a)).

According to the interview with eyewitness, the tsunami slightly overtopped the dock of the harbor but did not inundate out of the port. Possible causes of this discrepancy may be local effect of tsunami source mechanisms and the condition of harbor oscillation related to the size and shape of the bay.

In the town of Talcahuano, the tsunami penetrated with up to 2-3 m of flow depth (Figure. 6). After inspect-ing the structural damage in the town, some washed-away structures were found, but it was limited within the port facilities (north-west) and industrial area (south-west). Most of the structural damage in the town was likely to be caused by ground shaking, but minor damage, e.g. bending shutters of commercial buildings and broken windows.

3.2 Inspection of satellite images

Inspecting pre and post event satellite images and ground photos helps to understand multi aspects of tsuna-mi disaster. Figure. 7 is the comparison of pre and post event satellite images in Talcahuano. We acquired the pre-tsunami image from GoogleEarth (QuickBird image taken on 13 April, 2009), and used WorldView-2 pan-sharpened composite image as post-tsunami image. From post-tsunami image and field survey, we found the tumbled ship at the west of waterway in Tulcahuano bay that has been stably stood in the bay (even though it was not in use). In the coastal marsh, considerable changes of shoreline and tsunami debris are seen in the satellite images, and it was found from the ground photos (Figure. 8) that the coastal sand were eroded by inland penetration of tsunami.

3.3 Detection of salt-water penetration

Since salt-water penetration causes death of vegetation, sometimes it is used as a clear indicator of tsunami inundation. Using a specific feature of vegetation, i.e. strong absorption of visible red-band and strong reflection of nir-band, NDVI is defined by Equation (1) using the reflectance of near infrared and visible red bands.

$$NDVI=(\text{Near infrared} - \text{Red})/(\text{Near infrared} + \text{Red}) \quad (1)$$

Here, we focused on the eastern bank of the canal in Talcahuano. Figure. 9 indicates the area of investigation and illustrates the result of detecting tsunami penetration by the analysis of WorldView-2 pan-sharpened multi-spectral image and the multi spectral camera (Tetracam ADC3). As shown in the ground photos (Figures. 9 A and B), considerable inundation was found on the western bank of the canal while the eyewitness testified that the tsunami slightly overtopped the eastern bank (no inundation in houses). Using the multi spectral camera that takes visible red, green and near infrared bands, we first calculated NDVI at the top of the bank where the tsunami did not overtop (Figure. 9B). As a result, we found that NDVI of the dead vegetation be-comes less than 0.3. Using the threshold value determined by the spectral camera, we discuss the salt-water penetration on the eastern bank of the canal. Figure. 9 (c) shows the distribution of NDVI calculated from the post-tsunami WorldView-2 image (pan-sharpened). NDVI indicates lower value on the western bank (inundated) while relatively higher value on eastern bank (not inundated), and these features are quite consistent with the ground photos A and B.

3.4 Tumbes, Puerto Ingles and Llico

Tumbes locates and Puerto Ingles are the coastal communities, which were isolated by the limited road access. Figure.10 represents the overview of tsunami height measurements. Tsunami attacked these communities with up to 11 m height and caused significant damage. Along the coast from Tumbes to Puerto Ingles, the tsunami was particularly devastating to demolish the houses of isolated villages (Figure.11). Some survivors mentioned that the first wave was withdrawal and the 2nd wave was the largest. Having the experience and lessons from the 1960 Chilean tsunami, most of the village people evacuated to the hill immediately after the ground shaking. They mentioned that the tsunami in 1960 was witnessed only as receded sea and did not cause inundation.

3.5 Dichato

Dichato is a coastal village of approximately 3,000 inhabitants (Census 2002), which belongs to the municipality of Tome, located 37 km north of the city of Concepcion. Having a beautiful sandy beach, Dichato was very popular in summer for water sports and recreation. Attacked by the tsunami, Dichato became one of the most

devastated towns. According to Dichato-Tome Emergency office, 405 families living in camps, and 1223 families were affected on their properties. Figure. 14 represents the measured tsunami run-up height and flow depths. The tsunami penetrated approximately 800 m inland to 10 m altitude. Figures. 15 and 16 illustrates the devastating damage in Dichato. In this area, most of the houses were washed away and the tsunami left considerable amount of debris. According to the eyewitness who watched the tsunami from 8-story building, the first wave of tsunami hit at 5:00 (AM) after most of the people evacuated. In addition, he said that the tsunami attack was at least 3 times and the 3rd wave was the largest. The other eyewitness said that the tsunami did not come first from the sea, but from the backside with not so much power (first wave).

Number of fatality and missing reported is 66 and the surviving resident believe that most of the victims are not from Dichato but tourists or different regions, also heart attack elders or drunken people. This is mainly because the residents of Dichato knew about the possible tsunami after the earthquake and had evacuation drills.

4. SUMMARY

In summary, the results of our survey provide a dataset of tsunami run-up and inundation heights, flow depths and extent of inundation at approximately 150 points. The survey extent was from Dichato to Llico, the areas mostly devastated by the tsunami.

The tsunami inundation heights and flow depths were well recorded and will be used as a constraint in developing tsunami source model to comprehend the features of tsunami propagation and coastal inundation. Also, we collected the eyewitness accounts to describe the picture of tsunami attack. Most of the eyewitnesses said that the largest tsunami did not occur in the first wave.

Throughout the trip, we found that many of survivors knew the past event 1960 and evacuated immediately after the ground shaking. Again we found that education and passing the lessons from the past event is highly valued to mitigate the tsunami fatalities.

Acknowledgements:

This research was sponsored in part by Japan Science and Technology Agency (JST) thorough the project of Science and Technology Research Partnership for Sustainable Development (SATREPS).

References:

Ruegg, J.C., A. Rudloff, C. Vigny, R. Madariaga, J.B. de Chabalier, J. Campos, E. Kausel, S. Barrientos, D. Dimitrov, Interseismic strain accumulation measured by GPS in the seismic gap between Constitucion and Concepcion in Chile, Physics of the Earth and Planetary Interiors, 175, pp.78-85, 2009.

U.S. Geological Survey, <http://earthquake.usgs.gov/earthquakes/eqinthenews/2010/us2010tfan/>

West Coast/Alaska Tsunami Warning Center, NOAA, <http://wcatwc.arh.noaa.gov/previous.events/Chile_02-27-10/Tsunami-02-27-10.htm>

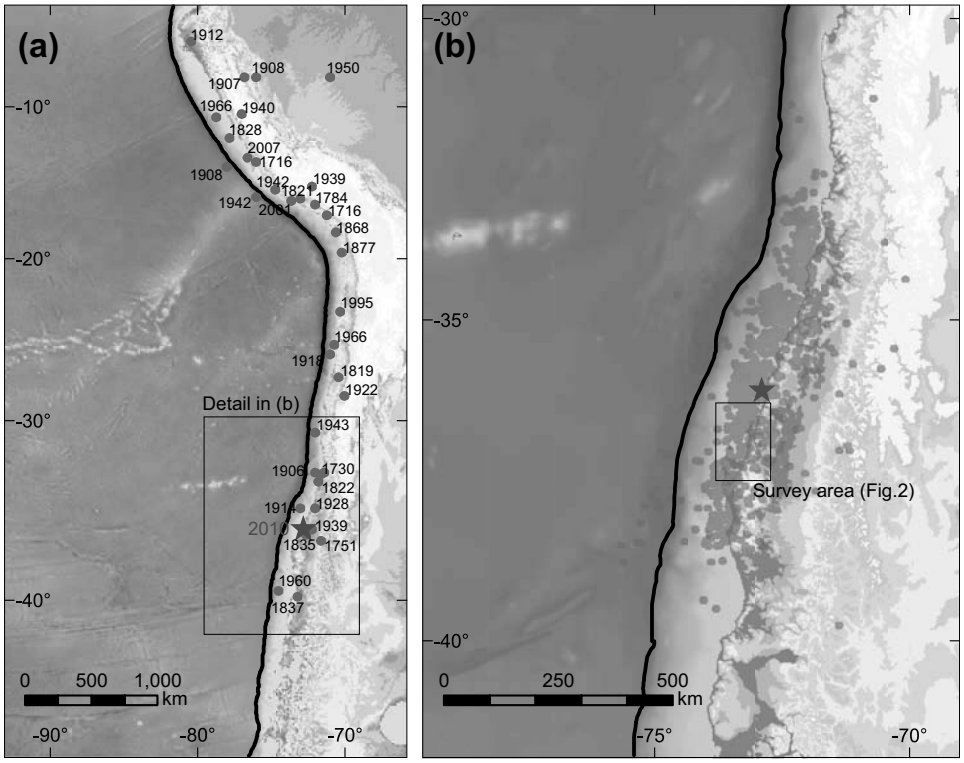


Figure1 (a) Significant earthquakes of more than M8 since 1700 and the epicenter of the 27 February 2010 Chile earthquake. (b) Mainshock (red star) and aftershocks of the 2010 Chilean earthquake (gray dots) during one day since the mainshock occurred.

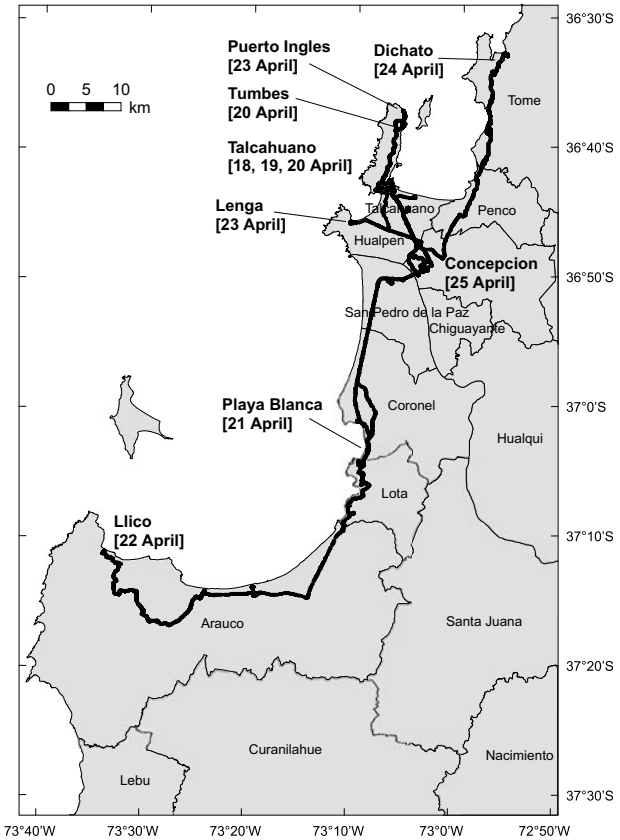


Figure 2 The route and area of the post-tsunami field survey in Biobio region.

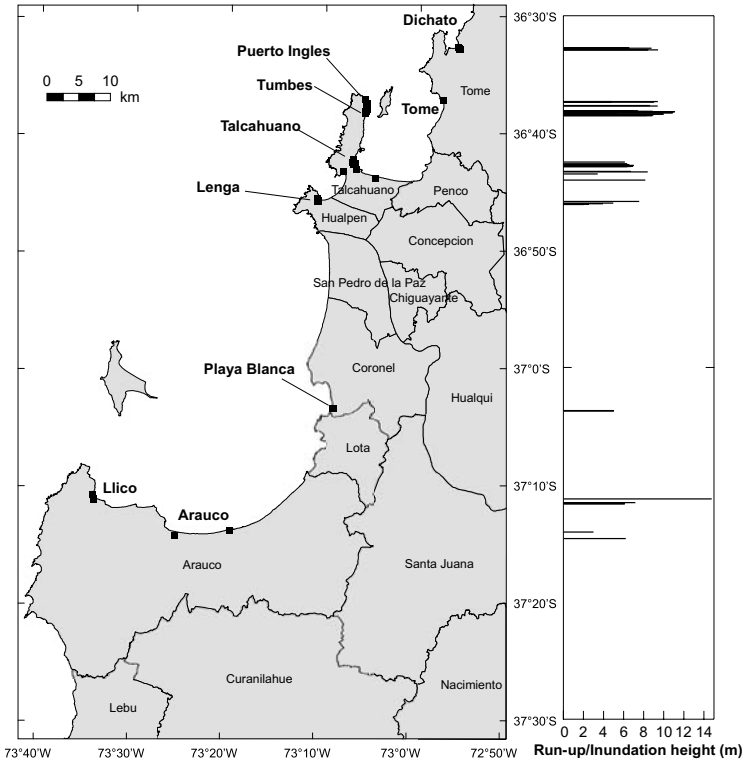


Figure3 Longshore distribution of inundation and run-up height above the astronomical tide level when the tsunami arrived. Tide correction was made by using tide table in Talcahuano.

Table 1 Acquired satellite images for the use of inspection in the tsunami- affected area.

Acquired area	Sensor or [Source]	Acquisition date
Talcahuano	WorldView-2	6 March, 2010
Talcahuano	QuickBird [Google]	13 April, 2009
Dichato	QuickBird [Google]	5 March, 2010
Dichato	QuickBird [Google]	26 April, 2006
Llico	GeoEye-1 [Google]	8 October, 2009

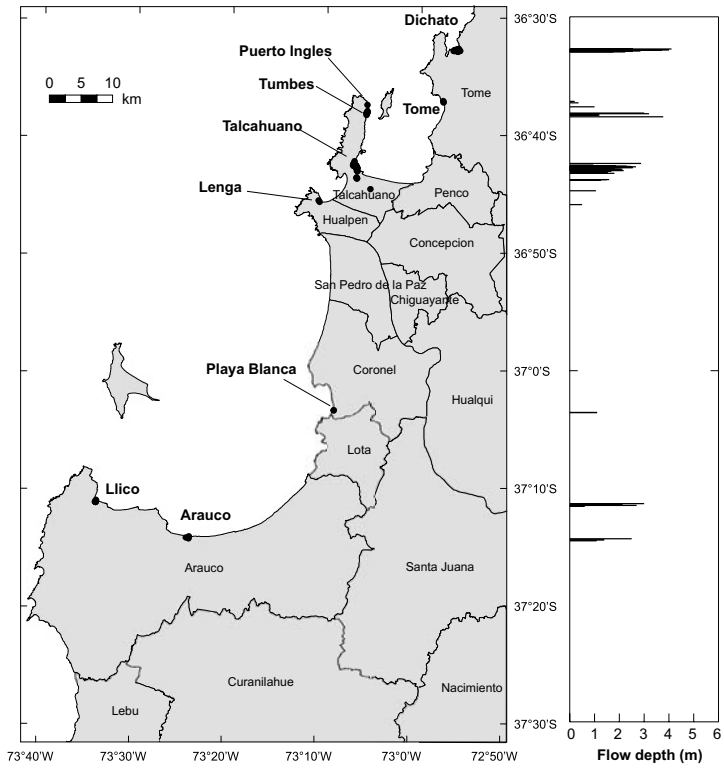


Figure 4 Longshore distribution of measured flow depths, which were measured as a height of watermark of tsunami penetration above the ground level.

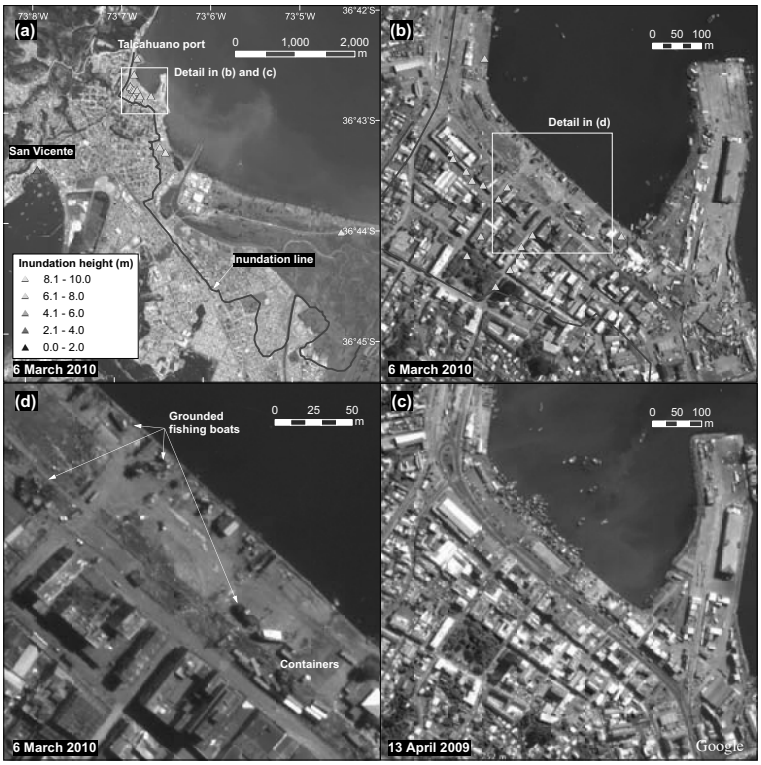


Figure 5 (a) Result of tsunami height measurement in Talcahuano. The red line indicates the extent of inundation zone which was obtained by the interview with CATOE (Centro de Alertamiento Temprano y Oficina de Emergencia). (b) Damage in Talcahuano found in the post-event satellite image (WorldView-2). (c) Satellite image of Talcahuano before the tsunami attack (13 April 2009, from Google) (d) Close-up view of port of Talcahuano. Grounded fishing boats and drifted containers were seen.

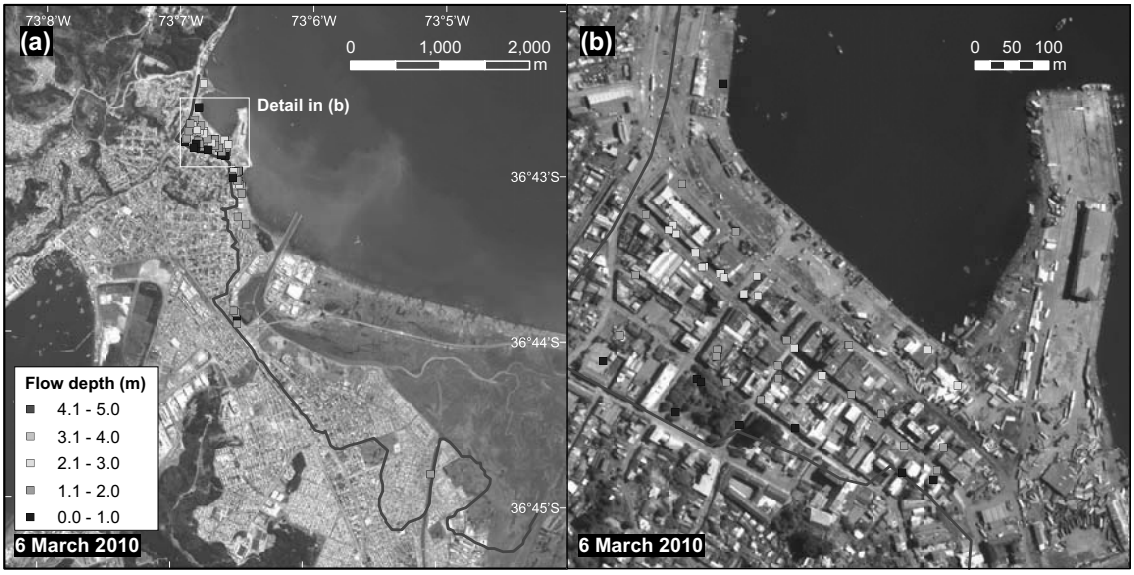


Figure 6 Result of tsunami flow depth measurement in the town of Talcahuano. The tsunami penetrated approximately 100 m inland with the flow depth of up to 2-3 m.

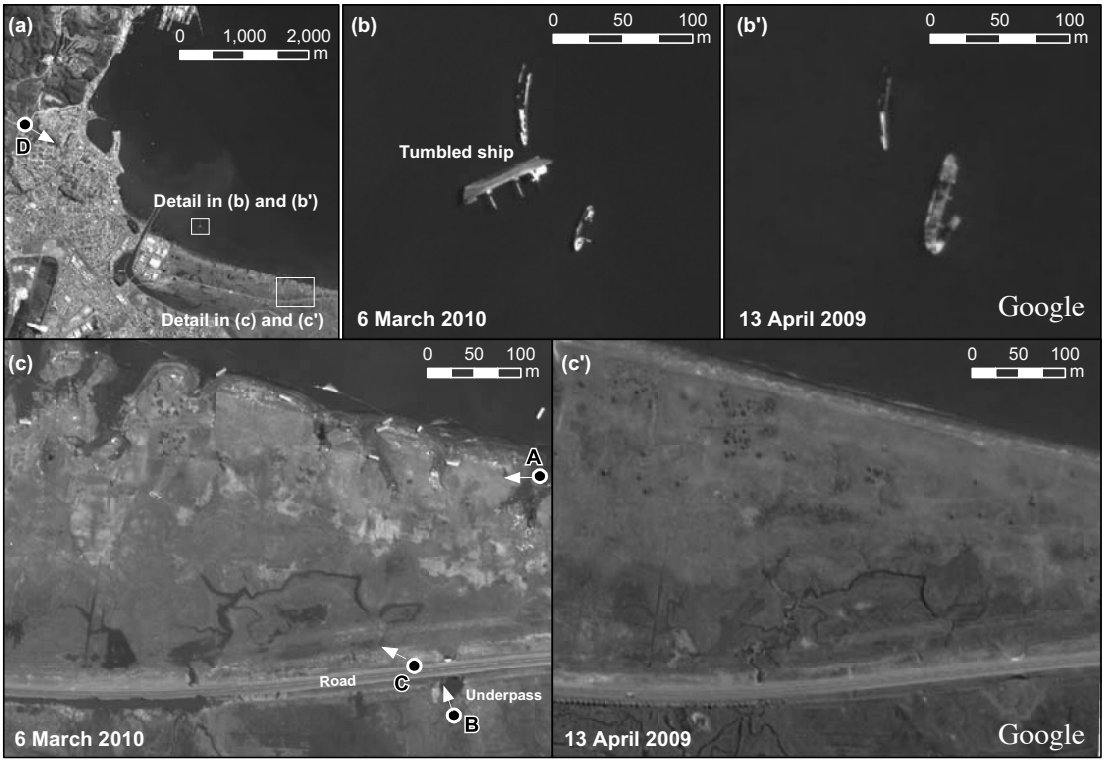


Figure 7 Pre and post event satellite images in Talcahuano. Points A to D represent the position of ground photos taken by the authors (Figure 8). White arrow is approximate direction of the camera focus. (a) Overview of Talcahuano port. (b) and (b') A 70m-long tumbled ship found the east of waterway. (c) and (c') Considerable change of coastline and drifted containers in the coastal marsh.

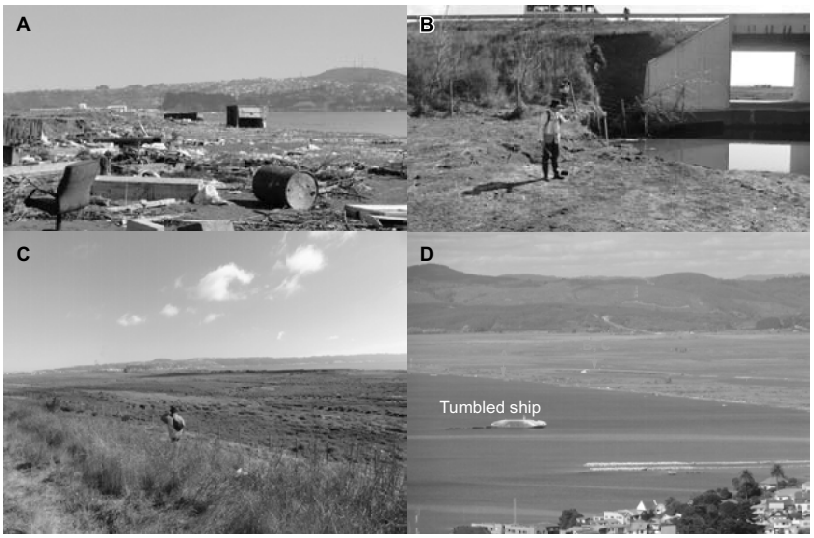


Figure 8 Ground photos in Talcahuano taken by the authors. Each point is identified in Figure 7. A : Tsunami debris and drifted containers in the coastal marsh. B : Erosion by the tsunami inundation found at the underpass. C : Overview of the coastal marsh inundated by the tsunami. D : Panoramic view of the coastal marsh from the hill.

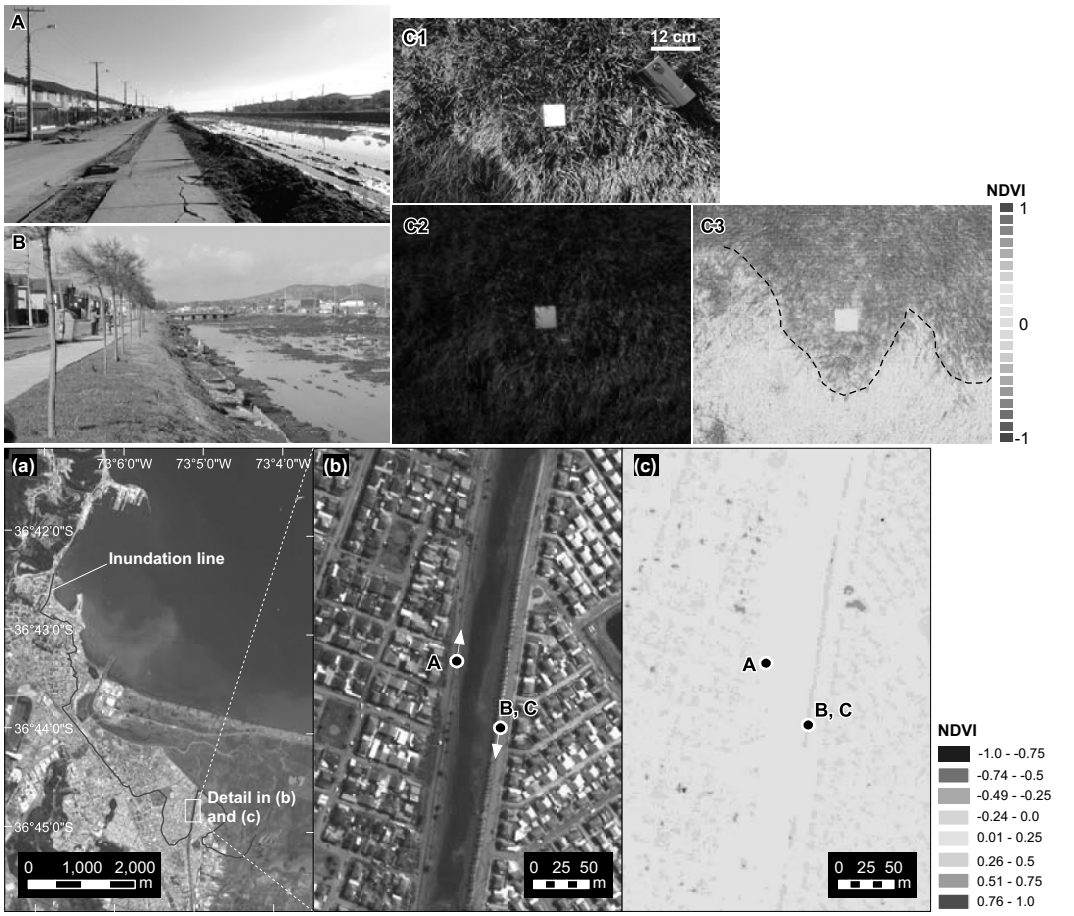


Figure 9 (a) Inspection area of saltwater penetration, (b) Pan-sharpened multi-spectral image of WorldView-2 acquired on 6 March 2010. A, B and C is the point of ground photos, White arrow is approximate direction of camera focus. (c) Spatial distribution of NDVI Western. A and B : Ground photos taken on the western and eastern bank of the canal respectively. C1 is the ground photo for inspecting vegetation activity (Same position as B). C2 and C3 : False color composite image and NDVI taken by the multi spectral camera (Tetracam ADC3). White plate is the reflector used for calibration.

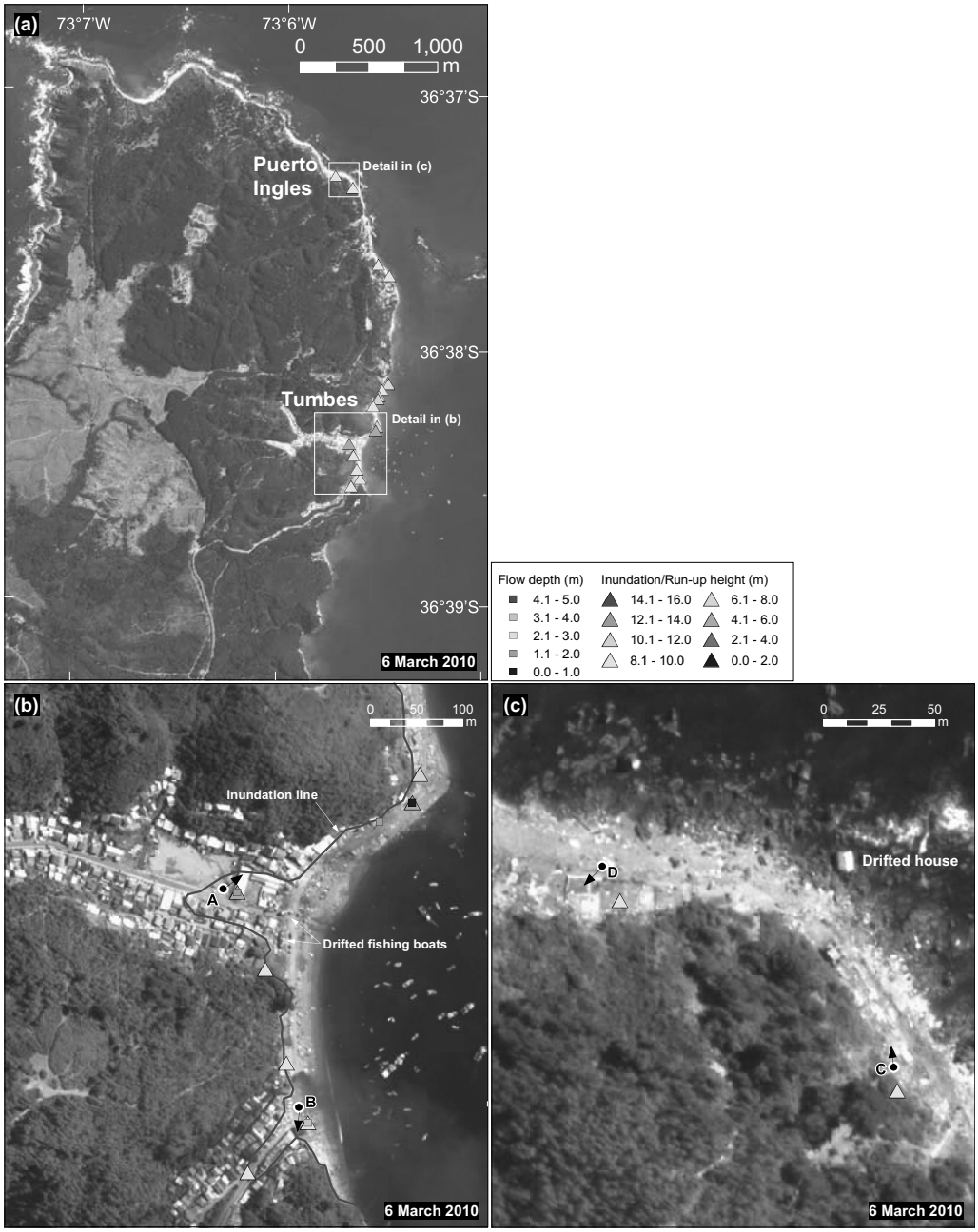


Figure 10 (a) Overview of tsunami measurements (inundation and run-up heights) in Tumbes and Puerto Ingles. (b) Detailed features of the measurements and the damage in Tumbes. (c) Devastated damage in Puerto Ingles. Point A to D is the position of ground photos in Figure 11 respectively with the arrow of focus direction.

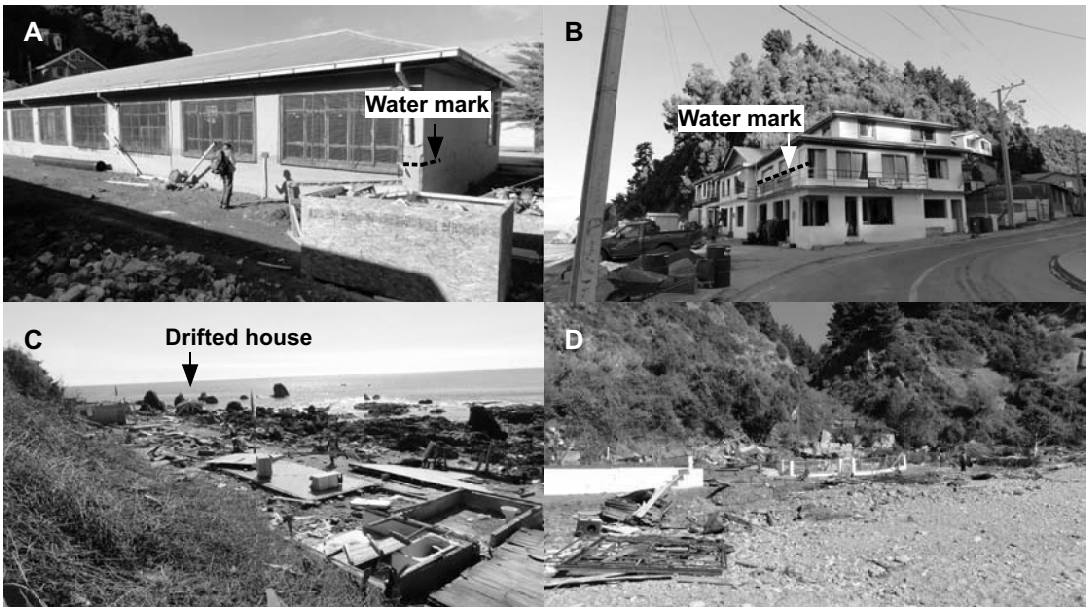


Figure 11 Ground photos from Tumbes (A, B) and from Puerto Ingles (C, D). A : Watermark on school building. B : Watermark on the house of Tumbes, C and D : Completely devastated village of Puerto Ingles.



Figure 12. Result of tsunami height measurement in Llico. Point A to D are the position of ground photos with the arrow of focus direction shown in Figure 13.

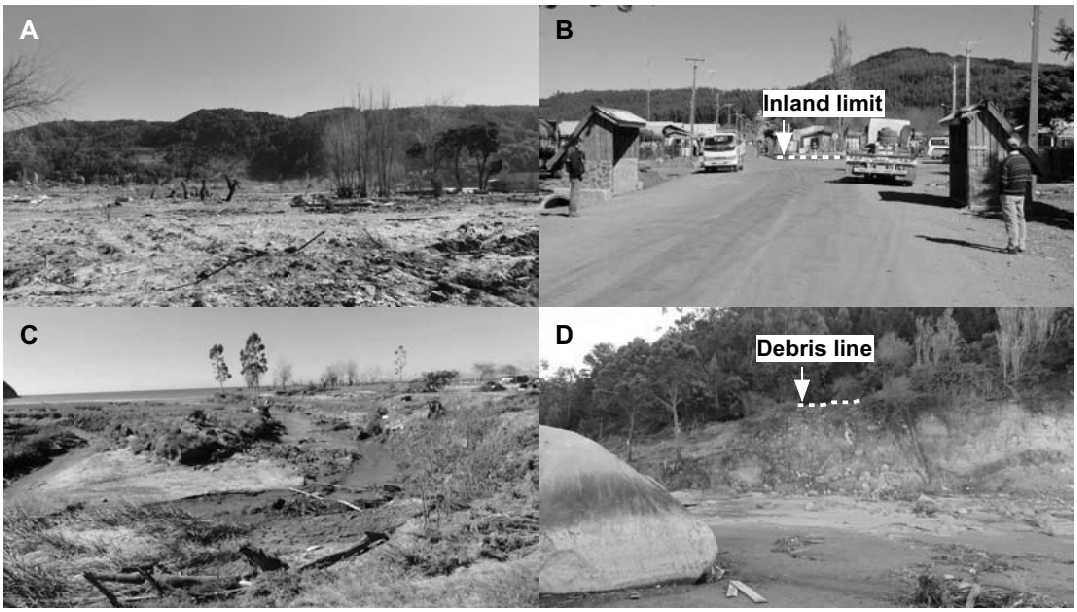


Figure 13 Ground photos from Llico. A : Completely devastated village. In the village, there were around 60 houses before tsunami. Almost all the houses were washed-away. B : Inland limit of tsunami inundation that is approximately 400 m from the shoreline. C : Tsunami run-up along the river. D : Tsunami debris line above 14.8 m pre-tsunami sea level.



Figure 14 Tsunami height, flow depth and extent of inundation in Dichato.



Figure 15 Pre and post event satellite images of the most devastated area in Dichato. Points A to G represent the position of ground photos taken by the authors (Figure 16). White arrow is approximate direction of the camera focus.



Figure 16 Ground photos from Dichato. A and B : Most devastated area. Only the unit of bathroom is remained. C : Damage on a bridge and erosion by tsunami inundation. D: Withstanding house, but significant damage. E : Drifted boat. F : Watermark on the house (approximately 2 m of flow depth). G : Panoramic view of the town of Dichato.

8CUEE CONFERENCE PROCEEDINGS
8th International Conference on Urban Earthquake Engineering
March 7-8, 2011, Tokyo Institute of Technology, Tokyo, Japan

FIELD SURVEY FOR 2010 CHILEAN EARTHQUAKE AND TSUNAMI DISASTER IN PORTS AND COASTS

Shigeo Takahashi[1)], Takahiro Sugano[1)], Takashi Tomita[1)], Taro Arikawa[1)], Daisuke Tatsumi[1)], Hiroaki Kashima[1)], Susumu Murata[2)], Yoshihiro Matsuoka[2)], and Tomoaki Nakamura[3)]

1) Asia-Pacific Center for Coastal Disaster Research, Port and Airport Research Institute, Japan
2) Coastal Development Institute of Technology
3) Nagoya University

Abstract: At 3:34 in February 27, 2010, an earthquake of Mw = 8.8 occurred offshore of central Chile and a tsunami attacked the Chilean coasts. This is a report of a survey conducted by a Japanese team from April 23 to 30. Major results of the survey are as follows: 1) Huge tsunami inundation heights were measured in the surveys: very high at Robinson Crusoe Island (6-16 m), very high at Dichato and Talcahuano (6-9 m), and moderate at Valdivia (1-2 m). 2) Although the tsunami was huge, the casualties were less than 500, relatively small compared with previous tsunami disasters since many people evacuated after the earthquake. 3) Similar devastating damages to those in previous tsunami disasters were found in the surveys. Talcahuano port was damaged significantly. Nearly 700 containers were washed away causing secondary damages by their drifting.

1. INTRODUCTION

A joint survey team from Japan conducted a disaster survey of the Chilean coasts after the 2010 Chilean Earthquake and Tsunami from April 23 to 30. The team consisted of nine members from the Port and Airport Research Institute, Coastal Development Institute of Technology, and Nagoya University. This is a brief report of the survey.

Chile (Republic of Chile) is located in the southern hemisphere, on the opposite side of the earth from Japan. It covers a narrow (less than 200 km) but very long (more than 4000 km) territory in the South American continent. The territory is twice that of Japan and the population is 16 million, with 6 million people living in Santiago, the capital city. Santiago is located at 33 degrees latitude, the same as that of Fukuoka City, Japan, in the northern hemisphere. The central district of Chile including Santiago has a Mediterranean climate with a dry summer (December to Feb.) and a rainy winter (June to August).

Chile faces a subduction zone of the Peru-Chile Trench between the Nazca Plate and the South American Plate and has many earthquakes and tsunamis. It has suffered from 71 large earthquakes (M 7.0 and larger) during the last 200 years. Among them, 13 earthquakes caused casualties of more than 50. Large earthquakes with tsunamis occurred in 1835, 1928 and 1939 near Concepcion. The huge 1835 earthquake and tsunami disaster in the area is described in the book on the Beagle's circumnavigation of the globe written by Charles Darwin(1839).

In 1960, a huge earthquake with a magnitude of 9.5, the largest in the 20th century, occurred near Valdivia The tsunami induced by the earthquake impacted not only the Chilean coasts but also all coasts of the Pacific Ocean. Devastating disasters in Japan and the United States led to international cooperation to establish an early warning system for distant tsunamis.

2. CHILEAN EARTHQUAKE and TSUNAMI

At 3:34 in February 27, 2010 (15:34 Japan standard time), an earthquake of Mw = 8.8 occurred offshore of central Chile. The epicenter was 335 km southwest of Santiago, and 105 km northeast of Concepcion at a depth of 30 km. The shaking along the coasts of central Chile was very strong and buildings and roads were damaged in these areas. The weather was fine and it was relatively light due to the full moon.

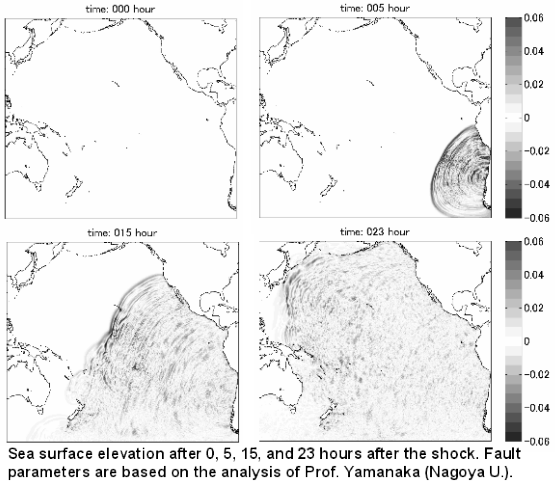


Figure 1 Calculated tsunami propagation

Immediately after the earthquake at 3:46 a tsunami warning was issued from PTWC (Pacific Tsunami Warning Center) to Chile and Peru. The tide in the coasts at that time was ebb tide (about 50 cm below the mean water level) at 4 o'clock and the high tide (about 50 cm above the mean water level) was to be at 10 o'clock. At 4:00 (16:00 Japan standard time), JMA (Japan Meteorological Agency) issued the first information on the distant tsunami. Figure 1 shows the results of the numerical simulation of tsunami propagation in the Pacific Ocean. The tsunami traveled more than 17,000 km within a day and hit the Japanese coast. Casualties in Chile due to the disaster were more than 500 and most of them were presumably due to the tsunami.

3. SURVEY METHOD

3.1 Preparation of Survey

After the earthquake, many disaster surveys were conducted by the Chilean government and local organizations in addition to international survey teams. The Asian Pacific Center for Coastal Disaster Research (APAC-CDR) of the Port and Airport Research Institute started to gather information on the earthquake and tsunami with the cooperation of the Japanese Ministry of the Land Infrastructure, Transport and Tourism. The Japan Society of Civil Engineers with the cooperation of Architectural Institute of Japan, the Japan Association for Earthquake Engineering and the Japanese Geotechnical Society decided to conduct a disaster survey in Chile from the end of March(Kawashima and Imamura, 2010). Two members from APAC-CDR, namely Drs. Sugano and Arikawa, could join the survey team with recommendations from Professors Kitagawa of Keio University, Midorikawa of Tokyo Institute of Technology, Kawashima of Tokyo Institute of Technology, and Imamura of Tohoku University. The joint survey team was organized to conduct more detailed surveys in the port and coast areas to extend the field survey results. The survey team had much help and advice including from Professor Emeritus K. Horikawa(1961) of the University Tokyo who had visited Chile just after the 1960 Chilean Earthquake and Tsunami.

Many organizations in Japan responded to the emergency of the distant tsunami after the JMA early warning. Many people were evacuated from the coasts, and in some areas, inundation occurred. APAC-CDR of PARI together with the Ministry of Land, Infrastructure, Transport and Tourism gathered information on the distant tsunami and conducted field surveys of the tsunami damage in Japan from March 4 to 6. For example, a tsunami height of more than 2 m was measured by the tsunami survey of APAC-CDR and the Tohoku Regional Bureau of the Ministry.

3.2 Objective and Itinerary of Survey

The joint survey for the disaster in ports and coasts in Chile was conducted from April 22 to May 2. The survey had two objectives. The first one was to reveal the nature of the disaster in coastal areas due to the Earthquake and Tsunami. Future tsunami disasters can be predicted more precisely using knowledge accumulated of actual disasters. The second objective was to enhance the cooperative relationship between Chile and Japan for disaster mitigation measures.

The survey was conducted by two groups. The disaster outline survey was conducted to reveal the overall view of the disaster in central Chile from Valparaiso to Valdivia including Robinson Crusoe Island. The Concepcion survey investigated the details of the disaster near Talcahuano Port including Concepcion Bay and San Vicente Bay. Figure 2 shows the map in central Chile, where Concepcion is located 340 km south of Santiago, Valdivia is 750 km south of Santiago and Robinson Crusoe Island is 670 km West of Valparaiso. The itinerary of the survey was as follows:

April 23: Visits to Chile office of Japan International Cooperation Agency (JICA), Japanese Embassy at Santiago, and Chilean Ministry of Public Works

April 24-28 Concepcion survey (Dichato, Tome, Penco, Talcahuano and Huachipato Steel Company) and Disaster outline survey (Robinson Crusoe Island, Valdivia areas)

April 28 pm Workshop at Concepcion University

April 29 Discussion at Valparaiso University

April 30 JICA and Japanese Embassy

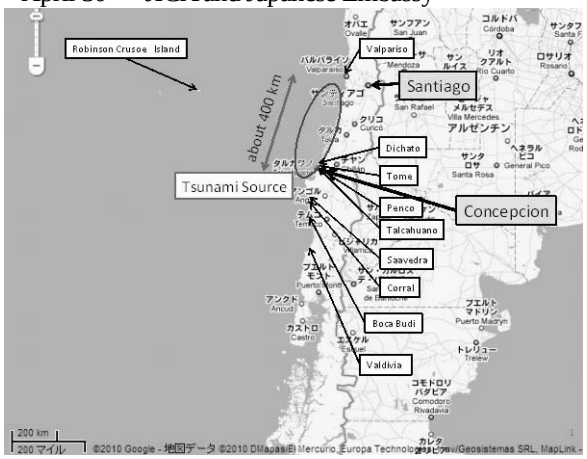


Figure 2 Map of Central Chile

The surveys were conducted with the kind cooperation of the Japanese Embassy and JICA Chile Office and the JICA Global Environment Department in Tokyo and the Japanese Ministry of Land, Infrastructure, Transport and Tourism. The survey at each location was conducted with the cooperation of many people from the Chilean Government, private companies, and universities. This enabled intensive investigation although the time was very limited.

4. DAMAGE IN EACH CITY

4.1 Talcahuano

Concepcion is a city in Province of Concepcion of

Region of Bio Bio and the second largest city in Chile. The city had moved from the Penco area to the present location due to the tsunami disaster in 1751. Talcahuano is a port city near Concepcion with a population of 250 thousand. Figure 3 shows the map near Talcahuano including Concepcion Bay and San Vicente Bay. Talcahuano Port is located in Concepcion bay with a large Navy base which could not be entered this time. Tome and Penco are located on the east coast of Concepcion Bay while Huachipato Steel Company is located in San Vicente Bay. Dichato is a little to the north of Concepcion Bay.

Photo 1 shows the south district of Talcahuano Port after the tsunami attack. The 680 containers stored in a wharf in the south district had all drifted shoreward from the wharf due to the first tsunami attack and 30% of the containers were moved into sea by the receding tsunami. Some of the containers collided with houses causing secondary damage. Many ships were moved onto the land or sank into the sea as can be seen in Photo 2. Drifting of containers and ships can be a major cause of disasters in coastal cities. This needs to be investigated further with numerical simulation of the drifting of containers and the collision mechanism of the containers.

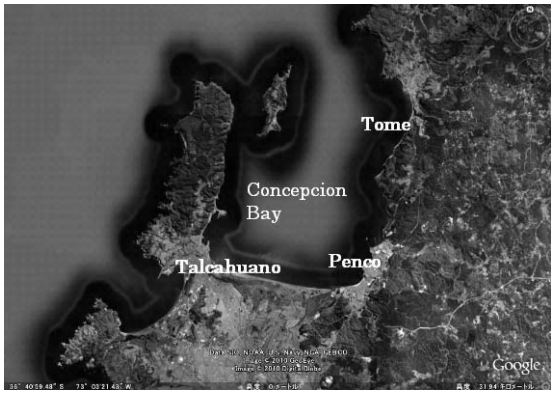


Figure 3 Concepcion Bay (from Google Earth)



Photo 1 Scattered containers at Talcahuano Port (Copyright: The International Federation of Red Cross and Red Crescent Societies (IFRC))



Photo 2 Damaged ships at Talcahuano Port (on April 27, 2010)

Huachipato steel mill is located along the coast of San Vicente Bay. The tsunami did not run up to the industrial zone which is located more than 5 m above sea level. The tsunami in the bay was relatively small compared with that in Concepcion Bay. However, although the tsunami damage was small, the damage due to shaking was significant and the recovery was only partial even after 2 months from the earthquake. The damage due to shaking will be explained later in this paper.

The recovery of the port seems to be slow. Recovery of the port and adjacent industrial areas is vital for the recovery of the economy of the city.

4.2 Dichato

Dichato village is a part of Tome City and is located in Coliumo Bay (above Concepcion Bay). The village has a long sandy beach and is a resort village with a population of more than 3000. There is a river in the middle of the village which flows into the bay through the beach. The area near the river is relatively low.

The tsunami arrived at the beach from the baymouth with a height of 8 to 9 m. The first wave arrived 40 to 50 minutes after the earthquake which could be seen from the highlands. The largest one was the fourth wave at around 7:30. Photo 3 shows the tsunami flowing into the village. The tsunami impacted the low-lying areas near the river in the town. Since the inundation depth was more than 4 m, all the houses were washed away. In the relatively high areas set apart from the river, the damage was limited as the inundation depth was less than 1 m.

There were 18 casualties, which was relatively small considering the tsunami height. Since the village was attacked by the 1960 tsunami, many people remembered the disaster and escaped to the highland areas nearby. Many tourists were in the village since the day was the Saturday at the end of the vacation season. Some of them did not know the danger of the tsunami and did not escape. Many of them did not know where the evacuation places were, and there was much confusion including the traffic jams in the town

with people using cars to escape. Drifting cars were seen with people inside. Unfortunately, the tsunami alert was canceled too quickly and some people returned to their houses and were involved in the tsunami attack.



Photo 3 Tsunami intrusion into Dichato

4.3 Penco

As mentioned above, Penco was the old Concepcion. It is located on the east coast of Concepcion Bay. The city has suffered from many tsunami disasters. It has a long sandy beach and is protected by a relatively high bank behind the beach used for a railway.

The first wave did not exceed the railway bank but the wave at around 7:30 exceeded the bank and inundated the town. Figure 4 shows the inundation depth measured along a road perpendicular to the bank. The ground level is lower than the bank and the overtopping water became a strong current penetrating 300 m into the town although the height of the overtopping water above the bank was less than 1 m. The overtopping water destroyed the front line of the houses and carried cars and boats through the road.

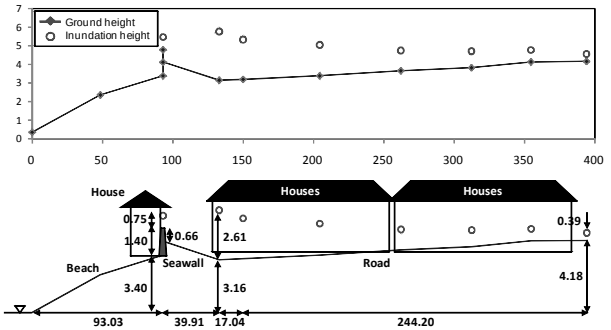


Figure 4 Ground height and inundation height at Penco

4.4 Robinson Crusoe Island

Robinson Crusoe Island (Juan Fernandez Island) is the largest island of the Juan Fernández archipelago, more than 600 km west of Valparaiso. It is a volcanic island surrounded by steep cliffs and inhabitable areas are very limited. Six hundred people live in the village of San Juan Bautista in Cumberland Bay, which faces the mainland where the earthquake was generated.

Three major tsunami waves are said to have attacked the bay. The first and the second were not very large and the inundation was limited to near the shore. The third wave at 4:20 was a huge one of more than 15 m. The arrival times of the first and second waves were 10 to 20 minutes before the third wave.

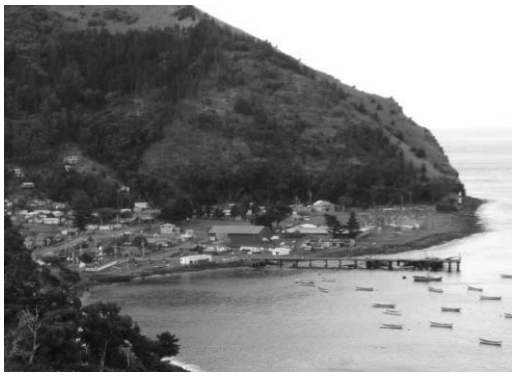




Photo-4 Before and After the tsunami at Robinson Crusoe Island (from Professor Patricio Winckler Grez of U.Valparaiso)



Photo-5 Beach at Robinson Crusoe Island (from Dr. Hector Saldias Rodreguez)

The maximum measured inundation depth was 7.6 m and the maximum tsunami height was 16.4 m. Clearly, a tsunami of more than 15 m attacked the village. Photo 4

compares the village before and after the attacks. The ground up to 200 m from the sea in the village is relatively low with a mild slope and then the slope becomes very steep. The low area near the sea was totally demolished by the tsunami especially since most of the houses were made of wood. A great amount of debris can be seen in Photo 5.

5. SUMMARY OF EARTHQUAKE DAMAGE

5.1 Shaking

The earthquake occurred in the subduction zone between the Nazca and South American Plates. The moment magnitude Mw was 8.8 according to the report of USGS (US Geological Survey). The general characteristics of the shaking on Chilean Coasts is a short predominant period of less than 0.5 s according to many observations but a long duration time of more than 60 s. This is the reason for the non-devastating damage to buildings and infrastructures although the magnitude was large.

5.2 Damage to Port Facilities

Failures of gravity and pile type quay walls at land reclamation sites were seen in the ports. Photo 6 shows the damage to a gravity type quay wall in Talcahuano Port where the retaining wall moved about 50 cm shoreward and the apron behind the wall settled down about 1 m. The through-wash effect of backfill sand can be seen due to tsunami and tidal changes. A seawall of the block masonry type was not damaged as seen in Photo 7. The gravity type (sheet pile type) quay walls were considered to have been destroyed due to deterioration since the shaking was considered to be not very large and liquefaction did not occur due to the relatively large diameter of the reclaimed sand. Similar damage can be seen in Photo 8 at Talcahuano Port.

Photo 9 shows a large piled jetty which was damaged slightly due to residual movement of the ground as in Photo 10 and shear damage to the pile heads as in Photo 11 which were under repair. The wheels of the ship unloaders on the pier had moved due to shaking as can be seen from Photo 12. It should be noted that the anchor of the unloader penetrated the plate of the superstructure, which was not seen even in Kobe port after the Hanshin-Awaji Great Earthquake although the unloaders had derailed significantly. This difference seems to be due to the difference in the superstructures of a piled pier and a concrete caisson pier. A seismically isolated structure should be introduced for unloaders to prevent derailing. It should be noted that the tsunami was low here and did not cause visible damage.

Since the propagation speed of the shaking was large (3000-6000 m/s) and the facilities were first attacked by shaking and then by tsunami waves, it is necessary to investigate the combined effects to the coastal facilities. One of the objectives of the survey was to reveal the combined effects to the coastal structures. Through the survey, we could not find any obvious case of the combined effects. Further investigation is needed using physical and numerical experiments.

5.3 Privatization of Port Facilities and Seismic Design

In Chile, from the beginning of 1980, many public services were privatized, such as electric power supply, telecommunication, banking, and steel, airline and shipping industries. Services such as expressways, airports and seaports are also being operated as concessions. Ports are operated by private companies of European capital. Although public funds are limited for the development of ports, the modernization of port operations using IT is being encouraged by privatization. The privatization is the so-called concession method where private companies invest in the construction of port facilities and operate the port for a certain period of time. Port operation should naturally maximize the benefit. However, it is very important to prepare for disasters, which is usually forgotten. Business continuity planning is essential for long-term port operation.

The survey revealed the absence of public design standards for port facilities in Chile, with the facilities being constructed based on consideration of the concession companies. If these companies or the design consulting companies have no experience in dealing with earthquakes they often do not possess the know-how to deal properly with the effects of earthquakes and tsunamis.



Photo 6 Damage to gravity type quay wall at Talcahuano Port



Photo 7 Block masonry type seawall at Talcahuano Port



Photo 8 Sheet pile quay wall at Talcahuano Port



Photo 9 Large piled jetty of Huachipato Steel Company



Photo 10 Deformation of crane rails on the jetty



Photo 11 Damage to the pile head of the jetty (ϕ 900 mm)



Photo 12 Anchor of unloader penetrating the jetty superstructure

5.4 Recovery Process and Ports

Ports can be used as a base for recovery from disaster to enhance the recovery since sea routes can substitute for transportation using roads and railways and emergency supplies can be stored in ports. In Japan, the government has a recovery plan utilizing ports as recovery bases. In Chile, ports are not expected to function as recovery bases and thus were not used in this manner. Cooperation of ports and local government is needed to expedite recovery from disaster.

6. SUMMARY OF TSUNAMI DAMAGE

6.1 Measured Water Marks

Figure 5 shows the measured water marks during the survey including detailed data around Talcahuano. The symbol (+) indicates the run-up height which is significantly affected by the topography while the symbol (●) indicates the inundation height without the effect of topography. It was confirmed that the inundation height was very large, 6 to 10 m near the hypocentral region as expected from the large magnitude of the earthquake. The inundation height decreased according to the distance from the hypocentral region, but was still high at Corral near Valdivia. On Robinson Crusoe Island, the inundation height was significantly high at 6 to 15 m.

The inundation height was confirmed to change significantly due to the topography as suggested from previous disasters. For example, the tsunami height at Talcahuano port was large compared with those at Tome and Penco even in the same Concepcion Bay. The tsunami height at Conception Bay was much larger than that at San Vicente Bay although they are located very close to each other. The reasons should be investigated through numerical simulations.

6.2 Evacuation and Casualties

Most people in the coastal areas felt the strong shaking and escaped. In some areas, like in Talcahuano, the evacuation was hampered due to damage by the strong shaking including cracks in the roads. Some people in areas where the shaking was not very strong, like Corral and

Saavedra, did not escape and even visited the coasts to see the tsunami. On Robinson Crusoe Island, most of the people were asleep and did not notice the shaking. Some people felt the shaking and/or saw the first and second tsunami waves and then evacuated together with their neighbors. The warning came to the island just before the tsunami attack and did not function sufficiently.

Unfortunately, the tsunami warning was cancelled after the first tsunami wave. However, most of the people believed that a tsunami comes in three waves and remained away for hours. Some people including children returned home but encountered the following tsunami in Talcahuano and more than 10 people died after returning home in Dichato. In Dichato, 7000 people were there at night and 50 people died or went missing. The rate was less than 1%.

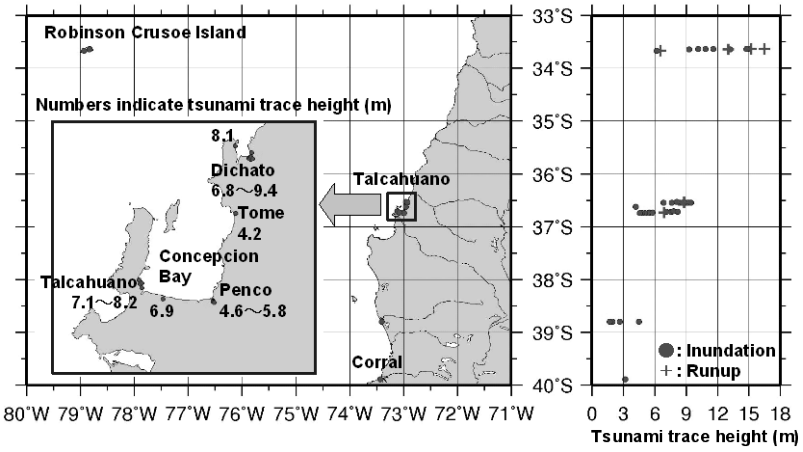


Figure 5 Measured tsunami water marks

Figure 6 shows the houses of the victims on Robinson Crusoe Island. It should be noted that many people lived near the edge of the inundation areas. The inundation boundary was actually a cliff or steep slope and they could not climb up the cliff but escaped using the roads indicated by yellow lines in the figure. During the evacuation, some were caught by the tsunami. Many of them were carried into sea by the tsunami and some were saved by boats. About 600 people lived in the village and 160 in the inundation areas. Sixteen people were killed, and the rate of 10% is relatively high, confirming the importance of proper early warning.

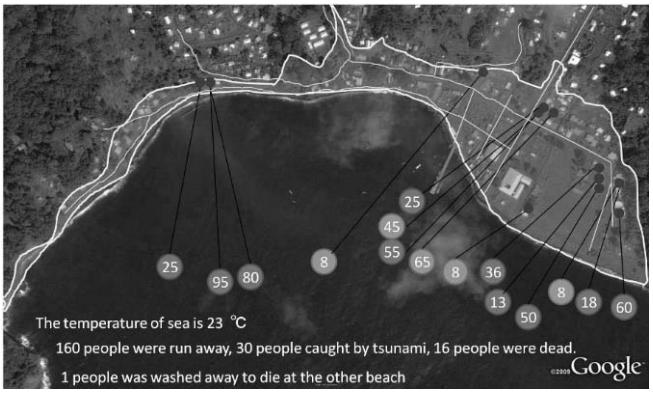


Figure 6 Places where victims were found at Robinson Crusoe Island (the number indicates the age, red color indicates female and blue, male)

6.3 Drifting Objects

Drifting of ships and containers is an important issue in a tsunami disaster. For example, in the Indian Ocean Tsunami, many ships drifted onto land. In the Chile tsunami, the drifting of a mass of containers occurred for the first time, involving 680 containers. Many ships also drifted and cars were found in the sea in Talcahuano and in other towns. Secondary damages including the collision of containers occurred in many places. Sunken objects hindered the navigation of ships and delayed the recovery of port activities. Numerical simulation of the drifting of a container is being investigated and will be checked with the field data obtained for this tsunami disaster.

7. CONCLUSIONS

Major results of the survey are as follows:

1) The earthquake occurred in the subduction zone between the Nazca and South American Plates with Mw =8.8 . The general characteristics of the shaking on Chilean Coasts is a short predominant period of less than 0.5 s according to many observations but a long duration time of more than 60 s. This is the reason for the non-devastating damage to buildings and infrastructures in the ports although the magnitude was large. One of the objectives of the survey was to reveal the combined effects of shaking and tsunami to the coastal structures. Through the survey, we could not find any obvious case of the combined effects. Further investigation is needed using physical and numerical experiments.
2) Huge tsunami inundation heights were measured in the surveys: very high at Robinson Crusoe Island (6-16 m), very high at Dichato and Talcahuano (6-9 m), and moderate at Valdivia (1-2 m). The maximum height occurred not with the first wave but the 3-5th waves. The tsunami inundation height changes significantly depending on the topography (for example, the south beach of Talcahuano (San Vicente Bay) is very low compared with that on the north side of Talcahuano (Concepcion Bay.) It should be noted that these are not unusual features of tsunamis. Obvious combined damage effect due to shaking and tsunami was not observed in the survey.
3) Although the tsunami was huge, the casualties were relatively small compared with previous tsunami disasters since many people evacuated after the earthquake. Sixteen

people were killed on Robinson Crusoe Island; it was difficult to transmit the warning as the earthquake occurred during the night.

4) Similar devastating damages to those in previous tsunami disasters were found in the surveys. For example, almost all the houses were washed away where the tsunami height exceeded 8 m and about 50% of the houses were damaged by a tsunami of 4 m. Wooden houses were very weak and reinforced concrete buildings were relatively strong.
5) Talcahuano port was damaged significantly. Nearly 700 containers were washed away causing secondary damages by their drifting. Many ships were also damaged. The quay walls were severely damaged by earthquake shaking. Early recovery of the port and industry areas near the port is vital for the economic recovery of the areas around Concepcion.

In addition to the field survey, the survey team discussed technical cooperation with various organizations in Chile, including Concepcion University, Valparaiso University and Catolica University, in addition to the Japanese Embassy, the JICA office in Santiago and the Chilean Ministry of Public Works. Knowledge on tsunami has accumulated in Japan due to repeated tsunami disasters(CDIT, 2010; Murata et.al., 2010; PIANC WG53, 2010). Knowledge on disaster mitigation developed further after the Kobe Earthquake disaster. Japanese experiences with disasters should contribute to disaster mitigation in Chile.

Acknowledgements:

Field survey is only possible with help of many people. All the members of the survey team would like to express their sincere appreciation to the people in Chile and Japan for their kind help and cooperation.

References:

Kawashima, K., and Imamura, F. (2010): The survey results of 2010 Chilean Earthquake and Tsunami, Rept. of JSCE, Vol. 95, No. 5, pp.30-33 (in Japanese).

Horikawa, K. (1961): The outline of Tsunami Survey in Chile, Kaigan, Vol. 28, pp.1-5 (in Japanese).

Darwin, C. (1839): Narrative of the surveying voyages of His Majesty's Ships Adventure and Beagle between the years 1826 and 1836, describing their examination of the southern shores of South America, and the Beagle's circumnavigation of the globe. Journal and remarks. 1832-1836.

Coastal Development Institute of Technology(CDIT) (2010): Terrible Tsunami, Maruzen Planet Publisher, 55p.(in Japanese)

Murata, S., Imamura, F., Katoh, k., Takahashi, S., and Takayama, T.(2010) Tsunami – To Survive from Tsunami, World Scientific, 302p.

PIANC WG53 Report: Mitigation of Tsunami Disaster in Ports, to be published in 2010.

8CUEE CONFERENCE PROCEEDINGS
8th International Conference on Urban Earthquake Engineering
March 7-8, 2011, Tokyo Institute of Technology, Tokyo, Japan

THE TSUNAMI OF CAMANA 2001

Cesar Jimenez[1)], Bruno Adriano[2)], Shunichi Koshimura[3)], and Yushiro Fujii[4)]

1) Assistant Professor, University of San Marcos UNMSM, Peru
2) Researcher, CISMID, National University of Engineering, Peru
3) Associate Professor, Department of Civil Engineering, Tohoku University, Japan
4) International Institute of Seismology and Earthquake Engineering, Japan
cjimenez@pucp.edu.pe, badrianoo@uni.edu.pe, koshimura@tsunami2.civil.tohoku.ac.jp, fujii@kenken.go.jp

Abstract: On 23 June 2001, at 15:33 local time, the Camaná city and all the peruvian southern region were hit by a strong earthquake of magnitude 8.4 Mw and maximal intensity VIII in Mercalli scale, the epicenter was located on the sea in the forefront of Ocoña (Arequipa). 15 minutes later a localized tsunami was generated, which destroyed the seaside town of Camana and caused the death of 24 people and 62 missing people. With the help of numerical modeling TIME and the use of computers, it is possible to make the numerical simulation of tsunami and to obtain parameters such as arrival times, run up (maximal height of flooding), synthetic tidal gage recordings and flooding maps, which will be useful for disaster mitigation for the corresponding authorities.

1. INTRODUCTION

A tsunami is a series of water waves of great length (with periods ranging from 5 to 60 minutes, or higher), generated by mechanisms such as volcanic explosions on islands, underwater landslides, falling rocks or bays ocean and tectonic movements associated with earthquakes. An earthquake tsunami generator is usually associated with subduction zones. Since many of these areas are along the Pacific Rim, the vast majority of tsunamis occur in the Pacific Ocean.

Tsunamis are classified in the place of arrival to the coast, according to the distance (or travel time) from their place of origin, in:

a) Local Tsunami, if the place of arrival on the coast is very near or within the area of generation (defined by the area of seafloor displacement) of the tsunami, or less than one hour travel time from the beginning.

b) Distant Tsunamis, if the place of arrival is more than 1000 km away from the zone of generation or end-opposite shores across the Pacific Ocean and about half a day or more of the tsunami travel time from that area (Jimenez, 2008).

According to the testimonies of survivors, shortly before the earthquake a refolding of the sea in some places and then the earthquake on 15 minutes started the tsunami destroyed the resort of Camaná. This was a small local tsunami that affected only Camaná coastal resorts. The height of the waves reached up to 7 m in some places, with a run-up to 7 m and a maximum flooding distance of 1350 m. There were 24 dead and 2 missing and large losses. This tunamigenic earthquake is the strongest since 1868 in the southern region of Peru. The period of recurrence of this type of event for the region of Peru and northern Chile is of 100 years (Kulikov et al., 2005).

The parameters obtained by the Geophysical Institute of Peru (IGP) were:

Local Time = 15h 33m 23 June 2001
Latitude = -16.20 º
Longitude = -73.75 º
Depth = 29 km
Magnitude Mw = 8.4
Intensity = VIII Ocoña, Camana
Location: 82 miles north west of Ocoña (Arequipa)

1.1 Area of study

Camana province is located in the Midwestern part of the Arequipa region to 172 km from the capital of the Department of Arequipa, and has about 56 thousand inhabitants. This is the first city that sent the conqueror Francisco Pizarro founded. Predominant economic activity is agriculture. Bounded on the north by the province Condesuyos, province of Castilla, Arequipa province (San Juan de Siguas) for the north-west province Caravelí and Penthouse, on the south by the Pacific Ocean on the east by the province of Islay. In 2001 a strong earthquake rocked the region and a tsunami devastated the coastal resorts of the city of Camana.

2. FOCAL PARAMETERS CALCULATION

From the empirical relationship of Papazachos 2004, between the seismic moment magnitude Mw and the focal parameters: length L (km), width W (km), and displacement

U (cm) of the failure to subduction zones :

$$\log(L) = 0.55M - 2.19$$
$$\log(W) = 0.31M - 0.63 \qquad (1)$$
$$\log(U) = 0.64M - 2.78$$

The following results were obtained for Mw = 8.4:

Rupture length	L = 269 km
Rupture width	W = 94 km
Fault displacement:	U = 3.9 m

The seismic moment Mo is defined as: Mo = μLWU = $4.9*10^{21}$ Nm, where μ = 4.5*1010 N/m2 is the modulus of the medium. Talandier 1993, provides a relationship between seismic moment Mo and the destructive potential of a tsunami. The value of Mo indicates that the Camana earthquake generated a small tsunami (Talandier, 1993). However, it was destructive in the area of the coastal resorts due to the vulnerability of buildings.

Table 1. Classification of tsunamis according Talandier.

Value range	Tsunami type
Mo < 10^{21} N.m	No tsunami was generated
10^{21} < Mo < $5*10^{21}$ N.m	Small tsunami
$5*10^{21}$ < Mo < $2*10^{22}$ N.m	Potencially destructive
Mo > $2*10^{22}$ N.m	Great and destructive

3. DATA AND SELECTION OF THE DOMAIN OF INTEGRATION

To model the tsunami flood zones need the following information:

a) Global bathymetry grid.- To simulate the largest where the tsunami spread. The data are taken Etopo2 model with a resolution of 3.6 km (Smith, 2006).

b) Local bathymetry.- These fine details are obtained from drilling conducted in the area.

c) Local topography.- To model the flooding caused by the tsunami. Data are taken on-site survey and satellite survey data SRTM 90 (Jarvis et al., 2006).

With all these data we obtain a digital elevation model and proceeds to draw 4 nested grids: A, B, C and D (see Figure 1). Where grid A is the largest and contains the area of rupture. The grid D is the smallest, but the data are finest and contains the region where we want to evaluate the flood. The boundaries of the grid are:

```
region_a = [-20    -13      282.0     290.0 ];
region_b = [-17    -15.8    285.5     287.5 ];
region_c = [-17    -16.2    286.5     287.5];
region_d = [-16.85 -16.59 287.258    287.373];
```

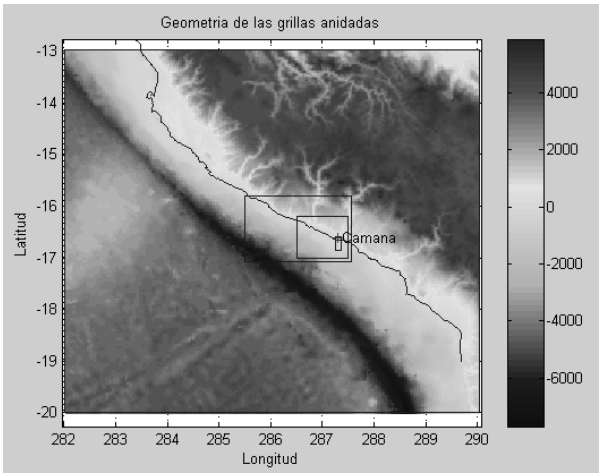


Fig. 1 Nested grids for the present model

4. TSUNAMI GENERATION PHASE

For an earthquake generates a tsunami is necessary to meet the following requirements:

a) The epicenter of the earthquake, or a majority of its rupture area, is under the seabed at a depth less than 60 km (shallow earthquake).

b) Occurring in a sink edge of tectonic plates in the sea, ie the failure to have vertical movement and is not just lateral strike slip motion.

c) The earthquake releases enough energy in a certain period of time and this is efficiently transmitted. In general, magnitude Mw > 7.0.

The initial condition of tsunami (strain field due to displacement or fault line) is determined using the model of Mansinha and Smylie (1971) assuming an instantaneous deformation of the ocean's surface equal to the vertical component of the strain field of the bed ocean. This is a model of fracture and requires knowledge of the earthquake focal mechanism (Okal, 2002). It has been considered the following values:

Strike angle = 301º
Dip angle = 20º
Slip angle = 90º

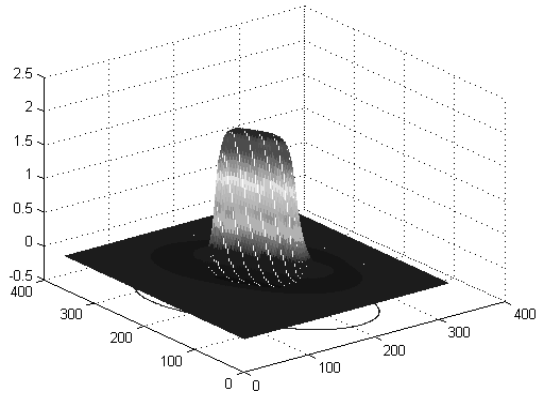


Fig. 2 Model of initial co-seismic deformation.

For this model the maximum height of the deformation is of 2.04 m. This creates the "piston effect" that destabilizes the water column causing tsunami waves.

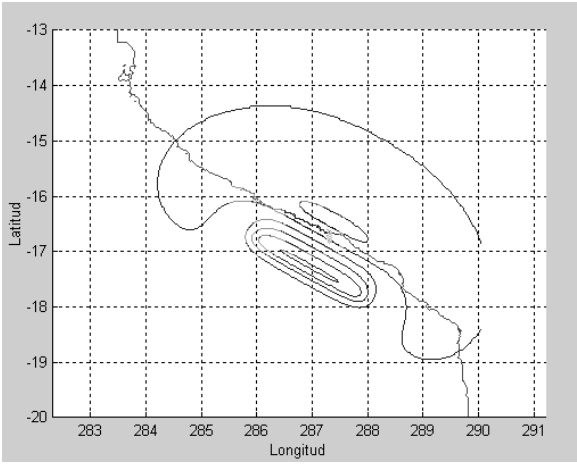


Fig. 3 Contours of initial co-seismic deformation.

Using the inversion of the tsunami waveforms from tidal gauge stations is possible to get the source parameters for a heterogeneous slip model as shown in Figure 4 (Adriano, 2010).

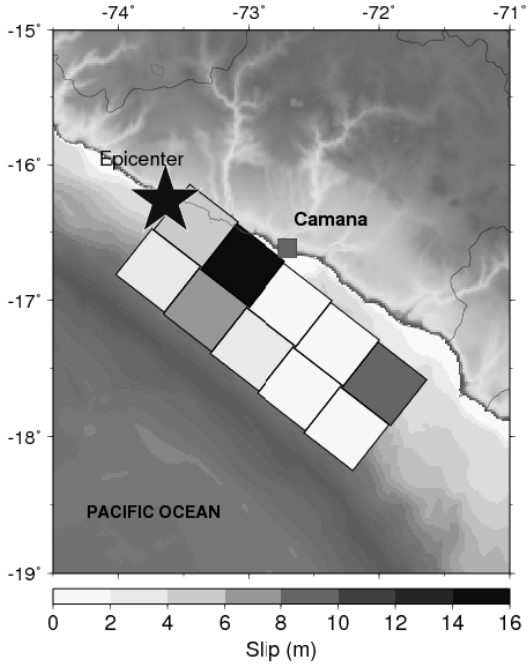


Fig. 4 Heterogeneous slip model from inversion of tsunami waveform data (Adriano, 2010).

5. PROPAGATION PHASE OF TSUNAMI

The propagation of the tsunami is simulated with the model of Goto and Ogawa (1982) that integrates the shallow water equations by the numerical method of finite differences. The TIME model (and other models) uses the linear equations for the propagation of the tsunami through the ocean floor in shallow water:

$$\frac{\partial \eta}{\partial t} + \nabla . \vec{U} = 0 \qquad (2)$$

$$\frac{\partial \vec{U}}{\partial t} + gh\nabla \eta = 0 \qquad (3)$$

where η is the disturbance of sea level, U represents the velocity field, g is the acceleration of gravity, h is the depth and t is time. In Figure 5 shows the initial stage of propagation of tsunami waves for the homogeneous slip model.

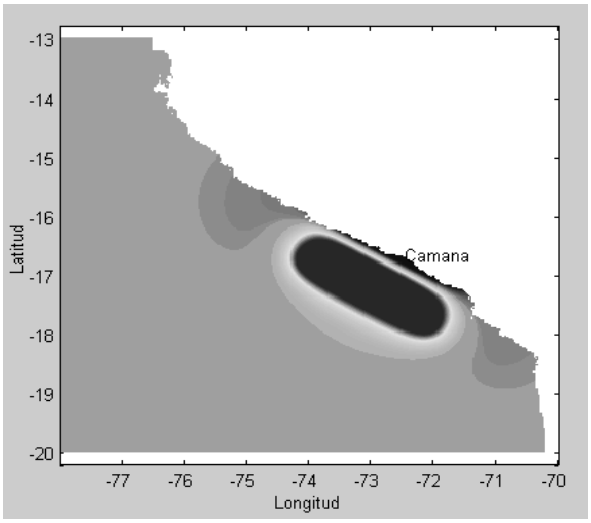


Fig. 5 Start time of Tsunami Propagation

6. INUNDATION PHASE OF TSUNAMI

The height reached by a tsunami, upon reaching the coast is due to the interaction of various physical and morphological factors such as characteristics of waves at sea, bathymetry, seabed slope, configuration of the sea boundary, diffraction, refraction, reflection, dispersion of the normal modes of resonance of the coastal formations and the formation of bores on beaches, estuaries and coastal lagoons. These factors determine that the arrival of the tsunami on the coastline is a complex process, which generates significant differences in height of the tsunami even over short distances along the coast.

In Figure 6 shows that the maximum wave height (according to model) to the shoreline was 9 m at the position corresponding to -72.75 degrees longitude (outside the area of interest: grid D). The maximum wave height is 7 m.

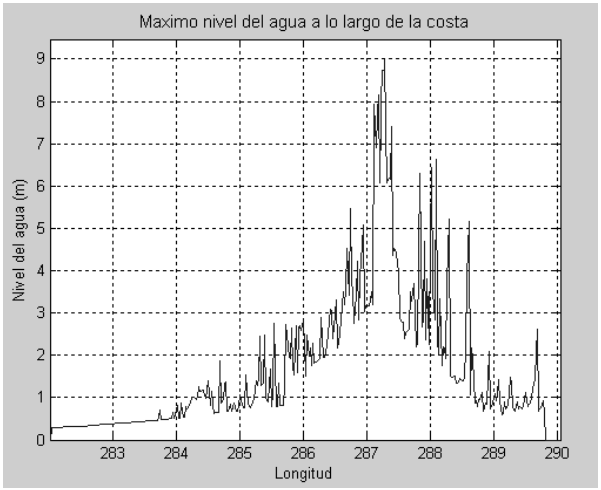


Fig. 6 Maximum wave height along the coast.

In Figure 7, we can see a tsunami inundation map according to the homogeneous slip model for Camana area. The narrow strip for the seaside resort (right side) is completely flooded, with the South Panamerican highway and the adjacent hills as boundary. The maximum horizontal inundation distance is about 1350 m, according to this model.

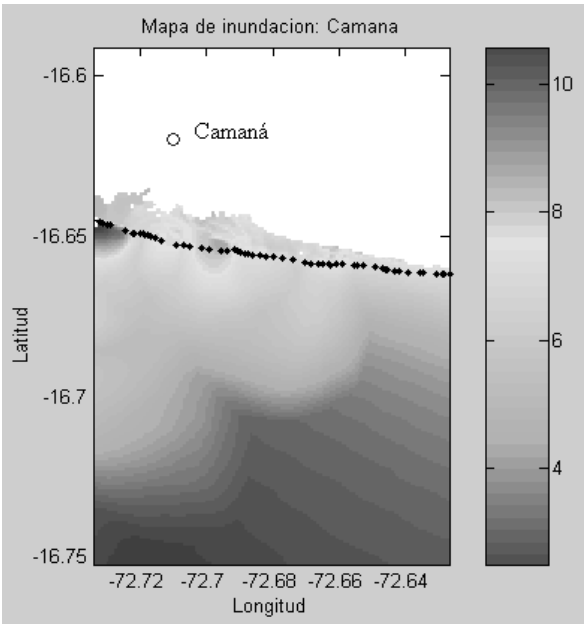


Fig. 7 Flooding map from the homogeneous slip model (scale in meter).

In Figure 8, we can see the inundation map for the heterogeneous slip model. This means that the tsunami would reach to Camana city, that did not happen, and this is because the values obtained for the slip amount on the northern part of the fault in the Tsunami waveform inversion model (for to get the heterogeneous slip model) are overestimated (Adriano, 2010).

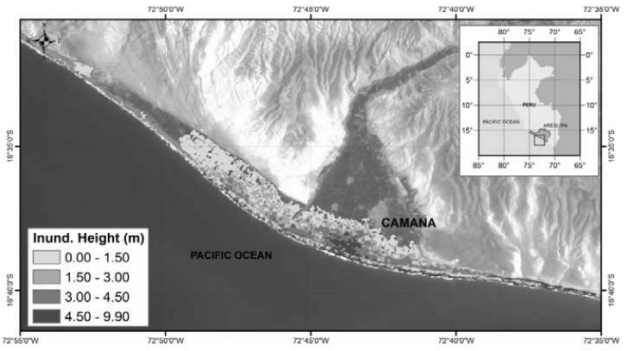


Fig. 8 Flooding map from the heterogeneous slip model (Adriano, 2010).

Figure 9 shows an aerial photograph in which is traced the flooding observed, it appears that the homogeneous slip model agrees quite closely with the observation in situ, thus validating this modeling tsunami inundation.



Fig. 9 Flooding map as in-situ (Source: DHN)

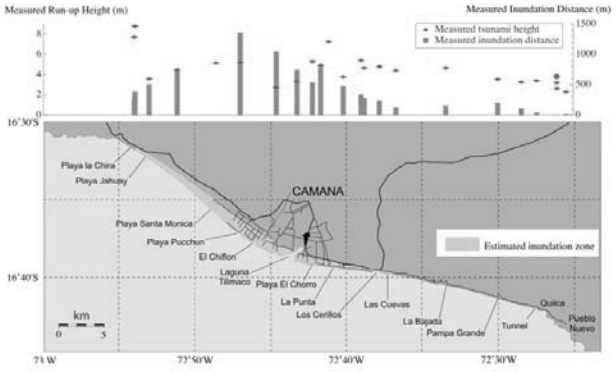


Fig. 10 Measured inundation distances (ITST)

In Figure 11 shows a synthetic waveform (tidal meter) located in the region of the grid D. The peak of the first wave arrives about 12 minutes and the next largest wave arrives at 28 min. The maximum wave height is about 7 m (which is consistent with the observation in situ). After 3

hours the wave amplitude has been reduced to little more than 1 m.

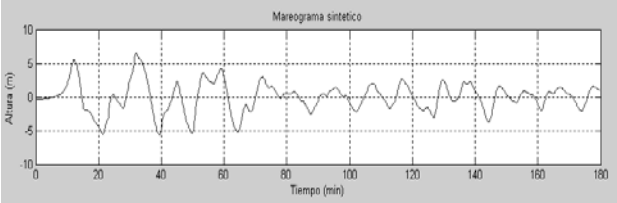


Fig.11 Synthetic waveform tsunami from a virtual tidal station located in the coastline of the flood region.

7. CONCLUSIONS

Camana City is well located, but not the coastal resort in an area that is highly vulnerable to the occurrence of a tsunami, which means that in future similar event may occur as in 2001.

The value of seismic moment Mo = $4.9*10^{21}$ Nm calculated in this work indicates that the earthquake of Camana 2001 generated small but destructive tsunami.

For a local tsunami, the arrival time of the first wave will be about 12 minutes, which provides little time for evacuation. However, not always the first wave is the largest.

The run-up (maximum flood height) reached a height of 7 m on average, implying that some places like the resort, would be potential flood spots.

The results in this paper are a mathematical physical model to some extent validated by field data and evidence.

The relevant authorities should develop plans for disaster mitigation in the event of an earthquake and tsunami. The coastal population must learn to be forewarned before the occurrence of these events.

References

Jiménez, C., Ortega, E. 2008. Cálculo de la Inundación del Maremoto del Callao de 1746. Revista de Investigación de Física, vol. 11, Nº 1, p. 20-26

Kulikov, E., Rabinovich, A., Thomson, R. 2005. Estimation of Tsunami Risk for the Coasts of Peru and Northern Chile. Natural Hazards vol. 35, p. 185-209.

Papazachos, B., 2004. Global relations between seismic fault parameters and moment magnitude of Earthquakes. Bulletin of the Geological Society of Greece vol. XXXVI, p. 1482-1489.

Talandier J., 1993. French Polynesia Tsunami Warning Center (CPPT). Natural Hazards and Earth System Sciencies 7, p. 237-256.

Smith, W., Sandwell, D. 2006. (ETOPO2v2) 2-minute Gridded Global Relief Data. National Oceanic and Atmospheric Administration, National Geophysical Data Center. http://www.ngdc.noaa.gov/mgg/fliers/ 06mgg01.html

Jarvis A., Reuter, A. Nelson, E. Guevara, 2006. Hole-filled seamless SRTM data V3, International Centre for Tropical Agriculture (CIAT), available from http://srtm.csi.cgiar.org.

Mansinha, L., Smylie, E. 1971. The displacement field of inclined faults. Bulletin of the Seismological Society of America, V. 61, No 5, pp. 1433-1440.

Okal, E., Dengler, L. 2002. Field Survey of the Camaná, Peru Tsunami of 23 June 2001. Seismological Research Letters, vol. 73, number 6, p. 907-920.

Adriano, B., 2010. Validation of Tsunami Inundation Modelling for the June 23, 2001 Peru earthquake. Master paper, Tsukuba University, Japan.

Goto and Ogawa, 1992. Numerical Method of Tsunami simulation with the leap-frog scheme. Tohoku University.

8CUEE CONFERENCE PROCEEDINGS
8th International Conference on Urban Earthquake Engineering
March 7-8, 2011, Tokyo Institute of Technology, Tokyo, Japan

ON SUBMARINE LANDSLIDE CAUSED BY THE SURUGA BAY EARTHQUAKE

Hiroyuki Matsumoto[1], Toshitaka Baba[2], and Yoshiyuki Kaneda[3]

1) Research Scientist, Japan Agency for Marine-Earth Science and Technology, Japan
2) Technical Engineer, Japan Agency for Marine-Earth Science and Technology, Japan
3) Project Leader, Japan Agency for Marine-Earth Science and Technology, Japan
hmatsumoto@jamstec.go.jp

Abstract: On 11 August, 2009, at 05:07 JST, a moderate-to-large earthquake took place in the Suruga Bay of central Japan. It struck two deep ocean water pipes in the near source area, of which the temperature and the turbidity of deep ocean water respectively became higher and larger than usual right after the earthquake, inferring that some damages have happened on the water pipes due to the earthquake. In the meantime, we carried out two in-situ surveys in order to reveal damages of the water pipes and its cause. The first survey was done by using ROV "Hyper-Dolphin", which contained the visual surveys. As a result, we have discovered one water pipe at least 2 kilometers downstream from the original position. The second survey by R/V "Natsushima" was done in order to reproduce the bathymetry map in the source area. Comparing with the topography obtained before the earthquake, we can recognize an erosion pattern near the water pipe, whereas a sediment pattern has been found in the downstream, suggesting possibly a submarine landslide trace caused by the earthquake. This submarine landslide might contribute to the tsunami excitation, which still cannot be interpreted by the seismic faulting alone.

1. INTRODUCTION

On 11 August, 2009 at 05:07 JST, a moderate-to-large earthquake took place, of which the magnitude was 6.5 and the hypocenter depth was 23 km in the Suruga Bay, central Japan. According to the preliminary report of Japan Metrological Agency (JMA, 2009), maximum seismic intensity was recorded to be 6 in the near source area, e.g., Izu, Yaizu, Makinohara, and Omaezaki cities. This earthquake is referred as the Suruga Bay earthquake here after. JMA issued the information for Tokai earthquake for the first time immediately after the Suruga Bay earthquake. The mechanism of the Suruga Bay earthquake was the thrust fault type with NNE-SSW lateral component (Fig. 1). The hypocenter is located in the subducting Philippine Sea plate and this was the typical intra plate earthquake. After shocks' distribution implies that the fault plate extended 20 km x 20 km.

The human and material disasters have been occurred at Shizuoka, Kanagawa, Tokyo and Nagano prefectures during the Suruga Bay earthquake. Among them, a land slide was occurred at the bank edge of the Tomei high way in Makinohara city. Fisheries, port and harbor structures were also damaged. Liquefaction was occurred at the Yaizu port. And a water pipe facility operated by Shizuoka prefecture exists in the source area of the Suruga Bay earthquake. Both the temperature and the turbidity sudden changes were observed after the Suruga Bay earthquake. We postulated that something has happened to the water pipe.

In the meantime, Japan Agency for Marine-Earth Science and Technology carried out in-situ two surveys; the first survey was to observe the water pipe, the second survey was to obtain bathymetry after the earthquake and the last survey is to do high resolution bathymetric mapping within a half year after the Suruga Bay earthquake. This paper describes the report of two surveys performed in the near source area of the Suruga Bay earthquake.

2. SURUGA BAY DEEP-SEA WATER PIPE AND ITS DAMAGE

Shizuoka prefecture has been operating two deep-sea water pipes off Yaizu city since 2001 and getting two different layered deep-sea waters. The shallower water pipe reaches 397 meters deep and the other deeper one reaches 687 meters deep. Deep-sea water is used for not only scientific and technological researches but also resources of original foods, which contributes to the local industrial development. Two water pipes have been deployed from Yaizu port parallel to eastward offshore. Length of two water pipes are 3.3 kilometers and 7.3 kilometers for 397 m and 687 m water pipes as shown Fig. 1. Water pipe is made by seamless high density polyethylene (HDPE) armored by steel. Though diameters are slightly different between 397 m and 687 m water pipes, proof load is about 2 kN. Sluice gates attached with 7.5 meters high truss scaffold are deployed at the end of the both water pipes.

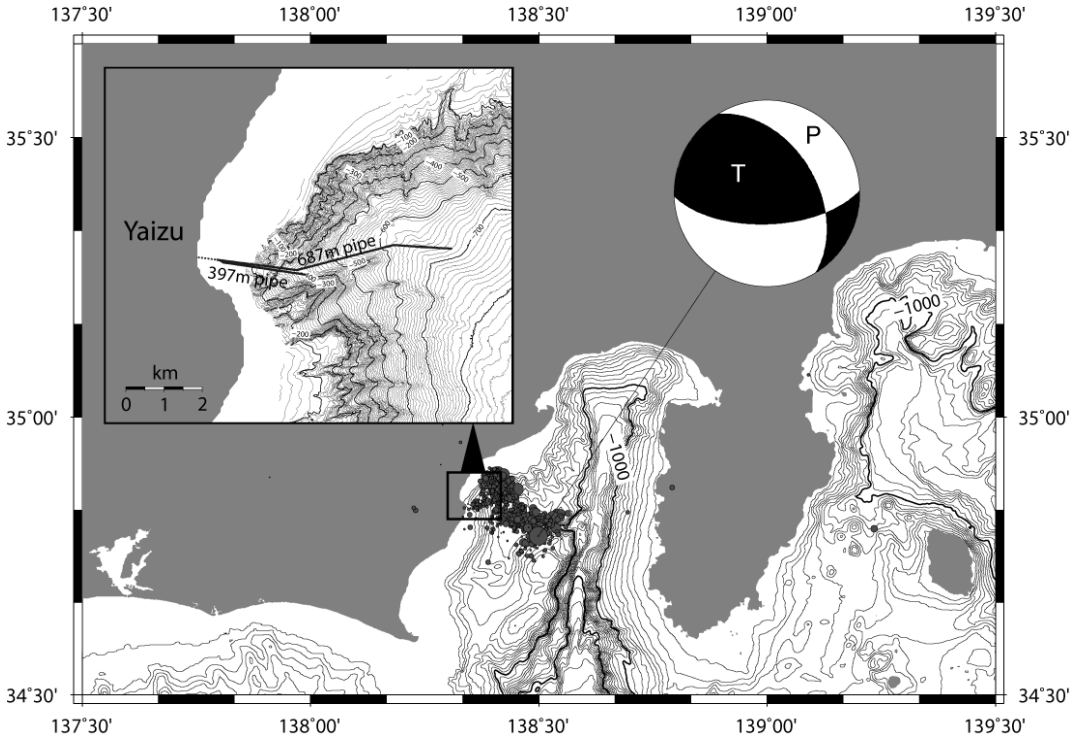


Figure 1 Map showing the epicenter of the earthquake taken place on 11 August, 2009 and the water pipes deployed in the Suruga Bay

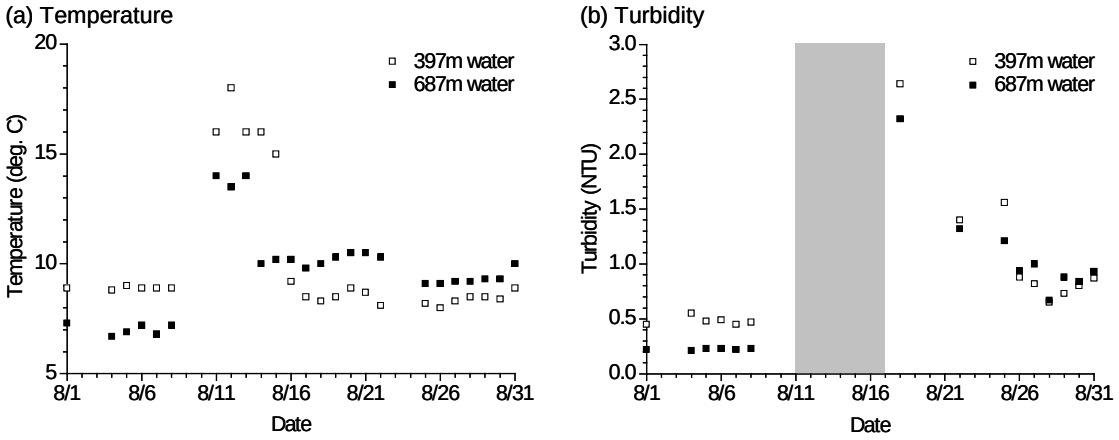


Figure 2 Time histories of deep-sea water on August, 2009 regarding (a) temperature and (b) turbidity. Note that data was saturated during the shaded period.

Basically, temperature and turbidity of deep-sea water are instrumentally measured once a day at the water pipe landing station. Figure 2 shows the time histories of deep-sea waters' temperature and turbidity on August 2009. Figure 2 (a) represents the temperature, in which it usually remained 9 degree C and 7 degree C for 397 m and 687 m waters, respectively. After the Suruga Bay earthquake, however, they changed 15 to 18 degree C and 13 to 14 degree C once, and high temperature continued for four days. On 16 August, the temperature of 397 m water was recovered, but that of 687 m water was still kept 9 degree C. Although the deeper 687 m water must be lower than the shallower 397 m water, thermal inversion occurred after the earthquake.

On the other hand, according to the turbidity data observed by 2100P produced by HACH Company in Fig. 2 (b), it remained 0.2 NTU and 0.5 NTU for 397 m water and 687 m water, respectively. But, they were saturated the dynamic range during a week after the earthquake, and it was impossible to measure the data. And about 0.5 NTU higher turbidity than the usual continued even after it became possible to do it again.

Continuous abnormal temperature increase and high turbidity from the 687 m water pipe implied that something happened to the 687 m water pipe.



Figure 3 Research Vessel "Natsushima"

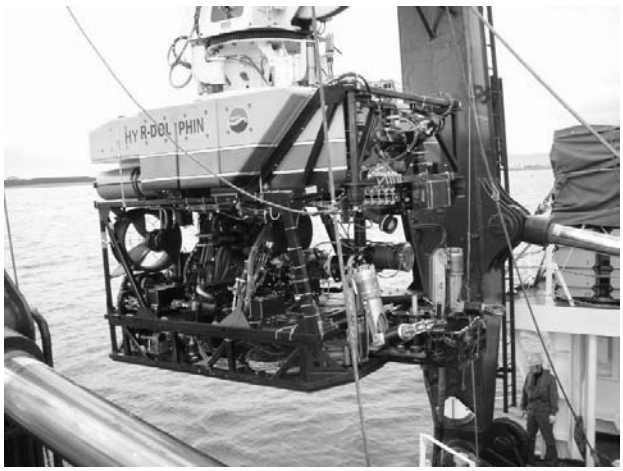


Figure 4 Remotely Operated Vehicle "Hyper-Dolphin"

3. IN-SITU SURVEY OF THE EARTHQUAKE SOURCE AREA

3.1. Overview

JAMSTEC planned to conduct two surveys in order to understand what happened in the near source area during the Suruga Bay earthquake both by using Research Vessel "Natsushima" (Fig. 3). The first survey was to carry out visual survey of the water pipes by Remotely Operated Vehicle "Hyper-Dolphin" (Fig. 4), and the second survey was to obtain bathymetry data by multi-narrow beam echo sounder equipped by "Natsushima".

3.2. "Hyper-Dolphin" survey

Because any damages have been considered to be taken place on the 687 m water pipe as mentioned previous section, two ROV's dives were carried out in order to know where to be damaged and the actual condition of the water pipe on 13 and 14 December 2009. ROV "Hyper-Dolphin" is carried by R/V "Natsushima", which can move flexibly under the water equipped with plural cameras to do visual survey. Figure 5 shows the "Hyper Dolphin" dive tracks after reaching the seabed measured by super short base line (SSBL) positioning system by "Natsushima".

The first dive, i.e., 1066 dive on 13 December was carried out at the water depth 200 to 300 meters. This is because the temperature from the 687 m water pipe is higher than that from 397 m water pipe after the earthquake. Damage has been take place at the shallower location than 397 m. "Hyper-Dolphin" dived across two water pipes, but it could cross the 397 m water pipe only. At last we could not find the 687 m water pipe during this dive, suggesting the 687 m water pipe has been moved away. Figure 6 shows the 397 m water pipe found by "Hyper-Dolphin". Half of 240 mm diameters pipe has been buried under the seabed. Moreover, we found 397 m water pipe has been suspended like a bridge at the submarine canyon.

The second dive, i.e., 1067 dive, on 14 December was carried out in order to find the sluice gate at the end of the 687 m water pipe. Figure 5 shows the dive track in which "Hyper-Dolphin" started to dive 200 m south from the pipe end. However, the sonar did detect nothing at the point of the 687 m water pipe end, and nothing could be found. Another survey line was made parallel to the first track to cross the 687 m water pipe again, but we could not find the 687 m water pipe. Then "Hyper -Dolphin" turned to westward and came across the 687 m water pipe denoted by A in Fig. 5. This is 500 meters away from the original water pipe laid position. After finding the 687 m water pipe, "Hyper-Dolphin" move to SE i.e., downstream along the water pipe. Debris has been deposited relatively on the SW side against the water pipe where "Hyper-Dolphin" came across the 687 m water pipe. We also found the wreck of submerged ship on the way as shown in Fig. 7. The further offshore "Hyper-Dolphin" proceeded, the more frequent the 687 m water pipe was lost and up cropping. At last we lost the 687 m water pipe at water depth of 782 meters denoted by B in Fig. 5. Section between A and B is the current 687 m water pipe location, but it is still unknown how the NW end of the 687 m water pipe is laid. After the visual survey by "Hyper-Dolphin", we have realized that the 687 m water pipe at least 2 km has been washed away toward the offshore from the original position.

3.2. "Natsushima" survey

It has become clear that the 687 m water pipe has been washed away offshore after the "Hyper-Dolphin" dives. Bathymetry survey by multi-narrow beam echo sounder equipped by "Natsushima" was carried out from 26 through 31 December 2009 in order to reveal the cause of 687 m water pipe washed away. Multi-narrow beam echo sounder used in the present survey is SeaBat 8160, Reson inc. Principal of multi-narrow beam echo sounder is simply described as follows. An acoustic beam is periodically transmitted to the seabed from the bottom of the ship. Hydrophone array receives the acoustic beams reflected from the seabed in order to determine the distance between the ship and the seabed. The bathymetry map is

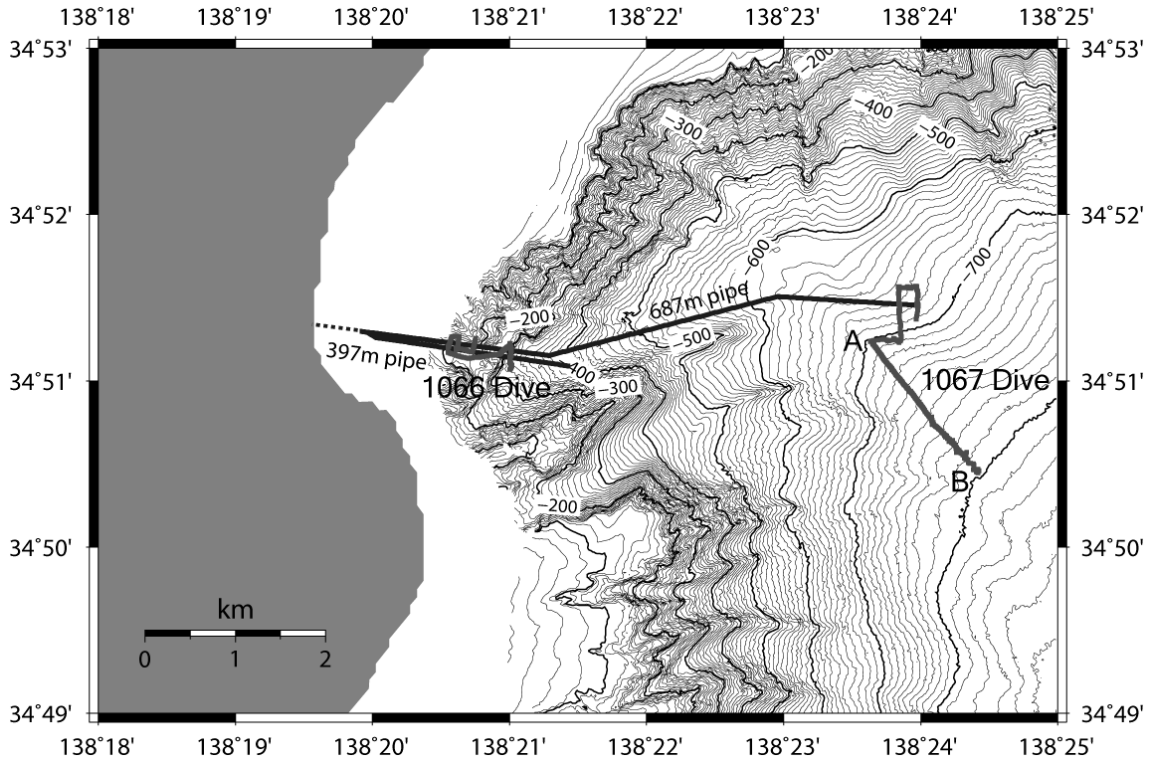


Figure 5 Dive tracks of ROV "Hyper-Dolphin" and the location of the water pipes



Figure 6 397 m water pipe observed by ROV "Hyper-Dolphin" during the 1066 dive



Figure 7 687 m water pipe and submerged ship found during the 1067 dive

made based on this procedure. In 2004, "Natsushima" also carried out bathymetry survey by using the same equipment, and it makes us possible to compare the bathymetry obtained before and after the earthquake. But it is noted that the resolution of bathymetry obtained before the earthquake is not good enough, because ship speed "Nastsushima" was relatively high. Moreover, area obtained the bathymetry is not completely coincident each other.

Ship track of "Natsushima", i.e., survey line by multi-narrow beam echo sounder in addition to the obtained bathymetry after the earthquake are superposed in Fig. 8. A lot of submarine canyons at the edge of the spur shaped by fan exist on the continental slope in the Suruga Bay (Otsuka, 1982). And the deep-sea water pipes are laid along one submarine canyon.

Difference between bathymetry dataset obtained before and after the Suruga Bay earthquake has been reproduced and its enlarged view in near the 687 m water pipe is shown in Fig. 9. Original laid position of the 687 m water pipe and the current water pipe location by "Hyper-Dolphin" are also drawn in Fig. 9.

Since contour lines are very close near submarine canyons and the resolution is not so good before the earthquake, it is difficult to evaluate the deformation due to the earthquake. Ignoring such topographies, difference is significantly large at the terrace around the depth of 600

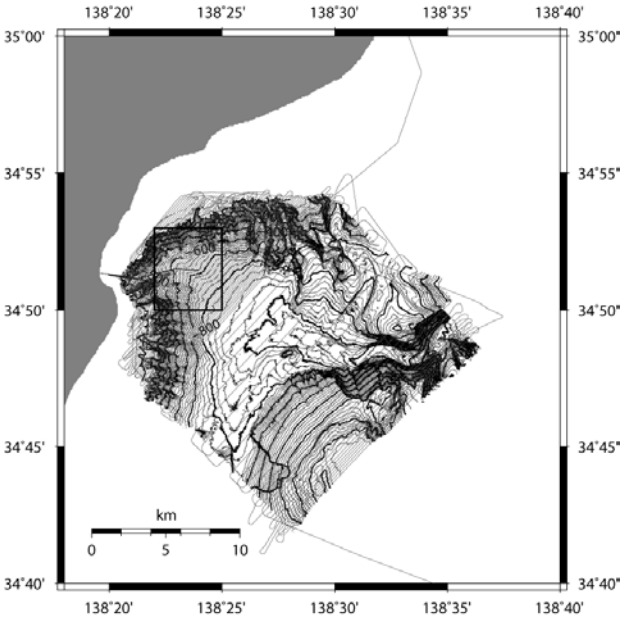


Figure 8 Bathymetry survey result by multi-narrow beam echo sounder of R/V "Natsushima"

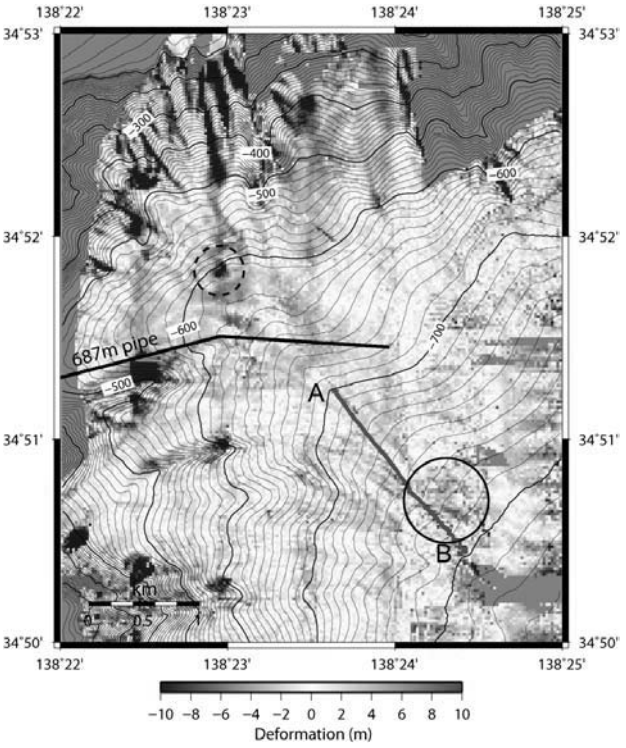


Figure 9 Difference between bathymetries obtained before/after the earthquake

meters near the 687 m water pipe denoted by dashed circle in Fig. 9. About 10 meter subsidence is appeared there and 3 to 5 meters subsidences aside. Contour lines are retrieved suggesting erosion pattern were taken place. This means that the submarine landslide has been taken place at this location. Turbidity current due to the submarine landslide flew SE along the submarine canyon, and washed away the 687 m water pipe laid at 900 m downstream. Location where "Hyper-Dolphin" lost the 687 m water pipe became uplift pattern denoted by solid circle in Fig. 9. This suggests that the turbidity originated by the submarine landslide has been deposited there.

4. CONCLUSING REMARKS

Deep-sea water pipes deployed in the near source area of the Suruga Bay earthquake occurred on 11 August 2009 have been damaged. For deepen understanding how the accidents have been happened and its cause, two surveys were carried out in December 2009. Two survey results are conclusively summarized as follows,

(1) Among two deep-sea water pipes, 687 m water pipe at least 2 kilometers has been washed away from the original position by visual survey by ROV "Hyper-Dolphin" during the 2009 Suruga Bay earthquake. Broken point separated from originals is still unknown.

(2) Bathymetry mapping by R/V "Natsushima" has revealed that the submarine landslide origin is possibly located at the northward upstream of the 687 m water pipe, where an erosion pattern is obviously visible. The current 687 m water pipe is covered with debris including that from the submerged ship.

It is worthwhile noted that the submarine cable located in the Suruga trough, about 100 km south from the earthquake source has been also damaged after 15 hours and 52 min after the Suruga Bay earthquake. Turbidity current due to the submarine landslide might reach there.

Entire damages of the deep-sea water pipes due to the submarine landslide earthquake have not been revealed in the preset surveys. Further survey and qualitative studies are necessary in the near source area, which may contribute to other similar submarine life lines such as submarine cable etc and mitigate their damages.

Acknowledgements:

The preliminary report of the series of JAMSTEC survey has been published by Matsumoto et al. (2010). We thank Hitoshi Hotta, exective director of JAMSTEC for his effort to carry out series of in-situ surveys. Some figures were prepared using GMT software (Wessel and Smith, 1995).

References:

Japan Meteorological Agency (2009), "Monthly report on earthquake and volcanoes in Japan, August 2009", 42-67. (in Japanese)

Matsumoto, H., Baba, T., Kashiwase, K., Kaneda, Y., Misu, T. and Hori. T. (2010), "Damage of deep water pipes due to the Suruga Bay earthquake on 11 August, 2009", *J. Japan Soc. Civil Eng., Ser. B2 (Coastal Eng.)*, **66**, 1341-1345. (in Japanese)

Otsuka, K. (1982), "Submarine sediment slide found on the west slope of the Senoumi-tai North Bank in western Suruga Bay, central Honshu, Japan", *Geosci. Repts. Shizuoka Univ.*, **7**, 87-95. (in Japanese)

Shizuoka Prefecture (2009), "Report of the Suruga Bay earthquake" No.4. (in Japanese)

Wessel, P. and Smith W. H. F. (1995), "New version of the Generic Mapping Tools released," *EOS Trans. AGU*, **76**, 329.

8CUEE CONFERENCE PROCEEDINGS
8th International Conference on Urban Earthquake Engineering
March 7-8, 2011, Tokyo Institute of Technology, Tokyo, Japan

NUMERICAL MODEL OF DYNAMICS OF COMPRESSIBLE OCEAN IN TSUNAMI SOURCE: SENSITIVITY TO INPUT PARAMETERS

Sergey V. Kolesov

Research junior, Physics Faculty, M.V.Lomonosov Moscow State University, Russia
kolesov@ocean.phys.msu.ru

Abstract: In this study 3D numerical model of compressible ocean behavior in a tsunami source is considered. The model is based on the linear potential theory of ideal homogeneous compressible fluid in the field of gravity. The water layer is bounded with free surface above and with absolutely rigid moving bottom below. Dynamic bottom displacement is specified as vector velocity field. The explicit finite-difference scheme on a rectangular grid is used to solve the problem. Testing of numerical model with use of exact analytical solution of the problem in the case of horizontal flat bottom is described. Taking the 2003 Tokachi-Oki tsunamigenic earthquake as an example the role of horizontal components of dynamic bottom deformation is examined.

1. INTRODUCTION

The issue of accounting for the compressibility of water in the problem of tsunami generation has been raised repeatedly in the literature (e.g. Miyoshi 1954, Sells 1965, Kajiura 1970, Nosov 2000, Ohmachi et al. 2001, Nosov et al. 2007, Gisler 2008, Ohmachi and Inoue 2010). In case of a horizontal absolutely rigid bottom a compressible ocean behaves as an waveguide which is characterized by a discrete set of normal frequencies

$$\nu_n = c(1+2n)/4H, \qquad (1)$$

where $n = 0,1,2,3...$, H is the ocean depth and c is the sound speed in water.

When JAMSTEC (Japan Agency for Marine-Earth Science and Technology) deployed a real-time observatory at the continental slope close to the islands of Japan (Hirata et al. 2002), it became possible to investigate a tsunami formation, including hydroacoustic phenomena, just at its source. 3D numerical model taking into account dynamic bottom deformations and water compressibility was created with the intent to reproduce in-situ measured bottom pressure variations during 2003 Tokachi-Oki earthquake (Kolesov et al. 2010). During simulation it becomes clear, that calculation results are rather sensitive to input parameters. The goal of present study is to test the model on the exact analytical solution and investigate the role of horizontal components of bottom deformation.

2. 3D NUMERICAL MODEL

Let us consider a layer of an ideal incompressible homogeneous liquid of variable depth $H(x,y)$ in the field of gravity. We assume the calculation domain to be small enough to neglect the sphericity of the Earth. The origin of the Cartesian reference frame $0xyz$ is on the unperturbed free surface, the $0z$ axis is directed vertically upward. To describe elastic oscillations of water column we shall resolve the problem with respect to the velocity potential $F(x,y,z,t)$ (Landau, Lifshitz, 1987):

$$\frac{\partial^2 F}{\partial t^2} - c^2 \Delta F = 0, \qquad (2)$$

$$\frac{\partial^2 F}{\partial t^2} = -g\frac{\partial F}{\partial z}, \quad z = 0, \qquad (3)$$

$$\frac{\partial F}{\partial \vec{\mathbf{n}}} = (\vec{u}, \vec{\mathbf{n}}), \quad z = -H(x,y), \qquad (4)$$

where $\vec{\mathbf{n}}$ is the unit vector normal to the bottom surface, $\vec{u} \equiv (u_x, u_y, u_z)$ is the velocity vector of bottom deformation. We assume the deformation of the basin bottom takes place during a time interval τ, upon which the basin bottom stops. Bottom deformations are assumed small, thus depth H and vector normal $\vec{\mathbf{n}}$ do not depend on time. Free surface displacement and dynamic pressure can be easily obtained using the following formulae:

$$\xi = -\frac{1}{g}\frac{\partial F}{\partial t}\Big|_{z=0}, \qquad (5)$$

$$p(x,y,z,t) = -\rho\frac{\partial F}{\partial t}, \qquad (6)$$

where ρ is the density of liquid. After the time moment $t = \tau$, i.e. when the bottom deformation stops, we can try to describe a gradual damping of hydroacoustic waves due to their absorption in the bottom. This can be archived by changing boundary condition (4) from “fully reflective” to the semi-transparent one:

$$\frac{\partial F}{\partial \vec{n}} = \frac{\partial F}{\partial t}\frac{1}{c}\frac{R_A - 1}{R_A + 1}, \qquad (7)$$

where R_A is amplitude reflection coefficient at the "water-bottom" boundary for a normally incident hydroacoustic wave. Generally, amplitude reflection coefficient R_A depends on parameters of the ground in particular site. In this study the value of $R_A = 0.89$ was taken.

The equations (2)-(7) are solved numerically with use of traditional explicit Finite Difference scheme (z-leveled model, rectangular grid). As a condition for stability of the scheme a well-known CFL criterion is used.

More comprehensive model description and numerical scheme implementation peculiarities can be found in following papers (Nosov and Kolesov 2007, Kolesov et al. 2010).

3. RESULTS AND DISCUSSION

Let us consider the case of a flat horizontal bottom. Due to simple shape of basin, boundary condition (4) could be rewritten in following form:

$$\frac{\partial F}{\partial z} = \frac{\partial \eta}{\partial t}, \quad z = -H, \qquad (8)$$

where η is bottom deformation. As a source of the waves, let us choose a cylindrically symmetric deformation of the bottom with duration τ:

$$\eta(r,t) = \sin\frac{\pi t}{\tau} e^{-\frac{r^2}{R^2}} \left(\Theta(t) - \Theta(t-\tau)\right), \qquad (9)$$

where R is the radius of the source, Θ is the Heaviside step function. Analytic solution of a cylindrically symmetric problem (2), (3), (8) obtained in Nosov (2000), allows us to calculate the free surface displacement as follows:

$$\xi(r,t) = -g^{-1}\int_0^\infty dk \int_{s-i\infty}^{s+i\infty} dp\, p \exp(pt)\, J_0(kr)\, A(p,k), \qquad (10)$$

$$A(p,k) = -\frac{p\, k\, \Psi(p,k)}{\alpha\left[\mathrm{sh}(\alpha h) + p^2 g^{-1}\alpha^{-1}\mathrm{ch}(\alpha h)\right]},$$

$$\Psi(p,k) = \frac{1}{2\pi\pi}\int_0^\infty dr \int_0^\infty dt\, \eta(r,t)\, r\, J_0(kr) \exp(-pt), \qquad (11)$$

$$\alpha^2 = k^2 + p^2 c^{-2}.$$

Integrals in (11) for a bottom deformation (9) can be easily calculated analytically. Integrals in (10) are calculated numerically.

For the numerical simulation a calculation domain with size of 220x220 km and depth 5.6 km was chosen. Number of grid nodes was varied within the following bounds: horizontal — from 200 to 800, vertical — from 20 to 80. Duration of the bottom deformation was τ=3.7 and 37 s. For the chosen depth source with short duration effectively excite only acoustic waves, source with long duration — only gravitational waves. Horizontal size of bottom deformation R was chosen to be equal the water layer depth H. Generally, the size of tsunami source area is much bigger than the depth of the ocean. Such a small source is chosen to demonstrate the model efficiency on horizontal discontinuities of small scale.

At the first stage, the influence of the grid horizontal spacing in the accuracy of the numerical solution was studied. The results are shown in Fig. 1. It's easy to see that the numerical model reproduces the amplitude of both acoustic (short-period) and gravitational waves. Over time, the accumulation of the phase difference between the analytical and numerical solutions becomes visible. The smallest phase difference corresponds to the most detailed resolution the grid, principally vertical resolution.

Simulation with a fixed number of nodes in the horizontal and variable in the vertical direction is shown on the Fig. 2. As in the previous case, the choice of spatial grid step does not significantly affects on the amplitude of oscillations. It is notable, that a phase difference tends to grow with reducing of the vertical resolution of the grid. Test calculations showed that for a correct reproduction of the amplitude characteristics it is sufficient 20 grid nodes vertically. Of course, vertical spatial step must satisfy following relation: $\Delta z < cT_{min}$, where T_{min} is the minimum period of acoustic waves generated by the source. To minimize the phase difference we should maximize vertical resolution of the grid. The choice of horizontal grid spacing is determined by the scale of the horizontal discontinuities of the source. In the simulation shown in Fig. 1, the horizontal steps $\Delta x = \Delta y \approx 1$km ($N_x = N_y = 200$) is sufficient to adequately reproduce the waves generated by a source with radius $R = H = 5.6$km.

From figures 1 and 2 one can conclude that the phase difference is accumulated over time for both acoustic and gravitational waves. However, accumulation for acoustic waves goes faster. Velocity of gravitational waves as well as the period of the acoustic waves depends on the depth of the water layer. The peculiarity of the finite difference method is that the approximation of boundary conditions utilizes 2-3 vertical nodes and, thus, reduces the true depth. A simple estimation shows that the error in determining the depth in sole node over time T will lead to the phase difference for the acoustic waves:

$$\Delta\Phi_a = \left(\frac{c}{4(H+\Delta z)} - \frac{c}{4H}\right) 2\pi T \qquad (12)$$

and for gravitational waves:

$$\Delta\Phi_g = \left(\frac{\sqrt{gH}}{L} - \frac{\sqrt{g(H+\Delta z)}}{L}\right) 2\pi T \qquad (13)$$

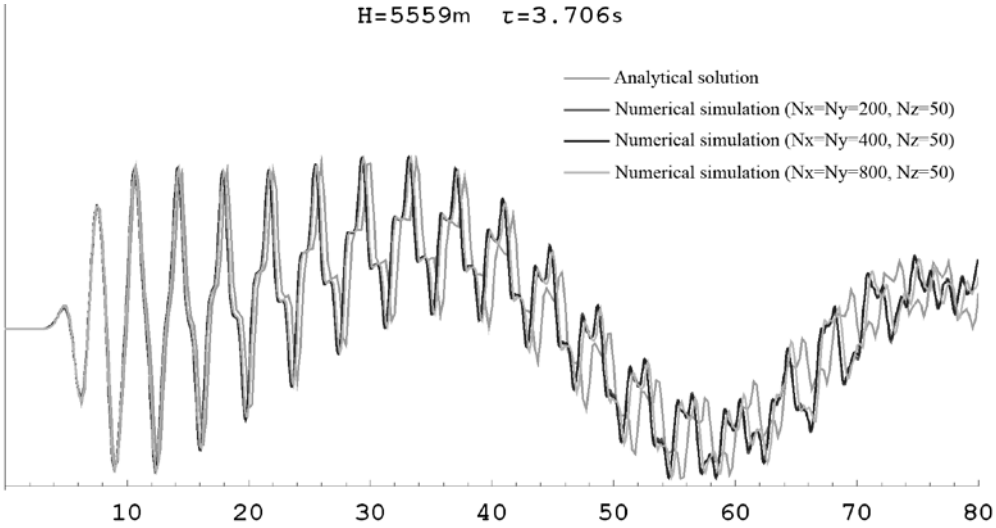


Figure 1. Free surface displacement in the center of calculation domain: influence of horizontal grid resolution.

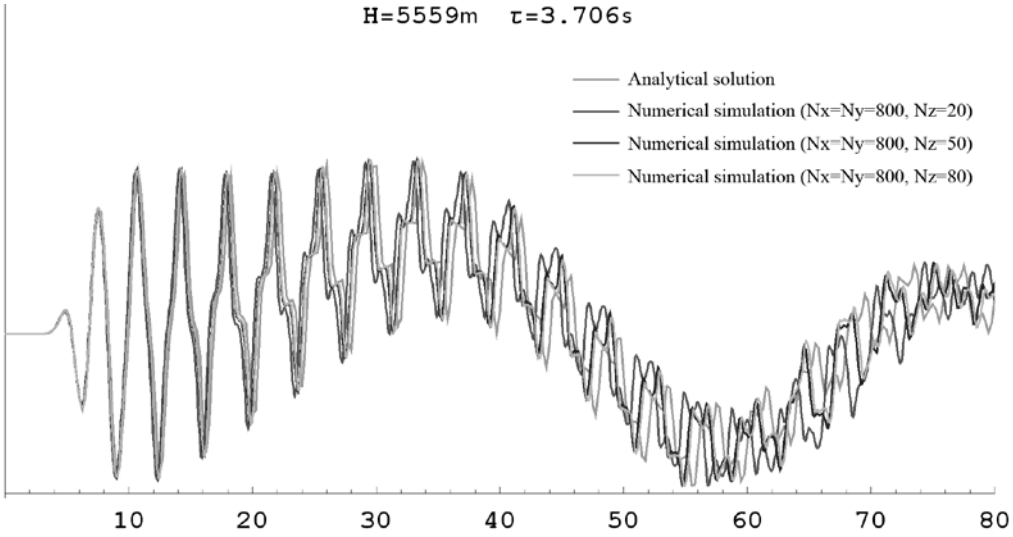


Figure 2. Free surface displacement in the center of calculation domain: influence of vertical grid resolution.

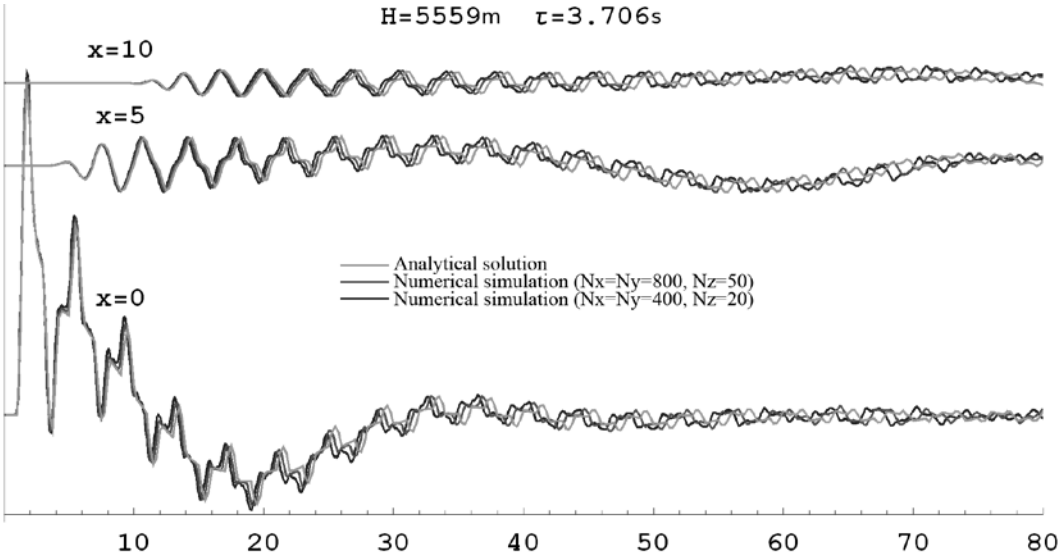


Figure 3. Free surface displacement at different distance from the center: fast bottom motion.

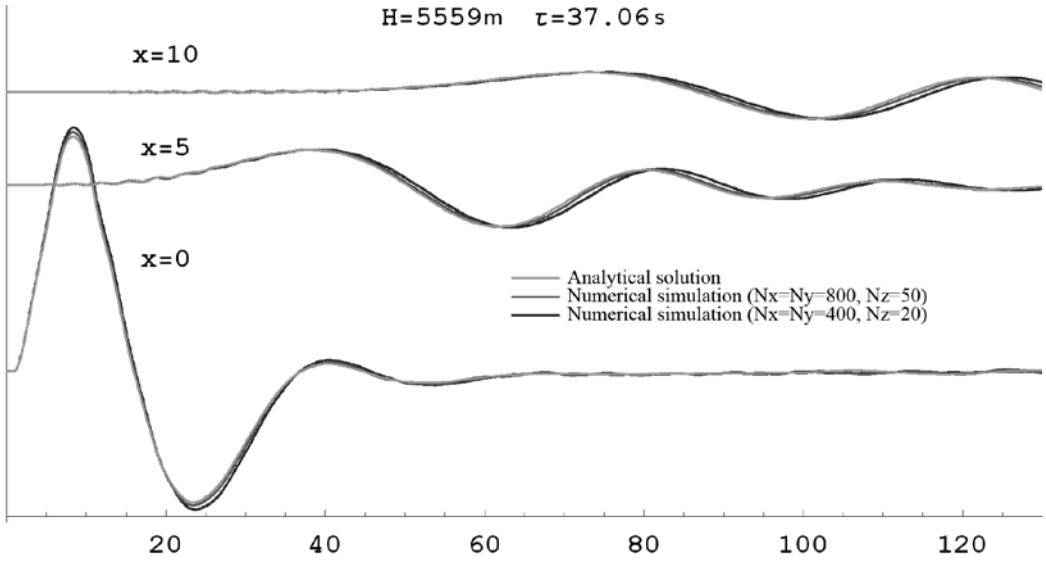


Figure 4. Free surface displacement at different distance from the center: slow bottom motion.

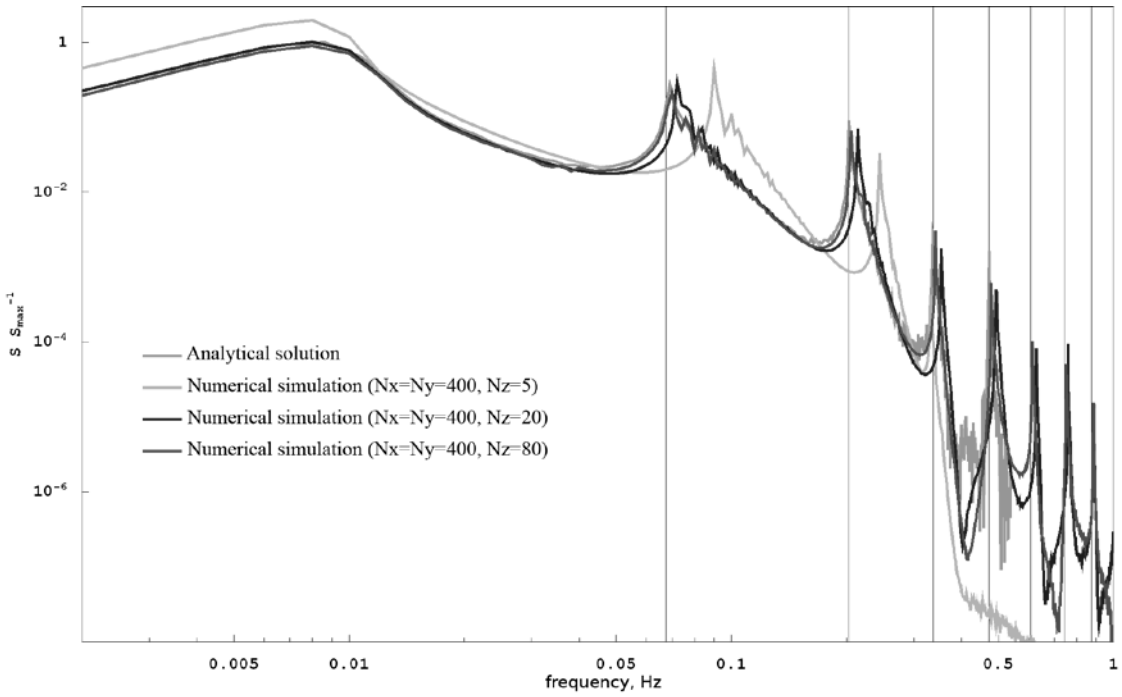


Figure 5. Normalized frequency spectra of free surface displacement in the center of calculation domain. Time series were calculated numerically and analytically at .bottom displacement duration of 3.7s. Vertical grid lines stand for the position of the normal frequencies of water layer.

In this particular case, if the computational domain has vertical resolution of 20 and 19 nodes, the phase difference between the first mode of elastic oscillations at 2π will be achieved at the 20th period. Same phase difference of gravitational waves will be achieved at the 39th period. It worth to note that the period of the gravitational waves is usually much longer than the period elastic oscillations of the water layer, it is obvious that the significant phase difference of acoustic waves will occur much earlier.

Fig. 3 presents a comparison of analytical and numerical solutions at three points away from the center at $0,\ 5H$ and $10H$. Calculations performed using the numerical model presented for large and small number of nodes in the computational grid. The numerical model shows good coincidence with the exact analytical solution, especially with greater number of grid nodes. A similar calculation but with longer duration of bottom deformation is shown in Fig. 4. In this case, we have a prevailing component of the gravitational wave motion. As one can see under these conditions the numerical model gives a nearly perfect coincide with the analytical solution.

Comparison of normalized energy spectra of the numerical and analytical solution is presented on Fig. 5. Normalization was carried out at maximum level, corresponding to the analytical solution. Vertical grid lines stand for the normal frequencies of water layer. It is seen that the numerical model precisely describes the frequency characteristics of the system. Accuracy of calculation increases with better vertical resolution of the grid. Cut-off of the spectrum of the analytical solution and the spectrum of numerical simulation with the least number of grid nodes could be explained by a low sampling rate of the data.

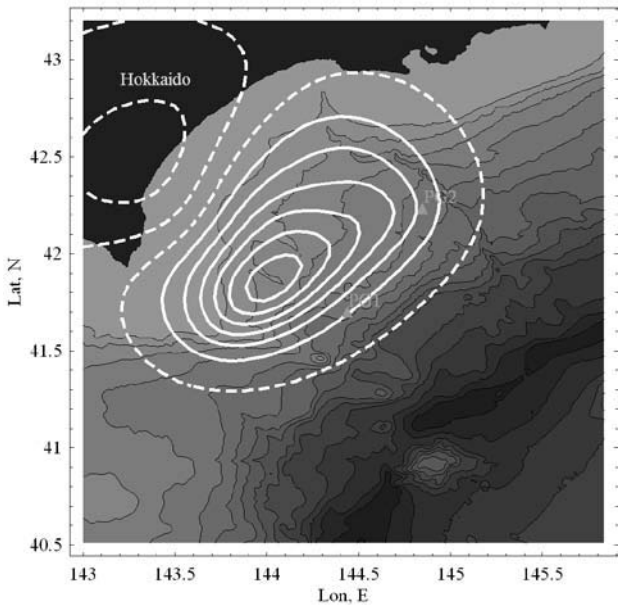


Figure 6. Computational domain. Vertical coseismic bottom deformation is shown by solid (uplift) and dashed (subsidence).

To examine the role of horizontal components of dynamic bottom deformation the simulation of the 2003 Tokachi-Oki tsunamigenic earthquake was performed. Fig. 6 depicts a computational domain with bathymetry, residual bottom deformation and points of virtual bottom pressure sensors. Computational area dimension was approximately 220x320 km (301x301 nodes); the number of vertical nodes was 15 with the spatial step 535 m. The dynamic bottom deformation was computed using fault model proposed in Koketsu et al. (2004). The calculation technique and parameters of the fault and ground are described in papers (Ohmachi et al. 2001, Kolesov et al. 2010). The duration of bottom motion was 128 seconds. Despite the fact that PG1 and PG2 points correspond to bottom cable stations deployed by JAMSTEC, in this study these points are chosen just for example. The ability of the numerical model to reproduce the in situ measured signal was discussed in Kolesov et al. (2010).

Two series of calculation was performed. First one using three-component dynamic bottom deformation ($\vec{u} \equiv (u_x, u_y, u_z)$), second one using only vertical velocity component ($\vec{u} \equiv (0, 0, u_z)$). Time-history of bottom pressure variations was recorded for both points PG1 and PG2. In Fig. 7 elastic oscillations generated by three-component source are plotted with red, blue curve stands for difference between synthetic signals, generated by both sources, in other words this is contribution of horizontal components of bottom deformation into resulting signal. It's clearly evident that mentioned contribution is almost negligible.

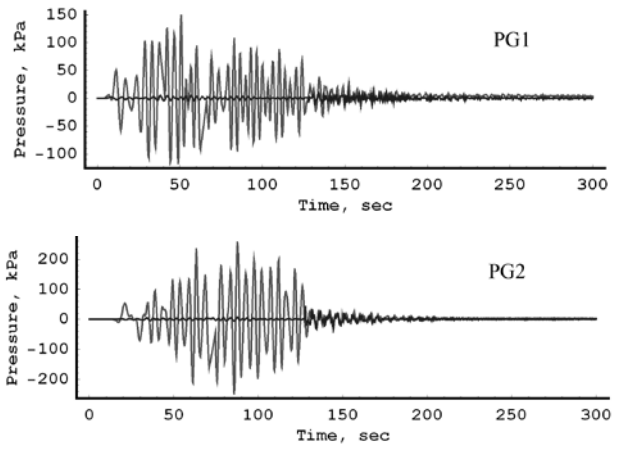


Figure 7. Bottom pressure variations in points PG1 and PG2. Acoustic waves from three-component source are shown with red, contribution of horizontal components are shown with blue.

4. CONCLUSIONS

3D numerical model was tested with use of exact analytical solution of the problem in the case of horizontal flat bottom. Good coincidence between analytical and numerical simulations was found. Numerical model

reproduces both amplitude and frequency characteristics of the system. Vertical grid resolution seems to be the most important parameter affecting the accuracy of calculations. The contribution of horizontal components of dynamic bottom deformation into hydroacoustic effects in tsunami source turned out to be small.

Acknowledgements:

This work was supported by the Russian Foundation for Basic Research (project 10-05-92102).

References:

Gisler, G. R. (2008), "Tsunami simulations," *Annu. Rev. Fluid Mech*., **40**, 71–90.

Hirata, K., Aoyagi, M., Mikada, H., Kawaguchi, K., Kaiho, Y., Iwase, R., Morita, S., Fujisawa, I., Sugioka, H., Mitsuzawa, K., Suyehiro, K., Kinoshita, H., and Fujiwara, N. (2002), "Real-time geophysical measurements on the deep seafloor using submarine cable in the southern Kurile subduction zone," *IEEE J. of Oceanic Eng*., **27** (2), 170-181.

Kajiura, K. (1970), "Tsunami source, energy and the directivity of wave radiation," *Bull. Earthq. Res. Inst. Tokyo Univ*., **48**, 835-869.

Koketsu, K., Hikima K., Miyazaki, S. and Ide, S. (2004), "Joint inversion of strong motion and geodetic data for the source process of the 2003 Tokachi-oki, Hokkaido, earthquake," *Earth Planets Space*, **56**(3), 329-334.

Kolesov S., Bolshakova, A., Inoue, S., Matsumoto, H., Nosov, M., and Ohmachi, T. (2010), "Numerical simulation of hydroacoustic effects in tsunami source," *Joint Conference Proceedings, 7th International Conference on Urban Earthquake Engineering (7CUEE) & 5th International Conference on Earthquake Engineering (5ICEE), March 3-5, 2010, Tokyo Institute of Technology, Tokyo, Japan*, 1687-1692.

Landau, L. D., and Lifshitz, E. M. (1987), "Fluid Mechanics, V.6 of Course of Theoretical Physics, 2nd English edition. Revised.," (Pergamon Press, Oxford - New York – Beijing – Frankfurt - San Paulo – Sydney – Tokyo - Toronto.

Miyoshi, H. (1954), "Generation of the tsunami in compressible water (Part I)," *J. Oceanology. Soc. Japan*, **10**, 1-9.

Nosov, M. A. and Kolesov, S. V. (2007), "Elastic oscillations of water column in the 2003 Tokachi-oki tsunami source: in-situ measurements and 3-D numerical modelling," *Natural Hazards and Earth System Sciences*, **7**, 243-249.

Nosov, M. A. (2000) "Tsunami generation in a compressible ocean by vertical bottom motions," *Izvestiya - Atmospheric and Ocean Physics*, **36** (5), 661-669.

Nosov, M. A., Kolesov, S. V., Denisova, A. V., Alekseev, A. B., and Levin, B. W. (2007), "On the near-bottom pressure variations in the region of the 2003 Tokachi-Oki tsunami source," *Oceanology*, **47**(1), 26-32.

Ohmachi, T. and Inoue, S. (2010), "Dynamic tsunami generation process observed in the 2003 Tokachi-oki Japan earthquake," *Advances in Geosciences - Ocean Science*, **18**, 159-168.

Ohmachi, T., Tsukiyama, H., and Matsumoto, H. (2001) "Simulation of tsunami induced by dynamic displacement of seabed due to seismic faulting," *Bulletin of the Seismological Society of America*, **91** (6), 1898-1909.

Sells, C.C.L. (1965), "The effect of a sudden change of shape of the bottom of a slightly compressed ocean," *Phil. Trans. Roy. Soc. London (A)*, **258**, 495-528.

8CUEE CONFERENCE PROCEEDINGS
8th International Conference on Urban Earthquake Engineering
March 7-8, 2011, Tokyo Institute of Technology, Tokyo, Japan

VALIDATION OF TSUNAMI INUNDATION MODELLING FOR THE JUNE 23, 2001 PERU EARTHQUAKE

Bruno Adriano[1], Shunichi Koshimura[2], and Yushiro Fujii[3]

1) Research Assistant, Japan Peru Center for Earthquake Engineering and Disaster Mitigation, Peru
2) Associate Professor, Disaster Control Research Center, School of Engineering, Tohoku University, Japan
3) Research Scientist, International Institute of Seismology and Earthquake Engineering, Building Research Institute, Japan
badrianoo@uni.edu.pe, koshimura@tsunami2.civil.tohoku.ac.jp, fujii@kenken.go.jp

Abstract: The validation of the tsunami inundation modeling for the June 23, 2001 Peru earthquake is carried out by using three different tsunami source models. The source parameters for this event have been estimated from seismological analysis. We use the Global Centroid Moment Tensor solution to estimate the first model. The second model was taken from the result of another seismic analysis, which determined the slip distribution of 40 subfault by using teleseismic broadband P-waves. The third model, called Tsunami Waveform Inversion Model, it is constructed in this study by using tsunami waveforms that were recorded at eleven tide gauge stations around the source region. In this model we determined the slip distribution in detail of 10 subfault segments. The numerical simulation of tsunami inundation is carried out. The inundation results from the three models are validated through comparison in terms of the run-up height and inundation distance with the field survey data measured around Camana city. The tsunami inundation modeling results in terms of the run-up height shows that the third model is more appropriate approximation compared to the field survey data, and in terms of the inundation distance the first model is more appropriate approximation.

1. INTRODUCTION

Due to the location in a highly seismic area, Peru has experienced some of the largest tsunamis that have occurred in the world. For example, the tsunami that occurred on June 23, 2001 in the southern part of Peru was generated by the earthquake of Mw 8.4.

The purpose of this study is to validate the tsunami inundation modelling of the June 23, 2001 Peru earthquake, in order to use it as model to create future tsunami hazard maps for the hazard assessment along the coastal area of Peru. In this study three different tsunami source models are simulated by tsunami inundation modeling and the results are validated through a comparison with field survey data in terms of the run-up height and inundation distance recorded along the coastal area of Camana city.

2. DATA AND METHOD

2.1 Bathymetry and Topography Data

In order to perform tsunami numerical modeling the computational area is divided into four domains to construct the nested grid system. The bathymetry data for the first to the third domains are interpolated from the General Bathymetry Chart of the Ocean (GEBCO) 30 arc-seconds grid data and for the fourth domain the bathymetry is generated from the nautical chart of Directorate of Hydrography and Navigation (DHN), Navy of Peru. The topography data for the first and second domains are interpolated from GEBCO, and for the third domain it is taken from the Shuttle Radar Topography Mission (SRTM) 3arc-second resolution data and for the fourth domain it was taken from the Thermal Emission and Reflection Radiometer (ASTER) 1 arc-second resolution data. Table 1 shows the boundary and resolution for each domain.

Table 1 Boundary, resolution and data source for each computational domain

Domain	Longitude		Latitude		Resolution
	Min.	Max.	Min.	Max.	arc-second
1	-78.00°	-70.00°	-19.00°	-11.00°	27
2	-74.00°	-72.00°	-18.00°	-16.00°	9
3	-73.15°	-72.40°	-17.00°	-16.25°	3
4	-72.92°	-72.58°	-16.75°	-16.50°	1

2.2 Tide Gauge Data

The June 23, 2001 Peru tsunami was recorded in several tide gauges around the world. In this study the tide gauge data are taken from the National Oceanic and Atmospheric Administration (NOAA)/Pacific Marine Environmental Laboratory (PMEL), Center for Tsunami

Research and are provided by the National Oceanic Services (NOS)/NOAA, Field Operation Division, Pacific Regional Office.

Among all tide gauge stations data, only eleven tide gauges are used as input data which has 1 minute data sampling, three tide gauge stations located in Peru and the rest of them located in Chile. In order to obtain the tsunami signal from each tide gauge data, firstly the initial time of the earthquake must be subtracted (T0 = 06/23 20:33:14 UTC, according to USGS). After that the astronomical signal must be estimated by fitting a polynomial regression model using the entire data. Then it can be removed from the original data. Finally these observed tsunami signals are compared with the synthetic tsunami signal obtained in the tsunami simulations.

2.3 Field Survey Data

The International Tsunami Survey Team (ITST) conducted a field survey along the area affected by the tsunami with the main purpose to examine the tsunami damage, to measure the tsunami run-up height and the extent of inundation and also to interview the eyewitnesses of the event. The measured tsunami run-up height, and inundation distance around Camana city done by the ITST (2001abc) are used in this study to validate the tsunami inundation model.

2.4 Tsunami Simulation

The numerical simulation is conducted by using TUNAMI-N2 (Tohoku University's Numerical Analysis Model for Investigation of Near-filed tsunami No.2) code based on shallow water theory and Cartesian coordinate system (Imamura, 1995), which was developed by Disaster Control Research Center (DCRC), Tohoku University, Japan. The computation time for the tsunami propagation is 3.5 hour. In order to satisfy the stability condition, the time step is 0.2 s. The tsunami inundation is calculated on the fourth domain using 1 arc-second of bathymetry and topography grid data (Table 2), and in this domain there are 1200 x 900 grid points along the longitude and latitude directions, respectively, for which the total computation time is 3.5 hours. The value of the Manning's roughness coefficient is assumed to be equal to 0.025 (Koshimura et al, 2009).

3. RESULTS AND DISCUSSION

3.1 Tsunami Source Models

The source parameters of the 2001 Peru earthquake have been estimated from two different seismological analyses, the Global Centroid Moment Tensor (GCMT) and Kikuchi and Yamanaka (2001). The results of these studies are used for two different models of Uniform Slip Model (USM) and Heterogeneous Slip Model (HSM). Another model called Tsunami Waveform Inversion Model (TWIM), estimated from tsunami waveform in this study is also used.

The USM is a single fault based on the GCMT solution which proposed some parameters of the seismic source (magnitude, strike, slip angle, centroid latitude and centroid longitude). By using the magnitude, it is possible to estimate the slip, length and width of the fault (Papazachos et al, 2004). Table 2 shows the magnitude and the source parameters for this simple model.

Table 2 Magnitude and source parameters for the Uniform Slip Model.

Magnitude (Mw)	Strike	Dip	Slip angle	Length (km)	Width (km)	Slip (m)	Top depth (km)
8.4	310°	18°	63°	270	95	4	29.6

The source parameters for the HSM are taken from the seismic inversion results by Kikuchi and Yamanaka (2001). They analyzed teleseismic broadband P waves retrieved from 24 seismic stations to determine the general source parameters. They determined the slip distribution in detail of 40 subfault segments in the rupture area of 150 km by 240 km (Figure 1). Each subfault segment has an area of 30 km x 30 km.

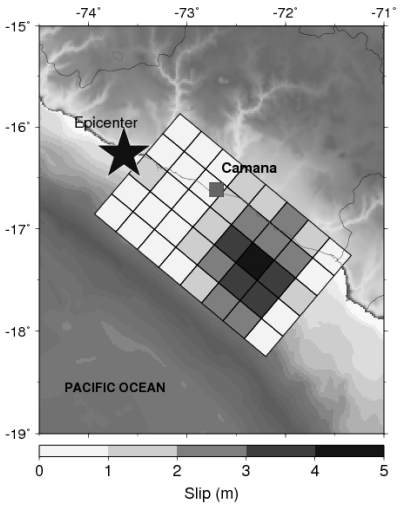


Figure 1 Slip distribution obtained by Kikuchi and Yamanaka (2001)

The source parameters for the TWIM are estimated by the inversion of the tsunami waveforms from tide gauge data (Satake, 1987). The computation area extends from 70°W to 85°W and 5°S to 35°S using GEBCO 30 arc-seconds bathymetry grid data, and consequently, there are 1800 x 3600 grid points along the longitude and latitude direction, respectively. The computation time for the tsunami numerical propagation is 4 hours. The time step is 2.0 s to satisfy the stability condition. The initial seafloor deformation for each subfault is calculated based on Okada (1985) and Tanioka and Satake (1996).

Figure 2 shows the spatial slip distribution obtained by the tsunami waveform inversion which is divided into ten subfault segments. The subfault size is 50 km x 50 km. The rupture area is 250 km by 100 km. Because of the spatial distribution of the stations around the fault area, the accuracy of the result in the southern part is better comparing to the

northern part. Therefore, this result is used to compute the initial seafloor deformation for the tsunami inundation model on Camana city that is located in the central part of the fault area. Table 3 shows the fault parameters obtained from the tsunami waveform inversion model.

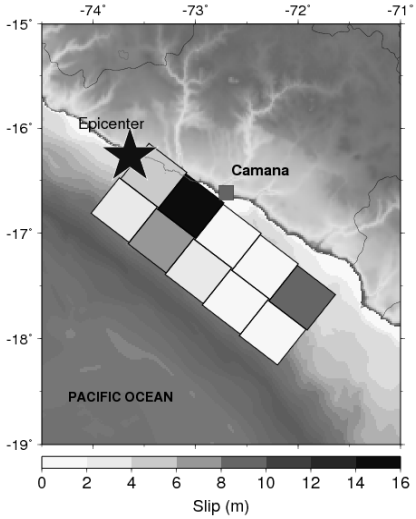


Figure 2 Results obtained from the tsunami waveform inversion

Table 3 Subfault parameters obtained from the tsunami waveform inversion

No.	Strike	Dip	Slip angle	Length (km)	Width (km)	Slip (m)	Error (m) +/-	Top depth (km)
1	308°	18°	63°	50	50	1.15	0.91	14.15
2	308°	18°	63°	50	50	0.35	0.43	14.15
3	308°	18°	63°	50	50	2.84	1.78	14.15
4	308°	18°	63°	50	50	7.78	4.79	14.15
5	308°	18°	63°	50	50	3.8	1.83	14.15
6	308°	18°	63°	50	50	8.38	4.18	29.6
7	308°	18°	63°	50	50	0.36	0.22	29.6
8	308°	18°	63°	50	50	0.68	2.01	29.6
9	308°	18°	63°	50	50	14.18	6.56	29.6
10	308°	18°	63°	50	50	5.92	2.89	29.6

3.2 Seafloor Deformation due to the Source Models

The initial seafloor deformation for each model was calculated by using the Okada (1985) formula (Figure 3). The spatial distribution of the uplift part is located offshore, while the subsidence part is extended towards the land area for all models.

Figure 4 shows the cross section of deformation height between 74.75°W and 71°W along the 17°S for each model. It shows that the uplift of the TWIM is higher than the USM and HSM, which is approximately two times compared with the uplift of the USM, and this is because the values obtained for the slip amount on the northern part of the fault in the TWIM are overestimated. The values of the subsidence from TWIM and UHM are approximately similar at about 0.5 m.

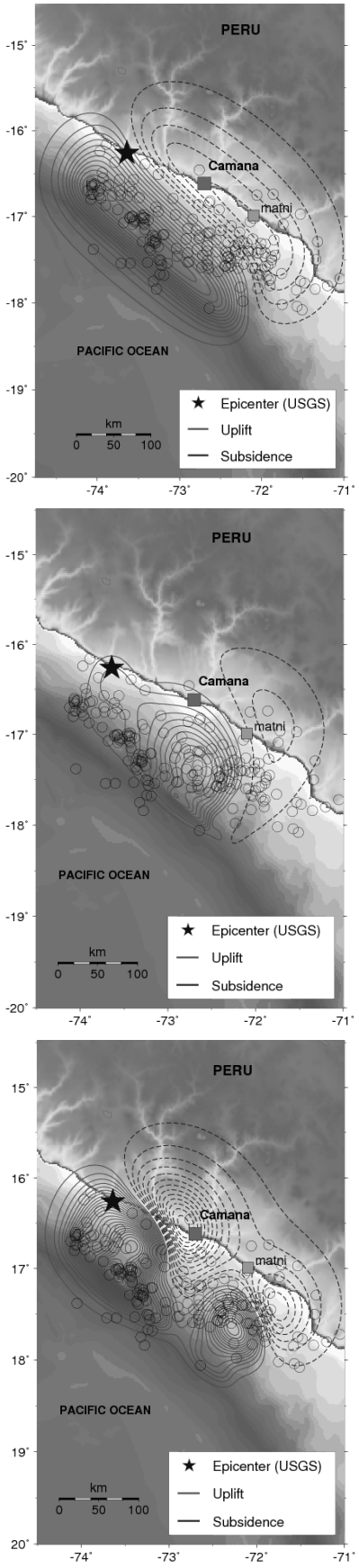


Figure 3 Seafloor deformation for each model top: USM, center: HSM and bottom: TWIM. Contour lines are drawn in every 0.1 m for uplift and subsidence part

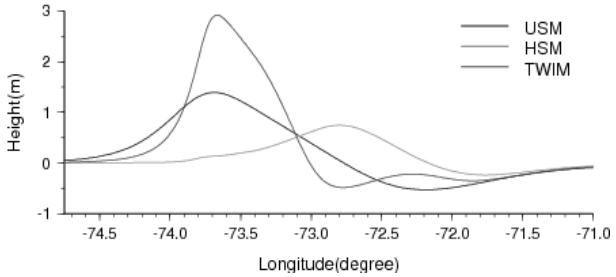


Figure 4 Cross section of seafloor deformation height for each model

3.3 Run-up Height and Inundation Distance

The calculated inundation results from each model are validated through a comparison with field survey data from ITST (2001abc) in terms of the run-up height and inundation distance. According to the ITST (2001abc), approximately 15 points were obtained for tsunami run-up height and inundation distance from the field survey.

The comparison between the computed and observed tsunami run-up height is shown in Figure 5. In general the computed tsunami run-up height along the coastline of Camana city from each model is underestimated compared to the measured run-up height. This might indicate the limitation of the tsunami inundation model using the shallow water approximation, and the possibility that the field data represents the extreme feature of tsunami run-up height, or lack of bathymetry and topography features in the model (Koshimura et al, 2009). However, the computed tsunami run-up height from the TWIM shows a better approximation on the southern part of Camana city from 72.61°W to 72.76°W.

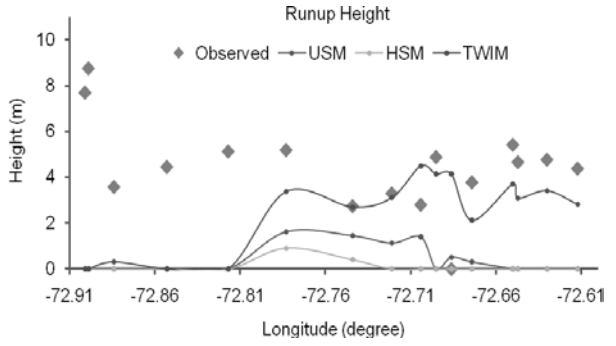


Figure 5 Comparison between the observed tsunami run-up height (gray diamond) and the computed tsunami run-up height from each model (line in blue: USM, line in green: HSM and line in red: TWIM)

The comparison between the computed and observed inundation distance is shown in Figure 6. It shows that the result from the HSM is underestimated on the entire area around Camana city. Figure 6, also shows that the result from the TWIM is overestimated predominantly on the south from 72.61°W to 72.81°W. However, the result from the USM fitted better, this is predominantly shown on the southern part of coastline of Camana city from 72.61°W to 72.81°W. This also might indicate the possibility that the field survey data represents the extreme feature of the tsunami inundation distance in the northern part of Camana city (from 72.81°W to 72.91°W).

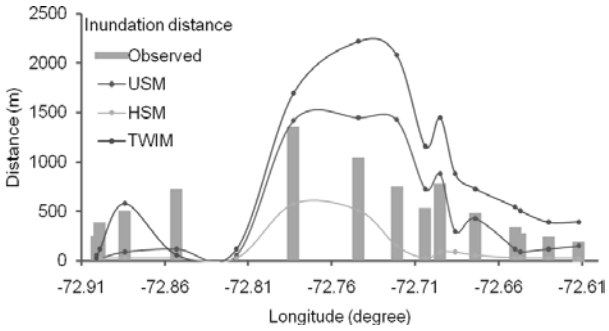


Figure 6 Comparison between observed tsunami inundation distance (gray bar) and computed tsunami inundation distance, from each model (line in blue: USM, line in green: HSM and line in red: TWIM)

I order to investigate the reason of underestimation of run-up height and inundation distance, we compare the real topography image and the topography data used in this study. The cross section shown in Figure 7 covers from 16.54°S, 72.91°W to 16.53°S, 72.90°W on the northern part of Camana city and shows a hill that is approximately 10 m height which does not exist in the real topography. This represents an incompatibility between the real topography and topography data used in this study, indicating that calculated tsunami waves less than 6 m at the coast line cannot pass through the hill.

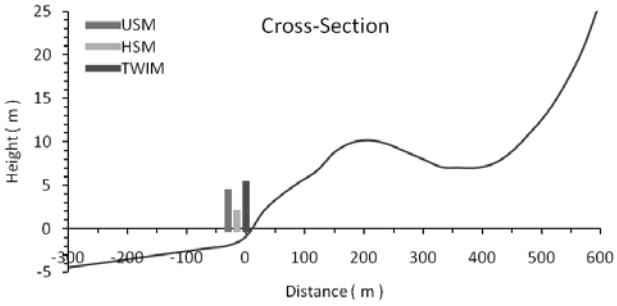


Figure 7 Cross section of topography and bathymetry data on the northern part of Camana city. Blue, green and red bars show calculated tsunami height al coast from USM, HSM and TWIM, respectively

3. CONCLUSIONS

The tsunami numerical modeling is performed using three different models for the June 23, 2001 Peru earthquake, based on the shallow water approximation and by using four computational domains that are connected with nested grid system. The results of tsunami inundation modeling in terms of the run-up height around Camana city shows that the third model from the Tsunami Waveform Inversion Model is more appropriate approximation compared to the field survey. In terms of the inundation distance the first model of

the Uniform slip model is more appropriate approximation. Considering the accuracy of the bathymetry and topography data, the third model can be used as tsunami source of June 23, Peru earthquake. However, we may need to improve the tsunami source inversion results. And also, topography and bathymetry data should be investigate and be improved.

Acknowledgements:

I would like to express my heartiest gratitude and sincere thanks to Dr. Fumihiko Imamura, the Disaster Control Research Center (DCRC) Tohoku University, and Dr. Bunichiro Shibazaki, the International Institute of Seismology and Earthquake Engineering (IISEE), for the guidance, and for the suggestion in the development of this study.

References:

Imamura, F., (1995), "Review of the tsunami simulation with a finite difference method, Long Wave Run-up Models", *Word Science*, 25-42.

ITST, 2001a, Report of the June 23, 2001 Peruvian Tsunami Field Survey of the International Tsunami Survey Team (ITST),

ITST, 2001b, Impacts of the 2001 Peru Tsunami in Camana, International Tsunami Symposium Proceedings, 409.

ITST, 2001c, The Peruvian tsunami of 23 June 2001 : Preliminary report by the International Tsunami Survey Team, International Tsunami Symposium Proceedings, 377-378.

Kikuchi, M. and Yamanaka, Y., (2001), "Near Coast of Peru earthquake (Mw 8.2) on June 23, 2001", EIC seismological note: 105.

Koshimura, S., Oie, T., Yanagisawa, H. and Imamura, F., 2009, "Developing fragility functions for tsunami damage estimation using numerical model and post-tsunami data from Banda Aceh, Indonesia", *Coastal Engineering Journal*, **51**(3), 243-273.

Okada, Y., (1985), "Surface Deformation Due to shear and Tensile Faults in Half-space", *Bulletin Seismological Society of America*, **75**(4), 1135-1154.

Papazachos, B, C., Scordilis E. M., Panagiotopoulos D. G., and Karakaisis G. F., (2004), "Global Relation Between Seismic Fault Parameter and Moment Magnitude of Earthquake", *Bulletin of the Geological Society of Greece Vol. XXXVI Proceedings of the 10th International Congress*, Thessaloniki, April 2004.

Satake, K. (1987), "Inversion of tsunami waveform for the estimation of a fault heterogeneity method and numerical experiments", *Journal of Physics of the Earth*, **35**, 241-254.

Tanioka, Y., and Satake K., (1996), "Tsunami generation by horizontal displacement of ocean bottom", *Geophysical Research Letters*, **23**, 891-894.

8CUEE CONFERENCE PROCEEDINGS
8th International Conference on Urban Earthquake Engineering
March 7-8, 2011, Tokyo Institute of Technology, Tokyo, Japan

THE TSUNAMI VULNERABILITY ASSESSMENT IN PERU USING THE INDEX OF POTENTIAL TSUNAMI EXPOSURE

Hideaki Yanagisawa[1)], Koshimura Shunichi[2)], Yuji Yagi[3)], Yushiro Fujii[4)], Gaku Shoji[5)], and Cesar Jimenez[6)]

1) Tokyo electric power services co., ltd., Japan
2) Associate Professor, Department of Civil Engineering, Tohoku University, Japan
3) Associate professor, Department of Life and Environmental Sciences, University of Tsukuba, Japan
4) International Institute of Seismology and Earthquake Engineering, Japan
5) Associate professor, Department of Engineering Mechanics and Energy, University of Tsukuba, Japan
6) Directorate of Hydrography and Navigation, Peru

h-yanagi@tepsco.co.jp, koshimura@tsunami2.civil.tohoku.ac.jp, yagi-y@geol.tsukuba.ac.jp, fujii@kenken.go.jp, gshoji@kz.tsukuba.ac.jp, cesarsud86@hotmail.com

Abstract: Tsunami vulnerability assessment along the coast of Peru was carried out based on the modeling of the 2001 Camana tsunami. We first conducted field survey of the 2001 Canama tsunami to measure tsunami flow depth and topography of the Camana coast. Based on the field observation, we found that 1 - 3 m of tsunami flow depth inundated the Camana coast and caused significant damage on houses. We then modeled the 2001 Camana tsunami using nonlinear shallow-water theory to examine the validation of a tsunami modeling. As a result, our numerical model is consistent with measured data. Developing the tsunami hazard scenarios, we examined potential tsunami hazard in Peruvian coast using the probability of potential tsunami exposure. Consequently, we found that Lima and Callao face a high risk of major tsunami disaster.

1. INTRODUCTION

Peruvian coast is one of the most important seismologic regions in the world. In the Peru-Chile border region, the largest earthquakes with moment magnitude close to 9.0 occurred in 1604, 1868 and 1877. In recent years, large earthquakes with moment magnitude more than 8.0 occurred in 2001 and 2007. These earthquakes have accompanied large tsunamis which were responsible for extensive property and human damage in Peruvian coast. To develop the effective countermeasure against the tsunamis, the area prone to be tsunami damage should be determined considering tsunami hazards, population and frequency of earthquakes. The purpose of this study is to provide vulnerability assessment to possible tsunami damage for the coastal area of Peru.

According to Koshimura et al.,(2009), tsunami hydrodynamic feature such as tsunami height is greatly related to damage ratio of human or buildings. Therefore, the accurate estimation of tsunami hazards is much required to conduct tsunami vulnerability assessment. We thus estimate tsunami hazards using numerical simulation to determine the detail of tsunami hydraulic feature. We first conduct the modeling of 2001 Camana tsunami to validate the numerical model. We then conduct vulnerability assessment developing tsunami hazard scenarios using population data, the fragility function of human damage and the computed tsunami hazards.

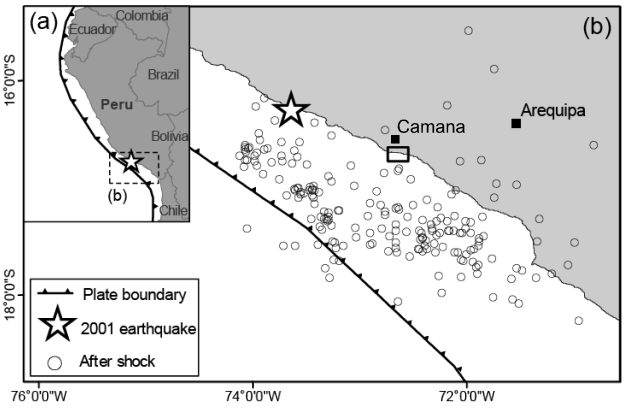


Figure 1 Map of southern coast of Peru showing the epicenter and after shocks of 2001 earthquake. The survey area is shown in the solid line.

2. FIELD SURVEY OF 2001 CAMANA TSUNAMI

2.1 Study area

On June 2001, a major earthquake of moment magnitude 8.4 generated a destructive tsunami that hit the southern coast of Peru (Fig. 1). The tsunami killed at least 25 people with additional 62 missing in the Camana area (Jaffe et al., 2003). Tsunami runup height around Camana area were estimated to have been approximately 3 - 8 m and the tsunami inundation distance extended more than 1 km inland

from coast (Okal et al., 2002). Nine years after the tsunami damage, some destroyed houses have been left derelict in the coast of Camana city, which was once the developed beach resort area. To find the evidence of 2001 tsunami, we conducted field investigation at the coast of Camana city.

2.2 Results of field survey

Although 9 years have passed since the tsunami impact, water marks of the tsunami have been remained on walls of some damaged houses. Figure 2 shows the tsunami flow depth inferred from the water marks on damaged houses and witness of the tsunami. The tsunami flow depth is the measuring water depth above the ground. These results show that 1.6 – 3.1 m tsunami inundated the beach resort area. The residential area on flat land stretches approximately 0.3－1.0 km inland so that the tsunami could have easily inundated the overall flat area and caused significant damage to houses (Fig. 2). We also found the trace of damage on the foundation of the house caused by tsunami wave erosion, which is mostly the same as it was when the tsunami attacked (Fig. 3). From field observation 9 years after the tsunami damage in Camana, we found valid data to estimate the tsunami flow.

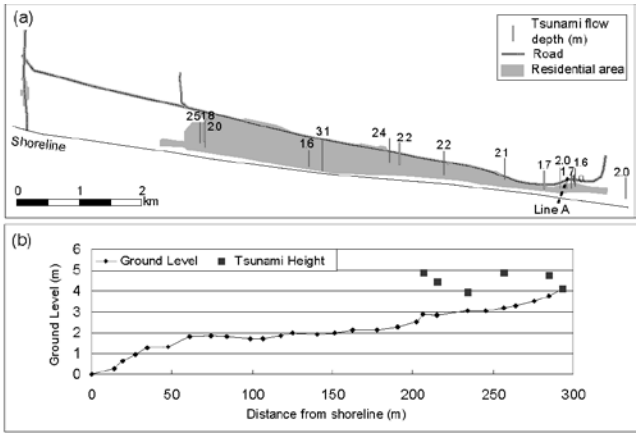


Figure 2 (a) Tsunami flow depth at the coast of Camana city (b) Cross-section view of the ground level with the tsunami heights along the Line A

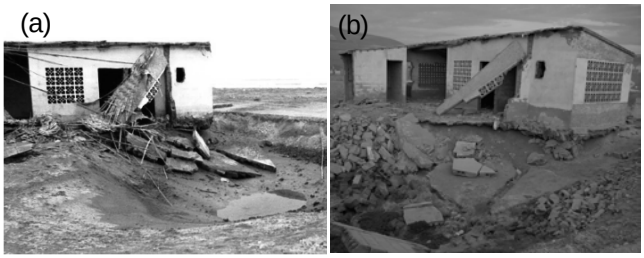


Figure 3 Damaged house and destruction of the foundation in (a) 2001 (Dengler, 2001) and (b) 2010

3. NUMERICAL MODELING OF 2001 CAMANA TSUNAMI

3.1 Fault parameter

The 2001 earthquake ruptured a portion of the plate boundary between the Pacific and Nazca Plates. According to Harvard CMT catalog, the magnitude of 2001 earthquake is estimated to be *Mw*8.4 ($M_0 = 4.67 \times 10^{21} N/m$). To determine the fault length and width, we applied the empirical relationships between moment magnitude *Mw*, fault length *L* and width *W* obtained by Papazachos et al (2004) as equation (1) and (2).

$$Log(L) = 0.5Mw - 2.19 \quad (1)$$
$$Log(W) = 0.31Mw - 0.63 \quad (2)$$

Using the fault area *A* (=*L*×*W*) and scalar moment M_0, the fault displacement *D* is determined by equation (3).

$$M_0 = \mu DA \quad (3)$$

where μ is the rigidity. Table 1 shows the determined fault parameters for 2001 earthquake. We applied the fault depth, angle of strike, dip and slip acquired by Harvard University. For the initial conditions of the tsunami modeling, we estimated the vertical seismic deformation of the land and sea bottom using the theory of Manshinha and Smylie (1971). We assumed instantaneous displacement of the sea surface identical to the vertical seafloor displacement.

3.2 Modeling of tsunami propagation and inundation

To validate a tsunami modeling, we performed numerical simulation of the 2001 Camana tsunami. Tsunami propagation in coastal areas was simulated based on the nonlinear shallow-water theory, which includes the bottom friction in the form of Manning's formula. For tsunami modeling, we made 1350 m grid digital bathymetry/topography data, interpolated from the data provided by the General Bathymetry Chart of the Oceans (GEBCO) Digital Atlas. In addition to GEBCO, we compiled local bathymetric/topography data of southern Peru provided by Directorate of Hydrography and Navigation (DHN), Shuttle Radar Topography Mission (SRTM) data and our measured data to construct merged bathymetry/topography data. The grid size varies from 1350 m to 50 m, constructing a nested grid system.

We compared measured tsunami runup heights with computed values. The local tsunami runup height is the result of measuring the water marks above the astronomical tide level when the tsunami arrived. According to Okal et al. (2002) and this study, totally 25 points of local tsunami

Table 1 Fault parameters for the 2001 Camana tsunami

Mw	Origin of the fault (°)		Length	Width	Dislocation	Dip	Slip	Strike	Depth
	Latitude	Longitude	(km)	(km)	(m)	(°)	(°)	(°)	(km)
8.4	-18.40	-72.30	260	95	4.1	18	63	310	29.6

runup height and inundation flow depth were obtained in the study area. The inundation flow depth (above ground level) is changed to the tsunami runup height using the compiled topography data acquired by this study. The validation of the model is performed by K and κ proposed by Aida (1978) as equations (4), (5) and (6).

$$\log K = \frac{1}{n}\sum_{i=1}^{n} \log K_i \tag{4}$$

$$\log \kappa = \sqrt{\frac{1}{n}\sum_{i=1}^{n} (\log K_i)^2 - (\log K)^2} \tag{5}$$

$$K_i = R_i / H_i \tag{6}$$

where R_i and H_i are the measured and modeled values of tsunami runup height at point *i*. JSCE (2002) empirically provides the guideline for a tsunami numerical modeling suggesting that $0.95 < K < 1.05$ and $\kappa < 1.45$ as the threshold of valid tsunami source to develop the tsunami hazard assessment.

3.3 Numerical results of 2001 Camana tsunami

To validate our numerical results, we compared measured tsunami runup heights with maximum tsunami runup heights computed from our model. Figure 4 shows the special distribution of the computed maximum tsunami runup height. The tsunami run up averagely 5 meters along the coast of Camana. Figure 5 shows the comparison between measured and computed tsunami runup height. The numerical results were approximately consistent with the measured data, excluding the higher values resulting from water splashing. Our model is sufficiently satisfied with the value of JSCE (2002) (K=0.98, κ=1.34). This finding confirms that our numerical model can be used with confidence to develop the tsunami hazard scenarios.

4. VULNERABILITY ASSESSMENT IN PERUVIAN COAST

4.1 Development of tsunami hazard scenario

During the past 430 years, the 11 largest earthquakes (from *Mw* 8.0 to 8.8) with accompanying large tsunamis have occurred along the plate boundary between the Pacific and Nazca Plates near the Peruvian coast (e.g., Dorbath et al., 1990; Kulikov et al., 2005). To estimate tsunami hazards, we assumed 53 earthquake scenarios with *Mw*8.0, 8.2, 8.4, 8.6, 8.8 along the plate boundary (Fig. 6). Based on the modeling of 2001 tsunami, the fault length, width and displacement of each moment magnitude were determined by equations (1), (2) and (3). The remaining parameters were determined using example of 2001 earthquake (table 2). Tsunami propagation was simulated based on the nonlinear shallow-water theory using spherical coordinate system, which includes the bottom friction in the form of Manning's formula. Here, we used 0.5 sec grid digital bathymetry/topography data provided by GEBCO.

To estimate potential human damage, we used the

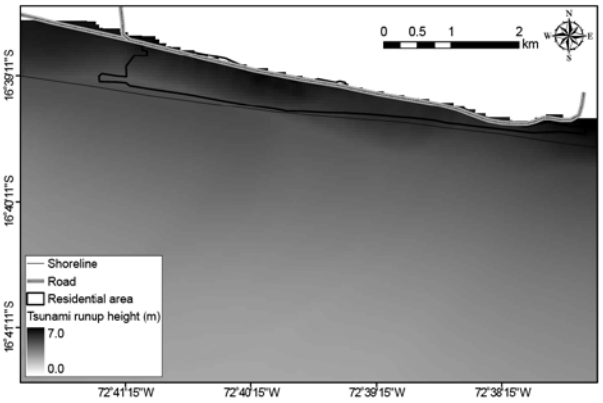


Figure 5 Comparison between measured tsunami runup height and computed maximum tsunami heights. The black outline square presents the higher value resulting from water splashing (Okal et al., 2002)

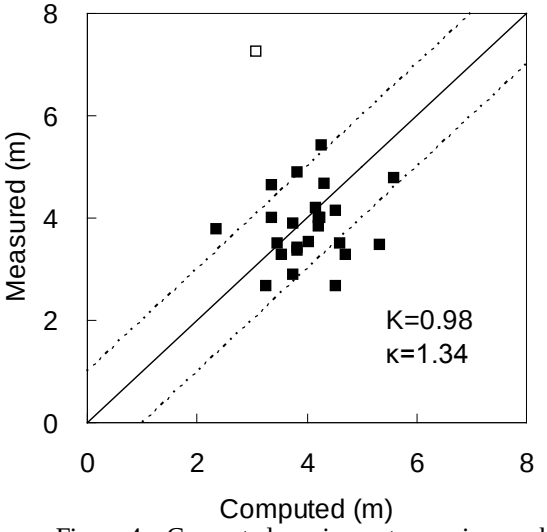


Figure 4 Computed maximum tsunami runup height

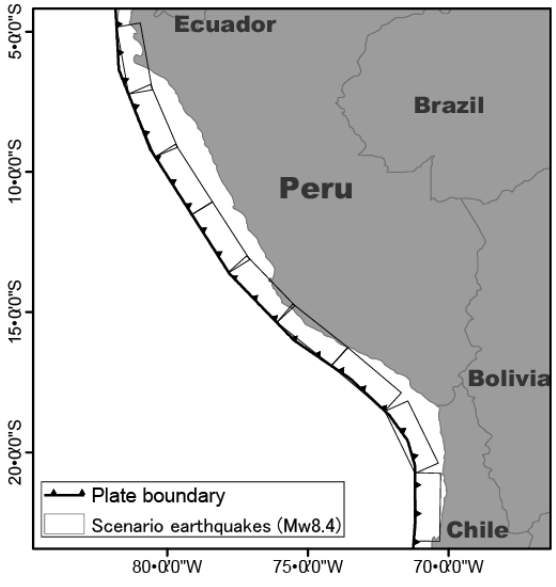


Figure 6 Scenario earthquakes for tsunami vulnerability assessment in the case of *Mw*8.4

following fragility function, which is the relationship between the computed maximum tsunami runup height η and the ratio of human damage $\alpha(\eta)$, which was acquired by the analysis of damage of the 2004 Indian Ocean tsunami (Koshimura et al, 2009).

$$\alpha(\eta) = \Phi\left[(\eta - \mu)/\sigma\right] \qquad (7)$$

where Φ is the cumulative density function of a standard normal distribution, μ and σ are the mean and standard deviation of η ($\mu = 5.37$, $\sigma = 0.72$). Using the Geographic Information System (GIS), we estimated the Potential Tsunami Exposure (*PTE*) multiplying the human damage ratio $\alpha(\eta)$ by global grid population data at shoreline (Ork Ridge National Laboratory, 2006). We further estimate the *t* year probability of exceedance using Poisson process as equation (8),

$$P\left[PTE \geq a; t\right] = 1 - \exp(-\lambda t) \qquad (8)$$

where $P\left[PTE \geq a; t\right]$ is the probability that *PTE* will exceed *a* value at least once in the 50-year, and λ is annual frequency of occurrence. We simply estimated λ by the following equation,

$$\lambda = \sum_{m=1}^{n} \frac{N\left[PTE \geq a\right]}{N_m} \times \frac{1}{n} \times \frac{1}{T} \qquad (9)$$

where $N\left[PTE \geq a\right]$ is the number of scenarios in each magnitude that *PTE* exceeds *a* value, N_m is the number of scenarios in each magnitude, *n* is the number of magnitude (=5) and *T* is the average return period. Here, we assumed that the frequency of occurrence of earthquakes in each magnitude is constant because Peruvian coast is lacking in certain data of the largest earthquakes.

4.2 Results and Discussion

Figure 7 shows the 50 year probability of exceedance when *PTE* will exceed 100 people. This result indicated that the coast of Lima and Callao face a high risk of major tsunami disaster (P > 10%). These results provide basic information for the tsunami disaster prevention planning. However, this study is preliminary assessment to detect area prone to be tsunami damage. Thus, additional studies are required to conduct a detailed assessment of the possible tsunami damage in the highest tsunami-risk areas.

Acknowledgements:

The authors acknowledge support from M. Estrada and H. Yanagisawa. This research was supported in part by the JST-JICA project of Science and Technology Research Partnership for Sustainable Development (SATREPS).

Table 2 Fault parameters for scenario earthquakes

Mw	Length (km)	Width (km)	Dislocation (m)	Dip (°)	Slip (°)	Depth (km)
8.0	160	70	2.4	18	90	30
8.2	210	80	3.3	18	90	30
8.4	270	95	4.3	18	90	30
8.6	350	110	5.7	18	90	30
8.8	450	125	7.7	18	90	30

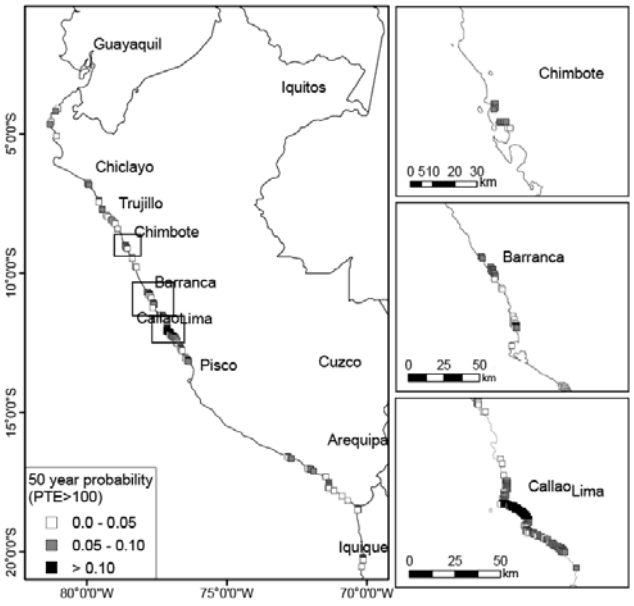


Figure 7 50 year probability of exceedance of Potential tsunami exposure (PTE) along the coast of Peru

References:

Jaffe, B. E., Gelfenbaum, G., Rubin, D. M., Peters, R., Anima, R., Swensson, M., Olcese, D., Anticona, L. B., Gomes, J . C. and Riega, P. C. (2003), "Identification and Interpretation of Tsunami Deposits from the June 23, 2001 Peru Tsunami," *Proceedings of the International Conference on Coastal Sediments 2003*, CD-ROM Published by World Scientific Publishing Corp and East Meets West Productions, Corpus Christi, TX, USA, ISBN 981-238-422-7, 13p.

Kulikov, E. A., Rabinovich, A. B. and Thomson, R. E. (2005), "Estimation of Tsunami Risk for the Coasts of Peru and Northern Chile," Natural Hazards, **35**, 185-209, DOI 10.1007/s11069-004-4809-3.

Okal, E. A., Dengler, L., Araya, S., Borrero, J. C., Gomer, B. M., Koshimura, S., Laos, G., Olcese, D., Modesto, O. F., Swensson, M., Titov, V. V. and Vegas, F. (2002), "Field Survey of the Camana, Peru Tsunami of 23 June 2001, " *Seismological Research Letters*, **73**(6), 907-920.

Papazachos, B. C., Scordilis, E. M., Panagiotopoulos, D. G., Papazachos, C. B. and Karakaisis, G. F. (2004), "Global Relations Between Seismic Fault Parameters and Moment Magnitude of Earthquakes, " *Bulletin of Geological Society of Greece*, vol. XXVI, 1482-1489.

Dorbath, L., Cisternas, A. and Dorbath, C. (1990), "Assessment of the Size of Large and Great Historical Earthquakes in Peru," *Bulletin of the Seismological Society of America*, **80**(3), 551-576.

Aida, I. (1778), "Reliability of A Tsunami Source Model Derived from Fault Parameters," *Journal of Physics of the Earth*, **26**, 73-75.

Manshinha, L. and Smylie, D. E. (1971), "The Displacement Field of Inclined Faults," *Bulletin of the Seismological Society of*

America, **61**, 1433-1440.
Koshimura, S., Namegaya, Y. and Yanagisawa, H. (2009), "Tsunami Fragility - A New Measure to Assess Tsunami Damage," *Journal of Disaster Research*, **4**(6), 479-488.
Japan Society of Civil Engineers. (2002), "Tsunami Assessment Method for Nuclear Power Plants in Japan," http://www.jsce.or.jp/committee/ceofnp/Tsunami/eng/JSCE_Tsunami_060519.pdf, 72p.

8CUEE CONFERENCE PROCEEDINGS
8th International Conference on Urban Earthquake Engineering
March 7-8, 2011, Tokyo Institute of Technology, Tokyo, Japan

WALKING EXPERIMENT CONSIDERING SCATTERED GOODS AND BLACKOUT IN WALKWAYS OF HIGH RISE BUILDINGS AFTER AN EARTHQUAKE

Akihiko Hokugo[1)], Ai Sekizawa[2)], Hiroaki Notake[3)], U Hiroi[4)], and Daisuke Ooiwa[4)]

1) Professor, Research Center for Urban Safety and Security, Kobe University, Japan
2) Professor, Graduate School of Global Fire and Technology, Tokyo University of Science, Japan
3) Senior Research Engineer, Institute of Technology, Shimizu Corporation, Japan
4) Assistant Professor, Fire and Disaster Management Laboratory, The University of Tokyo, Japan
hokugo@kobe-u.ac.jp, sekizawa@rs.kagu.tus.ac.jp, notake_hiroaki@shimz.co.jp
hiroi@fse.t.u-tokyo.ac.jp, ooiwa@fse.t.u-tokyo.ac.jp

Abstract: Today, the structural safety of buildings has been improved with a resulting improvement in quake resistance. There are, however, many mid-to-high-rise buildings, not only in big cities like Tokyo, Osaka or Nagoya, and it is necessary to think about measures to keep fixtures and furniture inside from moving or tipping during a long-period ground motion as the higher floors of these buildings are expected to generate the floor response during an earthquake. This study attempted to re-create the impact of evacuation obstacles such as scattered goods and blackout on people's evacuation behavior in a building at the time of an earthquake. The authors conducted experimental study on walking speed in the presence of obstacle and blackout on a walkway assuming evacuation in high rise buildings.

1. INTRODUCTION

Modern high-rise buildings, which have been increasing rapidly, are securely constructed regarding both quake and fire resistance. However, secondary elements such as ceilings and partitions may be damaged together with interior and/or articles inside the rooms, although the main structural elements are not damaged at all due to a moderate earthquake. Moreover, fire protection systems such as sprinklers are particularly vulnerable to strong earthquake motion. Nevertheless, there are a very few reports of the impact of obstacles and blackout on the evacuation road, while many studies on evacuation behavior during the fire in a high-rise building have been done so far. Human behavior and walking speed caused by scattered obstacles and blackout require more investigation for the case of evacuation during the fire or other possible emergency after an earthquake. The authors, therefore, conducted real scale experiments to observed and measure the impact of scattered goods and blackout on the walkway using the simulated corridors assuming evacuation after an earthquake in a high rise building.

2. SCATTERED GOODS EXPERIMENTS

2.1 Assumption of the Experiments

The walking experiment, as shown in Figure 1 was conducted based on several conditions. Table 1 shows the scattering density of goods from nothing 0% up to 90% in

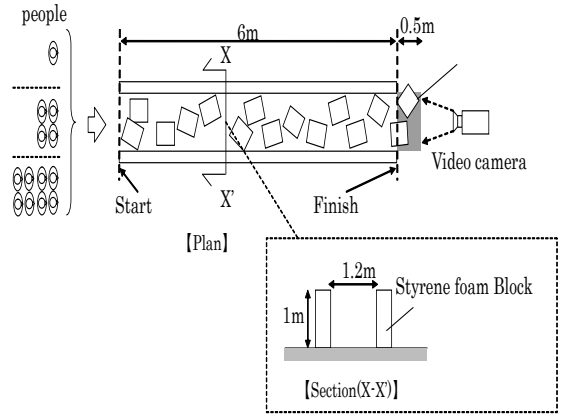




Figure 1 Appearance of Conditions in the Experiments

coverage for each case. The Number of participants was 48 and all of them were young students consisting of 30 male students and 18 female students. They participated each case in a random manner. They instructed to walk the lane like the evacuation drill “not rash” but “promptly evacuate” in each case including free walking.

Table 1 Conditions of Cases in the Experiments

Case No.	Scattering Density of Goods on a Walkway	Number of Persons who walk together
1	A(30%)	1
2	B(60%)	1
3	C(90%)	1
4	D(60%+ broken acrylic boards)	1
5	B (60%)	4
6	C (90%)	4
7	B (60%)	8
8	C (90%)	8

2.2 Results on “speed”

Figure 2 indicates the results of the experiments for a single walking in each condition of scattered density, in which the average walking speed and its band within±1σ(standard deviation) are shown. As the scattered density increases, the walking speed decreases substantially. It is worth noting that the walking speed goes drastically down by 57% to compare with the case of no obstacles in the case of scattering density of only 30%. And, the walking speeds in the cases of larger density of scattered goods does not drop so much from the level in the case A (30%) to the largest case C (90%).

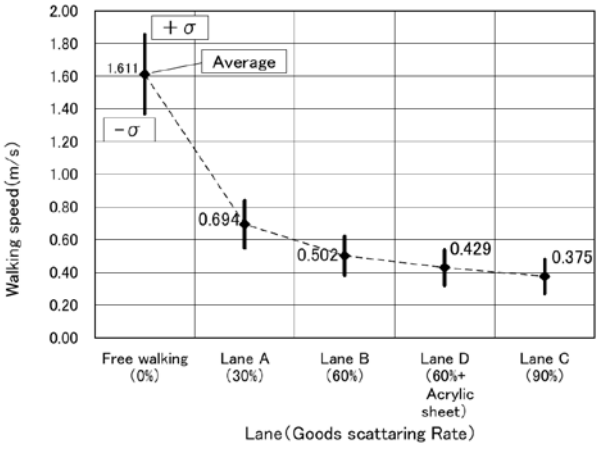


Figure 2 Average Waling Speed in Different Density of Scattered Goods



Figure 3 Free waling along 20m lane



Figure 4 Acrylic sheet imitating broken glass

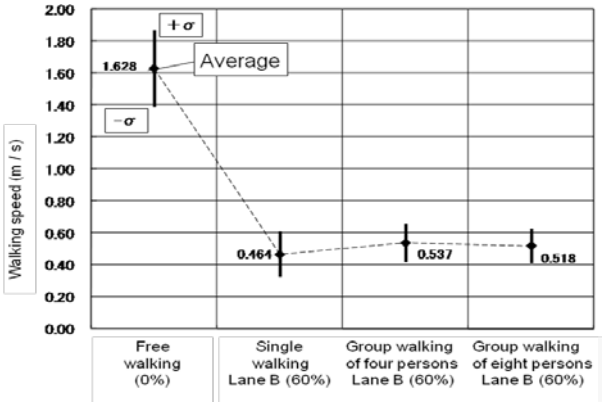


Figure 5 Average Waling Speed in condition of single walking and group walking of four and eight

The Figure 5 indicates the results of the experiments in condition of single walking and group walking of four and eight for Lane B of 60% scattered density, in which the average walking speed and its band within±1σ(standard deviation) are shown.



Figure 6 Group walking of four persons



Figure 7 Group walking of eight persons

2.3 Results on “Questionnaire”

We questioned the participants in the experiments. In this questionnaire, we asked chiefly the following personal attributes and feelings.

・Age, Sex, Height, Clothes, Height of heel, Custom of

Sports

・Difficult to Walk
・Feeling about Obstacles
・Fear in the Walking

If they were difficult to walk, they answered “5”(most difficult). In Figure 8, this ratio is shown by dark-red color. And if they were easy to walk, they answered “1”(most easy), this ratio is shown by light-blue color.

Figure 9 show what they felt most nuisance. Acrylic boards is most nuisance, big obstacles (cardboard box) follow and small obstacles (plastic bottle) have a small influence on walking.

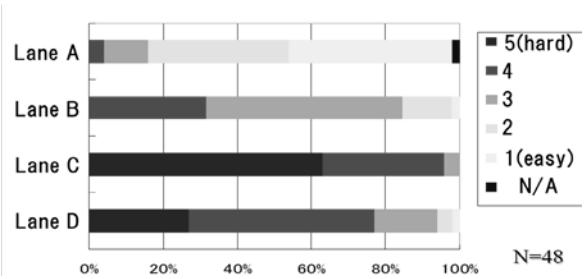


Figure 8 Difficult to Walk in Each Lanes

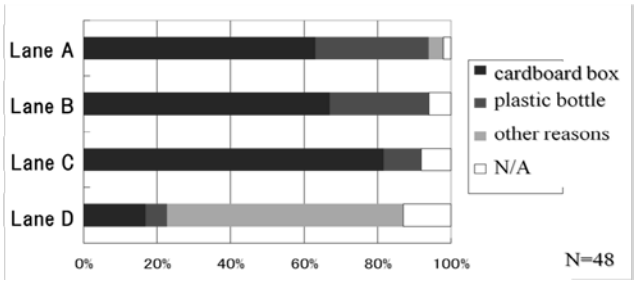


Figure 9 Obstacle have Some Influence on Walking

Table 2 Average walking speed and SD by factors

N = 48

Factor		Sex	N	Free walk [m/s](SD)	Lane A [m/s](SD)	Lane B [m/s](SD)	Lane C [m/s](SD)	Lane D [m/s](SD)
Total		Male	30	1.59(0.24)	0.73(0.14)	0.53(0.12)	0.41(0.09)	0.48(0.09)
		Female	18	1.65(0.25)	0.64(0.14)	0.45(0.1)	0.32(0.19)	0.35(0.09)
Body height	150cm - 160cm	Female	12	1.68(0.25)	0.61(0.14)	0.45(0.08)	0.31(0.1)	0.34(0.09)
	160cm - 170cm	Female	6	1.58(0.26)	0.7(0.13)	0.46(0.14)	0.33(0.13)	0.37(0.08)
		Male	10	1.5(0.26)	0.71(0.12)	0.52(0.11)	0.42(0.1)	0.46(0.11)
	170cm -	Male	20	1.63(0.22)	0.74(0.14)	0.54(0.13)	0.4(0.08)	0.48(0.08)
Height of shoe heel	Under 3cm	Male	30	1.59(0.24)	0.73(0.14)	0.53(0.13)	0.41(0.09)	0.48(0.09)
		Female	11	1.58(0.2)	0.65(0.15)	0.42(0.1)	0.32(0.11)	0.32(0.07)
	3cm -	Female	7	1.76(0.3)	0.62(0.15)	0.5(0.08)	0.32(0.1)	0.4(0.09)
Time for exercising	Under 15 minutes	Male	11	1.51(0.27)	0.7(0.13)	0.5(0.11)	0.37(0.1)	0.44(0.1)
		Female	15	1.62(0.26)	0.65(0.14)	0.44(0.19)	0.33(0.11)	0.35(0.07)
	15 – 60 minutes	Male	4	1.49(0.12)	0.58(0.14)	0.48(0.16)	0.43(0.1)	0.47(0.11)
		Female	2	1.72(0.19)	0.51(0.16)	0.43(0.04)	0.25(0.05)	0.25(0.06)
	60 minutes -	Male	15	1.67(0.21)	0.79(0.19)	0.57(0.11)	0.42(0.08)	0.5(0.08)
	Unknown	Female	1	1.91(—)	0.74(—)	0.66(—)	0.32(—)	0.52(—)
Earthquake experience	No experience	—	19	1.69(0.27)	0.71(0.15)	0.51(0.13)	0.37(0.1)	0.45(0.11)
	Light experience	—	21	1.57(0.21)	0.68(0.14)	0.52(0.12)	0.38(0.18)	0.42(0.12)
	Mid-Heavy experience	—	8	1.52(0.22)	0.68(0.13)	0.44(0.09)	0.38(0.07)	0.41(0.07)

3. BLACKOUT EXPERIMENTS

3.1 Assumption of the Experiments

The walking experiment using emergency electric lighting, as shown in Figure 10 was conducted based on several conditions. Table 3 shows patterns of lighting for each case. The Number of participants was 24 and all of them were young male students. They participated each case in a random manner. They instructed to walk the lane like the evacuation drill “not rash” but “promptly evacuate” in each case including free walking.

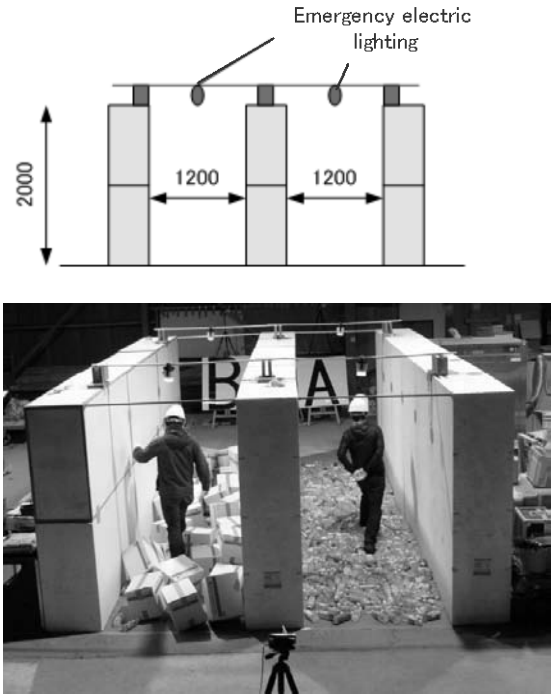


Figure 10 Appearance of Conditions in the Experiments using emergency electric lighting

Table 3 Conditions of Cases in the Experiments

Case No.	Lane	Scattering Density	Lighting Condition	Experimental proceduer
1	A	60%	250 Lux	Constant (normal light)
2	B	60%	250 Lux	Constant (normal light)
3	A	60%	1 Lux	Switch off normal light at the start
4	B	60%	1 Lux	Switch off normal light at the start
5	A	60%	1 Lux	Constant (emergency light)
6	B	60%	1 Lux	Constant (emergency light)
7	A	60%	0-1 Lux	Constant (half of emergency light)
8	B	60%	0-1 Lux	Constant(half of emergency light)



Figure 11 Appearance of Conditions in the Experiments (1 Lux with emergency light)



Figure 12 Appearance of Conditions in the Experiments (0-1 Lux with half of emergency lights switched off)

3.2 Results on “speed”

Figure 13 indicates the results of the experiments for a single walking in each condition of lighting, in which the average walking speed and its band within±1σ(standard deviation) are shown.

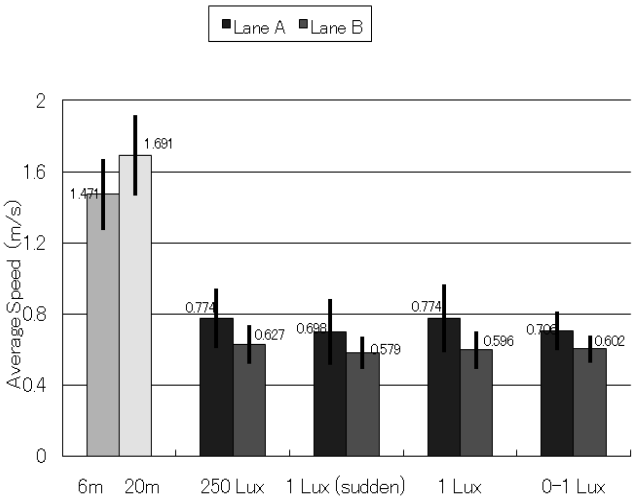


Figure 13 Average Waling Speed in Different Lighting Conditions

In reduced light, the walking speed decreases slightly but It is worth noting that the walking speed goes down by only 10% in case of emergency lighting with sudden switching off normal lighting. The effectiveness of emergency lighting was demonstrated in this experiment.

3.3 Results on "Questionnaire"

We questioned the participants in the experiments. In this questionnaire, we asked chiefly the following personal attributes and feelings.

- Age, Height, Clothes
- Feeling about Obstacles
- Fear in the Walking

If they felt fear in the walking, they answered "5"(most scary). In Figure 14, this ratio is shown.

Figure 15 show what they felt most nuisance. Switching off lighting has small influence on walking because there were still emergency lightings (1 Lux).

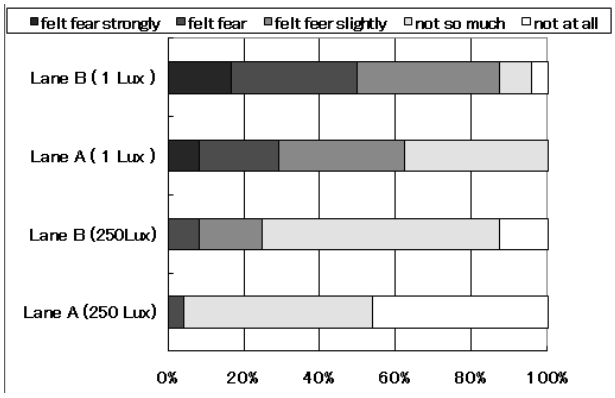


Figure 14 Fear at walking in each condition (N=24)

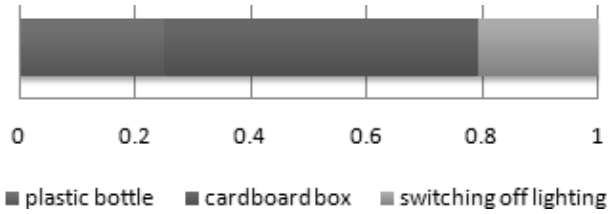


Figure 15 Obstacle at walking in each condition (N=24)

4. CONCLUSIONS

As the result of this experiment study, following points were found out.

1. As the goods scattered density increases, the walking speed decreases substantially. It is worth noting that the walking speed goes drastically down compare with the case of no obstacles. And, the walking speeds in the cases of larger density of scattered goods does not drop so much. The influence of broken glass is high.
2. The size of obstacle affects the walking speed. Small obstacle affects less.
3. In reduced light, the walking speed decreases slightly. The effectiveness of emergency lighting was demonstrated in this experiment.

Acknowledgements:

The authors acknowledge support from the JSPS Grants-in-Aid for Scientific Research (B) and the participation of students of Graduate School of Engineering, Kobe University whose names are Ms. Liu Chang and Mr. Takayuki Kaneko.

References:

Akihiko Hokugo, Takuyuki Kaneko, Ai Sekizawa, Syuji Kakegawa, Hiroaki Notake (2010), A Study on Evacuation Simulation after Earthquake in Consumer Facilities, Fifth International Conference on Pedestrian and Evacuation Dynamics.

U Hiroi, Ai Sekizawa, Akihiko Hokugo, Takayuki Kaneko, Liu Chang, HiroakiI Notake and Daisuke oiwa (2010), Experimental Study on Walking Speed in the Presence of Obstacles on a Walkway assuming Fire Evacuation in a Department Store, The 8th Asia-Oceania Symposium for Fire Science and Technology.

8CUEE CONFERENCE PROCEEDINGS
8th International Conference on Urban Earthquake Engineering
March 7-8, 2011, Tokyo Institute of Technology, Tokyo, Japan

CONSTRUCTIVE LOOP MODEL OF MANAGEMENT FOR PRE-QUAKE MITIGATION AND POST-QUAKE REHABILITATION

Haruyuki Fujii

Associate Professor, Department of Architecture, Tokyo Institute of Technology, Japan
hfujii@arch.titech.ac.jp

Abstract: Management for pre-quake mitigation and post-quake rehabilitation requires prompt decision-making and acts under such an uncertain situation that resources and information, which can be used for management, are limited and rapidly changing. To deal with the situation, a constructive model of management is proposed. The loop is composed of three major processes, i.e., generation, analysis, and focusing. It is important to repeat the loop effectively for management to accomplish the preferable goal.

1. INTRODUCTION

The final goal of this study is to construct a computational schema of pre-quake mitigation management as well as post-quake rehabilitation management. This paper abstracts the characteristics of these managements and proposes a constructive loop model that is expected to facilitate management dealing with the characteristics.

2. PRE AND POST QUAKE MANAGEMENT

Management is the act and art of judiciously using means to accomplish and maintain the designated situation, the target situation, in other words. Management is significant in the circumstance that the situation would become less preferable than the target situation if management were not properly done. The target situation is not fully or strictly designated in advance to allow flexible decision-making in unexpected or uncertain situations.

Two major characteristics of pre and post quake management in question, i.e., incompleteness and situatedness, are described.

2.1 Incompleteness

Both the management for pre-quake mitigation, or mitigation management, and management for post-quake rehabilitation, or rehabilitation management deal with a similar situation. It is uncertain where an earthquake comes, how strong the earthquake is, and what kind of damages does the earthquake brings about. Even though it is true that many means of predicting those things are being developed, it is not perfectly guaranteed that we never come across any situation beyond the predictions.

The mitigation management and the rehabilitation management are different from each other in the sense that the resources, such as time, information, etc., are less limited in mitigation management than rehabilitation management and that the situation faced is changing too fast to deliberate on what the best move is.

A process of management is situated. Decisions in management have to be made on the basis of incomplete information. The crucial nature of management is that the concrete means to accomplish the goal have to be constructed on the basis of the current situation and the assumptions. The assumptions complement incomplete information acquired so far. They are made before the concrete means are determined. During management, information is updated as a new situation is experienced and some of the assumptions are modified if they are not compatible with the current situation.

Decision is made to determine what should be done in order to select promising means towards a preferable situation. Decision under rapidly changing situations in rehabilitating process after an earthquake has to be made on the basis of incomplete or uncertain information. The situations often require prompt actions to change them into preferable ones or to avoid making them worse. The decisions on what to do in those situations cannot afford to be made after deliberation on the basis of complete and certain information even though it is ideal to make decision after deliberation. Even if decisions are made on the basis of incomplete or uncertain information, it is desirable that the decisions are made so as to increase the possibility of accomplishing the preferable situations.

In the case of emergency, some decision-making should be done timely even though the decision has to be made under incomplete and uncertain information. It is, of course, wise to wait for the result of analysis of the situation on the basis of enough information only when it is clear that the result waited is essential for adequate decision-making and is

clear what to do depending on the result. The worst thing is to just wait for the situation where information for decision-making is complete and certain without any plan to do with the information waited. Commitment to selected hypothesis and the flexible attitude that is not afraid of the replacement of the hypotheses are the keys to decision-making under rapidly changing situation.

2.2 Situatedness

Management deals with the proximal features as well as the distal features describing the things involved in management. A proximal feature is the feature that articulates a distal feature. A distal feature is the feature that emerges as an appearance of the unified totality of proximal features. The proximal features are recognized as the constituents of the distal feature, but the distal feature cannot be well-defined in terms of the proximal features. It depends on the level of the granularity, scale, and abstraction adopted for the observation of the thing if a feature is proximal or distal. The classification is relative since the level of the observation changes.

It is hard to consider every important feature to construct the concrete means in advance. Some features that have not been considered are found to be important in a certain situation. This means that management should be constructive and have dialectic nature and that decisions are made as drawing the trajectory towards the goal and adjusting it to the situations encountered during execution of the means.

Therefore, it is important for a management plan to afford situated decision-making and on-the-fly acts. A management plan should consist of a general schema with the framework that is not affected by measure of uncertainty and a flexible part that leaves the rooms for making decision in an actual situation.

A schema defines the framework of a management plan, from which the concrete means are embodied, and formulates the mechanism underlies emergence of the expected situations upon the management. A schema is individualized in the sense that it is formed so as to fulfill particular expectations in a certain context. Adding some features to the general schema in accordance with the context forms an individual schema. A schema is an abstraction of the means to accomplish the goal and is expressed in the form of a plan, an agenda, a manual, etc.

3. PREREQUISITE OF A TASK IN MANAGEMENT

Let T0 be one of the main tasks in management. Suppose that the objective of T0 is to accomplish the target situation S(t'). When T0 is successfully done, we become aware that the current situation S(t) changes into the target situation S(t'). T0 would also let us be aware of the unexpected situation Ss(t') brought about by the interaction between the task and the environment.

A task has to satisfy the prerequisites so as to be done successfully. The prerequisites of T0 are S(t), which is needless to say, and Sp(t"). It is necessary for the success of T0 that situation S(1) and situation Sp(t") are satisfied. The figure depicts that Sp(t") is decomposed into Sp1(t1) and Sp2(t2), where Sp1(t1) and Sp2(t2) are coupled by the diamond with label "&" linked to Sp(t"). This means that Sp(t") is satisfied if both Sp1(t1) and Sp2(t2) are satisfied. Therefore, it is required for the success of T0 that all of S(t), Sp1(t1), and Sp2(t2) are satisfied. The figure also depicts that situation Sp2(t2) is substituted by situation Sp2a(t2) or situation Sp2b(t2), where Sp2a(t2) and Sp2b(t2) are coupled by the diamond with label "or" linked to Sp2(t2). This means that either Sp2a(t2) or Sp2b(t2) satisfies Sp2(t"). Situation Sp1(t1), Ts2a(t2), and Ts2b(t2) are satisfied if task Ts1, Ts2a, and Ts2b are successful, respectively.

It becomes clear from above discussion that it is important for a task to be executed in the situation where the prerequisites of the task are satisfied. It is also important that subtasks should be done successfully in order to confirm that the prerequisites are satisfied. If we have enough resources so as to execute the tasks and the subtasks completely, we should do so. If the resources in rapidly changing situations were limited, the tasks and subtasks would have to be sorted out.

One of crucial task in management is to sort out the tasks and the subtasks. It is important to select the promising ones under the situation that the resources, i.e., time, budget, information, etc., for confirming that their prerequisites are satisfied or that it is possible to make the prerequisite satisfied by executing the subtasks.

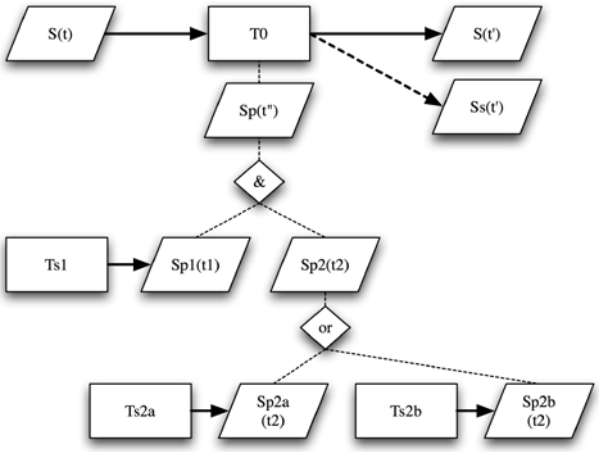


Figure 1. A Task and its Context

4. FEATURES INVOLVED IN MANAGEMENT

4.1 Feature Types

Things are differentiated from each other in terms of their features. A feature is expressed as a pair of a variable and its value. To define a feature is to select the variable and to determine the value among the alternatives. A process of management is formulated as a process where the features, which are designated to describe a preferable situation, are being acquired or maintained. The features are classified into five types with respect to the level of the accessibility and the level of granularity of the description of the things. Table below shows the classification.

Table 1. Classification of Features

	Proximal	*Distal*
Accessed	A-feature	-
Controlled	Dd-feature	-
Influenced	Di-feature	E-feature
Hardly Influenced	I-feature	I-feature

The level of accessibility is defined as follows. A feature is described as being accessed when the future is being specified by direct operation on it. A feature is described as being controlled when it cannot be accessed but is being indirectly but conclusively specified through the direct operation on one or more other features. A feature is described as being influenced when it cannot be controlled but is being affected as the consequence of the interaction between the result of the control of one or more other features and the environment. A feature is hardly influenced if it is not accessible, controlled, or influenced. The level of granularity of the description is defined by whether a feature is proximal or distal. This definition is relative since it depends on the abstraction level of observation whether a feature is proximal or distal. We assume that a feature can be directly determined or controlled if it is perceived as a proximal feature.

With respect to the levels, a feature is classified into on of an accessible feature, or A-feature, a directly deducible feature, or Dd-feature, an indirectly deducible feature, or Di-feature, an emergent feature, or E-feature, and an inaccessible feature, or I-feature, respectively. An E-feature is a distal feature whose proximal features are the A-features, D-features, and I-features. As it is relative to observation whether a feature is proximal or distal, a feature seen as an E-feature in an observation can be seen as another type of feature in another observation.

Table 2. Referents and Variable Type of Features

Features	*Referents*	*Variable Type*
A-feature	Structure	Design variable, Target Variable
Dd-feature	Behavior	Controlled variable, Target Variable
Di-feature	Behavior	Target variable
I-feature	Context	Context variable
E-feature	Function	Target variable

4.2 A Cycle in Management

Management is the combination of generation and analysis. The two parts are performed sequentially or synchronized with each other. In generation, a set of the means that is expected to have the potentiality to change the current situation into preferred one is formed. Generation produces a course of actions. In analysis, it is predicted what if the means are executed. The beliefs about causalities and information retrieved from the existing situations are used as grounds for the prediction. If it is convinced that the means have the expected potentiality on the basis of the consequence of prediction then a course of action to change the current situation into preferable one is determined. If not, the schema of the artifact and some beliefs are modified on the basis of the difference between the preferable situation and the predicted situation.

It is often the case that the significance of a thing being designed is described in terms of E-features promoted by the thing. In management, A-features are determined directly and D-features are controlled under the constraints described by I-features in the expectation that the E-features emerge upon the interaction among the features. An operation is specified in terms of A and Dd-features. The schema embodied by the artifact is described as the relation among A, Dd, Di, I, and E-features. Design explores the specific features towards the preferable situation as well as the relation among the features.

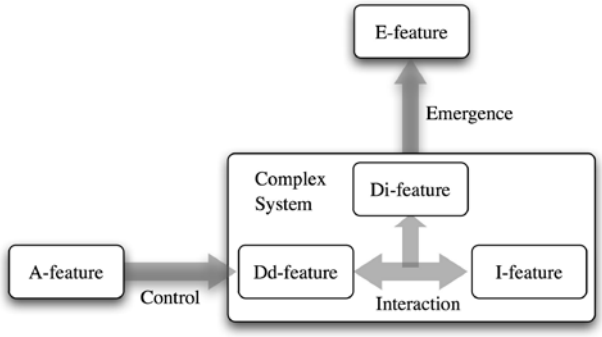


Figure 2. Relation among Features

1. To construct an image of a preferable situation expected to come true. The goal is described as the situation expected to be brought about.
2. To represent the preferable situation in terms of the features, to represent also the differences between the situation and the current situation and the things in common.
3. To assume the causalities associate the designable features with the target features, or to select or modify the causalities currently employed. The decisions are made on the basis of the decision-maker's beliefs about causalities related to the things in question and about the existing situations.
4. To set D-features to be expected to let the target features emerge.
5. To select or assume the mechanism expected to provide the D-features set above.
6. To determine A-features that embody the mechanism. It is desirable that decisions are made in the conviction that the expected phenomena will emerge with minimal unfavorable effects. If the effects are favorable then they may be expected explicitly in the succeeding decision-making. It is presupposed that an A-feature and a D-feature have a causal relation that an A-feature is the cause of a D-feature.
7. To produce actually or virtually the artifact that has the designable features set above.
8. To observe the interaction between the behaviors of the mechanism embodied and the environment. The secondary effects could be either favorable or unfavorable.
9. To evaluate whether the preferable situation emerges. If yes, then the process is done successfully, else, repeat from step 1.

4.3 Causalities Coupling Features

Management applies causalities to construct the schema as well as constructs causalities on the basis of the observation. The schema associating an artifact with the significance is formed with respect to causalities as well as causalities is modified constructively to understand the unexpected consequences of forming the schema.

Some A-features are determined on certain grounds. The relations among the features derived from causalities are consciously applied to form a schema with the conjecture that an artifact with the schema facilitates the expected features. It is essential for the success of schema forming to refer causalities that governs the features. It is important to do something with the consciousness and assumptions of existence of causalities. Causalities could be subjective, or private, in the sense that it represents personal understandings of the world formed through the experience. Even though it is subjective or private, it plays an important role to define the direction of design. To form a schema is to construct the hypothetical relations among the features.

Causalities are expressed in some ways.

(A) Some causality is expressed in the form of an equilibrium governing A-features, D-features, and I-features. The features must be in the same proximal level. A distal feature is not expressed in the equilibrium since a distal feature is defined as the feature that cannot be described by its proximal features completely.

(B) Some causality is expressed as qualitative or quantitative causalities between two things. A thing is expressed as the cause of the other thing, or a thing is expressed as the effect of the other thing. Procedural knowledge, which couples means and ends and is applied to plan a course of actions in generation, is expressed in this form. The relations between the emergent behavior of a system and the behavior of the constituents of the system are also expressed in this form.

At least one of the two things can be an action. When an action is the cause of the other thing, the thing is the result or consequence of the action. When an action is the effect of the other thing, the thing facilitates the action. Proximal features as well as distal features can characterize the things involved in this form of expression. The relations among the proximal features and the distal features are expressed by virtual causality. The notion of vertical causality refers to the causality among the features in the different conceptual level (Nakashima, Suwa, and Fujii 2007).

(C) The rest of causality is tacit and not expressed explicitly in the forms described above. It could be expressed implicitly in a narrative form. Intuitive beliefs about causalities, which determine which features should be focused in design, cannot be expressed in the form of either equilibrium or causality. The focused features are important to determine the direction of generation and analysis.

5. A CONSTRUCTIVE METHODOLOGY

Fujii, Nakashima, and Suwa have been constructing a model of a constructive methodology in design. In the broader sense, management is regarded as design since a promising course of means to accomplish the goal is designed and executed in management. The methodology enriches the process of problem solving so as to express the nature of the process of designing and to facilitate an innovative design. In innovative design, it is significant to find new design variables and to re-evaluate an evaluate function on-the-fly during design.

The core structure of the constructive methodology is composed of the cycles of three processes, i.e., generation, analysis, and focusing as shown in figure 1. Each of the processes traverses the layer of representation and that of entity or the current representation and the future representation. The current representation expresses the things currently recognized, while the future representation expresses the things expected to be realized.

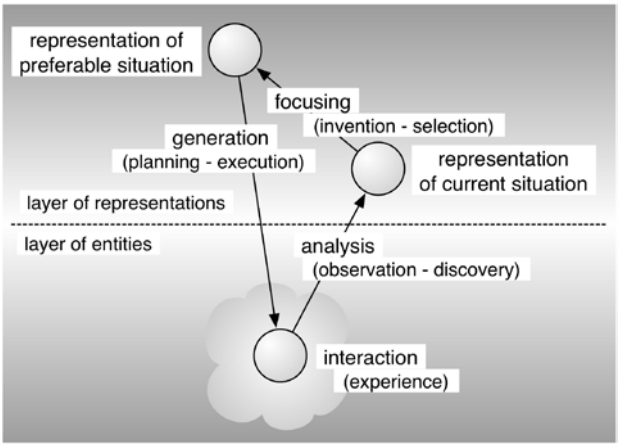


Figure 3. FNS loop.

The *generation* process is the process of embodying the future representation by synthesizing new formation of new and existing entities. The designer interacts with the environment by operating on the entities. The structure of the world changes as the result of the process and the expected phenomena depicted in the future representation and unexpected ones emerge as the consequence. This process has the intentionality of realizing the mechanism that is depicted in the future representation. It is intended to fabricate a situation that renders the future representation true. Operations towards the entity layer are executed with the expectation that the future representation. A process of generation in design is formulated as a process where relations among features are assumed and A-features are determined with respect to the relations.

The changes in the world structures are driven by the interaction between the direct operations in generation and the entities in the world. Since the entities constructs a complex system, it is theoretically impossible to foreseen the result and the consequence of generation completely. Therefore, interaction brings about unexpected changes in the layer of entities and provides an opportunity for a designer to find new design variables and to re-evaluate existing evaluation functions.

The designer predicts the conditional experiential consequences that would be logically or probably derived in accordance with certain inference rules if the selected hypothesis were true and the schema were embodied. Decision whether the schema should be embodied is made. If the decision is made, a course of actions to embody the schema is planned. Then, decision how the schema should be embodied is made.

The *analysis* process is the process of observing and depicting the result and consequence of the generation and the interaction. As the consequence of the process, the representation of the current formation of the entities and the emergent phenomena is made. The current representation is compared with the last future representation depicted just before this process. This process has the intentionality of understanding the current structure of the world. It is intended to narrate the experience in the current situation. The interpretation basically tends to remain the same as the interpretation in the previous cycle, but it is subject to change in focusing when unexpected things are observed and it is hard to express the things under the current interpretation. A process of analysis is formulated as a process where D-features are deduced from the A-features and it is predicted, on the basis of the assumptions, whether the expected E-features emerge upon the interaction among the A-features, the D-features, and the I-features or not.

The designer actually embodies the schema and verifies how far the predicted consequences are consistent with the experiential observations as estimating the proportion of truth of the hypothesis. Decisions whether the schema and the hypothesis are sensibly correct, or require some inessential modification to fulfills the intention, or must be rejected are made. If the second decision is made, then the direction of the modification is determined.

The *focusing* process is the process of depicting the next future representation of the mechanism on the basis of the current representation of mechanism acquired as and the differences between the current representation and the last future representation of the mechanism. Decisions on the acceptance of the assumptions and the adoption of the features are made. A course of actions in the next cycle is planned in this process. The direction of improving the designed artifact and the service given through the utilization of the artifact is decided. In an innovative design, new design parameters and the causalities coupling the entities and the parameters are constructed. It is intended to signify the current situation to construct the next cycle of generation, analysis, and focusing. Decisions on whether design has been completed, should be continued, or has to be stopped are made. The assumptions about the relations are modified to fill the gap between the prediction and the expectation in the succeeding generation process. The decisions on the direction of the modification are made. If the current representation is similar to the last future representation, it seems that the design is completed successfully.

The designer imagines, on the basis of the past and present experiences, how the situations will change if a certain schema is embodied. The designer invents some hypotheses that shall fulfills the will, and selects the one that seems promising. Decision which hypothesis should be the most promising and be adopted is made. A schema that is consistent with the hypothesis is formed. There is no logical way to invent or select the most plausible hypothesis and to design the consistent artifact. Even if we investigate the existing situations and correct a plenty of information on the current situation, we have to make decision with some intuition.

Either abduction or induction doesn't have logical inference rules that guarantee the truth of the consequences in spite that deduction does. Therefore, the success of design as well as scientific inquiry depends not only on the procedural schema like the rules of deductive reasoning but also on the heuristic capacities to be employed to select the most plausible hypothesis, to classify the empirical observations, and to imagine a course of action towards the goal.

6. CONCLUSIONS

A model of the constructive methodology of management for pre-quake mitigation and post-quake rehabilitation is proposed on the basis of two major nature of the management, i.e., incompleteness and situatedness.

Acknowledgment

Discussions given in this article are mostly the result of an on-going and long discussion with Hideyuki Nakashima (Future University – Hakodate) and Masaki Suwa (Keio University), and partially inspired by discussions with Yoshitsugu Aoki (Tokyo Institute of Technology).

References:

1) H. Fujii, H. Nakashima, and M. Suwa (2008), "Types of Intelligence in Architectural Design Processes - On the basis of a Phenomenological and Dialectic Model of Design Processes," *Proc. Ninth International Conference on Design & Decision Support Systems*, The Netherlands, CD-ROM.
2) H. Fujii, H. Nakashima, and M. Suwa (2008), "Aspects of Innovation in Constructive Methodology—Investigating Architecture as a Material ", Transactions of Information Processing Society of Japan, Vol. 49, No. 4, pp. 1571-1580, (in Japanese).
3) H. Fujii (2009), "Nature of Design from an Architectural Point of View", *Special Issue of Japanese Society for the Science of Design*, Vol. 16-2, No. 62, pp. 27-30.
4) H. Fujii and H. Nakashima (2010), Designing Action Know as Design, *Cognitive Studies*, Vol.17, No.3, pp.403-416, (in Japanese).
5) Nakashima, H. (2009), "Design of Constructive Design Process", *Special Issue of Japan Society for the Science of Design*, in press.
6) Nakashima, H., Suwa, M., and Fujii, H. (2007), "Vertical Causality (in Japanese)", *Proc. 24th Annual Meeting of Japanese Cognitive Science Society*,42-47.

8CUEE CONFERENCE PROCEEDINGS
8th International Conference on Urban Earthquake Engineering
March 7-8, 2011, Tokyo Institute of Technology, Tokyo, Japan

HUMAN BEHAVIOR OF BUILDING RECONSTRUCTION AND FIREPROOFING OF CITIES

Toshihiro Osaragi[1] and Yumi Nakata[2]

1) Associate Professor, Graduate School of Information Science and Engineering, Tokyo Institute of Technology, Japan
2) Graduate Student, Graduate School of Information Science and Engineering, Tokyo Institute of Technology, Japan

Abstract: The fireproofing of building structures is one of the most important issues in the field of disaster prevention planning. In the Tokyo metropolitan area, improving fireproofing is of great concern, since a devastating earthquake and subsequent fires could cause the widespread damage. In this study, we construct a probabilistic model that describes the conversion process of building structures. Using this model, we estimate the time-series changes of the building structures in an established city area and extract hazardous areas from the viewpoint of disaster prevention. In these areas, we simulate time-series changes in the building structures by applying urban- and building-regulations and evaluate the effectiveness and efficiency of these regulations for promoting fireproofing in potentially dangerous areas.

1. INTRODUCTION

1.1 Background and objectives

One of the most urgent issues in regional disaster planning is how to make the densely built parts of a city more resistant to fires. Planners in Tokyo took the lesson of the 1995 South Hyogo Prefecture Earthquake (Kobe earthquake), and, in 1996, drew up plans for recreating Tokyo as a "fire-proof city", with the objectives of updating fire-fighting resources in the locations with the most densely clustered wooden buildings and promoting the clearing of firebreaks. The plan was revised in 2003; simultaneously, architectural safety ordinances (new fire safety regulations) were introduced that continued to allow quasi-fire-resistant structures in some districts but placed severe fire-prevention requirements on wooden structures. However, there are still many areas in Tokyo that are quite vulnerable to fires following an earthquake. As a result, there is widespread and intense interest in policies for efficiently and effectively promoting fireproof or fire-resistant construction.

This paper presents a quantitative assessment—from a "micro" perspective of fireproofing processes of individual buildings in Tokyo—of what kinds of regulations and policies promote efficient and effective change-over to fireproof or fire-resistant construction, in what places and to what extent. First, a stochastic model that describes the processes of replacing buildings was built. Factors affecting the promotion of fireproofing were identified. Next, this model was used to predict changes in building structures over a span of many years; this provides a "handle" on the current fireproofing remodeling situation and identifies districts in which this progress is slow.

1.2 Previous Research

One method for reducing the area burned in a fire is to divide a continuously built-up urban area into small subzones separated by fireproofed strips that function as firebreaks. This is anticipated to be vital in densely built-up cities, where fires cannot be expected to naturally "burn themselves out". Tsukakoshi et al. (1984) and Fujimoto et al. (1989) have assessed the effectiveness of firebreaks in models for simulating the spread of fire and explored what forms of firebreaks were the most effective. Itoigawa (2004) argued that fire spread models must be expanded in order to obtain valid assessments of how various factors, including building construction, affect the spread of urban fires. These reports resemble the present paper in their attempts to examine how rebuilding and structural changes contribute to fireproofing. Hirota et al. (1997) considered that rights-of-way such as roadways could function as firebreaks, and investigated the benefits of fire-resistant construction, limits on building floors and specifications for roadway widths. They suggested that main roads and cross streets could be modified to divide areas effectively into subzones. This paper presents a quantitative assessment of the above processes, with views of the current state of progress in the fireproofing of buildings along streets of different widths, and a review of the effectiveness of urban- and building-regulations and policies in areas where fireproofing has lagged behind.

The tragic history of urban fires makes plain to the importance of promoting the use of incombustible materials in densely built wooden residential areas. Not only is there a risk of spread once a fire breaks out, but narrow streets are all too easily blocked by burning rubble from the collapse of

buildings, trapping fleeing victims. Nevertheless, efforts to install incombustible materials and widen streets have not gone very far. Machida et al. (2006) and Katsumata et al. (2006) conducted surveys of residents of densely built wooden residential areas and local public organizations to investigate the causes of delays in the fireproofing of deteriorating wooden residences. While they found problems in citizens' attitudes, they also noted that conversion was hampered by the legal status of lots and other physical factors. This paper considers the physical factors contributing to the probability of building reconstruction and presents a quantitative analysis of how these factors hamper fireproofing.

2. A STOCHASTIC RECONSTRUCTION MODEL

2.1 Components of a stochastic reconstruction model

In a typical fireproofing modification, a fire-prone wooden structure is demolished and replaced with a completely new fire-resistant building. The rebuilding event is modeled in this paper in two stages: the demolishing process and the structural change process (Figure 1). The *demolition model* designates buildings to be demolished, and the *structural conversion model* predicts the changes made to the structure of new buildings. The combination of these two is referred to as the "*stochastic reconstruction model*".

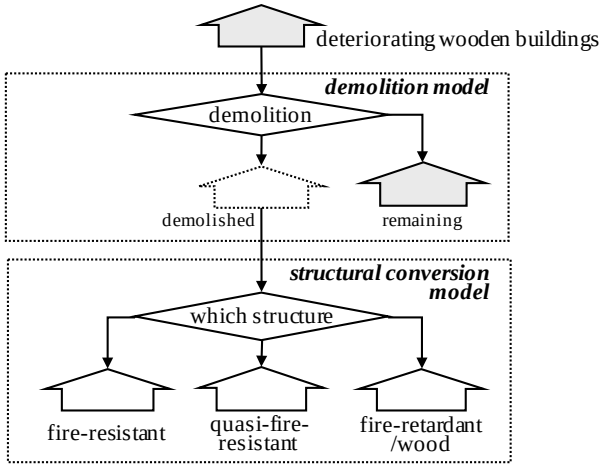


Figure 1 Stochastic reconstruction model

2.2 Demolition model and structural conversion model

The demolition model decides stochastically whether a building is to be dismantled at the following time step, depending on various factors (e.g., building attributes, the surroundings, urban- and building-regulations). The output takes a high value if there is a strong possibility that building j will be torn down by the next time point, and a low value if the building will probably be left as it is. u_j, the potential for building j to be demolished, is represented by the following linear model:

$$u_j = a_0 + \sum_k a_k x_{jk} \tag{1}$$

where x_{jk} is a variable expressing the attributes of building j, the surroundings, and regulations, and a_0 and a_k are unknown parameters. The probability p_j that building j will be demolished by the next time point is defined by the following binomial logit model:

$$p_j = \exp[u_j] \Big/ \left(1 + \exp[u_j]\right) \tag{2}$$

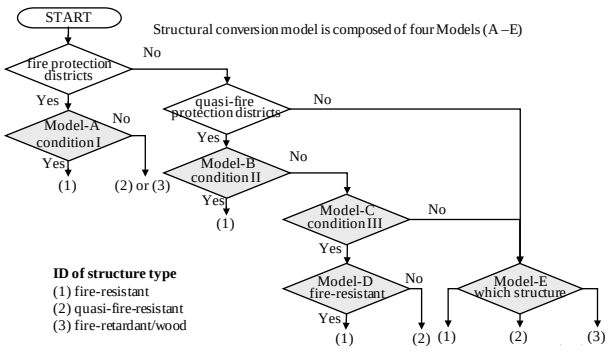
The structural conversion model is a stochastic model describing whether a newly constructed building will be fire-resistant, quasi-fire-resistant, or fire-retardant/wood construction, using nearly the same factors as above. When replacing buildings that meet conditions I - III in Figure 2 in fire-protection districts or quasi-fire-protection districts, however, the only permitted structural types are fire-resistant or quasi-fire-resistant. Thus, the model describes whether the conversion of a building that stands in a fire-protection district or quasi-fire-protection district meets conditions I - III.

The building is described by Models A - D in Figure 2, a diagram of the structural conversion model. In Equation (3), we define the fire-resistant potential v_j, whose value corresponds to the potential for building j to be rebuilt as a fire-resistant building:

$$v_j = b_0 + \sum_k b_k x_{jk} \tag{3}$$

where x_{jk} is a variable expressing the attributes of building j, the surroundings, and urban- and building-regulations, and b_0 and b_k are unknown parameters. The probability q_j that building j will become fire-resistant by the next time point is given, as above, by the binomial logit model as follows:

$$q_j = \exp[v_j] \Big/ \left(1 + \exp[v_j]\right) \tag{4}$$



Permission of structural types in fire-protection districts/ quasi-fire-protection districts

Regulations	Conditions	Size of building	Permitted structural types
Fire-protection districts	I	Number of floors ≧ 3 or Floor area>100㎡	(1)
	—	Others	(1) or (2)
Quasi-fire-protection districts	II	Number of floors ≧ 4 or Floor area>1500㎡	(1)
	III	Number of floors=3 or 500㎡<Floor area ≦ 1500㎡	(1) or (2)
	—	Others	(1) or (2) or (3)
No regulation	—		(1) or (2) or (3)

Figure 2 Structural conversion model

Model-E has three possible options for conversion — fire-resistant, quasi-fire-resistant or fire-retardant/ wood — and is constructed as follows. We insert the quasi-fire resistance potential w_j in addition to the fire resistance potential v_j. As in Equation (3), this model is linear and uses variables to express the attributes of building j, the surroundings, and urban- and building-regulations. The probability that building j will become fire-resistant and quasi-fire-resistant by the next time point is given by probabilities q_j and r_j respectively in the multinomial logit models:

$$q_j = \exp[v_j] \Big/ \left(1 + \exp[v_j] + \exp[w_j]\right), \qquad (5)$$

$$r_j = \exp[w_j] \Big/ \left(1 + \exp[v_j] + \exp[w_j]\right), \qquad (6)$$

$$where\ v_j = b_0 + \sum_k b_k x_{jk},\ w_j = c_0 + \sum_k c_k x_{jk}.$$

3. EXECUTING THE DEMOLITION MODEL AND THE STRUCTURAL CONVERSION MODEL

3.1 Study area and data for analysis

The region examined with these models was Setagaya Ward, Tokyo. Ward GIS data (1996; 2001) and applications for building plan approval were used. Since there were no direct connections between the building data and building plan approval data, these data were connected based on the spatial relationships of the same building-lot location. Information about building construction years is closely related to trends in the demolition of then-current structures. This is one of the integral factors in the remodeling process. The latter data set is incorporated in the construction year data. In addition, there is great potential for building reconstruction to occur simultaneously with divisions or consolidations of lots. A simulation of building renewals that includes lot division or consolidation may provide more useful information about these actions. A method proposed by Osaragi et al. (2005, 2006, 2007) was also used to compare lot shape changes between the two time points with GIS data in order to extract the lots that had been divided or consolidated.

3.2 Results of analysis by demolition model

Table 1 shows the results provided by the demolition model. The reader can see the following findings about the likelihood of a building to be demolished. (1) The most powerful of the many explanatory variables is the age of the building; the greater its age, the more likely a building is to be demolished. (2) The probability of demolition is increased when a lot is divided or combined with another. (3) The estimated value of [ratio of unused floor-area] is greater than 0, the greater the unused floor space, the more likely the building is to be demolished. (4) Since the estimated parameters of building area [0 - 50 m^2] is less than [50 - 150 m^2] and negative, the lower the area of a building, the less likely it is to be demolished. (5) The estimated parameters of lot area [100 - 200 m^2] is greater than 0, so buildings on smaller lots (about 100 m^2) are less likely to be demolished. (6) The estimated parameters of street frontage [0 - 2 m] is less than that of [2 - 6 m], so buildings on lots with bad connections to the adjoining street and illegal lots with insufficient frontage [0 - 2 m] tend not to be demolished. (7) The estimated parameters of street width [0 < 2 m] is less than 0, so buildings facing small streets in densely crowded neighborhoods have a low probability of being demolished. There is a common tendency for districts with the highest risk of fire spread to have the slowest progress in fireproofing.

Table 1 Estimators and fitness of demolition model

Explanation variables and categories		Estimated parameters	Wald statistics	Probability of insignificance
Age of building		0.110	2936.509	0.000
Structure before demolition	fire-resistant	-0.779	52.073	0.000
	quasi-fire-resistant	-0.634	72.878	0.000
	fire-retardant/wood	-0.681	180.366	0.000
Number of floors before demolition	1 floor	0.564	25.443	0.000
	2 floors	0.528	32.471	0.000
	over 4 floors	-0.552	17.772	0.000
Building type before demolition	commercial	-1.274	28.050	0.000
	house with shop	-1.582	47.712	0.000
	detached house	-1.995	82.519	0.000
	flat	-1.916	71.150	0.000
	factory	-1.523	38.020	0.000
Building area before demolition	0～50㎡	-0.439	24.595	0.000
	50-150㎡	-0.226	8.217	0.004
Division of building lot		0.961	375.908	0.000
Unification of building lot		0.849	267.769	0.000
Area of building lot	100 - 200㎡	0.158	20.417	0.000
Length of frontage of building lot	0-2m	-0.320	13.940	0.000
	2-6m	-0.240	18.560	0.000
Width of street	0-2m	-0.318	7.543	0.006
Land use regulation	high-rise residential	-0.135	8.729	0.003
	commercial	-0.445	7.660	0.006
Ratio of unused floor-area*		0.002	32.077	0.000
Ratio of detached house**		0.006	22.481	0.000
Gross building area ratio of building adjacent to 4m wide street**		-1.652	29.497	0.000
Ratio of bulk lots***		-0.712	12.496	0.000
Average of building age***		-0.091	9.242	0.002
Moving potential of household with income over 700 million yen		0.101	19.134	0.000
Constant		0.741	1.416	0.234

Fitness of estimated model

		Estimation		Fitting Ratio (%)
		remaining	demolished	
Obs.	remaining	7229	2978	70.8
	demolished	2575	7636	74.8
Total				72.8

* Ratio of unused floor-area= $\frac{(\text{legal floor-area-ratio} - \text{actual floor-area-ratio})}{\text{legal floor-area-ratio}} \times 100$

**Calculated in the area within 100 m from the building

***Calculated in the town where the building located

3.3 Results of analysis by structural conversion model

Table 2 shows the results of running the structural conversion model. Model-A predicts that buildings will be at least three floors high or will have at least 100 m^2 of floor space (Condition I) when they are rebuilt in fire-protection districts. In the Setagaya Ward fire-protection district, a large majority (95.8%) of the replaced buildings from 1996 to 2001 met Condition I. Thus, it can be predicted that reconstructed buildings in a fire-protection district will be fire-resistant structure.

The next is Model-B, which predicts that a building replacing an old, demolished building in a quasi-fire -protection district will be at least four floors high or have more than 1500 m^2 of floor space (Condition II). From the estimated values of the parameters, the buildings most likely to meet this condition—i.e., become fire-resistant structure —replace large buildings, are on lots that have just been consolidated, are on lots with unused ground, or have some other condition favoring the construction of large buildings; these buildings might also have good street connections.

Under Model-C, when a building is replaced in a quasi-fire-protection district, it is predicted to be at least three floors high or have a floor area between 500 m^2 and 1500 m^2 (Condition III). From the estimated values of the parameters, the buildings most likely to meet this condition are in districts zoned for high-rises to use land more efficiently, when the building is shared residential and commercial, the street connections are good and the lot area is comparatively small.

Model-D predicts whether a building will be replaced in accordance with Condition III, which indicates in a fire-resistant or quasi-fire-resistant structure. From the estimated values of the parameters, reconstructed buildings tend to be fire-resistant when their predecessors were fire-resistant and when there are many fire-resistant buildings in the vicinity. Conversely, when a lot is small or has inconvenient connections to the adjoining street, it tends to be built with a quasi-fire-resistant structure when predecessors are residential- commercial use or residential-industrial use.

Table 2 Estimators and fitness of structure transition model

Explanation variables and categories		Model-B			Model-C			Mode-D		
		Parameters	Wald	Probability	Parameters	Wald	Probability	Parameters	Wald	Probability
Present building meets condition II		3.276	8.416	0.004						
Present building meets condition III					2.292	89.914	0.000			
Structure before demolition	fire-resistant				1.312	29.612	0.000	1.385	31.070	0.000
	quasi-fire-resistant				0.448	9.218	0.002			
	fire-retardant/wood	-0.606	8.630	0.003	0.266	8.723	0.003			
Building type before demolition	residential-commercial				0.394	5.723	0.017			
	flat							-0.357	5.135	0.023
	residential-industrial							-1.050	4.830	0.028
Total floor area		0.006	36.510	0.000						
Area of building lot	0-100 ㎡				0.239	5.468	0.019	-1.101	16.086	0.000
	100-200 ㎡							-0.679	11.047	0.001
Perimeter length of building area					-0.006	18.623	0.000	0.011	8.567	0.003
Division of building lot		-1.359	20.756	0.000	0.775	70.922	0.000	-1.483	61.766	0.000
Consolidation of building lot		2.116	82.724	0.000	0.337	9.325	0.002	1.231	37.404	0.000
Length of frontage of building lot	0-2 m				-0.661	9.764	0.002			
	2-6 m	-1.558	17.110	0.000	-0.328	6.064	0.014			
	6-10 m	-0.678	5.503	0.019						
	10-14 m	-0.710	7.865	0.005						
Width of adjacent street	0-2 m				-0.538	7.881	0.005	-1.064	5.759	0.016
	2-4 m	-0.878	13.758	0.000	-0.236	8.637	0.003	-0.385	5.749	0.016
Ratio of unused floor-area*	continuous variable	0.009	14.084	0.000	0.005	20.722	0.000			
	over 160%							0.459	5.793	0.016
Land use regulation	First low-rise residential				-0.860	59.143	0.000			
	Second low-rise residential	-1.309	22.125	0.000						
	Neighborhood commercial	1.344	19.092	0.000						
Ratio of households over 65 years old*					-3.888	6.581	0.010			
Ratio of fire-resistant building*								4.365	11.524	0.001
Ratio of bulk area*					-2.490	24.053	0.000			
Ratio of buildings of 2-floor or less*					-3.080	21.021	0.000			
Constant		-1.377	9.194	0.002	3.148	28.664	0.000	-0.565	2.031	0.154
Fitting ratio (%)				85.3			70.8			74.3

Explanation variables and categories		Model-E (fire-resistant)			Model-E (quasi-fire-resistant)		
		Parameter	Wald	Probability	Parameter	Wald	Probability
Building structure before demolition	fire-resistant	3.895	232.979	0.000	0.904	16.295	0.000
	semi fire-resistant	0.991	13.802	0.000	1.230	151.630	0.000
	fire-retardant/wood	-0.448	5.839	0.016	-0.641	110.299	0.000
Area of building lot	0-100 ㎡	-0.573	4.999	0.025	-0.360	19.585	0.000
Perimeter length of building area		0.003	11.463	0.001	-0.003	14.772	0.000
Division of building lot		-0.774	12.700	0.000	0.084	1.450	0.228
Width of adjacent street	0-2 m	-0.626	1.747	0.186	-0.591	15.182	0.000
Ratio of unused floor-area*	35-80 %	0.334	4.805	0.028	0.151	7.198	0.007
Ratio of bulk area*		1.788	6.954	0.008	-0.315	1.077	0.299
Constant		-3.482	309.320	0.000	-0.299	13.152	0.000
Fitting ratio (%)							56.7

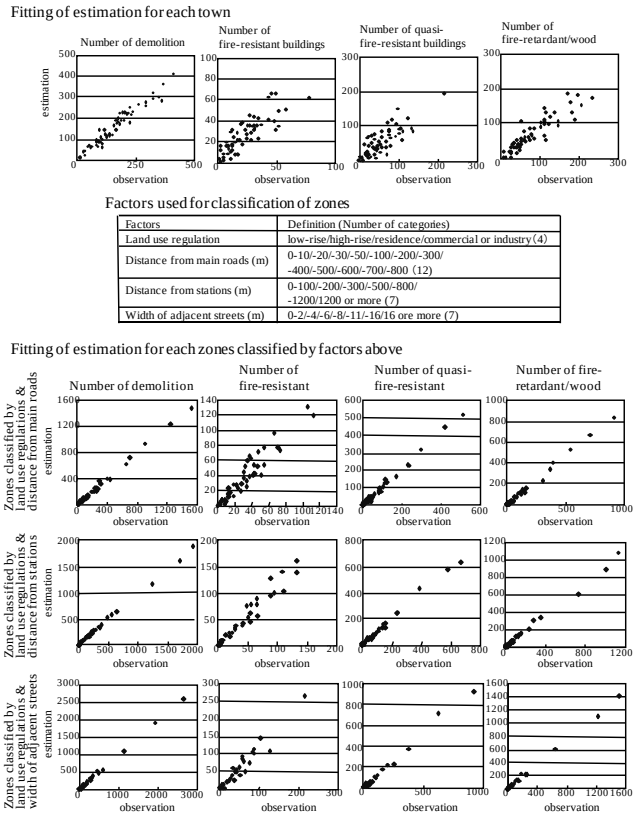
*regional variable observed in a town

Lastly, Model-E predicts whether a replacement building will have a fire-resistant, quasi-fire-resistant or fire-retardant/wooden structure when the original building is in a quasi-fire-protection district not in accordance with Conditions II and III or a district undesignated for fire-protection. From the estimated values of the parameters, when a building is fire-resistant or quasi-fire-resistant before demolition, it has a high probability of being rebuilt as fire-resistant or quasi-fire-resistant; however, when the lot is small, the building tends to be rebuilt with fire-retardant materials.

3.4 Compatibility of stochastic reconstruction model

The demolition model and structural conversion models were combined to create the stochastic reconstruction model and the compatibility of the combined model was validated. Here, the 1996 data were used as a base for predicting the demolitions, replacements and fireproofing upgrades from 1996 through 2001 to verify the accuracy of the model. The demolition model attempted to extract the buildings that were replaced and the stochastic reconstruction model attempted to predict the degree of fire-protection of their replacements. Because the results in Figure 3 combine multiple models, it is difficult to determine how accurate the predictions are for individual buildings. Nevertheless, if one examines the map by town (a subsection of a ward; there are 59 towns in Setagaya Ward), the model provides an accurate prediction of the number of demolished buildings. The prediction of structural conversions, however, was less accurate. One reason for this was that the errors in the estimates of the demolition model affected the structural conversion model.

At the same time, classification of zones by land use regulations, distance from main roads and railway stations, and width of the streets adjoining individual building lots and counting within the zones defined this way provided a more accurate count than estimates performed at each town.



Factors	Definition (Number of categories)
Land use regulation	low-rise/high-rise/residence/commercial or industry (4)
Distance from main roads (m)	0-10/-20/-30/-50/-100/-200/-300/ -400/-500/-600/-700/-800 (12)
Distance from stations (m)	0-100/-200/-300/-500/-800/ -1200/1200 or more (7)
Width of adjacent streets (m)	0-2/-4/-6/-8/-11/-16/16 ore more (7)

Figure 3 Fitness of stochastic reconstruction model

4. SIMULATION USING THE STOCHASTIC RECONSTRUCTION MODEL

4.1 Progress in fireproofing and extraction of most vulnerable areas

Figure 4 is a flow chart for the simulation. The stochastic reconstruction model was used to predict the replacement of buildings and changes in structure for a 30-year period beginning in 2001, assuming no control under urban- and building-regulations (the current regulations). The simulation results showed a predicted gradual rise in fire-resistant and quasi-fire-resistant buildings and a gradual decrease in fire-retardant/wooden structures.

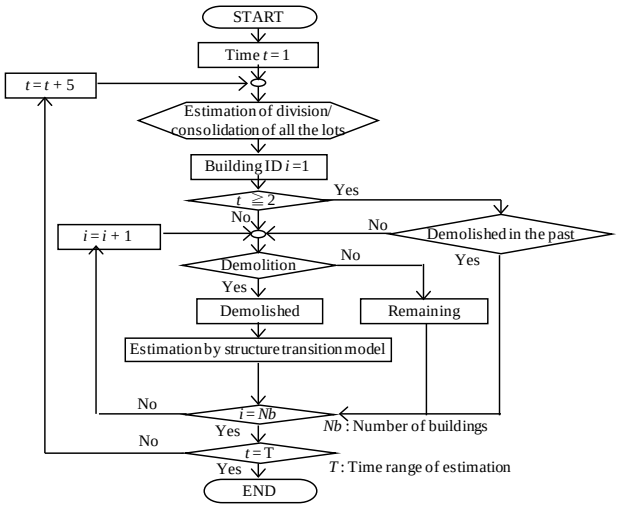


Figure 4. Flow chart of simulation

Next, districts were divided into several zones with respect to their distance from main roads, distance from railway stations, width of adjoining streets and land use regulations. Each zone was examined to find the rate of use of incombustible materials over the 30-year period and the mean rate of increase in use of incombustible materials. Figure 5 shows the results of that simulation. Over 70% of buildings were predicted to be fireproofed in the next 30 years in zones within 30 m of main roads excepting the low-, middle- and high-rise residential zones. In contrast, in the low-, middle- and high-rise residential zones, it was predicted to lag, with low rates of conversion. High rates of fire-resistant conversion were predicted for buildings within 30 m of main roads, but relatively low rates were expected beyond the 30 m line. Areas along main roads are expected to fulfill a role as firebreaks, so it will be important in low-, middle- and high-rise residential zones also to be adequately fireproofed.

Results of zones combining land use regulations and distance from railway stations showed increased levels of fireproofing in buildings closer to train stations. Again, however, in low-, middle- and high-rise-, residential zones were predicted to have low rates of fireproofing, even after 30 years. There are many transient occupants near railway stations, which makes safety that much more vital. Fireproofing should therefore be promoted in residential-use zones within 300 m of a station.

Factors of land use regulations and width of adjoining streets were also combined for simulation. A relatively large gain was predicted in fireproofing of buildings facing streets in the width range of 0 - 4 m, but the current rate of fireproofing among these buildings is so low that even after 30 years, the gain still resulted in a low overall level of fireproofing. Indeed, in low-rise residential zone, it showed only a small rise in fireproofing even when they were facing streets 6 m or more wide, with the same low rate of fireproofing after 30 years. From the viewpoint of preventing fire spread, it is essential to promote fireproofing of buildings near narrow streets. Since two functionalities are required—to serve as a firebreak and to serve as a route for evacuation of citizens—new policies are necessary to make aggressive improvements in the fire resistance of streets connecting to streets with widths of 6 - 8 m.

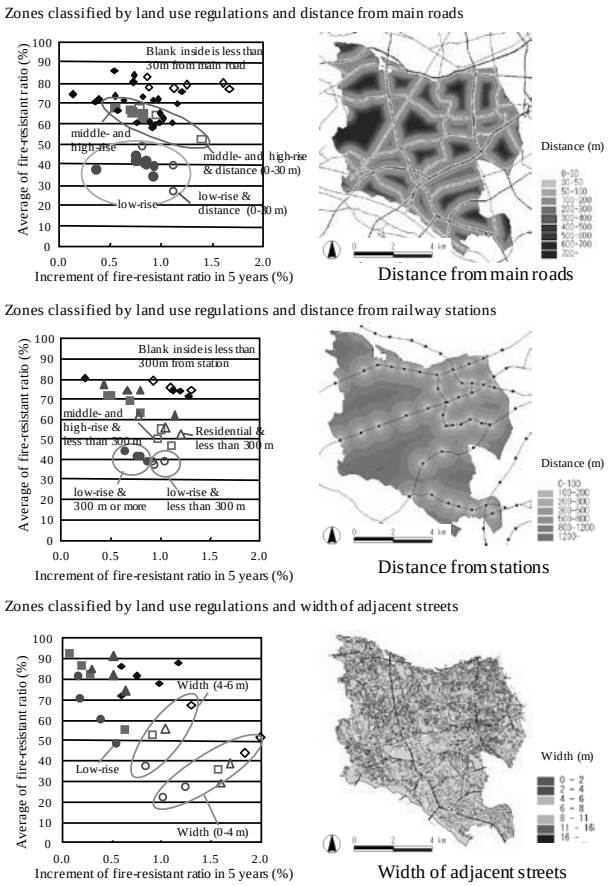


Figure 5. Average and increment of fire-resistant ratio in zones classified by factors

4.2 Assessment of influence of regulations and policies on fireproofing progress

Regulations and promotion policies that seem most effective for fireproofing of buildings were determined (26 total). They address (1) lot area; (2) lot connections to

adjoining street(s); (3) zoning; and (4) capacity factors. Next, the effects of each regulation and policy on the progress of fireproofing in the districts found in 4.1 to be the most vulnerable were predicted. These were compared with the consequences of not enforcing the regulations (the current situation) in order to observe which are most effective. Next, Fireproofing Promotion Plans were created using various combinations of the eight regulations found to be most effective; the benefits of each combination were assessed in terms of the "effect" and "efficiency".

It is more efficient to combine regulations and policies with special provisions for previously existing buildings that do not meet standards than to change zoning or capacity factors. This is because these buildings are then easier to replace under the special provisions of regulations and policies, and will then be replaced with fire-resistant or quasi-fire-resistant structures. If capacity factors are legally raised, there will be more fire-resistant buildings, but if capacity factors are loosened excessively, lot consolidation will be suppressed, promoting lot division; this would work against the final goal of increasing the number of fire-resistant buildings. Thus, planners must be cautious not to allow the outcome of deregulation to be the opposite of its desired effects.

Other effective policies apply minimum lot size regulations to entire districts to suppress lot divisions while promoting the construction of fire-resistant buildings. However, there are many cases in which lots are divided while wooden buildings are replaced; if minimum lot size regulations are enforced against small lots, lot division will be suppressed, potentially suppressing a large number of otherwise probable replacements of wooden buildings. Minimum lot size regulations are anticipated to be quite effective for forming favorable city lots, but caution must be exercised to promote the desirable replacement of deteriorating wooden buildings.

5. SUMMARY AND CONCLUSIONS

This paper presents a "micro" view of the process of fireproofing individual buildings in a city. A stochastic model was created to describe the process of building replacement in two parts: a demolition model and a structural conversion model. Real data were employed in model simulations, and the values of the estimated parameters revealed factors affecting the process of fireproofing of buildings.

Reconstruction simulations were carried out with data from existing city lots. These provided a view of progress in reconstruction of buildings assuming that current regulations and policies are continued without modification. Locations in particular need of faster reconstruction were identified.

Fireproofing promotion plans were created, combining a variety of different regulations and policies, and evaluated using the above model for effectiveness and efficiency. Regulations and policies resulting in the most effective increase in fireproofing were noted, as follows. (1) In order to promote more rapid building renewal, it is more efficient to enact regulations incorporating special, looser measures for existing buildings that do not meet current standards than simply to relax regulations on zoning or capacity factors. (2) Loosening restrictions on capacity factor generally encourages construction of fire-resistant structures, but it also suppresses the desirable consolidation of lots and promotes lot division. (3) Regulations on minimum lot size suppress lot division and promote construction of fire-resistant buildings, but also have the potential to suppress the replacement of wooden buildings that is likely to occur during lot division.

The results of the simulations with the stochastic reconstruction model created in this study demonstrated that fireproofing proceeds at different paces in different areas. Therefore, a key feature of these plans is to avoid uniform fireproofing policies affecting wide regions in favor of more localized approaches that are well tuned to each district's realities. The appropriate division and combination of lots will create a more safe and beautiful urban landscape.

References:

Tsukagosi, S. and Itoigawa, E. (1984), "Evaluation of fire blocking belt in the planning of urban fire prevention unit: Part 1 Estimation of fire load to fire blocking belt ", *Journal of Architectural Planning and Engineering, AIJ*, 340, 92-100.

Hirota, A., Iijima, H. and Tsuboi, Y. (1997), "A study on the effect of the strip zoning system: Present condition of the firebreak belt", *Journal of Architectural Planning and Engineering, AIJ*, 497, 129-135.

Ichikawa, F., Sakata, T. and Yoshikawa, T. (2004), "An analysis of accessibility to spaces for disaster refuge considering danger of street-blockades caused by collapse of buildings on evacuation routes", *Theory and applications of GIS*, 12(1), 47-56.

Machida, Y., Kawagishi, U., Kitano, K. and Ohmura, S. (2006), "Study on town development in densely populated wooden building district: Case study of Nogata area in Nakano-ku, Tokyo", *Summaries of Technical Papers of Annual Meeting, Architectural Institute of Japan*, F-1, 679-680.

Katsumata, W., Iida, N. and Taketani, S. (2006), "Study on exceptional permissions in the zoning code under the building standard law, to encourage rebuilding in densely built-up areas", *Summaries of Technical Papers of Annual Meeting, Architectural Institute of Japan*, F-1, 681-682.

Osaragi, T. and Inoue, T. (2005), "Modeling and analysis of lots consolidation in established city area", *Journal of Architectural Planning and Engineering, AIJ*, 592, 147-153.

Osaragi, T. and Inoue, T. (2006), "Potential and patterns of lots subdivision in established urban districts", *Journal of Architectural Planning and Engineering, AIJ*, 605, 151-157.

Osaragi, T. and Inoue, T. (2007), "The effects of minimum lot size regulation: Simulation of the lots subdivision and consolidation in established urban districts", *Journal of Architectural Planning and Engineering, AIJ*, 614, 199-204.

8CUEE CONFERENCE PROCEEDINGS
8th International Conference on Urban Earthquake Engineering
March 7-8, 2011, Tokyo Institute of Technology, Tokyo, Japan

STATIC AND DYNAMIC EMERGENCY EVACUATION GUIDANCE FOR COMPLEX BUILDING GEOMETRIES

Chih-Yuan Chu

Assistant Professor, Department of Civil Engineering, National Central University, Taiwan
jameschu@ncu.edu.tw

Abstract: The paper proposes a method for designing static and dynamic evacuation guidance in complex building spaces. A visibility graph is used to analyze the geometry of the building in a manner consistent with actual human behavior. The static evacuation sign installation locations and the associated evacuation direction information can then be found using the graph. However, the pre-determined, static emergency guidance does not respond to the real-time situations and may cause congestion in the event of evacuation. To address this problem, this paper further proposes a complementary method for planning dynamic emergency evacuation guidance using image process to support the static guidance system.

1. INTRODUCTION

The evacuation time of a building is one of the most critical measures of performance in its emergency design. In addition to building geometry, the design of the emergency guidance system is another key component that determines the time required for pedestrians to leave hazardous areas. The following sections introduce the proposed design methods for planning static and dynamic evacuation guidance.

2. STATIC EVACUATION GUIDANCE

Designing the static evacuation guidance is highly related to finding shortest paths in the presence of obstacles, which is a classic problem in computational geometry. The following theorem states the property of a shortest path from an origin to a destination in such space:

The shortest path from one point to another point among a set of disjoint polygonal obstacles is a polygonal path whose vertices (except for the origin and destination) are vertices of the obstacles.

The proof of the theorem can be found in de Berg et al. (2008). This theorem is very intuitive and can be illustrated with the following example. Consider a rope passing through two points with several obstacles between them. By assuming that the rope represents the correct path, the length of the path can be reduced by pulling on the rope from either end. When the rope cannot be pulled any further, the shortest path must be a polygonal line and its vertices are the vertices of the obstacles.

2.1 Visibility Graph and Shortest Path

A visibility graph is a network whose vertices are the vertices of obstacles and whose arcs connect all vertex pairs that are visible to each other. The rule for determining if two vertices are visible to each other is that a straight arc can be constructed between them without intersecting any obstacles. Based on the theorem, a visibility graph always contains the shortest paths from one vertex to another in complex building spaces. To find the shortest path between an origin–destination pair, new arcs are added to connect the origin and the vertices of the network visible to the origin. Similarly, new arcs are appended for the destination. When the graph is constructed, the shortest path between the origin and the destination can be found in the network using a shortest path algorithm such as Dijkstra's. See Ahuja et al. (1993) for examples of shortest path algorithms.

Figure 1 shows an example of a visibility graph. The black rectangles are the obstacles and the small squares are the candidate sign locations. The solid gray lines constitute the visibility graph and the green exit sign is the destination. The arcs are bidirectional except for arcs {e,b} and {g,d}. That is, corner b could be a candidate for sign installation from the location of corner e; however, e is not a candidate from the position of corner b because e is not on the shortest path from b to the exit or any other corner. The explanation for corners d and g is the same.

After the visibility graph is constructed, the next task is to find the shortest paths from all corners to the exit and the corresponding sign installation locations, which should be done with a many-to-one shortest path algorithm. Note that

the visibility is bidirectional; therefore, if one corner can be seen by another, the opposite is also true, and the distances for both directions would be identical. As a result, instead of running a many-to-one shortest path algorithm to find the shortest paths from all corners to the exit, a one-to-many shortest path algorithm is sufficient to find the shortest paths from the exit to all corners. The only required change is inverting the unidirectional arcs in the graph before running the shortest path algorithm and reversing the result of the shortest paths afterward. The shortest path from a corner to the exit can be easily traced.

2.2 Finding the Best Sign Location

Although signs could be installed at all vertices in the graph, only some of them would be useful for guiding pedestrians. We find the "best" corner for a pedestrian standing at a cell. The "best" corner and all the predecessor corners are marked until we reach the exit. The procedure is repeated for the complete building space. To simplify this step, the continuous space is discretized into 40 cm×40 cm cells, which is the average space a person occupies (Burstedde et al., 2001). After all cells are calculated, we remove all the corners that were never marked and their associated arcs. Finally, we install signs at all the remaining corners. To simplify the presentation, we assume that the range of visibility of a sign is unlimited. This assumption can easily be relaxed by adding relay signs between two distant signs. A detailed algorithm that determines which corners require sign installation can be found in Chu (2011).

In the procedure describe above, a "best" corner must be selected for the cell under consideration. It seems reasonable that pedestrians would select the signs closest to them. However, this criterion does not generate the shortest route to the exit. For example, in Figure 1, if pedestrians B and E start the evacuation by following the signs closest to them (b and f, respectively), they end up following paths b-a-exit and f-b-a-exit, respectively. On the other hand, pedestrians A, C, and D should not follow the signs that are closest to them. Instead, they should follow signs c, d, and b initially and evacuate via c-exit, d-c-exit, and b-a-exit for their shortest paths. Thus, the correct criterion for selecting the "best" corner for a sign is to find the corner such that the distance from the corner to the exit plus the distance between the cell and the corner the smallest. In the figure, these "best" corners selected for installing signs are colored red and their evacuation direction information is represented by the short blue arrows. In practice, this criterion does not cause too much confusion when there is only one exit because all the visible signs for a pedestrian should be pointing in the same direction and the pedestrian can determine the correct direction to move. For example, it should be evident for pedestrian D that b is the sign to follow because signs b, e, and f are all pointing to the left and, moreover, e and f both point to b. The remaining problem is how to ensure that pedestrians follow the "best" signs, which may not be as obvious as the closest ones to them. Additional information can be provided by measures such as text, color, and special signs visible only from a certain position. The appropriate equipment and technology to achieve this will be the subject of future research.

3. DYNAMIC EVACUATION GUIDANCE

The pre-determined, static emergency guidance introduced in Section 2 provides only static information of evacuation routes to exits and do not respond to the real-time situations. In the cases of large-scale evacuation, these evacuation routes are likely to be congested because a large number of pedestrians attempt to leave the hazardous areas at the same time. To address this problem, this paper further proposes a complementary method for planning dynamic emergency evacuation guidance to support the static guidance.

The technique of digital image processing is one of the key components in the identification of congestion in the event of evacuation. Because digital images are composed of pixels, it is required to convert the building under consideration into squares of equal-sized cells, which is identical to the discretization adopted in Section 2.2. Indeed, the model accuracy could be affected due to the discretization; it is emphasized that reducing the cell size is still possible if higher accuracy is required.

3.1 Identify congestion areas

Various studies have successfully adopted the techniques of image/video processing for pedestrian tracking and detection. For example, Hoogendoorn et al. (2003) and Helbing and Johansson (2007) are capable of detecting the positions of the pedestrians in a specific area. It follows that macroscopic measures such as density can also be calculated. They further combined various algorithms from different fields to extract the microscopic characteristics such as speed of each pedestrian over time. Therefore, the technologies of positioning the pedestrians in buildings are readily available and the spatial distribution of pedestrians that will be required in the follow procedures can be obtained through these techniques without difficulties.

The pedestrian simulation shown in Figure 2 is used to explain the problem of relying only on the static guidance in emergency evacuation. In the figure, the black areas represent the obstacles and the pedestrians are represented by gray areas. Stairways connecting to the ground floor are the exits and are marked with exit signs. To explain the methodology in detail, a 30 m×40 m space is selected in the lower right part of the figure and the following discussions will be focused on this area. As the selected area shows, the pedestrians are moving from north and west to leave the floor via the stairway following the static guidance. There are two sources of bottlenecks caused by the static guidance: pedestrians from north pass the same ticket gate to access the exit and all of those from west use the narrow space between the wall and a column. Because the

pedestrians follow the static guidance and all of them are taking the shortest paths, significant congestions are formed at the two bottlenecks. Without the dynamic guidance, the alternative routes are ignored and the evacuation process could be delayed.

The concept of the identification of congestion areas is treating the spatial distribution of the pedestrians as a binary image (i.e., black and white). Each pixel is equivalent to a small square of space, i.e. a cell, in the building. A congestion area implies a group of cells crowded with pedestrians and jamming and clogging are forming. Therefore, in terms of digital image processing, congestion can be identified by finding objects in a binary image converted from a pedestrian distribution. The standard procedure for identifying objects in image processing includes noise removal, erosion, and dilation.

When a pedestrian is moving without any pedestrians in the adjacent cells, it is clear that the pedestrian is able to walk freely and thus no congestion exists. In the sense of digital image processing, it is equivalent to a single dot in the image and can be seen as a noise. Because these scattered dots are not of interest for congestion identification, a noise removal algorithm can be used to eliminate them from the consideration. In this study, the commonly used *median filter* algorithm is adopted for this task. A median filter scans a neighborhood and uses the median value for all pixels in the neighborhood to replace the value of the pixel in the center of the neighborhood. This study selects a typical 5×5 neighborhood. Because the cell size chosen for this research is 40 cm×40 cm, the meaning of the selection is that if there are at least 13 persons in a 4 m^2 space (0.16 m^2× 25, equivalent to the density of 3.25 persons per m^2), the center cell of the space is considered congested. The threshold of 3.25 persons per m^2 is consistent with the jamming density reported in Jin (2002), which is 3.5 persons per m^2. Figure 3(a) and Figure 3(b) show the effect of a median filter. After the processing, pedestrians not in the congestion areas are removed from the image and only pedestrians in congestion areas remain. However, it can be seen from the figure that many small gaps and holes exist and theirs shapes are rather irregular. Because the planning of the guidance adopted in this paper depends on the polygonal obstacles and to avoid overly complicated dynamic guidance, it would be more effective if the identified areas have more regular shapes, preferably concave polygons; therefore, more processing is required.

After the step of noise removal, the next task is to search for major congestion areas with simple shapes in the facility. In the terminology of image processing, it is equivalent to finding objects of interest in an image, which can be done by smoothing out object outlines, filling small holes, and eliminating small projections in the image (Umbaugh, 2005). The common operations include erosion and dilation. Erosion shrinks objects by eroding their boundaries to simply their shapes in an image and dilation expands the objects for the loss of size in the step of erosion. By operating erosion and dilation in sequence, the objects with simpler shapes can be identified. When it is applied on the spatial distribution of pedestrians, the irregular shapes of small groups of pedestrians are smoothed out. Therefore, the planning of the adaptive guidance would not be affected by these relative small congestion areas. Figure 3(c) and Figure 3(d) show the effects of erosion and dilation respectively, and the results are the congestion areas that will be considered in the following procedure of adaptive guidance design. Finally, it should be emphasized that the parameters in the image processing algorithms determine the size and number of congestion areas. The appropriate parameters for different scenarios of emergency evacuation could be different and more research would be required for this topic.

3.2 Dynamic guidance

The main concept of the adaptive guidance is to consider the congestion areas identified above as virtual obstacles. A new static guidance considering both the original obstacles and the update-to-date congestion areas as obstacles is generated with the method proposed in Section 2. Due to the additional obstacles, the shortest paths to the exits and the optimal guidance would be different. By comparing the routes suggested by the original guidance system and the adaptive guidance, the required information to instruct the pedestrians to bypass the congestion areas can be determined. The procedure can be explained by Figure 3(a) and the congestion areas identified in Figure 3(d) are drawn in Figure 3(a) for comparison. As explained above, the pedestrians are moving toward to the exit from west and north. It can be seen from the pedestrian simulation shown in Figure 4 that the alternative guidance (arrows in the figure) instructs the pedestrians to bypass the congestion areas. One of the practical ways for implementing this adaptive guidance is to deploy staff members at appropriate locations and guide the pedestrians to use the less congested routes with vocal or gestural instruction. However, the mechanisms of providing the dynamic guidance is not specified in this study and still need more tests and experiments.

4. CONCLUSIONS

This paper has examined the design of the static and dynamic evacuation guidance system in complex building spaces. The static guidance designed with the proposed methodology has the following properties. First, at least one sign is visible from any point in the building; that is, all pedestrians are covered by the system. Second, each sign indicates the direction to the next sign via the shortest path to an exit. Most importantly, the system guides pedestrians to their closest exits via the shortest paths.

This paper further proposes a complementary method for planning dynamic emergency evacuation guidance to support the pre-determined, static guidance that does not respond to the real-time situations. Using the techniques of

digital image processing, the congestion areas in the building can be identified. By considering these areas as virtual obstacles, the dynamic guidance that instructs the pedestrians to take the alternative routes and bypass the congestion can be generated.

Acknowledgements:

The authors acknowledge the travel grant from the Center for Urban Earthquake Engineering (CUEE) in Tokyo Institute of Technology and the support from the National Science Council of Taiwan through research grant NSC 99-2628-E-008 -007.

References:

Ahuja, R. K., Magnanti, T. L., and Orlin, J. B. (1993). Network Flow: Theory, Algorithms, and Applications. Prentice-Hall, Inc.

Burstedde, C., Klauck, K., Schadschneider, A., and Zittartz, J. (2001). Simulation of pedestrian dynamics using two-dimensional cellular automation. Physica A, 295, 507–525.

Chu, C.-Y. (2011). "Optimal emergency evacuation guidance design for complex building geometries." working paper.

de Berg, M., Cheong, O., van Kreveld, M., and Overmars, M. (2008). Computational Geometry: Algorithms and Applications. Springer-Verlag, New York, NY, USA, 3 edition.

Golledge, R. (1999). Wayfinding behavior: Cognitive mapping and other spatial processes. Johns Hopkins Univ Pr. 16

Helbing, D. and Johansson, A. (2007). "Dynamics of crowd disasers: An empirical study." Physical Review E, 75, 046109–1–046109–7.

Hoogendoorn, S., Daamen, W., and Bovy, P. (2003). "Extracting microscopic pedestrian characteristics from video data." Transportation Research Board 2003 Annual Meeting CD-ROM.

Jin, T. (2002). "Visibility and human behavior in fire smoke." SFPE Handbook of Fire Protection Engineering, P. J. DiNenno, ed., National Fire Protection Association, Quincy, MA, USA, 3 edition, chapter 2-4, 2–42–2–53.

Umbaugh, S. (2005). Computer Imaging: digital image analysis and processing. CRC Press.

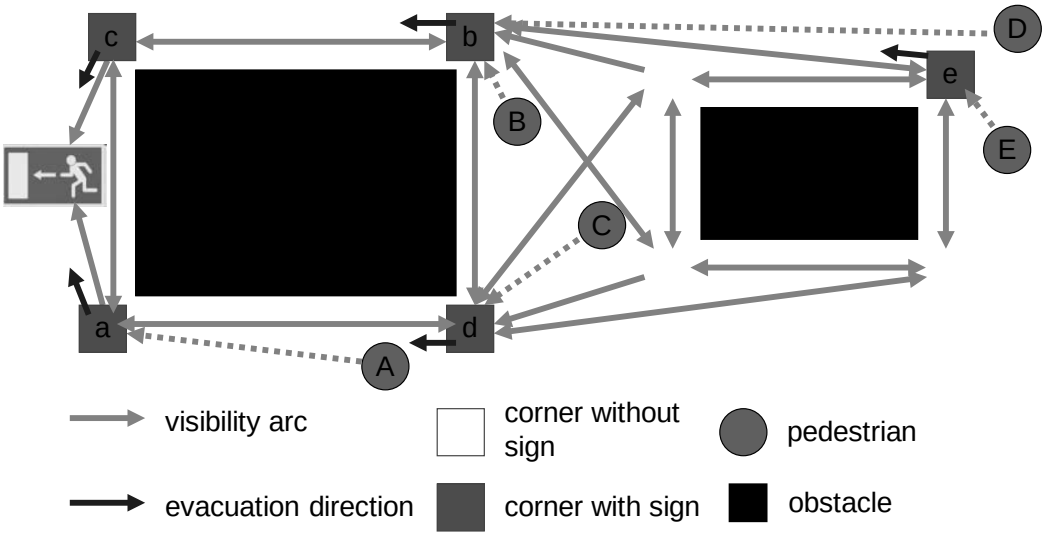


Figure 1. Visibility graph and sign installation

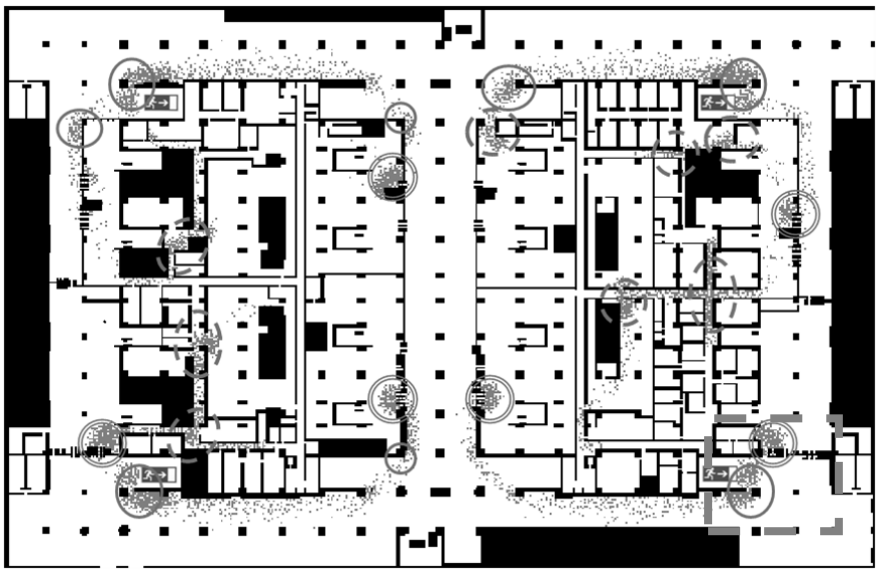
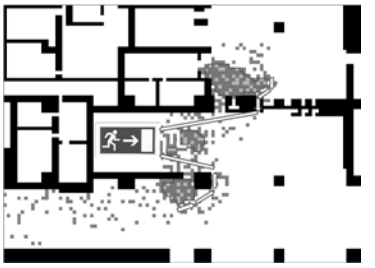
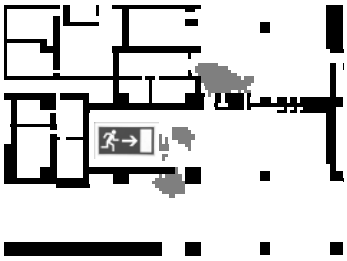


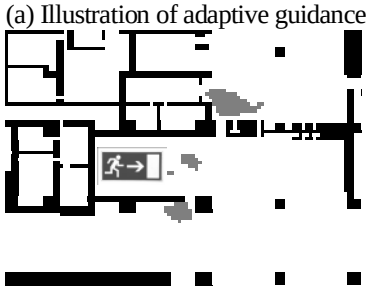
Figure 2. Building layout and simulation under only static guidance



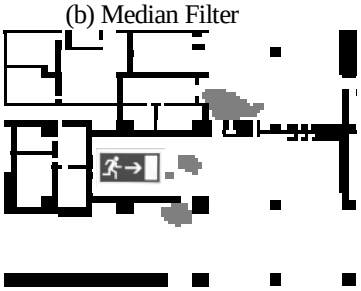
(a) Illustration of adaptive guidance



(b) Median Filter



(c) Erosion



(d) Dilation

Figure 3. Congestion detection and dynamic guidance

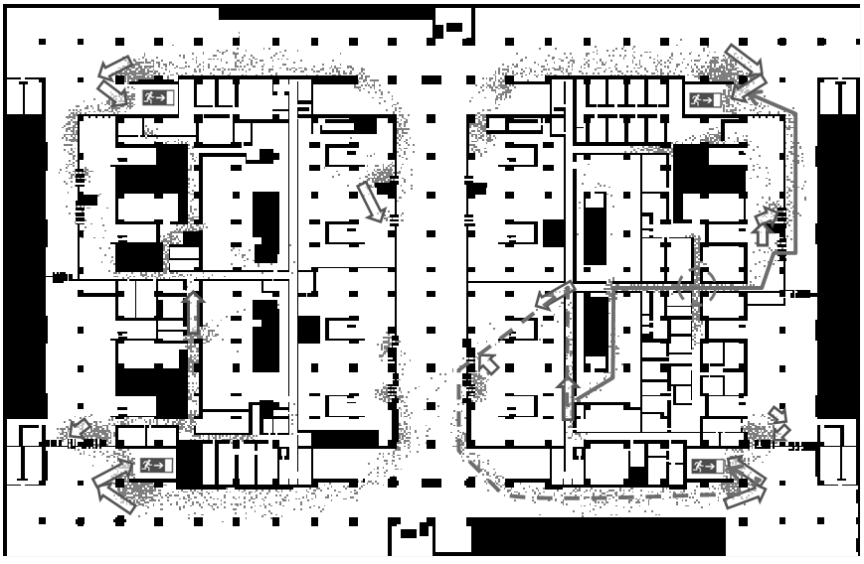


Figure 4. Simulation under both static and dynamic guidance

8CUEE CONFERENCE PROCEEDINGS
8th International Conference on Urban Earthquake Engineering
March 7-8, 2011, Tokyo Institute of Technology, Tokyo, Japan

RESIDENTS ADAPTATION OF POST DISASTER HOUSING: THE ROLE OF PHYSICAL ENVIRONMENT FOR SOCIAL INTERACTION

Syam Rachma Marcillia

Graduate Student, Department of Built Environment, Tokyo Institute of Technology, Japan
syam.r.aa@m.titech.ac.jp

Abstract: In this paper, physical adjustment of Java 2006 post disaster housing is investigated to understand its influence to the social interaction by examining and analyzing residents` usage, adjustments and attitude toward the housing. Two case studies for self-built and donated post disaster housing were investigated. An intensive and comprehensive onsite fieldwork research was conducted not only by encompassing questionnaires and interviews but also observation of residents' activities as well as physical changes they made to the original donated dome houses and site plan. The results suggested that residents tends to built their self-built housing to satisfy their needs of social interaction with others in the house while still maintain their privacy. Even in a restricted dome donated housing, the residents have the ability to be adapted to the physical environment misfits by adjusting their physical and behavior aspects in order to accommodate and maintain their previous social lifestyle. However, flexibility and open ended design in physical built environment would give an advantage in their critical transition to the new environment.
.

1. INTRODUCTION

Housing reconstruction efforts were made by many parties, NGO, government, etc after tsunami (Aceh, 2004) and earthquake (Java, 2006) disasters. But large scale of emergency development in a short time without cultural sensitivity resulted in rejection of ill planned and designed settlement. On the other hand, some community based reconstruction housing get a good response because of its open ended design that facilitate the cultural needs. These highlight the importance of understanding cultural background in the design of a dwelling

Social behavior is one of the important cultural backgrounds in Indonesia dwellings and Java specifically. For Javanese, a house is living environment that represent the philosophical concept of the society itself.

In previous researches, traditional `margersari` housing and other public housing consist of so called `core house` , the room pattern is `guest room`, bedroom` and kitchen. (Ikaputra, 1992). Most of the `core housing` alteration start with the expansion of double/triple size of `guests room` which is a `social space` then bedroom.(Yoyok Subroto, 1993). Another finding is the phenomena of 'guest area` appearance in temporary tents and house right after Java 2006 earthquake (Fig. 1a and 1b. Even their needs of functional room (bedroom, kitchen, etc) is not yet fulfill, but the importance to facilitate social behavior to be a part of the society is express and actualize through the activity in `guest room`. These show the importance of social factors in the Javanese dwellings.

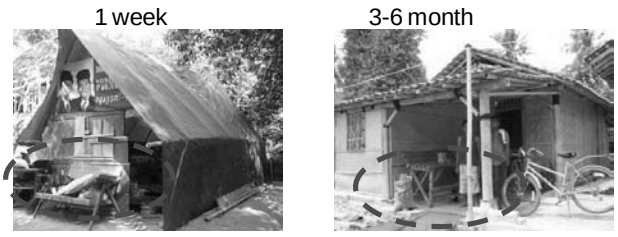


Figure 1: 1a and b Guest area appearances in temporary Java post disaster dwellings

There had been studies on how social behavior affect Indonesia domestic space (Java studies specifically). Some focused on how social interactions and its meaning influence the morphology of traditional dwellings (Tjahjono, 1989; Revianto, 1997) and others on its influence in the present non-traditional dwellings, such as public housing (Yoyok, 1993) or urban houses (Yulyta, 2008). Even though cultural changes in the society accompany the change in house, social behavior apparently still have influence in Indonesia dwellings. Correspondently, it is believed in this study also that the physical environment have influence to facilitate or inhibit certain social interaction that are necessary for the residents in Java 2006 post disaster housings.

In defining dwelling (housing), one can not only compare the physical artifacts encounters (Rapoport, 2005). Different culture had different perception and actualization of their dwelling. For most Javanese people, dwelling settings not only consist in the core house itself, but also the surrounding wells, streets, etc. as social space that accommodate various social behavior. In this study, data on physical setting as well as residents' behavior in self-built

and donated post disater housing are interpreted in the emphasis of the personal-social interaction activities to extract clearer basic relation between the social meanings, ideal, values with dwellings usage.

2. RESEARCH METHOD

Post disaster housing physical adjustments and residents' activities pattern was investigated as activities pattern can be 'the most useful entry point' for relating culture with the built environment (Rapoport, 1969). Two approaches were taken to analyze relationship between physical setting and social interaction behavior:

(A) The spatial development and adjustment for satisfying social interaction in constraint dwellings for both self-built and donated post disaster housing.

(B) The behavior adjustment and evaluation of mis-fit spaces in unchangeable dome donated post disaster housing.

2.1 Overview of Study Area

Two case studies were conducted according to the approaches above. First case is the Java earthquake 2006 self-built post disaster dwellings in three sub-villages of *Ketonggo, bawuran and Tegalrejo*、*Yogyakarta*. Two integrated surveys were taken within 2 years in order to see the development of temporary house to permanent house. In first survey, 39 respondents were chosen based on houses' condition after the earthquake where most houses destroyed and the permanent post disaster houses are rebuilt by themselves or based on their own design. Second survey targeted same respondents but only 33 respondents were re-surveyed.

Second case is donated dome post disaster housing in *New Ngelepen, Yogyakarta* . After Java earthquake May 27th 2006, in the original *Ngelepen* village, almost 50 houses were demolished by catastrophic landslide and the area declared as a geographically unbuildable land. As a result, the residents were relocated to *New Ngelepen* post disaster settlement, situated about 1,5km from the original village.

The *New Ngelepen* introduced house clusters site plan design where every 12 houses form a block that shared sanitation, electricity, public toilet/washing area and approach pathways. Dome monolithic with a hemispherical roof and a circular plan were introduced with concrete cast as a single and integral structure as the donated post disaster houses. The diameter of the house is 7 meters, two stories, with the total area about 38 square meters. The development of the houses began in October 10, 2006, and started to be occupied at the end of April 2007. These unique unchangeable dome house design and different settlement type from residents' original housing was investigated to understand its influence to residents' social interaction within the first 3 years occupancy. A total of 68% of the residents in 34 occupied dome houses were interviewed.

Both conditions are considered as 'constraint dwelling' because there is a change of situation from their previous 'preferred' living environment to their 'temporary' restricted condition. Table 1 shows the details of two case studies.

Table 1 Detail Description of Case Studies Areas

case	Java Post disaster dwellings		Dome Housing
Resident ethnic	Javanese 100%		Javanese 100%
Status	Owner 100%		House owner 100% Land borrower
Dwelling Design	Self-built post disaster temporary and permanent house build by self-design cognition		Donated dome housing with unchangeable limited size & differ design cognition with original house
Area type	Rural area, Yogyakarta, Java 3 sub villages (Ketonggo, Manggung and Tegalrejo). First survey obtained 39 data, only 33 data were re-attained.		Rural area, New Ngelepen, Yogyakarta, Java From total 71houses, only 51 lived in
Time survey	*First survey* in Nov.-Dec. 2006	*Second survey* in Nov.2008	August 2009

2.1 Data Questionnaires and Interview

Questionnaires, observation and in-depth interview with the residents were attained with the help of Gadjah Mada University volunteers. Each team consists of 2 people, one person was asked to sketch the house plan while the other interviews the resident. In Japan case, residents were interviewed and asked to draw their own house plan. Information acquired as follows:

a. Background
- Residents: age, sex, family, occupation, income, etc.
- House: structure, house age, land status, etc.

b. House plan: room space, size, etc

c. Space usage
- Personal activities in space which include: *personal biological needs* (eating, sleeping, etc), *entertainment* (watch TV, relaxing, etc), *work* (study, etc) and *household routines* (cooking, washing, etc).
- Interpersonal activities which include: location and behaviors in accepting different guest types in the house and interaction and frequency with neighbors.

d. Cognition of space on front/back, hidden/seen, public/private, flexibility, etc.

e. Evaluation of house, outdoor space and neighborhoods space (for dome housing)

3. RESEARCH RESULTS AND DISCUSSION

3.1 Importance of guest area and social interaction

From the survey in self-built post disaster housing 95% of the residents values traditional social behavior. Accepting guest activities in the house occurs 41% for everyday occasions and 90% residents involved in community gathering and accept large gathering guests in their house. Similar situations happen in dome post disaster housing. Approximately more than 95% for both heads of household and spouses said that they participate in community activities with their own willingness, while only less than 5% feel obligated to participate and null for no participation. High participation to community activities is supported by their perception on the importance of the value and existence

of community activities in their neighborhood. Approximately 65% head of household and 57% of spouses response is A "I feel that community activities are very important" and approximately only about 34% for both heads of household and spouses said that "they are neutral, don' t really have certain feeling". Unfortunately the incapability of dome house design to facilitates certain social interaction behavior results in the usage of outer space of the house and neighborhood as the `guest area` or `incidental social interaction space`



2.a Self-built housing



2.b dome housing

Fig.2 Accepting guest in Java 2006 post disaster housing

In self-built post disaster housing case where both temporary and permanent house is currently use by the residents, guest area is one of the earliest function that move to permanent house (Fig.3) . Expansion from temporary houses to permanent houses indicates the need of guest room increases by 5 times its original size and 3.6 times its original total room number (Fig. 4). Room modification also shows that it is important to have a separate formal guest area in the house (Fig.5). The expansion and separation tendency of guest area have relevant founding with public housing complex in Yogyakarta where most `core house` alteration cases started with the expansion of guest room to the front area and had doubled its original size (Yoyok, 1993). However, total room number and addition of bedroom modification is still the highest overall adjustments which also indicate a high need of private space although its average room size actually decreases (Fig.5).

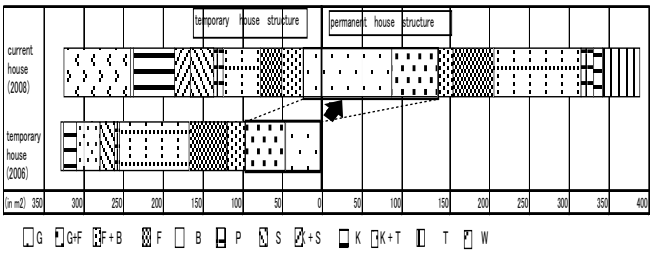


Figure 3 Size & function changes in self-built temporary to permanent

sub village	Ketonggo							Manggung							Tegalrejo													%	
Modif./Ques.	2	3	4	5	7	8	9	2	3	4	5	6	7	8	1	2	3	4	5	6	7	8	9	10	11	12	13	14	15		
G out to in				■	■													■	■			■			■	■			■	20.7	social space
Mf+B separate							■										■												■	24.1	
G+F separate	■	■				■		■		■	■			■					■			■		■			■		■	55.2	
addition B			■	■	■	■		■	■	■			■	■		■	■	■	■	■	■	■	■			■	■	■	■	79.3	private space
addition Pr			■			■			■				■			■	■	■	■	■	■	■	■			■	■	■	■	27.6	
addition S											■	■				■		■			■									24.1	
K out to in				■	■			■	■	■	■					■	■	■	■	■	■	■	■	■	■	■				58.6	support space
T out to in				■	■			■	■	■	■					■	■	■	■	■	■	■	■	■	■	■				51.7	
addition W	■							■																						21	

G = Guestroom Mf= Multifunction (Guest+Familyroo F= Familyroom B = Bedroom
Pr = Prayerroom S = Storage K = Kitchen T= Toilet/bath room W = Workroom

Figure. 5 Room modification in self-built housing

3.2 Cognition of spaces in dwellings

Cognitions of space are much related with the arrangement and allocation of 'self'(personal) and 'other'(interpersonal) space. Space pattern development in self-built housing also showed the existence of private/public spaces in simplest condition (Fig 6). These related to findings in Java case where residents' cognition of front/back area is associated to hidden/shown area to other people (Fig.7). This supported by previous research on traditional dwellings where front of house is outwardly-oriented domain where domestic prestige displayed in form of status differences and formality in meeting others (Revianto, 1997).

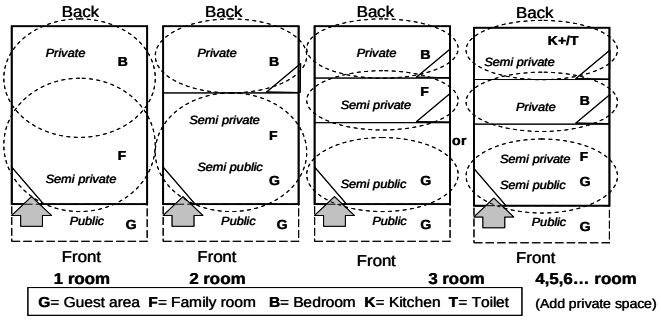


Figure 6 Development of private/public space pattern in self-built post disaster housing

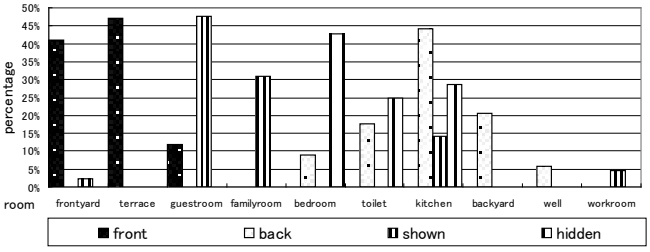


Figure 7 Spatial cognition and preferences in self built housing

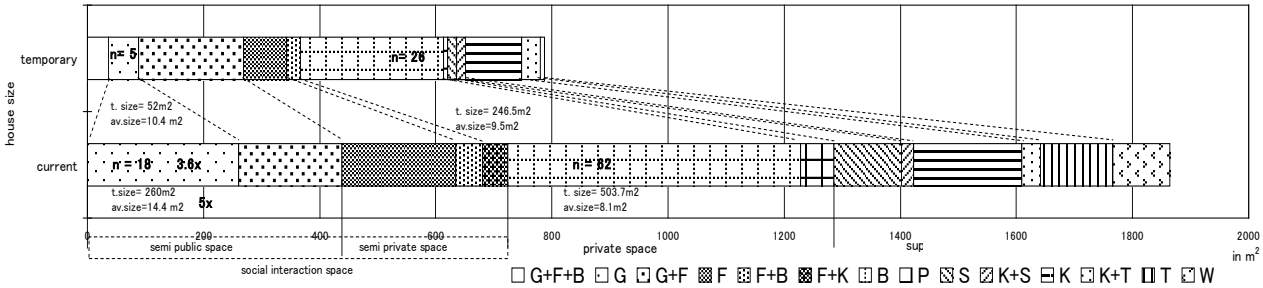
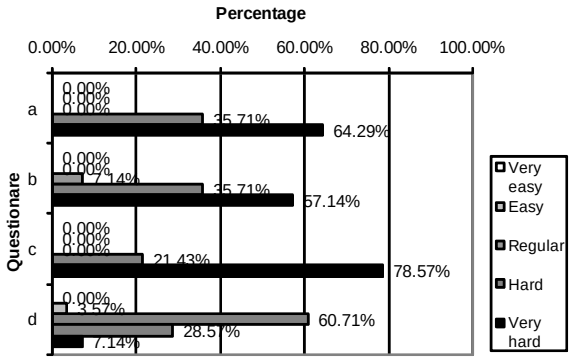


Figure 4 Size expansion from temporary to permanent in self-built houses

3.3 Misfit in Dome housing for Social Interaction.

From the residents‟ evaluation to their dome house design shows that "very hard" capability of residents to *"to change the order/function of the rooms"* (64%), *"to expand the room"*(57%), and *"to change the location of the doors or windows"* (76%). Only 61% for capability *"to give rooms addition"* shows *"regular"* capability (Figure 8). we can make a conclusion that flexibility in dome houses is one of the most complicated problems for the residents except for capability *"to give rooms addition"* although in reality it is also hard for the residents *"to make additional room that compatible with original donated house"*.



a. Easiness to change the order/function of the rooms.
b. Easiness to expand the original room
c. Easiness to change the location of the doors or windows.
d. Easiness to give rooms addition

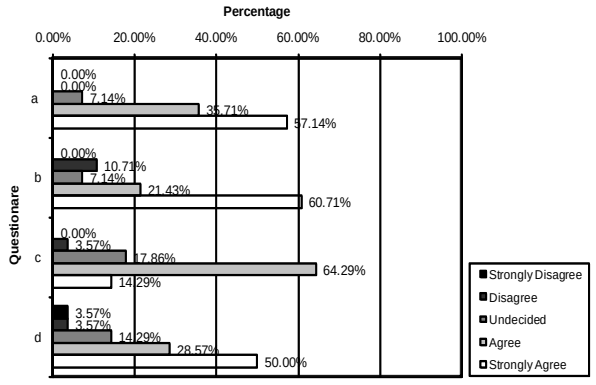
Figure 8 Residents' evaluation for dome house design flexibility

In Javanese traditional housing, a `guest room` hold an important role for social interaction within the house. The house contains both `self` and `others` domains that are interrelated (Revianto,1997). Inflexibility of the dome house design to provide enough social interaction space in the built-in less than 10m2 `guest area` had resulted in the usage of surrounding outer space or even the neighborhoods space.

Unfortunately, dome house outdoor site plan also have some misfit relating to its used as an extension space that facilitates the social interaction. Evaluation for house outdoor space shows *"very agree"* attitude toward statement *"it is better for each house to have private approach pathway"* (57%), *"there is not enough yard/room in the house to have social gathering"* (61%) and *"it is important to have a front terrace but the space available is not possible to made one"* (50%), while only 64% shows *"agree"* attitude toward statement *"each house should have own pathway from house to public toilet area"* (Figure 9).

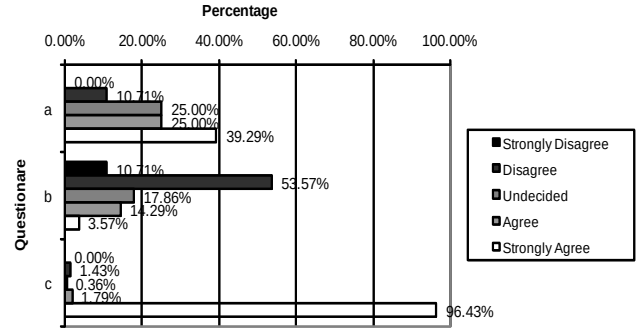
From house outdoor evaluation showed that there is not enough space for need of front terrace not large gathering space. Moreover, house outdoor design elements such as pathways that were design to promote social interaction infact only intrude their privacy.

Evaluation for neighborhood streets shows that more than 96% of the residents are *"very agree"* to the statement *"the house front yard space should be larger instead of larger street for better social gathering space"*. However evaluation for statement *"streets inside the neighborhood should not be too large so that cars and motors not easily pass by" were "disagree"* by more than 53% (Figure 10).



a. It is better for each house to have private approach pathway.
b. There is not enough yard/room in the house to have social gathering.
c. Each house should have own pathway from house to public toilet/washing area

Figure 9 Residents' evaluation for dome house outdoor space



a. neighborhood streets are too dangerous to leave children play by themselves.
b. streets inside the neighborhood should not be too large so that cars and motors not easily pass by
c. The house front yard space should be larger instead of larger street for

Figure 10 Residents' evaluation for dome house neighborhood

From the residents‟ evaluation we can presume that house outdoor space hold an important role in their social interaction activities. Typical Javanese rural dwellings had large yard that function not only for planting and drying laundry but as drying harvest crops, burning garbage, drying the corkwood, etc. It also hold important role as a socialization space. In daily life, housewives like to chats with the neighbors while looking after their little children playing in the house yard. Occasionally large social gathering are also done in house yard area such as wedding, trah‟ gathering, etc.

In *New Ngelepen*, the limitation of house inner and outdoor space made the residents use neighborhood‟s streets for their social activities. From the interview and observation, during the day little children were playing freely on the streets, while housewives chat on side of the streets. The streets were also used as social gathering spaces. Near neighborhood entrance, main street was painted as badminton field where youths and man gather in the evening to play badminton or just to hang around. Social gathering

that used to be facilitated in original dwellings but not possible in dome houses, now performed on the streets such as ruwahan", etc. Even once the streets were closed for one of the resident' s wedding ceremony.

4. CONCLUSIONS

In java 2006 self-built post disaster dwellings, physical changes and development from temporary to permanent such as size and room number expansion, space modification, function changes, show that guest area is inevitably an important social interaction space to be provided in the house. On the other hand, total room number and addition of bedroom is still the highest overall adjustments which also indicate a high need of private space. These show that both needs of social interaction space and private space are simultaneous exist. The duality spheres in the house also actualize in their cognition of spaces.

Respondents' cognitions of space are much related with the arrangement and allocation of 'self'(personal) and other'(interpersonal) space and how it is interrelated in spatial arrangement of fixed and semi-fixed elements of the house.. Although self-built and dome housing cases are different in physical conditions but both residents` cognition of private/public have the same tendency and this also related to their front/back, hidden/shown spaces for interaction.

In mis-fit and unchangeable spaces, social interactions are still facilitated and preserved by the respondents although it means that private space is intruded. As consequences some behavior adjustments are needed to be taken such as appointment of time and preparing of incidental `guest area`. Since dome house design was misfit and unchangeable then house outdoor space facilitates some of its social function. In some cases where certain activities cannot be done inside and outside the house space then neighborhood spaces such as streets, etc. will bear bigger role in facilitating these social interaction needs.

This research has once again highlighted the importance of social behavior in Javanese dwelling even at its constraint situation. Meaning, values and ideals of social behavior are reflected on their cognition of spaces in the dwellings as well as their behavior adjustments. It is necessary that even in constraint dwelling such as post disaster housing need to consider social behavior importance as culturally sensitive design for reconstruction recovery. Flexibility and open ended design in physical built environment would give an advantage in their critical transition to the new environment

Acknowledgements:

The author acknowledged support from G-COE Center for Urban Earthquake Engineering (CUEE) in Tokyo Institute of Technology for funding this research. A sincere thanks to Prof. Ryuzo Ohno for his support and guidance for this study. Last but not least, thanks to all Gadjah Mada Architecture students who helped me to do field survey and interviewed and to the people in New Ngelepen who are willing to help in this research.

References:

Bayulke, Nejat (1983). *Lessons to be Learned from Relocation of Villages and Use of Prefabricated Houses in Post-disaster Housing in Turkey*. Proceedings of the Seminar on Socio-Architectural Aspects of Housing in Earthquake-Prone Areas of Turkey, Ankara, the Scientific & Technical Research Council of Turkey Building Research Institute.

Birkman, J. et.al. (2007) *Rapid Vulnerability Assessment in Sri Lanka Post-Tsunami Study of Two Cities:Galle and Batticaloa.* SOURCE **(**Studies of the University: Research, Councel, Education). Paffenholz, Bornheim,Germany: Publication Series of UNU-EHS Vol.7/August 2007.

Dikmen, Nese (2006) *Relocation or Rebuilding in the Same Area: An Important Factor for Decision making For Post Disaster Housing Project.* Department of Architecture, Suleyman Demirel University

Feinstein, David (2008) *Energy Psychology in Disaster Relief*. The journal *Traumatology* (Vol 14, Issue 1, March 2008). IF Research Group, University of Montreal .

Ikaputra(2008). *Response to Localize the Imported Culture.* Proceeding of the 14 World Conference on Earthquake Engineering October 12-17, 2008, Beijing, China

Saraswati Titien. *"The Development of Architecture in Yogyakarta: Are the Reconstruction Buildings of Post-Earthquake Responsive?"*. Paper presented in the National Seminar of the Development of Architecture in Indonesia, Diponegoro University, Semarang, Indonesia, May 05, 2007.

8CUEE CONFERENCE PROCEEDINGS
8th International Conference on Urban Earthquake Engineering
March 7-8, 2011, Tokyo Institute of Technology, Tokyo, Japan

DEVELOPMENT OF A METHOD FOR DETECTING VULNERABLE AREA BY URBAN TEXTURE

Xue Ma[1] and Ryuzo Ohno[2]

1) Graduate student, Dept. of Build Environment, Tokyo Institute of Technology, Japan
2) Professor, Dept. of Build Environment, Tokyo Institute of Technology, Japan

Abstract: Accompanied by the high-speed urbanization, as a seismic active country, China has a great deal of requirements on disaster mitigation and prevention system. Especially after 2008 Wenchuan Earthquake, more and more attention has been attracting to this topic. Disaster mitigation parks as an essential part of the whole disaster mitigation system, which strengthen the capability of disaster prevention or mitigation measures such as evacuation, emergency action, urban safety, providing temporary home for victim of calamity. As an initial step in the development of disaster mitigation park system, to detect dangerous area and its vulnerability is the primal issue which can reflect the requirements for improving the areas in a city. The present research starts with learning the experiences of Japanese disaster mitigation parks system, and then compares the city conditions between Japan and China to discuss the necessity of development of a new system for Chinese city. In order to search those potential vulnerable urban areas of different type and to detect what might be their weaknesses under various damage situations, a measurement method of the "circulation spaces" is developed. Through a case study applied for the different areas in Tianjin city, this analysis method is proved to be useful for describing the vulnerability of each area.

1. INTRODUCTION

1-1 Background

China is a seismic active country. Since the beginning of the last century, China has had nearly 800 quakes with a magnitude of over 6 on the Richter scale. Especially after 1950, we experienced five very big earthquakes which caused big losses of life and property.

There are two features of damage caused by earthquakes in China. One is large number of fatalities caused by low building quality and low evacuation efficiency. The other is slow recovery after earthquake caused by the problems like no emergency responding system, the lack of rescue system and too long time taken in rebuilding.

This research focuses on developing a method for detecting dangerous area as an initial step towards establishing a planning method of disaster mitigation park system in China.

1-2 Definition of disaster mitigation park

The term of disaster mitigation parks was first used by Japanese. The original definition of disaster mitigation/prevention park is that those parks and sites which strengthen the ability of disaster prevention or mitigation when earthquake and secondary disasters happen, life and possessions are threaten. Here the ability of disaster prevention or mitigation means evacuation, emergency action, urban safety, temporary home for victim of calamity and homeless.

2. NECESSITY OF DEVELOPING DISASTER MITIGATION PARK SYSTEM IN CHINA

2-1 Japanese disaster mitigation system

Japan lies in one of the most seismically active areas of the world, and Japan already set up a serial of measures which consists of a comprehensive system facing to the earthquake. With relation to this research, the current disaster mitigation park system and vulnerability evaluation system in Japan could provide us useful suggestions.

The disaster mitigation park system as a part of the urban evacuation system basically built on the existing park system. It is classified as: 1) wide regional disaster mitigation center, 2) regional disaster mitigation center, 3) wide-regional evacuation site, 4) temporary evacuation site, 5) neighborhood evacuation site, and 6) evacuation path, green buffer from its function and scale.

The vulnerability evaluation system is applied for promoting preparations for earthquakes by enabling of the local government and the residents to understand the vulnerability of the community and providing basis for

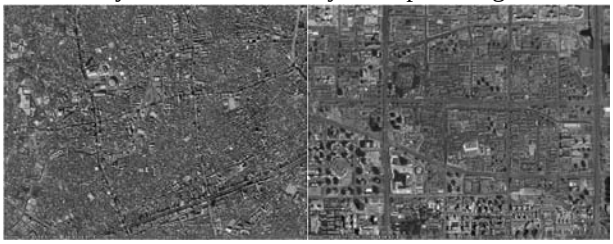


Figure 1 Typical urban texture in Japan and China

re-development under the aim of disaster-resistant city. This system in Tokyo, for instance, is applied to measure each district based on the basic information of building classification, aggregation and the type of ground structure. In accordance with the most threats in Tokyo, safety levels under dangers of building collapse and the spreading of fire are measured and ranked from low to high as level 1 to level 5. Finally, the integrated level of vulnerability is evaluated.

2-2 The disaster mitigation park system considering Chinese urban conditions

According to the physical and social conditions, different urban situation bring different demands and requirements on urban construction. Different cities may face with different potential dangers when earthquakes happen, consequently, the demands on disaster mitigation park spaces will be diverse also. When we consider setting up the disaster mitigation park system in Chinese city, it can't be simply copied from the Japanese system no matter how successful it performed when earthquake occurred in a Japanese city.

Compare with Japanese big cities, there are several significant differences in characters of Chinese cities which are shown in Table 1.

Table 1: Characteristics of urban areas in China and Japan

Characteristics	China	Japan
Building structure in vulnerable urban areas	Concrete/brick	Wooden-frame
Building type in vulnerable urban areas	6 floors/ high-rise (>18)	Low-rise (<10)
City Road pattern	Wide avenue divide urban area into superblock	Continuous pattern consist by dense and narrow street
Evacuation spaces system	Unplanned and inadequate	Planned
Concerned dangers	Building collapse Debris Safety during evacuation	Spreading of fire Building collapse

The network of road in Chinese city tends to use wide avenues as main road as contrasted with dense but narrow streets in Japan, which provides an easy identification of "super block" divided by it.

2-3 Process of developing disaster mitigation park system

Table 2: The green system in China is similar with one in Japan in terms of the system structure.

	CHINA	JAPAN		Area	Disaster Mitigation Park
Residential Pak	Group park	Block park (街区公園)	R=250 A=0.25	A>0.05	neighborhood evacuation site
	Street park	Neighbor park (近隣公園)	R=500 A=1-2	A>1	temporary evacuation site
	Zone park	Zone park (地区公園)	R=1000 A=4		
Urban Basic Pak	Urban park	Integrate park (総合公園)	A=10-50	A>10	wide-regional evacuation site
		Sport park (運動公園)	A=15-75	A>50	
Urban Extensive Park	Extensive park	Extensive park (広域公園)	A>50		regional disaster mitigation center
National Park	National Park	National Park (国営公園)	A>300(ha)		

There are two essential issues of developing a disaster mitigation park system: in one hand, the current green system and its relationship with disaster mitigation parks, from the comparison, connections can be made by its size and scale; And in the other hand, what is the demanding of disaster mitigation parks in target area?

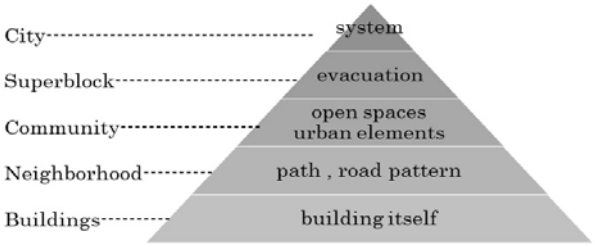


Figure 2 Urban elements and contents to be considered in different scales

We try to detect the dangerous area by examining urban elements in different scales. We classify the urban elements into 5 categories according to their scale: the buildings, the neighborhood, the community, the superblock, and city.

This research is basically concentrated on the scale of building and neighborhood. City has different sub-areas. In China the big avenues divides up the urban area into highly-recognizable sub-areas, the spaces inside one sub-area or between several areas usually show the similar road-pattern, building density and building size even height, thus show a curtain urban texture. We can recognize the difference in urban texture, and divide the urban area into sub-area, and based on each different features find out their potential dangers, and then we can propose a countermeasure by setting up the disaster mitigation parks system.

3. DEVELOPMENT OF A METHOD FOR EVALUATING CIRCULATION SPACE

3-1 Definition of circulation space

In this research, the state of circulation space is brought forward as criteria for evaluation of danger. It combines both outward and inward direction of movement, i.e. evacuation and access as well as usable spaces for staying. It means free movement or passage in a circuit inside particular area.

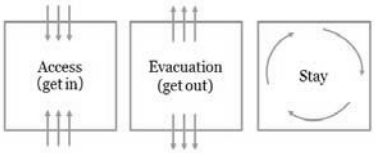


Figure 3 Three functions of circulation spaces

3-2 Measurement of space between buildings

After choosing target area, we draw network diagram

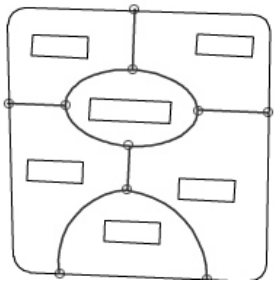


Figure 4 Network diagram

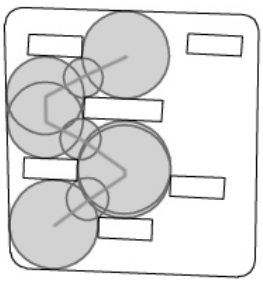
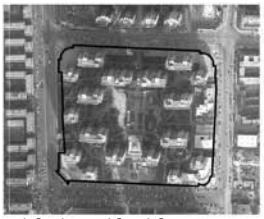


Figure 5 The circles drawn in the site plan

showing all possible circulation routes on the site plan in order to measure circulation spaces. Firstly, we identify the spaces where the junctions of network exist and draw circles of maximum size that fit into the identified spaces. Then the centre of circle is defined as a node of circulation route. Between two adjacent nodes, we draw circles of maximum size in the inflection point fit the spaces between buildings. With this method, we can describe the changing width of circulation spaces along the routes.

4. AN APPLICATION OF THE METHOD

4-1 Choosing target areas



A:High-rise residential area
Area: 8.37 ha/ Average height:60m/ Built year: after 1990/ Concrete



B:New low-rise residential area
Area: 8.16 ha/ Average height:15m/ Built year: after 1990/ Brick with shear wall



C:Old low-rise residential area
Area: 7.23 ha/ Average height:18m/ Built year: before 1990/ Concrete



D: Concession area
Area: 8.31 ha / Average height:10m/ Built year: after 1860/ Masonry



E: Traditional area
Area: 0.87 ha/ Average height:4m/ Built year: before 1990/ Masonry

Figure 6 Satellite image and circulation network

We choose the city of Tianjin, China as target city, which experienced the 1976 Tangshan earthquake with fatalities over 250,000. Five residential patterns are distinguished and picked out by different typical urban texture: high-rise building area (HB), new low-rise area (NL), old low-rise area (OL), historical concession (HC) area and old traditional (OT) area.

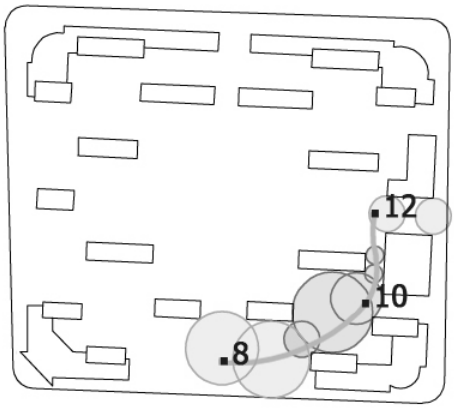
From each are, one residential site around 8ha in Chinese standard was chosen as a sample for applying the method.

4-2 Network in the target site

The outermost edge of buildings is connected to form the boundary of the chosen site. All the possible routes are marked including the city roads which pass through the site.

4-3 Measurement of circulation spaces

Category of width (radius) is set every 3 meter difference, the length of the route that belongs to each radius category are recorded.



	LL(total)	Radius
8	0	27.28
a1-f	26.04	12.86
10	29.01	28.42
a1-h	19.52	74.57
a1-i	21.06	95.63
A1-j	12.79	108.42
12	28.43	136.85

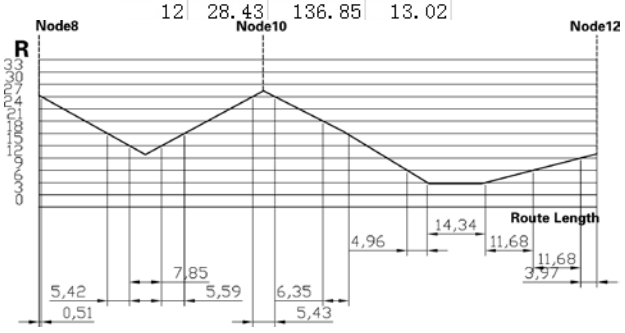


Figure 7 An example of measurement procedure of circulation spaces

from node 8 to 10 and 10 to 12 on the site A. At the node 8, the radius of the circle is 27m and towards node 10, it once reduce to 12m in the inflection point then increases up to 28m at the node 10.

Afterthen, the distribution frequency of the length that belongs to each category in all routes are collected as shown in Figure 8, the cumulative length of different radius is obtained in Figure 9.

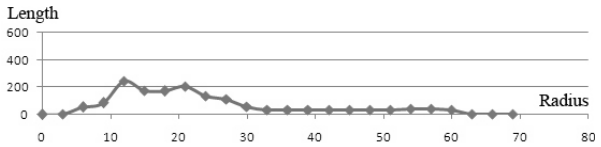


Figure 8: Analysis of circulation spaces on area A: Distribution frequency by radius

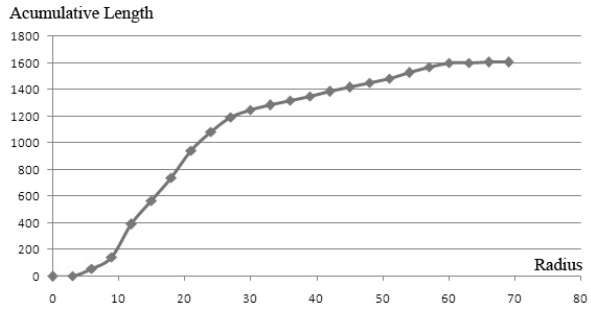


Figure 9: Analysis of circulation spaces on area A: Cumulative length by radius

4-4 Variation of circulation space under different building damage

We take the situation of surface damage and structure damage into consideration. Debris drop from the buildings have uncertain effecting area. Assuming that the width "W1"of surface damage effecting area is 10% of building's height, to judge if each circulation path still possible to be passed through. Once there is one point which radius is less the W1, then the whole route need to be removed. As Figure4-5 shows, there is one point with a radius 5.72m (<W1: 6m)on path 10-12, the circulation spaces locate on this path can't be taken into calculation.

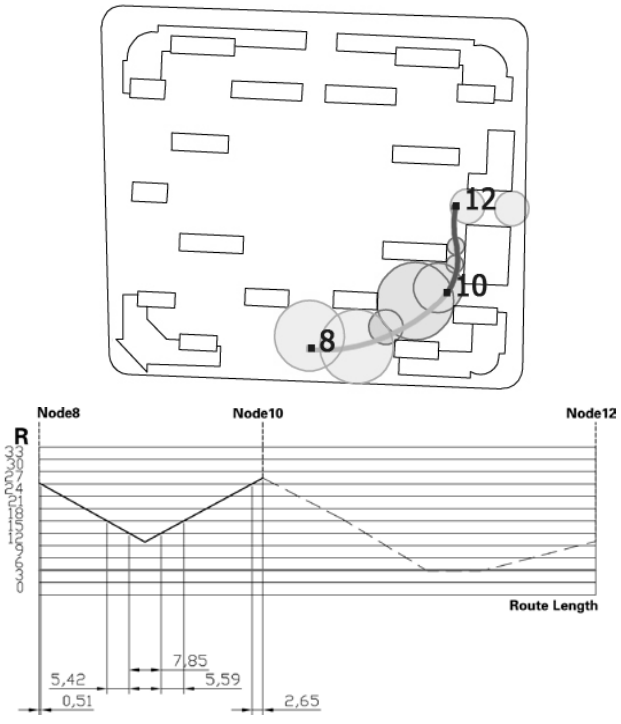


Figure 10: Analysis of circulation spaces of each path under damage situation under damage situation

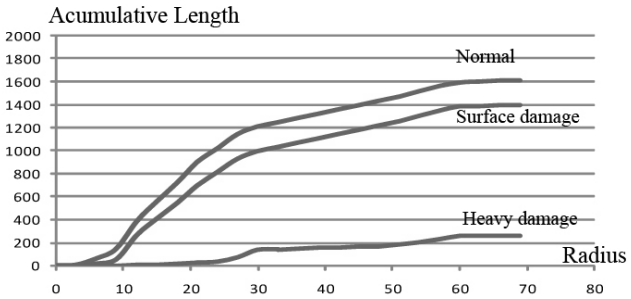


Figure 11: Analysis of circulation spaces of area A: Cumulative length of different radius

Using the same method, the situation of heavy damage takes width "W2" of effecting area which assumed as 30% of building's height. In the analysis of most areas, the surface damage just makes little influence but heavy damage triggers bigger influence.

4-5 Evaluation of circulation spaces for various usage

It is important that some circulation spaces over certain width can be used for temporary gathering for people or collecting or distributing emergency goods and materials. Besides, the situation on access of `fire engine also is can't be ignored. Even the fire is not easily to spread in Chinese city, fire engine is still significant towards the high risk of inside fire and rescue of trapped person. The same method can be used for measure those usable spaces. 4 meter (the minimal width for fire engine), 9 meter (two lanes for vehicle according to residential district index) and 18 meter are set separated as three standards.

4-6 Comparison of the target areas

Data under different damage situation of five areas are compared, showing the characters of each different type as Figure 12

Area (HB) possesses the widest circulation path. The total length is around 1600m. But it changes a lot when the heavy damage happen, only very limit but wide spaces in the center of the area are left.

Area (OL) performs best around in all the areas, the

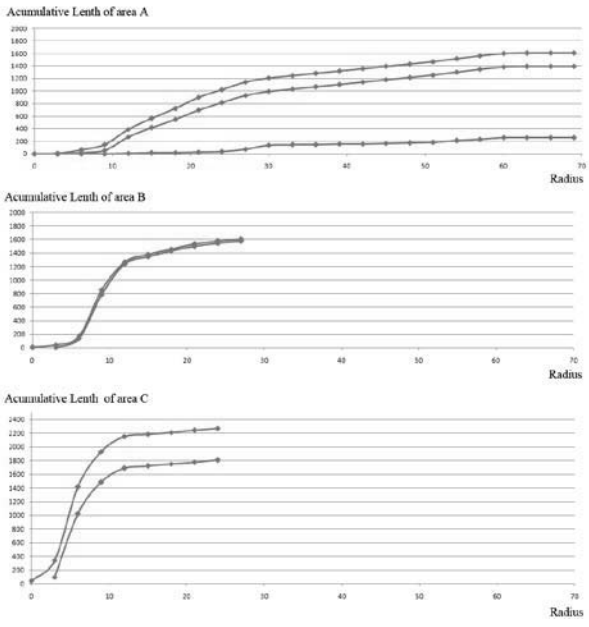




Figure 12: Analysis of circulation spaces on area A to area E: Cumulative length of different radius

circulation spaces are not affected when surface damage happen and just changes a little when heavy damage come. The total length is around 1600m.

The tendency of area (NL) is quite similar to area (OL) in the layout. But the influence of heavy damage present more distinct. However, its length exceeds almost 1/3 than area (OL) in the number of 2300m.

The (TC) area shows a dense pattern which is shown in the graph with a more than 2800m length. The width of circulation spaces is not more than 17m which changes a lot than those areas we mentioned above.

The (OT) area is quite special compare with all the other areas. It shows extremely dense and long circulation spaces. Several districts are picked up to make the analysis for it. Biggest radius is less than 5m while the total length reaches almost 5000m.

The comparison of usable circulation spaces under different damage level also shows a distinctive result in Figure13 .That blue express the normal situation, red shows the situation of surface damage as well as the green one

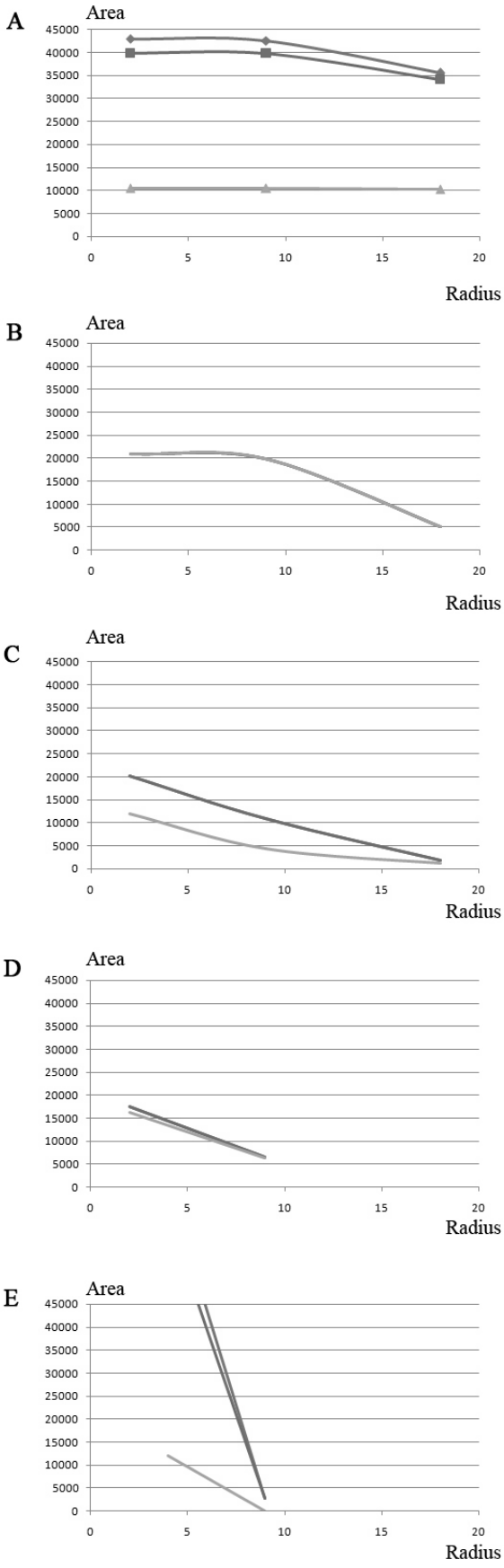


Figure 13: Analysis of usable spaces under different damage situation on area A to area E

shows the situation of heavy damage.

The horizontal axis indicates the certain width while the vertical axis states the area of usable circulation spaces.

Area (HB) has the biggest usable spaces on each certain width under normal state and surface damage. Area (NL) shows little changes under all situations. Although the usable spaces in area (OL) is not so abundant, but it suffers little decrease under damage. In area (OT), it doesn't look so good, Spaces wider than radius 4.5m is hard to be found and usable spaces over 4 meter declines to a great extent that means there is almost impossible for fire engine access when heavy damage happen.

5. CONCLUSION

This thesis is a part of the research that provides a basis for developing a planning method of disaster mitigation park system in China. The analysis result of measurement is expected to provide a numerical basis for the circulation spaces that is important criterion for judging the vulnerability in different areas.

Based on the result, suggestion and planning can be proposed directly towards the different urban areas. Later, the same method will be applied again to testify how the circulation spaces improve after the planning.

Acknowledgements:

The author acknowledged support from G-COE Center for Urban Earthquake Engineering (CUEE) in Tokyo institute of Technology for supporting this research. Last but not least, Thanks to Dr. Miura Hiroyuki and Ms. Soh huichen who helped me to process the satellite image.

References:

Oguchi, K. (2003), "Parks in case of disaster in Tokyo, Construction and plan of rescue and shelter (in Japanese)," *journal of the Japanese Institute of Landscape Architecture*, **66**(3), 208-212

Tsukada,S. (2008), "Analysis of the evaluation structure in design a ted manager system of urban park," *Journal of the Japanese Institute of Landscape Architecture* **73**(631), 1923-1928.

Matsuda,N. (2003), Urban park planning from the point of view of the safe and secure urban environment(in Japanese), *Journal of the Japanese Institute of Landscape Architecture*, **66**(3), 180-184

Asada,T, (2004)," Research on the condition of disaster prevention park sand it's directivity in Hiroshima (in Japanese)„" *Architecture institute of Japan*, **27**, 737-740

Gohta, M. (1990), "A Morphological Study of Open Space in Urban Space: Part 1 Quantitative Analysis using the Largest Empty Circle Method (in Japanese)," *Proceeding of annual conference*

Yasuyuki Yamada Japan Meteorological Agency, "Disaster mitigation system in Japan (2) - Earthquake and Tsunami Warning/Information in Japan."

8CUEE CONFERENCE PROCEEDINGS
8th International Conference on Urban Earthquake Engineering
March 7-8, 2011, Tokyo Institute of Technology, Tokyo, Japan

SOCIO ECONOMIC DISASTER RISK ASSESSMENT OF ASEAN COUNTRIES

Sushil Gupta[1] and Jerry Velasquez[2]

1) General Manager, Risk Modeling and Insurance, Risk Management Solutions, India
2) Regional Coordinator, United Nations International Strategy for Disaster Reduction, Asia Pacific, Thailand
velasquezg@un.org

Abstract: The countries of the Association of Southeast Asian Nations (ASEAN), which comprises Brunei, Cambodia, Indonesia, Laos, Malaysia, Myanmar, Philippines, Singapore, Thailand, and Vietnam, are geographically located in one of the most disaster prone regions of the world. Often these disasters transcend national borders and overwhelm the capacities of individual countries to manage them. Most countries in the region have limited financial resources and physical resilience. Because of this high vulnerability and the relatively small size of most of the ASEAN countries, it will be more efficient and economically prudent for the countries to cooperate in the areas of civil protection, and disaster preparedness and prevention. A synthesis report on ASEAN member states disaster risks was developed at the country and regional levels. This review also analyses trans-boundary disaster risks and their effects; projected losses in the absence of mitigation measures (Average Annual Loss, AAL and economic losses for different probabilities of exceedance), climate change assessment, population growth, economic development, and urban expansion. Disaster Risk assessments for all the countries and the region have been prepared and the review concludes with recommendations on the way forward for ASEAN disaster risk reduction.

1. INTRODUCTION

The countries of the Association of Southeast Asian Nations (ASEAN), which comprises Brunei, Cambodia, Indonesia, Laos, Malaysia, Myanmar, Philippines, Singapore, Thailand, and Vietnam, is geographically located in one of the most disaster prone regions of the world. The ASEAN region sits between several tectonic plates causing earthquakes, volcanic eruptions and tsunamis. The region is also located in between two great oceans namely the Pacific and the Indian oceans causing seasonal typhoons and in some areas, tsunamis. The countries of the region have a history of devastating disasters that have caused economic and human losses across the region. Almost all types of natural hazards are present, including typhoons (strong tropical cyclones), floods, earthquakes, tsunamis, volcanic eruptions, landslides, forest-fires, and epidemics that threaten life and property, and droughts that leave serious lingering effects.

Typhoons are the most prevalent hazard in the region, causing destruction to human life, buildings, agriculture and infrastructure alike, while causing flooding and landslides/mudslides. The region provides compelling evidence of the destructive power of such disasters. For example, the recent tropical cyclone Nargis of May 2008 in Myanmar killed over 133 thousand people, affected over 2.4 million people and caused an estimated economic loss of over $ 4 billion. Over 600 thousand hectares of agriculture land was flooded, killing about 50 per cent of the draught animals. In the same year, on June 21, 2008, Typhoon Fenghsen in the Philippines killed 573 and affected at least 4 million people in just four hours. In October 2009, cyclone Pepang (Parma) in the Philippines killed 539 people, affected 4.5 million and caused an estimated economic loss of $592 million.

Some of the major disasters of recent times in the region are: the December 26, 2004 Indian Ocean tsunami, September 16, 1990 Luzon earthquake (Philippines), May 26, 2006 Yogyakarta earthquake (Indonesia), June 1991 volcanic eruption of Mount Pinatubo (Philippines), 2005 (Thailand), and 1997 (Vietnam) droughts, September 2009 cyclone Ketsana (known as Ondoy in the Philippines), catastrophic flood of October 2008, and January 2007 flood (Vietnam), September 1997 forest-fire (Indonesia) and many others. Climate change is expected to exacerbate disasters associated with hydro-meteorological hazards.

Often these disasters transcend national borders and overwhelm the capacities of individual countries to manage them. Most countries in the region have limited financial resources and physical resilience. Furthermore, the level of preparedness and prevention varies from country to country and regional cooperation does not exist to the extent necessary. Because of this high vulnerability and the relatively small size of most of the ASEAN countries, it will be more efficient and economically prudent for the countries to cooperate in the areas of civil protection, and disaster preparedness and prevention.

With the aim of reducing ASEAN's vulnerability to the risk of disasters, the World Bank, United Nations International Strategy for Disaster Reduction (UNISDR), through the Global Facility for Disaster Risk Reduction (GFDRR), and in collaboration with other international partners have started support for implementing the ASEAN Agreement for Disaster Management Emergency Response (AADMER) to promote sustainable development in ASEAN region. The AADMER is a regional legally binding agreement that binds ASEAN Member States together to promote regional cooperation and collaboration in reducing disaster losses and intensifying joint emergency response to disasters in the ASEAN region. AADMER is also ASEAN's affirmation of its commitment to the Hyogo Framework for Action 2005-2015 (HFA). The HFA, endorsed by 168 countries, is coordinated by UNISDR to provide nations and communities the roadmap to disaster-proof the significant development gains.

To support ASEAN, the World Bank, UNISDR and ASEAN secretariat signed a tripartite Memorandum of Cooperation (MoC) on disaster risk reduction (DRR) in 2009. The MoC lays a framework for technical support from the World Bank and UNISDR to help the ASEAN secretariat formulate and implement strategies and action plans for disaster risk reduction and management. The objectives of this program include (i) building ASEAN's capacity in the areas of disaster risk reduction and climate change adaptation; (ii) mobilizing resources for the implementation of DRR initiatives in ASEAN; and (iii) helping ASEAN policy-makers gain knowledge of effective and practical ways to reduce disaster risks.

As part of the work of the tripartite MoC, the objective of this assignment is to develop a synthesis report on ASEAN member states' disaster risks by carrying out a desk review of already available reports, studies, maps, analyses and assessments regarding disaster risks at the country and regional levels. This 'desk review' also analyses trans-boundary disaster risks and their effects; projected losses in the absence of mitigation measures (Average Annual Loss, AAL and economic losses for different probabilities of exceedance), climate change assessment, population growth, economic development, and urban expansion. Disaster Risk assessments for all the countries and the region have been prepared and the review concludes with recommendations on the way forward for ASEAN disaster risk reduction.

2. METHODOLOGY

This synthesis report on ASEAN disaster risks has been prepared by carrying out a desk review of already available reports, studies, maps, analyses and assessments regarding disaster risks at the country and regional levels within the scope of the tripartite Memorandum of Cooperation (MoC) on Disaster Risk Reduction (DRR), between ASEAN Secretariat, the UNISDR and the World Bank. The MoC on DRR is a part of ASEAN Agreement for Disaster Management Emergency Response (AADMER), which is in line with the Hyogo Framework for Action 2005 – 2015 (HFA). The objective of this synthesis report is to carry a simplified quantitative risk assessment to determine the social and economic loss potentials and the likelihood of occurrence of different hazards at country and regional levels.

The review analyses and assesses disaster risk at country and regional levels, focusing on natural hazards such as earthquakes, tropical cyclonic storms (typhoons), floods, landslides, tsunamis, droughts, and forest fires. It analyses trans-boundary disaster risks (common risks) and their effects, and projected losses in the absence of mitigation measures (Average Annual Loss, AAL and economic losses for different probabilities of exceedance). The review also analyses climate change assessment, economic developments, and urban expansion and rural development in ASEAN countries.

ASEAN consists of the ten following countries - Brunei, Cambodia, Indonesia, Lao PDR, Malaysia, Myanmar, Philippines, Singapore, Thailand, and Vietnam. It covers a total land area of 4.48 million sq km and has a population of 593 million (2009). The People's Republic of China borders the region to the north, the Pacific Ocean and Papua New Guinea to the east, Australia to the southeast, the Indian Ocean to the south, Bay of Bengal and Andaman-Nicobar Islands (India) to the west and India and Bangladesh to the northwest.

The ASEAN region is geographically diverse and includes high hills and rugged mountains, elevated plateaus, highlands, floodplains, coastal plains and deltas. It is home to large river systems such as the Mekong and Ayeyarwady, and major water bodies such as the Tonle Sap and Lake Toba, the latter being the largest volcanic lake in ASEAN region. Most part of ASEAN has hot and humid tropical climate, an exception being the mountainous areas in the Indochina Peninsula that experience a milder temperature and drier landscape.

A major part of the population in the region lives in riverine plains, delta and coastal plains. Hence, the most populous areas are subjected to periodic and extensive hazards such as flood, tsunami, and cyclone. Moreover, the unique geographic and climatic conditions make ASEAN one of the world's most vulnerable regions to disasters caused by natural hazards as well as climate change impact. Almost every year, powerful typhoons that cause flooding and landslides batter the region. In addition, the region faces risk from earthquakes, volcanic eruptions, tsunamis, and forest fires that threaten life and property, and drought that leaves serious lingering effects.

A review of the existing hazard, vulnerability and economic loss data at country level was performed. The

main data sources consulted include the CRED EM-DAT, ADRC, NGDC, GSHAP, MRC, WAMIS, DWR, Munich Re, World Bank, UNISDR, GAR, InTerragate, IFNet, and CCFSC, DESINVENTAR, country specific reports and research papers were also reviewed.

The socio-economic data was analyzed along with the mortality risk for various hazards to quantify the vulnerability (ISDR, 2009). As most of the data available in the public domain are related to disasters rather than hazard risk, this study relied on the Global Assessment Report (GAR) preview platform database (GAR, 2009) for mortality risk for various hazards such as earthquake, flood, landslide, cyclone and drought; GSHAP hazard data for earthquake and NGI hazard data for landslide. The GAR preview platform (http://preview.grid.unep.ch) has created spatial data for the entire world using simplified modeling techniques. The hazard risk data for the region was extracted from this global data and graded into four/five categories of very high, high, medium and low/very low for earthquake, flood, landslide, drought, cyclonic storm, and multi-hazards. The hazard risk data were analyzed along with grid based population data to assess the population exposed to various hazard risks.

To analyze risk profiles at country and regional levels, reported economic disaster data (1970-2009) have been used. However, for earthquake and tsunami (1900-2009), a longer duration of disaster data have been used. Analyses of projected losses in the absence of mitigation measures expressed in the form of average annual loss (AAL) and economic loss potential for selected probabilities of exceedance have been carried out.

3. KEY FINDINGS

3.1 Disasters

The disasters risk assessment analyses show that in terms of human casualties, cyclonic storms are the dominant disaster risk in ASEAN followed by earthquakes, tsunamis, floods, epidemics, landslides, droughts, volcanic eruptions and forest-fires. During the last 40 years (1970-2009), 1,211 reported disasters have caused over 414,900 deaths. Out of the reported disasters, 36 per cent were floods, 32 per cent were cyclonic storms, 9 per cent were earthquakes, 8 per cent were epidemics, and 7 per cent were landslides. Cyclones (storms) caused the maximum number of deaths: over 184,000, followed by earthquakes (114,000) and tsunamis (83,600).

3.2 Vulnerability

The social vulnerability (SV) ranking of each country was estimated based on the average number of people killed per year per million (relative social vulnerability). The analysis of disaster data for the period 1970-2009 shows that the average number of people killed per year per million for ASEAN region is 17.5. In Myanmar, the relative SV is more than 3.5 times that of Indonesia (the second highest). In terms of relative SV ranking, Myanmar has the highest ranking followed by Indonesia, Philippines, Thailand, Vietnam, Lao PDR, Cambodia, and Malaysia. Due to paucity of disaster loss data, the SV ranking could not be carried out for Brunei and Singapore. The quantitative risk assessment performed in this study confirms the following risk patterns for the ASEAN countries:

- Cambodia: floods represent the dominant risk followed by droughts
- Indonesia: forest (wild) fires, earthquakes and tsunamis, and floods represent the dominant risks followed by volcanoes, droughts, and landslides
- Lao PDR: cyclonic storms, and floods are the dominant risks followed by droughts
- Malaysia: floods are the dominant risks followed by forest fires, tsunamis, and cyclonic storms
- Myanmar: cyclonic storms are the dominant risk followed by tsunamis, floods and forest-fires
- Philippines: typhoons (cyclonic storms) are the dominant risk followed by floods, earthquakes; volcanoes, droughts, and landslides
- Thailand: floods are the dominant risk followed by tsunamis, cyclonic storms, and droughts
- Vietnam: cyclonic storms, and floods are the dominant risk followed by droughts, and landslides
- Brunei and Singapore: no disaster data is available

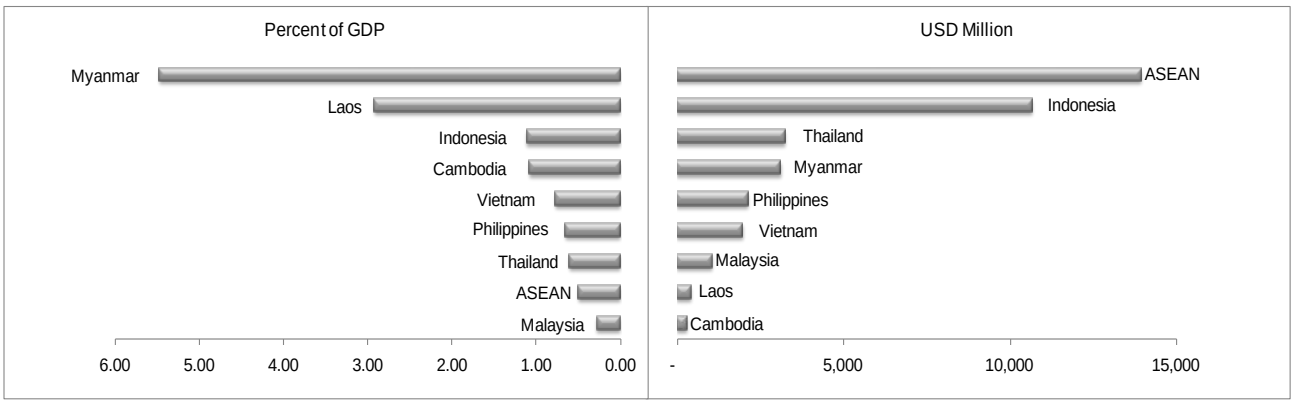


Figure A: Economic Loss Potential for annual probability of exceedance of 0.5 per cent

Disasters can have enormous economic consequences. The quantitative risk assessment performed in this study confirms that a catastrophic event with a 200-year return period (0.5 per cent annual probability of exceedance) would have a major impact on ASEAN countries' economies, some of which are already fragile. To gauge the potential economic impact, the economic vulnerability (EV) ranking of each country has been estimated in terms of likely economic losses that an event with a 200-year return period would cause as a percentage of that country's Gross Domestic Product (GDP PPP) (Figure A). According to this categorization, Myanmar has the highest EV ranking in the region, followed in descending order by Laos, Indonesia, Cambodia, Vietnam, Philippines, Thailand, and Malaysia.

Due to paucity of economic loss disaster data, the Average Annual Loss (AAL) and economic loss analysis for different probabilities of exceedance could not be carried out for Brunei and Singapore.

Urban areas are especially vulnerable to the adverse impact of disasters. Capital cities: Manila, Jakarta, Bangkok, Ha Noi, and Singapore are amongst the most populated cities in the ASEAN region and all are undergoing intense economic transformation. In terms of earthquake risk, Manila is at highest risk followed by Jakarta and Bangkok. In terms of flood risk, Manila is also at highest risk followed by Jakarta, Bangkok, and Ha Noi. In terms of tropical cyclonic risk, Manila is also at highest risk followed by Ha Noi, and Jakarta. In terms of overall risks from these hazards, Manila is at highest risk, followed by Jakarta, Bangkok, Ha Noi, Singapore, Kuala Lumpur, Naypyidaw, Phnom Penh, Vientiane, and Bandar Seri Begawan.

3.3 Climate Change Impacts

Climate change is considered as one of the most significant developmental challenges confronting ASEAN nations in the 21st century. According to the Intergovernmental Panel on Climate Change (IPCC, 2007) reports, the mean surface air temperature in Southeast Asia increased at the rate of 0.1 – 0.3°C per decade between 1951 and 2000. Following the global trend, the mean sea level is projected to rise by 40 cm on average by 2100 in comparison to 1990. Moreover, the region experiences decreasing rainfall and increasing sea levels (1–3 mm per year). The frequencies of extreme weather events like heat waves, heavy precipitation, and tropical cyclones have been increasing considerably. These climatic changes have brought massive flooding, landslides, and droughts in different regions and have caused extensive damage to property, assets, and human life. High concentration of population and intense economic activities in coastal areas, and a high dependence on agriculture and forestry in many countries of the region are making the situation more complex and may hinder the regions sustainable development.

Global Circulation Models addressing climate change do not present a uniform view of the impact of climate change on ASEAN as they have limited capabilities to forecast the present meteorological patterns. A high-resolution climate change model of the region appears to be more stable and predicts a temperature increase of 3 to 4 0C over the next 80 years.

Developing countries are especially vulnerable to climate change because of their geographic exposure, low incomes, and greater reliance on climate sensitive sectors such as agriculture. The cost of climate change in ASEAN could be as high as a 6-7 per cent loss in GDP by 2100 compared to what could have been achieved in a world without climate change.

4. WAY FORWARD

Based on the analyses, the review makes the following recommendations to reduce disaster risk in ASEAN:

4.1 Additional Analyses

Three levels of analyses are envisioned to refine the results presented in this report. These analyses should emphasize more on floods, typhoons (tropical cyclonic storms), and earthquakes and tsunamis, as they are the most damaging quick-onset disasters.

- Level 1: An analysis similar to this one based only on historical records should be repeated at a higher level of resolution. Instead of limiting the resolution of the analysis at the country level, a high-resolution grid (for example a 100-km grid) should be considered. Risk aggregation by hazard type and area would provide, at low cost, a much more refined picture of the risk than is offered by the present analysis.
- Level 2: On a second level, using the same methodology, worst-case scenarios should be considered for the highly populated cities. This analysis would provide a reasonable quantification of loss, given the occurrence of a particular disaster scenario. The uncertainty around the risk could then be bracketed by scientifically estimating the range of probability of occurrence of such scenarios. Such worst-case scenario studies can be used in preparation of city specific Disaster Management Plans (DMP).
- Level 3: On a third level, fully probabilistic analysis containing all the elements of standard risk analysis should be performed for the hazards and regions identified as high risk in levels 1 and 2.

Drought hazard should be addressed in the context of climate change and long-term adaptation strategies should be considered. Climate risk assessments study should merge traditional risk assessments with climate change assessments.

Use of Open Source Risk Models is recommended, in which probabilistic techniques are applied to the analysis of various natural hazards. At this level of analysis, hazard information is combined with exposure and vulnerability data allowing the user to determine the risk simultaneously on an inter-related multi-hazard basis. In recent years, several open source GIS-based multi-hazard risk platform has/are being developed. HAZUS-MH is a powerful risk assessment platform for analyzing potential losses from earthquakes, floods, and winds. CAPRA- Central American Probabilistic Risk Assessment is another GIS-based platform for risk analysis of earthquakes, tsunamis, tropical cyclones, floods, landslides, forest-fires, and volcanoes. HazSana'a and HazYemen are other two such open source GIS-based multi-hazard risk platform being developed for Sana'a city and Yemen country, respectively. These open source platform should build upon existing initiatives, with the objective of consolidating methodologies for hazard, exposure, and risk assessment, and raising risk management awareness in the region.

8CUEE CONFERENCE PROCEEDINGS
8th International Conference on Urban Earthquake Engineering
March 7-8, 2011, Tokyo Institute of Technology, Tokyo, Japan

SEISMIC RISK EVALUATION BASED ON DIGITAL MAPPING OF A ROMANIAN URBAN AREA

Ana-Maria Toma[1)] and Gabriela M. Atanasiu[2)]

1) Assistant Professor, M.Sc.(Eng), Ph.D. candidate, Multidisciplinary Centre of Structural Engineering & Risk Management, Technical University "Gheorghe Asachi" of Iasi
2) Professor, Ph.D., Multidisciplinary Centre of Structural Engineering & Risk Management, Technical University "Gheorghe Asachi" of Iasi
anamtoma@ce.tuiasi.ro, gabriela.atanasiu@gmail.com

Abstract: Natural disasters occur all over the world, regardless of the geographical region. A sustainable development of the built infrastructure of Romania needs a strategy of mitigating the natural disaster effects at country and region level, as stated in 2009 in a published report of United Nations Organization. This paper is presenting a risk evaluation methodology for the Iasi Municipality, a city of North Eastern Romania, characterized by an existing crowded infrastructure. The first step of research methodology is the F.E. analysis of specific classes of residential buildings widely used in Romanian cities. The structural models were subjected to Romanian earthquake scenarios, for monitoring their behavior for different degrees of degradation developed during their life span. The second stage of research is based on the evaluation of the structural vulnerability using the seismic risk index. The visualization of the specific risk of each structure in a selected urban sample is achieved by using NetSET software, a Geographic Information System, GIS, developed for Iasi municipality built infrastructure. The final results along with research study conclusions are useful to fully comprehend seismic vulnerability of the existing city building stock. This enables mapping the vulnerable areas affected by past earthquakes and also forecasting seismic risk, important features for decision makers.

1. INTRODUCTION

In order to help and support a community in managing an incoming disaster, it is necessary to understand and evaluate the risk that the potential danger holds. The process of risk assessment involves hazard assessment and vulnerability analysis. In the case of earthquakes, the seismic vulnerability represents the evaluation of the consequences that an earthquake has upon a community and the environment together with the time of response and recovery from the disaster (Wood et al. 2002).

This paper is presenting a risk evaluation methodology for the Iasi Municipality, a city of North Eastern Romania, characterized by an existing crowded infrastructure.

For the first step of the research methodology, the Finite Element Analysis of two specific classes of residential buildings was considered. The first type of structure is a four stories Load Bearing Masonry condominium (P+4 LBM) and the second one is a four stories building made of Precast Concrete Panels (P+4 PCP), as shown in Figure 1.

The second step of the research consists in evaluating the seismic vulnerability of the city building stock, based on

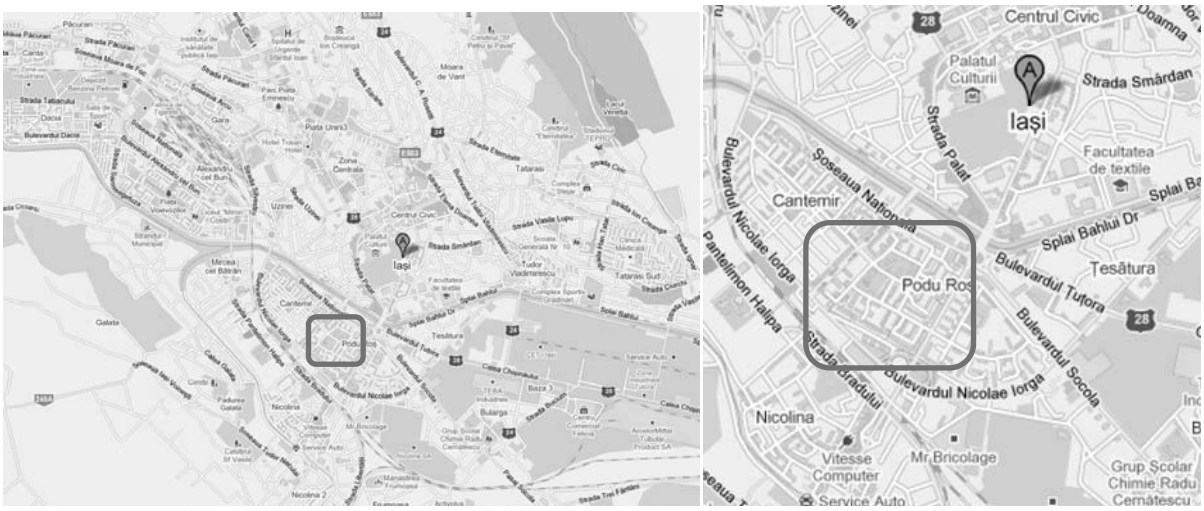


a) 4 stories Load Bearing Masonry condominium



b) 4 stories Precast Concrete Panel

Figure 1 Examples of structures frequently met in the urban areas in Romania, Iasi



a) General view of Iasi city, Romania b) Considered area sample

Figure 2 Selected urban sample for the city of Iasi, Romania, (www.maps.google.com)

the seismic risk index. For this purpose, the numerical models are subjected to different levels of degradations and their behavior to earthquake actions was closely monitored.

The visualization of specific risk of each structure in a selected urban sample, shown in Figure 2, is achieved by using a Geographic Information System (GIS) software. A GIS is an organized collection of hardware, software geographic data and personnel designed to efficiently capture, store, update, manipulate, analyze and display all forms of geographically referenced information (Lavakare and Krovvidi 2001). This methodology enables mapping the vulnerable areas affected by past earthquakes and forecasting the seismic risk, all important features for decision makers in case of disasters.

2. FINITE ELEMENT ANALYSIS

2.1 The Finite Element Models

The conventional design methods used in civil engineering are considered to be deterministic approaches. There is a wide range of applications of the deterministic method not only in civil engineering (Joshi and Mohan 2008) but also in weather forecasting and hurricane risk assessment (Emanuel et al. 2006). The deterministic approach of the evaluation is based on the modelling and numerical simulations using SAP2000 software, (Computers and Structures Inc. 2005).

In the case of the P+4 PCP, the materials used were C16/20 (NE 012-99) for the exterior walls and floors, C12/15 (NE 012-99) for the interior walls. The considered reinforcement was smooth stirrups made of OB37 steel (STAS 438/1-89) and ribbed bars for the tensile reinforcement made of PC60 steel (STAS 438/1-89).

In the case of P+4LBM, the material properties of the masonry are presented in Table 1. The values are in accordance with the Romanian design code CR 6-2006.

Shell elements were used to model the walls, floors and stair cases for both numerical models (Toma and Atanasiu 2010).

2.2 Analysis Cases

The analysis of the structures was made by subjecting the models to three types of actions: dead load, live loads and repetitive seismic loads. The loading cases were defined in accordance with Romanian standards, in agreement with Eurocode 0 (UTCB 2006).

The seismic actions have been introduced in the program in the form of time-history functions in terms of accelerations. The accelerograms chosen at this stage of the research were those corresponding to Vrancea earthquakes in Romania. A summary of the information with respect to the considered earthquakes is shown in Table 2 (Borcia 2007).

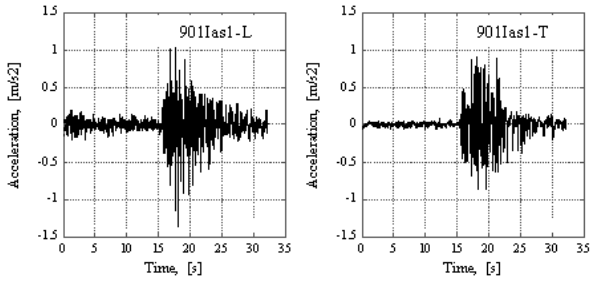
The earthquakes were chosen due to the fact that the considered types of structures were built starting from 1960 and are representative for the building stock for Romanian urban areas, as Iasi municipality.

Table 1 Material properties of masonry

Compressive Strength [MPa]	Modulus of Elasticity [MPa]	Poisson's Coefficient -
6.1	2870	0.2

Table 2 Earthquake scenarios considered in the present paper

No.	Earthquake Code	Station Code	Date:	Mw
1	771	-	1977.03.04	7.5
2	861	IAS2	1986.08.30	7.3
3	901	IAS1	1990.05.30	7.0
4	902	IAS2	1990.05.31	6.4
5	041	IAS4	2004.10.27	6.0



a) Longitudinal component b) Transversal component

Figure 3 The time history graphs for 1990 Vrancea earthquake recorded at the station IAS1 (Borcia, 2007)

Table 3 Classification of the structures based on the coefficient of degradation

Degradation state	Reference interval, δ_M
Minor degradations	0.0 – 0.2
Capital repairs needed	0.2 – 0.5
Irreparable	0.5 – 1
Total collapse	> 1.0

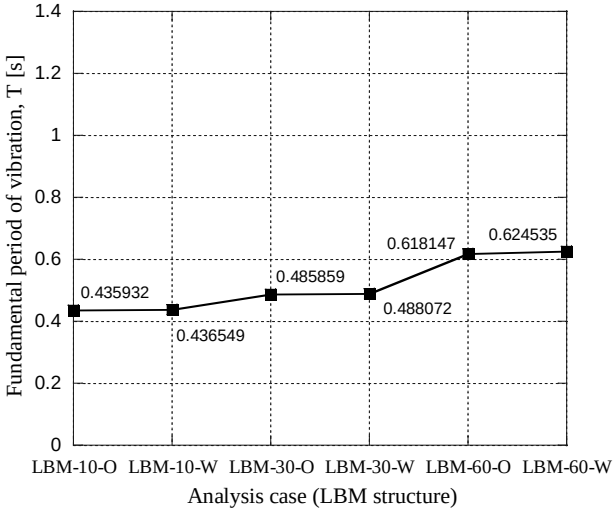


Figure 4 Variation of the fundamental period of vibration for the PCP model structure

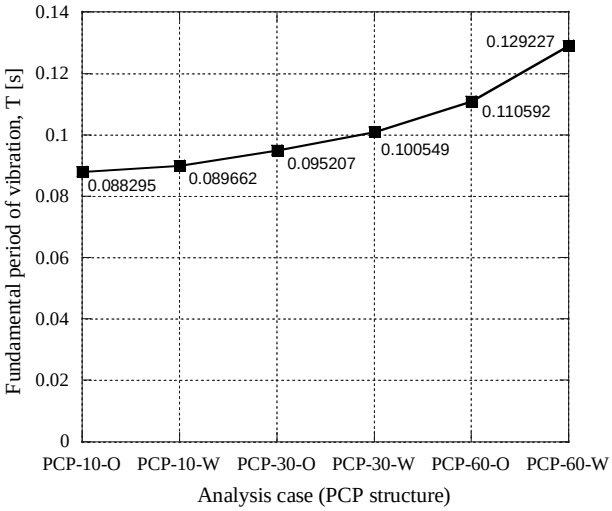


Figure 5 Variation of the fundamental period of vibration for the LBM model structure

An example of the longitudinal and transversal components of the time history graphs for a Vrancea earthquake, denoted as 901 (Table 2), is represented in Figure 3. The finite element program superposes the two components of the earthquake for a better representation of the real natural event.

The notations of the analysis cases are explained below for an easier understanding of the upcoming results. Each case has been denoted in the form: type of structure followed by a number and by a letter. The two types of structures considered in the analysis were LBM, load bearing masonry, and PCP, precast concrete panel, structures. The number following in the name of the analysis case indicate the percentage of damage considered for each case. Finally, the letter at the end of the analysis case name shows the location of the considered degradations: "O" for walls with openings (windows and doors) and "W" for all walls. For example, the analysis case denoted LBM-10-O refers to a load bearing masonry structure having 10% degradation in the walls with openings.

The main parameters of the present paper were the seismic loading scenarios, different degradation percentages applied to the structure as well as their assumed distribution in the numerical models. The considered degradation percentages were 10%, 30% and 60%. The behaviour of the structures under seismic excitations was investigated for two possible distributions scenarios of the degradations: the first scenario assumed that only the walls with openings were affected by degradations and the second scenario assumed that all the walls were affected by degradations. These degradations were introduced into the numerical models by means of stiffness modifiers (SAP 2000).

3. RESULTS AND DISCUSSIONS

3.1 Degradation Coefficient

The coefficient of degradation, equation 1, as defined by DiPasquale and Cakmak (1990), depends of the natural periods of vibration of the structure. The classification of the structures depending on the coefficient of degradation has been made according to the reference intervals shown in Table 3 (Patras and Patras 2002).

$$\delta_M = 1 - \frac{T_0}{T_{degr}} \quad (1)$$

where:

T_0 is the natural period of vibration of the structure in its initial state;

T_{degr} is the natural period of vibration of the structure in its degraded state.

The fundamental period of vibration for the LBM and PCP structures were 0.417 seconds and 0.085 seconds, respectively.

Table 4 Classification of the models from the first case study based on the degradation coefficient

Case study	δ_M	Degradation state
LBM-10-O	0.045	Minor degradations
LBM-10-W	0.046	
LBM-30-O	0.143	
LBM-30-W	0.147	
LBM-60-O	0.326	Capital repairs needed
LBM-60-W	0.333	

Table 5 Classification of the models from the second case study based on the degradation coefficient

Case study	δ_M	Degradation state
PCP-10-O	0.032	Minor degradations
PCP -10-W	0.047	
PCP -30-O	0.103	
PCP -30-W	0.151	
PCP -60-O	0.227	Capital repairs needed
PCP -60-W	0.339	

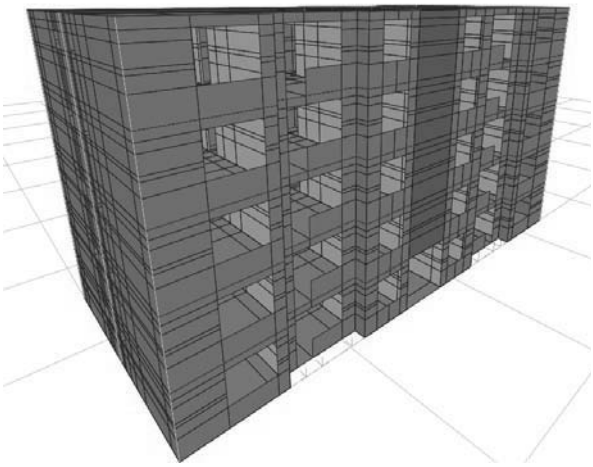


Figure 6 Finite element model for the LBM structure (SAP2000)

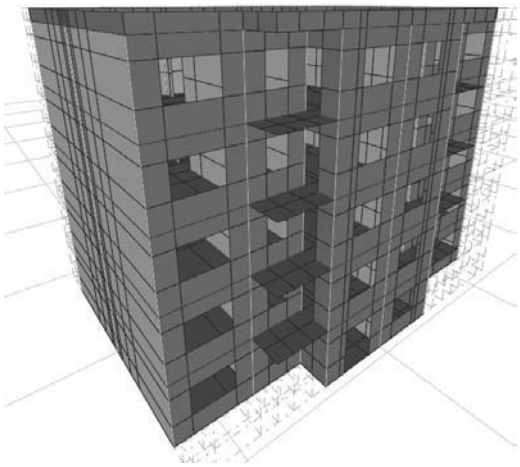


Figure 7 Finite element model for the PCP structure (SAP2000)

Figure 4 and Figure 5 show the variation of the fundamental period of vibration for the two structural models when all degradation percentages were considered for both distribution scenarios. It can be observed that the fundamental period of vibration increases for both types of structures with the increase of the degradation percentage. This can be explained by the decreased stiffness of the structure affected by degradations. Furthermore, a wider spread of the damage, from wall with openings only to all structural walls, causes further decrease in the overall stiffness of the structures.

The difference between the fundamental periods of vibrations for the two damage distribution scenarios increases with the increase in the considered amount of degradations. It ranges from 1.5% to 16.85% for the PCP case and from 0.1% to 1% for the LBM case.

The analysis cases can be classified to a degradation state by applying equation (1). The results are summarized in Table 4, for the LBM structure, and in Table 5, for the PCP structure. It can be observed that even though the classification of the analysis cases is similar for both scenarios, the LBM structure has slightly higher degradation coefficients especially for the more extended damage scenarios.

3.2 Peak Displacements

Figures 6 and 7 show the F.E. models considered in this paper. The structures were subjected to earthquake loads that occurred during their lifespan.

For each type of structure and for each damage percentage and damage distribution investigated in this research the peak displacements at the top were recorded during each earthquake excitation. The values are summarized in Table 6 for the LBM structure and in Table 7 for the PCP structure. Due to the limit space available, only the 30% damage analysis cases, with two distribution patterns of the degradations, are presented here. However, similar trends of the recorded data were observed for all other analysis cases.

From the analysis of the data presented in Tables 6 and 7, it can be concluded that the highest values of the peak displacements were obtained for the 1977 Vrancea earthquake (Table 2). At the same time, higher values for the peak displacements were obtained for the LBM structure compared with the PCP structure.

This can be explained by an increased stiffness of the PCP structure. An increased stiffness would result in a lower fundamental period of vibration, as presented in section 3.1.

Figures 8 and 9 show the variation of peak displacements for the LBM and PCP structures, respectively. The displayed results are for the undamaged state of the buildings. In both cases, it can be observed that the peak displacements in Y direction are larger than the ones in X direction. The Y direction is set along the shorter side of each structure (Figure 6 and 7, respectively). Therefore, a lower stiffness is expected with respect to Y axis. The analysis results confirm this assumption, as it can be observed from the data summarized in Tables 6 and 7. A similar trend was observed for the other analysis cases, as well.

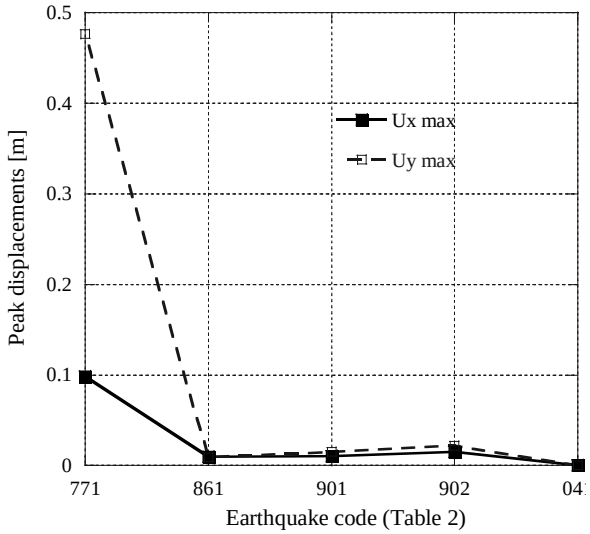


Figure 8 Peak displacements for LBM-0 analysis case

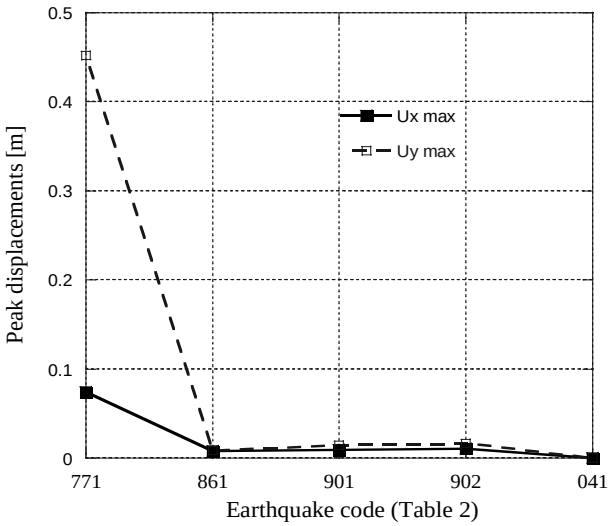


Figure 9 Peak displacements for PCP-0 analysis case

Table 6 Maximum displacements measured for the Load Bearing Masonry structure

Earthquake Code	LBM-0		LBM-30-O		LBM-30-W	
	Ux max [m]	Uy max [m]	Ux max [m]	Uy max [m]	Ux max [m]	Uy max [m]
771	0.098	0.477	0.098	0.470	0.100	0.471
861	0.0099	0.0092	0.0097	0.0098	0.0097	0.0094
901	0.0102	0.0151	0.0103	0.0158	0.0104	0.0159
902	0.0148	0.0221	0.0161	0.0189	0.0164	0.0195
041	0.00026	0.00029	0.00019	0.00023	0.000208	0.00021

Table **7** Maximum displacement measured for the Precast Concrete Panel structure

Earthquake Code	PCP-0		PCP-30-O		PCP-30-W	
	Ux max [m]	Uy max [m]	Ux max [m]	Uy max [m]	Ux max [m]	Uy max [m]
771	0.0746	0.452	0.0747	0.452	0.0747	0.452
861	0.008	0.0088	0.0083	0.0091	0.008	0.0088
901	0.0098	0.0145	0.0098	0.0145	0.0098	0.0144
902	0.0108	0.0168	0.0108	0.0168	0.0110	0.0168
041	0.00008	0.00009	0.00016	0.00011	0.00011	0.00012

A closer look at the values of displacements for the cases when a 30% damage was considered shows the fact that the peak values are almost the same, despite a different distribution of the degradations. It is the belief of the authors that this matter should be further investigated in more detail.

4. VISUALIZATION OF THE RESULTS IN A GIS ENVIRONMENT

The vulnerability of buildings, structures and population is dependent on their exposure to the hazard, which varies from location to location. The spatial characteristics of hazard and vulnerability justify the application of mapping and spatial technologies, such as Geographical Information Systems (GIS), remote sensing and photogrammetry in the risk assessment process (Lavakare and Krovvidi 2001).

In order to visualize the damaged structures from the considered urban sample, it is necessary to use a mapping Geographic Information System (GIS). GIS represents a system that joins two data bases. One data base operates with geometrical spatial objects and the second data base with the attributes of the information contained in the first one (Dimitriu 2001; Toma 2010). The main purpose of this system is analyzing and studying the information that is stored in its data bases. It can be a very powerful tool in complex decisions making.

4.1 NetSET Description

NetSET (**Net**work **S**patial **E**diting **T**ool) is a software package designed by a Romanian company from Iasi

(Ciobanu et al. 2005). It is a GIS application designed to solve important problems for the local public administration and economic agencies.

The software application is based on the widely used shape file format (.shp), compatible with any other GIS solutions on the market that are using the same format for storing vectorial map elements. NetSET package can perform various types of analyses based on implemented or user defined subroutines and has been successfully applied for viewing and analyzing risk data using the map of Iași city (Leon and Atanasiu 2007; Atanasiu et al. 2008; Atanasiu and Toma 2010).

4.2 Evaluation of Seismic Risk of the Iasi Urban Area using NetSET Map

In order to evaluate the seismic risk in a certain urban region, one should have data about the existing building stock, the earthquakes that have been registered in that area and the routes that firemen and medical teams must take in case of a disaster.

For the city of Iasi, building data came from experts' reports, field investigations and computer simulations (Toma and Atanasiu 2010; Atanasiu and Toma 2010). Inserting all the data in NetSET, a very clear picture of the seismic risk in the considered area can be obtained. For the first step, the user has to define the urban infrastructure, introducing for each building from the map the following data: the complete address, the structural type and height, type of foundation soil, the functional of the building and the year of construction, a.s.o. The buildings are then classified into four groups, depending on their degree of risk in case of an earthquake (Vișan and Hapurne 2008).

Figure 10 shows the urban sample area chosen for this research. The buildings in the area are colour coded depending on their structural type: precast concrete panels (light blue), load bearing masonry (red), frames (dark blue) and frames with shear walls (purple).

The degradation coefficient, (equation 1) obtained from numerical simulations or field survey to assess the damage of a structure can be also inserted into the program (Figure 11). Following the pre-programmed functions, the program can show the buildings depending on the degradation coefficient. The user can select to view only the buildings with a certain level of damage. Moreover, the program can display all the buildings for which a degradation coefficient is computed and display them with different colours depending on the values of the coefficient, as shown in Figure 12.

Also, with the help of this software, one can visualize the route that firemen or medical teams could take in case of an emergency situation, only by introducing the address of the place in need (Figure 13).

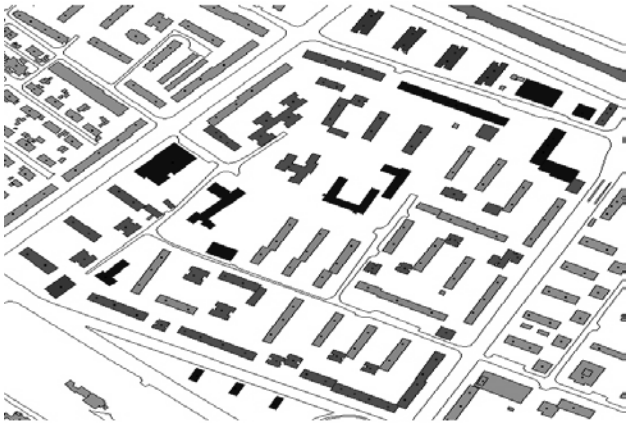


Figure 10 The chosen urban area sample

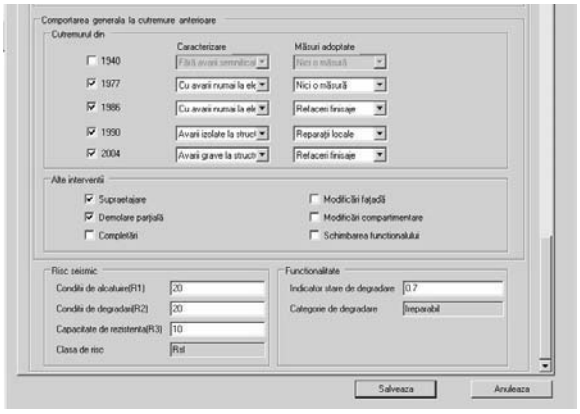


Figure 11 Type of data related to the degree of damage of a structure

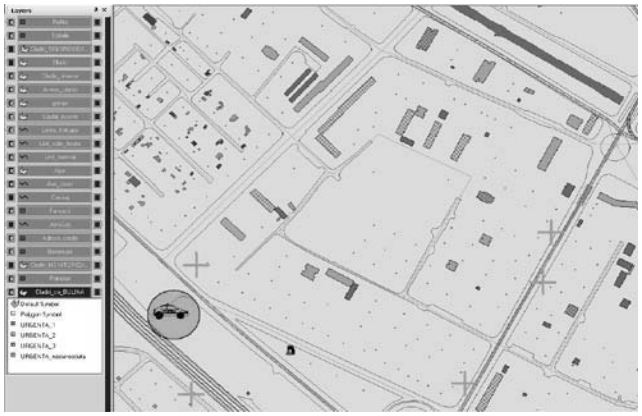


Figure 12 The chosen urban area sample



Figure 13 Sample of route displaying for fire fighters

5. CONCLUSIONS

The seismic vulnerability represents the evaluation of the consequences that an earthquake has upon a community and the environment together with the time of response and recovery from the disaster. In order to assess the vulnerability of a community it is necessary to visualize the damaged areas from the urban sample. For this purpose it is necessary to use a mapping Geographic Information System (GIS).

The deterministic approach of the seismic risk evaluation is based on the modelling and numerical simulations using SAP2000 software. This evaluation is conducted on two classes of building structures from Romanian building stock, subjected to seismic loads. The first construction class consists of a P+4 residential building made of precast concrete panels, while the second class is represented by a P+4 load bearing masonry structures. The degradation coefficient is computed based on the data obtained from the numerical simulation of the two models subjected to different earthquake loads, degrees of degradation and distribution of the damage throughout the structure.

Even though the obtained results are similar to those from field surveys, it is the belief of the authors that further improvements should be made to this approach. Currently, nonlinear numerical simulations are conducted for each type of structure in the chosen urban area sample. The analysis consists of nonlinear time history cases representing all the earthquakes that took place during the lifetime of the considered structure.

The results of the research are used for classifying the building structures based on their seismic risk index and the degree of degradations in order to fully comprehend and investigate the seismic vulnerability of the existing building stock. NetSET mapping system is used to visualise the present damaged areas. The results of this research work are used to improve the prediction functions of the software and make it become a powerful complex tool to help the society in case of future earthquakes. With its help, many scenarios can be simulated and, as a result, a better time response and management of situations in case of disasters will be provided.

Acknowledgements:

The present research is conducted within "The diagnosis of the vulnerability of the urban infrastructure to natural disasters and the k-management of the integrated risk – case study for the city of Iasi", Grant Aggreement No. 31065/2007, Romanian National Authority of Research, ANCS, Bucharest, Romania.

References:

Atanasiu, G.M. and Toma, A.-M. (2010), "Managing the seismic risk of some residential buildings of Romanian urban infrastructure", *Proceedings of the 14th European Conference on Earthquake Engineering*, Paper No. 439.

Atanasiu, G.M., Leon, F., Popa, B.F. and Doniga, C. (2008), "A computational approach for the assessment of seismic vulnerability based on the national data infrastructure", *Advanced Materials research*, **33**(37), 789-794.

Borcia, I.S. (2007), "Engineering measures of ground motion. Applications for 1977.03.04 INCERC record and for 1986.08.30 Cernavodă record", *Proceedings of the Syposium "Thirty Years from Romania Earthquake of March 4, 1977"*, Bucharest, Romania.

Ciobanu, A., Lefter, C., Ocheşel, A. and Gâlea, D. (2005), "GIS technologies and applications to monitoring the seismic risk for urban areas", in Atanasiu, G.M., Gâlea, D. (ed) *Monitorizarea GIS a riscului seismic urban*, Politehnium Printing House, Iaşi, Romania (in Romanian).

Computers and Structure Inc. (2005). SAP2000 Integrated Software for Structural Analysis & Design, Berkeley, California, USA. Available at: http://www.csiberkeley.com/products_SAP.html

CR 6-2006 (2006), "Design code for masonry structures", *Bucureşti: Monitorul Oficial al României, part I, nr. 807*, (in Romanian).

Dimitriu, G. (2001), "Geographical Information Systems GIS", Editura Albastră, Cluj – Napoca, Romania (in Romanian).

DiPasquale, E. and Cakmak, A.S. (1990), "Seismic damage assessment using linear models", *Soil Dynamics and Earthquake Engineering*, **9**(4), 194–215.

Emanuel, K., Ravela, S., Vivant, E. and Risi, C. (2006), "A statistical deterministic approach to hurricane risk assessment", *Bulletin of the American Meteorological Society*, **87**(3), 299-314.

Joshi, A. and Mohan, K. (2008), "Simulation of accelerograms from simplified deterministic approach for the 23rd October 2004 Niigata-ken Chuetsu, Japan earthquake", *Journal of Seismology*, **12**(1), 35-51.

Lavakare, A. and Krovvidi, A. (2001), "GIS & Mapping for Seismic Risk Assessment", *Proceedings of the National seminar on Habitat Safety against Earthquakes and Cyclones*, New Delhi.

Leon, F. and Atanasiu, G.M. (2007), "Seismic hazard analysis of Iasi city using geographic information systems", *Proceedings of Nordic Geographers Meeting 2007*, Bergen.

NE 012-99, (1999), "Design code for plain, reinforced and pre-stressed concrete structures" (in Romanian)

Patras, B. and Patras, M. (2002), "On the safety concept in buildings affected by repetable high earthquakes", *Ovidius University Annals of Constructions*, **1**(3), 4.

STAS 438/1-89 (1989), "Steel products for reinforced concrete. Hot rolled structural steel. Grades and quality technical requirement", *Romanian Committee for Science and Technology, Romanian Institute of Standardization*.

Toma, A.-M. (2010), "Using GIS visualization for the seismic risk assessment of the Romanian infrastructure", *The Bulletin of the Polytechnic Institute of Iassy, Constructions and Architecture Section*, **56**(3), 31-38.

Toma, A.-M. and Atanasiu, G.M. (2010), "Evaluation of the seismic vulnerability for P+4 residential buildings from the urban area of Iasi using the finite element method", *The Bulletin of the Polytechnic Institute of Iassy, Constructions and Architecture Section*, **56**(4), 97-109.

Universitatea Tehnică de Construcţii Bucureşti UTCB (2006), "CR 0 - 2005 Design code. The basis of structural design in civil engineering", *Bucureşti: Monitorul Oficial al României nr. 0148*, (in Romanian).

Vişan, D. and Hapurne, T. (2008), "Studiu de caz în eşantion urban din municipiul Iaşi", in Atanasiu, G.M. and Gâlea, D. (ed), 2nd edition, Politehnium Printing House, Iaşi, Romania (in Romanian).

Wood, N.J., Goof, J.W. and Goodwin R.F. (2002), "Vulnerability Assessment of a Port and Harbor Community to Earthquake and Tsunami Hazards", *Integrating Technical Expert and Stakeholder Input. Natural Hazards Review*, ASCE, **3**(4), 148-157.

8CUEE CONFERENCE PROCEEDINGS
8th International Conference on Urban Earthquake Engineering
March 7-8, 2011, Tokyo Institute of Technology, Tokyo, Japan

STRATEGIC FIREFIGHTING OPERATION TO MITIGATE FIRE DAMAGE RISK IN A NEAR-FIELD EARTHQUAKE IN THE METROPOLIS OF TOKYO –ANALYSIS OF THE RELATIONSHIP BETWEEN THE TIMING OF THE SWITCH TO FIREFIGHTING OPERATION AND DAMAGE REDUCTION–

Eiichi Itoigawa

Graduate School of Systems and Information Engineering, University of Tsukuba

Abstract: In response to fears that a near-field earthquake might occur in Tokyo, the Tokyo metropolitan government recently published the report, "Damage Estimates of an Earthquake with an Epicenter in the Tokyo Metropolitan Area." The report states that one of the main dangers is the extensive damage from fires that will result from such an earthquake. This study focuses on the timing of the switch from a local firefighting operation to a more wide-area firefighting operation, in which the limited available firefighting resources are used to deal with simultaneous outbreaks of fires in different locations. We discuss the relationship between the timing of the operation switch and the effect of the fire damage reduction quantitatively via simulation experiments under various conditions.

1. BACKGROUND AND PURPOSE OF THE STUDY

(1) Background of the Study

In response to fears regarding the impending risk that a near-field earthquake might occur in Tokyo, the Tokyo metropolitan government published in 2006 the report "Damage Estimates of an Earthquake with an Epicenter in the Tokyo Metropolitan Area."[1)]. According to this report, if an earthquake of a magnitude 7.3 were to occur at 18:00 on a winter day with an epicenter in the northern part of Tokyo Bay, which is considered to be highly probable and to cause extensive damage, the result could be more than 5,600 deaths, the complete collapse of 127,000 buildings, and other extensive damage.

One of the main factors causing such extensive damage is fire; among the various causes of damage resulting from large earthquakes, fire takes a significant toll regarding both human casualties and damage to buildings.

Whether or not fires resulting from a large earthquake spread through a city largely depends on initial countermeasures as well as town and city redevelopment for disaster prevention on ordinary days. Suppressing fires as quickly as possible is the most important measure for preventing catastrophic fires, and rapidly detecting a fire and extinguishing it immediately is the most important principle in fire prevention activities in an earthquake disaster. For this reason, bringing local firefighting resources to bear immediately at the initial stage of a large earthquake (each fire station handles local fires within its area with its own fire brigades) is considered to have considerable advantages; for example, each fire station can establish bases for receiving disaster reports and information collection at the initial stage of an earthquake disaster, when collection of detailed disaster outbreak information is assumed to be difficult due to congestion and disruption etc. of emergency service telephone lines (119 in Japan), making it easier to conduct flexible firefighting operations appropriate for the scale and conditions of the disaster.

On the other hand, in order to alleviate fire disasters across the entire Metropolis of Tokyo, it is necessary to deploy unified operations of all firefighting forces with a broader perspective in accordance with actual disaster conditions so as to promptly eliminate differences in fire fighting capabilities among regions due to various local characteristics, and operate all the currently available fire fighting forces efficiently.

From the above viewpoints, at a time of a large earthquake, it is thought to be advantageous to switch from operation of local firefighting units to a wider-area firefighting operation at a certain time in order to efficiently alleviate damage from spreading fires. However, switching too early, before a sufficient amount of detailed disaster information has been acquired, could result in biased allocation of the available fire brigades to fires breaking out immediately after the earthquake. Such a bias would likely lead to reduced operation efficiency due to concentration on already-detected fires, which delays handling undetected fires and fires breaking out later in areas with high risk of fire spreading; this has the risk of aggravating overall fire damage. Therefore, in order to operate the firefighting services efficiently, the relationship between the timing of the switch from local firefighting operations to more

wide-area firefighting operations and damage reduction must be quantified.

(2) Purpose of the Study

Against this background, this study focuses on the simultaneous outbreak of many fires, a significant cause of severe damage during a earthquake disaster, and it considers fire district units as wide-area operation units of firefighting services. On this basis, we clarify the relationship between the timing of the switch from local firefighting operations undertaken immediately after the occurrence of an earthquake to a district-wide firefighting operation effort, and the effect in alleviating fire damage. Thereby, this study aims to contribute to the examination of strategic firefighting operations to alleviate damage caused by the simultaneous outbreak of many fires in a near field earthquake in the Metropolis of Tokyo. Note that a fire district headquarters (hereinafter referred to as "district headquarters") analyzes the conditions of fires and fire brigade operation within its area based on reports from each fire station. However, it is expected that it will be increasingly difficult for the district headquarters to manage the operation of all fire brigades within its district in the most efficient manner as the number of fires increases, and such operation is thus not assumed under the current operations of firefighting services in an earthquake disaster. On the contrary, considering the purpose above, this study assumes that a district headquarters makes judgments on how to operate all fire brigades against fires occurring within its district and verifies the effects. We then verify the existence of more-effective approaches than the current fire fighting operation method, and attempt to obtain basic data that can be reflected on the future firefighting operations against earthquake disasters.

(3) Method of the Study

In this study, we will construct a simulation model that allows simulating the outbreak and spread of fires during an earthquake disaster, taking both local and district-wide firefighting operations into consideration. Furthermore, we will run simulation experiments in which we vary the timing of the switch from local firefighting operations to district operations under various conditions in order to analyze the relationship between the timing of the operation switch and the effect on the fire damage reduction.

2. CONSTRUCTION OF SIMULATION MODELS

(1) Overview of Simulation Models

In this study, we construct the simulation model shown in Figure 1 using a mesh model that expresses the conditions of the urban area (hereinafter referred to as the "mesh") in square zone units measuring 250m on a side, from a macroscopic viewpoint. Note that the data of the urban area conditions investigation by the Tokyo Fire Department[2] is used for all mesh unit data.

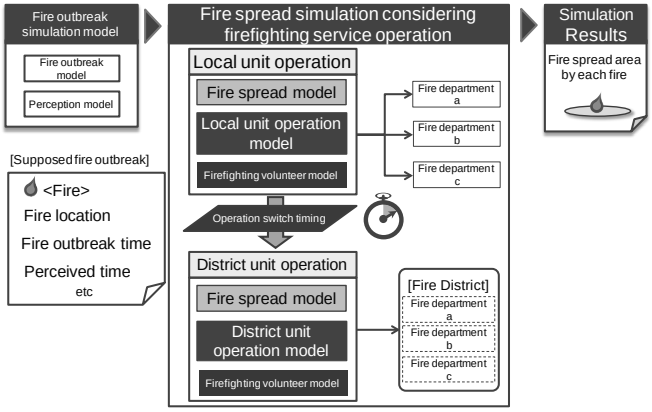


Figure 1 Overview of Simulation Models

The fire outbreak simulation model comprises a fire outbreak model and a perception model. In the fire outbreak model, locations of fires are assigned to the mesh units by probability based on the expected number of fires resulting from an earthquake[3] and, further, the starting time of each fire is assigned to each fire by probability based on the prediction function[4] derived from past earthquake fire cases. The perception model indicates the probable time required to detect each fire using the prediction function[4] obtained from the method and time of perception in past earthquakes.

The spreading fire simulation model, taking fire control services into consideration, comprises a spreading fire model and a fire brigade operation model (comprised of local unit operation model, district unit operation model, and firefighting volunteer model). The spreading fire model extracts the building-to-land ratio, ratio of roads, ratio of open space, etc. to building structures (wooden structures, fire-resistant structures, quasi-fireproof structures, and fireproof structures) for each mesh unit, and calculates the area of fire spreading for each fire, taking into consideration the speed of spread calculated using the rate of spreading equation (Tokyo Fire Defense Board equation 2001 (macro equation))[5] and fire spread prevention activities by fire brigades. The fire brigade operation model is to compute the dynamic state of fire brigades (including firefighting volunteers) in local firefighting operations and district operations. The timing of the switch from local firefighting operations to district operations can be set arbitrarily.

(2) Local Firefighting Operation Model

a) Number of Participating Fire Brigades

Past studies[4] indicate that, in local firefighting operations during the early stages of an earthquake disaster, specification of the number of participating brigades according to a ranking of the fire-spreading risk where the fire is breaking out[6] is effective in reducing the area of fire spreading. Based on this research result, the number of participating brigades per fire is determined by the ranking of the fire spreading risk, at the location of the fire, as shown in Table 1, and specified in advance.

Table 1 Number of Participating Brigades by Risk Rank of Fire Spread

Risk of fire spreading risk	Specified number of participating brigades
7 or more	3
5 or 6	2
4 or 3	1
2 or less	0 (no mobilization)

b) Priority of Mobilization at Fire

A fire brigade headquarters must decide "how many fire brigades in total should be sent to which fire from what district" in case of detected fires for which the specified number of brigades has not been committed yet (hereinafter called "fires requiring judgment") if it has standby teams or teams available to take on another fire after a fire has been extinguished (hereinafter, such teams are referred to as "mobilizable teams"). If there are multiple fires requiring judgment, fire brigades are committed to fires with higher rank of fire spreading risk first. If there are several fires requiring judgment with the same the rank of fire spreading risk, fire brigades are committed to fires detected earlier first.

c) Determination of Mobilized Fire Brigades

The fire brigades to be mobilized are selected among fire brigades belonging to the fire station that is in charge of the location of fire outbreak, in order of teams that can be mobilized closer to the fire in question. Fire brigades in the middle of firefighting shall not be moved to another fire location.

d) Mobilization Judgment Speed

So far, no existing studies have fully investigated the time required for mobilization judgment. In this model, therefore, we allowed setting the time required for one mobilization judgment Δt [min] as well as the number of fires for which mobilization judgment can be made simultaneously Np (hereinafter referred to as "number of fires for which mobilization judgment can be made"), to arbitrary values. With these two variables, we defined the speed of mobilization judgment as follows:

$$s_f = \frac{N_p}{\Delta t} \quad \text{[fires/min]} \qquad \cdots[5]$$

Note that it is reasonable to expect that the greater the number of fires requiring judgment, the longer the time required for mobilization judgment. Therefore, the time required for one mobilization judgment is set to be determined by the number of fires requiring judgment. In addition, if a new fire is detected while making mobilization judgment, the detected fire in question shall not be included in the currently performed mobilization judgment, but included in the subsequent fires requiring judgment.

e) Formation of Emergency Fire Brigades

There are two types of emergency fire brigades formed and mobilized to deal with fires at earthquake disasters (hereinafter referred to as "emergency fire brigade"): emergency pump teams and portable pump teams. Emergency pump teams and portable pump teams are organized around reserve fire engines equipped with pumps and portable pumps of each fire station and firefighters gathering at each fire station. The time required for firefighters to gather at each fire station is calculated by the assembly ratio curve for each fire station based on data from assembly trainings conducted assuming earthquake disasters; one emergency fire brigade can be formed with every 5 fire fighters that are gathered.

f) Settings of Fire Brigade Moving Speed etc.

When a fire brigade is dispatched to a fire, it immediately starts moving toward the location of the fire outbreak. The speed of the fire brigade etc. is set based on past studies[4), 7)], which closely examined traffic obstructions etc. experienced by fire brigades due to blocked roads, which posed an impediment to firefighting during the Great Hanshin-Awaji Earthquake Disaster.

(3) District Operation Model

a) Fire Brigade Operation Method in District Operation

Each time a mobilization judgment is made, fire brigades are dispatched to all detected fires in order to minimize the fire spreading.

b) Judgment of the Number of Mobilized Fire Brigades and Order of Mobilization Priority Order

The district headquarters makes mobilization judgment when there are detected fires that are spreading within the district and teams that can be mobilized are available. The algorithm used for the judgment is as follows.

If the un-besieged perimeter length of fire i is $L_i(t)$ at time t and the length $E_i(t)$ ($L_i(t) \geq E_i(t)$) is to be besieged for each fire, the enlarged fire spread area for all detected fires from time t to t+1 is expressed as follows:

$$\Delta S = \sum_{i=1}^{K(t)} ds_i = \sum_{i=1}^{K(t)} \frac{\{L_i(t) - E_i(t)\}}{2 \cdot r_i(t)} \{r_i(t+1)^2 - r_i(t)^2\} \qquad \cdots[6]$$

Here, $s_i(t)$ is the fire spread area at time t [m^2]
$L(t)$ is the un-besieged fire perimeter length at time t [m], $E(t)$ is the besieged perimeter length at time t [m]
$r(t)$ is the maximum radius of fire at time t [m], and
$K(t)$ is the number of already detected fires at time t [m]

At this point, define:

$$\frac{r_i^2(t+1) - r_i^2(t)}{r_i(t)} = U_i(t) \qquad \cdots[7]$$

Then, the objective function to minimize ΔS *is*:

$$\Delta S = \frac{1}{2}\sum_i U_i(t) \cdot L_i(t) - \frac{1}{2}\sum U_i(t) \cdot E_i(t) \to \min \qquad \cdots[8]$$

$$\Leftrightarrow \sum_i U_i(t) \cdot E_i(t) \to \max \qquad \cdots[9]$$

That is, in order to minimize the total growing area of the spreading fire, it is necessary to mobilize fire

brigades to fires with large U first. Note that, from equation [7], it can be confirmed that the greater the increase of fire spreading area per unit of time and the smaller the maximum radius of a fire, the greater the value of U becomes. This means that mobilizing fire brigades to fires with greater U first is equivalent to mobilizing fire brigades to "fires that spread quickly and are easy to besiege (greater siege perimeter length per brigade relative to fire perimeter length) preferentially," which is considered to be a reasonable judgment.

(4) Firefighting Volunteer Model

a) Operation of Firefighting Volunteers

In the firefighting volunteer model we construct in this study, firefighting squads organized by volunteer firefighters gathered after the occurrence of an earthquake are considered to be the smallest units available for firefighting. Firefighting squads are committed by the firefighting volunteer commander based on the instruction of the fire brigade headquarters. Based on past studies[4), 7)], the general properties of fire teams, such as settings of mobility etc., are set to be the same as for portable pump teams. Moreover, in view of the basic principle of firefighting volunteers that "our own town must be protected by ourselves," it is not considered appropriate to assume that such firefighting squads will be operated in wider areas. They are thus operated as in local firefighting operations (activities in a squad's own area of jurisdiction) even after the switching of the operation.

b) Time Required to Organize Firefighting Squads

Volunteer firefighters in wards of the Metropolis of Tokyo (hereinafter referred to as "branch firefighting volunteers") are classified into service-area volunteers and resident-area volunteers. Since an earthquake is assumed to break out at 18:00 in this study, we assume that only resident-area volunteers have time to gather.

The time for a firefighting squad to be formed is calculated and set based on the lead-time for branch firefighting volunteers to start gathering after an earthquake and the transportation time required for gathering.

The lead-time required for branch firefighting volunteers to confirm the safety of family members etc. and start gathering is assumed to be 15 minutes. This value is found from statistical analysis of questionnaire surveys targeting branch firefighting team commanders in wards of the Metropolis of Tokyo; 15 minutes corresponds to the median of the cumulative response ratio of time required for gathering at earthquake disaster stated by the branch firefighting squad commanders.

c) Transportation Time Required for Gathering

The area that branch firefighting team D_i is in charge of is defined as a circle having the equivalent area as the actual branch firefighting team zone (radius R_im) and the branch firefighting team headquarters is assumed to be located at the center. The firefighting squad members (total number of members m_i) that are able to gather at the fire station are assumed to be uniformly distributed within the branch firefighting team zone; immediately after the earthquake, they start to move toward the headquarters. The time required for the xth firefighting squad member to reach the headquarters, $t_{i,x(move)}$ min, is calculated as follows [14)]:

$$t_{i,x(move)} = \sqrt{\frac{x}{Dm_i}} \cdot \left(\frac{1.3R_i}{v_w} \right) \quad \cdots[14]$$

Where v_w is the assembling speed (set to 100 [m/min] on foot)

One firefighting squad is organized with every five firefighting volunteers that are gathered.

3. SIMULATION EXPERIMENTS

(1) Selection of Case Study Areas

For the simulated fire district, we will choose a fire district closest to the average in terms of density of fire occurrences assumed at the earthquake disaster scene and the ratio of fire brigade to the assumed number of fires within the jurisdiction of each local fire station among the eight fire districts having jurisdiction over the wards of the Metropolis of Tokyo. And Fire District "F" is chosen as the case study area in this study. (Figure 3)

(2) Parameter Settings

The time required for making a judgment at the local firefighting operation and at the district operation is presumed as shown in Table 2. We then conducted experiments in which we changed certain key parameters shown in Table 3 in order to understand the factors affecting the time for switching the method of operation and the effect on damage reduction. Note that the underlined values in Table 3 indicate the reference value of each parameter.

Table 2 Time Required for Mobilization Judgment

Number of fires requiring judgment	At local firefighting operation (min.)	At district operation (min.)
1 to 5	1	1
6 to 10	2	2
1 to 15	—	3
15 or more	—	4

Table 3 Parameter Settings

Factor	Parameter	Set value
Number of fires	Coefficient of expected number of fires	0.5 , <u>1.0</u>, 1.5
Speed of mobilization judgment	Number of fires for which mobilization judgment can be made	1 , <u>2</u> , 3
Operation of firefighting volunteer	Operation of firefighting volunteers	Yes, <u>No</u>

*Coefficient of expected number of fires: a coefficient by which the expected number of fires per mesh unit is multiplied in order to change the assumed number of fires.

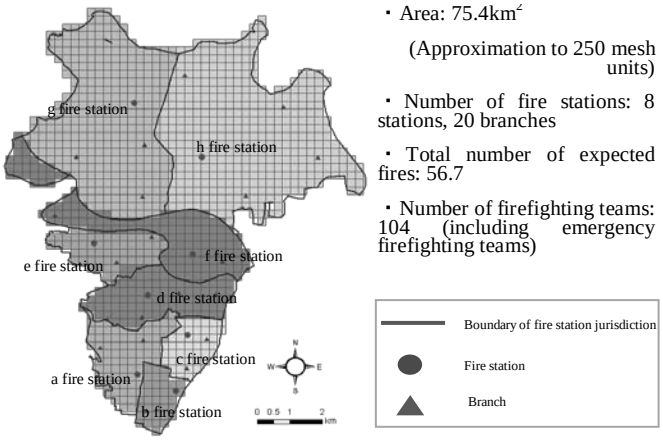


Figure 3 Map of Fire District "*F*"

4. RESULTS OF EXPERIMENTS AND ANALYSIS

(1) Basic Experiments

In order to first understand the trends of each evaluation index at each operation switch time, we conducted experiments based on the default scenario using the underlined values in Table 3 (Experiment 1).

Figure 4 shows the numbers of fires and detected fires by time of occurrence in the basic experiments. The result shows that approximately half of the fires start within five minutes after the occurrence of the earthquake, and the majority of fires are detected within 5 to 20 minutes after the occurrence of the earthquake. In addition, Figure 5 shows the relationship between the operation switching time following the earthquake and the area that fire spreads to within the district. The result shows that the fire spread area within the district is minimized when the operation is switched 25 minutes after the occurrence of the earthquake; if the switch takes place either earlier or later, the fire spread area would be greater.

a) Operation Switch Timing and Effect on Damage Reduction Seen from Entire District

Figure 6 shows the relationship between the fire spread area within the district and the ratio of extinguished fires within the district (ratio of fires extinguished by fire brigades relative to the number of fires breaking out within 180 minutes after the outbreak of the earthquake) when the operation switch timing is changed. The ratio of extinguished fires is higher and the fire spread area is smaller in the upper left part of the graph, which is more favorable.

Figure 6 indicates a strong negative correlation between the fire spread area and the ratio of extinguished fires in the district. From this result, in order to mitigate the fire spread area, it is considered important to operate firefighting services according to the principle of firefighting at an earthquake disaster called "early extinguishing of fires." That is, mobilizing fire brigades in more wide-area fire operations to deal with local fires with inferior firefighting services in early stages is considered effective in minimizing the fire spread area. With this measure, it becomes possible for a small number of fire brigades to extinguish fires quickly and be moved to other fires. Thus, the effect of preventing fire spreading per fire brigade can be increased to achieve more efficient firefighting operation.

However, if the operation is switched too early, the fire spread area in the district overall becomes greater and both the ratio of extinguished fires and the area where fire spreading is prevented per fire brigade become smaller. Here, comparing Figure 4 and Figure 5 for confirmation, it can be seen that the optimal time to switch operation seen from the entire district is slightly after the time when the number of detected fires by time within the district becomes the maximum. From this result, it is thought that if the operation is switched too early, the judgment about the operation of fire brigades cannot catch up with the fire detection, leading to delays in mobilization commands to the fire brigades. Thus, it becomes difficult to extinguish fires in the early stage and, as a result, the fire spread area will increase. On the other hand, if the operation switch is too late, taking actions against fires where firefighting services are insufficient is delayed, allowing the fire spread area to expand in the region in question and making early fire extinguishing difficult, and the fire spread area will increase.

From these considerations, we can say that local firefighting operations are effective in the period when a rush of reports and detections of fires come in after the outbreak of an earthquake. Then, when a certain period has elapsed after the occurrence of the earthquake and the peak of fire detections has passed, all firefighting services should be mobilized to switch to wider area operations as early as possible. Thereby, it is possible to extinguish fires in the early stage and mitigate damage caused by fire spreading.

b) Time of Operation Switch and Effect on Damage Reduction Seen by Jurisdiction of Fire Station

Figure 7 shows changes in the fire spread area by fire station jurisdiction when the operation method is switched 25 minutes after the outbreak of the earthquake as compared to no operation switching. The fire spread area was reduced in nearly all fire station jurisdictions, but the area increased in fire station jurisdiction b only, by approximately 27 percent. This result suggests that operation method switching can reduce the overall damage in a district, but it is accompanied by the risk of increased local damage.

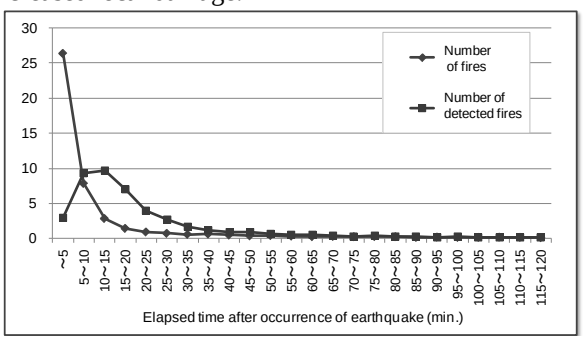


Figure 4 Number of Fires/Number of Detected Fires by Time (experiment 1)

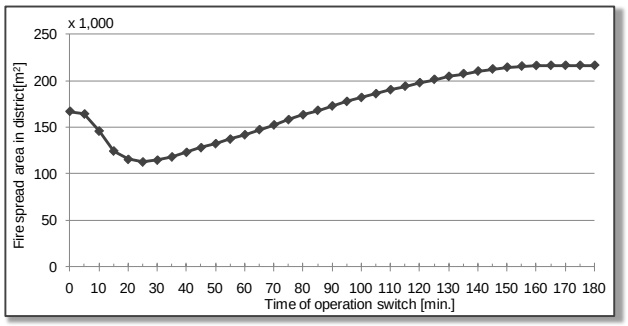


Figure 5 Operation Switch Time－Fire Spread Area in District (Experiment 1)

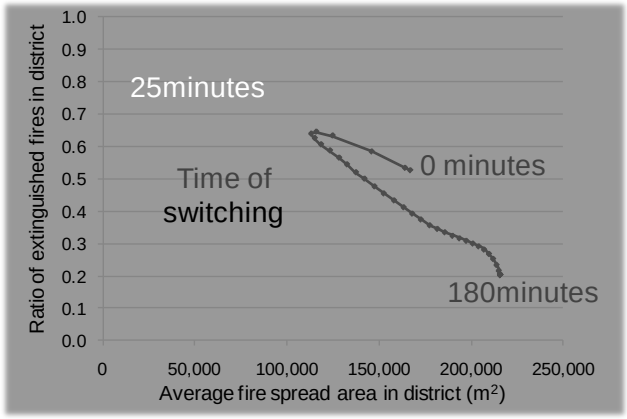


Figure 6 Average Fire spread area within District－Average Ratio of Fire Extinction

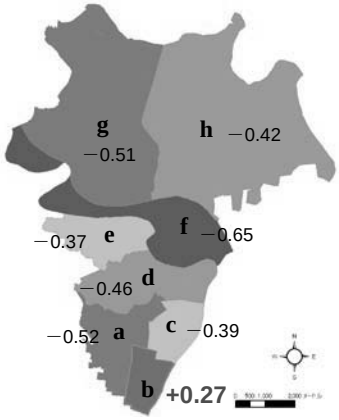


Figure 7 Rate of Change of Fire Spread Area due to Operation Switching (25 minutes)

The reasons why the fire spread area increased in fire station jurisdiction b only are thought to be found in the local characteristics of the jurisdiction and the district operation policy. Comparing the expected number of fires within the district on a five-point scale, fire station jurisdiction b is considered to have a relatively high risk of fires compared to other jurisdictions within the district, while the risk of fire spreading is low. In this study, we employed the district operation policy to "prioritize fires that spread quickly." For this reason, the risk of multiple fires is high in fire station jurisdiction b, but the priority on fires within the jurisdiction is lowered after switching the operation because the speed of fire spreading is relatively slow in this jurisdiction, which inhibited sending a large number of fire brigades, resulting in increased area of fire spreading. This result suggests the risk of allowing local fires to spread based on characteristics different from local characteristics such as speed of fire spreading, depending on the local characteristics and operation policy. It is thus considered important to identify areas with a high risk of fire spreading and the damage increase trend in such areas, when judging the timing of switching firefighting operations.

(2) Understanding the Influence of Mobilization Judgment

a) Speed of Mobilization Judgment in Local Firefighting Operations

In order to understand the impact of speed of mobilization judgment in local firefighting operations on the relationship between the operation switch timing and the effect on damage reduction, we conducted experiments with the same fire assumptions as in the default scenario, but we changed the number of fires for which mobilization judgment can be made during local firefighting operation. Even if the operation judgment speed of the local firefighting operation is changed, scarcely any difference could be recognized in the relationship between the operation switch timing and the fire spread area in the district.

b) Speed of Mobilization Judgment in District Operations

In order to understand the impact of speed of mobilization judgment in district operations on the relationship between the operation switch timing and damage reduction, we conducted experiments under the same fire assumptions as in the default scenario, but we changed the number of fires for which mobilization judgment can be made at district operation as shown in Table 4.

Figure 8 shows the relationship between the operation switch timing after the occurrence of the earthquake and the fire spread area in the district. It is seen that if the operation judgment speed in district operations becomes faster, the operation switch timing that minimizes the fire spread area in the district becomes earlier, and the risk of increased fire spread area if the judgment to switch operation is made too early also drops. The possible reason is that damage is reduced due to an earlier switch to district operation, because operation judgment can also be made relatively efficiently in the early period of earthquake disaster when fire detections peak. On the other hand, if number of fires for mobilization judgment is fewer, the efficiency of mobilization judgment is greatly affected by the number of detected fires. In particular, if the operation is switched too early during the initial period of an earthquake disaster, the efficiency of fire brigade operation judgment drops dramatically due to the high concentration of fire detections, manifesting itself directly in a higher amount of damage.

Table 4 Experimental Conditions (Experiments 4 and 5)

Experiment number	Coefficient of expected number of fires	Number of fires for which mobilization judgment can be made		Operation of firefighting volunteer
		Local firefighting operation	District operation	
4	1.0	2	1	None
5			3	

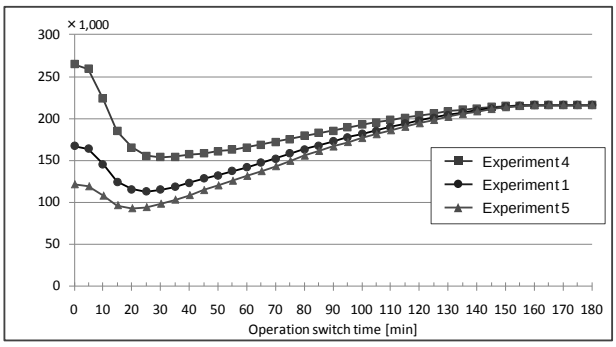


Figure 8 Operation Switch Timing －Average Fire spread area within District

(3) Understanding Influence of Number of Fires

In order to understand the influence of the number of fires on the relationship between the operation switch timing and the damage reduction, we conducted experiments under the some conditions changing the coefficient of expected number of fires.

From the results, it indicates that the operation switch timing that minimizes the fire spread area within the district does not change greatly in line with the number of fires. Moreover, when the number of fires is high, the difference in the area flame propagation due to the operation switch timing in the early period of the earthquake disaster becomes larger. The reason for this may be that if the number of fires is large, many fires break out before emergency fire brigades are formed and firefighting services become insufficient in some areas in the early stage after the occurrence of the earthquake, manifesting the effect of an early operation switch. If, however, the number of fires is large, the number of fire detections concentrated at the early stage of the earthquake disaster naturally also becomes large. For this reason, if the operation switch is performed too early, operation judgment made by the district headquarters will not catch up with the number of detected fires and the efficiency of mobilization becomes lower compared to local firefighting operation, which thus resulted in aggravating fire damage just as well.

(4) Influence of Operation of Firefighting Volunteers

In order to see the influence of the operation of firefighting volunteers on the operation switch timing and reduction of damage, we conducted experiments under the same fire assumptions as in the default scenario by operating firefighting volunteers, and compared the results. Table 5 shows the experimental conditions.

Looking at the area of fire spreading in the entire district, it is possible to reduce the fire spread area by approximately 40 to 50 percent, by means of firefighting volunteers, which confirms the considerable effect of these volunteers (See Figure 9). In particular, if the operation switch timing is earlier, the effect of the operation of firefighting volunteers to reduce the fire spread area becomes large. Moreover, if firefighting volunteers are used, the operation switch timing that minimizes the fire spread area takes place earlier and the difference in fire spread area due to the operation switch timing lessens in the early stage of an earthquake disaster. The reason for this is that, even if the operation method is switched at the early period of earthquake disaster when fire detections peak, if firefighting volunteers are mobilized, they are mobilized to nearby fires immediately after formation and prevent the spread of fire, compensating for the tentative drop of efficiency of mobilization judgment by the local firefighting department. This also has an advantage that required number of fire brigades can be sent out.

Moreover, it is possible to compensate for the disadvantages of switching the operation too early, causing a lack of firefighting services in certain areas in the district and focusing fire brigades on fires that broke out relatively early, for the same reasons as mentioned above. We thus consider that the spreading of fire will be suppressed even if the operation switch is made too early as well.

Table 5 Experimental Conditions (Experiment 8)

Experiment number	Coefficient of expected number of fires	Number of fires for which mobilization judgment can be made		Operation of firefighting volunteer
		Local firefighting operation	District operation	
8	1.0	2	2	Yes

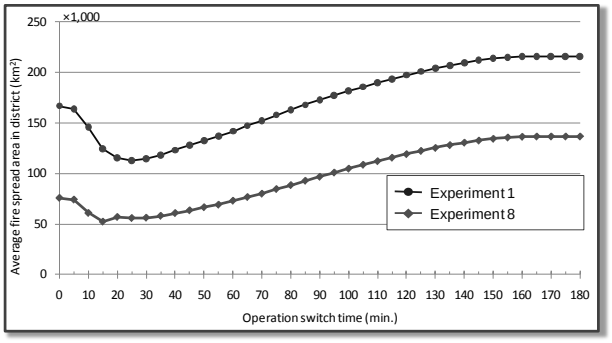


Figure 9 Number of Fires/Number of Detected Fires by Hour

5 CONCLUSION AND FUTURE ISSUES

(1) Conclusion

The conclusion drawn from this study is as follows.

a)Operation Switch Timing where an Effect on Damage Reduction Can Be Expected

Utilizing local firefighting operations in the initial phase of an earthquake disaster when reports (detections)

of many simultaneous fires peak, and switching to district operation as soon as possible after the peak of fire detections subsides some time after the outbreak of the earthquake, is effective to minimize fire damage. However, depending on the distribution of dangers of fires within a district, distribution of dangers of spreading of fires, or operation policies at district operation and the timing of operation switch, switching from local to district operation in an early stage involves a certain risk of increased local damages even though it reduces overall damages in the entire district. For this reason, it is necessary to identify areas with high risks of damage increase due to operation switching and the trends of damage increase in such areas in advance.

b) Influence of Speed of Mobilization Judgment

If the operation method is to be switched in the early stage after the outbreak of an earthquake, the judgment speed of mobilizing fire brigades by the district headquarters has a strong impact on the reduction of damages.

Thus, establishment of operation framework of fire brigades by the district headquarters in an early stage and repletion of command functions of the headquarters are effective.

c) Influence of Number of Fires

From a standpoint of wider area operation, the number of fires has little impact on the operation switch timing that minimizes the area of fire spreading. However, if the number of fires is great, the differences in the areas where fire is spreading become greater if the operation framework is switched during the initial stage of an earthquake disaster. If the operation framework is switched extremely early, in particular, there is a risk of significantly increasing fire damage. Moreover, if the number of fires is small, the later the operation is switched, the more difficult it becomes to conduct efficient firefighting operations; thus the effect on fire damage reduction is substantially reduced. Therefore, when the number of fires is anticipated to be small during the initial phase of an earthquake disaster, early operation switching should be examined in a proactive manner, and if the number of fires is projected to be great, careful judgment is required to switch operation at an early time.

d) Effect of Operation of Firefighting Volunteers

When wide-area fire brigades operate in combination with community-based firefighting activities by firefighting volunteers, a significant reduction of fire damage can be expected. Moreover, if firefighting activities by firefighting volunteers are conducted effectively, the risk of an increase in fire damage at the time of the operation switch to fire brigades in the initial phase of an earthquake disaster can be reduced.

(2) Future Issues

The future issues of this study are as follows.

a) Trials and Analyses in Multiple Fire Districts

The numeric values of effective operation switch timing shown in this study are applicable only when the operation method assumed in this paper is applied in a specified district. The same results are not assured if urban area conditions, firefighting service conditions, or disaster conditions are changed. This means that it is necessary to see how the relationship between the operation switch timing and damage reduction changes due to local characteristics of other fire districts, as well as understand the optimum operation switch timing for each district and risks involved in operation switching in the future.

b) Trials of Combinations of Various Operation Methods

This study examined the effects of combinations of a certain strategy (how to maneuver fire brigades), but diverse combinations of strategies at each operation are conceivable. From here on, it is necessary to model realistic operation strategies in touch with damage conditions at each operation and understand the relationship between the operation switch timing and damage reduction in these various combinations.

c) Consideration of Damage other than from Fires

During an earthquake disaster, all kinds of destruction is assumed to occur in addition to that caused by fires. When such things other than fires are included in the simulation models, it is necessary to take into account the possibility of fire brigades being unable to engage in firefighting or unable to start firefighting immediately, through evaluation of risks of outbreak of each type of disaster in chronological order.

d) Improvement of Simulation Model Accuracy

From now on, in order to improve the accuracy of the simulation models, it is required to closely examine impediments to firefighting, time required for making judgments on operation of fire brigades and so on, taking water supply and uncertainty into consideration, and to reflect the results in the simulation models.

References:

1) The Tokyo Metropolitan Disaster Management Council Earthquake Section: Estimation of Damage in Tokyo in a Near Field Earthquake of the Metropolis of Tokyo, the Disaster Prevention Management Department, Disaster Prevention Division, Tokyo Metropolitan Government Bureau Of General Affairs, 2006.5
2) Tokyo Fire Department: Survey Report on Urban Conditions in the Metropolis of Tokyo, Disaster Section, Disaster Division, Tokyo fire Department, 2005.3
3) Tokyo Fire Department: Measurement of Risk of Fire Outbreak by Region at Earthquake in the Metropolis of Tokyo (7th), Disaster Section, Disaster Division, Tokyo fire Department, 2006.3
4) Fire Prevention Council / Tokyo Fire Department: Examination of Effective Firefighting Framework at Earthquake, Ideal Firefighting Framework at Earthquake, P158-P253, 2003.3
5) Fire Prevention Council / Tokyo Fire Department: Development and Utilization Method of Disaster Prevention Performance Evaluation Methodology in Fires at Earthquake, 2001.3
6) Tokyo Fire Department: Measured Risk of Fire Spread at Earthquake in the Metropolis of Tokyo (7th), Disaster Section, Disaster Division, Tokyo Fire Department, 2007.9
7) Tokyo Metropolitan Disaster Management Council: Survey Report on Assumed Damage in Near-Field Earthquake in Tokyo (Damage Estimation Methodology), P219-P236, disaster prevention planning Division, Headquarters for disaster control, Tokyo Metropolitan Government Bureau of General Affairs, 1997

8CUEE CONFERENCE PROCEEDINGS
8th International Conference on Urban Earthquake Engineering
March 7-8, 2011, Tokyo Institute of Technology, Tokyo, Japan

RESCHEDULING TIMETABLES OF TAIWAN HIGH-SPEED RAIL SYSTEM USING OPTIMIZATION AND DECISION TREE

Ting-Wu Ho[1], Te-Che Chen[1], Nailah Firdausiyah[2], Chia-Ying Lin[1], Ssu-Min Tseng[1], and Chien-Cheng Chou[3]

1) PhD Student, Department of Civil Engineering, National Central University, Taiwan
2) Lecturer, Department of Civil Engineering, University of Brawijaya, Indonesia
3) Associate Professor, PhD student, Department of Civil Engineering, National Central University, Taiwan
993402004@cc.ncu.edu.tw, 983402008@cc.ncu.edu.tw, nailah_firdausiyah@yahoo.com, 993402003@cc.ncu.edu.tw, 983402006@cc.ncu.edu.tw, and ccchou@ncu.edu.tw

Abstract: Managing circulation of trains, including regular inspection, car cleaning times and turning back operations, has become important due to the scarcity of railway company resources. The Taiwan High-Speed Railway (THSR) already has cyclic patterns of daily train circulation, but these patterns have not been modeled yet. Moreover, based on a review of the literature, researchers in the railway field have never considered train circulation, especially in HSR systems, even though it is important. This research proposes a scheduling optimization model that has the capability to accommodate not only basic requirements such as railway topology, traffic rules, and user requirements, but also train circulation as well. Mixed integer and dynamic programming have been chosen to solve the model under CPLEX. In addition, railway systems are often characterized by high traffic density that is sensitive to disturbances; thus, rescheduling activity for updating an existing schedule in response to disruptions is needed. This research has presented the mathematical model to reschedule the timetable. Assumptions as well as input and output values are configured by using real data from THSR, which used two lines, 128 services, 29 trains, and eight stations. The model has obtained a timetable result as good as the real timetable in two hours (that is, 7442.51 second). Rescheduling results could determine the new timetable for calamity. Therefore, it could be a good simulation analysis for predicting the effect of disruptions on the timetable without doing real experiments such as trains being disordered and overtaken.

1. INTRODUCTION

Railway transportation plays an important role in the passenger and freight transportation market. The railway has grown by over 40% in both freight and passenger sectors over the past 10 years. All railway companies try to provide good services in order to satisfy their customers. One way to realize this is by improving the quality of the train control process or scheduling so that the railway company could optimize these services as well. In addition, the train timetable is the basis for performing the train operations. It contains information regarding the topology of the railway, train number and classification, arrival and departure times of trains at each station, arrival and departure paths, etc. More formally, the train scheduling problem is to find an optimal train timetable, subject to a number of operational and safety requirements. Due to the limited resources of railway companies, managing circulation of trains becomes important, including turning back operations, regular inspection and car cleaning times. Any solution that ignores train circulation requirements is unreasonable to train companies. The Taiwan High-Speed Railway System already has cyclic patterns of daily train circulation, but these patterns have not been modeled yet. Furthermore, based on the data in the contingency timetable, THSR prefers to cancel many trains and operates only two trains per hour in many cases of disturbances. On the other hand, creating an optimal timetable, which means optimal journey time, is important since the THSR Company has to preserve the maximal profit during disturbances. In addition, in order to mitigate the impact of disturbances instead of cancelling many trains on their system, THSR needs a method for analyzing how disturbances propagate within the original timetable and which actions to decide. In the end, the train operator could predict the effects of disruptions on the timetable without doing real experiments.

Train scheduling problems have been studied by researchers over the years. They have been formulated using operation research (OR)-based techniques including mixed integer programming and network optimization models. Among the solution techniques developed to solve the problems were branch and bound, heuristics, and Lagrangian relaxation. In addition, researchers have proposed some methods to solve scheduling problems as the Job-Shop problem, program evaluation and review technique, and satisfaction constraint.

The strengths and weaknesses of each method depend on research objectives. Many researchers prefer to use a heuristic method to speed up the computation time and direct the search towards a feasible solution, but a heuristic needs more evaluation in practice due to the optimality issue of the results. There is no guarantee that the heuristic will generate an optimal solution in every test case (Chiu et al. 2002). The scheduling and rescheduling problem in this research is formulated as mixed-integer-programming (MIP), in which some of the variables are real-valued and some are integer-valued. There are two ways to solve MIP: exact solution, including branch and bound, and dynamic programming and approximation, including heuristic and lagrangian relaxation techniques (Yan and Shih 2009). The most widely used method for solving MIP for exact solution is branch and bound, and no researchers have used dynamic programming as a solution technique, although it could obtain the optimal solution as well. Therefore, this research proposes the exact-solution algorithm, which is dynamic programming, to solve train-scheduling problems and get the optimal solution exactly.

2. FORMAT REQUIREMENTS

Suppose a railway system with r station, n trains going down and m trains going up. Minimizing the operation times for all trains means minimizing the journey times (arrival and departure times) for all trains going-down, initialized as i (1 to n) plus the journey time of trains going-up as j (1 to m) in every station (1 to r). Thus, the mathematical constraint for representing the objective function in this research is presented as Eq. (1) below:
Minimized total operation time

$$\sum_{i=1}^{i=n}\left(T_i A_r - T_i D_1\right) + \sum_{j=1}^{j=m}\left(T_j A_1 - T_j D_r\right) \qquad (1)$$

The variables of this research are journey time, arrival and departure time of all trains with travel time, station time, headway, car cleaning time, regular inspection time and turning back operation, as parameters. Travel time constraints restrict minimum time to travel between two contiguous stations (k to k+1) for all trains going up initialized as i (1 to n) and trains going down initialized as j (1 to m).

$$T_i A_{k+1} - T_i D_k \geq time\ i_{k\to(k+1)} \qquad (2)$$

As represented by Eq. (2), the arrival time for train i in the station k+1 minus departure time in the station k (origin station) should be greater or equal to the needed time for trains i to travel between two contiguous stations (k to k+1).

$$T_j A_k - T_j D_{k+1} \geq time\ j_{(k+1)\to k} \qquad (3)$$

The arrival time for train j in the station k minus departure time in station k+1 should be greater or equal to the needed time for trains j to travel between two contiguous stations (k+1 to k). This research uses minimum travel time between two contiguous stations, because different types of trains have different speeds and travel time would automatically differ. As explained before, running time is calculated from departure times in the timetable minus dwell times. Therefore, station time for each train i and j at station k (1 to r) should be greater than departure time minus arrival time, as shown in Eq. (4) and (5). This condition represents that the model uses maximum station time at each station, because not all trains will stop at every station.

$$T_i D_k - T_i A_k \leq TS_{i_k} + CS_{i_k} \qquad (4)$$

$$T_j D_k - T_j A_k \leq TS_{j_k} + CS_{j_k} \qquad (5)$$

Headway constraint restricts to the departure times differences between two consecutive trains in the same station. The headway time in this research is fixed to one value because we want to keep the time spacing between two trains exactly.

$$T_{t'} D_k - T_t D_k + INF \times Y_{t-t';k->(k+1)} \leq INF - headway \qquad (6)$$

$$T_{t'} D_k - T_t D_k + INF \times Y_{t-t';k->(k+1)} \geq headway \qquad (7)$$

$$T_{t'} A_{k+1} - T_t A_{k+1} + INF \times Y_{t-t';k->(k+1)} \leq INF - headway \qquad (8)$$

$$T_{i'} A_{k+1} - T_i A_{k+1} + INF \times Y_{t-t';k->(k+1)} \geq headway \qquad (9)$$

As represented by Eq. (6)-(9), $Y_{t\text{-}t';k->(k+1)}$ is the decision variable for the availability of track in one segment. The value is 1 if there is a track available between station k to k+1 and 0 otherwise. Travel time in line determines the total travel time for one train to travel through a line southbound

and northbound plus allowed time margin. Travel time in line determines the total travel time for one train to travel through a line southbound and northbound plus allowed time margin. Maximum travel time has been applied in the model; thus, the difference between arrival and departure time for one train in the same station should be less or equal to this travel time, as formulated in Eq. (10) and (11) below:

$$T_i A_r - T_i D_1 \le \left(1 + \partial/100\right) \times time\ i_{1 \to r} \quad (10)$$

$$T_j A_1 - T_j D_r \le \left(1 + \partial/100\right) \times time\ j_{r \to 1} \quad (11)$$

In the THSR system, allowed time margin was set to different numbers for different types of train. Therefore, this parameter would be a good input in sensitivity analysis to reveal the effects of changes in this parameter on objective value. Like many railway companies, THSR has a cyclic timetable in order to manage the resources comprising its infrastructure. In this research, it is assumed that the cycle time is 120 minutes (maximum travel time). Thus, if the headway time is set to 12 minutes, it means there are ten trains in the first cycle, and the next train (11th train) would be the same train as number one. It means the timetable at every two hours is the same pattern; the daily timetable is obtained by carrying out this pattern repeatedly. A train circulation model is needed to deal with these requirements. In the THSR system, train circulation takes 30 minutes maximum time, including car cleaning, regular car inspection, and turning back operations. Consequently, departure time for another train which will use the same track as those operations should be greater or equal to arrival time plus train circulation times as formulated in Eq. (12) and (13) below:

$$T_{i\left(j + \frac{traveltime}{headway}\right)} D_r \ge T_j A_1 + (InsT_1 + ClT_1 + TB_1) \quad (12)$$

$$T_{j\left(i + \frac{traveltime}{headway}\right)} D_r \ge T_i A_r + (InsT_r + ClT_r + TB_r) \quad (13)$$

If there were an event that required long travel times and headway between two contiguous trains, then the train circulation pattern would change as well.

3. RESULT

After the mathematical model for scheduling problem was formulated, a collection of data regarding scheduling requirements from the THSR Company began. Primary data was collected from interviews with senior engineers in the THSR Company, and secondary data was gathered from THSR documents including the Equipment and Facilities Operations Manual, and existing timetables from THSR. Mixed integer programming (MIP) methods and dynamic programming solution techniques have been used to solve the models with the CPLEX solver tool. The tests were operated in an Intel Core 2 Duo CPU 2Ghz with 2GB RAM.

The results showed 0% gap during the process, and the algorithm defined the results by cutting off the model. It means that the nodes were being solved during the branch and cut search. This value is typically computed by exceeding the cutoff value, and then the node can be pruned without the need to solve the node to optimality. Therefore, the computation time to solve the model is (7442.51 seconds) and performance time is 6,780 minutes as the optimal result of minimum total operation time in the THSR system. Compared to a real timetable, THSR has 6,420 minutes operation time in their system, thus the gap between these two timetables is 360 minutes or a 2.72% gap. It is caused by the difference in assumptions between the model and the real problem. In the THSR system, every type of train has its own speed to run among stations, whereas in the model this is not the case. The timetable diagram contains information regarding departure and arrival times of trains at each station. From the output departure and arrival times for each train at stations, we developed the timetable diagram in Figure 1. The new timetable for rescheduling is shown by Figure 2, that is a calamity in station 3 at time is 100.

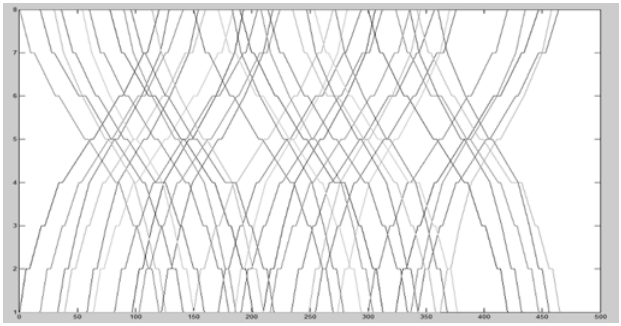


Figure 1 Timetable diagram for general event

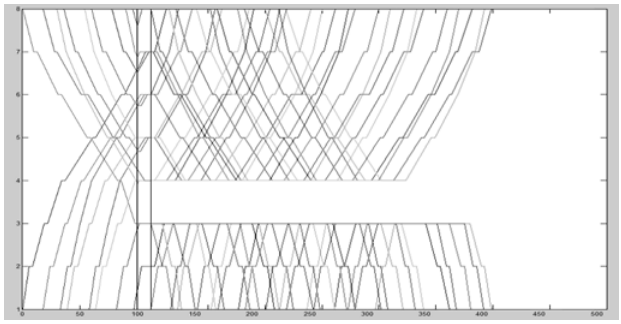


Figure 2 Timetable diagram of rescheduling for disaster

In the Figure 3, the train 1 and train 2 for southbound are not cross at all station. If the train 1 at station 2 delay 10 minutes, the timetable is shown in Figure 4, that bring the train 1 and train 2 occur the cross event at station 7.

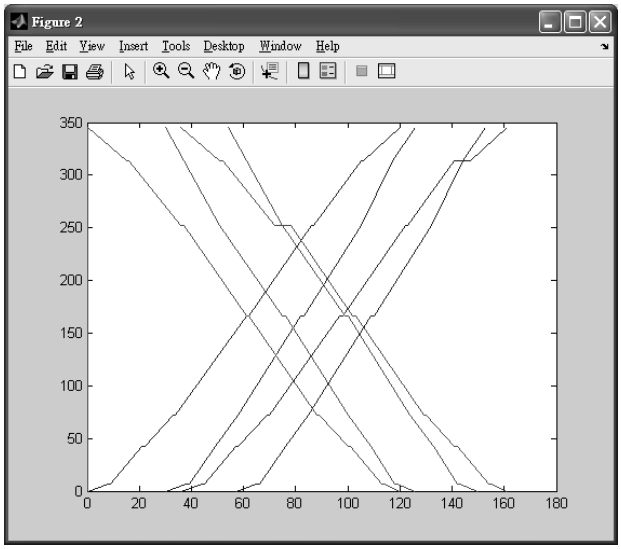


Figure 3 Timetable with no delay time event

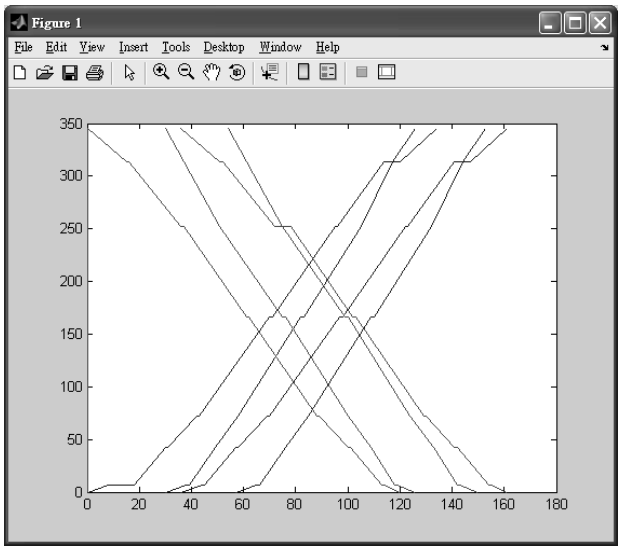


Figure 4 Timetable with delay 10 minutes on station 2 for train 1

We use the input and output patterns from mathematical model to build a decision tree using the J48 algorithm. The attributes of the decision tree as shown in Table 1. The TYPE represents the type of train with southbound and northbound, TNO represents the train number with 1 to 4, STATION represents the station number with 1 to 8, STOPT represents the delay time (minute) for a train stop at the station, and CLASS is the class of the decision tree. In the CLASS attribute, the ORG means the timetable for rescheduling is same with original timetable, T(t, t')NC means the train t and train t' are not occurring the cross event, and T(t, t')C(s) means the train t and train t' are occurring the cross event at after s stations. The decision tree algorithm selected with J48 algorithm, the result is shown in Table 2. Table 2 shown that is a very high accuracy for any number of stations and any number of trains, it can be explain that the proposed decision tree model can find the relation between the delay time and cross event.

Table 1 The attributes of tree model

Attribute	Range
TYPE	SB, NB
TNO	1, 2, 3, 4
STATION	1, 2, 3, 4, 5, 6, 7, 8
STOPT	+0, +1, +2, …, +10
CLASS	ORG, T(t, t')NC, T(t, t')C(s)

Table 2 The result of decision tree with J48 algorithm

Number of Station	Number of Train	Accuracy
8	4	85.22 %
8	8	87.09 %
10	8	70.31 %
10	4	76.22 %

4. CONCLUSIONS

This research developed an optimization model for designing timetables in high-speed railway systems that considers basic requirements as well as special requirements regarding train circulation, including car cleaning, regular inspection, and train turning back operations. The model could generate a good timetable result as good as a real timetable in two hours (7442.51 seconds). Furthermore, the model could generate train circulation patterns as illustrated in the timetable diagram results. The proposed decision

tree model can find the relation between the delay time and cross event. The rescheduling could be a good simulation analysis for predicting the effects of disruptions on the timetable without conducting real experiments.

Acknowledgements:
The authors would like to express sincere thanks to Mr. Te-Che Chen, who is a senior engineer at Taiwan High-Speed Railway Corporation and currently a Ph.D. student under the guidance of Dr. Chien-Cheng Chou, for providing real data and invaluable suggestions.

References:

Brännlund, U., Lindberg, P.O., Nõu, A. and Nilsson, J.E. (1998), "Railway Timetabling Using Lagrangian Relaxation." Transportation Science, 32(4), 358-369.

Caprara, A. (2001), "Solution of Real-World Train Timetabling Problems." Proceedings of the 34th Hawaii International Conference on System Sciences, 34(3), 3030.

Caprara, A., Monaci, M., Toth, P. and Guida, P. (2006) "A lagrangian heuristic algorithm for a real -world train timetabling problem." Discrete Applied Mathematics, 154, 738–753.

Carey, M. and Carville, S. (2003). "Scheduling and platforming trains at busy complex stations." Transportation Research Part A ,37, 195–224.

Castillo, E. (2008), "Timetabling Optimization of a Single Railway Track Line with Sensitivity Analysis." Sociedad de Estadística e Investigación Operativa, Top, 17, 256–287.

Chiu, C. K., et al. A Constraint-Based Interactive Train Rescheduling Tool. Kluwer Journal Academic Publishers, Vol. 7, 2002, pp. 167–198.

Kroon, L.G. and Peeters, L.W.P. (2003). "A variable trip time model for cyclic railway timetabling." Transportation Science, 37(2), 198-212.

Kroon, L.G., Maroti, G. and Helmrich, M.R. (2008). "Stochastic improvement of cyclic railway timetables." Transportation Research Part B, 42, 553-570.

Lee, Y. and Chen, C.Y. (2009), "A Heuristic for the Train Pathing and Timetabling Problem." Transportation Research, Part B(43), 837-861.

Mladenovic, S. and Cangalovic, M. (2007), "Heuristic Approach to Train Rescheduling." Yugoslav Journal of Operations Research, 1, 9-29.

Vieira, G.E., Herrmann, J.W. and Lin, E. (2003). "Rescheduling Manufacturing Systems: A Framework of Startegies, Policies, and Methods." Journal of Scheduling, 6, 39-62.

Yan, S. and Shih, Y.L. (2006), "Optimal Scheduling of Emergency Roadway Repair and Subsequent Relief Distribution." Computers & Operations Research Journal, 36, 2049-2066.

8CUEE CONFERENCE PROCEEDINGS
8th International Conference on Urban Earthquake Engineering
March 7-8, 2011, Tokyo Institute of Technology, Tokyo, Japan

Study of Self-risk Management of Local Residents for Earthquake Disaster

Masami Kobayashi

Professor, Graduate School of Global Environmental Studies, Kyoto University, Japan
mkoba@archi.kyoto-u.ac.jp

Abstract: Impending Nankeen Earthquake is published to be expected magnitude 8.4, event probability 60% in 30 years, by the Central Disaster Prevention Council. It is also announced that the forecasting of the event is difficult. Therefore the residents in affected areas have to be in safe places beforehand. Setting the research field on Saijyo-city, Ehime prefecture, which is designated as the Tonankai Nankai Earthquake Disaster Prevention Promote Area, we examined two topics. Topic 1 refers whether or not residents could know their personal damage risk of Nankai Earthquake from officially disclosed earthquake damage estimations (EDEs), examining the risk factors considered. Topic 2 refers the possible measures for residents to reduce their risk. Firstly, as a measure promoted by government, seismic retrofitting of wooden houses with official support is examined. Then, using questionnaire and governmental ledger, we investigated the households in which 'people vulnerable to disaster' are living in 'ineligible wooden housing'. Analyzing their situations of life risk at earthquake and their self-risk management, possible practical measures to reduce human damage are discussed.

1. INTRODUCTION

In Japan, government has taken measures with escape plan for residents based on 'earthquake damage estimation (EDE)', setting 'the Local Disaster Prevention Planning' which is obligation of local government by 'the Basic Law of the Natural Disasters'. But central government announced that forecast of impending of 'Nankai earthquake', which is published to be expected magnitude 8.4, event probability 50% in 30 years[1)], is difficult[2)]. As the residents in affected area could not escape just before the event, there are no ways of disaster prevention for residents but to be in safe place before the event. This is the reason why residents have to know their personal damage risk in order to take appropriate measures for their safety. This paper deals with two topics. The first topic refers whether or not residents could know their personal damage risk of Nankai earthquake from disclosed EDEs, by examining how risk factors are considered in EDEs. The second topic refers the possible measures for their self-risk management, by examining the measures promoted by government with official support. Setting research field on Saijo-city*, Ehime-prefecture in Japan, which is designated as the Tonankai & Nankai Earthquake Disaster Prevention Promotion Area (2003) by the central government, we investigated their EDEs and preparedness of the residents. In Saijo-city there are 2 EDEs disclosed in public by governments. They are Saijyo-city Disaster Prevention Planning (2006) based on Ehime-prefecture EDE (2002) obtained via Saijo-city official homepage and Central Government EDE (2003) via the central government official homepage. As for the residents, Ehime-prefecture the Basic Ordinance of the Disaster Prevention (2006)" is stating that 'measures taken by residents' selves are important' in the preceding sentence[3)]

*Saijo-city: Population 115,651, household 46,977, area 509.04km^2(2007.10)

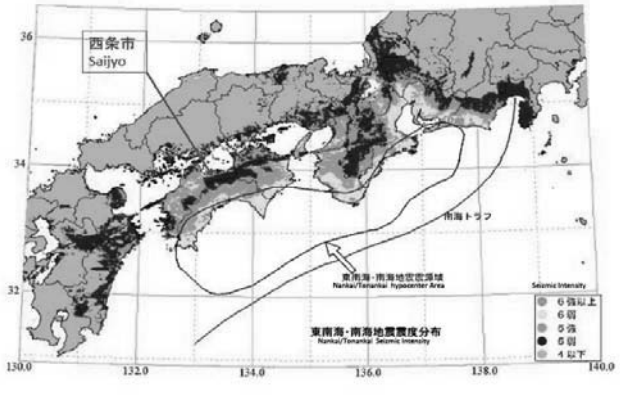


Fig.1 Location of Saijyo-City

2. TOPIC 1: To know personal damage risk of Nankai earthquake

Is it possible for each resident to know his/her personal damage risk from EDE (earthquake damage estimation) disclosed by government? It is examined how EDE is calculated, made outcome and described to public, what information is informed to residents, considering risk factor with each residents.

2.1 Major risk factors of human damage in earthquake disaster

From the tendency of recent earthquake hazard[4)5)], high-risk conditions are 1)big shake place, 2) old wooden building' and 3)escape difficulties such as the old or disabled people who stay inside for long time and are struck by building destruction. That is, major risk factors of earthquake damage are 'address', 'structure and age of housing' and 'existence or nonexistence of escape difficulties in housing', which are all personal information and each resident must have known his/her rate of each risk factor.

2.2 Informed content to residents

About the described way of Ehime-prefecture EDE, there are "estimated outcome" and "brief explanations of calculation way": but the detailed content of calculation way is not shown, and so residents couldn't calculate by themselves. The way of description of outcome is like this. Ground motion is expressed as distribution of classification of intensity on Ehime-prefecture map (scale about 1:700,000, 500m-mesh). Building damage is expressed as severe damage building–count, severe & moderate damage building-count, and the ratio of severe damage building and so on. Saijo-city is composed of 4 areas and building-count is shown as area total. The ratio is shown as the distribution of number per mesh on the map. The percentage is average in mesh nevertheless each house has different risk factor. Human damage is expressed as death people-count, which is shown as area total. Building damage and human damage are shown as total number of wide area or average of mesh area and they don't describe personal damage risk.

2.3 Calculation way

Ehime-prefecture EDE is calculated in 500m-mesh using 'governmental ledger (Fixed Asset Tax Rolls)' and 'prediction formula' developed from the Great Hanshin-Awaji Earthquake in 1995, in this case. The calculation has 4 steps: [1]Setting of expected Nankai earthquake→[2]Ground motion→[3]Building damage→ [4]Human damage. About building damage, 'the ratio of severe damage building' is determined by PGV (peak ground velocity) and 'structure and age of building'; PGV (peak ground velocity) is calculated by the mesh, building is counted by mesh with 'structure has 5 sections (Wood, Light-gauge Steel, Steel, RC/SRC, others)', 'age of buildings has 5 sections (-1951, 1952-1961, 1962-1972-1981, 1982-)'. Risk factor of building is considered at calculation level, but it is not at public description level; shown as average of mesh area. About human damage, it is calculated from risk factor of place and building, which is 'the ratio of severe damage building' and 'structure of housing (wood or the other'. It is not considering the risk factor of humans, just in a single uniform way, which does not have make sense.

2.4 Informed outcome

Central government EDE shows that about 5,000-6,400 severe damage of buildings, about 80-100 death of people in Ehime-prefecture, while Ehime-prefecture EDE shows 210,958 severe damage of buildings, and 2,556 death people. For example, used prediction formula 'correlation equation of ground motion & building damage' is different, that of Ehime-prefecture EDE[6)] is 'intensity & the ratio of the severe damage building', and that of Central Government EDE[7)] is 'peak ground velocity & the ratio of the severe damage building'.

2.5 Conclusion of Topic 1

Residents could not know personal damage risk from EDE disclosed by government. There are problems on the way of description to public and the way of calculation, and so, the informed contents are different. Personal damage risk is calculated by personal information (risk factor of building) and official information (prediction formula, ground motion and so on) which residents do not know. Personal information is used so the way of disclosing in public becomes 'obscure'. EDE should be disclosed so that each resident could know his/her personal damage risk and its calculation way. The future tasks are (1) development of tool for informing (e.g. inputting personal information on Web service, damage risk is calculated automatically), and (2) confirmation or unification of calculation way (Prediction formula is made from unitary event, and outcome is different by each prefecture).

3. TOPIC 2: Possible measures for self-risk management

Topic 2 refers to "What are possible measures for resident to practice their self-risk management".

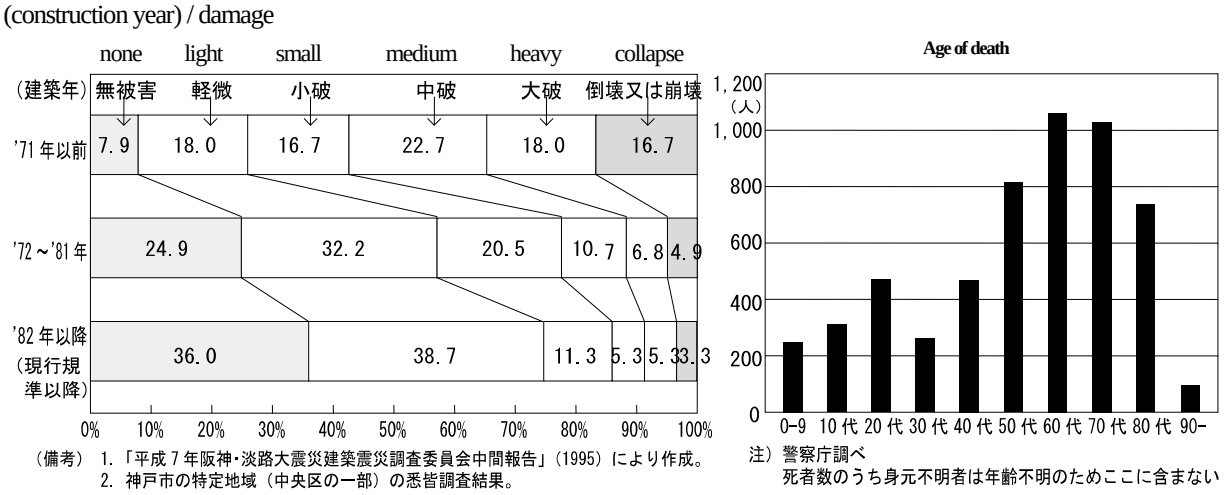


Fig.2 Variation of Wooden Building Damage by Construction Year (left) and Age of the dead (right) in Hanshin-Awaji Earthquake (1995)

図２ 激震地における建築年別の木造建物の被害(左)、阪神淡路大震災の年齢別死者数（右） 出典：阪神淡路大震災調査報告、(社)日本建築学会)

Table 1 Situation of the dead people at 'Niigata Chuetsu-oki Earthquake' (2007)

表１ 新潟県中越沖地震・死亡者の亡くなった状況（出典：朝日新聞('07.7.18)

死亡者	亡くなった状況
女 (81)	一人暮らし。2 階建て木造住宅が倒壊し、1 階にいて死亡
女 (79)	娘、孫と 3 人暮らし。2 階建て木造住宅の 1 階がつぶれて死亡
男 (76) 女 (72)	2 人暮らし。木造 2 階建て住宅の 1 階がつぶれて死亡
女 (78)	1 人暮らし。倒壊した住宅の屋根の下から発見される。救出されたが搬送先の病院で死亡
男 (83)	妻と長男夫婦との 4 人暮らし。居間でテレビを見ていたとき、木造 2 階建て住宅の 1 階がつぶれて死亡
男 (82)	長男夫婦と 3 人暮らし。木造住宅が倒壊して死亡
女 (71)	夫と 2 人暮らし。買い物に出かけ、木造 2 階建ての呉服店の倒壊に巻き込まれ死亡
男 (77)	夫と長男夫婦との 4 人暮らし。食事中、地震の揺れでいすから倒れ、搬送先の病院で死亡

Woman (81) in wooden house at 1F
Woman (79) in wooden house
Man (76) and woman (72) in wooden house at 1F
Woman (78) under roof of collapse
Man (83) in wooden house at 1F
Man (82) in wooden house
Woman (71) wooden store
Man (77) at hospital



Fig.3 Survey Area

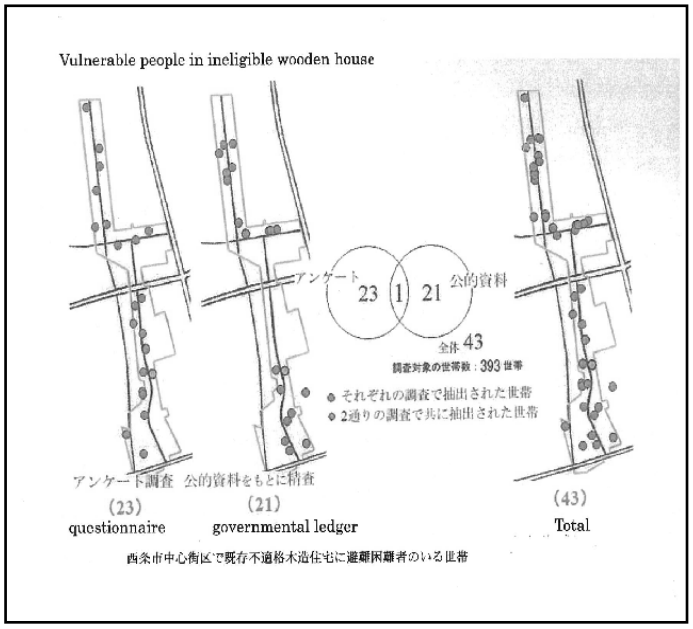


Fig.4 Vulnerable people in Ineligible Wooden House

3-1 Legally safe standard

In recent earthquake hazard, human damage has concentrated on old people living in old wooden building[4)5)]. (See Fig.2 and Table1) The building with pre code-revision (before 1981) is existing ineligible, which is often luck of seismic performance. Such housings are about 10,000,000 in Japan[8)]. Government has taken measures to especially 'ineligible wooden housing'. While, residents who are in difficulties to escape at disasters by themselves were defined as 'people vulnerable to disaster' by Central Government Guideline (2005), and government recognized necessity of support of their escape. This study investigated the number of households that are *'people vulnerable to disaster' living in 'ineligible wooden housing'*, in the central district of Saijyo-city on Sep. 2007. The research area (See Fig.3) has 1,538 people and 693 households are crowded with old wooden houses. The research way was with ① questionnaire to ask existence of 'people vulnerable to disaster', which is conformable to Central government guideline, and to check the same issues by ② the governmental ledger. We asked 11 neighborhood councils in the area to distribute the questionnaire sheets and 228 households (62.6%) have answered them. The outcome is ①23,②21,①∩②1,①∪②43, total is 1 in 14 households (43/228), not a few residents.(See Fig.4)

3-2 Official support

After the Great Hanshin-Awaji Earthquake, local government has taken measures for 'ineligible wooden housing' with official support about seismic retrofitting: subsidy for seismic diagnosis and seismic retrofitting. While, local government has taken measures for 'people vulnerable to disaster' with 'Escape Support Plan' which sets the way of rescue or leading to evacuation center for each of them immediately. But it is 'after the event (earthquake)', in case of surviving. After the event, there are 'Escape Support Plan', provision of temporary housing, reconstruction money and condolence money for bereaved families and so on, which are for residents with building or human damage. While before the event, official support is only about seismic retrofitting.

3-3 Measures promoted by government

Measure promoted by government is only 'seismic retrofitting' which can prevent unpredictable earthquake disaster. But it is unpopular to residents, there are mainly 4 reasons: (1) residents' economical burden, (2) botheration in regular life and deterioration of habitability (by decrease of open mouth and increase of wall), (3) trustless to effect, and (4) lack of information[9)]. Economical reason is big. The subsidy is often given only for the case to over the structural-overall score 1.0 (1.0 is standard of the Building Code), which needs structural calculation and adequate construction work by licensed person. And the government has taken stance of not using official money for contribution to personal property, so subsidy to housing is limited.

We also asked 228 households in the survey area with questionnaire 'Why don't you do seismic retrofitting?' The major reasons (multiple selections) are 1st: 'Non-dweller after several years' 49(21.5%) and 2nd: 'Economical burden' 40(17.5%). Among 21 households with 'people vulnerable to disaster' living in 'ineligible wooden housing', 20 households answered the reasons for not doing seismic retrofitting. Their major reasons are 'No dweller after several years' 7(35%), and 'economic burden' 7(35%). The average cost of seismic retrofitting for old wooden houses is reported as 1.76 million yen[3)].

Informed the brief explanation of Ehime-prefecture EDE within the questionnaire, 37 households hoped to consult about seismic retrofitting, so it was explained about official support to them with city officer, but only 1 household used seismic diagnosis and no household did seismic retrofitting.

3-4 Possible measures for self-risk management

Even if it is impossible to prevent earthquake disaster, it is possible to reduce human damage risk. The concept is to save human life. There are some possible measures for self-risk-management. Mitigation way is to make a space residents spend most of their time not to be destroyed severely, and also not to stay long time at high-risk space. Some examples are like these.

a) Simple seismic retrofitting**:** (e.g. Sumida, Tokyo) Official support could be applied to the case that seismic performance improved before, even if overall score doesn't over 1.0. It also could be applied to only bedrooms or living rooms.

b) Self-build or self order**:** These are based on each resident's judgment, so repair way or the contractor is chosen by themselves. These might not be taken place strictly following with legal standard.

c) Cooperation of each resident**:** For example, cooperative reconstruction by neighborhood. If residents unfulfilled with legal safety standard cooperate and build as 'community shelter' for pre-escape, there might be possibility of official support in future.

d) Application of seismic diagnosis**:** By seismic diagnosis, resident could know high-risk rooms so they could choose where to be in a day and sleeping time.

e) Application of public resources**:** To shorten time to

stay at high-risk housing, there is possibility by application of public resources (e.g. café, spa, community bus…etc.) available in regular life in neighborhood. The public buildings have seismic performance. Enriching public service and infrastructure to access, it is promoted to be out of high-risk space.

3-5 Conclusion of Topic 2

The measure promoted by government is about 'seismic retrofitting', which is exactly a way for disaster prevention. If the residents are living in 'ineligible wooden housing', they can receive official support, but it is unpopular though there are not a few 'people vulnerable to disaster' are living in 'ineligible wooden housing'. The main reason of unpopularity is economical burden (including 'non-dweller after several years), which is the outcome of Benefit/Cost (B/C) of the residents. Housing is personal property and so, measures shall be done by self-help, which is governmental consensus. However, considering with the concept to reduce personal risk of human damage, there are possible measures implemented by self-risk management. And measures which enable residents to choose could be increased if social and public resources are used for their safe places before the event. Future task is (1) sharing the same information of damage risk between government and the residents: presence of residents with high-risk, presence of old wooden houses unfulfilled with legal safety standard, and the rate of damage risk caused by the coupling of the two factors, (2) affordable activities for mitigation conducted by residents and government with official support. That is if the resident could check and obtain the rate of personal life risk in their houses at the coming earthquake by the disclosed EDEs which are personally accessed through internet at the governmental websites, for instance, it is possible for the residents to choose to judge their accessible safe place before the earthquake as well as 'acceptable size and expense for house retrofitting', considering their span of life expectancy.

References:

1） The Headquarters for Earthquake Research Promotion: "Overview of long term estimation of ocean-trench earthquake", Japan, 2008

2) Central Disaster Prevention Council: "Expert panel about Tokai earthquake (the 3rd conference note)", Japan, 2001

3) Ehime-prefecture: "Ehime-prefecture the Basic Ordinance of Disaster Prevention", preceding sentence, Japan, 2006

4) Architectural Institute of Japan: "Search Report of the Great Hanshin-Awaji Earthquake", Japan, 2000

5) Disaster Prevention Bureau of Niigata-prefecture Government: "Disaster damage of the Niigataken Chuetsu-oki Earthquake in 2007.7.16 (the 241st report)", Japan, 2008

6) J. Miyakoshi, Y. Hayashi, K. Tamura, N. Fukuwa: "Damage Ratio Functions of Buildings Using Damage Data of the 1995 Hyogo-ken Nanbu Earthquake", Proc. Of ICOSSAR'97, pp.349-354, 1997

7) Yamasaki's method (1999) (Central Disaster Prevention Council Homepage: http://www.bousai.go.jp/jishin/chubou/taisaku_nankai/nankai_top.html, Japan, pp.1-3, 2003

8) Ministry of Land, Infrastructure, Transport and Tourism (MLIT): "Handout of Earthquake Disaster Prevention Promotion for Housing and Building", Japan, 2005

9) Michiko Ootsuka, Traffic Policy Division of MLIT: "Actual state and Problem of Housing to Resist Earthquake", National Diet Library, IDDUE BRIEF NUMBER 568, Japan, 2007

8CUEE CONFERENCE PROCEEDINGS
8th International Conference on Urban Earthquake Engineering
March 7-8, 2011, Tokyo Institute of Technology, Tokyo, Japan

LONG-RUN EFFECTS OF A DISASTER: MEASURING THE ECONOMIC IMPACTS OF THE KOBE EARTHQUAKE

Yasuhide Okuyama

Center for Urban Earthquake Engineering, Tokyo Institute of Technology, and University of Kitakyushu, Japan
okuyama.y.ac@m.titech.ac.jp

Abstract: In 1995, the Great Hanshin-Awaji Earthquake, a.k.a. Kobe Earthquake, occurred in the second largest economic region of Japan, and its economic damages were accounted around 10 trillion yen (Okuyama et al., 1999). A catastrophic event in this magnitude would have surely created some long-run impacts on the regional economy as well as on the surrounding regions. In addition, the recovery and reconstruction activities would have affected the economic structure of the region and interdependencies between regions. While these long-run economic impacts are considered to be sizable, few studies have conducted to empirically measure or estimate such impacts, due to the significant noises in economic data disturbed by macroeconomic fluctuations and to the lack of detailed economic data on the damages and losses caused by the earthquake. At the same time, several cross-country and/or cross-hazard studies, for example Skidmore and Toya (2002) and Cuaresma et al. (2008), have been carried out to analyze whether or not long-run economic implications of disasters actually materialize, while their results are somewhat mixed. This paper presents an empirical investigation of long-run economic impacts of the Kobe earthquake, using econometric models.

1. INTRODUCTION

While significant progress has been made in recent years for the economic analysis of disasters, especially in the field of economic modeling for disaster impact (for example, Okuyama and Chang, 2004; and an excellent compilation of related papers by Kunreuther and Rose, 2004). Since the pioneering work by Dacy and Kunreuther (1969), a generalized framework for the economic analysis of natural disasters had been proposed (for example, Sorkin, 1982; and Albala-Bertrand, 1993). The recent advancements have been more toward empirical analysis and toward strategies for modeling extensions and modifications to fit them to disaster situations. This trend is due to improved data availability of disaster damages and losses and to increased multidisciplinary research activities about disasters, including sociology, economics, and psychology. At the same time, the uniqueness of each hazard and of its damages and impacts presents enormous challenges in economic modeling for disaster impact estimates; many issues remain unsolved to this date. In particular, while the domination of flow analysis models employed in the recent research indicates that the impacts of a catastrophic disaster spread over to other regions or nations through expanded trades between regions (Okuyama et al., 1999) and/or sometimes between nations (Okuyama, 2010), some other researchers claimed that the the impact estimation of even a large disaster ends up "insignificant total impacts." (Albala-Bertrand, 1993)

These arguments should have entertained the measurement of empirically observed disaster impacts; however, few studies, if non-existent, have done such study. Most of those studies estimating the impacts of a particular disaster after its occurrence only assessed the impacts based on the available input data and some economic models, like input-output models and so on. It appears considerably entangled to literary measure disaster impacts based on empirically available macroeconomic data, partly because the disaster statistics are not standardized even among developed countries and are even "somewhat crude measures," (Skidmore and Toya, 2002) and also because in usual macroeconomic indicators, such as gross domestic products or gross regional products, economic impacts of a particular disaster may be potentially hidden within macroeconomic fluctuations and may be more likely cancelled out between negative impacts from damages and positive impacts of recovery and reconstruction activities. At the same time, empirical measurement of disaster impacts is necessary and critical to improve the accuracy of and assure those impact estimates derived based on economic model, and to understand how a disaster affect economies in terms of readily available data and indices.

In this paper, the economic impacts of the Hanshin-Awaji Earthquake occurred in 1995 are measured empirically using the time-series data and econometric models. Next section briefly summarized the previous studies and findings related to economic impacts of natural disasters. Section 3 presents the econometric models for measurement and sets time frame for the case study. The results of model estimation and the discussions are presented

in Section 4. Section 5 concludes this paper with the discussion of findings and some remarks.

2. ECONOMIC IMPACTS OF NATURAL DISASTERS

Natural disasters can cause physical destructions to built-environment and networks, such as transportation and lifelines, and can also cause casualties and injuries to human lives. These damages are often called damages, and are by economics' definition the damages on stocks, which include physical and human capitals. Then, these damages lead to the interruptions of economic activities, such as production and/or consumption, and the losses from business interruptions are called the (first-order) losses of a disaster. At the same time, there is another term called higher-order effects, which take into account the system-wide impact of flow losses through interindustry relationships. (Rose, 2004). And, total impacts are the total of flow impacts, adding (first-order) losses and higher-order effects (Okuyama and Sahin, 2009). While some researchers critique that the higher-order effects of disaster are "more a possibility than a reality" (Albala-Bertrand, 1993, p. 104), the estimation of indirect effects has been attempted to "gauge individual and community vulnerability, evaluate the worthiness of mitigation, determine the appropriate level of disaster assistance, improve recovery decisions, and inform insurers of their potential liability" (Rose, 2004, p. 13).

The economic impacts of natural disasters have been studies in various contexts and with a range of time frames. Ex-ante analysis of a hypothetical and/or potential hazard occurrence is often done for the decision-making of preparedness and mitigation strategies; and ex-post analysis of actual hazards and disasters is usually carried out to investigate how the event affected the economy and to examine to what extent the relief efforts by various levels of public sector and by other institutions are needed. The impact studies of natural disasters can be also categorized between short-run impact analysis and long-run impact analysis. Short-run analysis of disaster impact studies intends to estimate the total (flow) impacts of a hazard, defined above, for the period of a few years, and usually employs input-output model, social accounting matrix, or computable general equilibrium model of a particular region, regions, or nation. By its nature, short-run analysis measures only flow changes and can distinguish between the negative impacts based on loss data and the positive impacts from recovery and reconstruction activities, which serve as intense demand injections to the region. Several shor-run analyses of disasters were compiled in Okuyama and Chang (2004) and the methodologies are summarized in Okuyama (2007). On the other hand, long-run analysis of disaster studies aims to measure the effects of damages on stock, which may affect the long-run growth path of the damaged region, resulted from the changes in physical and human capital accumulation level and technology replacement (Okuyama, 2003). The long-run analysis of disasters usually employs econometric models with time series data; and because of it, they cannot distinguish between negative and positive impacts of a disaster and can only derive net impacts. Notable studies in this line include Skidmore and Toya (2002), Rasmussen (2004), and Cuaresma et al. (2008). Comparing to short-run analysis, long-run analyses of natural disasters have been limited, due mainly to the significant noises in macroeconomic data and also to the difference in details and extent of damage data gathered over time.

3. EMPIRICAL MODELS FOR STATISTICAL TESTS AND MEASUREMENT OF THE IMPACT OF AN EARTHQUAKE

We employ the Hanshin-Awaji Great Earthquake (hereafter Kobe Earthquake),which occurred in 1995 at Kobe, Japan, as the case study for empirically measuring the trends of the total impact over time. In doing so, we construct time-series models for City of Kobe and Hyogo Prefecture that includes Kobe.

3.1 Recap of Kobe Earthquake

On January 17, 1995, the worst disaster in the postwar Japan struck the second largest region of Japan—the Kinki region. The City of Kobe and surrounding municipalities experienced massive destruction of houses, buildings, roads, rails, and infrastructure. The magnitude of this event can be shown with the following facts: according to the Hyogo Prefecture Government (2010), the number of casualties was 6,434; the number of injuries was 43,792; the number of evacuees was 316,678 (at its peak); and the number of damaged houses was about 640,000. The direct damages from this Kobe Earthquake were estimated at about 10 trillion yen (US$ 100 billion, as $1=100 yen), equivalent to about 2.1% of Japan's GDP and 11% of Kinki's GRP (Gross Regional Product) at that time. These direct damages were concentrated in the destruction of buildings (including houses and production facilities), transportation facilities, and utilities. Although the damaged area was geographically only 4% of Kinki, it included 15% of the Kinki's population. The damages to capital stocks were estimated about 0.8% of Japan's total (Okuyama et al., 1999).

3.2 Time-Series Models

In order to statistically analyze the total impact of the Kobe Earthquake using the empirical time-series data, a series of time-series models is constructed. The functional form of these models employs an autoregressive-distributed lag model (Hendry, 1995). This is because we are interested in the total impact of an exogenous shock (earthquake) on gross regional product (GRP), a flow measure of the economy, and also because we measure the total impact as departures from the long-run growth path of an economy. The general form of the linear autoregressive-distributed lag model can be written as follows:

$$y_t = \beta_1 z_t + \beta_2 y_{t-1} + \beta_3 z_{t-1} + \varepsilon_t$$

where y_t is the dependent variable, z_t is the independent variable. In this formulation, z_t can be used to control exogenous factors influencing the growth path of y_t. Any miscellaneous influences to y_t will be captured by ε_t, residuals.

Base on this formulation, three models are constructed to statistically measure and test the total impact of the Kobe Earthquake. The first model is for the City of Kobe where the earthquake struck and damaged most severely:

$$KOBE_t = \beta_0 + \beta_1 JPN_t + \beta_2 JPN_{t-1} + \beta_3 KOBE_{t-1} + \varepsilon_t \quad (1)$$

where $KOBE_t$ is the logarithm of GRP per capita for the City of Kobe at t, JPN_t is the logarithm of GDP for Japan at t. JPN_t and its lagged variable intend to control the macroeconomic trends, such as changes in inflation, interest rate, currency exchange rate, economic booms (bubble economy of mid and late 80's) and slumps (after early 90's), etc., of Japan. The second model is for the Hyogo Prefecture, which includes the City of Kobe and other cities and municipalities hit by the earthquake:

$$HYOGO_t = \beta_0 + \beta_1 JPN_t + \beta_2 JPN_{t-1} + \beta_3 HYOGO_{t-1} + \varepsilon_t \quad (2)$$

where $HYOGO_t$ is the logarithm of GRP per capita for the Hyogo Prefecture at t. As seen above, the basic structure of equation (2) is exactly the same as the one of equation (1). One of the assumptions here to use JPN_t and its lagged variable in the right hand side of equations (1) and (2) is that the earthquake did not impact on the Japan's GDP per capita. If it did, the inclusion of JPN_t in the right hand side may lead to the violation of residual distribution assumptions, and the models require some countermeasures, like instrumental variable or others, for estimation. In order for testing whether or not the earthquake impacted on Japan's GDP, the third model is constructed:

$$JPN_t = \beta_0 + \beta_1 JPN_{t-1} + \varepsilon_t \quad (3)$$

This form constitutes a univariate time-series model, a variant of the above linear auto-regressive lag model.

In order to test the hypothesis that the earthquake has some impact on the respective long-run growth path, dummy variables for the year when the earthquake occurred and subsequent years are added to each model.

3.3 Data and Period

The time series data used for the analysis was extracted from the Cabinet Office of Japan's web site.[1] The data are "National Accounts" for GDP, and "Prefectural Accounts" for GRPs. Since the Japanese government started collecting and releasing these statistics using the Systems of National Accounts (SNA) from 1975, the consistent time series data are also from 1975. Thus, the period of analysis for this study becomes during 1975 and 2006, which is the latest data point. Note that all the data that the Japanese government publishes are fiscal year base, and the Japanese fiscal year starts from April and ends at March of the next year. This implies that while the Kobe earthquake occurred in January, 1995, it is within the fiscal year 1994.

All the data are converted to the 2000 constant price. An overview of the trends of three variables, *JPN*, *HYOGO*, and *KOBE* are shown in Figure 1. The Japan's GDP per capita had steadily increased throughout the period, while the rate of growth had slowed down a bit after 1990, when the bubble economy bursted, and has regained some speed after 2002. Hyogo's GRP per capita is mostly lower than Japan's, and the rate of growth appears to parallel to the Japan's till 1993. The fiscal year 1994, when the Kobe earthquake occurred, shows a small dent, whereas 1995 and 1996 show sharp increases. At the same time, after 1997, the Hyogo's trend looks downward, until it turned to upward after 2004. The Kobe's growth path mirrors the Hyogo's, but the values are generally larger than not only Hyogo's but also Japan's. The dent of 1994 for Kobe is much larger than the Hyogo's, and the increase in 1995 is also higher. Unlike Hyogo's, however, Kobe seems not to turn the trend upward until 2006. This may be resulted partly from population changes in the City of Kobe after the earthquake.



Figure 1. Trends of per capita GDP and GRPs

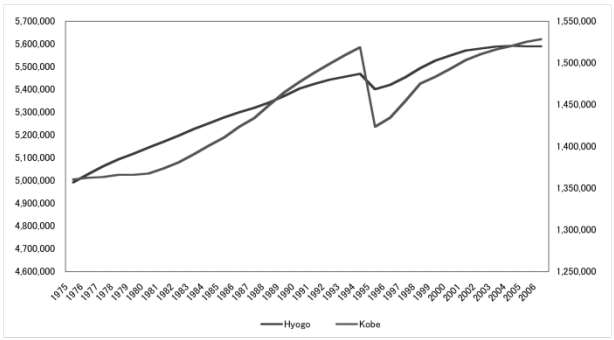


Figure 2. Trends of Population for Hyogo Prefecture and City of Kobe
(right vertical axis for Kobe and left vertical axis for Hyogo)

As displayed in Figure 2, after the sharp decline of its population in 1994, Kobe had struggled to regain its population to the pre-earthquake level until 2002, and the population increase has continued afterwards. On the other hand, the Hyogo Prefecture, including the City of Kobe, also lost their population in 1994, but it was not as sever as Kobe did in terms of the rate of change. Hyogo returned to its previous population level in 1998, and after 2003 their population trends appear flat. With these casual

[1] http://www.esri.cao.go.jp/jp/sna/toukei.html#kenmin (in Japanese)

observations, the effects of the Kobe Earthquake are apparent: a sharp negative impact in 1994, positive ones in the following few years, and some slumps afterwards until picking up the paces in the mid 2000s. We estimate these trends statistically in the following section to see whether or not this observation is supported statistically.

4. HYPOTHESIS TESTS AND ANALYSIS

In this section, a series of hypothesis tests are carried out to investigate whether or not the Kobe earthquake's total impact made statistically significant influence on the respective economy's long-run growth path. In addition, with the estimated long-run growth model, the earthquake's total impacts are measured for the period after the occurrence.

4.1 Hypothesis Tests

First, we test the hypothesis whether or not the earthquake had any statistical impact on the long-run growth path of Japanese's economy. Equation (3) above was estimated using the Japan's GDP data during 1976 and 2006[2]. Dummy variables for each year after fiscal year 1994 are included to see their statistical significance. The estimation results are shown in Table 1 below.

Table 1. Significance of the earthquake on GDP (JPN as dependent variable)

Variables	Model 3-1	Model 3-2	Model 3-3	Model 3-4	Model 3-5
Dependent variable	JPN	JPN	JPN	JPN	JPN
Constant	1.073*		1.165*	1.194*	1.307**
	(0.566)		(0.582)	(0.585)	(0.602)
JPN (t-1)	0.897***	1.002***	0.888***	0.885***	0.873***
	(0.056)	(0.002)	(0.057)	(0.058)	(0.059)
D94			0.095		0.105
			(0.120)		(0.121)
D95				0.106	0.116
				(0.121)	(0.122)
Number of observations	31	31	31	31	31
R-squared	0.90	0.90	0.90	0.90	0.90
BIC	-20.70	-20.61	-19.32	-19.40	-18.11

Standard error in parentheses.
* Significant at the 10% level.
** Significant at the 5% level.
*** Significant ar the 1% level.

Models 3-1 and 3-2 do not include any time dummy variables. Model 3-1 includes the constant term, β_0 in the above equation (3), and it is barely significant at 10% revel. While R-squared for both models are about the same, the value of BIC for Model 3-1 is slightly better than 3-2's, the models with time dummy variables include the constant, indicating a moving average process. Models 3-3, 3-4, and 3-5 include time dummy variables in different ways[3]. As seen above, however, these time dummy variables for the fiscal years 1994, when the earthquake occurred, and 1995, when the reconstruction activities were at their full swing, are not statistically significant in any of three models. Also, the inclusion of these dummy variables either does not improve the values of R-squared and of BIC. This is an indication that the Kobe earthquake did not influence and did not have any impacts on the long-run growth path of Japan. This also implies that the use of Japan's GDP as an independent variable to control macroeconomic influences in equations (1) and (2) can be rationalized, and does not cause the endogeneity problem.

Secondly, we estimate equation (2) to test the statistical significance of the earthquake impact on the Hyogo's economy. The results are shown in Table 2.

Table 2. Significance of the earthquake on GRP (HYOGO as dependent variable)

Variables	Model 2-1	Model 2-2	Model 2-3	Model 2-4	Model 2-5
Dependent variable	HYOGO	HYOGO	HYOGO	HYOGO	HYOGO
Constant	0.065				
	(0.044)				
JPN	0.602*	0.894***	0.856***	0.911***	0.907***
	(0.316)	(0.250)	(0.250)	(0.244)	(0.239)
JPN (t-1)	-0.354	-0.668**	-0.651**	-0.698**	-0.650**
	(0.335)	(0.263)	(0.261)	(0.256)	(0.251)
HYOGO (t-1)	0.686***	0.760***	0.783***	0.772***	0.725***
	(0.140)	(0.133)	(0.133)	(0.130)	(0.128)
D94			-0.037		
			(0.031)		
D95				0.048	
				(0.030)	
D96					0.057*
					(0.030)
Number of observations	31	31	31	31	31
R-squared	0.97	0.97	0.97	0.98	0.98
BIC	-60.59	-61.13	-60.21	-60.80	-61.40

Standard error in parentheses.
* Significant at the 10% level.
** Significant at the 5% level.
*** Significant ar the 1% level.

The results of Models 2-1 and 2-2 illustrate no statistical significance of constant term; thus the following estimations with time variables do not include the constant term in their models. The estimation with time dummy variables displays the mixed results. The dummy variables for the fiscal year 1994 when the earthquake occurred and the following fiscal year, 1995, are not statistically significant with large margins, while the dummy variable for the fiscal year, almost two years after the earthquake is statistically significant at 10% level with a small and positive coefficient value. The value of BIC with the 1996 dummy variable is marginally better than the model without time dummy variables. The interpretation of these results requires some caution. This anomaly of the fiscal year 1996 may or may not be caused by the earthquake, since we cannot distinguish between the impact from the earthquake and related activities, such as recovery and reconstruction activities, and the other influence specific to the Hyogo Prefecture in the current model structure. The coefficient for the 1996 dummy variable is positive and relatively small.

[2] 1975 data was lost due to the lag structure of the model. Thus, the number of sample for this and subsequent models becomes 31.

[3] Time dummy variables after the fiscal year 1996 were also implemented and estimated, but they appeared not statistically significant at all, either included separately or all together. Thus, the results for these cases are not included in this table. This tendency also found in the following HYOGO and KOBE cases; therefore, the tables below do not include those results, either.

This means the slight increase in the Hyogo's GRP, departing from the long-run growth path. If it were resulted from the earthquake related activities, however, this result implicates that the influence from such activities would have required some time, in this case around two years, to materialize in a larger region, the Hyogo Prefecture. Or, maybe, the total impact from the earthquake would have absorbed in a larger economy, canceling out between the negative impact from destructions and damages and the positive impact of demand injections through recovery and reconstruction activities for the fiscal years 1994 and 1995. Again, it is difficult to conclude how this positive departure in the fiscal year 1996 emerged.

Finally, the results of Kobe's model (1) are summarized in Table 3. Based on the Models 1-1 and 1-2, the constant term is not included in the following analysis, since the constant term in Model 1-1 is not significant and the model without constant term, Model 1-2, has the better BIC. Models 1-3 and 1-4 reveal that the fiscal years 1994 and 1995 are statistically different from the long-run growth model[4]. The coefficients are negative for 1994, when the earthquake occurred, and positive for 1995. These signs are consistent with the trend observation above and with disaster theory that the destructions by earthquake lead to the negative impacts on the economy, while the demand injection of recovery and reconstruction activities can create some positive impacts later on.

Table 3. Significance of the earthquake on GRP
(KOBE as dependent variable)

Variables	Model 1-1	Model 1-2	Model 1-3	Model 1-4	Model 1-5
Dependent variable	KOBE	KOBE	KOBE	KOBE	KOBE
Constant	0.030				
	(0.056)				
JPN	1.175***	1.291***	1.221***	1.298***	1.231***
	(0.352)	(0.272)	(0.258)	(0.203)	(0.181)
JPN (t-1)	-1.002**	-1.143***	-1.096***	-1.225***	-1.179***
	(0.379)	(0.268)	(0.254)	(0.201)	(0.179)
KOBE (t-1)	0.808***	0.852***	0.877***	0.919***	0.942***
	(0.138)	(0.110)	(0.104)	(0.083)	(0.074)
D94			-0.066**		-0.062***
			(0.031)		(0.022)
D95				0.119***	0.117***
				(0.025)	(0.022)
Number of observations	31	31	31	31	31
R-squared	0.97	0.97	0.98	0.98	0.99
BIC	-57.76	-59.32	-60.00	-67.27	-69.83

Standard error in parentheses.
* Significant at the 10% level.
** Significant at the 5% level.
*** Significant ar the 1% level.

We also tested the Model 1-5, which includes both the dummy variables of 1994 and 1995. The result indicates a better BIC value and the largest R-squared among the models we estimated. All the coefficients become statistically significant at 1% level, and the sign and size of them are consistent with the previous models. Unlike the Hyogo's case, it is less ambiguous that why 1994 and 1995 are dissociated with the Kobe's long-run growth path; these negative and positive departures are considered as the result from the occurrence of the Kobe Earthquake. However, if this is the case, we may encounter two potential problems: 1) the size of negative impact in 1994 is about a half of the 1995's positive impact, implying that the earthquake created net positive impact, i.e. net gain, in Kobe; and 2) the impacts of the earthquake and of the recovery and reconstruction activities appear lasted only two years. These problems are investigated in the following sub-section by measuring the total impacts of the earthquake using the time-series model.

4.2 Measuring the Impacts of the Kobe Earthquake

The total impact of the Kobe Earthquake is measured based on the model estimated above. Since Model 1-5 in Table 3 has the highest R-squared and the best BIC value, it is employed for this task as follows:

$$KOBE_t^{est} = b_1 JPN_t + b_2 JPN_{t-1} + b_3 KOBE_{t-1} + b_4 D_{94} + b_5 D_{95} \quad (4)$$

In order to measure the earthquake's impacts, it is often suggested to compare between the values with the earthquake, i.e. the actual GRP, and the projected values as if the earthquake never occurred; then, the differences between them become the changes made by the event. In this context, we can just compare the actual values with the fitted values based on equation (4) excluding two dummy variables, D_{94} and D_{95}, to calculate the impacts, as follows:

$$KOBE_t^{est} = b_1 JPN_t + b_2 JPN_{t-1} + b_3 KOBE_{t-1} \quad (5)$$

However, the equation (5) includes a lagged variable, $KOBE_{t-1}$, which represents the actual Kobe's GRP values containing the earthquake's influences after its occurrence. This may create a causality problem--for example, the projected 95 value is derived based on equation (5) using the actual 1994 GRP value, $KOBE_{94}$, including the earthquake's influence. Therefore, the projected 1995 GRP for KOBE without earthquake influences should not adopt the actual 1994 GRP value; rather, it should employ the estimated 1994 GRP, $KOBE_{94}^{est}$, in equation (5). This modifies the equation (5) to become as follows after 1995:

$$\left.\begin{aligned} KOBE_t^{est} &= b_1 JPN_t + b_2 JPN_{t-1} + b_3 KOBE_{t-1} \quad until\ 1994 \\ KOBE_t^{est} &= b_1 JPN_t + b_2 JPN_{t-1} + b_3 KOBE_{t-1}^{est} \quad after\ 1995 \end{aligned}\right\} \quad (6)$$

In this way, the impacts of earthquake are excluded in the projected values after 1994. The projected 'no-earthquake' values are compared with the fitted values derived using equation (4). This is because the residuals of Model 1-5, difference between actual and fitted values, include some other unknown disturbances specific to the City of Kobe than macroeconomic influences controlled by the Japan's GDP and its lagged term and the impacts of the earthquake controlled by dummy variables. Hence, the comparison between the fitted values and the projected 'no earthquake' values counts out those unknown disturbances.

The trends of actual (in blue), fitted (in red), and projected 'no-earthquake' cases (in yellow) are shown in

[4] Dummy variables for all other years after 1996 are not statistically significant.

Figure 3. The yellow trend line of no earthquake case departs from the red line of the fitted trends at 1994, when the earthquake occurred. The earthquake impact of 1994 is negative, as indicated with the dummy variable for 1994, D94 in equation (4). In the mean time, from 1995, the fitted values are greater than the no-earthquake ones till 2003, indicating the positive impacts, potentially from the demand injections of recovery and reconstruction activities within the City of Kobe. These positive impacts appear larger during 1995 and 1996 and gradually declining afterwards. After 2004, however, the difference becomes negative, implying the Kobe's economy is not performing well as the long-run growth path predicted. These last three years' negative impacts might be seen as a realization of the long-run effects caused by the earthquake, by which the Kobe's economy has become slump after the completion of reconstructions exogenously boosting the economy. These observations have to be investigated more closely and carefully with the empirical events and activities to make more insightful analysis.

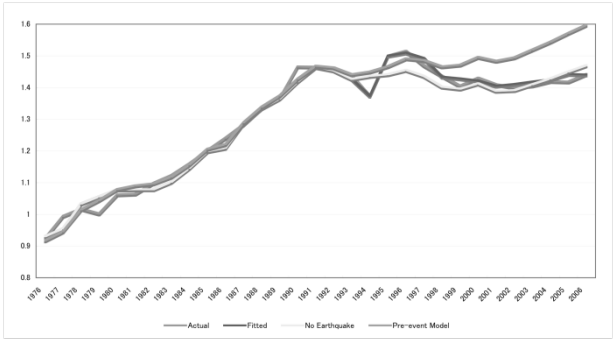


Figure 3. Comparison of Trends with and without the Kobe Earthquake
(logarithm of per capita GRP; 2000 constant price)

Figure 3 also accompanies another trend line in green. This trend is derived based on the estimated equation (1) but using only the time series data during 1975 and 1993. This projection is made because a usual way for the comparison between trends before and after an event or policy is to compare the projected trend based on the trends before the event with the actual trends after it, in order not to take into account the structural change caused potentially by the event. The estimation results of equation (1) with 1975-1993 data are displayed in Table 4 below. The constant term is again not statistically significant as in Model 1-6, so the final model (Model 1-7) does not include it. The sign of three coefficients in Model 1-7 are the same as ones in 1-5, while the size of them is smaller in Model 1-7 than ones in 1-5, indicating a relatively smooth trend. In fact, the trends of the Kobe's GRP per capita during 1975 and 1993 seem to have lesser fluctuations except the ones after 1990, when the bubble economy collapsed.

The projected trend based on Model 1-7 uses the similar data conversion after 1995 to the above case in equation (6), in order for counting out the earthquake's influences. The differences between the projected trends in green and the actual values after 1994 present quite large and increasing gaps. The initial impacts are negative one in 1994, like the previous result, and positive ones for a few years after 1995, while the positive impacts are short lived and the gap becomes negative and larger as time passes by. The projected trend line based on the pre-earthquake trend becomes upward after 2002, reflecting the trend of Japan's GDP included in the right hand side of Model 1-7.

Table 4. Comparison of KOBE Models for Different Period

Variables	Model 1-5	Model 1-6	Model 1-7
Dependent variable	KOBE	KOBE	KOBE
Estimation Period	1975-2006	1975-1993	1975-1993
Constant		0.005	
		(0.044)	
JPN	1.231***	1.091***	1.110***
	(0.181)	(0.298)	(0.248)
JPN (t-1)	-1.179***	-0.741**	-0.765**
	(0.179)	(0.343)	(0.267)
KOBE (t-1)	0.942***	0.672***	0.682***
	(0.074)	(0.184)	(0.160)
D94	-0.062***		
	(0.022)		
D95	0.117***		
	(0.022)		
Number of observations	31	18	18
R-squared	0.99	0.99	0.99
BIC	-69.83	-39.05	-40.48

Standard error in parentheses.
* Significant at the 10% level.
** Significant at the 5% level.
*** Significant ar the 1% level.

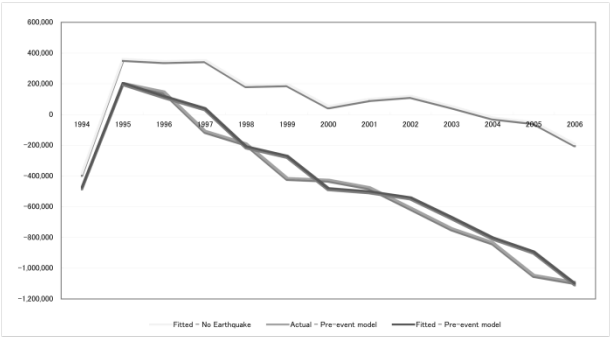


Figure 4. Comparison of Calculated Impacts
(difference in GRP; million yen in 2000 constant price)

These estimation results manifest considerable discrepancies in the measurement of the earthquake's total impacts, shown in Figure 4. The results based on Model 1-5 show the extended period, around nine years, of positive gains caused by recovery and reconstruction activities; on the other hand, the results based on Model 1-7, estimated using only the pre-earthquake period, present a short period of relatively small positive gains and the steady downward trends afterwards. The comparison of the estimated earthquake impacts over time is summarized in Table 5. The sum of estimated impacts, total net impact, during 1994 and 2006 becomes positive with Model 1-5, around 1 trillion yen, while it becomes negative with Model 1-7, about 6 trillion yen. With closer observations, both models derive the similar initial negative impact in 1994, around 400 to

470 million yen; the following positive gains from demand injections are quite diverse, ranging from about 1.8 trillion yen by Model 1-5 to around 360 million yen by Model 1-7--5 times difference; similarly, the long-run effects (losses) look contradictory, between 260 million yen loss by Model 1-5 and almost 6 trillion yen loss by Model 1-7--23 times separation.

Table 5. Comparison of Estimated Earthquake Impacts (million yen in 2000 constant price)

	Fitted - No Earthquake Model 1-5	Actual - Pre-event model Model 1-7	Fitted - Pre-event model Model 1-7
1994	-386,832	-474,010	-474,010
1995	361,370	204,745	204,745
1996	347,230	150,160	119,333
1997	353,664	-105,790	40,724
1998	191,053	-187,848	-206,814
1999	197,620	-412,783	-269,595
2000	52,479	-423,285	-479,035
2001	100,185	-472,264	-499,138
2002	120,476	-605,282	-540,081
2003	53,229	-740,395	-666,972
2004	-19,407	-831,489	-799,394
2005	-49,729	-1,043,062	-891,542
2006	-194,001	-1,089,740	-1,098,206
Total	1,127,336	-6,031,042	-5,559,985
Initial Impact	-386,832	-474,010	-474,010
Positive Gains	1,777,305	354,906	364,801
Long-run Losses	-263,137	-5,911,938	-5,450,777

How are these discrepancies caused? One potential explanation is that Model 1-5 includes the post-earthquake data of Kobe (1994-2006) for the coefficients estimation of long-run growth path, while Model 1-7 does not. This implies if any structural change specific to the Kobe economy arose after the earthquake, Model 1-7 cannot take into account, whereas Model 1-5 can. It has been reported that the earthquake's catastrophic destructions resulted some companies' bankrupt, some other companies' moving away from the Kobe area, other companies' changing the business practices, or some new companies' replacing the old and damaged ones, etc. These restructuring of the Kobe economy surely caused the structural change and interindustry relationships. In addition, when companies restore their old and damaged equipments and facilities, they might have replaced the damaged ones with newer and more sophisticated ones, causing technology update (Okuyama, 2003). The technology update alters productivity, influencing the production function of the Kobe economy. These changes are certainly economic consequences of the Kobe earthquake and specific to the Kobe economy. Therefore, while the estimates based on Model 1-5 sound more plausible, and appear consistent with the empirical observations and other studies (for example, Okuyama et al., 1999), it may be superficial not taking to account the long-run effects. If the estimate based on Model 1-7 is the case, the total impacts and long-run effects of the Kobe earthquake may be much larger and severer than what we derived previously with short-run models.

5. CONCLUSIONS

This study aimed to measure the total impacts of the Kobe Earthquake using the empirical time series data. Based on the econometric analyses, the estimated impacts have the negative initial impact in the year the earthquake occurred, followed by the positive gains resulted from the demand injections for recovery and reconstruction activities, and leading to the negative long-run effects due to the changes in economic structure of Kobe. In addition, the results appear consistent with the conventional disaster theory and other studies. Particularly, the estimation results of equations (1), (2), and (3) in Tables 1, 2, and 3 may potentially prove the Albala-Bertrand's (2007) claim that the economic impact of a disaster may not affect negatively the macro-economy in both short-term and long-term, and rather may concentrate on the local economy. Our results clearly show that earthquake's impacts on the long-run growth path are statistically significant only for Kobe, and not significant with Hyogo or Japan, larger economies.

These results are contradictory to the findings in other studies that analyze interregional impacts of disasters (for example, Okuyama et al., 1999 and Okuyama, 2010), suggesting that sizable impacts spill over to other regions through interregional and interindustry relationships. It turns out that this is exactly the evidence that the measurement of impacts using macroeconomic indicator, i.e. GDP or GRP, can derive only the net impacts, the sum of negative and positive impacts. The larger the economy becomes, the more these negative and positive impacts may offset each other and may become insignificant. For the further and more detailed analysis of the aftermath and how a disaster affects economy, net impact needs to be disaggregated to negative and positive impacts separately. This is because negative impact and positive gain affect the economy in many different ways, and because the extent of their effects may differ by its significance and over space. Careful examinations of these disaggregated impacts will provide important and useful information for decision making on preparedness and mitigation strategies for the future catastrophes and on recovery and reconstruction strategies of the next calamity.

This disaggregation of total impacts to negative and positive ones requires also to consolidate this line of empirical study for the bench mark with other economic evaluation models, such as input-output (I-O) model and computable general equilibrium (CGE) model and the standardized database of damages and losses caused by an earthquake and recovery and reconstruction activities. These evaluation models can estimate negative and positive impacts separately (or all together), and can disaggregate the impacts also over space and/or by income group, for example. At the same time, the accuracy of estimation by these evaluation models depends essentially on the accuracy of the input data--data of damages, losses, and recovery and reconstruction activities. As discussed above, in disaster research community, even the definition of damages and losses are vague. We need a standardized definition and

framework to collect the damage and loss data consistently, so that comparative study of disaster impact can be carried out and the historical data can be accumulated. In addition, as Greenberg et al. (2007) suggested, the standardization of evaluation models is also an urgent task. Of course, empirical measurement of economic impacts like this study should be also carried out for major disasters to investigate the long-run effects, which may be quite different from the short-run impact estimation.

Acknowledgement:

This research was supported by the JSPS Grant-in-Aid for Scientific Research (C) [21510199]. The author is also grateful for the participants in the session on Regional Economic Effects of Disasters at the 57th North American Meetings of the Regional Science Association International, for helpful and thoughtful comments and suggestions.

References:

Albala-Bertrand, J.-M. (2007) "Globalization and Localization: An Economic Approach", in H. Rodriguez, E.-L. Quarantelli, and R.-R. Dynes, eds., *Handbook of Disaster Research*. Springer, New York, 147-67.

Albala-Bertrand, J.M. (1993) *The Political Economy of Large Natural Disasters: With Special Reference to Developing Countries*. Oxford, UK: Clarendon Press.

Cuaresma, J.C., Hlouskova, J., and Obersteiner, M. (2008) "Natural Disasters as Creative Destruction?: Evidence from Developing Countries", *Economic Inquiry*, 46 (2), pp. 214-226.

Dacy , D.C. and H. Kunreuther. (1969) *The Economics of Natural Disasters*. New York: The Free Press.

Greenberg, M.-R., M. Lahr, and N. Mantell, (2007) "Understanding the Economic Costs and Benefits of Catastrophes and Their Aftermath: A Review and Suggestions for the U.S. Federal Government", *Risk Analysis* 27 (1), 83-96.

Hendry, D.F. (1995) *Dynamic Econometrics*. New York, NY: Oxford University Press.

Hyogo Prefecture Government. (2010) *Status of Recovery and Reconstruction after the Hanshin-Awaji Great Earthquake*. (in Japanese)

Kunreuther, H. and A. Rose. eds. (2004) *The Economics of Natural Hazards, Volume I & II*. Northampton, MA: Edward Elgar.

Okuyama, Y. (2003) Economics of Natural Disasters: a Critical Review, Research Paper 2003-12, Regional Research Institute, West Virginia University.

Okuyama, Y. (2007) "Economic Modeling for Disaster Impact Analysis: Past, Present, and Future", *Economic Systems Research*, 19 (2), pp. 115-124.

Okuyama, Y. (2010) "Globalization and Localization of Disaster Impacts: An Empirical Examination," *CEFifo Forum*, 11 (2): 56-66.

Okuyama, Y. and Chang, S.E. eds. (2004) *Modeling Spatial and Economic Impacts of Disasters*. New York: Springer.

Okuyama, Y. and S. Sahin (2009) "Impact Estimation of Disasters: A Global Aggregate for 1960 to 2007," Policy Research Working Paper 4963, the World Bank.

Okuyama, Y., G.J.D. Hewings, and M. Sonis, (1999) "Economic Impacts of an Unscheduled, Disruptive Event: A Miyazawa Multiplier Analysis," in G.J.D. Hewings, M. Sonis, M. Madden, and Y. Kimura eds., *Understanding and Interpreting Economic Structure*, Springer-Verlag: 113-144.

Rasmussen, T.N. (2004) Macroeconomic implications of natural disasters in the Caribbean, IMF Working Paper WP/04/224, International Monetary Fund.

Rose, A. (2004) "Economic Principles, Issues, and Research Priorities in Hazard Loss Estimation", in: Y. Okuyama and S.E. Chang eds. *Modeling Spatial and Economic Impacts of Disasters*. New York: Springer; 13-36.

Skidmore, M. and Toya, H. (2002) "Do Natural Disasters Promote Long-run Growth?" *Economic Inquiry*, 40 (4), pp. 664-687.

Sorkin, A.L. (1982) *Economic Aspects of Natural Hazards*. Lexington, MA: Lexington Books.

United Nations. (2008) *World Economic and Social Survey 2008: Overcoming Economic Insecurity*. New York, NY: UN.

8CUEE CONFERENCE PROCEEDINGS
8th International Conference on Urban Earthquake Engineering
March 7-8, 2011, Tokyo Institute of Technology, Tokyo, Japan

EARTHQUAKE PREPAREDNESS AND BCM IN JAPAN

Shinichi Okabe

Management Science and Technology, Graduate School of Engineering, Tohoku University
shinichi.okabe@tokiorisk.co.jp

Abstract: According to the Japanese Government Cabinet Office Survey 2010 on Disaster Management and BCM, among companies affected by any disasters, 60 % of them have been affected by earthquake, followed by 30% by flood. For last 70 years Japanese Government and private companies have been tackling natural disasters as high priority. In contrast, other country, like UK shows a very different picture. The UK Government's National Risk Register 2010 shows that attacks on transportation and crowed places, pandemic human disease, and severe whether come high in their frequency and impact assessment of the risks for the country. Those differences are reflected in BCM approaches in two countries. In Japan, companies tend to consider BCP for large disaster measures. Many companies approach BCM along pre-disaster measures for the facilities. On the other hand, the UK approach seems to focus more on ordinary business disruption incidents. This paper reviews Japan BCM approaches and earthquake preparedness. If a severe earthquake totally destroys key facilities, reasonably quick resumption of business would not be possible. Pre-earthquake measures are critical to minimize losses to the extent that BCM strategies would be effective to resume operation at the expected time frame.

1. INTRODUCTION

The Cabinet Office of Japanese Government has been conducting the surveys on Business Continuity Management(BCM) and Disaster Management(DM) in the private sector since 2008. About 1000 to 1500 companies from wide rage of industries have participated in the surveys. These reports show the current status of implementation of BCM and DM in Japan. This 2010 report tells 19% of the companies had been affected by disasters in the past. The ratios vary by company size as large company group (large G) 35%, middle company group (middle G) 19%, small company group (small G) 14%. Among those, 60% has been affected by earthquake, 33% by flood and 10% by fire. It is also noted that large G is more affected than other two groups, large: 78%, middle: 68%, small: 43%).

2. DISASTER MANAGEMENT PLAN AND BUSINESS CONTINUITY PLAN

Japan is a disaster prone country. Private companies have been spending resources to enhance resiliency for natural disasters and accidents. The 2010 survey report shows 54% (*)of companies have implemented Disaster Management Plan (DMP). There is a large difference by company sizes. 80% of large G have implemented DRP but only half of companies in middle G and small G. (* This ratio includes companies which are preparing DRP.)

The implementation of Business Continuity Plan (BCP) ratios(*) also vary by company size groups; large G: 58%, middle G: 27%, small G 22%. Between 2008 and 2010, DMP rations have not much changed but BCP ratios have increased in large G by 23%, middle G by 11%, small G by 10%. This indicates that companies which have already implemented DMP have been proceeding into BCP implementation. The companies which have not implemented DMP have not much changed.

The top disasters which those companies have prepared for by DRP are earthquake (88%), fire (78%), and flood (31%). The top disasters which are prepared for by BCP are earthquake (57%), fire (42%), and flood (20%). This clearly shows earthquake is the top concern

There are large differences in implementation of DMP and BCP in the main industries. Figure 1 shows DMP and BCP ratios of eight industries. There is correlation between implementation of DRP and BCP. Electricity and Gas come top by far and IT/Communication and Financial / Insurance follow. Retail is the lowest among those eight industries.

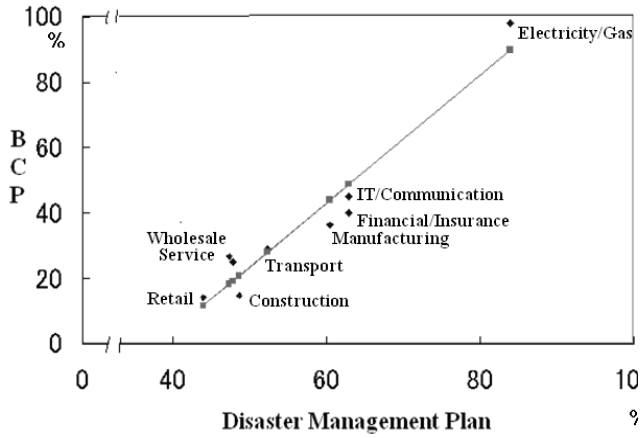


Figure 1 DRP and BCP implementation

The Cabinet Office 2008 survey shows high ratio of the companies throughout the industry which do not know BCP. The Figure 2 shows reverse correlation between DRP implementation and BCP recognition. Retail show lowest DRP implementation ratio and it show highest ratio of "Do not know BCP" The higher is the DMP implementation ratio, the lower the 'Don't know BCP" ratio. This indicates introducing DMP leads to knowledge of BCP. In other words DMP can be regarded as the grounding for BCP implementation.

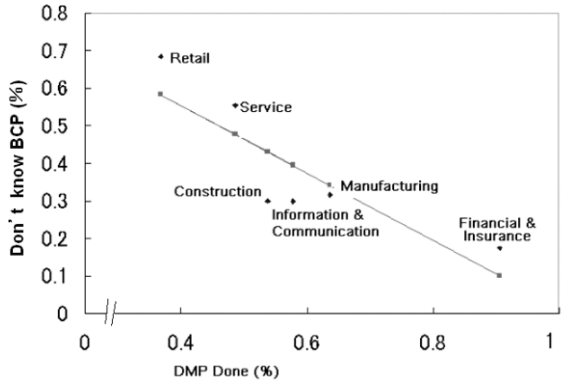


Figure2 DRP and BCP implementation

3. BCP IMPLEMENTATION STAGES OF MUNUFACTURING INDUSTRY

Based on the survey questions, BCP implementation processes are categorized in four stages; 1st: DRP done, 2nd: BCP Recognized, 3rd: BCP done and 4th: BCP done with BIA. This categorization assumes the implementation process that companies which implemented DRP would move to BCP recognition, BCP implementation and to BCP with BIA. BIA stands for Business Impact Analysis which is one of important key process during BCP planning in order to analyze potential impact to organization by disaster and identify the critical functions which should be resumed at highest priority to survive disasters.

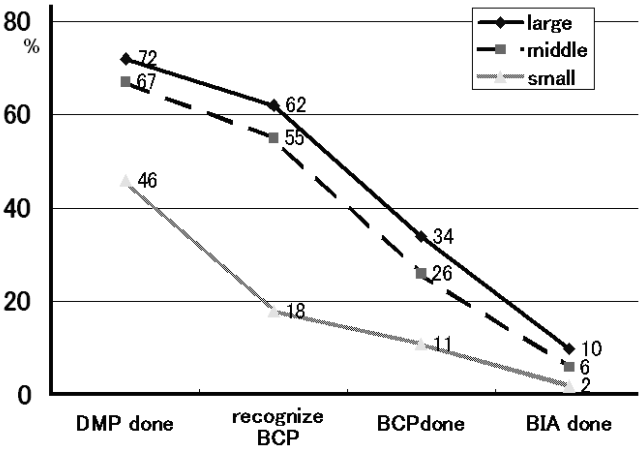


Figure 3 BCP implementation stages

The Figure 3 shows implementation ratios in the above 1st to 4th stages of manufacturing companies. It shows trends by the three company groups. The two graph lines of large and middle Gs show very similar trends but the small G's line is apart down and from the above two.

DRP is implemented by 72% of large G, 67% of middle G but only by 46% of small G. The 2nd / recognized BCP ratio is down from 1st / DRP done by about 10 points in large and middle G, but only 1/3 of small G. The 2nd /BCP implementation ratios from 3rd /BCP done of large G and middle G go down to half but to 1/4 in small G.

In order to promote BCP introduction, further analysis is needed to review the causes why there are such large gaps between ratios of 2nd / recognized BCP and 3rd / BCP done in all three groups.

Further more, among companies which answered that they have done BCP, only 1/3 of large G (10%), 1/4 of middle G (6%) and 1/5 of small G (2%) conducted BIA. BIA is a fundamental and required process during BCP planning. In other words, the companies which have not conducted BIA are not considered to have implemented BCP in the strict sense from BCP guidelines published by Cabinet Office of Japanese Government or major foreign BCM standards.

4. ANTI-EARTUQUAKE MEASURES AND BCP

The surveys ask questions on what kinds of earthquake damage mitigation measures are done, such as tip resistant measures for office equipment, anti-earthquake machinery/equipment fixation, anti-seismic reinforcement, compliance with seismic building code, relocation to seismic resistant building.

Those anti-earthquake measures have been done

traditionally through DRP. The Figure 4 shows implementation ratios of those anti-earthquake measures in five DPR and BCP implementation stages. In Figure 4, one stage before DRP done is added as no DRP which means DRP is not implemented.

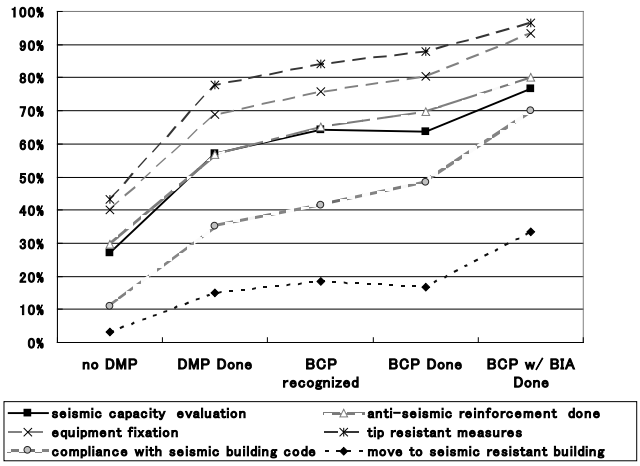


Figure 4 Anti-earthquake measures and BCP stages

The six graph lines of anti-earthquake measures show very similar trends. The implementation ratios of those measures become larger along the BCP stages advance. It is noted that the order of ratios is the same in six stages and it is considered that this would be an order of easier feasibility of those six measures. The companies start with implementing economically easier measures such as fixation of office equipment or machinery. The anti-seismic reinforcement measures of the buildings or complying with seismic building code are effective but require funds and time.

There are larger increases noted between stages between no DRP and DRP done and stages between BCP done and BCP with BIA than other two stages. In the last stage of BCP with BIA, 70% of companies have complied with new building code, which is a very significant measure for earthquake preparedness.

5. CASE STUDIES

Based upon the current status of DRP and BCP, are companies able to survive major earthquake or other natural disasters if they have implemented DMP and BCP? My answer would be "Maybe yes, if they are lucky"

The writer interviewed small to middle size companies which were damaged by earthquakes occurred in Niigata Pref. in 2004 and 2007. There are two successful recovery cases, one is Japanese sake (rice wine) brewery and another is a regional general hospital.

5.1 Japanese sake brewery

This company was severely damages as 70% of their buildings were totally collapsed and about 10,000 sake bottles waiting for shipment were broken. Fortunately, the earthquake hit on holiday and there were no injuries because nobody was working in the brewery. Top executive said that employees would have been dead or injured by collapsed buildings if the earthquake had hit during working hours. The building of bottling lines which was built in compliance with new building code withstood the earthquake without major damage.

The key infrastructure has been restored within shorter period of time than other affected area hit by the same earthquake. The company did not have alternate option for water supply but it was recovered within 20 days. The company was able to resume partial (less than 20%) production within a month.

The executive who was interviewed emphasized, from his learned lessons, that the critical process should be protected to be able to recover even if entire earthquake reinforcement measures are not financially feasible to the company.

5.2 A regional general hospital

In a regional hospital case, the main buildings (except one old one) were complied with seismic building code and not severely damaged. But walls fell, pipes above ceilings were broken and upper floors were flooded. Medical equipment fell and tipped over. The emergency generator which was supposed to run for two days with stored oil supply stopped after having operated for only 40 minutes. It was because that cooling water supply was cut off by breakage of pipes from the water tank. This unexpected electricity failure forced hospital staffs to manually support breathing of patients on a respirator.

But there were fortunate factors; the earthquake hit in the early evening on Saturday when there were not any scheduled operation and dialysis. And there were more staffs at the shift change from day to night shift. More than 200 hospitalized patients were safely transferred to lower levels by the trained hospital staffs. They had to temporarily rest on the floor until they were transferred to other hospitals. The hospital successfully managed keeping safety of patients and providing increasing out patients injured by the earthquake under such a severely disaster emergency situation.

From reviewing its recovery process, the hospital financially suffered substantial revenue reduction in addition to the heavy burden of restoration costs. The buildings were not severely damaged but the damage to equipment and rooms are substantial and hospital was not usable until repaired.

After nine day, outpatient treatment and dialysis were resumed. After 11day, half of hospitalized patients came back. But it took almost one month to resume operation because of the delayed oxygen equipment restoration. The operation is one of important revenue source for the hospital.

In addition, the hospital owns an adjacent nursing facility, which was a building with the foundation installed with seismic isolation rubber. It was proved very effective in this earthquake that this building was not damaged and internal equipment did not fall.

6. CONCLUSIONS

6.1 Disaster Management Plan

As shown in the above two case studies, the current status of DRP and BCP do not seem to sufficient for survival for middle to small companies. The traditionally disaster management measures are linked to premises and facilities (or mainly tangible properties such as building and equipment) As the above two cases show, critical operation should be protected or its expected damage should be reduced to the extent that resumption should be feasible within reasonable short time or acceptable period to the bottom line of the company. Therefore anti-earthquake measures such as compliance with anti-earthquake building codes are very critical. Such measures are absolutely necessary and without those measures, survival cannot be expected. For middle to small companies, such anti-earthquake measures are very costly and many companies cannot afford them. As long as such risk remains, the company has to make necessary measures through mid to long term plans.

6.2 Business Continuity Plan

The traditional Disaster Management Plan focuses on safety of human being and protection of assets. Even such measures can protect people and assets, they are not sufficient to protect business operations. The critical factors to protect and to resume business operations are not only tangible but also intangible and not only internal assets but also external services such as infrastructure and key parts/ material supplies. The current BCP which have been implemented by Japanese companies tend to be carried out in extension of DRP which have been closely tied with premises and locations. BCP requires out of location measures if there are no viable alternative options for business recovery within own premises.

BCP aims to protect business operation by implementing business continuity measures. Such measures are not limited to own properties. There are various key factors of critical functions depend. For example, among important infrastructure services, electricity is normally restored sooner than other services. But water supply needs longer period to restore water piping repair. The above sake maker case shows water supply was their bottle neck for recovery as the company did not have alternative source of water supply. But they were fortunate that water recovered to be able to resume partial operation within a month. Another food maker which was severely affected by the earthquake drilled a well for back up water supply within its premise.

In the hospital case, an emergency generator unexpectedly stopped due to lack of cooling water supply only after it ran for only 40 minutes. But the emergency generator system including cooling water supply pipes were damaged by earthquake. This was a blind spot. Even back up systems are installed, it is necessary to evaluate if such systems would survive disaster and could operate at disasters. And oxygen supply was critical to operations at hospital. The oxygen restoration substantially affected hospital financial bottom line.

In both cases, the recovery works by top managements and employees at the time of emergency deserve the praised for their efforts. But those two organizations did not implement BCP and did not have pre-measures which enabled to shorten the recovery time. As preparedness for disasters, DRP and BCP have common and overlapping factors. And if both DRP and BCP are coordinated for under the common goals, more effective measures would be feasible to minimize losses and damages.

References:

Cabinet Office, Government of Japan, 2005. “Business Continuity Guidelines 1st ed.,-Reducing the Impact of Disasters and Improving Responses to Disasters by Japanese Companies”

Sheffi, Y., 2005, The Resilient Enterprises MIT Press

Watanabe,K, 2009, Developing public-private partnership based business continuity management for increased community resilience, Vol 3, No4 335-344 Journal of Business Continuity and Emergency Planning (Journal Articles)

Forbes, N, Contingency planning for earthquakes in Asia, Vol 3, No4 356-367 Journal of Business Continuity and Emergency Planning (Journal Articles)

8CUEE CONFERENCE PROCEEDINGS
8th International Conference on Urban Earthquake Engineering
March 7-8, 2011, Tokyo Institute of Technology, Tokyo, Japan

QUANTITATIVE RISK ANALYSIS APPROACH FOR BCP (BUSINESS CONTINUITY PLANNING) DECISION MAKING AGAINST EARTHQUAKES

Satoru Nishikawa

Director of Regional Planning, Ministry of Land Infrastructure Transport and Tourism, Japan
nishikawa-s2iv@mlit.go.jp

Abstract: Business continuity is now being regarded as an important factor in management of enterprises. In order to draw BCP (Business Continuity Plan) for enterprises, and for the top executives to decide on necessary measures and investments, there is a need for a quantitative risk analysis method to evaluate their risk. Most of the enterprises are not stand-alone; they depend on Supply Chain (SC), for their operations. The business interruption time is a crucial factor in terms of economic loss. Two model enterprises each with three factories connected through series and parallel supply chain patterns are applied in comparing and analyzing the risk. The annual exceedance probability of business interruption time of these enterprises are calculated and compared. The business interruption time risk of series supply chain is greater than the parallel. Three alternative options, by provision of redundant nodes, for decreasing the risk are proposed. The annual exceedance probability of business interruption time of these location and supply chain types are calculated and compared. The options are examined from the viewpoint of BC Planning. This risk analysis method is proven to be realistic and functional. Through combining these factors a realistic risk analysis method for evaluating business interruption is proposed and is proven to be functional. This method may be applied for strategic location planning of supply chain dependent enterprises who wish to minimize their risk and to justify the necessary investments.

1. INTRODUCTION

Japan is facing imminent threats of possible large scale earthquakes such as the Tokai, the Tonankai & Nankai, the Japan Trench & Kuril Trench Type and the Tokyo Metropolitan Area Direct Beneath Earthquakes. All of these earthquakes are foreseen to occur within the next thirty years' time span and the economic damages from these earthquakes are feared to be gigantic. The economic damage by the 1995 Hanshin-Awaji (Kobe) Earthquake was estimated as 2% of the GDP of Japan, which did not seriously affect the Japanese economy and it was capable of providing sufficient capital for the recovery and reconstruction of Kobe. Whereas the economic damage by the Tokyo Metropolitan Area Direct Beneath Earthquake is estimated to claim approximately 1/5 to 1/4 of GDP, which may degrade the Japanese economy and bring socio-economic stagnation. How to minimize this economic damage by preventive measures? This is the challenge that we face and it is the race against time.

In April 2006, the Central Disaster Management Council chaired by the Prime Minister decided the Earthquake Disaster Reduction Strategy where it aims to halve the estimated human and economic damage within the next 10 years. One of the main pillars for reduction of economic damage is the adoption of Business Continuity Plans (BCP) by enterprises. The strategy calls for all of the large scale enterprises and half of the medium scale enterprises to adopt BCP. There have been many efforts paid to propagate BCP. The Cabinet Office issued the BCP guideline in 2005 and formed committees to encourage trade unions to formulate their own BCP guidelines to meet their characteristics. The Development Bank of Japan started a new low interest loan to encourage enterprises to adopt BCP in 2006. A non-profit organization BCAO was newly established in 2006 as a forum to promote BCP in Japan. Five years have passed; there is a big gap between the strategy and the reality regarding the adoption of BCP.

How can this gap be filled? One solution may be to clearly indicate the benefit of adopting BCP in quantitative terms so that the entrepreneurs who are skeptics may understand the value of BCP and agree to invest for preventive measures for business continuation. This paper focuses on the business interruption time (BIT) as an important factor in decreasing the economic damage from earthquakes and proposes quantitative analysis methods to assist decision making to introduce necessary measures to shorten BIT in case of earthquakes.

2. QUANTITATIVE RISK ANALYSIS METHOD to EVALUATE BIT of SUPPLY CHAIN DEPENDENT ENTERPRISE

2.1 Risks Facing Supply Chain (SC) Dependent Enterprises

Most of the modern enterprises are not stand-alone; they depend on supply chains (SC), for their operations. In

many of the competitive manufacturing industries, the management, for the sake of decreasing the cost of stockpiling and also to respond quickly to changing market demands, is shifting to the "Just in Time" procurement and manufacturing system. This system is based on the assumption that the SC to their factory functions without interruption. Therefore, once the SC is interrupted, they face the immediate risk of halt of operations. On the other hand, business continuity is now being regarded as an important factor in risk management of enterprises.

In the case of the Niigata-Chuetsu-Oki Earthquake on 16 July 2007 in Japan, an automobile engine piston ring manufacturer suffered serious damage. Since this manufacturer had a dominant share, most of the major automobile companies in Japan had to halt their assembly lines for one week, due to the fact that they did not have extra stock of piston rings in their hands. Since it was difficult to identify an alternate supplier for the sophisticated piston rings in a short period, the automobile companies sent their own engineers to this piston ring manufacturer to assist the quick restoration of the piston ring manufacturing lines. This is a typical example of a local disaster affecting production in other locations since they are SC connected. This incident demonstrated the need to consider the supply chain as an important factor in drawing BCP in such enterprises. Similar cases were seen in the October 2004 Niigata-Chuetsu Earthquake and in the 1995 Hanshin-Awaji Earthquake, where the direct damage to the factories hit by the earthquake spread to the enterprises located outside the affected area through the halt of the supply chain of parts and materials.

2.2 Necessity to Evaluate BIT of Supply Chain (SC) Dependent Enterprise

These cases call for the need to develop an earthquake risk evaluation method for business continuity planning of SC dependent enterprise. For such evaluation, multiple locations of the nodes of the SC system and the individual risks of the buildings on these locations need to be combined and considered. Not only the direct material damage by the earthquake to the nodes, but moreover the Business Interruption Time (BIT) of the enterprise is a crucial factor for the survival of the enterprise in the competitive market. The BIT is a crucial factor in terms of economic loss. If an enterprise halts its supply of products over a consumer acceptable timeframe, the consumer will be quickly taken over by rival enterprises and if the business resumption time exceeds a certain limit, the enterprise will no longer be able to return to the previous market. Therefore a method to quantify the BIT of the SC dependent system and to evaluate options to decrease the BIT is needed (Nishikawa et al. 2007).

This paper, proposes a quantitative risk evaluation method of BIT of SC dependent enterprise, and applies to model enterprises based in the Greater Tokyo Metropolitan Area. Also several alternative options to decrease the BIT is proposed and evaluated.

3. STRUCTURE of the RISK EVALUATION METHOD of BIT

There has been previous proposal and study on a method to evaluate earthquake damage risk of an enterprise who possesses a portfolio of multiple building assets in various locations (Fukushima et al. 2002). This method, by generating numerous possible scenario earthquakes (hereinafter earthquake events), estimates possible damage to the individual buildings and by summation of these damages calculates the damage risk of the portfolio. By expanding this methodology, 1) BIT of individual nodes of a SC is calculated according to each earthquake event and 2) by combining the results of BIT of individual nodes according to the supply chain pattern, thus generating event trees, the BIT of the SC dependent enterprise will be obtained.

3.1 Business Interruption Time of Individual Node

BIT of individual node *j* by earthquake event *i* shall be represented as $t_j(i)$ and is defined by equation (1) as follows.

$$t_j(i) = \sum_{k=0}^{4} [\, p_{j,k}(i) \cdot t_{j,k}(i)] \qquad (1)$$

k is the variable representing levels of damage as follows, *k*=0: no damage, *k*=1: slight damage, *k*=2: moderate damage, *k*=3: severe damage, *k*=4: collapse.

$t_{j,k}(i)$ represents BIT of node *j* by event *i* according to level of damage *k*.

$p_{j,k}(i)$ represents conditional probability of $t_{j,k}(i)$.

$p_{j,k}(i)$ is drawn from the fragility curve of individual node *j*.

3.2 Business Interruption Time of Supply Chain

BIT of SC by earthquake event *i* shall be represented as $t_{SC}(i)$ and is defined by equation (2) as follows.

$$t_{SC}(i) = \sum_{l=1}^{N} f[\mathbf{p}_l(i)] \cdot g[\mathbf{t}_l(i)] \qquad (2)$$

l is the variable representing individual end-branches of event trees.

N is the total number of end-branches.

$\mathbf{t}_l(i)$ represents the vector composed from $t_{j,k}(i)$ for end-branch case *l*.

$\mathbf{p}_l(i)$ represents the vector of conditional probability corresponding to $\mathbf{t}_l(i)$.

$f[\cdot]$ represents the conditional probability of occurrence of end-branch case *l* and is defined by equation (3) as a function of $\mathbf{p}_l(i)$.

$$f[\mathbf{p}_l(i)] = p_{1,k1} \times p_{2,k2} \times \cdots \times p_{n,kn} \qquad (3)$$

n represent the number of nodes composing the SC.

$g[\cdot]$ represents the BIT of SC for each end-branch and is a function of $\mathbf{t}_l(i)$. This function is determined by the connection pattern of the nodes of the SC. For a series SC the maximum, for a parallel SC the minimum, is chosen.

Fig.1 shows the outline of evaluation of BIT for each earthquake event. Fig.2 shows the procedure of the proposed BIT risk evaluation method. In order to consider the uncertainties, a Monte-Carlo simulation with ground motion strength and building strength as stochastic variables is applied.

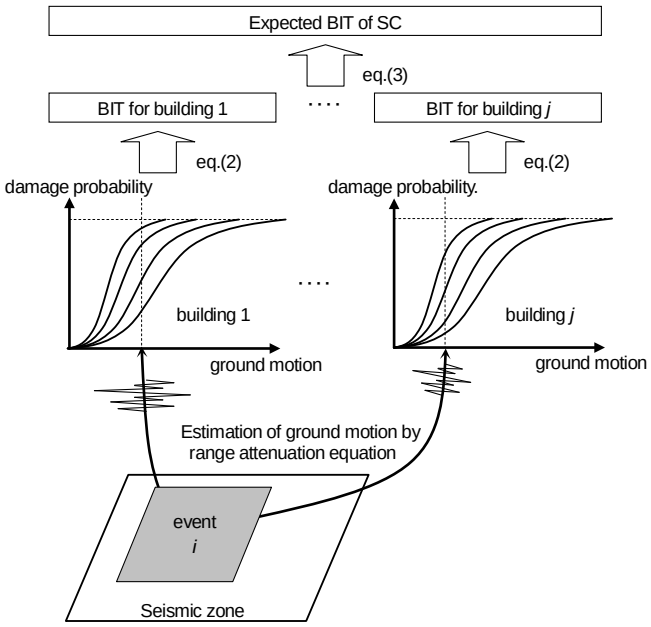


Fig.1 Outline of Evaluation Process of BIT of SC

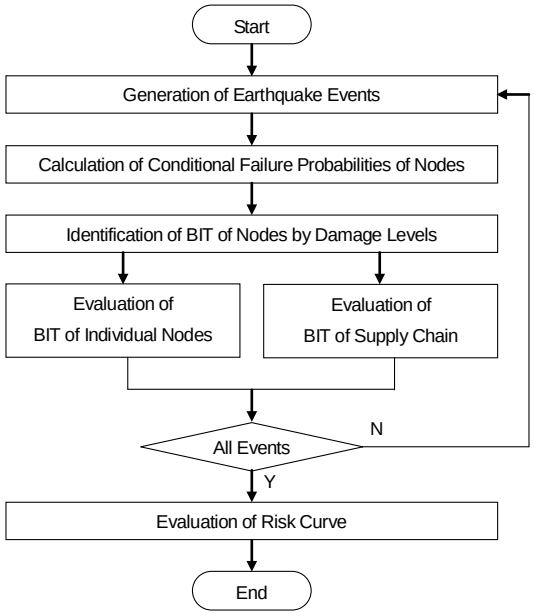


Fig.2 Flowchart of Risk Analysis of Supply Chain

4. APPLICATION to MODEL SUPPLY CHAIN

4.1 Setting of Model Supply Chain

Three nodes located in the Greater Tokyo Metropolitan Area were set as examples. The nodes are, Saitama, Chiba and Yokohama as shown in Fig.3. Based on the previous findings in (Fukushima et al. 2002) and (Sakamoto et al. 2006), the seismic strength of each nodes and BIT by damage level were set as shown in Table 1. Fig.4 shows the two connection patterns of the three nodes, series and parallel, as model SCs.

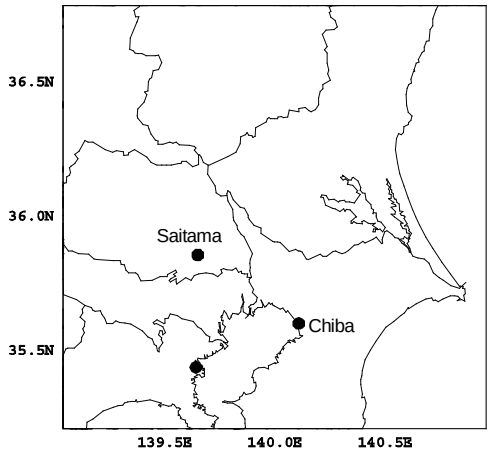


Fig.3 Location of Nodes of SC

Table 1 Fragility Curve and BIT by Level of Destruction

Damage Level	Characteristic Values of Fragility		BIT (day)
	Median (cm/s/s)	Log-normal Std. Deviation	
Slight	200	0.4	3
Moderate	600	0.4	15
Severe	1000	0.4	60
Collapse	1400	0.4	180

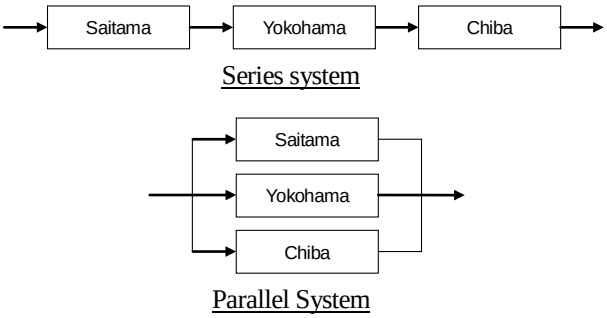


Fig.4 Supply Chain Models

4.2 Setting of Seismic Activity Model

Seismic activity zone model was set according to (Architectural Institute of Japan, 2004). Fig.5 shows the location of seismic sources and the seismic parameters are shown in Table 2. With reference to (Annaka & Yashiro 1998) attenuation relation of ground motion was calculated following the Annaka Model as shown in equation (4).

$$\log a = 0.61M + 0.00501h - 2.203\log d + 1.377 \quad (4)$$
$$d = \sqrt{\Delta^2 + 0.45h^2} + 0.22\exp(0.699M)$$

a stands for maximum ground acceleration, Δ for distance from the epicenter,

h for depth of seismic source, M for magnitude of the earthquake event.

Logarithmic standard deviation representing the variability of the range attenuation was set at natural logarithm 0.5.

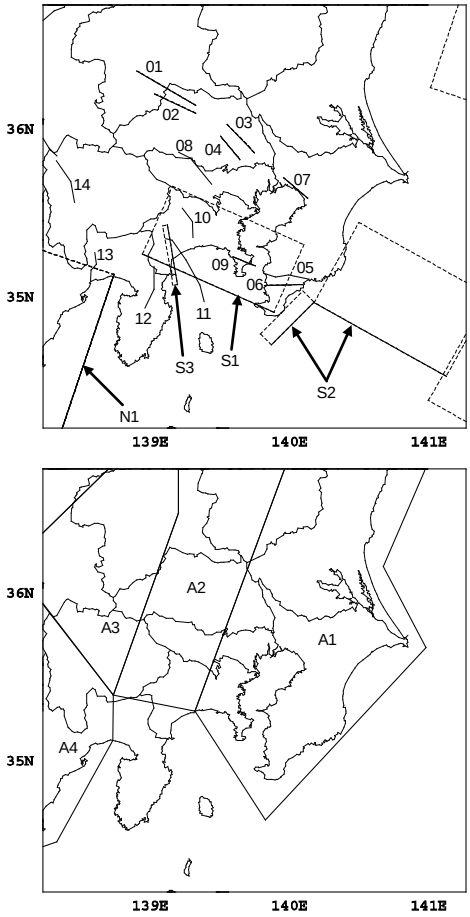


Fig.5 Location of Seismic Sources

Table 2 Parameters of Seismic Sources

Source Number	*Range of M*	Return Period (yr.)	Source Number	*Range of M*	Return Period (yr.)
01	7.0-7.6	1182	02	6.9-7.3	5212
03	7.0-7.4	79283	04	6.8-7.2	5931
05	7.1-7.5	2842	06	7.0-7.4	2639
07	6.8-7.2	5676	08	7.1-7.5	8710
09	6.6-7.0	1365	10	6.9-7.3	7239
11	7.5-7.9	1625	12	7.1-7.5	877
13	6.8-7.2	1917	14	7.1-7.5	2851
S1	7.8-8.2	200	S2	7.8-8.2	1000
S3	6.8-7.2	73	N1	7.6-8.0	130
Source Number	*Range of M*	*A-Value in G-R equation*	Source Number	*Range of M*	*A-Value in G-R equation*
A1	5.0-7.0	2.344	A2	5.0-7.0	4.235
A3	5.0-7.0	1.645	A4	5.0-7.0	2.344

b-Value in G-R equation for sources A1, A2, A3 and A4 is set 0.9.

5. BIT RISK CURVE of MODEL SUPPLY CHAIN

Risk Curve of BIT for the Parallel Model Supply Chain is shown in Fig.6. Risk Curve of BIT for the Series Model Supply Chain is shown in Fig.7. In these figures, the horizontal axis shows the 90 percentile exceedance of BIT(days), the vertical axis shows the annual exceedance probability. The bold line shows the risk curve of the SC, the thin lines show the risk curve of the different nodes.

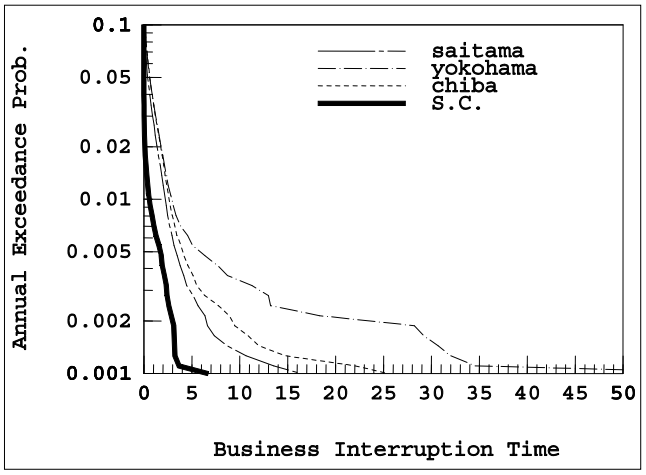


Fig.6 Risk Curve of Parallel SC

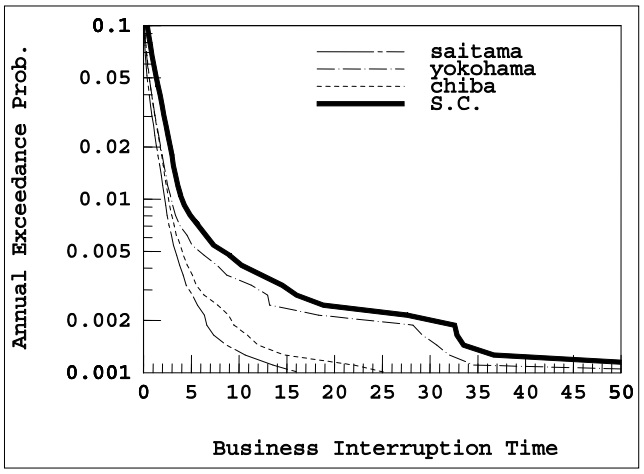


Fig.7 Risk Curve of Series SC

In Parallel SC, the SC halts only when all three nodes suffer damage at the same earthquake event. Therefore, as shown in Fig.6, the risk curve of the SC is smaller than any of the individual risk curve of the different nodes. In Series SC, if one or more of the three nodes suffers damage, the SC halts. Therefore, as shown in Fig.7, the risk curve of the SC is larger than any of the nodes and is strongly affected by node Yokohama which has the largest risk curve of the three.

Through the comparison of the two SC models, in order to decrease the BIT risk of a series supply chain, making the nodes parallel, in other words, providing alternates to the nodes would be effective. Since node Yokohama has the highest probability of

earthquake occurrence out of the three nodes, countermeasures to decrease the risk by node Yokohama need to be identified.

6. REDUCTION of BIT RISK by PROVISION of ALTERNATIVE NODES

6.1 Setting Alternatives of Nodes for Risk Reduction

In order to identify effective countermeasures to reduce the BIT risk of a series SC, three modified models are proposed, as shown in Fig.8. In Modification *A* an alternative node with same seismic strength for node Saitama is provided on the same location of the original node. In Modification *B* an alternative for node Yokohama is provided. In Modification *C* alternatives for all three nodes are provided.

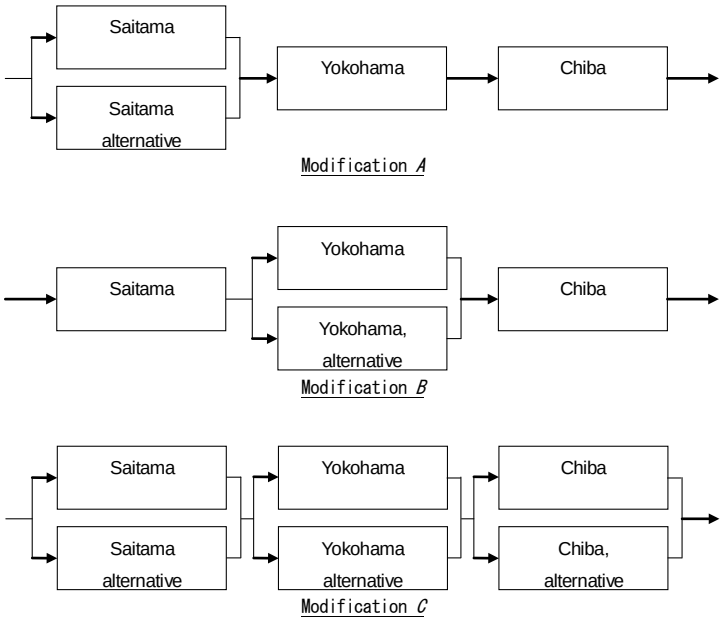


Fig.8 Modified Series SC by Provision of Alternative Nodes

6.2 Risk Curve of BIT of Series SC with Alternatives

Risk curve of BIT for modified series SC is shown on Fig.9, Fig.10 and Fig.11. By provision of alternative nodes, in all of the modified SC their risk curves are smaller than the original series SC. The probability of the two nodes on the same location suffering exactly the same level of damage is smaller than the probability of single node suffering the same level of damage. Therefore the provision of alternative node contributes to risk reduction of SC.

Fig.10 shows that provision of alternative node for Yokohama, which has the highest probability of earthquake occurrence, is effective for decreasing the risk curve. Fig.9 shows that provision of alternative node for Saitama, which has the lowest probability of earthquake occurrence, has limited effect for decreasing the risk curve. Fig.11 shows that provision of alternative nodes for all three locations gives the lowest risk curve of the three cases.

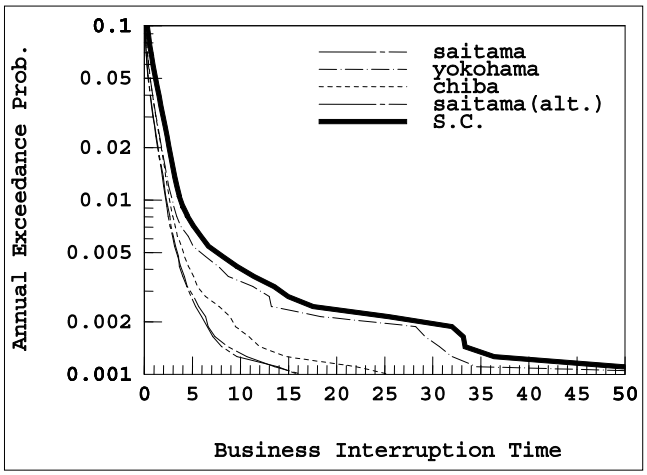


Fig.9 Risk Curve of Modification *A*

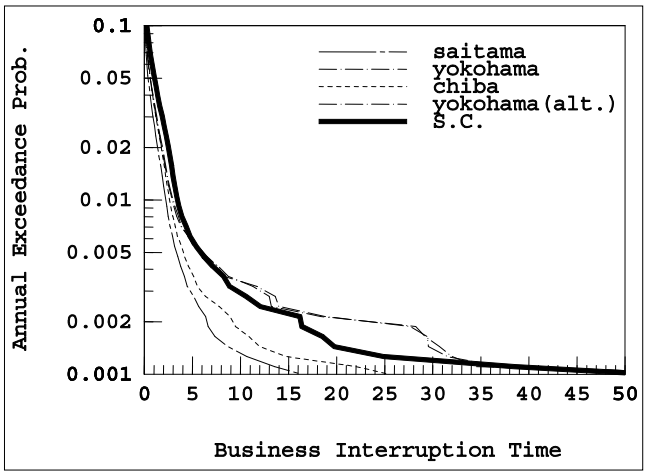


Fig.10 Risk Curve of Modification *B*

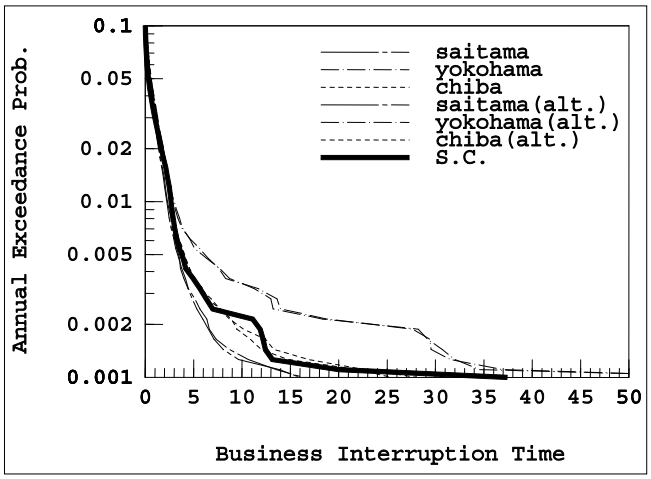


Fig.11 Risk Curve of Modification *C*

6.3 Effect of Provision of Alternative Nodes and Reflections for BCP

Fig.12 shows the comparison of the modified SC's BIT with the original series SC. The vertical axis is the annual exceedance probability, the horizontal axis is the ratio of BIT (modified SC's BIT divided by the original series SC's BIT).

For the domain where the annual exceedance probability is greater than 0.01, Modification *A* and Modification *B* do not demonstrate significant decrease of BIT risk. In this domain, high frequency & small scale earthquakes are dominant, thus provision of alternative for one location does not effectively decrease the BIT of the SC, since the remaining two locations will be frequently affected. Modification *C* demonstrates significant decrease of BIT risk since all three nodes are doubled.

For the domain where the annual exceedance probability is smaller than 0.005, Modification *B* demonstrates significant decrease of BIT risk. In this domain, low frequency & large scale earthquakes similar to the 1923 Great Kanto Earthquake are dominant. Yokohama has the high probability of being affected by such earthquake compared with Saitama and Chiba. Therefore provision of alternate node for Yokohama effectively decrease BIT risk. Whereas, Saitama has relatively low probability of being affected by such earthquake. Therefore provision of alternate node for Saitama (Modification *A*) does not effectively decrease BIT risk. Modification *C* decreases BIT risk, however, if the cost of providing alternative node is same in three locations, compared with Modification *B*, the benefit is relatively low in consideration of the necessary cost. If an enterprise with series SC with nodes in these three locations is to draw BCP to decrease it's BIT risk, the best option would be Modification *B*.

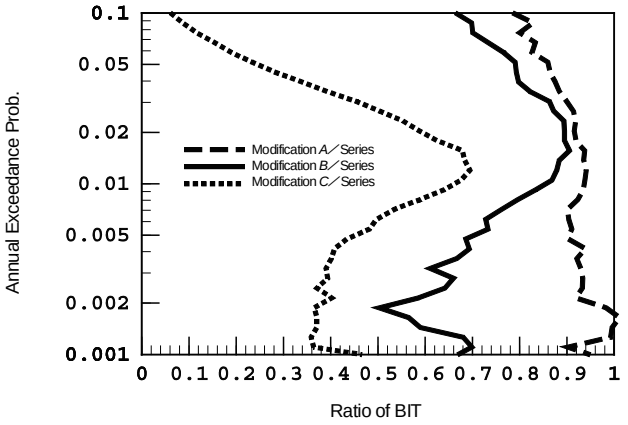


Fig.12 BIT Risk Reduction by Provision of Alternative Nodes

7. APPLICATION for STRATEGIC BUSINESS CONTINUITY PLANNING and DECISION MAKING

There are two main objectives for enterprises to draw BCP (Fig.13). First, to avoid the total halt of operations, even in case of disasters and maintain the minimal level of operations for business continuity. Second, to resume the operations to pre-disaster level within an acceptable timeframe from the viewpoint of corporate management in the competitive market.

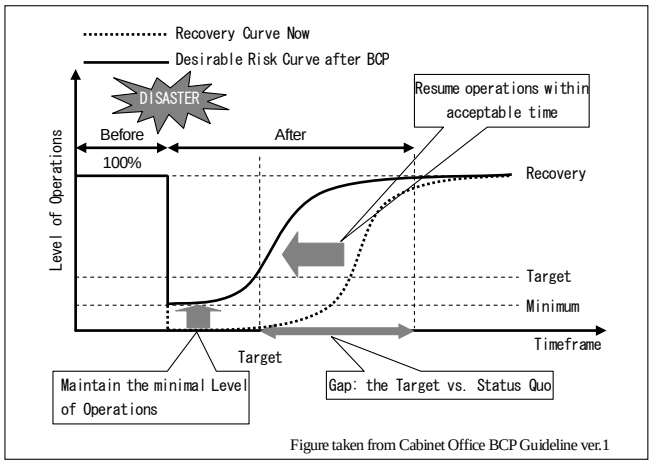


Fig.13 The Overall Concept of BCP

Let us suppose that a factory was hit by an earthquake. For the user of the product of the factory, his biggest interest would be when the factory would resume supply to him. If he sees that he cannot expect the supply within the timeframe he can wait, he will search for an alternative product or manufacturer. If the user decides that he cannot wait anymore, the factory will lose the user. Even if the factory resumes production afterwards, since the previous user is already taken by other manufacturer, the enterprise that runs the factory will have to pay marketing efforts to regain the user or to find new customers, which will require additional marketing costs. The longer the BIT, the marketing cost necessary will augment. If the BIT of the factory is further prolonged, the enterprise may no longer be able to return to the market. Thus BIT is an important factor for business continuity of an enterprise.

It might look like ideal to minimize BIT even in case of severe earthquakes. However it would require various investments to secure business continuation; seismic reinforcement or base isolation of buildings, stockpiling of abundant materials and parts, backup generators and fuel, additional water tanks, provisional contracts for backup offices, all of which might be just a burden for enterprises if they do not appreciate the value of BIT reduction. Enterprises need to identify the time limits for their customers to "wait" and plan to meet this time limit by choosing the good alternative for themselves.

The proposed method for evaluation of business interruption time for supply chain dependent enterprises will enable corporate executives to quantitatively appreciate the risks they face, support their decision making for countermeasures and justify the costs to reduce the risk. The proposed method is flexible to be adapted to various types of supply chain patterns. Furthermore, by decomposing the elements of the individual nodes of the supply chains, it can be further adapted to reflect the different types of operations by industry. Also by considering the connection routes between the nodes as one of the nodes, this method can be further fine-tuned.

The proposed method for analysis of alternatives for BIT risk reduction will enable corporate executives to compare options for reducing the risk and to draw strategies to fit their needs. Each enterprise has their own "limits" for BIT according to their type of business and their relation with the customers. Through comparison of the expected rate of reduction of probabilities to exceed their "limits" for BIT, the enterprises will be able to choose the best alternative to reduce their risk in balance with the costs incurred.

8. CONCLUSIONS

A quantitative risk evaluation method of BIT of SC dependent enterprise is proposed, and applied to model enterprises based in the Greater Tokyo Metropolitan Area. The risk curves of BIT for series and parallel supply chain are calculated and examined. Three alternative options to decrease the BIT risk of series SC are proposed and evaluated.

This method enables enterprises to quantitatively compare their options for decreasing their BIT risks. Taking into consideration the costs for these options, this method will be an effective tool for BC planning of supply chain dependent enterprise.

Through the application of this method, it is expected to decrease the possible business interruption time in future disasters and thus reduce the economic damage. The author hopes that these methods to be put into practice in the near future and contribute to the reduction of economic damage.

Acknowledgements:

The author would like thank Dr. Harumi Yashiro and Dr. Sei'ichiro Fukushima for their valuable advice and assistance in developing this analysis method.

References:

Nishikawa, S., Fukushima, S. and Yashiro H., "Proposal of a new Method for Risk Evaluation of Supply-Chain Dependent Business Continuation Plan", *Proceedings of the Annual Conference of the Institute of Social Safety Science*, Vol.21, (2007), pp.39-42.

Fukushima, S. and Yashiro H., "Seismic Risk Analysis on Portfolio of Buildings", *Journal of Architecture, Planning and Environmental Engineering*, No.552, (2002), pp.169-176.

Sakamoto, S. "Evaluation of Recovery Curve for Business Continuity Planning", *Report of Taisei Technology Center*, No.39, (2006), pp.05.1-05.5.

Architectural Institute of Japan, "Recommendations for Loads on Buildings", (Architectural Institute of Japan, 2004).

Annaka, T. and Yashiro, H., "A seismic source model with temporal dependencies of large earthquake occurrence for probabilistic seismic hazard analysis in Japan", Risk Analysis, (WIT PRESS, 1998), pp.233-242.

8CUEE CONFERENCE PROCEEDINGS
8th International Conference on Urban Earthquake Engineering
March 7-8, 2011, Tokyo Institute of Technology, Tokyo, Japan

"DISASTER PREVENTION" AND BUSINESS CONTINUITY: LINGUISTIC AND CULTURAL PITFALLS FOR IMPLEMENTING EFFECTIVE BCM IN JAPAN

Nathan Lee Rhoden[1)] and Shinji Hosotsubo[2)]

1) Director, Crisis Management & Preparedness Organization, Japan
2) Chairman, Crisis Management Education & Exercise Center, Japan

Abstract: Earthquakes loom large as a major hazard that must be taken into consideration when implementing Business Continuity Management (BCM) in Japan, yet earthquakes and other natural disasters are not the only issues which need to be addressed by Japanese organizations seeking viable continuity. Historically, Japan has fostered a sophisticated culture of Bosai (防災) or "Disaster Prevention," but the authors' research indicates that effective BCM can be hampered by this deeply ingrained cultural mindset. Part of the difficulty stems from the fact that the concept of "Disaster" has been translated into Japanese as Saigai (災害) which traditionally implies only natural disasters, whereas the English term, especially as defined within the BCM community, has a far broader meaning.

1. INTRODUCTION

Spurred by the need for improved Crisis Management in the wake of the 1995 Great Hanshin-Awaji Earthquake, the authors of this paper were among the earliest proponents of Business Continuity Management (BCM) in Japan. During that period, the phrase "Business Continuity" was still virtually unknown in Japan, and much of the early efforts to raise awareness and promote the concepts of BCM fell on deaf ears. Since that time there has been a kind of great-awakening, and BCM has even become a kind of buzzword among organizations in Japan.

Beginning in 2005, several official guidelines were issued by the Japanese government, including the "Business Continuity Guidelines" by Cabinet Office, and the "Guidelines to Formulate and Operate BCP for Small and Medium Enterprise" by the Small and Medium Enterprise Agency. In addition, in 2006, the Koizumi Administration announced targeted goals, stating that within 10 years it wanted "almost all large corporations, and more than half of medium-size firms" to have implemented BCM.[1]

Such government announcements carry considerable weight in Japan, so these events have caused a tremendous increase in interest about BCM. And, to satisfy this interest, a great many educational and instructional books have been published to supplement and provide commentary on the various official government guidelines.

Despite this new found interest in BCM, the authors' empirical research indicates that the vast majority of organizations attempting to implement BCM in Japan are not realizing its full benefits. In fact, top management at many organizations have come to perceive BCM as some kind of expensive boondoggle that they can ill afford in view of today's difficult economic climate.

This situation is quite regrettable, since at its effective best, BCM is a proven management methodology which can greatly aid top management in all times of crisis, including a poor economy. But, so far, fundamental misconceptions about the nature and purpose of BCM have generally limited its introduction to only relatively low management levels. Most of the top management in Japan remain unaware of its potential benefits, and therefore extremely few organizations have actually implemented effective BCM.

This paper attempts to explain some of the linguistic and cultural pitfalls that appear to be hampering the implementation of effective BCM in Japan, establish some of the key similarities between BCM and traditional Strategic Management, and point out why BCM can be especially useful in times of rapid change.

2. LINGUISTIC AND CULTURAL ISSUES

2.1 The Definition of Disaster

The word "disaster" has typically been translated into the Japanese term Saigai (災害), a term that is generally applied only to natural disasters.

Japan has long history of Bosai (防災) or "Disaster Prevention," and this concept is deeply ingrained into the Japanese culture. Business Continuity Management (BCM) shares its origins with a related discipline called "Disaster Recovery," and English language treatises on BCM frequently employ the word "disaster." Since this word is invariably translated as Saigai, many Japanese readers have been led to the misconception that BCM is just another (albeit potentially advanced) form of Bosai of "Disaster Prevention," and that BCM is also focused primarily on earthquakes and other natural disasters.

To the contrary, the BCM discipline has never been

particularly focused only on natural disasters per se, and its methodology is now increasingly being applied to completely non-physical events.[2]

Even in colloquial English the word "disaster" has a far broader meaning than natural disaster (e.g., "That meeting was a disaster." or "My party was a disaster."), and it is defined within much of the BCM community as:

"A sudden, unplanned catastrophic event causing unacceptable damage or loss. 1) An event that compromises an organization's ability to provide critical functions, processes, or services for some unacceptable period of time 2) An event where an organization's management invokes their recovery plans."[3]

The significance of this difference between the Japanese and English definitions lies in the fact that Japanese organizations typically have an existing Bosai or "Disaster Prevention" function which is usually positioned within their Soumu-Bu (総務部) or "General Affairs Department." And, this Bosai function is indeed focused almost entirely on preventing or mitigating the effects of natural disasters and fires. Therefore, when BCM is misperceived as also being primarily about natural disasters, it too is usually relegated to the "General Affairs Department."

According to the authors' extensive experience, positioning of the BCM function at this level within the hierarchical structure of a Japanese organization rarely results in effective BCM.

2.2 Risk Management vs. Crisis Management

Another related linguistic issue is how the Japanese term Kiki-Kanri (危機管理) has also been translated into English. While every Japanese-English dictionary translates the first portion of the term, Kiki (危機), as "Crisis," and the second portion of the term, Kanri (管理), as "Management," the complete term Kiki-Kanri has often been translated as "Risk Management."

As it happens, there is no obvious way to succinctly translate the word "Risk" into Japanese, making simple translation of the phrase "Risk Management" difficult, except by phonetic method. So, when the concepts of Risk Management were being introduced into Japan, it is likely that the well known (though often poorly understood) Japanese term Kiki-Kanri may have presented itself as a simple solution to this translation issue. And, it is even possible that the English words for "Risk" and "Crisis" were poorly understood and somehow equated. In any case, the authors' believe this additional bit of linguistic confusion has also hampered the implementation of effective BCM in Japan.

Risk Management and Crisis Management are not always well defined even within the English speaking world, and a detailed examination of the two concepts is beyond the scope of this paper. However, suffice it so say that the two disciplines are quite different, and in the authors' view, most Japanese possess a cultural propensity for Bosai or "Disaster Prevention" which makes them far more comfortable with the concepts found in Risk Management, and relatively uncomfortable with many of those in Crisis Management.

Risk Management tends to be a statistically driven discipline largely focused on known risks (whether natural or otherwise) and as such, tends to fit well with the Bosai cultural mindset which has, as its "core nature" the desire to, if possible, prevent natural disasters, even earthquakes. Bosai recognizes, of course, that where prevention is not yet possible, mitigation must be applied. However, the ultimate goal of the Bosai mindset is prevention.

On the other hand, to be at all effective, Business Continuity Management (BCM) must fully and unequivocally accept the concept of truly unknown risks, which are therefore inherently unpreventable.

The fact is that "disasters" (i.e. Events that compromise an organization's ability to provide critical functions, processes, or services.) will always occur. So, while cost effective prevention and/or mitigation efforts can play a significant role in BCM, there is a particular kind of high-level strategic planning found in effective BCM that is intended to counter even heretofore unknown risks, and has propelled towards the realm of Crisis Management.

2.3 Danger vs. Opportunity

The linguistic and cultural issues described above have had the unfortunate tendency to limit the implementation of BCM in such a way that its full benefits cannot be completely actualized in Japan due to inadequate top management understanding and participation.

BCM has, as its "core nature," the desire to successfully continue an organization's operations, under any and all circumstances. And presumably, the top management of any organization will share such a desire. Because of its highly strategic "core nature," effective BCM can serve a dual purpose. The fundamental principles embodied in effective BCM can be applied equally well to capitalizing on opportunities and growing an organization, as they can to "preventing disaster." Once fully empowered by top management, the BCM methodology becomes extremely useful to the day-to-day organization, whether or not it ever actually faces disaster. Effective BCM can enhance both the agility and the resiliency of the organization.

Perhaps such duality was understood by the ancients who developed the ideogram for Kiki (危機) or "Crisis." The first character (危) denotes the concept of danger, since it is also used as the first character of term Kiken (危険) or "Danger." Similarly, the second character (機) is used as the first character of the term Kikai (機会) which means "Opportunity" or "Chance," as in a chance meeting. Thus to the Japanese eye, their ideogram for crisis appears to embody a dual nature of both danger and opportunity.

3. STRATEGIC MANAGEMENT & BCM

3.1 "Full Scope" BCM

Lehman Brothers Holdings Inc. was founded in 1850 and stood for over 158 years. But, their sudden bankruptcy on September 15, 2008, led to a global business calamity that is referred to in Japan as the "Lehman Shock."

Within the international BCM community, the

Lehman's bankruptcy stands out, not as a failure of BCM, but as a highly visible example of the risk associated with having too limited a scope when applying the principles of BCM within an organization. Thus, the "Lehman Shock" can be said to officially mark the beginning of an already existing trend towards "Full Scope" (or "All-Risk") BCM.

Traditionally, even sophisticated practitioners of BCM, such as Lehman Brothers, have tended to limit the scope of their BCM to operational threats, since financial threats (such as the unprecedented tightening of short-term credit which led to the demise of Lehman Brothers), typically fell within the scope of their Risk Management Department.

Unfortunately, the discipline of Risk Management is singularly unsuited to the task of evaluating "unprecedented" risks, so the "Lehman Shock" has further accelerated the movement of effective BCM towards the realm of Crisis Management, or perhaps more precisely, towards the realm of Japanese Kiki-Kanri which has always tended to have a broad scope that encompasses all threats to an organization.

3.2 Strategic Management

The discipline of Strategic Management has never been in danger of being mistaken by Japanese top management as a form of Bosai, or "Disaster Prevention," yet it shares many important attributes with effective BCM.

Strategic Management asks and answers questions like "Which business should we be in?" and "How does being in this business add value to our customers?" Such questions and their answers are also crucial to effective BCM.

Strategic Management also provides direction to corporate values, corporate culture, corporate goals, and corporate missions, and these too are also crucial to effective BCM.

3.3 Corporate Strategy

Strategic Management can be illustrated as a pyramid with four levels of strategy as shown in Figure 1.

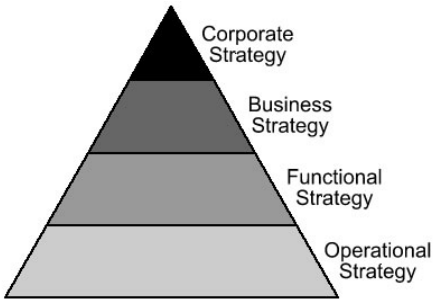


Figure 1 Strategic Pyramid with Corporate Strategy at its apex.

Like Strategic Management, which has Corporate Strategy at its apex, BCM has, at its highest level, the logical equivalent.

Just as Corporate Strategy is determined by corporate values, corporate culture, corporate goals, and corporate missions; these same values, culture, goals, and missions must determine the overall Business Continuity Strategy. Therefore, given this transitive relationship, Business Continuity Strategy (BCS) and Corporate Strategy must be essentially equivalent.

The establishment of an overall Business Continuity Strategy (BCS) by top management is essential to effective BCM. Just as Corporate Strategy drives all the lower levels of strategy within the pyramid of Strategic Management, it is the overall BCS which must drive all the lower levels of business continuity, functional recovery and operational recovery in BCM. Without a coherent BCS established with the full commitment of top management, all BCM efforts will likely be doomed to failure, or at best, be limited and ineffective.

The traditional pyramid of strategic hierarchy with Corporate Strategy at its apex may not be the best way to illustrate this point. Perhaps it is more useful to reconstruct the pyramid as shown in Figure 2. This figure better illustrates how Corporate Strategy (and BCS) must be established at the very foundation of the organization, and how it is upon this foundation that both Business Strategy and Business Continuity must be built.



Figure 2 Strategic Pyramid with Corporate Strategy as its foundation.

Given the strong foundation of a solid Corporate Strategy it is possible to establish successful business, functional, and operational strategies, but without a solid Corporate Strategy, all the other dependent strategies will collapse into rubble. Likewise, without the strong foundation of a solid BCS, it is impossible to establish effective (and cost effective) BCM.

The authors' empirical research indicates that in Japan the previously mentioned linguistic and cultural issues work together to limit top management understanding and involvement, which in turn weakens the foundation and limits effective BCM.

3.4 Structure Follows Strategy

Alfred Chandler, one of the pioneers of Strategic Management, emphasized the importance of a central strategy by stating quite succinctly that "Structure follows Strategy."[4]

Over the years, successful practitioners of BCM have arrived at this same conclusion, although perhaps from a different route. But, whatever the routes, the disciplines of BCM and Strategic Management have come to share many key principles and concepts in common.

3.5 Process Reengineering

Jay Barney conceived of strategy, within the context of Strategic Management, as assembling an optimum mix of resources (financial assets, human assets, technological assets) and configuring them in sustainable ways.[5] And, Michael Hammer and James Champy suggested that these resources should be restructured, so that an organization's assets are organized around whole processes rather than individual tasks. They named this concept Process Reengineering.[6]

The similarity to BCM methodology is striking. The Business Impact Analysis (BIA) is central to BCM methodology, and much of the initial analysis undertaken during a BIA involves thoroughly understanding an organization's processes, how those processes are developed from tasks, and how the various processes and tasks interrelate and sustain each other.

3.6 Core Competencies

Gary Hamel and C. K. Prahalad's best known contribution to the Strategic Management discipline is their concept of core competency, and they emphasize just how important it is to know the one or two key things that your organization does better than the competition.[7] And, John Kay further states that the role of Strategic Management is to identify core competencies, and then assemble a collection of assets that will increase value added and provide a competitive advantage.[8]

Again, these key concepts of Strategic Management parallel those of BCM. In addition to understanding the organization's processes as mentioned above, the Business Impact Analysis (BIA) also entails judicious prioritization of core competencies based on quantitative and qualitative analysis of just how those core competencies add value to stakeholders.

The BIA is essential to effective BCM because it allows for detailed strategic planning well in advance of a crisis, whether that crisis be a danger or an opportunity.

3.7 Core Values

Another key element of BCM involves establishing clear social, socioeconomic and ethical values that are well understood throughout the organization, and can provide vital guidance during times of crisis. How an organization comports itself under stress is an excellent indicator as to the depth and strength of its core values.

James Collins and Jerry Porras spent years conducting empirical research on successful organizations in hopes of determining just what makes a great organization "great." And, they finally uncovered one key underlying principle: "great organizations encourage and preserve a core ideology that sustains the organization." Strategy may change, and tactics will certainly change, but great organizations manage to maintain a constant set of core values.[9]

3.8 What is BCM?

Despite the misconceptions common in Japan, effective BCM is not about planning in advance for an earthquake, or some other kind of disaster that would have a negative impact on the organization, should it occur.

Effective BCM is about establishing and preserving core values that can endure the test of time, thoroughly understanding both the strengths and weaknesses of the organization's processes, and fully recognizing just how, and to whom, those processes can add the most value.

Ironically, once this kind of BCM has been established at the top management level, earthquake mitigation is often achieved by the organization as a kind of "free bonus." This is because effective BCM is indeed uniquely capable of minimizing, or possibly even preventing, impacts from all manner of disruptive events, including earthquakes.

But it is important to note that this kind of "free bonus" can only be received from one direction: top down, not bottom up. When implemented from the bottom up, for the purposes of earthquake mitigation, BCM rarely rises to the level where it can be perceived as a useful management methodology by top management.

Not only that, when implemented from the bottom up, BCM also commonly fails at even its stated goal of earthquake mitigation because it quickly reaches an impasse with top management over costs. Since bottom up BCM does not incorporate the true strategic thinking of top management, the earthquake mitigation "strategies" (more often tactics) proposed from the bottom up are typically deemed to be too expensive and unrealistic to be approved by top management.

This impasse is commonly overcome by compromising on lower cost earthquake mitigation tactics that are not only ineffective against all but nominal earthquake scenarios; they are usually completely useless against other threats such as pandemic. This is not effective BCM.

3.9 Positioning the BCM Department

In "Crisis Leadership," Ian Mitroff describes how and why Alfred P. Sloan changed the GM organizational structure by adding a new and previously unknown department at its top.[10]

When Sloan took over as CEO, GM was experiencing a crisis: it had no idea how many cars it was selling. The organization had grown so huge that it had lost control over its inventory, it couldn't get accurate and timely sales data from its dealers, and it had trouble getting the various car divisions to share their revenues with the central parent corporation.

Sloan solved this crisis through the creation of a Finance Department at the very top of the company. Today many might assume that Finance Departments have always been a part of corporate structures, but in actuality, Sloan established the world's first Finance Department less than a hundred years ago.

Similarly, if today's organizations are to survive their current crisis of a rapidly changing environment, they would be well served to establish a BCM Department at the highest level of their organizational structure.

Just as past leaders required financial savvy, today's leaders will require BCM savvy.

4. STRATEGIC CHANGE & BCM

4.1 The Age of Discontinuity

The phrase "Age of Discontinuity" was coined by Peter Drucker to describe how change disrupts the continuity of our society.[11] In periods of continuity, extrapolating from the past provides a reasonably useful and relatively accurate method for predicting the future. But in an Age of Discontinuity, extrapolating from the past is completely ineffective. Trends that exist today cannot be assumed to continue into the future.

Alvin Toffler is well known for predicting a trend towards accelerating rates of change.[12] In his popular books, Toffler describes how social and technological norms have increasingly shorter life spans, and he predicts society's increasing inability to cope with such constant change. He sees relentless change as the defining feature of our current civilization.[13]

Richard Pascale wrote that constant change requires that businesses continuously reinvent themselves.[14] He is famous for stating that "Nothing fails like success," meaning that yesterday's strengths become today's weaknesses.

Effective BCM can be highly useful in managing strategic change. Unlike Risk Management which tends to utilize relatively passive methods of prevention or mitigation, BCM incorporates proactive principles of Crisis Management that require rapid decision-making in times of rapid change, and rapid decision-making even when all the information desired for decision-making is not available.

The concept of "continuous reinvention" also has a strong correlation with BCM. A continuous improvement cycle is a fundamental part of the BCM methodology, and effective BCM can readily drive continuous reinvention as it constantly reevaluates the strengths and weaknesses of an organization's processes, and how, and to whom, those processes are adding value.

4.2 Scenario Planning

BCM methodology also employs scenario planning in a number of ways. The Business Impact Analysis (BIA) process utilizes multiple scenarios where impacts from the complete disruption of each discrete function or task that makes up of each of the organization's processes are evaluated individually, but on a non-threat-specific basis.

Threat-specific scenario planning is also used to evaluate the likely effectiveness of proposed, and often highly creative, Business Continuity Strategies (BCS). It is this kind of scenario planning found in BCM that can encourage the spirit of inquiry, the constructive conflict, and the healthy debate that is necessary for organizations to survive in an environment of constant change.

As Peter Schwartz put it, strategic outcomes can no longer be known in advance, so the sources of competitive advantage cannot be predetermined.[15] The rapid pace of change in the current environment makes the sustainability of competitive advantage too uncertain. But, scenario planning allows multiple outcomes to be explored, and their implications assessed.

According to Pierre Wack, scenario planning is about insight, complexity, and subtlety, not about formal analysis and numbers.[16] Effective BCM also shares these qualities, and in fact, strategic creativity is frequently the most important factor in achieving viable continuity

5. CONCLUSIONS

Far from being an expensive boondoggle, once understood and fully implemented by top management, effective Business Continuity Management (BCM) can actually be highly profitable, and help promote the growth of an organization, not just its continuity.

While BCM is not primarily about natural disasters, once it is incorporated into an organization's overall management strategy, it is uniquely effective in reducing, or even eliminating, the impacts from any business interruption.

Due to its effectiveness in times of rapid change, BCM has become an increasingly important methodology in the management of modern organizations.

Once BCM is better recognized by Japanese top management as the Strategic Management methodology that it is, Japanese organizations will also be able to implement BCM that is more strategically aligned with their business goals and thus begin to reap its true benefits.

References:

1. Central Disaster Prevention Council, "Countermeasure Strategies against Disaster by Inland Earthquake in the Capital City"
2. The Business Continuity Institute (2010), "Good Practice Guidelines"
3. The Disaster Recovery Journal and Disaster Recovery Institute International, "Glossary 2.0"
4. Chandler, Alfred (1962), "Strategy and Structure: Chapters in the history of industrial enterprise," Doubleday, New York
5. Barney, J. (1991) "Firm Resources and Sustainable Competitive Advantage," Journal of Management, vol 17, no 1
6. Hammer, M. and Champy, J. (1993), "Reengineering the Corporation," Harper Business, New York
7. Hamel, G. & Prahalad, C.K. (1990), "The Core Competence of the Corporation," Harvard Business Review, May-June
8. Kay, John (1993), "Foundations of Corporate Success," Oxford University Press, Oxford
9. Collins, James and Porras, Jerry (1994), "Built to Last," Harper Books, New York
10. Mitroff, Ian (2003), "Crisis Leadership - Planning for the Unthinkable," John Wiley, New York
11. Drucker, Peter (1968), "The Age of Discontinuity," Harper and Row, New York
12. Toffler, Alvin (1970), "Future Shock," Bantam Books, New York
13. Toffler, Alvin (1980), "The Third Wave," Bantam Books, New York
14. Pascale, Richard (1990), "Managing on the Edge," Simon and Schuster, New York
15. Schartz, Peter (1991), "The Art of the Long View," Doubleday, New York
16. Wack, Pierre (1985), "Scenarios: Uncharted Waters Ahead," Harvard Business Review, September-October

8CUEE CONFERENCE PROCEEDINGS
8th International Conference on Urban Earthquake Engineering
March 7-8, 2011, Tokyo Institute of Technology, Tokyo, Japan

TOKYO INLAND EARTHQUAKES AND BUSINESS CONTINUITY OF COMPANIES/ORGANIZATION

Hiroaki Maruya

Professor, Center for Urban Earthquake Engineering, Tokyo Institute of Technology, Japan,
Research Fellow, Research Institute of Construction and Economy, Japan,
Board Chairman, Business Continuity Advancement Organization, Japan
h-maruya@tiara.ocn.ne.jp

Abstract: Facing the threats of Tokyo Inland Earthquakes, both government and private organizations are required to equip their BCP (Business Continuity Plan). Even if the core government organizations were forced to move out of the central districts of Tokyo by their damage, they would stay in cities within the greater Tokyo region, such as Tachikawa, Yokohama, Saitama, etc. to preside over the recovery and reconstruction activities that should be their top priorities. Some private enterprises who think it is more advantageous to keep their headquarters in the greater Tokyo region would stay just like the core government organizations. On the other hand, many other enterprises would move their head office functions to major branches in cities such as Osaka and Nagoya, considering the constraining factors of securing houses for their workers, their commuting difficulty and so on. Therefore, it is meaningful for major cities outside of capital region including Osaka and Nagoya to make preparations to accept a part of private enterprises' core functions.

1. INTRODUCTION

Today the Japanese capital's core functions face threats such as Tokyo Inland Earthquakes, pandemic influenza and large-scale terrorism. To protect the national capital functions, there are some opinions that Tokyo's core functions should be dispersed into other areas of the country. The Japanese government is discussing continuously the dispersal of the Parliament House and other important government organizations out of Tokyo. However, no detail plan has been decided for capital function dispersal.

On the other hand, as countermeasures against these threats, both the government and private businesses in Tokyo are required to formulate BCP (Business Continuity Plan) to keep continuity of important activities in a time of disaster. The concept of Business Continuity is shown in Figure1.

The method of BCP includes selecting important operations, estimating damage to resources of organizations such as people, goods, money, information and systems that are essential to continue important operations, as well as securing alternative resources and/or reinforcing resources to reduce damage.

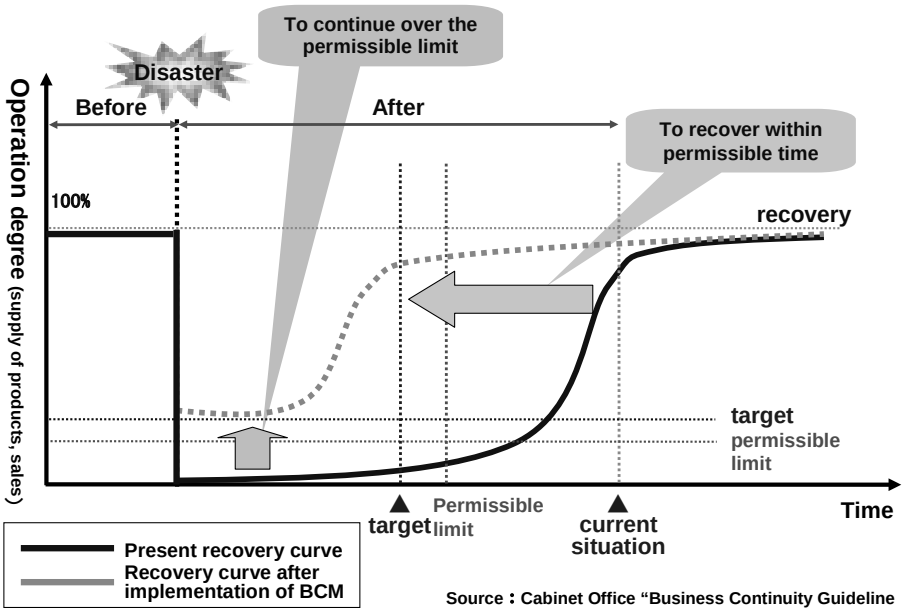
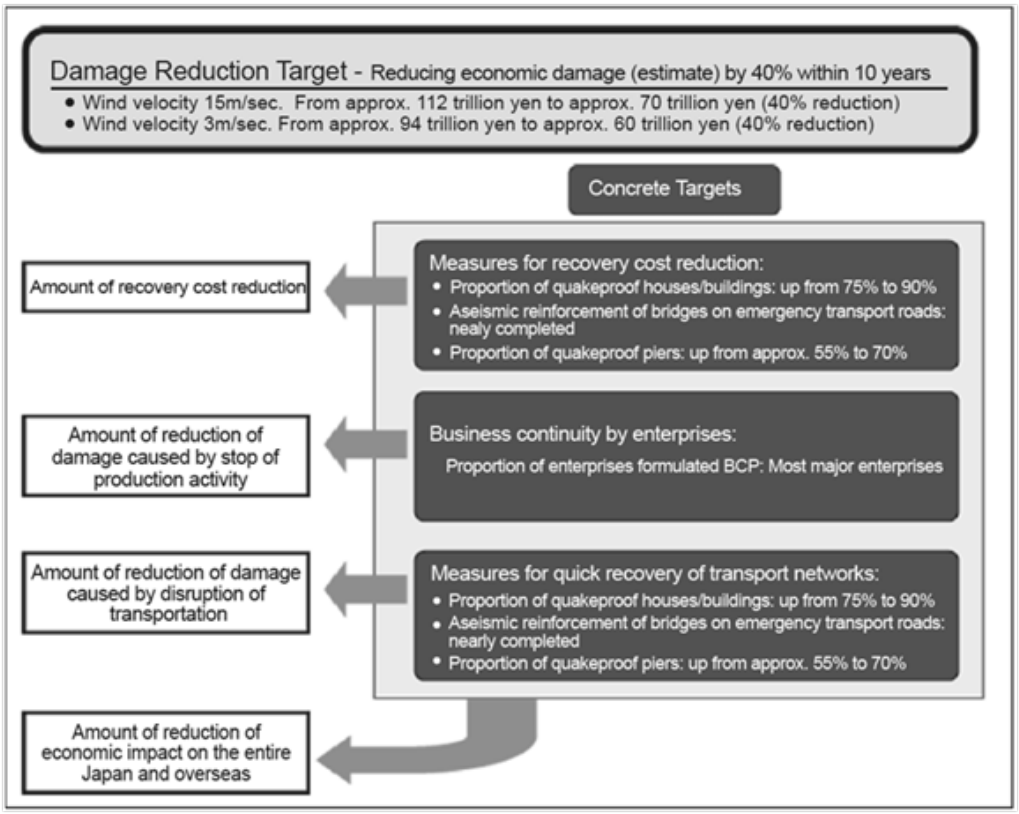
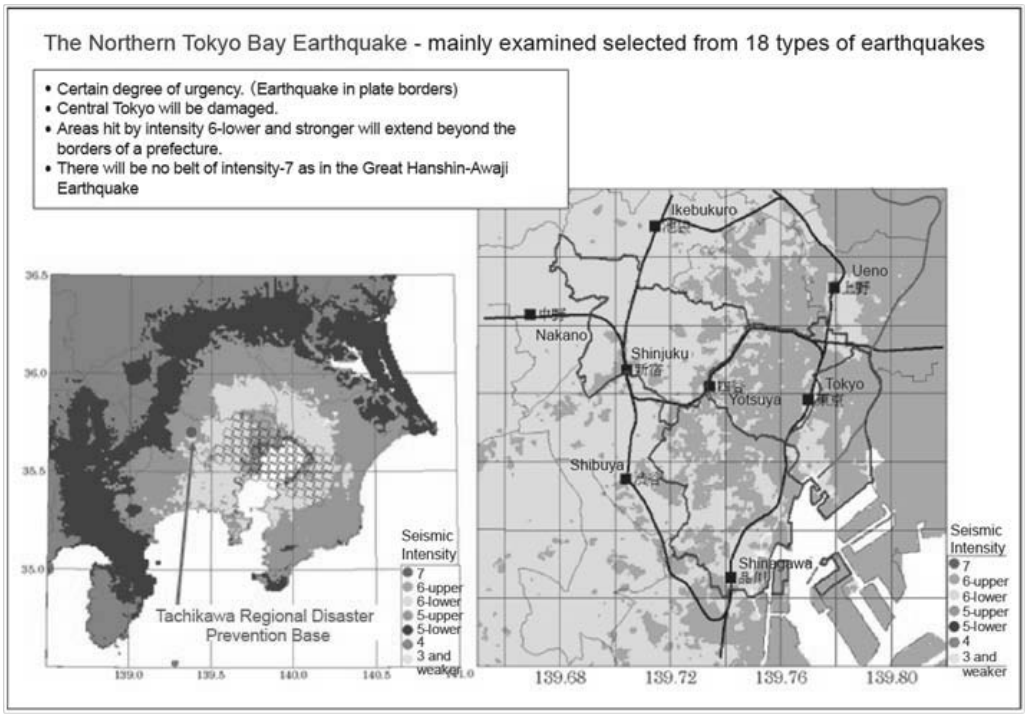


Figure 1 Concept of Business Continuity



Material of the Cabinet Office (Disaster Prevention)

Figure 2　Earthquake Disaster Prevention Strategy in Case of Tokyo Inland Earthquakes（Economic Damage）



Material of the Cabinet Office (Disaster Prevention)

Figure 3　Distribution of Seismic Intensity during the Northern Tokyo Bay Earthquake (7.3-magunitude)

2. Damages of Tokyo Inland Earthquakes

2.1 The Expected Worst Type

It is scientifically understood that in the greater Tokyo capital area, massive trench-type earthquakes with a magnitude of 8 or greater, like the Great Kanto Earthquake (1923), occur at intervals of 200-300 years. Additionally, it is estimated that smaller several types of Tokyo Inland Earthquakes (magnitude 7 (M7) class) occur before a M8 scale earthquake.

Japanese government published the estimation that a M7 class will occur in the probability of 70% in next 30 years.[1] The Central Disaster Management Council of Japanese government has carried out damage estimations for 18 types of Tokyo Inland Earthquakes (M7 class). The type whose epidemic center is at northern part of Tokyo Bay (assumed scale of M7.3 at 6pm in winter) is estimated to cause most serious damage. It would include a death toll of approximately 11,000 people, total collapse of 85,000 buildings and a maximum economic loss of 112 trillion yen. To reduce the economic loss, introduction of BCP to public and private organizations is positioned as one of the main countermeasures (Figure 2).

2.2 Distribution of a Seismic Intensity

Figure 3 shows maps of the seismic intensity distribution of the expected Tokyo Inland Earthquake whose epidemic center is at northern part of Tokyo Bay. On this earthquake, most places in east half of the central districts of Tokyo is predicted to experience a seismic intensity[2] 6-upper. The standard damages by the intensity 6-upper earthquakes are defined by Japan Meteorological Agency as in Table 1[3].

Table 1 The Standard Damage of Earthquakes of a Intensity 6-Upper

- One cannot stand. One cannot move unless crawling.
- A lot of the furniture moves unless it is not fixed, and Some of them fall down.
- Of many buildings, tiles on walls and windowpanes are damaged and drop.
- Most of fences made of blocks which are not reinforced are fall down.
- Some wooden houses with high quake resistance have crazing and cracks on walls.
- Many of wooden houses with low quake resistance have crazing and cracks on walls. A considerable number of those incline or fall down.
- Some steel reinforced concrete buildings with high quake resistance have crazing and cracks on walls, beams, pillars etc.
- Some steel reinforced concrete building with low quake resistance have diagonal or X-shaped crazing and cracks on walls, beams, pillars, etc. Of these, there are buildings that collapse caused by breaking down of pillars of the first floor or intermediate floors.

3. Substitution Places for the Central Districts of Tokyo

3.1 Business/ Operational Nucleus Cities

To de-centralize excessive “capital core functions” of the central districts of Tokyo, the concept of the “Business/Operational Nucleus Cities (BNCs)” have been introduced based on the “Act for the Promotion of Multipolar Pattern National Land Formation” in 1988. The act stipulates to choose BNCs from the area except the 23 wards area which are including the central districts of Tokyo.[4] At the time of a large-scaled disaster in Tokyo, BNCs are expected to play important role as substitute places for the organizations and enterprises located at the central districts of Tokyo.

Government has supported to develop and facilitate BNCs by systematic and financial methods. Among these, most effective method seems to be the transfer of ministries’ branch offices for Kanto region (i.e. several prefectures around Tokyo) from the central districts of Tokyo to some of BNCs such as Saitama City (north from Tokyo) and Yokohama City (southwest from Tokyo). Another BNC is Tachikawa (west from the central districts of Tokyo) where the alternative base of the Cabinet of Japanese government is prepared for the time of disaster. Others are Chiba City (east from Tokyo) and so on.

The distance from the center of Tokyo to each BNC which is scattered in Tokyo metropolitan area and three prefectures neighboring Tokyo (hereafter “the greater capital area”) is more than 30 kilo-meters. We can expect that for any type of Tokyo Inland Earthquake whose epidemic center is in the greater capital area, one or more BNCs would be safe without serious damage. In other words, it is not predicted that all of BNCs are simultaneously hit by seismic shaking of intensity 6-lower (the minimum seismic intensity to cause considerable damage) or over.

3.2 Substitute Headquarters for Government Organization

Presently, important buildings and facilities of the Japanese central government are mostly earthquake-resistant. On this reason, the present BCPs of the ministries’ head offices prepared against Tokyo Inland Earthquakes assumed that the ministries would be able to use their headquarter buildings with high probability.

However, we have to consider that the ministries may not be able to use their headquarters because of unexpected damage of building structure, outbreak of fire, troubles of electric power supply and telecommunication service breakage of sewage pipes, workers’ commuting problems and so on. Japanese BCP guidelines for central ministries[5] recommended that a substitute office is specified in each ministry’s BCP. For example, the substitute offices for Ministry of Land, Infrastructure, Transport and Tourism (MLIT) which is the first ministry to formulate BCP in Japan, are as follows; 1) Kanto Regional Survey Department, Geospatial Information Authority of Japan (Chiyoda Ward, Tokyo), 2) College of Land, Infrastructure, Transport and Tourism (Kodaira City, west from the central districts of Tokyo) . This college is near to the Tachikawa Regional

Disaster-prevention Base where the Cabinet would evacuate as mentioned above. Substitute offices of ministries of Japanese government are shown in Table 2.

Table 2 Substitute Offices for Ministries

Name of Ministry	Substitute Offices
Ministry of Land, Infrastructure, Transport and Tourism (MLIT)	1) Kanto Regional Survey Department, Geospatial Information Authority of Japan (Chiyoda Ward, Tokyo), 2) College of Land, Infrastructure, Transport and Tourism (Kodaira City, Tokyo)
Ministry of Internal Affairs and Communications	Local Autonomy College (Tachikawa City, Tokyo), Institute for Information and Communications Policy (Kokubunji City, Tokyo)
Ministry of Economy, Industry and Trade	Japan Patent Office (Chiyoda Ward, Tokyo)
Ministry of Agriculture, Forestry and Fisheries	Sanbancho Branch Government Office (Chiyoda Ward, Tokyo)
Ministry of the Environment	1) Chidorigafuchi National Cemetery Administration Office (Chiyoda Ward, Tokyo) 2) Kokyogaien National Garden Office (Chiyoda Ward, Tokyo) 3) Shinjuku Gyoen National Garden Office (Shinjuku Ward, Tokyo) 4) The National Environmental Research and Training Institute (Tokorozawa City, Saitama Prefecture)
Consumer Affairs Agency	Specific place is not published
Japan Coast Guard	Coast Guard Research Center (Tachikawa City, Tokyo) Yokohama Maritime Disaster Prevention Base (Yokohama City, Kanagawa Prefecture)
Japan Meteorological Agency	Secured in nearby (Chiyoda Ward, Tokyo)
Ministry of Education, Culture, Sports, Science and Technology	Considering Continuously
Ministry of Finance	To consider in future
Financial Service Agency	To consider in future
Ministry of Justice	Not referred
Ministry of Defense	Not referred
National Police Agency	Not referred
Japan Fair Trade Commission	Not referred

When a severe natural disaster hits Tokyo, it should be a top priority for most ministries to preside over the recovery and reconstruction activities in capital area. Although most of ministries do not specify the substitute offices outside of the 23 ward area of Tokyo in their present BCPs, the author expects that their branch offices for Kanto region in Saitama City or Yokohama City would be good candidates for the substitute offices. Small number of ministries might move their headquarters to some big cities such as Osaka, Nagoya, or Kobe, but they would secure their second headquarters in BCMs or other cities in the greater capital area.

However, above-mentioned story seems to be not applicable if the Diet decides to move to any cities outside of greater capital region. Some ministries would decide the place of substitute head office in the same cities which the Diets move to. Others would set up second headquarters in the same cities. As the BCP of the Diet has not been published yet, we cannot deny the probability of these, but the Diet member would prefer, in the author's anticipation, to stay nearby where the Cabinet is working for the reconstruction works.

3.3 Substitute Worksites for Large Enterprises

A portion of large enterprises acting nationwide in Japan would stay in the great capital region when they cannot use their headquarters and think it is more advantageous to keep their headquarters in the region. Examples of these companies are those whose business activities are deeply related to recovery and reconstruction projects in Tokyo. However, this expectation does not mean that most of the workers of these companies would necessarily keep staying in and around Tokyo. This point will be discussed in Chapter 4.

Other enterprises would move their head offices to other branches or factories in the cities outside of the greater Tokyo region such as Osaka, Nagoya and so on, if they feel difficult to operate as usual in the region. However parts of their operational functions would stay in BNCs or other cities in greater Tokyo region for the business activities in and around Tokyo.

4. Evacuation from Tokyo for Business Continuity Purpose

4.1 Necessity of Evacuation of People

For the business/operational continuity, it is not enough for each organization to secure their operations carried out by restricted members of emergency response team. It is also indispensable to recover all critical operations as soon as possible which are carried out by many other ordinal workers/officials. In initial several days after the quake, emergency response activities are very important, but after this period, each organization has to restart more important operations.

According to Damage Estimation by Tokyo Metropolitan Government, Tokyo Inland Earthquake at northern part of Tokyo Bay (scale of M7.3) would cause major damage on railways at 28 places[6]. The major damage needs civil engineering works to recover, and it ordinary takes at least several weeks. BCP of MLIT uses assumptions as follows: "In the area suffered from a seismic intensity 5-upper and more, rail way service would stop for 3 days, then, gradually recover. All railway service would recover in 30 days." Therefore, commuting problems of officials would be very serious for about a month or more in Tokyo area.

In addition, Government published the estimation of serious shortfalls of tentative housing.[7] In the worst case of Tokyo Inland Earthquakes (scale of M7.3, at northern part of Tokyo Bay at 6pm, in winter), the needs of tentative housing is expected to 1.62 million units of emergency dwelling in Tokyo metropolitan and three neighboring prefectures. However, by one month after the earthquake, supply would be only 1.26 million housing units including vacant private rental houses in Tokyo, its three neighboring prefectures and other prefectures nearby. This number apparently cannot meet the needs. Even by six months later, supply of 120 thousand emergency temporary houses, 310 thousand units of emergency repair of sufferers' houses and two thousand public rental housing are expected. Only if we include vacant private rental houses in Tokyo and above mentioned prefectures, we can finally fulfill the needs.

Considering these problems, evacuations of people living in the great capital area are very useful. Furthermore it would be necessary for large companies to transfer their workers/officials and their family to other business site outside of Tokyo as quickly as possible in order to retain business continuity.

4.2 Important Meaning of the Evacuation

Most of government officials and workers of enterprises in charge of recovery works would not be able to depart from Tokyo. In addition, workers in small and medium scaled companies which do not have substitute sites outside of Tokyo would be very difficult to go away from Tokyo. Therefore, the author thinks that larger companies having other business sites outside of Tokyo are requested to evacuate workers and their family from Tokyo to these sites. Important social effect of this evacuation is to make ease of shortfall of housing, commuting troubles, commodity supply restriction, etc. This evacuation seems to relate directly to social contribution and corporate social responsibility.

One of critical requirements for this evacuation is quickness and smoothness. To realize in very short period, Osaka, Nagoya, and other major cities in Japan would have important roles as recipients of evacuation. These cities are requested to supply sufficient workspace, business facilities, housing, school, nursery service and so on. Preparation in advance of these recipient cities seems to be highly desirable for the business continuity of companies based in Tokyo. For this preparation, the author would like to proposes a questionnaire survey to major companies in Tokyo to find out to which city and how much workers they expect to evacuate at the time of Tokyo Inland Earthquakes.

However, we should be careful that these sudden needs of work place, facilities, housing and so on in recipient cities would arise very fast after a Tokyo Inland Earthquake occurs, but in addition, the needs will start to decline as early as in several months or in several years at the longest. Therefore construction investment of additional offices and housing in the recipient cities may not cost-effective for the preparation of the evacuation. If the preparation activities cause major development projects in recipient cities, it would be, of course, welcomed by business associations in these cities. This may be one of the most difficult discussion points.

5. Conclusion

From the perspective of crisis management for natural disasters and other threats, it is apparently better that the nation's political and economic core functions do not concentrate in one place. However, in present-day Japan, both governmental and business functions are concentrated in Tokyo and the greater Tokyo region. Full-scale dispersion of those functions, if we could, would require a vast amount of money and time. Therefore, we must devise business and operational continuity methods based on present conditions in preparation for a crisis that may occur even in this year.

As mentioned above, all government organizations and private companies that have headquarters in central districts of Tokyo should secure substitute offices/sites as soon as possible. They should carefully study and decide the locations of substitute offices/sites. Their first option would be the places nearby in the central districts of Tokyo, since it is convenient for them to transfer from their headquarters to their substitute offices/sites. However, they should also secure the second substitute offices/sites in the places where one and the same disaster does not causes severe damage to both of their headquarter and substitute offices/sites simultaneously. Most of government organizations seem to select the places in the greater capital area, for example in BNCs. Private companies are expected to choose their substitute offices/sites in the greater capital region or out of this region based on the character of their business.

In addition, regardless of the place of substitute site, many of large companies in Tokyo are requested to consider quick evacuation of workers and their family from Tokyo to their substitute sites/office in other city far from Tokyo to avoid troubles caused by the quake until the recovery progresses sufficiently. Preparation for this evacuation in recipient cities are desirable.

References:

Cabinet Office (2007), "Business Continuity Guidelines for Ministries 1st edition (in Japanese, 中央省庁業務継続ガイドライン第１版)," http://www.bousai.go.jp/jishin/gyomukeizoku/pdf/gyoumu_guide_honbun070621.pdf

Cabinet Office (2008), "Report of Research Committee for Evacuation Method for Tokyo Inland Earthquakes (in Japanese, 首都直下地震避難対策等専門調査会報告)," http://www.bousai.go.jp/jishin/chubou/shutohinan/index.html

Disaster Management Council, Tokyo Metropolitan Government (2006), "Final Report of Damage Estimation in Tokyo by Tokyo Inland Earthquake (in Japanese, 首都直下地震による東京の被害想定最終報告)," http://www.bousai.metro.tokyo.jp/japanese/tmg/assumptioni01.pdf

The Headquarters for Earthquake Research (2010), "Result of Long-term Evaluation, Trench type Earthquake (in Japanese, 長期評価結果、海溝型地震)"

http://www.jishin.go.jp/main/choukihyoka/kaikou.htm
Japan Coast Guard (2008), "BCP of Japan Coast Guard (in Japanese)," http://www.kaiho.mlit.go.jp/bcp/index.html
JMA (Japan Meteorological Agency) (2008), "BCP of Japan Meteorological Agency (in Japanese)," http://www.jma.go.jp/jma/press/0804/01a/BCP.html
JMA (2011), Website of "Explanation Table of the Seismic Intensity Level of Japan Meteorological Agency (in Japanese, 気象庁震度関連階級解説表)," http://www.jma.go.jp/jma/kishou/know/shindo/kaisetsu.html
Ministry of Agriculture, Forestry and Fisheries (2008), "BCP of Ministry of Agriculture, Forestry and Fisheries (in Japanese)," http://www.maff.go.jp/j/saigai/keikaku/index.html#d-2
Ministry of Economy, Industry and Trade (2008), "BCP of Ministry of Economy, Industry and Trade (in Japanese)," http://www.meti.go.jp/press/20080613007/20080613007.html
Ministry of Internal Affairs and Communications (2008), "BCP of Ministry of Internal Affairs and Communications (in Japanese)," http://www.soumu.go.jp/menu_seisaku/kokumin/pdf/syobo_2.pdf
Ministry of the Environment (2008), "BCP of Ministry of the Environment (in Japanese)," http://www.env.go.jp/other/keizoku/
MLIT (Ministry of Land, Infrastructure, Transport and Tourism) (2007), "BCP of Ministry of Land, Infrastructure, Transport and Tourism (in Japanese)," http://www.mlit.go.jp/kisha/kisha07/05/050621_.html
MLIT (2011), Website of "Business/Operational Nucleus Cities (BNCs) (in Japanese , 業務核都市）" http://www.mlit.go.jp/crd/daisei/gyoumukaku/index.html

Notes

[1] Explained in the report: The Headquarters for Earthquake Research (2010)
[2] Japan Meteorological Agency Seismic Intensity Scale
[3] Explanations in Table 1 are tentative translation of JMA (2011) by the author. Official translation from Japanese to English has not been published.
[4] Defined in the website :MLIT (2011)
[5] Explained in the guidelines : Cabinet Office (2007)
[6] Explained in the report: Disaster Management Council, Tokyo Metropolitan Government (2006)
[7] Cabinet Office (2008), pp.7-8

8CUEE CONFERENCE PROCEEDINGS
8th International Conference on Urban Earthquake Engineering
March 7-8, 2011, Tokyo Institute of Technology, Tokyo, Japan

BUSINESS CONTINUITY PLANNING AT UNIVERSITIES - A CASE STUDY ON TOKYO-TECH SUZUKAKEDAI CAMPUS-

Hideki Kaji[1], Tatsuo Ohmachi[2], Saburoh Midorikawa[2], Hiroaki Maruya[1], and Masaki Fujioka[3]

1) Professor, Center for Urban Earthquake Engineering (CUEE), Tokyo Institute of Technology, Japan
2) Professor, Department of Built Environment, Tokyo Institute of Technology, Japan
3) Researcher, Center for Urban Earthquake Engineering (CUEE), Tokyo Institute of Technology, Japan
kaji@cuee.titech.ac.jp, ohmachi@enveng.titech.ac.jp, smidorik@enveng.titech.ac.jp, maruya-hi16@rice.or.jp, fujioka.m.aa@m.titech.ac.jp

Abstract: This paper introduces a case study of the university BCP for the early recovery of its education and research activities, which has been conducted on Suzukakedai Campus, Tokyo Institute of Technology, in 2009. The paper first discusses the reasons why the university needs BCP, mainly focusing on its social role and responsibility, with the aim of clarifying theoretical background for setting the major goals of the university BCP. The paper then proposes a method of identifying the priority activities which are essential for early recovery, and applies to the education and research activities of the Campus. On a base of the analysis, the earthquake warning system and the isolation tables for the priority equipment have been installed as practical measure in this case. Regarding with emergency responses, the paper examines the current guideline of Tokyo-Tech in terms of early recovery in emergency cases, and points out substantial defects disturbing early recovery of the university activities, which must be common with every university. The paper, thus, proposes a methodological guidance for university BCP which can be applied to universities in general.

1. INTRODUCTION

Most of universities in Japan are located in earthquake prone areas. Thus, once an earthquake occurs, the education and research activities of the universities will be interrupted, resulting in the delay of student's graduation and the severe setback on the advanced researches.

Needless-to-say, these negative effects may be enlarged as the interruption period becomes longer, and on the contrary, they can be minimized by early resumption. The concept of Business Continuity Planning (abbreviated by BCP hereafter) advocated by USA, aims at pursuing the minimum consequential loss of businesses after unexpected emergencies, such as natural disasters, terrorisms, contagion, and so on. The idea has been introduced to Japan since 2004 [*](Ministry of Cabinet Affairs 2005). The authors try to apply this concept to university activities taking the Suzukakedai Campus, Tokyo Institute of Technology, as a case study.

Suzukakedai Campus locates in the Tokyo Metropolitan region, where tectonic earthquakes occur around every 200 to 250 years and two to three active fault earthquakes underneath the area give sever damage to the region in this interval. Since the region has not suffered from any earthquake for the past 87 years since the last tectonic Kanto Earthquake in 1923, seismologists thus anticipate the occurrence of earthquakes by the active faults located underneath the area in very near future. In addition, the location of the Campus is also in the influential territory of Tokai earthquake.

The Campus is not particularly more earthquake-prone than other universities in Japan but rather it is a common fate with Japanese universities, and therefore the methodology applied in this paper may contribute to Japanese universities in general, which confront same problems.

2. WHY DO UNIVERSITIES NEED BCP?

The universities have similar characteristics with business enterprises in a sense that they are competitive each other for both student enrolment and advanced researches. In case of a university, however, some other reasons why it needs BCP may be argued from the view points of its fundamental function that is totally different from private businesses seeking their profit. The paper thus tries to take

[*] This paper was originally prepared to the 3rd Asia Conference on Earthquake Engineering, held in Bangkok, Thailand, 1-3, Dec., 2010, and has been revised based on the discussions and comments raised to the presentation there.

up the following five points for discussion.

The first argument is on the fulfillment of a contract with students. The primary function of a university is to provide educational services to students and to issue a certificate of graduation to those who have completed the given courses within scheduled period. These services are performed under the contract with students who may collaterally pay tuition fee to the university. The interruption of its services or a delay of given schedule is not only non-fulfillment of a contract but also causes severe disadvantages to the students, because the certificate issued by the university has a great social value as a guarantee of quality of the said student. It is also serious fault of the university which may lead to lose its social credit, resulting in severe influence on competitive student enrolment in future.

Secondly, the university has social responsibility to a nation and region for supplying human resources which the society requires. The interruption of university activities implies, in other words, a disorder of this supply system and may cause confusion to the governments or enterprises which regularly expect new human resources.

Thirdly, the university also bears responsibility for keeping its operation to those high school students who are preparing for an entrance examination. It is because, in recent society, the cultural structure in which people evaluate each other based on the certificate of graduation from the university as guarantee of individual quality is popularly established. Thus, the university education is regarded as a mean of individual career development rather than of pursuing scientific truth. In this sense, the university is already a part of social system in which it is expected to pursue its business. This relationship between the university and the society is a kind of a tacit understanding and thus the students preparing for the entrance examination have a tacit right under this understanding. It could therefore be said that the university should not be interrupted unilaterally at its own convenience.

Fourthly, more substantial argument may be drawn from the fundamental function of the university. The raison d'être of the university is no other than to provide higher and qualified education to the nation. The long term interruption of university businesses may cause deterioration of its academic performance in both education and researches, resulting in depreciation of quality of human resources on a country. It may sometimes lead to a national crisis when the said university is the leading academic center in teams of national policy of the country. In this sense, the promotion of the university BCP can be regarded as a part of the national strategy.

Finally, the university BCP is related to employment management, which is common with the enterprise BCP. The long term interruption of the university businesses may cause financial deterioration, resulting in dismissal of its employees, particularly in case of private universities.

As far as employment management, there is some other argument for supporting the importance of BCP. In general, the interruption of businesses of big companies may give the great influences on neighborhood market in the sense that demand for their sales might drastically decline and thus may cause bankruptcies of neighboring businesses leading to dismissal of their employments. However, here in this paper, the authors place it beyond discussion.

3. GOALS OF UNIVERSITY BCP

The goals of the university BCP can naturally be drawn from the above arguments. The pioneering attempt at a university BCP was the one of the "Business Resumption Planning at the University of California, Berkeley" (Sarah K. Nathe, 2005), which was adopted in late 2001 and practically commenced in 2006. The planning goal is to have the university open for business within 30 days of a major earthquake on the Hayward fault. The guidelines are in place to coordinate recovery efforts in four areas of university "business":

1) Inspecting, cleaning & repairing, and reoccupying buildings;
2) Roles and responsibilities of university employees during the recovery effort;
3) Resumption of instruction and research in departments; and
4) Recovery of information and communications systems.

Taking account of this example, the authors have identified the following five goals of the BCP for earthquake disaster at the Suzukakedai Campus on the base of arguments mentioned earlier:

[Goal 1] To secure students, faculty members, and other employees against earthquake disasters;

This goal is primarily for damage mitigation's sake, but the highest priority can also be placed on BCP. It is not only because rescue operations of human life overcome business continuity when human damage is severe, but also because the particular educational programs cannot be continued when the affected professors are not replaceable. Thus, the human resources are regarded as the most fundamental property in BCP.

[Goal 2] To graduate students as scheduled;

As argued earlier, it is a contract with students for a university to graduate them. And the university has social responsibility to a nation and region for supplying human resources which the society requires. In order for the university to perform this duty, particular businesses such as securing regular class hours, authorizing credits, acknowledging graduation, and so on should be continued without delay. Some supplemental businesses such as the issue of certificates, writing of recommendation letters, and assistance of job hunting should be accompanied as well.

[Goal 3] To enroll new students as scheduled;

Regular execution of entrance examination by the university implies to maintain the social system in which the university education is established as a mean of individual career development and its certificate of graduation is regarded as a guarantee of individual quality. The businesses directly

related to it include series of works on application for admission, execution of examination, marking, announcement of successful applicants, and so on. Some supplementary activities such as public guidance of university, distribution of application forms, and preparation of exam questions may also be performed.

[Goal 4] To ensure highly qualified education and researches;

All professors and researchers involve in very advanced and challenging researches, which are highly time competitive in a sense that new academic results can belong to the paper publisher based on the first come and first serve principle. Therefore, even a short interruption of performance may bring the severe setback in their respective academic fields. Needless-to-say, these setback may be enlarged as a resumption time becomes longer, and on the contrary, they can be caught up with easily by reducing recovery time.

[Goal 5] To ensure employment status of faculty members and other employees;

As an employer, the university supports the family lives of its employees. To secure their lives is basic responsibility for the organization. In particular, it would be vital for the university to protect from a brain drain of qualified resource persons.

4. PLANNING CONDITION

4.1 Possible Earthquakes

The first step of BCP is to clarify the possible earthquakes, which may cause damage to the Campus. In 2004, the Disaster Mitigation Division of Cabinet Office, Government of Japan, conducted overall earthquake damage estimate on the faults located in Metropolitan region. According to the result, the four events by the fault shown in table 1 and figure 1 possibly cause severe damage to the Campus. Among them, it is anticipated that Tachikawa fault may cause most severe damage to the Campus (figure 2).

Table 1 Possible earthquakes

Earthquake	Magnitude
1.Kanagawa east EQ (underneath Yokohama city)	M6.9
2. EQ underneath Kawasaki city	M6.9
3. EQ by Tachikawa fault	M7.3
4. EQ by Miura faults	M7.2

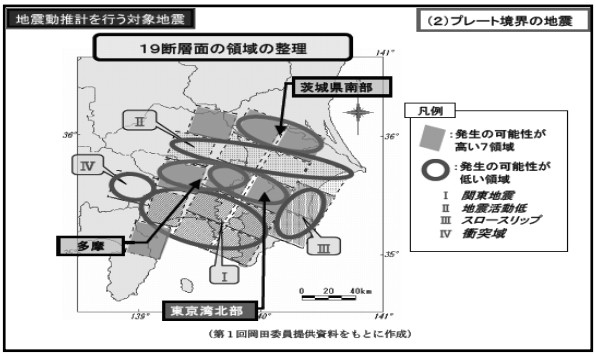


Figure 1 Location of faults

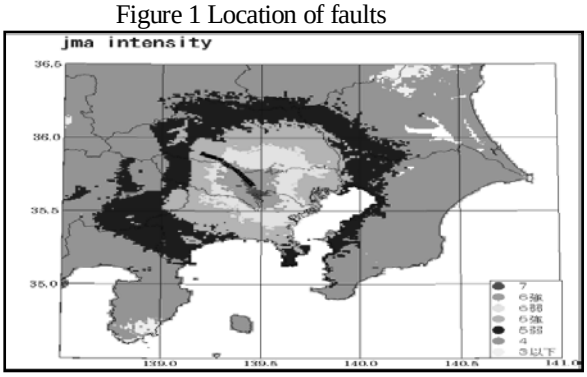


Figure2. Grand motion by Tachikawa fault

4.4 Target Resumption Date

The target resumption date of businesses is, in other words, the acceptable interruption period. But by whom is it acceptable? The argument made in the section 2 suggests variety of the stakeholders such as; by students, by society, by examinees, by a nation, and by its employees. Theoretically speaking, the interruption period has to be determined by all of them, but it would be hard enough.

Moreover situation is more complicate, because the acceptable period depends on the time when the event occurs and on the affected area and severity of damage. In fact, more time may be available when it occurs before a summer vacation, while time may be limited before the graduation season. The society may accept the delay of resumption when the affected area is extremely vast, and damage is so severe, while it does not tolerate long interruption in case of limited damage.

In summary, there is not clear criterion to determine a proper resumption date, and rather it may vary from a case to another. In order to formulate the BCP, however, the date has to be set up. So, after the example of University of California, Berkeley, the planning goal is determined to have the university open for business within 30 days after any possible earthquakes.

4.3 Educational Program at Suzukakedai Campus

The Suzukakedai campus of Tokyo Institute of technology consists of one undergraduate school and two graduate schools, with 2350 students in total.

As to the undergraduate school, the 3rd and 4th grade students of about 350 persons study in the two Departments of School of Bioscience and Biotechnology for their graduation thesis works.

One of two graduate schools is Graduate School of Bioscience and Biotechnology, which consists of five courses (departments) such as Life Science, Biological Sciences, Biological Information, Bioengineering, and Bimolecular Engineering, and about 450 students join in master and doctoral program. Another graduate school is Interdisciplinary Graduate School of Science and Engineering, which consists of 11 courses (departments) such as Innovative and Engineered Materials, Electronic

chemistry, Materials Science and Engineering, Environmental Science and Technology, Built Environment, Energy Science, Environmental Chemistry and Engineering, Electronics and Applied Physics, Mechano-Micro Engineering, Computational Intelligence and Systems Science, and Information Processing and about 1600 master and doctoral students are working.

4.4 Research Activities at Suzukakedai Campus

In the Suzukakedai campus, about 500 employees are working. Out of them, 400 persons are researchers such as professor, associate professor, lecturer, and research associate, and others are engineers and administrators. In addition, some more part time stuff joins. Most of researchers perform their research works under the above mentioned departments integrating with educational activities. Apart from these educational organizations, however, six research laboratories are in operation at the campus. They are; Chemical Resources Laboratory, Precision and Intelligence Laboratory, Materials and Structures Laboratory, Imaging Science and Engineering Laboratory, Frontier Research Center, and Center for Biological Resources and Informatics.

5. EXISTING GUIDELINE TO EMERGENCY RESPONSE AT TOKYO TECH

In order to resume the educational and research activities as quick as possible, protective measures avoiding fatal loss leading to a severe delay of recovery is vital. In this respect, the structure of university buildings has to be resistant to a earthquake and office furniture have to be fixed. As to the Suzukakedai Campus, retrofit of all buildings has been completed, and the fix of the office furniture is proceeding.

Such earthquake measures are also a part of BCP in broader sense. In other words, however, it is a common field with a traditional earthquake measurement. More substantial problems in terms of BCP rather lie in the guideline to emergency response, which is commonly prepared at any university.

5.1 Emergency Response System to Earthquake

One of the difficulties for establishing the emergency response system at university, the command system of the emergency operation has to be designed based on physical location or individual building where every damage event occurs. It must be, however, normally observed that research and educational activities of one department are scattered about several buildings in the Campus and to the contrary, there is a case where couples of departments share one building. It means that the regular administrative organization cannot be applied to the command system of emergency operation.

In case of the Suzukakedai Campus, the situation is not exceptional, and the guideline of emergency responses involves substantial faults, which must be common with other universities. As mentioned earlier, there are two undergraduate departments and sixteen graduate courses (departments) at Suzukakedai Campus. However, the numbers of research and educational buildings are thirty-one. Thus, the guideline of emergency responses at Tokyo Tech set “Self Defense Corps for Disaster (SDCD)” for individual building. These thirty-one SDCDs are placed under the command of the Emergency Headquarter (EH) which is supposed to be established just after the event by the ten members of the head of the schools, the research laboratories, and administration office. The problems identified through the careful examination of existing SDCD operations on the emergency case are as follows;

- Although emergency response operation will depend on the extent of damage, no clear criteria is described in the guideline for setting-up and operation procedure of an EH,
- The member of EH serves concurrently as a chief of two to four SDCDs. Though this arrangement aims to gather all information to the EH, the SDCD at the scene has to work without leader,
- There is no clear procedure for collecting damage information on the affected buildings, where dangerous experimental materials are normally dealt with, and most severely,
- No duty is given to SDCD to assure itself that the building in charge is safe for the building residents to reoccupy their respective office or laboratory and to resume their education and research activities. This point is vital for early recovery and resumption.

5.2 Amendment to the Guideline for BCP

On the basis of the existing guideline, an amendment to the guideline has been proposed from the view point of BCP as follows;

- To clarify the trigger criteria for setting-up an EH and for starting SDCD operation,
- To prepare the operation manuals at the different level of damage,
- To establish an independent operation system of SDCD at the affected scene under the command of the respective team leader at the early stage of the event,
- The EH to dispatch special team to investigate the leakage of dangerous materials on the base of the request made by the respective SDCD, and
- To formulate the clear procedure for the building residents to reoccupy their respective office or laboratory and to resume their education and research activities.

6. BCP FOR EDUCATION

As mentioned above, the guideline of emergency responses of Tokyo Tech regulates to form a special command system at the occurrence of an earthquake and all faculty members have to behave under the system. The guideline, however, does not cover measures for the educational program of the respective department such as resumption of the classes, authorization of credits for

graduation, or indispensable exceptional rules. Thus, each department has to set its own rules and emergency responses action plan of the following items.

(1) Commencement of emergency operation at the department
- To urgently hold the faculty meeting of the department,
- To make a rule on who calls the meeting since the chairman is not always available,
- To clarify beforehand the trigger event for holding the meeting, and
- To make a decision criterion which is different from normal majority rule, as only limited faculty members can attend.

(2) Inspection of damage and student life

(3) Resumption program of classes
- To reform the curriculum based on available faculty members,
- To establish information transmission system with the students, and
- To make a rotation program of faculty members including replacement with the injured.

(4) Execution of graduation and entrance examination
- To provides a particular works for fulfilling conditions for required educational period, and
- To apply the exceptional rule to authorization of credits with given criteria

(5) Recovery of experimental laboratories

(6) Public relations

7. BCP FOR RESEARCH ACTIVITIES

7.1 Survey of Current Activities and Damage Estimate

Whatever earthquake resistant measures are taken, physical damage to a set of experimental equipment in every laboratory cannot be avoidable to a certain extent once an earthquake occurs, as no perfect protective measure to keep all the equipment safely to the events exists. In order to clarify the current activities and working environment of the research laboratories, and also to estimate their loss and damage caused by an earthquake, the investigation of the following contents through a questionnaire survey and direct interview survey to research stuff is required.
- What kind of research works or experiments are in operation?
- What kinds of equipment and dangerous materials are used under what conditions?
- How much energy is normally in use?
- How far the researches would be influenced through one month interruption by earthquake?
- How long does it take for the researches to be resumed when major equipment is collapsed?

In this paper, “Frontier Research Center” where the five laboratories are currently performing their research works is taken as a case study.

7.2 Priority Preparatory Measures for Early Recovery

One of the principal ideas of BCP is to clarify the target resumption date, or acceptable period of interruption. In order to keep it, however, the function of some basic experimental equipment or law materials should be kept safely without collapse or deterioration by an earthquake. It is thus essential for BCP to identify the most fundamental function and to give priority investments beforehand to avoid fatal loss leading to a severe delay of recovery. In this paper, two criteria have been applied to identify such priority investment as follows:

Influence of Business Interruption
= (Acceptable period of interruption: 5 ranks)
× (Intent of influence: 5 ranks) (1)

Acceptable period of interruption:
Rank 1 – more than 30 days
Rank 2 – less than 3 weeks
Rank 3 – less than 2 weeks
Rank 4 – less than 1 week
Rank 5 – within 1 day

Intent of influence:
Rank 1 – no influence
Rank 2 – small influence
Rank 3 – certain influence
Rank 4 – large influence
Rank 5 – severe influence

Difficulty of Resumption
= (Acceptable time for repair: 5 ranks)
× (Possibility of repair: 3ranks) (2)

Acceptable time for repair:
Rank 1 – about 1 month
Rank 2 – about 3 months
Rank 3 – about 5 months
Rank 4 – about 6 months
Rank 5 – about 1year or more

Possibility of repair:
Rank 1 – possible
Rank 2 – hard to repair
Rank 3 – impossible

The result is shown in figure 3. Since Lab B-1 has been identified as the highest priority research program in a sense that both the difficulty of resumption and the influence of interruption are greatest, the recommendation of special investment to secure the research program has been proposed.

In addition to it, the following arrangements to be prepared beforehand have been recommended.
- To identify all resources that are required to achieve this target, including human resources, working space, experimental equipment and materials, energy, water and so on so force,
- To reserve spare parts or preferably a spare set of equipment,

- To establish priority repair agreement with a manufacturer,
- To reserve experimental materials, or to establish a purchase channel on them,
- To coordinate with electric company for priority energy supply,
- To coordinate with water supply agency for priority water supply, and
- To prioritize recovery order with emergency funding arrangement

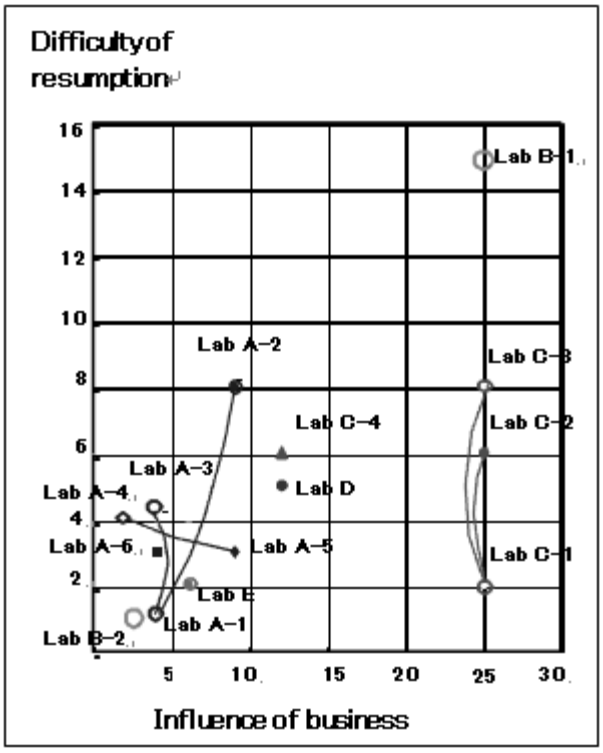


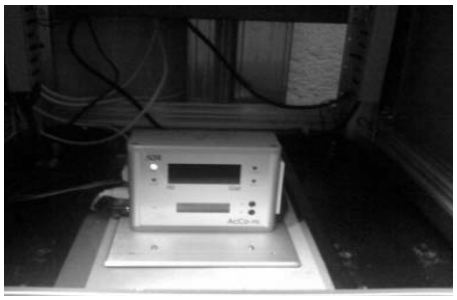
Figure 3 Laboratories on two criteria

7.3 Practical Measures

As to the first step of practical implementation of the BCP for the Campus, the isolation tables were installed to the instruments to which protective measures should be given as the top priority on the bases of the analysis in the previous section (Picture 1), and the special treatment to fix fundamental experiment instruments on the floor or to side wall. To be particularly highlighted, the Earthquake Early Warning System (EEWS) has been installed at the "Frontier Research Center" building (Picture 2, 3). The system is expected to catch P-wave and to give a warning of the occurrence of an earthquake 15 to 25 second before the reach of S-wave that causes major ground motion.



Picture1. Isolation table



Picture2. Seismogram



Picture3. Information board

8. CONCLUSIONS

In order for the BCP to be implemented effectively, the intensive involvement of the all stakeholders is vital. Therefore, some continuous program for promoting people's awareness must be provided in daily life. In addition, the activities of respective laboratories are not stable but are changing with some research cycles. It means that the BCP has to be up-dated on regular bases in order to catch up with these changes and to reflect new situations.

Lastly but not the least, the university also must need to prepare for accepting refugees who are escaping from neighboring calamity. It must definitely be a part of social responsibility of the university.

Acknowledgements:

The authors wish to express their gratitude for the support from Tokio Marine & Nichido Risk Consulting Co., Ltd. Japan. Without its support, the project would not become possible.

References

Disaster Mitigation Division of Cabinet Office (2004), "The Direct Damage Estimate of Underneath Earthquakes in Tokyo Metropolitan Region" ,

Disaster Mitigation Division of Cabinet Office, (2005), "The First Edition of Guideline of BCP – Towards Damage Mitigation and Capacity Building of Enterprises in Japan"

Sarah K. Nathe (2005), "Business Resumption Planning at the University of California, Berkeley", Paper presented at the 1st International Conference on Urban Disaster Reduction, Kobe

Japan Chamber of Commerce and Industry (2007), "Step-up

Guidance of BCP for Small and Medium Sized Enterprises”

8CUEE CONFERENCE PROCEEDINGS
8th International Conference on Urban Earthquake Engineering
March 7-8, 2011, Tokyo Institute of Technology, Tokyo, Japan

SEISMIC RISK AND DAMAGE COST ANALYSIS OF MID-RISE BASE ISOLATED BUILDINGS IN PERU

Luis A. Bedrinana[1)] and Taiki Saito[2)]

1) Assistant Researcher, Center for Earthquake Engineering Research and Disaster Mitigation (CISMID), Peru
2) Chief Research Engineer, International Institute of Seismology and Earthquake Engineering, Building Research Institute, Japan
luisbedrim@gmail.com, tsaito@kenken.go.jp

Abstract: The principal objective of this study is to evaluate the cost-effectiveness as well as the seismic safety of a base isolated building located in Peru. A methodology to evaluate quantitatively the seismic risk and the cost-effectiveness of a base isolated building during its lifetime is presented. The process starts with the hazard analysis and the earthquake ground motion generation in the studied area. Lima area is considered in this study. Series of artificial earthquake ground motions are generated by a stochastic method in the studied area. Then a preliminary seismic design of the target building is carried out, by using the Peruvian seismic code. To get the response distribution of the target building, several dynamic nonlinear analyses are performed by using the generated artificial motions as input waves. By assuming a structural response distribution, the seismic risk analysis is performed in terms of three structural parameters such as: interstory drift ratio (*IDR*), floor acceleration (*FA*) and the structural damage index (*DI*). The damage of the target building is evaluated by using a damage index. Finally, the cost-effectiveness of using base isolation system is examined, by comparing the exceedance probability of repair cost in the target building with and without base isolation during a given time period.

1. INTRODUCTION

Peru is an earthquake prone country, which has experienced many severe earthquakes in its history. Most of those severe earthquakes have been a big disaster, producing huge losses and fatalities. Most important problems noticed in buildings during these events, are: low resistance, high level of damage, and no protection of contents. To increase resistance in buildings several improvements have been made in the seismic code; however, there is no any regulation about damage limit levels in buildings in current codes. Moreover, current provisions do not provide any protection to nonstructural components, equipment and contents of buildings.

One of the best alternatives to reduce the damage and to provide protection of contents in buildings is the use of base isolation. Base isolation has proved to be a reliable technology to prevent damage in buildings and to increase the seismic performance; however current seismic provisions do not provide information of the real safety of base isolated buildings. Furthermore, in developing countries the use of base isolation is not wide due to the high construction cost of isolation system. So, a methodology to evaluate the real seismic safety and cost-effectiveness of the base isolation system is needed to meet current performance requirements in buildings. This methodology has to provide a rational basis and clear procedures to achieve the target in order to be used normally.

2. SEISMIC HAZARD AND EARTHQUAKE GROUND MOTION MODELING

Seismic hazard of studied area is determined using past earthquake data. The historical data of past earthquakes (Figure 1) from the Peruvian seismic catalog (Tavera et al. 2007) are used to model the earthquake occurrence of magnitude (*M*) and hypocentral distance (*R*) around Lima area.

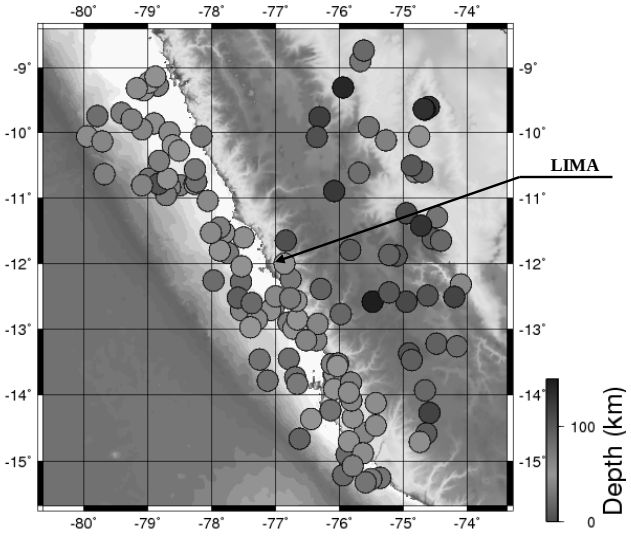


Figure 1 Distribution of earthquake epicenters around Lima from 1963 to 2005.

The earthquake occurrence of magnitude and hypocentral distance is modeled by a truncated G-R formula and the Beta probability function respectively as is shown in Figure 2. To generate the artificial ground motions, several sets of *M* and *R* are randomly generated according to their probability distributions by standard procedures. Then, each set of values of *M* and *R* is related to ground motions by means of an attenuation formula in terms of spectral acceleration for Peru subduction earthquakes. In this study the attenuation relationship for spectral acceleration in Peru is used (Chavez 2006), which was proposed for different soil conditions of the Peruvian coastal area.

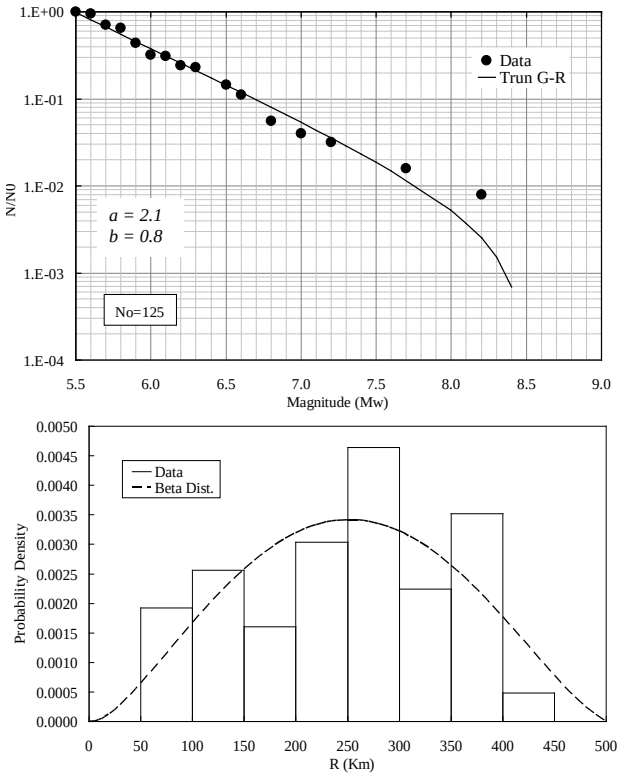


Figure 2 Earthquake occurrence of magnitude *M* and hypocentral distance *R* (1963 to 2005).

The artificial earthquake ground motions are generated as a nonstationary stochastic process compatible with the response spectrum calculated previously with the attenuation formula. By using the random vibration theory, a simple model of earthquake ground motion *A(t)* is expressed as a product of a wave *x(t)* from a stationary random process, with a power spectral density *PS(ω)*, and an intensity envelope function *E(t)* (Shibata 2010) as follows

$$A_{(t)} = E_{(t)}.x_{(t)} \tag{1}$$

In this study, the Jennings's intensity envelope function *E(t)* is used (Jennings et al. 1969). This function takes into account the transient effects in time of earthquake ground motions. The sample wave *x(t)* is generated by a combination of harmonic functions, with a given power spectral density *PS(ω)* (Gasparini et al. 1976). This power spectral density *PS(ω)* represents the importance of the harmonic function, in some specified band frequencies, and it matches the target spectrum defined previously. A total number of 800 artificial earthquake ground motions are generated for the studied area. Figure 3 shows the response spectrum of a sample generated wave (Sample 128) *RSX* which is compared with the target response spectrum *RST*.

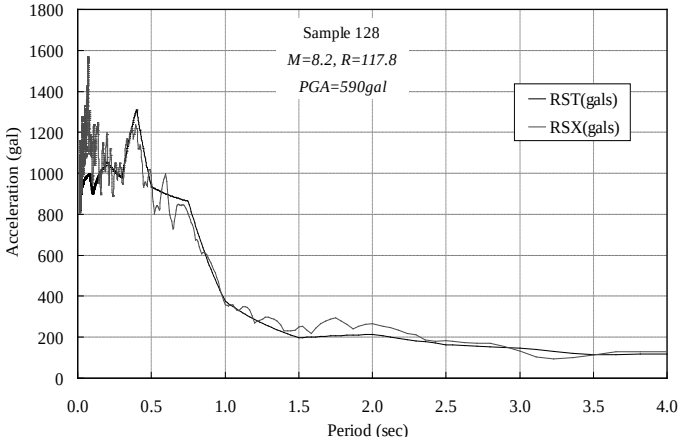


Figure 3 Comparison between target response spectrum and response spectrum of generated sample wave.

3. STRUCTURAL AND DAMAGE ANALYSIS

3.1 Target building

The target building for this study is an RC office building with 8 stories as is shown in Figure 4. This building is assumed to be located in Lima downtown and it is a representative mid-rise building. The concrete used in this building has a nominal strength of *f'c=21MPa*, and the nominal strength of steel is *fy=412MPa*. The total weight of the structure is around *46174kN*, and the fundamental period is 0.65s in X direction and 0.54s in Y direction. The target building is designed according to the Peruvian seismic code. The design base shear coefficient is 0.08 in X direction and 0.09 in Y direction.

3.2 Design of base isolation system

In this study, the equivalent SDOF method (Okamoto et al. 2002) is used to design the base isolation system in the target building. This method considers an isolated building as a rigid body moving with hysteretic properties of isolation devices, with a bilinear model. The lead rubber bearing LRB is used as isolation devices in this study. The total design yield force of the isolation system is set to 4% of the total weight and the design limit displacement is 300mm. Moreover, the design target period of the isolation system is 2.24s. Table 1 shows the dimensions of isolation devices.

3.3 Dynamic Analysis

To obtain structural response of the target building a series of nonlinear dynamic analyses are carried out, using artificial ground motions generated previously as input motions. These artificial ground motions represent future

earthquakes that would occur in the life cycle of the building. In this study structural uncertainty is assumed to be small compared with uncertainties of ground motions, and structural uncertainty is not taken into account. The nonlinear dynamic analyses are carried out in the building with conventional design as well as with base isolation.

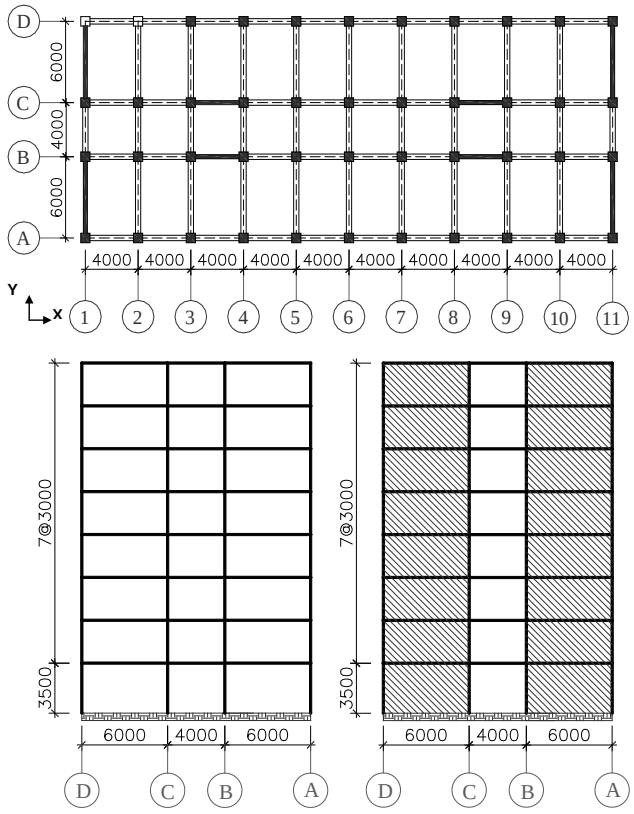


Figure 4 Plan and elevation view of the target building.

Table 1 Dimensions of isolation devices.

	LRB-600	LRB-500
Shear Modulus (N/mm2)	0.39	0.39
Shear Modulus lead (N/mm2)	0.59	0.59
Exterior Diameter (mm)	600	500
Interior Diameter (mm)	100	100
Thickness of rubber layer (mm)	4	3.5
Total rubber thickness (mm)	144 4 x 36	123 3.5 x 35
Steel layer thickness (mm)	2.5	2.5
Primary Shape Factor S1	37.5	35.7
Secondary Shape Factor S2	4.2	4.1
Number of Bearings	36	8

3.4 Damage Analysis

Additionally to the structural response in terms of *IDR* and *FA*, the structural damage in the target building is evaluated. To correlate the values of *IDR* with damage, the Park-Ang's damage index (1985) is used. This damage index considers earthquake damage in RC members is composed of the damage caused by the maximum displacement and the absorbed hysteretic energy. The damage index *DI* is expressed by.

$$DI = \frac{\delta_m}{\delta_u} + \beta_c \frac{Eh}{Q_y \delta_u} \tag{2}$$

Where Q_y the yield strength, Eh is the total hysteretic energy dissipated during earthquake, δ_m is the maximum drift during earthquake, δ_u is the ultimate drift under monotonic loads, and β_c is a constant.

Moreover, the overall damage of entire buildings is checked by means of the total damage index DI_T, (Park et al. 1985) as follows

$$DI_T = \sum \lambda_i DI_i \qquad \lambda_i = \frac{Eh_i}{\sum Eh_i} \tag{3}$$

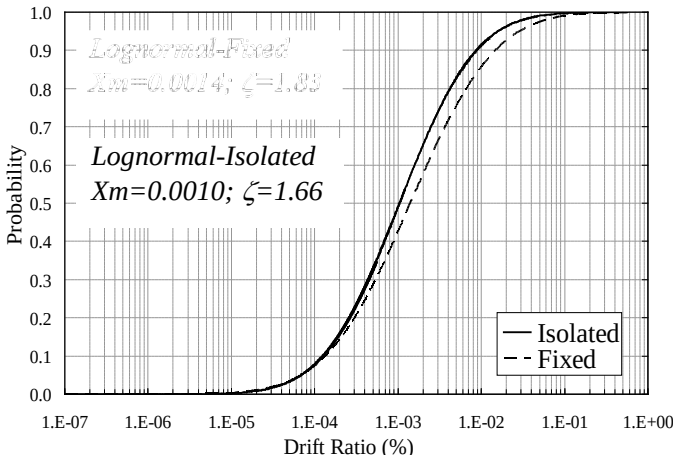


Figure 5 Lognormal distribution of *IDR* in 1st story.

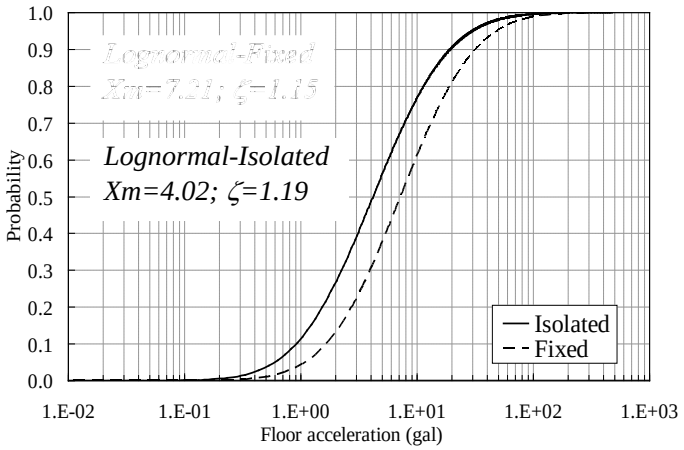


Figure 6 Lognormal distribution of *FA* in 1st story.

4. STRUCTURAL RESPONSE DISTRIBUTION

A total of 800 nonlinear dynamic analyses are carried out in the target building, with and without base isolation, by using artificial earthquake ground motions previously generated. With information of structural maximum response in each analysis, the probability distribution of the interstory drift ratio (*IDR*) and peak floor acceleration (*FA*) is obtained. The structural response is modeled by a lognormal distribution in this study and Figure 5 and Figure 6 show the distribution of *IDR* and *FA* respectively in the first story of the target building.

Based on the 800 values of maximum *IDR* showed previously, the damage index is calculated for each and every case. Park and Ang (1985) determined that the damage index is reasonably lognormal distributed. Figure 7 shows the lognormal probability distribution of total damage (DI_T) in the target building. It can be seen from this plot that structural damage in isolated building is considerably reduced. Additionally, the median value and the standard deviation of damage distribution of isolated building are lower than conventional one.

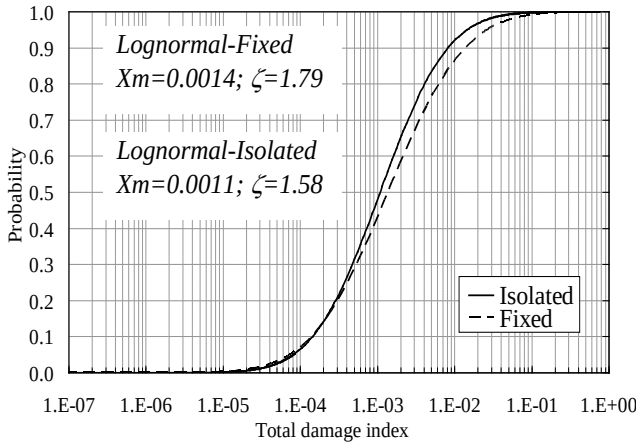


Figure 7 Probability distribution of DI_T.

5. SEISMIC RISK ANALYSIS

The seismic safety of a building can be quantified in terms of the exceedance probability of the structural response. To evaluate the exceedance probability of a random variable *X*, which represents structural response, the Poisson process model is used as is shown in Figure 8. If *X* is the random variable evaluated, $F_{(X)}$ is the cumulative distribution of *X*, and ν is the annual occurrence of the event; the exceedance probability that $X>X_m$ in t years is given as follows (Saito and Wen 1994)

$$p_f = P\left(X > X_m \middle| [0,t]\right) = 1 - \exp\left[-\nu t(1 - F(X_m)\right] \quad (4)$$

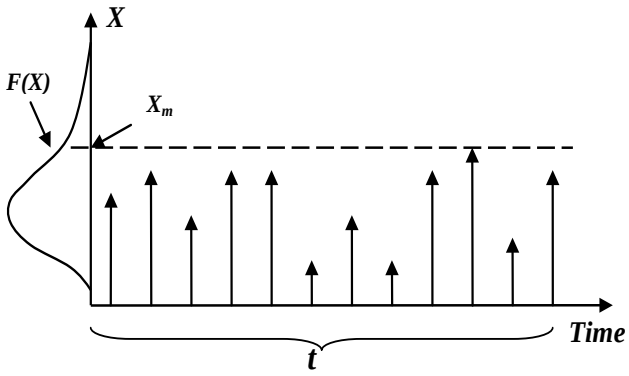


Figure 8 Exceedance probability of random variable based on the Poisson process.

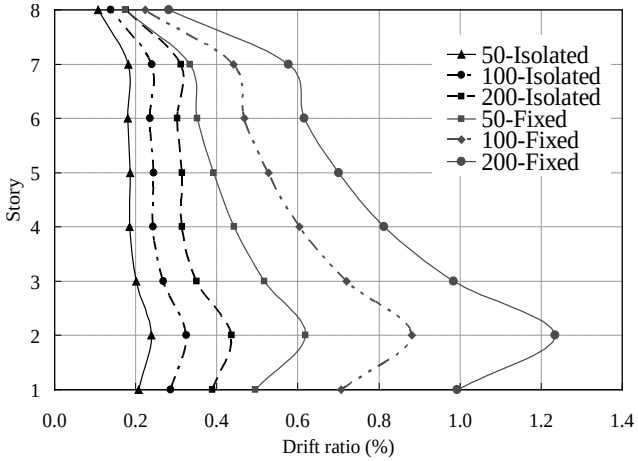


Figure 9 Values of *IDR* with 10% of exceedance probability in 50, 100 and 200 years.

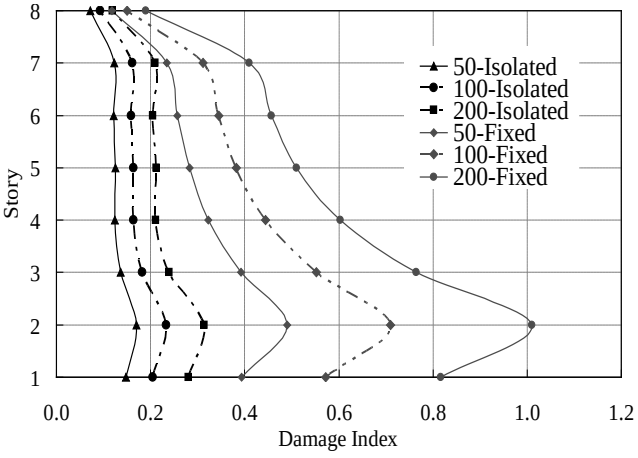


Figure 10 Values of *DI* with 10% of exceedance probability in 50, 100 and 200 years.

The seismic risk of the structure can be quantified in terms of exceedance probability of the structural response. To estimate the probability that the *IDR* will exceed some threshold value, the Poisson process model is assumed for the earthquake occurrence. The annual earthquake occurrence is $\nu=2.98$ in this study. Figure 9, shows the

values of *IDR* for the target building with 10% of exceedance probability. The values of *IDR* for isolated building are much lower than values for conventional building. So, it can be said that isolated building has better seismic safety than conventional building.

The seismic risk of the structure can be also quantified in terms of exceedance probability of damage index. The Poisson process model for earthquake occurrence is also used to obtain the probability that *DI* will exceed some threshold value. Figure 10 shows the values of *DI* with 10% of exceedance probability. It is observed that conventional building suffer large damage for long time periods and after 100 years there is a 10% exceedance probability to have a value of *DI* equal or more than 0.60. Damage in main structure is reduced by using the base isolation system, so the probabilities to have severe damage are significantly lower than the case of conventional building.

6. COST-EFFECTIVENESS ANALYSIS

In addition to the seismic risk analysis, the cost-effectiveness analysis of the target building, with and without base isolation, is carried out. In this study just the structural cost is taken into account, principally due to the lack of reliable data of nonstructural components, contents and maintenance of buildings in Peru. The cost-effectiveness is evaluated by a model which correlates damage index into structural repair cost of each story, so the total cost is the sum of repair cost in each story. In this study the model to correlate damage and repair cost is based on the proposal of Takahashi and Shiohara (1987). The repair cost is defined by the structural repair cost ratio R_S, which is the normalized repair cost by the cost of total replacing with new one. The repair cost ratio R_S is defined by

$$R_S = \begin{cases} 0.0; & DI < Dc \\ \dfrac{DI - Dc}{1 - Dc}; & Dc \le DI < 1 \\ 1.0; & DI \ge 1 \end{cases} \quad (5)$$

Where *Dc* is the minimum damage index in which repair work is necessary and a value of 0.01 is taken.

Results obtained in damage analysis are related to repair cost by the cost ratio. Using values of damage index with 10% of exceedance probability, the structural cost repair ratio can be obtained in every case. It is noticed from these tables that conventional building has large values of R_S; especially in long time intervals, it is observed that some stories need to be almost totally repaired. If the life time were 100 years; it would be expected a value of 37.1% for total cost ratio in the conventional building, which is about 4.7 times larger than value of isolated building.

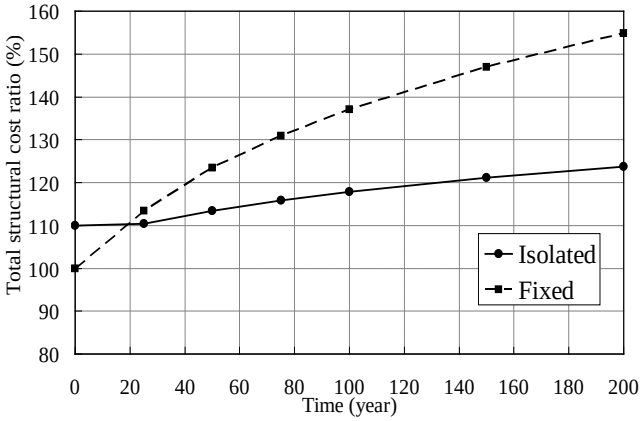


Figure 11 Expected values of total structural cost with 10% of exceedance probability in the lifetime of the building.

7. CONCLUSIONS

The methodology presented here is a useful tool to quantify the seismic risk and the cost effectiveness of base isolated buildings. Additionally this procedure could be extended to any kind of building structure.

The total damage in conventional building is considerably larger than isolated building. The expected value of the total damage index in 50 years, with 10% of exceedance probability, for the fixed building has a value of about 2.47 times larger than isolated one.

Although the initial total structural cost in the isolated building is larger than in fixed one, the total structural cost in isolated building is much smaller for long time interval. So, base isolated building is cheaper than fixed building during the lifetime of the target building.

It can be concluded that the seismic risk is much lower in isolated building; moreover, the cost-effectiveness in isolated building is better than fixed building, during lifetime period when large damage is expected.

An upgrade in seismic codes is needed in order to include probabilistic methodologies to evaluate the seismic risk of buildings.

Acknowledgements:

Special thanks are given to CISMID and its director Dr. Carlos Zavala for their valuable collaboration to this study. The information from the seismic catalog of Peru was provided by H. Tavera from the Geophysical Institute of Peru and the information of the attenuation equation was provided by J. Chavez; their collaboration is acknowledged. This study was supported by the Japanese Government through the Japan International Cooperation Agency (JICA). This financial support is gratefully acknowledged.

References:

Bedriñana L. A., Saito T., 2010, "Seismic risk and cost-effectiveness of base isolated buildings in Peru", Bulletin of IISEE, BRI, Japan.

Chavez J. A., 2006, "Attenuation relationships for Spectral Acceleration in Peru", Engineering Thesis, Faculty of Civil

Engineering, National University of Engineering, Lima. (In Spanish)
Gasparini D. A., Vanmarcke E. H., 1976, “Simulated earthquake ground motions compatible with prescribed response spectra”, Report R76-4, Dep. Civil Eng., MIT, Cambridge, Massachusetts.
Jennings P. C., Housner G. W., Tsai N. C., 1969, “Simulated Earthquake Motion for Design Purpose”, Proc. 4th WCEE, Santiago, Vol. I A1, 145-160.
Midorikawa M., Iiba M., Koshika N., Kani N., 2006, “Performance-Based Seismic Provisions for Seismically Isolated buildings in Japan”, Proc. 3rd ICUEE, Tokyo.
Park Y. J., Ang A. H–S, 1985, “Mechanistic Seismic Damage Model for Reinforced Concrete”, Jour. Struc. Eng., ASCE, Vol. 111, SE 4, 722-739.
Park Y. J., Ang A. H–S, Wen Y.K., 1985, “Seismic Damage Analysis of Reinforced Concrete Buildings”, Jour. Struc. Eng., ASCE, Vol. 111, SE 4, pp. 740-757.
Saito T., Wen Y. K., 1994, “Seismic Risk Evaluation of R.C. Buildings in Japan”, Report UILU-ENG-94-2003, Structural Research Series No 587, Univ. of Illinois, Illinois.
Shibata A., 2010, “Dynamic Analysis of Earthquake Resistant Structures”, Tohoku University Press, Sendai.
Takahashi N., Shiohara H., 2004, “Life Cycle Economic Loss due to Seismic Damage of Nonstructural elements”, Proc. 13th WCEE, Vancouver, paper No. 203.
Tavera H., Agüero C., Fernandez E., Rodriguez S., 2007, “Seismic Catalog of Peru”, Geophysical Institute of Peru, Lima. (In Spanish).
Trifunac, M.D. and Brady, A.G. (1975), “A Study on Duration of Strong Earthquake Ground Motion,” *Bulletin of the Seismological Society of America*, **65**(3), 581-626.

8CUEE CONFERENCE PROCEEDINGS
8th International Conference on Urban Earthquake Engineering
March 7-8, 2011, Tokyo Institute of Technology, Tokyo, Japan

AN INTEGRATED EARTHQUAKE IMPACT ASSESSMENT SYSTEM

Sheng-Lin Lin[1], Amr S. Elnashai[2], and Billie F. Spencer, Jr.[3]

1) Research Assistant, Dept. of Civil and Environmental Engineering, University of Illinois, Urbana, USA
2) Head, Professor, Dept. of Civil and Environmental Engineering, University of Illinois, Urbana, USA
3) Professor, Dept. of Civil and Environmental Engineering, University of Illinois, Urbana, USA
slin30@illinois.edu, aelnash@illinois.edu, bfs@illinois.edu

Abstract: NEES Integrated Seismic Risk Assessment Framework (NISRAF) combines several components in order to obtain the most reliable earthquake impact assessment results possible. The components are: hybrid simulation, free-field and structural sensor measurement, hazard characterization, system identification-based model updating technology, hybrid fragility analysis, and impact assessment packages. A software tool has been built and verified, concurrently, via application to an actual test bed in California. Impact assessment results using the generated hazard map and fragility curves correlated with field reports of the Northridge earthquake 1994. The novelty of the developed system is primarily the integration of components of earthquake impact assessment—most of which have not been deployed in such an environment before.

1. INTRODUCTION

The objective of research in earthquake engineering is to improve seismic loss estimation which aids in emergency planning, mitigation, response and recovery. Through field investigations after damaging earthquakes, along with theoretical and experimental studies, practitioners and researchers have substantially improved their understanding of the effects of earthquakes in the recent decades. Individual sub-disciplines have been focused on specific problems within the broad field of earthquake engineering. Examples of disciplinary developments are strong-motion measurements, system identification, model updating, structural performance evaluation through experimental and analytical simulations, fragility derivation, and the development of consequence estimation software.

The above component-specific studies allow researchers to focus on a particular problem at a fundamental level. Even though these specific studies have progressed considerably and produced mature research results, uncertainties remain in their outcomes not only because of their inherent characteristics, but also because of the interactions between them. For example, the derivation of fragility curves requires that a large amount of simulations be performed. It is essential to have an accurate structural model which closely represents the response of the real structure. In most fragility simulations, however, either a very simplified structural model is used or a complicated numerical model is used without being calibrated to measured response. Such methods, therefore, introduce significant and by-and-large unquantifiable uncertainties in the derived fragility curves. Moreover, the fragility curves heavily depend on input ground motions, particularly when the fragility curves are defined in terms of peak ground acceleration (PGA) (Kwon and Elnashai 2006). The ground motion is in turn influenced by source, path, and site characterization, each of which is a formidable challenge in its own right. The realism of both model and input is therefore essential to the accuracy and applicability of the ensuing fragility relationships.

Hazard, fragility, and inventory are the three major components of earthquake impact assessment. Among these, the inventory can be improved through the development and application of survey methods and technologies. This renders the accuracy of the assessment dependent on the reliability of the fragility curves and hazard characterization. Unquantifiable uncertainty and inaccuracies in the latter two components of hazard and fragility lead to earthquake impact assessments—that are unreliable and that do not form a viable basis for societal readiness.

2. METHODOLOGY

To reduce the above-mentioned uncertainties and unreliability in impact assessment, an integrated framework is proposed, developed, and verified via application to an actual test bed. Figure 1 illustrates the proposed framework and how its components are combined to achieve the main goal of this research. As can be seen, the proposed framework, referred to as NEES Integrated Seismic Risk Assessment Framework (NISRAF), integrates hybrid simulation with free-field and structure sensor measurements, hazard characterization analysis, system identification-based model updating technology, hybrid fragility analysis, and

earthquake impact assessment tools. The procedure is specifically proposed and programmed for ease of use.

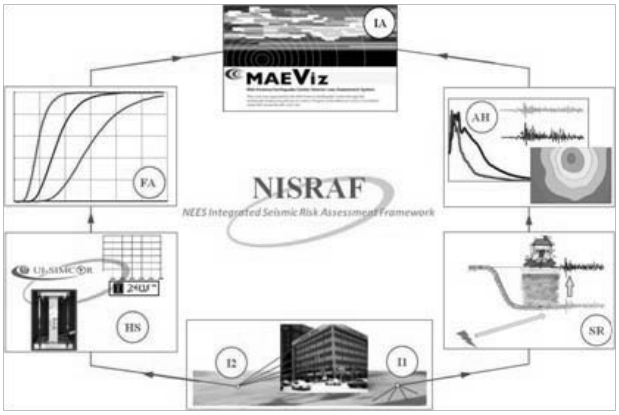


Figure 1 Schematic of the proposed integrated framework

In the schematic representation of the integrated framework given in Figure 1, free-field measurements (**I1**) along with nonlinear site response analysis (**SR**) are used to generate the advanced hazard map and ground motion records (**AH**). The measured and synthetic records are then used as seismic inputs in hybrid simulation and fragility analysis. Meanwhile, the structural model is calibrated with the measured structural response (**I2**). Next, hybrid simulations (**HS**) are performed with the most critical component of the structural system tested in the laboratory and the remainder of the structure simulated analytically. These simulations are conducted to derive the mean seismic intensity value (PGA, for example) of the corresponding performance limit state. The fragility curves (**FA**) of the structure are then generated using the hybrid simulation data and the dispersions from the literature. Finally, the derived fragility curves and the calibrated hazard map are fed into the impact assessment tools, such as MAEviz (MAE Center 2007) (**IA**) to evaluate the seismic losses.

The integration feature provides a chance to bring together all the sub-disciplines, capitalizing on the respective advances of each sub-discipline. This method of integration is not only intended to provide a tool, but it is also intended to stimulate the sub-communities of researchers to investigate the problems at the interfaces between them. Through this systematic and transparent framework, uncertainties from each sub-discipline can be managed more effectively and the use of the instrumentation will increase. For example, the reliability of probabilistic seismic hazard can be significantly improved through the use of free-field strong-motion measurements. Analytical and hybrid (analytical-experimental) simulations can be realistic due to calibration with system identification results from sensor measurements. The uncertainties resulting from deriving fragility relationships can be greatly reduced through the use of more reliable representation of hazard and more accurate structural models. Confidently, with seismic hazard from field measurements and fragility curves from more accurate models, NISRAF can significantly improve upon earthquake impact assessment results with higher reliability.

In the subsequent sections, the methodologies and techniques utilized in each component are discussed and then followed by application examples of the integrated framework.

3. ADVANCED METHODS UTILIZED IN NISRAF

To achieve a seamless integration and to arrive at an operational and verified system, several components were used innovatively, tailored to perform the role required by NISRAF.

3.1 Advanced Hazard Analysis Method

Owing to uncertainties from seismo-tectonic, earthquake energy attenuation and site conditions, it is difficult to describe accurately the hazard characterization. Many tools for seismic hazard analysis have been developed over the past decades. Among them, Deterministic Seismic Hazard Analysis (DSHA) and Probabilistic Seismic Hazard Analysis (PSHA) are the most commonly used methods, and both are generally implemented within the earthquake impact assessment packages. Due to the probabilistic nature and the simplified assumption for the local site effect, such as the use of site coefficients *Fa* and *Fv* (FEMA 2009), uncertainties remain in the procedure and outcome. To reduce these uncertainties, an advanced hazard characterization analysis approach, including site response analysis, is proposed.

As shown in Figure 2, this approach is composed of (i) seismic hazard analysis, (ii) synthetic ground motion generation, (iii) site response analysis and (iv) hazard map generation. First of all, the natural records are directly investigated to evaluate the hazard characterization. Synthetic records of different hazard levels are then generated for further use in hybrid simulation and fragility curve derivation. Subsequently, both the natural and synthetic records are ready to be modified to reflect the local site condition. DEEPSOIL (Hashash et al. 2009)—a 1-D site response analysis program—is implemented in NISRAF to conduct this analysis.

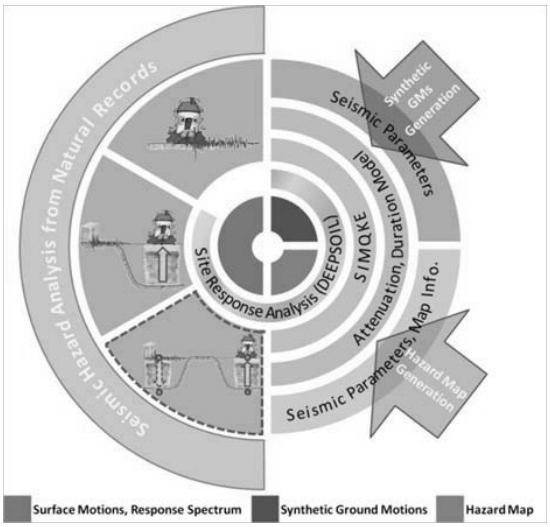


Figure 2 Methodology and procedure of the advanced hazard characterization analysis method

In addition to the seismic hazard analysis, synthetic ground motion generation and site response analysis, this advanced hazard analysis method also provides a function to generate hazard map, which is the exposure of the impact assessment.

3.2 Efficient Model Calibration Method

Finite element model simulation provides a powerful way to understand the response of structures. Unfortunately, even well constructed models may produce significant differences in some dynamic response predictions, in particular when the structure behaves nonlinearly. The difference is from the uncertainties of the material, boundary conditions and the contribution of the non-structural elements in the real structures. In order to overcome this drawback, a model calibration method based on the experimental or real response—which is composed of system identification and model updating techniques—is proposed. The following sections give an overview of these two techniques.

Among the many state-space based system identification methods, the Eigensystem Realization Algorithm (ERA) (Juang and Pappa 1985) is implemented in NISRAF due to its wide application and good performance in multi-input multi-output (MIMO) problems. Moreover, in order to filter out computational or noise modes, a two-step strategy is applied. Since more singular values are retained, more potentially genuine modes can be identified. In NISRAF, the dimension of the realized system N is increased until an adequate number of modes are included. For each particular order of a system, three commonly used mode accuracy indicators, namely, Modal Amplitude Coherence (MAC) (Juang and Pappa 1985), Extended Modal Amplitude Coherence (EMAC) and Modal Phase Colinearity (MPC) (Pappa and Elliott 1993) are used to filter out the computational or noise modes. The retained modes are then deemed trustable and a stabilization diagram is plotted for further confirmation.

Model updating aims to minimize the discrepancies between the numerical and real model by adjusting the stiffness and mass matrices. The objective function is formed as a linear combination of the natural frequency residuals and mode shape residuals, with different weighting factors for each residual.

$$F(x) = w_f \sum_{k=1}^{N_f} \left(\frac{f_{ak} - f_{ek}}{f_{ek}} \right)^2 + w_m \sum_{k=1}^{N_m} \frac{cos^{-1}(\sqrt{MAC_k})}{(\pi/2)} \quad (1)$$

f_{ak} and f_{ek} denote the analytical and experimental natural frequencies; w_f and w_m are weighting factors applied to the frequency residuals and mode shape residuals, respectively. *MAC* (Modal Assurance Criteria) is a measurement of mode shape discrepancy and is defined as (Allemang and Brown 1982):

$$MAC_i = \frac{(\emptyset_{ai}^T \emptyset_{ei})^2}{(\emptyset_{ai}^T \emptyset_{ai})(\emptyset_{ei}^T \emptyset_{ei})} \quad (2)$$

$\emptyset_{ai}$ and $\emptyset_{ei}$ are analytical and experimental mode shapes, respectively. *MAC* = 1 means $\emptyset_{ai}$ and $\emptyset_{ei}$ are perfectly matched; *MAC* = 0 means they are orthogonal. It is known that *MAC* is rather insensitive to the change of mode shape. It is also noted that the *MAC* is actually the square of the inner product between the two mode shape vectors. Therefore, the objective function for the mode shape residual is formed as the normalized angle between the two mode shape vectors, which are much more sensitive to the changes in the mode shape.

3.3 Advanced Hybrid Fragility Analysis Method

Fragility, or vulnerability, presents the probability of reaching or exceeding a specific performance level under a specific seismic hazard. Fragility curves relate the effects of seismic hazard to the damage of the structures. Through the application of fragility curves, losses from earthquake hazard can be estimated.

Generally, fragility curves are sub-divided into four categories based on data sources, namely, empirical, judgmental, analytical, and hybrid fragility curves (Rossetto and Elnashai 2003). Empirical fragility curves are developed through field investigations after earthquakes—are the most realistic. However, this observation data is scarce and clustered in the low damaged range. Judgmental fragility curves are based on expert opinion, and are therefore subjective. Unlike the empirical and judgmental fragility curves, analytical fragility curves are more general, curves are allowed to be generated for different limit states and different structural types, although at a higher computation cost. Due to this limitation, most analytical fragility curves are generated either by simplified models or by complicated models without calibration to the real structural response, which can result in uncertainties in these curves.

To reduce the uncertainties, an advanced hybrid fragility analysis method is proposed, as shown in Figure 3. In this hybrid approach, hybrid simulation, with critical element tested in the laboratory and the rest simulated in the calibrated finite element model, is conducted to evaluate the structural response. By scaling ground motions, several hybrid tests are performed to reach the target structural response. The PGA value of the scaled ground motion is then assigned as the mean PGA value for the current limit state. Here, the target structural response is defined for different limit states, such as interstory drift angle of 0.7% for immediate occupancy limit state for steel moment frame building. Finally, with the mean PGA values and the dispersions from similar structures found in the literature, the fragility curves are generated based on the lognormal distribution assumption.

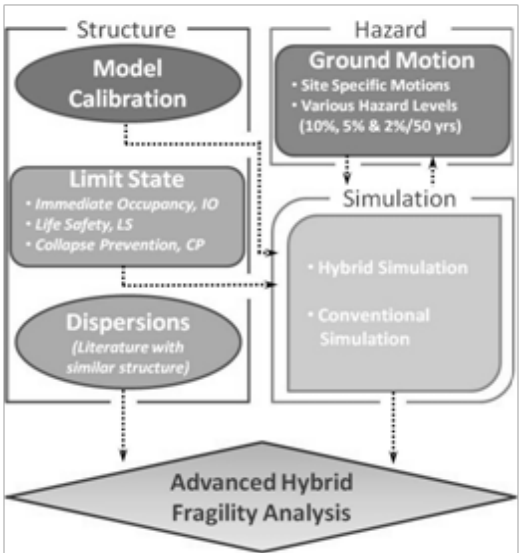


Figure 3 Methodology and procedure of the advanced hybrid fragility analysis method

4. NEES INTEGRATED SEISMIC RISK ASSESSMENT FRAMEWORK

NISRAF, a software platform with a graphical user interface (GUI) under the MATLAB environment, has been developed for the purpose of making impact assessment more efficient and more reliable. Several components—instrumentation, advanced hazard characterization, system identification, model updating, hybrid simulation, advanced hybrid fragility analysis and impact assessment tools—have been implemented and tailored with novel methods to build the seamless, transparent and extensible framework. Figure 4 presents several components with GUI implemented in NISRAF.

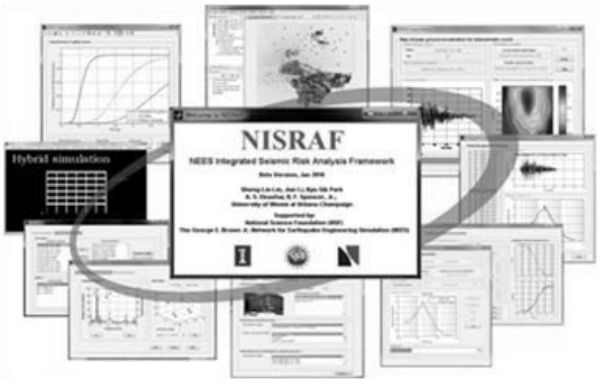


Figure 4 Components with GUI in NISRAF

There are several advanced features contained in this integrated framework. Among those features are:

- *Open source software with friendly GUI:* This software, as well as the source code, will be open to the public. The open source feature will allow NISRAF to be utilized efficiently, as well as improve its integrity and robustness.
- *Extensible and accessible:* In NISRAF, each component is developed separately (modularized), which facilitates understanding and maintenance. Most importantly, it is extensible and accessible to any latest research findings and program techniques.
- *Efficient and reliable impact assessment:* This is the first time that all the components for impact assessment are integrated and work seamlessly in just one software platform. Concurrently, the integrated feature brings the most advanced tools in order to obtain the most reliable earthquake impact assessment results possible. Surely, with these seamlessly-integrated and advanced technologies, which provide a more accurate hazard and structural model and hence generate superb fragility curves, the assessment of earthquake impact will be more efficient and more reliable than ever.

5. CASE STUDY

A six-story instrumented building in Burbank, California was selected to demonstrate NISRAF. This selected building is a steel moment resisting frame structure, in which the perimeter frames are the primary lateral load resisting system and the internal frames only resist the gravity load. Reference was made to Anderson and Bertero (1991) and Fumal et al. (1979) for more detailed information about this building and site condition, respectively. The building was instrumented by the California Strong Motion Instrumentation Program (CSMIP) in 1980 with 13 sensor channels. Several significant earthquakes were captured, including the 1987 Whittier earthquake, the 1991 Sierra Madre earthquake and the 1994 Northridge earthquake.

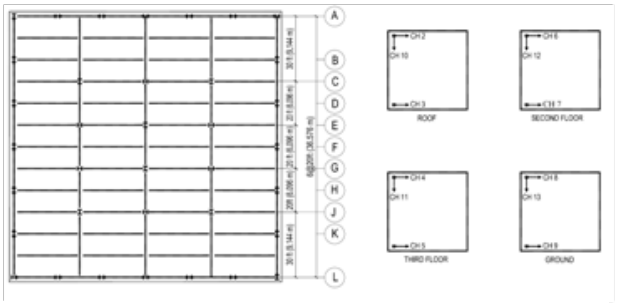


Figure 5 Plan view of Burbank building and sensors

The finite element model was built in ZEUS-NL platform (Elnashai et al. 2004). Due to the fact that only the perimeter frames are part of the lateral load resisting system, a 2-D frame was built to represent the entire structure. Section dimensions and material properties for each beam and column were based on design documents. Lumped masses were used and applied at the beam-column connections. Concrete slabs were modeled and connected to the steel girders using rigid elements to account for their contribution to stiffness.

5.1 Instrumentation

Many database centers archive tens of thousands of strong-motion records and structural sensor histories. To increase the utilization of this data, an interface with linkage

to several web databases, such as ANSS, Advanced National Seismic System; COSMOS, the Consortium of Organizations for Strong Motion Observation Systems; CESMD, Center for Engineering Strong Motion Data; and PEER, the Pacific Earthquake Engineering Research Center, was developed, which allows users to easily access to the database and to download any records of interest. Moreover, NISRAF allows users to create a project folder to archive the downloaded records and some basic information about this project. Figure 6 is an example, which shows the basic information of the Burbank building and the already-downloaded records.



Figure 6 Basic information of Burbank building archived in NISRAF

5.2 Hazard Characterization Analysis

Secondly, the hazard characterization at the Burbank site was performed by using both the downloaded free-field station records and the generated synthetic ground motion records. To generate the synthetic records for different hazard levels (e.g. 10%, 5%, and 2% probability of exceedance in 50 years), the deaggregation results were fed into the attenuation model to produce the response spectra and duration for SIMQKE (Gasparini and Vanmarcke 1976) to generate synthetic ground motions. Subsequently, DEEPSOIL was used to generate site specific ground motions. Figure 7 is the GUI, which shows the generated site specific ground motion as well as the hazard map in NISRAF.

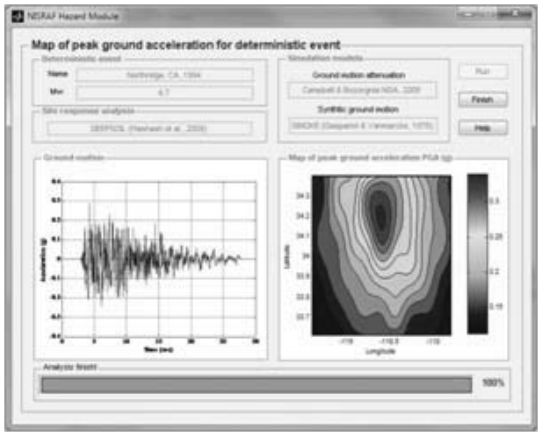


Figure 7 Site specific ground motions and hazard map generation in NISRAF

5.3 Model Calibration

The ERA method was performed on the Northridge earthquake records in order to identify the frequency of this building. At the beginning of the process, small values of EMAC and MPC were recommended since they are more sensitive to the noise modes compared to the MAC. Some genuine modes may be filtered out due to too large EMAC or MPC values. Hence, the information in the stabilization diagram was too limited to identify the natural frequencies. The values were then adjusted for multiple running of ERA to get a reasonable stabilization diagram. Eventually, the first and second bending modes were identified as 0.72 Hz and 2.14 Hz, respectively. The corresponding damping ratios were 3.37% and 6.71%.

Based on the identified information, model updating was performed. Young's modulus of steel (*Es*), lumped mass and effective width of concrete slab were selected as candidate parameters based on the sensitivity analysis. The optimization problem defined previously was solved by the Nelder-Mead method (Nelder and Mead 1965). Table 1 tabulates the structural frequencies of the identified, original and updated model. As can be seen, the errors between the identified and updated model reduced to 1% and 5.78% for the first and second natural frequency, respectively. With this refined finite element model, hybrid simulation was then conducted to yield a seismic response prediction with higher accuracy.

Table 1 Identify, original and updated models

Mode	ERA	Original FE		Updated FE	
	Freq. (Hz)	Freq. (Hz)	Error (%)	Freq. (Hz)	Error (%)
1	0.719	0.688	-4.31	0.712	-1.00
2	2.144	1.956	-8.77	2.020	-5.78

5.4 Hybrid Simulation

The calibrated building model along with ground motions from hazard characterization analysis were used to verify the integration of the hybrid simulation in NISRAF. The tuned 2-D structure was divided into two sub-structures, namely, the column (the lower part of the left exterior column at the first floor) and the frame (the remaining structure). The frame module was simulated in ZEUS-NL platform, while the column module—replaced by a small scale aluminum specimen—was tested in the laboratory using the NEES@UIUC (MUST-SIM) facility (Figure 8). Testing at small scale is acceptable here because the objective is to demonstrate the integration of hybrid simulation in NISRAF. Hybrid simulation, coordinated by UI-SIMCOR (Kwon et al. 2007) under the 1994 Northridge earthquake, was first conducted as the proof test prior to the generation of the hybrid fragility curves. Good agreement was found between the measured response during the Northridge earthquake and the responses from the hybrid simulation test, as shown in Figure 9.



Figure 8 Hybrid simulation setup using NEES facilities

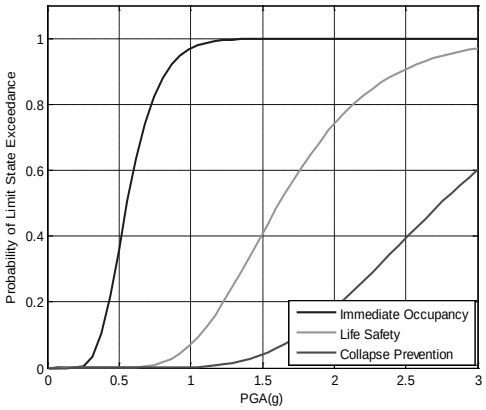


Figure 10 Fragility curves generated by NISRAF

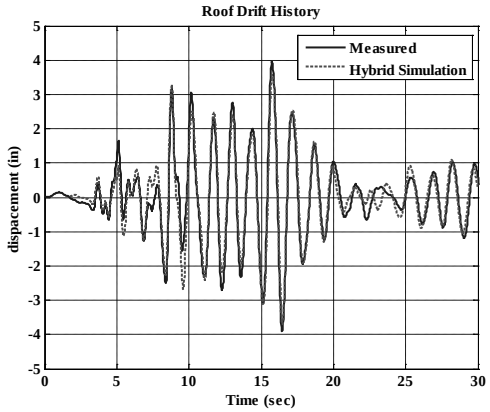


Figure 9 Comparison of the roof drift history between the measured and the hybrid simulation result

5.5 Hybrid Fragility Analysis

Hybrid simulation results under different synthetic ground motions (10%, 5% and 2% probability of exceedance in 50 years for immediate occupancy, life safety and collapse prevention performance level, respectively) were used to derive the mean PGA value for each performance level. Using these mean values, along with dispersions from previous studies with similar structures (Table 2), fragility curves were generated based on lognormal distribution assumption (Figure 10).

Table 2 Interstory drift angle, dispersion and mean PGA of different performance levels

Performance Level	Immediate Occupancy	Life Safety	Collapse Prevention
ISDA (%)*	0.7	2.5	5.0
Dispersion**	0.311	0.328	0.346
Mean PGA (g)***	0.545	1.627	2.777

**FEMA 2000b*

***FEMA 2000a, Cornell et al. 2002*

****Hybrid simulation results*

5.6 Impact Assessment

Finally, with the generated compatible hazard map and fragility curves, MAEviz under NISRAF was conducted to calculate earthquake impact losses. Table 3 lists the probabilities of exceeding limit states. As shown, only 15% probability for damage occurred in the immediate occupancy limit state. The results correlated with the post-earthquake report made by Applied Technology Council (ATC 2001), which reported slight damage observed to this building from the Northridge earthquake of 17 January 1994.

Table 3 NISRAF impact assessment results

Probability of exceeding limit state		
Immediate Occupancy	Life Safety	Collapse Prevention
0.15	0.00	0.00

6. APPLICATIONS OF REGIONAL IMPACT ASSESSMENT

The actual test bed in Burbank, California, the 6-story steel building was carried out to verify the framework as well as its components. This building example demonstrated not only the seamlessly-integrated, extensible and transparent framework, but it also showed that all the elements required for an accurate impact assessment can be performed under just one software platform. Consequently, the impact assessment result, which showed good agreement with the post-earthquake report, confirmed one of the advanced features of NISRAF—efficient and reliable impact assessment. Meanwhile, it also established that the proposed advanced methods—the hazard characterization analysis, the model calibration and the hybrid fragility analysis—were reliable. As a result of demonstration of this impact assessment on one individual building, the same procedures can be applied to other different building types, seismic code levels and construction materials, to perform regional impact assessment. Figure 11 is an example, which shows the regional impact assessment in Los Angeles area using NISRAF.

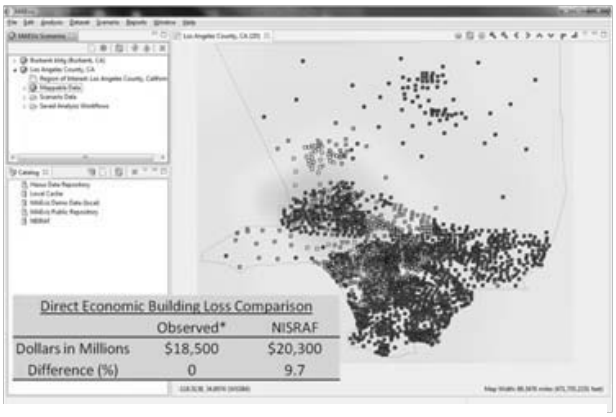


Figure 11 Regional impact assessment

7. CONCLUSIONS

NISRAF serves as a user-friendly software platform through which impact assessment can be efficiently and reliably performed by combining hazard (exposure) and fragility (sensitivity), to provide assessment of impact on the built environment at the regional scale. Concurrently, it extends the state-of-the-art hybrid simulation approach to fragility analysis, and proposes novel method for hazard characterization and model calibration. The successful completion of the development of the framework and verification of its components not only demonstrates that these objectives have been achieved, but also showcases the power and advantages offered by the George E. Brown, Jr. Network for Earthquake Engineering Simulation (NEES). For example, the hybrid simulation technique enables NISRAF to integrate testing capabilities at multiple NEES sites. The assessment thereby employs the strength of existing computational models and the expertise of individual research groups to explore previously unapproachable problems. Finally, the application of NISRAF will be a stimulus not only for geotechnical and structural earthquake engineers and impact assessment experts, but also for seismologists and structural control researchers improving their algorithms in order to pursue the ultimate goal of NEES under NEHRP: the assessment and mitigation of earthquake losses.

Acknowledgements:

This research was supported by National Science Foundation, Grant Number 0724172. The support is gratefully acknowledged.

References:

Allemang, R. J., and Brown, D. L. (1982), "A Correction Coefficient for Modal Vector Analysis, Proceedings," *International Modal Analysis Conference*, Orlando, FL, 110~116.

Anderson, J. C., and Bertero, V. V. (1991), "Seismic performance of an instrumented six-story steel building," Report UCB/EERC-91/11, University of California, Berkeley, U.S.A.

Applied Technology Council (ATC) (2001), "Database on the performance of structures near strong-motion recordings: 1994 Northridge, California, earthquake," Report No. ATC-38, Redwood City, CA.

Comerio, M. C., Landis, J. D., Firpo, C. J., and Monzon, J. P. (1996), "Residential Earthquake Recovery," California Policy Seminar, University of California, Berkeley, CA.

Cornell, C. A., Jalayer, F., Hamburger, R. O., and Foutch, D. A. (2002), "Probabilistic Basis for 2000 SAC Federal Emergency Management Agency Steel Moment Frame Guidelines," *Journal of Structural Engineering*, **128**(4): 526-533.

Elnashai, A. S., Papanikolaou V., and Lee, D. (2002), "Zeus NL – a system for inelastic analysis of structures," Mid-America Earthquake Center, University of Illinois at Urbana-Champaign, Program Release January 2004.

Federal Emergency Management Agency (FEMA) (2000a), "Recommended Seismic Design Criteria for New Steel Moment-Frame Buildings," Report No. FEMA-350, Washington D.C.

Federal Emergency Management Agency (FEMA) (2000b), "Prestandard and Commentary for the Seismic Rehabilitation of Building," Report No. FEMA-356, Washington D.C.

Federal Emergency Management Agency (FEMA) (2009), "NEHRP (National Earthquake Hazard Reduction Program) Recommended Seismic Provisions for New Buildings and Other Structures," Report No. FEMA P-750, Washington D.C.

Fumal, T. E., Gibbs, J. F., and Roth, E. F. (1979), "In-situ measurements of seismic velocity at 19 locations in the Los Angeles, California region," SMIP geotechnical report No. 131, U.S. Geological Survey.

Gasparini, D. A., and Vanmarcke, E. H. (1976), "Simulated Earthquake Motions Compatible with Prescribed Response Spectra, Evaluation of Seismic Safety of Buildings," Report No.2, Massachusetts Institute of Technology.

Hashash, Y., Groholski, D.R., Phillips, C.A., and Park, D. (2009), "DEEPSOIL V3.5beta, User Manual and Tutorial," Department of Civil and Environmental Engineering, University of Illinois at Urbana-Champaign, Urbana, IL.

Juang, J. N., and Pappa, R. S. (1985), "An eigensystem realization algorithm for modal parameter identification and model reduction," *Journal of Guidance, Control, and Dynamics*, **8**(5): 620-627.

Kempton, J. J. and Stewart, J. P. (2006), "Prediction Equations for Significant Duration of Earthquake Ground Motions Considering Site and Near-Source Effects," *Earthquake Spectra*, **22**(4), 985-1013.

Kwon, O. S., and Elnashai, A. S. (2006), "The effect of material and ground motion uncertainty on the seismic vulnerability curves of RC structure," *Engineering Structures*, **28**(2):289-303.

Kwon, O. S., Nakata, N., Park, K. S., Elnashai, A. S., and Spencer, B. J. (2007), "User Manual and Examples for UI-SIMCOR v2.6," Department of Civil and Environmental Engineering, University of Illinois at Urbana-Champaign, Urbana, IL.

Mid-America Earthquake Center (MAE Center) (2007), "Mid-America Earthquake Center Seismic Loss Assessment System, MAEviz v3.1.1," University of Illinois at Urbana-Champaign, Urbana, IL.

Nelder, J. A., and Mead, R. (1965), "A simplex method for function minimization," *Computer Journal*, **7**: 308-313.

Pappa, R. S., and Elliott, K. B. (1993). "Consistent-mode indicator for the eigensystem realization algorithm," *Journal of Guidance, Control, and Dynamics*, **16**(5): 852-858.

Power, M., Chiou, B., Abrahamson, N., Bozorgnia, Y., Shantz, T., and Roblee, C. (2008), "An Overview of the NGA Project," *Earthquake Spectra*, **24**(1): 3-22.

Rossetto, T., and Elnashai, A. (2003), "Derivation of Vulnerability Functions for European-type RC Structures Based on Observational Data," *Engineering Structures*, **25**(10):1241-1263

8CUEE CONFERENCE PROCEEDINGS
8th International Conference on Urban Earthquake Engineering
March 7-8, 2011, Tokyo Institute of Technology, Tokyo, Japan

LOCAL SITE EFFECTS ON DAMAGE OF HISTORICAL MONUMENTS IN ISTANBUL DURING THE 1894 MARMARA SEA, TURKEY, EARTHQUAKE

Masashi Morita[1)], Saburoh Midorikawa[2)], Atilla Ansal[3)], and Barbaros Çetiner[4)]

1) Post-Doctoral Research Fellow, Center for Urban Earthquake Engineering, Tokyo Institute of Technology, Japan
2) Professor, Dept. of Built Environment, Tokyo Institute of Technology, Japan
3) Professor, Dept. of Earthquake Engineering, Boğazici University: Kandilli Observatory and Earthquake Research Institute, Turkey
4) Graduate Student, ditto
mmorita@enveng.titech.ac.jp, smidorik@enveng.titech.ac.jp, ansal@boun.edu.tr, bacetiner@yahoo.com

Abstract: Istanbul, which is one of the World Heritage Sites, has been repeatedly struck by destructive earthquakes. This paper examines local site effects on damage of historical monuments in Istanbul during the 1894 Marmara Sea Earthquake. In order to understand local site conditions in Istanbul, microtremore measurements were conducted at 64 sites near monuments, which were damaged by 1894 Earthquake. By taking forms of H/V spectral ratio of microtremor and boring logs into consideration, 64 sites are classified into six groups. Then, a relation between damage of historical monuments and local site condition by a proposed site classification is examined. The result shows that damage degree of historical monuments is better correlated with the site class proposed in this study than the site class by IMM (2007).

1. INTRODUCTION

Istanbul, which is one of the mega cities in the world, has been repeatedly struck by destructive earthquakes because it is located at the west end of the North Anatolian Fault Zone. At the same time, Istanbul itself is designated a World Heritage Site because of many historical monuments and its cityscape. Therefore it is important for the earthquake disaster prevention of human lives and those monuments to investigate building damage caused by past earthquakes. Findings obtained from such historical facts and lessons are contributory to establish a better disaster protection and reduction system. From this view point, the main objectives in this paper are historical monuments in Istanbul damaged during the 1894 Marmara Sea Earthquake (Ms=7.3), which is the latest earthquake causing severe damage to Istanbul, as a case study.

Concerning to casualties and building damage, books and articles are published by several researchers (Ambraseys 2001, Ürekli 1999, Çalık 2003). These articles summarized damage of historical monuments with collecting records from many newspapers and journals of the day. Ansal *et al*. (1990) examined the distribution of building damage and the influence of local soil condition. However, the damage distribution was grossly compiled, and the discussion was limited to the damage of several important monuments. In the previous paper (Morita *et al*. 2010), damage of historical monuments and its distribution caused by 1894 Earthquake, which were obtained from the records of the day (Öztin 1994), were compared with the geology and site class in Istanbul (JICA *et al*. 2000, IMM 2007). As the result, a certain correlation between damage degrees and soil conditions was found.

In order to examine local site effects on damage of historical monuments in detail, microtremor measurements were conducted at total 64 sites near historical monuments in Istanbul, which were damaged by 1894 Earthquake. First, local site conditions based on the result of microtremor measurements in Istanbul are considered. Next, a new site class is proposed based on forms of H/V spectral ratios by microtremor and boring logs. After that, a relation between damage of historical monuments and local site conditions in accordance with a proposed site class is examined.

2. OUTLINE OF DAMAGE ON HISTORICAL MONUMENTS CAUSED BY 1894 EARTHQUAKE

The report by Öztin (1994) contains records of building damage in the area corresponding to Istanbul province at present. In cases that damaged parts of historical monuments such as a dome or walls were clearly written and damage degrees were described, it is possible to estimate their damage degrees. As referring to the damage criteria for masonry buildings by EMS-98 (ESC 1998) too, damage degrees of historical monuments are classified into four levels according to the criteria based on the damage description as shown in Table 1. DL4, DL3 and DL2 indicate totally collapsed, half collapsed or heavy damage, and partly collapsed or light damage respectively (Fig. 1). DL1 indicates that damage levels are not determined because of no detailed description about a damage degree.

As for eight important historical monument types such as mosque, minaret, church, Muslim seminary (*medrese*), school (*mekteb*), large commercial building (*han*), public bath (*hamam*) and mausoleum (*Türbe*), the locations of damaged historical monuments are identified. Figure 2 shows the distribution of all damaged historical monuments with damage levels on the site class map by Istanbul Metropolitan Municipality (IMM 2007). In this figure, locations of historical monuments, whose damage were not recorded, are also indicated as N/A for considering overall distribution of historical monuments in Istanbul at that time. The site class by IMM is determined by a combination of standard penetration test, relative density, S-wave velocity and thickness of topmost soil in accordance with the Turkish Regulation (Ministry of Public Works and Settlement 1997). In this criterion, Z1 means the hardest soil, Z4 means the softest soil and AF/O means artificial soil or other soils not defined by the regulation.

Damaged historical monuments mostly stood from the eastern to northwestern part of the city except at the middle of the northern coastal area. Along the southwestern coastal area, somewhat concentration of damaged historical monuments is also identified. With respect to damage degree, heavy damage occurred in the middle of southern

Table 1 Criteria for Damage Level of Historical Monument

Damage Degree		Descrieption of Damage	EMS98
Unknown	DL1	Described with only words yıkırmıştır (broken, fell down) çatlamiştır (cracked)	
Partly Collapsed (Light Damage)	DL2	bazı yerleri ... (some part ...) kısımen ... (a part ...) biraz ... (a little ...)	Grade 2 Grade 3
Half Collapsed (Heavy Damage)	DL3	haylice ... (a large part ...) ekser yerleri ... (most par t...) yarısı ... (half)	Grade 4
Totally Collapsed	DL4	harap olmuş (ruined) çökmüştır (collpsed all) tümüyle ... (totally ...)	Grade 5



Grand Bazaar (DL4) Amcazade Hüseyin Paşa Medrese (DL3)

Figure 1 Photos of Damaged Historical Monuments by 1894 Earthquake

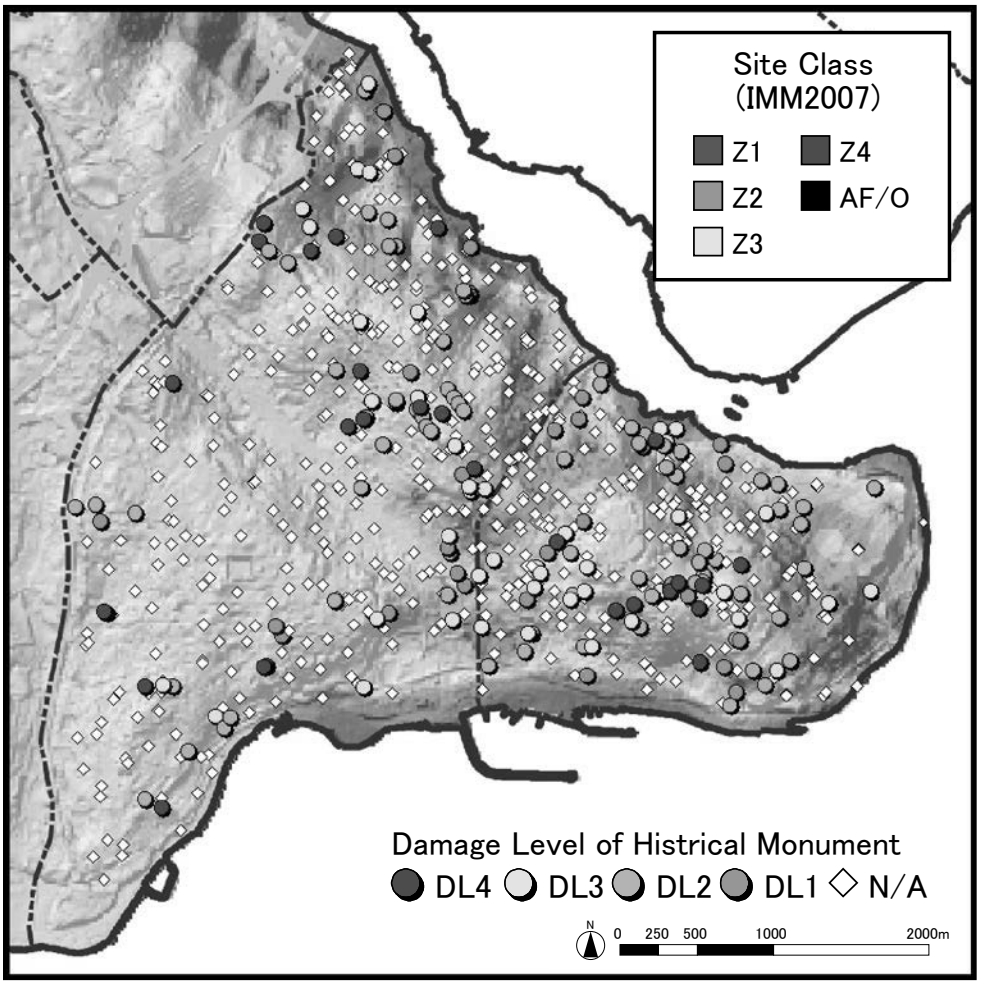


Figure 2 Distribution of All Damaged Historical Monuments with Damage Level on the Site Class Map (IMM 2007)

part of Istanbul. Figure 3 shows the ratio of all damaged historical monuments together with damage degrees and the classification criteria. The ratios of DL4 increase from Z1 to Z4 as 1.0%, 2.7%, 3.5% and 4.9% in order, and there is no historical monument which was totally collapsed in AF/O. Though the ratios of D3 also tend to increase from Z1 to AF/O as 3.5%, 5.4%, 4.0%, 7.3% and 15.4% in order, the ratio in Z3, which is the softer site class than Z2, decrease. In regard to total of damaged historical monuments, the ratio in Z1 is about 10%, the ratios in Z2 and Z4 are over 20% but the ratio of Z3 is less than 20 %. The ratio in AF/O exceeds 30%. Therefore, the ratio of heavily damaged historical monuments becomes high as soils become soft in general. However, in Z2 and Z3, opposite tendencies are appeared partly. It is suggested by this result that the site class by IMM doesn't indicate good correlation with damage levels of historical monuments.

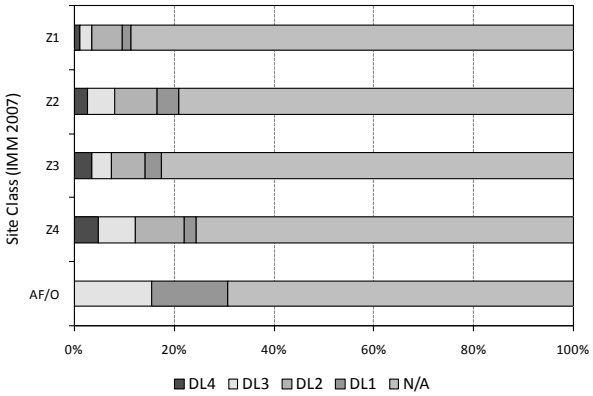


Figure 3 Ratio of All Damaged Historical Monuments in accordance with the Site Class (IMM2007)

3. OUTLINE OF MICROTREMOR MEASUREMENT IN ISTANBUL

In order to understand local site conditions of Istanbul in detail, microtremor measurements in Istanbul were carried out at total 64 points on March and October 2010. Measurement points for microtremor were selected close to historical monuments which were damaged by the 1894 Earthquake (Fig. 4). A high sensitive velocity seismometer was used for measurements. The microtremor instrument has 3 components that X directs to North-South, Y directs to East-West and Z directs to Up-Down component. At every measurement point, microtremor was usually recorded at least 4 times with 1/100 second sampling rate and 42.0 second data length. Fourier spectra of each component are calculated from records of microtremors.

For calculation, a unit of 20.48 seconds at each record was picked up by judging from waveform in the time domain in order to avoid noise parts. A Parzen window of 0.2-Hz bandwidth is adopted to obtain smooth spectra. After calculating Fourier spectra of each component, H/V spectral ratio of each record and average H/V spectral ratio were calculated at each measurement point. Figure 5 shows the results of H/V spectral ratios at several measurement points. From the average H/V spectral ratio in each measurement point, a predominant period and a peak value of H/V spectral ratio are obtained. Table 2 shows types of historical monuments, damage levels, predominant periods and peak values of H/V spectral ratios at each measurement point. Figure 6 shows the measurement points with predominant periods.



No. 17: Nişancı Paşa Hamam No. 13: Sultan Bayesit Mosque

Figure 4 Situation of Microtremor Measurement

Table 2 Result of Microtremor Measurement

No	Type	DL	Period	Peak
M1-1	MO	DL3	0.25	4.9
	MI	DL3		
M1-4	HA	DL1	0.21	3.6
M1-5	SC	DL3	0.19	1.9
M1-6	MO	DL3	0.10	1.7
M1-7	SC	DL4	0.24	1.7
M1-8	MO	DL2	1.14	2.1
	MI	DL2		
M1-10	MO	DL2	0.19	1.7
M1-11	SC	DL2	0.09	2.2
M1-12	MO	DL4	0.17	5.1
M1-13	MI	DL3	0.20	8.0
M1-14	CH	DL3	0.25	7.9
M1-15	MO	DL4	0.45	11.4
	MI	DL3		
M1-17	CH	DL4	0.60	11.6
M1-18	MO	DL4	0.60	12.1
	MI	DL4		
M1-19	PB	DL2	0.55	12.7
M2-1	MO	DL4	1.02	5.7
	MA	DL3		
M2-3	MI	DL1	0.89	6.4
M2-4	SC	DL1	0.89	4.4
M2-5	MO	DL4	0.85	7.7
	MI	DL4		
M2-6	SC	DL3		
M2-7	SC	DL2	1.08	4.6
M2-8	MO	DL2	1.02	6.1
M2-9	PB	DL4	1.02	6.5
M2-10	PB	DL2	0.82	4.9
M2-11	SC	DL3	0.82	5.4
M2-12	CH	DL2	0.76	4.4
M2-13	CH	DL2	0.89	6.7
M2-14	MO	DL4	0.93	7.5
M2-15	SC	DL2	0.98	6.1
M3-1	MO	DL3	0.22	6.7
M3-2	SC	DL1	0.34	9.2
M3-3	PB	DL2		
M3-5	MI	DL3	0.18	7.2

No	Type	DL	Period	Peak
M3-8	MO	DL3	0.18	3.8
M3-11	MO	DL2	0.18	2.8
M3-12	SC	DL3	0.17	8.7
M3-13	MI	DL2		
M3-14	SC	DL1	0.17	10.4
M3-15	MO	DL3	0.22	6.4
M3-16	SC	DL3	0.16	3.8
M3-18	MO	DL3	0.11	13.0
M3-20	MI	DL3	0.44	5.6
M3-21	SC	DL2		
M3-22	HA	DL3	0.43	8.0
M3-23	SC	DL2	0.34	14.3
M3-25	MO	DL4	0.29	8.1
1	MI	DL4	0.57	7.9
2	MI	DL1	0.57	6.9
3	MA	DL4	0.53	10.3
4	MO	DL4	0.53	7.9
	MI	DL2		
5	MI	DL3	0.45	7.3
6	MI	DL4	0.30	9.7
7	MO	DL2	0.32	7.6
8	MO	DL3	0.26	5.0
	MI	DL3		
9	MO	DL2	0.28	5.4
	MI	DL4		
	MA	DL2,1		
10	CH	DL1	0.11	2.3
11	HA	DL4	0.41	5.0
12	MO	DL3	0.40	6.7
13	MO	DL2	0.44	4.8
14	MI	DL4	0.46	5.9
15	MO	DL2	0.28	5.5
16	MI	DL2	0.27	5.1
17	PB	DL3	0.25	8.8
18	CH	DL1	0.16	4.9
19	MO	DL2	0.18	8.1
20	MO	DL2	0.18	7.0
21	PB	DL1	0.14	4.1
22	MO	DL2	0.12	4.0

Mo: Mosque, Mi: Minaret, Ma: Mausoleum, Ch: Church, PB: Public Bath, Ha: Commercial Building, SC: School

4. LOCAL SITE CONDITION BASED ON MICRO-TREMOR MEASURMENT

Predominant periods at all of measurement points range 0.1 to 1.1 second (Table 2). As shown in Figure 5 and Figure 6, in the northwestern and eastern part of Istanbul,

peaks of H/V spectral ratios at measurement points near the seashore (No. M1-10) are not clear and predominant periods of those points are short. At measurement points with increasing distance from the seashore (No. 8 and 1), peaks of H/V spectral ratios become clear and predominant periods become long. In southwestern part, peaks of H/V spectral ratios are very clear (No. M2-9) and predominant periods are over 1.0 second.

When predominant periods are compared with the site class by IMM, some measurement points where short predominant periods are obtained (No.M1-1, M1-4, 10, 18 and 22) are located on, or close to Z4 which is the softest soil. Around the seashore including these points, the site classes change from AF/O to Z2 rapidly within a short distance from the seashore line. In addition, Istanbul has a terrain with its many uphills and downhills. Especially, in the area around No.10, steep slopes run from the seashore. Judging from these topographical characteristics, it is presumed that subsurface structures in these areas are complex, and there is a possibility that a classification of sites was not performed correctly. Therefore, short predominant periods are obtained at points which are even close to Z4. Moreover, there are some points located on Z3, whose predominant periods are shorter than 0.5 second, in the eastern part of Istanbul. On the contrary, predominant periods and peak values of H/V spectral ratios at several points in the western part of Istanbul differ considerably with location though all of those sites are classified into Z3. That is, it is needed that Z3 occupying a great part of Istanbul should be considered in detail more.

Figure 7 shows the relation between damage levels of historical monuments and predominant periods at each point.

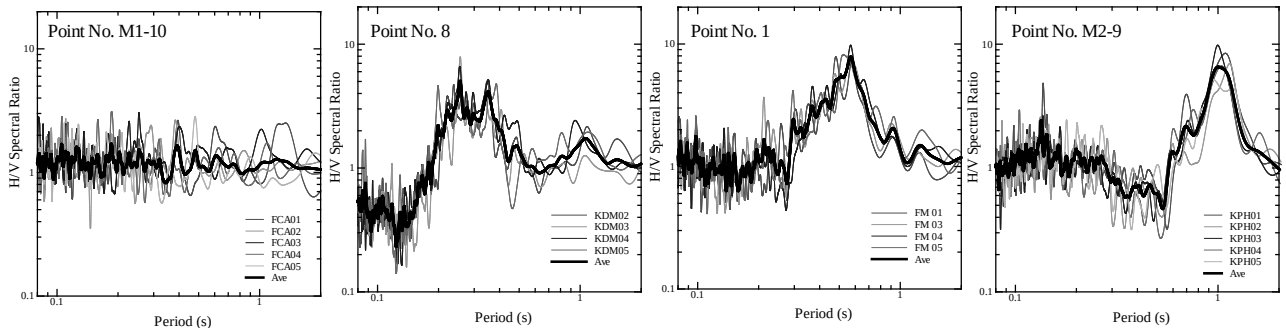


Figure 5 Examples of H/V Spectral Ratio

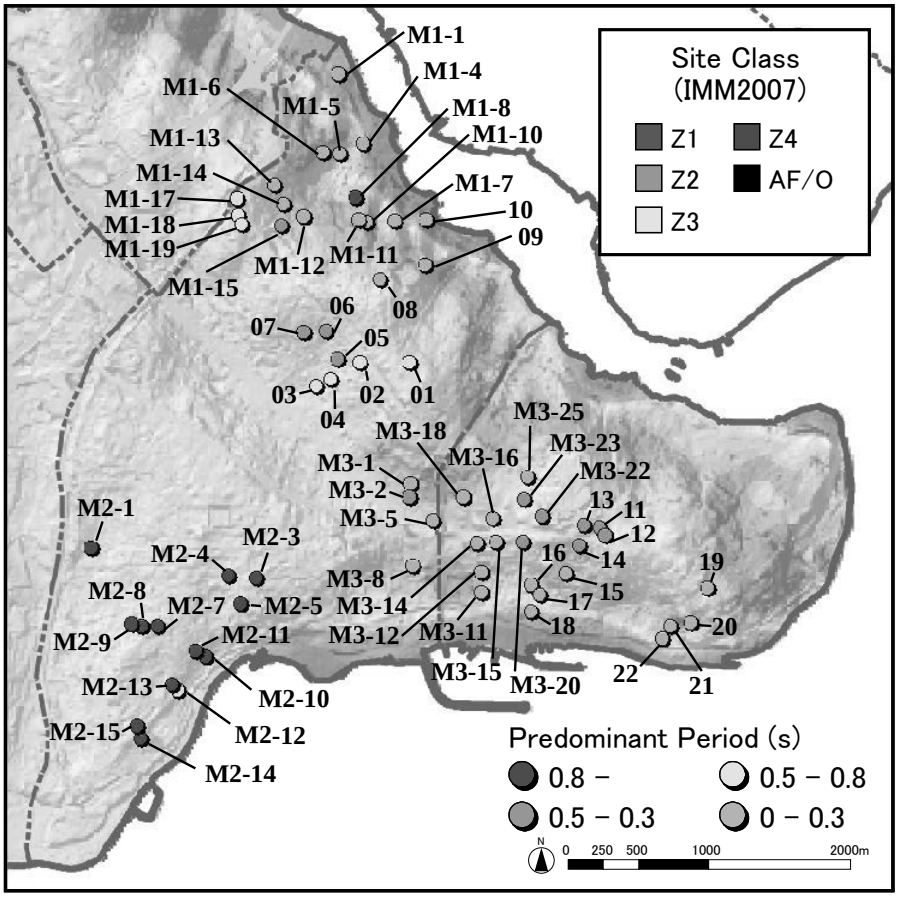


Figure 6 Measurement Point with Predominant Period

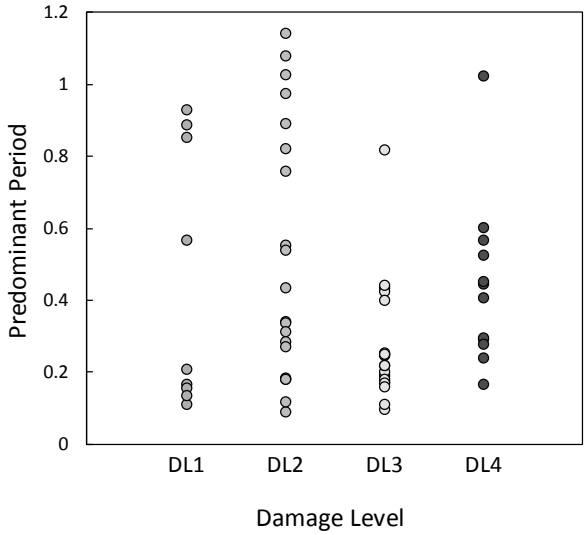


Figure 7 Relation between Damage Level of Historical Monument and Predominant Period

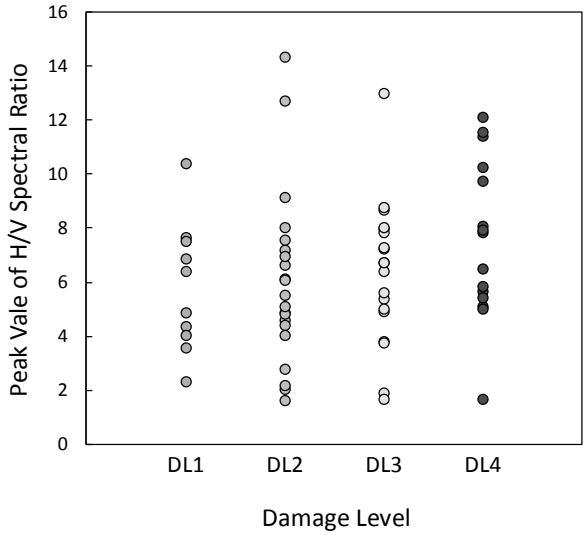


Figure 8 Relation between Damage Level of Historical Monument and Peak Value of H/V Spectral Ratio

Predominant periods range from 0.11 to 0.93 second in DL1, from 0.09 to 1.14 second in DL2, from 0.10 to 0.82 second in DL3 and from 0.17 to 1.02 second in DL 4. In addition, the longest predominant period is appeared in DL2. Therefore, damage levels of historical monuments don't tend to become heavy as predominant periods become long. This tendency applies to the relation between damage levels of historical monuments and peak values of H/V spectral ratios at each point as shown in Figure 8. From these results, it is needed that causes of damage should be considered with not only the result of microtremor measurements but also with more detailed information concerning to soils.

5. RELATION BETWEEN DAMAGE OF HISTORICAL MONUMENTS AND LOCAL SITE CONDITION

5.1 Re-Classification of Site based on Form Patterns of H/V Spectral Ratios and Boring Logs

In Istanbul, the boring investigation to a depth of 30 meters had been carried out at approximately 250-meter intervals. By using the result of microtremor measurement and the boring logs, site conditions of 17 measurement points, which are within 100 m from boring points, are re-classified. According to a similarity of form patterns of H/V spectral ratios basically, 17 selected points are classified into six groups. Figure 9 shows the result of classification and boring logs obtained from the nearest boring points at each selected point. Here, Trakya Formation of Lower Carboniferous age is composed of sandstone and siltstone. Bakırköy and Güngören Formations of Upper Miocene are mainly composed of loose clay and sand.

Group A: H/V spectral ratios don't have clear peaks. Around these points, Trakya Formation is deposited thickly under thin artificial fills. Therefore, Group A can be classified as the hardset soil group among six groups.

Group B: H/V spectral ratios are smooth mountainious forms with having a peak at short period side. Subsurface structures around these poins are mainly composed of artificial fills and Traky Formation with thin Güngören Formation between them. Looking at Point 19, Güngören Formation is deposited thickly at the nearest boring ponit. However, No. 19 is 72.0 m away from the boring point toward Z2 side (Fig. 4). Therefore, it is possible to think that the actual thickness of Güngören Formation at No. 19 is a little thiner.

Group C: H/V spectral ratios have two sharp peaks at short period side. Subsurface structures include alluvion in only this group. Looking at No. M1-4、alluvion is deposited thickly at the nearest boring point. However, No. M1-4 is 78.6 m away from the boring point in fact, and subsurface structures aroud No. M1-4 change rapidly (Fig. 4). Taking this situation into consideration, it is possible to think that the actual thickness of alluvion at No. M1-4 is a little thiner. Therefore, it is predictable that subsarface sturctures are composed of artificial fills and Trakya Formation with thin soft layer between them and tend to have distinct contrast of soil hardness at shallow depth whrere such a H/V spectral ratio is obtaied.

Group D: Thoguh predominant periods range from 0.2 to 0.6 second, peaks of H/V spectral ratios are not sharp. As for subsurface structures around these points, Güngören Formation are deposited thickly under thin artificial fills.

Group E: Though predominat preiods range from 0.2 to 0.6 second like Group D, peaks of H/V spectral ratios are very sharp. As for subsurface structures around these point, compositions of formations and their thickness are almost same as one in GroupD. Therefore, it is hard to distingish Group E from Group D by only boring logs.

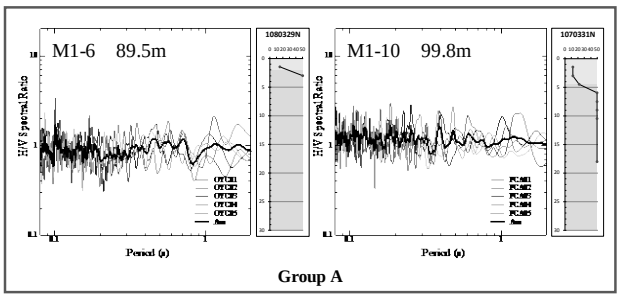


Figure 9 Grouping of 17 selected points

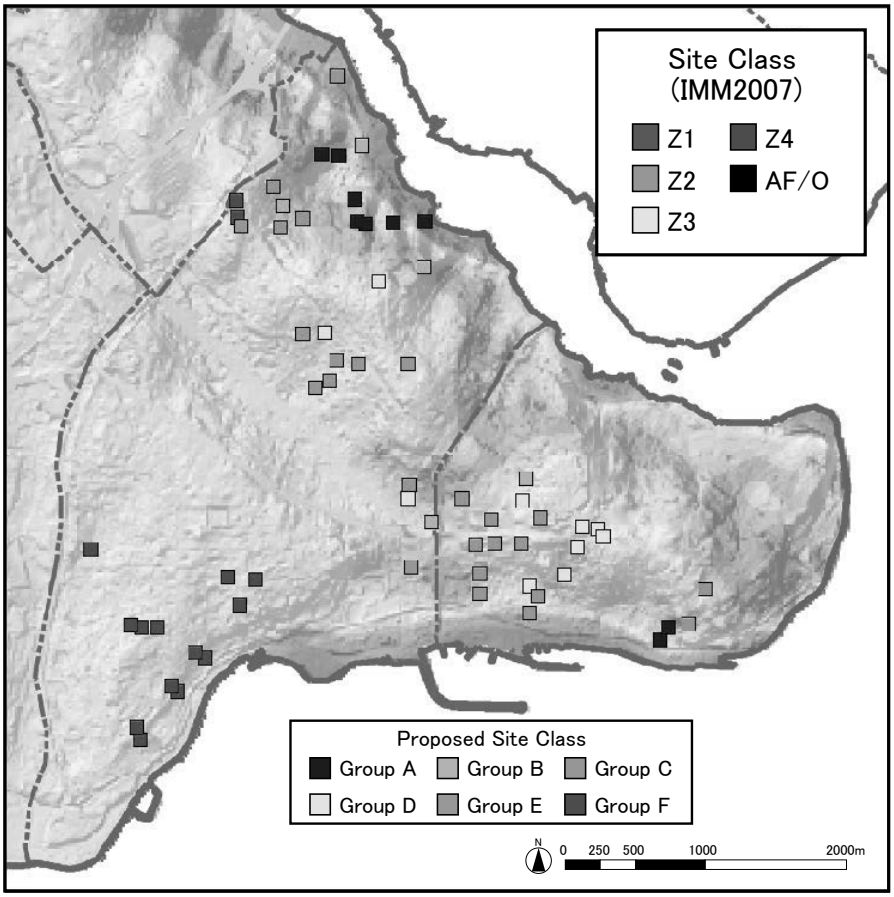


Figure 10 Proposed Site Class at Microtremor Measurement Point

Group F: Predominant periods range from 0.6 to 1.0 second, and peaks of H/V spectral ratios are very sharp. Subsurface structures aroud these points are composed of artifisial fills, Bakırköy Formation and Güngören Formation without Trakya Formation. Therefore, Group F can be classified as the softest soil group among six groups.

5.2 Comparison of Damage Degree of Historical Monuments with Site Class

Figure 10 shows the result that other 47 points were classified into the six groups which were obtained in the previous section. Points located on Z1 and Z2 in the northwestern part of Istanbul were classfied into GroupA and GroupB, which indicate hard soils amoung the six groups. Points in the eastern part were classified into 4 groups. It corresponeds to complicated soil conditions as shown by the site clss of IMM. Points located on Z3 in the wester part could be classfied into Group D, Group E and Group F. That is, the proposed site class in Istanbul are classified finely as the result of re-calssification is harmonized with the site class by IMM

As for the historical monuments closed to which microtemor measurements were conducted, the ratios of damaged historical monuments together with the damage degrees and the proposed site classification criteria is shown in Figure 11. The ratios over DL3 are about 30.0%, 57.1%, 55.6%, 45.5%, 68.8% and 57.9% in Group A to Group F respectively. The ratios of DL4 are about 10.0%, 7.1%, 22.2%, 27.3%, 25.0% and 42.1% in Group A to Group F respectively. It is clearly shown that damage degrees become heavy when soils are soft. Figure 12 shows the ratios of damaged historical monuments together with the damage degrees and the classification criteria by IMM. In Z4, there is no damaged historical monument, whose damage level is DL4. In Z2, the ratio of DL3 is the highest. Comparing to the site class by IMM, a correlation between damage of historical monuments and the proposed site class becomes better.

6. CONCLUDING REMARKS

This paper examines local site effects on damage of historical monuments in Istanbul during the 1894 Marmara Sea Earthquake. Microtremore measurements were conducted at 64 sites closed to historical monuments, which were damaged by 1894 Earthquake. According to forms of H/V spectral ratios of microtremor and boring logs, re-classification of sites in Istanbul was performed. Then, damage degrees of historical monuments were compared with the proposed site class in this study. As the result, the proposed site class shows a better correlation with damage degree of historical monuments than the site class by IMM.

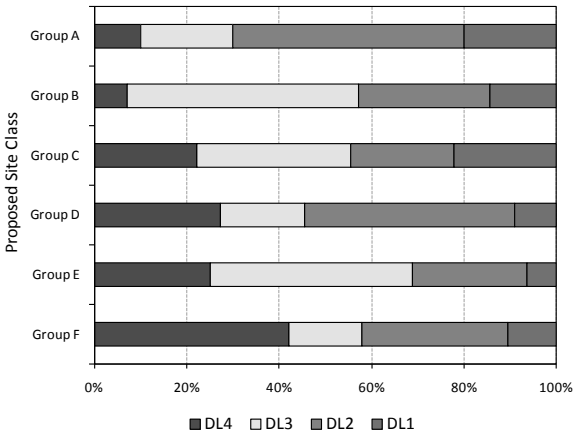


Figure 11 Ratio of Damaged Historical Monuments in accordance with the Proposed Site Class

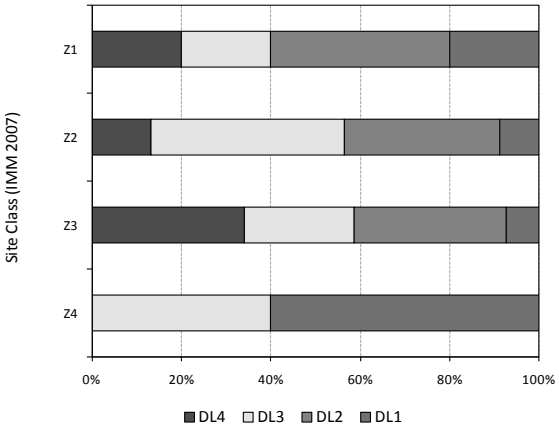


Figure 12 Ratio of Damaged Historical Monuments in accordance with the Site Class (IMM2007)

It is suggested by this result that there is a possibility to estimate building damage in accordance with a site class based on microtremor with relatively-accuracy even where boring logs are unavailable.

Acknowledgements:

This study is supported by the Global COE Program "International Urban Earthquake Engineering Center for Mitigating Seismic Mega Risk" in Tokyo Institute of Technology supported by Japan Ministry of Education, Culture, Sport, Science, and Technology (MEXT).

References:

Ambraseys, N.N. (2001), "The Earthquake of 10 July 1894 in the Gulf of Izmit (Turkey) and Its Relation to the Earthquake of 17 August 1999", *Journal of Seismology*, Vol. 5, pp.117-128

Ürekli, F. (1999), *The 1894 Earthquake in Istanbul*, Ankara (in Turkish)

Çalık, S. (2003), *An Anonymous Diary about the Destructive Earthquake of 1894 in Istanbul*, Istanbul (in Turkish)

Ansal, A. and Güneş, A.M. (1990), "The 1894 Earthquake of Istanbul", *3rd International Workshop on Historical Earthquakes in Europe*, Prague, Czechoslovakia, pp.263-271

Morita, M. and Midorikawa, S., (2010), "Distribution of Building Damage in Istanbul during the 1894 Marmara Sea, Turkey, Earthquake", *Joint Conference Proceedings 7CUEE & 5ICEE*, 813-820

Öztin, F., (1994), *The Report of the 10 July 1894 Istanbul Earthquake*, Ankara (in Turkish)

European Seismological Commission: *European Macroseismic Scale 1998 (EMS-98)*, 1998.

JICA and IMM, (2002), *The Study on a Disaster Prevention / Mitigation Basic Plan in Istanbul Including Seismic Microzonation in the Republic of Turkey*.

IMM, (2007), *Microzonation Maps and Reports (South Section of European Side)*, http://www.ibb.gov.tr/tr-TR/SubSites/IstanbulVeDeprem/Calismalarimiz/Pages/AnaSayfa.aspx

Ministry of Public Works and Settlement, Republic of Turkey (1997), "Regulation on Construction in Disaster Areas", *Resmi Gazete*, No.23098 (in Turkish)

8CUEE CONFERENCE PROCEEDINGS
8th International Conference on Urban Earthquake Engineering
March 7-8, 2011, Tokyo Institute of Technology, Tokyo, Japan

A STUDY ON EXPECTED DISTRIBUTION OF LEAD TIME BY EARTHQUAKE EARLY WARNING IN JAPAN

Hidetoshi Yoshinari[1], Miho Ohara[2], and Kimiro Meguro[3]

1) Graduate Student, Dpt. of Civil Engineering, The University of Tokyo, Japan
2) Associate Professor, Institute of Industrial Science, The University of Tokyo, Japan
3) Professor, Institute of Industrial Science, The University of Tokyo, Japan
yoshinari@risk-mg.iis.u-tokyo.ac.jp, ohara@iis.u-tokyo.ac.jp, meguro@iis.u-tokyo.ac.jp

Abstract: The Japan Meteorological Agency (JMA) was started the public service of earthquake early warning (EEW) since October 1st, 2007. The 2008 Iwate-Miyagi Inland Earthquake on June 14, 2008 was the first case that EEW could be successfully broadcasted before the arrival of strong tremors. However, the warning could not be provided before strong tremors to some areas near the hypocenters. The number of earthquakes that EEW was announced since October, 2007 is too limited to evaluate the effectiveness of EEW properly. Therefore, in this research, using the data of the past earthquakes' occurred from 1923 to 2007, expected lead times before S-waves were analyzed based on the assumption that EEW system had been operated before those earthquakes. In addition, the effect of increasing seismometers in the future was also simulated. Based on the results obtained in both current and future cases, regional characteristics of expected lead times of EEW and their damage mitigation effect in each region were revealed, and future strategies for making the best use of EEW were discussed.

1. INTRODUCTION

It is said that seismic activity around Japan is increasing. Japan has a high probability of big earthquakes such as Tokyo Metropolitan Inland Earthquake with magnitude around 7, Tokai, Tonankai, and Nankai Earthquakes with magnitude 8 or more in the near future. The Japan Meteorological Agency (JMA) has launched earthquake early warning (EEW) system for the public since Oct. 1st, 2007. This is a new system that quickly analyses seismic wave data observed by seismometers near an epicenter and provides prompt alerts which may reach people before the arrival of strong tremors (S-waves).

The 2008 Iwate-Miyagi Inland Earthquake on June 14, 2008 was the first case since October 2007 that EEW could be successfully broadcasted before the arrival of S-waves. The warning was widely provided by television, the radio and mobile phones. At the earthquake, however, the warning could not reach before S-waves in some areas near the epicenters. This situation was regarded as a failure of EEW among the general public although it was due to technological limitation of EEW methods in case of inland earthquakes. After the earthquake, some mass media questioned the meanings of EEW and unfortunately, this led to negative understanding on effectiveness of EEW among some of the general public.

According to JMA, EEW had announced to the public 17 times. The number of EEWs which were succeeded in being available before strong tremor is limited. In addition, EEW for advanced users had announced 111 earthquakes until Octber 2010 since it started. These numbers are statistically too limited to decide the effectiveness of EEW. It is important to provide quantitative data about expected lead time that EEW could provide before future earthquakes in order to promote proper understanding on its merits and limitations.

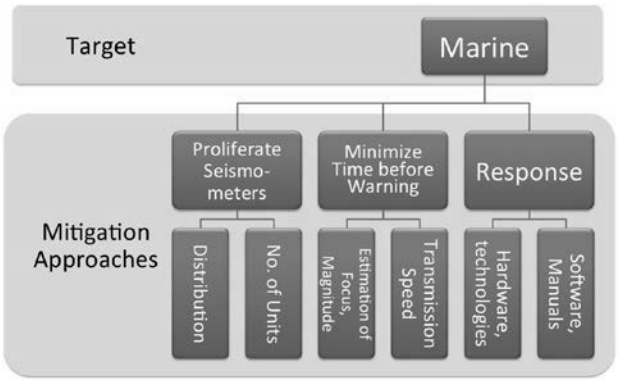


Figure 1 Target and Mitigation Approaches Considered in This Study

Technologies for announcing EEW are still renovating (Meguro, 2007). Figure 1 illustrates three approaches for making better use of EEW. The first approach is proliferation of seismometers, such as increasing the number of seismometers and densifing their network, which leads to

the prompt detection of an earthquake. The second is minimization of time before the warning, such as data transmissions and determination of a focus and magnitude of an earthquake. The last approach is response; in other words, how people can prepare for a strong tremor during lead times. Software approaches such as preparing manuals, are one part of the response. On the other hand, hardware approaches such as automatic response systems, play the other part.

In this study, using the past earthquakes occurred during 1923 to 2007, expected lead times before S-waves were analyzed on the assumption that the current EEW system had been operated before those earthquakes. According to the results, regional characteristics of expected lead times of EEW and their damage mitigation effect were revealed. In addition, the effect of increasing seismometers such as Ocean-bottom seismometers or Hi-Net by National Research Institute for Earth Science and Disaster Prevention (NIED) in the future was also simulated. Considering the results obtained in both current and future cases, future strategies for making the best use of EEW were discussed.

2. METHOD FOR CALCULATION

2.1 Data of Earthquakes Used

In this rstudy, data of 62,127 earthquakes with magnitude 4 or more occurred during 1927 to 2007 listed in "Report on Earthquakes and Volcanoes (Catalog)" by JMA was used. The number of earthquakes that EEW was announced since October, 2007 is too limited to evaluate the effectiveness of EEW properly. Then, the data of the past earthquakes was used in order to understand expected lead times that could be provided by EEW in future earthquakes.

Table 1 The Number of Earthquakes for Calculation

Year	M4	M5	M6	M7	M8	Total
1923–1966	6,505	2,673	620	348	7	10,153
1967–1980	4,637	1,496	287	83	5	6,508
1981–1990	5,911	3,607	459	12	0	9,989
1991–2000	13,660	6,772	657	22	1	21,112
2001–2007	9,074	4,799	482	28	2	14,385
Total	39,787	19,347	2,505	493	15	62,147

2.2 Locations of Seismometers

JMA uses 205 seismometers for providing initial alert of EEW as of November 2010. According to JMA, 774 seismometers of Hi-Net by National Research Institute for Earth Science and Disaster Prevention (NIED) are currently used only to double-check the location of the estimated hypocenter and the magnitude of a coming earthquake. Figure 2 shows the distribution of 205 JMA seismometers, and Fig. 3 shows that of Hi-Net. In the chapter 3, locations of JMA seismometers were used. The fourth chapter simulated the effect of increasing seismometers and 774 seismometers of Hi-Net were used for the calculation.



Figure 2 Distribution of JMA Seismometers



Figure 3 Distribution of Hi-Net Seismometers

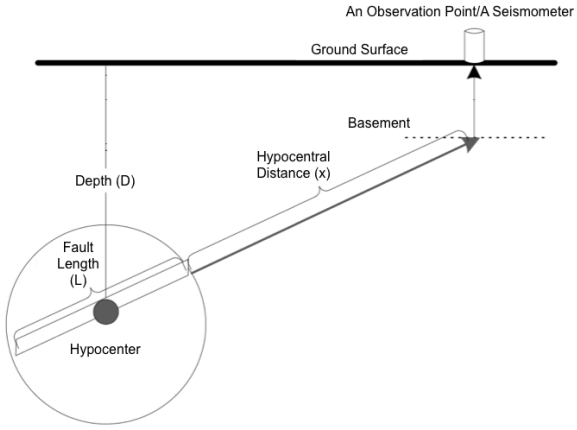
2.3 Method for Estimating Lead Time and Seismic Intensity

Japan has 47 prefectures and totally 1955 local municipalities under prefectures. This research estimated lead times and expected seismic intensities of the 62,147 past earthquakes at 1,955 local municipality offices all over Japan based on the assumption that EEW had been operated before those earthquakes. We regard the locations of 1955 local municipality as observation points. The procedure for estimation is same as the method currently used by JMA (2010).

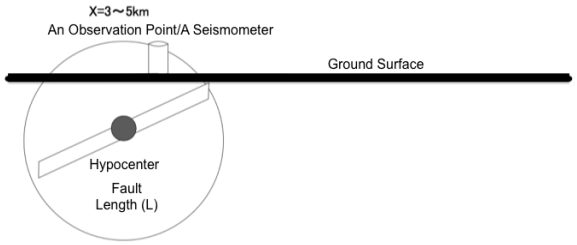
When an earthquake occurs, seismometers near its hypocenter detect ground vibration, and the location of hypocenter is estimated by using the data observed by these seismometers. Figure 4 illustrates a model of obtaining the distance between a hypocenter and the nearest seismometer or an observation point. The distance was calculated using equations, eqs. (1) to (9). Here, all the seismometers were assumed to be located at the ground surface because their depth was negligible for obtaining the distance to the hypocenter. Hypocenters were treated as fault planes as shown in Fig. 4 (a). In case that half of the fault length was longer than the distance between the hypocenter and an observation point / the nearest station, the distances were set

to be 3km as shown in Fig. 4 (b).

Next, expected times for P-wave to travel to the nearest seismometer and for S-wave to strike each observation point were calculated. Based on these time differences, lead time provided by EEW before the arrival of S-wave at the observation point was obtained. In the real procedure for announcing EEW, analysis for estimating the hypocenter takes several seconds, but this time lag was not considered in this paper in order to estimate the maximum effectiveness of EEW. The velocities of P-wave and S-wave varying according to depth level were used following the table by JMA.



(a) Case Where Distance Between An Observation Point / A Seismometer Is Smaller Than A Half of Fault Length



(b) Case Where Distance Between An Observation Point / A Seismometer Is Bigger Than A Half of Fault Length

Figure 4 Calculation Model for Deciding The Distance Between A Hypocenter and An Observation Point / The Nearest Station

$$a = \cos\phi \cdot \cos\theta \quad (1)$$

$$b = \cos\phi \cdot \sin\theta \quad (2)$$

$$c = \sin\phi \quad (3)$$

$$d = \cos\phi' \cdot \cos\theta' \quad (4)$$

$$e = \cos\phi' \cdot \sin\theta' \quad (5)$$

$$f = \sin\phi' \quad (6)$$

$$x = \sqrt{\{R \cdot \arccos(a \cdot d + b \cdot f + c \cdot e)\}^2 + D^2} - L/2 \quad (0 \le x) \quad (7)$$

$$x = 3 \quad (x < 0) \quad (8)$$

$$\log L = 0.5M - 1.85 \text{ (Utsu: 1977)} \quad (9)$$

θ, ϕ: Latitude, Longitude (rad), D: Depth(km), R: Radius (km), x: Minimum distance to fault(km), L: Length of fault

Then, expected seismic intensities at 1955 local municipality in case of the 62147 past earthquakes were calculated using equations of eqs. (10) to (13).

$$M_w = M_{JMA} - 0.171 \quad (10)$$

$$\log(PGV_{600}) = 0.58M_w + 0.0038D - 1.29 - \log(x + 0.028 \cdot 10^{0.50M_w}) - 0.002x \quad (11)$$

$$PGV = ARV_i \cdot PGV_i (= ARV_i \cdot 0.90 \cdot PGV_{600}) \quad (12)$$

$$I_{INSTRA} = 2.68 + 1.72\log(PGV) \pm 0.21 \quad (4 < I_{INSTRA} < 7) \quad (13)$$

M_w: Moment magnitude, M_{jma}: JMA magnitude, PGV_{600}: Maximum velocity at engineering bedrock (S-wave velocity is 600 m/s), PGV_i: Maximum velocity at land surface, ARV_i: Amplification factor between land surface and 30m depths

2.4 Method for Evaluating Damage Mitigation Effects

In Japan, earthquakes are categorized to 2 types; inland and marine earthquakes according their location of epicenters as described in Fig.1. As for increase of inland earthquakes, lead times are generally small because time lags between S-wave and P-wave are expected to be short. On the other hand, lead times of marine earthquakes whose epicenters are in the ocean might be much longer. Therefore, this research treats these two earthquake types separately.

This research estimated lead times and expected seismic intensities of the 62,147 past earthquakes with magnitude 4 or more at 1,955 local municipality offices in Japan. These results were summarized to the number of earthquakes in each prefecture according to the expected lead times and seismic intensities. The past earthquakes included both marine and inland earthquakes. The trends of expected lead time in both marine and inland earthquake types in each prefecture were analyzed. Moreover, regional characteristics of expected lead times of EEW and their damage mitigation effect were evaluated in each prefecture.

As mentioned in the chapter 1, proliferation of seismometers is vital for EEW improvement. Since only 205 seismometers are currently used for the initial alert of EEW, the distance between a hypocenter and a seismometer might be long in some area. This possibly causes a late detection of a future earthquake. If seismometers are proliferated, lead time generally increases because of the minimization of the distance. This research clarified the effectiveness of the proliferation of seismometers. The cases,

in which the number of seismometers was increased and their network was densified, were simulated. Comparing the results of these cases with the current situation, the effectiveness of lead times was evaluated.

3. ANALYSIS OF EXPECTED LEAD TIME OF EEW AT PAST EARTHQUAKES

In this chapter, lead times for the past earthquakes during 1923-2007 were analyzed based on the assumption that EEW had been operated before those earthquakes.

3.1 Expected Lead Time Distribution of EEW in Each Prefecture

The lead times and seismic intensities of EEW at the past earthquakes were calculated at 1,955 local municipality offices as explained in the chapter 2. Outcomes of calculations for municipalities in one prefecture were added up to be data of one prefecture. When several municipalities in one prefecture record shaking at an earthquake, the largest seismic intensity among the municipalities and its corresponding lead times were plotted on the figure. Figure 5 shows the distribution of the expected lead times in Kanagawa Prefecture. The horizontal axis means lead time, and the vertical axis shows the cumulative numbers of earthquakes whose lead times are more than the value on the horizontal axis. Cumulative curves for expected lead times were plotted according estimated seismic intensities from 4 to 7. The negative value of the horizontal axis infers that S-wave strikes before an EEW announcement. The seismic intensity 4(a) means the curve for EEW whose seismic intensity is simply estimated 4. The seismic intensity 4(b) means the curve whose maximum intensity outside the prefecture is 5- or more although the intensity inside that prefecture is 4.

3.3 Analysis on Regional Characteristics of Expected Lead Time of EEW

Japan is surrounded by 4 plates. Distances from ocean trenches could affect regional characteristics of the expected lead times in each prefecture differently. According to the expected lead times in each prefectures, 47 prefectures were classified into four typical types; Kanagawa, Iwate, Nagano, and Hokkaido's types.

First, Kanagawa type has relatively long lead times among all the prefectures. The cumulative number of earthquakes moderately decreased according to the length of lead time as shown in Fig.5 because the effect of marine earthquakes with long lead times was more strongly

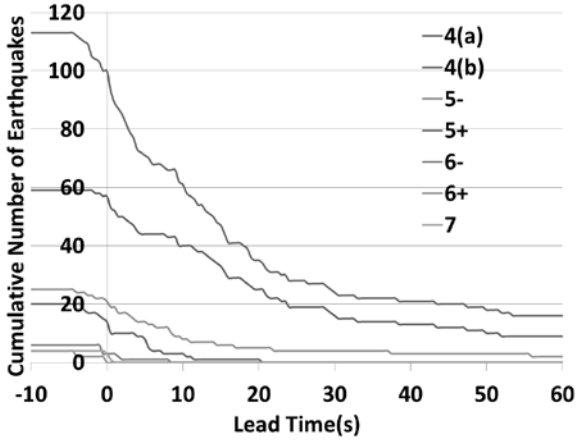


Figure 5 Expected Distribution of Lead Times in Kanagawa Prefecture

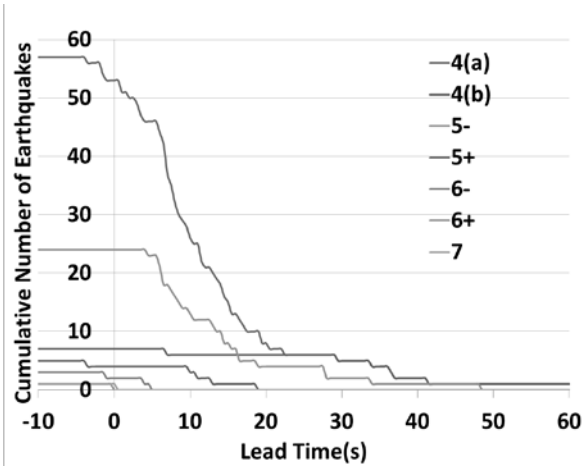


Figure 6 Expected Lead Times of EEW in Iwate Prefecture

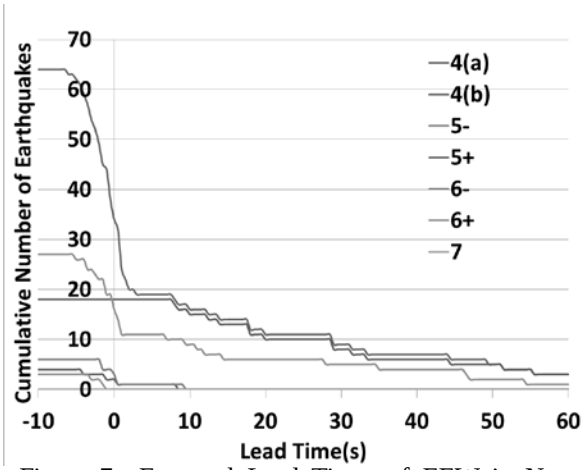


Figure 7 Expected Lead Times of EEW in Nagano Prefecture

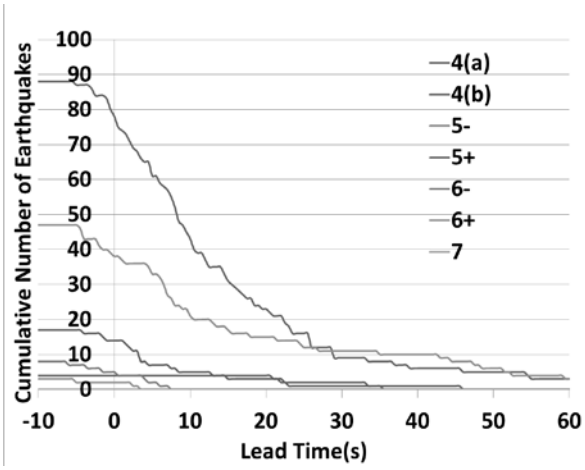


Figure 8 Expected Lead Times of EEW in Hokkaido Prefecture

reflected than that of inland earthquakes. Yamanashi, Osaka, Mie and Tokushima Prefectures were similar to this type. Osaka had longer lead times in case of inland earthquakes because of soft surface soils below Osaka area led to big seismic intensity at remote earthquakes with big magnitude. In this case, much longer lead time could be provided to respond against the coming shaking.

Second is Iwate type. Its expected lead times are not as long as Kanagawa type because Iwate prefecture is located near trenches. As shown in Fig.6, the cumulative number of earthquakes rapidly decreased as lead time was between 0 to 10 seconds. Fukushima Prefecture was also classified in the same type because curves of the lead time less than 20 seconds were especially similar to Iwate type. In prefectures with these characteristics, damage mitigation approaches within 10 seconds should be arranged.

Third is Nagano type. In this case, long lead time can not be expected as shown in Fig.7 because of frequent occurrence of inland earthquakes. In fact, 90 were inland earthquakes while the total number of earthquakes affecting Nagano Prefecture was 104; about 87% of the earthquakes with seismic intensities 4 or more were inland types in this area. Therefore, the curves dropped drastically around lead time 0 second because hypocenters were too close to the observation points. Consequently, damage mitigation approaches including automatic response systems, which are possibly applicable with in seconds, are extremely necessary to cope with these inland earthquakes. On the other hand, the gently decreasing line after that drop indicates this type also has long lead times in case of large earthquakes which occurred far away.

Finally, fourth is Hokkaido type. Because there is enough distance from trenches and troughs to obtain long lead time of EEW, the curves of this type moderately decreased from the top at lead time 0 second as shown in Fig.8. 113 of total 163 earthquakes which recorded seismic intensities 4 or more, occurred in ocean area, and the most of them had long lead times such as 30 seconds or more. All of the earthquakes with seismic intensities 5- were located at the boundary between North America plate and Eurasian plate. This characteristics show the effectiveness of damage mitigation approaches taking 10 seconds or more.

4 EVALUATION OF EFFECT OF USE OF MORE SEISMOMETERS FOR EEW

4.1 Effect of Use of Ocean-Bottom Seismometers

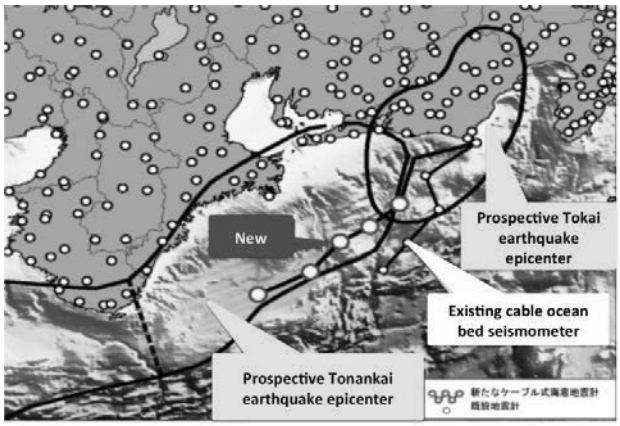
Table 3 Locations of Ocean-Bottom Seismometers

Seismometers Name	North Latitude	East Longitude	Altitude
TT1OBS	33.62	136.78	−2068m
TT2OBS	33.73	137.03	−2100m
TT3OBS	33.86	137.40	−1000m
TT4OBS	34.01	137.54	−1836m
TT5OBS	34.25	137.72	−1019m

In October 2008, JMA started to operate extra 5 ocean-bottom cable seismometers in Tokai and Tonankai area. In this section, the effect of using new 5 ocean-bottom seismometers in addition to the existing 205 seismometers was evaluated. Table 3 and Figure 9 show the locations of new ocean-bottom seismometers reported by JMA (2008).

Installing ocean-bottom seismometers aimed to increase lead times of EEW at the future earthquakes. In order to evaluate these effects, an index "E" was proposed to quantify the increase of lead time by using new ocean-bottom seismometers. It corresponds to the difference of the total area of lead time curves with/without ocean-bottom seismometer. Here, curves $f(t)$ of lead times in expected lead times figures were used.

Figure 9 Locations of Ocean-Bottom Seismometers



$$E = A - A_0 \tag{14}$$

$$A = \int f(t)dt \tag{15}$$

A_0: Area of lead time curves with the current systems without ocean-bottom seismometer, A: Area of lead time curves with ocean-bottom seismometers.

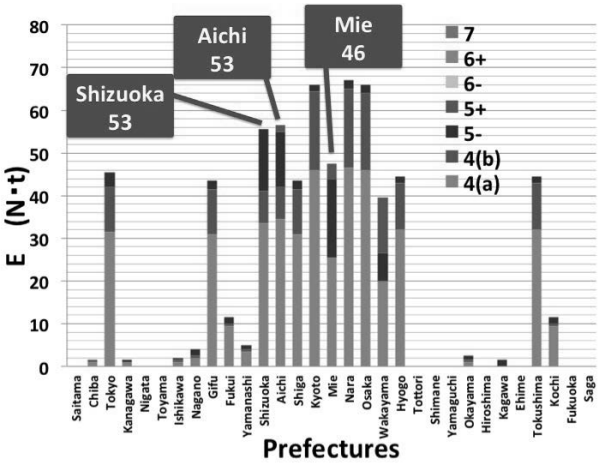


Figure 10 E Value in Each Prefecture with Ocean-Bottom Seismometers

Figure10 shows the value of index E for each prefecture in case that the ocean-bottom seismometers were used in addition to the current JMA ones. In the prefectures

near by Nankai Trough such as Shizuoka, Aichi, and Mie, the values of E were big especially with the seismic intensity 5- or more. Since these prefectures have shorter distance from the trough than the other prefectures, installing ocean-bottom seismometers is expected to have positive effect against strong earthquakes. Figure 11 shows the relationship between expected seismic intensities and the growth of the lead time that were achieved at the earthquakes by using ocean-bottom seismometers in Shizuoka Prefecture. In Fig.11, the total number of earthquakes with intensity 5- is 13, which is almost same as the other prefectures whose values of E were high. The highest growth of lead times by installing ocean-bottom seismometers was over ten seconds at the earthquake whose expected intensity in Shizuoka was 5-. Compared to the lead time growth in Mie as shown in Fig.12, most dots only slide to the right because of the distance decay with seismic intensities. Both prefectures are suffered from the 1944 Tonankai earthquake and the 1946 Nankai earthquake. These earthquakes were magnitude 7.9 and 8.0. However, both figures do not show the lead time growth in these earthquakes because added ocean-bottom seismometers are not so critically near by the epicenters of these two earthquakes.

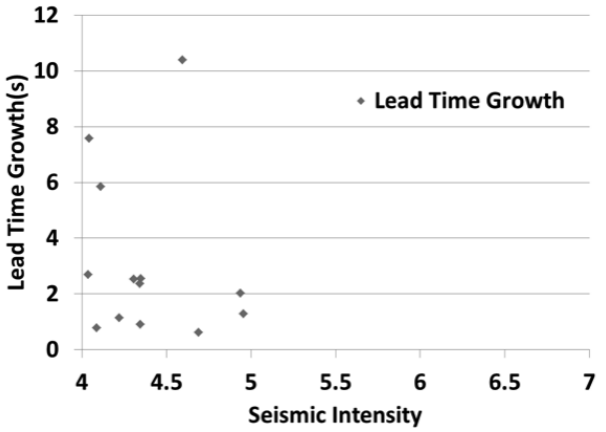


Figure 11 Lead Time Growth in Shizuoka

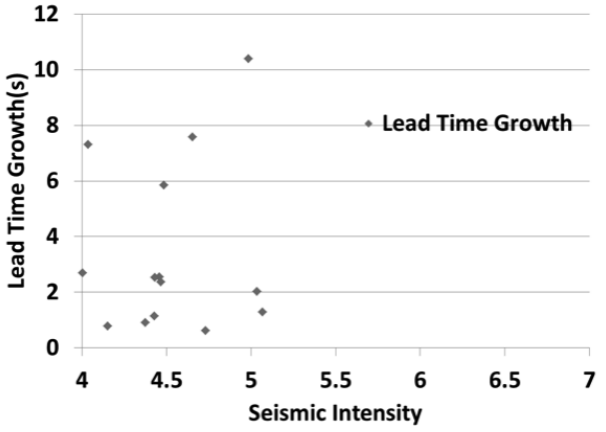


Figure 12 Lead Time Growth in Mie

4.2 Effect of Using Hi-Net

In this section, the effect of use of Hi-net was evaluated. Hi-Net has 774 seismometers operated by NIED. Index E for each prefecture was calculated by eqs.(14) and (15) in case that Hi-Net was used in addition to 210 seismometers including JMA and ocean-bottom seismometers.

Proper response to EEW is different according to the lead times available. If lead time before S-wave is few seconds, only automatic response systems could reduce the damage due to a coming earthquake. For example, automatic system for protecting important facilities, shutting down gas supply, stopping transportation systems, etc. could be effective. If about 10 seconds is provided as lead time, there is possibility for people to take some actions to protect themselves. As the lead time increase to be more than 10 seconds, more complicated actions for protecting properties and people become possible. Installing more seismometers aims to increase lead time at the future earthquakes. Increasing short lead time might have more impact than increasing long lead time; for example, growth of lead time from 0 to 5 seconds could be more meaningful than that of lead time from 30 to 35 seconds. It implies that the meaning of index E could be different according to the lead time. Then, three types of index E were proposed to understand the detail impact by installing new seismometers. They are $E_{0\text{-}5}$ that corresponds to the change of lead time curve during 0-5 seconds, $E_{0\text{-}10}$ during 0-10 seconds, and $E_{10\text{-}}$ during the lead time more than 10 seconds. The lead time is more demanded than the one of longer lead time.

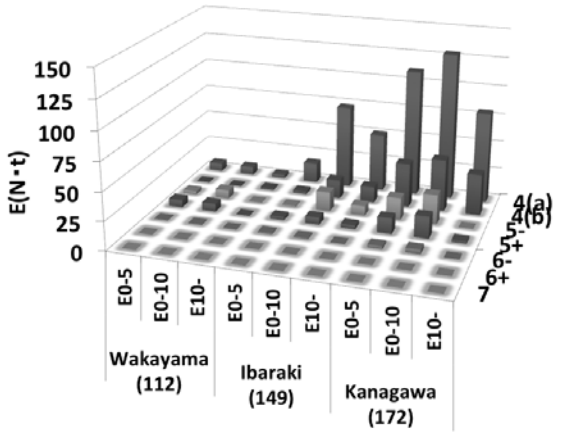


Figure 13 E Value in Wakayama, Ibaraki, Kanagawa with Hi-Net

Index $E_{0\text{-}5}$, $E_{0\text{-}10}$, and $E_{10\text{-}}$ for each prefecture were calculated in case that Hi-Net was used in addition to 210 seismometers including JMA and ocean-bottom seismometers. As a result, three typical types were observed; Kanagawa, Ibaraki, and Saitama types. Figure 13 shows the value of Index $E_{0\text{-}5}$, $E_{0\text{-}10}$, and $E_{10\text{-}}$ of three prefectures according to the seismic intensity. The numbers of total earthquakes in each prefecture are shown in the parentheses under prefecture names.

First, the Kanagawa type shows high $E_{0\text{-}5}$ and $E_{0\text{-}10}$; especially, $E_{0\text{-}5}$ was high enough to dominate the high percentage of $E_{0\text{-}10}$. It is said that use of Hi-Net will provide more opportunities whose lead times are 0 to 5 seconds.

These trends were observed not only for the earthquakes with intensity 4 but also for the earthquakes with seismic intensity 5- or more. In Kanagawa Prefecture, adding Hi-Net to the current EEW network was considered highly beneficial because it could totally achieve big growth of indexes E. Considering future use of Hi-Net, implementation of automatic response system had better be promoted in order to make better use of expected lead time.

Second, Ibaragi type shows the characteristics that $E_{0\text{-}10}$ and $E_{10\text{-}}$ are high instead of $E_{0\text{-}5}$. Use of Hi-Net will provide more opportunities whose lead times are more than 5 seconds. In order to use the benefit of Hi-Net, software approaches including human response might be effective as well as hardware approaches.

Third, Wakayama type has low value in each indexes E. The result shows that Hi-Net does not generally affect the lead time 0 to 60 even though the total number of earthquakes is 62. Therefore, the proliferation of seismometers needs more investigation on where to install, otherwise damage mitigation approaches can not improve.

In this chapter, index E evaluated the effect of increasing the lead time by using ocean-bottom seismometers or Hi-Net. In order to understand the effect of proliferations of seismometers, referring to both the expected lead time distribution and the value of index E is necessary. Based on the effect of installing Hi-Net on EEW damage mitigation approaches suitable for each prefectures were proposed in this section.

5. CONCLUSIONS

In this study, expected lead times of EEW were analyzed using the past earthquakes during 1923 to 2007 based on the assumption that EEW had been operated before those earthquakes. Based on the results obtained in the study, regional characteristics of expected lead times and their damage mitigation effects were revealed.

In addition, method for evaluating the effect of use of more seismometers was proposed defining three kinds of indexes E. Not only the currently-used 205 JMA seismometers, but also 5ocean-bottom seismometers and Hi-Net ones were taken into account for estimation. Finally, approaches to make suitable strategies for each area reflecting the characteristics of expected lead times were proposed.

At first, there are mainly four types in expected lead times with the current 205 JMA seismometers. Kanagawa and Hokkaido types expectedly have long lead times and are able to plan damage mitigation approaches sparing long time. However, in a hand, Kanagawa type does not suffer from earthquakes with intensity 5- or more. On the other hand, Hokkaido type has many 5+ earthquakes. On the contrary, both Iwate and Nagano types show shorter lead times even if each of them suffers from each type of earthquakes; inland and marine. In prefectures with these characteristics, damage mitigation approaches which are applicable within seconds should be considered.

Second, the effectiveness of ocean-bottom seismometers was analyzed using index E. Prefectures near by Nankai trough benefitted from these additional seismometers. Especially Shizuoka, Mie, and Aichi were so affected by these seismometers that they could maintain 10 seconds or more lead time growth.

Third, the effect of Hi-Net installing to EEW were studied. In this case, index E are taken apart to three; $E_{0\text{-}5}$, $E_{0\text{-}10}$, $E_{10\text{-}}$. Depending on the amount of indexes E, the effectiveness on expected lead times in the future was analyzes, and strategies considering this prospect were mentioned in this study.

Acknowledgements:

The authors acknowledge the Japan Meteorological Agency (JMA) for providing data of the past earthquakes as well as National Research Institute for Earth Science and Disaster Prevention (NIED) for Hi-Net data.

References:

Japan Meteorological Agency. (2008). “Hello! This is JMA!”. 4 Jan. 2011. http://www.jma.go.jp/jma/kishou/jma-magazine/0811/index.html

Japan Meteorological Agency. “Information of EEW service,” JMA Home Page. 19 Nov. 2010. http://www.seisvol.kishou.go.jp/eq/EEW/kaisetsu/joho/joho.html

Japan Meteorological Agency. “About The Number of EEW Announces,” JMA Home Page. 12 Dec. 2010. http://www.seisvol.kishou.go.jp/eq/EEW/kaisetsu/kensuu.pdf

Japan Meteorological Agency, Dep. of Earthquakes and Volcanoes, Administrative Division, Information Control. (2010). “Report of Earthquakes and Volcanoes (Catalog)” Chiyoda, Tokyo, Japan.

Meguro, K., Yukio Fujinawa. (2007). “緊急地震速報−揺れる前にできること-“ Tokyo Horei Syuppan.

Japan Meteorological Agency. (2008). “A Technical Reference about General Information of Earthquake Early Warning and Processing Method.” JMA Home Page. 12 Dec. 2010. http://www.seisvol.kishou.go.jp/eq/EEW/kaisetsu/Whats_EEW/reference.pdf

8CUEE CONFERENCE PROCEEDINGS
8th International Conference on Urban Earthquake Engineering
March 7-8, 2011, Tokyo Institute of Technology, Tokyo, Japan

AN AUTOMATED DECISION-MAKING SYSTEM FRAMEWORK FOR EARTHQUAKE EARLY WARNING SYSTEM APPLICATIONS

Stephen Wu[1], James L. Beck[2]

1) Graduate Student, Division of Engineering and Applied Science, California Institute of Technology, USA
2) Professor, Division of Engineering and Applied Science, California Institute of Technology, USA
stewu@caltech.edu, jimbeck@caltech.edu

Abstract: Earthquakes are one of the most unpredictable natural hazards but recently short-lead-time Earthquake Early Warning Systems (EEWS) have become practical with a system operating in Japan and another planned for operation in California in the next year or two. A few seconds to a minute or so of early warning is achievable. For example, if appropriate, an early warning can be broadcast to enhance the effectiveness of evacuations, water and gas supplies can be temporarily cut off, and other more advanced engineering applications may also be developed. Due to the limited warning time and the uncertainty of the information from an EEWS, applications that require real-time human decision-making are not practical. This motivates recent research to develop a robust automated rapid decision-making procedure for mitigation actions. A rational procedure is to initiate a potential loss-reduction action if, based on the incoming information from an EEWS, the expected loss from taking no action is greater than the expected loss from taking the mitigation action. To estimate the expected loss of a predicted event, it is proposed to use the recently developed PEER performance-based earthquake engineering methodology.

1. INTRODUCTION

Due to the high uncertainty of the stress and strength distributions within the tectonic plates on Earth, earthquakes are one of the most unpredictable natural hazards. Accurate prediction of when an earthquake will happen is still not possible, but the concept of earthquake early warning can be achieved because of the rapid development of computing power and network communication. *Earthquake Early Warning Systems* (EEWS) have been operating in several different regions. Japan has a long history of earthquake monitoring: Urgent Earthquake Detection and Alarm System (UrEDAS) of the Japan Railway Group is one of the first applications of EEWS and now most regions in Japan are covered by a public warning broadcast network operated by the Japan Meteorological Agency (JMA) (Allen et al. 2009b, Doi 2000, Yamazaki and Meguro and Noda 1998). In Mexico, warnings are issued to the general public as well. In Taiwan, Istanbul and Bucharest, warnings are released to one or more users outside the research community (Allen et al. 2009b). Currently, an EEWS, called the California Integrated Seismic Network (CISN) ShakeAlert System, is also under testing in California, USA.

Early warning systems are usually based on P-wave detection that exploits the slower transmission velocity of S-waves, the main destructive wave, relative to electronic signals and P-waves. Comparing to other natural hazard early warning systems, the main challenge of EEWS is the extremely short *lead time*, defined as the time elapsing between the moment when the occurrence of a catastrophic shaking event at a given location is known to be reasonably certain to occur and the moment it actually occurs (Gasparini et al. 2007). Therefore, it is necessary to develop an *Automated Decision-making System* (ADS), which can make fast rational decisions based on the information from an EEWS. Here, we use expected economic loss as a basis for rational decision-making, and the *Pacific Earthquake Engineering Research Center* (PEER) *Performance-Based Earthquake Engineering* (PBEE) methodology (Porter 2003) is used for seismic loss estimation during the decision process. However, due to the complexity of the methodology, such a decision process suffers from long computation times. In order to obtain a fast ADS framework, the concept of *Action Function* and *Surrogate Model* are utilized in this paper. Combining all these ideas, a complete ADS framework is presented.

2. BACKGROUND

2.1 Brief Overview of EEWS in California, USA

The CISN ShakeAlert System, as currently planned, combines the outputs of three early warning systems each based on a different theory: τ_c-P_d on-site algorithm, Earthquake Alarms Systems (ElarmS), and Virtual Seismologist (V-S) (see Fig.1). The τ_c-P_d on-site algorithm is based on observations from a single sensor with two key parameters: period parameter τ_c and high-pass filtered

displacement amplitude P_d. Vertical components of velocity and/or displacement data within the first three seconds window of P-waveforms is used to determine both parameters (Bose et al. 2009). On the other hand, ElarmS and V-S are regional network-based EEWS. ElarmS's earthquake location estimation is mainly based on a grid search to minimize arrival time residuals when there are more than 2 sensors triggered in the network. Its magnitude estimation relies on the amplitude and frequency content of the detected P-wave. Acceleration, velocity, displacement and predominant period (Allen and Kanamori 2003) are continuously determined from the vertical component of P-waves from all stations (Allen et al. 2009a). The V-S algorithm is based on a Bayesian method, which combines prior information with a likelihood function to narrow down the uncertainties. The V-S location estimation uses Voronoi Cells with a probabilistic approach. Its magnitude estimation relies on an attenuation model that is based on P-wave and S-wave envelopes (Cua and Heaton 2007). The likelihood function is formulated in terms of the attenuation model, while prior information, such as network topology, station health status, regional hazard maps, earthquake forecasts, etc., may be utilized to construct the prior probability density function (PDF). The PDF for the earthquake magnitude is then found by combining both likelihood function and prior PDF using Bayes' Theorem (Cua et al. 2009).

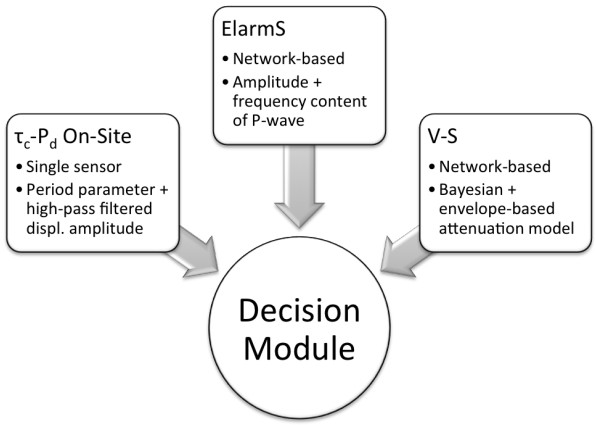


Figure 1 Structure of CISN Shake Alert System

All three systems receive data from the same CISN seismic network. Once a station is triggered within the network, each system will run its own algorithm to produce PDFs of earthquake magnitude and location estimation based on the received data signals. Then, all results will be integrated in a centralized module, called the Decision Module (Fig.1), which will produce a PDF for earthquake magnitude and location estimates based on the PDFs from all three systems.

2.2 Importance of ADS for Applications of EEWS

A few seconds to a minute of early warning can provide significant benefits to society. For example, through broadcasting an early warning of an earthquake, the efficiency of evacuation of at-risk structures or hazardous locations can be enhanced. Also, an automated action can be taken to mitigate the impending earthquake's impact on society, such as temporarily cutting off water and gas supplies. However, we believe that the true power of EEWS will only be achieved through more sophisticated engineering applications, which in many cases will involve mitigation actions that have significant resulting costs, including significant downtime losses caused by interference with normal operations. The decision of whether to activate such a mitigation action is a complicated tradeoff problem which, if time allowed, would best be done by human decision-making. Unfortunately, due to the limited warning time and the uncertainty in the predictions from EEWS, applications that involve human decision-making are not practical. Therefore, it is important to develop a decision-making system that can make rational decisions given uncertain predictions, as well as to make fast enough decisions in order to maximize available lead time for responding to the warning from the EEWS. This motivates the research presented here to develop a general framework of ADS. By using ADS, the utility of EEWS may be extended to cover a broader range of engineering applications. Hence, the impact of future large-scale earthquakes to society can be mitigated.

3. ADS FRAMEWORK

A decision is usually made between available choices by balancing different tradeoffs from the consequences of the choices. For EEWS applications, the automated system must choose whether to take mitigation actions or not based on a pre-determined criterion. In the simplest situation, the alternatives are **To Take Action** or **Not To Take Action**. Taking an action often leads to some kind of interruption to the operation of the facility, business or society, while not taking an action induces a risk of hazardous losses. To compare possibly disparate consequences, they need to be converted into a single metric, called here a *Decision Variable* (DV). Once we have a consistent metric for tradeoff comparisons, a rational decision-making procedure can be based on comparing the expected values of the DV, conditional on the EEWS data, for the two cases: action taken and action not taken. The decision criterion can be specified mathematically:

If smaller values of the chosen metric DV are preferred (i.e. it measures a negative/harmful event, such as economic loss or structural damage):

$$Take\ Action\ if\quad E_{\overline{A}}[DV|D(t)] \geq E_A[DV|D(t)] \quad (1)$$

If larger values of the chosen metric DV are preferred (i.e. it measures a positive/beneficial event, such as economic savings or structural damage avoidances):

$$Take\ Action\ if\quad E_{\overline{A}}[DV|D(t)] \leq E_A[DV|D(t)] \quad (2)$$

where:

$E_a[X|Y]$: $Expected\ value\ of\ X\ given\ Y\ for\ case$ "a"

$D(t)$: $Data\ from\ EEWS\ as\ a\ function\ of\ time\ (t)$

a: $\overline{A}\ or\ A$; $\overline{A}$: $Action\ not\ taken$; A: $Action\ taken$

3.1 Calculation of the Expected Values

Depending on the complexity of the mitigation actions in an EEWS application, the calculation of expected DV values may be difficult. In order to illustrate the complexity of the problem, a commonly used DV, economic loss, is chosen. Economic loss is a very suitable metric in many cases because it is able to quantify different types of losses. It is also the DV in the PEER PBEE methodology, as shown in Fig.2.

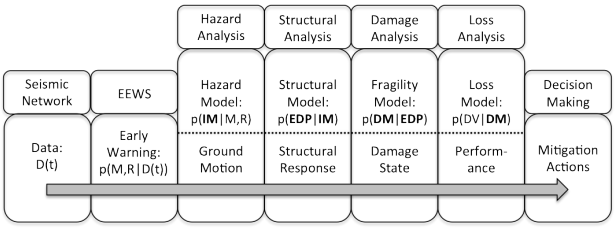


Figure 2 Information flow of PBEE-based EEWS (Grasso, Beck and Manfredi 2007)

In this figure, M and R are the magnitude and site-to-event distance of the incipient earthquake; **IM** is the ground shaking intensity measure; **EDP** is a vector of engineering demand parameters, and **DM** is a damage state measure for all the vulnerable components in the structure. Typical probability models for each analysis stage can be found, for example, in Goulet et al. (2007).

Using the PBEE methodology, the expected economic loss (denoted as DV in the following) can be calculated with the integral form as shown below (Goulet et al. 2007):

$$E_a[DV|D(t)] = \int DV\, p_a(DV|\boldsymbol{DM})\, p_a(\boldsymbol{DM}|\boldsymbol{EDP}) \ldots p_a(\boldsymbol{EDP}|\boldsymbol{IM}) p(\boldsymbol{IM}|M,R) p\big(M,R\big|D(t)\big) \ldots dDV d\boldsymbol{DM} d\boldsymbol{EDP} d\boldsymbol{IM} dM dR \quad (3)$$

Here, $p_a(x|y)$ denotes the PDF of x given y for case "a". Once all the PDFs are obtained from the models shown in Fig.2, the expected loss for both cases $\overline{A}$ and A are found. Then, a decision can be made based on (1) or (2).

Even though there is an explicit expression for calculating $E_a[DV|D(t)]$, there remains an important challenge for practical usage. Since it is not possible to analytically evaluate the integral for most practical applications, a numerical integration scheme that may require heavy computing power is necessary. As a result, the real-time decision-making process may not be fast enough for EEWS purpose. To solve this problem, the concepts of *Action Function* (AF) and *Surrogate Model* are introduced.

3.2 Action Function and Surrogate Model

In order to shorten the computational time for real-time decision-making, most parts of the expected loss calculation may be pre-calculated and stored in a computationally efficient form. This can be done by introducing the Action Function and a surrogate model. Let us first re-write (3) in a more compact form:

$$E_a[DV|D(t)] = \int E_a[DV|M,R]\, p(M,R|D(t)) dM dR$$

where

$$E_a[DV|M,R] = \int DV\, p_a(DV|\boldsymbol{DM})\, p_a(\boldsymbol{DM}|\boldsymbol{EDP}) \ldots p_a(\boldsymbol{EDP}|\boldsymbol{IM}) p(\boldsymbol{IM}|M,R) dDV d\boldsymbol{DM} d\boldsymbol{EDP} d\boldsymbol{IM}$$

is to be pre-computed. Define the Action Function (AF) by:

$$AF = E_{\overline{A}}[DV|M,R] - E_A[DV|M,R] \quad (4)$$

then from (1) and (2), the new form of the decision criterion becomes:

If smaller values of the chosen metric DV are preferred:

$$\text{Take Action if and only if} \quad E[AF|D(t)] \geq 0 \quad (5)$$

If larger values of the chosen metric DV are preferred:

$$\text{Take Action if and only if} \quad E[AF|D(t)] \leq 0 \quad (6)$$

where $E[AF|D(t)] = \int AF(M,R) p\big(M,R\big|D(t)\big) dM dR$

Note that AF in (4) can be pre-determined from the four probability models shown in Fig.2 because it is not related to real-time information from the EEWS. Therefore, all of the integrals giving AF can be pre-calculated so that AF(M,R) can be approximated by a surrogate model, thereby increasing the efficiency of calculating E[AF|D(t)]. It is expected that the EEWS in California will quantify the uncertainty in the predicted magnitude and location estimates by a Gaussian PDF p(M,R|D(t)), so we have chosen to use Gaussian radial kernel functions as a basis for a surrogate model for AF. Since both AF(M,R) and p(M,R|D(t)) have a Gaussian form, their product also has a Gaussian form and thus its integral can be written in an analytical form. The surrogate model regression scheme is chosen to be the relevance vector machine (RVM) because of its ability to provide a sparse and accurate regression model (Tipping 2001 and 2004, Tipping and Faul 2003, Bishop 2006). As a result, an efficient analytical form for E[AF|D(t)] can be obtained that significantly speeds up the real-time decision-making process.

3.3 ADS Framework Summary

Let us consider a simple EEWS application that contains only one mitigation action on a target structure/system. First, based on the PEER PBEE methodology, the Action Function is pre-calculated and approximated by the RVM using a Gaussian radial kernel basis. Next, as the EEWS starts to feed in earthquake estimates to ADS, E[AF|D(t)] is rapidly calculated as described above. An automated decision is then made based on (5) or (6) depending on the chosen DV, as well as the action time constraint:

Take back-up action or no action when $t_{left} < 0$

where $t_{left} = t_{EEWS} - t_{ADS} - t_{Act}$

t_{EEWS} = *remaining lead time from EEWS*

t_{ADS} = *average decision-making time delay*

t_{Act} = *time required to complete action*

The above time constraint checks if the remaining time is enough for completing the target mitigation action. If not,

then either no action is taken or, if there exists one, the back-up action is taken which is not as effective as the principal mitigation action but that can be implemented in sufficient time. Fig.3 shows a summary of the structure of the ADS framework. For more complicated applications, such as multiple mitigation actions, this framework can be extended.

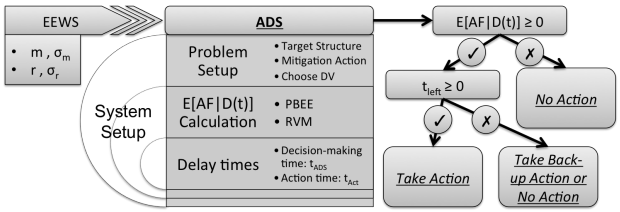


Figure 3 Structure of the ADS framework: m and r are the means of M and R; σ_m and σ_r are the standard deviations of M and R

4. CONCLUSION AND FUTURE WORK

The benefits and feasibility of EEWS is getting better appreciated throughout the world. It is expected that there will be one operating in California in a year or two. In order to maximize the benefits of EEWS, a fast ADS is essential to tackle the very short lead times. However, the whole process of rational decision-making requires a complicated model analysis and long computational times in general. Therefore, the only way to make it practical is to break up the computations so that many can be done prior to implementing ADS at a structure or facility. From the moment that EEWS releases warning information, the three main steps to achieve are performing the ground motion prediction at a chosen site, the response prediction for the target structure/system, and the loss/damage prediction. Since all three steps do not involve information from the EEWS, these can be done ahead of time and then approximated with a robust Bayesian surrogate model using the RVM. Combining the concepts of Action Function and the surrogate model, we can develop a fast ADS framework. The next step in our research is to investigate the framework for various case studies using past-earthquake data. We are currently doing so, but there remain some key challenges to apply the ADS framework. One of them is that it is difficult to quantify the benefit of a mitigation action. Over-estimating the benefit will increase the probability of taking a mitigation action when it should not have been done, while under-estimating will increase the probability of not acting when it is appropriate to do so. More research will be done on these kind of practical issues.

Acknowledgements:

The authors wish to thank Prof. Tom Heaton and Dr. Maren Böse for providing valuable information on recent EEWS development in California, USA.

References:

Allen, R.M. and Kanamori, H. (2003), "The Potential for Earthquake Early Warning in Southern California," *Science*, **300**(5620), 786-789.

Allen, R.M et al. (2009a), "Real-time earthquake detection and hazard assessment by ElarmS across California," *Geophysical Research Letters*, **36**(L00B08).

Allen, R.M et al. (2009b), "The Status of Earthquake Early Warning around the World: An Introductory Overview," *Seismological Research Letters*, **80**(5), 682-693.

Bishop, C.M. (2006), *Pattern Recognition and Machine Learning*, Springer Berlin Heidelberg.

Böse, M. et al. (2009), "Real-time Testing of the On-Site Warning Algorithm in Southern California and its Performance During the July 29 2008 Mw5.4 Chino Hills Earthquake," *Geophysical Research Letters*, **36**(L00B03).

Cua, G. and Heaton, T. (2007), "The Virtual Seismologist (VS) Method: a Bayesian Approach to Earthquake Early Warning," *Earthquake Early Warning Systems*, p.97-132.

Cua, G. et al. (2009), "Real-time Performance of the Virtual Seismologist Earthquake Early Warning Algorithm in Southern California," *Seismological Research Letters*, 80(5), 740-747.

Doi, K. (2000), "Earthquake early warning system in Japan," *Proceedings of Early Warning Systems for Natural Disaster Reduction*, 447-452.

Gasparini, P., Manfredi, G. and Zschau, J. editors (2007), *Earthquake Early Warning Systems*, Springer-Verlag Berlin Heidelberg.

Grasso, V.F., Beck, J.L. and Manfredi, G. (2007), "Automated Decision Procedure for Earthquake Early Warning," *Engineering Structures*, **29**(12), 3455-3463.

Goulet, C.A. et al. (2007), "Evaluation of the Seismic Performance of a Code-Conforming Reinforced-Concrete Frame Building---from Seismic Hazard to Collapse Safety and Economic Losses," *Earthquake Engineering and Structural Dynamics*, 36(13), 1973-1997.

Iervolino, I., Giorgio, M. and Manfredi, G. (2007), "Expected loss-based Alarm Threshold Set for Earthquake Early Warning Systems," *Earthquake Engineering and Structural Dynamics*, **36**(9), 1151-1168.

Kanamori, H. (2005), "Real-time Seismology and Earthquake Damage Mitigation," *Annual Review of Earth and Planetary Sciences*, **33**, 195-214.

Porter, K.A. (2003), "An Overview of PEER's Performance-Based Earthquake Engineering Methodology," *Applications of Statistics and Probability in Civil Engineering*, **1-2**, 973-980.

Tipping, M.E. (2001), "Sparse Bayesian Learning and the Relevance Vector Machine," *Journal of Machine Learning Research*, **1**(3), 211-244.

Tipping, M.E. (2004), "Bayesian Inference: An Introduction to Principles and Practice in Machine Learning," *Advanced Lectures on Machine Learning*, **3176**, 41-62.

Tipping, M.E. and Faul, A.C. (2003), "Fast Marginal Likelihood Maximization for Sparse Bayesian Models," *Proceedings of the Ninth International Workshop on Artificial Intelligence and Statistics*.

Yamazaki, F., Meguro, K. and Noda, S. (1998), "Developments of Early Earthquake Damage Assessment Systems in Japan," *Structural Safety and Reliability*, **1-3**, 1573-1580.